MINI-REVIEW / MINI-SYNTHÈSE

Self-assembly in Schiff base lanthanide complexes — From supramolecular dimers to coordination polymers[1]

Wanda Radecka-Paryzek

Abstract: A review is given of the latest contribution of the author's research group to the coordination chemistry of Schiff base polyaza macrocycles and acyclic salicylaldimines. Focus is placed on the effectiveness of lanthanides in supramolecular self-assembly of the components leading to the formation of compounds with unusual properties and structures.

Key words: Schiff base macrocycles, salicylaldimines, lanthanides, self-assembly, template synthesis.

Résumé : On passe en revue les contributions récentes du groupe de recherche de l'auteur à la chimie de coordination de bases de Schiff salicylaldimines acycliques et macrocycliques polyazotés. On met l'emphase sur l'efficacité des lanthanides dans l'autoassemblage supramoléculaire des composants qui conduisent à la formation de composés comportant des propriétés et des structures inhabituelles.

Mots-clés : bases de Schiff macrocycliques, salicylaldimines, lanthanides, autoassemblage, synthèse sur gabarit.

[Traduit par la Rédaction]

Introduction

Schiff bases have been known since 1864 when Hugo Schiff reported the condensation of primary amines with carbonyl compounds (1). Nowadays, the research field dealing with Schiff base coordination chemistry has expanded enormously. The importance of Schiff base complexes for bioinorganic chemistry, biomedical applications, supramolecular chemistry, catalysis and material science, separation and encapsulation processes, and formation of compounds with unusual properties and structures has been well-recognized and reviewed (2). In this paper, we would like to show, on the basis of the latest contribution of the author's research group, that although the coordination chemistry of Schiff bases is very rich, it still remains an interesting and unpredictable area. Our research effort for the last 30 years has been focused on the investigation of the coordination template effect in generating new supramolecular mono- and homo- or hetero-dinuclear polyaza and polyoxaaza Schiff base macrocyclic and acyclic complexes. We have found the lanthanide metal ions to be very effective templates in the synthesis of the complexes of this type (3). Lanthanides have little or no stereochemical requirements and can be accommodated by the particular constraints enforced by the template process. The structural versatility of the lanthanide complexes arises from the lack of strong crystal field effects for 4f-electronic configuration and from the large ionic radii of these metal ions. In the lanthanides, the 4f-orbitals are shielded by the 5s- and 5p-electrons, and their ionic radii decrease monotonically with the increasing atomic number (lanthanide contraction). The large ionic radii of the lanthanide ions together with the increased ionic character of the metal–ligand bonding in their complexes led to the generation of complexes with higher coordination numbers ranging from 8 to 12. The effective ionic diameters of the Ln(III) ions (Ln is symbol for any one of the lanthanides from lanthanum to lutetium) strongly depend on both the atomic number and the coordination number: a difference of about 0.4 Å is found between La(III) and Lu(III) and, for a given Ln(III) ion, between coordination numbers 8 and 12.

Received 17 March 2008. Accepted 6 May 2008. Published on the NRC Research Press Web site at canjchem.nrc.ca on 12 September 2008.

It is a privilege for me and a great pleasure to have an opportunity to dedicate this paper to Professor Richard J. Puddephatt, particularly in light of his outstanding leadership of an international group of postdoctoral fellows.

W. Radecka-Paryzek. Faculty of Chemistry, Department of Bioinorganic Chemistry, Adam Mickiewicz University, Grunwaldzka 6, 60-780 Poznań, Poland; (e-mail: wrp@amu.edu.pl).

[1]This article is part of a Special Issue dedicated to Professor R. Puddephatt.

 doi:10.1139/V08-109 © 2008 NRC Canada

The peculiar chemical, structural, spectroscopic, and magnetic properties of the trivalent lanthanide ions associated with their $4f^{1-14}$ configuration make them suitable for development of novel interesting systems relating to general chemistry and application.

Pentaazadentate Schiff base lanthanide macrocyclic complexes as a result of self-assembly process

The interest in exploring the encapsulation of the lanthanide elements by macrocycles has continually been increasing, as they can be used in imaging, medical and material processing as well as analytical, environmental, and telecommunication areas. These new applications of the macrocyclic systems, in particular those containing nitrogen-donor atoms, involve their use as supramolecular devices (4–7), bioinorganic probes for the active sites in metallobiomolecules (8, 9), as magnetic resonance imaging contrast-enhancing agents (10–24), chemotherapeutics (25–27), potential radioimmunopharmaceuticals for monoclonal antibody technology (28–33) and sensitizers for photodynamic therapy (34), and finally as synthetic nucleases for in vivo applications (35–40). While searching for new stable complexes of rare-earth elements in view of their potential applications, we have recently reported the first examples of lutetium and ytterbium macrocyclic complexes with the seven-coordination and pentagonal bipyramidal structure and their peroxo-bridged dimeric derivatives containing a biologically significant and unprecedented among lanthanide macrocyclic complexes planar side-on μ-η^2:η^2 coordination mode of the peroxide (41–44). Template reactions of 2,6-diacetylpyridine with 3,7-diazanonane-1,9-diamine were carried out in the presence of mixed lutetium or ytterbium chloride and perchlorate salts under argon (Scheme 1).

Recrystallization produced 16-membered macrocyclic complexes with an N_5 set of donor atoms as a result of a [1+1] Schiff base cyclocondensation. X-ray analysis reveals that these two complexes of formula $\{LnMe_2pyo[16]trieneN_5Cl_2\}ClO_4$, where Ln is Lu^{3+} or Yb^{3+} and $Me_2pyo[16]trieneN_5$ is 2,14-dimethyl-3,6,10,13,19-pentaazabicyclo[13.3.1]nonadeca-1(19),2,13,15,17-pentaene, are isostructural. The Lu(III) and Yb(III) are seven-coordinate with the pentagonal bipyramidal coordination geometry (Fig. 1) (41, 43).

These complexes show no tendency to include solvent molecules in either the metal coordination sphere or the crystal lattice. The electronic and steric requirements of central metal atoms appear to be fully satisfied by the coordination to the five nitrogen donors of the macrocycle and two chlorine donors. The organizational role of the lanthanide cation in the assembly of the pentaaza macrocycle was proved by the recovery of insoluble yellow materials of indefinite composition when the condensation of 2,6-diacetylpyridine with 3,7-diazanonane-1,9-diamine was carried out in the absence of the metal ion. The failure of this system to undergo complete condensation and cyclization confirms the importance of the metal ion in directing the steric course of the condensation process, which ultimately ends with ring closure.

UV–vis, NIR, ^{1}H NMR, and ESI spectral data reveal that the integrity of the complexes is maintained in solution. The

Scheme 1.

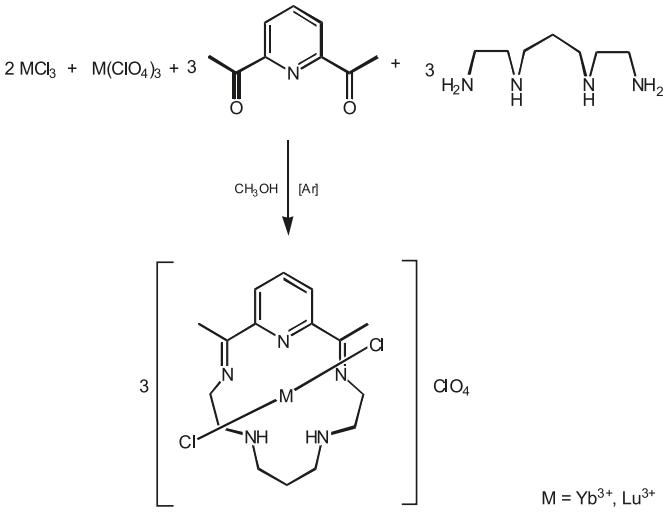

Fig. 1. Structure of 16-membered pentaazadentate macrocyclic lutetium(III) and ytterbium(III) complex cations.

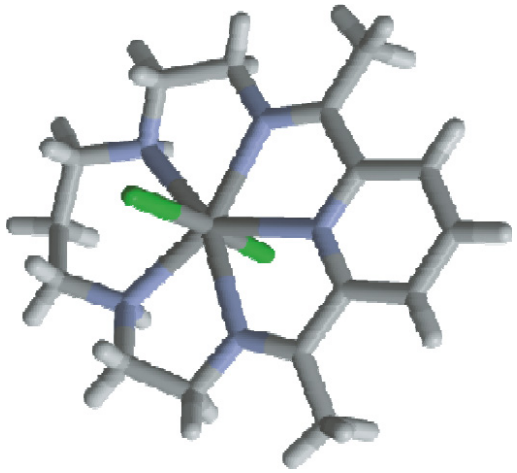

properties of this ytterbium complex were found to be very important and promising in the area of ytterbium physicochemistry. For the first time, the spectrum of the $^2F_{7/2} \rightarrow {}^2F_{5/2}$ transition has been obtained for a molecular complex of ytterbium with organic ligands in which all ligand-field components of the ground and excited state are well-displayed at room temperature (Fig. 2) (44).

These pentaaza macrocyclic complexes exhibit a structural similarity to lutetium texaphyrins, which have been tested as photosensitizers for use in the photodynamic treatment of recurrent breast cancer (LUTRIN), photoangioplastic reduction of atherosclerosis (ANTRIN), and light-based treatment of age-related macular degeneration (OPTRIN) (34). Moreover, Yb^{3+} complexes are now of increasing interest due to their potential application in various areas of biomedical sciences and technology as probes for fluoroimmunoassays, as effective therapeutic and diagnostic agents, in optical amplification, and in laser systems (45–51).

The template Schiff base condensation of 2,6-diacetylpyridine with 3,7-diazanonane-1,9-diamine carried out on air in the presence of the lutetium(III) ion followed by a slow crystallization process yielded, to our surprise, a

© 2008 NRC Canada

Fig. 2. Diffuse reflectance spectrum of 16-membered pentaazadentate macrocyclic ytterbium(III) complex at 295 K.

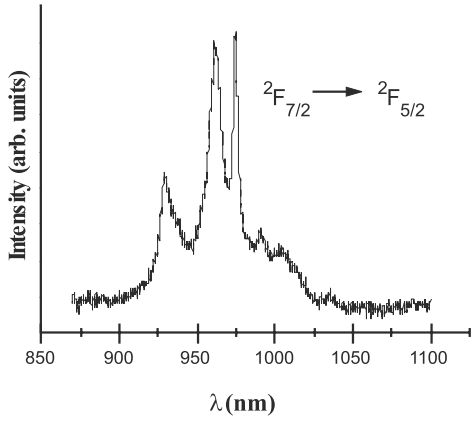

dimeric peroxo-bridged derivative of formula $[\{LuClMe_2pyo[16]trieneN_5\}_2(\mu\text{-}\eta^2\text{:}\eta^2\text{-}O_2)](ClO_4)_2$ with a planar side-on doubly bidentate coordination mode of the peroxide, unprecedented so far among lanthanide macrocyclic complexes (42). The isolation and definitive identification of an isostructural ytterbium(III) peroxo complex $[\{YbClMe_2pyo[16]trieneN_5\}_2(\mu\text{-}\eta^2\text{:}\eta^2\text{-}O_2)](ClO_4)_2$ allowed us to exclude the serendipity of this unexpected result of template cyclocondensation reaction (Fig. 3) (43, 44).

The complexes consist of two lanthanide(III) centers, five macrocycle nitrogen atoms make the equatorial plane of the coordination polyhedron, and the outer axial positions are filled by chlorine atoms. The position between the metal ions is occupied by the peroxide fragment. All Ln–O bond lengths are equivalent within the experimental error, clearly proving the planar side-on $\mu\text{-}\eta^2\text{:}\eta^2$ coordination mode of the peroxide. These results expand the unique series of compounds containing this particular coordination mode of the peroxide, which is considered biologically significant because it is known to occur in some oxyhemocyanins and it is postulated as a new mode of binding or activation of dioxygen in other biological systems. The first solid evidence for the formation of an entirely novel planar $\mu\text{-}\eta^2\text{:}\eta^2$-peroxide geometry was found in peroxo bis(trimethylsilyl)-amido dinuclear lanthanum species (52) and remained the only known and structurally characterized example of such a coordination mode of O_2^{2-} in lanthanide chemistry. The peroxo group showed previously unreported behaviour, acting as a symmetrical doubly bidentate bridge between the two metal atoms. The use of appropriately positioned, highly hindered tris(pyrazolyl)borate ligands made it possible to structurally establish this novel coordination mode of the peroxide in d-block element complexes (53). These $\mu\text{-}\eta^2\text{:}\eta^2$-peroxo dinuclear copper(II) complexes were found to have physicochemical properties strikingly similar to those of oxyhemocyanin. Subsequently, the crystal structure of oxyhemocyanin from the horseshoe crab (*Limulus polyphemus*) was solved, revealing the presence of precisely this type of $\mu\text{-}\eta^2\text{:}\eta^2$-peroxide moiety (54). In this case, accurate structural model compounds preceded the determination of the protein structure. Based on reports involving binuclear Cu(II) peroxo species, the formation of a $\mu\text{-}\eta^2\text{:}\eta^2$-peroxo intermediate was proposed as an attractive novel possibility for

Fig. 3. Structure of $\mu\text{-}\eta^2\text{:}\eta^2$-peroxo bridged 16-membered pentaazadentate macrocyclic lutetium(III) and ytterbium(III) complex cations.

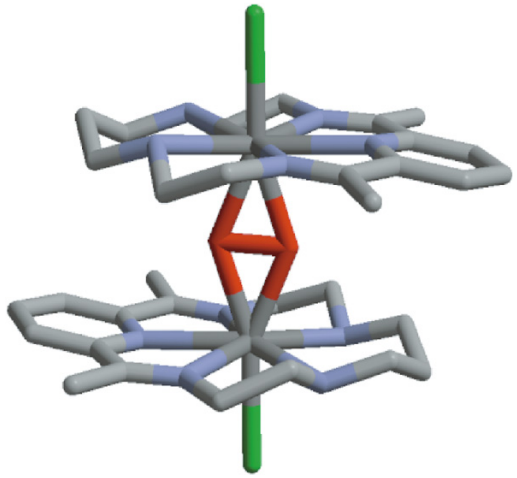

the mechanism of water oxidation and O_2 evolution during photosynthesis catalyzed by tetranuclear manganese clusters, although no such Mn complex has been synthesized yet (55). It seems worthy to note that the synthesis of the first lanthanum(III) and copper(II) $\mu\text{-}\eta^2\text{:}\eta^2$-peroxo complexes required severe conditions: treatment with H_2O_2 under anaerobic conditions or low-temperature (ca. –70 °C) direct dioxygen addition. The formation of Schiff base macrocyclic lanthanide $\mu\text{-}\eta^2\text{:}\eta^2$-peroxo complexes appears to be a result of a one-step template synthesis followed by slow crystallization in air. Moreover, the O–O bond distances in these complexes are consistent with the value observed in dinuclear Cu(II) $\mu\text{-}\eta^2\text{:}\eta^2$-peroxide bridged species, of interest as oxyhemocyanin and oxytyrosinase models (53, 56). By comparison, in previously mentioned first lanthanum(III) $\mu\text{-}\eta^2\text{:}\eta^2$-peroxo complex, the O–O bond distance was found to be extremely large, probably due to their artificial elongation caused by the effects of crystal decomposition (52).

Inclusion of an appropriate solvent molecule into the crystal structure of $[\{LnClMe_2pyo[16]trieneN_5\}_2(\mu\text{-}\eta^2\text{:}\eta^2\text{-}O_2)](ClO_4)_2$ ($Ln=Lu^{3+}$ or Yb^{3+}) peroxo dinuclear complexes generates a tetrameric supramolecular architecture in which the solvent-controlled self-assembly is observed (43, 44). To some extent at least, the shape, symmetry, and hydrogen bonding (or in more general terms: weak interactions) properties of the solvent molecule influence the resulting three-dimensional structure of the crystal (43, 44).

The building block of the crystal structure of the dioxane solvate of four $\mu\text{-}\eta^2\text{:}\eta^2$-peroxo bridged lutetium(III) and ytterbium(III) dimers is created by a centrosymmetric hydrogen-bonded tetramer of complexes, perchlorate anions, and dioxane molecule (Fig. 4) (42–44). The shape, symmetry, and hydrogen-bond accepting properties of dioxane are compatible with the shape and properties of the tetrameric network.

The two three-dimensional structures of crystals of $\mu\text{-}\eta^2\text{:}\eta^2$-peroxo ytterbium(III) complexes obtained from simple aromatic solvents, benzene (43) and toluene (44), are almost identical (in fact, the crystals are highly isomorphous). They contain chains of molecules connected by hydrogen bonds;

© 2008 NRC Canada

Fig. 4. The van der Waals radii representation of the building block of four μ-η^2:η^2-peroxo bridged lutetium(III) and ytterbium(III) complexes without (left) and with (right) the solvent dioxane molecule.

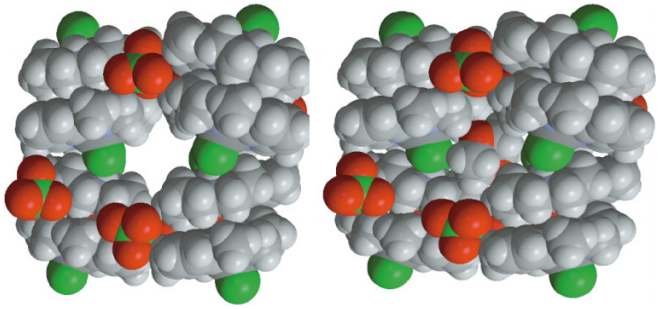

Fig. 5. The van der Waals radii representation of the building block of the μ-η^2:η^2-peroxo bridged ytterbium complex without (left) and with (right) a toluene or benzene molecule.

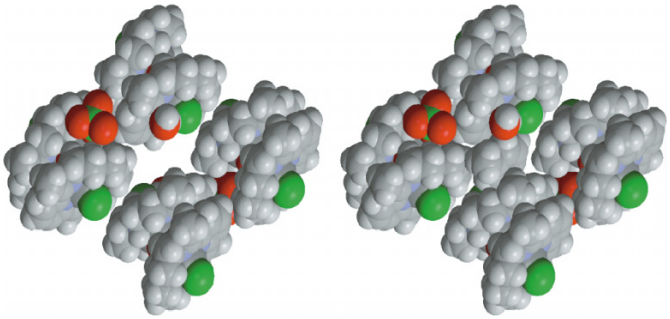

these chains are interconnected via perchlorate anions, and this tetrameric network can accommodate small flat molecules of the solvent. Because there are no specific interactions between these guest molecules and macrocyclic complex host, only very weak π-stacking, solvent molecules are highly disordered (Fig. 5) (43, 44).

Crystals of the methanol solvate of the ytterbium(III) complex are a very special case (44). The unit cell contains two different dimeric complex cations, four chloride, and four perchlorate anions and one methanol molecule. In one of them, formulated as $[\{Yb(H_2O)Me_2pyo[16]trieneN_5\}_2(\mu\text{-}\eta^2\text{:}\eta^2\text{-}O_2)]^{4+}$, there is a μ-$\eta^2$:$\eta^2$-peroxo bridge between the two Yb^{3+} centers, while the other, formulated as $[\{Yb(H_2O)Me_2pyo[16]trieneN_5\}_2(\mu\text{-}OH)_2)]^{4+}$, has two μ-OH hydroxyl bridges between the ytterbium ions. The molecule with a μ-η^2:η^2-peroxo bridge is similar to the previous ones except for the molecules occupying the axial positions (water molecules instead of chlorides). The molecule with two hydroxyl bridges is more folded. In both molecules, due to symmetry requirements, the central Yb–O–Yb–O fragments are exactly planar. The structural and spectral results afford some insight into the origin of the peroxo group. It seems reasonable to assume that the hydrolysis/oxidation of $\{LnMe_2pyo[16]trieneN_5Cl_2\}ClO_4$ occurs during the slow crystallization. The OH groups may replace axial chlorides in the coordination sphere of the metal ion yielding a di-μ-hydroxo species. These two OH groups may oxidatively form the peroxide and give rise to the complexes containing a planar side-on doubly bidentate coordination mode of the peroxide.

These results provide an interesting example of three-level inorganic self-organization involving templating as the first step of the assembly of well-defined supramolecular architectures of higher complexity. The lanthanide(III) ions serve as templates to orient the reacting groups of linear precursors in the desired conformation for the condensation process, which ultimately ends with the pentaaza macrocyclic Schiff base complexes. The stabilization of seven-coordination and pentagonal bipyramidal geometry in these complexes, relatively uncommon in the lanthanide series, seems to be a consequence of the "best fit" between the size of cations and the cavity of the macrocycle generated during the template process. In the dimerization step, these complexes are able to activate atmospheric oxygen and form the unique dimeric species linked through the biologically significant μ-η^2:η^2 peroxo bridge. The driving force underlying this unusual behaviour may be attributed to the stabilizing effect provided by the specific steric arrangement of the two macrocycles. In the crystal structure, packing as the next level of self-assembly is observed. The solvent molecules determine the three-dimensional disposition of the dimers. The supramolecular tetrameric network is created by the molecules of the peroxo complex acting as a host for the solvent guest.

Self-assembled salicylaldimine lanthanide complexes

Continuing our systematic investigation on the coordination template effect of lanthanides in generating supramolecular macrocyclic and acyclic Schiff base systems, we extended our studies to salicylaldimines. Transition-metal salicylaldimines have been studied broadly due to the number of applications in catalysis and material, biomimetic, and medicinal chemistry. They can be used as enantioselective epoxidation catalysts (57–61), components for the assembly of supramolecular architectures displaying interesting structures and properties (62–73), as models for active sites of metalloenzymes, and as therapeutic agents with superoxide dismutase and catalase activity (74–78). X-ray structure data reveal that, in the metal complexes of this type, the Schiff bases generally act as deprotonated tetradentate ligands with the N_2O_2 set of donor atoms capable of effective coordination in the planar fashion. Recently, we have communicated the definitive structural details correlated with spectral characterization of the salicylaldimine lanthanide nitrate complexes with unusual coordination mode (79, 80). These complexes are formed in situ in a one-step lanthanide promoted reaction between salicylaldehyde and rigid aromatic 4-methyl-1,3-phenylenediamine or flexible aliphatic 1,4-butanediamine (putrescine, biogenic amine) (Scheme 2).

They self-assemble into finite dimer or infinite two-dimensional coordination polymer depending on the type of diamine precursors.

In the crystal structure, the *N,N′*-bis(salicylidene)-4-methyl–1,3-phenylenediamine gadolinium(III) nitrate complex exists as a centrosymmetric dimer with 2:4 metal–ligand ratio (Fig. 6) (79).

The gadolinium(III) ions are nine-coordinate, and the geometry around the central ions can be described as a distorted tricapped trigonal prism. Each metal ion is ligated by

© 2008 NRC Canada

Scheme 2.

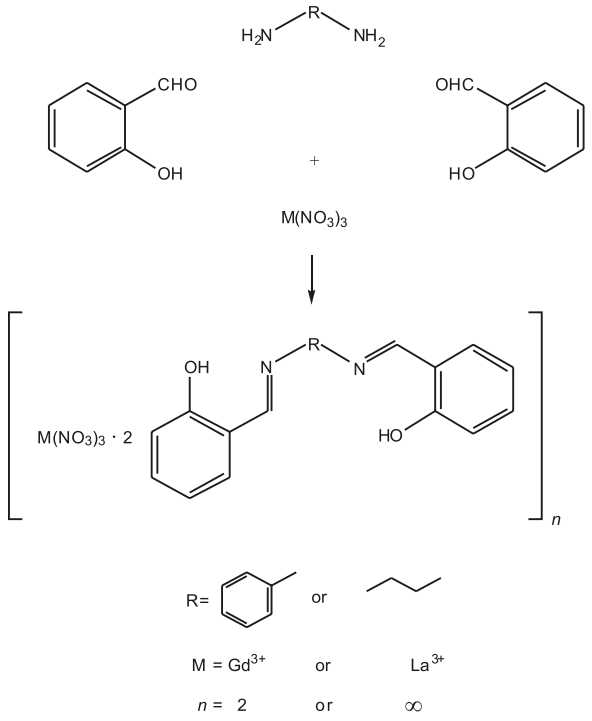

Fig. 6. Structure of the *N,N′*-bis(salicylidene)-4-methyl–1,3-phenylenediamine gadolinium(III) nitrate complex.

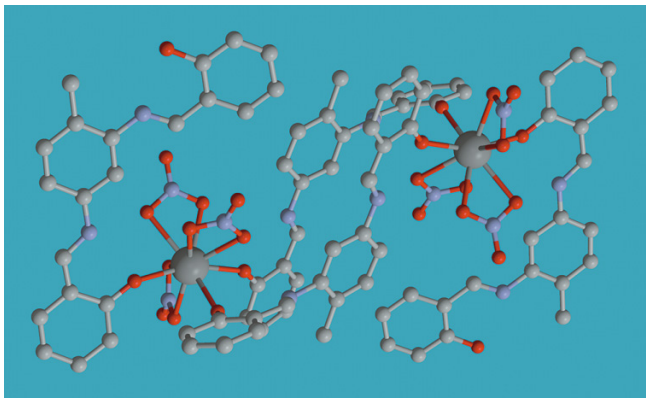

three bidentate nitrate counterions and three neutral salicylaldimine ligands that utilize only hydroxy oxygen atoms while the nitrogen atoms remain uncoordinated. The two ditopic O-donor ligands bridge the gadolinium ions, while the third ligand appears to involve only one oxygen atom in coordination. The second oxygen atom of this ligand does not take part in any intermolecular interactions.

The *N,N′*-bis(salicylidene)-1,4-butanediamine lanthanum(III) nitrate complex displays infinite two-dimensional polymeric structure composed of networks of ten-coordinated La(III) nodes linked by bridging neutral salicylaldimine ligands (Fig. 7) (80).

The coordination polyhedron around the lanthanum ions can be described as a distorted bicapped dodecahedron. Interestingly, only the oxygen atoms take part in the coordination; they come from three nitrate groups (six atoms) and from four neutral salicylaldimine ligand molecules (one oxygen from each molecule). This polymer might be described as composed of columns of dimers connected into chains, via the flexible parts of ligands.

Fig. 7. Structure of the *N,N′*-bis(salicylidene)-1,4-butanediamine lanthanum(III) nitrate complex.

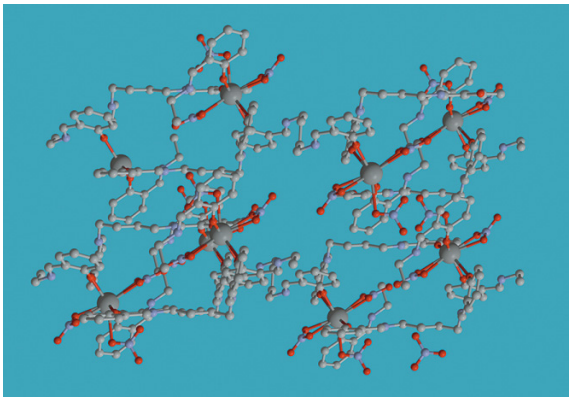

These two complexes provide the examples of a rare coordination pattern of salicylaldimine ligands revealed by X-ray crystallography and correlated with spectroscopic characterization. Salicylaldimine ligands use exclusively the oxygen atoms as donor atoms with the nitrogen atoms not being involved in coordination. All the hydroxy groups of the ligands do not undergo deprotonation. The observed profound changes in the C–O and C=N bond lengths of the ligands upon coordination are consistent with the zwitterionic, charge-separated form in which the positive and negative charges reside on the azomethine function and on the metal coordination sphere, respectively. This point is proved by the results of spectral characterization of these complexes with reference to the free ligands obtained separately and identified for comparison purposes. The neutral O-donor type of coordination is in a marked contrast to the dianionic tetradentate N_2O_2 donor-set arrangement typically found in salicylaldimine complexes. An inspection of the available data for the structures of the related tetradentate N_2O_2 salicylaldiminato metal complexes reveals that the effects on the bond lengths of the coordination of the metal ion through oxygen only are remarkably similar to those caused by the removal of protons by ionization and coordination of all oxygen and nitrogen atoms. Therefore, the coordination mode might have been incorrectly inferred from spectroscopic analysis alone. The characterization of the complexes by both X-ray crystallography and spectroscopic methods is found to be useful in guiding and confirming interpretations concerning coordination modes in similar complexes for which no crystal data are available.

It is worth noticing that these two lanthanide nitrate complexes were obtained in similar experimental conditions and display similar spectral properties; for both complexes, analytical data indicate 1:2 metal – salicylaldimine ligand ratio. Obviously, it is going to be very difficult to differentiate these two coordination frameworks without detailed structural information gained from single-crystal X-ray crystallography. In these complexes, the nitrate counterions act as bidentate chelators occupying six coordination sites around the lanthanide cations and leaving the remaining sites available for salicylaldimine coordination. The lanthanide ions

© 2008 NRC Canada

may thus be regarded as assembling and templating joints for the ligands formed through the self-assembly process including the metal template-induced Schiff base condensation as the first step of self-organization. It could account for the unusual coordination mode of salicylaldimines in these complexes. The high coordination number and hardness of lanthanide(III) centers along with the nature of ligand spacers (length, flexibility, aromacity) and counterions seem to have a crucial bearing on the building of inorganic supramolecular arrays.

Conclusion

These findings confirm that the results of supramolecular self-assembly processes are sometimes unexpected and surprising. Many interesting supramolecular structures could not have been predicted. However, their retrospective analysis may provide necessary information in the attempts to intentionally design new materials with specific functions and properties. The difficulty in controlling the coordination environments is especially seen in lanthanide ions, which display high and variable coordination numbers with little or no stereochemical preferences. The new lanthanide structures with peculiar characteristics hold the potential to become powerful tools used to define interesting features relating both to general chemistry and application.

Acknowledgements

I would like to express my deep gratitude to Professor Richard J. Puddephatt for his invaluable scientific guidance and advice, which I received during my stay as visiting scientist in the University of Western Ontario in 1985 (joining the group of Dick's desperados).

My thanks are due to the co-workers whose names appear in the references and to the referees for helpful comments. The financial support from the Polish Ministry of Science and Higher Education (grants 4T09A 05624 and N N204 031733) is appreciated.

References

1. H. Schiff. Ann. Suppl. **3**, 343 (1864).
2. P.A. Vigato and S. Tamburini. Coord. Chem. Rev. **248**, 1717 (2004).
3. W. Radecka-Paryzek, V. Patroniak, and J. Lisowski. Coord. Chem. Rev. **249**, 2156 (2005).
4. S.J. Dalgarno, M.J. Hardie, J.L. Atwood, J.E. Warren, and C.L. Raston. New J. Chem. **29**, 649 (2005).
5. M.K. Thompson, M. Vuchokv, and I.A. Kahwa. Inorg. Chem. **40**, 4332 (2001).
6. S. Faulkner and B.P. Burton-Pye. Chem. Commun. 259 (2005).
7. J.-C.G. Bünzli and C. Piguet. Chem. Rev. **102**, 1897 (2002).
8. D. Parker. Chem. Soc. Rev. **33**, 156 (2004).
9. H. Tsukube and S. Shinoda. Chem. Rev. **102**, 2389 (2002).
10. M. Botta. Eur. J. Inorg. Chem. 399 (2000).
11. M. Woods, S. Aime, M. Botta, J.A.K. Howard, J.M. Moloney, M. Navet, D. Parker, M. Port, and O. Rousseaux. J. Am. Chem. Soc. **122**, 9781 (2000).
12. F. Alhaique, I. Bertini, M. Fragai, M. Carafa, C. Luchinat, and G. Parigi. Inorg. Chim. Acta, **331**, 151 (2002).
13. S. Aime, L. Frullano, and S.G. Crich. Angew. Chem., Int. Ed. Engl. **41**, 1017 (2002).
14. P. Caravan, J.J. Ellison, T.J. McMurry, and R.B. Lauffer. Chem. Rev. **99**, 2293 (1999).
15. V. Comblin, D. Gilsoul, M. Hermann, V. Humblet, V. Jacques, M. Mesbahi, C. Sauvage, and J.F. Desreux. Coord. Chem. Rev. **185–186**, 451 (1999).
16. J.P. André, É. Tóth, H. Fischer, A. Seelig, H.R. Mäcke, and A.E. Merbach. Chem. Eur. J. **5**, 2977 (1999).
17. F.A. Dunand, R.S. Dickins, D. Parker, and A. Merbach. Chem. Eur. J. **7**, 5160 (2001).
18. S. Aime, D.D. Castelli, F. Fedeli, and E. Terreno. J. Am. Chem. Soc. **124**, 9364 (2002).
19. W. Li, G. Parigi, M. Fragai, C. Luchinat, and T.J. Meade. Inorg. Chem. **41**, 4018 (2002).
20. M. Woods, Z. Kovacs, S. Zhang, and A.D. Sherry. Angew. Chem., Int. Ed. **42**, 5889 (2003).
21. S. Zhang, R. Trokowski, and A.D. Sherry. J. Am. Chem. Soc. **125**, 15288 (2003).
22. F. Yerly, A. Borel, L. Helm, and A.E. Merbach. Chem. Eur. J. **9**, 5468 (2003).
23. L.V. Elst, M. Port, I. Raynal, C. Simonot, and R.N. Muller. Eur. J. Inorg. Chem. 2495 (2003).
24. K. Kimpe, T.N. Parac-Vogt, S. Laurent, C. Piérart, L.V. Elst, R.N. Muller, and K. Binnemans. Eur. J. Inorg. Chem. 3021 (2003).
25. K. Wang, R. Li, Y. Cheng, and B. Zhu. Coord. Chem. Rev. **190–192**, 297 (1999).
26. S.W.A. Bligh, N. Choi, C.F.G.C. Geraldes, S. Knoke, M. McPartlin, M.J. Sanganee, and T.M. Woodroffe. J. Chem. Soc. Dalton Trans. 4119 (1997).
27. L.A.D. Williams, R.C. Howell, R. Young, and I.A. Kahwa. Comp. Biochem. Physiol. Part C: Toxicol. Pharmacol. **128**, 119 (2001).
28. L. Thunus and R. Lejeune. Coord. Chem. Rev. **184**, 125 (1999).
29. H. Ali and J.E. van Lier. Chem. Rev. **99**, 2379 (1999).
30. D.A. Keire, Y.H. Jang, L. Li, S. Dasgupta, W.A. Goddard, and J.E. Shivel. Inorg. Chem. **40**, 4310 (2001).
31. S. Aime, M. Botta, M. Fasano, and E. Terreno. Chem. Soc. Rev. **27**,19 (1998).
32. W.A. Volkert and T.J. Hoffman. Chem. Rev. **99**, 2269 (1999).
33. M.J. Heeg and S.S. Jurisson. Acc. Chem. Res. **32**, 1053 (1999).
34. J.L. Sessler and R.A. Miller. Biochem. Pharmacol. **59**, 733 (2000).
35. J.K. Bashkin and L.A. Jenkins. Comments Inorg. Chem. **16**, 77 (1994).
36. K.G. Ragunathan and H.-J. Schneider. Angew. Chem., Int. Ed. Engl. **35**, 1219 (1996).
37. C. Liu, M. Wang, T. Zhang, and H. Sun. Coord. Chem. Rev. **248**, 147 (2004).
38. R. Häner and J. Hall. Antisense Nucl. Acid Drug Dev. **7**, 423 (1997).
39. S.W.A. Bligh, N. Choi, E.G. Evagorou, M. McPartlin, and K.N. White. J. Chem. Soc. Dalton Trans. 3169 (2001).
40. D.A. Voss Jr, L.A. Butterey-Thomas, T.S. Janik, M.R. Churchill, and J.R. Morrow. Inorg. Chim. Acta, **317**, 149 (2001).
41. W. Radecka-Paryzek, V. Patroniak, and M. Kubicki. Polyhedron, **22**, 2773 (2003).
42. V. Patroniak, M. Kubicki, and W. Radecka-Paryzek. J. Inclusion Phenom. Macrocyclic Chem. **49**, 121 (2004).
43. W. Radecka-Paryzek, V. Patroniak, and M. Kubicki. Inorg. Chem. Commun. **7**, 455 (2004).
44. V. Patroniak, M. Kubicki, A. Mondry, J. Lisowski, and W. Radecka-Paryzek. Dalton Trans. 3295 (2004).

© 2008 NRC Canada

45. I.K. Hemmilä. Applications of fluorescence in immunoassays. Wiley and Sons. New York. 1991.
46. M.H.V. Werts, J.W. Hofstraat, F.A.J. Geurts, and J.W. Verhoeven. Chem. Phys. Lett. **276**, 196 (1997).
47. M.P. Oude Wolbers, F.C.J.M. van Veggel, F.G.A. Peters, E.S.E. van Beelen, J.W. Hofstraat, F.A.J. Geurts, and D.N. Reinhoudt. Chem. Eur. J. **4**, 772 (1998).
48. D. Imbert, M. Cantuel, J.-C.G. Bünzli, G. Bernardinelli, and C. Piguet. J. Am. Chem. Soc. **125**, 15698 (2003).
49. R.S. Dickins, A.S. Batsanov, J.A.K. Howard, D. Parker, H. Puschamnn, and S. Salamano. Dalton Trans. 70 (2004).
50. S. Faulkner, M.-C. Carrié, S.J.A. Pope, J. Squire, A. Beeby, and P.G. Sammes. Dalton Trans. 1405 (2004).
51. Y. Hasegawa, T. Ohkubo, K. Sogabe, Y. Kawamura, Y. Wada, H. Nakashima, and S. Yanagida. Angew. Chem., Int. Ed. **39**, 357 (2000).
52. D.C. Bradley, J.S. Ghotra, F.A. Hart, M.B. Hursthouse, and P.B. Raithby. J. Chem. Soc. Dalton Trans. 1166 (1977).
53. N. Kitajima, K. Fujisawa, C. Fujimoto, Y. Moro-oka, S. Hashimoto, T. Kitagawa, K. Toriumi, K. Tatsumi, and A. Nakamura. J. Am. Chem. Soc. **114**, 1277 (1992).
54. K.A. Magnus, B. Hazes, H. Ton-That, C. Bonaventura, J. Bonaventura, and W.G.J. Hol. Proteins, **19**, 302 (1994).
55. K. Yachandra, K. Sauer, and M.P. Klein. Chem. Rev. **96**, 2927 (1996).
56. N. Kitajima and Y. Moro-oka. Chem. Rev. **94**, 737 (1994).
57. H. Jacobsen and L. Cavallo. Chem. Eur. J. **7**, 800 (2001).
58. P.G. Cozzi. Chem. Soc. Rev. **33**, 410 (2004).
59. E. Jacobsen. Acc. Chem. Res. **33**, 421 (2000).
60. T. Katsuki. Chem. Soc. Rev. **33**, 437 (2004).
61. N.S. Venkataramanan, G. Kuppuraj, and S. Rajagopal. Coord. Chem. Rev. **249**, 1249 (2005).
62. K. Binnemans, K. Lodewyckx, T. Cardinaels, T.N. Parac-Vogt, C. Bourgogne, D. Guillon, and B. Donnio. Eur. J. Inorg. Chem. **1**, 150 (2006).
63. D. Cunningham, P. McArdle, M. Mitchell, N.N. Chonchubhair, and M. O'Gara. Inorg. Chem. **39**, 1639 (2000).
64. W. Huang, H.-B. Zhu, and S.-H. Gou. Coord. Chem. Rev. **250**, 414 (2006).
65. R. Gheorghe, M. Andruh., J.-P. Costes, and B. Donnadieu. Chem. Commun. 2778 (2003).
66. X.Yiang and R.A. Jones. J. Am. Chem. Soc. **127**, 7686 (2005).
67. Z. Li and C. Jablonski. Inorg. Chem. **39**, 2456 (2000).
68. W.-K. Lo, W.-K. Wong, J. Guo, W.-Y. Wong, K.-F. Li, and K.-W. Cheah. Inorg. Chim. Acta, **357**, 4510 (2004).
69. J. He, Y.-G. Yin, X.-C. Huang, and D. Li. Inorg. Chem. Commun. **9**, 205 (2006).
70. L. Rigamonti, F. Demartin, A. Forni, S. Righetto, and A. Pasini. Inorg. Chem. **45**, 10976 (2006).
71. M. Yuan, F. Zhao, W. Zhang, Z.-M. Wang, and S. Gao. Inorg. Chem. **46**, 11235 (2007).
72. L. Mishra, R. Prajapati, K. Kimura, and S. Kobayashi. Inorg. Chem. Commun. **10**, 1040 (2007).
73. Z.-H. Ni, L.-F. Zhang, V. Tangoulis, W. Wernsdorfer, A.-L. Cui, O. Sato, and H.-Z. Kou. Inorg. Chem. **46**, 6029 (2007).
74. D.P. Riley. Chem. Rev. **99**, 2573 (1999).
75. J. Ziegler, T. Schuerle, L. Pasierb, C. Kelly, A. Elamin, K.A. Cole, and D.W. Wright. Inorg. Chem. **39**, 373 (2000).
76. A. Puglisi, G. Tabbi, and G. Vecchio. J. Inorg. Biochem. **98**, 969 (2004).
77. V. Daier, H. Biava, C. Palopoli, S. Shova, J.-P. Tuchagues, and S. Signorella. J. Inorg. Biochem. **98**, 1806 (2004).
78. F. Cisnetti, G. Pelosi, and C. Policar. Inorg. Chim. Acta, **360**, 557 (2007).
79. M.T. Kaczmarek, I. Pospieszna-Markiewicz, M. Kubicki, and W. Radecka-Paryzek. Inorg. Chem. Commun. **7**, 1247 (2004).
80. W. Radecka-Paryzek, I. Pospieszna-Markiewicz, and M. Kubicki. Inorg. Chim. Acta, **360**, 488 (2007).

© 2008 NRC Canada

REVIEW / SYNTHÈSE

B–N as a C–C substitute in aromatic systems[1]

Michael J.D. Bosdet and Warren E. Piers

Abstract: The substitution of isoelectronic B–N units for C–C units in aromatic hydrocarbons produces novel heterocycles with structural similarities to the all-carbon frameworks, but with fundamentally altered electronic properties and chemistry. Since the pioneering work of Dewar some 50 years ago, the relationship between B–N and C–C and the wealth of parent all-carbon aromatics has captured the imagination of organic, inorganic, materials, and computational chemists alike, particularly in recent years. New applications in biological chemistry, new materials, and novel ligands for transition-metal complexes have emerged from these studies. This review is aimed at surveying activity in the area in the past couple of decades. Its organization is based on ring size and type of the all-carbon or heterocyclic subunit that the B–N analog is derived from. Structural aspects pertaining to the retention of aromaticity are emphasized, along with delineation of significant differences in physical properties of the B–N compound as compared to the C–C parent.

Key words: boron–nitrogen heterocycles, aromaticity, organic materials, main-group chemistry.

Résumé : La substitution d'unités C–C par des unités B–N, dans des hydrocarbures aromatiques, conduit à la production de nouveaux hétérocycles comportant des similarités structurales avec tous les squelettes carbonés, mais dont la chimie et les propriétés électroniques sont fondamentalement modifiées. Depuis les travaux de pionnier de Dewar, il y a plus de cinquante ans, la relation entre B–N et C–C et la richesse de tous les produits aromatiques carbonés parents a capturé l'imagination des praticiens de la chimie organique, de la chimie inorganique, de la chimie des matériaux aussi bien que des chimistes théoriciens, particulièrement dans les années récentes. De nouvelles applications dans le domaine de la chimie biologique, des nouveaux matériaux et des nouveaux ligands pour les complexes de métaux de transition ont émergé de ces études. Cette revue est orientée vers une évaluation de l'activité dans ce domaine dans les deux dernières décades. Son organisation est basée sur la taille du cycle et sur le type de sous unité entièrement carbonée ou hétérocyclique à partir de laquelle l'analogue B–N est dérivé. Les aspects structuraux relatifs à la rétention de l'aromaticité sont mis en évidence, avec une délimitation des différences significatives dans les propriétés physiques du composé B–N par comparaison avec le composé C–C.

Mots-clés : hétérocycles bore–azote, aromaticité, matériaux organiques, chimie du groupe principal.

[Traduit par la Rédaction]

Introduction

The isoelectronic relationship between "B–N" and "C–C" has been appreciated and exploited for several decades. The substitution of one or more B–N fragments for C–C fragments in classic aromatic hydrocarbons was first explored in the seminal work of Dewar and co-workers in the 1950s and 1960s. More recent investigations have revealed the potential for boron-doped aromatic species in new generations of materials with desirable photophysical and electrochemical properties (1, 2) or biological activity (3). First hinted at via computational investigations, these improved properties have begun to be observed experimentally and with recent development of new methods for synthesizing BN substituted aromatic species, the potential for access to new compounds has reinvigorated research into elemental isomers (4) of classic aromatic species. The recent resurgence of interest in this field of research and the fact that 2008 is the 50th anniversary of Dewar's initial report (5) on a BN phenanthrene derivative has prompted this review. While the focus of this account is recent chemistry of analogues of aromatic hydrocarbons incorporating a BN moiety, some of the early work

Received 6 March 2008. Accepted 14 May 2008. Published on the NRC Research Press Web site at canjchem.nrc.ca on 17 September 2008.

Dedicated to Professor Dick Puddephatt, for his outstanding contributions to Inorganic Chemistry.

M.J.D. Bosdet and W.E. Piers.[2] University of Calgary, Department of Chemistry, 2500 University Dr. NW, Calgary, AB T2N 1N4, Canada.

[1]This article is part of a Special Issue dedicated to Professor R. Puddephatt.
[2]Corresponding author (e-mail: wpiers@ucalgary.ca).

 doi:10.1139/V08-110 © 2008 NRC Canada

summarized in the last review (6) will be briefly discussed to give context.

Perhaps, the quintessential BN hydrocarbon analog is borazine ($B_3N_3H_6$), commonly referred to as "inorganic benzene", an extreme in the continuum of BN for CC substitution in a six-membered aromatic ring. The chemical and physical properties of borazine are well-established, though the debate as to whether or not it can be referred to as "aromatic" continues (7). The sequential replacement of CC moieties for BN in six-membered and more complex aromatic systems has been less thoroughly investigated, and it is therefore interesting to consider the compounds that exhibit such sequential replacements and to elucidate the effects on their structural, electronic, and photophysical properties. As such, this review deals exclusively with compounds obtained by incompletely replacing CC for BN in conjugated systems. That is, fully heteroatomic analogues of cyclopentadienyl and benzene (i.e., borazine) are beyond the scope of this article and have not been included. The intent here is to focus on the intermediate range from organic to inorganic benzene and polycyclic species derived from these. Indeed, there have been numerous accounts examining borazine (8), fully heteroatomic BN-cyclopentadienyl analogues (9–11), linear BN-acenes (12–14), as well as the analogues of graphite, such as hexagonal boron nitride (15), but these will not be specifically addressed here. To further limit the scope of this review, the omission of graphitic structures composed of boron, carbon, and nitrogen commonly referred to as BCN materials, is justified on the basis that the materials so formed have an ill-defined arrangement of BN and CC moieties; that is, the heteroatom substitutions are not at prescribed positions (2, 16, 17). Investigations of BN substitution with "defined" locations in such structures will be addressed.

From the onset of BN aromatic chemistry, several groups have investigated the relative stabilities of the three possible C_4BN benzene isomers, with much the same findings (6, 18–20). The BN-benzene formed by adjacent BN substitution, the 1,2-isomer (Chart 1**a**), is by far the most stable owing to the complimentary π- and σ-donations from nitrogen and boron, respectively. The "disconnected" 1,4-isomer **b** has been predicted to be significantly less stable than **a**, though polycyclic derivatives are known. The least stable substitution pattern is the 1,3-isomer **c**, for which no classical uncharged bonding depiction can be drawn. Indeed, no examples of this isomer have been reported.

Based on atomic radii, the expected bond length for a B–N single bond is 1.58 Å, while that for a B=N double bond is 1.40 Å (21). Just as the CC bond lengths in benzene are intermediate in length between double and single bonds, the participation of the BN fragment in aromatic systems can also be anticipated to result in a bond length between that of a purely single or double bond. Clearly, this bonding situation is indicative of π-character, and as such an appropriate depiction of this bond is shown in Chart 2**b**, which also highlights the dipolar nature of this moiety. However, it has been shown that the B and N atoms do not become significantly polarized due to opposing σ- and π-electron polarizations (Chart 2**c**), and the net formal charges are actually quite similar, even resulting in a net negative charge at nitrogen (6, 22). Given the suppressed polarization, the resonance

Chart 1.

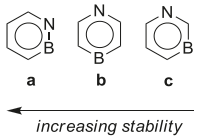

Chart 2.

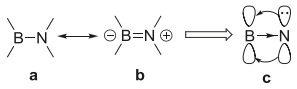

form shown in Chart 2**a** is also valid (and commonly depicted), and though it does not highlight the multiple bond character, this depiction will be used throughout this review for the sake of clarity.

In terms of organization, we classify and discuss BN heterocycles on the basis of the parent azaborinine ring only, and appended rings are considered as substituents on the core heteroaromatic ring of interest. That said, polycyclic systems are regularly referred to in such a way as to highlight their similarity to common aromatic compounds: BN-naphthalene, B_2N_2-triphenylene, and so forth. The abbreviated nomenclature for azaborinines proposed by Thakkar (20) has been adopted in this review, particularly as it pertains to $C_2B_2N_2$ rings. Thus, for example, in describing $C_2B_2N_2$ heterocycles, the first two numbers indicate the nitrogen atom positions, and the latter two indicate the boron atoms.

Six-membered rings

Heterocycles with one BN moiety: 1,2-azaborinines

Benzene analogues

The simplest ring to consider is 1,2-azaborinine, in which one CC pair of benzene has been substituted with a BN unit. As yet, the parent system has eluded isolation, though Dewar and co-workers were able to detect this species via mass spectroscopy (23). Their attempts at forming this parent ring led to rapid polymerization although the products of decomposition were ill-defined. The first substituted examples of this system were prepared by Dewar via desulfurization of **1** with Raney nickel to give **2** (Scheme 1) (5) and by White via dehydrogenation of azaboracyclohexane **3** giving phenyl-substituted **4** (Scheme 2) (24).

In 1980, new derivatives of BN-benzene were prepared by Gronowitz (25, 26), following the analogous desulfurization protocol to that originally utilized by Dewar (Scheme 3). Incorporating a non-fused thiophene moiety at the position α to boron, monodesulfurization yielded only the ethyl derivative **6**, which could then be reacted further to produce the target compound **7**, with an aliphatic, rather than aromatic, group at the α position. Note that utilizing the regioisomer **5**, Gronowitz was able to obtain the isomer **7** having an aliphatic substituent at position 4 as opposed to position 3 (26). Derivatives were assessed by UV-vis and NMR spectroscopies.

© 2008 NRC Canada

Scheme 1.

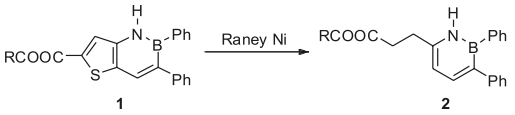

Scheme 2.

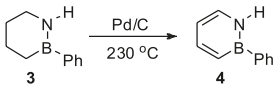

Scheme 3.

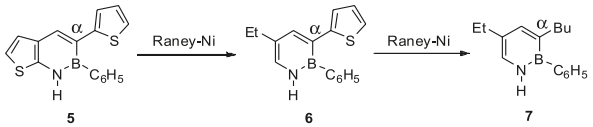

In 2000, a communication by Ashe reported the synthesis of **8a** via condensation of in situ generated allylboron dichloride with ethylallylamine, followed by installation of the B-phenyl group, ring-closing metathesis, and oxidation with DDQ (Scheme 4) (27). In the subsequent year, this same group reported the synthesis of compounds **8** via a ring-expansion reaction of **9** with CH_2Cl_2 and an appropriate lithium base (Scheme 5) (28); overall yields in this latter methodology showed a modest improvement (~35% vs. ~25%). Complexation with $Cr(CO)_3$ and $Mo(CO)_3$ showed compounds **8** to be viable π-ligands, and allowed the first crystallographic characterization of the BN-benzene ring. Here, the BN bond was found to be 1.466(6) Å, suggesting delocalized π-bonding.

The reaction of **10** (the conjugate base of **4**) with $[Cp^*RuCl]_4$ gave rise to mixed sandwich Ru complex **11** (Scheme 6) (29). The N atom of this complex could be protonated by acetic acid, and the acid was determined to have a pK_a of 9.21 ± 0.10 in 85% MeOH/H_2O. This complex was also examined for utility as a nucleophilic catalyst in the acylation of benzyl alcohol with phenylethylketene, but was found to have significantly lower activity than conventional catalysts.

Crystallographic analysis of a derivative of **4** without a directly coordinated metal was first accomplished by Ashe and co-workers in 2006 on the 2-($PhCr(CO)_3$) substituted compound **12** (Fig. 1, Scheme 7) (30). The B–N bond length of 1.430(5) Å was in the appropriate range for a BN double bond, while the bond lengths throughout this ring provided evidence for significant π delocalization. Complex **12** was formed as the thermodynamic product of **4** with $(MeCN)_3Cr(CO)_3$ in THF (Scheme 7), whereas the kinetic product was found to be **13**, suggesting that the phenyl ring serves as the better π-ligand to $Cr(CO)_3$. Conversely, the deprotonated analogues **14** and **15** exhibited the reverse haptotropic tendency, with 1,2-azaboratabenzene serving as the superior π-ligand in the anionic complexes. These migrations were determined to be largely intramolecular via deuterium-labeling studies.

Complimentary crystallographic data as well as reactivity towards electrophiles were communicated in 2007 by Ashe (31). This first investigation of classic aromatic substitution chemistry on a BN-benzene derivative (other than borazine)

Scheme 4.

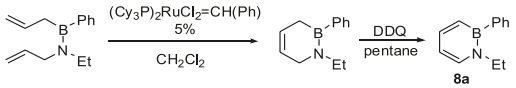

Scheme 5.

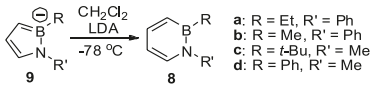

Scheme 6.

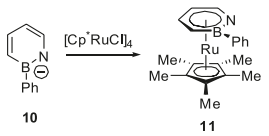

Fig. 1. The BN-benzene ring of **12**, with the –$PhCr(CO)_3$ moiety removed for clarity. Ring bond lengths as shown in **a** are reported in Å. The side-on view in **b** has the B–N bond in the foreground, with the substituents on B and N also omitted for clarity.

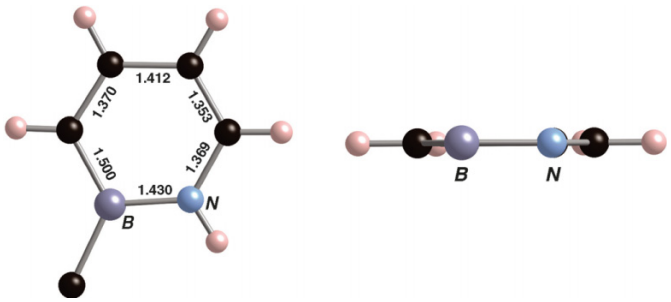

Scheme 7.

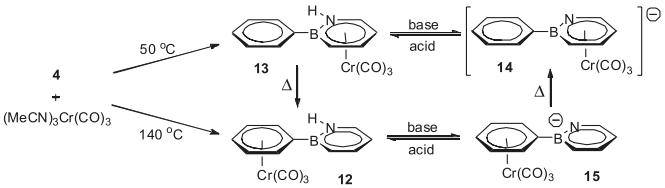

(32) revealed that the positions α (ortho) and γ (para) to boron were susceptible to electrophilic substitution (Scheme 8), in agreement with early investigations by Dewar on larger ring systems (vide infra) (33) as well as previous computations and predicted resonance stabilization (19). Compounds **16a–16c** and **17d–17e** were formed in poor-to-good yields (10%–91%).

Derivatization of the BN-benzene via nucleophilic substitution at boron was recently reported by Liu and co-workers (34). Thus, the reaction of chloro boron species **18** with several anionic nucleophiles, including H^-, proceeded in good yields (Scheme 9). A demonstration of the synthetic utility came with the formation of the BN analog of the hypolipidemic agent methyl 2-ethylphenoxyacetate **19i**, which was achieved through reaction of **18** with methyl glycolate.

© 2008 NRC Canada

Scheme 8.

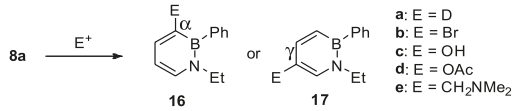

Scheme 9.

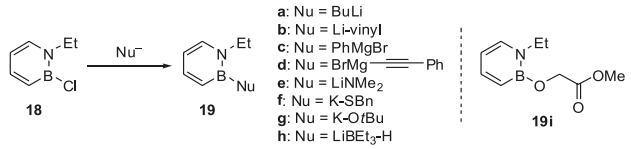

Bicyclic systems

Bicyclic aromatics incorporating the isoelectronic BN unit were first synthesized by Dewar, utilizing condensation reactions of BCl_3 with appropriate olefinic amines to give the framework **20** (Chart 3) (35). Dewar also introduced the internalized BN-naphthalene isomer **21**, via hydroboration/cyclization of di-3-butenylamine with subsequent dehydrogenation (33). Spectroscopic and reactivity studies on **21** substantiated the claims that aromaticity was retained upon heteroatom substitution in the rings. The stability of BN-naphthalene **21** to ambient atmosphere is noteworthy, as hydrolysis of **20** had been observed to be appreciable under such conditions; this highlights the chemical stability imparted by "internalizing" the heteroatoms at ring junctions.

The ring-closing metathesis methodology introduced by Ashe (vide supra) was extended to give access to the **3a**,**7a**-azaborindenyl framework, isoelectronic to the indenyl framework (Scheme 10) (36). A zirconium complex of this ligand was structurally analogous to that of the all-carbon indenyl-supported zirconocene in that the metal associated most strongly with the three non-bridgehead atoms of the five-membered ring. Complexation with $Cr(CO)_3$ showed the formally anionic five-membered ring to be coordinating in the thermodynamic product, just as in BN-benzene complex **14** (30). Competition studies with the zirconium complex in the presence of indene showed the all-carbon system to be a superior π-ligand with free **22** recovered.

A new synthetic route to the BN-naphthalene isomer **21** was introduced by Ashe and co-workers in 2006, utilizing their ring-expansion methodology (vide supra) from **22** (Scheme 10). Overall yields of 5.6%, while still far from desirable, represented an improvement on the 0.2% optimized yield of the original synthesis (33). Importantly, the fully unsubstituted BN-naphthalene **21** was assessed by X-ray diffraction, and found to be isostructural with naphthalene, having an analogous herringbone morphology dominated by CH-π interactions and no π-stacking. Furthermore, the short BN bond (1.461(1) Å) was again in the appropriate range for this moiety within an aromatic ring.

The BN-naphthalene isomer **20** was re-visited by Paetzold and co-workers in 2004 (37). Following the procedure originally outlined by Dewar, they were able to access both halogenated and alkylated (at B) derivatives via condensation of 2-aminostyrene with appropriate haloboranes (Scheme 11). Introduction of water to the chloro derivative **23a** resulted in an equilibrium mixture of the oxide **24** with the 2-hydroxy derivative **23d**. Such behaviour, in which the B–OH group serves as a protic acid, has been noted in several boron aromatics and has been taken as evidence for their aromatic stability, as boron more commonly serves as a Lewis acid under similar conditions (6).

Chart 3.

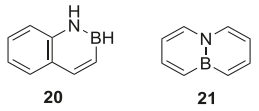

Scheme 10.

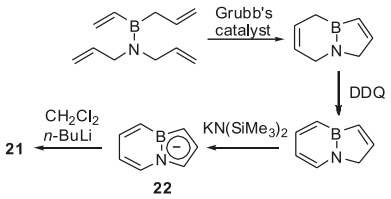

Scheme 11.

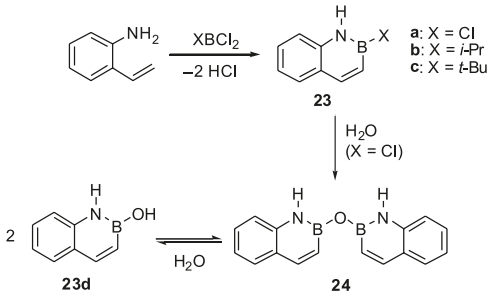

Using a different approach, derivatives were also obtained in an electrophilic addition of *N*-methyl aminoborane **25** to phenylacetylene, giving **26** (Scheme 12). Reaction of this derivative with $(MeCN)_3Cr(CO)_3$ afforded an η^6 complex with the transition-metal fragment associated with the annulated homoaromatic C6 ring only.

Kar and co-workers computed the stabilities of mono-BN-naphthalenes and determined the isomer **27** to be most stable (Chart 4) (12). Interestingly, this derivative is the "inverse" of isomer **20** (i.e., formed by interchanging B and N atoms), which was omitted from Kar's study. The internalized isomer **21** was third in this stability study, 2 kcal mol^{-1} higher in energy than **28** and almost equivalent in energy to **29**. The least stable variant was **30**, the inverse of **28**, though no rationale for this disparity was offered.

Tricyclic systems

Among the first BN isoelectronic aromatics synthesized by Dewar were the BN-phenanthrenes **31** (Scheme 13), which he studied extensively (5, 38, 39). The original synthesis involved condensation of 2-aminobiphenyl with BCl_3, followed by heating of the crude product to 170 °C with $AlCl_3$. Treatment of the chloride **31a** with $LiAlH_4$ afforded the unsubstituted **31b**, which was found to be air- and moisture-stable. Similar strategies produced analogues of anthracene incorporating two BN moieties (40). Recently, **31b** was utilized as a precursor in the interest of developing boron-doped mesophase pitches, with thermostability superior to that of carbonaceous materials (41).

© 2008 NRC Canada

Scheme 12.

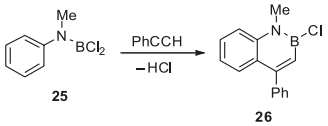

Chart 4.

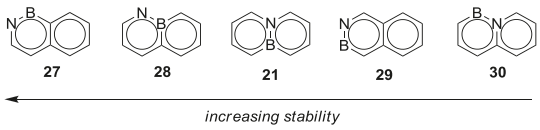

Scheme 13.

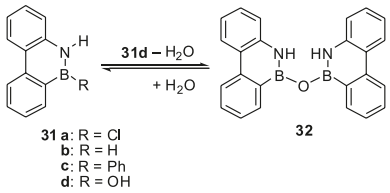

The hydroxy derivative **31d** was investigated in a crystal-engineering study by Philp and co-workers (42, 43), thus providing the first crystallographic analysis of Dewar's BN-phenanthrene framework and verifying the π character of the B–N bond. Drawing an analogy between BN aromatics and carboxylic acids, empirical predictions regarding the intermolecular behaviour were verified in the solid-state structure (Fig. 2), though the dimerization did not appear to be general. Their studies further utilized the ease of dehydration of **31d**, leading to the anhydride **32** (Scheme 13).

A different route into this BN-phenanthrene skeleton was attempted by Zanirato, who explored the reactivity of dichlorophenylborane with various aromatic azides (44). Formation of the transient Lewis acid–base adduct led to extrusion of dinitrogen with the simultaneous 1,2 shift of the phenyl group to the aryl nitrogen (Scheme 14). Intramolecular condensation with the loss of HCl resulted in the desired C_4BN framework. This methodology was found to lack generality, and in fact was successful only with thiophene derivatives giving **33** and its regioisomers; reaction with 2-azidobiphenyl produced a mixture of phenylated aminobiphenyl and carbazole.

Zanirato's work followed from work with Gronowitz on bisthiophene-annulated BN-benzene derivatives such as **33** (45). Several isomers were formed, differing in the orientation of the annulated thiophenes, though all were found to have comparable absorption features to that of benz-annulated derivatives **31**.

Dewar also introduced the isomer **34**, featuring "internalized" B and N atoms (Scheme 15) (46). Relatively little work was done on this species, despite the predicted stability of the ring system bearing heteroatoms at the ring junctions. The analogous reaction scheme was utilized by Dewar to access "internalized" BN- (47) and B_3N_3-triphenylenes (23).

Another isomeric BN-phenanthrene permutation, **36**, was reported in 2007 by Piers and co-workers (48). The new isomer, also featuring internalized heteroatoms, was formed via cycloisomerization of the transient alkynyl substituted borabenzene–pyridine adduct **35** (Scheme 16).

Fig. 2. Hydrogen-bonded dimer of **31d**, highlighting the similarity to the dimeric association of carboxylic acids in the solid state. Hydrogen atoms on the homoaromatic rings have been omitted for clarity.

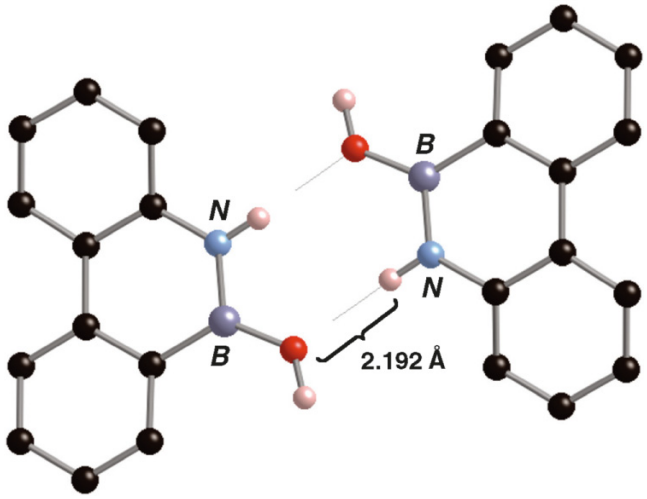

Scheme 14.

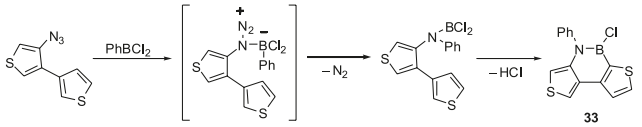

Scheme 15.

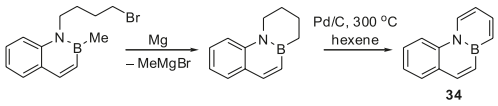

BN-phenanthrenes **36a**–**36e** were found to be stable to aqueous media but suffered decomposition upon prolonged exposure to molecular oxygen. Blue fluorescence was exhibited, with good quantum efficiencies (ϕ_f = 0.38–0.62). As with **36a**, the quantum yield of the isomer **31b** was also found to be significantly greater than that of the all-carbon analog, though the emission wavelength remained indicative of an "organic" fluorophore. That is, whereas the BN moiety of **36** clearly participated in the fluorescence event, the same cannot be said of this moiety in **31**, where the role was more that of an inorganic linker that orients the biphenyl chromophore. Crystallographic analysis revealed the BN bond to be slightly longer than is typical for BN aromatics (1.491(2) Å), but this is consistent with the elongation of the corresponding C–C bond in phenanthrene (49).

Dimeric BN-phenanthrene analogues have also been investigated (50). Compounds **37** and **38** were prepared in one step from the reaction of 2 equiv. of 2-ethynylpyridines with either 2,2′-(51) or 4,4′-diborabiphenyl precursors (Scheme 17) (52). In the crystal structure of **38**, the two BN-phenanthrene units were observed to be orthogonal to each other, resulting in no significant intra- or intermolecular π–π stacking interactions. Both compounds exhibited fluorescence that was significantly red-shifted relative to the monomer **36**, suggestive of communication between the BN-phenanthrene moieties. That these compounds were observed to be emissive is

© 2008 NRC Canada

Scheme 16.

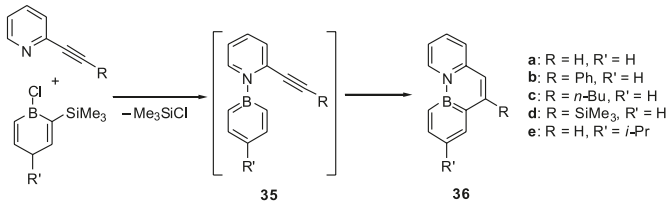

Scheme 17.

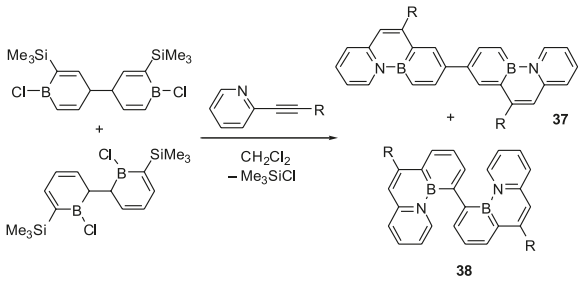

in contrast to B_2N_2-quaterphenyl analogues without "buttressing" ethene groups (vide infra).

Tetracyclic systems

The original BN-pyrene **39** was synthesized from 2,6-diaminobiphenyl by Dewar and co-workers following an analogous route to that for **31** (Chart 5) (35, 40). Interestingly, the isomer **40** could not be obtained in this manner, presumably due to deactivation of the C6 ring toward Friedel–Crafts substitution by the first cyclization event. Additionally, the BN-pyrene **41** was formed from 4-aminophenanthrene, albeit with some difficultly (53).

Philp and co-workers revisited the original synthesis in 2001, but also expanded on this system by incorporating solubilizing *t*-Bu groups in addition to forming the B-hydroxy (**42**) and methoxy derivatives (Scheme 18) (54). This investigation provided a crystallographic analysis, which again showed the π character of the B–N bond, with a distance of 1.427 Å. The formation of B–O–B anhydride oligomers **43** in solutions of **42** was assessed by MALDI-TOF, whereby it was shown that removal of trace water by 4 Å molecular sieves shifted the equilibrium to anhydride formation.

Again utilizing an ene-yne cycloisomerization strategy, Piers and co-workers reported the synthesis of **46** (Scheme 19) in which the BN moiety was fully encapsulated within an all-carbon framework (55). Starting from appropriately substituted 2,6-bis(alkynyl)pyridines, reaction with 4-alkyl-1-chloro-2-(trimethylsilyl)boracyclohexa-2,5-dienes gave **45** as the isolable product, though the transient borabenzene–pyridine adduct **44** could be isolated when R′ = –$SiMe_3$. Treatment of the intermediates **45** with catalytic $PtCl_2$ afforded the desired BN-pyrene analogues in good yields. As with **36**, the photophysical properties were found to be strongly influenced by the heteroatoms, giving green fluorescence in dilute solution, a bathochromic shift of ~120 nm compared with pyrene (56). As with the all-carbon analogue, **46a** was found to form excimers in concentrated cyclohexane solution, though the red-shift in excimer emission was much less pronounced than that observed with pyrene. The BN-pyrenes **46** were also found to undergo reversible one-electron reductions at potentials anodic to pyrene, and

Chart 5.

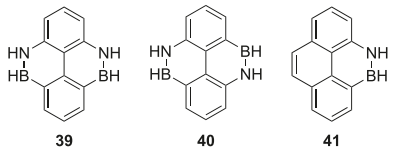

Scheme 18.

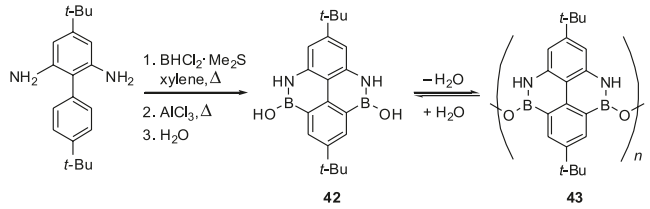

Scheme 19.

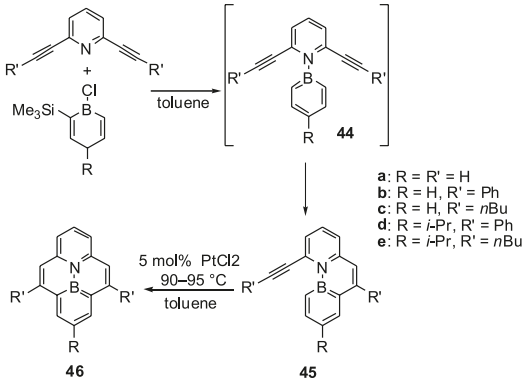

indeed radical anionic species were formed upon treatment with alkali metals.

As with the BN-phenanthrenes **37**, dimeric BN-pyrenes have been investigated (50). The emissive properties of derivatives **47a** and **47b** were found to deviate only slightly from the corresponding monomeric BN-pyrenes, despite the apparently extended π-system. The lack of π-communication between the two BN-pyrene units was attributed to the steric repulsion of the R substitutents, which forced the units to remain rigidly orthogonal to each other.

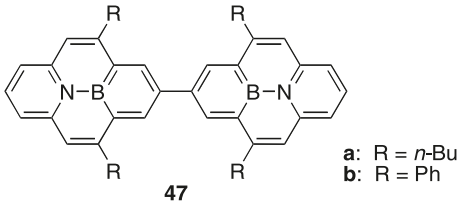

Nöth and co-workers formed the C_4BN framework within a tetracyclic framework via the cyclization of 9-fluorenylidene-tetramethylpiperidino-borane **48** with nitriles, giving rise to **49**, a BN analog of the PAH fluoranthene (Scheme 20) (57). The reaction was presumed to proceed by initial association of the Lewis basic nitrile nitrogen to the boron, followed by electrophilic attack of the nitrile carbon on the adjacent aromatic ring. Crystallographic analysis demonstrated the formed heterocyclic ring was not truly aromatic, as the endocyclic B–N bond in **49** was only slightly shorter than the exocyclic B–N bond (1.469(5) and 1.477(5) Å,

© 2008 NRC Canada

respectively), the former being somewhat longer than is typically realized in BN aromatics. Conversely, the C–B bond length of 1.490(5) Å was short, and indeed the ring consisted of alternating short and long bonds.

Heterocycles with two BN moieties

1,3-Diaza-2,4-diborinines

Of the $C_2B_2N_2$ aromatic ring structures, the 1,3-diaza-2,4-diborinine structure has been computed to be the most thermodynamically stable (20, 58). This result has not been borne out in synthetic work, though a few examples do exist. The benzene analogue **51** was reported first by Paetzold and co-workers and was formed from the 4 + 2 cycloaddition of dimethylacetylenedicarboxylate with diazadiboretidine **50** (Scheme 21) (59). No reaction was observed with less active dienophiles, such as 2-butyne or diphenylacetylene. Crystal structure analysis of **51** showed the ring to be highly twisted, with dihedral angles ranging from 7° to 29°, likely due to the bulky *t*-Bu substituents. Nevertheless, B–N bond lengths were in the range for typical structures (1.447(8)–1.460(8) Å).

A somewhat more generalized route to this ring system was first reported by Köster and Iwasaki and involved the dimerization of aromatic amine-borane adducts (Scheme 22) (60). The resulting B_2N_2-naphthalene **52** was readily susceptible to hydrolysis but stable to dry air. Notably, of the unsubstituted B_2N_2-naphthalenes, this isomer has been computed to be the most thermodynamically stable (12).

Work on this system since the time of the last review (6) has largely been accomplished by Frange and co-workers, who have investigated several such B_2N_2-naphthalenes with various substituents on the benzo and heteroaromatic rings. The crystal structure of methyl substituted **52** showed shortened, though alternating, B–N bond lengths of 1.405(4), 1.454(4), and 1.424(4) Å (61). The dihedral angles through the heteroaromatic ring show it to be significantly more planar than **51**, though still with minor puckering (maximum dihedral angle of 4.2°).

Frange's group extended the condensation methodology to include the formation of B_2N_2-phenanthrene **53** (62, 63) and B_2N_2-benz[*a*]anthracene **54** (Chart 6) (64). While not general, the formation of the "dimeric" 1,3,2,4 ring system (as opposed to the thermodynamic "trimeric" borazine products) was improved via the use of BBr_3 or BI_3 vs. the lighter haloboranes (61).

The reactivity of the heterocyclic framework **52** towards electrophilic metal centers has been investigated (65–67), and it was found that complexation occurred exclusively on the annulated homoaromatic C6 rings, giving a mixture of atropisomers. Bond lengths in the complexed ring were elongated by an average of 0.025 Å relative to the uncomplexed species, whereas in the heteroaromatic ring, bond lengths were increased by less than half this amount (67).

Bowser and co-workers have suggested that **55** (Chart 7), a bicyclic variant of the 1,3,2,4 ring system, may serve as a synthon for $C_{12}B_{24}N_{24}$ analogues of buckminsterfullerene (vide infra) (68, 69). While stoichiometrically appropriate, there have been no reports on the synthesis of either this precursor or the fullerene product. Additionally, this heterocyclic naphthalene isomer was not included in a computational study of the possible (and yet unknown) B_4N_4-naphthalenes, though the closely related **56** was deemed to have relatively low thermodynamic stability (12).

Scheme 20.

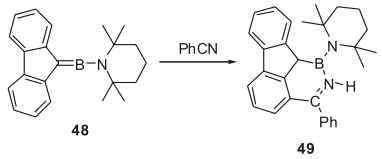

Scheme 21.

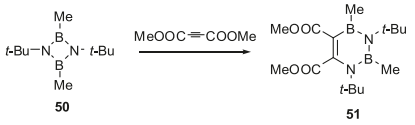

Scheme 22.

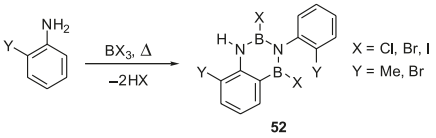

Chart 6.

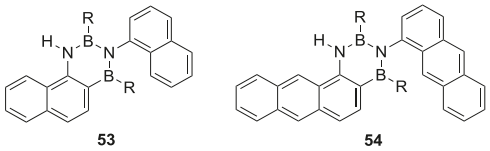

2,3-Diaza-1,4-diborinines

The 2,3-diaza-1,4-diborinine ring system was the first isolated example of an isoelectronic analogue of benzene with two BN units, despite computations suggesting this heterocycle to be less stable than the 1,3-diaza-2,4-diborinine ring by over 50 kcal/mol (20, 58). The substituted derivative **57** was achieved by Siebert via the reaction of thiadiborolenes with hydrazines, giving an air-sensitive liquid (Scheme 23) (70, 71). Crystals suitable for X-ray analysis were isolated at low temperature, and revealed a planar structure with endocyclic bond lengths indicative of a delocalized system, though the very short B–N bonds (1.387(4) Å) were closer to that of a pure B–N double bond. Subsequent treatment of **57** with $(MeCN)_3Cr(CO)_3$ afforded the corresponding η^6-$Cr(CO)_3$ complexes **58**, which were also studied crystallographically. Here, metal complexation in **58a** caused elongation of the B–N bonds to 1.41(2) and 1.44(1) Å, as well as a considerable upfield shift in the ^{11}B NMR resonance, from 33.9 (**57a**) to 22.8 (**58a**) ppm, both in accordance with the participation of the π-orbitals in the metal interaction.

The first polycyclic compounds with this ring system were B_2N_2-triphenylene analogues **59**–**61**, prepared by Piers

© 2008 NRC Canada

Chart 7.

55 **56**

et al. (51, 52). Formed via reaction of a 2,2′-diborabiphenyl precursor with pyridazine Lewis bases (Scheme 24), the polycyclic species were found to undergo (in most examples) two reversible one-electron reductions, and indeed radical anionic species were crystallograpically characterized for two derivatives upon reduction with $CoCp^*_2$. A marked increase in the B–N bond length was observed in going from the neutral species **59a** ($B–N_{avg.}$ = 1.458 Å) to the radical anion ($B–N_{avg.}$ = 1.484 Å), in agreement with the predicted B–N antibonding character of the SOMO (52). Derivatives **59a** and **60** were also found to be weakly fluorescent (ϕ_f = 0.02–0.08), with yellow–orange (**59a**) to green emission (**60**), which correlates well with the emissive efficiency of all-carbon triphenylene (ϕ_f = 0.07). Compounds **59b** and **61** were found to be non-fluorescent due to large twists imposed by steric interactions with protons α to boron, thereby disrupting the conjugation through the molecules.

1,4-Diaza-2,3-diborinines

Relatively few examples of the 1,4-diaza-2,3-diborinine ring system have been reported, and there are no examples of a monocyclic species, though calculations suggest that the ring should be more stable than the 2,3-diaza-1,4-diborinine ring by ~10 kcal/mol (20, 58). At the time of the previous review, there were only three examples of the 1,4-diaza-2,3-diborinine ring, all offered by Nöth and co-workers (6). Analogues of naphthalene (**63**), phenanthrene (**64**), and anthracene (**65**) were formed via condensation of dialkyldiborabis(dimethylamide)s with an appropriate *ortho*-diamino aromatic precursor (Chart 8) (72). It was later shown that complexation of **63** with $Cr(CO)_3$ occurred at the homoaromatic ring, as evidenced by the small downfield shift in the ^{11}B NMR and the considerable upfield shift of the aromatic protons in the ^1H NMR (73).

More recently, Cowley, Marder, and Norman prepared **66**, which can be considered an *oxo*-bridged dimer of the 1,4-diaza-2,3-diborinine heterocycle (74). This product resulted from the reaction of $B_2(OMe)_4$ with Li_2[dab] (dab = 1,4-di-*tert*-butyl-1,4-diazabutadiene), and was obtained as colourless crystals (Scheme 25). Though the focus of this account was the central B_4O_2 ring, the bond lengths for the external heterocycles were found to be in the appropriate ranges for typical BN compounds, with average distances of 1.429, 1.405, and 1.338(3) Å for B–N, N–C, and C–C bonds, respectively. Notably, this is the only reported crystal structure of a six-membered aromatic ring incorporating a B–B bond, which was found to be 1.683(3) Å. Comparison with average B–B lengths of 1.731 Å in similar structures having a B_4O_2 ring with acyclic groups on the B atoms shows that the B–B distances of **66** are appreciably shortened (75), presumably due to conjugation through these atoms. Furthermore, the

Scheme 23.

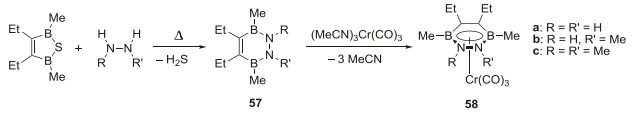

57 **58**

Scheme 24.

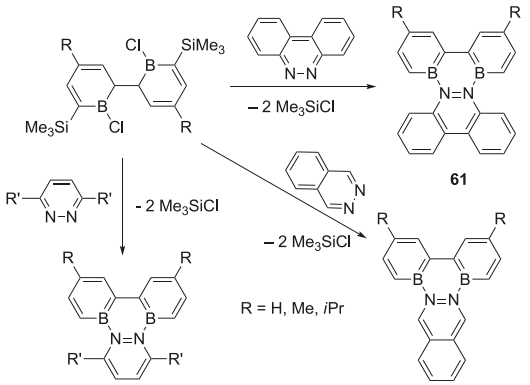

59a: R' = H
59b: R' = Ph

60 **61**

Chart 8.

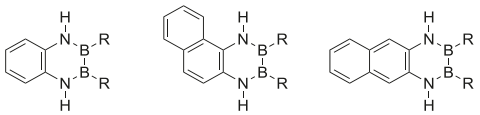

63 **64** **65**

$C_2B_2N_2$ ring in **66** was found to be planar, with a maximum dihedral angle of 4.5°.

1,5-Diaza-2,4-diborinines

The only example of the 1,5-diaza-2,4-diborinine ring system was reported by Roesler and co-workers in 2006 (76). The six π-electron ring **67** was achieved in two steps starting from the condensation of a trimethylsilyl formamidinate with 1,1-bis(methylchloroboryl)ethane in the presence of trimethylsilyl triflate (Scheme 26). Crystallographic analysis of both **67** and deprotonated **68** revealed a planar arrangement of the ring atoms, though the relatively long B–N bond lengths (avg. = 1.498 Å) suggested that the π electrons were distributed over hetero-allyl fragments (B_2C^- and N_2C^+) rather than being fully delocalized around the ring. This bonding situation was previously predicted using MNDO calculations (58), though more recent analysis of the electronic structure suggests some degree of aromaticity (77).

Five-membered rings

Cyclopentadiene analogues with one BN moiety

Numerous studies have considered the influence of incorporating BN into fullerene and nanotube frameworks. It is

© 2008 NRC Canada

Scheme 25.

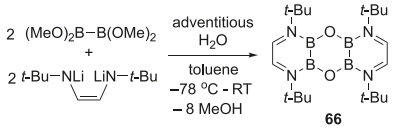

Scheme 26.

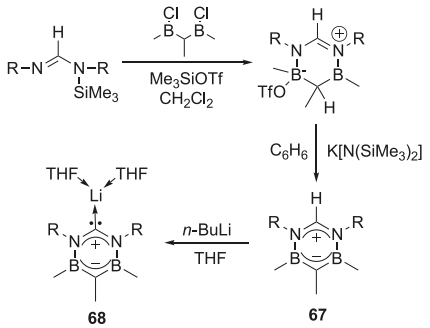

thus useful to consider not only BN substitution in six-membered rings, but also five-membered rings.

The BN analogue of the cyclopentadienyl anion (Cp), 1,2-azaborolyl (abbreviated here as Ab), was first reported by Schmid in the 1980s (78). His compounds were formed via deprotonation of **69** with LTMP affording the lithium salts **70**, which were subsequently ligated to numerous transition metals via salt elimination (Scheme 27). The sandwich complexes **71** displayed predictable bonding arrangements in the solid state. Thus, complexes with relatively electron-rich metals, such as Co and Ni, had significantly diminished interaction with the donor N atom of the Ab ring, to such an extreme in the nickelocene analog that the bonding was more accurately depicted as η^3, in which the BN unit served as a linker for an allyl ligand. Conversely, the sandwich complex formed with Fe showed delocalized bonding throughout the ligand and as such the Ab ring was appreciably isoelectronic and isosteric with Cp. The *meso* and *rac* diastereomers formed in these syntheses were formed in equal proportions and were thus energetically equivalent.

Schmid has also reported complexes of Ab with main-group elements. One such study addressed the structural behaviour of beryllocene, taking advantage of the diastereomeric Ab_2Be complexes to better assess both solid-state and solution behaviour (79). As in beryllocene, Ab_2Be was found to assume η^5 binding to one ligand, and η^1 bonding to a carbon atom of the other. Upon isolating by fractional crystallization one of the Ab_2Be diastereomers and storing this in C_6D_6 or toluene-d_8 for five days, a 1:1 mixture of diastereomers was re-established. Further, the mixed complex AbCpBe **72** could be formed by combining solutions of Ab_2Be and Cp_2Be. These results suggested that dissociation of one of the ligated rings was occurring to give an ion pair (Scheme 28). This was confirmed by variable temperature (VT)-NMR experiments, as well as the observation that THF solutions of AbCpBe were significantly conductive.

More recently, the groups of Ashe and Fu have reported more synthetically useful methodologies to the BN–Cp framework. In 2000, the former group employed the ruthenium-catalyzed ring-closing metathesis of a vinyl/allyl substituted aminoborane to give the cyclic heterocycle **73**, which upon deprotonation gave the desired 1,2-azaborolyl **9d** (Scheme 29) (27). Fu's method was very similar to that of Schmid, but involved treatment of the B–Cl heterocycle **74** with various nucleophiles prior to salt metathesis (Scheme 30) (80), thereby introducing a "tunability" at boron. Indeed, the donor properties as a function of Nu could be monitored by measuring the CO stretching frequencies of $Cr(CO)_3$ complexes **77** via IR spectroscopy. Both groups reported the facile coordination of the BN–Cp analogue to various transition metals, including Zr, Ru, and Co, giving analogues of known Cp complexes (27, 80, 81).

Scheme 27.

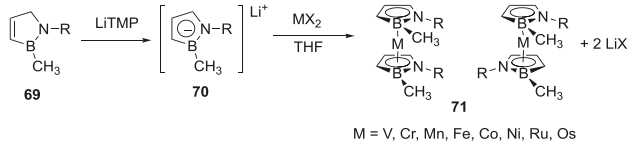

Fu has also generated enantiopure iron(II) complexes with the Ab ligand and shown them to be viable in promoting highly stereoselective aldol reactions (82). Starting from complex **78**, a racemic mixture of the B–OH compounds **79** could be achieved (Scheme 31), which was subsequently resolved by chiral HPLC.

Cyclopentadiene analogues with two BN moieties

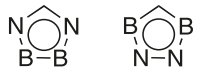

A heterocyclic Cp analogue with two BN moieties was first communicated by Roesler and co-workers (83, 84). Thus, condensation of $MeCH(RBCl)_2$ with di*iso*propylhydrazine afforded **80**, which was subsequently deprotonated with an appropriate alkali-metal base to give **81** (Scheme 32). All alkali-metal salts were observed to exist as sandwich complexes in the solid state, though none via η^5 coordination. This is in contrast to analogous η^5 Cp complexes, and coupled with the longer metal–ligand atom distances, suggests that the heterocycles are poorer π ligands than Cp. Endocyclic B–C and B–N bonds lengths were comparable to those in other BN heterocycles (1.50 Å and 1.46 Å avg., respectively), though the N–N bond lengths of 1.45–1.46 Å were indicative of a single bond. Slight deviations from planarity in the ring were noted in the structures of **81c** and **81d**.

Reaction of the alkali-metal salts **81** with group 12 metal dihalides resulted in sandwich complexes **82**, which demonstrated η^1:η^1 (M′ = Hg, Cd) or η^3:η^3 (M′ = Zn) binding centered at the ring carbon atom (83, 85). While structurally comparable to bis cyclopentadienyl analogues, the lessened σ character of the ring carbon in the heterocyclic complexes suggested increased π stabilization through the electron-deficient boron atoms relative to that afforded by the cyclopentadienyl ligand.

The B_2N_2 N-heterocyclic carbene **84** also recently reported by Roesler and co-workers (86), while formally isoelectronic to Cp, was found to be non-aromatic

© 2008 NRC Canada

Scheme 28.

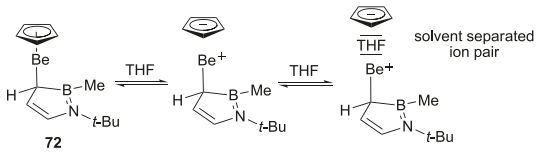

Scheme 29.

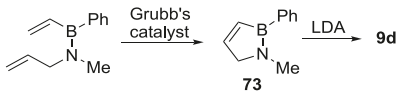

Scheme 30.

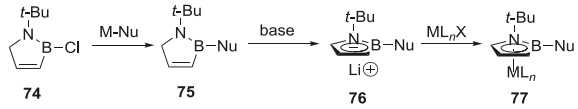

Scheme 31.

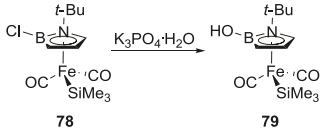

(Scheme 33). Specifically, the use of dimethylamino substituents at boron resulted in short exocyclic B–N bonds (1.377 Å avg.) and long endocyclic B–N bonds (1.465 Å avg.), and as such, the resulting heterocycle mirrored the bonding parameters of *iso*-propyl substituted N-heterocyclic carbenes; this was indeed reflected in the chemical behaviour of the B_2N_2 heterocycle. A subsequent computational study further verified the non-aromatic nature of **84** (77).

BN substitution in classic heteroaromatic compounds

BN analogues of pyrazole, indole, and indolizine

Monocyclic pyrazole analogues

Diazaboroles are formed by the replacement of CC with BN in pyrrole. The first examples of this ring system without annulated rings were the work of Niedenzu (87) and Schmid (88). The synthesis and reactivity of these rings were the subject of a review in 2001 (89), and as such, only a few examples prior to that date are provided for comparison to other BN heterocycles.

The first $Cr(CO)_3$ complexes were reported in 1977 by the group of Schmid (90, 91). In these investigations, the *N*-phenyl heterocycle formed the phenyl-complexed derivative **85** as opposed to η^5 coordination to the heteroaromatic ring. Without phenyl substituents, η^5 bound **86** was formed, and subsequent treatment with $NOPF_6$ afforded the cationic nitrosyl complex **87** (Scheme 34) (91).

Scheme 32.

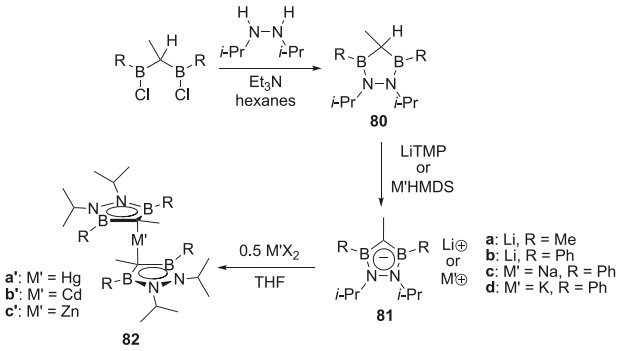

Scheme 33.

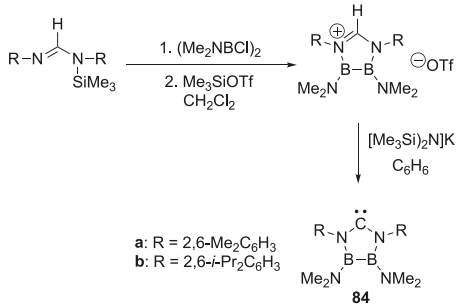

Subsequent work by Schmid led to a crystallographic analysis of the derivative **89**, which verified the planar geometry and sp^2 hybridization of the ring atoms (92). In the case of precursor **88**, dehydrogenation also resulted in dimerization to give **90** (Scheme 35), though the two rings were canted out of conjugation in the solid-state structure.

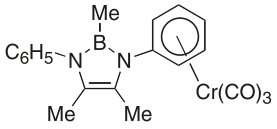

85

More recently, Weber and co-workers have investigated bis(diazaborole) compounds with bridging aromatic groups (93). Thus, phenyl- and biphenyl-bridged derivatives **91a** and **91b** were characterized by multinuclear NMR, UV–vis, and fluorescence spectroscopies, though only **91b** was found to be emissive. Additionally, a 1,3,5-trisubstituted benzene derivative was reported and crystallographically characterized. Cyclic voltammetry showed that compounds **91** undergo irreversible oxidation.

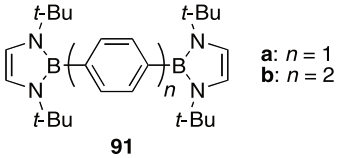

91

Ferrocenyl derivatives **92** and **93** were obtained by the reaction of (dibromoboryl)ferrocene or 1,1′-bis(dibromoboryl)ferrocene with diazabutadienes, followed by sodium amalgam reduction (Scheme 36) (94). Solid-state structures

© 2008 NRC Canada

Scheme 34.

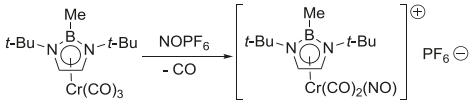

Scheme 35.

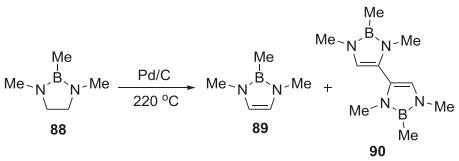

showed the absence of conjugation between the BN-pyrrole and the cyclopentadienyl ligands, though the heterocycles did serve as electron donors, leading to cathodic shifts in the oxidation potential of the iron center.

A relatively new line of investigation concerning this framework has been directed at producing boron heterocycles that are anionic and isoelectronic to Arduengo-type carbenes. Carbenes of this type are known to have some aromatic character, though this is a relatively minor contributor to the overall stability of the molecule (95). Initial computations by Schoeller suggested that Group IIIa carbenes of this ilk were viable synthetic targets, with boron retaining significant electron density (96). The carbene analogue boronide **96** was presumed as an intermediate in reductions of bromide **94** with alkali metals, which produced a mixture of **97** and **98** (Scheme 37) (97); no confirmatory evidence or further investigation of the novel species was provided in this report.

Subsequently, Yamashita and Nozaki succeeded in isolating and structurally characterizing the boryl anion **100** in 2006 (Scheme 38) (98). The lithium salt was obtained by reduction of 2,6-di*iso*propylphenyl substituted **99** with lithium naphthalide, and was structurally characterized. While formally a carbene analogue, the planar structure and shortened intracyclic bonds of **100** supports the existence of a delocalized π electron system (99). The boron center was protonated in the presence of water, giving borane **101**.

Polycyclic pyrazole analogues

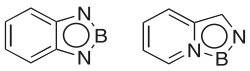

Much more extensively studied than their monocyclic counterparts are the bicyclic diazaborinine derivatives, which are BN derivatives of indole; in fact, this was the very first BN aromatic formed (100). The chemistry of this heterocycle was extensively reviewed by Fritsch (6), though there has been renewed interest in this system, as the appended benzene ring tends to enhance the emissive quantum efficiencies relative to the monocyclic BN-pyrroles (89).

A particularly facile synthesis of this ring system is the condensation of an *ortho*-phenylenediamine with boronic acids, a reaction that has even been shown to occur smoothly in the solid state (101). A useful synthon for various B-substituted analogues is **102a**, which can be obtained by

Scheme 36.

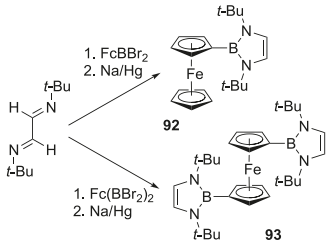

Scheme 37.

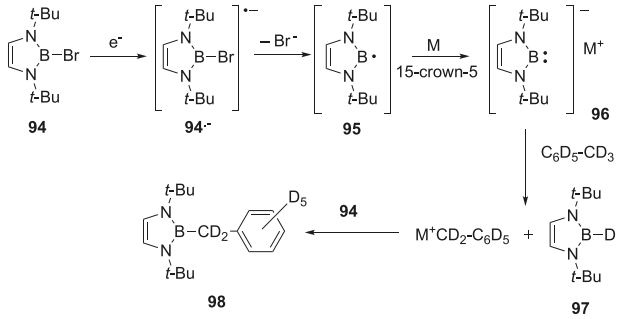

Scheme 38.

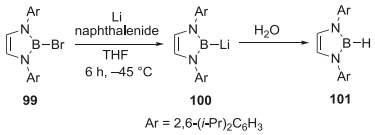

treating *N*,*N*′-diethyl-*o*-phenylenediamine with BBr_3, followed by CaH_2 (Scheme 39) (102). Thus, reaction of **102a** with AgCN or MeLi gave rise to B-cyano (**102b**) and B-methyl (**102c**) derivatives, respectively, whereas reaction with Na/K alloy gave the dimer **103**.

An interesting route to this heterocycle involved the thermally induced reductive transposition of B and C in borane adducts of 1,3-benzazoles **104** to give 1,3,2-benzazaboroles **105** (Scheme 40) (103). Isolobal products were formed, such that the X–C(sp^2)–N(sp^2)–B(sp^3) fragment became X–B(sp^2)–N(sp^2)–C(sp^3) (X = NH, O, S), as evidenced, in particular, by the marked downfield shift in the ^{11}B NMR (from approximately –22 to 23 ppm). In the case of the borane adduct of 1-ethyl-2-(*o*-methoxyphenyl)benzimidazole **106**, transposition was accompanied by loss of methane to give the tetracyclic product **107** (Scheme 41).

Parent complex **108** was functionalized at the nitrogen atoms by treatment with 2 equiv. of BuLi, affording **109**, which was subsequently quenched with Me_3SiCl to give **110** (Scheme 42) (104).

In 2002, Maruyama and Kawanishi reported the synthesis and photophysical properties of bis(diazaboroles) **111** and the more extensively conjugated derivatives **112** and **113** (Chart 9) (105). Compounds **111** and **112** were found to fluoresce violet–blue with excellent quantum efficiencies; **111b** had a quantum yield near unity. Phenalene-type derivative **113** was found to be non-emissive. Oxidation potentials for **111a**–**111c** were obtained and reflected the electron withdrawing/releasing nature of the substituents; these molecules were not stable to electrochemical reduction.

© 2008 NRC Canada

Scheme 39.

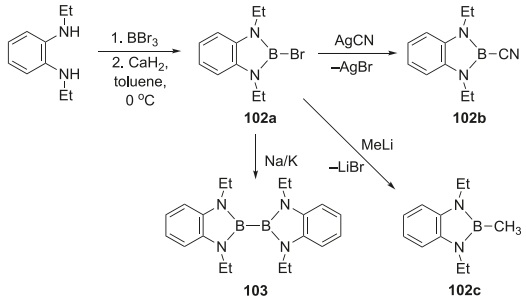

Scheme 40.

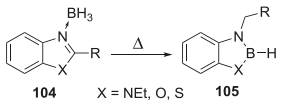

A series of BN-indole derivatives substituted or bridged by thiophene moieties were studied by Weber and coworkers in 2006 (Chart 10) (106). Compounds **114**–**115** were obtained via salt elimination from **102a** (Scheme 39) and lithiated thiophenes. Biphenyl bridged **118** was also investigated and had the largest Stokes shift (123 nm) of all compounds in this study. Bisthiophene derivative **117** was characterized crystallographically and showed the 1,3,2-benzodiazaborole group to be planar with BN bond lengths of 1.431(5) and 1.440(4) Å. Additionally, **114a** and **114b** were found to serve as fluoride-ion sensors, as monitored by the reversible quenching of fluorescence upon addition of *n*-Bu_4NF.

Alkyne-functionalized examples of both BN-pyrroles and BN-indoles were achieved, again via salt-elimination protocols (107). Successful formation of the terminal alkyne **120** came by way of the B-cyano derivative **119** (Scheme 43), though the same reaction with **122** led to an ethylenediamine-linked dimer **123** (Scheme 44) (102). Alkyne-bridged species **121** was accessible from **120**, and these were observed to undergo two oxidative processes, suggesting communication between the two heterocycles across the C_2 bridge.

Polymeric species incorporating this BN heterocycle have also been investigated (108). Polyacenaphthalene with diazaborole side chains was formed by thalliation of the parent polymer with thallium trifluoroacetate, followed by borylation and hydration to give a polymer with boronic acid functions on ca. 30% of the acenaphthalene units (Scheme 45). Subsequent treatment with *p*-nitro-*o*-phenylenediamine gave polymer **124**.

In follow-up work, this bicyclic BN aromatic was more intimately incorporated into the polymer chain, giving rise to photoluminescent polyphenylene derivatives (109). Thus, Suzuki coupling of 1,4-dibromo-2,3-phenylenediamine with 2,7-bis(1,3,2-dioxaborolan-2-yl)-9,9′-dioctylfluorene gave copolymer **125** in high yields. Reaction with aryl boronic acids gave the polymer **126**, with >80% incorporation of the boron substituents (Scheme 46). Polymer **126** exhibited both higher quantum efficiencies and higher oxidation potentials than **125**, clearly manifesting the benefits of incorporation of BN functions into these frameworks.

Scheme 41.

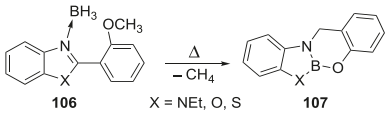

Scheme 42.

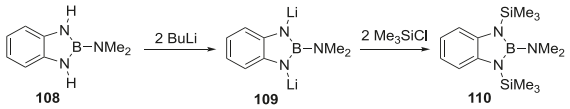

Chart 9.

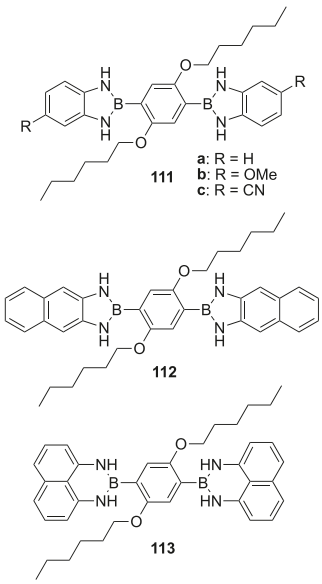

Chart 10.

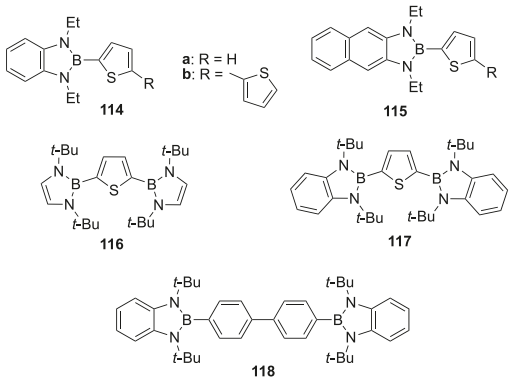

Habereder and Nöth used salt elimination strategies to access derivatives **128** with Group 14 elements in the interest of preparing versatile intermediates for organic chemistry via oxidative addition to Pt(0) (Scheme 47) (110). Examples of all were obtained and crystallographically characterized, though only the trimethylstannyl derivative **128d** was observed to undergo oxidative addition of the B–E bond to $(\eta^2\text{-}C_2H_4)Pt(PPh_3)_3$, giving the cis Pt complex. The bromo-derivative **127** was the only other heterocycle to oxidatively add to the Pt(0) reagent but gave the trans product.

© 2008 NRC Canada

Scheme 43.

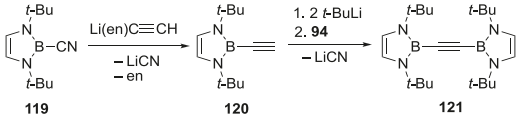

Scheme 44.

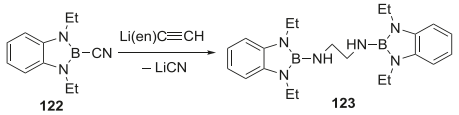

Scheme 45.

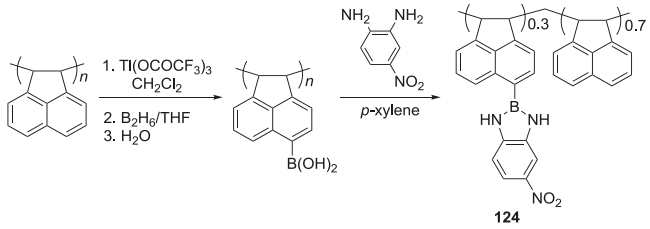

The oxidative addition of the B–CN bond of **129** to palladium(0) was studied by Suginome and co-workers (111). Thus, in the presence of 5 mol% Pd catalyst, alkynes could be cyanoborated in near quantitative yields, giving substituted acrylonitriles **130** (Scheme 48). Good regioselectivities were observed with unsymmetrical alkynes. Mechanistic studies corroborated the reversible nature of the oxidative addition (112).

Rhodium-catalyzed hydroborations of terminal olefins with **131** were investigated by Hadebe and Robinson, and showed the diazaborinine to be a competent reagent for functionalization of olefins (113). No reaction with internal olefins was observed. Further, **131** was particularly robust relative to the more common pinacol- and catechol-boranes, as no disproportionation of the borane was observed. The resistance of **131** towards forming metal boryl complexes has also been noted in the case of Ru(II) (114), though Hartwig was able to crystallographically characterize a family of boryl-bridged Ru dimers with the *N*-methyl derivatives **131a** and **131b** (115).

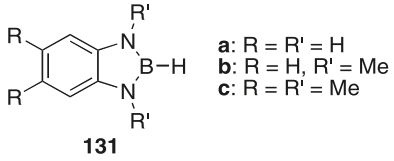

a: R = R' = H
b: R = H, R' = Me
c: R = R' = Me

A BN analogue of indolizine was first reported by Weber and co-workers in 2001 (116). Reaction of a pyridine carbaldimine with BBr_3 afforded the bicyclic diazaborolium salt **132**, which was subsequently reduced with excess sodium amalgam to give **133** in good yield (Scheme 49). Heterocycle **133** could be readily converted into a number of different B-substituted derivatives by standard means. Crystallographic analysis of the B-cyano derivative revealed alternating bond lengths in the pyridine ring but an overall planar structure with BN bond lengths of 1.420(2) and 1.429(2) Å. Attempts to form diazomethane complexes were marginally successful, as the products could not be purified (117). Similarly, a ferrocenyl derivative analogous to **92** was formed but also proved relatively unstable (94).

Scheme 46.

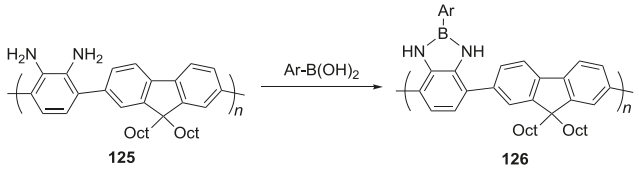

Scheme 47.

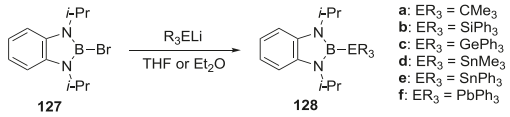

Scheme 48.

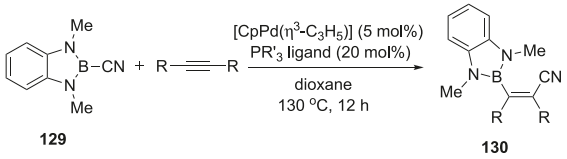

Chart 11.

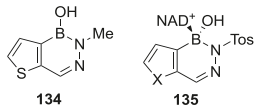

BN analogues of pyridine and related polycycles

An interesting class of heteroaromatic compounds arising from BN substitution is the BN-isoquinoline series, formed by the conceptual annulation of a (hetero)aromatic ring to a BN-pyridine analogue. First reported by Dewar (118), these compounds have been extensively studied as antibacterial agents since the late 1960s, and more recently have also been found to inhibit the growth of yeast cells (119). The mechanism of action has been increasingly well-understood, though detailed discussion of the biochemical activity is deferred to the recent literature (3, 120–123). Crystallographic analysis of the 2-methyl substituted 2,3,1-benzodiazaborine **134** showed the rings to be planar, with a B–N distance of 1.433(3) Å (124), though Baldock and co-workers were able to characterize the tetrahedral borate complex **135** in the active site of enoyl reductase (Chart 11), indicating that the Lewis acidity of the B center is important in the function of these compounds (121). Thus, in the presence of NAD^+ the molecule forms a borate complex, which binds strongly to the active site of enoyl reductase. Replacement of the BN moiety with CC resulted in an analogue devoid of biological activity (125), demonstrating the key importance of the B-hydroxy group.

© 2008 NRC Canada

Scheme 49.

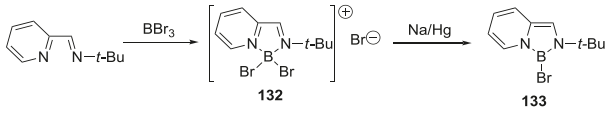

Scheme 50.

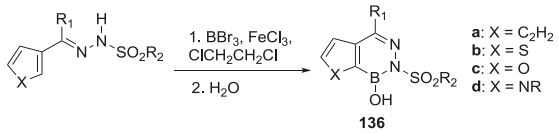

Scheme 51.

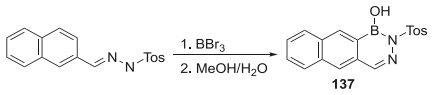

Chart 12.

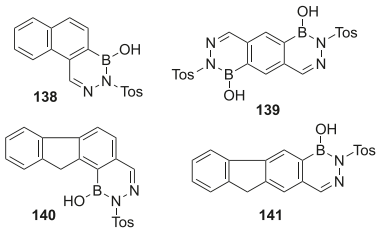

The original synthesis involved reaction of *ortho*-formylbenzeneboronic acids with hydrazine or its derivatives (118). Müller and Grassberger independently reported an alternative, more versatile route, which made use of a Lewis acid to promote the electrophilic attack of trihaloboranes on (organosulfonyl)hydrazones of (hetero)aromatic aldehydes and ketones, giving the target compounds **136** (Scheme 50) (125, 126). This route was tolerant to numerous functional groups on the (hetero)aromatic ring, though yields were significantly diminished with electron-withdrawing groups. Attempts by Müller to form tricyclic derivatives of this ilk resulted in the formation of anthracene-type derivative **137** only (Scheme 51), with no evidence of the conceivable phenanthrene-type analog (126). Grassberger reported the synthesis of another phenanthrene-type isomer **138**, as well as bifunctional **139** and tetracyclic analogues **140** and **141** (Chart 12) (125) using similar methodologies.

Numerous derivatives of this framework were reported by Gronowitz, most with an annulated thiophene moiety, as in **136b** (127). Reactivity of the BN-isoquinolines towards various electrophiles was extensively discussed in both Gronowitz's and Fritsch's reviews (6, 127).

Desulfurization of thiophene annulated derivatives such as **136b** with Raney nickel afforded BN-pyridine analogues **142** (Scheme 52), which were found to be much more stable than related BN-benzene derivatives and less polar than corresponding pyridines (128, 129). Indeed, Doerksen and Thakkar have recently calculated the polarity to be less than 0.71 D (11). Of the 10 possible BN-pyridines, these researchers found this N–N–B isomer to be 23.4 kcal/mol higher in energy than the isomer with N–B–N bonding.

Scheme 52.

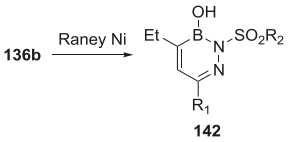

Scheme 53.

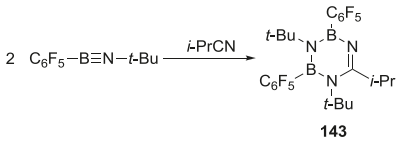

Scheme 54.

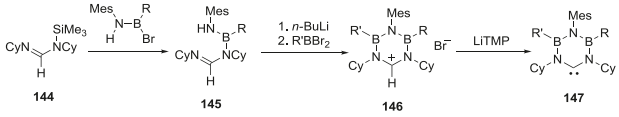

Scheme 55.

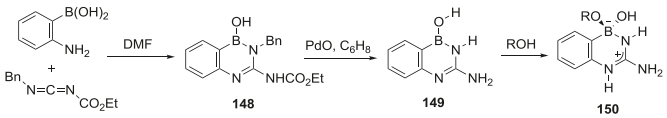

Substitution of two pyridine CC units with BN via the cycloaddition of *iso*propylnitrile to iminoborane **143** leads to formation of a B_2N_2-pyridine (Scheme 53) (130). In the solid-state structure, some degree of bond alternation was evident, though all were within the range expected for a delocalized π system (1.415–1.450 Å). The synthesis was not general and depended strongly on the nitrile used. Notably, this was computed to be the most stable substitution pattern of 16 possible B_2N_2-pyridines (11).

A related ring system was recently investigated by Bertrand as a heterocyclic carbene precursor (Scheme 54) (131). Derivatives without amino substituents at boron were prepared by reacting *N*-silylated formamide **144** with an appropriately substituted aminoborane, giving **145**. Deprotonation with *n*BuLi followed by the introduction of R′BBr_2 gave cationic **146**, which could be converted to the carbene **147** with LiTMP. Here, the reported structure was isoelectronic to benzene as opposed to pyridine, and π-electron delocalization was evident in the solid-state structure with B–N bond lengths of 1.43–1.44 Å. Indeed, electronic-structure calculations suggest some degree of aromaticity in this heterocyclic carbene (95). Upon introduction of 0.5 equiv. of bis(μ-chlorocyclooctadienerhodium), **147** served as a strong σ donor to the metal centre (131).

Groziak and co-workers have also investigated several BN heteroaromatic derivatives, and highlighted some similarities to biologically relevant molecules. Thus, condensation of 2-aminophenylboronic acid with 1-benzyl-3-(ethoxycarbonyl)carbodiimide afforded the BN-quinoline **148**, from which purine analogue **149** could be obtained via catalytic transfer hydrogenolysis (Scheme 55) (132). Exposure of **149** to weak nucleophiles, such as water or methanol, resulted in reversible 1,4-addition to the B and transannular N, giving **150**. More derivatives of this heterocyclic system, including

© 2008 NRC Canada

Chart 13.

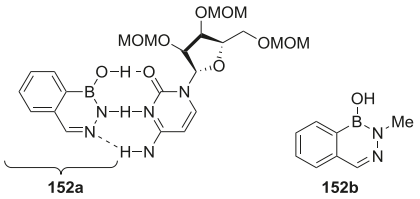

152a 152b

151, were synthesized by an analogous condensation procedure and tested for activity against *M. tuberculosis* by Martin and co-workers, though **151** was found to be quite ineffective (133).

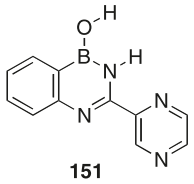

151

In 1997, both the solid-state and solution hydrogen-bonding interactions of BN-isoquinolines were assessed, and similarities to the hydrogen-bonding motifs of nucleic acids were found (134). Specifically, hydroxy compound **152a** was shown to participate in hydrogen-bonding interactions with 2′,3′,5′-tri-*O*-(methoxymethyl)cytidine in the solid state, and in solution as demonstrated by VT-NMR spectroscopy (Chart 13). The hydrogen bonding was disrupted in the 2-methyl substituted derivative **152b** (124).

Groziak also reported the construction of derivative **153**, which, via intramolecular hydrogen bonding, resembled the tetracyclic molecule estrogen, both in solution and in the solid state (135). The maintenance of a downfield-shifted ^{1}H NMR resonance for BO*H* in DMSO-d_6 solution was indicative of a strong hydrogen bond in solutions, while X-ray crystallography established this interaction in the solid state.

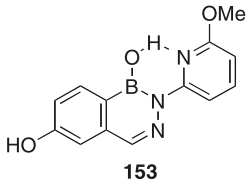

153

Another ring system, which was hoped to have biological significance was the bicyclic BN-quinazoline **154** (Scheme 56), due to a resemblance to purine compounds (136). The reaction of lithium tris(trimethylenedioxyboryl)methide with 4,6-dichloro-5-formylpyrimidine, followed by treatment with liquid ammonia at 75 °C gave low yields of the desired product, though **154** proved exceedingly difficult to purify and characterize.

BN substitution in graphene morphologies

The graphene allotropes of carbon are well-known to exhibit interesting properties. Numerous computational investigations have examined the influence on doping these structures with boron and nitrogen, where interest stems from the possibility of tuning electronic properties by mixing appropriate stoichiometries of conductive (graphite) and insulating (boron nitride) species (2, 137, 138).

Scheme 56.

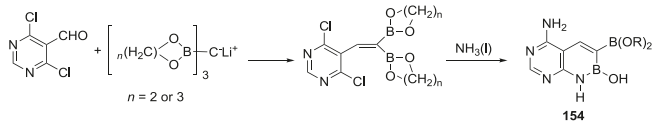

Chart 14.

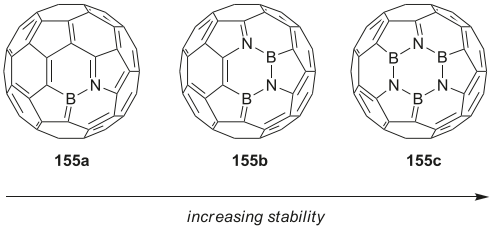

BN fullerenes

There have been numerous investigations of BN as a CC substitute in fullerenes, and much the same stability rules have been computed: greater stability is attained in substituting a contiguous BN unit as opposed to disconnected B and N atoms, and there is a preference for maximizing the number of B–N bonds when more than one CC group is replaced (139). For BN-fullerenes, the preferred site of BN substitution can be specifically located at the site of attachment between two six-membered rings, as in **155a** (Chart 14) (140, 141). Introduction of a second BN moiety favourably continues the alternating BN substitution within one of the hexagons (**155b**), while the third BN completes the six-membered ring, essentially forming the encapsulated borazine **155c** (142). The sequential introduction of more than three BN pairs has been investigated by Kar and co-workers by semi-empirical MNDO (142) and density functional theory (143), and similar substitution rules apply. Additionally, the requirement for maximizing the number of B–N bonds was found to result in the separation of heteroatom and carbon domains in more highly substituted analogues (143). In the case of $C_{48}B_6N_6$ isomers, the two structures containing two borazine rings on opposing sides of the molecule were found to be lowest in energy, with the S_6 symmetric isomer being lower in energy than the very similar D_3 isomer by only 2.9 kcal/mol (144). This result is in much better agreement with Kar's substitution rules than a previous study on the structures of $C_{48}B_6N_6$ isomers (145).

In general, BN-fullerenes are expected to exhibit lower HOMO–LUMO gaps, with the major contributor being higher energy HOMO levels (142). This suggests that the BN doped fullerenes should be more readily oxidized than C_{60}. More recent work suggests that this should be true for heterofullerenes with 10 or less BN units incorporated, while more highly heteroatom-substituted fullerenes may have a larger band gap than C_{60}, owing to higher LUMO levels (146). This trend was also observed in a recent time-dependent density functional theory study on the absorption properties of some B_xN_x-fullerenes (147). Hirsch, Thiel, and co-workers used nucleus independent chemical shift (NICS) calculations to show that the lower BN analogues ($C_{58}BN$,

© 2008 NRC Canada

Chart 15.

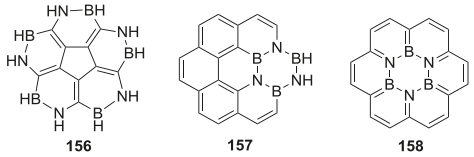

156 157 158

$C_{54}(BN)_3$, and $C_{48}(BN)_6$) should be more aromatic than all-carbon fullerene, whereas $C_{12}(BN)_{24}$ should be slightly less aromatic (148).

In light of the predicted destabilizing effects of B–B and N–N bonds in any of these heteroaromatic systems, the derivative $C_{12}(BN)_{24}$ represents the most highly BN-substituted derivative, which may be formed without forming any such bonds. It has been shown by numerous computational methods that this derivative should be stable, with a larger HOMO–LUMO gap than C_{60} (68, 69, 149–151), and minimal structural deviation (<5%) from that of the all-carbon analogue (150).

Isoelectronic BN substitution has also been investigated in other fullerene morphologies. Substitution in small fullerenes having anywhere from 20 to 50 atoms has been computed by several groups, from mono-BN (152, 153) to derivatives having "BN-belts" (154, 155) (as is found in $C_{12}(BN)_{24}$). Additionally, there has been one investigation of a $C_{129}BN$ bisfullerene (156). All of these investigations suggest that incorporation of BN significantly alters the electronic properties of the molecules without great structural perturbation.

BN nanotubes

The effect of BN-doping in armchair single-walled carbon nanotubes (ASWCNTs) was recently investigated by AM1 methods by Zhang and co-workers (157). Their studies reiterated the importance of inserting a BN pair as opposed to isolated B and N atoms in mono-substituted ASWCNTs, while in di- and tri-BN-substituted species, isomers with sequential B–N–B–N and B–N–B–N–B–N contacts in a single ring were the thermodynamically favoured derivatives, just as in the substituted fullerenes (vide supra). Additionally, ionization potentials (IPs) were lowered and electron affinities (EAs) increased with increasing BN incorporation, resulting in larger HOMO–LUMO gaps relative to the all-carbon derivatives.

Computations on other morphologies

Substitution to give BN-corannulenes and BN-coronenes has been investigated by a couple of groups. Disch and Schulman found that substituting the five peripheral HCCH moieties of corannulene with HBNH units, giving **156** (Chart 15), drastically reduced the inversion barrier to less than 1 kcal/mol (158). Türker determined the effect of replacing an entire benzene unit from the periphery of coronenes with borazine and found the resulting structure **157** to be thermodynamically viable, with little influence on the HOMO–LUMO gap (159). In the same year, Fowler and co-workers investigated the structure and magnetic properties of internally borazine-substituted coronene **158**. Their computations predicted a planar D_{3h} structure with an internal diatropic ring current, as opposed to the paratropic internal ring current of coronene. They found the structure not only to be viable but also to possess an aromaticity very similar to that of the parent hydrocarbon (160). It has been proposed that the electronic eigenvalues of larger BN aromatics, such as coronenes, may be readily predicted via density functional theory (161).

Chart 16.

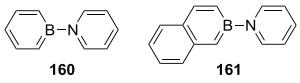

160 161

Finally, Tanaka and co-workers computed the HOMO–LUMO gap for BN-substituted polyperylene **159**, essentially a polymeric form of **21** (162). The isoelectronic substitution was found to decrease the band gap relative to the all-carbon system, by lowering the ionization potential and raising the electron affinity.

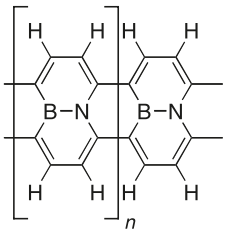

159

Other isoelectronic analogues of conjugated hydrocarbons

Intercyclic BN sustitution

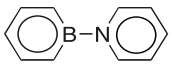

The borabenzene–pyridine system **160** represents another mode of B–N substitution in aromatic systems (Chart 16). Specifically, the B–N pair substitutes a formal C–C single bond, and indeed the B–N bond lengths in these systems tend to be indicative of a B–N single bond. Nonetheless, the heteroatoms play a key role in the properties of the aromatic systems, and as such, they are worthy of comment here.

Reviews of borabenzene and boratabenzene chemistry were published in 1986 (163) and again in 2001 (164). The borabenzene–pyridine adduct was first described by Herberich in 1970, and the $Cr(CO)_3$ complex of this in 1985 by Schmid (165). Since the last review, investigations into the reactivity of this heteroaromatic framework have been largely the efforts of the group of Piers (vide infra) (166).

Schmid reported the synthesis of 2-boranaphthalene and its pyridine adduct **161** (167). The B–N bond of this adduct was notably shorter than that of **160**, which was attributed to extended conjugation between the ring systems. The $Cr(CO)_3$ complex was also reported, and was found, via crystallography, to be η^6 bound to the borabenzene ring, rather than the homoaromatic benzo ring (165).

Piers and co-workers have attempted to exploit known reactivity patterns in these adducts to development methods for systematic functionalization of these heterocycles. For example, the carbon atoms α to boron are prone to

© 2008 NRC Canada

Scheme 57.

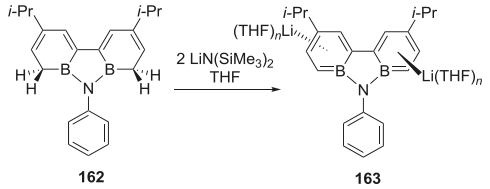

Scheme 58.

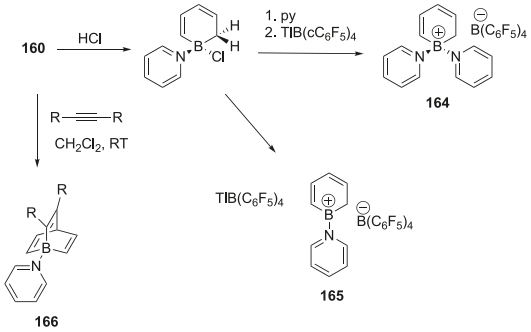

electrophilic attack, including protonation. They were thus able to access the dianionic B_2N analogue of fluorene **163** via **162** in the reaction depicted in Scheme 57 (168, 169). They also studied the reactivity of the parent compound **160** with pyridinium salts, giving access to rare examples of both four-coordinate boronium **164** and three-coordinate borenium ions **165** (Scheme 58) (170). Additionally, they discovered a new reactivity pattern for borabenzenes upon analysis of the frontier orbitals of the adduct **160**; these computations suggested that the HOMO of **160** was well-suited to serve as a diene for Diels–Alder-type reactivity, and indeed cycloadducts **166** were formed upon reaction with various dienophiles (Scheme 58). The products were dubbed "borabarrellene" adducts, highlighting the analogy to all-carbon barrellene.

More extended borabenzene–pyridine adducts have also been investigated by Piers' group, giving rise to B_2N_2 analogues of *ortho*- and *para*-quaterphenyl (Chart 17) (50). Two analogues of *p*-quaterphenyl, **167** and **168**, were investigated, and both were found to be non-fluorescent, in contrast to the parent hydrocarbon. The crystal structure of **167** showed it to possess a helical twist of the aromatic groups, hindering communication between the aromatic rings. The molecular structure of *o*-quaterphenyl analogue **169** demonstrated intramolecular π-stacking of the pyridine moieties, though this forced the aromatic rings out of coplanarity, and as such, this derivative was also found to be non-fluorescent.

Disconnected B–N substitution: 1,4-azaborinines

The installation of B and N at disconnected ring positions has been computed to give rise to isoelectronic aromatic species, which are thermodynamically less stable than the more widely studied adjacent 1,2 substitution pattern (18–20). While a monocyclic derivative has not been reported, the 1,4

Chart 17.

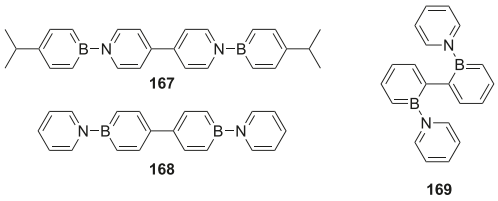

Scheme 59.

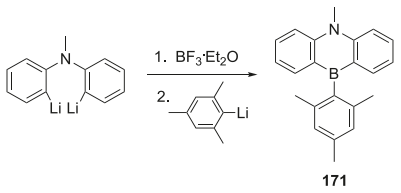

system is viable and was first reported by Maitlis as the anthracene analogue **170** (171). In the presence of base, the corresponding borate was formed, though this could be reversed by re-acidification.

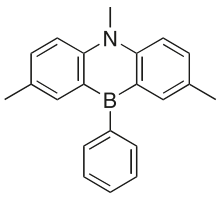

Crystallographic analysis of **170** was first reported by Reikhsfel'd and co-workers (172, 173) and suggested significant participation of the B atom in the conjugated system; in particular, the endocyclic B–C bonds (1.512 Å avg.) were found to be considerably shorter than the exocyclic B–C_{phenyl} bond (1.594 Å). Further, despite the potential donor–acceptor behaviour of the heteroatoms, they found no evidence of a transannular B···N bonding interaction.

This same anthracene core was synthesized a few years later by Clark via the reaction of 2,2′-dilithiodiphenylmethylamine with $BF_3{\cdot}Et_2O$, followed by treatment with mesityl lithium (Scheme 59) (174). The crystal structure of the resulting BN-anthracene analogue **171** showed the tricylic system to be quite planar, with endocyclic C–B bonds slightly shorter than those in triphenylborane (1.537 Å avg.). That said, the ^{11}B NMR chemical shift of 54.0 ppm was in the same region as triphenylborane, prompting them to assign this ring as a conjugated C=C–N–C=C unit bridged by boron, despite the shortened B–C bonds. This same group also mentioned the synthesis of a pentacyclic derivative, though no confirming evidence or data was provided (19).

Some interesting examples of the 1,4-substitution pattern have recently been reported by Kawashima and co-workers (Scheme 60) (175–177). The pentacene analogue **172** was found to be highly fluorescent (ϕ_f = 0.69) and was air- and moisture-stable, owing to the steric protection of the mesityl groups at boron. A crystallographic study of **172** showed it to be quite planar, though no significant intermolecular interactions could be discerned, presumably due to the large, out-of-plane mesityl substituents. The methodology was ex-

© 2008 NRC Canada

Scheme 60.

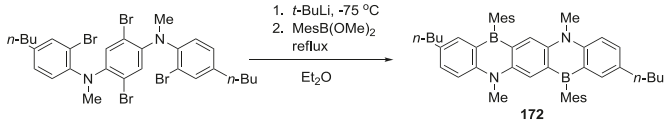

Chart 18.

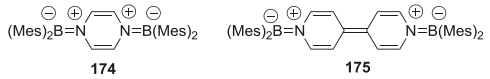

tended to give heptacene derivative **173**, which exhibited the expected bathochromic shifts in both absorption and emission spectra. Further, derivatives of **172** functionalized with carbazol-9-yl groups were found to have near-unity quantum efficiencies (176).

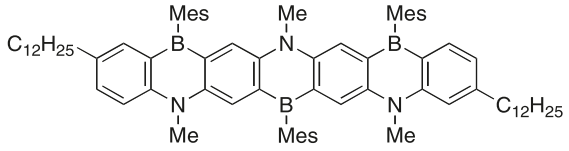

Exocyclic BN substitution

Some further interesting examples of BN substitution for CC were disclosed by Kaim and co-workers (178, 179). Thus, exocyclic substitution of Thiele's and Chichibabin's hydrocarbons incorporated the BN moiety in a conjugated quinoidal, rather than aromatic, framework (Chart 18) (double bonds have been included to highlight the π-character of this exocyclic bond). This π distribution was verified crystallographically for compound **174**, with B–N bond lengths of 1.444(3) Å, and alternating single and double C–C bonds. Both **174** and **175** were found to undergo reversible one-electron oxidations, and indeed, the radical cations formed could be studied by EPR and ENDOR spectroscopies. The extremely small hyperfine coupling constants supported the substantial π-character in the B–N bonds, as well as significant π-electron delocalization in the radical cation as compared with the neutral system.

Aminoboratabenzene complexes reported by Bazan and by Herberich can also be regarded as conjugated BN systems with an exocyclic BN π bond. Indeed, crystalline derivatives of complexes such as **176** exhibit very short BN bonds (1.396(6) Å), with intra-ring delocalization centered on the carbon atoms, as shown by the η^5 bonding arrangement with Zr (180). Additionally, in the case of **176**, the *N*-isopropyl groups were observed to be diastereotopic by virtue of restricted rotation about BN, further confirming the π character of the B–N bond. (181). A more detailed discussion of these compounds is deferred to Fu's review (164).

Other systems

Chart 19 shows some miscellaneous systems that have been reported or proposed. The unique 18-π-electron aromatic ring **177** was proposed by Fowler and co-workers (182). The optimized geometry and magnetic properties computed by ab initio methods supported the potential for aromaticity. The stability of BN derivatives of benzyne were

Chart 19.

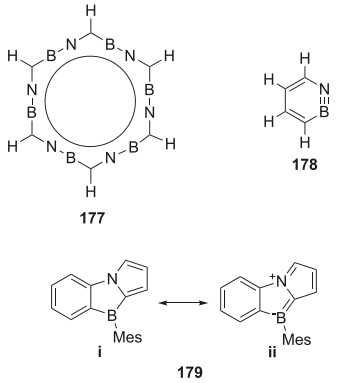

recently investigated by Fazen and Burke (183). They surmised that azaborine **178** was the most stable derivative

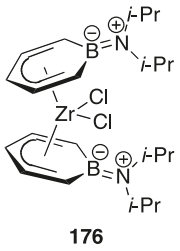

formed by replacing a pair of carbon atoms, and that it was significantly aromatic.

To date, there has been only one investigation of a BN *anti*-aromatic compound, which was communicated by Kaufmann in 1999 (184). Their reported 8-mesityl-8-borafluorazene **179** was found to be air- and moisture-sensitive, though thermally tolerant (purified by high vacuum distillation at 140 °C). High-level ab initio calculations on their compound suggested some contribution of resonance form **ii**, in agreement with the computed electronic distribution of the parent 12-π-electron benzopentalene (Chart 19).

Summary and concluding remarks

Azaborinine compounds have been the focus of numerous computational studies, many of which have addressed the validity of classifying such molecules as "aromatic". Chemically, this classification seems justified, since the tricoordinate boron in these rings is generally much less Lewis acidic than a typical borane. Heterocyclic B–OH derivatives often behave like Brönsted acids rather than Lewis acids, and the rings themselves are more likely to undergo electrophilic substitution than addition reactions. Indeed, most BN aromatics are amenable to classic electrophilic aromatic substitution chemistry, as has been extensively examined. The electropositive nature of the B atom renders the ortho and para positions susceptible to attack by electrophiles, while nucleophilic substitution at B–X (X = Cl, Br) represents a facile means of tuning electronics in the heteroaromatics. Furthermore, the rings serve as suitable π-donors towards metal centres, particularly tricarbonylchromium(0) fragments, forming complexes that are structurally comparable to complexes with corresponding

© 2008 NRC Canada

hydrocarbon aromatics. The case for aromaticity in isoelectronic BN analogues is bolstered by the intermediacy of the bond lengths between single and double bonding as well as the planar nature of the heterocycles. The inability to isolate any examples of unsubstituted BN- or B_2N_2-benzene analogues has made direct comparisons with benzene or borazine impossible, though qualitative evaluations do support the classification as aromatic species.

While there have been significant advances in aromatic BN chemistry in the decades since the last review (6), several of the BN-substituted benzene derivatives remain to be synthesized. Most notable is the 1,3-azaborinine ring, which represents a significant synthetic challenge due to its predicted instability. While the 1,4-azaborinine ring has been achieved in heterocyclic acenes, the monocyclic species remains elusive. A fully unsubstituted derivative of this system may be particularly exigent and could be prone to polymerization. Of the yet unknown B_2N_2-benzene analogues, the 1,4,2,5-, 1,3,2,5-, and 1,4,2,6-diazadiborinine ring structures are the most likely to be achievable based on computed stabilities (20, 58). The former is a particularly interesting challenge, as it is the only remaining B_2N_2 derivative with substitution by BN pairs that has not yet been synthesized.

Though relatively little computational work has been done on the BN-cyclopentadienyl analogues, there are isomers here too that have yet to be prepared experimentally. Specifically, there have been no reports of either 1,3-azaborylyl or 1,3-diaza-2,4-diborylyl rings, though Kaufmann's antiaromatic compound **179** could arguably be considered a representative of the former. It should be noted that predicted properties of the possible BN-substituted pyrroles, pyrazoles, and furans has been reported (11). Studies on BN-cyclopentadienyl derivatives have largely been with the intent of producing Cp surrogates. On the other hand, studies of six-membered BN-containing rings have traditionally been less focused on applications, though resurgence in studies comes from the promise of materials with interesting properties, with compounds such as Piers' BN-phenanthrenes or Kawashima's BN-acenes validating this potential. The substitution of CC by an isoelectronic BN moiety thus remains both of intense fundamental interest and of high potential for furnishing novel materials for applications in a variety of areas.

Acknowledgements

WEP would like to thank the Piers group colleagues who have contributed to our efforts in this area over the past several years; they are named in the cited references. The authors would like to thank Thomas Wood, Lauren Mercier, and Prof. Shih-Yuan Liu (University of Oregon) for reading the manuscript and providing helpful comments. The work described here from the Piers group was funded by NSERC's Discovery Grant Program; MJDB thanks NSERC for PGS funding and the Alberta Ingenuity Fund for a Studentship.

References

1. (*a*) C.D. Entwistle and T.B. Marder. Chem. Mater. **16**, 4574 (2004); (*b*) C.D. Entwistle and T.B. Marder. Angew. Chem., Int. Ed. **41**, 2927 (2002); (*c*) T.B. Marder. Angew. Chem., Int. Ed. **47**, 242 (2008).
2. M. Kawaguchi. Adv. Mater. **9**, 615 (1997).
3. C. Baldock, G. De Boer, J.B. Rafferty, A.R. Stuitje, and C.R. Rice. Biochem. Pharmacol. **55**, 1541 (1998).
4. H.-B. Zhou, K.W. Nettles, J.B. Bruning, Y. Kim, A. Joachimiak, S. Sharma, K.E. Carlson, F. Stossi, B.S. Katzenellenbogen, G.L. Greene, and J.A. Katzenellenbogen. Chem. Biol. **14**, 659 (2007).
5. M.J.S. Dewar, V.P. Kubba, and R. Pettit. J. Chem. Soc. 3073 (1958).
6. (*a*) A.J. Fritsch. *In* Special topics in heterocyclic chemistry. Vol. 30. 1977. p. 381; (*b*) M.J.S. Dewar. Prog. Boron Chem. **1**, 235 (1964).
7. R. Islas, E. Chamorro, J. Robles, T. Heine, J.C. Santos, and G. Merino. Struct. Chem. **18**, 833 (2007) and refs. cited therein.
8. *In* Gmelins Handbuch der Anorganischen Chemie, Borazine and Its Derivatives. Verlag Chemie, Weinheim, Germany. 1978. p. 48.
9. H. Nöth, W. Winterstein, W. Kaim, and H. Bock. Chem. Ber. **112**, 2494 (1979).
10. B. Maouche and J. Gayoso. Int. J. Quantum Chem. **23**, 891 (1983).
11. R.J. Doerksen and A.J. Thakkar. J. Phys. Chem. A, **103**, 2141 (1999).
12. T. Kar, D.E. Elmore, and S. Scheiner. J. Mol. Struct. (Theochem), **392**, 65 (1997).
13. A.K. Phukan, R.P. Kalagi, S.R. Gadre, and E.D. Jemmis. Inorg. Chem. **43**, 5824 (2004).
14. P.K. Chattaraj and D.R. Roy. J. Phys. Chem. A, **111**, 4684 (2007).
15. J.H. Edgar. Properties of Group III nitrides. IEE. London, UK. 1994.
16. R. Ma, D. Golberg, Y. Bando, and T. Sasaki. Phil. Trans. R. Soc. Lond. A, **362**, 2161 (2004).
17. M.N. Uddin, I. Shimoyama, Y. Baba, T. Sekiguchi, K.G. Nath, and M. Nagano. J. Appl. Phys. **89**, 084902 (2006).
18. S.T. Massey and R.W. Zoellner. Int. J. Quantum Chem. **39**, 787 (1991).
19. M. Kranz and T. Clark. J. Org. Chem. **57**, 5492 (1992).
20. R.J. Doerksen and A.J. Thakkar. J. Phys. Chem. A, **102**, 4679 (1998).
21. P. Paetzold. Pure Appl. Chem. **63**, 345 (1991).
22. K. Niedenzu. Angew. Chem., Int. Ed. **3**, 86 (1964).
23. K.M. Davies, M.J.S. Dewar, and P. Rona. J. Am. Chem. Soc. **89**, 6294 (1967).
24. D.G. White. J. Am. Chem. Soc. **85**, 3634 (1963).
25. S. Gronowitz and I. Ander. Chem. Scr. **15**, 135 (1980).
26. S. Gronowitz and I. Ander. Chem. Scr. **15**, 145 (1980).
27. A.J. Ashe, III and X. Fang. Org. Lett. **2**, 2089 (2000).
28. A.J. Ashe, III, X. Fang, and J.W. Kampf. Organometallics, **20**, 5413 (2001).
29. J. Pan, J.W. Kampf, and A.J. Ashe. Organometallics, **23**, 5626 (2004).
30. (*a*) J. Pan, J.W. Kampf, and A.J. Ashe, III. Organometallics, **25**, 197 (2006); (*b*) J. Pan, J. Wang, M.M. Banaszak Holl, J.W. Kampf, and A.J. Ashe, III. Organometallics, **25**, 3463 (2006).
31. J. Pan, J.W. Kampf, and A.J. Ashe, III. Org. Lett. **9**, 679 (2007).
32. B. Chiavarino, M.E. Crestoni, and S. Fornarini. J. Am. Chem. Soc. **121**, 2619 (1999).

© 2008 NRC Canada

33. M.J.S. Dewar and R. Jones. J. Am. Chem. Soc. **90**, 2137 (1968).
34. A.J.V. Marwitz, E.R. Abbey, J.T. Jenkins, L.N. Zakharov, and S.-Y. Liu. Org. Lett. **9**, 4905 (2007).
35. M.J.S. Dewar and R. Dietz. J. Chem. Soc. 2728 (1959).
36. A.J. Ashe, III, H. Yang, X. Fang, and J.W. Kampf. Organometallics, **21**, 4578 (2002).
37. P. Paetzold, C. Stanescu, J.R. Stubenrauch, M. Bienmüller, and U. Englert. Z. Anorg. Allg. Chem. **630**, 2632 (2004).
38. M.J.S. Dewar and V.P. Kubba. J. Am. Chem. Soc. **83**, 1757 (1961).
39. M.J.S. Dewar and P.J. Grisdale. J. Org. Chem. **28**, 1759 (1963).
40. S.S. Chissick, M.J.S. Dewar, and P.M. Maitlis. Tetrahedron Lett. **23**, 8 (1960).
41. A.V.K. Westwood, R. Brydson, R. Coult, M.A. Fox, B. Rand, and K. Wade. Carbon, **40**, 2157 (2002).
42. K.D.M. Harris, B.M. Kariuki, C. Lambropoulos, D. Philp, and J.M.A. Robinson. Tetrahedron, **53**, 8599 (1997).
43. J.M.A. Robinson, B.M. Kariuki, D. Philp, and K.D.M. Harris. Tetrahedron Lett. **38**, 6281 (1997).
44. P. Zanirato. J. Organomet. Chem. **293**, 285 (1985).
45. S. Gronowitz, I. Ander, and P. Zanirato. Chem. Scr. **22**, 55 (1983).
46. M.J.S. Dewar, C. Kaneko, and M.K. Bhattacharjee. J. Am. Chem. Soc. **84**, 4884 (1962).
47. G.C. Culling, M.J.S. Dewar, and P.A. Marr. J. Am. Chem. Soc. **86**, 1125 (1964).
48. M.J.D. Bosdet, C.A. Jaska, W.E. Piers, T.S. Sorensen, and M. Parvez. Org. Lett. **9**, 1395 (2007).
49. J. Trotter. Acta Cryst. **16**, 605 (1963).
50. C.A. Jaska, W.E. Piers, R. McDonald, and M. Parvez. J. Org. Chem. **72**, 5234 (2007).
51. D.J.H. Emslie, W.E. Piers, and M. Parvez. Angew. Chem., Int. Ed. (2003).
52. C.A. Jaska, D.J.H. Emslie, M.J.D. Bosdet, W.E. Piers, T.S. Sorensen, and M. Parvez. J. Am. Chem. Soc. **128**, 10885 (2006).
53. M.J.S. Dewar and W.H. Poesche. J. Org. Chem. **29**, 1757 (1964).
54. P.R. Ashton, K.D.M. Harris, B.M. Kariuki, D. Philp, J.M.A. Robinson, and N. Spencer. J. Chem. Soc., Perkin Trans. 2, 2166 (2001).
55. M.J.D. Bosdet, W.E. Piers, T.S. Sorensen, and M. Parvez. Angew. Chem., Int. Ed. **46**, 4940 (2007).
56. R.S. Becker. Theory and interpretation of fluorescence and phosphorescence. J. Wiley Sons. New York. 1969.
57. E.P. Mayer and H. Nöth. Chem. Ber. **126**, 1551 (1993).
58. S.T. Massey and R.W. Zoellner. Inorg. Chem. **30**, 1063 (1991).
59. P. Schreyer, P. Paetzold, and R. Boese. Chem. Ber. **121**, 195 (1988).
60. R. Köster and K. Iwasaki. Adv. Chem. Ser. **42**, 157 (1964).
61. A. Thozet, S. Allaoud, T. Zaïr, A. Karim, and B. Frange. J. Organomet. Chem. **406**, 269 (1991).
62. A. Rizzo and B. Frange. J. Organomet. Chem. **76**, 1 (1974).
63. S. Allaoud and B. Frange. Phosphorus and Sulfur, **28**, 129 (1986).
64. B. Frange. Bull. Soc. Chim. 2165 (1973).
65. S. Allaoud, A. Karim, A. Mortreux, F. Petit, and B. Frange. J. Organomet. Chem. **379**, 89 (1989).
66. S. Allaoud, S. Conté, B. Fenet, B. Frange, F. Robert, F. Sécheresse, and A. Karim. J. Organomet. Chem. **469**, 59 (1994).
67. B. Abouhamza, M. Ait Ali, S. Allaoud, O. Blacque, B. Frange, and A. Karim. Acta Cryst. **C57**, 796 (2001).
68. J.R. Bowser, D.A. Jelski, and T.F. George. Inorg. Chem. **31**, 154 (1992).
69. X. Xia, D.A. Jelski, J.R. Bowser, and T.F. George. J. Am. Chem. Soc. **114**, 6493 (1992).
70. W. Siebert and R. Full. Angew. Chem., Int. Ed. **15**, 45 (1976).
71. W. Siebert, R. Full, H. Schmidt, J. von Seyerl, M. Halstenberg, and G. Huttner. J. Organomet. Chem. **191**, 15 (1980).
72. H. Nöth and P. Fritz. Z. Anorg. Allg. Chem. **324**, 129 (1963).
73. R. Goetze and H. Nöth. J. Organomet. Chem. **145**, 151 (1978).
74. C.J. Carmalt, W. Clegg, A.H. Cowley, F.J. Lawlor, T.B. Marder, N.C. Norman, C.R. Rice, O.J. Sandoval, and A.J. Scott. Polyhedron, **16**, 2325 (1997).
75. W. Maringgele, M. Noltemeyer, and A. Meller. Organometallics, **16**, 2276 (1997).
76. T.D. Forster, K.E. Krahulic, H.M. Tuononen, R. McDonald, M. Parvez, and R. Roesler. Angew. Chem., Int. Ed. **45**, 6356 (2006).
77. A. Kausamo, H.M. Tuononen, K. Krahulic, and R. Roesler. Inorg. Chem. **47**, 1145 (2008).
78. G. Schmid. Comments Inorg. Chem. **4**, 17 (1985); and refs. cited therein.
79. G. Schmid, O. Boltsch, and R. Boese. Organometallics, **6**, 435 (1987).
80. S.-Y. Liu, I.D. Hills, and G.C. Fu. Organometallics, **21**, 4323 (2002).
81. A.J. Ashe, III, H. Yang, and F.J. Timmers. Eur. Patent WO 03-087-114 (A1). 23 October 2003.
82. S.-Y. Liu, I.D. Hills, and G.C. Fu. J. Am. Chem. Soc. **127**, 15352 (2005).
83. H.V. Ly, T.D. Forster, D. Maley, M. Parvez, and R. Roesler. Chem. Commun. 4468 (2005).
84. H.V. Ly, T.D. Forster, A.M. Corrente, D.J. Eisler, J. Konu, M. Parvez, and R. Roesler. Organometallics, **26**, 1750 (2007).
85. H.V. Ly, T.D. Forster, M. Parvez, R. McDonald, and R. Roesler. Organometallics, **26**, 3516 (2007).
86. K.E. Krahulic, G.D. Enright, M. Parvez, and R. Roesler. J. Am. Chem. Soc. **127**, 4142 (2005).
87. J.S. Merriam and K. Niedenzu. J. Organomet. Chem. **51**, C1 (1973).
88. L. Weber and G. Schmid. Angew. Chem., Int. Ed. **13**, 467 (1974).
89. L. Weber. Coord. Chem. Rev. **215**, 39 (2001).
90. G. Schmid and J. Schulze. Angew. Chem., Int. Ed. **16**, 249 (1977).
91. J. Schulze and G. Schmid. Chem. Ber. **114**, 495 (1981).
92. G. Schmid, M. Polk, and R. Boese. Inorg. Chem. **29**, 4421 (1990).
93. L. Weber, I. Domke, C. Schmidt, T. Braun, H.-G. Stammler, and B. Neumann. Dalton Trans. 2127 (2006).
94. L. Weber, I. Domke, H.-G. Stammler, and B. Neumann. Eur. J. Inorg. Chem. 4715 (2005).
95. H.M. Tuononen, R. Roesler, J.L. Dutton, and P.J. Ragogna. Inorg. Chem. **46**, 10693 (2007).
96. A. Sundermann, M. Reiher, and W.W. Schoeller. Eur. J. Inorg. Chem., 305 (1998).
97. L. Weber, M. Schnieder, and P. Lönnecke. J. Chem. Soc., Dalton Trans. 3459 (2001).
98. (*a*) Y. Segawa, M. Yamashita, and K. Nozaki. Science (Washington, DC), **314**, 113 (2006); (*b*) T.B. Marder. Science, **314**, 69, (2006); (*c*) H. Braunschweig. Angew. Chem., Int. Ed. **46**, 1946 (2007).
99. The aromatic character of **101** was also supported by electronic structure computations in reference 77.
100. D. Ulmschneider and J. Goubeau. Chem. Ber. **90**, 2733 (1957).

© 2008 NRC Canada

101. G. Kaupp, M.R. Naimi-Jamal, and V. Stepanenko. Chem. Eur. J. **9**, 4156 (2003).
102. (*a*) L. Weber. Coord. Chem. Rev. **252**, 1, (2008); and refs. cited therein; (*b*) L. Weber, H.B. Wartig, H.-G. Stammler, and B. Neumann. Z. Anorg. Allg. Chem. **627**, 2663 (2001).
103. I.I. Padilla-Martínez, N. Andrade-López, M. Gama-Goicochea, E. Aguilar-Cruz, A. Cruz, R. Contreras, and H. Tlahuext. Heteroatom Chem. **7**, 323 (1996).
104. U. Braun, T. Habereder, H. Nöth, H. Piotrowski, and M. Warchhold. Eur. J. Inorg. Chem., 1132 (2002).
105. S. Maruyama and Y. Kawanishi. J. Mater. Chem. **12**, 2245 (2002).
106. L. Weber, V. Werner, I. Domke, H.-G. Stammler, and B. Neumann. Dalton Trans. 3777 (2006).
107. L. Weber, A. Penner, I. Domke, H.-G. Stammler, and B. Neumann. Z. Anorg. Allg. Chem. **633**, 563 (2007).
108. A.A.H.A. Al-Kadhumi, P. Hodge, B.J. Hunt, and F.G. Thorpe. React. Polym. **7**, 15 (1987).
109. I. Yamaguchi, B.-J. Choi, T.-A. Koizumi, K. Kubota, and T. Yamamoto. Macromolecules, **40**, 438 (2007).
110. T. Habereder and H. Nöth. Appl. Organometal. Chem. **17**, 525 (2003).
111. M. Suginome, A. Yamamoto, and M. Murakami. Angew. Chem., Int. Ed. **44**, 2380 (2005).
112. M. Suginome, A. Yamamoto, T. Sasaki, and M. Murakami. Organometallics, **25**, 2911 (2006).
113. S.W. Hadebe and R.S. Robinson. Eur. J. Org. Chem. 4898 (2006).
114. G.J. Irvine, W.R. Roper, and L.J. Wright. Organometallics, **16**, 2291 (1997).
115. J.M. Murphy, J.D. Lawrence, K. Kawamura, C. Incarvito, and J.F. Hartwig. J. Am. Chem. Soc. **128**, 13684 (2006).
116. L. Weber, M. Schnieder, R. Boese, and D. Bläser. J. Chem. Soc., Dalton Trans. 378 (2001).
117. L. Weber, H.B. Wartig, H.-G. Stammler, and B. Neumann. Organometallics, **20**, 5248 (2001).
118. M.J.S. Dewar and R.C. Dougherty. J. Am. Chem. Soc. **86**, 433 (1964).
119. B. Pertschy, G. Zisser, H. Schein, R. Köffel, G. Rauch, K. Grillitsch, C. Morgenstern, M. Durchschlag, G. Högenauer, and H. Bergler. Mol. Cell. Biol. **24**, 6476 (2004).
120. G. Högenauer and M. Woisetschläger. Nature (London, UK), **293**, 662 (1981).
121. C. Baldock, J.B. Rafferty, S.E. Sedelnikova, P.J. Baker, A.R. Stuitje, A.R. Slabas, T.R. Hawkes, and D.W. Rice. Science (Washington, DC), **274**, 2107 (1996).
122. C.W. Levy, C. Baldock, A.J. Wallace, S.E. Sedelnikova, R.C. Viner, J.M. Clough, A.R. Stuitje, A.R. Slabas, D.W. Rice, and J.B. Rafferty. J. Mol. Biol. **309**, 171 (2001).
123. K.F.M. Pasqualoto and M.M.C. Ferreira. QSAR Comb. Sci. **7**, 629 (2006); and refs. cited therein.
124. P.D. Robinson, M.P. Groziak, and L. Chen. Acta Cryst. **C54**, 71 (1998).
125. M.A. Grassberger, F. Turnowsky, and J. Hildebrandt. J. Med. Chem. **27**, 947 (1984).
126. B.W. Müller. Helv. Chim. Acta, **61**, 325 (1978).
127. S. Gronowitz. Chem. Heterocycl. Compd. **30**, 1252 (1994).
128. J. Namtvedt and S. Gronowitz. Acta Chem. Scand. **22**, 1373 (1968).
129. These compounds have been reviewed previously. See references 6 and 127.
130. C. Klöfkorn, M. Schmidt, T. Spaniol, T. Wagner, O. Costisor, and P. Paetzold. Chem. Ber. **128**, 1037 (1995).
131. C. Präsang, B. Donnadieu, and G. Bertrand. J. Am. Chem. Soc. **127**, 10182 (2005).
132. M.P. Groziak, A.D. Ganguly, and P.D. Robinson. J. Am. Chem. Soc. **116**, 7597 (1994).
133. M.C. Davis, S.G. Franzblau, and A.R. Martin. Bioorg. Med. Chem. Lett. **8**, 843 (1998).
134. M.P. Groziak, L. Chen, L. Yi, and P.D. Robinson. J. Am. Chem. Soc. **119**, 7817 (1997).
135. P.D. Robinson and M.P. Groziak. Acta Cryst. **C55**, 1701 (1999).
136. D.S. Matteson, M.S. Biernbaum, R.A. Bechtold, J.D. Campbell, and R.J. Wilcsek. J. Org. Chem. **43**, 950 (1978).
137. Y. Miyamoto, A. Rubio, M.L. Cohen, and S.G. Louie. Phys. Rev. B, **50**, 4976 (1994).
138. K. Suenaga, C. Colliex, N. Demoncy, A. Loiseau, H. Pascard, and F. Willaime. Science (Washington, DC), **278**, 653 (1997).
139. Z. Chen, K. Ma, H. Zhao, Y. Pan, X. Zhao, A. Tang, and J. Feng. J. Mol. Struct. (Theochem), **466**, 127 (1999).
140. Z. Chen, K. Ma, L. Chen, H. Zhao, Y. Pan, X. Zhao, A. Tang, and J. Feng. J. Mol. Struct. (Theochem), **452**, 219 (1998).
141. K.A. Yee, H. Yi, S. Lee, S.K. Kang, J.S. Song, and S. Seong. Bull. Korean Chem. Soc. **24**, 494 (2003).
142. J. Pattanayak, T. Kar, and S. Scheiner. J. Phys. Chem. A, **105**, 8376 (2001).
143. T. Kar, J. Pattanayak, and S. Scheiner. J. Phys. Chem. A, **107**, 8630 (2003).
144. E. Emanuele, F. Negri, and G. Orlandi. Inorg. Chim. Acta, **360**, 1052 (2007).
145. M.R. Manaa, R.-H. Xie, and V.H. Smith. Chem. Phys. Lett. **387**, 101 (2004).
146. R.-H. Xie, G.W. Bryant, G. Sun, T. Kar, Z. Chen, V.H. Smith, Y. Araki, N. Tagmatarchis, H. Shinohara, and O. Ito. Phys. Rev. B, **69**, 201403 (2004).
147. C.N. Ramachandran and N. Sathyamurthy. J. Phys. Chem. A, **111**, 6901 (2007).
148. Z. Chen, H. Jiao, A. Hirsch, and W. Thiel. J. Org. Chem. **66**, 3380 (2001).
149. J. Liu, M. Huang, and B. Gu. Chinese Phys. Lett. **9**, 581 (1992).
150. K. Kobayashi and N. Kurita. Phys. Rev. Lett. **70**, 3542 (1993).
151. H.-M. Yin, R.-Q. Zhang, B.-H. Yang, K.-L. Han, and G.-Z. He. Int. J. Quantum Chem. **84**, 363 (2001).
152. J. Pattanayak, T. Kar, and S. Scheiner. J. Phys. Chem. A, **108**, 7681 (2004).
153. H.Y. Rao and Z.G. Le. Chinese Chem. Lett. **15**, 246 (2004).
154. X. Xu, Z. Shang, G. Wang, R. Li, Z. Cai, and X. Zhao. J. Phys. Chem. A, **109**, 3754 (2005).
155. F. Liu, L. Meng, and S. Zheng. J. Phys. Chem. B, **110**, 6666 (2006).
156. Y. Zheng, J. Zhang, and G. Gahungu. J. Phys. Chem. A, **110**, 9921 (2006).
157. C. Zhang, R. Li, D. Zhang, Z. Shang, G. Wang, Y. Liang, Y. Xing, Y. Pan, Z. Cai, X. Zhao, and C. Liu. J. Mol. Struct. (Theochem), **765**, 1 (2006).
158. R.L. Disch. J. Am. Chem. Soc. **116**, 1533 (1994).
159. L. Türker. J. Mol. Struct. (Theochem), **584**, 135 (2002).
160. E. Steiner, P.W. Fowler, R.G. Viglione, and R. Zanasi. Chem. Phys. Lett. **355**, 471 (2002).
161. V. Marcon, O. A. van Lilienfeld, and D. Andrienko. J. Chem. Phys. **127**, 064305 (2007).
162. K. Tanaka, S. Yamanaka, K. Ueda, S. Takeda, and T. Yamabe. Synth. Met. **20**, 333 (1987).
163. G.E. Herberich and H. Ohst. Adv. Organomet. Chem. **25**, 199 (1986).

© 2008 NRC Canada

164. G.C. Fu. Adv. Organomet. Chem. **47**, 101 (2001).
165. R. Boese, N. Finke, T. Keil, P. Paetzold, and G. Schmid. Z. Naturforsch. B, **40**, 1327 (1985).
166. The groups of Herberich, Fu, and Bazan have maintained an interest in the use of borabenzene derivatives as isoelectronic surrogates for cyclopentadienyl in catalyst development. See for example: (*a*) X. Zheng and G.E. Herberich. Eur. J. Inorg. Chem. 2175 (2003); (*b*) G.C. Fu. J. Org. Chem. **69**, 3245 (2004); (*c*) J.S. Rogers, X. Bu, and G.C. Bazan. Organometallics, **19**, 3948 (2000).
167. R. Boese, N. Finke, J. Henkelmann, G. Maier, P. Paetzold, H.P. Reisenauer, and G. Schmid. Chem. Ber. **118**, 1644 (1985).
168. I. Ghesner, W.E. Piers, M. Parvez, and R. McDonald. Organometallics, **23**, 3085 (2004).
169. I. Ghesner, W.E. Piers, M. Parvez, and R. McDonald. Can. J. Chem. **84**, 1 (2006).
170. I. Ghesner, W.E. Piers, M. Parvez, and R. McDonald. Chem. Commun. 2480 (2005).
171. P.M. Maitlis. J. Chem. Soc. 425 (1961).
172. V.K. Bel'skii, S.V. Nesterova, and V.O. Reikhsfel'd. Zh. Struct. Khim. **28**, 186 (1987).
173. Y.F. Sigolaev, S.G. Semenov, V.O. Reikhsfel'd, and S.K. Bel'skii. Teor. Eksp. Khim. **26**, 221 (1990).
174. M. Kranz, F. Hampel, and T. Clark. J. Chem. Soc., Chem. Commun. 1247 (1992).
175. T. Agou, J. Kobayashi, and T. Kawashima. Org. Lett. **8**, 2241 (2006).
176. T. Agou, J. Kobayashi, and T. Kawashima. Chem. Commun. 3204 (2007).
177. T. Agou, J. Kobayashi, and T. Kawashima. Chem. Eur. J. **13**, 8051 (2007).
178. A. Lichtblau, W. Kaim, A. Schulz, and T. Stahl. J. Chem. Soc., Perkin Trans. 2, 1497 (1992).
179. A. Lichtblau, H. Hausen, W. Schwarz, and W. Kaim. Inorg. Chem. **32**, 73 (1993).
180. G.C. Bazan, G. Rodriguez, A.J. Ashe III, S. Al-Ahmad, C. Muller. J. Am. Chem. Soc. **118**, 2291 (1996).
181. G.E. Herberich, B. Schmidt, and U. Englert. Organometallics, **14**, 471 (1995).
182. A. Soncini, P.W. Fowler, I. Cernusak, and E. Steiner. Phys. Chem. Chem. Phys. **3**, 3920 (2001).
183. P.J. Fazen and L.A. Burke. Inorg. Chem. **45**, 2494 (2006).
184. K. Albrecht and D.E. Kaufmann. J. Chem. Research (S), 264 (1999).

© 2008 NRC Canada

An improved synthesis of sitophilure[1]

Cuifen Lu, Junqi Nie, Guichun Yang, and Zuxing Chen

Abstract: The asymmetric synthesis of sitophilure was carried out in 8 steps, with 42% overall yield and 97% enantiomeric excess from propionaldehyde. The synthesis relied on an approach employing an asymmetric acyl-thiazolidinethione propionate aldol reaction to establish two stereogenic centers.

Key words: sitophilure, thiazolidinethione, chiral auxiliary, synthesis.

Résumé : Utilisant le propionaldéhyde comme produit de départ, on a réalisé une synthèse asymétrique du sitophilure en huit étapes, avec un rendement global de 42% et un excès énantiomérique de 97%. La synthèse repose sur une approche dans laquelle on utilise une réaction asymétrique aldolique acyl-propionate de thiazolidinethione pour générer deux centres stéréogéniques.

Mots-clés : sitophilure, thiazolidinethione, auxiliaire chiral, synthèse.

[Traduit par la Rédaction]

Introduction

The rice weevil *Sitophilus oryzae L.* and the maize weevil *Sitophilu zeamaais M.* are both pests that cause commercially serious damage to stored cereal grains. Effective, cost-efficient grain weevil management could be accomplished by monitoring the pest populations with pheromone-baited insect traps and applying control methods only when pest densities reach economic thresholds. Their common aggregation pheromone, sitophilure, was identified by Schmuff et al. (1) as (4*R*, 5*S*)-5-hydroxy-4-methyl-3-heptanone. A synthesis of the four sitophilure stereoisomers was reported by Mori (2) to clarify the stereochemistry–bioactivity relationship. Bioassay of Mori's samples by Walgenbach et al. (3) revealed (4*S*,5*R*) stereoisomer **1** to be the pheromone sitophilure (Fig. 1). Since effective and cost-efficient control of both maize and rice weevils populations can be foreseen with the aid of the aggregation pheromone, several total syntheses of the racemic and the natural forms of sitophilure **1** have been published (4).

Carbon–carbon bond-forming reactions involving asymmetric aldol additions have emerged as powerful tools in organic synthesis. As demonstrated by the pioneering work of Evans et al. (5), Heathcock and co-workers (6), and Crimmins et al. (7), additions of enolates of acyl oxazolidinones, oxazolidinethiones, and thiazolidinethiones to aldehydes can be highly effective at selectively generating enantiomerically pure *syn* and *anti* aldol products. Among these chiral auxilaries, 4-mono substituted thiazolidinethiones derived from natural amino acids are more useful in asymmetric synthesis because they can be removed from the thiazolidinthiones after completion of the chiral induction easily (8). For these reasons, we have chosen to pursue this line of work and applied this system to the synthesis of the pheromone sitophilure using 4-monosubstituted thiazolidinethiones as chiral auxiliary (Scheme 1). In comparison with the published syntheses, this synthesis is very short and the overall yield very high.

Results and discussion

As shown in Scheme 1, we used 4-benzyl-1,3-thiazolidine-2-thione as starting material. Acylation of thiazolidinethione by propionyl chloride using DMAP as catalyst at room temperature afforded *N*-acylthiazolidinthiones **2** in 95% yield (7*a*). Compound **2** was treated with $TiCl_4$, *N*,*N*-diisopropylethylamine (DIPEA), and *N*-methylpyrrolidone (NMP) in turn, and the resulting complex reacted with propionaldehyde to give alcohol **3** in 98% yield (7*c*). The aldol product could be easily protected with *tert*-butyldimethylsilyl chloride (TBDMSCl) using lutidine as base (9). The compound, obtained by the protection of **3**, was reduced to alcohol **4** with sodium borohydride in the presence of ethanol. Oxidation of alcohol **4** with $Py{\cdot}O_3$ in the presence of DIPEA gave aldehyde **5** in 84% yield. Compound **5** was treated with excess EtMgBr to give a diastereoisomeric mixture of alcohols **6** (4*c*). The diastereoisomeric mixtures were not separated and were directly treated with pyridinium chlorochromate (PCC) and anhydrous sodium acetate in CH_2Cl_2, affording a ketone. Deprotection of the TBS group with tetrabutylammonium fluoride afforded sitophilure **1** (89% yield, 42% overall yield, and 97% ee, based on the reported rotation of +27.0) (2).

Received 8 December 2007. Accepted 18 February 2008. Published on NRC Research Press Web site at canjchem.nrc.ca on 27 May 2008.

C. Lu,[2] J. Nie, G. Yang, and Z. Chen. Ministry of Education, Key Laboratory for the Synthesis and Application of Organic Functional Molecules & School of Chemistry and Chemical Engineering, Hubei University, Wuhan 430062, China.

[1]This article is part of a Special Issue dedicated to Professor R. Puddephatt.

[2]Corresponding author (e-mail: lucf@hubu.edu.cn)

 doi:10.1139/V08-032 © 2008 NRC Canada

Fig. 1. Sitophilure **1.**

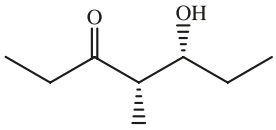

1

Scheme 1. Improved synthesis of sitophilure **1**. Reagents and conditions: a) DMAP (0.2 equiv.), Et_3N (1.2 equiv.), propionyl chloride (1.3 equiv.), CH_2Cl_2, RT, 3 h; b) $TiCl_4$ (1.05 equiv.), DIPEA (1.1 equiv.), NMP (2.0 equiv.), propionaldehyde (1.1 equiv.), CH_2Cl_2, 0 °C, 3 h; c) TBDMSCl (2.5 equiv.), lutidine (1.5 equiv.), CH_2Cl_2, RT, 3 h; d) $NaBH_4$ (4.0 equiv.), EtOH, 0 °C, 1 h; e) Py·SO_3 (3.7 equiv.), DIPEA (2.3 equiv.), CH_2Cl_2, 0 °C, 3 h; f) EtMgBr (2.8 equiv.), Et_2O, –78 °C ~ RT, 2 h; g) PCC (1.5 equiv.), NaOAc (0.3 equiv.), CH_2Cl_2, RT, 4 h; h) Bu_4NF (1.0 equiv.), THF, RT, 18 h.

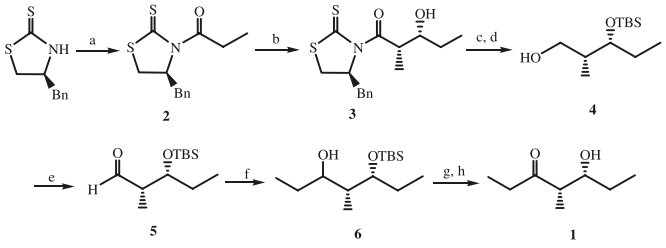

Conclusion

In summary, an efficient synthesis (8 steps, 42% overall yield, and 97% enantiomeric excess) of enantiomerically enriched sitophilure **1** was developed from propionaldehyde using 4-benzyl-1,3-thiazolidine-2-thione as chiral auxiliary.

Experimental

General

All organic solvents and base were dried by standard methods. TLCs were performed on precoated plates of silica gel HF254 (0.5 mm, Yantai, China). Flash column chromatography was performed on silica gel H (Yantai, China). Melting points were measured on a WRS-1A digital melting point apparatus and are uncorrected. Optical rotations were determined with a PerkinElmer Model 241 MC polarimeter. IR spectra were recorded on an IR-spectrum one (PE) spectrometer. ^{1}H NMR (600 MHz) and ^{13}C NMR (150 MHz) spectra were recorded on a Varian Unity INOVA 600 spectrometer in $CDCl_3$ using TMS as internal standard. Mass spectra were recorded on Finnigan LCQ DUO MS system.

Synthesis of (*S*)-4-benzyl-3-propionyl-1, 3-thiazolidine-2-thione (2)

To a solution of the thiazolidinethione (7.5 g, 35.89 mmol) in dry CH_2Cl_2 (150 mL) at room temperature was added DMAP (0.88 g, 7.18 mmol) and triethylamine (6.0 mL, 43.06 mmol). Freshly distilled propionyl chloride (4.1 mL, 46.65 mmol) was added dropwise over 5 min and the mixture was stirred for 3 h at room temperature. The reaction mixture was quenched into saturated NH_4Cl (25 mL) and the organic phase was separated. The aqueous layer was extracted with CH_2Cl_2 (50 mL) and the organic extracts were combined, washed with aqueous saturated $NaHCO_3$ and brine, dried over $MgSO_4$, and the solvent was evaporated. The crude product was recrystallized from CH_3CN to yield a yellow solid **2** (9.03 g, 95%), mp 101.1–101.5 °C. IR (KBr, cm^{-1}): 1703, 1261, 1163, 1033, 759, 706. ^{1}H NMR (600 MHz, $CDCl_3$) δ: 7.27-7.35 (m, 5H), 5.38 (m, 1H), 3.21 (dd, *J* = 9.6 Hz, 3.6 Hz, 1H), 3.13 (dd, *J* = 10.8 Hz, 7.2 Hz, 1H), 3.05 (dd, *J* = 10.8 Hz, 2.4 Hz, 1H), 2.88 (dd, *J* = 10.2 Hz, 3.0 Hz, 1H),1.19 (t, *J* = 7.2 Hz, 3H). ^{13}C NMR (150 MHz, $CDCl_3$) δ: 202.5, 174.8, 137.4, 130.0, 129.3, 69.1, 37.3, 33.0, 32.3, 9.8.

Synthesis of (*S*)-4-benzyl-3-((2′S, 3′*R*)-3′-hydroxy-2′-methylpentanoyl)-thiazolidine-2-thione (3)

To solution of compound **2** (4.99 g, 18.82 mmol) in anhyd. CH_2Cl_2 (100 mL) at 0 °C under N_2 was added $TiCl_4$ (2.17 mL, 19.76 mmol), and the solution was stirred for 15 min. DIPEA (3.60 mL, 20.70 mmol) was added dropwise to the mixture, and the solution was stirred for 40 min. NMP (3.61 mL, 37.65 mmol) was added at 0 °C and the mixture was stirred for an additional 10 min. Freshly distilled propionaldehyde (1.51 mL, 20.70 mmol) was then added to the enolate. The reaction was allowed to stir for 2 h followed by the addition of satd. NH_4Cl (10 mL). The organic layer was separated and the aqueous layer was extracted with CH_2Cl_2 (50 mL). The combined organic layers were dried over anhyd. $MgSO_4$, filtered and concentrated, the crude product was purified by column chromatography on silica gel (*n*-hexane/EtOAc, 10:1 *v*/*v*) to afford a yellow oil **3** (5.95 g, 98%). $[\alpha]_D^{25}$ = +130.3° (c 1.30, $CHCl_3$). IR (KBr, cm^{-1}): 3344, 2963, 1693, 1260, 1164, 743, 701. ^{1}H NMR (600 MHz, $CDCl_3$) δ: 7.12–7.27 (m, 5H), 5.25 (m, 1H), 4.43 (m, 1H), 3.77 (m, 1H), 3.31 (dd, *J* = 6.6 Hz, 4.8 Hz, 1H), 3.13 (dd, *J* = 9.6 Hz, 3.6 Hz, 1H), 2.95 (dd, *J* = 10.2 Hz, 2.4 Hz, 1H), 2.80 (d, *J* = 11.4 Hz, 1H), 1.46 (q, *J* = 7.2 Hz, 1H), 1.37 (q, *J* = 6.0 Hz, 1H), 1.16 (d, *J* = 7.2 Hz, 3H), 0.87 (t, *J* = 7.2 Hz, 3H). ^{13}C NMR (150 MHz, $CDCl_3$) δ: 201.2, 178.1, 136.2, 129.3, 128.9, 128.8, 128.7, 127.2, 73.5, 68.7, 42.7, 37.9, 31.9, 27.1, 10.2, 10.1.

Synthesis of (2*R*, 3*R*)-3-(*t*-butyldimethylsilanyloxy)-2-methyl-1-pentanol (4)

To a stirred solution of **3** (4.89 g, 15.13 mmol) in CH_2Cl_2 (50 mL) was added lutidine (2.65 mL, 22.74 mmol) and *t*-butyldimethylsilyl chloride (4.56 g, 37.77 mmol). After stirring for 3 h at room temperature, the reaction mixture was diluted with CH_2Cl_2 and washed with CH_2Cl_2 (50 mL) and brine. The organic layers were dried over $MgSO_4$, filtered, and concentrated in vacuum to give a green oil product (5.30 g). The green oil product (5.30 g, 14.18 mmol) was dissolved in anhyd. ethanol (50mL) and treated with sodium borohydride (2.25 g, 14.25 mmol) with cooling (ice-water bath) and stirring. After stirring for 1 h, 1 N HCl was added to quench the reaction. The reaction mixture was extracted with ethyl acetate and dried over $MgSO_4$. The solvent was evaporated and the crude product was purified by column chromatography on silica gel (*n*-hexane/EtOAc, 5:1 *v*/*v*) to afford a colorless oil **4** (2.92 g, 72%). $[\alpha]_D^{25}$ = +6.68° (c 1.30, $CHCl_3$) [lit. value (4*c*) $[\alpha]_D^{25}$ = +6.65° (c 1.30,

© 2008 NRC Canada

$CHCl_3$)]. IR (KBr, cm^{-1}): 3362, 2959, 1463, 1254. ^1H NMR (600 MHz, $CDCl_3$) δ: 3.61 (m, 2H), 3.44 (m, 1H), 2.43 (s, 1H), 1.91 (m, 1H), 1.44 (m, 2H), 0.83 (s, 9H), 0.74 (t, J = 7.2 Hz, 3H), 0.02 (m, 6H). ^{13}C NMR (150 MHz, $CDCl_3$) δ: 66.0, 39.2, 25.8, 25.2, 18.0, 11.8, 10.7, -4.4, -4.6.

Synthesis of 3-(*t*-butyldimethylsilanyloxy)-2-methylpentanal (5)

A solution of Py·SO_3 (1.88 g, 11.80 mmol) in dry DMSO (15 mL) was added dropwise to a solution of **4** (0.74 g, 3.19 mmol) and DIPEA (4.5 mL, 27.2 mmol) in dry CH_2Cl_2 (5 mL) and stirred in an ice-water bath. The mixture was stirred for 3 h, added to brine, and extracted with ether. The combined organic fractions were dried over $MgSO_4$, filtered and concentrated in vacuum, and the residue was chromatographed on silica gel (*n*-hexane/EtOAc, 10:1 *v*/*v*) to yield a colorless oil **5** (0.62 g, 84%). $[\alpha]_D^{25}$ = +22.9° (c 2.4, $CHCl_3$) [lit. value (10) $[\alpha]_D^{25}$ = +22.7° (c 2.4, $CHCl_3$)]. IR (KBr, cm^{-1}): 2959, 1727, 1463, 1258. ^1H NMR (600MHz, $CDCl_3$) δ: 9.73 (s,1H), 4.01 (m, 1H), 2.42 (m, 1H), 1.49 (m, 2H), 1.02 (m, 3H), 0.84 (s, 9H), 0.03 (m, 6H). ^{13}C NMR (150 MHz, $CDCl_3$) δ: 205.3, 73.3, 50.7, 27.3, 25.7, 17.9, 10.0, 7.4, –4.3, –4.8.

Synthesis of (3*R*,4*R*,5*RS*)-5-(*t*-butyldimethylsilanyloxy)-4-methyl-3-heptanol (6)

To a cooled (–78 °C) solution of **5** (0.50 g, 2.17 mmol) in ether (10 mL) was added ethylmagnesium bromide (2 mL, 6 mmol of a 3.0 mol/L solution in Et_2O) over a 5 min period under N_2. After the addition, the cooling bath was removed, the reaction mixture was allowed to warm to room temperature, and stirred for an additional 2 h. Saturated aq. NH_4Cl (10 mL) was added to quench the reaction. The reaction mixture was extracted with CH_2Cl_2 (20 mL) and dried over $MgSO_4$, filtered and concentrated, the crude product was purified by column chromatography (*n*-hexane/EtOAc, 10:1 *v*/*v*) to afford a colorless oil **6** (0.47 g, 83%). IR (KBr, cm^{-1}): 3441, 1463, 1259. ^1H NMR (600 MHz, $CDCl_3$) δ: 3.67 (m, 1H), 3.55 (m, 1H), 2.52 (s, 1H), 1.42–1.46 (m, 5H), 0.83 (t, J = 7.2 Hz, 3H), 0.79 (s, 9H), 0.76 (t, J = 7.2 Hz, 3H), 0.72 (t, J = 7.2Hz, 3H), 0.02 (m, 6H). ^{13}C NMR (150 MHz, $CDCl_3$) δ: 79.2, 76.8, 38.2, 27.9, 27.5, 25.8, 18.0, 10.4, 9.8, 5.3, –3.7, –4.6.

Synthesis of (4*S*,5*R*)-5-hydroxy-4-methyl-3-pentanone(1)

To a solution of pyridinium chlorochromate (0.47 g, 2.23 mmol) and anhydrous sodium acetate (0.04 g, 0.44 mmol) in CH_2Cl_2 (10 mL) was added **6** (0.37 g, 1.44 mmol) at room temperature. The reaction was stirred for 4 h, followed by the addition of ether (20 mL). The resulting solution was filtered through a column of silica, dried over $MgSO_4$, and concentrated under reduced pressure. The residue (0.36 g) was dissolved in anhyd. THF (15 mL) and treated with tetrabutyl ammonium fluoride (0.37 g, 1.41 mmol). The resulting solution was stirred for 18 h before being diluted with ether (20 mL). The mixture was washed with satd. aq. NH_4Cl and brine, dried over $MgSO_4$, filtered, and concentrated, and the crude product was purified by column chromatography (*n*-hexane/EtOAc, 10:1 *v*/*v*) to afford a colorless oil **1** (0.18 g, 89%), $[\alpha]_D^{25}$ = +26.3° (c 1.24, Et_2O) [lit. value (2) $[\alpha]_D^{25}$ = +27.0° (c 1.24, Et_2O)]. IR (KBr, cm^{-1}): 3445, 2959, 2930, 1710, 1462, 1255. ^1H NMR (600 MHz, $CDCl_3$) δ: 3.75 (m, 1H), 3.55 (s, 1H), 2.51 (m, 1H), 1.29–1.50 (m, 4H), 1.06 (d, J = 3.6 Hz, 3H), 0.98 (t, J = 7.2 Hz, 6.6 Hz, 3H), 0.88 (t, J = 7.2 Hz, 3H). ^{13}C NMR (150 MHz, $CDCl_3$) δ: 216.6, 72.5, 49.2, 34.7, 26.7, 11.5, 10.2, 9.9.

Acknowledgements

This work is supported by the National Natural Sciences Fundation of China (No. 20772026) and the Natural Sciences Foundation of Hubei Province (2007ABA031).

References

1. N.R. Schmuff, J.K. Phillips, W.E. Burkholder, H.M. Fales, C.W. Chen, P.P. Roller, and M. Ma. Tetrahedron Lett. **25**, 1533 (1984).
2. K. Mori and T. Ebata. Tetrahedron, **42**, 4421(1986).
3. C.A. Walgenbach, J.K. Phillips, W.E. Burkholder, G.G.S. King, K.N. Slessor, and K. Mori. J. Chem. Ecol. **13**, 2159 (1987).
4. (*a*) E.J. Corey, R. Imwinkelried, S. Pikul, and Y.B. Xiang. J. Am. Chem. Soc. **111**, 5493 (1987); (*b*) J. Razkin, A. González, P. Gil. Tetrahedron: Asymmetry, **7**, 3479 (1996); (*c*) R.A. Pilli, V.B. Riatto, and J. Braz. Chem. Soc. **10**, 363 (1999).
5. (*a*) D.A. Evans, J. Bartroli, and T.L. Shih. J. Am. Chem. Soc. **103**, 2127 (1981); (*b*) D.A. Evans, C.W. Downey, J.T. Shaw, and J.S. Tedrow. Org. Lett. **4**, 1127 (2002).
6. (*a*) M.A. Walker and C.H. Heathcock. J. Org. Chem. **56**, 5747 (1991); (*b*) B.C. Raimundo and C.H. Heathcock. Synlett, **12**, 1213 (1995).
7. (*a*) M.T. Crimmins and K. Caudhary. Org. Lett. **2**, 775 (2000); (*b*) M.T. Crimmins, B.W. King, E.A. Tabet, and K. Caudhary. J. Org. Chem. **66**, 894 (2001); (*c*) M.T. Crimmins and J. She. Synlett, **8**, 1371 (2004); (*d*) M.T. Crimmins and D.J. Slade. Org. Lett. **8**, 2191(2006).
8. Y.K. Wu, Y.P. Sun, Y.Q. Yang, Q. Hu, and Q. Zhang. J. Org. Chem. **69**, 6141 (2004).
9. G. Cainelli, M. Contento, D. Giacomini, and M. Panunzio. Tetrahedron Lett. **26**, 937 (1985).
10. D.E. Cane, W. Tan, and W.R.Ott. J. Am. Chem. Soc. **115**, 527 (1993).

© 2008 NRC Canada

DFT mechanistic studies on the epoxidation of cyclohexene by non-heme tetraaza manganese complexes[1]

Alicja Haras and Tom Ziegler

Abstract: Herein, we report density functional calculations on the epoxidation of cyclohexene with H_2O_2 activated by $(Me_2EBC)MnCl_2$ (Me_2EBC stands for 4,11-dimethyl-1,4,8,11-tetraazabicyclo[6.6.2]hexadecane). The computed energy landscapes for different interaction modes of cyclohexene with the Mn^{IV}-hydroperoxo complex and the Mn^{V}-oxo species support recent experimental findings by Busch and co-workers [J. Am. Chem. Soc. **127**, 17170 (2005)], according to which the Mn^{IV}-hydroperoxo species is the active complex for olefin epoxidation. Thus, the dominant olefin epoxidation pathway is via direct transfer of the distal protonated oxygen of the hydroperoxo adduct without changes in the oxydation state of its tetravalent metal centre, i.e., the mechanism commonly observed in the uncatalyzed epoxidation by peracids. The homolytic decomposition of the O–OH bond in the active manganese complex leading to the Mn^{V}-oxo species is found to be the only epoxidation pathway that could possibly compete with the O_β transfer from the hydroperoxo adduct. However, the generated Mn^{V}-oxo is shown to be a rather poor oxidant resulting in low yields of the target epoxy cyclohexane.

Key words: epoxidation, density functional theory, permanganic acid, peracid.

Résumé : Dans ce travail, on rapporte les résultats de calculs effectués sur la base de la théorie de la fonction de densité pour la réaction d'époxydation du cyclohexène, à l'aide de H_2O_2 catalysé par le $(Me_2EBC)MnCl_2$ (Me_2EBC = 4,11-diméthyl-1,4,8,11-tétraazabicyclo[6.6.2]hexadécane). L'énergie calculée pour les paysages des divers modes d'interaction du cyclohexène avec le complexe Mn(IV)-hydroperoxo et l'espèce Mn(V)-oxo est en accord avec les résultats expérimentaux obtenus récemment par Busch et al. [J. Am. Chem. Soc, **127**, 17170 (2005)] selon lesquels l'espèce Mn(IV)-hydroperoxo est le complexe actif pour l'époxydation de l'oléfine. En conséquence, la voie réactionnelle principale dominante pour l'époxydation de l'oléfine implique un transfert direct de l'oxygène protoné distal de l'adduit hydroperoxo, sans changements de l'état d'oxydation de sont centre métallique tétravalent, c'est-à-dire le mécanisme généralement observé dans l'époxydation par les peracides non catalysée. La décomposition homolytique de la liaison O–OH du complexe activé du manganèse conduisant à la formation de l'espèce Mn(V)-oxo serait la seule voie d'époxydation qui pourrait entrer en compétition avec le transfert O_β à partir de l'adduit hydroperoxo. Toutefois, on a démontré que l'entité Mn(V)-oxo qui est générée est un mauvais oxydant qui ne conduit qu'à de faibles rendements de l'époxycyclohexane recherché.

Mots-clés : époxydation, théorie de la fonction de densité, acide permanganique, peracide.

[Traduit par la Rédaction]

Introduction

The development of an efficient route of oxygen transfer into an olefin double bond with hydrogen peroxide as the epoxidizing agent has been a long term goal in organic syntheses (1, 2). Such a process would be an enviroment-friendly alterative to the existing technologies for epoxide production. Unfortunately, the oxidant itself is not sufficiently active, and transition-metal complexes that might serve as catalysts for the process can rather easily undergo homolytic or heterolytic decomposition. The tetraaza-macrocyclam manganese systems proposed by Busch and co-workers (3–6) and shown in Fig. 1 are the first known examples (5) of manganese complexes that can generate a Mn–OOH adduct active and stable enough to directly epoxidize terminal olefins as demonstrated by oxygen-labelling experiments performed by Busch and co-workers (3, 4).

Received 18 January 2008. Accepted 17 March 2008. Published on the NRC Research Press Web site at canjchem.nrc.ca on 11 June 2008.

Dedicated to Professor R.J. Puddephatt on the occasion of his 65th anniversary.

A. Haras and T. Ziegler.[2] Department of Chemistry, University of Calgary, University Drive 2500, Calgary, AB T2N 1N4, Canada.

[1]This article is part of a Special Issue dedicated to Professor R. Puddephatt.
[2]Corresponding author (e-mail: ziegler@ucalgary.ca).

 doi:10.1139/V08-065 © 2008 NRC Canada

Fig. 1. Crystallographic structure (4) and schematic display of the $(Me_2EBC)Mn^{IV}(OH)_2^{2+}$ cation. Hydrogen atoms are omitted for clarity.

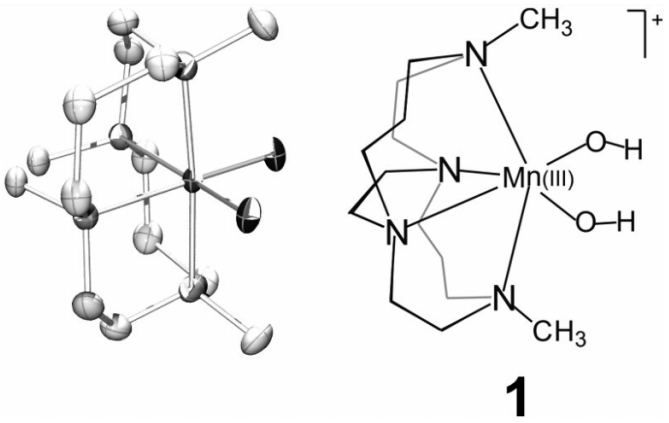

In the present work, we present DFT calculations on the epoxidation of cyclohexene in the presence of the novel Mn(II) complexes bearing the bridged cyclam tetraaza ligand (see Fig. 1). The chosen substrate (olefin) was taken as the smallest among the various olefins epoxidized by Busch and coworkers (4), since it is the most convenient for theoretical studies. We concentrate our attention on the tetravalent manganese-hydroperoxo adduct, $(Me_2EBC)Mn^{IV}(O)(OOH)^+$, as the acive epoxidizing agent. Based on experimental findings (4), the complex formulated as "permanganic acid" was proposed to be formed under catalytic conditions from $(Me_2EBC)Mn^{IV}(O)(OH)^+$ according to eq. [1] at pH < 7.

$$[1] \quad (Me_2EBC)Mn^{IV}(O)(OH)^+ + H_2O_2 \leftrightarrow (Me_2EBC)Mn^{IV}(O)(OOH)^+ H_2O$$

It is the objective of the present study to understand the unique behaviour of the Busch system as a catalyst for epoxidation of olefins by hydrogen peroxide. To this end we shall explore why the manganese-hydroperoxo adduct $(Me_2EBC)Mn^{IV}(O)(OOH)^+$, as observed by Busch and coworkers, serves as the oxygen transfer agents rather than the $(Me_2EBC)Mn^{V}$-oxo and $(Me_2EBC)Mn^{IV}$-oxo species. We present here a detailed study of the different reaction channels for cyclohexene epoxidized in the presence of **1** of Fig. 1 involving $(Me_2EBC)Mn^{IV}(O)(OOH)^+$ as well as $(Me_2EBC)Mn^{V}$-oxo species.

Model and method

The crystallographic structure of the studied manganese tetraaza catalyst without the counterion (PF^-_6) is displayed in Fig. 1.

The "butterfly"-like structure of the catalytic system has a distorted octahedral geometry with the bridged cyclam ligand coordinated to the metal centre through the four nitrogen atoms. The Mn–N bond distances are not equal, ranging from 2.115 to 2.327 Å. In the basal plane formed by manganese and two nitrogens bridged by an ethylene group, there are two additional coordination sites at the metal centre occupied by chlorine atoms in the starting complex. Under catalytic conditions, the two Cl atoms are exchanged with oxygen-containing ligands that can further serve as an oxygen source in the cyclohexene epoxidation process. Different from the in-plane nitrogens, the two out-of-plane N atoms with methyl groups (labelled as N′) are not bridged to each other. Overall, the system has a C_2 symmetry with the symmetry axis bisecting the Cl–Mn–Cl and the N′–Mn–N′ angles (see Fig. 2).

Fig. 2. Schematic structure of the $(Me_2EBC)Mn^{IV}(OH)_2^{2+}$ complex with the two symmetry axes.

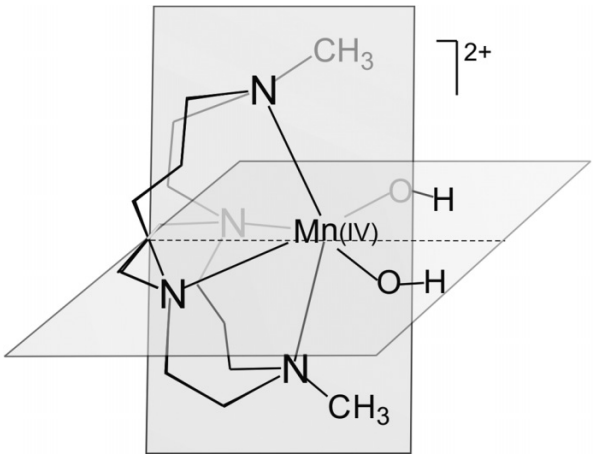

All spin-unrestricted DFT computations presented here have been carried out with the program package ADF 2006.01 (7). The complexes considered here were high-spin with all d electrons unpaired. Geometry optimzations at the BP86 level of theory (8–10) with the DZ basis sets for H and the DZP basis sets for Mn, C, O, and N have been performed to calculate the energies and structures involved in the studied processes. The inner cores of manganese (1s 2s 2p) as well as the carbon, nitrogen, and oxygen (1s) shell have been treated by the frozen core approximation. Neither thermochemistry corrections nor corrections for zero-point vibration energy have been applied. Transition states TS1–TS6 all had a Hessian with a single negative eigenvalue. Solvent effects (acetone/water mixture in 4:1 ratio) have been systematically estimated using the COSMO continuum model as inplemented in ADF (11). The dielectric constant employed had a value of 68. The atomic radii of manganese (2.4 Å), nitrogen (1.4 Å), carbon (2.3 Å), oxygen (1.4 Å), and hydrogen (1.16 Å) have been used for construction of the cavity in the solvent (12, 13). Geometry optimizations were carried out without constraints.

Results and discussion

Epoxidation with $(Me_2EB)Mn^{IV}(O)(OOH)^+$

We begin the computational investigations of cyclohexene epoxidation with **1** as the catalyst by exploring possible stable conformers of **1**. The first conformation **1a** of Fig. 3 has the hydrogen on the β-oxygen pointing away from the α′-oxygen, whereas the second conformation **1b** displays a bonding interaction between the β-hydrogen and the α′-oxygen. The difference in relative energy of **1a** and **1b** was calculated to be 7 kcal/mol (1 cal = 4.184 J) in favour of **1b**.

We have also explored the interconversion of **1a** and **1b**. We find a barrier of 16.8 kcal/mol in going from the more stable conformation **1b** over the transition state shown as

© 2008 NRC Canada

Fig. 3. Two stable configurations of **1** along with transition state for their interconversion (1 cal = 4.184 J).

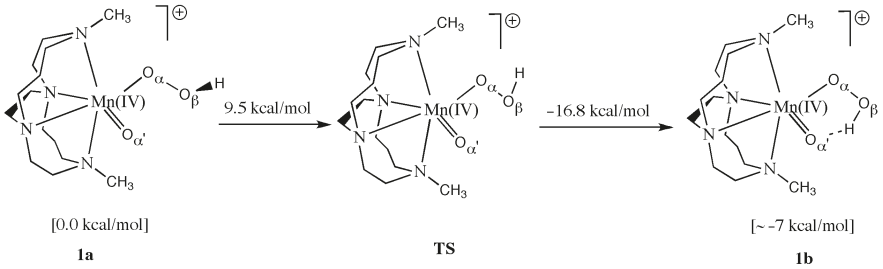

Fig. 4. Transition-state geometries for the symmetric and asymmetric O_β uptake from **1b**. Bonds in the process of breaking or forming are shown with dashed lines; bond distances are in Å.

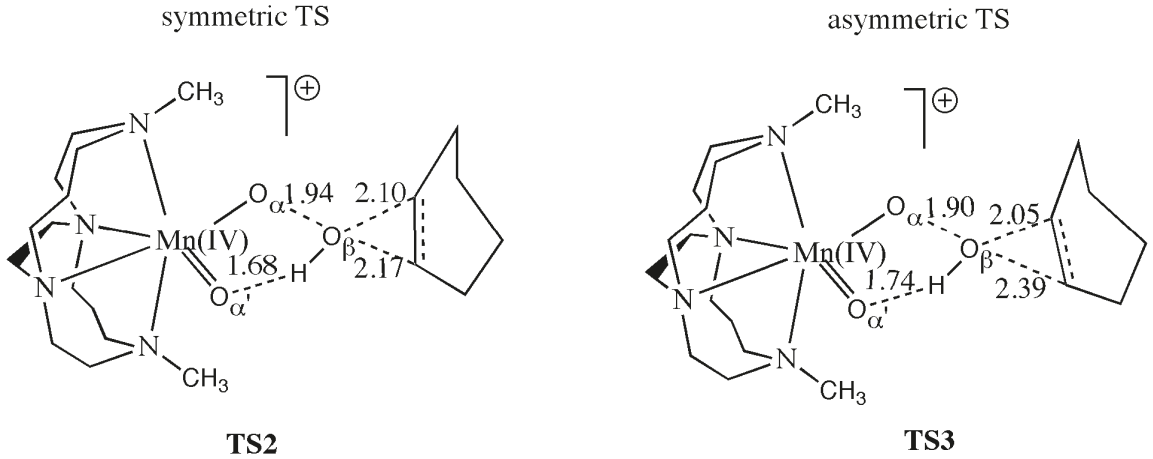

TS1 in Fig. 3 to **1a**. In TS1, the hydrogen bond is completely broken. An additional factor is the loss of conjugation between the occupied p_π orbitals on the two oxygens and empty d orbitals on the metal center. This loss is responsible for the barrier in going from **1a** to **1b**.

By looking at the structures of the two conformers of **1**, it is clear that the higher stability of **1b** is a result of the weak hydrogen interactions between the distal hydrated oxygen in OOH and its neighbouring oxo group. The close proximity of the two groups directly coordinated to the metal centre makes the complex structurally similar to the organic peracids widely used in oxygen-transfer reactions. It is thus possible that **1** of Fig. 3 epoxidizes olefins in a way similar to that observed for peracids. To explore this possibility, we shall now turn to the reaction of **1** with cyclohexene.

Scheme 1 presents all the studied reaction pathways for the direct epoxidation of cyclohexene by **1**. As one can notice, an oxygen atom can be directly transferred from the studied manganese hydroperoxo complex either via the concerted or the stepwise mechanism. Moreover, the presence of two distinct oxygen atoms in the hydroperoxo group coordinated to the metal centre increases the number of possible reaction channels for epoxidation by a factor of two. For simplicity, the oxygen atom that is directly coordinated to the metal centre and the distal protonated oxygen will be referred to thereafter as O_α and O_β, respectively.

Let us concentrate first on the O_β transfer. In the presence of **1b**, the mechanism would be analogeous to the one observed in the case of the uncatalyzed olefin epoxidation by peroxy acids, known in organic chemistry as the Prilezahev reaction (14), in which the oxygen uptake is accompanied by

Scheme 1. All studied reaction paths for the direct cyclohexene epoxidation by **1**.

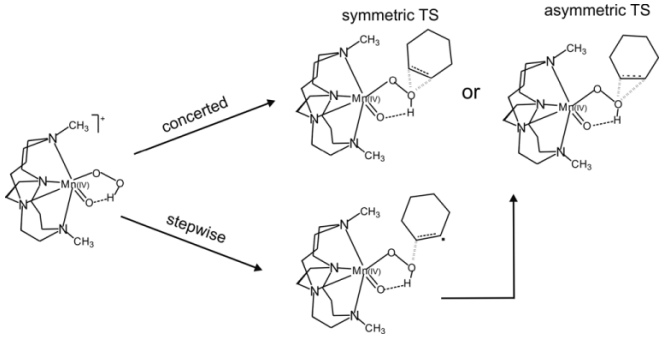

simultaneous transfer of H to the neighbouring oxo group. When the process takes place in the presence of **1a**, there must be transfer of the H atom from O_β to another oxygen before the oxygen transfer can take place. The explored potential energy surfaces for the synchronous (TS2 of Fig. 4) and the asynchronous O_β (TS3 of Fig. 4) uptakes with **1b** reveal rather low energy barriers in both cases (10.75 and 9.2 kcal/mol, respectively). On route to the transition state, a precomplex is formed that is stabilized relative to the separate reactants by 7–8 kcal/mol. In the transiton state structures shown in Fig. 4, the reacting oxygen atom and the carbon atoms from the olefin double bond are within 2 Å. At the same time, the O–O bond in the OOH group coordinated to the metal centre is elongated to 1.9 Å, and the distance between the hydrogen atom at O_β and the O'_α group is reduced to 1.7 Å, indicating the onset of an H–O bond.

© 2008 NRC Canada

Scheme 2. Catalytic cycle for the most facile O_β uptake from the more stable conformer of **1**.

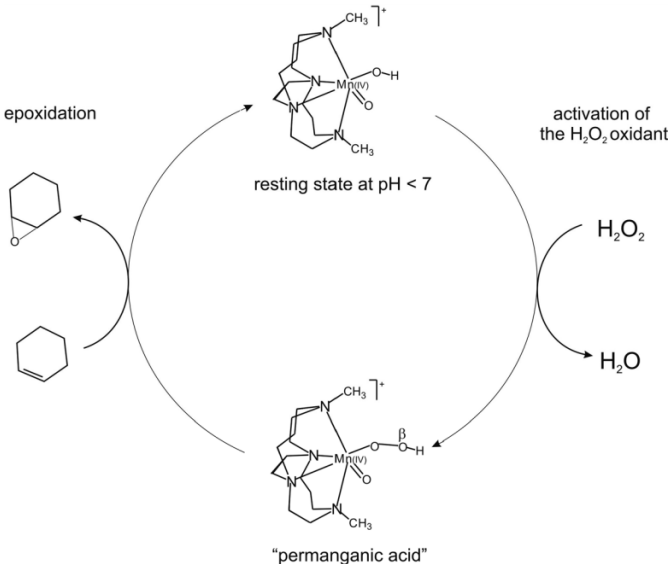

Although one might expect that the coordination of the tetraaza ligand coordinated to the metal centre via four nitrogen atoms would somehow be influenced by epoxidation, there are no significant ligand deformations observed in the identified TS geometries. After passing the transition states, the transfer of the H atom to the O'_α group is spontaneous, resulting in the formation of epoxy cyclohexane and regeneration of the $(Me_2EBC)Mn^{IV}(O)(OH)^+$ unit from which the active hydroperoxo complex is formed. The overall catalytic cycle for the process is displayed in Scheme 2.

We have also explored passways involving the transfer of O_β in **1a** to the olefin. However, attempts to make the necessary transfer of hydrogen from O_β to O'_α prior to the β-oxygen uptake by olefin were unsucessful. Thus, all the explored pathways resulted in a high energy process involving dissociation of the OH group from the active hydroperoxo complex. Consequently, we are lead to conclude that this process will lead to the decomposition of **1a** rather than to the epoxidation of cyclohexene.

Next, the reaction paths for the epoxidation by O_α were explored, again for both stable conformations of **1** (Scheme 3). Analyzing the less stable **1a**, one could imagine that the olefin uptake of O_α can be assisted by the formation of an adduct in which the distal oxygen of the hydroperoxo group weakly interacts with the metal centre. Such an interaction in the presence of olefin would further facilitate the O_α uptake and would lead to the regeneration of $(Me_2EBC)Mn^{IV}(O)(OH)^+$, which is a resting state under catalytic conditions and completes the catalytic cycle (Scheme 3).

Starting from the isolated reagents, the approaching olefin forms a precomplex that is stabilized by 6.0 kcal/mol both for the asymmetric attack as well as the symmetric interactions of O_α with the olefinic double bond. The asymmetric attack results in the transition state with no changes in the O–O distance of the OOH group but with elongation of the Mn–O bond to 2.63 Å. The first transition states for the asymmetric O_α uptake in the presence of **1a** and **1b** are destabilized by 42.2 kcal/mol with respect to the stable

Scheme 3. Possible reaction pathways for O_a uptake by cyclohexene from **1**.

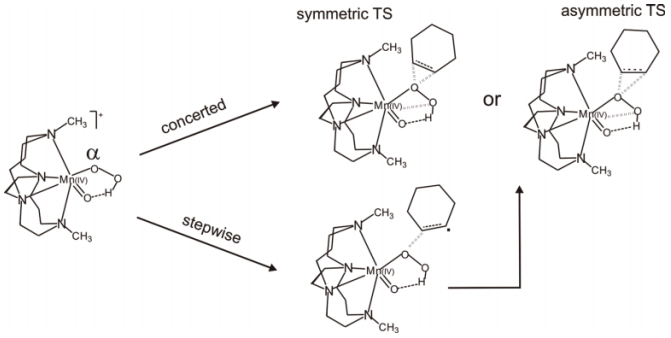

Fig. 5. Transition state for breaking the O–OH bond in **1b** (TS4). Bonds in the process of breaking or forming are shown with dashed lines; bond distances are in Å.

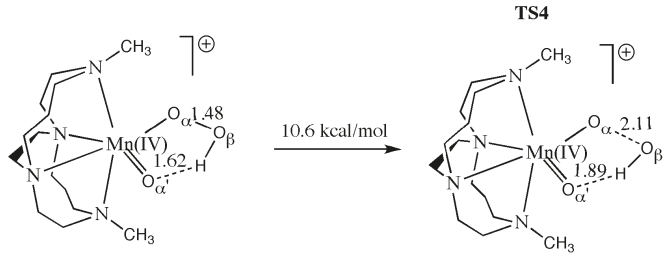

precomplexes. We note further that the attack by olefin on **1a** and **1b** leads to the same transition state because of the rapid rearrangement of **1a** once the olefin approaches the reactive oxygen. It is clear from our calculations that a direct attack of the OOH group coordinated to the **1b** metal center on the olefin is much more facile for the O_β oxygen than the O_α oxygen in **1**. We have for that reason not explored the O_α uptake process in full details (see Scheme 3).

Epoxidation with $(Me_2EBC)Mn^V(O)_2^+$

It is conceivable that the active $(Me_2EBC)Mn^{IV}(O)(OOH)^+$ complex can undergo homolytic decomposition of the O–OH bond to generate the $(Me_2EBC)Mn^V(O)_2^+$ system that can further participate in the epoxidation of cyclohexene. Some $Mn(O)_2$ units are well-known to be strong epoxidizing agents in the oxygen-transfer processes catalyzed by the Mn-heme and Mn-salen complexes studied extensively both by theoretical as well as experimental methods (14). We have as a consequence explored the energetics of breaking the O–OH bond in the more stable configuration of **1** as well as the potential of the resulting $(Me_2EBC)Mn^V(O)_2^+$ complex as an epoxidizing agent.

The optimized transition state TS4 for breaking the O–OH bond is situated 10.6 kcal/mol above the substrate complex with the $R(O_\alpha–O_\beta)$ reaction coordinate being elongated to 2.11 Å (see Fig. 5). The notable differences between the transition state geometry and the stable **1b** complex is the reduced distance between the β-hydrogen of the OOH ligand and the neighbouring O'_α group as well as the elongation of the O–O bond. Here, it is worth to notice that the obtained energy barrier is comparable to the one required to insert the

© 2008 NRC Canada

Scheme 4. All studied reaction paths for the cyclohexene epoxidation by the Mn^{V}-oxo species.

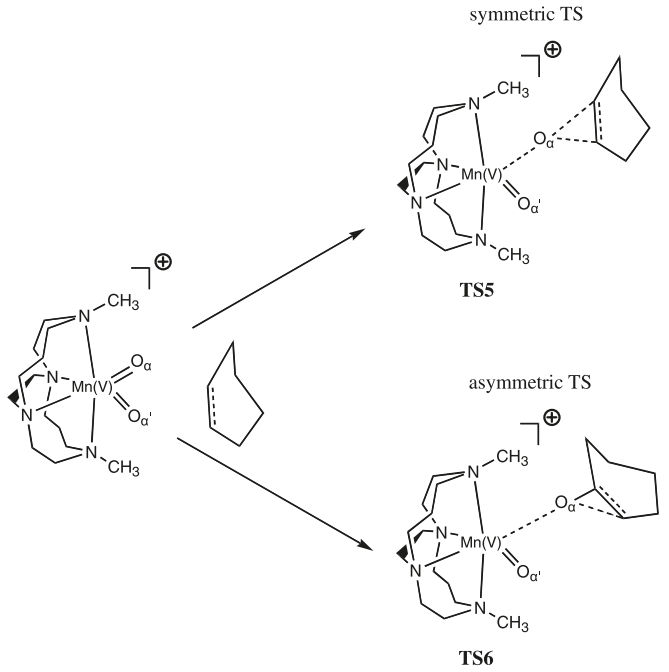

reactive O_β atom into the olefin double bond. This would suggest that the decomposition process can only be competitive to O_β epoxidation (Scheme 2) at low olefin concentrations. We note that Busch and co-workers never observed OH radicals or $Mn^{V}(O)_2^{+}$ species. Nevertheless, we shall in the following briefly examine whether an oxo group of the postulated $Mn^{V}(O)_2^{+}$ species can be transferred into the olefin double bond either in a sequential or concerted manner resulting in the reduced manganese centre. The studied possibilities are displayed in Scheme 4.

Starting from the symmetric interaction mode, the Mn^{V}-oxo species does not form any stable precomplex with the incoming cyclohexene, but there is a steady increase in energy observed once the distance between the reacting oxo group and the two carbon atoms of the olefinic double bond is reduced. At the distance of about 1.8 Å between the oxygen from the Mn^{V}-oxo and the two carbon atoms of the interacting double bond, the saddle point TS5 is located with the energy of 35.5 kcal/mol above the isolated reacting species. The identified transition-state geometry is very symmetric, as the bond to be broken between manganese and the reacting oxygen atom is similar (1.85 Å) to the two new bonds formed by the oxygen with cyclohexene (1.68 and 177 Å, TS5 of Fig. 6).

When the cyclohexene approach is asynchronous, the activation energy to form the first bond with the incoming olefin amounts to 16.4 kcal/mol (TS6 of Fig. 6). Again, the distance between the atoms forming a new bond in TS6 and the bond that is broken in the active manganese complexes are almost the same (1.77 and 1.74 Å, respectively), resulting in the formation of an intermediate with the olefin being oriented perpendicular to the basal plane formed by manganese and the two oxo groups coordinated to the metal centre. The formed intermediate product is very unstable with an energy of 13.4 kcal/mol above the reactants, which precludes the

Fig. 6. Synchronous (TS5) and asynchronous (TS6) transition states for epoxidation of cyclohexene by $(Me_2EBC)Mn^{V}$=O species.

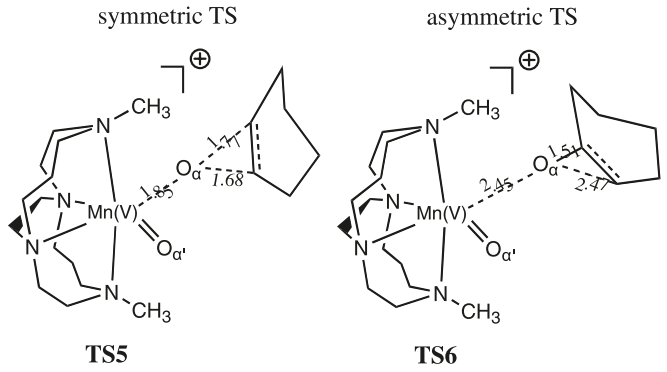

mechanism from being competitive to the uptake of O_β from the $(Me_2EBC)Mn^{IV}(O)(OOH)^{+}$ complex that is required to overcome an energy barrier of only 10 kcal/mol as shown in the preceding section.

Conclusions

We have, in the computational study present here, investigated the mechanistic aspects of cyclohexene epoxidation with H_2O_2 activated by the manganese tetraaza bridged cyclam catalyst **1**. Two active manganese complexes have been considered as the potential oxygen source: the tetravalent manganese hydroperoxo adduct, $LMn^{IV}(O)(OOH)^{+}$, **1**, in its two stable conformations, **1a** and **1b**, and the product from the homolytic decomposition of **1**, i.e., $LMn^{V}(O)_2^{+}$. We have probed different modes for the transfer of oxygen from the active manganese species into olefin. Our investigation has provided clear evidence in favour of the acid–base mechanism in which the transfer of the hydrated oxygen (O_β) of the coordinated OOH group to the metal center is accompanied by the simultaneous transfer of H to the proximal oxo group. The mechanism is facilitated by the unique architecture of the catalyst ligand, which orients the oxo and hydroperoxo ligands in a cis position relative to each other. It is interesting to note that the more stable configuration of the active manganese hydroperoxo complex **1b** closely resembles the one observed in peroxyacids allowing for the spontaneous hydrogen transfer to the neighbouring oxo group during the oxygen uptake process.

An analysis of the frontier orbitals (not shown) provides support for the stabilizing effect of the proximal oxo group on the π orbital of the reactive oxygen, which donated electrons into the π^* orbital on the olefin double bond. In addition, the high-valent manganese centre analogeously to the electron-withdrawing carbonyl group in peroxyacids tends to attract the electron density from the OOH ligand jointly promoting the transfer of its distal oxygen atom to the double bond of the incoming olefin.

Acknowledgements

We wish to thank the Procter & Gamble company for providing us with a crystallographic structure of the studied manganese system and for sharing with us details of the performed experimental research. The computations reported

© 2008 NRC Canada

here were carried out on the WestGrid high performance computing resources (www.westgrid.ca). T.Z. would like to thank the Canadian Government for a Canada Research Chair.

References

1. K.-T. Aye, G. Ferguson, A.J. Lough, and R.J. Puddephatt. Angew. Chem., Int. Ed. **28**, 767 (2003).
2. (*a*) B.S. Lane and K. Burgess. Chem. Rev. **103**, 2457 (2003); (*b*) N. Mizuno and K. Yamaguchi. The Chemical Record, **6**, 12 (2006).
3. G.Yin, M. Buchalova, A.M. Danby, Ch.M. Perkins, D. Kitko, J.D. Carter, W.M. Scheper, and D.H. Busch. J. Am. Chem. Soc. **127**, 17170 (2005).
4. G.Yin, J.M. McCormick, M. Buchalova, A.M. Danby, K. Rodgers, V.W. Day, K. Smith, Ch.M. Perkins, D. Kitko, J.D. Carter, W.M. Scheper, and D.H. Busch. Inorg. Chem. **45**, 8052 (2006).
5. G.Yin, M. Buchalova, A.M. Danby, Ch.M. Perkins, D. Kitko, J.D. Carter, W.M. Scheper, and D.H. Busch. Inorg. Chem. **45**, 3467 (2006).
6. T.J. Hubin, J.M. McCormick, N.W. Alcock, and D.H. Busch. Inorg. Chem. **40**, 435 (2001).
7. (*a*) E.J. Baerends, D.E. Ellis, and P. Ros. Chem. Phys. **2**, 41 (1973); (*b*) E.J. Baerends and P. Ros. Chem. Phys. **2**, 52 (1973); (*c*) G. te Velde and E.J. Baerends. J. Comput. Phys. **99**, 84 (1992); (*d*) C.G. Fonseca, O. Visser, J.G. Snijders, G. te Velde, and E.J. Baerends. *In* Methods and techniques in computational chemistry. METECC-95. Available from http://theochem.chem.rug.nl/publications/Abstracts.html#255.
8. A.D. Becke. Phys. Rev. A, **38**, 3098 (1988).
9. J.P. Perdew. Phys. Rev. B, **34**, 7406 (1986).
10. J.P. Perdew. Phys. Rev. B, **33**, 8822 (1986).
11. C. Pye and T. Ziegler. Theor. Chem. Acc. **101**, 396 (1999).
12. M-H. Baik, C.K. Schauer, and T. Ziegler. J. Am. Chem. Soc. **124**, 11167 (2002).
13. T. Wondimagegn, K. Vanka, Z. Xu, and T. Ziegler. Organometallics, **23**, 2651 (2004).
14. S.L.H. Rebelo, M.M. Pereira, Q.M.M. Simões, M.G.P.M.S. Neves, and J.A.S. Cavaleiro. J. Catal. **234**, 76 (2005).

© 2008 NRC Canada

Gold complexes of ditelluridoimidodiphosphinate ligands — Reversible oxidation of Au(I) to Au(III) via insertion of gold into a phosphorus–tellurium bond[1]

Dana J. Eisler, Stuart D. Robertson, and Tristram Chivers

Abstract: The reaction of (THT)AuCl with (TMEDA)Na[N($TePR_2$)$_2$] (R = Ph, *i*-Pr, *t*-Bu) produces a series of gold (III) complexes of the type [{R_2PNP(Te)R_2}Au(μ-Te)]$_2$ (**4a**, R = *i*-Pr; **4b**, R = Ph; **4c**, R = *t*-Bu) rather than the expected homoleptic Au(I) complexes of the ditelluridoimidodiphosphinate ligands. A combination of solution- and solid-state NMR studies shows that both cis and trans isomers of **4a**–**4c** are formed in these reactions. X-ray structural determinations of the trans isomers of **4a**–**4c** reveal a centrosymmetric arrangement with a central four-membered Au_2Te_2 ring formed by the formal insertion of gold into a P–Te bond; this insertion process was shown to be reversible upon addition of PPh_3 to **4a** to give the monomeric gold(I) complex $Ph_3PAu[N\{TeP(i\text{-}Pr)_2\}_2]$. The X-ray structure of *cis*-**4b** is also described.

Key words: gold, tellurium, redox, X-ray structures, imidodiphosphinate.

Résumé : La réaction du (THT)AuCl avec le (TMEDA)Na[N($TePr_2$)$_2$] (R = Ph, *i*-Pr et *t*-Bu) conduit à la formation d'une série de complexes d'or(III) du type [{R_2PNP(Te)R_2}Au(μ-Te)]$_2$ (**4a**, R = *i*-Pr; **4b**, R = Ph; **4c**, R = *t*-Bu) plutôt qu'aux complexes homoleptiques Au(I) des ligands ditelluridoimidodiphosphinate. Une combinaison d'études RMN en solution et à l'état solide a permis de montrer que dans ces réactions il y a formation des isomères cis- et trans- des produits **4a**–**4c**. Des déterminations de structures par diffraction des rayons X des isomères trans- des produits **4a**–**4c** indiquent qu'ils existent dans un arrangement centrosymétrique, avec un cycle central à quatre membres de Au_2Te_2 obtenu par l'insertion formelle d'or dans la liaison P-Te; on a démontré que ce processus d'insertion est réversible par addition de PPh_3 au produit **4a** qui conduit à la formation du complexe monomère d'or(I), $Ph_3PAu[N\{TeP(i\text{-}Pr)_2\}_2]$. On décrit aussi la structure du produit *cis*-**4b** telle que déterminée par diffraction des rayons X.

Mots-clés : or, tellure, redox, structures déterminées par diffraction des rayons X, imidodiphosphinate.

[Traduit par la Rédaction]

Introduction

Prior to 2002, the chemistry of dichalcogenidoimidodiphosphinate ligands of the type **1** was restricted to derivatives in which E = O, S, or Se. A number of uses or potential uses for metal complexes of these inorganic analogues of acetylacetonates have been identified in review articles (1–3), e.g., as luminescent materials or lanthanide shift reagents, as well as in metal extraction processes. In the last 5–6 years, a renaissance of the interest in such metal complexes has occurred as a result of (*i*) extensive studies by O'Brien and co-workers, which have demonstrated that metal complexes of the selenium analogue of **1a** are suitable single-source precursors for the deposition of pure thin films of metal selenides by using CVD techniques (4) and (*ii*) the discovery of a synthesis of alkali-metal derivatives of the ditellurido derivatives **1a**–**1c** (5–7). The latter development has opened the door to investigations of the fundamental chemistry of these tellurium-containing ligands, as well as applications of their metal complexes as single-source precursors for binary metal tellurides that are of interest for use, inter alia, in solar cells (CdTe, HgTe) or infrared detectors (SnTe), and as thermoelectric materials (Sb_2Te_3, Bi_2Te_3) (8).

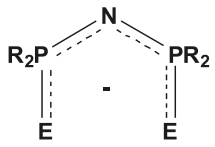

1a (E = Te, R = *i*-Pr)

1b (E = Te, R = Ph)

1c (E = Te, R = *t*-Bu)

Received 10 March 2008. Accepted 10 April 2008. Published on the NRC Research Press Web site at http://canjchem.nrc.ca on 11 June 2008.

Dedicated to Professor Dick Puddephatt in recognition of his outstanding contributions to chemistry in Canada.

D.J. Eisler, S.D. Robertson, and T. Chivers.[2] Department of Chemistry, University of Calgary, Calgary, AB T2N 1N4, Canada.

[1]This article is part of a Special Issue dedicated to Professor R. Puddephatt.

[2]Corresponding author (e-mail: chivers@ucalgary.ca).

 doi:10.1139/V08-074 © 2008 NRC Canada

Scheme 1.

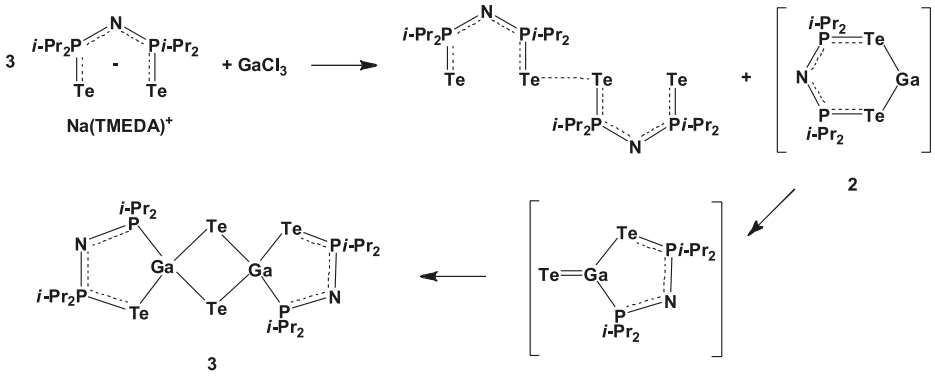

Investigations of the redox behaviour of **1a** revealed new aspects of the well-studied chemistry of dichalcogenidoimidodiphosphinate ligands in which one-electron oxidation with iodine produces the dimeric ditelluride $TePR_2NR_2PTe–TePR_2NPR_2Te$ (**2**: R = *i*-Pr) (see Scheme 1) with an elongated central tellurium–tellurium bond (9). Similar dichalcogenides are also obtained upon oxidation of the disulfido and diselenido ligands (**1**: E = S, R = *t*-Bu; E = Se, R = *i*-Pr, *t*-Bu) (7). In the case of **1c**, however, a structural isomer comprised of a contact ion pair in which a $[(TeP\text{-}t\text{-}Bu_2)_2N]^-$ anion is Te, Te chelated to one Te atom of an incipient cyclic cation $[(TeP\text{-}t\text{-}Bu_2)_2N]^+$ is obtained (7). The five-membered cations $[(EPR_2)_2N]^+$ (E = S, Se, Te; R = *i*-Pr, *t*-Bu) are obtained, as iodide salts, by two-electron oxidation of the corresponding anions with iodine (7, 10).

Homoleptic complexes of **1a** with group 12 (Zn, Cd, Hg) and group 15 (Sb, Bi) metals are obtained via metathesis with the appropriate metal halide (6), and the cadmium and antimony complexes have been shown to be effective single-source precursors for pure CdTe (11) and Sb_2Te_3 (12) thin films, respectively, using the technique of aerosol-assisted chemical vapour deposition (AACVD) (8). Homoleptic complexes may also be prepared for coinage metals, although the ditellurido ligands **1a** and **1b** give rise to higher oligomers with silver(I) (specifically, a hexamer for **1a** and a tetramer for **1b**) (13) compared to the trimeric complexes observed for **1** (E = S, Se; R = *i*-Pr) (14). Interestingly, the ditellurido ligands in both copper(I) and silver(I) complexes exhibit the ability to act as doubly bridging ligands, a feature that brings two metal centres in close proximity suggesting the possibility of metallophilic (d^{10}–d^{10}) interactions. The strong reducing power of **1a** is evident in the reaction of the sodium salt with AuCl, which immediately deposits a gold mirror; however, this reduction may be pre-empted by the addition of PPh_3, leading to the isolation of the monomeric gold(I) complex $Ph_3PAu[N\{TeP(i\text{-}Pr)_2\}_2]$ (13). Although tellurium occurs in combination with gold in certain minerals (e.g., krennerite, $AuTe_2$), only a few gold–tellurium complexes have been structurally characterized. Some representative examples include the ternary gold tellurium halides AuTeI (15) and $AuTe_2X$ (X = Cl, I) (16), the tetrameric gold(I) tellurolate $Au_4[TeC(SiMe_3)_3]_4$ (17), the monomeric gold(I) tellurolate $Ph_3PAu[TeC(SiMe_3)_3]$ (17), and a variety of binary gold–tellurium anions, e.g. $Au_4Te_4^{4-}$ (18), $Au_3Te_4^{3-}$ (19), and $AuTe_7^{3-}$ (20).

Another fascinating difference between the behaviour of the ditellurido ligand **1a** and the dithio or diselenido analogues (**1**: E = S, Se; R = *i*-Pr) is observed in the reactions with group 13 dihalides (21). For example, the reaction of $GaCl_3$ with 3 equiv. of Na(TMEDA)**1a** produces the dimeric complex $\{Ga(\mu\text{-}Te)[i\text{-}Pr_2P(Te)NPi\text{-}Pr_2]\}_2$ (3) as a mixture of cis and trans isomers, together with a high yield of the ditelluride **2**. As indicated in Scheme 1, the formation of the four-membered Ga_2Te_2 ring in **3** was proposed to occur via initial formation of the homoleptic gallium(III) complex $Ga[N\{TeP(i\text{-}Pr)_2\}]_3$, followed by reductive elimination and formation of the gallium(I) complex $Ga[N\{TeP(i\text{-}Pr)_2\}]$ (**2**). Subsequent rearrangement of this Ga(I) complex to the corresponding gallatellurone followed by dimerisation gives **3** in which the gallium centres are P, Te-chelated by the monotellurido $[TePR_2PNPR_2]^-$ (R = *i*-Pr) ligand. The synthesis of the lithium derivative of this anion and its use as an in situ reagent for the preparation of homoleptic complexes of group 12 metals has been reported recently (22).

To determine whether a more labile two-electron donor than PPh_3 would allow the formation of oligomeric gold complexes of ditelluridoimidodiphosphinate ligands similar to those observed for Cu(I) and Ag(I) (13), we have investigated the reactions of the sodium salts of **1a–1c** with the soluble gold(I) complex (THT)AuCl (THT = tetrahydrothiophene). Interestingly, these reactions give rise to the formation of the gold (III) complexes $[\{R_2PNP(Te)R_2\}Au(\mu\text{-}Te)]_2$ (**4a**, R = *i*-Pr; **4b**, R = Ph; **4c**, R = *t*-Bu) rather than the expected homoleptic Au(I) complexes of **1a–1c**. The characterisation of these new gold(III) complexes in the solid state by X-ray structural determinations and ^{31}P NMR spectroscopy (**4a**) and in solution by multinuclear (^1H, ^{31}P, and ^{125}Te) NMR spectroscopy is discussed.

Results and discussion

The 1:1 reaction of the ditelluridoimidodiphosphinate anions **1a**–**1c**, as their sodium salts, with (THT)AuCl proceeds rapidly in dichloromethane at room temperature producing deeply coloured solutions of the gold complexes **4a**–**4c**, as depicted in Scheme 2. While the *iso*-propyl complex **4a** is moderately soluble in THF and CH_2Cl_2, the phenyl and *tert*-butyl derivatives **4b** and **4c** exhibit poor solubility in common organic solvents. The complexes **4a**–**4c** were all obtained in high purity as crystalline solids, which are stable to

© 2008 NRC Canada

Scheme 2.

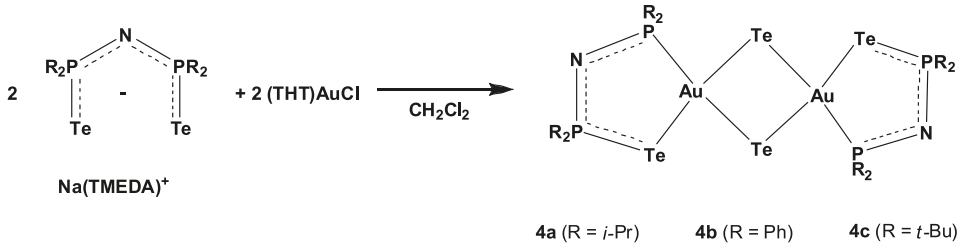

light, air, and moisture in the solid state, but decompose slowly (weeks) in solution at room temperature. The purity of the bulk crystalline samples was confirmed in each case by elemental analysis.

X-ray diffraction studies were carried out on crystalline samples of all three complexes **4a**–**4c**. The most significant difference between the structures involves the substituents on the phosphorus centres, and so the structure of *trans*-**4b** is shown in Fig. 1 as a representative example; a selection of geometrical parameters is given in Table 1. In each case, it was found that the complexes adopt a dimeric structure, which is comprised of a central $[Au_2Te_2]^{2+}$ four-membered ring bound to two monotelluridoimidodiphosphinate anions $[R_2P(Te)NPR_2]^-$ (22) that are arranged in a trans fashion (Fig. 1). A similar structure has been observed previously in the gallium complex **3** (Scheme 1), although in that case, the metal centres are tetrahedral, whereas the gold centres in the complexes **4a**–**4c** are approximately square-planar.

The solid-state structures of the complexes **4a**–**4c** clearly indicate that the gold centres have been oxidized from Au(I) to Au(III). This oxidation formally involves insertion of Au(I) into a phosphorus–tellurium bond of the ditelluridoimidodiphosphinate ligand, with concomitant reduction of one of the P(V) centres to P(III). Oxidation of Au(I) to Au(III) with reagents such as alkyl halides and halogens is well-documented and known to be facile (23). Oxidation by chalcogens has been observed before in the reaction of AuCN with Na_2Se_5, which produced $[Au_2Se_2(Se_4)_2]^{2-}$ (24) containing an Au_2Se_2 ring similar to the central Au_2Te_2 ring observed in the complexes **4a**–**4c**. However, the current work appears to be the only example of the oxidation of Au(I) to Au(III) by insertion into a phosphorus–chalcogen bond. The formation of the Au_2Te_2 ring in **4a**–**4c**, presumably via the initial production of a gold(I) complex of **1a**–**1c**, parallels the transformation depicted in Scheme 1 for the generation of a Ga_2Te_2 ring, except that the Ga(I) complex is generated by reductive elimination rather than an initial metathesis.

As expected for Au(III) (d^8 configuration), the geometry at the gold centres is square-planar, although there are significant deviations from the ideal 90° angles, which likely arise from the softness of the Au–P and Au–Te bonds (Table 1). Regardless of the deviation from the ideal angles, the sum of the bond angles is near 360° for all three complexes (*trans*-**4a**, 359.93°; *trans*-**4b**, 360.60°; *trans*-**4c**, 359.81°). In each case, the most acute angle is the endocyclic Te(2)–Au(1)–Te(2A) angle [*trans*-**4a**, 78.34(4)°; *trans*-**4b**, 79.18(2)°; *trans*-**4c**, 74.75(4)°], while the widest angles are those involving P(2)–Au(1)–Te(2) [*trans*-**4a**, 98.95(7)°; *trans*-**4b**, 97.43(4)°; *trans*-**4c**, 104.66(6)°]. The increase in this latter angle, and compression of the former angles, correlates with an increase in the bulk of the substituents on the phosphorus centres, and may arise from unfavourable steric interactions between these groups and the central Au_2Te_2 ring. The Au–Te–Au angles in the planar four-membered Au_2Te_2 ring in *trans*-**4a**–**4c** are larger than the corresponding Te–Au–Te angles by 23.3–30.5° leading to transannular distances of 3.20–3.35 Å that are well within the sum of van der Waals radii for two tellurium atoms (4.40 Å). For comparison, the Te—Te separation in the four-

Fig. 1. Thermal ellipsoid diagram of complex *trans*-**4b**. Hydrogen atoms have been removed for clarity. Symmetry transformations used to generate equivalent atoms: –*x*, –*y*, –*z*.

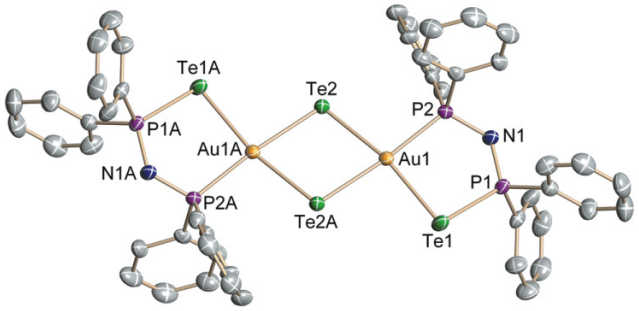

Table 1. Selected bond distances and angles for *trans*-**4a**, *trans*-**4b**, and *trans*-**4c**.

	trans-**4a**	*trans*-**4b**	*trans*-**4c**
Distances [Å]			
Au1—P2	2.365(3)	2.357(2)	2.377(2)
Au1—Te1	2.625(1)	2.6197(8)	2.6267(9)
Au1—Te2	2.628(1)	2.6149(8)	2.649(1)
Au1—Te2A	2.644(1)	2.6446(9)	2.6334(8)
P1—Te1	2.456(3)	2.464(2)	2.474(2)
P1—N1	1.588(8)	1.583(5)	1.589(6)
P2—N1	1.630(7)	1.621(5)	1.634(6)
Te2—Te2A	3.330(8)	3.352(7)	3.2067(9)
Angles [°]			
P2–Au1–Te1	93.82(7)	92.14(4)	94.91(6)
P2–Au1–Te2	98.95(7)	97.43(4)	104.66(6)
Te1–Au1–Te2A	88.82(4)	91.85(3)	85.49(4)
Te2–Au1–Te2A	78.34(4)	79.18(2)	74.75(4)
P2–Au1–Te2A	177.23(6)	173.79(4)	176.96(5)
Te1–Au1–Te2	166.05(3)	168.43(2)	160.02(2)
Au1–Te2–Au1A	101.66(3)	100.82(2)	105.25(2)

© 2008 NRC Canada

Fig. 2. Thermal ellipsoid diagram for one of the two crystallographically independent molecules of the complex *cis*-**4b**. Hydrogen atoms have been removed for clarity.

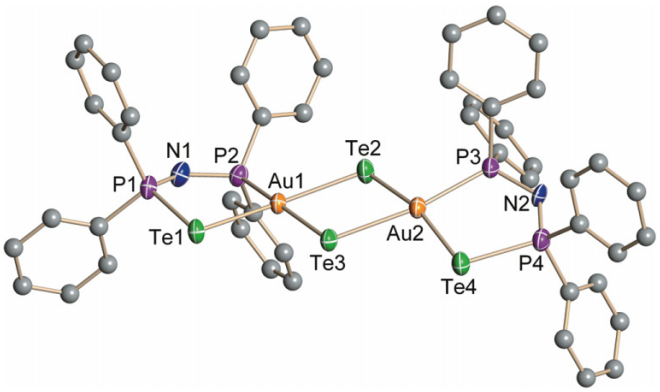

membered Au_2Te_2 rings in AuTeI is 3.235 Å (15). The Au—Te bond lengths fall in a very narrow range for all three complexes [2.6149(8)–2.649(1) Å] and are similar to other reported Au–Te distances (14–20).

During this work, it was found that rapid crystallization of **4b** from concentrated THF or CH_2Cl_2 solutions resulted in the formation of two distinct crystal morphologies: deep red, rhombohedral plates and orange rectangular plates, the latter of which were identified as *trans*-**4b** by determination of the unit cell. An X-ray crystallographic study on a rhombohedral plate revealed the presence of the cis isomer of complex **4b** (Fig. 2). There are two crystallographically independent, but chemically equivalent, molecules of *cis*-**4b** present in the asymmetric unit, which have very similar metrical parameters.

The geometrical parameters of *cis*-**4b** are similar to those observed for *trans*-**4b**. The geometry of the gold(III) centres is best described as distorted square-planar, with significant deviations from the ideal 90° bond angles (Table 2). The most compressed angles are those contained within the central Au_2Te_2 ring [Te2–Au1–Te3, 78.60(5)°; Te2–Au2–Te3, 78.28° (5)], while the widest angles are P2–Au1–Te2, 98.1(1)° and P3–Au2–Te2, 96.2(1)°. The Au–Te bond distances [range: 2.612(2)–2.655(2) Å] are similar to those observed in the trans complexes of **4a**–**4c**. Like the trans complexes of **4a**–**4c**, the four-membered Au_2Te_2 ring of *cis*-**4b** is planar, with the Au–Te–Au bond angles more than 20° larger than the Te–Au–Te angles. As a consequence, the transannular Te–Te distance is 3.35 Å, which is virtually identical to that of *trans*-**4b**. Regardless of the similarity between the cis and trans structures, there is a clear preference in the solid state for the trans isomer. Slow crystallization of all of the complexes **4a**–**4c** consistently resulted in the isolation of the trans isomer in the solid state; only a single crystal morphology was observed and random testing of multiple crystals from each sample using X-ray crystallography provided exclusively the unit cell for the trans isomer. All attempts to isolate crystals of *cis*-**4a** and *cis*-**4c** were unsuccessful.

The solution-state NMR spectra obtained for the complexes **4a**–**4c** revealed the presence of two closely related species in solution. For example, in the ^{31}P NMR spectra, two sets of phosphorus resonances, with very similar chemical shifts and coupling constants, were observed in each case. However, the two species were not present in equal quantities, but in a ratio of nearly 2:1 in each case. The observed spectroscopic data can be explained by the presence of both the cis and trans isomers in solution, with one isomer clearly predominating. While it is tempting to assign the resonances of the major component present in solution to the trans isomer, solid-state NMR studies suggest that it is the cis isomer that predominates in solution.

Table 2. Selected bond distances and angles for *cis*-**4b**, molecule **1**.

Distances [Å]	
Au1—P2	2.345(4)
Au1—Te1	2.627(2)
Au1—Te3	2.645(1)
Au2—Te3	2.655(2)
P1—Te1	2.458(5)
P1—N1	1.58(2)
P3—N2	1.60(1)
Te2—Te3	3.347(2)
Au2—P3	2.357(5)
Au1—Te2	2.612(2)
Au2—Te2	2.620(2)
Au2—Te4	2.634(2)
P4—Te4	2.461(5)
P2—N1	1.61(2)
P4—N2	1.61(2)
Angles [°]	
P2–Au1–Te1	93.3(1)
P2–Au1–Te2	98.1(1)
Te1–Au1–Te3	90.73(5)
Te2–Au1–Te3	78.60(5)
Te2–Au1–Te1	166.40(4)
P2–Au1–Te3	173.8(1)
Au1–Te2–Au2	100.23(4)
P3–Au2–Te–4	92.8(1)
P3–Au2–Te2	96.2(1)
Te3–Au2–Te4	93.77(5)
Te2–Au2–Te3	78.28(5)
Te2–Au2–Te4	166.67(5)
P3–Au2–Te3	171.4(1)
Au1–Te3–Au2	102.03(5)

The solid-state ^{31}P NMR spectrum of a crystalline sample of **4a** grown slowly from dichloromethane is compared with the solution-state spectrum in Fig. 3. It is clear from these two spectra that the isomer that predominates in the solid state is, in fact, the minor component present in solution. The unit cell was determined for multiple crystals from this solid-state sample, and in each case the presence of the trans isomer was confirmed. It should be noted that the solid-state ^{31}P NMR spectrum indicates that there is a small quantity of the cis isomer present in the sample. Nonetheless, crystals of the cis isomer could not be detected visually or by crystallographic methods. In contrast, the solid-state ^{31}P NMR spectrum obtained on a sample of **4b** that had been rapidly crystallized showed that the ratio of the two isomers was largely unchanged from that present in solution. This obser-

© 2008 NRC Canada

Fig 3. (Top) Solution ^{31}P NMR spectrum of complex **4a** showing the mixture of cis and trans isomers. (Bottom) Solid-state ^{31}P NMR spectrum (11 kHz) of slowly crystallized **4a**.

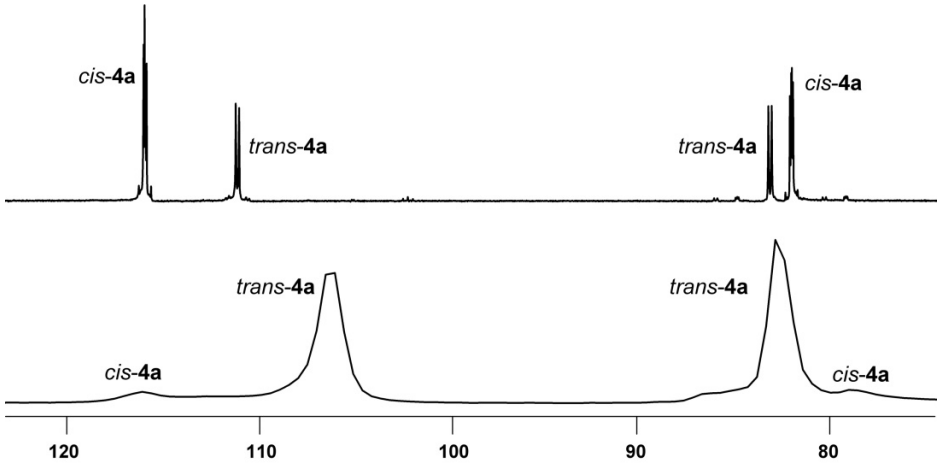

Scheme 3.

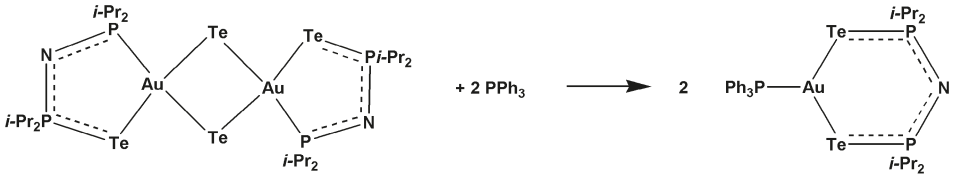

vation, in conjunction with the relative quantities of crystals of *cis*- and *trans*-**4b** noted in rapidly crystallized samples, also suggests that it is the cis isomer that is the major component in solution. Although it is possible that the trans isomer crystallizes preferentially, leaving the cis isomer in solution, the ^{31}P NMR spectrum obtained for a single crystal of *trans*-**4a** was found to be identical to that of bulk samples of **4a**, with the two sets of resonances in a 2:1 intensity ratio. Thus, it is clear that the cis and trans isomers are readily able to interconvert in solution, although the mechanism by which this occurs is not clear.

Finally, we note a minor difference in the ^{31}P NMR spectra of the cis and trans isomers. The trans isomers exhibit one set of mutually coupled doublets, whereas the resonances for the cis isomers exhibit second-order behaviour and appear as more complex multiplets, as observed for the related square-planar complexes *cis*-[M{$Ph_2P(E)NPPh_2$}$_2$] (M = Pd, Pt; E = S, Se) (25).

In light of the facile oxidation of Au(I) to Au(III) observed in this work and the previous observation that Ph_3P stabilizes a homoleptic Au(I) complex of **1a** (13), we decided to investigate the reaction of **4a** with Ph_3P. Addition of Ph_3P to solutions of **4a** resulted in the immediate and quantitative formation of the known complex Ph_3PAu[N{TeP(*i*-$Pr)_2$}$_2$] (13), which was identified by ^{31}P NMR spectroscopy (Scheme 3). To further confirm the identity of the complex, it was shown that the addition of an authentic sample of Ph_3PAu[N{TeP(*i*-$Pr)_2$}$_2$] to the solution used to obtain the NMR spectrum resulted only in an increase in the intensity of the NMR resonances; no additional resonances were observed.

Conclusions

The reaction of the soluble Au(I) complex (THT)AuCl with the ditelluridoimidodiphosphinate complexes **1a–1c** was found to produce the stable dimeric complexes **4a**–**4c**, in which the gold centres have been oxidized to Au(III). This oxidation involves the formal insertion of the gold centres into a phosphorus–tellurium bond and converts a ditelluridoimidodiphosphinate ligand to a monotelluridoimidodiphosphinate with the formation of an Au_2Te_2 ring. The insertion of a metal centre into a P–Te bond has been observed previously in the formation of the gallium complex {Ga(μ-Te)[*i*Pr_2P(Te)NP*i*Pr_2]}$_2$ (3). Taken together, these results indicate that reactions of the ditellurido ligands **1a**–**1c** with metals that have two easily accessible oxidation states, separated by two units, may be complicated by redox chemistry. The reversibility of the redox chemistry that was observed in the current work is unprecedented and may have significant implications in the formation of metal complexes of ditelluridoimidodiphosphinate ligands; in particular, an investigation of the possible occurrence of a similar process for the gallium(III) complex **3** is warranted.

Experimental section

Reagents and general procedures

Solvents were dried and distilled before use: *n*-hexane, THF, and toluene (Na/benzophenone); CH_2Cl_2 (calcium hydride). The ditelluridoimidodiphosphinate complexes **1a** (6), **1b** (5), and **1c** (7) and the complex (THT)AuCl (26) were prepared according to the literature procedures. The handling of air- and moisture-sensitive materials was performed

© 2008 NRC Canada

under an atmosphere of argon gas using standard Schlenk techniques or a glovebox. ^{1}H, ^{31}P, and ^{125}Te NMR spectra were collected using a Bruker AC-300, AMX-300, or DRX-400 spectrometer, and chemical shifts are reported relative to Me_4Si (^{1}H), 85% H_3PO_4 (^{31}P), and Te_2Ph_2 (^{125}Te). Solid-state ^{31}P NMR spectra were collected on a Bruker AM300 wide-bore spectrometer in a 4 mm tube, and chemical shifts are reported relative to $(NH_4)H_2PO_4$. The Analytical Services Laboratory of the Department of Chemistry, University of Calgary, provided elemental analyses.

Preparation of [(*i*-Pr$_2$PNP(Te)*i*-Pr$_2$)Au(μ-Te)]$_2$ (4a)

A solution of **1a** (0.200 g, 0.31 mmol) in CH_2Cl_2 (25 mL) was added to a darkened flask containing a solution of (THT)AuCl (0.100 g, 0.31 mmol) in CH_2Cl_2 (15 mL), resulting in the immediate formation of a dark red solution. The mixture was stirred for 15 min and then filtered through Celite. The solution was stored at –30 °C for 72 h giving dark red crystals of **4a**, suitable for X-ray analysis (0.158 g, 0.11 mmol, 73%). ^{1}H NMR (D_8-THF) δ: 2.35 (m $(CH_3)_2CH$, *trans*-**4a**), 2.25 (m, $(CH_3)_2CH$, *cis*-**4a**), 1.23 (m, $(CH_3)_2CH$, *cis*-**4a**, *trans*-**4a**). ^{31}P NMR (D_8-THF) δ: 113.94 (m, *P*Au, *cis*-**4a**), 108.88 (d, $^{2}J_{PP}$ = 29 Hz, *P*Au, *trans*-**4a**), 80.70 (d, $^{2}J_{PP}$ = 29 Hz, $^{1}J_{TeP}$ = 946 Hz, *P*Te, *trans*-**4a**), 79.15 (m, $^{1}J_{TeP}$ = 948 Hz, *P*Te, *cis*-**4a**). ^{125}Te NMR δ: 292.0 (d, $^{1}J_{TeP}$ = 950 Hz, P*Te*, *trans*-**4a**), 281.0 (d, $^{1}J_{TeP}$ = 943 Hz, P*Te*, *cis*-**4a**), –38.4 (s, μ-Te, *trans*-**4a**), –397.4 (s, μ-Te, *cis*-**4a**). Solid-state ^{31}P NMR δ: 116.17 (*P*Au, *cis*-**4a**), 106.15 (*P*Au, *trans*-**4a**), 82.27 (*P*Te, *trans*-**4a**), 78.28 (*P*Te, *cis*-**4a**). Anal. calcd. for $C_{24}H_{56}Au_2N_2P_4Te_4$ (%): C 20.58, H 4.03, N 2.00; found: C 21.06, H, 3.94, N 1.95.

Preparation of [(Ph$_2$PNP(Te)Ph$_2$)Au(μ-Te)]$_2$ (4b)

A solution of **1b** (0.243 g, 0.31 mmol) in CH_2Cl_2 (25 mL) was added to a darkened flask containing a solution of (THT)AuCl (0.100 g, 0.31 mmol) in CH_2Cl_2 (15 mL), resulting in the immediate formation of a dark green solution. The mixture was stirred for 15 min and then filtered through Celite, concentrated to ~15 mL and then stored at –30 °C for 24 h giving crystalline **4b** (0.112 g, 0.07 mmol, 43%). ^{1}H NMR (D_8-THF) δ: 7.69, 7.35 (m, Phenyl-*H*; *cis*-, *trans*-**4b**). ^{31}P NMR (CD_2Cl_2) δ: 78.29 (m, *P*Au, *cis*-**4b**), 70.21 (d, $^{2}J_{PP}$ = 80 Hz, *P*Au, *trans*-**4b**), 30.41 (m, $^{1}J_{TeP}$ = 982 Hz, *P*Te, *cis*-**4b**), 30.22 (d, $^{2}J_{PP}$ = 80 Hz, $^{1}J_{TeP}$ = 982 Hz, *P*Te, *trans*-**4b**). Anal. calcd. for $C_{48}H_{40}Au_2N_2P_4Te_4$ (%): C 34.46, H 2.41, N 1.67; found: C 34.56, H, 2.19, N 1.61. X-ray quality crystals of *trans*-**4b** were grown by slow evaporation of a solution of the complex in CH_2Cl_2. A suitable crystal for X-ray analysis of the complex *cis*-**4b** was obtained from a concentrated solution of the complex in THF.

Preparation of [(*t*-Bu$_2$PNP(Te)*t*-Bu$_2$)Au(μ-Te)]$_2$ (4c)

A solution of **1c** (0.218 g, 0.31 mmol) in CH_2Cl_2 (30 mL) was added to a darkened flask containing a solution of (THT)AuCl (0.100 g, 0.31 mmol) in CH_2Cl_2 (30 mL), resulting in the immediate formation of a dark red solution. The mixture was stirred for 15 min and then filtered through Celite. The solution was concentrated to ~30 mL and stored at –30 °C for 72 h giving crystalline **4c** (0.080 g, 0.05 mmol, 34%). ^{1}H NMR (CD_2Cl_2) δ: 1.39, (m, $C(CH_3)_3$, *cis*-**4c**), 1.18 (m, $C(CH_3)_3$, *trans*-**4c**). ^{31}P NMR (CD_2Cl_2) δ: 129.17 (m, *P*Au, *cis*-**4c**), 124.14 (d, $^{2}J_{PP}$ = 27 Hz, *P*Au, *trans*-**4c**), 94.71 (d, $^{2}J_{PP}$ = 27 Hz, $^{1}J_{TeP}$ = 980 Hz, *P*Te, *trans*-**4c**), 94.02 (m, $^{1}J_{TeP}$ = 980 Hz, *P*Te, *cis*-**4c**). Anal. calcd. for $C_{32}H_{72}Au_2N_2P_4Te_4$ (%): C 25.40, H 4.80, N 1.85; found: C 25.43, H, 4.48, N 1.75. X-ray quality crystals of *trans*-**4c** were grown by slow evaporation of a solution of the complex in CH_2Cl_2.

X-ray structural analyses

Crystal data for *trans*-**4a**, *trans*-**4b**, *cis*-**4b**, and *trans*-**4c** are summarized in Table 3.[3] A suitable crystal of the complex was selected, coated in Paratone oil, and mounted on a glass fibre. Data were collected at 173 K (273 K = 0 °C) on a Nonius Kappa CCD diffractometer using Mo Kα radiation (λ = 0.71073 Å) via ω and φ scans. The unit-cell parameters were calculated and refined from the full data set. Crystal cell refinement and data reduction were carried out using the Nonius DENZO package. After data reduction, the data were corrected for absorption using SORTAV (27). The structures were solved using the automated Patterson routine within SHELXS-97 (28) and refinement was carried out on F^2 against all independent reflections by the full-matrix least-squares method using the SHELXL-97 program (29). The hydrogen atoms were calculated geometrically and were riding on their respective atoms unless otherwise noted. For the complexes *trans*-**4a**, *trans*-**4b**, and *trans*-**4c**, all non-hydrogen atoms were refined with anisotropic thermal parameters. In each case, only one-half of the molecule was located in the difference Fourier map as the molecule is situated around a centre of symmetry. In the case of complex *cis*-**4b**, the crystals diffracted weakly, and so a relatively poor-quality dataset was obtained. The complex crystallizes with two chemically equivalent, but crystallographically independent, molecules in the asymmetric unit. Four of the phenyl substituents were disordered and each was modelled as an isotropic 50:50 mixture with geometric restraints; all other phenyl rings were constrained to be regular hexagons and were refined with isotropic thermal displacement parameters. The lattice-bound THF molecules were poorly ordered, and each was modelled as an isotropic 50:50 mixture with geometric restraints. Due to the low quality of the data, only the Au, Te, P, and N atoms making up the core of the structure were refined with anisotropic thermal displacement parameters.

Acknowledgements

We thank Jamie Ritch for collection of the X-ray data for the complex *cis*-**4b** and the Natural Sciences and Engi-

[3] Supplementary data for this article are available on the journal Web site (canjchem.nrc.ca) or may be purchased from the Depository of Unpublished Data, Document Delivery, CISTI, National Research Council Canada, Ottawa, ON K1A 0R6, Canada. DUD 3762. For more information on obtaining material, refer to cisti-icist.nrc-cnrc.gc.ca/irm/unpub_e.shtml. CCDC 680164–680167 contain the crystallographic data for this manuscript. These data can be obtained, free of charge, via www.ccdc.cam.ac.uk/conts/retrieving.html (Or from the Cambridge Crystallographic Data Centre, 12 Union Road, Cambridge CB2 1EZ, UK; fax +44 1223 336033; or deposit@ccdc.cam.ac.uk).

© 2008 NRC Canada

Table 3. Crystallographic data for complexes *trans*-**4a**, *trans*-**4b**, *cis*-**4b**, and *trans*-**4c**.

Crystal	*trans*-**4a**	*trans*-**4b**	*cis*-**4b**	*trans*-**4c**
Empirical formula	$C_{24}H_{56}Au_2N_2P_4Te_4$	$C_{48}H_{40}Au_2N_2P_4Te_4$	$C_{48}H_{40}Au_2N_2P_4Te_4{\cdot}(C_4H_8O)$	$C_{32}H_{72}Au_2N_2P_4Te_4$
Formula mass	1400.92	1673.03	1745.14	1513.13
Colour, habit	Red, block	Orange, plate	Red, plate	Orange, plate
Crystal size (mm)	0.14 × 0.14 × 0.08	0.08 × 0.06 × 0.04	0.10 × 0.08 × 0.04	0.10 × 0.08 × 0.05
Crystal system	Triclinic	Triclinic	Triclinic	Triclinic
Space group	*P*-1	*P*-1	*P*-1	*P*-1
Z	1	1	4	1
a (Å)	8.1864(7)	9.8966(2)	12.1688(3)	8.3382(5)
b (Å)	9.7477(8)	11.0948(3)	19.5417(5)	11.2270(5)
c (Å)	13.901(1)	12.5300(4)	24.6410(6)	13.6625(9)
α (°)	108.625(5)	105.451(2)	108.317(1)	72.509(3)
β(°)	92.495(4)	93.450(2)	90.033(2)	76.957(3)
γ (°)	112.270(3)	110.369(2)	102.362(1)	70.899(3)
Collection ranges	$-9 \le h \le 9$ $-11 \le k \le 11$ $-16 \le l \le 16$	$-12 \le h \le 12$; $-14 \le k \le 14$; $-16 \le l \le 16$	$-12 \le h \le 12$; $-20 \le k \le 20$; $-25 \le l \le 25$	$-10 \le h \le 10$; $-14 \le k \le 14$; $-17 \le l \le 17$
Volume (Å^3)	955.49(14)	1225.23(6)	5419.2(2)	1141.13(12)
$D_{calcd.}$ (Mg/m^3)	2.435	2.267	2.139	2.202
μ (mm^{-1})	10.846	8.480	7.675	9.090
F(000)	640	768	3232	704
θ range for data collection (°)	3.15–25.03	2.57–27.50	2.62–21.97	2.76–26.37
Observed reflections	13619	22307	81792	18224
Independent reflections	3349 (R_{int} = 0.092)	5603 (R_{int} = 0.070)	13210 (R_{int} = 0.105)	4659 (R_{int} = 0.093)
Data/restraints/ parameters	3349/0/171	5603/0/271	13210/125/604	4659/0/211
Maximum shift/error	0.00	0.00	0.00	0.00
GooF on F^2	1.046	1.030	1.041	1.035
Final *R* indices [$I > 2\sigma(I)$][a]	0.0440, 0.1005	0.0367, 0.0745	0.0531, 0.1125	0.0445, 0.0983
R indices (all data)[b]	0.0598, 0.1089	0.0554, 0.0817	0.0925, 0.1298	0.0703, 0.1106
Largest diff. peak and hole (e Å^{-3})	1.519 and –3.275	1.046 and –2.216	2.194 and –1.953	1.251 and –3.497

[a] $R_1 = [\Sigma||F_o|-|F_c||]/[\Sigma|F_o|]$ for $[I > 2\sigma(I)]$.
[b] $wR_2 = \{[\Sigma w(F_o^2-F_c^2)^2]/[\Sigma w(F_o^2)^2]\}^{1/2}$ (all data).

neering Research Council of Canada (NSERC) for financial support.

References

1. I. Haiduc. *In* Comprehensive coordination chemistry II. *Edited by* J.A. McCleverty and T.J. Meyer. Elsevier Ltd., Amsterdam. 2003. pp. 323–347.
2. C. Silvestru and J.E. Drake. Coord. Chem. Rev. **223**, 117 (2001).
3. T.Q. Ly and J.D. Woollins. Coord. Chem. Rev. **176**, 451 (1998).
4. For selected examples, see: (*a*) M. Afzaal, D. Crouch, M.A. Malik, M. Motevalli, P. O'Brien, J.H Park, and J.D. Woollins. Eur. J. Inorg. Chem. 171 (2004); (*b*) M. Afzaal, D. Crouch, M.A. Malik, M. Motevalli, P. O'Brien, and J.H. Park. J. Mater. Chem. **13**, 2761 (2003); (*c*) D.J. Crouch, P.M. Hatton, M. Helliwell, P. O'Brien, and J. Raftery. Dalton Trans. 2761 (2003).
5. G.G. Briand, T. Chivers, and M. Parvez. Angew. Chem., Int. Ed. **41**, 3468 (2002).
6. T. Chivers, D.J. Eisler and J.S. Ritch. Dalton Trans. 2675 (2005).
7. J.S. Ritch, T. Chivers, D.J. Eisler, and H.M. Tuononen. Chem. Eur. J. **13**, 4643 (2007).
8. J.S. Ritch, T. Chivers, M. Afzaal, and P. O'Brien. Chem. Soc. Rev. **30**, 1622 (2007).
9. T. Chivers, D.J. Eisler, J.S. Ritch, and H.M. Tuononen. Angew. Chem., Int. Ed. **44**, 4953 (2005).
10. (*a*) J. Konu, T. Chivers, and H.M. Tuononen. Chem. Commun. 1634 (2006); (*b*) J. Konu, T. Chivers, and H.M. Tuononen. Inorg. Chem. **45**, 10678 (2006).
11. S.S. Garje, J.S. Ritch, D.J. Eisler, M. Afzaal, P. O'Brien, and T. Chivers. J. Mater. Chem. **16**, 966 (2006).
12. S.S. Garje, D.J. Eisler, J.S. Ritch, M. Afzaal, P. O'Brien, and T. Chivers. J. Am. Chem. Soc. **128**, 3120 (2006).
13. M.C. Copsey, A. Panneerselvam, M. Afzaal, T. Chivers, and P. O'Brien. Dalton Trans. 1528 (2007).
14. M. Afzaal, D. J. Crouch, P. O'Brien, J. Raftery, P. J. Skabara, A. J. P. White, and D. J. Williams. J. Mater. Chem. **14**, 233 (2004).
15. J. Fenner and D. Mootz. J. Solid State Chem. **24**, 367 (1978).
16. H. M. Haendler, D. Mootz, A. Rabenau and G. Rosenstein. J. Solid State Chem. **10**, 175 (1974).
17. P.J. Bonasia, D.E. Gindelberger, and J. Arnold. Inorg. Chem. **32**, 5126 (1993).
18. R.C. Haushalter. Angew. Chem., Int. Ed. **24**, 432 (1985).
19. C.J. Warren, D.M. Ho and A.B. Bocarsly. J. Am. Chem. Soc. **115**, 6416 (1993).
20. D.M. Smith, L.C. Roof, M.A. Ansari, J.M. McConnachie, J.C. Bollinger, M.A. Pell, R.J. Salm, and J.A. Ibers. Inorg Chem. **35**, 4999 (1996).
21. M.C. Copsey and T. Chivers. Chem. Commun. 4938 (2005).

© 2008 NRC Canada

22. J.S. Ritch and T. Chivers. Dalton Trans. 957 (2008).
23. (*a*) J.P. Fackler, Jr. Polyhedron. **16**, 1 (1997); (*b*) W.E. van Zyl, J.M. Lopez-de-Luzuriaga, J.P. Fackler, Jr., and R.J. Staples. Can. J. Chem. **79**, 896 (2001); (*c*) D. Schneider, O. Schuster, and H. Schmidbaur. Dalton Trans. 1940 (2005).
24. M.G. Kanatzidis and S.P. Huang. Inorg. Chem. **28**, 4667 (1989).
25. P. Bhattacharyya, A.M.Z. Slawin, D.J. Williams, and J.D. Woollins. J. Chem. Soc. Dalton Trans. 3189 (1995).
26. R. Uson, A. Laguna, and M. Laguna. Inorg. Synth. **26**, 85 (1986).
27. (*a*) R.H. Blessing. Acta Cryst. **A51**, 33 (1995); (*b*) R.H. Blessing. J. Appl. Cryst. **30**, 421 (1997).
28. G.M. Sheldrick, SHELXS-97 [computer program]. Program for solution of crystal structures, University of Göttingen, Germany, 1997.
29. G.M. Sheldrick, SHELXL-97 [computer program]. Program for refinement of crystal structures, University of Göttingen, Germany, 1997.

© 2008 NRC Canada

Catalytic synthesis of carbon nanotubes from the decomposition of methane over a Ni–Co/La_2O_3 catalyst[1]

Long Chen, Haitao Liu, Keli Yang, Jiankang Wang, and Xiaolai Wang

Abstract: The production of multi-walled carbon nanotubes (MWNTs) by the catalytic chemical vapour deposition (CCVD) method was examined over a series of Ni–Co/La_2O_3 catalysts with methane as the carbon source. The catalyst composition and the reaction conditions were optimized by analyzing the effluent gas with gas chromatography. Various techniques, such as X-ray diffraction (XRD), Transmission electron microscopy (TEM), Raman spectra, and Thermal gravimetric analysis (TGA) were used to characterize the catalysts and products. The results indicate that the unreduced catalyst 30Ni–10Co/La_2O_3 showed the highest activity for methane decomposition, and the highest carbon yield, being 624.2%, was obtained over this catalyst at 700 °C after 60 min of reaction with hydrogen as carrier gas. TGA results suggest that the purity of carbon nanotubes (CNTs) can reach up to 98 wt% after a single-step purification by hydrochloric acid.

Key words: carbon nanotubes, catalytic chemical vapour deposition, methane decomposition, Ni–Co/La_2O_3 catalyst.

Résumé : On a examiné la production de nanotubes de carbones à parois multiples (NTCPM) par la méthode de déposition de vapeur chimique catalytique (DVCC) sur une série de catalyseurs de Ni-Co/La_2O_3, en n'utilisant que du méthane comme source de carbone. On a optimisé les conditions réactionnelles et la décomposition du catalyseur en procédant à l'analyse des gaz effluents par chromatographie gazeuse. La caractérisation des catalyseurs et des produits a été effectuée en utilisant diverses techniques, tels les patrons de diffusion des rayons X (DRX), la microscopie de transmission électronique (MTE), la spectrométrie Raman et l'analyse par thermogravimétrie (ATG). Les résultats indiquent que les catalyseurs non réduits, 30Ni-10Co/La_2O_3 présentent la plus grande activité pour la décomposition du méthane et le rendement le plus élevé en carbone, 624,2%, a été obtenu sur ce catalyseur, à 700 °C, après 60 minutes de réaction avec de l'hydrogène comme gaz porteur. Les résultats de ATG suggèrent que la pureté des nanotubes de carbone (NTC) peut atteindre 98% en poids après une seule purification avec de l'acide chlorhydrique.

Mots-clés : nanotubes de carbone, déposition de vapeur chimique catalytique, décomposition du méthane, catalyseur de Ni-Co/La_2O_3.

[Traduit par la Rédaction]

Introduction

Carbon nanotubes have been widely studied not only for their unique structural, electronic, and mechanical properties but also for their potential applications in electronic devices, displays, and in the field of hydrogen storage (1). To realize various applications of CNTs, large quantities of high-quality CNTs are inevitably necessary. Over the past decade, different production techniques have been developed, including arc discharge (2, 3), laser ablation (4, 5), and chemical vapour deposition (6–8). Among these techniques, the catalytic chemical vapour deposition (CCVD) method is regarded as the most promising method to commercialize the CNT growth owing to the advantages in its low cost, high yield, and easy control (9–11).

In the CCVD method, CNTs are produced from the thermal decomposition of the carbon-containing molecules on desirable metal catalyst (commonly, Fe, Co, and Ni). For nanotube nucleation and growth, it is crucial to select an effective catalyst with the appropriate size of active metal. Mixed metal oxides as perovskites have been recently investigated as the precursor of catalyst for CNT growth (12–16). Liang et al. (14) reported bulk synthesis of CNTs from CH_4 using La_2NiO_4 as the catalyst precursor. Liu et al. (13, 16) have utilized $LaCoO_3$ and $LaFeO_3$ as catalyst precursors for CNT growth. They obtained multi-walled carbon nanotubes on $LaCoO_3$ and bundles of single-walled carbon nanotubes on $LaFeO_3$. With these kinds of catalyst, some important advantages of preparing nanotubes are obvious. The product yield is higher and the reaction temperature is lower, com-

Received 10 October 2007. Accepted 15 April 2008. Published on the NRC Research Press Web site at http://canjchem.nrc.ca on 11 June 2008.

L. Chen, H. Liu, K. Yang, J. Wang, and X. Wang.[2] State Key Laboratory for Oxo Synthesis and Selective Oxidation, Lanzhou Institute of Chemical Physics, Chinese Academy of Sciences, Lanzhou 730000, P.R. China.
L. Chen, H. Liu, K. Yang, and J. Wang. The Graduate University of the Chinese Academy of Sciences, Beijing 100039, P.R. China.

[1]This article is part of a Special Issue dedicated to Professor R. Puddephatt.

[2]Corresponding author (e-mail address: chenlong2000_1984@126.com).

 doi:10.1139/V08-077 © 2008 NRC Canada

Table 1. Summary of reaction conditions and results.

Catalysts	Ni loading (wt%)	Co loading (wt%)	Reduction (yes or no)	Carrier gas	Carbon yield (%)
$40Ni/La_2O_3$	40	0	No	N_2	431
$30Ni–10Co/La_2O_3$	30	10	No	N_2	552
$20Ni–20Co/La_2O_3$	20	20	No	N_2	515.4
$10Ni–30Co/La_2O_3$	10	30	No	N_2	207.8
$40Co/La_2O_3$	0	40	No	N_2	290.4
$40Ni/La_2O_3$	40	0	Yes	N_2	350.2
$40Co/La_2O_3$	0	40	Yes	N_2	0
$30Ni–10Co/La_2O_3$	30	10	Yes	N_2	185.8
$40Ni/La_2O_3$	40	0	No	H_2	554.2
$40Co/La_2O_3$	0	40	No	H_2	190.4
$30Ni–10Co/La_2O_3$	30	10	No	H_2	624.2

pared with other methods. The diameter of the CNTs is uniform and their purification and separation is easy because La_2O_3 is easily dissolved in hydrochloric acid, so most of the residual catalyst can be eliminated from the CNT product.

In the present work, novel $Ni–Co/La_2O_3$ catalysts have been prepared to produce CNTs by the CCVD method with methane as the carbon source. By analyzing the effluent gas with gas chromatography, the catalytic activities of these catalysts were determined. The effects of Ni and Co content, hydrogen-reduction pretreatment, and carrier gas on the activity and stability of the catalysts were also investigated.

Experimental

Catalysts preparation

The catalysts were prepared by combustion synthesis, with citric acid as a foaming and combustion additive. The designation and metal loading of the catalysts studied herein are given in Table 1. For all the catalysts, the total Ni and Co metal loading was adjusted to 40 wt%. A high metal loading was chosen to obtain a longer catalytic activity (17). The catalysts were prepared as follows: to aqueous solutions of $Ni(NO_3)_2·6H_2O$, $Co(NO_3)_2·6H_2O$, and $La(NO_3)_3·6H_2O$ having the required amount of metals, stoichiometry amount of citric acid was added. The resulting gel was evaporated at 80 °C under vacuum until a viscous syrup was formed. The viscous syrup was dried at 120 °C for 5 h, and a foamy material was obtained. Then, the foamy material was directly burned in air at 500 °C for 1 h and subsequently calcined at 800 °C for 5 h, and finally ground into a fine powder.

Carbon nanotubes synthesis

Catalytic tests were carried out in a fixed-bed horizontal quartz tube reactor with an outer diameter of 30 mm and a length of 600 mm. Initially, 50 mg of catalyst powder was sprayed uniformly into a quartz boat, which was inserted in the center of the reactor. Two reaction modes were adopted. First, the unreduced catalysts were directly used to decompose methane at 700 °C. Second, the catalysts were first reduced by hydrogen at 700 °C for 30 min and then used to decompose methane at the same temperature. N_2 and H_2 were used as carrier gas with the flows of the mixture CH_4/N_2 and CH_4/H_2 of 30/30 ml/min and 30/6 ml/min, respectively. The reaction lasted for 60 min during which the effluent gas was sampled out for the gas chromatography analysis. After the reaction, the system was cooled to room temperature under N_2 protection. The as-prepared product was removed from the reactor, purified in concentrated hydrochloride solution and filtered. It was then washed with distilled water and dried at 120 °C.

The carbon yield was calculated based on the following equation: Carbon yield (%) = 100 $(M_{total} - M_{cat})/M_{cat}$, where M_{total} denotes the total mass of carbon product and catalyst after 60 min of reaction and M_{cat} is the mass of catalyst before reaction.

Materials characterization

The XRD patterns of the catalysts were recorded on a PANalytical X Pert PRO with Cu radiation at a scanning rate of 4°/min. The TEM images of samples were obtained on a JEOL-1200EX TEM operating at 80 KV. The TGA profiles were obtained on a PerkinElmer Diamond TG/DTA under a flow of air with the heating rate of 10 °C/min. Raman studies were performed on a Renishaw 1000 micro-Raman spectrometer using Ar^+ laser with the excitation of 514.5 nm.

Results and discussion

Characterization of the catalysts

Figure 1 shows the XRD patterns of the catalysts before reduction. In the XRD pattern of the catalyst $40Ni/La_2O_3$ (Fig. 1*a*), the diffraction peaks at 32.8°, 47.3° and 58.7° were those of $LaNiO_3$. The diffraction peaks due to NiO were observed at 2θ = 37.2°, 43.3°, and 62.9°. For the catalyst $40Co/La_2O_3$ (Fig. 1*b*), the diffraction peaks at 32.9°, 33.3°, and 47.5° were characteristic lines of $LaCoO_3$, and the diffraction peaks at 31.3°, 36.9°, and 65.4° corresponded to Co_3O_4 phase. In the XRD pattern of the catalyst $30Ni–10Co/La_2O_3$ (Fig. 1*c*), the diffraction peaks at 32.8°, 33.1°, and 47.4° were attributed to $LaNi_{0.6}Co_{0.4}O_3$. The presence of NiO in the catalyst was also observed. From the XRD patterns, it can be observed that the catalysts mainly exist in the form of perovskites $LaNiO_3$, $LaCoO_3$, or $LaNi_{0.6}Co_{0.4}O_3$ and metal oxides NiO or Co_3O_4. This is because at high calcination temperature, the transition metals and the rare earth ox-

© 2008 NRC Canada

Fig. 1. XRD patterns of the catalysts before reduction: (*a*) 40Ni/La_2O_3, (*b*) 40Co/La_2O_3, and (*c*) 30Ni–10Co/La_2O_3.

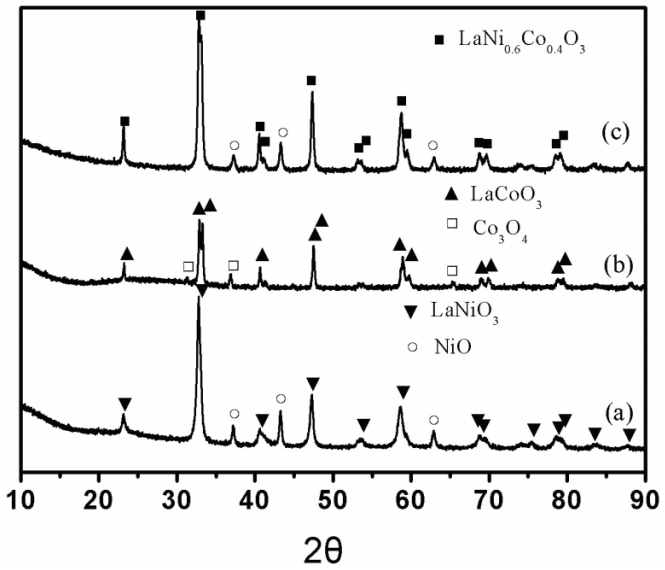

Fig. 2. XRD patterns of the catalysts after reduction: (*a*) 40Co/La_2O_3 and (*b*) 30Ni–10Co/La_2O_3.

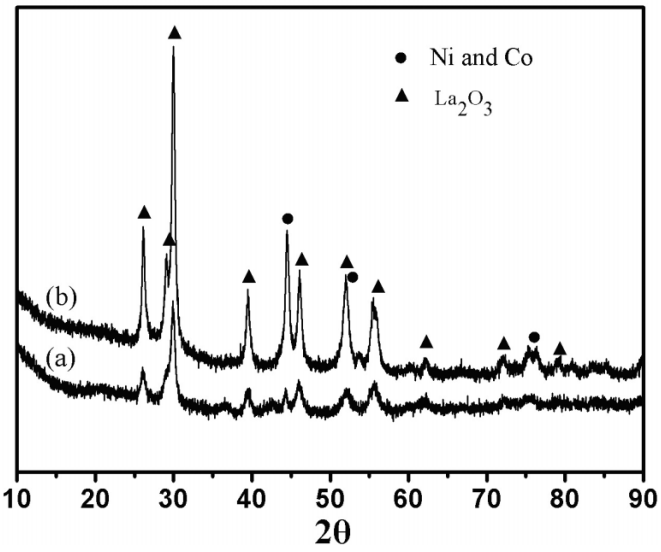

ide La_2O_3 can easily form perovskites, as already reported previously (12–16).

Figure 2 shows the XRD pattern of the catalysts 40Co/La_2O_3 and 30Ni–10Co/La_2O_3 after reduction. Compared with the unreduced catalyst (Fig. 1), the diffraction peaks due to perovskites $LaCoO_3$ and $LaNi_{0.6}Co_{0.4}O_3$ disappeared, and a new series of diffraction lines attributed to La_2O_3 appeared for the reduced catalysts. Ni and Co metal peaks were also observed in the samples at $2\theta = 44.5°$, 52.0°, and 76.3°, indicating the presence of Ni and Co particles. It is considered that the rare earth oxide La_2O_3 can prevent the transition metal from agglomerating and promote the dispersion of the nano-scale particle after reduction, which is frequently responsible for CNT growth (14).

Performance of the catalysts

Effects of Ni and Co content on carbon yield

The CNT synthesis was carried out by decomposition of CH_4 at 700 °C for 60 min. The yield of deposited carbon was measured by varying the content of Ni and Co in the Ni–Co/La_2O_3 catalysts to examine the effect of the catalyst composition on the activity of the catalysts. All the catalysts studied were not reduced before reaction, and N_2 was used as carrier gas. As shown in Table 1, with the nickel content in the catalyst increasing, the carbon yield slightly decreased from 290.4% to 207.8% over the catalysts 40Co/La_2O_3 and 10Ni–30Co/La_2O_3, respectively. Then, it increased to 515.4% over the catalyst 20Ni–20Co/La_2O_3. The highest carbon yield, being 552%, was obtained for the catalyst 30Ni–10Co/La_2O_3. Nevertheless, the carbon yield declined to 431% for the catalyst 40Ni/La_2O_3. Compared with the monometallic catalysts 40Ni/La_2O_3 and 40Co/La_2O_3, the bimetallic catalysts showed higher carbon yield except the catalyst 10Ni–30Co/La_2O_3. This suggests that the bimetallic catalysts are more active than the monometallic ones. The results reported here are consistent with the previous work (18–20). The catalytic activity of bimetallic catalyst is superior to that of monometallic catalyst because of its catalytic synergies in producing CNTs from CH_4.

Effects of hydrogen-reduction pretreatment

It is well-documented that prior reduction of catalysts with hydrogen is not necessary during the synthesis of CNTs by CCVD method, because it is commonly known that metal oxides will be reduced in the reaction environment by means of methane gas (21, 22). However, to the best of our knowledge, few studies reported the effects of hydrogen-reduction pretreatment on the activity of the catalysts. In this study, the effects of hydrogen-reduction pretreatment on the activity of the catalysts were examined over two monometallic catalysts 40Ni/La_2O_3 and 40Co/La_2O_3 and one bimetallic catalyst 30Ni–10Co/La_2O_3. Figure 3 shows the change of the methane conversion with time on stream in the methane decomposition at 700 °C. All the catalysts studied were not reduced before reaction, and N_2 was used as carrier gas. It should be pointed out that at the first contact of methane with these catalysts, no product was observed. After a period of time, the product H_2 was detected by chromatography, and we attributed this point to the beginning of the reaction. The contact of methane with these catalysts causes reduction of the metal-oxide species into small metal particles, which grow CNTs (21, 22). It is likely that there is a minimum particle size required for transition metals to grow CNTs through methane decomposition (23). At the first contact of methane with the catalysts, highly dispersed metal-oxide particles are reduced and aggregated into small metal particles. As soon as the particle size of the metals reaches that required to grow CNTs, the metal particles decompose methane to grow CNTs. As shown in Fig. 3, for all the catalysts, methane decomposition proceeded selectively to form hydrogen only as a gaseous product. Methane conversion was the highest at the beginning of the reaction, and it gradually decreased and finally terminated. It was also found that the catalytic activity was strongly dependent on the type of the catalysts and decreased in the order of 30Ni–10Co/La_2O_3

© 2008 NRC Canada

Fig. 3. Change of the methane conversion with time on stream in the methane decomposition over the unreduced catalysts at 700 °C. Carrier gas: N_2.

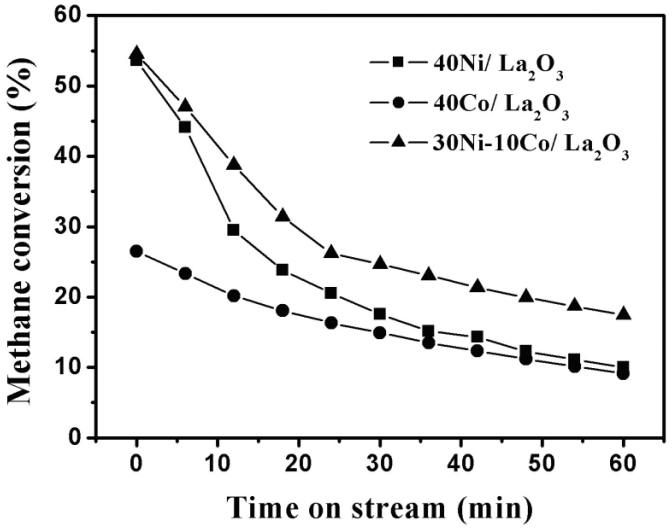

Fig. 4. Change of the methane conversion with time on stream in the methane decomposition over the reduced catalysts at 700 °C. Carrier gas: N_2.

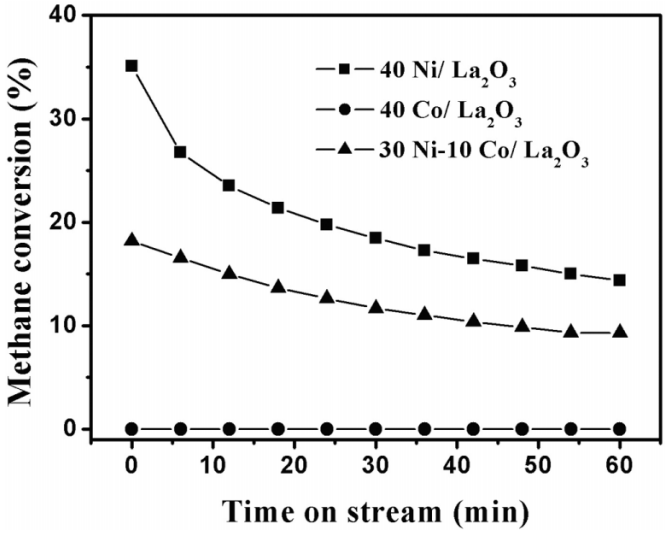

> $40Ni/La_2O_3$ > $40Co/La_2O_3$, which was in accordance with the carbon yield shown in Table 1.

For comparison, another series of the catalysts that had been reduced by hydrogen for 30 min before reaction were examined for methane decomposition, as shown in Fig. 4. The catalytic activity of the reduced catalysts decreased notably compared with that of the unreduced catalysts shown in Fig. 3. The catalyst $40Co/La_2O_3$ was almost inactive in methane decomposition. Correspondingly, the carbon yield declined to 185.8%, 350.2%, and 0 (Table 1) for the catalysts $30Ni–10Co/La_2O_3$, $40Ni/La_2O_3$, and $40Co/La_2O_3$, respectively. According to the experimental results presented above, we concluded that hydrogen-reduction pretreatment had a suppressing effect on the activity of the catalysts. The suppressing effect might be ascribed to the following reasons. First, the metal particles in the catalysts were aggregated during the period of the reduction to form large particles. According to Scherrer equation, the sizes of metal particles reached up to 23 and 26 nm for the catalysts $30Ni–10Co/La_2O_3$ and $40Co/La_2O_3$, respectively, after reduction (Fig. 2). Perhaps, these large particles caused the low catalytic activity for CNT synthesis and even no catalytic activity in the case of $40Co/La_2O_3$ (24, 25). Second, the lattice oxygen on the unreduced catalysts had positive effect on the activity of the catalysts, in presence of which the simultaneous catalyst reduction provided energy for the endothermic methane decomposition and consumed part of hydrogen and carbon (to the H_2O and CO), making the equilibrium of methane decomposition shift to the direction of hydrogen and CNT production in a much higher reaction rate (21).

Effects of carrier gas

In the CCVD method, H_2 is often used as carrier gas, especially when a liquid hydrocarbon like xylene, toluene, or benzene is used as the carbon source. Here, the effects of the H_2 as carrier gas on the activity of the catalysts were examined. Figure 5 shows the change of the methane conversion with time on stream in the methane decomposition at

Fig. 5. Change of the methane conversion with time on stream in the methane decomposition over the unreduced catalysts at 700 °C with H_2 as Carrier gas. Inset shows the conversion of methane as a function of time on stream in the methane decomposition over the unreduced catalyst $30Ni–10Co/La_2O_3$, with N_2 and H_2 as carrier gas, respectively.

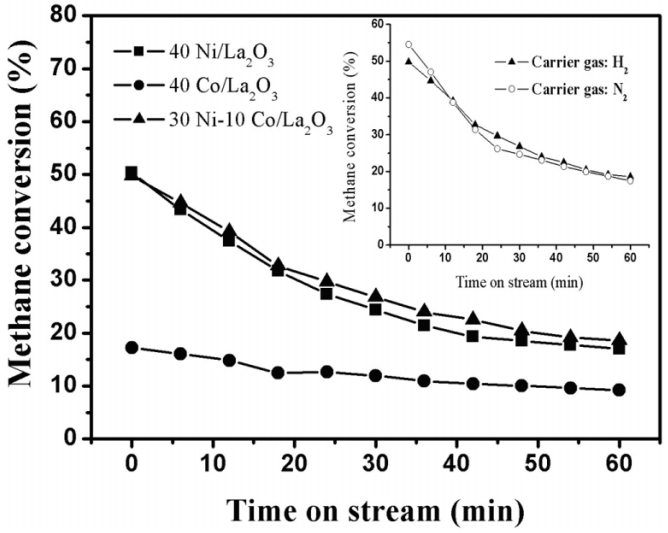

700 °C. All the catalysts studied were not reduced before reaction, and H_2 was used as carrier gas. As shown in Fig. 5, the catalytic activity of the catalysts also decreased in the order of $30Ni–10Co/La_2O_3$ > $40Ni/La_2O_3$ > $40Co/La_2O_3$. Compared with N_2 as carrier gas (Fig. 5, inset), although the initial activity of the catalyst $30Ni–10Co/La_2O_3$ decreased, the stability of the catalyst was slightly improved with H_2 as carrier gas. Generally, in the CCVD method, CNT growth involves the decomposition of hydrocarbons on one side of a nanometer-sized catalyst particle, subsequent diffusion of carbon atoms through the volume or surface of the particle, and then precipitation of CNTs on its other side (8). For continuous growth of CNTs, the decomposition rate of hy-

© 2008 NRC Canada

Fig. 6. TEM images of as-grown CNTs produced by catalytic decomposition of CH_4 at 700 °C over (*a*) and (*b*) 40Ni/La_2O_3, (*c*) and (*d*) 40Co/La_2O_3, (*e*) and (*f*) 30Ni–10Co/La_2O_3. All the catalysts used were not reduced before reaction, and the carrier gases were N_2 for (*a*) (*c*) (*e*) and H_2 for (*b*) (*d*) (*f*).

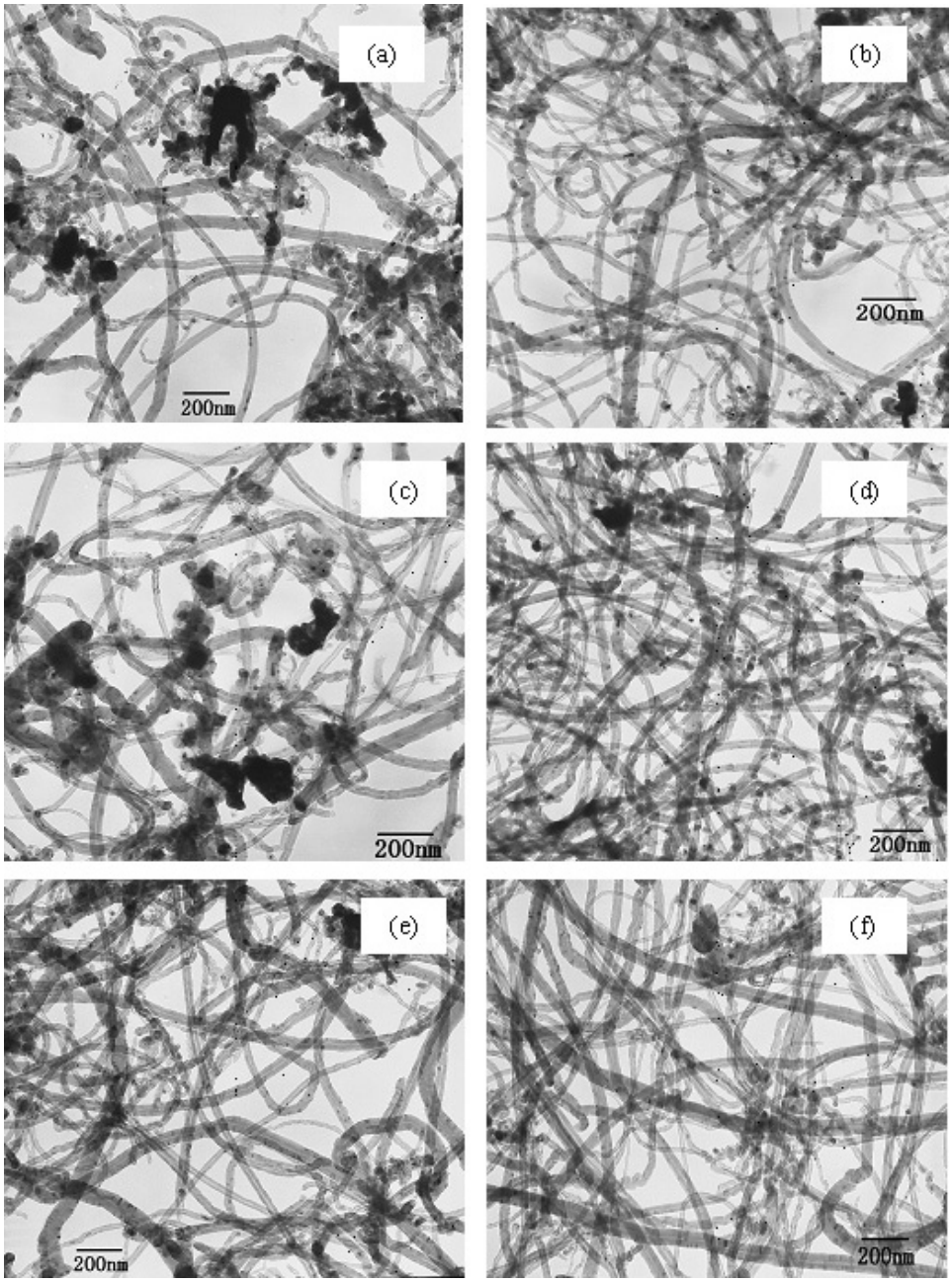

drocarbons must match well with the diffusion rate of carbon atoms. The formation of encapsulated carbon is regarded as the main reason for the deactivation of the catalysts. The results in Fig. 5 imply that the role of H_2 as carrier gas is to limit or alleviate the poisoning of the metal catalysts by elemental carbon, which can explain why the stability of the catalysts was improved with H_2 as carrier gas. After 60 min reaction, the carbon yields were 624.2%, 554.2%, and 190.4% for the catalysts 30Ni–10Co/La_2O_3, 40Ni/La_2O_3, and 40Co/La_2O_3, respectively. It should be pointed out that the carbon yield for the catalyst 30Ni–10Co/La_2O_3 is remarkably high. Compared with the data reported earlier (17, 26, 27), the presently observed carbon yield indicates that the activity of the catalyst 30Ni–10Co/La_2O_3 is very good for the growth of CNTs.

Characterization of the CNTs

The morphology of the carbon products obtained was characterized by TEM. Figure 6*a*–6*f* shows TEM images of as-grown CNTs synthesized by methane decomposition at 700 °C over the unreduced catalysts with N_2 and H_2 as carrier gas, respectively. It was observed that dense multi-walled carbon nanotubes were grown on the surfaces of all the catalysts. The morphologies of the MWNTs produced over these catalysts were similar to each other with relatively uniform diameters from 10 to 60 nm. Some catalyst particles

© 2008 NRC Canada

were found to be present at the tip of the CNTs, which suggested that the growth of the CNTs in the present work followed the tip growth mechanism (28). In the TEM measurement, some impurities such as amorphous carbon and carbon nanofibers were also observed in the samples, and the purity of CNTs was always higher for the carbon deposit synthesized with H_2 as carrier gas than for that synthesized with N_2 as carrier gas, which suggested that hydrogen could inhibit the formation of less-ordered and thermodynamically stable impurities so that the more-ordered and thermodynamically stable CNTs could be produced (29).

Raman spectroscopy is a useful technique for the characterization of CNTs. Figure 7 shows the Raman spectra of the CNTs grown over 30Ni–10Co/La_2O_3 with N_2 and H_2 as carrier gas, respectively. For all the Raman spectra, three major bands were observed, representing D, G, and 2D bands. The D band, observed at 1350 cm^{-1}, is known as either the disorder induced due to the wall disorder or the presence of amorphous carbon deposited on the outer surface of nanotubes (30). The G band, observed at 1590 cm^{-1}, can be attributed to the degree of graphitization of CNTs (30). The relative intensity ratio of D band to G band is known as an index to determine the structure of CNTs (31). It is found that the CNTs deposited on the catalyst with H_2 as carrier gas show smaller I_D/I_G ratio as compared with those with N_2 as carrier gas. This reveals that H_2 as carrier gas could provoke the formation of better graphitized CNTs and inhibit the formation of amorphous carbon in the products, which is consistent with TEM characterization discussed before.

Purification after the synthesis process is a very important part of the CNT production process. It involves the separation and the removal of the catalytic particles, support material, and amorphous particles from CNTs. We studied the purification of the CNTs by hydrochloric acid. Figure 8 shows TGA curves of the raw and purified CNTs produced by methane decomposition at 700 °C over the catalyst 30Ni–10Co/La_2O_3 with H_2 as carrier gas. These curves are very useful for the characterization of CNTs, since they provide simple and direct evidence for the purity grade and structural characteristics of the obtained CNT samples. For the raw sample, the slight mass loss occurred at 352 °C was due to the combustion of amorphous carbon present in the sample. The significant mass loss in TGA curve, which started near 521 °C and ended at about 612.4 °C was mainly attributed to oxidation of CNTs. The remaining quantity was 6.6 wt%, which was the mass of oxidized catalyst with La_2O_3. For the purified sample, the 98 wt% mass loss in TG curve was mainly attributed to oxidation of CNTs, and the 2 wt% residual could be assigned to the metallic particles that were either covered by a carbon cage or were located inside the tubes, being thus protected from acid attack (32). Thus, after a single-step purification by hydrochloric acid, most of the impurities were eliminated, and the purity of CNTs reached up to 98 wt%. The high purity of CNTs is achieved in this study owing to the fact that the use of La_2O_3 as catalyst support simplifies somewhat the purification process because it is easily dissolved in hydrochloric acid. However, in the case of zeolite or silica, which is widely used as catalyst support for CNT synthesis, only concentrated hydrofluoric acid can dissolve the support material. That is quite harmful for the integrity of the nanotubes themselves (33).

Fig. 7. Raman spectra for CNTs grown over 30Ni–10Co/La_2O_3 catalyst with N_2 and H_2 as carrier gas, respectively: (*a*) N_2 (*b*) H_2.

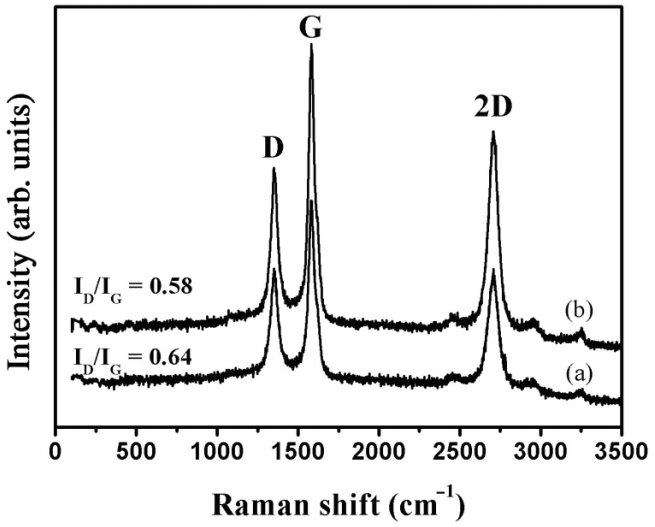

Fig. 8. TGA curves of the raw and purified CNTs produced by catalytic decomposition of CH_4 at 700 °C over the 30Ni–10Co/La_2O_3 catalyst with H_2 as carrier gas.

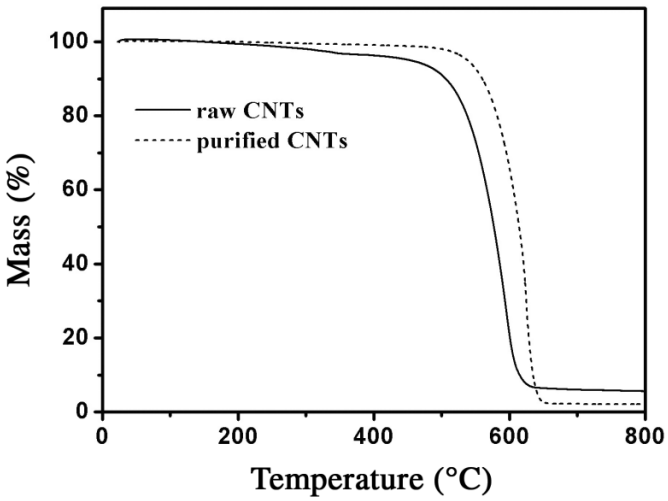

Conclusion

Novel Ni–Co/La_2O_3 catalysts have been prepared to produce CNTs by the CCVD method with methane as the carbon source. The effects of Ni and Co content, hydrogen-reduction pretreatment, and carrier gas on the activity and stability of the catalysts were investigated. The results indicate that the unreduced catalyst 30Ni–10Co/La_2O_3 showed the highest activity for methane decomposition and the carbon yields, being 552% and 624.2%, were obtained over this catalyst at 700 °C with nitrogen and hydrogen as carrier gas, respectively. The aggregation of metal particles and the lack of lattice oxygen caused the reduced catalysts to show lower catalytic activity than the unreduced ones. Hydrogen as carrier gas could limit or alleviate the poisoning of the metal

© 2008 NRC Canada

catalysts by elemental carbon and inhibit the formation of the impurities; thus, it improved the stability of the catalysts and reduced the quantity of the impurities present in the products. After a single-step purification by hydrochloric acid, the purity of the CNTs produced by methane decomposition over the unreduced catalyst 30Ni–10Co/La_2O_3 with hydrogen as carrier gas can reach up to 98 wt%, which makes the catalyst a very promising industrial product to produce high-quality CNTs on a large scale and at a low cost.

References

1. M. Paradise and T. Goswami. Mater Design **28**, 1477 (2007).
2. T.W. Ebbesen and P.M. Ajayan. Nature (London, UK), **358**, 220 (1992).
3. Y. Ando, X. Zhao, S. Inoue, T. Suzuki, and T. Kadoya. Diam. Relat. Mater. **14**, 729 (2005).
4. T. Guo, P. Nikolaev, A. Thess, D.T. Colbert, and R.E. Smalley. Chem. Phys. Lett. **243**, 49 (1995).
5. W.K. Maser, E. Munoz, A.M. Benito, M.T. Martinez, G.F. de la Fuente, Y. Maniette, E. Anglaret, and J.L. Sauvajol. Chem. Phys. Lett. **292**, 587 (1998).
6. J.F. Colomer, G. Bister, I. Willems, Z. Konya, A. Fonseca, G. Van Tendeloo, and J.B.Nagy. Chem. Commun. **14**, 1343 (1999).
7. Y. Soneda, L. Duclaux, and F. Béquin. Carbon, **40**, 965 (2002).
8. H. Dai, A.G. Rinzler, P. Nikolaev, A. Thess, D.T. Colbert, and R.E. Smalley. Chem. Phys. Lett. **260**, 471 (1996).
9. V. Ivanov, J.B. Nagy, P. Lambin, A. Lucas, X.B. Zhang, X.F. Zhang, D. Bernaerts, G. Van Tendeloo, S. Amelincks, and J. Van Landuyt. Chem. Phys. Lett. **223**, 329 (1994).
10. W.Z. Li, S.S. Xie, L.X. Qian, B.S. Chang, B.S. Zou, W.Y. Zhou, R.A. Zhou, and G. Wang. Science (Washington, DC), **274**, 1701 (1996).
11. Z.F. Ren, Z.P. Huang, J.W. Xu, J.H. Wang, P. Bush, M.P. Siegal, and P.N. Provencio. Science (Washington, DC), **282**, 1105 (1998).
12. M. Kuras, R. Roucou, and C. Petit. J. Mol. Catal. A: Chem. **265**, 210 (2006).
13. B.C. Liu, L.Z. Gao, Q. Liang, S.H. Tang, M.Z. Qu, and Z.L. Yu. Catal. Lett. **71**, 225 (2001).
14. Q. Liang, L.Z. Gao, Q. Li, S.H. Tang, B.C. Liu, and Z.L. Yu. Carbon, **39**, 897 (2001).
15. H. Li, Q. Liang, L.Z. Gao, S.H. Tang, Z.Y. Cheng, B.L. Zhang, Z.L. Yu, C.F. Ng, and C.T. Au. Catal. Lett. **74**, 185 (2001).
16. B.C. Liu, S.H. Tang, Z.L. Yu, B.L. Zhang, T. Chen, and S.Y. Zhang. Chem. Phys. Lett. **357**, 297 (2002).
17. A.K.M. Fazle Kibria, Y.H. Mo, K.S. Nahma, and M.J. Kimb. Carbon, **40**, 1241 (2002).
18. E. Flahaut, A. Govindaraj, A. Peigney, C.H. Laurent, A. Rousset, and C.N.R. Rao. Chem. Phys. Lett. **300**, 236 (1999).
19. A.M. Cassell, J.A. Raymakers, J. Kong, and H. Dai. J. Phys. Chem. B. **103**, 6484 (1999).
20. M. Su, B. Zheng, and J. Liu. Chem. Phys. Lett. **322**, 321 (2000).
21. W. Qian, T. Liu, F. Wei, Z. Wang, and Y. Li. Appl. Catal. A. **258**, 121 (2004).
22. L.B. Avdeeva, D.I. Kochubey, and Sh.K. Shaikhutdinov. Appl. Catal. A. **177**, 43 (1999).
23. Y. Chen, S. Ciuparu, S. Lim, Y. Yang, G. L. Haller, and L. Pfefferle. J. Catal. **226**, 351 (2004).
24. L. Zhou, K. Ohta, K. Kuroda, N. Lei, K. Matsuishi, L. Gao,T. Matsumoto, and J. Nakamura. J. Phys. Chem. B, **109**, 4439 (2005).
25. S. Takenaka, M. Ishida, M. Serizawa, E. Tanabe, and K. Otsuka. J. Phys. Chem. B, **108**, 11464 (2004).
26. K. Hernadi, A. Fonseca, J.B. Nagy, D. Bernaerts, and A. Lucas. Carbon, **34**, 1249 (1996).
27. P.E. Anderson and N.M. Rodriguez. J. Mater. Res. **14**, 2912 (1999).
28. S. Amelinckx, X.B. Zhang, D.Bernaters, X.F. Zhang, V. Ivanov, and J.B. Nagy. Science (Washington, DC), **267**, 635 (1995).
29. W. Wasel, K. Kuwana, P.T.A. Reilly, and K. Saito. Carbon, **45**, 833 (2007).
30. S-P. Chai, S.H. Sharif Zein, and A.R. Mohamed. Appl. Catal. A, **326**, 173 (2007).
31. S. Reich, C. Thomsen, and J. Maultzsch. Carbon nanotubes: basic concepts and physical properties. Wiley-VCH. Germany. 2004.
32. L.A. Montoro, P. Corio, and J.M. Rosolen. Carbon, **45**, 1234 (2007).
33. A. Fonseca, K. Hernadi, P. Piedigrosso, J.F. Colomer, K. Mukhopadhyay, R. Doome, S. Lazarescum, L.P. Biro, Ph. Lambin, P.A. Thiry, D. Bernaerts, and J.B. Nagy. Appl. Phys. A, **67**, 11 (1998).

© 2008 NRC Canada

A DFT investigation into the origin of regioselectivity in palladium-catalyzed allylic amination[1]

Marco Zimmer De Iuliis, Iain D.G. Watson, Andrei K. Yudin, and Robert H. Morris

Abstract: The addition of amines or aziridines to prenylacetate is catalyzed by palladium phosphine complexes. The first-formed products have recently been shown to be the branched olefins $R_2NCMe_2CH{=}CH_2$, R = alkyl, or R_2 = 1,2-C_6H_{10}, for example. DFT calculations using the MPW1K functional were performed on reactions of the suspected intermediate η^3-prenyl complex $[Pd(\eta^3\text{-}Me_2CCHCH_2)(PH_3)_2]^+$ with dimethylamine and ethylene imine. The activation barrier for the nucleophilic attack by the amine or the aziridine is calculated to be similar for either the sterically hindered site of the π-allyl ligand to produce the branched olefin complex or the unhindered site to give the linear olefin complex. Therefore, these calculations do not reveal the experimentally observed preference for attack. This observation, along with the experimental observation of lack of isomerization of the branched olefin product of the aziridine reactions, appears to rule out the intermediacy of a π-allyl complex $[Pd(\eta^3\text{-}Me_2CCHCH_2)L_2]^+$, L = phosphine or L_2 = diphosphine in the C–N bond-forming reaction.

Key words: allyl palladium, amine, aziridine, DFT, mechanism, catalysis.

Résumé : L'addition d'amines ou d'aziridines à l'acétate de prényle est catalysée par les complexes des phosphines de palladium. Il a été démontré récemment que les premiers produits formés sont des oléfines ramifiées, telles les $R_2NCMe_2CH{=}CH_2$ dans lesquelles R = alkyle ou R_2 = 1,2-C_6H_{10}. On a effectué des calculs théoriques de la fonctionnelle de densité à l'aide d'une fonction MW1K sur les réactions de l'intermédiaire prévu, le complexe η^3-prényle $[Pd(\eta^3\text{-}Me_2CCHCH_2)(PH_3)_3]^+$ avec la diméthylamine et l'éthylèneimine. On a calculé que la barrière d'activation à l'attaque nucléophile par l'amide ou l'aziridine est semblable que ce soit pour le site stériquement empêché du ligand π-allyle à produire la complexe à oléfine ramifiée ou le site non empêché à donner le complexe de l'oléfine linéaire. Ces calculs ne permettent donc pas de confirmer la préférence observée expérimentalement pour cette attaque. Cette observation ainsi que l'observation expérimentale que l'oléfine ramifiée des réactions de l'aziridine ne conduit pas à une isomérisation semble éliminer la possibilité que le complexe π-allyle $[Pd(\eta^3\text{-}Me_2CCHCH_2)L_2]^+$, L = phosphine ou L_2 = diphosphine, soit un intermédiaire dans la réaction de formation de la liaison C–N.

Mots-clés : allylpalladium, amine, aziridine, calculs théoriques de la fonctionnelle de densité, mécanisme, catalyse.

[Traduit par la Rédaction]

Introduction

Transition-metal-catalyzed allylic substitution has found broad applications in synthesis (1–3). Efficient catalysts are available to carry out allylic alkylation with high degrees of efficiency and selectivity, and chiral ligands can be employed to effect the reaction, affording products with high enantioselectivities (1). The use of nitrogen nucleophiles (4) in allylic amination enables the synthesis of allylamines, fundamental building blocks in organic chemistry. Allylamines are important synthetic intermediates for a range of biologically active compounds (1) such as α- and β-amino acids (5) and alkaloids (6). The generally accepted mechanism is thought to proceed by nucleophilic attack of Pd(0) at an allyl position of an olefinic compound and an oxidative addition to produce a cationic π-allyl palladium complex. The key step is proposed to be the subsequent nucleophilic attack by the amine nucleophile at the π-allyl palladium complex, resulting in formation of the allylamine product (Scheme l) (7).

There are two possible sites for nucleophilic attack at an unsymmetrical allyl π system, leading to distinct regioisomeric products. The regiochemistry of attack in allylic substitution varies greatly with respect to the metal, ligands, nucleophile, and allyl substituent type. For example, if there is an electron-accepting substituent (R) on the allyl group, then attack at the more substituted position is preferred (8–10). In contrast, if R is an electron-donating group, attack at the less substituted position is more favoured (11–15). Therefore, it was surprising to find that for the addition of amines or aziridines to prenylacetate catalyzed by palladium phosphine complexes, the first-formed products were found to be the branched olefins $R_2NCMe_2CH{=}CH_2$ where R is

Received 27 February 2008. Accepted 10 April 2008. Published on the NRC Research Press Web site at canjchem.nrc.ca on 17 June 2008.

This article is dedicated to Professor Richard Puddephatt on the occasion of his 65th birthday and in recognition of his outstanding contributions to chemistry in Canada.

M. Zimmer De Iuliis, I.D.G. Watson, A.K. Yudin,[2] and R.H. Morris.[2] Davenport Research Laboratories, Department of Chemistry, The University of Toronto, 80 St. George Street, Toronto, ON M5S 3H6, Canada.

[1]This article is part of a Special Issue dedicated to Professor R. Puddephatt.

[2]Corresponding authors (e-mail: ayudin@chem.utoronto.ca; rmorris@chem.utoronto.ca).

 doi:10.1139/V08-078 © 2008 NRC Canada

Scheme 1. Proposed mechanism of Pd-catalyzed allylic amination.

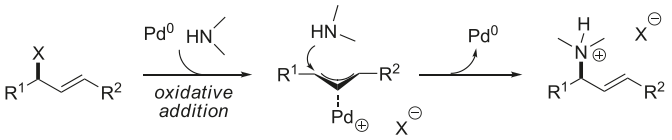

Me or R_2 is 1,2-C_6H_{10}, or other substituents (16–18). A possible explanation is that a π-allyl complex such as the η^3-prenyl palladium complex **A** forms (Scheme 2) (19, 20) and is attacked preferentially by an amine nucleophile at position *a* in complex **A** to give initially the branched product under basic conditions (18). This is followed by a branched to linear (b/l) isomerization to form the thermodynamically more stable linear product (16, 17). It was later found that protic acid generated during the reaction is the prerequisite for product isomerization (18). Palladium coordination to the double bond of the protonated allylamine initiates ionization of the kinetically favoured branched product (Scheme 2). Surprisingly, the unsubstituted aziridine nucleophiles gave only the kinetic branched products and these did not undergo the b/l isomerization (16, 17).

We were interested in determining the reasons behind the b/l isomerization by utilizing DFT calculations, with particular regard to the Pd-coordinated intermediates. Density functional theoretical (DFT) calculations have been found to be very useful in exploring reaction mechanisms and the origin of selectivities found in transition-metal-catalyzed processes. In particular, DFT calculations have been used to study attack of nucleophiles on η^3-allylpalladium complexes containing phosphine ligands (21–24), phosphorus–nitrogen ligands (25, 26), and chlorine and amine ligands (25, 27–29).

One such study by Delbeq et al. investigated the regioselectivity of nucleophilic attack by NH_3 on three model complexes with substituted η^3-allyl ligands; one of which was an η^3-prenyl ligand (30). They found that, in the gas phase, attack at the substituted carbon is always favoured. This trend was rationalized based on the interaction of the HOMO and LUMO of the η^3-allyl species with the HOMO of the NH_3; that is, the larger the coefficient in the LUMO on a carbon in the direction of attack, the more selective the nucleophile is for that particular carbon.

We wondered if attack at the key η^3-palladium π-allyl complex **A** (Scheme 2) explains the reasons for the observed b/l ratios and the isomerization of the branched products to the linear product, but only in the case of amine and not aziridine. Also, does a switch in nucleophile from a simple amine to an aziridine cause a change in the regiochemistry of attack at complex **A**? This study was based on a model η^3-prenyl palladium catalyst using $HNMe_2$ and HNC_2H_4 as the aminating agents. To the best of our knowledge, this is the first mechanistic DFT study of allylic amination of an η^3-prenyl palladium complex using these nucleophiles.

Computational details

All calculations were performed using Gaussian03 (31). The calculations were performed on a workstation with two

Scheme 2. Possible mechanism for the branched-to-linear isomerization of allylamines in Pd-catalyzed allylic aminations

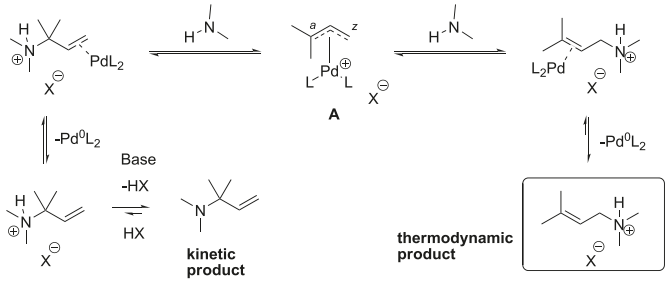

2.8 GHz Opteron X2 processors with 4 GB of RAM using the Red Hat Linux Enterprise Edition operating system. All calculations used the MPW1K density functional method, since it has been shown to provide accurate barrier heights for thermochemical kinetics (32–34). The MPW1PW91 method was also used for the complete system, resulting in the same findings. Palladium was treated with the SDD basis set to include relativistic effects and an effective core potential and H, C, N, and P were treated with the triple zeta basis set 6-311++G**, which includes diffuse functionals and additional p orbitals on H as well as additional d orbitals on C, N, and P. The structures were optimized in the gas phase at 1 atm of pressure and 298 K (1 atm = 101.325 kPa, 0 °C = 273 K). Full vibrational analyses were performed on the optimized structure to obtain values of ΔG, ΔH, and ΔS. The QST2 or QST3 method was utilized to locate transition states. All transition states were found to have one imaginary frequency. The calculated atomic polar tensor (APT) charges are used. The APT charge is the derivative of the forces on the atoms with respect to an applied external electric field and yields atomic charges that more accurately reflect the charge distribution rather than individual atomic charges (35).

Solvation by tetrahydrofuran (THF) was modeled using the polarized continuum model (PCM). Single-point energy calculations were performed on the gas-phase optimized structures. The following modifications to the PCM model were used: the bondi radii were used to specify explicit hydrogen atoms and scfvac keyword was added to calculate $\Delta G_{solvation}$. The default solvent parameters included in Gaussian03 were used for THF. PCM solvation has been successfully utilized to calculate solvation free energies of neutral and ionic organic and inorganic molecules (36–40). This method has also been effectively applied to the investigation of organometallic reaction mechanisms (41–45).

Supporting information about this work includes lists of atomic coordinates for all of the calculated structures, details of the calculation of solvation energies, and results using the MPW1PW91 method.[3]

Results and discussion

The starting point for our calculations was the optimization of the palladium(II) η^3-allyl complex $[Pd(\eta^3\text{-}Me_2CCHCH_2)(PH_3)_2]^+$ (**1**, Fig. 1). A simplification made to

[3] Supplementary data for this article are available on the journal Web site (canjchem.nrc.ca) or may be purchased from the Depository of Unpublished Data, Document Delivery, CISTI, National Research Council Canada, Ottawa, ON K1A 0R6, Canada. DUD 3764. For more information on obtaining material, refer to cisti-icist.nrc-cnrc.gc.ca/irm/unpub_e.shtml.

© 2008 NRC Canada

Table 1. Comparison of selected bond lengths and angles of some palladium prenyl diphosphine crystal structures and that of the model structure calculated. All distances are listed in Å and all angles are

Parameter	$[Pd(C_5H_9)(dppe)][OTf]$ (49)	$[Pd(C_5H_9)(dppf)][BF_4]$ (49)	$[Pd(C_5H_9)(DPEphos)][BF_4]$ (49)	$[Pd(C_5H_9)(PH_3)_2]^+$
Pd—C1	2.174(7)	2.152(16)	2.161(7)	2.14
Pd—C2	2.185(9)	2.192(15)	2.21(1)	2.16
Pd—C3	2.253(7)	2.291(18)	2.37(1)	2.27
Pd—P1	2.2930(16)	2.313(6)	2.336(1)	2.34
Pd—P2	2.2959(16)	2.331(9)	2.379(2)	2.33
Pl–Pd–P2	85.77(6)	101.2(3)	103.93(6)	102.8

Fig. 1. Calculated structure (I) and a schematic representation (II) of **1**. Selected APT charges for **1** (ESU): C1 0.13, C2 = –0.06, and C3 = 0.43.

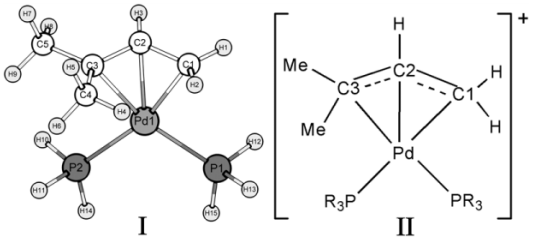

the real system $[Pd(\eta^3\text{-}Me_2CCHCH_2)(PR_3)_2]^+$ is the use of PH_3 for the phosphine ligands. Experimentally, modification of the sterics by varying the phosphine groups R did not greatly affect the conversion or the selectivity. For example, the b/l ratio changed little between different phosphine bidentate ligands, such as BINAP (bite angle of 92.8°, 8/92 b/l ratio) and Xantphos (bite angle of 104.6°, 4/96 b ratio), or monodentate ligands, such as PPh_3 (cone angle 145° (46)) and $P(OEt)_3$ (cone angle of 109° (47)) (16). Both the model complex and the actual catalysts are cationic, which aids in the activation of the allyl group for nucleophilic attack (48). Another simplification was to ignore the role of the acetate or chloride counter ions.

In Table 1, the calculated geometry of the model complex is compared to that of the structures of prenyl η^3-allyl phosphine palladium complexes determined by single-crystal X-ray diffraction. The agreement is quite good. For the remainder of this paper, C1 will denote the sterically less hindered, terminal carbon of the prenyl ligand, C2 will denote the central carbon, and C3 will denote the sterically hindered, methyl substituted carbon.

Of note is the difference between the Pd–C1 and Pd–C3 distances in Table 1. A previous theoretical study (25) attributed this difference to phosphine ligand asymmetry, but this is not the case here. An X-ray study of $[Pd(\eta^3\text{-prenyl})(\text{diphosphine})]^+$ complexes (49) concluded that the Pd–C3 distance was long due to steric effects, but we find the same lengthening in $[Pd(\eta^3\text{- preny1})(PH_3)_2]^+$ where there is no steric interaction between the phosphines and the η^3-prenyl ligand. Branchadell et al. have attributed the difference to the nature of the substituents on the allyl group (50). They reported that if a methoxy group (electron-donating) is present on a terminal allyl carbon, then the other terminal carbon will have the shortest Pd–C bond of the allyl ligand. Conversely, if a nitro group (electron-withdrawing) is bound to a terminal allyl carbon, the nitro-bound carbon will have the shortest metal–carbon bond. In the structure reported here,

Fig. 2. Effect of electron-donating groups bound to the terminal carbon on molecular orbitals of the allyl ligand.

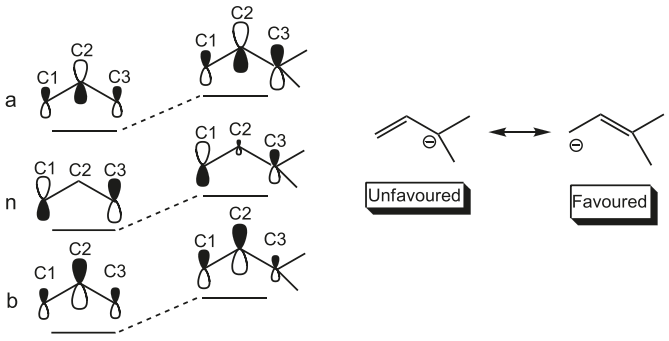

the methyl groups are ineffective in stabilizing negative charge at C3 (Fig. 2). This allows a stronger interaction between the metal and C1. The left hand side of Fig. 2 shows a schematic representation of the MOs of the allyl ligand. Addition of methyl groups onto the parent allyl fragment causes an increase in the orbital energies and allows for mixing of the various orbitals, since the ligand is no longer symmetric. The asymmetry causes polarization of n–π orbital towards C1 and results in the short Pd–C1 distance.

The calculated charge distributions for complex I are shown in Fig. 1. The charges are not distributed evenly over C1, C2, and C3. C3 has a charge equal to 0.45, which is more than 0.3 ESU greater than either C1 or C2, making it more susceptible to nucleophilic attack.

Nucleophilic attack of dimethylamine

The calculated reaction pathway for the nucleophilic attack of $HNMe_2$ on **1** is outlined in Scheme 3. The reaction pathway for nucleophilic attack by NH_3 was also calculated for comparison with the results of Delbeq et al. (30). There are two possible sites of attack for the amine: either C1, which is the sterically unhindered site and is shown in the right-hand side, or C3, which is the sterically hindered site, on the left-hand side.

Both reaction pathways were found to involve three essential steps. The first involves the approach of the $HNMe_2$ to either C1 or C3. The second step is the formation of a transition state for the nucleophilic attack in which a new C–N bond is formed. Finally, there is the formation of the palladium(0) olefin complex. In considering the reaction coordinate diagram for $HNMe_2$ attack, the sum of the calculated free energies of **1** and $HNMe_2$ will be used as the zero energy reference point, and all other energies will be relative to this value (Fig. 3).

© 2008 NRC Canada

Scheme 3. Calculated reaction pathway for $HNMe_2$ attack on the π-allyl complex **1**.

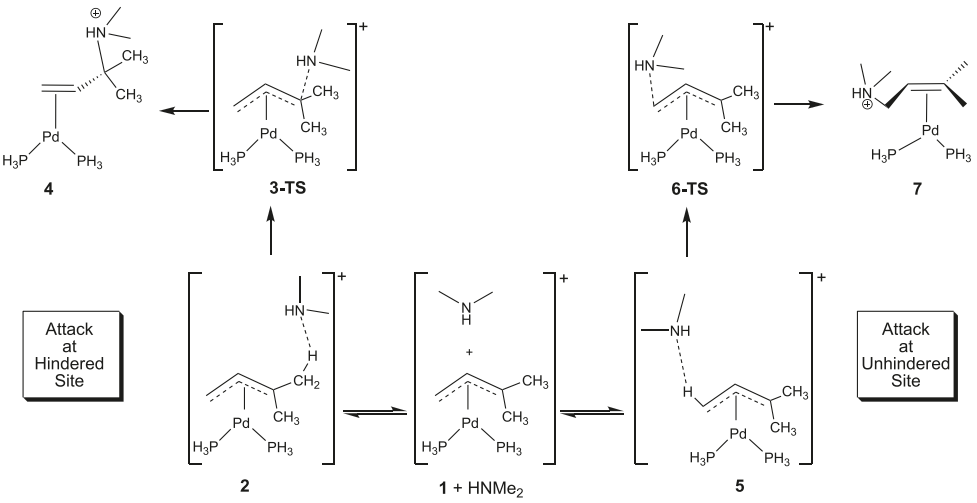

Fig. 3. Reaction coordinate diagram (free energies at 298 K, 1 atm) for the reaction of $HNMe_2$ (black lines) and NH_3 (grey lines) with the π-allyl complex **1** in the gas phase (solid line) and with THF solvation (dotted line).

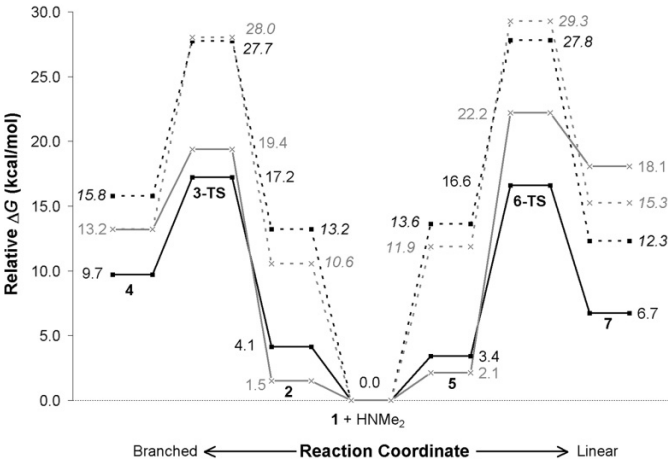

We will first examine the left-hand side of Scheme 3, leading to the branched allylamine. A weakly interacting adduct **2** with a linear N1···H17–C5 interaction provides a metastable starting point (Fig. 4). The C1–C2 and C2–C3 bond distances of the η^3-allyl system have the same value of 1.41 Å, which indicates that at this point in the reaction, there is still a delocalized π system present. In **2**, N1 is negative, at –0.59 ESU while the charge on C3 is 0.53, which suggests that attack of N1 on C3 is electrostatically favourable (Fig. 4).

In the gas phase, the free energy of **2** is 4.1 kcal/mol greater than the starting reactants, while in solution it is 13.2 kcal/mol. The increase in free energy is due to the loss of entropy in going from free reactants to this adduct.

The reaction progresses from **2** to the transition state for the attack of $HNMe_2$ on C3 (**3-TS**). In this case, the N1–C3 distance is 2.23 Å, and the $HNMe_2$ is oriented directly above the plane of the prenyl cation. The methyl groups on C3 are pushed downward toward the palladium and below the plane created by C1, C2, and C3. Also of note is the "slipped" nature of the π-prenyl ligand. The Pd–C3 distance is now 2.84 Å, which is more than 0.6 Å longer than either Pd–C2 or Pd–C1. This rearrangement allows for the maximum orbital overlap of the attacking nucleophile on the electrophile (Fig. 5) (51). There are only minor changes in the Pd–P distances and the Pl–Pd–P2 angle throughout the reaction.

The charges in the transition state are dramatically different from those of **2**. The charge on C3, where a new C–N bond is forming, has increased from 0.50 to 1.33 ESU, and N1 has become more negative, going to –0.72. A noticeable trend in both complexes **2** and **3** is that the charges of N1, C3, C2, and C1 alternate between negative (N1, C2) and positive (C3, C1). This is true for all of the structures calculated. The activation energy calculated for attack on the hindered site, which corresponds to the free energy of **3-TS**, is 17.2 kcal/mol in the gas phase and 27.7 kcal/mol in solution. Animation of the single imaginary frequency, 199*i* cm^{-1} shows the N1–C3 bond shortening with the geometry of C3 going from nearly planar to tetrahedral.

The product of attack is the palladium(0) olefin complex **4**. In this case, C1 and C2 form a C=C double bond of 1.41 Å, while C3 and C2 form a single bond with a bond length of 1.51 Å. The charges have been re-distributed on N1 and C3 to reflect the new C–N bond that has formed, with the N1 now = –0.50 and C3 = 0.57 ESU. The relative energy of **4** is 9.7 kcal/mol in the gas phase and 15.8 kcal/mol in solution. Other steps in the catalytic cycle would have to drive this endothermic reaction if this mechanism is operating.

We now turn to the right-hand side of Scheme 3 in which $HNMe_2$ attacks C1 to yield the linear product. Structural diagrams of **5**, **6-TS**, and **7** are shown in Fig. 6 along with selected geometric parameters and APT charges.

The starting point for attack on the less hindered carbon C1 is a weak adduct **5**. The N1–H2 distance is 2.36 Å and the N1–H2–C1 angle is 171.2°. The charge on C1 is 0.09 ESU, which is 0.41 ESU less than that of C3 in **2**, the analogous structure for branched attack. The charges of N1 are similar in both **2** and **5**. The relative free energy of **5** is greater than the free reactants by a similar amount to that of **2** both in the gas and solution phases (Fig. 3). **6-TS** is very similar in structure to **3-TS**, with a N1–C1 distance of 2.10 Å and the slipping of allyl ligand such that the C1–Pd

© 2008 NRC Canada

Fig. 4. Calculated Structures of **2**, **3-TS**, and **4**. Selected bond distances (Å) and angles (°): **2**: P1—Pd = 2.34, P2—Pd = 2.33. Pd—C1 = 2.14, Pd—C2 = 2.16. Pd—C3 = 2.28, N1···H7 = 2.33, P1–Pd–P2 = 103.5. **3-TS**: P1—Pd = 2.36, P2—Pd = 2.31. Pd—C1 = 2.08, Pd—C2 = 2.19, Pd—C3 = 2.84, N1—C3 = 2.23, P1–Pd–P2 = 104.0. **4**: P1—Pd = 2.34, P2—Pd = 2.34, Pd—C1 = 2.09, Pd—C2 = 2.14, Pd—C3 = 3.14, N1—C1 = 1.57, P1–Pd–P2 = 102.9. Selected APT charges (ESU): **2**: C1 = 0.15, C2 = –0.08, C3 = 0.50, N1 = –0.62. **3-TS**: C1 = 0.36. C2 = –0.55, C3 = 1.33, N1 = –0.72. **4**: C1 = 0.19. C2 = –0.05, C3 = 0.57, N1 = –0.50.

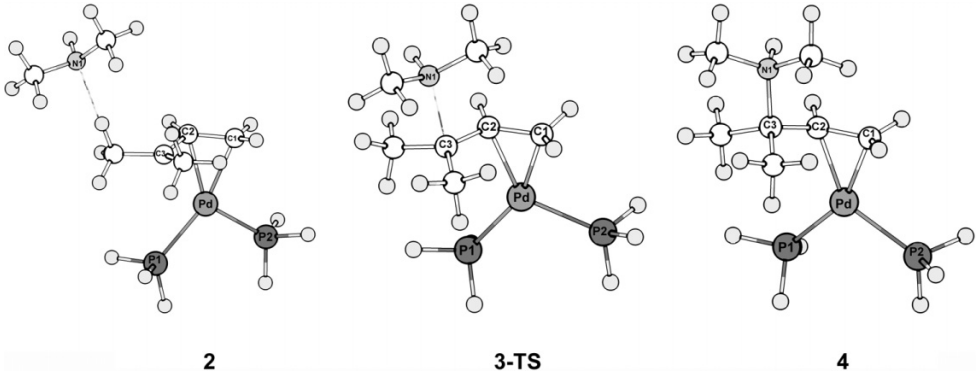

Fig. 5. Molecular orbital diagram for **3-TS** showing the HOMO-5 orbital with constructive orbital overlap between C3 and N1.

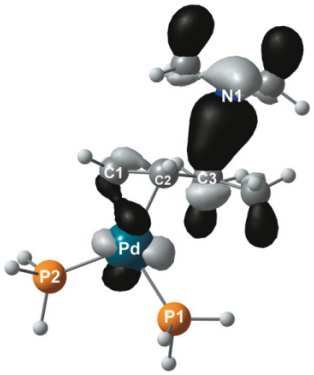

bond is elongated compared with the Pd–C2 and Pd–C3 bonds. The charge distribution changes to reflect the C–N bond formation. C1 and N1 are highly polarized with charges of 1.16 and –0.84 ESU, respectively, reflecting the electrostatic attraction of the nucleophilic N1 to the electrophilic C3. The activation energy for attack on C1 is 16.6 kcal/mol in the gas phase and 27.8 kcal/mol in solution. Again, this value does not differ significantly from that for **3-TS**. Animation of the imaginary frequency, 292*i* cm^{-1}, shows N1 approaching C1 and the planar geometry of C1 changing to tetrahedral.

The palladium(0) linear olefin complex **7** has a C=C double bond of length = 1.41 Å formed between C3 and C2, with a C–C single bond between C1 and C2. The polarized charges observed in **6-TS** have been re-distributed, with C1 having a 0.49 ESU charge and N1 with –0.50 ESU. These charges are very similar to those of the branched olefin product **4**. The relative free energy for **7** is greater than the reactants by 6.7 kcal/mol in the gas phase and 12.3 in solution. Compared with **4**, **7** is more stable by 3.0 kcal/mol in the gas phase and 3.5 kcal/mol in solution.

To determine the relative energies of the uncomplexed branched vs. linear allylammonium products, the energy-minimized conformations of simplified isomeric protonated allylamines were calculated. The difference in the calculated total energy was 8.5 kcal/mol in the gas phase and 8.9 kcal/mol in THF, with the linear *N*-allylammonium having a lower calculated total energy (Fig. 7). The greater degree of olefin substitution is likely the reason for the lower energy of the linear allylamine, a result of increased hyperconjugation. Therefore, the calculated energy-minimized conformers of the protonated branched and linear allylamines verify that the linear allylamine is the thermodynamic product of the reaction.

These results indicate that for attack on η^3-prenyl palladium complex **A**, neither of the calculated pathways is significantly energetically different. The same reaction pathway using NH_3 as a nucleophile also shows that the energy barrier for attack at either side is equally favourable. This is not the conclusion that Delbeq et al. arrived upon in their study; however, the DFT method and basis sets utilized in the current study are different. Delbeq et al used the B3LYP method, since it was shown to yield results similar to the MP2 method (52). However, since the principle focus of the present study is to determine if there is a preference for attack at either end of an unsymmetrical π-allyl palladium complex, the MPW1K method was utilized, since it has been optimized for kinetics (32–34). The basis sets employed by Delbeq et al (LANL2DZ ecp for Pd and P, D95V* for C and N, and D95V for H) are double zeta rather than triple zeta and do not include diffuse functionals, which were included here by using the 6-311++G** basis set for H, N, C, and P.

Experimentally, formation of the branched allylamine is observed initially, with high selectivity. The reaction pathway of Scheme 2 does not explain this kinetic preference because the calculated barriers to re-isomerization are similar for the branched and linear allylamines. Since experimental observations show high selectivity, it is unlikely that the mechanism calculated here is operating, and therefore, these results indicate that other allyl-palladium complexes may be responsible for the observed results.

Nucleophilic attack of aziridine

The reaction proceeds in an analogous way to the amine attack and is shown in Scheme 4. Again, the left-hand side details attack on the hindered site at C3 while the right-hand side depicts attack on the unhindered site at C1. The reaction

© 2008 NRC Canada

Scheme 4. Reaction pathway for HNC_2H_4 attack on the π-allyl complex **1**.

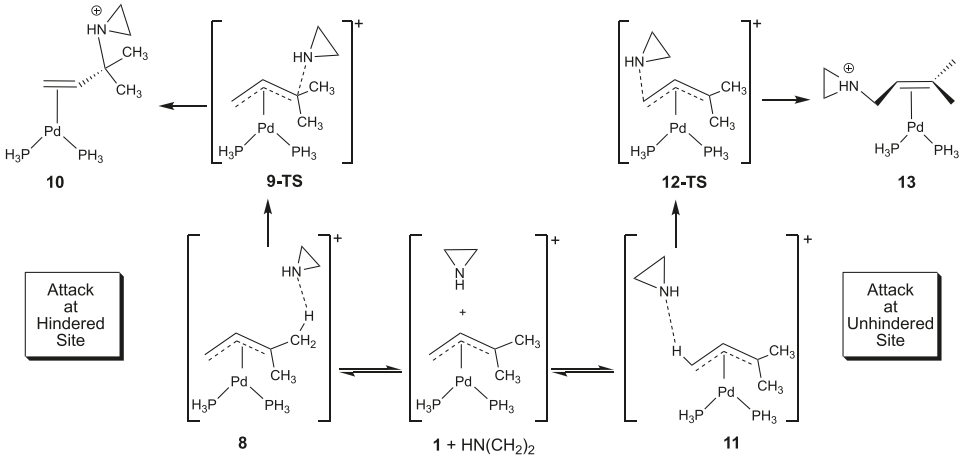

Fig. 6. Calculated Structures of **5**, **6-TS**, and **7**. Selected bond distances (Å) and angles (°): **5**: P1—Pd = 2.34, P2—Pd = 2.33, Pd—C1 = 2.15, Pd—C2 = 2.16, Pd—C3 = 2.26, N1···H2 = 2.36, P1–Pd–P2 = 103.3. **6-TS**: P1—Pd = 2.32, P2—Pd = 2.36, Pd—C1 = 2.57, Pd—C2 = 2.16, Pd—C3 = 2.15, N1—C1 = 2.10, P1–Pd–P2 = 103.7. **7**: P1—Pd = 2.33. P2—Pd = 2.35, Pd—C1 3.01, Pd—C2 = 2.13, Pd—C3 = 2.13, N1—C1 = 1.53, Pl–Pd–P2 = 104.3. Selected APT charges (ESU): **5**: C1 = 0.09, C2 = – 0.06, C3 = 0.43, N1 = –0.56. **6-TS**: C1 = 1.16, C2 = –0.42, C3 = 0.58, N1 = –0.84. **7**: C1 = 0.49, C2 = –0.12, C3 = 0.44, N1 = –0.50.

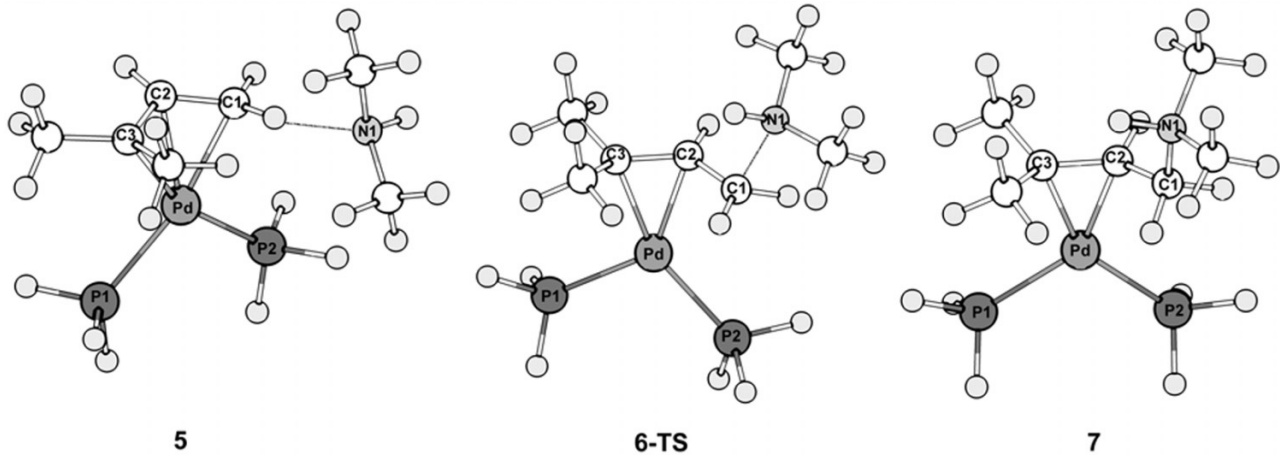

Fig. 7. Relative stabilities of decomplexed isomeric allyl ammonium products in the gas phase.

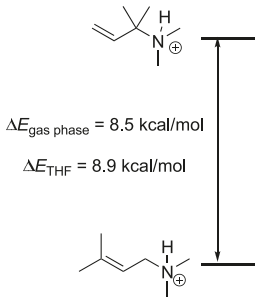

profile diagram for HNC_2H_4 attack is shown in Fig. 8, with the free energy of **1** plus that of free HNC_2H_4 as the zero reference point.

Attack at C3 begins with an adduct, **8**, shown in Fig. 9. N1 is an average of 2.54 Å away from protons of the methyls bound to C3. There is a small degree of slippage of the π-prenyl ligand with C3 now 0.15 Å farther away from the Pd centre than C2 or C3. Comparing the APT charges of **1** and **8**, there is an increase in charge on C3 from 0.45 to

Fig. 8. Reaction coordinate diagram (free energies at 298 K) for the reaction of HNC_2H_4 with the π-allyl complex **1** in the gas phase (solid line) and with THF solvation (dotted line).

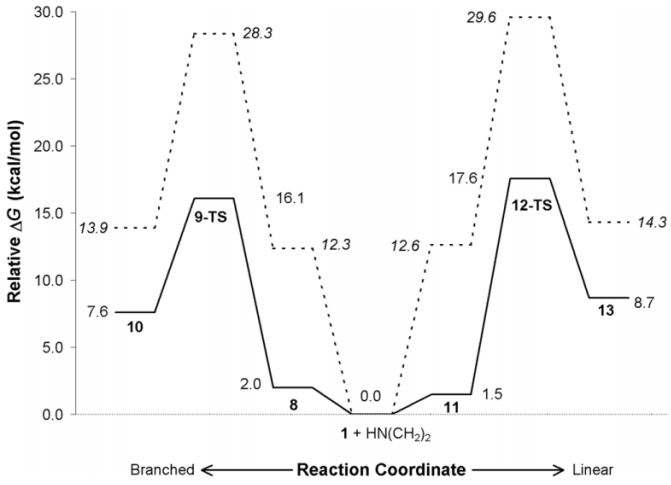

© 2008 NRC Canada

Fig. 9. Calculated Structures of **8**, **9-TS**, and **10**. Selected bond distances (Å) and angles (°): **8**: P1—Pd = 2.33, P2—Pd = 2.34, Pd—C1 = 2.14, Pd—C2 = 2.16, Pd—C3 = 2.28, N1···H7 = 2.60, N1···H8 = 2.46, P1–Pd–P2 = 103.3. **9-TS**: P1—Pd = 2.31, P2—Pd = 2.35, Pd—C1 = 2.08. Pd—C2 = 2.17, Pd—C3 = 2.86, N1—C1 = 2.15, P1–Pd–P2 = 104.3. **10**: P1—Pd = 2.34, P2—Pd = 2.34. Pd—C1 = 2.01, Pd—C2 = 2.12, Pd—C3 = 3.12, N1—C1 = 1.54, P1–Pd–P2 = 104.0. Selected APT charges (ESU): **8**: C1 = 0.09. C2 = –0.08, C3 = 0.50, N1 = –0.53. **9-TS**: C1 = 0.35, C2 = –0.56, C3 = 1.40, N1 = –0.80. **10** : C1 = 0.16, C2 = –0.02, C3 = 0.59, N1 = –0.54.

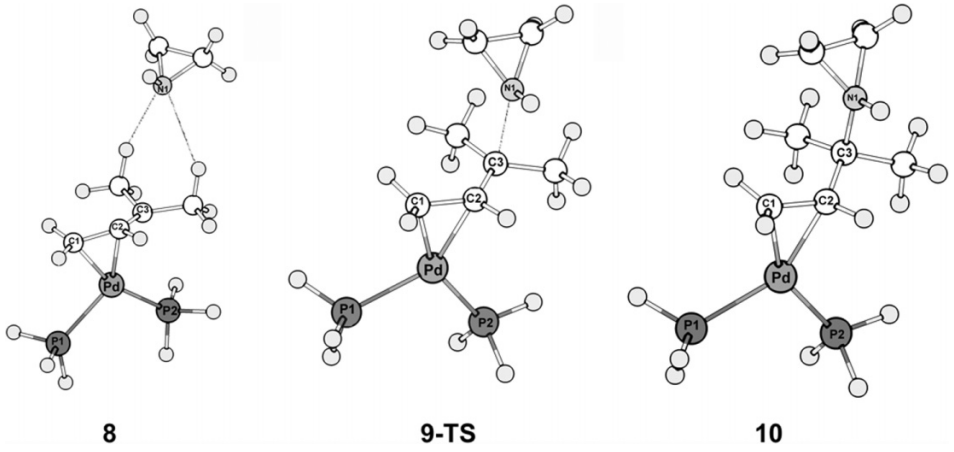

Fig. 10. Calculated Structures of **11**, **12-TS**, and **13**. Selected bond distances (Å) and angles (°): **11**: P1—Pd = 2.34, P2—Pd = 2.33, Pd—C1 = 2.15, Pd—C2 = 2.16, Pd—C3 = 2.26, N1···H2 = 2.28, P1–Pd–P2 = 103.6. **12-TS**: P1—Pd = 2.33, P2—Pd = 2.36, Pd—C1 = 2.61, Pd—C2 = 2.16, Pd—C3 = 2.15, N1—C1 = 2.02, P1–Pd–P2 = 103.2. **13**: P1—Pd = 2.33, P2—Pd = 2.35. Pd—C1 = 3.02, Pd—C2 = 2.12, Pd—C3 = 2.13, N1—C1 = 1.50, P1–Pd–P2 = 104.2. Selected APT charges (ESU): **11**: C1 = 0.09, C2 = –0.06, C3 = 0.43, N1 = –0.53. **12-TS**: C1 = 1.26, C2 = –0.44, C3 = 0.59, N1 –0.88. **13**: C1 = 0.55, C2 = –0.12, C3 = 0.45, N1 = –0.57.

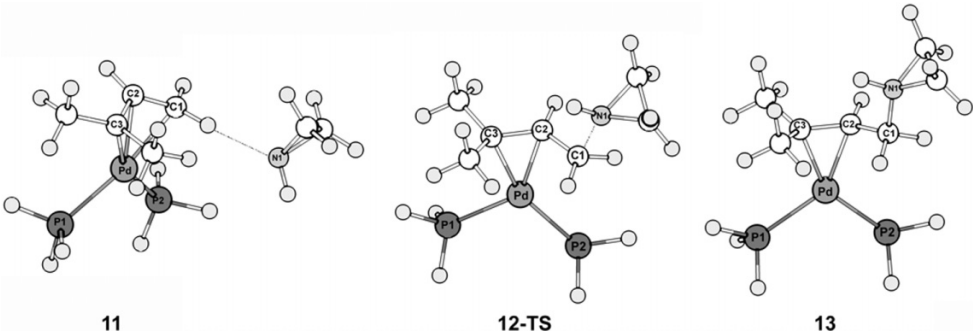

0.50 ESU, showing that the interaction has caused some polarization, making the C3 more electrophilic. As in the case of the amine attack, **8** has a greater relative energy, 2.0 kcal/mol in the gas phase and 16.1 kcal/mol in solution, than the free reactants.

In the transition state, **9-TS**, the aziridine nitrogen is 2.15 Å from C3 and is oriented directly above the plane of the η^3-preny1 ligand. The methyl groups on C3 are also beginning to bend away from the incoming aziridine. The slippage of the π-prenyl ligand is now very evident, as C3 is now more than 0.65 Å farther from the Pd than either C2 or C3. The APT charges in **9-TS** reflect the electrophilic and nucleophilic characters of C3, 1.40 ESU, and N, –0.80 ESU, respectively. Animation of the single imaginary frequency, 239*i* cm^{-1}, shows the C3–N1 distance decreasing and the methyl groups on C3 bending away from the incoming aziridine. **9-TS** is 16.1 kcal/mol in the gas phase, and 28.3 kcal/mol in solution, higher than the free reactants, which corresponds to the activation energy for this reaction. Thus, the barrier for attack of aziridine on C3 (**9-TS**) in the gas phase is 1 kcal/mol less than that of the amine attack on C3 (**3-TS**). It is 0.6 kcal/mol higher in THF solution. Finally, there is the formation of the branched olefin complex **10**, which has a C=C double bond between C2 and C1 (1.41 Å). The APT charges are no longer as polarized and are similar in magnitude to those of **8**. The relative free energy of **10** is 7.6 kcal/mol in the gas phase and 13.9 kcal/mol greater than the free reactants. These are slightly (~2 kcal/mol) higher than the analogous energies for $HNMe_2$ attack on C3.

Looking at the right-hand side of Scheme 4, we may examine attack at C1. The initial adduct, **11**, involves the interaction of the nitrogen of HNC_2H_4 with one of the protons on C1 (Fig. 10). The features of the reaction are very similar to those of the amine attack on C1.

The imaginary frequency of **12-TS** is 336*i* cm^{-1}. In **12-TS**, C1 is more than 0.45 Å farther away from the Pd than either C2 or C3, and there is a high degree of polarization of the charges of C1 (1.26 ESU) and N1 (–0.88 ESU). The activation barrier for the attack on the unhindered side is calculated to be 17.6 kcal/mol in the gas phase and 29.6 kcal/mol in solution, only 1.5 kcal/mol higher than that of the attack on the hindered side. Similar to the left-hand side, the reaction ends with the formation of an olefin palladium(0) com-

© 2008 NRC Canada

Fig. 11. Relative stabilities of decomplexed isomeric allyl aziridinium products in the gas phase.

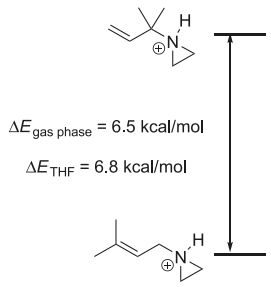

plex, which lies 8.7 kcal/mol and 14.3 kcal/mol higher in energy than the free reactants.

The difference in the calculated total energies of the uncomplexed protonated linear and branched allyl aziridines is 6.5 kcal/mol in the gas phase and 6.8 kcal/mol in THF, with linear allyl aziridinium having a lower calculated total energy (Fig. 11). These results agree with those of the protonated allylamine regioisomers. Indeed, the linear allyl aziridine would be the thermodynamic product if isomerization occurred between these substrates.

Experiments show that with cyclohexene imine as the nucleophile, the branched product is observed in high yields with only a small fraction of the linear product, yet our calculations on the mechanism of unsubstituted aziridine attack at η^3-prenyl palladium complex **A** provide no evidence for such a selectivity. Therefore, as with the calculations of the allylamine complexes, these results indicate that other reaction intermediates must be responsible for the observed results.

Conclusions

The mechanism of nucleophilic attack of $HNMe_2$ and HNC_2H_4 on the model complex $[Pd(\eta^3\text{-}Me_2CHCH_2)(PH_3)_2]^+$ (**1**) found here by computation involves at least three steps. First, there is the interaction of the nucleophile with hydrogens of the η^3-prenyl ligand. Next is the transition state, in which the π- prenyl ligand is slipped and C–N bond formation occurs (**3-TS**, **6-TS**, **9-TS**, and **12-TS**). The slippage is known to facilitate orbital overlap with the incoming nucleophile (51). Finally, a palladium(0) olefin complex is formed (**4**, **7**, **10**, and **13**).

The calculated activation barriers for attack at either C1 or C3 by either $HNMe_2$ or HNC_2H_4 differ by about 1 kcal/mol. Therefore, there does not appear to be a preferred site of attack on the π-allyl in $[Pd(\eta^3\text{-}Me_2CHCH_2)(PH_3)_2]^+$ according to Scheme 2. This suggests that there may be a different palladium intermediate that causes the initial, selective formation of the branched products observed experimentally. Work is underway to look for alternative mechanisms, for example, those that involve the counter anion or an η^1- allyl complex (16), as well as to verify that that the use of PH_3 in this study is justified.

Examining the relative energies of the decomplexed *N*-allylammonium and *N*-allylaziridinium products, it is found that the linear isomer is more stable than the branched counterpart by at least 5 kcal/mol, and hence isomerization to the linear product should occur when either $HNMe_2$ or HNC_2H_4 is the nucleophile. However, experimentally, it is found that the branched aziridine adduct does not isomerize. This observation is not explained by the mechanism of Scheme 2 involving the intermediate $[Pd(\eta^3\text{-}Me_2CHCH_2)(PH_3)_2]^+$. Hence, alternative mechanisms and reaction intermediates still to be discovered are responsible for the observed selectivities.

Acknowledgements

We thank the Natural Sciences and Engineering Research Council of Canada (NSERC) for Discovery Grants to AKY and RHM and Prof. D. Gusev for suggesting the use of the MPW1K density functional method.

References

1. B.M. Trost and M.L. Crawley. Chem. Rev. **103**, 2921 (2003).
2. B.M. Trost. Chem. Pharm. Bull. **50**, 1 (2002).
3. B.M. Trost and D.L. vanVranken. Chem. Rev. **96**, 395 (1996).
4. A. Ricci. Modern amination methods. Wiley-VCH. Weinheim, Germany. 2000.
5. K. Burgess, L.T. Liu, and B. Pal. J. Org. Chem. **58**, 4758 (1993).
6. L.A. Paquette and S.M. Leit. J. Am. Chem. Soc. **121**, 8126 (1999).
7. J.-E. Bäckvall. *In* Metal-catalyzed cross-coupling reactions. 2nd ed. *Edited by* A.d. Meijere and F. Diederich. Wiley. Weinheim, Germany. 2004. pp. 479–530.
8. B.M. Trost, L. Weber, P.E. Strege, T.J. Fullerton, and T.J. Dietsche. J. Am. Chem. Soc. **100**, 3416 (1978).
9. B.M. Trost and P.E. Strege. J. Am. Chem. Soc. **97**, 2534 (1975).
10. P.S. Pregosin and R. Salzmann. Coord. Chem. Rev. **155**, 35 (1996).
11. W.R. Jackson and J.U.G. Strauss. Tetrahedron Lett. **16**, 2591 (1975).
12. J. Tsuji. Palladium reagents and catalysts. Wiley. Chichester, UK. 1995.
13. K. Ogura, N. Shibuya, and H. Iida. Tetrahedron Lett. **22**, 1519 (1981).
14. B. Principato, M. Maffei, C. Siv, G. Buono, and G. Peiffer. Tetrahedron, **52**, 2087 (1996).
15. Y. Yamamoto, M. Al-Masum, and A. Takeda. J. Chem. Soc., Chem. Commun. 831 (1996).
16. I.D.G. Watson and A.K. Yudin. J. Am. Chem. Soc. **127**, 17516 (2005).
17. I.D.G. Watson, S.A. Styler, and A.K. Yudin. J. Am. Chem. Soc. **126**, 5086 (2004).
18. I. Dubovyk, I.D.G. Watson, and A.K. Yudin. J. Am. Chem. Soc. **129**, 14172 (2007).
19. C. Amatore, E. Génin, A. Jutand, and L. Mensah. Organometallics, **26**, 1875 (2007).
20. B. Åkermark, G. Åkermark, L.S. Hegedus, and K. Zetterberg. J. Am. Chem. Soc. **103**, 3037 (1981).
21. O. Piechaczyk, C. Thoumazet, Y. Jean, and P.l. Floch. J. Am. Chem. Soc. **128**, 14306 (2005).
22. M. García-Iglesias, E. Bunuel, and D. J. Cárdenas. Organometallics, **25**, 3611 (2006).
23. K.J. Szabó. Chem. Soc. Rev. **30**, 136 (2001).
24. H. Fujimoto and T. Suzuki. Int. J. Quan. Chem. **74**, 735 (1999).
25. P.E. Blöchl and A. Togni. Organometallics, **15**, 4125 (1996).
26. F. Robert, F. Delbecq, C. Nguefack, and D. Sinou. Eur. J. Inorg. Chem. 351 (2000).

© 2008 NRC Canada

27. D. Tang, X. Luo, W. Shen, and M. Li. Theochem, **716**, 79 (2005).
28. O.Y. Tkachenko and A.P. Belov. J. Struct. Chem. **45**, 417 (2004).
29. I. Mácsari and K.J. Szabó. Chem. Eur. J. **7**, 4097 (2001).
30. F. Delbecq and C. Lapouge. Organometallics, **19**, 2716 (2000).
31. M.J. Frisch, G.W. Trucks, H.B. Schlegel, G.E. Scuseria, M.A. Robb, J.R. Cheeseman, V.G. Zakrzewski, J.A. Montgomery Jr., R.E.Stratmann, J.C. Burant, S. Dapprich, J.M. Millam, A.D. Daniels, K.N. Kudin, M.C. Strain, O. Farkas, J. Tomasi, V. Barone, M. Cossi, R. Cammi, B. Mennucci, C. Pomelli, C. Adamo, S. Clifford, J. Ochterski, G.A. Petersson, P.Y. Ayala, Q. Cui, K. Morokuma, D.K. Malick, A.D. Rabuck, K. Raghavachari, J.B. Foresman, J. Cioslowski, J.V. Ortiz, B.B. Stefanov, G. Liu, A. Liashenko, P. Piskorz, I. Komaromi, R. Gomperts, R.L. Martin, D.J. Fox, T. Keith, M.A. Al-Laham, C.Y. Peng, A. Nanayakkara, C. Gonzalez, M. Challacombe, P.M.W. Gill, B.G. Johnson, W. Chen, M.W. Wong, J.L. Andres, M. Head-Gordon, E.S. Replogle and J.A. Pople. Gaussian03 [computer program]. Rev. D01. Gaussian, Inc., Pittsburgh, PA. 2001.
32. Y. Zhao, N. González-García, and D.G. Truhlar. J. Phys. Chem. A. **109**, 2012 (2005).
33. Y. Zhao, J. Pu, B.J. Lynch, and D.G. Truhlar. Phys. Chem. Chem. Phys. **6**, 673 (2004).
34. Y. Zhao and D.G. Truhlar. J. Phys. Chem. A, **109**, 5656 (2005).
35. J. Cioslowski. J. Am. Chem. Soc. **111**, 8333 (1989).
36. X.S. Lopez, M.A. Dejaegere, and M. Karplus. **124**, 5010 (2002).
37. Y. Fu, L. Liu, R.C. Li, R. Liu, and Q.X. Guo. J. Am. Chem. Soc. **126**, 814 (2004).
38. J.R. Pliego and J.M. Riveros. J. Phys. Chem. A, **106**, 7424 (2002).
39. M.H. Baik, C.K. Schauer, and T. Ziegler. **124**, 11167 (2002).
40. Y.H. Takano and K.N. Houk. J. Chem. Theory Comput. **1**, 70 (2005).
41. G. Kovacs and I. Papai. Organometallics, **25**, 820 (2006).
42. C.P. Casey, J.B. Johnson, S.W. Singer, and Q. Cui. J. Am. Chem. Soc. **127**, 3100 (2005).
43. T. Marino, N. Russo, and M. Toscano. J. Am. Chem. Soc. **127**, 4242 (2005).
44. T. Nowroozi-Isfahani, D.G. Musaev, F.E. McDonald, and K. Morokuma. Organometallics, **24**, 2921 (2005).
45. G.P. Schubert and I. Pápai. J. Am. Chem. Soc. **125**, 14847 (2003).
46. C.A. Tolman. Chem. Rev. **77**, 313 (1977).
47. K.A. Bunten, L. Chen, A.L. Fernandez, and A.J. Poë. Coord. Chem. Rev. **233-234**, 41 (2002).
48. R.H. Crabtree. The organometallic chemistry of the transition metals. 2nd ed. John Wiley & Sons, Inc.. New York, NY. 1994.
49. R.J. van. Haaren, K. Goubitz, J. Fraanje, G.P.F. van Strijdonck, H. Oevering, B. Coussens, J.N. H. Reek, P.C.J. Kamer, and P.W.N.M. van Leeuwen. Inorg. Chem. **40**, 3363 (2001).
50. V. Branchadell, M. Moreno-Manãs, F. Pajuelo, and R. Pleixats. Organometallics, **18**, 4934 (1999).
51. O. Eisenstein and R. Hoffmann. J. Am. Chem. Soc. **103**, 4308 (1981).
52. D.A. Singleton, S.R. Merrigan, J. Liu, and K.N. Houk. J. Am. Chem. Soc. **119**, 3385 (1997).

© 2008 NRC Canada

DFT studies of the σ-donor/π-acceptor properties of $[SnCB_{10}H_{11}]^-$ and its relationship to $[SnCl_3]^-$, CO, PF_3, $[SnB_{11}H_{11}]^{2-}$, $SnC_2B_9H_{11}$, and related $SnC_2B_nH_{n+2}$ compounds[1]

Mark A. Fox, Todd B. Marder, and Lars Wesemann

Abstract: The 1,2-carbastanna-closo-dodecaborate, $[SnCB_{10}H_{11}]^-$, was found via DFT calculations to have intermediate σ-donor/π-acceptor properties between those of $[SnB_{11}H_{11}]^{2-}$ and 3,1,2-$SnC_2B_9H_{11}$, and quite similar HOMO and LUMO energies and shapes to those of $[SnCl_3]^-$, which is a stronger σ-donor and weaker π-acceptor than CO or PF_3. The non-carbon containing cluster $[SnB_{11}H_{11}]^{2-}$ is shown to be a very strong donor, whereas the dicarbon cluster 3,1,2-$SnC_2B_9H_{11}$ is a poor σ-donor but good Lewis acid, consistent with experimental results. Thus, these systems can be tuned across a very wide range via isolobal replacement of $[BH]^-$ for CH vertices. The higher negative charge in the non-carbon-containing systems, as well as the fact that boron is more electropositive than carbon, contribute to the increased energies of both HOMO and LUMO in the stannaboranes compared to the stannacarboranes, explaining their relative donor and acceptor properties.

Key words: DFT calculations, tin, borane cluster.

Résumé : Sur la base de calculs théoriques effectués par la méthode de la fonctionnelle de la densité (DFT), nous mettons en évidence les propriétés donneur σ/accepteur π du 1,2-carbastanna-*closo*-dodécaborate, $[SnCB_{10}H_{11}]^-$, sont intermédiaires entre celles de $[SnB_{11}H_{11}]^{2-}$ et celles de 3,2,1-$SnC_2B_9H_{11}$. Les énergies et les formes de l'orbitale la plus haute occupée (HOMO) et de l'orbitale la plus basse vacante (LUMO) sont quelque peu similaires à celles de $[SnCl_3]^-$, qui est plus donneur σ et moins accepteur π que CO ou PF_3. Nous montrons que, en accord avec les données expérimentales, l'agrégat non carboné $[SnB_{11}H_{11}]^{2-}$ est un très bon donneur σ, au contraire de $SnC_2B_9H_{11}$ qui est un mauvais donneur σ mais un bon acide de Lewis. Ainsi, il est possible de jouer de façon importante sur les propriétés de tels systèmes par le remplacement isolobal de sommets $[BH]^-$ par des sommets CH. La charge négative plus importante dans les systèmes non carbonés, ainsi que le fait que le bore soit plus électropositif que le carbone, contribuent à l'augmentation des énergies des HOMO et LUMO dans les stannaboranes, comparée aux stannacarboranes, expliquant leurs propriétés de donneurs et d'accepteurs relatives.

Mots-clés : calculs théoriques de la fonctionnelle de densité, étain, agrégat de borane.

Introduction

Recently, one of us reported the synthesis and coordination chemistry of the new 1,2-carbastanna-closo-dodecaborate, $[SnCB_{10}H_{11}]^-$ (1). We were intrigued by the structure of the unusual dianion $[Rh(PPh_3)_2(SnCB_{10}H_{11})_3]^{2-}$ (**1**), which has a trigonal bipyramidal (tbp) geometry with axial PPh_3 ligands and equatorial anionic $SnCB_{10}H_{11}$ ligands (Scheme 1). It was formed from the reaction of Wilkinson's catalyst $[Rh(PPh_3)_3Cl]$ with three equivalents of the anion $[SnCB_{10}H_{11}]^-$. In a d^8-ML_5 trigonal bipyramidal Rh(I) complex, it is well known that the strongest σ-donors occupy axial positions, whereas the strongest π-acceptors occupy equatorial positions, the latter owing to the fact that the HOMO for a C_{2v}-d^8-ML_4 fragment is a π-orbital lying in the equatorial plane (2). Thus, it would appear that the anionic $[SnCB_{10}H_{11}]^-$ ligand must be a reasonably strong π-acceptor. It was noted that the structure resembles that proposed for $[Rh(CNcy)_2(SnCl_3)_3]^-$, for which the authors had pointed out (3) that the $SnCl_3$ must be the stronger π-acceptor and CNcy (cyclohexyl isonitrile) must be the stronger σ-donor. In addition, we noted the similarity of the value for the $J_{Rh\text{-}P}$ for **1**, 88 Hz, to that reported for $[Rh(PPh_3)_2(CO)_3]^+$ (**2**), 72 Hz (4) which also has a (fluxional) tbp geometry,

Received 1 April 2008. Accepted 23 April 2008. Published on the NRC Research Press Web site at canjchem.nrc.ca on 1 August 2008.

Dedicated to Professor Richard J. Puddephatt in recognition of his outstanding and extensive contributions to many areas of inorganic chemistry.

M.A. Fox[2] and T.B. Marder.[2] Department of Chemistry, Durham University, South Road, Durham, DH1 3LE, UK.
L. Wesemann. Institüt fur Anorganishe Chemie, Universität Tübingen, Auf der Morgenstelle 18, D-72076 Tübingen, Germany.

[1]This article is part of a Special Issue dedicated to Professor Richard J. Puddephatt.

[2]Corresponding authors (e-mail: m.a.fox@durham.ac.uk, todd.marder@durham.ac.uk).

 doi:10.1139/V08-081 © 2008 NRC Canada

Scheme 1. Schematic representations of the key compounds discussed in the paper. Solid circles represent C–H vertices whereas open circles represent B–H vertices.

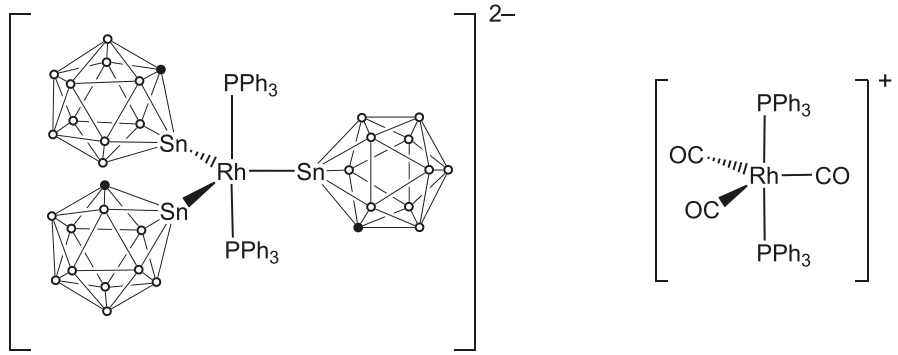

1 **2**

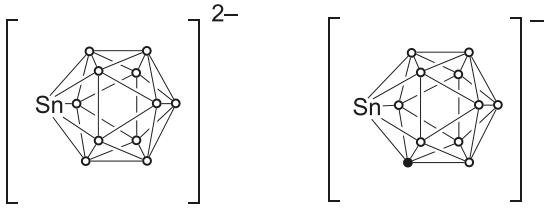

$SnB_{11}H_{11}^{2-}$ 2,1-$SnCB_{10}H_{11}^{-}$ 3,1,2-$SnC_2B_9H_{11}$

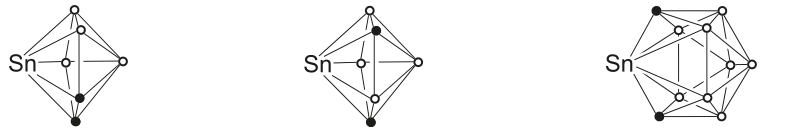

1,2,3-$SnC_2B_4H_6$ 1,2,4-$SnC_2B_4H_6$ 1,2,3-$SnC_2B_8H_{10}$

4,1,6-$SnC_2B_{10}H_{12}$ 4,1,2-$SnC_2B_{10}H_{12}$

with axial PPh_3 groups and equatorial CO ligands, as expected. That the $J_{Rh\text{-}P}$ value for **1** was slightly larger than that for **2** suggested that the $[SnCB_{10}H_{11}]^-$ ligand was probably a stronger σ-donor and weaker π-acceptor than CO. Nonetheless, it was clear that the $[SnCB_{10}H_{11}]^-$ ligand must be a reasonably strong π-acceptor for all three of them to occupy equatorial positions. Before we begin a detailed examination of the frontier orbitals of the $[SnCB_{10}H_{11}]^-$ ligand, it is worth pointing out that the isoelectronic dianionic stannaborane $[SnB_{11}H_{11}]^{2-}$ ligand is strongly nucleophilic at the tin center (5, 6), exhibits an extremely strong trans-influence, and forms numerous transition metal coordination complexes (7, 8), including such unusual homoleptic species as $[M(SnB_{11}H_{11})_4]^{4-}$ and $[M(SnB_{11}H_{11})_6]^{8-}$ (M = Ni, Pd, Pt) (9), the latter complexes involving the Group 10 metals in their formal IV oxidation state. In contrast, the neutral analogue 3,1,2-$SnC_2B_9H_{11}$ is distinctly electrophilic (10, 11). Considering this to be a possible stable stannylene analogue, as early as 1976, one of us attempted to coordinate it to photochemically generated $Cr(CO)_5(THF)$, but we were unsuc-

© 2008 NRC Canada

cessful in obtaining evidence for a Cr–Sn complex (12). Indeed, it is now known that 1,2-Me_2-3,1,2-$SnC_2B_9H_9$ is capable of binding either one or two N, O, or P-ligands at the Sn-center to provide slipped-stannacarboranes (13, 14). Likewise, C-substituted analogues of the smaller $SnC_2B_4H_6$ system also bind ligands such as 2,2′-bipyridine and 2,2′-bipyrimidine (15–18), but do not react with BH_3·THF or BF_3 to form adducts (19). The lack of σ-donating ability of the $SnC_2B_4H_{6-n}R_n$ systems was ascribed to the diffuse nature of the exo-polyhedral lone pair on the tin center (19) and to the symmetric electron distribution in some of the lower-lying filled MOs which the authors associated with the Sn "lone pair" (15). In their MNDO calculations on $SnC_2B_4H_6$, the authors indicated that the HOMO is localized on the cage borons (15). We show below, via DFT MO calculations, that $[SnCB_{10}H_{11}]^-$ has σ-donor/π-acceptor properties intermediate between those of $[SnB_{11}H_{11}]^{2-}$ and 3,1,2-$SnC_2B_9H_{11}$, and quite similar HOMO and LUMO energies and shapes to those of $[SnCl_3]^-$, a stronger σ-donor and weaker π-acceptor than CO or PF_3. We also report the shapes, energies, and atomic compositions of the orbitals for these systems as well as for related dicarbastannaboranes (13–24).

Computational details

All ab initio computations were carried out with the Gaussian 03 package (25). The geometries of the six compounds described here were optimized using the B3LYP functional (26) with no symmetry constraints. The basis sets used here were 6-31G* for all atoms (27) except for Sn, for which the LANL2DZ basis set (28) incorporating pseudopotentials was employed. Frequency calculations were performed using these optimized geometries at the same levels of theory, and the lack of any imaginary frequencies confirms that all optimized geometries are true minima. The MO diagrams and orbital contributions were generated with the aid of the Gabedit (29) and GaussSum (30) packages, respectively. Total energies in hartrees for the compounds are $[SnB_{11}H_{11}]^{2-}$: –283.572 67, [2,1-$SnCB_{10}H_{11}]^-$: –296.873 90, 3,1,2-$SnC_2B_9H_{11}$: –310.000 74, 1,2-Me_2-3,1,2-$SnC_2B_9H_9$: –388.620 55, 1,2,3-$SnC_2B_8H_{10}$: –284.532 53, 1,2,3-$SnC_2B_4H_6$: –182.631 95, 1,2,4-$SnC_2B_4H_6$: –182.655 17, 4,1,6-$SnC_2B_{10}H_{12}$: –335.459 61, 1,6-Me_2-4,1,6-$SnC_2B_{10}H_{10}$: –414.083 63, 1,2-μ-($CH_2CH{=}CHCH_2$)-4,1,2-$SnC_2B_{10}H_{12}$: –490.260 82, $[SnCl_3]^-$: –1384.204 88, PF_3: –640.956 47, and CO: –113.309 45. The computed Sn bond distances in Å for 1,2,4-$SnC_2B_4H_6$ are Sn–C(2,4): 2.412, Sn–B(3): 2.467, and Sn–B(5,6): 2.431. Calculated Sn bond distances in Å for 1,2-μ-($CH_2CH{=}CHCH_2$)-4,1,2-$SnC_2B_{10}H_{10}$ are Sn–C(1,2): 2.437, Sn–B(3,6): 2.434, and Sn–B(7,10): 2.380, using a cage numbering scheme described elsewhere (31).

Calculated NMR shifts at the GIAO-B3LYP level were obtained from the optimized geometries using the same basis sets. Theoretical ^{11}B chemical shifts at the GIAO-B3LYP level were referenced to B_2H_6 (16.6 ppm) and converted to the usual BF_3·OEt_2 scale: $\delta(^{11}B) = 110.0 - \sigma(^{11}B)$. The ^{13}C and ^1H chemical shifts were referenced to TMS: $\delta(^{13}C) = 189.1 - \sigma(^{13}C)$; $\delta(^1H) = 32.15 - \sigma(^1H)$. Agreements between observed and calculated ^{11}B (and ^{13}C) NMR shifts generated from optimized geometries are generally very good for heteroboranes (32). Agreements between observed and calculated ^1H NMR shifts in heteroboranes are often not as good owing to a narrow ppm range (ca. 12 ppm) and substantial solvent effects on ^1H shift measurements (33). Calculated ^1H NMR shifts for the hydrogens attached to cage carbons are also in very good agreement with observed data. However, hydrogens attached to cage borons have been assigned only for one closo-carbastannaborane, 1,2,3-$SnC_2B_8H_{10}$, and in this case the agreement between computed and observed shifts is surprisingly poor. Agreements between observed and calculated ^{119}Sn NMR shifts are poor owing to two factors: the ^{119}Sn NMR shift measurements depend strongly on the solvent, and the pseudopotentials and the basis set for Sn used to compute ^{119}Sn NMR shifts are not considered to be appropriate (34).

Results and Discussion

Our main interest in these systems was to compare the frontier orbitals and σ-donor/π-acceptor abilities of a series of isolectronic stannaboranes and stannacarboranes containing one tin and zero, one, or two carbon atoms in the cage and, especially, to examine those of $[SnCB_{10}H_{11}]^-$, which seemed, on the basis of the reported structure of the rhodium complex **1**, vide supra, to have both good σ-donor and good π-acceptor properties (1). The metal complexes and borane ligands of interest here are shown in Scheme 1. Optimized geometries of $[SnB_{11}H_{11}]^{2-}$ and [2,1-$SnCB_{10}H_{11}]^-$ at the DFT level of theory are in excellent agreement with their X-ray-determined molecular structures (1, 6) as demonstrated by a comparison of bond lengths involving the tin atom listed in **Table 1.** However, the dicarbastannaborane, 3,1,2-$SnC_2B_9H_{11}$, and its dimethyl derivative have not been structurally characterized. The optimized geometry of 3,1,2-$SnC_2B_9H_{11}$ reveals a slipped Sn vertex with Sn–C bonds being longer than Sn–B bonds, and the trend of the Sn vertex slippage is evident on going from $[SnB_{11}H_{11}]^{2-}$ to [2,1-$SnCB_{10}H_{11}]^-$ and 3,1,2-$SnC_2B_9H_{11}$.

Plots of the frontier orbitals of $[SnB_{11}H_{11}]^{2-}$, $[SnCB_{10}H_{11}]^-$, and 3,1,2-$SnC_2B_9H_{11}$ are displayed in **Fig. 1,** and their energies and coefficients (on Sn, CH, upper belt BH, lower belt BH, and unique BH vertices) are given in Tables 2–4, respectively. For comparison, the frontier orbitals of the well-known π-acceptor ligands $[SnCl_3]^-$, PF_3, and CO are displayed in Fig. 2, and their energies are given in **Tables 5–7,** respectively. These all have non-degenerate, σ-symmetry HOMOs and degenerate, π-symmetry LUMOs, and the similarity of their orbitals is quite obvious. Their σ-donating ability decreases and their π-accepting ability increases in the order $[SnCl_3]^-$, PF_3, and CO, as evidenced by the orbital energies listed in Tables 5–7.

Noting that $[SnB_{11}H_{11}]^{2-}$ has five-fold symmetry, belonging to the point group C_{5v}, and that the LUMO is thus doubly degenerate (shown in Fig. 1 and Table 2 as LUMO and LUMO+1 for consistency), whereas for $[SnCB_{10}H_{11}]^-$ and 3,1,2-$SnC_2B_9H_{11}$, the only symmetry element is a mirror plane, and thus, in the C_s point group, there are no degeneracies, one can still see right away the general similarities of the orbital shapes. It is important to note also that for $[SnB_{11}H_{11}]^{2-}$, while the HOMO is largely of π-symmetry and is heavily localized on the upper belt of the cage, lying

© 2008 NRC Canada

Table 1. Comparison of Sn-B and Sn-C bond distances between optimised gas-phase and reported experimental solid-state geometries, where available.

	Bond	Experimental	Calculated
$[SnB_{11}H_{11}]^{2-}$	Sn–B (averaged)[a]	2.385(4)	2.395
$[SnCB_{10}H_{11}]^{-}$	Sn–C(1)[b]	2.466(5)	2.445
	Sn–B(3,6) (averaged)	2.415(6)	2.402
	Sn–B(7,11) (averaged)	2.380(5)	2.372
3,1,2-$SnC_2B_9H_{11}$	Sn–C(1,2)		2.515
	Sn–B(4,7)		2.399
	Sn–B(8)		2.345
1,2-Me_2-3,1,2-$SnC_2B_9H_9$	Sn–C(1,2)		2.546
	Sn–B(4,7)		2.383
	Sn–B(8)		2.323
1,6-Me_2-4,1,6-$SnC_2B_{10}H_{10}$	Sn–C(1)[c]	2.411(3)	2.396
	Sn–B(2)	2.639(4)	2.616
	Sn–B(3)	2.592(4)	2.585
	Sn–B(7)	2.453(4)	2.427
	Sn–C(6)	2.672(4)	2.678
	Sn–B(10)	2.425(4)	2.403
2-Me_3Si-1,2,3-$SnC_2B_4H_5$	Sn–C(2)[d]	2.518(5)	2.488
	Sn–C(3)	2.475(6)	2.456
	Sn–B(4)	2.432(7)	2.438
	Sn–B(5)	2.397(8)	2.404
	Sn–B(6)	2.431(7)	2.434

[a]Ref. 6.
[b]Ref. 1.
[c]Ref. 22. Poor quality X-ray structural data for 4,1,6-$SnC_2B_{10}H_{12}$ have also been reported.
[d]Refs. 13 and 15.

at nearly the same energy are two degenerate and effectively σ-symmetry orbitals. Thus, we will consider the HOMO-1 and HOMO-2 orbitals for this ligand as those suitable for σ-donation to a metal center. We can see from Table 2 that the HOMO-1 and HOMO-2 orbitals are comprised of a mixture of mainly Sn and the top belt of the cage, but lie at very high energy (+1.43 eV), and are thus both strong donor levels, well above that of $[SnCl_3]^-$ (–2.45 eV). The degenerate LUMO orbitals are of π-symmetry, but are also quite high in energy, lying at +7.23 eV, well above those of CO (–0.59 eV), and are thus too high to act as π-acceptor levels, although they are almost completely localized on Sn.

An examination of the two carbon-containing cages, $[SnCB_{10}H_{11}]^-$ and 3,1,2-$SnC_2B_9H_{11}$, shows that they have very similar frontier orbitals (Fig. 1) comprising an essentially σ-symmetry HOMO and the non-degenerate π-symmetry LUMO and LUMO+1 levels. While the σ-symmetry HOMO in each case is slightly "tipped" towards the carbon vertices, nonetheless these are of suitable symmetry and have at least modest (46% and 39%, respectively) Sn-content to act as potential σ-donors. For comparison, the σ-donor HOMO levels of $[SnCl_3]^-$, PF_3, and CO are 45% localized on Sn, 64% localized on P, and 90% localized on C, respectively. Thus, while the HOMO of 3,1,2-$SnC_2B_9H_{11}$ lies at –7.33 eV, which is below that of $[SnCl_3]^-$ (–2.45 eV), but above those of PF_3 (–8.78 eV) and CO (–10.11 eV), the combination of relatively low energy and diminished content on the potential donor atom make this a poor σ-donor. In contrast, the LUMO and LUMO+1 energies of 3,1,2-$SnC_2B_9H_{11}$ are well below those of any of the "conventional" π-acceptor ligands, and are 87 and 76% localized on Sn, which makes them directly susceptible to nucleophilic attack by one or two Lewis basic ligands.

Now it is useful to consider the case of $[SnCB_{10}H_{11}]^-$ in more detail. Both the HOMO and LUMO/LUMO+1 orbital energies are between those of $[SnB_{11}H_{11}]^{2-}$ and 3,1,2-$SnC_2B_9H_{11}$, and their Sn-contents are 46, 84, and 77%, respectively, (cf. $[SnCl_3]^-$, for which the Sn-content of the HOMO is 45%, and the degenerate LUMO is 95%). A comparison of the orbital energies of $[SnCB_{10}H_{11}]^-$ and $[SnCl_3]^-$ is also informative, and we see that these are also quite similar; the HOMOs are –2.87 eV and –2.45 eV, respectively, and the LUMOs are +2.45 and +2.93 for the former and +3.25 eV for the latter. $[SnCB_{10}H_{11}]^-$ would be expected to be a slightly poorer σ-donor and slightly better π-acceptor than $[SnCl_3]^-$, but the differences are both small. Thus, $[SnCB_{10}H_{11}]^-$ and $[SnCl_3]^-$ are very similar ligands, with regard both to their energies and to the orbital overlaps with a metal center. Therefore, it is not surprising to find that it is possible to prepare trigonal bipyramidal Rh(I) complexes bearing three $[SnCB_{10}H_{11}]^-$ ligands, or that they should all lie in the equatorial plane, as expected for strong π-acceptor ligands.

While only one cage geometry of each of the closo systems, the $[SnB_nH_n]^{2-}$ dianions and the $[SnCB_nH_{n+1}]^-$ anions, is known, there are many different geometries of $SnC_2B_nH_{n+2}$ clusters with n = 4, 8, 9, and 10 reported in the literature (13–24). Molecular structures of dicarbastannaboranes with n = 4 and n = 10 have been structurally characterised (13, 15, 18, 22) and optimized geometries for each

© 2008 NRC Canada

Fig. 1. Frontier orbitals for $[SnB_{11}H_{11}]^{2-}$, $[SnCB_{10}H_{11}]^{-}$, and 3,1,2-$SnC_2B_9H_{11}$. Note that for $[SnB_{11}H_{11}]^{2-}$, LUMO and LUMO+1 constitute a degenerate pair, in contrast to $[SnCB_{10}H_{11}]^{-}$ and 3,1,2-$SnC_2B_9H_{11}$, for which there are no degeneracies.

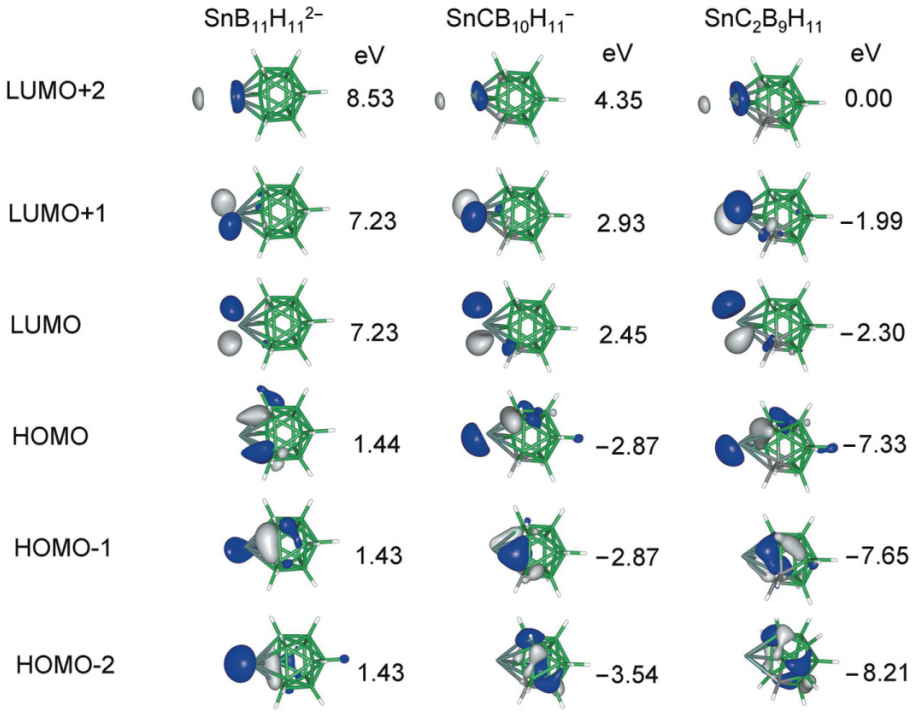

Fig. 2. Frontier orbitals for $[SnCl_3]^{-}$, PF_3, and CO. Note that orbitals labelled HOMO-1 and HOMO-2 are a degenerate pair as are LUMO and LUMO+1.

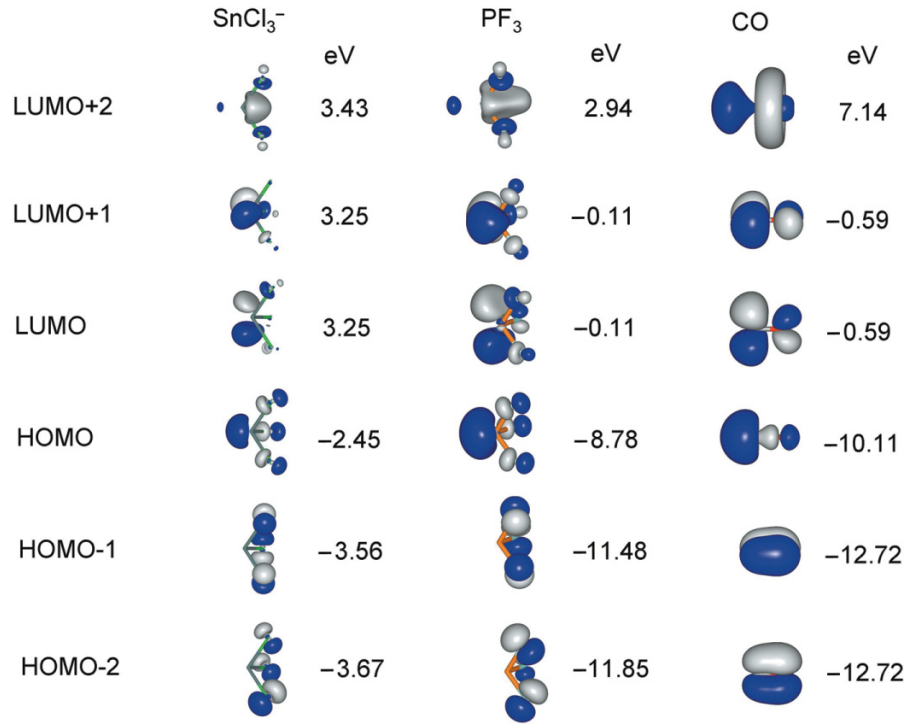

system are in very good agreement with experimental data (Table 1). The crystallographically determined molecular structures of the supraicosahedral stannacarboranes, 4,1,6-$SnC_2B_{10}H_{12}$ and 1,6-Me_2-4,1,6-$SnC_2B_{10}H_{10}$, contain asymmetrical geometries in the solid state which are in excellent agreement with optimized "gas-phase" calculated geometries, as shown in Table 1 for the Sn–C and Sn–B bond lengths in 1,6-Me_2-4,1,6-$SnC_2B_{10}H_{10}$ (22). One cage carbon is a 4-connected vertex and the other carbon is a 5-connected vertex. Agreement between experimental and optimized geometries for 2-Me_3Si-1,2,3-$SnC_2B_4H_5$ is also very good as shown in Table 1 (13, 15). The slippage of the Sn

© 2008 NRC Canada

Table 2. Molecular orbital coefficients and energies for $[SnB_{11}H_{11}]2–$.

MO	Orbital	eV	Sn	BH(upper)	BH(lower)	BH(unique)
41	**L+4**	**9.50**	**0**	**57**	**42**	**1**
40	**L+3**	**9.50**	**0**	**57**	**42**	**1**
39	L+2	8.53	75	16	9	0
38	**L+1**	**7.23**	**81**	**10**	**6**	**4**
37	**LUMO**	**7.23**	**81**	**10**	**6**	**4**
36	HOMO	1.44	23	57	16	4
35	H-1	1.43	32	48	15	5
34	H-2	1.43	53	27	14	6
33	**H-3**	**0.71**	**0**	**56**	**44**	**0**
32	**H-4**	**0.71**	**0**	**56**	**44**	**0**

Note: Degenerate levels are shown in boldface.

Table 3. Molecular orbital coefficients and energies for $[SnCB_{10}H_{11}]^–$.

MO	Orbital	eV	Sn	CH	BH(upper)	BH(lower)	BH(unique)
41	L+4	5.23	1	2	49	47	1
40	L+3	5.08	6	11	39	43	1
39	L+2	4.35	69	5	14	11	1
38	L+1	2.93	77	2	8	8	5
37	LUMO	2.45	84	5	2	7	3
36	HOMO	–2.87	46	2	30	16	7
35	H-1	–2.87	20	1	58	17	4
34	H-2	–3.54	12	3	48	34	3
33	H-3	–3.80	0	0	28	63	8
32	H-4	–3.90	5	2	31	48	15

Table 4. Molecular orbital coefficients and energies for 3,1,2-$SnC_2B_9H_{11}$.

MO	Orbital	eV	Sn	CH	BH(upper)	BH(lower)	BH(unique)
41	L+4	0.78	4	5	39	51	1
40	L+3	0.41	5	23	23	45	3
39	L+2	0.00	66	9	11	12	2
38	L+1	–1.99	76	8	2	11	3
37	LUMO	–2.30	87	2	2	7	2
36	HOMO	–7.33	39	3	32	18	9
35	H-1	–7.65	14	11	48	24	3
34	H-2	–8.21	1	3	26	64	6
33	H-3	–8.32	1	2	40	44	13
32	H-4	–8.41	2	1	32	56	10

Table 5. Molecular orbital coefficients and energies for $[SnCl_3]^–$.

MO	Orbital	eV	Sn	Cl_3
33	**L+4**	**9.67**	**97**	**3**
32	**L+3**	**9.67**	**97**	**3**
31	L+2	3.43	87	13
30	**L+1**	**3.25**	**95**	**5**
29	**LUMO**	**3.25**	**95**	**5**
28	HOMO	–2.45	45	55
27	H-1	–3.56	0	100
26	**H-2**	**–3.67**	**2**	**98**
25	**H-3**	**–3.67**	**2**	**98**
24	H-4	–3.97	0	100

Note: Degenerate levels are shown in boldface.

Table 6. Molecular orbital coefficients and energies for PF_3.

MO	Orbital	eV	P	F_3
26	L+4	8.1	94	6
25	L+3	6.21	106	–5
24	L+2	2.94	92	8
23	**L+1**	**–0.11**	**92**	**8**
22	**LUMO**	**–0.11**	**92**	**8**
21	HOMO	–8.78	64	36
20	H-1	–11.48	0	100
19	**H-2**	**–11.85**	**4**	**96**
18	**H-3**	**–11.85**	**4**	**96**
17	H-4	–12.81	4	96

Note: Degenerate levels are shown in boldface.

© 2008 NRC Canada

Table 7. Molecular orbital coefficients and energies for CO.

MO	Orbital	eV	C	O
12	**L+4**	**13.93**	**100**	**0**
11	**L+3**	**13.93**	**100**	**0**
10	L+2	7.14	144	–43
9	**L+1**	**–0.59**	**76**	**24**
8	**LUMO**	**–0.59**	**76**	**24**
7	HOMO	–10.11	90	10
6	**H-1**	**–12.72**	**27**	**73**
5	**H-2**	**–12.72**	**27**	**73**
4	H-3	–15.51	21	79
3	H-4	–31.51	26	74

Note: Degenerate levels are shown in boldface.

Table 8. Calculated LUMO and HOMO energies for known dicarbastannaboranes.

Compound	LUMO	HOMO
1,2,3-$SnC_2B_4H_6$[a]	–1.64	–6.73
1,2,4-$SnC_2B_4H_6$[b]	–1.69	–6.93
1,2,3-$SnC_2B_8H_{10}$[c]	–2.25	–7.32
3,1,2-$SnC_2B_9H_{11}$[d]	–2.30	–7.33
4,1,6-$SnC_2B_{10}H_{12}$[e]	–2.55	–7.37
1,2-μ-($CH_2CH{=}CHCH_2$)-4,1,2-$SnC_2B_{10}H_{10}$[f]	–2.72	–7.22

[a]Ref. 20.
[b]For 2,4-$(Me_3Si)_2$-1,2,4-$SnC_2B_4H_4$ see ref. 21.
[c]Ref. 23.
[d]Refs. 10 and 11.
[e]Ref. 22.
[f]For 1,2-[μ-$C_6H_4(CH_2)_2$]-4,1,2-$SnC_2B_{10}H_{10}$ see ref. 24.

Table 9. Comparison of calculated and observed (where available) ^{11}B, ^{13}C and ^{1}H NMR chemical shifts.

Compound	^{11}B,*^{13}C* (calcd)	^{11}B,*^{13}C* (exptl)	^{1}H (calcd)	^{1}H (exptl)
$[SnB_{11}H_{11}]^{2-}$	–7.6 (B12)	–5.5 (B12) (Ref.7)	2.38 (B12H)	
	–12.3 (B2-6)	–10.9 (B2-6)	1.97 (B7-11H)	
	–14.7 (B7-11)	–12.2 (B7-11)	1.30 (B2-6H)	
$[2,1\text{-}SnCB_{10}H_{11}]^{-}$	–6.6 (B12)	–6.0 (1B) (Ref. 1)	2.58 (B9H)	3.53 (1H) (Ref. 1)
	–7.6 (B9)	–7.1 (1B)	2.45 (B12H)	2.20 (1H)
	–9.6 (B7,11)	–8.3 (2B)	2.39 (B8,10H)	2.11 (2H, B8,10H)
	–11.5 (B8,10)	–10.5 (2B, B8,10)	2.36 (B4,5H)	2.04 (2H)
	–16.2 (B4,5)	–14.6 (2B)	1.74 (B3,6H)	1.38 (2H, B3,6H)
	–16.8 (B3,6)	–15.3 (2B, B3,6)	1.52 (B7,11H)	0.99 (2H)
	51.5	*51.8*	1.66 (CH)	1.76 (CH)
3,1,2-$SnC_2B_9H_{11}$	–2.0 (B9,12)		3.06 (B9,12H)	
	–5.6 (B8)	–6.8 (Ref. 11)	2.98 (B6H)	
	–8.0 (B10)		2.90 (B10H)	
	–12.1 (B5,11)		2.78 (B5,11H)	
	–14.0 (B6)	–13.8	2.12 (B8H)	
	–15.8 (B4,7)		1.92 (B4,7H)	
	47.7		2.74 (CH)	
1,2-Me_2-3,1,2-$SnC_2B_9H_9$	–2.6 (B9,12)		2.99 (B9,12H)	
	–3.4 (B6)	–3.9 (4B) (Ref.14)	2.98 (B5,11H)	
	–3.8 (B8)		2.85 (B6H)	
	–6.9 (B5,11)	–5.9 (2B)	2.72 (B10H)	
	–10.1 (B4,7)	–8.5 (2B)	2.42 (B4,7H)	
	–10.7 (B10)	–12.4 (1B)	1.91 (B8H)	
	72.2 (cage C)	*69.4 (cage C)*	2.02 (CH_3)	1.69 (CH_3) (Ref. 14)
	25.4 (CH_3)	*26.5 (CH_3)*		
4,1,6-$SnC_2B_{10}H_{12}$	17.8 (B3)[a]		4.69 (B8H)[a]	
	15.8 (B8)	11.3 (1B)(Ref. 22)	4.63 (B2H)	
	9.5 (B11)	10.7 (2B)	3.96 (B13H)	
	8.5 (B2)	9.1 (2B)	4.29 (B3H)	
	7.5 (B9)		4.10 (B9H)	
	6.9 (B13)		3.81 (B12H)	
	6.0 (B7)	7.3 (3B)	3.60 (B7H)	
	1.9 (B12)		3.05 (B11H)	
	–3.4 (B10)		1.41 (B10H)	
	–13.4 (B5)	–6.3 (2B)	0.91 (B5H)	
			7.08 (C1H)	5.51 (CH) (Ref. 22)

© 2008 NRC Canada

Table 9. (*concluded*).

Compound	^{11}B,*^{13}C* (calcd)	^{11}B,*^{13}C* (exptl)	^{1}H (calcd)	^{1}H (exptl)
	118.3 (C1)	*92.3*	3.94 (C6H)	
	65.2 (C6)			
4,1,6-$SnC_2B_{10}H_{12}$	11.4 (B8,13)[b]	11.3 (1B) (Ref. 22)	4.63 (B2H)[b]	
	9.5 (B11)	10.7 (2B)	4.33 (B8,13H)	
	8.5 (B2)	9.1 (2B)	4.10 (B9H)	
	7.5 (B9)		3.60 (B7H)	
	7.2 (B3,10)	7.3 (3B)	3.05 (B11H)	
	6.0 (B7)		2.85 (B3,10H)	
	–5.8 (B5,12)	–6.3 (2B)	2.36 (B5,12H)	
	90.1	*92.3*	5.51 (C1,6H)	5.51 (CH) (Ref. 22)
1,2,3-$SnC_2B_8H_{10}$	–0.6 (B8,9)	0.5 (B8,9) (Ref.23)	3.42 (B10,11H)	3.83 (B8,9H) (Ref. 23)
	–1.8 (B4,5,6,7)	0.2 (B4,5,6,7)	3.15 (B8,9H)	2.48 (B4,5,6,7H)
	–7.1 (B10,11)	–6.1 (B10,11)	3.15 (B4,5,6,7H)	1.96 (B10,11H)
	105.8		6.22 (CH)	6.28 (CH)

[a]Computed values are based on the ground-state optimized "gas-phase" and experimental "solid-state" asymmetric geometry.
[b]Computed values are based on fluxionality between two ground-state asymmetric geometries in solution. Shifts for the pairs C1/6, B8/13, B5/12, B3/10 and their exo-hydrogens are averaged.

vertices for the 2-Me_3Si-1,2,3-$SnC_2B_4H_5$ geometries is rather less pronounced than for the optimized geometries of 3,1,2-$SnC_2B_9H_{11}$ and 1,2-Me_2-3,1,2-$SnC_2B_9H_9$.

Geometry optimizations of known $SnC_2B_nH_{n+2}$ systems with n = 4, 8, and 10 were carried out and the electronic structures at these geometries were examined. The orbitals and their energies for these neutral systems are all similar to 3,1,2-$SnC_2B_9H_{11}$ (Table 8). This is perhaps not surprising as these systems exhibit similar Lewis acid properties. On this basis, the unknown non-icosahedral $[SnB_nH_n]^{2-}$ and $[SnCB_nH_{n+1}]^-$ ligands would be expected to have similar donor and acceptor properties to those of the icosahedral systems $[SnB_{11}H_{11}]^{2-}$ and $[SnCB_{10}H_{11}]^-$, respectively.

If ^{11}B and ^{13}C NMR shifts computed from an optimized geometry of a heteroborane at the DFT or MP2 level of theory show a very good correlation with its experimental solution-state NMR data, then the optimized geometry is considered the best representation of its molecular structure in solution (32). Comparison of the observed and computed ^{11}B and ^{13}C NMR data listed in Table 9 reveals that the optimized geometries of the 12-vertex dicarbastannaboranes 3,1,2-$SnC_2B_9H_{11}$ and 1,2-Me_2-3,1,2-$SnC_2B_9H_9$ with slipped tin vertices are also likely to be found in solution.

However, the calculated ^{11}B and ^{13}C NMR data from the asymmetrical "gas-phase" optimized geometry of the supraicosahedral system 4,1,6-$SnC_2B_{10}H_{12}$ are in poor agreement with the observed solution NMR data (22). This 13-vertex dicarbastannaborane 4,1,6-$SnC_2B_{10}H_{12}$ is fluxional in solution, interconverting between two mirror-related isomers of the asymmetric geometry via a double diamond-square process with a C_s symmetry transition state (22). Averaging of the computed NMR shifts of the relevant pairs of atoms gave very good agreement with the experimental values listed in Table 9, consistent with the fluxionality of the supraicosahedral cluster taking place in solution. The 11-vertex dicarbastannaborane 1,2,3-$SnC_2B_8H_{10}$ has the expected closo-11-vertex geometry based on the excellent agreement between the experimentally-assigned solution state (23) and the computed ^{11}B NMR data (Table 9). The optimized geometry reveals short Sn–C bond distances of 2.265 and long Sn–B bond distances of 2.695 Å compared to the corresponding bond distances listed in Table 1. Of interest are the calculated ^{13}C NMR chemical shifts for the two 4-connected carbon vertices in 1,2,3-$SnC_2B_8H_{10}$ (105.8 ppm) and the 4-connected carbon vertex in 4,1,6-$SnC_2B_{10}H_{12}$ (118.3 ppm) which are significantly different from those 5-connected vertices in other stannacarboranes (47.7-65.2 ppm) listed in Table 9.

Conclusions

DFT MO calculations show that $[SnCB_{10}H_{11}]^-$ has intermediate σ-donor/π-acceptor properties between those of the very strong σ-donor $[SnB_{11}H_{11}]^{2-}$ and the poor donor but good Lewis acid 3,1,2-$SnC_2B_9H_{11}$, and quite similar HOMO and LUMO energies and shapes to those of $[SnCl_3]^-$, a stronger σ-donor and weaker π-acceptor than CO or PF_3. Other $SnC_2B_nH_{n+2}$ systems show similar HOMO and LUMO energies to those of 3,1,2-$SnC_2B_9H_{11}$, both well below those of $[SnCB_{10}H_{11}]^-$, and are thus capable of binding one or two σ-donor ligands, but are poor σ-donors themselves. In contrast, the frontier orbital energies of $[SnB_{11}H_{11}]^{2-}$ are quite high in energy, resulting in excellent σ-donor but poor π-acceptor behavior, accounting for the strong trans-influence of this ligand, and its ability to stabilize metals in unusually high oxidation states. The higher negative charge in the non-carbon-containing systems, as well as the fact that boron is more electropositive than carbon, contribute to the increased energies of both HOMO and LUMO in the stannaboranes compared to the stannacarboranes, explaining their relative donor and acceptor properties.

Acknowledgements

We thank Durham University for access to its High Performance Computing Cluster, on which these calculations were carried out, and Professor Zhenyang Lin (The Hong

© 2008 NRC Canada

Kong University of Science and Technology) for helpful discussions.

References

1. D. Joosten, I. Weissinger, M. Kirchmann, C. Maichle-Mössmer, F.M. Schappacher, R. Pöttgen, and L. Wesemann. Organometallics, **26**, 5696 (2007).
2. A.R. Rossi and R. Hoffmann. Inorg. Chem. **14**, 365 (1975).
3. M. Kretschmer, P.S. Pregosin, and J. Rüegger. J. Organomet. Chem. **241**, 87 (1983).
4. (*a*) J.A. Long, T.B. Marder, P.E. Behnken, and M.F. Hawthorne. J. Am. Chem. Soc. **106**, 2979 (1984); (*b*) see also: R.R. Schrock and J.A. Osborn. J. Am. Chem. Soc. **93**, 2397 (1971).
5. R.W. Chapman, J.G. Kester, K. Folting, W.E. Streib, and L.J. Todd. Inorg. Chem. **31**, 979 (1992).
6. T. Gädt and L. Wesemann. Z. Anorg. Allg. Chem. **633**, 693 (2007).
7. T. Marx, L. Wesemann, S. Dehnen, and I. Pantenburg. Chem. Eur. J. **7**, 3025 (2001).
8. (*a*) T. Gädt and L. Wesemann. Organometallics, **26**, 2474 (2007); (*b*) S. Hagen, H. Schubert, C. Maichle-Mössmer, I. Pantenburg, F. Weigend, and L. Wesemann. Inorg. Chem. **46**, 6775 (2007); (*c*) T. Gädt and L. Wesemann. Dalton Trans. 328 (2006); (*d*) T. Gädt, L Eichele, and L. Wesemann. Dalton Trans. 2706 (2006); (*e*) S. Hagen, L. Wesemann, and I. Pantenburg. Chem. Commun. **8**, 1013 (2005); (*f*) T. Marx, B. Mosel, I. Pantenburg, S. Hagen, H. Shulze, and L. Wesemann. Chem. Eur. J. **9**, 4472 (2003); (g) S. Hagen, I. Pantenburg, F. Weigend, C. Wickleder, and L. Wesemann. Angew. Chem. Int. Ed. **42**, 1501 (2003); (h) L. Wesemann, S. Hagen, T. Marx, I. Pantenburg, M. Nobis, and D. Drießen-Hölscher. Eur. J. Inorg. Chem. 2261 (2002).
9. (*a*) M. Kirchmann, K. Eichele, F.M. Schappacher, R. Pöttgen, and L. Wesemann. Angew. Chem. Int. Ed. **47**, 963 (2008); (*b*) For a Highlight, see: S. Aldridge. Angew. Chem. Int. Ed. **47**, 2348, (2008).
10. (*a*) R.L. Voorhees and R.W. Rudolph. J. Am. Chem. Soc. **91**, 2173 (1969); (*b*) R.W. Rudolph and V. Chowdhry. Inorg. Chem. **13**, 248 (1974).
11. R.W. Rudolph, R.L. Voorhees, and R.E. Cochoy. J. Am. Chem. Soc. **92**, 3351 (1970).
12. T.B. Marder and M.F. Hawthorne. Unpublished work.1976.
13. A.H. Cowley, P. Galow, N.S. Hosmane, P. Jutzi, and N.C. Norman. J. Chem. Soc. Chem. Commun. 1564 (1984).
14. P. Jutzi, P. Galow, S. Abu-Orabi, A.M. Arif, A.H. Cowley, and N.C. Norman. Organometallics, **6**, 1024 (1987).
15. N.S. Hosmane, P. de Meester, N.N. Maldar, S.B. Potts, S.S.C. Chu, and R.H. Herber. Organometallics, **5**, 772 (1986).
16. R.D. Barreto, T.P. Fehlner, and N.S. Hosmane. Inorg. Chem. **27**, 453 (1988).
17. (*a*) U. Siriwardane, N.S. Hosmane, and S.S.C. Chu. Acta Crystallogr. **C43**, 1067 (1987); (*b*) J.A. Maguire, G.P. Ford, and N.S. Hosmane. Inorg. Chem. **27**, 3354 (1988); (*c*) N.S. Hosmane, M.S. Islam, U. Siriwardane, J.A. Maguire, and C.F. Campana. Organometallics, **6**, 2447 (1987).
18. N.S. Hosmane, R.D. Barreto, M.A. Tolle, J.J. Alexander, W. Quintana, U. Siriwardane, S.G. Shore, and R.E. Williams. Inorg. Chem. **29**, 2698 (1990).
19. N.S. Hosmane, N.S. Sirmokadam, and R.H. Herber. Organometallics, **3**, 1665 (1984).
20. K.-S. Wong and R.N. Grimes. Inorg. Chem. **16**, 2053 (1977).
21. N.S. Hosmane, L. Jia, H. Zhang, and J.A. Maguire, Organometallics, **13**, 1411 (1994).
22. N.M.M. Wilson, D. Ellis, A.S.F. Boyd, B.T. Giles, S.A. Macgregor, G.M. Rosair, and A.J. Welch. Chem. Commun. 464 (2002).
23. K. Nestor, B. Štíbr, T. Jelínek, and J.D. Kennedy. J. Chem. Soc. Dalton Trans. 1661 (1993).
24. K.-H. Wong, H.-S. Chan, and Z. Xie. Organometallics, **22**, 1775 (2003).
25. M.J. Frisch, G.W. Trucks, H.B. Schlegel, G.E. Scuseria, M.A. Robb, J.R. Cheeseman, J.A. Montgomery, Jr., T. Vreven, K.N. Kudin, J.C. Burant, J.M. Millam, S.S. Iyengar, J. Tomasi, V. Barone, B. Mennucci, M. Cossi, G. Scalmani, N. Rega, G.A. Petersson, H. Nakatsuji, M. Hada, M. Ehara, K. Toyota, R. Fukuda, J. Hasegawa, M. Ishida, T. Nakajima, Y. Honda, O. Kitao, H. Nakai, M. Klene, X. Li, J.E. Knox, H.P. Hratchian, J.B. Cross, C. Adamo, J. Jaramillo, R. Gomperts, R.E. Stratmann, O. Yazyev, A.J. Austin, R. Cammi, C. Pomelli, J.W. Ochterski, P.Y. Ayala, K. Morokuma, G.A. Voth, P. Salvador, J.J. Dannenberg, V.G. Zakrzewski, S. Dapprich, A.D. Daniels, M.C. Strain, O. Farkas, D.K. Malick, A.D. Rabuck, K. Raghavachari, J.B. Foresman, J.V. Ortiz, Q. Cui, A.G. Baboul, S. Clifford, J. Cioslowski, B.B. Stefanov, G. Liu, A. Liashenko, P. Piskorz, I. Komaromi, R.L. Martin, D.J. Fox, T. Keith, M.A. Al-Laham, C.Y. Peng, A. Nanayakkara, M. Challacombe, P.N.W. Gill, B. Johnson, W. Chen, M.W. Wong, C. Gonzalez, and J.A. Pople. Gaussian 03. Revision C.02 [computer program]. Gaussian, Inc., Wallingford, Conn. 2004.
26. (*a*) A.D. Becke. J. Chem. Phys. **98**, 5648 (1993); (*b*) C. Lee, W. Yang, and R.G. Parr. Phys. Rev. B, **37**, 785 (1988).
27. (*a*) G.A. Petersson and M.A. Al-Laham. J. Chem. Phys. **94**, 6081 (1991); (*b*) G.A. Petersson, A. Bennett, T.G. Tensfeldt, M.A. Al-Laham, W.A. Shirley, and J. Mantzaris. J. Chem. Phys. **89**, 2193 (1988).
28. (*a*) T.H. Dunning Jr. and P.J. Hay. *In* Modern theoretical chemistry. Vol. 3. *Edited by* H. F. Schaefer III. Plenum, New York.1976; (*b*) P.J. Hay and W.R. Wadt. J. Chem. Phys. **82**, 270 (1985); (*c*) W.R. Wadt and P.J. Hay. J. Chem. Phys. **82**, 284 (1985); (*d*) P.J. Hay and W.R. Wadt. J. Chem. Phys. **82**, 299 (1985).
29. A.-R. Allouche. Gabedit 2.1.0. CNRS and Université Claude Bernard, Lyon1, France. 2007. Available from http://gabedit.sourceforge.net.
30. N.M. O'Boyle and J.G. Vos. GaussSum 1.0. Dublin City University, Ireland. 2005. Available from http://gausssum.sourceforge.net.
31. R. McIntosh, D. Ellis, J. Gil-Lostes, K.J. Dalby, G.M. Rosair, and A.J. Welch. Dalton Trans. 1842 (2005).
32. (*a*) M. Bühl and P.v.R. Schleyer. J. Am. Chem. Soc. **114**, 477 (1992); (*b*) M.A. Fox, A.E. Goeta, A.K. Hughes, and A.L. Johnson. J. Chem. Soc. Dalton Trans. 2132 (2002).
33. (*a*) E.S. Alekseyeva, A.S. Batsanov, L.A. Boyd, M. A. Fox, T.G. Hibbert, J.A.K. Howard, J.A.H. MacBride, A. Mackinnon, and K. Wade. Dalton Trans. 475 (2003)*;* (*b*) A.R. Turner, H.E. Robertson, K.B. Borisenko, D.W.H. Rankin, and M.A. Fox. Dalton Trans. 1310 (2005).
34. (*a*) J. Campbell, H.P.A. Mercier, H. Franke, D.P. Santry, D.A. Dixon, and G.J. Schrobilgen. Inorg. Chem. **41**, 86 (2002); (*b*) Y. Mizuhata, N. Takeda, T. Sasamori, and N. Tokitoh. Chem. Commun. 5876 (2005).

© 2008 NRC Canada

Exploring the utility of a new chiral phosphoramidite *P,N*-ligand derived from (*R*)-BINOL and 7-azaindole in asymmetric catalysis[1]

Dominik Wechsler and Mark Stradiotto

Abstract: Lithiation of 7-azaindole, followed by quenching with [(*R*)-(1,1′-binaphthalene-2,2′-diyl)]chlorophosphite afforded the new chiral phosphoramidite **1** in 92% isolated yield. Treatment of 0.5 equiv. of $[(COD)MCl]_2$ (M = Rh, Ir; COD = η^4-1,5-cyclooctadiene) with 2 equiv. of **1** afforded the corresponding [(κ^1-*P,N*-**1**)(κ^2-*P,N*-**1**)MCl] complexes in 68% (**2a**, Rh) and 72% (**2b**, Ir) yield, while treatment of $(PPh_3)_3RhCl$ with 1 equiv. of **1** afforded [(PPh_3)(κ^2-*P,N*-**1**)RhCl] (**3**) as an analytically pure solid in 74% isolated yield. In examining the reaction of **1** with a mixture of 0.5 equiv. of $[(COD)RhCl]_2$ and 1 equiv. of $AgBF_4$, an inseparable mixture of [(κ^2-*P,N*-**1**)$_2$Rh]$^+BF_4^-$ (**4a**) and [(COD)(κ^2-*P,N*-**1**)Rh]$^+BF_4^-$ (**5a**) was generated. Under analogous conditions employing $[(COD)IrCl]_2$, the complex [(COD)(κ^2-*P,N*-**1**)Ir]$^+BF_4^-$ (**5b**) was obtained in 86% isolated yield. Treatment of 0.5 equiv. of [(η^3-allyl)$PdCl]_2$ with **1** afforded [(η^3-allyl)(κ^2-*P,N*-**1**)Pd]$^+Cl^-$ (**6**) in 86% isolated yield. The application of **1** in platinum group metal-mediated asymmetric chemical transformations, including alkene hydrogenation and hydroboration, ketone hydrosilylation, and allylic alkylation, was examined.

Key words: chiral, ligand, phosphoramidite, asymmetric catalysis.

Résumé : La lithiation du 7-azaindole, suivie d'un piégeage avec du chlorophosphite de [(*R*)-(1,1′-binaphtalène-2,2′-diyle) conduit à la formation du nouveau phospharamidite chiral, **1**, avec un rendement de 92% en produit isolé. Le traitement de 0,5 équiv. de $[(COD)MCl]_2$ (M= Rh, Ir; COD = η^4-cycloocta-1,5-diène) avec deux équiv. de **1** conduit à la formation des complexes correspondants [κ^1-*P,N*-**1**)(κ^2-*P,N*-**1**)MCl avec des rendements de 68% (**2a**, Rh) et de 72% (**2b**, Ir) alors que le traitement de $(PPh_3)_3RhCl$ avec 1 équiv. de **1** conduit à la formation du [(PPh_3)(κ^2-*P,N*-**1**)(RhCl] (**3**) qui a été isolé avec un rendement de 74% sous la forme d'un solide analytiquement pur. La réaction du produit **1** avec un mélange de 0,5 équiv. de $[(COD)RhCl]_2$ et un équiv. de $AgBF_4$ conduit à un mélange inextricable de [(κ^2-*P,N*-**1**)$_2$Rh]$^+BF_4^-$ et de [(COD)(κ^2-*P,N*-**1**)Rh]$^+BF_4^-$ (**5a**); dans des conditions impliquant l'utilisation du $[(COD)IrCl]_2$, on obtient le complexe [(COD)(κ^2-*P,N*-**1**)Ir]$^+BF_4^-$ (**5b**) avec un rendement isolé de 86%. Le traitement de 0,5 équiv. de [(η^3-allyl)$PdCl]_2$ avec le produit **1** conduit à la formation du produit [(η^3-allyl)(κ^2-*P,N*-**1**)Pd]$^+Cl^-$ (**6**) avec un rendement d 86% en produit isolé. On a examiné l'application du composé **1** dans les transformations chimiques asymétriques catalysées par un métal du groupe du platine, y compris les réactions d'hydrogénation et d'hydroboration des alcènes, d'hydrosilylation de cétones et d'alkylation allylique.

Mots-clés : chiral, ligand, phosphoramidite, catalyse asymétrique.

[Traduit par la Rédaction]

Introduction

Transition metal-catalyzed asymmetric synthesis represents one of the most effective approaches for the preparation of chiral non-racemic molecules on both benchtop and industrial scales (1). Platinum-group metal (PGM) complexes supported by chiral, heterobidentate *P,N*-ligands have proven particularly effective in mediating important transformations of this type, including the asymmetric addition of E–H bonds to unsaturated substrates (E = H, B, Si, etc.) and the enantioselective formation of C–C linkages (2). As a result, the pursuit of chiral *P,N*-ligands that can enable new and (or) improved asymmetric substrate transformations represents an important theme of modern catalysis research.

One facet of our research program focuses on the development of novel *P,N*-ligands for use in metal-mediated catalytic applications (3). In building upon this theme and encouraged by the utility of monodentate phosphoramidite (MonoPhos) ligands (4) as well as rigid κ^2-*P,N* phosphinooxazoline (PHOX) ligands (5) in PGM catalysis, we identified potentially bidentate chiral phosphoramidite ligands derived from 7-azaindole as attractive and readily prepared synthetic targets. Notably, while two reports by Woolins and

Received 3 April 2008. Accepted 23 April 2008. Published on the NRC Research Press Web site at canjchem.nrc.ca on 16 July 2008.

We dedicate this article to Professor Richard Puddephatt, in recognition of his widespread contributions to chemical research in Canada.

D. Wechsler and M. Stradiotto.[2] Department of Chemistry, Dalhousie University, Halifax, NS B3H 4J3, Canada.

[1]This article is part of a Special Issue dedicated to Professor Richard J. Puddephatt.

[2]Corresponding author (e-mail: mark.stradiotto@dal.ca).

 doi:10.1139/V08-092 © 2008 NRC Canada

co-workers (6) and Burrows et al. (7) document the PGM coordination chemistry of achiral κ^2-*P*,*N*-(7-aza-*N*-indolyl)phosphines, the preparation and application in asymmetric catalysis of chiral variants of such ligands has not been reported. Herein we report on the synthesis and characterization of a new chiral phosphoramidite ligand **1**, a preliminary account of the Rh, Ir, and Pd coordination chemistry of this ligand, and the application of **1** in PGM-mediated asymmetric chemical transformations including alkene hydrogenation and hydroboration, ketone hydrosilylation, and allylic alkylation.

Experimental

General Considerations

All manipulations were conducted in the absence of oxygen and water under an atmosphere of dinitrogen, either by use of standard Schlenk methods or within an mBraun glovebox apparatus, utilizing glassware that was oven-dried (130 °C) and evacuated while hot prior to use. Celite was oven-dried for 5 d and then evacuated for 24 h prior to use. The non-deuterated solvents tetrahydrofuran, diethyl ether, benzene, toluene, hexanes, and pentane were deoxygenated and dried by sparging with dinitrogen gas, followed by passage through a double-column solvent purification system purchased from mBraun Inc. Tetrahydrofuran and diethyl ether were purified over two alumina-packed columns, while benzene, toluene, hexanes, and pentane were purified over one alumina-packed column and one column packed with copper-Q5 reactant. All solvents used within the glovebox were stored over activated 4 Å molecular sieves. CD_2Cl_2 (Cambridge Isotopes) was degassed by using three repeated freeze–pump–thaw cycles, dried over CaH_2 for 7 days, distilled in vacuo, and stored over 4 Å molecular sieves for 24 h prior to use. C_6D_6 (Cambridge Isotopes) was degassed by using three repeated freeze–pump–thaw cycles and then dried over 4 Å molecular sieves for 24 h prior to use; styrene (Sigma-Aldrich, containing 10–15 ppm 4-*tert*-butylcatechol as inhibitor) was degassed in a similar manner, but was not stored over molecular sieves. Ph_2SiH_2 (Gelest, shipped under argon) was not degassed and was dried over 4 Å molecular sieves for 24 h prior to use. Hydrogen (99.999%, UHP Grade) gas was obtained from Air Liquide and was used as received. [(*R*)-(1,1′-binaphthalene-2,2′-diyl)]chlorophosphite (8) and (±)-(*E*)-1,3-diphenylprop-2-enyl acetate (9) were prepared by the use of literature procedures, while the transition metal reagents and silver salts were purchased from Strem Chemicals Inc. All purchased and prepared solid reagents were dried in vacuo for 24 h prior to use. Otherwise, all other commercial reagents were obtained from Sigma-Aldrich or Fluka and were used as received. ^{1}H, ^{13}C, and ^{31}P NMR characterization data were collected at 300 K on a Bruker AV-500 spectrometer operating at 500.1, 125.8, and 202.5 MHz (respectively) with chemical shifts reported in parts per million downfield of $SiMe_4$ (for ^{1}H and ^{13}C) or 85% H_3PO_4 in D_2O (for ^{31}P). ^{1}H and ^{13}C NMR chemical shift assignments are made on the basis of data obtained from ^{13}C-DEPT, ^{1}H-^{1}H COSY, ^{1}H-^{13}C HSQC, and ^{1}H-^{13}C HMBC NMR experiments. In some cases, fewer than expected unique ^{13}C NMR resonances were observed, despite prolonged acquisition times. Elemental analyses were performed by Canadian Microanalytical Service Ltd., Delta, British Columbia, Canada.

Synthesis of 1

A 1.6 mol/L hexanes solution (pre-cooled to –35 °C) of *n*-BuLi (0.51 mL, 0.82 mmol) was added dropwise to a vial containing a magnetically stirred solution (pre-cooled to –35 °C) of 7-azaindole (0.097 g, 0.82 mmol) in THF (4 mL), producing a colorless solution. The reaction mixture was stirred for 0.75 h at ambient temperature, followed by cooling to –35 °C. A pre-cooled (–35 °C) mixture of [(*R*)-(1,1′-binaphthalene-2,2′-diyl)]chlorophosphite (0.29 g, 0.82 mmol) and THF (5 mL) was then transferred slowly to the reaction mixture via Pasteur pipette. Upon completion of transfer, the resulting mixture was stirred for 2 h, after which the THF and other volatile materials were removed in vacuo. The residue was dissolved in a mixture of diethyl ether (4 mL) and benzene (2 mL) and filtered through Celite. The filtrate was dried in vacuo yielding **1** as an analytically pure, white solid (0.33 g, 0.76 mmol, 92%). ^{1}H NMR (C_6D_6) δ: 8.42 (d of d, $^3J_{HH}$ = 4.5 Hz, *J* = 1.5 Hz, 1H, C4-H or C6-H Aza.), 7.61 (d, $^3J_{HH}$ = 8.5 Hz, 1H, C-H Naph.), 7.57 (d, $^3J_{HH}$ = 9.0 Hz, 1H, C-H Naph.), 7.55 (d, $^3J_{HH}$ = 4.0 Hz, 1H, C-H Naph.), 7.53 (d, $^3J_{HH}$ = 4.5 Hz, 1H, C-H Naph.), 7.45 (d, $^3J_{HH}$ = 7.5 Hz, 1H, C6-H or C4-H Aza.), 7.41 (d, $^3J_{HH}$ = 8.5 Hz, 1H, C-H Naph.), 7.32 (d, $^3J_{HH}$ = 2.0 Hz, 1H, C-H Naph.), 7.30 (d, $^3J_{HH}$ = 2.5 Hz, 1H, C-H Naph.), 7.17–7.10 (m, 2H, C-H Naph.), 6.97 (m, 1H, C-H Naph.), 6.93 (m, 1H, C-H Naph.), 6.81 (d of d, $^3J_{HH}$ = 5.0 Hz, $^3J_{HH}$ = 8.0 Hz, 1H, C5-H Aza.), 6.76 (d, $^3J_{HH}$ = 4.0 Hz, 1H, C2-H or C3-H Aza.), 6.65 (d, $^3J_{HH}$ = 9.0 Hz, 1H, C-H Naph.), 5.92 (d of d, $^3J_{HH}$ = 4.0 Hz, *J* = 1.0 Hz, C3-H or C2-H Aza.). ^{13}C{^{1}H} NMR (C_6D_6) δ: 152.8 (d, *J* = 16.0 Hz, quat Aza.), 148.4 (quat Naph.), 148.0 (d, *J* = 4.2 Hz, quat Naph.), 143.7 (C4 or C6 Aza.), 133.0 (quat Naph.), 132.6 (quat Naph.), 131.7 (quat Naph.), 131.4 (quat Naph.), 131.1 (C-H Naph.), 130.1 (C-H Naph.), 128.5 (C-H Naph.), 128.4 (C-H Naph.), 128.2 (C6 or C4 Aza.), 127.0 (C-H Naph.), 126.9 (C-H Naph.), 126.5 (C-H Naph.), 126.4 (C-H Naph.), 126.2 (d, *J* = 4.3 Hz, C2 or C3 Aza.), 125.2 (C-H Naph.), 125.1 (C-H Naph.), 124.5 (d, *J* = 5.4 Hz, quat Aza.), 123.6 (quat Naph.), 122.3 (quat Naph.), 121.5 (C-H Naph.), 121.3 (C-H Naph.), 117.7 (C5 Aza.), 104.2 (C3 or C2 Aza.). ^{31}P{^{1}H} NMR (C_6D_6) δ: 133.8. Anal. calcd. for $C_{27}H_{17}P_1N_2O_2$: C 74.98; H 3.97; N 6.48. Found: C 74.58; H 3.93; N 6.26.

Synthesis of 2a

To a vial containing a magnetically stirred solution of **1** (0.056 g, 0.13 mmol) in THF (2 mL) was added dropwise a solution of $[(COD)RhCl]_2$ (0.016 g, 0.032 mmol) in THF (2 mL). The reaction mixture was stirred for 1 h, after which the solvent and other volatiles were removed in vacuo. The residue was washed with pentane (2 mL) and dried in vacuo, yielding **2a** as a pale yellow solid (0.044 g, 0.044 mmol, 68%). ^{1}H NMR (C_6D_6) δ: 9.34 (1H, C-H), 8.50–8.45 (m, 2H, C-Hs), 8.40 (d, $^3J_{HH}$ = 8.8 Hz, 1H, C-H), 7.68–7.63 (m, 2H, C-Hs), 7.60 (d, *J* = 8.75 Hz, 1H, C-H), 7.55–7.45 (m, 3H, C-Hs), 7.41 (d, $^3J_{HH}$ = 8.1 Hz, 1H, C-H), 7.35 (d, $^3J_{HH}$ = 8.2 Hz, 1H, C-H), 7.30–7.26 (m, 2H, C-Hs), 7.23 (d, $^3J_{HH}$ = 8.6 Hz, 1H, C-H), 7.13 (m, 1H, C-H), 7.07–6.98 (m, 3H, C-Hs), 6.97–6.82 (m, 4H, C-Hs), 6.81–6.75 (m, 2H, C-Hs),

© 2008 NRC Canada

6.71 (m, 1H, C-H), 6.57–6.50 (m, 2H, C-Hs), 6.41 (m, 1H, C-H), 6.21 (d, $^3J_{HH}$ = 8.8 Hz, 1H, C-H), 6.11 (d, $^3J_{HH}$ = 3.5 Hz, 1H, C-H), 5.96 (d, $^3J_{HH}$ = 8.7 Hz, 1H, C-H), 5.80–5.75 (m, 2H, C-H). $^{13}C\{^1H\}$ NMR (C_6D_6) δ: 151.8 (quat), 148.8 (quat), 148.4 (quat), 147.9 (quat), 143.1 (C-H), 142.9 (C-H), 132.8 (quat), 132.2 (quat), 132.1 (quat), 132.1 (quat), 131.9 (quat), 131.8 (quat), 131.0 (quat), 130.7 (quat), 130.6 (C-H), 130.2 (C-H), 129.8 (C-H), 129.4 (C-H), 129.3 (C-H), 129.0 (C-H), 128.8 (C-H), 128.2 (C-H), 128.2 (C-H), 128.1 (C-H), 128.0 (C-H), 127.2 (C-H), 127.0 (C-H), 126.9 (C-H), 126.8 (C-H), 126.3 (C-H), 125.8 (C-H), 125.8 (C-H), 125.4 (C-H), 125.3 (C-H), 124.7 (C-H), 124.5 (C-H), 123.6 (C-H), 123.6 (quat), 123.1 (quat), 122.3 (quat), 121.9 (quat), 121.3 (quat), 120.8 (C-H), 120.3 (C-H), 118.5 (quat), 117.5 (C-H), 117.3 (C-H), 108.0 (C-H), 103.6 (C-H). $^{31}P\{^1H\}$ NMR (C_6D_6) δ: 146.6 (d of d, $^1J_{PRh}$ = 275.2 Hz, $^2J_{PP}$ = 64.5 Hz), 140.0 (d of d, $^1J_{PRh}$ = 309.3 Hz, $^2J_{PP}$ = 64.2 Hz). Anal. calcd. for $C_{54}H_{34}Cl_1P_2N_4O_4Rh_1$: C 64.64; H 3.41; N 5.59. Found: C 64.55; H 3.74; N 5.48.

Synthesis of 2b

A procedure analogous to that described for the synthesis of **2a** was employed, using $[(COD)IrCl]_2$ (0.048 g, 0.072 mmol) in THF (2 mL). Complex **2b** was isolated as a light brown solid (0.11 g, 0.10 mmol, 72%). ^1H NMR (C_6D_6) δ: 9.51 (br s, 1H, C-H), 8.42 (d, $^3J_{HH}$ = 8.7 Hz, 1H, C-H), 8.37–8.34 (m, 2H, C-H), 7.89 (br s, 1H, C-H), 7.67 (d, *J* = 8.75 Hz, 1H, C-H), 7.62 (d, *J* = 8.75 Hz, 1H, C-H), 7.55–7.49 (m, 3H, C-H), 7.42 (d, $^3J_{HH}$ = 8.1 Hz, 1H, C-H), 7.36 (d, $^3J_{HH}$ = 8.2 Hz, 1H, C-H), 7.32–7.28 (m, 2H, C-H), 7.25 (d, $^3J_{HH}$ = 8.6 Hz, 1H, C-H), 7.06–7.02 (m, 2H, C-H), 6.98–6.89 (m, 4H, C-H), 6.88–6.83 (m, 2H, C-H), 6.82–6.78 (m, 2H, C-H), 6.71 (m, 1H, C-H), 6.59–6.52 (m, 2H, C-H), 6.39 (m, 1H, C-H), 6.27 (d, $^3J_{HH}$ = 8.8 Hz, 1H, C-H), 6.15 (d, $^3J_{HH}$ = 3.3 Hz, 1H, C-H), 5.96 (d, $^3J_{HH}$ = 8.8 Hz, 1H, C-H), 5.93 (d, $^3J_{HH}$ = 3.5 Hz, 1H, C-H), 5.75 (d, $^3J_{HH}$ = 2.9 Hz, 1H, C-H). $^{13}C\{^1H\}$ NMR (C_6D_6) δ: 151.4 (quat), 148.7 (quat), 148.5 (quat), 147.7 (quat), 142.8 (C-H), 141.0 (C-H), 132.8 (quat), 132.3 (quat), 132.2 (quat), 132.0 (quat), 131.7 (quat), 130.9 (quat), 130.6 (C-H), 130.4 (C-H), 129.9 (C-H), 129.4 (C-H), 128.7 (C-H), 128.1 (C-H), 128.1 (C-H), 127.3 (C-H), 127.1 (C-H), 127.0 (C-H), 126.9 (C-H), 126.3 (C-H), 125.7 (C-H), 125.4 (C-H), 125.2 (C-H), 125.1 (C-H), 124.6 (C-H), 124.5 (C-H), 124.3 (quat), 123.6 (C-H), 123.1 (quat), 122.2 (quat), 121.8 (quat), 121.2 (quat), 120.9 (C-H), 120.6 (C-H), 118.6 (quat), 117.4 (C-H), 117.1 (C-H), 107.8 (C-H), 103.3 (C-H). $^{31}P\{^1H\}$ NMR (C_6D_6) δ: 107.6 (d, $^2J_{PP}$ = 63.4 Hz), 104.3 (d, $^2J_{PP}$ = 63.5 Hz). Anal. calcd. for $C_{54}H_{34}Cl_1P_2N_4O_4Ir_1$: C 59.36; H 3.14; N 5.13. Found: 59.79; H 3.46; N 4.91.

Synthesis of 3

To a vial containing a magnetically stirred solution of **1** (0.047 g, 0.11 mmol) in THF (2 mL) was added dropwise a solution of $(PPh_3)_3RhCl$ (0.10 g, 0.11 mmol) in THF (2 mL), and the reaction mixture was stirred for 2 h. Pentane (10 mL) was added to the reaction mixture, causing the product to precipitate. The supernatant was decanted away and the precipitate washed with pentane (2 mL). The solid was dried in vacuo, yielding **3** as a yellow-brown solid (0.065 g, 0.081 mmol, 74%). ^1H NMR (C_6D_6) δ: 9.97 (d, $^3J_{HH}$ = 5.3 Hz, 1H, C-H), 7.99–7.91 (m, 6H, C-Hs), 7.79 (br s, 1H, C-H), 7.57 (d, $^3J_{HH}$ = 8.2 Hz, 1H, C-H), 7.44 (d, $^3J_{HH}$ = 8.85 Hz, 1H, C-H), 7.42 (d, $^3J_{HH}$ = 8.2 Hz, 1H, C-H), 7.31 (d, $^3J_{HH}$ = 8.6 Hz, 1H, C-H), 7.26 (d, $^3J_{HH}$ = 8.8 Hz, 1H, C-H), 7.08–7.20 (m, 3H, C-Hs), 7.03 (m, 1H C-H), 6.93 (d, $^3J_{HH}$ = 8.8 Hz, 1H, C-H), 6.91–6.83 (m, 3H, C-Hs), 6.80–6.76 (m, 8H, C-Hs), 6.58 (m, 1H, C-H), 5.91 (d, $^3J_{HH}$ = 3.7 Hz, 1H, C-H), 5.80 (d, $^3J_{HH}$ = 3.6 Hz, 1H, C-H). $^{13}C\{^1H\}$ NMR (C_6D_6) δ: 154.3 (d, *J* = 24.3 Hz, quat), 148.5 (d, J = 14.6 Hz, quat), 147.8 (d, *J* = 7.2 Hz, quat), 143.7 (C-H), 136.1 (quat), 135.7 (quat), 135.3 (C-H), 135.2 (C-H), 132.7 (m), 131.6 (quat), 131.3 (quat), 130.4 (C-H), 130.2 (C-H), 129.5 (C-H), 128.9 (C-H), 128.4 (C-H), 128.2 (C-H), 127.4 (C-H), 126.9 (m), 126.5 (C-H), 125.8 (C-H), 125.4 (C-H), 124.9 (C-H), 124.8 (m), 122.3 (m), 122.1 (C-H), 121.8 (C-H), 118.2 (d, *J* = 6.3 Hz, quat), 117.4 (C-H), 107.8 (C-H). $^{31}P\{^1H\}$ NMR (C_6D_6) δ: 135.4 (d of d, $^1J_{PRh}$ = 322.0 Hz, $^2J_{PP}$ = 64.7 Hz, 1P, PN), 43.4 (d of d, $^1J_{PRh}$ = 159.8 Hz, $^2J_{PP}$ = 64.7 Hz, PPh_3). Anal. calcd. for $C_{45}H_{32}Cl_1P_2N_2O_2Rh_1$: C 64.86; H 3.87; N 3.36. Found: 64.99; H 4.13; N 3.01.

Synthesis of 5b

To a vial containing a magnetically stirred suspension of $[(COD)IrCl]_2$ (0.074 g, 0.11 mmol) in THF (2 mL) was added a suspension of $AgBF_4$ (0.043 g, 0.22 mmol) in THF (2 mL). An orange solution was generated immediately along with a white precipitate. The supernatant solution was separated from the precipitate by filtration through Celite, and the solution was transferred to a vial containing a magnetically stirred solution of **1** (0.095 g, 0.22 mmol) in THF (2 mL). The reaction mixture was stirred for an additional 3 h at ambient temperature, during which the solution developed a red-orange coloration. The reaction mixture was then filtered through a plug of Celite, followed by removal of the solvent and other volatiles in vacuo to yield **5b** as a bright red-orange solid (0.16 g, 0.19 mmol, 86%). ^1H NMR (CD_2Cl_2) δ: 8.43 (d, $^3J_{HH}$ = 8.0 Hz, 1H, C-H), 8.31 (d, $^3J_{HH}$ = 5.5 Hz, 1H, C-H), 8.24 (d, $^3J_{HH}$ = 9.0 Hz, 1H, C-H), 8.21 (d, $^3J_{HH}$ = 8.5 Hz, 1H, C-H), 8.15–8.10 (m, 2H, C-Hs), 7.76 (d, $^3J_{HH}$ = 9.0 Hz, 1H, C-H), 7.68–7.60 (m, 3H, C-Hs), 7.47–7.39 (m, 5H, C-Hs), 7.14 (d, $^3J_{HH}$ = 4.0 Hz, 1H, C-H), 6.43 (d of d, *J* = 2.0 Hz, *J* = 3.5 Hz, 1H, C-H), 6.04 (br s, 1H, COD), 5.98 (br s, 1H, COD), 4.19 (br s, 1H, COD), 4.13 (br s, 1H, COD), 2.52–2.18 (m, 8H, COD). $^{13}C\{^1H\}$ NMR (CD_2Cl_2) δ: 156.9 (quat), 146.8 (d, *J* = 13.7 Hz, quat), 145.8 (d, *J* = 7.0 Hz, quat), 142.4 (C-H), 135.1 (C-H), 132.4 (quaJune 24, 2008t), 132.2 (quat), 132.1 (C-H), 132.0 (C-H), 128.8 (C-H), 128.8 (C-H), 127.5 (2 C-Hs), 127.0 (C-H), 127.0 (C-H), 126.7 (C-H), 126.6 (C-H), 124.6 (d, *J* = 6.0 Hz, C-H), 122.3 (quat), 122.0 (quat), 121.1 (d, *J* = 8.3 Hz, quat), 120.0 (C-H), 119.8 (C-H), 119.7 (C-H), 111.9 (C-H), 70.3 (m, C-H), 62.2 (C-H), 33.2 (CH_2), 33.0 (CH_2), 29.0 (CH_2), 28.8 (CH_2). $^{31}P\{^1H\}$ NMR (CD_2Cl_2) δ: 115.3. Anal. calcd. for $C_{35}H_{29}P_1N_2O_2B_1F_4Ir_1$: C 51.26; H 3.57; N 3.42. Found: 51.24; H 3.78; N 2.99.

Synthesis of 6

To a vial containing a magnetically stirred solution of **1**(0.078 g, 0.18 mmol) in THF (1 mL) was added dropwise a solution of $[(\eta^3\text{-allyl})PdCl]_2$ (0.033 g, 0.090 mmol) in THF

© 2008 NRC Canada

(2 mL). The reaction mixture was stirred for 0.5 h, and the solvent and other volatiles were removed in vacuo yielding **6** as a yellow solid (0.092 g, 0.15 mmol, 86%). ^{1}H NMR (CD_2Cl_2) δ: 8.60 (d of d, $^3J_{HH}$ = 5.0 Hz, J = 1.4 Hz, 1H, C4-H or C6-H Aza.), 8.19 (d, $^3J_{HH}$ = 8.9 Hz, 1H, C-H), 8.09 (d, $^3J_{HH}$ = 8.3 Hz, 1H, C-H), 8.06–8.03 (m, 2H, C-Hs), 7.98 (d, $^3J_{HH}$ = 8.9 Hz, 2H, C-Hs), 7.62–7.57 (m, 2H, C-Hs), 7.51–7.45 (m, 2H, C-Hs), 7.44–7.39 (m, 2H, C-Hs), 7.34 (d of d, 1H, $^3J_{HH}$ = 5.0 Hz, $^3J_{HH}$ = 7.9 Hz, C5-H Aza.), 7.15 (d of d, 1H, $^3J_{HH}$ = 8.80 Hz, J = 0.7 Hz, C-H), 6.71 (d of d, 1H, $^3J_{HH}$ = 3.8 Hz, J = 1.6 Hz, C2-H or C3-H Aza.), 6.55 (d, $^3J_{HH}$ = 3.8 Hz, 1H, C3-H or C2-H Aza.), 5.83 (m, 1H, allyl), 3.94 (br s, 4H, allyl). ^{13}C{^{1}H} NMR (CD_2Cl_2) δ: 152.5 (C3a or C7a Aza.), 152.3 (C7a or C3a Aza.), 147.5 (m, quat), 146.9 (d, J = 4.9 Hz, quat), 143.3 (C4 or C6 Aza.), 132.4–131.9 (m, quat), 131.5 (C-H), 131.1 (C-H), 130.4 (C-H), 128.7–128.6 (m, aryl C-H and allyl C-H), 127.0 (m, C-Hs), 126.9 (C-H), 126.1 (m, C-Hs), 123.0 (quat), 122.6 (quat), 121.7 (d, J = 2.0 Hz, C-H), 120.3 (C-H), 118.8 (C5 Aza.), 107.5 (C3 or C2 Aza.). ^{31}P{^{1}H} NMR (CD_2Cl_2) δ: 133.1. Anal. calcd. for $C_{30}H_{22}Cl_1P_1N_2O_2Pd_1$: C 58.53; H 3.61; N 4.55. Found: 58.11; H 3.63; N 4.03.

General protocol for the metal-catalyzed hydrogenation experiments

A solution of metal (M = Rh or Ir) precursor (0.025 mmol in 0.5 mL) and **1** (1.2 equiv. relative to M; 0.030 mmol in 0.5 mL) in the desired solvent were combined to give a 0.025 mol/L solution of the catalyst (based on M). The solution was allowed to equilibrate for 0.75 h, at which point methyl 2-acetamidoacrylate (0.50 mmol in 0.5 mL) was added by use of an Eppendorf pipette. The mixture was placed in glass reactor cell, which was equipped with a magnetic stir bar and sealed under nitrogen with a PTFE valve. The cell was transferred to a Schlenk line, and the mixture was degassed by use of three freeze–pump–thaw cycles, followed by the addition of ca. 1 atm of H_2 (1 atm = 101.325 kPa), while magnetically stirring the solution. At the desired sampling time, the reaction mixture was concentrated in vacuo and extracted with diethyl ether (2 mL). The catalyst was removed by passing the diethyl ether extract through a plug of silica (0.6 cm × 2 cm) from which a clear, colorless solution eluted. This solution was transferred to a GC vial and sealed. Quantitative data were obtained from chiral GC-FID analysis using a Varian CHIRAL-L-VAL column.

General protocol for the metal-catalyzed hydroboration experiments

The general protocol employed herein for the hydroboration of styrene with HBpin has been described elsewhere (10). For reactions in which HBcat was employed, pinacol (2.1 equiv.) was added to the reaction mixture after 24 h followed by stirring for an additional 24 h. The subsequent work up procedure employed was the same as that undertaken for reactions involving HBpin.

General protocol for the metal-catalyzed hydrosilylation experiments

A solution of metal precursor (0.045 mmol in 0.75 mL) and **1** (1.2 equiv.; 0.054 mmol in 0.75 mL) in the desired solvent were combined to give a 0.030 mol/L solution of the catalyst (based on the metal). The solution was allowed to equilibrate for 0.75 h, at which point the ketone (0.90 mmol) was added by use of an Eppendorf pipette. The vial was then sealed, shaken vigorously, and cooled to –35 °C. Subsequently, pre-cooled (–35 °C) Ph_2SiH_2 (1.6 mmol) was added dropwise by use of an Eppendorf pipette to the reaction mixture, and the vial was then sealed and the reaction mixture was magnetically stirred for 18 h at ambient temperature. The reaction mixture was then cooled to 0 °C, and 1 mol/L HCl (5 mL) and acetone (5 mL) were added. The mixture was stirred for 1.5 h at 0 °C followed by 0.5 h at ambient temperature. A solution of saturated sodium bicarbonate was added, and the reaction mixture was stirred until no more gas evolution was observed (approx. 0.25 h). The reaction mixture was extracted with diethyl ether (2 × 5 mL). The combined organic layers were dried over Na_2SO_4, and the catalyst was removed by passing the solution through a plug of alumina (0.6 cm × 2 cm) from which a clear, colorless solution eluted. This solution was transferred to a GC vial and sealed. Products were identified by use of GC-MS while quantitative data were obtained from chiral GC-FID analysis by using a Supelco BETA-DEX 120 column.

Representative protocol for the metal-catalyzed allylic alkylation experiments

A 0.020 mol/L stock solution of catalyst was prepared by adding [(η^3-allyl)PdCl]$_2$ (0.0073 g, 0.020 mmol) in THF (1 mL) to ligand **1** (0.017 g, 0.040 mmol) in THF (1 mL), followed by stirring for 0.5 h. A 0.40 mol/L stock solution of the substrate was prepared by dissolving (±)-(*E*)-1,3-diphenylprop-2-enyl acetate (0.27 g, 1.1 mmol) in THF (2.7 mL). A 0.12 mL aliquot was taken from each of the two stock solutions and combined; this reaction mixture was stirred for 0.25 h and was then diluted with THF to a total volume of 12 mL to produce a final substrate concentration of 0.004 mol/L. Dimethyl malonate (6.6 μL, 0.058 mmol, 1.1 equiv.), *N*,*O*-bis(trimethylsilyl)acetamide (14.1 μL, 0.058 mmol, 1.1 equiv.), and KOAc (catalytic amount) were added to the reaction mixture, and the resulting suspension was stirred at 24 °C for 72–100 h. The reaction mixture was then concentrated in vacuo, passed through a short silica gel column (0.6 cm × 5 cm), and eluted with diethyl ether/hexanes (2:1). A portion of the eluent was transferred to a GC vial and sealed, while the remaining eluent was concentrated in vacuo. The reaction products were identified by use of GC-MS, while quantitative data were obtained from GC-FID analysis using a Supelco DB200 column. The enantiomeric excess of **11** was determined by use of ^{1}H NMR methods through the addition of Eu(hfc)$_3$ (8–10 mg) in $CDCl_3$ (0.6 mL) to the reaction sample. Isomer assignments are given on the basis of literature data (11).

Results and discussion

Ligand synthesis and coordination chemistry

The new chiral phosphoramidite **1** was prepared in 92% isolated yield (Scheme 1) via lithiation of 7-azaindole, followed by quenching with [(*R*)-(1,1′-binaphthalene-2,2′-diyl)]chlorophosphite prepared from the commercially available reagents *R*-BINOL and PCl_3. Prior to evaluating the

© 2008 NRC Canada

Scheme 1. Synthesis of the new chiral *P,N*-ligand 1.

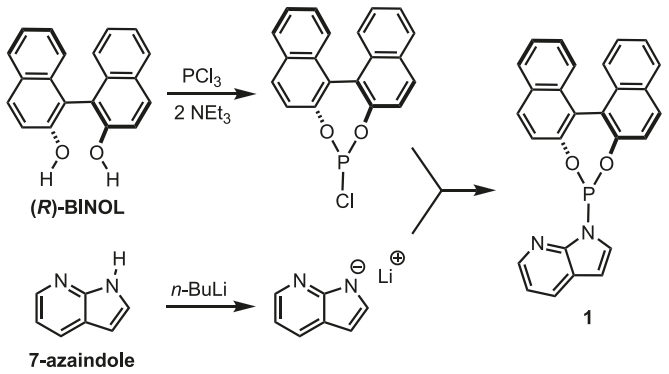

Scheme 2. Reactivity of 1 with $[(COD)MCl]_2$ or $(PPh_3)_3RhCl$ (M = Rh, Ir; COD = η^4-1,5-cyclooctadiene).

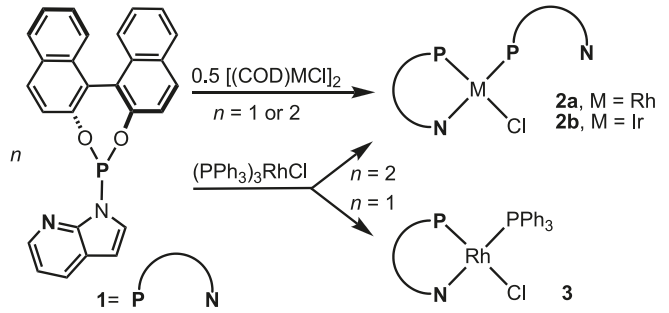

utility of **1** as a chiral ancillary ligand in PGM-mediated catalysis, we sought to examine the coordination chemistry of this new ligand. Treatment of 0.5 equiv. of $[(COD)MCl]_2$ (M = Rh, Ir; COD = η^4-1,5-cyclooctadiene) with 1 equiv. of **1** did not afford $[(COD)(\kappa^1\text{-}\mathbf{1})MCl]$; instead, a clean mixture of 0.5 equiv. of $[(\kappa^1\text{-}P,N\text{-}\mathbf{1})(\kappa^2\text{-}P,N\text{-}\mathbf{1})MCl]$ **2a** and **2b** and 0.25 equiv. of unreacted $[(COD)MCl]_2$ was observed by use of NMR spectroscopic methods (Scheme 2). Compounds **2a** and **2b** are observed as the only phosphorus-containing product when a **1**/M ratio of 2:1 is employed, thereby allowing for the convenient isolation of **2a** and **2b** as analytically pure solids in 68% (**2a**, Rh) and 72% (**2b**, Ir) yields, respectively. The observation of ^{31}P-^{31}P coupling between the magnetically non-equivalent phosphorus centers in the ^{31}P NMR spectra of **2a** and **2b** (as well as the clearly discernable ^{103}Rh coupling in the case of **2a**) is consistent with the existence of P-M-P′ linkages in **2a** and **2b**. Moreover, the cis-disposition of the phosphorus fragments in **2a** and **2b** as depicted in Scheme 2 is in keeping with the magnitude of the observed $^2J_{PP}$ value (ca. 64 Hz) for these complexes. Whereas **2a** is also formed upon treatment of $(PPh_3)_3RhCl$ with 2 equiv. of **1**, the use of only 1 equiv. of **1** under similar conditions afforded $[(PPh_3)(\kappa^2\text{-}P,N\text{-}\mathbf{1})RhCl]$ **3** as an analytically pure solid in 74% isolated yield.

In the pursuit of $[(COD)(\kappa^2\text{-}P,N\text{-}\mathbf{1})M]^+X^-$ complexes (M = Rh, Ir), the reaction of **1** with mixtures of 0.5 equiv. of $[(COD)MCl]_2$ and 1 equiv. of $AgBF_4$ in THF was examined. For M = Rh, NMR analysis revealed the formation of an inseparable mixture of $[(\kappa^2\text{-}P,N\text{-}\mathbf{1})_2Rh]^+BF_4^-$ **4a** and $[(COD)(\kappa^2\text{-}P,N\text{-}\mathbf{1})Rh]^+BF_4^-$ **5a** (12) as depicted in Scheme 3. Compound **4a** was also observed as a major phosphorus-

Scheme 3. Reactivity of 1 with $[(COD)MCl]_2/AgBF_4$ (M = Rh, Ir; COD = η^4-1,5-cyclooctadiene) and $[(\eta^3\text{-allyl})PdCl]_2$.

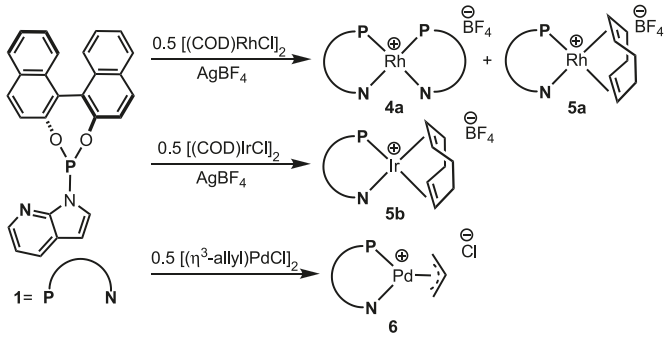

containing product in such reactions when the **1**/Rh ratio was reduced to 0.5:1. Conversely, reactions employing **1**:Ir in a 1:1 ratio afforded $[(COD)(\kappa^2\text{-}P,N\text{-}\mathbf{1})Ir]^+BF_4^-$ **5b** as the major product, thereby allowing for the isolation of this species in 86% yield.

The ability of **1** to form 1:1 complexes with Pd was confirmed upon treatment of 0.5 equiv. of $[(\eta^3\text{-allyl})PdCl]_2$ with **1**; the corresponding salt $[(\eta^3\text{-allyl})(\kappa^2\text{-}P,N\text{-}\mathbf{1})Pd]^+Cl^-$ **6** was obtained as an analytically pure solid in 86% isolated yield (Scheme 3). While shortly following dissolution the ^{31}P NMR spectrum of **6** exhibits a single resonance at 133.1 ppm, a new signal at 129.4 ppm was observed to grow in over the course of 3 h. Although we are presently unable to comment definitively regarding the relationship between these two phosphorus-containing species, the propensity of $[(\eta^3\text{-allyl})(\kappa^2\text{-}P,N)Pd]^+X^-$ complexes to exhibit complicated dynamic behavior is well-established (13). Having briefly explored the coordination chemistry of **1** with Rh, Ir, and Pd, the utility of this new chiral *P,N*-ligand in PGM-mediated asymmetric synthesis was surveyed. For convenience, catalyst complexes were prepared in situ by using an appropriate metal precursor in combination with **1** (except where noted).

Asymmetric hydrogenation

The Rh- and Ir-mediated asymmetric hydrogenation of methyl-2-acetamidoacrylate **7** to afford **8** (eq. [1]) under mild conditions (24 °C, ca. 1 atm H_2, 5.0 mol% Rh or Ir) was selected as a preliminary catalytic test reaction to use in benchmarking the performance of **1** (14); key results of these hydrogenation studies are collected in Table 1. Control experiments confirmed the ability of catalyst mixtures derived from 0.5 $[(COD)RhCl]_2$ and $AgBF_4$ in THF (without added **1**) to mediate the reduction of **7** (Table 1, entry 1–1). Under analogous conditions employing 6.0 mol% of **1** (1.2 equiv. relative to Rh), the quantitative reduction of **7** was also achieved, affording **8** in 65% ee (Table 1, entry 1–2). However, increasing the amount of **1** to 12.0 mol% (Table 1, entry 1–3) in such transformations was found to diminish both the conversion (78%) and the enantioselectivity (50% ee), possibly because of the preferential formation of less effective catalytic intermediates derived from $[(\kappa^2\text{-}P,N\text{-}\mathbf{1})_2Rh]^+BF_4^-$ **4a**. On the basis of this postulate and in light of the established preference of **1** to form **4a** (and not $[(COD)(\kappa^2\text{-}P,N\text{-}\mathbf{1})Rh]^+BF_4^-$ **5a**) when combined with $[(COD)Rh(THF)_2]^+BF_4^-$ (vide supra), it is likely that the results featured in entry 1–2 (Table 1) do not truly reflect the

© 2008 NRC Canada

Table 1. Hydrogenation of methyl 2-acetamidoacrylate.

Entry	Metal precursor (5.0 mol%)	Mol% of **1** added	Solvent	%[a]	% ee[b]
1–1	$[(COD)Rh(THF)_2]^+BF_4^-$	0	THF	>99	<1
1–2	$[(COD)Rh(THF)_2]^+BF_4^-$	6.0	THF	>99	65
1–3	$[(COD)Rh(THF)_2]^+BF_4^-$	12.0	THF	78	50
1–4	$[(COD)Ir(THF)_2]^+BF_4^-$	0	CH_2Cl_2	>99	<1

Note: Conditions: 24 °C, 1 atm H_2. $[(COD)M(THF)_2]^+BF_4^-$ prepared in situ from 0.5 $[(COD)MCl]_2$ and $AgBF_4$ in THF (M = Rh, Ir and COD = η^4-1,5-cyclooctadiene).

[a]Percent conversion based on the consumption of methyl-2-acetamidoacrylate (**7**) at 24 h.

[b]Enantiomeric excess of **8** determined on the basis of chiral GC-FID data.

performance of the target pre-catalyst complex **5a** alone; rather, the previously discussed coordination chemistry studies indicate that each of $[(COD)Rh(THF)_2]^+BF_4^-$, **4a**, and **5a** are likely to be present as pre-catalysts under these experimental conditions. In this regard, the inherent enantioselectivity of **5a** is likely underestimated, owing to the significant background reactivity associated with $[(COD)Rh(THF)_2]^+BF_4^-$ (Table 1, entry 1–1) and the generally inferior performance of **4a**, as based on entry 1–3. In an effort to possibly promote the formation of **5a**, the reaction solvent was changed to CH_2Cl_2; however, all such reactions employing $[(COD)Rh(THF)_2]^+BF_4^-$ (pre-formed in THF) in combination with 0, 1.2, or 2.4 equiv. of **1** relative to Rh afforded no conversion of the alkene substrate (15). Similarly, the pre-formed Rh complex **3** proved to be catalytically inactive in either THF or CH_2Cl_2. While $[(COD)Ir(THF)_2]^+BF_4^-$ mediated the quantitative conversion of **7** to **8** in CH_2Cl_2 (Table 1, entry 1–4), the activity of Ir in this chemistry was completely inhibited by the addition of 1.2 equiv. of **1** for reactions carried out in CH_2Cl_2 or THF.

[1] 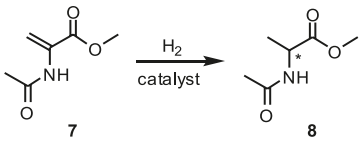

Asymmetric hydroboration

The asymmetric hydroboration of styrene (16) employing either pinacolborane (HBpin) or catecholborane (HBcat) was selected as an alternative E–H addition reaction with which to evaluate the ability of **1** to promote chemo-, regio-, and enantioselectivity in PGM-mediated catalysis (eq. [2] and Table 2). For reactions employing HBpin, catalyst mixtures derived from 5.0 mol% $[(COD)_2Rh]^+BF_4^-$ and 5.5 mol% **1** were found to exhibit modest selectivity towards the desired branched isomer **9a** over the linear isomer **9b** at substrate concentrations of 0.19 mol/L (Table 2, entry 2–1) and 0.046 mol/L (Table 2, entry 2–2); inferior selectivity was noted for analogous reactions in which HBcat was used (Table 2, entries 2–3 and 2–4). Unfortunately, no enantioselectivity (in **9a**) was achieved in the aforementioned hydroboration reactions, and analogous reactions employing 5.0 mol% $[(COD)_2Ir]^+BF_4^-$ and 5.5 mol% **1** afforded exclusively the linear product **9b**.

Table 2. Rhodium-catalyzed addition of HBpin and HBcat to styrene.

Entry	Borane[a]	Substrate conc. (mol/L)	Branched: linear[b] (**9a**:**9b**)
2–1	HBpin	0.19	73:27
2–2	HBpin	0.046	68:32
2–3	HBcat	0.19	60:40
2–4	HBcat	0.046	61:39

Note: Conditions: –30 °C for 24 h; 5.0 mol% $[(COD)_2Rh]^+BF_4^-$; 5.5 mol% **1**; borane-to-styrene ratio of 1.2:1; THF. For all experiments >95% conversion of styrene was achieved.

[a]HBpin = pinacolborane; HBcat = catecholborane.

[b]Product ratio on the basis of GC-FID data, rounded to the nearest percent. In all cases, other boron-containing products represented <3% of the total product distribution. No enantioselectivity was achieved in these reactions, on the basis of chiral GC-FID data.

Table 3. Addition of diphenylsilane to acetophenone.

Entry	Metal precursor (5.0 mol% Rh)	Mol% of **1** added	Solvent	%[a]	% ee[b]
3–1	$[(COD)RhCl]_2$	6.0	THF	50	32
3–2	$[(COD)RhCl]_2$	12.0	THF	<1	N/D
3–3	$[(COD)Rh(THF)_2]^+BF_4^-$	6.0	THF	69	28
3–4	$[(COD)Rh(THF)_2]^+BF_4^-$	12.0	THF	24	19

Note: Conditions: 24 °C. $[(COD)Rh(THF)_2]^+BF_4^-$ prepared in situ from 0.5 $[(COD)RhCl]_2$ and $AgBF_4$ in THF (COD = η^4-1,5-cyclooctadiene).

[a]Percent conversion based on the consumption of ketone at 18 h.

[b]Enantiomeric excess of **10** determined on the basis of chiral GC-FID data, rounded to the nearest percent (N/D = not determined).

[2] 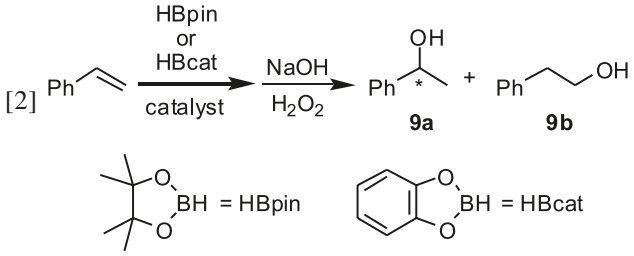

Asymmetric hydrosilylation

The asymmetric hydrosilylation of ketones represents an appealing synthetic route to chiral secondary alcohols. While highly effective PGM catalysts for this challenging enantioselective transformation are relatively few, a report by Tao and Fu (17) highlights the utility of appropriately designed chiral *P*,*N*-ligands in Rh-catalyzed transformations of this type. Key results of our investigation of asymmetric hydrosilylation of acetophenone with Ph_2SiH_2 (eq. [3]) in THF are collected in Table 3. In preliminary experiments using a catalyst mixture comprised of 0.25 mol% $[(COD)RhCl]_2$ and 6.0 mol% **1**, 50% conversion of the ketone was achieved; however, the derived secondary alcohol formed upon acidic workup was obtained in only 32% ee (Table 3, entry 3–1). When employing catalyst mixtures featuring **1**/Rh in a 2:1 ratio, no conversion was achieved (Table 3, entry 3–2), thereby indirectly suggesting that **2a** is

© 2008 NRC Canada

Table 4. Palladium-catalyzed allylic alkylation.

Entry	Substrate conc. (mol/L)	Mol% of **1** added	Solvent	Ratio[a]	Time (h)	%[b]	% ee[c]
4–1	0.2	5.0	CH_2Cl_2	1:1.1	24	>99	24 (R)
4–2	0.04	5.0	CH_2Cl_2	1:1.1	24	85	43 (R)
4–3	0.2	5.0	CH_2Cl_2	1:3	24	>99	22 (R)
4–4	0.04	5.0	CH_2Cl_2	1:3	24	>99	40 (R)
4–5	0.2	5.0	THF	1:1.1	24	96	40 (R)
4–6	0.04	5.0	THF	1:1.1	24	93	57 (R)
4–7	0.2	5.0	THF	1:3	24	>99	15 (R)
4–8	0.04	5.0	THF	1:3	24	81	38 (R)
4–9	0.004	2.5	THF	1:1.1	100	49	70 (R)
4–10	0.004	5.0	THF	1:1.1	100	>99	66 (R)
4–11	0.004	10.0	THF	1:1.1	100	61	17 (S)
4–12	0.004	15.0	THF	1:1.1	100	10	7 (S)

Note: Conditions: 24 °C; 2.5 mol% $[(\eta^3\text{-allyl})PdCl]_2$ and stated amount of **1**.

[a]Ratio of (±)-(*E*)-1,3-diphenylprop-2-enyl acetate to dimethyl malonate.

[b]Percent conversion to **11** based on the consumption of (±)-(*E*)-1,3-diphenylprop-2-enyl acetate.

[c]Product distribution determined on the basis of ^{1}H NMR integration of the product mixture after the addition of the chiral shift reagent Eu(hfc)$_3$, rounded to the nearest percent (error ± 5%); the major isomer is indicated in parentheses.

an ineffective pre-catalyst for this transformation. While the use of 5.0 mol% $[(COD)Rh(THF)_2]^+BF_4^-$ in combination with **1** (6.0 or 12.0 mol%) afforded a correspondingly more active catalyst system (Table 3, entries 3–3 and 3–4), only modest enantioselectivities (<30% ee) were achieved.

[3] 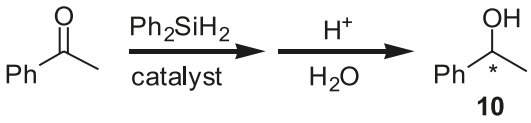

10

Asymmetric allylic alkylation

The Pd-mediated asymmetric allylic alkylation of (±)-(*E*)-1,3-diphenylprop-2-enyl acetate with dimethyl malonate (eq. [4]) is a well-established C–C bond forming reaction that is used commonly as a means of benchmarking the utility of chiral *P*,*N*-ligands in enantioselective catalysis (13, 18). Table 4 summarizes some key results of our catalytic studies employing catalyst mixtures of derived from 2.5 mol% $[(\eta^3\text{-allyl})PdCl]_2$ and **1** under standard conditions (18a) employing *N*,*O*-bis(trimethylsilyl)acetamide (BSA) and a catalytic amount of potassium acetate as base. In a preliminary catalytic survey (5.0 mol% **1**, 24 h), the influence of solvent (CH_2Cl_2, THF), substrate concentration (0.2 mol/L, 0.04 mol/L), and the ratio of (±)-(*E*)-1,3-diphenylprop-2-enyl acetate to dimethyl malonate (1:1.1, 1:3) on conversion and enantioselectivity was examined (Table 4, entries 4–1 to 4–8). Whereas a number of experimental conditions were identified that could provide >99% conversion to **11**, reactions employing 0.04 mol/L (±)-(*E*)-1,3-diphenylprop-2-enyl acetate and 1.1 equiv. of dimethyl malonate in THF (Table 4, entry 4–6) afforded what we viewed as the best balance between conversion (93%) and enantioselectivity (57%). Schenkel and Ellman (19) have reported that improved enantioselectivity in Pd-catalyzed asymmetric allylic alkylation can be achieved by conducting the reaction under dilute conditions. In this context, a series of catalytic reactions were carried out employing a substrate concentration of 0.004 mol/L and in which the amount of added **1** was varied (0.5, 1.0, 2.0, and 3.0 equiv. relative to Pd; Table 4, entries 4–9 to 4–12). While a 1:1 ratio of **1**/Pd (Table 4, entry 4–10) produced the most effective catalyst system, resulting in >99% conversion (after 100 h) and affording *R*-**11** in 66% ee, it is noteworthy that the catalyst system obtained, when employing 2.0 or 3.0 equiv. of **1** relative to Pd, exhibits a modest preference for the formation of the opposite enantiomer *S*-**11** (Table 4, entries 4–11 and 4–12). Although these preliminary results are somewhat promising, it is important to recognize that the overall performance of **1** in the Pd-mediated enantioselective synthesis of **11** is not competitive with the best chiral *P*,*N*-ligands, including PHOX (5) and alternative phosphoramidite ligands (20), which offer >99% conversion and >95% ee for this enantioselective transformation (18a).

[4] 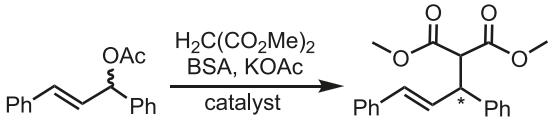

11

Summary and conclusions

In conclusion, we have reported herein on the synthesis and characterization of a new chiral heterobidentate phosphoramidite ligand **1**, which is easily prepared in high yield from the commercially available reagents 7-azaindole, *R*-BINOL, and PCl_3. Preliminary coordination chemistry studies confirm the ability of **1** to form isolable κ^2-*P*,*N* complexes with Rh, Ir, and Pd. However, in the course of such synthetic studies, Rh (and in some cases Ir) exhibited a marked propensity to form M(**1**)$_2$ complexes; such behavior may contribute in part to the generally lacklustre catalytic performance exhibited by mixtures of **1** and Rh precursor complexes in the asymmetric addition of E–H fragments (E = H, B, Si) to unsaturated substrates. While under certain conditions, mixtures of **1** and $[(\eta^3\text{-allyl})PdCl]_2$ proved capable of mediating the addition of dimethyl malonate to

© 2008 NRC Canada

(±)-(*E*)-1,3-diphenylprop-2-enyl acetate with >99% conversion and a maximum ee of 66%, the rather low enantioselectivity achieved suggests that **1** is not competitive with more well-established chiral *P*,*N*-ligands for such asymmetric transformations.

Acknowledgement

Acknowledgment is made to Dalhousie University (including the Department of Chemistry and the Industry Liaison and Innovation Office for a Research Innovation Award for MS), the Natural Sciences and Engineering Research Council of Canada (for a postgraduate scholarship for DW), and the Springboard Atlantic Network for their generous support of this work. We also thank Drs. Michael Lumsden and Katherine Robertson (Atlantic Region Magnetic Resonance Center, Dalhousie) for assistance in the acquisition of NMR data.

References

1. (*a*) N.B. Johnson, I.C. Lennon, P.H. Moran, and J.A. Ramsden. Acc. Chem. Res. **40**, 1291 (2007); (*b*) V. Farina, J.T. Reeves, C.H. Senanayake, and J.J. Song. Chem. Rev. **106**, 2734 (2006); (*c*) H.-U. Blaser, B. Pugin, and F. Spindler. J. Mol. Cat. A, **231**, 1 (2005); (*d*) H.-U. Blaser, F. Spindler, and M. Studer. Appl. Cat. A, **221**, 119 (2001).
2. For selected reviews, see: (*a*) K. Källström, I. Munslow, and P. G. Andersson. Chem. Eur. J. **12**, 3194 (2006); (*b*) P.J. Guiry and C.P. Saunders. Adv. Synth. Catal. **346**, 497 (2004); (*c*) G. Chelucci, G. Orrù, and G.A. Pinna. Tetrahedron, **59**, 9471 (2003); (*d*) K.N. Gavrilov and A.I. Polosukhin. Russ. Chem. Rev. **69**, 661 (2000).
3. For selected references to catalysts supported by *P*,*N*-indene and related ligands, see: (*a*) R.J. Lundgren, M.A. Rankin, R. McDonald, and M. Stradiotto. Organometallics, **27**, 254 (2008); (*b*) R.J. Lundgren, M.A. Rankin, R. McDonald, G. Schatte, and M. Stradiotto. Angew. Chem. Int. Ed. **46**, 4732 (2007); (*c*) B.M. Wile, R. McDonald, M.J. Ferguson, and M. Stradiotto. Organometallics, **26**, 1069 (2007); (*d*) J. Cipot, R. McDonald, M.J. Ferguson, G. Schatte, and M. Stradiotto. Organometallics, **26**, 594 (2007); (*e*) J. Cipot, C.M. Vogels, R. McDonald, S.A. Westcott, and M. Stradiotto. Organometallics, **25**, 5965 (2006).
4. (*a*) A.J. Minnaard, B.L. Feringa, L. Lefort, and J.G. de Vries. Acc. Chem. Res. **40**, 1267 (2007); (*b*) J.G. de Vries and L. Lefort. Chem. Eur. J. **12**, 4722 (2006).
5. G. Helmchen and A. Pfaltz. Acc. Chem. Res. **33**, 336 (2000).
6. H.L. Milton, M.V. Wheatley, A.M.Z. Slawin, and J. D. Woolins. Inorg. Chem. Commun. **7**, 1106 (2004).
7. A.D. Burrows, M.F. Mahon, and M.Varrone. Dalton Trans. 4718 (2003).
8. R. Sablong, C. Newton, P. Dierkes, and J.A. Osborn. Tetrahedron Lett. **37**, 4933 (1996).
9. I.D.G. Watson and A.K. Yudin. J. Am. Chem. Soc. **127**, 17516 (2005).
10. D. Wechsler, M.A. Rankin, R. McDonald, M.J. Ferguson, G. Schatte, and M. Stradiotto. Organometallics, **26**, 6418 (2007).
11. G. Brenchley, M. Fedouloff, M.F. Mahon, K.C. Molloy, and M. Wills. Tetrahedron, **51**, 10581 (1995).
12. $^{31}P\{^{1}H\}$ NMR (CD_2Cl_2) δ: 148.6 (d, $^{1}J_{RhP}$ = 280.0 Hz, **4a**), 130.7 (d, $^{1}J_{RhP}$ = 270.4 Hz, **5a**).
13. P.S. Pregosin and R. Salzmann. Coord. Chem. Rev. **155**, 35 (1996).
14. For an overview of the Rh-mediated asymmetric hydrogenation of alkenes bearing polar functional groups, see: I.D. Gridnev and T. Imamoto. Acc. Chem. Res. **37**, 633 (2004).
15. By comparison, a recently reported phosphine-phosphoramidite ligand afforded >99% conversion and >99% ee in the Rh-catalyzed asymmetric hydrogenation of dehydroamino acid esters in CH_2Cl_2: J.-D. Huang, X.-P. Hu, Z.-C. Duan, Q.-H. Zeng, S.-B. Yu, J. Deng, D.-Y. Wang, and Z. Zheng. Org. Lett. **8**, 4367 (2006).
16. For reviews on metal-mediated asymmetric hydroboration, see: (*a*) A.-M. Carroll, T.P. O'Sullivan, and P.J. Guiry. Adv. Synth. Catal. **347**, 609 (2005); (*b*) C.M. Crudden and D. Edwards. Eur. J. Org. Chem. 4695 (2003).
17. B. Tao and G.C. Fu. Angew. Chem. Int. Ed. **41**, 3892 (2002).
18. (*a*) B.M. Trost and D.L. Van Vranken. Chem. Rev. **96**, 395 (1996); (*b*) P. von Matt, G.C. Lloyd-Jones, A.B.E. Minidis, A. Pfaltz, L. Macko, M. Neuburger, M. Zehnder, H. Rüegger, and P.S. Pregosin. Helv. Chim. Acta, **78**, 265 (1995).
19. L.B. Schenkel and J.A. Ellman. Org. Lett. **5**, 545 (2003).
20. For a recent example, see: O. Pàmies, M. Diéguez, and C. Claver. Adv. Synth. Catal. **349**, 836 (2007).

© 2008 NRC Canada

Synthesis of platinum(II) cyclometallated compounds derived from imines containing pyridyl or pyrimidyl groups[1]

Margarita Crespo, Craig M. Anderson, and Joseph M. Tanski

Abstract: The reaction of compounds $[Pt_2Me_4(\mu\text{-}SMe_2)_2]$ and *cis*-$[PtPh_2(SMe_2)_2]$ with ligands 4-(2′-C_5H_4N)$C_6H_4CHNCH_2CH_2NMe_2$ (**1a**) and 4-(3′,5′-$C_4H_3N_2$)$C_6H_4CHNCH_2CH_2NMe_2$ (**1b**) carried out in acetone at room temperature produced compounds in which the imines act as bidentate [*N,N*′] ligands. Analogous compounds could be obtained in refluxing methanol when *cis*-$[PtCl_2(DMSO)_2]$ was used as starting material. The corresponding cyclometallation processes leading to platinum(II) compounds with a tridentate [*C,N,N*′] ligand took place under different reaction conditions, except for metallation of **1a** with *cis*-$[PtPh_2(SMe_2)_2]$, which could not be achieved. All compounds were characterized by usual techniques and [PtMe{4-(3′,5′-$C_4H_3N_2$)$C_6H_3CHNCH_2CH_2NMe_2$}] (**3bMe**) was also characterized crystallographically.

Key words: platinum, imines, pyridyl, pyrimidyl, cyclometallation, crystal structure.

Résumé : Opérant en solution dans l'acétone et à la température ambiante on a effectué la réaction des produits $[Pt_2Me_4(\mu\text{-}SMe_2)_2]$ et *cis*-$[PtPh_2(SMe_2)_2]$ avec les ligands 4-(2′-C_5H_4N)$C_6H_4CHNCH_2CH_2NMe_2$ (**1a**) et 4-(3′,5′-$C_4H_3N_2$)$C_6H_4CHNCH_2CH_2NMe_2$ (**1b**) et on en a isolé des produits dans lesquels les imines agissent comme des ligands [*N,N*′]-bidentates. On a aussi pu obtenir des composés analogues en opérant dans le méthanol au reflux en présence de *cis*-$[PtCl_2(dmso)_2]$ utilisé comme substrat. Les processus de cyclométallation correspondants qui conduisent à la formation de composés du platine(II) avec un ligand tridentate [*C,N,N*′] se produit aussi dans des conditions réactionnelles différentes, mais la métallation du composé **1a** par le *cis*-$[PtPh_2(SMe_2)_2$ ne peut pas être réalisée. On a caractérisé tous les produits par les techniques usuelles et on a fait appel à la diffraction des rayons X pour caractériser le [PtMe{4-(3′,5′-$C_4H_3N_2$)$C_6H_3CHNCH_2CH_2NMe_2$}] (**3bMe**).

Mots-clés : platine, imines; pyridyle, pyrimidyle, cyclométallatation, structure cristalline.

[Traduit par la Rédaction]

Introduction

Cycloplatinated compounds have been a topic of interest in the last years as a consequence of the wide range of their potential applications in many areas (1–8). In spite of the large number of this type of compound described so far, the factors that control the cyclometallation process are not fully understood. Besides gross electronic and steric factors, subtle differences in the substituents of the ligands to be metallated can be decisive in the course of the reaction (9, 10). Following our studies of cycloplatination of imines containing aromatic groups such as benzene (11, 12), thiophene (13), furane (14), naphthalene (15), phenanthrene and anthracene (16), and biphenyls (17, 18), we now report the reactions of imines derived from 4-(2-pyridyl)benzaldehyde (**1a**) and 5-(4-formylphenyl)pyrimidine (**1b**) with metallating agents $[Pt_2Me_4(\mu\text{-}SMe_2)_2]$, *cis*-$[PtPh_2(SMe_2)_2]$ and *cis*-$[PtCl_2(DMSO)_2]$. The aim of this study is to evaluate the influence of pyridyl or pyrimidyl substituents in the aryl group as well as of the metallating substrate used in the synthesis of novel platinacycles. For all these systems, the labile sulfide or sulfoxide ligands should be easily replaced by the two nitrogen atoms of the ligands leading to isolation of [*N,N*′] coordination compounds. The intramolecular C–H bond activation may occur through either oxidative addition or electrophilic substitution pathways (19). Moreover, the presence of one or two nitrogen atoms in the aromatic moiety introduces reactive sites on the ligands and allows further chemical reactions of the corresponding cyclometallated compounds (20).

Received 1 April 2008. Accepted 23 April 2008. Published on NRC Research Press Web site at canjchem.nrc.ca on 17 July 2008.

We are pleased to contribute this paper to the Special Issue recognizing the outstanding scientific career of Richard J. Puddephatt, who we hold in the highest esteem and continues to influence and inspire our own work.

M. Crespo.[2] Departament de Química Inorgànica, Universitat de Barcelona, Barcelona, Spain.
C.M. Anderson.[2] Department of Chemistry, Bard College, Annandale-on-Hudson, NY 12504, USA.
J.M. Tanski. Department of Chemistry, Vassar College, Poughkeepsie, NY 12604, USA.

[1]This article is part of a Special Issue dedicated to Professor R.J. Puddephatt.

[2]Corresponding authors (e-mail: margarita.crespo@qi.ub.es, canderso@bard.edu).

 doi:10.1139/V08-084 © 2008 NRC Canada

Chart 1.

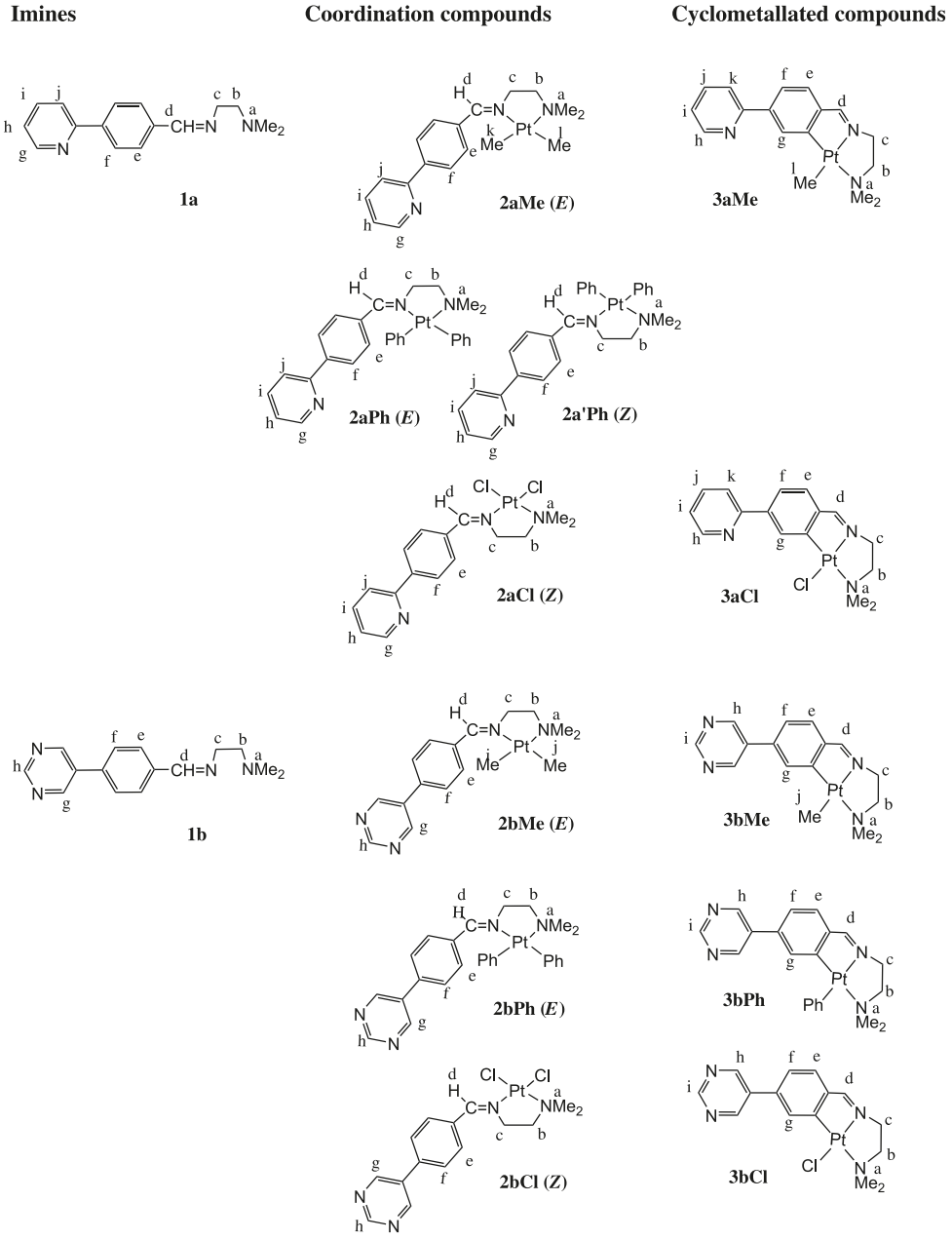

Results and discussion

Ligands 4-(2′-C_5H_4N)$C_6H_4CHNCH_2CH_2NMe_2$ (**1a**) and 4-(3′,5′-$C_4H_3N_2$)$C_6H_4CHNCH_2CH_2NMe_2$ (**1b**) were prepared from the condensation reactions of *N,N*-dimethylethylenediamine and the corresponding aldehyde carried out in toluene at room temperature. The resulting imines were characterized by ^{1}H NMR spectroscopy.

Reactions of ligands 1a and 1b with $[Pt_2Me_4(\mu\text{-}SMe_2)_2]$

The reactions of $[Pt_2Me_4(\mu\text{-}SMe_2)_2]$ with potentially tridentate ligands **1a** and **1b** carried out in acetone at room temperature produced the compounds $[PtMe_2\{4\text{-}(2'\text{-}C_5H_4N)\text{-}C_6H_4CHNCH_2CH_2NMe_2\}]$ (**2aMe**) and $[PtMe_2\{4\text{-}(3',5'\text{-}C_4H_3N_2)C_6H_4CHNCH_2CH_2NMe_2\}]$ (**2bMe**), respectively, in which the imines act as bidentate [*N,N*′] ligands (see Chart 1).

Compound **2aMe** was characterized by elemental analyses, mass spectrometry, and ^{1}H NMR spectra. Compound **2bMe** was characterized in solution by NMR spectroscopy but it could not be isolated in a pure form, since further reaction at room temperature produces the corresponding cyclometallated compound **3bMe** within 1 h (see below). In the ^{1}H NMR spectra, two distinct resonances appear in the methyl region, both coupled with ^{195}Pt. The one at higher field with a larger coupling to ^{195}Pt is assigned to the methyl trans to the NMe_2 moiety (see Table 1). The coordination of the ligand through both nitrogen atoms is confirmed by the coupling of both amine and imine protons to platinum. The *J*(H–Pt) values for the imine proton indicate an *E* conformation of the imine as previously observed for analogous compounds (11–18).

Intramolecular activation of C–H bonds followed by

© 2008 NRC Canada

Table 1. Selected ^{1}H NMR data.

	δ(NMe_2) [^3J(H–Pt)]	CH=N [^3J(H–Pt)]	Me–Pt [^2J(H–Pt)][a]	Me–Pt [^2J(H–Pt)][b]
2aMe	2.84 (19)	9.03 (45)	0.25 (90)	0.63 (84)
2bMe	2.85 (20)	9.07 (42)	0.21 (90)	0.64 (84)
2aPh	2.67 (17)	8.84 (44)	—	—
2a′Ph	2.62 (21)	8.43 (28)	—	—
2bPh	2.67 (18)	8.87 (43)	—	—
2aCl	3.14[c]	9.58 (52)	—	—
2bCl	3.15[c]	9.57[c]	—	—
3aMe	2.86 (20)	8.64 (58)	—	1.06 (79)
3bMe	2.87 (21)	8.68 (59)	—	1.04 (78)
3bPh	2.80 (21)	8.56 (57)	—	—
3aCl	2.91 (12)	8.13 (141)	—	—
3bCl	2.93 (14)	8.43 (140)	—	—

Note: δ in ppm, J in Hz.
[a]Me trans to NMe_2.
[b]Me trans to CH=N.
[c]Coupling to ^{195}Pt was not observed.

methane elimination to yield [*C,N,N′*] cycloplatinated compounds took place at room temperature for **2bMe** and when a toluene solution of compound **2aMe** was refluxed for 2 h. Compounds **3aMe** and **3bMe** were characterized by mass spectrometry, NMR spectroscopy, and elemental analyses. In addition, **3bMe** was also characterized crystallographically. In the ^{1}H NMR spectra, the methyl ligand, the dimethylamino, and the imine groups are coupled to platinum, and the values of the coupling constants are in the usual range for analogous compounds (11–18). In agreement with previous data, the J(H–Pt) values of the imine group increase from the coordination compounds to the cyclometallated compounds (see Table 1). In addition, the aromatic proton adjacent to the metallation site is also coupled to platinum and provides evidence of the cyclometallation process.

Imine **1a** derived from 4-(2-pyridyl)benzaldehyde could in principle produce binuclear compounds either mono- or doubly-cyclometallated such as **4a** and **5a** shown in Chart 2. Doubly cyclometallated compounds have been described for both platinum and palladium (21, 22). With this aim, the reaction of $[Pt_2Me_4(\mu\text{-}SMe_2)_2]$ with an equimolar amount of imine **1a** was carried out in acetone.

Unfortunately, the obtained orange solid was too insoluble for NMR or mass spectra and could only be characterized by elemental analyses, which were consistent with formation of **4a**. This result indicates the ability of imine **1a** to participate in further reactions through the pyridyl nitrogen atom. Attempts to produce a doubly cyclometallated compound using longer reaction times in acetone at room temperature or refluxing a toluene suspension of compound **4a** for several hours gave insoluble materials that could not be identified. Because of the difficulties arising from the low solubility of these binuclear compounds, no further studies were carried out.

Reactions of ligands 1a and 1b with *cis*-$[PtPh_2(SMe_2)_2]$

The reactions carried out in acetone at room temperature produced compounds $[PtPh_2\{4\text{-}(2'\text{-}C_5H_4N)C_6H_4CHNCH_2CH_2NMe_2\}]$ (**2aPh**) and $[PtPh_2\{4\text{-}(3',5'\text{-}C_4H_3N_2)C_6H_4CHNCH_2CH_2NMe_2\}]$ (**2bPh**) in good yields. The obtained compounds were characterized by elemental analyses, mass spectrometry, and ^{1}H NMR spectroscopy. As for the compounds above, the coordination of the ligand through both nitrogen atoms is confirmed by the coupling of both amine and imine protons to platinum, and the J(H–Pt) values for the imine proton indicate an *E* conformation.

Chart 2.

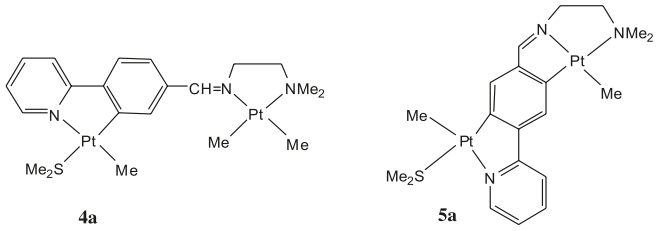

Formation of the corresponding cyclometallated compounds was attempted by refluxing toluene solutions of **2aPh** or **2bPh** for 6 h, a method previously reported for the synthesis of analogous compounds with biphenyl ligands (18), which consists in intramolecular activation of a $C_{aromatic}$–H bond along with elimination of benzene. Using this procedure for **2bPh**, the corresponding [*C,N,N′*] cyclometallated compound $[PtPh\{4\text{-}(3',5'\text{-}C_4H_3N_2)C_6H_3CHNCH_2CH_2NMe_2\}]$ (**3bPh**) was obtained as an orange red solid. Compound **3bPh** was characterized by elemental analyses, mass spectrometry, and NMR spectra. As shown in Table 1, the coupling constant of the imine proton to platinum increases slightly compared with compound **2bPh** as a result of the formation of a metallacycle. Under the same experimental conditions, the analogous compound **3aPh** was not obtained, since red solutions were formed, and the NMR spectra taken for the final residue show only intense aldehyde signals, which indicate hydrolysis of the imine bond, along with peaks for unidentified products. Hydrolysis of imines with adventitious water in the solvent has been reported under metallation conditions with palladium or platinum substrates (23, 24). Using shorter refluxing times did not improve the results. Therefore, the synthesis of cyclometallated compound **3aPh** was attempted under milder conditions such as stirring at room temperature a solution of **2aPh** in acetone. After several hours, a new compound was formed and its spectral data, in particular a small value of J(H–Pt) for the imine proton (J(H–Pt) = 27.9 Hz), suggest isomerization of the imine from the initial *E* conformation observed in **2aPh** to the less congested *Z* form leading to compound **2a′Ph**. After 24 h, the ratio **2a′Ph/2aPh** is 0.54:1.00, and the amount of **2a′Ph** increases slowly up to a ratio of ~ 1.00:1.00 after 5 days in solution. No evidence of formation of the expected cyclometallated compound is observed in the ^{1}H NMR spectra, while small amounts of the aldehyde are formed. Isomerization from the most favoured *E* conformation of the free ligand to the *Z* conformation upon coordination to a platinum centre has been previously observed for analogous systems (18) and can be explained by the steric crowding in the coordination sphere of the platinum(II) centre, which is minimized through this conformational change. It has to be noted, however, that the adequate arrangement for producing cyclometallation at the aromatic group is the *E* conformation, since isomerization to the less

© 2008 NRC Canada

congested *Z* form places the aromatic group away from the platinum centre. Therefore, the reaction at room temperature was not a good strategy for cyclometallation of **2aPh**.

Reactions of ligands 1a and 1b with *cis*-[$PtCl_2(DMSO)_2$]

When equimolar amounts of *cis*-[$PtCl_2(DMSO)_2$] and ligand **1a** were refluxed in methanol for 5 h, the corresponding compound [$PtCl_2$\{\{4-(2′-C_5H_4N)$C_6H_4CHNCH_2CH_2NMe_2$\}] (**2aCl**) was obtained in good yield. As previously noticed for analogous systems (25), a *Z* conformation around the C=N bond is adopted with the imine proton close to the platinum nucleus, which is evidenced in the ^{1}H NMR spectrum by the downfield shift of the imine signal (δ = 9.58 ppm). This fact suggests that coordination of a bidentate ligand to a $PtCl_2$ moiety produces a conformational change from the most stable *E* conformation of the free ligand to the *Z,* and consequently *Z–E* isomerization should precede the cyclometallation step as previously reported for analogous systems. The corresponding reaction for ligand **1b** produced compound [$PtCl_2$\{4-(3′,5′-$C_4H_3N_2$)$C_6H_4CHNCH_2CH_2NMe_2$\}] (**2bCl**) as a rather insoluble impure solid; attempts to obtain **2bCl** in a pure form were unsuccessful because of its low solubility.

The most widely used conditions for converting compounds analogous to **2aCl** and **2bCl** into cycloplatinated derivatives are refluxing for several hours in either toluene or in a donor solvent such as methanol or ethanol, in some cases in the presence of an external base, which favours the formal elimination of HCl (25–30). When **2aCl** was treated with an equimolar amount of sodium acetate in refluxing methanol for 48 h, cyclometallated compound **3aCl** was produced. The process requires an initial step in which *Z* to *E* imine isomerization brings the aryl ring closer to platinum followed by the actual intramolecular C–H bond activation, which leads to a five-membered metallacycle.

Alternatively, **3aCl** could be obtained when equimolar amounts of *cis*-[$PtCl_2(DMSO)_2$], ligand **1a** and sodium acetate were refluxed in methanol for 48 h. This method was also used to obtain **3bCl**. The obtained yields were lower than those obtained for analogous compounds derived from biphenyl such as [PtCl\{4-$C_6H_5C_6H_3CHNCH_2CH_2NMe_2$\}] and [PtCl\{2-$C_6H_5C_6H_3CHNCH_2CH_2NMe_2$\}] (18). Furthermore, using prolonged reaction times, toluene–methanol mixtures, and higher reaction temperatures (26–30) did not improve the yields, since metallic platinum and high amounts of aldehyde were formed under these conditions. Compounds **3aCl** and **3bCl** were characterized by elemental analyses, mass spectrometry, and NMR spectra. In the ^{1}H NMR spectra, a significant increase in the coupling constant of the imine proton to platinum is observed upon cyclometallation. The obtained values shown in Table 1 are in the range reported for analogous cyclometallated compounds in which a chloro ligand is in a trans position to the imine (18). As a whole, analysis of the ^{1}H NMR data reported in Table 1 indicate that the *J*(H–Pt) values for the imine proton increase in the order: **2a′Ph** (28 Hz) < **2bMe**, **2bPh**, **2aPh**, **2aMe** (42–45 Hz) < **2aCl** (52 Hz) < **3bPh**, **3aMe**, **3bMe** (57–58 Hz) << **3aCl**, **3bCl** (140–141 Hz).

This sequence is consistent with the larger *J*(H–Pt) values expected for: (*i*) cyclometallated vs. non-cyclometallated compounds, (*ii*) imine moieties trans to a chloro ligand vs. trans to a methyl or a phenyl ligand, and (*iii*) *E* vs. *Z* conformation of the imine.

Table 2. Selected bond lengths (Å) and angles (°) with estimated standard deviations for compound **3bMe**.

Bond lengths (Å)	
Pt—C(8)	1.990(5)
Pt—N(1)	2.169(4)
N(1)—C(4)	1.499(7)
N(2)—C(5)	1.457(6)
C(6)—C(7)	1.447(7)
Pt—C(1)	2.074(5)
Pt—N(2)	2.017(4)
C(4)—C(5)	1.497(8)
N(2)—C(6)	1.279(6)
C(7)—C(8)	1.436(6)
Bond angles (°)	
C(8)–Pt–N(2)	81.1(2)
N(1)–Pt–N(2)	81.9(2)
C(1)–Pt–C(8)	97.7(2)
C(1)–Pt–N(1)	99.3(2)

Fig. 1. Molecular structure of compound **3bMe**.

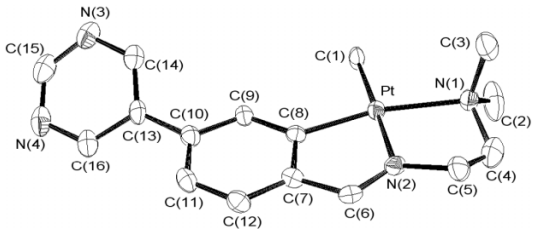

Crystal structure of 3bMe

Suitable crystals of **3bMe** were grown by slow diffusion of a CH_2Cl_2 solution into MeOH. The crystal structure is composed of discrete molecules separated by van der Waals interactions. Selected bond lengths and angles are given in Table 2, and a molecular view is shown in Fig. 1.[3]

The ligand behaves as [*C,N,N′*]-tridentate and a three fused [*6,5,5*] ring system containing a five-membered endo metallacycle is formed. A methyl ligand completes the square-planar coordination of the platinum atom. The metallacycle is approximately planar as suggested by the sum of internal angles, which is close to 540° (31) and nearly co-planar with both the metallated phenyl and the mean coordination plane. The dihedral angle between phenyl and pyrimidyl groups is 31.8(2)°, which suggests, aside from

[3] Supplementary data for this article are available on the journal Web site (canjchem.nrc.ca) or may be purchased from the Depository of Unpublished Data, Document Delivery, CISTI, National Research Council Canada, Ottawa, ON K1A 0R6, Canada. DUD 3774. For more information on obtaining material, refer to cisti-icist.nrc-cnrc.gc.ca/irm/unpub_e.shtml. CCDC 6792371 contains the crystallographic data for this manuscript. These data can be obtained, free of charge, via www.ccdc.cam.ac.uk/conts/retrieving.html (Or from the Cambridge Crystallographic Data Centre, 12 Union Road, Cambridge CB2 1EZ, UK; fax +44 1223 336033; or deposit@ccdc.cam.ac.uk).

© 2008 NRC Canada

packing effects, a compromise between van der Waals repulsion of the ortho hydrogen atoms and the co-planarity required for resonance extended to both aryl rings. Tilt angles ranging from 10.4° to 49.9° have been obtained for biphenyl systems in analogous platinum(II) and platinum(IV) cyclometallated compounds (17, 18). Bond lengths and angles are in the expected range for analogous compounds (11–13, 15–18). The Pt–NMe_2 distance is longer (2.169(4) Å) than the Pt–NCH (2.017(4) Å), which is consistent with the relatively weak coordinating ability of tertiary amines for platinum. Bond angles at platinum are close to the ideal value of 90°, and the smallest angles correspond to those involving the tridentate ligand with "bite" angles C(8)–Pt–N(2) and N(1)–Pt–N(2) being 81.1(2)° and 81.9 (2)°, respectively.

Conclusions

The results here presented indicate that [*C,N,N′*] cyclometallated compounds derived from **1a** and **1b** can be easily obtained when $[Pt_2Me_4(\mu\text{-}SMe_2)_2]$ is used as a metallation agent. The presence of two nitrogen atoms in the pyrimidyl substituent in **1b** facilitates the reaction, which takes place under milder conditions than for **1a**. When *cis*-$[PtPh_2(SMe_2)_2]$ is used as starting material, the corresponding [*C,N,N′*] cyclometallated compound could only be obtained for the more activated **1b** ligand. For both substrates $[Pt_2Me_4(\mu\text{-}SMe_2)_2]$ and *cis*-$[PtPh_2(SMe_2)_2]$, the mechanism consists of oxidative addition followed by elimination of methane (32) or benzene (33), and therefore, the presence of an additional nitrogen atom, more electronegative than a carbon atom, should have a similar activating effect in both cases.

The failure to produce cyclometallation of ligand **1a** with *cis*-$[PtPh_2(SMe_2)_2]$ is however unexpected taking into account that this metallation agent was effective for 4-biphenylimine and even for the more sterically demanding 2- biphenylimine (17, 18), and that, in this case, the presence of one nitrogen atom in **1a** should facilitate the process. Based on the observed presence of aldehyde in the attempted cyclometallation reaction, we might assume that ligand **1a** is more prone to experience hydrolysis than the corresponding biphenyl ligands. This fact along with the lower reactivity of *cis*-$[PtPh_2(SMe_2)_2]$ vs. $[Pt_2Me_4(\mu\text{-}SMe_2)_2]$ (18) may account for the observed results.

When *cis*-$[PtCl_2(DMSO)_2]$ was used as starting material, the corresponding [*C,N,N′*] cyclometallated compounds could also be obtained, although with poor yields. As previously indicated for analogous systems (18, 25), the greater steric requirements of chloro vs. methyl or phenyl ligands in the platinum substrate leads to a *Z* conformation of the imine group in the [*N,N′*] compounds, and therefore, *Z* to *E* isomerization should precede the cyclometallation. Moreover, the lower yields compared with those obtained for biphenyl ligands (18) could be related to the higher proclivity of ligands **1a** and **1b** to hydrolysis as well as to the reduced reactivity towards an electrophilic reagent expected for ligands containing electron-withdrawing substituents.

As a whole, the above results indicate that pyridyl or pyrimidyl substituents on the aryl group may have a decisive influence in the cyclometallation process, which is attributed more to electronic than to steric effects, since the substituents are away from the metallation position. In addition to determining the success and ease of the cyclometallation, these substituents emphasize the differences observed when different metallating agents such as $[Pt_2Me_4(\mu\text{-}SMe_2)_2]$, *cis*-$[PtPh_2(SMe_2)_2]$, and *cis*-$[PtCl_2(DMSO)_2]$ are used, which is further evidence of the different mechanisms operating for such substrates (19). Further work aimed at evaluating the ability of free pyridyl or pyrimidyl groups in the new compounds to coordinate a second metallic fragment is in progress.

Experimental

General

NMR spectra were performed at the Unitat de RMN d'Alt Camp de la Universitat de Barcelona using Mercury 400 and Varian 300 spectrometers and referenced to $SiMe_4$. δ values are given in ppm and *J* values in Hz. *J*(H–Pt) values were measured at 300 MHz to avoid errors arising from broadening of the ^{195}Pt satellites observed at 400 MHz. Labelling of the compounds is as shown in Chart 1. ES-mass spectra were performed at the Servei d'Espectrometria de Masses de la Universitat de Barcelona using a VG-Quattro spectrometer. Microanalyses were performed by the Servei de Recursos Científics i Tècnics de la Universitat Rovira i Virgili (Tarragona).

All starting materials were purchased from commercial sources and used as received. Toluene was distilled from sodium–benzophenone. Compounds $[Pt_2Me_4(\mu\text{-}SMe_2)_2]$ (34), *cis*-$[PtPh_2(SMe_2)_2]$ (35, 36), and *cis*-$[PtCl_2(DMSO)_2]$ (37) were prepared according to literature methods.

Preparation of the compounds

Compounds **1** were prepared by the reaction of equimolar amounts of *N*,*N*-dimethylethylenediamine and the corresponding aldehyde in toluene (20 mL). The mixture was stirred for 1 h and dried over Na_2SO_4. The solvent was removed in a rotary evaporator to yield yellow oils.

4-(2′-C_5H_4N)$C_6H_4CHNCH_2CH_2NMe_2$ (1a)

Obtained from 0.5 g (2.90×10^{-3} mol) of 4-(2-pyridyl)benzaldehyde and 0.26 g of *N*,*N*-dimethylethylenediamine. Yield: 0.5 g (67%). ^1H NMR (400 MHz, $CDCl_3$) δ: 2.32 [s, 6H, H^a], 2.67 [t, *J*(H–H) = 7.2, 2H, H^b], 3.78 [td, *J*(H–H) = 7.2, 0.8, 2H, H^c], 7.26 [m, 1H, H^h], 7.77 [m, 2H, $H^{i,j}$], 7.84 [d, *J*(H–H) = 8.4, 2H, H^f], 8.05 [d, *J*(H–H) = 8.4, 2H, H^e], 8.37 [s, 1H, H^d], 8.71 [dt, *J*(H–H) = 4.4, 1.4, 1H, H^g].

4-(3′,5′-$C_4H_3N_2$)$C_6H_4CHNCH_2CH_2NMe_2$ (1b)

Obtained from 0.4 g of 5-(4-formylphenyl)pyrimidine (2.17×10^{-3} mol) and 0.19 g of *N*,*N*-dimethylethylenediamine. Yield: 0.4 g (72%). ^1H NMR (400 MHz, $CDCl_3$) δ: 2.34 [s, 6H, H^a], 2.69 [t, *J*(H–H) = 7.2, 2H, H^b], 3.80 [t, *J*(H–H) = 7.2, 2H, H^c], {7.64 [d, *J*(H–H) = 8.4, 2H], 7.89 [d, *J*(H–H) = 8.4, 2H], $H^{e,f}$}, 8.38 [s, 1H, H^d], 8.98 [s, 2H, H^g], 9.23 [s, 1H, H^h].

© 2008 NRC Canada

[PtMe$_2${4-(2′-C$_5$H$_4$N)C$_6$H$_4$CHNCH$_2$CH$_2$NMe$_2$}] (2aMe)

Compound **2aMe** was obtained from 88 mg (3.49×10^{-4} mol) of ligand **1a** and 100 mg (1.74×10^{-4} mol) of compound [Pt$_2$Me$_4$(μ-SMe$_2$)$_2$] in acetone (20 mL). The mixture was stirred for 30 min at room temperature. **2aMe** was obtained as an orange solid upon removal of the acetone in a rotary evaporator and washing of the residue with ether (3×2 mL).

Yield: 150 mg (90%). ^{1}H NMR (400 MHz, CDCl$_3$) δ: 0.25 [s, ^2J(Pt–H) = 90, 3H, H^k], 0.63 [s, ^2J(Pt–H) = 84, 3H, H^l], 2.71 [t, J(H–H) = 5.2, 2H, H^b], 2.84 [s, ^3J(H–Pt) = 19, 6H, H^a], 4.07 [t, J(H–H) = 5.2, 2H, H^c], 7.76–7.79 [m, 3H, H^{h,i,j}], {8.01 [d, J(H–H) = 8.2, 2H], 8.37 [d, J(H–H) = 8.2, 2H],H^{e,f}}, 8.70 [d, J(H–H) = 5.2, 1H, H^g], 9.03 [s, ^3J(Pt–H) = 45, 1H, H^d]. ES (+)-MS (MeCN – H$_2$O): 504 [M – Me + MeCN], 489 [M – 2Me + MeCN], 463 [M – Me], 448 [M – 2Me]. Anal. found: C, 44.5; H, 5.9; N, 8.5. Calcd. for C$_{18}$H$_{25}$N$_3$Pt: C, 45.18; H, 5.26; N, 8.78 (%).

[PtMe$_2${4-(3′,5′-C$_4$H$_3$N$_2$)C$_6$H$_4$CHNCH$_2$CH$_2$NMe$_2$}] (2bMe)

Compound **2bMe** was obtained following the same procedure from 18 mg of ligand **1b** and 20 mg (0.35×10^{-4} mol) of compound [Pt$_2$Me$_4$(μ-SMe$_2$)$_2$] in acetone (10 mL). Compound **2bMe** could be characterized in solution, and within an hour, produces **3bMe** (see below).

^{1}H NMR (400 MHz, CDCl$_3$) δ: 0.21 [s, ^2J(Pt–H) = 90, 3H, H^i], 0.64 [s, ^2J(Pt–H) = 84, 3H, H^j], 2.72 [m, 2H, H^b], 2.85 [s, ^3J(H–Pt) = 20, 6H, H^a], 4.11 [m, 2H, H^c], {7.60 [d, J(H–H) = 8.4, 2H], 8.45 [d, J(H–H) = 8.4, 2H], H^{e,f}}, 9.00 [s, 2H, H^g], 9.07 [s, ^3J(Pt–H) = 42, 1H, H^d], 9.24 [s, 1H, H^h].

[PtPh$_2${4-(2′-C$_5$H$_4$N)C$_6$H$_4$CHNCH$_2$CH$_2$NMe$_2$}] (2aPh)

Compound **2aPh** was obtained as a yellow solid following the same procedure as for **2aMe** from 48 mg (0.19 mmol) of ligand **1a** and the equimolar amount of compound *cis*-[PtPh$_2$(SMe$_2$)$_2$] (90 mg) in acetone (10 mL).

Yield: 80 mg (70%). ^{1}H NMR (400 MHz, CDCl$_3$) δ: 2.67 [s, ^3J(Pt–H) = 17, 6H, Me^a], 2.79 [t, J(H–H) = 5.0, 2H, H^b], 4.21 [t, J(H–H) = 5.0, 2H, H^c], {6.28 [t, J(H–H) = 7.0, 1H], 6.38 [t, J(H–H) = 7.4, 2H], 6.81 [t, J(H–H) = 7.2, 1H], 6.93 [m, 4H], 7.23 [ddd, J(H–H) = 7.6, 4.8, 1.2, 1H], 7.48 [d, J(H–H) = 8.0, 2H], 7.55–7.58 [m, 3H], 7.73 [td, J(H–H) = 7.6, 2, 1H], 8.14 [d, J(H–H) = 8.4, 2H], 8.65 [ddd, J(H–H) = 4.4, 1.6, 1.0, 1H]}, 8.84 [s, ^3J(Pt–H) = 44, 1H, H^d]. ES (+)-MS (MeCN – H$_2$O): 603 [M + H], 525 [M – Ph], 448 [M – 2Ph]. Anal. found: C, 54.5; H, 4.9; N, 6.5. Calcd. for C$_{28}$H$_{29}$N$_3$Pt·H$_2$O: C, 54.18; H, 5.03; N, 6.77 (%). Isomerization to **2a′Ph** (*Z* isomer) took place in acetone at room temperature. ^{1}H NMR (400 MHz, CDCl$_3$) δ: 2.62 [s, ^2J(Pt–H) = 21, 6H, Me^a], 2.76 [t, J(H–H) = 6.0, 2H, H^b], 4.02 [td, J(H–H) = 6.0, 2,0, 2H, H^c], 8.43 [s, ^3J(Pt–H) = 28, 1H, H^d].

[PtPh$_2${4-(3′,5′-C$_4$H$_3$N$_2$)C$_6$H$_4$CHNCH$_2$CH$_2$NMe$_2$}] (2bPh)

Compound **2bPh** was obtained as a yellow solid following the same procedure as for **2aMe** from 48.3 mg (0.19 mmol) of ligand **1b** and the equimolar amount of compound *cis*-[PtPh$_2$(SMe$_2$)$_2$] (90 mg) in acetone (10 mL).

Yield: 90 mg (78%). ^{1}H NMR (400 MHz, CDCl$_3$) δ: 2.67 [s, ^3J(Pt–H) = 18, 6H, Me^a], 2.80 [t, J(H–H) = 5.0, 2H, H^b], 4.20 [t, J(H–H) = 5.0, 2H, H^c], {6.34–6.36 [m, 2H], 6.80 [t, J(H–H) = 8.0, 2H], 6.89–6.92 [m, 3H], 7.12 [d, J(H–H) = 8.4, 2H], 7.44–7.46 [m, 3H], 8.12 [d, J(H–H) = 8.0, 2H], 8.81 [s, 2H], 9.20 [s, 1H], aromatics}, 8.87 [s, ^3J(Pt–H) = 43, 1H, H^d]. ES (+)-MS (MeCN – H$_2$O): 604 [M + H], 526 [M – Ph], 449 [M – 2Ph]. Anal. found: C, 53.2; H, 4.8; N, 9.0. Calcd. for C$_{27}$H$_{28}$N$_4$Pt: C, 53.72; H, 4.67; N, 9.28 (%).

[PtCl$_2${4-(2′-C$_5$H$_4$N)C$_6$H$_4$CHNCH$_2$CH$_2$NMe$_2$}] (2aCl)

Compound **2aCl** was obtained from 150 mg (3.50×10^{-4} mol) of *cis*-[PtCl$_2$(DMSO)$_2$] and the equimolar amount (90.0 mg) of **1a** after refluxing the mixture in methanol for 5 h. On cooling, a light yellow solid is formed.

Yield: 120 mg (65%). ^{1}H NMR (400 MHz, CDCl$_3$) δ: 2.70 [t, ^2J(H–H) = 6.0, 2H, H^b], 3.14 [s, 6H, Me^a], 4.09 [td, ^2J(H–H) = 6.0, 2.0, 2H, H^c], 7.33 [ddd, J(H–H) = 6.8, 4.8, 2, 1H, H^h], 7.64 [d, ^3J(H–H) = 8.4, 2H, H^e or H^f], 7.80–7.82 [m, 2H, H^i, H^j], 8.13 [d, ^3J(H–H) = 8.4, 2H, H^e or H^f], 8.73 [dt, J(H–H) = 4.8, 2, 1H, H^g], 9.58 [s, ^3J(Pt–H) = 52, 1H, H^d]. ESI-MS: 520 [M + H], 484 [M – Cl]. Anal. found: C, 36.2; H, 3.7; N, 8.0. Calcd. for C$_{16}$H$_{19}$Cl$_2$N$_3$Pt·H$_2$O: C, 35.76; H, 3.94; N, 7.82 (%).

[PtCl$_2${4-(3′,5′-C$_4$H$_3$N)C$_6$H$_4$CHNCH$_2$CH$_2$NMe$_2$}] (2bCl)

Compound **2bCl** was obtained as an insoluble impure solid following the procedure reported above for **2aCl**.

^{1}H NMR (400 MHz, CDCl$_3$) δ: 2.72 [m, 2H, H^b], 3.15 [s, 6H, Me^a], 4.08 [t ^2J(H–H) = 6.0, 2H, H^c], 7.73–7.76 [m, 4H], 8.99 [s, 2H,], 9.29 [s, 1H], 9.57 [s, 1H, H^d].

[PtMe{4-(2′-C$_5$H$_4$N)C$_6$H$_3$CHNCH$_2$CH$_2$NMe$_2$}] (3aMe)

Compound **3aMe** was obtained after refluxing a toluene solution (20 mL) containing 50 mg of compound **2aMe** for 2 h. Toluene was totally removed, and the residue was recrystallized from CH$_2$Cl$_2$–MeOH to yield **3aMe** as a red solid.

Yield: 40 mg (83%). ^{1}H NMR (400 MHz, CDCl$_3$) δ: 1.06 [s, ^2J(Pt–H) = 79, 3H, H^l], 2.86 [s, ^3J(H–Pt) = 20, 6H, H^a], 3.19 [t, J(H–H) = 5.2, 2H, H^b], 4.09 [t, J(H–H) = 5.2, 2H, H^c], 7.19 [m, 2H, H^{i,j}], {7.37 [d, J(H–H) = 8.0, 2H], 7.82 [d, J(H–H) = 8.0, 2H],H^{e,f}}, 7.73 [d, J(H–H) = 6.8, 1H, H^k], 8.07 [d, J(H–H) = 2, ^3J(Pt–H) = 67, 1H, H^g], 8.64 [s, ^3J(H–Pt) = 58, 1H, H^d], 8.67 [d, J(H–H) = 4.8, 1H, H^h]. ES (+)-MS (MeCN – H$_2$O): 488 [M – Me + MeCN], 462 [M]. Anal. found: C, 44.0; H, 4.7; N, 8.5. Calcd. for C$_{17}$H$_{21}$N$_3$Pt: C, 44.15; H, 4.58; N, 9.09 (%).

[PtMe{4-(3′,5′-C$_4$H$_3$N$_2$)C$_6$H$_3$CHNCH$_2$CH$_2$NMe$_2$}] (3bMe)

Compound **3bMe** was obtained from 89 mg (3.49×10^{-4} mol) of ligand **1b** and 100 mg (1.74×10^{-4} mol) of compound [Pt$_2$Me$_4$(μ-SMe$_2$)$_2$] in acetone (20 mL). The mixture was stirred for 1 h at room temperature, metallic platinum was filtered off, and acetone was removed in a rotary evaporator. Red crystals of **3bMe** were obtained upon recrystallization of the residue from CH$_2$Cl$_2$–MeOH.

Yield: 100 mg (62%). ^{1}H NMR (400 MHz, CDCl$_3$) δ: 1.04 [s, ^2J(Pt–H) = 78, 3H, H^j], 2.87 [s, ^3J(H–Pt) = 21, 6H, H^a], 3.21 [t, J(H–H) = 6.0, 2H, H^b], 4.12 [td, J(H–H) = 6.0, 1.2, 2H, H^c], 7.16 [dd, J(H–H) = 7.6, 1.6, 1H, H^f], 7.38 [d, J(H–H) = 7.6, ^4J(H–Pt) = 10, 1H, H^e], 7.82 [d, J(H–H) = 2.0, ^3J(H–Pt) = 65, 1H, H^g], 8.68 [s, ^3J(H–Pt) = 59, 1H, H^d],

© 2008 NRC Canada

8.97 [s, 2H, H^h], 9.17 [s, 1H, H^i]. ES (+)-MS (MeCN – H_2O): 489 [M – Me + MeCN], 463 [M], 448 [M – Me]. Anal. found: C, 41.0; H, 4.3 N, 11.7. Calcd. for $C_{16}H_{20}N_4Pt$: C, 41.47; H, 4.35; N, 12.09 (%).

[PtPh{4-(3′,5′-$C_4H_3N_2$)$C_6H_3CHNCH_2CH_2NMe_2$}] (3bPh)

Compound **3bPh** was obtained from 50 mg (8.3×10^{-5} mol) of **2bPh** in 20 mL of toluene. The mixture was refluxed for 6 h, and toluene was removed in a rotary evaporator. The residue was washed with ether to yield an orange–red solid.

Yield: 33 mg (76%). ^{1}H NMR (400 MHz, $CDCl_3$) δ: 2.80 [s, ^3J(H–Pt) = 21, 6H, H^a], 3.24 [t, J(H–H) = 6.0, 2H, H^b], 4.11 [td, J(H–H) = 6.0, 1.2, 2H, H^c], 6.95 [tt, J(H–H) = 7.4, 1.6, 1H, *p*-Ph], 7.10 [t, J(H–H) = 7.4, 2H, *m*-Ph], 7.15 [dd, J(H–H) = 7.4, 1.6, 1H, H^g], 7.32 [d, J(H–H) = 1.6, 1H, H^e], 7.37 [d, J(H–H) = 8, 1H, H^f], 7.55 [dd, J(H–H) = 8, 1.6, ^3J(H–Pt) = 59, 2H, *o*-Ph], 8.56 [s, ^3J(H–Pt) = 57, 1H, H^d], 8.79 [s, 2H, H^h], 9.10 [s, 1H, H^i]. ES (+)-MS (MeCN – H_2O): 973 [2M – Ph], 526 [M]. Anal. found: C, 48.7; H, 4.2; N, 10.2. Calcd. for $C_{21}H_{22}N_4Pt$: C, 48.00; H, 4.22; N, 10.66 (%).

[PtCl{4-(2′-C_5H_4N)$C_6H_3CHNCH_2CH_2NMe_2$}] (3aCl)

Compound **3aCl** was prepared from 50 mg (9.6×10^{-5} mol) of **2aCl** and the equimolar amount of $Na(CH_3COO)$ (8 mg) after refluxing the mixture in methanol for 48 h. The reaction mixture was cooled, filtered to remove unreacted materials, and concentrated to dryness. The obtained residue was recrystallized in dichloromethane–methanol to yield an orange solid.

Yield: 15 mg (32%). ^{1}H NMR (400 MHz, $CDCl_3$) δ: 2.91 [s, ^3J(H–Pt) = 12, 6H, H^a], 3.11 [t, ^2J(H–H) = 6.0, 2H, H^b], 3.97 [t, ^2J(H–H) = 6.0, 2H, H^c], 7.22 [ddd, J(H–H) = 7.6, 5.0, 1.2, 1H, H^i], 7.32 [d, ^3J(H–H) = 8.0, 1H, H^k], 7.74 [td, J(H–H) = 7.6, 1.6, 1H, H^j], 7.79 [dd, J(H–H) = 8, 1.6, 1H, H^e], 7.87 [d, ^3J(H–H) = 8.0, 1H, H^f], 8.13 [s, ^3J(Pt–H) = 141, 1H, H^d], 8.18 [d, ^4J(H–H) = 1.6, 1H, H^g], 8.67 [dd, J(H–H) = 5.0, 1.6, 1H, H^h]. ES (+)-MS (MeCN – H_2O): 447 [M – Cl]. Anal. found: C, 37.6; H, 4.1; N, 8.5. Calcd. for $C_{16}H_{18}ClN_3Pt{\cdot}H_2O$: C, 38.36; H, 4.02; N, 8.39 (%).

[PtCl{4-(3′,5′-$C_4H_3N_2$)$C_6H_3CHNCH_2CH_2NMe_2$}] (3bCl)

Compound **3bCl** was prepared from 100 mg (2.37×10^{-4} mol) of *cis*-[$PtCl_2(DMSO)_2$], 60.2 mg of **1b**, and 20 mg of sodium acetate after refluxing the mixture in methanol for 48 h. The reaction mixture was cooled, filtered to remove unreacted materials, and concentrated to dryness. The obtained residue was recrystallized in dichloromethane–pentane to yield an orange solid.

Yield: 20 mg (17.4%). ^{1}H NMR (400 MHz, $CDCl_3$) δ: 2.93 [s, ^3J(H–Pt) = 14, 6H, H^a], 3.15 [t, ^2J(H–H) = 6.0, 2H, H^b], 4.15 [td, ^2J(H–H) = 6.0, 1.2, ^3J(H–Pt) = 34, 2H, H^c], 7.21 [dd, J(H–H) = 8.0, 2.0, 1H, H^e], 7.39 [d, ^3J(H–H) = 8.0, 1H, H^f], 7.98 [d, J(H–H) = 2.0, 1H, H^g], 8.43 [t, J(H–H) = 1.2, ^3J(Pt–H) = 140, 1H, H^d], 9.02 [s, 2H, H^h], 9.19 [s, 1H, H^i]. ES (+)-MS (MeCN – H_2O): 503 [M + H_2O]. Anal. found: C, 33.3; H, 3.5; N, 9.5. Calcd. for $C_{15}H_{17}ClN_4Pt{\cdot}CH_2Cl_2$: C, 33.78; H, 3.37; N, 9.85 (%).

Table 3. Crystallographic and refinement data for compound **3bMe**.

Formula	$C_{16}H_{20}N_4Pt$
FW	463.45
T (K)	125(2)
Wavelength (Å)	0.71073
Crystal system	Monoclinic
Space group	$P2_1/c$
a (Å)	11.0787(8)
b (Å)	16.981(1)
c (Å)	8.1766(6)
β (°)	94.310(1)
V (Å^3)	1533.9(2)
Z	4
$D_{calcd.}$ (g/cm^3)	2.007
Abs. coeff. (mm^{-1})	9.146
θ range (°)	1.84–28.28
% Completeness to θ max	99.4
Data collected, unique	19507, 3781 (R_{int} = 0.0561)
Data, restraints, parameters	3781, 0, 193
GOF on F^2	1.023
R_1, wR_2 (F^2, $I > 2\sigma(I)$)	0.0295, 0.0574
R_1, wR_2 (F^2, all data)	0.0465, 0.0624
Peak and hole, e/Å^{-3}	1.522 and –0.792

4a

Compound **4a** was prepared from 22 mg (8.7×10^{-5} mol) of ligand **1a** and 50 mg (8.7×10^{-5} mol) of compound [$Pt_2Me_4(\mu\text{-}SMe_2)_2$] in acetone (20 mL). The mixture was stirred for 5 h at room temperature, and the resulting orange solid was filtered.

Yield: 60 mg (92%). **4a** was too insoluble for NMR or mass spectra. Anal. found: C, 33.3; H, 4.9 N, 5.2. Calcd. for $C_{21}H_{34}N_3Pt_2S$: C, 33.60; H, 4.56; N, 5.60 (%).

5a

The preparation of compound **5a** was attempted using a procedure consisting of refluxing a toluene suspension of compound **4a** for 2 h. The obtained solid was too insoluble for NMR or mass spectra, and the elemental analysis was not consistent with the expected formula. An alternative procedure detailed below gave analogous results: 25 mg (5.2×10^{-5} mol) of compound **3a** and 15 mg (2.6×10^{-5} mol) of compound [$Pt_2Me_4(\mu\text{-}SMe_2)_2$] were allowed to react in acetone at room temperature for 16 h. The resulting insoluble solid was filtered. Yield: 30 mg (79%, based on the expected formula $C_{20}H_{30}N_3Pt_2S$).

X-ray structure determination

X-ray diffraction data were collected on a Bruker APEX 2 CCD platform diffractometer (Mo Kα, λ = 0.71073 Å) at 125 K (0 °C = 273.15 K). A suitable crystal was mounted in a nylon loop with Paratone–*N* cryoprotectant oil. During data examination and space-group determination with XPREP, the σ(I) values were normalized and multiplied by a factor of 0.5. The structure was solved using direct methods and standard difference map techniques, and was refined by full-matrix least-squares procedures on F^2 with SHELXTL (Version 6.14) (38). All non-hydrogen atoms were refined

© 2008 NRC Canada

anisotropically. Hydrogen atoms were included in calculated positions and were refined using a riding model. Crystal data and refinement details are presented in Table 3.

Acknowledgements

We thank the Ministerio de Ciencia y Tecnología (project: CTQ2006-02007/BQU (MC)), Bard College, Vassar College, and The National Science Foundation (Grant NSF 0521237 to JMT (PI) and CMA) for financial support.

References

1. A.D. Ryabov. Synthesis, 233 (1985).
2. J. Dupont, M. Pfeffer, and J. Spencer. Eur. J. Inorg. Chem. 1917 (2001).
3. J. Dupont, C.S. Consorti, and J. Spencer. Chem. Rev. **105**, 2527 (2005).
4. I. Omae. Coord. Chem. Rev. **248**, 995 (2004).
5. P. Espinet, M.A. Esteruelas, L.A. Oro, J.L. Serrano, and E. Sola. Coord. Chem. Rev. **117**, 215 (1992).
6. C. Navarro-Ranninger, I. López-Solera, J.M. Pérez, J.R. Masaguer, and C. Alonso. Appl. Organomet. Chem. **7**, 57 (1993).
7. M. Albrecht and G. van Koten. Angew. Chem. Int. Ed. **40**, 3750 (2001).
8. I. Omae. J. Organomet. Chem. **692**, 2608 (2007).
9. A. Zucca, M.A. Cinellu, M.V. Pinna, S. Stoccoro, G. Minghetti, M. Manassero, and M. Sansoni. Organometallics, **19**, 4295 (2000).
10. A. Zucca, S. Stoccoro, M.A. Cinellu, G. Minghetti, M. Manassero, and M. Sansoni. Eur. J. Inorg. Chem. 3336 (2002).
11. C.M. Anderson, M. Crespo, M.C. Jennings, A.J. Lough, G. Ferguson, and R.J. Puddephatt. Organometallics, **10**, 2672 (1991).
12. M. Crespo, M. Martinez, J. Sales, X. Solans, and M. Font-Bardía. Organometallics, **11**, 1288 (1992).
13. C. Anderson, M. Crespo, M. Font-Bardía, A. Klein, and X. Solans. J. Organomet. Chem. **601**, 22 (2000).
14. C. Anderson and M. Crespo. J. Organomet. Chem. **689**, 1496 (2004).
15. M. Crespo, M. Font-Bardia, S. Pérez, and X. Solans. J. Organomet. Chem. **642**, 171 (2002).
16. M. Crespo and E. Evangelio. J. Organomet. Chem. **689**, 1956 (2004).
17. M. Crespo, M. Font-Bardia, and X. Solans. J. Organomet. Chem. **691**, 444 (2006).
18. M. Crespo, M. Font-Bardia, and X. Solans. J. Organomet. Chem. **691**, 1897 (2006).
19. A.D. Ryabov. Chem. Rev. **90**, 403 (1990).
20. C.K. Koo, Y.M. Ho, C.F. Chow, M.H.W. Lam, T.C. Lau, and W.Y. Wong. Inorg. Chem. **46**, 3603 (2007).
21. J.W. Slater and J.P. Rourke. J. Organomet. Chem. **688**, 112 (2003).
22. A. Zucca, A. Doppiu, M.A. Cinellu, S. Stoccoro, G. Minghetti, and M. Manassero. Organometallics, **21**, 783 (2002).
23. J. Bravo, C. Cativiela, R. Navarro, and E.P. Urriolabeitia. J. Organomet. Chem. **650**, 157 (2002).
24. C. López, A. Caubet, S. Pérez, X. Solans, M. Font-Bardia, and E. Molins. Eur. J. Inorg. Chem. 3974 (2006).
25. M. Crespo, M. Font-Bardia, J. Granell, M. Martinez, and X. Solans. Dalton Trans. 3763 (2003).
26. A. Capapé, M. Crespo, J. Granell, M. Font-Bardia, and X. Solans. J. Organomet. Chem. **690**, 4309 (2005).
27. A. Capapé, M. Crespo, J. Granell, M. Font-Bardia, and X. Solans. Dalton Trans. 2030 (2007).
28. L. Ding, D.P. Zou, and Y.J. Wu. Polyhedron, **17(15)**, 2511 (1998).
29. C. López, A. Caubet, S. Pérez, X. Solans, and M. Font-Bardia. Chem. Commun. 540 (2004).
30. Y.J. Wu, L. Ding, H.X. Wang, Y.H. Liu, H.Z. Yuan, and X.A. Mao. J. Organomet. Chem. **535**, 49 (1997).
31. H.F. Klein, S. Camadanli, R. Beck, D. Leukel, and U. Flörke. Angew. Chem. Int. Ed. **44**, 975 (2005).
32. C.M. Anderson, R.J. Puddephatt, G. Ferguson, and A.J. Lough. J. Chem. Soc., Chem. Commun. **18**, 1297 (1989).
33. M. Crespo, M. Font-Bardia, and X. Solans. Organometallics, **23**, 1708 (2004).
34. C.J. Levy, G.S. Hill, M.J. Irwin, L.M. Rendina, and R.J. Puddephatt. Inorg. Synth. **32**, 149 (1998).
35. D. Song and S. Wang. J. Organomet. Chem. **648**, 648 (2002).
36. M. Rashidi, Z. Fakhroeian, and R.J. Puddephatt. J. Organomet. Chem. **406**, 261 (1990).
37. V.Y. Kukushin, A.J.L. Pombeiro, C.M.P. Ferreira, and L.I. Elding. Inorg. Synth. **33**, 189 (2002).
38. G.M. Sheldrick. Acta Cryst. A64, 112 (2008).

© 2008 NRC Canada

Oxalate bridged heteronuclear compounds containing MM quadruple bonds (M = Mo and W) and their radical cations[1]

Malcolm H. Chisholm and Nathan J. Patmore

Abstract: The heteronuclear MM quadruply bonded oxalate bridged compound $[(t\text{-}BuCO_2)_3MoW]_2(\mu\text{-}C_2O_4)$ **(I)** has been prepared from the reaction between $MoW(O_2Ct\text{-}Bu)_4$ and oxalic acid and characterized by elemental analysis, ^{1}H NMR and UV-vis spectroscopy, and electrochemical studies. Single electron oxidation of **I** by reaction with $Ag^+PF_6^-$ leads to the formation of the kinetically labile radical cation $\mathbf{I}^+$, which has been characterized by UV-vis, NIR, and EPR spectroscopy. The latter results are compared with the properties of their related homonuclear Mo_4- and W_4-oxalate bridged compounds and their respective radical cations. The spectroscopic features of the related radical cations $[(t\text{-}BuCO_2)_6Mo_xW_y(\mu\text{-}C_2O_4)]^+$, where x = 1, 2, 3 and $y = 4 - x$, are also described with the conclusion that the $[(t\text{-}BuCO_2)_3Mo_2(\mu\text{-}C_2O_4)W_2(O_2Ct\text{-}Bu)_3]^+$ and $[(t\text{-}BuCO_2)_3Mo_2(\mu\text{-}C_2O_4)MoW(O_2Ct\text{-}Bu)_3]^+$ cations are valence trapped on the Robin and Day scheme for the classification of mixed valence compounds.

Key words: molybdenum, tungsten, mixed valence.

Résumé : La réaction du $MoW(O_2Ct\text{-}Bu)_4$ avec l'acide oxalique permet de préparer le composé hétéronucléaire MM, à liaison quadruple et pont d'oxalate, $[(t\text{-}Bu(CO_2)_3MoW]_2(\mu\text{-}C_2O_4)$, **I**, qu'on a caractérisé par analyse élémentaire, par spectroscopie UV-vis et RMN du ^{1}H ainsi que par des études électrochimiques. La réaction d'oxydation du composé **I** par un électron à l'aide du $Ag^+PF_6^-$ conduit à la formation du cation radical cinétiquement labile, $\mathbf{I}^+$, qu'on a caractérisé par spectroscopies RPE et UV-vis et proche infrarouge. On a comparé ces derniers résultats aux propriétés de leurs composés homonucléaires apparentés Mo_4- et W_4- liés à l'oxalate et leurs cations radicaux respectifs. On décrit aussi les caractéristiques spectroscopiques des cations radicaux apparentés $[(t\text{-}Bu(CO_2)_6Mo_xW_y(\mu\text{-}C_2O_4)]^+$ dans lesquels x = 1,2,3 et $y = 4 - x$ et on en conclut que les cations $[(t\text{-}Bu(CO_2)_3Mo_2(\mu\text{-}C_2O_4)W_2(O_2C\text{-}tBu)_3]^+$ et $[(t\text{-}Bu(CO_2)_3Mo_2(\mu\text{-}C_2O_4)MoW(O_2C\text{-}tBu)_3]^+$ sont liés par leur valence dans le schéma de Robin et Day de classification des composés de valence mixte.

Mots-clés : molybdène, tungstène, valence mixte.

[Traduit par la Rédaction]

Introduction

Electron transfer and electron delocalization are closely related phenomena, and each is fundamental to numerous chemically, physically, and biologically important processes (1). Indeed, in a molecular system the interconversion of valence-trapped and fully delocalized states corresponds to a molecular switch being "off" or "on", respectively, although it should be recognized that molecular systems and assemblies may never fully replicate the properties of solid-state inorganic based semiconductor (SiMOS) devices. It is, however, easily recognized that molecules can more easily store and impart data and signal recognition at the subnanamoter scale than any solid state device. Thus, the desire to develop molecular electronic and infomatic devices is a topic of considerable focus in current research (2). An understanding of how redox active centers (X) interact in molecular bridged systems (X-bridge-X) in their neutral, singly oxidized and (or) reduced and photoexcited states is thus of fundamental importance, be the redox active center a metal or an organic moiety.

In this paper we describe our studies of oxalate bridged MM quadruply bonded complexes where the redox active metal centers M = Mo or W. Specifically, we examine the heteronuclear complexes containing Mo_xW_y where x = 1, 2, and 3 in relation to $y = 4 - x$ (3, 4).

Received 14 February 2008. Accepted 23 May 2008. Published on the NRC Research Press Web site at canjchem.nrc.ca on 7 Aguust 2008.

Dedicated to Professor R. J. Puddephatt in appreciation of his pioneering contributions to inorganic and organometallic chemistry.

M.H. Chisholm[2] and N.J. Patmore.[3] Department of Chemistry, The Ohio State University, 100 W. 18th Ave., Columbus, OH 43210, USA

[1]This article is part of a Special Issue dedicated to Professor Richard J. Puddephatt.
[2]Corresponding author (e-mail: chisholm@chemistry.ohio-state.edu).
[3]Present address: Department of Chemistry, University of Sheffield, Sheffield S3 7HF, Great Britain.

 doi:10.1139/V08-093 © 2008 NRC Canada

Results and discussion

Preparations

In our previous studies, we have prepared the oxalate bridged compounds according to the reaction outlined in eq. [1] (3, 4). The desired tetranuclear compound was isolated by its preferential precipitation from toluene in what is otherwise an equilibrium mixture of products and reactants.

[1] $$2M_2(O_2Ct\text{-}Bu)_4 + HO_2CCO_2H \xrightarrow[\text{Toulene}]{25°C} [(t\text{-}BuCO_2)_3M_2]_2(\mu\text{-}O_2CCO_2) + 2t\text{-}BuCO_2H$$

In this study, the well-characterized compound $[(t\text{-}BuCO_2)_3MoW]_2(\mu\text{-}O_2CCO_2)$ (**I**) was similarly prepared from the known compound $MoW(O_2Ct\text{-}Bu)_4$ (5) and its reaction with oxalic acid. The other mixed metal containing complexes shown in Scheme 1 were prepared similarly but were not separable in a pure manner from their respective derivatives of the combinations of starting materials. For example, the complex $[(t\text{-}BuCO_2)_3Mo_2(\mu\text{-}O_2CCO_2)W_2(O_2Ct\text{-}Bu)_3]$ (**II**) was formed in the reaction between oxalic acid and a 1:1 equivalent of the respective homonuclear complexes $M_2(O_2Ct\text{-}Bu)_4$ (M = Mo or W), eq. [2], but was not separable from the homometallic M_4-oxalate bridged compounds $[(t\text{-}BuCO_2)_3Mo_2]_2(\mu\text{-}O_2CCO_2)$ (**V**) and $[(t\text{-}BuCO_2)_3W_2]_2(\mu\text{-}O_2CCO_2)$ (**VI**). The ^1H NMR spectrum of the products indicated a near statistical distribution of products in a 1:2:1 ratio. Spectroscopically, however, the Mo_2W_2-oxalate compound **II** and its radical cation $\mathbf{II}^+$, formed in situ by oxidation with $Ag^+PF_6^-$, were detectable in the presence of the known spectral features of the homometallic compounds. Similarly in reactions employing $M_2(O_2Ct\text{-}Bu)_4$ (M = Mo or W) and $MoW(O_2Ct\text{-}Bu)_4$ with oxalic acid, eqs. [3] and [4], the heterometallic species containing Mo_3W-oxalate (**III**) and W_3Mo-oxalate (**IV**) can be identified along with their radical cations formed by single electron oxidation.

[2] $$4Mo_2(O_2Ct\text{-}Bu)_4 + 4W_2(O_2Ct\text{-}Bu)_4 + 4HO_2CCO_2H \xrightarrow[\text{Toulene}]{25°C} [Mo_2]\text{-}O_2CCO_2\text{-}[Mo_2] + 2[Mo_2]\text{-}O_2CCO_2\text{-}[W_2] + [W_2]\text{-}O_2CCO_2\text{-}[W_2]$$

[3] $$4Mo_2(O_2Ct\text{-}Bu)_4 + 4MoW(O_2Ct\text{-}Bu)_4 + 4HO_2CCO_2H \xrightarrow[\text{Toulene}]{25°C} [Mo_2]\text{-}O_2CCO_2\text{-}[Mo_2] + 2[Mo_2]\text{-}O_2CCO_2\text{-}[MoW] + [MoW]\text{-}O_2CCO_2\text{-}[MoW]$$

[4] $$4W_2(O_2Ct\text{-}Bu)_4 + 4MoW(O_2Ct\text{-}Bu)_4 + 4HO_2CCO_2H \xrightarrow[\text{Toulene}]{25°C} [MoW]\text{-}O_2CCO_2\text{-}[MoW] + 2[W_2]\text{-}O_2CCO_2\text{-}[MoW] + [W_2]\text{-}O_2CCO_2\text{-}[W_2]$$

where $M_2 = (t\text{-}BuCO_2)_3M_2$

Scheme 1.

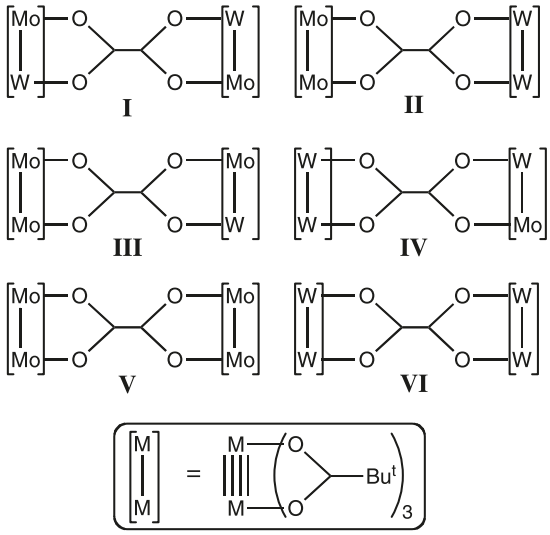

Due to the synthetic constraints associated with compounds **II**–**IV** (eqs. [2–4]), the only well-defined and fully characterized heterometallic compound is the $(MoW)_2$-oxalate bridged complex **I** and its radical cation $\mathbf{I}^+$. The nature of the other heterometallic species are inferred based on spectroscopic properties of mixtures.

Electronic structure calculations

Given that compounds **II**–**IV** cannot be isolated cleanly from other product combinations, the calculated electronic structure and spectroscopic features will be of help in interpreting their properties. Calculations employing density functional theory (DFT) using the Gaussian 2003 suite of programs were performed on the formate substituted model compounds $[(HCO_2)_6Mo_xW_y(\mu\text{-}C_2O_4)]^{0/+}$, where $x = 0$ (**VI′**), 1 (**IV′**), 2 (**I′** and **II′**), 3 (**III′**), 4 (**V′**) and $y = 4 - x$. The structure of each complex was determined by geometry optimization, and in each instance the oxalate bridge in the ground state structure adopted a planar configuration. The planar bridge maximizes MM′-δ to oxalate-π* backbonding. For compound **I′**, there are two possible geometric forms of a planar oxalate core that can be termed as the syn (C_{2v} symmetry) and anti (C_{2h} symmetry) isomers with respect to the Mo atoms. The syn form of **I′** would be expected to have an overall dipole moment due to the polarity of the MoW bond. The calculated ground state energy, electronic structure, and spectroscopic properties of both isomers are nearly identical, and hence only the properties of the anti isomer are reported.

For all of the oxalate bridged M4-containing compounds, the HOMO-1 and the HOMO are the in-phase and out-of-phase MM δ-orbital combinations, respectively. They interact with the oxalate π-system as shown in Scheme 2, and of these two interactions the one involving the oxalate π* orbital is the most important, based on energy considerations. The Mo_2-δ^* orbital is lower in energy than the unoccupied oxalate-π* orbital, and for complexes containing Mo_2 cores (**II′**, **III′**, **V′**) the LUMO is a Mo_2-δ*. Due to the decrease in electronegativity for tungsten, the δ^* orbitals of MoW and W_2 cores are higher in energy than for Mo_2, and the LUMO is the oxalate-π* orbital for complexes **I′**, **IV′** and **VI′**. A ta-

© 2008 NRC Canada

Table 1. Selected calculated spectroscopic data for compounds **I′**–**VI′** and their associated radical cations **I′**$^{+}$–**VI′**$^{+}$.

Compound	Calcd. MM′-δ to oxalate-π* transition		Calcd. HOMO-1 to SOMO transition for the *radical cation*	
	λ_{max} (nm)	Oscillator strength	λ_{max} (nm)	Oscillator strength
I′ ({MoW}$_2$)	498	0.4233	1275	0.2199
II′ (Mo_2W_2)	489	0.6198	1305	0.2129
III′ (Mo_3W)	468	0.4487	1352	0.2255
IV′ (W_3Mo)	513	0.5772	1226	0.2001
V′ (Mo_4)	449	0.5147	1421	0.2303
VI′ (W_4)	529	0.7222	1180	0.1776

Scheme 2.

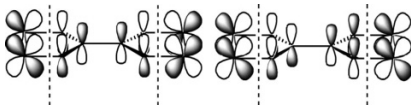

ble of the calculated frontier MO energies and assignments for all complexes is given in the Supplementary Data.[4]

The calculated electronic absorption spectra show intense MM′-δ to oxalate-π* MLCT (metal to ligand charge transfer) transitions for all compounds in the visible region, summarized in Table 1. MLCT transitions involving W are predicted to be more intense, and the general trend of MLCT absorption *energy* follows the order Mo_2 > MoW > W_2. This reflects the smaller HOMO–oxalate-π* gaps due to the higher energy of MoW-δ and W_2-δ orbitals and greater radial extension of the W 5d orbitals, features that have been discussed in other studies of [(*t*-$BuCO_2$)$_3M_2$]$_2$(μ-dicarboxylate) systems (6). For the radical cations, the energy, intensity, and shape of the charge resonance band (HOMO-1 to SOMO transition) can be used to quantify the extent of electron delocalization (7, 8). The calculated energies of the HOMO-1 to SOMO (δ to δ) absorptions of the radical cation mixed-valence species **I′**$^{+}$–**VI′**$^{+}$, calculated from the geometry optimized structures, are also included in Table 1. The trends predicted by the gas-phase calculations are observed experimentally in solution (see later in Figs. 1 and 2), though the observed spectral features are all red-shifted.

[(*t*-$BuCO_2$)$_3$MoW]$_2$(μ-O_2CCO_2) and its radical cation

The compound **I**, formed in a reaction related to eq. [1] but involving MoW(O_2C*t*-Bu)$_4$, is a purple microcrystalline compound only sparingly soluble in benzene and toluene but more soluble in the polar solvents THF and DMSO. The compound was characterized by ^{1}H NMR and MALDI-TOF spectroscopy and elemental analysis.

The intense color of compound **I** in THF is due to the fully allowed HOMO to LUMO electronic transition, which is MLCT involving a MoW-δ combination and the oxalate bridge π* orbital. The electronic absorption spectrum is shown in Fig. 1, where a comparison is made with the

Fig. 1. Electronic absorption spectra of **I** (black), **V** (red), and **VI** (blue) in THF at room temperature.

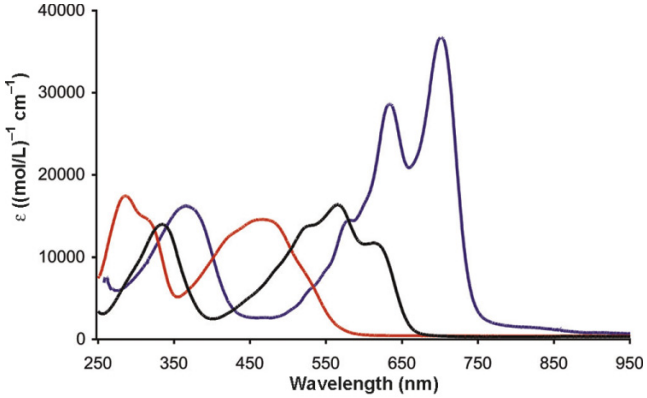

Fig. 2. Electronic absorption spectra of **I** (gray) and **I**$^{+}$$PF_6^{-}$ (black) in THF at room temperature. The inset shows an expansion of the charge resonance band region for **I**$^{+}$$PF_6^{-}$, including the bands of **V**$^{+}$$PF_6^{-}$ (red) and **VI**$^{+}$$PF_6^{-}$ (blue) for comparison. The spectral feature at ca. 4400 cm^{-1} corresponds to a sample cell absorption.

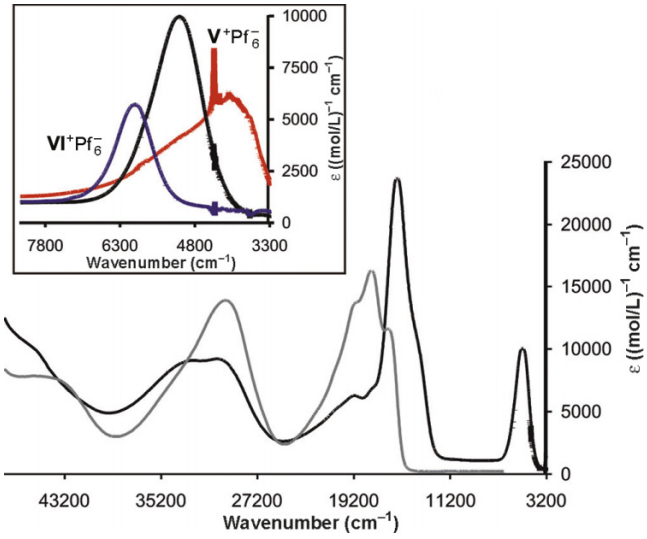

[4] Supplementary data for this article are available on the journal Web site (canjchem.nrc.ca) or may be purchased from the Depository of Unpublished Data, Document Delivery, CISTI, National Research Council Canada, Ottawa, ON K1A 0R6, Canada. DUD 3782. For more information on obtaining material refer to cisti-icist.nrc-cnrc.gc.ca/irm/unpub_e.shtml.

© 2008 NRC Canada

Table 2. Summary of electrochemical data for oxalate bridged hetero- and homonuclear compounds **I**–**VI** (Scheme 1) alongside related dinuclear tetracarboxylate species.

Compound	$E_{1/2}(1)$ (V) [a]	$E_{1/2}(2)$ (V) [a]	$\Delta E^{1/2}$ (mV)	K_c [b]	Ref.
$Mo_2(O_2Ct\text{-}Bu)_4$	–0.04	—	—	—	9
$MoW(O_2Ct\text{-}Bu)_4$	–0.48	—	—	—	9
$W_2(O_2Ct\text{-}Bu)_4$	–0.70	—	—	—	9
I ($\{MoW\}_2$)	–0.53	0.02	544	1.6×10^9	This work
II (Mo_2W_2)	–0.63	0.34[c]	966[c]	2.1×10^{16}	This work
III (Mo_3W)	–0.34	0.31[c]	648[c]	9.0×10^{10}	This work
IV (W_3Mo)	–0.78	–0.16[c]	620[c]	5.4×10^4	This work
V (Mo_4)	–0.03	+0.25	280	5.4×10^4	4, 5
VI (W_4)	–1.26	–0.54	717	1.3×10^{12}	4, 5

[a]Values obtained in 0.1 mol/L n-Bu_4NPF_6/THF solutions at 298 K and referenced relative to the Fc/Fc^+ redox couple.
[b]Determined according to the equation $K_c = \exp(\Delta E_{1/2}/25.69)$ (10).
[c]Estimated values extrapolated from superposition of coincidental redox waves from other redox active species.

Table 3. NIR absorption spectral data for the oxalate bridged radical cations in THF.

Compound	$\overline{V}_{max}$ (cm^{-1})	$\Delta\upsilon_{1/2}$ (expt., cm^{-1})	$\Delta\upsilon_{1/2}$ (calcd., cm^{-1})[a]	H_{ab} (cm^{-1})	Ref.
$\mathbf{V}^+PF_6^-$ (Mo_4)	4050	2196[b]	3059	2025	3, 4
$\mathbf{I}^+PF_6^-$ ($\{MoW\}_2$)	5110	1191	3436	2555	This work
$\mathbf{VI}^+PF_6^-$ (W_4)	6000	877	3722	3000	3, 4

[a]$\Delta\upsilon_{1/2}$ (calcd.) = $[2310\ \overline{V}_{max}]^{1/2}$ from ref. 13.
[b]Non-symmetrical absorption, hence band-width determined from the high-energy side of the band to avoid low-energy cutoff effects.

respective homometallic Mo_4 (**V**) and W_4 (**VI**) containing complexes. The intermediate energy of this electronic transition is consistent with the calculated trend in M_2-δ orbital energies and the electrochemical oxidation potentials.

Electrochemical studies by both cyclic voltammetry and differential pulse voltammetry reveal two oxidation waves for **I**, the first being reversible on the electrochemical timescale and the second being quasi-reversible. The first oxidation potential and the separation between the first and the second $\Delta E_{1/2}$ are intermediate between the respective homometallic compounds **V** and **VI**. Electrochemical data for these compounds are summarized in Table 2.

The single oxidation of compound **I** in THF was carried out by reaction with one equivalent of $AgPF_6$, and the radical cation $\mathbf{I}^+PF_6^-$ was characterized by both its electronic absorption spectrum and by EPR spectroscopy.

Oxidation of **I** to $\mathbf{I}^+$ causes a red shift of the intense MLCT band and the generation of a low-energy absorption in the near-infrared (NIR) that corresponds to a HOMO-1 → SOMO (δ → δ) transition. The spectra of **I** and $\mathbf{I}^+$ in THF are compared in Fig. 2. The low energy band at 5110 cm^{-1} is readily assignable to a charge resonance band of a Class III fully delocalized radical cation on the Robin and Day scheme (11) for mixed valence complexes, based upon the intensity and narrower than predicted peak width of the transition (12). The extent of electronic coupling can be quantified by the cross coupling matrix element, H_{ab}, that is determined by application of Hush theory (13) to the transition. The H_{ab} value for $\mathbf{I}^+PF_6^-$ of 2555 cm^{-1} is, as expected, intermediate between that observed for $\mathbf{V}^+PF_6^-$ (2025 cm^{-1}) and $\mathbf{VI}^+PF_6^-$ (3000 cm^{-1}). The NIR spectra for these mixed-valence species are compared in the inset in Fig. 2, and the spectroscopic data for the charge resonance bands of the radical cations summarized in Table 3.

The EPR spectrum of $\mathbf{I}^+PF_6^-$ in 2-MeTHF at 250 K is shown in Fig. 3. This isotropic spectrum shows a central signal at g = 1.868 due to the presence of the isotopomers $(MoW)_2$ with spin inactive nuclei and a satellite spectrum arising from the presence of ^{183}W (I = 1/2, 14.5% natural abundance) and $^{95/97}Mo$ (I = 5/2, 25.4% total natural abundance). The EPR spectrum is entirely consistent with a fully delocalized electron in a δ combination orbital for the $(MoW)_2^+$ moiety. Notably, the hyperfine coupling to $^{95/97}Mo$, I = 5/2 is larger than in the related $\mathbf{V}^+PF_6^-$ Mo_4-containing radical cation, while the coupling to ^{183}W, I = 1/2 is smaller than in the $\mathbf{VI}^+PF_6^-$ W_4-containing cation. These data are summarized in Table 4 and clearly indicate the polarized nature of the MoW δ-orbital, as seen in the respective $MoW(O_2Ct\text{-}Bu)^+PF_6^-$ radical cation (9). On a relative scale, Mo(2+) is more electronegative than W(2+). This is largely a result of the more effective shielding of the valence electrons by the number of core electrons and is seen in the fact that oxidizing powers of the cations follows the order $Cr^{6+} > Mo^{6+} > W^{6+}$ for the d^0 metal ions in their oxides MO_3 and their oxometallate anions MO_4^{2-}.

© 2008 NRC Canada

Table 4. Hyperfine coupling constants (Gauss) for the oxalate bridged MM radical cations in 2-MeTHF.

Compound	A_{iso} $^{95/97}$Mo	A_{iso} ^{183}W	g_{av}	Ref.
$Mo_2(O_2Ct\text{-}Bu)_4$ $^+PF_6^-$	27		1.9	9
$MoW(O_2Ct\text{-}Bu)_4{}^+PF_6^-$	44	31	1.9	9
$W_2(O_2Ct\text{-}Bu)_4{}^+PF_6^-$		51	1.8	9
$\mathbf{I}^+PF_6^-$ ($\{MoW\}_2$)	25	20	1.9	This work
$\mathbf{II}^+PF_6^-$ (Mo_2W_2)		48	1.8	This work
$\mathbf{III}^+PF_6^-$ (Mo_3W)	—[a]	—[a]	1.9	This work
$\mathbf{IV}^+PF_6^-$ (W_3Mo)	—[a]	—[a]	1.8	This work
$\mathbf{V}^+PF_6^-$ (Mo_4)	15		1.9	3, 4
$\mathbf{VI}^+PF_6^-$ (W_4)		31	1.8	3, 4

[a]Hyperfine coupling constants could not be resolved because of coincident signals from other species in solution.

Fig. 3. The X-band EPR spectrum of $\mathbf{I}^+PF_6^-$ in 2-MeTHF at 250 K.

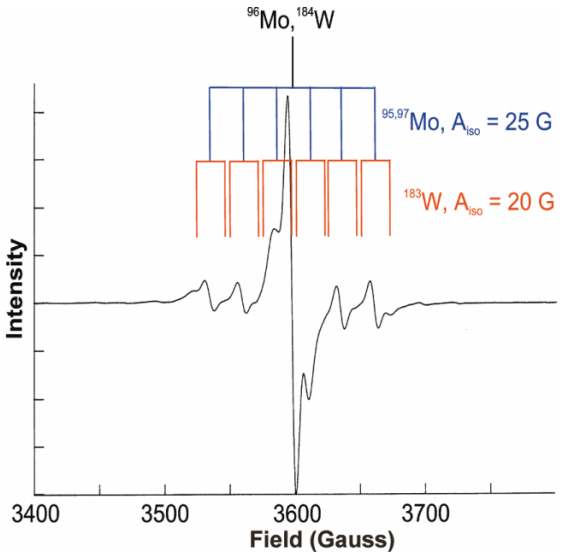

Fig. 4. Differential pulse voltammograms in 0.1 mol/L $NBu^n{}_4PF_6$/THF solutions of the product mixtures formed from the intended synthesis of **IV** (top), **II** (middle), and **III** (bottom).

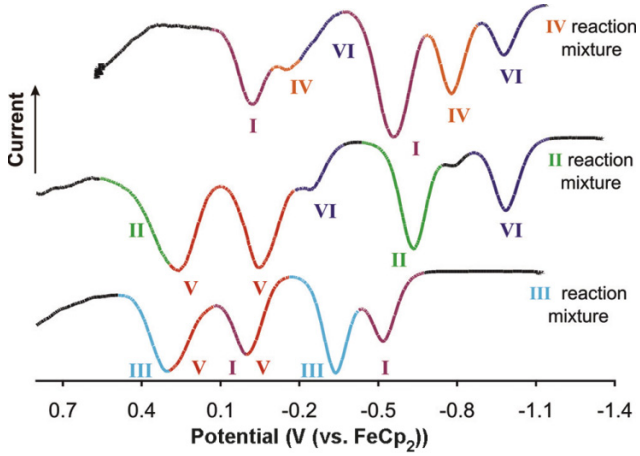

The radical cations of II, III, and IV

The reaction between a 1:1:1 mixture of $Mo_2(O_2Ct\text{-}Bu)_4$, $W_2(O_2Ct\text{-}Bu)_4$, and oxalic acid (eq. [2]) gives a mixture of the previously characterized homometallic M_4-oxalate bridged complexes (**V** and **VI**) in addition to the Mo_2W_2-oxalate bridged compound **II**. ^{1}H NMR spectroscopy shows a statistical mixture of the products is formed, indicating that the reaction of both $Mo_2(O_2Ct\text{-}Bu)_4$ and $W_2(O_2Ct\text{-}Bu)_4$ with oxalic acid proceeds with similar kinetics. The cyclic voltammogram of this mixture (Fig. 4) shows six oxidation waves, four of which are associated with the known homonuclear compounds **V** and **VI**. The remaining two oxidation waves at –0.63 and 0.34 V represent successive oxidation of the W_2 and Mo_2 units of compound **II**. The Mo_3W-oxalate (**III**) and W_3Mo-oxalate (**IV**) compounds were prepared in a similar fashion (eqs. [3] and [4]), and the redox potentials of the compounds extrapolated from the reaction mixtures is shown in Fig. 4 and summarized in Table 2.

For the spectroscopic studies on the radical cation $\mathbf{II}^+PF_6^-$, just enough $Ag^+PF_6^-$ was added in situ to preferentially oxidize **VI** and **II** by one electron, preventing formation of the $\mathbf{V}^+PF_6^-$ radical cation that could further complicate the spectra. The notable spectroscopic features of the new mixed valence ion are the absence of any electronic absorption band in the region 7000–3000 cm^{-1} and a signal in the EPR spectrum at g = 1.831 with coupling to ^{183}W (A_{iso} = 48 G). This, together with the relative intensities of the satellites in the EPR spectrum and the absence of any hyperfine coupling to $^{95/97}$Mo, is a clear indication of this mixed valence complex being valence-trapped. The W_2 center is oxidized and the unpaired electron resides in a W_{2-} δ orbital.

Unfortunately, because of similar g values and overlapping spectra for the $\mathbf{III}^+$ and $\mathbf{I}^+$ radical cations, reliable values for the $^{95/97}$Mo and ^{183}W coupling constants could not be obtained from the EPR spectrum of $\mathbf{III}^+PF_6^-$. No absorption bands were observed in the NIR region 7000–3000 cm^{-1} for $\mathbf{III}^+PF_6^-$, indicating that the radical cation is likely to be valence-trapped with the single electron residing in a polarized MoW-δ orbital.

In contrast, the spectroscopic features of the W_3Mo-containing $\mathbf{IV}^+PF_6^-$ radical cation may be classified as mixed valence fully delocalized or Class III on the Robin and Day scheme (11), based upon the appearance of low

© 2008 NRC Canada

energy electronic absorption bands in the region 7000–3000 cm^{-1} (see Supplementary Data).[4] As expected, the absorption falls in an energy region between the $\mathbf{I}^+$ and $\mathbf{VI}^+$ bands. The EPR spectrum of this mixture is once again sufficiently complicated that assignment of the hyperfine coupling constants to $^{95/97}$Mo and ^{183}W could not be made.

Concluding remarks

The spectroscopic features of the mixed metal complex **I** and its radical cation $\mathbf{I}^+$ are, as expected, intermediative between the respective homometallic complexes and their radical cations. The mixed valence radical cation $\mathbf{I}^+$ can be classified as fully delocalized on the Robin and Day scheme (11), and from the hyperfine satellite spectrum we can see that greater electron density lies on the Mo atoms. This is consistent with the observed polarization of the single electron toward the Mo atom in the $MoW(O_2Ct\text{-}Bu)_4^+$ δ^1 orbital (10). The properties of the $[W_3Mo]^+$-containing ion, $\mathbf{IV}^+$, is also indicative of Class III behavior, whilst the $[Mo_2W_2]^+$- and $[Mo_3W]^+$-containing ions, $\mathbf{II}^+$ and $\mathbf{III}^+$, are valence-trapped. The latter might well have been anticipated given that the first oxidation potential of the homometallic complexes $M_2(O_2Ct\text{-}Bu)_4$ differ by ~0.5 V for Mo = Mo and W. Compound **I**, having a planar ground state due to (MoW) to oxalate π^* back-bonding, can exist as two geometric forms that could be termed with respect to the Mo atoms as syn and anti. Given the polarity of the MoW quadruple bond the former, the syn geometric isomer would be expected to have a dipole moment. In the present study the spectroscopic features do not allow us to distinguish between these, and regrettably the kinetic lability of these species toward decomposition has not allowed us to interrogate this by single crystal X-ray crystallography.

Experimental section

Physical procedures

Because of the air sensitive nature of the reactants and products, all experimental manipulations were performed under nitrogen and argon atmospheres. Solvents were distilled prior to use over the appropriate drying agent. The Schlenk flasks containing the reaction mixtures were centrifuged, as opposed to filtered, to improve the reaction yield. The compounds $Mo_2(O_2Ct\text{-}Bu)_4$ (14), $MoW(O_2Ct\text{-}Bu)_4$ (6), $W_2(O_2Ct\text{-}Bu)_4$ (15), $[(t\text{-}BuCO_2)_3Mo_2(\mu\text{-}O_2CCO_2)W_2(O_2Ct\text{-}Bu)_3]$ (**II**) (16), $[(t\text{-}BuCO_2)_3Mo_2]_2(\mu\text{-}O_2CCO_2)$ (**V**) (4), and $[(t\text{-}BuCO_2)_3W_2]_2(\mu\text{-}O_2CCO_2)$ (**VI**) (4), were prepared according to literature procedures. The radical cations were synthesized by addition of a stoichiometric amount of $AgPF_6$ to solutions of the neutral compounds immediately prior to spectroscopic measurements.

Microanalysis was performed by Atlantic Microlab, Inc. Electronic absorption spectra were recorded on a PerkinElmer Lambda 900 UV–vis and NIR spectrometer, with nitrogen purging, employing IR quartz cells with 1.00 mm path lengths and sample concentrations of ~10^{-4} mol/L. A 400 MHz Bruker DPX Avance spectrometer was used to record ^{1}H NMR spectra that were referenced to residual protio signals of d_8-THF at δ 3.58 and 1.73 ppm. Electrochemical measurements were performed using a Princeton Applied Research (PAR) 173A potentiostat-galvanostat equipped with a PAR 176 current-to-voltage converter using 0.1 mol/L solutions of $n\text{-}Bu_4NPF_6$ in THF. The voltammetric cell was equipped with a platinum wire auxiliary electrode, a platinum working electrode, and a pseudo-reference electrode consisting of a silver wire in 0.1 mol/L $n\text{-}Bu_4NPF_6$/THF separated from the bulk solution by a Vycor tip. The potentials are referenced internally to the $FeCp_2^{0/+}$ couple by the addition of a small amount of $FeCp_2$ to the solutions. X-band EPR spectra were recorded using a Bruker ESP300 electron spin resonance spectrometer. Temperature regulation was achieved by employing a Bruker Variable Temperature unit.

Preparation of $[(MoW)(O_2Ct\text{-}Bu)_3]_2(\mu\text{-}O_2CCO_2)$ (I)

A suspension of $MoW(O_2Ct\text{-}Bu)_4$ (250 mg, 0.37 mmol) and oxalic acid (16 mg, 0.18 mmol) in 5 mL of toluene was stirred for 10 days in a Schlenk flask, during which a purple precipitate formed. The purple precipitate was isolated by centrifugation of the Schlenk flask, then washed with two aliquots of toluene and one aliquot of hexane, before drying in vacuo. Yield 151 mg (67%). UV-vis (0.478 mmol/L in THF, 295 K, values of $\varepsilon \times 10^{-3}$ are given in parentheses): 615 (11.4), 565 (16.0), 525 (13.4), 334 (13.7), 221 (7.6) nm. ^{1}H NMR (THF-d_8) δ: 1.40 (s, 38H), 1.42 (s, 18H). Elemental anal. calcd. for $Mo_2W_2O_{16}C_{32}H_{54}$: C 30.64, H 4.34; found: C 30.65, H 4.45. MALDI-TOF calcd. monoisotopic MW for $Mo_2W_2O_{16}C_{32}H_{54}$: 1258.05 (M+); found, 1257.77.

Preparation of $[(t\text{-}BuCO_2)_3Mo_2(\mu\text{-}O_2CCO_2)MoW(O_2Ct\text{-}Bu)_3]$ (III)

A Schlenk flask was charged with $MoW(O_2Ct\text{-}Bu)_4$ (125 mg, 0.18 mmol), $Mo_2(O_2Ct\text{-}Bu)_4$ (109 mg, 0.18 mmol), and oxalic acid (16 mg, 0.18 mmol). Toluene (2 mL) was added and the suspension stirred for 10 days, during which a purple precipitate formed. The precipitate was isolated by centrifugation, then washed with toluene (2 × 10 mL aliquots) and hexane (1 × 10 mL aliquot), before drying in vacuo. Yield 159 mg. The ^{1}H NMR of the product mixture displayed a number of peaks in the range 1.40–1.46 ppm. The MALDI-TOF spectrum of the product mixture showed peaks corresponding to **V** [calcd. monoisotopic MW, 1085.96 (M^+); found 1086.02], **I** [calcd. monoisotopic MW, 1258.05 (M^+); found 1258.23] as well as compound **III** [calcd. monoisotopic MW, 1172.01 (M^+); found, 1172.09]. Assuming the products **V**, **III**, and **I** formed a 1:2:1 statistical mixture, the elemental anal. calcd. for $Mo_3W_1O_{16}C_{32}H_{54}$: C 32.95, H 4.67; found: C 32.85, H, 4.58.

Preparation of $[(t\text{-}BuCO_2)_3W_2(\mu\text{-}O_2CCO_2)MoW(O_2Ct\text{-}Bu)_3]$ (IV)

Toluene (2 mL) was added to a Schlenk flask charged with $MoW(O_2Ct\text{-}Bu)_4$ (125 mg, 0.18 mmol), $W_2(O_2Ct\text{-}Bu)_4$ (141 mg, 0.18 mmol) and oxalic acid (16 mg, 0.18 mmol). The suspension stirred for 10 days, during which a blue precipitate formed. The precipitate was isolated by centrifugation, then washed with toluene (2 × 10 mL aliquots) and hexane (1 × 10 mL aliquot), before drying in vacuo. Yield 123 mg. The ^{1}H NMR of the product mixture displayed a number of peaks in the range 1.37–1.42 ppm. The MALDI-TOF spectrum of the product mixture showed peaks corre-

© 2008 NRC Canada

sponding to **I** [calcd. monoisotopic MW, 1258.05 (M^+); found 1258.18], **VI** [calcd. monoisotopic MW, 1430.14 (M^+); found 1430.43], as well as compound **IV** [calcd. monoisotopic MW, 1342.25 (M^+); found 1342.33].

Electronic structure calculations

Molecular and electronic structure calculations on the neutral model compounds **I′–VI′** and the radical cations **I′$^+$–VI′$^+$**, were performed using density functional theory as implemented in the Gaussian 2003 suite of programs (17). The B3LYP functional (18) was used along with the 6–31G* basis set for O, C, H^{19}, and SDD energy-consistent pseudopotentials for Mo and W (19). All geometries were fully optimized and confirmed to be minima on the potential energy surface using harmonic vibrational frequency analysis. Electronic absorption spectra were predicted using the time-dependent DFT (TD-DFT) method.

Acknowledgements

We thank the National Science Foundation for financial support of this work. The Ohio Supercomputer Center is gratefully acknowledged for computational resources.

References

1. R.J.H. Clark, P. Day, and N.S. Hush. Phil. Trans. Roy. Soc. A, **366**, 5, (2008).
2. C. Joachim and M. Ratner (*Special Feature Editors*). Proc. Nat. Acad. Sci. U.S.A. **102**, 8800 (2005).
3. R.H. Cayton, M.H. Chisholm, J.C. Huffman, and E.B. Labkovsky. J. Am. Chem. Soc. **113**, 8709 (1991).
4. B.E. Bursten, M.H. Chisholm, R.J.H. Clark, S. Firth, C.M. Hadad, A.M. MacIntosh, P.J. Wilson, P.M. Woodward, and J.M. Zaleski. J. Am. Chem. Soc. **124**, 3050 (2002).
5. V. Katovic, J.L. Templeton, R.J. Hoxmeler, and R.E. McCarley. J. Am. Chem. Soc. **97**, 5300 (1975).
6. M.H. Chisholm and N.J. Patmore. Acc. Chem. Res. **40**, 19 (2007).
7. B.S. Brunschwig, C. Creutz, and N. Suttin. Chem. Soc. Rev. **31**, 168, (2002).
8. S.F. Nelson. Chem. Eur. J. **6**, 581 (2001).
9. M.H. Chisholm, J.S. D'Acchioli, B.D. Pate, and N.J. Patmore. Inorg. Chem. **44**, 1061 (2005).
10. D.E. Richardson and H. Taube. Inorg. Chem. **20**, 1278 (1981).
11. M.B. Robin and P. Day. Adv. Inorg. Radiochem. **10**, 247 (1967).
12. N.S. Hush. Prog. Inorg. Chem. **8**, 391 (1967).
13. A.G. Brignole and F.A. Cotton. Inorg. Synth. **13**, 81 (1972).
14. D.J. Santure, J.C. Huffman, and A.P. Sattelberger. Inorg. Chem. **24**, 371 (1985).
15. M.H. Chisholm, J.S. D'Acchioli, C.M. Hadad, and N.J. Patmore. Dalton Trans. 1852 (2005).
16. M.J. Frisch, G.W.Trucks, H.B. Schlegel, G.E. Scuseria, M.A. Robb, J.R. Cheeseman, J.A. Montgomery Jr., T. Vreven, K.N. Kudin, J.C. Burant, J.M. Millam, S.S. Iyengar, J. Tomasi, V. Barone, B. Mennucci, M. Cossi, G. Scalmani, N. Rega, G.A. Petersson, H. Nakatsuji, M. Hada, N. Ehara, K. Toyota, R. Fukuda, J. Hasegawa, M. Ishida, T. Nakajima, Y. Honda, O. Kitao, H. Nakai, M. Klene, X. Li, J.E. Knox, H.P. Hratchian, J.B. Cross, C. Adamo, J. Jaramillo, R. Gomperts, R.E. Stratmann, O. Yazyev, A.J. Austin, R. Cammi, C. Pomelli, J.W. Ochterski, P.Y. Ayala, K. Morokuma, G.A. Voth, P. Salvador, J.J. Dannenberg, V.G. Zakrzewski, S. Dapprich, A.D. Daniels, M.C. Strain, O. Ortiz, Q. Cui, A.G. Baboul, S. Clifford, J. Cioslowski, B.B. Stefanov, G. Liu, A. Liashenko, P. Piskorz, I. Komaroami, R.L. Martin, D.J. Fox, T. Keith, M.A. Al-Laham, C.Y. Peng, A. Nanayakkara, M. Challacombe, P.M.W. Gill, B. Johnson, W. Chen, M.W. Wong, C. Gonzalez, and J.A. Pople. Gaussian 03 [computer program]. Gaussian, Inc., Pittsburgh, PA. 2003.
17. (*a*) A.D. Becke. Phys. Rev. A, **38**, 3098 (1988); (*b*) A.D. Becke. J. Chem. Phys. **98**, 5648 (1993); (*c*) C. Lee, W. Yang, and R.J. Parr. Phys. Rev. B. Condens. Matter, **37**, 785 (1988).
18. W.J. Hehre, L. Radom, P.v.R. Schleyer, and J.A. Pople. Ab initio molecular orbital theory. J. Wiley and Sons, New York. 1986.
19. D. Andrae, U. Hauessermann, M. Dolg, and H. Preuss. Theor. Chim. Acta, **77**, 123 (1990).

© 2008 NRC Canada

A weakly coordinating anion as a tripodal "Br_3"-ligand for platinum(IV) — Structure of [(*closo*-$CB_{11}H_6Br_6$)$PtMe_3$][1]

Antonio G. De Crisci, Jesse Kleingardner, Alan J. Lough, Anna Larsen, and Ulrich Fekl

Abstract: Synthesis, structure, and NMR spectroscopic data for [(*closo*-$CB_{11}H_6Br_6$)$PtMe_3$] are reported. This neutral platinum(IV) complex contains the *closo*-$CB_{11}H_6Br_6^-$ anion bonded to the trimethylplatinum(IV) cation via three boron-bound bromines. *Closo*-$CB_{11}H_6Br_6^-$, which often acts as weakly coordinating or even non-coordinating anion, adopts here a role still very rare for this anion: it acts as a tripodal capping ligand enabling a pseudo-octahedral geometry at a d^6 metal center. Three bromines from the lower hemisphere of the hexahalogenated carboranate coordinate to Pt(IV), and distortions from ideal octahedral angles at Pt are marginal (<3°). Pt-Br bond lengths are 2.7279(18), 2.7129(17), and 2.7671(18) Å. Using the $^2J_{PtH}$ coupling constant of Pt-bonded methyl groups (79.0 Hz) as indicator of the donor strength of the tripodal cap, the prediction is obtained that *closo*-$CB_{11}H_6Br_6^-$ is a relatively weak donor toward the trimethylplatinum(IV) cation. Ligand competition equilibria can be expected to depend on both the intrinsic donor strengths of competing ligands and on the effects of charge and geometry. We observe that *closo*-$CB_{11}H_6Br_6^-$ is capable of replacing acetone from $Me_3Pt(acetone)_3^+$, whereas BF_4^- counterion is unable to replace acetone under similar conditions.

Key words: non-coordinating anion, platinum(IV), trimethyl, *closo*-carboranate, tripodal, trans-influence, NMR spectroscopy.

Résumé : On a réalisé la synthèse et on a déterminé la structure et les données de spectroscopie RMN relative au [(*closo*-$CB_{11}H_6Br_6$)$PtMe_3$]. Ce complexe neutre de platine(IV) contient un anion *closo*-$CB_{11}H_6Br_6^-$ lié à un cation triméthylplatine(IV) par le biais de trois atomes de bore liés à des atomes de brome. L'anion *closo*-$CB_{11}H_6Br_6^-$ qui agit souvent comme un anion de coordination faible, qui est même quelquefois non coordinant, adopte dans notre cas un rôle encore plus rare pour cet anion, à savoir celui de ligand tripode qui sert de cap et qui permet d'avoir une géométrie pseudo-tétraédrique au niveau d^6 du centre métallique. Les trois atomes de brome de la partie inférieure de l'hémisphère du carboranate hexahalogéné se lient par coordination au Pt(IV) et les distorsions par rapport aux angles octaédriques idéaux au niveau du platine sont marginales (<3°), alors que les longueurs des liaisons Pt-Br sont de 2,7279(18), 2,7129(17) et 2,6771(18) Å. Utilisant la constante de couplage $^2J_{PtH}$ des groupes méthyles liés au platine (79,0 Hz) comme indicateur de la force du cap trigonal, on arrive à la prédiction que l'anion *closo*-$CB_{11}H_6Br_6^-$ est un donneur relativement faible par rapport au cation triméthylplatine(IV). On peut s'attendre à ce que l'équilibre de compétition pour le ligand dépende à la fois des forces intrinsèques comme donneurs des ligands en compétition et sur les effets de charge et de géométrie. On a observé que l'anion *closo*-$CB_{11}H_6Br_6^-$ est capable de remplacer l'acétone du complexe $Me_3Pt(acétone)_3^+$ alors que le contre-ion BF_4^- n'est pas capable de remplacer l'acétone dans de telles conditions.

Mots-clés : anion non coordinant, platine(IV), triméthyle, *closo*-carboranate, tripode, influence *trans*, spectroscopie RMN.

[Traduit par la Rédaction]

Introduction

The development of noncoordinating (or very weakly coordinating) anions has led to tremendous progress in the field of highly Brønsted-acidic or Lewis-acidic species (1). *Closo*-carboranates (2) have proven excellent alternatives to tetraarylborates. Furthermore, the *closo*-carboranate framework seems to be nontoxic (3). Carboranates have recently

Received 6 February 2008. Accepted 23 April 2008. Published on the NRC Research Press Web site at canjchem.nrc.ca on 9 August 2008.

A.G. De Crisci and U. Fekl.[2] Department of Chemical and Physical Sciences, University of Toronto Mississauga, Mississauga, ON L5L 1C6, Canada.
J. Kleingardner and A. Larsen.[2] Department of Chemistry, Ithaca College, Ithaca, NY 14850, USA.
A.J. Lough. X-ray Crystallography Lab, University of Toronto, Toronto, ON M5S 3H6, Canada.

[1]This article is part of a Special Issue dedicated to Professor Richard J. Puddephatt.
[2]Corresponding authors (e-mail: alarsen@ithaca.edu, ulrich.fekl@utoronto.ca).

 doi:10.1139/V08-085 © 2008 NRC Canada

been used, for example, as counter-anions for the isolation of reactive silylium ions (4), as well as to furnish inert conjugate bases for superacids used to obtain crystalline hydronium ions and protonated arenes (5). Cluster anions such as *closo*-$CB_{11}H_{12}^-$ and substituted derivatives often act as noncoordinating or very weakly coordinating anions in systems containing transition metals (2, 6, 7). Cases do exist, however, where *closo*-carboranates coordinate to metal centers. Even for the rather electron-deficient carboranate *closo*-$CB_{11}H_6Br_6^-$, examples have been reported recently where coordination to metals occurs, and it is just beginning to become clear to which metals this carboranate may bind and under which conditions. The ability of *closo*-$CB_{11}H_6Br_6^-$ to coordinate should depend on the metal in question, its oxidation state, and its ligand environment. The vast majority of examples where metal coordination to *closo*-$CB_{11}H_6Br_6^-$ and closely related carboranates occurs involve the highly Lewis-acidic Ag(I) (8, 9). A few d^8 metal examples are known where coordination to rhodium(I) (7*a*) or iridium(I) (7*a*) could be observed. However, only very recently (2007) a crystallographically characterized example was reported where $CB_{11}H_6Br_6^-$ acted as a tripodal ligand toward a d^6 metal center, namely toward a rhodium(III) dihydride supported by an additional tricyclohexylphosphine (10). The question arises as to whether the ability of *closo*-$CB_{11}H_6Br_6^-$ to act as a tripodal cap for an octahedral complex may be extended to other platinum group metals. An excellent candidate is the trimethylplatinum(IV) unit, an often very stable moiety. A recent determination of the Lewis-acidity of the Me_3Pt^+ unit found it to be moderately Lewis-acidic (11). We can now report here that a stable pseudo-octahedral complex is formed when *closo*-$CB_{11}H_6Br_6^-$ reacts with a good source of the Me_3Pt^+ synthon.

Results and discussion

Synthesis

A salt metathesis of the cesium carboranate (12) [Cs][*closo*-$CB_{11}H_6Br_6$] with tetrameric trimethylplatinum(IV) triflate (13), a good source of the Me_3Pt^+ synthon, in a weakly coordinating nonpolar solvent (such as benzene) forms the highly soluble [(*closo*-$CB_{11}H_6Br_6$)$PtMe_3$] in quantitative yield, while insoluble cesium triflate (CsOTf = $Cs(F_3CSO_3)$) precipitates. In dry form, the compound is isolated as a shiny white microcrystalline powder. While we avoided exposing the compound to significant amounts of water, we found it very stable towards air or oxygen. We found no decomposition in noncoordinating solvents at room temperature and very little decomposition on a sample that was heated to 60 °C in CD_2Cl_2 for 8 months! Considering that many trimethylplatinum(IV) complexes undergo carbon–carbon reductive elimination (to form ethane) rather readily, the inertness of [(*closo*-$CB_{11}H_6Br_6$)$PtMe_3$] towards reductive elimination may appear surprising at first but is entirely in agreement with our current very detailed knowledge of reductive elimination in platinum(IV) systems: sp^3-sp^3 carbon–carbon reductive elimination from platinum(IV) is always *relatively* slow, for example, much slower than carbon–hydrogen reductive elimination in comparable methyl(hydrido) systems (14). Two factors have major influence on the barrier to C–C reductive elimination: (*i*) the ease of formation of a five-coordinate intermediate (15) and (*ii*) electronic effects, namely the donor strength of the spectator ligands. Alkyl–alkyl reductive elimination from Pt(IV) generally requires that the complex can assume a five-coordinate geometry (14–18), and the barrier to forming such a five-coordinate geometry contributes to the overall barrier for reductive elimination. While the ground-state geometry of [(*closo*-$CB_{11}H_6Br_6$)$PtMe_3$] is six-coordinate and octahedral (see below), a five-coordinate geometry should be accessible (if the tripodal carboranate partially dechelates) and only slightly uphill. Electronic effects are most likely responsible for the inertness observed here: for C–C reductive elimination to be fast, the coordination environment has to contain strongly donating spectator ligands (such as phosphines (14, 16, 17) systems having a less donating nitrogen-based ligand enviroment are comparably resistant to reductive elimination) (17), and the observed lack of reductive elimination for [(*closo*-$CB_{11}H_6Br_6$)$PtMe_3$] indicates that *closo*-$CB_{11}H_6Br_6^-$ acts as a rather weakly donating spectator ligand.

X-ray crystal structure

Crystals suitable for X-ray diffraction were obtained by slowly reducing the volume of a saturated dichloromethane solution of [(*closo*-$CB_{11}H_6Br_6$)$PtMe_3$] under nitrogen. Data were collected on a Nonius-Kappa CCD diffractometer at 150(1) K, and the crystal structure was solved by direct methods and refined on F^2 against all reflections.[3] Crystal data are summarized in Table 1. The structure contains discrete units of molecular [(*closo*-$CB_{11}H_6Br_6$)$PtMe_3$], shown in Fig. 1 (selected distances and angles in the legend). The most striking feature is the almost perfectly pseudo-octahedral environment of platinum(IV), where deviations from ideal angles are less than 3°. The average of the three Pt-Br distances (2.7279(18), 2.7129(17), 2.7671(18) Å) is 2.74 Å. This is 8% longer than the Pt-Br distance for Br^- ion coordinated to platinum(IV) in a terminal fashion (2.5394(6) Å for Pt-Br in a bromotriorganylplatinum(IV) complex chelated by a substituted bipyridine (19)) but only 3% longer than the Pt-Br distance in tetrameric trimethylplatinum(IV) bromide (20), which contains triply bridging bromide (2.67(1) Å).

Coupling constant correlation

The trimethylplatinum(IV) unit is a convenient tool to gauge the donor strength of coordinated ligands (21). *Trans*-influence effects weaken a Pt-CH_3 bond proportionally to the donor strength of the ligand *trans* to it, an effect that transmits into the $^2J_{PtH}$ coupling constant of the methyl.

[3] Supplementary data for this article are available on the journal Web site (canjchem.nrc.ca) or may be purchased from the Depository of Unpublished Data, Document Delivery, CISTI, National Research Council Canada, Ottawa, ON K1A 0R6, Canada. DUD 3775. For more information on obtaining material refer to cisti-icist.nrc-cnrc.gc.ca/irm/unpub_e.shtml. CCDC 676243 contains the crystallographic data for this manuscript. These data can be obtained, free of charge, via www.ccdc.cam.ac.uk/conts/retrieving.html (Or from the Cambridge Crystallographic Data Centre, 12 Union Road, Cambridge CB2 1EZ, UK; fax +44 1223 336033; or deposit@ccdc.cam.ac.uk).

© 2008 NRC Canada

Table 1. Crystal and structure refinement for [(*closo*-$CB_{11}H_6Br_6$)$PtMe_3$].

Empirical formula	$C_4H_{15}B_{11}Br_6Pt$
Formula weight	856.62
Temperature (K)	150(2)
Wavelength (Å)	0.710 73
Crystal system	Monoclinic
Space group	$P\ 2_1/c$
a (Å)	11.3965(9)
b (Å)	11.8815(4)
c (Å)	14.8355(10)
α (°)	90
β (°)	90.16
γ (*)	90
V (Å^3)	2008.8(2)
Z	4
D_{calcd} (Mg/m^3)	2.832
Absorption coefficient (mm^{-1})	18.902
F(000)	1528
Crystal size	0.10 mm × 0.08 mm × 0.06 mm
Theta range for data collection	2.75°–25.00°
Index ranges	$-13 \le h \le 13$, $-14 \le k \le 14$, $-12 \le l \le 17$
Reflections collected	3491
Independent reflections	3491 [R(int) = 0.145]
Completeness to theta = 25.00°	98.5%
Absorption correction	Semi-empirical from equivalents
Max. and min. transmission	0.359 and 0.139
Refinement method	Full-matrix least-squares on F^2
Data, restraints, parameters	3491, 0, 213
Goodness-of-fit on F^2	1.033
Final R indices [$I>2\sigma(I)$]	R_1 = 0.0581, wR_2 = 0.1344
R indices (all data)	R_1 = 0.0746, wR_2 = 0.1445
Largest diff. peak and hole (e, Å^{-3})	2.751, –3.516

Capping the three positions *trans* to the *fac*-trimethyls in a trimethylplatinum(IV) complex with three strongly donating phosphine donors leads to a very low coupling constant, and $^2J_{PtH}$ = 55 Hz is observed for the complex containing the tris(phosphino)borate $PhB(CH_2PPh_2)_3^-$ (22). Having three relatively donating nitrogen donors normally leads to a $^2J_{PtH}$ around 72 Hz. The $^2J_{PtH}$ coupling constant is sensitive to fairly subtle electronic effects related to the donor strength of the ligand. For example, $^2J_{PtH}$ = 72 Hz is observed in the presence of the tris(pyrazolyl)methane cap *trans* to $PtMe_3$ (23), whereas $^2J_{PtH}$ = 70 Hz is observed in the presence of the more electron-rich tris(3,5-dimethylpyrazolyl)borate cap *trans* to $PtMe_3$ (21c). An analogous complex having trifluoromethyl groups instead of methyl groups on the pyrazolates is less donating because of inductive effects, and an increased $^2J_{PtH}$ is observed for the Pt methyls, namely 75.4 Hz (21c). Among the weakest donors toward platinum(IV) are oxygen donors, and a weakly coordinating "O_3" environment typically leads to a $^2J_{PtH}$ value for platinum trimethyls between 76 and 82 Hz (21c). The 82 Hz extreme value belongs to trimethylplatinum(IV) in the tetrameric structure $\{Me_3Pt(OTf)\}_4$, which contains octahedral platinum(IV) and triply bridging triflate (13, 24). The $^2J_{PtH}$ value for the methyls in the aqua complex $Me_3Pt(OH_2)_3^+$ is 80.6 Hz (25). The coupling constant observed for [(*closo*-$CB_{11}H_6Br_6$)$PtMe_3$], 79.0 Hz (in benzene-d_6), leads us to conclude that the "Br_3" environment is roughly as donating toward Pt(IV) as an oxygen-donor environment. It will be of interest to investigate how efficiently *closo*-$CB_{11}H_6Br_6^-$ competes for the Me_3Pt^+ unit if other relatively weakly donating ligands are present in an equilibrium mixture.

Ligand competition experiments

We feel that the $^2J_{PtH}$ of the platinum-bound methyls is a reasonable indicator of the ligand donor strength because of *trans*-influence arguments, as discussed above. Regarding the strengths of the ligand-metal interactions in a thermodynamic sense, as measured in complexation equilibria, we would expect that a semi-quantitative prediction should be possible based on donor strength judged by $^2J_{PtH}$. An absolutely accurate prediction cannot be expected, in particular in cases where $^2J_{PtH}$ values are very similar and in cases where a competition between ligands bearing different charges or having very different steric requirements is considered. To test our hypothesis that donor strengths as indicated by $^2J_{PtH}$ have significant value for predicting complexation equilibria, we performed several experiments where *closo*-$CB_{11}H_6Br_6^-$ was competing against other ligands for complexation to Me_3Pt^+. We reacted [(*closo*-$CB_{11}H_6Br_6$)$PtMe_3$], which contains a tripodal monoanionic ligand, with the tripodal monoanionic ligand $CpCo[P(O)(OCH_3)_2]_3^-$ ("Kläui ligand", added as the sodium

© 2008 NRC Canada

Fig. 1. Molecular structure of [(*closo*-$CB_{11}H_6Br_6$)$PtMe_3$], using 30% probability thermal ellipsoids. Selected distances (Å) and angles (°): Pt1–C2 2.006(17); Pt1–C3 2.047(18); Pt1–C4 2.036(18); Pt1–Br1 2.7279(18); Pt1–Br4 2.7129(17); Pt1–Br5 2.7671(18); Br1–B1 1.961(15); Br2–B4 1.968(19); Br3–B5 1.979(19); C2-Pt1-C4 89.1(7); C2-Pt1-C3 88.1(7); C4-Pt1-C3 88.3(8); C2-Pt1-Br4 178.2(6); C4-Pt1-Br4 92.3(5); C3-Pt1-Br4 92.9(5); C2-Pt1-Br1 92.8(5); C4-Pt1-Br1 94.0(6); C3-Pt1-Br1 177.6(5).

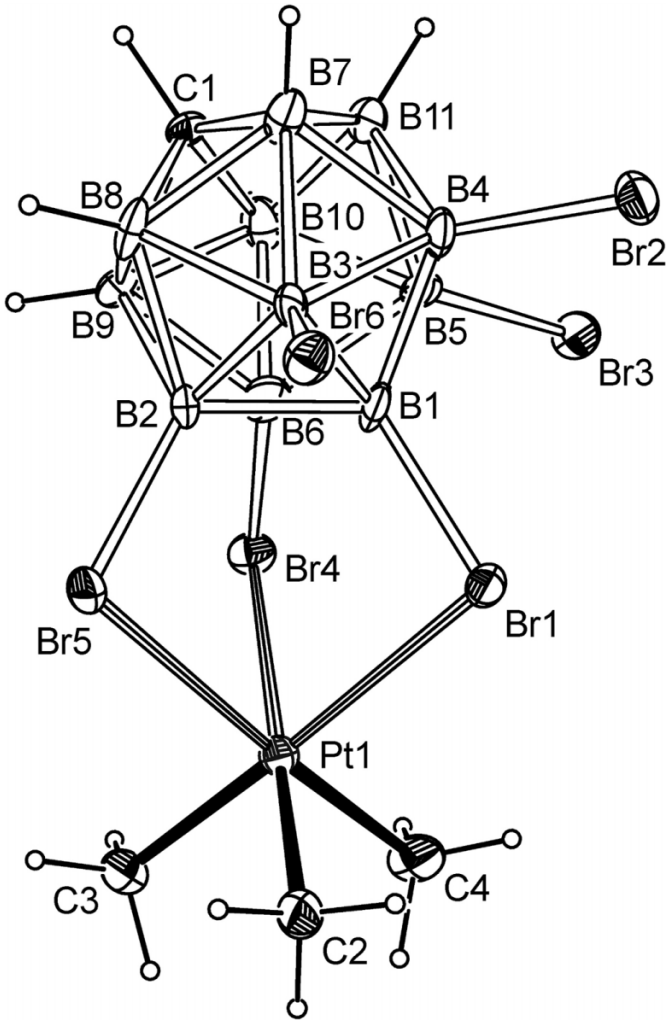

salt; Cp = η^5-C_5H_5). Based on $^2J_{PtH}$ arguments, it would be expected that the Kläui ligand is more donating ($^2J_{PtH}$ = 78.5 Hz *trans* to Kläui ligand; $^2J_{PtH}$ = 79.3 Hz *trans* to *closo*-$CB_{11}H_6Br_6^-$ in 1,2-dichloroethane-d_4). In agreement with this prediction, we observed that addition of 1 equiv. of Kläui ligand led to complete decoordination of *closo*-$CB_{11}H_6Br_6^-$ and to formation of {CpCo[P(O)$(OCH_3)_2$]$_3$$PtMe_3$}, as observed by ^{1}H and ^{11}B NMR spectra (26). On the other hand, it would be interesting to test for competition equilibria between *closo*-$CB_{11}H_6Br_6^-$ and ligands where $^2J_{PtH}$ predicts lower donor strength than *closo*-$CB_{11}H_6Br_6^-$. We are not aware of any ligand that complies with the above $^2J_{PtH}$ requirement *and* is tripodal *and* monoanionic. We therefore decided to use neutral monodentate ligands to test for their ability to coordinate to Pt(IV) and release *closo*-$CB_{11}H_6Br_6^-$ as a noncoordinating anion. $^2J_{PtH}$ arguments would predict that acetone is less donating than $CB_{11}H_6Br_6^-$ ($^2J_{PtH}$ = 79.8 Hz *trans* to acetone, in $Me_3Pt(acetone)_3^+$; $^2J_{PtH}$ = 79.3 Hz *trans* to *closo*-$CB_{11}H_6Br_6^-$; 1,2-dichloroethane-d^4 solvent). Although acetone is charge-neutral, such that there does exist some electrostatic bias towards carboranate-coordination, it still can be expected that a neutral molecule should replace the carboranate if that neutral molecule were vastly more donating than the carboranate. Even after addition of 38 equiv. of acetone to a solution containing [(*closo*-$CB_{11}H_6Br_6$)$PtMe_3$] (3.5 mmol/L in 1,2-dichloroethane-d^4), we observe no carboranate decoordination (^{11}B NMR) and no acetone coordination to Pt (^{1}H NMR). To test for whether a more donating solvent, as judged by $^2J_{PtH}$, leads to carboranate replacement, we used tetrahydrofuran (thf), which we would predict to be more coordinating than *closo*-$CB_{11}H_6Br_6^-$ ($^2J_{PtH}$ = 76.8 Hz in $Me_3Pt(thf)_3^+$ compared with 79.3 Hz for [(*closo*-$CB_{11}H_6Br_6$)$PtMe_3$] in 1,2-dichloroethane-d_4). In accord with this prediction, we observed rapid decoordination of *closo*-$CB_{11}H_6Br_6^-$ when titrating in small amounts of thf to the platinum complex (3.6 mmol/L in 1,2-dichloroethane-d^4), and after the addition of 38 equiv. of thf, the carboranate was essentially fully decoordinated (96%; after addition of 48 equiv. of thf, 100% decoordination was achieved). It seems, indeed, that donor strengths, as judged by $^2J_{PtH}$, have bearing on competition equilibria. Regarding acetone versus a weakly coordinating anion, again it is significant that $Me_3Pt(acetone)_3^+$ can be obtained reliably using a BF_4^- counter-ion and even crystallized (29). In contrast, $Me_3Pt(acetone)_3^+$ cannot be obtained using *closo*-$CB_{11}H_6Br_6^-$ anion. We confirmed this by reacting [$Me_3Pt(acetone)_3$][BF_4] with 0.87 equiv. of [Cs][*closo*-$CB_{11}H_6Br_6$], where we observed partial acetone substitution and carboranate coordination. It should be interesting to compare the coordinating ability of *closo*-$CB_{11}H_6Br_6^-$ with the coordinating ability of triflate. Both anions are generally regarded as weakly coordinating, and it is known for both anions that they can coordinate to the trimethylplatinum(IV) unit; triflate-coordination to trimethylplatinum(IV) is well-known (13, 24), and *closo*-$CB_{11}H_6Br_6^-$ coordination to trimethylplatinum(IV) has been shown in the present work. While $^2J_{PtH}$ for Pt-Me is 82.0 Hz in tetrameric trimethyl platinum triflate, {$Me_3Pt(O_3SCF_3)$}$_4$, $^2J_{PtH}$ of 79.0 Hz is observed for [(*closo*-$CB_{11}H_6Br_6$)$PtMe_3$] (both in CD_2Cl_2), which would indicate that the carboranate is more donating. When we reacted [(*closo*-$CB_{11}H_6Br_6$)$PtMe_3$] with 0.97 equiv. of a soluble triflate salt, (NBu_4)(F_3CSO_3), in 340 µL of 1,2-dichloroethane-d^4, we observed partial decoordination (57%) of the *closo*-$CB_{11}H_6Br_6^-$ anion in the equilibrium mixture, and both the carboranate and triflate were effectively competing for the trimethylplatinum(IV) moiety. Qualitatively, we conclude that triflate and *closo*-$CB_{11}H_6Br_6^-$ are of very similar coordinating ability toward trimethylplatinum(IV); if triflate were much more donating, 97% of the carboranate would have been released as free noncoordinating anion, as opposed to the 57% free carboranate observed. We remain with a qualitative conclusion regarding the triflate versus *closo*-$CB_{11}H_6Br_6^-$ competition, since the tetrameric nature of trimethylplatinum triflate leads to a rather complex reaction stoichiometry instead of a straightforward ligand-for-ligand substitution. The reaction

© 2008 NRC Canada

stoichiometry is as follows: 4 [(*closo*-$CB_{11}H_6Br_6$)$PtMe_3$] + 4 NBu_4^+ + 4 $F_3CSO_3^-$ → $\{Me_3Pt(O_3SCF_3)\}_4$ + 4 NBu_4^+ + 4 $CB_{11}H_6Br_6^-$. For practical purposes, the coordinating ability of *closo*-$CB_{11}H_6Br_6^-$ toward Me_3Pt^+ may be described as "less coordinating than the Kläui ligand, approximately as coordinating as triflate, more coordinating than tetrafluoroborate". It should be noted here that this *relatively* high propensity of *closo*-$CB_{11}H_6Br_6^-$ to coordinate to Me_3Pt^+ is likely due to the fact that the bromine donors, "soft" donor atoms, are relatively good ligands for a soft metal such as platinum. Geometric reasons certainly contribute as well, since the Br_3 donor "cap" enables an octahedral geometry for platinum(IV).

Summary and conclusion

The brominated carboranate *closo*-$CB_{11}H_6Br_6^-$ acts as a tripodal Br_3 donor ligand cap in the new compound [(*closo*-$CB_{11}H_6Br_6$)$PtMe_3$], made using a salt metathesis of the cesium carboranate [Cs][closo-$CB_{11}H_6Br_6$] with tetrameric trimethylplatinum(IV) triflate in nonpolar solvents, where the precipitation of insoluble cesium triflate provides the driving force. The Br_3 donor cap enables an octahedral geometry for platinum(IV). *Closo*-$CB_{11}H_6Br_6^-$ is among the weakly donating ligands towards $PtMe_3^+$ but in effect more coordinating, in this particular system than tetrafluoroborate, since it substitutes acetone from $Me_3Pt(acetone)_3^+$. In contrast, the BF_4^- counter-ion is unable to replace acetone under similar conditions. A reasonable estimate of the donor strengths of ligands for trimethylplatinum(IV) can be obtained using the $^2J_{PtH}$ coupling constant seen for the Pt-bound methyls, and such an approach appears to have qualitative and (or) semi-quantitative predictive power for ligand competition equilibria.

Experimental section

General information, reagents, and precursors

All manipulations involving organometallic compounds were carried out with the use of vacuum line and dry glove box using oven-dried glassware and J. Young NMR tubes. ^1H and $^{13}C\{^1H\}$ NMR spectra were obtained on a on Varian Gemini 200 MHz, Bruker Avance III 400 MHz NMR, or Unity Inova Varian 500 MHz spectrometers (Mississauga, platinum complexes) or JEOL 400 MHz NMR spectrometer (Ithaca, cesium carboranates).[3] ^{19}F NMR data were recorded on a Bruker Avance III 400 MHz NMR (Mississauga) spectrometer at 376 MHz and referenced to an internal standard, neat trifluoroacetic acid (capillary within the sample tube) set at δ 78.50 ppm. $^{11}B\{^1H\}$ and ^{11}B NMR spectra were taken on a JEOL 400 MHz NMR (Ithaca) and Bruker Avance III 400 MHz NMR (Mississauga) spectrometer and referenced relative to neat $BF_3{\cdot}OEt_2$ (capillary within the sample tube) set at δ 0 ppm. All NMR spectra were taken at 20 °C unless otherwise noted. Solvent peaks were used as reference: ^1H (δ, ppm, dichloromethane-d_2, 5.32; 1,2-dichloroethane-d_4, 3.72; benzene-d_6, 7.16; acetone-d_6, 2.05), ^{13}C (δ, ppm, dichloromethane-d_2, 53.8; benzene-d_6, 128.0; acetone-d_6, 29.8 (-*C*D_3)). CD_2Cl_2 (obtained from Cambridge Isotopes, 99.9% D), $ClCD_2CD_2Cl$ and CH_2Cl_2 were dried over CaH_2 and vacuum-transferred before use. $(CD_3)_2CO$ (99.9% D) and $(CH_3)_2CO$ was dried over activated 3 Å molecular sieves. C_6D_6 (99.5% D) and $(CD_3)_2CO$ were purchased from Cambridge Isotopes. Trifluoroacetic acid, 1,2-dichloroethane-d_4, (99% D), fluorene (98%) were purchased from Sigma-Aldrich. Iodotrimethylplatinum (99.8%) was purchased from Strem Chemicals. Decaborane, used for the synthesis (27) of $CsCB_{11}H_{12}$, precursor for [Cs][*closo*-$CB_{11}H_6Br_6$], was purchased from Katchem spol. s.r.o. (Ltd.), Czech Republic. Silver trifluoromethanesulfonate, silver tetrafluoroborate (98%), and tetrabutylammonium trifluoromethanesulfonate (≥99.0%) and all other chemicals where a supplier is not explicitly mentioned were purchased from Sigma-Aldrich (≥99.8%). Tetrahydrofuran (THF) and benzene (protio and deuterated) were dried over sodium-benzophenone and vacuum-transferred before use. Elemental analyses were conducted at Analytical Laboratory for Environmental Science and Research Training (ANALEST), Toronto, ON, Canada. Cs[*closo*-$CB_{11}H_6Br_6$] was synthesized using the literature method (12) from $CsCB_{11}H_{12}$ (27). It was obtained in 75% yield and found to be analytically pure by elemental analysis (Calcd. for [Cs][*closo*-$CH_6B_{11}Br_6$]: C 1.60, H 0.81; found: C 1.90, H 1.07) and NMR (^1H NMR (500 MHz, $(CD_3)_2CO$) δ: 3.07–1.82 (6H, br, B-H); $^{13}C\{^1H\}$ NMR (125 MHz, $(CD_3)_2CO$) δ: 41.71 (C_{cage}); $^{11}B\{^1H\}$ NMR (128.34 MHz, $(CD_3)_2CO$, 22 °C) δ: –2.0 (s, 1B, Br-*B* opposite to carbon apex), –9.8 (s, 5B, Br-*B* of lower ring), –20.3 (s, 5B, H-*B*)). The tetrameric trimethylplatinum(IV) triflate precursor was synthesized using literature methods in THF solvent (13). $\{Me_3Pt(OTf)\}_4$: ^1H NMR 500 MHz, (C_6D_6) δ: 1.49 (9H, s+d, Pt-Me_3, $^2J_{PtH}$ = 82.0 Hz); $^{13}C\{^1H\}$ NMR (125 MHz, C_6D_6) δ: –9.71 (s+d, Pt-Me_3, J_{PtC} = 827.5 Hz); ^{19}F NMR (376 MHz, C_6D_6) δ: –79.10 (s, 3F).

[(*closo*-$CB_{11}H_6Br_6$)$PtMe_3$]

[Cs][*closo*-$CB_{11}H_6Br_6$] (11.4 mg, 749.3 g/mol, 0.0153 mmol) was added to a 540 µL of benzene-d_6 solution containing $\{Me_3Pt(OTf)\}_4$ (6.0 mg, 0.0154 mmol in Pt) and shaken for 30 s. Sonication of the solution aids in the dissolution of $CsCB_{11}H_6Br_6$. The reaction was monitored by ^1H NMR spectroscopy using the platinum methyl signal and was completed within 1 h. The solvent was removed under vacuum and extracted with dichloromethane (where CsOTf is insoluble). The residue was washed with 1 mL portions of dichloromethane, allowing CsOTf to settle between each washing. Removal of the solvent yielded the product as white crystals. NMR conversion is quantitative, isolated yield is 73%. ^1H NMR 500 MHz, (C_6D_6) δ: 3.3–1.9 (5H, br, B_{cage}-H), 1.66 (1H, s, C_{cage}-H), 1.17 (9H, s+d, Pt-Me_3, $^2J_{PtH}$ = 79.0 Hz). $^{13}C\{^1H\}$ NMR (125 MHz, CD_2Cl_2) δ: 45.10 (s, C_{cage}), 4.42 (s+d, Pt-Me_3, J_{PtC} = 714.25 Hz). $^{11}B\{^1H\}$ NMR 128.38 MHz, (CD_2Cl_2, 25 °C) δ: 0.6 (s, 1B, Br-*B* opposite to carbon apex, –8.9 (s, 5B, Br-*B* of lower ring), –20.2 (s, 5B, H-*B*). ^{11}B NMR 128.38 MHz, (CD_2Cl_2, 25 °C) δ: 0.6 (s, 1B, Br-*B* opposite to carbon apex, –8.9 (s, 5B, Br-*B* of lower ring), –20.2 (br d, 5B, H-*B*, $^1J_{BH}$ = 169 Hz). All NMR data indicate an apparent three-fold rotational symmetry of the $PtMe_3$ unit and an apparent five-fold symmetry of the boranate cage, in contrast to the approximate C_s symmetry of the molecule in the crystal structure. We suggest that the $PtMe_3$ unit rapidly migrates around the (brominated) lower rim of the cage, as proposed by Weller

© 2008 NRC Canada

and co-workers (10) for rhodium(III) complexes of the same carboranate. Calcd. for $C_4H_{15}B_{11}Br_6Pt$: C 5.61, H 1.77, N 0.00; found: C 5.73, H 1.74, N not detected.

Ligand competition experiments

General considerations

All competition experiments were conducted in 1,2-dichloroethane-d_4 at room temperature (25 °C) in J. Young NMR tubes. Reactions were monitored using ^{1}H, ^{11}B, and ^{11}B{1H} NMR. Fluorene (unless otherwise stated) was employed as an internal standard for the fully relaxed ^{1}H NMR with a delay time of D_1 = 60 s. Neat BF_3-Et_2O was used as the internal reference (capillary in tube) for the ^{11}B and ^{11}B{^{1}H} NMR and set to 0 ppm. To increase accuracy for those competition experiments where not a solid sample (μg balance) was added but rather a liquid via 2.0 microliter syringe, ^{1}H NMR spectral integration (with sufficient relaxation delay for the acquisition) was used in conjunction with an added internal standard (fluorene). ^{11}B NMR spectroscopy is very useful for demonstrating whether the carboranate is coordinated or not to trimethylplatinum. When the carboranate is decoordinated to some extent in an equilibrium mixture, two species are seen in the ^{11}B NMR spectrum, the coordinated species and that of the noncoordinated species. The noncoordinated species exhibits the most pronounced upfield shift on two peaks of its three-peak spectrum. The two ^{11}B peaks that shift the most on going from the coordinated to noncoordinated (or vice versa) are the peaks at the Br-*B* opposite to carbon apex and that of the lower Br-*B* ring (the peaks that contain the Me_3Pt moiety). These peaks experience an upfield shift of approximately 2.5 ppm and 1.2 ppm, respectively, when the carboranate becomes decoordinated. The third ^{11}B peak, belonging to the "upper ring" (5 BH), remains virtually unchanged (± 0.1 ppm).

Solution data for [(closo-$CB_{11}H_6Br_6$)$PtMe_3$]

^{1}H NMR 400 MHz, ($ClCD_2CD_2Cl$) δ: 3.4–1.5 (5H, br, B_{cage}-H), 2.98 (overlap with B_{cage}-H region, 1H, s, C_{cage}-H), 1.84 (overlap with B_{cage}-H region, 9H, s+d, Pt-Me_3, $^2J_{PtH}$ = 79.3 Hz). ^{11}B{^{1}H} NMR 128.38 MHz, ($ClCD_2CD_2Cl$, 25 °C) δ: 0.6 (br s, 1B, Br-*B* opposite to carbon apex, –9.0 (s, 5B, Br-*B* of lower ring), –20.5 (br s, 5B, H-*B*).

Solution data for [Cs][closo-$CB_{11}H_6Br_6$]

^{11}B{^{1}H} NMR 128.38 MHz, ($ClCD_2CD_2Cl$, 25 °C) δ: –2.0 (br s, 1B, Br-*B* opposite to carbon apex), –10.2 (br s, 5B, Br-*B* of lower ring), –20.6 (br s, 5B, H-*B*)).

Competition Experiment with Kläui Ligand (Sodium(cyclopentadienyl) tris(dimethylphosphito)cobaltate(I))

To a solution containing 1.09 mg (0.001 27 mmol) of [(*closo*-$CB_{11}H_6Br_6$)$PtMe_3$] and 1.23 mg (0.007 40 mmol) of fluorene in 470 μL of 1,2-dichloroethane-d_4 (0.002 71 mol/L in Pt) was added the Kläui ligand ([Na][(CpCo[P(O)-$(OCH_3)_2]_3$], FW: 474.1 g/mol) in approximately 0.3 to 0.4 equiv. per Pt per titrant, aided with sonication. A total of 2.08 equiv. were added. After adding 1 equiv. of Kläui ligand, the carboranate becomes fully decoordinated and a different Pt species is observed in quantitative yield in the ^{1}H NMR. The newly formed species has a ^{1}H NMR shift value of 0.92 ppm and $^2J_{PtH}$ = 78.5 Hz, in contrast with the starting [(*closo*-$CB_{11}H_6Br_6$)$PtMe_3$] with a chemical shift value of 1.84 ppm and $^2J_{PtH}$ = 79.3 Hz. After adding more than one equiv. of ligand, the ^{1}H displays two Kläui Cp ligand environments, namely that of the coordinated [Me_3Pt(CpCo[P(O)$(OCH_3)_2]_3$)] at 5.15 ppm and an additional peak belonging to the Cp ligand of the free [Na][(CpCo[P(O)$(OCH_3)_2]_3$] at 5.37 ppm (28). The ^{11}B{^{1}H} NMR shows that the new noncoordinated species has chemical shift values similar to those of [Cs][*closo*-($CB_{11}H_6Br_6$)] in the same solvent, leading us to conclude that the noncoordinated carboranate species is [Na][*closo*-($CB_{11}H_6Br_6$)]. ^{11}B spectra, internally referenced (BF_3-Et_2O), were also acquired, and they confirm that during the titration the amount of [(*closo*-$CB_{11}H_6Br_6$)$PtMe_3$] decreases, whereas a new species grows in. ^{11}B{^{1}H} shows that peak at the Br-*B*, opposite to the carbon apex, has shifted from +0.60 ppm to –2.10 ppm on going from the coordinated to noncoordinated *closo*-$CB_{11}H_6Br_6^-$, while the peak at Br-*B* of the lower ring, the ring which contains the Me_3Pt^+, shifts from –9.06 ppm to –10.36 ppm on going from the coordinated to noncoordinated *closo*-$CB_{11}H_6Br_6^-$, while the B-H ring peaks remain virtually unchanged at –20.51 ppm. The largest ^{11}B shifts observed are those that contain the Me_3Pt^+ bound moiety.

Competition experiment with THF

To a solution containing 1.73 mg (0.002 02 mmol) of [(*closo*-$CB_{11}H_6Br_6$)$PtMe_3$], 2.37 mg (0.0143 mmol) of fluorene in 560 μL of 1,2-dichloroethane-d_4 (0.00361 mol/L in Pt) was added THF (peaks appear as broad singlets at 3.65 ppm and 1.79 ppm) in amounts corresponding to approximately 8 equiv. per Pt, until *closo*-$CB_{11}H_6Br_6^-$ becomes fully decoordinated. It is interesting to note that it required 7.9 μL (0.0974 mmol) of thf (or 48 equiv.) per Pt to fully decoordinate the carboranate. Observed is the formation of a new species, assigned as $Me_3Pt(thf)_3^+$, with a chemical shift of 1.23 ppm for the Pt-methyl and $^2J_{PtH}$ = 76.8 Hz, clearly distinct from the starting [(*closo*-$CB_{11}H_6Br_6$)$PtMe_3$] having its methyl resonance at 1.84 ppm ($^2J_{PtH}$ = 79.3 Hz). The ^{11}B NMR spectrum confirms that the carboranate becomes noncoordinating, where the chemical shifts of the new species are very similar to [Cs][*closo*-($CB_{11}H_6Br_6$)] in the same solvent, which confirms the assignment as noncoordinating *closo*-$CB_{11}H_6Br_6^-$. The internally referenced (BF_3-Et_2O). The ^{11}B{^{1}H} NMR spectrum shows that peak at Br-*B* opposite to the carbon apex has shifted upfield 2.59 ppm to δ –2.15 ppm on going from the coordinated to noncoordinated *closo*-$CB_{11}H_6Br_6^-$, while the peak at Br-*B* of the lower ring, the ring which contains the Me_3Pt^+, has shifted upfield 1.28 ppm to δ –10.25 ppm on going from the coordinated to noncoordinated *closo*-$CB_{11}H_6Br_6^-$, while the B-H ring peaks remains virtually unchanged at –20.60 ppm.

Competition experiment with acetone

In a similar fashion to the thf experiment, the acetone experiment was conducted. To a solution containing 1.67 mg (0.001 95 mmol) of [(*closo*-$CB_{11}H_6Br_6$)$PtMe_3$], 1.57 mg (0.009 45 mmol) of fluorene in 560 μL of 1,2-dichloroethane-d_4 (0.003 48 mol/L in Pt) was added 5.3 μL

© 2008 NRC Canada

(0.0722 mmol) of acetone (peak appears as a singlet at 2.08 ppm), which is approximately 38 equiv. per Pt. The ^{1}H NMR shows a slightly broadened $PtMe_3$ environment at with a chemical shift value of 1.82 ppm, and a $^2J_{PtH}$ is unresolved (because of overlap of the carbon satellites of the added acetone and a broadening of the Me_3Pt peaks), compared with the starting material of chemical shift value of 1.84 ppm. The $^{11}B\{^1H\}$ spectrum shows *one* species *only* and is that of the starting coordinated carboranate ligand, [(*closo*-$CB_{11}H_6Br_6$)$PtMe_3$], with slight broadening of base peaks for the two B-Br peaks directly coordinated to the Me_3Pt^+ moiety. The internally referenced (BF_3-Et_2O) $^{11}B\{^1H\}$ shows that the peak at Br-*B* opposite to the carbon apex has shifted slightly upfield 0.264 ppm to broad singlet at δ 0.25 ppm (compared with a approximately 2.6 ppm upfield shift for full decoordination experiments), while the peak at Br-*B* of the lower ring, the ring which contains the $[Me_3Pt]^+$, has shifted upfield 0.09 ppm to δ –9.13 ppm, while the B-H ring peaks remains virtually unchanged at –20.54 ppm). The data show that substantial decoordination of the carboranate does not occur. The very small chemical shift differences that are observed may indicate a weak outer-sphere association of acetone.

Competition experiment with NBu_4OTf

This experiment was performed using an accurate analytical mass balance with a ± 0.01 mg error. To a solution containing 1.33 mg (0.001 55 mmol) of [(*closo*-$CB_{11}H_6Br_6$)$PtMe_3$] was added 0.59 mg (0.001 51 mmol, 0.97 equiv. per Pt, FW: 391.53 g/mol) of NBu_4OTf in 340 µL (0.00456 mol/L in Pt) of 1,2-dichloroethane-d_4. The $^{11}B\{^1H\}$ spectrum shows the partial decoordination in a 43:57 ratio of coordinated-to-noncoordinated. The decoordinated species $^{11}B\{^1H\}$ peaks appear at –2.05 ppm, –10.25 ppm, and –20.65 ppm in the given reaction conditions.

Reverse competition experiment with $[Me_3Pt(acetone)_3][BF_4]$

The tris-acetone complex was prepared using modified literature methods (11, 29), similar to the preparation of $[Me_3Pt(benzaldehyde)_3][BF_4]$ but using acetone instead of benzaldehyde and using 1,2-dichloroethane-d_4 instead of dichloromethane-d_2 solvent. ^{1}H NMR 400 MHz, ($ClCD_2CD_2Cl$) δ: 2.24 (18H, s), 1.48 (9H, s+d, Pt-Me_3, $^2J_{PtH}$ = 79.8 Hz). $^{11}B\{^1H\}$ NMR 128.38 MHz, ($ClCD_2CD_2Cl$, 25 °C) δ: –1.52 (s, 1B, BF_4). Titrating in 0.21 to 1.87 equiv. of [Cs][*closo*-$CB_{11}H_6Br_6$] into a 420 µL solution of 1,2-dichloroethane-d_4 (0.0227 mol/L in Pt) containing 4.77 mg (0.009 52 mmol) of $[Me_3Pt(acetone)_3][BF_4]$ (FW: 501.23 g/mol), partial decoordination of the acetone complex occurs as shown by the ^{1}H NMR shift of acetone moving upfield from 2.24 ppm to 2.10 ppm. A new Me_3Pt species at 1.78 ppm, appears downfield from the starting species. Due to the relative broadness of the Pt satellites, it is difficult to accurately assess the $^2J_{PtH}$. Also formed is an insoluble precipitate, consistent with a reaction forming insoluble $CsBF_4$. The $^{11}B\{^1H\}$ NMR spectrum shows the disappearance of the sharp BF_4 peak at or near the equivalence point of Cs salt addition. Despite the broadened nature of the $^{11}B\{^1H\}$ spectrum, it shows that there are two *distinct* species present in solution at the 1.8 equivalence point, assigned as [(*closo*-$CB_{11}H_6Br_6$)$PtMe_3$] at $^{11}B\{^1H\}$ } 0.1 ppm, –9.32 ppm, and –20.48 ppm, as well as free, excess [Cs][*closo*-$CB_{11}H_6Br_6$] at –2.02 ppm, –10.17 ppm, and –20.48 ppm.

Crystallography[3]

The crystal was refined as a non-merohedral twin with the ratio of the twin components refining to 0.818(2):182(2). In addition, a large electron density peak located in the final difference Fourier map refined to the equivalent of ca. 5% of a Pt atom. Hence the structure was refined as containing "whole molecule disorder" with only the Pt atom being refined over two sites. The refined occupancies of the maximum and minimum components are 0.951(3) and 0.049(3). All other atoms were refined with full occupancy.

Acknowledgment

Funding by the Natural Science and Engineering Research Council (NSERC) of Canada, the Canadian Foundation of Innovation, and the University of Toronto (Connaught Foundation) is gratefully acknowledged (UF), as well as a PRF 44692.01-GB award from the American Chemical Society and the Cottrell College Award CC6755 from Research Corporation (AL). We thank Dr. Gordon K. Hamer and Dr. Peter Mitrakos (Mississauga) for assistance with the NMR instruments. We thank Ms. Elzbieta Stepowska (Mississauga) for assisting in the synthesis of [{Me_3PtOTf}$_4$].

References

1. I. Krossing and I. Raabe. Angew. Chem. Int. Ed. **43**, 2066 (2004).
2. C.A. Reed. Acc. Chem. Res. **31**, 133 (1998).
3. W.H. Sweet, A.H. Soloway, and R.L. Wright. J. Pharmacol. Exp. Ther. **137**, 263 (1962).
4. (*a*) K.-C. Kim, C.A. Reed, D.W. Elliott, L.J. Mueller, F. Tham, L.J. Lin, and J.B. Lambert. Science (Washington, D.C.), **297**, 825 (2002); (*b*) S.P. Hoffmann, T. Kato, F.S. Tham, and C.A. Reed. Chem. Commun. (Cambridge, U.K.), 767 (2006).
5. Leading references (review): C.A. Reed. Chem. Commun. (Cambridge, U.K.), 1669 (2005).
6. S. Körbe, P.J. Schreiber, and J. Michl. Chem. Rev. **106**, 5208 (2006).
7. (*a*) C. Douvris and C.A. Reed. Organometallics, **27**, 807 (2008); (*b*) T.M. Douglas, E. Molinos, S.K. Brayshaw, and A.S. Weller. Organometallics, **26**, 463 (2007); (*c*) N.J. Patmore, M.F. Mahon, J.W. Steed, and A.S. Weller. J. Chem. Soc. Dalton Trans. 277 (2001); (*d*) S.M. Ivanova, S.V. Ivanov, S.M. Miller, O.P. Anderson, K.A. Solntsev, and S.H. Strauss. Inorg. Chem. **38**, 3756 (1999); (*e*) A.J. Lupinetti, M.D. Havighurst, S.M. Miller, O.P. Anderson, and S.H. Strauss. J. Am. Chem. Soc. **121**, 11920 (1999).
8. N.J. Patmore, C. Hague, J.H. Cotgreave, M.F. Mahon, C.G. Frost, and A.S. Weller. Chem. Eur. J. **8**, 2088 (2002).
9. (*a*) D.J. Liston, Y.J. Lee, W.R. Scheidt, and C.A. Reed. J. Am. Chem. Soc. **111**, 6643 (1989); (*b*) D.J. Liston, C.A. Reed, C.W. Eigenbrot, and W.R. Scheidt. Inorg. Chem. **26**, 2739 (1987); (*c*) Z. Xie, C.-H. Tsang, F. Xue, and T.C.W. Mak. J. Organomet. Chem. **577**, 197 (1999).
10. E. Molinos, S.K. Brayshaw, G. Kociok-Köhn, and A.S. Weller. J. Chem. Soc. Dalton Trans. 4829 (2007).
11. V. Hsieh, A.G. De Crisci, A.J. Lough, and U. Fekl. Organometallics, **26**, 938 (2007).

© 2008 NRC Canada

12. T. Jelínek, J. Plešek, S. Heřmánek, and B. Štíbr. Collect. Czech. Chem. Commun. **51**, 819 (1986); see also http://www.reedgrouplab.ucr.edu/documents/Carborane%20Synthesis.htm.
13. J.C. Baldwin and W.C. Kaska. Inorg. Chem. **18**, 686 (1979).
14. D.M. Crumpton-Bregel and K.I. Goldberg. J. Am. Chem. Soc. **125**, 9442 (2003).
15. For C–C coupling from isolated five-coordinate platinum(IV) complexes, please see: (*a*) A.T. Luedtke and K.I. Goldberg. Inorg. Chem. **46**, 8496 (2007); (*b*) U. Fekl and K.I. Goldberg. J. Am. Chem. Soc. **124**, 6804 (2002).
16. B.S. Williams and K.I. Goldberg. J. Am. Chem. Soc. **123**, 2576 (2001).
17. G.S. Hill, G.P.A.Yap, and R.J. Puddephatt. Organometallics, **18**, 1408 (1999).
18. M.P. Brown, R.J. Puddephatt, and C.E.E. Upton. J. Chem. Soc. Dalton Trans. 2457 (1974).
19. C.S.A. Fraser, H.A. Jenkins, M.C. Jennings, and R.J. Puddephatt. Organometallics, **19**, 1635 (2000).
20. W. Massa, G. Baum, B.-S. Seo, and J. Lorberth. J. Organomet. Chem. **352**, 415 (1988).
21. (*a*) T.G. Appleton, H.C. Clark, and L.E. Manzer. Coord. Chem. Rev. **10**, 335 (1973); (*b*) V.K. Jain, G.S. Rao, and L. Jain. Adv. Organomet. Chem. **27**, 113 (1987); (*c*) U. Fekl, R. van Eldik, S. Lovell, K.I. Goldberg. Organometallics, **19**, 3535 (2000).
22. J.C. Thomas and J.C. Peters. Polyhedron, **23**, 489 (2004).
23. P.K. Byers, A.J. Canty, B.W. Skelton, and A.H. White. Organometallics, **9**, 826 (1990).
24. S. Schlecht, J. Magull, D. Fenske, and K. Dehnicke. Angew. Chem. Int. Ed. **36**, 1994 (1997).
25. K. Kite, J.A.S. Smith, and E.J. Wilkins. J. Chem. Soc. A., 1744 (1966).
26. (*a*) $\{CpCo[P(O)(OCH_3)_2]_3PtMe_3\}$ has been previously reported and structurally characterized, please see: R.E. Marsh, W.P. Schaefer, D.K. Lyon, J.A. Labinger, and J.E. Bercaw. Acta Cryst. C, **48**, 1603 (1992); (*b*) For the closely related $\{CpCo[P(O)(O\mathbf{C_2H_5})_2]_3PtMe_3\}$, please see: A. Nettle, M. Valderrama, R. Contreras, M. Scotti, K. Peters, H.G. von Schnering, and H. Werner. Polyhedron, **7**, 2095 (1988).
27. J. Plešek, T. Jelínek, E. Drdakova, S. Heřmánek, and B. Štíbr. Collect. Czech. Chem. Commun. **49**, 1559 (1984).
28. It seems that, aided by the relative nonpolarity of the NMR solvent, the excess Kläui ligand ($[Na][(CpCo[P(O)(OCH_3)_2]_3]$) present after more than 1 equiv. (relative to Pt) has been added, partially associates with the "free" Na^+ of the $[Na][closo\text{-}(CB_{11}H_6Br_6)]$ in the titration solution. This results in a slight downfield shift (by 0.36 ppm) of the Cp protons in such excess Kläui ligand, where the resonance is observed at 5.36 ppm as opposed to the 5.00 ppm value observed for the pure ligand $[Na][(CpCo[P(O)(OCH_3)_2]_3]$ in the same solvent. Solution data of Kläui ligand, ($[Na][(CpCo[P(O)(OCH_3)_2]_3]$, in the absence of extra sodium: ^{1}H NMR 400 MHz, ($ClCD_2CD_2Cl$) δ: 5.00 (5H, s, Cp ligand), 3.54 (18H, dd, J_{HH} = 3.8, 6.5 Hz).
29. H. Junicke, C. Bruhn, D. Ströhl, R. Kluge, and D. Steinborn. Inorg. Chem. **37**, 4603 (1998).

© 2008 NRC Canada

Alkyne adducts of paramagnetic and diamagnetic tripalladium clusters supported by dppm ligands[1]

Cyril Cugnet, Sophie Dal Molin, David Brevet, Dominique Lucas, Yves Mugnier, Pierre D. Harvey, and René T. Boeré

Abstract: The unsaturated redox-active cluster $[Pd_3(dppm)_3(CO)]^{n+}$ (n = 0,1, or 2) reacts with ethylene dicarboxylic esters and a variety of terminal acetylenes (but not PhC≡CPh) in all three charge states. In particular, the radical cations $[Pd_3(dppm)_3(CO)(RC{\equiv}CR')]^{\cdot+}$ can be produced by several routes: one-electron electrochemical reduction of the dication adducts, comproportionation of the neutral and dicationic adducts, as well as the direct complexation of alkyne to the known radical cation $[Pd_3(dppm)_3(CO)]^{\cdot+}$. Compared with the latter, each of the adducts have significantly extended lifetimes and classify as persistent radicals in solution. The alkyne adducts have been characterized by voltammetry (cyclic and rotating disk electrode), by UV–vis titrations and by MALDI-TOF mass spectra from dithranol matrices. Isotropic solution EPR spectra of the adducts with R = R′ = MeOC(O) and EtOC(O), as well as those with R′ = H and R = C_6H_5, FC_6H_4, $HC{\equiv}CC_6H_4$, and EtO have been obtained. Full line shape fitting simulations demonstrate that all display coupling to six different ^{31}P (I = 1/2) and to one to three ^{106}Pd (I = 5/2) nuclei. The $A(^{31}P)$ values range from a low of 3.0×10^4 to a high of 180.5×10^4 cm^{-1}; this variation is caused by changes in the contribution of P s orbitals to the SOMO resulting from structural distortions of the Pd_3P_6 core upon alkyne coordination.

Key words: electrochemistry, redox state, electron paramagnetic resonance, catalytic model, palladium, bridging phosphine.

Résumé : Le cluster insaturé $[Pd_3(dppm)_3(CO)]^{n+}$ (n = 0,1, ou 2) réagit, quelle que soit sa charge, sur des dérivés acétyléniques de formule générale RCCR′ comme des di-esters acétyléniques et sur une variété de dérives acétyléniques vrais R′CCH mais pas sur PhC≡CPh pour conduire aux adduits $[Pd_3(dppm)_3(CO)(RCCR')]^{n+}$ (n = 0,1,2). En particulier les radicaux cations $[Pd_3(dppm)_3(CO)(RC{\equiv}CR')]^{\cdot+}$ peuvent être générés par plusieurs voies : soit par réduction monoélectronique de l'adduit dicationique correspondant $[Pd_3(dppm)_3(CO)(RC{\equiv}CR']^{2+}$ soit par une réaction d' antidismutation entre l'adduit neutre et l'adduit dicationique et enfin par la complexation directe de l'alcyne sur l'espèce monocationique paramagnétique électrogénéré $[Pd_3(dppm)_3(CO)]^{\cdot+}$. Comparé à ce dernier, chacun des adduits paramagnétiques obtenus sont beaucoup plus stables et peuvent donc être plus facilement caractérisés en solution. Les différentes méthodes mises en oeuvre pour la caractérisation des adduits reposent sur la voltammétrie cyclique et sur électrode tournante, la spectroscopie UV–visible, la spectrométrie de masse (MALDI-TOF) et par analyse RPE, méthode pour laquelle des spectres des adduits $[Pd_3(dppm)_3(CO)(RC{\equiv}CR')]^{\cdot+}$ avec R = R′ = MeOC(O) and EtOC(O) d'une part et avec R′ = H, R = C_6H_5, FC_6H_4, $HC{\equiv}CC_6H_4$ et EtO d'autre part, ont été obtenus avec une bonne résolution. La simulation des spectres a permis de tirer toutes les constantes de couplage aux six atomes de phosphore ^{31}P (I = 1/2) et avec un, deux ou trois des atomes de palladium ^{106}Pd (I = 5/2). Pour expliquer la variation importante des différentes valeurs des constantes $A(^{31}P)$ qui correspond à 3.0×10^4 pour la valeur la plus faible à 180.5×10^4 cm^{-1} pour celle la plus élevée, un changement de la contribution de l'orbitale s du phosphore à l'orbitale SOMO, est retenue qui résulte d'une distorsion structurale du cœur Pd_3P_6 par coordination de l'alcyne.

Mots-clés : électrochimie, état redox, résonance paramagnétique électronique, modèle catalytique, palladium, cluster, diphosphine.

Received 25 March 2008. Accepted 23 May 2008. Published on the NRC Research Press Web site at canjchem.nrc.ca on 12 August 2008.

This article is dedicated to Professor Richard J. Puddephatt in recognition of his significant contributions to Canadian Chemistry.

C. Cugnet, S.D. Molin, D. Brevet, D. Lucas, and Y. Mugnier.[2] Institut de Chimie Moléculaire de l'Université de Bourgogne (ICMUB), UMR CNRS 5260, Faculté des Sciences Mirande, Université de Bourgogne, 9 Avenue Alain Savary, BP 47870, 21078 Dijon CEDEX, France.
P.D. Harvey.[2] Département de Chimie, Université de Sherbrooke, Sherbrooke, QC J1K 2R1, Canada.
R.T. Boeré.[2] Department of Chemistry and Biochemistry, University of Lethbridge, Lethbridge, AB T1K 3M4, Canada.

[1]This article is part of a Special Issue dedicated to Professor R. Puddephatt.
[2]Corresponding authors (e-mail: yves.mugnier@u-bourgogne.fr; Pierre.Harvey@USherbrooke.ca; boere@uleth.ca).

 doi:10.1139/V08-105 © 2008 NRC Canada

Introduction

Puddephatt and co-workers (1–3) first reported a convenient synthetic route to trifluoracetate and hexafluorophosphate salts of the cyclic tripalladium cluster $[Pd_3(dppm)_3(\mu_3\text{-}CO)]^{2+}$ in which each diphenylphosphinomethane (dppm) ligand bridges two Pd atoms. These workers also reported structural characterization of the former by X-ray crystallography (1–3). This interesting complex is formed from Pd(II) precursors via a redox reaction and is both electronically delocalized with an average Pd oxidation state of 2/3 and coordinatively unsaturated. The approximately planar Pd_3P_6 core is surrounded by a "picket fence" of ligand phenyl rings (Scheme 1), creating a cavity on the side opposite to the triply bridged carbonyl ligand. A wide variety of ligands and ions are able to occupy this cavity, including small anions, Cl^- (2, 4–6), Br^- (7), I^- (3), and larger ions, PF_6^- (8), NO_3^- (9), $CF_3CO_2^-$ (1, 8), and $PO_2F_2^-$, that appear to be held in place by electrostatic attraction to the positively charged core (10). The delocalized electronic structure of the $[Pd_3(dppm)_3(\mu_3\text{-}CO)]^{2+}$ cluster leads to a rich redox chemistry that we have investigated through an exhaustive electrochemical study that led inter alia to the discovery of the persistent radical cation $[Pd_3(dppm)_3(\mu_3\text{–}CO)]^{\cdot+}$ (11). This success may be contrasted with the initial failure to reduce this compound by chemical means (1).

The $[Pd_3(dppm)_3(CO)]^{2+}$ system has been thoroughly studied because it represents an excellent solution-phase model for a close-packed metal surface with Pd atoms in triangular relationship (3, 12, 13). We have discovered both stoichiometric and catalytic reactivity under conditions of reductive electrochemical activation with halocarbons and acid halides (7, 10, 14, 15). Thus, reducing the positive charge at the Pd_3P_6 centre is postulated to decrease the attraction of the cluster counterions, thereby increasing reactivity towards neutral substrates. When alkynes are employed, we demonstrated a stronger affinity for binding to the cluster in lower oxidation states, which enables the quantitative reversal of binding from the alkynes by monoanionic ligands such as I^- or NO_3^- after reoxidation of the adducts (16). In this initial study, the persistence of the $[Pd_3(dppm)_3(CO)]^+$ monocation radical state was shown to be significantly extended in $[Pd_3(dppm)_3(CO)(RC{\equiv}CR')]^{\cdot+}$ for two alkynes with quite different properties, PhC≡CH and $MeCO_2C{\equiv}CCO_2Me$. This increase in stability was attributed to the protection from outside contaminants provided by the coordinated alkynes (Scheme 1).

We have now extended the study of such alkyne adducts to six different examples with quite different electronic and steric properties (Chart 1). In this paper we compare the electrochemical responses of the six alkyne adducts in stepwise reduction first with the paramagnetic monocations and subsequently with neutral clusters. The alkyne-containing monocation radicals, all of which have enhanced stability over the parent species, have been unambiguously characterized using electron paramagnetic resonance (EPR) spectroscopy. The "parent" radical cation $[Pd_3(dppm)_3(CO)]^{\cdot+}$ (**1b**), displays a symmetric septet pattern with intensities in the expected Pascal's triangle ratios for six equivalent $I = 1/2$ nuclei (10). Despite relatively broad main lines, satellite signals are observed extending from the outer set of lines attributable to the equal-intensity sextet that is expected from, on-average, a single ^{105}Pd nucleus per trimer (22.2% natural abundance). By comparison, each of the alkyne adduct monocations **2b**–**7b** display EPR spectra that clearly demonstrate the presence of one major species in solution that has significantly reduced symmetry, consistent with coordination of the alkyne to the "open" face of the cluster.

Scheme 1. Alkyne adducts with $n = 2, 1, 0$.

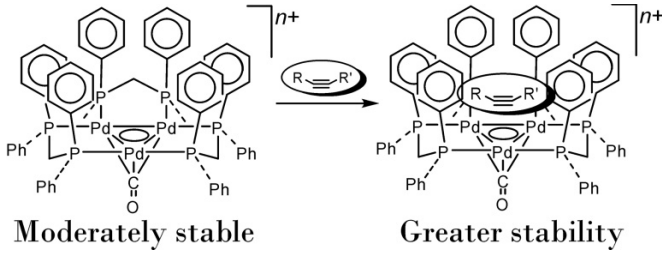

Chart 1. Composition of the ethynyl adducts; precise location and coordination of the CO and RC≡CR′ ligands is uncertain.

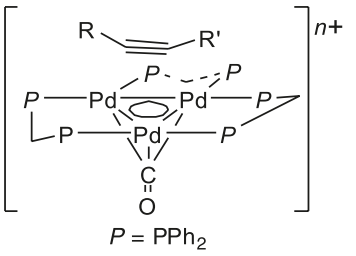

1 Without alkyne
2 R = R' = EtO(CO)
3 R = R' = MeO(CO)
4 R = Ph, R' = H
5 R = 4-FC_6H_4, R' = H
6 R = 4-PhC≡CC_6H_4, R' = H
7 R = EtO, R' = H
a, n=2; **b**, n=1; **c**, n=0

These EPR spectra are important because it has not yet been possible to obtain crystal structures of any of these alkyne adducts because of their limited stability over very long periods of time. However, the structure of the CO-displaced monocation $[Pd_3(dppm)_3(O_2CCF_3)(MeCO_2C{\equiv}CCO_2Me)]^+$ demonstrates significant distortion of the Pd_3P_6 frame and the generation of a square-planar geometry at one of the three metal atoms where the trifluoroacetate ligand is coordinated trans to one of the alkyne C atoms (17). This demonstrates that significant symmetry lowering can accompany substrate activation, though in each of our examples decarbonylation does not occur and therefore the substrate coordination can be reversed.

Results and discussion

Reversible adduct formation

The formation of the alkyne adducts was monitored by UV–vis spectroscopy, as demonstrated in the earlier work (16). In addition, the diamagnetic alkyne adducts $[Pd_3(dppm)_3(CO)(RC{\equiv}CR')]^{2+}$ could be characterized from evaporation of the THF solutions without removal of the electrolyte by means of MALDI ionization. The resulting mass spectra fit in most cases for gas-phase species of the type $[Pd_3(dppm)_3(RC{\equiv}CR')]^+$, i.e., through loss of the CO ligand, although in one case, $[Pd_3(dppm)_3(CO)(FC_6H_4C{\equiv}CH)]^+$, the CO ligand is retained. The results of the MALDI-TOF MS experiments are summarized in Table 1. Attempts to verify the presence of CO by IR spectroscopy were inconclusive (see discussion in ref. 16). The complete reversibility of the alkyne coordination demonstrates, however, that the

© 2008 NRC Canada

Table 1. MALDI-TOF mass spectrometric data (monopositive ion peaks) from the dication alkyne adducts.

	Fragment							
Complex	$Pd_2(dppm)_2$	$Pd_3(dppm)_2$	$Pd_3(dppm)_3$–$P(Ph)_4CH_2$	$Pd_3(dppm)_3$–PPh_2[a]	$Pd_3(dppm)_3$	$Pd_3(dppm)_3$ (RCCR′)	$Pd_3(dppm)_3$ (CO)RCCR′)	Additional peaks
1a	980	1083	1122[a]	1286	1470	—	—	—
2a	976	1083	1118	1280–1306	1470	1640	—	—
3a	976	1083	1119	1286	1470	1613	—	—
4a	982	1088	1123	1287	1472	1573	—	—
5a	981	1087	1122	1288	1472	—	1617	—
6a	982	—	1122	1286	1471	—	—	1722[b]
7a	979[c], 994[c]	1049[c], 1065[c]	1122	1286	1471	1540[d]	1648[c]	1795[e]

[a]Assignment tentative.
[b]$Pd_3(dppm)_3(RCCR)_2$.
[c]Very strong peaks observed.
[d]Very weak peaks observed.
[e]Ion pair with PF_6^-

$[Pd_3(dppm)_3(CO)]^{n+}$ moiety is retained within the timescale of the electrochemistry under the conditions utilized in our studies.

Voltammetric and electrolytic study

Corroboration of alkyne adduct formation is provided by electrochemistry. A typical experiment can be exemplified from rotating disk electrode (RDE) voltammetry as follows. The parent cluster $[Pd_3(dppm)_3(CO)]^{2+}$ (as the PF_6^- salt) exhibits two reversible one-electron waves A_1 and A_2 (Fig. 1) at –0.210 and –0.470 V, respectively, which correspond to sequential one-electron reductions of the dication to the monocation and on to the neutral cluster $[Pd_3(dppm)_3(CO)]^0$. In the presence of alkyne, two new reversible one-electron reduction waves, P_1 and P_2, corresponding to the following two reactions, replace the original waves.

[1] $$[Pd_3(dppm)_3(CO)(RCCR')]^{2+} + 1e^- \rightleftarrows [Pd_3(dppm)_3(CO)(RCCR')]^+ \quad (P_1/P_1')$$

[2] $$[Pd_3(dppm)_3(CO)(RCCR')]^+ + 1e^- \rightleftarrows [Pd_3(dppm)_3(CO)(RCCR')]^0 \quad (P_2/P_2')$$

Electrolysis performed at the potential of the first wave consumes one electron-equivalent yielding the monocationic species $[Pd_3(dppm)_3(CO)(RCCR')]^{\cdot+}$, which exhibits reduction wave P_2 and oxidation wave P_1' by RDE voltammetry (Fig. 1). After electrolysis at the potential of wave P_2, two electron-equivalents are consumed and the RDE voltammetry of the resulting solution shows two oxidation waves P_1' and P_2' characteristic of the neutral cluster $[Pd_3(dppm)_3(CO)(RCCR')]^0$ (Fig. 1).

A more interesting way to obtain the paramagnetic monocationic cluster can be performed as follows: electrolysis is performed directly at the potential of the second wave P_2, but after a quantity of electricity equal to one electron has been passed, the electrolysis is stopped, whereupon the monocationic cluster is obtained. Its formation can be explained from comproportionation of the neutral and dicationic clusters as indicated in the following reactions:

Fig. 1. Rotating disk electrode voltammograms of $[Pd_3(dppm)_3(CO)]^{2+}$ in THF–NBu_4PF_6 solution. (*a*) $[Pd_3(dppm)_3(CO)]^{2+}$ alone. (*b*) $[Pd_3(dppm)_3(CO)]^{2+}$ with 2 equiv. of $C_6H_6O_4$ and a delay of 45 min. (*c*) After electrolysis at –0.3 V and consumption of one electron. (*d*) After electrolysis at –1 V and consumption of one further electron.

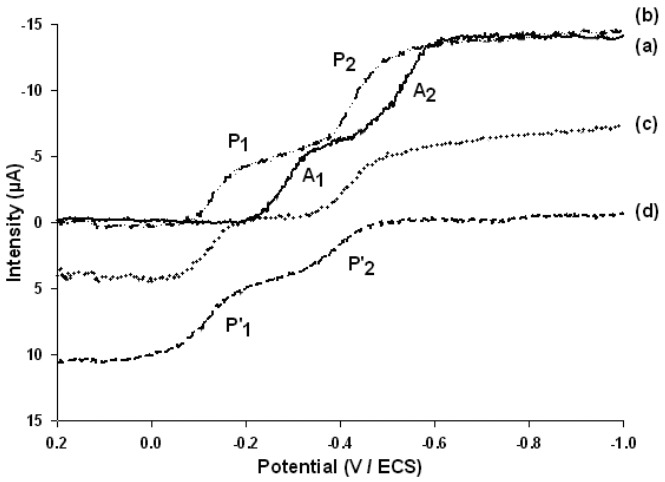

[3] $$[Pd_3(dppm)_3(CO)(RCCR')]^{2+} + 2e^- \rightleftarrows [Pd_3(dppm)_3(CO)(RCCR')]^0$$

[4] $$[Pd_3(dppm)_3(CO)(RCCR')]^{2+} + [Pd_3(dppm)_3(CO)(RCCR')]^0 \rightleftarrows 2[Pd_3(dppm)_3(CO)(RCCR')]^+$$

A third variant for preparing the monocationic clusters consists of first producing $[Pd_3(dppm)_3(CO)]^{\cdot+}$ by one-electron reduction of the parent dicationic cluster and then adding RC≡CR′. Here too, the initial oxidation and reduction waves A_1' and A_2 become oxidation and reduction steps P_1' and P_2, according to the reaction

[5] $$[Pd_3(dppm)_3(CO)]^+ + RCCR' \rightarrow [Pd_3(dppm)_3(CO)(RCCR')]^+$$

© 2008 NRC Canada

Scheme 2. Feasible routes to $[Pd_3(dppm)_3(CO)(RCCR')]^{+}$.

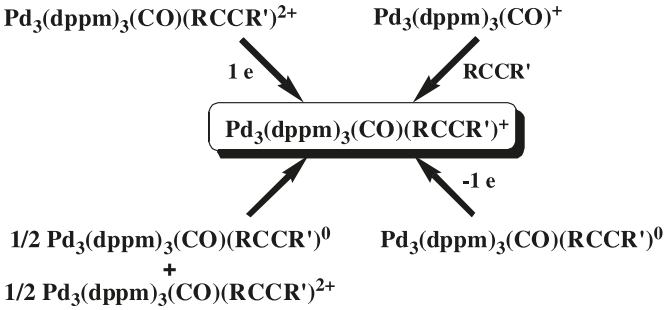

The various approaches that successfully lead to the monocationic paramagnetic clusters are summarized in Scheme 2.

In the case of the bifunctional alkyne $HC{\equiv}CC_6H_4C{\equiv}CH$, formation of a tetracationic diadduct such as $[\{Pd_3(dppm)_3(CO)\}_2(HCCC_6H_4CCH)]^{4+}$ does not occur, since in the presence of 0.5 equiv of alkyne, reduction peaks A_1, P_1, A_2, and P_2 are all detected by cyclic voltammetry in the reaction mixture. On the other hand, it is interesting to note that no interaction occurs between $[Pd_3(dppm)_3(CO)]^{n+}$ and PhC≡CPh, since reduction waves A_1 and A_2 are not modified even in the presence of an excess of PhC≡CPh. Steric hindrance from the two bulky substituents seems to be a likely explanation for this observation.

If we now compare the redox potentials of **1**–**7** (Table 2), we see that the two alkyne ester adducts are reduced *more easily* than the parent cluster **1** in both processes, whereas **4**–**7** are all *more difficult* to reduce. This is consistent with the electron-deficient alkyne esters acting as net withdrawers of electron density, whereas the aryl and alkoxy alkynes act as net electron donors to the palladium cluster. A measure of these donating and withdrawing effects can be estimated by calculating the (vertical) first ionization energies of the alkynes using semiempirical PM3 calculations. These are graphed against the P_1/P_1' and P_2/P_2' potentials in Fig. 2. Reasonable linear fits are observed (R^2 values of 0.84 and 0.86, respectively), although the $C_2H_5OC{\equiv}CH$ adduct **7** is in poor agreement (either the calculated ionization energy is wrong, or the redox potentials are not what we would expect for this system). The similarity in the slopes of the two lines reflects the consistency of the ΔE for the two processes, which is 0.34 ± 0.03 V for the alkyne adducts. Note that this ΔE is considerably larger than what is observed for the parent cluster **1** (0.22 V).

EPR characterization of the monocations

Bulk one-electron reductive electrolyses of $[Pd_3(dppm)_3(CO)(RC{\equiv}CR')]^{2+}$ adducts lead to the corresponding paramagnetic monocations **2b**–**7b**, all of which are stable for several hours in solution at room temperature (RT). Each of the six adducts that we have investigated can be simulated using combinations of hyperfine coupling constants (hfcc) for six different ^{31}P nuclei. The EPR parameters determined by simulation and measurement are summarized in Table 3 along with those previously determined for **1b**. Spectral traces of the new complexes are provided in Figs. 3–6; for similar diagrams of the previously reported **1b** (10) and **3b** and **4b** (16) see the indicated references.

Table 2. Voltammetric data for the complexes (in volts).

Complex[a]	Alkyne	E_0 (P_1/P_1')	E_0 (P_2/P_2')
1	None	–0.210	–0.470
2	$(EtO_2CC)_2$	–0.099	–0.402
3	$(MeO_2CC)_2$	–0.102	–0.401
4	PhC≡CH	–0.272	–0.632
5	FC_6H_4CCH	–0.356	–0.682
6	$HCCC_6H_4CCH$	–0.310	–0.680
7	EtOC≡CH	–0.322	–0.692

[a]Alkyne adducts of $[Pd_3(dppm)_3(CO)]^{2+}$ measured in THF–$^nBu_4NPF_6$ at room temperature on a 3 mm diameter GC electrode vs. SCE.

Fig. 2. Correlation of the (*a*) first and (*b*) second reduction potentials of $[Pd_3(dppm)_3(CO)(RC{\equiv}CR')]^{2+}$ with the vertical first ionization energies of the alkynes from PM3 calculations.

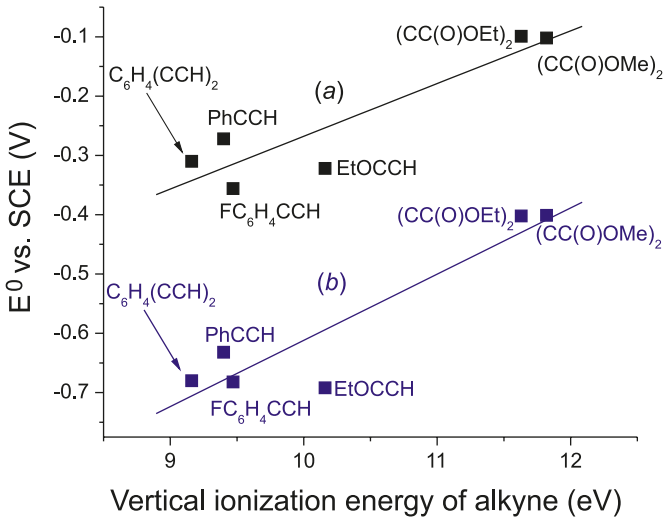

The experimental spectrum measured for the diethyl acetylene dicarboxylate complex **2b** is displayed in Fig. 3*a*. There are several features that apply to all the EPR spectra measured for the alkyne adducts. First of all, the spectra cover a large field–frequency range, which in the case of **2b** encompasses more than 40 mT and for some of the other adducts closer to 50 mT and are significantly distorted in the high-field branches. This asymmetry in the continuous wave (CW) spectra can safely be attributed to motional line broadening, a phenomenon that is common for relatively large paramagnetic molecules in X-band EPR spectroscopy (18, 19) that undergo slow tumbling on the EPR timescale.

The simulation (Fig. 3*b*) was obtained by a computerized line-fitting procedure as implemented in the software WinSim version 0.98 using a simplex minimization algorithm and starting from approximate hfcc obtained from measurements taken off the experimental spectrum (20). It can be seen that there is excellent agreement between the calculated and simulated spectra, with most of the large and small features in the measured spectrum accounted for other than the effect of the motional line broadening. Because of the expected symmetry of dispersive EPR signals, the computer line fitting can be restricted to the low-field half of the spectrum; hfcc are extracted from the simulations, as are the line widths (Table 3). Excellent agreement is obtained for all the spectra using purely Lorentzian line shapes, which sug-

© 2008 NRC Canada

Table 3. Table of EPR data obtained for the monocation radicals of the tripalladium clusters.

	EPR data (10^4 cm^{-1})											
Complex	*A*(P1)	*A*(P2)	*A*(P3)	*A*(P4)	*A*(P5)	*A*(P6)	$\sum A$(P)	*A*(Pd1)	*A*(Pd2)	*A*(Pd3)	LW	g^a
1b[b]	74.0	74.0	74.0	74.0	74.0	74.0	444.2	7.6	7.6	7.6	6.5	2.065
2b	180.5	105.5	37.9	37.9	37.9	7.0	406.7	9.2	0.0	0.0	5.0	2.036
3b[c]	180.3	105.4	37.9	37.9	37.9	7.0	406.3	10.4	0.0	0.0	5.5	2.038
4b[c]	160.0	100.3	43.1	34.0	22.9	8.0	368.4	12.2	3.7	0.0	4.8	2.032
5b	158.4	101.4	42.4	34.0	23.0	8.3	367.7	16.7	3.4	0.0	4.8	2.033
6b	160.4	97.7	43.8	34.3	22.8	7.7	366.7	10.3	0.0	0.0	5.5	2.032
7b	154.1	117.5	17.8	12.7	12.0	3.0	317.0	10.2	10.23	10.23	5.1	2.039

Note: hfcc *A*/*hc* and line width (LW) in units of 10^4 cm^{-1} are obtained from digital simulations using WinSim version 0.98 (20).
[a]*g* values are nondimensional.
[b]Taken from ref. 10.
[c]Taken from ref. 16.

Fig. 3. (*a*) Experimental and (*b*) simulated EPR spectra of $[Pd_3(dppm)_3(CO)\{CH_3CH_2OC(O)C\}_2]^{\bullet+}$ (**2b**) recorded in THF–$^nBu_4NPF_6$ at ambient temperature. The experimental spectrum is broadened at high field because of slow tumbling and has been corrected for baseline drift.

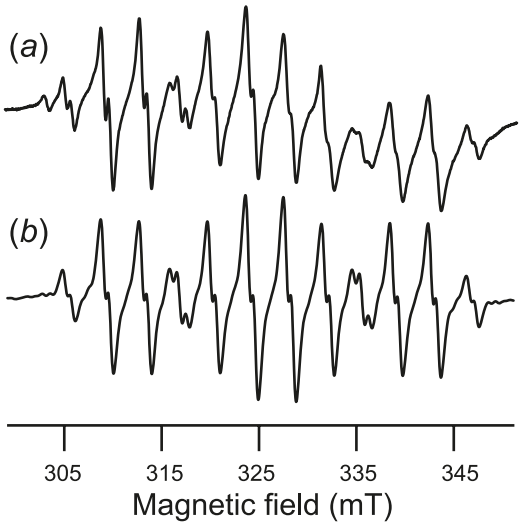

Fig. 4. (*a*) Experimental and (*b*) simulated EPR spectra of $[Pd_3(dppm)_3(CO)(FC_6H_4C{\equiv}CH)]^{\bullet+}$ (**5b**) recorded in THF–$^nBu_4NPF_6$ at ambient temperature. The experimental spectrum is broadened at high field because of slow tumbling and has been corrected for baseline drift.

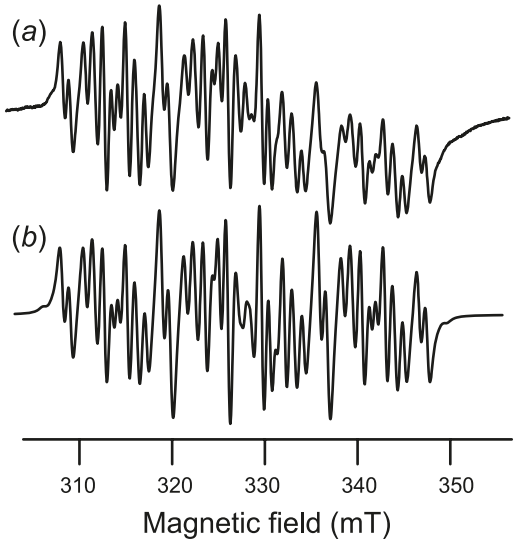

gests that there is little residual coupling to other nuclei in the spectra of any of these radical cations.

The hfcc to ^{31}P thus obtained for the two acetylene dicarboxylate containing cation radicals **2b** and **3b** comprise one very large, one medium, three small and apparently identical, and one very small value, ranging from 180.5×10^4 to 7.0×10^4 cm^{-1}. We say "apparently identical" because the lines are quite broad (the line width parameter used in the simulations is ca. 5×10^4 cm^{-1}) so that small variations in coupling will not be observable. When we compare the spectra of these two complexes with that of the parent cation radical **1b**, for which all six ^{31}P hfcc are 74.0×10^4 cm^{-1}, we note that ΣA(P) does not differ greatly (ca. 406 or 407 vs. 444×10^4 cm^{-1}), so that the total size of coupling to phosphorus seems to remain similar, but the *distribution* thereof among the six phosphorus nuclei is very strongly perturbed.

The experimental and simulated spectrum of 4-fluorophenylethyne complex **5b**, obtained by a very similar procedure, is presented in Fig. 4. Here too all the large and small features of the experimental spectrum have been accurately captured by the full line shape simulation, which also employs a Lorentzian line shape. As seen for **2b**, there are one large, one medium, three similar *but not identical*, and one very small hfcc values. The loss of (approximate) equivalence of the middle three coupling constants has a dramatic effect on the appearance of the spectrum, which looks much more complex than that shown in Fig. 3. Almost all the *A*(P) values are smaller than in **2b** and **3b**, so that ΣA(P) is now noticeably smaller. Note also that the parameters for **4b** and **5b** are quite similar, suggesting that the coordination of the PhC≡CH unit is only mildly affected by *para* fluorine substitution.

The experimental and simulated spectrum of the *p*-diethynylbenzene complex **6b** is shown in Fig. 5. Here too the fit between the measured and experimental spectrum is generally excellent, although there is a slight mismatch for a few lines at the centre of the spectrum. In all likelihood the discrepancy can be attributed to a line width effect because this spectrum seems to be somewhat more strongly affected

© 2008 NRC Canada

Fig. 5. (*a*) Experimental and (*b*) simulated EPR spectra of $[Pd_3(dppm)_3(CO)(HC{\equiv}CC_6H_4C{\equiv}CH)]^{\cdot+}$ (**6b**) recorded in THF–$^n Bu_4NPF_6$ at ambient temperature. The experimental spectrum is broadened at high field because of slow tumbling and has been corrected for baseline drift.

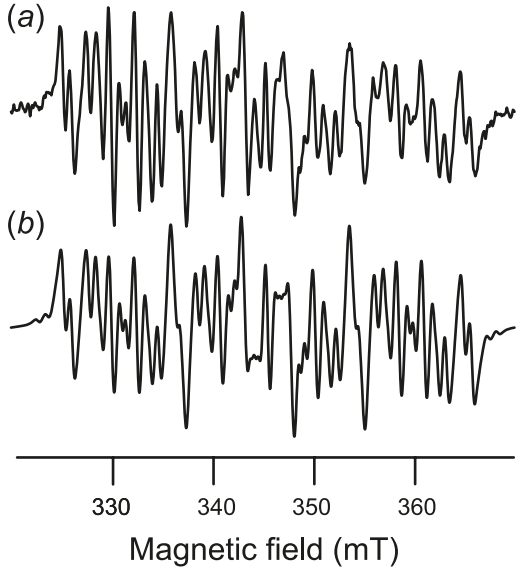

Fig. 6. (*a*) Experimental and (*b*) simulated EPR spectra of $[Pd_3(dppm)_3(CO)(CH_3CH_2OC{\equiv}CH)]^{\cdot+}$ (**7b**) recorded in THF–$^n Bu_4NPF_6$ at ambient temperature. The experimental spectrum is broadened at high field because of slow tumbling and has been corrected for baseline drift. The features indicated by the arrows in the experimental spectrum appear to be associated with hyperline coupling to the ^{106}Pd nuclei.

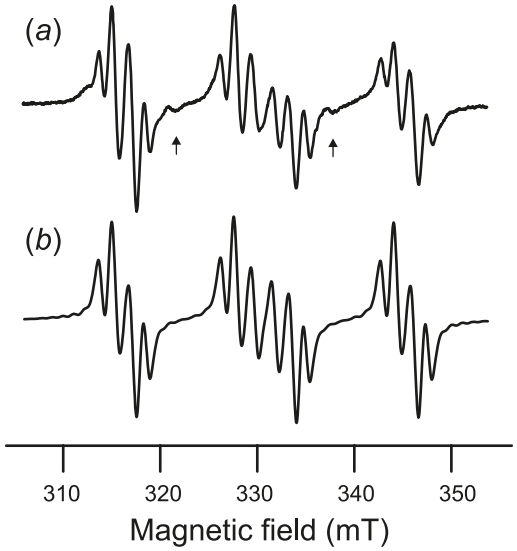

by motional broadening than those of the others, an effect that may be associated with the extended length of the 4-$HC{\equiv}CC_6H_4$ "tail" causing slower tumbling in solution. It seems certain, however, from the close agreement between the parameters for **6b**, **5b**, and **4b** that only one of the two alkyne groups in this ligand interacts with the Pd_3 centre, a conclusion that substantiates the evidence provided by voltammetry (see previous discussion). The second alkyne group will then presumably act through normal aryl substituent influences on the coordinated moiety.

The spectrum and simulation obtained for the monoethoxyethyne complex **7b** is shown in Fig. 6. This spectrum has a deceptively simple appearance, since the complex does not, in fact, have very similar hfcc values. As observed for the three ArylC≡CH complexes **4b**, **5b**, and **6b**, here too there are two larger, three medium, and one very small coupling, except that all the values are smaller (other than that of A(P2), which is larger and hence the most similar to A(P1)). Consistently, ΣA(P) is the smallest of the series.

In each of these complexes, the evidence from the good simulations achieved and the use of Lorentzian line shapes suggests that the unpaired electron spin does not get significantly redistributed in the different monocation radicals. Thus, we have to look elsewhere for the origin of the observed variation in ΣA(P) for the six adducts. A possible source of this effect is suggested by the different X-ray crystal structures mentioned in the Introduction (albeit for derivatives of the dication $[Pd_3(dppm)_3(\mu_3\text{-}CO)]^{+2}$). Whereas all these complexes retain the planar Pd_3 framework, ligand substitution leads to variable amounts of distortion of phosphorus positions out of the plane of the three metal atoms. On the reasonable assumption that similar distortions apply in **2**–**7**, subtle changes in the s- and p-orbital contributions of different phosphorus atoms to the singly occupied molecular orbital (SOMO) will occur. By comparison to the parent complex, some of the P nuclei gain and some lose the s-orbital contribution that is essential for hfcc via the Fermi contact mechanism (19). There is a ca. 30% *decrease* in $\Sigma A(^{31}P)$ from the parent complex **1b** to the monoethoxyethyne complex **7b**, whereas there is no good reason to think that these differing ligands lead to a redistribution of spin density of such magnitude away from the P nuclei. This also points, we believe, to variations in geometry that affect the amount of s-orbital contributions to the SOMO.

In addition to the $A(^{31}P)$ values, each of these spectra show evidence of the presence of the 22.2% abundant ^{105}Pd nuclei, but the complexity of the spectra and broad lines greatly limit the accuracy with which we can assign these hfcc values. Finally, there is a significant change in the g value between **1b** and *all* the alkyne adducts, but amongst the different adducts no meaningful pattern seems to be present. The variation in g values most likely reflects differences in the population of the excited states of these radical cations (19).

Conclusions

The tripalladium cluster $[Pd_3(dppm)_3(CO)]^{2+}$ first prepared by Puddephatt and co-workers (1–3) has in our hands been shown to be redox-active with stepwise and reversible reduction first to a monocation radical and subsequently to a neutral cluster. Coordination of alkynes to the framework causes significant variation in the E_0 values for both the P_1/P_1' and P_2/P_2' processes. The unambiguous identification of the monocation radicals by EPR spectroscopy provides strong evidence for the correctness of the proposed mechanisms deduced by voltammetry. Finally, the reversible nature of the alkyne coordination and the dependency thereof on redox state suggests the possibility of developing a "molecular

© 2008 NRC Canada

shuttle" in which $[Pd_3(dppm)_3(CO)]^{n+}$ could transport alkynes through a cell as a result of a charge gradient. The exploitation of this idea is a subject of ongoing research in our laboratories.

Experimental

General procedures

The solvent tetrahydrofuran was distilled over Na-benzophenone under protection of Ar. Alkynes were obtained from Sigma-Aldrich and were used as received. The $[Pd_3(dppm)_3(CO)](PF_6)_2$ salt was prepared according to a literature procedure (1, 21). The UV–vis spectra were acquired on a Varian Cary 50 spectrophotometer. MALDI-TOF mass spectra were obtained on a Bruker ProFLEX III spectrometer using 1,8-dihydroxy-10*H*-anthracen-9-one (dithranol) as matrix. The EPR spectra were acquired on a Bruker Elexsys E500 spectrometer.[3]

Electrochemistry and EPR spectroscopy

All manipulations were performed using Schlenk techniques in an atmosphere of dry oxygen-free argon. The supporting electrolyte, $^nBu_4NPF_6$, was degassed under vacuum before use and then dissolved to a concentration of 0.2 mol L^{-1}. For cyclic voltammetry experiments, the concentrations of the analyte were slightly less than 1×10^{-3} mol L^{-1}. Voltammetric analyses were carried out in a standard three-electrode cell using an EG&G Princeton Applied Research (PAR) model 263A potentiostat, interfaced to a computer running Electrochemistry Power Suite software. The reference electrode was a saturated calomel electrode (SCE) separated from the solution by a sintered glass disk. The auxiliary electrode was a platinum wire. For all voltammetric measurements, the working electrode was a vitreous carbon disk (nominal diameter = 3 mm). Under these conditions, when operating in THF, the formal potential for the ferrocene (+/0) couple was found to be +0.56 V vs. the SCE. Controlled potential electrolysis was performed with an Amel 552 potentiostat coupled with an Amel 721 electronic integrator. Bulk electrolyses were performed in a cell with three compartments separated by glass frits of medium porosity. Carbon gauze was used as the working electrode, a platinum plate was used as the counter electrode, and a saturated calomel electrode was used as the reference electrode.

Acknowledgments

Financial support by the Natural Sciences and Engineering Research Council of Canada (NSERC) and the Centre national de recherche scientifique (CNRS, UMR 5260) is gratefully acknowledged.

References

1. L. Manojlović-Muir, K.W. Muir, B.R. Lloyd, and R.J. Puddephatt. J. Chem. Soc. Chem. Commun. 1336 (1983).
2. L. Manojlović-Muir, K.W. Muir, B.R. Lloyd, and R.J. Puddephatt. J. Chem. Soc. Chem. Commun. 536 (1985).
3. B.R. Lloyd, L. Manojlović-Muir, K.W. Muir, and R.J. Puddephatt. Organometallics, **12**, 1231 (1993).
4. A.L. Balch, B.J. Davis, and M.M. Olmstead. J. Am. Chem. Soc. **112**, 8592 (1990).
5. D.G. Holah, A.N. Hughes, E. Krysa, G.J. Spivak, M.D. Havighurst, and V.R. Magnuson. Polyhedron, **16**, 2353 (1997).
6. P.D. Harvey, R. Provencher, J. Gagnon, T. Zhang, D. Fortin, K. Hierso, M. Drouin, and S.M. Socol. Can. J. Chem. **74**, 2268 (1996).
7. D. Lucas, F. Lemaitre, B. Gallego-Gomez, C. Cugnet, P. Richard, Y. Mugnier, and P.D. Harvey. Eur. J. Inorg. Chem. 1011 (2005).
8. R. Provencher, K.T. Aye, M. Drouin, J. Gagnon, N. Boudreault, and P.D. Harvey. Inorg. Chem. **33**, 3689 (1994).
9. D. Brevet, D. Lucas, P. Richard, A. Vallat, Y. Mugnier, and P.D. Harvey. Can. J. Chem. **84**, 243 (2006).
10. F. Lemaitre, D. Lucas, K. Groison, P. Richard, Y. Mugnier, and P.D. Harvey. J. Am. Chem. Soc. **125**, 5511 (2003).
11. D. Brevet, D. Lucas, H. Cattey, F. Lemaitre, Y. Mugnier, and P.D. Harvey. J. Am. Chem. Soc. **123**, 4340 (2001).
12. J. Tsui (*Editor*). Palladium in organic synthesis. *In* Topics in organomettalic chemistry. Vol. 14. Springer Gmbh, Berlin. 2005. p. 332.
13. R.J. Puddephatt and J. Xiao. Met. Clusters Chem. **2**, 605 (1996).
14. F. Lemaitre, D. Lucas, Y. Mugnier, and P.D. Harvey. J. Org. Chem. **67**, 7537 (2002).
15. D. Brevet, Y. Mugnier, F. Lemaitre, C.D. Lucas, S. Samreth, and P.D. Harvey. Inorg. Chem. **42**, 4909 (2003).
16. S.D. Molin, C. Cugnet, D. Brevet, D. Lucas, Y. Mugnier, D. Fortin, R.T. Boeré, and P.D. Harvey. Organometallics, **26**, 5209 (2007).
17. M. Rashidi, G. Schoettel, J.J. Vital, and R.J. Puddephatt. Organometallics, **11**, 2224 (1992).
18. M.A. Bennett, S.K. Bhargava, J.F. Boas, R.T. Boeré, A.M. Bond, A.J. Edwards, S.-X. Guo, A. Hammerl, J.R. Pilbrow, S.H. Privér, and P. Schwerdtfeger. Inorg. Chem. **44**, 2427 (2005).
19. J.A. Weil, J.R. Bolton, and J.E. Wertz. Electron paramagnetic resonance: elementary theory and practical applications. Wiley-Interscience, New York. 1994.
20. D.R. Duling. WinSim (version 0.98, 2002) software. J. Magn. Reson. B, **104**, 105 (1994).
21. B.R. Lloyd and R.J. Puddephatt. Inorg. Chim. Acta, **90**, L77 (1984).

[3] Supplementary material for this article (experimental parameters used for the determination of the EPR spectra of the $[Pd_3(dppm)_3(CO)(RC{\equiv}CR')]^+$ adducts) are available on the journal Web site (canjchem.nrc.ca) or may be purchased from the Depository of Unpublished Data, Document Delivery, CISTI, National Research Council Canada, Ottawa, ON K1A 0R6, Canada. DUD 3786. For more information on obtaining material refer to cisti-icist.nrc-cnrc.gc.ca/csm/unpub_e.shtml.

© 2008 NRC Canada

Study of aerobic oxidation of phenyl Pt^{II} complexes (dpms)Pt^{II}Ph(L) (dpms = di(2-pyridyl)methanesulfonate; L = water, methanol, or aniline)[1]

Julia R. Khusnutdinova, Peter Y. Zavalij, and Andrei N. Vedernikov

Abstract: Oxidation of phenyl Pt^{II} complexes K[(dpms)$Pt^{II}Ph_2$], **1**, (dpms)Pt^{II}Ph(MeOH), **2**, (dpms)Pt^{II}Ph(OH_2), **3**, and methyl Pt^{II} complex (dpms)Pt^{II}Me(NH_2Ph), **6**, with O_2 in aqueous or methanol solutions under ambient conditions leads to corresponding (dpms)Pt^{IV}R(X)OH complexes (R = X = Ph, **7**; R = Ph, X = OH, **8**; R = Ph, X = OMe, **9**; R = Me, X = NHPh; **11**; dpms = di(2-pyridyl)methanesulfonate). Complexes **7–9** could be isolated in high yield. Complex **11** as well as its phenyl analogue (dpms)Pt^{IV}Ph(NHPh)OH, **10** can be prepared in high yield by oxidation of corresponding (dpms)Pt^{II}R(NH_2Ph) with H_2O_2 in methanol. Phenyl Pt^{II} complexes (dpms)Pt^{II}Ph(HX) derived from HX = aniline and DMSO, **4** and **5**, respectively, are inert toward O_2. The rate of oxidation of **1–5** with O_2 decreases in the order **1** > **3** ≈ **2** » **4**, and **5** is unreactive. Methyl analogues are significantly more reactive compared with their phenyl counterparts. Proposed mechanism of oxidation with O_2 includes formation of anionic species (dpms)Pt^{II}R(X)$^-$ responsible for reaction with dioxygen. Attempts at C–O and C–N reductive elimination from phenyl Pt^{IV} complexes **7–10** do not lead to phenyl derivatives PhX at 80–100 °C, consistent with the results of the DFT estimates of corresponding activation barriers, ΔG^0 exceeding 28 kcal/mol.

Key words: platinum phenyl complexes, oxidation, dioxygen, aqueous solution, mechanism.

Résumé : L'oxydation des complexes phénylés du Pt(II), K[(dpms)$Pt^{II}Ph_2$], **1**, (dpms)Pt^{II}Ph(MeOH), **2**, (dpms)Pt^{II}Ph(OH_2), **3**, ainsi que du complexe méthylé du Pt(II), (dpms)Pt^{II}Me(NH_2Ph), **6**, effectuée avec de l'oxygène (O_2), en solutions aqueuses ou méthanoliques et dans des conditions ambiantes, conduit à la formation des dérivés (dpms)Pt^{IV}R(X)OH correspondants (R = X = Ph, **7**; R = Ph, X = OH, **8**; R = Ph, X = OMe, **9**; R = Me, X = NPh, **11**; dpms = di(2-pyridyl)méthanesulfonate). Les complexes **7–9** ont été isolés avec des rendements élevés. Le complexe **11** ainsi que son analogue phénylé, (dpms)Pt^{IV}Ph(NHPh)OH, **10**, peuvent être préparés avec d'excellents rendements par oxydation du (dpms)Pt^{II}R(NH_2Ph) avec du H_2O_2 dans le méthanol. Les complexes phénylés du Pt(II), (dpms)Pt^{II}Ph(HX), dans lesquels X représente l'aniline (**5**) et le DMSO (**6**) sont inertes vis-à-vis de l'oxygène. Les vitesses d'oxydation des produits **1-5** par l'oxygène diminuent dans l'ordre **1** > **3** ≈ **2** > **4,5** (inerte). Les analogues méthylés sont sensiblement plus réactifs que leurs analogues phénylés. Le mécanisme d'oxydation proposé pour l'action de l'oxygène implique la formation d'espèces anioniques (dpms)Pt^{II}R(X)$^-$ qui seraient responsables de la réaction avec le dioxygène. Les essais réalisés entre 80 et 100°C en vue d'effectuer une élimination réductrice C–O et C–N à partir des complexes phénylés **7-10** n'ont pas conduit à la formation de dérivés phénylés, PhX; ces résultats sont en accord avec les résultats d'évaluations, faites à l'aide de la théorie de la densité fonctionnelle (TDF), des barrières d'activation correspondantes, ΔG^0, qui seraient supérieures à 28 kcal/mol.

Mots-clés : complexes phénylés du platine, oxydation, dioxygène, solution aqueuse, mécanisme.

[Traduit par la Rédaction]

Introduction

The use of oxygen as the terminal oxidant for selective transition-metal-mediated functionalization of organic substrates is an important practical goal (1). One of the possible approaches to selective aerobic CH functionalization may include a sequence of the following transformations: (*i*) selective CH activation with a Pt^{II} complex, (*ii*) aerobic conversion of resulting hydrocarbyl Pt^{II} to a Pt^{IV} complex, and (*iii*) reductive elimination of organic products from the Pt^{IV} intermediate (Scheme 1).

Recently, we reported facile aerobic dpms-enabled (2) functionalization of alkyl Pt^{II} complexes in water leading to methanol (3), methyl ether (4), and olefin oxides (5, 6).

Received 27 March 2008. Accepted 14 May 2008. Published on the NRC Research Press Web site at canjchem.nrc.ca on 19 August 2009.

Dedicated to Professor Richard Puddephatt.

J.R. Khusnutdinova, P.Y. Zavalij, and A.N. Vedernikov.[2] Department of Chemistry and Biochemistry, University of Maryland, College Park, MD 20742, USA.

[1]This article is part of a Special Issue dedicated to Professor R. Puddephatt.

[2]Corresponding author (e-mail: avederni@umd.edu).

 doi:10.1139/V08-108 © 2008 NRC Canada

Scheme 1. Aerobic Pt^{II}-mediated CH functionalization.

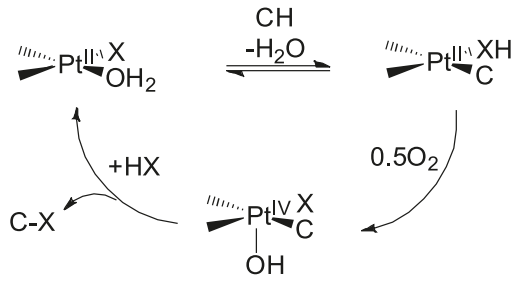

Chart 1. dpms Ligand and derived phenyl Pt^{II} complexes.

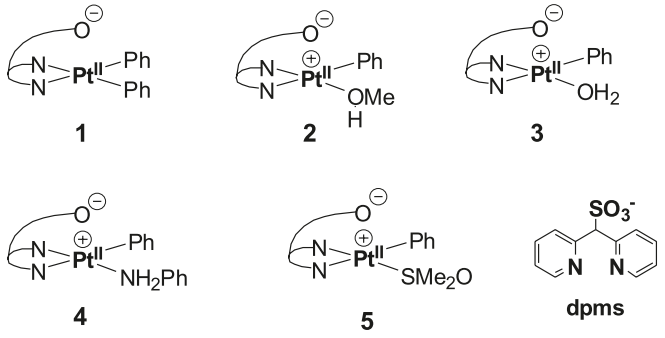

These transformations include selective aerobic conversion of Pt^{II} alkyls to isolable Pt^{IV} hydroxo alkyl complexes with subsequent clean reductive C–O elimination of a functionalized alkane product from a Pt^{IV} center. A similar reaction sequence might also be probed for aryl Pt derivatives. Aromatic CH activation with Pt^{II} (7, 8) complexes is well-established, but oxidation of monohydrocarbyl $Pt^{II}Ar$ and diaryl $Pt^{II}Ar_2$ complexes with O_2 was never observed. Slow aerobic oxidation of a mixed alkyl aryl (tmeda)-Pt^{II}(Ph)Me complex in methanol was reported but reaction products were not characterized (9). In this work, we present first examples of clean aerobic conversion of an anionic diphenyl Pt^{II} and several neutral monohydrocarbyl Pt^{II}Ph(HX) complexes to corresponding Pt^{IV}Ph derivatives (Chart 1), all enabled by dpms ligand. We also report results of attempted C(sp^2)–O and C(sp^2)–N reductive elimination from derived Pt^{IV}Ph species in water and (or) some organic solvents.

Results and discussion

(dpms)Pt^{II} Complexes 2–6

Methanol complex (dpms)Pt^{II}Ph(MeOH) (**2**) can be synthesized by reductive elimination of benzene from diphenyl Pt^{IV} hydride complex (dpms)$Pt^{IV}Ph_2H$ in methanol at 50 °C (eq. [1]). The latter complex can be prepared by protonation of anionic diphenyl Pt^{II} species K[(dpms)$Pt^{II}Ph_2$], **1** (2). Due to the poor solubility of the hydride, elevated temperatures and a prolonged time (5 h) are required to bring reaction to completion. In contrast to (dpms)$Pt^{IV}Ph_2H$, the methanol adduct **2** is soluble in warm MeOH. As a result, the reaction endpoint can be readily recognized when the entire solid disappears. Other solvento complexes studied in this work, **3**, HX = H_2O; **4**, HX = $PhNH_2$; and **5**, HX = Me_2SO, can be prepared most conveniently by a ligand exchange between methanol complex **2** and an appropriate ligand HX (eq. [2]; R = Ph).

Fig. 1. ORTEP plots (50% probability ellipsoids) for complexes **4** (*a*) and **11** (*b*).

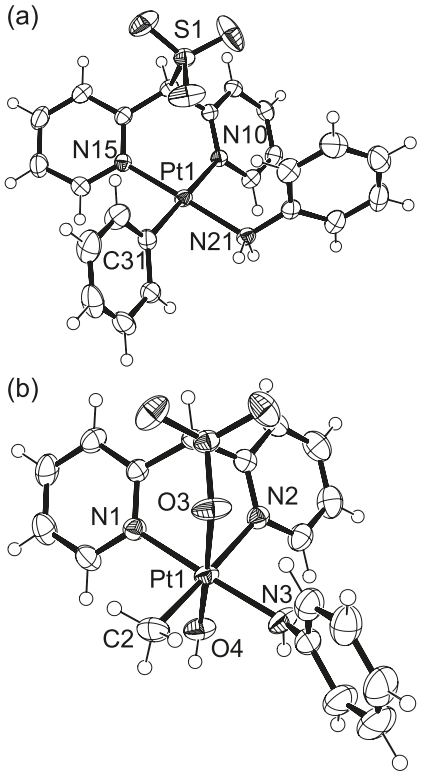

[1] (dpms)$Pt^{IV}Ph_2H$ + MeOH → (dpms)Pt^{II}Ph(MeOH) + PhH

[2] (dpms)Pt^{II}R(MeOH) + HX → (dpms)Pt^{II}R(HX) + MeOH

For instance, dissolution of **2** in water or DMSO produces quantitatively the corresponding aqua or DMSO adducts. The aniline derivative **4** can be synthesized by reacting **2** with 17 equiv. of aniline in methanol solution. Complexes **2** and **4** were prepared in an analytically pure form.

All complexes **2–5** were characterized by ^{1}H NMR spectroscopy and electrospray ionization mass spectrometry (ESI-MS). Poor solubility of **2–4** in cold methanol or water prevented us from obtaining high quality ^{13}C NMR spectra. Two sets of signals originating from pyridyl protons could be found in NMR spectra of **2–5**, indicating the presence of two non-equivalent pyridyl fragments and a low C_1 molecular symmetry of these complexes. In particular, two readily recognizable most downfield-shifted ^{1}H NMR signals of pyridyl ortho protons integrating as 1H each could be found in spectra of **2–5** in the range of 8–9 ppm. The signals appear as virtual doublets with characteristic small H–H coupling constant $^3J_{HH}$ = 5–6 Hz.

Complex **4** was characterized by single-crystal X-ray diffraction. X-ray quality crystals of **4** could be obtained by slow crystallization from a reaction mixture. Platinum atom in complex **4** has an idealized square-planar environment (Fig. 1*a*). The Pt1–N15 bond, which is trans to aniline ligand, is 2.024(3) Å long and is shorter than Pt1–N10, 2.102(3) Å, which is trans to phenyl, consistent with a

© 2008 NRC Canada

Chart 2. Products of oxidation of complexes **1**–**4** and **6**.

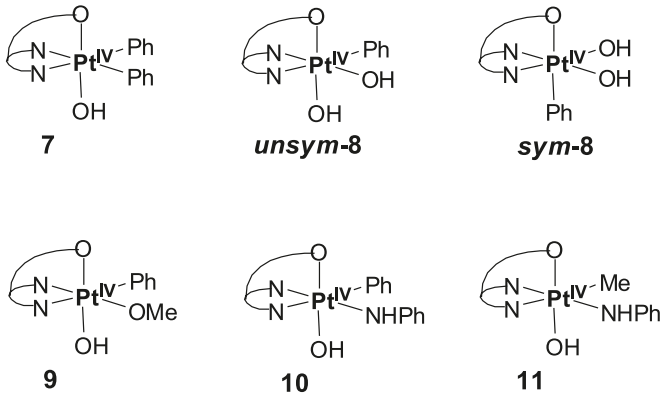

stronger trans influence of the phenyl compared with aniline ligand (10). The Pt1–N21 distance between the metal and the nitrogen atom of the aniline ligand is 2.066(3) Å. Both NH bonds of the aniline ligand point away from the sulfonate group. The shortest Pt1–sulfonate oxygen contact is non-bonding, 3.186 Å.

The mode of coordination of DMSO ligand to the metal in complex **5** could be established by IR spectroscopy. IR spectra of **5** exhibit the presence of the ν(S=O) band of S-coordinated DMSO at 1131 cm^{-1}, typical for S-coordinated DMSO complexes (11).

Solvento complexes derived from water, **3**, and methanol, **2**, are air-sensitive, whereas aniline derivative **4** and DMSO adduct **5** are stable under air. Reactivity of phenyl (dpms)Pt^{II} solvento complexes **2**–**4** toward O_2 will be compared with that of their methyl analogues (dpms)Pt^{II}Me(HX) (vide infra) whose aerobic oxidation chemistry was reported recently (HX = H_2O (3), MeOH (4)). The aniline methyl Pt^{II} complex (dpms)Pt^{II}Me(NH_2Ph) (**6**) was unknown and was prepared in this work.

For the preparation of **6**, a procedure similar to that utilized for its phenyl analogue **4** was used (eq. [2]; R = Me). Upon mixing of methanolic solutions of (dpms)Pt^{II}Me(MeOH) (4) with 1.2 equiv. of aniline and removal of the solvent, the target compound could be isolated as a colourless solid in 87% yield.

^{1}H NMR spectral patterns of **6** in D_2O are consistent with the C_1 molecular symmetry. The spectrum shows the presence of a Pt^{II}Me group resonance at 0.79 ppm (J_{195PtH} = 72 Hz) integrating as 3H, a singlet of the dpms ligand CH bridge at 5.91 ppm integrating as 1H, a set of partially overlapping signals of the aniline phenyl group, and signals of two non-equivalent pyridyl fragments. Two virtual doublets of ortho H atoms of two pyridyls integrating as 1H each can be observed at 8.14 ppm (J = 5.5 Hz) and 8.73 ppm (J = 5.9 Hz, $^3J_{195PtH}$ = 56 Hz). ESI-mass spectrum of aqueous solution of **6** shows single ^{195}Pt-derived peak with m/z = 553.1 (calculated for (dpms)$^{195}Pt^{II}$Me(NH_2Ph)·H^+, $C_{18}H_{20}N_3SO_3{}^{195}$Pt, 553.1).

(dpms)Pt^{IV} Complexes — Oxidation of (dpms)Pt^{II}R complexes with O_2 in water or methanol

Diphenyl complex sym-*(dpms)$Pt^{IV}Ph_2$(OH) (7)*

Oxidation of K[(dpms)$Pt^{II}Ph_2$] (2) with O_2 in water is facile and is complete in about 2 h at 22 °C. The target compound, *sym*-(dpms)$Pt^{IV}Ph_2$(OH), **7** (Chart 2) is poorly soluble in the reaction medium and can be isolated in an analytically pure form by filtration from the strongly alkaline aqueous solution containing KOH (eq. [3]).

[3] $$2\ K[(dpms)Pt^{II}Ph_2] + O_2 + 2\ H_2O \rightarrow 2\ sym\text{-}(dpms)Pt^{IV}Ph_2(OH) + 2\ KOH$$

Complex **7** dissolved in DMSO-d_6 exhibits in its ^{1}H NMR spectrum a broad singlet at 2.56 ppm with ^{195}Pt satellites (J = 36 Hz) integrating as 1H and corresponding to the Pt^{IV}(OH) proton. A doublet of doublets at 8.30 ppm (J = 5.5, 1.5 Hz) integrating as 2H, which is seen in the most downfield region of the spectrum was assigned to the pyridyl ortho protons. Accordingly, there are nine signals corresponding to two symmetry-related pyridyls and two symmetry-related phenyl ligands in the aromatic region of the ^{13}C NMR spectrum of **7**, evidencing the mirror symmetry of the product.

High reactivity of anionic diphenyl Pt^{II} complex **1** toward O_2 in aqueous solution and the retention of the planar arrangement of the four donor atoms at the Pt center upon oxidation of **1** to mirror symmetric **7** are similar to the behaviour of the dimethyl analogue K[(dpms)$Pt^{II}Me_2$] in its reaction with O_2 (2). Based on the stereochemical outcome of these reactions and also reactions including (dpms)Pt^{II}Me(HX), HX = H_2O (3), L = MeOH (4) and (dpms)$Pt^{II}(C_2H_4OH)OH^-$ (5), we suggest that the mechanisms of oxidation of these complexes might be also similar (Scheme 2; X = Me or Ph, steps **b**–**d** only) (5).

Scheme 2. Plausible mechanism of aerobic oxidation of (dpms)Pt^{II} complexes.

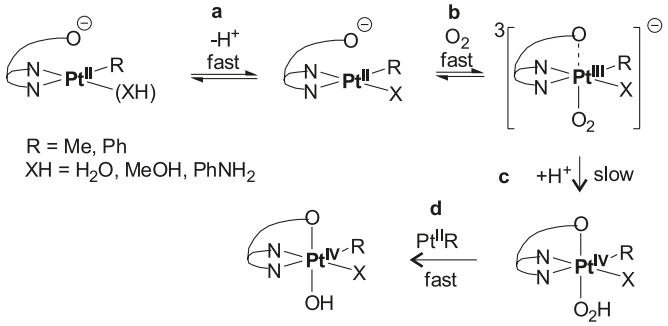

The mechanism presented in Scheme 2 was discussed previously (5) and is based on the idea of the axial attack of electrophilic O_2 at Pt^{II} center (9) that allows to account for the retention of the configuration at the Pt atom in the course of oxidation reaction. At the same time, we presume that in the case of neutral monophenyl complexes (dpms)Pt^{II}Ph(HX) only anionic species (dpms)Pt^{II}Ph$(X)^-$ can accept such an attack as it was shown previously for some monoalkyl analogues (5).

Notably, aerobic oxidation of diphenyl Pt^{II} complexes to form $Pt^{IV}Ph_2$ products has never been reported. In particular, (tmeda)$Pt^{II}Ph_2$ is unreactive toward O_2. In contrast, presumably electron-richer mixed-ligand phenyl methyl analogue (tmeda)Pt^{II}(Ph)Me can be oxidized with O_2 (9). Hence, the presence of the pendant axial sulfonate group (see Fig. 1*a*, for example) in anionic (dpms)Pt^{II} species is sufficient to raise energy levels of neutral $Pt^{II}Ph_2$ fragment and enable

© 2008 NRC Canada

electron transfer between Pt^{II} atom present in complex **1** and dioxygen (Scheme 2, steps **b**–**c**) (5).

***Phenyl dihydroxo complex* unsym-*(dpms)Pt^{IV}Ph(OH)$_2$* (8)**

Solutions of aqua complex **3** in water react slowly with O_2 at atmospheric pressure and ambient temperature to produce colourless unsymmetrical phenyl dihydroxo complex *unsym*-(dpms)$Pt^{IV}Ph(OH)_2$, *unsym*-**8** (Chart 2), that can be isolated in an analytically pure form in 93% yield (eq. [4]):

[4] $$2\ (\text{dpms})Pt^{II}Ph(OH_2) + O_2 \rightarrow 2\ \textit{unsym}\text{-}(\text{dpms})Pt^{IV}Ph(OH)_2$$

The presence of two non-equivalent pyridyl groups and hence the C_1 molecular symmetry of *unsym*-**8** are evident from data of ^{1}H and ^{13}C NMR spectroscopy in aqueous and DMSO solutions of *unsym*-**8**. Interestingly, two hydroxo ligands present in this complex give rise to two individual signals that integrate as 1H each and appear as broad singlets at 1.45 ppm (no resolved ^{195}Pt satellites) and 2.99 ppm ($^2J_{195PtH}$ = 30 Hz). Based on the analogy with complex **7**, the latter signal might be assigned to the proton of the axial OH ligand of complex *unsym*-**8**, whereas the signal at 1.45 ppm might be assigned to the proton of the equatorial OH ligand. Aqueous solutions of **8** acidified with HBF_4 show the presence of monoprotonated species **8**·H^+, *m*/*z* = 556.1 (calculated for (dpms)^{195}PtPh(OH)$_2$·H^+, $C_{17}H_{17}N_2SO_5{}^{195}Pt$, 556.1).

The rate of reaction in eq. [4] is much slower than that for K[(dpms)$Pt^{II}Ph_2$] (eq. [3]); an estimated half-life of **3** is 8.8 h. This fact may be related to the neutral character of **3** in contrast to anionic complex **1**, and therefore, a much lower fraction of anionic hydrocarbyl (dpms)Pt^{II} species is available for attack with O_2 in the case of **3**.

As in the case of bishydrocarbyl complexes K[(dpms)$Pt^{II}R_2$], R = Me or Ph, aerobic oxidation of monohydrocarbyl species (dpms)$Pt^{II}R(OH_2)$ leads to Pt^{IV} hydroxo derivatives *unsym*-(dpms)$Pt^{IV}R(OH)_2$ for both R = Me (3, 5) and Ph. Based on available estimates of half-life of (dpms)$Pt^{II}R(OH_2)$ measured under identical conditions in neutral aqueous solutions at 22 °C, the reactivity of complexes (dpms)$Pt^{II}R(OH_2)$ decreases in the order Me ($\tau_{1/2} \approx$ 15min) (5) > Ph ($\tau_{1/2} \approx$ 8.8 h). Assuming that mechanisms of these aerobic oxidation reactions are also similar (Scheme 2, steps **a**–**d**), this difference can be related to the electron-poorer character of the phenyl complex **3**. On one hand, electron-poorer complex **3** is more acidic than its methyl analogue. That increases the fraction of anionic (dpms)$Pt^{II}R(OH)^-$ species available for reaction with O_2 (5) and makes complex **3** more reactive. On the other hand, an electron-poorer Pt^{II} center in anionic intermediate (dpms)$Pt^{II}Ph(OH)^-$ is more difficult to oxidize that leads to an overall lower reactivity of the phenyl aqua complex **3**.

Notably, no *mono*phenyl Pt^{II} complexes were known that are able to react with O_2 to produce Pt^{IV}Ph derivatives. As in the case of complex **1**, we assume that the anionic pendant sulfonate tail present in dpms ligand allows to raise energy levels of neutral Pt^{II}Ph(OH) fragment to an extent, which is sufficient to enable electron transfer from Pt^{II} atom present in this species to O_2.

Taking these considerations into account, one can suggest that methanol analogue of aqua adduct **3**, complex **2** containing an almost equally acidic but more donating methanol ligand will be more reactive toward O_2. This was proven correct in the experiments described below.

***Phenyl hydroxo methoxo complex (dpms)Pt^{IV}Ph(OH)(OMe)* (9)**

Oxidation of methanol phenyl complex **2** was performed in methanol at ambient temperature. In the course of the reaction, solid complex **2** dissolves to produce a more soluble colourless hydroxo methoxo phenyl complex (dpms)Pt^{IV}Ph(OH)(OMe), **9**. The product was isolated in analytically pure form in 91% yield (eq. [5]).

[5] $$2\ (\text{dpms})Pt^{II}Ph(MeOH) + O_2 \rightarrow 2\ (\text{dpms})Pt^{IV}Ph(OH)(OMe)$$

According to ^{1}H NMR spectroscopy, complex **9** in DMSO-d_6 exhibits a broad singlet of the Pt^{IV}(OH) proton at 2.52 ppm integrating as 1H and a singlet of the methoxo ligand at 2.94 ppm with discernible ^{195}Pt satellites ($^3J_{195PtH}$ = 33 Hz) integrating as 3H. An ESI-mass spectrum of solution of **9** in MeOH acidified with HBF_4 shows the presence of a peak with *m*/*z* = 570.1 that corresponds to a monoprotonated species (dpms)^{195}PtPh(OCH$_3$)(OH)·H^+, (calculated for $C_{18}H_{19}N_2SO_5{}^{195}Pt$, 570.1).

Assuming that oxidation of methanol adducts (dpms)$Pt^{II}R(MeOH)$ proceeds via similar mechanisms for R = Me and Ph and implies retention of the configuration of both R and MeO ligands at the Pt center, complex **9** was tentatively assigned the same configuration (see Chart 2) as the product of aerobic oxidation of the methyl analogue. In the latter case, as established by a single-crystal X-ray diffraction analysis of the reaction product, (dpms)Pt^{IV}Me(OMe)OH methyl and methoxo fragments retain their positions in the equatorial plane of the product (4).

Half-life of complex **2** (eq. [5]) determined at 22 °C and 1 atm (1 atm = 101.325 kPa) partial pressure of O_2 was estimated to be 5.5 h. This result means that the reactivity of methanolic solutions of **2** is slightly higher than that of aqueous solutions of its aqua-analogue **3**.

A comparison of reactivity of analogous methanol complexes (dpms)$Pt^{II}R(HX)$, HX = MeOH, R = Me and Ph shows that the methanol phenyl complex **2** is less reactive compared with the electron-richer methanol methyl complex: Me ($\tau_{1/2}$ < 1 h) (4) > Ph ($\tau_{1/2} \approx$ 5.5 h). The same trend was observed for aqua complexes, HX = H_2O, R = Me and Ph.

Considering oxidation of the aniline derivatives **4** and **6** with O_2, one can expect poor reactivity because the acidity of aniline is many orders of magnitude lower than that of H_2O or MeOH that serve as ligands in species **2** and **3** (12). Hence, anionic intermediates (dpms)$Pt^{II}R(NHPh)^-$ required for oxidation may be available in exceedingly low concentrations only. Similarly, dimethylsulfoxide ligand present in adduct **5** is even less acidic than aniline. Therefore, complex **5** may be even less reactive toward O_2. Reactivity of aniline adducts **4** and **6** as well as that of DMSO adduct **5** toward O_2 was tested in the following experiments.

© 2008 NRC Canada

Phenylamido complexes (dpms)Pt^{IV}Ph(NHPh)(OH) (10) and (dpms)Pt^{IV}Me(NHPh)(OH) (11)

Methanolic solutions of complexes **4** and **5** are inert toward O_2. No changes were observed by ^{1}H NMR spectroscopy as well as no new species were detected by ESI-MS after 7 days of exposure of the above solutions to O_2 (1 atm) at ambient temperature.

To be able to test reductive elimination chemistry of an amido phenyl (dpms)Pt^{IV}(OH) complex, which can be derived from the aniline adduct **4**, oxidation of **4** was performed with hydrogen peroxide (eq. [6]).

[6] $$(dpms)Pt^{II}Ph(PhNH_2) + H_2O_2 \rightarrow (dpms)Pt^{IV}Ph(NHPh)(OH) + H_2O$$

Treatment of complex **4** dissolved in methanol with 2.5 equiv. of 30% H_2O_2 produced complex **10** in a quantitative yield, according to ^{1}H NMR spectroscopy. The colourless product could be precipitated with diethyl ether and isolated in an analytically pure form in 90% yield.

Phenylamido phenyl Pt^{IV} complex **10** was fully characterized by ^{1}H and ^{13}C NMR spectroscopy and ESI-mass spectrometry. ^{1}H NMR spectrum of **10** in DMSO-d_6 solutions shows two broad singlets, one at 3.01 ppm and another at 4.36 ppm integrating as 1H each that can be attributed to OH and NH protons, respectively. Both ^{1}H and ^{13}C NMR spectra reveal a low C_1 molecular symmetry of **10**. ESI-mass spectra of **10** dissolved in methanol exhibit single ^{195}Pt-derived peak at m/z = 631.1 that corresponds to (dpms)^{195}PtPh(NHPh)(OH)H$^+$ (calculated for $C_{23}H_{22}N_3O_4{}^{195}$Pt S, 631.1).

Based on presumed common mechanism of oxidation of (dpms)Pt^{II}R(HX) species, R = Me and Ph, the configuration of complex **10** at the Pt atom was assumed to be the same as for its methyl analogue **11** (Chart 2; vide infra).

Reactivity of an analogous methyl Pt^{II} aniline adduct **6** toward O_2 was also tested. Notably, upon stirring of aqueous solution of **6** under O_2 atmosphere (1 atm) at an ambient temperature, slow oxidation leading to complex (dpms)Pt^{IV}Me(NHPh)(OH), **11**, (Chart 2) was evident by ^{1}H NMR spectroscopy and ESI-mass spectrometry (eq. [7]). The reaction half-life was estimated to be 30 h.

[7] $$2\ (dpms)Pt^{II}Me(PhNH_2) + O_2 \rightarrow 2\ (dpms)Pt^{IV}Me(NHPh)(OH)$$

Similar to **10**, complex **11** could be prepared by oxidation of methanolic solution of **6** with 1.1 equiv. of H_2O_2. The reaction is quantitative by NMR spectroscopy.

Aqueous solutions of **11** are weakly basic (pH ≈ 9) presumably due to reversible protonation on the nitrogen atom of the phenylamido ligand.

As in the case of phenyl Pt^{II} complex **10**, the ^{1}H NMR spectrum of **11** in DMSO-d_6 shows the presence of two broad singlets at 2.22 ppm and 4.17 ppm, corresponding to OH and NH fragments, respectively. Both ^{1}H and ^{13}C NMR spectroscopy suggests a low C_1 molecular symmetry of complex **11**. ESI-mass spectra of aqueous solutions **11** exhibit single ^{195}Pt-derived peak with m/z = 569.1 (calculates for (dpms)^{195}PtMe(NHPh)(OH)·H$^+$, $C_{18}H_{20}N_3SO_4{}^{195}$Pt, 569.1).

X-ray quality crystals of **11** could be obtained by slow diffusion of ether vapours into solution of **11** in methanol. The structure of complex **11** reveals the presence of a Pt atom in a slightly distorted octahedral environment (Fig. 1*b*). As in the case of the Pt^{II}Ph aniline adduct **4**, the Pt1–N2 bond trans to hydrocarbyl is longer than the Pt1–N1 bond trans to phenylamido ligand, 2.189(3) Å vs. 2.089(3) Å, respectively. The Pt1–N3 bond with formally anionic phenylamido ligand is about 0.05 Å shorter than the Pt–N bond in the Pt^{II} adduct **4** with neutral aniline ligand, 2.018(3) Å. One of the sulfonate oxygen atoms in the Pt^{IV} complex **11** is bound to the metal with a short Pt1–O3 distance of 2.102(3) Å.

The configuration of complex **11** shows that the methyl and phenylamido fragments retain their equatorial positions in the course of oxidation of the Pt^{II} precursor **6** with H_2O_2.

Different ability of aniline-derived methyl and phenyl (dpms)Pt^{II} complexes **4** and **6** to react with O_2 in water is remarkable. Though the acidity of coordinated aniline may be expected to be many orders of magnitude lower compared with that of Pt^{II}-bound water or methanol ligands, corresponding anionic phenylamido Pt^{II} species (dpms)Pt^{II}R(NHPh)$^-$ required for reaction with O_2 (Scheme 2, steps **b**–**c**) may still be available in sufficient concentration in the case of R = Me. At the same time, the electron-poorer nature of phenyl ligand might be responsible for precluding a facile electron transfer between the Pt^{II} center in (dpms)Pt^{II}R(NHPh)$^-$ and dioxygen.

Finally, the inertness of complex **5** toward O_2 is consistent with its virtual inability to produce an anionic phenyl Pt^{II} complex required for aerobic reaction (Scheme 2, step **a**).

Attempted reductive elimination from (dpms)Pt^{IV}Ph complexes

It is assumed that C–X reductive elimination from Pt^{IV} center (X = O, N, C, H) is most facile if it proceeds via five-coordinate intermediates with a coordination vacancy trans to the hydrocarbyl being eliminated (13, 14). The ability of a d^6 metal complex to produce low-coordinate transients and therefore the presence of a good leaving group may be critical for fast reductive elimination chemistry at a Pt^{IV} center. The best leaving group available in (dpms)Pt^{IV} complexes **7**–**11** is the sulfonate but it is cis to hydrocarbyl ligands in all of the complexes. As a result, reductive elimination from **7**–**11** might be expected to be preceded by their isomerization. Indeed, when alkyl (dpms)Pt^{IV}(OH) complexes with an alkyl group cis to the sulfonate are submitted to reductive elimination experiments, intermediates with the alkyl trans to the sulfonate are actual reactive species involved in C–O reductive elimination reactions. These species can be detected by NMR spectroscopy in reaction mixtures and, in a number of cases, isolated in analytically pure form (3–6). Whereas C(sp^3)–X elimination from Pt^{IV} can operate an S_N2 (X = O, N) (15, 16) or a recently discovered direct C(sp^3)–O elimination mechanism (6), in the case of aryl Pt^{IV} derivatives, a direct C(sp^2)–X elimination was observed only (17). Hence, a direct C(sp^2)–X reductive elimination from complexes **7**–**10** might be expected.

Heating complex **7** in DMSO at 100 °C for 6 days resulted in clean isomerization to *unsym*-**7** featuring one of the phenyl groups in the axial position. No other products were detected in the solution.

Similarly, unsymmetrical phenyl dihydroxo complex **8** dissolved in water and exposed to 100 °C for 3 days cleanly

© 2008 NRC Canada

produced the more stable isomer *sym*-**8** with the aryl in the axial position (half-life ≈ 12.5 h). No other products were found. The latter complex is C_s symmetric, according to ^{1}H and ^{13}C NMR spectroscopy and produces the same signal in ESI-mass spectra as its unsymmetrical precursor.

To probe the effects of solvent and pH on reactivity of *sym*-**8**, its samples were submitted to C–O reductive elimination in DMSO and also acidic and alkaline aqueous solutions at 100 °C. No changes were detected in these solutions by ^{1}H NMR spectroscopy after 5 days, suggesting that the Gibbs activation energy for direct C–O elimination from Pt^{IV} exceeds 30 kcal/mol in all these cases.

Reductive elimination reactions from complexes **9** and **10** were probed in aprotic DMSO-d_6, CD_3CN, and DMF-d_7.

In the case of **9** in DMSO-d_6 solution slow formation of a single Pt^{II} complex **5-*d*$_6$** and methanol was detected by ^{1}H NMR spectroscopy and ESI-MS at 100 °C. No anisole or phenol was detected. The reaction was clean and involved presumably the solvent as a reductant (eq. [8]).

[8] $$(dpms)Pt^{IV}Ph(OMe)OH + 2\ Me_2SO \rightarrow (dpms)Pt^{II}Ph(dmso) + MeOH + Me_2SO_2$$

A complex mixture of unidentified products formed in DMF-d_7 and CD_3CN solutions of **9** at 100 °C already after several hours, but no anisole or phenol was detected by ^{1}H NMR spectroscopy either.

Phenylamido complex **10** in CD_3CN solution produced a soluble Pt^{II} complex $(dpms)Pt^{II}Ph(CD_3CN)$ along with a complex mixture of solids of unknown composition after 5 h at 80 °C. No diphenylamine or phenol was detected by ^{1}H NMR spectroscopy.

Similarly, a complex mixture of products not containing diphenylamine formed when a solution of complex **10** in DMF-d_7 was heated at 80 °C for 24 h. ESI-MS spectra of acidified reaction mixtures diluted with methanol exhibited a peak of unreacted starting material, *m*/*z* 631.1, and two new peaks with *m*/*z* = 1225.2 and *m*/*z* = 613.1 that might be assigned to a mono- and doubly-protonated dinuclear species $[(dpms)_2Pt^{IV}{}_2Ph_2(\mu\text{-}NPh)(\mu\text{-}NHPh)]^+$ (calcd. $C_{46}H_{39}N_6O_6{}^{195}Pt_2S2$ 1225.1) and $[(dpms)_2Pt^{IV}{}_2Ph_2(\mu\text{-}NHPh)_2]^{2+}$ (calcd. 613.1), respectively.

Therefore, none of complexes **7**–**10** reacted via Pt^{IV}–Ph bond cleavage, and none can be used for arene CH functionalization such as the one shown in Scheme 1. Oxidation of a solvent (complex **9** in DMSO) or, presumably phenylamido ligand (complex **10** in MeCN), or formation of insoluble polynuclear complexes (complex **10** in DMF) was seen instead.

Our DFT estimates of the Gibbs activation energy for the "direct" C–O or C–N elimination from $(dpms)Pt^{IV}Ph$ phenyl complexes **8**–**10** provided high barriers for these reactions. In particular, the Gibbs activation energy for PhOH elimination from *sym*-**8** is 29.4 kcal/mol. The same value was found for PhOMe elimination from an isomer of complex **9** with phenyl ligand in the axial position. Finally, the Gibbs activation energy for Ph_2NH elimination from an isomer of complex **10** with the axial $Pt^{IV}Ph$ group is 28.7 kcal/mol. Hence, the results of DFT modeling are qualitatively consistent with our experimental observations.

Summary

Though none of the Pt^{IV} phenyl complexes $(dpms)Pt^{IV}Ph(X)OH$ exhibited C–X reductive elimination chemistry in the temperature range of 20–100 °C, results of this study may be important for understanding of factors affecting reactivity of hydrocarbyl Pt^{II} complexes toward O_2. When observed, aerobic oxidation of dipyridylmethanesulfonate monohydrocarbyl Pt^{II} complexes $(dpms)Pt^{II}R(HX)$ derived from water, methanol, and aniline (HX) leads to Pt^{IV} hydroxo complexes $(dpms)Pt^{IV}Ph(X)OH$. This reactivity depends both on the solvento ligand HX and the donicity of the hydrocarbyl R. Among phenyl Pt^{II} species, the anionic diphenyl complex is the most reactive, whereas aniline and DMSO adducts are inert: X = Ph > MeO ≈ HO » PhNH, DMSO. In turn, methyl derivatives are more reactive than their phenyl counterparts, R = Me > Ph; even the aniline adduct can be oxidized with O_2 when R = Me.

Experimental section

General

All manipulations were carried out under purified argon using standard Schlenk and glovebox techniques. All reagents for which synthesis is not given are commercially available from Sigma-Aldrich, Acros, Alfa Aesar, or Pressure Chemicals and were used as received without further purification. Potassium di(2-pyridyl)methanesulfonate was synthesized as described previously (2). DMSO-d_6, CD_3CN, DMF-d_7, and CD_3OD from Cambridge Isotope Laboratories were dried over CaH_2, vacuum-transferred, and stored in Teflon-sealed flasks in an argon-filled glovebox. Water was deaerated by repeating freezing-pumping cycles and stored under argon in a Teflon-sealed Schlenk flask in a glovebox. ^{1}H (400 MHz) and ^{13}C NMR (125 MHz) spectra were recorded on a Bruker AVANCE 400 or Bruker DRX-500 spectrometers. Chemical shifts are reported in ppm and referenced to residual solvent resonance peaks. IR spectra were recorded on a JASCO FT/IR 4100 spectrometer. ESI-MS experiments were performed using a JEOL AccuTOF-CS instrument. Elemental analyses were carried out by Chemisar Laboratories Inc., Guelph, Canada.[3]

Computational details

Theoretical calculations in this work have been performed using density functional theory (DFT) method (18), specifically functional PBE (19), implemented in an original program package "Priroda" (20). In PBE calculations, relativistic Stevens–Basch–Krauss (SBK) effective core potentials (ECP) (21), optimized for DFT calculations, have been used. Basis set was 311-split for main-group elements with one additional polarization p-function for hydrogen and additional two polarization d-functions for elements of higher periods. Full geometry optimization has been performed without constraints on symmetry. For all species under investigation, frequency analysis has been carried out.

[3] Caution: methanol flash point is 12 °C and is lower under pure O_2 atmosphere.

© 2008 NRC Canada

All minima have been checked for the absence of imaginary frequencies. All transition states possessed just one imaginary frequency. Using method of intrinsic reaction coordinate, reactants, products, and the corresponding transition states were proven to be connected by a single minimal energy reaction path.

Preparation of (dpms)Pt^{II}Ph(MeOH) (2)

(dpms)PtPh$_2$H (184 mg, 306 μmol), prepared according to the literature procedure (2), in MeOH (30 mL) was placed into a 100 mL Schlenk tube equipped with a stirring bar under an argon atmosphere, and the reaction mixture was stirred at 50 °C. Colourless solution formed after 5 h. The solution was filtered under argon, reduced in volume to 2–3 mL under vacuum, and the resulting suspension was cooled down to –20 °C. White precipitate of **2** was filtered, washed with cold methanol, and dried under vacuum for 12 h. Yield: 127 mg, 75%. White solid, oxidizes in air, poorly soluble in methanol, dissolves in water and DMSO with the loss of methanol ligand and formation of (dpms)PtPh(OH$_2$) and (dpms)PtPh(DMSO), respectively.

IR (KBr) ν: 3394 (w, br), 3046 (w), 2949 (w), 2764 (w), 1602 (w), 1572 (w), 1480 (w), 1438 (w), 1252 (m), 1168 (m), 1033 (s), 767 (m), 742 (m), 702 (m), 687 (m) cm^{-1}. ^{1}H NMR (CD$_3$OD, 22 °C) δ: 6.02 (s, 1H), 6.86–6.92 (m, 1H), 6.98 (vt, *J* = 7.5 Hz,), 7.04 (ddd, *J* = 7.8, 5.7, 1.5 Hz, 1H), 7.43 (dd, *J* = 7.5, 1.1 Hz, $^3J_{PtH}$ = 32 Hz, 2H), 7.62 (ddd, *J* = 7.9, 5.4, 1.6 Hz, 1H), 7.80 (dd, *J* = 7.9, 1.5 Hz, 1H), 7.94 (d, *J* = 7.8 Hz, 1H), 7.98 (td, *J* = 7.8, 1.6 Hz, 1H), 8.11 (td, *J* = 7.9, 1.7 Hz, 1H), 8.43 (dd, *J* = 5.7, 1.7 Hz, 1H), 8.81 (d, *J* = 5.4 Hz, 1H). ^{13}C spectrum of (dpms)PtPh(MeOH) could not be obtained due to its low solubility in methanol. ESI of dilute solution in methanol, *m*/*z* 554.1. Calculated for (dpms)Pt^{II}Ph(MeOH)·H$^+$, $C_{23}H_{21}N_3O_3{}^{195}$PtS: 554.1. Anal. found: C, 39.36; H, 3.47; N, 5.19. Calcd. for $C_{18}H_{19}N_2O_4$PtS: C, 39.06; H, 3.28; N, 5.06.

Preparation of (dpms)Pt^{II}Ph(OH$_2$) (3)

(dpms)PtPh(MeOH) (20 mg, 36 μmol) and 20 mL of deaerated water were placed into a 50 mL round-bottomed flask and stirred at room temperature until complete dissolution of the starting material. ^{1}H NMR spectrum of the sample diluted with D$_2$O recorded after 20 min showed complete conversion of **2** into (dpms)PtPh(OH$_2$) and 1 equiv. of methanol. The mixture was evaporated to dryness, and the resulting solid was dried under vacuum for 8 h. Yield: 19 mg, 97%. White solid, oxidizes in air, poorly soluble in water.

^{1}H NMR (D$_2$O, 22 °C) δ: 6.08 (s, 1H), 6.98–7.12 (m, 4H), 7.23 (d, *J* = 7.5 Hz, 2H), 7.63 (ddd, *J* = 7.7, 5.5, 1.3 Hz, 1H), 7.77 (dd, *J* = 7.7, 1.5 Hz, 1H), 7.89 (d, *J* = 7.9 Hz, 1H), 8.01 (td, *J* = 7.7, 1.6 Hz, 1H), 8.10 (td, *J* = 7.7, 1.5 Hz, 1H), 8.31 (dd, *J* = 6.0, 1.5 Hz, 1H), 8.74 (vd, *J* = 5.5 Hz, 1H). ^{13}C spectrum of (dpms)PtPh(OH$_2$) could not be obtained due to its low solubility in water. ESI of aqueous solution, acidified with HBF$_4$, *m*/*z* 540.1. Calculated for (dpms)PtPh(OH$_2$)·H$^+$, $C_{17}H_{17}N_2O_4{}^{195}$PtS: 540.1.

Preparation of (dpms)Pt^{II}Ph(NH$_2$Ph) (4)

(dpms)PtPh(MeOH) (65 mg, 117 μmol) was placed into a 10 mL vial equipped with a stirring bar. Deaerated methanol (2 mL) and 185 mg of aniline (2 mmol, 17 equiv.) were added, and a white suspension was stirred at RT. (dpms)PtPh(MeOH) dissolved after 10 min, and the target complex (dpms)PtPh(NH$_2$Ph) formed as large crystals. The reaction mixture was placed into a freezer at –20 °C for 4 h. White precipitate of **4** was filtered off, washed with 0.5 mL of cold methanol, and dried under vacuum for 12 h. Yield: 60 mg (97.6 μmol), 83%. White solid, poorly soluble in methanol and water.

IR (KBr) ν: 3494 (w, br), 3056 (w), 2828 (w), 1603 (w), 1573 (w), 1494 (w), 1436 (w), 1252 (m), 1222 (m) 1166 (m), 1031 (s), 757 (m), 686 (m) cm^{-1}. ^{1}H NMR (D$_2$O, 22 °C) δ: 6.00 (s, 1H), 6.94–7.00 (m, 1H), 7.01–7.16 (m, 6H), 7.20–7.27 (m, 3H), 7.31 (d, *J* = 7.1 Hz, $^3J_{PtH}$ = 40 Hz, 2H), 7.77 (vd, *J* = 7.8 Hz, 2H), 7.89 (td, *J* = 7.8, 1.4 Hz, 1H), 7.98 (td, *J* = 7.8, 1.6 Hz, 1H), 8.34 (dd, *J* = 6.0, 1.4 Hz, 1H), 8.43 (dd, *J* = 5.6, 1.6 Hz, 1H). ^{13}C spectrum of (dpms)PtPh(MeOH) could not be obtained due to its low solubility. ESI of solution in MeOH/H$_2$O (1:1 *v*/*v*), *m*/*z* 615.1. Calculated for (dpms)PtPh(NH$_2$Ph)·H$^+$, $C_{23}H_{22}N_3O_3{}^{195}$PtS: 615.1. Anal. found: C, 44.63; H, 3.27; N, 6.61. Calcd. for $C_{23}H_{21}N_3O_3$PtS: C, 44.95; H, 3.44; N, 6.84.

Preparation of (dpms)Pt^{II}Ph(dmso) (5)

(dpms)PtPh(MeOH) (55.6 mg, 100 μmol) and 5 mL of dry degassed DMSO were placed into a 25 mL Schlenk tube under an argon atmosphere. The reaction mixture was stirred for 1 h at RT to produce a clear solution. The solvent was removed by vacuum distillation. The resulting solid was washed with cold methanol and ether and dried under vacuum for 24 h at 65 °C. Yield: 51.1 mg, 85%. White solid, soluble in methanol and DMSO. The complex is stable in MeOH solutions at RT for several days; ligand exchange occurs in DMSO-d_6 solutions to give (dpms)PtPh(DMSO-d_6) ($\tau_{1/2}$ = 1.2 h at RT).

IR (KBr) ν: 3048 (w), 2924 (w), 1606 (w), 1574 (w), 1483 (w), 1435 (w), 1231 (m), 1167 (m), 1131 (m), 1031 (s), 765 (m), 685 (m) cm^{-1}. The ν(S=O) band of S-coordinated dimethylsulfoxide at 1131 cm^{-1} is missing in IR spectra of other Pt^{II} sulfonate complexes reported here. The frequency is typical for Me$_2$SO ligand coordinated to a metal through the sulfur atom (11) and similar to S=O frequency of (dpms)Pt(dmso)(OH) (1127 cm^{-1}) (6).

^{1}H NMR (CD$_3$OD, 22 °C) δ: 3.07 (s, $^3J_{195PtH}$ = 36 Hz, 3H), 3.19 (s, $^3J_{195PtH}$ = 30 Hz, 3H), 6.17 (s, 1H), 6.90 (td, *J* = 7.3, 1.3 Hz, 1H), 7.01 (t, *J* = 7.3, 1.3 Hz, 1H), 7.17–7.27 (m, 2H), 7.39 (d, *J* = 7.3, $^3J_{195PtH}$ = 40 Hz, 1H), 7.58 (ddd, *J* = 7.9, 5.5, 1.3 Hz, 1H), 7.70 (d, *J* = 7.3 Hz, $^3J_{195PtH}$ = 35 Hz, 1H), 7.95 (d, *J* = 7.9 Hz, 1H), 7.98 (d, *J* = 7.9 Hz, 1H), 8.04 (td, *J* = 7.9, 1.5 Hz, 1H), 8.12 (td, *J* = 7.9, 1.5 Hz, 1H), 8.30 (dd, *J* = 5.5, 1.5 Hz, $^3J_{195PtH}$ = 55 Hz, 1H), 9.11 (dd, *J* = 5.5, 1.5 Hz, $^3J_{195PtH}$ = 23 Hz, 1H). ^{1}H NMR (DMSO-d_6, 22 °C) δ: 3.06 (s, $^3J_{195PtH}$ = 30 Hz, 3H), 3.09 (s, $^3J_{195PtH}$ = 30 Hz, 3H), 6.20 (s, 1H), 6.86 (td, *J* = 7.4, 1.5 Hz, 1H), 6.97 (t, *J* = 7.4, 1H), 7.16 (td, *J* = 7.4, 1.5 Hz, 1H), 7.28 (ddd, *J* = 7.9, 5.5, 1.1 Hz, 1H), 7.35 (d, *J* = 7.4, $^3J_{195PtH}$ = 30 Hz, 1H), 7.58 (ddd, *J* = 7.9, 5.5, 1.1 Hz, 1H), 7.62 (d, *J* = 7.4, $^3J_{195PtH}$ = 30 Hz, 1H), 7.90 (d, *J* = 7.9 Hz, 1H), 7.93 (d, *J* = 7.9 Hz, 1H), 8.06 (td, *J* = 7.9, 1.4 Hz, 1H), 8.10–8.17 (m, 2H), 8.98 (dd, *J* = 5.5, 1.4 Hz, 1H). ^{13}C NMR (DMSO-d_6, 22 °C) δ: 43.8 (CH$_3$), 44.4 (CH$_3$), 75.4, 124.1, 124.4, 127.3, 128.1 (Cq), 128.2, 129.3, 136.3, 137.3, 140.1,

© 2008 NRC Canada

140.8, 151.5, 152.5 (Cq), 153.2, 154.0 (Cq). Carbon assignments were made from DEPT experiments. ESI of solution in methanol acidified with HBF_4, *m/z* 600.1. Calculated for (dpms)PtPh(Me_2SO)·H^+, $C_{19}H_{21}N_2S_2O_4{}^{195}Pt$: 600.1. (dpms)PtPh(DMSO-d_6): ESI of solution in methanol acidified with HBF_4, *m/z* 606.1. Calculated for (dpms)PtPh((CD_3)$_2$SO)·H^+, $C_{19}H_{15}D_6N_2S_2O_4{}^{195}Pt$: 606.1.

Preparation of (dpms)$Pt^{II}Me(NH_2Ph)$ (6)

Solution of (dpms)PtMe(MeOH) (192 μmol) in deaerated methanol (10 mL), prepared from isomeric hydrides (dpms)$PtMe_2H$ (91.4 mg, 192 μmol) (5), was placed in a 50 mL Schlenk tube and combined with distilled aniline (18.1 mg; 194 μmol, 1.01 equiv.). The mixture was stirred at room temperature for 15 min. According to ^{1}H NMR, ligand exchange was complete in 15 min. The reaction mixture was evaporated to dryness; the resulting colourless solid was washed with ether and dried under vacuum for 6 h. Yield: 92.9 mg, 87%. White solid, soluble in methanol and water, slowly oxidizes in air.

^{1}H NMR (D_2O, 22 °C) δ: 0.79 ($^2J_{195PtH}$ = 72 Hz, 3H), 5.91 (s, 1H), 7.05–7.33 (m, 6H), 7.38 (m, 1H), 7.74 (vd, *J* = 7.8 Hz, 2H), 7.88 (vt, *J* = 7.8 Hz, 1H), 8.03 (vt, *J* = 7.8 Hz, 1H), 8.14 (d, *J* = 5.5 Hz, 1H), 8.73 (d, *J* = 5.9 Hz, $^3J_{195PtH}$ = 56 Hz, 1H). ESI-MS of aqueous solution of (dpms)PtMe(NH_2Ph), *m/z* observed: 553.1. Calcd. for (dpms)PtMe(NH_2Ph)·H^+, $C_{18}H_{20}N_3SO_3{}^{195}Pt$: 553.1.

Preparation of *sym*-(dpms)$Pt^{IV}Ph_2OH$ (7) by oxidation of K(dpms)$Pt^{II}Ph_2$ (1) with O_2

K[(dpms)$PtPh_2$] (55.9 mg, 88 μmol) (2) was dissolved in 2 mL of deaerated water and placed into a 10 mL vial equipped with a magnetic stirring bar. The vial was filled with O_2, and the solution was stirred at room temperature for 2 h. No K(dpms)$PtPh_2$ was detected in solution after that time; the solution pH was ~12. White precipitate was filtered off and washed with water until neutral reaction of the filtrate. The product was dried under vacuum for 6 h. Yield: 47.0 mg, 87%. White solid, soluble in dichloromethane and DMSO, insoluble in water.

IR (KBr) ν: 3583 (w, br), 3055 (w), 2981 (w), 1604 (w), 1574 (w), 1472 (w), 1449 (w), 1294 (m), 1203 (w), 1143 (s), 1025 (m), 981 (s), 736 (m), 695 (m) cm^{-1}. ^{1}H NMR (DMSO-d_6, 22 °C) δ: 2.56 (br s, $^2J_{195PtH}$ = 36 Hz, 1H), 6.89 (s, 1H), 6.92–7.04 (m, 6H), 7.34 (dd, *J* = 8.0, 1.7 Hz, $^3J_{195PtH}$ = 30 Hz, 4H), 7.65 (ddd, *J* = 7.8, 5.5, 1.2 Hz, 2H), 8.08 (d, *J* = 7.8 Hz, 2H), 8.23 (td, *J* = 7.8, 1.5 Hz, 2H), 8.30 (dd, *J* = 5.5, 1.5 Hz, 2H). ^{13}C NMR (DMSO-d_6, 22 °C) δ: 70.7, 124.9, 125.9, 126.4 (Cq), 126.5, 127.3, 130.9, 141.8, 149.6, 151.4 (Cq). Quaternary carbon assignments are from DEPT experiment. ESI of solution in MeOH/CH_2Cl_2 (1:1 *v/v*) acidified with HBF_4, *m/z* 616.1. Calculated for (dpms)$PtPh_2$(OH)·H^+, $C_{23}H_{21}N_2SO_4{}^{195}Pt$: 616.1. Anal. found: C, 44.81; H, 3.45; N, 4.24. Calcd. for $C_{23}H_{20}N_2O_4PtS$: C, 44.88; H, 3.27; N, 4.55.

Preparation of *unsym*-(dpms)$Pt^{IV}Ph(OH)_2$ (8) by oxidation of (dpms)$Pt^{II}Ph(OH_2)$ with O_2

(dpms)PtPh(MeOH) (99.1 mg, 179 μmol) and 100 mL of deaerated water were placed into 250 mL round-bottomed flask. This suspension was stirred for 30 min under argon. Resulting clear solution was stirred under O_2 at room temperature. After 48 h, the solution was reduced in volume to 1 mL under vacuum. Resulting suspension was left at 5 °C for 1 h. White precipitate was filtered off, washed with 0.5 mL of cold water, and dried under vacuum for 8 h. Yield: 92.3 mg, 93%. White solid, very soluble in water, methanol, and DMSO.

IR (KBr) ν: 3548 (w, br), 3070 (w), 2928 (w), 1607 (w), 1574 (w), 1481 (w), 1445 (w), 1301 (m), 1210 (w), 1142 (s), 1027 (w), 966 (s), 737 (m), 698 (s) cm^{-1}. ^{1}H NMR (DMSO-d_6, 22 °C) δ: 1.45 (br s, 1H), 2.99 (br s, $^2J_{195PtH}$ = 30 Hz, 1H), 6.93 (s. 1H), 7.03–7.23 (m, 5H), 7.60 (ddd, *J* = 7.8, 5.5, 1.3 Hz, 1H), 7.88–8.00 (m, 2H), 8.06 (dd, *J* = 7.8, 1.3 Hz, 1H), 8.09 (d, *J* = 7.8 Hz, 1H), 8.26 (td, *J* = 7.8, 1.5 Hz, 1H), 8.33 (td, *J* = 7.8, 1.5 Hz, 1H), 8.96 (dd, *J* = 5.5, 1.5 Hz, 1H). ^{1}H NMR (D_2O, 22 °C) δ: 6.84 (s, 1H), 7.03 (d, *J* = 8.0 Hz, $^3J_{195PtH}$ = 20 Hz, 2H), 7.22–7.35 (m, 3H), 7.58 (ddd, *J* = 7.9, 5.9, 1.3 Hz, 1H), 7.97 (ddd, *J* = 7.9, 5.5, 1.2 Hz, 1H), 8.03 (dd, *J* = 5.9, 1.4 Hz, 1H), 8.10 (dd, *J* = 7.9, 1.3 Hz, 1H), 8.16 (d, *J* = 7.9 Hz, 1H), 8.29 (td, *J* = 7.9, 1.4 Hz, 1H), 8.35 (td, *J* = 7.9, 1.4 Hz, 1H), 8.95 (dd, *J* = 5.5, 1.4 Hz, 1H). ^{13}C NMR (DMSO-d_6, 22 °C) δ: 70.7, 125.6, 126.2, 126.5, 126.8, 127.1, 127.3 (Cq), 127.6, 132.2, 141.9, 142.7, 148.3, 149.5 (Cq), 151.1, 152.7 (Cq). Quaternary carbon assignments are from DEPT experiment. ESI of solution in MeOH/H_2O (1:1 *v/v*) acidified with HBF_4, *m/z* 556.1. Calculated for (dpms)PtPh(OH)$_2$·H^+, $C_{17}H_{17}N_2SO_5{}^{195}Pt$: 556.1. Anal. found: C, 36.48; H, 3.29; N, 4.74. Calcd. for $C_{17}H_{16}N_2O_5PtS$: C, 36.76; H, 2.90; N, 5.04.

Preparation of (dpms)$Pt^{IV}Ph(OMe)(OH)$ (9) by oxidation of (dpms)$Pt^{II}Ph$(MeOH) with O_2

(dpms)PtPh(MeOH) (98.2 mg, 177 μmol) in 75 mL of dry methanol was placed into a 250 mL round-bottomed flask equipped with a magnetic stirring bar. The flask was filled with O_2, and the reaction mixture was stirred vigorously at RT. After 40 h, the clear solution was reduced in volume to ~0.3 mL under vacuum. Resulting suspension was left at –20 °C for 1 h. White precipitate was filtered off, washed with small amount of cold methanol, and dried under vacuum for 12 h. Yield: 91.8 mg, 91%. White solid, soluble in methanol and DMSO.

IR (KBr) ν: 3318 (w, br), 3031 (w), 2976 (w), 2817 (w), 1606 (w), 1573 (w), 1483 (w), 1446 (w), 1298 (s), 1210 (m), 1147 (s), 1027 (m), 974 (s), 742 (s), 696 (s) cm^{-1}. ^{1}H NMR (DMSO-d_6, 22 °C) δ: 2.52 (br s, 1H), 2.94 (s, $^3J_{195PtH}$ = 33 Hz, 3H), 6.95 (s, 1H), 7.04–7.31 (m, 5H), 7.60 (ddd, *J* = 7.9, 5.8, 1.5 Hz, 1H), 7.92 (dd, *J* = 5.8, 1.5 Hz, 1H), 7.96 (ddd, *J* = 7.9, 5.5, 1.2 Hz, 1H), 8.07 (dd, *J* = 7.9, 1.2 Hz, 1H), 8.09 (d, *J* = 7.9 Hz, 1H), 8.27 (td, *J* = 7.9, 1.5 Hz, 1H), 8.34 (td, *J* = 7.9, 1.5 Hz, 1H), 8.95 (dd, *J* = 5.5, 1.5 Hz, 1H). ^{1}H NMR (CD_3OD, 22 °C) δ: 2.66 (s, $^3J_{195PtH}$ = 27 Hz, 3H), 6.67 (s, 1H), 7.10–7.28 (m, 5H), 7.53 (ddd, *J* = 7.8, 5.5, 1.5 Hz, 1H), 7.92 (ddd, *J* = 7.8, 5.5, 1.2 Hz, 1H), 8.02–8.14 (m, 3H), 8.24 (td, *J* = 7.8, 1.5 Hz, 1H), 8.30 (td, *J* = 7.8, 1.5 Hz, 1H), 9.01 (dd, *J* = 5.5, 1.5 Hz, 1H). ^{13}C NMR (DMSO-d_6, 22 °C) δ: 57.3 (CH_3), 70.7, 125.6, 126.1, 126.3, 126.7, 127.0, 127.8, 129.3 (Cq), 131.4, 141.9, 142.7, 148.0, 149.6 (Cq), 151.5, 152.4 (Cq). Assignments of carbon peaks are made from DEPT experiments. ESI of solution in MeOH acidified with HBF_4, *m/z* 570.1. Calculated for

© 2008 NRC Canada

(dpms)PtPh(OCH_3)(OH)·H^+, $C_{18}H_{19}N_2SO_5{}^{195}Pt$: 570.1. Anal. found: C, 37.79; H, 3.41; N, 4.77. Calcd. for $C_{18}H_{18}N_2O_5PtS$: C, 37.96; H, 3.19; N, 4.92.

Attempted oxidation of (dpms)Pt^{II}Ph(NH_2Ph) (4) and (dpms)Pt^{II}Ph(dmso) (5) with O_2

Solution of (dpms)PtPh(NH_2Ph) (2 mg, 3 μmol) in 2 mL of CD_3OD was placed into a 10 mL round-bottomed flask equipped with a magnetic stirring bar. The flask was filled with oxygen, and the solution was stirred vigorously at room temperature. According to ^{1}H NMR, the starting material remained unchanged after 7 days. No traces of (dpms)Pt^{IV}Ph(NHPh)(OH) or other products were detected in the solution by ESI-MS; no precipitate formed.

An analogous procedure was used for attempted oxidation of (dpms)PtPh(dmso) (2 mg, 3 μmol) in CD_3OD (1 mL) with O_2. According to ^{1}H NMR, after 7 days of stirring under O_2 at RT, only starting material (dpms)Pt^{II}Ph(dmso) was present in solution; no other products were detected in the amounts exceeding 2%; no precipitate formed.

Preparation of (dpms)Pt^{IV}Ph(NHPh)(OH) (10)

(dpms)PtPh(NH_2Ph) (53.8 mg, 87.5 μmol) and 2 mL of MeOH were placed into a 10 mL vial equipped with a stirring bar, and 25 μL of 30% aq. H_2O_2 were added slowly upon stirring. Stirring continued for 1 h at RT. Solid (dpms)PtPh(NH_2Ph) dissolved, and reddish solution formed. The yield of **10** is quantitative according to ^{1}H NMR spectroscopy. Ether (2 mL) was slowly added to the solution, and the resulting mixture was stored for 1 day at RT. Crystalline precipitate of (dpms)PtPh(NHPh)(OH) was filtered off, washed with ether and pentane; yield: 36 mg. An additional fraction of the product was obtained by evaporation of the filtrate. Dry solid was washed with water (10 mL), ether (5 mL), and pentane (5 mL) and dried under vacuum for 10 h; yield: 13.9 mg. Combined yield: 50 mg (79 μmol), 90%.

IR (KBr) ν: 3555 (w, br), 3050 (w), 2970 (w), 1592 (w), 1574 (w), 1489 (w), 1298 (m), 1207 (w), 1145 (s), 1026 (m), 980 (s), 760 (s), 695 (s) cm^{-1}. ^{1}H NMR (DMSO-d_6, 22 °C) δ: 3.01 (br s, 1H), 4.36 (br s, 1H), 6.28–6.40 (m, 1H), 6.44–6.70 (m, 4H), 6.95 (s, 1H), 6.97–7.06 (m, 3H), 7.07–7.27 (m, 2H), 7.59 (ddd, J = 7.8, 5.5, 1.1 Hz, 1H), 7.78–7.84 (m, 1H), 7.97 (d, J = 5.5 Hz, 1H), 8.08 (d, J = 7.8 Hz, 1H), 8.10 (d, J = 7.8 Hz, 1H), 8.25 (td, J = 7.8, 1.3 Hz, 1H), 8.29 (td, J = 7.8, 1.3 Hz, 1H), 8.90 (d, J = 4.3 Hz, 1H). ^{1}H NMR (CD_3OD, 22 °C) δ: 6.57 (s, 1H), 6.65–6.79 (m, 3H), 6.92 (d, J = 7.8 Hz, 2H), 7.02–7.13 (m, 3H), 7.19 (dd, J = 7.7, 1.9 Hz, $^3J_{195PtH}$ = 23 Hz, 2H), 7.45–7.54 (m, 2H), 8.03 (d, J = 7.8 Hz, 1H), 8.04 (d, J = 7.6 Hz, 1H), 8.08 (d, J = 5.8 Hz, 1H), 8.13 (td, J = 7.8, 1.5 Hz, 1H), 8.17 (td, J = 7.6, 1.5 Hz, 1H), 8.60 (d, J = 5.6 Hz, 1H). ^{13}C NMR (DMSO-d_6, 22 °C) δ: 70.4, 115.6, 118.7, 125.4, 125.8, 126.3, 126.8, 127.2, 127.7, 127.8, 128.2 (Cq), 131.6, 141.8, 142.6, 149.0, 150.0 (Cq), 150.9, 152.1 (Cq), 155.4 (Cq). Quaternary carbon assignments were made based on DEPT experiment. ESI of solution in methanol, m/z 631.1. Calculated for (dpms)PtPh(NHPh)(OH)·H^+, $C_{23}H_{22}N_3O_4{}^{195}PtS$: 631.1. Anal. found: C, 43.52; H, 3.26; N, 6.33. Calcd. for $C_{23}H_{21}N_3O_4PtS$: C, 43.81; H, 3.36; N, 6.66.

Preparation of (dpms)Pt^{IV}Me(NHPh)(OH) (11)

Distilled aniline (33.3 mg, 358 μmol, 1.2 equiv.) was added to a solution of (dpms)PtMe(MeOH) prepared from 140.1 mg (295 μmol) isomeric hydrides (dpms)$PtMe_2H$ and 15 mL MeOH (5). According to ^{1}H NMR, the ligand exchange was complete in 15 min to give (dpms)PtMe(NH_2Ph), which was used in the next step without isolation. The mixture was placed into an ice bath; 35 mg of 30% H_2O_2 (~308 μmol) were slowly added to the stirred reaction mixture. Mixture turned yellow immediately after addition of H_2O_2. According to ^{1}H NMR, oxidation was complete in less than 15 min to give (dpms)PtMe(NHPh)(OH) quantitatively. The resulting solution was reduced in volume to 2 mL; the product was precipitated with 6 mL of ether, filtered off, and dried under vacuum for 3 h. Yield: 106.2 mg, 63%. The product is soluble in methanol, DMSO, and water; aqueous solutions have weakly basic reaction (pH ~9).

IR (KBr) ν: 3548 (w, br), 3087 (w), 2973 (w), 1592 (w), 1489 (w), 1448 (w), 1296 (m), 1212 (m), 1154 (s), 980 (m), 750 (m), 688 (m) cm^{-1}. ^{1}H NMR (DMSO-d_6, 22 °C) δ: 2.22 (br s, 1H), 4.17 (br s, 1H), 6.40–6.87 (m, 5H), 7.26 (s, 1H), 7.68–7.77 (m, 1H), 7.80 (ddd, J = 7.9, 5.7, 1.2 Hz, 1H), 8.02 (d, J = 7.9 Hz, 1H), 8.06 (d, J = 7.9 Hz, 1H), 8.23 (td, J = 7.9, 1.9 Hz, 1H), 8.30 (td, J = 7.9, 1.2 Hz, 1H), 8.63 (dd, J = 5.7, 1.2 Hz, 1H), 8.67–8.77 (m, 1H). ^{1}H NMR (CD_3OD, 22 °C) δ: 2.19 ($^2J_{195PtH}$ = 68 Hz, 3H), 6.49 (s, 1H), 6.82 (m, 1H), 6.90 (m, 2H), 7.07 (d, J = 7.7 Hz, 2H), 7.41 (ddd, J = 7.7, 5.8, 1.1 Hz, 1H), 7.77 (ddd, J = 8.0, 5.8, 1.2 Hz, 1H), 7.96 (d, J = 7.7 Hz, 1H), 8.02 (d, J = 7.7 Hz, 1H), 8.07 (td, J = 7.7, 1.5 Hz, 1H), 8.23 (td, J = 7.7, 1.5 Hz, 1H), 8.33 (d, J = 5.8 Hz, 1H), 8.67 (d, J = 5.8 Hz, 1H). ^{13}C NMR (DMSO-d_6, 22 °C) δ: 2.2 ($^1J_{195PtC}$ = 606 Hz), 70.4, 116.0, 119.4, 125.8, 126.7, 126.9, 128.0, 128.2, 141.5, 142.4, 148.3, 149.7, 150.0, 152.2, 155.8. ESI-MS of aqueous solution of (dpms)PtMe(NHPh)(OH), m/z observed: 569.1. Calcd. for (dpms)PtMe(NHPh)(OH)·H^+, $C_{18}H_{20}N_3SO_4{}^{195}Pt$: 569.1. Anal. found: H, 3.24; C, 38.18; N, 6.97; S, 5.50. Calcd. for $C_{18}H_{19}O_4N_3PtS$, H, 3.37; C, 38.03; N, 7.39; S, 5.64.

Oxidation of (dpms)Pt^{II}Me(NH_2Ph) (6) with O_2

(dpms)Pt^{II}Me($PhNH_2$) (40 mg, 72 μmol) and 10 mL of water were placed into a 50 mL round-bottomed flask equipped with a magnetic stirring bar. The flask was filled with O_2, and the solution was stirred vigorously under O_2 atmosphere at room temperature. According to ^{1}H NMR spectroscopy, slow oxidation occurred to give (dpms)PtMe(NHPh)(OH) as the only Pt^{IV} product. The reaction half-life is ~30 h at RT. Signals corresponding to protonated starting material (m/z 553.1) and oxidation product (dpms)Pt^{IV}Me(NHPh)(OH) (m/z 569.1) were detected by ESI-MS.

Isomerization of unsym-(*dpms*)Pt^{IV}Ph$(OH)_2$ (unsym-8) into sym-(dpms)Pt^{IV}Ph$(OH)_2$ (sym-8)

Solution of *unsym*-(dpms)PtPh$(OH)_2$ (103 mg, 180 μmol) in water (30 mL) was placed into a 50 mL round-bottomed flask equipped with a magnetic stirring bar and a condenser. The mixture was heated at 100 °C. After 70 h, the reaction mixture was reduced in volume to ~1 mL under vacuum and

© 2008 NRC Canada

Table 1. X-ray data for the complexes **4** and **11**.

Compound	**4**	**11**
Formula	$C_{23}H_{21}N_3O_3PtS{\cdot}2CH_3OH$	$C_{18}H_{19}N_3O_4PtS$
FW	678.66	568.51
Crystal system	Monoclinic	Monoclinic
Space group	*P2/n*	$P2_1/c$
a (Å)	9.9681(6)	8.530(2)
b (Å)	8.7798(5)	11.102(3)
c (Å)	28.8445(16)	19.457(5)
α (°)	90	90
β (°)	90.6590(10)	90.916(4)
γ (°)	90	90
Volume (Å^3)	2524.2(3)	1842.4(8)
Z	4	4
$D_{(calcd.)}$ (Mg/m^3)	1.786	2.050
Abs. coeff. (mm^{-1})	5.682	7.759
F(000)	1336	1096
No. of reflns./ind.reflns.	47802/5791	22924/4408
Abs. corr.	Semi-empirical	Semi-empirical
No. of data/restr./params.	5791/31/336	4408/1/267
R1, wR^2 (I > 2σ(I))	0.0244, 0.0583	0.0231, 0.0588

left at 5 °C for 1 h. White precipitate was filtered off and dried under vacuum for 6 h. Yield: 94 mg, 91%.

IR (KBr) ν: 3500 (w, br), 3062 (w), 2964 (w), 1607 (w), 1574 (w), 1475 (w), 1441 (w), 1267 (m), 1205 (m), 1146 (s), 996 (m), 736 (m), 691 (m) cm^{-1}. ^{1}H NMR (DMSO-d_6, 22 °C) δ: 2.32 (br s, $^2J_{195PtH}$ = 26 Hz, 2H), 6.38 (d, *J* = 7.3 Hz, $^3J_{195PtH}$ = 35 Hz, 2H), 6.74 (s, 1H), 6.87 (vt, *J* = 7.3 Hz, 2H), 7.04 (vt, *J* = 7.3 Hz, 1H), 7.65 (ddd, *J* = 7.8, 5.8, 1.3 Hz, 2H), 8.06 (d, *J* = 5.8 Hz, 2H), 8.08 (d, *J* = 7.8 Hz, 2H), 8.31 (td, *J* = 7.8, 1.3 Hz, 2H). ^{1}H NMR (D_2O, 22 °C) δ: 6.72 (s, 1H), 6.85–7.22 (m, 4H), 7.26 (vt, *J* = 7.3 Hz, 1H), 7.63 (ddd, *J* = 8.0, 5.9, 1.3 Hz, 2H), 8.09 (dd, *J* = 5.9, 1.4 Hz, 2H), 8.14 (dd, *J* = 8.0, 1.3 Hz, 2H), 8.33 (td, *J* = 8.0, 1.4 Hz, 2H). ^{13}C NMR (DMSO-d_6, 22 °C) δ: 72.1, 125.9, 126.3, 127.2, 127.4, 128.0, 132.5, 142.3, 149.8, 150.9.

Attempted reductive elimination from *sym*-(dpms)Pt^{IV}Ph$_2$(OH) (*sym*-7) in DMSO-d_6 solution

A sample of *sym*-(dpms)PtPh$_2$(OH) (2 mg, 3.2 μmol) was dissolved in dry DMSO-d_6 (0.7 mL), and solution was placed into an NMR Young tube under an argon atmosphere. The Young tube was heated at 100 °C in a silicon-oil bath. The only reaction observed was isomerization of **7** into corresponding unsymmetrical isomer (half-life is 26 h). After 6 days, the isomerization was complete, yield of *unsym*-**7** > 97% by ^{1}H NMR spectroscopy. No biphenyl or phenol were detected.

^{1}H NMR (DMSO-d_6, 22 °C) δ: 1.37 (br s, 1H), 6.65 (d, *J* = 8.2 Hz, $^3J_{195PtH}$ = 44 Hz, 2H), 6.78 (s, 1H), 6.88–7.12 (m, 6H), 7.20–7.39 (m, 2H), 7.59 (ddd, *J* = 7.9, 5.9, 1.5 Hz, 1H), 7.65 (ddd, *J* = 7.9, 5.7, 1.3 Hz, 1H), 8.00 (dd, *J* = 5.7, 1.5 Hz, 1H), 8.08 (d, *J* = 7.9 Hz, 1H), 8.14 (dd, *J* = 7.9, 1.5 Hz, 1H), 8.20 (dd, *J* = 5.9, 1.5 Hz, 1H), 8.25 (td, *J* = 7.9, 1.5 Hz, 1H), 8.34 (td, *J* = 7.9, 1.5 Hz, 1H). ^{13}C NMR (DMSO-d_6, 22 °C), δ: 71.9, 124.3, 125.1, 125.5, 125.8, 126.9, 127.1, 127.3, 127.4, 128.4, 128.7, 132.7, 133.8, 141.6, 142.6, 148.7, 150.3, 152.7, 152.9.

Attempted reductive elimination from *sym*-(dpms)Pt^{IV}Ph(OH)$_2$ (*sym*-8)

Four samples of *sym*-(dpms)PtPh(OH)$_2$ (2.5 mg each, 4.5 μmol) were dissolved in neutral D_2O (0.8 mL), 50 mmol/L solution of HBF_4 in D_2O (0.8 mL), 11 mmol/L NaOD/D_2O solution (0.8 mL), and DMSO-d_6 (0.8 mL) under argon. The solutions were placed into NMR Young tubes and Teflon-sealed. Residual solvent peaks were used as internal standards. The solutions were heated at 100 °C. According to ^{1}H NMR spectroscopy, concentration of *sym*-(dpms)PtPh(OH)$_2$ remained unchanged after 5 days; no products were detected by ^{1}H NMR.

Attempted reductive elimination from (dpms)Pt^{IV}Ph(OH)(OMe) (9)

Reaction in DMSO-d_6

A sample of (dpms)PtPh(OMe)(OH) (2 mg, 3.5 μmol) was dissolved in 0.7 mL of DMSO-d_6. The solution was placed into an NMR Young tube and Teflon-sealed under argon. The solution was heated at 80–100 °C, periodically cooled down to room temperature and analyzed by ^{1}H NMR. Slow reaction occurred at 80 °C with a half-life of ~47 h. The reaction continued at 100 °C with a half-life of 4.5 h; quantitative formation of only one platinum-containing product, (dpms)PtPh(DMSO-d_6), was observed. ^{1}H NMR of the product was identical to that of (dpms)PtPh(DMSO-d_6) obtained by dissolving (dpms)Pt(MeOH) in DMSO-d_6; ESI of acidified solution diluted with methanol showed the presence of a signal with *m/z* = 606.1 (calcd. For (dpms)PtPh(C_2D_6SO)H$^+$, $C_{19}H_{15}D_6N_2S_2O_4{}^{195}$Pt, *m/z* 606.1). One equivalent of methanol was released into solution, according to ^{1}H NMR spectroscopy.

Reactions in DMF-d_7 *and* CD_3CN

Analogous procedure was applied to reactions in DMF-d_7 and CD_3CN as solvents. NMR Young tubes with the samples were heated at 100 °C and periodically monitored by ^{1}H

© 2008 NRC Canada

NMR. Formation of a complex mixture of unidentified products was evident by ^{1}H NMR spectroscopy.

Attempted reductive elimination from (dpms)Pt^{IV}Ph(NHPh)(OH) (10)

Reaction in CD_3CN

A sample of (dpms)PtPh(NHPh)(OH) (3 mg, 5 μmol) and 0.7 mL of CD_3CN were placed into an NMR Young tube and Teflon-sealed under argon. The reaction mixture was heated at 80 °C for 5 h; dark precipitate and dark-coloured solution formed. The only product present in the solution after 5 h was (dpms)PtPh(CD_3CN), according to ^{1}H NMR spectroscopy and ESI-MS. Characteristics of the product are identical to those of (dpms)PtPh(CD_3CN) obtained by dissolving (dpms)PtPh(MeOH) in CD_3CN.

^{1}H NMR (CD_3CN, 22 °C) δ: 5.82 (s, 1H), 6.92–7.03 (m, 4H), 7.24 (dd, J = 7.5, 1.5 Hz, $^3J_{195PtH}$ = 45 Hz, 2H), 7.52 (ddd, J = 7.9, 5.5, 1.5 Hz, 1H), 7.74 (dd, J = 7.9, 1.5 Hz, 1H), 7.85 (d, J = 7.9 Hz, 1H), 7.97 (td, J = 7.9, 1.5 Hz, 1H), 8.07 (td, J = 7.9, 1.5 Hz, 1H), 8.15 (dd, J = 5.7, 1.5 Hz, $^3J_{195PtH}$ = 63 Hz, 1H), 8.85 (dd, J = 5.5, 1.5 Hz, 1H). ESI of acidified solution diluted with methanol exhibited only one peak, m/z 566.1 (Calcd. for (dpms)^{195}PtPh(CD_3CN)H$^+$, $C_{19}H_{15}D_3N_3O_3{}^{195}$PtS: 566.1).

The precipitate formed in the reaction mixture was dissolved in DMSO-d_6; ^{1}H NMR spectrum of the resulting solution showed the presence of a complex mixture of unidentified products. No diphenylamine was detected by ^{1}H NMR.

Reaction in DMF-$\mathbf{d_7}$

Upon heating at 60 °C, the starting material slowly disappeared, and an insoluble product formed. After heating the sample at 80 °C for 24 h, complex mixture of product formed in DMF-d_7 solution and a dark precipitate.

X-ray structure determinations

The X-ray intensity data were measured at 220(2) K (0 K = 273.15 °C) on a three-circle diffractometer system equipped with Bruker Smart1000 CCD area detector using a graphite monochromator and a Mo Kα fine-focus sealed tube (λ = 0.71073 Å) operated at 50 kV and 40 mA. Details of the data collections and structure refinements are given in Table 1. Supplementary information for this article is available on the Web.[4]

Acknowledgements

We thank the University of Maryland, the Donors of the American Chemical Society Petroleum Research Fund (PRF#42307-AC3), and the NSF (CHE-0614798) for the financial support of this work.

References

1. (*a*) T. Punniyamurthy, S. Velusamy, and J. Iqbal. Chem. Rev. **105**, 2329 (2005); (*b*) S.S. Stahl. Angew. Chem., Int. Ed. **43**, 3400 (2004).
2. A.N. Vedernikov, J.C. Fettinger, and F. Mohr. J. Am. Chem. Soc. **126**, 11160 (2004).
3. A.N. Vedernikov, S.A. Binfield, P.Y. Zavalij, and J.R. Khusnutdinova. J. Am. Chem. Soc. **128**, 82 (2006).
4. J.R. Khusnutdinova, P.Y. Zavalij, and A.N. Vedernikov. Organometallics, **26**, 3466 (2007).
5. J.R. Khusnutdinova, P.Y. Zavalij, and A.N. Vedernikov. Organometallics, **26**, 2402 (2007).
6. J.R. Khusnutdinova, L. Newman, P.Y. Zavalij, Y.-F. Lam, and A.N. Vedernikov. J. Am. Chem. Soc. **130**, 2174 (2008).
7. A.E. Shilov and G.B. Shulpin. Chem. Rev. **97**, 2879 (1997).
8. M. Lersch and M. Tilset. Chem. Rev. **105**, 2471 (2005).
9. V.V. Rostovtsev, L.M. Henling, J.A. Labinger, and J.E. Bercaw. Inorg. Chem. **41**, 3608 (2002).
10. (*a*) J.P. Collman, L.S. Hegedus, J.R. Norton, and R.G Finke. Principles and applications of organotransition metal chemistry. University Science Books. Sausalito, CA. 1987; (*b*) B.J. Coe and S.J. Glenwright. Coord. Chem. Rev. **203**, 5 (2000).
11. K. Nakamoto. Infrared and raman spectra of inorganic and coordination compounds. Part II: Applications in coordination, organometallic, and bioinorganic chemistry. 5th Ed. Wiley. New York. 1997.
12. M.B. Smith and J. March. March's advanced organic chemistry: reactions, mechanisms, and structure. 5th Ed. Wiley. New York. 2001.
13. B.S. Williams, A.W. Holland, and K.I. Goldberg. J. Am. Chem. Soc. **121**, 252 (1999).
14. D.M. Crumpton-Bregel and K.I. Goldberg. J. Am. Chem. Soc. **125**, 9442 (2003).
15. G.A. Luinstra, J.A. Labinger, and J. E. Bercaw. J. Am. Chem. Soc. **115**, 3004 (1993).
16. B.S. Williams and K.I. Goldberg. J. Am. Chem. Soc. **123**, 2576 (2001).
17. A. Yahav-Levi, I. Goldberg, A. Vigalok, and A.N. Vedernikov. J. Am. Chem. Soc. **130**, 724 (2008).
18. R.G. Parr and W. Yang. Density functional theory of atoms and molecules. Oxford University Press. Oxford, UK. 1989.
19. J.P. Perdew, K. Burke, and M. Ernzerhof. Phys. Rev. Lett. **77**, 3865 (1996).
20. (*a*) D.N. Laikov. Chem. Phys. Lett. **281**, 151 (1997); (*b*) D.N. Laikov and Yu.A. Ustynyuk. Russ. Chem. Bull. **54**, 820 (2005).
21. (*a*) W.J. Stevens, H. Basch, and M. Krauss. J. Chem. Phys. **81**, 6026 (1984); (*b*) W.J. Stevens, H. Basch, M. Krauss, and P. Jasien. Can. J. Chem. **70**, 612 (1992); (*c*) T.R. Cundari and W.J. Stevens. J. Chem. Phys. **98**, 5555 (1993).

[4] Supplementary data for this article are available on the journal Web site (canjchem.nrc.ca) or may be purchased from the Depository of Unpublished Data, Document Delivery, CISTI, National Research Council Canada, Ottawa, ON K1A 0R6, Canada. DUD 3796. For more information on obtaining material, refer to cisti-icist.nrc-cnrc.gc.ca/irm/unpub_e.shtml. CCDC 683095 and 683096 contain the crystallographic data for this manuscript. These data can be obtained, free of charge, via www.ccdc.cam.ac.uk/conts/retrieving.html (Or from the Cambridge Crystallographic Data Centre, 12 Union Road, Cambridge CB2 1EZ, UK; fax +44 1223 336033; or deposit@ccdc.cam.ac.uk).

© 2008 NRC Canada

The synthesis and X-ray crystal structures of rare earth(III) perfluoroadipate complexes — Novel coordination polymers[1]

Glen B. Deacon, Winfried Elgersma, Rita Harika, Peter C. Junk, Brian W. Skelton, and Allan H. White

Abstract: A representative series of polymeric hydrated lanthanoid perfluoroadipates $[Ln_2(pfad)_3(H_2O)_n]\cdot mH_2O$ (Ln = La, Ce, Nd, Gd, Yb) has been prepared from the reaction of perfluoroadipic acid with either the appropriate lanthanoid oxide or $Ce_2(CO_3)_3$ in water. X-ray crystal structures showed $[Ln_2(pfad)_3(H_2O)_{10}]\cdot 4H_2O$ (La, Nd) to be two-dimensional inorganic polymers, which contain nine-coordinate Ln atoms to which are attached five water molecules and four carboxylate oxygen atoms. Two pfad ligands bridge two Ln atoms through one carboxylate group, the other being free, whilst one pfad ligand bridges four Ln atoms in a μ_4-($\eta^1,\eta^1/\eta^1,\eta^1$) manner. In two-dimensional polymeric $[Yb_2(pfad)_2(H_2O)_8](pfad)\cdot 6H_2O$, each eight-coordinate ytterbium atom has four water ligands and four carboxylate oxygen donor atoms. The two carboxylate ligands bind in a μ_4-($\eta^1,\eta^1/\eta^1,\eta^1$) manner, and there is one pfad counter-ion per two ytterbium atoms. These structures show features quite different from those of many lanthanoid adipate complexes $[Ln_2(ad)_3(H_2O)_n]\cdot mH_2O$, but there is no F-Ln coordination. From the reaction of $[Nd_2(pfad)_3(H_2O)_{10}]\cdot 4H_2O$ with benzene-1,2-disulfonic acid (H_2bds), the mixed ligand complex $[Nd_2(bds)_2(pfad)(H_2O)_8]$ was isolated. This is a one-dimensional polymer featuring $Nd_2(bds)_2$ units linked together by μ-η^2,η^2 pfad ligands. Each Nd atom is nine-coordinate with three sulfonate oxygen donors, two carboxylate oxygen atoms, and four water ligands, and the bds ligands bind in the new μ-$\eta^2(O,O')$,$\eta^1(O'')$ manner for Ln complexes. Surprisingly, $[Na_2pfad]$ was isolated unhydrated from water, the six-coordinate Na atoms being coordinated by four carboxylate oxygen atoms and two (C)-F atoms in an octahedral array. The ligands are duodecadentate, each $-CF_2CO_2$ unit binding to five different sodium ions through four oxygen and one α-F atom with the second α-F atom bound to a sodium ion in a OC(O)CF-Na chelate ring.

Key words: rare earths, lanthanoid, X-ray crystal structures, adipates, carboxylates.

Résumé : On a préparé une série représentative de perfluoroadipates de lanthanoïdes hydratés et polymères $[Ln_2(pfad)_3(H_2O)_n]\cdot mH_2O$ (Ln = La, Ce, Nd, Gd, Yb) en faisant réagir de l'acide perfluoroadipique avec l'oxyde de lanthanoïde approprié ou avec du $Ce_2(CO_3)_3$ dans l'eau. Les structures cristallines déterminées par diffraction des rayons X montrent que les dérivés $[Ln_2(pfad)_3(H_2O)_{10}]\cdot 4H_2O$ (Ln = La, Nd) sont des polymères inorganiques bidimensionnels qui contiennent des atomes de Ln nonacoordinés auxquels sont liés cinq molécules d'eau et quatre atomes d'oxygène provenant du carboxylate. Deux ligands pfad servent de pont entre deux atomes de Ln par le biais d'un groupe carboxylate et l'autre est libre alors qu'un ligand pfad sert de pont à quatre atomes de Ln d'une manière $\mu_4(\eta^1,\eta^1/\eta^1,\eta^1)$. Dans le composé $[Yb_2(pfad)_2(H_2O)_8)\cdot 6H_2O$, chaque atome d'ytterbium octacoordiné est associé à quatre molécules d'eau agissant comme ligands alors que quatre atomes d'oxygène de groupes carboxylates agissent comme donneurs. Les deux ligands carboxylates se lient d'une façon $\mu_4(\eta^1,\eta^1/\eta^1,\eta^1)$ et il y a un contre ion pfad pour deux atomes d'ytterbium. Ces structures présentent des caractéristiques fort différentes de celles observées avec plusieurs complexes de $[Ln_2(ad)_3(H_2O)_n]\cdot mH_2O$, mais on n'observe aucune coordination F-Ln. La réaction du $[Nd_2(pfad)_3(H_2O)_{10}]\cdot 4H_2O$ avec l'acide benzène-1,2-disulfonique (H_2bds) permet d'isoler le complexe $[Nd_2(bds)_2(pfad)(H_2O)_8]$. Ce produit est un polymère unidimensionnel comportant des unités $Nd_2(bds)_2$ liées ensemble par des ligands pfad μ-η^2,η^2. Chaque atome de Nd est nonacoordiné par trois atomes d'oxygène donneurs du sulfonate, deux atomes d'oxygène de carboxylate et

Received 11 April 2008. Accepted 15 May 2008. Published on the NRC Research Press Web site at canjchem.nrc.ca on 16 August 2009.

Dedicated to Professor Richard Puddephatt in recognition of his outstanding contribution to inorganic and organometallic chemistry.

G.B. Deacon,[2] W. Elgersma, R. Harika, and P.C. Junk.[2] Monash University, School of Chemistry, Clayton, Victoria 3800 Australia,
B.W. Skelton and A.H. White. The University of Western Australia, School of Biomedical, Biomolecular and Chemical Sciences, Chemistry M313, Crawley 6009, Western Australia.

[1]This article is part of a Special Issue dedicated to Professor R.J. Puddephatt.

 doi:10.1139/V08-104 © 2008 NRC Canada

quatre ligands d'eau alors que les ligands bds se lient d'une nouvelle façon, μ-η^2(O,O′),η^1(O,O″), D'une façon surprenante, le produit [Na_2pfad] a pu être isolé non hydraté à partir d'une solution aqueuse et les six atomes de sodium sont coordinés d'une façon octaédrique par quatre atomes d'oxygène de carboxylates et deux atomes (C)–F. Les ligands sont des duodécadentate dans lesquels chaque unité $-CF_2CO_2$ se lie à cinq ions sodium différents par le biais de quatre atomes d'oxygène et un atome α de fluor et un deuxième atomes α de fluor qui est lié à un ion sodium dans un noyau chélate de structure OC(=O)CFNa.

Mots-clés : terres rares, lanthanoïde, structures cristallines déterminées par diffraction des rayons X, adipates, carboxylates.

[Traduit par la Rédaction]

Introduction

Carboxylate ions are popular ligands for lanthanoid ions (1–5), as their binding mode versatility makes them suitable to satisfy the high coordination appetite of the large lanthanoid ions (6). Di- and poly-carboxylate ions are common building blocks for the construction of molecular frameworks and coordination polymers (7–9), including those of lanthanoid ions (4, 10). The use of aromatic carboxylates optimizes control in crystal engineering owing to their structural rigidity. Nevertheless, the flexibility of alkanedicarboxylates is an attraction in building rare earth polymeric coordination networks. Thus, adipate (hexanedioate) ions have given rise to a wide range of rare earth polymers (11–22), even based on "simple" hydrated rare earth adipates [$Ln_2(ad)_3(H_2O)_n$]. Thus, the following crystallographically distinct species have been defined: [$Ln_2(ad)_3(H_2O)_4$]·$6H_2O$ (Ln = Pr (12, 14), Nd (12, 14), La (11), Ce (12, 13)), [$Ln_2(ad)_3(H_2O)_4$]·H_2O (Ln = Nd, Sm (12)), [$Ln_2(ad)_3(H_2O)_4$] (Ln = Gd (12), Eu (15), Dy (16)), [$Ln_2(ad)_3(H_2O)_2$]·$4H_2O$·H_2ad (Ln = Nd (17–19), Pr, Ce (13), La (17)), [$Nd_2(ad)_3(H_2O)_2$]·H_2O (14, 20), [$Ln_2(ad)_3(H_2O)_2$] (Ln = Nd (20), Ce (21)), [$Ln_2(ad)_3(H_2O)_2$]·bpy (Ln = Pr (18), Eu (22), bpy = 4,4′-bipyridine), [$Pr_4(ad)_6(H_2O)_4$]·H_2O (18), [$Eu_4(ad)_6(H_2O)_2$]·$2H_2O$ (15). In addition, the complexes [Ln(ad)(H_2O)$_5$]X (Ln = Gd, Er; X = NO_3; Ln = Er, X = Cl (17)) have been isolated, as well as a mixed oxalate–adipate complex (23) and a mixed metal (La–Cu) species (24). The coordination number nine predominates with occasional examples of ten (14, 19–21) and a mixed eight- and nine-coordinate complex (17). Early to mid lanthanoid elements dominate the complexes studied, but nine-coordinate [Er(ad)(H_2O)$_4$]X (X = Cl, NO_3) complexes, a different composition, provide exceptions.

We now report a detailed study of the structures of lanthanoid perfluoroadipates encompassing virtually the whole range of Ln^{3+} sizes, as well as the structure of sodium perfluoroadipate, a metathesis synthon, and a mixed perfluoroadipate–benzene-1,2-disulfonate complex. As perfluoroadipic acid is a much stronger acid than adipic acid, reduced donor properties of the carboxylate groups might be expected and might impinge on coordination polymer formation. In addition, C-F-Ln binding is possible, as has been previously detected for perfluoroalkyl groups (25,26), and it is known that in encapsulation of La^{3+} in a cage with fluoroaromatic, and N and O donors, F–La bonds are shorter than N(O)–La bonds (27).

Results and discussion

Syntheses

Initially studied in this work was the preparation and structural characterization of the sodium salt of perfluoroadipic acid [Na_2(pfad)] (**1**), which was conveniently prepared by the treatment of perfluoroadipic acid with NaOH in ethanol (eq. [1]). Colourless single crystals were obtained upon slow evaporation of the reaction mixture.

$$[1] \quad 2NaOH + H_2pfad \xrightarrow{EtOH} [Na_2(pfad)] + 2H_2O$$

The compound was originally intended as a metathesis reagent for the synthesis of lanthanoid perfluoroadipates, but a more convenient route based on the high acidity of perfluoroadipic acid is now preferred.

Treatment of Ln_2O_3 or $Ce_2(CO_3)_3$ with perfluoroadipic acid in water under reflux conditions led to the formation of complexes of the type $Ln_2(pfad)_3{\cdot}xH_2O$ (Ln = La, (**2**); Ce, (**3**); Nd, (**4**); Gd, (**5**); Yb (**6**)) (eq. [2]). Single crystals of the complexes [$Ln_2(pfad)_3(H_2O)_{10}$]·$4H_2O$ (Ln = La, (**2**); Nd, (**4**)) and [$Yb_2(pfad)_2(H_2O)_8$](pfad)·$6H_2O$ (Ln = Yb, (**6**)) were obtained upon cooling of the reaction mixture, and their structures were characterized by X-ray crystallography (see below).

$$[2] \quad Ln_2O_3 + 3H_2pfad \xrightarrow{H_2O} [Ln_2(pfad)_3(H_2O)_x]{\cdot}yH_2O + 3H_2O$$

Single crystals of [$Nd_2(bds)_2(pfad)(H_2O)_8$] (**7**) were obtained by a fortuitous synthesis from the treatment of Nd_2O_3 (contaminated with H_2pfad) with benzene-1,2-disulfonic acid (H_2bds). A deliberate synthesis of **7** was possible by the reaction of $Nd_2(pfad)_3$ with a stoichiometric amount of H_2bds (28) (eq. [3]). The reaction of $Nd_2(bds)_3$ (28) with H_2pfad did not yield **7**. These preparative observations suggest that the disulfonic acid is a stronger acid than perfluoroadipic acid.

$$[3] \quad Nd_2(pfad)_3 + 2H_2bds + 8H_2O \rightarrow [Nd_2(bds)_2(pfad)(H_2O)_8] + 2H_2pfad$$

Microanalyses and (or) metal analyses of **2**, **4**, and **6** indicate less water than in the X-ray determined composition, hence the compounds effloresce readily. Thus **3** and **5**, which were not investigated crystallographically, may have more water when freshly isolated than indicated by analysis. The ability of the compounds to retain water on standing increases with increasing atomic number, as attested by the an-

© 2008 NRC Canada

alytical compositions **2**, **3**·6H_2O, **4**·9H_2O, **5**, **6**·12H_2O. The visible and near IR spectra of complexes **4**, **6**, and **7** showed the features expected for the appropriate Ln^{3+} ion (29, 30). The main peak or cluster exhibited in the negative electrospray mass spectra (solvent = methanol/water), for all of the complexes of the type $Ln_2(pfad)_3$ in aqueous methanol, was assigned to $[Ln(pfad)_2]^-$ species, resulting from the breakdown of the polymeric structures (below). The mass spectra of the $Ln_2(bds)_3$·xH_2O complexes showed a similar feature (28), viz., $[Ln(bds)_2]^-$. ^{19}F NMR spectra and IR data provided further support for the structural features of **1**–**7**. Two fluorine resonances were exhibited in the ^{19}F NMR spectra, consistent with the two different fluorine chemical environments within the structures. The lack of paramagnetic shifting for the resonances of **3**–**6** suggests substantial ionization of the pfad ligands, a reflection of weak donor ability and (or) little transmission of the paramagnetic affect beyond the carboxyl group, owing to weak coordination. The IR spectra of **2**–**6** showed two distinct ν(OH) absorptions, the higher (3658–3628 cm^{-1}) attributable to coordinated water, and the lower, broader band (3397–3382 cm^{-1}) attributable to lattice water. Carboxylate absorptions are assigned at ca. 1670 cm^{-1} ($\nu_{as}(CO_2)$) and ca. 1460 cm^{-1} ($\nu_s(CO_2)$), and ν(CF) at 1187–1179 and 1127–1123 cm^{-1}.

X-ray crystal structures

Single crystal X-ray structure determinations have been conducted for **1**, **2**, **4**, **6**, and **7**. The structures of the lanthanoid complexes, the main theme of the paper, are discussed first.

For the lanthanum complex **2**, the results of the X-ray study are consistent with its formulation as $[La_2(pfad)_3(H_2O)_{10}]$·4$H_2O$ (the water molecules being secured by location and refinement of all hydrogen atoms). The neodymium complex **4** is isomorphous, with the series presumably extending beyond Nd to some as yet undefined limit short of the Ln = Yb analogue $[Yb_2(pfad)_2(H_2O)_8](pfad)$·6$H_2O$ **6**, which, although isostoichiometric, is of a different structural form. The La and Nd pair crystallize with one half of the formula unit, comprising the asymmetric unit of the structure. This entails one lanthanoid atom, seven water molecules, and one and a half ligands. Ligand 1 is fully independent, but ligand 2 is disposed with its central bond located on a crystallographic inversion centre. The lanthanoid atoms are nine-coordinate, with tricapped trigonal prismatic stereochemistry. Water molecules O(1,2,4) provide the capping atoms, water molecules O(3,5) and carboxylate O(211) one of the trigonal faces, and carboxylate O(111,112^i,212^{ii}) the other (Fig. 1*a*, Table 1). All Ln–O bond lengths are similar for both sets of donor atoms and tightly ranged throughout (≤0.12 Å) for both **2** and **4**, the differences between the two sets of values being consistent with expectations of the lanthanoid contraction. The lanthanoid atoms are linked into a two-dimensional polymer normal to *c* by the perfluoroadipate ligands, which bridge in different manners, successive layers being linked by hydrogen bonding (Fig. 1*b*). A string of lanthanoid atoms is linked along *a* by centrosymmetric $Ln(OCO)_2Ln$ units, alternately composed of pairs of ligand 2 and ligand 1 carboxylate units. The ligand 2 bridges are of interest, the Ln-O-C linkages being quasi-linear, with the associated Ln···Ln distances longer than in the unit bridged by the carboxylate 1 units, where Ln-O-C are more usual in their values. Ligand 1 displays μ-η^1:η^1 coordination through one carboxylate group, with the other being free. By contrast, centrosymmetric ligand 2 bridges μ-η^1:η^1 through both carboxylate groups. Seemingly, the water molecule and carboxylate oxygen atoms are similar in their coordinating capacity, components of both types being coordinated and uncoordinated. Thus, the water molecules O(6,7), and the carboxylate comprised of C(16) and O(161,162), are noncoordinating. Hydrogen bonding (Table 2) occurs to oxygen atoms of both types. Torsion angles are essentially trans throughout the fluorocarbon strings except for C(21)-C(22)-C(23)-C(23′), which is 60.2(1)°. All fluorine atoms are >3.7Å from the Ln atoms and are noncoordinating.

Although the ytterbium derivative **6** is isostoichiometric, it has a different structure, which can be represented as $[Yb_2(pfad)_2(H_2O)_8](pfad)$·6$H_2O$, although it forms a polymer of the same dimensionality. Again, the asymmetric unit of the structure is a single lanthanoid atom, seven water molecules, and one and a half ligands (Fig. 2*a*, Tables 3 and 4). The last component, however, is comprised of three halves of three independent perfluoroadipate ions. However, of the three available carboxylate groups, only two are involved in coordination, utilizing all oxygen atoms again as bridging groups, but this time both link the same pair of lanthanoid atoms and extend from there to create a web in two dimensions (Fig. 2*b*). They exhibit μ-η^1:η^1 binding of both carboxylate groups. The third ligand does not coordinate through any of its oxygen atoms but serves to link the two-dimensional sheet in the third dimension by hydrogen bonds from coordinated water molecules at either end. The ytterbium environment, in keeping with the diminished ionic radius, is now eight-coordinate with a square-antiprismatic arrangement. Interestingly, the two square faces of the coordination polyhedron are comprised in each case of either water molecule oxygen atoms O(1–4), or carboxylic oxygen atoms O(111,112^i,211,212^i), <Ln–O> 2.35(4) (range: 2.305(2)–2.388(2)), 2.29(3) (2.263(2)–2.334(2) Å), respectively, and the resulting (centrosymmetric) unit is $[(H_2O)_4Yb(OCO)_4Yb(OH_2)_4]$). The carboxylate oxygen faces of the two ytterbium atoms that they bridge are eclipsed (Yb···Yb 4.5698(3) Å). The hydrogen-bonding array is less inclusive than in the La–Nd complexes, some involving fluorine rather than oxygen atoms. The effect of the strut-like nature of the uncoordinated anion 3 between successive sheets (made up of binuclear units linked by extended struts) is that voids are created, occupied by the uncoordinated water molecules. Torsions in the C-C-C-C (non-central) components of the perfluoroadipate strings are –177.9(2) (string 2), 58.2(3)° (string 3); in string 1, disorder of the central atom is such that the linkage across the inversion centre appears to be C-*C*-*C*′-C with a torsion of 62.3(4)°.

It is reasonable to conclude that the cerium complex **3** is isostructural with **2** and **4** as Ce^{3+} is of intermediate size between La^{3+} and Nd^{3+}, but speculation as to the structure of the gadolinium derivative **5** would be premature.

The structures of the lanthanoid perfluoroadipate (pfad) complexes are compared with those of lanthanoid adipates

© 2008 NRC Canada

Fig. 1. (*a*) The lanthanum environment in $[La_2(pfad)_3(H_2O)_{10}]\cdot 4H_2O$ **2**. Compound **4** is isomorphous. (*b*) Unit cell contents of **[**$La_2(pfad)_3(H_2O)_{10}]\cdot 4H_2O$ **2** projected down *a*.

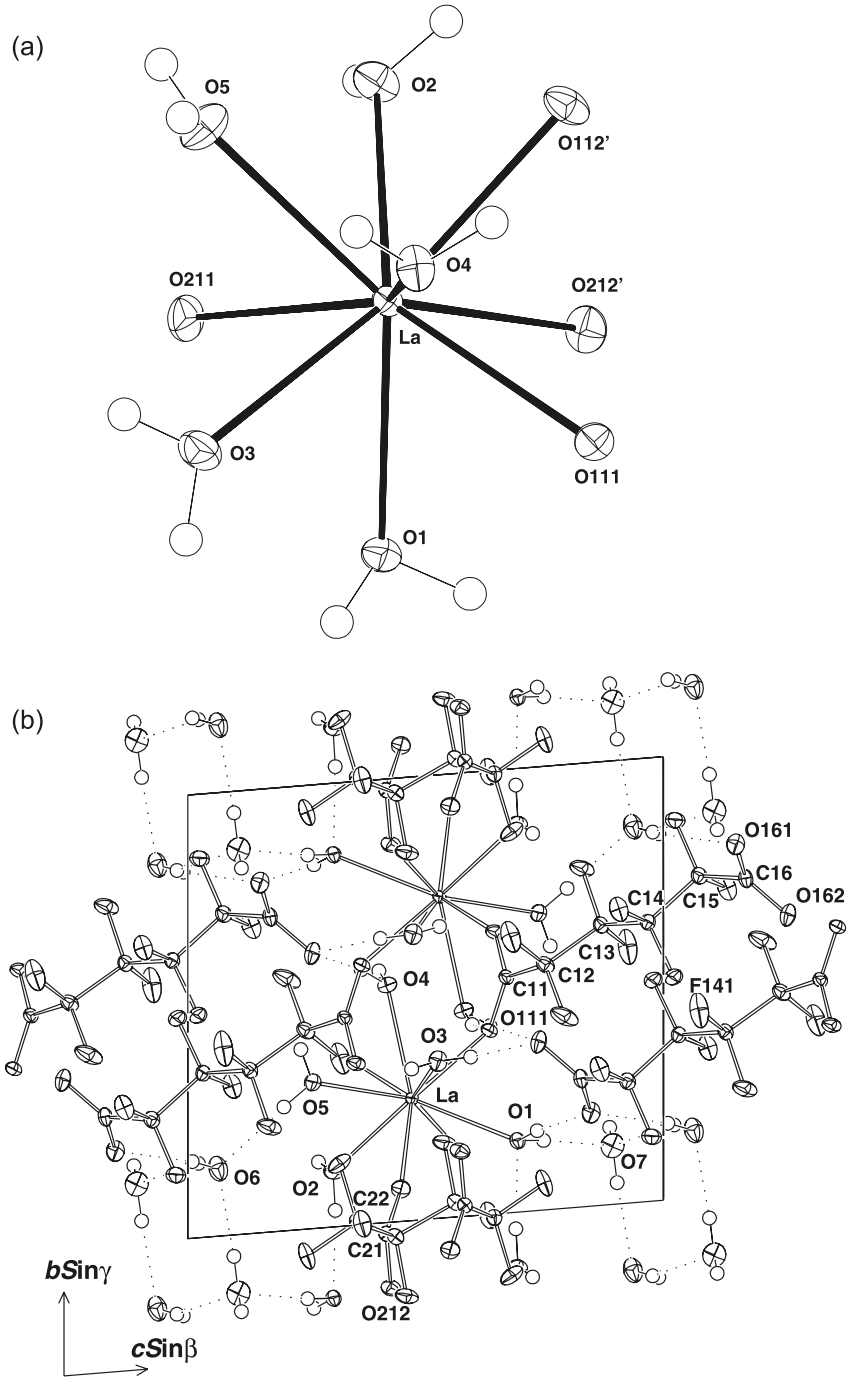

(ad) in Table 5. Despite the large number of $[Ln_2(ad)_3(H_2O)_n]\cdot mH_2O$ structures (11–23), there are none for heavier lanthanoids beyond Dy, the two erbium structures being for $[Er(ad)(H_2O)_5]X$ (X = Cl, NO_3) (20) species. Thus, the present structure of $[Yb_2(pfad)_2(H_2O)_8](pfad)\cdot 6H_2O$ (**6**) is unique at this time. What is striking on comparing the pfad and ad structures is the far more extensive coordination of water in the former with $5H_2O$/La, Nd (**2**, **4**) and $4H_2O$/Yb **6**, whereas $2H_2O$/Ln is the maximum observed in the ad species (11–16). This can be attributed to the weaker donor ability of the pfad ligand owing to the electron-withdrawing properties of the fluorine substituents. Unlike the sodium derivative **1**, there is no C-F-metal binding to reinforce the carboxylate coordination. Furthermore, the μ_4-(η^1,η^1/η^1,η^1) coordination mode, ubiquitous in **2**, **4**, and **6**, has only been observed in two ad complexes, viz. $[Ln_2(ad)_3(H_2O)_2]\cdot$bpy (Ln = Pr, Eu), which, oddly, each contain a noncoordinating 4,4′-bipyridine molecule in the lattice (18, 22). Unique to the present Ln complexes is observation of the μ-(η^1,η^1/–) coordination mode, in which one carboxylate group remains uncoordinated. In ad complexes of non-lanthanoid metals bound at only one end, the free

© 2008 NRC Canada

Table 1. Metal atom environments $[Ln_2(pfad)_3(H_2O)_{10}]\cdot 4H_2O$, Ln = La, **2**; Nd, **4**.

Atom	*r*	O(2)	O(3)	O(4)	O(5)	O(111)	O(211)	O(112^{i})	O(212^{ii})
O(1)	2.6143(8)	118.53(3)	71.64(3)	121.41(3)	135.81(3)	73.21(3)	69.87(3)	138.77(3)	69.13(3)
	2.555(1)	118.30(4)	71.85(4)	120.70(4)	135.79(5)	73.11(4)	69.55(4)	138.93(4)	69.19(4)
O(2)	2.5715(9)		133.96(3)	120.00(3)	70.62(3)	132.79(3)	68.53(3)	64.23(3)	73.52(3)
	2.518(1)		132.74(5)	120.98(4)	70.08(5)	133.17(4)	68.23(5)	64.87(4)	73.34(5)
O(3)	2.5583(9)			70.51(3)	73.55(3)	93.15(3)	75.39(3)	139.50(3)	140.15(3)
	2.498(1)			70.03(5)	73.25(5)	94.01(4)	74.69(5)	139.47(5)	140.62(5)
O(4)	2.5879(9)				69.20(3)	66.11(3)	136.37(3)	69.78(3)	126.43(3)
	2.532(1)				69.63(5)	66.24(4)	136.01(4)	70.42(4)	127.35(4)
O(5)	2.5391(9)					135.27(3)	75.70(3)	85.25(3)	143.55(3)
	2.480(1)					135.78(4)	75.73(5)	85.09(5)	142.87(5)
O(111)	2.5534(8)						143.07(3)	77.97(3)	69.20(3)
	2.507(1)						142.66(4)	77.95(4)	69.54(5)
O(211)	2.4920(8)							132.59(3)	97.20(3)
	2.446(1)							132.94(5)	96.61(5)
O(112^{i})	2.5376(8)								73.43(3)
	2.482(1)								73.76(5)
O(212^{ii})	2.5253(8)								
	2.466(1)								

Note: Values for the Ln = Nd derivative are given below those for the Ln = La adduct. Transformations of the asymmetric unit; i: $1-x$, $1-y$, $1-z$ and ii: $1-x$, $\bar{y}$, $1-z$. Ln-O(111)-C(11): 134.74(7), 134.7(1); Ln-O(211)-C(21) 170.12(8), 169.8(1); Ln-O(112^{i})-C(11^{i}) 142.79(7), 142.7(1); Ln-O(212^{ii})-C(21^{ii}) 131.88(7), 133.0(1)°. Ln···Ln^{i}, Ln^{ii} are 5.8416(2), 5.4077(2) (Ln = La); 5.7688(4), 5.3732(4) Å (Ln = Nd).

Table 2. Hydrogen bonding $[Ln_2(pfad)_3(H_2O)_{10}]\cdot 4H_2O$ (Ln = La, **2**; Nd, **4**).

Atoms	Distance (Å)
O(1), H(1A)···O(7)	2.769(2), 1.85(3)
	2.767(2), 1.83(5)
H(1B)···O(161^{iii})	2.739(1), 1.93(3)
	2.748(2), 1.93(5)
O(2), H(2A)···O(112^{i})^{a}	2.716(1), 2.37(3)
	2.682(2), 2.41(5)
H(2B)···O(1^{ii})	2.809(1), 1.97(3)
	2.817(2), 1.90(4)
O(3), H(3A)···O(162^{iii})	2.735(1), 1.89(3)
	2.741(2), 1.94(4)
H(3B)···F(122^{iv})	3.307(1), 2.54(3)
	3.312(2), 2.51(5)
O(4), H(4A)···O(111^{i})	2.854(1), 2.03(3)
	2.839(2), 1.96(5)
H(4B)···O(162^{v})	2.736(1), 1.94(3)
	2.735(2), 1.80(6)
O(5), H(5A)···O(162^{v})	3.044(1), 2.29(3)
	3.019(2), 2.23(4)
H(5B)···O(6)	2.848(2), 2.03(3)
	2.852(2), 2.01(5)
O(6), H(6A)···O(7^{v})	2.884(2), 2.08(3)
	2.820(3), 2.09(4)
H(6B)···O(161^{iv})	2.863(2), 2.04(3)
	2.878(2), 2.03(4)
O(7), H(7A)···F(151^{vi})	3.108(2), 2.28(5)
	3.084(3), 2.30(7)
H(7B)···O(6^{ii})	2.817(2), 1.93(4)
	2.820(3), 1.95(3)

Note: Transformations of the asymmetric unit (see Table; iii: $\bar{x}$, $1-y$, $2-z$; iv: $\bar{x}$, $1-y$, $1-z$; v: x, y, $z-1$; vi: $1-x$, $1-y$, $2-z$. [a]O(2,112^{i}) are in the coordination sphere of the same lanthanoid.

carboxylate group is protonated (31, 32). Both of these features and the observation of a free pfad^{2-} ion in **6** also reflect the weaker donor ability of pfad than ad.

For the neodymium mixed ligand complex **7**, the results of the single crystal X-ray study are consistent with the formulation $[Nd_2(bds)_2(pfad)(H_2O)_8]$, one half of the binuclear formula unit comprising the asymmetric unit of the structure. The array is an infinite one-dimensional polymer (Figs. 3*a*, 3*b*)). About the nine-coordinate neodymium atom of tricapped trigonal prismatic stereochemistry (Table 6), a disulfonate ligand acts as a chelate through one oxygen atom of each sulfonate group (seven-membered ring), and a single oxygen atom from another disulfonate ligand is also bound. The coordination sphere is completed by four unidentate water molecules and a chelating carboxylate group. Pairs of metal centres are linked (*i*) by centrosymmetric pfad ligands (one-half per asymmetric unit), each end behaving as a chelate giving overall μ-η^2:η^2 coordination (Figs. 3*a*, 3*b*), and (*ii*) about other inversion centres by one of the non-chelating sulfonate oxygen atoms from each ligand, forming eight-membered (NdOSONdOSO-) rings (Figs. 3*a*, 3*b*). The benzene-1,2-disulfonate ligand binds in a μ-η^2(O,O′);η^1(O″) manner, a new disposition towards lanthanoid ions, though the seven-membered chelation component is known in Ln complexes (28, 33) and μ-η^2(O,O′);η^2(O″,O‴) binding is also known (33). Torsions in the adipate chain are 180° (necessarily) in the central C–C bond and 163.8(2)° in the adjacent. All hydrogen atoms form strong hydrogen bonds (Table 7), linking adjacent chains of the polymer predominantly to sulfonate but also to carboxylate and other water molecule oxygen atoms.

The sodium salt is unsolvated $[Na_2(pfad)]$ **1**, one-half of the formula unit comprising the asymmetric unit of the structure; the anion is disposed with its mid-point at a crystallographic inversion centre, the other backbone torsion in C(3)-C(2) being –175.87(6)° with C(3)-C(2)-C(1)-O(11,21)

© 2008 NRC Canada

Fig. 2. (*a*) The centrosymmetric binuclear core. (*b*) Unit cell contents of $[Yb_2(pfad)_2(H_2O)_8](pfad)\cdot 6H_2O$ **6** projected down *c*.

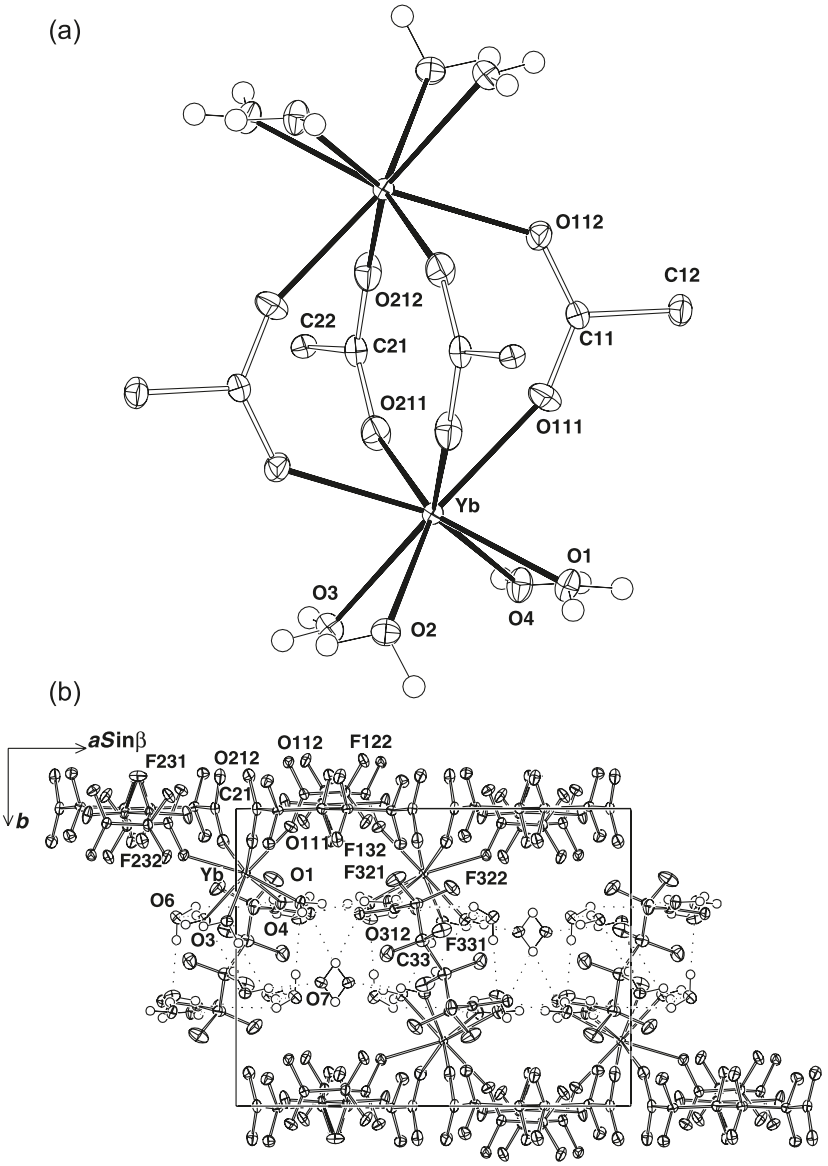

Table 3. Selected geometries $[Yb_2(pfad)_4(H_2O)_8](pfad)\cdot 6H_2O$ **6**: ytterbium environment.

Atom	*r*	O(2)	O(3)	O(4)	O(111)	O(112^i)	O(211)	O(212^i)
O(1)	2.305(2)	70.29(6)	112.09(6)	72.12(6)	79.75(6)	140.06(5)	144.00(6)	78.66(6)
O(2)	2.369(2)		71.00(6)	110.12(6)	143.00(6)	76.28(6)	140.99(6)	78.90(6)
O(3)	2.388(2)			71.99(5)	142.92(5)	75.49(5)	76.20(6)	141.16(5)
O(4)	2.349(2)				79.41(6)	142.04(5)	78.13(6)	143.53(6)
O(111)	2.280(2)					118.77(6)	75.22(6)	74.26(6)
O(112^i)	2.334(2)						75.56(6)	73.95(5)
O(211)	2.263(2)							117.78(7)
O(212^i)	2.271(2)							

Note: Yb$^{(i)}$-O(m1n)-C(m1) (mn = 11,12,21,22) are: 157.8(2), 133.6(1), 141.7(2), 147.3(2)°. Transformation i is $\bar{x},\bar{y},\bar{z}$.

being –82.06(8), 98.23(8)°. The structure is polymeric, comprising sheets of CF_2 moieties disposed about $x = 0$ (Fig. 4*a*). The sodium environment is unusual (Table 8). Unsurprisingly it involves both oxygen atoms of the anion, both of these bridging symmetry-related cations, clustered to one side of the coordination sphere, comprising four coordination sites. The environment is made up to six-coordinate by the approaches of a pair of α-fluorine atoms from different anions at distances of <2.6 Å (Fig. 4*b*). The C–F bond lengths for those are 1.3574(9), 1.3580(9), cf. those at C(3) of 1.3420(10), 1.3431(10) Å, F-C-F being 106.71(6), 108.45(7)° respectively. Each perfluoroadipate ligand is

© 2008 NRC Canada

Fig. 3. (*a*) Unit cell contents of $[Nd_2(bds)_2(pfad)(H_2O)_8]$ **7** projected down *a*. (*b*) A single polymeric strand.

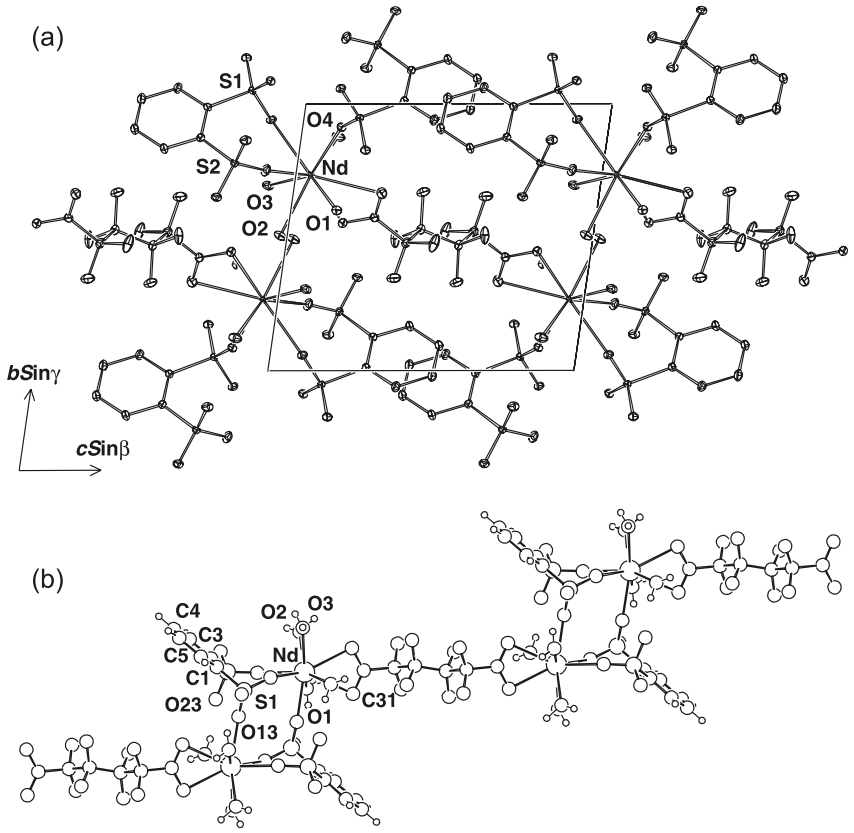

Table 4. Selected geometries $[Yb_2(pfad)_4(H_2O)_8](pfad)\cdot 6H_2O$ **6**: hydrogen bonding.

Atoms	Distance (Å)
O(1), H(1A)···O(4)	2.740(2), 2.67(2)
H(1B)···O(5)	2.761(2), 1.99(2)
O(2), H(2A)···O(7^{i})	2.749(3), 1.97(2)
H(2B)···O(3^{i})	2.925(2), 2.08(2)
O(3), H(3A)···O(211)	2.872(2), 2.73(2)
H(3B)···O(7^{i})	2.726(2), 1.92(2)
O(4), H(4A)···O(311)	2.896(2), 2.13(2)
H(4B)···O(312^{ii})	2.749(2), 1.93(2)
O(5), H(5A)···F(221^{iii})	2.939(2), 2.54(3)
H(5B)···F(231^{iii})	3.042(2), 2.27(2)
O(6), H(6A)···O(5^{i})	2.749(3), 2.00(1)
H(6B)···O(312^{ii})	2.787(2), 2.05(2)
O(7), H(7A)···O(311)	2.744(2), 1.92(2)
H(7B)···F(122^{iv})	2.992(2), 2.17(2)

Note: Transformations of the asymmetric unit: i: $\bar{x}$, 1 – *y*, $\bar{z}$. ii: 1/2 – *x*, *y*, 1/2 – *z*. iii: $\bar{x}$, $\bar{y}$, $\bar{z}$. iv: *x*, 1 + *y*, *z*.

duodecadentate. Each carboxylate oxygen atom of the centrosymmetric ion bridges two different sodium ions resulting in μ_4-η^1:η^1:η^1:η^1 binding of each carboxylate group. Both α-F atoms bind to sodium ions, one to a sodium also ligated by one of the adjacent carboxylate oxygen atoms, and one to a sodium otherwise unattached to this primary ligand. Overall, each ligand is attached to ten different sodium ions. No water is coordinated or present in the lattice despite crystallization from aqueous solution.

During the course of this work, crystals of perfluoroadipic acid were grown from aqueous solution. The X-ray crystal structure of this compound had been previously published (34), data being measured at room temperature using a single counter instrument. It crystallizes as the dihydrate $H_2pfad\cdot 2H_2O$, one half of the formula unit comprising the asymmetric unit of the structure with the centre of the central C–C bond of the molecule at *y* = 0.72 lying disposed on a crystallographic *2*-axis in space group *C*2/*c*. The unit cell contents are shown in projection down the short crystallographic axis *b* in Fig. 5*a*, the molecule quasi-normal to that axis disposed about a plane at ca. *y* = 0.72, together with the water molecule. Interactions with inversion and (or) screw related entities at ca. 0.28 through the associated hydrogen atoms result in a hydrogen-bonded web about the plane *x* = 0.25 (Fig. 5*b*). The acidic hydrogen atom is associated with carboxylate O(1) (C(1)-O(1,2) 1.287(1), 1.211(1) Å; O(1)-C(1)-O(2) 128.01(7), C(2)-C(1)-O(1,2) 111.62(7), 120.37(7); O(1)-H(1) 0.97(2) Å, H(1)-O(1)-C(1) 111.4(1)°), and hydrogen-bonds to the water-molecule oxygen atom (H(1)···O(3)(*x*, 1–*y*, 1/2+*z*) 1.54(2) Å). Within the water molecule, O(3)–H(3A,B) are 0.85(1), 0.83(1) Å respectively, with H(3A)-O(3)-H(3B) 109.8(1)°, the two hydrogen atoms hydrogen-bonding to different and (or) symmetry-related O(2) (O(2)···H(3A) 1.98(2), O(2)···H(3B) (1/2 – *x*, 1/2 – *y*, 1 – *z*) 2.13(1) Å). The torsion angle in C(2)-C(3) of the acid backbone is –163.99(7), with C(3)-C(2)-C(1)-O(1,2) –62.0(1), 118.8(1) and C(2)-C(3)-C(3′)-C(2′) –159.08(6)°. There are some similarities between the structures of the sodium salt **1** and the acid dihydrate $H_2pfad\cdot 2H_2O$ (Figs. 4*a*, 5*a*).

© 2008 NRC Canada

Table 5. Coordination numbers and binding geometries for lanthanoid adipates (11–22).

Complex	Coord No.	Lanthanoid	Binding
$[Ln_2(ad)_3(H_2O)_4]\cdot 6H_2O$	9	La, Ce, Pr, Nd	μ_4-(η^2,η^1/η^2,η^1) + 2 × μ_3-(η^1,η^1;η^2)
$[Ln_2(ad)_3(H_2O)_4]\cdot H_2O$	9	Nd, Sm	μ-(η^2/η^2) + 2 × μ_3-(η^2,η^1/η^2)
$[Ln_2(ad)_3(H_2O)_4]$	9	Gd, Eu, Dy	μ-(η^2/η^2) + 2 × μ_3-(η^2,η^1/η^2)
$[Ln_2(ad)_3(H_2O)_4]\cdot 4H_2O\cdot H_2ad$	10	La, Ce, Pr, Nd	μ-(η^2/η^2) + 2 × μ_4-(η^2,η^1/η^2,η^1)
$[Nd_2(ad)_3(H_2O)_2]\cdot H_2O$	9	Nd	μ_4-(η^2,η^1/η^2,η^1) + 2 × μ_4-(η^2,η^1/η^1,η^1)
$[Ln_2(ad)_3(H_2O)_2]$	9	Nd, Ce	μ_4-(η^2,η^1/η^2,η^1) + 2 × μ_4-(η^2,η^1/η^1,η^1)
$[Ln_2(ad)_3(H_2O)_2]\cdot$bpy	9	Pr, Eu	μ_4-(η^1,η^1/η^1,η^1) + 2 × μ_4-(η^2,η^1/η^2,η^1)
$[Pr_4(ad)_6(H_2O)_4]\cdot H_2O$	9, 10	Pr	μ-(η^2/η^2) + 5 × μ_4-(η^2,η^1/η^2,η^1)
$[Eu_4(ad)_6(H_2O)_2]\cdot 2H_2O$	8, 9	Eu	3 x μ_4-(η^2,η^1/η^1,η^1) + 3 × μ_4-(η^2,η^1/η^2,η^1)
$[Ln(ad)(H_2O)_5]X$; X=Cl,NO_3	9	Er, Gd	μ-(η^2/η^2)
$[Ln_2(pfad)_3(H_2O)_{10}]\cdot 4H_2O$	9	La, Nd	μ_4-(η^1,η^1/η^1,η^1) + 2 × μ-(η^1,η^1/-)
$[Yb_2(pfad)_2(H_2O)_8](pfad)\cdot 6H_2O$	8	Yb	2 × μ_4-(η^1,η^1/η^1,η^1) + free pfad

Note: bpy = 4,4′-bipyridine.

Table 6. Selected geometries $[Nd_2(bds)_2(pfad)(H_2O)_8]$ **7**: neodymium environment.

Atom	*r*	O(21)	O(1)	O(2)	O(3)	O(4)	O(31)	O(32)	O(13^i)
O(11)	2.470(1)	68.74(6)	134.48(5)	118.08(6)	71.15(5)	72.44(6)	137.20(6)	138.25(6)	75.07(5)
O(21)	2.418(2)		72.65(6)	72.97(6)	99.40(6)	139.75(6)	142.01(6)	135.86(6)	82.32(6)
O(1)	2.553(2)			70.42(5)	139.55(6)	134.03(6)	88.31(5)	65.05(6)	76.79(5)
O(2)	2.446(2)				69.38(6)	137.61(6)	69.70(6)	102.94(6)	143.44(6)
O(3)	2.486(2)					77.41(6)	73.94(5)	120.72(6)	142.75(5)
O(4)	2.464(2)						76.46(6)	72.12(6)	77.84(6)
O(31)	2.570(2)							50.30(5)	125.75(6)
O(32)	2.655(2)								76.54(3)
O(13^i)	2.421(2)								

Note: Transformation of the asymmetric unit; i: 1 – *x*, 2 – *y*, $\bar{z}$. Nd-O(11,21)-S(1,2) are 142.9(1), 169.3(1)°; the neodymium atom lies 2.338(5) Å out of the C_6 aromatic plane of the chelating ligand and 3.183(4) Å of the bridging ligand.

Table 7. Hydrogen bonding in $[Nd_2(bds)_2(pfad)(H_2O)_8]$ **7**.

Atoms	Distance (Å)
O(1), H(1A)···O(22^i)	2.700(2), 1.92(5)
H(1B)···O(12^{ii})	2.768(2), 2.00(5)
O(2), H(2A)···O(3^{iii})	2.907(3), 2.20(7)
H(2B)···O(1^i)	2.721(2), 1.97(5)
O(3), H(3A)···O(31^{iii})	2.742(3), 1.93(4)
H(3B)···O(23^{iv})	2.796(2), 2.07(5)
O(4), H(4A)···O(23^{ii})	2.842(2), 2.05(3)
H(4B)···O(12^i)	2.919(3), 2.15(5)

Note: Transformations of the asymmetric unit; i: 1 – *x*, 1 – *y*, $\bar{z}$; ii: 1 – *x*, 2 – *y*, $\bar{z}$; iii: 2 – *x*, 1 – *y*, $\bar{z}$; iv: *x* + 1, *y*, *z*; v: 2 – *x*, 2 – *y*, $\bar{z}$.

Conclusions

Lanthanoid complexes of the perfluoroadipate ligand show different structures to those of the many for lanthanoid adipates. $[Ln_2(pfad)_3(H_2O)_{10}]\cdot 4H_2O$ (Ln = La or Nd) (**2**, **4**) and $[Yb_2(pfad)_2(H_2O)_8](pfad)\cdot 6H_2O$ (**6**) exhibit more coordinated water than in adipate counterparts, and there is no adipate complex with a free dicarboxylate counterion as in the ytterbium complex **6**. The predominant pfad binding mode in **2**, **4**, **6**, viz., μ_4-η^1,η^1/η^1,η^1 is rarely seen in ad coordination to Ln^{3+}, and the μ-η^1,η^1/– single end binding observed for **2** and **4** has no counterpart in lanthanoid adipate coordination. Many of the features of pfad binding are consistent with it being a weaker donor than ad. In the mixed ligand complex **7**, a new binding mode to Ln^{3+} of the benzene-1,2-disulfonate ion was observed. It is reasonable to conclude the cerium complex **3** is isostructural with **2** and **4**, as Ce^{3+} is of intermediate size between La^{3+} and Nd^{3+}, but speculation as to the structure of the gadolinium derivative **5** would be premature.

Experimental

General procedures

The rare earth oxides used were purchased from Grace Davison Chemicals, Unilab, Riedel de Haën and Allied Signal, cerium(III) carbonate was from Sigma-Aldrich, the perfluoroadipic acid was from Bristol Organic Limited, and dipotassium 1,2-benzenedisulfonate was from Sigma-Aldrich. 1,2-benzenedisulfonic acid was prepared as outlined in the literature (33), but using the anhydrous compound instead of dipotassium 1,2-benzenedisulfonic acid monohydrate. The metal analyses were adapted from the method described previously (35) but without the need of an acid digestion. The Campbell Microanalytical Laboratory of the University of Otago, New Zealand, performed the microanalyses. Listed IR data using a PerkinElmer 1600 FTIR spectrometer are of Nujol and hexachlorobutadiene mulls for the region 4000–650 cm^{-1} (only for the sulfo-

© 2008 NRC Canada

Fig. 4. (*a*) Unit cell contents of Na_2(pfad) **1** projected down *b*. (*b*) The sodium environment in Na_2(pfad) **1**.

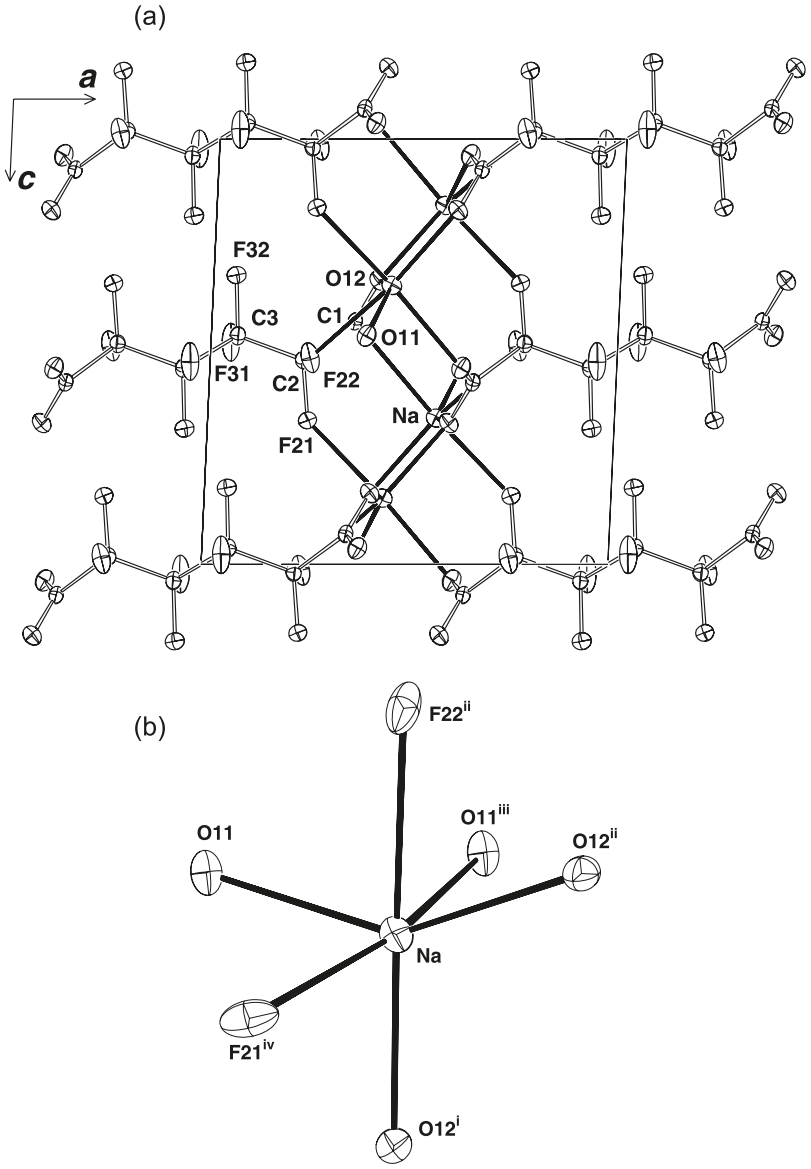

Table 8. The sodium atom environment Na_2(pfad) **1**.

Atom	*r*	O(12^{i})	O(12^{ii})	O(11^{iii})	F(21^{iv})	F(22^{ii})
O(11)	2.2793(7)	101.82(3)	146.39(3)	87.38(2)	78.46(2)	82.11(2)
O(12^{i})	2.2980(7)		111.78(2)	101.27(3)	78.11(2)	172.80(3)
O(12^{ii})	2.3124(7)			85.47(2)	108.52(3)	64.57(2)
O(11^{iii})	2.3723(7)				165.30(3)	84.84(2)
F(21^{iv})	2.5801(7)					96.95(2)
F(22^{ii})	2.5489(7)					

Note: Transformations of the asymmetric unit; i: 1 – *x*, *y* – 1/2, 1/2 – *z*; ii: *x*, *y* – 1, *z*; iii: 1 – *x*, $\bar{y}$, 1 – *z*; iv: *x*, 1/2 – *y*, *z* – 1/2; v: 1 – *x*, 1/2 + *y*, 1/2 – *z*; vi: *x*, 1 + *y*, *z*. Na···Na^{iii}, Na^{i} are 3.3643(7), 3.6983(4) Å, with C(1)-O(11,12) 1.2445(9), 1.2441(9). C(1)-O(11)-Na,Na^{iii} are 136.92(6), 119.63(5), Na-O(11)-Na^{iii} 92.62(2) (Σ 349.2); C(1)-O(12)-Na^{v,vi} are 124.84(5), 125.76(5), Na^{vi}-O(12)-Na^{v} 106.68(2).

nates). ^{1}H NMR spectra were recorded at 400 MHz with a Bruker DRX400 spectrometer. Electrospray mass spectra were recorded with a Bruker BioApec 47e FTMS with a 4.7T superconducting magnet and fitted with an analytica electrospray source. Only metal-containing peaks are quoted. Visible and near IR spectra were recorded with a Varian Cary 17 spectrophotometer. Molar absorption coefficients (ε) are given in mol dm^{-3} cm^{-1}.

Synthesis of [Na_2(pfad)] (1)

Perfluoroadipic acid (2.91 g, 10.0 mmol) was dissolved in ethanol (50 mL) and then added to NaOH (0.82g) dissolved

© 2008 NRC Canada

Fig. 5. (*a*) Unit cell contents of H_2pfad·$2H_2O$, projected down *b*. (*b*) The hydrogen-bonded web about the plane $x = 0.25$.

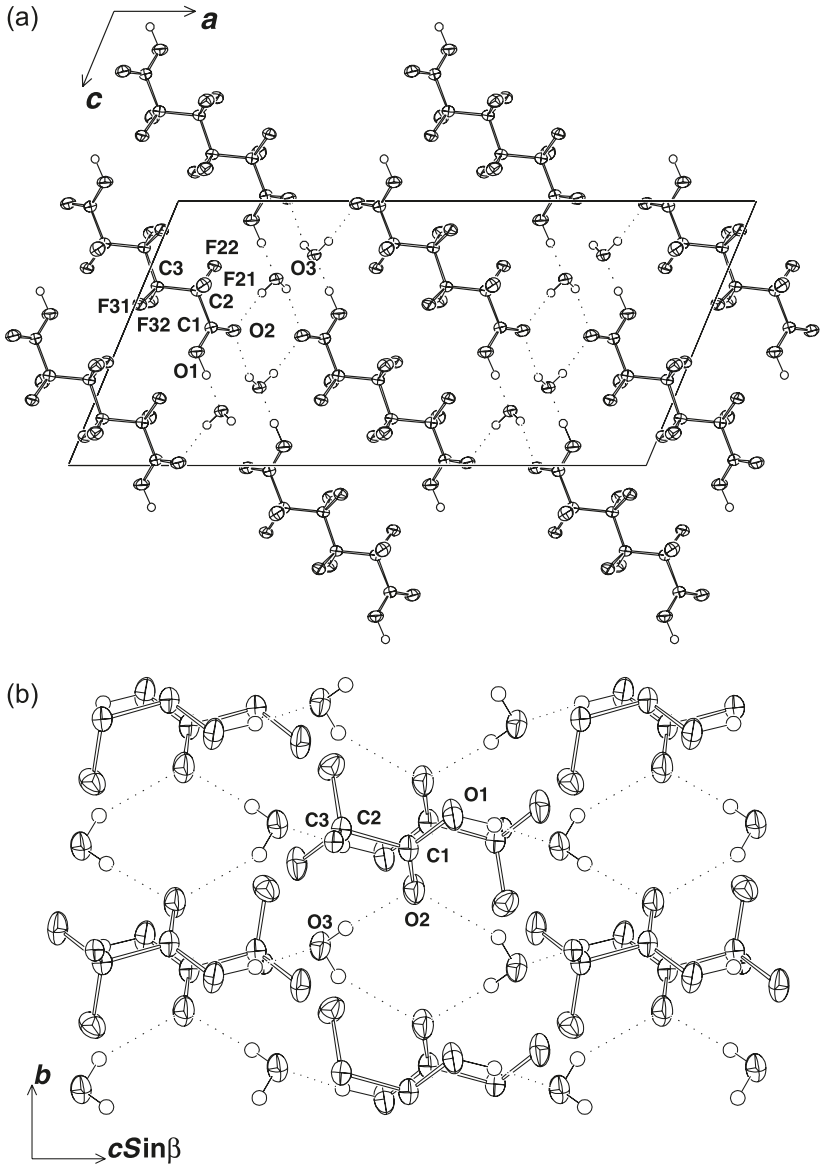

in ethanol (50 mL), which formed a white solid on standing. Yield 2.23 g (67%). IR (cm^{-1}): 3362w, 1699s, 1400vs. (br), 1194s, 1123s, 818s, 722m, 653s. ^{19}F NMR (D_2O) δ: –116.4 (m, 4F, CF_2CO_2), –122.1 (m, 4F, CF_2CF_2). *m*/*z* (-ve ES, 35v): 311 (100%, $[NaL]^-$).

General syntheses of $[Ln_2(pfad)_3]$ derivatives

Perfluoroadipic acid and the appropriate lanthanoid(III) oxide (or cerium carbonate, $Ce_2(CO_3)_3.11H_2O$) were refluxed in water. The mixture was then filtered though a Celite pad and the water was evaporated to dryness. The crude product was then redissolved in the minimum amount of water and refiltered though Celite, and the solvent was removed until the solution became viscous when it was left to crystallize. The product was then collected and drained on a sinter.

Synthesis of $[La_2(pfad)_3(H_2O)_{10}]·4H_2O$ (2)

Lanthanum(III) oxide (1.04 g, 3.19 mmol) and perfluoroadipic acid (1.39 g, 4.79 mmol) were brought to reflux in water (50 mL) by heating for 12 h. After the work-up of the mixture, single colourless crystals of **2** were obtained and characterized by X-ray crystallography. Yield 1.48 g (74%). IR (cm^{-1}): 3635m, 3487m (br), 1657s, 1460vs, 1179vs, 1127s, 808m, 722m, 653m. ^{19}F NMR (D_2O) δ: –116.46 (m, 12F, CF_2CO_2), –122.07 (m, 12F, CF_2CF_2). *m*/*z* (–ve ES, 35v): 465 (11%, $[La(pfad)F_2]^-$), 715 (100, $[La(pfad)_2]^-$), 1073 (5, $[La_3(pfad)_6H]^{2-}$), 1096 (5, $[La_3(pfad)_6(HCO_2)H_2]^{2-}$), 1286 (7, $[La_4(pfad)_7]^{2-}$). Elemental anal. calcd. for $La_2(pfad)_3(H_2O)_6$, $C_{18}H_{12}F_{24}La_2O_{18}$ (%): La 22.22; found: La 22.08.

Synthesis of $[Ce_2(pfad)_3(H_2O)_{10}]·4H_2O$ (3)

Cerium carbonate, $Ce_2(CO_3)_3·11H_2O$ (2.94 g, 7.38 mmol) and perfluoroadipic acid (2.78 g, 9.58 mmol) were heated to reflux in water (100 mL) for 12 h. Single colourless crystals of **3** were obtained after the work-up of the solution. Yield 2.98 g (75%). IR (cm^{-1}): 3628m, 3397m (br), 1662s, 1460vs, 1179s, 1126s, 808m, 722m, 652m. ^{19}F NMR (D_2O)

© 2008 NRC Canada

Table 9. Crystal and refinement data.

Crystal	**1**	**2**	**4**	**6**	**7**	H_2pfad·$2H_2O$[a]
Empirical formula	$C_6F_8Na_2O_4$	$C_{18}H_{28}F_{24}La_2O_{26}$	$C_{18}H_{28}F_{24}Nd_2O_{26}$	$C_{18}H_{28}F_{24}O_{26}Yb_2$	$C_{18}H_{24}F_8Nd_2O_{24}S_4$	$C_6H_6F_8O_6$
Formula mass	334.0	1394.3	1404.9	1462.5	1193.1	326.1
Crystal system	Monoclinic	Triclinic	Triclinic	Monoclinic	Triclinic	Monoclinic
Space group	$P2_1/c$	$P\bar{1}$	$P\bar{1}$	$P2/n$	$P\bar{1}$	$C2/c$
a (Å)	8.8242(5)	9.7883(5)	9.7332(8)	13.7567(8)	7.8666(7)	22.021(4)
b (Å)	6.1120(4)	10.4743(5)	10.3814(8)	10.3012(6)	9.7700(9)	5.0815(8)
c (Å)	9.1905(6)	10.6252(5)	10.5723(8)	14.8097(9)	11.348(1)	10.869(2)
α (°)	90	85.285(1)	84.938(2)	90	80.404(2)	90
β (°)	92.591(2)	88.840(1)	88.659(2)	96.939(1)	76.818(3)	112.666(3)
γ (°)	90	70.147(1)	70.151(2)	90	83.097(2)	90
V (Å^3)	495.17(5)	1021.1(1)	1000.9(2)	2083.2(2)	834.2(1)	1122.3(3)
D_{calcd} (Mg m^{-3})	2.24	2.26	2.33	2.33	2.37	1.93
Z	2	1	1	2	1	4
Absorption coeff. (μ) (mm^{-1})	0.34	2.3	2.8	4.7	3.5	0.24
Crystal dimensions (mm)	0.19 × 0.14 × 0.06	0.20 × 0.16 × 0.13	0.48 × 0.30 × 0.15	0.20 × 0.14 × 0.10	0.30 × 0.15 × 0.11	0.19 × 0.16 × 0.05
$T_{(min/max)}$	0.70	0.70	0.56	0.73	0.69	0.76
$2\theta_{max}$ (°)	75	75	75	75	75	75
N_t	10 231	20 353	20 046	43 382	17 155	11 578
N (R_{int})	2594 (0.020)	10322 (0.016)	9935 (0.031)	10973 (0.041)	8519 (0.057)	2948 (0.027)
N_o	2165	9987	9601	8356	7789	2027
$R1$	0.036	0.018	0.030	0.028	0.031	0.032
$wR2$	0.11	0.049	0.081	0.060	0.082	0.092
a (b)	0.072, 0.061	0.0266, 0.5918	0.060, 0.990	0.0289	0.0444	0.052
S	1.05	1.10	1.06	0.95	1.04	0.98

Note: Compounds **2** and **4** are isomorphous.
[a]A previous study has been recorded at room temperature, using a single counter instrument (34). In **6**, the central CF_2 group was modelled as disordered over two sets of sites, occupancies 0.5.

δ: –116.57 (m, 12F, C**F**$_2$CO$_2$), –122.17 (m, 12F, C**F**$_2$C**F**$_2$). *m/z* (–ve ES, 35v): 466 (11%, [Ce(pfad)F$_2$]$^-$), 716 (100, [Ce(pfad)$_2$]$^-$), 1074 (5, [Ce$_3$(pfad)$_6$H]$^{2-}$), 1097 (4, [Ce$_3$(pfad)$_6$(HCO$_2$)H$_2$]$^{2-}$), 1288 (7, [Ce$_4$(pfad)$_7$]$^{2-}$). Elemental anal. calcd. for Ce$_2$(pfad)$_3$(H$_2$O)$_6$, $C_{18}H_{12}Ce_2F_{24}O_{18}$ (%): C 17.26, H 0.97, Ce 22.37; found: C 17.31, H 0.91, Ce 22.00.

Synthesis of [Nd$_2$(pfad)$_3$(H$_2$O)$_{10}$]·4H$_2$O (4)

Neodymium oxide (1.08 g, 3.21 mmol) and perfluoroadipic acid (1.39 g, 4.79 mmol) were added to water (50 mL) and the mixture was brought to reflux for 12 h. After work-up of the reaction mixture, pink crystals formed and were established to be **4** by X-ray crystallography. Yield 1.48 g (70%). Visible/near IR [λ_{max}, nm (ε), H$_2$O]: 329 (3), 347 (5), 354 (7), 427 (2), 461 (2), 469 (2), 475 (2), 512 (4), 521 (8), 575 (15), 679 (2), 732 (9), 740 (15), 794 (22), 799 (13), 864 (7), 889 (2). IR (cm^{-1}): 3635m, 3396m (br), 1752m, 1666vs, 1606s, 1456vs, 1179vs, 1127vs, 807m, 726w, 652m. ^{19}F NMR (D$_2$O) δ: –116.45 (m, 12F, C**F**$_2$CO$_2$), –122.07 (m, 12F, C**F**$_2$C**F**$_2$). *m/z* (–ve ES, 35v): 468 (11%, [Nd(pfad)F$_2$]$^-$), 718 (100, [Nd(pfad)$_2$]$^-$), 1080 (5, [Nd$_3$(pfad)$_6$H]$^{2-}$), 1103 (5, [Nd$_3$(pfad)$_6$(HCO$_2$)H$_2$]$^{2-}$), 1296 (9, [Nd$_4$(pfad)$_7$]$^{2-}$). Elemental anal. calcd. for Nd$_2$(pfad)$_3$(H$_2$O)$_9$, $C_{18}H_{18}F_{24}Nd_2O_{21}$ (%): C 16.44, H 1.38, Nd 21.94; found: C16.47, H 1.03, Nd 21.76.

Synthesis of [Gd$_2$(pfad)$_3$(H$_2$O)$_{12}$] (5)

Gadolinium oxide (1.16 g, 3.20 mmol) and perfluoroadipic acid (1.39 g, 4.79 mmol) were heated to reflux for 12 h in water (50 mL). Upon work-up of the solution, a white powdery product was collected and analysed to be **5**. Yield 1.04 g (47%). IR (cm^{-1}): 3638m, 3392m (br), 1670 s, 1460vs, 1178s, 1127s, 809m, 625m. ^{19}F NMR (D$_2$O) δ: –116.24 (m, 12F, C**F**$_2$CO$_2$), –122.50 (m, 12F, C**F**$_2$C**F**$_2$). *m/z* (–ve ES, 35v): 734 (100%, [Gd(pfad)$_2$]$^-$), 1100 (4, [Gd$_3$(pfad)$_6$H]$^{2-}$), 1126 (8, [Gd$_3$(pfad)$_6$(CO$_2$)H$_2$]$^{2-}$), 1323 (8, [Gd$_4$(pfad)$_7$]$^{2-}$). Elemental anal. calcd. for $C_{18}H_{24}F_{24}Gd_2O_{24}$ (%): Gd 21.55; found: Gd 22.96.

Synthesis of [Yb$_2$(pfad)$_2$(H$_2$O)$_8$](pfad)·6H$_2$O (6)

Ytterbium oxide (1.26 g, 3.20 mmol) and perfluoroadipic acid (1.39 g, 4.79 mmol) were brought to reflux in water (50 mL) for 12 h. The work-up product was found to be **6** by X-ray determination. Yield 1.14 g (50%). IR (cm^{-1}): 3658m, 3382m, 1753s, 1666s, 1464vs, 1187s, 1124s, 808m, 721s, 658m. ^{19}F NMR (D$_2$O) δ: –116.41 (m, 12F, C**F**$_2$CO$_2$), –122.04 (m, 12F, C**F**$_2$C**F**$_2$). *m/z* (–ve ES, 35v): 500 (7%, [Yb(pfad)F$_2$]$^-$), 750 (100, [Yb(pfad)$_2$]$^-$), 1123 (7, [Yb$_3$(pfad)$_6$H]$^{2-}$), 1146 (8, [Yb$_3$(pfad)$_6$(HCO$_2$)H$_2$]$^{2-}$), 1354 (8, [Yb$_4$(pfad)$_7$]$^{2-}$). Visible/near IR [λ_{max}, nm (ε), H$_2$O]: 938 (2), 974 (5). Elemental anal. calcd. for Yb$_2$(pfad)$_3$(H$_2$O)$_{12}$, $C_{18}H_{24}F_{24}O_{24}Yb_2$ (%): Yb 24.26; found: Yb 24.67.

© 2008 NRC Canada

Synthesis of $[Nd_2(bds)_2(pfad)(H_2O)_8]$ (7)

Neodymium(III) perfluoroadipate (0.50 g, 0.37 mmol) was heated to reflux with 1,2-benzenedisulfonic acid (1.8 g, 7.54 mmol) in water (30 mL) for 24 h. Work-up was as for **2**, but ethanol was also added to induce crystallization. Pink single crystals of **7** were obtained, collected, and crystallographically characterized. The bulk product was found to be $[Nd_2(bds)_2(pfad)(H_2O)_7]$. Yield 0.54 g (93%), mp >360 °C. IR (cm^{-1}): 3388s (br), 2961w, 2922w, 2856w, 1644s, 1431m, 1417s, 1224vs, 1196vs, 1173vs, 1131vs, 1119vs, 1081s, 1062vs, 1038s, 1012s, 872m, 818m, 778s, 757m, 690s, 658s. ^{1}H NMR (D_2O) δ: 7.31 (m, 4H, **H**4,5), 7.64 (m, 4H, **H**3,6). ^{19}F NMR (D_2O) δ: –116.46 (m, 4F, C**F**$_2$CO$_2$), –122.10 (m, 4F, C**F**$_2$C**F**$_2$). *m*/*z* (–ve ES, 50v): 616 (100%, $[Nd(bds)_2]^-$), 668 (49, $[Nd(bds)(pfad)]^-$), 720 (8, $[Nd(pfad)_2]^-$), 899.5 (10, $[Nd_3(bds)_2(pfad)_3(MeO)]^{2-}$), 951 (4). Visible/near IR [λ_{max}, nm (ε), H_2O]: 327 (16), 338 (14), 347 (16), 354 (18), 427 (7), 461 (6), 469 (6), 475 (6), 512 (8), 522 (12), 575 (19), 679 (4), 732 (12), 740 (17), 794 (25), 799 (17), 865 (9), 889 (3). Elemental anal. calcd. for $C_{18}H_{22}F_{16}Nd_2O_{23}S_4$ (%): C 18.40, H 1.89, Nd 24.55; found: C 18.36, H 2.01, Nd 24.50. The compound was initially fortuitously obtained from what was considered to be neodymium oxide (0.62 g) and 1,2-benzenedisulfonic acid (0.62 g, 2.61 mmol) in water (30 mL) at reflux for 24 h. Reaction of $Nd_2(C_6H_4(SO_3)_2\text{-}1,2)_3$ with $HO_2C(CF_2)_4CO_2H$ did not yield **7**.

Structure determinations

Full spheres of CCD area-detector diffractometer data were measured (Bruker AXS instrument, ω-scans, monochromatic Mo Kα radiation, λ = 0.710 73 Å, T *ca.* 153K) yielding $N_{t(otal)}$ reflections, these merging to N unique (R_{int} cited) after "empirical"/multiscan absorption correction (proprietary software), N_o with $I > 2\sigma(I)$ being considered "observed". All reflections were used in the full matrix refinements on F^2, refining anisotropic displacement parameter forms for the non-hydrogen atoms, $(x, y, z, U_{iso})_H$ being refined for 1,2,7 (reflection weights: $(\sigma^2(F^2) + (aP)^2 (+ bP))^{-1}$ ($P = (F^2_o + 2F^2_c/3)$). Neutral atom complex scattering factors were employed within the SHELXL 97 program (36). Pertinent results are given above (Table 9) and in the tables and figures, the latter showing 50% displacement envelope probability amplitudes for the non-hydrogen atoms, where hydrogen atoms, where shown, have arbitrary radii of 0.1 Å. Where metal atom environment tables are presented in matrix form, r (Å) is the metal···ligand atom distance, with other entries being the angles (°) subtended at the metal atom by the relevant atoms at the head of the row and columns. Full cif. depositions, excluding structure factor amplitudes are supplied in the Supplementary data.[3]

Acknowledgements

The Australian Research Council is acknowledged for financial support.

References

1. F.A. Hart. *In* Comprehensive coordination chemistry. Vol. 3. *Edited by* G. Wilkinson, R.D. Gillard, and J.A. McCleverty. Pergamon, Oxford, UK. 1987. p. 1082.
2. E.R. Birnbaum. *In* Gmelin handbook of inorganic chemistry. Vol. D5. *Edited by* T. Moeller and E. Schleitzer-Rust. Springer-Verlag, Berlin. 1984.
3. G. Meyer. J. Alloys Compd. **300**, 113 (2000).
4. S. Cotton. *In* Comprehensive coordination chemistry II. Vol. 3. *Edited by* J.A. McCleverty, T.J. Meyer, and G.F.R. Parkin. Elsevier, Oxford. 2004. Chap. 3.2.
5. A. Ouchi, Y. Suzuki, Y. Ohki, and V. Koizumi. Coord. Chem. Rev. **92**, 29 (1988).
6. S.A. Cotton. C.R. Chimie, **8**, 129 (2005).
7. K. Biradha. CrystEngComm. **5**, 374 (2003).
8. D. Braga, L. Brammer, and N.R. Champness. CrystEngComm. **7**, 1 (2005).
9. L. Brammer. Chem. Soc. Rev. **33**, 476 (2004).
10. J.-C. Bünzli and C. Piguet. Chem. Rev. **102**, 1897 (2002).
11. Y.-Q. Zheng, L.-X. Zhou, and J.-L. Lin. Z. Krist. New Cryst. Struct. **216**, 351 (2001).
12. A. Dimos, D. Tsaousis, A. Michaelides, S. Skailika, S. Golhen, L. Ouahab, C. Didierjean, and A. Aubry. Chem. Mater. **14**, 2616 (2002).
13. Z.-G. Sun, Y.-P. Ren, L.-S. Long, R.-B. Huang, and L.-S. Zheng. Inorg. Chem. Commun. **5**, 629 (2002).
14. G. Piente, G. Echeveroia, F. Sives, E.V. Brussau, J.C. Pedregosa, G.E. Narda, and J. Elena. C.R. Chimie, **8**, 1469 (2005).
15. Y.J. Kim, M. Suh, and D.-Y. Jung. Inorg. Chem. **43**, 245 (2004).
16. D.T. deLill, W.W. Brennessel, L.A. Borkowski, N.S. Gunning, and C.L. Cahill. Acta Cryst. Sect. E Struct. Rep. Online, **61**, m1343 (2005).
17. C. Bromant, H. Flemig, W. Nika, I. Pantenburg, and G. Meyer. Z. Anorg. Allg. Chem. **632**, 851 (2005).
18. D.T. Lill, N.S. Gunning, and C.L. Cahill. Inorg. Chem. **44**, 258 (2005).
19. L.-M. Duan, L. Ye, Y.-B. Liu, F.-T. Xie, J.-H. Yu, and J.-Q. Xu. Pol. J. Chem. **79**, 1835 (2005).
20. L.A. Borkowski and C.L. Cahill. Inorg. Chem. Comm. **7**, 725 (2004).
21. L.-M. Duan, J.-Q. Xu, F.-T. Xie, Y.-B. Liu, and H. Ding. Inorg. Chem. Commun. **7**, 216 (2004).
22. G.-Y. Dong, J.-H. Dou, S.-Y. Ge, L. Lin, Y.-B. Zheng, and Z.-R. Wei. Chin. J. Str. Chem. **24**, 69 (2005).
23. M. Dan, G. Coltereau, and C.N.R. Rao. Solid State Sciences, **7**, 437 (2005).
24. A.D. Gutland, A. Hallen, J.W. Kampf, and V.L. Pecoraro. J. Am. Chem. Soc. **123**, 6211 (2001).
25. W.J. Evans, D.G. Giarikos, M.A. Johnston, M.A. Greci, and J.W. Ziller. J. Chem. Soc. Dalton Trans. 520 (2002).
26. D.C. Bradley, H. Chudzyriska, M.E. Hammond, M. Hursthouse, M. Montevalli, and V. Ruower. Polyhedron, **11**, 375 (1992).
27. H. Takemura, S. Nakashima, N. Kori, M. Yatsutaki, T. Shinmyozu, and T. Inazu. J. Am. Chem. Soc. **123**, 9293 (2001).
28. G.B. Deacon, R. Harika, P.C. Junk, B.W. Skelton, and A.H. White. New J. Chem. **31**, 634 (2007).

[3] Supplementary data for this article are available on the journal Web site (canjchem.nrc.ca) or may be purchased from the Depository of Unpublished Data, Document Delivery, CISTI, National Research Council Canada, Ottawa, ON K1A 0R6, Canada. DUD 3785. For more information on obtaining material refer to cisti-icist.nrc-cnrc.gc.ca/irm/unpub_e.shtml. CCDC numbers 622506 (compound **2**), 622507 (compound **4**), 622508 (compound **6**), 622509 ($H_2pfad{\cdot}2H_2O$), 622510 (compound **1**), and 609829 (compound **7**) contain the crystallographic data for this manuscript. These data can be obtained, free of charge, via www.ccdc.cam.ac.uk/conts/retrieving.html (Or from the Cambridge Crystallographic Data Centre, 12 Union Road, Cambridge CB2 1EZ, UK; fax +44 1223 336033; or deposit@ccdc.cam.ac.uk).

© 2008 NRC Canada

29. C.H. Evans. Biochemistry of the lanthanoids. Plenum, New York. 1990.
30. D.C. Stewart and D. Kato. Anal. Chem. **30**, 2 (1958).
31. H.-Z. Xie, D.-Y. Wei, and Y.-Q. Zheng. Acta Crystallogr. C, **61**, m419 (2005).
32. J.-L. Lin and Y.-Q. Zheng. Acta Crystallogr. C, **61**, m501 (2005).
33. G.B. Deacon, A. Gitlits, G. Zelesny, D. Stellfeldt, and G. Meyer. Z. Anorg. Allg. Chem. **625**, 764 (1999).
34. R. Centore and A. Tuzi. Z. Kristallogr. New Cryst. Struct. **214**, 526 (1999).
35. J.E. Cosgriff, G.B. Deacon, and B.M. Gatehouse. Aust. J. Chem. **46**, 1881 (1993).
36. G.M. Sheldrick. SHELXL 97 [computer program]. University of Göttingen, Germany. 1997.

© 2008 NRC Canada

Synthesis and electrochemical properties of bimetallic η^5-indenyl ruthenium complexes[1]

Quan Yuan Hu and Guochen Jia

Abstract: Treatment of RuCl(dppm)(η^5-C_9H_7) with alkynes HC≡C(C_6H_4)$_n$C≡CH (n = 1, 2) in the presence of $TlPF_6$ and *t*-BuONa affords the bimetallic ruthenium acetylide complexes [(η^5-C_9H_7)(dppm)Ru]$_2$(μ-C≡C(C_6H_4)$_n$C≡C). Reactions of the hydride complex RuH(dppm)(η^5-C_9H_7) with HC≡C(C_6H_4)$_n$C≡CH (n = 1, 2) in refluxing toluene give the bimetallic ruthenium alkenyl complexes [(η^5-C_9H_7)(dppm)Ru]$_2$(μ-CH=CH(C_6H_4)$_n$CH=CH). The electrochemical properties of the new complexes have been investigated by cyclic voltammetry, which reveals that the organic spacer –CH=CHC_6H_4CH=CH– is more effective than –C≡CC_6H_4C≡C– in mediating electronic communication between the two ruthenium moieties.

Key words: ruthenium, bimetallic, acetylide, insertion, electrochemistry.

Résumé : La réaction du RuCl(dppm)(η^5-C_9H_7) avec les alcynes HC≡C(C_6H_4)$_n$C≡CH (n = 1, 2), en présence de $TlPF_6$ et de *t*-BuONa conduit à la formation des bimétalliques d'acétylures de ruthénium, [η^5-C_9H_7)(dppm)Ru]$_2$[μ-C≡C(C_6H_4)$_n$C≡C]. Les réactions de l'hydrure complexe RuH(dppm)(η^5-C_9H_7) avec le HC≡C(C_6H_4)$_n$C≡CH (n = 1, 2), dans le toluène au reflux, conduit à la formation des complexes bimétalliques d'alcénylruthénium [(η^5-C_9H_7)(dppm)Ru]$_2$[μ-C=C(C_6H_4)$_n$C=C]. Les propriétés électrochimiques des nouveaux complexes ont été évaluées par voltampérométrie cyclique et elles révèlent que par rapport au groupe organique d'espacement –C≡C(C_6H_4)$_n$C≡C–, le groupe –C=C(C_6H_4)$_n$C=C– permet une meilleure communication électronique entre les deux portions contenant du ruthénium.

Mots-clés : ruthénium, bimétallique, acétylure, insertion, électrochimie.

[Traduit par la Rédaction]

Introduction

Bimetallic complexes with a π-conjugated hydrocarbon bridge have attracted much interest for their synthesis and physical properties (1). Examples of common conjugated bimetallic complexes include acetylide complexes $L_nMC{\equiv}C(C{\equiv}C)_mC{\equiv}CML_n$ (2, 3) and $L_nMC{\equiv}C(CH{=}CH)_mC{\equiv}CML_n$ (4), and alkenyl complexes $L_nMCH{=}CH(CH{=}CH)_mCH{=}CHML_n$ (5, 6). Electrochemical properties of many of these carbon-rich bimetallic complexes have been investigated to evaluate whether electron delocalization takes place or whether electronic communication occurs.

Received 8 March 2008. Accepted 23 April 2008. Published on the NRC Research Press Web site at canjchem.nrc.ca on 15 August 2008.

Dedicated to Professor Richard J. Puddephatt, a respected mentor and valued friend, in recognition of his outstanding contributions to science.

Q.Y. Hu[2] and G. Jia.[3] Department of Chemistry, The Hong Kong University of Science and Technology, Clear Water Bay, Kowloon, Hong Kong.

[1]This article is part of a Special Issue dedicated to Professor R. Puddephatt.

[2]Present address: Ministry of Education Key Laboratory for the Synthesis and Application of Organic Functional Molecules, College of Chemistry and Chemical Engineering, Hubei University, Wuhan 430062, Hubei Province, P. R. China.

[3]Corresponding author (e-mail: chjiag@ust.hk).

Organic spacers play an important role in mediating electronic communication. To study the effect of organic spacers, it is desirable to have bimetallic complexes with the same metal moieties but different organic bridges. The diethynyl units –C≡C(C_6H_4)$_n$C≡C– (7–9) and divinyl units –CH=CH(C_6H_4)$_n$CH=CH– (10) are often used as a bridge in constructing bimetallic or polymetallic complexes. However, bimetallic complexes with the same metal moieties containing these bridging ligands are rare. In this work, we have obtained bimetallic complexes with the same metal moiety Ru(dppm)(η^5-C_9H_7) linked by –C≡C(C_6H_4)$_n$C≡C– or –CH=CH(C_6H_4)$_n$CH=CH– (n = 1, 2), using precursors RuCl(dppm)(η^5-C_9H_7) (11) and RuH(dppm)(η^5-C_9H_7) (12) as the starting materials. We have also investigated the electrochemical properties of the new complexes by cyclic voltammetry. The details of the investigations are reported in this paper.

Results and discussion

Synthesis of metal complexes

Treatment of RuCl(dppm)(η^5-C_9H_7) (**1**) with 1 equiv. $TlPF_6$ in THF gave a solution of the putative intermediate [Ru(THF)(dppm)(η^5-C_9H_7)]PF_6 (**2**), which reacted with HC≡CC_6H_4C≡CH at refluxing temperature in the presence of *t*-BuONa to give a brown solution, from which the bimetallic σ-alkynyl complexes [(η^5-C_9H_7)(dppm)Ru]$_2$(μ-C≡CC_6H_4C≡C) (**3**) (Scheme 1) can be isolated.

A similar reaction between **2** and HC≡C$C_6H_4C_6H_4$C≡CH gave the bimetallic complex [(η^5-C_9H_7)(dppm)Ru]$_2$(μ-

 doi:10.1139/V08-106 © 2008 NRC Canada

Scheme 1.

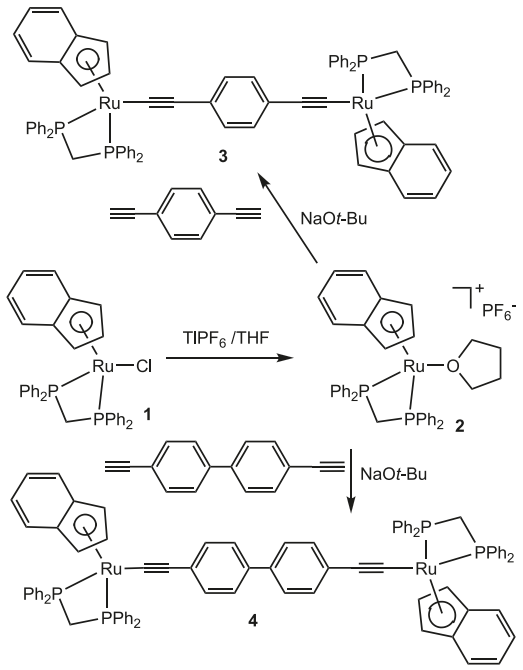

Scheme 2.

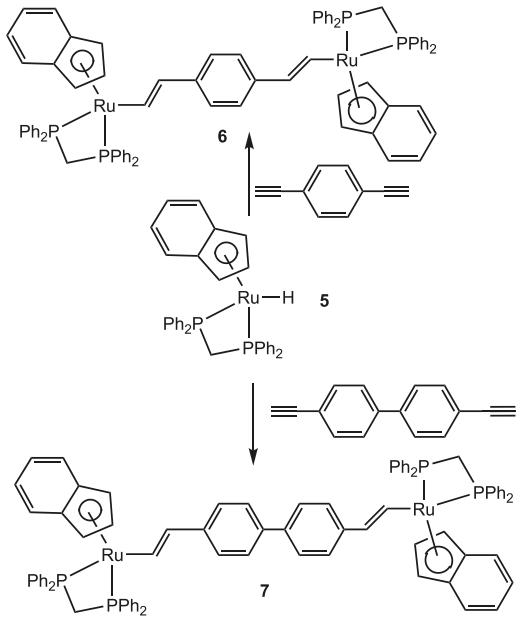

C≡CC$_6$H$_4$C$_6$H$_4$C≡C) (**4**). Attempts to prepare complexes **3** and **4** by the reactions of RuCl(dppm)(η^5-C$_9$H$_7$) with HC≡CC$_6$H$_4$C≡CH or HC≡CC$_6$H$_4$C$_6$H$_4$C≡CH in the presence of $NaPF_6$ and NEt_3 were unsuccessful.

The bimetallic acetylide complexes **3** and **4** have been characterized analytically and spectroscopically. The IR spectra exhibit a characteristic υ(C≡C) peak at 2070 and 2074 cm^{-1} for **3** and **4**, respectively. The $^{31}P\{^1H\}$ NMR spectra in $CDCl_3$ show a singlet at 17.8 ppm for **3** and 17.6 ppm for **4**, indicating the chemical equivalence of the phosphorus atoms. The chemical shifts are close to those of Ru(C≡CC(Ph) = CH$_2$)(η^5-C$_9$H$_7$)(dppm) (13), Ru(C≡CPh)(η^5-C$_9$H$_7$)(dppm) (14), and Ru(C≡CC$_6$H$_4$NO$_2$-4)(η^5-C$_9$H$_7$)(dppm) (15) (being 19.50, 19.02, and 18.79 ppm, respectively). The $^{13}C\{^1H\}$ NMR spectra display a characteristic triplet signal of RuC_α at 117.5 ppm for **3** and 116.6 ppm for **4** with a $^3J_{CP}$ of ~22.5 Hz. The resonance of C_β of RuC$_\alpha$≡C_β appears as a singlet at 112.3 ppm for **3** and 112.2 ppm for **4**. In the ^1H and $^{13}C\{^1H\}$ NMR spectra, the chemical shifts of the signals associated with the indenyl and dppm ligands are similar to those of the known mononuclear compounds Ru(C≡CR)(dppm)(η^5-C$_9$H$_7$) (13–15).

The hydrido complex RuH(η^5-C$_9$H$_7$)(dppm) (**5**) is known to undergo insertion reactions with alkynes RC≡CR to give σ-alkenyl complexes Ru(CR=CHR)(η^5-C$_9$H$_7$)(dppm) (16). Thus, we expect that the reaction of RuH(η^5-C$_9$H$_7$)(dppm) with HC≡CRC≡CH may give bimetallic complex [(η^5-C$_9$H$_7$)(dppm)Ru]$_2$(μ-CH=CHRCH=CH). Indeed, reaction of RuH(η^5-C$_9$H$_7$)(dppm) (**5**) with 0.5 equiv. of HC≡CC$_6$H$_4$C≡CH in toluene at refluxing temperature leads to a brown solution from which the bimetallic σ-alkenyl complex [(η^5-C$_9$H$_7$)(dppm)Ru]$_2$(μ-CH=CHC$_6$H$_4$CH=CH) (**6**) can be isolated as a red solid (Scheme 2). Similar reaction between RuH(η^5-C$_9$H$_7$)(dppm) and HC≡CC$_6$H$_4$C$_6$H$_4$C≡CH gave the analogous complex [(η^5-C$_9$H$_7$)(dppm)Ru]$_2$(μ-CH=CHC$_6$H$_4$C$_6$H$_4$CH=CH) (**7**). As monitored by $^{31}P\{^1H\}$ NMR spectroscopy, compared to the reaction of RuH(η^5-C$_9$H$_7$)(dppm) with phenylacetylene (80 °C, 3 h) (16*a*), complete formation of bimetallic complexes **6** and **7** requires a higher temperature and a longer time, especially for the formation of **6**, due to steric effect.

Complexes **6** and **7** have been characterized by elemental analysis and NMR ($^{31}P\{^1H\}$, ^1H, and $^{13}C\{^1H\}$) spectroscopy. The spectroscopic data associated with indenyl and dppm ligands are similar to those of Ru(*E*-CH=CHR)(η^5-C$_9$H$_7$)(dppm) (16). The $^{31}P\{^1H\}$ NMR spectra show a singlet at δ 22.5 ppm for **6** and at 21.4 ppm for **7**. The trans stereochemistry of the alkenyl ligand is indicated by the ^1H NMR data. In particular, the ^1H NMR spectrum of **6** in $CDCl_3$ shows the signals of RuC_αH and RuCH=CH_β at 7.78 and 5.79 ppm, respectively, with a $^3J_{HH}$ of 16.2 Hz. The ^1H NMR spectrum of **7** in $CDCl_3$ shows the signals of RuC_αH and RuCH=CH_β at 8.12 and 5.93 ppm with a $^3J_{HH}$ of 16.2 Hz. The magnitude of the $^3J_{HH}$ coupling constants supports the trans geometry of RuCH=CH double bond. In the $^{13}C\{^1H\}$ NMR spectrum of **6** in CD_2Cl_2, the signals of the alkenyl ligand appear at 147.5 (C$_\alpha$) and 139.5 (C$_\beta$) ppm. For complex **7**, the C$_\alpha$ and C$_\beta$ signals of the alkenyl ligand appear at 153.4 and 138.8 ppm, respectively.

Electrochemical properties

To study the electrochemical properties of complexes **3**, **4**, **6**, and **7**, their cyclic voltammograms were collected in CH_2Cl_2 supported by *n*-Bu$_4$NPF$_6$ at 25 °C with a scanning rate of 20 mV/s. The results are collected in Table 1, where the potentials are referenced to that of Fc/Fc$^+$.

The cyclic voltammogram of **3** in CH_2Cl_2 exhibits two reversible waves at 0.053 and 0.241 V vs. Fc/Fc$^+$. These two oxidation waves can be attributed to the formation of [(η^5-C$_9$H$_7$)(dppm)RuC≡CC$_6$H$_4$C≡CRu(dppm)(η^5-C$_9$H$_7$)]$^+$ and [(η^5-C$_9$H$_7$)(dppm)Ru=C=C=C$_6$H$_4$=C=C=Ru(dppm)(η^5-C$_9$H$_7$)]$^{2+}$ (Scheme 3). The peak separation of the two waves is 0.195 V, implying the presence of metal–metal interaction. Similar results have been observed for related homobimetallic com-

© 2008 NRC Canada

Table 1. Electrochemical data for complexes **3**, **4**, **6**, and **7**.

Complex	E_p^a (V)	E_p^c (V)	$E_{1/2}$ (V)	n-Bu_4NPF_6 (mol/L)
3	0.101	0.005	0.053	0.10
	0.296	0.186	0.241	
4	–0.080	–0.154	–0.117	0.50
6	–0.269	–0.343	–0.306	0.50
	–0.013	–0.087	–0.050	
7	–0.285	–0.359	–0.322	0.50

Note: $E_{1/2} = (E_p^a + E_p^c)/2$.

plexes, such as $Cl(dppm)_2RuC{\equiv}CC_6H_4C{\equiv}CRu(dppm)_2Cl$ ($E_{1/2}$ = –0.30 and 0.00 V vs. Fc/Fc^+) (9a), $Cl(dppm)_2OsC{\equiv}CC_6H_4C{\equiv}COs(dppm)_2Cl$ ($E_{1/2}$ = –0.51 and –0.21 V vs. Fc/Fc^+) (9a), $Cl(dppe)_2RuC{\equiv}CC_6H_4C{\equiv}CRu(dppe)_2Cl$ ($E_{1/2}$ = 0.15 and 0.51 V vs. SCE) (9*b*), $[(\eta^5\text{-}C_5Me_5)(dppe)FeC{\equiv}CC_6H_4C{\equiv}CFe(dppe)(\eta^5\text{-}C_5Me_5)]$ ($E_{1/2}$ = –0.315 and –0.050 V vs. SCE) (9c), and $Cl(depe)_2FeC{\equiv}CC_6H_4C{\equiv}CFe(depe)_2Cl$ (9*a*) ($E_{1/2}$ = –0.63 and –0.47 V vs. Fc/Fc^+), where the peak separations are 0.30, 0.30, 0.36, 0.265, and 0.16 V, respectively.

Similarly, the cyclic voltammogram of **6** in CH_2Cl_2 also exhibits two reversible waves at –0.306 and –0.050 V vs. Fc/Fc^+ with a peak separation of 0.256 V. The two oxidation waves can be attributed to the generation of $[(\eta^5\text{-}C_9H_7)(dppm)RuCH{=}CHC_6H_4CH{=}CHRu(dppm)(\eta^5\text{-}C_9H_7)]^+$ and $[(\eta^5\text{-}C_9H_7)(dppm)Ru{=}CHCH{=}C_6H_4{=}CH\text{-}CH{=}Ru(dppm)(\eta^5\text{-}C_9H_7)]^{2+}$ (Scheme 4). The peak potentials suggest that it is easier to oxidize complex **7** ($E_{1/2}$ = –0.306 and –0.050 V vs. Fc/Fc^+, respectively) than complex **3** ($E_{1/2}$ = 0.053 and 0.241 V vs. Fc/Fc^+, respectively). The observation of a peak separation of 0.256 V for **6** clearly indicates a communication between the two ruthenium centers in **6**. The value is bigger than that of complex **3** (0.195 V), which has the conjugated bridge –C≡C–C_6H_4–C≡C–. The results reveal that –CH=CHC_6H_4CH=CH– is more efficient in mediating electron transfer or electronic delocalization than –C≡CC_6H_4C≡C– in homobimetallic complexes.

In contrast, the cyclic voltammograms of the acetylide complex **4** and the vinyl complex **7** only exhibit one reversible oxidation wave at –0.117 V vs. Fc/Fc^+ and –0.322 V vs. Fc/Fc^+, respectively. Apparently, the biphenyl group reduces the interaction between the two ruthenium moieties. The peak potentials again suggest that it is easier to oxidize the vinyl complex **7** than the analogous acetylide complex **4**.

In summary, we have successfully prepared bimetallic complexes $[(\eta^5\text{-}C_9H_7)(dppm)Ru]_2(\mu\text{-}C{\equiv}C(C_6H_4)_nC{\equiv}C)$ (n = 1, 2) and $[(\eta^5\text{-}C_9H_7)(dppm)Ru]_2(\mu\text{-}CH{=}CH(C_6H_4)_nCH{=}CH)$ (n = 1, 2). Cyclic voltammetry studies reveal that complexes bridged with –C≡CC_6H_4C≡C– or –CH=CHC_6H_4CH=CH– show two reversible redox waves, while complexes bridged with –C≡$CC_6H_4C_6H_4$C≡C– or –CH=$CHC_6H_4C_6H_4$CH=CH– exhibit one reversible redox wave. The studies also suggest that the organic spacer –CH=CHC_6H_4CH=CH– is better than –C≡CC_6H_4C≡C– in mediating electronic communication between the two ruthenium moieties.

Experimental section

All manipulations were carried out at room temperature under a nitrogen atmosphere using standard Schlenk techniques unless otherwise stated. Solvents were distilled under nitrogen from sodium benzophenone (hexane, ether, and THF), sodium (benzene), or calcium hydride (CH_2Cl_2). The starting materials $RuCl(dppm)(\eta^5\text{-}C_9H_7)$ (11) and $RuH(dppm)(\eta^5\text{-}C_9H_7)$ (12) were prepared following the procedures described in literature. All other reagents were used as purchased from Sigma-Aldrich Chemical Co., USA.

Microanalyses were performed by M-H-W Laboratories (Phoenix, AZ). ^1H, $^{13}C\{^1H\}$, and $^{31}P\{^1H\}$ spectra were collected on a Bruker ARX 300 MHz spectrometer. ^1H and ^{13}C NMR chemical shifts are referenced relative to TMS, and ^{31}P NMR chemical shifts are referenced relative to 85% H_3PO_4. FTIR spectra were recorded on a PerkinElmer Spectrum-One spectrometer. MS spectra were recorded on a Finnigan TSQ7000 spectrometer. The electrochemical measurements were performed with a CHI 660 potentiostat. A three-component electrochemical cell was used with a glassy-carbon electrode as the working electrode, a platinum wire as the counter electrode, and an Ag/AgCl electrode as the reference electrode. The cyclic voltammograms were collected with a scan rate of 20 mV/s in CH_2Cl_2 containing 0.10 or 0.50 mol/L n-Bu_4NPF_6 as the supporting electrolyte. The peak potentials reported are referenced to the ferrocene/ferrocenium redox couple (Fc/Fc^+).

Scheme 3. Electrochemical redox process of complex **3**.

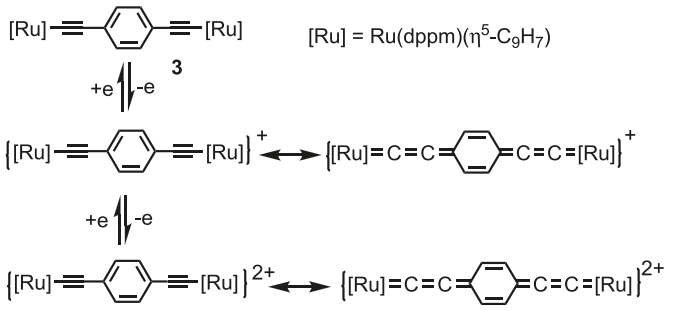

Scheme 4. Electrochemical redox process of complex **6**.

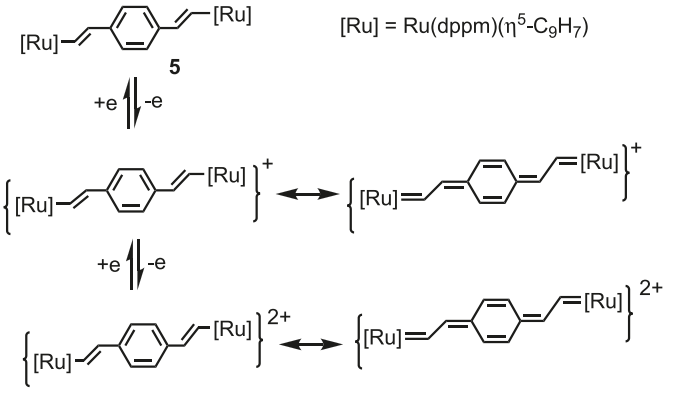

[$(\eta^5$-$C_9H_7)$(dppm)Ru]$_2(\mu$-C≡CC_6H_4C≡C) (3)

A mixture of $RuCl(dppm)(\eta^5\text{-}C_9H_7)$ (456 mg, 0.717 mmol) and $TlPF_6$ (250 mg, 0.717 mmol) was stirred in THF (20 mL) for 2 h and then filtered. To the filtrate was added 1,4-diethynylbenzene (40 mg, 0.32 mmol) and a solution of *t*-BuONa (100 mg, 1.04 mmol) in THF (10 mL). The mixture was refluxed for 3 h and then filtered through Celite.

© 2008 NRC Canada

The solvent was removed under vacuum. The residue was washed with CH_3OH (5 × 10 mL) and then recrystallized twice from CH_2Cl_2/hexane (1:5) and dried under vacuum to give a brown solid. Yield: 195 mg, 46%. FTIR (KBr, cm^{-1}): $\upsilon_{(C\equiv C)}$ = 2070. $^{31}P\{^1H\}$ NMR (CD_2Cl_2, 121.48 MHz) δ: 17.8 (s). ^1H NMR (CD_2Cl_2, 300.13 MHz) δ: 7.70–7.13 (br m, 52 H, 40 H of PPh, 4 H of C_6H_4, 8 H of C_9H_7), 5.80 (m, 4 H, C_9H_7), 5.46 (m, 2 H, C_9H_7), 4.71 (dt, J_{HH} = 13.8 Hz, $^2J_{HP}$ = 9.6 Hz, 2 H, PCHP), 4.35 (dt, J_{HH} = 13.8 Hz, $^2J_{HP}$ = 11.8 Hz, 2 H, PCHP). $^{13}C\{^1H\}$ NMR (CD_2Cl_2, 75.46 MHz) δ: 138.5–127.8 (m, C_6H_4, PC_6H_5), 124.8 (s, C_9H_7), 123.4 (s, C_9H_7), 117.5 (t, $^3J_{CP}$ = 22.5 Hz, RuC), 112.3 (s, RuC≡*C*), 107.2 (s, C_9H_7), 89.1 (s, C_9H_7), 67.7 (s, C_9H_7), 49.9 (t, $^2J_{CP}$ = 23.4 Hz, PCH_2P). Anal. calcd. for $C_{78}H_{62}P_4Ru_2$: C, 70.58; H, 4.71; found: C, 70.22; H, 4.42. FAB-MS: *m*/*z* = 1326.6 (calcd. 1326.2).

[(η^5-C_9H_7)(dppm)Ru]$_2$(μ-C≡C$C_6H_4C_6H_4$C≡C) (4)

A mixture of RuCl(dppm)(η^5-C_9H_7) (1.40 g, 2.20 mmol) and $TlPF_6$ (0.77 g, 2.20 mmol) was stirred in THF (25 mL) for 2 h and then filtered. To the filtrate was added HC≡C$C_6H_4C_6H_4$C≡CH (202 mg, 1.00 mmol) and a solution of *t*-BuONa (200 mg, 2.08 mmol) in THF (15 mL). The mixture was refluxed for 2 h and then filtered through Celite. The solvent was removed under vacuum. The residue was washed with CH_3OH (5 × 10 mL) and then recrystallized twice from CH_2Cl_2/CH_3OH (1:4) and dried under vacuum to give a brown solid. Yield: 0.75 g, 54 %. FTIR (KBr, cm^{-1}): $\upsilon_{(C\equiv C)}$ = 2074. $^{31}P\{^1H\}$ NMR (CD_2Cl_2, 121.48 MHz) δ: 17.6 (s). ^1H NMR (CD_2Cl_2, 300.13 MHz) δ: 7.78–7.10 (br m, 56 H, 40 H of PPh, 8 H of C_9H_7 and 8 H of C_6H_4), 5.84 (m, 4 H, C_9H_7), 5.49 (m, 2 H, C_9H_7), 4.75 (dt, J_{HH} = 13.8 Hz, $^2J_{HP}$ = 9.6 Hz, 2 H, PCHP), 4.38 (dt, J_{HH}= 13.8 Hz, $^2J_{HP}$ = 11.8 Hz, 2 H, PCHP). $^{13}C\{^1H\}$ NMR (CD_2Cl_2, 75.46 MHz) δ: 142.2–128.7 (m, C_6H_4 and PC_6H_5), 124.6 (s, C_9H_7), 123.3 (s, C_9H_7), 116.6 (t, $^3J_{CP}$ = 22.5 Hz, RuC), 112.2 (s, RuC≡*C*), 106.8 (s, C_9H_7), 88.7 (s, C_9H_7), 67.5 (s, C_9H_7), 49.7 (t, $^2J_{CP}$ = 23.6 Hz, PCH_2P). Anal. calcd. for $C_{84}H_{66}P_4Ru_2$: C, 71.89; H, 4.74; found: C, 71.44; H, 4.35. FAB-MS: *m*/*z* = 1402.5 (calcd. 1402.2).

[(η^5-C_9H_7)(dppm)Ru]$_2$(μ-CH=CHC_6H_4CH=CH) (6)

A mixture of RuH(dppm)(η^5-C_9H_7) (0.51 g, 0.85 mmol) and 1,4-diethynylbenzene (0.05 g, 0.40 mmol) in toluene (20 mL) was refluxed for 12 h, and the solvent was removed under vacuum. The residue was washed with hexane (3 × 10 mL) and then recrystallized twice from CH_2Cl_2/hexane (1:4) and dried under vacuum to afford a yellow solid. Yield: 0.47 g, 89%. $^{31}P\{^1H\}$ NMR (CD_2Cl_2, 121.48 MHz) δ: 22.5 (s). ^1H NMR (CD_2Cl_2, 300.13 MHz) δ: 7.78 (dt, $^3J_{HH}$ = 16.2 Hz, $^3J_{HP}$ = 5.4 Hz, 2 H, RuCH), 7.57–6.77 (br m, 52 H, 40 H of PPh, 4 H of C_6H_4, 8 H of C_9H_7), 5.79 (d, J_{HH} = 16.2 Hz, 2 H, RuCH=C*H*), 5.51 (m, 4 H, C_9H_7), 5.29 (m, 2 H, C_9H_7), 4.33 (dt, J_{HH}= 13.8 Hz, $^2J_{HP}$ = 9.6 Hz, 2 H, PCHP), 3.94 (dt, J_{HH}= 13.8 Hz, $^2J_{HP}$ = 11.4 Hz, 2 H, PCHP). $^{13}C\{^1H\}$ NMR (CD_2Cl_2, 75.46 MHz) δ: 147.5 (t, $^2J_{CP}$ = 15.5 Hz, Ru*C*H=CH), 139.5 (t, $^3J_{CP}$ = 4.6 Hz, RuCH=*CH*), 139.4–128.0 (m, PC_6H_5), 137.7 (s, C_6H_4), 124.1 (s, C_9H_7), 123.1 (s, C_6H_4), 122.6 (s, C_9H_7), 108.4 (s, C_9H_7), 90.2 (s, C_9H_7), 68.4 (s, C_9H_7), 49.3 (t, $^2J_{CP}$ = 21.8 Hz, PCH_2P). Anal. calcd. for $C_{78}H_{66}P_4Ru_2$: C, 70.36; H, 5.00; found: C, 69.93; H, 5.03. FAB-MS: *m*/*z* = 1329.9 (calcd. 1330.2).

[(η^5-C_9H_7)(dppm)Ru]$_2$(μ-CH=C$HC_6H_4C_6H_4$CH=CH) (7)

A mixture of RuH(dppm)(η^5-C_9H_7) (100 mg, 0.166 mmol) and HC≡C$C_6H_4C_6H_4$C≡CH (15 mg, 0.074 mmol) in toluene (10 mL) was refluxed for 3 h, and the solvent was removed under vacuum. The residue was washed with hexane (3 × 10 mL) and then recrystallized twice from CH_2Cl_2/hexane (1:4) and dried under vacuum to afford a yellow solid. Yield: 92 mg, 88%. $^{31}P\{^1H\}$ NMR ($CDCl_3$, 121.50 MHz) δ: 21.4 (s). ^1H NMR ($CDCl_3$, 300.13 MHz) δ: 8.12 (dt, $^3J_{HH}$ = 16.2 Hz, $^3J_{HP}$ = 5.8 Hz, 2 H, RuCH), 7.52–7.00 (br m, 56 H, 40 H of PPh, 8 H of C_9H_7 and 8 H of C_6H_4), 6.94 (d, J_{HH} = 8.1 Hz, 4 H, C_6H_4), 5.93 (d, J_{HH} = 16.2 Hz, 2 H, RuCH=C*H*), 5.55 (m, 4 H, C_9H_7), 5.31 (m, 2 H, C_9H_7), 4.42 (dt, J_{HH} = 13.8 Hz, $^2J_{HP}$ = 9.6 Hz, 2 H, PCHP), 4.04 (dt, J_{HH} = 13.8 Hz, $^2J_{HP}$ = 11.4 Hz, 2 H, PCHP). $^{13}C\{^1H\}$ NMR ($CDCl_3$, 75.48 MHz) δ: 153.4 (t, $^2J_{CP}$ = 15.5 Hz, Ru*C*H=CH), 140.6 (s, C_6H_4), 139.5–128.0 (m, PC_6H_5), 138.8 (t, $^3J_{CP}$ = 4.6 Hz, Ru RuCH=CH), 137.7 (s, C_6H_4), 135.9 (s, C_6H_4), 125.8 (s, C_9H_7), 124.3 (s, C_9H_7), 124.0 (s, C_6H_4), 123.0 (s, C_6H_4), 108.6 (s, C_9H_7), 90.4 (s, C_9H_7), 68.6 (s, C_9H_7), 49.3 (t, $^2J_{CP}$ = 21.7 Hz, PCH_2P). Anal. calcd. for $C_{84}H_{70}P_4Ru_2$: C, 71.68; H, 5.02; found: C, 71.24; H, 4.95.

Acknowledgment

We acknowledge financial support from the Hong Kong Research Grants Council (Grant No. HKUST601306).

References

1. (*a*) M.I. Bruce and P.J. Low. Adv. Organomet. Chem. **50**, 179 (2004); (*b*) S. Szafert and J.A. Gladysz. Chem. Rev. **103**, 4175 (2003); (*c*) N.J. Long, and C.K. Williams. Angew. Chem., Int. Ed. **42**, 2586 (2003); (*d*) F. Paul and C. Lapinte. Coord. Chem. Rev. **178**, 431 (1998); (*e*) U.H.F. Bunz. Angew. Chem., Int. Ed. Engl. **35**, 969 (1996); (*f*) S. Lotz, P.H. van Rooyen, and R. Meyer. Adv. Organomet. Chem. **37**, 219 (1995); (*g*) N.J. Long. Angew. Chem., Int. Ed. Engl. **34**, 21 (1995); (*h*) M.D. Ward, Chem. Soc. Rev. 121 (1995); (*i*) H. Lang. Angew. Chem., Int. Ed. Engl. **33**, 547 (1994); (*j*) W. Beck, B. Niemer, and M. Wieser. Angew. Chem., Int. Ed. Engl. **32**, 923 (1993).
2. For recent work on bimetallic complexes with a C_x bridge, see for example: (*a*) M.I. Bruce, K. Costuas, T. Davin, J.F. Halet, K.A. Kramarczuk, P.J. Low, B.K. Nicholson, G.J. Perkins, R.L. Roberts, B.W. Skelton, M.E. Smith, and A.H. White. Dalton Trans. 5387 (2007); (*b*) L. de Quadras, E.B. Bauer, J. Stahl, F. Zhuravlev, F. Hampel, and J.A. Gladysz. New J. Chem. **31**, 1594 (2007); (*c*) M.I. Bruce, K. Costuas, B.G. Ellis, J.F. Halet, P.J. Low, B. Moubaraki, K.S. Murray, N. Ouddai, G.J. Perkins, B.W. Skelton, and A.H. White. Organometallics, **26**, 3735 (2007); (*d*) J. Stahl, W. Mohr, L. de Quadras, T.B. Peters, J.C. Bohling, J.M. Martín-Alvarez, G.R. Owen, F. Hampel, and J.A. Gladysz. J. Am. Chem. Soc. **129**, 8282 (2007); (*e*) L. Quadras, E.B. Bauer, W. Mohr, J.C. Bohling, T.B. Peters, J.M. Martín-Alvarez, F. Hampel, and J.A. Gladysz. J. Am. Chem. Soc. **129**, 8296 (2007).
3. Additional examples: (*a*) M.I. Bruce, K. Costuas, T. Davin, B.G. Ellis, J.F. Halet, C. Lapinte, P.J. Low, M.E. Smith, B.W.

© 2008 NRC Canada

Skelton, L. Toupet, and A.H. White. Organometallics, **24**, 3864 (2005); (*b*) M.I. Bruce, B.G. Ellis, M. Gaudio, C. Lapinte, G. Melino, F. Paul, B.W. Skelton, M.E. Smith, L. Toupet, and A.H. White. Dalton Trans. 1601 (2004); (*c*) G.L. Xu, G. Zou, Y.H. Ni, M.C. DeRosa, R.J. Crutchley, and T. Ren. J. Am. Chem. Soc. **125**, 10057 (2003); (*d*) V.W.W. Yam, K.M.C. Wong, and N.Y. Zhu. Angew. Chem., Int. Ed. **42**, 1400 (2003); (*e*) F. Coat, F. Paul, C. Lapinte, L. Toupet, K. Costuas, and J.F. Halet. J. Organomet. Chem. **683**, 368 (2003); (*f*) H.J. Jiao, K. Costuas, J.A. Gladysz, J.F. Halet, M. Guillemot, L. Toupet, F. Paul, and C. Lapinte. J. Am. Chem. Soc. **125**, 9511 (2003).

4. See for example: (*a*) L.B. Gao, S.H. Liu, L.Y. Zhang, L.X. Shi, and Z.N. Chen. Organometallics, **25**, 506 (2006); (*b*) M. Akita, Y. Tanaka, C. Naitoh, T. Ozawa, N. Hayashi, M. Takeshita, A. Inagaki, and M.C. Chung. Organometallics, **25**, 5261 (2006); (*c*) Y. Shi, G.T. Yee, G. Wang, and T. Ren. J. Am. Chem. Soc. **126**, 10552 (2004).
5. (*a*) H.P. Xia and G. Jia. Organometallics, **16**, 1 (1997); (*b*) H.P. Xia, R.C.Y. Yeung, and G. Jia. Organometallics, **16**, 3557 (1997); (*c*) H.P. Xia, R.C.Y. Yeung, and G. Jia, Organometallics, **17**, 4762 (1998); (*d*) S.H. Liu, Y.H. Chen, K.L. Wan, T.B. Wen, Z.Y. Zhou, M.F. Lo, I.D. Williams, and G. Jia. Organometallics, **21**, 4984 (2002); (*e*) S.H. Liu, H.P. Xia, T.B. Wen, Z.Y. Zhou, and G. Jia. Organometallics, **22**, 737 (2002); (*f*) S.H. Liu, Q.Y. Hu, P. Xue, T.B. Wen. I.D. Williams, and G. Jia. Organometallics, **24**, 769 (2005).
6. Additional examples: (*a*) N. Rajapakse, B.R. James, and D. Dolphin. Can. J. Chem. **68**, 2274 (1990); (*b*) R.M. Bullock, F.R. Lemke, and D.J. Szalda. J. Am. Chem. Soc. **112**, 3244 (1990); (*c*) F.R. Lemke, D.J. Szalda, and R. M. Bullock. J. Am. Chem. Soc. **113**, 8466 (1991); (*d*) M.B. Sponsler. Organometallics, **14**, 1920 (1995); (*e*) B.A. Etzenhouser, Q. Chen, and M.B. Sponsler. Organometallics, **13**, 4176 (1994); (*f*) B.A. Etzenhouser, M.D. Cavanaugh, H.N. Spurgeon, and M.B. Sponsler. J. Am. Chem. Soc. **116**, 2221 (1994); (*g*) M.C. Chung, X. Gu, B.A. Etzenhouser, A.M. Spuches, P.T. Rye, S.K. Seetharaman, D.J. Rose, J. Zubieta, and M.B. Sponsler. Organometallics, **22**, 3485 (2003); (*h*) X. Niu, L. Gopal, M.P. Masingale, D.A. Braden, B.S. Hudson, and M.B. Sponsler. Organometallics, **19**, 649 (2000); (*i*) H.H. Fox, J.K. Lee, L.Y. Park, and R.R. Schrock. Organometallics, **12**, 759 (1993).
7. Recent examples: (*a*) L.B. Gao, J. Kan, Y. Fan, L.Y. Zhang, S.H. Liu, and Z.N. Chen. Inorg. Chem. **46**, 5651 (2007); (*b*) S.I. Ghazala, F. Paul, L. Toupet, T. Roisnel, P. Hapiot, and C. Lapinte. J. Am. Chem. Soc. **128**, 2463 (2006); (*c*) M. Samoc, N. Gauthier, M.P. Cifuentes, F. Paul, C. Lapinte, and M.G. Humphrey. Angew Chem., Int. Ed. **45**, 7376 (2006); (*d*) A. Klein, O. Lavastre, and J. Fiedler. Organometallics, **25**, 635 (2006); (*e*) L. Medei, L. Orian, O.V. Semeikin, M.G. Peterleitner, N.A. Ustynyuk, S. Santi, C. Durante, A. Ricci, and C.L. Sterzo. Eur. J. Inorg. Chem. **45**, 2582 (2006); (*f*) M.I. Bruce, P.J. Low, F. Hartl, P.A. Humphrey, F. de Montigny, M. Jevric, C. Lapinte, G.J. Perkins, R.L. Roberts, B.W. Skelton, and A.H. White. Organometallics, **24**, 5241 (2005); (*g*) F. de Montigny, G. Argouarch, K. Costuas, J.F. Halet, T. Roisnel, L. Toupet, and C. Lapinte. Organometallics, **24**, 4558 (2005).
8. (*a*) M.A. MacDonald, R.J. Puddephatt, and G.P.A. Yap. Organometallics, **19**, 2194 (2000); (*b*) M.J. Irwin, J.J. Vittal, and R.J. Puddephatt. Organometallics, **16**, 3541 (1997); (*c*) M.J. Irwin, G. Jia, N.C. Payne, and R.J. Puddephatt. Organometallics, **15**, 51 (1996); (*d*) G. Jia, R.J. Puddephatt, J.D. Scott, and J.J. Vittal. Organometallics, **12**, 3565 (1993).
9. Additional examples: (*a*) M.C.B. Colbert, J. Lewis, N.J. Long, P.R. Raithby, M. Younus, A.J. P. White, D.J. Williams, N.N. Payne, L. Yellowless, D. Beljonne, N. Chawdhury, and R.H. Friend. Organomeallics, **17**, 3034 (1998); (*b*) O. Lavastre, J. Plass, P. Bachmann, S. Guesmi, C.Moinet, and P.H. Dixneuf. Organometallics, **16**, 184 (1997); (*c*) N. Le Narvor, and C. Lapinte. Organometallics, **14**, 634 (1995).
10. (*a*) J. Maurer, B. Sarkar, B. Schwederski, W. Kaim, R.F. Winter, and S. Zalis. Organometallics, **25**, 3701 (2006); (*b*) J. Maurer, R.F. Winter, B. Sarkar, J. Fiedler, and S. Zalis. Chem. Commun. 1900 (2004); (*c*) B. Gomez-Lor, A. Santos, M. Ruiz, and A.M. Echavarren. Eur. J. Inorg. Chem. 2305 (2001); (*d*) G. Jia, W.F. Wu, R.C.Y. Yeung, and H.P. Xia. J. Organomet. Chem. **539**, 53 (1997); (*e*) A. Santos, J. Lopez, J. Montoya, P. Noheda, A. Romero, and A.M. Echavarren. Organometallics, **13**, 3605 (1994).
11. Preparation of RuCl(dppm)(η^5-C_9H_7): (*a*) L.A. Oro, M.A. Ciriano, M. Campo, C. Foces-Foces, and F.H. Cano. J. Organomet. Chem. **289**, 117 (1985); (*b*) M.P. Gamasa, J. Gimeno, C. Gonzalez-Bernardo, B.M. Martin-Vaca, D. Monti, and M. Bassetti. Organometallics, **15**, 302 (1996).
12. Preparation of RuH(dppm)(η^5-C_9H_7): M.I. Bruce, M.G. Humphrey, A.G. Swincer, and R.C. Wallis. Aust. J. Chem. **37**, 1747 (1984).
13. V. Cardierno, M.P. Gamasa, J. Gemeno, M. Gonzalez-Cueva, E. Lastra, J. Borge, S. Garcia-Granda, and E. Prez-Carreno. Organometallics, **15**, 2137 (1996).
14. M.P. Gamasa, J. Gemeno, B. Martin-Vaca, J. Borge, S. Garcia-Granda, and E. Prez-Carreno. Organometallics, **13**, 4045 (1994).
15. V. Cadierno, S. Conejero, M.P. Damasa, J. Gimeno, I. Asselberghs, S. Houbrechts, K. Clays, A. Persoon, J. Borge, and S. Garcia-Granda. Organometallics, **18**, 582 (1999).
16. (*a*) M. Bassetti, P. Casellato, M.P. Gamasa, J. Gimeno, C. Gonzalez-Bernardo, and B. Martin-Vaca. Organometallics, **16**, 5470 (1997); (*b*) M.P. Gamasa, J. Gimeno, and B.M. Martin-Vaca. Organometallics, **17**, 3707 (1998).

© 2008 NRC Canada

Synthesis, characterization, and reactivity of a novel thallium arylspiroboronate ester[1]

Nathan R. Halcovitch, Christopher M. Vogels, Andreas Decken, and Stephen A. Westcott

Abstract: Addition of 3,5-di-*tert*-butylcatechol (butcat) to solutions of $H_3B{\cdot}SMe_2$ gave the novel diboron species $B_2(butcat)_3$ (**2**) in moderate to high yields. Compound **2** reacts with Tl(acac) to give butcatB(acac) (**4**) and $Tl(Bbutcat_2)$ (**5**). Attempts to abstract the chlorides from $[(dppb)Rh(\mu\text{-}Cl)]_2$ (where dppb = 1,4-bis(diphenylphosphino)buthane) using **5** led to the unusual dimer $[(dppb)Rh(\mu\text{-}Cl)_2(\mu\text{-}Tl)Rh(dppb)][Bbutcat_2]$ (**6**), which contains an unsymmetrical Rh–Tl–Rh bridge.

Key words: arylspiroboronate ester, non-coordinating anion, rhodium, thallium.

Résumé : L'addition du 3,5-di-*tert*-butylcatéchol (butcat) à des solutions de $H_3B{\cdot}SMe_2$ conduit à la formation de nouvelles espèces de dibore, $B_2(butcat)_3$ (**2**), avec des rendements allants de modérés à élevés. Le composé **2** réagit avec le Tl(acac) pour conduire à la formation de butcatB(acac) (**4**) et de $Tl(Bbutcat_2)$ (**5**). Des essais effectués en vue d'utiliser le produit (**5**) pour enlever les ions chlorures à partir du $[(dppb)R(\mu\text{-}Cl)]_2$ (dans lesquels dppb = 1,4-bis(diphénylphosphino)buthane) ont conduit à la formation du dimère inhabituel $[(dppb)Rh(\mu\text{-}Cl)_2(\mu\text{-}Tl)Rh(dppb)][Bbutcat_2]$ (**6**) qui comporte un pont asymétrique Rh–Tl–Rh.

Mots-clés : ester d'acide arylspiroboronique, anion non coordinant, rhodium, thallium.

[Traduit par la Rédaction]

Introduction

The transition metal catalysed hydroboration of alkenes and alkynes has become a well-established technique in organic synthesis (1). One of the most active and selective groups of catalyst precursors for hydroborations using catecholborane (HBcat; cat = 1,2-$O_2C_6H_4$) are those derived from addition of diphosphines to $Rh(acac)(coe)_2$ (acac = acetylacetonato and coe = cyclooctene) (2). The actual catalyst resting state using these systems is believed to be a zwitterionic complex of the type $Rh(\eta^6\text{-}catBcat)(P_2)$ (where P_2 = diphosphine), arising from the redistribution of substituents on HBcat. The arylspiroboronate ester anion $Bcat_2^-$ is bound to the rhodium centre via one of the arene rings as shown in Fig. 1. In an elegant study, Marder and co-workers have found that addition of B_2cat_3 to $Rh(acac)(P_2)$ led to the zwitterionic complexes $Rh(\eta^6\text{-}catBcat)(P_2)$ in high yields, along with concomitant formation of acacBcat (3). The diboron species B_2cat_3 can be generated as a decomposition product in nucleophilic reactions with HBcat or when HBcat is heated at elevated temperatures (4). This species can also be prepared by the direction addition of catechol to solutions of $BH_3{\cdot}THF$ (5).

We have begun a detailed investigation into the synthesis of other zwitterionic complexes containing this arylspiroboronate ester ligand (6) and expanding the role of this class of ligand in organometallic chemistry. The limiting factor in using this methodology lies in the rather small number of metal acetylacetonato complexes, compared with the more common metal halides. As such, we have prepared a novel thallium arylspiroboronate ester compound for its use in reactions with metal halides. Initial results are presented herein.

Received 31 March 2008. Accepted 14 April 2008. Published on the NRC Research Press Web site at cjc.nrc.ca on 15 August 2009.

This paper is dedicated to Dr. R.J. Puddephatt in recognition of his numerous outstanding contributions to organometallic chemistry.

N.R. Halcovitch, C.M. Vogels, and S.A. Westcott.[2] Department of Chemistry, Mount Allison University, Sackville, NB E4L 1G8, Canada.
A. Decken.[3] Department of Chemistry, University of New Brunswick, Fredericton, NB E3B 5A3, Canada.

[1]This article is part of a Special Issue dedicated to Professor R. Puddephatt.

[2]Corresponding author (e-mail: swestcott@mta.ca).
[3]Corresponding author for X-ray crystallography (e-mail: adecken@unb.ca).

Results and discussion

We have found that reactions of B_2cat_3 with Tl(acac) affords the desired thallium salt $Tl(Bcat_2)$ (**1**) in high yields. The use of thallium salts to abstract metal halides is a well-documented and established technique in organometallic chemistry (7). Unfortunately, compound **1** was insoluble in all organic solvents, and all attempts to use this compound to abstract metal halides proved unsuccessful. We then decided to prepare the analogous diboron species using commercially available 3,5-di-*tert*-butylcatechol (butcat), where the two bulky alkyl groups were chosen to increase solubility in organic solvents. Addition of this diol to solutions of

 doi:10.1139/V08-107 © 2008 NRC Canada

Fig. 1. Zwitterionic rhodium diphosphine complexes.

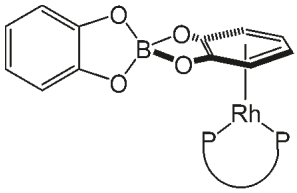

$BH_3{\cdot}SMe_2$ gave the corresponding diboron analogue $B_2(butcat)_3$ (**2**) in moderate to high yields (up to 85%). Compound **2** appears to be a mixture of isomers, as ascertained by the different number of *tert*-butyl groups in the ^1H NMR spectrum. Although attempts to characterize **2** by X-ray diffraction proved unsuccessful, we were able to grow suitable crystals of **3**, where the bridging catecholato unit was replaced by a minor impurity in 3,5-*tert*-butylcatechol that is difficult to separate from the starting material, viz 4-*tert*-butylcatechol. The molecular structure of one of the molecules in the asymmetric unit for **3** is shown in Fig. 2 (8).[4] Crystallographic data for **3** are given in Table 1.

Addition of Tl(acac) to a solution of **2** (Scheme 1) in toluene gave high yields (82%) of compound **5**, $Tl(Bbutcat_2)$, along with concomitant formation of the mixed species butcatB(acac) (**4**). Compound **4** has a peak in the ^{11}B NMR spectrum at δ 8 ppm characteristic of a four-coordinate boron atom bonded to four oxygen atoms. A single-crystal X-ray diffraction study was also conducted on **4** to confirm the formation of this by-product, the molecular structure of which is shown in Fig. 3. The boron–oxygen bond lengths for the catecholato group of B(1)–O(1), 1.450(4), and B(1)–O(2), 1.436(4), are slightly shorter than those for the acac group with B(1)-O(3), 1.505(4), and B(1)-O(4), 1.500(4), respectively, but are similar to those reported earlier (9).

Compound **5** has been characterized by a number of physical methods including multinuclear NMR spectroscopy. The ^1H NMR spectrum for **5** shows two peaks for the different *tert*-butyl groups at δ 1.35 and 1.26 ppm. This observation is in agreement with the $^{13}C\{^1H\}$ NMR spectrum with peaks at δ 34.9 and 34.5 ppm for the quaternary carbons and δ 32.4 and 30.2 ppm for the corresponding methyl groups. The ^{11}B NMR spectrum shows a sharp singlet at δ 13 ppm for the four-coordinate boron atom.

We then decided to examine the reactivity of **5** with $[(P_2)Rh(\mu\text{-}Cl)]_2$ in an attempt to generate complexes of the type $Rh(\eta^6\text{-}butcatBbutcat)(P_2)$. Interestingly, we have found that addition of **5** to a mixture of $[RhCl(coe)_2]_2$ and 2 equiv. of 1,4-bis(diphenylphosphino)butane (dppb) did not lead to the expected zwitterionic product, but gave the novel thallium bridged dimer $[(dppb)Rh(\mu\text{-}Cl)_2(\mu\text{-}Tl)Rh(dppb)][Bbutcat_2]$ (**6**) as the only new rhodium containing species. The $^{31}P\{^1H\}$ NMR data for **6** consists of a doublet at δ 40.2 ppm with coupling to rhodium with J_{PRh} = 178 Hz. The ^{11}B NMR resonance remains at ca. 14 ppm for the noncoordinated

Fig. 2. The molecular structure of **3** with ellipsoids drawn at 50% probability level. Hydrogen atoms are omitted for clarity. Selected bond distances (Å) and angles (°): B(1)–O(3), 1.355(4); B(1)–O(1), 1.378(4); B(1)–O(2), 1.392(4); B(2)–O(6), 1.358(4); B(2)–O(5), 1.389(4); B(2)–O(4), 1.389(4); O(3)-B(1)-O(1), 127.1(3); O(3)-B(1)-O(2), 120.0(3); O(1)-B(1)-O(2), 112.8(3); O(6)-B(2)-O(5), 120.6(3); O(6)-B(2)-O(4), 126.3(3); O(5)-B(2)-O(4), 113.1(2).

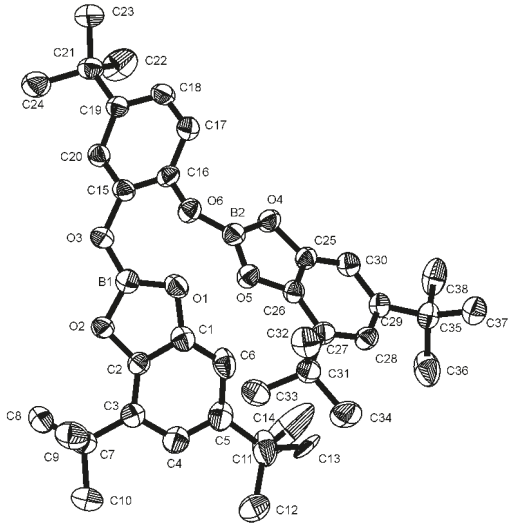

$Bbutcat_2$ anion (10). Complex **6** has also been characterized by a single-crystal X-ray diffraction study, the molecular diagrams of which are shown in Figs. 4–6. Complexes containing thallium transition metal bonds, particularly with Tl(I), are quite rare (11). Indeed, to the best of our knowledge, only one rhodium–thallium complex has been characterized structurally (11*b*). This heterobimetallic complex, $[TlRh_4(\mu\text{-}pyS_2)_2(cod)][PF_6]$ (where pyS = 2,6-pyridineditholate and cod = 1,5-cyclooctadiene), has an almost linear arrangement for the Rh–Tl–Rh subunit with roughly equivalent Rh–Tl bond distances of 2.7686(9) and 2.7706(9) Å. Complex **6** is remarkable, however, in that the Tl bridge is unsymmetrical. Indeed, the Rh–Tl bonds are disparate at Tl(1)–Rh(1), 2.8050(4) Å, and Tl(1)–Rh(2), 3.1234(4) Å, with an angle of Rh(1)–Tl(1)–Rh(2), 68.042(7)°. Metal $M(d^8)$–Tl(I)–$M(d^8)$ units with bridging thallium atoms have also been reported previously for $[Ir_2Tl(CO)_2Cl_2\{\mu\text{-}Ph_2PCH_2)_2AsPh\}_2]$ (11*c*) and $[(H_3N)_2Pt(1\text{-}MeT)_2Tl(1\text{-}MeT)_2Pt(NH_3)_2]^+$ (1-MeT = 1-methylthymine anion) (11*d*), where the bonding in these molecules has been rationalized in terms of the stereoactive $6s^2$ thallium inert pair where the thallium atom acts a Lewis acid to metal centre and a Lewis base to the other. The observation that *both* rhodium centres are distorted square-planar configurations, however, does not support this bonding motif, nor is there any evidence of asymmetry seen in the solution spectra of the complex. The asymmetry in **6** may be a result of a solid-state phenomenon

[4] Supplementary data for this article are available on the journal Web site (canjchem.nrc.ca) or may be purchased from the Depository of Unpublished Data, Document Delivery, CISTI, National Research Council Canada, Ottawa, ON K1A 0R6, Canada. DUD 3795. For more information on obtaining material refer to cisti-icist.nrc-cnrc.gc.ca/cms/unpub_e.shtml. CCDC numbers 682774–68776 contain the crystallographic data for this manuscript. These data can be obtained, free of charge, via www.ccdc.cam.ac.uk/conts/retrieving.html (Or from the Cambridge Crystallographic Data Centre, 12 Union Road, Cambridge CB2 1EZ, UK; fax +44 1223 336033; or deposit@ccdc.cam.ac.uk).

© 2008 NRC Canada

Table 1. Crystallographic data, collection parameters, and observed data for **3**, **4**, and **6**.

Compound	**3**	**4**	**6**
Chemical formula	$C_{19}H_{27}BO_4$	$C_{38}H_{52}B_2O_6$	$C_{92}H_{118}BCl_2O_6P_4Rh_2Tl$
Formula mass	330.22	626.42	1935.64
Crystal dimensions (mm^3)	0.275 × 0.20 × 0.025	0.45 × 0.45 × 0.20	0.57 × 0.40 × 0.20
Crystal system	Monoclinic	Orthorhombic	Monoclinic
Space group	*P*2(1)/*c*	*Pna*2(1)	*P*2(1)/*n*
Z	4	8	4
a (Å)	17.166(5)	16.858(4)	15.748(2)
b (Å)	10.825(3)	20.756(5)	31.128(4)
c (Å)	10.262(3)	20.866(5)	18.045(2)
α (°)	90	90	90
β (°)	101.577(4)	90	94.085(2)
γ (°)	90	90	90
Volume ($Å^3$)	1868.1(9)	7301(3)	8823.2(19)
D_{calcd} (mg m^{-3})	1.174	1.140	1.457
T (K)	198(1)	173(1)	173(1)
Radiation (λ = 0.710 73Å)	Mo Kα	Mo Kα	Mo Kα
μ (mm^{-1})	0.080	0.074	2.376
Total reflections collected	12 422	47 360	61 035
Total unique reflections	4171	8478	19 789
No. of variables	237	873	935
θ (°)	1.21–27.50	1.37–27.50	1.31–27.50
GoF on F^2	1.017	1.110	1.051
$R_1{}^a$ ($I > 2\sigma(I)$)	0.0563	0.0476	0.0337
$wR_2{}^b$ (all data)	0.1699	0.1360	0.0822
Largest diff. peak, hole (e, Å)	0.234, –0.206	0.432, –0.302	2.783, –1.842

[a] $R1 = \sum\|F_o|-|F_c\|/\sum|F_o|$.

[b] $wR2 = \{\sum[w(F_o^2 - F_c^2)2]/\sum(F_o^4)\}^{1/2}$; where $w = 1/[\sigma^2(F_o^2) + (0.066P)^2 + (02976P)]$ for **3**, $w = 1/[\sigma^2(F_c^2) + (0.0516P)^2 + (2.5455P)]$ for **4**, and $w = [\sigma^2(F_o^2) + (0.0391P)^2 + (4.9242P)]$ for **6**, where $P = (\max(F_o^2,0)) + 2F^{2c})3$.

Scheme 1. Preparation of the thallium salt $Tl(Bbutcat_2)$ (**5**).

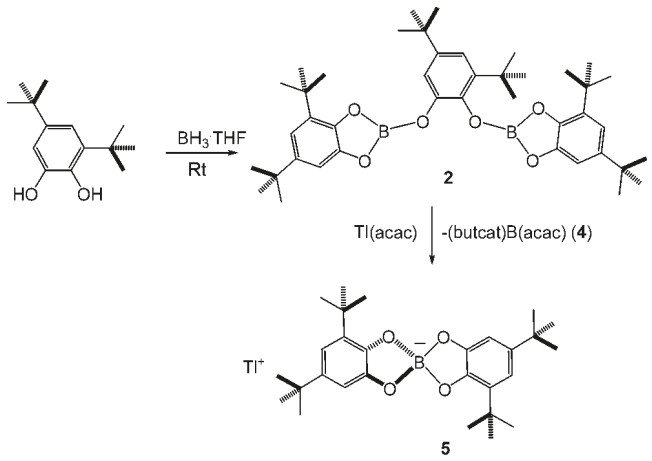

Fig. 3. The molecular structure of **4** with ellipsoids drawn at 50% probability level. Hydrogen atoms are omitted for clarity. Selected bond distances (Å) and angles (°): B(1)–O(2), 1.436(4); B(1)–O(1), 1.450(4); B(1)–O(4), 1.500(4); B(1)–O(3), 1.505(4); O(1)–C(1), 1.379(3); O(2)–C(2), 1.385(3); O(3)–C(15), 1.304(3); O(4)–C(17), 1.302(3); O(2)-B(1)-O(1), 108.3(2); O(2)-B(1)-O(4), 111.3(2); O(1)-B(1)-O(4), 109.4(3); O(2)-B(1)-O(3), 110.0(3); O(1)-B(1)-O(3), 110.2(2); O(4)-B(1)-O(3), 107.6(2).

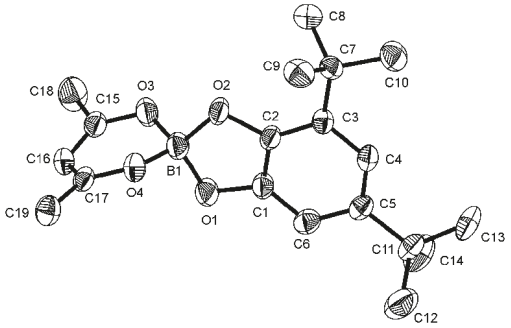

arising from close contact between two phenyl groups from the phosphine ligands with the bridging thallium atom (Fig. 5). Thallium–arene interactions have been reported previously where the hapticity of the arene ring can vary from η^1 to η^6 (12). In the case of **6**, the two phenyl rings are coplanar, and it appears that in one arene ring there are three "short" Tl–C bonds (Tl(1)–C(7), 3.1728(29); Tl(1)–C(8), 3.3866(32); and Tl(1)–C(12), 3.4849(34)) and three "long" Tl–C interactions (Tl(1)–C(9), 3.8870(35); Tl(1)–C(10), 4.1531(36); and Tl(1)–C(11), 3.9539(37)), whereas the other has "two" short (Tl(1)–C(35), 3.2701(29); and Tl(1)–C(36), 3.2086(31)) and four "long" (Tl(1)–C(37), 3.5663(36); Tl(1)–C(38), 3.9320(40); Tl(1)–C(39), 3.9754(38); and Tl(1)–C(40), 3.6745(34)) interactions. An η^3 bonding mode was reported recently for Tl[ArNC(*t*-Bu)NAr] (Ar = 2,6-*i*-Pr-C_6H_3) (12*b*), and bond distances in **6** are within the range reported for these other examples.

© 2008 NRC Canada

Fig. 4. The molecular structure of the cation in **6** with ellipsoids drawn at 50% probability level. Hydrogen atoms and solvent molecules (MeOH and hexane) have been omitted for clarity. Selected bond distances (Å) and angles (°): Tl(1)–Rh(1), 2.8050(4); Tl(1)–Rh(2), 3.1234(4); Rh(1)–P(1), 2.2213(8); Rh(1)–P(2), 2.2232(8); Rh(1)–Cl(2), 2.3825(7); Rh(1)–Cl(1), 2.4303(8); Rh(2)–P(3), 2.2106(8); Rh(2)–P(4), 2.2294(8); Rh(2)–Cl(2), 2.4086(8); Rh(2)–Cl(1), 2.4375(8); Rh(1)-Tl(1)-Rh(2), 68.042(7); P(1)-Rh(1)-P(2), 99.06(3); P(1)-Rh(1)-Cl(2), 91.71(3); P(2)-Rh(1)-Cl(2), 162.36(3); P(1)-Rh(1)-Cl(1), 169.53(3); P(2)-Rh(1)-Cl(1), 88.37(3); Cl(2)-Rh(1)-Cl(1), 82.97(3); P(1)-Rh(1)-Tl(1), 91.39(2); P(2)-Rh(1)-Tl(1), 102.65(2); Cl(2)-Rh(1)-Tl(1), 90.93(2); Cl(1)-Rh(1)-Tl(1), 79.73(2); P(3)-Rh(2)-P(4), 92.94(3); P(3)-Rh(2)-Cl(2), 173.61(3); P(4)-Rh(2)-Cl(2), 92.39(3); P(3)-Rh(2)-Cl(1), 93.04(3); P(4)-Rh(2)-Cl(1), 168.97(3); Cl(2)-Rh(2)-Cl(1), 82.28(3); P(3)-Rh(2)-Tl(1), 91.36(2); P(4)-Rh(2)-Tl(1), 115.72(2); Cl(2)-Rh(2)-Tl(1), 83.144(19); Cl(1)-Rh(2)-Tl(1), 73.384(19); Rh(1)-Cl(1)-Rh(2), 86.25(2); Rh(1)-Cl(2)-Rh(2), 87.97(3).

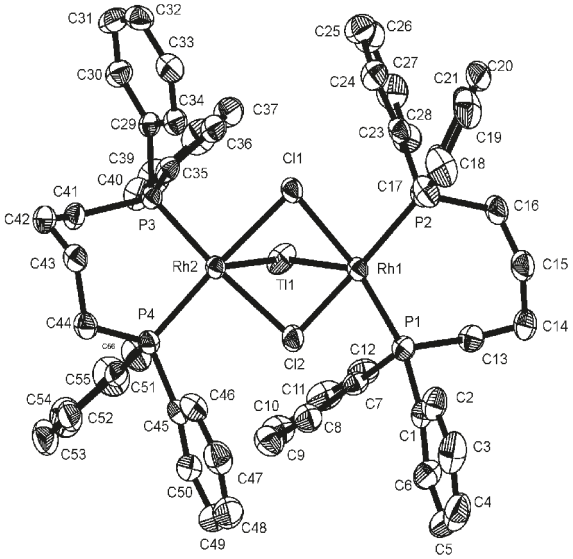

Fig. 5. An alternate view of the cation in **6** showing the thallium–arene interactions, with ellipsoids drawn at 50% probability level. Hydrogen atoms, solvent molecules (MeOH and hexane), and some of the phenyl rings have been omitted for clarity. Selected bond distances (Å): Tl(1)–C(7), 3.1728(29); Tl(1)–C(8), 3.3866(32); Tl(1)–C(9), 3.8870(35); Tl(1)–C(10), 4.1531(36); Tl(1)–C(11), 3.9539(37); Tl(1)–C(12), 3.4849(34); Tl(1)–C(35), 3.2701(29); Tl(1)–C(36), 3.2086(31); Tl(1)–C(37), 3.5663(36); Tl(1)–C(38), 3.9320(40); Tl(1)–C(39), 3.9754(38); Tl(1)–C(40), 3.6745(34).

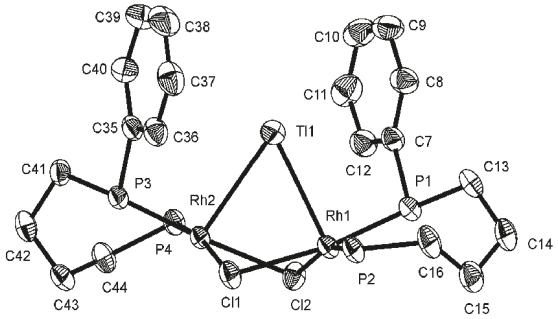

Fig. 6. The molecular structure of the anion in **6** with ellipsoids drawn at 50% probability level. Hydrogen atoms and solvent molecules (MeOH and hexane) have been omitted for clarity. Selected bond distances (Å) and angles (°): O(1)–C(57), 1.365(3); O(1)–B(1), 1.488(4); O(2)–C(62), 1.374(3); O(2)–B(1), 1.490(4); O(3)–C(71), 1.364(3); O(3)–B(1), 1.478(4); O(4)–C(76), 1.361(4); O(4)–B(1), 1.471(4); O(4)-B(1)-O(3), 105.4(2); O(4)-B(1)-O(1), 113.5(3); O(3)-B(1)-O(1), 109.4(2); O(4)-B(1)-O(2), 111.2(3); O(3)-B(1)-O(2), 113.4(2); O(1)-B(1)-O(2), 104.2(2).

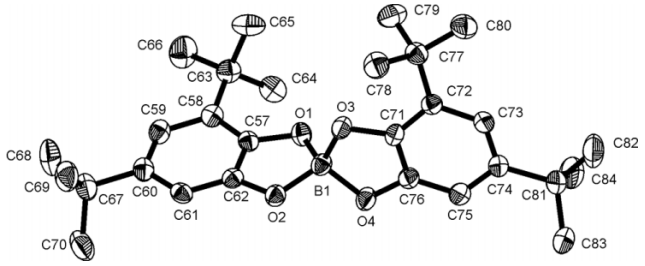

The long Rh···Rh separation of 3.3274(4) Å suggests no significant interaction exists between the two d^8 metal centres (13). The bond distances and angles in the noncoordinating $Bbutcat_2^-$ anion are well within those observed for other arylspiroboronate esters derived from catechols (14).

Interestingly, all attempts (elevated temperatures and different solvents) to abstract the chlorides from $[(dppb)Rh(\mu\text{-}Cl)]_2$ using **5** proved unsuccessful, even with reactions utilizing microwave radiation. We are in the process of examining the unusual bonding in complex **6** in more detail and will report our findings in due course. Initial results show that addition of **5** to $[RhCl(coe)_2]_2$ and other diphosphines all give products with similar ^{31}P coupling constants to **6**. As considerable research has focused on the development of novel catalyst systems containing noncoordinating or weakly coordinating counteranions (15), we have also begun an in-depth look at the use of this thallium salt with other metal halides.

Conclusion

We have found that addition of 3,5-di-*tert*-butylcatechol (butcat) to solutions of $H_3B{\cdot}SMe_2$ gave the novel diboron species $B_2(butcat)_3$ (**2**) in moderate to high yields. Compound **2** reacts readily with Tl(acac) to give butcatB(acac) (**4**) and $Tl(Bbutcat_2)$ (**5**). Attempts to abstract the chloride from $[(dppb)Rh(\mu\text{-}Cl)]_2$ using this new thallium salt led to the formation of an unusual dimer $[(dppb)Rh(\mu\text{-}Cl)_2(\mu\text{-}Tl)Rh(dppb)][Bbutcat_2]$ (**6**), which contains a unique unsymmetrical Rh–Tl–Rh bridge. All attempts to remove the chloride ligands proved unsuccessful and future work will investigate the ability of this bulky $Bbutcat_2^-$ anion to bind to other metal centres.

Experimental

General

Reagents and solvents used were purchased from Sigma-Aldrich Chemicals. NMR spectra were recorded on a JEOL JNM-GSX270 FT spectrometer. ^1H NMR chemical shifts are reported in ppm and referenced to residual solvent protons in

© 2008 NRC Canada

deuterated solvent at 270 MHz. ^{11}B NMR chemical shifts are reported in ppm and are referenced to $BF_3{\cdot}OEt_2$ as an external standard at 87 MHz. ^{13}C NMR chemical shifts are referenced to solvent carbon resonances as internal standards at 68 MHz and are reported in ppm. ^{31}P NMR chemical shifts are reported in ppm and are referenced to H_3PO_4 as an external standard at 109 MHz. Multiplicities are reported as singlet (s), doublet (d), triplet (t), multiplet (m), broad (br), and overlapping (ov). All reactions were carried out under an atmosphere of dinitrogen. Microanalyses for C and H were carried out at Guelph Chemical Laboratories (Guelph, Ontario). $[RhCl(coe)_2]_2$ was prepared by an established method (16).

Tl(Bcat$_2$) (1)

To a stirred THF (5 mL) solution of thallium(I) acetylacetonate (0.20 g, 0.66 mmol) was added a THF (5 mL) solution of B_2cat_3 (0.23 g, 0.66 mmol). The reaction was allowed to proceed for 18 h at which point a white precipitate was collected by suction filtration and washed with THF (2 × 3 mL) to afford **1**. Yield: 0.25 g (88%); mp: decomposes above 350 °C (decomp.). Spectroscopic NMR data (in DMSO-d_6): ^{1}H NMR δ: 6.47 (br ov m, Ar); ^{11}B NMR δ: 13 (sharp); ^{13}C{^{1}H} NMR δ: 152.1, 117.8, 108.2. Anal. calcd. (%) for $C_{12}H_8BO_4Tl$ (431.39): C 33.41, H 1.87; found: C 33.25, H 1.81.

B$_2$butcat$_3$ (2)

To a stirred toluene (10 mL) solution of 3,5-di-*tert*-butylcatechol (5.97 g, 0.027 mol) was added a 2.0 mol/L toluene solution of $Me_2S{\cdot}BH_3$ (9.0 mL, 0.018 mol). The reaction was heated at reflux for 18 h at which point the solvent was removed under vacuum. The residual sticky solid was triturated with hexane (2 × 5 mL) and collected by suction filtration to afford **2** as a white solid. Yield: 7.83 g (85%). FT-IR (Nujol): 2951, 2935, 2910, 2862, 1462, 1410, 1377, 1363, 1300, 1263, 1223, 1209, 1142, 1126, 976, 856. Spectroscopic NMR data (in $CDCl_3$): ^{1}H NMR δ: 7.29 (d, J = 2.0 Hz, 1H, Ar), 7.19 (d, J = 2.0 Hz, 1H, Ar), 7.02 (d, J = 1.5 Hz, 1H, Ar), 6.91 (d, J = 1.7 Hz, 1H, Ar), 6.89 (d, J = 1.5 Hz, 1H, Ar), 6.51 (d, J = 1.7 Hz, 1H, Ar), 1.42 (s, 9H, *t*-Bu), 1.35 (s, 9H, *t*-Bu), 1.34 (s, 9H, *t*-Bu), 1.28 (s, 9H, *t*-B), 1.18 (s, 9H, *t*-Bu), 1.10 (s, 9H, *t*-But); ^{13}C{^{1}H} NMR δ: 147.6, 147.5, 146.5, 145.3, 145.0, 143.5, 143.2, 143.0, 140.5, 140.1, 134.6, 134.4, 119.4, 116.4, 116.2, 115.7, 107.4, 107.1, 35.5, 35.0, 34.8, 34.7, 34.3, 34.1, 31.8, 31.7, 31.6, 30.2, 29.7, 29.4; ^{11}B NMR δ: 21 (br). Anal. calcd. (%) for $C_{42}H_{60}B_2O_6$ (682.64): C 73.89, H 8.88; found: C 74.22, H 8.53.

butcatB(acac) (4)

To a stirred toluene (10 mL) suspension of $B_2butcat_3$ (2.00 g, 2.92 mmol) was added thallium(I) acetylacetonate (0.88 g, 2.92 mmol) as a solid. The reaction was allowed to proceed for 18 h at which point a white precipitate was collected by suction filtration. Upon storing the toluene filtrate at –30 °C, a white solid precipitated and was collected by suction filtration. The solid was washed with hexane (2 × 1 mL) to afford **4**. Yield: 0.53 g (55%); mp: 220–222 °C. FT-IR (Nujol): 2980, 2829, 1556, 1471, 1444, 1375, 1288, 1265, 1240, 1205, 1097, 1009, 947, 854, 802, 723, 658. Spectroscopic NMR data (in $CDCl_3$): ^{1}H NMR δ: 6.77 (s, 2H, Ar), 6.00 (s, 1H, C*H*C(O)CH$_3$), 2.30 (s, 6H, CHC(O)C*H*$_3$), 1.41 (s, 9H, *t*-Bu), 1.29 (s, 9H, *t*-Bu); ^{13}C{^{1}H} NMR δ: 191.3, 149.8, 145.6, 142.2, 131.6, 113.8, 105.5, 102.2, 34.8, 34.4, 32.1, 29.9, 24.5; ^{11}B NMR δ: 8 (sharp). Anal. calcd. (%) for $C_{19}H_{27}BO_4$ (330.23): C 69.11, H 8.24; found: C 69.16, H 8.37.

Tl(Bbutcat$_2$) (5)

To a stirred toluene (10 mL) suspension of $B_2butcat_3$ (2.00 g, 2.92 mmol) was added thallium(I) acetylacetonate (0.88 g, 2.92 mmol) as a solid. The reaction was allowed to proceed for 18 h at which point a white precipitate was collected by suction filtration and washed with toluene (2 × 5 mL) to afford **5**. Yield: 1.57 g (82%); mp: 212 °C (decomp.). Spectroscopic NMR data (in $CDCl_3$): ^{1}H NMR δ: 6.81 (s, 4H, Ar), 1.35 (s, 18H, *t*-Bu), 1.26 (s, 18H, *t*-Bu); ^{13}C{^{1}H} NMR δ: 149.1, 147.0, 142.1, 132.8, 114.8, 106.1, 34.9, 34.5, 32.4, 30.2; ^{11}B NMR δ: 13 (sharp). Anal. calcd. (%) for $C_{28}H_{40}BO_4Tl$ (655.80): C 51.28, H 6.15; found: C 51.53, H 6.33.

[(dppb)Rh(μ-Tl)Rh(dppb)][(Bbutcat$_2$)] (6)

To a stirred toluene (10 mL) suspension of $[RhCl(coe)_2]_2$ (0.50 g, 0.70 mmol) was added a toluene (10 mL) solution of dppb (0.59 g, 1.40 mmol) and the reaction was allowed to proceed for 2 h. To the clear burgundy solution, TlBbutcat$_2$ (1.00 g, 1.53 mmol) was added as a solid and the mixture was stirred for 18 h. Following filtration to remove a small amount of precipitate, the volume of the clear orange solution was decreased to 5 mL under vacuum. The solution was stored at –30 °C whereupon an orange precipitate was collected by suction filtration and washed with hexane (2 × 3 mL) to afford **6**. Yield: 0.62 g (45%); mp: 215 °C (decomp.). FT-IR (Nujol): 2952, 2919, 2856, 1459, 1432, 1231, 1185, 1095, 1071, 1027, 993, 904, 846, 740, 697, 655. Spectroscopic NMR data (in THF-d_8): ^{1}H NMR δ: 7.48 (br m, 16H, Ar), 7.32–7.19 (ov m, 24H, Ar), 6.52 (d, J = 1.7 Hz, 2H, Ar), 6.44 (d, J = 1.7 Hz, 2H, Ar), 2.36 (br m, 8H, C*H*$_2$), 1.36 (s, 18H, *t*-Bu), 1.19 (s, 18H, *t*-Bu), 0.88 (m, 8H, C*H*$_2$); ^{13}C{^{1}H} NMR δ: 152.0, 148.2, 137.6, 135.8 (t, J_{CP} = 23.5 Hz, *C*-P), 133.1 (br), 129.6, 128.2, 125.1, 110.2, 103.8, 34.5, 33.8, 31.8, 29.3, 27.8 (t, J_{CP} = 12.8 Hz, *C*H$_2$-P), 22.1; ^{11}B NMR δ: 14 (sharp); ^{31}P{^{1}H} NMR δ: 40.2 (d, J_{PRh} = 178 Hz). Anal. calcd. (%) for $C_{84}H_{96}BCl_2O_4P_4Rh_2Tl$ (1785.78): C 56.49, H 5.43; found: C 55.72, H 5.38.

X-ray crystallography

Crystals of **3** were grown from saturated hexane solutions, crystals of **4** from saturated diethyl ether solutions, and crystals of **6** from saturated methanol solutions layered with hexanes, all at –30 °C. Single crystals were coated with Paratone-N oil, mounted using a glass fibre, and frozen in the cold stream of the goniometer. A hemisphere of data were collected on a Bruker AXS P4/SMART 1000 diffractometer using ω and θ scans with a scan width of 0.3° and exposure times of 30 s (**3**), 40 s (**4**), and 10 s (**6**). The detector distances were 5 cm. The data were reduced (SAINT) (17) and corrected for absorption (SADABS). The structures were solved by direct methods and refined by full-matrix least-squares on F2(SHELXTL). One of the *tert*-butyl

© 2008 NRC Canada

groups of **3** was disordered and the site occupancy determined using an isotropic model as 0.9 (C(12)-C(14)) and 0.1 (C(12a)-C(14a)) and fixed in subsequent refinement cycles. Likewise, one of the *tert*-butyl groups in **4** was disordered and the site occupancy determined using an isotropic model as 0.60 (C(12)-C(14)) and 0.4 (C(12′)-C(14′)) and fixed in subsequent refinement cycles. All non-hydrogen atoms were refined using anisotropic displacement parameters. Hydrogen atoms were included in calculated positions and refined using a riding model. Hexane solvent molecules in **6** were modeled using disordered electron densities.

Acknowledgements

This paper is dedicated to Dr. R.J. Puddephatt in recognition of his outstanding contributions to chemistry. Thanks are gratefully extended to the Natural Sciences and Engineering Research Council (NSERC) of Canada, Canada Research Chairs Programme, Canadian Foundation for Innovation–Atlantic Innovation Fund, and Mount Allison University for financial support. We also thank Roger Smith and Dan Durant for their expert technical assistance and anonymous reviewers for helpful comments, especially with respect to bonding in complex **6**.

References

1. (*a*) K. Burgess and M.J. Ohlmeyer. Chem. Rev. **91**, 1179 (1991); (*b*) C.M. Crudden and D. Edwards. Eur. J. Org. Chem. 4695 (2003); (*c*) I. Beletskaya and A. Pelter. Tetrahedron, **53**, 4957 (1997); (*d*) J.M. Brown. Modern rhodium catalyzed organic reactions. *Edited by* P.A. Evans. Wiley-VCH, Weinheim. 2004; (*e*) C. Fu, M. Beller, and C. Bolm. Transition metals for organic synthesis. Wiley-VCH, Weinheim. 1998; (*f*) C.M. Vogels and S.A. Westcott. Curr. Org. Chem. **9**, 687 (2005); (*g*) P.J. Guiry, M. McCarthy, P.M. Lacey, C.P. Saunders, S. Kelly, and D.J. Connolly. Curr. Org. Chem. **4**, 821 (2000).
2. (*a*) S.A. Westcott, H.P. Blom, T.B. Marder, and R.T. Baker. J. Am. Chem. Soc. **114**, 8863 (1992); (*b*) P. Nguyen, R.B. Coapes, A.D. Woodward, N.J. Taylor, J.M. Burke, J.A.K. Howard, and T.B. Marder. J. Organomet. Chem. **652**, 77 (2002); (*c*) R.T. Baker, P. Nguyen, T.B. Marder, and S.A. Westcott. Angew. Chem. Int. Ed. Engl. **34**, 1336 (1995); (*d*) C.M. Vogels, A. Decken, and S.A. Westcott. Can. J. Chem. **84**, 146 (2006).
3. (*a*) R.B. Coapes, F.E.S. Souza, R.L. Thomas, J.J. Hill, and T.B. Marder. Chem. Commun. (Cambridge), 614 (2003); (*b*) C. Dai, E.G. Robins, A.J. Scott, W. Clegg, D.S. Yufit, J.A.K. Howard, and T.B. Marder. Chem. Commun. (Cambridge), 1983 (1998).
4. S.A. Westcott, H.P. Blom, T.B. Marder, R.T. Baker, and J.C. Calabrese. Inorg. Chem. **32**, 2175 (1993).
5. J.V.B. Kanth, M. Periasamy, and H.C. Brown. Org. Process Res. Dev. **4**, 550 (2000).
6. (*a*) S.J. Geier, E.E. Chapman, D.I. McIsaac, C.M. Vogels, A. Decken, and S.A. Westcott. Inorg. Chem. Commun. (Cambridge, U.K.), **9**, 788 (2006); (*b*) D.I. McIsaac, S.J. Geier, C.M. Vogels, A. Decken, and S.A. Westcott. Inorg. Chim. Acta, **359**, 2771 (2006).
7. R.P. Hughes, T. Le Husebo, S.M. Maddock, A.L. Rheingold, and I.A. Guzei. J. Am. Chem. Soc. **119**, 10231 (1997).
8. E. Barnea, T. Andrea, M. Kapon, and M.S. Eisen. J. Am. Chem. Soc. **126**, 5066 (2004).
9. (*a*) H. Höpfl, N. Pérez Hernández, S. Rojas Líma, R. Santillan, and N. Farfán. Heteroat. Chem. **9**, 359 (1998); (*b*) A.T. Balaban, I. Haiduc, H. Höpfl, N. Farfán, and R. Santillan. Main Group Met. Chem. **19**, 385 (1996).
10. H Nöth and B. Wrackmeyer. *In* Nuclear magnetic resonance spectroscopy of boron compounds. Springer-Verlag, Berlin. 1978.
11. (*a*) P. Pyykö. Chem. Rev. **97**, 597 (1997); (*b*) M.A. Casado, J.J. Pérez-Torrente, J.A. López, M.A. Ciriano, F.J. Lahoz, and L.A. Oro. Inorg. Chem. **38**, 2482 (1999); (*c*) A.L. Balch, J.K. Nagle, M.M. Olmstead, and P.E. Reedy, Jr. J. Am. Chem. Soc. **109**, 4123 (1987); (*d*) O. Renn, B. Lippert, and I. Mutikainen. Inorg. Chim. Acta, **208**, 219 (1993); (*e*) V.J. Catalano, B.L. Bennett, R.L. Yson, and B.C. Nol. J. Am. Chem. Soc. **122**, 10056 (2000); (*f*) H.-B. Song, Z.-Z. Zhang, Z. Hui, C.-M. Che, and T.C.W. Mak. Inorg. Chem. **41**, 3146 (2002); (g) L.R. Falvello, J. Forniés, R. Garde, A. García, E. Lalinde, M.T. Moreno, A. Steiner, M. Tomás, and I. Usón. Inorg. Chem. **45**, 2543 (2006); (*h*) W. Chen, F. Liu, K. Matsumoto, J. Autschbach, B. Le Guennic, T. Ziegler, M. Maliarik, and J. Glaser. Inorg. Chem. **45**, 4526 (2006).
12. (*a*) J.C. Thomas and J.C. Peters. Inorg. Chem. **42**, 5055 (2003); (*b*) C. Jones, P.C. Junk, J.A. Platts, D. Rathmann, and A. Stasch. Dalton Trans. 2497 (2005); (*c*) S.H. Strauss, M.D. Noirot, and O.P. Anderson. Inorg. Chem. **25**, 3850 (1986); (*d*) M.D. Noirot, O.P. Anderson, and S.H. Strauss. Inorg. Chem. **26**, 2216 (1987); (*e*) N. Oberbeckmann-Winter, P. Braunstein, and R. Welter. Organometallics, **23**, 6311 (2004); (*f*) E.J. Fernández, A. Laguna, J.M. López-de-Luzuriaga, M.E. Olmos, and J. Pérez. Chem. Commun. (Cambridge), 1760 (2003); (*g*) P.J. Schebler, C.G. Riordan, I.A. Guzei, and A.L. Rheingold. Inorg. Chem. **37**, 4754 (1998); (*h*) Y. Sarazin, N. Kaltsoyannis, J.A. Wright, and M. Bochmann. Organometallics, **26**, 1811 (2007); (*i*) R.S. Mathur, T. Drovetskaya, and C.A. Reed. Acta Crystallogr. Sect. C: Cryst. Struct. Commun. **53**, 881 (1997); (*j*) Y. Sarazin, D.L. Hughes, N. Kaltsoyannis, J.A. Wright, and M. Bochmann. J. Am. Chem. Soc. **129**, 881 (2007); (*k*) S.E. Matthews, N.H. Rees, V. Felix, M.G.B. Drew, and P.D. Beer. Inorg. Chem. **42**, 729 (2003); (*l*) H. Schmidbaur, W. Bublak, B. Huber, J. Hofmann, and G. Muller. Chem. Ber. **122**, 265 (1989); (*m*) W. Frank, D. Kuhn, S. Muller-Becker, and A. Razavo. Angew. Chem. Int. Ed. Engl. **32**, 90 (1993); (*n*) W. Frank, G. Korrell, and G.J. Reiss. J. Organomet. Chem. **506**, 293 (1996); (*o*) L.H. Gade. Dalton Trans. 267 (2003); (*p*) C. Janiak. Coord. Chem. Rev. **163**, 107 (1997).
13. (*a*) S.S. Oster and W.D. Jones. Polyhedron, **23**, 2959 (2004); (*b*) G. Canepa, C.D. Brandt, K. Ilg, J. Wolf, and H. Werner. Chem. Eur. J. **9**, 2502 (2003); (*c*) K.A. Bunten, D.H. Farrar, A.J. Poë, and A. Lough. Organometallics, **21**, 3344 (2002); (*d*) B. Richter, A.L. Spek, G. van Koten, and B.-J. Deelman. J. Am. Chem. Soc. **122**, 3945 (2000); (*e*) K. Wang, M.E. Goldman, T.J. Emge, and A.S. Goldman. J. Organomet. Chem. **518**, 55 (1996); (*f*) P. Hofmann, C. Meier, W. Hiller, M. Heckel, J. Riede, and M.U. Schmidt. J. Organomet. Chem. **490**, 51 (1995); (*g*) R.C. Schnabel and D.M. Roddick. Inorg. Chem. **32**, 1513 (1993); (*h*) M.D. Curtis, W.M. Butler, and J. Greene. Inorg. Chem. **17**, 2928 (1975); (*i*) G.E. Ball, W.R. Cullen, M.D. Fryzuk, and B.R. James. Organometallics, **10**, 3767 (1991).
14. (*a*) C.M. Vogels, A. Decken, and S.A. Westcott. Can. J. Chem. **84**, 146 (2006); (*b*) N.C. Norman, A.G. Orpen, M.J. Quayle, and E.G. Robins. Acta Crystallogr. Sect. C: Cryst. Struct. Commun. **56**, 50 (2000); (*c*) W. Clegg, M.R.J. Elsegood, T.B.

© 2008 NRC Canada

Marder, C. Dai, N.C. Norman, N.L. Pickett, and E.G. Robins. Acta Crystallogr. Sect C: Cryst. Struct. Commun. **55**, 733 (1999); (*d*) X. Heand and J.F. Hartwig. J. Am. Chem. Soc. **118**, 1696 (1996); (*e*) A. Downard, M. Nieuwenhuyzen, K.R. Seddon, J-A. van den Berg, M.A. Schmidt, J.F.S. Vaughan, and U. Welz-Biermann. Cryst. Growth Des. **2**, 111 (2002); (*f*) T. Miyazaki, M. Sugawara, H. Danjo, and T. Imamoto. Tetrahedron Lett. **45**, 9341 (2004); (*g*) S.H. Chikkali, D. Gudat, F. Lissner, M. Nieger, and T. Schleid. Dalton Trans. 3906 (2007).

15. (*a*) J. Cipot, R. McDonald, M.J. Ferguson, G. Schatte, and M. Stradiotto. Organometallics, **26**, 594 (2007); (*b*) B.M. Wile, R. McDonald, M.J. Ferguson, and M. Stradiotto. Organometallics, **26**, 1069 (2007); (*c*) J. Cipot, D. Wechsler, M. Stradiotto, R. McDonald, and M.J. Ferguson. Organometallics, **22**, 5185 (2003); (*d*) B.M. Wile, R.J. Burford, R. McDonald, M.J. Ferguson, and M. Stradiotto. Organometallics, **25**, 1028 (2006); (*e*) M.A. Rankin, R. McDonald, M.J. Ferguson, and M. Stradiotto. Angew. Chem. Int. Ed. **44**, 3603 (2005); (*f*) R.E. LaPointe, G.R. Roof, K.A. Abboud, and J. Klosin. J. Am. Chem. Soc. **122**, 9560 (2000); (*g*) J.D. Feldman, J.C. Peters, and T.D. Tilley. Organometallics, **21**, 4050 (2002); (*h*) T.J. Barbarich, S.M. Miller, O.P. Anderson, and S.H. Strauss. J. Mol Catal. A: Chem. **128**, 289 (1998); (*i*) J.L. Priego, L.H. Doerrer, L.H. Rees, and M.L.H. Green. Chem. Commun. (Cambridge), 779 (2000); (*j*) R.T. Tjahjanto and J. Beck. Z. Naturforsch. B: Chem. **62B**, 1291 (2007); (*k*) S.H. Strauss. Chem. Rev. **93**, 927 (1993); (*l*) I. Krossing and I. Rabbe. Angew. Chem. Int. Ed. **43**, 2066 (2004); (*m*) C.A. Reed. Acc. Chem. Res. **31**, 133 (1998); (*n*) J. Tang, J.S. Costa, A. Pevec, B. Kozlevcar, C. Massera, O. Roubeau, I. Mutikainen, U. Turpeinen, P. Gamez, and J. Reedijk. Cryst. Growth Res. **8**, 1005 (2008).

16. A. van der Ent and A.L. Onderdelinden. Inorg. Synth. **14**, 92 (1973).

17. (*a*) Bruker AXS, Inc. SAINT [computer program], Version 6.02. Bruker AXS, Inc., Madison, Wisconsin. 1997–1999; (*b*) G.M. Sheldrick. SADABS [computer program]. Bruker AXS, Inc., Madison, Wisconsin. 1999; (*c*) G.M. Sheldrick. SHELXTL [computer program], Version 5.1. Bruker AXS, Inc., Madison, Wisconsin. 1997.

© 2008 NRC Canada

Synthesis and structures of palladium(II) and platinum(II) complexes containing heterocyclic thiolate ligands formed by cycloaddition reactions of coordinated azides[1]

Angela Fleischer, Alexander Roller, Vladimir B. Arion, Bernhard K. Keppler, and Fabian Mohr

Abstract: The phosphine-stabilized azido complexes $[M(N_3)_2(PTA)_2]$ (M = Pd, Pt; PTA = 1,3,5-triaza–7-phosphaadamantane) were prepared in high yields by a ligand exchange reaction from *cis*-$[Pd(N_3)_2(tmeda)]$ and *cis*-$[Pt(N_3)_2(cod)]$, respectively. The Pd and Pt complexes $[M(N_3)_2(PTA)_2]$ undergo cycloaddition reactions with various isothiocyanates to give complexes containing anionic, S-coordinated tetrazole-thiolate ligands of the type *trans*-$[M(SCN_4R)_2(PTA)_2]$ (M = Pd, Pt; R = Et, allyl, Me, Ph). The molecular structures of several of these derivatives were determined by X-ray crystallography.

Key words: palladium, platinum, thiolate, heterocycle, azide, cycloaddition.

Résumé : On a préparé les complexes azido stabilisés par une phosphine $[M(N_3)_2(PTA)_2]$ [M= Pd, Pt; PTA = 1,3,5-triaza-7-phosphaadamantane] avec des rendements élevés en procédant à une réaction d'échange de ligand à partir respectivement du *cis*-$[Pd(N_3)_2(tmeda)]$ et *cis*-$[Pt(N_3)_2(cod)]$. Les complexes du Pd et du Pt $[M(N_3)_2(PTA)_2]$ subissent des réactions de cycloaddition avec divers isothiocyanates pour conduire à la formation de complexes contenant des ligands anioniques tétrazole-thiolate, S-coordinés, du type *trans*-$[M(SCN_4R)_2(PTA)_2]$ (M = Pd, Pt; R = Et, allyle, Me, Ph). Les structures molécules de plusieurs de ces dérivés ont été déterminées par la diffraction des rayons X.

Mots-clés : palladium, platine, thiolate, hétérocycle, azide, cycloaddition.

[Traduit par la Rédaction]

Introduction

Azido complexes of palladium stabilized by phosphine ligands were first reported by Beck et al. in 1965 (1). In a series of papers, the group showed that the coordinated azido groups undergo cycloaddition reactions with nitriles, alkynes, and isothiocyanates to give metal-coordinated tetrazolates (Chart 1) (2–6). Since then, several groups have studied reactions of phosphine-stabilized Pd and, to a much lesser extent, Pt azido complexes with various nitriles and isocyanides. In contrast, cycloaddition reactions with isothiocyanates have only recently been studied in detail (7–9). These results show that the resulting heterocycle is S-coordinated to the metal (Chart 1) rather than N-coordinated, as originally suggested by Beck and co-workers in 1972 (5). A computational study of the reaction mechanism leading to the S-coordinated tetrazole-thiolato complex has also been carried out (10).

We have been exploring the structures and reactivity of precious metal complexes containing the water-soluble phosphine ligand 1,3,5-triaza–7-phosphaadamantane (PTA) (11–14). In this context, water-soluble Pt(II) complexes containing heterocyclic thiolate ligands showed promising in vitro cytotoxicity against various tumour cell lines (15). To generate a library of new water-soluble Pd and Pt complexes with a variety of substituted tetrazole-thiolates from one common precursor, we investigated the cycloaddition of isothiocyanates to PTA-stabilized Pd and Pt azido complexes. Some preliminary results of this study are reported herein.

Received 9 April 2008. Accepted 14 May 2008. Published on the NRC Research Press Web site at canjchem.nrc.ca on 27 August 2008.

This article is dedicated to my mentor and friend Dick Puddephatt in recognition of his outstanding contributions to the chemistry of the precious metals.

F. Mohr.[2] Fachbereich C–Anorganische Chemie, Bergische Universität Wuppertal, 42119 Wuppertal, Germany.
A. Fleischer, A. Roller, V.B. Arion, and B.K. Keppler. Institut für Anorganische Chemie, Universität Wien, 1090 Wien, Austria.

[1]This article is part of a Special Issue dedicated to Professor R. Puddephatt.
[2]Corresponding author: (e-mail: fmohr@uni-wuppertal.de).

Results and discussion

The PTA stabilized Pd and Pt bis(azido) complexes $[M(N_3)_2(PTA)_2]$ (M = Pd **1**, Pt **2**) are readily prepared in high yields by displacement of the tmeda or cod ligands from *cis*-$[Pd(N_3)_2(tmeda)]$ and *cis*-$[Pt(N_3)_2(cod)]$, respectively. Both complexes are poorly soluble in water and insoluble in chlorinated solvents, acetone, and alcohols, but readily soluble in DMSO. The $^{31}P\{^1H\}$ NMR spectra of

 doi:10.1139/V08-115 © 2008 NRC Canada

Chart 1.

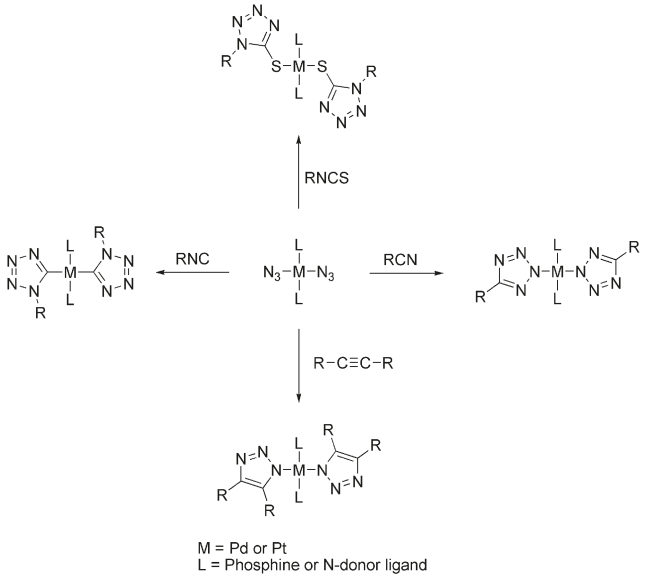

Scheme 1.

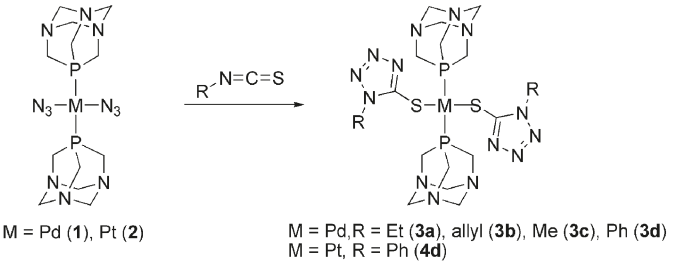

Fig. 1. Molecular structure of complex **3a**. Ellipsoids show 50% probability levels. Hydrogen atoms have been omitted for clarity. Selected bond distances (Å) and angles (°): Pd1–P1 2.3054(4), Pd1–S1 2.3434(4), S1–C7 1.7250(15), C7–N5 1.3348(18), C7–N4 1.3485(18), N4–N7 1.3576(17), N7–N6 1.2934(18); P1–Pd1–S1 89.390(13), C7–S1–Pd1 100.88(5).

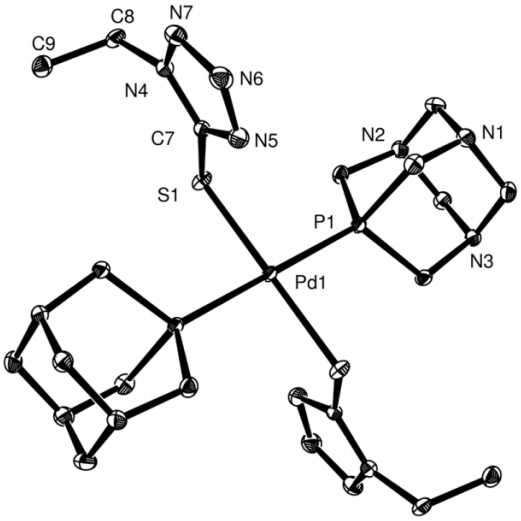

complexes **1** and **2** show singlet resonances at –29.90 and –59.09 ppm, respectively. The IR spectra of both compounds show strong bands between 2020 and 2050 cm^{-1} due to the coordinated azido ligand. The positive ion ES-MS spectra of both complexes show a single, intense peak with *m/z* of 527 (**1**) and 616 (**2**), corresponding to the Na adduct of the molecular ions. The observed isotopic distribution patterns are in perfect agreement with the proposed formulas. Attempts to obtain X-ray diffraction quality crystals of these complexes failed, as the initially yellow or colorless DMSO solutions darkened and eventually decomposed to give a metallic mirror over a period of 2–3 days. However, the solid samples are stable in air at ambient temperatures for months.

Complex **1** reacts with the isothiocyanates RNCS (R = Et, allyl, Me, Ph) in CH_2Cl_2 at room temperature over a period of ca. 18 h to give orange solutions, which, upon layering with Et_2O, afford crystals of the Pd tetrazole-thiolato complexes *trans*-[$Pd(SCN_4R)_2(PTA)_2$] (R = Et **3a**, allyl **3b**, Me **3c**, Ph **3d**) after several days (Scheme 1).

The structures of complexes **3a**, **3b**, and **3d** were determined by X-ray crystallography, and in addition, ^1H and $^{31}P\{^1H\}$ NMR spectra were recorded. Since we were at this stage not interested in isolating bulk samples of the materials, only NMR scale experiments were performed, and thus no other analytical techniques were used to characterize the compounds. In the case of the Me derivative (**3c**), the crystals were of poor quality so only ^1H and $^{31}P\{^1H\}$ NMR spectra are available for this compound. The $^{31}P\{^1H\}$ NMR spectra of complexes **3a**–**3d** consist of a singlet resonance at ca. –56 ppm, which is shifted by ca. 27 ppm from that of the azido precursor. These chemical shifts are very similar to those observed in other Pd PTA complexes containing thiolate ligands (14). The ^1H NMR spectra of complexes **3a**–**3d** show, in addition to the signals from the tetrazole substituents, a singlet and an AB-quartet because of the PCH_2N and NCH_2N protons of the PTA ligands, respectively. The proposed structures of the complexes were confirmed by X-ray diffraction studies of compounds **3a**, **3b**, and **3d**; the molecular structures are shown in Figs. 1–3.

In all three complexes, the palladium is coordinated by two tetrazolate-thiolates (via the sulfur atom) and two PTA ligands in a square planar geometry with a *trans* configuration. The Pd–P and Pd–S bond distances of (ca. 2.30 and 2.34 Å, respectively) are very similar to those observed in other PTA complexes of palladium containing thiolate ligands, e.g., *trans*-[$Pd(SPyridine)_2(PTA)_2$] (14). The C–S bond lengths of ca. 1.72 Å are also similar to those observed in other tetrazole-thiolate complexes of Pd (7) but shorter than in Pd complexes containing pyridine thiolate ligands (1.75 Å) (14).

It was also attempted to prepare analogous complexes using the Pt precursor [$Pt(N_3)_2(PTA)_2$] **2**. In this case, however, the cycloaddition reaction was considerable slower (ca. 2–3 days were required for all of complex **2** to be consumed), compared with the Pd series. This difference in reaction rate between Pd and Pt complexes has also been observed by Kim et al. (7). Furthermore, it was only possible to obtain crystalline material for the product derived from phenyl isothiocyanate (**4d**) upon layering the sample with Et_2O. The spectroscopic data of complex **4d** is essentially identical to that of its Pd congener **3d**. The $^1J_{Pt\text{-}P}$ coupling constant of

© 2008 NRC Canada

Fig. 2. Molecular structure of complex **3b**. Ellipsoids show 50% probability levels. Hydrogen atoms have been omitted for clarity. Selected bond distances (Å) and angles (°): Pd1–P1 2.2949(4), Pd1–S1 2.3328(4), S1–C7 1.7213(14), C7–N5 1.3472(18), C7–N4 1.3345(18), N4–N7 1.3672(18), N7–N6 1.2944(1); P1–Pd1–S1 93.400(13), C7–S1–Pd1 104.14(5).

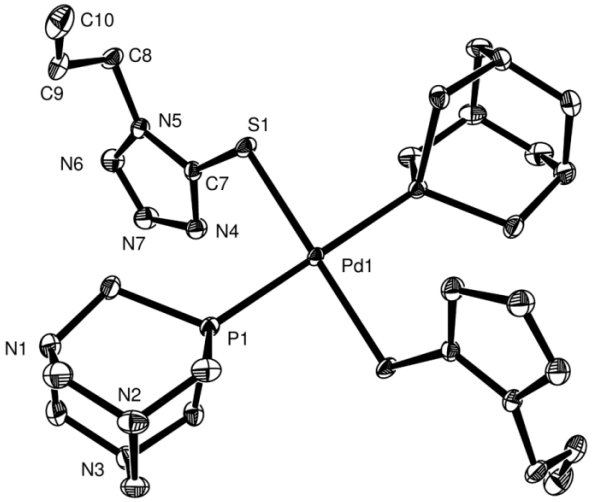

Fig. 3. Molecular structure of complex **3d**. Ellipsoids show 50% probability levels. Hydrogen atoms have been omitted for clarity. Selected bond distances (Å) and angles (°): Pd1–P1 2.3018(7), Pd1–S1 2.3406(6), S1–C7 1.717(3), C7–N4 1.349(3), C7–N7 1.324(3), N4–N5 1.365(3), N5–N6 1.292(3); P1–Pd1–S1 90.98(2), C7–S1–Pd1 101.29(9).

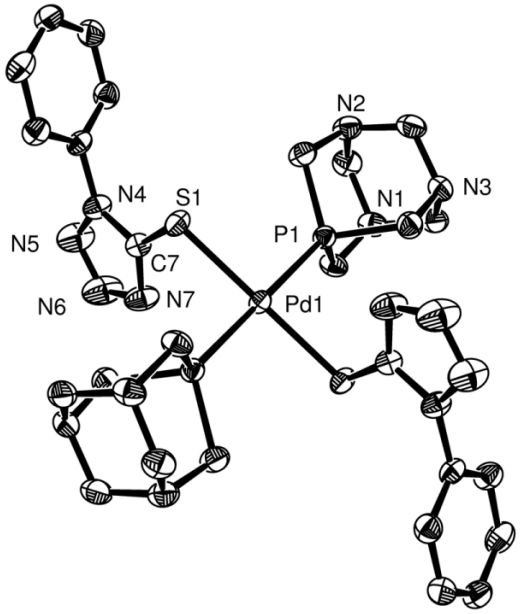

2458 Hz observed in the $^{31}P\{^{1}H\}$ NMR spectrum of **4d** is consistent with a *trans* configuration, similar to what has been reported for other *trans* Pt complexes containing PTA and thiolate ligands (15). This trans geometry was confirmed by X-ray crystallography; the molecular structure of **4d**·CH_2Cl_2 is shown in Fig. 4.

Fig. 4. Molecular structure of complex **4d**·CH_2Cl_2. Ellipsoids show 50% probability levels. Hydrogen atoms and the disordered CH_2Cl_2 molecule have been omitted for clarity. Selected bond distances (Å) and angles (°): Pt1–P1 2.2897(10), Pt1–S1 2.3393(9), S1-C7 1.717(4), C7–N4 1.331(5), C7–N1 1.355(5), N4–N3 1.364(5), N3–N2 1.282(5); P1–Pt1–S1 87.21(3), C7–S1–Pt1 102.44(13).

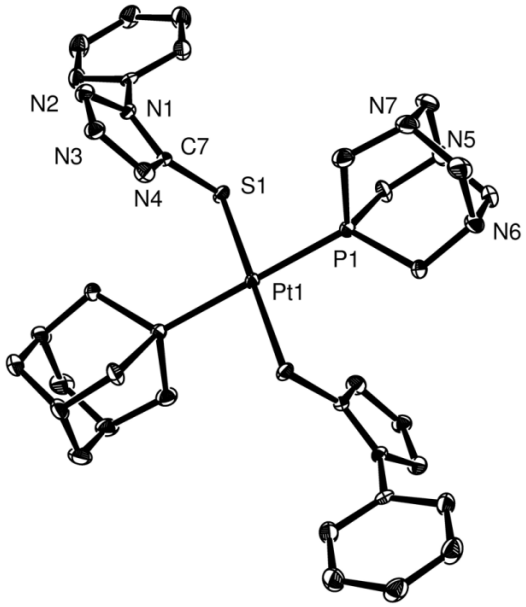

The molecular structure of **4d** is very similar to that of the Pd derivative **3d**: Pt shows square planar coordination geometry with a *trans* arrangement of pairs of identical ligands. Bond lengths and angles in **4d** are also typical for complexes of this kind.

In conclusion, we have shown that the reaction of various isothiocyanates with a PTA-stabilized Pd azido complex gives *trans* Pd complexes containing anionic, S-coordinated tetrazole-thiolate ligands. This coordination mode of the cycloaddition product was confirmed by crystallographic studies. In the case of platinum, the same reaction occurs, but the rate of the reaction is considerably slower. Further work is currently in progress to develop a suitable preparation method for larger quantities of these complexes and to study their biological activity.

Experimental

PTA (1,3,5-triaza–7-phosphaadamantane), *cis*-[$Pt(N_3)_2$(cod)] (cod = 1,5-cyclooctadiene), and *cis*-[$Pd(N_3)_2$(tmeda)] (tmeda = *N*,*N*,*N*′,*N*′-tetramethylethylenediamine) were prepared following published procedures (16, 17). All solvents and chemicals were sourced commercially and used as received. ^{1}H, ^{13}C, and $^{31}P\{^{1}H\}$ NMR spectra were recorded on a Bruker Avance III 500 MHz instrument using residual solvent signals as reference. Mass spectra (ES-MS positive ion mode) were measured on a Bruker Esquire 3000 spectrometer and IR spectra on a Bruker FT-IR instrument as KBr disks. Elemental analyses were carried out by staff of the microanalytical laboratory of the Institute of Inorganic Chemistry at the University of Vienna.

© 2008 NRC Canada

$[Pd(N_3)_2(PTA)_2]$ (1)

To a CH_2Cl_2 solution of *cis*-$[Pd(N_3)(tmeda)]$ (0.300 g, 1.142 mmol) was added a solution of PTA (0.359 g, 2.284 mmol) in CH_2Cl_2 (15 mL). After stirring the mixture for 2 h, the yellow solid was isolated by filtration, washed with Et_2O, and dried. Yield: 0.496 g, 86%. IR (KBr disk, cm^{-1}) ν (N_3): 2040, 2019. ^1H NMR (500 MHz, DMSO-d_6, 25 °C, ppm) δ: 4.47 (AB quart, J = 12.6 Hz, 12 H, NCH_2N), 4.35 (s, 12 H, PCH_2P). $^{13}C\{^1H\}$ NMR (126 MHz, DMSO-d_6, 25 °C, ppm) δ: 51.30 (br s, PCH_2N), 71.64 (s, NCH_2N). $^{31}P\{^1H\}$ NMR (202 MHz, DMSO-d_6, 25 °C, ppm) δ: –29.90. ES-MS *m/z*: 527 $[M + Na]^+$. Calcd. for $C_{12}H_{24}N_{12}P_2Pd$ (504.77): C 28.55, H 4.79, N 33.30; found C 28.72, H 4.81, N 33.06.

$[Pt(N_3)_2(PTA)_2]$ (2)

To a suspension of *cis*-$[Pt(N_3)_2(cod)]$ (0.100 g, 0.258 mmol) in CH_2Cl_2 was added PTA (0.081 g, 0.516 mmol). After stirring for ca. 2 h, the colourless solid was isolated by filtration, washed with Et_2O, and dried to give 0.129 g (84%) of the complex. IR (KBr disk, cm^{-1}) ν(N_3): 2052, 2036. ^1H NMR (400 MHz, DMSO-d_6, 25 °C, ppm) δ: 4.46 (AB quart, J = 12.6 Hz, 12 H, NCH_2N), 4.25 (s, 12 H, PCH_2P). $^{31}P\{^1H\}$ NMR (162 MHz, DMSO-d_6, 25 °C, ppm) δ: –59.09 ($J_{Pt\text{-}P}$ = 3140 Hz). ES MS *m/z*: 616 $[M + Na]^+$. Calcd. for $C_{12}H_{24}N_2P_2Pt$ (593.42): C 24.29, H 4.08, N 28.32; found C 24.50, H 4.03, N 28.39.

Preparation of the cycloaddition products

To a suspension of $[M(N_3)_2(PTA)_2]$ (M = Pd, Pt) (25 mg) in CH_2Cl_2 (5 mL) was added an excess (ca. 0.2 mL) of RNCS (R = Et, allyl, Me, Ph). The mixture was left to stir for ca. 18 h at room temperature during which all solid had dissolved. Et_2O was carefully layered onto the solution and after standing for 2–4 days, crystals could be harvested. NMR data was obtained by re-dissolving the crystals in a suitable deuterated solvent. In case of the Pt derivative, the reaction required much longer time (assessed by the time taken for **2** to completely dissolve), and crystals were only obtained when using phenyl isothiocyanate. Using this procedure the following compounds were prepared.

***trans*-$[Pd\{SCN_4(Et)\}_2(PTA)_2]$ (3a)**

Orange crystals. ^1H NMR (500 MHz, $CDCl_3$, 25 °C, ppm) δ: 4.34–4.43 (m, 18 H, NCH_2N, CH_3CH_2N), 4.15 (s, 12 H, PCH_2P), 1.58 (t, J = 7.3 Hz, 6 H, CH_3CH_2N). $^{31}P\{^1H\}$ NMR (202 MHz, $CDCl_3$, 25 °C, ppm) δ: –56.12.

***trans*-$[Pd\{SCN_4(CH_2CHCH_2)\}_2(PTA)_2]$ (3b)**

Orange crystals. ^1H NMR (500 MHz, $CDCl_3$, 25 °C, ppm) δ: 5.98–6.09 (m, 2 H, $NCH_2CH{=}CH_2$) 5.39 (d, J = 10.1 Hz, 2 H, $NCH_2CH{=}CH_2$), 5.32 (d, J = 17.0 Hz, 2 H, $NCH_2CH{=}CH_2$), 4.96 (d, J = 5.9 Hz, 4 H, $NCH_2CH{=}CH_2$), 4.38 (AB quart, J = 12.6 Hz, 12 H, NCH_2N), 4.14 (s, 12 H, PCH_2P). $^{31}P\{^1H\}$ NMR (202 MHz, $CDCl_3$, 25 °C, ppm) δ: –55.84.

***trans*-$[Pd\{SCN_4(Me)\}_2(PTA)_2]$ (3c)**

Yellow crystals. ^1H NMR (500 MHz, $CDCl_3$, 25 °C, ppm) δ: 4.33–4.49 (m, 12 H, NCH_2N), 4.16 (s, 12 H, PCH_2P), 4.00 (s, 6 H, Me). $^{31}P\{^1H\}$ NMR (202 MHz, $CDCl_3$, 25 °C, ppm) δ: –56.25.

trans-*$[Pd\{SCN_4(Ph)\}_2(PTA)_2]$ (3d)*

Orange crystals. ^1H NMR (500 MHz, $CDCl_3$, 25 °C, ppm) δ: 7.87 (d, J = 7.6 Hz, 4 H, *o*-Ph), 7.60 (t, J = 7.6 Hz, 4 H, *m*-Ph), 7.54 (t, J = 7.3 Hz, 2 H, *p*-Ph), 4.36 (AB quart, J = 13.2 Hz, 12 H, NCH_2N), 4.16 (s, 12 H, PCH_2P). $^{31}P\{^1H\}$ NMR (202 MHz, $CDCl_3$, 25 °C, ppm) δ: –55.61.

trans-*$[Pt\{SCN_4(Ph)\}_2(PTA)_2]$ (4d)*

Colourless crystals. ^1H NMR (500 MHz, $CDCl_3$, 25 °C, ppm) δ: 7.84 (d, J = 7.6 Hz, 4 H, *o*-Ph), 7.62 (t, J = 6.9 Hz, 4 H, *m*-Ph), 7.56 (t, J = 7.3 Hz, 2 H, *p*-Ph), 4.37 (AB quart, J = 13.2 Hz, 12 H, NCH_2N), 4.17 (s, 12 H, PCH_2P). $^{31}P\{^1H\}$ NMR (202 MHz, $CDCl_3$, 25 °C, ppm) δ: –63.80 ($J_{P\text{-}Pt}$ = 2458 Hz).

X-ray crystal structure determinations[3]

X-ray diffraction quality crystals of compounds **3a**, **3b**, **3d**, and **4d**·CH_2Cl_2 were mounted in a cryoloop with a drop of oil and placed into the cold stream (100 K) of a Bruker X8 APEX II CCD diffractometer with graphite-monochromated Mo Kα radiation (λ = 0.710 73 Å), controlled by a Pentium-based PC running the SAINT software package (18). Single crystals were positioned at 40 mm from the detector and 1843, 2075, 1599, and 4656 frames were measured, each for 70, 20, 70, and 5 s over 1° scan width for **3a**, **3b**, **3d**, and **4d**·CH_2Cl_2, correspondingly. Crystal data, data collection parameters, and structure refinement details for **3a**, **3b**, **3d**, and **4d**·CH_2Cl_2 are given in Table 1. The structures were solved by direct methods and refined on F^2 by full-matrix least-squares techniques using the SHELXTL software package (19, 20); scattering factors were taken from the literature (21). The co-crystallized CH_2Cl_2 molecule in **4d**·CH_2Cl_2 was found disordered over two positions with site occupation factors 0.61:0.39. The disorder was solved by using SADI and EADP restraints. All non-hydrogen atoms were refined with anisotropic displacement parameters. Hydrogen atoms were placed at calculated positions or localized on difference Fourier maps and isotropically refined. Calculated hydrogen atoms have assigned thermal parameters equal to either 1.5 (methyl hydrogen atoms) or 1.2 (non-methyl hydrogen atoms) times the thermal parameters of the atom to which they were attached. The graphics were prepared by using ORTEP (22).

Acknowledgements

FM thanks the University of Vienna and Bernhard Keppler for a visiting professorship. To Bernhard and all the members of his research group many thanks for access to all

[3] Supplementary data for this article are available on the journal Web site (canjchem.nrc.ca) or may be purchased from the Depository of Unpublished Data, Document Delivery, CISTI, National Research Council Canada, Ottawa, ON K1A 0R6, Canada. DUD 3806. For more information on obtaining material refer to cisti-icist.nrc-cnrc.gc.ca/cms/unpub_e.shtml. CCDC 688299–688302 contain the crystallographic data for this manuscript. These data can be obtained, free of charge, via www.ccdc.cam.ac.uk/conts/retrieving.html (Or from the Cambridge Crystallographic Data Centre, 12 Union Road, Cambridge CB2 1EZ, UK; fax +44 1223 336033; or deposit@ccdc.cam.ac.uk).

© 2008 NRC Canada

Table 1. Crystallographic and refinement details of complexes **3a**, **3b**, **3d**, and **4d**·CH_2Cl_2.

Compound	**3a**	**3b**	**3d**	**4d**·CH_2Cl_2
Formula	$C_{18}H_{34}N_{14}P_2PdS_2$	$C_{20}H_{34}N_{14}P_2PdS_2$	$C_{26}H_{34}N_{14}P_2PdS_2$	$C_{28}H_{38}Cl_4N_{14}P_2PtS_2$
FW	679.05	703.07	775.13	1033.67
Crystal system	Triclinic	Triclinic	Monoclinic	Monoclinic
Space group	*P*-1	*P*-1	$P2_1/n$	$P2_1/c$
a (Å)	6.354 10(10)	6.253 40(10)	9.316 2(3)	10.899 8(9)
b (Å)	10.549 5(3)	9.779 7(2)	11.729 2(6)	18.024 0(13)
c (Å)	10.937 8(3)	12.424 9(3)	21.741 0(10)	9.837 1(8)
α (°)	106.484(2)	99.106(2)	90	90
β (°)	92.9180(10)	101.1290(10)	92.048(3)	100.500(5)
γ (°)	106.8810(10)	103.4310(10)	90	90
V (Å^3)	665.62(3)	708.57(3)	1609.63(13)	1900.2(3)
Z	1	1	2	2
D_{calcd} (g cm^{-3})	1.694	1.648	1.599	1.807
μ (mm^{-1})	1.014	0.955	0.850	4.212
F(000)	348	360	792	1024
Reflections	22 043	26 570	48 582	134 597
Unique Reflections (R_{int})	3887 (0.0363)	4154 (0.0385)	4716 (0.0980)	4369 (0.0539)
Parameters	169	178	205	239
θ range (°)	2.40–30.08	2.48–30.05	2.56–30.09	2.21–27.50
R_1 ($I > 2\sigma(I)$)[a]	0.0211	0.0218	0.0394	0.0309
wR_2 (all data)[b]	0.0587	0.0515	0.0920	0.0782
GOF[c]	1.009	1.055	0.984	1.080
Largest diff. peak, hole (e Å^{-3})	0.509, –0.388	0.699, –0.406	0.821, –1.166	1.612, –1.667

[a] $R_1 = \Sigma||F_o| - |F_c|| / \Sigma|F_o|$.
[b] $wR_2 = \{\Sigma[w (F_o^2 - F_c^2)^2] / \Sigma[w(F_o^2)^2]\}^{1/2}$.
[c] GOF = $\{\Sigma[w(F_o^2 - F_c^2)^2] / (n - p)\}^{1/2}$, where *n* is the number of reflections and *p* is the total number of parameters refined.

the facilities and for making my stay in Vienna so enjoyable and productive.

References

1. W. Beck, K. Feldl, and E. Schuierer. Angew. Chem. Int. Ed. Engl. **4**, 439 (1965).
2. W. Beck, W.P. Fehlhammer, P. Pöllmann, and H. Schächl. Chem. Ber. **102**, 1976 (1969).
3. W. Beck, W.P. Fehlhammer, H. Bock, and M. Bauder. Chem. Ber. **102**, 3637 (1969).
4. W. Beck, K. Burger, and W.P. Fehlhammer. Chem. Ber. **104**, 1816 (1971).
5. P. Kreutzer, J.C. Weis, H. Böhme, T. Kemmerich, W. Beck, C. Spencer, and R.Z. Mason. Naturforsch, **27B**, 745 (1972).
6. P. Kreutzer, J.C. Weis, H. Bock, J. Erbe, and W. Beck. Chem. Ber. **116**, 2691 (1983).
7. Y.J. Kim, J.T. Han, S. Kang, W.S. Han, and S.W. Lee. Dalton Trans. 3357 (2003).
8. Y.J. Kim, X. Chang, J.T. Han, M.S. Lim, and S.W. Lee. Dalton Trans. 3699 (2004).
9. Y.J. Kim, S.H. Lee, S.H. Lee, S.I. Jeon, M.S. Lim, and S.W. Lee. Inorg. Chim. Acta, **358**, 650 (2005).
10. K. Lee, Y.J. Kim, and K.K.J. Baeck. Organomet. Chem. **690**, 4319 (2005).
11. F. Mohr, E. Cerrada, and M. Laguna. Organometallics, **25**, 644 (2006).
12. F. Mohr, S. Sanz, E. Vergara, E. Cerrada, and M. Laguna. Gold Bull. **36**, 212 (2006).
13. F. Mohr, S. Sanz, E.R.T. Tiekink, and M. Laguna. Organometallics, **25**, 3084 (2006).
14. E. Vergara, S. Miranda, F. Mohr, E. Cerrada, E.R.T. Tiekink, P. Romero, and M. Laguna. Eur. J. Inorg. Chem. 2926 (2007).
15. S. Miranda, E. Vergara, F. Mohr, D. de Vos, E. Cerrada, A. Mendía, and M. Laguna. Inorg. Chem. **47**, 5641 (2008).
16. D.J. Daigle. Inorg. Synth. **32**, 40 (1998).
17. Y.J. Kim, J.C. Choi, and K.H. Park. Bull. Korean Chem. Soc. **15**, 690 (1994).
18. Saint-Plus (version 7.06a) and APEX2 [computer programs]. Bruker Nonius AXS Inc., Madison, Wisc., USA. 2004.
19. G.M. Sheldrick. SHELX–97 [computer program]. Program for crystal structure solution. University of Göttingen, Göttingen, Germany. 1997.
20. G.M. Sheldrick. SHELXL–97 [computer program]. Program for crystal structure refinement. University of Göttingen, Göttingen, Germany. 1997.
21. International tables for X-ray crystallography. Vol. *Edited by* C. Kluwer. Academic Press, Dodrecht, The Netherlands. 1992. Tables 4.2.6.8 and 6.1.1.4.
22. G.K. Johnson. Report ORNL–5138. Oak Ridge National Laboratory, Oak Ridge, Tenn., USA. 1976.

© 2008 NRC Canada

Octahedral perfluoroalkyl complexes of Ir(III) formed by oxidative addition of perfluoroalkyl iodides to Ir(acac)$(CO)_2$[1]

Hui Huang, N. Raluca Hurubeanu, Cheryl J. Bourgeois, Sue-Mei Cheah, Jian Yuan, Arnold L. Rheingold, and Russell P. Hughes

Abstract: Oxidative addition of primary, secondary, or benzylic perfluoroalkyl iodides (R_F–I) to the phosphine free Ir(I) precursor Ir(acac)(CO)**2 1** (acac = 2,4-pentanedionato) proceeds smoothly to afford octahedral Ir(III) products Ir(acac)(I)(R_F)$(CO)_2$, A combination of X-ray crystallographic studies and solution spectroscopy shows that these products are the result of overall trans-addition of the C–I bond to iridium, probably a result of thermodynamic control; evidence for a kinetic product resulting from net cis-addition is obtained in one case. Treatment of the Ir(III) compounds with AgOTf (Tf = CF_3SO_3) illustrates that the iodo ligand is replaced by triflate with retention of stereochemistry at Ir. The resulting triflate complexes are inert to displacement by H_2O or H_2. The Ir(III) products exhibit very high CO stretching frequencies in the IR, indicating that the CO ligands may be non-classical. A quantitative estimation of the degree of backbonding to the CO ligands in these compounds, and a comparison of the π-acceptor properties of CO and fluoroalkyl ligands, is made using an approach based on Density Functional Theory (DFT) and Natural Bond Orbital analyses.

Key words: iridium, fluoroalkyl, oxidation, carbonyl, DFT.

Résumé : L'addition oxydante d'iodures primaires, secondaires ou benzyliques perfluoroalkylés (R_F–I) sur le précurseur Ir(I) sans phosphine, Ir(acac)$(CO)_2$ (**1**) (acac = 2,4-pentanedionato), s'effectue sans problème et elle conduit à la formation de produits Ir(III) octaédriques Ir(acac)((I)(R_F)$(CO)_2$. Des études cristallographiques par diffraction des rayons X et d'autres réalisées par spectroscopie en solution permettent de montrer que ces produits sont le résultat d'une addition nette *trans* de la liaison C–I sur l'iridium, probablement sous l'influence d'un contrôle thermodynamique; dans un cas, on a toutefois été en mesure de mettre en évidence d'un produit cinétique résultant d'une addition nette *cis*. Le traitement des composés Ir(III) avec du AgOTf (Tf = CF_3SO_3) permet d'illustrer que le ligand iodo est remplacé par le triflate avec rétention de la stéréochimie au niveau de l'iridium. Les complexes triflates qui en résultent sont inertes aux déplacements par l'eau ou l'hydrogène. Les produits Ir(III) présentent des spectres infrarouges dans lesquels les fréquences d'élongation du CO sont très élevées, ce qui suggère que les ligands CO ne sont pas classiques. Faisant appel à la théorie de la densité fonctionnelle et une analyse des orbitales de liaison naturelle, on a fait une évaluation quantitative du degré de retour de liaison vers les ligands CO dans ces composés ainsi qu'une comparaison des propriétés des ligands CO et fluoroalkyles comme accepteurs π.

Mots-clés : iridium, fluoroalkyle, oxydation, carbonyle, théorie de la densité fonctionnelle (TDF).

[Traduit par la Rédaction]

Introduction

The oxidative addition of carbon–halogen bonds to low-valent transition metal complexes is a fundamental organometallic reaction that plays a key role in many useful catalytic transformations (1). An important example is the addition of CH_3I to *cis*-$[MI_2(CO)_2]^-$ (M = Rh or Ir) in the carbonylation of methanol to form acetic acid (2–6). Corresponding oxidative addition of a large variety of substrates to square-planar d^8 complexes of platinum has also been a subject of great interest and the source of a great many significant contributions from the Puddephatt group over the

Received 30 April 2008. Accepted 17 June 2008. Published on the NRC Research Press Web site at canjchem.nrc.ca on 27 August 2008.

Dedicated to Professor Richard J. Puddephatt in recognition of his outstanding contributions to inorganic and organometallic chemistry.

H. Huang, N.R. Hurubeanu, C.J. Bourgeois, S.-M. Cheah, J. Yuan, R.P. Hughes.[2] Department of Chemistry, Dartmouth College, Hanover, NH 03755, USA.
A.L. Rheingold. Department of Chemistry and Biochemistry, University of California, San Diego, CA 92093, USA.

[1]This article is part of a Special Issue dedicated to Professor R. Puddephatt.
[2]Corresponding author (e-mail: rph@dartmouth.edu).

 doi:10.1139/V08-114 © 2008 NRC Canada

Scheme 1.

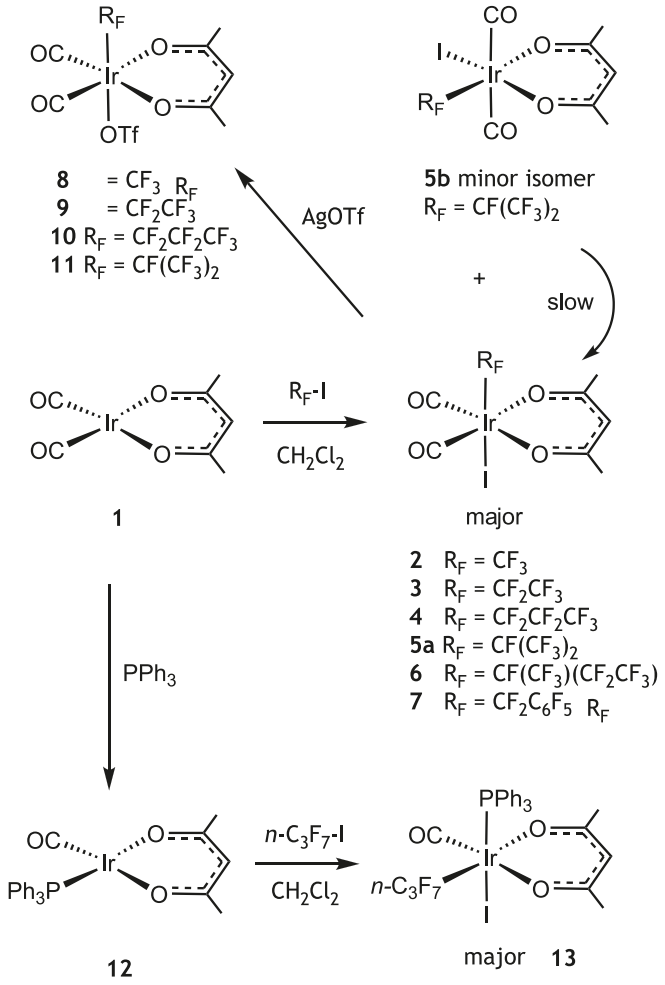

past three decades, only representative examples of which are referenced here (7–27). Our group has had a long-standing interest in using analogous oxidative addition reactions of perfluoroalkyl iodides, based on reactions originally reported in the 1960s (28, 29), to prepare perfluoroalkyl complexes of the late transition metals, including iridium (30–32), rhodium (31–36), palladium (37, 38), and platinum (39–43).

The square-planar iridium(I) complex **1** (Scheme 1) (44) is a commercially available catalyst for anti-Markovnikov arylation of olefins and olefin isomerization (45) and has been broadly employed to prepare other organometallic complexes through ligand substitution (46, 47) or cluster formation (48, 49). Simple oxidative addition reactions to this 16-electron complex do not appear to have been reported. Here, we report syntheses, reactivity, and DFT studies of a series of new perfluoroalkyl iridium complexes, obtained by oxidative addition of **1** with perfluoroalkyl iodides, which have been characterized spectroscopically, and in some cases, crystallographically.

Results and discussion

Synthesis and molecular structure of 1

Despite being known for four decades and being a compound of some synthetic utility (vide supra), the molecular structure of **1** has apparently not been determined accurately. A search of the Cambridge Structure Database (50) revealed a single report (code ACRHCO) of a 12% structure with no deposited coordinates, resulting from a Ph.D. thesis (51). In our hands, when **1** was synthesized according to the reported method (52), good quality crystals were obtained and were subjected to a single-crystal X-ray diffraction study. An ORTEP is shown in Fig. 1, details of the crystal data are presented in Table 1, and selected bond lengths and angles for the coordination sphere of Ir are given in Table 2. The intramolecular structure is unremarkable, but the crystal packing diagram shown in Fig. 2 reveals the expected face-to-face stacking of the individual planar molecules to give a linear chain structure with an Ir–Ir separation of 3.192 Å. Despite the absence of a deposited crystal structure, several studies of phenomena resulting from intermolecular interactions in the solid-state structure of this molecule have already been reported (53–58).

Fig. 1. ORTEP diagram of **1** with ellipsoids drawn at the 30% probability level. Hydrogen atoms are omitted for clarity. Selected bond lengths and angles are presented in Table 2.

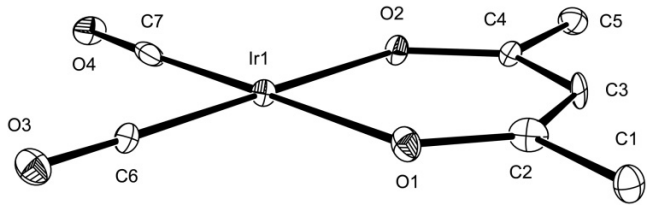

Oxidative addition of perfluoroalkyl iodides to 1

Treatment of **1** with primary, secondary, and benzylic perfluoroalkyl iodides (R_F–I) in CH_2Cl_2 at room temperature afforded oxidative addition of the R_F–I bond to give the Ir(III) complexes **2**–**7** in excellent yields as shown in Scheme 1. Crystal structures were obtained for complexes **4** and **5**; ORTEP diagrams are presented in Figs. 3 and 4, respectively, and details of the crystal data and structure determinations are presented in Table 1. Selected bond lengths and angles for the coordination sphere of Ir are given in Table 2.

The structures establish an approximate octahedral coordination around iridium, with the fluoroalkyl and iodo ligands mutually trans to each other. Analogous trans-stereochemistry for the oxidative addition of fluoroalkyl iodides to square-planar compounds has previously been observed in reactions of Pt(II) complexes (37, 42, 59).

As previously observed for Pd(II) (38) and other Ir(III) (30) complexes, the Ir–R_F bond length to the primary fluoroalkyl group in **4** [2.093(5) Å] is significantly shorter than that to the much bulkier (60) secondary fluoroalkyl in **5** [2.139(3) Å]. The Ir–C(O) bond lengths in **4** [1.893(5), 1.907(5) Å] and **5** [1.897(4), 1.900(4) Å] are slightly longer than those in the Ir(I) precursor **1** [1.856(10), 1.883(14) Å], while the Ir–O(acac) bond lengths in **4** [2.037(3), 2.037(3) Å] and **5** [2.031(2), 2.035(2) Å] are slightly shorter than those in **1** [2.053(6), 2.078(8) Å]; both these features are consistent with formal oxidation at iridium and less backbonding from Ir → CO. A more quantitative discussion of the degree of backbonding to the CO ligands is presented later. The Ir–I bond lengths for **4** [2.7363(4) Å] and **5**

© 2008 NRC Canada

Table 1. Summary of crystallographic data for **1**, **4**, **5a**, **8**, **9**, and **13**.

Compound	**1**	**4**	**5a**	**8**	**9**	**13**
Formula	$C_7H_7IrO_4$	$C_{10}H_7F_7IIrO_4$	$C_{10}H_7F_7IIrO_4$	$C_9H_7F_6IrO_7S$	$C_{10}H_7F_8IrO_7S$	$C_{27}H_{22}F_7IIrO_3P$
Formula mass	347.33	643.26	643.26	565.41	615.42	877.52
Space group	*P*-1	*P*2(1)/*n*	*P*2(1)/*n*	*P*2(1)/*n*	*P*-1	*P*2(1)/*c*
a (Å)	6.3387(15)	11.5266(12)	10.5998(12)	9.3487(10)	8.4781(8)	13.507(5)
b (Å)	7.6501(17)	11.9579(13	11.6832(13)	12.7522(14)	9.8173(10)	11.672(4)
c (Å)	9.102(2)	11.5760(12	13.2202(14)	12.9532(14)	11.5359(11)	18.783(6)
α (°)	106.776(3)	90	90	90	75.2520(10)	90
β (°)	90.686(3)	98.415(2)	110.084(2)	100.129(2)	76.5010(10)	106.124(6)
γ (°)	100.288(3)	90	90	90	67.5830(10)	90
V (Å^3)	414.83(17)	1593.9(3)	1537.6(3)	1520.2(3)	848.32(14)	2844.6(16)
Z	2	4	4	4	2	4
$D_{calcd.}$ (g cm^{-3})	2.781	2.681	2.779	2.470	2.409	2.049
μ (mm^{-1})	16.062	10.399	10.780	9.019	8.108	5.909
Temp. (K)	100(2)	173(2)	173(2)	208(2)	208(2)	208(2)
Diffractometer	Bruker Smart Apex CCD					
Radiation	Mo Kα (0.71073 Å)					
Crystal size (mm)	0.50 × 0.15 × 0.05	0.10 × 0.07 × 0.05	0.15 × 0.10 × 0.10	0.29 × 0.27 × 0.25	0.33 × 0.28 × 0.18	0.40 × 0.20 × 0.20
F(000)	316	1168	1168	1056	576	1664
Measured reflns.	5325	13434	12862	9543	14067	19232
Independent reflns.	1519	3710	3595	3483	2967	6709
$R(F)$ (%)[a]	0.0436	0.0303	0.0230	0.0324	0.0328	0.0511
$R(wF^2)$ (%)[b]	0.1058	0.0679	0.0525	0.0720	0.0804	0.1276

[a] $R = \sum||F_o| - |F_c||/\sum|F_o|$.
[b] $R(wF^2) = \{\sum[w(F_o^2 - F_c^2)^2]/\sum[w(F_o^2)^2]\}^{1/2}$; $w = 1/[\sigma^2(F_o^2) + (aP)^2 + bP]$, $P = [2F_c^2 + \max(F_o,0)]/3$.

Table 2. Selected bond lengths (Å) and angles (°) for iridium complexes.

Compound	1	**4**	**5a**	**8**	**9**	**13**
Ir–R_F	—	2.093(5)	2.139(3)	2.039(5)	2.049(6)	2.076(8)
Ir–CO	1.856(10)	1.893(5)	1.897(4)	1.916(5)	1.919(6)	1.843(8)
	1.883(14)	1.907(5)	1.900(4)	1.917(5)	1.920(6)	—
Ir–O(acac)	2.053(6)	2.037(3)	2.031(2)	2.013(3)	2.016(4)	2.038(5)
	2.078(8)	2.037(3)	2.035(2)	2.014(3)	2.024(4)	2.225(6)
Ir–I	—	2.7363(4)	2.7205(3)	—	v	2.7202(8)
Ir–OTf	—	—	—	2.184(3)	2.154(4)	—
$C_α$–F	—	1.359(6)	1.398(4)	1.306(6)	1.356(8)	1.557(11)
	—	1.375(6)	—	1.316(6)	1.367(8)	1.369(8)
	—	—	—	1.326(6)	—	—
$C_β$–F	—	1.354(6)	1.338(4)	—	1.321(9)	1.402(12)
	—	1.342(6)	1.339(4)	—	1.352(8)	1.360(11)
	—	—	1.332(4)	—	1.300(9)	—
	—	—	1.338(4)	—	—	—
	—	—	1.337(4)	—	—	—
	—	—	1.329(4)	—	—	—
C–O (CO)	1.132(12)	1.131(6)	1.123(4)	1.118(6)	1.124(8)	1.139(9)
	1.105(15)	1.122(6)	1.125(4)	1.118(6)	1.120(7)	—
X–Ir–R_f	—	172.49(13)	173.67(8)	171.95(16)	172.7(2)	99.2(2)
C(O)–Ir–C(O)	89.2(5)	91.7(2)	92.63(14)	94.3(2)	91.7(2)	—
Ir–PPh_3	—	—	—	—	—	2.3445(16)
PPh_3–Ir–I	—	—	—	—	—	168.49(4)

[2.7205(3) Å] are essentially the same. As previously observed in Pd(II) complexes (38), the secondary α-C–F bond lengths in **4** [1.359(6), 1.375(6) Å] are shorter than the tertiary α-C–F bond length in **5** [1.398(4) Å].

Solution spectroscopy is also consistent with trans-stereochemistries for compounds **2**–**5a** and **7**. Observation of a single methyl resonance for the acac CH_3 groups is consistent with a structure having a plane of symmetry perpendicu-

© 2008 NRC Canada

Fig. 2. Packing diagram for **1** with ellipsoids drawn at the 30% probability level.

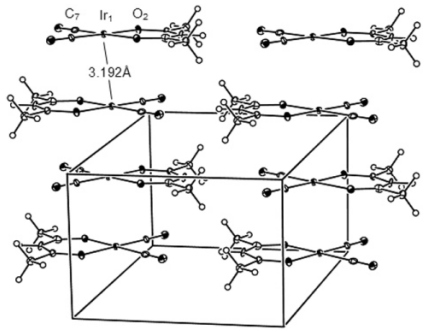

Fig. 3. ORTEP diagram of **4** with ellipsoids drawn at the 30% probability level. Hydrogen atoms are omitted for clarity. Selected bond lengths and angles are presented in Table 2.

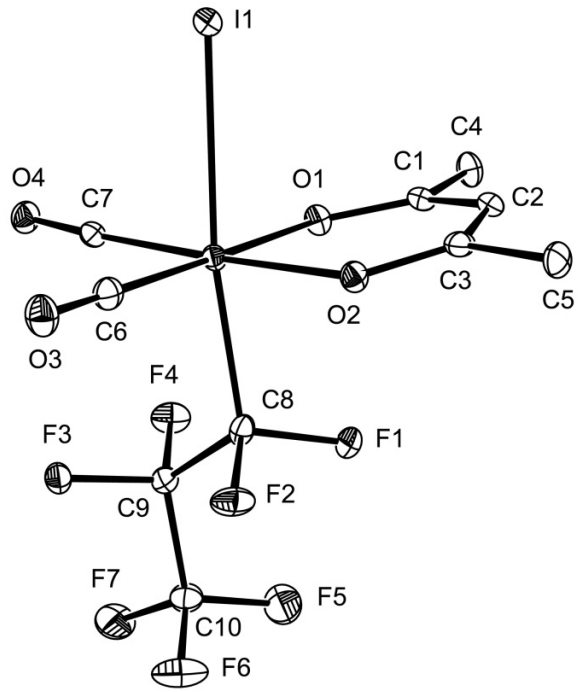

lar to the acac plane, and observation of symmetry equivalent α-CF_2 fluorines in **4** or β-CF_3 groups in **5a** is only consistent with a plane of symmetry including the α-carbon of the fluoroalkyl group. Only the illustrated trans-stereochemistries satisfy both these requirements. The overall structure of compound **6** is not unambiguously defined by spectroscopy, as the stereocenter at the α-carbon precludes any symmetry planes, yet only one CH_3 group is observed for the acac ligand; we assume that this arises due to accidental isochronicity of these methyl resonances and that the structure of **6** is analogous to those of its relatives. Curiously, in the reaction of **1** with perfluoro-*iso*-propyl iodide, a second set of transient peaks was observed in the reaction mixture; only a single CF_3 resonance was observed in the ^{19}F NMR spectrum and two methyl resonances were observed in the ^1H NMR spectrum. These observations are only consistent with the structure of this second compound being **5b** (Scheme 1). These peaks disappear over a short

Fig. 4. ORTEP diagram of **5a** with ellipsoids drawn at the 30% probability level. Hydrogen atoms are omitted for clarity. Selected bond lengths and angles are presented in Table 2.

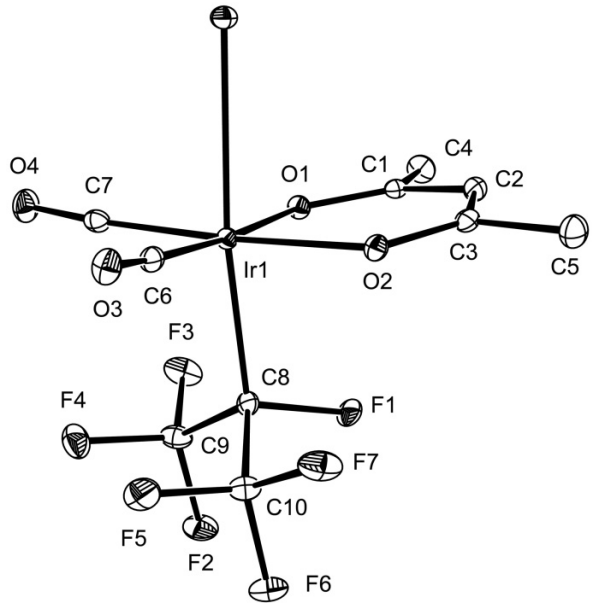

time, leaving **5a** as the only isolable product. This observation suggests that, at least in the case of perfluoro-*iso*-propyl iodide, the kinetic stereochemistry of oxidative addition is cis, and perhaps that in all cases described here, the final observed trans-stereochemistry may be the result of thermodynamic control. It is interesting to note that cis oxidative addition was reported in the oxidative addition of perfluoro-*n*-propyl iodide to Rh(acac)L_2 (L = PPh_3, $PMePh_2$) to give compounds **14** (61) but that trans-stereochemistries are the demonstrable kinetically controlled norm for oxidative addition of perfluoroalkyl iodides to Pt(II) systems (37, 42).

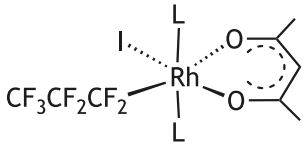

14 (L = PPh_3, $PMePh_2$)

We have shown previously that the iodide ligand in Cp*Ir(PMe_3)(R_F)(I) compounds is easily substituted by triflate on treatment with AgOTf, to give Cp*Ir(PMe_3)(R_F)(OTf) complexes, in which the triflate ligand can readily be substituted by water to give cationic Cp*Ir(PMe_3)(R_F)(OH_2)][OTf] compounds (32). These water compounds proved to be useful precursors for heterolytic activation of H_2, with subsequent hydrogenolysis of α-CF bonds to liberate hydrofluorocarbon products (62, 63). To see whether analogous reactivity could be observed in triflates derived from the systems described here, compounds **2**–**5a** were treated with AgOTf in CH_2Cl_2 to afford the corresponding triflate analogues **8**–**11** (Scheme 1). Crystal structures of **8** and **9** were carried out; ORTEP diagrams are provided in Figs. 5 and 6, respectively. Crystallographic

© 2008 NRC Canada

Fig. 5. ORTEP diagram of **8** with ellipsoids drawn at the 30% probability level. Hydrogen atoms are omitted for clarity. Selected bond lengths and angles are presented in Table 2.

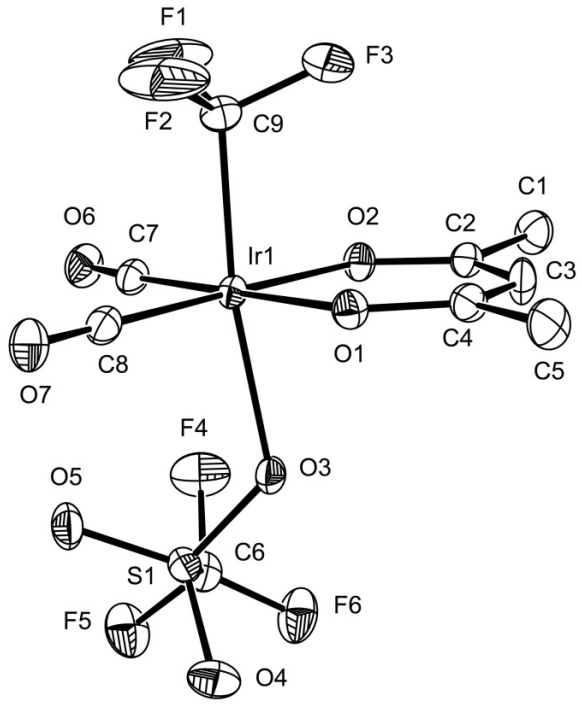

Fig. 6. ORTEP diagram of **9** with ellipsoids drawn at the 30% probability level. Hydrogen atoms are omitted for clarity. Selected bond lengths and angles are presented in Table 2.

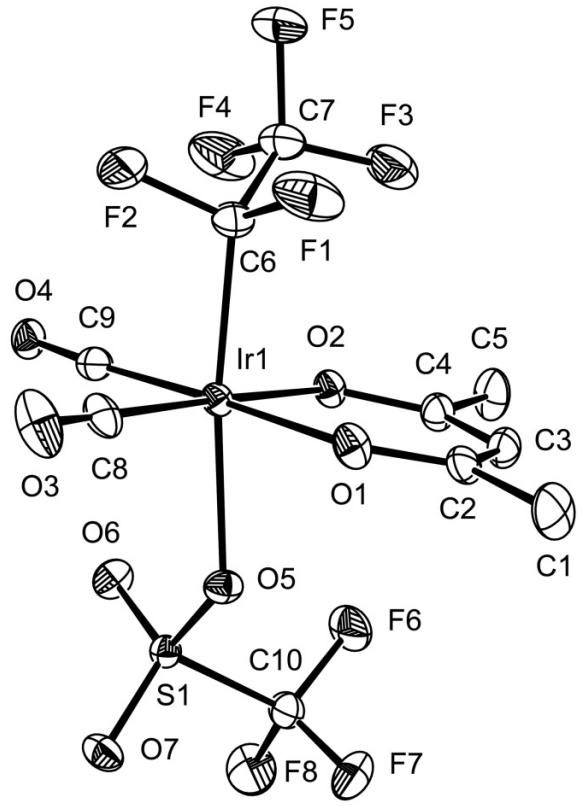

Fig. 7. ORTEP diagram of **13** with ellipsoids drawn at the 30% probability level. Hydrogen atoms are omitted for clarity. Selected bond lengths and angles are presented in Table 2.

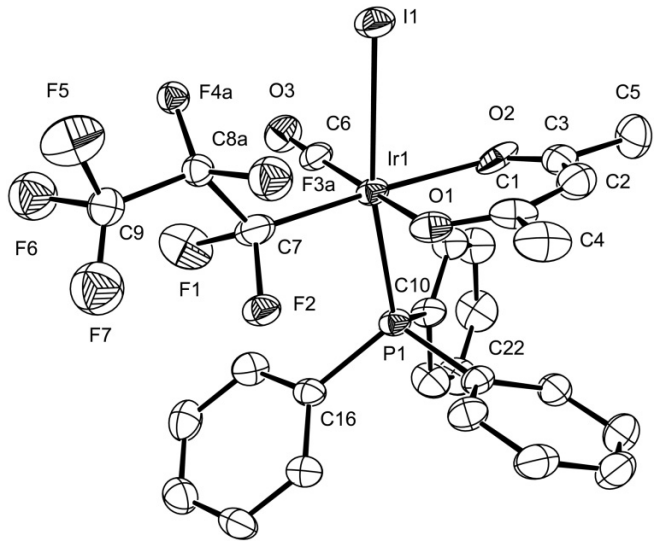

data are presented in Table 1 and selected bond lengths and angles in Table 2.

The crystal structures confirm the trans-stereochemistries of **8** and **9**, and solution NMR data are also consistent with this stereochemistry for all compounds **8**–**11**; replacement of iodide with triflate clearly proceeds via a mechanism in which overall stereochemistry at iridium is retained. However, no reaction of these compounds with either water or H_2 was observed, in contrast to our previous observations on pentamethylcyclopentadienyl analogues (62, 63) and in contrast with the observations of Eisenberg on dicationic Ir(III)–CF_3 complexes (64). Compounds **8**–**11** appear to possess the classic inertness expected for low spin d^6 compounds of the third transition series.

Finally, **1** was treated with 1 equiv. of PPh_3 to prepare the phosphine analogue **12** (Scheme 1) according to the reported method (44). Treatment of **12** with perfluoro-*n*-propyl iodide resulted in smooth oxidative addition, but NMR spectroscopy of the reaction mixture showed the presence of two isomeric products whose relative concentration did not change with time. Crystallization afforded single crystals of the major isomer, whose structure was obtained by X-ray diffraction and shown to be **13** (Scheme 1). An ORTEP diagram is presented in Fig. 7; crystallographic details are in Table 1, and selected bond lengths and angles in Table 2. The structure shows the perfluoropropyl group cis to iodide and also cis to PPh_3, with these three ligands adopting a mutually meridional configuration. The structure of the minor isomer remains unknown.

Computational studies

The expected increase in the IR stretching frequencies of the CO ligands is observed on formation of compounds **2**–**7** from **1**; values of ν_{CO} are shown in Table 3. It is interesting to note that in the Ir(III)–iodo complexes **2**–**7**, one of the CO stretching vibrations (ν_{sym}) occurs at a value higher than that of free CO (2143 cm^{-1}), illustrating that in these phosphine-donor-free Ir(III) complexes, the CO ligands may be non-

© 2008 NRC Canada

Table 3. Values of ν_{CO} (cm^{-1} in CH_2Cl_2).

Compound	ν_{CO} (cm^{-1})
1	2072, 1994
2	2150, 2106
3	2148, 2105
4	2145, 2103
5a	2149, 2104
6	2147, 2104
7	2147, 2104
8	2168, 2125
9	2167, 2125
10	2167, 2125
11	2169, 2129

classical (65–67), and that relatively little backbonding from Ir → CO π* may be present. Replacement of iodide by the more electronegative triflate ligand in compounds **8**–**11** increases ν_{CO} even further, but there is no significant effect on the CO frequencies by changing the fluoroalkyl ligand structure (CF_3, primary, or secondary).

The advent of density functional theory (DFT) (68–71), natural bond orbital (NBO) (72, 73), and natural population analysis (NPA) (74) as powerful tools for probing electronic structure in main-group and transition metal compounds(75) led us to apply these methods to representative compounds discussed here.

Four compounds were studied by DFT/NBO. The structures of starting material **1**, **2**, **3**, and **5a**, containing representative CF_3, primary (C_2F_5) and secondary [$(CF_3)_2CF$] ligands were optimized using the B3LYP functional with the LACV3P**++ basis set, as implemented in the Jaguar suite of programs(76); extended core potentials were used for Ir and I, with all other atoms treated using a 6–311G**++ basis set. For compounds **1** and **5a**, this procedure reproduced the crystallographically determined bond lengths within 0.02 Å and angles within 1°. The computed structures were confirmed as energy minima by calculating the vibrational frequencies by second derivative analytic methods and confirming the absence of negative frequencies. The use of second-order perturbative NBO analysis for estimating metal–ligand backbonding interaction energies (ΔE_{bb}), obtained from the off-diagonal Fock matrix element expressed in the NBO basis, has been thoroughly described and is now well-established (77–79). In our molecules, appropriate values of ΔE_{bb} reflect the energies of delocalization of the three formal "lone pairs" on Ir [the non-bonding d_{xy}, d_{xz}, and d_{yz} orbitals of d^6 Ir(III) in the NBO analysis] into the π* antibonding orbitals of the two CO ligands. Corresponding delocalization energies from the same metal orbital set into the C–F or C–C σ* antibonding orbitals on the α-carbon of the fluoroalkyl ligand can likewise be obtained. These values of ΔE_{bb} for compounds **1, 2, 3,** and **5a** are presented in Table 4, which also tabulates the natural charges from the NPA on iridium and the CO ligand atoms arising from the NBO treatment (80).

The data in Table 4 clearly show that when square-planar **1** reacts with fluoroalkyl iodides to form the oxidative addition products, the iridium is indeed oxidized, with an approximate doubling of the positive charge at the metal center. The carbon atoms of the CO ligands become more positive while the corresponding O atoms become more negative, resulting in a more polar CO ligand relative to the corresponding situation in **1**. This increase in positive charge on iridium results in a dramatic reduction in backbonding from Ir → CO (π*), illustrated by the loss of one third of the corresponding delocalization energy (ΔE_{bb}). The changes in formal charges on Ir and the CO ligand atoms are independent of the fluoroalkyl ligand. The fluoroalkyl ligands themselves are very weak π-acceptors compared to CO. The number of fluorines on the α-carbon dominates the extent of backbonding, with CF_3 being the best; replacement of the acceptor C–F (σ*) orbitals with C–C (σ*) orbitals results in progressively poorer π-acceptor properties. The relative π-acceptor properties of CF_3 and CO agree well with those recently reported for Mn and Tc carbonyl complexes (77), and it is clear that in a competition for backbonding with CO ligands, fluoroalkyl ligands fare poorly. We concur with other authors that the increase in CO stretching frequencies on oxidation of a metal center results from two factors: increased polarization of the C–O bond and reduced population of CO π* antibonding orbitals (81).

Table 4. NPA charges on Ir and CO ligands, and Ir–CO and Ir–R_F backbonding interaction energies (ΔE_{bb} kcal/mol).

Compound	**1**	**2**	**3**	**5a**
Ir → C–O (π*)	96.5	64.1	68.2	70.4
Ir → α-C–F (σ*)	—	6.5	4.9	2.5
Ir → α-C–C (σ*)	—	—	1.0	1.8
Total Ir → R_F (σ*)	—	6.5	5.9	4.3
Charge on Ir	+0.26	+0.50	+0.51	+0.52
Charge on CO (C)	+0.57	+0.65	+0.64	+0.64
Charge on CO (O)	–0.44	–0.38	–0.38	–0.38

Experimental

General data

Air-sensitive reactions were performed in oven-dried glassware using standard Schlenk techniques under an atmosphere of nitrogen, which was deoxygenated over BASF catalyst and dried over Aquasorb or in a Braun drybox. Methylene chloride, hexanes, diethyl ether, tetrahydrofuran, and toluene were dried over an alumina column under nitrogen (82). NMR spectra were recorded on a Varian Unity Plus 300 or 500 FT spectrometer. ^1H NMR spectra were referenced to the protio impurity in the solvent: C_6D_6 (7.16 ppm), CD_2Cl_2 (5.32 ppm). ^{19}F NMR spectra were referenced to external $CFCl_3$ (0.00 ppm). $^{13}C\{^1H\}$ NMR spectra were referenced to the deuterium solvent. Coupling constants are reported in units of Hertz and are absolute values. IR spectra were recorded on a PerkinElmer FTIR 1600 Series spectrophotometer. Elemental analyses were performed by Schwartzkopf (Woodside, NY) and X-ray crystallographic analyses at the University of California, San Diego.

$IrCl_3 \cdot xH_2O$ (Pressure Chemicals), Hacac and *sec*-C_4F_9–I (Alfa Aesar), AgOTf, and R_F–I (R_F = CF_3, C_2F_5, *n*-C_3F_7, *i*-C_3F_7, $CF_2C_6F_5$) (Synquest) were commercially available. Ir(acac)$(CO)_2$ (52) and Ir(acac)(CO)(PPh_3) (44) were prepared using literature procedures.

© 2008 NRC Canada

Computations

Structures were optimized at the DFT (B3LYP) level of theory, using ECP values on Ir and I atoms and a 6–311G**++ basis set for all other atoms, as implemented by Jaguar, versions 6.5 and 7.0 (76). Optimized geometries are provided in the Supplementary Data.[3] NPA (72–75) were carried out at the B3LYP level of theory using the NBO program (80), also implemented as part of the Jaguar suite. As part of the NBO program, second-order perturbation analysis was used to estimate metal–ligand backbonding energies (ΔE_{bb}) with the overall value obtained by summing all second-order perturbation $E(2)$ terms between the relevant metal d-orbital donor lone pair and the appropriate π* C–O or σ* C–F or σ* C–C acceptor orbitals

$Ir(CO)_2(acac)$ (1) (52)

IR (hexane, cm^{-1}): 2074, 1999; IR (CH_2Cl_2, cm^{-1}): 2072, 1994. ^1H NMR (C_6D_6, 500 MHz, 25 °C) δ: 5.07 (s, H, CH), 1.54 (s, 6H, $2CH_3$). Crystals suitable for X-ray diffraction were grown from CH_2Cl_2/hexanes.

$Ir(CO)_2(acac)(CF_3)$(I) (2)

CF_3I was bubbled into a yellow CH_2Cl_2 (15 mL) solution of $Ir(CO)_2(acac)$ (174 mg, 0.500 mmol) for 5 s. The solution turned brown-red gradually, then back to yellow again. After 6 h, IR showed no peak for starting materials. The solvent was removed under vacuum to give a yellow solid, which was crystallized from CH_2Cl_2/hexane at –30 °C to give yellow crystals (230 mg, 86%). IR (CH_2Cl_2, cm^{-1}): 2150 (s), 2106 (vs). ^1H NMR (C_6D_6, 500 MHz, 25 ºC) δ: 5.10 (H, s, CH), 1.53 (6H, s, $2CH_3$). ^{19}F NMR (C_6D_6, 470 MHz, 25 °C) δ: –22.4 (F, s, CF_3). Anal. calcd. for $C_8H_7F_3IIrO_4$ (%): C 17.69, H 1.30; found (%): C 17.77, H 1.38.

$Ir(CO)_2(acac)(CF_2CF_3)$(I) (3)

C_2F_5I was bubbled into a yellow CH_2Cl_2 (15 mL) solution of $Ir(CO)_2(acac)$ (87 mg, 0.250 mmol) for 5 s. The solution turned brown-red gradually, and was allowed to react overnight to give a brown solution. IR showed the reaction had finished. The solvent was removed under vacuum to give a brown solid, which was crystallized from CH_2Cl_2/hexane at –30 °C to give a yellow crystalline solid (128 mg, 86%). IR (CH_2Cl_2, cm^{-1}): 2148 (s), 2105 (vs). ^1H NMR (C_6D_6, 300 MHz, 25 °C) δ: 5.11 (H, s, CH), 1.54 (6H, s, $2CH_3$). ^{19}F NMR (C_6D_6, 282.2 MHz, 25 °C) δ: –83.7 (s), –91.0 (s). Anal. calcd. for $C_9H_7F_5IIrO_4$ (%): C 18.22, H 1.19; found (%): C 18.82, H 1.07.

$Ir(CO)_2(acac)(CF_2CF_2CF_3)$(I) (4)

To a yellow CH_2Cl_2 (20 mL) solution of $Ir(CO)_2(acac)$ (274 mg, 0.790 mmol) was added n-C_3F_7–I (0.11 mL, 0.79 mmol) at 0 °C. The colour turned to yellow → orange → yellow over 5 min. After 4.5 h, ^{19}F NMR showed some residual peaks for n-C_3F_7–I, and the mixture was allowed to react overnight to give a light yellow solution. The solvent was removed to give a light orange-yellow solid, which was crystallized from CH_2Cl_2/hexane at –30 °C to give a yellow crystalline solid (439 mg, 86%). The solid was recrystallized from ether/hexane at –60 °C to give crystals suitable for X-ray diffraction. IR (hexane, cm^{-1}): 2145 (s), 2103 (s). ^1H NMR (C_6D_6, 500 MHz, 25 °C) δ: 5.09 (H, s, CH), 1.52 (6H, s, $2CH_3$). ^{19}F NMR (C_6D_6, 470 MHz, 25 °C) δ: –79.3 (3F, t, $^3J_{FF}$ = 11 Hz, CF_3); –89.3 (2F, q, $^3J_{FF}$ = 11 Hz, α-CF_2); –118.7 (2F, s, β-CF_2). Anal. calcd. for $C_{10}H_7F_7IIrO_4$ (%): C 18.67, H 1.10; found: C 18.84, H 1.22.

$Ir(CO)_2(acac)[CF(CF_3)_2]$(I) (5a, 5b)

To a yellow CH_2Cl_2 (20 mL) solution of $Ir(CO)_2(acac)$ (204 mg, 0.600 mmol) was added i-C_3F_7–I (0.09 mL, 0.6 mmol) at 0 °C. There was no apparent colour change, and the mixture was allowed to react overnight to give a light yellow solution. IR showed no peak for starting materials, and two sets of ^1H and ^{19}F NMR signals, corresponding to two product isomers **5a** (major) and **5b** (minor) were observed. On standing at room temperature, the mixture evolved to give only **5a**. The solvent was removed to give a yellow solid (292 mg, 82%), which was recrystallized from ether/hexane at –60 °C to give crystals suitable for X-ray diffraction.

5a

IR (hexane, cm^{-1}): 2145 (s), 2103 (s); IR (CH_2Cl_2, cm^{-1}): 2149 (s), 2104 (s). ^1H NMR (C_6D_6, 500 MHz, 25 °C) 5.04 (H, s, CH), 1.51 (6H, s, $2CH_3$). ^{19}F NMR (C_6D_6, 470 Hz, 25 °C) δ: –71.0 (d, 6F, $^3J_{FF}$ = 10 Hz, CF_3), –166.8 (sept, 1F, $^3J_{FF}$ = 10 Hz, CF).

5b

^1H NMR (C_6D_6, 500 MHz, 25 °C) 5.14 (H, s, CH), 1.54 (3H, s, CH_3), 1.49 (3H, s, CH_3). ^{19}F NMR (C_6D_6, 470 Hz, 25 °C) δ: –70.5 (6F, d, $^3J_{FF}$ = 10 Hz, CF_3), –179.8 (1F, sept, $^3J_{FF}$ = 10 Hz, CF).

Anal. calcd. for $C_{10}H_7IIrF_7O_4$ (%): C 18.67, H 1.10; found: C 18.74, H 1.20.

$Ir(CO)_2(acac)[CF(CF_3)(CF_2CF_3)]$(I) (6)

To a CH_2Cl_2 (30 mL) solution of $Ir(CO)_2(acac)$ (34.7 mg, 0.1 mmol) was added sec-C_4F_9I (0.02 mL), and an immediate colour change from yellow to orange was observed. The mixture was stirred at room temperature for 2 h, and the solvent was removed to give a yellow-orange solid, which was recrystallized from CH_2Cl_2/hexane at –30 °C to give a yellow crystalline solid (253 mg, 76%). IR (CH_2Cl_2, cm^{-1}): 2147 (s), 2104 (s). ^1H NMR (C_6D_6, 300 MHz, 25 °C) δ: 5.01 (1H, s, CH), 1.49 (6H, s, CH_3). ^{19}F NMR (C_6D_6, 282 MHz, 25 °C) δ: –69.67 (3F, s, γ-CF_3); –79.41 (3F, s, β-CF_3); –106.3 (F, d, $^2J_{FF}$ = 302 Hz, CF_A); –111.4 (F, d, $^2J_{FF}$ = 302

[3] Supplementary data for this article are available on the journal Web site (canjchem.nrc.ca) or may be purchased from the Depository of Unpublished Data, Document Delivery, CISTI, National Research Council Canada, Ottawa, ON K1A 0R6, Canada. DUD 3803. For more information on obtaining material, refer to cisti-icist.nrc-cnrc.gc.ca/cms/unpub_e.shtml. CCDC numbers 685793–685798 contain the crystallographic data for this manuscript. These data can be obtained, free of charge, via www.ccdc.cam.ac.uk/conts/retrieving.html (Or from the Cambridge Crystallographic Data Centre, 12 Union Road, Cambridge CB2 1EZ, UK; fax +44 1223 336033; or deposit@ccdc.cam.ac.uk).

© 2008 NRC Canada

Hz, CF_B); –169.22 (F, s, CF). Anal. calcd. for $C_{11}H_7F_9IIrO_4$ (%): C 19.06, H 1.02; found: C 19.46, H 1.44.

$Ir(CO)_2(acac)(CF_2C_6F_5)(I)$ (7)

To a CH_2Cl_2 (30 mL) solution of $Ir(CO)_2(acac)$ (56 mg, 0.16 mmol) was added C_7F_7I (0.03 mL), and an immediate colour change from yellow to orange was observed. The mixture was stirred at room temperature for 2 h, and the solvent was removed to give a yellow-orange solid, which was recrystallized from CH_2Cl_2/hexane at –30 °C to give a yellow crystalline solid (34 mg, 75%). IR (CH_2Cl_2, cm^{-1}): 2147 (s), 2104 (s). ^1H NMR (C_6D_6, 300 MHz, 25 °C) δ: 4.66 (1H, s, CH), 1.29 (6H, s, CH_3). ^{19}F NMR (C_6D_6, 282 MHz, 25 °C) δ: –37.62 (2F, s, CF_2); –141.4 (2F, s, *o*-CF); –149.9 (F, s, *p*-CF); –161.1 (2F, s, *m*-CF). Anal. calcd. for $C_{14}H_7F_7IIrO_4$ (%) C 24.32, H 1.02; found (%): C, 24.76, H 1.34.

$Ir(CO)_2(acac)(CF_3)(OTf)$ (8)

To a CH_2Cl_2 (10 mL) suspension of AgOTf (104 mg, 0.405 mmol) was added a yellow CH_2Cl_2 (10 mL) solution of $Ir(CO)_2(acac)(CF_3)(I)$ (200 mg, 0.368 mmol) at room temperature. The solution was stirred overnight to give a yellow solution and yellow precipitate. The solution was filtered to give a pale yellow solution. The solvent was removed under vacuum to give a white solid with some dark brown impurities, which was recrystallized by CH_2Cl_2/hexane to give yellow crystals suitable for X-ray diffraction (182 mg, 87%). IR (CH_2Cl_2, cm^{-1}): 2168 (s), 2125 (vs). ^1H NMR (C_6D_6, 300 MHz, 25 °C) δ: 5.02 (H, s, CH), 1.48 (6H, s, $2CH_3$). ^{19}F NMR (C_6D_6, 282 MHz, 25 °C) δ: –15.5 (3F, s, CF_3), –77.3 (3F, s, OTf). Anal. calcd. for $C_9H_7F_6IrO_7S$ (%): C 19.12, H 1.25; found (%): C 19.54, H 1.66.

$Ir(CO)_2(acac)(CF_2CF_3)(OTf)$ (9)

To a CH_2Cl_2 (5 mL) suspension of AgOTf (130 mg, 0.510 mmol) was added a CH_2Cl_2 (10 mL) solution of $Ir(CO)_2(acac)(C_2F_5)(I)$ (260 mg, 0.440 mmol) at room temperature. The white AgOTf turned quickly to a brown-yellow solid, and after 1 h the solution was filtered to give a yellow solution. The solvent was removed to give a yellow solid, which was recrystallized from CH_2Cl_2/hexane at –30 °C to give yellow crystals suitable for X-ray diffraction (220 mg, 86%). IR (CH_2Cl_2, cm^{-1}): 2167 (s), 2125 (vs). ^1H NMR (C_6D_6, 300 MHz, 25 °C) δ: 5.03 (H, s, CH), 1.53 (6H, s, $2CH_3$). ^{19}F NMR (C_6D_6, 282 MHz, 25 °C) δ: –77.3 (3F, s, CF_3), –78.0 (3F, s, OTf), –83.6 (2F, s, CF_2). Anal. calcd. for $C_{10}H_7F_8IrO_7S$ (%): C 19.52, H 1.15; found (%): C 19.64, H 1.21.

$Ir(CO)_2(acac)(CF_2CF_2CF_3)(OTf)$ (10)

$Ir(CO)_2(I)(n\text{-}C_3F_7)(acac)$ (221 mg, 0.343 mmol) and AgOTf (106 mg, 0.412 mmol) were stirred in CH_2Cl_2 (15 mL) overnight to give a pale yellow solution with a pale yellow precipitate, which was filtered to give a yellow solution. The solvent was removed to give a yellow solid, which was recrystallized from CH_2Cl_2/hexane at –30 °C to give yellow crystals (206 mg, 91%). IR (CH_2Cl_2, cm^{-1}): 2167 (s), 2125 (s). ^1H NMR (C_6D_6, 500 MHz, 25 °C) δ: 5.03 (H, s, CH), 1.53 (6H, s, $2CH_3$). ^{19}F NMR (C_6D_6, 470 MHz, 25 °C) δ: –76.9 (d, $^4J_{FF}$ = 11 Hz, α-CF_2), –77.3 (3F, s, OTf), –79.6 (3F, t, $^4J_{FF}$ = 11 Hz, CF_3), –119.3 (2F, s, β-CF_2). Anal. calcd. for $C_{11}H_7F_{10}IrO_7S$ (%): C 19.85, H 1.06; found (%): C 20.20, H 1.11.

$Ir(CO)_2(acac)[(CF(CF_3)_2](OTf)$ (11)

A mixture of $Ir(CO)_2(I)(i\text{-}C_3F_7)(acac)$ (214 mg, 0.333 mmol) and AgOTf (100 mg, 0.33 mmol) was stirred in CH_2Cl_2 (15 mL) overnight to give a pale yellow solution with pale yellow precipitate, which was filtered to give a yellow solution. The solvent was removed to give a yellow solid (200 mg, 90%), which was recrystallized from CH_2Cl_2/hexane at –30 °C to give yellow crystals. IR (CH_2Cl_2, cm^{-1}): 2169 (s), 2129 (s). ^1H NMR (C_6D_6, 500 MHz, 25 °C) δ: 4.87 (H, s, CH), 1.47 (6H, s, $2CH_3$). ^{19}F NMR (C_6D_6, 470 MHz, 25 °C) δ: –70.7 (6F, d, $^3J_{FF}$ = 9 Hz, $2CF_3$), –77.1 (3F, s, OTf), –145.7 (F, hept, $^3J_{FF}$ = 9 Hz, CF). Anal. calcd. for $C_{11}H_7F_{10}IrO_7S$ (%): C 19.85, H 1.06; found (%): C 19.64, H 1.30.

$Ir(CO)(PPh_3)(acac)(CF_2CF_2CF_3)(I)$ (13)

To a yellow CH_2Cl_2 (10 mL) solution of $Ir(CO)(PPh_3)(acac)$ (50 mg, 0.086 mmol) was added excess $n\text{-}C_3F_7$–I (0.05 mL, 0.38 mmol) at 0 °C. The reaction was monitored by ^{19}F NMR and IR. After 90 minutes, ^{19}F NMR showed two sets of peaks for two different isomers. IR (CH_2Cl_2) showed no peak for $Ir(CO)(PPh_3)(acac)$. The solvent was removed under vacuum to give a yellow solid, which was recrystallized through slow evaporation from hexane/ether solution to give crystals of the major isomer (70 mg, 93%).

Major

IR (CH_2Cl_2, cm^{-1}): 2063 (s). ^1H NMR (C_6D_6, 500 MHz, 25 °C) δ: 7.58–7.41 (15H, m, PPh_3), 5.09 (H, s, CH), 1.70 (3H, s, CH_3), 1.67 (3H, s, CH_3). ^{19}F NMR (C_6D_6, 470 Hz, 25 °C) δ: –67.6 (F, mq, J_{FF} = 264 Hz, α-F), –72.6 (F, mq, $^2J_{FF}$ = 264 Hz, α-F), –80.0 (3F, t, $^3J_{FF}$ = 13 Hz, CF_3), –112.7 (F, mq, $^2J_{FF}$ = 282 Hz, β-F), –114.6 (F, mq, $^2J_{FF}$ = 282 Hz, β-F). $^{31}P\{^1H\}$ NMR (CD_2Cl_2, 202 MHz, 25 °C) δ: –4.89 (P, d, $^3J_{PF}$ = 34 Hz, PPh_3).

Minor

IR (CH_2Cl_2, cm^{-1}): 2063 (s). ^1H NMR (C_6D_6, 500 MHz, 25 °C) δ: 7.90–7.81 (15H, m, PPh_3), 5.71 (H, s, CH), 2.03 (3H, s, CH_3), 1.98 (3H, s, CH_3). ^{19}F NMR (C_6D_6, 470 MHz, 25 °C) δ: –71.4 (F, mq, $^2J_{FF}$ = 265 Hz, α-F), –93.4 (F, mq, $^2J_{FF}$ = 265 Hz, α-F), –80.2 (3F, t, $^3J_{FF}$ = 11 Hz, CF_3), –117.5 (F, mq, $^2J_{FF}$ = 288 Hz, β-F), –122.2 (F, mq, $^2J_{FF}$ = 289 Hz, β-F). $^{31}P\{^1H\}$ NMR (CD_2Cl_2, 202 MHz, 25 °C) δ: –17.4 (P, d, $^3J_{PF}$ = 24 Hz, PPh_3). Anal. calcd. for $C_{27}H_{22}F_7IIrO_3P$ (%): C 36.95, H 2.53; found (%): C 37.27, H 3.17.

Acknowledgements

RPH is grateful to the National Science Foundation for generous financial support and to Professor Clark Landis (University of Wisconsin-Madison) for encouragement and consultation on the computational work.

© 2008 NRC Canada

References

1. J.P. Collman, L.S. Hegedus, J.R. Norton, and R.G. Finke. Principles and applications of organotransition metal chemistry. University Science Books, Mill Valley, CA. 1987.
2. D. Forster. Adv. Organomet. Chem. **17,** 255 (1979).
3. T.W. Dekleva and D. Forster. Adv. Catal. **34,** 81 (1986).
4. M.J. Howard, M.D. Jones, M.S. Roberts, and S.A. Taylor. Catal. Today, **18,** 325 (1993).
5. A. Haynes, B.E. Mann, G.E. Morris, and P.M. Maitlis. J. Am. Chem. Soc. **115,** 4093 (1993).
6. G.J. Sunley and D.J. Watson. Catal. Today, **58,** 293 (2000).
7. F. Zhang, M.E. Broczkowski, M.C. Jennings, and R.J. Puddephatt. Can. J. Chem. **83,** 595 (2005).
8. M.C. Janzen, M.C. Jennings, and R.J. Puddephatt. Inorg. Chem. **42,** 4553 (2003).
9. M.C. Janzen, H.A. Jenkins, L.M. Rendina, J.J. Vittal, and R.J. Puddephatt. Inorg. Chem. **38,** 2123 (1999).
10. M. Rashidi, A.R. Esmaeilbeig, N. Shahabadi, S. Tangestaninejad, and R.J. Puddephatt. J. Organomet. Chem. **568,** 53 (1998).
11. C.R. Baar, H.A. Jenkins, J.J. Vittal, G.P.A. Yap, and R.J. Puddephatt. Organometallics, **17,** 2805 (1998).
12. C.R. Baar, G.S. Hill, J.J. Vittal, and R.J. Puddephatt. Organometallics, **17,** 32 (1998).
13. L.M. Rendina and R.J. Puddephatt. Chem. Rev. **97,** 1735 (1997).
14. C.J. Levy and R.J. Puddephatt. J. Am. Chem. Soc. **119,** 10127 (1997).
15. C.J. Levy, J.J. Vittal, and R.J. Puddephatt. Organometallics, **15,** 2108 (1996).
16. C.J. Levy and R.J. Puddephatt. J. Chem. Soc., Chem. Commun. 2115 (1995).
17. C.J. Levy, R.J. Puddephatt, and J.J. Vittal. Organometallics, **13,** 1559 (1994).
18. K.T. Aye, J.J. Vittal, and R.J. Puddephatt. J. Chem. Soc., Dalton Trans. 1835 (1993).
19. S. Achar, J.D. Scott, and R.J. Puddephatt. Organometallics, **11,** 2325 (1992).
20. R.J. Puddephatt. Pure Appl. Chem. **62,** 1161 (1990).
21. K.T. Aye, L. Gelmini, N.C. Payne, J.J. Vittal, and R.J. Puddephatt. J. Am. Chem. Soc. **112,** 2464 (1990).
22. C.M. Anderson, R.J. Puddephatt, G. Ferguson, and A.J. Lough. J. Chem. Soc., Chem. Commun. 1297 (1989).
23. P.K. Byers, A.J. Canty, M. Crespo, R.J. Puddephatt, and J.D. Scott. Organometallics, **7,** 1363 (1988).
24. P.K. Monaghan and R.J. Puddephatt. Organometallics, **5,** 439 (1986).
25. R.J. Puddephatt and J.D. Scott. Organometallics, **4,** 1221 (1985).
26. R.H. Hill and R.J. Puddephatt. J. Am. Chem. Soc. **107,** 1218 (1985).
27. J.K. Jawad and R.J. Puddephatt. J. Chem. Soc., Dalton Trans. 1466 (1977).
28. R.B. King, P.M. Treichel, and F.G.A. Stone. J. Am. Chem. Soc. **83,** 3593 (1961).
29. J.A. McCleverty and G. Wilkinson. J. Chem. Soc. 4200 (1964).
30. R.P. Hughes, J.M. Smith, L.M. Liable-Sands, T.E. Concolino, K.-C. Lam, C. Incarvito, and A.L. Rheingold. J. Chem. Soc., Dalton Trans. 873 (2000).
31. C.J. Bourgeois, R.P. Hughes, T.L. Husebo, J.M. Smith, I.M. Guzei, L.M. Liable-Sands, L.N. Zakharov, and A.L. Rheingold. Organometallics, **24,** 6431 (2005).
32. R.P. Hughes, D.C. Lindner, J.M. Smith, D. Zhang, C.D. Incarvito, K.-C. Lam, L.M. Liable-Sands, R.D. Sommer, and A.L. Rheingold. J. Chem. Soc., Dalton Trans. 2270 (2001).
33. A.A. Bowden, R.P. Hughes, D.C. Lindner, C.D. Incarvito, L.M. Liable-Sands, and A.L. Rheingold. J. Chem. Soc., Dalton Trans. 3245 (2002).
34. R.P. Hughes, D.C. Lindner, A.L. Rheingold, and L.M. Liable-Sands. J. Am. Chem. Soc. **119,** 11544 (1997).
35. R.P. Hughes, T.L. Husebo, A.L. Rheingold, L.M. Liable-Sands, and G.P.A. Yap. Organometallics, **16,** 5 (1997).
36. R.P. Hughes, D.C. Lindner, L.M. Liable-Sands, and A.L. Rheingold. Organometallics, **20,** 363 (2001).
37. R.P. Hughes, M.A. Meyer, M.D. Tawa, A.J. Ward, A. Williamson, A.L. Rheingold, and L.N. Zakharov. Inorg. Chem. **43,** 747 (2004).
38. R.P. Hughes, J.S. Overby, A. Williamson, K.-C. Lam, T.E. Concolino, and A.L. Rheingold. Organometallics, **19,** 5190 (2000).
39. R.P. Hughes, R.B. Laritchev, L.N. Zakharov, and A.L. Rheingold. Organometallics, **24,** 4845 (2005).
40. R.P. Hughes, A.J. Ward, A.L. Rheingold, and L.N. Zakharov. Can. J. Chem. **81,** 1270 (2003).
41. R.P. Hughes, J.S. Overby, K.-C. Lam, C.D. Incarvito, and A.L. Rheingold. Polyhedron, **21,** 2357 (2002).
42. R.P. Hughes, J.T. Sweetser, M.D. Tawa, A. Williamson, C.D. Incarvito, B. Rhatigan, A.L. Rheingold, and G. Rossi. Organometallics, **20,** 3800 (2001).
43. R.P. Hughes, A. Williamson, C.D. Incarvito, and A.L. Rheingold. Organometallics, **20,** 4741 (2001).
44. F. Bonati and R. Ugo. J. Organomet. Chem. **11,** 341 (1968).
45. T. Matsumoto and H. Yoshida. Catal. Lett. **72,** 107 (2001).
46. C. Buron, L. Stelzig, O. Guerret, H. Gornitzka, V. Romanenko, and G. Bertrand. J. Organomet. Chem. **664,** 70 (2002).
47. V. Miranda-Soto, J.J. Pérez-Torrente, L.A. Oro, F.J. Lahoz, M.L. Martín, M. Parra-Hake, and D.B. Grotjahn. Organometallics, **25,** 4374 (2006).
48. J.A. Camerano, M.A. Casado, M.A. Ciriano, F.J. Lahoz, and L.A. Oro. Organometallics, **24,** 5147 (2005).
49. F. Li and B.C. Gates. J. Phys. Chem. B, **108,** 11259 (2004).
50. Cambridge Structural Database (CSD), May 2007 update, http://www.ccdc.cam.ac.uk.
51. G.C. Oldham. Ph.D. thesis. University of North Carolina at Chapel Hill. 1968. p. 106.
52. D. Roberto, E. Cariati, R. Psaro, and R. Ugo. Organometallics, **13,** 4227 (1994).
53. H. Kunkely, and A. Vogler. Inorg. Chem. Commun. **8,** 119 (2005).
54. A. Vasquez, F.E. Wagner, U. Klein, J. Moser, G. Wortmann, H.J. Keller, and A. Bolz. J. Phys. Colloques, 519 (1976).
55. R. Aderjan, H.J. Keller, H.H. Rupp, F.E. Wagner, and U. Wagner. J. Chem. Phys. **64,** 3748 (1976).
56. L.V. Interrante and F.P. Bundy. J. Chem. Soc. D, 584 (1970).
57. L.F. Ballard and J.J. Wortman. J. Appl. Phys. **41,** 4232 (1970).
58. L.K. Monteith, L.F. Ballard, C.G. Pitt, B.K. Klein, L.M. Slifkin, and J.P. Collman. Solid State Commun. **6,** 301 (1968).
59. H.C. Clark and J.D. Ruddick. Inorg. Chem. **9,** 2556 (1970).
60. B.E. Smart. *In* Chemistry of organofluorine compounds II. *Edited by* M. Hudlicky and A. Pavlath. 1995. Publisher, Location.
61. A.J. Mukhedkar, V.A. Mukhedkar, M. Green, and F.G.A. Stone. J. Chem. Soc. A, 3166 (1970).
62. R.P. Hughes, S. Willemsen, A. Williamson, and D. Zhang. Organometallics, **21,** 3085 (2002).
63. R.P. Hughes and J.M. Smith. J. Am. Chem. Soc. **121,** 6084 (1999).
64. P.J. Albietz, Jr., J.F. Houlis, and R. Eisenberg. Inorg. Chem. **41,** 2001 (2002).
65. H. Willner and F. Aubke. Organometallics, **22,** 3612 (2003).

© 2008 NRC Canada

66. A.J. Lupinetti, S.H. Strauss, and G. Frenking. Prog. Inorg. Chem. **49,** 1 (2001).
67. S.H. Strauss. J. Chem. Soc., Dalton Trans. 1 (2000).
68. P. Hohenberg and W. Kohn. Phys. Rev. **136,** B864 (1964).
69. W. Kohn and L.J. Sham. Phys. Rev. **140,** A1133 (1965).
70. T.R. Cundari. Comprehensive Organometallic Chemistry III, **1,** 639 (2007).
71. J.N. Harvey. Annu. Rep. Prog. Chem., Sect. C, **102,** 203 (2006).
72. J.P. Foster and F. Weinhold. J. Am. Chem. Soc. **102,** 7211 (1980).
73. A.E. Reed, L.A. Curtiss, and F. Weinhold. Chem. Rev. **88,** 899 (1988).
74. A.E. Reed, R.B. Weinstock, and F. Weinhold. J. Chem. Phys. **83,** 735 (1985).
75. F. Weinhold and C.R. Landis. Valency and bonding: a natural bond orbital donor–acceptor perspective. Cambridge University Press. Cambridge. 2005.
76. Jaguar [computer program]. Version 7.0. Schrödinger, LLC, New York, NY. 2007.
77. T. Leyssens, D. Peeters, A.G. Orpen, and J.N. Harvey. Organometallics, **26,** 2637 (2007).
78. T. Leyssens and D. Peeters. J. Org. Chem. **73,** 2725 (2008).
79. T. Leyssens, D. Peeters, A.G. Orpen, and J.N. Harvey. New J. Chem. **29,** 1424 (2005).
80. NBO 5.0 [computer program]. Theoretical Chemistry Institute, University of Wisconsin, Madison. 2001.
81. A.S. Goldman and K. Krogh-Jespersen. J. Am. Chem. Soc. **118,** 12159 (1996).
82. A.B. Pangborn, M.A. Giardello, R.H. Grubbs, R.K. Rosen, and F.J. Timmers. Organometallics, **15,** 1518 (1996).

© 2008 NRC Canada

Structural and spectroscopic studies of some adducts of silver(I) salts with ethylenethiourea[1]

Graham A. Bowmaker, Narongsak Chaichit, Chaveng Pakawatchai, Brian W. Skelton, and Allan H. White

Abstract: Syntheses, single crystal X-ray structural and spectroscopic characterizations are described for a variety of adducts of silver salts with ethylenethiourea (etu). Ag_2SO_4/etu (1:6) is isomorphous with its previously studied copper(I) counterpart, the $[Ag(S\text{-etu})_3]^+$ species disposed with their silver atoms on crystallographic 3-axes, one of the two independent cations being slightly perturbed by a distant *O*-sulfate approach along that axis. In AgCl/etu (1:3), the silver atom is in a four-coordinate $ClAgS_3$ environment, while $AgNO_3$/etu (1:3) takes the form $[(etu)_2Ag(\mu\text{-}S\text{-}etu)_2Ag(etu)_2](NO_3)_2$. AgBr/etu (1:2) is binuclear $[(etu)_2Ag(\mu\text{-}Br)_2Ag(etu)_2)]$, unlike its previously studied copper counterpart, which is $[(etu)BrCu(\mu\text{-}S\text{-}etu)_2CuBr(etu)]$. AgCl/etu (4:6) is an interesting ionic polymer $[ClAg_4(etu)_6]_{(\infty|\infty)}Cl_3$, containing a novel one-dimensional polymeric cation. Bands in the far IR spectra of these compounds are assigned to ν(AgS) and ν(AgX) (X = halogen) modes, and a correlation between ν(AgS) and the Ag–S bond length *d*(AgS) is established for silver complexes involving the etu ligand.

Key words: silver, sulfur ligands, X-ray crystal structure, coordination chemistry, complexes.

Résumé : On décrit les synthèses, les caractérisations spectroscopiques et par diffraction des rayons X d'une variété d'adduits de sels d'argent à l'éthylènethiourée (etu). L'adduit Ag_2SO_4/etu (1:6) est isomorphe avec sa contrepartie cuivreuse, Cu(I), étudiée antérieurement et les espèces $[Ag(S\text{-etu})_3]^+$ sont disposées d'une façon telle que les atomes d'argent sont sur les 3-axes cristallographiques, l'un des deux cations indépendants étant faiblement perturbé par une approche distant du *O*-sulfate le long de cet axe. Dans le cas de l'adduit AgCl/etu (1:3), l'atome d'argent se trouve dans un environnement tétracoordiné $ClAgS_3$, alors que le cas de l'adduit $AgNO_3$/etu (1:3), prend la forme $[(etu)_2Ag(\mu\text{-}S\text{-}etu)_2Ag(etu)_2](NO_3)_2$. L'adduit AgBr/etu (1:2) est binucléaire $[(etu)_2Ag(\mu\text{-}Br)_2Ag(etu)_2]$, contrairement à sa contrepartie cuivreuse, Cu(I), étudiée antérieurement, qui est de la forme $[(etu)BrCu(\mu\text{-}S\text{-}etu)_2CuBr(etu)]$. L'adduit AgCl/etu (4:6) est un polymère ionique intéressant $[ClAg_4(etu)_6]_{(\infty|\infty)}Cl_3$ qui contient un nouveau cation polymère monodimensionnel. On a attribué les bandes du spectre infrarouge éloigné aux modes ν(AgS) et ν(AgX) (X = halogène) et, pour les complexes impliquant un ligand etu, on a établi une corrélation entre ν(AgS) et la valeur de la longueur de la liaison AgS, *d*(AgS).

Mots-clés : argent, ligands sulfurés, structure cristalline par diffraction des rayons X, chimie de coordination, complexes.

[Traduit par la Rédaction]

Introduction

Sulfur-donor ligands derivative of thiourea (tu) have been utilized in a variety of forms to access coordination complexes, most notably of type B or "soft" metal ions. In its simplest form, the ligand is unsubstituted, $SC(NR_2)_2$, R = H, but it may be obtained with diverse R, which may entail incorporation of the nitrogen atoms into heterocyclic rings; these, if saturated, behave as "normal" unidentate donors, but, if unsaturated, aromatic, or otherwise deprotonated, then the now unsubstituted nitrogen atom(s) may also attain donor capability. We exclude these last from present considerations, focussing only on *S*-donor forms in the "simpler" substituted thiourea ligands, xtu (Scheme 1) in their complexes with metal(I) systems. In the adducts with simple salts of gold(I), the structural chemistry of the considerable

Received 8 April 2008. Accepted 30 May 2008. Published on the NRC Research Press Web site at cjan.nrc.ca on 29 August 2008.

Dedicated to Professor Richard Puddephatt in appreciation of his outstanding contributions to Chemistry.

G.A. Bowmaker.[2] Department of Chemistry, University of Auckland, Private Bag 92019, Auckland, New Zealand.
N. Chaichit. Department of Physics, Faculty of Science and Technology, Thammasat University, Pathumthani 12121, Thailand.
C. Pakawatchai. Department of Chemistry, Prince of Songkla University, Hat Yai 90112 Thailand.
B.W. Skelton, and A.H. White. School of Biomedical, Biomolecular and Chemical Sciences, Chemistry M313, The University of Western Australia, Crawley 6009, Western Australia.

[1]This article is part of a Special Issue dedicated to Professor Richard J. Puddephatt.

[2]Corresponding author (e-mail: ga.bowmaker@auckland.ac.nz).

 doi:10.1139/V08-112 © 2008 NRC Canada

Scheme 1.

etu

xtu = mtu (R, R' = H; R'' = Me
dmtu (R = H; R', R'' = Me
tmtu (R, R', R'' = Me)
detu (R = H; R', R'' = Et)

array of structurally characterized compounds is dominated by that of linearly coordinated two-coordinate S-Au-S systems; with copper(I) and silver(I), the coordination number may rise as high as (quasi-tetrahedral) four, and indeed, four unidentate *S*-coordinated thiourea ligands are to be found in the hexafluorosilicate(IV) salt, $[Cu(tu)_4]_2(SiF_6)$ (1–3*a*). No counterpart $[Ag((x)tu)_4]^+$ example has yet been so defined for silver(I), the highest AgX/xtu stoichiometry thus far structurally authenticated being 1:3, although formation of a complex $[Ag(etu)_4](NO_3)$ (etu = ethylenethiourea = imidazolidine-2-thione; $(CH_2NH)_2CS$; see Scheme 1) was claimed in an early study (4). Adducts AgX/xtu (1:3) may be found in mononuclear or binuclear form. The latter are found with non-coordinating or feebly coordinating anions as ionic $[(xtu)_2Ag(\mu\text{-}S\text{-}xtu)_2Ag(xtu)_2]^{2+}$ arrays, for adducts of silver(I) perchlorate with tu (5), dmtu (6), etu (7), [dmtu = $(MeHN)_2CS$]. Mononuclear arrays, also essentially ionic, with (only distant contacts of the anion to) a trigonal planar silver(I) atom, $[Ag(xtu)_3]^+X^-$ are found for the cyclic 1-methylimidazole-2-thione (Hmimt) (8), tetrahydro-1,3-pyridine-2-thione (thpt) (9), X = NO_3, tfs = trifluoromethanesulfonate, respectively. With (pseudo-)halide or other soft anion, the X becomes coordinated, yielding four-coordinate $[XAg(xtu)_3]$, defined for X = Cl/tu (preliminary data only) (10) or MeNH·CS·NH_2 (mtu) (11), $(EtNH)_2CS$ (Br/detu) (12), I/detu (13), HS/Et_2N·CS·NH·COPh (14). For adducts of 1:2 stoichiometry, mononuclear species have been defined, both as ionic arrays $[AgL_2]^+X^-$ with linear two-coordinate silver(I) atoms, for X/xtu = ClO_4/etu (15) and NO_3/Et_2N·CS·NC(Ph)NH_2 (16), although the NO_3/MeCONH·CS·NH_2 adduct (17) contains a polymeric cation with one of the ligands μ_2-S and three-coordinate silver(I). The SCN/tu adduct is molecular $[(NCS)Ag(tu)_2]$ (18), with three-coordinate silver(I), the etu analogue weakly dimerizing (19). Polymers involving coordination of a less "innocent" anion are found for the Cl/tu (20) and Cl/etu (21) adducts, the chloride and one ligand being terminal donors in four-coordinate silver(I) environments, but in the Br/thpt adduct (22), all ligands bridge, leaving the bromide ions uncoordinated. The Br/etu adduct (21) is binuclear $[L_2Ag(\mu\text{-}Br)_2AgL_2]$, while the perchlorate/dmtu adduct has a one-dimensional polymeric cation (6). The CN/tu adduct has one ligand and the cyanide bonding terminally in a four-coordinate silver atom environment in a one-dimensional polymer (23); CN/tu, mtu, dmtu, $(Me_2N)_2CS$ (tmtu), etu all form adducts of 1:1 stoichiometry with diverse types of cyanide and xtu donor ligands about four-coordinate silver(I) atoms, except in the AgCN/tmtu adduct, which is ···LAg(CN)LAg(CN)··· with the silver atom three-coordinate (23). The adduct of AgI/Hmimt is of 1:0.5 stoichiometry and has a two-dimensional polymeric sheet structure with ligand (sulfur) and halide both bridging and the silver atom four-coordinate (24).

In the above context, we record the results of a number of our own studies with the ligand etu, also exploring the behaviour of the sulfate anion as donor or otherwise, in these contexts; all ligands derivative of thiourea behave as unidentate or bridging *S*-donor ligands in the present array of compounds, none of the nitrogen atoms behaving as donors, although the NH hydrogen atoms are widely involved in hydrogen-bonding interactions that may be influential in determining the form of the product. These compounds have also been studied by IR spectroscopy to establish correlations between the structures and the vibrational spectra, particularly in the far IR region where metal–sulfur and metal–halogen bands are expected to occur. Two of the compounds (AgCl/etu (1,2:3)) have been the subject of a preliminary communication (25).

Experimental

Syntheses

Ag_2SO_4/etu (1:6)

A mixture of silver(I) sulfate (0.62 g, 2 mmol) and ethylenethiourea (1.23 g, 12 mmol) in water (20 ml) was heated until all of the solid material dissolved. Colourless crystals of the product separated upon cooling. Yield 1.70 g (92%). Anal. calcd. for $C_{18}H_{36}Ag_2N_{12}O_4S_7$: C 23.38, H 3.92, N 18.18; found: C 23.4, H 4.1, N 18.3%.

$AgNO_3$/etu (1:1.5)

A hot solution of ethylenethiourea (0.31 g, 3 mmol) in water (10 mL) was added to a hot solution of $AgNO_3$ (0.34 g, 2 mmol) in water (10 mL). A colourless, fibrous mass of product formed upon cooling. Yield 0.63 g (97%). Anal. calcd. for $C_{4.5}H_9AgN_4OS_{1.5}$: C 16.73, H 2.81, N 17.34; found: C 17.0, H 3.3, N 17.3%.

$AgNO_3$/etu (2:6)

A hot solution of silver(I) nitrate (0.34 g, 2 mmol) in water (5 mL) was added to a hot solution of ethylenethiourea (0.63 g, 6 mmol) in water (5 mL). Colourless crystals of the product separated upon cooling. Yield 0.60 g (62%). Anal. calcd. for $C_{18}H_{36}Ag_2N_{14}O_6S_6$: C, 22.69, H 3.81, N 20.58; found: C 22.6, H 3.9, N 20.5%.

$AgNO_3$/etu (1:4)

A hot solution of silver(I) nitrate (0.34 g, 2 mmol) in water (5 mL) was added to a hot solution of ethylenethiourea (1.02 g, 10 mmol) in water (5 mL). Colourless crystals of the product separated upon cooling. Yield 1.00 g (87%). Anal. calcd. for $C_{12}H_{24}AgN_9O_3S_4$: C 24.91, H 4.18, N 21.79; found: C 24.4, H 4.4, N 21.1%. Calcd. for $C_{12}H_{26}AgN_9O_4S_4$ (the monohydrate): C 24.16, H 4.39, N 21.13.

AgCl/etu (4:6)

A mixture of silver(I) chloride (0.29 g, 2 mmol) and ethylenethiourea (0.31 g, 3 mmol) in water (10 mL) was heated to boiling with stirring and filtered while hot to re-

© 2008 NRC Canada

move a slightly grey insoluble residue. Colourless crystals of the product separated upon cooling. Yield 0.19 g (32%). Anal. calcd. for $C_{18}H_{36}Ag_4Cl_4N_{12}S_6$: C 18.23, H 3.06, N 14.17; found: C 18.4, H 3.3, N 14.2%.

AgCl/etu (1:3)

A mixture of silver(I) chloride (0.29 g, 2 mmol) and ethylenethiourea (0.62 g, 6 mmol) in water (10 mL) was heated to boiling with stirring until all of the solids had dissolved. The resulting hot solution was diluted with water (10 mL) and allowed to stand. Colourless crystals of product separated upon standing overnight. Yield 0.70 g (78%). Anal. calcd. for $C_9H_{18}AgClN_6S_3$: C 24.03, H 4.03, N 18.68; found: C 24.1, H 4.1, N 18.6%.

AgBr/etu (2:4)

A mixture of silver(I) bromide (0.38 g, 2 mmol) and ethylenethiourea (1.23 g, 12 mmol) in water (25 mL) was heated to boiling with stirring until all of the solids had dissolved. The resulting hot solution was diluted with water (10 mL) and allowed to stand. Colourless crystals of product separated upon standing. Yield 0.60 g (76%). Anal. calcd. for $C_{12}H_{24}Ag_2Br_2N_8S_4$: C 18.38, H 3.09, N 14.29; found: C 18.6, H 3.3, N 14.35%.

AgBr/etu (1:3)

A mixture of silver(I) bromide (0.38 g, 2 mmol) and ethylenethiourea (0.82 g, 8 mmol) in water (15 mL) was heated to boiling with stirring and filtered while hot to remove an insoluble yellow residue. Colourless crystals of product separated upon standing. Yield 0.64 g (81%). Anal. calcd. for $C_9H_{18}AgBrN_6S_3$: C 21.87, H 3.67, N 17.00; found: C 21.7, H 3.8, N 16.7%. A sample of this compound was ground in an agate mortar and pestle with a small amount of water, just sufficient to form a paste, and the IR spectrum of the dried product showed that it had converted completely to a mixture of the 1:2 complex and uncomplexed etu.

AgI/etu (1:0.5)

A hot solution of potassium iodide (0.33 g, 2 mmol) in water (10 mL) was added to a hot solution of silver nitrate (0.34 g, 2 mmol) and ethylenethiourea (0.61 g, 6 mmol) in water (10 mL). There was an immediate dense white precipitate. The mixture was filtered while warm and the product was washed with water. Yield 0.56 g (99%). Anal. calcd. for $C_{1.5}H_3AgINS_{0.5}$: C 6.30, H 1.06, N 4.90; found: C 6.6, H 1.2; N 5.0%.

Structure determinations

Full spheres of CCD area-detector diffractometer data were measured (ω-scans, monochromatic Mo Kα radiation, λ = 0.710 73 Å) yielding $N_{t(otal)}$ reflections, these merging to N unique (R_{int} cited) after "empirical"/multiscan absorption correction (proprietary software), N_o with $F > 4\sigma(F)$ being considered "observed". Anisotropic displacement parameter forms were refined (full matrix on F^2) for the non-hydrogen atoms, hydrogen atom treatment following a riding model unless otherwise noted (reflection weights: $(\sigma^2(F^2) + (aP)^2 + bP)^{-1}$ ($P = (F_o + 2F_c)/3$)). Neutral atom complex scattering factors were employed within the SHELXL 97 program (26). Pertinent results are given below and in the Tables and Figures, the latter showing 50% (low temperature) or 20% (room temperature) displacement envelopes for the non-hydrogen atoms, hydrogen atoms, where shown, having arbitrary radii of 0.1 Å.[3]

Crystal/refinement data

AgCl/etu (1:3)

$C_9H_{18}AgClN_6S_3$, M = 449.8; rhombohedral, space group $R3c$ (C_{3v}^6, No. 161) (hexagonal setting), a = 14.7380(1) Å, c = 12.2965(1) Å, V = 2313 Å^3; D_{calcd} (Z = 6) = 1.937 g cm^{-3}; μ_{Mo} = 1.9 mm^{-1}; specimen = 0.33 mm × 0.24 mm × 0.20 mm; $T_{min/max}$ = 0.81; $2\theta_{max}$ = 87°; N_t = 49899, N = 3907 (R_{int} = 0.023), N_o = 3807; R_1 = 0.015, wR_2 = 0.037 (a = 0.021, b = 0.951); S = 1.10. $|\Delta\rho_{max}|$ = 0.3 e Å^{-3}; x_{abs} = –0.016(11); T ca. 100 K.

AgCl/etu (4:6)

$C_{18}H_{36}Ag_4Cl_4N_{12}S_6$, M = 1186.3; othorhombic, space group $C222_1$ (D_2^5, No. 20), a = 15.9435(2) Å, b = 16.2883(2) Å, c = 14.6276(2) Å, V = 3799 Å^3; D_{calcd} (Z = 4) = 2.074 g cm^{-3}; μ_{Mo} = 2.7 mm^{-1}; specimen = 0.40 mm × 0.30 mm × 0.30 mm; $T_{min/max}$ not recorded; $2\theta_{max}$ = 57°; N_t = 12883, N = 4621 (R_{int} = 0.019), N_o = 4361; R_1 = 0.036, wR_2 = 0.092 (a = 0.0491, b = 13.687); S = 1.09. $|\Delta\rho_{max}|$ = 1.9 e Å^{-3}; x_{abs} = 0.01(4); T ca. 298 K.

AgBr/etu (2:4)

$C_{12}H_{24}Ag_2Br_2N_8S_4$, M = 784.2; monoclinic, space group $P2_1/n$ (C_{2h}^5, No. 14; variant), a = 8.975(1) Å, b = 10.457(1) Å, c = 13.158(2) Å, β = 103.421(2)°, V = 1201 Å^3; D_{calcd} (Z = 2) = 2.168 g cm^{-3}; μ_{Mo} = 5.3 mm^{-1}; specimen = 0.32 mm × 0.22 mm × 0.18 mm; $T_{min/max}$ = 0.71; $2\theta_{max}$ = 57°; N_t = 13226, N = 2968 (R_{int} = 0.025), N_o = 2743; R_1 = 0.019, wR_2 = 0.049 (a = 0.0278, b = 0.4579); S = 1.13. $|\Delta\rho_{max}|$ = 1.02 e Å^{-3}; T ca. 153 K. This structure has been previously determined at room temperature (21).

$AgNO_3$/etu (2:6)

$C_{18}H_{36}Ag_2N_{14}O_6S_6$, M = 952.7; monoclinic, space group $P2_1/n$, a = 6.544(2) Å, b = 23.300(9) Å, c = 11.792(3) Å, β = 100.69(2)°, V = 1767 Å^3; D_{calcd} (Z = 2) = 1.791 g cm^{-3}; μ_{Mo} = 1.52 mm^{-1}; specimen = 0.48 mm × 0.42 mm × 0.32 mm; $T_{min/max}$ = 0.83; $2\theta_{max}$ = 50°; N = 3058, N_o = 2720; R_1 = 0.029, wR_2 = 0.067 (a = 0.0104, b = 2.0506); S = 1.10. $|\Delta\rho_{max}|$ = 0.46 e Å^{-3}; T ca. 295 K. Data were measured using a single counter instrument; a Gaussian absorption correction was applied.

[3] Supplementary data for this article are available on the journal Web site (canjchem.nrc.ca) or may be purchased from the Depository of Unpublished Data, Document Delivery, CISTI, National Research Council Canada, Ottawa, ON K1A 0R6, Canada. DUD 3802. For more information on obtaining material refer to cisti-icist.nrc-cnrc.gc.ca/cms/unpub_e.shtml. CCDC 675959, 675960, 681829, 683354, and 683355 contain the crystallographic data for this manuscript. These data can be obtained, free of charge, via www.ccdc.cam.ac.uk/conts/retrieving.html (Or from the Cambridge Crystallographic Data Centre, 12 Union Road, Cambridge CB2 1EZ, UK; fax +44 1223 336033; or deposit@ccdc.cam.ac.uk).

© 2008 NRC Canada

Fig. 1. The two cations of $[Ag(etu)_3]_2(SO_4)$, showing the interaction of one with the sulfate, and the associated hydrogen-bonding.

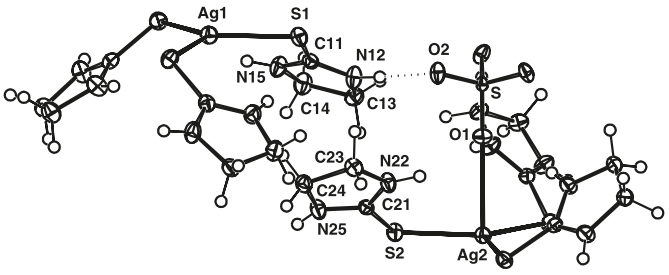

Ag_2SO_4/etu (1:6)

$C_{18}H_{36}Ag_2N_{12}O_4S_7$, M = 924.8; rhombohedral, space group $R3c$, a = 12.998(2) Å, c = 34.675(7) Å, V = 5073 Å^3; D_{calcd} (Z = 6) = 1.816 g cm^{-3}; μ_{Mo} = 1.64 mm^{-1}; specimen = 0.56 mm × 0.45 mm × 0.27 mm; $T_{min/max}$ = 0.72; $2\theta_{max}$ = 56°; N_t = 18947, N = 2839 (R_{int} = 0.022), N_o = 2815; R_1 = 0.014, wR_2 = 0.038 (a = 0.0221, b = 4.3079); S = 1.10. $|\Delta\rho_{max}|$ = 0.29 e Å^{-3}; x_{abs} = 0.03(2); T ca. 153 K. The structure is isomorphous with the previously determined copper(I) counterpart (27).

IR spectroscopy

IR spectra were recorded at 4 cm^{-1} resolution on dry powders using a PerkinElmer Spectrum 100 FT-IR spectrometer equipped with a Universal ATR sampling accessory, or on Nujol mulls between KBr plates using a PerkinElmer Spectrum 1000 Fourier transform IR spectrometer. Far IR spectra were recorded at 4 cm^{-1} resolution using a Nicolet 8700 FTIR spectrometer on samples suspended in Polythene disks.

Results and Discussion

Syntheses

In an early study of silver(I)/etu complexes involving aqueous solution syntheses, Morgan and Burstall suggested the existence of AgX/etu (1:n) complexes with n = 3, 2, 1 for X = Cl, Br, I, respectively (4), but our initial studies of these complexes showed that the situation is more complicated than this. Thus, syntheses from aqueous 1:3 AgCl/etu solutions initially yielded crystals of a 1:1.5 complex, shown by a single crystal X-ray study to be $[ClAg_4(etu)_6]Cl_3$ (see below). IR studies of the products of mechanochemical syntheses established the existence of the 1:3 chloride complex (25), and this was subsequently prepared as a crystalline solid from aqueous solution by the method described in the Experimental section above. While the chloride complex could be obtained from a 1:3 AgCl/etu reaction mixture, the bromide could only be obtained from solutions containing excess etu because of the low solubility of AgBr in the reaction medium, and there was a strong tendency for the 1:2 complex to crystallize, particularly from less concentrated solutions; the 1:3 complex was obtained on only one occasion, and mechanochemical treatment of this compound with water showed that it is unstable with respect to the 1:2 complex and etu under ambient conditions (see Experimental). This is in contrast to the situation for the 1:3 chloride, which

Fig. 2. A molecule of $[ClAg(etu)_3]$ projected down the Cl–Ag bond, coincident with a crystallographic 3-axis.

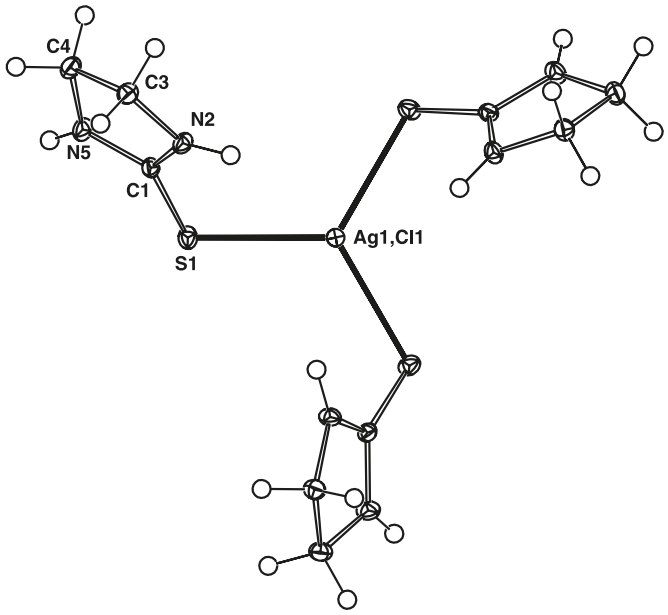

can be prepared by mechanochemical synthesis from a mixture of the 1:1.5 complex and 1.5 equivalents of etu in the presence of water (25). No AgCl/etu complex of composition between 1:3 and 1:1.5 could be prepared from aqueous solution, in agreement with mechanochemical experiments that demonstrated the non-existence of a 1:2 complex (25). This contrasts with a previous report that claims the existence of such a complex, but which was unsupported by elemental analysis or structural data (21). The 1:0.5 AgI/etu complex was prepared by reaction of one equivalent of potassium iodide with an aqueous solution of $[Ag(etu)_4](NO_3)$ (see Experimental). The low ligand content in the product has been attributed to dissociation during washing of an unstable 1:2 complex, whose existence was established by a mechanochemical method (25).

Morgan and Burstall reported the formation of 1:1.5 and 1:4 $AgNO_3$/etu complexes (4). The present study confirmed the existence of the 1:1.5 complex, which forms very thin fibrous crystals that were unsuitable for single crystal X-ray studies and resulted in the identification of a 1:3 complex, whose structure is described below. Attempts to prepare a 1:4 complex resulted in products with lower than the required C, H, and N composition, despite the use of a 1:5 ratio of reactants, the crystals again not being appropriate for X-ray work.

Crystal structures

Silver(I) sulfate, crystallized with etu (in 1:6 ratio) from aqueous solution, forms a 1:6 adduct, shown by the results of the single crystal X-ray study to be isomorphous with its previously studied copper(I) counterpart (27). The silver complex is the same as a recently reported compound obtained from dimethylformamide solution (28). There are two independent cations in the structure, each disposed with the metal atom on a crystallographic 3-axis, lying closely coplanar with the S_3 plane of the three symmetry related ligands, with the metal atom of cation 2 approached by one of

© 2008 NRC Canada

Table 1. Selected geometries for $AgNO_3$/etu $(1:3)_2$.

Bond distances (Å)	
Ag–S(1)	2.723(1)
Ag–S(2)	2.530(1)
Ag–S(1^i)	2.559(1)
Ag–S(3)	2.557(1)
Ag···Ag^i	3.3067(8)
S(1)···S(1^i)	4.122(3)
Bond angles (°)	
S(1)-Ag-S(2)	103.94(3)
S(1^i)-Ag-S(2)	112.61(3)
S(1)-Ag-S(3)	104.77(3)
S(1^i)-Ag-S(3)	117.66(3)
S(1)-Ag-S(1^i)	102.58(3)
S(2)-Ag-S(3)	113.28(3)
Ag-S(1)-C(11)	95.2(1)
Ag-S(2)-C(21)	106.3(1)
Agi-S(1)-C(11)	106.4(1)
Ag-S(3)-C(31)	103.7(1)
Ag-S(1)-Ag^i	77.42(3)
Out-of-(C_3N_2) plane deviations (δ, Å) of the silver atoms	
Plane 1 (Ag)	2.787(5)
Plane 2	0.624(9)
Plane 1 (Ag^i)	0.296(7)
Plane 3	0.724(9)
Dihedral angles (°) of the C_3N_2 planes to the Ag_2S_2 plane	
Plane 1	82.1(1)
Plane 2	83.1(1)
Plane 3	51.5(1)
Hydrogen-bonding interactions (Å)	
O(1)···N, H(32^{ii})	2.953(5), 2.1
O(3)···N, H(15)	2.906(4), 2.1

Note: In the nitrate ion, N-O(1,2,3) are: 1.211(5), 1.237(6), 1.234(5) Å, with opposed angles 118.7(3), 122.9(4), 118.4(4)°. Transformations of the asymmetric unit i: 2 – *x*, 1 – *y*, 1 - *z*; ii: *x* – 1/2, 1 1/2 – *y*, *z* – 1/2.

the sulfate oxygen atoms (Fig. 1), which, together with the sulfur atom, also lies on the 3-axis. In the copper complex, Cu(1)–S(1) is 2.246(2) Å; Cu(2)–S(2) is 2.269(2) with Cu(2)···O(1) 2.834(8) Å; Cu(1,2) lie out of their associated S_3 planes by 0.014(1) and 0.103(1) Å (the latter toward O(1)). In the present structure, Ag(1)–S(1) is 2.4680(6) Å, with Ag(1) 0.081(1) Å out of the $S(1)_3$ plane, S(1)–Ag(1)–S(1′) being 119.811(2)°; Ag(2)–S(2) is 2.5059(5) Å, Ag(2) 0.082(1) Å out of the $S(2)_3$ plane, S(2)–Ag(2)–S(2′) 119.893(2)° and Ag(2)–O(1) 2.791(2) Å, shorter than the Cu–O counterpart distance. The C_3N_2 ligand planes (χ2 2098, 523) make dihedral angles of 35.44(6)° and 44.49(5)° to their associated S_3 planes. As usual in such complexes, the NH hydrogen atoms of the ligand hydrogen-bond intra- or inter-species-wise to the anion or sulfur atoms of other ligands; thus N,H(12)···O(2) 2.787(2), 1.9 (see Fig. 1); N,H(15)···S(1)(1 – *x* + *y*, 1 – *x*, *z*) 3.589(2), 2.7; N,H(22)···O(1) 3.018(2), 2.2; N,H(25)···O(2)(1/3 – *x* + *y*, 2/3 + *y*, 1/6 + *z*) 2.840(2), 2.0 Å. S–O(1,2) are 1.477(2) and 1.479(2) Å and Ag–S–C 105.1(1)° and 103.0(1)°.

Fig. 3. (*a*) Projection of the unit cell contents of $[(etu)_2Ag(\mu\text{-}S\text{-}etu)_2Ag(etu)_2](NO_3)_2$ down *a*. (*b*) The $[(etu)_2Ag(\mu\text{-}Br)_2Ag(etu)_2]$ dimer. Ag–Br,Br^i are 2.8005(3) and 2.8320(3) Å; Ag–S(1,2) 2.4818(6) and 2.4846(5) Å; Br-Ag-S(1,2) 114.60(2)° and 110.16(2)°; Br^i-Ag-S(1,2) 105.35(2)° and 108.83(2)°; S(1)-Ag-S(2) 123.67(2)°; Br-Ag-Br^i 87.72(2)°; Ag-Br-Ag^i 92.27(1)°, Br···H(12,22) 2.6, 2.7 Å (est.) (i = 1 – *x*, – *y*, 1 – *z*). Ag···Ag^i, Br···Br^i are 4.0609(5), 3.9032(5) Å.

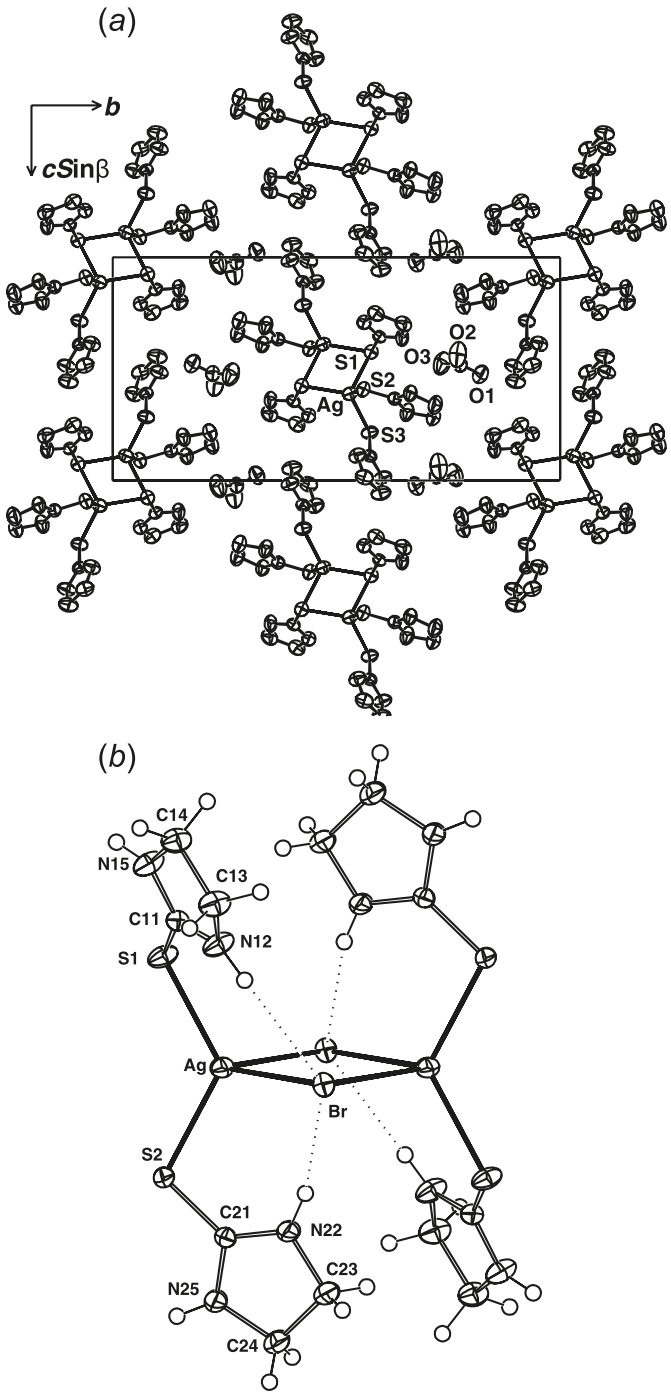

© 2008 NRC Canada

Fig. 4. (*a*) Unit cell contents of $[ClAg_4(etu)_6]Cl_3$ projected down *c*. (*b*) Projection of part of the complex cation $[ClAg_4(etu)_6]_{(\infty|\infty)}^{+}$.

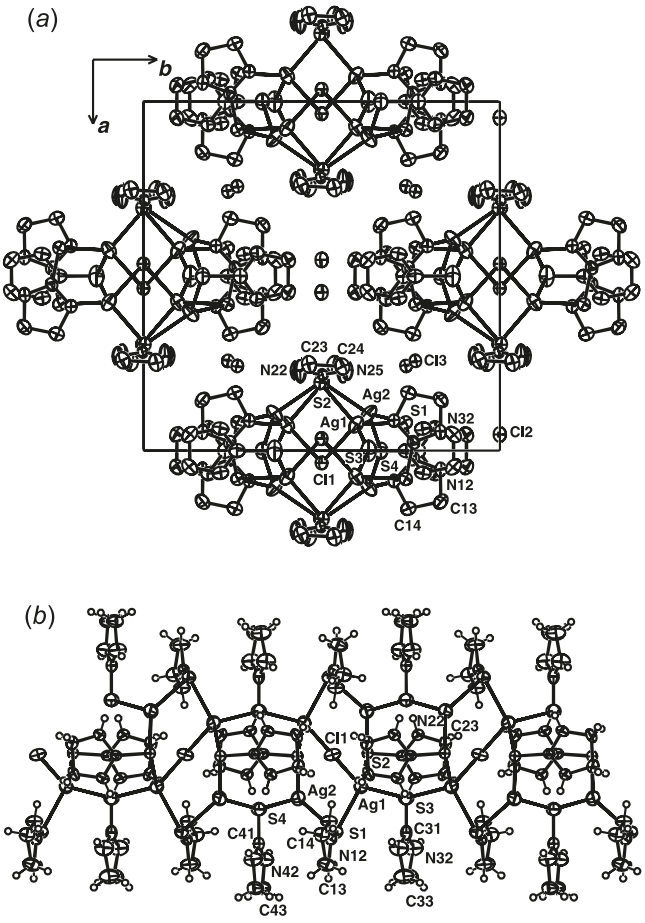

The geometry about the silver atoms in Ag_2SO_4/etu (1:6) may be compared with that found in $[ClAg(etu)_3]$ where the anion firmly coordinates, and the complex is similarly disposed on three-fold axes of the same space group, there being only one independent complex in this case, (Fig. 2). Ag–S,Cl are 2.5468(2), 2.8295(2) Å, with S–Ag–S,Cl 117.534(3)°, 99.126(5)°, with intramolecular N,H(2)···Cl 3.2306(5), 2.40 Å (est.). The silver atom lies 0.40(1) Å above the S_3 plane and 1.192(2) Å out of the ligand plane, the latter making a dihedral angle of 63.82(3)° with the S_3 plane. It is of interest to compare the geometry of the present complex with that of molecule 2 of the preceding sulfate complex, wherein there is an interchange of the approaching axial donor from hard to soft ligand, the distortion from trigonal planar geometry being greater in the present chloride, despite the longer Ag–X distance.

The 1:3 adduct of $AgNO_3$ with etu crystallizes as a binuclear array, $[(etu)_2Ag(\mu\text{-}S\text{-}etu)_2Ag(etu)_2](NO_3)_2$, one half of that unit comprising the asymmetric unit of the structure, the cation being centrosymmetric (Table 1, Fig. 3*a*) and the anion uncoordinated, as in the perchlorate counterpart (7); in binuclear AgBr/etu (1:2) (Fig. 3*b*), the Ag···Ag′ distance is greatly increased consequent on replacement of the bridging sulfur atom by the bromide atom. This latter structure provides a remarkable contrast with counterpart copper(I) systems, where, on passing from similarly binuclear CuX/xtu

Fig. 5. Far IR spectra of (*a*) ethylenethiourea, (*b*) $[Ag(etu)_3]_2(SO_4)$, (*c*) $[Ag_2(etu)_6](NO_3)_2$. Bands assigned as ν(AgS) are labelled with their wavenumbers.

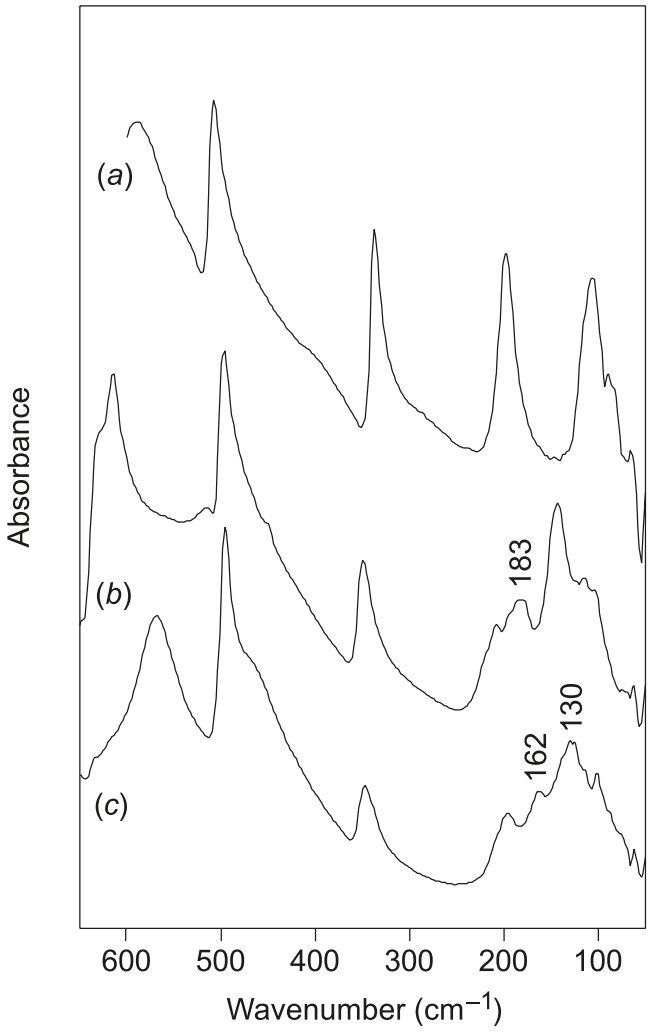

$(1:3)_2$ arrays (e.g. X = ClO_4, xtu = etu (29)) to CuBr/xtu $(1:2)_2$ species, it is a terminal xtu ligand that is replaced by the bromine atom (3*b*), perhaps dependent to some extent on the niceties of the associated hydrogen bonds evident in all such structures, which must play some part in their relative stabilities.

Notwithstanding the low AgCl/L ratio in AgCl/etu (1:1.5), we find uncoordinated chloride ions as companions to a novel one-dimensional polymeric cation, oriented along *c*. One $(AgCl_{(2|2)})_2(etu)_3$ formula unit (Table 2, Fig. 4) comprises the asymmetric unit of the structure. Of the two independent silver atoms, one, Ag(1) is four-coordinated by a chloride atom Cl(1), the latter disposed on a crystallographic 2-axis that bridges a pair of such symmetry-related silver atoms and three sulfur atoms from three independent etu ligands, one of the those, S(3), also disposed on a 2-axis and bridging to a symmetry-related silver atom (different to that related by the Cl(1) bridge). S(1,2) are also bridging, to diverse Ag(2). Ag(2) is three-coordinated (angle sum: 359.4°) by three etu ligand sulfur atoms, all bridging. Cl(1) bridges the two Ag(1) atoms of an eight-membered macrocycle

© 2008 NRC Canada

Table 2. Selected geometries for AgCl/etu $(2:3)_2$.

Bond distances (Å)[a]			
Ag(1)-Cl(1)	2.744(1)	Ag(2)···Ag(1)	3.2033(6)
Ag(1)-S(1)	2.576(1)	Ag(2)-S(1)	2.559(1)
Ag(1)-S(2)	2.558(1)	Ag(2)-S(4)	2.6347(6)
Ag(1)-S(3)	2.6067(6)	Ag(2)-S(2^{i})	2.528(1)
Bond angles (°)			
Cl(1)-Ag(1)-S(1)	106.62(3)	S(1)-Ag(2)-S(4)	108.11(5)
Cl(1)-Ag(1)-S(2)	100.00(4)	S(1)-Ag(2)-S(2^{i})	129.97(4)
Cl(1)-Ag(1)-S(3)	106.13(4)	S(4)-Ag(2)-S(2^{i})	121.34(5)
S(1)-Ag(1)-S(2)	127.03(4)	Σ	359.4
S(1)-Ag(1)-S(3)	103.72(6)	Ag(1)-Cl(1)-Ag(1^{i})	100.96(6)
S(2)-Ag(1)-S(3)	111.69(4)		
Ag(1)-S(1)-C(11)	102.3(2)	Ag(1)-S(2)-C(21)	104.0(1)
Ag(2)-S(1)-C(11)	100.1(2)	Ag(2^{i})-S(2)-C(21)	100.9(1)
Ag(1)-S(1)-Ag(2)	77.18(4)	Ag(1)-S(2)-Ag(2^{i})	96.09(4)
Ag(1)-S(3)-C(31)	102.59(5)	Ag(2)-S(4)-C(41)	102.02(4)
Ag(1)-S(3)-Ag(1^{ii})	154.8(1)	Ag(2)-S(4)-Ag(2^{iii})	155.96(8)
Out-of-(SC_3N_2) plane deviations (δÅ) of the silver atoms			
Ag(1)/1	1.196(7)	Ag(2)/1	–1.947(5)
Ag(1)/2	1.821(6)	Ag(2^{i})/2	1.381(7)
Ag(1)/3	2.505(3)	Ag(2)/4	1.476(7)
Hydrogen-bonding interactions (Å)			
Cl(1)···N, H(15)	3.411(3), 2.4	Cl(3)···N, H(22^{iv})	3.167(5), 2.3
Cl(2)···N, H(12)	3.153(5), 2.3	N, H(25)	3.166(5), 2.5
		N, H(32)	3.129(5), 2.4
		N, H(42^{v})	3.152(5), 2.3

Note: Transformations of the asymmetric unit i: *x*, 1 – *y*, 1 – *z*; ii: 2 – *x*, *y*, 1/2 – *z*; iii: 2 – *x*, *y*, 1 1/2 – *z*; iv: 1 1/2 – *x*, 1/2 + *y*, 1 1/2 – *z*; v: 1 1/2 – *x*, 1 1/2 – *y*, 1/2 + *z*; vi: 1 1/2 – *x*, 1 1/2 – *y*, *z* – 1/2.
[a]Also: Ag(2)···Cl(3^{vi}) 3.030(1) Å.

Fig. 6. Correlation between ν(MS) and the M–S bond length *d*(MS) for $[Ag(etu)_3]_2(SO_4)$ (●) and $[Ag_2(etu)_6](NO_3)_2$ (■) (this work) and for $[Cu(etu)_3]_2(SO_4)$ (▲) and $[Cu(etu)_4](NO_3)$ (▼) (Refs. 27 and 32).

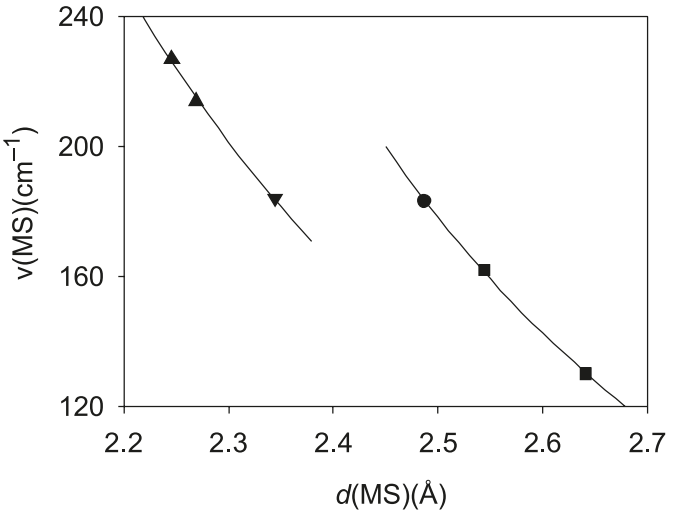

through the centre of which its two-fold axis (parallel to *a*) passes, thus $\{S(2),Ag(1),S(1),Ag(2)\}_2$. A second 2-axis, parallel to *b*, passes through the S–C bonds of ligands 3,4 generating a second eight-membered ring $\{S(3),Ag(1),S(2),Ag(2)(x, 1 – y, 1 – z), S(4)(x, 1 –y, 1 – z)\}_2$, the polymer being generated by a fusion of alternating ring types through successive unit cells. (All sulfur atoms are μ_2). In projection down *c*, it is seen that the polymeric array is sheathed in stacks of quasi-parallel ring planes of ligands 1,3,4 (C_3N_2/C_3N_2 interplanar dihedral angles: 1/3 49.0(2)°, 5.5(2)°, 3/4 35(3)°) up *c* and on the *b* faces of the column, while ligands 2 sheath the polymer, lying quasi-parallel to *c* on the *a* face, reinforced with intra-polymer hydrogen bonds from the NH hydrogen atoms of ligand 1 to Cl(1), but the remainder to the lattice anions, Cl(2,3).

IR spectroscopy

The far IR spectra of the etu ligand and the two complexes $[Ag(etu)_3]_2(SO_4)$ and $[Ag_2(etu)_6](NO_3)_2$ are shown in Fig. 5. Ethylenethiourea shows bands due to internal vibrational modes at 337 and 198 cm^{-1}; an additional band at 106 cm^{-1} has been assigned as a lattice mode (30). Previous studies of the far IR and Raman spectra of thiourea and ethylenethiourea complexes have shown that the metal–sulfur stretching modes ν(MS) occur in the region 170-330 cm^{-1} (27, 30-32). The bands at 208 cm^{-1} in the sulfate and 196 cm^{-1} in the nitrate are assigned to the ligand band that occurs at 198 cm^{-1} in the uncomplexed ligand. The band at 183 cm^{-1} in the sulfate and 162 cm^{-1} in the nitrate are as-

© 2008 NRC Canada

Fig. 7. Far IR spectra of (*a*) $[ClAg_4(etu)_6]Cl_3$, (*b*) $[Br_2Ag_2(etu)_4]$, (*c*) $[IAg(etu)_{0.5}]$. Bands assigned as ν(AgS) or ν(AgX) are labelled with their wavenumbers.

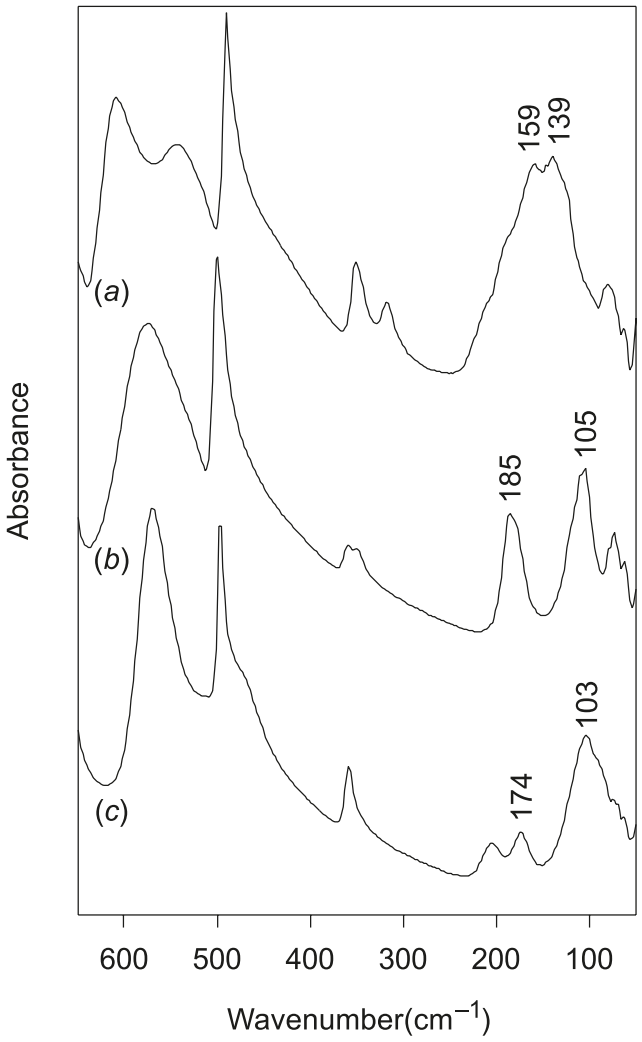

signed to the ν(AgS) vibrations involving the terminal etu ligands in these complexes. As expected, these occur at lower wavenumbers than the ν(CuS) modes previously assigned in related copper(I) complexes (27). The nitrate complex also contains bridging etu ligands with longer Ag–S bonds (see above), which should give rise to ν(AgS) bands at lower wavenumber than those involving the terminal etu ligands. The peak at 130 cm^{-1} in the spectrum of $[Ag_2(etu)_6](NO_3)_2$ (Fig. 5*c*) is assigned to vibrations of this type, and the dependence of the ν(AgS) vibrational frequencies on the mean Ag–S bond lengths shown in Fig. 6 supports this assignment. As has been shown previously in the case of the related copper(I) complexes (32), the data in Fig. 6 can be fitted to an equation of the form,

$$[1] \qquad \nu\ (cm^{-1}) = b(r\ (Å))^{-m}$$

with b = 11 450 and 33 360, and m = 4.85 and 5.71 for the copper(I) and silver(I) complexes, respectively. Similar correlations have previously been found for the Cu–X bonds in a range of copper(I) and silver(I) halide complexes with phosphine and amine ligands, and an increase in the values

Fig. 8. Far IR spectra of (*a*) $[ClAg(etu)_3]$ and (*b*) $[BrAg(etu)_3]$. Bands assigned as ν(AgX) are labelled with their wavenumbers.

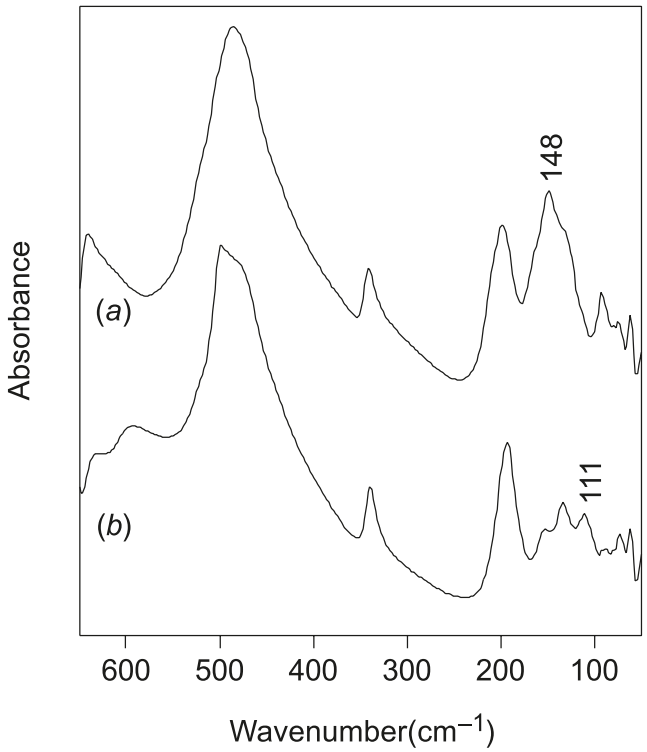

of the b and m parameters from copper to silver was observed in these cases as well (33, 34).

The far IR spectrum of $[ClAg_4(etu)_6]Cl_3$ is shown in Fig. 7*a*. According to the correlation for Ag–S bonds in eq. [1], six ν(AgS) bands are expected to occur in the range 120–170 cm^{-1}, while the corresponding correlation for Ag–Cl bonds (34) predicts ν(AgCl) at 131 cm^{-1}. The strong, broad absorption band in the range 120–170 cm^{-1} is therefore assigned to overlapping ν(AgS) and ν(AgCl) bands, the complexity of absorption in this region reflecting the complex molecular structure of this compound. By contrast, the far IR spectrum of the strucurally much simpler compound $[Br_2Ag_2(etu)_4]$ shows only two, well- resolved bands in the 100–200 cm^{-1} region (Fig. 7*b*). The Ag–S bonds are very nearly equal in length, with a mean value of 2.483 Å, corresponding to ν(AgS) = 185 cm^{-1} (eq. [1]). Likewise, the Ag–Br bonds are all similar in length, with a mean value of 2.816 Å, which corresponds to ν(AgBr) = 105 cm^{-1}. These two predicted frequencies correspond exactly to the observed values 185 and 105 cm^{-1}, which are therefore assigned as ν(AgS) and ν(AgBr), respectively. The far IR spectrum of $[IAg(etu)_{0.5}]$ is shown in Fig. 7*c*. ν(AgS) and ν(AgI) are assigned at 174 and 103 cm^{-1} respectively. The structure of this compound is not known at present, but one possibility is suggested by that of the closely related compound $[Ag_2I_2(Hmimt)]_n$, which has a polymeric sheet structure containing planar four-membered $Ag_2(\mu_3\text{-}I)_2$ rings, which are linked to form ladders that are bridged by the Hmimt ligands.

The far IR spectra of $[XAg(etu)_3]$ (X = Cl, Br) are shown in Fig. 8. ν(AgX) are 148 and 111 cm^{-1} for X = Cl and Br respectively.

© 2008 NRC Canada

Fig. 9. IR spectra in the ν(NH) region of (*a*) $[ClAg_4(etu)_6]Cl_3$, (*b*) $[Br_2Ag_2(etu)_4]$, (*c*) $[ClAg(etu)_3]$, (*d*) $[BrAg(etu)_3]$. The highest wavenumber ν(NH) bands are labelled with their wavenumbers.

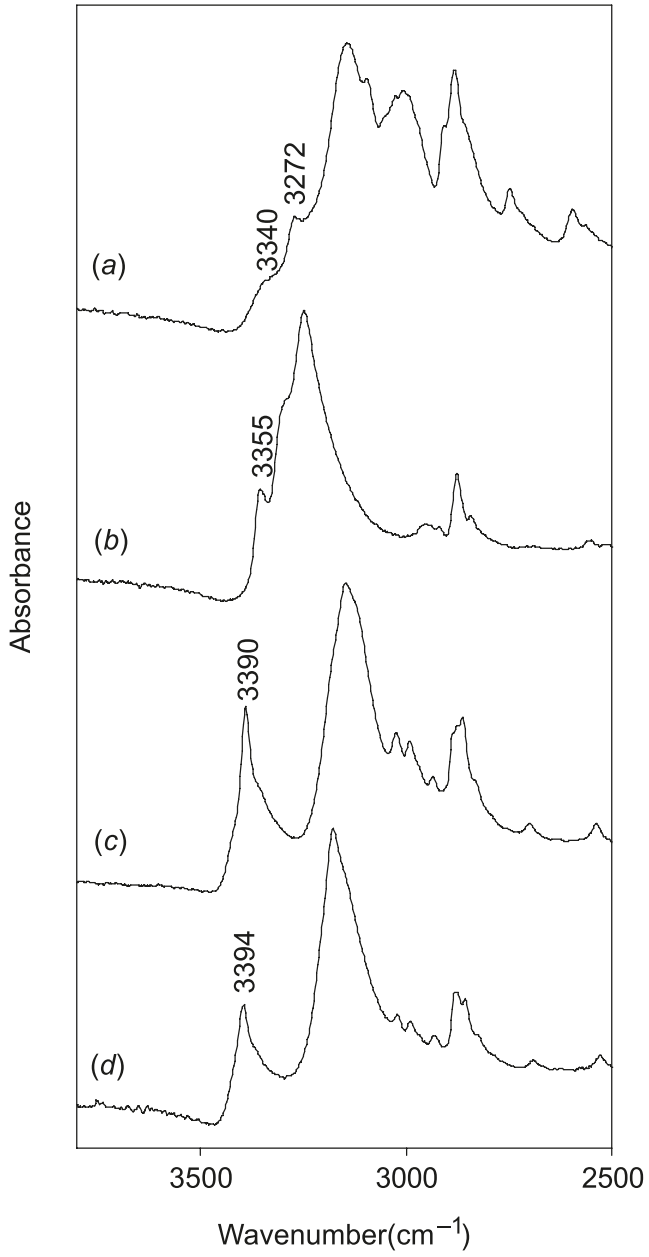

The mid IR spectra contain bands due to the coordinated thiourea ligand, and the bands in the ν(NH) region are particularly sensitive to changes in stoichiometry and structure (25). The spectra of $[ClAg_4(etu)_6]Cl_3$, $[Br_2Ag_2(etu)_4]$, $[ClAg(etu)_3]$, and $[BrAg(etu)_3]$ in the ν(NH) region are shown in Fig. 9. Particularly noticeable is the variation in the position of the highest wavenumber ν(NH) band with increasing etu/AgX ratio. This is attributed to changes in the degree of hydrogen bonding; the N-H hydrogens are involved to varying degrees in hydrogen bonding with the halogen atoms in the structure, and in $[ClAg(etu)_3]$ there is a clear distinction between the hydrogen atoms that are involved in hydrogen bonding to the chlorine atom and those that are not (Fig. 2). The band at 3390 cm^{-1} is assigned to the non hydrogen-bonded N-H hydrogen in this complex. A similar pattern of bands in the spectrum of $[BrAg(etu)_3]$ indicates that this complex is isostructural with the chloride. We have previously shown that the ν(NH) bands in these types of complex are useful for identifying different kinds of complex. The presence of a band at 3357 cm^{-1} in the spectrum of AgI/etu (1:2) is indicative of of a complex with a structure similar to that of the Br analogue, $[Br_2Ag_2(etu)_4]$ (25).

A band in the mid IR spectrum of $AgNO_3$/etu (1:4) at 1634 cm^{-1}, which has no counterpart in the spectra of the other complexes, is assigned to the bending mode of H_2O, present as water of crystallization. This complex is thus formulated as the monohydrate $[Ag(etu)_4](NO_3)\cdot H_2O$, which is consistent with its elemental analysis (see Experimental). The mid IR spectra of the three nitrate complexes $[Ag(etu)_4](NO_3)\cdot H_2O$, $[Ag_2(etu)_6](NO_3)_2$ and $AgNO_3$/etu (1:1.5) contain bands due to the nitrate ion and the coordinated thiourea ligand. Bands due to the $\nu_3(E')$ mode of nitrate, which occurs at about 1380 cm^{-1} in the uncomplexed ion in KNO_3 (35), are obscured by strong bands due to the etu ligand in this region. However, the nitrate $\nu_2(A_2'')$ band is clearly visible in all three cases, occurring at 826, 826, and 819 cm^{-1} respectively. The first two are close to the value of 828 cm^{-1} for the uncomplexed ion (35), and this is consistent with the crystal structure in the case of $[Ag_2(etu)_6](NO_3)_2$. The significantly lower value of this frequency observed for $AgNO_3$/etu (1:1.5) suggests that the nitrate is incorporated in the silver coordination environment in this complex.

Conclusion

Syntheses, single crystal X-ray structural, and spectroscopic characterizations are described for a variety of adducts of silver salts with ethylenethiourea. Ag_2SO_4/etu (1:6) is isomorphous with its previously studied copper(I) counterpart, while $AgNO_3$/etu (1:3) takes the form $[(etu)_2Ag(\mu\text{-}S\text{-}etu)_2Ag(etu)_2](NO_3)_2$, for which there is no published copper(I) counterpart. In AgCl/etu (1:3), the silver atom is in a four-coordinate $ClAgS_3$ environment. AgBr/etu (1:2) is binuclear $[(etu)_2Ag(\mu\text{-}Br)_2Ag(etu)_2)]$, unlike its previously studied copper counterpart, which is $[(etu)BrCu(\mu\text{-}S\text{-}etu)_2CuBr(etu)]$. AgCl/etu (4:6) is an interesting ionic polymer $[ClAg_4(etu)_6]_{(\infty|\infty)}Cl_3$, containing a novel one-dimensional polymeric cation. Bands in the IR spectra in the ν(NH) region prove to be particularly sensitive to the composition and structure of the halide complexes. Bands in the far IR spectra are assigned to ν(AgS) and ν(AgX) (X = halogen) modes, and a correlation between ν(AgS) and the Ag–S bond length *d*(AgS) is established for silver complexes involving the etu ligand. Subsequent work on the $AgNo_3$/etu (1:4) complex produced crystals that were suitable for an X-ray structure determination, which confirmed that the compound is $[Ag(etu)_4](NO_3)\cdot H_2O$ as formulated above (3*a*).

References

1. G.W. Hunt, N.W. Terry, and E.L. Amma. Cryst. Struct. Comm. **3**, 523 (1974).

© 2008 NRC Canada

2. G.W. Hunt, N.W. Terry, and E.L. Amma. Acta Crystallogr. Sect. B, **35**, 1235 (1979).
3. (*a*) G.A. Bowmaker, J.V. Hanna, C. Pakawatchai, B.W. Skelton, Y. Thanyasirikul, and A.H. White. Z. Anorg. Allg. Chem. In press; (*b*) G.A. Bowmaker, J.V. Hanna, C. Pakawatchai, B.W. Skelton, Y. Thanyasirikul, and A.H. White. Inorg. Chem. Manuscript in preparation.
4. G.T. Morgan and F.H. Burstall. J. Chem. Soc. 143 (1928).
5. M.R. Udupa and B. Krebs. Inorg. Chim. Acta, **7**, 271 (1973).
6. C. Pakawatchai, K. Sivakumar, and H.-K. Fun. Acta Crystallogr. Sect. C, **52**, 1954 (1996).
7. F.-F. Jian, P.-P, Sun, H.-L. Xiao, and K. Jiao. Wuji Huaxue Xuebao **19**, 979 (2003) (CCDC: EXONOU).
8. J.S. Casas, E. Garcia Martínez, A. Sánchez, A. Sánchez González, J. Sordo, U. Casellato, and R. Graziani. Inorg. Chim. Acta, **241**, 117 (1996).
9. P.G. Jones. CCDC private communication: BIBXIU.
10. M. Nardelli, L. Cavalca, and A. Braibanti. Gazz. Chim. Ital. **87**, 907 (1957).
11. T.C. Lee and E.L. Amma. J. Cryst. Mol. Struct. **2**, 117 (1972).
12. C. Pakawatchai, S. Saithong, P. Sudkeaw, U. Tooptakong, and J.H. Charmant. X-ray Structure Analysis Online. **21**, x211 (2005).
13. H.-K. Fun, I.A. Razak, C. Pakawatchai, C. Khaokong, S. Chantrapromma, and S. Saithong. Acta Crystallogr. C, **54**, 453 (1998).
14. U. Braun, R. Richter, J. Sieler, A.I. Yanovsky, and Yu.T. Struchkov. Z. Anorg. Allg. Chem. **529**, 201 (1985).
15. J. Sola, A. López, R.A. Coxall, and W. Clegg. Eur. J. Inorg. Chem. 4871 (2004).
16. U. Braun, J. Sieler, R. Richter, B. Hettich, and A. Simon. Z. Anorg. Allg. Chem. **557**, 134 (1988).
17. F.-F. Jian, H.L. Xiao, and P.-S. Zhao. Jiegou Huaxue, **23**, 486 (2004).
18. M.R. Udupa, G. Henkel, and B. Krebs. Inorg. Chim. Acta, **18**, 173 (1976).
19. M.B. Ferrari, G.G. Fava, and M.E.V. Tani. Cryst. Struct. Comm. **10**, 571 (1981).
20. E.A. Vizzini, I.F. Taylor, and E.L. Amma. Inorg. Chem. **7**, 1351 (1968).
21. L.P. Battaglia, A. Bonamartini Corradi, and M. Nardelli. Croat. Chem. Acta, **57**, 545 (1984).
22. P.C. Zachariadis, S.K. Hadjikakou, N. Hadjiliadis, S. Skoulika, A. Michaelides, J. Balzarini, and E. De Clercq. Eur. J. Inorg. Chem. 1420 (2004).
23. F.B. Stocker, D. Britton, and V.G. Young, Jr. Inorg. Chem. **39**, 3479 (2000).
24. A. Beheshti, W. Clegg, N.R. Brooks, and F. Sharafi. Polyhedron, **24**, 435 (2005).
25. G.A. Bowmaker, N. Chaichit, C. Pakawatchai, B.W. Skelton, and A.H. White. Dalton Trans. 2926 (2008).
26. G.M. Sheldrick. SHELXL-97 [computer program]. University of Göttingen, Göttingen, Germany, (1997).
27. G.A. Bowmaker, C. Pakawatchai, B.W. Skelton, P. Thavornyutikarn, Y. Wattanakanjana, and A.H. White. Aust. J. Chem. **47**, 15 (1994). (See also: L.P. Battaglia, A.B. Corradi, M. Nardelli, M.E.V. Tani. J. Chem. Soc. Dalton Trans. 143 (1976).)
28. D. Jia, Y. Zhang, J. Deng, and M. Ji. J. Coord. Chem. **60**, 833 (2007).
29. E.S. Raper, J.D. Wilson, and W. Clegg. Inorg. Chim. Acta, **194**, 51 (1994).
30. D.M. Adams and J.B. Cornell. J. Chem. Soc. A, 884 (1967).
31. C.D. Flint and M. Goodgame. J. Chem. Soc. A, 744 (1966).
32. R.C. Bott, G.A. Bowmaker, C.A. Davis, G.A. Hope, and B.E. Jones. Inorg. Chem. **37**, 651 (1998).
33. G.A. Bowmaker, P.C. Healy, J.D. Kildea, and A.H. White. Spectrochim. Acta A, **44**, 1219 (1988).
34. G.A. Bowmaker, Effendy, J.D. Kildea, and A.H. White. Aust. J. Chem. **50**, 577 (1997).
35. K. Nakamoto. *In* Infrared and Raman spectra of inorganic and coordination compounds. Part A. 5th Ed. Wiley, NY. 1997. p. 182.

© 2008 NRC Canada

Ferrocenyl phosphine–oxazaphospholidine oxide ligands for the Suzuki–Miyaura coupling of hindered aryl bromides and chlorides[1]

Daniele Vinci, Nelson Martins, Ourida Saidi, John Bacsa, Amadeu Brigas, and Jianliang Xiao

Abstract: A series of ferrocenyl oxazaphospholidine phosphines that differ electronically and sterically were investigated as ligands for the Suzuki–Miyaura cross-coupling reactions. One of these compounds, **1**, was shown to be highly effective in the coupling reactions of bulky aryl bromides with boronic acids when combined with $Pd(OAc)_2$, while another, **2**, was capable of coupling aryl chlorides with boronic acids. However, these ligands were less effective in asymmetric induction.

Key words: Suzuki–Miyaura coupling, ferrocenyl phosphines, aryl bromides, aryl chlorides, palladium.

Résumé : Une série de ferrocényl oxazaphospholidine phosphines qui présentent des différences tant électroniques que stériques a été étudiée comme ligands pour les réactions de couplage croisé de Suzuki–Miyaura. On a montré qu'un de ces composés, **1**, lorsqu'il est combiné au $Pd(OAc)_2$, est très efficacle dans les réactions de couplage de bromures d'aryles avec des acides boroniques alors que le composé **2** permet d'effectuer le couplage de chlorures d'aryles avec les acides boroniques. Toutefois, ces ligands sont moins efficaces dans l'induction asymétrique.

Mots-clés : couplage de Suzuki–Miyaura, ferrocényl phosphines, bromures d'aryles, chlorures d'aryles, palladium.

[Traduit par la Rédaction]

Introduction

The palladium-catalyzed cross-coupling reactions of organoboron compounds and organic halides or triflates have emerged as a powerful and general methodology for the formation of carbon–carbon bonds (1–7). Advances in recent years have made the reactions scalable and cost effective (8). However, methods that are generally applicable to the synthesis of bulky and axially chiral biaryls, common structural motifs in natural products and chiral ligands, are still rare (9–17). Although reasonably good results in the enantioselective Suzuki coupling have been achieved using P^N ligands based on biaryl and ferrocene backbones, the reaction times, scope of substrates, and catalyst loadings remain to be improved (18, 19).

Suzuki–Miyaura coupling of hindered aryl bromides and chlorides is a particularly challenging area of research. Recently, new and improved catalytic systems for the coupling of these demanding substrates have been developed and described (20–28). In particular, biaryl monophosphine ligands have proven to be highly effective, partially meeting the requirement of increased catalytic performance (29). However, there remain some key issues that need to be addressed; these include problems such as hydrolysis of Pd–Ar complexes, slow transmetalation or slow trans to cis isomerization of intermediate palladium species, leading to the formation of unwanted byproducts (18, 29–34).

Ferrocene-based ligands have been employed successfully in many catalytic transformations (35) due to their ease of functionalization and the stability of most of its derivatives. Its proven record in homogeneous catalysis has been demonstrated. The Suzuki–Miyaura reaction is no exception to this trend (36, 37). Recently, we reported a new series of ferrocenyl-phosphine ligands that were synthesized by ortholithiation of (2*R*,4*S*,5*R*)-3,4-dimethyl-2-ferrocenyl-5-phenyl-[1,3,2]oxazaphospholidine 2-oxide (Scheme 1) (38). Herein, we present our findings on the application of the ligands **1**–**4** in the Suzuki–Miyaura reactions.

Received 27 March 2008. Accepted 30 May 2008. Published on the NRC Research Press Web site at canjchem.nrc.ca on 3 September 2008.

Dedicated to Professor Dick Puddephatt for his outstanding contributions to chemistry and mentoring.

D. Vinci, N. Martins, O. Saidi, J. Bacsa, and J. Xiao.[2] Department of Chemistry, University of Liverpool, Liverpool L69 7ZD, U.K.
N. Martins and A. Brigas. C CIQA, Faculdade de Ciências e Tecnologia, Universidade do Algarve, 8005-139 Faro, Portugal.

[1]This article is part of a Special Issue dedicated to Professor R. Puddephatt.
[2]Corresponding author (e-mail: j.xiao@liv.ac.uk).

 doi:10.1139/V08-113 © 2008 NRC Canada

Scheme 1. Ferrocenyl phosphino ligands synthesized by ortho-lithiation and examined in this study.

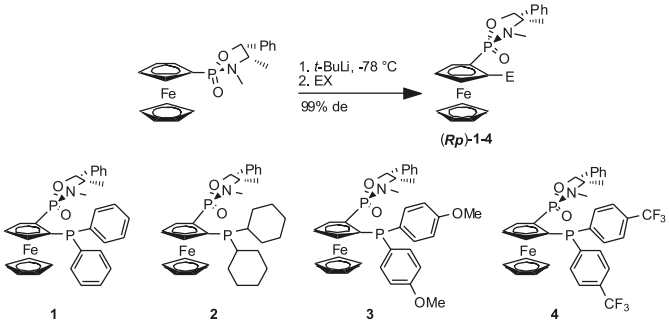

Experimental[3]

Procedures for Suzuki–Miyaura coupling reactions

The coupling of 1-bromo-2-methoxynaphthalene with 1-naphthalene boronic acid to give 2-methoxy-1,1′-binaphthyl, **5**, is described as a typical example. An oven-dried carousel reaction tube was charged with 1-naphthalene boronic acid (0.75 mmol), CsF (1.5 mmol), **1** (10 μmol), and $Pd(OAc)_2$ (5 μmmol). The aryl bromide (0.5 mmol) was introduced at this stage (or after degassing by injection through a rubber septum in case of a liquid). The reaction vessel was evacuated and backfilled with N_2. This process was repeated five times, after which dioxane (3 mL) was introduced. The reaction mixture was then heated at 100 °C for 4 h. After cooling down to ambient temperature, the conversion was determined from the crude ^{1}H NMR, and isolated yield was obtained after a standard work-up and purification by flash chromatography (100% hexane). The product 2-methoxy-1,1′-binaphthyl, **5**, was obtained in 98% yield. Analytic details: mp 106 to 107 °C. ^{1}H NMR ($CDCl_3$, 400 MHz, ppm) δ: 3.75 (s, 3H), 7.14 (d, 1H, J = 8.8 Hz), 7.19–7.28 (m, 2H), 7.30–7.33 (m, 2H), 7.42–7.47 (m, 3H), 7.61 (t, 1H, J = 7.7 Hz), 7.86 (d, 1H, J = 8.0 Hz), 7.93 (d, 1H, J = 8.0 Hz), 7.94 (d, 1H, J = 8.0 Hz), 7.97 (d, 1H, J = 8.8 Hz). ^{13}C NMR ($CDCl_3$, 100 MHz, ppm) δ: 56.8, 113.8, 123.2, 123.5, 125.5, 125.5, 125.7, 125.8, 126.2, 126.4, 127.7, 127.8, 128.2, 128.4, 129.0, 129.4, 132.9, 133.7, 134.2, 134.5, 154.6. MS *m/z*: 284 (M^+). The products **6**–**19** were obtained in a similar manner.

X-ray structural determination of Pd-1

The complex **Pd-1** was synthesized by heating $PdCl_2(PhCN)_2$ with **1** in dry dichloromethane with a 91% yield. ^{1}H NMR ($CDCl_3$, 400 MHz, ppm) δ: 0.78 (s, br, 3H), 2.00 (d, 3H, J = 11.2 Hz), 3.69 (m, 1H), 4.15 (br, 1H), 4.75 (s, 5H), 4.80 (br, 1H), 4.83 (br, 1H), 5.70 (br, 1H), 7.30–7.90 (m, 15H). ^{31}P NMR ($CDCl_3$, 162 MHz, ppm) δ: 16.4(s), 46.6(s). HR-MS (ES+) *m/z*: calcd. for $C_{32}H_{31}{}^{37}Cl^{54}FeNO_2P_2Pd$: 719.9920, $C_{32}H_{31}{}^{35}Cl^{56}FeNO_2P_2Pd$: 719.9903 $[M - Cl]^+$; found: 719.9918.

Single crystal X-ray data were collected on a Bruker D8 diffractometer with an APEX detector using graphite monochromated Mo Kα radiation (λ = 0.710 73 Å). The crystal was cooled to T = 110(2) K. A total of 19537 reflections was collected with $2\theta_{max}$ = 55.1°. Of these reflections, 13146 were unique (R_{int} = 0.0406). The reflection data were integrated using SAINT v6.45a (39). The data were corrected for absorption, decay, and other errors using SADABS V2007-2 (40). The structure was solved by direct methods and refined using SHELX (41). X-SEED (42), a graphical interface to SHELX, was used to generate representations of the crystal structure.

Crystal data: $2(C_{32}H_{31}Cl_2FeNO_2P_2Pd)$, C_7H_5N, $CHCl_3$, M = 1701.38, orange block, 0.20 mm × 0.20 mm × 0.10 mm, monoclinic, space group $P2_1$ (No. 4), a = 9.4590(19), b = 19.219(4), c = 19.677(4) Å, β = 96.99(3)°, V = 3550.5(12) Å^3, Z = 2, $D_{calcd.}$ = 1.591 g/cm^3, F_{000} = 1720. Final GoF = 1.011, $R1$ = 0.0517, $wR2$ = 0.1042, R indices based on 10244 reflections with $I > 2\sigma(I)$ (refinement on F^2), 842 parameters, 1 restraint, μ = 1.266 mm^{-1}. Absolute structure parameter = –0.00(2).

Table 1. Suzuki coupling with $Pd(OAc)_2$ and ligands **1**–**4**.

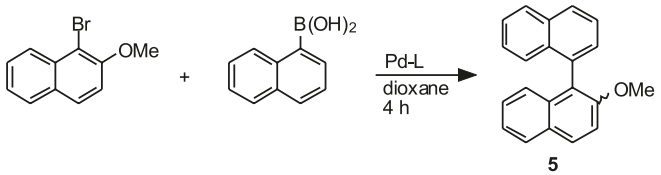

Entry	Ligand	L/Pd ratio	Conv. (%)	Yield (%)[a]
1	**1**	2	>99	98
2	**1**	1	78	63
3	**2**	2	55	50
4	**2**	1	>99	94
5	**3**	2	91	90
6	**3**	1	78	76
7	**4**	2	97	91
8	**4**	1	90	79
9[b]	**1**	2	61	54
10[b]	**2**	1	27	21
11[b]	**3**	2	39	22
12[b]	**4**	2	53	39
13	$FcPPh_2$	2	22	8

Note: Reaction conditions: 1.0 equiv. of aryl bromide, 1.5 equiv. of boronic acid, 3.0 equiv. of CsF, 1 mol% $Pd(OAc)_2$, 105 °C, 4 h in dioxane.

[a]Isolated yields; hydrolysis products were observed in the case of low yields.

[b]Reaction time: 1 h.

Results and discussion

Ligand screening

The ligands **1**–**4** are hemilabile, with P^O chelation to Pd being the most likely. Sterically and electronically, however, they show different behaviour, and it was of interest to see

[3] Supplementary data for this article are available on the journal Web site (canjchem.nrc.ca) or may be purchased from the Depository of Unpublished Data, Document Delivery, CISTI, National Research Council Canada, Ottawa, ON K1A 0R6, Canada. DUD 3800. For more information on obtaining material refer to cisti-icist.nrc-cnrc.gc.ca/cms/unpub_e.shtml. CCDC 691402 contains the crystallographic data for this manuscript. These data can be obtained, free of charge, via www.ccdc.cam.ac.uk/conts/retrieving.html (Or from the Cambridge Crystallographic Data Centre, 12 Union Road, Cambridge CB2 1EZ, UK; fax +44 1223 336033; or deposit@ccdc.cam.ac.uk).

© 2008 NRC Canada

Fig. 1. The X-ray structure of **Pd-1**. Selected bond distances (Å) and angles (°): Pd(1)–O(2) 2.071(4), Pd(1)–P(1) 2.229(2), Pd(1)–Cl(2) 2.262(2), Pd(1)–Cl(1) 2.364(2); O(2)-Pd(1)-P(1) 88.93(14), O(2)-Pd(1)-Cl(2) 172.8(1), P(1)-Pd(1)-Cl(2) 89.94(7), O(2)-Pd(1)-Cl(1) 88.4(1), Cl(2)-Pd(1)-Cl(1) 92.77(7).

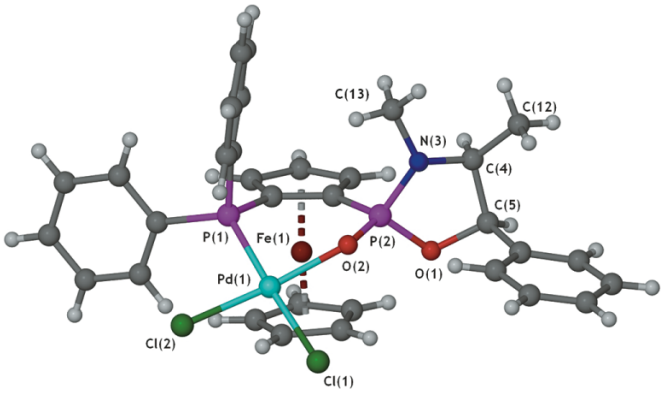

how this difference would impact the palladium-catalyzed Suzuki coupling. At the outset, we examined the coupling between the sterically hindered 1-bromo-2-methoxynaphthalene and 1-naphthalene boronic acid and compared the results with a similar but less bulky phosphine. The results are reported in Table 1.

As can be seen, ligand **1** showed excellent results when the ligand/catalyst ratio was set to 2. The reaction was complete after 4 h and the coupling product was recovered in 98% yield after purification by column chromatography (Table 1, entry 1). At a lower concentration of ligand, the reaction slowed down, lowering the yield to 63% (Table 1, entry 2). In contrast, the reaction with ligand **2** was found to go to completion when a 1/1 ligand/palladium (L/Pd) ratio was used (Table 1, entry 4). At higher concentrations, the rate dropped dramatically (Table 1, entry 3). Ligands **3** and **4** show similar behaviour and their results are somewhat similar to those obtained with the ligand **1**. To better appreciate the differences among the ligands, the coupling time was reduced. As is seen from the entries 9–12 in Table 1, the ligand **1** gave the best yields, and it appears that an electron rich phosphine does not benefit the coupling. The coupling was considerably less efficient with the less bulky ligand $FePPh_2$ (Fc = ferrocenyl) (Table 1). Thus, the oxazaphospholidine moiety of **1**–**4**, in combination with the phosphine group, is able to stabilize the active palladium species and accelerate the reaction rate. The differences between **1** and **2** could partially be explained by assuming a stable, active Pd species requires two equivalents of **1** but only one equivalent of the bulkier **2** (43).

The X-ray crystal structure of the complex, **Pd-1**, formed between **1** and $PdCl_2(PhCN)_2$, confirms that **1** behaves as a chelating ligand, with both the phosphorus atom and the phosphoryl oxygen atom of the oxazaphospholidine ring coordinating to the Pd(II) centre (Fig. 1). The compound crystallizes in the chiral space group $P2_1$ with 2 **Pd-1** molecules, a benzonitrile, and a chloroform molecule in the asymmetric unit, but the two organometallic molecules are chemically and nearly structurally identical. Examination of the orientation of the two molecules and the crystal packing reveals no missing symmetry elements, and the refined absolute structure parameter is further evidence that the crystals are indeed chiral. The molecular structure of one of the two molecules is shown in Fig. 1. The coordination geometry about the Pd(II) atom is square planar, with P, O, and the two Cl atoms cis to each other. The two Pd–Cl bonds are noticeably different [2.262(2) and 2.364(2) Å]. The longer Pd–Cl bond, which is trans to P(1), is likely to be due to the stronger trans effect of a P atom than an O atom. The three chiral centres of P(2), C(4), and C(5) have *R*, *S*, and *R* configurations, respectively. The complex is also planar chiral with a *R* configuration.

Table 2. Suzuki coupling of sterically hindered partners with **1**.

Entry	ArBr	$ArB(OH)_2$	Yield (%)	Product
1	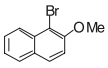		98	**5**
2			93	**6**
3			91	**7**
4	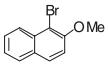		97	**8**
5			97	**9**
6			96	**10**
7	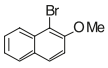	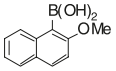	12[a]	**11**
8	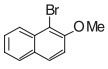	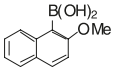	43[a,b]	**11**

Note: Reaction conditions: 1.0 equiv. of aryl bromide, 1.5 equiv. of boronic acid, 3 equiv. of CsF, 100 °C in dioxane, 1 mol% $Pd(OAc)_2$, 2 mol% **1**. Yield refers to isolated yields.

[a]Hydrolysis product was observed.

[b]NEt_3 (3 equiv.) and toluene as solvent were used.

During the Suzuki coupling, the phosphoryl oxygen could dissociate from the palladium to facilitate the transmetalation and recoordinate to induce a faster reductive elimination. This may well be the case with the bulkier **2**. In the case of **1**, **3**, and **4**, however, the need for 2 equiv. of ligand for a more efficient coupling appears to suggest that the phosphoryl oxygen is replaced by the phosphine group of a second ligand.

Aryl bromides as substrates

One of the biggest challenges in the use of a Suzuki–Miyaura reaction is the coupling of hindered substrates. Since the ligand **1** afforded the best results in the coupling of 1-bromo-2-methoxynaphthalene and 1-naphthalene boronic acid, its catalytic activity towards other hindered substrates was studied. The results of the coupling of various sterically

© 2008 NRC Canada

Table 3. Suzuki coupling of aryl chlorides using **2**.

Entry	ArCl	$ArB(OH)_2$	Time (h)	Yield (%)	Product
1			1	96	**12**
2			18	96[a]	**12**
3			8	92	**13**
4			8	93	**14**
5			8	93	**15**
6			8	97	**16**
7			8	91	**17**
8			24	97	**18**
9			24	84	**19**
10			24	89	**7**

Note: Reaction conditions: 1.0 equiv. of aryl chloride, 1.5 equiv. of boronic acid, 3.0 equiv. of CsF, 105 °C in dioxane, 1 mol% $Pd(OAc)_2$, 1 mol% ligand **2**. Yield refers to isolated yields.
[a]$Pd(OAc)_2$ (0.1 mol%).

hindered aryl bromides and sterically hindered aryl boronic acids employing ligand **1** are reported in Table 2.

The couplings involving the formation of the trisubstituted biaryls proceeded smoothly to completion. The reactions were complete after 4 h and no hydrolysis byproducts were observed in the crude mixtures. However, the reaction leading to tetra-substituted biaryl compounds resulted in low yields (Table 2, entries 7 and 8), and a significant amount of hydrolysis product, 2-methoxynaphthalene.

The important factor that impedes the coupling of partners in entry 7 of Table 2 is likely to be the increased steric bulk of the boronic acid, which makes the transmetallation difficult. This may in turn give preference to protonolysis of the Pd–Ar intermediate, leading to the hydrolysis product. Accordingly, a combination of CsF and NEt_3 as base and a nonprotic solvent like toluene afforded some improvement in the conversion. The yield increased from 12% to 43% (Table 2, entry 8), although 2-methoxynaphthalene was still observed.

Aryl chlorides as substrates

To find the best ligand for these substrates, we screened the ligands **1–4** for the coupling of the activated 4-chloroacetophenone with phenylboronic. In sharp contrast to the coupling of the bromides, only the ligand **2** was found to give satisfactory results; hence, the other ligands were not studied further. Apparently, a more electron-rich ligand is needed for the aryl chlorides, which are expected to be less reactive in the oxidative addition at Pd(0) than the corresponding bromides. The results of the coupling reactions obtained with **2** are summarized in Table 3.

The reaction between 4-chloroacetophenone and phenylboronic acid at 105 °C using 1 mol% of Pd and 1 equiv. of **2** was complete in just 1 h (Table 3, entry 1). Reducing the amount of palladium to 0.1 mol% resulted in a predictable decrease of the reaction rate; complete conversion was reached after 18 h (Table 3, entry 2). Increasing the steric bulk on the boronic acid also resulted in a decrease in the reaction rate (Table 3, entry 3). Although the coupling of the 4-chloroacetophenone with 2-tolylboronic acid also occurred at a 0.1 mol% Pd loading, the reaction took more than one day to reach completion. The rest of the reactions were therefore performed using 1 mol% Pd.

As can be seen from Table 3, going from an activated chloride to a deactivated one like 2-chlorotoluene, the yield was not affected under the conditions employed. The coupling of sterically hindered boronic acids, such as 1-naphthylboronic acid and 2-tolylboronic acid (Table 3, entries 6 and 7), ran smoothly to completion after 8 h. However, a further increase in the steric bulk of the chlorides did eventually affect the reaction rate. Thus, with 2-chloro-meta-xylene as substrate, the coupling reactions went to completion only after 24 h (entries 8–10). The results obtained with **2** are better than or comparable with those obtained using related electron-rich ferrocenyl phosphines (44, 45).

Table 4. Asymmetric Suzuki coupling.

Entry	Ligand	L/Pd	T (°C)	Time (h)	Conv. (%)	Ee (%)[a]
1	**1**	2	70	12	85	26 (*R*)
2	**1**	1	50	12	78	18 (*R*)
3	**2**	1	50	12	55	7 (*S*)
4	**2**	1	70	12	>99	9 (*S*)
5	**2**	2	70	7	80	27 (*R*)
6	**3**	2	70	12	84	14 (*R*)
7	**4**	2	70	12	92	3 (*R*)

Note: Reaction conditions: 1.0 equiv. of aryl bromide, 1.5 equiv. of boronic acid, 3.0 equiv. of CsF, dioxane, 5 mol% $Pd(OAc)_2$.
[a]Determined by HPLC using a DAICEL OJ column (90/10 hexane/iPrOH).

Asymmetric coupling

So far, few catalysts have been developed for asymmetric Suzuki cross-coupling reactions (18, 19). In the course of this study, we examined the ligands **1–4** for the asymmetric coupling of 1-naphthylboronic acid and 1-bromo-2-methoxynaphthylboronic acid. The reaction conditions are slightly different from the ones reported in Table 1. The conversions and ee values obtained are reported in Table 4.

Ligand **1** yielded a 85% conversion and 26% ee as its best results (Table 4, entry 1). Decreasing the temperature or the L/Pd ratio did not bring about any amelioration. Although the ligand **2** was previously found to give a higher activity using a lower L/Pd ratio (Table 1, entry 4), it gave a higher enantioselectivity (27% ee) when 2 equiv. of the ligand were used (Table 4, entry 5). Most notably, the configuration of the product was reversed in the case of the latter, suggesting that the active catalyst varies with the L/Pd ratio. The higher ee for the L/Pd ratio of 2 is probably due to

© 2008 NRC Canada

the formation of a Pd-diphosphine species, which increases the steric bulk around the palladium. Ligand **4**, the electron-poor analogue of **1**, afforded the poorest enantioselectivity, which may partly stem from its ease of dissociation from the metal centre. However, it is difficult to draw conclusions relating the electronic and steric properties of ligand with the asymmetric induction observed, not least because there are probably more than one active catalytic species operating in the reaction media.

Conclusion

This paper presents results on the application of a series of electronically and sterically varied ferrocenyl ligands to the Suzuki–Miyaura cross-coupling reactions of aryl bromides and chlorides. Ligands **1** and **2** were proven to generate very effective catalysts for the coupling of sterically hindered partners. However, ligand **1** was ineffective in the coupling of aryl chlorides. For these substrates, including deactivated ones, the bulkier, electron-rich ligand **2** was necessary. A strong dependence of the catalytic activity on the L/Pd ratio was observed and this varied with the nature of the ligand. In contrast with **1**, an active catalyst was formed when 1 equiv. of **2** relative to the palladium was used, a scenario reminiscent of those observed with other bulky, electron-rich phosphines (43). The satisfying performance of the ligands in terms of reaction rates and substrate scope could partly be ascribed to the presence of the oxazaphospholidine moiety, which renders the ligand to be potentially hemilabile during the catalysis, thereby stabilizing the active palladium species. These ligands were also shown to induce enantioselection in the Suzuki coupling reaction; however, their performance remains to be improved in this respect.

Acknowledgements

We gratefully acknowledge Johnson Matthey and the Fundação para a Ciência e a Tecnologia (SFRH/BD/17262/2004 NM) for financial support.

References

1. A. Suzuki. Acc. Chem. Res. **15**, 178 (1982).
2. A. Suzuki. Pure Appl. Chem. **57**, 1749 (1985).
3. N. Miyaura and A. Suzuki. J. Synth. Org. Chem. Jpn. **46**, 848 (1988).
4. A. Suzuki. Pure Appl. Chem. **63**, 419 (1991).
5. N. Miyaura and A. Suzuki. J. Synth. Org. Chem. Jpn. **51**, 1043 (1993).
6. A. Suzuki. Pure Appl. Chem. **66**, 213 (1994).
7. N. Miyaura and A. Suzuki. Chem. Rev. **95**, 2457 (1995).
8. S. Liu and J. Xiao. J. Mol. Catal. A: Chem. **270**, 1 (2007).
9. G. Bringmann, R. Walter, and R. Weirich. Angew. Chem. Int. Ed. **29**, 977 (1990).
10. T.G. Gant and A.I. Meyers. Tetrahedron, **50**, 2297 (1994).
11. A.I. Meyers, J.R. Flisak, and R.A. Aitken. J. Am. Chem. Soc. **109**, 5446 (1987).
12. K. Kamikawa and M. Uemera. Synlett, 938 (2000).
13. M. Uemura, A. Daimon, and Y. Hayashi. J. Chem. Soc. Chem. Commun. 1943 (1995).
14. K. Kamikawa, A. Tachibana, S. Sugimoto, and M. Uemura. Org. Lett. **3**, 2033 (2001).
15. G. Bringmann, M. Breuning, and S. Tasler. Synthesis, **4**, 525 (1999).
16. G. Bringmann and D. Menche. Acc. Chem. Res. **34**, 615 (2001).
17. K.C. Nicolaou, H. Li, C.N.C. Boddy, J.M. Ramanjulu, T.Y. Yue, S. Natarajan, X.J. Chu, S. Brase, and F. Rubsam. Chem. Eur. J. **5**, 2584 (1999).
18. J. Yin and S.L. Buchwald. J. Am. Chem. Soc. **122**, 12051 (2000).
19. M. Genov, A. Almorin, and P. Espinet. Chem. Eur. J. **12**, 9346 (2006).
20. S.D. Walker, T.E. Barder, J.R. Martinelli, and S.L. Buchwald. Angew. Chem. Int. Ed. **43**, 1871 (2004).
21. J. Yin, M.P. Rainka, X.X. Zhang, and S.L. Buchwald. J. Am. Chem. Soc. **124**, 1162 (2002).
22. J.P. Wolfe and S.L. Buchwald. Angew. Chem. Int. Ed. **38**, 2413 (1999).
23. J.P. Wolfe, R.A. Sinjer, B.H. Yang, and S.L. Buchwald. J. Am. Chem. Soc. **121**, 9550 (1999).
24. D.W. Old, J.P. Wolfe, and S.L. Buchwald. J. Am. Chem. Soc. **120**, 9722 (1998).
25. N. Gurbuz, I. Ozdemir, S. Demir, and B. Centinkaya. J. Mol. Catal. **209**, 23 (2004).
26. S.D. Cho, H.K. Kim, H.S. Yim, M.R. Kim, J.K. Lee, J.J. Kim, and Y.J. Yoond. Tetrahedron, **63**, 1345 (2007).
27. T.E. Barder, S.D. Walker, J.R. Martinelli, and S.L. Buchwald. J. Am. Chem. Soc. **127**, 4685 (2005).
28. N. Marion, O. Navarro, J. Mei, E.D. Steven, N.M. Scott, and S.P. Nolan. J. Am. Chem. Soc. **128**, 4101 (2006).
29. K. Billingsley and S.L. Buchwald. J. Am. Chem. Soc. **129**, 3358 (2007).
30. A.N. Cammidge and K.V.L. Crépy. Chem. Commun. 1723, (2000).
31. A.N. Cammidge and K.V.L. Crépy. Tetrahedron, **60**, 4377 (2004).
32. A.M. Herrbach, O. Baudoin, D. Guénard and F. Guéritte. J. Org. Chem. **68**, 4897 (2003).
33. A.S. Castanet, F. Colobert, P.E Broutin, and M. Obringer. Tetrahedron: Asymmetry, **13**, 659 (2002).
34. N. Hadei, E.A.B. Kantchev, C.J. O'Brien, and M.G. Organ. Org. Lett. **7**, 1991 (2005).
35. R.G. Arrayas, J. Adrio, and J.C. Carretero. Angew. Chem. Int. Ed. **45**, 7674 (2006).
36. F.Y. Kwong, W.H. Lam, C.H. Yeung, K.S. Chan, and A.S.C. Chan. Chem. Commun. 1922 (2004).
37. T.E. Pickett, F.X. Roca, and C.J. Richards. J. Org. Chem. **68**, 2592 (2003).
38. D. Vinci, N. Mateus, X. Wu, F. Hancock, A. Steiner, and J. Xiao. Org. Lett. **2**, 215 (2006).
39. Bruker AXS, Inc. SAINT-PLUS. Version 6.45a [computer program]. Bruker AXS Inc., Madison, Wisconsin. 2005.
40. Bruker AXS, Inc. SADABS. Version 2007-2 [computer program]. Bruker AXS Inc., Madison, Wisconsin. 2007.
41. G.M. Sheldrick. SHELXL-97 [computer program]. University of Göttingen, Germany. 1997.
42. L.J. Barbour. J. Supramol. Chem. **1**, 189 (2001).
43. I.D. Hills, M.R. Netherton, and G.C. Fu. Angew. Chem. Int. Ed. **42**, 5749 (2003).
44. J.F. Jensen and M. Johannsen. Org. Lett. **5**, 3025 (2003).
45. C. Baillie, L. Zhang, and J. Xiao. J. Org. Chem. **69**, 7779 (2004).

© 2008 NRC Canada

Synthesis and organic group transfer of organodiplatinum complex with a 1,2-bis(diphenylphosphino)ethane ligand[1]

Nobuyuki Komine, Tomoko Ishiwata, Jun-ya Kasahara, Erino Matsumoto, Masafumi Hirano, and Sanshiro Komiya

Abstract: A series of homometallic alkyl- and phenyldinuclear complexes containing one platinum–platinum bond, (dppe)RPt–Pt(η^5-Cp)(CO) (R = Me, Et, CH_2CMe_3, Ph), have been prepared by oxidative addition of the Pt–C bond of PtR(η^5-Cp) to Pt(styrene)(dppe), and were characterized by spectroscopic methods and (or) X-ray structure analysis. The geometry at Pt with a dppe ligand is square planar, and the carbonyl and Cp ligand of the Pt(η^5-Cp)(CO) moiety lie orthogonal to the coordination plane of former platinum. Competitive organic group transfer reactions along the Pt–Pt bond in these complexes took place to give PtR(η^5-Cp)(CO) and PtR(η^1-Cp)(dppe) on thermolysis. Alkyl or aryl transfer from Pt with a dppe ligand were enhanced by addition of olefin, whereas treatment with CO and tertiary phosphine ligands causes Cp transfer from Pt(η^5-Cp)(CO).

Key words: organoplatinum–platinum complex, organic group transfer.

Résumé : On a préparé une série de complexes alkyl- et phényldinucléaires homométalliques contenant une liaison platine-platine, (dppe)RPt-Pt(η^5-Cp)(CO) (R = Me, Et, CH_2CMe_3, PH) par le biais d'une réaction d'addition oxydante de la liaison Pt-C du PtR(η^5-Cp) sur du Pt(styrène)(dppe) et on les a caractérisés par des méthodes spectroscopiques ainsi que par des analyses de structure par diffraction des rayons X. La géométrie au niveau du Pt portant un ligand dppe est plan carré et le groupement carbonyle et le ligand Cp de la portion Pt(η^5-Cp)(CO) se trouve en position orthogonale par rapport au plan de coordination du premier atome de platine. Il se produit des réactions compétitives de transfert des groupes organiques le long de la liaison Pt-Pt de ces complexes et elles conduisent à la formation de PtR(η^5-Cp)(CO) et PtR(η^5-Cp)(dppe) par thermolyse. Les transferts de groupes alkyles ou aryles à partir des dérivés de Pt portant le ligand dppe sont rendus plus fréquents par l'addition d'oléfine alors que des traitements par du CO ou des ligands phosphines tertiaires provoquent des transfert de Cp du Pt(η^5-Cp)(CO).

Mots-clés : complexe organique de platine–platine, transfert de groupe organique.

[Traduit par la Rédaction]

Introduction

The cooperative effect in multimetallic catalysis is one of the most intriguing and interesting unsolved problems at the molecular level both in homo- and heterogeneous catalyses (1). As the simplest model for active intermediates in various transition metal catalyzed reactions promoted by heterometallic catalysts, we previously reported the synthesis and some reactions of heterodinuclear organometallic complexes containing group 10 metals, having both M–R and M–M′ bonds, $L_nRM–M'L'_m$ (M = Pt, Pd; M′ = Mo, W, Co, Fe, Mn, Re; R = Me, Et, Ph, H, Ac, allyl; L_n = cod, dppe, bpy, phen, tmeda; L′ = η^5-Cp, CO) (2). They show unique reactions such as organic group transfer between different metal centers (2*a*, 2*c*, 2*d*, 2*e*, 2*h*, 2*k*, 2*q*), significant acceleration of β-hydrogen elimination (2*f*, 2*i*), enhanced CO insertion reactions into the Pd–C bond (2*g*, 2*l*), and regio- and stereoselective insertion reactions of thiiranes into the Pt–Mn (or –Re) bond controlled by an ancillary alkyl ligand (2*j*). On the other hand, organoplatinum- (or palladium-) cobalt complexes show catalytic activities in carbonylation of thietane (2*m*) and copolymerization of aziridine and CO (2*p*, 2*s*). Among these reactions, organic group transfer reactions attract interest as a simple model for easy σ-organic group movement on the heterometallic catalyst surface. The process is found to be essentially reversible and is regarded as reductive elimination of transition metal and organic groups at the transition metal. In most of the complexes we have investigated, an organic group on the platinum metal moves to other metals with small electronegativity. In this work, we investigated the synthesis and reaction of homometallic

Received 3 April 2008. Accepted 20 May 2008. Published on the NRC Research Press Web site at canjchem.nrc.ca on 9 September 2008.

This paper is dedicated to Professor Richard Puddephatt for his great contributions in Organometallic Chemistry.

N. Komine, T. Ishiwata, J. Kasahara, E. Matsumoto, M. Hirano, and S. Komiya.[2] Department of Applied Chemistry, Graduate School of Engineering, Tokyo University of Agriculture and Technology, 2–24–16 Nakacho, Koganei, Tokyo.

[1]This article is part of a Special Issue dedicated to Professor R. Puddephatt.

[2]Corresponding author (e-mail: komiya@cc.tuat.ac.jp).

 doi:10.1139/V08-111 © 2008 NRC Canada

alkyl- and aryl-dinuclear complexes containing one platinum–platinum bond (3). These complexes were synthesized by oxidative addition of the Pt–C bond of PtR(η^5-Cp)(CO) to a platinum(0) complex containing a 1,2-bis(diphenylphosphino)ethane ligand (dppe). In these dinuclear complexes, two competitive organic group transfers took place simultaneously and the reaction selectivity was controlled by additives such as olefins, carbon monoxide, and phosphine lignads.

Results and discussion

Synthesis and characterization of alkyl- (or phenyl-) platinum–platinum complexes

Treatment of the zero-valent platinum complex, Pt(η^2-CH_2=CHPh)(dppe) (**1**) with carbonyl(η^5-cyclopentadienyl)methylplatinum, PtMe(η^5-Cp)(CO) (**2a**) (4), prepared by treatment of PtMe(η^1-Cp)(cod) with CO, smoothly gave methyldiplatinum complex, (dppe)MePt–Pt(η^5-Cp)(CO) (**3a**), in 62% yield in benzene at room temperature (eq. [1]). Similar reactions with other organoplatinum complexes PtR(η^5-Cp)(CO) (R = Et (**2b**), CH_2CMe_3 (**2c**), Ph (**2d**)) also gave the corresponding organodiplatinum complexes, (dppe)RPt–Pt(η^5-Cp)(CO) (R = Et (**3b**), CH_2CMe_3 (**3c**), Ph (**3d**)). These complexes **3a**–**3d** were characterized by ^{1}H and ^{31}P{^{1}H} NMR and IR spectroscopies and elemental analysis. Single crystals of complexes **3a** and **3c** suitable for X-ray structure analysis were obtained by recrystallization from Et_2O or toluene–hexane. Figure 1 depicts an ORTEP drawing of **3a** and **3c** showing the formation of both Pt–Pt and C–Pt bonds by oxidative addition of the Pt–C bond to Pt(0). The Pt(1)–Pt(2) bond distances for **3a** and **3c** are 2.6415(10) and 2.6489(5) Å, respectively. The Pt(1)–C(1) bond distances for **3c** (2.136(9) Å) is slightly longer than for **3a** (1.98(2) Å). The geometry of the Pt metal coordinated by 1,2-bis(diphenylphosphino)ethane is essentially square planar, where the Pt(η^5-Cp)(CO) moiety and the methyl or neopentyl group are placed cis to each other. This square planar geometry is consistent with the d^8 configuration of Pt(II). The carbonyl and Cp ligands in these complexes lie orthogonal to the coordination plane of the Pt metal bearing a 1,2-bis(diphenylphosphino)ethane ligand. The Pt(2)–C(33)–O(1) [177(2)°] linkage in **3a** and Pt(2)–C(37)–O(1) [176.5(8)°] linkage in **3c** are linear compared with the corresponding linkages of heterodinuclear complexes, suggesting that these carbonyl ligands have no bridging interaction with Pt metal coordinated with dppe.

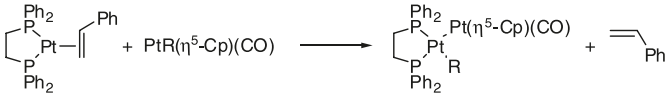

1a

[1]

R = Me (**2a**)
Et (**2b**)
CH_2CMe_3 (**2c**)
Ph (**2d**)

R = Me (**3a**) (62%)
Et (**3b**) (68%)
CH_2CMe_3 (**3c**) (64%)
Ph (**3d**) (72%)

The IR spectra of **3a**–**3d** show a strong ν(CO) band at ca. 1940 cm^{-1}. The value is considerably lower than that for the known Pt(II) complex PtMe(η^5-Cp)(CO) (2036 cm^{-1}) (3*a*), suggesting strong π back-donation from the Pt metal. From these data, the actual oxidation state of the Pt metal with dppe and an organic group and of the Pt metal with CO and Cp ligands were calculated to be close to two and zero, respectively, though the formal oxidation state of each is one.

Fig. 1. Molecular structures of (dppe)MePt–Pt(η^5-Cp)(CO) (**3a**) and (dppe)(Me_3CCH_2)Pt–Pt(η^5-Cp)(CO) (**3c**). All hydrogen atoms and solvent are omitted for clarity. Elipsoids represent 50% probability. Selected bond distances (Å) for **3a**: Pt(1)–Pt(2) 2.6415(10), Pt(1)–P(1) 2.210(5), Pt(1)–P(2) 2.290(5), Pt(1)–C(1) 1.98(2), Pt(2)–C(33) 1.73(2), C(33)–O(1) 1.20(3). Selected bond angles (°) for **3a**: Pt(2)–Pt(1)–C(1) 86.8(6), P(1)–Pt(1)–P(2) 86.51(18), P(1)–Pt(1)–C(1) 91.3(7), Pt(2)–Pt(1)–P(2) 95.50(13), Pt(2)–C(33)–O(1) 177(2). Selected bond distances (Å) for **3c**: Pt(1)–Pt(2) 2.6489(5), Pt(1)–P(1) 2.221(2), Pt(1)–P(2) 2.298(2), Pt(1)–C(1) 2.136(9), Pt(2)–C(37) 1.777(10), C(37)–O(1) 1.151(12). Selected bond angles (°) for **3c**: Pt(2)–Pt(1)–C(1) 91.6(2), P(1)–Pt(1)–P(2) 85.63(8), P(1)–Pt(1)–C(1) 88.9(2), Pt(2)–Pt(1)–P(2) 93.77(6), Pt(2)–C(37)–O(1) 176.5(8).

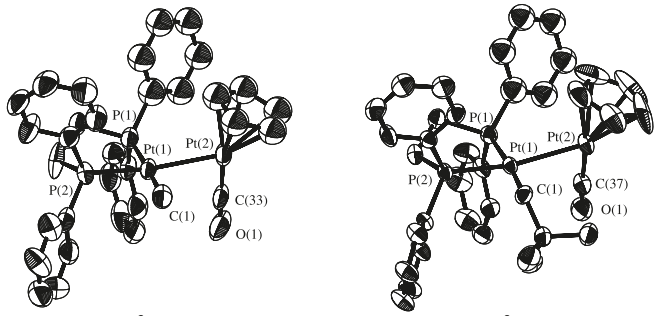

The ^{31}P{^{1}H} NMR spectrum of **3a** shows two sets of resonances centered at δ 43.0 and 51.1, both of which are accompanied by two ^{195}Pt satellite peaks. No apparent P–P coupling is observed. The P–Pt coupling constants for the resonance at δ 43.0 (3377 and 950 Hz) are smaller than those for the resonance at δ 51.1 (1733 and 125 Hz), suggesting that the former signal is assigned to the P nucleus *trans* to the methyl ligand and the latter *trans* to Pt, since the *trans* influence of the methyl is larger than that of Pt metal (2*b*, 2*c*, 2*d*). A large second coupling constant (950 Hz) for the resonance at δ 51.1 is also consistent with the *trans* configuration between this P and Pt nuclei. ^{31}P{^{1}H} NMR spectra of complexes **3b**–**3d** showed similar patterns. All observations of two ^{195}Pt satellites in ^{31}P nuclei are consistent with the dinuclear structure with a Pt–Pt bond.

The ^{1}H NMR spectrum of **3a** in benzene-d_6 shows a double doublet with ^{195}Pt satellite for the methyl group, owing to couplings with two different P nuclei at room temperature. Cp protons in **3a** appear as a singlet at δ 5.58. The *ortho* protons of Ph in the dppe ligand are observed as two separated sets of multiplets at δ 7.7 and 7.9, each with 4H intensity. Inequivalency of the two phosphorus nuclei in dppe of **3a** is consistent with the structural result. The phenyl analogue **3d** also show similar results. On the other hand, the ethyl complex **3b** shows broad signals for the ethyl and the *ortho* protons of phenyl in the dppe ligand at room temperature. When the temperature is raised to 70 °C, clear signals consisting of a double quartet (2H) and a double triplet (3H) with Pt satellites owing to the ethyl ligand and two multiplets (4H each) for the *ortho* protons are observed. The

© 2008 NRC Canada

Scheme 1. Rotation of platinum–platinum bond.

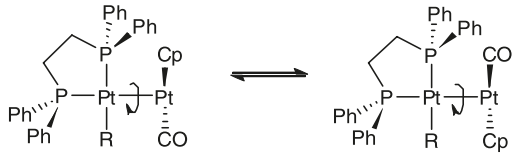

results indicate that these complexes involve some fluxionality in solution without Pt–P bond rupture. When these complexes in acetone-d_6 are cooled to –40 °C, two multiplets for the *ortho* protons further split to four multiplets with 2H intensity, though unfortunately the ethyl signals are not well resolved. The result suggests that four aryl groups in dppe become magnetically inequivalent at low temperature. Such a situation becomes more clear for the ^{1}H NMR of neopentyl derivative **3c**: four separated *ortho* protons are observed at room temperature. Furthermore, methylene signals owing to the neopentyl group appear as an AB quartet that further splits into double doublets by coupling with two P nuclei with Pt satellites. Observation of the diastereotopic methylene signals indicates that **3c** is stereochemically rigid as shown by X-ray structure analysis, where CO and Cp ligands are fixed above and below the square planar coordination plane of Pt metal with dppe ligand. Therefore the observed fluxionality in **3a** and **3b** is considered to be due to the rotation of the Pt–Pt bond without any bond dissociation (Scheme 1). The qualitative ease of the Pt–Pt bond rotation decreases in the order **3a**≈**3d** > **3b** > **3c**, reflecting the increase of steric bulkiness of the alkyl ligands. The importance of steric bulk in the dinuclear system is also previously reported in the structural study of alkyl, acyl, and hydrido heterodinuclear complexes (2*r*).

To clarify the polarization of the platinum–platinum bond, reactions of methyl and ethylplatinum–platinum complexes with an electrophile were investigated (eq. [2]). The reaction of methylplatinum–platinum complex **3a** with methyl iodide in acetone-d_6 gave PtMe(η^5-Cp)(CO) (**1a**, 86%) and PtMeI(dppe) (**4a**, 95%) but no PtI(η^5-Cp)(CO) or $PtMe_2$(dppe) (eq. [2]). A similar result was obtained for the reaction of **3a** with EtI and **3b** with MeI. These results indicate that Pt with dppe is essentially electrophilic and Pt with CO is nucleophilic in both cases, being consistent with Pt(II)–Pt(0) formalism, and also with IR and X-ray structural data.

[2]

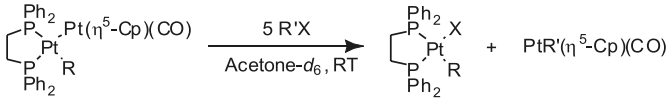

R = Me (**3a**)	R'X = MeI	8 h	95% (**4a**)	86% (**1a**)
	EtI	55 h	98% (**4a**)	56% (**1b**)
Et (**3b**)	MeI	25 h	96% (**4b**)	80% (**1a**)

Controlled organic group transfer along the platinum–platinum bond

Thermolysis of 3a–3d

Thermolysis of organodiplatinum complexes **3a**–**3d** (Scheme 2) was carried out and the results are summarized in Table 1. Heating of methyl complex **3a** in C_6D_6 at 70 °C

Scheme 2. Controlled organic group transfer along platinum–platinum bond.

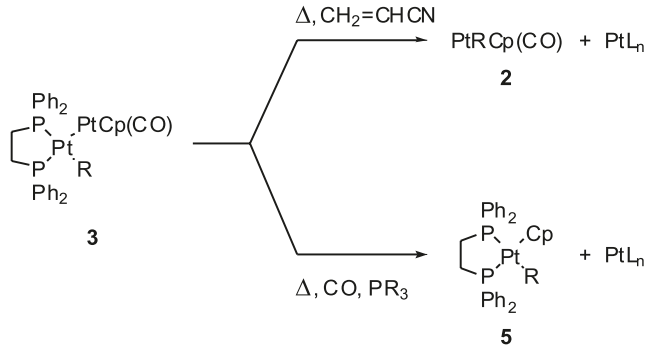

led to the migration of the Cp ligand to the other Pt atom giving PtMe(η^1-Cp)(dppe) (**5a**) in 55% yield with a small amount of PtMe(η^5-Cp)(CO) (**2a**) (Table 1, entry 1). The progress of the thermolysis of **3a** monitored by ^{1}H NMR indicated that **2a** and **5a** were formed simultaneously in the same ratio. Thermolysis of ethyl complex **3b** at 70 °C also gave PtEt(η^1-Cp)(dppe) (30%) accompanied by the evolution of ethylene (59%) (entry 2). Only a trace of **2b** was detected. In contrast, heating of neopentyl derivative **3c** in C_6D_6 at 70 °C led to the migration of the neopentyl ligand to the other Pt atom giving Pt(CH_2CMe_3)(η^5-Cp)(CO) (**2c**) (Table 1, entry 3) preferentially. Phenyl derivative **3d** was relatively stable and when thermolysis of **3d** was performed under similar conditions, PtPh(η^1-Cp)(dppe) (**5d**) was formed in lower yield and no **2d** was detected (entry 4). These results show that reductive elimination occurs at both Pt metals giving PtR(η^5-Cp)(CO) and PtR(η^1-Cp)(dppe). **3c** favors the organic transfer from square planar Pt but Cp ligand selectively moves to square planar Pt in the cases of **3a**, **3b**, and **3d**. In other words, reductive elimination at square planer Pt is preferred for the former, but that of Pt and Cp at the Pt(CO) site for the latter. These results are in sharp contrast with the previously reported thermal reductive elimination of the alkyl or aryl and transition metal at Pt in L_2RPt–M(η^5-Cp)L_n giving only MR(η^5-Cp)L_n (2*a*, 2*c*, 2*d*, 2*e*), in which β-hydrogen elimination of ethylplatinum–molybdenum (or –tungsten) complexes (2*d*, 2*i*) and no Cp transfer were observed. Unfortunately, corresponding Pt(0) products were not identified. The stronger electron-donating property of the neopentyl ligand may accelerate the reductive elimination (5). The origin of the present selectivity difference of organic group transfer is not clear at present and further detailed kinetic and theoretical studies are required.

Organic group transfer assisted by olefins, carbon monoxide, or phosphine ligands

When the organodiplatinum complexes **3a**–**3d** were treated with olefins, CO, and tertiary phosphine ligands, organic transfer reactions were enhanced. Results of the reactions at room temperature are also summarized in Table 1.

Treatment of **3a** with 5 equiv. of acrylonitrile in C_6D_6 gave **2a** (35%) and **5a** (19%) in 2 h, showing acceleration of methyl transfer at the square planar platinum site (Table 1, entry 5) (6). Reaction with methyl acrylate also produced a similar result, though the rate was relatively slow (Table 1, entry 6). Styrene showed no large effect on reductive elimi-

© 2008 NRC Canada

Table 1. Organic group transfer of organoplatinum–platinum complex with a 1,2-bis(diphenylphosphino)ethane ligand.

						Yield (%)	
Entry	Complex	Additive	Temp.	Time	Conv. (%)	**2**	**5**
1	**3a**	None	70 °C	25 h	83	7	55
2[a]	**3b**	None	70 °C	25 h	92	Trace	43
3	**3c**	None	70 °C	6 h	74	47	Trace
4	**3d**	None	70 °C	24 h	53	0	18
5	**3a**	CH_2=CHCN (5 eq)	RT	2 h	65	35	19
6	**3a**	CH_2=CH(CO_2Me) (5 eq)	RT	24 h	50	21	19
7	**3a**	CH_2=CHPh (5 eq)	RT	24 h	16	2	10
8	**3b**	CH_2=CHCN (5 eq)	RT	22 h	55	37	13
9	**3c**	CH_2=CHCN (5 eq)	RT	24 h	24	15	4
10	**3d**	CH_2=CHCN (5 eq)	RT	1.5 h	56	56	1
11	**3a**	CO (1 atm)	RT	Instant	100	13	59
12	**3c**	CO (1 atm)	RT	4 h	76	20	41
13	**3d**	CO (1 atm)	RT	2 h	97	25	67
14	**3a**	dppe (5 eq)	RT	Instant	0	0	52
15	**3a**	PPh_3 (10 eq)	RT	Instant	2	0	94

Note: Reactions were performed in C_6D_6.
[a]Evolution of ethylene (59%).

Scheme 3. A possible mechanism for controlled organic group transfer along platinum–platinum bond.

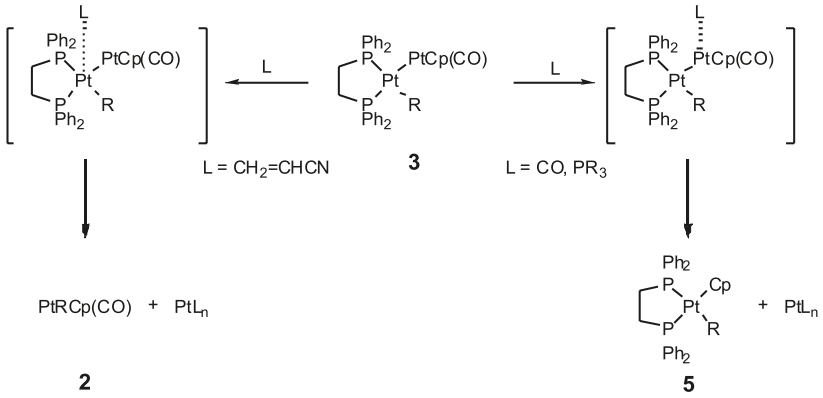

nation (Table 1, entry 7). A similar trend was also observed in the reactions of **3b** and **3d** (Table 1, entries 8 and 10). No significant effect was observed for the neopentyl derivative **3c** (Table 1, entry 9). These results can be reasonably understood by the coordination of these substituted olefins to the square planar platinum atom enhancing the reductive elimination of PtR(η^5-Cp)(CO) complexes, similar to the organic transfer of heterodinuclear organoplatinum complexes assisted by electron deficient olefins, which was previously reported by us (2*a*, 2*c*, 2*d*, 2*e*). Coordination of electron-deficient olefins to the square planar platinum complexes enhances the reductive elimination. Therefore the relatively electron-rich styrene showed no significant effect. The low acceleration by added acrylonitrile to the neopentyl complex **3c** could be due to the fact that the sterically bulky neopentyl ligand discourages coordination. The importance of steric bulkiness of the neopentyl ligand is also discussed in the NMR study (vide supra).

In contrast, reaction of a C_6D_6 solution of **3a**, **3c**, **3d** with CO (1 atm) at room temperature afforded PtR(η^1-Cp)(dppe) (R = Me (**5a**), CH_2CMe_3 (**5c**), Ph (**5d**)) as the major product (Table 1, entries 11–13). When **3a** was treated with a tertiary phosphine ligand such as 1,2-bis(diphenylphosphino)ethane (dppe) or PPh_3 in C_6D_6 at room temperature, selective Cp group transfer took place to give only PtMe(η^1-Cp)(dppe) (**5a**) in high yield (Table 1, entries 14, 15).

Possible mechanism for controlled organic group transfer along platinum–platinum bond

As shown in Scheme 3, competitive organic group transfer reactions along the Pt–Pt bond in organodiplatinum complexes (dppe)RPt–Pt(η^5-Cp)(CO) take place to give PtR(η^5-Cp)(CO) and PtR(η^1-Cp)(dppe) on thermolysis. The reaction was enhanced by the coordination of additives such as olefin, CO, and tertiary phosphine ligands. The selectivity of the reaction is affected by the coordination site of the added substrate. Specifically, the organic group transfer at square planar platinum is favored by interaction with electron-deficient olefin, whereas Cp group transfer from Pt(η^5-Cp)(CO) to PtR(dppe) is enhanced by tertiary phosphine ligands or carbon monoxide. Probably, these ligands favor the

© 2008 NRC Canada

coordination at the Pt(η^5-Cp)(CO) site to enhance the Cp migration, while preferred coordination of π-accepting ligands such as acrylonitrile to the Pt metal with an electron-donating dppe ligand gives PtR(η^5-Cp)(CO). The acceleration effect of added olefin on the alkyl transfer reaction is well established in the reductive elimination of square planar diorganonickel (or palladium) complexes (7) and heterodinuclear organometallic complexes containing platinum (2*a*, 2*c*, 2*d*). The observed selective reaction caused by ligands could be due to the thermodynamic stability of products. For example, reductive elimination at the (dppe)Pt site favors Pt(0) product such as Pt(olefin)(dppe) rather than a putative complex Pt(olefin)$(CO)_n$ with ligands with all strong π-back-donation. Further detailed study including a theoretical approach is required to clarify the origin of this selectivity.

Experimental

General

All manipulations were carried out under dry nitrogen or argon atmosphere using standard Schlenk and vacuum line techniques. Solvents (benzene, toluene, hexane, and THF) were refluxed over and distilled from sodium benzophenone ketyl under N_2. Deuterated solvents were degassed by three freeze-pump-thaw cycles and then vacuum-transferred from appropriate drying agents (C_6D_6 from sodium wire, acetone-d_6 from drierite). The zero-valent platinum complex, Pt(η^2-CH_2=CHPh)(dppe) was prepared by the reaction of PtI_2(dppe) with $NaBH_4$ in the presence of a large excess of the styrene according to the analogous literature method (2*k*). PtR(η^1-Cp)(cod) were prepared by the reaction of PtRCl(cod) and NaCp according to the analogous literature methods with modifications (3). PtR(η^1-Cp)(dppe) (R = Me (**5a**), Et (**5b**), CH_2CMe_3 (**5d**), Ph (**5e**)) were prepared for assignment, according to the analogous literature methods (8). NMR spectra were recorded on a JEOL LA-300 spectrometer (300.4 MHz for ^{1}H, 121.6 MHz for ^{31}P). Chemical shifts were reported in ppm downfield from TMS for ^{1}H and from 85% H_3PO_4 in D_2O for ^{31}P. IR spectra were recorded on a JASCO FT–IR-410 spectrometer using KBr disks. Elemental analyses were carried out with a Perkin-Elmer 2400 series II CHN analyzer.

Synthesis of organoplatinum–platinum complexes

As a typical procedure, the oxidative addition of methyl(η^5-cyclopentadienyl)(monocarbonyl)platinum complex (**2a**) to the zero-valent platinum complex, Pt(η^2-CH_2=CHPh)(dppe) (**1**) to afford (dppe)MePt–Pt(η^5-Cp)(CO) (**3a**) is described. PtMe(η^5-Cp)(CO) was first prepared by treating PtMe(η^1-Cp)(cod) (69.9 mg, 0.169 mmol) with CO and dissolving it in benzene (3 mL). This was then added to a solution of Pt(η^2-CH_2=CHPh)(dppe) (105.2 mg, 0.1507 mmol) in benzene (10 mL). The reaction mixture was stirred at room temperature for 1 h. After the solution was concentrated under reduced pressure, excess hexane was added to give a yellow powder. The product was filtered, washed with hexane, and dried under vacuum at room temperature. Recrystallization from ether gave yellow crystals (yield: 62%). IR (KBr, cm^{-1}) ν(CO): 1933. ^{1}H NMR (C_6D_6, RT, 300.4 MHz) δ: 1.6–1.8 (m, 4H, dppe CH_2), 1.80 (dd, $^3J_{PH}$ = 7.4, 5.1 Hz, $^2J_{PtH}$ = 64.9 Hz, 3H, PtCH_3), 5.58 (m, 5H, *Cp*), 6.8–7.3 (m, 12H, *m,p-Ph*), 7.66 (m, 4H, *o-Ph*), 7.80 (m, 4H, *o-Ph*). ^{1}H NMR (acetone-d_6, RT, 300.4 MHz) δ: 1.01 (dd, $^3J_{PH}$ = 7.6, 4.9 Hz, $^2J_{PtH}$ = 66.4 Hz, 3H, PtCH_3), 2.15–2.42 (m, 4H, dppe CH_2), 5.25 (m, 5H, *Cp*), 7.40–7.65 (m, 12H, *m,p-Ph*), 7.70–7.95 (m, 8H, *o-Ph*). ^{31}P{^{1}H} NMR (C_6D_6, RT, 121.6 MHz) δ: 41.7 (s, $^1J_{PtP}$ = 3289 Hz, $^2J_{PtP}$ = 1010 Hz), 51.7 (s, $^1J_{PtP}$ = 1702 Hz, $^2J_{PtP}$ = 132 Hz). ^{31}P{^{1}H} NMR (acetone-d_6, RT, 121.6 MHz) δ: 43.0 (s, $^1J_{PtP}$ = 3377 Hz, $^2J_{PtP}$ = 950 Hz), 51.1 (s, $^1J_{PtP}$ = 1733 Hz, $^2J_{PtP}$ = 125 Hz). Anal. calcd. for $C_{39}H_{38}OP_2Pt_2$: C 48.05, H 3.93; found: C 47.69, H 3.99.

(dppe)EtPt–Pt(η^5-Cp)(CO) (3b)

140.3 mg (0.1372 mmol, 73%). IR (KBr, cm^{-1}) ν(CO): 1934. ^{1}H NMR (C_6D_6, 70 °C, 300.4 MHz) δ: 1.55–2.00 (m, 4H, dppe CH_2), 1.56 (dt, $^3J_{PtH}$ = 45.6 Hz, $^2J_{HP}$ = 10.8 Hz, $^3J_{HH}$ = 7.8 Hz, 3H, PtCH$_2$CH_3), 2.62 (dq, $^2J_{PtH}$ = 71.5 Hz, $^2J_{PH}$ = 14.7 Hz, $^2J_{HH}$ = 7.2 Hz, 2H, PtCH_2CH$_3$), 5.61 (m, 5H, *Cp*), 7.02–7.23 (m, 12H, *m,p-Ph*), 7.60–7.87 (m, 8H, *o*-Ph). ^{31}P{^{1}H} NMR (C_6D_6, 70 °C, 121.6 MHz) δ: 42.0 (s, $^1J_{PtP}$ = 3453 Hz, $^2J_{PtP}$ = 977 Hz, $^3J_{PP}$ = 3.6 Hz), 49.3 (s, $^1J_{PtP}$ = 1480 Hz, $^2J_{PtP}$ = 141 Hz, $^3J_{PP}$ = 3.6 Hz). Anal. calcd. for $C_{41}H_{42}OP_2Pt_2$: C 48.72, H 3.79; found: C 49.10, H 4.22.

(dppe)(Me_3CCH_2)Pt–Pt(η^5-Cp)(CO) (3c)

106.5 mg (0.1119 mmol, 64%). IR (KBr, cm^{-1}) ν(CO): 1941. ^{1}H NMR (C_6D_6, RT, 300.4 MHz) δ: 1.28 (s, 9H, CH$_2$CMe_3), 1.4–1.9 (m, 4H, dppe CH_2), 2.75 (td, $^2J_{HH}$ = $^3J_{PH}$ = 11.7 Hz, $^3J_{PH}$ = 8.4 Hz, $^2J_{PtH}$ = 52.3 Hz, 1H, CH_2CMe$_3$), 2.92 (ddd, $^2J_{HH}$ = 11.7 Hz, $^3J_{PH}$ = 7.8, 3.3 Hz, $^2J_{PtH}$ = 72.7 Hz, 1H, CH_2CMe$_3$), 5.56 (m, 5H, *Cp*), 7.0–7.2 (m, 12H, *m*, *p*-Ph), 7.53 (m, 2H, *o*-Ph), 7.63 (m, 2H, *o*-Ph), 7.70 (m, 2H, *o*-Ph), 7.79 (m, 2H, *o*-Ph). ^{31}P{^{1}H} NMR (C_6D_6, RT, 121.6 MHz) δ: 40.7 (d, $^1J_{PtP}$ = 3408 Hz, $^2J_{PtP}$ = 1860 Hz, $^2J_{PP}$ = 3.6 Hz), 50.8 (d, $^1J_{PtP}$ = 1508 Hz, $^2J_{PtP}$ = 175 Hz, $^2J_{PP}$ = 3.6 Hz).

(dppe)PhPt–Pt(η^5-Cp)(CO) (3d)

49.9 g (0.052 mmol, 31%). IR (KBr, cm^{-1}) ν(CO): 1947. ^{1}H NMR (C_6D_6, RT, 300.4 MHz) δ: 1.6–1.8 (m, 4H, dppe CH_2), 5.42 (m, 5H, *Cp*), 6.9–7.3 (m, 15H, *m,p*-Ph, dppe *m*, *p*-Ph), 7.47 (m, 4H, dppe *o*-Ph), 7.68 (t, $^3J_{HH}$ = $^3J_{PH}$ = 7.1 Hz, $^3J_{PtH}$= 45.7 Hz, 2H, *o*-Ph), 7.96 (m, 4H, dppe *o*-Ph). ^{1}H NMR (acetone-d_6, RT, 300.4 MHz) δ: 2.15–2.42 (m, 4H, dppe CH_2), 5.61 (m, 5H, *Cp*), 6.45 (t, $^3J_{HH}$ = 7.4 Hz, 1H, *p*-Ph), 6.67 (td, J_{HH} = 7.4, 1.7 Hz, 2H, *m*-Ph), 7.11 (td, $^3J_{HH}$ = $^3J_{PH}$ = 7.4 Hz, $^3J_{HH}$ = 1.7 Hz, $^3J_{PtH}$= 45.4 Hz, 2H, *o*-Ph), 7.54–7.62 (m, 16H, dppe *o,m,p*-Ph), 7.90–8.05 (m, 4H, dppe *o*-Ph). ^{31}P{^{1}H} NMR (C_6D_6, RT, 121.6 MHz) δ: 37.4 (s, $^1J_{PtP}$ = 3185 Hz, $^2J_{PtP}$ = 995 Hz), 48.2 (s, $^1J_{PtP}$ = 1645 Hz, $^2J_{PtP}$ = 127 Hz). ^{31}P{^{1}H} NMR (acetone-d_6, RT, 121.6 MHz) δ: 43.0 (s, $^1J_{PtP}$ = 3272 Hz, $^2J_{PtP}$ = 960 Hz), 47.6 (s, $^1J_{PtP}$ = 1655 Hz, $^2J_{PtP}$ = 127 Hz).

Reactions with alkyl halide

A typical procedure for **3a** with methyl iodide in acetone-d_6 is given. Acetone-d_6 (0.5 mL) was vacuum-transferred to an NMR tube (5 mmϕ × 180 mm) containing **3a** (5.3 mg, 5.9×10^{-3} mmol), and 1,4-dioxane was added as an internal standard to the solution. Then 1 equivalent of methyl iodide

© 2008 NRC Canada

was introduced into the NMR tube. NMR spectra were periodically measured to follow the reactions. Results are summarized in Table 1.

Thermolysis

A typical procedure for **3a** in C_6D_6 is given. C_6D_6 (0.5 mL) was vacuum-transferred to an NMR tube containing **3a**, and 1,4-dioxane was added as an internal standard to the solution. Then the NMR tube was heated on oil bath. NMR spectra were periodically measured to follow the reactions. Results are summarized in Table 1.

Reactions with olefin or phosphine ligand

A typical procedure for **3a** in C_6D_6 is given. C_6D_6 (0.5 mL) was vacuum-transferred to an NMR tube containing **3a**, and 1,4-dioxane was added as an internal standard to the solution. Then olefin or phosphine ligand was introduced into the NMR tube. NMR spectra were periodically measured to follow the reactions. Results are summarized in Table 1.

Reactions with CO

A typical procedure for **3a** is given. C_6D_6 (0.5 mL) was vacuum-transferred to an NMR tube containing **3a**, and 1,4-dioxane was added as an internal standard to the solution. The solution was degassed by freeze-pump-thaw cycles and CO (0.1 MPa) was introduced. NMR spectra were periodically measured to follow the reaction. Results are summarized in Table 1.

X-ray structure data[3]

The crystallographic data were measured on a Rigaku RASA-7R four-circle diffractometer using Mo Kα (λ = 0.710 69 Å) radiation with a graphite crystal monochromator at –73 °C. A single crystal was selected by means of a polarized microscope and mounted in a capillary tube (GLASS, 0.7 mmϕ), which was sealed by small flame torch, or onto a glass capillary with Paraton N oil. The unit cell dimensions were obtained by a least-squares fit of 20 centered reflections. Intensity data were collected using the ω-2θ technique to a maximum 2θ of 55.0°. The scan rates were 16.0 deg/min. Three standard reflections were monitored in every 150 reflections. Intensities were corrected for Lorentz and polarization effects. The data were processed using the Crystal Structure (9, 10) crystallographic software package. The structure of **3a** and **3c** was solved by Patterson methods (DIRDIF99 PATTY). An absorption correction for **3c** was applied with the program PSI SCAN method. All non-hydrogen atoms were found on difference maps.

(dppe)MePt–Pt(η^5-Cp)(CO) (3a)

For complex **3a**, all non-hydrogen atoms were refined with anisotropic displacement parameters except for one of the phenyl rings of dppe, Cp ring atoms, and the incorporated solvent molecule, which were treated as a fixed group. Crystallographic data: **3a**·Et_2O: $C_{37}H_{42}O_2P_2Pt_2$, FW: 970.83, triclinic. *P*1 (No. 2) *a*: 11.952(7) Å, *b*: 18.217(16) Å, *c*: 8.955(2) Å, α: 101.24(5)°, β: 99.72(3)°, γ: 71.37(7)°. *V*: 1800.1(19) Å^3. *Z*: 2. D_{calcd}: 1.791 g cm^{-3}. 5356 unique reflections with $I > 3\sigma(I)$. R_1: 0.080, wR_2: 0.099.

(dppe)(Me$_3$CCH$_2$)Pt–Pt(η^5-Cp)(CO) (3c)

For complex **3c**, all non-hydrogen atoms were refined with anisotropic displacement parameters except for one of the phenyl rings of dppe and the incorporated solvent molecule. The solvent molecule was refined with isotropic displacement parameters, and one phenyl ring of dppe was treated as a fixed group. Crystallographic data: **3c**·$2C_6H_6$: $C_{49}H_{52}OP_2Pt_2$, FW: 1109.08, monoclinic. $P2_1/n$ (No. 14) *a*: 11.61(7) Å, *b*: 20.43(9) Å, *c*: 18.67(6) Å, β = 91.8(3)°. *V*: 4425.1(346) Å^3. *Z*: 4, D_{calcd}: = 1.665 g·cm^{-3}. 7679 unique reflections with $I > 3\sigma(I)$. R_1: 0.0462, wR_2: 0.0622.

Acknowledgement

This work was financially supported by a Grant-in-Aid for Scientific Research from the Ministry of Education, Sports, Culture, Science, and Technology, Japan.

References

1. (*a*) Metal clusters in chemistry. P. *Edited by* Braunstein, L.A. Oro, and P.R. Raithby. Wiley-VCH, Weinheim, Germany. 1999; (*b*) Catalysis by di- and polynuclear metal cluster complexes. *Edited by* R.D. Adams and F.A. Cotton. Wiley-VCH, New York. 1998; (*c*) M.J. Chetcuti. *In* Comprehensive organometallic chemistry II. Vol. 10. *Edited by* R.D. Adams. Pergamon Press, Oxford, UK. 1995; (*d*) The chemistry of metal cluster complexes. *Edited by* D.F. Shriver, H. Kaesz, and R.D. Adams. VCH, New York. 1990.
2. (*a*) S. Komiya and I. Endo. Chem. Lett. 1709 (1988); (*b*) K. Miki, N. Kasai, I. Endo, and S. Komiya. Bull. Chem. Soc. Jpn. **62**, 4033 (1989); (*c*) A. Fukuoka, T. Sadashima, I. Endo, N. Ohashi, Y. Kambara, T. Sugiura, and S. Komiya. Organometallics, **13**, 4033 (1994); (*d*) A. Fukuoka, T. Sadashima, T. Sugiura, X. Wu, Y. Mizuho, and S. Komiya. J. Organomet. Chem. **473**, 139 (1994); (*e*) S. Komiya, I. Endo, A. Fukuoka, and M. Hirano. Trends Organomet. Chem. **1**, 223 (1994); (*f*) A. Fukuoka, T. Sugiura, T. Yasuda, T. Taguchi, M. Hirano, and S. Komiya. Chem. Lett. 329 (1997); (*g*) A. Fukuoka, S. Fukagawa, M. Hirano, and S. Komiya. Chem. Lett. 377 (1997); (*h*) T. Yasuda, A. Fukuoka, M. Hirano, and S. Komiya. Chem. Lett. 29 (1998); (*i*) S. Komiya, T. Yasuda, A. Fukuoka, and M. Hirano. J. Mol. Cat. A **159**, 63 (2000); (*j*) S. Komiya, S. Muroi, M. Furuya, and M. Hirano. J. Am. Chem. Soc. **122**, 170 (2000); (*k*) N. Komine, H. Hoh, M. Hirano, and S. Komiya. Organometallics, **19**, 5251 (2000); (*l*) A. Fukuoka, S. Fukagawa, M. Hirano, N. Koga, and S. Komiya. Organometallics, **20**, 2065 (2001); (*m*) M. Furuya, S. Tsutsuminai, H. Nagasawa, N. Komine, M. Hirano, and S. Komiya. Chem. Commun. (Cambridge), 2046 (2003); (*n*) S. Tsutsuminai, N. Komine, M. Hirano, and S. Komiya.

[3] Supplementary data for this article are available on the journal Web site (canjchem.nrc.ca) or may be purchased from the Depository of Unpublished Data, Document Delivery, CISTI, National Research Council Canada, Ottawa, ON K1A 0R6, Canada. DUD 3798. For more information on obtaining material refer to cisti-icist.nrc-cnrc.gc.ca/cms/unpub_e.shtml. CCDC 683196 and 683197 contain the crystallographic data for this manuscript. These data can be obtained, free of charge, via www.ccdc.cam.ac.uk/conts/retrieving.html (or from the Cambridge Crystallographic Data Centre, 12 Union Road, Cambridge CB2 1EZ, UK; fax +44 1223 336033; or deposit@ccdc.cam.ac.uk).

© 2008 NRC Canada

Organometallics, **22**, 4238 (2003); (*o*) S. Tsutsuminai, N. Komine, M. Hirano, and S. Komiya. Organometallics, **23**, 44 (2004); (*p*) N. Komine, S. Tanaka, S. Tsutsuminai, Y. Akahane, M. Hirano, and S. Komiya. Chem. Lett. **2004**, 33, 858; (*q*) A. Kuramoto, K. Nakanishi, T. Kawabata, N. Komine, M. Hirano, and S. Komiya. Organometallics, **25**, 311 (2006); (*r*) N. Komine, S. Tsutsuminai, H. Hoh, T. Yasuda, M. Hirano, and S. Komiya. Inorg. Chem. Acta **359**, 3699 (2006); (*s*) S. Tanaka, H. Hoh, Y. Akahane, S. Tsutsuminai, N. Komine, M. Hirano, and S. Komiya. J. Organomet. Chem. **692**, 26 (2007); (*t*) N. Komine, S. Tsutsuminai, M. Hirano, and S. Komiya. J. Organomet. Chem. **692**, 4486 (2007); (*u*) N. Komine, T. Hirota, M. Hirano, and S. Komiya. Organometallics, **27**, 2145 (2008).

3. (*a*) J. Fornies, F. Martinez, R. Navarro, M.C. Frias, and R. Usón. Inorg. Chimica Acta, **132**, 217 (1987); (*b*) H. Jun and R.J. Angelici. Organometallics, **13**, 2454 (1994); (*c*) E. Alonso, J. Casas, F.A. Cotton, X. Feng, J. Forniés, C. Fortuño, and M. Tomas. Inorg. Chem. **38**, 5034 (1999); (*d*) S. Cristofani, P. Leoni, M. Pasquali, F. Eisentraeger, and A. Albinati. Organometallics, **19**, 4589 (2000); (*e*) J. Forniés, P. Espinet, C. Fortuño, M. Tomas, and R. Usón. J. Chem. Soc. Dalton Trans. 1583 (1989).
4. (*a*) H.C. Clark and A. Shaver. Can. J. Chem. **54**, 2068 (1976); (*b*) G.A. Anderson, Organometallics, **5**, 1903 (1986).
5. (*a*) K. Tatsumi, R. Hoffmann, A. Yamamoto, and J.K. Stille. Bull. Chem. Soc. Jpn. **54**, 1857 (1981); (*b*) J.J. Low and W.A. Goddard III. J. Am. Chem. Soc. **108**, 6115 (1986); (*c*) J.J. Low and W.A. Goddard III. Organometallics, **5**, 609 (1986).
6. Acetonitrile (5 equiv.) showed no effect on reductive elimination; therefore the reaction was enhanced by coordination of the C=C bond of acrylonitrile.
7. (*a*) T. Yamamoto, A. Yamamoto, and S. Ikeda. J. Am. Chem. Soc. **93**, 3350 (1971); (*b*) T. Yamamoto, A. Yamamoto, and S. Ikeda. J. Am. Chem. Soc. **93**, 3360 (1971); (*c*) J. Lau and R. Sustmann. Tetrahedron Lett. **26**, 4907 (1985); (*d*) R. Sustmann and J. Lau. Chem. Ber. **119**, 2531 (1986).
8. (*a*) T.G. Appleton and M.A. Bennett. Inorg. Chem. **17**, 738 (1978); (*b*) G. K. Anderson. Organometallics, **5**, 1903 (1986).
9. CrystalStructure [computer program]. Version 3.8.0. Rigakuand Rigaku/MSC, The Woodlands, Tex., USA. 2000–2007.
10. J.R. Carruthers, J.S. Rollett, P.W. Betteridge, D. Kinna, L. Pearce, A. Larsen, and E. Gabe. CRYSTALS, Issue 11 [computer program]. Chemical Crystallography Laboratory, Oxford, UK. 1999.

© 2008 NRC Canada

Reactivity of $IrCl(PPh_3)_3$ with diphenylacetylene — A direct route to 1-iridaindene[1]

Joyanta Choudhury, Sanjay Pratihar, Arnab Kumar Maity, and Sujit Roy

Abstract: The 1-iridaindene complex, $Ir[C_8H_5(Ph\text{-}2)]Cl(PPh_3)_2$ (**2**), has been prepared from the reaction of $IrCl(PPh_3)_3$ with PhC≡CPh by a novel direct cycloiridation reaction. A plausible mechanistic pathway has been suggested involving π-coordination assisted *ortho*- C–H activation and subsequent alkyne hydroiridation reaction to provide the five-member iridacycle.

Key words: iridium, diphenylacetylene, C–H activation, cyclometallation, metallacycle.

Résumé : On a préparé le complexe du 1-iridaindène, $Ir[C_8H_5(ph\text{-}2)]Cl(PPh_3)_2$ (**2**), par réaction du $IrCl(PPh_3)_3$ avec le PhC≡CPh par une nouvelle réaction de cycloiridation directe. On propose une voie mécanistique plausible impliquant une activation du C–H en *ortho* qui serait assistée par une coordination π et qui serait suivie par une réaction d'hydroiridation de l'alcyne conduisant à la formation de l'iridacycle à cinq chaînons.

Mots-clés : iridium, diphénylacétylène, activation d'une liaison C–H, cyclométallation, métallacycle.

[Traduit par la Rédaction]

Introduction

Metallacycles are important synthons as well as intermediates in many catalytic organic and organometallic reactions (1–12). Iridaindene motifs can be viewed as metallacyclopentadienes that are intermediates in metal-mediated [2+2+2] cyclotrimerization of alkynes to provide aromatic six-membered rings (13–18). There are also examples of [2+2+1] cyclotrimerization reactions with the intermediacy of metallacyclopentadienes (19–25). Moreover, the metallacyclopentadiene complexes are utilized for the synthesis of metallabenzenes, which are interesting structural units, compared with simple aromatics (26–28). To our knowledge, a direct and unassisted route for the preparation of such metallacycles by the activation of organic precursors with appropriate metal complexes is hitherto unknown. The more common routes involve (*i*) an indirect transmetallation method, which commonly uses organomercury compounds and (*ii*) carbon monoxide assisted cyclocarbonylation using alkynes or allenes leading to metallacyclopentadienones.

With specific reference to iridium, an iridaindene complex $Ir[C_8H_5(Ph\text{-}2)](C_5H_5)(P^iPr_3)$ was prepared earlier from $Ir(PhC{\equiv}CPh)(C_5H_5)(P^iPr_3)$ via the formation of a vinyl complex $Ir(PhC{=}CHPh)(OCOCF_3)(C_5H_5)(P^iPr_3)$ by CF_3COOH and subsequent reaction with NH_4PF_6 in methanol (29). Recently, Wright and co-workers (30) reported a transmetallation route for the synthesis of a substituted 1-iridaindene $Ir[C_8H_5(Ph\text{-}3)]Cl(PPh_3)_2$ (**1**) from the corresponding organomercury compound $Hg(CH{=}CPh_2)_2$ and $IrHCl_2(PPh_3)_3$ (Scheme 1*a*). Earlier, they isolated **1** as a side product from the reaction of $Hg(CH{=}CPh_2)_2$ and $IrCl(CS)(PPh_3)_2$ in only 20% yield (Scheme 1*b*) (31).

Our recent interest in iridium chemistry, particularly on the activation and coupling of organic functionalities (32–37) led us to investigate the activation of alkynes. Herein we report the first example of a direct cycloiridation from the reaction of $IrCl(PPh_3)_3$ with PhC≡CPh, leading to a new air-stable 1-iridaindene complex, $Ir[C_8H_5(Ph\text{-}2)]Cl(PPh_3)_2$ (**2**). We also describe the structural characterization of **2** by single crystal X-ray diffraction and propose a plausible mechanism involving C–H activation followed by ring closure.

At this point it should be noted that our result is quite interesting because the 16-electron iridium(I) complex $IrCl(PPh_3)_3$ was reported earlier to react with various alkynes. With terminal alkynes, the oxidative addition products resulted (38). But in the case of diphenylacetylene, the π-complex, $IrCl(PhC{\equiv}CPh)(PPh_3)_2$ (**3**), was reported to be formed (vide ^{1}H NMR and IR) with the substitution of one phosphine ligand (Scheme 2*a*) (38). The complex **3** was also synthesized as yellow crystals by the reaction of $IrCl(N_2)(PPh_3)_2$ with diphenylacetylene (Scheme 2*b*) (39).

Results and discussion

The reaction of $IrCl(PPh_3)_3$ with diphenylacetylene in refluxing benzene was accompanied by a gradual color change from yellow to red, which is noticeable to the naked eye within 4–6 h. Ex-situ UV–vis monitoring of the solution in benzene showed the appearance of a new peak at 510 nm. After reflux for 18 h, evaporation of the solvent in vacuum and subsequent recrystallization of the resulting solid resi-

Received 5 April 2008. Accepted 31 May 2008. Published on the NRC Research Press Web site at canjchem.nrc.ca on 9 September 2008.

J. Choudhury, S. Pratihar, A. Kumar Maity and S. Roy.[2] Organometallics and Catalysis Laboratory, Chemistry Department, Indian Institute of Technology, Kharagpur 721302, India.

[1]This article is part of a Special Issue dedicated to Professor Richard J. Puddephatt.

[2]Corresponding author (e-mail: sroy@chem.iitkgp.ernet.in).

 doi:10.1139/V08-119 © 2008 NRC Canada

Scheme 1.

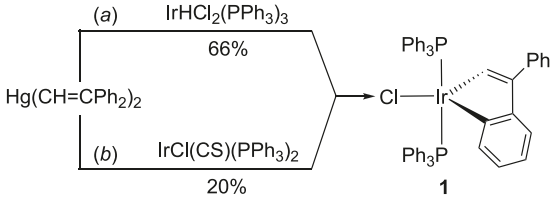

Scheme 2.

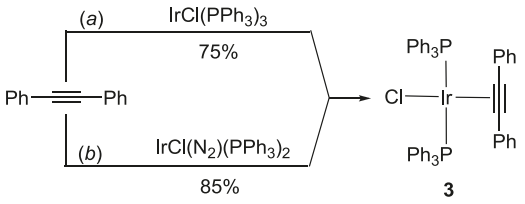

Scheme 3.

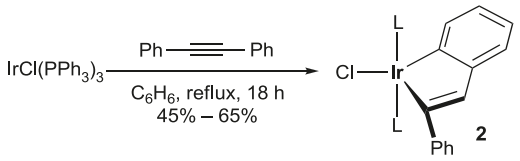

due from chloroform/ethanol or dichloromethane/ethanol afforded **2** as deep red block-like air-stable crystals, the 1st crop yield being 45%–65% (Scheme 3).

The IR spectrum of **2** in KBr discs shows no characteristic peak for coordinated alkyne. The $\nu_{C\equiv C}$ frequency in IR of the known η^2-alkyne complex **3** appears within 1850–1865 cm^{-1} (31, 32). In the ^1H NMR spectrum of **2**, there is a clean signature for the resonances of the iridaindene fragment. The sharp singlet at 5.65 ppm is assigned to the resonance of the C*H* of the five-membered iridacycle. The remaining four protons of the iridaindene six-membered ring resonate as an unresolved doublet of doublet at 5.99 ppm ($J_{H\text{-}H}$= 7.2, 7.6 Hz), a doublet at 6.10 ppm ($J_{H\text{-}H}$ = 7.2 Hz), an apparent triplet at 6.43 ppm (formally doublet of doublet, $J_{H\text{-}H}$ = 7.2, 7.2 Hz), and a doublet at 6.91 ppm ($J_{H\text{-}H}$ = 7.6 Hz), respectively. In the ^{13}C NMR spectrum, the signals of two carbon atoms bonded to iridium, viz., vinyl-*C*(Ph)Ir and aryl-*C*Ir appear as unresolved triplets at 133.9 and 145.9 ppm, respectively. The assignment is made according to a literature comparison (31). The carbon atoms of the iridaindene six-membered ring and phenyl substituent of iridaindene resonate separately as singlets between 120.1 and 133.0 ppm. The ^{31}P NMR signal appears at 22.78 ppm.

A single crystal of **2** suitable for an X-ray diffraction study was obtained by slow diffusion of ethanol into a chloroform solution of the compound at room temperature. The solid-state molecular structure of **2** is illustrated in Fig. 1. The structure contains a $CHCl_3$ molecule as solvent of crystallization. The geometry around the iridium atom is trigonal bipyramidal with axial phosphines (∠P1-Ir01-P2 = 176.73(16)°), while the equatorial plane is occupied by the chlorine atom and the two carbon atoms (∠Cl01-Ir01-C01 = 133.1(5)°, ∠Cl01-Ir01-C08 = 149.6(6)°, ∠C01-Ir01-C08 = 77.3(8)°). The iridaindene ring is found to be planar, while

Fig. 1. ORTEP representation for the molecular structure of **2·CHCl$_3$** (50% thermal ellipsoids). H atoms have been omitted for clarity. Selected bond lengths (Å) and angles (°): Ir(01)–P(1), 2.349(4); Ir(01)–P(2), 2.341(4); Ir(01)–Cl(01), 2.411(4); Ir(01)–C(01), 2.00(2); Ir(01)–C(08), 2.035(15); C(06)–C(07), 1.42(3); C(01)–C(06), 1.40(2); C(07)–C(08), 1.36(3); ∠P(1)-Ir(01)-P(2), 176.73(16); ∠Cl(01)-Ir(01)-C(01), 133.1(5); ∠Cl(01)-Ir(01)-C(08), 149.6(6); ∠C(01)-Ir(01)-C(08), 77.3(8).

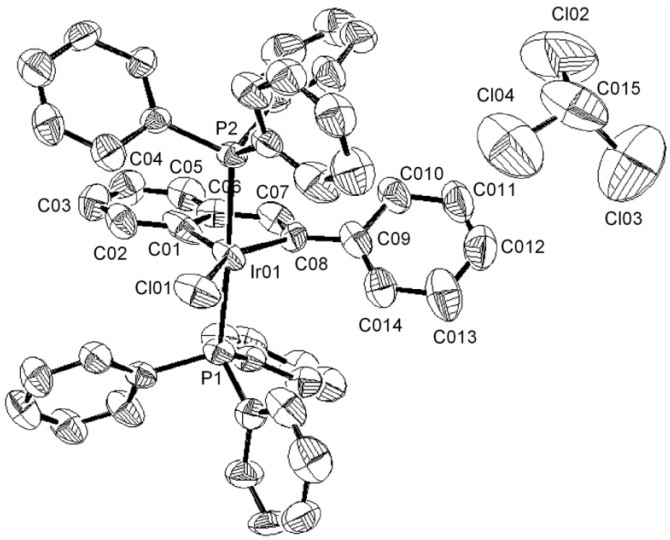

the phenyl group at the 2 position is slightly tilted away from the plane. In the five-membered iridacycle, the two Ir–C bond lengths are 2.00(2) and 2.035(15) Å, which signify some degree of multiple bond nature instead of single bond character. The other three C–C bond lengths within this ring are 1.42(3) Å (C06–C07), 1.40(2) Å (C01–C06), and 1.36(3) Å (C07–C08), indicating little delocalization within the ring. The two triphenylphosphine ligands are mutually trans with Ir–P distances of 2.349(4) and 2.341(4) Å. The Ir–Cl distance is 2.411(4) Å.

To gain some insight into the plausible mechanistic pathway of this cycloiridation process, the aliquots from a 1:1 reaction mixture of $IrCl(PPh_3)_3$ and PhC≡CPh in C_6D_6 at 30, 60, and 90 °C (oil-bath temperature) were subjected to ^1H NMR spectral analysis. The formation of complex **2** was observed only under reflux conditions, as revealed from the appearance of new and characteristic peaks at 5.50, 5.84, 5.98, 6.25, and 6.37 ppm due to the iridaindene fragment. These characteristic peaks were observed at slightly downfield region in $CDCl_3$ solution of **2** (see the Experimental section). The temperature effect suggests that sufficient thermal energy was required for the C–H activation–cycloiridation to take place.

A plausible route for the formation of **2** is suggested in Scheme 4, invoking prior dissociation of a phosphine ligand from $IrCl(PPh_3)_3$ in solution, followed by the π coordination of the alkyne ligand forming the complex **A**. This proximal π-alkyne coordination in **A** adopts one of the alkyne phenyl rings, such that the iridium center can access the *ortho* C–H bond for the purpose of orthometallation. Though alkyne is less well-known to serve such a role of tethering for orthometallation, compared with other donor groups such as carbonyl, halide, or amine (40, 41), recently Hill et al. (42)

© 2008 NRC Canada

Scheme 4.

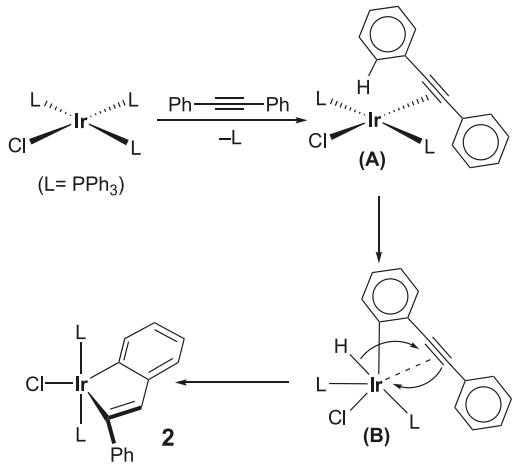

Scheme 5.

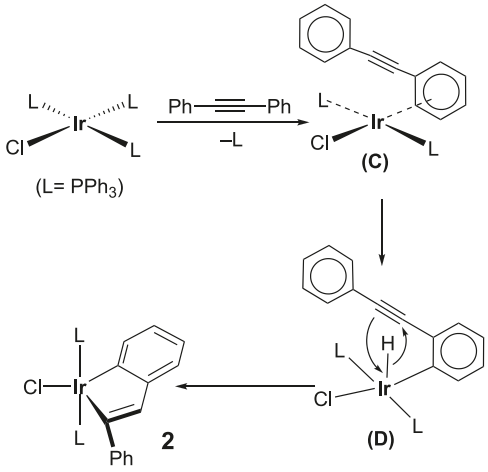

proposed such a phenomenon during the formation of a ruthenaindenone complex. Accordingly, in our proposal the iridium-hydride intermediate **B** resulting from the *ortho* C–H activation then undergoes alkyne hydroiridation to generate the iridacycle **2**. At this stage we cannot rule out another alternative mechanism (Scheme 5), involving the η^2 alkyne as dead-end, with the coordination of iridium to phenyl group leading to the hypothetical intermediate **C**. The latter, upon *ortho* C–H insertion, would produce intermediate **D**, which subsequently converts to the iridacycle **2**. Complexes featuring the binding of a phenyl group of diphenylacetylene to the metal in a η^2- or η^6-fashion (as in intermediate **C**, vide Scheme 5) have precedents in the literature. Examples from late transition metal complexes include $[Os(NH_3)_5(\eta^2\text{-}C_6H_5C{\equiv}CPh)](OTf)_2$ (43) and $[CpRu(\eta^6\text{-}C_6H_5C{\equiv}CPh)](OTf)$ (44). Two examples of η^6-bound diphenylacetylene complexes of early transition metals are $[(CO)_3Cr(\eta^6\text{-}C_6H_5C{\equiv}CPh)]$ (45) and $[(CO)_3Mo(\eta^6\text{-}C_6H_5C{\equiv}CPh)]$ (46). Recently, Legzdins and co-workers reported the formation of tungsten complexes of the type **D** having a pendent dead η^2-alkyne moiety (40). The observation of selective *ortho* C–H activation may be due to the driving force of the subsequent ring-closure reaction to a stable product, whereas the insertion into *meta* or *para* C–H bonds would be reversible.

The possibility of catalysis in the presence of traces of acid impurity (29) in our reaction mixture was also considered. We ruled out this possibility because even in the presence of 1 equiv. of Na_2CO_3, the reaction of $IrCl(PPh_3)_3$ with diphenylacetylene proceeded well, leading to the formation of the desired iridacycle **2**.

In summary, we have demonstrated here a direct cycloiridation reaction leading to an iridaindene molecule that is poised towards further functionalization of the activated indene moiety to useful organic end-product(s). A plausible mechanistic pathway has also been suggested involving π-coordination assisted *ortho* C–H activation and subsequent alkyne hydroiridation reaction to provide the five-membered iridacycle. Work is underway to explore the generality of the reaction, the reactivity of the iridacycle, and deducing the mechanism.

Experimental

General

All preparations and manipulations have been performed under a dry, oxygen-free argon atmosphere using standard vacuum lines and Schlenk techniques. All solvents have been dried and distilled by standard methods and previously deoxygenated in the vacuum line. ^1H (400 MHz), ^{13}C NMR (100 MHz), and ^{31}P NMR (162 MHz) spectra were recorded on Bruker Avance II 400 MHz spectrometer at 300 K. Tetramethylsilane was used as internal reference for ^1H and ^{13}C, while H_3PO_4 was used as external reference for ^{31}P NMR. FT-IR (4000-500 cm^{-1}; using KBr pellets) spectra were obtained using a PerkinElmer FTIR Spectrometer (Spectrum RX-I). UV–vis spectra were recorded in a Chemito Spectroscan UV 2600 spectrophotometer using HPLC-grade benzene. Elemental analyses were performed on PerkinElmer Instruments 2400 Series II CHNS/O Analyzer. $IrCl(PPh_3)_3$ was prepared according to literature procedure (47). Diphenylacetylene (Lancaster, 99%) either used directly or after recrystallization from ethanol, yielded identical results. All other chemicals were obtained commercially and used without further purification.

Synthesis and characterization details of 2[3]

In a typical example, $IrCl(PPh_3)_3$ (0.1 mmol, 101 mg) and diphenylacetylene (0.3 mmol, 54 mg) were placed in a Schlenk flask under argon. Following dissolution in dry benzene (3 ml), the solution was refluxed for 18 h. The color of the solution gradually changed from yellow to deep red. After this period, the solvent was removed under vacuum at 300 K, and the resulting solid residue was recrystallized

[3] Supplementary data for this article are available on the journal Web site (canjchem.nrc.ca) or may be purchased from the Depository of Unpublished Data, Document Delivery, CISTI, National Research Council Canada, Ottawa, ON K1A 0R6, Canada. DUD 3810. For more information on obtaining material refer to cisti-icist.nrc-cnrc.gc.ca/cms/unpub_e.shtml. CCDC 652721 contains the crystallographic data for this manuscript. These data can be obtained, free of charge, via www.ccdc.cam.ac.uk/conts/retrieving.html (Or from the Cambridge Crystallographic Data Centre, 12 Union Road, Cambridge CB2 1EZ, UK; fax +44 1223 336033; or deposit@ccdc.cam.ac.uk).

© 2008 NRC Canada

from chloroform/ethanol to give iridaindene **2** as deep red block-like crystals (68 mg, 65%), mp 282–284 °C (dec).

UV–vis (benzene) λ_{max} (nm) (ε (mol/L)$^{-1}$cm^{-1})): 364 (10 000), 510 (640). IR (KBr, cm^{-1}): 694 (s), 743(s), 1094(s), 1435(s), 1483(s). ^{1}H NMR (400 MHz, $CDCl_3$, ppm) δ: 7.10–7.57 (m, P(C_6H_5)$_3$, and 3H′s of C_6H_5, 33H), 6.96–7.02 (m, 2H′s of C_6H_5, 2H), 6.91 (d, $J_{H\text{-}H}$= 7.6 Hz, *H*05, 1H), 6.43 (dd, $J_{H\text{-}H}$= 7.2, 7.2 Hz, *H*03, 1H), 6.10 (d, $J_{H\text{-}H}$= 7.2 Hz, *H*02, 1H), 5.99 (dd, $J_{H\text{-}H}$= 7.2, 7.6 Hz, *H*04, 1H), 5.65 (s, *H*07, 1H). ^{13}C{^{1}H} NMR (100 MHz, $CDCl_3$, ppm) δ: 127.4 (t, $^{2,4}J_{CP}$= 5.1 Hz, *o*-C_6H_5P), 129.3–129.8 (m, *i*-C_6H_5P and *p*-C_6H_5P), 134.9 (t, $^{3,5}J_{CP}$= 5.1 Hz, *m*-C_6H_5P), 120.1, 121.8, 122.1, 126.4, 127.1, 127.8, 133.0 (all singlet signals are for *C*H of iridaindene six-membered ring and Ph substituent of iridaindene); 133.9 (unresolved t, $^2J_{CP}$= 7.9 Hz, iridaindene *C*2Ph), 139.5 (s, iridaindene *C*3H), 144.5 (s, quat. C), 145.9 (unresolved t, $^2J_{CP}$= 6.9 Hz, iridaindene *C*Ir), 160.3 (s, quat. C). N.B. in ^{1}H and ^{13}C NMR spectra, peaks due to the solvated $CHCl_3$ appeared at 7.27 and 77.0 ppm, respectively. ^{31}P NMR (162 MHz, $CDCl_3$, ppm) δ: 22.78. Anal. calcd. for $C_{50}H_{40}ClP_2Ir.CHCl_3$: C 58.35, H 3.94; found: C 57.82, H 4.36.

X-ray structure determination of 2·$CHCl_3$

Single crystals of **2** suitable for X-ray diffraction study were obtained from slow diffusion of ethanol into a solution of **2** in chloroform or dichloromethane at room temperature. A suitable deep-red blocklike crystal of the complex **2** obtained from $CHCl_3$/EtOH solution was subjected to an Enraf Nonius Turbo CAD4 diffractometer with Graphite monochromated Mo Kα (λ= 0.710 73 Å). Unit cell parameters were obtained from a least-square refinement of 25 reflections. The structure was solved by SHELXS-97 and refined by full-matrix least squares on F^2 with SHELXL-97 methods (48, 49). The non-hydrogen atoms were refined anisotropically. All calculations were performed using WinGX crystallographic software package (50). Crystallographic data as well as structure solution and refinement details for **2**: $C_{50}H_{40}Cl_1P_2Ir_1.CHCl_3$; triclinic, P-1; a = 10.3295(15) Å, b = 12.4243(19) Å, c = 17.544(3) Å; α = 94.005(11)°, β = 98.539(13)°, γ = 98.581(12)°; V = 2191.9(6) Å^3; Z = 2; T = 293(2) K; λ (Mo K α) = 0.710 73 Å; D_{calc} = 1.591 mg/m^3; μ = 3.398 mm^{-1}; F(000) = 1044; Θ (min–max) = 1.18–25.00°; independent reflection = 6440; R_{int} = 0.0201; T (min, max) = 0.6124, 0.7727; data, restraints, parameters = 6440, 0, 524; final R indices ($I>2\sigma(I)$) R_1 = 0.0711, wR_2 = 0.1693; R indices (all data) R_1 = 0.1339, wR_2 = 0.2386; GOF on F^2 = 1.137.

Acknowledgements

SR thanks the Department of Science and Technology (DST), New Delhi, for research grant inclusive of a post-doctoral fellowship to JC. Financial assistance from Council of Scientific and Industrial Research (CSIR) (fellowship to SP) and University Grants Commission (UGC) (fellowship to AKM) is also acknowledged. While submitting this work to this special issue of CJC, SR likes to fondly express his gratitude to Dick for the cheerful years spent at the RJP lab two decades ago.

References

1. I. Omae. Coord. Chem. Rev. **248**, 995 (2004).
2. M. Catellani, G.P. Chiusoli, and M. Costa. J. Organomet. Chem. **500**, 69 (1995).
3. G.P. Chiusoli. J. Mol. Catal. **41**, 75 (1987).
4. J. Dehand and M. Pfeffer. Coord. Chem. Rev. **18**, 327 (1976).
5. M.E. van der Boom and D. Milstein. Chem. Rev. **103**, 1759 (2003).
6. V. Ritleng, C. Sirlin, and M. Pfeffer. Chem. Rev. **102**, 1731 (2002).
7. G. Dyker. Angew. Chem. Int. Ed. **38**, 1698 (1999).
8. P.R. Sharp. J. Organomet. Chem. **683**, 288 (2003).
9. J.R. Bleeke. Acc. Chem. Res. **40**, 1035 (2007).
10. U. Rosenthal, V.V. Burlakov, M.A. Bach, and T. Beweries. Chem. Soc. Rev. **36**, 719 (2007).
11. C.W. Landorf and M.M. Haley. Angew. Chem. Int. Ed. **45**, 3914 (2006).
12. L.J. Wright. Dalton. Trans. 1821 (2006).
13. J.P. Collman, J.W. Kang, W.F. Little, and M.F Sullivan. Inorg. Chem. **7**, 1298 (1968).
14. T. Takahashi, Z. Xi, A. Yamazaki, Y. Liu, K. Nakajima, and M. Kotora. J. Am. Chem. Soc. **120**, 1672 (1998).
15. T. Takahashi, R.Y. Tsai, Y. Li, K. Nakajima, and M. Kotora. J. Am. Chem. Soc. **121**, 11093 (1999).
16. R.J. Baxter, G.R. Knox, P.L. Pauson, and M.D. Spicer. Organometallics, **18**, 197 (1999).
17. R. Diercks, B.E. Eaton, S. Gurtzgen, S. Jalisatgi, A.J. Matzger, R.H. Radde, and K.P.C. Vollhardt. J. Am. Chem. Soc. **120**, 8247 (1998).
18. N. Agenet, V. Gandon, K.P.C. Vollhardt, M. Malacria, and C. Aubert. J. Am. Chem. Soc. **129**, 8860 (2007).
19. J.M. O'Connor, K. Hiibner, R. Merwin, P. Gantzel, A.L. Rheingold, and B.S. Fong. J. Am. Chem. Soc. **119**, 3631 (1997).
20. E.S. Johnson, G.J. Balaich, P.E. Fanwick, and I.P. Rothwell. J. Am. Chem. Soc. **119**, 11086 (1997).
21. H.J. Kim, N.S. Choi, and S.W. Lee. J. Organomet. Chem. **616**, 67 (2000).
22. G. Moran, M. Green, and A.G. Orpen. J. Organomet. Chem. **250**, C15 (1983).
23. J. Moreto, K. Maruya, P.M. Bailey, and P.M. Maitlis. J. Chem. Soc. Dalton Trans. 1341 (1982).
24. W.S. Han and S.W. Lee. Organometallics, **24**, 997 (2005).
25. E. Becker, K. Mereiter, M. Puchberger, R. Schmid, K. Kirchner, A. Doppiu, and A. Salzer. Organometallics, **22**, 3164 (2003).
26. E. Álvarez, M. Paneque, M.L. Poveda, and N. Rendón. Angew. Chem. Int. Ed. **45**, 474 (2006).
27. C.S. Chin and H. Lee. Chem. Eur. J. **10**, 4518 (2004).
28. C.S. Chin, H. Lee, and M.-S. Eum. Organometallics, **24**, 4849 (2005) and refs. cited therein.
29. H. Werner and A. Höhn. J. Organomet. Chem. **272**, 105 (1984).
30. A. Bierstedt, G.R. Clark, W.R. Roper, and L.J. Wright. J. Organomet. Chem. **691**, 3846 (2006).
31. G.-L. Lu, W.R. Roper, L.J. Wright, and G.R. Clark. J. Organomet. Chem. **690**, 972 (2005).
32. J. Choudhury, S. Podder, and S. Roy. J. Am. Chem. Soc. **127**, 6162 (2005).
33. M. Banerjee and S. Roy. J. Mol. Catal. A, **246**, 231 (2006).
34. J. Choudhury and S. Roy. J. Organomet. Chem. **692**, 5614 (2007).
35. S. Podder, J. Choudhury, U.K. Roy, and S. Roy. J. Org. Chem. **72**, 3100 (2007).
36. S. Podder, J. Choudhury, and S. Roy. J. Org. Chem. **72**, 3129 (2007).

© 2008 NRC Canada

37. J. Choudhury and S. Roy. J. Mol. Catal. A, **279**, 37 (2008).
38. M.A. Bennett, R. Charles, and P. J. Fraser. Aust. J. Chem. **30**, 1213 (1977).
39. J.P. Collman and J.W. Kang. J. Am. Chem. Soc. **89**, 844 (1967).
40. J.Y.K. Tsang, M.S.A. Buschhaus, P. Legzdins, and B.O. Patrick. Organometallics, **25**, 4215 (2006).
41. X. Li, P. Chen, J.W. Faller, and R.H. Crabtree. Organometallics, **24**, 4810 (2005).
42. A.F. Hill, M. Schultz, and A.C. Willis. Organometallics, **23**, 5729 (2004).
43. W.D. Harman, J.F. Wishart, and H. Taube. Inorg. Chem. **28**, 2411 (1989).
44. B. Chaudret, X. He, and Y. Huang. J. Chem. Soc. Chem. Commun. 1844 (1989).
45. S.P. Tunik, A.V. Vlasov, A.B. Nikol'skii, G.L. Starova, S. Ooi, H. Nakai, and T. Sato. J. Organomet. Chem. **464**, 71 (1994).
46. A.N. Nesmeyanov, V.V. Krivykh, V.S. Kaganovich, and M.I. Rybinskaya. J. Organomet. Chem. **102**, 185 (1975).
47. R. Acharyya, F. Basuli, R-Z. Wang, T.C.W. Mak, and S. Bhattacharya. Inorg. Chem. **43**, 704 (2004).
48. G.M. Sheldrick. SHELXS-97 [computer program]. University of Göttingen, Göttingen, Germany, 1997.
49. G.M. Sheldrick. SHELXL-97 [computer program]. University of Göttingen, Göttingen, Germany, 1997.
50. L.J. Farrugia. J. Appl. Cryst. **32**, 837 (1999) (WinGX Version 1.70.00. An integrated system of Windows programs for the solution, refinement, and analysis of single crystal X-ray diffraction data).

© 2008 NRC Canada

$Pt(2,2'\text{-bpy})(O_2CCF_3)_2$ as a terminator for $[Ag(O_2CCF_3)]_n$ aggregates — Syntheses and structures of heterobimetallic $Pt^{II}Ag^{I}$ complexes[1]

Yi Sun, Bryan Ross, Rui-Yao Wang, and Suning Wang

Abstract: The reactions between $Pt(2,2'\text{-bpy})(O_2CCF_3)_2$ and $Ag(O_2CCF_3)$ have been found to consistently produce heterobimetallic complexes where the $[Pt(2,2'\text{-bpy})]^{2+}$ unit acts as a terminator for various $[Ag(O_2CCF_3)]_n$ aggregates. The stoichiometry and the structure of the heterobimetallic complex obtained is dependent on the ratio of $Pt(2,2'\text{-bpy})(O_2CCF_3)_2$ and $Ag(O_2CCF_3)$ used in the synthesis. When a 1:1 ratio of Pt/Ag was used, a heteronuclear complex $Pt_2Ag_2(2,2'\text{-bpy})_2(O_2CCF_3)_6$ (**1a**) was obtained where the four metal ions have a linear Pt-Ag-Ag-Pt arrangement. Molecules of **1a** stack in the crystal lattice via intermolecular Pt···Pt interactions to form a linear 1D extended structure. A structural isomer of **1a**, $Pt_2Ag_2(2,2'\text{-bpy})_2(O_2CCF_3)_6$ (**1b**), where the four metal ions have an "L"-shaped arrangement was also identified and characterized, which forms a zig-zag 1D extended structure via intermolecular Pt···Pt interactions. When the 1:2 and the 1:3 ratios of Pt/Ag were used, heteronuclear complexes $Pt_2Ag_4(2,2'\text{-bpy})_2(O_2CCF_3)_8$ (**2**) and $Pt_2Ag_6(2,2'\text{-bpy})_2(O_2CCF_3)_{10}$ (**3**) were isolated, respectively, where the Ag(I) ions form cyclic structures with the $Pt(2,2'\text{-bpy})(O_2CCF_3)_2$ units at the terminal positions. Further increase of the amount of $Ag(O_2CCF_3)$ used in the synthesis did not lead to the isolation of larger aggregates. The structures of compounds **1a**, **1b**, **2**, and **3** were determined by single-crystal X-ray diffraction analyses. ^{19}F NMR spectroscopic analysis established that these heterobimetallic complexes undergo dynamic exchanges in solution.

Key words: heterobimetallic complexes, structure, silver, platinum, metal-metal interaction.

Résumé : On a observé que les réactions du $Pt(2,2'\text{-bpy})(O_2CCF_3)$ avec le $Ag(O_2CCF_3)$ conduisent d'une façon systématique à la formation de complexes bimétalliques dans lesquels l'entité $[Pt(2,2'\text{-bpy})]^{2+}$ agit comme unité terminale de divers agrégats $[Ag(O_2CCF_3)]_n$. La stoechiométrie et la structure de complexe hétérobimétallique obtenu dépend du rapport entre les quantités de $Pt(2,2'\text{-bpy})(O_2CCF_3)_2$ et de $Ag(O_2CCF_3)$ utilisés dans la synthèse. Avec un rapport Pt:Ag égal à l'unité, on obtient un complexe $Pt_2Ag_2(2,2'\text{-bpy})_2(O_2CCF_3)_6$ (**1a**) dans lequel les quatre ions métalliques Pt-Ag-Ag-Pt forment un arrangement linéaire. Les molécules de **1a** s'empilent dans le réseau cristallin par le biais d'interactions Pt···Pt intramoléculaires qui forment une structure linéaire unidimensionnelle étendue. On a aussi mis en évidence la présence et caractérisé un isomère de structure du produit **1a**, $Pt_2Ag_2(2,2'\text{-bpy})_2(O_2CCF_3)_6$ (**1b**) dans lequel les quatre ions métalliques adoptent un arrangement en forme de « L » et qui forment une structure étendue unidimensionnelle en zigzag par le biais d'interactions Pt···Pt intramoléculaires. Avec des rapports de Pt:Ag égaux à 2 ou 3, on a isolé respectivement les complexes hétéronucléaires $Pt_2Ag_4(2,2'\text{-bpy})_2(O_2CCF_3)_8$ (**2**) et $Pt_2Ag_6(2,2'\text{-bpy})_2(O_2CCF_3)_{10}$ (**3**) dans lesquels les ions Ag(I) forment des structures cycliques avec des unités $Pt(2,2'\text{-bpy})(O_2CCF_3)_2$ en positions terminales. Une utilisation dans les synthèses de quantités plus grandes de $Ag(O_2CCF_3)$ ne conduit pas à la formation d'agrégats plus gros. On a déterminé les structures des composés **1a**, **1b**, **2** et **3** par les techniques de diffraction des rayons X par un cristal unique. Une analyse par RMN du ^{19}F a permis d'établir que ces complexes hétérobimétalliques donnent lieu à des échangent dynamiques en solution.

Mots-clés : complexes hétérobimétalliques, structure, argent, platine, interaction métal-métal.

[Traduit par la Rédaction]

Introduction

Coordination polymers have attracted much research attention recently because of their various potential applications in materials science, catalysis, etc. (1). One key challenge in coordination polymer synthesis is the control of the stoichiometry, the structure, and the chain length of the polymeric species (1). The most commonly used strategy in coordination polymer synthesis is the use of a linker ligand or hydrogen bonds that direct the propagation of the extended structure (1). In heterobimetallic coordination polymers, achieving effective control of the stoichiometry and the structure of the polymeric species becomes more com-

Received 28 April 2008. Accepted 22 May 2008. Published on the NRC Research Press Web site at canjchem.nrc.ca on 10 September 2008.

Y. Sun, B. Ross, R.-Y. Wang, and S. Wang.[2] Department of Chemistry, Queen's University, Kingston, ON K7L 3N6, Canada.

[1]This article is part of the Special Issue dedicated to Professor Richard J. Puddephatt.

[2]Corresponding author (e-mail: wangs@chem.queensu.ca).

 doi:10.1139/V08-129 © 2008 NRC Canada

plex and challenging. Therefore, useful synthetic protocols that allow controlled and systematic syntheses of coordination polymers or oligomers, especially the heterobimetallic ones, are always highly desired to the coordination polymer and solid-state inorganic chemistry community. Silver(I) acetate and analogues are well-known to have the tendency to form various aggregates in the solid state via the carboxylate bridge (2). Many structures that contain aggregates of $[Ag(O_2CR)]_n$ have been reported in the literature (2). We have recently discovered serendipitously that the Pt(2,2′-bpy)$(O_2CCF_3)_2$ complex can be used effectively as a chelate ligand for binding to Ag(I) ions and for controlling the size of the $[Ag(O_2CCF_3)]_n$ aggregates, which in turn allows the controlled and easy synthesis of a number of new heterobimetallic Pt–Ag complexes without the use of any linker ligands other than the $CF_3CO_2^-$ anion in the starting metal complexes. The synthetic and structural details of the new heterobimetallic complexes are reported herein.

Experimental

All reactions were performed under an inert atmosphere of dry N_2 with standard Schlenk techniques, unless otherwise noted. All starting materials were purchased from Sigma-Aldrich Chemical Co. and used without further purification. CH_2Cl_2 was distilled over P_2O_5, Et_2O was purified using a solvent purification system (Innovation Technologies Co.). Deuterated solvents such as CD_2Cl_2 (Cambridge Isotopes) were used as received without further drying. NMR spectra were recorded on a Bruker Avance 400 spectrometer (400.13 MHz for ^{1}H, 100.62 MHz for ^{13}C, 376.50 MHz for ^{19}F), chemical shifts are referenced to the residual solvent peaks and have been reported in parts per million (ppm) relative to TMS (^{1}H and ^{13}C) and $CFCl_3$ (^{19}F). Elemental analyses were performed at the Analytical Laboratory for Environmental Science Research, Department of Chemistry, University of Toronto, Toronto, Ontario and Canadian Microanalytical Service LTD, Delta, BC. Pt(2,2′-bpy)Cl_2 was prepared by a modified method described in the literature (3).

Preparation of Pt(2,2′-bpy)$(O_2CCF_3)_2$

To a solution in a Schlenk flask containing 0.422 g (1.0 mmol) of Pt(2,2′-bpy)$(Cl)_2$ and 120 mL of CH_2Cl_2 was added 0.454 g (2.0 mmol) of $Ag(O_2CCF_3)$. The reaction mixture was stirred at 25 °C for 2 h in the dark. The precipitation was filtered and the filtrate was concentrated to ~10 mL under a reduced pressure, followed by the addition of diethyl ether to precipitate the product. Collection and drying under vacuum gave a light yellow solid, 470 mg (81%) of Pt(2,2′-bpy)$(O_2CCF_3)_2$. ^{1}H NMR (400 MHz, CD_2Cl_2, ppm) δ: 8.61 (d, ^3J = 8.0 Hz, 2H, py), 8.26 (t, ^3J = 8.0 Hz, 2H, py), 8.02 (d, ^3J = 8.0 Hz, 2H, py), 7.67 (t, ^3J = 8.0 Hz, 2H, py). ^{19}F NMR (376.50 MHz, CD_2Cl_2, ppm) δ: –176.0. Anal. calcd. for $C_{14}H_8F_6N_2O_4Pt$: C, 29.13, H 1.40, N 4.85; found: C 29.25, H 1.48, N 4.76.

Preparation of Pt_2Ag_2(2,2′-bpy)$_2(O_2CCF_3)_6$ (1a)

A CH_2Cl_2 (15 mL) solution of Pt(2,2′-bpy)$(O_2CCF_3)_2$ (20 mg, 0.035 mmol) was mixed with a CH_2Cl_2 (15 mL) solution of $Ag(O_2CCF_3)$ (7.7 mg, 0.035 mmol). Slow evaporation of the solvents afforded yellow crystals of **1a**, 16 mg (58%), mp 125–126 °C. ^{1}H NMR (400 MHz, CD_2Cl_2, ppm) δ: 8.52 (d, ^3J = 8.0 Hz, 2H, py), 8.27 (t, ^3J = 8.0 Hz, 2H, py), 8.03 (d, ^3J = 8.0 Hz, 2H, py), 7.67 (t, ^3J = 8.0 Hz, 2H, py). ^{19}F NMR (376.50 MHz, CD_2Cl_2, ppm) δ: –174.2, –175.8. IR (KBr disk, cm^{-1}) ν(COO$^-$): 1713s, 1691s, 1409m. Anal. calcd. for $C_{32}H_{22}Ag_2F_{18}N_4O_{12}Pt_2$: C 23.99, H 1.38, N 3.50; found: C 23.76, H 1.03, N 3.49.

Compound **1b** has the same formula as that of **1a**. It was isolated as a minor product from the reaction of Pt(B2bpy)Cl_2, B2bpy = 5,5′-bis[B(mesityl)$_2$]-2,2′-bpy (4) with excess $Ag(O_2CCF_3)$ in CH_2Cl_2 where the B–C bond on the B2bpy ligand was cleaved by the Ag(I) ion. Mechanistic investigation on this B–C bond cleavage reaction will be reported in due course. We have not been able to produce compound **1b** in a logical synthesis. All synthetic attempts led to the isolation of the isomer **1a**. The ^{1}H NMR of **1b** is identical to that of **1a**.

Preparation of Pt_2Ag_4(2,2′-bpy)$_2(O_2CCF_3)_8$ (2)

In the same manner as for the preparation of **1a**, 20 mg (0.035 mmol) of Pt(2,2′-bpy)$(O_2CCF_3)_2$ was mixed with 16 mg (0.070 mmol) of $Ag(O_2CCF_3)$ in 50 mL of CH_2Cl_2. Slow evaporation of the solvent afforded yellow crystals of **2**, 18 mg (51%), mp > 235 °C dec. ^{1}H NMR (400 MHz, CD_2Cl_2, ppm) δ: 8.47 (d, ^3J = 8.0 Hz, 2H, py), 8.27 (t, ^3J = 8.0 Hz, 2H, py), 8.03 (d, ^3J = 8.0 Hz, 2H, py), 7.67 (t, ^3J = 8.0 Hz, 2H, py). ^{19}F NMR (376.50 MHz, CD_2Cl_2, ppm) δ: –174.1, –175.7. IR (KBr disk, cm^{-1}) ν(COO$^-$): 1712s, 1683s, 1409m. Anal. calcd. for $C_{36}H_{24}Ag_4F_{24}N_4O_{16}Pt_2$: C 21.13, H 1.18, N 2.74; found: C 20.78, H 0.77, N 2.42.

Preparation of Pt_2Ag_6(2,2′-bpy)$_2(O_2CCF_3)_{10}$ (3)

In the same manner as for the preparation of **1a**, 20 mg (0.035 mmol) of Pt(2,2′-bpy)$(O_2CCF_3)_2$ was mixed with 23 mg (0.105 mmol) of $Ag(O_2CCF_3)$ in 60 mL of CH_2Cl_2. Slow evaporation of the solvents afforded yellow crystals of **3**, 20 mg (46%), mp 142–144 °C. ^{1}H NMR (400 MHz, CD_2Cl_2, ppm) δ: 8.49 (d, ^3J = 8.0 Hz, 2H, py), 8.27 (t, ^3J = 8.0 Hz, 2H, py), 8.03 (d, ^3J = 8.0 Hz, 2H, py), 7.67 (t, ^3J = 8.0 Hz, 2H, py). ^{19}F NMR (376.50 MHz, CD_2Cl_2, ppm) δ: –174.1, –175.7. IR (KBr disk, cm^{-1}) ν(COO$^-$): 1710s, 1681s, 1407m. Anal. calcd. for $C_{40}H_{26}Ag_6F_{30}N_4O_{20}Pt_2$: C 19.29, H 1.05, N 2.25; found: C 19.21, H 0.61, N 2.42.

X-ray crystallographic analyses

Single crystals of compounds **1a**, **1b**, **2**, and **3** were mounted on glass fibers in a brass pin, and the data were collected on a Bruker AXS Apex II single-crystal X-ray diffractometer with graphite-monochromated Mo Kα radiation operating at 50 kV and 30 mA at 180 K. No significant decay was observed during the data collection. Data were processed on a Pentium PC using Bruker AXS SHELXTL software package (version 6.14). Empirical absorption corrections were applied to all crystals. The crystals of **1a**, **1b**, and **2** belong to the triclinic space group *P*-1, while the crystals of **3** belong to the monoclinic space group *C*2/*c*. The structures were solved by direct methods. Some of the CF_3 groups in these complexes display rotational disorders that were modeled and refined successfully. All non-hydrogen atoms were refined anisotropically except some of the disor-

© 2008 NRC Canada

Table 1. Crystallographic data.

Compound	**1a**	**1b**	**2**	**3**
Formula	$C_{32}H_{16}N_4O_{12}F_{18}Ag_2Pt_2$	$C_{32}H_{16}N_4O_{12}F_{18}Ag_2Pt_2$	C_{36} H_{16} $F_{24}N_4O_{16}Pt_2Ag_4$	$C_{40}H_{16}N_4O_{20}F_{30}Ag_6Pt_2$
Formula mass	1596.41	1596.41	2038.19	2479.97
Space group	*P*-1	*P*-1	*P*-1	*C*2/*c*
a (Å)	8.82850(10)	11.0279(7)	10.6486(2)	21.6149 (4)
b (Å)	11.7750(2)	12.6504(8)	11.2390(2)	10.9268(2)
c (Å)	12.1268(2)	16.3352(10)	12.0023(2)	25.1217(4)
α (°)	63.5890(10)	79.2570(10)	111.9140(10)	90
β (°)	89.7240(10)	80.2800(10)	105.3960(10)	98.7640(10)
γ (°)	68.1070(10)	71.1710(10)	91.4610(10)	90
V (Å^3)	1027.79 (3)	2104.6 (2)	1272.29 (4)	5864.01 (18)
Z	1	2	1	4
D_{calcd} (g cm^{-3})	2.579	2.519	2.66	2.809
μ (mm^{-1})	7.871	7.687	7.144	6.883
$2\theta_{max}$ (°)	52	52	52	52
Reflections collected	7 675	22 203	10 471	18 063
Reflections used (R_{int})	4002 (0.0175)	8240 (0.0294)	4899 (0.0165)	5746 (0.0205)
No. of variables	325	589	415	479
Final R [$I > 2\sigma$ (I)][a,b]	R_1 = 0.0210, wR_2 = 0.0510	R_1 = 0.0450, wR_2 = 0.1168	R_1 = 0.0248, wR_2 = 0.0611	R_1 = 0.0224, wR_2 = 0.0490
R (all data)	R_1 = 0.0223, wR_2 = 0.0517	R_1 = 0.0569, wR_2 = 0.1254	R_1 = 0.0260, wR_2 = 0.0618	R_1 = 0.0240, wR_2 = 0.0495
GOF on F^2	1.041	1.027	1.014	1.108

[a] $R_1 = \Sigma [|F_o| - |F_c|] / \Sigma |F_o|$.
[b] $wR_2 = \{\Sigma [w(F_o^2 - F_c^2)] / \Sigma (wF_o^2)\}^{1/2}$; $w = 1 / [\sigma^2(F_o^2) + (0.075P)^2]$, where P = [max. (F_o^2, 0) + $2F_c^2$] / 3.

Table 2. Selected bond lengths and angles.

Compound	Bond lengths (Å)		Bond angles (°)	
1a	Pt(1)–N(2)	1.986(3)	N(2)-Pt(1)-N(1)	81.49(13)
	Pt(1)–N(1)	1.987(3)	N(2)-Pt(1)-O(3)	176.90(12)
	Pt(1)–O(3)	2.026(3)	N(1)-Pt(1)-O(3)	95.52(13)
	Pt(1)–O(1)	2.029(3)	N(2)-Pt(1)-O(1)	93.48(12)
	Ag(1)–O(6′)	2.321(3)	N(1)-Pt(1)-O(1)	174.93(12)
	Ag(1)–O(5)	2.340(3)	O(3)-Pt(1)-O(1)	89.52(12)
	Ag(1)–O(4)	2.502(3)	O(6′)-Ag(1)-O(5)	125.47(11)
	Ag(1)–O(2)	2.537(3)	O(6′)-Ag(1)-O(4)	78.52(11)
	Ag(1)–Pt(1)	2.8412(3)	O(5)-Ag(1)-O(4)	154.09(11)
	Ag(1)–Ag(1′)	2.8570(5)	O(6′)-Ag(1)-O(2)	156.13(11)
			O(5)-Ag(1)-O(2)	77.56(11)
			O(4)-Ag(1)-O(2)	77.74(11)
1b	Pt(1)–N(2)	1.963(8)	N(2)-Pt(1)-N(1)	81.0(4)
	Pt(1)–N(1)	1.979(8)	N(2)-Pt(1)-O(12)	96.3(4)
	Pt(1)–O(12)	2.017(7)	N(1)-Pt(1)-O(12)	176.6(3)
	Pt(1)–O(1)	2.046(7)	N(2)-Pt(1)-O(1)	173.7(4)
	Pt(2)–N(4)	1.984(7)	N(1)-Pt(1)-O(1)	92.7(3)
	Pt(2)–N(3)	1.987(7)	O(12)-Pt(1)-O(1)	90.0(3)
	Pt(2)–O(10)	2.029(6)	N(4)-Pt(2)-N(3)	81.1(3)
	Pt(2)–O(5)	2.031(6)	N(4)-Pt(2)-O(10)	177.0(3)
	Ag(1)–O(4)	2.301(8)	N(3)-Pt(2)-O(10)	97.2(3)
	Ag(1)–O(7)	2.321(8)	N(4)-Pt(2)-O(5)	96.0(3)
	Ag(1)–O(11)	2.361(7)	N(3)-Pt(2)-O(5)	176.7(3)
	Ag(2)–O(8)	2.279(7)	O(10)-Pt(2)-O(5)	85.6(3)
	Ag(2)–O(3)	2.288(7)	O(4)-Ag(1)-O(7)	90.9(3)
	Ag(2)–O(6)	2.394(7)	O(4)-Ag(1)-O(11)	139.2(3)
	Ag(2)–O(9)	2.499(7)	O(7)-Ag(1)-O(11)	129.5(3)

© 2008 NRC Canada

Table 2 (*concluded*).

Compound	Bond lengths (Å)		Bond angles (°)	
	Ag(1)–Pt(1)	2.9149(7)	O(8)-Ag(2)-O(3)	103.6(3)
	Ag(2)–Pt(2)	2.9061(6)	O(8)-Ag(2)-O(6)	140.1(3)
	Ag(1)–Ag(2)	2.9607(8)	O(3)-Ag(2)-O(6)	102.0(3)
			O(8)-Ag(2)-O(9)	126.2(3)
			O(3)-Ag(2)-O(9)	94.3(3)
			O(6)-Ag(2)-O(9)	81.2(3)
2	Pt(1)–N(2)	1.982(4)	N(2)-Pt(1)-N(1)	81.00(15)
	Pt(1)–N(1)	1.983(4)	N(2)-Pt(1)-O(2)	95.30(15)
	Pt(1)–O(2)	2.030(3)	N(1)-Pt(1)-O(2)	176.30(15)
	Pt(1)–O(6)	2.033(3)	N(2)-Pt(1)-O(6)	176.94(13)
	Ag(1)–O(3)	2.236(3)	N(1)-Pt(1)-O(6)	97.59(15)
	Ag(1)–O(5′)	2.39(2)	O(2)-Pt(1)-O(6)	86.09(15)
	Ag(1)–O(1)	2.396(3)	O(3)-Ag(1)-O(5′)	102.4(4)
	Ag(1)–O(5″)	2.41(2)	O(3)-Ag(1)-O(1)	158.14(14)
	Ag(1)–O(7′)	2.464(3)	O(5′)-Ag(1)-O(1)	94.9(4)
	Ag(2)–O(4)	2.153(3)	O(3)-Ag(1)-O(5″)	116.8(4)
	Ag(2)–O(7)	2.206(3)	O(5′)-Ag(1)-O(5″)	14.5(5)
	Ag(1)–Pt(1)	2.9516(4)	O(1)-Ag(1)-O(5′)	81.3(4)
	Ag(1)–Ag(2)	2.9315(5)	O(3)-Ag(1)-O(7)	114.50(13)
			O(5′)-Ag(1)-O(7)	86.8(5)
			O(1)-Ag(1)-O(7)	79.35(12)
			O(5A)-Ag(1)-O(7)	79.4(4)
3	Pt(1)–N(2)	1.981(3)	N(2)-Pt(1)-N(1)	80.96(13)
	Pt(1)–N(1)	1.981(3)	N(2)-Pt(1)-O(1)	177.68(12)
	Pt(1)–O(1)	2.028(3)	N(1)-Pt(1)-O(1)	96.72(12)
	Pt(1)–O(3)	2.036(3)	N(2)-Pt(1)-O(3)	97.74(12)
	Ag(1)–O(5)	2.205(3)	N(1)-Pt(1)-O(3)	178.15(11)
	Ag(1)–O(4)	2.374(3)	O(1)-Pt(1)-O(3)	84.58(11)
	Ag(1)–O(8′)	2.449(3)	O(5)-Ag(1)-O(4)	158.62(11)
	Ag(1)–O(2)	2.461(3)	O(5)-Ag(1)-O(8′)	113.42(10)
	Ag(2)–O(9)	2.241(3)	O(4)-Ag(1)-O(8′)	75.98(9)
	Ag(2)–O(6)	2.278(3)	O(5)-Ag(1)-O(2)	109.45(11)
	Ag(2)–O(7)	2.345(3)	O(4)-Ag(1)-O(2)	85.66(10)
	Ag(3)–O(10)	2.121(3)	O(8′)-Ag(1)-O(2)	103.13(10)
	Ag(3)–O(8)	2.163(3)	O(9)-Ag(2)-O(6)	124.75(12)
	Ag(3)–O(4′)	2.576(3)	O(9)-Ag(2)-O(7)	147.60(10)
	Ag(1)–Pt(1)	2.8865(3)	O(6)-Ag(2)-O(7)	87.20(11)
	Ag(1)–Ag(2)	3.2170(4)	O(10)-Ag(3)-O(8)	171.73(11)
	Ag(2)–Ag(3)	2.9638(5)	O(10)-Ag(3)-O(4	110.97(11)
	Ag(2)–Ag(3′)	3.3205(5)	O(8)-Ag(3)-O(4	77.05(9)
	Ag(3)–Ag(3′)	3.3027(7)		

dered F atoms. The positions of hydrogen atoms were calculated, and their contributions in structural factor calculations were included. The crystal data are provided in Table 1. Selected bond lengths and angles are given in Table 2.

Results

Syntheses and characterization of the heterobimetallic complexes

Three new heterobimetallic complexes $Pt_2Ag_2(2,2'\text{-bpy})_2(O_2CCF_3)_6$ (**1a**), $Pt_2Ag_4(2,2'\text{-bpy})_2(O_2CCF_3)_8$ (**2**), and $Pt_2Ag_6(2,2'\text{-bpy})_2(O_2CCF_3)_{10}$ (**3**) were obtained from the reactions of $Pt(2,2'\text{-bpy})(O_2CCF_3)_2$ and $Ag(O_2CCF_3)$ in 1:1, 1:2, and 1:3 ratios, respectively, as yellow crystals in moderate yields. Attempts were made to achieve Pt–Ag complexes that have more than 3 Ag(I) per Pt(II) by increasing the amount of $Ag(O_2CCF_3)$ used in the reaction, relative to that of $Pt(2,2'\text{-bpy})(O_2CCF_3)_2$. However, these attempts only led to the isolation of compound **3**. It is conceivable that larger heterobimetallic molecules did form when a greater amount of $Ag(O_2CCF_3)$ was used. However, the problem we encountered was that as the amount of $Ag(O_2CCF_3)$ increased, more insoluble products formed that were very difficult to separate

© 2008 NRC Canada

Fig. 1. The DSC diagram of **1a** with two heating and two cooling cycles (heating and cooling rate = 5.0 min.)

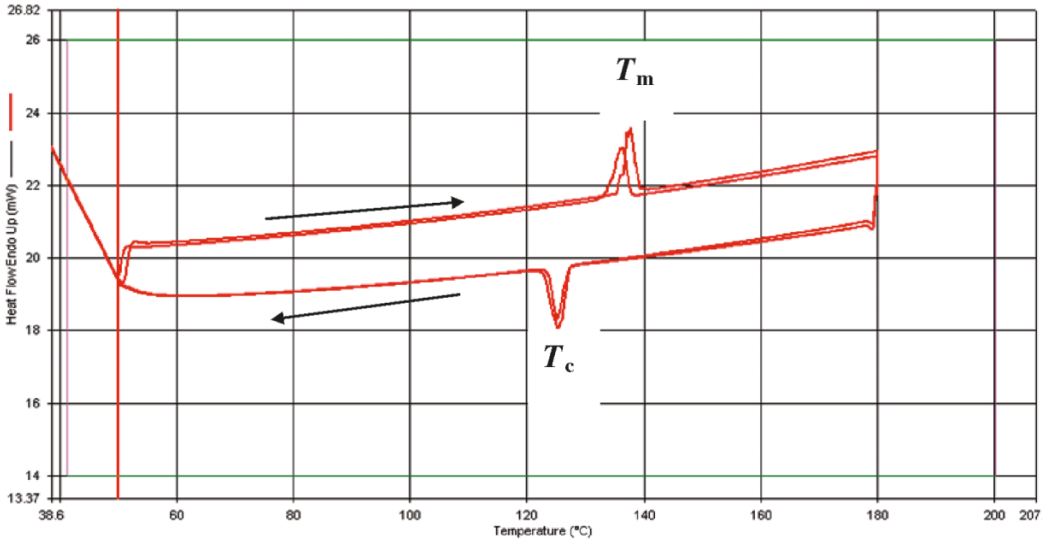

and characterize. Compound **1b**, a crystal isomer of **1a**, was isolated as a minor product from the reaction of Pt(B2bpy)Cl_2 with excess Ag(O_2CCF_3), where B2bpy = 5,5′- bis[B(mesityl)$_2$]-2,2′-bpy (4). Our investigation has established that the Ag(I) ion played a key role in the B–C bond cleavage in this reaction, and the details will be reported in due course. All our attempts to obtain compound **1b** via logical syntheses led to the isolation of compound **1a**. The compositions of all compounds were established by elemental analysis and ^{19}F NMR spectroscopic study. The ^{1}H NMR spectra for **1a**, **2**, and **3** in CD_2Cl_2 are nearly identical, with only a small notable difference for the chemical shift of the 6-H atoms on the 2,2′-bpy ring, an indication that the chemical environment for the 2,2′-bpy ligand in these complexes is similar. Compounds **1a** and **1b** have identical ^{1}H NMR spectra, supporting the notion that they have the same structure in solution. DSC diagrams of **1a** did not show any phase transition up to 180 (mp ~126) as shown in Fig. 1, an indication that **1a** and **1b** do not interconvert in the solid state. ^{19}F NMR spectra display two distinct and identical ^{19}F peaks at ca. –174 and ca. –176 ppm that were observed for all compounds at ambient temperature with the ratio of integrated intensities (1:2 for **1a** (**1b**), 1:1 for **2**, and 3:2 for **3**), which match well with the ratio of the number of $CF_3CO_2^-$ anions associated with Ag(I) and Pt(II), respectively, as used in the reaction for each compound. However, they are similar to those of the starting materials Ag(O_2CCF_3) (–174.1 ppm) and Pt(2,2′-bpy)(O_2CCF_3)$_2$ (–176.0 ppm), respectively, an indication that these complexes likely dissociate or undergo a dynamic exchange in solution. Indeed, as shown in Fig. 2, variable temperature ^{19}F NMR data showed that both peaks broaden with a decrease of temperature, confirming the presence of dynamic exchange processes. Due to the poor solubility of our complexes in common organic solvents, $^{107/109}$Ag and ^{195}Pt NMR studies were not possible. The IR spectra of compounds **1a**, **2**, and **3** have similar patterns. The carboxylate peak at 1712 cm^{-1} has two shoulder peaks (1731 and 1683 cm^{-1}) with somewhat different intensity ratios for each compound (see Supplementary Data).[3] None of the heterobimetallic complexes display luminescence at ambient temperature or at 77 K. The crystal structures of the new complexes were established by the single-crystal X-ray diffraction experiments and are shown schematically in Chart 1.

Crystal structures

Structures of 1a and 1b

The structures of Pt_2Ag_2(2,2′-bpy)$_2$(O_2CCF_3)$_6$ (**1a**) and its crystal isomer **1b** are shown in Figs. 3, 4, and 5, respectively. Both complexes consist of two Pt(II) ions, two Ag(I) ions, and six carboxylate anions. The two Pt(2,2′-bpy)(O_2CCF_3)$_2$ units act as chelate ligands to two Ag(I) ions. The structure of **1a** has a crystallographically imposed inversion center symmetry. The four metal ions have a linear Pt-Ag-Ag-Pt arrangement with the Pt(1)-Ag(1)-Ag(1′) angle being 173.12(2)° and two $CF_3CO_2^-$ ligands bridging every two metal ions. The Pt(1)–Ag(1) distance of 2.8412(3) Å in **1a** is fairly short and less than the sum of the atomic radii (2.83 Å), supporting the presence of Pt–Ag interactions (5). Similar Pt–Ag separation distances are known in the literature (6, 7). The Ag(1)–Ag(1′) separation distance of 2.8570(5) Å is longer than the Ag–Ag distance in metallic silver (2.889 Å) (5), indicating weak Ag–Ag interactions. Other reported Ag–Ag distances where metal–metal interactions were considered to occur range from 2.740 to 3.085 Å (2). The coordination geometry of the Pt center is square planar with normal Pt–N and Pt–O bond lengths. The Ag center has a highly distorted octahedral geometry with one Pt and one Ag atoms occupying the 5th and the 6th positions. The Ag–O bond lengths in **1a** range from 2.323(3) to 2.537(3) Å compared well with those observed in related complexes (2). In the crystal lattice, mole-

[3] Supplementary data for this article are available on the journal Web site (canjchem.nrc.ca) or may be purchased from the Depository of Unpublished Data, Document Delivery, CISTI, National Research Council Canada, Ottawa, ON K1A 0R6, Canada. DUD 3820. For more information on obtaining material refer to cisti-icist.nrc-cnrc.gc.ca/cms/unpub_e.shtml. CCDC 691135–691138 contain the crystallographic data for this manuscript. These data can be obtained, free of charge, via www.ccdc.cam.ac.uk/conts/retrieving.html (Or from the Cambridge Crystallographic Data Centre, 12 Union Road, Cambridge CB2 1EZ, UK; fax +44 1223 336033; or deposit@ccdc.cam.ac.uk).

© 2008 NRC Canada

Chart 1.

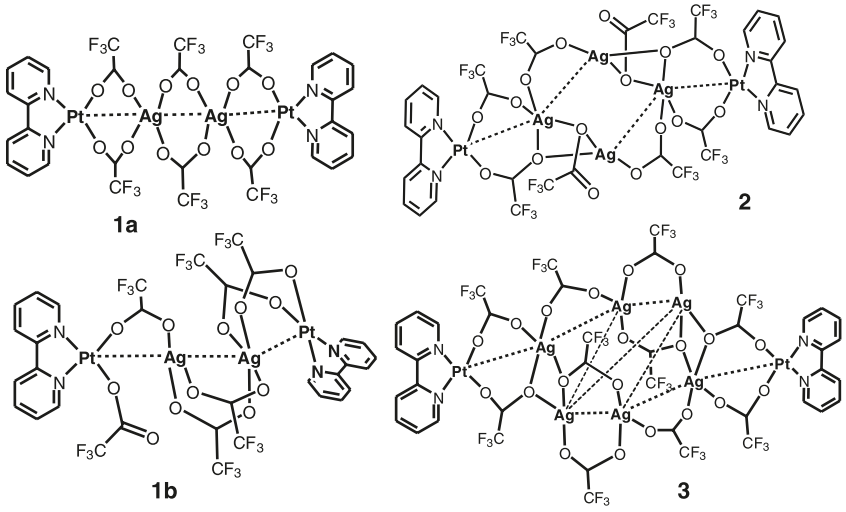

Fig. 2. ^{19}F NMR spectra of compound **2** in CD_2Cl_2 at 193– 273 K.

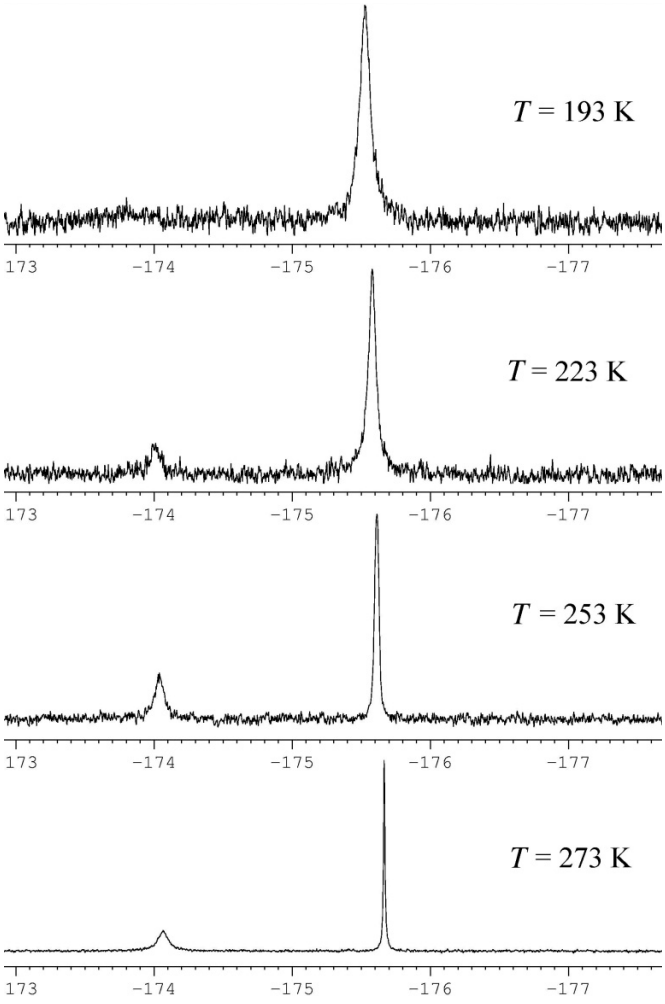

cules of **1a** form extended linear chains via weak intermolecular Pt··Pt interactions as indicated by the Pt(1)–Pt(1′) separation distance of 3.381(1) Å. The 1D metal chain of **1a** is not fully insulated by the $CF_3CO_2^-$ ligands, as shown by the space-filling diagram in Fig. 4.

Fig. 3. The crystal structure of **1a** (top) and the extended 1D structure (bottom) showing Pt··Pt interactions (right). For clarity, all non-metal atoms are shown in stick styles and only one set of fluorine atoms are shown for the disordered CF_3 groups.

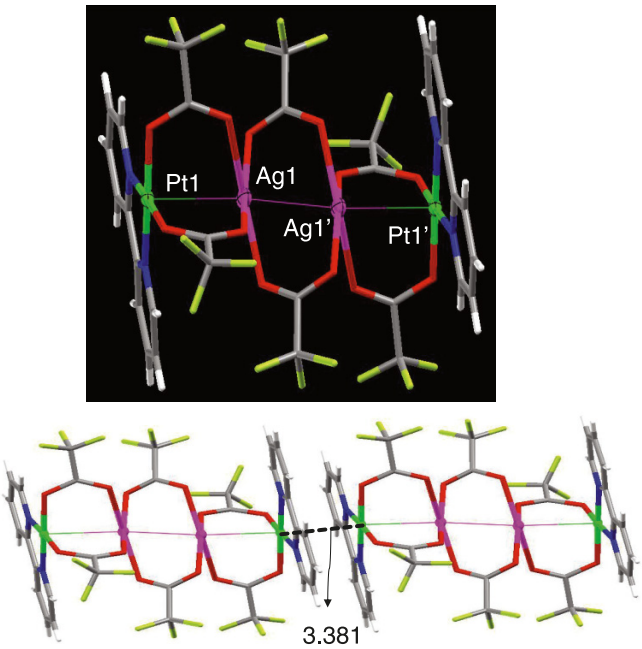

In contrast to the linear structure **1a**, the four metal ions in **1b** have an "L"-shaped arrangement with the Pt(1)-Ag(1)-Ag(2) and Pt(2)-Ag(2)-Ag(1) angles being 163.93(3)° and 110.13(3)° respectively. The metal–metal separation distances in **1b** are much longer than those in **1a** (Pt(1)–Ag(1) = 2.9149(7), Pt(2)–Ag(2) = 2.9061(6), Ag(1)–Ag(2) = 2.9607(8) Å) because of the increased steric interactions among the ligands. The Ag(1) center is three-coordinate with the Ag(1)–O bond lengths being 2.302(6) to 2.362(5) Å, while the Ag(2) center is four-coordinate with the Ag(2)–O bond lengths being 2.283(5) to 2.498(5) Å. The carboxylate groups that span two metal centers are all oriented approximately *cis* to each other instead of *trans*, as observed in **1b**. One of the carboxylates on the Pt(1) center acts as a termi-

© 2008 NRC Canada

Fig. 4. A space-filling view of the diagram shown in Fig. 3 (bottom) showing that the "metallic wire" is not fully insulated by the trifluoroacetate ligands.

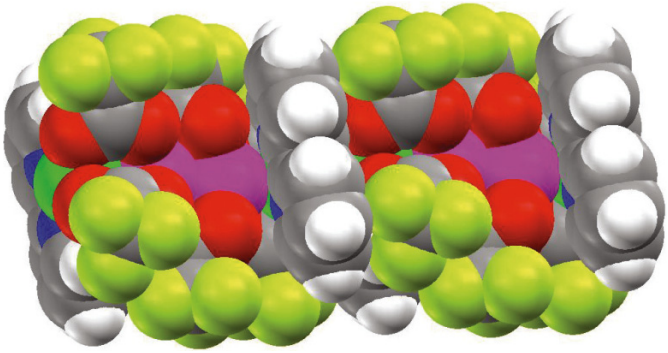

Fig. 5. The crystal structure of **1b** (top) and the extended 1D structure (bottom) showing Pt···Pt interactions (right). For clarity, all non-metal atoms are shown in stick styles and only one set of fluorine atoms are shown for the disordered CF_3 groups.

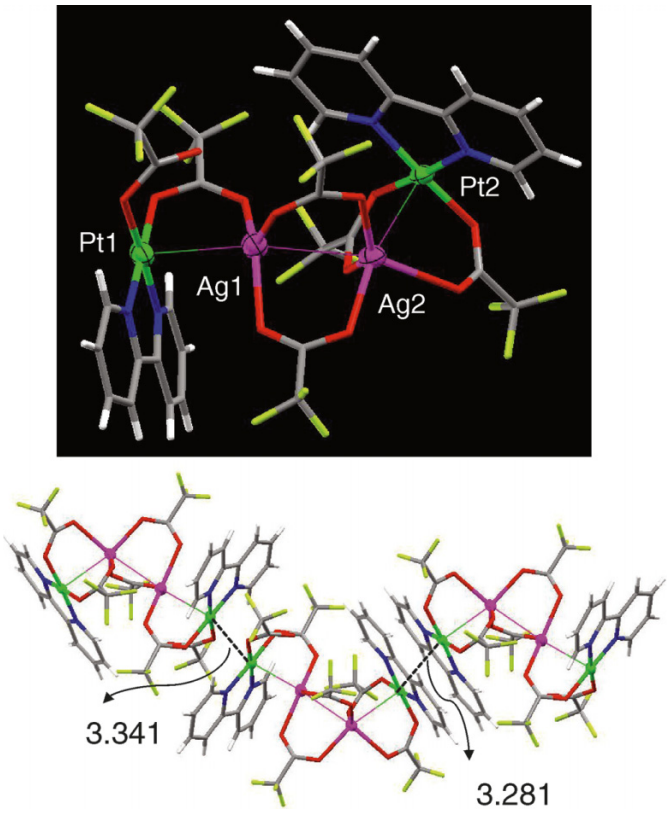

nal ligand (the non-coordinate oxygen atom on this ligand is 2.86 Å away from the Ag(1) center). In the crystal lattice, molecules of **1b** form an extended zig-zag chain via intermolecular Pt···Pt interactions (Pt(1)···Pt(1′) = 3.341(1), Pt(2)···Pt(2′) = 3.281(1) Å). Based on the results of our attempts to reproduce the structure **1b** that consistently led to the formation of **1a**, **1b** may be the less common form among the two structural isomers in the solid state.

Fig. 6. The crystal structure of **2** (top) and the extended 1D structure (bottom) showing Pt···Pt interactions (right). For clarity, all non-metal atoms are shown in stick styles and only one set of fluorine atoms are shown for the disordered CF_3 groups.

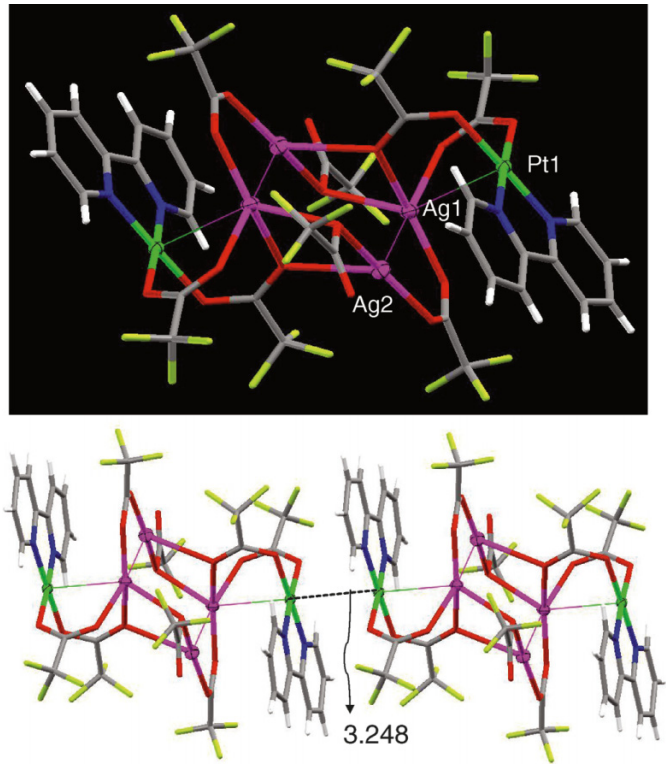

Structure of 2

The structure of compound **2** is shown in Fig. 6. Compound **2** has a crystallographically imposed inversion center. There are four Ag(I) ions and two Pt(II) centers in **2**. As observed in **1a** and **1b**, the $[Pt(2,2'\text{-bpy})]^{2+}$ units are at the terminal positions of the cluster. The four Ag(I) ions have a rectangular arrangement with two short and two long Ag–Ag separation distances (Ag(1)–Ag(2) = 2.9315(4) and Ag(2)–Ag(1′) = 3.729(1) Å). The Pt(1)–Ag(1) distance is 2.9565(4) Å, longer than those in **1a** and **1b**. The 8 $CF_3CO_2^-$ ligands display three different bonding modes, (η^2, μ_2)–, (η^2, μ_3)–, and (η, μ_2)–. The Ag(1) atoms are three-coordinate while the Ag(2) atoms are four-coordinate. In the crystal lattice, molecules of **2** form an extended one dimensional structure via intermolecular Pt···Pt interactions (3.248(1) Å).

Structure of 3

The structure of **3** is shown in Fig. 7. The molecule of **3** possesses a crystallographically imposed inversion center with 6 Ag(I) ions that have an elliptical arrangement and two $[Pt(2,2'\text{-bpy})]^{2+}$ units at the terminal positions. Two of the carboxylates display an η^2,μ_3-bonding mode, while the remaining carboxylates have the typical η^2,μ_2-bonding modes. The Pt(1)–Ag(1) distance is fairly short at 2.8865(3) Å. The Ag(1)–Ag(2) and Ag(2)–Ag(3) separation distances are 3.2170(4) and 2.9638(5) Å, respectively. Short Ag–Ag distances are also found between Ag(2)–Ag(3′) (3.3204(5) Å) and Ag(3)–Ag(3′) (3.3027(7) Å). In the crystal lattice, molecules of **3** also form an extended one dimensional structure

© 2008 NRC Canada

Fig. 7. The crystal structure of **3** (top) and the extended structure (bottom) showing Pt···Pt interactions (right). For clarity, all non-metal atoms are shown in stick styles and only one set of fluorine atoms are shown for the disordered CF_3 groups.

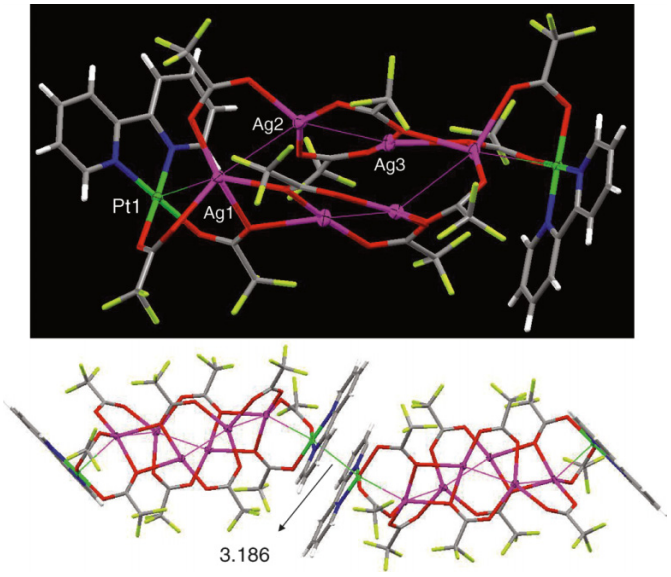

via intermolecular Pt···Pt interactions (3.1859(3) Å). Two of the oxygen atoms bound to the Ag(3) center have an O-Ag-O angle of 171.74(11)° and significantly much shorter Ag–O bond lengths (2.121(3) and 2.163(3) Å) than others in **3**, which can be attributed to the much weaker Ag–O bond by the 3rd oxygen atom (Ag–O = 2.576(3) Å) on the same Ag center.

Discussion

The structures of **1a**, **1b**, **2**, and **3** demonstrate that the Pt(2,2′-bpy)$(O_2CCF_3)_2$ group is capable of forming various heterobimetallic PtAg complexes with Ag(O_2CCF_3) in different Pt/Ag ratios. Most importantly is that these structures show that the Pt(2,2′-bpy) unit allows the size control of the Ag(I) aggregate formed by acting as a terminating agent. Although the formation mechanism of the new bimetallic Pt–Ag complexes has not been understood, the Pt(2,2′-bpy)$(O_2CCF_3)_2$ molecule consistently acts as a bidentate chelate ligand to bind to a Ag(I) ion in all structures. The structures of the Ag(I) aggregates within these new bimetallic complexes, and the carboxylate bonding modes resemble many previously known examples in the literature (2). Although it is difficult to predict the exact structure of the $[Ag(O_2CCF_3)]_n$ aggregate for a given number of Ag(I) ions because of the flexible coordination number and geometry around the Ag(I) center and the multiple bonding modes of the carboxylate ligands, as shown by the distinctly different structures of **1a** and **1b**, our investigation shows that it is possible to control the stoichiometry and the size of the aggregate by using the Pt(2,2′-bpy) unit. This may have value in the controlled formation of Ag(I) or Ag–Pt(II) nanoparticles. A number of heterobimetallic Pt–Ag complexes are previously known in the literature (6, 7), however, none are based on the simple trifluoroacetate and 2,2′-bipyridine ligands, and none show any logical size control of the cluster or aggregate formed. It is important to point out that molecules **1a**, **1b**, **2**, and **3** are in general elongated along the Pt–Pt vector (the intramolecular Pt–Pt separation distances for **1a**, **1b**, **2**, and **3** are 8.53, 7.35, 8.93, and 13.06 Å, respectively). The capping or the terminating location of the Pt(2,2′-bpy) group is in general along the long axis of the molecule. In other words, the terminating effect of the Pt unit seems highly directional (one dimensional in all our compounds). We in fact have examined a number of crystals obtained from the syntheses of compounds **2** and **3** to see if other structural variations exist. As yet, no new structures have been found. Crystal lattice packing efficiency and solubility may be important factors in the formation of the crystal structures reported here. The directionality of the terminating group can be at least partially attributed to the intermolecular Pt···Pt attraction, which is persistent in all four structures. Square planar Pt(II) complexes are well-known to form highly anisotropic one-dimensional structures in the solid state via Pt···Pt interactions (1*c*, 8). The intermolecular Pt···Pt separation distances in crystals **1a**–**3** are within the typical range reported previously for one dimensional Pt(II)-extended structures (1*c*, 7, 8). Nonetheless, when the central core contains a large number of Ag(I) ions such as the case in **3**, two-dimensional structures via two-dimensional intermolecular Pt···Pt interactions are conceivable. The lack of such two-dimensional structures in our systems may be attributed to the fact that Ag(O_2CCF_3) has the tendency to form one-dimensional chain structures via the carboxylate bridge (2). If the carboxylate anion is replaced by other anionic ligands, such as $CF_3SO_3^-$, achieving two- or three-dimensional extended structures directed by intermolecular Pt···Pt interactions may be possible.

In summary, three new heterobimetallic Pt–Ag complexes have been synthesized and fully characterized. The Pt(2,2′-bpy)$(O_2CCF_3)_2$ group has been found to play a key role in the selective formation of the target complex. The intermolecular Pt···Pt attractions have been found to direct the assembly of the one-dimensional extended structures of the heterobimetallic complexes. Two distinct structures for $Pt_2Ag_2(O_2CCF_3)_6$ have been observed. Our results establish that it is possible to control the stoichiometry and the size of the heterobimetallic clusters by using the Pt(2,2′-bpy)$(O_2CCF_3)_2$ molecule as the terminating group. The applicability of this strategy to other heterobimetallic systems will be investigated by our group.

Acknowledgment

We thank the Natural Sciences and Engineering Research Council of Canada for financial support.

References

1. (*a*) D.W. Bruce and D. O'Hare (*Editors*). Inorganic materials. 2nd ed. John Wiley and Sons, New York, USA. 1996; (*b*) J.W. Steed and J.L. Atwood. Supramolecular chemistry. John Wiley and Sons, New York, USA. 2000; (*c*) J.S. Miller. (*Editor*). Extended linear chain Compounds. Vol. I. Plenum, New York, USA. 1982; (*d*) D. Tanaka and S. Kitagawa. Chem. Mater. **20**, 922 (2008); (*e*) S. Kitagawa and R. Matsuda. Coord. Chem. Rev, **251**, 2490 (2007); (*f*) B.D. Chandler, G.D. Enright, K.A. Udachin, S. Pawsey, J.A. Ripmeester, D.T. Cramb, and G.K.H.

© 2008 NRC Canada

Shimizu. Nature-Materials, **7**, 229 (2008); (*g*) S.A. Dalrymple and G.K.H. Shimizu. J. Am. Chem. Soc. **129**, 12114 (2007); (*h*) C.A. Wheaton, M.C. Jennings, and R.J. Puddephatt. J. Am. Chem. Soc. **128**, 15370 (2006); (*i*) N.C. Habermehl, F. Mohr, D.J. Eisler, M.C. Jennings, and R.J. Puddephatt. Can. J. Chem. **84**, 111 (2006); (*j*) C.A. Wheaton and R.J. Puddephatt. Angew. Chem. Int. Ed. **46**, 4461 (2007); (*k*) M.-C. Brandys and R.J. Puddephatt. J. Am. Chem. Soc. **123**, 4839 (2001); (*l*) C.-D. Wu, L. Zhang, and W. Lin. Inorg. Chem. **45**, 7278 (2006); (*m*) C. Seward, W. L. Jia, R.Y. Wang, G.D. Enright, and S. Wang. Angew. Chem. Int. Ed. **43,** 2933 (2004); (*n*) J. Pang, E.J.-P. Marcotte, C. Seward, R.S. Brown, and S. Wang. Angew. Chem. Int. Ed. **40**, 4042 (2001); (*o*) M. Eddaoudi, D.B. Moler, H. Li, B. Chen, T.M. Reineke, M. O'Keeffe, and O.M. Yaghi. Acc. Chem. Res. **34**, 319 (2001); (*p*) S.G. Telfer, R. Kuroda, J. Lefebvre, and D.B. Leznoff. Inorg. Chem., **45**, 4592 (2006).

2. (*a*) E.V. Karpova, A.I. Boltalin, Y.M. Korenev, and S.I. Troyanov. Koord. Khim. **25**, 70 (1999); (*b*) X.L. Zhao, Q.M. Wang, and T.C.W. Mak. Inorg. Chem. **42**, 7872 (2003); (*c*) L. Zhao and T.C.W. Mak. J. Am. Chem. Soc. **127**, 14966 (2005); (*d*) X.L. Zhao and T.C.W. Mak. Polyhedron, **24**, 940 (2005); (*e*) J. Powell, M.J. Horvath, A. Lough, A. Philips, and J. Brunet. Dalton Trans. 637 (1998); (*f*) K. Vehlow, K. Köhler, S. Blechert, S. Dechert, and F. Meyer. Eur. J. Inorg. Chem. 2727 (2005); (*g*) L. Brammer, M.D. Burgard, C.S. Rodger, J.K. Swearingen, and N.P. Rath. Chem. Comm. 2468 (2001).
3. G.R. Newkome, K.J. Theriot, F.R. Fronczek, and B. Villar. Organometallics, **8**, 2513 (1989).
4. Y. Sun, N. Ross, S.B. Zhao, K. Huszarik, W. L. Jia, R.Y. Wang, D. Macartney, and S. Wang. J. Am. Chem. Soc. **129,** 7510 (2007).
5. J. Emsley. The Elements. 2nd ed. Oxford University Press, Oxford, UK. 1991.
6. (*a*) G. Douglas, M.C. Jennings, L. Manojlovic-Muir, and R.J. Puddephatt. Inorg. Chem. **27**, 4516 (1988); (*b*) J. Forni, A. Martin, R. Navarro, V. Sicilia, P. Villarroya, and A.G. Orpen. Dalton Trans. 3721 (1998); (*c*) D.E. Janzen, L.F. Mehne, D.G. VanDerveer, and G.J. Grant. Inorg. Chem. **44**, 8182 (2005); (*d*) N. Oberbeckmann-Winter, X. Morise, P. Braunstein, R. Welter. Inorg. Chem. **44**, 1391 (2005); (*e*) R. Us, J. Forni, M. Tom, J.M. Casas, F.A. Cotton, and L.R. Falvello. J. Am. Chem. Soc. **107**, 2556 (1985); (*f*) R. Us, J. Forni, B. Menj, F.A. Cotton, L.R. Falvello, and M. Tom. Inorg. Chem. **24**, 4651 (1985).
7. (*a*) A. Erxleben and B. Lippert. Dalton Trans. 2329 (1996); (*b*) F. Zamora, H. Witkowski, E. Freisinger, J. Müller, B. Thormann, A. Albinati, and B. Lippert. Dalton Trans. 175 (1999); (*c*) B. Lippert and D. Neugebauer. Inorg. Chem. **21**, 451 (1985).
8. (*a*) P. Du, J. Schneider, W.W. Brennessel, and R. Eisenberg. Inorg. Chem. **47**, 69 (2008); (*b*) T.J. Wadas, Q.M. Wang, Y.J. Kim, C. Flaschenreim, T.N. Blanton, and R. Eisenberg. J. Am. Chem. Soc. **126**, 16841 (2004).

© 2008 NRC Canada

Tungsten coordination chemistry of 1,4-bisdiphenylphosphinobutadiyne — Synthesis of coordination macrocycles and factors controlling diyne cycloaddition[1]

Jordan A. Tsui, Timothy M. Bolton, and Brian T. Sterenberg

Abstract: The 1:1 reaction of $[W(CO)_4(2\text{-picoline})_2]$ (**1**) with $Ph_2PC{\equiv}C\text{-}C{\equiv}CPPh_2$ (**2**) led to $\{[cis\text{-}W(CO)_4]_2(\mu\text{-}Ph_2PC_4PPh_2)_2\}$ (**3**), in which two bis(diphenylphosphino)butadiyne ligands bridge two tetracarbonyltungsten centres. Reaction of **1** with excess **2** led to $[cis\text{-}W(CO)_4(Ph_2PC_4PPh_2\text{-}\kappa^1\text{-}P)_2]$ (**4**), in which two dangling bis-phosphines are coordinated to one metal centre, and reaction of **2** with two equivalents of **1** led to $\{[W(2\text{-picoline})(CO)_4]_2(\mu\text{-}Ph_2PC_4PPh_2)\}$ (**5**), in which one ligand bridges two tungsten centres. Combination of **4** and **5** led to the trimeric complex $\{[cis\text{-}W(CO)_4]_3(\mu\text{-}Ph_2PC_4PPh_2)_3\}$ (**6**), in which three tetracarbonyltungsten centres are bridged by three bisdiphenylphosphinobutadiyne ligands. The dimeric complex **3** showed no reactivity towards alkyne cycloaddition; however, the trimeric complex **6** undergoes cycloaddition at moderate temperatures to form $\{[W(CO)_4]_3[\mu_3\text{-}C_{12}(Ph_2P)_6]\}$ (**8**), which contains a cyclododecatrienetriyene ring. Comparison of structural data for the template complexes **3** and **6**, as well that of previously described platinum template complexes, suggests that alkyne cycloaddition reactions are favoured by proximity of the alkynyl carbons α to phosphorus in adjacent ligands.

Key words: coordination chemistry, diyne, cycloaddition, templated reaction, tungsten.

Résumé : La réaction 1:1 du $[W(CO)_4(2\text{-picoline})]$ (**1**) avec le $Ph_2PC{\equiv}C\text{–}C{\equiv}CPPh_2$ (**2**) conduit à la formation du produit $\{[cis\text{-}W(CO)_4]_2(\mu\text{-}Ph_2PC_4PPh_2)_2\}$ (**3**) dans lequel deux ligands bis(diphénylophosino)butadiynes agissent comme ponts entre deux centres tétracarbonyltungstène. La réaction du produit **1** avec un excès de **2** conduit à la formation de $[cis\text{-}W(CO)_4(Ph_2PC_4PPh_2\text{-}\kappa^1\text{-}P)_2]$ dans lequel deux bisphosphines pendantes sont coordinées à un centre métallique alors que la réaction de **2** avec deux équivalents de **1** conduit à la formation de $\{[W(2\text{-picoline})(CO_4)]_2(\mu\text{-}Ph_2PC_4PPh_2)\}$, **5**, dans lequel un ligand sert de pont entre deux centres tungstènes. La combinaison des produits **4** et **5** conduit à la formation du complexe trimère $\{[cis\text{-}W(CO)_4]_3(\mu\text{-}Ph_2PC_4PPh_2)_3\}$, **6**, dans lequel trois centres tétracarbonyltungstène sont liés à trois ligands bisdiphénylphosphinobutadiyne. Le complexe dimère **3** ne présente aucune réactivité vis-à-vis d'une cycloaddition d'alcyne; toutefois, le complexe trimère **6** conduit à une cycloaddition à température modérée avec formation de $\{[W(CO)_4]_3[\mu_3\text{-}C_{12}(Ph_2P)_6]\}$, **8**, qui contient un noyau cyclododécatrièneтriyne. Une comparaison des données structurales des complexes gabarits **3** et **6** avec ceux des complexes gabarits du platine décrits antérieurement suggère que les réactions de cycloaddition de l'alcyne sont favorisées par la proximité des atomes de carbone alcynyles α au phosphore dans les ligands adjacents.

Mots-clés : chimie de coordination, diyne, cycloaddition, réaction sur gabarit, tungstène.

[Traduit par la Rédaction]

Introduction

The construction of large macrocycles of controlled shape including triangles and squares by combining transition metal centres with rigid bi- or polydentate ligands is receiving increased attention (1–19). In addition to their inherent beauty, these macrocyclic structures have potential applications as catalysts (20, 21) and sensors (22). Our interest in coordination macrocycles stems from the potential of metal coordination to template unique reactions of unsaturated backbones of ligand substrates. Metal templation has been applied to many synthetic challenges including macrocycles (23), catenanes, and rotaxanes (24). Templation has also been used to control cycloaddition reactions of alkenes and

Received 1 April 2008. Accepted 10 June 2008. Published on the NRC Research Press Web site at canjchem.nrc.ca on 13 September 2008.

Dedicated to Professor Richard J. Puddephatt in recognition of his contributions to organometallic chemistry.

J.A. Tsui, T.M. Bolton, and B.T. Sterenberg.[2] Department of Chemistry and Biochemistry, University of Regina, Regina, SK S4S 0A2, Canada.

[1]This article is part of a Special Issue dedicated to Professor Richard J. Puddephatt.
[2]Corresponding author (e-mail: brian.sterenberg@uregina.ca).

 doi:10.1139/V08-123 © 2008 NRC Canada

Scheme 1.

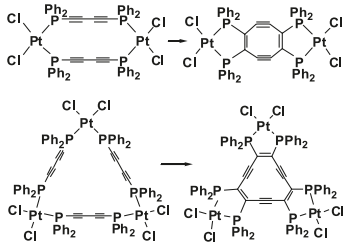

alkynes; however, in most cases, the substrate–template interaction used has been hydrogen bonding (25). We are exploring the use of metal coordination in template cycloaddition reactions, particularly cycloaddition reactions of unsaturated phosphines. This approach has been used previously to control reactivity of the alkyne units in alkynyl phosphines (26–31).

As a part an ongoing project, we have been examining the coordination chemistry of bis(diphenylphosphino)butadiyne (32). The phosphino groups of this substrate readily coordinate to a variety of transition metals (33–36). By using the appropriate metal template molecule, the spatial relationship between the reactive diyne functionalities in two or more substrate molecules can be controlled, allowing for selective cycloaddition reactions. In the absence of metal coordination, this substrate polymerizes to a material containing enyne units (37). In a previous paper (38), we showed that coordination of two or three substrate molecules to a $PtCl_2$ template fragment resulted in cycloaddition to form either a novel cyclooctadienediyne ring or a cyclododecatienetriyne ring (Scheme 1). Surprisingly, a very similar $Pt(CH_3)_2$ fragment did not induce the cycloaddition reaction under the same mild conditions. At that point, it was not obvious which structural parameters of the template complexes controlled the cycloaddition reaction.

The major disadvantage of the $PtCl_2$ system is the very poor solubility of the metal complexes, which prevented us from exploring the potentially interesting spectroscopy of the highly coloured cyclooctadienediyne ring complex. The poor solubility also made it impossible to control product distribution between the dimeric and trimeric template complexes. As a result, we set out to find a metal template fragment that would lead to soluble metal complexes as products. In addition, by surveying a number of different metal templates, we were aiming to better understand the structural features of the template complexes that control the cycloaddition reaction. A clear understanding of these factors will allow us to expand the range of metal-templated reactions to other unsaturated phosphine containing substrates.

Our work with platinum complexes suggests that bringing the substrate molecules into close enough proximity to react requires *cis*-coordination with a 90° or smaller angle between two phosphine ligands at the metal complex. In the platinum system, this was achieved by *cis* coordination of the phosphine moieties to a square planar metal centre. The same relative arrangement of phosphine ligands could also be achieved in a *cis*-octahedral metal complex. In this paper, we report our investigation of the coordination chemistry of bis-diphenylphosphinobutadiyne with *cis*-octahedral tungsten complexes. Some tungsten coordination chemistry of

Scheme 2.

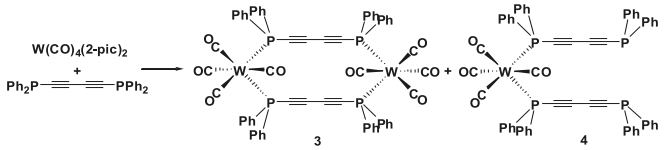

bis-diphenylphosphinobutadiyne has been reported; however in these complexes only one ligand was used to bridge two tungsten centres (32). Although the octahedral geometry of the tungsten fragment in the targeted template complexes provides the same 90° angle between the two substrate molecules as the square planar $PtCl_2$ template, the larger atomic radius of tungsten and the steric influence of the octahedral metal centre are expected to affect the geometrical relationship of the substrate molecules. We will use this comparison as a probe of the effect of the structural parameters of the template complexes on the reactivity of the diyne substrates.

Results

The tungsten precursor used for this work was [*cis*-$W(CO)_4$(2-picoline)$_2$] (**1**) (39), which provides an octahedral W(0) centre with two labile *cis* ligands. The *ortho* methyl groups in the 2-picoline ligands make them more labile than the pyridine ligands in [*cis*-$W(CO)_4(py)_2$], allowing substitution reactions to take place under milder conditions. A one-to-one reaction of **1** and $Ph_2PC{\equiv}C\text{-}C{\equiv}CPPh_2$ (**2**) at 60°C led to a mixture of two phosphine complexes in a 2:1 ratio (Scheme 2). The reaction mixture also contained unidentified tungsten carbonyl decomposition products, as indicated by IR spectroscopy. The two phosphine complexes were readily isolated using column chromatography. The first of these compounds was shown to be the anticipated dimer [{*cis*-$W(CO)_4$}$_2$(μ-$Ph_2PC_4PPh_2$)$_2$] (**3**), in which two substrate molecules bridge two tungsten centres. The ^{31}P NMR spectrum of **3** shows a singlet at δ 2.80 with ^{195}W satellites and $^1J_{WP}$ of 241 Hz. An ORTEP diagram of the molecular structure is shown in Fig. 1. Each tungsten centre is coordinated by four carbonyls and two phosphines, which are *cis* to each other. The overall complex has a twisted boat shaped configuration, with both tungsten centres directed to the same side of complex. This configuration results in alkyne centre-to-centre distances of 3.499 and 3.482 Å. For comparison, alkyne centre-to-centre distances in analogous platinum complexes range from 3.236 to 3.38 Å.

The second reaction product was [*cis*-$W(CO)_4$($Ph_2PC_4PPh_2$-κ^1-P)$_2$] (**4**), in which two equivalents of the bisphosphine ligand coordinate to one tungsten centre. This product is favoured by excess phosphine ligand. However, it cannot be formed independently of Compound **3** and requires purification by column chromatography. The ^{31}P NMR spectrum of **3** shows two peaks at δ 1.3 and –30.0. The first peak shows tungsten satellites, and the chemical shift is similar to that of **2**, consistent with a $W(CO)_4P_2$ unit. The second peak is very close to that of the free ligand (δ –29.2) and is attributed to the dangling phosphines. There was no evidence of trimer formation in this reaction, as was observed in the platinum system (38). The apparent deficiency of tungsten in the isolated products of the 1:1 reaction resulted

© 2008 NRC Canada

Fig. 1. ORTEP diagram showing the molecular structure of Compound **3**. Hydrogen atoms have been omitted for clarity.

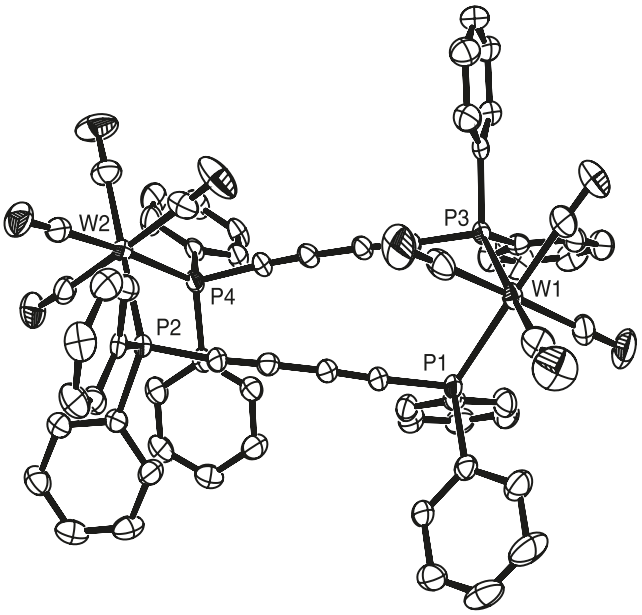

from the decomposition of **2** into other tungsten carbonyl complexes, which do not contain the phosphines ligand.

The kinetics of the 2-picoline–phosphine substitution reactions were studied to allow us to optimize the synthetic reactions. The substitution of the two 2-picoline ligands at each tungsten centre for phosphine ligands occured in two distinct steps with very different rates. Substitution of the first 2-picoline ligand at tungsten occured rapidly at room temperature, with both ends of the ligand coordinating to tungsten to form the intermediate $[W(2\text{-picoline})(CO)_4]_2(\mu\text{-}Ph_2PC_4PPh_2)$ (**5**) (Scheme 3). This reaction was first order in metal complex, consistent with a dissociative substitution mechanism, which is expected for 18-electron W(0) complexes (40). The half-time for the disappearance of **2** at 0°C was 18 minutes, so preparative reactions to form **5** were run for 3 hr (10 half lives).

The second substitution step, which leads to **3**, occured much more slowly at room temperature, typically requiring several days to go to completion. At 0°C, the second substitution was suppressed completely. Because of the long reaction times, the kinetics of the second substitution were not studied in detail. The disparate rates between the first and second substitution steps allowed us to isolate compound **5** by reacting the ligand with two equivalent of the tungsten precursor at 0°C. The dimer **3** could also be formed free of compound **4** by stirring the ligand with $[cis\text{-}W(CO)_4(2\text{-picoline})_2]$ (**1**) at 0°C for 3 h to form **5**, and then heating to 60°C for 1.5 h to coordinate the second ligand (Scheme 3). Isolated yield after chromatography and recrystalization was 44%.

Our ability to isolate compounds **4** and **5** allowed us to conceive a convergent route to a larger coordination macrocycle. Reaction of compound **5**, in which one ligand is coordinated to two metal complexes, with compound **4**, in which two equivalents of ligand are coordinated to one metal complex, led to a mixture of the dimer **3** and a new compound,

Scheme 3.

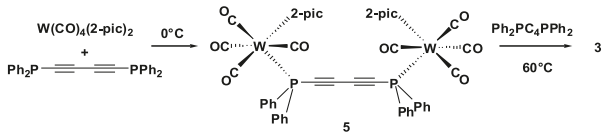

Scheme 4.

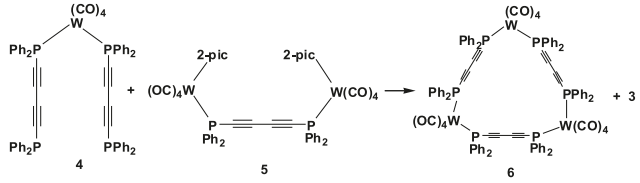

which has been identified as the trimeric complex $[\{cis\text{-}W(CO)_4\}_3(\text{-}Ph_2PC_4PPh_2)_3]$ (**6**) (Scheme 4). The three-fold symmetry of **6** means that its spectroscopic parameters are nearly identical to those of **3**, with a ^{31}P chemical shift of δ 3.0, and nearly super-imposable IR spectra. The formation of significant quantities of **3** in the reaction suggests that phosphine–phosphine displacement reactions are competitive with the phosphine–picoline substitution reactions. The reaction was optimized for temperature and solvent, and it was shown that higher temperatures favour the formation of **3**. The optimal reaction conditions were room temperature and THF solvent, which gave a mixture of **3** (dimer) and **6** (trimer) in a 3:5 ratio. Darkly coloured material formed in the reaction suggests that some decomposition is also occuring. Although a lower temperature might increase the proportion of **6**, below room temperature the reaction becomes too slow to be useful. The isolated yield of **6** after chromatography is 12%. The low isolated yield is a result of decomposition during reaction and decomposition on the column.

An ORTEP diagram of the molecular structure of **6** is shown in Fig. 2. The molecule adopts a helical structure, with each diyne unit crossing the plane formed by the three tungsten atoms. A side view of the molecule, emphasizing the helical structure is shown in Fig. 3. The helical nature of the molecule means that it is chiral, and the compound crystallizes the chiral space group $P2_13$, indicating that the two enantiomers crystallize independently. However, the two types of crystals could not be visually distinguished. The conformation of **6** brings the alkyne moieties of adjacent phosphines much closer together than those in the dimer **3**, with an alkyne centre-to-centre distance of 3.335 Å, compared with 3.499 Å in the dimer. The shorter alkyne-alkyne distance in the trimer suggests that it may be more reactive towards cycloaddition.

An alternate convergent route to the trimeric complex involves reaction of **4** with two equivalents of $[cis\text{-}W(CO)_4(2\text{-picoline})_2]$ (**1**) to form **7** (Scheme 5). Although the first step of this route was successful, reaction of **7** with an additional equivalent of the ligand **1** did not close the ring, but instead led primarily to the dimer **3**.

Heating the dimeric compound **3** to temperatures up to 140°C did not result in any cycloaddition reaction. In fact, compound **3** is thermally very robust and shows no significant decomposition at this temperature. Similarly, photolysis

© 2008 NRC Canada

Fig. 2. ORTEP diagram showing the molecular structure of Compound **6**. Hydrogen atoms and co-crystalized solvent have been omitted for clarity. The molecule lies on a crystallographic three-fold axis meaning that the three tungsten centres are crystallographically equivalent.

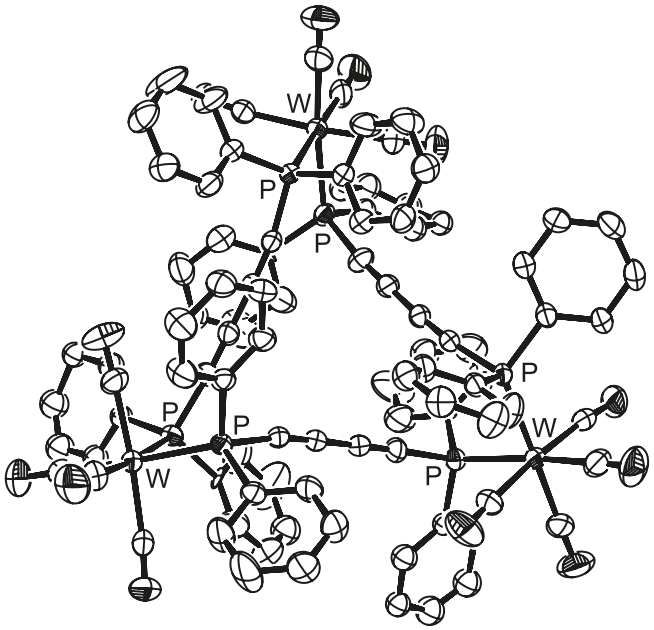

Fig. 3. Side view of the molecular structure of Compound **6** emphasizing its helical structure. Phenyl groups have been omitted for clarity.

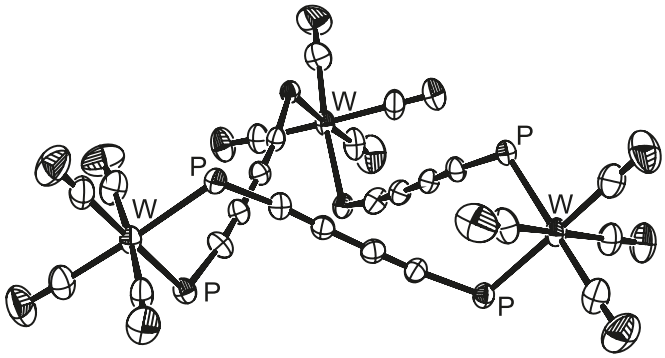

Scheme 5.

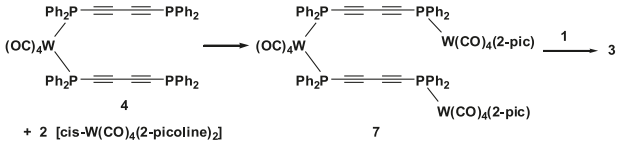

resulted in no reaction. The stability of **3** toward cycloaddition is not surprising given the large separation between the alkynes on adjacent phosphines.

In contrast, compound **6** underwent slow reaction over several weeks at room temperature if exposed to light. More rapid reaction could also be thermally induced by heating to 60°C. Compound **8**, the product of the reaction, has been assigned as the tungsten complex of the phosphine substituted cyclododecatrienetriyne ring, which results from the 4+4+4

Scheme 6.

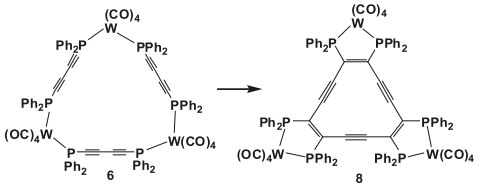

cycloaddition of the three diynes (Scheme 6). It is analogous to the product observed in the Pt system. Although crystals were grown, twinning problems could not be resolved, so **8** has been characterized spectroscopically and by analogy to the Pt complexes. Upon cycloadditon, the ^{31}P chemical shift changed from δ 3.0 to δ 60.1. This large chemical shift change is a result of the conversion of the alkynyl substituent on the phosphine to an alkenyl substituent. The alkynyl substituent is strongly deshielding, while the alkenyl substituent is shielding, resulting in the large downfield shift (41). A nearly identical downfield shift was observed in the cycloaddition reactions of the analogous platinum complexes (38).

The IR spectrum of **8** shows the characteristic pattern for the *cis*-$W(CO)_4$ moiety, indicating that the metal geometry is unchanged. However, the C≡C stretch observed in **6** has disappeared as a result of the transformation of the unsymmetrical IR-active alkynes in **6**, into symmetrical, IR inactive alkyne in **8**. The carbonyl region of the ^{13}C NMR spectrum of **8** shows two carbonyl peaks as expected for this metal geometry (*cis* and *trans* with respect to the phosphines). The spectrum also shows a single alkene carbon resonance at δ 155.7 and a single alkyne carbon resonance at δ 106.2, rather than the two chemically non-equivalent alkyne carbons expected in the diyne structure, supporting the formation of the cyclododecatrienetriyne ring. The alkene carbons show one-bond and two-bond couplings to phosphorus of 46 and 31 Hz. For comparison, the alkene carbons of diphenylvinyl phosphine show coupling constants of 24 and 14 Hz (42). The alkyne carbon is also coupled to phosphorus with a two-bond coupling constant of 23 Hz.

The UV–vis spectrum of **8** is very broad and generally uninformative; however, a comparison with the spectrum of the precursor, complex **6**, reveals changes that result from the formation of the 12-membered ring. Compound **6** shows a single broad peak centred at 350 nm (ε 4000 $(mol/L)^{-1}cm^{-1}$). Compound **8** shows peaks at 280 nm (ε 17000 $(mol/L)^{-1}cm^{-1}$), 350 nm (ε 3000 $(mol/L)^{-1}cm^{-1}$), and 500 nm (ε 400 $(mol/L)^{-1}cm^{-1}$). The peaks at 280 and 500 nm can clearly be attributed to the ring since the remaining chromophores are the same in both compounds. For comparison, the spectrum of the parent cyclododecatrienetriyne ring shows peaks at 239 nm (ε = 38700), 247.5 nm (ε 57200), and 457 nm (ε 177) (43, 44).

Discussion

Table 1 summarizes key structural parameters in template complexes of $Ph_2PC_4PPh_2$ (**2**). It is apparent from the data that the primary structural parameter that determines the reactivity of templated alkynes is the α-carbon–α-carbon separation, rather than M–P bond lengths or alkyne centre-to-centre distances or angles. The cycloaddition reaction is ob-

© 2008 NRC Canada

Table 1. Structural parameters for metal template complexes of $Ph_2PC_4PPh_2$ (**2**).

Compound	Avg. *d*(M–P) (Å)	*d*(αC-αC) (Å)	Alkyne–alkyne distance (Å)	Alkyne–alkyne angle (°)	Cycloaddition	Temperature[a]	Reference
$W(CO)_4$ dimer	2.504	3.582	3.499	19.6	No	—	This work
$W(CO)_4$ trimer	2.504	3.165	3.335	79.4	Yes	RT	This work
$PtMe_2$ dimer	2.278	3.3215	3.304	34	No	—	38
$PtMe_2$ trimer	2.280	3.216	3.384	85	Yes	80 °C	38
$PtCl_2$ trimer	2.230	3.021	3.236	81.0	Yes	< 0 °C	38
$PtCl_2$ dimer[b]	—	—	—	—	Yes	< 0 °C	38

[a]Lowest temperature at which cycloaddition is observed. Temperatures for preparative reactions are higher.
[b]The $PtCl_2$ dimer was not structurally characterized because its cycloaddition reaction occurs too quickly.

served in all template complexes where this distance is approximately 3.2 Å or lower. This distance also appears to correlate well with the temperature required to induce cycloaddition. Template complexes with shorter α-carbon–α-carbon separation undergo cycloaddition at lower temperatures. The separation between the α carbons on adjacent alkynyl phosphine ligands is controlled by the metal–phosphorus distance and by the relative rotations of the two phosphine ligands (rotation about the M–P bond). The first parameter is readily controlled by the choice of metal. However, the second parameter depends on the overall conformation of the template complex, and is thus harder to predict and control. The trimeric complexes have a stronger tendency to adopt a conformation that brings the α carbons closer together. We are currently using the dimeric tungsten complex **3** to test if the conformation can be affected by substitution of carbonyls for larger ligands, or by oxidative addition to form 7-coordinate tungsten.

Compound **4**, which has two dangling bis-phosphine ligands, also provides us with an opportunity to form heterobimetallic complexes by reaction with another metal precursor. By combining large radius tungsten with a smaller radius metal such as platinum, we may be able to induce unique cycloaddition reactions. This work is underway and will be published in a subsequent paper. Compound **5**, in which one diyne substrate is coordinated to two metal complexes, will allow us to mix the diyne ligand with other phosphine-substituted substrates to template other reactions, including alkene–alkyne cycloadditions, and additions across the triple bonds.

In summary, we have synthesised bimetallic and trimetallic tungsten coordination macrocycles of bis(diphenylphosphino)butadiyne. We have used the structural parameters and reactivity of these complexes, along with those of the related platinum macrocycles, to elucidate the structural relationships that support diyne cycloaddition reactions.

Experimental section

All procedures were carried out under nitrogen using standard Schenk techniques. Dichloromethane and hexane were purified using solvent purification columns containing alumina (dichloromethane) or alumina and copper catalyst (hexane and toluene). THF was distilled from sodium–benzophenone under a dinitrogen atmosphere. Deuterated chloroform was vacuum distilled from P_2O_5. The NMR spectra were recorded in $CDCl_3$ at 300.1 MHz (^1H), 121.5 MHz ($^{31}P\{^1H\}$), or 75.5 ($^{13}C\{^1H\}$). The compounds $W(CO)_6$, Ph_2PCl, hexachlorobutadiene, 2-picoline, and *n*-BuLi (2.5 M in hexane) were purchased from Sigma-Aldrich and used as received.

Synthesis of [*cis*-$W(CO)_4$(2-picoline)$_2$] (1)

This compound was prepared according to the method developed by Tosh and Mihichuk (39). The compound $[W(CO)_6]$ (2.00 g, 5.68 mmol) was dissolved in 2-picoline (10 mL) in a flask equipped with a reflux condenser. The resulting solution was degassed by purging with N_2 for 10 min. The solution was heated at 130°C and the reaction progress was monitored by FTIR until product formation was complete (5–6 hr, ν(CO): 2006, 1875, 1870sh, 1825 cm^{-1}). The solution was cooled to rt and the product was precipitated as a bright yellow microcrystalline solid by rapid addition of hexane (40 mL). Yield: 2.007 g, 4.163 mmol, 73%.

Synthesis of $Ph_2PC_4PPh_2$ (2)

This compound was prepared according to a procedure developed by Martin-Redondo et al. (38). A solution of *n*-BuLi (51 mL of 2.5 M in hexane, 128 mmol) in THF (80 mL) was cooled to –78°C and protected from light. A solution of hexachlorobutadiene (5.0 mL, 32 mmol) in THF (20 mL) was added dropwise over a period of 30 min. Once addition was complete, the solution was stirred for an additional 15 min at –78°C, warmed to rt over 15 min, then stirred for 2 h at rt. The reaction mixture was again cooled to –78°C and PPh_2Cl (11.5 mL, 64 mmol) was added dropwise via syringe over a period of 30 min. Once addition was complete, the solution was stirred for 15 min at –78°C, warmed to rt over 15 min, and then stirred for 15 min at rt. The solution was hydrolyzed with water (40 mL). The organic phase was separated, dried over $MgSO_4$ and charcoal, and filtered. The solvent was removed in vacuo to leave behind a black, viscous residue. The residue was extracted into dichloromethane (50 mL) and passed through a florisil column (1.5 cm × 15 cm) to remove viscous black material. The column was washed three times using dichloromethane (25 mL). The extracts were combined, the solvent was removed in vacuo, and the residue was recrystallized from CH_2Cl_2–hexane at –25°C. Yield: 6.294 g, 15.04 mmol, 47%.

Synthesis of {[$W(CO)_4$]$_2$(μ-$Ph_2PC_4PPh_2$)$_2$} (3)

A Schlenk tube was charged with $Ph_2PC_4PPh_2$ (**2**, 100 mg, 0.239 mmol) and [*cis*-$W(CO)_4$(2-picoline)$_2$] (**1**) (115 mg, 0.239 mmol), cooled to 0°C, and protected from light. THF

© 2008 NRC Canada

(10 mL) was added and the resulting solution was stirred at 0°C for 2.5 h, and then heated under reflux for 1.5 h. The solution was cooled to rt and solvent was removed in vacuo. The residue was extracted into CH_2Cl_2 (10 mL) and passed through a short florisil column. The solvent was removed and the residue was extracted into a minimal quantity of CH_2Cl_2. Addition of hexane (20 mL) resulted in the precipitation of **3** as a pale yellow microcrystalline solid, which was washed twice with hexane (5 mL) and dried under vacuum. Yield: 75 mg, 0.052 mmol, 44%. X-ray quality crystals of **3** were grown by slow diffusion of hexane into a CH_2Cl_2 solution. IR (CH_2Cl_2, cm^{-1}) ν: 2089s (C≡C), 2026s (CO), 1930sh (CO), 1909s (CO). ^1H NMR δ: 7.26–7.4 (m, C_6H_5), 7.5–7.7 (m, C_6H_5). $^{13}C\{^1H\}$ NMR δ: 203.9 (2nd order mult., ^1J(WC) = 148 Hz, *trans*-W(CO)), 201.4 (t, ^2J(PC) = 7 Hz, ^1J(WC) = 126 Hz, *cis*-W(CO)), 134.4 (2nd order mult., Ph), 131.6 (2nd order mult., Ph), 130.46 (s, Ph), 128.8 (2nd order mult., Ph), 92.1 (2nd order mult., PC≡C), 80.5 (2nd order mult., PC≡C). $^{31}P\{^1H\}$ NMR δ: 2.8 (s, ^1J(WP) = 241 Hz). Anal. calcd. for $C_{64}H_{40}O_8P_4W_2$: C 53.81, H 2.82; found: C 53.93, H 2.80.

Synthesis of {[W(CO)$_4$](Ph$_2$PC$_4$PPh$_2$-*K^1*-*P*)$_2$} (4)

A Schlenk tube was charged with $Ph_2PC_4PPh_2$ (**2**, 260 mg, 0.622 mmol) and [*cis*-W(CO)$_4$(2-picoline)$_2$] (**1**) (**1**, 100 mg, 0.207 mmol), cooled to 0°C and protected from light. THF (40 mL) was added via syringe and the mixture was stirred for 2.5 h at 0 °C, and then heated to 60 °C for 1.5 h. The solution was cooled to rt and the solvent was removed in vacuo. The residue was shown to be a mixture of {[W(CO)$_4$](Ph$_2$PC$_4$PPh$_2$)$_2$} **4** and {[W(CO)$_4$]$_2$(μ-Ph$_2$PC$_4$PPh$_2$)$_2$} **3** in approximately 2:1 ratio. Column chromatography was used to isolate **4** (silica gel, ethyl acetate – hexane 10:90 gradient to 20:80). Fractions containing **4** were collected and solvent was removed, resulting in a microcrystalline solid, which was used without further purification. Yield: 97 mg, 0.086 mmol, 41%. IR (CH_2Cl_2, cm^{-1}) ν: 2079w (CC), 2027s (CO), 1939sh (CO), 1913s (CO). ^1H NMR δ: 7.24–7.4 (m, C_6H_5), 7.5–7.66 (m, C_6H_5). $^{13}C\{^1H\}$ NMR δ: 204.0 (2nd order mult., ^1J(WC) = 53 Hz, *trans*-W(CO)), 201.3 (t, ^2J(PC) = 14 Hz, ^1J(WC) = 127 Hz, *cis*-W(CO)), 134.6 (2nd order mult., Ph), 133.1 (s, Ph), 132.8 (s, Ph), 131.7 (2nd order mult., Ph), 130.1 (s, Ph), 129.6 (s, Ph), 128.9 (2nd order mult., Ph), 128.6 (2nd order mult., Ph), 92.0 (2nd order mult., WPC≡C), 90.4 (2nd order mult. C≡CP), 84.511 (s, C≡CP), 84.276 (s, WPC≡C). $^{31}P\{^1H\}$ NMR δ: 1.3 (s, ^1J(WP) = 242 Hz), –29.2 (s). Anal. calcd. for $C_{60}H_{40}O_4P_4W$: C 63.62, H 3.56; found: C 63.36, H 3.58.

Synthesis of {[W(CO)$_4$(CH$_3$C$_5$H$_4$N)]$_2$(μ-Ph$_2$PC$_4$PPh$_2$)} (5)

A Schlenk tube was charged with $Ph_2PC_4PPh_2$ (100 mg, 0.239 mmol) and [*cis*-W(CO)$_4$(2-picoline)$_2$] (**1**) (230 mg, 0.479 mmol), cooled to 0°C and protected from light. Dichloromethane (15 mL) was added via syringe and the resulting solution was stirred for 3 h at 0 °C. The solvent was removed in vacuo and the residue was extracted into a minimum quantity of CH_2Cl_2. Rapid addition of hexane (20 ml) resulted in the precipitation of an oily yellow powder, which was washed twice with hexane and dried under vacuum. Yield: 239 mg, 0.200 mmol, 83.5%. IR (CH_2Cl_2, cm^{-1}) νCO: 2015s, 1900sh, 1886s, 1856s. ^1H NMR δ: 8.78 (d, ^2J(HH) = 5.6 Hz, $CH_3C_5H_4N$), 7.5–7.7 (m, Ph, $CH_3C_5H_4N$), 7.25–7.4 (m, Ph), 7.07 (d, ^2J(HH) = 7.9 Hz, $CH_3C_5H_4N$), 6.67 (m, $CH_3C_5H_4N$), 2.64 (s, $CH_3C_5H_4N$). ^{13}C NMR δ: 208.8 (d, ^2J(PC) = 3 Hz, *cis*-W(CO)), 208.1 (d, ^2J(PC) = 35 Hz, *trans*-W(CO)), 204.2 (d, ^2J(PC) = 8 Hz, axial W(CO)), 162.2 (2-picoline), 157.6 (2-picoline), 137.8 (2-picoline), 133.7 (Ph), 133.0 (Ph), 132.3 (Ph) 132.1(Ph), 130.74 (Ph), 130.71(Ph), 129.1(Ph), 129.0 (Ph), 126.3(2-picoline). 121.9(2-picoline), 91.3 (dd, ^2J(PC) = 11 Hz, ^3J(PC) = 4 Hz, PC≡C), 79.6 (d, ^1J(PC) = 55 Hz, PC≡C), 30.7 (s, CH_3). ^{31}P NMR δ: 12.28 (s, ^1J(WP) = 244.4 Hz).

Synthesis of {[W(CO)$_4$]$_3$(μ-Ph$_2$PC$_4$PPh$_2$)$_3$} (6)

A Schlenk tube was charged with {[W(CO)$_4$](Ph$_2$PC$_4$-PPh$_2$-*K^1*-*P*)$_2$} (**4**, 100 mg, 0.088 mmol) and {[W(CO)$_4$(CH$_3$C$_5$H$_4$N)]$_2$(μ-Ph$_2$PC$_4$PPh$_2$)} (**5**, 106 mg, 0.088 mmol) and protected from light. THF (7 mL) was added and the resulting solution was stirred for 5 days. The solvent was removed in vacuo. The ^{31}P NMR spectrum showed the residue to be a mixture of **3** and **6** (3:5). The residue was separated by column chromatography (silica gel, THF–hexane 40:60). Three bands were isolated and identified as **3**, **6**, and **8**. Fractions containing **6** were collected and the solution was concentrated under reduced pressure until yellow precipitate formed. The supernatant was decanted and the product was dried under vacuum. Yield: 23 mg, 0.011 mmol, 12%. The low yield of **6** is attributed to decomposition during the reaction, and decomposition on the column primarily via conversion to **8**. X-ray quality crystals were grown by slow diffusion of hexane into a CH_2Cl_2 solution of **6**. UV–vis (ε 4000 $M^{-1}cm^{-1}$): 350 nm. IR (CH_2Cl_2 solution, cm^{-1}) ν: 2088w (CC), 2023s (CO), 1930sh (CO), 1908s (CO). ^1H δ: 7.5–7.7 (m, C_6H_5), 7.26–7.4 (m, C_6H_5). ^{31}P NMR δ: 3.0 (s, ^1J(WP) = 243 Hz).

Synthesis of {[W(CO)$_4$]$_3$[μ$_3$-C$_{12}$(Ph$_2$P)$_6$]} (8)

Pure samples of **6** were converted to **8** by heating CH_2Cl_2 solutions at 60°C for 2.5 h in a closed tube. The ^{31}P NMR spectrum showed quantitative conversion of **6** to **8**. Because the isolated yield of **6** was so low, however, the most efficient preparative synthesis of **8** was to repeat the procedure given above for the preparation of **6**, but to collect and isolate fractions containing **8**. X-ray quality crystals of **8** were grown by slow diffusion of hexane into CH_2Cl_2 solutions of **8**; however twinning problems could not be resolved, so a successful structure of **8** could not be obtained. UV–vis $\lambda_{max}(\varepsilon)$: 280 (17000), 350 (3000), 500 (400). IR (CH_2Cl_2, cm^{-1}) ν_{CO}: 2021s, 1925sh, 1905s. ^1H NMR δ: 7.18–7.25 (m, C_6H_5), 7.02–7.14 (m, C_6H_5). $^{13}C\{^1H\}$ NMR δ: 207.2 (dd, ^2J(CP) = 25 Hz, ^2J(CP) = 6 Hz, *trans*-W(CO)), 200.7 (t, ^2J(PC) = 6 Hz, *cis*-W(CO)), 153.3 (dd, ^1J(PC) = 46 Hz, ^2J(PC) = 31 Hz, PC=CP), 133.2 (dd, ^1J(PC) = 42 Hz, ^4J(PC) = 3, *ipso* Ph), 131.5 (s, Ph), 131.3 (s, Ph), 130.4 (s, Ph), 128.9 (s, Ph), 128.7 (s, Ph), 106.1 (d, $^2J_{PC}$ = 23 Hz, C≡C). ^{31}P NMR δ: 60.1 (s, ^1J(WP) = 237 Hz). Anal. calcd. for $C_{96}H_{60}O_{12}P_6W_3$: C 53.81, H 2.82; found: C 53.81, H 2.71.

Kinetics measurements

The kinetics of the reaction of [W(CO)$_4$(2-picoline)$_2$] (**1**) with $Ph_2PC{\equiv}C\text{-}C{\equiv}CPPh_2$ (**2**) were monitored via in-situ ATR IR spectroscopy (ReactIR™, SiComp probe, Mettler

© 2008 NRC Canada

Table 2. Crystal data for compounds **3** and **6**.

Compound	**3**	**6**·C_6H_{14}
Empirical formula	$C_{64}H_{40}O_8P_4W_2$	$C_{96}H_{60}O_{12}P_6W_3$·C_6H_{14}
Formula weight	1428.54	2142.92
Crystal system	Triclinic	Cubic
Space group	$P\bar{1}$	$P2_13$
a (Å)	14.300(2)	21.568(2)
b (Å)	14.683(2)	21.568(2)
c (Å)	15.841(2)	21.568(2)
α (°)	67.714(2)	90
β (°)	67.625(3)	90
γ (°)	79.325(3)	90
V (Å^3)	2842.7(6)	10033(1)
Z	2	4
D_{calcd} (mg/m$^{3)}$	1.669	1.490
μ (Mo Kα) (mm^{-1})	1.669	3.584
Reflections collected	25 437	87 933
Independent reflections	25 437	7 684
Data, restraints, parameters	25 437, 0, 704	7 684, 10, 425
Goodness-of-fit on F^2	1.014	1.241
R_1	0.0413	0.0335
wR_1	0.1055	0.0854
R_2	0.0502	0.0372
wR_2	0.1100	0.0868
Res. diff. peak, hole (e Å^{-3})	1.925, –1.838	0.881, –0.446
Flack parameter	—	0.012(8)

Toledo AutoChem, 2002). In a typical experiment, $[W(CO)_4(2\text{-picoline})_2]$ (**1**) (100 mg, 0.207 mmol) was dissolved in 5 ml of CH_2Cl_2. The solution was cooled to 0°C and IR spectra were recorded at 3 min intervals. Solid $Ph_2PC{\equiv}C\text{-}C{\equiv}CPPh_2$ (**2**) (43 mg, 0.207, 0.10 mmol) was added to the solution. The reaction was monitored for 270 min. The resulting spectral data was deconvoluted using ConcIRT™ (Mettler-Toledo Autochem, 2002), which identified two major components, $[W(CO)_4(2\text{-picoline})_2]$ (**1**) and $\{[W(CO)_4(CH_3C_5H_4N)]_2(\mu\text{-}Ph_2PC_4PPh_2)\}$ (**5**). The disappearance of **1** was fitted to first order kinetics by plotting the ln of the relative concentration of **1** vs. t. The reaction rate was independent of the concentration of $Ph_2PC{\equiv}C\text{-}C{\equiv}CPPh_2$ (**2**). Full details of the kinetic studies are given in the Supplementary Data.[3]

X-ray crystallography

Suitable crystals of compounds **3** and **6** were mounted on glass fibres. Programs for diffractometer operation, data collection, cell indexing, data reduction and absorption correction were those supplied by Bruker AXS Inc., Madison, WI. Diffraction measurements were made on a PLATFORM diffractometer/SMART 1000 CCD using graphite-monochromated Mo-Kα radiation at –80°C. The unit cell was determined from randomly selected reflections obtained using the SMART CCD automatic search, centre, index, and least-squares routines. Integration was carried out using the program SAINT and an absorption correction was performed using SADABS. The crystal used for data collection on Compound **3** was found to display non-merohedral twinning. Both components of the twin were indexed with the program CELL_NOW. The second twin component can be related to the first component by 180º rotation about the [1 –1 0] axis in both real and reciprocal space. Integrated intensities for the reflections from the two components were written into a SHELXL-93 HKLF 5 reflection file with the data integration program SAINT (version 7.06A), using all reflection data (exactly overlapped, partially overlapped, and non-overlapped). The data were corrected for absorption through use of a multi-scan model, as implemented in the program TWINABS. Crystal data and collection parameters are listed in Table 2. Structure solution was carried out using the SHELX97 (45) suite of programs and the WinGX graphical interface (46). Initial solutions were obtained by direct methods and refined by successive least-squares cycles. The structure of **6** contained two disordered phenyl groups which were modeled using two different phenyl group rotations and restrained to regular hexagons. One pair of disordered phenyl rings was modeled with isotropic thermal parameters, while the other could be successfully refined anisotropically. The structure also contained highly disordered solvent molecules lying on symmetry special positions, which were mod-

[3] Supplementary data for this article are available on the journal Web site (canjchem.nrc.ca) or may be purchased from the Depository of Unpublished Data, Document Delivery, CISTI, National Research Council Canada, Ottawa, ON K1A 0R6, Canada. DUD 3813. For more information on obtaining material refer to cisti-icist.nrc-cnrc.gc.ca/cms/unpub_e.shtml. CCDC 692890 and 692891 contain the crystallographic data for this manuscript. These data can be obtained, free of charge, via www.ccdc.cam.ac.uk/conts/retrieving.html (or from the Cambridge Crystallographic Data Centre, 12 Union Road, Cambridge CB2 1EZ, UK; fax +44 1223 336033; or deposit@ccdc.cam.ac.uk).

© 2008 NRC Canada

eled using two partially occupied *n*-hexane molecules. Hydrogen atom for the disordered solvent molecules could not be modeled. Despite the disorder problems, the overall structure quality is very good.

Acknowledgements

This work was financially supported by a Natural Sciences and Engineering Research Council of Canada (NSERC) (Discovery Grant to BTS, USRA to JAT), Canada Foundation for Innovation (CFI), and the University of Regina. The authors also thank Robert McDonald and Mike Ferguson (University of Alberta) for X-ray data collection.

References

1. H. Jude, H. Disteldorf, S. Fischer, T. Wedge, A.M. Hawkridge, A.M. Arif, M.F. Hawthorne, D.C. Muddiman, and P.J. Stang. J. Am. Chem. Soc. **127**, 12131 (2005).
2. N.L.S. Yue, M.C. Jennings, and R.J. Puddephatt. Inorg. Chem. **44**, 1125 (2005).
3. F.A. Cotton, C. Lin, and C.A. Murillo. Proc. Natl. Acad. Sci. U.S.A. **99**, 4810 (2002).
4. N. Das, P.J. Stang, A.M. Arif, and C.F. Campana. J. Org. Chem. **70**, 10440 (2005).
5. H. Jude, D.J. Sinclair, N. Das, M.S. Sherburn, and P.J. Stang. J. Org. Chem. **71**, 4155 (2006).
6. M.R.J. Elsegood, M.B. Smith, and P.M. Staniland. Inorg. Chem. **45**, 6761 (2006).
7. S. Ghosh and P.S. Mukherjee. J. Org. Chem. **71**, 8412 (2006).
8. J. Zhang, R.F. Cai, Z.X. Chen, and X.G. Zhou. Inorg. Chem. **46**, 321 (2007).
9. M. Ferrer, A. Gutierrez, M. Mounir, O. Rossell, E. Ruiz, A. Rang, and M. Engeser. Inorg. Chem. **46**, 3395 (2007).
10. S. Ghosh and P.S. Mukherjee. Organometallics, **26**, 3362 (2007).
11. L.P. Ma, J. Zhang, R.F. Cai, Z.X. Chen, and X.G. Zhou. Dalton Trans. 2718 (2007).
12. Y.F. Han, Y.H. Lin, W.G. Ha, L.H. Weng, and G.X. Jin. Organometallics, **26**, 5848 (2007).
13. Y.M. Na, T.H. Noh, I.S. Chun, Y.A. Lee, J. Hong, and O.S. Jung. Inorg. Chem. **47**, 1391 (2008).
14. B.H. Northrop, A. Glockner, and P.J. Stang, J. Org. Chem. **73**, 1787 (2008).
15. M. Chas, D. Abella, V. Blanco, E. Pia, G. Blanco, A. Fernandez, C. Platas-Iglesias, C. Peinador, and J.M. Quintela. Chem. Eur. J. **13**, 8572 (2007).
16. C.H.M. Amijs, G.P.M. van Klink, and G. van Koten. Dalton Trans. 308 (2006).
17. D. Kim, J.H. Paek, M.J. Jun, J.Y. Lee, S.O. Kang, and J.J. Ko. Inorg. Chem. **44**, 7886 (2005).
18. R. Lin, J.H.K. Yip, K. Zhang, L.L. Koh, K.Y. Wong, and K.P. Ho. J. Am. Chem. Soc. **126**, 15852 (2004).
19. P. Thanasekaran, R.T. Liao, Y.H. Liu, T. Rajendran, S. Rajagopal, and K.L. Lu. Coord. Chem. Rev. **249**, 1085 (2005).
20. M. Fujita, Y.J. Kwon, S. Washizu, and K. Ogura. J. Am. Chem. Soc. **116**, 1151 (1994).
21. J. Kuwabara, C.L. Stern, and C.A. Mirkin. J. Am. Chem. Soc. **129**, 10074 (2007).
22. M.J.E. Resendiz, J.C. Noveron, H. Disteldorf, S. Fischer, and P.J. Stang. Org. Lett. **6**, 651 (2004).
23. Z.R. Laughrey and B.C. Gibb. Top. Curr. Chem. **249**, 67 (2005).
24. F. Aricó, J.D. Badjic, S.J. Cantrill, A.H. Flood, K.C.-F. Leung, Y. Liu, and J.F. Stoddart. Top. Curr. Chem. **249**, 203 (2005).
25. L.R. MacGillivray, G.S. Papaefstathiou, T. Friscic, D.B. Varshney, and T.D. Hamilton. Top. Curr. Chem. **284**, 201 (2004).
26. A. Garcia, J. Gomez, E. Lalinde, and M.T. Moreno. Organometallics, **25**, 3926 (2006).
27. J. Fornies, A. Garcia, B. Gil, E. Lalinde, and M.T. Moreno. Dalton Trans. 3854 (2004).
28. A. García, E. Lalinde, and M.T. Moreno. Eur. J. Inorg. Chem. **2007**, 3553 (2007).
29. A. García, J. Gómez, E. Lalinde, and M.T. Moreno. Organometallics, **25**, 3926 (2006).
30. A.J. Carty, N.J. Taylor, and D.K. Johnson. J. Am. Chem. Soc. **101**, 5422 (1979).
31. D.K. Johnson, T. Rukachaisirikul, Y. Sun, N.J. Taylor, A.J. Canty, and A.J. Carty. Inorg. Chem. **32**, 5544 (1993).
32. C.J. Adams, M.I. Bruce, E. Horn, and E.R.T. Tiekink. J. Chem. Soc. Dalton Trans. 1157 (1992).
33. M. Semmelmann, D. Fenske, and J.F. Corrigan. J. Chem. Soc. Dalton Trans. 2541 (1998).
34. C.J. Adams, M.I. Bruce, E. Horn, B.W. Skelton, E.R.T. Tiekink, and A.H. White. J. Chem. Soc. Dalton Trans. 3299 (1993).
35. M.I. Bruce, P.J. Low, M.Z. Ke, B.D. Kelly, B.W. Skelton, M.E. Smith, A.H. White, and N.B. Witton. Aust. J. Chem. **54**, 453 (2001).
36. M.J. Went. Polyhedron, **14**, 465 (1995).
37. F. Carré, N. Devylder, S.G. Dutremez, C. Guerin, B.J.L. Henner, A. Jolivet, V. Tomberli, and F. Dahan. Organometallics, **22**, 2014 (2003).
38. M.P. Martin-Redondo, L. Scoles, B.T. Sterenberg, K.A. Udachin, and A.J. Carty. J. Am. Chem. Soc. **127**, 5038 (2005).
39. E.K. Tosh. Ring-opening metathesis polymerisation reactions of norbornene and norbornadiene using *cis*-$W(CO)_4(C_5H_5N)_2$ and $W(CO)_3I_2(\eta^2$-dppm) as catalysts. M.Sc. thesis. University of Regina, Regina, Sask. 2006.
40. J.A.S. Howell and P.M. Burkinshaw. Chem. Rev. **83**, 557 (1983).
41. E. Fluck and G. Heckmann. *In* Phosphorus-31 NMR spectroscopy in stereochemical analysis. *Edited by* J. G. Verkade and L. D. Quin. VCH, Deerfield Beach. 1987. p. 61.
42. C.E. Anderson, D.C. Apperley, A.S. Batsanov, P.W. Dyer and J. A. K. Howard. Dalton Trans. 4134 (2006).
43. F. Sondheimer, R. Wolovsky, P.J. Garratt, and I.C. Calder. J. Am. Chem. Soc. **88** (1966).
44. K.G. Untch and D.C. Wysocki. J. Am. Chem. Soc. **88**, 2608 (1966).
45. G.M. Sheldrick. SHELX97 [computer program]. Institüt für Anorganische Chemie der Universität, Tammanstrasse 4, D-3400 Göttingen, Germany, 1998.
46. L.J. Farrugia. J. Appl. Cryst. **32**, 837 (1999).

© 2008 NRC Canada

Formation of a [2]rotaxane and [2]catenane based on $PdBr_2L_2$ as a template[1]

Barry A. Blight, James A. Wisner, and Michael C. Jennings

Abstract: Previous studies have determined that neutral palladium(II) dibromide complexes template the formation of [2]pseudorotaxanes, albeit with weaker affinities than the analogous palladium(II) dichloride species. Here, the self-assembly of both [2]rotaxane (**2**) and [2]catenane (**5**) were attempted using a $PdBr_2L_2$ centre as the template, resulting in the desired interlocked structures. The structures were confirmed by NMR spectroscopy, CSI-MS, and single crystal X-ray diffraction analyses. [2]Rotaxane **2** was isolated in 53% and [2]catenane **5** in 41% yields. The lower yields observed in comparison to the chloride analogues can be attributed to the reduced template effect of the palladium(II) dibromide subunits, caused by both the poor steric fit of the bromides in the isophthalamide cleft and bromide's reduced capacity as a hydrogen bond acceptor.

Key words: rotaxane, catenane, hydrogen bonding, interlocked, supramolecular chemistry.

Résumé : Des études antérieures ont permis de déterminer que les complexes de dibromure de palladium(II) neutre peuvent être utilisés comme gabarit pour la formation de [2]pseudorotoxanes, même si leur affinité est plus faible que celle des espèces analogues à base de dichlorure de palladium(II). Dans ce travail, on a tenté de réaliser l'autoassemblage du [2]rotoxane (**2**) et du [2]caténane (**5**) en utilisant un gabarit à base de $PdBr_2I_2$ et on a obtenu les structures comportant les interrelations désirées. Les structures ont été confirmées par spectroscopie RMN, par spectrométrie de masse avec ionisation par nébulisation à froid (SM-INF) et par des analyse de diffraction des rayons X par un cristal unique. On a isolé le [2]rotoxane (**2**) avec un rendement de 53% et le [2]caténane (**5**) avec un rendement de 41%. Ces rendements plus faibles que ceux obtenus avec les analogues chlorés peuvent être attribués à l'effet de gabarit réduit des unités de dibromure de palladium(II) qui est provoqué par le mauvais ajustement stérique des bromures dans les espaces disponibles de l'isophtalamide ainsi que par la capacité réduite du bromure comme accepteur d'une liaison hydrogène.

Mots-clés : rotaxane, caténane, liaison hydrogène, interrelié, chimie supramoléculaire.

[Traduit par la Rédaction]

Introduction

The study of interlocked molecules (e.g., rotaxanes and catenanes) (1), conceptual precursors to molecular machines (2), has largely been possible because of the potentially high yields of products that self-assemble by applying modern template-based synthetic methods (1, 2). In this context, the use of transition metals in these assemblies generally falls into one of two categories. The metal may be used as a reversible connection point in the backbone of one or more of the components (3). Alternatively, the metal can participate in the template process to organize accompanying ligands in a desired spatial arrangement (4). The simultaneous use of the metal in both roles is rare but offers a possible route to further simplify syntheses of these interlocked products (5).

Received 31 March 2008. Accepted 11 April 2008. Published on the NRC Research Press Web site at canjchem.nrc.ca on 16 September 2008.

B.A. Blight, J.A. Wisner,[2] and M.C. Jennings. Department of Chemistry, The University of Western Ontario, London, ON N6A 5B7, Canada.

[1]This article is part of a Special Issue dedicated to Professor R. Puddephatt.

[2]Corresponding author (e-mail: jwisner@uwo.ca).

We have previously reported a study (6) that examined the complexation of *trans*-bis-pyridine palladium(II) dihalide axles by the well-known isophthalamide-based macrocycle **1** (7). Their combination resulted in [2]pseudorotaxane formation, employing second-sphere coordination of the halide ligands (hydrogen-bond acceptors) by the isophthalamide clefts (hydrogen-bond donors) of **1** as the template. It was concluded that the size of the $PdCl_2$ subunit of a *trans*-$PdCl_2Py_2$ axle was a complimentary fit to the size of the hydrogen-bond donating macrocyclic cavity (K_a = 5000 $(mol/L)^{-1}$ in $CDCl_3$ at 298 K). Nitrogen-based ligand exchange allowed us to then apply this template strategy in the facile self-assembly of palladium(II) dichloride templated [2]rotaxane (8) and [2]catenane superstructures (9).

Anion recognition studies by Crabtree and co-workers (10), Smith and co-workers (11), Beer and co-workers (12), and Gale and co-workers (13) have demonstrated that neutral isophthalamide-based acyclic receptors associate with a variety of anions through hydrogen bonding in solution. Studies specifically examining isophthalamide–halide complexation in solution revealed an inferior affinity for bromide compared with chloride, which can be rationalized by a reduced hydrogen-bond acceptor ability and a poorer steric fit of bromide anions for such receptors. [2]Pseudorotaxanes formed between **1** and a *trans*-$PdBr_2Py_2$ axle exhibit a similarly reduced affinity (K_a = 750 $(mol/L)^{-1}$ in $CDCl_3$ at 298 K) in

 doi:10.1139/V08-126 © 2008 NRC Canada

Scheme 1. Syntheses of [2]rotaxane **2** and [2]catenane **5**. Aromatic protons are labeled identically to the previously reported $PdCl_2$-based structures (8, 9) to aid in discussion of their respective ^1H NMR spectra.

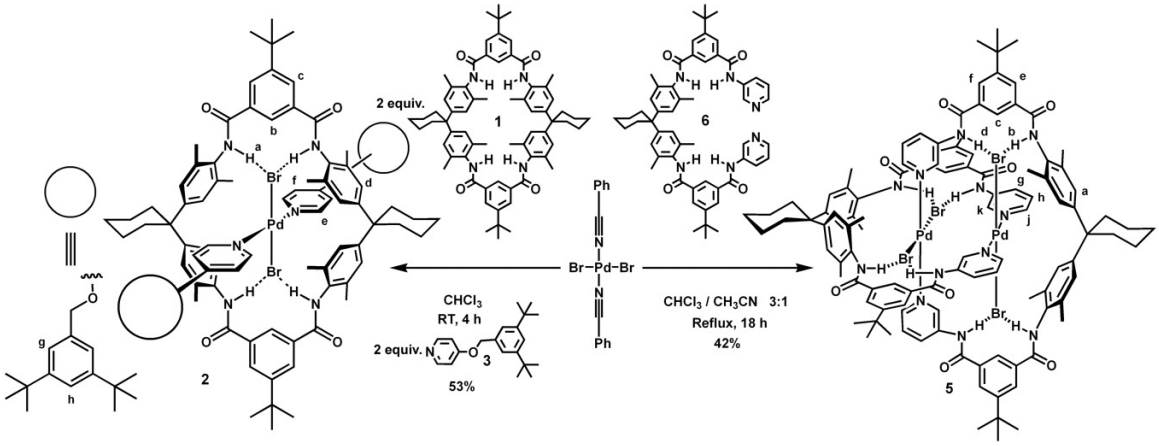

comparison with the chloride analogue, which can be explained using similar arguments (6). To date, however, there are no literature examples of bromide anions or ligands acting as, or in, the organizational template to form a finite interlocked structure. We sought to examine this potential phenomenon by observing whether bromide can indeed be used to template interlocked products, and, if so, how they compare structurally to other bromide-bound isophthalamide-based receptors. Herein, we describe the syntheses and characterization of a [2]rotaxane (**2**) and [2]catenane (**5**) templated by second-sphere coordination of palladium(II) dibromide complexes via hydrogen bonding (Scheme 1) and rendered interlocked through first-sphere ligation.

Results and discussion

[2]Rotaxane (2)

Ligand substitution of benzonitrile from *trans*-bis-benzonitrile palladium(II) dibromide (14) by sterically demanding pyridine co-ligands (4-(3,5-di-tert-butylbenzyl)-oxypyridine) **3** (8) in the presence of **1** (2 equiv.) results in the synthesis of interlocked **2** in modest yields (Scheme 1). Its preparation proceeds via dissolution of the above three components in chloroform and allowing them to stir for 4 h at room temperature. After selective crystallization of macrocycle **1** and precipitation of the remaining liquor's contents into hexanes, flash column chromatography was required to separate the product from the reaction mixture, affording [2]rotaxane **2** in 53% yield.

Comparison of the ^1H NMR spectra of the free components macrocycle **1** and dumbbell **4** with the pale yellow powder isolated from chromatography supported the expected interlocked geometry in solution (Fig. 1). Hydrogen-bonding interactions with the bromide ligands result in the deshielding of the macrocyclic amide protons (H_a $\Delta\delta = 0.94$ ppm). As a consequence of the interpenetrated nature of the structure, both pyridyl-protons (H_e $\Delta\delta = -1.44$ ppm, H_f $\Delta\delta = -0.55$ ppm) are shifted upfield from the frequency of their free components due to C-H$\cdots\pi$ interactions with the diphenylcyclohexyl sidewalls of the macrocycle, which also results in deshielding of the diphenylcyclohexyl arene protons (H_d $\Delta\delta = 0.23$ ppm). Cold spray ionization mass spectrometry (CSI-MS) confirmed the presence of the solvated

Fig. 1. The aromatic region of the ^1H NMR spectra (600 MHz, $CDCl_3$, 298 K) of free macrocycle **1** (top), [2]rotaxane **2** (middle), and free dumbbell **4** (bottom). Illustrated are the observed perturbations in chemical shift between free and interlocked components (dashed lines). COSY, and ROESY NMR experiments were performed to determine individual ^1H NMR spectroscopic assignments.

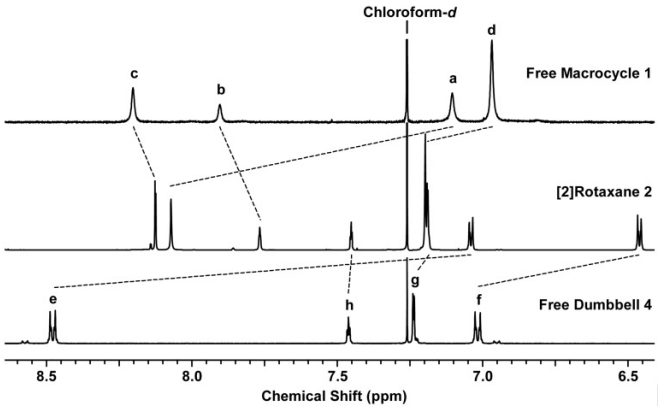

superstructure with ions of $[M - Br]^+$ at 1797.9 amu and $[M - 2Br]^{2+}$ at 858.5.3 amu, signals that do not appear in solutions of **1** and (or) **4** subjected to the same conditions.

Determination of the solid-state structure by single crystal X-ray diffraction analysis confirmed the solution evidence for the interlocked geometry (Fig. 2). Colorless plate-like single crystals were grown by slow diffusion of diisopropylether into a concentrated chloroform solution of **2**. The anticipated interlocked architecture crystallized in space group *P*(-1) and contained structural similarities to isophthalamide–bromide complexes in the existing literature (10–13). In these cases, hydrogen-bond contacts are slightly longer (3.42 to 3.63 Å) than the sums of the Van der Waals radii (3.40 Å), with the exception of one isophthalamide–bromide conjugate reported by Smith and co-workers (3.28 and 3.39 Å) and are in agreement with those measured in **2**. The larger size of bromide anions (or ligands) also causes each amide nitrogen from these examples, including **2**, to deviate from coplanarity from the central isophthalamide ring in the direction of bromide (by >20°) resembling a perching-type geometry. This also results in a 2.11 Å dis-

© 2008 NRC Canada

Fig. 2. Stick representation of [2]rotaxane **2** in the solid state. All methyl, cyclohexyl, and *t*-butyl groups of the macrocycle and all C-H hydrogen atoms have been removed for clarity. Hydrogen bonds and weak contacts have been represented by yellow dashed lines. Color code: C gray, H white, N blue, O red, Br orange, Pd teal.

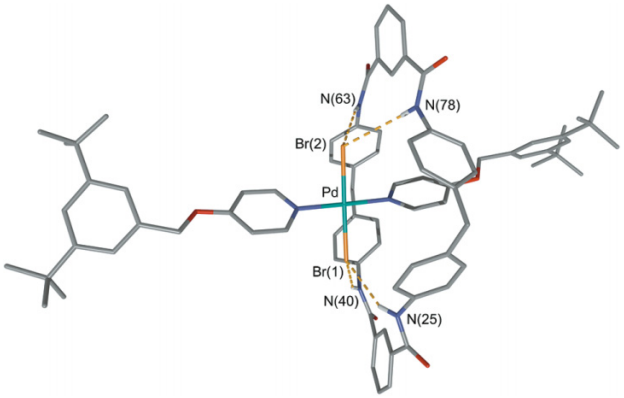

placement of the palladium centre from the least-squares plane of the macrocyclic ring (plane defined by the four carbonyl carbons), caused by the poor steric fit of the bromide ligands in the isophthalamide clefts of **1**. The dissymmetric geometry of **2**, in the solid state, prompted us to investigate its potential shuttling activity in solution (15). However, low temperature ^{1}H NMR showed no sign of exchange broadening down to –50 °C (248 K). Contact distances and angles of interest include: N(25)···Br(1) = 3.46 Å (N-H···Br = 156°), N(40)···Br(1) = 3.45 Å (N-H···Br = 153°), N(63)···Br(2) = 3.57 Å (N-H···Br = 164°), N(78)···Br(2) = 3.67 Å (N-H···Br = 150°).

[2]Catenane (5)

[2]Catenane **5** is designed to employ a *trans*-bidentate ligand **6** (9) that incorporates the structural components of both macrocycle **1** and the required pyridine co-ligands (Scheme 1). A chloroform–acetonitrile solution of **6** and *trans*-bis-benzonitrile palladium(II) dibromide (14) were refluxed for 18 h. The reaction mixture was concentrated, precipitated into hexanes to remove residual benzonitrile, and the resulting orange solid subjected to column chromatography to afford [2]catenane **5** (a yellow powder) in 41% yield.

^{1}H NMR spectral comparison of the reaction product to the previously synthesized Pd_2Cl_4-based [2]catenane (9) confirmed in solution that the desired interlocked geometry was likely obtained using palladium(II) dibromide to template [2]catenane formation (Fig. 3). Similar chemical shifts of protons H_a, H_b, H_e, H_f, H_g, H_h, H_j, and H_k between **5** and its Pd_2Cl_4-counterpart lead us to this conclusion. In this case, however, H_h is more shielded ($\Delta\delta$ = –0.32 ppm) and H_j is less shielded ($\Delta\delta$ = 0.13 ppm) than observed in the Pd_2Cl_4-based [2]catenane, which may be attributed to stronger and (or) more frequent C-H···π interactions of H_h (resulting in weaker interactions with H_j) with the diphenylcyclohexyl cavity of the opposing macrocycle. Unexpectedly, amide proton H_d is extremely shielded ($\Delta\delta$ = –0.87 ppm) and H_c deshielded ($\Delta\delta$ = 1.07 ppm) in comparison with the Pd_2Cl_4-[2]catenane, and although examination of the ^{1}H NMR evi-

Fig. 3. The aromatic region of the ^{1}H NMR spectra (600 MHz, 298 K) of Pd_2Cl_4-[2]catenane (top), and [2]catenane **5** (bottom). Individual proton assignments are compared between the two superstructures (dashed lines). NOESY, and ROESY NMR experiments were performed to determine individual ^{1}H NMR assignments.

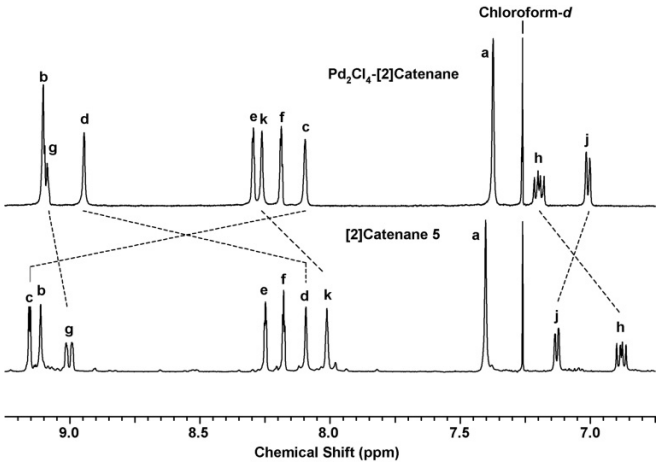

dence could not explain these two proton assignments, a reasonable explanation presented itself upon receipt of the solid-state structure. CSI-MS also confirmed the presence of [2]catenane **5** in solution with ions of $[M + H]^+$ at 2300.8 amu and $[M + 2H]^{2+}$ at 1150.3 amu. Compound **5** was then dissolved in 1 mol/L of DMSO-d_6 and monitored by ^{1}H NMR spectroscopy in an attempt to disassemble it into its degenerate macrocyclic components. Unfortunately, the system completely degrades under these conditions, giving rise to a mixture of unidentifiable polymeric materials.

Orange platelike single crystals were grown from a concentrated chloroform solution of **5** by slow diffusion of diisopropyl ether crystallizing in space group *P*2(1)/*c* and subjected to single crystal X-ray diffraction analysis. Structural elucidation of **5** established the desired interlocked geometry in the solid state (Fig. 4), which unexpectedly contained two exotopically arranged amide functionalities (with respect to the NH groups) in the structure of *macrocycle B* (all eight amide NHs of the Pd_2Cl_4-[2]catenane are endotopic). We posit that competition for hydrogen-bond acceptors ($PdBr_2$ subunits and the carbonyl-oxygen atoms in the backbone of each macrocyclic component) by the hydrogen-bond donating clefts results in an overall geometry containing a blend of structural elements from Crabtree's isophthalamide–bromide complex (10) and the amide-based [2]catenanes of Hunter (16), Vögtle and co-workers (17), and Leigh and co-workers (18) in the solid state.

The isophthalamide subunit of *macrocycle A* participates in the mutual recognition of Br(2B) (N(17A)···Br(2B) = 3.37 Å (N-H-Br = 165°), N(32A)···Br(2B) = 3.36 Å (N-H-Br = 166°)), resembling those of the isophthalamide–bromide conjugates previously discussed (10–13), as well as **2**. The second isophthalamide subunit of *macrocycle A* bifurcates O(69B) of *macrocycle B* with its NH groups (N(55A)···O(69B) = 3.75 Å (N-H-O = 158°), N(70A)···O(69B) = 2.95 Å (N-H-O = 171°), while the exotopically arranged NHs of *macrocycle B* are independently engaged in hydrogen bonding with adjacent *macrocycle A* units through the crystal lattice (N(32B)···O(57A) =

© 2008 NRC Canada

Fig. 4. Stick representation of [2]catenane **5** in the solid state. All C-H hydrogen atoms, methyl, cyclohexyl, and *t*-butyl groups have been removed for clarity. Hydrogen bonds and weak contacts have been represented by yellow dashed lines. Color code: C gray, H white, N blue, O red, Br orange, Pd teal.

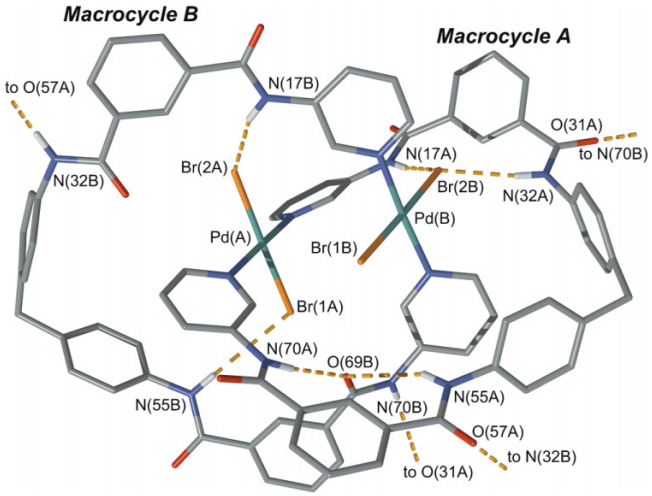

2.91 Å (N-H-O = 158°), N(70B)···O(31A) = 2.98 Å (N-H-O = 141°)) and are both features of the mentioned amide-based [2]catenanes in the solid state. Each isophthalamide subunit of *macrocycle B* is singularly engaged in weak hydrogen-bond contacts with the opposing bromide ligands of *macrocycle A* (N(17B)···Br(2A) = 3.67 Å (N-H-Br = 151°), N(55B)···Br(2A) = 3.99 Å (N-H-Br = 155°). As in **2,** the Br-Pd-Br subunits in **5** are also too large for the macrocyclic cavity, which forces the displacement of each $PdBr_2$ from the centre of its respective host macrocycle (macrocyclic-plane-A···Pd(B) = 1.48 Å, macrocyclic-plane-B···Pd(A) = 2.40 Å). This results in perched geometries of both $PdBr_2$ subunits in the mouths of their respective macrocyclic components, with all amides engaged in bromide–ligand contacts deviating from coplanarity with their respective isophthalamide phenyl ring (>20°) but one. Finally, from the solid-state structure we can postulate that the unusual upfield ^{1}H NMR shift of H_d (N(32A), N(55A), N(32B), N(55B)) is likely due to this hydrogen-bond competition resulting in increased exposure to the bulk solvent, while the downfield shift of H_c (C(21A), C(59A), C(21B), C(59B)) may be the result of positioning in the deshielding cone of a neighboring endotopically arranged carbonyl-oxygen atom.

Conclusion

In summary, palladium(II) dibromide metal centres have been used successfully to self-assemble both a [2]rotaxane and [2]catenane despite the reduced magnitude of the template interactions present in comparison with previously reported palladium(II) dichloride analogues. The reduced ability of the macrocycle to hydrogen bond to the bromide ligands of the metal complex gives rise to distortions of the resulting interlocked molecules from the planned template geometry, yielding recognizable structural elements from other known isophthalamide-containing supramolecules in the solid state. The [2]catenane generated using the PdBr2 template was unstable to attempts to dissociate the two catenated rings, using DMSO as a competitive solvent for both hydrogen bonding and ligand exchange.

Experimental

General

All reactions were performed in dry solvents and under an inert $N_{2(g)}$ atmosphere. All organic reagents, including palladium(II) dibromide, were purchased from Sigma-Aldrich Chemical Company and all were used without further purification. 1D NMR spectral analyses of **4** for characterization purposes were performed on a Varian Mercury 400MHz instrument. 1D NMR and 2D NMR spectral analyses of **2** and **5** or individual assignments were performed on a Varian Inova 600MHz instrument. Cold-spray ionization mass determinations were performed with Micromass LCT instrumentation with carrier gases cooled to 200 K.

X-ray crystallographic analyses

Single crystal X-ray diffraction data, for both **2** and **5** (grown from a concentrated chloroform solution of **2** or **5** by slow vapor diffusion of diisopropyl ether), was obtained from a programmed hemisphere scan routine on a Nonius Kappa-CCD diffractometer. The unit cell parameters were calculated and refined from the full data set. Crystal cell refinement and data reduction were carried out using DENZO (Nonius B.V., 1998). The data were scaled using SCALEPACK (Nonius B.V., 1998). The solution for **2** was solved by Patterson methods, and the solution for **5** by direct methods, followed by difference Fourier syntheses to find the remaining atoms in each subsequent structure. Refinement was with full-matrix least-squares methods using SHELXTL-NT 6.1 (G.M. Sheldrick, Madison, Wisconsin, USA, 2000). The organic material and the metal center(s) were very well resolved in both structures. All of the non-hydrogen atoms were refined with anisotropic thermal parameters. The hydrogen atom positions were calculated geometrically and were included as riding on their respective carbon atoms. A summary of the data collection, solution, and refinement parameters are listed in Table 1.[3]

Procedures

[2]Rotaxane (2)

Macrocycle **1** (50 mg, 0.049 mmol) and *trans*-bis-benzonitrile palladium(II) dibromide (14) (12 mg, 0.025 mmol) were dissolved in chloroform (10 mL) in a 25 mL round-bottomed flask and stirred for 10 min. 4-(3,5-Di-*tert*-

[3] Supplementary data for this article are available on the journal Web site (canjchem.nrc.ca) or may be purchased from the Depository of Unpublished Data, Document Delivery, CISTI, National Research Council Canada, Ottawa, ON K1A 0R6, Canada. DUD 3817. For more information on obtaining material refer to cisti-icist.nrc-cnrc.gc.ca/cms/unpub_e.shtml. CCDC 672440 (**2**) and 672439 (**5**) contain the crystallographic data for this manuscript. These data can be obtained, free of charge, via www.ccdc.cam.ac.uk/conts/retrieving.html (Or from the Cambridge Crystallographic Data Centre, 12 Union Road, Cambridge CB2 1EZ, UK; fax +44 1223 336033; or deposit@ccdc.cam.ac.uk).

© 2008 NRC Canada

Table 1. Crystal data, solution, and refinement parameters for [2]rotaxane **2** and [2]catenane **5**.

Compound	**2**	**5**
CCDC number	672440	672439
Empirical formula	$C_{122}H_{164}Br_2Cl_6N_6O_8Pd$	$C_{122}H_{146}Br_4Cl_3N_{12}O_{9.5}Pd_2$
	(**2**·2 $CHCl_3$·2 isopropyl ether)	(**5**·1 $CHCl_3$·1.5 isopropyl ether)
Formula mass	2321.51	2571.3
Crystal description	Colorless plates	Orange plates
Crystal size (mm)	0.50 × 0.06 × 0.04	0.33 × 0.10 × 0.05
Crystal system	Triclinic	Monoclinic
Space group	P (-1)	*P*2(1)/*c*
a (Å)	17.415(2)	15.2868(5)
b (Å)	20.501(3)	32.6803(12)
c (Å)	21.0011(17)	24.8098(8)
α (°)	107.372(6)	90
β (°)	100.449(6)	95.628(2)
γ (°)	113.911(5)	90
Z	2	4
V (Å^3)	6 136.3(12)	12 334.7(7)
D_{calcd} (gcm^{-3})	1.256	1.385
μ (mm^{-1})	0.988	1.712
Independent reflections (R_{int})	20 709 (0.0780)	21 137 (0.187)
Data, restraints, parameters	20 709, 0, 1340	21 137, 22, 1370
Goodness-of-fit on F^2	1.056	0.921
Final R_1 [$F^2 > 2\sigma F^2$]	0.0985	0.091
Final wR_2 [$F^2 > 2\sigma F^2$]	0.1836	0.2089
Final R_1 (all data)	0.219	0.3346
Final wR_2 (all data)	0.2404	0.2959
Residuals peak, hole (e, Å^3)	0.994, –0.794	1.248, –0.784

butylbenzyl)-oxypyridine **3** (15 mg, 0.049 mmol) was dissolved in chloroform (2 mL) and added dropwise via pipette. The solution was stirred for 4 h, followed by cooling in the freezer to selectively crystallize unreacted macrocycle. The precipitate was isolated via vacuum filtration, and volume of the filtrate reduced under reduced pressure to approximately 2 mL of solvent. This concentrated solution was then added dropwise to a beaker of hexanes to precipitate the product away from the high-boiling benzonitrile. The precipitate was collected via vacuum filtration. The crude product was then chromatographed (5% EtOAc in DCM, leading band) to afford 24 mg (0.013 mmol, 53% yield) of pure [2]rotaxane **2**. ^{1}H NMR ($CDCl_3$, 600 MHz) δ: 8.13 (d, 4H, 6 Hz), 8.07 (s, 4H), 7.77 (t, 4H, 6 Hz), 7.45, (t, 2H, 5 Hz), 7.20 (s, 8H), 7.19 (d, 4H, 5 Hz), 7.04 (d, 4H, 12 Hz), 6.46 (d, 4H, 12 Hz), 5.07 (s, 4H), 2.48 (bs, 8H), 2.10 (s, 24H), 1.70 (bs, 8H), 1.57 (bs, 4H), 1.37 (s, 18H), 1.30 (s, 36H). ^{13}C NMR ($CDCl_3$, 600 MHz) δ: 166.13, 166.00, 153.49,152.91, 151.91, 135.11, 134.53, 133.11, 131.56, 129.00, 123.38, 123.11, 121.70, 112.20, 71.82, 35.26, 34.90, 34.73, 31.40, 31.36, 31.20, 22.79, 19.30, 19.19. LR CSI-MS (MeOH matrix in $CHCl_3$) $[M - 2Br]^{2+}$ *m*/*z*: 858.5.3, $[M - Br]^+$ *m*/*z*: 1797.9.

Dumbbell (4)

In a 10 mL round-bottomed flask, *trans*-bis-benzonitrile palladium(II) dibromide (14) (40.0 mg, 0.085 mmol) was dissolved in dry acetonitrile (3 mL) and allowed to stir for 5 minutes. 4-(3,5-Di-*tert*-butylbenzyl)-oxypyridine **3** (14) (50.5 mg, 0.17 mmol) was dissolved in dry acetonitrile (1 mL) and added dropwise to the bulk solution. The reaction was stirred for 30 min to allow ample time for precipitation of the desired product. The product was isolated via vacuum filtration (65.1 mg, 0.076mmol, 88% Yield). ^{1}H NMR ($CDCl_3$, 400 MHz) δ: 8.48 (d, 4H, 8 Hz), 7.46 (t, 2H, 4 Hz), 7.24 (d, 4H, 4 Hz), 7.02 (d, 4H, 8 Hz), 5.10 (s, 4H), 1.34 (s, 36H). ^{13}C NMR ($CDCl_3$, 400 MHz) δ: 166.28, 154.90, 151.51, 133.42, 123.09, 122.31, 111.89, 71.69, 34.88, 31.39. LR-ESI MS (MeOH matrix in $CHCl_3$) $[M - Br]^+$ *m*/*z*: 781.2, $[M - 2Br + H]^+$ *m*/*z*: 699.3.

[2]Catenane (5)

Dipyridyl ligand **6** (50 mg, 0.057 mmol) was dissolved in a 3:1 chloroform/acetonitrile solvent mixture (10 ml). A chloroform solution (2 ml) of *trans*-bis-benzonitrile palladium(II) dibromide (14) (27 mg, 0.057 mmol) was added dropwise to the reaction mixture, and the reaction refluxed for 18 h. The crude reaction mixture was filtered through celite to remove any precipitate, and solvent removed under reduced pressure. The resulting solid was dissolved in a minimum amount of dichloromethane and precipitated into hexanes to remove residual benzonitrile. The precipitate was collected via vacuum filtration and the crude product was then chromatographed (5% EtOAc in DCM, leading band) to afford 27 mg (0.012 mmol, 42% yield) of pure [2]catenane **5**. ^{1}H NMR ($CDCl_3$, 600 MHz) δ: 9.16 (d, 4H, 1.8 Hz), 9.12 (s, 4H), 9.01 (d, 4H, 8.4 Hz), 8.26 (dd, 4H, 1.8 and 1.8 Hz), 8.18 (dd, 4H, 1.8 Hz and 1.8 Hz), 8.09 (s, 4H), 8.02 (s, 4H), 7.40 (s, 8H), 7.14 (d, 4H, 5.4 Hz), 6.88 (dd, 4H, 8.4 Hz and 5.4 Hz) 2.61 (bs, 8H), 2.22 (s, 24H), 1.77 (bs 8H), 1.61 (bs,

© 2008 NRC Canada

4H), 1.34 (s, 36H). ^{13}C NMR ($CDCl_3$, 600 MHz) δ: 165.48, 164.78, 153.68, 148.22, 146.41, 143.20, 138.25, 135.45, 134.35, 133.50, 131.52, 130.49, 129.75, 129.17, 126.27, 125.93, 120.67, 44.98, 35.19, 34.63, 31.03, 26.34, 22.79, 19.34. LR CSI-MS (MeOH matrix in $CHCl_3$) $[M + 2H]^{2+}$ *m/z*: 1150.3, $[M + H]^+$ *m/z*: 2300.8.

Acknowledgements

We are grateful for the financial support provided by the Natural Sciences and Engineering Research Council of Canada and the University of Western Ontario.

References

1. (*a*) G. Schill. Catenanes, rotaxanes and knots. Academic Press, New York, USA. 1971; Molecular catenanes, rotaxanes, and knots. *Edited by* J.P. Sauvage and C.O. Dietrich-Buchecker Wiley-VCH, Weinheim, Germany. 1999; (*b*) F. Arico, T. Chang, S.J. Cantrill, S.I. Khan, and F.J. Stoddart. Chem. Eur. J. **11**, 4655 (2005); (*c*) C.A. Schalley. J. Phys. Org. Chem. **17**, 967 (2004); (*d*) S.J. Loeb and J.A. Wisner. Angew. Chem. Int. Ed. **37**, 2838 (1998); (*e*) C.A. Hunter. J. Am. Chem. Soc. **114**, 5303 (1992); (*f*) C. Reuter, R. Schmieder, and F. Vögtle. Pure Appl. Chem. **72**, 2233 (2000); (*g*) H. Adams, F.J. Carver, and C.A. Hunter. Chem. Commun. 809 (1995); (*h*) B. Therrien, A. Hori, M. Tominaga, and M. Fujita. Acc. Chem. Res. **38**, 369 (2005); (*i*) X.-Y. Li, J. Illigen, M. Nieger, S. Michel, and C.A. Schalley. Chem. Eur. J. **9**, 1332 (2003); (*j*) A.-M. Fuller, D.A. Leigh, P.J. Lusby, A.M.Z. Slawin, and D.B. Walker. J. Am. Chem. Soc. **127**, 12612 (2005); (*k*) M.R. Sambrook, P.D. Beer, J.A. Wisner, R.L. Paul, and A.R. Cowley. J. Am. Chem. Soc. **126**, 15364 (2004); (*l*) A.L. Hubbard, G.J.E. Davidson, R.H. Patel, J.A. Wisner, and S.J. Loeb. Chem. Commun. 138 (2004).
2. (*a*) E.R. Kay, D.A. Leigh, and F. Zerbetto. Angew. Chem. Int. Ed. **46**, 72 (2007) and refs. cited therein; (*b*) A. Mateo-Alonso, C. Ehli, G.M. Aminur Rahman, D.M. Guldi, G. Fioravanti, M. Marcaccio, F. Paolucci, and M. Prato. Angew. Chem. Int. Ed. **46**, 3521 (2007); (*c*) F. Durola and J.-P. Sauvage. Angew. Chem. Int. Ed. **46**, 3537 (2007); (*d*) W. Abraham, K. Buck, M. Orda-Zgadzaj, S. Schmidt-Schaeffer, and U.-W. Grummet. Chem. Commun. 3094 (2007); (*e*) V. Aucagne, J. Berna, J.D. Crowley, S.M. Goldup, K.D. Haenni, D.A. Leigh, P.J. Lusby, V.E. Ronaldson, A.M.Z. Slawin, A. Viterisi, and D.B. Walker. J. Am. Chem. Soc. **129**, 11950 (2007); (*f*) S. Saha, A.H. Flood, J.F. Stoddart, S. Impellizzeri, S. Silvi, M. Venturi, and A. Credi. J. Am. Chem. Soc. **129**, 12159, (2007); (*g*) J.D. Crowley, D.A. Leigh, P.J. Lusby, R.T. McBurney, L.-E. Perret-Aebi, C. Petzold, A.M.Z. Slawin, and M.D. Symes. J. Am. Chem. Soc. **129**, 15085 (2007); (*h*) S.J. Vella, J. Tiburcio, and S.J. Loeb. Chem. Commun. 4752 (2007).
3. (*a*) M. Fujita, F. Ibukuro, H. Hagihara, and K. Ogura. Nature, **367**, 720, (1994); (*b*) M. Fujita, F. Ibukuro, K. Yamaguchi, and K. Ogura. J. Am. Chem. Soc. **117**, 4175 (1995); (*c*) K.-I. Yamashita, M. Kawano, and M. Fujita. J. Am. Chem. Soc. **129**, 1850 (2007); (*d*) I. Yoon, M. Narita, T. Shimizu, and M. Asakawa. J. Am. Chem. Soc. **126**, 16740, (2004); (*e*) C.O. Dietrich-Buchecker, N. Geum, A. Hori, M. Fujita, S. Sakamoto, K. Yamaguchi, and J.-P. Sauvage. Chem. Comun. 1182 (2001); (*f*) R.S. Wylie and D.H. Macartney. Supramol. Chem. **3**, 29 (1993); (*g*) K.-Y. Chang, H.-Y. Jang, and K.-S. Jeong. Chem. Eur. J. **9**, 1535 (2003); (*h*) H. Ogino. J. Am. Chem. Soc. **103**, 1303 (1981); (*i*) M. Chas, E. Pia, R. Toba, C. Peinador, and J.M. Quintela. Inorg. Chem. **45**, 6117 (2006); (*j*) M. Chas, V. Blanco, C. Peinador, and J.M. Quintela. Org. Lett. **9**, 675 (2007); (*k*) V. Blanco, M. Chas, D. Abella, C. Peinador, and J.M. Quintela. J. Am. Chem. Soc. **129**, 13878 (2007); (*l*) M.J. Gunter, N. Bampos, K.D. Johnstone, and J.K.M. Sanders. New J. Chem. **25**, 166 (2001); (*m*) G.J.E. Davidson, S.J. Loeb, N.A. Parekh, and J.A. Wisner. J. Chem. Soc. Dalton Trans. 3135 (2001); (*n*) K. Kim. Chem. Soc. Rev. **31**, 96 (2002); (*o*) S.Y. Chang and K.-S. Jeong. J. Org. Chem. **68**, 4014 (2003); (*p*) C.O. Dietrich-Buchecker, B. Colasson, M. Fujita, A. Hori, N. Geum, S. Sakamoto, K. Yamaguchi, and J.-P. Sauvage. J. Am. Chem. Soc. **125**, 5717 (2003).
4. (*a*) C.O. Dietrich-Buchecker and J.-P. Sauvage. Tetrahedron. Lett. **24**, 5095 (1985); (*b*) C.O. Dietrich-Buchecker and J.-P. Sauvage. J. Am. Chem. Soc. **106**, 3043 (1984); (*c*) B. Mohr, M. Weck, J.-P. Sauvage, and R.H. Grubbs. Angew. Chem Int. Ed. Engl. **36**, 1308 (1997); (*d*) J.-C. Chambron, V. Heitz, and J.-P. Sauvage. J. Chem. Soc. Chem. Commun. 1131 (1992); (*e*) J.-C. Chambron, V. Heitz, and J.-P. Sauvage. J. Am. Chem. Soc. **115**, 12378 (1993); (*f*) P. Gavina and J.-P. Sauvage. Tetrahedron Lett. **38**, 3521 (1997); (*h*) L. Hogg, D.A. Leigh, P.J. Lusby, A. Morelli, S. Parsons, and J.K.Y. Wong., Angew. Chem. Int. Ed. **43**, 1218 (2004); (*i*) A.-M. Fuller, D.A. Leigh, P.J. Lusby, I.D.H. Oswald, S. Parsons, and D.B. Walker. Angew. Chem. Int. Ed. **43**, 3914 (2004); (*j*) A.-M. Fuller, D.A. Leigh, P.J. Lusby, A.M.Z. Slawin, and D.B. Walker. J. Am. Chem. Soc. **127**, 12612 (2005); (*k*) D.A. Leigh, P.J. Lusby, A.M.Z. Slawin, and D.B. Walker. Chem. Commun. 4919 (2005); (*l*) A.-M. Fuller, D.A. Leigh, P.J. Lusby, A.M.Z. Slawin, and D.B. Walker. J. Am. Chem. Soc. **127**, 12619 (2005); (*m*) J.C. Loren, P. Gantzel, A. Linden, and J.S. Siegel. Org. Biomol. Chem. **3**, 3105 (2005); (*n*) M. Hutin, C.A. Schalley, G. Bernardinelli, and J.R. Nitschke. Chem. Eur. J. **12**, 4069 (2006); (*o*) M. Ammann, A. Rang, C.A. Schalley, and P. Bäuerle. Eur. J. Org. Chem. 1940 (2006); (*p*) K.S. Chichak, S.J. Cantrill, A.R. Pease, S.-H. Chiu, G.W.V. Cave, J.L. Atwood, and J.F. Stoddart. Science, **304**, 1308 (2004).
5. (*a*) C.P. McArdle, M.J. Irwin, M.C. Jennings, and R.J. Puddephatt. Angew. Chem. Int. Ed. **38**, 3376 (1999); (*b*) C.P. McArdle, J.J. Vittal, and R.J. Puddephatt. Angew. Chem. Int. Ed. **39**, 3819 (2000); (*c*) C.P. McArdle, M.C. Jennings, J.J. Vittal, and R.J. Puddephatt. Chem. Eur. J. **7**, 3572 (2001); (*d*) N.C. Habermehl, F. Mohr, D.J. Eisler, M.C. Jennings, and R.J. Puddephatt. Can. J. Chem. **84**, 111 (2006); (*e*) M.E. Padilla-Tosta, O.D. Fox, M.G.B. Drew, and P.D. Beer. Angew. Chem. Int. Ed. **40**, 4235 (2001); (*f*) W.W.H. Wong, J. Cookson, E.A.L. Evans, E.J.K. McInnes, J. Wolowska, J.P. Maher, P. Bishop, and P.D. Beer. Chem. Commun. 2214 (2005); (*g*) J. Cookson and P.D. Beer. Dalton Trans. 1459 (2007).
6. B.A. Blight, K.A. Van Noortwyk, J.A. Wisner, and M.C. Jennings. Angew. Chem. Int. Ed. **44**, 1499 (2005).
7. C. Fischer, M. Nieger, O. Mogck, V. Böhmer, R. Ungaro, and F. Vögtle. Eur. J. Org. Chem. **1**, 155 (1998).
8. B.A. Blight, J.A. Wisner, and M.C. Jennings. Chem. Commun. 4593 (2006).
9. B.A. Blight, J.A. Wisner, and M.C. Jennings. Angew. Chem. Int. Ed. **46**, 2835 (2007).
10. (*a*) K. Kavallieratos, S.R. de Gala, D.J. Austin, and R.H. Crabtree. J. Am. Chem. Soc. **119**, 2325 (1997); (*b*) K. Kavallieratos, C.M. Bertao, D.J. Austin, and R.H. Crabtree. J. Org. Chem. **64**, 1675 (1999).
11. (*a*) J.M. Mahoney, A.M. Beatty, and B.D. Smith. J. Am. Chem. Soc. **123**, 5847 (2001); (*b*) A.V. Koulov, J.M. Mahoney,

© 2008 NRC Canada

A.M. Beatty, and B.D. Smith. Org. Biomol. Chem. **1**, 27 (2003); (*c*) J.M. Mahoney, R.A. Marshall, A.M. Beatty, B.D. Smith, S. Camiolo, and P.A. Gale. J. Supramol. Chem. **1**, 289 (2001); (*d*) J.M. Mahoney, J.P. Davis, and B.D. Smith. J. Org. Chem. **68**, 9819 (2004); (*e*) J.M. Mahoney, G.U. Nawaratna, A.M. Beatty, P.J. Duggan, and B.D. Smith. Inorg. Chem. **43**, 5902 (2004).

12. (*a*) J.A. Wisner, P.D. Beer, and M.G.B. Drew. Angew. Chem. Int. Ed. **40**, 3606 (2001); (*b*) J.A. Wisner, P.D. Beer, N.G. Berry, and B. Tomapatanaget. Proc. Nat. Acad. Sci. **99**, 4983 (2002); (*c*) M.R. Sambrook, P.D. Beer, J.A. Wisner, R.L. Paul, A.R. Crowley, F. Szemes, and M.G.B. Drew. J. Am. Chem. Soc. **127**, 2292 (2005); (*d*) J.A. Wisner, P.D. Beer, M.G.B. Drew, and M.R. Sambrook. J. Am. Chem. Soc. **124**, 12469 (2002); (*e*) M.R. Sambrook, P.D. Beer, M.D. Lankshear, R.F. Ludlow, and J.A. Wisner. Org. Biomol. Chem. **4**, 1529 (2006); (*f*) K.-Y. Ng, A.R. Cowley, and P.D. Beer. Chem. Commun. 3676 (2006).
13. (*a*) P.A. Gale. Acc. Chem. Res. **39**, 465 (2006); (*b*) P.V. Santacroce, J.T. Davis, M.E. Light, P.A. Gale, J.C. Iglesias-Sanchez, P. Prados, and R. Quesada. J. Am. Chem. Soc. **129**, 1886 (2007).
14. (*a*) C. Tessier and F.D. Rochon. Inorg. Chim. Acta, **295**, 25 (1995); (*b*) G.B. Kauffman. Inorg. Synth. **7**, 249 (1970); (*c*) M.M. Olmstead, P.-P. Wei, A.S. Ginwalla, and A.L. Balch. Inorg. Chem. **39**, 4555 (2000).
15. B.A. Blight, J.A. Wisner, and M.C. Jennings. Inorg. Chem. **46**, 8445 (2007).
16. (*a*) C.A. Hunter. J. Am. Chem. Soc. **114**, 5303 (1992); (*b*) H. Adams, F.J. Carver, and C.A. Hunter. J. Chem. Soc. Chem. Commun. 809 (1995).
17. (*a*) S. Ottens-Hildebrandt, M. Nieger, K. Rissanen, J. Rouvinen, S. Meier, G. Hardera, and F. Vögtle. J. Chem. Soc. Chem. Commun. 777 (1995); (*b*) Q.-Y Li,. E. Vogel, A.H. Parham, M. Nieger, M. Bolte, R. Fröhlich, P. Saarenketo, K. Rissanen, and F. Vögtle. Eur. J. Org. Chem. 4041 (2001).
18. A.G. Johnston, D.A. Leigh, R.J. Pritchard, and M.D. Deegan. Angew. Chem. Int. Ed. Engl. **34**, 1209 (1995).

© 2008 NRC Canada

Dinuclear organoplatinum(II) complexes containing *N*-methylbenzamide[1]

Michael G. Crisp and Louis M. Rendina

Abstract: The preparation and characterization of cationic, dinuclear complexes of the type *trans*-[$Pt(PPh_3)_2$(σ-C_6H_4NHMe)-μ-L-$Pt(PPh_3)_2$(σ-C_6H_4NHMe)]$(OTf)_2$ (L = 4,4′-bipyridine, 4,7-phenanthroline, 4,4′-dipyrazolylmethane, and 1,1′-diphenyl-4,4′-dipyrazolylmethane; OTf = trifluoromethanesulfonate (triflate)) containing two C^3-*N*-methylbenzamide ligands are described. The key structural feature of the cationic complexes is the presence of two convergent amide groups that may allow for charge-assisted, H-bonding interactions in solution with suitable heteroaromatic guest molecules such as nucleobases.

Key words: organoplatinum(II) complex, organometallic host, dinuclear complex, *N*-methylbenzamide.

Résumé : On décrit la préparation et la caractérisation de complexes cationiques dinucléaires du type *trans*-[$Pt(PPh_3)_2$ (σ-C_6H_4NHMe)-μ-L-$Pt(PPh_3)_2$(σ-C_6H_4NHMe)]$(OTf)_2$ [L= 4,4′-bipyridine; 4,7-phénanthroline; 4,4′-dipyrazolylméthane; et 1,1′-diphényl-4,4′-dipyrazolylméthane; OTf = trifluorométhanesulfonate (triflate)] contenant deux ligands C^3-*N*-méthylbenzamide. La caractéristique structurale clé des complexes cationiques est la présence de deux groupes amides convergents qui, en solution, peuvent favoriser des interactions de liaisons hydrogènes assistées par des charges avec des molécules hôtes hétéroaromatiques appropriées, telles des nucléobases.

Mots-clés : complexe organique du platine(II), hôte organométallique, complexe dinucléaire, *N*-méthylbenzamide.

[Traduit par la Rédaction]

Introduction

There is great interest in the study of synthetic receptors for the selective binding of nucleobases (1, 2), owing to their many important functional roles in biological systems, e.g., intracellular energy transfer, signal transduction, and nucleic-acid synthesis. Various modes of hydrogen-bonding recognition have been shown to occur between nucleobases and simple carboxylic acids, for example, and it has been demonstrated that many aromatic carboxylic acids preferentially bind Hoogsteen sites, whereas aliphatic carboxylic acids bind preferentially at the Watson–Crick site (3, 4). In addition to hydrogen-bonding, π-stacking is usually found to augment the interaction involving aromatic hosts and nucleobase guests, and both macrocyclic and non-macrocyclic molecular receptors containing hydrogen-bonding and (or) π-stacking binding domains have been studied previously (5–18), all of which have the capacity to target nucleobases such as adenine and its derivatives. Theoretical studies have also complemented the work (10, 11).

Macrocyclic nucleobase receptors can discriminate their guest molecule by attributes such as size, electronic properties, nature of the hydrogen-bonding groups, and the π-stacking surface area (5, 6, 12). In contrast, non-macrocyclic "molecular tweezers" possess two binding sites with convergent functionality, which are linked together by a spacer unit (7–9, 13–18). Molecular tweezers usually possess one or more hydrogen-bonding functionalities, such as carboxylic acids or amides, and, in some cases, converging aromatic surfaces that have the capacity to undergo π-stacking interactions. Organometallic complexes in which direct coordination of adenine to the metal centre is augmented by H-bonding and π-stacking interactions are also known (19, 20), but to our knowledge there exist no examples of where metal coordination does not play a key role in the recognition motif. Instead, the formation of strong H-bonding interactions with the guest molecule is the result of the complementary shape of the cationic host, which can be further augmented by charge assistance (21).

We have previously reported the preparation, pK_a data, and X-ray structures of σ-arylplatinum(II) complexes bearing carboxylic acid functionalities (22–24) some of which have been shown to possess interesting supramolecular properties in non-aqueous solution, e.g., the formation of discrete, multimeric cyclic arrays with nanoscale dimensions (24). The use of a protection–deprotection strategy was required in the oxidative addition reactions involving aryl iodides bearing a carboxylic acid functionality owing to their high reactivity with platinum(0) precursor compounds. Furthermore, in some cases, we found that carboxylic acids

Received 5 May 2008. Accepted 14 June 2008. Published on the NRC Research Press Web site at canjchem.nrc.ca on 16 September 2008.

Dedicated to Prof. R.J. Puddephatt, FRS, on the occasion of his retirement and in recognition of his many outstanding contributions to organometallic chemistry.

M.G. Crisp. School of Chemistry and Physics, The University of Adelaide, Adelaide SA 5005, Australia.
L.M. Rendina.[2] School of Chemistry, The University of Sydney, Sydney, NSW 2006, Australia.

[1]This article is part of a Special Issue dedicated to Professor R. Puddephatt.
[2]Corresponding author: (e-mail: rendina@chem.usyd.edu.au).

 doi:10.1139/V08-116 © 2008 NRC Canada

Scheme 1.

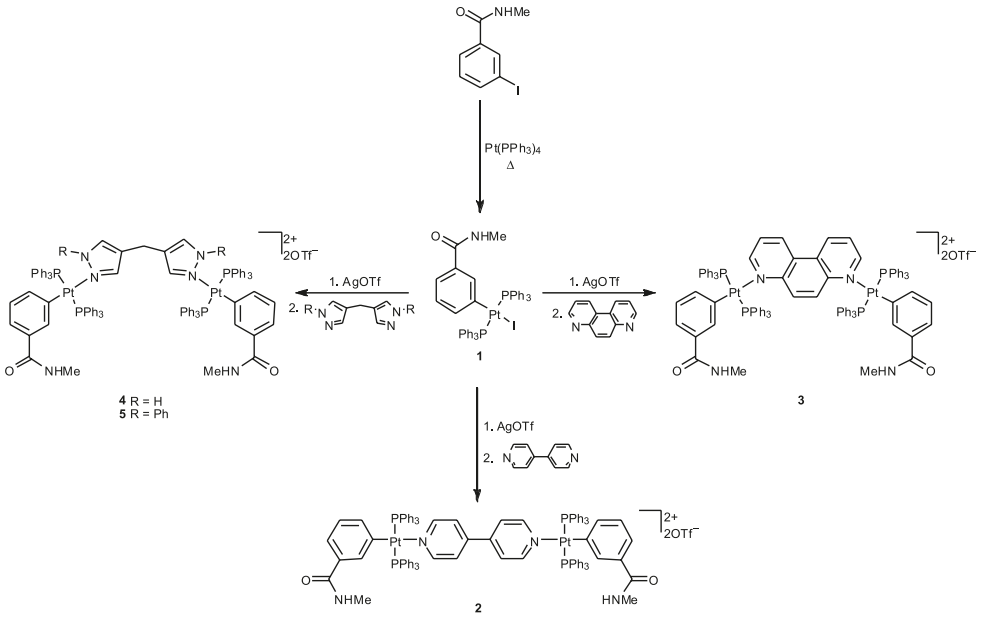

readily H-bonded to counter-ions (e.g., triflate) both in low-polarity solvents and in the solid-state, thus markedly complicating the assembly and (or) molecular-recognition studies (22, 23). The use of N-substituted σ-benzamide ligands instead of pyridine carboxylic acids was expected to address many of these issues largely because of the markedly lower acidity of the amide N–H group compared with that of a carboxylic acid. Herein, we describe the synthesis and characterization of dinuclear organoplatinum(II) derivatives bearing convergent *N*-methylamide functionalities for potential application as molecular receptors for nucleobases.

Results and discussion

The oxidative addition of the C–I bond of 3-iodo-*N*-methylbenzamide to $Pt(PPh_3)_4$ proceeded cleanly to afford the iodoplatinum(II) complex **1** in good yield (Scheme 1). The ^{1}H NMR spectrum of **1** displayed four distinct signals at δ 6.67, 6.72, 6.24, and 6.96 ppm, which are assigned to the H^2, H^4, H^5, and H^6 protons of the σ-aryl ligand, respectively. The methyl protons of the NHMe group appeared as a doublet at δ 2.76 ppm ($^3J_{HH}$ = 4.8 Hz), and the NH proton appeared as a broad multiplet at δ 4.98 ppm. Complex **1** was readily converted to the labile triflato derivative by the use of AgOTf. Two equivalents of this species were then treated immediately with 1 equiv. of the bridging bidentate, N-donor ligand 4,4′-bipyridine, 4,7-phenanthroline, 4,4′-dipyrazolylmethane, or 1,1′-phenyl-4,4′-dipyrazolylmethane to form the desired diplatinum(II) complexes (**2**–**5**) in good yield and purity (Scheme 1).

Complex **2** displayed a doublet signal in the ^{1}H NMR spectrum at δ 7.03 ppm ($^3J_{HH}$ = 7.5 Hz), which is attributed to the H^6 proton of the σ-aryl ligand. The signal due to the H^4 proton appeared as a doublet at δ 6.81 ppm ($^3J_{HH}$ = 7.5 Hz), and the H^5 proton gave rise to a triplet signal at δ 6.39 ppm ($^3J_{HH}$ = 7.8 Hz). The ortho protons of the 4,4′-bipyridine were masked by the PPh_3 signals at δ 7.34–7.19 ppm, whilst the meta hydrogens appeared at δ 6.83 ppm as a distinct signal, which is assigned to the XX′ portion of a AA′XX′ spin system. The NMR spectra of **3** were measured in CD_2Cl_2 solution instead of $CDCl_3$ as the complex was found to dissociate to afford free 4,7-phenanthroline over a period of a few hours at room temperature in $CDCl_3$ but remained stable for indefinite periods in CD_2Cl_2 solution. This effect has been previously observed in the ESI-MS of these and related complexes (vide infra) (22–25), and it is most probably the result of the strong trans effect associated with the σ-aryl ligand. Interestingly, a Pd_6 hexagon prepared from 4,7-phenanthroline and dinuclear organopalladium(II) precursor complexes appears to remain intact both in solution and in the gas phase despite the presence of a σ-aryl ligand located trans to the coordinated N-atom (26).

The assignment of the aromatic proton resonances in **2**–**5** was facilitated by 2D ^{1}H COSY (correlation spectroscopy) NMR experiments at 600 MHz, whereby distinct cross-peaks were observed for coupled protons of the σ-aryl ring systems, as seen in the NMR spectrum of **4** (Fig. 1). For this complex, protons H^4 and H^6 appeared as doublets at δ 6.77 and δ 7.00 ppm, respectively. The H^5 proton appeared as a triplet ($^3J_{HH}$ = 7.2 Hz) at δ 6.35 ppm. The signal due to H^2 appeared as a sharp singlet at δ 6.10 ppm. The N–Me protons appeared as a doublet at δ 2.83 ppm ($^3J_{HH}$ = 4.8 Hz), and the amide N–H proton gave rise to a broad singlet at δ 6.01 ppm. The signal due to the methylene bridge protons appeared as a sharp singlet at δ 2.53 ppm, and the N–H signal of the pyrazolyl ring was located downfield at δ 12.45 ppm.

Compared to the ^{1}H NMR spectrum of complex **4**, the related complex **5** had many broad unresolved signals, with all the σ-aryl signals appearing as broad singlets. This effect is most likely related to the dynamic phenomena of analogous platinum(II) species (23), whereby free rotation of the 1,1′-diphenyl-4,4′-dipyrazolylmethane ligand about the Pt–N bond is restricted owing to the considerable steric interactions between the N–Ph group and the bulky PPh_3 ligands. This proposal is also supported by the fact that the related 4,4′-dipyrazolylmethane complex **4** does not exhibit this re-

© 2008 NRC Canada

Fig. 1. Expanded ^{1}H COSY NMR spectrum (600 MHz) of **4** in $CDCl_3$ solution showing key couplings and peak assignments for the σ-aryl protons.

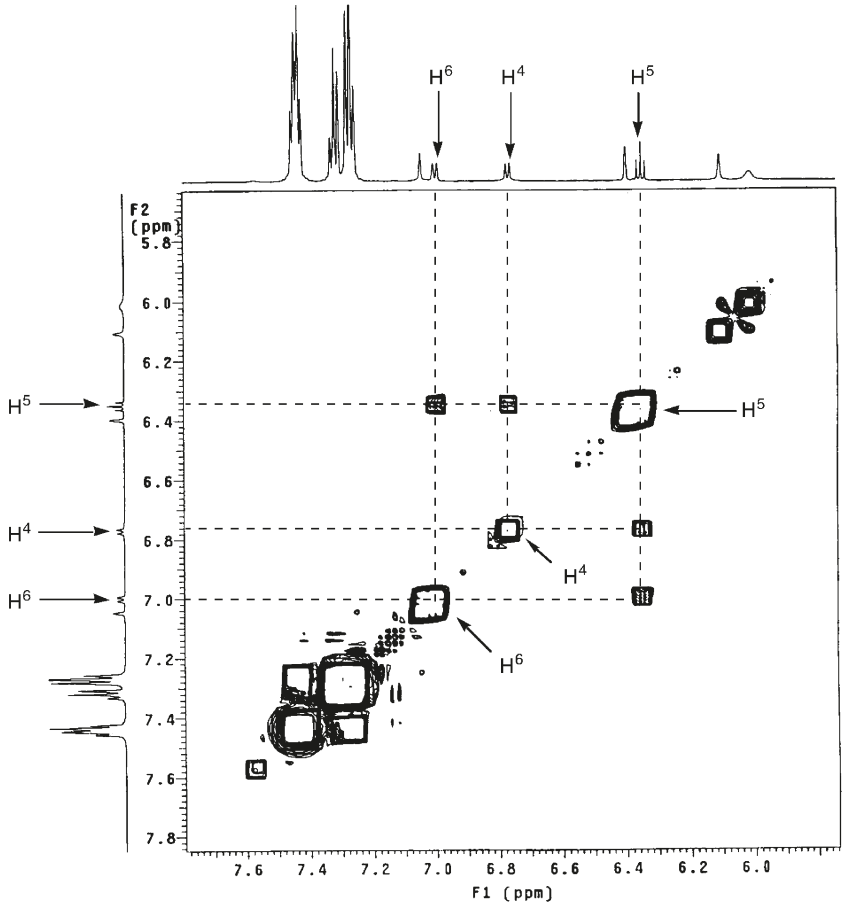

lated NMR behaviour, suggesting that in this case there exists free rotation around the Pt–N bond.

All complexes prepared in this work displayed a sharp singlet between δ 20–25 ppm in the $^{31}P\{^1H\}$ NMR spectrum, and it was always flanked by ^{195}Pt satellite signals. The magnitude of $^1J_{PtP}$ (~3000 Hz) for all complexes falls in the range that is expected for trans-substituted σ-arylplatinum(II) complexes (28, 29). Only minor differences were observed in the magnitude of $^1J_{PtP}$ upon substitution of the iodo ligand with N-donor ligands, largely because the ^{195}Pt–^{31}P coupling is predominantly influenced by the nature of the trans ligand (PPh_3).

Positive ion ESI-MS studies failed to show any evidence of an intact species in the spectra of **2**–**5** and, instead, the N-donor ligands (L) were readily lost, and peaks corresponding to $[M–OTf–L]^+$ were observed. The strong trans-effect associated with the σ-aryl ligand would account for the facile labilization of the N-donor ligand in the gas phase, and similar behaviour has also been observed in the ESI-MS of related systems (22–25).

Conclusion

In this work, we have demonstrated the facile synthesis of organplatinum(II) complexes bearing convergent H-bonding amide functionalities by exploiting an oxidative addition reaction involving a platinum(0) precursor. The low reactivity of the amide N–H group ensures that unwanted side reactions involving the N–H bond do not occur, and C–I bond cleavage is favoured exclusively. We are in the process of investigating the "molecular chelation" properties of selected complexes with various guest molecules, such as derivatives of purine bases, including adenine and guanine. Indeed, preliminary molecular modelling studies (SYBYL force field) demonstrate that a stable 1:1 species between **4** and adenine is feasible in the gas phase in which the exocyclic NH_2, N-7, and N-1 atoms of the guest molecule are all involved in strong H-bonding interactions with both amide groups of the complex, and we are currently investigating the host–guest chemistry of **2**–**5** and related complexes in various solvents. The results of this work will be reported in due course.

Experimental

All complexes were synthesised under a N_2 atmosphere using standard Schlenk techniques. All solvents were dried and purified in the following manner: CH_2Cl_2 was distilled from CaH_2, and toluene was pre-dried over $CaSO_4$ followed by distillation from sodium. The solvents were stored under N_2 over 4 Å molecular sieves.

All 1D NMR spectra were recorded at 298 K by means of a Varian Gemini 2000 NMR spectrometer with an Oxford 300 MHz magnet (^{1}H at 300.10 MHz, ^{31}P at 121.50 MHz);

© 2008 NRC Canada

2D NMR (^{1}H COSY) spectra were recorded by using a 600 MHz magnet. ^{1}H NMR chemical shifts were reported in ppm relative to tetramethylsilane (TMS). ^{31}P{^{1}H} NMR spectra were referenced to sealed external standard of 85% phosphoric acid. IR spectra were recorded as Nujol mulls in the range 4000–400 cm^{-1} on a PerkinElmer FTIR spectrophotometer. ESI-MS were obtained by means of a Finnegan LCQ mass spectrometer in the positive-ion mode using HPLC-grade MeOH as the solvent. Elemental analysis was performed by CMAS (Chemical and Microanalytical Services, Pty. Ltd.), Belmont, Victoria.

3-Iodo-*N*-methylbenzamide (27), tetrakis(triphenylphosphine)platinum(0) (30), 4,4′-dipyrazolylmethane (31), and 1,1′-phenyl-4,4′-dipyrazolylmethane (32) were prepared and purified according to the literature procedures.

Trans-iodo(*N*-methylbenzamide-*C*^{3})bis(triphenylphosphine)platinum(II) (1)

3-Iodo-*N*-methylbenzamide (0.110 g, 0.402 mmol) was placed in a Schlenk flask with $Pt(PPh_3)_4$ (0.500 g, 0.402 mmol). Toluene (20 mL) was added to the flask, and the solution was stirred for 16 h at 80 °C. Hexane (20 mL) was slowly added to the solution to precipitate the product, which was collected by filtration to afford **1** as a colourless, microcrystalline solid (0.344 g, 88%). IR (Nujol): 1632 ν(C=O) cm^{-1}. ^{1}H NMR ($CDCl_3$) δ: 7.56–7.22 (m, 30H, PPh_3), 6.96 (d, 1H, $^3J_{HH}$ = 7.5 Hz, $^1J_{PtH}$ = 29.3 Hz, H^6), 6.72 (d, 1H, $^3J_{HH}$ = 8.4 Hz, H^4), 6.67 (s, 1H, $^1J_{PtH}$ = 28.8 Hz, H^2), 6.24 (t, 1H, $^3J_{HH}$ = 7.8 Hz, H^5), 4.98 (br m, 1H, NH), 2.76 (d, 3H, $^3J_{HH}$ = 4.8 Hz, NCH_3). ^{31}P{^{1}H} NMR ($CDCl_3$) δ: 22.0 ($^1J_{PtP}$ = 3029 Hz). Anal. calcd. for $C_{44}H_{38}INOP_2Pt$: C, 53.89; H, 3.91; N, 1.43. Found: C, 53.37; H, 3.85; N, 1.45.

Trans-μ-4,4′-bipyridinebis[(*N*-methylbenzamide-*C*^{3})bis(triphenylphosphine) platinum(II)] bis(triflate) (2)

Complex **1** (0.400 g, 0.401 mmol) was treated with AgOTf (0.103 g, 0.401 mmol) in CH_2Cl_2 (25 mL), and the reaction mixture was stirred at room temperature for 3 h in the absence of light. AgI was then removed by filtration through Celite filter aid. 4,4′-Bipyridine (0.031 g, 0.201 mmol) was added to the clear solution and then stirred overnight at room temperature. The solvent was reduced in vacuo to afford **2** as a colourless, microcrystalline solid (0.260 g, 60%). IR (Nujol): 1655 ν(C=O) cm^{-1}. ^{1}H NMR ($CDCl_3$) δ: 7.34–7.19 (m, 60H, PPh_3), 7.03 (d, 2H, $^3J_{HH}$ = 7.5 Hz, H^6), 6.83 (s, 2H, H^2), 6.83 (XX′ portion of AA′ XX′, 4H, H_m), 6.81 (d, 2H, $^3J_{HH}$ = 7.5 Hz, H^4), 6.39 (t, 2H, $^3J_{HH}$ = 7.8 Hz, H^5). ^{31}P{^{1}H} NMR ($CDCl_3$) δ: 20.9 ($^1J_{PtP}$ = 3008 Hz). Anal. calcd. for $C_{44}H_{38}INOP_2Pt$: C, 55.56; H, 3.92; N, 2.59. Found: C, 55.62; H, 3.51; N, 2.64.

Trans-μ-4,7-phenanthrolinebis[*N*-methylbenzamide-*C*^{3})bis(triphenylphosphine) platinum(II)] bis(triflate) (3)

Following a procedure similar to that described for complex **2**, complex **1** (0.400 g, 0.401 mmol) was treated with AgOTf (0.103 g, 0.401 mmol) followed by the addition of 4,7-phenanthroline (0.036 g, 0.201 mmol) to afford **3** as a colourless, microcrystalline solid (0.360 g, 55%). IR (Nujol): 1641 ν(C=O) cm^{-1}. ^{1}H NMR (CD_2Cl_2) δ: 9.40 (d, 2H, $^3J_{HH}$ = 9.3 Hz, H^{1,10}), 9.07 (d, 1H, $^3J_{HH}$ = 4.2 Hz, H^{3,8}), 9.05 (s, 2H, H^{5,6}), 7.41–7.11 (m, 20H, PPh_3), 6.88 (d, 2H, $^3J_{HH}$ = 7.8 Hz, H^{14}), 6.38 (t, 2H, $^3J_{HH}$ = 8.1 Hz, H^{15}), 5.96 (br s, 2H, NH), 2.84 (d, 6H, $^3J_{HH}$ = 4.8 Hz, NMe). ^{31}P{^{1}H} NMR (CD_2Cl_2) δ: 19.5 ($^1J_{PtP}$ = 3003 Hz). Anal. calcd. for $C_{102}H_{84}F_6N_4O_8P_4Pt_2S_2$: C, 56.04; H, 3.87; N, 2.56. Found: C, 55.94; H, 3.45; N, 2.18.

Trans-μ-4,4′-dipyrazolylmethanebis[(*N*-methylbenzamide-*C*^{3})bis(triphenylphosphine)platinum(II)] bis(triflate) (4)

Following a procedure similar to that described for **2**, complex **1** (0.400 g, 0.401 mmol) was treated with AgOTf (0.103 g, 0.401 mmol) followed by the addition of 4,4′-dipyrazolylmethane (0.029 g, 0.201 mmol) to afford **4** as a colourless, microcrystalline solid (0.369 g, 81%). IR (Nujol): 1643 ν(C=O), 3400 ν(N–H) cm^{-1}. ^{1}H NMR ($CDCl_3$) δ: 12.45 (s, 2H, pyrazolyl NH), 7.45–7.25 (m, 60H, PPh_3), 7.04 (s, 2H, H^9), 7.00 (d, 2H, $^3J_{HH}$ = 7.8 Hz, H^6), 6.77 (t, 2H, $^3J_{HH}$ = 7.2 Hz), 6.40 (s, 2H, H^2), 6.35 (t, 2H, $^3J_{HH}$ = 7.2 Hz, H^5), 6.10 (s, 2H, H^{10}), 6.01 (m, 2H, amide NH), 2.83 (d, 6H, $^3J_{HH}$ = 4.8 Hz, NHMe), 2.53 (s, 2H, CH_2). ^{31}P{^{1}H} NMR ($CDCl_3$) δ: 20.8 ($^1J_{PtP}$ = 3022 Hz). Anal. calcd. for $C_{97}H_{84}F_6N_6O_8P_4Pt_2S_2$: C, 54.09; H, 3.93; N, 3.90. Found: C, 53.98; H, 4.09; N, 3.71.

Trans-μ-(1,1′-phenyl-4,4′-dipyrazolylmethane)bis[(*N*-methylbenzamide- C^3)bis(triphenylphosphine)platinum(II)] bis(triflate) (5)

Following a procedure similar to that described for **2**, complex **1** (0.400 g, 0.401 mmol) was treated with AgOTf (0.103 g, 0.401 mmol) followed by the addition of 1,1′-phenyl-4,4′-dipyrazolylmethane (0.060 g, 0.201 mmol) to afford **5** as a colourless, microcrystalline solid (0.129 g, 54%). ^{1}H NMR ($CDCl_3$) δ: 6.94 (br s, 2H, H^6), 6.69 (br s, 2H, H^2), 6.58 (br s, 2H), 6.25 (br s, 2H, H^5), 5.70 (m, 2H, NH), 3.11 (s, 2H, CH_2), 2.84 (d, 6H, $^3J_{HH}$ = 4.5 Hz, NHMe), 7.64–7.28 (m, 60H, PPh_3). ^{31}P{^{1}H} NMR ($CDCl_3$) δ: 25.0 ($^1J_{PtP}$ = 3084 Hz). Anal. calcd. for $C_{109}H_{92}F_6N_6O_8P_4Pt_2S_2$: C, 56.77; H, 4.02; N, 3.64. Found: C, 56.57; H, 4.09; N, 3.49.

Acknowledgements

We thank Mr Phil Clements (The University of Adelaide) for assistance with the NMR experiments. We also thank Johnson–Matthey for the generous loan of platinum salts. The authors wish to acknowledge funding of the work by the Australian Research Council (ARC).

References

1. S.R. Perumalla, E. Suresh, and V.R. Pedireddi. Angew. Chem., Int. Ed. **44** (2005) 7752.
2. S. Sivakova and S.J. Rowan Chem. Soc. Rev. **32** (2005) 9.
3. P. Rao, S. Ghosh, and U.J. Maitra. Phys. Chem. B, **103** (1999) 4528.
4. G.J. Lancelot. J. Am. Chem. Soc. **99** (1977) 7037.
5. B. Askew, P. Ballester, C. Buhr, K.S. Jeong, S. Jones, K. Parris, K. Williams, and J. Rebek, Jr., J. Am. Chem. Soc. **111** (1989) 1082.
6. S. Goswami, D. Van Engen, and A.D. Hamilton. J. Am. Chem. Soc. **111** (1989) 3425.
7. S.C. Zimmerman and W. Wu. J. Am. Chem. Soc. **111** (1989) 8054.

© 2008 NRC Canada

8. J.C. Adrian and C.S. Wilcox. J. Am. Chem. Soc. **111** (1989) 8055.
9. L. Yu and H.-J. Schneider. Eur. J. Org. Chem. (1999) 1619.
10. I. Alkorta, J. Elguero, S. Goswami, and R. Mukherjee. J. Chem. Soc., Perkin Trans. 2, (2002) 894.
11. S. Topiol and G. Talbot, J. Am. Chem. Soc. **112** (1990) 8734.
12. Y. Hisamatsu, H. Takami, N. Shirai, S. Ikeda, and K. Odashima. Tetrahedron Lett. **48** (2007) 617.
13. H. Nemoto, T. Kawano, N. Ueji, M. Bando, M. Kido, I. Suzuki, and M. Shibuya. Org. Lett. **2** (2000) 1015.
14. M.M. Conn, G. Deslongchamps, J. de Mendoza, and J. Rebek, Jr. J. Am. Chem. Soc. **115** (1993) 3548.
15. K.S. Jeong, T. Tjivikua, A. Muehldorf, G. Deslongchamps, M. Famulok, and J. Rebek, Jr. J. Am. Chem. Soc. **113** (1991) 201.
16. K. Williams, B. Askew, P. Ballester, C. Buhr, K.S. Jeong, S. Jones, and J. Rebek, Jr. J. Am. Chem. Soc. **111** (1989) 1090.
17. S.C. Zimmerman, W. Wu, and Z. Zeng. J. Am. Chem. Soc. **113** (1991) 196.
18. R. Güther, M. Nieger, and F. Vögtle. Angew. Chem., Int. Ed. **32** (1993) 601.
19. J.E. Kickham, S.J. Loeb, and S.L. Murphy. Chem. Eur. J. **3** (1997) 1203.
20. J.E. Kickham, S.J. Loeb, and S.L. Murphy. J. Am. Chem. Soc. **115** (1993) 7031.
21. D. Braga and F. Grepioni. Acc. Chem. Res. **33** (2000) 601.
22. M.G. Crisp, E.R. Tiekink, and L.M. Rendina. Inorg. Chem. **42** (2003) 1057.
23. D.P. Gallasch, E.R.T. Tiekink, and L.M. Rendina. Organometallics, **20** (2001) 3373.
24. N.C. Gianneschi, E.R.T. Tiekink, and L.M. Rendina. J. Am. Chem. Soc. **122** (2000), 8474.
25. M.G. Crisp, S.M. Pyke, and L.M. Rendina. J. Organomet. Chem. **607** (2000) 222.
26. J.R. Hall, S.J. Loeb, G.K.H. Shimizu, and G.P.A. Yap. Angew. Chem., Int. Ed. **37** (1998) 121.
27. D.P. Gallasch, S.L. Woodhouse, and L.M. Rendina. J. Organomet. Chem. **689** (2004) 1288.
28. P.S. Pregosin and R.W. Kunz. ^{31}P and ^{13}C NMR of transition-metal complexes. Springer. Berlin. 1979.
29. G.K. Anderson, H.C. Clark, and J.A. Davies. Organometallics, **1** (1982) 64.
30. R. Ugo, F. Cariati, and G. La Monica. Inorg. Synth. **11** (1968) 105.
31. S. Trofimenko. J. Am. Chem. Soc. **92** (1970) 5118.
32. I.L. Finar and G.H. Lord. J. Chem. Soc. (1959) 1819.

© 2008 NRC Canada

Top-down meets bottom-up — Electron-beam induced metalorganic deposition of amorphous iron oxide nanostructures[1]

Simon Trudel and Ross H. Hill

Abstract: We present the use of a metalorganic precursor, iron(III) 2-ethylhexanoate, as a precursor for the electron-beam induced deposition of amorphous iron oxide nanostructures. Exposing this precursor to an area dose of 1.560 mC/cm^2 with 10 keV electrons affords a material that can be developed and was determined to be amorphous iron oxide when examined by TEM, electron diffraction, and energy dispersive X-ray spectroscopy. Single point exposure yields free-standing hollow nanorods with diameters from 85 to 255 nm controlled by the exposure dose. The patterning of sub 40 nm nanowires with low (<3 nm) line edge and width roughnesses is also presented.

Key words: electron beam lithography, amorphous iron oxide, nanotubes, nanowires, coordination polymer precursor.

Résumé : Dans ce travail, on propose l'utilisation d'un composé organométallique, le 2-éthylhexanoate de Fe(III), comme précurseur pour le dépôt de nanostructures d'oxyde de fer induit par un faisceau d'électron. Lorsqu'on expose ce précurseur à une dose superficielle de 1,560 mC/cm^2 à l'aide d'électrons à 10 keV, il se forme un matériau qui peut être développé et qui, sur la base de la microscopie électronique à transmission (MET), la diffraction des électrons et la spectroscopie des rayons X à dispersion d'énergie, serait de l'oxyde de fer amorphe. Des expositions en un seul point conduisent à la formation de nanotiges de diamètres variant de 85 à 225 nm et contrôlés par la dose d'exposition. On rapporte aussi les résultats obtenus en vue de déterminer les patrons des nanofils de tailles inférieures à 40 nm comportant des lisières et des largeurs de rugosité faibles (<3 nm).

Mots-clés : lithographie à faisceau électronique, oxyde de fer amorphe, nanotubes, nanofils, précurseur d'une polymère de coordination.

[Traduit par la Rédaction]

Introduction

In this contribution, we report on the electron-beam metalorganic deposition (EMOD) of amorphous metal oxide nanostructures, including nanowires and nanotubes. As an example, we demonstrate the deposition of iron oxide nanostructures using radiation sensitive iron(III) 2-ethylhexanoate.

Several metal oxides are technologically important materials, and the controlled patterned deposition of nanostructures made of such materials is thus relevant to the fabrication of nanoscaled devices (1–4). For example, nanowire structures are attractive for several devices (3, 5). However, the controlled placement of nanowires onto surfaces remains challenging. In conventional microfabrication, metal oxide nanostructures can be used as ultrathin resists (6) and etch-resistant top-side resists (7).

Iron oxide nanostructures are attractive for applications as magnetic elements in spintronic devices (8–10) and can be used as catalysts for the controlled deposition of single-walled carbon nanotubes (11). However, no control over the position of these iron oxide nanostructures was achieved when the nanostructures were deposited onto substrates, as they were deposited from suspensions of preformed nanostructures (8–11).

Iron oxide nanostructures have been deposited lithographically by introducing $Fe(CO)_5$ in the gas phase in the path of the focused electron beam (12, 13). The material was either amorphous (13) or nanocrystalline (12) iron oxide, depending on whether the carrier gas was water vapour or oxygen, respectively.

Previous work within our group has extensively explored the use of metal 2-ethylhexanoates for the lithographic photochemical metalorganic deposition (PMOD) of metal oxides (14, 15) and nanocomposites (16). These precursors are sensitive to ultraviolet light. Upon irradiation, the molecule is destabilized and will fragment, ultimately losing its ligands as volatile organic products. In air, a metal oxide is obtained. Upon developing in an appropriate solvent, unconverted precursor in the unexposed areas is removed, leaving a pattern of the metal oxide on the substrate.

Received 26 March 2008. Accepted 24 June 2008. Published on the NRC Research Press Web site at canjchem.nrc.ca on 18 September 2008.

This article is dedicated to Dick Puddephatt in recognition of his many contributions as a person, an educator, and a scientist.

S. Trudel and R.H. Hill[2]. 4D LABS and Department of Chemistry, Simon Fraser University, 8888 University Drive, Burnaby, BC V5A 1S6, Canada.

[1]This article is part of a Special Issue dedicated to Professor Richard J. Puddephatt.

[2]Corresponding author: (e-mail: rhill@sfu.ca).

 doi:10.1139/V08-124 © 2008 NRC Canada

An alternative approach to the patterning of nanostructures is the use of an electron beam to induce a chemical reaction in a precursor, as in PMOD. EMOD is a convenient approach to the direct, controlled patterning of functional materials onto surfaces. For example, materials such as conducting PdC (17) and Pd (18), Au nanoparticles (19), etch-resistant titanium oxide (7), superconducting Y-Ba-Cu oxide (20), ferromagnetic Fe-Co containing ceramics (21), and uranium oxide for X-ray masks (22) have been prepared using metalorganic precursors. This approach to the patterning of functional materials is at the convergence of the "top-down" and "bottom-up" technologies. It uses traditional micro-fabrication tools to modify and "assemble" molecular building blocks into the desired material. A post-development thermal treatment is usually required to obtain the final material (7, 18–21).

Experimental

Chemicals, substrates, and intruments

The metalorganic precursor iron(III) 2-ethylhexanoate was purchased from Strem as a solution in mineral spirits. Silicon substrates were purchased from WaferNet. The CaF_2 disk used for the acquisition of the FTIR spectrum was purchased from Wilmad.

Fourier-transform infrared (FTIR) spectra were obtained on a BOMEM Michelson 120 FTIR spectrophotometer operating at a 4 cm^{-1} resolution, whose sample chamber was maintained under a nitrogen atmosphere. Spectroscopic ellipsometry measurements were carried with a Jobin-Yvon UVISEL NIR phase modulated ellipsometer. Measurements were carried out every 5 nm from 300 to 900 nm. The measured spectrum was fit using the DeltaPsi2 software, using a Forouhi–Bloomer model (23). Electron beam exposure and SEM imaging was carried out in a Raith e-LINE system, equipped with a field-emission electron gun. All writing was done by performing a raster of vector scans of the Gaussian shaped electron beam as the stage remained fixed. Atomic force microscopy (AFM) was carried out using a Thermo Microscopes Explorer microscope and Microlever Si_3N_4 cantilevers. Transmission electron microscopy (TEM) was carried out on a FEI Tecnai 20 operating at an acceleration voltage of 200 kV, equipped with an EDAX energy dispersive X-ray spectroscopy unit.

Preparation of precursor thin film and e-beam exposure

A solution containing 15% by weight of the precursor in methyl *iso*-butylketone (MIBK) was used to saturate the surface of an approximately 2 cm × 2 cm piece of [100] oriented silicon. The silicon substrate was then spun to disperse the precursor (6000 rpm, 60 s). This yielded a highly uniform, optical quality precursor thin film. Spectroscopic ellipsometry measurements indicate a precursor thin film thickness of ~240 nm (see Fig. S1).[3] This precursor thin film was loaded into the electron beam lithography system. Electrons accelerated to 10 keV were used to expose this precursor thin film, using a beam current of 235 pA. Area, line, and point doses (in units of mC/cm^2, nC/cm, and pC, respectively) were used to control the exposure. The sample was developed by dipping the substrate into MIBK maintained at 19 °C, for a period of 3 s. The sample was blown dry under a stream of nitrogen and inspected by scanning electron microscopy (SEM). Contact-mode AFM images were also acquired.

The same procedure was used to spin coat a thin film of iron(III) 2-ethylhexanoate on a CaF_2 disk.

Preparation of TEM samples

Samples suitable for TEM investigation were prepared as described above, except the thin film of iron(III) 2-ethylhexanoate was coated on a 75 nm thick Si_3N_4 membrane TEM grid (SPI Supplies), and that a beam current of 126.8 pA was used. The sample was inspected using TEM in bright field (BF) imaging and electron diffraction mode, as well as scanning TEM using a high-angle annular dark field (HAADF) detector.

Results

The FTIR spectrum of a thin film of iron(III) 2-ethylhexanoate is shown in Fig. 1. The observed absorption bands are associated with symmetric and asymmetric vibrations of the C–O groups of the ligand, 2-ethylhexanoate, and 2-ethylhexanoic acid. The absorption bands at 1690, 1589, and 1553 cm^{-1} are tentatively assigned as the asymmetric stretches, and the absorption bands at 1460 and 1424 cm^{-1} as symmetric stretches.

The absorption band at 1690 cm^{-1} is associated to coordinated acid (14). The binding mode of the acid can be determined based on the difference between the asymmetric and symmetric absorption bands (24). Bridging and bidentate binding modes are observed in this thin film. The presence of bridging binding modes suggests that an oligomeric (or polymeric) form of iron(III) 2-ethylhexanoate is present in the thin film. The proposed molecular structure of this coordination polymer is shown in Scheme 1. This coordination polymer tentatively contains chains propagated via bridging carboxylates. This type of polymer has been suggested in previous studies of PMOD using metal 2-ethylhexanoates (14).

We examined arrays of elements exposed to various doses (Fig. 2*a*) to determine the dose required for patterning large areas with a 10 kV acceleration voltage. Figure 2*a* shows an SEM image of a region that was exposed with seven different doses. The central elongated element was exposed with a dose of 1.560 mC/cm^2. The top of the image, where three elements were exposed with doses of 12.5, 25, and 50% the

[3] Supplementary Data includes spectroscopic ellipsometry fit spectra (Fig. S1) and best fit parameters (Table S1), measured hight of large areas as a function of exposure dose (Fig. S2), SEM images of nanowires patterned with different line doses (Fig. S3), a scheme showing the difference between LER and LWR (Scheme S1), and the equations used to calculate LER and LWR (SE-1 and SE-2). Supplementary data for this article are available on the journal Web site (canjchem.nrc.ca) or may be purchased from the Depository of Unpublished Data, Document Delivery, CISTI, National Research Council Canada, Ottawa, ON K1A 0R6, Canada. DUD 3814. For more information on obtaining material refer to cisti-icist.nrc-cnrc.gc.ca/cms/unpub_e.shtml.

© 2008 NRC Canada

Fig. 1. FTIR spectrum of an iron(III) 2-ethylhexanoate precursor thin film on CaF_2.

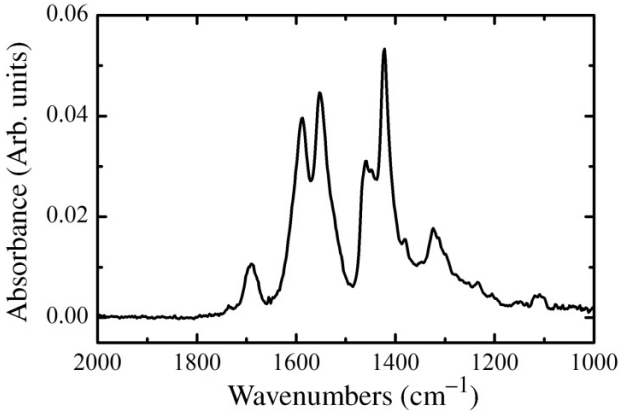

Scheme 1. Proposed structure of oligomeric (or polymeric) iron(III) 2-ethylhexanoate precursor. R = CH(Et)Bu.

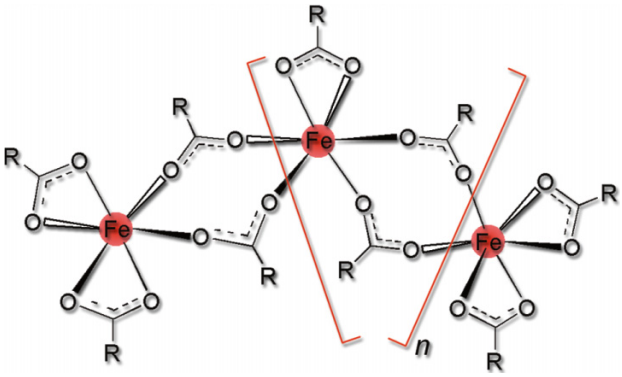

Fig. 2. (*a*) SEM image of elements exposed with doses of (from left to right, top to bottom) 0.195, 0.390, 0.780, 1.560, 3.120, 6.240, and 12.480 mC/cm^2. (*b*) SEM image of 31 nm wide wire on silicon (exposure dose = 34.2 nC/cm).

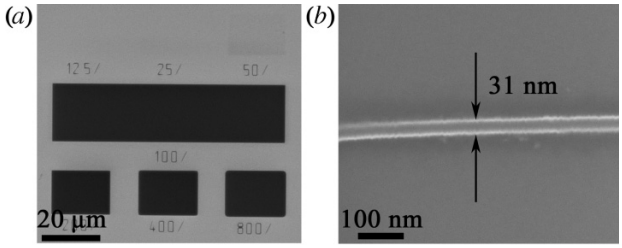

dose of 1.560 mC/cm^2, showed no material remained on the silicon surface after development. The bottom image shows elements exposed with 2, 4, and 8 times the dose of 1.560 mC/cm^2. While material is deposited, rounding at the corner of these elements suggest over-exposure. As such, we determined that a dose of 1.560 mC/cm^2 is required for patterning areas.

The thickness of large areas exposed to various doses were measured by AFM (see Fig. S2).[3] At a dose of 1.4 mC/cm^2, the thickness is ~58 nm. The thickness increases with increasing exposure dose to a maximum of ~110 nm at a dose of 2.8 mC/cm^2. Further increases in dose results in a decrease in the thickness of the structure. Above

Fig. 3. Normal distribution of 41 line width measurements, made every ~30 nm along the line segment of the SEM image shown in the inset.

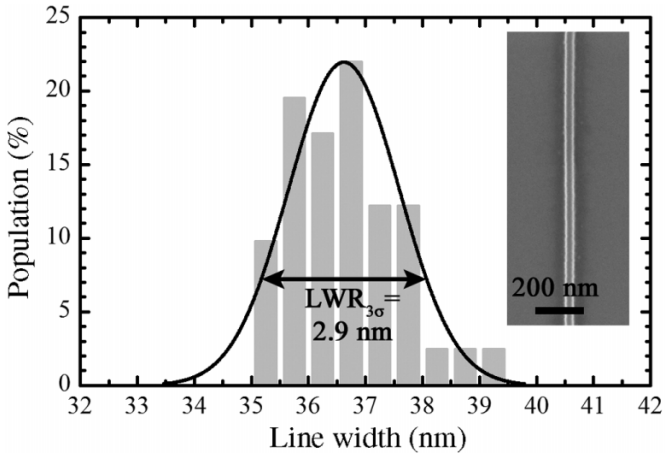

a dose of 10 mC/cm^2, the thickness of the feature is independent of dose and about ~40 nm. This result is consistent with the formation of an insoluble material that densifies with further exposure.

This dose compares favorably to other EMOD precursors. For example, precursors containing high atomic number metals such as palladium(II) acetylacetonate and polystyrene-based gold(I) thiolate require doses of 4 and 9.8 mC/cm^2 at 10 and 20 kV, respectively, (17, 19), while mixtures of metal neodecanoates used for the deposition of $YBa_2Cu_4O_x$ required a dose of 1.200 mC/cm^2 at 25 kV (20). Our reported dose of 1.560 mC/cm^2 for iron(III) 2-ethylhexanoate is essentially the same as the dose of 1.500 mC/cm^2 at 10 kV reported by Henderson and co-workers (7) for the patterning of sub-100 nm lines using the closely related titanium(IV) di-*n*-butoxide bis(2-ethylhexanoate).

Henderson also reports that a pre-exposure bake can improve by a factor of almost seven the sensitivity of this titanium precursor. This may be an avenue to decrease the required dose to print in our system, even though it may be expected that the effect of a pre-exposure thermal treatment may not be as pronounced as with a thermally sensitive alkoxide-based precursor.

The deposition of 31 nm wide nanowires on a silicon substrate was achieved when the iron(III) 2-ethylhexanoate thin film was exposed with a dose of 34.2 nC/cm (Fig. 2*b*). The width of the deposited nanowires could be controlled by varying the exposure dose (see Fig. S3).[3] Using the EMOD approach described in this paper, we have patterned 37 nm wide nanowires with line-edge roughness (LER$_{3\sigma}$) and linewidth roughness (LWR$_{3\sigma}$) of 2.7 and 2.9 nm, respectively, (see eqs. SE-6 and 7 as well as Scheme S1).[3] The LWR measurements are shown in Fig. 3.

In the same fashion, features could be patterned by exposing single spots for a predetermined dwell time (Fig. 4*a*). Such features appear to be dots, but on closer examination of such features exposed with a lower dose, elongated structures can be seen instead of dots (Fig. 4*b*). The diameter of the pillar could be tuned by changing the exposure dose. The diameter roughly depends on the logarithm of the dose (Fig. 4*c*). The height of the standing pillars seems to be in-

© 2008 NRC Canada

Fig. 4. (*a*) SEM image of pillars on silicon. The dose increases from 0.19 (bottom) to 1.34 pC (top). (*b*) Standing and fallen pillars. (*c*) Diameter of the obtained pillar as a function of exposure dose.

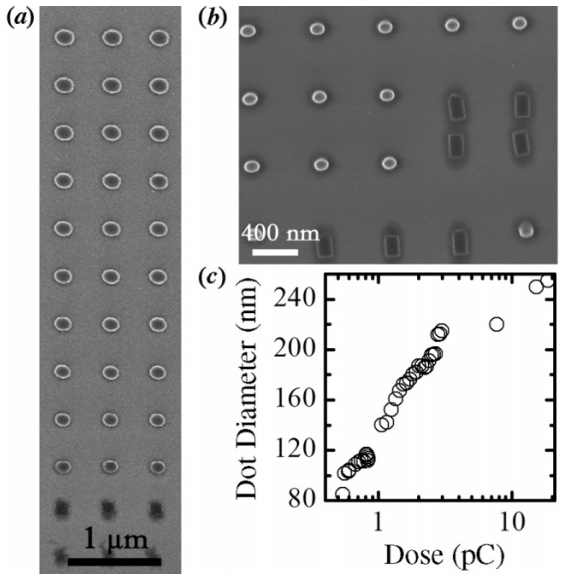

Fig. 5. AFM images of dot arrays. (*a*) Image at the threshold dose, which is ~0.504 pC. The dose increases from left (~0.204 pC) to right (~0.588 pC). Images taken for dots exposed below (*b*) and above (*c*) the threshold dose.

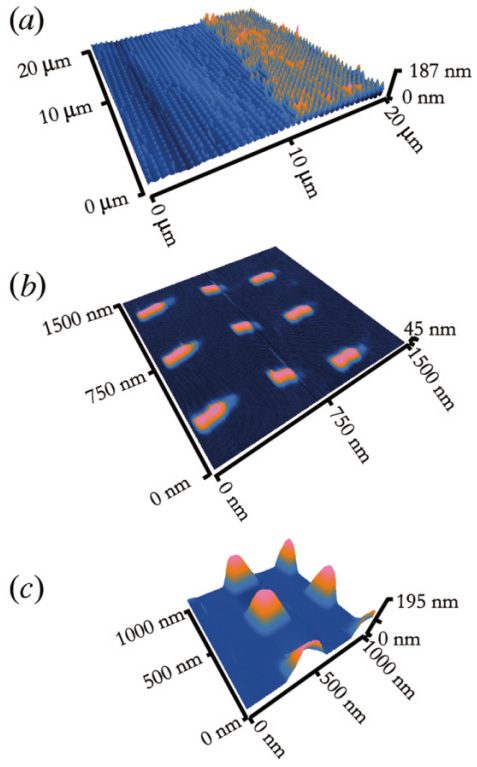

dependent of exposure dose as seen from AFM imaging (Fig. 5*a*) and is more likely to be a function of the precursor film thickness. The precursor thickness can be controlled by adjusting the spin-coating conditions.

Fig. 6. (*a*) HAADF-STEM image of patterned area and associated electron diffraction. The bright area is the material deposited by EMOD. (*b*) Energy dispersive X-ray spectroscopy of areas highlighted in (*a*). The top spectrum corresponds to the area labelled *T* in (*a*), while the bottom spectrum corresponds to the area labelled *B*. The peaks are attributed to C *K* (●), N *K* (○), O *K* (■), Fe $L_{1,2,3}$ (□), Si K_{α} (◆), and Fe $K_{\alpha/\beta}$ (*) X-ray lines.

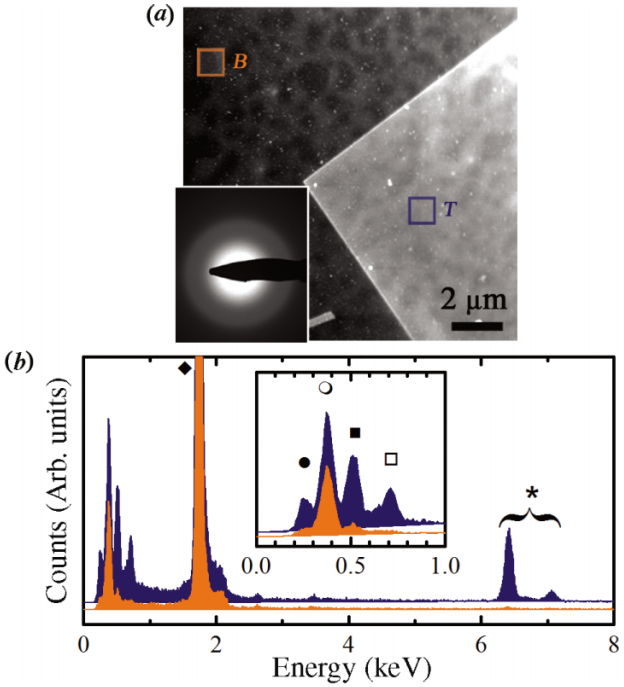

We believe spot exposure leads to the deposition of pillar structures, and that the elongated features are actually pillars fallen onto their side. This was verified by AFM. Representative images are shown in Fig. 5. A large area view of an exposed dot array is shown in Fig. 5*a*, in which the exposure dose increases from left to right from ~0.204 to ~0.588 pC. It is clear that below a threshold dose (~0.504 pC), the structures have fallen over. For example, Fig. 5*b* shows fallen nanopillars, similar to the elongated features shown in Fig. 4*b*. Above this dose, free standing nanopillars are obtained (Fig. 5*c*), similar to the circular features seen by SEM in Fig. 4*b*.

The falling of the pillars is possibly due to mechanical failure during the development. The preferential alignment of the fallen pillars might suggest that failure occurs during the drying step where a stream of gas flowing in one direction is used. Based on SEM and AFM imaging, we estimate the 85 nm wide pillars have an aspect ratio of ~2.5.

Samples prepared on 75 nm thick Si_3N_4 membranes were inspected using TEM. A large area view is shown in Fig. 6*a*. The electron diffraction pattern showed no features apart from diffuse scattering, which suggests an amorphous product is obtained (Fig. 6*a*, inset). The same area was examined by energy dispersive X-ray analysis. In addition to the lines due to the Si_3N_4 substrate (N *K* and Si *K*α), lines were observed for C *K*, O *K*, and Fe $L_{1,2,3}$ and $K_{\alpha/\beta}$ X-ray emission. This indicates that the deposited material is iron oxide with some carbon. It is unclear whether the carbon is due to residual iron(III) 2-ethylhexanoate or comes from the develop-

© 2008 NRC Canada

Fig. 7. (*a*) HAADF-STEM image of patterned lines on Si_3N_4 membrane. The line in the inset is 22 nm wide. (*b*) HAADF-STEM and BF-TEM (inset) images of single dot exposures.

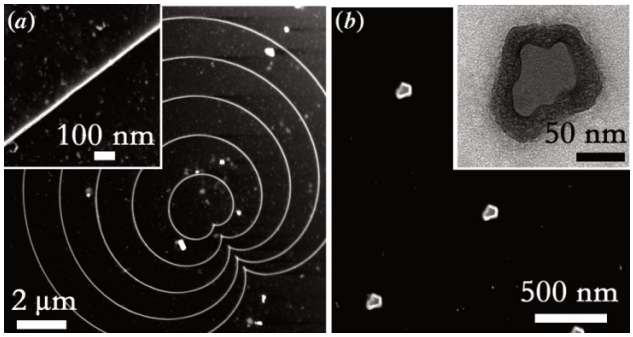

ment process. However, the presence of carbon is not unexpected as full conversion of the precursor is not required for development to be feasible. The production of an amorphous metal oxide is consistent with our previous observations of PMOD using metal 2-ethylhexanoate precursors (14, 15). While EMOD was carried out under high vacuum (~5×10^{-6} mbar, 1 bar = 100 kPa), we believe the deposited material is readily oxidized when removed from the chamber of the exposure tool and exposed to air. We are currently designing experiments to carry out the characterization of the deposited product (obtained by either of PMOD or EMOD) in the absence of oxygen.

Nanowires patterned on thin substrates are shown in Fig. 7*a*. The inset of this figure shows a 22 nm wide nanowire. The amount of backscattered and secondary electrons generated through electron–solid interactions will depend on the thickness as well as the atomic number of the substrate material (25). It is expected that fewer backscattered and secondary electrons are generated when a thin, lower atomic number Si_3N_4 membrane is used as a substrate (when compared with a bulk silicon substrate). This explains the lower line widths observed on the silicon nitride membrane.

Imaging of the pillar structures using TEM and STEM shows a modulation of the averaged density of material within an individual pillar. In a BF-TEM image (Fig. 7*b*, inset), the center of the pillar appears as brighter than the ~20 nm at the periphery of the pillar, without however being as bright as the surrounding unpatterned areas. A similar modulation in the density of material can be seen in a HAADF-STEM image, although the contrast is inverted between the BF and DF images (Fig. 7*b*). We believe the irregular, but reproducible, shape of the pillar is due to the crude electron-beam astigmatism correction used when this sample was patterned. A series of pillars exposed to different exposure doses are shown in Figs. 8*a*–8*f*. It can be seen in this series of images that at low doses, the pillar does not have a central feature (Fig. 8*a*). As higher doses are used, the central features increase in diameter, as does the outer diameter of the pillar.

Fig. 8. Pillar structures obtained with various exposure doses indicated below each image. The field of view is the same in all images, and the scale bars = 50 nm.

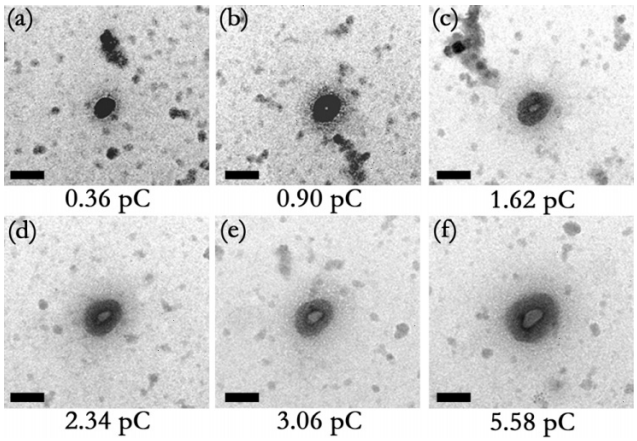

Discussion

Line edge and line width resolutions

One of the major resolution problems currently encountered with organic resists are the line-edge roughness (LER) and the line-width roughness (LWR). The LWR represents the uniformity of the line width, while the LER represents how smooth the edge of a patterned line is (see Scheme S1).[3]

The effect of the LER/LWR on semiconducting devices has been demonstrated to be in general detrimental to device performance. The threshold voltage and the off-state current leakage are both dependent on the LER/LWR in sub 100 nm devices (26–29). The off-state leakage current now accounts for as much power consumption as the actual use of the device and is a major challenge to further microprocessor miniaturization (30). As such, lithographic methods with low line edge and line width roughnesses are desirable.

A multitude of factors have been attributed as contributing to the LER and LWR in organic resists, such as the type, molecular weight, and the dispersity of the polymer resists; the concentration, distribution, and diffusibility of the photoacid generator; the development time; the swelling of the resists; and finally the LER/LWR of the photomask itself (when photolithography is carried out), to name but a few (31, 32). These defects are then transferred from the resist to the substrate/patterned material during the subsequent etch step (33). For example, LER values of 5 to 15 and 6 to 17 nm for chemically amplified UV-5 (34) and UV-6 (35) resists have been reported, respectively. Sub 9 nm LER values were reported for PMMA (3.5 to 7 nm) (35) and polyphenol resists with and without photoacid generators (2.3 to 8.4 nm) (36).

The method presented here is capable of achieving sub 3 nm LER and LWR. When considering the factors that contribute to LER/LWR in organic resists, it is apparent that many of them are not applicable to our metalorganic deposition method. For instance, no photogenerated acid is used. The size of organic polymer molecules used as resists is such that the removal of a single molecule during the development step can affect the edge roughness. In our system, small molecules are used, and as such the effect of the removal of single molecules is far less noticeable in terms of edge roughness. Our method requires very short (~3 s) development times, and a metal oxide material is far less likely to uptake solvent. This greatly minimizes swelling.

In our system, the deposited metal oxide can be used directly as a device-active component, or it can be used as an

© 2008 NRC Canada

Scheme 2. Proposed mechanism for the formation of free-standing iron oxide nanotubes. On the left-hand side, a low exposure dose yields free-standing, solid pillar. On the right-hand side, a higher exposure dose leads to heating of the core and the thermal evaporation of material (shown as dotted arrows), leaving a free-standing nanotube on the substrate.

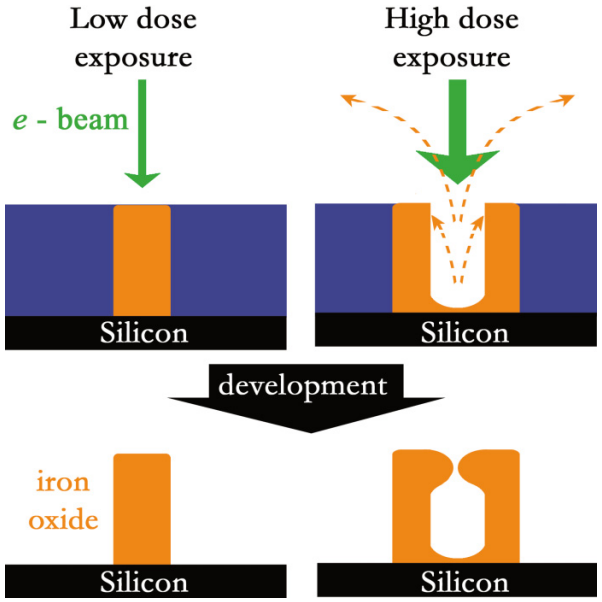

utlrathin top-side resist. In both instances, a low LER/LWR is expected in the final structure.

Patterning of free-standing nanotubes

The observation of two different regions in the BF-TEM images of pillars (see Figs. 7 and 8) could be interpreted as either due to (*i*) two different materials (either compositionally or – density), (*ii*) different crystallinity, or (*iii*) modulation of *overall* averaged density of material. No indication of materials other than iron oxide was found, and the whole structure was seen to be amorphous when inspected using high-resolution TEM and electron diffraction. However, if the total amount of a given material changes within the structure, with less material present in the middle, images as those presented here would be expected. As such, we suggest the pillars are partially hollowed.

The dependence of the diameter of the interior region with exposure dose is consistent with our expectation for thermal evaporation from the core leading to hollowing of the pillar (see Scheme 2). As the exposure dose increases, the outer diameter of the pillar increases. If only a low exposure dose is used, a solid pillar is obtained, as shown in Fig. 8*a* and depicted on the left hand side of Scheme 2. If the pillar is subjected to a higher dose, local heating occurs in the central region where the primary beam is hitting the newly formed iron oxide. This ultimately leads to electron beam induced thermal evaporation of material from the central region of the pillar, yielding a free-standing nanotube (Scheme 2, right hand side). Incomplete thermal evaporation of the core will probably leave some material in the core of the nanotube. Capping of the nanotube is also expected. This can be due to a collapse of the edge of the nanotube or to the redeposition of thermally evaporated material at the lip of the nanotube, or a combination of both.

The observed TEM and STEM images are consistent with the model presented above. Presumably, the increased overall density of the interior of these features with respect to the supporting membrane is associated with the capping of the nanotube by iron oxide. Capping is also consistent with the SEM and AFM images presented here. Thus, we suggest that the pillars are hollow, free standing iron oxide nanotubes.

Conclusions

We have shown the deposition of sub 100 nm iron oxide nanostructures using electron beam metalorganic deposition. Sub 40 nm nanowires with low line edge and line width roughness were patterned onto silicon surfaces. This method has the advantage over the deposition from the gas phase that the amount of deposit is easily controlled through the initial coating process. The process itself can be conducted on standard e-beam lithography tools without modification.

The patterning of free-standing, hollow nanotubes when using electron beam metalorganic deposition is, to our knowledge, unprecedented. The use of electron beam lithography affords the tunability of the external diameter of the nanotube, as well as the ability to address the position of the nanotube. The preparation of such structures with positional control is hard to achieve using either top- down or bottom-up fabrication strategies.

Acknowledgements

We thank the Canadian Foundation for Innovation, the Natural Science and Engineering Research Council of Canada, the British Columbia Knowledge Development Fund, and Simon Fraser University for financial support. We thank the clean room staff of 4D LABS for technical assistance.

References

1. P. Nguyen, H.T. Ng, T. Yamada, M.K. Smith, J. Li, J. Han, and M. Meyyappan. Nano Lett. **4**, 651 (2004).
2. L. Francioso, A. Forleo, A.M. Taurino, and P. Siciliano. Proc. SPIE-Int. Soc. Opt. Eng. **6589**, 658913 (2007).
3. Y. Xia, P. Yang, Y. Sun, Y. Wu, B. Mayers, B. Gates, Y. Yin, F. Kim, and H. Yan. Adv. Mater. **15**, 353 (2003).
4. Z. Wang, J. Hu, A.P. Suryavanshi, K. Yum, and M.-F. Yu. Nano Lett. **7**, 2966 (2007).
5. M. Law, J. Goldberger, and P.D. Yang. Annu. Rev. Mater. Sci. **34**, 83 (2004).
6. T. Tsutsumi, K. Ishii, H. Hiroshima, S. Hazra, M. Yamanaka, I. Sakata, H. Taguchi, E. Suzuki, and K. Tomizawa. J. Vac. Sci. Technol. B, **18**, 2640 (2000).
7. A. Jeyakumar, C.L. Henderson, P. Roman Jr., and S. Suh. J. Vac. Sci. Technol. B, **21**, 3157–3161 (2003).
8. Z.-M. Liao, Y.-D. Li, J. Xu, J.-M. Zhang, K. Xia, and D.-P. Yu. Nano Lett. **6**, 1087 (2006).
9. Z. Liu, D. Zhang, and C. Zhou. Mater. Res. Soc. Symp. Proc. **853E**, I6.7.1 (2005).
10. D. Zhang, Z. Liu, S. Han, C. Li, B. Lei, M.P. Stewart, J.M. Tour, and C. Zhou. Nano Lett. **4**, 2151 (2004).

© 2008 NRC Canada

11. Y. Li, W. Kim, Y. Zhang, M. Rolandi, D. Wang, and H. Dai. J. Phys. Chem. B, **105**, 11424 (2001).
12. M. Shimijo, M. Takeguchi, and K. Furuya. Nanotechnology, **17**, 3637 (2006).
13. M. Shimijo, M. Takeguchi, K. Mitsuishi, M. Tanaka, and K. Furuya. Jpn. J. Appl. Phys. Part 1, **46**, 6247 (2007).
14. H. Zhu and R. H. Hill. J. Non-Cryst. Solids **311**, 174 (2002).
15. S. Trudel, G. Li, X. Zhang, and R.H. Hill. J. Photopolym. Sci. Technol. **19**, 467 (2006).
16. S. Trudel, C.H.W. Jones, and R.H. Hill. J. Mater. Chem. **17**, 2206 (2007).
17. T. Stark, T. Mayer, D. Griffis, and P. Russell. J. Vac. Sci. Technol. B, **9**, 3475–3478 (1991).
18. T. Bhuvana and G.U. Kulkarni. ACS Nano, **2**, 457 (2008).
19. M.K. Corbierre, J. Beerens, and R.B. Lennox. Chem. Mater. **17**, 5774 (2005).
20. J. Mantese, A.B. Catalan, A.H. Hamdi, A.L. Micheli, and K. Studer-Rabeler. Appl. Phys. Lett. **53**, 526 (1988).
21. S.B. Clendenning, S. Aouba, M.S. Rayat, D. Grozea, J.B. Sorge, P.M. Brodersen, R.N.S. Sodhi, Z.-H. Lu, C.M. Yip, M.R. Freeman, H.E. Ruda, and I. Manners. Adv. Mater. **16**, 215 (2004).
22. R.H. Hill, A.A. Avey, S.L. Blair, M. Gao, and B.J. Palmer. Mater. Chem. Phys. **43**, 233 (1996).
23. A.R. Forouhi and I. Bloomer. Phys. Rev. B: Condens. Matter, **34**, 7018 (1986).
24. K. Nakamoto. Infrared and Raman spectra of inorganic and coordination compounds. Part A, 5th Ed. John Wiley and Sons Inc., New York. 1997.
25. M.A. McCord and M.J. Rooks. Handbook of microlithography, micromachining, and microfabrication. *Edited by* P. Rai-Choudhury. SPIE Press, Bellingham, Wash., USA. 1997.
26. C.H. Diaz, H.-J. Tao, Y.-C. Ku, A. Yen, and K. Young. IEEE Electron Device Lett. **22**, 287 (2001).
27. A. Yamaguchi, K. Ichinose, S. Shimamoto, H. Fukuda, R. Tsuchiya, K. Ohnishi, H. Kawada, and T. Iizumi. Proc. SPIE-Int. Soc. Opt. Eng. **5375**, 468 (2004).
28. K. Shibata, N. Izumi, and K. Tsujita. Proc. SPIE-Int. Soc. Opt. Eng. **5375**, 865 (2004).
29. J.Y. Lee, J. Shin, H.-W. Kim, S.-G. Woo, H.-K. Cho, W.-S. Han, and J.-T. Moon. Proc. SPIE-Int. Soc. Opt. Eng. **5376**, 426 (2004).
30. N.S. Kim, T. Austin, D. Blaauw, T. Mudge, K. Flautner, J.S. Hu, M.J. Irwin, M. Kandemir, and V. Narayanan. Computer, **36**, 68 (2003).
31. F.M. Houlihan, D. Rentkiewicz, G. Lin, D. Rahman, D. Mackenzie, A. Timko, T. Kudo, C. Anyadiegwu, M. Thiyqarqjan, S. Chiu, A. Romano, R.R. Dammel, and M. Padmanaban. J. Photopolym. Sci. Technol. **19**, 327 (2006).
32. G. Lee, T.-S. Eom, C. Bok, C. Lim, S.-C. Moon, and J. Kim. Proc. SPIE-Int. Soc. Opt. Eng. **5753**, 390 (2005).
33. H. Namatsu, M. Nagase, T. Yamaguchi, K. Yamazaki, and K. Kurihara. J. Vac. Sci. Technol. B, **16**, 3315 (1998).
34. Y. Ma and F. Cerrinaa. J. Vac. Sci. Technol. B, **23**, 1096 (2005).
35. Y. Ma and G. Tsvid. J. Vac. Sci. Technol. B, **21**, 3124 (2003).
36. A. Atsuko Yamaguchi, H. Fukuda, T. Arai, J. Yamamoto, T. Hirayama, D. Shiono, H. Hada, and J. Onodera. J. Vac. Sci. Technol. B, **23**, 2711 (2005).

© 2008 NRC Canada

Zinc and iron complexes of a helix-directing (1*R*,2*R*)-cyclohexyl salen ligand with phenanthryl sidearms[1]

Alexander V. Wiznycia, John Desper, and Christopher J. Levy

Abstract: A symmetrical salen ligand is formed by the condensation of (1*R*,2*R*)-diaminocyclohexane with 4-hydroxy-3-phenanthrenecarboxaldehyde. Crystallographic characterization of the metal complexes (Zn^{II}, Fe^{II}, and Fe^{III}) show 1:1 mixtures of diastereomeric *M* and *P* helical molecules. ECD spectra of the Zn^{II} complex combined with DFT simulations strongly suggest that the *M* conformation is dominant in solution. This is supported by ^{1}H and ^{13}C NMR data, which are consistent with a single species in solution.

Key words: zinc, iron, ECD, DFT, salen complexes.

Résumé : La condensation du (1*R*,2*R*)-diaminocyclohexane avec le 4-hydroxyphénanthracène-3-carboxaldéhyde conduit à la formation d'un ligand salen symétrique. La cristallisation cristallographique des complexes métalliques (Zn^{II}, Fe^{II} et Fe^{III}) montre la présence de mélanges 1:1 de molécules hélicoïdales *M* et *P* diastéréoisomères. Les spectres de DCE du complexe de Zn(II), combinés aux résultats de calculs suivant la théorie de la théorie de la fonctionnelle de densité (TFD) suggèrent que la conformation *M* est prépondérante en solution. Cette conclusion est appuyée par les données de RMN du ^{1}H et du ^{13}C qui sont en accord avec la présence d'une seule entité en solution.

Mots-clés : zinc, fer, DCE, TFD, complexes salen.

[Traduit par la Rédaction]

Introduction

The helix is an important chiral motif in natural systems, and there is increasing development of helical transition metal complexes and related supramolecular structures (1). A simple single-stranded monohelical complex can be constructed by wrapping a multidentate ligand around a metal centre. For resolved chiral ligands there will generally be a preference for either the plus (*P*) or minus (*M*) conformation of the helix. In previous studies we have examined monohelical complexes based on salen ligands with chiral backbones and polyaromatic sidearms (2). In this report we extend this work and detail our results for systems with the (1*R*,2*R*)-cyclohexyl backbone and phenanthryl sidearms. X-ray structural characterization combined with electronic circular dichroism (ECD) spectroscopy and DFT spectral simulations indicate an unusual solution to solid state optical switching of diastereomeric helical conformations for these complexes (2, 3).

Received 1 April 2008. Accepted 3 June 2008. Published on the NRC Research Press Web site at canjchem.nrc.ca on 23 September 2008.

We are delighted to contribute to this special issue recognizing the outstanding scientific career of Richard J. Puddephatt, who has been a mentor and an inspiration in science and in life.

A.V. Wiznycia, J. Desper, and C.J. Levy.[2] Department of Chemistry, Kansas State University, 111 Willard Hall, Manhattan, Kansas 66506, USA.

[1]This article is part of a Special Issue dedicated to Professor R. Puddephatt.

[2]Corresponding author: C.J. Levy (e-mail: clevy@ksu.edu).

Results and discussion

Synthesis

The ligand (*R*,*R*)-**1** was prepared by condensation of the aldehyde precursor, 4-hydroxy-3-phenanthrenecarbox-aldehyde, with (1*R*,2*R*)-diaminocyclohexane [(*R*,*R*)-DAC] in ethanol (Scheme 1). (*R*,*R*)-**1** was then metalated by combination with the appropriate metal chloride in the presence of excess sodium methoxide (Scheme 1). A solvent mixture (CH_2Cl_2/ethanol or THF/ethanol) in the metalation reactions allowed for sufficient solubility of the metal salt and the deprotonated ligand (formed in situ) for reactions to be completed in reasonable times. Dissolution of the crude products in THF followed by precipitation and washings with CH_2Cl_2 and EtOH yielded pure products. The Fe^{III} complex had considerably lower solubility than the M^{II} complexes, and the crude product was only partially redissolved in THF, resulting in a lower yield for this compound. The metalation reactions do not proceed in the absence of base, but triethylamine can be used in place of sodium methoxide. Product isolation from MeOH/NaOMe is generally easier than from $HNEt_3Cl/NEt_3$ via solubility protocols, making NaOMe the preferred base for these reactions. Drying of the M^{II} complexes in vacuo yields compounds without coordinated solvent or additional solvent of crystallization, as indicated by combustion analysis and NMR spectroscopy.

 doi:10.1139/V08-125 © 2008 NRC Canada

Table 1. Crystal data for the ligand and its complexes.

Crystal	(*rac*)-**1**	(*R*,*R*)-**2**(py)	(*R*,*R*)-**3**(py)	(*R*,*R*)-**4**
Formula	$C_{36}H_{30}N_2O_2$	$C_{41}H_{33}N_3O_2Zn$	$C_{41}H_{33}Fe\ N_3O_2$	$C_{36}H_{28}ClFeN_2O_2$
Formula mass (g mol^{-1})	522.62	665.07	655.55	611.90
Colour, habit	Yellow, prism	Black, plate	Black, plate	Orange, plate
Crystal dimensions (mm)	0.15 × 0.25 × 0.35	0.10 × 0.20 × 0.30	0.15 × 0.40 × 0.40	0.15 × 0.30 × 0.45
Crystal system	Triclinic	Monoclinic	Monoclinic	Monoclinic
Space group	*P*(-1)	$P2_1$	$P2_1$	$P2_1$
Z	4	4	4	4
a (Å)	9.9861(9)	8.4421(4)	8.386(3)	10.9436(6)
b (Å)	14.1047(11)	20.4458(10)	20.709(7)	20.7678(11)
c (Å)	18.9046(15)	17.8670(8)	17.704(6)	12.3169(7)
α (°)	87.046(5)	90	90	90
β (°)	84.757(5)	95.085(3)	94.86(2)	94.813(3
γ (°)	86.979(5)	90	90	90
Collection ranges	$-12 \le h \le 12$, $-17 \le k \le 18$, $-24 \le l \le 22$	$-9 \le h \le 10$, $-26 \le k \le 27$, $-23 \le l \le 23$	$-11 \le h \le 11$, $-26 \le k \le 25$, $-22 \le l \le 21$	$-14 \le h \le 12$, $-27 \le k \le 27$, $-15 \le l \le 14$
T (K)	173(2)	173(2)	203(2)	173(2)
Volume (Å^3)	2645.0(4)	3071.8(3)	3063.3(17)	2789.4(3)
D_{exp} (Mg m^{-3})	1.312	1.438	1.421	1.457
μ (mm^{-1})	0.081	0.843	0.536	0.674
Radiation	Mo Kα	Mo Kα	Mo Kα	Mo Kα
F(000)	1104	1384	1368	1268
θ range for data collection (°)	2.45–27.15	2.4–25.6	2.25–27.0	1.66–28.28
Observed reflections	19 157	27 171	35 237	35 811
Independent reflections	11 481	13 665	11 319	11 585
R_{int}	0.1082	0.0424	0.0487	0.0433
R_1[a]	0.0740	0.0377	0.0360	0.0313
wR_2[a]	0.1826	0.0768	0.0784	0.0767
R_1 (all data)	0.1151	0.0724	0.0562	0.0372
wR_2 (all data)	0.2034	0.0860	0.0852	0.0802
GOF on F^2	1.015	0.874	0.955	1.042
Absolute structure parameter	N/A	–0.20(13)	–0.31(15)	–0.015(8)

[a] $R_1 = \Sigma\|F_o| - |F_c\| / \Sigma|F_o|$ for $F_o > 2\sigma(F_o)$ and $wR_2 = \{\Sigma[w(F_o^2 - F_c^2)^2] / \Sigma[w(F_c^2)]\}^{1/2}$.

Scheme 1. Synthesis of the ligand (*R*,*R*)-**1** and its divalent metal complexes.

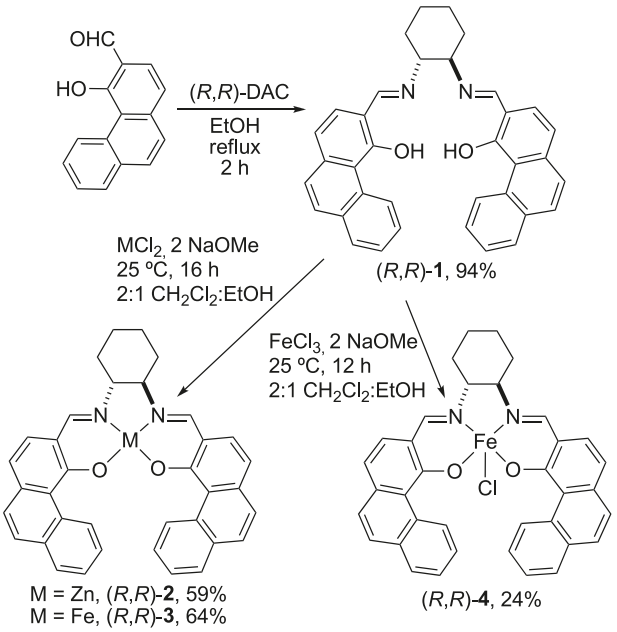

X-ray structural characterization

Crystal data for the structures reported in this article are presented in Table 1.

Crystals of the ligand (*R*,*R*)-**1** suitable for X-ray analysis could not be grown under the conditions examined, but solvent diffusion techniques did produce good quality crystals of (*rac*)-**1**. The structure shows two distinct molecules with the *R*,*R* configuration in the unit cell: they differ in both the sidearm positions and the arrangement of the acidic protons (Fig. 1). Molecule A has one sidearm roughly parallel and one roughly perpendicular to the cyclohexyl ring. There are two N–H···O hydrogen-bonding interactions such that the molecule exists in the di(keto-amine) form. Molecule B has both sidearms roughly perpendicular to the cyclohexyl backbone but in opposite orientations, resulting in pseudo-C_2 symmetry. In this tautomer there is one N–H···O and one O–H···N hydrogen bond. The O–H···N moiety is characterized by the position of the hydrogen as well as the shorter N=C and longer O–C bonds, compared with those associated with the N–H···O units (Fig. 1). The keto-amine to enol-imine isomerization indicated here is well-known for aromatic Schiff bases (4). The two molecules with *S*,*S* configuration (not shown) are related to the *R*,*R* molecules by the centre of inversion in the centrosymmetric P(-1) space group.

© 2008 NRC Canada

Table 2. Selected molecular parameters for the metal complexes.

Crystal	(*R*,*R*)-**2**(py), M = Zn(II)		(*R*,*R*)-**3**(py), M = Fe(II)		(*R*,*R*)-**4**, M = Fe(III)	
	M	*P*	*M*	*P*	*M*	*P*
Bond lengths (Å)						
M–N41/Cl1	2.089(4)	2.083(4)	2.126(3)	2.116(3)	2.2342(7)	2.2260(7)
M–N15	2.066(5)	2.093(5)	2.077(4)	2.092(3)	2.0772(18)	2.0910(18)
M–N35	2.061(4)	2.069(5)	2.081(3)	2.078(4)	2.078(2)	2.0755(19)
M–O5	1.978(4)	1.973(4)	1.943(3)	1.953(3)	1.8880(16)	1.8891(16)
M–O25	1.995(4)	1.982(4)	1.966(3)	1.965(3)	1.9010(16)	1.9055(16)
C5–O5	1.295(7)	1.297(7)	1.301(5)	1.311(5)	1.320(3)	1.288(5)
C15–N15	1.270(7)	1.274(7)	1.282(5)	1.285(5)	1.280(3)	1.284(2)
C16–N15	1.470(6)	1.475(6)	1.465(4)	1.468(4)	1.468(3)	1.526(3)
C16–C36	1.540(5)	1.518(6)	1.520(4)	1.524(4)	1.527(3)	1.470(3)
C36–N35	1.470(6)	1.477(5)	1.474(4)	1.473(4)	1.475(3)	1.472(3)
C35–N35	1.278(7)	1.278(7)	1.282(5)	1.296(5)	1.290(3)	1.290(3)
C25–O25	1.289(7)	1.284(7)	1.312(3)	1.302(5)	1.314(3)	1.322(3)
Angles (°)						
O5-M-O25	96.57(17)	95.27(17)	103.49(13)	102.24(13)	96.10(7)	96.58(7)
O5-M-N15	87.80(18)	86.83(17)	86.86(14)	86.90(13)	86.59(7)	86.78(8)
N15-M-N35	79.13(19)	79.04(19)	78.93(14)	78.84(14)	76.89(7)	76.94(7)
N35-M-O25	87.98(17)	88.36(17)	86.05(13)	85.12(13)	86.56(7)	85.72(7)
M out-of-plane	0.435	0.432	0.344	0.347	0.517	0.492
N15-C16-C36-N35	43.4(4)	43.4(4)	43.2(6)	42.9(3)	47.8(2)	47.3(2)
phen-phen	48.8	54.0	47.9	53.7	11.2	12.0
(C1-C6)-(C7-C12)	5.5	10.6	6.83	10.91	11.3	14.4
(C21-C26)-(C27-C32)	6.4	3.5	7.47	4.04	12.1	8.5

Note: The atom-numbering scheme of the ligand framework is the same for all three complexes. The *M* and *P* conformers have the same numbering schemes, with a 1 appended to the label for the *M* conformer and a 2 appended to the labels for the *P* conformer in the associated CIF files.

Fig. 1. Thermal ellipsoid plot (50%) of (*R*,*R*)-**1** from the structure of (*rac*)-**1**. Selected bond lengths (Å): N11–H11 1.04(3), N11–C115 1.293(3), C102–O112 1.307(3), N12–H12 1.10(3), N12–C215 1.289(3), C202–O212 1.305(3), N21–H21 1.13(2), N21–C315 1.285(3), C302–O312 1.297(3), N22–C415 1.279(3), O412–H22 0.86(3), C402–O412 1.341(3).

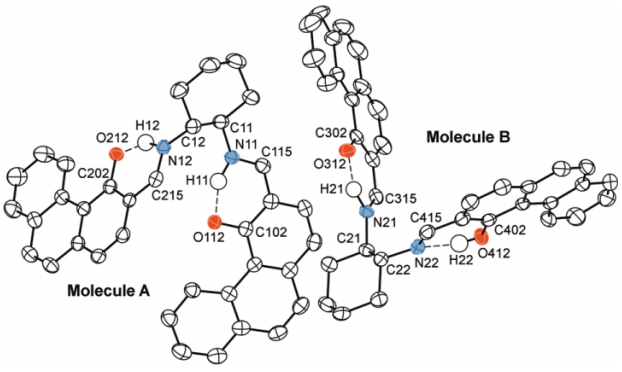

The Zn^{II}, Fe^{II}, and Fe^{III} complexes all crystallize in the $P2_1$ space group. In each case, the metal centre has a distorted square pyramidal geometry with the metal sitting above the square plane of donors by 0.34–0.52 Å. There are also two distinct diastereomeric conformations, *M* and *P*, that are in a 1:1 ratio and are related by a pseudo-inversion centre. Each form has diequatorial cyclohexyl backbones, and there is little difference in the N-C-C-N dihedral between them (Table 2). Instead, it is the pivoting of the phenanthryl arms about the C-O-Zn linkages and the accompanying tilting of the phenanthryl rings that relates the two conformers.

Looking at the structures in more detail, the Zn^{II} and Fe^{II} complexes are very similar (Fig. 2): both have axial pyridine donors and closely comparable bond lengths and angles (Table 2). This isostructural relationship is not unexpected, given the similar sizes of the divalent ions and strong (largely ionic) bonding to the phenoxide donors. The phenanthryl arms of both the Zn^{II} and Fe^{II} complexes are significantly tilted with respect to one another. For (*R*,*R*)-**2**(py) the interplanar angles are 48.8° (*M*) and 54.0° (*P*), while for (*R*,*R*)-**3**(py) the angles are 47.9° (*M*) and 53.7° (*P*). It appears that the repulsive steric interactions between the edge and face of the two phenanthryl groups are not sufficient to force them into a more coplanar arrangement. However, these interactions do contribute to significant curvature of the phenanthryl rings away from one another. A measure of curvature is the interplanar angle between the phenol and terminal rings of each phenanthryl group: this is 5.5° and 6.4° for the *M* helix and 3.5° and 10.6° for the *P* helix of (*R*,*R*)-**2**(py). The same trend is seen for (*R*,*R*)-**3**(py) (Table 2).

Some insight into the preference for the 1:1 crystallization of diastereomeric helices may be obtained from examining the crystal packing of (*R*,*R*)-**2**(py). Along the crystallographic *a* axis are arranged columns of molecules with the same conformation and orientation. The arrangement of stacks of *M* and *P* molecules in the crystallographic *bc* plane is shown in Fig. 2*d*. Although columns of homohelical molecules is an efficient packing motif, the axial pyridine ligands

© 2008 NRC Canada

Fig 2. (*a*) Thermal ellipsoid plot (50%) of (*R*,*R*)-**2**(py) showing the relative positions of the two conformers in the unit cell. (*b*) Space-filling plots of the *P* and *M* conformers of (*R*,*R*)-**2**(py). (*c*) Thermal ellipsoid plot (50%) of (*R*,*R*)-**3**(py) showing the relative positions of the two conformers in the unit cell. (*d*) Crystal packing of (*R*,*R*)-**2**(py) viewed down *a*. (*e*) Crystal packing of (*R*,*R*)-**2**(py) viewed down *b*.

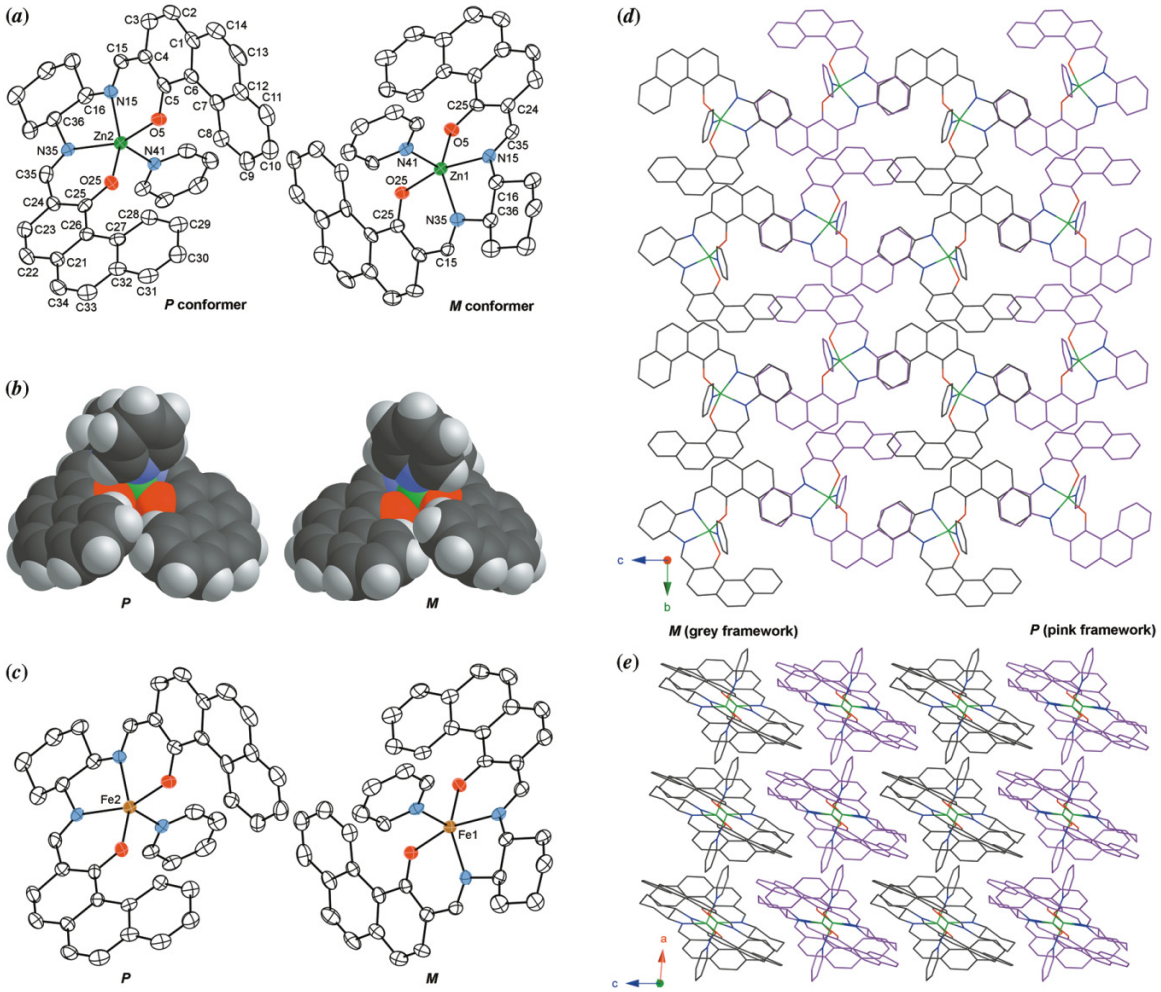

do not allow the close approach required for effective space-filling. This is compensated for by partial interlocking of adjacent *M* and *P* molecular stacks: the sidearm termini of *M* molecules are located over the cyclohexyl rings or sidearm termini of molecules with the *P* conformation (Figs. 2*d* and 2*e*). The interlocking of alternate stacks appears to be an important factor favouring the observed 1:1 *M*/*P* composition of the crystal. The iron complex (*R*,*R*)-**3**(py) has the same packing arrangement as (*R*,*R*)-**2**(py).

The Fe^{III} complex (*R*,*R*)-**4** has the same general molecular structure (Fig. 3) as seen for the divalent metal complexes, except that there is now an axial chloro ligand and the interplanar angles between the phenathryl rings are considerably smaller (11.2° for *M* and 12.0° for *P*). The flatter nature of this complex can be readily understood in terms of the stronger M–O bonding for the Fe^{III} complex, which pulls the phenathryl groups closer to one another and increases edge-to-face repulsions, forcing the rings to be more parallel. The lower steric requirements of the axial chloro compared with the pyridine is also a likely factor here. The curvature of the sidearms for (*R*,*R*)-**4** is 12.1° and 11.3° for the *M* conformer and 14.4° and 8.5° for the *P* conformer. The greater degree of curvature seen here is consistent with the closer proximity of the phenathryl rings to one another compared with the divalent complexes.

The crystal packing in (*R*,*R*)-**4** is significantly different than for the divalent metal complexes. Here there is a close 1:1 pairing between the *M* and *P* conformers: they have parallel molecular planes and are rotated 180° with respect to each other. This arrangement can be seen in Fig. 3*a*, and it allows for the helices to pack efficiently because of the complementary shape matching.

NMR Characterization

The ^{1}H and ^{13}C spectra of the ligand (*R*,*R*)-**1** are consistent with a single C_2 symmetric species in solution. The ^{1}H spectrum shows 9 resonances in the 7–11 ppm range, consistent with the aromatic and N=CH signals of a single species. Notable signals in this range are the imine N=C-H protons at 8.61 ppm and the signal at 10.61 ppm, which is due to the bay region hydrogens at the 5-positions of the phenanthryl rings. The bay protons are affected by edge position aromatic deshielding and anisotropic deshielding from the hydroxyl group at the nearby 4-position (5). The

© 2008 NRC Canada

Fig. 3. (*a*) Thermal ellipsoid plot (50%, depth fading) of (*R*,*R*)-**4** showing the relative positions of the two conformers in the unit cell. (*b*) Space-filling plots of the *P* and *M* conformers of (*R*,*R*)-**4**.

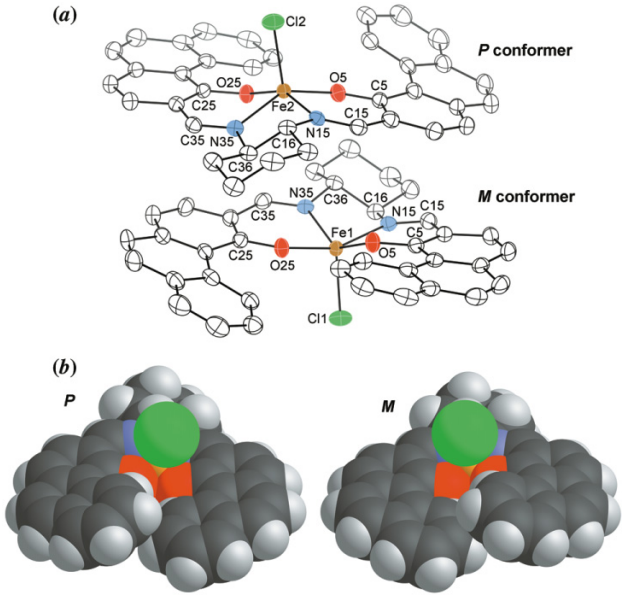

Fig. 4. Top: ECD spectrum of (*R*,*R*)-**1** in THF (2.5×10^{-5} mol/L). Bottom: electronic spectra of (*R*,*R*)-**1** (2.5×10^{-5} mol/L) in 1:1 THF/MeOH, THF, and, cyclohexane.

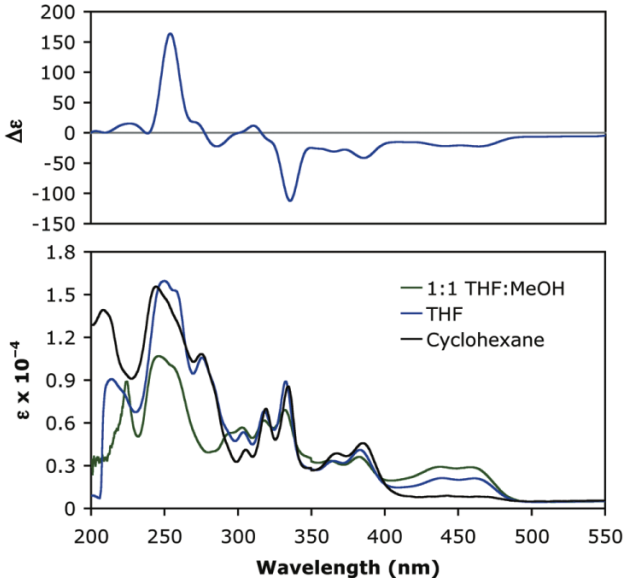

intramolecularly hydrogen-bonded protons appear at 15.97 ppm. While tautomerization is evident from the crystal structure, only an averaged ^{1}H NMR signal is observed, due to rapid proton transfer.

The diamagnetic Zn^{II} complex (*R*,*R*)-**2** has ^{1}H and ^{13}C spectra similar to those of the uncomplexed ligand and they show signals consistent with a C_2 symmetric molecule in solution. The most notable differences with the ligand ^{1}H spectrum are the absence of the phenolic resonance and the significant downfield shift of the bay region proton to 11.79 ppm. This shift is mainly the result of increased anisotropic deshielding by the phenoxide donor at the 4-position (5). The most significant aspect of the spectra of this complex is that they are not consistent with the 1:1 diastereomeric mixture in solution, unless rapid equilibration of *M* and *P* conformers is occurring. This is unlikely, given the significant molecular motions of large groups that would be required. Further support for this conclusion is provided by the –90 °C ^{1}H NMR spectrum of (*R*,*R*)-**2**, which shows signals for only one metal complex. A minor set of signals consistent with another helical conformation is not resolved at this temperature. Thus, the NMR spectra suggest that there is predominantly one thermodynamically favoured conformation in solution (>95%).

The paramagnetic iron complexes have broad ^{1}H NMR spectra over a wide chemical shift range (–28 to +42 and –3 to +17 for (*R*,*R*)-**3** and (*R*,*R*)-**4**, respectively), and ^{1}H-^{1}H couplings are not resolved. However, the number of signals present for each of these complexes is consistent with one major C_2 symmetric complex in solution. Just as for the Zn^{II} complex, the NMR data of the iron complexes are at odds with the solid state structures, which show a 1:1 *M*/*P* mixture.

Electronic and ECD spectroscopy

Neutral uncomplexed Schiff bases and salens can exist as an equilibrium mixture of keto-amine and the enol- imine tautomers, and the differences in electronic spectra of the two species is often diagnostic (4). The most notable difference is a lower energy $\pi \rightarrow \pi^*$ transition for the ketone compared with that of the imine. This is evident in the electronic spectrum of (*R*,*R*)-**1**: the ketone bands appear at 438 and 461 nm, while the imine bands are at 365 and 383 nm. The position of the equilibrium can be shifted by a change in solvent polarity, with more polar solvents favouring the keto-amine isomer, as has been seen for other Schiff bases (4). Figure 4 shows the electronic spectra collected in cyclohexane, THF, and a 1:1 MeOH/THF mixture. A progression to a larger proportion of keto-amine isomer in this series is seen and is especially evident in the 350–500 nm region.

The electronic and ECD spectra of (*R*,*R*)-**2** and (*R*,*R*)-**3** (Fig. 5) are similar in appearance, with the iron complex having broader absorptions, especially in the ECD spectrum. The low-energy envelope (350–460 nm) is attributable primarily to the π-π^* transition of the imine groups and is shifted to lower energy compared with the free ligand, as expected (6). The negative Cotton effect associated with this transition confirms a diequatorial 1*R*,2*R* configuration and non-coplanar imines (7). The appearance of the 200–380 nm spectral region is consistent with that of substituted phenanthrenes (8). The ECD spectra show strong signals, suggesting that there is one dominant helical form in solution, as opposed to a pseudo-racemic 1:1 *M*/*P* mixture (as observed in the solid). This is supported by DFT simulated spectra (Fig. 5*c*), which show a good match between the experimental spectrum of (*R*,*R*)-**2** and the simulated spectrum of the *M* conformer. Correspondingly, the *P* conformer simulated spectrum resembles the mirror image of both the experimental spectrum and the *M* conformer simulated spectrum.

DFT calculations (B3LYP/6-31G(d,p)) for (*R*, *R*)-**2**(py) indicate that the *M* conformer is thermodynamically favoured over the *P* conformer. The calculated energy difference is 2.5 kcal mol^{-1} (1 cal = 4.184 J) based on the crystal struc-

© 2008 NRC Canada

Fig. 5. (*a*) Electronic spectra and (*b*) ECD spectra of (*R*,*R*)-**2** (2.5×10^{-5} mol/L) and (*R*,*R*)-**3** (2.0×10^{-5} mol/L) in THF ($\Delta\varepsilon$ is in units of $(mol/L)^{-1}\ cm^{-1}$). (*c*) Simulated ECD spectra of the *M* and *P* forms of (*R*,*R*)-**2** (rotational strength is in 10^{-40} esu cm erg G^{-1}).

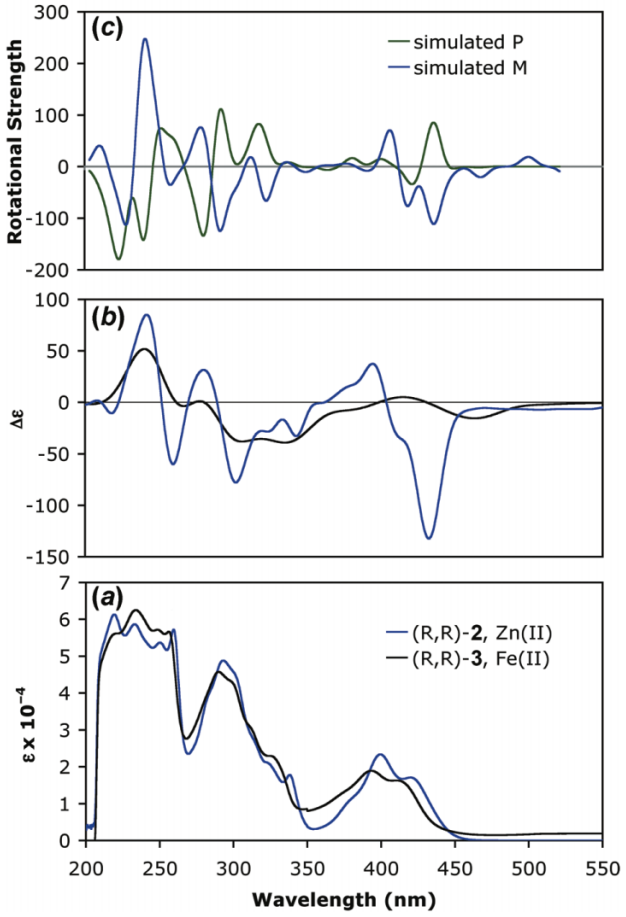

ture geometries and 1.5 kcal mol^{-1} based on AM1 minimized structures. This suggests that the *M* conformer is the major species in solution, consistent with the conclusion from the ECD simulations.

Experimental section[3]

General methods

The sidearm precursor 4-hydroxy-3-phenanthrenecarboxaldehyde was synthesized as reported previously (2). All air and (or) moisture sensitive compounds were manipulated using standard Schlenk techniques or in a glove box under a nitrogen atmosphere (9). All solvents were stored under vacuum over sodium benzophenone ketyl, magnesium, or calcium hydride prior to use. Solvents used in metalation reactions were degassed before use and inert gas was purified by passing through 4 Å molecular sieves and Engelhard Q5 catalyst. UV–vis data were collected on a Varian Cary 500 spectrometer and CD data were collected using a JASCO 720 Spectropolarimeter. Solution samples for these techniques were prepared using dried spectroscopic grade tetrahydrofuran, and solutions were loaded into a 1.00 cm quartz cell. UV–vis and CD data were collected at ambient temperature. NMR data were collected on a Varian Unity 400 MHz spectrometer using the residual solvent protons as an internal standard.

ECD simulations

All DFT computations relating to ECD spectroscopy were carried out using version 2005.0 lb of the Amsterdam density functional (ADF) software suite. Minimized geometries were obtained from crystallographic data employing a triple-ζ Slater-type basis set, including one polarization function (TZP) and the Vosko–Wilk–Nusair (10) (VWN) local density approximation. The addition of a second polarization function yielded minimal, if any, improvement in the results. For Zn, the 1s, 2s, and 2p orbitals were kept frozen. For C, N, and O, only the 1s orbital was kept frozen. The same TZP basis set and other parameters were utilized in the spectroscopic computations. Excitation energies and rotational strengths were calculated for the first 250 non zero strength transitions of (*R*,*R*)-**2**. When compared with experimental data, it is evident that the energies are overestimated by an average of ca. 0.1 eV. This is not unexpected given the approximations inherent in the LDA functional employed (11). In view of the overestimation, a 0.1 eV correction was applied to the calculated energies. Gaussian shaped distributions were subsequently generated from the computed data using a line width ($\Delta\lambda_{1/2}$) of 11 nm, and the simulated spectra were obtained by superposition of the individual Gaussian curves.

3,3′-[(1*R*,2*R*)-1,2-Cyclohexanediylbis-(nitrilomethylidyne)]bis-4-phenanthrenol (*R*,*R*)-1

A mixture of (1*R*,2*R*)- diaminocyclohexane (0.39 g, 3.4 mmol) and 4-hydroxy-3-phenanthrenecarboxaldehyde (1.50 g, 6.80 mmol) in ethanol (80 mL) was refluxed for 2 h. The resulting suspension was filtered while hot, and the yellow precipitate was collected, washed with boiling ethanol (40 mL), and dried in vacuo to give (*R*,*R*)-**1** (1.662 g, 94% yield). ^{1}H NMR ($CDCl_3$, 400 MHz) δ: 1.50–1.63 (m, 2 H, CH), 1.82–1.94 (m, 2 H, CH), 1.95–2.04 (m, 2 H, CH), 2.17–2.25 (m, 2 H, CH), 3.46–3.55 (m, 2 H, CH), 7.07 (d, 2 H, *J* = 8.3 Hz, CH), 7.14 (d, 2 H, *J* = 8.3 Hz, CH), 7.54–7.61 (m, 4 H, CH), 7.68–7.73 (m, 2 H, CH), 7.79 (d, 2 H, *J* = 8.7 Hz, CH), 7.84 (dd, 2 H, *J* = 1.2, 7.9, CH), 8.32 (d, 2 H, *J* = 3.7 Hz, CH), 10.09 (d, 2 H, *J* = 8.7 Hz, CH), 15.42 (br, s, 2 H, OH). ^{13}C NMR ($CDCl_3$, 100 MHz) δ: 24.51, 33.07, 70.51, 114.15, 118.08, 121.06, 125.95, 127.11, 127.33, 128.47, 129.25, 129.25, 130.68, 131.88, 132.59, 137.29, 165.09, 167.92. Anal. calc. for $C_{36}H_{30}N_2O_2$: C 82.73, H 5.79, N 5.36; found: C 82.62, H 6.01, N 5.36.

3,3′-[*trans*-1,2-Cyclohexanediylbis-(nitrilomethylidyne)]bis-4-phenanthrenol (*rac*)-1

The procedure for (*R*,*R*)-**1** was followed using *trans*-1,2-diaminocyclohexane in place of the *R*,*R* enantiomer to give *rac*-**1** (0.339 g, 96% yield). ^{1}H and ^{13}C NMR spectra were

[3] Supplementary data for this article are available on the journal Web site (canjchem.nrc.ca) or may be purchased from the Depository of Unpublished Data, Document Delivery, CISTI, National Research Council Canada, Ottawa, ON K1A 0R6, Canada. DUD 3815. For more information on obtaining material refer to cisti-icist.nrc-cnrc.gc.ca/cms/unpub_e.shtml.

© 2008 NRC Canada

identical to that of compound (*R*,*R*)-**1**. Anal. calc. for $C_{36}H_{30}N_2O_2$: C 82.73, H 5.79, N 5.36; found: C 82.41, H 5.82, N 5.37. Single crystals suitable for X-ray analysis were grown by slow diffusion of hexanes into a solution of *rac*-**1** in methylene chloride.

(*R*,*R*)-2 (Zn^{II} complex of (*R*,*R*)-1)

Anhydrous zinc(II) chloride (0.079 g, 0.58 mmol), sodium methoxide (0.093 g, 1.73 mmol), and (*R*,*R*)-**1** (0.30 g, 0.58 mmol) were suspended in a 2:1 mixture of methylene chloride/ethanol (15 mL). After stirring for 12 h, the reaction mixture was concentrated to a yellow solid that was then dissolved into THF (20 mL). The solution was filtered to remove fine insoluble solids, and the clear filtrate was diluted with ethanol (40 mL). Stirring for 3 h resulted in the gradual formation of a yellow precipitate. The precipitate was collected and washed consecutively with methylene chloride (5 mL) and ethanol (5 mL) to afford (*R*,*R*)-**2** (0.200 g, 59% yield). ^{1}H NMR (pyridine-d_5, 400 MHz) δ: 1.20–1.34 (m, 4 H, CH), 1.79 (br, s, 2 H, CH), 2.31 (br, s, 2 H, CH), 3.22 (br, s, 2 H, CH), 7.30 (d, 2 H, *J* = 8.2 Hz, CH), 7.57–7.66 (m, 4 H, CH), 7.80–7.87 (m, 4 H, CH), 7.96 (d, 2 H, *J* = 8.6 Hz, CH), 8.01 (d, 2 H, *J* = 7.9 Hz, CH), 8.63 (s, 2 H, CH), 11.79 (d, 2 H, *J* = 8.5 Hz, CH). ^{13}C NMR (pyridine-d_5, 100 MHz) δ: 25.08, 28.79, 66.31, 114.43, 117.48, 125.31, 125.69, 128.36, 128.55, 128.95, 130.04, 130.84, 133.31, 134.26, 134.98, 138.71, 166.27, 174.70. Anal. calc. for $C_{36}H_{28}N_2O_2Zn$: C 73.79, H 4.82, N 4.78; found: C 73.60, H 5.01, N 4.68. Lowering and raising (–90 to +50 °C) the temperature of a 1:1 CD_2Cl_2/pyridine-d_5 solution did not appreciably change the spectra, and no exchange was evident. Single crystals of (*R*,*R*)-**2** suitable for X-ray analysis were grown via slow cooling from boiling pyridine.

(*R*,*R*)-3 (Fe^{II} complex of (*R*,*R*)-1)

Anhydrous iron(II) chloride (0.073 g, 0.58 mmol), sodium methoxide (0.093 g, 1.7 mmol), and (*R*,*R*)-**1** (0.30 g, 0.58 mmol) were suspended into a 2:1 mixture of methylene chloride/ethanol (15 mL). After stirring for 12 h, the solvent was removed in vacuo to give a green-brown solid. The solid was dissolved into THF (15 mL), and the solution was filtered to remove fine insoluble solids. The resulting clear filtrate was diluted with ethanol (45 mL) and stirred for 30 min, resulting in the formation of a purple precipitate. This was collected and then suspended into methylene chloride (10 mL). After stirring for 15 min, the solid was recollected and dried in vacuo to afford (*R*,*R*)-**3** (0.21 g, 64% yield). ^{1}H NMR (pyridine-d_5, 400 MHz) δ: –25.11 (br, s, 2 H, CH), –11.69 (s, 2 H, CH), –4.80 (br, s, 2 H, CH), –3.28 (s, 2 H, CH), 1.66 (s, 2 H, CH), 5.26 (s, 2 H, CH), 10.13 (s, 2 H, CH), 10.90 (s, 2 H, CH), 17.14 (s, 2 H, CH), 24.61 (s, 2 H, CH), 40.42 (br, s, 2 H, CH). Anal. calcd. for $C_{36}H_{28}N_2O_2Fe$: C 75.01, H 4.90, N 4.86; found: C 74.94, H 5.00, N 4.71. Single crystals suitable for X-ray analysis were grown by slow diffusion of methanol into a pyridine solution of (*R*,*R*)-**3**.

(*R*,*R*)-4 (Fe^{III} complex of (*R*,*R*)-1)

Anhydrous iron(III) chloride (0.093 g, 0.56 mmol), sodium methoxide (0.093 g, 1.7 mmol), and (*R*,*R*)-**1** (0.29 g, 0.56 mmol) were suspended into a 2:1 mixture of THF/ethanol (15 mL) and stirred for 12 h. The solvent was removed in vacuo, and THF (80 mL) was added to the resulting solid. After stirring for 15 min, the insoluble material was removed by filtration and the red-black solution was diluted with ethanol (80 mL). Upon concentration to 1/2 volume, a black precipitate formed that was collected and dried in vacuo to afford (*R*,*R*)-**4** (0.082 g, 24%). The ^{1}H NMR spectrum consisted of broad overlapping signals that were not readily assignable. Anal. calcd. for $C_{36}H_{28}N_2O_2FeCl$: C 70.66, H 4.61, N 4.58; found: C 70.40, H 4.34, N 4.52. Single crystals suitable for X-ray analysis were grown by slow diffusion of diethyl ether into a methylene chloride solution of (*R*,*R*)-**4**.

Conclusions

Two diastereomeric conformers crystallize in a 1:1 ratio for each of the metal complexes. This is an unusual assembly mode, which has been observed in only a few systems, (12,13), in addition to our previous studies of an analogous Fe^{II} complex with an extended benz[*a*]anthryl sidearm (2). For the complexes of (*R*,*R*)-**1,** the adoption of *pseudo*-enantiomeric helical conformers is favoured in the crystalline solid. This appears to be the result of more efficient packing when *M* and *P* helices, which have complementary shapes, can associate in the crystal. For these complexes the packing forces can dominate the crystal composition since the conformers readily interconvert and the energy difference between them is small (~2 kcal mol^{-1}). However, the energy difference is large enough that the thermodynamically preferred *M* conformer dominates in solution. Thus, there is a solution to solid chiral switching that occurs for these complexes, although the rate of the process is as yet unknown. We are currently investigating other metal complexes of (*R*,*R*)-**1** and examining their utility as asymmetric catalysts.

Acknowledgements

This work is supported by the National Science Foundation under grant number CHE-0349258 and by Kansas State University.

References

1. (*a*) C. Piguet, G. Bernardinelli, G. Hopfgartner. Chem. Rev. **97**, 2005 (1997); (*b*) H.C. Aspinall. Chem. Rev. **102**, 1807 (2002); (*c*) M. Albrecht. Chem. Rev. **101**, 3457 (2001).
2. (*a*) A.V. Wiznycia, J. Desper, C.J. Levy. Chem. Commun. 4693 (2005); (*b*) Inorg. Chem. **45**, 10034 (2006); (*c*) Dalton Trans. 1520 (2007).
3. For examples see: (*a*) H. Jiang, C. Dolain, J.-M Léger, H. Gornitzka, and I. Huc. J. Am. Chem. Soc. **126**, 1034 (2004); (*b*) Q. Yu, T.E. Baroni, L. Liable-Sands, A.L. Reingold, A.S. Borovik. Tetrahedron Lett. **39**, 6831 (1998).
4. (*a*) H. Ünver. Spectrosc. Lett. **34**, 783 (2001); (*b*) H. Joshi, F.S. Kamounah, G. Zwan, C. Gooijer, L. Antonov. J. Chem. Soc. Perkin Trans. 2, 2303 (2001); (*c*) R. Herzfeld and P. Nagy. Spectrosc. Lett. **32**, 57 (1999); (*d*) J. Császár. Acta Phys. Chem. **25**, 129 (1979); (*e*) J. Charette, G. Faltlhansl, and Ph. Teyssie. Ph. Teyssie Spectrochim. Acta, **20**, 597 (1964).

© 2008 NRC Canada

5. (*a*) K.L. Platt, F. Oesch. J. Org. Chem. **47**, 5321 (1982) and refs. cited therein; (*b*) R.M. Letcher. Org. Magn. Res. **16**, 220 (1981).
6. (*a*) Y.-L. Zhang, W.-J. Ruan, X.–J. Zhao, H.-G Wang, and Z.–A. Zhu. Polyhedron, **22**, 1535 (2003); (*b*) A. Pasini, M. Gullotti, and R. Ugo. J. Chem. Soc. Dalton Trans. 346 (1977); (*c*) E. Szlyk, A. Surdykowski, M. Barwiolek, and E. Larsen. Polyhedron, **21**, 2711 (2002). (*d*) E. Szlyk, A. Surdykowski, M. Barwiolek, and E. Larsen. Trans. Metal Chem. **25**, 670 (2000).
7. R.C. Felicio, E.T.G. Cavalheiro, and E.R. Dockal. Polyhedron, **20**, 261 (2001).
8. (*a*) S. Akiyama, M. Nakagawa, and K. Nishimoto. Bull. Chem. Soc. Jpn. **44**, 1054 (1971); (*b*) M.M. Husain, M.S. Khan, and Z.H. Khan. Spectrochim. Acta A, **56**, 2741 (2000).
9. B.J.C. Burger and J.E. Bercaw. *In* New developments in the synthesis, manipulation and characterization of organometallic compounds. Edited by A. Wayda and M.Y. Darensbourg. American Chemical Society, Washington, DC, 1987. Vol. 357.
10. S.H. Vosko, L.Wilk, and M. Nusair. Can. J. Phys. **58**, 1200 (1980).
11. A. Rosa, G. Ricciardi, O. Gritsenko, and E. J. Baerends. *In* Principles and applications of density functional theory in inorganic chemistry. Edited by I.N. Kaltsoyannis and J.E. McGrady. Springer, Berlin, Germany. 2004. p. 112, 49.
12. (*a*) C. Mazet and L.H. Gade. Inorg. Chem. **42**, 210 (2003); G. Baum, E.C. Constable, D. Fenske, C.H. Housecroft, T. Kulke, M. Neuburger, and M. Zehnder. J. Chem. Soc. Dalton Trans. 945 (2000); (*b*) G. Baum, E.C. Constable, D. Fenske, C.E. Housecroft, and T. Kulke. Chem. Commun. 2659 (1998) and 195 (1999).
13. (*a*) R.W. Saalfrank, H. Maid, F. Hampel, and K. Peters. Eur. J. Inorg. Chem. 1859 (1999); (*b*) R.W. Saalfrank, O. Struck, K. Peters, and H.G. von Schnering. Inorg. Chim. Acta, **222**, 5 (1994).

© 2008 NRC Canada

Unexpectedly different reactions of $[(arene)Mn(CO)_3]^+$ cations (arene = trindane, indane, tetralin, or dibenzosuberane) with potassium *t*-butoxide — C-H insertions, haptotropic shifts, dimerization, or elimination[1]

Nada Reginato, Laura E. Harrington, Yannick Ortin, and Michael J. McGlinchey

Abstract: [(η^6-Trindane)$Mn(CO)_3$][BF_4] (**1**) reacts with *tert*-BuOK in THF in the presence of alkyl halides (CH_2=$CHCH_2Br$, CH_3I) to yield the corresponding (η^6-$C_{15}H_{18}$)$Mn(CO)_2X$, where X = Br (**3**) or I (**4**). In contrast, **1** and *tert*-BuOK react, in the presence of a donor ligand, to generate (η^5-$C_{15}H_{15}$)$Mn(CO)_2L$, where L = CO (**7**), $P(OMe)_3$ (**8**), or PPh_3 (**9**), in which the metal has migrated from the central ring onto a peripheral ring that has lost three hydrogens; [(η^6-indane)$Mn(CO)_3$][BF_4] behaves similarly. A mechanism is proposed in which the initially formed (η^6-trindane)$Mn(CO)_2CO_2$-*tert*-Bu suffers the loss of CO_2 and isobutene to yield the hydride, (η^6-trindane)$Mn(CO)_2H$, that in turn undergoes three successive C-H insertions with concomitant loss of two molecules of dihydrogen. In contrast, [(η^6-tetralin)$Mn(CO)_3$][PF_6] (**17**) and [(η^6-dibenzosuberane)$Mn(CO)_3$][BF_4] (**23**) each suffer deprotonation at a benzylic site. In the first case, the zwitterion formed attacks its progenitor to yield a tetralenyl-substituted (η^5-cyclohexadienyl)$Mn(CO)_3$ complex (**21**); however, for the dibenzosuberane complex (**23**) the elimination product (**28**) is stable. X-ray crystal structures are reported for **3**, **4**, **7**, **8**, **23**, **28**, and for the phosphite complexes [(η^6-trindane)$Mn(CO)\{P(OMe)_3\}_2$][BF_4] (**15**) and [(η^6-tetralin)$Mn(CO)_2\{P(OMe)_3\}$][PF_6] (**20**).

Key words: arene–manganese, organometallic cations, deprotonations, X-ray crystallography.

Résumé : Le [(η^6-trindane)$Mn(CO)_3$[BF_4] (**1**) réagit avec le *tert*-BuOK, dans le THF, en présence d'halogénures d'alkyles (CH_2=$CHCH_2Br$ et le CH_3I) pour conduire à la formation des (η^6-$C_{15}H_{18}$)$Mn(CO)_2X$ dans lesquels X = Br (**3**) ou I (**4**). Par opposition, le composé **1** réagit avec la *tert*-BuOK, en présence d'un ligand donneur, pour générer les complexes (η^5-$C_{15}H_{15}$)$Mn(CO)_2L$ dans lesquels L = CO (**7**), $P(OMe)_3$ (**8**) ou PPh_3 (**9**) alors que le métal a migré du noyau central vers un noyau périphérique avec perte de trois atomes d'hydrogène; Le [(η^6-indane)$Mn(CO_3)$][BF_4] se comporte de la même manière. On propose un mécanisme dans lequel l'entité (η^6-trindane)$Mn(CO)_2CO_2$-*tert*-Bu subit une perte de CO_2 et d'isobutène pour fournir l'hydrure (η^6-trindane)$Mn(CO)_2H$ qui subit à son tour trois insertions successives de C-H avec la perte concomitante de deux molécules de dihydrogène. Par ailleurs, le [(η^6-tétraline)$Mn(CO)_3$][PF_6] (**17**) et le [(η^6-dibenzosubérane)$Mn(CO)_3$[BF_4] (**23**) subissent chacun une déprotonation au niveau du site benzylique. Dans le premier cas, le zwitterion qui est formé attaque son progéniteur pour conduire à la formation d'un complexe (η^5-cyclohexadiényl)$Mn(CO)_3$ portant un substituant tétralényle (**21**); toutefois, pour le complexe avec le dibenzosubérane (**23**), le produit d'élimination (**28**) est stable. Faisant appel à la diffraction des rayons X, on a déterminé et on décrit les structures cristallines des composés **3**, **4**, **7**, **8**, **23** et **28** ainsi que celles des complexes de phosphite, [(η^6-trindane)$Mn(CO)\{P(OMe_3\}_2$][BF_4] (**15**) et [(η^6-tétraline)$Mn(CO)_2\{P(OMe_3\}$][BF_6] (**20**),

Mots-clés : arène-manganèse, cations organométalliques, déprotonations, cristallographie par diffraction des rayons X.

[Traduit par la Rédaction]

Received 31 March 2008. Accepted 14 May 2008. Published on the NRC Research Press Web site at canjchem.nrc.ca on 3 October 2008.

This article is dedicated to Professor Richard Puddephatt, an outstanding chemist, an inspiring teacher, and a valued friend.

N. Reginato and L.E. Harrington. Department of Chemistry, McMaster University, Hamilton, ON L8S 4M1, Canada.
Y. Ortin and M.J. McGlinchey.[2] School of Chemistry and Chemical Biology, University College Dublin, Belfield, Dublin 4, Ireland.

[1]This article is part of a Special Issue dedicated to Professor Richard J. Puddephatt.
[2]Corresponding author (e-mail: michael.mcglinchey@ucd.ie).

 doi:10.1139/V08-122 © 2008 NRC Canada

Introduction

As part of a program directed towards an organometallic route to sumanene (1), we began to develop the organometallic chemistry of tri(cyclopentano)benzene (trindane) (2, 3), a tetracyclic substructure of the target molecule. To this end, we chose to attempt the alkylation of all six *exo*-benzylic positions of (η^6-trindane)ML_n using the now classic Astruc methodology (4). Since Eyman and co-workers (5) have already shown that [(hexamethylbenzene)$Mn(CO)_3$]$^+$ readily undergoes abstraction of a benzylic proton to yield the corresponding cyclohexadienyl system that reacts with electrophiles to functionalize the benzylic site (5), we decided to study the reactions of [(η^6-trindane)$Mn(CO)_3$] [BF_4] (**1**) and [(η^6-trindane)$Fe(C_5H_5)$][PF_6] (**2**) with potassium *tert*-butoxide, and subsequently with alkyl halides. However, as reported in a preliminary communication (6), the reactions of **1** led to unexpected rearrangement products. We now describe these studies more fully, and also report how the reactions have been extended to the analogous [(η^6-arene)$Mn(CO)_3$]$^+$ systems, whereby the five-membered rings in trindane or indane have been replaced by six- and seven-membered rings in tetralin and dibenzosuberane, respectively.

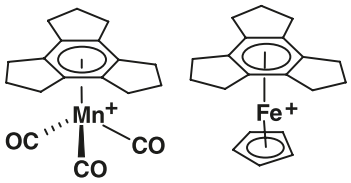

1 **2**

Results and discussion

The activation of benzylic sites by incorporation of a π-complexed organometallic moiety is a well-established phenomenon, and has been attributed to a combination of the electron-withdrawing effect of the metal and the resonance stabilization of the conjugate base (7). Typically, molecules of the type (η^6-arene)ML_n, where ML_n is $Cr(CO)_3$, $Mn(CO)_3^+$, or $Fe(C_5H_5)^+$, undergo ready deprotonation at benzylic positions; subsequent treatment with alkyl halides leads to attack at the benzylic site. Particularly elegant examples are provided by Jaouen et al.'s (8) specific functionalization at the 6β position in (3-methoxyestradiol)[α-$Cr(CO)_3$], and by Astruc's (9) systematic construction of organometallic dendrimers. Another very ingenious application that takes advantage of the steric blocking of one face of the arene by a metal tripod is the preparation of an artificial receptor, whereby trindane was benzylated at the three *exo*-wingtip positions (10).

Reactions of [(η^6-trindane)$Fe(C_5H_5)$][PF_6]

In light of these precedents, [(η^6-trindane)$Fe(C_5H_5)$][PF_6] (**2**) and *tert*-BuOK were mixed as dry solids and then treated with excess allyl bromide (or methyl iodide) in THF in the hope that all six *exo*-benzylic sites would be alkylated. In a previous study (2), we had noted that the corresponding reaction of **2** and *tert*-BuOK in the presence of DMSO-d_6 yielded dodeca-deuterated **2** as the major product; that is, all twelve benzylic positions, both exo and endo, had undergone exchange. Interestingly, use of either allyl bromide or methyl iodide again led to extensive multiple alkylation, and mass spectrometric data indicated the incorporation of at least ten, and possibly twelve, allyl or methyl substituents. After many attempts to obtain a sample of the polymethylated complex appropriate for an X-ray study, data sets were acquired on several crystals of rather poor quality, but disorder problems have so far prevented the satisfactory resolution of these structures.

Reactions of [(η^6-trindane)$Mn(CO)_3$][BF_4]

Since an $M(CO)_3$ moiety (M = Cr, Mn) has been shown to generate a larger cone angle than an $Fe(C_5H_5)$ fragment (11), the tripodal group $Mn(CO)_3^+$ was selected as an activating agent, not only to enhance the acidity at the benzylic positions but in addition to act as a stereodirecting group by blocking one π-face of the arene ligand. Consequently, our focus switched to the manganese cation, **1**, which, when mixed with *tert*-BuOK as dry solids, and then treated with excess allyl bromide in THF furnished after chromatographic separation a deep red crystalline material whose NMR, mass, and IR spectra indicated it to be (η^6-trindane)$Mn(CO)_2Br$ (**3**). The analogous reaction of **1**, *tert*-BuOK, and methyl iodide gave the corresponding (η^6-trindane)$Mn(CO)_2I$ (**4**).

The X-ray crystal structures of **3** and **4** appear in Figs. 1*a* and 1*b*, respectively, and are reminiscent of the geometry previously reported for (η^6-C_6Me_6)$Mn(CO)_2Cl$ whereby the tripod is staggered relative to the alkyl substituents (12). Moreover, the cyclopentene rings in **3** (and **4**) adopt envelope conformations such that the "wingtip" methylene groups are folded endo with respect to the plane of the central six-membered ring, as was previously found in both (η^6-trindane)$Cr(CO)_3$ and [(η^6-trindane)$RuCl_2${$P(OMe)_3$}] (2, 3). The structures of **3** and **4** may also be compared with the known complexes [tri(cyclohexano)benzene]ML_n, where ML_n = $Cr(CO)_3$ or $Mn(CO)_3^+$, whereby the $M(CO)_3$ unit displays the typical staggered orientation and the peripheral rings exhibit the "half-boat" conformation (13).

Another structural feature of interest for compounds **3** and **4** is that, in each case, the central ring is slightly folded such that the arene carbons C(1) and C(2), trans to the halogen atom, are slightly closer to the manganese atom than are the other four carbons [i.e., C(3), C(4), C(5), C(6)]. Whether this folding is attributable to packing effects, or to the weaker trans influence of the halide, is not clear; however, it parallels the folding found in (η^6-C_6Me_6)$Mn(CO)_2Cl$. The manganese atoms in **3** and **4** are located 1.677 and 1.678 Å, respectively, below the centroid of the six-membered ring, slightly closer than is found in (η^6-C_6Me_6)$Mn(CO)_2Cl$ (1.706(3) Å) (12). The Mn–CO bond lengths are normal (1.781(8)–1.802(10) Å), the Mn-C-O angles are slightly less than 180°, and the Mn-ring-carbon distances range from 2.133(7) to 2.230(4) Å.

As expected, the carbonyl IR stretching frequencies in the series (η^6-trindane)$Mn(CO)_2X$ decrease as a result of the transformation from a cationic to a neutral species: X = Cl (1980, 1931 cm^{-1}), X = Br (1971, 1927 cm^{-1}), X = I (1973, 1926 cm^{-1}). The starting material, [(η^6-trindane)$Mn(CO)_3$][BF_4] (**1**) exhibits carbonyl stretches at 2056 and 1997 cm^{-1}. These data are similar to the ν_{CO} values previously reported for (η^6-C_6Me_6)$Mn(CO)_2X$ complexes: 1972, 1920 cm^{-1}; 1971,

© 2008 NRC Canada

Fig. 1. (*a*) The molecular structure of (η^6-trindane)$Mn(CO)_2Br$ (**3**) showing the staggered orientation of the tripodal $Mn(CO)_2Br$ moiety. (*b*) The molecular structure of (η^6-trindane)$Mn(CO)_2I$ (**4**) illustrating the envelope conformation of the peripheral rings. Thermal ellipsoids are shown at the 30% probability level.

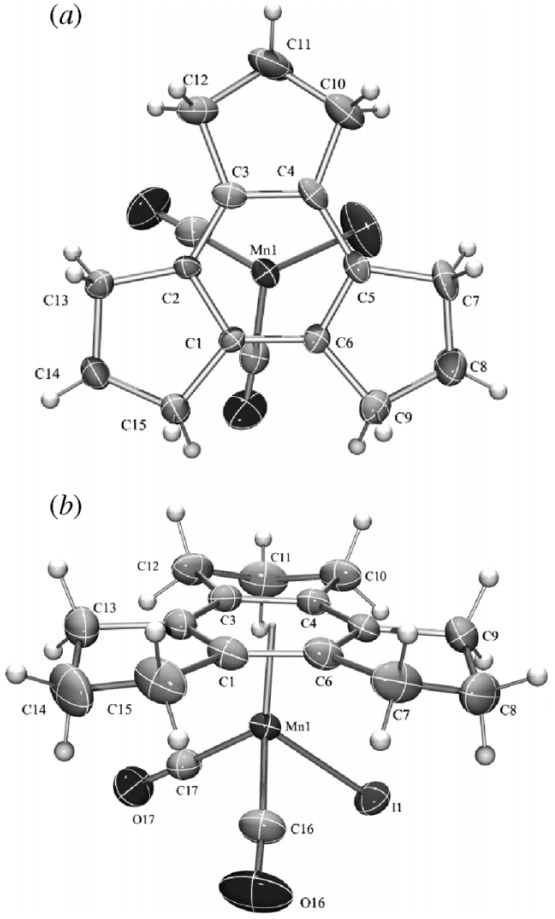

1921 cm^{-1}; and 1968, 1920 cm^{-1}; where X = Cl, Br, and I, respectively (12).

Since replacement of a carbonyl by a phosphine or a halide in $[(\eta^6\text{-}C_6Me_6)Mn(CO)_3]^+$ normally requires either photolysis or use of Me_3NO (14, 15), it was somewhat surprising that the formation of the (η^6-trindane)$Mn(CO)_2X$ species, **3** and **4**, should have occurred so readily. Moreover, because (η^6-C_6Me_6)$Mn(CO)_2H$ is known to yield (η^6-C_6Me_6)$Mn(CO)_2Cl$ in the presence of CCl_4 or $CHCl_3$ (but not CH_2Cl_2) (12), one is tempted to invoke the intermediacy of (η^6-trindane)$Mn(CO)_2H$ (**5**). Eyman and co-workers (16) have shown that (η^6-C_6Me_6)$Mn(CO)_2I$ reacts with *tert*-butyllithium to yield thermally stable (η^6-C_6Me_6)$Mn(CO)_2H$, apparently via loss of isobutene from the presumed *tert*-butyl intermediate. Furthermore, as the cationic complexes $[(\eta^6\text{-arene})Mn(CO)_3]^+$, (arene = C_6H_6 or C_6Me_6), are known to react with methoxide in methanol to yield the rather unstable esters, (η^6-arene)$Mn(CO)_2CO_2Me$ (17), one might propose that a reaction between **1** and *tert*-BuOK could generate the *tert*-butyl ester (**6**) that readily eliminates both isobutene and carbon dioxide via a very favorable six-membered transition state to produce **5**, as depicted in Scheme 1. Interestingly, treatment of **1** with *tert*-BuOK in CH_2Cl_2 gave (η^6-trindane)$Mn(CO)_2Cl$, suggesting that **5** is more reactive than $(C_6Me_6)Mn(CO)_2H$ towards alkyl halides.

Scheme 1. Proposed mechanism of formation of **3** and **4**.

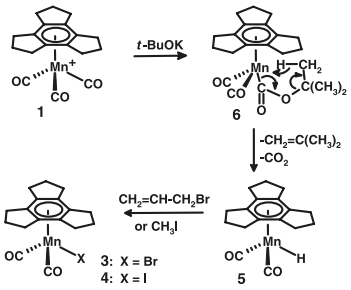

Although it is well established that $(C_6Me_6)Mn(CO)_2H$ can be prepared by treatment of $(C_6Me_6)Mn(CO)_2Br$ with $[Bu_4N][BH_4]$ (12), numerous attempts to synthesize (η^6-trindane)$Mn(CO)_2H$ from the corresponding bromide **3** by this route, or to detect the hydride signal by NMR at low temperature, were unsuccessful. Consequently, we chose to try to intercept the purported hydride **5**, either as (trindane)$Mn(CO)(PR_3)H$, or as the formyl complex (trindane)$Mn(CO)(CHO)(PR_3)$, in the absence of RBr.

When the cation **1** and *tert*-BuOK were treated with trimethyl phosphite in THF and allowed to stir at 40 °C for 20 h, to our surprise, the two products isolated after chromatographic separation, were yellow crystalline materials **7** and **8** whose ^1H and ^{13}C NMR spectra indicated that the three-fold symmetry of the trindane ligand had been broken. The mass spectra of **7** and **8** exhibited parent peaks at *m*/*z* = 334 and 430, respectively, indicating a molecular formula of $(C_{15}H_{15})Mn(CO)_2L$, where L = CO for **7**, and L = $P(OMe)_3$ for **8**. Both products were definitively characterized by X-ray crystallography as η^5-indenyl complexes in which the manganese has migrated from the central arene onto a five-membered ring that has evidently lost three hydrogens. The analogous complex (**9**), where L = PPh_3, is also accessible in this manner. Likewise, the corresponding reactions of [(η^6-indane)$Mn(CO)_3$][BF_4] (**10**) and *tert*-BuOK yield the known complexes (η^5-indenyl)$Mn(CO)_2L$, where L = $P(OMe)_3$ or PPh_3 (18). The IR spectra of **7** (ν_{CO} absorptions at 2016 and 1934 cm^{-1}) and **8** (ν_{CO} at 1944 and 1876 cm^{-1}) each exhibit two carbonyl bands, and are in accord with those of the closely analogous systems (η^5-C_5H_5)$Mn(CO)_3$ (ν_{CO} at 2025 and 1938 cm^{-1}) and (η^5-C_5H_5)$Mn(CO)_2[P(OMe)_3]$ (ν_{CO} at 1948 and 1884 cm^{-1}).

The structures of the rearranged molecules **7** and **8** are shown in Figs. 2*a* and 2*b*, respectively, and reveal in each case a "piano stool" structure with the $Mn(CO)_2L$ tripod coordinated in an η^5-fashion to a peripheral five-membered ring. The manganese atoms in **7** and **8** lie 1.824 and 1.797 Å, respectively, below the centroid of the five-membered ring. The Mn-to-cyclopentadienyl-carbon distances range from 2.114(2) to 2.235(2) Å, and are comparable to those reported for (η^5-cyclopenta[*def*]phenanthrenyl)$Mn(CO)_3$ (19).

In Scheme 2, a mechanistic rationale to account for these novel products is offered. We suggest that in the absence of an alkyl halide, the initially generated (trindane)$Mn(CO)_2H$ (**5**) undergoes a hydrogen migration (presumably via an agostic interaction) from an *endo*-benzyl site onto the metal thus producing the cyclohexadienyl complex (**11**) that in turn

© 2008 NRC Canada

Fig. 2. (*a*) Molecular structure of $(C_{15}H_{15})Mn(CO)_3$ (**7**). (*b*) Molecular structure of $(C_{15}H_{15})Mn(CO)_2[P(OMe)_3]$ (**8**). Thermal ellipsoids are shown at the 30% probability level.

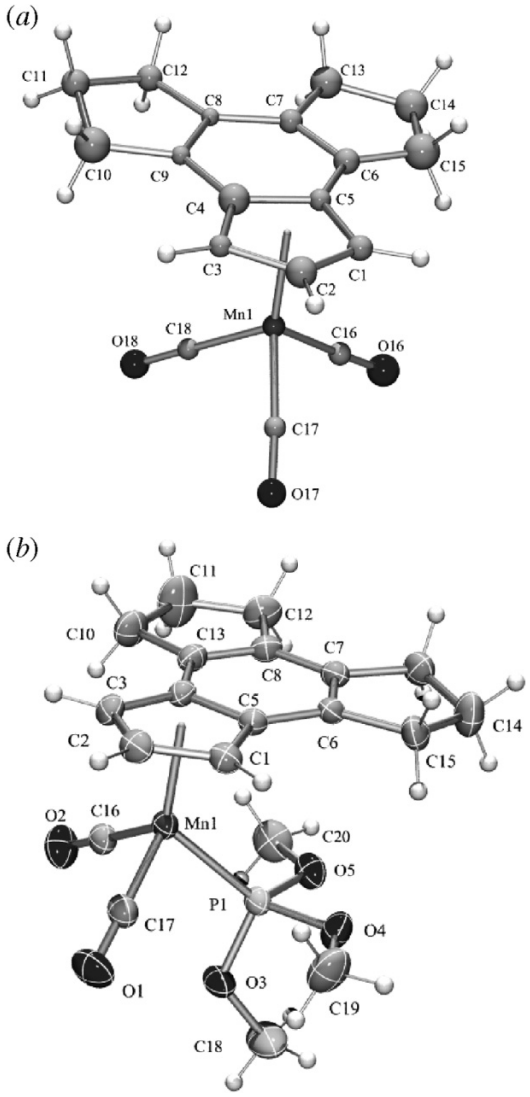

loses dihydrogen to give **12**. A second *endo*-benzyl hydrogen migration to yield the isoindene framework (**13**) is followed by the final hydrogen migration producing **14**. Loss of dihydrogen and incorporation of either a carbonyl or a phosphite ligand would give the observed products **7** or **8**, respectively.

In seeking a precedent for the proposal outlined above, we note the report by Crabtree and Parnell (20) wherein $[(\eta^6\text{-indane})Ir(PPh_3)_2]^+$ undergoes dehydrogenation and an η^6-to-η^5 haptotropic shift at 80 °C to furnish $[(\eta^5\text{-indenyl})Ir(PPh_3)_2(H)]^+$. Moreover, Ustynyuk and co-workers (21) have shown that $(\eta^5\text{-indenyl})Cr(CO)_3Me$ undergoes a "ricochet reaction" in which the methyl is delivered onto the five-membered ring and the tricarbonylchromium fragment migrates to the six-membered ring, as depicted in Scheme 3. Density functional theory calculations by these workers indicate that the reaction proceeds through an isoindene structure in which the chromium is bonded to the diene portion of the six-membered ring and one double bond of the

Scheme 2. Proposed mechanism of formation of **7**, **8**, and **9**.

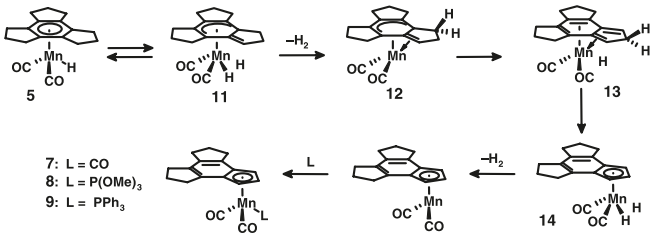

Scheme 3. "Ricochet" inter-ring haptotropic rearrangement.

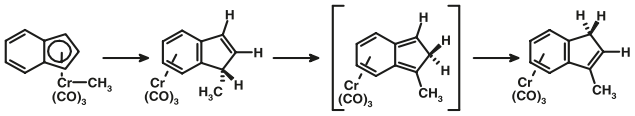

cyclopentadiene ring and provide some justification for the structures **12** and **13** proposed in Scheme 2.

Other (trindane)ML_3 complexes (M = Mn, Re)

With the aim of selectively deprotonating only the *exo*-benzylic positions of trindane, we chose to replace one or more of the carbonyl ligands in **1** with somewhat more sterically demanding phosphite substituents, even though such an approach could diminish the acidic character of the benzylic sites. Thus, treatment of $[(\eta^6\text{-trindane})Mn(CO)_3][BF_4]$ (**1**) with trimethyl phosphite and trimethylamine N-oxide furnished a yellow crystalline solid that was characterized spectroscopically and by X-ray crystallography as $[(\eta^6\text{-trindane})Mn(CO)\{P(OMe)_3\}_2][BF_4]$ (**15**). The IR spectrum displayed a single carbonyl stretch at 1911 cm^{-1}, similar to that previously reported for $[(\eta^6\text{-}C_6Me_6)Mn(CO)\{P(OMe)_3\}_2][PF_6]$ (14). Figure 3*a* depicts the cationic portion of **15**, which has the conventional piano stool structure typical of half-sandwich complexes; the carbonyl and the two trimethyl phosphite ligands adopt a staggered conformation relative to the carbon atoms of the arene ring, and the manganese atom is located 1.724 Å below the centroid of the arene. The Mn–C (arene) bond lengths range from 2.194(4) to 2.237(3) Å, the Mn-CO and two Mn-P distances are 1.772(4), 2.1996(12), and 2.2174(14) Å, respectively, and the Mn-C-O angle is reduced to 173.9(4)°. As far as we are aware, the only other (arene)manganese-bisphosphite complex to have been crystallographically characterized is $[(\eta^6\text{-toluene})Mn(CO)\{P(OEt)_3\}_2][PF_6]$ (22); the bis-chelated di-tertiary phosphine, $[(\eta^6\text{-}C_6H_6)Mn(CO)\{\eta^2\text{-}PPh_2(CH_2)_3PPh_2\}][PF_6]\cdot 2CH_3CN$ and $(\eta^5\text{-}C_6Me_6H)Mn(CO)[P(OMe)_3]_2$ have also been reported (23, 24).

Figure 3*b* shows a space-filling view of **15** that emphasises the degree of crowding on the endo side of the complexed trindane ligand, thus restricting access to that face. However, because of the rather poor yield (11%) of **15**, deprotonation or other further reactions of this system were not investigated. This low yield follows the trend observed for analogous compounds such as $[(\eta^6\text{-toluene})Mn(CO)\{P(OR)_3\}_2][PF_6]$ where R is Me or Et (22). Likewise, treatment of $[(\eta^6\text{-toluene})Mn(CO)_3][PF_6]$ with Me_3NO and PPh_3 failed to bring about substitution of the carbonyl groups by triphenylphosphine (24).

In the hope that the hydride $(\eta^6\text{-trindane})Re(CO)_2H$ might show enhanced stability relative to its manganese counter-

© 2008 NRC Canada

Fig. 3. (*a*) Molecular structure of the cation [(η^6-trindane)Mn(CO){P(OMe)$_3$}$_2$]$^+$ (**15**). Thermal ellipsoids are shown at the 30% probability level. (*b*) Space-filling view of **15** accentuating the degree of crowding induced by the tripodal fragment.

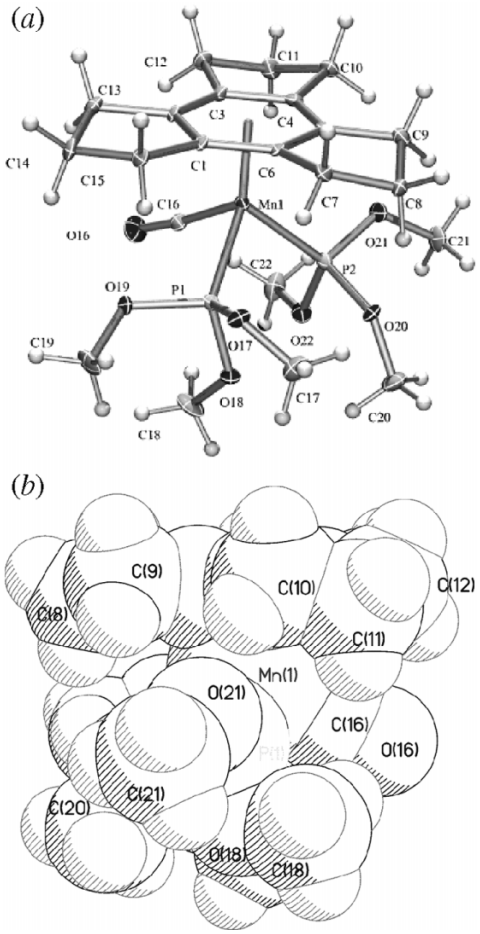

part **5**, it was deemed worthwhile to attempt the synthesis of the analogous [(η^6-trindane)Re(CO)$_3$]$^+$ cation (**16**). Indeed, **16** can be prepared from BrRe(CO)$_5$, AlCl$_3$, and trindane, but the yield, as is sometimes the case with arene–rhenium complexes (14), is very poor (2%). Nevertheless, the [(η^6-trindane)Re(CO)$_3$]$^+$ cation was readily characterized by IR (ν_{CO} at 2058 and 1966 cm^{-1}) and by electrospray mass spectrometry, which gave rise to distinctive molecular ion peaks at *m*/*z* 467 and 469 that exhibited the 37:63 isotopic abundance ratio diagnostic for the presence of ^{185}Re and ^{187}Re. Moreover, the ^{1}H NMR spectrum exhibited the four chemical environments characteristic of trindane metal carbonyl complexes.

Reactions of [(η^6-tetralin)Mn(CO)$_3$][PF$_6$]

To probe the generality of the reaction leading to formation of a hydride intermediate, as in (η^6-trindane)Mn(CO)$_2$H, and the possibility of dehydrogenation concomitant with a haptotropic shift, the corresponding six-membered tetrahydronaphthalene (tetralin) system was synthesized and treated with potassium *tert*-butoxide and trimethyl phosphite. Following the literature precedent (25), tetralin was treated with bromo(pentacarbonyl)manganese in the presence of aluminum trichloride; subsequent anion exchange furnished [(η^6-tetralin)Mn(CO)$_3$][PF$_6$] (**17**) in 80% yield. We are aware of only one report on the reactivity of the cation **17**, whereby Lee and co-workers (25) found that nucleophilic addition afforded adducts at the α-position, as in **18**, except when treated with MeMgBr in THF at 0 °C, which also yielded the acyl compound **19** (Scheme 4). Related studies by Sweigart and co-workers (26) on hormonal steroidal systems bearing a [Mn(CO)$_3$]$^+$ moiety on the aromatic A ring likewise underwent exo addition at C-1 when treated with a range of nucleophiles.

Scheme 4. Reactions of [(η^6-tetralin)Mn(CO)$_3$]$^+$ (**17**) with nucleophiles.

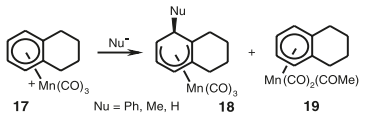

The reaction of [(η^6-tetralin)Mn(CO)$_3$][PF$_6$] (**17**) with *tert*-BuOK and P(OMe)$_3$ in THF gave, even after repeated chromatographic separations, multiple products each in such low yield as to preclude definitive identification. As a result of the complexity of the reaction, it was decided to investigate the effects of each reagent separately to help clarify their roles in the overall reaction. When trimethyl phosphite in THF was added to [(η^6-tetralin)Mn(CO)$_3$][PF$_6$] in the dark, no change was observed, as monitored by in situ IR spectroscopy. However, when exposed to sunlight, the reaction yielded a yellow crystalline solid that was identified by ^{1}H, ^{13}C, and ^{31}P NMR and mass spectrometry as [(η^6-tetralin)Mn(CO)$_2${P(OMe)$_3$}][PF$_6$] (**20**); the assignment was verified by means of a single crystal X-ray diffraction study. The molecule exhibited carbonyl IR stretches at 2008 and 1961 cm^{-1}, and ^{31}P NMR resonances for each of the phosphorus environments, i.e., for the trimethyl phosphite ligand and the hexafluorophosphate anion.

As shown in Figs. 4*a* and 4*b*, the tripodal [Mn(CO)$_2${P(OMe)$_3$}] unit lies in an essentially staggered orientation, typical of such polycyclic manganese complexes (26). The cyclohexene ring adopts a twisted half-chair conformation, with one of the homobenzylic ring carbon atoms lying below, and the other lying above, the molecular plane defined by the arene ring, which is itself planar. The manganese atom is located 1.679 Å below the plane of the arene ring, and the Mn-C(arene) distances range from 2.179(2) to 2.207(2) Å. The hexafluorophosphate anion was disordered, and two orientations were found.

X-ray crystal structures of related systems in which the tetralin fragment is bound to a Cr(CO)$_3$ moiety have been reported by Schmalz and co-workers (27). Moreover, these workers investigated the regioselectivity of the deprotonation/alkylation process. Their data revealed that, in the case of two competing exo hydrogen atoms having comparable steric environments, it is not necessarily the *exo*-benzylic hydrogen atom that adopts a pseudoaxial position that is preferentially abstracted. It was concluded that the conformation of the chromium tricarbonyl tripod may influence the regioselectivity of benzylic deprotonation in chiral (arene)Cr(CO)$_3$ complexes (27), as had been suggested previously (28).

Treatment of [(η^6-tetralin)Mn(CO)$_3$][PF$_6$] (**17**) with potassium *tert*-butoxide in THF afforded a yellow-orange oil that,

© 2008 NRC Canada

Fig. 4. (*a*) Molecular structure of the cation in [(η^6-tetralin)Mn(CO)$_2${P(OMe)$_3$}][PF$_6$] (**20**); (*b*) Bird's eye view of **20** illustrates the staggered orientation of the tripodal manganese fragment. Thermal ellipsoids are shown at the 30% probability level.

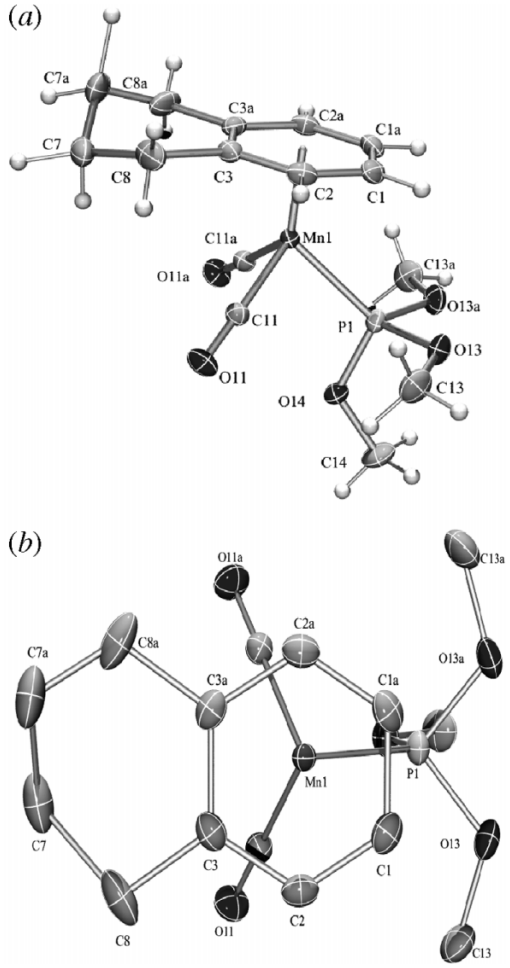

despite repeated efforts, did not yield a crystalline product. Nevertheless, the mass spectrometric and IR data provide strong evidence that the product may be assigned as the tetralenyl-substituted cyclohexadienyl manganese complex **21**. Carbonyl IR absorptions at 2007 and 1927 cm^{-1} (neat) are indicative of a (cyclohexadienyl)Mn(CO)$_3$ system. For example, nucleophilic attack on [(tetralin)Mn(CO)$_3$]$^+$ by hydride, methyl, or phenyl gave the 4-exo-substituted compounds (**18**) that exhibited ν_{CO} peaks (in NaCl) at 2000/1910 cm^{-1}, 2000/1920 cm^{-1}, and 2004/1916 cm^{-1}, respectively, (25). Chemical ionization data for **21** revealed an [M + H]$^+$ peak at *m*/*z* 403, followed by loss of 131 corresponding to $C_{10}H_{11}$. Subsequent fragmentation revealed the presence of a tricarbonylmanganese moiety. Because of considerable peak overlap, the ^{1}H and ^{13}C NMR spectra of **21** have not yet been fully assigned unequivocally, however, efforts to grow X-ray quality crystals are continuing.

A straightforward mechanistic proposal to account for the formation of **21** is depicted in Scheme 5. Deprotonation of [(η^6-tetralin)Mn(CO)$_3$][PF$_6$] by *tert*-BuOK to yield the zwitterionic species **22** (perhaps better represented by the η^5 structure **22a**) can be followed by nucleophilic attack on **17**; subsequent loss of the [Mn(CO)$_3$]$^+$ moiety leads directly to **21**.

Scheme 5. Proposed mechanism for the formation of **21**.

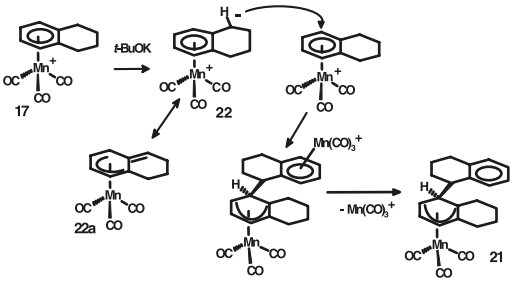

Scheme 6. Possible rearrangement reactions of **23** and **25**.

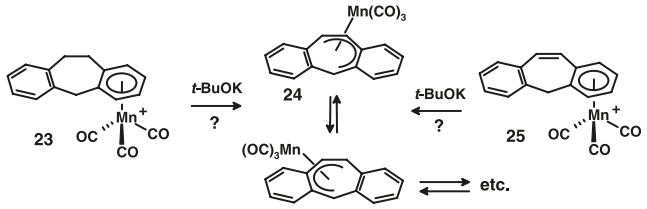

Reactions of [(η^6-dibenzosuberane)Mn(CO)$_3$][BF$_4$]

In light of the previously described reactions of the cations [(η^6-trindane)Mn(CO)$_3$]$^+$ (**1**) and [(η^6-indane)Mn(CO)$_3$]$^+$ (**10**) with *tert*-BuOK and P(OMe)$_3$, whereby dehydrogenation of a five-membered ring and concomitant haptotropic shifts yield η^5 complexes, we chose to extend this study to include systems in which the manganese-complexed arene ring was joined to a seven-membered ring. If the reaction of [(η^6-dibenzosuberane)Mn(CO)$_3$][BF$_4$], **23**, were to proceed in a manner analogous to that of the trindane system, **1**, then one might anticipate loss of three hydrogen atoms from the central ring and formation of a (η^5-dibenzocycloheptatrienyl)Mn(CO)$_3$ complex, such as **24**, which might exhibit a fluxional process (Scheme 6) that would equilibrate the two six-membered rings. It has previously been reported that deprotonation of (η^6-benzocycloheptatriene)Cr(CO)$_3$ leads to an η^6-to-η^5 haptotropic shift such that the metal, which was originally located on the arene ring, is now bonded in an η^5 fashion in the seven-membered ring (29). If an analogous migration were to occur upon deprotonation of [(η^6-dibenzosuberene)Mn(CO)$_3$]$^+$, **25**, the centrally bonded manganese in **24** would presumably exhibit fluxionality, as does (η^5-C$_7$H$_7$)Mn(CO)$_3$ (30).

To this end, [(η^6-dibenzosuberane)Mn(CO)$_3$][BF$_4$] (**23**) was prepared by reaction of dibenzosuberane, bromopentacarbonylmanganese, and silver tetrafluoroborate in dichloromethane and was characterized spectroscopically and by X-ray crystallography. Electrospray mass spectrometry revealed a parent ion at *m*/*z* 333, with fragmentation peaks at 277 and 249 corresponding to loss of two and three carbonyls, respectively. The carbonyl IR stretching vibrations peaks at 2065 and 2014 cm^{-1} are typical of arene–manganese tricarbonyl cations, and the ^{1}H and ^{13}C NMR spectra reveal the presence of one coordinated and one uncoordinated arene ring, and three methylene groups; in each case the methylene protons are rendered nonequivalent by the presence of the metal tripod on one face of the molecule. The X-ray crystal structure of **23** is shown in Figs. 5*a* and 5*b* and reveals that the [Mn(CO)$_3$] fragment is situated on the con-

© 2008 NRC Canada

Fig. 5. (*a*) Molecular structure of the [(η^6-dibenzosuberane)Mn-$(CO)_3$]$^+$ cation in **23**, illustrating the positioning of the $Mn(CO)_3$ tripod on the concave face of the ligand. (*b*) Bird's eye view showing the eclipsed orientation of the tripod. Thermal ellipsoids are shown at the 30% probability level.

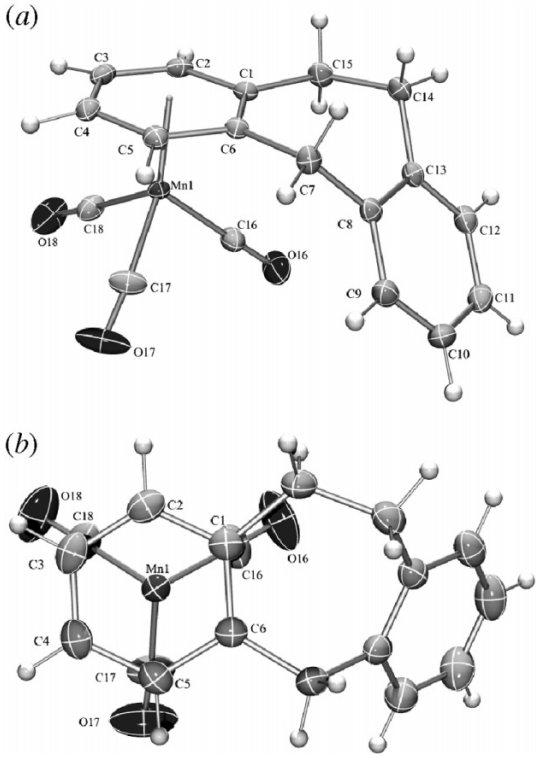

cave face of the tricyclic dibenzosuberane skeleton. The interplanar angle between the two arene rings in **23** is 129°, somewhat larger than the corresponding angle (123°) found in uncomplexed dibenzosuberane (31).

This result contrasts with the structures of the previously reported (η^6-dibenzosuberane)$Cr(CO)_3$ and (η^6-dibenzosuberone)$Cr(CO)_3$ in which the metal tripod lies on the exo (convex) side of the ligand, but follows the example of (η^6-dibenzosuberanol)$Cr(CO)_3$, which, like **23**, places the metal on the endo (concave) face (32). In the manganese case, this preference for the concave face may be a consequence of the need to pack both the organometallic cation and the tetrafluoroborate counterion as efficiently as possible.

It is common for polycyclic molecules that are π-complexed to metal fragments to fold away from the metal: examples include both α- and β-$Cr(CO)_3$ complexes of O-methyl podocarpate (33), as well as ruthenium (34), chromium (35), and manganese (26) derivatives of estradiol and estrone. Other crystallographically characterized molecules that contain manganese and the suberane skeleton are the carbene complex, **26**, and the η^2-ketene derivative, **27** (36).

Treatment of the (dibenzosuberane)tricarbonylmanganese cationic complex (**23**) with potassium *tert*-butoxide and trimethyl phosphite yielded, after chromatographic separation, a number of products in quantities too small to characterize unambiguously. Consequently, as was done in the case of [(η^6-tetralin)$Mn(CO)_3$][PF_6], each reagent was treated separately with [(η^6-dibenzosuberane)$Mn(CO)_3$][BF_4]. Although, in the absence of light, trimethyl phosphite alone did

Fig. 6. Molecular structure of (η^5-$C_{15}H_{13}$)$Mn(CO)_3$ (**28**); thermal ellipsoids are shown at the 30% probability level.

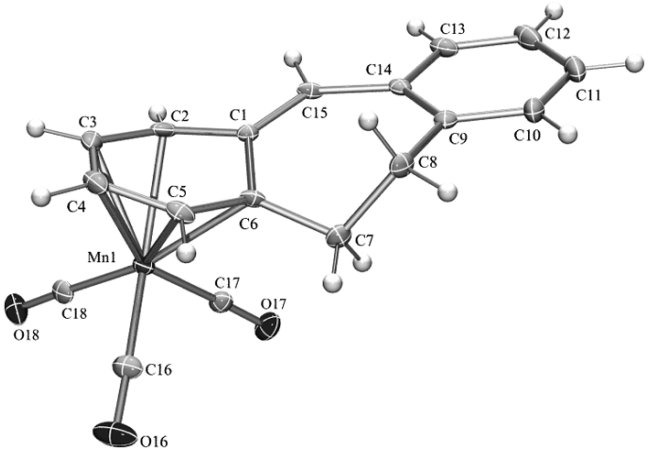

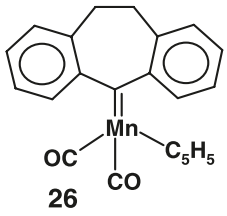

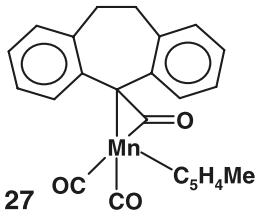

not lead to substitution of a carbonyl ligand, the reaction of **23** with *tert*-BuOK in THF gave as the major product an orange powder exhibiting carbonyl IR absorptions at 2022 and 1950 cm^{-1} and a parent peak in the mass spectrum at *m*/*z* 332. This material was characterized by X-ray crystallography as (η^5-$C_{15}H_{13}$)$Mn(CO)_3$ (**28**), in which deprotonation of the benzylic proton had occurred resulting in generation of a double bond in the central seven-membered ring. The structure of compound **28** appears in Fig. 6 and shows that the metal tripod is coordinated in an η^5-fashion to one of the outer six-membered rings, such that the manganese is located 1.718 Å below the ring.

The manganese-dienyl carbon bond distances in **28** range from 2.126(5) to 2.287(5) Å, typical for cyclohexadienyl manganese complexes, while the C(1)–C(15) bond length of 1.358(6) Å is significantly shorter than C(1)–C(6) (1.468(6) Å), and indicates double bond character. The carbon–carbon distances of the cyclohexadienyl ring average 1.407 Å and the cyclohexadienyl unit exhibits a deviation from planarity of only 0.002 Å, but the distortion from planarity of the cyclohexadienyl ring, i.e., the angle between planes C(2)-C(3)-C(4)-C(5)-C(6) and C(2)-C(1)-C(6) is 31°. This dihedral angle θ is smaller than is found in (η^5-C_6H_7)$Mn(CO)_3$ (43°) (37) or *endo*-(η^5-C_6Me_6H)$Mn(CO)_2${$P(OMe)_3$} (47.5°) (14) but is similar to those observed in the polycyclic systems **29** and **30**, derived from naphthalene or anthracene, in which the cyclohexadienyl ring is bent through 36° and 33°, respectively (38, 39).

The product derived from the reaction of [(η^6-dibenzosuberane)$Mn(CO)_3$][BF_4] (**23**) with potassium *tert*-butoxide is reminiscent of the behavior of the [(η^6-fluorene)ML_n]$^+$ cation (**31**) [ML_n = Fe(C_5H_5) or $Mn(CO)_3$], which upon deprotonation yielded (η^5-fluorenyl)ML_n, (**32**) (40, 41). In principle, these neutral molecules can be represented either

© 2008 NRC Canada

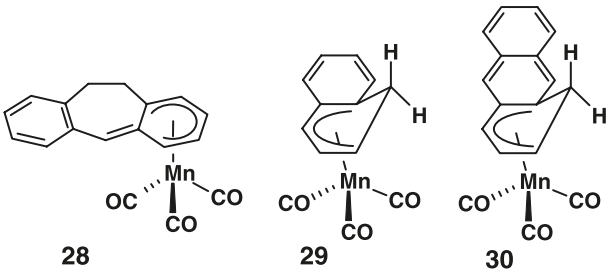

as zwitterions or as possessing a formal double bond in the central ring, as in **32′**. However, the X-ray crystal structures probably favored the latter interpretation in which the cyclohexadienyl ring is folded through 11° (Fe) or 15° (Mn), and the bond from the ring junction carbon to the benzylic carbon is 1.38 Å (Fe) (40) or 1.37 Å (Mn) (41). The (fluoradene)Ru(C_5Me_5) complexes **33** and **34** behave similarly (42). When (η^5-fluorenyl)ML_n (**32**), where ML_n = $Mn(CO)_3$ or Fe(C_5H_5), is heated, the organometallic moiety undergoes a haptotropic shift onto the central five-membered ring to produce **35** (41). As shown in Scheme 7, analogous behavior has also been reported for the (8,9-dihydrocyclopenta[*def*]phenanthrenyl)$Mn(CO)_3$ complexes **36** and **37** (19). Interestingly, the η^6-to-η^5 haptotropic shift of the organometallic fragment in the (cyclopenta[*def*]phenanthrenyl)$Mn(CO)_3$ complexes **38** and **39** occurs readily at –40 °C, and this has been rationalized in terms of the enhanced aromatic character of the transition state (43).

Why are the reactions so different?

We must now ask ourselves why the arene–manganese tricarbonyl cations **1**, **17**, and **23** possessing five-, six-, or seven-membered rings, respectively, exhibit such different behavior when treated with *tert*-BuOK. The trindane (or indane) system apparently yields a metal hydride that subsequently suffers a series of hydrogen eliminations, presumably via agostic interactions with suitably positioned benzylic hydrogens. The tetralin complex **17** appears to undergo proton abstraction to generate a nucleophile that can attack its progenitor, whereas deprotonation of the dibenzosuberane-complexed cation **23** yielded a stable elimination product.

Evidently, there can be competition between deprotonation at a benzylic site and nucleophilic attack by the alkoxide at a carbonyl ligand. Moreover, even if a manganese-hydride were to be generated in each case, one must then consider not only the ease or difficulty of forming an agostic Mn···H···C linkage, but also the strength of the manganese-to-ligand binding subsequent to the haptotropic shift. Taking the X-ray crystallographic data for (η^6-trindane)$Mn(CO)_2Br$ (**3**), [(η^6-tetralin)$Mn(CO)_2${P($OMe)_3$}]$^+$ (**20**), and [(η^6-dibenzosuberane)$Mn(CO)_3]^+$ (**23**), we note that the Mn-to-benzyl *endo*-H distances generally lie in the range 3.42–3.52 Å, considerably longer than might be anticipated for a manganese···hydrogen agostic interaction (~1.8 Å) (44). However, manganese-hydrogen agostic interactions have been invoked by Cooper and co-workers (38) to explain the fluxional behavior of the anthracenyl complex **29** whereby an endo benzylic hydrogen undergoes a 1,4 migration via the metal center. In that case, the metal-hydrogen distance in the ground state was determined crystallographically to be 3.13 Å, but such a process requires a flattening of the six-membered ring and an elongation of the C–H bond.

Scheme 7. Haptotropic shifts in polycyclic systems.

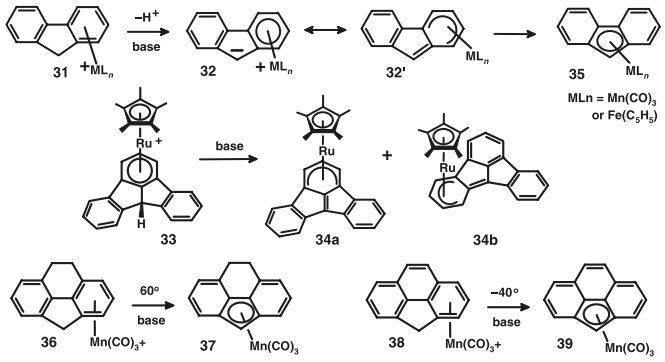

The transformation of (η^6-trindane)$Mn(CO)_2H$ (**5**) into (η^5-$C_{15}H_{15}$)$Mn(CO)_3$ (**7**) involves C-H and Mn-H cleavage with concomitant formation of a manganese–carbonyl bond and two molecules of dihydrogen. The requisite bond energies are BE(C-H) 413 kJ mol^{-1}, BE(Mn-H) 288 kJ mol^{-1} [calculated value (45)], BE(H-H) 436 kJ mol^{-1}, and BE(Mn-CO) ~190 kJ mol^{-1}(46). Thus, cleavage of three C–H bonds and one Mn–H bond has an energy cost of approximately 1527 kJ mol^{-1} of which only ~1060 kJ mol^{-1} are recovered as one Mn–CO and two H–H bonds. The overall free energy change must be controlled by the stronger bonding of the manganese to the five-membered ring and, of course, by the very favorable increase in entropy brought about by the liberation of two moles of dihydrogen.

The complex [(η^6-trindane)$Mn(CO)_3]^+$ (**1**) preferentially undergoes nucleophilic attack by the *tert*-butoxide anion on a metal carbonyl ligand, whereas in the tetralin and dibenzosuberane complexes, **17** and **23**, deprotonation at a benzylic site is favored. Steric considerations would suggest that in **23** the positioning of the metal tripod on the concave face of the dibenzosuberane ligand seriously hinders the approach of a relatively bulky *tert*-butoxide; in contrast, the $Mn(CO)_3$ moiety in the trindane complex **1** is staggered with respect to the five-membered rings, and the alkoxide can readily gain access to a carbonyl ligand. Upon removal of a benzylic proton from [(η^6-dibenzosuberane)$Mn(CO)_3]^+$, the resulting neutral species **28** is sufficiently flexible to allow the seven-membered ring to fold away from the metal and so adopt a conventional η^5-cyclohexadienyl conformation; this molecular deformation may be more difficult for the deprotonated tetralene complex **22**, which therefore retains its nucleophilic character and attacks the starting material to yield the "dimeric tetralenyl" η^5-cyclohexadienyl product **21**.

To conclude, the reactions of potassium *tert*-butoxide with the arene manganese tricarbonyl cations derived from trindane, indane, tetralin, or dibenzosuberane yield very different products and pose interesting mechanistic questions.

Experimental section

General procedures

All reactions were carried out under an atmosphere of dry nitrogen employing conventional benchtop and glovebag techniques. Silica gel (particle size 20–45 μm) was employed for flash column chromatography. Radial chromatog-

© 2008 NRC Canada

raphy was performed using a Chromatotron (7942T, Harrison Research, Inc.) with silica-coated plates (TLC grade 7749 with gypsum binder and fluorescent indicator; thickness: 1, 2, or 4 mm). ^{1}H, ^{13}C, and ^{31}P NMR data were acquired on Bruker Avance 500, 300, or 200 MHz spectrometers, and chemical shifts are given relative to residual ^{1}H or ^{13}C solvent signal, or externally referenced relative to 85% H_3PO_4 in D_2O. IR spectra were recorded on a Bio-Rad FTS-40 single beam spectrometer using KBr pellets or NaCl windows. In situ IR spectra were recorded on an ASI Applied Systems ReactIR 1000 with a SiComp probe. Mass spectrometric data were obtained on a Finnigan EI/CI mass spectrometer system, using direct electron impact and chemical ionization methods. The positive ion electrospray mass spectra were obtained on a Micromass Quattro LC triple quadrupole mass spectrometer. Melting and decomposition points were measured on a Fischer-Johns melting point apparatus and are not corrected. Microanalytical data are from Guelph Chemical Laboratories (Guelph, Ontario) or from the Microanalytical Laboratory at University College Dublin.

[(η^6-Trindane)$Mn(CO)_3$][BF_4] (**1**) and [(η^6-trindane)Fe(C_5H_5)][PF_6] (**2**) were prepared as previously described (2). Following the literature procedure (47), dibenzosuberane was obtained in 77% yield by reduction of dibenzosuberone with iodine and hypophosphorous acid in acetic acid.

Reaction of [(η^6-trindane)$Mn(CO)_3$][BF_4] with *tert*-BuOK and allyl bromide

A three-neck round-bottomed flask equipped with a side-arm, condenser, septum, and stir bar was charged with [(η^6-trindane)$Mn(CO)_3$][BF_4] (**1**) (0.500 g, 1.18 mmol) and *tert*-BuOK (1.33 g, 11.87 mmol) and held under vacuum for 3 h at 40 °C. A solution of allyl bromide (1.02 mL, 11.8 mmol) in THF (25 mL) was added via cannula, under N_2, and produced a green solution that was maintained at 40 °C, which eventually turned brownish-orange. After 20.5 h, the solvent was removed under reduced pressure and the pinkish-red residue was dissolved in CH_2Cl_2, filtered, and extracted with H_2O (3 × 10 mL). The organic layers were combined, dried with Na_2SO_4, and filtered, and the solvent was removed by rotary evaporation. After drying under vacuum, **3** was obtained as a dark red powder (0.077 g, 0.198 mmol; 17%), mp 128–130 °C (dec). IR (NaCl windows, $CDCl_3$, cm^{-1}) ν_{CO}: 1971(s), 1927 (s). ^{1}H NMR (200 MHz, CD_2Cl_2) δ: 2.76 (br, 12H, benzylic CH_2), 2.04 (br, 6H, wingtip CH_2). ^{13}C NMR (50 MHz, CD_2Cl_2) δ: 110.3 (aromatic C), 30.1 (benzylic CH_2), 24.1 (wingtip CH_2). Mass spectrum (MS) (DEI, *m/z* (%)): 198 (100, $[C_{15}H_{18}]^+$), 115 (5, $[C_9H_7]^+$). (As with (C_6Me_6)$Mn(CO)_2Br$, no parent ion was detectable; only peaks attributable to the ligand were observed.) Anal. calcd. for $C_{17}H_{18}MnBrO_2$ (%): C 52.47, H 4.66; found: C 52.04, H 4.92. A crystal suitable for an X-ray diffraction study was obtained by slow evaporation of dichloromethane at room temperature under an atmosphere of nitrogen.

Alternative route to (η^6-trindane)$Mn(CO)_2Br$ (3)

The second synthesis of **3** is based on the previously reported preparation of (η^6-C_6Me_6)$Mn(CO)_2Br$ (12). [(η^6-Trindane)$Mn(CO)_3$][BF_4] (0.501 g, 1.18 mmol), Me_3NO (0.107 g, 1.29 mmol), and (n-Bu)$_4$NBr (0.566 g, 1.433 mmol) were combined in a two-neck round-bottomed flask. The system was evacuated, flushed with N_2 (three times), and CH_2Cl_2 (25 mL) was added. The resulting red solution was left to stir under N_2 for 2 h, after which time the solvent was removed under reduced pressure. The crude product was chromatographed on a silica gel column (eluent hexane/acetone 50:50) affording **3** (0.425 g, 1.092 mmol, 93%). NOTE: trimethylamine *N*-oxide hydrate ($Me_3NO{\cdot}2H_2O$) was dehydrated by azeotroping the water from a toluene solution.

Reaction of [(η^6-trindane)$Mn(CO)_3$][BF_4] with *tert*-BuOK and methyl iodide

Analogously to the preparation of **3**, [(η^6-trindane)-$Mn(CO)_3$][BF_4] (0.513 g, 1.21 mmol), *tert*-BuOK (2.65 g, 23.6 mmol), and methyl iodide (1.47 mL, 23.6 mmol) in THF (25 mL) produced a purple solution that eventually turned yellow-cream. Work-up was as above, and separation by rotary chromatography (Chromatotron, eluent hexane/CH_2Cl2 20:80) yielded (η^6-trindane)$Mn(CO)_2I$ (**4**) (0.078 g, 0.18 mmol; 15%). IR (NaCl windows, $CDCl_3$, cm^{-1}) ν_{CO}: 1973 (s), 1926 (s). ^{1}H NMR (500 MHz, $CDCl_3$) δ: 2.80 (m, 12H, benzylic CH_2), 2.09 (br, 6H, wingtip CH_2). ^{13}C NMR (125 MHz, $CDCl_3$) δ: 108.8 (aromatic C), 30.1 (benzylic CH_2), 23.7 (wingtip CH_2). MS (DEI, *m/z* (%)): 380 (40, [M – 2CO]$^+$), 253 (10, [M – 2CO – I]$^+$), 198 (100, $[C_{15}H_{18}]^+$). Anal. calcd. for $C_{17}H_{18}MnIO_2$ (%): C 46.81, H 4.16; found: C 47.02, H 4.32. A crystal suitable for an X-ray diffraction study was obtained by slow evaporation of dichloromethane at room temperature under an atmosphere of nitrogen.

Reaction of [(η^6-trindane)$Mn(CO)_3$][BF_4] with *tert*-BuOK and trimethyl phosphite

Likewise, [(η^6-trindane)$Mn(CO)_3$][BF_4] (0.500 g, 1.18 mmol), *tert*-BuOK (2.65 g, 23.6 mmol), and $P(OMe)_3$ (2.78 mL, 23.6 mmol) in THF (30 mL) produced a red solution that eventually turned orange-brown. Workup was as above, and chromatography on a silica gel column (eluent hexane/CH_2Cl2 70:30) yielded two fractions, (η^5-$C_{15}H_{15}$)$Mn(CO)_3$ (**7**) (0.080 g, 0.240 mmol; 20%), mp 87–90 °C and (η^5-$C_{15}H_{15}$)$Mn(CO)_2P(OMe)_3$] (**8**) (0.055 g, 0.130 mmol; 11%), mp 124–126 °C.

Data for **7**: ^{1}H NMR (200 MHz, $CDCl_3$) δ: 5.03 (d, 2H, CH), 4.94 (t, 1H, CH), 2.93 (m, 4H, benzylic CH_2), 2.79 (m, 4H, benzylic CH_2), 2.13 (m, 4H, wingtip CH_2). ^{13}C NMR (50 MHz, $CDCl_3$) δ: 225.4 (Mn-CO), 139.4 (C6/C9 or C7/C8, C=C), 135.2 (C6/C9 or C7/C8, C=C), 101.1 (C4/C5), 87.4 (C2, CH), 69.7 (C1/C3, CH), 32.1 (benzylic CH_2), 25.5 (wingtip CH_2), 32.1 (benzylic CH_2). Anal. calcd. for $C_{18}H_{15}MnO_3$ (%): C 64.68, H 4.52; found: C 65.01, H 4.67. After numerous attempts, yellow crystals were grown from chloroform at 0 °C under an atmosphere of nitrogen, but were not of ideal quality. Nevertheless, an X-ray diffraction study was undertaken and the molecular structure was determined.

Data for **8**: IR (NaCl windows, $CDCl_3$, cm^{-1}) ν_{CO}: 1944 (s), 1876 (s). ^{1}H NMR (500 MHz, $CDCl_3$) δ: 4.84 (m, 3H, CH), 3.38 (d, $^3J_{H\text{-}P}$ = 11.7 Hz, 9H, OCH_3), 3.04 (m, 2H, benzylic CH_2), 2.92 (m, 2H, benzylic CH_2), 2.84 (m, 2H, benzylic CH_2), 2.75 (m, 2H, benzylic CH_2), 2.16 (m, 4H, wingtip CH_2). ^{13}C NMR (125 MHz, $CDCl_3$) δ: 137.9 (C6/C9 or C7/C8, C=C), 135.8 (C6/C9 or C7/C8, C=C), 100.9

© 2008 NRC Canada

(C4/C5), 87.0 (C2, CH), 68.7 (C1/C3, CH), 51.1 (OCH_3), 32.2 (benzylic CH_2), 31.8 (benzylic CH_2), 24.6 (wingtip CH_2). ^{31}P NMR (81.04 MHz, $CDCl_3$) δ: 211.6 (s). MS (DEI, *m/z* (%)): 430 (11, $[M]^+$), 374 (100, $[M - 2CO]^+$), 281(21, $[M - 2CO - 3(OMe)]^+$), 251 (51, $[M - 2CO - P(OMe)_3^+$), 195 (44, $[(C_{15}H_{15})]^+$). Anal. calcd. for $C_{20}H_{24}MnO_5P$ (%): C 55.82, H 5.62; found: C 55.45, H 5.96. A yellow crystal suitable for an X-ray diffraction study was grown from chloroform at 0 °C under an atmosphere of nitrogen.

Reaction of [(η⁶-trindane)Mn(CO)₃][BF₄] with *tert*-BuOK and triphenylphosphine

Analogously to the preparation of **8**, [(η⁶-trindane)$Mn(CO)_3$][BF_4] (0.500 g, 1.182 mmol), *tert*-BuOK (2.65 g, 23.6 mmol), THF (30 mL), and PPh_3 (619 g, 23.6 mmol) yielded three fractions after separation on a Chromatron (eluent hexane/CH_2Cl2 90:10): PPh_3, (η⁵-$C_{15}H_{15}$)$Mn(CO)_3$ (**7**), and (η⁵-$C_{15}H_{15}$)$Mn(CO)_2[PPh_3]$ (**9**) (0.060g, 0.1056 mmol; 9%), mp 179–180 °C (dec). IR (NaCl windows, $CDCl_3$, cm^{-1}) ν_{CO}: 1929 (s), 1862 (s). ^1H NMR (500 MHz, $CDCl_3$) δ: 7.31 (m, 15H, aromatic CH), 4.60 (d, 2H, CH), 4.47 (m, 1H, CH), 2.51 (m, 8H, benzylic CH_2), 2.08 (m, 4H, wingtip CH_2). ^{13}C NMR (125 MHz, $CDCl_3$) δ: 138.1, 137.8, 136.1, 133.1 ($J_{C\text{-}P}$ = 10.4 Hz), 129.5, 128.1 ($J_{C\text{-}P}$ = 9.3 Hz), 100.7 (C4/C5), 89.0 (C2, CH), 70.7 (C1/C3, CH), 32.3 (benzylic CH_2), 32.0 (benzylic CH_2), 24.6 (wingtip CH_2). ^{31}P NMR (81.04 MHz, $CDCl_3$) δ: 94.3. MS (DEI, *m/z* (%)): 569 (100, $[M + H]^+$), 512 (58, $[M - 2CO]^+$), 195 (62, $[C_{15}H_{15}]^+$); (CI, NH_3, *m/z* (%)): 569 (100, $[M + H]^+$), 512 (58, $[M - 2CO]^+$), 195 (63, $[C_{15}H_{15}]^+$). Anal. calcd. for $C_{35}H_{30}MnO_2P$ (%): C 73.94, H 5.28; found: C 74.18, H 5.49.

Preparation of [(η⁶-indane)Mn(CO)₃][BF₄] (10)

A mixture of $Mn(CO)_5Br$ (1.08 g, 4.029 mmol) and $AgBF_4$ (0.78 g, 4.029 mmol) in dry CH_2Cl_2 (40 mL) was heated at reflux for 3 h under nitrogen and then cooled to room temperature. To the reaction mixture, a solution of indane (0.493 mL, 4.029 mmol) in dry CH_2Cl_2 (10 mL) was added, and the reaction mixture was heated at reflux for 18 h. After cooling and filtration, the filtrate was passed through Celite and concentrated to approximately one-third its volume under reduced pressure, and excess hexane (80 mL) was added. The resulting yellow solid was filtered and dried in vacuo to furnish **10** (0.658 g, 1.918 mmol, 50%). IR (NaCl windows, $CDCl_3$, cm^{-1}) υ_{CO}: 2065 (s), 2008 (s). ^1H NMR (200 MHz, CD_2Cl_2) δ: 6.53 (m, 4H, aromatic), 3.03 (m, 4H, benzylic CH_2), 2.44 (m, 1H, wingtip CH_2), 2.10 (m, 1H, wingtip CH_2). ^{13}C NMR (50 MHz, CD_2Cl_2) δ: 227.2 (Mn-CO), 99.3 (aromatic C), 98.2 (aromatic C), 32.2 (benzylic CH_2), 23.7 (wingtip CH_2). MS (positive ESI, *m/z* (%)): 258 (M + 1, 24% of $[M]^+$), 257 (100, $[M]^+$), 229 (5.3, $[M - CO]^+$), 201 (2.7, $[M - 2CO]^+$), 173 (1.9, $[M - 3CO]^+$). Anal. calcd. for $C_{12}H_{10}O_3MnBF_4$ (%): C 41.90, H 2.93; found: C 41.69, H 2.76.

Reaction of [(η⁶-indane)Mn(CO)₃][BF₄] with *tert*-BuOK and triphenylphosphine

Following the procedure for **3**, [(η⁶-indane)$Mn(CO)_3$][BF_4] (0.106 g, 0.3089 mmol), *t*-BuOK (0.693 g, 6.178 mmol), and PPh_3 (1.620 g, 6.178 mmol) in THF (35 mL) produced a reddish-orange solution. Work-up yielded (η⁵-indenyl)$Mn(CO)_2PPh_3$ (0.017 g, 0.0348 mmol, 11%). IR (NaCl windows, $CDCl_3$, cm^{-1}) ν_{CO}: 1934 (s), 1866 (s), lit. (18); (nujol) υ_{CO}: 1931(s), 1863 (s). ^1H NMR (300 MHz, CD_2Cl_2) δ: 7.09 (m, 19H, aromatic C and CH=CH), 4.65 (m, 3H, Cp). ^{13}C NMR (75 MHz, $CDCl_3$) δ: 232.8 (Mn-CO), 133.7, 133.5, 130.1, 128.6, 128.5, 126.1, 125.9, 90.1 (Cp), 72.9 (Cp). ^{31}P NMR (81.05 MHz, CD_2Cl_2) δ: 92.4 (s). MS (DEI, *m/z* (%)): 488 (6, $[M]^+$), 432 (92, $[M - 2CO]^+$), 377 (1, $[M - 2CO - Mn]^+$), 115 (100, $[C_9H_7]^+$).

Reaction of [(η⁶-indane)Mn(CO)₃][BF₄] with *tert*-BuOK and trimethyl phosphite

As for the reaction with triphenylphosphine, [(η⁶-indane)$Mn(CO)_3$][BF_4] (0.500 g, 1.457 mmol), *t*-BuOK (3.27 g, 29.0 mmol), and $P(OMe)_3$ (619 g, 23.6 mmol) in THF (30 mL) yielded (η⁵-indenyl)$Mn(CO)_2[P(OMe)_3]$ (0.001 g, 2.857 mmol, 2%). IR (NaCl windows, $CDCl_3$, cm^{-1}) ν_{CO}: 1950 (s), 1881 (s). ^1H NMR (200 MHz, $CDCl_3$) δ: 7.40 (m, 2H, CH=CH), 7.02 (m, 2H, CH=CH), 4.97 (m, 2H, CH), 4.83 (m, 1H, CH), 3.42 (d, 9H, $^3J_{C\text{-}P}$ = 11.7 Hz, OCH_3). ^{31}P NMR (81.05 MHz, CD_2Cl_2) δ: 211.4 (s). MS (DEI, *m/z* (%)): 350 (12, $[M]^+$), 322 (5, $[M - CO]^+$), 294 (100, $[M - 2CO]^+$), 170 (29, $[C_9H_7Mn]^+$), 115 (41, $[C_9H_7]^+$).

Preparation of [(η⁶-trindane)Mn(CO){P(OMe)₃}₂][BF₄] (15)

[(η⁶-Trindane)$Mn(CO)_3$][BF_4] (0.463 g, 1.095 mmol) and Me_3NO (0.173 g, 2.307 mmol) were stirred in CH_2Cl_2 (55 mL) under N_2. To the yellow solution was added $P(OMe)_3$ (0.20 mL, 1.696 mmol) whereupon the solution turned red instantaneously. The solution was allowed to stir under N_2 for 6 h at room temperature, the solvent was removed under pressure, and the crude material was purified by chromatographic separation on a silica gel column (eluent CH_2Cl_2/acetone 90:10) giving rise to two fractions. The first fraction was identified as trindane and the second was **15** (0.071 g, 0.115 mmol, 11%). IR (NaCl windows, $CDCl_3$, cm^{-1}) υ_{CO}: 1911 (s). ^1H NMR (300 MHz, CD_2Cl_2) δ: 3.71 (t, 18H, $^3J_{P\text{-}H}$ = 5.0 Hz, $P(OMe)_3$), 2.74 (m, 12H, benzylic CH_2), 2.08 (m, 6H, wingtip CH_2). ^{13}C NMR (75 MHz, CD_2Cl_2) δ: 111.7 (aromatic C), 54.5 (OCH_3), 30.4 (benzylic CH_2), 23.2 (wingtip CH_2). ^{31}P NMR (121.51 MHz, CD_2Cl_2) δ: 185.5 (s). MS (positive ESI, *m/z* (%)): 529 (100, $[M^+]$), 405 (3, $[M - P(OMe)_3]^+$), 377 (8, $[M - P(OMe)_3 - CO]^+$). Anal. calcd. for $C_{22}H_{36}MnO_7P_2$ (%): C 42.88, H 5.89; found: C 42.69, H 5.86. A sample suitable for single-crystal X-ray diffraction was obtained by crystallization from dichloromethane by slow evaporation under nitrogen at room temperature.

Preparation of [(η⁶-trindane)Re(CO)₃][PF₆] (16)

In a 100 mL round-bottomed flask, $BrRe(CO)_5$ (0.944 g, 2.324 mmol), trindane (0.765 g, 3.864 mmol), $AlCl_3$ (1.630 g, 12.22 mmol), and petroleum ether (55 mL) were heated at reflux under nitrogen for 16.5 h. The solution was cooled in an ice-bath, followed by addition of an ice-water slush (25 mL). The petroleum ether layer was decanted, and the remaining water layer was washed with cold diethyl ether followed by the addition of excess NH_4PF_6 in water (5 mL). The resultant white precipitate (0.028 g, 0.0456 mmol, 2%) was filtered and washed with cold water

© 2008 NRC Canada

and methanol. IR (KBr pellet, cm^{-1}) υ_{CO}: 2052 (s), 1956 (s). IR (NaCl windows, $CDCl_3$, cm^{-1}) υ_{CO}: 2058 (s), 1966 (s). ^1H NMR (500 MHz, CD_2Cl_2) δ: 3.38 (m, 6H, benzylic CH_2), 2.95 (m, 6H, benzylic CH_2), 2.44 (m, 3H, wingtip CH_2), 1.91 (m, 3H, wingtip CH_2). ^{13}C NMR (125.773 MHz, CD_2Cl_2) δ: 185.7 (Mn-CO), 118.7 (aromatic C), 30.4 (benzylic CH_2), 24.7 (wingtip CH_2). MS (positive ESI, *m/z* (%)): 469 (100, $[M]^+$).

Attempted synthesis of $[(\eta^6\text{-}(CH_3)_{12}C_{15}H_6)FeCp][PF_6]$

$[(\eta^6\text{-}C_{15}H_{18})FeCp][PF_6]$ (**2**) (0.124 g, 0.267 mmol) and potassium *tert*-butoxide (7.20 g, 64 mmol) were stirred together under vacuum for 3 h, and a solution of methyl iodide (3.98 mL, 64 mmol) in freshly distilled THF (60 mL) was introduced by syringe. The solution became deep red in colour and continued to change colour (dark purple to mauve to pink) until the solution remained yellowish-cream in colour. After 48 h under nitrogen at 40 °C in the dark, the product was worked up as before, and chromatographed on an alumina neutral column (eluent hexane/acetone 90:10) to afford three orange products. The ^1H and ^{13}C NMR spectra of each fraction still indicated a mixture of compounds. Similarly positive ESI mass spectrometric data exhibited signals at *m/z* 459, 473, and 487 corresponding to the incorporation of 10, 11, and 12 methyls, respectively. Two samples suitable for structural determination by single-crystal X-ray diffraction were obtained by recrystallization from hexanes/acetone mixture; however, the structure has not been satisfactorily refined as a result of a disorder in the trindane fragment.

Attempted synthesis of $[(\eta^6\text{-}(CH_2CHCH_2)_{12}C_{15}H_6)FeCp][PF_6]$

Similarly, $[(\eta^6\text{-}C_{15}H_{18})FeCp][PF_6]$, **2**, (0.233 g, 0.502 mmol), potassium *tert*-butoxide (13.5 g, 120 mmol), and allyl bromide (10.43 mL, 120 mmol) in THF (60 mL) became deep red in colour and continued to change colour (pink to violet to mauve) until the solution remained yellowish-cream in colour. After work-up, the crude product was chromatographed on an alumina neutral column (eluent hexane) affording two yellow products. The ^1H and ^{13}C NMR spectra of each fraction still indicated a mixture of compounds. Similarly positive ESI mass spectrometric data exhibited signals consistent with the incorporation of 12 allyl groups at *m/z* 799, followed by consecutive losses of multiples of 40 to a *m/z* of 319 (which corresponds to $[(\eta^6\text{-}C_{15}H_{18})FeCp]^+$).

Preparation of $[(\eta^6\text{-tetralin})Mn(CO)_3][PF_6]$ (17)

As described in the literature (25), $Mn(CO)_5Br$ (1.97 g, 7.16 mmol), $AlCl_3$ (1.91 g, 14.3 mmol), tetralin (1.88 mL, 0.0138 mmol), and cyclohexane (50 mL) were heated at reflux for 5 h under N_2. The solution was cooled, followed by the addition of ice-cold H_2O (40 mL). To the aqueous layer, NH_4PF_6 (2.21 g, 0.0138 mmol) was added, yielding a yellow precipitate that was filtered and dried under vacuum. The product (2.383 g, 5.73 mmol, 80%) was recrystallized from a mixture of acetone and diethyl ether. Complete spectroscopic assignment of this compound had not been published prior to this study. IR (NaCl windows, $CDCl_3$, cm^{-1}) υ_{CO}: 2068 (s), 2025 (s), 2003 (s), lit. (25) (NaCl) υ_{CO}: 2056 (s), 2016 (s). ^1H NMR (200 MHz, acetone-d_6) δ: 6.84 (s, 4H, CH), 3.13 (m, 4H, CH_2), 2.30 (m, 4H, CH_2). ^{13}C NMR (50 MHz, acetone-d_6) δ: 216.9, 119.5, 101.9, 99.8, 28.2, 21.6. MS (positive ESI, *m/z* (%)): 271 (100, $[M]^+$), 243 (8, $[M - CO]^+$), 214 (23, $[M - 2CO]^+$), 187 (7, $[M - 3CO]^+$).

Reaction of $[(\eta^6\text{-tetralin})Mn(CO)_3][PF_6]$ with trimethyl phosphite

A 100 mL Schlenk flask equipped with a side arm and stir bar was charged with $[(\eta^6\text{-tetralin})Mn(CO)_3][PF_6]$ (**17**) (0.902 g, 2.168 mmol) and evacuated and purged with N_2 three times. A solution of THF (30 mL) containing $P(OMe)_3$ (5.11 mL, 43.4 mmol) was added dropwise under N_2, the solution was yellow in colour. The solution was stirred for 20 h under N_2 and the solvent was then removed under reduced pressure. The residue was dissolved in CH_2Cl_2 and hexanes, a precipitate formed, and it was filtered. The remaining solution was chromatographed on a silica gel column (eluent 100% hexane) affording **20**, a yellow compound (0.658 g, 1.285 mmol, 59%), mp 86–88 °C. IR (NaCl windows, $CDCl_3$, cm^{-1}) υ_{CO}: 2008 (s), 1961 (s). ^1H NMR (200 MHz, $CDCl_3$) δ: 5.94 (m, 4H, aromatic CH), 3.70 (t, 9H, $^3J_{H\text{-}P}$ = 11.6 Hz, OCH_3), 2.73 (m, 4H, CH_2), 1.79 (m, 4H, CH_2). ^{13}C NMR (50 MHz, $CDCl_3$) δ: 220.3 (d, $^2J_{C\text{-}P}$ = 43.2 Hz, Mn-CO), 113.9 (C1/C6), 97.8 (C2/C5 or C3/C4), 96.7 (C2/C5 or C3/C4), 54.1 (d, $^2J_{C\text{-}P}$ = 7.3 Hz, OCH_3), 27.5 (C7/C10), 21.1 (C7/C10). ^{31}P NMR (81.04 MHz, $CDCl_3$) δ: 182.1 (s, $P(OMe)_3$), –167.4 (septet, PF_6). MS (positive ESI, *m/z* (%)): 367 (100, $[M^+]$), 311 (19, $[M - 2CO]^+$). Anal. calcd. for $C_{15}H_{21}MnO_5P_2F_6$ (%): C 35.17, H 4.13; found: C 35.51, H 3.96. A sample suitable for single-crystal X-ray diffraction was obtained by crystallization from chloroform by slow evaporation under an atmosphere of nitrogen at room temperature.

Reaction of $[(\eta^6\text{-tetralin})Mn(CO)_3][PF_6]$ with *tert*-BuOK

A round-bottomed flask equipped with a side arm and stir bar was charged with $[(\eta^6\text{-tetralin})Mn(CO)_3][PF_6]$ (**17**) (0.952 g, 2.288 mmol) and *t*-BuOK (5.14 g, 45.8 mmol) and evacuated and purged with N_2 three times. This was followed by the addition of THF (30 mL) under N_2, which produced a dark orange-brown solution, which was stirred for 6 h under N_2. The solvent was removed under reduced pressure and the residue was dissolved in methylene chloride. Hexanes were added to the solution and, after filtration, the solvent was removed by rotary evaporation yielding a yellow-orange oil that was separated on a Chromatotron (eluent hexane with gradual addition of CH_2Cl_2) furnishing **21** (0.114 g, 0.284 mmol, 12%). IR (NaCl windows, neat, cm^{-1}) υ_{CO}: 2007 (s), 1927 (s). MS (CI, NH_3, *m/z* (%)): 403 (100, $[M + 1]^+$), 271 (57, $[M - C_{10}H_{11}]^+$), 187 (3, $M - C_{10}H_{11} - 3CO]^+$, 131 (8, $[C_{10}H_{11}]^+$).

Preparation of $[(\eta^6\text{-dibenzosuberane})Mn(CO)_3][BF_4]$ (23)

A mixture of $Mn(CO)_5Br$ (1.90 g, 6.92 mmol) and $AgBF_4$ (1.48 g, 7.61 mmol) in dry CH_2Cl_2 (50 mL) was heated at reflux for 3 h under nitrogen and then cooled to room temperature. To the reaction was added a solution of dibenzosuberane (1.78 g, 9.20 mmol) in dry CH_2Cl_2 (15 mL), and the mixture was heated at reflux overnight. After cooling and filtration, the filtrate was passed through Celite and concentrated to approximately one-third its volume under reduced pressure, and excess hexane (100 mL)

© 2008 NRC Canada

Table 1. Crystallographic collection and refinement parameters for **3**, **4**, **7**, and **8**.

Compound	**3**	**4**	**7**	**8**
Empirical formula	$C_{17}H_{18}O_2BrMn$	$C_{17}H_{18}O_2IMn$	$C_{18}H_{15}O_3Mn$	$C_{20}H_{24}O_5PMn$
Formula weight	389.16	436.15	334.24	430.30
Temperature (K)	299(2)	299(2)	173(2)	299(2)
Wavelength (Å)	0.71073	0.71073	0.71073	0.71073
Crystal system	Monoclinic	Orthorhombic	Monoclinic	Monoclinic
Space group	$P2_1/c$	*Pbca*	*C*2/*c*	$P2_1/c$
a (Å)	9.8049(13)	14.408(3)	16.567(18)	9.7325(17)
b (Å)	8.8852(13)	15.080(2)	9.919(14)	22.355(4)
c (Å)	18.682(3)	15.264(3)	18.524(26)	9.6052(17)
α (°)	90	90	90	90
β (°)	94.825(3)	90	98.09(5)	106.484(5)
γ (°)	90	90	90	90
Volume ($Å^3$)	1621.8(4)	3316.4(10)	3013.7(68)	2003.9(6)
Z	4	8	8	4
$D_{calcd.}$ (Mg/m^3)	1.594	1.747	1.473	1.426
Absorption coefficient (mm^{-1})	3.278	2.659	0.885	0.766
F(000)	784	1712	1376	896
Crystal size (mm)	0.06 × 0.08 × 0.24	0.14 × 0.28 × 0.33	0.04 × 0.22 × 0.42	0.08 × 0.33 × 0.35
Theta range for data collection (°)	2.08–23.25	2.37–24.99	2.40–24.99	1.82–27.50
Index ranges	$-10 \geq h \geq 10$ $-9 \geq k \geq 9$ $-20 \geq l \geq 20$	$-16 \geq h \geq 17$ $-17 \geq k \geq 17$ $-18 \geq l \geq 18$	$-21 \geq h \geq 20$ $-7 \geq k \geq 11$ $-21 \geq l \geq 16$	$-12 \geq h \geq 12$ $-28 \geq k \geq 26$ $-12 \geq l \geq 11$
Reflections collected	10 041	23 135	2 507	17 829
Independent reflections	2318 [*R*(int) = 0.0907]	2919 [*R*(int) = 0.0323]	1717 [*R*(int) = 0.2486]	4584 [*R*(int) = 0.0300]
Absorption correction	SADABS	SADABS	SADABS	SADABS
Refinement method	Full-matrix least-squares on F^2	Full-matrix least-squares on F^2	Full-matrix least-squares on F^2	Full–matrix least–squares on F^2
Data/restraints/parameters	2318/0/191	2919/0/192	1679/0/199	4584/0/245
Goodness-of-fit on F^2	1.075	1.053	1.080	1.030
Final *R* indices [$I > 2\sigma(I)$]	*R*1 = 0.0560, *wR*2 = 0.1326	*R*1 = 0.0412, *wR*2 = 0.1159	*R*1 = 0.1455, *wR*2 = 0.3683	*R*1 = 0.0350, *wR*2 = 0.0876
R indices (all data)	*R*1 = 0.1070, *wR*2 = 0.1582	*R*1 = 0.0490, *wR*2 = 0.1237	*R*1 = 0.1943, *wR*2 = 0.4620	*R*1 = 0.0528, *wR*2 = 0.0947
Extinction coefficient	0.0000(5)		0.0000(9)	
Absolute structure parameter				
Largest diff. peak and hole ($e \cdot Å^{-3}$)	0.464 and –0.436	0.756 and –0.1.292	1.304 and –1.241	0.252 and –0.214

was added. The resulting yellow solid was filtered and dried under vacuum furnishing **23** (0.301 g, 0.718 mmol, 10%), mp 218–220 °C. IR (NaCl windows, $CDCl_3$, cm^{-1}) υ_{CO}: 2065 (s), 2014 (s). ^{1}H NMR (500 MHz, acetone-d_6) δ: 7.38 (d, 1H, *J* = 7.3 Hz, H7/H10), 7.31 (m, 2H, H8, H9), 7.25 (t, 1H, *J* = 7.1, H7/H10), 7.13 (d, 1H, *J* = 6.6 Hz, H1/H4), 6.91 (t, 1H, *J* = 6.3 Hz, H2/H3), 6.58 (t, 2H, *J* = 6.3 Hz, H1/H3 or H2/H4), 4.48 (d, 1H, *J* = 15.5 Hz, H11a/H11b), 4.31 (d, 1H, *J* = 15.5 Hz, H11a/H11b), 3.44 (m, 3H, H6a/H6b, H5a/H5b), 3.27 (m, 1H, H6a/H6b, H5a/H5b). ^{13}C NMR (125 MHz, acetone-d_6) δ: 216.4 (Mn-CO), 139.6 (C12/C15), 138.6 (C12/C15), 130.2 (C8/C9), 129.8 (C7/C10), 129.4 (C8/C9), 128.0 (C7/C10), 123.7 (C14/C15), 118.6 (C14/C15), 105.5 (C1/C4), 103.1 (C2/C3), 100.6 (C2/C3), 97.3 (C2/C3 or C2/C4), 38.4 (C11), 32.1 (C5/C6). MS (positive ESI, *m*/*z* (%)): 333 (100, [M^+]), 277 (6.15, [M – 2CO]$^+$), 249 (17.75, [M – 3CO]$^+$). Anal. calcd. for $C_{18}H_{14}MnO_3BF_4$ (%): C 51.47, H 3.36; found: C 51.48, H 3.51. A sample suitable for structural determination by single-crystal X-ray diffraction was obtained by crystallization from acetone at room temperature.

Reaction of [(η^6-dibenzosuberane)$Mn(CO)_3$][BF_4] with *tert*-BuOK

A round-bottomed flask equipped with a side arm and stir bar was charged with [(η^6-dibenzosuberane)$Mn(CO)_3$][BF_4] (**23**) (0.377 g, 0.90 mmol) and *t*-BuOK (2.02 g, 18.0 mmol) and evacuated and purged with N_2 three times. This was followed by the addition of THF (25 mL) under N_2, which produced a dark red-brown-orange solution, which was stirred for 4 h under N_2. The solvent was removed under reduced pressure and the residue was dissolved in ether. Water (40 mL) was added to the ether solution and extracted with ether (2 × 10 mL). The organic layers were combined, dried with $MgSO_4$, and filtered. The solvent was removed by rotary evaporation yielding a red-orange material that was separated on a Chromatotron (eluent hexane with gradual addition of CH_2Cl_2) furnishing **28**, as an orange powder

© 2008 NRC Canada

Table 2. Crystallographic collection and refinement parameters for **15**, **20**, **23**, and **28**.

Compound	**15**	**20**	**23**	**28**
Empirical formula	$C_{22}H_{36}O_7P_2MnBF_4$	$C_{15}H_{21}O_5P_2F_6Mn$	$C_{18}H_{14}O_3MnBF_4$	$C_{18}H_{13}O_3Mn$
Formula weight	616.20	512.20	420.04	332.22
Temperature (K)	173(2)	173(2)	173(2)	173(2)
Wavelength (Å)	0.71073	0.71073	0.71073	0.71073
Crystal system	Triclinic	Orthorhombic	Monoclinic	Monoclinic
Space group	$P\bar{1}$	*Pnma*	$P2_1/n$	*C*2
a (Å)	9.3299(19)	15.694(5)	7.733(2)	25.577(14)
b (Å)	11.082(2)	10.991(4)	7.774(2)	6.255(3)
c (Å)	12.969(3)	11.735(4)	28.795(7)	9.362(5)
α (°)	97.600(3)	90	90	90
β (°)	94.229(3)	90	96.660(4)	107.230(8)
γ (°)	91.929(3)	90	90	90
Volume (Å^3)	1324.2(5)	2024.4(11)	1719.4(7)	1430.5(14)
Z	2	4	4	4
$D_{calcd.}$ (Mg/m^3)	1.545	1.681	1.623	1.543
Absorption coefficient (mm^{-1})	0.688	0.889	0.825	0.932
F(000)	640	1040	848	680
Crystal size (mm)	0.18 × 0.42 × 0.44	0.32 × 0.45 × 0.70	0.12 × 0.28 × 0.42	0.03 × 0.05 × 0.50
Theta range for data collection (°)	1.59 to 27.52	2.17 to 27.69	1.42 to 27.50	1.67 to 27.51
Index ranges	$-12 \geq h \geq 11$ $-14 \geq k \geq 14$ $-16 \geq l \geq 15$	$-20 \geq h \geq 18$ $-14 \geq k \geq 14$ $-14 \geq l \geq 15$	$-9 \geq h \geq 10$ $-9 \geq k \geq 10$ $-37 \geq l \geq 37$	$-32 \geq h \geq 32$ $-8 \geq k \geq 8$ $-12 \geq l \geq 11$
Reflections collected	11 886	16 907	14 780	6 352
Independent reflections	5981 [*R*(int) = 0.0259]	2455 [*R*(int) = 0.0419]	3936 | [*R*(int) = 0.0290]	2802 [*R*(int) = 0.0604]
Absorption correction	SADABS	SADABS	SADABS	SADABS
Refinement method	Full-matrix least-squares on F^2	Full-matrix least-squares on F^2	Full-matrix least-squares on F^2	Full-matrix least-squares on F^2
Data/restraints/parameters	5981/0/334	2452/0/222	3935/0/240	2802/0/200
Goodness-of-fit on F^2	1.047	1.164	1.051	1.034
Final *R* indices [$I > 2\sigma(I)$]	*R*1 = 0.0368, *wR*2 = 0.0938	*R*1 = 0.0343, *wR*2 = 0.0882	*R*1 = 0.0481, *wR*2 = 0.1208	*R*1 = 0.0520, *wR*2 = 0.0925
R indices (all data)	*R*1 = 0.0455, *wR*2 = 0.0988	*R*1 = 0.0469, *wR*2 = 0.0991	*R*1 = 0.0588, *wR*2 = 0.1272	*R*1 = 0.0894, *wR*2 = 0.1044
Extinction coefficient		0.0000(3)	0.0001(7)	0.0000(7)
Absolute structure parameter				0.50(3)
Largest diff. peak and hole (e•Å^{-3})	0.423 and –0.358	0.538 and –0.712	1.033 and –1.215	0.412 and –0.372

(0.131 g, 0.395 mmol, 44%). IR (NaCl windows, $CDCl_3$, cm^{-1}) υ_{CO}: 2022 (s), 1950 (s). ^{1}H NMR (500 MHz, CD_2Cl_2) δ: 7.05 (m, 4H, aromatic CH), 5.61 (t, 1H, *J* = 5.1 Hz, CH), 5.18 (t, 1H, *J* = 6.3 Hz, CH), 5.09 (d, 1H, *J* = 5.3 Hz, CH), 4.41 (d, 1H, *J* = 7.3 Hz, CH), 4.10 (s, 1H, CH), 3.23 (m, 2H, CH_2), 2.47 (m, 2H, CH_2). ^{13}C NMR (125 MHz, CD_2Cl_2) δ: 222.4 (Mn-CO), 138.7, 133.5, 130.1, 129.5, 126.6, 125.3, 106.7, 100.3, 98.6, 74.8, 74.6, 60.8, 38.0, 36.4, 32.9. MS (DEI, *m*/*z* (%)): 332 (2, $[M]^+$), 276 (3.2, $[M - 2CO]^+$), 248 (3.2, $[M - 3CO]^+$), 193 (100, $[C_{15}H_{13}]^+$). Anal. calcd. for $C_{18}H_{13}MnO_3$ (%): C 65.06, H 3.92; found: C 65.45, H 3.96. A rod-shaped, orange crystalline sample suitable for structural determination by single-crystal X-ray diffraction studies was grown from dichloromethane by slow evaporation under an atmosphere of nitrogen at room temperature.

X-ray crystal structure determinations[3]

X-ray crystallographic data (see Tables 1 and 2) were collected from single crystal samples, each of which was mounted on a glass fibre. Data were collected using a P4 Bruker diffractometer, equipped with a Bruker SMART 1K charge coupled device (CCD) area detector, using the program SMART (48), and a rotating anode, using graphite-

[3] Supplementary data for this article are available on the journal Web site (canjchem.nrc.ca) or may be purchased from the Depository of Unpublished Data, Document Delivery, CISTI, National Research Council Canada, Ottawa, ON K1A 0R6, Canada. DUD 3811. For more information on obtaining material refer to cisti-icist.nrc-cnrc.gc.ca/cms/unpub_e.shtml. CCDC 681235 (**3**), 681234 (**4**), 681228 (**7**), 681233 (**8**), 681232 (**15**), 681231 (**20**), 681230 (**23**), and 681229 (**28**) contain the crystallographic data for this manuscript. These data can be obtained, free of charge, via www.ccdc.cam.ac.uk/conts/retrieving.html (Or from the Cambridge Crystallographic Data Centre, 12 Union Road, Cambridge CB2 1EZ, UK; fax +44 1223 336033; or deposit@ccdc.cam.ac.uk).

© 2008 NRC Canada

monochromated Mo Kα radiation (λ = 0.71 073 Å). The crystal-to-detector distance was 4.987 cm, and the data collection was carried out in 512 × 512 pixel mode, utilizing 2 × 2 pixel binning. The initial unit cell parameters were determined by a least-squares fit of the angular settings of the strong reflections, collected by a 12° scan in 40 frames over three different sections of reciprocal space (160 frames in total). A hemisphere of data was collected with high redundancy, to better than 0.8 Å resolution at 153 K. Upon completion of the data collection, the first 40 frames were recollected to improve the decay correction analyses. Processing was carried out using the program SAINT (49), which applied Lorentz and polarization corrections to the three-dimensionally integrated diffraction spots. The program SADABS (50), was utilized for the scaling of the diffraction data, the application of a decay correction, and an empirical absorption correction based on redundant reflections for the data set. The structures were solved by using the direct-methods procedure in the Bruker SHELXTL program library (51), and refined by full-matrix least-squares methods on F^2 with anisotropic thermal parameters for all nonhydrogen atoms. Hydrogen atoms were either found and added from the difference map, and allowed to refine isotropically, or were added as fixed contributors at calculated positions, with isotropic thermal parameters based on the carbon atom to which they were bonded.

The structure of **3** exhibited a disorder between one of the carbonyl groups and a bromine atom and hence, the occupancy of the two conformations was allowed to refine as a free variable (final ratio of approximately 70:30). Likewise, the final structure of **4** was based on a disorder model in which the $Mn(CO)_2I$ tripod could exist in two conformations. The occupancy of the two conformations was allowed to refine as a free variable (final ratio of approximately 88:12). In the case of $[(\eta^6\text{-tetralin})Mn(CO)_2P(OMe)_3][PF_6]$ (**20**) the molecule lies on a crystallographic mirror plane; thus only half of the molecule was refined and the other half was generated by the mirror plane. This arises because of a disorder between C(7) and C(7a) such that there are two twisted half-chair conformations. Also, the anion was disordered, and two orientations were found for the PF_6 anion.[3]

Acknowledgements

Financial support from the Natural Sciences and Engineering Research Council of Canada (NSERC), from Science Foundation Ireland, and from University College Dublin, is gratefully acknowledged. Mass spectra were acquired courtesy of Dr. Kirk Green of the McMaster Regional Mass Spectrometry Facility. We also thank Dr. James F. Britten for X-ray crystallographic advice.

References

1. (*a*) G. Mehta, S.R. Shah, and K. Ravikumar. J. Chem. Soc. Chem. Commun. 1006 (1993); (*b*) H. Sakurai, T. Daiko, and T. Hirao. Science (Washington, D.C.), **301**, 1878 (2003).
2. H.K. Gupta, P.E. Lock, and M.J. McGlinchey. Organometallics, **16**, 3628 (1997).
3. H.K. Gupta, P.E. Lock, D.W. Hughes, and M.J. McGlinchey. Organometallics, **16**, 4355 (1997).
4. (*a*) J.-R. Hamon, J.-Y. Saillard, A. Le Beuze, M.J. McGlinchey, and D. Astruc. J. Am. Chem. Soc. **104**, 7549 (1982); (*b*) C. Valério, E. Alonso, J. Ruiz, J.-C. Blais, and D. Astruc. Angew. Chem. Int. Ed. Engl. **38**, 1747 (1999), and refs. cited therein.
5. (*a*) D.M. LaBrush, D.P. Eyman, N.C. Baenziger, and L.M. Mallis. Organometallics, **10**, 1026 (1991); (*b*) J.L. Moler, D.P. Eyman, J.M. Neilson, A.M. Morken, S.J. Schauer, and D.B. Snyder. Organometallics, **12**, 3304 (1993).
6. N. Reginato and M.J. McGlinchey. Organometallics, **20**, 4147 (2001).
7. (*a*) S. Sun, C.A. Dullaghan, and D.A. Sweigart. J. Chem. Soc. Dalton Trans. 4493 (1996); (*b*) R.D. Pike and D.A. Sweigart. Coord. Chem. Rev. **187**, 183 (1999).
8. G. Jaouen, S. Top, A. Laconi, D. Couturier, and J. Brossard. J. Am. Chem. Soc. **106**, 2207 (1984).
9. D. Astruc. Acc. Chem. Res. **33**, 287 (2000), and refs. cited therein.
10. H.-J. Choi, Y.S. Park, S.H. Yun, H.-S. Kim, C.S. Cho, K. Ko, and K.H. Ahn. Org. Lett. **4**, 795 (2002).
11. (*a*) H.K. Gupta, S. Brydges, and M.J. McGlinchey. Organometallics, **18**, 115 (1999); (*b*) S. Brydges, L.E. Harrington, and M.J. McGlinchey. Coord.Chem. Rev. **233–234**, 75 (2002).
12. R.J. Bernhardt, M.A. Wilmoth, J.J. Weers, D.M. LaBrush, D.P. Eyman, and J.C. Huffman. Organometallics, **5**, 883 (1986).
13. L.H.P. Gommans, L. Main, and B.K. Nicholson. J. Organomet. Chem. **346**, 385 (1988).
14. L.A.P. Kane-Maguire and D.A. Sweigart. Inorg. Chem. **18**, 700 (1979).
15. R.J. Bernhardt and D.P. Eyman. Organometallics, **3**, 1445 (1984).
16. P.J. Schlom, A.M. Morken, D.P. Eyman, N.C. Baenziger, and S.J. Schauer. Organometallics, **12**, 3461 (1993).
17. (*a*) P.J.C. Walker and R.J. Mawby. Inorg. Chim. Acta, **7**, 621 (1973); (*b*) There is an early report of *t*-Bu-OCO-$Co(CO)_4$: R.F. Heck. J. Organomet. Chem. **2**, 195 (1964).
18. R.B. King. J. Organomet. Chem. **23**, 527 (1970).
19. A. Decken, J.F. Britten, and M.J. McGlinchey. J. Am. Chem. Soc. **115**, 7275 (1993).
20. R.H. Crabtree and C.P. Parnell. Organometallics, **3**, 1727 (1984).
21. O.I. Trifonova, E.A. Ochertyanova, N.G. Akhmedov, V.A. Roznyatovsky, D.N. Laikov, N.A. Ustynyuk, and Y.A. Ustynyuk. Inorg. Chim. Acta, **280**, 328 (1998).
22. F. Rose-Munch, C. Susanne, C. Renard, E. Rose, and J.Vaissermann. J. Organomet. Chem. **519**, 253 (1996).
23. D.A. Brown, W.K. Glass, K.M. Kreddan, D. Cunningham, P.A. McArdle, and T. Higgins. J. Organomet. Chem. **418**, 91 (1991).
24. D.B. Snyder, S.J. Schauer, D.P. Eyman, J.L. Moler, and J.J. Weers. J. Am. Chem. Soc. **115**, 6718 (1993).
25. T.-Y. Lee, S.S. Lee, Y.K. Chung, and S.W. Lee. J. Organomet. Chem. **486**, 141 (1995).
26. (*a*) K. Woo, G.B. Carpenter, and D.A. Sweigart. Inorg. Chim. Acta, **220**, 297 (1994); (*b*) K. Woo, P.G. Williard, D.A. Sweigart, N.W. Duffy, B.H. Robinson, and J. Simpson. J. Organomet. Chem. **487**, 111 (1995).
27. T. Volk, D. Bernicke, J.W. Bats, and H.-G. Schmalz. Eur. J. Inorg. Chem. 1883 (1998).
28. M.J. McGlinchey. Adv. Organomet. Chem. **34**, 285 (1992), and refs. cited therein.
29. A. Ceccon, A. Gambaro, and A. Venzo. J. Organomet. Chem. **281**, 221 (1985).
30. T. Whitesides and R. Budnik. Inorg. Chem. **15**, 874 (1976).

© 2008 NRC Canada

31. P.J.P. Reboul, B. Cristau, and G. Pèpe. Acta Crystallogr. **B37**, 394 (1981).
32. W. Weissensteiner, O. Hofer, and U.G. Wagner. J. Org. Chem. **53**, 3988 (1988).
33. (*a*) R.C. Cambie, G.R. Clark, A.C. Gourdie, P.S. Rutledge, and P.D. Woodgate. J. Organomet. Chem. **297**, 177 (1985); (*b*) B. Mailvaganam, R.E. Perrier, B.G. Sayer, B.E. McCarry, R.A. Bell, and M.J. McGlinchey. J. Organomet. Chem. **354**, 325 (1988).
34. R.M. Moriarty, Y.-Y. Ku, U.S. Gill, R. Gilardi, R.E. Perrier, and M.J. McGlinchey. Organometallics, **8**, 960 (1989).
35. A. Vessières, S. Top, A.A. Ismail, I.S. Butler, M. Louer, and G. Jaouen. Biochemistry, **27**, 6659 (1988).
36. W.A. Herrmann, J. Plank, G.W. Kriechbaum, M.L. Ziegler, H. Pfisterer, J.L. Atwood, and R.D. Rogers. J. Organomet. Chem. **264**, 327 (1984).
37. M.R. Churchill and S. Scholer. Inorg. Chem. **8**, 1950 (1969).
38. J.M. Veauthier, A. Chow, G. Fraenkel, S.J. Geib, and N.J. Cooper. Organometallics, **19**, 3942 (2000).
39. J.M. Veauthier, A. Chow, G. Fraenkel, S.J. Geib, and N.J. Cooper. Organometallics, **19**, 661 (2000).
40. (*a*) P.M. Treichel and J.W. Johnson. Inorg. Chem. **16**, 749 (1977); (*b*) P.M. Treichel, K.P. Fivizzani, and K.J. Haller. Organometallics, **1**, 931 (1982).
41. (*a*) J.W. Johnson and P.M. Treichel. J. Chem. Soc. Chem. Commun. 688 (1976); (*b*) J.W. Johnson and P.M. Treichel. J. Am. Chem. Soc. **99**, 1427 (1977); (*c*) E. Kirillov, S. Kahlal, T. Roisnel, T. Georgelin, J.-Y. Saillard, and J.-F. Carpentier. Organometallics, **27**, 387 (2008).
42. A. Xia, J.P. Selegue, A. Carrilo, and C.P. Brock. J. Am. Chem. Soc. **122**, 3973 (2000).
43. S. Brydges, N. Reginato, L.P. Cuffe, C.M. Seward, and M.J. McGlinchey. C. R. Chim. **8**, 1497 (2005).
44. M. Brookhart and M.L.H. Green. J. Organomet. Chem. **250**, 395 (1983).
45. E. Folga and T. Zeigler. J. Am. Chem. Soc. **115**, 5169 (1993).
46. J.K. Klassen, M. Selke, A.A. Sorensen, and G.K. Yang. J. Am. Chem. Soc. **112**, 1267 (1990).
47. L.D. Hicks, J.K. Han, and A.J. Fry. Tetrahedron Lett. **41**, 7817 (2000).
48. Bruker AXS, Inc. SMART. Release 5.611 [computer program]. Bruker AXS, Inc., Madison, Wis. 2000.
49. Bruker AXS, Inc. SAINT. Release 6.02a [computer program]. Bruker AXS, Inc., Madison, Wis. 2000.
50. G.M. Sheldrick. SADABS [computer program]. Bruker AXS Inc., Madison, Wis. 2000.
51. G.M. Sheldrick. SHELXTL. Version 5.1 [computer program]. Bruker AXS, Inc., Madison, Wis. 1998.

© 2008 NRC Canada

A microporous alkaline-earth phosphonate sustained by one-dimensional inorganic and organic units[1]

Ramanathan Vaidhyanathan, Amir H. Mahmoudkhani, and George K.H. Shimizu

Abstract: The single-crystal X-ray structure of a microporous alkaline-earth phosphonate incorporating a new triphosphonate ligand is presented. $Sr_2(H_2L)(CH_3OH)(H_2O)_4$, where L = 1,3,5-tris(4-phosphonophenyl)benzene, crystallizes in triclinic space group *P*-1 (a = 6.9230(4) Å, b = 15.3370(9) Å, c = 16.1930(11) Å, α = 62.201(3)°, β = 85.288(4)°, γ = 86.665(4)°). The solid is sustained by cooperative interactions between both one-dimensional inorganic and organic columns and forms a two-fold interpenetrated microporous structure. Gas and vapour sorption experiments confirm the microporosity. Based upon the sustaining interactions, this compound can serve as a model for more porous structures as extension of its structure disfavours further interpenetration.

Key words: metal–organic framework, coordination polymer, phosphonate, microporous, alkaline earth.

Résumé : Faisant appel à la diffraction des rayons X par un cristal unique, on a déterminé la structure cristalline d'un phosphonate de terre alcaline microporeuse incorporant un nouveau ligand triphosphonate. Le $Sr_2(H_2L)(CH_3OH)(H_2O)_4$ dans lequel L = 1,3,5-tris(4-phosphonophényl)benzène cristallise dans le groupe d'espèce *P*-1 [a = 6,9230(4) Å, b = 15,3370(9) Å et c = 16,1930(11) Å, α = 62,201(3)°, β = 85,288(4)° et γ = 86,665(4)°]. Le solide est soutenu par des interactions coopératives entre les colonnes unidimensionnelles inorganiques et organiques et il forme une structure microporeuse binaire dans laquelle on observe une interpénétration. Des expériences de sorption de gaz et de vapeur confirment la microporosité. Sur la base des interactions de soutien, ce composé peut servir de modèle pour des structures plus poreuses puisque l'extension de sa structure défavorise d'autre interpénétration.

Mots-clés : squelette organométallique, polymère de coordination, phosphonate, microporeux, terre alcaline.

[Traduit par la Rédaction]

Introduction

With the illustration that network coordination compounds can sustain permanent pores (1) has come an interest in the design principles for such materials (2) and a concurrent upsurge in the coordination chemistry of new ligands for their formation. The majority of research in this area has focused on polycarboxylate or polypyridyl ligands (3). The phosphine group is not a widely examined functionality for the formation of networks. Much of the available literature comes from the Puddephatt group who have reported numerous elegant examples of phosphine-based coordination polymers illustrating the breadth of different discrete and infinite assemblies possible (4). They have also conducted research on the dynamics of assembly (and disassembly) of coordination polymers (5). Most of our work has concerned sulfonate frameworks (6), which can range from highly flexible (**6a**–**6d**) to robust (**6e**, **6f**) even when sustained by H-bonding (7). There is a structural analogy with this group to the phosphonate chemistry illustrated by a predisposition to layered solids as well as observed intercalation phenomena (8). Also, both represent "adaptable" functionalities (9).

Phosphonates are strongly ligating functional groups that readily coordinate to a wide range of metal ions (10). Owing to the strength of these interactions, phosphonate groups have been extensively examined as ligands for the formation of porous solids (10). With most simple phosphonate ligands, the default structure observed is a layered motif, and many efforts have been made to perform chemistry in between the layers of these materials (11). With the potential of the layers to swell with solvation, the gallery height and hence chemical confinement of species can be variable. Pillaring the layers can form pores, with appropriate spacer phosphate or phosphonate groups between pillars, but these pores can be irregular (12). Simple linear diphosphonates typically will not yield a porous structure (13); however, we

Received 24 May 2008. Accepted 27 June 2008. Published on the NRC Research Press Web site at canjchem.nrc.ca on 4 October 2008.

This paper is dedicated to Professor Richard Puddephatt for his great contributions in Organometallic Chemistry.

R. Vaidhyanathan, A.H. Mahmoudkhani, and G.K.H. Shimizu.[2] Department of Chemistry, University of Calgary, Calgary, AB T2N 1N4, Canada.

[1]This article is part of a Special Issue dedicated to Professor R. Puddephatt.
[2]Corresponding author (e-mail: gshimizu@ucalgary.ca).

 doi:10.1139/V08-130 © 2008 NRC Canada

have recently reported an exception with 2,5-dihydroxy-1,4-benzenediphosphonate (14).

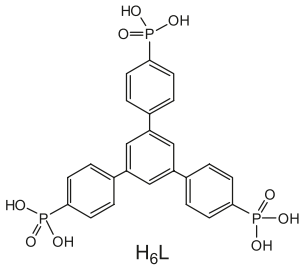

H_6L

Several polyphosphonate ligands have been reported, which have been designed to direct the metal phosphonate aggregate away from a layered motif and generate pores (15–17). A challenge with this strategy is that, with the various coordination modes/protonation states accessible to a RPO_3^{2-} group and the strength of its ligation, solids can readily precipitate in an amorphous state. While these materials may be porous, they would not be amenable to characterization by X-ray diffraction and likely possess a high dispersity of pore sizes. However, under appropriate conditions, crystalline and porous phosphonates have been attained (16), more typically with divalent metal ions (17), as more highly charged ions increase the likelihood of a less ordered, albeit more robust solid. Here, we report an alkaline-earth phosphonate framework with the new ligand 1,3,5-tris(4-phosphonophenyl)benzene, H_6L. The ligand possesses a rigid and sizeable trigonal core, which makes formation of an efficiently packed layered motif impossible. With Sr^{2+}, a doubly interpenetrated, three-dimensional crystalline solid is obtained, $Sr_2(H_2L)(CH_3OH)(H_2O)_4$, **1**. Gas and vapour sorption studies confirm permanent porosity. The structure is sustained by both one-dimensional inorganic and π-stacked organic columns, which mutually reinforce one another. The structure also presents a starting point for design of larger pore crystalline materials.

Experimental[3]

General

NMR spectra in solution were recorded on a Bruker WP-200 instrument at 200 MHz for ^1H and 50.3 MHz for ^{13}C and referenced internally to residual solvent peaks. Solid-state ^{31}P NMR spectra were recorded in a 2.5 mm MAS probe at 25 °C on a Bruker AMX300 spectrometer operating at a resonance frequency of 121.50 MHz. Thermal analysis (TG–DSC) data were recorded on a Netzsch STA 449C apparatus with a heating rate of 5 °C /min using an aluminum pan as a reference standard in N_2 atmosphere. Water vapour adsorption/desorption and CO_2 adsorption/desorption at room temperature were also studied on the same instrument. Infrared spectra were recorded on a Nicolet Nexus 470 FTIR spectrometer in the range of 4000–400 cm^{-1} by using dry KBr pellets containing about 1%–2% of the sample. The adsorption isotherm of CO_2 was carried out at 273 K using an Autosorb-1 from Quantachrome. Samples were outgassed at 120 °C for 24 h under vacuum before each measurement.

Synthesis of 1,3,5-tris(4-phosphonophenyl)benzene (H_6L)

The phosphonate diethylester of L was prepared using a slight modification of the Michaelis–Arbuzov reaction by following a published process (18). Tris(4-bromophenyl)benzene (1.2 g, 2.2 mmol), anhyd. $NiCl_2$ (28 mg, 0.22 mmol), and 80 mL of 1,3-diisopropylbenzene were added to a 250 mL three-necked flask fitted with reflux condenser, N_2 inlet, and an addition funnel. The flask was fitted into a regulated heating mantle with magnetic stirring. Triethylphosphite (2.3 mL, 13.2 mmol) and 1,3-diisopropylbenzene (20 mL) were transferred into addition funnel. The system was purged with N_2 for 10 min and kept under static atmosphere of the inert gas. The solution was brought to reflux when triethylphosphite solution was added over a period of 3 h. The mixture was refluxed for 24 h and allowed to cool overnight. The resulting dark black solution was vacuum distilled to remove the excess triethylphosphite and the solvent. The product was extracted using 50 mL $CHCl_3$. Removing the solvent by rotary evaporation leaving a yellow oily viscous liquid of the product with 84% yield (1.3 g). ^{31}P NMR: 19.42 (methanol-d_4) or 18.48 (acetone-d_6 or $CDCl_3$) ppm. ^1H NMR (acetone-d_6): 7.81–8.23 (m, 15H), 4.11 (p, 12H), 1.29 (t, 18H). EI-MS *m/z*: (M + H) 715.3 (100%), 658.1, 578.4, 529.1, 448.1, 366.2, 241.2, 155.1.

Hydrolysis of the diethyl ester using concentrated HCl afforded the corresponding phosphonic acid as a white powder at 90% yield. IR (KBr pellet, cm^{-1}): 3398 w br, 2920 w, 2146 w br, 1595 m, 1489 m, 1438 w, 1380 w, 1143 m, 1074 m, 1008 s, 932 m, 887 w sh, 812 s, 723 m, 677 w, 558 w, 526 w, 483 w, 431 w. ^{13}C NMR (methanol-d_4): 145.22, 145.17, 143.10, 132.89, 132.67, 128.34, 128.19, 126.83. Solid-state CP MAS ^{31}P NMR: 19.10 ppm.

Synthesis of $Sr_2(H_2L)(CH_3OH)(H_2O)_4$ (1)

Compound **1** can be synthesized as a poorly crystalline solid by a reaction of H_6L with $Sr(OH)_2$, $SrCl_2$, or $SrCO_3$. Efforts to crystallize the compound by redissolving it in dilute hydrochloric acid and slow evaporation were unsuccessful. However, crystallinity can be improved by prolonged hydrothermal dissolution of the powder at elevated temperatures, as followed by PXRD. By careful examination of variation of reactants ratio, a reaction of $Sr(OH)_2$ with H_6L at 1:1 ratio was found to be promising. Crystals of **1** were grown hydrothermally by a reaction of H_6L (200 mg, 0.36 mmol) and $Sr(OH)_2$ (44 mg, 0.36 mmol) in a mixture of distilled water (7 mL) and methanol (3 mL) in a Teflon-lined Parr autoclave with the capacity of 23 mL. A temperature program is used as the following: rising from RT to 140 °C (30 min), isothermal at 140 °C for 2 day, and cooling to room temp during 3 day. Colourless needle crystals were ob-

[3] Supplementary data for this article are available on the journal Web site (canjchem.nrc.ca) or may be purchased from the Depository of Unpublished Data, Document Delivery, CISTI, National Research Council Canada, Ottawa, ON K1A 0R6, Canada. DUD 3831. For more information on obtaining material, refer to cisti-icist.nrc-cnrc.gc.ca/cms/unpub_e.shtml. CCDC 656597 contains the crystallographic data for this manuscript. These data can be obtained, free of charge, via www.ccdc.cam.ac.uk/conts/retrieving.html (Or from the Cambridge Crystallographic Data Centre, 12 Union Road, Cambridge CB2 1EZ, UK; fax +44 1223 336033; or deposit@ccdc.cam.ac.uk).

© 2008 NRC Canada

Table 1. Crystal data and structure refinement for compound **1**.

Empirical formula	Sr_2 $(CH_3OH)(H_2L)(H_2O)_4$
Formula mass	812.62
T (K)	173(2)
λ (Å)	0.710 73
Crystal system, space group	Triclinic, *P*-1
a (Å)	6.9230(4)
b (Å)	15.3370(9)
c (Å)	16.1930(11)
α (°)	62.201(3)
β (°)	85.288(4)
γ (°)	86.665(4)
V (Å^3), Z	1515.39(16), 2
$D_{calcd.}$ (Mg/m^3)	1.781
Absorption coefficient (mm^{-1})	3.745
F(000)	814
Crystal size (mm)	0.60 × 0.08 × 0.04
Theta range for data collection	2.95° to 26.11°
Index ranges	$-8 \le h \le 8$, $-18 \le k \le 18$, $-19 \le l \le 19$
Reflections collected	20 463
Independent reflections	5798 [R(int) = 0.132]
Completeness to θ = 26.11°	96.1%
Refinement method	Full-matrix least-squares on F^2
Data, restraints, parameters	5798, 7, 420
Goodness-of-fit on F^2	1.042
Final R indices [$I > 2\sigma(I)$]	R_1 = 0.058, wR_2 = 0.137
R indices (all data)	R_1 = 0.085, wR_2 = 0.154
Largest diff. peak, hole (e Å^{-3})	1.411, –1.669

tained and kept in mother liquor. Crystals turn opaque after 24 h even sitting in mother liquor and quickly desolvate when removed from solution. IR (KBr pellet, cm^{-1}): 3396 s br, 2339 w sh, 1635 w sh, 1599 m, 1556 w, 1499 w, 1439 w, 1383 w, 1139 m, 1061 m, 970 m, 899 w, 818 m, 694 m, 574 w. Solid-state CP MAS ^{31}P NMR: 12.86 ppm.

X-ray crystallography

A colourless needle crystal of **1** with dimension of 0.6 × 0.08 × 0.04 mm^3 was mounted on the tip of a glass capillary using oil technique. Data were collected on a Nonius Kappa CCD fitted with an Oxford Cryosystem Series 700 Cryostream low-temperature device with graphite monochromated Mo Kα radiation (λ = 0.71 073 Å). The data were integrated using DENZO SMN (19) and processed using DENZOX (19). Absorption effects were empirically corrected by Gaussian quadrature using Sortav (20). Full-matrix least-squares refinement on F^2 was carried out using SHLEXL97 (21). All calculations were carried out using the WinGX software package (22). The results are summarized in Table 1. Selected bond distances and angles are in Table 2.

Results and discussion

Structure of 1

The ligand H_6L was prepared using a slight modification of the Michaelis–Arbuzov reaction (18). Sr^{2+} complexes of L

Table 2. Selected bond lengths and angles for Compound **1**.

Bond lengths (Å)	
Sr(1)—O(23)	2.484(4)
Sr(1)—O(22)	2.515(4)
Sr(1)—O(1W)	2.551(6)
Sr(1)—O(4W)	2.592(5)
Sr(1)—O(33)	2.593(4)
Sr(1)—O(5)	2.693(4)
Sr(1)—O(12)	2.754(4)
Sr(1)—O(32)	2.858(4)
P(1)—O(12)	1.503(4)
P(1)—O(13)	1.521(5)
P(1)—O(11)	1.576(4)
P(1)—C(11)	1.801(6)
P(2)—O(23)#1	1.499(4)
P(2)—O(22)	1.521(4)
P(2)—O(21)	1.558(4)
P(2)—C(21)	1.797(6)
Sr(2)—O(32)	2.452(4)
Sr(2)—O(33)#2	2.478(4)
Sr(2)—O(2W)	2.556(4)
Sr(2)—O(12)#2	2.579(4)
Sr(2)—O(22)#2	2.593(4)
Sr(2)—O(23)	2.661(4)
Sr(2)—O(3W)	2.738(16)
Sr(2)—O(5)	2.740(5)
P(3)—O(32)	1.502(5)
P(3)—O(33)	1.507(4)
P(3)—O(31)	1.550(4)
P(3)—C(31)	1.805(7)
Bond angles (°)	
O(23)–Sr(1)–O(22)	136.64(13)
O(23)–Sr(1)–O(1W)	72.74(16)
O(22)–Sr(1)–O(1W)	69.40(15)
O(23)–Sr(1)–O(4W)	83.58(15)
O(22)–Sr(1)–O(4W)	92.15(15)
O(1W)–Sr(1)–O(4W)	112.84(18)
O(23)–Sr(1)–O(33)	128.79(13)
O(22)–Sr(1)–O(33)	71.10(12)
O(1W)–Sr(1)–O(33)	89.03(17)
O(4W)–Sr(1)–O(33)	146.25(15)
O(23)–Sr(1)–O(5)	70.14(13)
O(22)–Sr(1)–O(5)	153.11(13)
O(1W)–Sr(1)–O(5)	134.37(16)
O(4W)–Sr(1)–O(5)	88.44(15)
O(33)–Sr(1)–O(5)	94.03(13)
O(23)–Sr(1)–O(12)	144.15(14)
O(22)–Sr(1)–O(12)	72.32(13)
O(1W)–Sr(1)–O(12)	141.40(15)
O(4W)–Sr(1)–O(12)	73.05(14)
O(33)–Sr(1)–O(12)	73.97(13)
O(5)–Sr(1)–O(12)	82.19(13)
O(23)–Sr(1)–O(32)	76.11(12)
O(22)–Sr(1)–O(32)	117.57(13)
O(1W)–Sr(1)–O(32)	81.80(16)
O(4W)–Sr(1)–O(32)	150.21(15)
O(33)–Sr(1)–O(32)	53.75(12)
O(5)–Sr(1)–O(12)	64.37(13)
O(12)–Sr(1)–O(32)	112.37(12)

© 2008 NRC Canada

Table 2 (*concluded*).

O(32)–Sr(2)–O(33)#2	129.34(14)
O(32)–Sr(2)–O2W	84.12(16)
O(33)#2–Sr(2)–O(2W)	74.89(16)
O(32)–Sr(2)–O(12)#2	150.03(14)
O(33)#2–Sr(2)–O(12)#2	79.05(14)
O(2W)–Sr(2)–O(12)#2	96.80(15)
O(32)–Sr(2)–O(22)#2	119.96(13)
O(33)#2–Sr(2)–O(22)#2	71.68(12)
O(2W)–Sr(2)–O(22)#2	146.43(15)
O(12)#2–Sr(2)–O(22)#2	74.06(13)
O(32)–Sr(2)–O(23)	80.47(13)
O(33)#2–Sr(2)–O(23)	127.92(12)
O(2W)–Sr(2)–O(23)	157.18(16)
O(12)#2–Sr(2)–O(23)	88.41(13)
O(22)#2–Sr(2)–O(23)	56.29(11)
O(32)–Sr(2)–O(3W)	61.1(3)
O(33)#2–Sr(2)–O(3W)	77.1(3)
O(2W)–Sr(2)–O(3W)	98.9(4)
O(12)#2–Sr(2)–O(3W)	146.8(3)
O(22)#2–Sr(2)–O(3W)	76.7(4)
O(23)–Sr(2)–O(3W)	88.3(4)
O(32)–Sr(2)–O(5)	69.25(14)
O(33)#2–Sr(2)–O(5)	154.27(14)
O(2W)–Sr(2)–O(5)	91.89(15)
O(12)#2–Sr(2)–O(5)	80.78(13)
O(22)#2–Sr(2)–O(5)	117.49(12)
O(23)–Sr(2)–O(5)	66.94(12)
O(3W)–Sr(2)–O(5)	127.5(3)

Note: Symmetry transformations used to generate equivalent atoms, #1: $x + 1, y, z$; #2: $x - 1, y, z$.

can be synthesized as a poor solid by a reaction of H_6L with $Sr(OH)_2$, $SrCl_2$, or $SrCO_3$. Efforts to crystallize the compound by dissolution in dilute hydrochloric acid and slow evaporation were unsuccessful. Crystallinity can be improved by prolonged hydrothermal dissolution of the powder at elevated temperatures; however, loss of water from the structure results in a slight change of lattice parameters, as followed by PXRD and the material loses crystallinity after 24 h. Crystals suitable for single-crystal X-ray diffraction were grown hydrothermally by a reaction of H_6L and $Sr(OH)_2$.

The three-dimensional structure of **1** is built up from the linking of one-dimensional SrO chains by the organophosphonate ligand, L, into a three-dimensional honeycomb-like net (Fig. 1). The inorganic backbone is composed of face-sharing SrO_8 monocapped pentagonal biprisms. The two crystallographically independent Sr centers are each coordinated by five phosphonate oxygen atoms (Sr–O = 2.450(4)–2.854(4) Å), a μ_2 bridging methanol oxygen (Sr–O5 = 2.693(7), 2.742(7) Å), and two water molecules (Sr–O = 2.551(6)–2.736(6) Å). The phosphonate groups of L show two different binding modes, while P1 binds only through one oxygen to two different Sr centers, P2 and P3 each bind through two of their oxygens to three different Sr centers. Thus, each ligand connects to three different SrO chains and vice versa. Such connectivities result in a three-dimensional framework with large one-dimensional channels (19.34(1) × 14.83(1) Å) along the *a* axis visible in Fig. 1. Parts of the channels are lined by the hydrophobic phenyl rings of L, and the rest by the polar phosphonate groups. From any single one-dimensional inorganic column, the three pendant organic groups of L are separated by 6.92(1) Å along the *a* axis, a distance suited to including another aromatic ring. Considering these one-dimensional inorganic columns as infinite SBUs, structure **1** can be described as having a hms rod packing (23). From examination of a single net, the structure appears three-dimensionally porous; however, both the large pores and spacing between L molecules are sufficient to allow two-fold interpenetration of the structure (Fig. 2). This interpenetration results in the efficient pi-stacking of only the central aryl rings of L molecules from different nets (centroid–centroid distance = 3.52(1) Å), which serve to augment the stability of the framework. The two independent nets are offset by 60° so that while the central aryl rings of L are pi-stacked, clefts remain between the three peripheral aryl rings (Fig. 2, inset). The spacing of these rings is well-suited to enclathrate another aromatic ring, and so this was examined along with other sorption features.

Fig. 1. Space-filling representation of the structure of **1** showing the channels present along the *a* axis (19.36 × 14.83 Å) The hexagonal layer is connected by one-dimensional SrO columns.

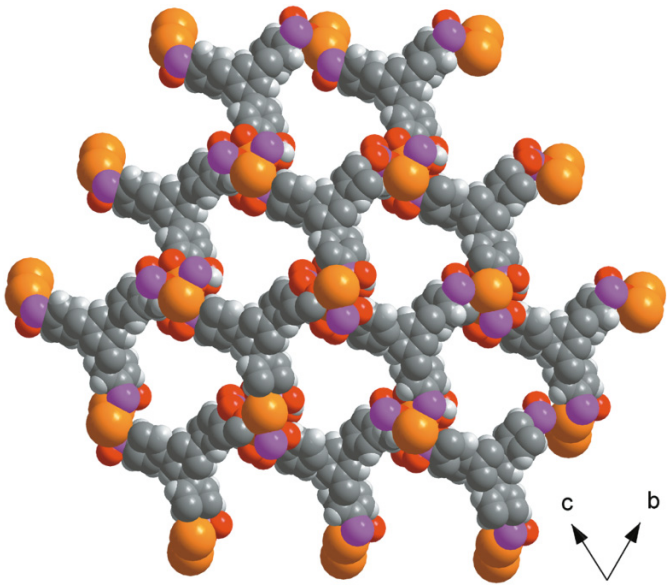

Stability, porosity, and guest inclusion of 1

The stability of **1** was examined using thermogravimetric analysis carried out under N_2 atmosphere. Compound **1** exhibits a two-step mass loss of 13.54% observed in the temperature region of 65–400 °C, corresponding to the loss of four water molecules and the methanol (13.64% calcd.). All experiments to show that **1** sorbed aromatic molecules failed to show any uptake, even with benzene. The gas sorption isotherm of **1** using CO_2 indicated that it is porous, giving a Type 1 isotherm with significant hysteresis evident (Fig. 3). The BET fit gave a surface area of 146 m^2/g. This is a modest value for a surface area, but this is due to the interpenetrated structure. In a separate experiment, the reversible

© 2008 NRC Canada

Fig. 2. Wireframe diagram showing the relation of the two interpenetrated nets (shown in red and blue). The inset is a space-filling diagram of the pi-stacking down the *a* axis of the central arene ring of staggered L molecules that further augments the stability.

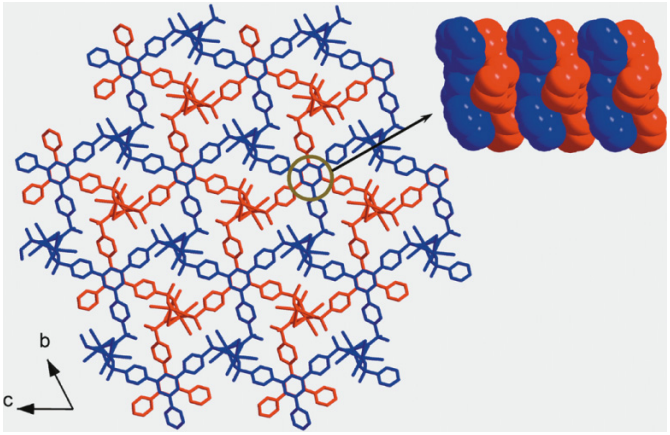

Fig. 3. CO_2 sorption and desorption isotherm for **1** at 273 K.

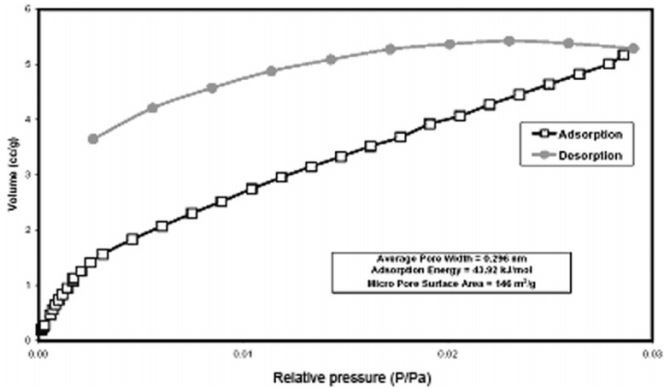

Fig. 4. Reversible uptake of water vapour by **1** upon successive heating and hydration cycles (water vapour introduced as flow gas) as monitored by thermogravimetry: blue, mass; red, temperature; green, DSC.

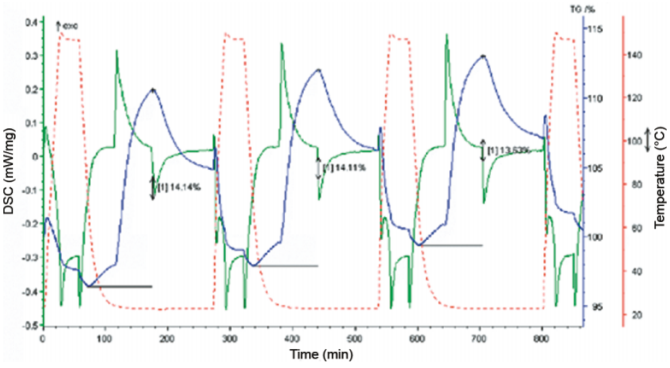

uptake of water vapour by **1** was examined over three heating–cooling cycles from 25 to 150 °C. Compound **1** takes up 14.14%, 14.11%, and 13.63% in the successive cycles (Fig. 4). Carbon dioxide uptake was investigated by heating **1** up to 100 °C in dry N_2 on the TG, to lose solvent

Fig. 5. CO_2 uptake by **1**. The blue trace shows the thermogravimetric analysis of a sample of **1** heated to first desolvate the sample. CO_2 was introduced at 50 min.

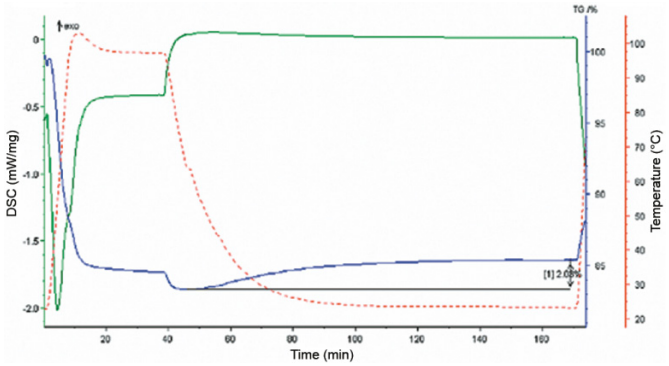

Fig. 6. IR spectrum of **1** before (top) and after (bottom) exposure to CO_2 gas. Peaks at ~2350 cm^{-1} correspond to the asymmetric stretch of CO_2.

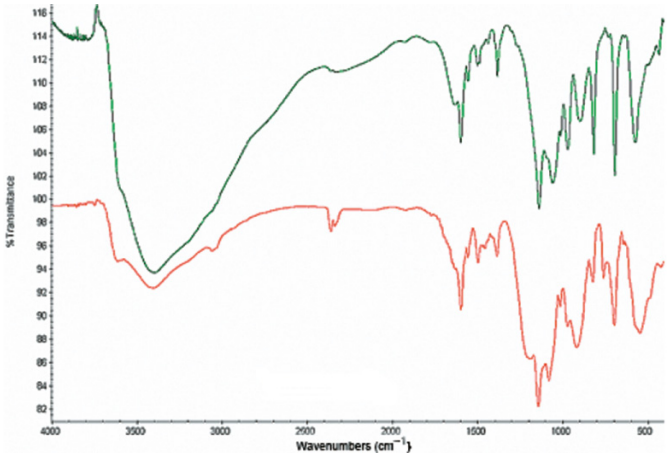

molecules, and then it was allowed to stand at RT under CO_2 for 2 h (Fig. 5). A 2% mass gain, corresponding to 0.4 mol of CO_2/formula unit, was observed. IR spectroscopy (Fig. 6) corroborated the presence of CO_2 in the samples as shown by the growth of peaks at 2350 cm^{-1}. Over three sorption–desorption cycles in the temperature range of 25 to 300 °C, a 2.5%–3% CO_2 uptake was observed. This observation of selective CO_2 uptake by this material is intriguing given the global interest in CO_2 sequestration and the recent work concerning application of MOFs for this target (24).

Design implications

With respect to phosphonate ligands in general, the coordination to metals is not so regular as to offer any zero-dimensional or one-dimensional aggregates (25) that could truly be called SBUs. The ligand L was designed specifically to disfavour a densely packed solid, and the rigid trigonal core directs the formation of a two-fold interpenetrated microporous structure. The framework is stabilized both by the one-dimensional inorganic columns, which could be regarded as infinite SBUs (23), and pi-stacked central aryl groups of L molecules that result from the two-fold interpenetration. The topology of **1** has design implications. The obvious means of increasing porosity would be to add

© 2008 NRC Canada

additional phenyl spacers in L off the core. With the π-stacked L molecules being specifically enabled by two-fold interpenetration, lengthening the pendant arms in L would not lead to a more interpenetrated structure, as with diamondoid networks (26), without compromising the stabilizing π-stacked column. Thus, porosity should be able to be systematically enhanced. Furthermore, an extension of this thinking would be that any planar aromatic polyphosphonate, trigonal or not, would favour the formation of one-dimensional alkaline-earth phosphonate columns likely augmented by π-stacked aromatics. Thus, **1** provides several structural insights on how phosphonate SBUs can be used to form more porous solids.

Conclusions

A new alkaline-earth phosphonate has been presented. The topology is that of hexagonal sheets linked in one-dimension by inorganic columns. Small clefts are present in the structure giving a degree of microporosity as confirmed by gas adsorption. Compound **1** has an affinity for CO_2 (albeit a small capacity) as confirmed by gravimetry and IR experiments. The topology of this network should allow extension of the ligand L to form larger pore solids without increasing the likelihood of higher degrees of interpenetration that would offset any increase to the pore volume.

Acknowledgements

GKHS thanks the Natural Sciences and Engineering Research Council (NSERC) of Canada and DRDC Atlantic of the Department of National Defence for funding.

References

1. H. Li, M. Eddaoudi, M. O'Keeffe, and O.M. Yaghi. Nature (London, UK), **402**, 276 (1999).
2. (*a*) S. Kitagawa, R. Kitaura, and S.I. Noro. Angew. Chem., Int. Ed. **43**, 2334 (2004); (*b*) O.M. Yaghi, M. O'Keeffe, N.W. Ockwig, H.K. Chae, M. Eddaoudi, and J. Kim. Nature (London, UK), **423**, 705. (2003); (*c*) C. Janiak. Dalton Trans. 2781 (2003); (*d*) D. Bradshaw, J.B. Claridge, E.J. Cussen, T.J. Prior, M.J. Rossensky. Acc. Chem. Res. **38**, 273 (2005); (*e*) Y.E. Lee, S.Y. Jang, and M.P. Suh. J. Am. Chem. Soc. **127**, 6374 (2005).
3. (*a*) A.Y. Robin and K.M. Fromm. Coord. Chem. Rev. **250**, 2127 (2006); (*b*) W. Mori and S. Takamizawa. J. Solid State Chem. **152**, 120 (2000); (*c*) C.N.R. Rao, S. Natarajan, and R. Vaidhyanathan. Angew. Chem., Int. Ed. **43**, 1466 (2004); (*d*) B.L. Chen, C. Liang, J. Yang, D.S. Contreras, Y.L. Clancy, E.B. Lobkovsky, O.M. Yaghi, and S. Dai. Angew. Chem., Int. Ed. **45**, 1390 (2006); (*e*) D.N. Dybtsev, H. Chun, S.H. Yoon, D. Kim, and K. Kim, J. Am. Chem. Soc. **126**, 32 (2004).
4. (*a*) C.A. Wheaton and R.J. Puddephatt. Angew. Chem., Int. Ed. **46**, 4461 (2007); (*b*) M.C. Brandys and R.J. Puddephatt. J. Am. Chem. Soc. **124**, 3946 (2002); (*c*) C.Q. Zhao, M.C. Jennings, and R.J. Puddephatt. J. Coord. Chem. **61**, 31 (2008).
5. (*a*) T.J. Burchell and R.J. Puddephatt. Inorg. Chem. **44**, 3718 (2005); (*b*) N.L.S. Yue, M.C. Jennings, and R.J. Puddephatt. Chem. Commun. 4792 (2005); (*c*) T.J. Burchell, D.J. Eisler, and R.J. Puddephatt. Inorg. Chem. **34**, 5550 (2004); (*d*) T.J. Burchell, D.J. Eisler, M.C. Jennings, and R.J. Puddephatt. Chem. Commun. 2228 (2003).
6. (*a*) B.D. Chandler, G.D. Enright, S. Pawsey, J.A. Ripmeester, D.T. Cramb, and G.K.H. Shimizu. Nat. Mater. **7**, 229 (2008); (*b*) D.J. Hoffart, S.A. Dalrymple, and G.K.H. Shimizu. Inorg. Chem. **44**, 8868 (2005); (*c*) B.D. Chandler, A.P. Côté, D.T. Cramb, J.M. Hill, and G.K.H. Shimizu. Chem. Commun. 1900 (2002); (*d*) S.K. Mäkinen, N.J. Melcer, M. Parvez, and G.K.H. Shimizu. Chem. Eur. J. **7**, 5176 (2001); (*e*) S.A. Dalrymple and G.K.H. Shimizu. Chem. Eur. J. **8**, 3010 (2002); (*f*) A.P. Côté and G.K.H. Shimizu. Chem. Eur. J. **9**, 5361 (2003).
7. (*a*) S.A. Dalrymple and G.K.H. Shimizu. J. Am. Chem. Soc. **129**, 12114 (2007); (*b*) S.A. Dalrymple and G.K.H. Shimizu. Chem. Commun. 2224 (2002); (*c*) S.A. Dalrymple and G.K.H. Shimizu. Supramol. Chem. **15**, 591 (2003).
8. (*a*) L.J. May and G.K.H. Shimizu. Chem. Mater. **17**, 217 (2005); (*b*) A.P. Côté, M.J. Ferguson, K.A. Khan, G.D. Enright, A.D. Kulynych, S.A. Dalrymple, and G.K.H. Shimizu. Inorg. Chem. **41**, 287 (2002).
9. G.K.H. Shimizu. J. Solid State Chem. **178**, 2519 (2005).
10. (*a*) K. Maeda. Micropor. Mesopor. Mater. **73**, 47 (2002); (*b*) M.A. Occelli and H. Robson. Expanded clays and other microporous solids. Academic Press, New York. 1992; (*c*) A. Clearfield. Prog. Inorg. Chem. **47**, 371 (1998); (*d*) G.B. Hix, A. Turner, B.M. Kariuki, M.Tremayne, and E. Maclean. J. Mater. Chem. **12**, 3220 (2002).
11. (*a*) M.A. Petruska, B.H. Watson, M.W. Meisel, D.R. Talham. Chem. Mater. **14**, 2011 (2002); (*b*) S.S. Bao, G.S. Chen, W. Yin, Y.Z. Li, L.M. Zheng, and Q.H. Luo. Inorg. Chem. **45**, 1124 (2006); (*c*) X. Tang, N. Yao, and M.E. Thompson. Supramol. Sci. **4**, 35 (1997).
12. (*a*) G. Alberti, F. Marmottini, S. Murcia-Mascarós, and R. Vivani. Angew. Chem., Int. Ed. **33**, 1594 (1994); (*b*) N.J. Clayden. J. Chem. Soc. Dalton Trans. 1877 (1987).
13. (*a*) K.J. Frink, R. Wang, J.L. Colón, and A. Clearfield. Inorg. Chem. **30**, 1438 (1991); (*b*) G. Cao and T.E. Mallouk. Inorg. Chem. **30**, 1434 (1991).
14. For an exception, see: J. Liang and G.K.H. Shimizu. Inorg. Chem. **30**, 1434 (2007).
15. M.V. Vasylyev, E.J. Wachtel, R. Popovitz-Biro, and R. Neumann. Chem. Eur. J. **12**, 3507 (2006).
16. (*a*) O.R. Evans, H.L. Ngo, and W.B. Lin. J. Am. Chem. Soc. **123**, 10395 (2001); (*b*) H.L. Ngo and W.B. Lin. J. Am. Chem. Soc. **124**, 14298 (2002).
17. (*a*) J.M. Taylor, A.H. Mahmoudkhani, and G.K.H. Shimizu. Angew. Chem., Int. Ed. **46**, 795 (2007); (*b*) D. Kon, J. Zoñ, J. McBee, and A. Clearfield. Inorg. Chem. **46**, 977 (2006).
18. M.M. Gómez-Alcántara, A. Cabeza, M. Martínez-Lara, M.A.G. Aranda, R. Suau, N. Bhuvanesh, and A. Clearfield. Inorg. Chem. **43**, 5283 (2004).
19. Z. Otwinowski and W. Minor. Processing of X-ray diffraction data collection in oscillation mode. *In* Methods in enzymology. Vol. 276. Macromolecular crystallography, Part A. *Edited by* C.W. Carter Jr and R.W. Sweet. Academic Press. New York. 1997. pp. 307–326.
20. R.H. Blessing. J. Appl. Crystalogr. **30**, 421 (1997).
21. G.M. Sheldrick. SHELXL97 [computer program]. Release 97–2. University of Göttingen, Germany. 1997.
22. L.J. Farrugia. J. Appl. Crystallogr. **32**, 837 (1999).
23. N.L. Rosi, J. Kim, M. Eddaoudi, B.L. Chen, M. O'Keeffe, and O.M. Yaghi. J. Am. Chem. Soc. **127**, 1504 (2005).
24. B. Wang, A. P. Côté, H. Furukawa, M. O'Keeffe, and O.M. Yaghi. Nature (London, UK), **453**, 207 (2008).
25. (*a*) M.I. Khan and J. Zubieta. Prog. Inorg. Chem. **43**, 1 (1995); (*b*) V. Chandrasekhar, P. Sasikumar, R. Boomishankar, and G. Anantharaman. Inorg. Chem. **45**, 3344 (2006); (*c*) Y. Yang, J.

© 2008 NRC Canada

Pinkas, M. Noltemeyer, H.-G. Schmidt, and H.W. Roesky. Angew. Chem., Int. Ed. **38**, 664 (1999); (*d*) W.F. Ruettinger, D.M. Ho, and G.C. Dismukes. Inorg. Chem. **38**, 1036 (1999); (*e*) E. Dumas, C. Sassoye, K.D. Smith, and S.C. Sevov. Inorg. Chem. **41**, 4029 (2002); (*f*) C. Lei, J.-G. Mao, Y.-Q. Sun, H.-Y. Zeng, and A. Clearfield. Inorg. Chem. **42**, 6157 (2003); (*g*) V. Chandrasekhar and S. Kingsley. Angew. Chem., Int. Ed. **39**, 2320 (2000).

26. (*a*) M.J. Zaworotko. Chem. Soc. Rev. **23**, 283 (1994); (*b*) K.M.E. Jones, A.H. Mahmoudkhani, B.D. Chandler, and G.K.H. Shimizu. CrystEngComm, **8**, 303 (2006).

© 2008 NRC Canada

Synthesis and photophysical properties of naphthyl-, phenanthryl-, and pyrenyl-appended bis(pyridyl)triazine ligands and their Zn(II) and Ru(II) complexes[1]

Francesco Nastasi, Frédérique Loiseau, Sebastiano Campagna, Elaine A. Medlycott, Marie-Pierre Santoni, and Garry S. Hanan

Abstract: A family made of four bis(pyridyl)triazine ligands with appended aryl rings, including three fused aromatic rings, have been synthesized, and their corresponding homoleptic Ru(II) and Zn(II) complexes have been prepared and characterized by several means. The free ligands 2,4-di(2-pyridyl)-6-phenyl-1,3,5-triazine (**L1**); 2,4-di(2-pyridyl)-6-(1-naphthyl)-1,3,5-triazine (**L2**); 2,4-di(2-pyridyl)-6-(9-phenanthryl)-1,3,5-triazine (**L3**); and 2,4-di(2-pyridyl)-6-(1-pyrenyl)-1,3,5-triazine (**L4**) were formed in triazine ring-forming reactions from the reactions of the cyano-functionalized aromatic rings with $LiNMe_2$ followed by the addition of 2 equiv. of 2-cyanopyridine. The metal complexes examined in this study are the homoleptic Ru(II) complexes $Ru(\mathbf{L1})_2^{2+}$ (**2a**), $Ru(\mathbf{L2})_2^{2+}$ (**2b**), $Ru(\mathbf{L3})_2^{2+}$ (**2c**), and $Ru(\mathbf{L4})_2^{2+}$ (**2d**) and Zn(II) complexes $Zn(\mathbf{L1})_2^{2+}$ (**3a**), $Zn(\mathbf{L2})_2^{2+}$ (**3b**), $Zn(\mathbf{L3})_2^{2+}$ (**3c**), and $Zn(\mathbf{L4})_2^{2+}$ (**3d**). Also, crystallographic data for the free ligands and Zn(II) and Ru(II) complexes have been obtained in some cases. The redox behaviour and absorption spectra of all the species have been investigated, together with the luminescence properties of the free ligands at room temperature in fluid solution and of the Ru(II) complexes both at room temperature in fluid solution and at 77 K in rigid matrix. The redox data indicate that the free ligands are reduced twice at relatively mild potentials (< –2.30 V vs. SCE), with the first reduction almost independent of the nature of the substituted aryl group. The UV absorption spectra of all the compounds are dominated by intense spin-allowed π–π* transitions mainly centered on the bis(pyridyl)triazine moiety; however, in **L2**–**L4**, moderately intense intraligand charge-transfer (ILCT) bands are also present. Such bands are red-shifted in the Zn(II) compounds, while they are obscured in the Ru(II) species by the more intense spin-allowed metal-to-ligand charge-transfer (MLCT) bands. The free ligands exhibit interesting emission properties, ranging from fluorescence from π–π* states to excimeric (in **L4**) and ILCT (in **L2** and **L3**) emission. In the Ru(II) complexes, strong emission is found at 77 K from triplet MLCT states. For **2c** and **2d**, the emissive MLCT states are mixed with low-lying triplet ligand-centered states.

Key words: triazine ligands, ruthenium complexes, zinc complexes, ILCT emission.

Résumé : On a effectué la synthèse d'une famille formée de quatre ligands bis(pyridyl)triazine portant des noyaux aromatiques, y compris trois noyaux aromatiques dont on a préparé et caractérisé les complexes homoleptiques correspondants du Ru(II) et du Zn(II). Les ligands libres 2,4-di(2-pyridyl)-6-phényl-1,3,5-triazine (**L1**), 2,4-di(2-pyridyl)-6-(1-naphtyl)-1,3,5-triazine (**L2**), 2,4-di(2-pyridyl)-6-(9-phénanthryl)-1,3,5-triazine (**L3**) et 2,4-di(2-pyridyl)-6-(1-pyrényl)-1,3,5-triazine (**L4**) ont été obtenus par des réactions conduisant à des triazines et impliquant l'action du $LiNMe_2$ sur des cyano portés par noyaux aromatiques fonctionnalisés, suivie par l'addition de deux équivalents de 2-cyanopyridine. Les complexes métalliques examinés dans cette étude sont les complexes homoleptiques du Ru(II), $Ru(\mathbf{L1})_2^{2+}$ (**2a**), $Ru(\mathbf{L2})_2^{2+}$ (**2b**), $Ru(\mathbf{L3})_2^{2+}$ (**2c**) et $Ru(\mathbf{L4})_2^{2+}$ (**2d**) et du Zn(II), $Zn(\mathbf{L1})_2^{2+}$ (**3a**), $Zn(\mathbf{L2})_2^{2+}$ (**3b**), $Zn(\mathbf{L3})_2^{2+}$ (**3c**) et $Zn(\mathbf{L4})_2^{2+}$ (**3d**). Dans certains cas, on a aussi obtenu des données cristallographiques pour les ligands libres et des complexes du Zn(II) et du Ru(II). On a étudié le comportement redox et les spectres d'absorption de toutes les

Received 3 April 2008. Accepted 10 June 2008. Published on the NRC Research Press Web site at canjchem.nrc.ca on 11 October 2008.

This paper is dedicated to Professor Richard Puddephatt for his great contributions in Organometallic Chemistry.

F. Nastasi and S. Campagna. Dipartimento di Chimica Inorganica, Chimica Analitica e Chimica Fisica, Università di Messina, 98166 Messina, Italy.
F. Loiseau. Département de Chimie Moléculaire, UMR CNRS 5250, ICMG– FR 2607, Université Joseph Fourier, BP-53, 38041 Grenoble CEDEX 9, France
E.A. Medlycott, M.-P. Santoni, and G.S. Hanan.[2] Department of Chemistry, Université de Montréal, Montréal, QC H3T 1J4, Canada.

[1]This article is part of a Special Issue dedicated to Professor R. Puddephatt.
[2]Corresponding author (e-mail: garry.hanan@umontreal.ca).

 doi:10.1139/V08-134 © 2008 NRC Canada

espèces, de même que les propriétés de luminescence des ligands libres, à la température ambiante et en solution fluide ainsi que celles des complexes du Ru(II) tant à la température ambiante, en solution fluide, que celles à 77 K, dans une matrice solide. Les données redox indiquent que les ligands libres sont réduits deux fois à des potentiels relativement faibles (< –2,30 V vs SCE) et que la première réduction est pratiquement indépendante de la nature du substituant aryle. La région UV des spectres d'absorption de tous les composés est dominée par d'intenses transitions π–π* permises par les spins et centrés principalement sur la portion bis(pyridyl)triazine; toutefois, dans les ligands **L2**–**L4**, on observe aussi la présence de bandes de transfert de charge intraligand (TCIL) d'intensité moyenne. Ces bandes sont déplacées vers le rouge dans les composés du Zn(II) alors que dans les espèces Ru(II) elles sont obscurcies par les bandes de transfert de charge métal à ligand (TCML) permises par les spins et de grande intensité. Les ligands libres possèdent des propriétés d'émission intéressantes allant de la fluorescence des états π–π* aux émissions excimères (dans **L4**) et aux bandes de transfert de charge intraligand (dans **L2** et **L3**). Dans les complexes du Ru(II), à 77 K, on observe une émission intense de transfert de charge métal à ligand à partir des états triplets. Pour les composés **2c** et **2d**, les états d'émission TCML sont mixtes avec des états triplets de basse énergie centrés sur le ligand.

Mots-clés : ligands de triazine, complexes du ruthénium, complexes du zinc, émission de transfert de charge intraligand (TCIL).

[Traduit par la Rédaction]

Introduction

Complexes of polypyridine ligands have been the subject of intense research because of their promising photophysical properties and potential applications in areas of light-harvesting devices, luminescent sensors, and photocatalysis. In particular, complexes of d^6 transition-metal ions show promise in these fields because of their relatively long excited-state lifetimes and emission through low-lying MLCT (metal-to-ligand charge-transfer) states (1–5). Over the last two decades, there has been considerable efforts to optimize the photophysical properties of Ru(II) complexes based on 2,2′:6′,2″-terpyridine (tpy) (2, 6). Indeed, the tridentate motif offers synthetic advantages over bidentate ligands based on 2,2′-bipyridine (bpy), as the latter creates stereocentres in metal complexes with octahedral geometry. Consequently, in larger polynuclear systems, the separation of diastereomers can be problematic despite synthetic advances in the purification of isomers (7, 8). Unfortunately, Ru(II) tpy-type complexes have poor photophysical properties, as the steric strain imposed in N–N–N coordination in tridentate ligand lowers the energy of non-emissive, metal-centred (MC) states, which can be thermally accessed at room temperature. Synthetic strategies have been developed to overcome the deactivation of MLCT excited states, primarily focusing on manipulating the energy of ^{3}MLCT states relative to ^{3}MC states. Alternatively, ligand systems have been developed with low energy emissive intraligand charge-transfer (ILCT) states (9). The excited-state energy of the ILCT state in Ru(II) complexes, or complexes of other transition-metal ions, must be significantly lower in energy than the MLCT/MC states to influence the excited-state lifetime (10–14). Alternatively, d^{10} Zn(II) metal ions can be employed to study the ILCT emission, as these polypyridine complexes of such metal ions do not exhibit MLCT or MC states at low energies, and their eventual emission can involve ILCT states (13–16). An ILCT transition requires a coordinating motif to acts as an electron acceptor and an appended organic group to act as an electron donor. Tpy is typically an electron acceptor, and a variety of organic groups act as the electron donor. Fused aromatic rings have previously been employed as the organic, electron donating motif, as they offer interesting properties in the excited state through excimer and exciplex formation as well as offering a means of aggregating cations in the solid state through π–π interactions (12, 14, 15, 17–19). Herein, we report the synthesis and characterization of a family of triazine ligands with fused aromatic rings appended. The absorption spectra and redox properties of free ligands and of their Zn(II) and Ru(II) complexes are also discussed, together with the luminescence properties of free ligands and Ru(II) complexes.

Results and discussion

Synthesis

The ligands were synthesized by using a slightly modified version of a previously reported procedure (see Supplementary data for full ligand structures) (20, 21).[3] $LiNMe_2$ was generated in situ through the slow addition of *n*-BuLi to $HNMe_2$ in anhyd. diethylether. On addition of the cyano-precursors, an amidinate intermediate formed, which was converted to the appropriate triazine ligand by the addition of 2 equiv. of 2-cyanopyridine. The reaction proceeded slower than previously reported syntheses for non-symmetric triazine ligands and with slightly lower yields. The presence of the adjacent fused aromatic ring may lead to a stabilized amidinate intermediate by intramolecular H-bonding with the $C{=}N^-$ motif, which interferes with the cyclization reaction (Scheme 1).

Complexes **2** were synthesized by addition of $RuCl_3{\cdot}3H_2O$ to 2 equiv. of the ligand, with 3 equiv. of $AgNO_3$ in EtOH. The complexes were purified by column chromatography followed by anion exchange to afford complexes **2b**–**2d** in 56%, 23%, and 11% yields, respectively. The Zn(II) complexes were synthesized by the addition of $Zn(ClO_4)_2{\cdot}6H_2O$ to a solution of the appropriate ligand in acetonitrile at reflux for 15 min. Precipitation of the product by the addition

[3] Supplementary data for this article are available on the journal Web site (canjchem.nrc.ca) or may be purchased from the Depository of Unpublished Data, Document Delivery, CISTI, National Research Council Canada, Ottawa, ON K1A 0R6, Canada. DUD 3836. For more information on obtaining material, refer to cisti-icist.nrc-cnrc.gc.ca/cms/unpub_e.shtml.

© 2008 NRC Canada

Scheme 1. Synthesis of ligands **L1**–**L4** and the complexation of the ligands to form the Ru(II) complexes **2a**–**2d** and Zn(II) complexes **3a**–**3d**.

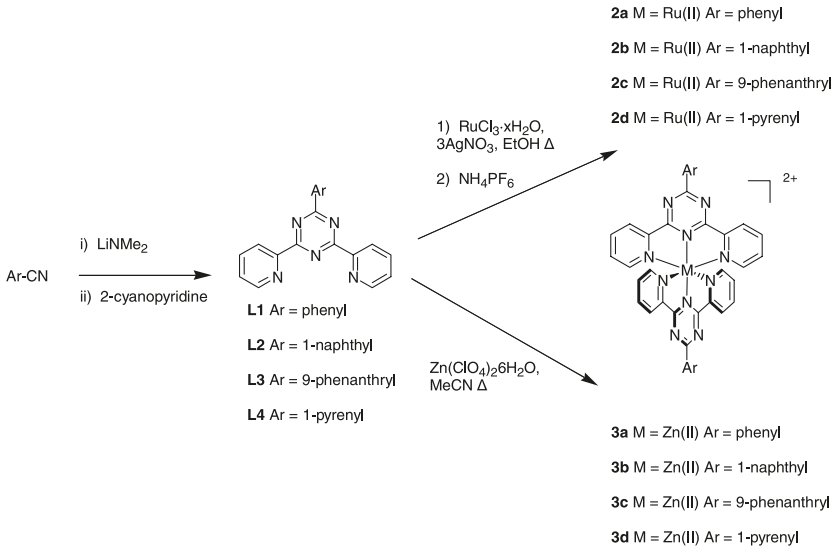

of diethyl ether afforded the complexes **3a**–**3d** in 68%, 55%, 74%, and 84% yields, respectively. The complexes were characterized in solution by ^{1}H NMR and in the solid state by elemental analyses.

On complexation to the Ru(II) or Zn(II) metal ions, the pyridyl and pyrenyl signals of ligands are both shifted to lower field owing to the electron-withdrawing effect of the metal ions (Fig. 1). The Zn(II) ion in complex **3d** has a greater electron-withdrawing effect on the pyridyl protons closest to the metal centre ($H_{5,5''}$ and $H_{6,6''}$) when compared with the Ru(II) complex **2d**. Complex **3d** has limited solubility and reaches saturation point in solution very rapidly as compared with **2d** presumably owing to aggregation caused by the pyrenyl group.

Fig. 1. ^{1}H NMR spectra of **L4** in $CDCl_3$ (above), **2d** (middle), and **3d** (below) in CD_3CN. $H_{3,3''}$, $H_{4,4''}$, $H_{5,5''}$, and $H_{6,6''}$ refer to the pyridyl protons.

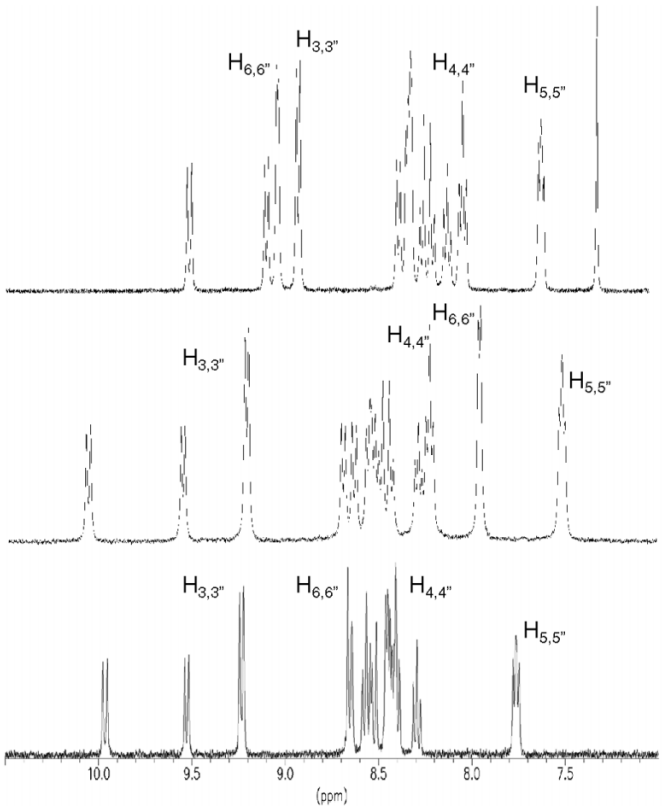

Solid-state structures

Crystals suitable for analyses of **L2** were obtained by slow diffusion of hexane into a concentrated solution of **L2** in chloroform. One molecule of water is found in the asymmetric unit with H-bonding to *N*-pyridyl atoms with N–H distances of 2.15 and 2.14 Å. Significant face-to-face π-stacking interactions are observed in the extended lattice with each triazine ring overlaying pyridyl rings above and below the plane with centroid-to-centroid distances of 3.6–3.8 Å (Fig. 2).

Attempts to crystallize **2b** and **3b** as the PF_6 and ClO_4 salts, respectively, were unsuccessful. Red crystals of **2b** were obtained by addition of excess NH_4BF_4 in methanol to a concentrated solution of **2b** in acetonitrile followed by slow diffusion of isopropyl ether. The complex crystallized in the monoclinic space group *P*2(1)/*n* with two cations, four anions, (three PF_6^- anions and one BF_4^- anion) and four molecules of acetonitrile. The Zn(II) complexes could be synthesized as the PF_6^- salts according to a literature procedure (22), and crystals of **3b** were obtained as the PF_6^- salt by slow diffusion of isopropyl ether into an acetonitrile solution of the complex. Complex **3b** crystallized in the non-centrosymmetric space group *P*2(1) with two cations, four PF_6 counter-ions and three acetonitrile solvent molecules. In both crystal structures, significant π-stacking interactions were observed in the extended lattice between naphthyl groups and coordinating pyridyl rings with centroid-centroid distances of 3.66 and 3.71 Å for complex **2b** and 3.89 and 3.96 Å in complex **3b** (Fig. 3). The use of non-covalent interactions to aggregate functional assemblies through crystal engineering is appealing as conventional, covalent ap-

© 2008 NRC Canada

Fig. 2. ORTEP representation of solid-state structure **L2** with H_2O solvent molecule (left) and pyridyl-triazine π-stacking interaction (right). Thermal ellipsoids are set at 30%.

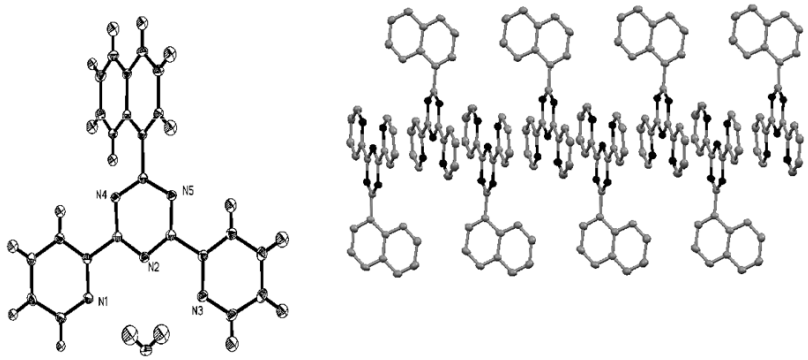

Fig. 3. ORTEP representations of π-stacking interactions in the solid-state structures of **2b** and **3b**. Thermal ellipsoids are set at 30%. Anions and solvent molecules of crystallization were omitted for clarity.

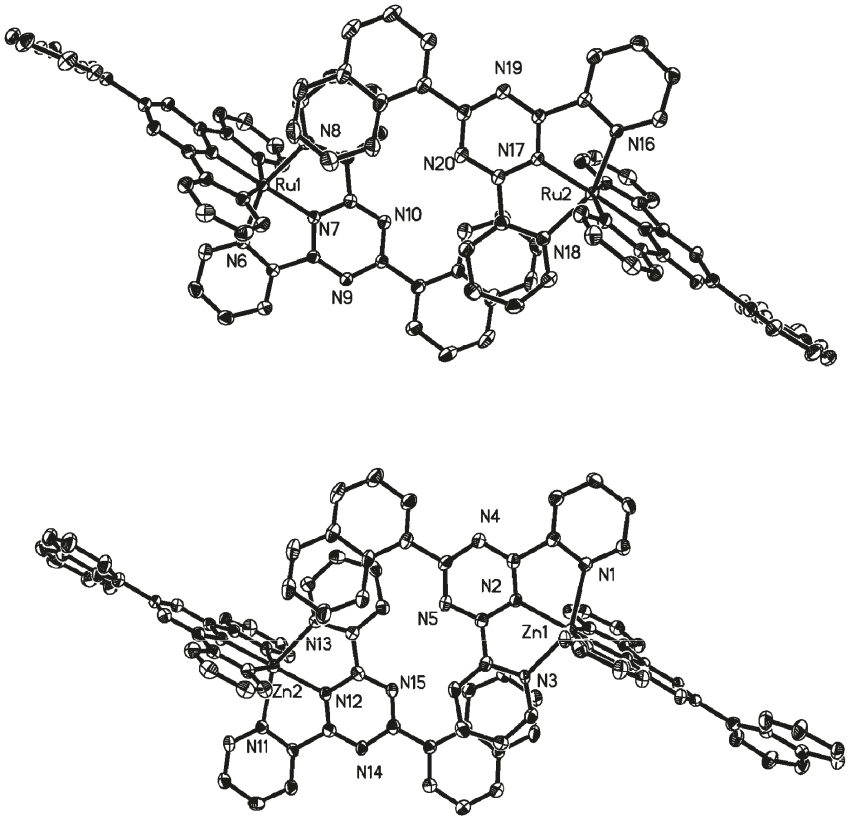

proaches require multistep syntheses (4, 17, 19, 22). Naphthyl-pyridyl, π-stacking interactions were previously observed in naphthyl-appended tpy-based Ru(II) and Fe(II) complexes (19). We previously reported similar interactions in the solid-state structure of complex **2c** in which phenanthryl groups π-stack with pyridyl groups (20). The naphthyl groups twist away from the central triazine rings by 16.6°–36.9° in complex **2b** and 21.5°–29.1° in complex **3b** for the four ligands of the two cations. Intramolecular C–H–N(triazine) H-bonding interactions are still favouring minimal twisting of the naphthyl group relative to the triazine ring and thereby favouring significant mixing of molecular orbitals.

The M–N bond distances in both **2b** and **3b** are shorter to the central triazine ring compared with the terminal pyridyl rings as expected owing to the constrained bite angle imposed by tridentate ligands. The Ru–N bond distances, 1.97–1.98 Å to the central triazine ring and 2.09–2.11 Å to the terminal pyridyl rings, are in agreement to those previously reported for related Ru(II) complexes of triazine-based ligands (20, 21). The Zn–N bond distances are slightly longer and similar to those reported for tpy-type ligands (22).

Electrochemical properties

The redox data for the ligands and their complexes are gathered in Table 1. The redox data of ligands **L1**, **L2**, and **L4** are reported in DMF owing to their poor solubility in acetonitrile. In all of the ligands, an initial reversible

© 2008 NRC Canada

Table 1. Half-wave potentials for ligands **L** and complexes **2** and **3**. Data are in acetonitrile at 200 mV s^{-1} vs. SCE, unless otherwise stated.

Compound	$E_{1/2}$(oxidation)		$E_{1/2}$(reduction)			
L1[a]			–1.42(84)	–2.25(irr)		
L2[a]			–1.41(82)	–2.17(irr)		
L3[b]			–1.42(86)	–2.15(irr)		
L4[a]	1.54 (irr)		–1.40(75)	–1.84(96)	–2.17(irr)	
2a[c]	1.51(81)		–0.71(65)	–0.88(69)	–1.51(74)	–1.75(78)
2b	1.52(84)		–0.73(63)	–0.89(68)	–1.52(67)	–1.75(80)
2c[b]	1.52(85)		–0.72(74)	–0.89(77)	–1.52(79)	–1.75(90)
2d	1.46(irr)	1.66(irr)	–0.75(68)	–0.89(69)	–1.51(88)	–1.74(irr)
3a			–0.79(80)	–0.91(84)	–1.60(86)	–1.77(78)
3b			–0.80(67)	–0.91(77)	–1.59(78)	–1.75(74)
3c[b]			–0.81(irr)	–0.86(104)	–1.52(103)	–1.73(108)
3d	1.45 (irr)		–0.76(68)	–0.87(76)	–1.52(irr)	

[a]In DMF.
[b]From ref. 20.
[c]From ref. 21.

triazine-based reduction is observed at –1.40 to –1.42 V vs. SCE. The negligible potential difference among all four ligands indicates that the aryl substituent on the triazine has little influence on this process. A second triazine-based reduction is observed at –2.15 to –2.17 V in **L2**–**L4**. This same reduction shifts to a more negative potential in **L1** (–2.25 V), indicating the LUMO +1 molecular orbital involves non-negligible mixing of the aromatic and triazine motifs. An additional pyrenyl-based reduction is observed in **L4** at –1.84 V. No oxidative processes are observed in **L1**–**L3** within the solvent potential limits. However, the pyrene motif is oxidized at +1.54 V in **L4**, which is more positive than the tpy-pyrene ligand (+1.49 V) owing to the stabilizing effect of the electron-deficient triazine ring (12). However, overall a lower energy HOMO–LUMO gap is estimated by electrochemistry: 2.94 V for **L4** as compared to 3.15 V for tpy-pyrene (12).

The oxidative potentials for the Ru(II)/(III) couple in complexes **2a**–**2c** are in agreement with those previously reported for Ru(II) complexes of triazine ligands (20, 21). However, in complex **2d**, the pyrene motif is oxidized prior to the Ru(II) centre at +1.46 V, and the Ru(II)/(III) couple is consequently at a more positive potential and irreversible. In the Zn(II) complex **3d**, the pyrene motif is oxidized at +1.45 V. The electron-withdrawing effect of metal coordination results in significant positive shifts in the potentials for the triazine-based reductions for both Ru(II) complexes **2a**–**2d** and Zn(II) complexes **3a**–**3d**. Each triazine ligand has two reductions giving a total of four reductions for complexes **2a**–**2d** and **3a**–**3c**.

Absorption spectra

The absorption spectral data for the ligands and their complexes are gathered in Table 2. Figure 4 shows the absorption spectra of some representative compounds. At wavelengths shorter than 350 nm, ligand-based spin-allowed π–π* transitions dominate the spectra. However, less intense bands are also present at longer wavelengths even for the free ligands, particularly for **L2**–**L4**. These bands are assigned to aryl-to-bis(pyridyl)triazine charge-transfer transitions (intraligand charge transfer, ILCT). Compound **L1** does not exhibit a similar low energy absorption band, since the phenyl group is a worse electron-donor group compared with the other fused aromatic rings. On metal complexation, such ILCT bands are expected to shift to lower energy, since the bipyridyltriazine orbitals are stabilized by metal coordination. This is clearly evidenced in the Zn(II) complexes, which exhibit ILCT absorption bands that extend to the visible, in particular for complexes **3b**–**3d** (see Fig. 4, bottom). The ILCT transitions are red-shifted in comparison to Zn(II) tpy complexes with fused aromatic rings (17), as a consequence of the better acceptor properties of the bis(pyridyl)triazine group compared with the terpy. In Ru(II) complexes **2a**–**2d**, the ILCT bands are largely obscured by the spin-allowed metal-to-ligand charge-transfer (MLCT) transitions, which are responsible for the relatively strong absorption bands in the 450–560 nm region (Table 2, Fig. 4, middle). However, the absorption in the 450–560 nm region increases on passing from **2a** (not shown in Fig. 4, middle) and **2b** to **2c**, and even further on going to **2d**, which exhibits a maximum at lower energy than the other complexes. This cannot be attributed only to contribution of the ILCT

Table 2. Absorption data in acetonitrile.

	λ_{max} (nm) (ε, ((mol/L)$^{-1}$ cm^{-1} × 10^{-3}))
L1[a]	243 (25.0); 276 (40.8)
L2	217 (55.8); 243 (27.9); 277 (21.9); 325 sh (9.6)
L3	250 (56.8), 270(35.1), 325 sh (11.4)
L4	240 (27.7); 285 (17.2); 370 (9.6); 400 (7.2)
2a[b]	242 (24.4); 284 (73.2); 481 (24.6)
2b	211 (88.4); 274 (50.8); 487 (20.6)
2c	250 (91.9); 271 (83.7); 345 (24.3); 490(30.3)
2d	236 (79.9); 272 (76.5); 380 (20.0); 532(43.8)
3a	249 (25.1); 293 (57.2)
3b	211 (121.8); 254 (49.1); 277 (47.7); 293 sh (38.2);388 (18.7)
3c	253 (77.9); 276 sh, 390 (14.9)
3d	238 (89.7); 257 (52.6); 268 (54.9); 281 (44.6); 297 (46.0); 394 (14.4): 460 (27.9)

[a]From ref. 20.
[b]From ref. 21.

© 2008 NRC Canada

Fig. 4. Top: absorption spectra of **L2**, **L3**, and **L4**. Middle: absorption spectra of **2b**, **2c**, and **2d**. Bottom: absorption spectra of **3a** and **3b**. All the spectra are in acetonitrile.

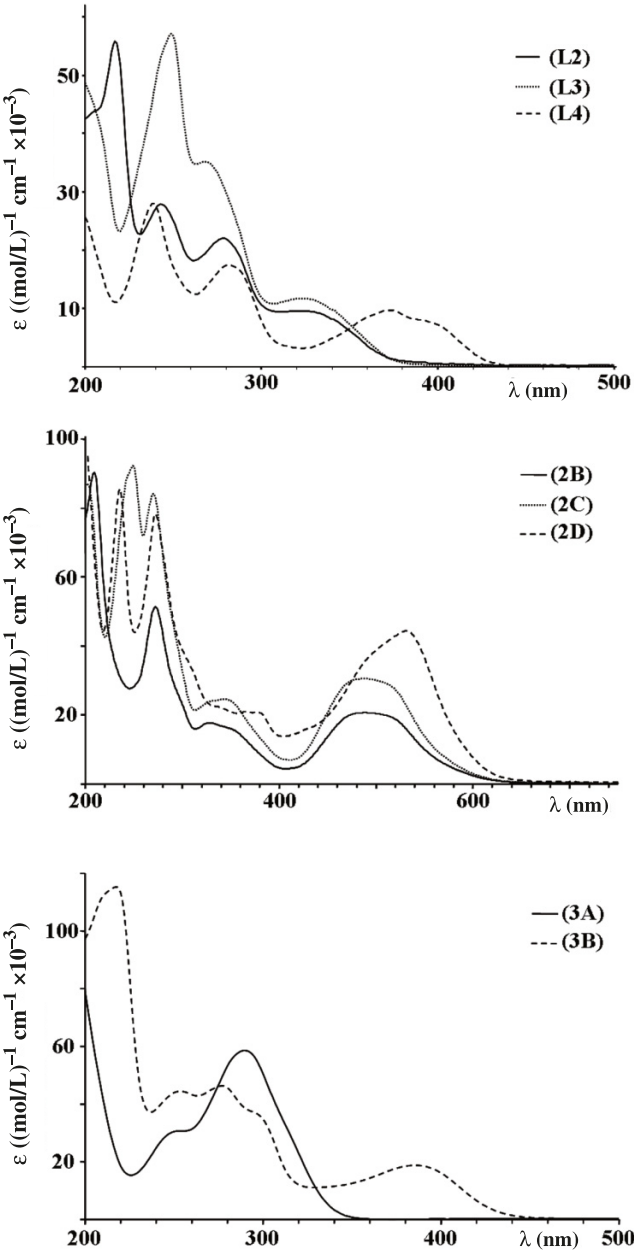

bands in the visible, since the lowest energy bands in **3d**, assigned to the ILCT transition, maximizes at 460 nm, with negligible contribution at wavelengths longer than 500 nm. Most likely, it is the intensity of the spin-allowed MLCT bands, which increases in the series.

The absorption spectra of all the compounds are stable for at least three days and do not exhibit any significant dependence on the concentration, within the range investigated ($8 \times 10^{-6} - 5 \times 10^{-5}$ mol/L).

Luminescence properties

The luminescence properties of the free ligands were studied in air-equilibrated acetonitrile solutions at room temperature. The luminescence data of the ligands are collected in Table 3, and the emission spectra of **L2**, **L3**, and **L4** are shown in Fig. 5.

Table 3. Luminescence properties of the free ligands.

	λ_{max} (nm)	τ (ns)
L1	414	1.7
L2	450	2.6
L3	376 sh	20 (67%), 2.3(33%)
	470	2.0
L4	384, 406	22 (85%), 1.7 (15%)
	471	2.2

Note: In acetonitrile at 298 K. The percentage of the decay in the biexponential analysis is reported in parentheses. The excitation wavelength is 308 nm.

Fig. 5. Emission spectra of **L2**, **L3**, and **L4** in acetonitrile.

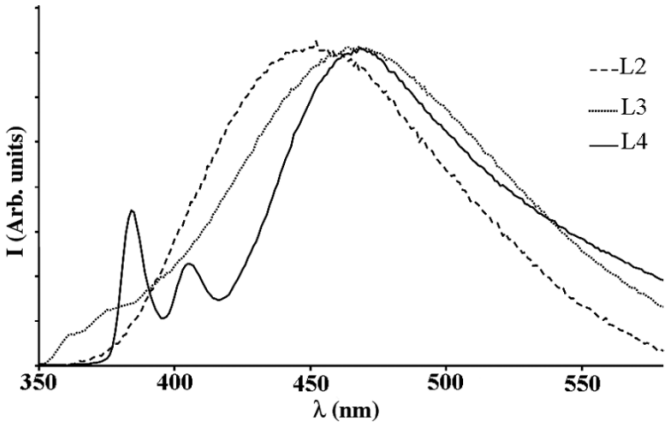

L1 is weakly emissive, with an unstructured emission with a maximum at 414 nm in acetonitrile with an excited-state lifetime of 1.7 ns. The emission is assigned to fluorescence from the π–π* singlet state, with only a partial phenyl-to-bis(pyridyl)triazine charge-transfer character.

L2 exhibits a broad band with maximum at 450 nm and a lifetime of 2.6 ns. The emission is too low-lying to be π–π* fluorescence from the naphthalene subunit (23, 24), and also too much red-shifted from that of **L1** to be π–π* fluorescence mainly involving the bis(pyridyl)triazine. In fact, naphthalene derivatives often exhibit a low-energy emission of excimeric nature. However, naphthalene excimer emission is normally in the range of 400–425 nm (23, 24). On the basis of such comments, we assign the emission of **L2** to a (naphthalene-to-bis(pyridyl)triazine) intraligand charge-transfer (ILCT) excited state. Such a state should be very sensitive to the presence of protons, since the acceptor subunit is protonable; indeed, addition of triflic acid leads to disappearance of the 450 nm emission band. As testified by the change in the absorption spectrum of **L2** upon triflic acid addition (see Supplementary data, Fig. S1: the ILCT absorption band is significantly red shifted), protonation of the acceptor subunit leads to a stabilization of the ILCT level, which apparently becomes non emissive.[3]

As far as **L3** is concerned, an emission band is present with maximum at 470 nm and 2.0 ns lifetime. However, on the blue-edge of the emission band, another emission feature appears, structured (see Fig. 5). When the emission decay is

© 2008 NRC Canada

Fig. 6. Change of the emission spectrum of **L3** upon protonation. Concentration of **L3** is 7.1×10^{-6} mol/L, and concentration of H^+ is 1.95×10^{-3} mol/L (molar ratio of **L3**:$H^+$is 1:3), (λ_{exc} = 303 nm, the isosbestic point).

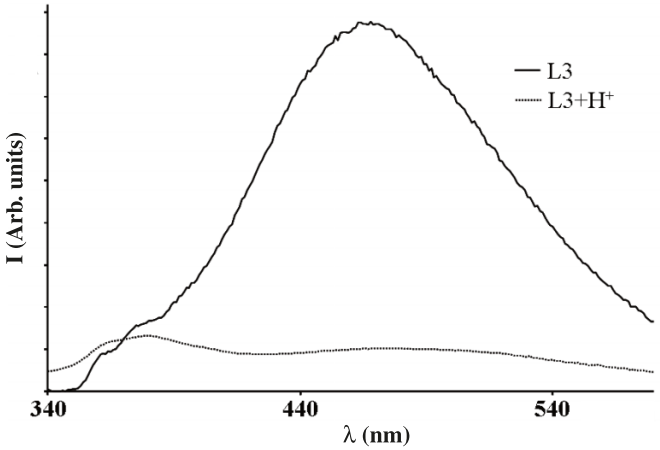

Fig. 7. Change of the emission spectrum of **L4** upon protonation. Concentration of **L4** is 4.9×10^{-6} mol/L, and concentration of H^+ is 1.95×10^{-3} mol/L (molar ratio of **L4**:$H^+$is 1:3), (λ_{exc} = 340 nm).

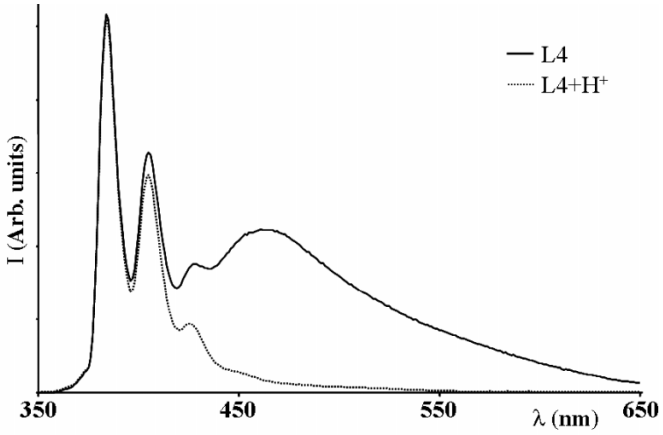

analyzed at 380 nm, a biexponential decay is found (see Table 3), with a long-lived component (20 ns) following a short-lived component (2.3 ns). The short-lived component is assigned to the contribution of the emission with a maximum at 470 nm, and indeed its lifetime agrees with the monoexponential decay recorded at 470 nm (Table 3), whereas the longer-lived component is assigned to the structured emission taking place in the range of 350–400 nm. This latter emission is attributed to fluorescence from the phenanthryl-based π–π* singlet, and the dominant, lower-energy emission is attributed to the ILCT excited state. To support such an assignment, phenanthrene fluorescence in polar solvents is reported to occur at 347 nm with a lifetime of 60.7 ns (24, 25), values in good agreement with those obtained for our substituted phenanthrene species. As for **L2**, protonation stabilizes the ILCT level of **L3**, leading to red shift of the low-energy absorption band and disappearence of the ILCT emission (Figs. S2 and 6).[3]

L4 clearly exhibits a double emission: a structured band, with a maximum at 380 nm, and a broad emission with maximum at about 470 nm (Table 3, Fig. 5). The higher energy emission is assigned to the π–π* singlet state of the pyrenyl subunit, which is reported to occur at about 375 nm in polar solvents (24, 26), and the lowest-energy emission is assigned to the excimer. Indeed, pyrene excimeric emission is reported to occur at the same energy (23). Moreover, the eventual ILCT emission should occur at significantly lower energy than 470 nm, as the ILCT level in **L4** is stabilized compared with the same level in **L3** (see absorption spectra) (27). A supporting experiment for the assignment of the low-energy emission of **L4** to an excimeric state is also the concentration dependence of the emission spectrum; indeed on increasing concentration (e.g., from 5×10^{-6} mol/L to 2×10^{-5} mol/L), the low-energy emission band significantly increases with respect to the high-energy emission feature. As for what found for **L3**, the analysis of the emission decay at 480 nm yields a monoexponential behaviour, while analysis of the decay at 380 nm gives a biexponential behaviour, with the shorter-lived component corresponding (within the experimental uncertainties) to the 480 nm emission lifetime (Table 3).

As for **L2** and **L3**, addition of triflic acid leads to disappearance of the lower-energy band, while the higher-energy π–π* (monomeric) emission remains unaffected (Fig. 7; for the changes on absorption spectrum upon acid addition, see Supplementary data).[3] Whereas the emission changes upon acid addition of **L4** are experimentally equivalent to those of **L3**, their interpretation is slightly different, as the origin of the 470 nm broad emission is different in the two compounds. In principle, proton addition is not expected to have a direct effect on excimer formation; in this case, it could change the association constant for excimer formation, since the pyrene "substituent" (i.e., the bis(pyridyl)triazine subunit) is protonable, and the excimer would become positively charged. However, if this would happen, the monomer emission would increase, and this is not found experimentally; therefore, protonation seems to not affect monomer/excimer ratio. This strongly suggests that the consequence of the protonation is that the ILCT state, potentially a quencher for both monomer and excimer emission, is displaced to lower energy, thereby increasing the driving force for the quenching process(es). This is supported by the effect of protonation on the absorption spectrum of **L4** (see Supplementary data).[3] It is suggested that quenching of the excimer emission of **L4** upon acid addition can be attributed to deactivation of the excimer to the proton-stabilized ILCT state (non emissive), which in the protonated species is significantly lower-lying than the excimeric state, where it was almost isoenergetic in the non-protonated species, so that the change in driving force is significant (it would pass from a very small value to a significant value). Most likely, the monomer emission is already partially quenched in **L4** by the ILCT state and increasing the driving force for this quenching process as a consequence of protonation has only negligible effects on monomer emission. However, this explanation should be considered as tentative, since we cannot perform quantitative calculations based on the effective driving force values, which are unknown.

Unfortunately, the study of the luminescence properties of the Zn(II) complexes **3a**–**3d** gave non reproducible results,

© 2008 NRC Canada

Table 4. Luminescence of the Ru(II) complexes.

	λ_{max} (nm)[a]	τ (μs)
2a[b]	672	1.4
2b	665	1.5
2c	665	24
2d	690	25

Note: In EtOH/MeOH 4:1 (*v*/*v*) at 77 K. The excitation wavelength is 408 nm.
[a]Higher-energy feature.
[b]From ref. 21.

most likely since the compounds were poorly stable at the concentrations used for the luminescence experiments (lower than 8×10^{-6} mol/L), a somewhat not unexpected behaviour for Zn(II) polypyridine complexes (15). Luminescence properties of the Zn(II) compounds **3a**–**3d** are therefore not investigated here.

Ru(II) polypyridine complexes based on tridentate ligands are very weakly emitting at room temperature (Table 4) because of the presence of a low-lying metal-centered (MC) state, which deactivates the potentially luminescent MLCT state (2, 3, 5, 28). This is evidently even more true for Ru(II) complexes of bis(pyridyl)triazine ligands, as this ligand has probably a weaker ligand field strength than tpy, like the absence of room-temperature emission of other homoleptic Ru(II) complexes based on substituted bis(pyridyl)triazine ligands seems to suggest (21). As a matter of fact, **2b**, **2c**, and **2d** are not luminescent at all at room temperature, and **2a** (21) is only weakly luminescent (λ = 710 nm, τ = 8 ns, $\Phi = 9 \times 10^{-5}$). All of the four Ru(II) complexes are emissive at 77 K from their lowest energy MLCT triplet (Table 4, Fig. 8), demonstrating that the MC state is no longer populated in this condition. The emission is partially structured, as expected for a MLCT emission at low temperature (29, 30), and the vibrational progression is typical of C=C and C=N stretching. However, the 77 K emission properties of **2a**–**2d** show interesting differences, the larger one being the longer lifetimes (one order of magnitude longer, see Table 4) exhibited by **2c** and **2d** compared with **2a** and **2b**. The reason for such longer lifetimes can have two origins: (*i*) delocalization of the MLCT state towards the larger phenanthryl and pyrenyl moieties, which can be coplanar with the triazine ring, so that the geometry of the excited state becomes closer to the geometry of the ground state, decreasing Franck–Condon factor for radiationless decay; (*ii*) mixing of the MLCT state with a closely-lying, longer-lived ligand-centered (^{3}LC) state. This ^{3}LC state could be the triplet of the ILCT state, which is expected to be lower in energy for the phenanthryl- and pyrenyl-containing ligands. In fact, hypothesis (*i*) would suggest that the first reduction potentials of **2c** and **2d** are less negative than those of the other two ruthenium(II) complexes, but this is not the case (see Table 1). Moreover, delocatization of the MLCT state over the aryl moieties should red shift the emission spectrum of **2c** compared with **2a** and **2b**, and this is not experimentally found. For these reasons, hypothesis (*ii*) appears to be preferred. At this point, it should be recalled that the presence of closely-lying states have already been reported to be able to influence the dynamics of the luminescent level, even at 77 K and without affecting the energy of the emitting level (31).

Fig. 8. Luminescence properties of **2b**, **2c**, and **2d** in EtOH/MeOH 4:1 (*v*/*v*) at 77 K.

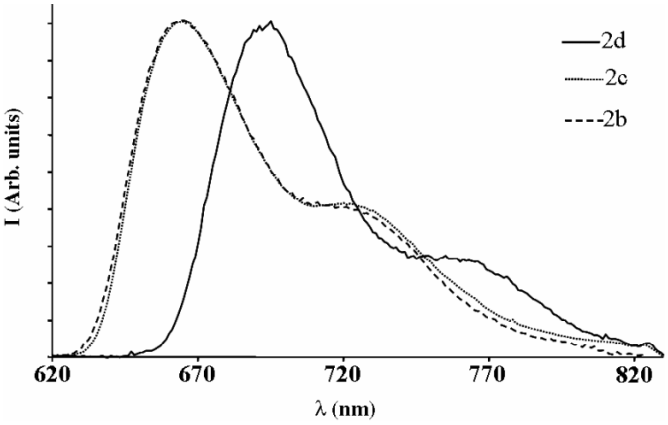

Conclusion

Introducing fused aromatic rings to the triazine-based tridentate ligands offers a means to significantly stabilize the ILCT band compared with their analogous systems based on tpy. As a consequence, room-temperature emission studies of **L2**–**L4** indicate that some of their emissive excited states have significant charge-transfer character. In the case of **L4**, an excimer emission is also found. On complexation, the ILCT states are red-shifted in the Zn(II) complex, as clearly evidenced by the absorption spectra. Unfortunately, luminescence of the Zn(II) complexes cannot be investigated, since the compounds are poorly stable at the low concentrations needed for luminescence experiments. In Ru(II) complexes, the potentially emissive MLCT excited states are quenched at room temperature by the presence of low-lying metal-centered states, whereas MLCT emission takes place at 77 K in rigid matrix with (for **2c** and **2d**) some contribution from closely lying LC (most likely, ILCT) triplet states.

Experimental section

General methods and equipment

NMR spectra were recorded in CD_3CN at RT on a Bruker AV400 spectrometer at 400 MHz for ^{1}H NMR and at 100 MHz for ^{13}C NMR. Chemical shifts are reported in ppm relative to residual solvent protons (1.93 ppm for acetonitrile-d_3) and the carbon resonance of the solvent. Absorption spectra were measured on a Cary 500i UV–vis NIR spectrophotometer. Luminescence spectra were obtained with a Horiba Jobin–Yvon Fluoromax P spectrofluorimeter equipped with a Hamamatsu R3896 photomultiplier and were corrected for photomultiplier response using a program purchased with the fluorimeter. Emission lifetimes were measured with an Edinburgh OB-900 single-photon counting spectrometer equipped with a Hamamatsu PLP-2 laser diode (pulse width at 408 nm, 59 ps) and with a PicoQuant PDL 800-D pulsed laser diode (pulse width at 308 nm, 50 ps). The emission decay traces (emission lifetimes measured at about the emission maximum wavelengths) were analyzed

© 2008 NRC Canada

by Marquadt algorithm. For each measurement, at least five determinations were carried out.

Electrochemical measurements were carried out in argon-purged acetonitrile at RT with a BAS CV50W multipurpose equipment interfaced to a PC. The working electrode was a Pt electrode. The counter electrode was a Pt wire, and the pseudo-reference electrode was a silver wire. The reference was set using an internal 1 mmol/L ferrocene/ferrocinium sample at 395 mV vs. SCE in acetonitrile and 432 mV in DMF. The concentration of the compounds was about 1 mmol/L. Tetrabutylammonium hexafluorophosphate was used as supporting electrolyte, and its concentration was 0.10 mol/L. Cyclic voltammograms were obtained at scan rates of 50, 100, 200, and 500 mV/s. For irreversible oxidation processes, the cathodic peak was used as *E*, and the anodic peak was used for irreversible reduction processes. The criteria for reversibility were the separation of approximately 60 mV between cathodic and anodic peaks, the close to unity ratio of the intensities of the cathodic and anodic currents, and the constancy of the peak potential on changing scan rate. The number of exchanged electrons was measured with OSWV and by taking advantage of the presence of ferrocene used as the internal reference.

Experimental uncertainties are as follows: absorption maxima, ±2 nm; molar absorption coefficient, 10%; emission maxima, ±5 nm; excited-state lifetimes, 10%; and redox potentials, ±10 mV.

Synthesis

Compounds **L1**, **L3**, **2a**, **2c**, and **3c** were synthesized as previously described (20, 21).

General procedure for L2 and L4

n-BuLi (1.6 mol/L in hexanes, 1.1 equiv.) was added dropwise to a stirred solution of $HNMe_2$ (2 mol/L in THF, 1.1 equiv.) in anhyd. Et_2O under an inert atmosphere. The mixture was stirred for 20 min until a white suspension formed and the cyano-arene (1 equiv.) was added to the mixture. The mixture was stirred for 4 h further followed by addition of 2-cyanopyridine (2 equiv.). The reaction mixture was stirred overnight and worked up by stirring for 30 min in air followed by removal of Et_2O under reduced pressure. The residue was recrystallized three times from water:ethanol and the solid collected, washed with diethyl ether to yield **L2** as a white solid in 35% yield and **L4** as a yellow solid in 26% yield.

L2

As per the general procedure using *n*-BuLi (1.6 mol/L in hexanes, 5.1 mL, 8.1 mmol), $HNMe_2$ (2 mol/L in THF, 4.1 mL, 8.1 mmol), 9-cyanophenathrene (1.50 g, 7.39 mmol), and 2-cyanopyridine (1.44 mL, 15.0 mmol) in 150 mL anhyd. ether. ^{1}H NMR (400 MHz, $CDCl_3$): 9.07 (d, 1H, J = 8.6 Hz) H_{nap}; 8.99 (dd, 2H, J = 4.3, 0.5 Hz) $H_{6,6''}$; 8.86 (d, 2H, J = 8.0 Hz) $H_{3,3''}$; 8.58 (d, 1H, J = 7.3 Hz) H_{nap}; 8.09 (d, 1H, J = 8.2 Hz) H_{nap}; 7.99 (m, 3H) $H_{4,4''}$, H_{nap}; 7.67 (2H, m) $2H_{nap}$; 7.60 (3H, m) $H_{5,5''}$, H_{nap}. ^{13}C NMR (400 MHz, $CDCl_3$): 124.59, 124.80, 125.31, 125.83,126.21, 127.20, 128.42, 130.83, 130.87, 132.35, 132.87, 133.76, 136.92, 150.03, 152.84, 170.95, 175.00. Anal. calcd. $C_{23}H_{15}N_5 \cdot H_2O$: C 72.8, H 4.5, N 18.5; found: C 72.6, H 4.6, N 18.5.

L4

As per the general procedure using *n*-BuLi (1.6 mol/L in hexanes, 5.1 mL, 8.1 mmol), $HNMe_2$ (2 mol/L in THF, 4.1 mL, 8.1 mmol), 1-cyanopyrene (1.68 g, 7.42 mmol), and 2-cyanopyridine (1.44 mL, 15.0 mmol) in 150 mL anhyd. ether. ^{1}H NMR ($CDCl_3$, 400 MHz): 9.51 (d, J = 10 Hz, 1H) H_{py}; 9.12 (d, J = 8 Hz, 1H), H_{py}; 9.06 (d, J = 4 Hz, 2H) $H_{6,6''}$; 8.94 (d, J = 8 Hz, 2H) $H_{3,3''}$; 8.39–8.07 (m, 7H) $7H_{py}$; 8.05 (td, J = 2 Hz, 8 Hz, 2H) $H_{4,4''}$; 7.61 (dd, J = 5 Hz, 6 Hz, 2H) $H_{5,5''}$. ^{13}C NMR (100 MHz, $CDCl_3$): 124.19, 124.49, 124.65, 124.84, 125.56, 125.82, 125.89, 126.09, 127.07, 128.90, 129.07, 129.33, 129.73, 130.27, 130.30, 130.84, 133.63, 136.82, 150.22, 153.13, 171.15, 175.46, 176.75. Anal. calcd. $C_{29}H_{18}N_5 \cdot 0.5H_2O$: C 78.4, H 4.1, N 15.8; found: C 78.7, H 3.3, N 15.5.

Ruthenium triazine complexes 2b and 2d

$RuCl_3 \cdot 3H_2O$ (0.032 g, 0.12 mmol) was added to a stirred solution of the appropriate ligand (0.24 mmol) in EtOH (15 mL). The mixture was stirred at RT for 15 min and then heated to reflux for 1 h. The reaction mixture was cooled and satd. KPF_6 (aq., 5 mL) was added. The solution was diluted with a 100 mL of water and the red solid collected and injected onto a silica column and eluted with acetone/water/KNO_3(satd.) 9:0.9:0.1. The nitrate salt was metathesized to the PF_6 salt by the addition of NH_4PF_6 and the solvent removed under reduced pressure. The product was collected by dissolving the solid in acetonitrile and precipitated by addition to water and recrystallized from acetonitrile/ether to afford **2b** and **2d** as red solids.

2b

Red solid, 56%. ^{1}H NMR (400 MHz, CD_3CN): 9.68 (d, J = 9 Hz, 2H) H_{nap}; 9.11 (d, J = 7 Hz, 4H) $H_{3,3''}$; 9.09 (m, 2H) H_{nap}; 8.40 (d, J = 8 Hz, 2H) H_{nap}; 8.23 (d, J = 8 Hz, 2H) H_{nap}; 8.17 (td, J = 8 Hz, 1 Hz, 4H) $H_{4,4''}$; 7.90–7.98 (m, 4H) H_{nap}; 7.88 (d, J = 6 Hz, 4H) $H_{6,6''}$; 7.81 (t, J = 8 Hz, 2H) H_{nap}; 7.46 (td, J = 6, 2Hz, 4H) $H_{5,5''}$. HR-MS: M^{2+} ($-2PF_6$) = 462.0845. Anal. calcd. $C_{46}H_{30}N_{10}RuP_2F_{12} \cdot 4H_2O$: C 46.6, H 3.2, N 11.8; found: C 46.4, H 2.7, N 11.7.

2d

Red solid, 11%. ^{1}H NMR (400 MHz, CD_3CN): 10.03 (d, J = 10 Hz, 2H) H_{pyrene}; 9.52 (d, J = 8.3 Hz, 2H) H_{pyrene}; 9.18 (d, J = 8 Hz, 4H) $H_{3,3''}$; 8.66 (d, J = 8 Hz, 2H) H_{pyrene}; 8.60 (d, J = 9.3 Hz, 2H) H_{pyrene}; 8.38–8.53 (m, 8H) $4H_{pyrene}$; 8.25 (t, J = 7 Hz, 2H) H_{pyrene}; 8.19 (t, J = 8 Hz, 4H) $H_{4,4''}$;7.92 (d, J = 5 Hz, 4H) $H_{6,6''}$; 7.47 (dd, J = 6 Hz, 6Hz, 4H) $H_{5,5''}$. Anal. calcd. $C_{58}H_{38}N_{10}RuP_2F_{12} \cdot 2H_2O$: C 53.7, H 2.9, N 10.8; found: C 53.7, H 2.4, N 10.2.

Zinc triazine complexes 3a, 3b, and 3d

$Zn(ClO_4)_2 \cdot 6H_2O$ (0.05 mmol, 0.018 g) was added to a stirred solution of the appropriate ligand (0.1 mmol) in MeCN (15 mL). The mixture was refluxed for 15 min, cooled, and the solvent removed under reduced pressure. The solid was recrystallized from ethanol, followed by pre-

© 2008 NRC Canada

cipitation in acetonitrile/diethyl ether to yield complexes **3a**–**3d**.

3a

White solid, 68%. ^{1}H NMR (400 MHz, CD_3CN): 9.14 (d, J = 8Hz, 2H) $H_{2'',6''}$; 9.05 (d, J = 7 Hz, 2H) $H_{3,3''}$; 8.31 (t, J = 8 Hz, 2H) $H_{4,4''}$; 8.24 (d, J = 4 Hz, 2H) $H_{6,6''}$; 7.93 (t, J = 7 Hz, 1H) $H_{4''}$; 7.80 (t, J = 7 Hz, 2H) $H_{3'',5''}$; 7.64 (dd, J = 6 Hz, 7 Hz, 2H) $H_{5,5''}$. Anal. calcd. $C_{38}H_{26}Cl_2N_{10}O_8Zn$: C 51.5, H 3.0, N 15.8; found: C 51.7, H 3.2, N 16.1.

3b

Yellow solid, 55%. ^{1}H NMR (400 MHz, CD_3CN): 9.50 (d, J = 9 Hz, 1H) H_{nap}; 9.09 (d, J = 8 Hz, 2H) $H_{3,3''}$; 9.05 (d, J = 7 Hz, 1H) H_{nap}; 8.43 (d, J = 8 Hz, 1H) H_{nap}; 8.30–8.34 (m, 4H) $H_{4,4''}$, $H_{6'6''}$; 8.20 (d, J = 8 Hz, 1H) H_{nap}; 7.90–7.93 (m, 2H) $2H_{nap}$; 7.78 (t, J = 7 Hz, 1H) H_{nap}; 7.69 (dd, J = 5 Hz, 6 Hz, 2H) $H_{5,5''}$. Anal. calcd. $C_{46}H_{30}C_{12}N_{10}O_8Zn{\cdot}H_2O$: C 55.0, H 3.2, N 13.9; found: C 55.1, H 3.6, N 14.1.

3d

Orange solid, 84%. ^{1}H NMR (400 MHz, CD_3CN): 9.93 (d, J = 9 Hz, 1H) H_{pyrene}; 9.49 (d, J = 9 Hz, 1H) H_{pyrene}; 9.19 (d, J = 8 Hz, 2H) $H_{3,3''}$; 8.60–8.63 (m, 2H) $2H_{pyrene}$; 8.47–8.54 (m, 3H) $3H_{pyrene}$; 8.35–8.41 (m, 5H) H_{pyrene}, $H_{4,4''}$, $H_{6,6''}$; 7.72 (dd, J = 6 Hz, 6Hz, 2H) $H_{5,5''}$. Anal. calcd. $C_{58}H_{34}Cl_2N_{10}O_8Zn{\cdot}H_2O$: C 60.4, H 3.2, N 12.2; found: C 60.5, H 3.4, N 12.3.

Acknowledgements

The authors (GSH, EM, MPS) would like to thank the Natural Sciences and Engineering Research Council of Canada (NSERC) and the Université de Montréal for financial support. EAM thanks the ICCS for funding. SC thanks the University of Messina and MIUR (PRIN project) for funding. FL thanks the CNRS for an "ATIP Jeunes Chercheurs" funding. Johnson Matthey PLC is thanked for a loan of $RuCl_3$. The authors would also like to thank F. Bélanger-Gariépy for assistance with X-ray analyses.

References

1. X.-Y. Wang, A. Del Guerzo, and R.H. Schmehl. J. Photochem. Photobiol. C, **5**, 55 (2004).
2. J.P. Sauvage, J.P. Collin, J.C. Chambron, S. Guillerez, C. Coudret, V. Balzani, F. Barigelletti, L. De Cola, and L. Flamigni. Chem. Rev. **94**, 993 (1994).
3. E. Baranoff, J.-P. Collin, L. Flamigni, and J.-P. Sauvage. Chem. Soc. Rev. **33**, 147 (2004).
4. (*a*) J.H. Alstrum-Acevedo, M.K. Brennaman, T.J. Meyer. Inorg. Chem. **44**, 6802 (2005); (*b*) M. Grätzel. Inorg. Chem. **44**, 6841 (2005).
5. (*a*) V. Balzani, A. Juris, M. Venturi, S. Campagna, and S. Serroni. Chem. Rev. **96**, 759 (1996); (*b*) S. Campagna, F. Puntoriero, F. Nastasi, G. Bergamini, and V. Balzani. Top. Curr. Chem. **280**, 117 (2007).
6. (*a*) E.A. Medlycott and G.S. Hanan. Coord. Chem. Rev. **250**, 1763 (2006); (*b*) E.A. Medlycott and G.S. Hanan. Chem. Soc. Rev. **34**, 133 (2005).
7. T.J. Rutherford, D.A. Reitsma, and F.R. Keene. J. Chem. Soc. Dalton Trans. 3659 (1994).
8. F.M. MacDonnell and S. Bodige. Inorg. Chem. **35**, 5758 (1996).
9. A.I. Baba, J.R. Shaw, J.A. Simon, R.P. Thummel, and R.H. Schmehl. Coord. Chem. Rev. **171**, 43 (1998).
10. A.C. Benniston, A. Harriman, D.J. Lawrie, and A. Mayeux. Phys. Chem. Chem. Phys. **6**, 51 (2004).
11. S. Baitalik, X.-Y. Wang, and R.H. Schmehl. J. Am. Chem. Soc. **126**, 16304 (2004).
12. W. Leslie, R.A. Poole, P.R. Murray, L.J. Yellowlees, A. Beeby, and J.A.G. Williams. Polyhedron, **23**, 2769 (2004).
13. J.F. Michalec, S.A. Bejune, and D.R. McMillin. Inorg. Chem. **39**, 2708 (2000).
14. J.F. Michalec, S.A. Bejune, D.G. Cuttell, G.C. Summerton, J.A. Gertenbach, J.S. Field, R.J. Haines, and D.R. McMillin. Inorg. Chem. **40**, 2193 (2001).
15. G. Albano, V. Balzani, E.C. Constable, M. Maestri, and D.R. Smith. Inorg. Chim. Acta, **277**, 225 (1998).
16. X.-Y. Wang, A. Del Guerzo, and R.H. Schmehl. Chem. Commun. 2344 (2002).
17. H. Krass, E.A. Plummer, J.M. Haider, P.R. Barker, N.W. Alcock, Z. Pikramenou, M.J. Hannon, and D.G. Kurth. Angew. Chem., Int. Ed. **40**, 3862 (2001).
18. K.K. Patel, E.A. Plummer, M. Darwish, A. Rodger, and M.J. Hannon. J. Inorg. Biochem. **91**, 220 (2002).
19. H.-S. Chow, E.C. Constable, C.E. Housecroft, M. Neuburger, and S. Schaffner. Dalton Trans. 2881 (2006).
20. E.A. Medlycott and G.S. Hanan. Inorg. Chem. Commun. **10**, 229 (2007).
21. (*a*) E.A. Medlycott, G.S. Hanan, F. Loiseau, and S. Campagna. Chem. Eur. J. **13**, 2837 (2007); (*b*) M.I.J. Polson, E.A. Medlycott, G.S. Hanan, L. Mikelsons, N.J. Taylor, M. Watanabe, Y. Tanaka, F. Loiseau, R. Passalacqua, and S. Campagna. Chem. Eur. J. **10**, 3640 (2004); (*c*) M.I.J. Polson, N.J. Taylor, and G.S. Hanan. Chem. Commun. 1356 (2002).
22. N.W. Alcock, P.R. Barker, J.M. Haider, M.J. Hannon, C.L. Painting, Z. Pikramenou, E.A. Plummer, K. Rissanen, and P. Saarenketo. Dalton–Trans. 1447 (2000).
23. M. Klissinger and J. Michl. Excited states and photochemistry of organic molecules. VCH. New York. 1995.
24. Handbook of photochemistry. 3rd ed. *Edited by* M. Montalti, A. Credi, L. Prodi, and M.T. Gandolfi. CRC. Boca Raton, FL. 2006.
25. G.P. Bluemer and M. Zander. Z. Naturforsch. **34A**, 909 (1979).
26. M. Zander. Z. Naturforsch. **33A**, 998 (1978).
27. However, we cannot exclude that an ILCT emission also takes place in **L4**, obscured by the more intense excimeric emission.
28. T.J. Meyer. Pure Appl. Chem. **58**, 1193 (1986) and refs. cited therein.
29. G.A. Crosby. Acc. Chem. Res. **8**, 231 (1975).
30. (*a*) A. Juris, V. Balzani, F. Barigelletti, S. Campagna, P. Belser, and A. von Zelewsky. Coord. Chem. Rev. **84**, 85 (1988); (*b*) Y. Chen and T.J. Meyer. Chem. Rev. **98**, 1439 (1998).
31. G. Guglielmo, V. Ricevuto, A. Giannetto, and S. Campagna. Gazz. Chim. Ital. **119**, 457 (1989).

© 2008 NRC Canada

Mechanistic investigations of bipyrimidine-promoted palladium-catalyzed allylic acetoxylation of olefins[1]

Bo-Lin Lin, Jay A. Labinger, and John E. Bercaw

Abstract: Several pyridine-like ligands were found to improve $Pd(OAc)_2$-catalyzed allylic oxidation of allylbenzene to cinnamyl acetate by *p*-benzoquinone in acetic acid. The best ligand examined, bipyrimidine, was used to identify the catalyst precursor for this system, (bipyrimidine)$Pd(OAc)_2$, which was fully characterized. Mechanistic studies suggest the reaction takes place through disproportionation of (bipyrimidine)$Pd(OAc)_2$ to form a bipyrimidine-bridged dimer, which reacts with olefin to form a Pd^{II}-olefin adduct, followed by allylic C–H activation to produce (η^3-allyl)Pd^{II} species. The (η^3-allyl)Pd^{II} intermediate undergoes a reversible acetate attack to generate a Pd^0-(allyl acetate) adduct, which subsequently reacts with *p*-benzoquinone to release allyl acetate and regenerate (bipyrimidine)$Pd(OAc)_2$. No KIE is observed for the competition experiment between allylbenzene-d_0 and allylbenzene-d_5 (CD_2=$CDCD_2C_6H_5$), suggesting that allylic C–H activation is not rate-determining. Catalytic allylic acetoxylations of other terminal olefins as well as cyclohexene were also effected by (bipyrimidine)$Pd(OAc)_2$.

Key words: olefin, palladium catalysis, allylic C–H oxidation, *p*-benzoquinone, bipyrimidine.

Résumé : On a observé que plusieurs ligands apparentés à la pyridine améliorent l'oxydation allylique de l'allylbenzène en acétate de cinnamyle par la *p*-benzoquinone dans l'acide acétique et catalysée par le $Pd(OAc)_2$. On a utilisé le meilleur ligand étudié, la bipyrimidine, pour identifier le précurseur du catalyseur pour ce système, le (bipyrimidine)$Pd(OAc)_2$, qui a été complètement caractérisé. Des études mécanistiques suggèrent que la réaction se produit par le biais d'une réaction de dismutation du (bipyrimidine)$Pd(OAc)_2$ qui conduit à la formation d'un dimère à pont bipyrimidine qui réagit avec l'oléfine pour conduire à un adduit Pd(II)-oléfine, le tout suivi de l'activation du C–H allylique conduisant à la formation de l'espèce (η^3-allyl)Pd(II). L'intermédiaire (η^3-allyl)Pd(II) subit une attaque réversible par l'ion acétate qui génère un adduit Pd°-(acétate d'allyle) qui réagit subséquemment avec la *p*-benzoquinone pour libérer l'acétate d'allyle et régénérer le (bipyrimidine)$Pd(OAc)_2$. On n'observe aucun effet isotopique cinétique pour l'expérience de compétition entre l'allylbenzène-d_0 et l'allylbenzène-d_5 (CD_2=$CDCD_2C_6H_5$); ce résultat suggère que l'activation allylique n'est pas l'étape cinétiquement déterminante. Les acétoxylations allyliques catalytiques du cyclohexène et d'autres oléfines terminales sont aussi affectées par le (bipyrimidine)$Pd(OAc)_2$.

Mots-clés : oléfine, catalyseur de palladium, oxydation de C–H allylique, *p*-benzoquinone, bipyrimidine.

[Traduit par la Rédaction]

Introduction

The selective oxidation of allylic C–H bonds offers a valuable approach to the construction of complex molecules (1). While earlier catalysts based on copper or selenium suffer from problems, such as limited substrate scope, low yields, and poor selectivities (2), extensive work on systems based on Pd(II) has led to some remarkably selective allylic C–H activations and oxidations (3, 4). The solvent often plays a key role in achieving selective oxidation to allyl acetates: in neat acetic acid, only symmetrical cyclic olefins are selectively oxidized with $Pd(OAc)_2$ (5), whereas terminal olefins can be selectively oxidized in DMSO/acetic acid (6), and yields can be further improved in dimethylacetamide (DMA) (7). The combination of Pd(II) with sulfoxide ligands also selectively oxidizes terminal olefins (8); this reaction has been successfully applied for catalytic allylic aminations (9) and macrolactonizations (10).

To date, no catalytic system has been reported to selectively oxidize both terminal and internal olefins to allyl acetates. Furthermore, in no case has the active catalytic species been characterized, which complicates the study and understanding of reaction mechanisms and impedes further development of new catalysts. Herein, we disclose a well-defined new catalyst precursor, (bipyrimidine)$Pd(OAc)_2$, that effects selective allylic acetoxylations of terminal olefins and

Received 17 April 2008. Accepted 2 July 2008. Published on the NRC Research Press Web site at canjchem.nrc.ca on 15 October 2008.

This paper is dedicated to Professor Richard Puddephatt for his great contributions in Organometallic Chemistry.

B.-L. Lin, J.A. Labinger,[2] and J.E. Bercaw.[2] Arnold and Mabel Beckman Laboratories of Chemical Synthesis, California Institute of Technology, Pasadena, CA 91125, USA.

[1]This article is part of a Special Issue dedicated to Professor R. Puddephatt.

[2]Corresponding authors (e-mail: jal@caltech.edu, bercaw@caltech.edu).

 doi:10.1139/V08-133 © 2008 NRC Canada

cyclohexene in acetic acid, and offer evidence for its mechanism of operation.

Experimental

All starting materials are commercially available and used as received without any further purification. $[(\eta^3\text{-}1\text{-phenylallyl})PdCl]_2$ (11) and $[(\eta^3\text{-}1\text{-phenylallyl})Pd(OAc)]_2$ (12) were synthesized according to literature procedures. Allylbenzene-d_5 ($C_6H_5CD_2CD{=}CD_2$) was synthesized by a modified literature procedure (13) where allyl bromide-d_5 was used instead of allyl bromide-d_0. Unless otherwise noted, all manipulations were carried out in air. ^1H and ^{13}C NMR spectra were recorded at room temperature on Varian Mercury 300 (^1H, 299.8 MHz; ^{13}C, 125.9 MHz) spectrometers. NMR spectra were referenced to residual solvent peak ($CDCl_3$: ^1H, 7.26 ppm; ^{13}C, 77.23 ppm; CD_3COOD: ^1H, 2.04 ppm) and reported in parts per million (ppm). Multiplicities were reported as follows: singlet (s), doublet (d), doublet of doublets (dd), doublet of triplets (dt), triplet (t), quartet (q), multiplet (m), and broad resonance (br). GC measurements were taken on an Agilent 6890 series GC instrument with an Agilent HP-5 column. The X-ray structure was obtained at Caltech X-ray Crystallography Laboratory. High-resolution mass spectra were obtained at Caltech Mass Spectrometry Laboratory. Reaction yields are corrected for the purities of the starting materials.

(Bipyrimidine)$Pd(OAc)_2$ (1)

A solution of 25 mg $Pd(OAc)_2$ and 17.8 mg bipyrimidine (BPM) in 4.5 mL glacial acetic acid was stirred for 30 min, resulting in a clear yellow solution. After removing the solvent under vacuum, $(BPM)Pd(OAc)_2$ (**1**) was obtained as a yellow powder, pure enough for NMR analyses. A yellow crystal of $[(BPM)Pd(OAc)_2{\cdot}H_2O]$ was obtained by slow evaporation of a chloroform solution of a 1:1:1 mixture of BPM, $Pd(OAc)_2$, and acetic acid under air. ^1H NMR ($CDCl_3$) δ: 9.20 (dd, 2H, $^3J_{HH}$ = 4.8 Hz, $^4J_{HH}$ = 2.2 Hz), 8.68 (dd, 2H, $^3J_{HH}$ = 5.7 Hz, $^4J_{HH}$ = 2.2 Hz), 7.73 (dd, 2H, $^3J_{HH}$ = 5.7 Hz, 4.8 Hz), 2.13 (s, 6H). ^{13}C NMR ($CDCl_3$) δ: 178.9, 160.5, 157.6, 124.2, 23.3. HR-MS (FAB+) *m/z* calcd. for $C_{10}H_9N_4O_2Pd^+$: $(M - OAc)^+$ 322.9796; found: 322.9774.[3]

General procedure for allylic oxidation (Table 2, entries 1, 2, 3, 5, and 6)

A solution of 25 mg $Pd(OAc)_2$ and 17.6 mg BPM in 4.5 mL glacial acetic acid was stirred for ~30 min, followed by sequential additions of 10 equiv. of olefin and 20 equiv. of benzoquinone. The mixture was heated at 70 °C with stirring, in a 20 mL glass vial sealed with a Teflon-lined cap and PTFE tape. After the reported time, the reaction mixture was cooled to room temperature in a water bath and neutralized with 50 mL of an aqueous solution of 6.2 g NaOH. The resultant mixture was extracted with 3 × 100 mL CH_2Cl_2. Organic portions were combined and dried over $MgSO_4$. Volatiles were removed under vacuum. The resultant oil was further purified by flash silica-gel column chromatography.

trans-*Cinnamyl acetate (Table 2, entry 1)*

Allylbenzene: 98% pure. Reaction time: 34 h. Eluent: 1:10 (*v/v*) EtOAc/hexanes. The product was isolated as a mixture of cis and trans isomers. Mass: 146 mg; overall yield: 76%; NMR yield of the trans isomer: 72%. ^1H NMR ($CDCl_3$) δ: 7.20–7.45 (m, 5H), 6.60–6.71 (d, 1H, $^3J_{HH}$ = 15.9 Hz), 6.24–6.35 (dt, 1H, $^3J_{HH}$ = 15.9 Hz, 6.6 Hz), 4.71–4.76 (dd, 2H, $^3J_{HH}$ = 6.6 Hz, $^4J_{HH}$ = 1.3 Hz), 2.11 (s, 3H). ^{13}C NMR ($CDCl_3$) δ: 171.1, 136.4, 134.4, 128.9, 128.3, 126.9, 123.4, 65.3, 21.3. HR-MS (FAB+) *m/z* calcd. for $C_{11}H_{12}O_2$: 176.0837; found: 176.0832.

trans-p-*Methylcinnamyl acetate (Table 2, entry 2)*

p-Allyltoluene: 99% pure. Reaction time: 32 h 46 min. Eluent: 1:10 (*v/v*) EtOAc/hexanes. The product was isolated as a mixture of cis and trans isomers. Mass: 165 mg; overall yield: 78%; NMR yield of the trans isomer: 75%. ^1H NMR ($CDCl_3$) δ: 7.26–7.32 (d, 2H, $^3J_{HH}$ = 8.1 Hz), 7.10–7.17 (d, 2H, $^3J_{HH}$ = 8.1 Hz), 6.58–6.68 (d, 1H, $^3J_{HH}$ = 15.9 Hz), 6.18–6.30 (dt, 1H, $^3J_{HH}$ = 15.9 Hz, 6.6 Hz), 4.68–4.76 (dd, 2H, $^3J_{HH}$ = 6.6 Hz, $^4J_{HH}$ = 1.3 Hz), 2.35 (s, 3H), 2.10 (s, 3H). ^{13}C NMR ($CDCl_3$) δ: 171.1, 138.2, 134.5, 133.6, 129.6, 126.8, 122.3, 65.5, 21.5, 21.3. HR-MS (FAB+) *m/z* calcd. for $C_{12}H_{14}O_2$: 190.0994; found: 190.0995.

trans-p-*Methoxycinnamyl acetate (Table 2, entry 3)*

p-Methoxyallylbenzene: 98% pure. Reaction time: 16 h. Eluent: 1.5:10 (*v/v*) EtOAc/hexanes. The product was isolated as a mixture of cis and trans isomers. Mass: 118 mg; overall yield: 53%; NMR yield of the trans isomer: 50%. ^1H NMR ($CDCl_3$) δ: 7.30–7.36 (d, 2H, $^3J_{HH}$ = 8.4 Hz), 6.82–6.89 (d, 2H, $^3J_{HH}$ = 8.4 Hz), 6.55–6.64 (d, 1H, $^3J_{HH}$ = 15.3 Hz), 6.10–6.21 (dt, 1H, $^3J_{HH}$ = 15.3 Hz, 6.6 Hz), 4.66–4.74 (dd, 2H, $^3J_{HH}$ = 6.6 Hz, $^4J_{HH}$ = 1.3 Hz), 3.80 (s, 3H), 2.09 (s, 3H). ^{13}C NMR ($CDCl_3$) δ: 171.2, 159.8, 134.3, 129.2, 128.1, 121.0, 114.2, 65.6, 55.5, 21.3. HR-MS (FAB+) *m/z* calcd. for $C_{12}H_{14}O_3$: 206.0943; found: 206.0952.

1-Acetoxy-trans-*2-decene (Table 2, entry 5)*

Reaction time: 20 h. Eluent: 1:10 (*v/v*) EtOAc/hexanes. The product was isolated as a mixture of allylic acetates along with (1-acetoxy-)3-, 4-, and 5-decenes. Both ^1H NMR and GC gave the estimated ratio of allylic acetates (sum of *trans*-primary allylic acetate, *cis*-primary allylic acetate, and secondary allylic acetate) to other isomers to be ~3.8. Only 1-acetoxy-*trans*-2-decene was fully characterized. Mass: 171 mg; overall yield: 78%; NMR yield of 1-acetoxy-*trans*-2-decene: 54%. ^1H NMR ($CDCl_3$) δ: 5.70–5.83 (m, 1H), 5.49–5.62 (m, 1H), 4.47–4.53 (dd, 2H, $^3J_{HH}$ = 6.6 Hz, $^4J_{HH}$ = 1 Hz), 2.06 (s, 3H), 1.92–2.08 (m, 2H), 1.27 (br s, 10H), 0.87 (t, 3H, $^3J_{HH}$ = 6.9 Hz). ^{13}C NMR ($CDCl_3$) δ: 171.1, 137.0, 123.9, 65.6, 32.5, 32.0, 29.6, 29.3, 29.1, 22.9, 21.3, 14.3. HR-MS (FAB+) *m/z* calcd. for $C_{12}H_{14}O_2$: 198.1620; found: 198.1625.

1-Acetoxy-3-cyclohexyl-trans-*2-propene (Table 2, entry 6)*

Allylcyclohexane: 96% pure. Reaction time: 20 h. Eluent: 1:10 (*v/v*) EtOAc/hexanes. The product was isolated as a mixture of allylic acetates, 3-cyclohexylidenepropyl acetate, and 3-cyclohexenylpropyl acetates. The ratio of allylic acetates (sum of *trans*-primary allylic acetate, *cis*-primary allylic acetate, and secondary allylic acetate) to other isomers was estimated to be ~6.2 by ^1H NMR and GC. Only 1-acetoxy-3-cyclohexyl-*trans*-2-propene was fully characterized. Mass: 150 mg; overall yield: 77%; NMR yield of 1-acetoxy-3-cyclohexyl-*trans*-2-propene: 65%. ^1H NMR

© 2008 NRC Canada

Table 1. Nitrogen ligand effects on $Pd(OAc)_2$-catalyzed allylic acetoxylation of allylbenzene.

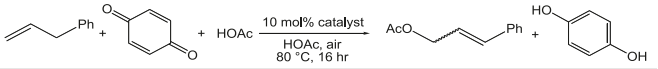

Entry	Catalyst	Yield[a,b]
1	10 mol% $Pd(OAc)_2$	13%
2	10 mol% $Pd(OAc)_2$ + 10 mol% 2,2′-bipyrimidine	76%
3	10 mol% $Pd(OAc)_2$ + 20 mol% pyridine	35%
4	10 mol% $Pd(OAc)_2$ + 10 mol% 1,10-phenanthroline	47%
5	10 mol% $Pd(OAc)_2$ + 10 mol% 2,2′-bipyridine	—[c]

Note: General experimental procedure: A mixture of catalyst, 0.7 mL glacial acetic acid, allylbenzene, 1 equiv. BQ, and 20 µL nitrobenzene (internal standard for GC) is stirred and heated in a sealed vial at 80 °C for 16 h.

[a]Sum of *cis* and *trans* isomers; GC yields.

[b]Conversions of allylbenzene: entry 1–3, 100%; entry 4, 87%; entry 5, 3%.

[c]No product detected.

($CDCl_3$) δ: 5.66–5.75 (dd, 1H, $^3J_{HH} \approx 15.6$ Hz, 6.3 Hz), 5.44–5.55 (dtd, 1H, $^3J_{HH} = 15.6$ Hz, 6.6 Hz, $^4J_{HH} = 1.1$ Hz), 4.46–4.52 (d, 2H, $^3J_{HH} = 6.6$ Hz), 2.05 (s, 3H), 1.84–2.05 (m, 1H), 0.94–1.79 (m, 10H). ^{13}C NMR ($CDCl_3$) δ: 171.1, 142.4, 121.5, 65.8, 40.6, 32.7, 26.3, 26.2, 21.3. HR-MS (FAB+) *m/z* calcd. for $C_{11}H_{18}O_2$: 182.1307; found: 182.1313.

Allyl acetate (Table 2, entry 4)

A 5 mL round-bottom flask was charged with 27.1 mg (BPM)$Pd(OAc)_2$ (10 mol%), 153 mg BQ (2 equiv.), 20 µL nitrobenzene, and 2.2 mL glacial acetic acid. Propylene (15.7 mL, 1 atm) was then condensed into the flask by liquid nitrogen after degassing (1 atm = 101.325 kPa). The mixture was stirred and heated at 70 °C for 24 h. An aliquot of the reaction mixture was taken and filtered through a short pipette of silica gel with Et_2O as the eluent for GC analysis. The GC-peak area of allyl acetate relative to nitrobenzene was used to calculate the yield. Allyl acetate was the only allylic oxidation product observed by ^1H NMR. GC Yield: 45%.

Cyclohexenyl acetates (Table 2, entry 7)

The general procedure above was followed, except for the use of 20 equiv. of cyclohexene and 24 equiv. of benzoquinone, and heating at 80 °C. After 24 h, the mixture was cooled to room temperature by water bath and neutralized by 6.2 g NaOH in 50 mL H_2O. The resultant mixture was extracted by 3 × 100 mL CH_2Cl_2. Organic portions were combined and dried over $MgSO_4$. Volatiles were removed under vacuum. The resultant oil was further purified by reduced-pressure distillation. A ~2.8:1 mixture of cyclohex-2-enyl acetate and cyclohex-3-enyl acetate was obtained. Mass: 160 mg; overall yield: 51.3%.

Cyclohex-2-enyl acetate

^1H NMR ($CDCl_3$) δ: 5.87–5.98 (m, 1H), 5.63–5.73 (m, 1H), 5.18–5.27 (m, 1H), 2.03 (s, 3H), 1.53–2.45 (m, 6H). ^{13}C NMR ($CDCl_3$) δ: 171.0, 132.9, 125.9, 68.3, 28.5, 25.1, 21.6, 19.1. HR-MS (FAB+) *m/z* calcd. for $C_8H_{12}O_2$: 140.0837; found: 140.0841.

Cyclohex-3-enyl acetate

^1H NMR ($CDCl_3$) δ: 5.62–5.67 (m, 1H), 5.51–5.60 (m, 1H), 4.93–5.03 (m, 1H), 2.03 (s, 3H), 1.53–2.45 (m, 6H).

Table 2. (Bipyrimidine)$Pd(OAc)_2$-catalyzed allylic acetoxylation of olefins.

Entry	Olefin	Temp. (°C)	Time (h)	Major product (NMR yield)	Overall yield[a]
1		70	34	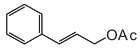 (72%)	76%
2	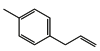	70	33	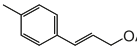 (75%)	78%
3	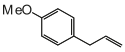	70	16	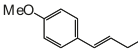 (50%)	53%
4		70	24		45%
5		70	20	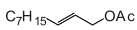 (54%)	77%
6		70	20	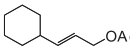 (65%)	77%
7		80	24	(33%)	51%

Note: Entry 1–6: 10 mol% catalyst loading and 2 equiv. BQ; Entry 7: 5 mol% catalyst loading and 1.2 equiv. BQ; All reactions except 4 and 7 are near completion.

[a]Product isolated as a mixture of isomers: Entries 1–3: *cis*- + *trans*-1° allyl acetates; Entries 5–7: C=C bond migration results in minor products such as homoallyl acetates; Entries 5 and 6: small amounts of 2° allyl acetates observed.

Fig. 1. X-ray crystallographic structure and the crystal packing of [(bipyrimidine)$Pd(OAc)_2 \cdot H_2O$] (see Supplementary data).[3]

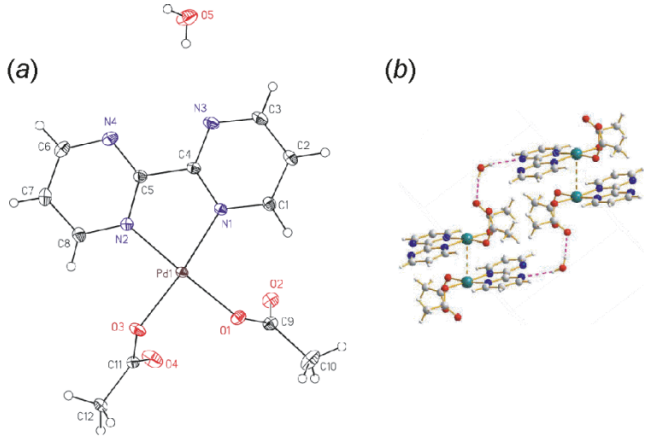

Scheme 1.

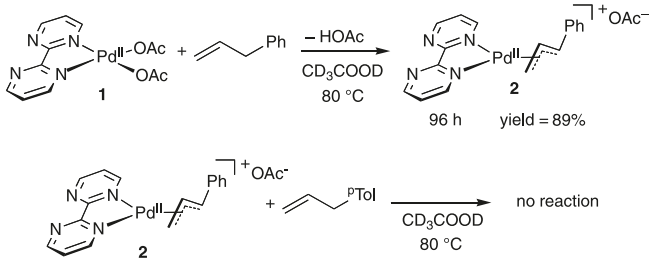

© 2008 NRC Canada

Table 3. Crystal data and structure refinement for [(BPM)Pd(OAc)$_2$·H$_2$O]

Empirical formula	$C_{12}H_{12}N_4O_4Pd·H_2O$
Formula mass	400.67
Crystallization solvent	Dichloromethane
Crystal habit	Block
Crystal size (mm)	0.36 × 0.31 × 0.27
Crystal colour	Yellow
λ Mo Kα (Å)	0.710 73
Temperature (K)	100(2)
a (Å)	9.6974(3)
b (Å)	14.9781(4)
c (Å)	10.0106(3)
β (°)	98.7400(10)
V (Å^3)	1437.14(7)
Z	4
Crystal system	Monoclinic
Space group	$P2_1/n$
$D_{calcd.}$ (Mg/m^3)	1.852
F(000)	800
θ range for data collection	2.47° to 44.89°
Completeness to θ = 44.89°	77.7%
Index ranges	$-18 \le h \le 17$, $-29 \le k \le 29$, $-17 \le l \le 17$
Reflections collected	28 065
Independent refl.	9164 [R_{int} = 0.0588]
Absorption coefficient (mm^{-1})	1.321
Absorption correction	None
Max. and min. transmission	0.7168 and 0.6477
Hydrogen placement	Difference Fourier map
Data, restraints, parameters	9164, 0, 255
Treatment of hydrogen atoms	Unrestrained
Goodness-of-fit on F^2	1.485
Final *R* indices [$I > 2\sigma(I)$, 7498 refl.]	R_1 = 0.0305, wR_2 = 0.0664
R indices (all data)	R_1 = 0.0393, wR_2 = 0.0678
Max shift/error	0.004
Average shift/error	0.000
Largest diff. peak and hole (e Å^{-3})	1.503 and –1.576

^{13}C NMR ($CDCl_3$) δ: 171.0, 127.0, 123.9, 70.0, 30.9, 27.5, 23.5, 21.6.

[(Bipyrimidine)Pd(η^3-1-phenylallyl)]$^+$(OAc)$^-$ (2)

Route 1

A mixture of 8.6 mg (BPM)Pd(OAc)$_2$ and 29.5 μL allylbenzene in 0.7 mL CD_3COOD was heated in a J–Young NMR tube under nitrogen at 80 °C for 96 h. The yield of compound **2** based on Pd was 89%, as estimated by ^{1}H NMR.

Route 2

A 2:1 ratio of AgOAc (3.8 mg) and [(η^3-1-phenylallyl)PdCl]$_2$ (5.5 mg) was stirred in 1 mL of acetone at room temperature for 30 min. After filtering off the precipitate, solvent was pumped away under vacuum. To the resultant yellow solid was added 3.6 mg BPM and 0.7 mL CD_3COOD. ^{1}H NMR shows that [(BPM)Pd(η^3-1-phenylallyl)]$^+$(OAc)$^-$ was formed quantitatively. Unfortunately, compound **2** is not isolable owing to rapid decomposition to Pd metal in the absence of acetic acid. ^{1}H NMR (CD_3COOD) δ: 9.24 (br s 4H), 7.78 (br s 2H), 7.46–7.82 (m, 5H), 6.59 (app dt, 1H, $^3J_{HH}$ = 12.3 Hz, 7.2 Hz), 5.06 (d, 1H, $^3J_{HH}$ = 12.3 Hz), 4.68 (d, 1H, $^3J_{HH}$ = 7.2 Hz), 3.87(d, 1H, $^3J_{HH}$ = 12.3 Hz). HR-MS (FAB+) *m*/*z* calcd. for $C_{17}H_{15}N_4Pd^+$: (M – OAc)$^+$ 381.0332; found: 381.0343.

(Bipyrimidine)[Pd(OAc)$_2$]$_2$ (3)

3.6 mg BPM and 10 mg Pd(OAc)$_2$ (2 equiv.) were mixed with 0.7 mL CD_3COOD. A clear yellow solution was obtained after stirring for 2 h. The solution contained an equilibrated mixture of Pd(OAc)$_2$, (BPM)Pd(OAc)$_2$ (**1**), and (BPM)[Pd(OAc)$_2$]$_2$ (**3**). The equilibrium constant was estimated to be ~25 mol^{-1} L by ^{1}H NMR. NMR yield of compound **3** based on BPM: 35%. ^{1}H NMR (CD_3COOD) δ: 8.75 (d, 4H, $^3J_{HH}$ = 5.7 Hz), 7.78 (t, 2H, $^3J_{HH}$ = 5.7 Hz). MS (MALDI) *m*/*z* calcd. for $C_{16}H_{18}N_4Pd_2^+$: (M$^+$) 605.919; found: 605.7228.

[(Bipyrimidine)Pd(η^3-2-propenyl)]$^+$(OAc)$^-$

To a solution of compound **1** in 0.7 mL CD_3COOD was added 2.4 μL allyl acetate (1 equiv.). After degassing, the solution was heated at 80 °C for 15 h. According to the ^{1}H NMR spectrum, ~50% of the starting material was converted to [(BPM)Pd(η^3-2-propenyl)]$^+$. ^{1}H NMR (CD_3COOD) δ: 9.32 (br s 4H), 7.99 (br s 2H), 6.03–6.19 (tt, 1H, $^3J_{HH}$ = 6.6 Hz, 12.6 Hz), 4.72–4.76 (dd, 2H, $^2J_{HH}$ = 1.3 Hz, $^3J_{HH}$ = 6.6 Hz), 3.60–3.72 (d, 2H, $^3J_{HH}$ = 12.6 Hz). HR-MS (FAB+) *m*/*z* calcd. for $C_{11}H_{11}N_4Pd^+$: (M – OAc)$^+$ 305.0019; found: 305.0044.

Exchange between *trans*-cinnamyl acetate and CD_3COOD

A mixture of compound **2** and 10 μL *trans*-cinnamyl acetate (3 equiv.) in 0.7 mL CD_3COOD was heated in a J–Young NMR tube under nitrogen at 80 °C. After 16 h 5 min, 20% of the starting $PhCH{=}CHCO_2CH_3$ was converted to $PhCH{=}CHCO_2CD_3$. No change of compound **2** was detected. Control experiments were carried out under similar conditions except that compound **2** was absent or replaced by an equimolar amount of NaOAc. In neither case was acetate scrambling detected by ^{1}H NMR.

Competition between allylbenzene-d_0 and allylbenzene-d_5

A mixture of 4.3 mg (BPM)Pd(OAc)$_2$ (~5 mol%), 10 μL nitrobenzene (internal standard), 15 μL allylbenzene-d_0, 15 μL allylbenzene-d_5, 25 mg BQ, and 0.35 mL CH_3COOH was heated in a sealed vial with stirring at 80 °C. Aliquots (~5 μL) were taken at certain times by microsyringe for GC analysis. The GC signals of allylbenzene-d_0 and allylbenzene-d_5 are fully separated, but those of the two isotopologs of *trans*-cinnamyl acetate are not.

Results and discussion

The oxidation of allylbenzene by *p*-benzoquinone (BQ) in acetic acid at 80 °C, with Pd(OAc)$_2$ as the catalyst, leads to only a 13% yield of cinnamyl acetate (100% consumption of allylbenzene). Several other unidentified products, probably

© 2008 NRC Canada

Scheme 2.

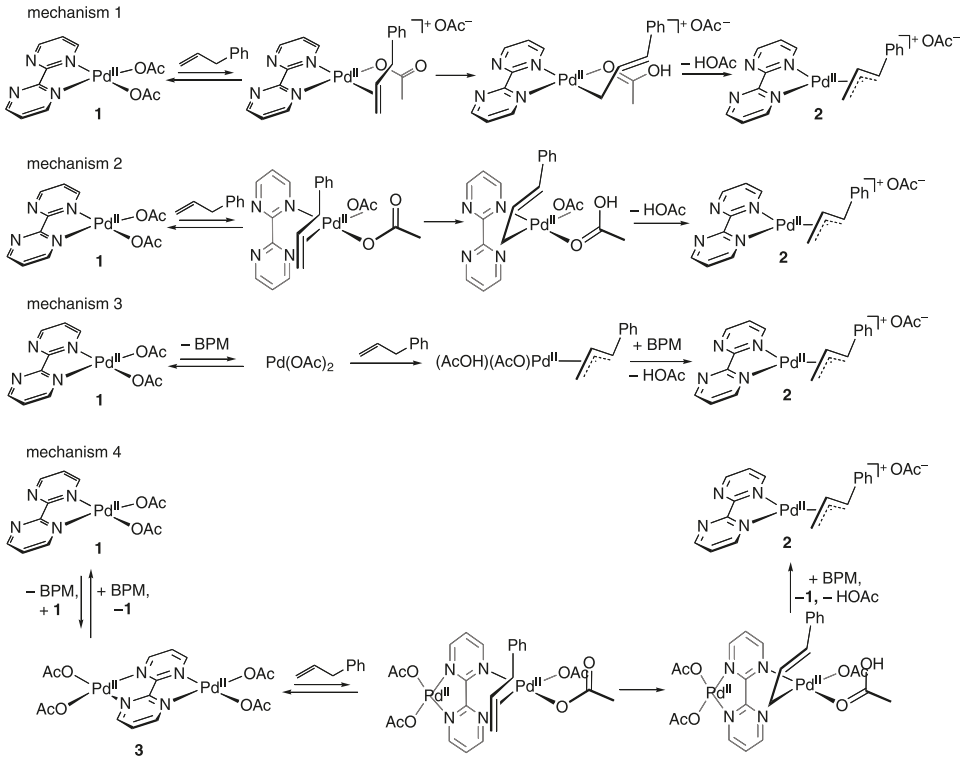

Scheme 3.

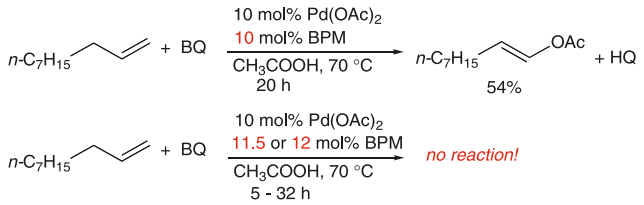

Scheme 4.

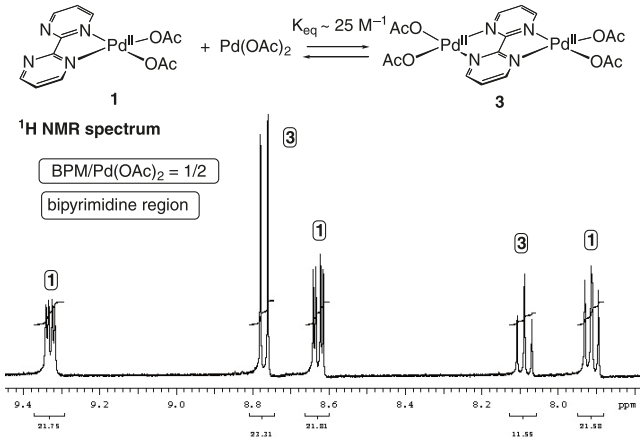

including the same Wacker-type products previously reported from reaction at 40 °C (6b), are observed. The selectivity for cinnamyl acetate is significantly improved by the addition of pyridine-like nitrogen ligands (with the exception of 2,2′-bipyridine, which shuts down the reaction) (Table 1). Among the ligands tested, bipyrimidine (BPM) is the best, leading to a 76% yield of cinnamyl acetate in 16 h at 80 °C.

Studies of substrate scope (Table 2) indicate that both benzylic C–H and methoxy groups are compatible with the acetoxylation (Table 2, entries 2 and 3). Unfortunately, the yield for olefins with alkyl groups at the allylic position (Table 2, entries 5 and 6) suffers from olefin isomerization, giving byproducts such as homoallylic acetates. Cyclohexene is also an active substrate for the reaction, producing a mixture of cyclohex-2-enyl acetate and cyclohex-3-enyl acetate (~ 2.8:1) (Table 2, entry 7). Interestingly, cyclohex-2-enyl acetate becomes the only allylic oxidation product if (1,10-phenanthroline)$Pd(OAc)_2$ or *bis*(oxazoline)$Pd(OAc)_2$ (14) is used as the catalyst.

The reaction of bipyrimidine with $Pd(OAc)_2$ in CD_3COOD forms $(BPM)Pd(OAc)_2$ (**1**) in quantitative yield after 30 min at room temperature, as monitored by ^1H NMR. A crystal structure for $(BPM)Pd(OAc)_2 \cdot H_2O$ was obtained (Fig. 1; Table 3).[3] Heating $(BPM)Pd(OAc)_2$ with allylbenzene (10 equiv.) in CD_3COOD at 80 °C for ~4 day affords $[(BPM)Pd(\eta^3\text{-}1\text{-phenylallyl})]^+(OAc)^-$ (**2**), the product

[3] Supplementary data for this article are available on the journal Web site (canjchem.nrc.ca) or may be purchased from the Depository of Unpublished Data, Document Delivery, CISTI, National Research Council Canada, Ottawa, ON K1A 0R6, Canada. DUD 3834. For more information on obtaining material refer to cisti-icist.nrc-cnrc.gc.ca/cms/unpub_e.shtml. CCDC 634014 contains the crystallographic data for this manuscript. These data can be obtained, free of charge, via www.ccdc.cam.ac.uk/conts/retrieving.html (Or from the Cambridge Crystallographic Data Centre, 12 Union Road, Cambridge CB2 1EZ, UK; fax +44 1223 336033; or deposit@ccdc.cam.ac.uk).

© 2008 NRC Canada

Fig. 2. Effect of BPM to $Pd(OAc)_2$ ratio on allylic oxidation of allylbenzene by benzoquinone, $Pd(OAc)_2$ fixed to be 5 mol%. Upper graph: initial rates of the disappearance of allylbenzene relative to that of n(BPM)/n(Pd) = 1.1; lower graph: appearance of cinnamyl acetate.

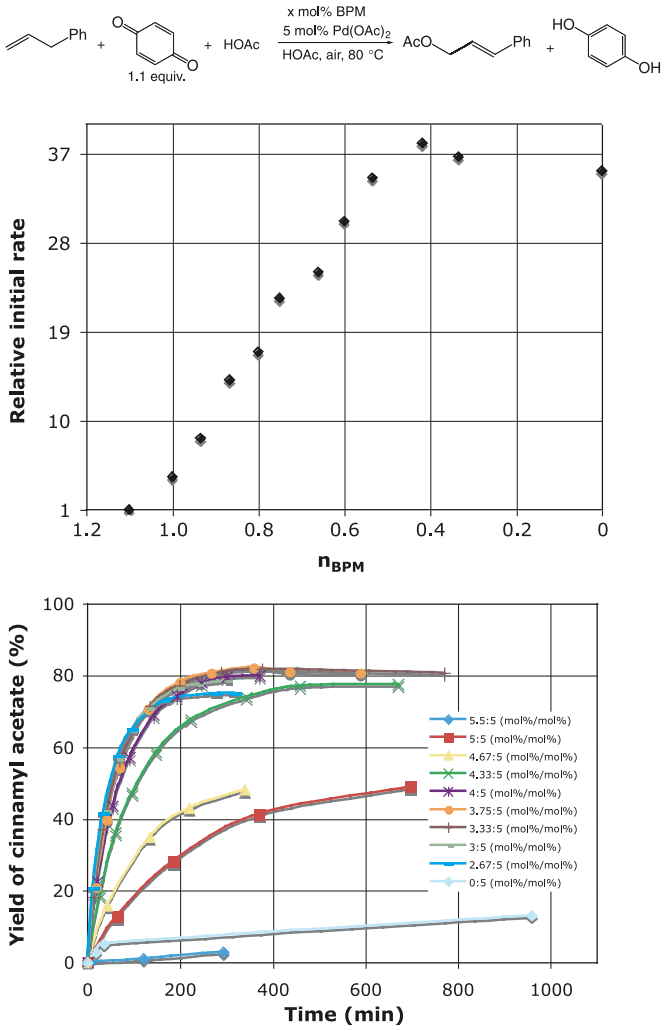

of allylic C–H activation, in ~89% yield (Scheme 1). Furthermore, the allylic C–H activation is irreversible, because neither olefin exchange nor deuterium incorporation into the allyl fragment is observed after heating **2** with *p*-allyltoluene in CD_3COOD at 80 °C for 15 h (Scheme 1). Similar irreversibility was also proposed for the sulfoxide–$Pd(OAc)_2$ system (8).

The reaction between allylbenzene and (BPM)$Pd(OAc)_2$ could occur via the displacement by the olefin of either an acetate or a coordinated BPM nitrogen to form a Pd(II)–olefin adduct, followed by allylic C–H activation to form **2** (Scheme 2, mechanisms 1 and 2). For either mechanism, addition of excess BPM should not have a significant effect on the reaction rate (a mixture of $Pd(OAc)_2$ and 1.15 equiv. BPM in CD_3COOD affords 1 equiv. (BPM)$Pd(OAc)_2$ and 0.15 equiv. free BPM (NMR)). However, no reaction is seen for allylbenzene or 1-decene when a slight excess (≤20 mol% relative to $Pd(OAc)_2$) of BPM is added (Scheme 3), clearly ruling out either mechanism for the acetoxylation.

Fig. 3. Oxidation of (η^3-allyl)Pd^{II} by benzoquinone is independent of the concentration of benzoquinone.

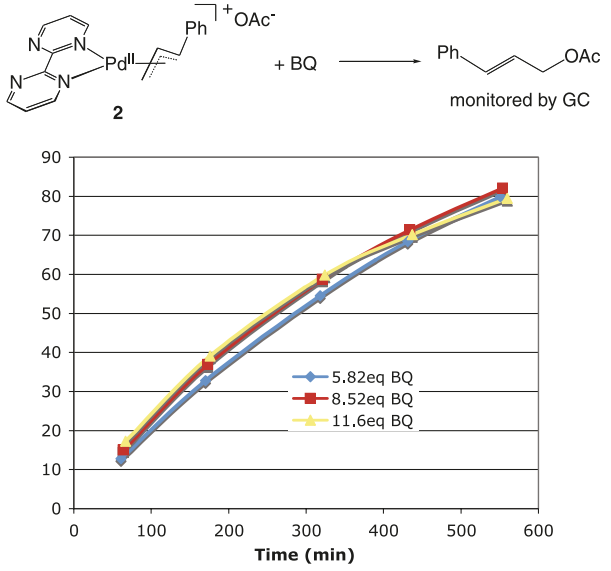

Scheme 5.

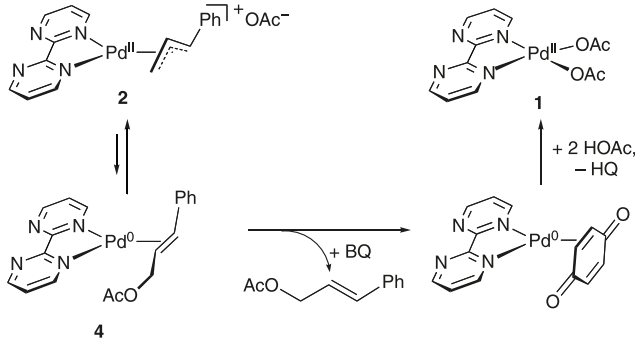

Scheme 6.

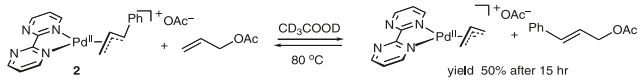

Scheme 7.

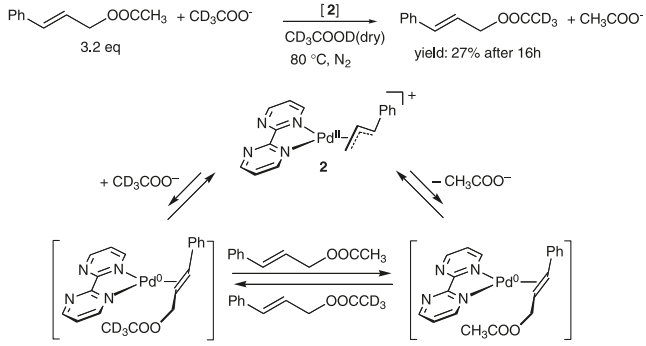

Full dissociation of BPM from (BPM)$Pd(OAc)_2$, forming $Pd(OAc)_2$, which then catalyzes the reaction, would be consistent with the inhibitory effect of excess BPM (Scheme 2,

© 2008 NRC Canada

Scheme 8.

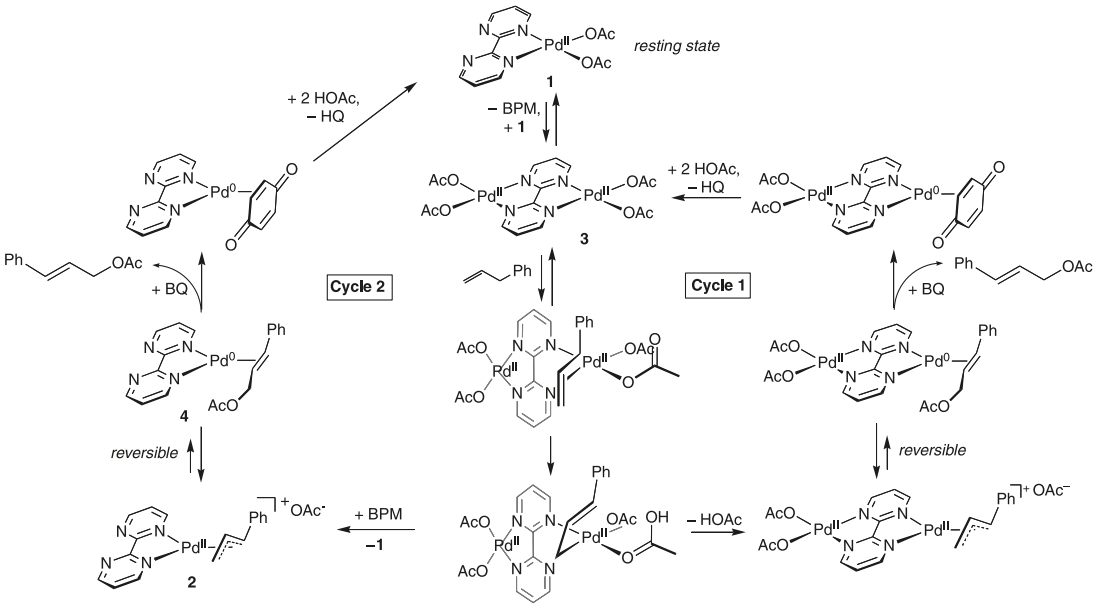

mechanism 3), but this is also unlikely to be the mechanism because $Pd(OAc)_2$ does not lead to selective allylic oxidation under current catalytic conditions (Table 1, entry 1). The nonselective oxidation catalyzed by $Pd(OAc)_2$ must originate in the allylic C–H activation of allylbenzene by $Pd(OAc)_2$ rather than a subsequent step, because the solvolysis of $[(\eta^3\text{-1-phenylallyl})Pd(OAc)]_2$ in wet acetic acid at 75 °C quantitatively forms allylic oxidation products (allylic acetates and cinnamaldehyde; the latter results from water as the nucleophile) (15).

In a further experiment, a mixture of $(BPM)Pd(OAc)_2$ and $Pd(OAc)_2$ in CD_3COOD (generated in situ by combining $Pd(OAc)_2$ and BPM in a 2:1 ratio) reacts to form a new species, characterized by ^{1}H NMR and MALDI as the BPM-bridged $Pd(OAc)_2$ dimer **3** (Scheme 4). The reaction does not reach 100% conversion, but equilibrates with K_{eq} ~ 25 mol^{-1} L, as estimated by ^{1}H NMR. The resultant mixture reacts with allylbenzene under air *at room temperature* to form an η^3-allyl species, cinnamyl acetate, and palladium black.

We propose that dimer **3** is the active species for the reaction with allylbenzene, because the $Pd(OAc)_2$-only system results in less selective oxidation of allylbenzene, while heating is required for the reaction between $(BPM)Pd(OAc)_2$ and allylbenzene. According to our proposal, in the latter reaction, small amounts of dimer and free BPM are formed via disproportionation of $(BPM)Pd(OAc)_2$, explaining the inhibition by excess BPM. The coordination of a second equivalent of $Pd(OAc)_2$ to BPM would be expected to weaken a Pd–N bond and thus facilitate the coordination of olefin; the Pd–olefin adduct subsequently undergoes allylic C–H activation to form **2** (Scheme 2, mechanism 4). This mechanism is further supported by the observation that the initial consumption rate of allylbenzene increases as the ratio of BPM to $Pd(OAc)_2$ decreases; the best overall yields (~82%) were obtained by combining 3–4 mol% BPM with 5 mol% $Pd(OAc)_2$ (Fig. 2).

Fig. 4. No significant KIE is observed for competition reaction between allylbenzene-d_0 and allylbenzene-d_5.

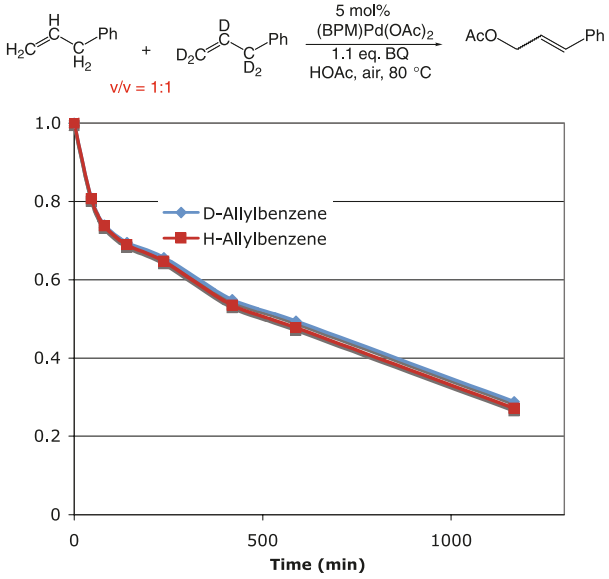

Although **2** is stable in CD_3COOD at 80 °C, the addition of benzoquinone (BQ) releases cinnamyl acetate (16) and generates $(BPM)Pd(OAc)_2$ and hydroquinone (HQ). It has been proposed that coordination of benzoquinone to Pd^{II} induces acetate attack (8, 17), but we find that the rate of the reaction between **2** and benzoquinone in acetic acid is independent of the benzoquinone concentration when at least 5.8 equiv. are used (Fig. 3), which argues against this mechanism.

Instead, we believe that reversible attack of acetate at the η^3-allyl moiety (18) occurs in the absence of benzoquinone to form the (unobservable) Pd^0(allyl acetate) species **4** (Scheme 5). Such a route is suggested by the reaction between allyl acetate and **2** in CD_3COOD, which generates

© 2008 NRC Canada

cinnamyl acetate and [(BPM)Pd(η^3-propenyl)]$^+$(OAc)$^-$ (Scheme 6), and by the fact that **2** catalyzes exchange of labeled and unlabeled acetate between *trans*-cinnamyl acetate and CD_3COOD (Scheme 7). (BPM)Pd^0(cinnamyl acetate) complex **4** then reacts with BQ to release cinnamyl acetate and form (BPM)Pd^0(BQ) (19), followed by a redox reaction with acetic acid to generate (BPM)$Pd(OAc)_2$ and hydroquinone (HQ) to complete the catalytic cycle (Scheme 5).

Scheme 8 shows a mechanism consistent with all current observations. Allylic C–H activation of allybenzene by dimer **3** leads to a dimeric (η^3-allyl)Pd^{II} complex, which can react either with benzoquinone to release cinnamyl acetate and regenerate the active dimer **3** (Scheme 8, cycle 1), or with free BPM (generated from the disproportionation) to form the monomeric (η^3-allyl)Pd^{II} **2**, followed by reaction with benzoquinone to release cinnamyl acetate and regenerate (BPM)$Pd(OAc)_2$ (Scheme 8, cycle 2). We assume that the mechanistic inferences from the stoichiometric reactions described above, which would be rigorously applicable only to the monomeric intermediates in cycle 2, most probably would be valid for the analogous dimeric intermediates of cycle 1 as well.

If cycle 2 is the dominant pathway, the rate-determining step for the whole catalytic cycle must occur before the formation of (η^3-allyl)Pd^{II} because the only Pd species observed by ^{1}H NMR during the reaction is (BPM)$Pd(OAc)_2$. In addition, the BPM inhibitory effect suggests a pre-equilibrium between (BPM)$Pd(OAc)_2$ and **3**. Therefore, either the olefin coordination or allylic C–H activation would be rate-determining. A competition experiment using a 1:1 (*v*/*v*) ratio of allylbenzene-d_0 and allylbenzene-d_5 (CD_2=$CDCD_2C_6H_5$) shows no kinetic isotope effect for the consumption rate of allylbenzene (Fig. 4), suggesting olefin coordination rather than C–H activation is rate-determining.

However, if cycle 1 is the dominant pathway, we cannot rule out the possibility that acetate attack on the dimeric (η^3-allyl)Pd^{II} complex is rate-determining. In that case, the dimeric (η^3-allyl)Pd^{II} complex would be the major species *within* the actual catalytic cycle, but it could still be unobservable if the equilibrium between **1** and **3** strongly favours the former. Since at present we do not know which cycle is dominant, we cannot conclusively identify the rate-determining step.

In summary, we have reported (BPM)$Pd(OAc)_2$ as a well-defined new catalyst for allylic C–H oxidation of olefins. Mechanistic studies have provided insight to understand the catalysis and led to further improvement of the reaction yield for the oxidation of allylbenzene. More studies are underway to explore the potential of the dimeric species and its derivatives in catalytic allylic C–H oxidations.

Acknowledgement

We thank Dr. Michael W. Day and Lawrence M. Henling for performing the X-ray crystallographic analysis. B.-L. Lin also thanks George S. Chen for suggestions in preparing the manuscript. This work has been generously supported by BP through the MC^2 program.

References

1. For examples, see the following review: J. Eames and M. Watkinson. Angew. Chem., Int. Ed. **40**, 3567 (2001).
2. (*a*) Copper: M.S. Kharasch and G. Sosnovsky. J. Am. Chem. Soc. **80**, 756 (1958); (*b*) Selenium: M.A. Umbreit and K.B. Sharpless. J. Am. Chem. Soc. **99**, 5526 (1977).
3. (*a*) Selective stoichiometric activation of allylic C–H bonds of olefins to form (η^3-allyl)Pd^{II}: B.M. Trost and P.J. Metzner. J. Am. Chem. Soc. **102**, 3572 (1980); (*b*) DMSO-promoted selective stoichiometric oxidation of 1-butene to but-2-enyl acetate: W. Kitching, Z. Rappoport, S. Winstein, and W.G. Young. J. Am. Chem. Soc. **88**, 2054 (1966).
4. Pd-catalyzed selective oxidations of α,β-enones (or ketals) to 1,4-enediones: J.-Q. Yu and E.J. Corey. J. Am. Chem. Soc. **125**, 3232 (2003).
5. (*a*) J.E. McMurry and P. Kocovsky. Tetrahedron Lett. **25**, 4187 (1984); (*b*) S. Hansson, A. Heumann, T. Rein, and B. Akermark. J. Org. Chem. **55**, 975 (1990); (*c*) C.G. Jia, P. Müller, and H. Mimoun. J. Mol. Catal. A: Chem. **101**, 127 (1995).
6. (*a*) R.C. Larock and T.R. Hightower. J. Org. Chem. **58**, 5298 (1993); (*b*) M.S. Chen and M.C. White. J. Am. Chem. Soc. **126**, 1346 (2004).
7. (*a*) D. Clark, P. Hayden, and R.D. Smith. Discussions Faraday Soc. **46**, 98 (1968); (*b*) T. Mitsudome, T. Umetani, N. Nosaka, K. Mori, T. Mizugaki, K. Ebitani, and K. Kaneda. Angew. Chem., Int. Ed. **45**, 481 (2006).
8. M.S. Chen, N. Prabagaran, N.A. Labenz, and M.C. White. J. Am. Chem. Soc. **127**, 6970 (2005).
9. K.J. Fraunhoffer and M.C. White. J. Am. Chem. Soc. **129**, 7274 (2007).
10. K.J. Fraunhoffer, N. Prabagaran, L.E. Sirois, and M.C. White. J. Am. Chem. Soc. **128**, 9032 (2006).
11. N. Marion, O. Navarro, J.-G. Mei, E.D. Stevens, N.M. Scott, and S.P. Nolan. J. Am. Chem. Soc. **128**, 4101 (2006).
12. W. Kitching, T. Sakakiyama, Z. Rappoport, P.D. Sleezer, S. Winstein, and W.G. Young. J. Am. Chem. Soc. **94**, 2329 (1972).
13. J. Ichihara. Chem. Commun. 1921(1997).
14. Preliminary screening of the following enantiopure ligands at 60 °C did not, however, lead to significant enantioselectivity: (–)-sparteine, (4*S*)-Bz-Box, (4*S*)-^{t}Bu-Box, and (*S*)-(–)-BINAP.
15. W. Kitching, T. Sakakiyama, Z. Rappoport, P.D. Sleezer, S. Winstein, and W.G. Young. J. Am. Chem. Soc. **94**, 2329 (1972).
16. A small amount of 1-phenylallyl acetate (~9%) is also formed during the reaction. More detailed mechanistic studies are underway to reconcile this observation with the proposed mechanism.
17. J.E. Bäckvall, R.E. Nordberg, and D. Wilhelm. J. Am. Chem. Soc. **107**, 6892 (1985).
18. A similar equilibrium was also proposed for (PCy_3)Pd(allyl)(OAc): T. Yamamoto, O. Saito, and A. Yamamoto. J. Am. Chem. Soc. **103**, 5600 (1981).
19. (*a*) Mixing $Pd(dba)_2$, BPM, and BQ in acetone forms (BPM)Pd(BQ): R.A. Klein, P. Witte, R. van Belzen, J. Fraanje, K. Goubitz, M. Numan, H. Schenk, J.M. Ernsting, and C.J. Elsevier. Eur. J. Inorg. Chem. 319 (1998); (*b*) BQ could be viewed as an electron-deficient olefin. For a detailed mechanistic study of olefin exchange on Pd^0, see: S.S. Stahl, J.L. Thorman, N. de Silva, I.A. Guzei, and R.W. Clark. J. Am. Chem. Soc. **125**, 12 (2003).

© 2008 NRC Canada

Kaolinite–poly(methacrylamide) intercalated nanocomposite via in situ polymerization[1]

Tamer A. Elbokl and Christian Detellier

Abstract: The preparation and characterization of a kaolinite–methacrylamide intercalation compound was achieved by a guest-displacement method, the direct treatment of a dimethylsulfoxide (DMSO) pre-intercalate with an aqueous solution of methacrylamide under mild conditions, giving intercalation ratios up to 92% and an expansion of 0.53 nm of the interlayer space. The DMSO molecules were fully displaced from the interlayer space by methacrylamide. Only partial intercalation could be obtained with *N*-methylformamide (NMF) pre-intercalate. After intercalation, the monomer was thermally polymerized at 100 or 150 °C with various heating times. XRD, FTIR, ^{13}C CP/MAS NMR, and thermogravimetric analysis confirmed that polymerization was partially achieved in the interlayer spaces, while the layered structure of kaolinite was maintained, constraining the polymer in an interlayer space of 0.57 nm in the *c*-direction. In good agreement with the TG data, elemental analysis gave a stoichiometry of $Al_2Si_2O_5(OH)_4{\cdot}(C_4H_7NO)_{0.52}$ for the thermally treated methacrylamide intercalate, corresponding to a ratio of one methacrylamide unit per two kaolinite structural units. The thermal stability of the methacrylamide intercalate was increased after thermal treatment and polymerization.

Key words: kaolinite, intercalation, nanocomposites, aluminosilicates, layered materials, interlayer polymerization, poly(methacrylamide).

Résumé : La préparation et la caractérisation d'un composé d'intercalation de la kaolinite avec la méthacrylamide ont été obtenues par une méthode de déplacement d'une molécule hôte, soit par le traitement direct d'un pré-intercalat de diméthylsulfoxide (DMSO) par une solution aqueuse de méthacrylamide sous des conditions douces. Des rapports d'intercalation de 92% furent obtenus avec une expansion de 0,53 nm de l'espace interfoliaire. Les molécules de DMSO furent complètement déplacées de l'espace interfoliaire par la méthacrylamide. Seulement une intercalation partielle put être obtenue à partir d'un pré-intercalat de *N*-méthylformamide. Après intercalation, le monomère fut polymérisé thermiquement à 100 ou 150 °C sous divers temps de chauffage. La diffraction des rayons X, l'IRTF, la RMN PC/RAM du ^{13}C et l'analyse thermogravimétrique ont confirmé que la polymérisation avait été obtenue partiellement dans l'espace interfoliaire, alors que la structure de la kaolinite était maintenue, contraignant le polymère dans un espace interfoliaire de 0,57 nm dans la direction *c*. En bon accord avec les données gravimétriques, l'analyse élémentaire a fourni une stoéchiométrie $Al_2Si_2O_5(OH)_4{\cdot}(C_4H_7NO)_{0.52}$ pour l'intercalat de méthacrylamide thermiquement traité, correspondant à un rapport d'une unité de méthacrylamide pour deux unités structurales de kaolinite. La stabilité thermique de l'intercalat de méthacrylamide est accru par le traitement thermique et la polymérisation.

Mots-clés : kaolinite, intercalation, nanocomposites, matériaux en couches, polymérisation interfoliaire, poly(méthacrylamide).

[Traduit par la Rédaction]

Introduction

A variety of organic–inorganic nanohybrid materials have been prepared and characterized in recent years (1). Among them, polymer nanocomposites, such as polymer–layered silicate (PLS), have become an effective alternative to conventional polymer composites in many applications. They exhibit enhanced mechanical and thermal properties, decreased gas permeability, improved flame-retardation properties, and increased solvent resistance (2, 3). Smectites have been widely used for the preparation of PLS nanocomposites. In general, two types of polymer–layered clay nanocomposites can be obtained, intercalates and exfoliates (4–7). Melt intercalation is the most common method of synthesis of PLS nanocomposites, as it is applicable to a wide range of polymers. Other strategies include in situ polymerization of a previously intercalated monomer and solution polymerization.

Received 21 April 2008. Accepted 24 July 2008. Published on the NRC Research Press Web site at canjchem.nrc.ca on 22 October 2008.

This paper is dedicated to Professor Richard Puddephatt for his great contributions in Organometallic Chemistry.

T.A. Elbokl and C. Detellier.[2] Center for Catalysis Research and Innovation and Department of Chemistry, University of Ottawa, Ottawa, ON K1N 6N5, Canada.

[1]This article is part of a Special Issue dedicated to Professor R. Puddephatt.
[2]Corresponding author (e-mail: dete@uottawa.ca).

 doi:10.1139/V08-142 © 2008 NRC Canada

Smectites are the most used class of phyllosilicates for the elaboration of nanohybrid and nanocomposite materials due to their swelling properties, their high exchange capacity, and surface area. On the other hand, the interlayer chemistry of kaolinite (Kao), one of the most abundant clay minerals on Earth, is much less developed.

Kaolinite is a 1:1 layered dioctahedral aluminosilicate, characterized by the chemical composition $Al_2Si_2O_5(OH)_4$ (8*a*). The individual layers are linked together through hydrogen bonds between the aluminol groups of the octahedral sheet on one side, and the siloxane macrorings of the tetrahedral sheets on the other side. They are also linked by the strong dipole interactions between the non-centrosymmetric layers (8*b*). These structural characteristics result in interlayer spaces that are not easily accessible by guest molecules. Consequently, kaolinite is not yet commonly used as the inorganic component of nanocomposites.

However, a few examples of intercalated kaolinite–polymer nanocomposites have been reported so far (9–18*a*). Direct intercalation from the melt was achieved in a few cases (9, 13). Other kaolinite–polymer nanocomposites were obtained either by the intercalation of the monomer followed by polymerization (10, 11, 14, 15, 17) or by direct intercalation of the polymer using a guest-displacement method (16).

In this paper, the synthesis of a new kaolinite–methacrylamide intercalation compound was achieved by direct treatment of an intermediate with an aqueous solution of methacrylamide. The surface modification of kaolinite particles by (trimethoxysilyl)propylmethacrylate (A174) followed by copolymerization with methacrylamide acid monomers has been reported (18*b*). However, in this work, for the first time, a kaolinite–poly(methacrylamide) intercalated nanocomposite was synthesized by in situ polycondensation of the pre-intercalated methacrylamide monomer. Methacrylamide (Chart 1) was first intercalated into kaolinite by a guest-displacement method, using kaolinite–dimethylsulfoxide (Kao–DMSO) as an effective intermediate. The intercalated monomer adopted a monolayer arrangement between the layers, confirmed by XRD analysis. Free-radical polymerization of methacrylamide was reported in the interlamellar spaces of Na-montmorillonite (19). Herein, the polymerization was achieved by thermal treatment of kaolinite–methacrylamide intercalation compound at ~150 °C for 2 h in air atmosphere. ^{13}C MAS NMR analysis confirmed the polymerization with the presence of residual monomeric species in the interlamellar space. The polymerization product had a high thermal stability, compared with the kaolinite–methacrylamide intercalation compound, as evidenced by thermogravimetric analysis. Analyses results confirmed the feasibility of the synthesis of an intercalated Kao–polymer nanocomposite, using in situ polymerization strategy.

Experimental

Chemicals and reagents

All chemicals used were of reagent-grade quality and were not further purified. Methacrylamide (C_4H_7NO, 98%) was obtained from Sigma-Aldrich and was used without further purification. Well-crystallized kaolinite from Georgia (labeled KGa-1b) was obtained from the Source Clays Repository of the Clay minerals Society (Purdue University, West Lafayette, Indiana, USA). This was purified according to previously reported sedimentation techniques (20), and the < 2 μm size fraction was used.

Chart 1.

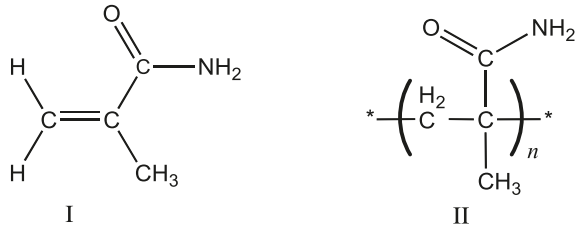

Analysis and characterization

XRD powder patterns were obtained on a Philips PW 3710 diffractometer using a generator voltage of 45 kV and a generator current of 40 mA. Typically, a step size of 0.04° (2θ) was used with a dwell time of 0.5 s/step in a continuous scan mode. The sample was spun during the acquisition, and a 12 mm automatic divergence slit was used together with a 0.2 mm fixed receiving slit, 1° secondary antiscatter slit, and a 10 mm fixed incident-beam mask. The ratio of intercalation (RI) was calculated as an approximation from the relative intensities of the (001) reflections of the organo-kaolinite phase and of the residual kaolinite phase.

Infrared spectra were acquired on a Thermo–Nicolet Nexus 670 FTIR spectrometer under dry air using 32–256 scans with a resolution of 2–4 cm^{-1}. The samples were prepared as KBr pellets from 50 mg of a mixture of 0.25–0.5 wt% sample in KBr. Peak positions were either picked manually or automatically, using the instrument installed software.

^{13}C CP/MAS NMR spectra were obtained on a Bruker ASX-200 instrument operating at 50.31 MHz at a spinning rate of 4.0–5.0 kHz and a contact time of 2 ms in most cases. The spectra were referenced to adamantane at δ = 38.4 ppm.

^{29}Si CP/MAS NMR spectra were obtained on a Bruker AVANCE-500 instrument operating at 99.35 MHz at a spinning rate of 6.0 kHz and a contact time of 8–10 ms. The spectra were referenced to tetramethylsilane (TMS) at 0.0 ppm.

All thermal analyses (TG, DTA, and DTG) were carried out on an SDT 2960 Simultaneous DSC–TGA instrument (TA Instruments) under air flow (100 mL min^{-1}) at a heating rate of 10–20 °C min^{-1}. Approximately 10–20 mg samples were used for each run. In all cases, the given TG mass-loss data were determined approximately.

Organic elemental analyses (CHNOS; combustion analysis) were performed on selected samples by Chemisar Laboratories Inc., Guelph, Ontario, Canada.

Preparation and characterization of Kao–DMSO intercalate

Kao–DMSO intercalate was typically prepared by mixing 20 g of KGa-1b with 100 mL of DMSO in a sealed container for a sufficient time (2 month) with occasional stirring to achieve maximum intercalation. The product was vacuum-filtered and washed with 1,4-dioxane to remove excess DMSO and then air-dried to yield an off-white powder.

© 2008 NRC Canada

Table 1. Summary of product codes, reaction conditions, and product X-ray characterization for the preparation of kaolinite–methacrylamide nanohybrids.

	Reaction conditions[a]		Product X-ray characterization	
Produced nanohybrid code	Starting material (SM)[b]	t_r[c] (h)	d_{001}[d] (Å)	RI[e] (%)
Kao–MAC1	Kao–NMF	22	12.6	9
Kao–MAC2	Kao–DMSO	21	12.5	50.3
Kao–MAC3	Kao–DMSO	67	12.5	92.0
Kao–MAC4	Kao–DMSO	48	12.5	91.4
Kao–MAC5	Kaolinite (KGa-1b)	72	7.15	—

Note: Reaction details are given in the Experimental section.
[a]All reactions took place at ambient temperature, and the reaction medium was 10% methacrylamide solution *w*/*v*, in all cases.
[b]Kaolinite (Kao), methacrylamide (MAC), *N*-methyl formamide (NMF), and dimethyl sulfoxide (DMSO).
[c]Approximate reaction time.
[d]The specified interlayer distance (d) is that of the principal product phase calculated using (00l) reflections; d_{001} reflections of the residual unexpanded kaolinite (d_{001K}) always gave a value of ~7.15 Å.
[e]Ratio of intercalation is the ratio of the intensities of the d_{001} reflection of the modified phase over the sum total of all the d_{001} reflections of the modified phase(s) and residual unexpanded kaolinite.

XRD: d_{001} = 11.16 Å (100.0), d_{001}(Kao) = 7.15 Å (9.7), d_{002} = 5.6 Å (4.2), d_{003} = 3.72 Å (45.7), d_{002}(Kao) = 3.57 Å (14.6), d_{004} = 2.8 Å (1.8), d_{060} = 1.49 Å (7.6), RI = 0.91–0.98 (various samples).

Preparation of Kao–NMF intercalate

Approximately 20 g of KGa-1b were mixed with 100 mL of *N*-methyl formamide in a sealed container for a sufficient time (~1 month) with occasional stirring to achieve maximum intercalation. After that, the product was filtered and washed with 1,4-dioxane to remove excess NMF and then air-dried. A representative sample gave XRD: d_{001} = 10.71 Å (100.0), d_{001}(Kao) = 7.15 Å (18.9), d_{002} = 5.28 Å (0.6), d_{003} = 3.58 Å (71.7), RI = 0.87.

Preparation of Kao–MAC by the reaction of methacrylamide with Kao–NMF (Kao–MAC1)

Kao–MAC1 was prepared by the displacement of NMF from the Kao–NMF intercalate with methacrylamide (Sigma-Aldrich). The mixture of Kao–NMF (1 g) and an aqueous solution of methacrylamide (10% *w*/*v*, 100 mL) was stirred for 22 h at room temperature, and the product was vacuum-filtered, washed with 2-propanol, and air-dried to yield an off-white powder. Prolonged reaction times did not increase the ratio of intercalation, since NMF was de-intercalated with the recovery of pristine kaolinite.

Preparation of Kao–MAC by the reaction of methacrylamide with Kao–DMSO (Kao–MAC2, –MAC3, and –MAC4)

In a series of experiments, Kao–MAC was prepared by displacing DMSO with methacrylamide. A mixture of Kao–DMSO (1 g) and an aqueous solution of methacrylamide (10% *w*/*v*, 100 mL) was stirred for 21, 67, and 48 h, respectively, at room temperature, and the products were vacuum-filtered, washed with 2-propanol, and air-dried. Prolonged reaction times had a positive effect on the ratio of intercalation with the optimum reaction time being ≈ 48 h.

The reaction of methacrylamide with KGa-1b

A mixture of KGa-1b (1 g) and an aqueous solution of methacrylamide (10% *w*/*v*, 100 mL) was stirred for 72 h at room temperature, and the product was vacuum-filtered, washed with 2-propanol, and air-dried to yield an off-white powder. XRD showed that no reaction has taken place, as the d_{001} observed was that of the pure kaolinite = 7.15 Å.

Results and discussion

Synthesis and XRD analysis

The preparation of the Kao–methacrylamide (MAC) intercalate was carried out at room temperature using what can be described as a "soft guest-displacement method" (21), most effectively from the DMSO intercalate of kaolinite by direct treatment with 10% aqueous solution of methacrylamide (98%, Sigma-Aldrich). First, a kaolinite–DMSO intercalation compound (abbreviated as Kao–DMSO) or a kaolinite – *N*-methyl formamide (Kao–NMF) was prepared as an intermediate according to the methods reported previously (22, 23). Table 1 summarizes the product names and codes, the reaction conditions, and the d_{001} values of the resulting materials. In the case of kaolinite (KGa-1b) as starting material, kaolinite was fully recovered, and the characteristic d_{001} reflection could be observed at ~7.2 Å. However, when the Kao–DMSO was used as an intermediate, a reflection at 12.5 Å was observed, indicative of the methacrylamide intercalation into the interlamellar spaces of kaolinite, since Kao–DMSO intercalate exhibits a d_{001} reflection at ~11.1 Å (24) (see Fig. 1). In a typical reaction, 1–2 g of Kao–DMSO intercalate were mixed with ~50–100 mL of 10% solution (*w*/*v*) of methacrylamide (MAC). The mixture was stirred at room temperature for a given period of time, followed by the reaction workup (washing with excess 2-propanol, vacuum filtration, and drying in vacuum). The ratio of intercalation was up to ~92%. Another intercalate was used as a starting material, Kao–NMF. The production of materials with d_{001} = 12.6 Å was observed when the Kao–NMF intercalate was used (d_{001} = 10.8 Å for Kao–NMF), but with a ratio of intercalation as low as 9%. It is worth noting that the reaction was unsuccessful from the melt, as methacrylamide sublimes at the melting temperature.

X-ray powder patterns of the starting materials (kaolinite and Kao–DMSO) and of the materials resulting from a typical reaction are shown in Fig. 1, for the range of 2–18° (2θ).

© 2008 NRC Canada

Fig. 1. XRD powder diffraction patterns (2θ = 2°–18°) of (*a*) kaolinite, (*b*) Kao–DMSO, and (*c*) Kao–MAC (d_{002} of the intercalate is marked by an asterisk).

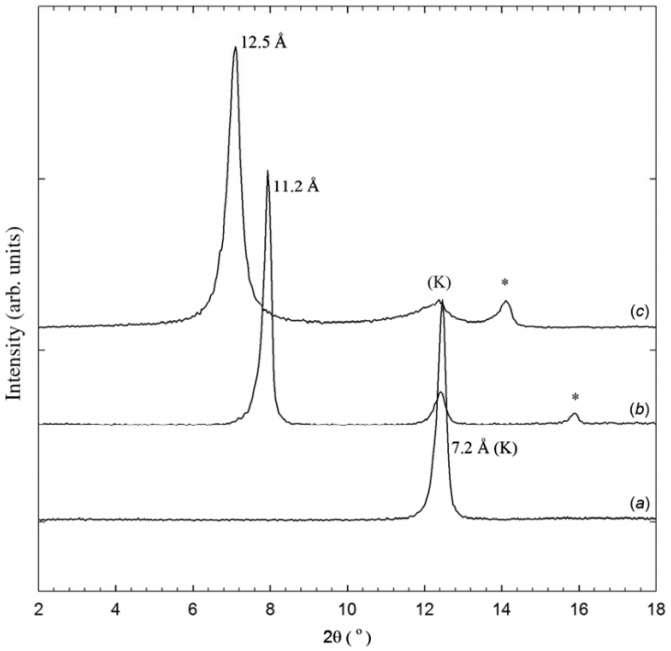

Notably, the layered structure of kaolinite remains largely unaffected, as the d_{060} reflection remains at 1.49 Å, characteristic of a dioctahedral clay mineral (not shown). The d_{001} reflection of the Kao–MAC intercalate corresponds to an expansion in the interlamellar distances by ~5.3 Å (subtracting a kaolinite layer thickness of 7.2 Å from the observed d_{001}). Since the ^{13}C NMR results show the complete disappearance of the intermediate organic intercalate (DMSO) after the reaction (see later sections), the expansion can be attributed only to the intercalation of the amide.

Methacrylamide can be polymerized in aqueous solutions in the presence of a free-radical initiator, e.g., benzoyl peroxide (19). Thermal treatment is used in this study to polymerize the intercalated amide in the interlamellar spaces without using an initiator. Figure 2 shows powder XRD patterns of Kao–MAC sample before and after thermal treatment. The sample was heated at a rate of 4 °C min^{-1} in a programmable furnace and then kept for 2 h at 150 °C or 30 h at 100 °C. The samples were allowed to cool to room temperature, and their XRD powder patterns were recorded. Heating the samples at higher temperatures would cause the intercalated kaolinite layers to collapse as a result of the deintercalation of the amide (see TG Section).

Thermal treatment (Fig. 2) causes the polymerization of methacrylamide molecules into the interlayer spaces. This can be observed by a slight expansion of the interlayer spacing from 12.5 Å to 12.9 Å for the polymerization product Kao–PMAC.

FTIR analysis

Detailed assignments of the major observed bands in the FTIR spectra of the produced nanohybrids before and after polymerization are given in Table 2.

The O–H stretching patterns for Kao–MAC and Kao–PMAC (Figs. 3*b* and 3*c*, respectively) are significantly different from the starting material, Kao–DMSO (Fig. 3*a*) (25). The Kao–DMSO band at 3665 cm^{-1} disappeared completely, and new bands appeared for Kao–MAC at ~3652, 3639, 3602, and 3547 cm^{-1}, suggesting the formation of a new pattern of strong H-bonding in the interlayer space between the intercalated methacrylamide molecules and the hydroxyls of the aluminol surface. After thermal treatment, the intensity of the band at 3652 cm^{-1} was greatly reduced, and the bands at 3602 and 3547 cm^{-1} disappeared. The NH stretching bands, characteristic of a primary amide, can be observed before and after the heat treatment (see Table 2). In both cases, the asymmetric and symmetric CH stretching bands are observed in the range of ~2980–2930 cm^{-1}.

Fig. 2. XRD powder diffraction patterns (2θ = 2°–18°) of Kao–MAC (*a*) before and (*b*) after thermal treatment.

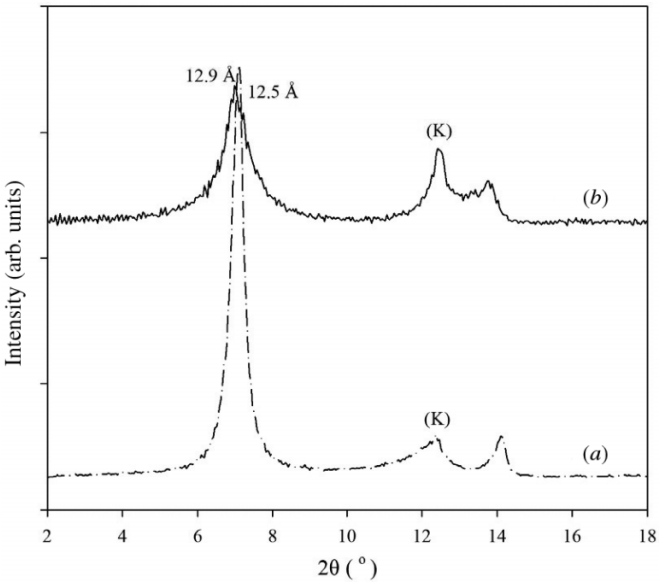

The FTIR spectra for the intercalation products before and after thermal treatment are depicted in Figs. 4*a* and 4*b*, respectively. The C=O stretching band was observed at ~1663 cm^{-1} in both cases. CH deformation bands and CN stretching bands are also observed in the range of ~1380–1460 cm^{-1} in both cases. Also, δ(NH) band is observed at ~1580 cm^{-1} (19, 26). The major change in the IR spectrum after heating is that the band at ~1620 cm^{-1}, attributed to the C=C stretching of the intercalated monomer, was considerably reduced after thermal treatment (Fig. 4), thus verifying that polymerization took place upon thermal treatment.

Solid-state NMR analysis

^{13}C NMR analysis

To identify the nature of the intercalated molecules, the results of ^{13}C NMR CP/MAS experiments (50.31 MHz) on the produced Kao–MAC nanohybrid and the intercalated Kao–PMAC nanocomposite were studied. The spectra are stacked in Fig. 5. The observed ^{13}C chemical shifts for the starting material (Kao–DMSO) are in agreement with literature data (see Fig. 5*a*) (27).

The ^{13}C NMR spectrum of the produced Kao–MAC nanohybrid confirmed the intercalation of methacrylamide in the interlayer spaces, and it is shown in Fig. 5*b*.

© 2008 NRC Canada

Table 2. FTIR absorbances in the 4000–1200 cm^{-1} range and their assignments for the Kao–MAC intercalate and the polymerization product (Kao–PMAC).

Wavenumber (cm^{-1})		
Kao–MAC	Kao–PMAC	Assignments
3696 (vs)	3696 (vs)	ν(O–H) (outer)
3652 (vs), 3639 (vs)	3638 (vs)	ν(O–H) (H-bonded)
3621 (vs)	3622 (vs)	ν(O–H) (inner)
3602 (w, sh), 3547 (m)	3554 (m), 3540 (m, br)	ν(O–H) (H-bonded)
3493 (s), 3360 (m, br), 3191 (w, br)	3498 (m, br), 3387 (m, br), 3203 (w)	ν(N–H) (as. and sym.)
3091 (w, br)	—	C–H as. stretch (unsaturated)
2954 (vw), 2928 (vw)	2954 (vw), 2932 (vw)	ν(CH_2) asymmetric and symmetric stretching (saturated)
1663 (vs)	1663 (vs)	ν(C=O)
1615 (vs)	1622 (sh)	ν(C=C)
1588 (s)	1591 (m)	δ(N–H) (scissors)
1407 (m)	1410 (m)	ν(C–N)
1456 (m), 1385 (m)	1457 (m), 1386 (m)	δ(CH_2) deformation bands

Note: The absorptions are designated as weak (w), medium (m), strong (s), very weak (vw), very strong (vs), shoulder (sh), and broad (br).

Fig. 3. FTIR spectra (4000–2600 cm^{-1}) of (*a*) Kao–DMSO, (*b*) Kao–MAC, and (*c*) Kao–PMAC.

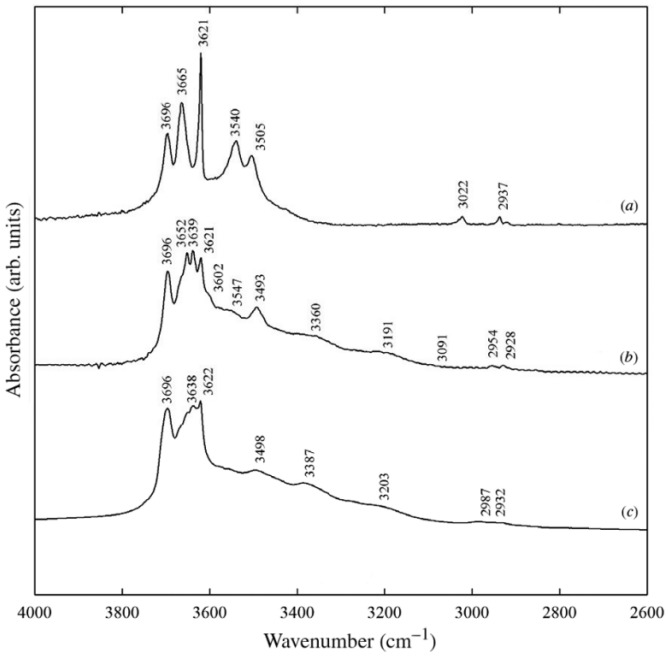

Fig. 4. FTIR spectra (2000–1200 cm^{-1}) of (*a*) Kao–MAC and (*b*) Kao–PMAC.

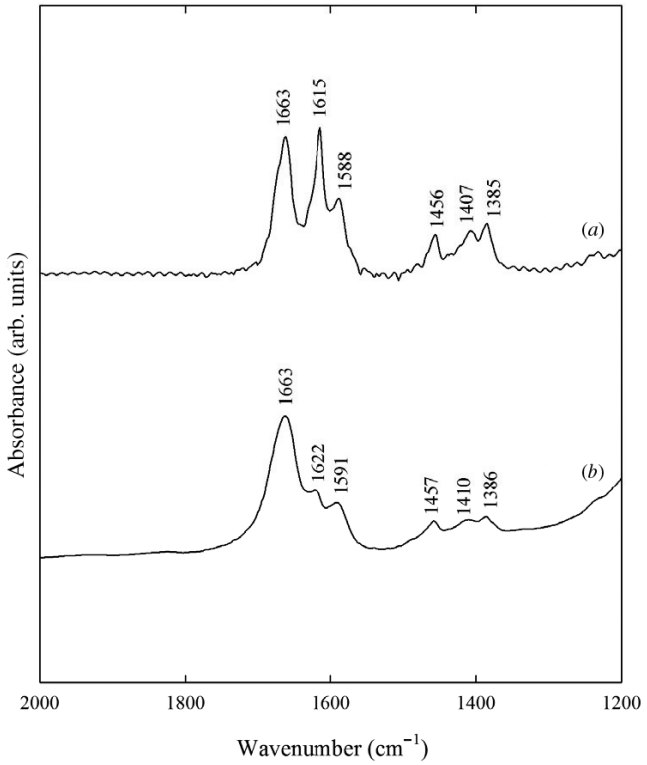

Methacrylamide signals can be observed at ~19.0 ppm (methyl carbon), and two signals at ~126 and 139 ppm are unambiguously attributed to the unsaturated carbons of the methacrylamide molecule. The signal at ~171 ppm is attributed to the amide carbonyl groups. No DMSO resonances were detected in the spectrum, indicating the complete displacement of the intermediate by methacrylamide (28, 29).

^{13}C NMR spectroscopy also confirmed the polymerization of methacrylamide by both the 150 °C and the 100 °C treatments. The spectra in Figs. 5*c* and 5*d* belong to the heat treated Kao–MAC intercalate at 150 °C and 100 °C, respectively. The main features in the spectra of the polymerized samples are the shift of the carbonyl signal to ~183 ppm and the appearance of new signals at ~45 and 55 ppm, attributed to the saturated carbons of the polymeric chain. These signals are in excellent agreement with the values reported in the literature (28, 29) for poly(methacrylamide). The presence of residual amounts of monomer indicates partial polymerization.

^{29}Si CP/MAS NMR

The ^{29}Si CP/MAS NMR spectrum (99.35 MHz) of kaolinite is given in Fig. 6*a*, displaying two well-resolved signals at –91.5 and –90.9 ppm. The ^{29}Si CP/MAS spectrum of Kao–DMSO intercalate is given in Fig. 6*b*. In addition to the residual signals of unexpanded kaolinite, one signal is observed at –92.7 ppm. Figure 6*c* gives the ^{29}Si CP/MAS

© 2008 NRC Canada

Fig. 5. Solid-state ^{13}C CP/MAS NMR spectra (50.32 MHz) of (*a*) Kao–DMSO, (*b*) Kao–MAC before thermal treatment, (*c*) Kao–MAC after heating at 150 °C for 2 h, and (*d*) Kao–MAC after heating at 100 °C for 30 h.

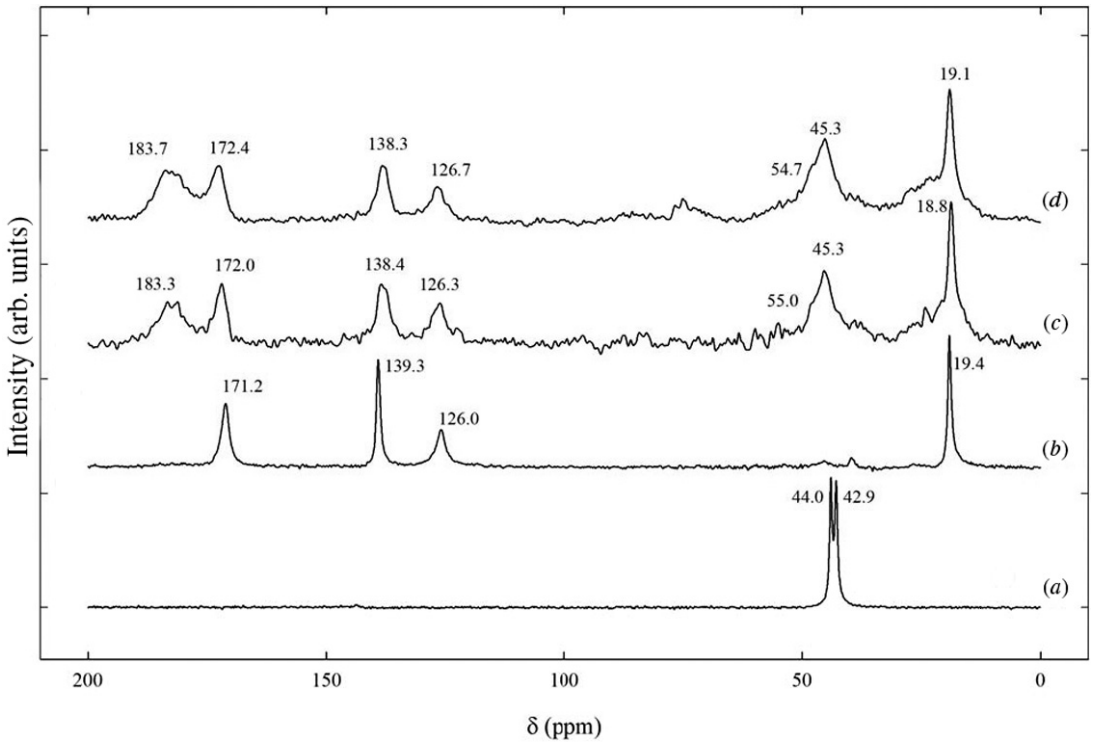

NMR spectra of the methacrylamide intercalate. The signal is slightly shifted to –92.9 ppm, and the signals due to the unexpanded kaolinite can also be observed, indicating a similar perturbation of the silicon environment by the intercalated methacrylamide molecules to that observed for the Kao–DMSO (30–32).

Fig. 6. ^{29}Si MAS NMR spectra (99.35 MHz) of (*a*) kaolinite, (*b*) Kao–DMSO, and (*c*) Kao–MAC.

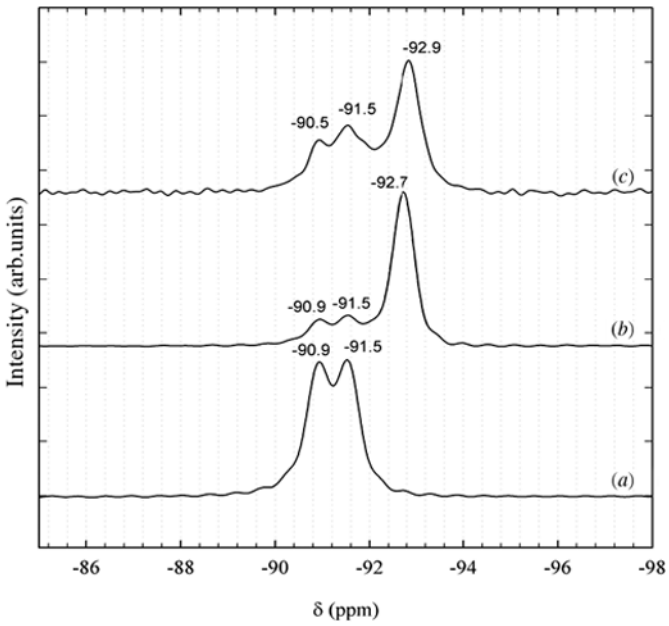

Thermogravimetric analysis

The TG thermogram of the Kao–MAC intercalate in air atmosphere is exhibited in Fig. 7*b*. The compound showed thermal stability comparable with that of the Kao–DMSO (Fig. 7*a*). The results also confirmed the displacement of DMSO molecules by methacrylamide in the interlayer spaces. In the case of Kao–MAC, the dehydroxylation step is observed at ~492 °C (see Fig. 8*a*), amounting to ~13% dehydroxylation mass loss. An additional mass loss (~14%) is observed with a maximum near 172 °C in the DTG, corresponding to the loss of the organic moieties via deintercalation. The final mass loss of ~1.0% is attributed to the trapped carbonaceous residue of the decomposed methacrylamide, released with the spinel-phase crystallization observed in this case near 935 °C (33).

The thermogram of the polymerized intercalated methacrylamide sample with prior thermal treatment shows enhanced thermal stability compared with the Kao–monomer sample (Fig. 7*c*). The dehydroxylation stage of kaolinite, giving rise to 13% mass loss, can be observed with a maximum at 503 °C in the DTG trace (Fig. 8*b*), which is similar to other reported dehydroxylation temperatures for Kao–polymer intercalated nanocomposites (9, 13, 16). Moreover, the mass-loss stage due to the decomposition of the organic material was shifted to a much-higher temperature with two signals in the DTG at 246 and 398 °C, with a total mass loss of ~13%. Also, the amount of the carbonaceous residue is increased to ~2.5%. The enhanced thermal stability of the polymerized sample Kao–PMAC, compared with the Kao–MAC sample, is an indication that the polymerization of methacrylamide was achieved in the interlamellar space by thermal treatment.

© 2008 NRC Canada

Fig. 7. TG curves (RT to 1100 °C) of (*a*) Kao–DMSO, (*b*) Kao–MAC, (*c*) Kao–PMAC, and (*d*) kaolinite.

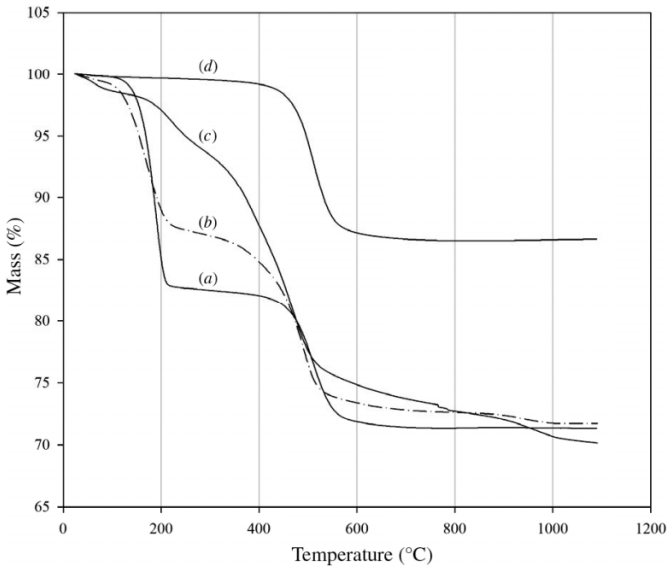

Fig. 8. DTG curves (RT to 1100 °C) of (*a*) Kao–MAC and (*b*) Kao–PMAC.

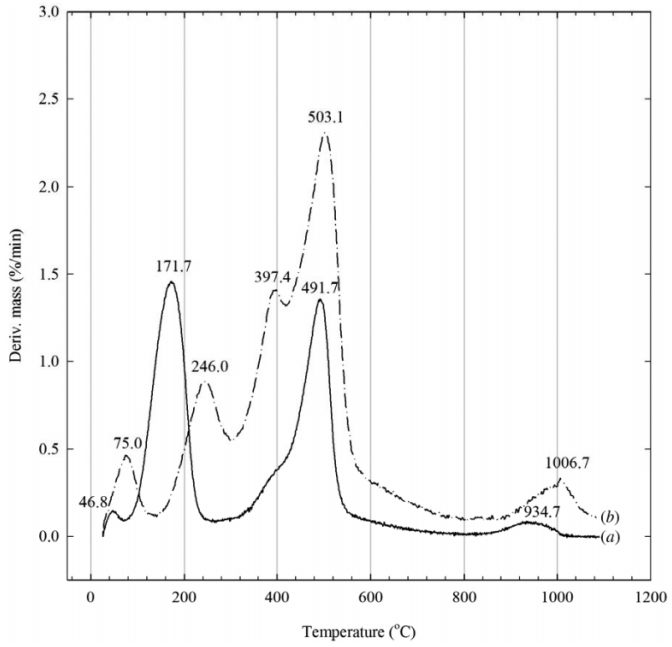

Elemental analysis

Elemental analyses were performed on a typical Kao–MAC sample and on the polymerized sample (after thermal treatment). Kao–MAC sample gave C 8.72%, H 2.37%, and N 2.60%. Thus, the calculated stoichiometry of this sample, based on the average of the results, is $Al_2Si_2O_5(OH)_4 \cdot (C_4H_7NO)_{0.66}$. Notably, this sample was free of the residual co-intercalated DMSO. After heat treatment, Kao–PMAC sample gave C 6.24%, H 2.16%, and N 1.84%. Similarly, the stoichiometry of this sample is $Al_2Si_2O_5(OH)_4 \cdot (C_4H_7NO)_{0.52}$. The higher average occupancy value of ~0.66 unit of MAC per unit cell of kaolinite, compared with that of the polymerized sample (0.52), is expected because of the partial de-intercalation upon heat treatment.

Conclusion

The preparation and characterization of a kaolinite–methacrylamide intercalation compound was achieved by direct treatment of a DMSO pre-intercalate with an aqueous solution of methacrylamide under mild conditions. The DMSO molecules were fully displaced from the interlayer space by methacrylamide. Only partial intercalation could be obtained with an NMF pre-intercalate. After intercalation, the monomer was thermally polymerized. XRD, spectroscopic, and thermogravimetric analysis confirmed that polymerization was partially achieved in the interlayer spaces.

This study confirms the feasibility of using in situ polymerization as a method to obtain intercalated nanocomposites from kaolinite. The intercalation of polymers in kaolinite to create nanohybrid materials, based on this abundant and non-centrosymmetric mineral, is a direction in the development of the interlayer chemistry of kaolinite. Joined to the intercalation of large organic cations, such as in the case of imidazolium ionic liquids (34), and to the functionalization of the interlayer aluminol surfaces by silanization (35) or by grafting of organic units (36), these studies demonstrate the potential of kaolinite as a promising raw material for the design of new advanced materials.

Acknowledgments

This work was financially supported by a Discovery Grant of the Natural Sciences and Engineering Research Council of Canada (NSERC). Dr. Glenn A. Facey is thanked for recording the NMR spectra.

References

1. K.J. Shea, J. Moreau, D.A. Loy, R.J.P. Corriu, and B. Boury. Functional hybrid materials. *Edited by* P. Gómez-Romero and C. Sanchez. Wiley-VCH, Weinheim, Germany. 2004.
2. G.W. Beall. Polymer-clay nanocomposites. *Edited by* T.J. Pinnavaia and G.W. Beall. John Wiley and Sons, West Sussex, UK. 2000.
3. K.A. Carrado. *In* Advanced polymeric materials: structure–property relationships. *Edited by* S.G. Advani and G.O. Shonaike. CRC Press LLC, Boca Raton, Fla., USA. 2003. pp. 349–396.
4. M. Alexandre and P. Dubois. Mater. Sci. Eng. **28**, 1 (2000).
5. P.C. LeBaron, Z. Wang, and T.J. Pinnavaia. Appl. Clay Sci. **15**, 11 (1999).
6. E.P. Giannelis. Appl. Organometal. Chem. **12**, 675 (1998).
7. M. Zanetti, S. Lomakin, and G. Camino. Macromol. Mater. Eng. **279**, 1 (2000).
8. (*a*) S.W. Bailey (*Editor*). Reviews in mineralogy: Hydrous phyllosilicates. Mineralogical Society of America, Wash., USA. 1988; (*b*) R.F. Giese. Bull. Miner. **105**, 417 (1982).
9. J.E. Gardolinski, L.C.M. Carrera, M.P. Cantao, and F. Wypych. J. Mater. Sci. **35**, 3113 (2000).
10. Y. Sugahara, S. Satokawa, K. Kuroda, and C. Kato. Clays Clay Miner. **36**, 343 (1988).
11. Y. Sugahara, S. Satokawa, K. Kuroda, and C. Kato. Clays Clay Miner. **38**, 137 (1990).

© 2008 NRC Canada

12. Y. Sugahara, T. Sugiyama, T. Nagayama, K. Kuroda, and C. Kato. J. Ceram. Soc. Jpn **100**, 413 (1992).
13. J.J. Tunney and C. Detellier. Chem. Mater. 8 927 (1996).
14. A. Matsumura, Y. Komori, T. Itagaki, Y. Sugahara, and K. Kuroda. Bull. Chem. Soc. Jpn **74**, 1153 (2001).
15. T. Itagaki, Y. Komori, Y. Sugahara, and K. Kuroda. J. Mater. Chem. **11**, 3291 (2001).
16. Y. Komori, Y. Sugahara, and K. Kuroda. Chem. Mater. **11**, 3 (1999).
17. (*a*) T.A. Elbokl and C. Detellier. J. Phys. Chem. Solids, **67**, 950 (2006); (*b*) X. Jia, Y. Li, B. Zhang, Q. Cheng, and S. Zhang. Mater. Res. Bull. **43**, 611 (2008); (*b*) B. Zhang, Y. F. Li, X.B. Pan, X. Jia, and X.L. Wang. J. Phys. Chem. Solids, **68**, 135 (2007).
18. (*a*) Y. Komori, Y. Sugahara, and K. Kuroda. J. Mater. Chem. **9**, 3081 (1999); (*b*) A. Gültek, T. Seçkin, Y. Önal, and M.G. Içduygu. Turk. J. Chem. **26**, 925 (2002).
19. M. Önaland and M. Çelik. Mater. Lett. **60**, 48 (2006).
20. M.L. Jackson, L.D. Whittig, and R.P. Pennington. Soil Sci. Soc. Am. Proc. **14**, 77 (1949).
21. T.A. Elbokl and C. Detellier, J. Colloid Interface Sci. **323**, 338 (2008).
22. B.K.G. Theng. *In* The chemistry of clay-organo reactions. Adam Hilger, London, UK. 1974. p. 239.
23. J.J. Tunney and C. Detellier. Can. J. Chem. **75**, 1766 (1997).
24. G.W. Brindley and G. Brown (*Editors*). Crystal structures of clay minerals and their X-ray identification: interlayer and intercalation complexes of clay minerals. Mineralogical Society, London, UK. 1984.
25. (*a*) V.C. Farmer (*Editor*). *In* The infrared spectra of minerals. Mineralogical Society, London, UK. 1974. pp. 331–363; (*b*) V.C. Farmer and J.D. Russell. Spectrochim. Acta, **2**0 1149 (1964).
26. B. Smith. Infrared spectral interpretation: a systematic approach. CRC press, Wash., USA. 1999.
27. (*a*) M.J. Duer, J. Rocha, and J.J. Klinowski. J. Am. Chem. Soc. **114**, 6867 (1992); (*b*) S. Hayashi. Clays Clay Miner. **45**, 724 (1997).
28. A.J. Brandolini and D.D. Hills. NMR spectra of polymers and polymer additives. CRC Press, Wash., USA. 2000.
29. (*a*) M. Stein. J. Appl. Polym. Sci. **46**, 2217 (1992); (*b*) T. Kameda and M. Tsukada. Macromol. Mater. Eng. **291**, 877 (2006).
30. (*a*) M. Mägi, E. Lippmaa, A. Samoson, G. Engelhardt, A.-R. Grimmer. J. Phys. Chem. **88**, 1518 (1984); (*b*) S. Hayashi, T. Ueda, K. Hayamizu, and E. Akiba. J. Phys. Chem. **96**, 10922 (1992); (*c*) P.F. Barron, R.L. Frost, J.O. Skjemstad, and A.J. Koppi. Nature, **302**, 49 (1983).
31. (*a*) J.G. Thompson. Clays Clay Miner. **33**, 173 (1985); (*b*) J.G. Thompson. Clays Clay Miner. **32**, 233 (1984).
32. J.G. Thompson and P.F. Barron. Clays Clay Miner. **35**, 38 (1987).
33. (*a*) C.M. Earnest. The application of differential thermal analysis and thermogravimetry to the study of kaolinite clay minerals. PerkinElmer thermal analysis application study. Vol. 3. PerkinElmer, Connecticut. 1980; (*b*) P.J. Sanchez-Soto, A. Justo, and J.L. Perez-Rodriguez. J. Mater. Sci. **29**, 1276 (1994); (*c*) L.A. Perez-Maqueda, J.L. Perez-Rodriguez, G.W. Scheiffele, A. Justo, and P.J. Sanchez-Soto. J. Therm. Anal. **39**, 1055 (1993).
34. S. Letaief and C. Detellier. J. Mater. Chem. **17**, 1476 (2007), and refs. cited therein.
35. I.K. Tonlé, T. Diaco, E. Ngameni, and C. Detellier. Chem. Mater. **19**, 6629 (2007).
36. (*a*) S. Letaief and C. Detellier. Chem. Commun. 2613 (2007); (*b*) S. Letaief and C. Detellier. Can. J. Chem. **86**, 1 (2008), and refs. cited therein.

© 2008 NRC Canada

Phenylsilane dehydrocoupling and addition to styrene catalyzed by (R-indenyl)Ni(phosphine)(methyl) complexes[1]

Yaofeng Chen and Davit Zargarian

Abstract: This report describes the synthesis and characterization of the Ni–Me complexes (R-indenyl)Ni(PR′$_3$)Me (R = 1-*i*-Pr, 1-SiMe$_3$, and 1,3-(SiMe$_3$)$_2$; R′= Me, Ph) and outlines their catalytic reactivities in the dehydrogenative oligomerization of PhSiH$_3$ and its addition to styrene in the absence of initiators/activators. Observation of higher hydrosilylation activities for PPh$_3$-based compounds featuring bulky substituents on the indenyl ligand confirms earlier suggestions that phosphine dissociation is an important component of the catalytic cycle for this reaction. In contrast, oligomerization of PhSiH$_3$ is more facile with PMe$_3$-based precursors and independent of the steric bulk of the indenyl ligand, implying that this reaction does not involve phosphine dissociation. These conclusions are consistent with the variable-temperature ^{1}H NMR spectra of {1,3,-(SiMe$_3$)$_2$-indenyl}Ni(PR′$_3$)Me and various structural parameters observed in the solid-state structures of {1,3,-(SiMe$_3$)$_2$-indenyl}Ni(PPh$_3$)Me, {1,3,-(SiMe$_3$)$_2$-indenyl}Ni(PMe$_3$)Cl, and {1-SiMe$_3$-indenyl}Ni(PMe$_3$)Me.

Key words: nickel-indenyl complexes, hydrosilylation, hydrosilane oligomerization.

Résumé : Ce rapport présente la synthèse et la caractérisation des complexes (R-indényle)Ni(PR′$_3$)Me (R = 1-*i*-Pr, 1-SiMe$_3$ et 1,3-(SiMe$_3$)$_2$; R′= Me et Ph) ainsi que la réactivité catalytique de ces composés dans l'oligomérisation déshydrogénative du PhSiH$_3$ et dans son addition au styrène en absence d'un initiateur ou d'un activateur. L'observation des plus grandes activités d'hydrosilylation chez les composés à base de PPh$_3$ et portant des substituants volumineux sur le ligand indényle indique que le cycle catalytique implique la dissociation de la phosphine. D'ailleurs, l'oligomérisation du PhSiH$_3$ est plus facile avec les composés à base de la PMe$_3$ et indépendante de la taille des substituents de l'indényle, ce qui semble indiquer que cette réaction n'implique pas la dissociation de la phosphine. Ces conclusions sont concordantes avec d'autres observations tirées des spectres RMN ^{1}H à températures variables des composés {1,3,-(SiMe$_3$)$_2$-indényle}Ni(PR′$_3$)Me et des études des structures des composés {1,3,-(SiMe$_3$)$_2$-indényle}Ni(PPh$_3$)Me, {1,3,-(SiMe$_3$)$_2$-indényle}Ni(PMe$_3$)Cl et {1-SiMe$_3$-indényle}Ni(PMe$_3$)Me.

Mots-clés : composés nickel-indényles, hydrosilylation, oligomérisation des hydrosilanes.

[Traduit par la Rédaction]

Introduction

Recent reports have shown that the complexes IndNi(L)X (Ind= indenyl and its substituted derivatives; L= neutral ligands such as phosphines or *N*-heterocyclic carbenes; X= anionic ligands such as halides, alkyls, triflate, and so forth) (1) promote the polymerization of ethylene (2), alkynes (3), or PhSiH$_3$ (4) in the presence of activators such as methylaluminoxanes. The in situ activation of these precursors can also be done using cationic initiators, such as AgBF$_4$, NaBPh$_4$, or AlCl$_3$, all of which generate the electronically unsaturated and highly electrophilic cations [IndNi(PR$_3$)]$^+$ (5); these intermediates promote the oligomerization of some olefins (6) as well as the hydrosilylation of olefins and ketones (7). Cationic species can also be generated in the absence of initiators by using the precursors (*i*-Pr-Ind)Ni(PPh$_3$)(OSO$_2$CF$_3$) (8) or [(η^5,η^1-Ind^NR$_2$)Ni(PR$_3$)]$^+$ (^ = various side chains tethering the amine moiety to the Ind ligand) (9), or by heating the complexes [IndNi(PR$_3$)$_2$]$^+$ bearing bulky phosphine ligands (10).

A number of recent studies have shown that of the reactions promoted by IndNi(PR$_3$)X, only those involving hydrosilanes can proceed in the absence of activators/initiators. Thus, the Ni–Me complexes (1-Me-Ind)Ni(PR$_3$)Me (R = Me, Ph, Cy) act as single-component precursors for the dehydrogenative oligomerization of PhSiH$_3$ (11), whereas the Ni–Cl complexes (R-Ind)Ni(PPh$_3$)Cl promote the addition of PhSiH$_3$ to styrene in the absence of any activator/initiator (12). The available mechanistic information indicates that these reactions are sensitive to the steric bulk and (or)

Received 1 May 2008. Accepted 7 July 2008. Published on the NRC Research Press Web site at canjchem.nrc.ca on 24 October 2008.

This paper is dedicated to Professor Richard Puddephatt for his great contributions in Organometallic Chemistry.

Y. Chen[2] and D. Zargarian.[3] Département de Chimie, Université de Montréal, Montréal, QC H3C 3J7, Canada.

[1]This article is part of a Special Issue dedicated to Professor R. Puddephatt.

[2]Present address: Shanghai Institute of Organic Chemistry, Chinese Academy of Science, 354 Fenglin Road, Shanghai 200032, P.R. China.

[3]Corresponding author (e-mail: zargarian.davit@umontreal.ca).

 doi:10.1139/V08-132 © 2008 NRC Canada

Scheme 1.

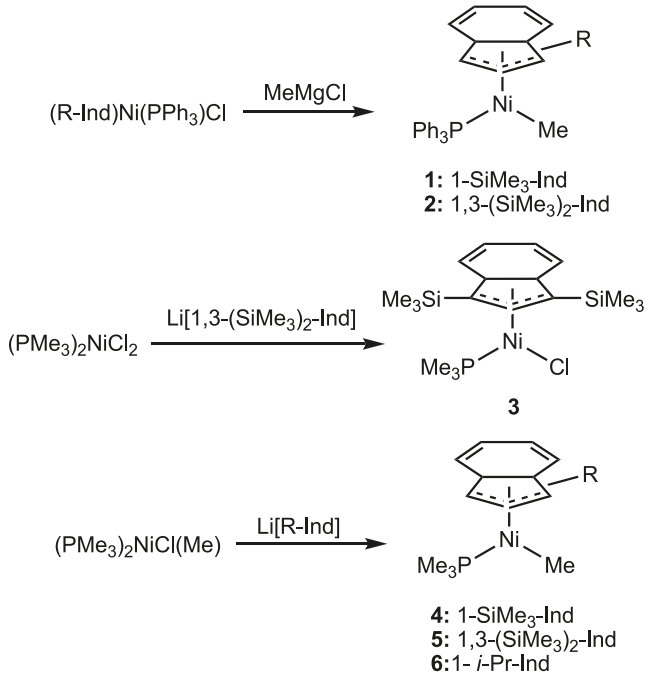

nucleophilicity of the phosphine ligand, the rates following the order $PMe_3 > PPh_3 > PCy_3$ for silane oligomerization (11) and $PPh_3 > PMe_3$ for the hydrosilylation (7). The latter reaction is also favoured by compounds featuring bulkier indenyl ligands (1,3-$(SiMe_3)_2$-Ind > 1-$SiMe_3$-Ind > 1-Me-Ind) (13). These and a number of other observations led us to propose that the hydrosilylation requires the dissociation of the phosphine ligand (12).

As a continuation of our studies on the structure–activity relationships in Ni–indenyl complexes, we have prepared a new series of IndNi(PR_3)Me complexes and studied their structures and reactivities in the oligomerization of $PhSiH_3$ and its addition to styrene as a function of Ind substituents and the phosphine ligands. This report presents the synthesis, characterization, and reactivity studies for the complexes (1-$SiMe_3$-Ind)Ni(PPh_3)Me (**1**), {1,3-$(SiMe_3)_2$-Ind}Ni(PPh_3)Me (**2**), {1,3-$(SiMe_3)_2$-Ind}Ni(PMe_3)Cl (**3**), (1-$SiMe_3$-Ind)Ni(PMe_3)Me (**4**), {1,3-$(SiMe_3)_2$-Ind}Ni(PMe_3)Me (**5**), and {1-*i*-Pr-Ind}Ni(PMe_3)Me (**6**), including the X-ray diffraction studies for **2**–**4**.

Results and discussion

Syntheses

Reaction of (R-Ind)Ni(PPh_3)Cl with MeMgCl gave the corresponding Ni–Me complexes in moderate yields (Scheme 1; R = 1-$SiMe_3$ (**1**, 73%), 1,3-$(SiMe_3)_2$-Ind (**2**, 66%)), but this approach did not work well for the preparation of the analogous PMe_3 complexes because of the difficult purification of the analogous Ni–Cl precursors. For instance, reacting equimolar quantities of Li[1,3-$(SiMe_3)_2$-Ind] and Ni$(PMe_3)_2Cl_2$ gave the desired {1,3-$(SiMe_3)_2$-Ind}Ni(PMe_3)Cl (**3**) in ~50% crude yield. As noted previously, however, the main challenge in the synthesis of Ni–indenyl compounds bearing PMe_3 is avoiding a side reaction that generates Ni$(PMe_3)_4$ and reducing the yield of the desired product (14). Removal of the PMe_3 released during the synthesis by periodic pumping of the reaction mixture helps minimize this decomposition pathway, but does not eliminate it altogether. In the case of **3**, the presence of small quantities of Ni$(PMe_3)_4$ in the reaction mixture complicated the purification, since both species appear to be highly soluble in most solvents, including hexane. However, solution NMR spectra and X-ray analysis of crystals obtained by removal of the oily impurities helped establish the identity of this compound unambiguously (vide infra).

The difficult purification of **3** encouraged us to seek an alternative pathway to the desired Ni–Me compounds. We found that the direct reaction of Li[R-Ind] with $(PMe_3)_2$NiCl(Me) gave reasonable yields of (R-Ind)Ni(PMe_3)Me (Scheme 1; R = 1-$SiMe_3$ (**4**, 87%), 1,3-$(SiMe_3)_2$-Ind (**5**, 64%), *i*-Pr (**6**, 77%)). The purification of **5** was also challenging, but **4** and **6** were obtained in good purity. The characterization of compounds **1**–**6** by solution NMR spectra and, in the case of **2**–**4**, by X-ray diffraction studies was straightforward, as described below.

NMR characterization

All of the complexes showed a single resonance in their $^{31}P\{^1H\}$ NMR spectra at chemical shifts that are characteristic of each type of complex. Thus, **1** and **2** gave singlets at ~47 and 44 ppm, respectively (cf. 48 ppm for (1-Me-Ind)Ni(PPh_3)Me) (15), **3** gave a singlet at ~ –18 ppm (cf. –11 ppm for (1-Me-Ind)Ni(PMe_3)Cl) (14), and **4**–**6** gave singlets at ~ –9 (**5**) and –4 ppm (**4** and **6**) (cf. –3.7 ppm for (1-Me-Ind)Ni(PMe_3)Me) (11).

The ^1H NMR spectra showed a number of characteristic signals for the Ni–Me moiety (~ –0.7 ppm), the $SiMe_3$ substituents (~0.3–0.5 ppm), the PMe_3 ligand (~0.6–0.8 ppm), and H2 of the Ind ligands (~6.1–6.7 ppm). It is interesting to note that methylation of the Ni–Cl bond shifts δ H2 upfield in {1,3-$(SiMe_3)_2$-Ind}Ni(PMe_3)X (from 6.72 to 6.13 ppm), {1,3-$(SiMe_3)_2$-Ind}Ni(PPh_3)X (from ~7 to 6.33 ppm), and (1-$SiMe_3$-Ind)Ni(PPh_3)X (from 6.65 to 6.42 ppm). This upfield shift likely arises from the greater delocalization induced in the five-membered ring moiety of the Ind ligands in Ni–alkyl vs. Ni–halide derivatives (1, 15). Finally, the phenyl rings of the PPh_3 ligand exert some shielding influence on H3 of the Ind ligand that is evident from a comparison of the δH3 in **1** (4.23 ppm) vs. **4** (4.62 ppm) and **6** (4.44 ppm).

We studied the variable-temperature ^1H NMR spectra of **2** and **5** (Fig. 1) and compared them to those of {1,3-$(SiMe_3)_2$-Ind}Ni(PPh_3)Cl to probe the issue of phosphine lability in the Ni–Me derivatives. It is worthwhile to recall that the low-temperature spectra of {1,3-$(SiMe_3)_2$-Ind}Ni(PPh_3)Cl showed a gradual sharpening of the $^{31}P\{^1H\}$ signal as well as the splitting of the ^1H singlet due to the $Si(CH_3)_3$ protons (Fig. 1*a*). The relatively small $\Delta G^{\ddagger}$ value of ~10 kcal/mol (1 cal = 4.184 J) calculated for this exchange process, as well as a number of parameters from the solid-state structure of {1,3-$(SiMe_3)_2$-Ind}Ni(PPh_3)Cl, convinced us that the dynamic exchange observed for this compound was caused by a rapid dissociation/re-association of the PPh_3 ligand as opposed to the hindered rotation of the 1,3-$(SiMe_3)_2$-Ind ligand (12). The lability of the PPh_3 ligand was ascribed to the significant steric interaction with the $SiMe_3$ substituents.

© 2008 NRC Canada

Fig. 1. The variable-temperature ^{1}H NMR spectra (toluene-d_8, 400 MHz) for {1,3-$(SiMe_3)_2$Ind}Ni(PPh_3)Cl (*a*), {1,3-$(SiMe_3)_2$Ind}-Ni(PPh_3)Me (**2**, *b*), and {1,3-$(SiMe_3)_2$Ind}Ni(PMe_3)Me (**5**, *c*).

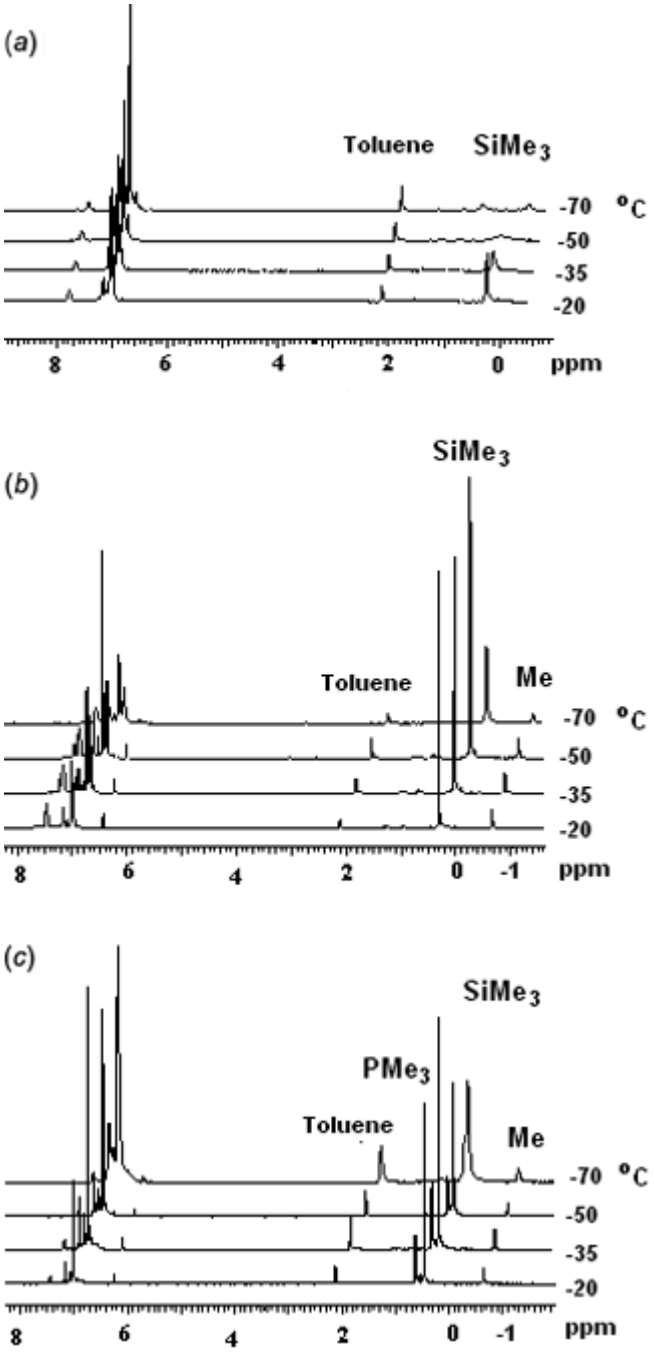

In contrast to the above discussed temperature-dependence of the {1,3-$(SiMe_3)_2$-Ind}Ni(PPh_3)Cl spectra, low-temperature spectra of the Ni–Me derivatives **2** and **5** showed no change in the linewidths of the ^{31}P signals or the multiplicities of the Si(CH_3)$_3$ singlets (Figs. 1*b* and 1*c*) down to –70 °C. These observations can be understood when we consider that methylation of the Ni–Cl bond is anticipated to reinforce the Ni–P bond strength and increase the delocalization of bonding in the five-membered-ring moiety of the Ind ligands; these changes would, in turn, lead to less facile phosphine dissociation and a less hindered Ind rotation. Since the NMR spectra indicate that the exchange process responsible for the equivalence of the $SiMe_3$ substituents in **2** and **5** is faster than the corresponding process in the Ni–Cl complex {1,3-$(SiMe_3)_2$-Ind}Ni(PPh_3)Cl, we conclude that these observations are more consistent with the rapid rotation of the 1,3-$(SiMe_3)_2$-Ind ligand as opposed to a dissociation/re-association of PR_3. The lower lability of their phosphine ligands should influence the hydrosilylation activities of the Ni–Me compounds (vide infra).

Solid-state structures

Single crystals obtained for **2**–**4** allowed us to examine their solid-state structures, which were found to be free of disorder and refined to a good degree of precision, as reflected in the *R* values of 3.77% (**2**), 4.16% (**3**), and 3.62% (**4**). The ORTEP diagrams for these compounds are shown in Fig. 2, and a selection of structural parameters is listed in Table 1; the full list of structural refinement parameters and the crystal data are provided as Supplementary data.[4]

In all three compounds, the coordination geometry around the Ni atom can be described as distorted square-planar, with the largest distortion arising from the small C1–Ni–C3 angles of ~67°. As commonly observed in this family of complexes (1), the Ind–Ni interaction in **2**–**4** is primarily through the allylic carbons, while the Ni–C bond distances for the benzo carbons are longer. This "slippage" away from an ideal η^5 hapticity is attributed to the tendency of Ni(II) to favour forming 16-electron complexes.

Another common type of slippage in this family of complexes is the so-called "sideways slippage", which is reflected in the unsymmetrical Ni–C bonds involving the allylic carbons (Ni–C1 > Ni–C3) and caused by the unequal trans influences of the PR_3 and X ligands (X= halides, phthalimidato, thiolato, triflato, and so forth). Little or no "sideways slippage" is evident in the PMe_3 compounds **3** and **4** (ΔNi–C(1,3) is within 6 esd values), which is consistent with the similar trans influences of PR_3 and Me ligands (1). On the other hand, complex **2** exhibits fairly different Ni–C bond lengths (ΔNi–C(1,3) = 50 × esd). We suspect that this anomalous elongation of the Ni–C3 bond in **2** is due primarily to the steric repulsion between PPh_3 and its neighbouring $SiMe_3$ group. This repulsion is also manifested in the greater C3–Ni–P angle in **2** (111°) compared with **3** (106°) and **4** (104°). Similar observations have been noted for the analogous complexes {$(SiMe_3)_n$-Ind}Ni(PPh_3)Cl (n = 1 or 2) (12).

Finally, the shorter Ni–P bond distance in **4** relative to **2** is consistent with both the greater nucleophilicity of PMe_3 and the larger Tolman cone angle for PPh_3, whereas the shorter

[4] Supplementary data for this article are available on the journal Web site (canjchem.nrc.ca) or may be purchased from the Depository of Unpublished Data, Document Delivery, CISTI, National Research Council Canada, Ottawa, ON K1A 0R6, Canada. DUD 3832. For more information on obtaining material, refer to cisti-icist.nrc-cnrc.gc.ca/cms/unpub_e.shtml. CCDC 686331, 686332, and 686333 contain the crystallographic data for this manuscript. These data can be obtained, free of charge, via www.ccdc.cam.ac.uk/conts/retrieving.html (Or from the Cambridge Crystallographic Data Centre, 12 Union Road, Cambridge CB2 1EZ, UK; fax +44 1223 336033; or deposit@ccdc.cam.ac.uk).

© 2008 NRC Canada

Fig. 2. ORTEP diagrams for complexes **2** (*a*), **3** (*b*), and **4** (*c*). Thermal ellipsoids are shown at the 30% probability level. Hydrogen atoms are omitted for clarity.

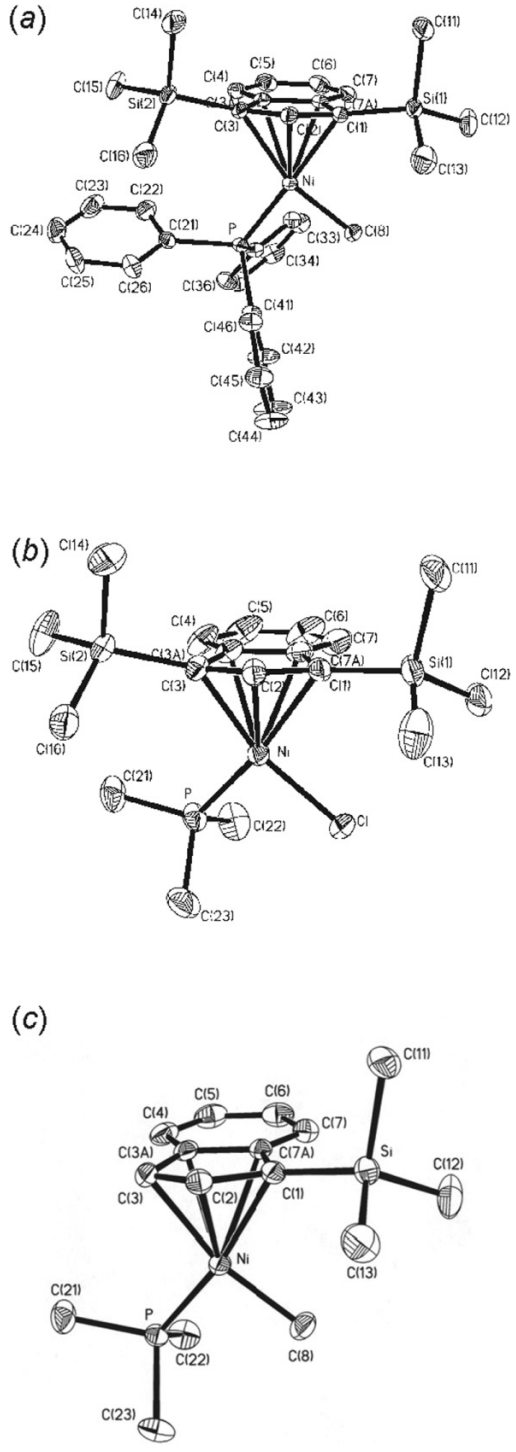

Ni–P bond in **4** relative to **3** reflects the tendency of the Ni–alkyl compounds to form stronger Ni–P interactions compared to their Ni–Cl counterparts (17). To the extent that solid state bond distances can correlate with the kinetic labilities of phosphines, the shorter Ni–P distance in **4** signals lower hydrosilylation activities for this complex (vide infra).

Table 1. Structural parameters for complexes **2**–**4**.

	2 (X= C8)	**3** (X= Cl)	**4** (X= C8)
Ni—C(1)	2.1013(14)	2.108(3)	2.0999(15)
Ni—C(2)	2.0910(14)	2.056(2)	2.0812(16)
Ni—C(3)	2.1763(14)	2.097(3)	2.1098(16)
Ni—C(3a)	2.3015(14)	2.308(3)	2.3075(16)
Ni—C(7a)	2.2700(15)	2.313(3)	2.2887(15)
Ni—X	1.9591(16)	2.1915(8)	1.9456(19)
Ni—P	2.1343(4)	2.1671(8)	2.1129(5)
Si(1)—C(1)	1.8634(15)	1.873(3)	1.8662(16)
Si(2)—C(3)	1.8684(16)	1.883(3)	—
C(1)—C(2)	1.428(2)	1.412(4)	1.431(2)
C(2)—C(3)	1.423(2)	1.418(4)	1.404(2)
C(1)—C(7a)	1.466(2)	1.470(5)	1.463(2)
C(3)—C(3a)	1.457(2)	1.469(4)	1.440(3)
C(3a)—C(7a)	1.434(2)	1.422(5)	1.428(2
X–Ni–C(1)	93.82(6)	96.64(8)	98.66(8)
X–Ni–P	88.07(5)	90.85(3)	90.05(7)
C(1)–Ni–P	173.24(5)	165.21(10)	170.21(5)
X–Ni–C(3)	160.13(6)	163.36(8)	165.32(8)
P–Ni–C(3)	111.60(4)	105.71(8)	104.47(5)
C(1)–Ni–C(3)	66.98(6)	67.63(11)	66.70(6)
ΔNi—C^a (Å)	0.15	0.21	0.19

Catalytic reactivities

The hydrosilylation activities of the Ni–Me complexes were examined for comparison with those of the corresponding Ni–Cl precursors. In addition, we hoped to determine the influence of factors such as nature of the phosphine ligand and the Ind substituents on these reactivities. The addition of $PhSiH_3$ to styrene was selected as a model system to allow comparison to our previous studies. The catalysis is initiated by the direct reaction of $PhSiH_3$ with the Ni–Me moiety, obviating the need for an activator/initiator. The main product of this reaction, $PhCH(Me)(SiPhH_2)$, arises from regioselective (>95%) α-addition of the silyl moiety (eq. [1]); as will be discussed later, appreciable quantities of silane oligomers, $(PhSiH)_n$, are also produced in some cases (vide infra). The catalytic runs were carried out at room temperature with Ni/styrene/$PhSiH_3$ ratios of 1:50:75 or 1:100:125; the excess of $PhSiH_3$ was meant as a compensation for its possible loss in the competitive silane oligomerization side reaction, thus ensuring the availability of sufficient quantities of silane for the desired hydrosilylation reaction. Analysis of the products and quantification of the yields were done according to previously published procedures (12).

[1] 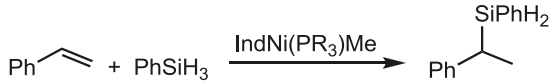

The results of the catalytic hydrosilylation reactions are shown in Table 2. The main point arising from the data is that the Ni–Me derivatives studied display more or less the same level of hydrosilylation activity as their analogous $IndNi(PPh_3)Cl$ complexes when the latter are used in the absence of any initiators (18). For instance, the addition of $PhSiH_3$ to styrene using the complexes $\{1,3\text{-}(SiMe_3)_2\text{-}Ind\}Ni(PPh_3)X$ under the same conditions proceeded with an 82% yield with X = Cl (12) vs. 79% with X = Me (Run 4). The similar catalytic activities of the Ni–Me and Ni–Cl pre-

© 2008 NRC Canada

Table 2. Hydrosilylation of Styrene with $PhSiH_3$ catalyzed by $IndNi(PR_3)Me$.

Run	Ind	PR_3	Ni:Styrene:$PhSiH_3$	Time (h)	Conversion (%)
1	1-Me-Ind	PPh_3[a]	1:50:75	5	37
2	1-$SiMe_3$-Ind	PPh_3	1:50:75	5	26
3	1,3-$(SiMe_3)_2$-Ind	PPh_3	1:50:75	5	74
4	1,3-$(SiMe_3)_2$-Ind	PPh_3	1:100:125	5	79
5	1-Me-Ind	PMe_3[b]	1:100:125	3	18
				5	22
6	1-*i*-Pr-Ind	PMe_3	1:100:125	3	29
				5	31
7	1-$SiMe_3$-Ind	PMe_3	1:100:125	3	11
				5	14
8	1,3-$(SiMe_3)_2$-Ind	PMe_3	1:100:125	3	35
				5	36

Note: Unless otherwise specified, the catalytic runs were conducted at room temperature in 394 mL of benzene using 5 μmol of the Ni precursor.
[a]The runs using PPh_3-based precursors gave traces only of cyclic and linear $(PhSiH)_n$ oligomers.
[b]The runs using PMe_3-based precursors gave variable quantities of cyclic and linear $(PhSiH)_n$ oligomers.

catalysts can be rationalized by noting that both of these precursors generate the same catalytically active intermediates beyond the initiation step.

Inspection of the data listed in Table 2 indicates that the PPh_3 derivatives are more active than their corresponding PMe_3 counterparts (Runs 1–3 vs. 5, 7, and 8), particularly for the precursors featuring the bulky 1,3-$(SiMe)_3$-Ind ligand, the most effective pre-catalyst being complex **2** (Runs 3 and 4). These observations confirm that hydrosilylation activity correlates with steric bulk of the Ind ligand (1,3-$SiMe_3$-Ind > 1-*i*-Pr-Ind > 1-Me-Ind) and phosphine lability (PPh_3 > PMe_3; Ni–Me < Ni–Cl). Interestingly, the Ni:substrate ratio does not appear to have a significant impact on the reactivities (Run 3 vs. 4).

As mentioned above, the PMe_3-based precursors exhibit lower hydrosilylation activities because of the less labile Ni–PMe_3 (12). On the other hand, the PMe_3-based complexes are efficient promoters of the competitive dehydrocoupling of $PhSiH_3$ (eq. [2]), whereas their PPh_3 counterparts are nearly inactive for this reaction; this implies that the dehydrocoupling does not require phosphine dissociation. Upon a closer examination of the silane dehydrocoupling reaction with the $IndNi(PMe_3)Me$ precursors, we found that the outcome of the catalysis was virtually independent of the specific Ind ligand used (Table 3). This implies that all of the $IndNi(PMe_3)Me$ precursors generate the same intermediate (e.g., $Ni^0(PMe_3)_n$) that acts as the active catalyst for the Si–Si bond formation reaction. It is worth noting that previous studies in our group have shown that most $Ni^0(PR_3)_n$ react with $PhSiH_3$ to produce mixtures of cyclic and linear oligomers (19), but the involvement of in situ generated Ni^0 species in the present studies has not been confirmed.

[2] $$PhSiH_3 \xrightarrow[-\ H_2]{IndNi(PMe_3)Me} (PhSiH)_n$$

Conclusion

This study supports our earlier observation that phosphine dissociation is an important step in the addition of $PhSiH_3$ to styrene catalyzed by IndNi(phosphine)X. It follows that PPh_3 derivatives are better catalyst precursors compared to their PMe_3 counterparts, and that bulky indenyl ligands facilitate the catalysis, presumably by favouring the phosphine dissociation step. Contrary to our expectation that stronger Ni–P interactions in the Ni–Me derivatives (supported by both solution and solid-state data) should mean a less facile phosphine dissociation step and hence lower hydrosilylation activities in these complexes, reactivity data showed that the nature of the ligand X (Cl or Me) has no significant impact on the catalysis. Studies are in progress to elucidate the intimate mechanisms of hydrosilylation and silane oligomerization reactions as catalyzed by indenyl–nickel complexes.

Table 3. Dehydrocoupling of $PhSiH_3$ catalyzed by $IndNi(PMe_3)Me$.

	$(PhSiH)_n$			
Ind	M_w	M_n	M_w/M_n	% lin
1-Me-Ind	1197	1172	1.02	79
1-*i*-Pr-Ind	1206	1180	1.02	87
1- $SiMe_3$-Ind	1362	1283	1.06	82
	1439[a,b,c]	1331	1.08	66
	1283[a,c]	1223	1.05	82
	1354[b,c]	1272	1.06	67
	1318[c]	1252	1.05	87
1,3-$(SiMe_3)_2$-Ind	1254	1216	1.03	88

Note: Unless otherwise indicated, the catalytic runs were conducted by stirring the Ni precursor (18 μmol) and $PhSiH_3$ (200 equiv.) in toluene (0.25 mL) at –35 °C for 7 day.
[a]This experiment was run in THF.
[b]This experiment was run at 25 °C.
[c]This experiment was run for 4 days.

Experimental section

General

All manipulations were performed under nitrogen atmosphere using standard Schlenk techniques and a glovebox. Dry, oxygen-free solvents were employed throughout. The Ni precursors $Ni(PR_3)_2Cl_2$ were prepared from $NiCl_2{\cdot}6H_2O$ and PPh_3 or $NiCl_2$ and PMe_3, respectively. The syntheses of 1-$SiMe_3$-IndH and 1,3-$(SiMe_3)_2$-IndH and their Ni deriva-

© 2008 NRC Canada

tives (1-$SiMe_3$-Ind)Ni(PPh_3)Cl and {1,3-($SiMe_3$)$_2$-Ind}Ni(PPh_3)Cl have been described previously;12 1-*i*-Pr-IndH and Li[*i*-Pr-Ind] were prepared as described previously (3*b*, 6*a*). Ni(PMe_3)$_2$MeCl (21) was prepared by reacting Ni(PMe_3)$_2$Cl$_2$ with 1 equiv. of MeMgCl in THF at –30 °C, and characterized by ^{1}H NMR and ^{31}P NMR spectroscopy. All other reagents used in the experiments were obtained from commercial sources and used as received. A Bruker ARX 400 spectrometer was used for recording ^{1}H (400 MHz), ^{13}C{H^1}(100.56 MHz), and ^{31}P{H^1}(161.92 MHz). Unless otherwise noted, the NMR spectra were recorded at 25 °C. The elemental analyses were performed by the Laboratoire d'Analyse Élémentaire (Université de Montréal). The molecular masses of $(PhSiH)_n$ oligomers were measured by a Waters 1525 GPC system with a refractive-index detector, using THF as eluent and polystyrene standards.

(1-$SiMe_3$-Ind)Ni(PPh_3)Me (1)

MeMgCl (0.43 mL of a 3 mol/L solution in THF, 1.30 mmol) was added dropwise to a stirring solution of (1-$SiMe_3$-Ind)Ni(PPh_3)Cl (0.64 g, 1.18, in 40 mL of Et_2O) at room temperature. The reaction mixture was stirred for 30 min after the addition was completed, the solution was concentrated to about 5 mL under vacuum, and the resulting residue was extracted into hexane (40 mL). The extracts were concentrated to about 8 mL and cooled to –30 °C to give a brown solid (0.45 g, 73% yield).

^{1}H NMR (C_6D_6): 7.38 (d, $^3J_{H–H}$ = 8.0 Hz; H4 or H7), 7.35 (m; aromatic protons of PPh_3), 7.28 and 7.05 (t, $^3J_{H–H}$ = 7.6 Hz; H5 and H6), 7.00 (m; aromatic protons of PPh_3), 6.81 (d, $^3J_{H–H}$ = 8.0 Hz; H4 or H7), 6.42 (s; H2), 4.23 (s; H3), 0.53 (s; Si(CH_3)$_3$), –0.52 (d, $^3J_{P–H}$ = 6.0 Hz; Ni–CH_3). ^{13}C{H^1} NMR ($CDCl_3$): 134.2 (d, $^1J_{P–C}$ = 43 Hz; C_{ipso}), 133.9 (d, $^2J_{P–C}$ = 11 Hz; C_{ortho}), 128.9 (C_{para}), 128.1 (d, $^3J_{P–C}$ = 10 Hz; C_{meta}), 125.0, 124.0, 122.9, 121.5, 118.9, and 117.7 (C3A, C4, C5, C6, C7and C7A), 106.3 (d, $^2J_{C–P}$ = 6 Hz; C2), 82.0 (d, $^2J_{C–P}$ = 9 Hz; C3), 82.0 (d, $^2J_{C–P}$ = 12 Hz; C1), 0.2 (–$SiMe_3$), –24.4 (d, $^2J_{P–C}$ = 27 Hz; Ni–CH_3). ^{31}P{H^1} NMR (C_6D_6): 47.1 (s). Anal. calcd. for $C_{31}H_{33}Ni_1P_1Si_1$: C, 71.14; H, 6.36. Found: C, 70.29; H, 6.62.

{1,3-($SiMe_3$)$_2$-Ind}Ni(PPh_3)Me (2)

MeMgCl (0.35 mL of a 3 mol/L solution in THF, 1.05 mmol) was added dropwise to a stirring solution of {1,3-($SiMe_3$)$_2$-Ind}Ni(PPh_3)Cl (0.59 g, 0.95 mmol, in 30 mL of Et_2O) at room temperature. The reaction mixture was stirred for 30 min after the addition was complete, the solvent was removed under vacuum, and the residue was extracted with hexane (~60 mL). The extracts were concentrated to ~5 mL and allowed to stand at room temperature, which gave a brown solid (0.41 g, 66% yield). Single crystals of this compound were grown from cold, concentrated hexane solutions and subjected to X-ray diffraction studies.

^{1}H NMR (C_6D_6): 7.49–7.41 (m; PPh_3), 7.06–6.98 (m; aromatic protons of Ind and PPh_3), 6.33 (s; H2), 0.28 (s; Si(CH_3)$_3$), –0.70 (d, $^3J_{P–H}$ = 7.0 Hz; Ni–CH_3). ^{13}C{H^1} ($CDCl_3$): 134.4 (d, $^2J_{P–C}$ = 11 Hz; C_{ortho}), 134.3 (d, $^1J_{P–C}$ = 43 Hz; C_{ipso}), 129.8 (C_{para}), 128.0 (d, $^3J_{P–C}$ = 10 Hz; C_{meta}), 125.8, 121.9 and 120.7 (C3A, C7A, C5, C6, C4 and C7), 112.1 (C2), 87.9 (C1 and C3), 0.5 ($SiMe_3$), –24.4 (d, $^2J_{P–C}$ = 28 Hz; Ni–CH_3). ^{31}P{H^1} NMR (C_6D_6): 44.0 (s). Anal. calcd. for $C_{34}H_{41}Ni_1P_1Si_2$: C, 68.57; H, 6.94. Found: C, 67.94; H, 7.13.

{1,3-($SiMe_3$)$_2$-Ind}NiPMe_3Cl (3)

A THF solution (100 mL) of Li[1,3-($SiMe_3$)$_2$-Ind] (0.611 g, 2.29 mmol) was added dropwise to a stirring solution of Ni(PMe_3)$_2$Cl$_2$ (0.646 g, 2.29 mmol, in 30 mL of THF) at room temperature. The reaction vessel was placed under vacuum for 30 s at regular intervals (following the addition of each 15 mL aliquot of the Li[1,3-($SiMe_3$)$_2$-Ind] solution) to remove the free PMe_3 released from the reaction (inefficient removal of PMe_3 results in the decomposition of the product and the formation of side-products such as Ni(PMe_3)$_4$). The reaction mixture was stirred for 10 min after the addition was complete, then the solvent was removed under vacuum, and the resulting residue was extracted with hexane (~15 mL). The extracts were concentrated to about 3 mL and allowed to stand at room temperature, which gave red crystals that were covered with a viscous oil (0.457 g, 51% crude yield). Repeated attempts to purify this product were not successful due to the high solubility of the desired product and the main impurity (Ni(PMe_3)$_4$).

^{1}H NMR (C_6D_6): 7.02–6.91 (m; H4, H5, H6 and H7), 6.72 (s; H2), 0.83 (d, $^2J_{P–H}$ = 9.0 Hz; P–CH_3), 0.33 (s; Si(CH_3)$_3$). ^{13}C{H^1} NMR (C_6D_6): 134.4, 125.8 and 120.1 (C3A, C7A, C5, C6, C4 and C7), 116.0 (C2), 86.0 (C1 and C3), 15.3 (d, $^1J_{P–C}$ = 28 Hz; P–CH_3), 0.4 (Si(CH_3)$_3$). ^{31}P{H^1} NMR (C_6D_6): –18.1 (s).

(1-$SiMe_3$-Ind)Ni(PMe_3)Me (4)

A THF solution (30 mL) of Li[1-($SiMe_3$)Ind] (0.232 g, 1.19 mmol) was added dropwise to a stirring THF (30 mL) solution of Ni(PMe_3)$_2$MeCl (0.297 g, 1.13 mmol) at RT. The reaction vessel was placed under vacuum for 30 s at regular intervals (following the addition of each ~7 mL aliquot of the Li[1-($SiMe_3$)Ind] solution) to remove the free PMe_3 released from the reaction (inefficient removal of PMe_3 results in the decomposition of the product and the formation of side-products such as Ni(PMe_3)$_4$). The reaction mixture was stirred for 10 min after the addition was complete, the solvent was removed under vacuum, and the residue was extracted with 20 mL hexane. The solution was concentrated to about 5 mL and cooled to –78 °C to yield a dark red solid (0.332 g, 87% yield).

^{1}H NMR (C_6D_6): 7.51 (d, $^3J_{H–H}$= 7.6 Hz; H4 or H7), 7.14–7.12 (m; aromatic protons of Ind), 7.04 (t, $^3J_{H–H}$ = 7.0 Hz; H5 or H6), 6.27 (bs; H2), 4.62 (b s; H3), 0.60 (d, $^2J_{P–H}$ = 9.1 Hz; P–CH_3), 0.50 (s; Si(CH_3)$_3$), –0.64 (d, $^3J_{P–H}$ = 6.4 Hz; Ni–CH_3). ^{13}C{H^1} NMR (C_6D_6): 126.6, 125.4, 123.1, 122.0, 119.6 and 117.4 (C3A, C7A, C5, C6, C4 and C7), 106.6 (C2), 81.7 (d, $^2J_{C–P}$ = 11 Hz; C1), 76.9 (C3), 16.5 (d, $^1J_{P–C}$ = 28 Hz; P–CH_3), 0.6 ($SiMe_3$), –28.4 (d, $^2J_{P–C}$ = 28 Hz; Ni–CH_3). ^{31}P{H^1} NMR (C_6D_6): –3.5 (s). Anal. calcd. for $C_{16}H_{27}Ni_1P_1Si_1$: C, 57.00; H, 8.07. Found: C, 57.37; H, 8.06.

{1,3-($SiMe_3$)$_2$-Ind}Ni(PMe_3)Me (5)

The procedure used for preparation of complex **4** was used here with Li[1,3-($SiMe_3$)$_2$-Ind] (0.351 g, 1.32 mmol) and Ni(PMe_3)$_2$MeCl (0.328 g, 1.25 mmol). The reaction

© 2008 NRC Canada

mixture was stirred for 10 min after the addition was complete, and then the solvent was removed under vacuum. Recrystallization attempts were unsuccessful because products are highly soluble in non polar solvents such as toluene and hexane. The residue was sublimated at 85–95 °C at 3 Torr (1 Torr = 101 325/760 Pa), and the initially obtained oily solid ((Ni(PMe_3)$_4$)) was cleaned and the sublimation restarted to collect the target product as a dark brown solid (0.301 g, 64% yield).

^{1}H NMR (C_6D_6): 7.45–7.43 and 6.99–6.96 (m; aromatic protons of Ind), 6.13 (s; H2), 0.64 (d, $^2J_{P-H}$ = 9.2 Hz; P–CH_3), 0.42 (s; Si(CH_3)$_3$), –0.71 (d, $^3J_{P-H}$ = 7.2 Hz; Ni–CH_3). ^{13}C{^{1}H} NMR (C_6D_6): 126.4, 122.2 and 121.4 (C3A, C7A, C5, C6, C4 and C7), 111.2 (C2), 87.1 (C1 and C3), 16.3 (d, $^1J_{P-C}$ = 29; P–CH_3), 1.2 ($SiMe_3$), –29.6 (d, $^2J_{P-C}$ = 31 Hz; Ni–CH_3). ^{31}P{^{1}H} NMR (C_6D_6): –8.6 (s). Anal. calcd. for $C_{19}H_{35}Ni_1P_1Si_2$: C, 55.75; H, 8.62. Found: C, 53.83; H, 8.85.

(1-*i*-Pr-Ind)Ni(PMe_3)Me (6)

The procedure used for preparation of complex **4** was used here with Li[1-*i*-Pr-Ind] (0.214 g, 1.30 mmol) and Ni(PMe_3)$_2$MeCl (0.310 g, 1.18 mmol) to give the target complex as a dark red solid (0.277 g, 77% yield).

^{1}H NMR (C_6D_6): 7.21–7.00 (m; aromatic protons of Ind), 6.15 (b s, H2), 4.44 (b s; H3), 2.87 (septet, $^3J_{H-H}$ = 6.8 Hz; C*H*Me_2), 1.39 and 1.35 (d, $^3J_{H-H}$ = 6.8 Hz, CH(CH_3)$_2$), 0.65 (d, $^2J_{P-H}$ = 9.0 Hz; P–CH_3), –0.77 (d, $^3J_{P-H}$ = 6.4 Hz; Ni–CH_3). ^{13}C{^{1}H} NMR (C_6D_6): 122.4, 122.1, 121.5, 120.2, 116.8 and 116.8 (C3A, C7A, C5, C6, C4 and C7), 100.8 (d, $^2J_{C-P}$ = 12 Hz; C1), 97.3 (C2), 70.2 (C3), 25.3 (*i*Pr–CH), 23.8 (*i*Pr–CH_3), 21.1 (*i*Pr–CH_3), 16.5 (d, $^1J_{P-C}$ = 28 Hz; P–CH_3), –22.2 (d, $^2J_{P-C}$ = 25 Hz; Ni–CH_3). ^{31}P{^{1}H} NMR (C_6D_6): –4.0 (s). Anal. calcd. for $C_{16}H_{25}Ni_1P_1$: C, 62.59; H, 8.21. Found: C, 61.93; H, 8.20.

General procedure for catalytic runs

The catalytic runs were carried out by stirring the substrates and the Ni precursors in benzene (hydrosilylations) or toluene (dehydrogenative oligomerizations) at the specified temperatures. The characterization of the products and yield determinations were done on the basis of NMR and GC–MS, as described in our previous report (12).

X-ray crystallographic studies

Crystals suitable for X-ray diffraction studies were obtained by recrystallization of the purified solids (for **2** and **4**) or crude material (for **3**) from hexane solutions. The crystallographic data were collected on a Bruker AXS SMART 2K diffractometer with graphite-monochromated Cu Kα radiation (λ = 1.54178 Å) at 220(2) K, using SMART (20). Cell refinement and data reduction were done using SAINT (21). A SADABS (22) absorption correction was applied. The structures were solved by direct methods using SHELXS97 (23) and difmap synthesis using SHELXL97 (24); the refinements were done on F^2 by full-matrix least squares. The PPh_3 and Cl groups in **2** are disordered. Details of data collection and refinement are listed in Table 1, while a selection of structural parameters is listed in Table 2. Complete crystallographic data for these structures are included in the Supplementary data.[4]

Acknowledgement

The authors are grateful to the Natural Sciences and Engineering Research Council of Canada (NSERC) for financial support of this work.

References

1. For a review on the structures, characterization, and reactivities of group 10 metal indenyl complexes, see: D. Zargarian. Coord. Chem. Rev. **157**, 233 (2002).
2. (*a*) M.-A. Dubois, R. Wang, D. Zargarian, J. Tian, R. Vollmerhaus, Z. Li, and S. Collins. Organometallics, **20**, 663 (2001); (*b*) L.F. Groux, D. Zargarian, L.C. Simon, and J.B.P. Soares. J. Mol. Catal. A: Chem. **193**, 51 (2003).
3. (*a*) R. Wang, F. Belanger-Gariepy, and D. Zargarian. Organometallics, **18**, 5548 (1999); (*b*) R. Wang, L.F. Groux, and D. Zargarian. J. Organomet. Chem. **660**, 98 (2002); (*c*) E. Rivera, R. Wang, X.X. Zhu, D. Zargarian, and R. Giasson. J. Mol. Catal. A, **325**, 204 (2003).
4. F.G. Fontaine, T. Kadkhodazadeh, and D. Zargarian. Chem. Commun. 1253 (1998).
5. R. Vollmerhaus, F. Belanger-Gariepy, and D. Zargarian. Organometallics, **16**, 4762 (1997).
6. (*a*) M.-A. Dubois. M.Sc. Thesis. Universite de Montreal. 2000; (*b*) H.-M. Sun, W.-F. Li, X. Han, Q. Shen, and Y. Zhang. J. Organomet. Chem. **688**, 132 (2003); (*c*) W.-F. Li, H.-M. Sun, Q. Shen, Y. Zhang, and K.-B. Yu. Polyhedron, **23**, 1473 (2004).
7. F.-G. Fontaine, R.-V. Nguyen, and D. Zargarian. Can. J. Chem. **81**, 1299 (2003).
8. R. Wang, L.F. Groux, and D. Zargarian. Organometallics, **21**, 5531 (2002).
9. (*a*) L.F. Groux, F. Belanger-Gariepy, D. Zargarian, and R. Vollmerhaus. Organometallics, **19**, 1507 (2000); (*b*) L.F. Groux and D. Zargarian. Organometallics, **20**, 3811 (2001); (*c*) L.F. Groux and D. Zargarian. Organometallics, **22**, 3124 (2003); (*d*) L.F. Groux and D. Zargarian. Organometallics, **22**, 4759 (2003).
10. M. Jimenez-Tenorio, M.C. Puerta, I. Salcedo, P. Valerga, S.I. Costa, L.C. Silva, and P.T. Gomes. Organometallics, **23**, 3139 (2004).
11. F.G. Fontaine and D. Zargarian. Organometallics, **21**, 401 (2002).
12. Y. Chen, C. Sui-Seng, S. Boucher, and D. Zargarian. Organometallics, **24**, 149 (2005).
13. For instance, the addition of $PhSiH_3$ to styrene catalyzed by IndNi(PPh_3)Cl in the absence of any activator/initiator gives yields of 7% (1-Me-Ind), 56% (1-$SiMe_3$-Ind), and 82% (1,3-($SiMe_3$)$_2$-Ind) (see ref. 12). It is important to emphasize, however, that for reactions run in the presence of initiators/activators, the steric bulk has little or no favourable influence on the reactivities unless the Ind ligand is substituted at both 1- and 3-positions. For instance, the addition of $PhSiH_3$ to styrene catalyzed by the combination of (1-R-Ind)Ni(PPh_3)Cl and $NaBPh_4$ is no more effective with R = *i*-Pr (61%) than Me (69%) (see ref. 7). This can be understood by recalling that the complexes (1-R-Ind)Ni(PPh_3)X always adopt a configuration that places the PPh_3 ligand away from the more bulky Ind substituent to avoid steric congestion (see ref. 1); hence, placing a substituent at the 1-position has no advantage for increasing the lability of the phosphine ligand or the catalytic activities.
14. F.-G. Fontaine, M.-A. Dubois, and D. Zargarian. Organometallics, **20**, 5145 (2001).

© 2008 NRC Canada

15. T.A. Huber, M. Bayrakdarian, S. Dion, I. Dubuc, F.G.-Belanger, and D. Zargarian. Organometallics, **16**, 5811 (1997).
16. F.-G. Fontaine and D. Zargarian. Organometallics, **21**, 401 (2002).
17. Ni–PR_3 interactions in IndNi(PR_3)X compounds can be understood in the following terms. Relatively soft X ligands like alkyls result in more effective interactions and shorter Ni–P bonds, whereas harder X ligands such as halides give less effective and longer Ni–P bonds. An alternative explanation for the less effective Ni–X bonds is in terms of cis-labilizing interactions between the occupied d_{z2} orbital on Ni and the lone pair of electrons on ligands X (halide, OR, NR_2, and so forth).
18. It should be added that the Ni–Cl precursors form much more efficient catalysts when used in conjunction with cationic initiators such as $NaBPh_4$ (12).
19. M. Morissette. M.Sc. Dissertation. Universite de Montreal. 2001.
20. R. Wang, L.F. Groux, and D. Zargarian. J. Organomet. Chem. **660**, 98 (2002).
21. H.F. Klein and H.H. Karsch. Chem. Ber. **105**, 2628 (1972).
22. SMART [computer program]. Release 5.059. Bruker molecular analysis research tool. Bruker AXS Inc. Madison, WI. 1999.
23. SAINT [computer program]. Release 6.06. Integration software for single crystal data. Bruker AXS Inc. Madison, WI. 1999.
24. G.M. Sheldrick. SADABS [computer program]. Bruker area detector absorption corrections. Bruker AXS Inc. Madison, WI. 1997.
25. G.M. Sheldrick. SHELXS [computer program]. Program for the solution of crystal structures. University of Goettingen, Germany. 1997.
26. G.M. Sheldrick. SHELXL [computer program]. Program for the refinement of crystal structures. University of Goettingen, Germany. 1997.

© 2008 NRC Canada

Approaches to alkane functionalization with Tp′Pt and (nacnac)Pt reagents[1]

Nathan M. West and Joseph L. Templeton

Abstract: In this perspective article we give an overview of our studies of C–H activation with platinum over the past decade. The scorpionate ligand Tp′ (Tp′ = hydrotris(3,5-dimethylpyrazolyl)borate) has exhibited the ability to stabilize both Pt(IV) and Pt(II) complexes due to flexibility between κ^3 and κ^2 binding modes. Control of the Tp′ coordination mode and Pt oxidation state is tightly coupled with acid/base chemistry. This ability allowed us to model a spectrum of intermediates in C–H activation reactions, including Pt(IV) alkyl hydrides, five-coordinate Pt(IV) silyl hydrides, and Pt(II) benzene complexes. We have been able to observe sturdy Pt(II) benzene complexes and probe their equilibria with the respective C–H activated Pt(IV) species in the presence of an added ligand. We have also taken steps toward functionalizing hydrocarbons with Tp′Pt by dehydrogenation of alkanes and by arylation of olefins. We have recently turned to bidentate nacnac (nacnac = N-phenyl-β-enamineimine) ligands in the hopes of catalytically functionalizing hydrocarbons.

Key words: C–H activation, reductive elimination, Tp′Pt, five-coordinate, β-diiminate.

Résumé : Dans cet article de perspective, on donne une vue d'ensemble de nos études sur l'activation des liaisons C–H par le platine qui ont été réalisées sur une période de quarante ans. Le ligand scorpionate, Tp′ (Tp′ = hydroxytris(3,5-diméthylpyrazolyl)borate a montré une habilité à stabilizer les complexes tant du Pt(IV) que ceux du Pt(II) en raison de la flexibilité entre les modes de fixation κ^3 et κ^2. Le contrôle du mode de coordination du Tp′ et l'état d'oxydation du platine sont fortement couplés avec la chimie acide/base. Cette habilité nous a permis de faire un modèle des spectres d'intermédiaires dans les réactions d'activation d'une liaison C–H, dont les hydrures d'alkyle-platine(IV), d'hydrures pentacoordinés de silyle-platine(IV) et de complexes Pt(II)-benzène. Il a été possible d'observer les complexes solides de Pt(II)-benzène et d'étudier leurs équilibres avec les espèces respectives de liaisons C–H activées par le platine(IV), en présence d'un ligand ajouté. On a aussi tenter de fonctionnaliser des hydrocarbures à l'aide du Tp′Pt en procédant à la déshydrogénation d'alcanes et l'arylation d'oléfines. Dans le but de fonctionnaliser des hydrocarbures d'une façon catalytique, on s'est récemment tourner vers les ligands bidentates nacnac (nacnac = *N*-phényl-β-énamineinimine).

Mots-clés : activation de liaisons C–H, élimination réductrice, Tp′Ph, pentacoordination, β-diiminate.

[Traduit par la Rédaction]

Introduction

Platinum-catalyzed C–H functionalization

Selective oxidation of alkanes has been an important goal for decades. This challenging reaction continues to attract widespread attention as fossil fuels are consumed and the price of energy soars (1). Even as fossil fuel supplies are depleted, alkanes from petroleum, particularly natural gas, remain abundant (1–4). Alkanes have high C–C and C–H bond strengths and are relatively inert (3, 5, 6). Dehydrogenation of alkanes can be accomplished thermally, but only at high temperatures (5). Radical oxidation reactions are capable of alkane functionalization, but they are not regioselective; furthermore, the partially oxidized products have weaker C–H bonds than the starting alkane, so they are poised to undergo overoxidation (7, 8).

Because of the expense required to capture, transport, and store gases, methane, the primary component of natural gas, is not being fully exploited as a fuel source. Low cost direct conversion of methane to a liquid fuel would allow its use as an alternative to traditional fossil fuels. The chemical reactivity limitations of alkanes have prevented industrial syntheses of methanol directly from methane; it is currently formed from syngas (H_2/CO). Organometallic reagents have demonstrated the ability to selectively activate and oxidize the C–H bonds of alkanes without overoxidation; further development of these catalysts may allow for the selective functionalization of alkanes under mild conditions (2, 3, 5–7, 9–18).

One of the first examples of alkane functionalization was Shilov and co-workers's report (18) of the oxidation of

Received 16 April 2008. Accepted 5 July 2008. Published on the NRC Research Press Web site at canjchem.nrc.ca on 30 October 2008.

This paper is dedicated to Professor Richard Puddephatt for his great contributions in Organometallic Chemistry.

N.M. West and J.L. Templeton.[2] Department of Chemistry, University of North Carolina at Chapel Hill, Chapel Hill, NC 27599-3290, USA.

[1]This article is part of a Special Issue dedicated to Professor R. Puddephatt.

[2]Corresponding author (e-mail: joetemp@unc.edu).

 doi:10.1139/V08-141 © 2008 NRC Canada

Scheme 1. Shilov oxidation of methane to methanol.

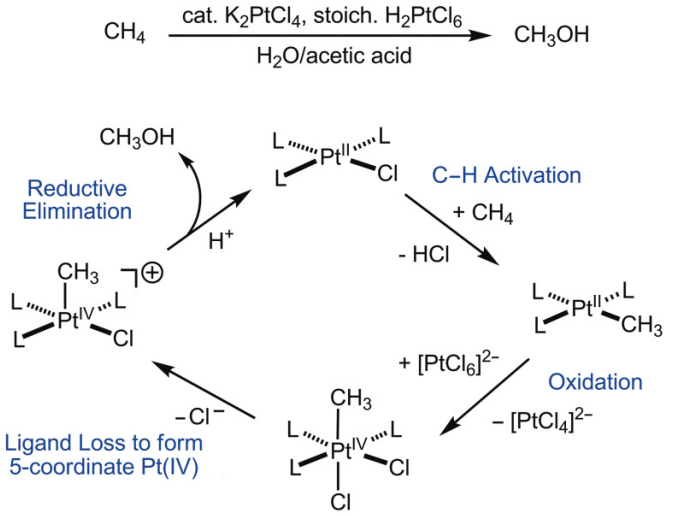

methane to methanol catalyzed by Pt(II) (Scheme 1). Good selectivity for methane activation was observed and many research groups have since focused on studying d^8 metal reagents for alkane functionalization. Recent successes have intensified research efforts directed toward methane oxidation catalysts based on platinum (16).

The Shilov system is impractical due to the stoichiometric consumption of Pt(IV) as the oxidant. There have been significant improvements in utilizing cheaper oxidants, but no industrially feasible process for converting methane to methanol has been discovered. The most successful methane oxidation system reported to date is a bipyrimidine ligated Pt(II) catalyst used in fuming sulfuric acid (Scheme 2), which gives high yields of the methanol surrogate $MeOSO_3H$. Economic factors and harsh reaction conditions, however, have prevented it from being utilized industrially (16). Despite considerable strides, there continues to be a need to study the activation and functionalization of alkanes in the hope of developing a catalyst for selective alkane oxidation (5, 19).

The mechanism of the Shilov oxidation, studied extensively by Bercaw and Labinger (5), is proposed to proceed by three key steps: oxidative addition of the C–H bond to Pt(II) followed by loss of a proton, oxidation of a Pt(II)Me species to a Pt(IV)Me intermediate, and reductive elimination of C–X (X = OH, Cl) (8). Reactive five-coordinate species are proposed as key intermediates formed from C–H activation and leading to C–X bond formation, respectively. An array of bidentate nitrogen ligands has been used to stabilize Pt(II) intermediates relevant to the Shilov oxidation. Monomethyl Pt(II) species, like the one involved in the catalytic oxidation, can often be formed by protonation of a dimethyl Pt precursor since methane loss results in many cases. If D^+ is used rather than H^+ then scrambling of the deuterium into the remaining Pt bound methyl group occurs, indicating that reductive elimination and oxidative addition of CH_4 are reversible and a σ-methane adduct must be involved (Scheme 3) (20, 21).

Isolation of five-coordinate intermediates involved in C–H activation, particularly alkyl hydrides, has proven challenging due to their propensity to undergo reductive elimination

Scheme 2. Catalytica system for methane oxidation by platinum.

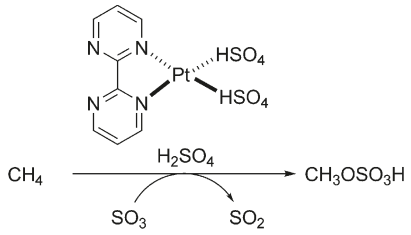

Scheme 3. Modeling Pt(II) intermediates with α-diimine ligands.

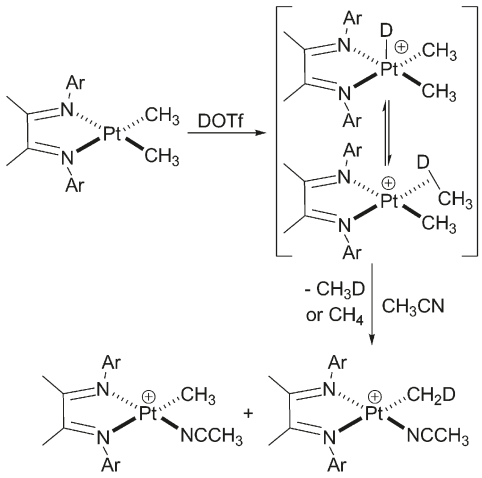

(22, 23). To access these Pt(IV) species we have employed scorpionate tris(pyrazolyl)borate ligands. These ligands are capable of binding in a κ^2 fashion in Pt(II) square-planar compounds, but they can coordinate in a κ^3 fashion to stabilize Pt(IV) octahedral complexes after oxidative addition of Pt(II).

Discussion

Accessing models of reactive Pt(IV) intermediates via reactions of Tp′PtMe$_2$H

The Pt(II) precursors [K][TpPtMe$_2$] Tp (Tp = hydridotris(pyrazolyl)borate) and [K][Tp′PtMe$_2$] Tp′ (Tp′ = hydridotris(3,5-dimethylpyrazolyl)borate) can be protonated with weak acids to form a five-coordinate dialkylhydride, which is immediately trapped by the third arm of the pyrazolyl borate ligand before elimination of methane can occur. The results of these reactions were the first thermally stable Pt(IV) complexes with cis alkyl hydride ligands, TpPtMe$_2$H and Tp′PtMe$_2$H; the latter was structurally characterized (24, 25). Wick and Goldberg (26) reported that addition of the Lewis acid $B(C_6F_5)_3$ to the anionic dimethyl Pt(II) precursor [K][Tp′PtMe$_2$] results in methide abstraction to form the Tp′PtMe fragment and then C–H activation of alkane solvent forms stable Pt(IV) alkyl hydride complexes (Scheme 4). Other tridentate nitrogen donor ligands have also demonstrated the ability to stabilize Pt(IV) species by inhibiting the formation of five-coordinate species (27–31). Early Tp′Pt chemistry was reviewed in Activation and functionalization of C–H bonds (32).

Thermolysis of Tp′PtMe$_2$H in arene solvent resulted in loss of methane at temperatures above 100 °C. Methane loss

© 2008 NRC Canada

Scheme 4. Stabilization of Pt(IV) alkyl hydrides with Tp′.

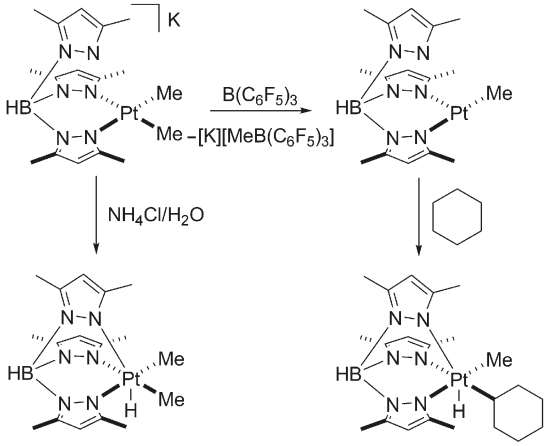

is followed by arene C–H activation, and formation of an aryl alkyl hydride Pt(IV) complex results. This complex then loses a second equivalent of methane to ultimately produce a diaryl hydride complex as the final product (33). The high temperatures required for reductive elimination reflect the stability of the six-coordinate Pt(IV) complex that is anchored by the tridentate Tp′ ligand. The thermodynamic parameters for elimination of the first equivalent of methane are $\Delta H^{\ddagger} = 35.0 \pm 1.1$ kcal/mol and $\Delta S^{\ddagger} = 13 \pm 3$ cal/mol deg (34). If the complex is thermolyzed in deuterated benzene, a mixture of methane isotopologs is observed. The first equivalent of methane eliminated is CH_4, but the second equivalent is a mixture of CH_3D, CH_2D_2, and CHD_3 (CD_4 may be present but it is invisible by ^{1}H NMR). If reductive coupling of methane were irreversible only CH_3D would be observed; the presence of methane isotopologs indicates that reductive coupling of methane to form a sigma Pt(CH_4) complex is reversible. This reductive coupling within the coordination sphere was examined by thermolysis of Tp′PtMe$_2$D at temperatures well below 100 °C, and Tp′PtMe(CH_2D)H was formed with no loss of methane. The thermodynamic parameters for this process are $\Delta H^{\ddagger} = 26 \pm 1$ kcal/mol and $\Delta S^{\ddagger} = 1 \pm 4$ cal/mol deg. The significantly lower barrier to reductive coupling to form methane than for elimination of methane indicates that it is dissociation of methane that is rate limiting; the activation entropy values also support this.

Reductive elimination of methane from Tp′PtMe$_2$H via protonation

Addition of strong acid to Tp′PtMe$_2$H resulted in protonation and dechelation of one of the Tp′ arms from the platinum center. The resulting five-coordinate complex reductively eliminates methane, even at –78 °C, and forms [(Hpz*)HB(pz*)$_2$Pt(Me)(solv)]$^+$, which binds a variety of trapping ligands (35). This low temperature pathway to reductive elimination of methane provided a useful alternative to high temperature thermolysis for the synthesis of Pt(II) products. The protonated Tp′ ligand is ineffective at stabilizing Pt(IV) alkyl hydride complexes, so the Tp′ ligand combines with acid/base chemistry to model both Pt(IV) and Pt(II) intermediates in the Shilov oxidation. Addition of D$^+$ to the dimethyl hydride complex resulted in no deuterium incorporation into either the Pt methyl groups or the evolved methane, so protonation of the Pt–N bond at nitrogen is the only detectable process. Note that protonation of Tp′PtMe$_2$D resulted in the loss of both CH_3D and CH_4 along with scrambling of deuterium into the remaining Pt methyl group. With one Tp′ arm protonated, reductive coupling to form methane is rapid and reversible and precedes methane elimination. Here, too, a sturdy sigma adduct of methane forms as an intermediate after reductive coupling builds the C–H link.

Scheme 5. Nucleophilic attack of the CO ligand in Tp′PtMeCO.

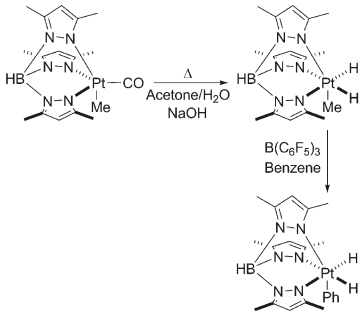

Moving from Tp′PtMe$_2$H to Tp′PtMeH$_2$ (36) and from Tp′PtMeH$_2$ to Tp′PtH$_3$ (37, 38) was accomplished by heating Tp′Pt(R)CO (R = Me, H) in acetone and water in the presence of base (Scheme 5). Haskel and Keinan (39) first reported a similar procedure for converting TpPtMeCO to TpPtMeH$_2$. Our modified procedure included the addition of a base, which increased the reaction rate. Presumably, the CO ligand is attacked by hydroxide and then elimination of CO_2 reduces the metal and allows for protonation by water. This reaction represents one half of the water-gas shift reaction, which interconverts H_2O and CO with H_2 and CO_2, respectively. Hydrogen formation from the Pt(IV) dihydride complex would complete the water-gas shift cycle.

The methyl dihydride species Tp′PtMeH$_2$ can be converted into an aryl dihydride Tp′PtArH$_2$ by gentle heating with $B(C_6F_5)_3$ in arene solvent (33). Methane loss and arene C–H activation occur yielding the desired compound.

Reversible C–H activation of a coordinated benzene complex

We have used thermolysis experiments to study C–H activation of benzene at high temperatures, but protonation makes it possible to observe arene C–H activation at low temperatures. Protonation of Tp′Pt(Ph)(H)$_2$ at low temperatures leads to reductive elimination of benzene, but below –30 °C the benzene remained in the inner coordination sphere in an η^2 fashion as evident in the crystal structure of [κ^2-HTp′Pt(H)(C_6H_6)][BAr′$_4$] (40, 41). Such η^2-coordinated benzene complexes had been previously observed by NMR (42). They bear some similarities to the elusive coordinated alkane adducts that precede alkane C–H activation. These η^2-benzene complexes undergo rapid and reversible C–H activation to form an unobserved five-coordinate Pt(IV) phenyl dihydride intermediate. The equilibrium lies far toward the Pt(II) benzene complex on the left, but activation of the C–H bonds was confirmed by spin-saturation transfer experiments in the ^{1}H NMR that showed exchange between the platinum hydride and the benzene protons (Scheme 6).

Five-coordinate Pt(IV) complexes are proposed as intermediates in most Pt(II)/Pt(IV) oxidative addition/reductive

© 2008 NRC Canada

Scheme 6. Reversible C–H activation of a coordinated benzene molecule.

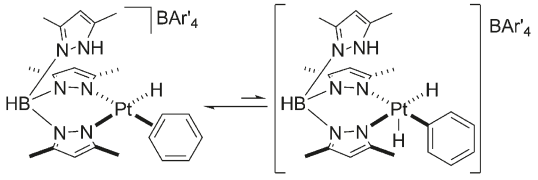

Scheme 7. Trapping of a five-coordinate phenyl dihydride intermediate with CH_3CN.

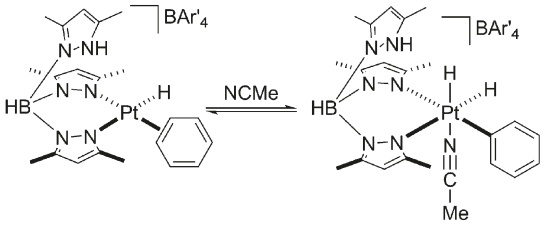

elimination processes, but only a handful of five-coordinate Pt(IV) complexes have been either directly observed or isolated (43). While we could not directly observe the five-coordinate species formed from C–H activation of benzene, we have spectroscopic and chemical reactivity evidence to support its existence. Several isolated examples of five-coordinate Pt(IV) complexes contain the $PtMe_3$ fragment (44–48); one is built around a (N-N)$Pt(SiMe_3)Me_2$ framework (49) and another is formulated as [κ^2-HTp′$Pt(H)_2(SiR_3)$][BAr′4] (50). Of these five-coordinate Pt(IV) complexes, the only one formed by bond activation is the latter complex, which was formed by oxidative addition of the Si–H bond in $HSiR_3$ to Pt(II) in [κ^2-HTp′Pt(H)(solv)][BAr'_4].

The barrier to arene C–H activation was determined by line broadening measurements on the platinum hydride signal and was found to have a $\Delta G^{\ddagger}$ of 12.7 kcal/mol at 241 K with $\Delta H^{\ddagger}$ = 11.7 ± 0.5 cal/mol deg and $\Delta S^{\ddagger}$ = –3.8 ± 2 cal/mol deg. The phenyl benzene complex [κ^2-HTp′Pt(Ph)(C_6H_6)][BAr'_4] had a $\Delta G^{\ddagger}$ of 12.9 kcal/mol at 241 K, while the deuterated version, [κ^2-HTp′Pt(C_6D_5)(C_6D_6)][BAr'_4], had a $\Delta G^{\ddagger}$ of 13.6 kcal/mol at 241 K.

It is important to note that addition of excess benzene to a solution of [κ^2-HTp′Pt(H)(C_6H_6)][BAr'_4] did not result in the exchange of free and coordinated benzene; alkenes, on the other hand, easily displace the benzene (vida infra). Furthermore, formation of [κ^2-HTp′Pt(H)(solv)][BAr′4] via protonation of Tp′$PtMeH_2$ in the presence of benzene did not result in the formation of a Pt-benzene adduct. The kinetic reluctance of benzene to trap the putative [κ^2-HTp′Pt(H)(solv)]$^+$ cation is almost certainly due to the energetic cost of breaking the aromaticity of benzene to coordinate it to the metal. Aromaticity also helps explain the low barrier to C–H activation because the phenyl group regains its aromaticity during conversion from η^2 to being σ-bound to the metal.

Given the stability of the benzene hydride complex at low temperatures we hypothesized that the addition of a weak ligand might allow us to trap the proposed five-coordinate Pt(IV) phenyl dihydride, but not displace the coordinated benzene. Upon addition of acetonitrile to [κ^2-HTp′Pt(H)(C_6H_6)][BAr'_4] below –30 °C we observed a mixture of the six-coordinate Pt(IV) phenyl dihydride nitrile adduct [κ^2-HTp′$Pt(H)_2$(Ph)($NCCH_3$)][BAr′4], in which the two hydrides were inequivalent, and the four-coordinate [κ^2-HTp′Pt(H)(C_6H_6)][BAr'_4] (51). In the dihydride complex, one hydride resided trans to acetonitrile and one was trans to a pyrazolyl nitrogen. The hydride trans to the acetonitrile resonated at –23.4 ppm and had a $^1J_{Pt\text{-}H}$ value of 1525 Hz, whereas the other hydride resonated at –19.4 ppm and had $^1J_{Pt\text{-}H}$ equal to 1279 Hz; the large coupling constant of the hydride at –23.4 indicated that the acetonitrile was weakly bound.

Thus, the nitrile trapping result substantiated the existence of the unobserved five-coordinate intermediate. The two compounds, square planar Pt(II) and octahedral Pt(IV), are in dynamic equilibrium and the six-coordinate acetonitrile product is favored by only 0.3 kcal/mol at 230 K (Scheme 7). Not surprisingly, as the nucleophilicity of the nitrile is increased the equilibrium shifts towards the six-coordinate species; at 201 K the K_{eq} value for *p*-OMe benzonitrile is 17.0 compared to 0.54 for *p*-CF_3 benzonitrile. For CH_3CN, *p*-OMe benzonitrile, and *p*-CF_3 benzonitrile ΔH° values of –5.9, –5.0, and –4.0 kcal/mol were determined, respectively, indicating that the more electron rich alkyl nitriles favor Pt(IV) more than the aryl nitriles. This result couples with ΔS° values near –20 cal/mol deg to indicate that nitrile coordination to the metal is the key element that determines the equilibrium constant.

Trapping of five-coordinate alkyl dihydride and trihydride species with added ligand

We have used similar trapping methods to study five-coordinate intermediates involved in reductive elimination of methane. Protonation of the methyl dihydride complex at a low temperature followed by addition of acetonitrile resulted in trapping to form an observable six-coordinate Pt(IV) dihydride species, [κ^2-HTp′$Pt(H)_2$(Me)(NCMe)][BAr'_4] (38). As in the benzene case, the two hydrides were inequivalent with one trans to the nitrile and one trans to a pyrazolyl nitrogen. One hydride appeared at –24.0 ppm with a $^1J_{Pt\text{-}H}$ of 1496 Hz and the other at –20.7 ppm with a $^1J_{Pt\text{-}H}$ of 1265 Hz; these values are similar to those of the trapped phenyl dihydride species. This product was the only one formed, and while it may be in equilibrium with a σ methane adduct, we did not observe such a species (Scheme 8).

Once again, trapping with nitrile supplied evidence for the intermediacy of a five-coordinate species involved in C–H activation. Methane elimination occurred to form [κ^2-HTp′Pt(H)(NCMe)][BAr'_4] when the six-coordinate Pt(IV) methyl dihydride acetonitrile adduct was allowed to reach temperatures above –30 °C. Assuming that nitrile loss is essential for reductive coupling to form the C–H bond of methane from a five-coordinate species, the σ-methane ligand is not easily displaced by the trapping the acetonitrile ligand at low temperatures. Note that we observed no elimination of dihydrogen; this was also true when Tp′$PtMeH_2$ was protonated without added trapping ligand.

One of our goals has been to study reductive elimination, or lack thereof, of hydrogen from the Tp′Pt(IV) system in hopes of learning why we do not observe H_2 loss from

© 2008 NRC Canada

Scheme 8. Trapping of a five-coordinate methyl dihydride intermediate with CH_3CN.

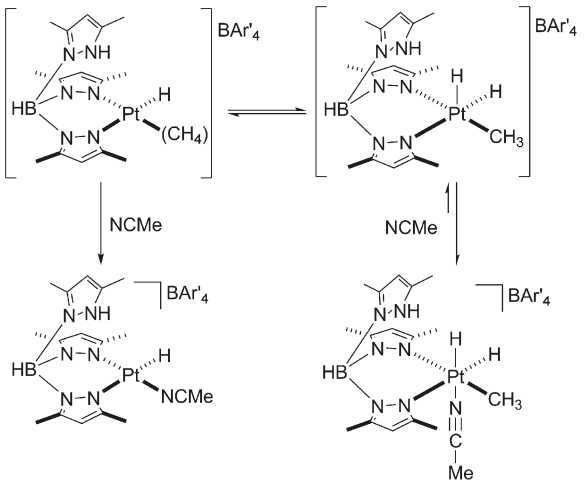

Tp′Pt(R)$(H)_2$ (R = Me, Ph). To stack the deck in favor of H_2 elimination we began by studying the trihydride, Tp′PtH_3, because it has no alkane option for reductive elimination. Protonation of the trihydride complex with $[H(OEt_2)_2][BAr'_4]$ did not result in reductive elimination of H_2; rather, it formed an unidentified species, which decomposes to regenerate starting material and Pt black. In an attempt to identify the unidentified species, we added acetonitrile as a trapping reagent as we had done in the other low temperature reductive elimination studies. Once again the trapping ligand worked beautifully, and the result was a quantitative formation of $[\kappa^2$-HTp′Pt$(H)_3$(NCMe)$][BAr'_4]$. The compound displayed one unique and two equivalent hydrides by ^{1}H NMR, with chemical shifts of –24.1 ppm for the unique hydride and –20.0 ppm for the two equivalent hydrides. Warming the complex did not result in reductive elimination of hydrogen; only starting material was detected.

Different results were obtained when CO was used as the trapping ligand in place of acetonitrile. The CO coordinated to the metal, forming the six-coordinate trihydride $[\kappa^2$-HTp′Pt$(H)_3$(CO)$][BAr'_4]$ just as the nitrile did, but now upon warming, reductive elimination of hydrogen occured and the Pt(II) hydride product, $[\kappa^2$-HTp′Pt(H)(CO)$][BAr'_4]$, formed (Scheme 9). The six-coordinate precursor species displayed one hydride signal at –12.3 ppm with a $^1J_{Pt\text{-}H}$ of 1126 Hz and two equivalent hydrides appeared at –17.5 ppm with a $^1J_{Pt\text{-}H}$ of 1114 Hz. The downfield of the unique hydride trans to CO indicated that it resided trans to a strong π-acid ligand. Kinetic measurements of the H_2 elimination yielded thermodynamic parameters of $\Delta H^{\ddagger}$ = 23.0 (1.0) kcal/mol and $\Delta S^{\ddagger}$ = 24.5 (4.0) cal/mol deg. The positive entropy and the exclusion of other possible mechanisms lead us to believe that H_2 reductive elimination occurs directly from the six-coordinate trihydride carbonyl complex and that *dissociation* of H_2 is rate limiting. Thermal reductive elimination of methane from Tp′$PtMe_2H$ proceeds with rate-limiting dissociation as well. This hydrogen forming reaction is a rare example of reductive elimination from a six-coordinate Pt(IV) species; reductive elimination typically occurs from a five-coordinate Pt(IV) species (52). We believe the strong π-acid properties of the CO ligand promote hydrogen formation.

Scheme 9. Possible reaction coordinate for carbon monoxide promoted hydrogen elimination from $[HTp'PtH_3]^+$.

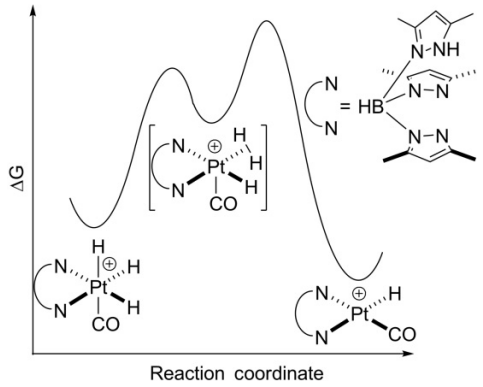

The nitrile adduct is presumably too electron rich to support formation and elimination of H_2.

Re-examination of the protonation and trapping of Tp′$PtMeH_2$ using CO instead of acetonitrile yielded different results. When CO was used, both methane and hydrogen were eliminated. The ratio of methane loss to hydrogen loss was about 5:1. While methane loss still dominates, this result further supports the claim that H_2 elimination is favored by the π-acid character of the CO ligand. An attractive hypothesis is that H_2 loss can occur from a saturated six-coordinate intermediate, while reversible CO binding allows methane to be eliminated from an unsaturated five-coordinate intermediate.

Olefin insertion into the Pt-phenyl bond of Tp′PtPh(olefin)

While mechanistic studies of C–H activation are essential for intelligent design of future catalysts, the C–X (X = C, heteroatom) bond formation required for functionalizing molecules often proves even more challenging. To this end we were eager to explore C–C bond forming reactions for hydrocarbon functionalization. We decided to probe olefin insertion reactions as a means to form new C–C bonds.

Low temperature protonation/deprotonation has been used to synthesize Tp′Pt(ethylene)(Ph) complexes starting from the diphenyl hydride reagent, Tp′$PtPh_2H$. An X-ray crystal structure of the ethylene phenyl complex was obtained, and as anticipated in view of the π-acidity of ethylene, the Tp′ ligand was found to be coordinated in a κ^3 manner (53). The three Pt–N bond distances are 2.14, 2.17, and 2.22 Å and the ethylene is oriented orthogonal to the Pt–C phenyl bond. The ethylene C=C double bond has been lengthened to 1.43 Å due to back-bonding into the π* orbital from the metal. All of these features indicate that formulating the complex as a Pt(IV) octahedral compound with a metallacyclopropane ring is useful even though the classic Pt(II) olefin formulation is of course a legitimate description, too.

Heating this complex resulted in insertion of ethylene into the Pt–Ph bond, and this was quickly followed by oxidative addition of an ortho C–H bond on the phenyl ring to yield the observed product, a Pt(IV) metallacycle hydride complex (Scheme 10). The reaction was promoted at room temperature by the addition of the Lewis acid $B(C_6F_5)_3$, which facili-

© 2008 NRC Canada

Scheme 10. Metallacycle formation by ethylene insertion into the Pt–Ph bond.

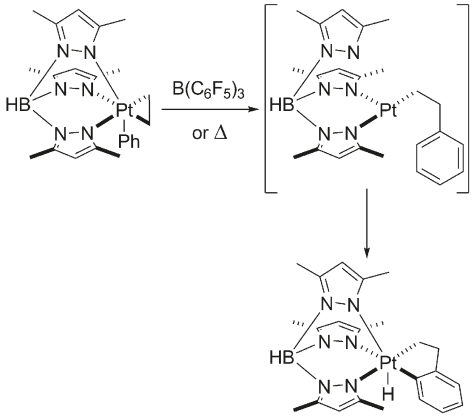

tates dechelation of one Tp′ arm. This indicated that removal of one Tp′ arm to form a five-coordinate intermediate was essential to the insertion process. The crystal structure of the ethylene complex shows it to be compatible with a Pt(IV) formulation, and this may be one way to rationalize the relative ease of insertion. Within the Pt(IV) formalism mentioned above, this net insertion reaction could be considered to be a reductive elimination forming a new C–C bond, and of course reductive eliminations from Pt(IV) often require formation of a five-coordinate intermediate to proceed. Within this Pt(IV) framework the generation of a five-coordinate intermediate and the ease of migration of the phenyl group to the adjacent methylene carbon are well precedented reactions.

The thermodynamic stability of these metallacycle compounds was further demonstrated by thermolytic C–H activation of ethyl benzene. Thermolysis of Tp′PtMe$_2$H with borane in ethyl benzene led to formation of the same metallacyclic product as the one formed from the insertion of ethylene into the Pt–Ph bond. The first step in the reaction with ethyl benzene is presumably reversible arene C–H activation, and once an ortho C–H bond is activated, the ethyl group is positioned for activation of a methyl C–H bond to yield the observed product. Even though activation at an ortho position is initially unfavorable because of steric interactions (21, 41, 54, 55), it eventually occurs. It then accounts for the final product because of the thermodynamic driving force favoring metallacycle formation.

When propylene was used as the coordinated olefin instead of ethylene, three platinum products were obtained: a 2,1 insertion product and both diastereomers of the 1,2 insertion product. Initially, the 2,1 product was obtained as the major product, but if the mixture of products was heated to 80 °C, isomerization eventually yielded the 1,2 insertion products as the major products. It is not surprising that the 2,1 (anti-Markovnikov) product is the kinetic product and the 1,2 (Markovnikov) product is the thermodynamic product, but it is surprising that interconversion of these isomers has a barrier of only 26.5 kcal/mol (Scheme 11). These low barriers to C–C coupling and C–C cleavage were encouraging signs that the complex may catalyze the hydroarylation of olefins, but the thermodynamic well associated with the

Scheme 11. Energy diagram for the interconversion of propylene insertion products.

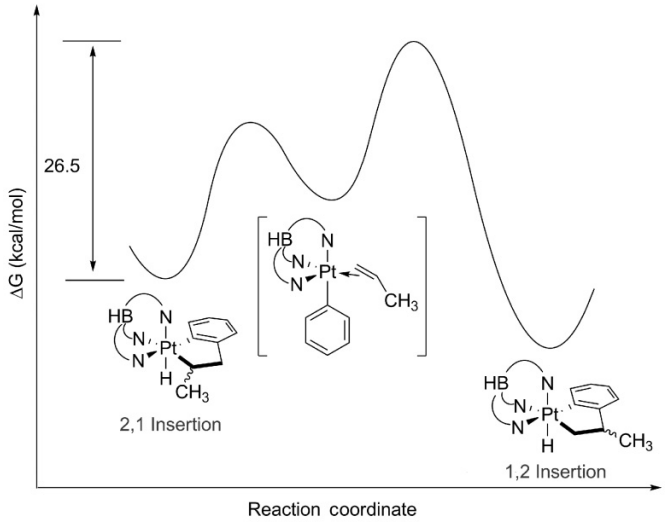

ortho C–H activation product proved too great to overcome by addition of external arene, and catalysis did not occur.

Lewis acid assisted thermal C–H activation of alkanes

Thus far we have discussed three different ways in which Tp′Pt derivatives can oxidatively add and reductively eliminate C–H bonds: high temperature thermolysis of a Pt(IV) alkyl hydride, low temperature protonation of a Pt(IV) alkyl hydride, and direct generation of Tp′PtR from a Pt(II) precursor. Another method is a hybrid of the low and high temperature routes to C–H activation following elimination of methane from a Pt(IV) alkyl hydride. Reductive elimination and C–H activation starting from Tp′PtMe(R)H were catalyzed by the Lewis acid $B(C_6F_5)_3$. The Lewis acid works in the same manner as H^+ in that it promotes formation of a reactive five-coordinate species, which can eliminate methane. The difference is that the Lewis acid reversibly binds to a Tp′ arm (catalysis by trace H^+ cannot be ruled out). Following methane elimination, the Lewis acid can decoordinate from Tp′ to form the reactive Tp′Pt(R) (R = Me, H, Ar) fragment, which can activate C–H bonds of the solvent. Addition of the borane Lewis acid allowed C–H activation of alkane or arene solvents between 25 and 50 °C (33, 56), far milder conditions than the 110 °C temperature required for direct thermal activation of arenes (34). Stirring the borane reagent with Tp′Pt(Me)(H)$_2$ in arene solvent facilitated methane elimination and benzene C–H activation.

When high temperature thermolyses of Tp′PtMe$_2$H were performed in alkane solvents only Pt black was isolated, but small amounts of olefins were also observed in solution indicating that some C–H activation was occurring (34). Lewis acid catalyzed C–H activation can be accomplished with Tp′PtMe$_2$H under milder conditions, and this allowed isolation of Tp′Pt(η^2-olefin)(H) complexes from reaction with alkanes. These products form from oxidative addition of an alkane C–H bond to Tp′PtMe followed by reductive elimination of a second equivalent of methane to form Tp′Pt(alkyl). This Pt(II) alkyl fragment then undergoes β-H elimination to form the observed η^2-olefin hydride complexes. Monitoring

© 2008 NRC Canada

Scheme 12. Dehydrogenation of cyclohexane with Tp′PtMe$_2$H.

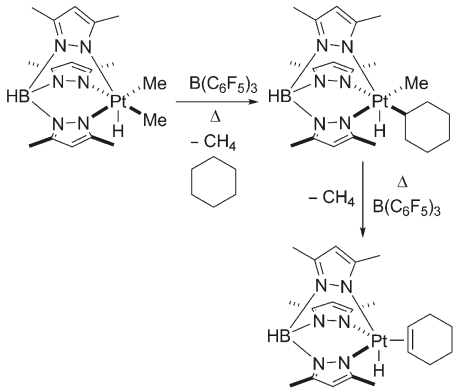

Scheme 13. Ether dehydrogenation by (nacnac)PtMe

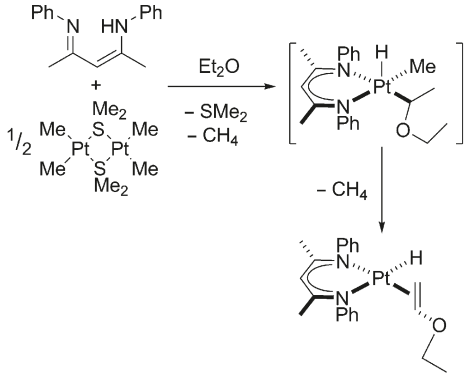

the reactions by ^{1}H NMR allowed observation of the unsymmetrical intermediate, Tp′Pt(Me)(alkyl)(H), for which the hydride had a chemical shift and Pt coupling constant similar to the parent Tp′PtMe$_2$H values (Scheme 12).

Alkane dehydrogenation is one of the simplest ways to functionalize alkanes; the alkenes formed from dehydrogenation are far more useful reagents than the parent alkanes. Alkenes are heavily used in polymer synthesis, and numerous basic organic reactions are available for functionalization or oxidation of alkenes. In contrast, few selective reactions are available with alkane reagents. Recently, alkane dehydrogenation has been utilized as a key step in alkane metathesis as described by Goldman et al. (57). While alkane dehydrogenation has been successfully catalyzed with various Rh and Ir reagents (58–61), only a few examples of alkane dehydrogenation with Pt have been reported (45, 62–65), and only one platinum example is catalytic (66).

Activation of *n*-pentane by Tp′PtMe$_2$H/B(C$_6$F$_5$)$_3$ appeared to favor oxidative addition of primary C–H bonds, initially forming the intermediate Tp′Pt(Me)(*n*-pentyl)(H) (56). Elimination of the second equivalent of methane from this complex and subsequent β-H elimination would yield the 1-pentene isomer of the η^2-olefin hydride complex. Selective formation of this isomer is desirable in part because the internal olefin isomers are favored thermodynamically and thus it is difficult to isolate only the terminal isomer. In addition, only the terminal isomer can be used for copolymerization with other olefins. While the major product of pentane dehydrogenation was the 1-pentene isomer, the 2-pentene isomer slowly appeared (56). So the reaction appeared to be kinetically selective for the formation of 1-pentene, but the α-olefin isomerized to the internal olefin as the reaction continues. This is typical for transition metal mediated alkane dehydrogenation as these systems tend to favor primary C–H bond activation (67), but they also tend to catalyze alkene isomerization (68, 69).

The complex Tp′Pt(H)(neohexene) was tested for catalytic activity toward transfer dehydrogenation of alkanes in the presence of B(C$_6$F$_5$)$_3$. Neohexene was used as the hydrogen acceptor and cyclohexane as the alkane to be dehydrogenated. Stoichiometric dehydrogenation of both neohexane and cyclohexane by Tp′PtMe$_2$H/B(C$_6$F$_5$)$_3$ was facile. Displacement of neohexene from Tp′Pt(H)(neohexene) by cyclohexene occured, forming Tp′Pt(H)(cyclohexene). While individual steps required for transfer dehydrogenation proceed, no transfer dehydrogenation catalysis of cyclohexane has been observed. This may be due to complications that arise from the presence of a large excess of alkene or from undesired reactions with the borane.

Alkane dehydrogenation with a (nacnac)PtMe fragment

To find a more active system for catalytic C–H bond functionalization we moved away from the tridentate Tp′ ligand to the monoanionic bidentate nacnac (nacnac = bis-*N*-aryl-β-enamineimine) ligand. This bidentate ligand will stabilize square planar Pt(II) complexes but not octahedral Pt(IV) complexes; this should enhance catalytic activity as we want reductive elimination from Pt(IV) intermediates to be facile. A bidentate ligand obviates the need for an external promoter, such as borane, to remove the third Tp′ arm and generate five-coordinate Pt(IV) intermediates.

Goldberg and co-workers (44, 45, 70) have reported several five-coordinate (nacnac)PtMe$_3$ complexes in which the nacnac ligand contained aryl groups with bulky alkyl substituents at the ortho positions. These complexes reductively eliminated ethane under mild conditions. Once the complexes had eliminated ethane, they could activate C–H bonds either in the ortho-alkyl substituent of the nacnac ligand or in an alkane solvent molecule. The olefin complexes resulting from alkane dehydrogenation were not susceptible to facile associative ligand exchange due to the bulky ortho groups on the *N*-phenyls blocking access to the metal. Slow ligand substitution rates prevented these complexes from functioning as catalysts for transfer dehydrogenation of alkanes.

We chose to use a nacnac ligand with no ortho substituents on the phenyl groups to allow access to the metal in hopes of promoting facile associative ligand exchange. Stirring Me$_4$Pt$_2$(μ-SMe$_2$)$_2$ with nacnacH (*N*-aryl, aryl = phenyl) in *n*-pentane overnight resulted in C–H activation and dehydrogenation of pentane to form (nacnac)Pt(H)(1-pentene) (Scheme 13) (65). Unlike the Tp′ case, this 1-pentene complex did not isomerize to the 2-pentene analog, and only the 1-pentene complex was observed. More surprising was the observation that conducting the reaction in Et$_2$O rather than pentane resulted in dehydrogenation of ether to form an ethyl vinyl ether hydride platinum complex (65).

It is clear from the selectivity for 1-pentene that primary C–H bond activation is favored when linear alkanes are

© 2008 NRC Canada

used, but this is not the case for the reaction with ethers. Reaction with THF results in dehydrogenation to yield the 2,3-dihydrofuran complex selectively; the double bond forms adjacent to the oxygen atom. Dehydrogenation of the partially deuterated ether reagent, $CH_3CD_2OCH_2CH_3$, produces both (nacnac)Pt(H)(CH_2=CDOEt) and (nacnac)Pt(H)(CH_2=CHOCD_2CH_3), as well as CH_4 and CH_3D. The absence of Pt-D products confirms that the initial site of C–H activation is the C–H bond α to oxygen (65).

Addition of alkene to these complexes results in rapid olefin exchange at room temperature; indeed, removal of the ortho substituents from the nacnac *N*-aryl groups exposes the metal and allows rapid associative ligand exchange. Given that olefin exchange is facile in these complexes, we attempted to catalyze transfer dehydrogenation with (nacnac)Pt(H)(neohexene). The reaction was quite slow, but we were able to observe about two turnovers in the dehydrogenation of either diethyl ether or tetrahydrofuran. This limited activity is a small step in the right direction.

Conclusions

The flexibility of the Tp′ ligand has allowed us to isolate Pt(IV) intermediates and to study C–H bond activation processes. Building from our knowledge of C–H bond tranformations, we have achieved reductive H–H bond formation from Tp′PtRH_2. We have also seen encouraging results relevant to functionalization of hydrocarbons. Arylation of olefins proceeds under surprisingly mild conditions. Moving to the bidentate nacnac ligand bound to platinum provides the potential for catalytic transfer dehydrogenation of hydrocarbons with some functional group tolerance.

Acknowledgements

We would like to acknowledge and thank our co-workers at the University of North Carolina who contributed to this research throughout the years: Stacy O'Reilly, Stefan Reinartz, Cynthia Norris-Kostelansky, and Margaret MacDonald. We would also like to thank M. S. Brookhart and Karen Goldberg for collaboration. We thank the National Science Foundation (NSF) for funding (CHE-0717086).

References

1. G.A. Olah. Angew. Chem. Int. Ed. **44**, 2636 (2005).
2. R.A. Periana, G. Bhalla, W.J. Tenn, K.J.H. Young, X.Y. Liu, O. Mironov, C.J. Jones, and V.R. Ziatdinov. J. Mol. Catal. A: Chem. **220**, 7 (2004).
3. A.E. Shilov and G.B. Shul'pin. Chem. Rev. **97**, 2879 (1997).
4. G.W. Huber, S. Iborra, and A. Corma. Chem. Rev. **106**, 4044 (2006).
5. J.A. Labinger and J.E. Bercaw. Nature (London), **417**, 507 (2002).
6. B.A. Arndtsen, R.G. Bergman, T.A. Mobley, and T.H. Peterson. Acc. Chem. Res. **28**, 154 (1995).
7. M. Lersch and M. Tilset. Chem. Rev. **105**, 2471 (2005).
8. S.S. Stahl, J.A. Labinger, and J.E. Bercaw. Angew. Chem. Int. Ed. **37**, 2181 (1998).
9. R.H. Crabtree. J. Chem. Soc. Dalton Trans. 2437 (2001).
10. U. Fekl and K.I. Goldberg. *In* Advances in inorganic chemistry: Including bioinorganic studies. Vol 54. Academic Press. 2003. p. 259.
11. C.G. Jia, T. Kitamura, and Y. Fujiwara. Acc. Chem. Res. **34**, 633 (2001).
12. A. Sen. Acc. Chem. Res. **31**, 550 (1998).
13. G. Dyker. Angew. Chem. Int. Ed. **38**, 1699 (1999).
14. Y. Guari, S. Sabo-Etienne, and B. Chaudret. Eur. J. Inorg. Chem. 1047 (1999).
15. R.A. Periana, O. Mironov, D. Taube, G. Bhalla, and C.J. Jones. Science (Washington, D.C.), **301**, 814 (2003).
16. R.A. Periana, D.J. Taube, S. Gamble, H. Taube, T. Satoh, and H. Fujii. Science (Washington, D.C.), **280**, 560 (1998).
17. J.A. Labinger. J. Mol. Catal. A: Chem. **220**, 27 (2004).
18. N.F. Gol'dshleger, V.V. Es'kova, A.E. Shilov, and A.A. Shteinman. Russ. J. Phys. Chem. **46**, 785 (1972).
19. H. Arakawa, M. Aresta, J.N. Armor, M.A. Barteau, E.J. Beckman, A.T. Bell, J.E. Bercaw, C. Creutz, E. Dinjus, D.A. Dixon, K. Domen, D.L. DuBois, J. Eckert, E. Fujita, D.H. Gibson, W.A. Goddard, D.W. Goodman, J. Keller, G.J. Kubas, H.H. Kung, J.E. Lyons, L.E. Manzer, T.J. Marks, K. Morokuma, K.M. Nicholas, R. Periana, L. Que, J. Rostrup-Nielson, W.M.H. Sachtler, L.D. Schmidt, A. Sen, G.A. Somorjai, P.C. Stair, B.R. Stults, and W. Tumas. Chem. Rev. **101**, 953 (2001).
20. L. Johansson and M. Tilset. J. Am. Chem. Soc. **123**, 739 (2001).
21. H.A. Zhong, J.A. Labinger, and J.E. Bercaw. J. Am. Chem. Soc. **124**, 1378 (2002).
22. L.M. Rendina and R.J. Puddephatt. Chem. Rev. **97**, 1735 (1997).
23. F.B. Zhang, E.M. Prokopchuk, M.E. Broczkowski, M.C. Jennings, and R.J. Puddephatt. Organometallics, **25**, 1583 (2006).
24. A.J. Canty, A. Dedieu, H. Jin, A. Milet, and M.K. Richmond. Organometallics, **15**, 2845 (1996).
25. S.A. O'Reilly, P.S. White, and J.L. Templeton. J. Am. Chem. Soc. **118**, 5684 (1996).
26. D.D. Wick and K.I. Goldberg. J. Am. Chem. Soc. **119**, 10235 (1997).
27. H.A. Jenkins, G.P.A. Yap, and R.J. Puddephatt. Organometallics, **16**, 1946 (1997).
28. E.M. Prokopchuk, H.A. Jenkins, and R.J. Puddephatt. Organometallics, **18**, 2861 (1999).
29. A.N. Vedernikov and K.G. Caulton. Angew. Chem. Int. Ed. **41**, 4102 (2002).
30. E.M. Prokopchuk and R.J. Puddephatt. Organometallics, **22**, 787 (2003).
31. J.G. Hinman, C.R. Baar, M.C. Jennings, and R.J. Puddephatt. Organometallics, **19**, 563 (2000).
32. C.M. Norris and J.L. Templeton. *In* ACS symposium series 885: Activation and functionalization of C–H bonds. *Edited by* K.I. Goldberg and A.S. Goldman. American Chemical Society, Washington, D.C. 2004. p. 303.
33. S. Reinartz, P.S. White, M. Brookhart, and J.L. Templeton. Organometallics, **20**, 1709 (2001).
34. M.P. Jensen, D.D. Wick, S. Reinartz, P.S. White, J.L. Templeton, and K.I. Goldberg. J. Am. Chem. Soc. **125**, 8614 (2003).
35. S. Reinartz, P.S. White, M. Brookhart, and J.L. Templeton. Organometallics, **19**, 3854 (2000).
36. S. Reinartz, M.H. Baik, P.S. White, M. Brookhart, and J.L. Templeton. Inorg. Chem. **40**, 4726 (2001).
37. S. Reinartz, P.S. White, M. Brookhart, and J.L. Templeton. Organometallics, **19**, 3748 (2000).
38. N.M. West, S. Reinartz, P.S. White, and J.L. Templeton. J. Am. Chem. Soc. **128**, 2059 (2006).

© 2008 NRC Canada

39. A. Haskel and E. Keinan. Organometallics, **18**, 4677 (1999).
40. S. Reinartz, P.S. White, M. Brookhart, and J.L. Templeton. J. Am. Chem. Soc. **123**, 12724 (2001).
41. C.M. Norris, S. Reinartz, P.S. White, and J.L. Templeton. Organometallics, **21**, 5649 (2002).
42. L. Johansson, M. Tilset, J.A. Labinger, and J.E. Bercaw. J. Am. Chem. Soc. **122**, 10846 (2000).
43. R.J. Puddephatt. Angew. Chem. Int. Ed. **41**, 261 (2002).
44. U. Fekl, W. Kaminsky, and K.I. Goldberg. J. Am. Chem. Soc. **123**, 6423 (2001).
45. U. Fekl, W. Kaminsky, and K.I. Goldberg. J. Am. Chem. Soc. **125**, 15286 (2003).
46. S.M. Kloek and K.I. Goldberg. J. Am. Chem. Soc. **129**, 3460 (2007).
47. A.T. Luedtke and K.I. Goldberg. Inorg. Chem. **46**, 8496 (2007).
48. S.-B. Zhao, G. Wu, and S. Wang. Organometallics, **27**, 1030 (2008).
49. D. Karshtedt, J.L. McBee, A.T. Bell, and T.D. Tilley. Organometallics, **25**, 1801 (2006).
50. S. Reinartz, P.S. White, M. Brookhart, and J.L. Templeton. J. Am. Chem. Soc. **123**, 6425 (2001).
51. C.M. Norris and J.L. Templeton. Organometallics, **23**, 3101 (2004).
52. D.M. Crumpton-Bregel and K.I. Goldberg. J. Am. Chem. Soc. **125**, 9442 (2003).
53. M.G. MacDonald, C.N. Kostelansky, P.S. White, and J.L. Templeton. Organometallics, **25**, 4560 (2006).
54. F.B. Zhang, C.W. Kirby, D.W. Hairsine, M.C. Jennings, and R.J. Puddephatt. J. Am. Chem. Soc. **127**, 14196 (2005).
55. L. Johansson, O.B. Ryan, C. Romming, and M. Tilset. J. Am. Chem. Soc. **123**, 6579 (2001).
56. C.N. Kostelansky, M.G. MacDonald, P.S. White, and J.L. Templeton. Organometallics, **25**, 2993 (2006).
57. A.S. Goldman, A.H. Roy, Z. Huang, R. Ahuja, W. Schinski, and M. Brookhart. Science (Washington, D.C.), **312**, 257 (2006).
58. C.M. Jensen. Chem. Commun. 2443 (1999).
59. K. Zhu, P.D. Achord, X. Zhang, K. Krogh-Jespersen, and A.S. Goldman. J. Am. Chem. Soc. **126**, 13044 (2004).
60. I. Gottker-Schnetmann and M. Brookhart. J. Am. Chem. Soc. **126**, 9330 (2004).
61. S.A. Kuklin, A.M. Sheloumov, F.M. Dolgushin, M.G. Ezernitskaya, A.S. Peregudov, P.V. Petrovskii, and A.A. Koridze. Organometallics, **25**, 5466 (2006).
62. A.N. Vedernikov, J.C. Huffman, and K.G. Caulton. New J. Chem. **27**, 665 (2003).
63. M.W. Holtcamp, L.M. Henling, M.W. Day, J.A. Labinger, and J.E. Bercaw. Inorg. Chim. Acta, **270**, 467 (1998).
64. G.S. Chen, J.A. Labinger, and J.E. Bercaw. Proc. Natl. Acad. Sci. U.S.A. **104**, 6915 (2007).
65. N.M. West, P.S. White, and J.L. Templeton. J. Am. Chem. Soc. **129**, 12372 (2007).
66. T. Yamakawa, T. Fujita, and S. Shinoda. Chem. Lett. 905 (1992).
67. A.J. Vetter, C. Flaschenriem, and W.D. Jones. J. Am. Chem. Soc. **127**, 12315 (2005).
68. F. Liu, E.B. Pak, B. Singh, C.M. Jensen, and A.S. Goldman. J. Am. Chem. Soc. **121**, 4086 (1999).
69. D. Morales-Morales, R. Redon, C. Yung, and C.M. Jensen. Inorg. Chim. Acta, **357**, 2953 (2004).
70. U. Fekl and K.I. Goldberg. J. Am. Chem. Soc. **124**, 6804 (2002).

© 2008 NRC Canada

Bonding and structures of copper-aminopyridine complexes — High-resolution electron spectroscopy and ab initio calculations[1]

Xu Wang and Dong-Sheng Yang

Abstract: Copper complexes of *x*-aminopyridine (*x* = 2, 3, 4) were prepared in a laser vaporization supersonic molecular beam source and identified using laser photoionization time-of-flight mass spectrometry. These complexes were studied by pulsed-field ionization zero electron kinetic energy (ZEKE) spectroscopy and second-order Møller-Plesset perturbation theory. Three structures formed by Cu binding to the pyridine nitrogen (σ_α), the amino nitrogen (σ_β), and the pyridine ring (π) were considered by the theoretical calculations, but only the σ_α structures with Cu binding to the pyridine nitrogen were confirmed by the spectroscopic measurements. Adiabatic ionization energies and metal-ligand and ligand-based vibrational frequencies of the σ_α complexes were measured from the ZEKE spectra, and the metal-ligand bond energies of the neutral and ionized complexes were predicted by the theory. The ionization energies of the Cu complexes are about 20 000 cm^{-1} lower than that of bare Cu atom. This ionization energy shift is the result of the stronger Cu^+-ligand bonding because of the additional charge-dipole interaction in the ion. Although the three complexes are formed by Cu coordination to the pyridine nitrogen atom, the position of the amino group affects the metal-ligand bonding strengths in both neutral and ionized species. These effects include the structural resonance and hydrogen bonding in the neutral complexes and the electric dipole moment and bidentate bonding in the ions.

Key words: photoelectron, PFI-ZEKE, ab initio, copper aminopyridine.

Résumé : On a préparé les complexes de cuivre de x-aminopyridine (x = 2, 3, 4) dans une source de faisceau moléculaire supersonique à vaporisation laser et on les a identifiés par spectrométrie de masse en temps de vol avec photoionisation au laser. On a étudié ces complexes par spectroscopie d'énergie cinétique électronique zéro (« ZEKE ») avec ionisation à champ pulsé ainsi que par la théorie de perturbation de Møller-Plesset du deuxième ordre. Pour les calculs théoriques, on a considéré trois structures formées par du cuivre se liant à l'azote de la pyridine (σ_α), l'azote de l'amine (σ_β) et le noyau pyridine (π); seules les structures σ_α du cuivre se liant à l'azote de la pyridine ont pu être confirmées par des mesures spectroscopiques. On a mesuré les énergies d'ionisation adiabatique et les fréquences de vibration métal-ligand ainsi que celles de vibrations basées sur le ligand des complexes σ_α à partir des spectres « ZEKE » alors que les énergies de liaison métal-ligand des complexes neutres et ionisés ont été calculés sur une base théorique. Les énergies d'ionisation des complexes du cuivre sont environ 20 000 cm^{-1} plus faibles que celles de l'atome de cuivre nu. Ce déplacement de l'énergie d'ionisation résulte d'une liaison Cu^+-ligand plus forte causée par l'interaction supplémentaire charge-dipôle dans l'ion. Même si les trois complexes se forment par une coordination du cuivre à l'atome d'azote de la pyridine, les positions différentes du groupe amino affecte les forces de liaison métal-ligand tant dans les espèces neutres qu'ionisées. Ces effets incluent la résonance structurale et la liaison hydrogène dans les complexes neutres et le moment électrique dipolaire ainsi que la liaison bidentate dans les ions.

Mots-clés : photoélectronique, « PFI-ZEKE », ab initio, cuivre-aminopyridine.

[Traduit par la Rédaction]

Introduction

Copper is a bioessential element in biology, whereas nitrogen is the fourth most common element in living systems, after carbon, hydrogen, and oxygen. Thus, the chemistry and biochemistry of the copper–nitrogen interaction have attracted considerable interest over the past decades (1–3). To probe fundamental interactions between a copper atom or ion and nitrogen-containing organic molecules, we have recently studied the bonding and structures of a series of coordinately unsaturated, transient copper complexes of amines (4–7) and aromatic nitrogen systems (8–10). In Cu-

Received 10 June 2008. Accepted 26 August 2008. Published on the NRC Research Press Web site at canjchem.nrc.ca on 5 November 2008.

This paper is dedicated to Professor Richard Puddephatt for his great contributions in Organometallic Chemistry.

X. Wang, and D.-S. Yang.[2] Department of Chemistry, University of Kentucky, Lexington, KY 40506-0055, USA.

[1]This article is part of a Special Issue dedicated to Professor Richard J. Puddephatt.
[2]Corresponding author (e-mail: dyang0@uky.edu).

 doi:10.1139/V08-146 © 2008 NRC Canada

methylamine complexes, the N atom binds to Cu through the lone-pair electrons in the N sp^3 hybrid orbital (6). Although ethylenediamine possesses two N binding sites, the structure of Cu-ethylenediamine was determined to be in a hydrogen-bond stabilized monodentate configuration (5). Interestingly, single methyl substitution of the amino hydrogen atom leads to a bidentate structure, with Cu binding to both N atoms (4). The change from the monodentate to the bidentate mode arises from the competition between copper coordination and hydrogen bonding. The pyridine molecule contains a nitrogen atom and an aromatic ring, thus it can function as a σ donor, a π acceptor, or a π donor. However, only the σ structure was predicted by MP2 theory and confirmed by pulsed-field ionization zero electron kinetic energy (ZEKE) spectroscopy (8). By introducing another nitrogen atom into different mutual positions of the aromatic ring, we predicted a π bonding structure for the neutral Cu-pyrimidine complex and three Cu^+-diazine ions using the MP2 calculations (10). However, our ZEKE measurements have only observed the σ structure for both neutral and ionic Cu-diazine complexes (10).

In this work, we have extended the ZEKE study to the Cu complexes with aminopyridines. These ligands have two types of nitrogen atoms for σ bonding: one is in the pyridine ring with lone-pair electrons in the sp^2 hybrid orbital and the other is in the amino group with lone-pair electrons in the sp^3 hybrid orbital (Figure 1). In addition to the two σ bonding sites, the aromatic pyridine ring in these ligands may offer π binding sites as well. It would be interesting to examine how these binding sites compete with each other to form stable Cu complexes. Previously, bond energies of alkali ion-aminopyridines were measured by threshold collision-induced dissociation, and the σ bonding structures of these ions were predicted by the MP2 method (11). Vibrational spectra of M^{2+}-aminopyridine complexes (M = Mn, Co, Ni, Cu, or Cd) in condensed phases were measured by nujol mulls or KBr FT-IR spectroscopy and analyzed in terms of σ bonding structures (12–15). On the other hand, the π bonding mode was identified for 2-aminopyridine·Ar_n van der Waals complexes by resonance-enhanced multiphoton ionization and ZEKE–mass-analyzed threshold ionization spectroscopy and ab initio calculations (16, 17). In this paper, we report the ZEKE spectra of Cu complexes with 4-aminopyridine (4-AP), 3-aminopyridine (3-AP), and 2-aminopyridine (2-AP). Adiabatic ionization energies (AIEs) and metal-ligand and ligand-based vibrational frequencies were measured from the ZEKE spectra. The structures of these complexes were determined by comparing the spectra with the MP2 calculations and spectral simulations.

Experimental and computational methods

The experimental setup has been described in a previous publication (18). The Cu complexes were prepared by reactions of Cu atoms with the *x*-AP ligands (*x* = 2, 3, and 4) (Sigma-Aldrich, 98%–99%) in molecular beams. The metal atoms were produced by pulsed laser vaporization of a Cu rod (Alfa Aesar, 99.9%) with the second harmonic output of a Nd:YAG laser (Quanta-Ray GCR-3, 532 nm, ~3 mJ) in the presence of He or Ar gas (Scott-Gross, ultra high purity) at ~50 psi (6.894 757 kPa). The carrier gas was delivered by a piezoelectric pulsed valve (19). The metal rod was translated and rotated by a motor-driven mechanism to ensure each laser pulse ablated a fresh surface. Since 4-AP is a solid (mp 155–158 °C) and has a low vapor pressure at room temperature, a Cu oven installed inside the molecular beam chamber was used to obtain sufficient ligand vapor. Although 3-AP and 2-AP are also solids (mp 65 and 57–60 °C, respectively), they have sufficient vapor pressures at ambient temperature. Therefore, these two ligands were placed in a glass bulb without heating, which was also installed inside the molecular beam chamber.

Fig. 1. Structural isomers of aminopyridines.

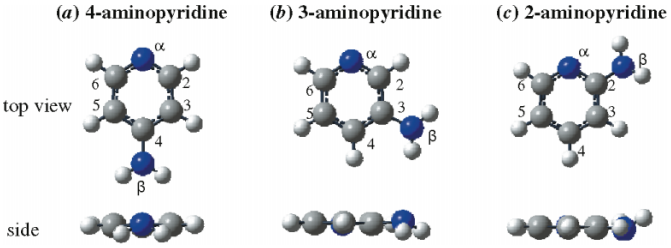

The Cu-(*x*-AP) complexes in the molecular beams were identified by photoionization time-of-flight mass spectrometry. Ionization was carried out by a frequency-doubled dye laser (Lumonics, HD-500), pumped by a XeCl excimer laser (Lumonics, PM-884) or the third harmonic output of a Nd:YAG laser (Continuum, Surelite III). The production of the 1:1 metal-ligand complexes was maximized by optimizing the timing and power of the vaporization and photoionization lasers, the amount of the ligand vapor, and the reservoir pressure of the carrier gas. Prior to ZEKE experiments, ionization thresholds of these complexes were measured by recording the ion signals as a function of the laser wavelength. ZEKE electrons were produced by phototexcitation of the neutral complexes to high-lying Rydberg states, followed by a 3 μs delayed, 1.2 V cm^{-1}, and 100 ns pulsed-electric-field ionization of these Rydberg states. A small dc field of ~0.08 V cm^{-1} was applied to help separate ZEKE from kinetic electrons produced by direct photoionization. The pulsed electric field was generated by a delay pulse generator (Stanford Research System, DG535). The ion and electron signals were detected by a dual microchannel plate detector (Galileo), amplified by a preamplifier (Stanford Research System, SR445), averaged by a gated integrator (Stanford Research System, SR250), and recorded in a laboratory computer. Laser wavelengths were calibrated against vanadium atomic transitions in regions of the ZEKE spectra (20). The field dependence of the ZEKE signal was not measured because of the limited size of the ZEKE signal. However, the energy shift from the small electric field has been shown to be smaller than the spectral linewidth (21).

Calculations of molecular geometries and vibrational frequencies were carried out by using the MP2/6-311+G(d,p) method, implemented in the GAUSSIAN 03 program (22). Multidimensional Franck–Condon (FC) factors were computed from the equilibrium geometries, harmonic frequencies, and normal modes of the neutral and ionic complexes (23, 24). The Duschinsky effect (25) was considered to account for normal mode differences between the neutral molecule and ion in the FC calculations. Spectral broadening

© 2008 NRC Canada

Fig. 2. Structural isomers, relative electronic energies, adiabatic ionization energies (AIE), and bond dissociation energies (D_0) of (*a*) Cu-(4-aminopyridine), (*b*) Cu-(3-aminopyridine), and (*c*) Cu-(2-aminopyridine) from MP2/6-311+G(d,p) calculations. The bond distances are in angstroms. Cu–N distances are given for the σ structures, and Cu-ring vertical distances are given for the π structures.

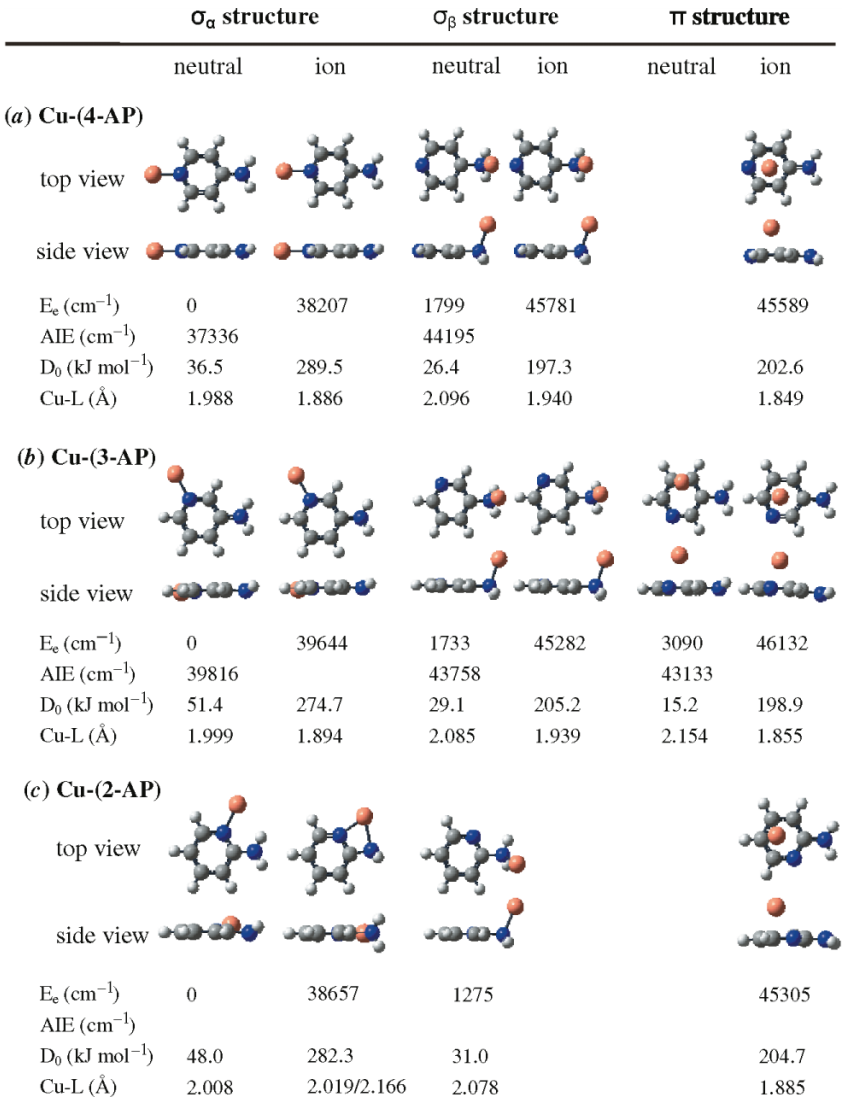

was simulated by giving each line a Lorentzian line shape with the linewidth of the experimental spectrum. Boltzmann distributions were used to simulate spectra at specific vibrational temperatures.

Equilibrium structures

In our computational survey of the minimum energy structures for the Cu-(*x*-AP) complexes, a π and two σ (σ_α and σ_β) configurations were considered for both neutral and ionic species. The π complex is formed by Cu binding atop of the pyridine ring, whereas the σ_α and σ_β complexes are formed by Cu binding to the pyridine nitrogen (N_α) or the amino nitrogen (N_β). These structures are presented in Figure 2, along with predicted electronic, ionization, and dissociation energies.

Cu-(4-AP)

The σ_α structure of Cu-(4-AP) has C_s symmetry, where the Cu and amino N_β atoms are nearly coplanar to the pyridine ring, and the two N_β–H bonds slightly bend out of the pyridine plane. This out-of-plane bending has also been found in the free ligand, and it is due to the sp^3 hybridized nature of the N_β atom, which tends to remain a tetrahedral configuration. The Cu–N_α distance is calculated to be 1.988 Å by the MP2 theory, which is slightly shorter than that in Cu-pyridine (2.005 Å) predicted previously at the same level of theory (8). However, the bond energy of this Cu–N_α bond is about 10.9 kJ mol^{-1} smaller than that of Cu-pyridine (47.4 kJ mol) (8).

The σ_β structure also belongs to the C_s point group and is ~1800 cm^{-1} less stable than the σ_α structure. This structure has a more distorted amino group because of Cu coordination to the N_β atom. The Cu–N_β bond has a longer distance (2.096 Å) and smaller dissociation energy than the Cu–N_α bond. It is also weaker than the Cu–N bond in the Cu-NH_3 complex (26), because of the larger steric repulsion from the pyridine ring. Like the σ_α structure, the pyridine-ring geometry remains virtually the same as that in the free ligand. This small perturbation on the ligand geometry has been found in other heterocyclic Cu complexes (8, 10).

© 2008 NRC Canada

Upon ionization, the Cu–N distance shrinks by 0.102 Å in the σ_α structure and 0.156 Å in the σ_β structure, respectively. The smaller Cu–N distances in the ionic complexes are due to the reduced repulsion between Cu $4s^1$ and N lone-pair electrons and the additional charge-dipole attraction. Interestingly, although the σ_α structure undergoes a smaller reduction in the Cu–N bond length, it has a larger increase in the C–N bond energy than the σ_β structure upon ionization. The larger increase of the bond energy from the neutral species to the ion leads to a lower AIE for the σ_α structure (38 270 cm^{-1}) than for the σ_β structure (45 781 cm^{-1}). Moreover, the Cu^+–N_α bond in the σ_α ion is predicted to be 30.8 kJ mol^{-1} stronger than that in Cu^+-pyridine, but the Cu–N bond energies in the corresponding neutral species have the opposite order (8). This difference is due to a so-called π resonance delocalization effect, which induces more negative charge on the N_α atom in 4-AP than the nitrogen atom in pyridine. The larger negative charge on N_α leads to an increased repulsion towards the Cu $4s^1$ electron but an enhanced attraction towards the Cu^+ ion. On the other hand, the Cu^+–N σ_β bond in the σ_β structure is much weaker than that in Cu^+-NH_3, indicating that the electron withdrawing and steric effects from the pyridine ring play an important role in this ion bonding. Therefore, the metal-ligand bonding strengths in these σ structures are determined by π resonance delocalization, electron withdrawing, and steric effects.

Like Cu-pyridine (8), a computational search for a stable π structure of the neutral Cu-(4-AP) complex is not successful. However, a π ion is located about 7400 cm^{-1} above the σ_α ion. The vertical distance between Cu^+ and pyridine ring is calculated to be 1.849 Å. The Cu^+-(4-AP) dissociation energy in this π structure (202.6 kJ mol^{-1}) is slightly larger than the Cu^+–N_β bond in the σ_β structure (197.3 kJ mol^{-1}) but much smaller than the Cu^+–N_α bond in the σ_α structure (289.5 kJ mol^{-1}).

Cu-(3-AP)

The σ_α structure of Cu-(3-AP) has a slightly longer Cu–N_α distance but a stronger bond compared with the Cu-(4-AP) σ_α complex. Similar to Cu-(4-AP), both the Cu and N_β atoms in the Cu-(3-AP) σ_α structure are nearly coplanar to the pyridine ring, the amino group is slightly tilted from this plane, and the local geometry of the amino group is almost identical to that in the free ligand. The σ_β structure of Cu-(3-AP) has a higher energy, a longer Cu–N distance, and a more distorted amino group than its σ_α structure. As in Cu-(4-AP), ionization reduces the Cu–N distances and thus increases the bond energies for both the σ_α and σ_β structures.

Unlike 4-AP, the 3-AP ligand forms a stable π structure with a Cu atom. This π structure is located 3090 cm^{-1} above the lowest-energy σ_α structure. The Cu atom is closest to the two carbon atoms that are bound to N_α, and the vertical Cu-ring distance is calculated to be 2.154 Å. The longer Cu-ring distance in the π structure than the Cu–N bonds in the σ structures suggests a weaker metal-ligand π interaction. Ionization of the π structure moves the Cu^+ ion towards the pyridine-ring center and reduces the vertical Cu^+-ring distance to 1.855 Å. The decrease of the Cu^+-ring distance is the result of the additional electrostatic interaction between the Cu^+ ion and the π surface of the ligand. Consequently, the resultant π ion is much more strongly bonded (198.9 kJ mol^{-1}) than the corresponding neutral structure (15.2 kJ mol^{-1}). The bond dissociation energy of the Cu^+-(3-AP) π ion is comparable to that of the Cu^+-(4-AP) counterpart.

The existence of the stable π structure in the neutral Cu-(3-AP) indicates that π electrons in the 3-AP ring are more delocalized and the ligand has higher aromaticity than 4-AP and 2-AP. This finding echoes our previous study of Cu-diazine complexes, where only pyrimidine (1,3-diazine) forms a stable π structure with a Cu atom (10).

Cu-(2-AP)

Due to the close proximity of the two nitrogen atoms, 2-AP may exhibit bonding capabilities different from the other two aminopyridines. In our computational search, we considered two σ configurations for both neutral and ionized forms: (*i*) Cu binding to the N_α atom with the amino group fixed in the same orientation as that in the free ligand and (*ii*) Cu binding to both N_α and N_β atoms, where the amino group is rotated by 90° so that the N_β lone-electron pair orbital points to the N_α atom. For the neutral complexes, only the geometry optimization of initial guess (*i*) is converged to a local minimum-energy σ_α structure. The geometry optimization of initial guess (*ii*) results in a transition-state energy structure, with an imaginary frequency of 330*i* cm^{-1}. In the σ_α structure, the Cu atom binds to the N_α atom, the N_β atom is nearly coplanar to the pyridine ring, and each N_β–H bond is slightly tilted out of the plane. Moreover, the Cu atom bends out of the ring plane by about 10° to minimize the repulsion from the amino group. The Cu–Nα distance is slightly longer than those of the Cu-(4-AP) and Cu-(3-AP) σ_α structures, whereas the bond energies are in the order of Cu-(4-AP) < Cu-(2-AP) < Cu-(3-AP). The monodentate Cu-(2-AP) σ_β structure is predicted to be 1275 cm^{-1} higher in energy than the σ_α structure. This σ_β structure has a similar Cu–N distance and bond dissociation energy to those of the Cu-(4-AP) and Cu-(3-AP) σ_β structures. For the ionized species, only the bidentate configuration is converged, where the Cu^+ ion binds to both N_α and N_β atoms. No monodentate structure was predicted for the ion. The bidentate ion has C_s symmetry, with Cu^+ being coplanar to the pyridine ring. In spite of the bidentate binding, the bond energy of Cu^+-(2-AP) is 7 kJ mol^{-1} smaller than that of the monodentate Cu^+-(4-AP) σ_α structure, possibly because of ample strain on the Cu^+-N_α-C-N_β four-membered ring. This ring strain also explains the longer Cu^+–N distances in the bidentate Cu^+-(2-AP) ion than those in the monodentate neutral Cu-(2-AP) or the Cu-(4-AP) and Cu-(3-AP) σ_α ions.

A π ion of Cu^+-(2-AP) is located, where the Cu^+ ion is closest to the C_5 atom. The vertical Cu^+-ring distance and bond dissociation energy are predicted to be nearly the same as those in the Cu^+-(4-AP) and Cu^+-(3-AP) π ions. Thus, the mutual position between the N_β atom in the amino group and the N_α atom in the pyridine ring has no significant effect on the π bonding of these substituted pyridines.

ZEKE spectra and vibrational analysis

Cu-(4-AP)

Figure 3*a* shows the ZEKE spectrum of Cu-(4-AP) seeded in He carrier gas. The first strong peak at 41 377 (5) cm^{-1} has a linewidth of 6 cm^{-1} and is assigned to the 0-0 transi-

© 2008 NRC Canada

tion between the ground vibronic levels of the neutral and ionic complexes. Above the 0-0 transition, the spectrum displays a main progression (ν^n_0) of 260 cm^{-1} intervals with up to four vibrational quanta. Superimposed on the 260 cm^{-1} progression are a number of satellite peaks separated by 15 and 36 cm^{-1} intervals from the respective ν^n_0 bands and an additional progression formed by the combination of 210 and 260 cm^{-1} intervals ($\nu^n_0\omega^j_i\delta^t_s$). Below the 0-0 transition, the spectrum displays a strong band at 193 cm^{-1} with two small bands on the higher energy side ($\nu^0_l\omega^n_n\delta^m_m$). To identify the transitions from excited vibrational levels of the neutral complex, ZEKE measurements were carried out with Ar carrier, and the spectrum is presented in Figure 4*a*. In this spectrum, the intensities of the $\nu^n_0\omega^j_i\delta^t_s$ and $\nu^0_l\omega^n_n\delta^m_m$ bands are largely diminished because of lower vibrational temperatures of the Ar-seeded Cu-(4-AP) complex; the spectral linewidth is reduced from 6 to 4 cm^{-1} because of lower rotational temperatures, and several additional cold bands that overlapped with hot bands in Figure 3*a* are now resolved. These include the peak at 565 cm^{-1} above the band origin (τ^1_{b0}), the combination of the 260 cm^{-1} spacing with a 514 cm^{-1} interval ($\tau^1_{a0}\nu^n_0$), and the combination of 260 and 790 cm^{-1} intervals ($\rho^1_0\nu^n_0$).

To assign the observed vibrations in the ZEKE spectra of Cu-(4-AP), we first compare the measured frequencies with those of Cu-alkylamines (4–7, 26), -pyridines (8), and -diazines (10). The metal-ligand stretching frequencies are in the range of 430–470 cm^{-1} for Cu^+-alkylamines and 265–275 cm^{-1} for Cu^+-pyridines and –diazines. Thus, the 260 cm^{-1} progression in the Cu-(4-AP) ZEKE spectra can be assigned to the Cu^+-(4-AP) stretching vibration of the σ_α structure. This progression should not be due to the Cu^+-(4-AP) stretch of the σ_β structure, because the Cu^+-N stretch of the σ_β structure would have a frequency similar to those in Cu^+-alkylamines (i.e., ≥400 cm^{-1}). Moreover, the spectral profile of Cu-(4-AP) seeded in He is very similar to those of the Cu-pyridine and -diazine complexes seeded in the same carrier. For the Cu-pyridine and -diazine complexes, satellite bands around the metal-ligand stretching progression have been assigned to the sequence transitions of the Cu-ring in-plane and (or) out-of-plane bends and the neutral Cu-ring stretch. Thus, the sequence peaks labeled by $\nu^n_o\omega^j_i\delta^t_s$ and $\nu^o_l\omega^n_n\delta^m_m$ in Figure 3*a* may be assigned to such bending and stretching modes as well. On the other hand, in comparison with the FT-IR spectroscopic measurement of Cu^{2+}-(4- AP)$_2$Ni(CN)$_4$ (13), the 514, 565, and 790 cm^{-1} intervals in the ZEKE spectra may arise from a C–H out-of-plane bend and two ligand-based out-of-plane distortions.

To analyze the ZEKE spectra in more detail, we compare the measurements with theoretical calculations. In our MP2 calculations, both σ_α and σ_β structures are predicted to be local minima for the neutral and ionized Cu-(4-AP) complexes, but only a π ion is found. Since the energy difference between σ_α and σ_β is small, both structures may have been produced in the molecular beam. In our spectral analysis, we thus consider both σ isomers by comparing the measured and calculated AIEs, vibrational frequencies, and FC intensities. Transitions between two different isomers are excluded, because such transitions are expected to have a very different FC intensity profile from the experimental spectra. The AIEs of the σ_α and σ_β complexes are calculated to be 37 336

Fig. 3. Experimental ZEKE spectrum of Cu-(4-aminopyridine) seeded in (*a*) He carrier and simulations of the (*b*) σ_α, and (*c*) σ_β structures at 50 (for vibrational mode smaller than 100 cm^{-1}) and 150 K (for those 200 cm^{-1} or greater).

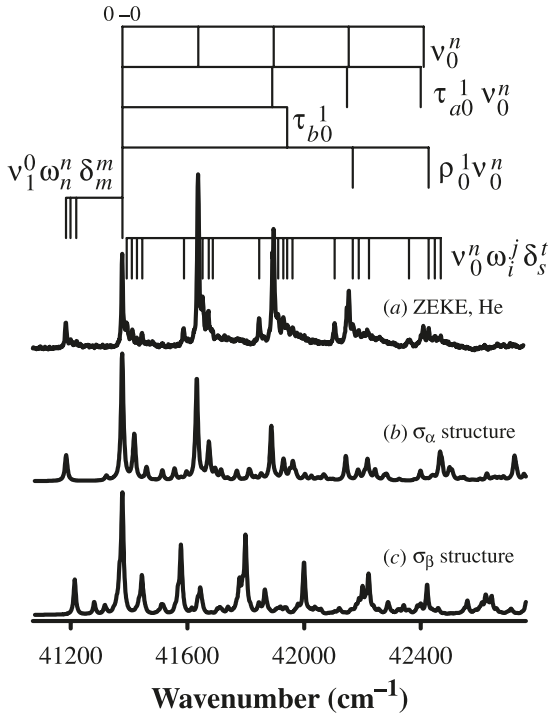

Fig. 4. Experimental ZEKE spectrum of Cu-(4-aminopyridine) seeded in (*a*) Ar carrier and simulations of the (*b*) σ_α, and (*c*) σ_β structures at 10 K.

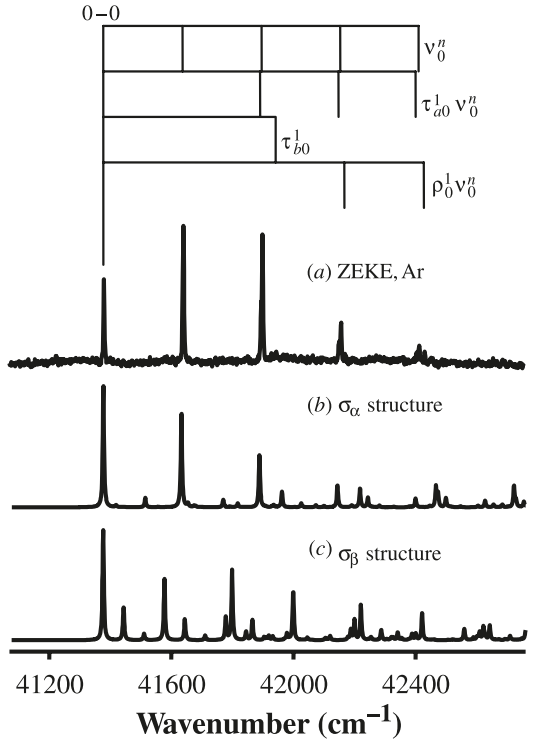

© 2008 NRC Canada

and 44 195 cm^{-1}. Our previous studies have shown that MP2 calculations typically underestimate the AIEs of Cu-molecule complexes by about 3000 cm^{-1} (4, 6, 8–10). If the 3000 cm^{-1} correction is employed, the AIEs are estimated to be 40 336 cm^{-1} for the σ_α structure and 47 195 cm^{-1} for the σ_β structure, respectively. It is clear that the corrected theoretical AIE value of the σ_α structure matches better the measured value of 41 377 cm^{-1}, and the σ_α structure is most likely the ZEKE carrier.

Figures 3 and 4 compare the experimental ZEKE spectra to the spectral simulations of the σ_α and σ_β structures. Since the thermal population of excited vibrational levels depends on vibrational frequencies, simulations of hot band intensities may require different temperatures for various vibrational modes. We have found that the best temperatures for simulating the hot band intensities of the ZEKE spectrum with He carrier (Fig. 3*a*) are 50 K for vibrational modes smaller than 100 cm^{-1} and 150 K for those 200 cm^{-1} or larger. For the ZEKE spectrum with Ar carrier (Fig. 4a), since no vibrational hot bands are clearly observed, a very low temperature (10 K) is used in our simulations. The simulation of the σ_α structure (Fig. 4*b*) shows a main progression of 256 cm^{-1} intervals, which matches well to the observed 260 cm^{-1} progression. On the other hand, the simulation of the σ_β structure (Fig. 4*c*) displays three progressions with 67, 201, and 422 cm^{-1} intervals, none of which match the experimental observations. Moreover, the hot band positions and intensities in the simulation of the σ_α structure (Fig. 3*b*) exhibit better agreement with the experimental observation (Fig. 3*a*) than those of the σ_β structure (Fig. 3*c*). Thus, these comparisons in vibrational frequencies and intensities suggest again that the σ_α structure is the carrier of the ZEKE spectra.

Based on the overall good agreement between the experimental spectra and simulations of the σ_α structure, the 260 cm^{-1} major progression is attributed to the transitions from the ground vibrational level of the Cu-(4-AP) σ_α neutral complex to symmetric stretching levels of the Cu^+-(4-AP) σ_α ion. The stretching frequency in the neutral Cu-(4-AP) is measured to be 193 cm^{-1}. A least-squares fit of the peak positions of ν^n_0 to $G(\nu) = \omega^+_S(\nu^+ + 1/2) + x^+_{SS}(\nu^+ + 1/2)^2$ yields a harmonic frequency of 261.1(5) cm^{-1} and an anharmonicity of –0.6 (1) cm^{-1} for the Cu^+–N_α stretching mode. The 15 and 36 cm^{-1} intervals arise from $\Delta v = 0$ sequence transitions of the Cu-ring out-of-plane and in-plane bending vibrations, respectively, and the 210 cm^{-1} interval is from the $v^+ = 3 \leftarrow v = 1$ transition of the Cu-ring in-plane bend. The neutral and ionic Cu-ring in-plane bending frequencies are derived to be 56 and 89 cm^{-1}, respectively. Moreover, the 514, 565, and 790 cm^{-1} intervals are assigned to the vibrational frequencies of a C–H out-of-plane bend (ρ^+) and two ligand out-of-plane distortions (τ_a^+ and τ_b^+) in the ion, which have nearly the same frequencies as those of Cu^{2+}-$(4Apy)_2Ni(CN)_4$ (13). The complete assignment for each peak is listed in Table 1.

Cu-(3-AP)

The ZEKE spectra of Cu-(3-AP) seeded in He and Ar carriers are presented in Figs. 5*a* and 6*a*, respectively. Both spectra have a similar spectral profile to and slightly narrower linewidths (5 cm^{-1} in He and 4 cm^{-1} in Ar) than those of Cu-(4-AP). The 0-0 band is located at 42 541(5) cm^{-1}, 1164 cm^{-1} higher in energy than that of Cu-(4-AP). The main progression labeled ν^n_0 has an interval of 268 cm^{-1}. Superimposed on the main progression are sequence transitions with at 29 cm^{-1} separations. Additionally, the spectrum shows a small peak at 131 cm^{-1} above the band origin and its combinations with 268 cm^{-1} intervals ($w^1_0\nu^n_0$). The ZEKE spectrum of the helium-seeded complex shows a fairly strong hot band at 194 cm^{-1} below the 0-0 transition and a small peak 29 cm^{-1} above the 194 cm^{-1} transition ($\nu^n_1 w^m_m$). In the spectrum with Ar carrier, none of these hot bands is observed. From these two spectra, two progressions consisting of 268 cm^{-1} intervals combined with 482 ($\tau^1_{ao}\nu^n_0$) or 564 cm^{-1} ($\tau^1_{bo}\nu^n_0$) spacing are found to be overlapped with some of the sequence transitions. In comparison with the spectra of Cu-(4-AP), the 268 and 194 cm^{-1} intervals are assigned to the Cu^+-(3-AP) and Cu-(3-AP) stretching modes, the 484 and 564 cm^{-1} intervals to ligand-based vibrations, and the sequence bands to Cu-(3-AP) bends.

The spectral simulations of the Cu-(3-AP) σ_α, σ_β, and π structures at 60/150 and 10 K are presented in Figs. 5*b*, 5*c*, 5*d* and 6*b*, 6*c*, 6*d*), respectively. Similar to Cu-(4-AP), the temperature of 50 K is used to simulate hot bands for vibrational modes smaller than 100 cm^{-1} and 150 K is used for those 200 cm^{-1} or larger. A comparison of the experimental and calculated spectra excludes the contributions from both σ_β and π structures to the observed spectrum. On the other hand, the simulation from the σ_α structure matches the experimental spectrum quite well. Moreover, the AIE values of σ_α, σ_β and π structures are predicted to be 42 816, 46 758, and 46 133 cm^{-1}, respectively, by the MP2 method (after the 3000 cm^{-1} correction). The AIE of the σ_α structure (42 816 cm^{-1}) has the best match with the experimental value of 42 541 cm^{-1}. Therefore, the observed spectrum is attributed to the σ_α structure of the Cu-(3-AP) complex. The 268 and 194 cm^{-1} intervals are attributed to the ionic (ν^+) and neutral (ν) metal-ligand stretching frequencies. A least-squares fit of the peak positions of ν^n_0 to $G(\nu) = \omega^+_S(\nu^+ + 1/2) + x^+_{SS}(\nu^+ + 1/2)^2$ yields a harmonic frequency of 271.6 (11) cm^{-1} and an anharmonicity of –1.1 (2) cm^{-1} for the ion stretching mode. The 482 and 564 cm^{-1} intervals are attributed to two (3-AP) out-of-plane distortions (τ_a^+ and τ_b^+), whereas the 131 cm^{-1} interval is assigned to the Cu^+-(3-AP) out-of-plane bending excitation (ω^+). One of the ligand out-of-plane distortions (τ_b^+) is mixed with an NH_2 wagging motion. Due to the limited size of the ZEKE signal, these peaks were not observed in the ZEKE spectrum with Ar carrier gas. From the calculated FC factors, the sequence bands are attributed to both Cu-(3-AP) in-plane (δ) and out-of-plane bending (ω) vibrations. These hot bands overlap each other because the calculated differences between the neutral and ionic in-plane bending vibrations ($\delta^+ - \delta = 30$ cm^{-1}) and between the neutral and ionic out-of-plane bending vibrations ($\omega^+ - \omega = 28$ cm^{-1}) are very close to each other. The experimental frequency difference is 29 cm^{-1} between these ionic and neutral bending vibrations. Thus, the frequency of the neutral Cu-(3-AP) out-of-plane bend is estimated to be 102 cm^{-1}.

Cu-(2-AP)

The ZEKE spectrum of Cu-(2-AP) (Fig. 7) shows a

© 2008 NRC Canada

Table 1. ZEKE peak positions (cm^{-1}) and assignments of the Cu-aminopyridine complexes.

Cu-(4-AP)		Cu-(3-AP)		Cu-(2-AP)	
Positions	Assignments	Positions	Assignments	Positions	Assignments
41 184	ν^0_1	42 347	ν^0_1	43 745	0^0_0
41 199	$\nu^0_1\omega^1_1$	42 378	$\nu^0_1\omega^1_1$	43 793	ω^1_1
41 219	$\nu^0_1\delta^1_1$	42 541	0^0_0	43 886	?
41 377	0^0_0	42 570	$\omega^1_1\delta^1_1$	43 944	?
41 392	ω^1_1	42 613	ν^1_1	44 006	ν^1_0
41 410	δ^1_1	42 666	ω^1_0	44 052	$\nu^1_0\omega^1_1$
41 427	$\omega^1_1\delta^1_1$	42 691	ω^2_1	44 188	τ^1_{a0}
41 445	δ^2_2/ν^1_1	42 809	ν^1_0	44 266	ν^2_0
41 588	δ^3_1	42 838	$\nu^1_0\omega^1_1/\nu^1_0\delta^1_1$	44 400	τ^1_{b0}
41 637	ν^1_0	42 929	$\nu^1_0\omega^1_0$	44 449	$\tau^1_{a0}\nu^1_0$
41 652	$\nu^1_0\omega^1_1$	42 943	$\nu^1_0\delta^1_0$	44 527	ν^3_0
41 673	$\nu^1_0\delta^1_1$	42 957	$\nu^1_0\omega^2_1$	44 633	τ^2_{a0}
41 687	$\nu^1_0\omega^1_1\delta^1_1$	43 023	τ^1_{ao}	44 707	$\tau^1_{a0}\nu^2_0$
41 705	$\nu^1_0\delta^2_2$	43 076	ν^2_0	44 894	$\tau^2_{a0}\nu^1_0$
41 846	$\nu^1_0\delta^3_1$	43 105	$\nu^2_0\omega^1_1/\nu^2_0\delta^1_1/\tau^1_{bo}$	44 915.2	$^4D^0_{1/2} \leftarrow {}^2S_{1/2}$
41 891	τ^1_{ao}	43 137	$\tau^1_{b0}\omega^1_1/\delta^1_1$	44 966	$\tau^1_{a0}\nu^3_0$
41 896	ν^2_0	43 212	$\nu^2_0\omega^1_0/\nu^2_0\omega^2_1$		
41 911	$\nu^2_0\omega^1_1$	43 283	$\tau^1_{a0}\nu^1_1$		
41 929	$\nu^2_0\delta^1_1$	43 343	ν^3_0		
41 942	$\nu^2_0\omega^1_1\delta^1_1/\tau^1_{bo}$ [a]	43 372	$\nu^3_0\omega^1_1/\nu^3_0\delta^1_1/\tau^1_{bo}\nu^1_0$		
41 960	$\nu^2_0\delta^2_2$	43 401	$\tau^1_{bo}\nu^1_0\omega^1_1/\tau^1_{b0}\nu^1_0\delta^1_1$		
41 986	$\nu^2_0\omega^2_0$	43 466	$\nu^3_0\omega^1_0$		
42 105	$\nu^2_0\delta^3_1$	43 489	$\nu^3_0\omega^2_1$		
42 147	$\tau^{1a}_o\nu^1_0$	43 604	ν^4_0		
42 153	ν^3_0	43 638	$\nu^4_0\omega^1_1/\nu^4_0\delta^1_1/\tau^1_{bo}\nu^2_0$		
42 167	$\nu^3_0\omega^1_1/\rho^1_0$ [a]	43 661	$\tau^1_{bo}\nu^2_0\omega^1_1/\tau^1_{b0}\nu^2_0\delta^1_1$		
42 187	$\nu^3_0\delta^1_1$	43 864	ν^5_0		
42 222	$\nu^3_0\delta^2_2$	43 903	$\nu^5_0\omega^1_1$		
42 360	$\nu^3_0\delta^3_1$				
42 400	$\tau^1_{ao}\nu^2_0/\tau^2_{ao}$				
42 410	ν^4_0				
42 427	$\nu^4_0\omega^1_1/\rho^1_0\nu^1_0$ [a]				
42 448	$\nu^4_0\delta^1_1$				
42 468	$\nu^4_0\delta^2_2$				

[a] Transitions from excited vibrational levels are observed only with He carrier.

broader linewidth (~20 cm^{-1}) and a lower signal/noise ratio compared with the spectra of Cu-(4-AP) and Cu-(3-AP). The spectrum displays a 0-0 transition at 43 745 (5) cm^{-1}, a major vibrational progression of 261 cm^{-1} (ν^n_0) with three quanta, a progression of 446 cm^{-1} (τ_a) with two quanta, an interval of 658 cm^{-1} (τ_b), and a few combinational bands of the 261 and 446 cm^{-1} intervals. In addition, it exhibits a partially resolved sequence transition at about 51 cm^{-1} to the higher energy side of the 0-0 and ν^1_0 peaks. In comparison with the spectra of the other two Cu-aminopyridine complexes discussed above, the 261 cm^{-1} progression is easily assigned to the Cu^+-(2-AP) stretching vibrations; the 446 and 658 cm^{-1} intervals are attributed to the (2-AP) out-of-plan distortions (τ_a^+ and τ_b^+) and the 51 cm^{-1} sequence bands are ascribed to transitions between the first vibrational levels of the Cu^+/Cu-(2-AP) out-of-plane bending mode (ω^+ – ω). In addition, the peak labeled with an asterisk is a Cu atomic transition, while two small peaks labeled with question marks remain to be assigned.

Although both nitrogen atoms in 2-AP may bind with a Cu atom to form a bidentate complex, the observation of vibrational modes similar to those in Cu-(4-AP) and Cu-(3-AP) indicates that the Cu-(2-AP) complex has monodentate binding as well. This observation is consistent with our MP2 prediction of the σ_α structure for the neutral complex. However, the bidentate ion structure predicted by the MP2 calculations is not observed in our ZEKE experiment. This is because a change from the neutral monodentate structure to the ion bidentate structure would give a spectrum with a much longer FC profile than what is observed in the experiment. Furthermore, if the ion is a bidentate σ structure, the ionization energy of the Cu-(2-AP) complex should be sig-

© 2008 NRC Canada

Fig. 5. Experimental ZEKE spectrum of Cu-(3-aminopyridine) seeded in (*a*) He carrier and simulations of the (*b*) σ_α, (*c*) σ_β, and (*d*) π structures at 50 (for vibrational mode smaller than 100 cm^{-1}) and 150 K (for those 200 cm^{-1} or greater).

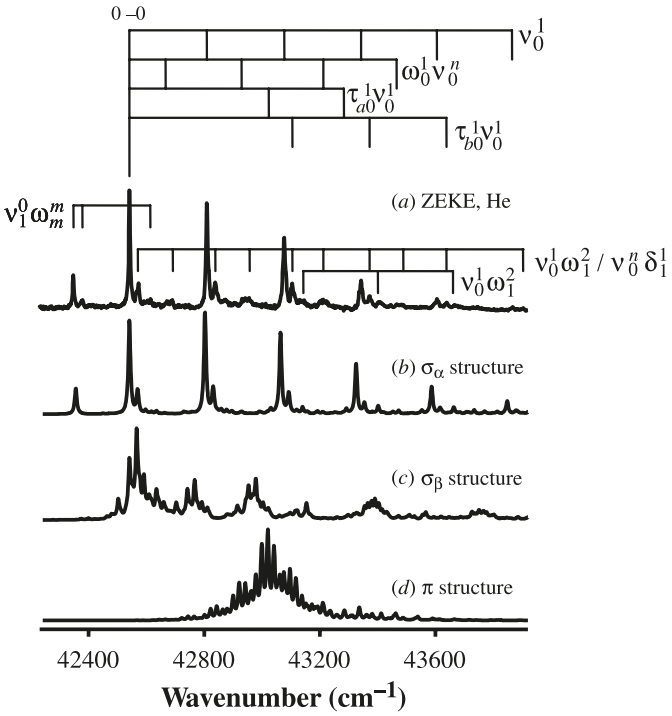

Fig. 6. Experimental ZEKE spectrum of Cu-(3-aminopyridine) seeded in (*a*) Ar carrier and simulations of the (*b*) σ_α, (*c*) σ_β, and (*d*) π structures at 10 K.

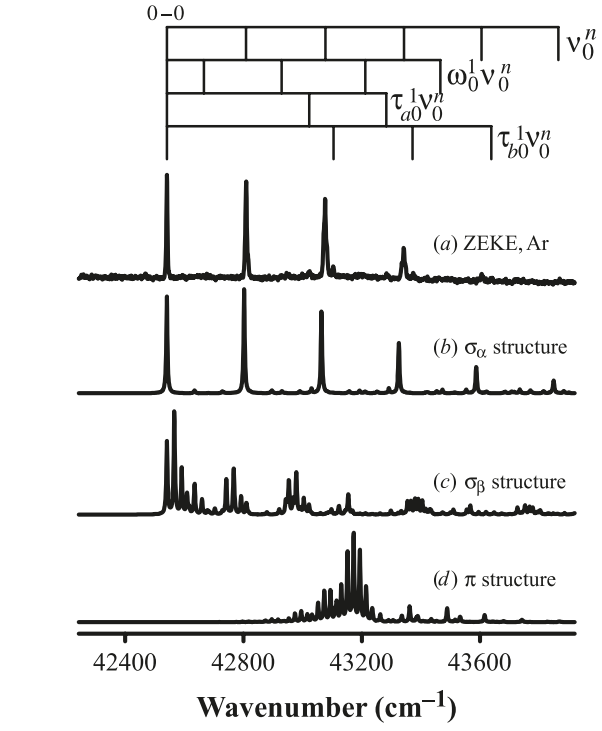

Fig. 7, Experimental ZEKE spectrum of Cu-(2-aminopyridine) seeded in the 1:1 He/Ar mixture.

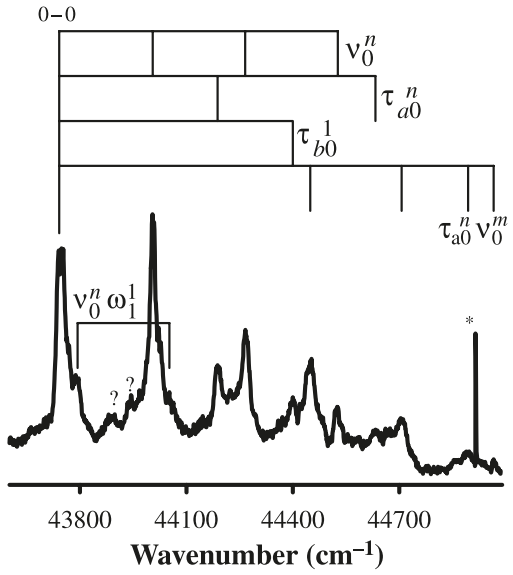

nificantly lower than those of Cu-(4-AP) or Cu-(3-AP) (4). Therefore, both AIE and FC profiles observed in the ZEKE spectrum indicate that the ion should have a σ_α structure as its corresponding neutral complex. Unfortunately, such a monodentate ion was not predicted by our theoretical calculations.

Ionization and bond energies

Table 2 summarizes the AIEs, metal-ligand bond energies, and vibrational frequencies from the ZEKE spectra and MP2/6-311+G(*d,p*) calculations of the σ_α Cu-aminopyridine complexes. The MP2 method predicts well the Cu-(*x*-AP) stretching and (*x*-AP)-based vibrational frequencies, but suffers relative large errors for the low-frequency Cu-(*x*-AP) bending modes. With the +3000 cm^{-1} correction, the theory also produces nicely the AIE values for these complexes. Since our MP2 calculations failed to locate a σ_α structure for Cu^+-(2-AP), no comparisons between the theory and experiment can be made for the ionization energy of Cu-(2-AP) and vibrational frequencies of Cu^+-(2-AP).

The measured AIEs of Cu-(*x*-AP) are 43 745, 42 541, and 41 377 cm^{-1}, with x = 2, 3 and 4, respectively. These values are 20 000 cm^{-1} (~240 kJ mol^{-1}) lower than the ionization energy of bare Cu atom [IE(Cu) = 62 317 cm^{-1}] (27). The large AIE shift arises from much stronger metal-ligand binding in the ion than in the neutral species, and the stronger ion bonding is due to the additional charge-dipole interaction. Because the metal-ligand bond energy in the neutral complex (36–51 kJ mol^{-1}) is only a small fraction of that in the corresponding ion (Table 2), the electrostatic interaction must be the major bonding force in these Cu-aminopyridine ions. The measured AIEs are in the order Cu-(4-AP) < Cu-(3-AP) < Cu-(2-AP), with an increment of ~1200 cm^{-1}. This small increment is consistent with the similar σ_α bonding in all these complexes. On the other hand, these AIE variations reveal subtle differences among the three aminopyridines. Although their polarizabilities are expected to be similar, the

© 2008 NRC Canada

Table 2. Adiabatic ionization energies (AIE, cm^{-1}), metal-ligand bond energies (D_0/D_0^+, kJ mol^{-1}), and vibrational frequencies (cm^{-1}) of the Cu-aminopyridine σ-complexes from ZEKE measurements and MP2/6-311+G(*d,p*) calculations.

		Mode	ZEKE[a]	MP2
Cu-(4-AP)	AIE		41 377	40 336[b]
	D_0^+/D_0			289.5 / 36.5
	Cu-(4-AP) stretch	ν^+/ν	261[b]/193	256 / 192
	Cu-(4-AP) o.p. bend	ω^+/ω	$\omega^+ - \omega = 15$	67 / 27
	Cu-(4-AP) i.p. bend	δ^+/δ	89/56	151 / 116
	(4-AP) o.p. distortion	τ_a^+	514	502
	(4-AP) o.p. distortion	τ_b^+	565	558
	C–H o.p. bend	ρ^+	790	784
Cu-3AP	AIE		42 541	42 816[c]
	D_0^+/D_0			274.7 / 51.4
	Cu-(3-AP) stretch	ν^+/ν	271[c]/194	262 / 185
	Cu-(3-AP) o.p. bend	ω^+/ω	131/102	94 / 66
	Cu-(3-AP) i.p. bend	δ^+/δ	$\delta^+ - \delta = 29$	141 / 111
	(3-AP) o.p distortion	τ_a^+	482	489
	NH_2 wag & (3-AP) o.p. distortion	τ_b^+	564	522
Cu-2AP	AIE		43 745	
	D_0^+/D_0			/ 48.0
	Cu-(2-AP) stretch	ν^+	261	
	Cu-(2-AP) o.p. bend	ω^+/ω	$\omega^+ - \omega = 51$	
	(2-AP) o.p. distortion	τ_a^+	446	
	(2-AP) o.p. distortion	τ_b^+	658	

[a]The uncertainty of the AIE values is ~5 cm^{-1}; o.p. = out-of-plane; i.p. = in-plane.
[b]With +3000 cm^{-1} correction.
[c]Harmonic frequencies from least-squares fits.

electric dipole moments are rather different and in the order of 4-AP (3.72 D) > 3-AP (3.18 D) > 2-AP (2.13 D), as predicted by our MP2 calculations. However, the dipole-induced interaction does not appear to play a major role in the metal-ligand bonding of the neutral complexes, because the Cu-(*x*-AP) bond energies are in a different order, i.e., D_0 [Cu-(3-AP) = 51.4 kJ mol^{-1}] > D_0 [Cu-(2-AP) = 48.0 kJ mol^{-1}] > D_0 [(Cu-(4-AP) = 36.5 kJ mol^{-1}]. Thus, beside the dipole moment of the molecule, the binding variations may be attributed to other possible factors, such as resonance, chelation, and steric effects. Among these factors, the resonance effect in 4- and 2-AP leads to resonance structures with an additional negative charge on the pyridine N_α atom and thus increases repulsion to the Cu $4s^1$ electron in the Cu-(4-AP) and Cu-(2-AP) σ_α structures. Unlike 4- and 2-AP, no such resonance structures exist in 3-AP, and thus the electron repulsion should be smaller in the neutral Cu-(3-AP) σ_α structure. Our MP2 calculations predict more negative charged N_α atoms and smaller metal-ligand bond dissociation energies in Cu-(4-AP) and Cu-(2-AP) than that of Cu-(3-AP), suggesting that the resonance effect plays a large role in the bonding of the neutral complexes. Between Cu-(4-AP) and Cu-(2-AP), the ortho-substituted complex is more strongly bound than the para-substituted one. The stronger bonding of Cu-(2-AP) is surprising at first glance. However, a careful examination of the predicted σ_α structures reveals that the distance (2.53 Å) of the Cu atom to one of the H atoms in the amino group of Cu-(2-AP) is much shorter than that (2.95 Å) to the closet H atom in the pyridine ring of Cu-(4-AP). Since the 2.53 Å distance is smaller than the sum of the Cu and H van der Waals radii (2.60 Å) (28), interaction must exist between the two atoms. Therefore, the stronger Cu-(2-AP) bond may be the result of the additional hydrogen bonding. This Cu···H bonding in Cu-(2-AP) is also evident from the predicted opposite charges on Cu (–0.01) and H (+0.27). On the other hand, the calculated charges on the Cu and H atoms are 0.03 and 0.14 in Cu-(4-AP).

For the σ_α ions, the bond energy of Cu^+-(4-AP) is predicted to be larger than that of Cu^+-(3-AP), which is consistent with the stronger charge-dipole interaction and resonance effect in the para-substituted complex. For Cu^+-(2-AP), our MP2 calculations were not able to locate a minimum energy σ_α structure. Instead, the calculations predict a bidentate structure with Cu^+ coordination to both pyridine and amino nitrogen atoms. The Cu^+-ligand bond energy of this bidentate structure is slightly lower than that of Cu^+-(4-AP) but larger than that of Cu^+-(3-AP).

Conclusion

Vibrationally resolved ZEKE spectra and minimum energy structures are reported for the three Cu-(*x*-aminopyridine) complexes, where *x* = 2, 3, and 4. The ionization energies of these complexes are much lower than that of bare Cu atom and in the order of the decreasing energy for the 2-, 3-, and 4-aminopyridines. These energy shifts indicate much stronger metal-ligand bonding in the ion than that in the neutral species, and the increased ion bonding is largely due to the charge-dipole interaction. The most stable

© 2008 NRC Canada

structures of these complexes are formed by Cu coordination to the nitrogen atom in the pyridine ring. The major metal-ligand binding force is the σ Cu-N interaction in the neutral complexes and the charge-dipole interaction in the ions. The binding differences among the three neutral complexes arise from the resonance effect in the ortho- and para-substituted complexes and the additional Cu··H hydrogen bonding in the ortho-substituted species. The small differences among the ions are due to different dipole moments and chelation effects of these ligands.

Acknowledgments

We are grateful for support from the Experimental Physical Chemistry Program of the National Science Foundation. We also acknowledge additional support from donors of the Petroleum Research Fund of the American Chemical Society and Kentucky Science and Engineering Foundation.

References

1. W. Kaim and J. Rall. Angew. Chem. Int. Ed. Engl. **35**, 43 (1996).
2. W. Kaim. Dalton Trans. 761 (2003).
3. R.H. Holm, P. Kennepohl, and E.I. Solomon. Chem. Rev. **96**, 2239 (1996).
4. X. Wang and D.-S. Yang J. Phys. Chem. A, **110**, 7568 (2006).
5. X. Wang and D.-S. Yang. J. Phys. Chem. A, **108**, 6449 (2004).
6. J. Miyawaki, K. Sugawara, S. Li, and D.-S. Yang. J. Phys. Chem A, **109**, 6697 (2005).
7. S. Li, B. R. Sohnlein, D.-S. Yang, J. Miyawaki, and K.-I. Sugawara. J. Chem. Phys. **122**, 214316/1 (2005).
8. X. Wang, B.R. Sohnlein, S. Li, J.F. Fuller, and D.-S. Yang. Can. J. Chem. **85**, 714 (2007).
9. X. Wang, J.S. Lee, and D.-S. Yang. J. Phys. Chem. A **110**, 12777 (2006).
10. X. Wang, J.S. Lee, and D.-S. Yang. J. Chem. Phys. **125**, 014309/1 (2006).
11. M.T. Rodgers. J. Phys. Chem. A, **105**, 8145 (2001).
12. S. Akyuz. J. Mol. Struct. **449**, 23 (1998).
13. S. Akyuz. J. Mol. Struct. **482-483**, 171 (1999).
14. A. Topacli and S. Bayari. Spectrochim. Acta Part A, **57A**, 1385 (2001).
15. S. Akyuz. J. Supramol. Chem. **2**, 401 (2003).
16. S.J. Baek, K.-W. Choi, Y.S. Choi, and S.K. Kim. J. Phys. Chem. A, **107**, 4826 (2003).
17. D.E. Belcher and M.C.R. Cockett. Chem. Phys. Lett. **398**, 539 (2004).
18. G.K. Rothschopf, J.S. Perkins, S. Li, and D.-S. Yang. J. Phys. Chem. A, **104**, 8178 (2000).
19. D. Proch adn T. Trickl. Rev. Sci. Instrum. **60**, 713 (1989).
20. C.E. Moore. Atomic Energy Levels. National Bureau Standards, Wash., USA. 1971.
21. B.R. Sohnlein and D.-S. Yang. J. Chem. Phys. **124**, 134305 (2006).
22. M. J. Frisch, G.W. Trucks, H.B. Schlegel, G.E. Scuseria, M.A. Robb, J.R. Cheeseman, J.A. Montgomery Jr., T. Vreven, K.N. Kudin, J.C. Burant, J.M. Millam, S.S. Iyengar, J. Tomasi, V. Barone, B. Mennucci, M. Cossi, G. Scalmani, N. Rega, G.A. Petersson, H. Nakatsuji, M. Hada, M. Ehara, K. Toyota, R. Fukuda, J. Hasegawa, M. Ishida, T. Nakajima, Y. Honda, O. Kitao, H. Nakai, M. Klene, X. Li, J. E. Knox, H.P. Hratchian, J.B. Cross, V. Bakken, C. Adamo, J. Jaramillo, R. Gomperts, R.E. Stratmann, O. Yazyev, A.J. Austin, R. Cammi, C. Pomelli, J.W. Ochterski, P.Y. Ayala, K. Morokuma, G.A. Voth, P. Salvador, J. J. Dannenberg, V.G. Zakrzewski, S. Dapprich, A. D. Daniels, M.C. Strain, O. Farkas, D.K. Malick, A.D. Rabuck, K. Raghavachari, J.B. Foresman, J.V. Ortiz, Q. Cui, A.G. Baboul, S. Clifford, J. Cioslowski, B.B. Stefanov, G. Liu, A. Liashenko, P. Piskorz, I. Komaromi, R.L. Martin, D.J. Fox, T. Keith, M.A. Al-Laham, C.Y. Peng, A. Nanayakkara, M. Challacombe, P.M.W. Gill, B. Johnson, W. Chen, M.W. Wong, C. Gonzalez, and J.A. Pople. GAUSSIAN 03. Revision C.02 [computer program]. Gaussian Inc., Wallingford, Conn., USA. 2004.
23. D.-S. Yang, M.Z. Zgierski, D.M. Rayner, P.A. Hackett, A. Martinez, D.R. Salahub, P.-N. Roy, and T. Carrington Jr. J. Chem. Phys. **103**, 5335 (1995).
24. A. Berces, M.Z.Zgierski, and D.-S. Yang. Computational Molecular Spectroscopy. Wiley, New York, USA. 2000.
25. F. Duschinsky. Acta Physicochim. URSS **7**, 551 (1937).
26. J. Miyawaki and K. Sugawara. J. Chem. Phys. **119**, 6539 (2003).
27. D.R. Lide. CRC Handbook of Chemistry and Physics. 88th ed. CRC Press, Boca Raton, Fla., USA. 2008.
28. Available from http://www.webelements.com.

© 2008 NRC Canada

A mechanistic study of the addition of alkynes to Brook silenes[1]

Kaarina K. Milnes and Kim M. Baines

Abstract: The addition of the alkyne-containing mechanistic probes (*trans*-2-phenylcyclopropyl)ethyne, (*trans,trans*-2-methoxy-3-phenylcyclopropyl)ethyne, and (*trans,trans*-2-methoxy-1-methyl-3-phenylcyclopropyl)ethyne (**1a**–**1c**) to a Brook silene 2-(1-adamantyl)-2-trimethylsiloxy-1,1-bis(trimethylsilyl)-1-silene (**14**) was examined. When alkyne **1a** was added to the silene, an ene adduct was observed; however, addition of alkyne **1c** to **14** gave a mixture of silacyclobutenes and silacycloheptenes. The regiochemistry of the phenyl and methoxy substituents on the seven-membered ring of the silacycloheptenes provides convincing evidence for the formation of a biradical intermediate along the reaction pathway.

Key words: Brook silene, alkyne, cycloaddition, reaction mechanism, mechanistic probe.

Résumé : On a étudié l'addition d'alcynes contenant des sondes mécanistiques, le (*trans*-2-phénylcyclopropyl)éthyne, le (*trans,trans*-2-méthoxy-3-phénylcyclopropyl)éthyne et le (*trans,trans*-2-méthoxy-1-méthyl-3-phénylcyclopropyl)éthyne (**1a**–**1c**) à un silène de Brook, le 2-(1-adamantyl)-2-triméthylsiloxy-1,1-bis(triméthylsilyl)-1-silène (**14**). Lorsque l'alcyne **1a** est additionné au silène, on observe la formation d'un adduit ène; toutefois, l'addition de l'alcyne **1c** au silène **14** conduit à la formation d'un mélange de silacyclobutènes et de silacycloheptènes. La régiochimie des substituants phényle et méthoxy sur le cycle à sept chaînons des silacycloheptènes fournit des données convaincantes de la formation d'un intermédiaire biradicalaire au cours de la voie réactionnelle.

Mots-clés : silène de Brook, alcyne, cycloaddition, mécanisme réactionnel, sonde mécanistique.

[Traduit par la Rédaction]

Introduction

There has been recent interest in the use of silenes as reagents in organic synthesis because of their highly regioselective cycloaddition reactions and the variety of transformations that the silicon can subsequently facilitate (1). In addition to their potential use in organic synthesis, the cycloaddition reactions of silenes have been critical for the synthesis of many new silacycles that have not been readily available by any other route (2). Furthermore, the cycloaddition reactions of silenes have played a central role in the development of silene chemistry, as they usually occur cleanly and in high yield, and thus these reactions have been used to provide indirect evidence for transient silenes (2). To fully exploit these important transformations, it is necessary to increase our understanding of their mechanisms.

In this work, we investigate the mechanism of the cycloaddition of alkynes to Brook silenes $(Me_3Si)_2Si{=}C(R)(OSiMe_3)$ (Scheme 1) (2). Brook silenes are a special class of relatively nonpolar silenes, which are important since they are one of the few stable silenes that can be easily synthesized (2). The products derived from the reactions of Brook silenes are, in general, the same as those derived from polar silenes; however, the rate constants for the reactions of Brook silenes appear to be less (2*c*). As with polarized silenes, the products formed from the addition of alkynes to Brook silenes are silacyclobutenes or, possibly, ene adducts if the silene or the alkyne contain an α-hydrogen (2). In an attempt to probe the mechanism of alkyne addition to silenes, Brook and co-workers (3) examined the addition of phenylacetylene and trimethylsilylacetylene to a mixture of the *E*- and *Z*-isomers of $(Me_3Si)(R)Si{=}C(1\text{-}Ad)(OSiMe_3)$, R = Mes (2,4,6-trimethylphenyl) or Tip (2,4,6-triisopropylphenyl); the E/Z ratio of the silene isomers was known but not assigned. In all cases, the ratio of the two isomeric silacyclobutenes produced was found to be identical to the E/Z ratio of the starting silene mixture. It was concluded that these results were, therefore, only consistent with a concerted mechanism of addition of the alkyne to the silene. Ishikawa and co-workers (4) have also examined the addition of alkynes to Brook silenes, both experimentally and theoretically, and in several cases implicate the involvement of biradical intermediates; however, unambiguous evidence for the intermediacy of biradicals was never obtained.

Received 21 April 2008. Accepted 24 July 2008. Published on the NRC Research Press Web site at canjchem.nrc.ca on 6 November 2008.

This paper is dedicated to Professor Richard Puddephatt for his many valued contributions in to Canadian science.

K.K. Milnes and K.M. Baines.[2] Department of Chemistry, University of Western Ontario, London, ON N6A 5B7, Canada.

[1]This article is part of a Special Issue dedicated to Professor Richard J. Puddephatt.

[2]Corresponding author (e-mail: kbaines2@uwo.ca).

 doi:10.1139/V08-145 © 2008 NRC Canada

Scheme 1.

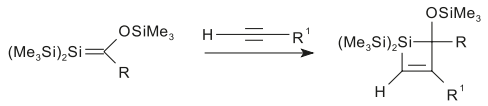

In the past few years, our group has investigated the use of molecular probes as a means of examining the mechanism of alkyne addition to group 14 (di)metallenes (5). We have developed alkynes **1b** and **1c** as mechanistic probes designed to undergo regiochemically distinct rearrangements to differentiate between the formation of α-cyclopropylvinyl radical and ionic intermediates (6). To exemplify, the α-cyclopropylvinyl radical (**2**), derived from alkyne **1b** or **1c**, rapidly ring opens toward the phenyl substituent yielding a benzyl radical. In contrast, the corresponding α-cyclopropylvinyl cation (**3**) undergoes ring-opening rearrangement selectively toward the methoxy substituent (Scheme 2). The analogous anion, as modeled by α-(*trans*-2-phenylcyclopropyl)vinyllithium (**4**) is stable towards ring opening (6*a*). Thus, an efficient method for distinguishing between the formation of all plausible intermediates has been established. (*trans*-2-Phenylcyclopropyl)ethyne **1a**, which does not contain a methoxy substituent on the cyclopropyl ring, undergoes ring-opening rearrangement toward the phenyl substituent when either a radical or a cation is generated at the α-cyclopropylvinyl position (6). Thus, alkyne **1a** is able to detect the formation of a reactive intermediate; however, there will be no structural differentiation observed in the products that are formed.

To examine the mechanism of the addition of alkynes to Brook silenes, we added cyclopropyl alkynes **1a**–**1c** to the Brook silene $(Me_3Si)_2Si{=}C(t\text{-}Bu)(OSiMe_3)$ (**5**) (7). When alkyne **1a** is added to silene **5**, the only products formed are two diastereomers of allene **6** (R^1 = H) (Scheme 3); however, when alkynes **1b** and **1c** are added to silene **5**, either allene **7** (R^1 = OMe), silacyclobutene **8** (R = H), and silacycloheptene **10**, or silacyclobutene **9** (R = Me) and silacycloheptenes **11** and **12** are formed, respectively. The products **6**–**12** have at least two stereocentres, and thus, two or more diastereomers of the products are typically observed, as indicated by the lower case letters following the compound numbers. Presumably, silacycloheptenes **10**, **11**, and **12** are formed by the reaction of intermediate silacyclohepta-1,2-dienes **13a** and **13b** (R = H or Me) with silene **5**.

In silacycloheptenes **10**, **11**, and **12**, the cyclopropyl ring has clearly undergone ring expansion. Using a variety of spectroscopic techniques, the phenyl substituent was found to be α and the methoxy group was found to be β to the former silenic carbon in all the silacycloheptenes. Because of the placement of the phenyl substituents on the 7-membered ring of silacycloheptenes **10**, **11**, and **12**, it was concluded that alkynes **1b** and **1c** must add to silene **5** to give an initial 1,4-biradical. The 1,4-biradical intermediate can then cyclize, forming silacyclobutenes **8** and **9** or undergo ring-opening rearrangement toward the phenyl substituent forming a 1,7-biradical intermediate. Cyclization of the 1,7-biradical intermediate yields silacyclohepta-1,2-diene (**13**). The addition of a second equivalent of silene **5** to **13** produces silacycloheptenes **10**, **11**, and **12**. Although these results provide evidence for the nature of the intermediate formed during the addition of alkynes to Brook silenes, it is important to remember that Brook silenes are a special class of relatively nonpolar silenes, and thus a generalization of the mechanism of addition of alkynes to all silenes cannot be based on these results. Nonetheless, we wished to explore the generality of these observations, and we now report on the addition of cyclopropyl alkynes **1a**–**1c** to a second example of a Brook silene, $(Me_3Si)_2Si{=}C(1\text{-}Ad)(OSiMe_3)$ (**14**) (8).

Scheme 2.

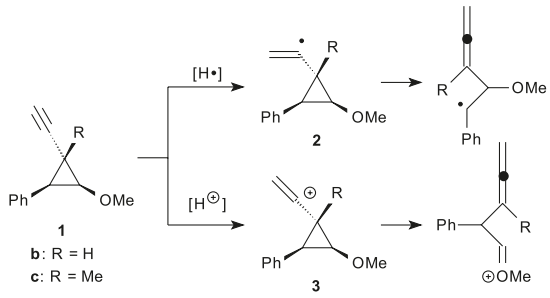

Results and discussion

Irradiation of 1-adamantanecarbonyltris(trimethylsilyl)-silane (**15**) in the presence of (*trans*-2-phenylcyclopropyl)-ethyne **1a** produces a diastereomeric mixture of allenes **16a** and **16b** (53:47), as revealed by ^{1}H NMR spectroscopy (Scheme 4). When alkyne **1a** is added to a solution of preformed silene **14** in the dark, the same product mixture was obtained in a similar ratio.

Irradiation of acylsilane **15** in the presence of alkyne **1c** produced a mixture of six diastereomers of silacycloheptene **17a**–**17f** and two diastereomers of silacyclobutene **18a** and **18b** (in ratios of 12:13:32:5:17:2:9:10) as revealed by ^{1}H NMR spectroscopy (Scheme 5). When alkyne **1c** is added to a solution of the preformed silene in the dark, the same product mixture was obtained in a similar ratio. Chromatographic separation of the crude product mixture yielded a mixture of silacycloheptenes **17a**–**17f** (14:17:34:8:24:3) and a mixture of silacyclobutenes **18a** and **18b** (56:44). Further chromatographic separation of the silacycloheptenes **17a**–**17f** yielded silacycloheptenes **17a** and **17b** (58:42) and silacycloheptenes **17c**–**17f** (65:14:19:2). Despite several attempts, no one compound could be isolated from the mixtures.

Allenes **16a** and **16b**, silacycloheptenes **17a**–**17f**, and silacyclobutenes **18a** and **18b** were identified by ^{1}H, ^{13}C, gCOSY, ^{1}H-^{13}C gHSQC and gHMBC, and ^{1}H-^{29}Si gHMBC NMR spectroscopy and mass spectrometry. The spectroscopic features that allowed for the elucidation of the structures of compounds **16a**, **16b**, **17a**–**17f**, **18a**, and **18b** are very similar to those seen for the products derived from the addition of alkynes **1a**–**1c** to silene **5** (7). For **17a**–**17e**, the phenyl substituent was found to be α and the methoxy substituent was found to be β to the former silenic carbon. Silacycloheptene **17f** was only present in a small amount, and as a consequence, not all the diagnostic correlations were evident in the NMR spectral data; however, the ^{1}H NMR spectral data for **17f** is very similar to that of the other

© 2008 NRC Canada

Scheme 3.

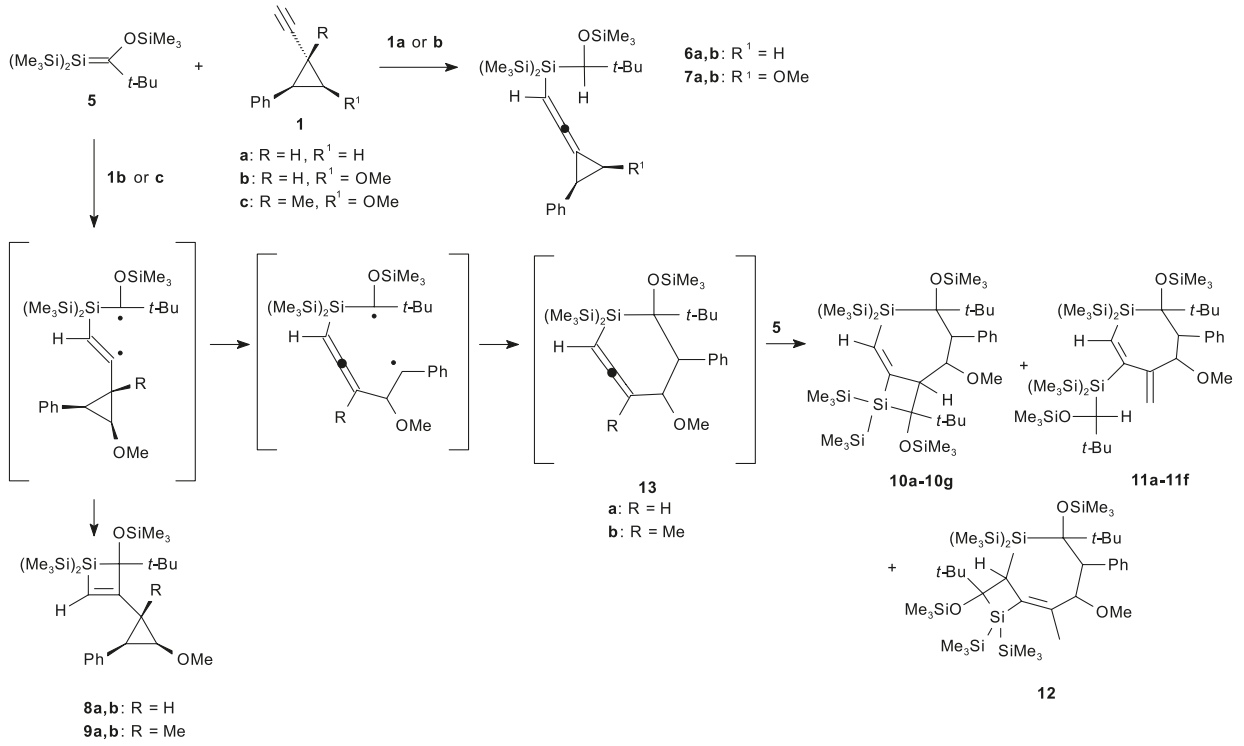

Scheme 4.

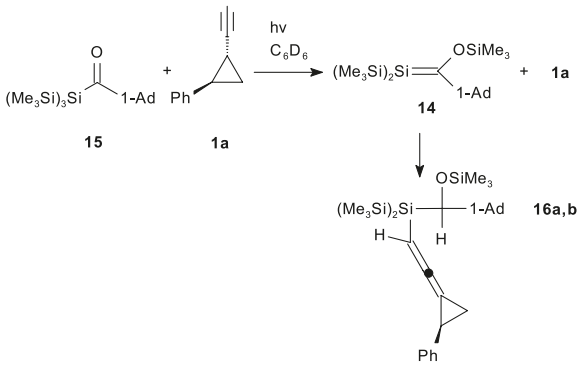

Scheme 5.

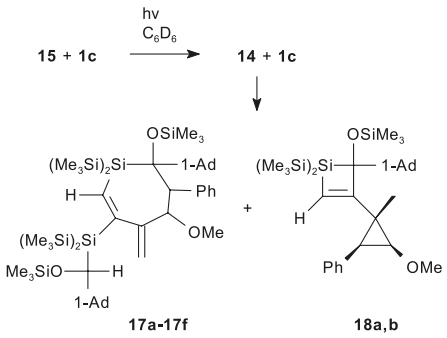

diastereomers of **17**, and therefore, its regiochemistry was assumed to be the same as **17a**–**17e**.

The formation of allenes **16a** and **16b** from the addition of alkyne **1a** to silene **14** is best described as a pericyclic ene-addition, as previously reported for the formation of allenes **6** and **7** (Scheme 3, R^1 = H or OMe) from the addition of alkynes **1a** and **1b** to silene **5** (7).

From the structure of silacycloheptenes **17a**–**17f**, it is evident that the cyclopropyl ring has undergone ring expansion. The location of the phenyl substituent on the carbon next to the former silenic carbon is *only* consistent with a mechanism that involves the formation of an α-cyclopropylvinyl *radical* intermediate during the course of the addition of alkyne **1c** to silene **14**: alkyne **1c** must add to the silene to give a 1,4-biradical intermediate that can cyclize forming silacyclobutenes **18a** and **18b** or ring open towards the phenyl substituent to yield a 1,7-biradical intermediate (Scheme 6). Ring closure of the 1,7-biradical intermediate yields silacyclohepta-1,2-diene (**19**), which apparently reacts with a second equivalent of silene via an ene addition to give the observed products **17a**–**17f**. The ene adduct is also likely derived from a biradical intermediate. The addition of alkyne **1c** to silene **14** did not afford a product analogous to **12** (Scheme 3), presumably because of steric effects.

The addition of alkyne **1b** to silene **14** was attempted several times, both by co-irradiation of the alkyne and acylsilane **15** and by addition of the alkyne to the preformed silene; however, a complex mixture of products was formed each time. The addition of alkyne **1b** to the related silene $(Me_3Si)_2Si{=}C(t\text{-Bu})(OSiMe_3)$ **5** yielded the bicycle **10**, where a second equivalent of silene **5** adds to the allene moiety of **13a**, presumably via the biradical intermediate **21a** (Scheme 7) (7). Only one regioisomer of **10** is formed, likely because of steric factors. The addition of silene **14** to the transient silacyclohepta-1,2-diene (**20**) may also form a biradical **21b** (R = 1-Ad) (Scheme 7). Biradical **21b** has no viable reaction pathways; it cannot disproportionate, and the

© 2008 NRC Canada

Scheme 6.

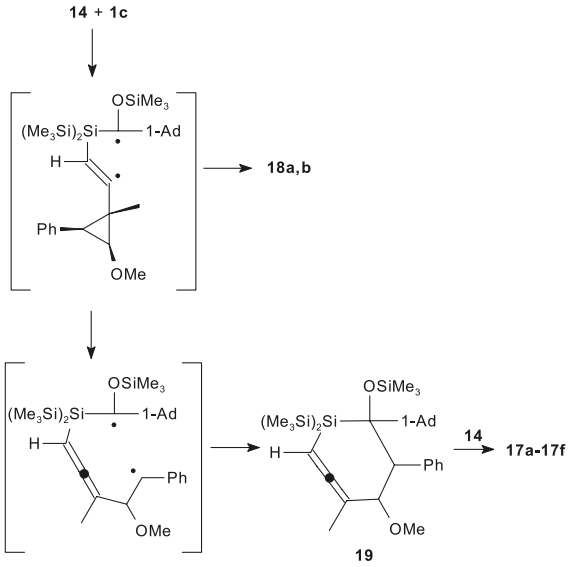

Scheme 7.

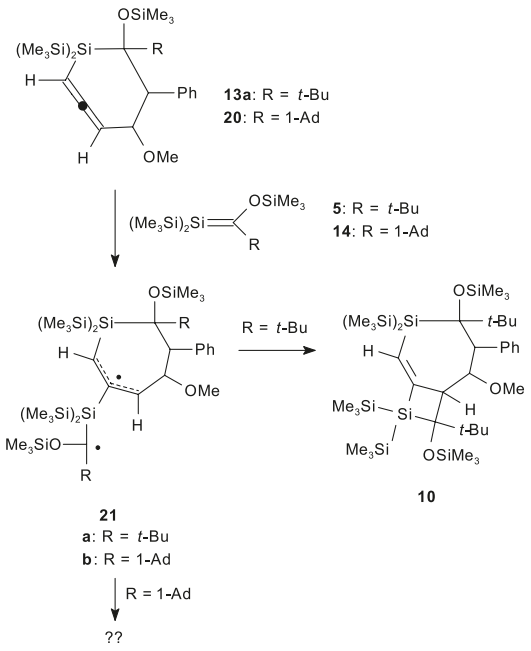

bulk of the adamantyl group apparently impedes cyclization to give a fused ring system. Thus, a complicated mixture of products is obtained when alkyne **1b** was added to silene **14**. The separation and characterization of the many products formed was not pursued.

Conclusions

The structure of silacycloheptenes **17a**–**17f**, resulting from the addition of alkyne **1c** to silene **14**, clearly indicates that the cyclopropyl ring has undergone a ring-opening rearrangement. Based on the location of the phenyl and methoxy substituents on the 7-membered ring in silacycloheptenes **17a**–**17f**, it can be concluded that the intermediate formed is an α-cyclopropylvinyl radical.

Table 1. Comparison of the product ratios obtained by the addition of alkynes **1a**–**1c** to $(Me_3Si)_2Si{=}C(R)(OSiMe_3)$.

		Silene	
Reaction	**Product**	**R= 1-Ad**	**R= t-Bu** (7)
Silene + 1a	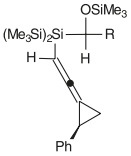	100	100
Silene + 1b	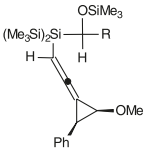	0	48
	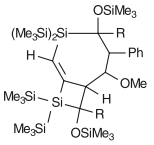	0	35
	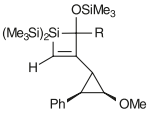	0	17
Silene + 1c	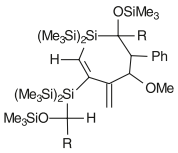	81	68
	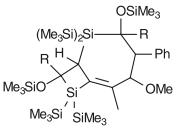	0	11
	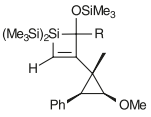	19	21

The results presented in this report are very similar to those obtained previously (7); a summary of the product ratios obtained in the addition of alkynes **1a**–**1c** to the two silenes is presented in Table 1. The most significant difference is seen in the reactivity of silenes **5** and **14** toward alkyne **1b**. The *t*-butyl silene **5** reacts cleanly with the alkyne to form allenes **7a** and **7b**, silacyclobutenes **8a** and **8b**, and silacycloheptenes **10a**–**10g**. In contrast, the adamantyl silene **14** does not react cleanly with alkyne **1b**, and no products were isolated. Both silenes react with alkyne **1a** to give stereoisomers of an allenic silane (i.e., **6a** and **6b** from **5** or **16a** and **16b** from **14**) as the only products. With alkyne **1c**, a silacyclobutene (i.e., **9a** and **9b** from **5** or **18a** and **18b** from **14**) is formed in approximately the same relative amount. The remaining material is converted to the ring-opened silacyclohepta-1,2-diene (i.e., **13a** or **20**), which adds a second equivalent of the silene, most likely via a biradical that can disproportionate to give a silacycloheptene with an exocyclic methylene group (i.e., **11a**–**11f** from **5** or **17a**–**17f** from **14**) or undergo ring closure in the case of silene **5** (i.e.,

© 2008 NRC Canada

10a–**10g**). Interestingly, the additional steric bulk of the adamantyl group does not influence the reactivity of the initially formed 1,4-biradical; the ratio of silacyclobutene to silacycloheptene products remains the same, ~ 20:80. However, the bulky adamantyl group does influence the course of the reaction of the silacyclohepta-1,2-diene with an additional equivalent of silene: no fused ring products are obtained, presumably because of steric effects; only disproportioned products are observed.

Given that the addition of alkynes **1a**–**1c** to Brook silene **5** gave similar results, we are increasingly confident that the addition of the triple bond of alkynes to Brook silenes involves a biradical intermediate. Not surprisingly, the bulk of the alkyl substituent on the carbon of the silene does not alter the mechanism of the reaction. However, if the alkyne has an α-hydrogen, as in the case of alkyne **1a**, allenes such as **16a** and **16b** may be formed. It is likely that these products are formed by a concerted pericyclic ene-addition (7).

Experimental

General details

All reactions were performed in flame-dried Schlenk tubes, or NMR tubes sealed with a septum, under an inert atmosphere of argon. Irradiations were carried out using three 100 W mercury spot lamps (Blak-Ray B-100AP series; λ > 350 nm); the NMR tubes were cooled in a cold water jacket (~6 °C). Benzene-d_6 was distilled from LAH prior to use and stored over 4 Å molecular sieves. Acylsilane **15** (8), silene **14** (8), and alkynes **1a**–**1c** (6*a*) were prepared according to the previously reported procedures.

The NMR standards used are as follows: residual C_6D_5H (7.15 ppm) for ^{1}H NMR spectra and C_6D_6 central transition (128.0 ppm) for ^{13}C NMR spectra; Me_4Si as an external standard, 0 ppm, for ^{1}H-^{29}Si gHMBC spectra. IR spectra were recorded (cm^{-1}) from thin films. Mass spectra were obtained using an ionizing voltage of 70 eV, and the data are reported in mass-to-charge units *m*/*z*.

Irradiation of acylsilane 15 and alkyne 1a

A solution of acylsilane **15** (91 mg, 0.22 mmol) and alkyne **1a** (35 mg, 0.24 mmol) dissolved in C_6D_6 (1.5 mL) was irradiated for 3.5 h. ^{1}H NMR spectroscopic analysis of the crude product revealed a mixture of diastereomeric allenes **16a** and **16b** contaminated with small amounts of impurities and unreacted alkyne **1a**. The crude product was purified by preparative thin layer chromatography (silica gel, hexanes) yielding allenes **16a** and **16b** (53:47, 54 mg) as a pale yellow oil (44% yield). **16a** and **16b**: IR (cm^{-1}) 2945 (s), 2904 (s), 2848 (m), 1987 (s), 1603 (w), 1445 (m), 1240 (s), 1045 (s), 835 (s), 692 (m). **16a**: ^{1}H NMR (C_6D_6) δ: 7.16–7.19 (m, Ph*H*), 7.02–7.07 (m, Ph*H*), 5.60 (q, 1H, *H*C=C=C, *J* = 4.9 Hz), 3.70 (s, 1H, Me_3SiOCH), 2.78 (dt, 1H, PhC*H*, *J* = 8.1, 4.7 Hz), 1.99 (br s, 3H, Ad-C*H*), 1.79–1.90 (m, 1H, CH_2), 1.67–1.69 (br m, 12H, Ad-CH_2), 1.67–1.69 (m, 1H, CH_2) (9), 0.35 (s, 9H, $SiMe_3$), 0.34 (s, 9H, $SiMe_3$), 0.11 (s, 9H, $OSiMe_3$); ^{13}C NMR (C_6D_6) δ: 196.82 (C=*C*=C), 141.54 (*i*-Ph*C*), 128.54 (*m*-Ph*C*), 126.91 (*o*-Ph*C*), 126.44 (*p*-Ph*C*), 84.00 (Me_3OSiCH), 83.83 (H*C*=C=C), 76.06 (HC=C=*C*) (10), 41.24 (Ad-CH_2), 38.07 (4° Ad-*C*), 37.42 (Ad-CH_2), 29.05 (Ad-*C*H), 26.11 (Ph*C*H), 18.12 (CH_2), 1.38 ($OSiMe_3$), 1.30 (2 × $SiMe_3$); ^{29}Si NMR (C_6D_6) δ: 14.5 ($OSiMe_3$), –15.0 (2 × $SiMe_3$), –48.1 ($Si(SiMe_3)_2$). **16b**: ^{1}H NMR (C_6D_6) δ: 7.16–7.19 (m, Ph*H*), 7.02–7.07 (m, Ph*H*), 5.52 (q, 1H, *H*C=C=C, *J* = 4.9 Hz), 3.90 (s, 1H, Me_3SiOCH), 2.82 (dt, 1H, PhC*H*, *J* = 7.6, 4.9 Hz), 1.99 (br s, 3H, Ad-C*H*), 1.79–1.90 (m, 2H, CH_2), 1.67–1.69 (br m, 12H, Ad-CH_2), 0.32 (s, 9H, $SiMe_3$), 0.29 (s, 9H, $OSiMe_3$), 0.18 (s, 9H, $SiMe_3$); ^{13}C NMR (C_6D_6) δ: 196.25 (C=*C*=C), 140.93 (*i*-Ph*C*), 128.53 (*m*-Ph*C*), 127.06 (*o*-Ph*C*), 126.44 (*p*-Ph*C*), 83.77 (H*C*=C=C), 81.76 (Me_3OSiCH), 76.10 (HC=C=*C*) (10), 41.36 (Ad-CH_2), 38.01 (4° Ad-*C*), 37.39 (Ad-CH_2), 29.05 (Ad-*C*H), 26.02 (Ph*C*H), 17.42 (CH_2), 1.59 ($OSiMe_3$), 0.84 ($SiMe_3$), 0.44 ($SiMe_3$); ^{29}Si NMR (C_6D_6) δ 14.2 ($OSiMe_3$), –15.3 ($SiMe_3$), –15.7 ($SiMe_3$), –47.7 ($Si(SiMe_3)_2$). **16a** and **16b**: HR EI-MS for $C_{31}H_{52}OSi_4$ (M^+) (*m*/*z*): calcd. 552.3095; found 552.3102.

Irradiation of acylsilane 15 and alkyne 1c

Two solutions of acylsilane **15** (201 mg, 0.49 mmol; 200 mg, 0.49 mmol) and alkyne **1c** (148 mg, 0.80 mmol; 147 mg, 0.79 mmol) dissolved in C_6D_6 (1.5 mL for each) were simultaneously irradiated. The progress of the reactions was monitored by ^{1}H NMR spectroscopy. After 24 h of irradiation, the two reaction mixtures were combined and the solvent was removed by rotary evaporation (649 mg); a mixture of silacycloheptenes **17a**–**17f** and silacyclobutenes **18a** and **18b** in a ratio of 12:13:32:5:17:2:9:10, respectively, was obtained, as determined by ^{1}H NMR spectroscopy. The ratio of the combined products was the same as the ratio of the individual reaction mixtures. Chromatographic separation of the crude mixture (silica gel, hexanes/CH_2Cl_2 7:3) yielded a mixture of silacycloheptenes **17a**–**17f** (14:17:34:8:24:3, 327 mg, 0.32 mmol) and a mixture of silacyclobutenes **18a** and **18b** (56:44, 41 mg, 0.07 mmol). A portion of the mixture of silacycloheptenes **17a**–**17f** (206 mg, 0.20 mmol) was further separated by chromatography (two preparative plates, silica gel, hexanes/CH_2Cl_2 5:1, hexanes/CH_2Cl_2 9:1) yielding a mixture of silacycloheptenes **17a** and **17b** (58:42, 32 mg, 0.03 mmol), and silacycloheptenes **17c**–**17f** (65:14:19:2, 31 mg, 0.03 mmol). Further separation of silacycloheptenes **17c**–**17f** was attempted with little success. In general, no one compound could be separated from the mixture, and thus the compounds were characterized as mixtures. **17a** and **17b** (colourless crystals): IR (cm^{-1}) 2906 (s), 2850 (m), 1452 (w), 1247 (s), 1109 (w), 1043 (s), 837 (s), 745 (m), 684 (w); **17a**: ^{1}H NMR (C_6D_6) δ: 8.21 (br s), 7.07–7.28 (br m) (all Ph*H*), 6.64 (s, 1H, SiC(*H*) = CSi), 5.39 (s, 1H, C=CH_2), 5.02 (br s, 1H, C=CH_2), 4.48 (br s, 1H, MeOC*H*), 4.36 (s, 1H, Me_3SiOCH), 3.77 (d, 1H, PhC*H*, *J* = 2.4 Hz), 3.15 (s, 3H, MeO), 1.65–2.40 (br m, all Ad-C*H*), 0.62 (s, 9H, $SiMe_{3linear}$), 0.51 (s, 18H, 2 × $SiMe_3$), 0.49 (s, 9H, $SiMe_3$), 0.25 (s, 9H, $OSiMe_{3linear}$), 0.06 (s, 9H, $OSiMe_{3cyclic}$); ^{13}C NMR (C_6D_6) δ: 158.87 (SiC(H) = *C*Si), 151.61 (*C*=CH_2), 142.24 (Si*C*(H) = CSi), 137.11 (br s, *i,o*-Ph*C*), 127.50, 127.43, 126.48 (all Ph*C*), 115.07 (C=*C*H_2), 103.1 (Me_3SiOC_{cyclic}) (11), 81.22 (MeO*C*H), 80.66 (Me_3SiOCH), 66.13 (Ph*C*H), 56.11 (MeO), 42.19 (4° Ad-C_{cyclic}), 41.17, 40.93, 40.15, 37.30, 37.18, 29.22 (all Ad-*C*) (12), 5.53 ($OSiMe_{3cyclic}$), 4.17 ($SiMe_3$), 3.31 ($SiMe_3$), 2.99 ($SiMe_3$), 2.45 ($SiMe_3$), 2.40 ($SiMe_3$) (13); ^{29}Si NMR (C_6D_6) δ: 13.5 ($OSiMe_{3linear}$), 6.2 ($OSiMe_{3cyclic}$), –15.3, –17.0 (2 ×

© 2008 NRC Canada

*Si*Me$_3$), –12 to –20 (2 × *Si*Me$_3$) (1), –20.7 (*Si*(SiMe$_3$)$_{2cyclic}$), –33.3 (*Si*(SiMe$_3$)$_{2linear}$); **17b**: ^{1}H NMR (C$_6$D$_6$) δ: 7.37 (br s), 7.07–7.28 (br m) (all Ph*H*), 6.71 (s, 1H, SiC(*H*) = CSi), 5.50 (br s, 1H, C=C*H*$_2$), 5.00 (br s, 1H, C=C*H*$_2$), 4.53 (br s, 1H, MeOC*H*), 4.28 (br s, 1H, Me$_3$SiOC*H*), 3.85 (d, 1H, PhC*H*, *J* = 1.8 Hz), 3.16 (s, 3H, MeO), 1.65–2.40 (br m, all Ad-C*H*), 0.60 (s, 9H, SiMe$_3$), 0.50 (s, 9H, SiMe$_3$), 0.49 (s, 9H, SiMe$_3$), 0.38 (s, 9H, SiMe$_3$), 0.28 (s, 9H, OSiMe$_{3linear}$), 0.03 (s, 9H, OSiMe$_{3cyclic}$); ^{13}C NMR (C$_6$D$_6$) δ: 159.46 (SiC(H) = *C*Si), 150.47 (*C*=CH$_2$), 143.24 (Si*C*(H) = CSi), 137.11 (br s, *i,o*-Ph*C*), 127.50, 127.43, 126.48 (all Ph*C*), 115.07 (C=*C*H$_2$), 103.8 (Me$_3$SiO*C*$_{cyclic}$) (11), 82.48 (Me$_3$SiO*C*H), 81.22 (MeO*C*H), 65.83 (Ph*C*H), 56.26 (MeO), 42.19 (4° Ad-*C*$_{cyclic}$), 41.17, 40.93, 40.15, 37.30, 37.18, 29.22 (all Ad-*C*) (12), 5.53 (OSiMe$_{3cyclic}$), 4.21 (SiMe$_3$), 3.56 (SiMe$_3$), 3.02 (SiMe$_3$), 2.62 (OSiMe$_{3linear}$), 2.26 (SiMe$_3$) (13); ^{29}Si NMR (C$_6$D$_6$) δ 13.5 (O*Si*Me$_{3linear}$), 5.8 (O*Si*Me$_{3cyclic}$), –15.3, –16.8 (2 × *Si*Me$_3$), –12 to –20 (2 × *Si*Me$_3$) (14), –21.1 (*Si*(SiMe$_3$)$_{2cyclic}$), –33.3 (*Si*(SiMe$_3$)$_2$) (14). **17a** and **17b**: HR EI-MS for C$_{53}$H$_{98}$O$_3$Si$_8$ (M$^+$) (*m*/*z*): calcd. 1006.5670, found 1006.5639. **17c**–**17f** (colourless crystals): IR (cm^{-1}) 2905 (s), 2852 (m), 1452 (m), 1248 (s), 1102 (m), 1039 (s), 1000 (w), 837 (s), 746 (w), 683 (w); ^{1}H NMR (C$_6$D$_6$) δ: 7.92–7.96, 7.06–7.33 (br m, all Ph*H*, **17c**–**17f**), 6.72 (s, 1H, SiC(*H*) = CSi, **17c**), 6.58 (s, 1H, SiC(*H*) = CSi, **17d**), 6.53 (s, 1H, SiC(*H*) = CSi, **17e**), 6.42 (s, 1H, SiC(*H*) = CSi, **17f**), 5.66 (s, 1H, C=C*H*$_2$, **17d**), 5.60 (s, 1H, C=C*H*$_2$, **17d**), 5.50 (s, 1H, C=C*H*$_2$, **17c**), 5.43 (s, 1H, C=C*H*$_2$, **17c**), 5.40 (s, 1H, C=C*H*$_2$, **17f**), 5.30 (s, 1H, C=C*H*$_2$, **17e**), 4.87 (d, 1H, MeOC*H*, *J* = 6.0 Hz, **17c**), 4.81 (s, 1H, C=C*H*$_2$, **17f**) (15), 4.78 (d, 1H, MeOC*H*, *J* = 7.2 Hz, **17d**), 4.75 (br s, 1H, MeOC*H*, **17e**), 4.72 (br s, 1H, C=C*H*$_2$, **17e**), 4.68 (s, 1H, MeOC*H*, **17f**) (15), 4.38 (s, 1H, Me$_3$SiOC*H*, **17f**), 4.35 (s, 1H, Me$_3$SiOC*H*, **17e**), 4.34 (s, 1H, Me$_3$SiOC*H*, **17d**), 4.33 (s, 1H, Me$_3$SiOC*H*, **17c**), 4.11 (s, 1H, PhC*H*, **17e**), 4.10 (s, 1H, PhC*H*, **17f**), 3.75 (d, 1H, PhC*H*, *J* = 6.6 Hz, **17d**), 3.65 (d, 1H, PhC*H*, *J* = 6.0 Hz, **17c**), 3.36 (s, 3H, MeO, **17f**), 3.30 (s, 3H, MeO, **17e**), 3.14 (s, 3H, MeO, **17c**), 3.11 (s, 3H, MeO, **17d**), 1.46–2.13 (br m, all Ad-C*H*, **17c**–**17f**), 0.63, 0.59, 0.58, 0.564, 0.56, 0.55, 0.543, 0.535, 0.52, 0.42, 0.38, 0.33, 0.28, 0.27, 0.268, 0.266, 0.26 (s, all SiMe$_3$ and OSiMe$_3$, **17c**–**17f**); ^{13}C NMR (C$_6$D$_6$) δ: 162.0 (SiC(H) = *C*Si, **17e**) (11), 161.57 (SiC(H) = *C*Si, **17c** and **17d**), 155.9 (*C*=CH$_2$, **17d**) (11), 155.09 (*C*=CH$_2$, **17c**), 150.6 (*C*=CH$_2$, **17e**) (11), 144.80 (Si*C*(H) = CSi, **17c**), 143.23 (Si*C*(H) = CSi, **17d**), 142.75 (Si*C*(H) = CSi, **17e**), 141.23 (*i*-Ph*C*, **17d**), 141.02 (*i*-Ph*C*, **17c**), 139.41 (*i*-Ph*C*, **17e**), 134.46, 134.32 (**17c**), 134.07 (**17d**), 133.32 (**17c**), 133.02, 132.81 (**17e**), 127.23, 127.17 (**17c**), 126.96, 126.73, 126.56, 126.47, 126.24 (**17c**), 126.06 (all Ph*C*, **17c**–**17f**), 120.33 (C=*C*H$_2$, **17e**), 116.91 (C=*C*H$_2$, **17d**), 116.30 (C=*C*H$_2$, **17c**), 99.81 (Me$_3$SiO*C*$_{cyclic}$, **17c**), 97.93 (Me$_3$SiO*C*$_{cyclic}$, **17d**), 94.72 (Me$_3$SiO*C*$_{cyclic}$, **17e**), 84.03 (MeO*C*H, **17e**), 83.07 (MeO*C*H, **17d**), 82.76 (Me$_3$SiO*C*H, **17e**), 82.67 (MeO*C*H, **17c**), 82.37 (Me$_3$SiO*C*H, **17c**), 80.17 (Me$_3$SiO*C*H, **17d**), 64.53 (Ph*C*H, **17e**), 62.55 (Ph*C*H, **17d**), 61.05 (Ph*C*H, **17c**), 57.12 (MeO, **17d**), 56.66 (MeO, **17c**), 56.20 (MeO, **17e**), 43.9 (4° Ad-*C*, **17d**) (11), 43.64 (4° Ad-*C*, **17e**), 43.48 (4° Ad-*C*, **17c**), 41.11, 40.97, 40.75, 40.23, 39.89, 37.18, 37.10, 37.04, 36.90, 32.30, 30.16, 30.10, 29.79, 29.37, 29.29, 29.05 (all Ad-*C*, **17c**–**17f**), 6.27, 6.19, 5.90, 5.08, 4.61, 4.20, 4.16, 4.09, 3.96, 3.45, 3.32, 3.13, 2.62, 2.59, 2.48, 2.35, 2.29, 2.16, 1.36 (all SiMe$_3$ and OSiMe$_3$, **17c**–**17f**); ^{29}Si NMR (C$_6$D$_6$) δ: 13.6 (O*Si*Me$_{3linear}$, **17c**), 13.5–13.7 (O*Si*Me$_{3linear}$, **17d**–**17f**) (14), 6.0 (O*Si*Me$_{3cyclic}$, **17e**), 2.1–2.3 (O*Si*Me$_{3cyclic}$, **17d**, **17f**) (14), 2.2 (O*Si*Me$_{3cyclic}$, **17c**), –11.0, –13.4 (2 × SiMe$_{3cyclic}$, **17c**), –16.0, –17.0 (2 × *Si*Me$_3$, **17c**), –13 to –18 (SiMe$_3$, **17d**–**17f**) (14), –29.1 (*Si*(SiMe$_3$)$_2$, **17e**), –31.5, –31.9 (2 × *Si*(SiMe$_3$)$_2$, **17c**), –33.9 (*Si*(SiMe$_3$)$_2$, **17d**) (16). **17c**–**17f**: HR EI-MS for C$_{53}$H$_{98}$O$_3$Si$_8$ (M$^+$) (*m*/*z*): calcd. 1006.5670, found 1006.5631. **18a** and **18b** (white solid): IR (cm^{-1}) 2906 (m), 2851 (w), 1650 (m), 1499 (w), 1451 (w), 1250 (m), 1093 (m), 1035 (m), 836 (s), 752 (w), 698 (w); **18a**: ^{1}H NMR (C$_6$D$_6$) δ: 7.59–7.61 (m, 2H, *o*-Ph*H*), 7.21–7.26 (m, 2H, *m*-Ph*H*), 7.06–7.11 (m, 1H, *p*-Ph*H*), 6.04 (s, 1H, SiC(*H*) = C, $^2J_{H\text{-}Si}$ = 8.8 Hz), 3.35 (d, 1H, MeOC*H*, *J* = 7.2 Hz), 3.29 (s, 3H, MeO), 2.68 (d, 1H, PhC*H*, *J* = 7.2 Hz), 1.97–2.10, 1.79–1.85, 1.67–1.74 (m, Ad-C*H*), 1.47 (s, 3H, Me), 0.37 (s, 9H, SiMe$_3$), 0.33 (s, 9H, SiMe$_3$) (17), 0.297 (s, 9H, OSiMe$_3$); ^{13}C NMR (C$_6$D$_6$) δ: 167.81 (SiC(H) = *C*), 137.25 (*i*-Ph*C*), 131.06 (*o*-Ph*C*), 128.2 (*m*-Ph*C*) (11), 126.78 (Si*C*(H) = C), 126.09 (*p*-Ph*C*), 97.64 (Me$_3$SiO*C*), 70.88 (MeOC*H*), 58.76 (MeO), 42.9 (4° Ad-*C*) (11), 40.30 (Ad-*C*), 37.21 (Ad-*C*), 31.65 (*C*Me), 31.53 (Ph*C*H), 29.55 (Ad-*C*), 13.01 (Me), 3.51 (OSiMe$_3$), 1.93 (SiMe$_3$), 1.53 (SiMe$_3$); ^{29}Si NMR (C$_6$D$_6$) δ: 6.5 (O*Si*Me$_3$), –12 to –13 (2 × *Si*Me$_3$) (14), –27.0 (*Si*(SiMe$_3$)$_2$); **18b**: ^{1}H NMR (C$_6$D$_6$) δ: 7.65–7.66 (m, 2H, *o*-Ph*H*), 7.21–7.26 (m, 2H, *m*-Ph*H*), 7.06–7.11 (m, 1H, *p*-Ph*H*), 5.96 (s, 1H, SiC(*H*) = C, $^2J_{H\text{-}Si}$ = 9.2 Hz), 3.93 (d, 1H, MeOC*H*, *J* = 7.2 Hz), 3.25 (s, 3H, MeO), 2.20 (d, 1H, PhC*H*, *J* = 7.2 Hz), 1.97–2.10, 1.79–1.85, 1.67–1.74 (m, Ad-C*H*), 1.51 (s, 3H, Me), 0.36 (s, 9H, SiMe$_3$), 0.32 (s, 9H, SiMe$_3$) (17), 0.303 (s, 9H, OSiMe$_3$); ^{13}C NMR (C$_6$D$_6$) δ: 168.73 (SiC(H) = *C*), 137.25 (*i*-Ph*C*), 130.72 (*o*-Ph*C*), 128.2 (*m*-Ph*C*) (11), 126.09 (*p*-Ph*C*), 125.35 (Si*C*(H) = C), 98.06 (Me$_3$SiO*C*), 68.39 (MeOC*H*), 58.47 (MeO), 42.0 (4° Ad-*C*) (11), 40.30 (Ad-*C*), 38.17 (Ph*C*H), 37.21 (Ad-*C*), 30.83 (*C*Me), 29.55 (Ad-*C*), 11.27 (Me), 3.51 (OSiMe$_3$), 1.93 (SiMe$_3$), 1.53 (SiMe$_3$); ^{29}Si NMR (C$_6$D$_6$) δ: 6.5 (O*Si*Me$_3$), –12 to –13 (2 × *Si*Me$_3$), –25.8 (*Si*(SiMe$_3$)$_2$); **18a**, **18b**: HR EI-MS for C$_{33}$H$_{56}$O$_2$Si$_4$ (M$^+$) (*m*/*z*): calcd. 596.3357, found 596.3370.

General procedure for the addition of alkynes to silene 14

Excess alkyne **1a** or **1c** (1.5–4 equiv.) dissolved in hexanes or ether was added to silene **14** dissolved in the same solvent (8). The reaction mixture was left to stir overnight. The solvent was removed and the residue was placed under high vacuum to remove the excess alkyne. The residue was analyzed by ^{1}H NMR spectroscopy.

Acknowledgements

We thank the Natural Sciences and Engineering Research Council of Canada (NSERC), the University of Western Ontario, and the Ontario Photonics Consortium for financial support.

References

1. H. Ottosson and P.G. Steel. Chem. Eur. J. **12**, 1576 (2006).

© 2008 NRC Canada

2. (*a*) H. Ottosson and A.M. Eklöf. Coord. Chem. Rev. **252**, 1287 (2008); (*b*) L.E. Gusel'nikov. Coord. Chem. Rev. **244**, 149 (2003); (*c*) T.L. Morkin and W.J. Leigh. Acc. Chem. Res. **34**, 129 (2001); (*d*) T.L. Morkin, T.R. Owens, and W.J. Leigh. *In* The chemistry of organic silicon compounds. *Edited by* Z. Rappoport and Y. Apeloig. Wiley and Sons Ltd., New York. 2001. Chap. 17; (*e*) A.G. Brook and M.A. Brook. Adv. Organomet. Chem. **39**, 71 (1996); (*f*) T. Müller, W. Ziche, and N. Auner. *In* The chemistry of organic silicon compounds. *Edited by* Z. Rappoport and Y. Apeloig. Wiley and Sons Ltd., New York, 1998. Chap. 16; (*g*) G. Raabe and J. Michl. *In* The chemistry of organic silicon compounds. *Edited by* Z. Rappoport and Y. Apeloig. Wiley and Sons Ltd., New York. 1989. Chap. 17; (*h*) A.G. Brook and K.M. Baines. Adv. Organomet. Chem. **25**, 1 (1986); (*i*) G. Raabe and J. Michl. Chem. Rev. **85**, 419 (1985); (*j*) N. Wiberg. J. Organomet. Chem. **273**, 141 (1984); (*k*) L.E. Gusel'nikov and N.S. Nametkin. Chem. Rev. **79**, 529 (1979); (*l*) L.E. Gusel'nikov, N.S. Nametkin, and V.M. Vdovin. Acc. Chem. Res. **8**, 18 (1975).
3. (*a*) A.G. Brook, A. Baumegger, and A.J. Lough. Organometallics, **11**, 3088 (1992); (*b*) P. Lassacher, A.G. Brook, and A.J. Lough. Organometallics. **14**, 4359 (1995).
4. (*a*) A. Naka, H. Ohnishi, J. Ohshita, J. Ikadai, A. Kunai, and M. Ishikawa. Organometallics, **24**, 5356 (2005); (*b*) A. Naka, H. Ohnishi, I. Miyahara, K. Hirotsu, Y. Shiota, K. Yoshizawa, and M. Ishikawa. Organometallics, **23**, 4277 (2004); (*c*) A. Naka and M. Ishikawa. Chem. Lett. **3**, 364 (2002); (*d*) A. Naka, J. Ikadai, M. Shingo, K. Yoshizawa, Y. Kondo, S.-Y. Kang, and M. Ishikawa. Organometallics, **21**, 2033 (2002); (*e*) K. Yoshizawa, Y. Kondo, S.-Y. Kang, A. Naka, and M. Ishikawa. Organometallics, **21**, 3271 (2002); (*f*) A. Naka and M. Ishikawa. J. Organomet. Chem. **611**, 248 (2002); (*g*) A. Naka and M. Ishikawa. Organometallics, **19**, 4921 (2000); (*h*) A. Naka, M. Ishikawa, S. Matsui, J. Ohshita, and A. Kunai. Organometallics, **15**, 5759 (1996).
5. (*a*) S.E. Gottschling, K.K. Milnes, M.C. Jennings, and K.M. Baines. Organometallics, **24**, 3811 (2005); (*b*) S.E. Gottschling, M.C. Jennings, and K.M. Baines. Can. J. Chem. **83**, 1568 (2005).
6. (*a*) S.E. Gottschling, T.N. Grant, K.K. Milnes, M.C. Jennings, and K.M. Baines. J. Org. Chem. **70**, 2686 (2005); (*b*) K.K. Milnes, S.E. Gottschling, and K.M. Baines. Org. Biomol. Chem. **2**, 3530 (2004).
7. K.K. Milnes, M.C. Jennings, and K.M. Baines. J. Am. Chem. Soc. **128**, 2491 (2006).
8. (*a*) A.G. Brook, J.W. Harris, J. Lennon, and M. El Sheikh. J. Am. Chem. Soc. **101**, 83 (1979); (*b*) A.G. Brook, S.C. Nyburg, F. Abdesaken, B. Gutekunst, G. Gutekunst, R.K.M.R. Kallury, Y.C. Poon, Y.-M. Chang, and W. Wong-Ng. J. Am. Chem. Soc. **104**, 5667 (1982).
9. This signal is completely obscured by the signals assigned to the adamantyl ^{1}H's.
10. It was difficult to assign the ^{13}C signals at 76.06 and 76.10 ppm to a specific isomer, and thus the assignments may be reversed.
11. Chemical shift estimated from the ^{1}H-^{13}C gHMBC spectrum.
12. The adamantyl carbon signals were difficult to assign to a specific isomer, and thus the assignments may be reversed.
13. It was difficult to assign the $SiMe_3$ ^{13}C signals to a specific isomer, and thus the assignments may be reversed.
14. It was difficult to assign all ^{29}Si signals because of the extensive overlap of the signals.
15. The ^{1}H signals at 4.81 and 4.68 ppm were difficult to assign specifically to C=CH_2 or MeOC*H* for **17f**, and thus their assignment may be reversed.
16. Not all the expected ^{29}Si correlations could be observed because of the low percentage of some of the isomers of silacycloheptenes **17c**–**17f**.
17. The ^{1}H signals at 0.33 and 0.32 ppm were difficult to assign to a specific isomer, and thus their assignment may be reversed.

© 2008 NRC Canada

Synthesis and electrochemistry of new thienyl – Schiff base complexes[1]

A. Pietrangelo, B.N. Boden, M.J. MacLachlan, and M.O. Wolf

Abstract: The synthesis and characterization of nickel(II), copper(II), and vanadyl ($[V=O]^{2+}$) complexes of two new thienyl-substituted Schiff base ligands are reported. Cyclic voltammetry of some of these complexes showed oxidation waves, but none of the complexes formed conductive polymer films upon repeated cycling. UV–vis absorption spectroscopy shows that some of the complexes exhibit enhanced conjugation, and the radical cations formed on these chromophores appear to be too stable to undergo oxidative coupling.

Key words: Schiff base, salphen, conjugated polymer, electrochemistry.

Résumé : On a effectué la synthèse et on a caractérisé les complexes du nickel(II), du cuivre(II) et du vanadyle ($[V=O]^{2+}$) de deux ligands dérivés de bases de Schiff substituées par de groupes thiényles. La voltampérométrie cyclique a permis de montrer que quelques-uns de ces complexes présentent des vagues d'oxydation, mais aucun de ces complexes ne forme de films de polymères conducteurs après des cycles voltampérométriques répétés. La spectroscopie d'absorption UV/vis montre que certains de ces complexes donnent lieu à une conjugaison exaltée et que les cations radicaux qui se forment sur ces chromophores semblent trop stables pour subir des couplages oxydants.

Mots-clés : base de Schiff, salphène, polymère conjugué, électrochimie.

[Traduit par la Rédaction]

Introduction

Conjugated polymers containing metal complexes are of interest because they combine the electronic properties of a highly delocalized π-system with the catalytic, magnetic, and optical properties of a metal (1). Schiff base complexes are a particularly intriguing class of metal complexes because they have large second-order and third-order NLO responses, are stable to over 300 °C, and have electronic or magnetic characteristics that permit additional functionality, such as chemical sensing, catalysis, and supramolecular organization (2–4). Both conjugated and non-conjugated polymers incorporating Schiff base complexes have been reported (5). Schiff base complexes containing a range of transition metals with pendant thiophene units have been electropolymerized to generate conductive polymer films that exhibit catalytic, sensing, and nonlinear optical properties (6).

The groups of both Swager and Reynolds have synthesized thiophene-containing Schiff base monomers and studied their electropolymerization. Oxidative coupling of monomers **1** and **2** (M = Co) gave conductive polymers where the metal does not contribute to conductivity but is necessary for electropolymerization (6*b*). Changing the substituents on **2** from R = H to larger groups such as R = Ph increases interchain spacing resulting in a reduction in conductivity for Cu(II)-containing polymers (6*c*). Reynolds investigated electropolymerization of monomers **3** and **4**, and found that polymerization occurs at the phenylene group for **3** (6*f*, 6*g*). In the case of **4**, polymerization could occur at either the thienyl or phenylene ring, except when R = CH_3, in which case polymerization occurs exclusively through the oligothiophene moiety.

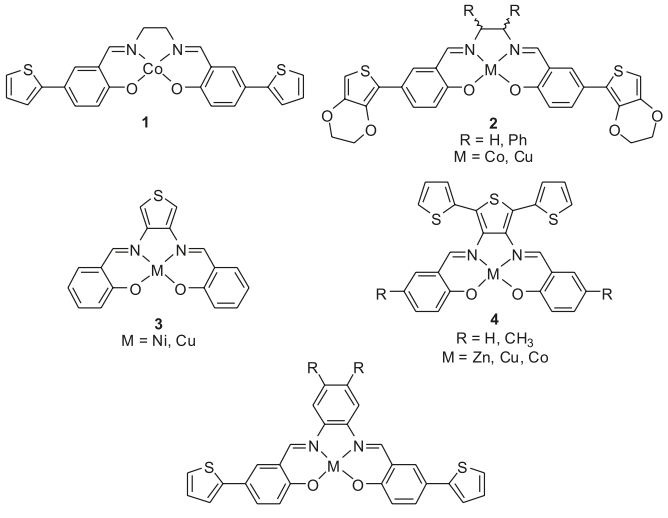

We recently reported the electropolymerization of substituted Schiff base complexes **5**–**7** in microgravity (6*a*). In some cases, improved film order was observed when film

Received 21 April 2008. Accepted 24 July 2008. Published on the NRC Research Press Web site at canjchem.nrc.ca on 12 November 2008.

A. Pietrangelo, B.N. Boden, M.J. MacLachlan,[2] and M.O. Wolf.[2] Department of Chemistry, University of British Columbia, Vancouver, BC V6T 1Z1, Canada.

[1]This article is part of a Special Issue dedicated to Professor R. Puddephatt.

[2]Corresponding authors (e-mail: mmaclach@chem.ubc.ca; mwolf@chem.ubc.ca).

 doi:10.1139/V08-143 © 2008 NRC Canada

growth occurred in the absence of gravity-driven convection currents as evidenced by higher χ^3 susceptibilities.

While electropolymerization is known for salphen complexes formed from 5-(2-thienyl)salicylaldehyde, such as **5**–**7**, it has not been studied for salphens made from 4-(2-thienyl)salicylaldehyde. In compounds with the general structure **A**, the relative meta arrangement between the thienyl and imine substituents on the phenyl ring leads to less effective conjugation than para arrangements (structure **B**). Visually it may be noted that the π-conjugation pathway between the thienyl substituents for **A** cannot be drawn with alternating single and double bonds in any important resonance structure, whereas in structure **B** the conjugation appears to be improved, inasmuch as this model is an indication of delocalization. Thus, we set out to probe whether 4-substituted structures polymerize and whether the resulting materials show significantly different electronic properties from those made from 5-substituted monomers.

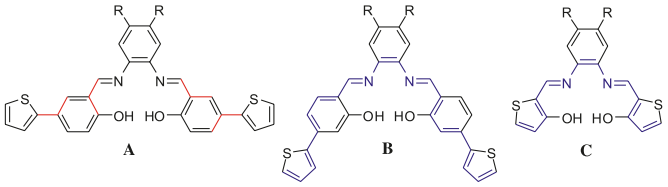

Another possible approach to a fully conjugated monomer involves replacing the terminal phenyl rings with thiophene groups, as in structure **C**. Here, we report a series of new conjugated monomers, along with electrochemistry and electronic absorption data.

Results and discussion

Synthesis

To prepare 4-(2-thienyl)salicylaldehyde **9**, 4-iodosalicylaldehyde **8** was coupled to 2-tributylstannylthiophene via Stille coupling affording **9** as a beige product in 92% yield (Scheme 1). Schiff base condensation of **9** with diamine **10a** gave salphen **11a** as an orange solid. With longer alkoxy chains, a longer reaction time was required for complete conversion to the product (**11b** and **11c**). The ^{1}H NMR spectrum of **11b** shows an imine resonance at δ 8.56 and a hydroxyl resonance at δ 13.34 (Fig. 1).

Heating **11b** at reflux in THF with the appropriate metal salt yielded the salphen metal complexes **12b**–**14b**. All three metal complexes crystallized readily, but the resulting crystals were thin and unsuitable for single crystal X-ray diffraction studies. The ^{1}H NMR spectrum of the diamagnetic Ni(II) complex **12b** was consistent with its structure, and all three complexes gave satisfactory mass spectrometry data and elemental analysis.

Thienolphenylenediimine (thienphen) complexes **19a** and **19b** were prepared by the route shown in Scheme 2. 3-Methoxythiophene **16** was prepared by Cu(I)-catalyzed Ullmann-type coupling of sodium methoxide with 3-bromothiophene **15** (7). Ortho-directed lithiation followed by quenching with DMF yielded 2-formyl-3-methoxythiophene **17** after work-up (8). Deprotection with BBr_3 afforded air-sensitive 2-formyl-3-hydroxythiophene **18** (9). Condensation

Scheme 1.

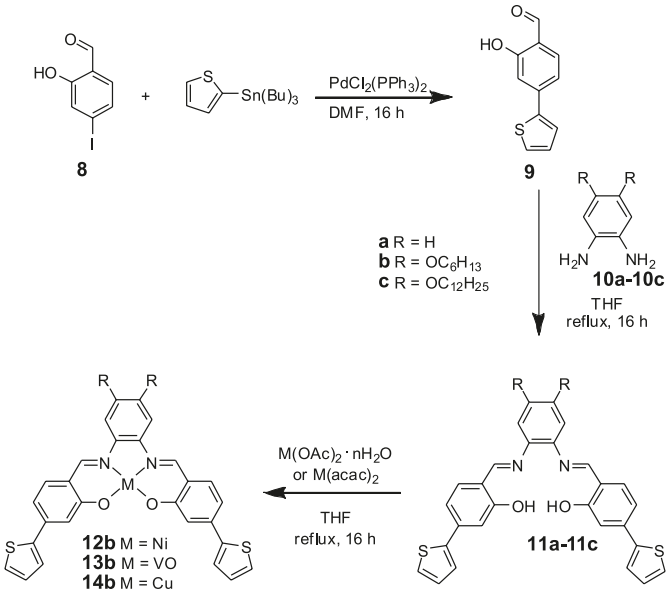

Fig. 1. ^{1}H NMR (300 MHz, $CDCl_3$) spectrum of **11b**.

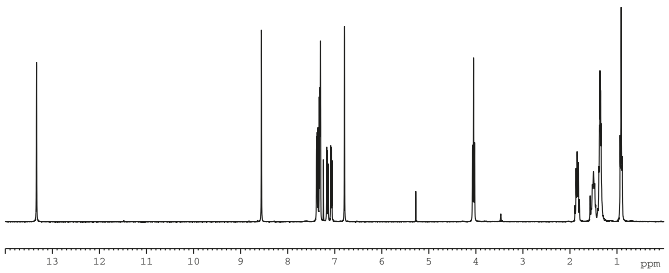

Scheme 2.

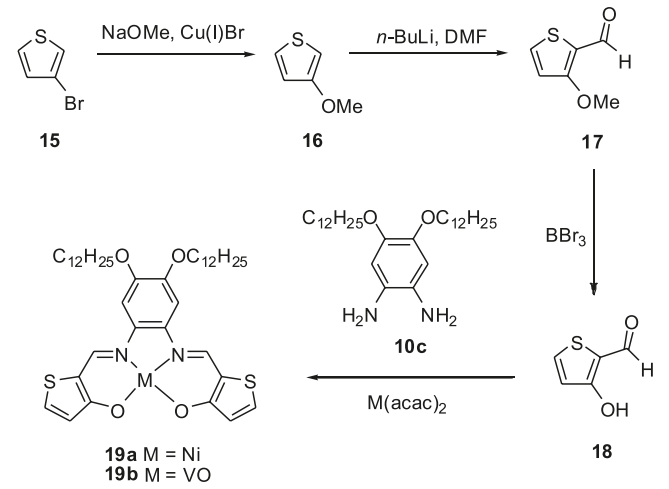

of **18** with diamine **10c** in the presence of a metal salt gave thienphen complexes **19a** and **19b** in 72% yield.

Electrochemistry

Electropolymerization of the three metal complexes **12b**–**14b** was attempted, but only the Ni(II) complex **12b** and Cu(II) complex **14b** showed oxidation waves within the solvent window. Repeated cycling through the first oxidation

© 2008 NRC Canada

Fig. 2. Cyclic voltammetry of **14b**. (*a*) 10 scans to 1.0 V. (*b*) 10 scans to 1.4 V. Only scans 1, 5 and 10 are shown. Pt-disc working electrode, 0.1 mol/L [*n*-Bu_4N]PF_6 in CH_2Cl_2, 100 mV/s scan rate.

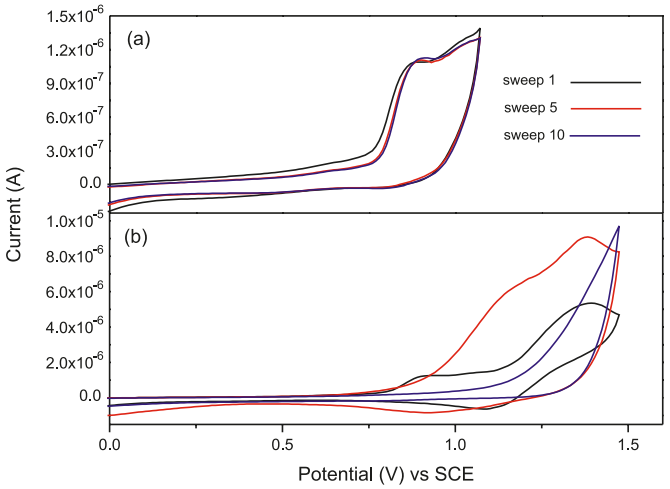

wave (~1 V vs. SCE) for both compounds resulted in identical cyclic voltammograms (CVs) on each sweep (Fig. 2*a*). No film growth was visible on either Pt-disc or gold-on-glass working electrodes. Cycling through both the first and second oxidation waves (1.4 V vs. SCE) resulted in significant changes in sequential CVs (Fig. 2*b*). An increase in current and positive shift of the oxidation wave was observed, along with the formation of a red film on the electrode surface. CVs of these films showed no oxidation or reduction features in the solvent window.

To explain these results, we consider the radical cations expected to form upon one electron oxidation of the dithienylsalphen monomers (Fig. 3). The radical cation in the oxidized species $\mathbf{B}^{\cdot+}$ is more delocalized than in the oxidized species $\mathbf{A}^{\cdot+}$; as a result, the radical cation of **B** may be stable enough to prevent polymerization. This explains the lack of polymerization observed when scanning only to the first oxidation wave in **12b** and **14b**. There are no known examples of electropolymerization of thiophene-substituted benzene with an imine para to the thienyl group. Upon scanning to higher potentials, a redox-inactive film is formed. The cyclic voltammetry differs from that observed upon electropolymerization of **5**–**7** where a lower potential feature attributed to reversible oxidation of the polymer backbone is observed. It is possible that at high potentials monomers **12b** and **14b** undergo coupling at the alkoxy substituted phenyl rings as has been observed previously in related species prepared by Reynolds and coworkers (6*f*, 6*g*).

Cyclic voltammetry of **19a** (Fig. 4) shows a quasi-reversible wave at 0.7 V vs. SCE, as well as two higher-potential irreversible waves. These waves are attributed to oxidation of the metal centre as well as ligand-based oxidations. No sign of electropolymerization is observed with repeated scanning to potentials up to 2.0 V. Complex **19b** also does not electropolymerize and shows an anodic wave at 0.9 V vs. SCE with a large associated cathodic wave. It is possible that the oxidized species generated here are also stabilized via resonance stabilization of the radical cations (Fig. 5).

Fig. 3. Formation of the radical cations of **A** and **B**, showing one resonance structure for each monomer.

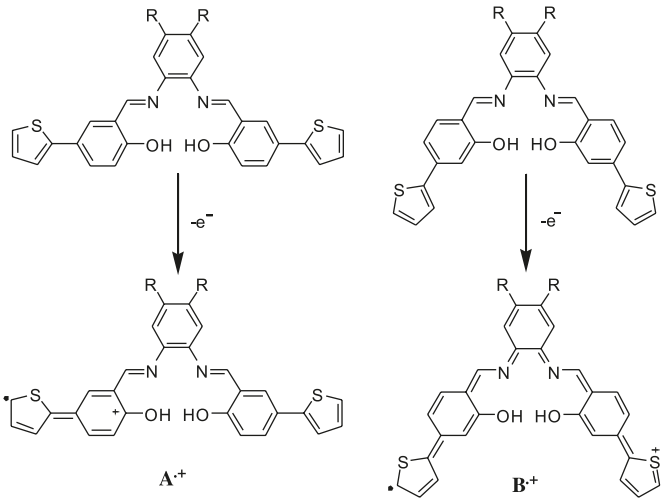

Fig. 4. Cyclic voltammetry of **19a**. The red trace (light trace in print version) shows scan reversal after the first oxidation wave; the black trace (heavy) shows a scan to 2 V. Pt-disc working electrode, 0.1 mol/L [*n*-Bu_4N]PF_6 in CH_2Cl_2, 100 mV/s scan rate.

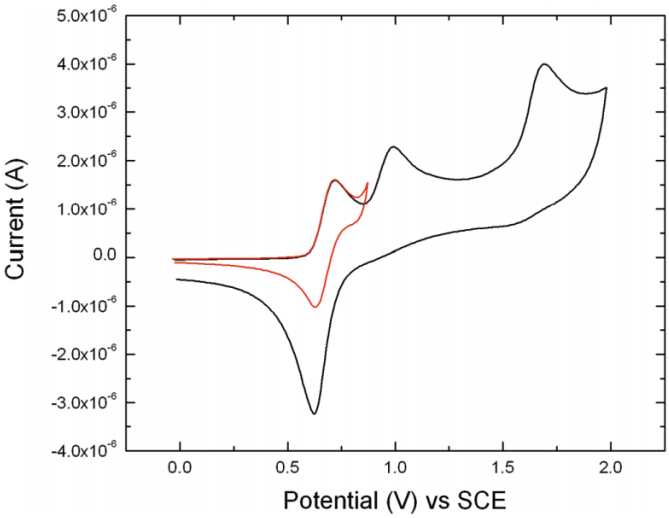

The electronic absorption spectra of the monomers can be used to provide insight into the degree of conjugation, because increased conjugation is expected to result in a bathochromic shift. The spectra for complexes **12b**–**14b** are shown in Fig. 6. At higher energy, the spectrum is dominated by peaks associated with the ligand (e.g., π–π* transitions) whereas the lower energy peaks are attributed to n–π* and metal-based transitions (metal to ligand charge transfer bands, d–d transitions). Comparison of UV–vis spectra of the 5-substituted monomers (**5**–**7**) with the corresponding 4-substituted species (**12b**–**14b**) reveals that, as expected, the low energy charge transfer absorption bands are shifted only slightly. The higher energy bands, on the other hand, are consistently shifted to lower energy in the 4-substituted monomers (cf. 320 nm for **5b** vs 350 nm for **12b**). These bands, attributed to π–π* transitions on the conjugated back-

© 2008 NRC Canada

Fig. 5. Formation of the radical cations of **19** (metal-based oxidation is not considered).

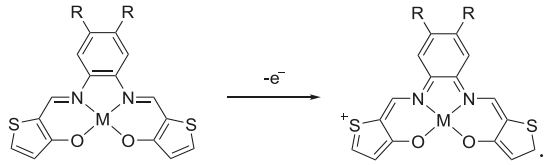

Fig. 6. Normalized absorption spectra of dithienylsalphen monomers in DCM (concentration 4.0 – 5.0 × 10^{-6} mol/L), where (*a*) **5b** (----), **12b** (—); (*b*) **6b** (----), **13b** (—); (*c*) **7b** (----), **14b** (—).

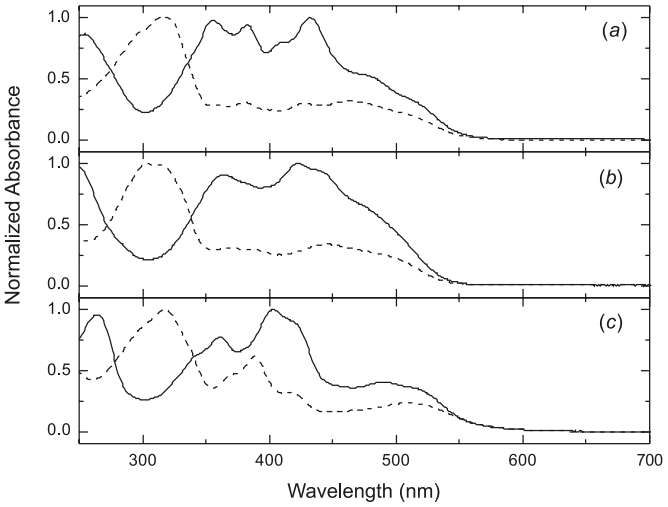

bone, shift in a manner consistent with enhanced conjugation.

The absorption spectra of **19a** and **19b** both have a higher energy band (~300 nm) attributed to the π–π* transition of the conjugated system (Fig. 7). This absorption is close in energy to the π–π* transition in **5b** and **6b** suggesting a similar extent of conjugation in these complexes. It is reasonable to conclude, based on these observations, that the conjugation is localized primarily over the diarylimine unit, regardless of whether the terminal aryl group is a substituted benzene or thiophene. The lower energy transitions in the spectra of **19a** and **19b** are attributed to CT transitions. The intensity of these transitions is comparable to the π–π* transition, possibly owing to an increase in the transition dipole moments as has been previously observed in similar complexes (10).

Conclusions

Two strategies for exploring the factors important in controlling electropolymerization of salphen complexes are reported. Extending the conjugation via substitution of the terminal phenyl ring at the 4-position with a thiophene group leads to a red-shift in the absorption spectrum, but results in species that do not electropolymerize. This is attributed to

Fig. 7. Absorption spectra of monomers in DCM (*a*) **19a** and (*b*) **19b**.

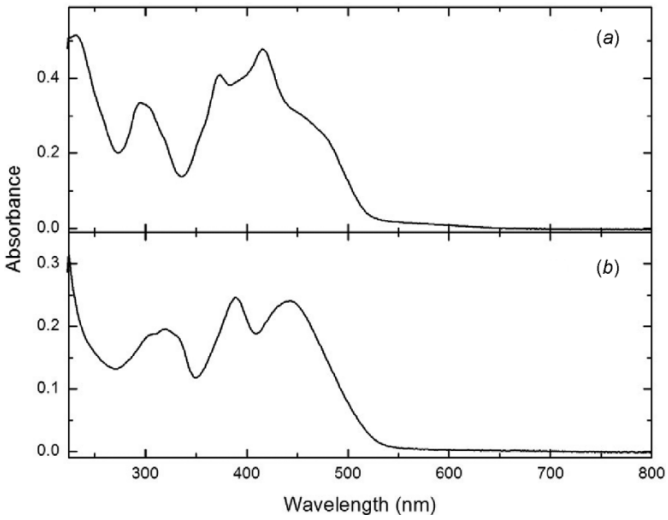

enhanced stabilization of the oxidized species owing to the extended conjugation. Similar observations were made for the thienolphenylenediimine complexes, and were also attributed to enhanced resonance stabilization of the oxidized species. Zotti has previously demonstrated that alkoxy-substituted hexathiophene oligomers do not polymerize well because of stabilization of the radical cation by the substituents (11). These results demonstrate that in order for electropolymerization to occur, the oxidized species cannot be too stable or the desired coupling reaction will not occur. The irreversibility of the oxidation waves associated with the organic groups suggests that other decomposition pathways may be available for the oxidized species. These results will guide future development of polymerizable thienyl – Schiff base complexes.

Experimental[3]

Compounds **8** (12) and **10a**–**10c** (13) were prepared according to literature procedures. Tetrahydrofuran (THF) was distilled over Na and benzophenone under N_2. All other chemicals were purchased from Sigma-Aldrich, TCI, or Fisher and used as received. All reactions were carried out under nitrogen unless otherwise noted. UV–vis spectra were obtained on a Varian Cary 5000 UV–vis NIR spectrometer using a 1 cm cuvette. Infrared spectra were obtained using KBr discs or on NaCl plates with a Bomem MB-100 spectrometer or a Nicolet 4700 FTIR spectrometer. ^{1}H NMR (300 or 400 MHz) and ^{13}C NMR (75.5 or 100.7 MHz) spectra were recorded on Bruker Avance 300 or Bruker Avance 400 spectrometers and were referenced internally to residual protonated solvent. Electrospray ionization (ESI) mass spectra were obtained on a Micromass LCT time-of-flight (TOF) mass spectrometer equipped with an electrospray ion source. Samples were analyzed in methanol–dichloromethane at 1 μmol/L. EI spectra were obtained with a double focusing

[3] Supplementary data for this article are available on the journal Web site (canjchem.nrc.ca) or may be purchased from the Depository of Unpublished Data, Document Delivery, CISTI, National Research Council Canada, Ottawa, ON K1A 0R6, Canada. DUD 3839. For more information on obtaining material refer to cisti-icist.nrc-cnrc.gc.ca/cms/unpub_e.shtml.

© 2008 NRC Canada

mass spectrometer (Kratos MS-50) coupled with a MASPEC data system with EI operating conditions of: source temperatures 120–220 °C and ionization energy 70 eV. Elemental analyses were obtained at the Microanalytical facility at the University of British Columbia. Melting points were recorded on a Fisher John's melting point apparatus.

Synthesis of 4-(2-thienyl)salicylaldehyde 9

A solution of 2-tributylstannylthiophene (8.0 mL, 25.2 mmol) in DMF (40 mL) was added to a mixture of 4-iodosalicylaldehyde **8** (4.095 g, 16.5 mmol) and trans-dichlorobis(triphenylphosphine) palladium (II) (0.606 g, 0.863 mmol). After heating for 16 h, the reaction solution was diluted with ether (100 mL) and washed with aqueous ammonium chloride (3 × 150 mL). The organic layer was filtered through silica and the solvent was removed under vacuum to obtain a beige solid, which was washed with hexanes and filtered to yield 3.088 g (0.794 mmol, 92%) of product; mp 92–94 °C. UV–vis (CH_2Cl_2, nm (L $mol^{-1}cm^{-1}$)): λ_{max} (ε): 331 (2.7×10^4). IR (KBr, cm^{-1}) ν: 3098, 3074, 2834, 2748, 1650, 1625, 1557, 1529, 1492, 1431, 1312, 1235, 1207, 1184, 995, 852, 800, 694. ^{1}H NMR (400 MHz, $CDCl_3$) δ: 11.12 (s, 1H, O*H*), 9.84 (s, 1H, C*H*O), 7.53 (d, 1H, *J* = 8.1 Hz, aromatic C*H*), 7.45 (d, 1H, *J* = 3.9 Hz, aromatic C*H*), 7.40 (d, 1H, *J* = 4.8 Hz, aromatic C*H*), 7.25 (dd, 1H, J_1 = 8.1 Hz, J_2 = 1.5 Hz, aromatic C*H*), 7.21 (s, 1H, aromatic C*H*), 7.11 (dd, 1H, J_1 = 4.8 Hz, J_2 = 3.9 Hz, aromatic C*H*). ^{13}C NMR (75.5 MHz, $CDCl_3$) δ: 195.7, 162.3, 142.7, 142.6, 134.5, 128.7, 127.7, 125.9, 119.8, 117.6, 114.1. ESI–MS *m*/*z*: 227 ($[M + Na]^+$). Anal. calcd. for $C_{11}H_8O_2S$: C 64.69, H 3.95; found C 64.30, H 3.99.

Synthesis of *N,N′*-Phenylenebis(4-(2-thienyl)salicylideneimine 11b

1,2-Dihexyloxy-4,5-diaminobenzene **10b** (0.297 g, 0.962 mmol) and 4-thienylsalicylaldehyde **9** (0.486 g, 2.37 mmol) were combined in a 100 mL Schlenk flask under nitrogen. To this mixture was added 20 mL of dry THF to form an orange solution. The solution was heated to reflux overnight and was cooled to room temperature, after which the volume of solution was reduced. Addition of methanol to the solution caused precipitation of an orange solid, which was collected on a Büchner funnel and washed with additional methanol. Yield: 0.587 g, 0.86 mmol, 89%. Compounds **11a** and **11c** were synthesized in an analogous fashion using **10a** and **10c** with yields of 0.355 g (0.66 mmol, 77%) and 0.525 g (0.61 mmol, 66%), respectively.

11a

^{1}H NMR (400 MHz, $CDCl_3$) δ: 13.21 (s, 2H, O*H*), 8.62 (s, 2H, *H*C=N), 7.39 (dd, 2H, J_1 = 3.7 Hz, J_2 = 1.0 Hz, aromatic C*H*), 7.36 (d, 2H, *J* = 8.0 Hz, aromatic C*H*), 7.35–7.32 (m, 6H, aromatic C*H*), 7.25 (m, 2H, aromatic C*H*), 7.17 (dd, 2H, J_1 = 8.0 Hz, J_2 = 1.7 Hz, aromatic C*H*), 7.08 (dd, 2H, J_1 = 5.0 Hz, J_2 = 3.7 Hz, aromatic C*H*). ^{13}C NMR (100.7 MHz, $CDCl_3$) δ: 162.9, 162.0, 143.6, 142.6, 139.3, 133.1, 128.4, 128.0, 126.5, 124.8, 119.8, 118.6, 116.9, 114.5. EI–MS: *m*/*z* = 480 (M^+). HRMS calcd for $C_{28}H_{20}N_2O_2S_2$: 480.09662; found: 480.09674.

11b

Mp 176–178 °C. UV–vis (CH_2Cl_2, nm (L $mol^{-1}cm^{-1}$)) λ_{max} (ε): 360 (5.0×10^4). IR (KBr, cm^{-1}) ν: 2950, 2928, 2853, 1608, 1510, 1375, 1263, 1189, 850, 804, 695. ^{1}H NMR (300 MHz, $CDCl_3$) δ: 13.34 (s, 2H, O*H*), 8.56 (s, 2H, *H*C=N), 7.39 (dd, 2H, J_1 = 3.7 Hz, J_2 = 0.9 Hz, aromatic C*H*), 7.35 (d, 2H, *J* = 8.0 Hz, aromatic C*H*), 7.32 (m, 4H, aromatic C*H*), 7.16 (dd, 2H, J_1 = 8.0 Hz, J_2 = 1.7 Hz, aromatic C*H*), 7.08 (dd, 2H, J_1 = 5.0 Hz, J_2 = 3.7 Hz, aromatic C*H*), 6.79 (s, 2H, aromatic C*H*), 4.05 (t, 4H, OCH_2), 1.86–0.88 (m, 22H, hexyl chain). ^{13}C NMR (75.5 MHz, $CDCl_3$) δ: 161.7, 161.1, 149.3, 143.7, 138.7, 135.6, 132.7, 128.4, 126.3, 124. 6, 118.8, 116.8, 114.3, 105.0, 70.0, 31.8, 29.5, 25.9, 22.8, 14.2. ESI–MS *m*/*z*: 681 ($[M + H]^+$). Anal. calcd. for $C_{40}H_{44}N_2O_4S_2$: C 70.56, N 4.11, H 6.51; found C 70.36, N 4.43, H 6.43.

11c

^{1}H NMR (400 MHz, $CDCl_3$) δ: 13.31 (s, 2H, O*H*), 8.58 (s, 2H, *H*C=N), 7.39 (d, 2H, *J* = 3.7 Hz, aromatic C*H*), 7.35 (d, 2H, *J* = 8.0 Hz, aromatic C*H*), 7.32 (m, 4H, aromatic C*H*), 7.17 (dd, 2H, J_1 = 8.0 Hz, J_2 = 1.6 Hz, aromatic C*H*), 7.08 (dd, 2H, *J* = 5.0 Hz, *J* = 3.7 Hz, aromatic C*H*), 6.81 (s, 2H, aromatic C*H*), 4.06 (t, 4H, OCH_2), 1.86–0.88 (m, 46H, dodecyl chain). ^{13}C NMR (100.7 MHz, $CDCl_3$) δ: 161.7, 161.0, 149.4, 143.6, 139.1, 135.2, 133.0, 128.4, 126.4, 124.7, 118.6, 116.9, 114.4, 105.0, 70.1, 32.2, 29.9, 29.9, 29.7, 29.6, 29.5, 26.3, 22.9, 14.3. EI–MS *m*/*z*: 848 (M^+). HRMS calcd. for $C_{52}H_{68}N_2O_4S2$: 848.46205; found: 848.46226.

12b

To a mixture of **11b** (0.137 g, 0.201 mmol) and nickel(II) acetate tetrahydrate (0.226 g, 0.908 mmol) was added 10 mL of distilled THF. The red solution was heated to reflux for 16 h. After cooling, MeOH was added to precipitate a red solid, which was subsequently filtered and washed with MeOH and petroleum ether. Yield: 0.095 g, 0.13 mmol, 64%; mp > 300 °C. UV–vis (CH_2Cl_2, nm (L $mol^{-1}cm^{-1}$)) λ_{max} (ε): 361 (4.3×10^4), 403 (5.6×10^4), 489 (2.2×10^4). IR (KBr, cm^{-1}) ν: 2953, 2930, 2859, 1607, 1584, 1501, 1475, 1438, 1362, 1282, 1188, 699. ^{1}H NMR (400 MHz, $CDCl_3$) δ: 7.87 (s, 2H, *H*C=N), 7.43 (s, 2H, aromatic C*H*), 7.39 (d, 2H, *J* = 3.4 Hz, aromatic C*H*), 7.32 (d, 2H, *J* = 5.0 Hz, aromatic C*H*), 7.26 (d, 2H, *J* = 8.3 Hz, aromatic C*H*), 7.07 (m, 2H, aromatic C*H*), 7.02 (s, 2H, aromatic C*H*), 6.88 (d, 2H, *J* = 8.3 Hz, aromatic C*H*), 3.97 (t, 4H, OCH_2), 1.81–0.88 (m, 22H, hexyl chain). ^{13}C NMR (75.5 MHz, $CDCl_3$) δ: 165.4, 151.4, 149.7, 144.0, 139.9, 136.3, 133.7, 128.4, 126.4, 124.8, 119.7, 117.9, 114.1 98.8, 64.2, 31.9, 29.4, 25.9, 22.8, 14.3. ESI–MS *m*/*z*: 759 ($[M + Na]^+$). Anal. calcd. for $C_{40}H_{42}N_2O_4S_2Ni$: C 65.13, H 5.74; found C 65.16, H 5.82.

13b

To a mixture of **11b** (0.166 g, 0.244 mmol) and vanadyl acetylacetonate (0.191 g, 0.720 mmol) was added 10 mL of distilled THF. The red solution was heated to reflux for 16 h. After cooling, the volume of the solution was reduced and MeOH was added to precipitate a red-brown solid. The product was subsequently filtered and washed with MeOH

© 2008 NRC Canada

and petroleum ether. Yield: 0.136 g, 0.18 mmol, 75%; mp 293 °C (dec.). UV–vis (CH_2Cl_2, nm (L $mol^{-1}cm^{-1}$)) λ_{max} (ε): 364 (4.6×10^4), 422 (5.0×10^4). IR (KBr, cm^{-1}) ν: 2956, 2927, 2857, 1604, 1577, 1509, 1479, 1430, 1377, 1275, 1191, 980, 696. ESI–MS *m/z*: 768 ($[M + Na]^+$). Anal. calcd. for **13b**·H_2O ($C_{40}H_{44}N_2O_6S_2V$): C 62.89, H 5.81, N 3.67; found C 63.09, H 5.87, N 3.91.

14b

To a mixture of **11b** (0.158 g, 0.232 mmol) and copper(II) acetylacetonate (0.186 g, 0.710 mmol) was added 20 mL of distilled THF. The brown solution was heated to reflux for 16 h. After cooling, the solution was reduced and MeOH was added to precipitate the product. Subsequent filtration afforded a red solid which was washed with MeOH and petroleum ether. The product was recrystallized from DCM and MeOH. Yield: 0.118 g, 0.16 mmol, 69%; mp > 300 °C. UV–vis (CH_2Cl_2, nm (L $mol^{-1}cm^{-1}$)) λ_{max} (ε): 356 (4.2×10^4), 383 (4.0×10^4), 432 (4.3×10^4). IR (KBr, cm^{-1}) ν: 2952, 2925, 2856, 1608, 1587, 1500, 1474, 1374, 1275, 1187, 696. MALDI-TOF-MS *m/z*:742 (M^+). Anal. calcd. for $C_{40}H_{42}N_2O_4S_2Cu$: C 64.71, H 5.70, N 3.77; found C 64.99, H 5.80, N 4.00.

19a

Under a nitrogen atmosphere, 3-hydroxy-2-formylthiophene **18** (200 mg, 1.56 mmol), 4,5-didodecyloxy-1,2-phenylenediamine **10c** (300 mg, 0.629 mmol), and nickel acetylacetonate tetrahydrate (232 mg, 0.932 mmol) were dissolved in anhydrous THF (40 mL) and heated to reflux for 48 h. The red solution was then cooled to room temperature and concentrated under vacuum. Addition of methanol to the solution precipitated a red solid, which was collected by centrifugation, then washed with methanol. The product was a red solid (300 mg, yield 63%); mp > 210 °C. UV–vis (CH_2Cl_2, nm (L $mol^{-1}cm^{-1}$)) λ_{max} (ε): 231 (27000), 295 (17500), 373 (21500), 416 (25000). IR (cm^{-1}) ν: 2918, 2850, 1600, 1571, 1518, 1487, 1469, 1443, 1338, 1281, 1190, 1142, 1076, 1041, 1032, 918, 812, 759, 698, 669, 593, 534, 466. ^{1}H NMR (400 MHz, DMSO-d_6) δ: 7.81 (2H, s, aromatic C*H*), 7.40 (2H, d, *J* = 5.7 Hz, aromatic C*H*), 6.97 (2H, s, aromatic C*H*), 6.58 (2H, d, *J* = 5.5 Hz, aromatic C*H*), 3.84 (4H, t, *J* = 6.7 Hz, OCH_2), 1.65 (4H, m, CH_2), 1.11 (36H, m, CH_2), 0.71 (6H, t, *J* = 6.8 Hz, CH_3). EI–MS *m/z*: 752 (M^+, 100%). Anal. calcd. for $C_{40}H_{58}S_2N_2O_4Ni$: C 63.74, H 7.76, N 3.72; found: C 63.35, H 7.90, N 4.08.

19b

The same procedure was used as for the preparation of **19a**. The product was isolated as a red solid, yield 72%; mp > 210 °C. UV–vis (CH_2Cl_2, nm (L $mol^{-1}cm^{-1}$)): λ_{max} (ε): 320 (14000), 388 (18000), 444 (17700). IR (cm^{-1}) ν: 2917, 2849, 1600, 1566, 1521, 1487, 1436, 1401, 1338, 1260, 1216, 1081, 1032, 982, 950, 796, 764, 720, 697, 681, 526, 489, 459. EI–MS *m/z*: 761 (M^+, 100%). Anal. calcd. for $C_{40}H_{58}N_2O_5S_2V$: C 63.05, H 7.67, N 3.68; found: C 62.89, H 7.74, N 3.95.

Electrochemistry

Cyclic voltammetry experiments were conducted using either a Pine AFCBP1 or Autolab potentiostat. The working electrode was a Pt disk, an indium tin oxide (ITO) thin film on glass, or Au (1000 Å) deposited on Si using a Cr (50 Å) adhesion layer. The counter electrode was a Pt mesh and the reference electrode a silver wire. An internal reference (decamethylferrocene) was added to correct the measured potentials with respect to saturated calomel electrode (SCE). $[(n\text{-}Bu)_4N]PF_6$ was used as a supporting electrolyte and was purified by triple recrystallization from ethanol and dried at 90 °C under vacuum for 3 days. Dichloromethane used for CV was purified by passing the solvent through an activated alumina tower. Polymerizations were carried out in a solution containing 0.1 mol/L electrolyte, and 1 mM monomer. Polymers were grown by cycling a potential between 0 V and the onset of monomer oxidation (= 1.6 V) for a total of 10 cycles, at a scan rate of 100 mV/s.

Acknowledgement

We thank the Canadian Space Agency (CSA) and Natural Sciences and Engineering Research Council of Canada (NSERC) for funding. We thank Dr. Bryan Sih for cyclic voltammetry measurements.

References

1. (*a*) M.O. Wolf. Adv. Mater. **13**, 545 (2001); (*b*) R.P. Kingsborough and T.M. Swager. Prog. Inorg. Chem. **48**, 123 (1999); (*c*) M.J. MacLachlan. Frontiers in Transition Metal-Containing Polymers. *Edited by* A. Abd-El-Aziz and I. Manners. John Wiley and Sons, Hoboken, NJ. 2007.
2. (*a*) P.G. Cozzi. Chem. Soc. Rev. **33**, 410 (2004); (*b*) P. Guerriero, S. Tamburini and P. A. Vigato. Coord. Chem. Rev. **139**, 17 (1995).
3. (*a*) P.G. Lacroix. Eur. J. Inorg. Chem. 339 (2001); (*b*) P.G. Lacroix, S. Di Bella, and I. Ledoux. Chem. Mater. **8**, 541 (1996).
4. For recent examples, see: (*a*) X. Lu, W.-Y. Wong, and W.-K. Wong. Eur. J. Inorg. Chem. 523 (2008); (*b*) S. Manivannan, R. Prabhakaran, K.P. Balasubramanian, V. Dhanabal, R. Karvembu, V. Chinnusamy, and K. Natarajan. Appl. Organomet. Chem. **21**, 952 (2007); (*c*) M.S. Shongwe, B.A. Al-Rashdi, H. Adams, M.J. Morris, M. Mikuriya, and G.R. Hearne. Inorg. Chem. **46**, 9558 (2007); (*d*) H. Zhou, Z.-H. Peng, Z.-Q. Pan, Y. Song, Q.-M. Huang and X.-L. Hu. Polyhedron, **26**, 3233 (2007).
5. (*a*) C.W. Leung and M.J. MacLachlan. J. Inorg. Organomet. Polym. Mater. **17**, 57 (2007); (*b*) D. Vitalini, P. Mineo, S. Di Bella, I. Fragala, P. Maravigna, and E. Scamporrino. Macromolecules, **29**, 4478 (1996).
6. (*a*) A. Pietrangelo, B.C. Sih, B.N. Boden, Z. Wang, Q. Li, K.C. Chou, M.J. MacLachlan, and M.O. Wolf. Adv. Mater. **20**, 2280 (2008); (*b*) R.P. Kingsborough and T.M. Swager. Adv. Mater. **10**, 1100 (1998); (*c*) R.P. Kingsborough and T.M. Swager. J. Am. Chem. Soc. **121**, 8825 (1999); (*d*) R.P. Kingsborough and T.M. Swager. Chem. Mater. **12**, 872 (2000); (*e*) J.L. Reddinger and J.R. Reynolds. Synth. Met. **84**, 225 (1997); (*f*) J.L. Reddinger and J.R. Reynolds. Macromolecules, **30**, 673 (1997); (*g*) J.L. Reddinger and J.R. Reynolds. Chem. Mater. **10**, 3 (1998); (*h*) T. Shioya and T.M. Swager. Chem. Commun. (Cambridge), 1364 (2002).
7. J. Sicé. J. Am. Chem. Soc. **75**, 3697 (1953).
8. (*a*) G. Henrio, G. Ple, and J. Morel. Comptes Rendus des Séances de l'Académie des Sciences, **278**, 125 (1974); (*b*) P.

© 2008 NRC Canada

Netchitailo, B. Decroix, J. Morel, and P. Pastour. J. Heterocyclic Chem. **15**, 337 (1978).
9. This compound has been previously prepared (see ref. 8*b*), but via deprotection with pyridine hydrochloride. We found that BBr_3 was more effective.
10. J. Gradinura, A. Forni, V. Druta, F. Tessore, S. Zecchin, S. Quici, and N. Garbalau. Inorg. Chem. **46**, 884 (2007).
11. G. Zotti, R.A. Marin, and M.C. Gallazzi. Chem. Mater. **9**, 2945 (1997).
12. C. Ma, A. Lo, A. Abdolmaleki, and M.J. MacLachlan. Org. Lett. **6**, 3841 (2004).
13. D.-H. Kim, M.J. Choi, and S.-K. Chang. Bull. Korean Chem. Soc. **21**, 145 (2000).

© 2008 NRC Canada

Synthesis and evaluation of the in vitro DNA-binding properties of chiral *cis*-dichloro(pyridyloxazoline)platinum(II) complexes[1]

David W. Dodd, Heather E. Toews, Michael J. Trevail, Michael C. Jennings, Robert H.E. Hudson, and Nathan D. Jones

Abstract: A series of chiral cis-dichloro(pyridyloxazoline)platinum(II) and palladium(II) complexes were synthesized and their reactivity towards a defined sequence of single-stranded and double-stranded DNA was investigated in comparison to cisplatin. The compounds differed in the nature and absolute configuration of the substituent at the *C*4 position of the oxazoline ring. The DNA-binding ability of these compounds was evaluated by HPLC analysis, post metal exposure, of enzymatic digests of an undecamer duplex containing one putative metallation site. Polyacrylamide gel electrophoresis (PAGE) and thermal denaturation confirmed the results of the HPLC analysis, which showed that the stereochemistry and character of the substituent at the *C*4 position of the oxazoline ring had little effect on DNA binding, possibly due to the formation of monofunctional adducts.

Key words: cisplatin, chiral, pyridyloxazoline, DNA-binding studies, platinum, palladium.

Résumé : On a réalisé la synthèse d'une série de complexes chiraux des *cis*-dichloro(pyridyloxazoline)platine(II) et palladium(II) et on a étudié leur réactivité, par comparaison au cisplatine, vis-à-vis une séquence définie d'ADN à un brin et à deux brins. Les composés diffèrent dans la nature et la configuration absolue du substituant dans la position *C*4 du noyau oxazoline. La capacité de liaison à l'ADN de ces composés a été évaluée par une analyse par chromatographie liquide à haute performance (CLHP) à la suite de l'exposition aux métaux, de mélanges obtenus par digestion enzymatique d'un duplex undécamère contenant un site putatif de métallation. Une électrophorèse sur gel de polyacrylamide (EGPA) et une dénaturation thermique ont permis de confirmer les résultats de l'analyse de CLHP qui avait montré que la stéréochimie et le caractère du substituant en position *C*4 du noyau oxazoline n'ont que peu d'effet sur la fixation sur l'ADN, probablement en raison de la formation d'adduits monofonctionnels.

Mots-clés : cisplatine, chiral, pyridyloxazoline, études de fixation d'ADN, platine, palladium.

[Traduit par la Rédaction]

Introduction

The serendipitous discovery of the antiproliferative properties of *cis*-dichlorodiammineplatinum(II) (cisplatin) over 30 years ago led to its eventual use as a chemotherapeutic agent (1). Today, cisplatin remains one of the most widely used drugs for the treatment of solid cell tumours (2). Motivated by cisplatin's effectiveness, similar treatments have been pursued; however, despite vigorous research towards this end, only a handful of successful analogues have been developed (3). While complexes of other metals, such as titanium, rhenium, ruthenium, and gallium, have shown promise as potential antineoplastic agents, the literature of metal anticancer therapeutics is dominated by platinum complexes (4). The efficacy of cisplatin in the treatment of carcinomata is almost universally thought to be due to its ability to form intrastrand adducts between adjacent purines in DNA (2–5).

The design principles of cisplatin analogues were described two years after the first clinical trials: the complexes should be neutral and four-coordinate with two coordination sites occupied by labile leaving ligands and two occupied by inert am(m)ine ligand(s) in a cis geometry (6).

Once cisplatin enters the cell, the lower intracellular chloride concentration permits dissociation of the halides resulting in the formation of an aquated platinum centre. This cationic species reacts predominantly with the *N*7 of guanine or adenine nucleobases (5). The guanine adduct is thought to be stabilized through hydrogen bonding of an ammine proton with the carbonyl oxygen of *C*6 making deoxyguanosine dinucleotide (-dGpdG-) the preferred target sequence (7). Binding to DNA in this fashion causes a kinking of the double helix and a widening of the minor groove; this can inhibit transcription and lead to apoptosis by inducing the

Received 21 April 2008. Accepted 30 May 2008. Published on the NRC Research Press Web site at canjchem.nrc.ca on 13 November 2008.

Dedicated to Prof. Dick Puddephatt on the occasion of his 65th birthday and in recognition of his outstanding contributions to chemistry.

D.W. Dodd, H.E. Toews, M.J. Trevail, M.C. Jennings, R.H.E. Hudson,[2] and N.D. Jones.[2] Department of Chemistry, The University of Western Ontario, London, ON N6A 5B7, Canada.

[1]This article is part of a Special Issue dedicated to Professor R. Puddephatt.

[2]Corresponding author (e-mail: robert.hudson@uwo.ca, njones26@uwo.ca).

 doi:10.1139/V08-131 © 2008 NRC Canada

binding of high mobility group (HMG) box proteins (5). Although cisplatin is indeed an effective drug, there are problems associated with prolonged dosages, such as toxicity and acquired resistance. Therefore, the search continues for improved platinum-based therapies.

While several thousand cisplatin analogues have been synthesized and tested for biological activity (8), only a select few have been entered into clinical trials. This has led many in the scientific community to believe that the search for Pt(II) chemotherapeutics is futile. Discovery of a drug suitable for clinical trials is a rare occurrence in every field, yet failure in cisplatin analogue discovery draws inordinate attention. Perhaps the reason for the reluctance to continue in this area is due to the remarkable simplicity of cisplatin itself: even minor substitutions cause drastic changes in efficacy. Although the structure of cisplatin is simple, the mode of action certainly is not, and many questions remain unanswered (5).

Although it is unlikely that a simple substitution of the ammine ligands will yield a complex with activity surpassing that of cisplatin, more elaborate changes, such as variation in the σ-donation character of the ligand and the introduction of chirality, could yield complexes with novel reactivities in vitro and corresponding cytostatic effects in vivo.

As DNA is a chiral molecule, binding of chiral platinum complexes results in diastereomeric adducts. Different binding affinities for enantiomeric complexes have been reported and (of no lesser importance) it has also been found that the diastereomeric adducts may be dealt with by cellular machinery in vastly different ways (9). For example, the *S,S*-enantiomer of (1,2-diaminocyclohexane)oxalatoplatinum(II) (Fig. 1, *S,S*-**I**) is significantly more mutagenic than the *R,R*-enantiomer, and consequently only the latter was entered into clinical trials (9, 10). Other examples of chiral DNA-binding Pt complexes that have been studied in detail include dichloro(*N*-methyl-2-aminomethylpyrrolidine)platinum(II) (Fig. 1, **II**) (10) and complexes involving 1,2-bis(aminomethyl)carbobicyclic ligands (Fig. 1, **III**) (11). Differences in reactivities of enantiomeric complexes towards DNA are rare (12).

Although hydrogen bonding involving coordinated NH groups has been considered necessary for cytostatic activity (13), there are examples of compounds lacking an NH proton that display significant antitumour effects (14, 15).

Pyridyloxazolines, derived from the condensation of a chiral β-amino alcohol with 2-cyanopyridine, are planar, bidentate ligands for platinum(II) and are necessarily bound cis (Fig. 2). The substituent at the α-position of the amino alcohol, *C*4 in the resultant oxazoline ring, can be varied greatly and inexpensively as the alcohols are obtained by the reduction of the corresponding enantiopure amino acids (16, 17).

Pyridyloxazoline Pt(II) complexes have found use in enantioselective enyne cyclizations (18), and the unsubstituted complex **6** has shown some promise as an anticancer therapeutic, displaying significant toxicity towards rat brain tumour cell lines in vitro (19). The palladium analogues have not been used in DNA-binding studies, but have been investigated as asymmetric catalysts for the intermolecular asymmetric Heck reaction (16).

Fig. 1. Chiral platinum complexes **I**–**III** studied as cisplatin analogues (9–11). Chiral centres are denoted by asterisks. X=O, CH_2, CH_2CH_2.

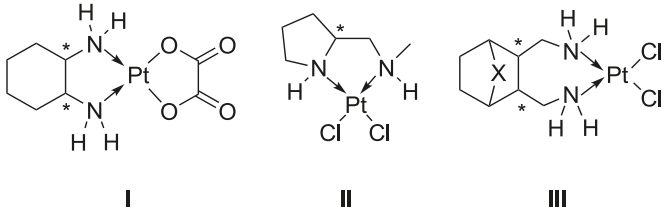

I **II** **III**

Fig. 2. Pyridyloxazoline platinum and palladium dichlorides employed in this study. The chiral centre is derived from the enantiomerically pure amino acid.

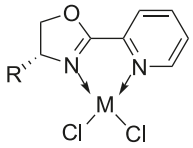

R-**1** R = iPr, M = Pt
R-**2** R = Bn, M = Pt
R-**3** R = Ph, M = Pt
R-**4** R = iPr, M = Pd

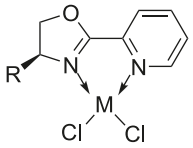

S-**1** R = iPr, M = Pt
S-**2** R = Bn, M = Pt
S-**3** R = Ph, M = Pt
S-**4** R = iPr, M = Pd
S-**5** R = sBu, M = Pt
6 R = H, M = Pt

In this work, binding of these complexes to a defined sequence of oligomeric double-stranded (ds) DNA containing one putative metallation site was investigated by HPLC analysis of enzymatic digests. The duplexes that were exposed to the metal complexes were also analyzed by thermal denaturation and polyacrylamide gel electrophoresis (PAGE). The difference in binding abilities between enantiomers and side-chain identity was investigated; the objective being to gain a better understanding of the structure–activity relationship of chiral platinum antineoplastic agents.

Experimental[3]

General

Pyridyloxazoline ligands (17) and the metal precursors $PdCl_2(PhCN)_2$ (20) and *cis*/*trans*-$PtCl_2(SMe_2)_2$ (21) were synthesized according to literature procedures and characterization data matched those of the known compounds. Platinum compounds **1**–**3**, **5**, and **6** were synthesized by a general procedure as outlined for *R*-**1**; spectral data for enantiomeric complexes were identical, as expected. Solution ^{1}H NMR spectra were collected using a Varian 400 spectrometer (400.09 MHz for ^{1}H and 100.61 MHz for ^{13}C) at RT in

[3] Supplementary data for this article are available on the journal Web site (canjchem.nrc.ca) or may be purchased from the Depository of Unpublished Data, Document Delivery, CISTI, National Research Council Canada, Ottawa, ON K1A 0R6, Canada. DUD 3818. For more information on obtaining material, refer to cisti-icist.nrc-cnrc.gc.ca/cms/unpub_e.shtml. CCDC 694283 contains the crystallographic data for this manuscript. These data can be obtained, free of charge, via www.ccdc.cam.ac.uk/conts/retrieving.html (Or from the Cambridge Crystallographic Data Centre, 12 Union Road, Cambridge CB2 1EZ, UK; fax +44 1223 336033; or deposit@ccdc.cam.ac.uk).

© 2008 NRC Canada

$CDCl_3$ (unless otherwise noted) and referenced to residual ^1H or ^{13}C in the deuterated solvent. Coupling constants are given in Hz. Elemental analyses were conducted by Chemisar Laboratories Inc., Guelph, ON. Denaturing polyacrylamide gels were cast and run according to literature procedures (22). The resultant gels were documented by colour digital photography over fluorescent TLC plates illuminated at 258 nm. For clarity, the image presented has been rendered in grayscale, inverted and contrast/brightness adjusted in Adobe Photoshop.

Optical rotations were recorded on an Atago Polax-2L polarimeter at a concentration of 1 g /100 mL at 589 nm in CH_2Cl_2 solution.

Stock solutions of the complexes (40 μmol/L) were prepared by dissolution in a minimum amount of DMF (<0.5 mL) followed by dilution with Milli-Q deionized water to 100 mL and stored at RT in the dark for no longer than 2 weeks. DNA was purchased from the University of Calgary DNA Services and used without further purification.

Syntheses

*Dichloro-2-[(4**R**)-4-**iso**-propyl-4,5-dihydro-1,3-oxazol-2-yl]pyridineplatinum(II) (**R**-1)*

The title complex was synthesized by the addition of *cis*/*trans*-$PtCl_2(SMe_2)_2$ (0.23 g, 0.60 mmol) to 5 mL of 1,2-dichloroethane containing a slight excess of pyridyl-oxazoline ligand (0.14 g, 0.72 mmol). The resultant yellow solution was heated to reflux for 4 h over which time it darkened in colour. The solvent was removed in vacuo and the remaining oil triturated with Et_2O (10 mL). Vacuum filtration gave 0.27 g (94%) of *R*-**1** as an orange/yellow powder. [α] = –65.0°. ^1H NMR δ: 9.51 (m, 1H, py), 8.17 (m, 1H, py), 7.76 (m, 1H, py), 7.63 (m, 1H, py), 5.00 (m, 1H, CH_2), 4.86 (m, 1H, CH), 4.71 (m, 1H, CH_2), 2.99 (m, 1H, CH), 0.98 (d, 3H, CH_3, ^3J = 7.1), 0.83 (d, 3H, CH_3, ^3J = 6.9). $^{13}C\{^1H\}$ NMR δ: 173.2, 149.7, 145.0, 139.4, 129.4, 126.6, 73.3, 68.2, 28.9, 18.9, 14.1. HRMS (ESI) calcd. for (M + Na) $C_{11}H_{14}N_2Cl_2ONaPt$: 477.0008; found: 477.0015. Anal. calcd. for $C_{11}H_{14}N_2Cl_2OPt$: C, 28.96; H, 3.09; N, 6.14%. Found: C, 28.90; H, 3.10; N, 6.21%.

*Dichloro-2-[(4**S**)-4-**iso**-propyl-4,5-dihydro-1,3-oxazol-2-yl]pyridineplatinum(II) (**S**-1)*

Yield: 94%. [α] = 70.0°. (ESI) calcd. for (M + Na) $C_{11}H_{14}N_2Cl_2ONaPt$: 477.0008; found: 476.9996. Orange plates suitable for X-ray diffraction analysis were provided by slow diffusion of Et_2O into a CH_2Cl_2 solution of the title complex.

*Dichloro-2-[(4**R**)-4-benzyl-4,5-dihydro-1,3-oxazol-2-yl]pyridineplatinum(II) (**R**-2)*

Yield: 72%. ^1H NMR δ: 9.63 (m, 1H, py), 8.15 (m, 1H, py), 7.67 (m, 1H, py), 7.39 (m, 1H, py), 7.27 (m, 5H, Ar), 5.01 (m, 1H, CH_2), 4.93 (m, 1H, CH), 4.85 (m, 1H, CH_2), 3.66 (dd, 1H, CH_2, ^2J = 13.9, ^3J = 10.7), 3.11 (dd, 1H, CH_2, ^2J = 13.9, ^3J = 5.8). $^{13}C\{^1H\}$ NMR δ: 173.9, 150.1, 145.3, 139.7, 135.9, 130.2, 129.5, 129.2, 127.6, 126.8, 64.5, 39.8. HRMS (ESI) calcd. for (M + Na) $C_{15}H_{14}N_2Cl_2ONaPt$: 526.0029; found: 526.0008. Anal. calcd. for $C_{15}H_{14}N_2Cl_2OPt$: C, 35.73; H, 2.80; N, 5.56%. Found: C, 36.02; H, 2.76; N, 5.54%.

*Dichloro-2-[(4**S**)-4-benzyl-4,5-dihydro-1,3-oxazol-2-yl]pyridineplatinum(II) (**S**-2)*

Yield: 68%. HRMS (ESI) calcd. for (M + Na) $C_{15}H_{14}N_2Cl_2ONaPt$: 526.0029; found: 526.0041. Anal. calcd. for $C_{15}H_{14}N_2Cl_2OPt$: C, 35.73; H, 2.80; N, 5.56%. Found: C, 36.03; H, 3.06; N, 5.52%.

*Dichloro-2-[(4R)-4-phenyl-4,5-dihydro-1,3-oxazol-2-yl]pyridineplatinum(II) (**R**-3)*

Yield: 94%. ^1H NMR δ: 9.45 (m, 1H, py), 8.20 (m, 1H, py), 7.86 (m, 1H, py), 7.62 (m, 1H, py), 7.38 (m, 5H, Ph), 5.88 (dd, 1H, CH_2, ^2J = 10.2, ^3J = 4.9), 5.46 (dd, 1H, CH, ^3J = 4.9, ^3J = 3.8), 4.92 (dd, 1H, CH_2, ^2J = 10.2, ^3J = 3.8). $^{13}C\{^1H\}$ NMR (CD_2Cl_2): δ: 174.3, 150.0, 149.6, 144.8, 139.5, 139.1, 130.3, 129.9, 129.1, 127.1, 126.8, 126.3, 81.1, 66.4. HRMS (ESI) calcd. for (M + Na) $C_{14}H_{12}N_2Cl_2ONaPt$: 511.9872; found: 511.9881. Anal. calcd. for $C_{14}H_{12}N_2Cl_2OPt$: C, 34.30; H, 2.47; N, 5.71%. Found: C, 34.53; H, 2.72; N, 5.52%.

*Dichloro-2-[(4**S**)-4-phenyl-4,5-dihydro-1,3-oxazol-2-yl]pyridineplatinum(II) (**S**-3)*

Yield: 92%. HRMS (ESI) calcd. for (M + Na) $C_{14}H_{12}N_2ONaCl_2Pt$: 511.9872; found: 511.9869. Anal. calcd. for $C_{14}H_{12}N_2Cl_2OPt$: C, 34.30; H, 2.47; N, 5.71%. Found: C, 34.56; H, 2.75; N, 5.73%.

*Dichloro-2-[(4**R**)-4-**iso**-propyl-4,5-dihydro-1,3-oxazol-2-yl]pyridinepalladium(II) (**R**-4)*

The title complex was synthesized as described in the literature. Characterization data matched those of the known compound (17).

*Dichloro-2-[(4**S**)-4-**iso**-propyl-4,5-dihydro-1,3-oxazol-2-yl]pyridinepalladium(II) (**S**-4)*

The title complex was made in the same way as *R*-**4**. Spectroscopic data matched those of the enantiomeric compound.

*Dichloro-2-[(4**S**)-4-**sec**-butyl-4,5-dihydro-1,3-oxazol-2-yl]pyridineplatinum(II) (5)*

Yield: 84%. ^{1}HNMR δ: 9.26 (d, 1H, py, ^3J = 5.5), 7.8 (dd, 1H, py, ^3J = 5.5, ^3J = 7.8), 7.76 (d, 1H, py, ^3J = 7.6), 7.56 (dd, 1H, py, ^3J = 7.8, ^3J = 7.6), 5.13 (m, 1H, CH_2), 4.87 (m, 1H, CH), 4.78 (m, 1H, CH_2), 2.75 (m, 1H, CH), 1.29 (m, 2H, CH_2), 1.00 (t, 3H, CH_3, ^3J = 7.4), 0.78 (d, 3H, CH_3, ^3J = 6.8). $^{13}C\{^1H\}$ NMR δ: 173.2, 149.8, 145.0, 139.3, 129.3, 126.5, 73.3, 66.9, 35.5, 26.5, 18.0, 11.9. HRMS (ESI) calcd. for (M + Na) $C_{12}H_{16}N_2ONaCl_2Pt$: 492.0185; found: 492.0177.

Dichloro-2-[4,5-dihydro-1,3-oxazol-2-yl]pyridineplatinum(II) (6)

The title compound has been previously made by a different route (19). Following the procedure for *R*-**1**, **6** was obtained in 72% yield. The limited solubility of this complex did not allow for the measurement of NMR spectral data. Anal. calcd. for $C_8H_8N_2Cl_2OPt$: C, 23.20; H, 1.95; N, 6.76%. Found: C, 23.50; H, 1.89; N, 6.66%.

© 2008 NRC Canada

Crystallography

An orange plate was cut loose and then mounted on a glass fibre. Data were collected at low temperature (–123 °C) on a Nonius Kappa-CCD area detector diffractometer with COLLECT (Nonius B.V., 1997–2002). The unit cell parameters were calculated and refined from the full data set. Crystal cell refinement and data reduction were carried out using HKL2000 DENZO-SMN (23). The absorption correction was applied using HKL2000 DENZO-SMN (SCALEPACK). The crystal data and refinement parameters of *S*-**1** are listed in Table 1.

The reflection data and systematic absences were consistent with a monoclinic space group: $P2_1$. The SHELXTL/PC V6.14 for Windows NT (Sheldrick, G.M., 2001) suite of programs was used to solve the structure by direct methods. Subsequent difference Fourier syntheses allowed the remaining atoms to be located. There were two independent molecules in the asymmetric unit. For this crystal, twinning was also an issue; it is discussed below. Only the heavy atoms (Pt, Cl) were refined anisotropically, as some of the lighter atoms became non-positive definite when they were allowed to refine freely. The hydrogen atom positions were calculated geometrically and were included as riding on their respective carbon atoms. The largest residue electron density peak (0.877 e/Å^3) was associated with one of platinum atoms. Full-matrix least-squares refinement on F^2 gave R_1 = 3.21 for 2σ data and wR_2 = 6.66 for all data (GooF = 1.021).

The structure was solved readily, but the initial refinement stalled at R = 12.9%. Further, the light atoms did not refine successfully with an anisotropic model. There were signs of non-merohedral twinning in the *E* statistics and the Fobs values were consistently higher than the *F* calculations. WinGX (24) was used to "detwin" the data. ROTAX (25) found the Twin Law, which turned out to be a 180° rotation about the direct lattice direction (100). "Make HKLF5" was used to generate the detwinned file used in further refinement.

The structure refinement improved considerably with better values for R_1, wR_2, GooF, standard uncertainties, and residual electron density. The final R_1 value came down to 3.21%. The final solution, however, could still not be refined completely anisotropically, and the light atoms were left isotropic in the refinement. The constant for the Twin Law refined to a value of 0.47309. All these points served to confirm the correct Twin Law was chosen.

Table 1. X-ray crystallographic structural parameters for compound *S*-**1**.

Crystal	*S*-**1**
Empirical formula	$C_{11}H_{14}Cl_2N_2OPt$
Formula mass	456.23
Colour, habit	Orange, plates
Crystal dimensions (mm)	0.17 × 0.15 × 0.10
Crystal system	Monoclinic
Space group	$P2_1$
Z	4
a (Å)	6.7455(3)
b (Å)	20.2782(9)
c (Å)	9.5172(4)
α (°)	90
β (°)	93.10(2)
γ (°)	90
Collection ranges	$-4 \le h \le 4$, $-24 \le k \le 24$, $-11 \le l \le 11$
T (K)	150(2)
V (Å^3)	1299.93(10)
$D_{calcd.}$ (Mg m^{-3})	2.331
Radiation	Mo Kα (λ = 0.71073 Å)
Absorption coeff. (μ) (mm^{-1})	11.189
Absorption correction	Semi-empirical from equivalents
F(000)	856
θ range for data collection (°)	2.94 to 25.03
Observed reflections	11811
Independent reflections	2550 (R_{int} = 0.0760)
Data, restraints, parameters	2550, 37, 171
Goodness-of-fit on F^2	1.023
Final R indices ($l > 2\sigma(l)$)	R_1 = 0.0321, wR_2 = 0.0664
R indices (all data)	R_1 = 0.0395, wR_2 = 0.0693
Absolute structure parameter	–0.009(18)
Largest diff. peak, hole (e, Å^3)	0.889, –0.702

Nuclease digest studies

Duplex DNA was prepared by heating a 1:1 mixture of the complementary sequences in 10 mmol/L $NaClO_4$ to 90 °C and allowing the solution to come slowly to RT. The solution was then cooled to 4 °C for 2 h. Both single- and double-stranded DNA (2 μmol/L) were reacted with the complexes in a 1:1 molar ratio in 200 μL of 10 mmol/L $NaClO_4$ for 48 h in the dark. The buffer was then adjusted to 50 mmol/L Tris, 20 mmol/L $MgCl_2$, pH 7.5. Bovine serum albumin (BSA) was added to a final concentration of 0.02 μg/mL, and the DNA was digested sequentially with bovine pancreas DNase I (Sigma, 36 U for 4 h), nuclease P1 (Sigma, 10 U for 18 h), and alkaline phosphatase (Promega, 20 U for 4 h). The samples were then heated to 90 °C for 2 min to denature the enzymes and centrifuged for 10 min at 10 000 g. The supernatant was analyzed at 254 nm by RP–HPLC on a Varian Microsorb 100 Å C18 column using a flow rate of 1 mL min^{-1} and a solvent system of 100:0 0.1 mol/L aqueous [Et_3NH][OAc] (pH 6.5):MeCN from 0–5 min followed by a linear ramp to 90:10 over a period of 20 min. Nucleoside peaks were identified by co-injection of standards. The areas under the peaks were found by integration and analyzed in relation to one another. These digests and the HPLC analyses thereof were carried out in triplicate.

Results and discussion

The modular nature of the pyridyloxazoline ligand scaffold, combined with its brief synthesis from readily available enantiopure starting materials and facile metal coordination, permitted the rapid development of small libraries of enantiomeric Pt(II) and Pd(II) complexes. The pyridyloxazoline ligands were made by the $ZnCl_2$-catalyzed coupling of 2-cyanopyridine with the β-amino alcohols, valinol, phenylalaninol, phenylglycinol, isoleucinol, and ethanolamine, respectively, using the procedure developed by Bolm et al. (Scheme 1) (17). The amino alcohols, except

© 2008 NRC Canada

Scheme 1. Synthesis of dichloro(pyridyloxazoline)metal(II) complexes.

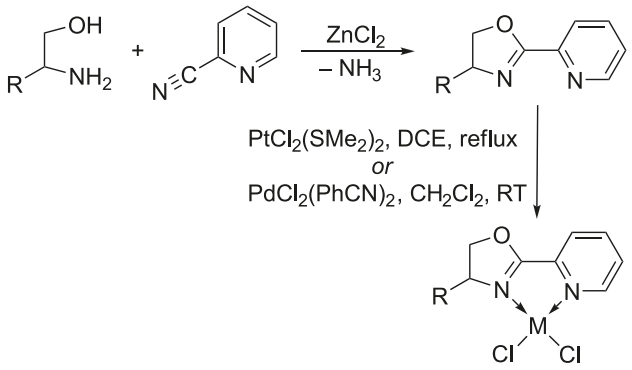

for ethanolamine, were themselves readily made by $NaBH_4/I_2$-reduction of both enantiomers of the corresponding amino acids, during which time no racemization occurs (26). The metal(II) complexes were made in good to excellent yields by the reaction of slight molar excesses of the ligands either with *cis*/*trans*-$PtCl_2(SMe_2)_2$ or *trans*-$PdCl_2(PhCN)_2$ in refluxing 1,2-dichloroethane or CH_2Cl_2 at RT. The complexes were yellow–orange, microcrystalline solids that were freely soluble in polar organic solvents, such as $CHCl_3$ and CH_2Cl_2, and insoluble in Et_2O and hexanes. All complexes were also sufficiently soluble in H_2O to allow DNA-binding studies.

The molecular structure of *S*-**1** is shown in Fig. 3; it is isostructural with the known analogous palladium derivative (16). As expected, the metal adopts an approximately square-planar coordination geometry, and the pyridyloxazoline ligand is roughly planar except for the *iso*-propyl substituent at the 4-position of the oxazoline ring, which projects prominently from one face of the complex and makes a torsion angle with it of ~62 °. The ligand has a "bite angle" of 79.711(4)°, which is nearly identical to that found for the palladium analogue, but unlike in that compound, whose M–oxazoline bond (2.017(5) Å) is significantly shorter than its M–pyridine bond (2.048(6) Å), there is no difference in the two M–N distances, which are both 2.015(11, 12) Å in *S*-**1**. However, there is, as in the palladium analogue, a significant difference in the M–Cl distances: in complexes of both metals, the M–Cl bond trans to the oxazoline ring is longer than that trans to the pyridine ring, which consistently suggests that oxazoline is a stronger field ligand than pyridine, and implies strong contribution from the resonance form that places a formal negative charge on the N atom of the free oxazoline.

The particular undecamer sequence chosen for the present studies (shown below) has been used by Lippard and coworkers to obtain a solution NMR structure of a platinated duplex and is known to adopt the typical B-form of DNA in the absence of platination (27). The putative metallation site is underscored.

Top: strand-5′-CTCTCGGTCTC-3′

Bottom: strand-3′-GAGAGCCAGAG-5′

After incubation of the ds DNA test sequence with complexes **1**–**6** and complete digestion of the oligonucleotides,

Fig. 3. Partial ORTEP representation of the molecular structure of *S*-**1**, with H atoms omitted for clarity. Thermal ellipsoids for Pt and Cl atoms are shown at 50 % probablility; all other atoms are refined isotropically (see Experimental section). Selected bond distances (Å) and angles (°), with estimated standard deviations in parentheses: Pt1–N1 2.015(11), Pt1–N11 2.015(12), Pt1–Cl11 2.2869(3), Pt1–Cl12 2.298(4), N1–Pt1–N11 79.711(4), Pt1–N11–C10–C12 61.629(19).

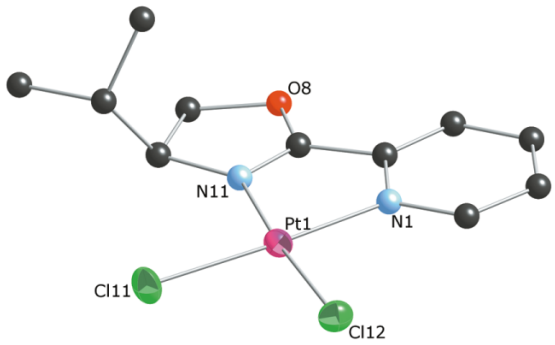

HPLC analyses were carried out. Nucleoside peaks were identified by the coinjection of standards, and integrated peak-area ratios were calculated. The ratios of nucleosides were calculated and analyzed as they are independent of reaction volume and concentration, are not influenced by volume of sample used for HPLC analysis, and eliminate errors associated with pipetting technique. Binding of cisplatin analogues to a ds DNA sequence is consistent with a marked decrease in dG/dC and a slight decrease in dA/dC because dG and dA are known to coordinate metal complexes. This dramatically shifts their retention times in RP–HPLC (28), although for the present work we did not conclusively identify the peaks belonging to metal–nucleoside adducts. The nucleoside peak-area ratios for the control digests conformed to the stoichiometry of the nucleosides within the DNA strands, given their relative absorptivities (extinction coefficients were obtained from ref. 29). The dG/dA ratio can be used as a measure of binding selectivity for dG over dA.

Results are shown in Fig. 4 for 1 equiv. of complex per duplex DNA. From the ratios of dG/dC, it can be seen that the pyridyloxazoline complexes tested are less reactive towards dG than cisplatin. From comparison with the control experiment, the composition of nucleosides is reduced in dG by ~40% and dA by ~8% upon exposure to cisplatin. Higher degrees of platination may be obtained by reaction at elevated temperatures with an excess of platinum salt (28) or through the use of bis-DMF/NO_3^- compounds (27). The low thermal stability of our test sequence precluded us from the use of the former and we avoided the latter as we wished not for complete saturation, but to determine the differences in binding between enantiomeric complexes. In all digests, dC/dT remains approximately constant implying that these bases are not reactive towards the platinum complexes, as expected (data not shown). Enantiomeric complexes showed no discernable patterns in their DNA-binding ability. In the case where R = *i*Pr [*R*-**1**: Δ(dG) = –32%; *S*-**1**: Δ(dG) = –23%], the *S* enantiomer is less reactive towards dG, but in the case where R = Ph [*R*-**2**: Δ(dG) = –16%; *S*-**2**: Δ(dG) = –23%], it is the *R* enantiomer that is less reactive. In the case

© 2008 NRC Canada

Fig. 4. Ratios of peak area for enzymatic digests of the undecamer duplex after exposure to no Pt containing compound (0), cisplatin (cisPt), and compounds **1**–**6**. Error bars are +/– 1 standard deviation.

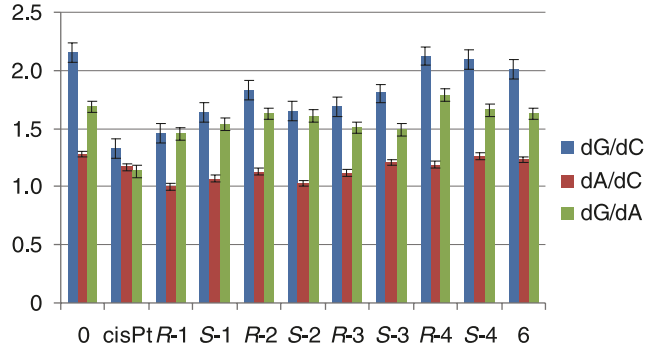

Fig. 5. Ratio of peak areas for the enzymatic digests of the bottom strand undecamer after exposure to no Pt containing compound (0), cisplatin (cisPt), and compounds **1** and **2**. Error bars are +/– 1 standard deviation.

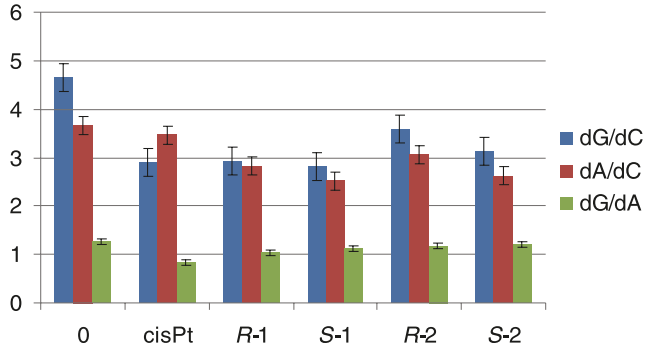

of R = Bn [*R*-**3**: Δ(dG) = –22%, *S*-**3**: Δ(dG) = –16%], there is little difference due to stereochemistry (Fig. 4). The unsubstituted ligand complex **6** (R = H) was the least reactive of the platinum complexes [Δ(dG) = –7%]; this was somewhat surprising as it was thought the decreased steric constraints would allow for greater DNA binding. It has been shown formerly that this compound has antineoplastic effects on cancer cells in vitro (19). The lack of binding in our study implies that this compound may have a different biological target and (or) mode of action. Both palladium complexes tested showed no significant deviations from the negative control [*R*-**4**: Δ(dG) = –1.4%; *S*-**4**: Δ(dG) = –3%]. Palladium complexes in a cis geometry are known to have lower binding affinities towards DNA than *cis*-dichloroplatinum compounds; however, the comparable trans-complexes often offer cytostatic effects surpassing that of cisplatin (30).

With respect to reactivity toward deoxyadenosine nucleosides in the context of duplex DNA, a parallel to the reactivity observed towards dG was found. For compound **1**, the *R*-enantiomer [Δ(dA) = –22%] was more reactive than the *S*-enantiomer [(Δ(dA) = –16%]; whereas for compound **2**, *R*-**2** [(Δ(dA) = –12%] was less reactive than *S*-**2** [(Δ(dA) = –19%]. For compound **3**, the reactivity of the *R*-stereoisomer [(Δ(dA) = –13%] was greater than that of the *S* [(Δ(dA) = –5%]. The loss of dA caused by compounds *R*-**4**, *S*-**4**, and **6** was modest at Δ(dA) = –7%, –1.5%, and –4%, respectively.

In the single-stranded digests, the lack of secondary structure should make the stereochemistry of the complexes less relevant. The complexes exhibited reactivity different from what was observed in the case of the duplex. In the reaction with the bottom strand (5′-GAGACCGAGAG-3′), where the only adjacent purines are dApdG, *R*-**1**, *S*-**1**, and *S*-**2** showed reactivity towards dG comparable to that of cisplatin, Δ(dG) = –37%, –39%, –33%, and –37%, respectively, Fig. 5. All complexes showed greater reactivity towards dA than cisplatin. Whereas cisplatin caused the loss of approximately 5% of dA, compounds *R*-**1**, *S*-**1**, *R*-**2**, and *S*-**2** reacted to a significantly greater extent causing the loss of 23%, 31%, 16%, and 29%, respectively. Decreased selectivity for dG is possibly due to the lack of an available NH proton. Of course, other electronic factors cannot be dismissed. Digests of the top strand (5′-CTCTCGGTCTC-3′) yielded very similar results to the duplex digestions where all compounds bound to dG less efficiently than cisplatin (data not shown).

Fig. 6. Denaturing polyacrylamide gel electrophoresis (PAGE) (negative exposure) of top strand (TS), bottom strand (BS), and double stranded (ds) DNA subjected to 1 equiv. of either *R*-**1**, cisplatin or no Pt. Lanes: 1: ds DNA, negative control; 2: ds DNA + cisplatin; 3: ds DNA + *R*-**1**; 4: BS, negative control; 5: TS, negative control; 6: BS + *R*-**1**; 7: TS + *R*-**1**; 8: BS + cisplatin; 9: TS + cisplatin.

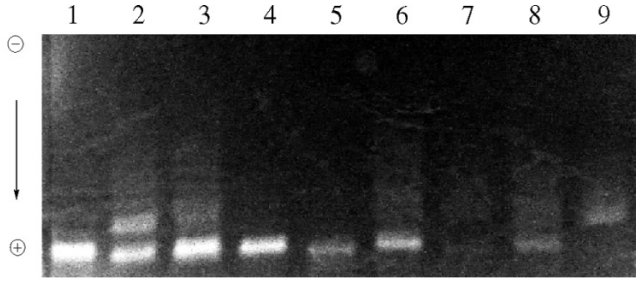

Thermal denaturation of platinated duplexes showed that cisplatin lowered the melting temperature (T_m) of the duplex, which is consistent with the formation of 1,2-intrastrand adducts (the stability of the duplex is compromised to the extent that a ΔT_m of –20 °C can be observed) (2, 31), while the pyridyloxazoline complexes decreased the T_m only very slightly (ΔT_m = 1–3 °C). This indicates that substantial duplex deformation is not occurring and implies that 1,2 adducts are likely not formed.

Denaturing polyacrylamide gel electrophoresis (PAGE) of the platinated ds and ss DNA again confirmed the generally low reactivity of the compounds. However, DNA platination is revealed by electrophoretic analysis of the reaction mixtures employing the most reactive compound used in this study (*R*-**1**), (Fig. 6). The accumulation of positive charge, which occurs after platination of the sequence, results in lower mobility of the oligonucleotide within the gel matrix.

A significant shifting of the bands in the lanes containing cisplatin was observed. The lanes containing the pyridyloxazoline complex *R*-**1** either showed one band identical to the control (no platinum) or two bands, the top band (corresponding to a platinated ss sequence) appearing very faintly.

© 2008 NRC Canada

It is possible that, if left for longer periods of time, the compounds tested may show differences in binding between enantiomers, as the diastereomeric adducts may be resolved towards the thermodynamic product. It was however found that the ratios after 36 h or 48 h of incubation were not substantially different.

In conclusion, the pyridyloxazoline complexes of Pt and Pd tested in this study likely did not form 1,2-adducts with DNA, but had a higher propensity towards the formation of complexes with dA than cisplatin. It was also found that the nature and absolute configuration of the substituent at *C*4 of the oxazoline ring had no systematic or simple and predictable effect on reactivity. The previous work demonstrating the antineoplastic effects of **6** (19) may imply that monofunctional adducts formed are pharmacologically relevant. In vivo or in vitro biological assays may, in turn, highlight whether the chirality of these complexes is pertinent in regards to their efficacy as anticancer agents.

Acknowledgements

The authors (RHEH, NDJ) are grateful to the Natural Sciences and Engineering Research Council of Canada (NSERC) and the University of Western Ontario for financial support.

References

1. B. Rosenberg. Interdiscip. Sci. Rev. **3**, 134 (1978).
2. E. Wong and C.M. Giandomenico. Chem. Rev. **99**, 2451 (1999).
3. N. Poklar, D.S. Pilch, S.J. Lippard, E.A. Redding, S.U. Dunham, and K.J. Breslauer. Proc. Natl. Acad. Sci. USA. **93**, 7606 (1996).
4. M.A. Jakupec, M. Galanski, V.B. Arion, C.G. Hartinger, and B.K. Keppler. Dalton Trans. 183 (2008).
5. Y. Jung and S.J. Lippard. Chem. Rev. **107**, 1387 (2007).
6. M.J. Cleare and J.D. Hoeschele. Bioinorg. Chem. **2**, 7792 (1973).
7. M. Benedetti, L.G. Marzilli, and G. Natile. Chem. Eur. J. **11**, 5302 (2005).
8. R.B. Weiss and M.C. Christian. Drugs, **46**, 360 (1993).
9. O. Delalande, J. Malina, V. Brabec, and J. Kozelka. Biophys. J. **88**, 4159 (2005).
10. T.W. Hambley, E.C.H. Ling, V.P. Munk, and M.S. Davies. J. Biol. Inorg. Chem. **6**, 534 (2001).
11. J.D. Mier-Vinué, M. Gay, A.M. Montaña, R. Sáez, V. Moreno, J. Kasparkova, O. Vrana, P. Heringova, V. Brabek, A. Boccarelli, M. Coluccia, and G. Natile. J. Med. Chem. **51**, 424 (2008).
12. G. Natile and L.G. Marzilli. Coord. Chem. Rev. **250**, 1315 (2006).
13. J. Reedijk. Chem. Commun. 801 (1996).
14. M.J. Bloemink, H. Engelking, N. Gütschow, S. Karentzopoulos, B. Krebs, and J. Reedijk. J. Inorg. Biochem. **59**, 222 (1995).
15. M.J. Bloemink, H. Engelking, S. Karentzopoulos, B. Krebs, and J. Reedijk. Inorg. Chem. **35**, 619 (1996).
16. D.W. Dodd, H.E. Toews, F.d.S. Carneiro, M.C. Jennings, and N.D. Jones. Inorg. Chim. Acta, **359**, 2850 (2006).
17. C. Bolm, K. Weickhardt, M. Zehnder, and T. Ranff. Chem. Ber. **124**, 1173 (1991).
18. M.P. Muñoz, J. Adrio, J.C. Carretero, and A.M. Echavarren. Organometallics, **24**, 1293 (2005).
19. N. Paschke, A. Röndigs, H. Poppenborg, J.E.A. Wolff, and B. Krebs. Inorg. Chim. Acta, **264**, 239 (1997).
20. F.R. Hartley. Organomet. Rev. A, **6**, 119 (1976).
21. G.S. Hill, M.J. Irwin, C.J. Levy, and R.J. Puddephatt. Inorg. Synth. **32**, 149 (1998).
22. A. Ellington and J.D. Pollard. Curr. Prot. Mol. Bio. 2.12.1–2.12.7 (1998).
23. Z. Otwinowski and W. Minor. Methods in enzymology: macromolecular crystallography. Part A. **276**, 307 (1997).
24. L.J. Farrugia. J. Appl. Cryst. **32**, 837 (1999).
25. R.I. Cooper, R.O. Gould, S. Parsons, and D.J. Watkin. J. Appl. Cryst. **35**, 168 (2002).
26. M.J. McKennon, A.I. Meyers, K. Drauz, and M. Schwarm. J. Org. Chem. **58**, 3568 (1993).
27. S.U. Dunham, C.J. Turner, and S.J. Lippard. J. Am. Chem. Soc. **120**, 5395 (1998)
28. L.G. Nikolcheva, C.M. Vogels, R.A. Stefan, H.A. Darwish, S.J. Duffy, R.J. Ireland, A. Decken, R.H.E. Hudson, and S.A. Westcott. Can. J. Chem. **81**, 269 (2003).
29. H.A. Sober, R.A. Harte, and E.K. Sober. CRC handbook of biochemistry and selected data for microbiology. 2nd ed. Chemical Rubber Co. Cleveland OH 1970. Section G.
30. S. Ray, R. Mohan, J.K. Singh, M.K., Samantaray, M.M. Shaikh, D. Panda, and P. Gosh. J. Am. Chem. Soc. **129**, 15042 (2007).
31. B. van Hemelryck, E. Guiettet, G. Chottard, J.-P. Girault, T. Huynh-Dinh, Y.-J. Lallemand, J. Igolen, and J.-C. Chottard. J. Am. Chem. Soc. **106**, 3037 (1984).

© 2008 NRC Canada

Synthesis and first X-ray structures of cobalt(II) and cobalt(III) complexes bearing 2,4-dioxo-alkanoic acid dialkylamide ligands[1]

Jian Wang, Nicholas A. Morra, Hongda Zhao, Jeffrey S.T. Gorman, Vincent Lynch, Robert McDonald, John F. Reichwein, and Brian L. Pagenkopf

Abstract: The aerobic oxidation of 5-hydroxy pentenes to *trans*-tetrahydrofurans (THFs), the Mukaiyama oxidation, has in recent years emerged as a powerful tool in synthetic chemistry. In this report we describe the first crystal structures of 2,4-dioxo-alkanoic acid dialkylamide complexes for both Co(II) and Co(III) salts. The Co(II) structures show an unprecedented arrangement of atoms, with a central $Co(II)(H_2O)_6$ flanked by two Co(II) atoms each coordinated with three anionic chelating ligands. The dimeric Co(III) structures show two anionic chelating ligands and bridging hydroxyl groups.

Key words: aerobic oxidation, trans-tetrahydrofuran (THF), cobalt, X-ray crystallography, oxidation, coordination.

Résumé : L'oxydation aérobique de 5-hydroxypentènes en *trans*-tétrahydrofuranes (THF), l'oxydation de Mukaiyama, est devenue au cours des années récentes un outil puissant. Dans ce travail, on décrit les structures cristallines de sels complexes de Co(II) et de Co(III) de dialkyamides de l'acide 2,4-dioxoalcanoïque. Les structures des sels du Co(II) présentent un arrangement d'atomes, inconnu jusqu'à maintenant, comportant un groupe central $Co(II)(H_2O)_6$ flanqué de deux atomes de Co(II) qui sont chacun liés à trois ligands chélatants anioniques. Les structures dimères du Co(III) comportent deux ligands chélatants anioniques et des groupes hydroxyles servant de ponts.

Mots-clés : oxydation aérobique, THF, cobalt, diffraction des rayons X, oxydation, coordination.

[Traduit par la Rédaction]

Introduction

Co(III) complexes of 2,4-dioxo-alkanoic acid dialkylamides are useful catalysts for the aerobic oxidation of olefins to peroxides or alcohols (1–5) and for the oxidative cyclization of 5-hydroxy pentenes to tetrahydrofurans (THFs) (6). In recent years, the stereoselective aerobic oxidation of 5-hydroxy pentenes to *trans*-THFs (henceforth the Mukiayama oxidation, Scheme 1) has emerged as a powerful tool in organic synthesis and has been strategically employed in the total synthesis of natural products by the groups of Wang et al. (7), Takahashi et al. (8), Evans et al. (9), and Pagenkopf and co-workers (10). Surprisingly, despite the obvious synthetic importance of these catalysts, there is little structural information available on transition metal 2,4-dioxo amide complexes, and to the best of our knowledge no X-ray structures of these species have been reported. In this paper we describe crystal structures of two Co(II) complexes and one Co(III) complex.

Scheme 1. Representative Mukaiyama oxidation.

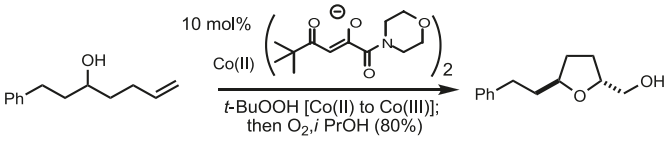

Experimental

General procedure for ligands 2

To a cooled (0 °C) solution of dialkylamine (10 mmol) and Et_3N (10 mmol) in CH_2Cl_2 (20 mL) was added ethyl oxalyl chloride (10 mmol). After stirring at room temperature (rt) for 16 h, the reaction mixture was washed with

Received 11 March 2008. Accepted 10 September 2008. Published on the NRC Research Press Web site at canjchem.nrc.ca on 15 November 2008.

J. Wang, N.A. Morra, and B.L. Pagenkopf.[2] Department of Chemistry, The University of Western Ontario, London, ON N6A 5B7, Canada.
H. Zhao, J.S.T. Gorman, V. Lynch,[3] **and J.F. Reichwein.** Department of Chemistry, The University of Texas at Austin, Austin, TX 78712, USA.
R. McDonald.[4] Chemistry Department, University of Alberta, Edmonton, AB T6G 2G2, Canada.

[1]This article is part of a Special Issue dedicated to Professor R. Puddephatt.
[2]Corresponding author (e-mail: bpagenko@uwo.ca).
[3]Corresponding author for questions concerning structures **3e** and **7** (e-mail: vmlynch@mail.utexas.edu).
[4]Corresponding author for questions concerning structure **9** (e-mail: Bob.McDonald@ualberta.ca).

 doi:10.1139/V08-151 © 2008 NRC Canada

Table 1. Crystallographic data collection parameters for **7**, **3e**, and **9**.

Complex	**3e**	**7**	**9**
Chemical formula	$C_{213}H_{218}Co_3N_6O_{22}$	$C_{141}H_{162}Co_3N_6O_{25}$	$C_{98.5}H_{110}Co_2N_4O_{14}$
Formula mass	3390.72	2517.56	1691.77
Crystal dimensions (mm)	0.32 × 0.26 × 0.15	0.50 × 0.14 × 0.11	0.53 × 0.27 × 0.15
Crystal system	Triclinic	Monoclinic	Monoclinic
Space group	$P\bar{1}$	$P2_1/n$	Ia
Z	2	2	4
a (Å)	17.9663(1)	16.5500(5)	24.6233(16)
b (Å)	23.9160(2)	20.8953(6)	13.1161(9)
c (Å)	24.1629(2)	19.1655(6)	29.4833(19)
α (°)	67.360(1)	90	90
β (°)	85.866(1)	98.326(2)	98.3545(10)
γ (°)	84.983(1)	90	90
Volume (Å^3)	9537.27(12)	6557.9(3)	9420.9 (11)
$D_{calcd.}$ (mg cm^{-3})	1.181	1.275	1.193
T (K)	153(2)	153(2)	193(2)
Radiation	MoKα (λ = 0.710 73)	MoKα (λ = 0.710 73)	MoKα (λ = 0.710 73)
μ (mm^{-1})	0.324	0.448	0.414
Total reflections collected	74 396	16 105	36 466
Total unique reflections	43 644 [R(int) = 0.0439]	8 560 [R(int) = 0.0606]	19 200 [R(int) = 0.0365]
Observed reflections [$I > 2\sigma(I)$]	16 105	74 396	15 217
$2\theta_{max}$ (α)	54.98	45	52.78
Goodness-of-fit on F^2	2.423	1.165	0.987
R_1 [$I > 2\sigma(I)$]	0.0847	0.0602	0.0504
wR_2 (all data)	0.1576	0.1373	0.129
Largest diff. peak and hole (e Å^{-3})	1.103 and –0.503	0.486 and –0.320	0.557 and –0.316

1 mol/L HCl (2×), satd. $NaHCO_3$, and brine and then dried ($MgSO_4$). Concentration in vacuo gave **1** as a white solid or colorless oil in quantitative yield, which was used without further purification.

A solution of *t*-BuOK (23 g, 205 mmol, 2.1 equiv.) in THF (180 mL) was added via cannula to a solution of pinacolone (12 mL, 96 mmol, 1.0 equiv.) and amide **1a** (18 g, 96 mmol, 1.0 equiv.) in THF (40 mL) over 40 min at rt. After 3 h, AcOH (20 mL, 350 mmol, 3.6 equiv.) was added over 5 min and the resulting heterogeneous mixture was filtered and the solids were washed with CH_2Cl_2. The filtrate was washed with $NaHCO_3$ and brine, dried, filtered, and concentrated. Purification of the resulting oil by flash chromatography (SiO_2, 50% EtOAc/hexanes) provided the title compound as a slightly yellow solid (18.1 g, 78%).

To a solution of **2** (7.0 mmol) in hexanes or benzene (**3a**) was added Co(II)(2-ethyl-hexanoate)$_2$ (3.5 mmol) solution in mineral spirits. The reaction mixture was stirred at rt for 8 h and hexane (ca. 70 mL) was added to induce precipitation. The solids were separated by centrifugation or filtration and washed with hexane.

Full characterization of Co(II) complexes by NMR was not possible because the salts are paramagnetic. Combustion analysis is significantly out of range because the number of water molecules within the powder varies and drying generally lead to decomposition. Attempts to record discrete melting points also lead to decomposition. Several of these complexes are known compounds, including **3a**, **3b**, and **3c** (3*a*, 11) (Table 1).

3a

Pink amorphous solids. MS (CI) *m*/*z*: 540 [M + H]$^+$, 242 [ligand + H]$^+$.

3b

Pink amorphous solids. MS (CI) *m*/*z*: 536 [M + H]$^+$, 240 [ligand + H]$^+$.

3c

Pink amorphous solids. MS (CI) *m*/*z*: 512 [M + H]$^+$, 228 [ligand + H]$^+$.

3d

Brownish peach colored amorphous solids. MS (CI) *m*/*z*: 760 [M + H]$^+$.

3e

Red crystals. MS (CI) *m*/*z*: 1064 [M + H]$^+$.

4

Pink amorphous solids. MS (CI) *m*/*z*: 676 [M + H]$^+$.

5

Reddish brown brittle foam. MS (CI) *m*/*z*: 732 [M + H]$^+$.

7

Red crystals. MS (CI) *m*/*z*: 732 [M + H]$^+$.

Synthesis and characterization of 9

To a mixture of **3d** (0.76 g, 1 mmol, 1.0 equiv.) in acetone (20 mL) was added 30% *w*/*w* H_2O_2 (1.2 mL, 10 mmol,

© 2008 NRC Canada

Scheme 2. Synthesis of Co(II) complexes.

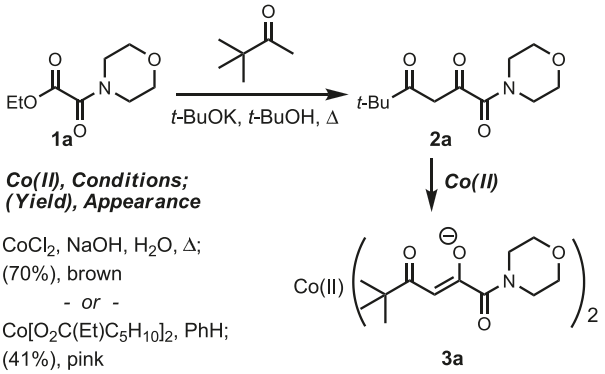

10 equiv.) at rt. After 15 h, the solution was concentrated under reduced pressure. TLC showed that the residue showed numerous spots. Flash chromatography over silica gel (25% EtOAc/hexanes) allowed separation of at least six distinct bands, one of which (R_f = 0.25, 40% EtOAc/hexanes) provided material that eventually crystallized. The crystal for X-ray analysis was grown from a vapor diffusion chamber containing EtOAc, toluene, and hexanes. ^{1}H NMR (600 MHz, C_6D_6) δ: 7.43 (d, J = 7.3 Hz, 4H), 7.24–7.20 (m, 8H), 7.15–7.08 (m, 8H), 7.00 (d, J = 7.1 Hz, 4H), 6.88–6.81 (m, 10H), 6.75 (t, J = 7.50, 4H), 6.53 (s, 2H), 6.34 (s, 2H), 6.26 (t, J = 7.3 Hz, 2H), 5.58 (d, J = 14.5 Hz, 2H), 5.29 (d, J = 15.4 Hz, 2H), 5.20 (d, J = 14.1 Hz, 2H), 4.28 (d, J = 16.8 Hz, 2H), 3.44–3.38 (m, 6H), 3.02 (d, J = 16.5 Hz, 2H), 1.26 (s, 18H), 1.01 (s, 18H), –3.39 (s, 1H), –3.72 (s, 1H). ^{59}Co NMR (144 MHz, C_6D_6) δ: 13364 (brs). Combustion calcd.: C 67.28, H 6.31, N 3.62; found: C 68.03, H 6.36, N 3.62.

Results and discussion

Cobalt(II) structures

Our initial efforts to employ the Mukaiyama oxidation in synthesis were complicated by fickle oxidation results as a consequence of inconsistent purity of the Co(II) complex. The first reports on Co(II) 2,4-dioxo-alkanoic acid amide complexes utilized $CoCl_2$ under aqueous alkaline conditions, but we found that such conditions caused decomposition of the morpholine amide **2a** (Scheme 2). The result was that the preparation of catalyst **3a** under the aqueous conditions provided a highly contaminated amorphous brown solid and attempts at purification proved fruitless. However, these difficulties were overcome by complexation under neutral conditions in organic solvent. When a solution of the free ligand **2a** in benzene was treated with 0.5 equiv. of Co(II)(2-ethyl hexanoate)$_2$, the initial dark blue color quickly dissipated and the resulting red solution was treated with hexane to precipitate the complex **3a**.

Table 2. Preparation of Co(II) complexes.

Entry	Co(II) Complex	#	Yield[a]
1	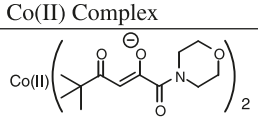	**3a**	99%
2	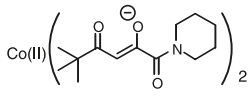	**3b**	75%
3	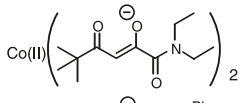	**3c**	59%
4	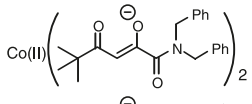	**3d**	59%
5	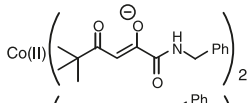	**4**	99%[b]
6	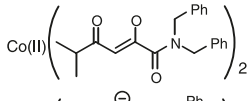	**5**	27%
7	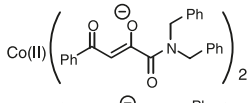	**6**	45%
8	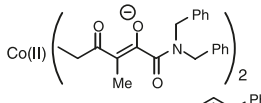	**7**	76%
9	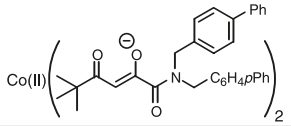	**3e**	23%

Note: The compounds shown are representative of the metal to ligand stoichiometry only, and are not meant to imply structure.
[a]Unoptimized yields of complexation.
[b]Poor solubility.

This modified procedure proved effective for the preparation of a variety of 2,4-dioxo amide complexes and these results are summarized in Table 2. Replacement of the morpholine with piperidine (**3b**), diethylamine (**3c**), or dibenzyl amine (**3d**) gave complexes as microcrystalline pink powders unsuitable for single crystal X-ray analysis. Of these, the dibenzyl amide **3d** displayed the most promising crystalline character, and in entries 5–7 of Table 2 the dibenzyl amide portion of the ligand was conserved while substitutions were made in place of the *tert*-butyl group. The methyl (**4**), isopropyl (**5**), and phenyl (**6**) analogs of **3d** were each prepared successfully, but they too failed to give crystals suitable for X-ray analysis.

A more substantial change was made by installing a methyl group at C(3) and, gratifyingly, the complex **7** was obtained as red crystals and the unusual X-ray structure of **7** is shown in Fig. 1.[5] Selected bond lengths and angles are reported in Table 3. There are three cobalt atoms present in the

[5] Supplementary data for this article are available on the journal Web site (canjchem.nrc.ca) or may be purchased from the Depository of Unpublished Data, Document Delivery, CISTI, National Research Council Canada, Ottawa, ON K1A 0R6, Canada. DUD 3859. For more information on obtaining material refer to cisti-icist.nrc-cnrc.gc.ca/cms/unpub_e.shtml. CCDC 203707 (**7**), 679940 (**3e**), and 203708 (**9**) contain the crystallographic data for this manuscript. These data can be obtained, free of charge, via www.ccdc.cam.ac.uk/conts/retrieving.html (Or from the Cambridge Crystallographic Data Centre, 12 Union Road, Cambridge CB2 1EZ, UK; fax +44 1223 336033; or deposit@ccdc.cam.ac.uk).

© 2008 NRC Canada

Fig. 1. (*a*) View of the complex **7**, $[(C_{21}H_{22}NO_3)_3Co]_2$-$Co(H_2O)_6$. The complex resides on a crystallographic inversion center at ½, ½, ½ with $Co(H_2O)_6$ at the center, which bridges a pair of $(C_{21}H_{22}NO_3)_3Co$ complexes via O-H···O hydrogen bonds (12). (*b*) View of **7** showing a single Co-ligand assembly and the central $Co(H_2O)_6$ with selected atoms labeled. Displacement ellipsoids are scaled to the 30% probability level. Hydrogen atoms and aromatic groups have been removed for clarity.

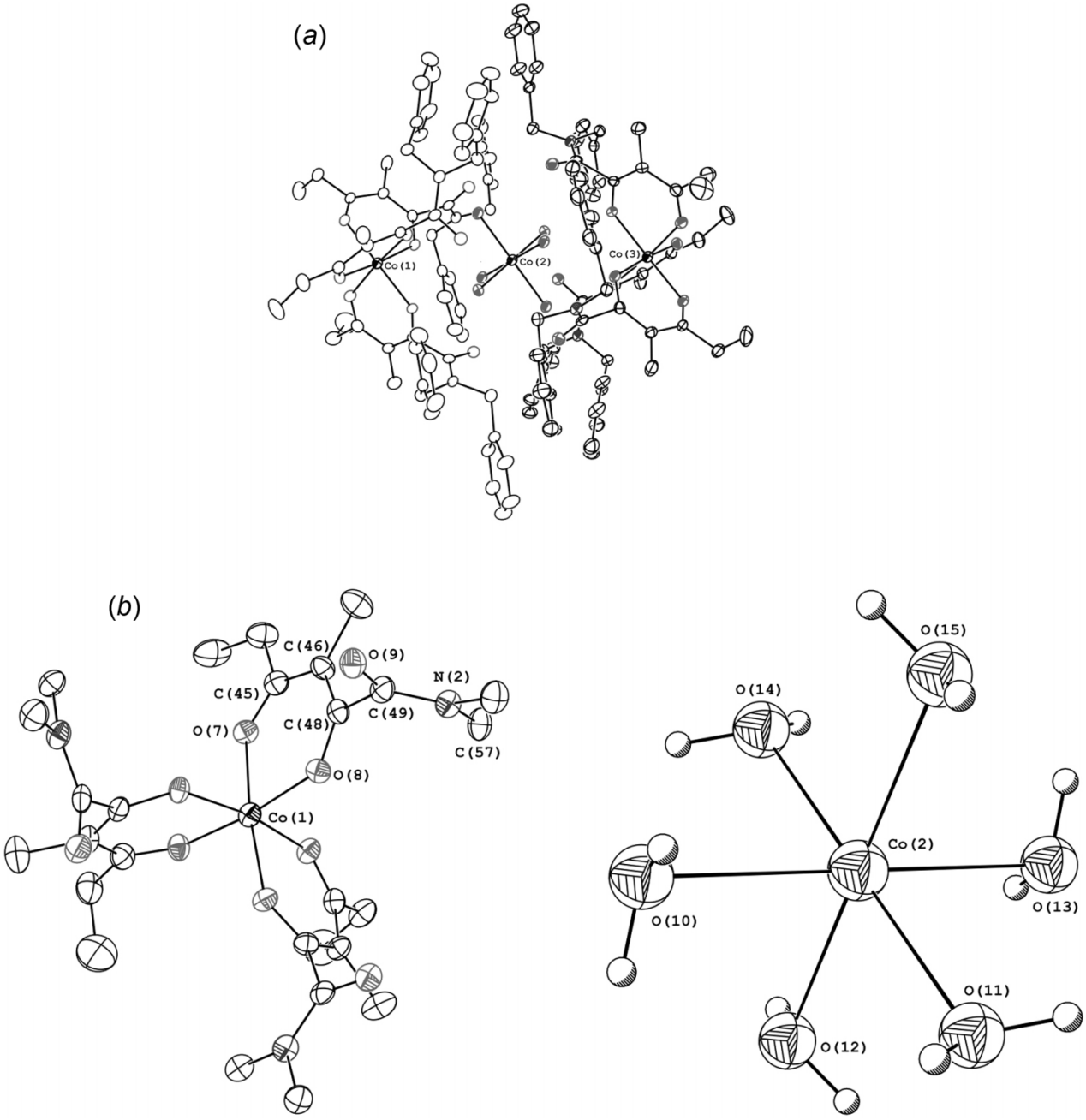

unit cell, each separated by 4.870 Å. The two outer cobalt atoms are each surrounded by three dioxoamide ligands and their negative charge is balanced by a central $Co(II)(H_2O)_6$. The dihedral angle between the amide carbonyl and the acac-like plane is 118(1)°, which might be expected to minimize A(1,3) strain with the C(3) methyl group. The unfavorable A(1,3) interaction was also evident in the ^1H NMR spectra of the metal-free ligand **8**, which in $CDCl_3$ existed as a 1:1 ratio of both the keto and enol forms (Scheme 3). In contrast, the preceding ligands existed primarily in the enol form. The distinctly different structure and behavior of ligand **8** compared with the others caused concern that the structure of **7** may be unique and not representative of the series.

To address concerns that the C(3) methyl may have lead to a structural anomaly, additional complexes more closely resembling **3d** were prepared. Of these, the biphenyl analog **3e** (Table 2, entry 9) formed crystals suitable for X-ray analysis (Fig. 2). Importantly, the major features of the two structures are conserved, including the arrangement of the three cobalt atoms and the angle of the amide. A minor difference is that the central cobalt in **3e** is surrounded by only

© 2008 NRC Canada

Fig. 2. View of the H-bound complex **3e**, $[(C_{34}H_{32}NO_3)_3Co]_2$-$Co(H_2O)_3$, showing the labeling scheme for selected atoms (12). Displacement ellipsoids are scaled to the 30% probability level. Hydrogen atoms and the aromatic groups have been removed for clarity. The three water molecules of the bis Co complex are H-bound to carbonyl oxygen atoms of the adjacent mono Co complex.

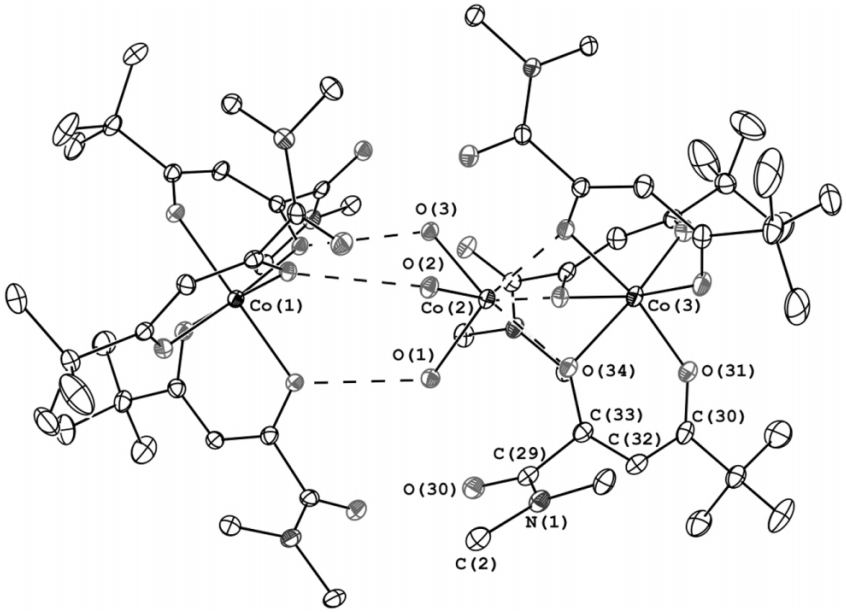

Table 3. Selected bond lengths and angles for **7**.

Bond lengths (Å)	
C(45)–C(46)	1.450(7)
C(45)–O(7)	1.246(6)
C(46)–C(48)	1.367(7)
C(48)–C(49)	1.535(7)
C(48)–O(8)	1.287(5)
C(49)–O(9)	1.236(6)
C(49)–N(2)	1.339(6)
Co(1)–O(7)	2.021(4)
Co(1)–O(8)	2.075(3)
N(2)–C(57)	1.471(6)
Bond angles (°)	
O(7)-C(45)-C(46)	124.3(5)
C(48)-C(46)-C(45)	121.4(5)
O(8)-C(48)-C(46)	129.2(4)
C(45)-O(7)-Co(1)	132.2(3)
C(48)-O(8)-Co(1)	125.9(3)
O(7)-Co(1)-O(8)	85.73(13)

Table 4. Selected bond lengths and angles for **3e**.

Bond lengths (Å)	
Co(3)–O(31)	2.058(2)
Co(3)–O(34)	2.091(2)
C(32d)–C(33)	1.407(4)
C(30d)–C(32)	1.379(4)
C(30d)–O(31)	1.285(3)
C(29)–O(30)	1.236(4)
C(29)–C(30)	1.515(4)
N(1)–C(2)	1.468(4)
N(1)–C(29)	1.349(4)
C(33)–O(34)	1.250(4)
Bond angles (°)	
C(33)-O(34)-Co(3)	125.1(2)
C(30)-O(31)-Co(3)	120.78(9)
O(31)-Co(3)-O(34)	86.88(8)
O(34)-C(33)-C(32)	123.4(3)
O(31)-C(30)-C(32)	127.4(3)
C(30)-C(32)-C(33)	125.8(3)

Scheme 3. Equilibrium disfavors the enol form.

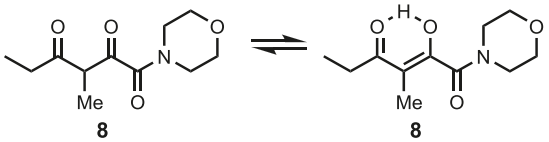

8 **8**

three water molecules, with the coordination sphere being fulfilled by dative bonding from a neighboring ligand. The distance between Co(1) and Co(2) was found to be 4.980 Å, Co(2) and Co(3) are separated by 2.926 Å. Bond lengths and angles of significance are reported in Table 4.

In both X-ray structures there are neutral donors, including water, surrounding the central cobalt atom. The reactions were run under an argon atmosphere using undried bulk solvents and this was presumably the origin of the water. To determine if additional water would facilitate crystallization, several complexation reactions were simply performed open to air. Remarkably, the preparation of **3d** under these conditions gave larger crystals that were easily obtained by filtration (instead of centrifugation). Importantly, no oxidation to Co(III) was observed under these conditions (TLC), whereas the analogous $Co(acac)_2$ species oxidize more readily.

© 2008 NRC Canada

Fig. 3. View of the complex **9**, $[(C_{34}H_{32}NO_3)_3Co]_2(\mu\text{-}OH)_2$, showing the labeling scheme for selected atoms (12). Nonhydrogen atoms are represented by Gaussian ellipsoids at the 30% probability level. Hydroxyl group hydrogen atoms are shown with arbitrarily small thermal parameters; all other hydrogens and aromatic groups have been removed for clarity.

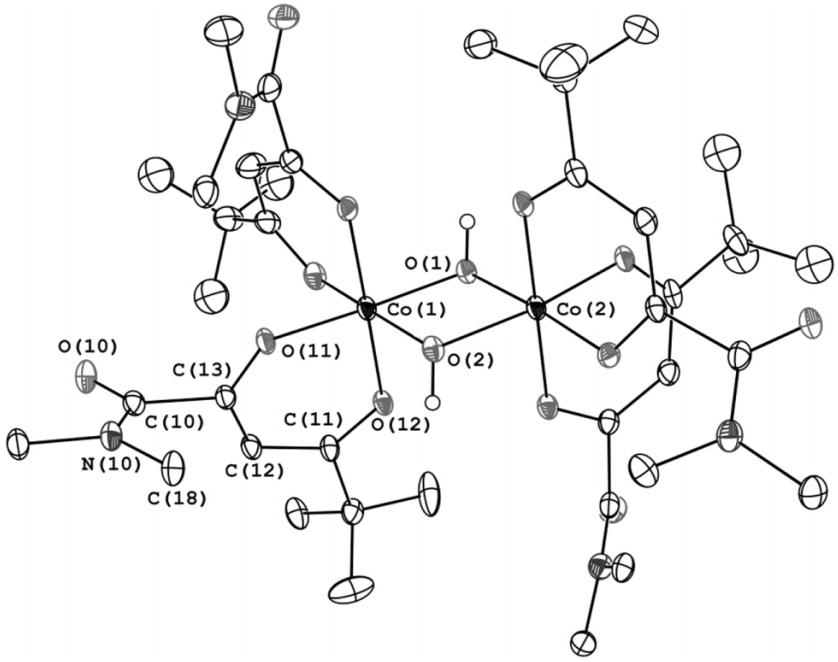

Cobalt(III) structure

Obtaining structural information about the Co(III) complexes (which are generated in situ for the Mukaiyama oxidation) might be more helpful in speculating about the nature of the active catalytic species. However, the Co(III) complexes are generally obtained as green oils or glasses. Efforts to grow crystals at –20 °C were promising, but the resultant crystals were not of suitable quality for X-ray analysis. The Co(III) complexes are stable to flash chromatography on silica gel and the complexes elute as numerous bands, some of which are readily separable while others are overlapping. We speculated one origin of these different bands to be diastereomeric complexation, and when separated the individual diastereomers might crystallize more easily. At rt individually eluted bands isomerize within a day or two to multiple species, as monitored by TLC. However, at –20 °C the isomerization is slowed dramatically and crystals suitable for X-ray crystallography were obtained from one of the more polar bands (R_f = 0.25, 40% EtOAc/hexanes) of compound **9** (the oxidized version of **3d**) (Fig. 3). In this binuclear cluster, the two central cobalt atoms are bridged by two hydroxyl groups and each cobalt is surrounded by two chelating ligands. Significant bond lengths and angles have been summarized in Table 5.

Table 5. Selected bond lengths and angles for **9**.

Bond lengths (Å)	
Co(1)–O(1)	1.903(2)
Co(1)–O(2)	1.904(2)
Co(1)–O(11)	1.888(2)
Co(1)–O(12)	1.887(2)
Co(2)–O(1)	1.903(2)
Co(2)–O(2)	1.918(2)
O(12)–C(13)	1.254(4)
O(11)–C(11)	1.284(4)
O(10)–C(10)	1.234(4)
C(12)–C(13)	1.415(4)
C(11)–C(12)	1.351(5)
C(10)–C(11)	1.541(4)
N(10)–C(10)	1.321(4)
N(10)–C(18)	1.486(4)
Bond angles (°)	
O(1)-Co(1)-O(2)	81.73(9)
O(1)-Co(1)-O(11)	174.77(10)
O(1)-Co(1)-O(12)	89.52(9)
Co(1)-O(1)-Co(2)	98.74(10)
Co(1)-O(2)-Co(2)	98.17(10)
Co(1)-O(11)-C(11)	120.3(2)
Co(1)-O(12)-C(13)	124.1(2)
O(12)-C(13)-C(12)	124.6(3)
O(11)-C(11)-C(12)	128.9(3)
C(11)-C(12)-C(13)	122.4(3)

Use of crystals in oxidative cyclizations

All of the new complexes reported in Table 2 possess some catalytic activity for the oxidation of γ-hydroxyl olefins to tetrahydrofurans. The complexes **3a** and **3d** have emerged as particularly useful catalysts and the decision to employ one versus the other is influenced by product polarity and chromatographic characteristics. Crystals of **9** were dissolved in *i*PrOH and appeared as a single spot by TLC. These crystals successfully catalyzed the oxidation shown in Scheme 1 (1 atm O_2, *i*PrOH, 50 °C, 16 h) in yields typically ranging from 70%–90%. Some spots isolated from the Co(III) species via chromatography were found to be inac-

© 2008 NRC Canada

tive under standard Mukaiyama oxidation conditions. Investigations are currently underway to determine the structural differences between the active and inactive Co(III) complexes.

Conclusions

A modified synthesis for the preparation of Co(II) complexes bearing 2,4-dioxo-alkanoic acid dialkylamide ligands has been reported and the resulting complexes are better precatalysts for the Mukaiyama oxidation compared with those prepared under aqueous alkaline conditions. X-ray structures for two of the Co(II) complexes have been solved and they revealed a unique arrangement of cobalt atoms in the unit cell, where two anionic clusters each containing one Co(II) atom surrounded by three negatively charged dioxoamide ligands flank a central Co(II) atom with neutral donors. Oxidation of the Co(II) salts with H_2O_2 gave green oils or glasses. Separation of the slowly equilibrating mixtures by flash chromatography on silica gel resulted in the isolation of a single diastereomer that lead to crystals suitable for X-ray analysis.

Acknowledgments

We thank the Natural Sciences and Engineering Research Council of Canada (NSERC), donors of the Petroleum Research Fund, and the DOD Prostate Cancer Research Program DAMD17-01-1-0109 for financial support. We also thank Professor Paul J. Ragogna and Jason Dutton for helpful discussions.

References

1. (*a*) S. Inoki, K. Kato, T. Takai, S. Isayama, T. Yamada, and T. Mukaiyama. Chem. Lett. **18**, 515 (1989); (*b*) T. Mukaiyama, S. Isayama, S. Inoki, K. Kato, T. Yamada, and T. Takai. Chem. Lett. **18**, 449 (1989).
2. K. Kato, T. Yamada, T. Takai, S. Inoki, and S. Isayama. Bull. Chem. Soc. Jpn. **63**, 179 (1990).
3. (*a*) S. Isayama and T. Mukaiyama. Chem. Lett. 18, 573 (1989); (*b*) S. Isayama. Bull. Chem. Soc. Jpn. **63**, 1305 (1990).
4. For examples of these catalysts being used in synthesis: (*a*) X.-X. Xu and H.-Q. Dong. J. Org. Chem. **60**, 3039 (1995); (*b*) T. Tokuyasu, A. Masuyama, M. Nojima, K.J. McCullough, H.-S. Kim, and Y. Wataya. Tetrahedron, **57**, 5979 (2001).
5. T. Mukaiyama. Aldrichimica Acta, **29**, 59 (1996).
6. (*a*) S. Inoki and T. Mukaiyama. Chem. Lett. 19, 67 (1990); (*b*) Z.-M. Wang, S.-K. Tian, and M. Shi. Tetrahedron Lett. **40**, 977 (1999); (*c*) S.-K. Tian, Z.-M. Wang, J.-K. Jiang, and M. Shi. Tetrahedron: Asymmetry, **40**, 551 (1999).
7. (*a*) Asimilobin: Z.M. Wang, S.K. Tian, and M. Shi. Tetrahedron Lett. **40**, 977 (1999); (*b*) Gigantetrocin A: Z.M. Wang, S.K. Tian, and M. Shi. Tetrahedron: Asymmetry, **10**, 667 (1999).
8. Mucocin: S. Takahashi, A. Kubota, and T. Nakata. Angew. Chem. Int. Ed. **41**, 4751 (2002).
9. Mucocin: P.A. Evans, J. Cui, S.J. Gharpure, A. Polosukhin, and H.R. Zhang. J. Am. Chem. Soc. **125**, 14702 (2003).
10. (*a*) Bullatacin: H.D. Zhao, J.S.T. Gorman, and B.L. Pagenkopf. Org. Lett. **8**, 4379 (2006); (*b*) Aplisiallene: J. Wang and B.L. Pagenkopf. Org. Lett. **9**, 3703 (2007).
11. M. Mukoyama, S. Isayama, K. Kato, S. Inoki, T. Yamada, and T. Takai. Japanese Patent 02121944, 1990.

© 2008 NRC Canada

Chemical synthesis and structural studies of thiol-capped gold nanoparticles[1]

Peng Zhang, Andy Yuan-Chi Chu, Tsun-Kong Sham, Yun Yao, and Shuit-Tong Lee

Abstract: We report the chemical synthesis and structural studies of thiol-capped Au nanoparticles (NPs) using extended X-ray absorption fine structures (EXAFS) and high-resolution transmission electron microscopy (HRTEM). Synthesis of Au NPs was conducted in one case in a toluene/water two-phase system using alkanethiols with varied hydrocarbon chain length (C6, C12, and C18), resulting in NPs of sizes ranging from 1.6 nm to 5.4 nm. Au L_3-edge EXAFS reveals a systematical trend of the local structure of Au in the NPs when the Au/S ratio and chain-length of thiols are varied. In another synthesis, thiol-capped Au NPs were prepared on the surface of silicon nanowires, which act as both substrates and reducing agents. HRTEM reveals that not only spherical particles but also very small quasi-1D nanostructures of Au were formed. The formation and structure of these Au NPs was discussed in terms of ligand and template effect associated with the silicon nanowire substrates.

Key words: thiol-capped Au nanoparticles, EXAFS, silicon nanowires, electroless deposition, quasi-1D Au nanostructures.

Résumé : On a réalisé la synthèse de nanoparticules (NP) d'or coiffées d'un thiol et on en a fait des études structurales en faisant appel à la méthode des structures fines d'absorption des rayons X étendue(SFAXE) et à la microscopie électronique de transmission à haute résolution (METHR). La synthèse des NP d'or a été réalisé, dans un cas, dans un système binaire toluène/eau et en utilisant des alcanethiols avec des chaînes carbonées de diverses (C6, C12 et C18) conduisant à des NP dont la taille allait de 1,6 à 5,4 nm. Les études de SFAXE à la limite L_3 révèlent la présence d'une tendance systématique de la structure locale de l'or dans les NP avec une variation du rapport Au/S et des longueurs des chaînes des thiols. Dans une autre méthode de synthèse, les NP d'or coiffées de thiol ont été préparées à la surface de nanofils de silicium qui agissent à la fois comme substrats et comme agents réducteurs. La METHR révèle qu'il y a formation non seulement de particules sphériques, mais aussi de très petites nanostructures quasi unidimensionnelles d'or. On discute de la formation et des structures de ces NP d'or en termes de ligand et d'effet de gabarit associé aux substrats nanofils de silicium.

Mots-clés : nanoparticules d'or coiffées d'un thiol, SFAXE, nanofils de silicium, dépôt sans électrode, nanostructures d'or quasi unidimensionnelles.

[Traduit par la Rédaction]

Introduction

During the past decade or so, thiol-capped gold nanoparticle (NP) has emerged as a prototype of nanostructured materials whose important role can be found in a variety of fundamental and applied areas (1). Particularly, because of the very high stability of Au clusters (oxidation-resistant) and strong Au–S bonding, the synthesis of very small thiol-capped has recently been possible (2, 3). The availability of these highly stable small NPs provides important opportunities for studies to understand the structure–property relationship of materials whose dimensions approach the lower limit of nanostructured materials, i.e., in the range of 0.5–2 nm. Meanwhile, rapid advancement in modern instrumental techniques, including a variety of high-resolution microscopic and spectroscopic methods, especially synchrotron-based techniques, opens up new avenues for unveiling the structure and properties of these nanomaterials with considerable details (4–7).

In this article, results from chemical synthesis and structural studies of thiol-capped Au NPs will be presented using synchrotron-based extended X-ray absorption fine structure (EXAFS) and high-resolution transmission electron microscopy (HRTEM). EXAFS studies of dodecanthiol-stabilized Au NPs have been recently reported by a number of groups (8–11). Comparing with the reported results, the new findings in the present work can be found in two areas. Synthetically, we prepared Au NPs with not only the classic

Received 31 March 2008. Accepted 7 July 2008. Published on the NRC Research Press Web site at canjchem.nrc.ca on 15 November 2008.

P. Zhang.[2] Department of Chemistry, Dalhousie University, Halifax, NS B3H 4J3, Canada.
A.Y-C. Chu and T.K. Sham.[3] Department of Chemistry, The University of Western Ontario, London, ON N6A 5B7, Canada.
Y. Yao and S.T. Lee. Center of Super-Diamond and Advanced Films (COSDAF), City University of Hong Kong, Hong Kong, P.R. China.

[1]This article is part of a Special Issue dedicated to Professor R. Puddephatt.
[2]Corresponding author (e-mail: peng.zhang@dal.ca).
[3]Corresponding author (e-mail: tsham@uwo.ca).

 doi:10.1139/V08-135 © 2008 NRC Canada

Scheme 1. A schematic illustration of the preparation of Au NPs capped with alkanethiols ($C_{18}SH$, $C_{12}SH$, and C_6SH) in solutions.

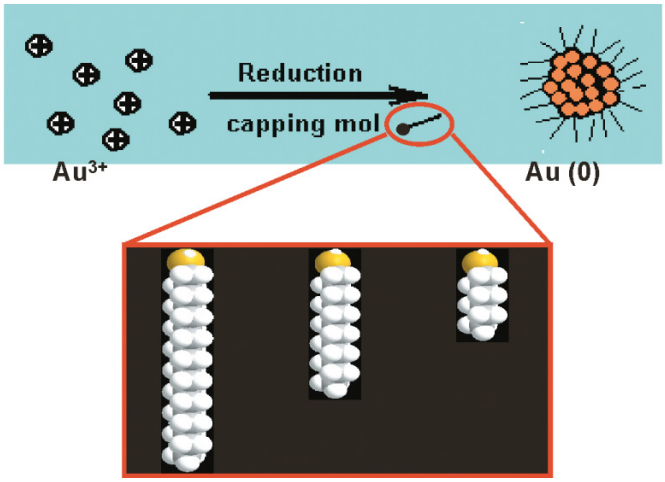

two-phase method (12), but also a recently developed strategy using thiol/silicon nanowires as capping ligands/nano-template (13). Particularly, the formation of quasi-1D Au NPs self-aligned on the surface of silicon nanowires was observed. From the perspective of structural analysis, experimental and simulated EXAFS were utilized to probe the structure of Au NPs capped with not only dodecanethiol but also hexanethiol and octadecylthiol. Based on these results, implications for tailoring the structure of Au NPs using wet chemical synthetic methods are discussed.

Experimental methods

The two-phase synthesis of Au NPs was conducted using the Brust method (12), which is schematically illustrated in Scheme 1. Typically, a $HAuCl_4$ aqueous solution (30 mL, 0.03 mol/L) was mixed with a toluene solution of tetraoctylammonium bromide (80 mL, 0.05 mol/L). The two-phase mixture was vigorously stirred until the aqueous phase becomes colourless, indicating that the $HAuCl_4$ compound was all transferred to the toluene phase. Next, the aqueous phase was removed and desired amount of alkanethiol (*n*-hexanethiol, *n*-dodecylthiol, and *n*-octadecylthiol) was added to the toluene phase. With vigorous stirring, freshly prepared aqueous $NaBH_4$ solution (25 mL, 0.4 mol/L) was added slowly to reduce all the Au(III) to Au(0). After further stirring for another 3 h, the toluene phase from the reaction mixture was collected and purified by the alcohol-precipitation method.

The electroless deposition of thiol-capped Au NPs on silicon nanowires (SiNWs) has been described previously (13, 14). Briefly, the SiNWs were prepared by a thermal evaporation method, producing nanowires several micrometers long with diameters of 20–30 nm. Then, stock solutions containing $HAuCl_4$ and thiol derivative (tiopronin) were prepared with the desired Au/S ratio (6:1) and concentrations (1 mmol/L $HAuCl_4$). Next, SiNWs (5% hydrofluoric acid treated for 2 min) were placed into the $HAuCl_4$/organosulfur solution for 5 min. After this, the Au/SiNWs were rinsed with distilled water several times to remove the unreacted chemicals and were allowed to dry in air.

Table 1. The average size and standard size deviation of C_6SH-, $C_{12}SH$-, and $C_{18}SH$-stabilized Au NPs. The results of $C_{12}SH$-stabilized Au NPs were taken from ref. 9.

	Au/S = 1:3	Au/S = 1:1	Au/S = 6:1
C_6SH	1.8±0.3 nm	2.4±0.5 nm	5.4±0.7 nm
$C_{12}SH$	1.6±0.3 nm	2.4±0.5 nm	4.0±0.6 nm
$C_{18}SH$	1.6±0.2 nm	1.9±0.4 nm	3.2±0.5 nm

The Au L_3-edge EXAFS measurements were conducted at the Pacific Northwest Consortium X-ray Operation Research (PNC-XOR) ID-20B beamline of the Advanced Photon Source (APS) at Argonne National Laboratory. The analysis of EXAFS data was performed using the WinXAS program with a standard procedure described previously (15). The FEFF8 (16) simulation was conducted using models of a symmetric Au_{55} cluster with and without 24 sulfur atoms on the three-fold hollow sites on the Au (111) surface of the cluster. High-resolution electron microscope measurements of Au NPs on Si nanowries were carried out using a JEOL 2010F (McMaster University) or a Philips CM200 FEG electron microscopy (City University of Hong Kong) operated at 200 kV.

Results and discussion

Size, morphology, and structure of the Au NPs prepared with two-phase method

For the Au NPs prepared with the two-phase method, the NP size can be controlled by varying either the Au/S ratio or the size of the alkanethiol molecules, or both. The general principle for the size control of Au NPs lies in the effectiveness of thiol-capping ligands in protecting the Au nuclei/clusters from aggregation and the concentration of the capping ligand in the vicinity of the nucleation site. The more effective and concentrated the ligands are, the smaller NPs will result. Therefore, the use of either a lower Au/S ratio in the starting materials or alkanethiols with a longer hydrocarbon chain can often lead to the production of smaller NPs (9).

Table 1 presents the size information of Au NPs synthesized by varying both the Au/S ratio and the chain length of thiols obtained from TEM, and the trend was confirmed by XRD. In Fig. 1, representative TEM images of *n*-dodecylthiol-capped NPs with Au/S ratios of 1:3, 1:1, and 6:1 are also shown. From Table 1, the trend of size dependence on concentration ratio (across the row) and ligand chain length (down the column) is apparent. For example, it can be seen that the use of $C_{18}SH$ or a Au/S ratio of 1:3 can generate the smallest NPs, whereas the use of C_6SH or a Au/S ratio of 6:1 result in the biggest particles. It is also noted that the control of NP size by varying the hydrocarbon chain length of thiols has the widest size range for the series of a Au/S ratio of 6:1. This is understandable in that when the concentration of the capping ligands is low, the size of the NP can grow larger before it is fully capped, and the diffusion rate of the ligand to the nucleation site is a factor. In contrast, when the highest concentration of thiols is used (Au/S = 1:3), the effect of chain length of capping molecules is much less significant, since the S-end of the molecules is

© 2008 NRC Canada

Fig. 1. Representative TEM images of $C_{12}SH$-capped Au NPs with Au/S ratios of (*a*) 1:3, (*b*) 1:1, and (*c*) 6:1 taken from ref. 9.

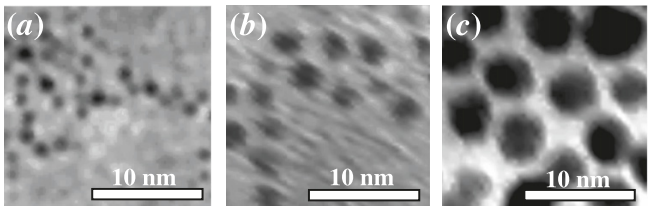

Fig. 2. Normalized FT-EXAFS of $C_{12}SH$-capped Au NPs with Au/S ratios of 1:3, 1:1, and 6:1 and bulk Au. Some baselines are shifted vertically for clarity. k-EXAFS range: 3–12 $Å^{-1}$. The distances are phase-uncorrected.

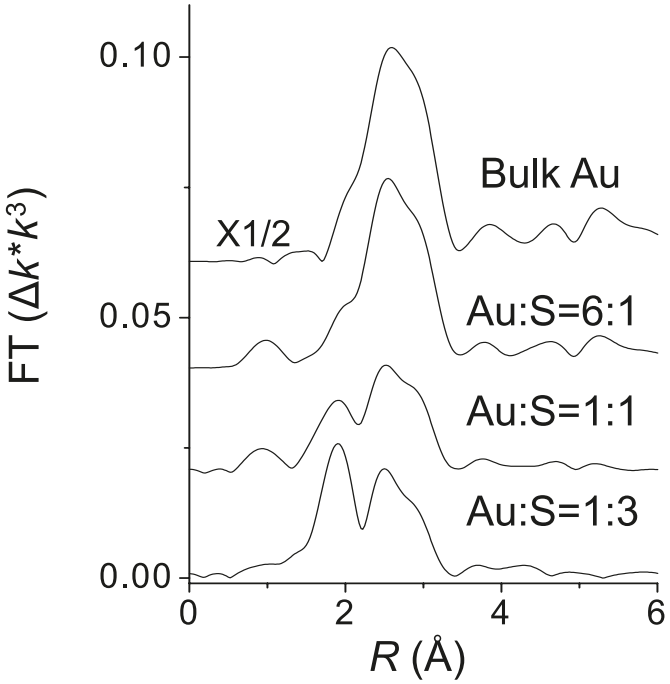

the same and there are abundant ligand molecules in the vicinity of the nucleation site.

To study comparatively the local structure of the NPs, we used EXAFS to investigate two series of samples selected from Table 1 (same ligand, $C_{12}SH$, different ratio and same ratio, 1:3, different ligands). Figure 2 shows the Fourier Transform (FT) of the Au L_3-edge EXAFS (with k^3 weighting) of $C_{12}SH$-capped NPs with Au/S ratios of 1:3, 1:1, and 6:1. Figure 3 depicts the FT-EXAFS of Au NPs with a Au/S ratio of 1:3 and different alkanethiols (C_6SH, $C_{12}SH$, and $C_{18}SH$). It should be noted that the peak position in the radial distribution (FT-EXAFS) is related to the real interatomic distance by a small phase correction. The peak positions are henceforth referred to as "phase uncorrected". The magnitude of the FT is mainly proportional to the coordination number for the same atomic pair. As can be seen in Table 1, the FT-EXAFS in Fig. 2 mainly reflect the NP size effect (same capping ligands), whereas in Fig. 3, the surface capping effect can be revealed as the differently capped NPs are nearly the same size. To assist the analysis, the Au L_3-

Fig. 3. FT-EXAFS of C_6SH, $C_{12}SH$ and $C_{18}SH$-capped Au NPs with a Au/S ratio of 1:3. k-EXAFS range: 3–12 $Å^{-1}$. The distances are phase-uncorrected.

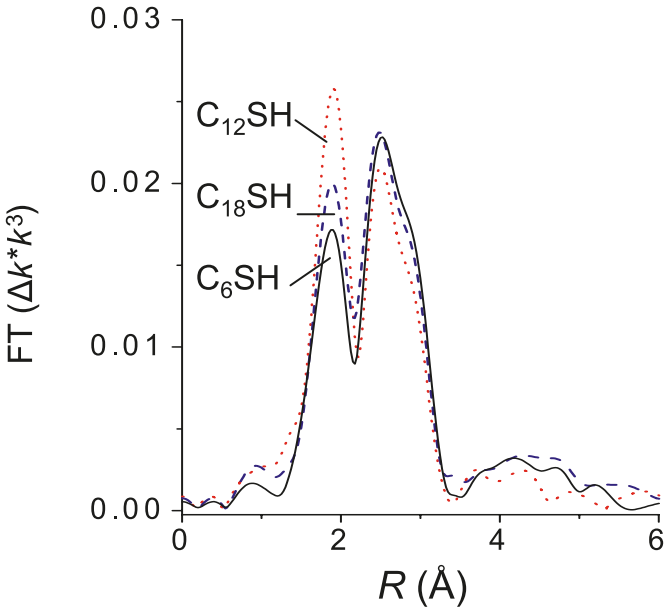

edge EXAFS was also simulated using the FEFF 8 code and the results are shown in Fig. 4. The simulated EXAFS and its FT are used below to interpret the experimental data presented in Figs. 2 and 3.

In Fig. 2, a couple of interesting observations are noted. First, the amplitude of the Au–Au bonding peak in the region of 2.5–3 Å corresponds to the inter-atomic distance of the nearest Au neighbour of the Au absorber in the NP (after a small phase correction). The magnitude of this peak decreases gradually with the size of Au. Second, a new peak at ~2 Å emerges as the NPs become smaller. The first observation is relatively easy to understand. As the NP size decreases, there are less Au neighbour atoms (on average) due to the higher fraction of surface Au atoms. As a result, the EXAFS intensity (amplitude of the FT), which is mainly determined by the Au–Au coordination number, decreases with the NP size (17). The second observation has been reported by a number of groups, and the peak at ~2 Å (phase uncorrected) has been assigned to Au–S bonding on the NP surface (8–11, 15). However, as shown in Fig. 2, this assignment has been challenged by the fact that bulk Au also shows a shoulder in the same region (~2 Å). To provide unambiguous evidence for the origin of the resonance peak at ~2 Å for the thiol-capped Au NPs, we next discuss the simulated EXAFS of three model clusters.

Figure 4*a* shows cross section of the plain Au_{55} model used for the FEFF simulation of FT-EXAFS. Five representative sites (center and 1^{st}–4^{th} shells) were used as the absorber for the simulation. The FT-EXAFS of each site for the model clusters $Au_{55}(SR)_{24}$, $Au_{55}(SR)_8$, and Au_{55} are presented in Figs. 4*b*, 4*c*, and 4*d*, respectively. The final simulated spectra were generated by weight-averaging the EXAFS of Au atoms in each shell of the model clusters. For the average FT-EXAFS shown in Fig. 4*e*, all three model clusters exhibit identical Au–Au bonding peak in the region of 2.5–3 Å. Meanwhile, a peak at ~2 Å is also observed for

© 2008 NRC Canada

Fig. 4. Simulated FT-EXAFS of $Au_{55}(SR)_{24}$, $Au_{55}(SR)_8$, and Au_{55}. (*a*): Part of a Au_{55} model illustrating the five representative sites for the FEFF simulations. (*b–d*): Site-specific simulations of $Au_{55}(SR)_{24}$ (*b*), $Au_{55}(SR)_8$ (*c*), and Au_{55} (*d*) by selecting each representative site illustrated in (*a*) as the absorber. (*e*): Weight-averaged FT-EXAFS of the three model clusters (for the simulation method, see refs. 18 and 19). The thiolate ligands, represented with $–SCH_3$ groups in the figure, were placed on the Au (111) surface with a Au–S distance of 2.3 Å. In the simulations, only gold and sulfur atoms were included in the input files.

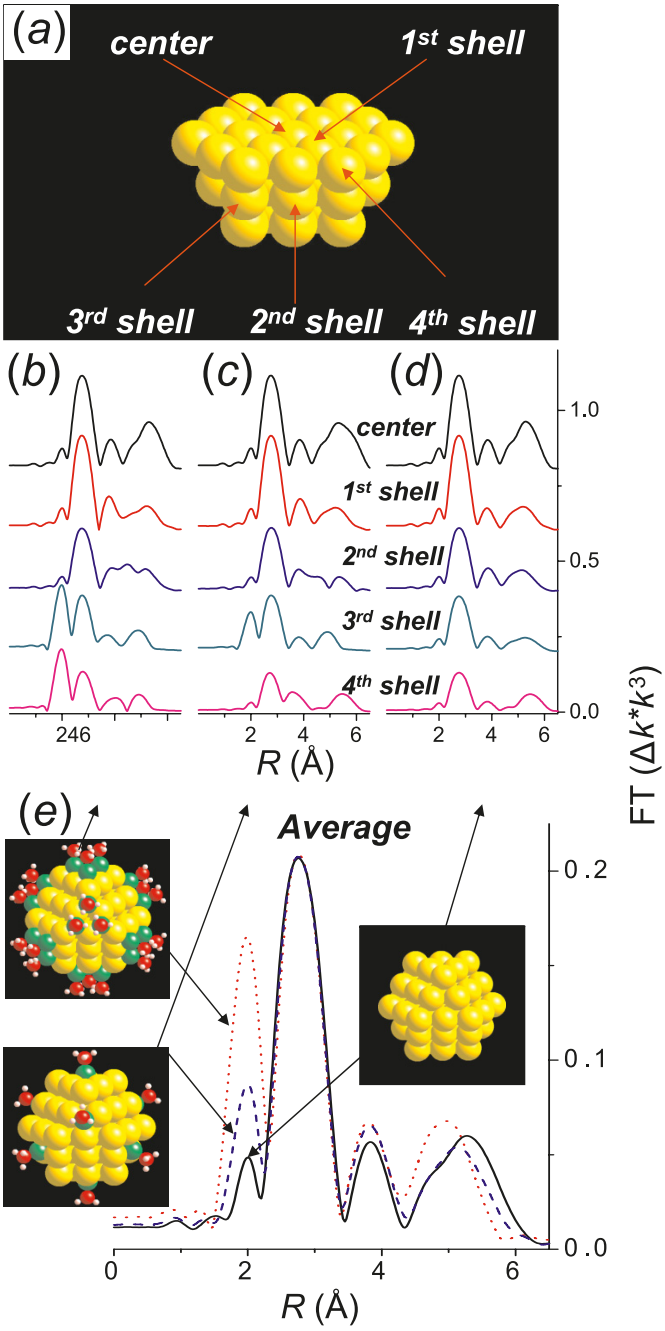

all the three clusters. Specifically, the intensity of this peak is very low for Au_{55} albeit observable. It increases by a factor of ~2 for $Au_{55}S_8$ and a factor of ~4 for $Au_{55}S_{24}$. The results in Fig. 4 indicate that the FT-EXAFS peak at ~2 Å is closely associated with the Au–S bonds of thiol-capped Au NPs and its intensity increases with the number of Au–S bonds on the NP surface. Thus, the intensity of this peak observed in Fig. 2 can be accounted for by the existence of more Au–S bonds on the surface of smaller Au NPs relative to the Au atoms in the core of the NP. Meanwhile, the results in Fig. 4 also suggest that the small but observable peak in this region associated with the Au–Au bonding may also need to be considered. This is particularly true for bigger particles with lower Au/S ratio, such as the largest NPs (Au/S = 6:1) shown in Fig. 2.

Returning to Fig. 3, we see the FT-EXAFS of three smallest Au NPs (1.6–1.8 nm) prepared using the same Au/S ratio (1:3), but capped with different alkanethiol molecules (C_6SH, $C_{12}SH$, and $C_{18}SH$). The sample C_6SH–Au and $C_{18}SH$–Au show Au–Au bonding peaks (in the region of 2.5–3 Å) of essentially the same intensity, which are slightly more intense than that of $C_{12}SH$–Au. The Au–S peak in region of ~2 Å is apparent for all NPs although there is some intensity variation. The EXAFS results suggest that $C_{12}SH$–Au is slightly smaller than the other two. This result, though somewhat different from the TEM results provided in Table 1 (C_6SH–Au = 1.8 nm, $C_{12}SH$–Au = 1.6 nm, $C_{18}SH$–Au = 1.6 nm), is understandable if one considers that TEM-based size information was obtained by counting NPs from a very small area in the sample (<100 nm × 100 nm), whereas EXAFS was collected from an area in the sample of 10^8 times bigger (>1 mm × 1 mm). Therefore, EXAFS can be considered as a measurement of the bulk of the samples, whereas TEM measurement is only sampling an extremely small fraction of the samples. In addition, the small difference of the NP sizes determined by TEM (1.6 nm vs. 1.8 nm) is within the experimental uncertainty of the measurement.

Figure 3 also reveals that the intensity of Au–S peak at ~2 Å decreases in the order of $C_{12}SH$–Au > $C_{18}SH$–Au > C_6SH–Au. The fact that the Au–S peak for $C_{18}SH$–Au is more intense than that of C_6SH–Au suggests a higher packing density of $C_{18}SH$ on the Au NPs than that of C_6SH, as they are of the same size according to EXAFS results. The mechanism for the highest Au–S peak intensity of $C_{12}SH$–Au among the three samples cannot be unambiguously accounted for. It can arise from the slightly smaller NP size (by EXAFS data) or still higher packing density of $C_{12}SH$ on the surface of Au NPs. The chain configuration and its effect on self assembly as well as NP size distribution may also play a role. Further experiment has to be conducted to reach a more satisfactory conclusion.

Morphology of Au NPs prepared on Si nanowires

Now, we report the second synthetic method for the preparation of thiol-capped Au NPs based on a recently developed electroless deposition method using HF-refreshed silicon nanowire (SiNWs) as reducing agent and substrate (13, 14). The mechanism is illustrated in Scheme 2. We have shown that the use of SiNWs in reaction with $HAuCl_4$ in the absence of thiols can lead to the formation of Au NPs of 20–30 nm (13). In comparison, in the presence of thiols, much smaller NPs whose surfaces are chemically functionalized with organic groups can be formed on SiNWs (see

© 2008 NRC Canada

Scheme 2. A schematic illustration of the preparation of Au NPs on silicon nanowires. (*a*) No capping molecules. (*b*) In the presence of capping thiol.

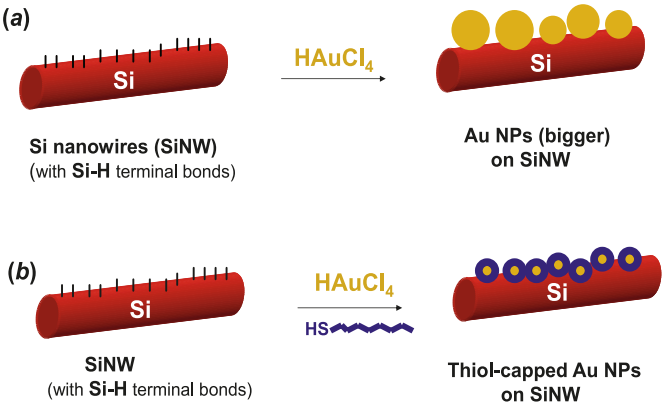

Fig. 5. TEM (*a*) and HRTEM (*b*) images of Au NPs on SiNWs. (*b*) Inset: a lattice-resolved Au NP. Scale bar: 2 nm.

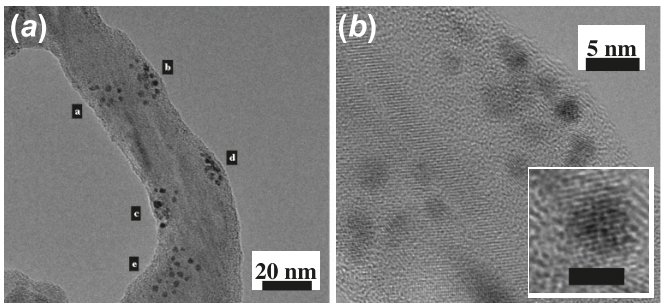

Scheme 2). In Fig. 5, it can be observed that Au NPs of 2–4 nm are formed on the surface of SiNWs. Measurement of lattice spacing of the NPs in Fig. 5*b* yields a value of 0.23 nm, consistent with the value of fcc Au.

Interestingly, we found that in some areas on SiNWs, very small non-spherical NPs were formed, as is shown in Fig. 6*a*. These NPs seem to self-assemble into quasi-1D nanostructure along the SiNW template. The STEM image in Fig. 6*b* and EDX (Energy Dispersive X-ray) spectroscopy data in Fig. 6*c* verify that these quasi-1D nanostructures are gold. Figures 6*d* and 6*e* show the HRTEM images of these quasi-1D Au NPs. The length of each rod-like Au NP is about 3–5 nm long and the width is about 0.8 nm. In the HRTEM image shown in Fig. 6*e*, the lattice fringe of SiNWs can be clearly visualized. However, the atomic structure of Au NPs (darker in colour) cannot be resolved. Instead, only amorphous structure originated from silicon oxide can be seen in the area where the quasi-1D Au NPs were formed. STEM shows similar results. It thus suggests that these very small Au NPs are buried by the oxide layer of SiNWs substrate. The presence of these small self-assemble NPs appears puzzling at first glance but can be understood in terms of the morphology of the SiNW and the HF refreshing process. SiNWs used in these reactions were prepared by the disproportionation of SiO, which usually lead to the formation of SiNW with an oxide sheath and core-shell type morphology (20). HF treatment usually cannot remove the surface oxide completely providing sporadic clean regions along the surface-oxide core-SiNW interface (21). These are

Fig. 6. TEM (*a*), STEM (*b*), EDX (*c*), and HRTEM (*d–e*) of quasi-1D Au nanostructures on SiNWs.

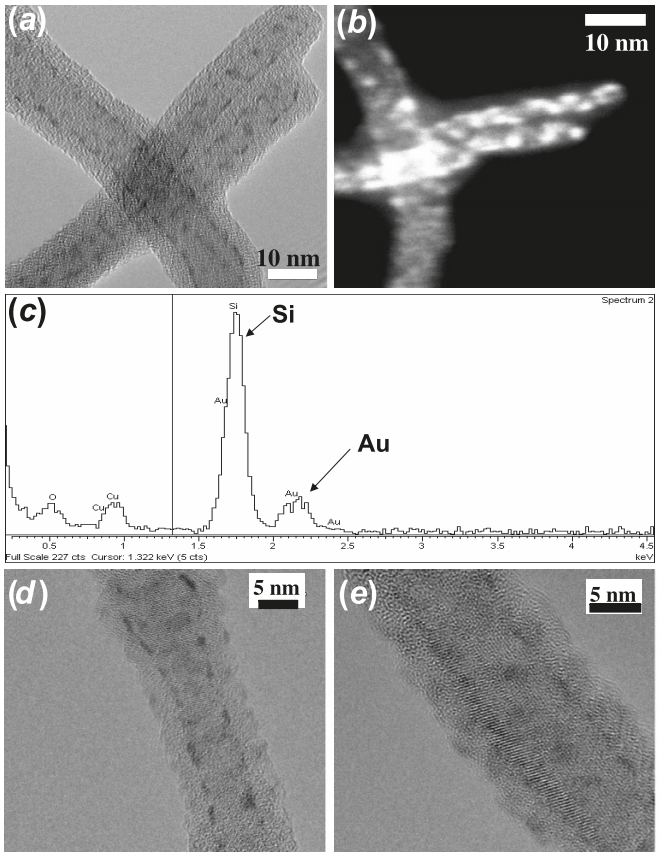

the most active regions for the reductive formation of Au NPs. It should also be noted that in addition to Si–H, clean Si on the surface can participate in the reduction of Au, producing oxide in the process. Thus, Au NPs on SiNW are likely to line up along the silicon oxide and core Si interface and encapsulated by amorphous oxide, which also terminates further growth of Au NPs.

Conclusion

We have used two chemical synthetic methods to prepare thiol-capped Au NPs. The size of Au NPs prepared with the two-phase method can be controlled in the range of 1.6–5.4 nm by varying the chain length of alkanethiols and (or) Au/S molar ratio in the staring materials. EXAFS reveals the trend of how the NP structure changes when these two factors are varied. FEFF8 simulations were used to unambiguously confirm the origin of FT-EXAFS peak of the thiol-capped Au NPs at ~2 Å, which has been assigned to Au–S bonding in the literature. In the second synthesis, both thiols and SiNWs were used to prepare substrate-supported Au NPs. It was found that both spherical and rod-like quasi-1D Au NPs were formed. HRTEM studies verify that these quasi-1D nanostructures are indeed gold. However, the atomic structure of these subnanometer-sized rod-like NPs has not been resolved, since they are buried by the oxide layer associated with the SiNW substrate and the reduction process.

© 2008 NRC Canada

Acknowledgements

The research at the UWO is financially supported by the Natural Sciences and Engineering Research Council of Canada (NSERC), Canada Foundation for Innovation (CFI), Ontario Innovation Trust (OIT), and Canada Research Chair (CRC) program (T.K. Sham). Research conducted at Dalhousie University is supported by NSERC and Dalhousie University. The APS is funded by the US Department of Energy (DOE) under contract No. W-31–109-Eng-38. The PNC-XOR operation is funded in part by an NSERC Major Facilities Access (MFA) grant. Research at the City University of Hong Kong is supported by a Competitive Earmarked Research Grant (CERG) (CityU 1294/03E) from the Research Grant Council of Hong Kong, SAR, China. We thank Dr. R.A. Gordon for technical support in EXAFS measurements.

References

1. M.C. Daniel and D. Astruc. Chem. Rev. **104**, 293 (2004).
2. L.D. Menard, S.P. Gao, H.P. Xu, R.D. Twesten, A.S. Harper, Y. Song, G.L. Wang, A.D. Douglas, J.C. Yang, A.I. Frenkel, R.G. Nuzzo, and R.W. Murray. J. Phys. Chem. B, **110**, 12874 (2006).
3. R.L. Donkers, D. Lee, and R.W. Murray. Langmuir, **20**, 1945 (2004).
4. E.M. Hunt, Z.L. Wang, N.D. Evans, and J.M. Hampikian. Micron, **29**, 191 (1998).
5. A.I. Frenkel, C.W. Hills, and R.G. Nuzzo. J. Phys. Chem. B, **105**, 12689 (2001).
6. T.K. Sham, P.S.G. Kim, and P. Zhang. Solid State Commun. **138**, 553 (2006).
7. T.K. Sham. Int. J. Nanotechnol. **5**, 1194 (2008).
8. D. Zanchet, H. Tolentino, M.C.M. Alves, O.L. Alves, and D. Ugarte. Chem. Phys. Lett. **323**, 167 (2000).
9. P. Zhang and T.K. Sham. Phys. Rev. Lett. **90**, 245502 (2003).
10. A.I. Frenkel, S. Nemzer, I. Pister, L. Soussan, T. Harris, Y. Sun, and M.H. Rafailovich. J. Chem. Phys. **123**, 184701 (2005).
11. C. Lopez-Cartes, T.C. Rojas, R. Litran, D. Martinez-Martinez, J.M. de la Fuente, S. Penades, and A. Fernandez. J. Phys. Chem. B, 109 8761 (2005).
12. M. Brust, M. Walker, D. Bethell, D.J. Schiffrin, and R. Whyman. J. Chem. Soc. Chem. Commun. 801 (1994).
13. P. Zhang, X.T. Zhou, Y.H. Tang, and T.K. Sham. Langmuir, **21**, 8502 (2005).
14. X.H. Sun, N.B. Wong, C.P. Li, S.T. Lee, P.S.G. Kim, and T.K. Sham. Chem. Mater. **16**, 1143 (2004).
15. P. Zhang and T.K. Sham. Appl. Phys. Lett. **81**, 736 (2002).
16. A.L. Ankudinov, B. Ravel, J.J. Rehr, and S.D. Conradson. Phys. Rev. B, **58**, 7565 (1998).
17. The EXAFS amplitude is depending on the scattering amplitude of the backscattering atom, bond length, coordination number, and Debye–Waller factor (vibration), and in this case, the only factor that varies is the coordination number.
18. D. Bazin, D. Sayers, J.J. Rehr, and C. Mottet. J. Phys. Chem. B, **101**, 5332 (1997).
19. A.L. Ankudinov, J.J. Rehr, J.J. Low, and S.R. Bare. J. Chem. Phys. **116**, 1911 (2002).
20. P.S.G. Kim, Y.H. Tang, T.K. Sham, and S.T. Lee. Can. J. Chem. **85**, 695 (2007).
21. T.K. Sham, S.J. Naftel, P.S.G. Kim, R. Sammynaiken, Y.H. Tang, I. Coulthard, A. Moewes, J.W. Freeland, Y.F. Hu, and S.T. Lee. Phys. Rev. B, **70**, 045313 (2004).

© 2008 NRC Canada

Unusual coordination behaviour of the ferrocenyl-terpyridine ligand with group 11 complexes[1]

Javier E. Aguado, M. Concepción Gimeno, Peter G. Jones, and Antonio Laguna

Abstract: Complexes of the ligand Fcterpy (Fcterpy = 4′-ferrocenyl-2,2′:6′,2′-terpyridine) with group 11 metals display different coordination modes. The reaction with complexes $[Cu(NO_3)(PPh_3)_2]$ or $[M(OTf)(PR_3)]$ (OTf = trifluoromethylsulphonate) gives the species $[M(Fcterpy)(PR_3)]X$ (M = Cu, X = PF_6, PR_3 = PPh_3 (**1**); M = Ag, X = OTf, PR_3 = PPh_3 (**2**), PPh_2Me (**3**); M = Au, X = OTf, PR_3 = PPh_3 (**4**)) in which the ligand is coordinated as a tridentate chelate to the metal. Treatment with $[Cu(NCMe)_4]PF_6$ or Ag(OTf) in 1:1 molar ratio gives the dinuclear complexes $[M_2(Fcterpy)_2]X_2$ (M = Cu (**5**), Ag (**6**)), in which the ligand is tetradentate because the central pyridine group is bonded to two metals. The reaction with the gold(I) complex $[Au(C_6F_5)(tht)]$ (tht = tetrahydrothiophene) leads to the first example of a terpyridine ligand bonded to three metal atoms, $[Au_3(C_6F_5)_3(Fcterpy)]$ (**7**); in the product of the corresponding reaction with the gold(III) derivative $[Au(C_6F_5)_3(OEt_2)]$ to give $[Au(C_6F_5)_3(Fcterpy)]$ (**8**), the ligand is monodentate, which is also unusual for a terpyridine ligand.

Key words: copper, silver, gold, terpyridine, ferrocene derivatives

Résumé : Les complexes du ligand Fcterpy [Fcterpy = 4′-ferrocényl-2,2′:6′,2′-terpyridine] avec les métaux du groupe 11 présentent divers modes de coordination. Les réactions avec des complexes $[Cu(NO_3)(PPh_3)_2]$ ou $[M(OTf)(PR_3)]$ (Otf = trifluorométhylsulfonate) conduisent à des espèces $[M(Fcterpy)(PR_3)]X$ [M = Cu; X = PF_6; PR_3 = PPh_3 (**1**); M = Ag; X = OTf; PR_3 = PPh_3 (**2**); PPh_2R (**3**); M = Au; X = OTf; PR_3 = PPh_3 (**4**)] dans lesquels le ligand est coordiné au métal sous la forme de chélate tridentate. Le traitement avec du $[Cu(NCME)_4]PF_6$ ou du Ag(OTf), dans un rapport molaire de 1:1, conduit à la formation de complexes binucléaires $[Me_2(Fcterpy)_2]X_2$ (M = Cu (**5**); Ag (**6**)] dans lesquels le ligand est tétradentate parce que le groupe pyridine central est lié à deux métaux. La réaction avec le complexe d'or(I) $[Au(C_6F_5)(tht)]$ (tht = tétrahydrothiophène) conduit au premier exemple d'un ligand terpyridine lié à trois atomes métalliques, $[Au_3(C_6F_5)_3(Fcterpy)]$ (**7**); dans le produit de la réaction correspondante avec le dérivé d'or(III) $[Au(C_6F_5)_3(OEt_2)]$ conduisant à la formation de $[Au(C_6F_5)_3Fcterpy)]$ (**8**), le ligand est sous la forme monodentate qui est inhabituelle pour un ligand terpyridine.

Mots-clés : cuivre, argent, or, terpyridine, dérivés du ferrocène.

[Traduit par la Rédaction]

Introduction

The coordination chemistry of terpyridine ligands with various metals has been the subject of numerous studies, inspired by the exciting photophysical properties of metal–polypyridyl complexes (1). In these compounds, the terpyridine generally acts as a chelating planar tridentate ligand; only in some examples does it act as a bidentate ligand with a non-coordinating residue (2). In the last few years, interesting spiral arrays have been prepared with these ligands that, by twisting, can accommodate more than one metal center. Thus, some examples have been prepared with silver in which the terpy is bonded to two different metal centers in a supramolecular structure (3). We have previously communicated another coordination mode in which the three nitrogen atoms are bonded to three different metals in the complex $[Au_3(C_6F_5)_3(Fcterpy)]$ (4). Few terpyridine complexes of gold have been described and these are gold(III) derivatives, such as $[AuX(Rterpy)]^{2+}$ (X = Cl, OH; R = H, SMe, PhOMe) (5–8), or $[Au(CN)_2Br(\eta^2\text{-terpy})]$ (9) (terpy = terpyridine), in which the ligand acts a tridentate or bidentate chelate. For silver and copper, more examples have been described including complexes of the type $[M(PR_3)_2(terpy)]X$ (M = Cu, Ag) (10).

Here we report complexes with the group 11 metals and a substituted terpyridine ligand, 4′-ferrocenyl-2,2′:6′,2′-terpyridine (Fcterpy) (11). Several coordination modes have been achieved, including tridentate chelate in complexes of the type $[M(Fcterpy)(PR_3)]X$ (M = Cu, Ag, Au), tetradentate in the homoleptic species $[M_2(Fcterpy)_2]X_2$ (M = Cu, Ag), which represent the first examples of dinuclear rather than

Received 21 May 2008. Accepted 10 September 2008. Published on the NRC Research Press Web site at canjchem.nrc.ca on 6 January 2009.

Dedicated to Professor Richard Puddephatt.

J.E. Aguado, M.C. Gimeno,[2] and A. Laguna. Departamento de Química Inorgánica, Instituto de Ciencia de Materiales de Aragón, Universidad de Zaragoza – C.S.I.C., E-50009 Zaragoza, Spain.
P.G. Jones. Institut für Anorganische und Analytische Chemie der Technischen Universität, Postfach 3329, D-38023 Braunschweig, Germany.

[1]This article is part of a Special Issue dedicated to Professor R. Puddephatt.
[2]Corresponding author (e-mail: gimeno@unizar.es).

 doi:10.1139/V08-148 © 2008 NRC Canada

Scheme 1. Synthesis of the Fcterpy ligand.

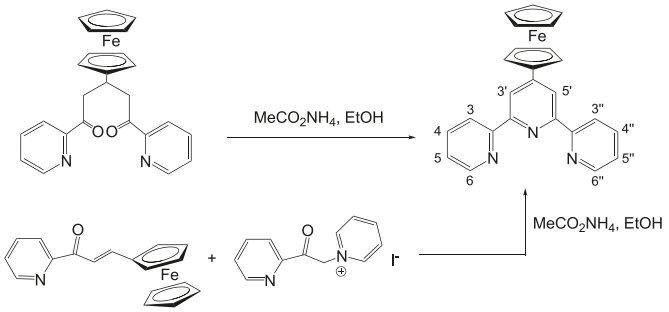

Fig. 1. Structure of compound Fcterpy showing the atom labelling scheme. Displacement parameter ellipsoids represent 50% probability surfaces. Radii are arbitrary; H atoms are omitted for clarity.

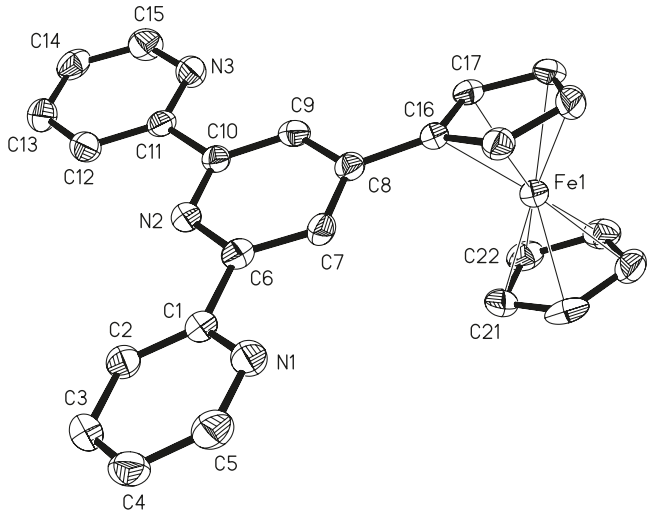

the usual polymeric derivatives, or monodentate in the gold(III) compound $[Au(C_6F_5)_3(Fcterpy)]$.

Results and discussion

The ligand 4′-ferrocenyl-2,2′:6′,2′-terpyridine (Fcterpy) has been synthesized by aromatization of a 3-ferrocenyl-1-bis(2-pyridyl)pentane-1,5-dione, previously obtained by reaction of ferrocenaldehyde and 2-acetylpyridine, or by aromatization of the corresponding enone with a pyridonium iodide salt (see Scheme 1) as has been previously described (11). The crystal structure of this ligand has been established and the molecule is shown in Fig. 1. A selection of bond lengths and angles are collected in Table 1. The overall bond lengths and angles are within the normal values found in this type of compound (12). The cyclopentadienyl rings are almost eclipsed. In the terpyridine moiety the aromatic rings are almost coplanar themselves, but not with the cyclopentadienyl ring; the dihedral angle formed by the nitrogen atoms and the cyclopentadienyl ring is 161.6°. The nitrogen atoms of the external pyridine rings are pointed in the opposite direction to that of the central one. This configuration changes upon coordination of the ligand.

The reaction of the Fcterpy ligand with $[Cu(NO_3)(PPh_3)_2]$ or $[Ag(OTf)(PR_3)]$ or $[Au(OTf)(PPh_3)]$ affords the complexes $[Cu(PPh_3)(Fcterpy)]NO_3$ (**1**), $[Ag(PR_3)(Fcterpy)]OTf$ (PR_3 = PPh_3 (**2**), PPh_2Me (**3**)), or $[Au(PPh_3)(Fcterpy)]OTf$ (**4**) (see Scheme 2). The IR spectra for these compounds show the absorptions of the ferrocenyl terpyridine unit as those arising from the aromatic pyridine and cyclopentadienyl rings around 1607 (s), 1586 (s), 1104 (s), and 820 (s) cm^{-1}. In addition, complex **1** shows the absorptions of the nitrate group at 1725 (w), 1090 (m), 1026 (m), 1000 (w), and 827 (m) cm^{-1} and complexes **2**–**4** show the bands arising from the ionic trifluoromethylsulfonate anion at around 1262 (vs), 1223 (m), 1147 (vs), and 1030 (vs) cm^{-1}. Because the ^1H NMR spectra of all complexes show the presence of the ligand Fcterpy, it is useful to compare the resonances with those present in the free ligand. The ligand shows two multiplets for the α and β protons of the substituted cyclopentadienyl group and a singlet for the unsubstituted cyclopentadienyl unit; the proton signals for the terpyridine are a doublet of doublets for the pair 5–5″, a doublet of triplets for the pair 4–4″, a singlet for 3′–5′, and doublets for the pairs 3–3″ and 6–6″. The resonances for the coordinated ligand in complexes **1**–**4** resemble those in the free ligand but with a different chemical shift and not so well defined, and in some cases the resonances overlap with those of the phenylic protons. For complex **3**, a doublet at 1.91 ppm for the methyl protons coupled to the phosphorus atom is observed. The $^{31}P\{^1H\}$ NMR spectra shows a singlet for complexes **1** and **4**, whereas for compounds **2** and **3** a broad resonance appears at room temperature and splits into two doublets at –55 °C, because of the coupling of the phosphorus atom with the two silver nuclei with spin 1/2, ^{109}Ag (48.17%) and ^{107}Ag (51.83%). The mass spectra show in all the complexes the cationic molecular peak $[M(PR_3)(Fcterpy)]^+$ at *m/z* = 742 (18%, **1**), 786 (34%, **2**), 724 (36%, **3**), and 876 (45%, **4**), although for the copper and silver complexes the most abundant peaks correspond to the species $[M(Fcterpy)]^+$.

Table 1. Bond lengths and angles for the ligand Fcterpy.

Bond lengths (Å)	
N(1)–C(5)	1.337(3)
N(1)–C(1)	1.346(3)
N(2)–C(10)	1.335(3)
N(2)–C(6)	1.344(4)
N(3)–C(15)	1.336(3)
N(3)–C(11)	1.338(3)
Bond angles (°)	
C(5)-N(1)-C(1)	116.8(2)
C(15)-N(3)-C(11)	116.9(2)
N(1)-C(1)-C(2)	122.4(2)
N(1)-C(1)-C(6)	116.6(2)
N(1)-C(5)-C(4)	124.4(3)
N(2)-C(6)-C(7)	122.8(2)
N(2)-C(6)-C(1)	115.9(2)
C(10)-N(2)-C(6)	117.6(2)
N(2)-C(10)-C(9)	122.7(2)
N(3)-C(11)-C(10)	116.7(2)
N(2)-C(10)-C(11)	116.7(2)
N(3)-C(15)-C(14)	124.5(3)

© 2008 NRC Canada

Scheme 2. (*i*) $[Cu(NO_3)(PPh_3)_2]$ or $[Ag(OTf)(PR_3)]$ or $[Au(OTf)(PPh_3)]$; (*ii*) $[Cu(NCMe)_4]PF_6$ or Ag(OTf); (*iii*) 3 $[Au(C_6F_5)(tht)]$; (*iv*) $[Au(C_6F_5)_3(OEt_2)]$.

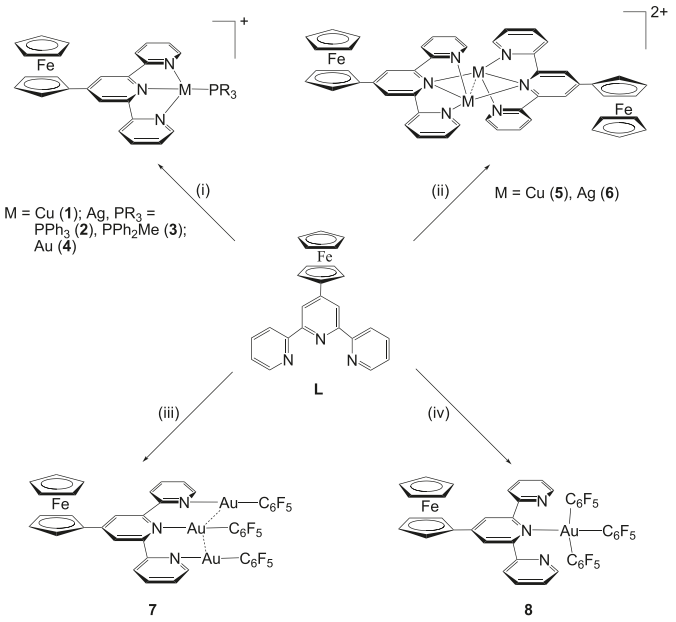

The silver complexes have been structurally characterized, showing that the metal center is bonded to the three nitrogen atoms of the terpyridine unit, although the shortest bond is with the central nitrogen atom; we assume analogous structures for the copper and gold complexes. However in the gold complex the metal could be far more strongly bonded to the central nitrogen atom and make only very short contacts with the others, given the high tendency of gold to form two-coordinate derivatives. No crystal structure for gold(I) complexes with terpyridine ligands has been carried out, with the exception of the trinuclear complex **7**. The structures of complexes **2** and **3** have been established by X-ray diffraction and are shown in Figs. 2 and 3, respectively. A selection of bond lengths and angles are collected in Tables 2 and 3. The structure for complex **2** shows that the silver center coordinates to the three nitrogen atoms of the terpyridine moiety and to the triphenylphosphine, and although it is tetra-coordinated, the geometry is far from tetrahedral. The silver atom is located 0.11 Å out of the plane formed by the four donor atoms, P, N11, N21, and N31, and only 0.057 Å out of the trigonal plane of the P, N21, and N31 atoms. The Ag–N distances are 2.302(4), 2.435(4), and 2.492(4) Å, the shortest being to the central nitrogen atom. The angles N–Ag–P are 117.53(9) and 109.91(11)°, which corresponds to normal values found in trigonal planar complexes (13); consequently the N–Ag–N angles are very narrow, 68.98(13) and 68.35(14)°. Two of the phenyl rings are disordered in mutually perpendicular positions, although this disorder is not shown in Fig. 2. The structure of complex **3** is similar, with Ag–N distances 2.332(4), 2.421(4), and 2.488(5) Å, again with the shortest to the central pyridine ring. The geometry around the silver center is more distorted than in complex **2**; the Ag atom lies 0.27 Å out of the plane formed by the four coordinated atoms and 0.11 Å out of the plane of the N1, N3, and P atoms. The phosphorus atom is located further from the plane formed by the terpyridine and

Fig. 2. Structure of the cation of compound **2** showing the atom numbering scheme. Displacement parameter ellipsoids represent 30% probability surfaces. Radii are arbitrary; H atoms are omitted for clarity.

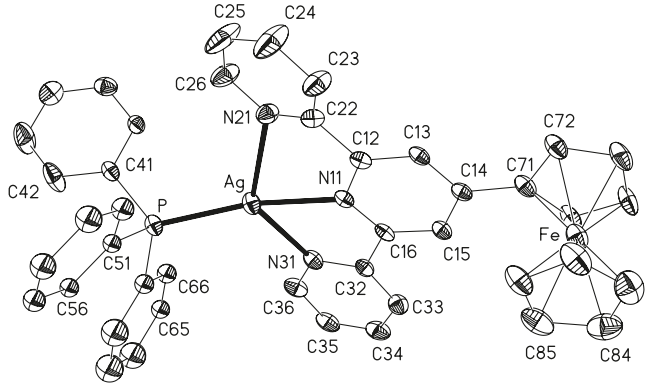

Fig. 3. Structure of the cation of compound **3** showing the atom numbering scheme. Displacement parameter ellipsoids represent 30% probability surfaces. Radii are arbitrary; H atoms are omitted for clarity.

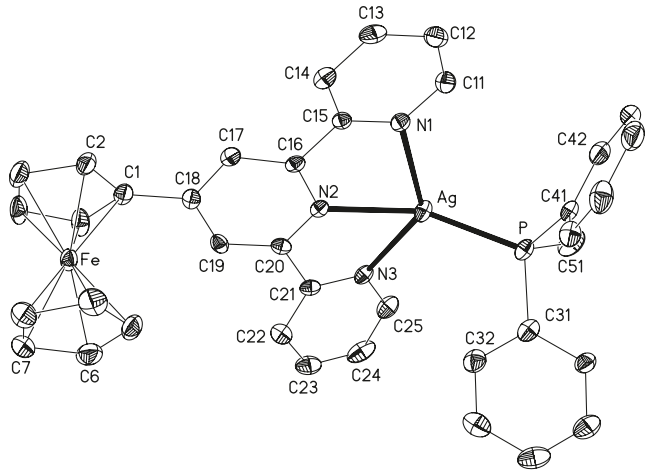

the silver atom than in complex **2**, with an N2–Ag–P angle of 152.06(11)° compared to 158.65(9)° in **2**. These structures are different from the previously reported complexes of stoichiometry $[M(terpy)(PPh_3)_2]^+$, which consist of discrete monomers of distorted trigonal-bipyramidal geometry, with the metal atoms coordinated to the distal terpyridine pyridyl rings [Cu-N 2.386(3), 2.535(4); Ag–N 2.614(2), 2.561 (2)Å] in axial sites (10). The coordination spheres are completed by the binding of the central pyridyl nitrogen atoms [Cu-N(2) 2.102(3), Ag–N(2) 2.457(2)Å] and two PPh_3 phosphorus atoms, which together define the equatorial planes.

The reaction of the ligand with an equimolar amount of $[Cu(NCMe)_4]PF_6$ or Ag(OTf) gives compounds with the stoichiometry [M(Fcterpy)]X (M = Cu, X = PF_6 (**5**); M = Ag, X = OTf (**6**)). The IR spectra show the typical absorptions of the Fcterpy ligand; the copper species show the absorption of the hexafluorophosphate at 640 (s) cm^{-1}, whereas the silver derivative presents the absorptions for the trifluoromethylsulfonate at 1259 (vs), 1223 (m), 1115 (vs),

© 2008 NRC Canada

Table 2. Selected bond lengths and angles for complex **2**.

Bond lengths (Å)	
Ag–N(11)	2.302(4)
Ag–N(31)	2.435(4)
Ag–P	2.3710(14)
Ag–N(21)	2.492(4)
Bond angles (°)	
N(11)-Ag-P	158.65(9)
N(11)-Ag-N(21)	68.35(14)
N(11)-Ag-N(31)	68.98(13)
P-Ag-N(21)	109.91(11)
P-Ag-N(31)	117.53(9)
N(31)-Ag-N(21)	132.38(13)

Table 3. Selected bond lengths and angles for complex **3**.

Bond lengths (Å)	
Ag–N(2)	2.332(4)
Ag–N(1)	2.421(4)
Ag–P	2.3783(16)
Ag–N(3)	2.488(5)
Bond angles (°)	
N(2)–Ag–P	152.06(11)
N(2)-Ag-N(3)	67.72(15)
N(2)-Ag-N(1)	69.22(15)
P-Ag-N(3)	111.19(11)
P-Ag-N(1)	113.70(11)
N(1)-Ag-N(3)	134.47(14)

and 1029 (vs) cm^{-1}. The ^1H NMR spectra also exhibit different ligand chemical shifts for the silver and copper derivatives; the copper species shows a broad resonance at 8.2 ppm for all the protons of the Fcterpy ligand. In the mass spectrum of complex **5** the peaks arising from $[Cu(Fcterpy)]^+$, $[Cu_2(Fcterpy)_2]^{2+}$, and $[Cu_2(Fcterpy)](PF_6)^+$ appear at m/z = 480 (100%), 960 (9%), and 1129 (15%); for complex **6** similar peaks at m/z = 524 ($[Ag(Fcterpy)]^+$, 100%), 941 ($[Ag(Fcterpy)_2]^+$, 12%), and 1119 ($[Ag_2(OTf)(Fcterpy)_2]^+$, 4%) are observed. These data could imply a dinuclear structure with two metal atoms and two ferrocenyl-terpyridine ligands. The previously reported complexes that contain a terpyridine ligand and silver atoms are usually polymeric species in which the silver center bonds asymmetrically to the terpyridine units, giving a polymeric chain structure or a helical structure for the ligand *t*-BuPh-terpy (14). In our ligand the presence of a more bulky group, the ferrocenyl unit, makes the structure different. Several crystals of complex **6** proved to be of low quality, small and poorly diffracting, but the molecule can be recognised in the structure solution and corresponds to a dinuclear derivative in which the ferrocenyl-terpyridine ligand has an unusual role; central pyridine is bonded to the two silver atoms, in a coordination mode described as "crevice" (see Scheme 1) that has only recently been reported for silver (10). We assume a similar structure for the copper species although we can not rule out other possibilities.

The reaction of the ferrocenyl-terpyridine ligand with three equivalents of $[Au(C_6F_5)(tht)]$ in dichloromethane leads to the synthesis of the compound $[Au_3(C_6F_5)_3(\eta^3\text{-Fcterpy})]$ (**7**), which has been previously communicated and represents the first example of a terpyridine ligand bonded to three metal atoms (4) The treatment of the ligand with the gold(III) derivative, $[Au(C_6F_5)_3(OEt_2)]$, gives an orange solid $[Au(C_6F_5)_3(Fcterpy)]$ (**8**). The IR spectrum shows the typical absorptions arising from the pentafluorophenyl groups bonded to gold(III) at 1509 (vs), 965 (vs), 821 (m), and 794 (vs) cm^{-1}. The ^{19}F NMR spectrum also confirms the presence of an $Au(C_6F_5)_3$ moiety because six resonances appear, three for the pentafluorophenyl rings in a mutually *trans* position and the other three for the other pentafluorophenyl ring (ratio 2:1). The ^1H NMR spectrum presents the resonances for the ferrocenyl-terpyridine, shifted compared to the free ligand. The protons of the ferrocenyl and terpyridine unit have the same pattern as in the free ligand and, consequently, we assume a symmetrical coordination. Furthermore, since gold(III) is mainly square planar and pentacoordination is not easily achieved, we propose a coordination of the gold(III) center to the central pyridine group.

Electrochemistry

The electrochemical behaviour of the ligand Fcterpy and some of these complexes has been studied by cyclic voltammetry at a platinum electrode in CH_2Cl_2. The ligand Fcterpy undergoes a reversible one-electron oxidation process at 0.64 eV; this is based on the ferrocene unit although at higher potential than the ferrocene itself. The cyclic voltammogram of the gold derivative **8**, at a scan rate of 100 mV s^{-1}, shows an essentially reversible wave arising from the oxidation-reduction of the ferrocene moiety at slightly lower potential than the free ligand, 0.61 eV. The copper(I) and silver(I) compounds $[M(PPh_3)(Fcterpy)]^+$ show, in addition to the wave from the ferrocene oxidation at 0.54 and 0.59 eV, respectively, a more anodic irreversible wave that can be assigned to the one electron oxidation of Cu^+ to Cu^{2+} and Ag^+ to Ag^{2+} at 0.70 and 1.12 eV. The dinuclear silver derivative $[Ag_2(Fcterpy)_2](OTf)_2$ also shows a quasi reversible wave for the oxidation-reduction of the ferrocene moieties at 0.60 eV and it is possible to distinguish two oxidation waves at 1.08 and 1.17 eV for the two Ag^+ atoms.

Experimental section[3]

Reagents and general procedures

Infrared spectra were recorded in the range 4000–200 cm^{-1} on a PerkinElmer 883 spectrophotometer using Nujol mulls

[3] Supplementary data for this article are available on the journal Web site (canjchem.nrc.ca) or may be purchased from the Depository of Unpublished Data, Document Delivery, CISTI, National Research Council Canada, Ottawa, ON K1A 0R6, Canada. DUD 3856. For more information on obtaining material refer to cisti-icist.nrc-cnrc.gc.ca/cms/unpub_e.shtml. CCDC 688756–688758 contain the crystallographic data for this manuscript. These data can be obtained, free of charge, via www.ccdc.cam.ac.uk/conts/retrieving.html (Or from the Cambridge Crystallographic Data Centre, 12 Union Road, Cambridge CB2 1EZ, UK; fax +44 1223 336033; or deposit@ccdc.cam.ac.uk).

© 2008 NRC Canada

between polyethylene sheets. C, H, N, and S analyses were carried out with a PerkinElmer 2400 microanalyzer. Mass spectra were recorded on a VG Autospec, with the liquid secondary-ion mass spectra (LSIMS) technique, using nitrobenzyl alcohol as matrix. NMR spectra were recorded on a Varian Unity 300 spectrometer and a Bruker ARX 300 spectrometer in $CDCl_3$, unless otherwise stated. Chemical shifts are cited relative to $SiMe_4$ (^1H, external), $CFCl_3$ (^{19}F, external), and 85% H_3PO_4 (^{31}P, external). Cyclic voltammetric experiments were performed by employing an EG&G PARC Model 273 potentiostat. A three-electrode system was used, consisting of a platinum disk working electrode, a platinum wire auxiliary electrode, and a saturated calomel reference electrode. The measurements were carried out in CH_2Cl_2 solutions with 0.1 mol/L Bu_4NPF_6 as a supporting electrolyte. Under the present experimental conditions, the ferrocenium–ferrocene couple was located at 0.47 V vs. SCE. The starting materials Fcterpy (11), $[Au(C_6F_5)(tht)]$ (15), $[Ag(OTf)(PR_3)]$ (16), $[Cu(NO_3)(PPh_3)_2]$ (17), $[Cu(NCMe)_4]PF_6$ (17), and $[Au(C_6F_5)_3(OEt_2)]$ (18) were prepared according to published procedures. $[Au(OTf)(PPh_3)]$ was obtained by reaction of $[AuCl(PPh_3)]$ (19) with Ag(OTf) in dichloromethane and used in situ. All other reagents were commercially available.

Preparation of $[Cu(PPh_3)(Fcterpy)]NO_3$ (1)

To a solution of Fcterpy (0.041 g, 0.1 mmol) in 20 mL of dichloromethane was added $[Cu(NO_3)(PPh_3)_2]$ (0.063 g, 0.1 mmol) under an argon atmosphere, and the mixture was left to react for 40 min. Evaporation of the solvent to ca. 2 mL and addition of hexane gave a deep red solid of complex **1**; yield 53%. ^1H NMR δ: 4.09 (s, 5H, C_5H_5), 4.63 (m, 2H, C_5H_4), 5.0 (m, 2H, C_5H_4), 6.9–7.5 (m, 15H + 4H, Ph + H5,H5″ + H6,H6″), 7.66 (t, 2H, *J*(HH) = 7.45 Hz, H4,H4′), 7.97 (d, 2H, *J*(HH) = 8.06 Hz, H3,H3″), 8.01 (s, 2H, H3′,H5′). ^{31}P NMR {^1H} δ: 1.2 (s, 1 P, PPh_3). MS *m*/*z*: 742 (18%, $[Cu(PR_3)(Fcterpy)]^+$), 480 (100%, $[Cu(Fcterpy)]^+$). Anal.calcd.. for $C_{43}H_{34}CuFeN_4O_3P$: C 64.14, H 4.25, N 6.95; found: C 64.53, H 4.62, N 6.74.

Preparation of $[Ag(PR_3)(Fcterpy)]OTf$ (PR_3 = PPh_3 (2) and PPh_2Me (3))

To a solution of Fcterpy (0.041 g, 0.1 mmol) in 20 mL of dichloromethane was added $[Ag(OTf)(PPh_3)]$ (0.051 g, 0.1 mmol) or $[Ag(OTf)(PPh_2Me)]$ (0.045 g, 0.1 mmol) and the mixture was left to react for 40 min. Evaporation of the solvent to ca. 2 mL and addition of hexane gave deep red solids of complex **2** or **3**. Complex **2**: yield, 92%. ^1H NMR δ: 4.10 (s, 5H, C_5H_5), 4.54 (m, 2H, C_5H_4), 5.08 (m, 2H, C_5H_4), 7.2–7.4 (m, 15H, Ph), 7.45 (d, 2H, *J*(HH) = 7.33 Hz, H5,H5″), 7.97 (t, 2H, *J*(HH) = 7.69 Hz, H4,H4′), 8.17 (d, 2H, *J*(HH) = 4.17 H6,H6″), 8.21 (s, 2H, H3′,H5′), 8.45 (d, 2 H, *J*(HH) = 7.92 Hz, H3,H3″). ^{31}P NMR {^1H, –55 °C} δ: 12.3 (2d, 1 P, *J*(^{109}AgP) = 707, *J*(^{107}AgP) = 615 Hz, PPh_3). MS *m*/*z*: 786 (34%, $[Ag(PPh_3)(Fcterpy)]^+$), 524 (100%, $[Ag(Fcterpy)]^+$). Anal. calcd. for $C_{44}H_{34}AgF_3FeN_3O_3PS$: C 56.43, H 3.65, N 4.48, S 3.42; found: C 56.57, H 3.70, N 4.72,S 3.20. Complex **3**; yield 80%. ^1H NMR δ: 1.91 (d, 3H, *J*(HP) = 6 Hz, Me), 4.45 (s, 5H, C_5H_5), 4.84 (m, 2H, C_5H_4), 5.35 (m, 2H, C_5H_4), 7.2–7.4 (m, 10H, Ph), 7.41 (2H, H5,H5″), 7.89 (t, 2H, *J*(HH) = 7.57 Hz, H4,H4′), 7.98 (s, 2H, H3′,H5′), 7.98 (s, 2H, H3′,H5′), 8.37 (d, 2H, *J*(HH) = 3.91 Hz, H6,H6″). ^{31}P NMR {^1H, –55 °C) δ: –6.7 (2d, 1 P, *J*(^{109}AgP) = 733 Hz, *J*(^{107}AgP) = 631 Hz, PPh_2Me). MS *m*/*z*: 724 (36%, $[Ag(PPh_2Me)(Fcterpy)]^+$), 524 (100%, $[Ag(Fcterpy)]^+$). Anal.calcd. for $C_{39}H_{32}AgF_3FeN_3O_3PS$: C 53.56, H 3.68, N 4.80, S 3.66; found: C 53.69, H 3.71, N 5.12, S 3.83.

Preparation of $[Au(PPh_3)(Fcterpy)]OTf$ (4)

To a solution of Fcterpy (0.041 g, 0.1 mmol) in 20 mL of dichloromethane was added $[Au(OTf)(PPh_3)]$ (0.060 g, 0.1 mmol) and the mixture was left to react for 40 min. Evaporation of the solvent to ca. 2 mL and addition of hexane gave a deep red solid of complex **4**; yield 65%. ^1H NMR δ: 4.31 (s, 5H, C_5H_5), 4.67 (m, 2H, C_5H_4), 5.30 (m, 2H, C_5H_4), 7.2–7.5 (m, 15H + 2H, Ph + H5,H5″), 7.89 (m, 2H, H4,H4′), 8.59 (m, 2H, H6,H6″), 8.32 (m, 2 H, H3,H3″), 8.71 (s, 2H, H3′,H5′). ^{31}P NMR{^1H} δ: 33.6 (s, 1P, PPh_3). MS *m*/z: 876 (45%, $[Au(PPh_3)(Fcterpy)]^+$). Anal. calcd. for $C_{44}H_{34}AuF_3FeN_3O_3PS$: C 51.52, H 3.34, N 4.09, S 3.12; found: C 51.74, H 3.44, N 4.10, S 3.31.

Preparation of $[M_2(Fcterpy)_2]X_2$ (M = Cu, X = PF_6 (5) and M = Ag, X = OTf = (6))

To a solution of Fcterpy (0.041 g, 0.1 mmol) in 20 mL of dichloromethane was added $[Cu(NCMe)_4]PF_6$ (0.038 g, 0.1 mmol), at 0 °C and under an argon atmosphere, or Ag(OTf) (0.025 g, 0.1 mmol), and the mixture was left to react for 30 min. Evaporation of the solvent to ca. 2 mL and addition of hexane gave deep red solids of complexes **5** or **6**. Complex **5**: yield 53%. ^1H NMR δ: 4.10 (s, 5H, C_5H_5), 5.06 (m, 2H, C_5H_4), 4.52 (m, 2H, C_5H_4), 8.2 (m, 10H, terpy). MS *m*/*z*: 1129 (15%, $[Cu_2(Fcterpy)_2](PF_6)^+$), 960 (9%, $[Cu_2(Fcterpy)_2]^+$), 480 (100%, $[Cu(Fcterpy)]^+$). Anal. calcd. for $C_{50}H_{38}Cu_2F_{12}Fe_2N_6P_2$: C 47.98, H 3.06, N 6.71; found: C 47.97, H 3.27, N 7.03. Complex **6**: yield 61%. ^1H NMR δ: 4.19 (s, 5H, C_5H_5), 4.65 (m, 2H, C_5H_4), 5.32 (m, 2H, C_5H_4), 7.43 (dq, 2H, *J*(HH) = 5.0, 1.1 Hz, H5,H5″), 8.06 (dt, 2H, *J*(HH) = 7.69, 1.71 Hz, H4,H4′), 8.31 (d, 2H, *J*(HH) = 5.0 Hz, H6,H6″), 8.48 (d, 2 H, *J*(HH) = 8.05 Hz, H3,H3″), 8.51 (s, 2H, H3′,H5′). MS *m*/*z*: 1119 (4%, $[Ag_2(OTf)(Fcterpy)_2]^+$), 941 (12%, $[Ag_2(Fcterpy)_2]^+$), 524 (100%, $[Ag(Fcterpy)]^+$). Anal. calcd. for $C_{52}H_{38}Ag_2F_6Fe_2N_6O_6S_2$: C 46.31, H 2.84, N 6.23, S 4.75; found: C 46.55, H 3.02, N 6.37, S 4.66.

Preparation of $[Au(C_6F_5)_3(Fcterpy)]$ (8)

To a solution of Fcterpy (0.041 g, 0.1 mmol) in 20 mL of dichloromethane was added $[Au(C_6F_5)_3(OEt_2)]$ (0.077 g, 0.1 mmol) at 0 °C and under an argon atmosphere, and the mixture was left to react for 40 min. Evaporation of the solvent to ca. 2 mL and addition of hexane gave a deep red solid of complex **8**; yield 63%. ^1H NMR δ: 4.15 (s, 5H, C_5H_5), 4.57 (m, 4H, C_5H_4), 5.04 (m, 4H, C_5H_4), 7.51 (m, 2H, H5,H5″), 8.01 (s, 2H, H3′,H5′), 8.03 (m, 2H, H3,H3″), 8.40 (m, 2H, H4, H4′), 8.69 (d, 2H, *J*(HH) = 5.13, H6,H6″). ^{19}F NMR δ: –121.6 (m, 6F, *m*-F), –156.4 (t, 2F, *p*-F, *J*(FF) = 21.12 Hz), –156.7 (t, 1F, *p*-F, *J*(FF) = 21.33 Hz), –160.8 (m, 4F, *o*-F), –161.9 (m, 2F, *o*-F). Anal. calcd. for $C_{43}H_{19}AuF_{15}FeN_3$: C 46.30, H 1.71, N 3.76; found: C 46.25, H 1.54, N 3.49.

© 2008 NRC Canada

Table 4. X-ray data for the compound Fcterpy and complexes **2** and **3**.

Compound	Fcterpy	**2**·0.59 H_2O	**3**·1/2 CH_2Cl_2
Formula	$C_{50}H_{38}Fe_2N_6$	$C_{44}H_{35.19}AgF_3FeN_3O_{3.6}PS$	$C_{39.5}H_{33}AgClF_3N_3O_3PS$
M_r	834.56	947.25	916.89
Habit	Red prism	Red tablet	Red prism
Crystal size (mm)	0.20 × 0.20 × 0.12	0.40 × 0.20 × 0.20	0.40 × 0.30 × 0.25
Crystal system	Monoclinic	Tetragonal	Triclinic
Space group	$P2_1/c$	$I4_1/a$	$P\bar{1}$
a (Å)	7.7987(8)	29.326(3)	11.397(2)
b (Å)	22.030(2)	29.326(3)	12.093(2)
c (Å)	11.3629(11)	18.561(2)	15.574(3)
α (°)	90	90	108.38(3)
β (°)	107.306(2)	90	105.79(3)
γ (°)	90	90	98.61(3)
V (Å^3)	1863.8(3)	15964(3)	1893.8(6)
Z	2	16	2
D (Mg m^{-3})	1.487	1.577	1.608
μ (mm^{-1})	0.826	1.007	1.125
F(000)	864	7680	926
T (°C)	–173	–100	–100
$2\theta_{max}$	51	50	50
Reflections collected	10 474	8828	7569
Independent reflections	3462	7006	6469
Transmissions	0.8522–0.9074	0.704–0.816	0.885–0.968
R_{int}	0.052	0.035	0.032
Parameters	302	466	482
Restraints	0	393	2
$wR(F^2$, all refl.)	0.09	0.088	0.131
$R(I, > 2\sigma(I))$	0.039	0.043	0.05
S	0.936	0.822	0.917
Max. Δρ (e Å^{-3})	0.499	0.599	1.36

Crystal structure determinations

Crystals were mounted in inert oil on glass fibers and transferred to the cold gas stream of a Bruker Smart 1000 CCD (Fcterpy) or Siemens P4 (**2**, **3**) diffractometer equipped with a low-temperature attachment. Data were collected using monochromated Mo Kα radiation (λ = 0.710 73 Å) and scan type ω, or ω and ϕ. Absorption corrections based on psi-scans (**2**, **3**) or multiple scans with the program SADABS (20) (Fcterpy), were applied. The structures were refined on F^2 using the program SHELXL-97 (21). All non-hydrogen atoms were refined anisotropically. Hydrogen atoms were included using a riding model. A special refinement was required for **2**: Two rings of the PPh_3 ligand are disordered over two positions and were refined isotropically. A peak of ca. 3 e/Å^3 was interpreted as a partially occupied water site. It is also involved in a contact of ca. 2.9 Å to itself, which could represent an H bond. Further details of the data collection and refinement are given in Table 4.

Acknowledgments

We thank the Dirección General de Investigación Científica y Técnica (CTQ2007–67273-C02–01) for financial support.

References

1. E. C. Constable. Adv. Inorg. Chem. Radiochem. **30**, 69 (1986).
2. See for example: (*a*) G. B. Deacon, J. M. Patrick, B. W. Skelton, N. C. Thomas, and A. H. White. Aust. J. Chem. **37**, 929 (1984); (*b*) N. C. Thomas and J. Fischer. J. Coord. Chem. **21**, 119 (1990); (*c*) E. C. Constable, M. J. Hannon, A. M. W. Cargill Thompson, D. A. Tocher, and J. V. Walker. Supramol. Chem. **3**, 243 (1993); (*d*) R. C. Chotalia, E. C. Constable, M. J. Hannon, and D. A. Tocher. J. Chem. Soc. Dalton Trans. 3571 (1995).
3. See for example: (*a*) K. T. Potts, M. Keshavarz, K. F. S. Tham, H. D. Abruña, and C. R. Arana. Inorg. Chem. **32**, 4422 (1993); (*b*) E. C. Constable, A. J. Edwards, M. J. Hannon, and P. R. Raithby. J. Chem. Soc. Chem. Commun. 1991 (1994); (*c*) G. Baum, E. C. Constable, D. Fenske, C. E. Housecroft, and T. Kulke. Chem. Commun. (Cambridge), 2659 (1998); (*d*) G. Baum, E. C. Constable, D. Fenske, C. E. Housecroft, T. Kulke, M. Neuburger, and M. Zehnder. J. Chem. Soc. Dalton Trans. 945 (2000); (*e*) M. H. Hannon, C. L. Painting, E. A. Plummer, L. J. Childs, and N. W. Alcock. Chem. Eur. J. **8**, 2225 (2002); (*f*) Y. Cui and C. He. J. Am. Chem. Soc. **125**, 16202 (2003).
4. J. E. Aguado, M. J. Calhorda, M. C. Gimeno, and A. Laguna. Chem. Commun. 3355 (2005).

© 2008 NRC Canada

5. L. S. Hollis and S. J. Lippard. J. Am. Chem. Soc. **105**, 4293 (1983).
6. H.-Q. Liu, T. C. Cheung, S. M. Peng, and C.-M. Che. J. Chem. Soc. Chem. Commun. 1787 (1995).
7. B. Pitteri, G. Marangoni, F. Visentin, T. Bobbo, V. Bertolasi, and P. Gilli. J. Chem. Soc. Dalton Trans. 677 (1999).
8. U. Sampath, W. C. Putnam, T. A. Osiek, S. Touami, J. Xie, D. Cohen, A. Cagnolini, P. Droege, D. Klug, C. L. Bernes, A. Modak, J. K. Bashkin, and S. S. Jurisson. J. Chem. Soc. Dalton Trans. 677 (1999).
9. V. Ferreti, P. Gilli, V. Bertolasi, G. Marangoni, P. Pitteri, and G. Ghessa. Acta Crystallogr. Sect. C, **48**, 814 (1992).
10. (*a*) Effendy, F. Marchetti, C. Pettinari, R. Pettinari, B. W. Skelton, and A. H. White. Inorg. Chim. Acta, **360**, 1414 (2007); (*b*) C. Di Nicola, Effendy, F. Marchetti, C. Pettinari, B. W. Skelton, and A. H. White. Inorg. Chim. Acta, **360**, 1433 (2007); (*c*) E. W. Ainscough, A. M. Brodie, S. L. Ingham, and J. M. Waters. J. Chem. Soc. Dalton Trans. 215 (1994).
11. E. C. Constable, A. J. Edwards, R. Martínez-Mánez, P. R. Raithby, and A. M. W. Cargill Thompson. J. Chem. Soc. Dalton Trans. 645 (1994).
12. U. Siemeling, U. Vorfeld, B. Neumann, H.-G. Stammler, M. Fontani, and P. Zanello. J. Organomet. Chem. **637**, 733 (2001).
13. (*a*) E. M. Barranco, O. Crespo, M. C. Gimeno, P. G. Jones, A. Laguna, and C. Sarroca. J. Chem. Soc. Dalton Trans. 2523 (2001); (*b*) O. Crespo, M. C. Gimeno, P. G. Jones, and A. Laguna. J. Chem. Soc. Dalton Trans. 4583 (1996).
14. P. K.-K. Ho, S.-M. Peng, K.-Y. Wong, and C.-M. Che. J. Chem. Soc. Dalton Trans. 1829 (1996).
15. R. Usón, A. Laguna, and M. Laguna. Inorg. Synth. **26**, 85 (1989).
16. M. Bardají, O. Crespo, A. Laguna, and A. K. Fischer. Inorg. Chim. Acta, **304**, 7 (2000).
17. G. J. Kubas. Inorg. Synth. **19**, 90 (1979).
18. R. Usón, A. Laguna, M. Laguna, J. Jiménez, and E. Durana. Inorg. Chim. Acta, **168**, 89 (1990).
19. R. Usón and A. Laguna. Inorg. Synth. **21**, 71 (1982).
20. G. M. Sheldrick. SADABS [computer program]. University of Göttingen, Göttingen, Germany. 1996.
21. G. M. Sheldrick. SHELXL-97 [computer program]. University of Göttingen, Göttingen, Germany. 1997.

© 2008 NRC Canada

Probing solid iminobis(diorganophosphine chalcogenide) systems with multinuclear magnetic resonance[1]

Bryan A. Demko and Roderick E. Wasylishen

Abstract: A ^{31}P and ^{77}Se solid-state NMR investigation of the iminobis(diorganophosphine chalcogenide) HN(R_2PE)$_2$ (R = Ph, ^{i}Pr; E = O, S, Se) systems is presented. The NMR results are discussed in terms of the known HN(R_2PE)$_2$ structures available from X-ray crystallography. The phosphorus chemical shift tensors are found to be sensitive to the nature of the alkyl and chalcogen substituents. The nature of the R group also influences the selenium chemical shift tensors of HN(R_2PSe)$_2$ (R = Ph, ^{i}Pr), which are shown to be sensitive to hydrogen bonding in the dimer structure of HN(Ph$_2$PSe)$_2$ and to the presence of disorder in the case of HN(^{i}Pr$_2$PSe)$_2$. Scalar relativistic ZORA DFT nuclear magnetic shielding tensor calculations were performed yielding the orientations of the corresponding chemical shift tensors. A theoretical investigation into the effect of the E-P···P-E "torsion" angle on the phosphorus and selenium chemical shift tensors of a truncated HN(Me$_2$PSe)$_2$ system indicates that the electronic effect of the alkyl group on the respective nuclear magnetic shielding tensors are more important than the steric effect of the E-P···P-E torsion angle.

Key words: iminobis(diorganophosphine chalcogenide), solid-state NMR, ^{31}P NMR, ^{77}Se NMR, ZORA DFT.

Résumé : On a effectué une étude basée sur les RMN du ^{31}P et du ^{77}Se à l'état solide d'iminobis(chalcogénure de diorganophosphine) HN(R_2PE)$_2$ (R = Ph, ^{i}Pr; E = O, S, Se). On discute des résultats de la RMN en fonction de structures HN(R_2PE)$_2$ connues, disponibles à partir de la diffraction des rayons X. On a trouvé que les tenseurs du déplacement chimique du phosphore sont sensibles à la nature du groupe alkyle et des substituants chalcogènes. La nature du groupe R influence aussi les tenseurs du déplacement chimique du sélénium de HN(R_2PSe)$_2$ (R = Ph, ^{i}Pr) et on a démontré qu'ils sont aussi sensibles à la liaison hydrogène dans la structure dimère du HN(Ph$_2$PSe)$_2$ et à la présence de désordre dans le cas du HN(^{i}Pr$_2$PSe)$_2$. On a effectué des calculs de théorie de la fonctionnelle de densité ZORA scalaires relativistiques du tenseur de blindage magnétique qui ont permis d'obtenir les orientations correspondantes des tenseurs de déplacements chimiques. Une investigation théorique de l'effet de l'angle de torsion E-P···P-E sur les tenseurs du déplacement chimique du phosphore et du sélénium d'un système HN(Me$_2$PSe)$_2$ tronqué indique que l'effet électronique du groupe alkyle sur les tenseurs respectifs de blindage magnétique nucléaire sont plus importants que l'effet stérique de l'angle de torsion E-P···P-E.

Mots-clés : iminobis(chalcogénure de diorganophosphine), RMN à l'état solide, RMN du ^{31}P, RMN du ^{77}Se, calculs de théorie de la fonctionnelle de densité ZORA.

[Traduit par la Rédaction]

Introduction

The coordination of monoanionic bidentate ligands with metal and non-metal centers continues to provide a vast area of research interest. Acetylacetonate (acac) and its β-diketonate derivatives represent the ideological figurehead of monoanionic bidentate coordination chemistry (1). Recently, β-diketonate precursors have been utilized in the fabrication of metal oxide thin films (2) and other chemical vapor deposition applications (3). Interest in related metal chalcogenide materials has spurred the investigation of monoanionic bidentate ligands possessing the corresponding elements of Group 16. Some sulfur- and selenium-containing ligands such as dialkyldichalcogenophosphates, dialkyldichalcogenophosphinates, and dialkyldichalcogenocarbamates have appeared in the literature (4–6); however, their small chalcogen–chalcogen interatomic distances result in the formation of complexes primarily in an anisobidentate fashion (*7*). The iminobis(diorganophosphine chalcogenide) compounds, the so-called non-carbon (main group) analogues of acetylacetone, offer the opportunity to vary the donor chalcogen atom. Also, variation of the alkyl group in these ligands is more easily accessible than for the organic

Received 13 June 2008. Accepted 25 August 2008. Published on the NRC Research Press Web site at canjchem.nrc.ca on 21 November 2008.

This paper is dedicated to Professor Richard J. Puddephatt in honour of his outstanding contributions to Canadian chemistry.

B.A. Demko and R.E. Wasylishen.[2] Department of Chemistry, Gunning–Lemieux Chemistry Centre, University of Alberta, Edmonton, AB T6G 2G2, Canada.

[1]This article is part of a Special Issue dedicated to Professor R. Puddephatt.

[2]Corresponding author (e-mail: roderick.wasylishen@ualberta.ca).

 doi:10.1139/V08-150 © 2008 NRC Canada

Scheme 1. Similarities between the structures of acetylacetone and the iminobis(diorganophosphine chalcogenide) systems.

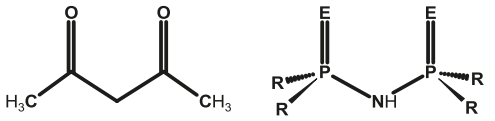

analogues (8). The fine-tuning available for specific metal complexation permits comparisons between the bonding in organic and inorganic analogues, knowledge widely sought throughout the chemistry community (9). While not isoelectronic, acac and dichalcogenoimidodiphosphinate systems are closely related (Scheme 1). An early example of the Group 10 complexes of $[N(Ph_2PSe)_2]^-$ contained heterocyclic MSe_2P_2N rings that were puckered (10), unlike those of acetylacetonate that contain planar six-membered rings (11, 12). This difference has been attributed to the ability of the dichalcogenoimidodiphosphinate ligands to form delocalized systems utilizing low lying d orbitals (10, 13, 14). The structures of these complexes are known to depend on the choice of chalcogen, alkyl group, and metal (13, 15–19). Often, the complexes exhibit symmetrical coordination patterns with the donor chalcogen atoms (8, 20).

Numerous reviews of the versatile dichalcogenoimidodiphosphinate ligands exist in the literature (15, 21–23). In addition to applications as single-source precursors for solid-state metal chalcogenide materials (4–6, 20, 24–29), these bidentate ligands have found uses in the search for stereochemically active lone pairs (10, 19, 30–32), in catalysis (33–35), and in metal extraction processes (15, 36–39), as lanthanide shift reagents (40, 41), luminescent materials (42), and as enzyme mimetics (43–45).

Despite the considerable interest in the properties and chemistry of the complexes of dichalcogenoimidodiphosphinate ligands, relatively little is known about the neutral iminobis(diorganophosphine chalcogenide) $HN(R_2PE)_2$ derivatives (46). Characterization of these systems has predominantly been performed by X-ray crystallography (10, 31, 47–53), often accompanied by IR (31, 54–57), Raman (56, 57), and (or) solution NMR spectroscopy (10, 31, 47, 54, 58). Solid-state NMR, being potentially more informative than solution NMR spectroscopy, would appear to be an appropriate technique for characterizing the $HN(R_2PE)_2$ ligands. Recently, we have demonstrated the use of solid-state NMR spectroscopy in the characterization of the metal(II) complexes of the $[N(^iPr_2PSe)_2]^-$ ligand (59, 60). Herein we present a solid-state ^{31}P and ^{77}Se NMR investigation of the $HN(R_2PE)_2$ (E = O, S, Se; R = Ph, ^{i}Pr) systems representing the first solid-state NMR investigation of the iminobis(diorganophosphine chalcogenides). Comparisons of the solid-state NMR results obtained herein with those of the $M[N(^iPr_2PSe)_2]_2$ complexes previously investigated are made, where appropriate (59, 60).

Experimental

Sample preparation

The phenyl and isopropyl variants of bis(diorganophosphino)amine $HN(R_2P)_2$ were prepared via the condensation reaction between hexamethyldisilazane $HN(SiMe_3)_2$ and the appropriate chlorodiorganophosphine R_2PCl (Sigma-Aldrich) (55, 61). Briefly, R_2PCl in toluene is added dropwise to a hot toluene solution of $HN(SiMe_3)_2$ and is maintained above 80 °C for at least two hours to remove the chlorotrimethylsilane by-product by distillation. Oxidation to the corresponding iminobis(diorganophosphine chalcogenide) was achieved from the subsequent reaction with hydrogen peroxide in an ice bath (55, 62) and via reflux with either elemental sulfur (55) or elemental selenium (10, 20). X-ray crystal structures from the literature, for each of the investigated iminobis(diorganophosphine chalcogenide) systems, $HN(R_2PE)_2$ (E = O; R = Ph (*50*) and ^{i}Pr (31), E = S; R = Ph (50–52) and ^{i}Pr (47), E = Se; R = Ph (10) and ^{i}Pr (31)), have been previously reported.

NMR experiments

Solid-state NMR investigations of powdered samples of $HN(R_2PE)_2]_2$ (E = O, S, Se; R = Ph, ^{i}Pr) were obtained using 4.70 T, 7.05 T, and 11.75 T NMR spectrometers. The samples were packed in 4 mm (7.05 T and 11.75 T) and 7.5 mm (4.70 T) o.d. zirconium oxide rotors and were placed within probes suitable for magic angle spinning, MAS, NMR experiments. A ramped amplitude cross polarization (RACP) pulse sequence was used to acquire all spectra (63). Two-pulse phase-modulation (TPPM) (64) and proton decoupling fields of approximately 60 kHz were utilized. The ^{31}P NMR spectra were referenced with respect to 85% aq. H_3PO_4 by setting the isotropic ^{31}P NMR peak of solid $(NH_4)H_2PO_4$ to 0.81 ppm (65). Selenium-77 NMR spectra were referenced to Me_2Se (l) by setting the isotropic peak of solid ammonium selenate $(NH_4)_2SeO_4$ to 1040.2 ppm (65, 66).

Solid-state ^{31}P NMR experiments were performed at Larmor frequencies of 81.0, 121.6, and 202.5 MHz, and at spinning frequencies ranging from 3.0 to 7.2 kHz. A total of between 64 and 128 scans were acquired per spectrum. Contact times between 1.5 and 6.5 ms, and pulse delays between 600 and 840 s for $HN(Ph_2PE)_2$ systems and between 7 and 18 s for the $HN(^iPr_2PE)_2$ systems were employed.

Solid-state ^{77}Se NMR measurements were performed at Larmor frequencies of 38.2, 57.3, and 95.4 MHz, and at spinning frequencies ranging from 2.0 to 14.0 kHz. A total of between 384 and 16 384 scans were acquired per spectrum. Contact times between 6.5 and 10.0 ms, and pulse delays between 600 and 840 s for $HN(Ph_2PE)_2$ species and between 5 and 14 s for the $HN(^iPr_2PE)_2$ systems were employed.

The principal components of the respective phosphorus and selenium chemical shift tensors, $\delta_{11} \geq \delta_{22} \geq \delta_{33}$, were determined from the experimental spectra using the procedure of Herzfeld and Berger (67, 68). All experimental solid-state NMR spectra were simulated using the determined values with the program WSOLIDS (69) to assess the quality of the obtained parameters. This procedure results in errors of ±0.2 ppm in the isotropic chemical shift, $\delta_{iso} = (1/3)(\delta_{11} + \delta_{22} + \delta_{33})$, and errors in the principal components of approximately 1%–3% of the span, $\Omega = \delta_{11} - \delta_{33}$, of the respective chemical shift tensors. Another useful quantity for describing the appearance of chemical shift powder patterns is the skew, $\kappa = 3(\delta_{22} - \delta_{iso})/\Omega$, where axial symmetry is described by $\kappa = +1$ or -1 (70).

© 2008 NRC Canada

DFT computations

Theoretical calculations of NMR parameters were performed on isolated molecules. Cartesian coordinates of the atoms were generated from the reported crystal structures placing hydrogen atoms at idealized locations (r_{CH} = 1.08 Å (R = Ph), 1.09 Å (R = ^{i}Pr)). Magnetic shielding tensors σ were calculated using the NMR module (71–73) of the Amsterdam density functional (ADF) program package (74–78). The Vosko–Wilk–Nusair (79) local density approximation with the Becke88–Perdew86 (80–82) generalized gradient approximation were used for the exchange-correlation functional. Scalar relativistic corrections were carried out based on the implementation of the zero-order regular approximation (ZORA) formalism (83–86). Triple-ζ doubly polarized (TZ2P) Slater-type ZORA basis sets were used for all atoms except for hydrogen, where double-ζ quality (DZ) basis functions were utilized. The corresponding phosphorus and selenium chemical shift tensors were obtained from the magnetic shielding tensors using the relationship,

$$[1] \qquad \delta_{ii}(\text{sample}) = \frac{\sigma_{\text{iso}}\ (\text{ref}) - \sigma_{ii}(\text{sample})}{1 - \sigma_{\text{iso}}\ (\text{ref})}$$

where σ_{iso}(ref) is the isotropic shielding of a standard reference. The absolute shielding scale for ^{31}P has been determined, and the value of σ_{iso} (85% aq. H_3PO_4) has been established to be 328.35 ppm (87). We have previously investigated the selenium chemical shift tensors in a wide range of selenium-containing compounds and used the value of 1580 ppm determined therein for the isotropic reference shielding of a neat liquid of dimethyl selenide at 23 °C (*88*).

Results and discussion

A common difference between the R = Ph and R = ^{i}Pr structures of the HN(R_2PE)$_2$ systems is that while the EPNPE backbones in iminobis(diphenylphosphine chalcogenide) species are oriented *anti*, the HN(^{i}Pr$_2$PE)$_2$ (E = O, S, Se) molecules all possess *gauche* conformations (Fig. 1). X-ray diffraction studies of each of the iminobis(diorganophosphine chalcogenides) investigated here indicate that the crystals contain one molecule in the asymmetric unit. The reported structure for HN(Ph_2PO)$_2$ contains an inversion center providing chemical equivalence between the two phosphorus atoms such that only a single phosphorus chemical shift tensor is expected for this sample. The remaining samples investigated, HN(Ph_2PE)$_2$ (E = S, Se) and HN(^{i}Pr$_2$PE)$_2$ (E = O, S, Se), do not possess any symmetry elements within their respective molecular structures providing chemical equivalence between the two phosphorus (or two selenium) atoms, thus two distinct phosphorus (or selenium) chemical shift tensors are expected in the experimental NMR spectra. The obtained phosphorus chemical shift tensors for the iminobis(diorganophosphine chalcogenide) systems are presented first, followed by the results of a solid-state ^{77}Se NMR study on HN(R_2PSe)$_2$ (R = Ph, ^{i}Pr). As the syntheses of the phenyl-derivatized species were reported prior to the isopropyl variants, the results for HN(Ph_2PE)$_2$ will precede those for HN(^{i}Pr$_2$PE)$_2$. The extracted NMR parameters are discussed in terms of the known molecular structures, highlighting the impact in the choice of R group and (or) chalcogen where applicable. DFT computations are used to provide the orientations of the phosphorus and selenium nuclear magnetic shielding tensors.

Fig. 1. Common conformations encountered in iminobis(diorganophosphine chalcogenide), HN(R_2PE)$_2$ (E = O, S, Se), systems.

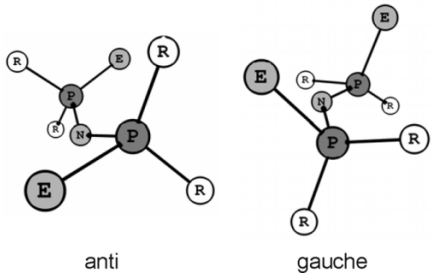

Solid-state ^{31}P NMR

The ^{31}P NMR parameters obtained for each of the HN(R_2PE)$_2$ (E = O, S, Se; R = Ph, ^{i}Pr) samples investigated are given in Table 1, along with theoretical calculations of the corresponding phosphorus chemical shift tensors. Experimental solid-state ^{31}P NMR spectra for HN(R_2PO)$_2$, HN(R_2PS)$_2$, and HN(R_2PSe)$_2$ are given in Figs. 2, 5, and 6, respectively.

HN(R_2PO)$_2$ (R = Ph, ^{i}Pr)

For the phenyl derivative, the imidodiphosphinic acid tautomer $Ph_2P(OH)NP(O)Ph_2$ (50) was found instead of the initially hypothesized HN(Ph_2PO)$_2$ structure (48, 49), which possesses an acidic N-H proton. As a result, $Ph_2P(OH)NP(O)Ph_2$ has a considerably different structure from the other iminobis(diorganophosphine chalcogenide) systems investigated that all display acidic N-H protons. Similar to the HN(Ph_2PE)$_2$ (E = S, Se) molecules that possess a solid-state structure in which the EPNPE backbone adopts an *anti* conformation, $Ph_2P(OH)NP(O)Ph_2$ is *trans* with an O-P···P-O "torsion" angle of 180° (50). However, unique to the $Ph_2P(OH)NP(O)Ph_2$ system is a linear P-N-P angle of 180° (50). The solid-state ^{31}P NMR spectrum is given, along with its simulation, in Fig. 2*a*. Contrary to the single phosphorus environment expected from the crystal structure of $Ph_2P(OH)NP(O)Ph_2$ (50), two phosphorus chemical shift tensors were extracted (Table 1), which possess isotropic chemical shifts and spans that differ by more than 20 ppm despite the two tensors possessing similar skews. As the ^{31}P NMR spectrum (not shown) of a chloroform solution of $Ph_2P(OH)NP(O)Ph_2$ displays only a single peak, the solid sample investigated, as obtained from a methylene chloride – hexanes recrystallization, must be of a different polymorph of $Ph_2P(OH)NP(O)Ph_2$ than the reported structure from a crystal grown in glacial acetic acid (50).

Phosphorus chemical shift tensors from the DFT computations of a single $Ph_2P(OH)NP(O)Ph_2$ unit from the reported crystal structure (50) (Table 1) produce comparable values of δ_{iso}, δ_{ii}, Ω, and κ with the experimentally determined parameters; however, they do not predict an equally large difference between the two respective isotropic chemical shifts. This discrepancy is likely a result of using the geometry from the reported crystal structure, which is not entirely representative of the actual solid-state structure of the solid

© 2008 NRC Canada

Table 1. Solid-state ^{31}P NMR parameters for HN(R_2PE)$_2$ (E = O, S, Se; R = Ph, ^{i}Pr).

E	R		δ_{iso} (ppm)	δ_{11} (ppm)	δ_{22} (ppm)	δ_{33} (ppm)	Ω (ppm)	κ	^1J(Se,P)$_{iso}$[a] (Hz)
O	Ph	(Exptl.)	8.2	79.6	13.3	–68.2	147.8	0.10	
			28.4	109.5	38.6	–62.8	172.3	0.18	
		(Calcd.)	19.0	85.7	35.8	–64.6	150.3	0.34	
			24.4	127.4	51.6	–105.9	233.3	0.35	
	^{i}Pr	(Exptl.)	52.5	101.8	101.8	–46.0	147.8	1.00	
			57.7	112.7	89.2	–28.8	141.5	0.67	
		(Calcd. a)	62.2	137.9	124.0	–75.2	213.1	0.87	
			68.9	144.3	123.9	–61.4	205.7	0.80	
		(Calcd. b)	59.1	131.1	122.3	–76.2	207.3	0.92	
			69.1	144.7	124.0	–61.4	206.1	0.80	
S	Ph	(Exptl.)	54.7	155.7	77.5	–69.2	224.9	0.30	
			57.1	164.0	92.7	–85.5	249.5	0.43	
		(Calcd.)	75.4	203.9	129.2	–106.9	310.8	0.52	
			76.5	195.3	118.0	–83.8	279.1	0.45	
	^{i}Pr	(Exptl.)	89.1	155.0	121.7	–9.4	164.4	0.60	
			90.6	163.0	118.5	–9.7	172.7	0.48	
		(Calcd.)	102.2	206.1	142.6	–41.9	248.0	0.49	
			108.2	190.3	164.3	–29.9	220.2	0.76	
Se	Ph	(Exptl.)	48.9	149.5	62.5	–65.2	214.7	0.19	–720
			52.4	160.4	79.9	–83.1	243.5	0.34	–740
		(Calcd.)	98.6	235.0	139.3	–78.6	313.6	0.39	
			101.8	249.3	153.9	–97.8	347.1	0.45	
	^{i}Pr	(Exptl.)	88.8	152.0	113.7	0.7	151.3	0.49	–740
			91.1	160.4	110.3	2.6	157.8	0.36	–735
		(Calcd. a)	129.8	245.8	170.2	–26.5	272.3	0.44	
			130.3	215.2	192.8	–17.1	232.3	0.81	
		(Calcd. b)	129.9	243.4	170.9	–24.6	268.0	0.46	
			130.5	225.2	184.4	–18.3	243.5	0.66	

[a]For directly bonded selenium-77 and phosphorus-31 spin pairs; signs of $^1J(^{77}Se,^{31}P)_{iso}$ are known to be negative for numerous analogous systems (95, 96).

sample investigated, as well as the neglect of intermolecular effects including potential hydrogen bonding between $Ph_2P(OH)NP(O)Ph_2$ molecules. Additionally, the computations indicate that the phosphorus bearing the hydroxyl group is more shielded than the P=O phosphorus in $Ph_2P(OH)NP(O)Ph_2$. The calculated orientations of the two phosphorus chemical shift tensors are also different, as shown in Fig. 3*a*. The computed P-OH phosphorus chemical shift tensor is oriented with δ_{11} perpendicular to the local O-P-N plane, and δ_{33} approximately parallel to the P-N vector with δ_{22} within the O-P-N plane and perpendicular to P-N. The calculated P=O phosphorus chemical shift tensor places δ_{11} perpendicular to the local O-P-N plane, while in contrast δ_{33} is oriented nearly parallel to the P-O vector with δ_{22} within the O-P-N plane and perpendicular to P-O. The orientation of the P=O phosphorus chemical shift tensor is similar to what is consistently found for tris-organophosphine oxides (89).

One of the largest differences between HN(^{i}Pr$_2$PO)$_2$ and $Ph_2P(OH)NP(O)Ph_2$ is that iminobis(diisopropylphosphine oxide) possesses an acidic N-H proton leading to a P-N-P angle of 130° (31). The *gauche* conformation of HN(^{i}Pr$_2$PO)$_2$, reflected in a 52° O-P···P-O "torsion" angle, yields a chain-like arrangement of HN(^{i}Pr$_2$PO)$_2$ units in its solid state structure (31). The X-ray structure of HN(^{i}Pr$_2$PO)$_2$ displays some disorder in that one methyl carbon on one isopropyl group possesses two 50% occupancy sites (31). There exists three spinning sideband manifolds corresponding to three discernable signals in the ^{31}P MAS spectrum of HN(^{i}Pr$_2$PO)$_2$ given in Fig. 2*b*; however, as one of the three signals is significantly less intense than the other two it is considered to be a minor impurity in the sample rather than resulting from disorder in the structure. The impurity can be readily identified in Fig. 2*b* by comparison of the experimental with the simulated spectrum. The two isotropic phosphorus chemical shifts obtained (Table 1) are in good agreement with the ^{31}P NMR value from a chloroform solution of HN(^{i}Pr$_2$PO)$_2$, i.e., 55.5 ppm (31). The phosphorus environments are deshielded with respect to those of $Ph_2P(OH)NP(O)Ph_2$ and possess slightly smaller spans and larger positive skews. The steric or electronic source of this difference will be discussed later. One phosphorus environment indicates an axially symmetric chemical shift tensor despite there being no symmetry reasons for attaining this axial symmetry. Methods for obtaining accurate principal components of the chemical shift tensor from spectra of MAS samples are known to have the greatest difficulty with axially or near axially symmetric species (90).

Calculated phosphorus chemical shift tensors were obtained for both of the 50% occupancy structures (31), labeled "a" and "b" in the Table 1. Both phosphorus chemical shift tensors computed for each of the two structures are in

© 2008 NRC Canada

Fig. 2. (*a*) RACP MAS ^{31}P NMR spectrum (lower trace) for $Ph_2P(OH)NP(O)Ph_2$ and its simulation (upper trace). Experimental conditions: 11.75 T, 64 scans, MAS at 3.0 kHz, 10 Hz of line broadening, 3.0 ms contact time, and 900 s recycle delay. (*b*) RACP MAS ^{31}P NMR spectrum (lower trace) for $HN(^iPr_2PO)_2$ and its simulation (upper trace). Experimental conditions: 11.75 T, 128 scans, MAS at 3.0 kHz, 10 Hz of line broadening, 3.0 ms contact time, and 18 s recycle delay. The isotropic peaks are marked with an asterisk (*).

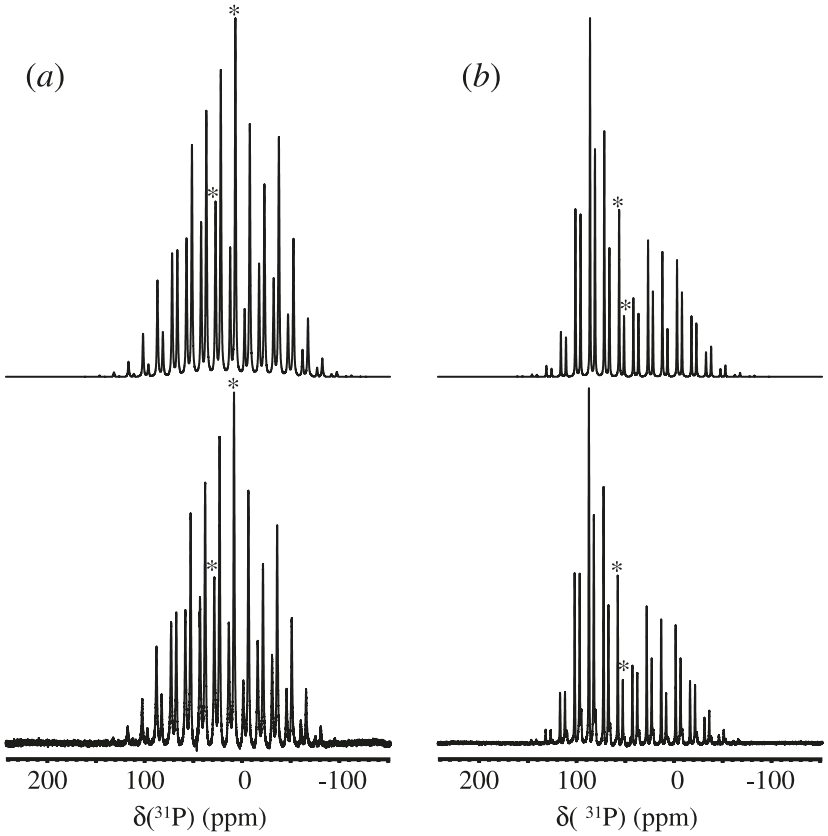

reasonable agreement with the experimental values. The values of δ_{ii}(calcd.) are quite similar for structures "a" and "b", suggesting that the presence of disorder in the methyl group does not significantly affect the phosphorus shielding in $HN(^iPr_2PO)_2$. This is consistent with the solid-state ^{31}P NMR spectrum (Fig. 2*b*) where no discernable difference in the obtained line widths or line shapes of the two phosphorus environments was detected. In contrast to the calculated orientations of the phosphorus chemical shift tensors in $Ph_2P(OH)NP(O)Ph_2$, all phosphorus tensors for $HN(^iPr_2PO)_2$ are oriented similarly (Fig. 3*b*). The computations place δ_{33} approximately along the O-P vector, and δ_{22} perpendicular to the local O-P-N plane, with δ_{11} perpendicular to O-P within the O-P-N plane.

$HN(R_2PS)_2$ (R = Ph, ^{i}Pr)

The *anti* conformation of $HN(Ph_2PS)_2$, with a S-P···P-S torsion angle of 156° is similar to that of $Ph_2P(OH)NP(O)Ph_2$, while the P-N-P angle of 133° is consistent with a PNP backbone that possesses a protonated nitrogen (50–52). The solid state structure consists of two $HN(Ph_2PS)_2$ molecules hydrogen bonded to form dimer pairs (Fig. 4) (50–52). The ^{31}P NMR parameters obtained from the RACP MAS spectrum for $HN(Ph_2PS)_2$ (Fig. 5*a*) are given in Table 1. The isotropic chemical shifts obtained are in good agreement with the solution ^{31}P NMR values of 55.1 ppm in THF (54) and 58.2 ppm in $CDCl_3$ (58). The phosphorus chemical shift tensors of $HN(Ph_2PS)_2$ describe phosphorus nuclei that are more deshielded, possess larger spans, and have slightly more positive values of κ than those obtained for $Ph_2P(OH)NP(O)Ph_2$.

The DFT computations were performed on a dimer of $HN(Ph_2PS)_2$ units. The calculated principal components of the respective phosphorus chemical shift tensors slightly overestimate the corresponding experimental values. The orientations of the two calculated phosphorus chemical shift tensors (Fig. 3*c*) are nearly identical and most closely resemble those calculated for the P=O phosphorus of $Ph_2P(OH)NP(O)Ph_2$, with δ_{33} approximately parallel to the P-S vector, δ_{11} perpendicular to the local S-P-N plane, and δ_{22} nearly within the S-P-N plane perpendicular to P-S. These orientations are consistent with those obtained for tris-organophosphine sulfide systems (89) and similar to those found in tetramethyldiphosphine disulfide (91).

Similar to that of $HN(^iPr_2PO)_2$, the structure of $HN(^iPr_2PS)_2$ contains a 132° P-N-P angle; however, the S-P···P-S torsion angle is slightly larger at 79° and the X-ray structure reports no evidence of disorder (47). The solid-state ^{31}P NMR spectrum of $HN(^iPr_2PS)_2$ is given in Fig. 5*b*. The isotropic chemical shifts for the two phosphorus environments are in good agreement with the value of 91.2 ppm reported for $HN(^iPr_2PS)_2$ in $CDCl_3$ (47). Similar to the chemical shift tensors describing the phosphorus shielding of $HN(Ph_2PS)_2$ and $Ph_2P(OH)NP(O)Ph_2$, the two phosphorus

© 2008 NRC Canada

Fig. 3. Calculated phosphorus chemical shift tensor orientations for (*a*) $Ph_2P(OH)NP(O)Ph_2$, (*b*) $HN(^iPr_2PO)_2$, (*c*) $HN(Ph_2PS)_2$, (*d*) $HN(^iPr_2PS)_2$, (*e*) $HN(Ph_2PSe)_2$, and (*f*) $HN(^iPr_2PSe)_2$.

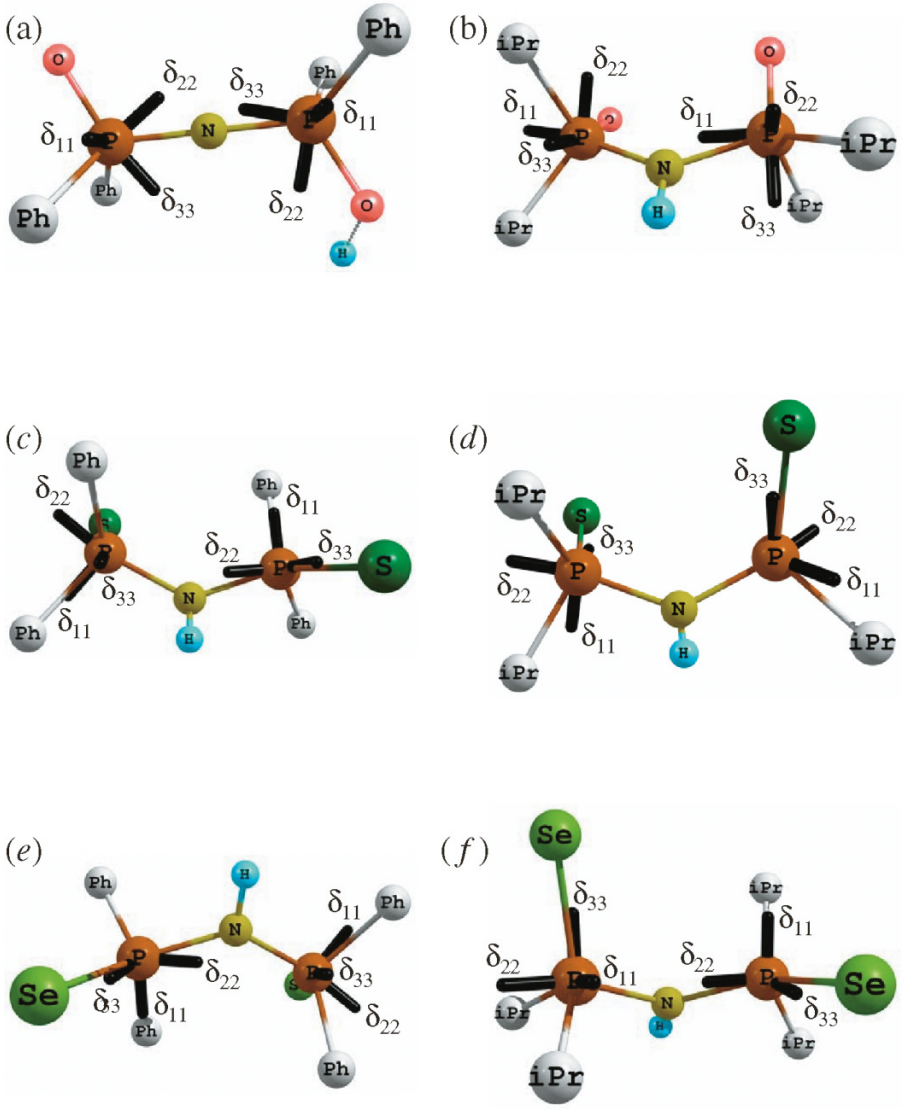

Fig. 4. Dimer structure of $HN(Ph_2PE)_2$ (E = S, Se).

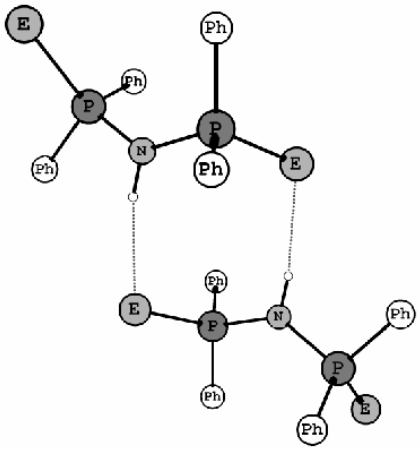

environments of $HN(^iPr_2PS)_2$ are more deshielded and possess larger spans than those for $HN(^iPr_2PO)_2$. Solution ^{31}P NMR for the mixed chalcogen system $^iPr_2P(O)NHP(S)^iPr_2$ displays a comparable difference in the values of $\delta_{iso}(^{31}P)$, 54.8 and 90.9 ppm (31). Additionally, as with the E = O compounds, the phosphorus sites in $HN(^iPr_2PS)_2$ are more deshielded and have larger positive skews than the phenyl derivative.

Calculated phosphorus chemical shift tensors for $HN(^iPr_2PS)_2$ are given in Table 1. The computed values of δ_{iso}, δ_{ii}, Ω, and κ are in reasonable agreement with the experimentally obtained parameters. As observed with the calculated orientation of the tensors in $HN(^iPr_2PO)_2$, the two phosphorus chemical shift tensors for $HN(^iPr_2PS)_2$ (Fig. 3*d*) are approximately identical and place δ_{33} nearly parallel to the E-P vector; however, the directions of δ_{11} and δ_{22} are essentially reversed in $HN(^iPr_2PS)_2$ with respect to $HN(^iPr_2PO)_2$, with δ_{11} perpendicular to the local S-P-N plane and δ_{22} within the S-P-N plane perpendicular to S-P.

© 2008 NRC Canada

Fig. 5. (*a*) RACP MAS ^{31}P NMR spectrum (lower trace) for $HN(Ph_2PS)_2$ and its simulation (upper trace). Experimental conditions: 11.75 T, 64 scans, MAS at 3.0 kHz, 10 Hz of line broadening, 3.0 ms contact time, and 900 s recycle delay. (*b*) RACP MAS ^{31}P NMR spectrum (lower trace) for $HN(^iPr_2PS)_2$ and its simulation (upper trace). Experimental conditions: 11.75 T, 128 scans, MAS at 3.0 kHz, 5 Hz of line broadening, 3.0 ms contact time, and 9 s recycle delay. The isotropic peaks are marked with an asterisk (*).

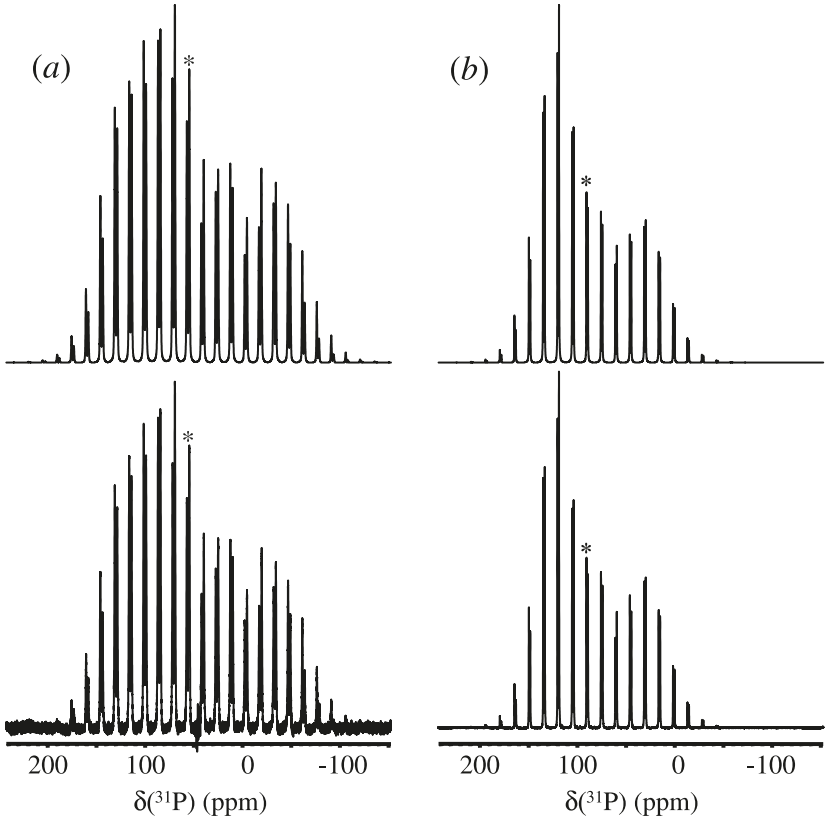

$HN(R_2PSe)_2$ (R = Ph, ^{i}Pr)

Isomorphous with $HN(Ph_2PS)_2$, the dimer structure of $HN(Ph_2PSe)_2$ possesses an *anti* conformation with a Se-P···P-Se torsion angle of 154° and a P-N-P angle of 132° (10). The phosphorus chemical shift parameters, along with an estimation of the one-bond selenium–phosphorus indirect spin–spin coupling constant $^1J(^{77}Se,^{31}P)_{iso}$ from the MAS ^{31}P NMR spectrum (Fig. 6*a*) are reported in Table 1. The values of $\delta_{iso}(^{31}P)$ and $^1J(^{77}Se,^{31}P)_{iso}$ obtained are in good agreement with those from ^{31}P NMR of methylene chloride and chloroform solutions of $HN(Ph_2PSe)_2$, 53.0 ppm and (–)793 Hz (10), and 53.2 ppm (58), respectively. The principal components of the phosphorus chemical shift tensors are very similar to those found for $HN(Ph_2PS)_2$ (Table 1) indicating that the impact of exchanging oxygen for sulfur in $HN(Ph_2PE)_2$ is larger than exchanging sulfur for selenium.

The phosphorus chemical shift tensors were calculated for a dimer of $HN(Ph_2PSe)_2$ molecules (10). The calculations overestimate the values of δ_{iso} and Ω, indicating that scalar relativistic effects may not be sufficient to accurately describe the shielding environment for $HN(Ph_2PSe)_2$, and that spin–orbit relativistic effects may be important. Similar to those of $HN(Ph_2PS)_2$, the calculated orientations of the phosphorus chemical shift tensors in $HN(Ph_2PSe)_2$ (Fig. 3*e*) place δ_{11} perpendicular to the local Se-P-N plane, δ_{33} approximately along the P-Se vector, and δ_{22} within the Se-P-N plane perpendicular to P-Se. This orientation is similar to that found for tris-organophosphine selenides (89).

The structure of $HN(^iPr_2PSe)_2$ more closely resembles that of $HN(^iPr_2PS)_2$ with an 80° Se-P···P-Se torsion angle and a P-N-P angle of 131° (31). However, similar to the structure of $HN(^iPr_2PO)_2$, the selenium analogue was refined where the location of one methyl carbon on one isopropyl group contained two 50% occupancy locations (31). The isotropic chemical shifts and $^1J(^{77}Se,^{31}P)_{iso}$ values extracted (Table 1) from the simulation of the solid-state ^{31}P NMR spectrum of $HN(^iPr_2PSe)_2$ (Fig. 6*b*) are in good agreement with those from a chloroform solution ^{31}P NMR study, 89.5 ppm and (–)757 Hz (31). Similar to the solid-state ^{31}P NMR spectrum of $HN(^iPr_2PO)_2$ (Fig. 2*b*), no evidence for the disorder in the methyl group was detected in the corresponding spectrum for iminobis(diisopropylphosphine selenide). As with the phosphorus chemical shift tensors of $HN(Ph_2PE)_2$ (E = S, Se), the two tensors for $HN(^iPr_2PSe)_2$ are comparable to those found for $HN(^iPr_2PS)_2$ (Table 1). The isotropic phosphorus chemical shifts of the mixed chalcogen compound $^iPr_2P(S)NHP(Se)^iPr_2$ from a chloroform solution ^{31}P NMR study are also very similar at 89.2 and 92.1ppm (31).

Phosphorus chemical shift tensors were calculated for both of the 50% occupancy structures (31), labeled "a" and "b" in Table 1. The scalar relativistic calculated phosphorus

© 2008 NRC Canada

Fig. 6. (*a*) RACP MAS ^{31}P NMR spectrum (lower trace) for $HN(Ph_2PSe)_2$ and its simulation (upper trace). Experimental conditions: 11.75 T, 64 scans, MAS at 3.0 kHz, 10 Hz of line broadening, 3.0 ms contact time, and 900 s recycle delay. (*b*) RACP MAS ^{31}P NMR spectrum (lower trace) for $HN(^iPr_2PSe)_2$ and its simulation (upper trace). Experimental conditions: 11.75 T, 128 scans, MAS at 3.0 kHz, 10 Hz of line broadening, 3.0 ms contact time, and 18 s recycle delay. The isotropic peaks are marked with an asterisk (*).

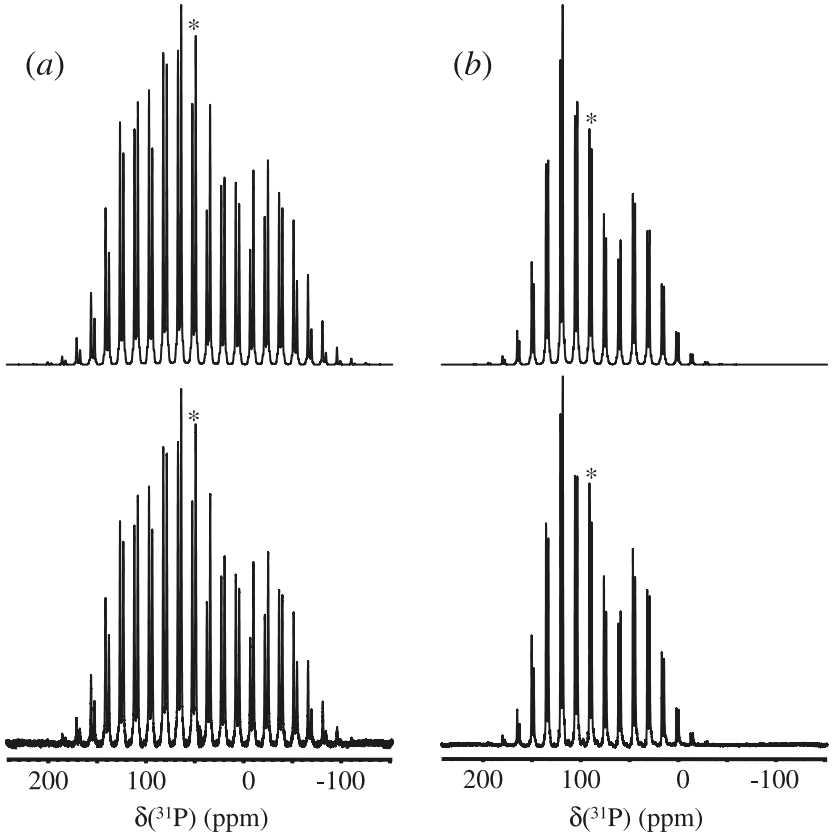

chemical shift tensors for $HN(^iPr_2PSe)_2$, as with those for $HN(Ph_2PSe)_2$, overestimate the experimental values. Analogous to those for $HN(^iPr_2PO)_2$, the calculated phosphorus chemical shift tensors for $HN(^iPr_2PSe)_2$ structures "a" and "b" are nearly identical and suggest that evidence for the disorder is unlikely to come from the solid-state ^{31}P NMR spectrum. As with the calculated orientations of the phosphorus chemical shift tensors in $HN(^iPr_2PO)_2$, all four tensors for iminobis(diisopropylphosphine selenide) are identical, as shown in Fig. 3*f*. They are all oriented similarly to those of $HN(^iPr_2PS)_2$ with δ_{33} near the P-Se vector, δ_{11} perpendicular to the local Se-P-N plane, and δ_{22} within the Se-P-N plane perpendicular to the P-Se vector.

Solid-state ^{77}Se NMR

The solid-state ^{77}Se NMR spectrum for $HN(Ph_2PSe)_2$ is given in Fig. 7*a* and the ^{77}Se NMR parameters extracted from its simulation are reported in Table 2. The values of $^1J(^{77}Se,^{31}P)_{iso}$ obtained are in agreement with those from solution ^{31}P NMR (10) and with our solid-state ^{31}P NMR values (Table 1) above. Similar to the large difference in isotropic phosphorus chemical shifts observed for $Ph_2P(OH)NP(O)Ph_2$, there is a significant difference between the two values of δ_{iso}(Se) in $HN(Ph_2PSe)_2$. The spans of the selenium chemical shift tensors are both larger than any of the phosphorus chemical shift tensors, which is consistent with the less symmetric environment of selenium in the iminobis(diorganophosphine chalcogenide) systems and the larger chemical shift range of selenium with respect to that of phosphorus (92, 93).

The dimer structure of $HN(Ph_2PSe)_2$ (Fig. 4) was used to calculate the selenium chemical shift tensors. The computed principal components are in good agreement with the experimental values, particularly in the difference in shielding between the two chemical shift tensors. The calculations indicate that the selenium that participates in hydrogen bonding between the two $HN(Ph_2PSe)_2$ molecules is less shielded than the selenium that is not involved in hydrogen bonding. The calculated orientations of the two selenium chemical shift tensors are also different (Fig. 8*a*). For the selenium involved in hydrogen bonding between the dimers, δ_{33} is nearly parallel to the Se-P vector, δ_{11} is perpendicular to the local Se-P-N plane, and δ_{22} is within the Se-P-N plane perpendicular to Se-P. The selenium that is not involved in hydrogen bonding possesses a chemical shift tensor that orients δ_{22} approximately along Se-P, with δ_{11} perpendicular to the local Se-P-N plane, and δ_{33} within the Se-P-N plane perpendicular to Se-P.

The ^{77}Se NMR parameters obtained from the solid-state ^{77}Se NMR spectrum for $HN(^iPr_2PSe)_2$ (Fig. 7*b*) are given in Table 2. The two $^1J(^{77}Se,^{31}P)_{iso}$ obtained are in good agreement with the reported values from solution (31) and solid-

© 2008 NRC Canada

Fig. 7. (*a*) RACP MAS ^{77}Se NMR spectrum (lower trace) for HN($Ph_2PSe)_2$ and its simulation (upper trace). Experimental conditions: 11.75 T, 384 scans, MAS at 3.0 kHz, 50 Hz of line broadening, 10.0 ms contact time, and 840 s recycle delay. (*b*) RACP MAS ^{77}Se NMR spectrum (lower trace) for HN($^i Pr_2PSe)_2$ and its simulation (upper trace). Experimental conditions: 11.75 T, 5288 scans, MAS at 6.0 kHz, 50 Hz of line broadening, 6.5 ms contact time, and 14 s recycle delay. The isotropic peaks are marked with an asterisk (*).

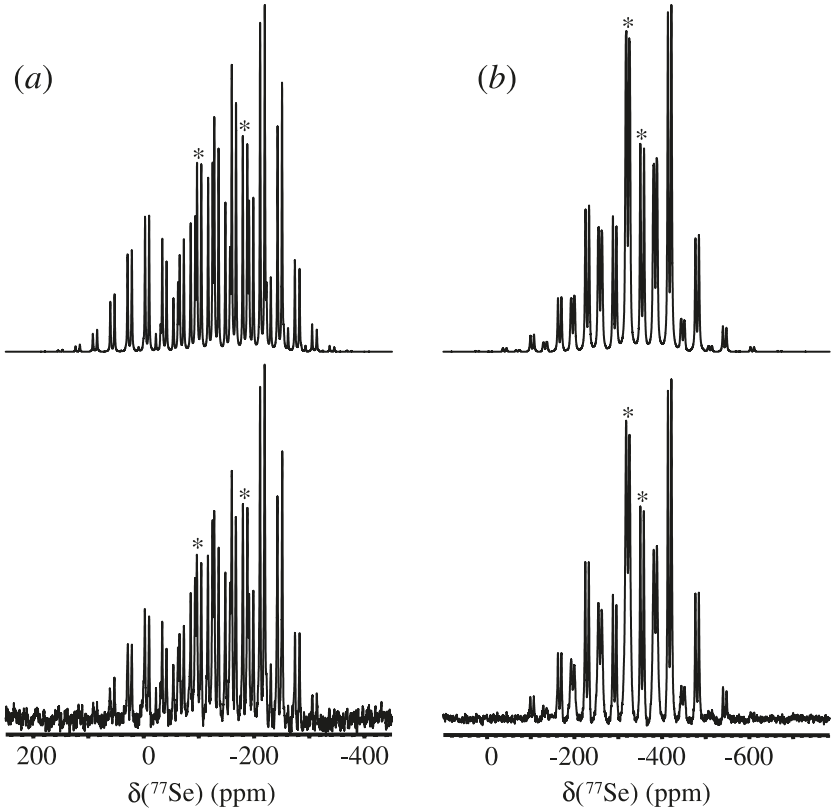

state (above) ^{31}P NMR. Unlike those for HN($Ph_2PSe)_2$, the two isotropic selenium chemical shifts for iminobis(diisopropylphosphine selenide) are more shielded and significantly closer together. In contrast to the solid-state ^{31}P NMR spectra for HN($^i Pr_2PE)_2$ (E = O, Se), the solid-state ^{77}Se NMR spectrum for HN($^i Pr_2PSe)_2$ appears to be sensitive to the disorder of the methyl group in the structure (31). Figure 9 displays the isotropic region of the solid-state ^{77}Se NMR spectra for HN($R_2PSe)_2$ (R = Ph, ^{i}Pr), where one of the two J-coupled isotropic peaks for HN($^i Pr_2PSe)_2$ is visibly broader than the other.

The two calculated selenium chemical shift tensors for each of the two 50% occupancy structures also suggest that the impact of the disorder of the methyl group should be more pronounced in the solid-state ^{77}Se NMR spectrum; however, the calculations indicate that both selenium environments should be influenced by the disorder. The calculations predict that the selenium environment that is furthest from the methyl group should be affected more than the proximal selenium. The calculated orientations of the selenium chemical shift tensors (Fig. 8*b*) are identical for structures "a" and "b", yet distinct. The chemical shift tensor for the selenium distal to the methyl disorder is oriented such that δ_{33} is nearly along the Se-P vector, δ_{11} is perpendicular to the local Se-P-N plane, while δ_{22} lies within the Se-P-N plane perpendicular to Se-P. The selenium nearest the methyl disorder possesses a calculated chemical shift tensor that also places δ_{11} approximately perpendicular to the local Se-P-N plane; however, the P-Se vector nearly bisects the δ_{22}-Se-δ_{33} angle within the Se-P-N plane.

Iminobis(diorganophosphine selenide) vs. diselenoimidodiphosphinato complexes

Upon comparison with the phosphorus and selenium chemical shift tensors of the M[N($^i Pr_2PSe)_2]_2$ complexes previously investigated (59, 60), there are some consistent changes in the calculated orientations of the phosphorus and selenium chemical shift tensors of HN($^i Pr_2PSe)_2$ upon deprotonation and complexation with a cationic center. The phosphorus chemical shift tensors in the diselenoimidodiphosphinato complexes are all oriented similarly, with δ_{33} nearly parallel to the P-N bond vector, δ_{11} perpendicular to the local Se-P-N vector, and δ_{22} within the Se-P-N plane perpendicular to the P-N vector (59, 60). This is in contrast to the majority of the phosphorus chemical shift tensors where δ_{33} is nearly parallel to the P-E vector, and most closely resembles the orientation of the phosphorus chemical shift tensor for the P-OH environment in $Ph_2P(OH)NP(O)Ph_2$. The change in the orientation of the selenium chemical shift tensor upon complexation is not quite as predictable. When [N($^i Pr_2PSe)_2]^-$ is coordinated with a Group 10 (Pd or Pt) or 12 (Zn, Cd or Hg) metal center, the orientation of the selenium chemical shift tensor remains essentially identical to that found in HN($^i Pr_2PSe)_2$ with δ_{33} nearly parallel to the P-Se vector, δ_{11} perpendicular to the local Se-P-N plane, and δ_{22} perpendicular to the P-Se vector (59, 60). However, when

© 2008 NRC Canada

Table 2. Solid-state ^{77}Se NMR parameters for HN(R_2PSe)$_2$ (R = Ph, ^{i}Pr).

R		δ_{iso} (ppm)	δ_{11} (ppm)	δ_{22} (ppm)	δ_{33} (ppm)	Ω (ppm)	κ	^1J(Se,P)$_{iso}$[a] (Hz)
Ph	(Exptl.)	–184	–41	–219	–291	250	–0.42	–800
		–101	79	–146	–236	317	–0.43	–740
	(Calcd.)	–201	–30	–248	–325	295	–0.48	
		–115	97	–133	–331	408	–0.13	
^{i}Pr	(Exptl.)	–355	–135	–419	–511	376	–0.51	–760
		–322	–179	–352	–435	256	–0.36	–720
	(Calcd. a)	–495	–140	–609	–735	595	–0.58	
		–436	–222	–512	–575	353	–0.64	
	(Calcd. b)	–518	–307	–608	–638	331	–0.82	
		–465	–265	–528	–603	337	–0.55	

[a]For directly bonded selenium-77 and phosphorus-31 spin pairs; signs of $^1J(^{77}Se,^{31}P)_{iso}$ are known to be negative for numerous analogous systems (95, 96).

Fig. 8. Calculated orientations of the selenium chemical shift tensors for (*a*) HN($Ph_2PSe)_2$ and (*b*) HN($^iPr_2PSe)_2$.

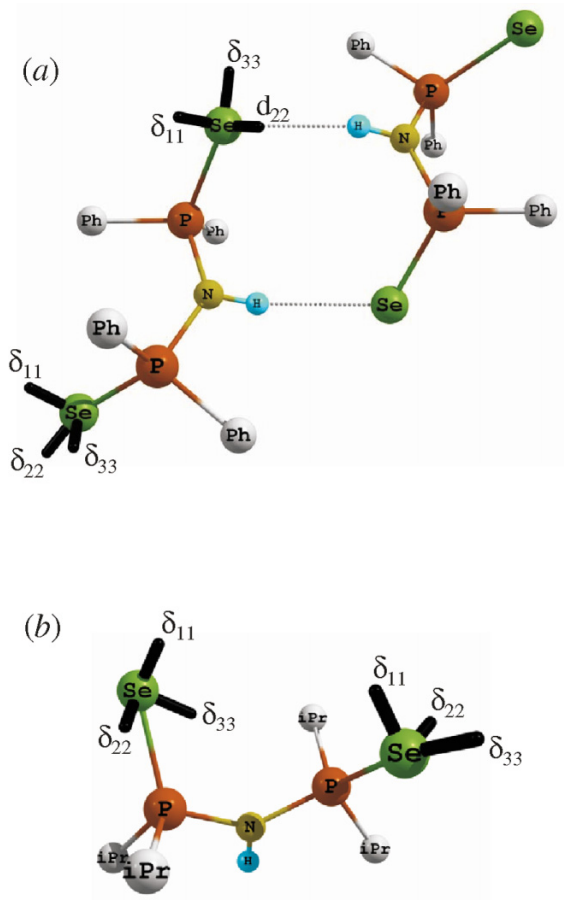

coordinated to a Group 16 (Se or Te) center, the orientation of the selenium chemical is significantly different in that δ_{33} is directed nearly parallel to the Se-Se or Te-Se vector, δ_{11} nearly parallel to the Se-P vector, and δ_{22} perpendicular to the Se-Se-P/Te-Se-P plane (60).

The influence of the *E*-P···P-*E* torsion angle on ^{31}P and ^{77}Se NMR parameters

From Table 1, it is clear that the phosphorus environments in the HN($Ph_2PE)_2$ (E = O, S, Se) systems, which all possess

Fig. 9. Isotropic region of the ^{77}Se NMR spectrum for (*a*) HN($Ph_2PSe)_2$ and (*b*) HN($^iPr_2PSe)_2$ (lower traces) and their simulations (upper traces).

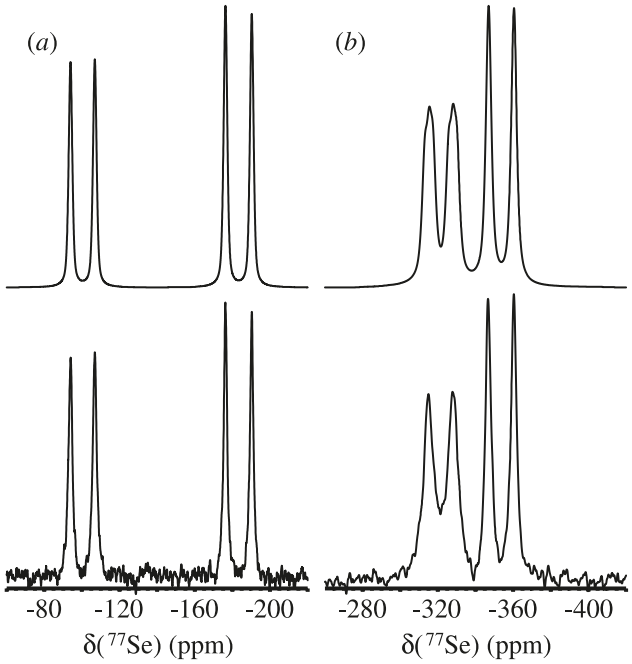

anti *E*-P···P-*E* torsion angles, are all more shielded than their HN($^iPr_2PE)_2$ counterparts that have *gauche* torsion angles. Conversely, in Table 2 the selenium nuclei of HN($Ph_2PSe)_2$ are both less shielded than those of HN($^iPr_2PSe)_2$. The consistent differences observed in the isotropic chemical shifts between the phenyl and isopropyl variants of HN($R_2PE)_2$ (E = O, S, Se) are likely to arise from a combination of the electronic effects of the chosen R group and the common steric differences between the structures. To probe the nature of these differences, nuclear magnetic shielding calculations were performed on a truncated system, HN($Me_2PSe)_2$. The HN($Me_2PSe)_2$ structure was achieved by replacing the isopropyl groups of one of the two 50% occupancy structures of HN($^iPr_2PSe)_2$ with methyl groups. Figure 10 displays the effect of rotation about the *E*-P···P-*E* torsion angle from an eclipsed orientation of 0° to a *trans* conformation of 180° in 15° increments. For both the computed phosphorus

© 2008 NRC Canada

Fig. 10. Effect of rotation about the *E*-P···P-*E* torsion angle for $HN(Me_2PSe)_2$ on (*a*) $\delta_{iso}(^{31}P)$ and (*b*) $\delta_{iso}(^{77}Se)$.

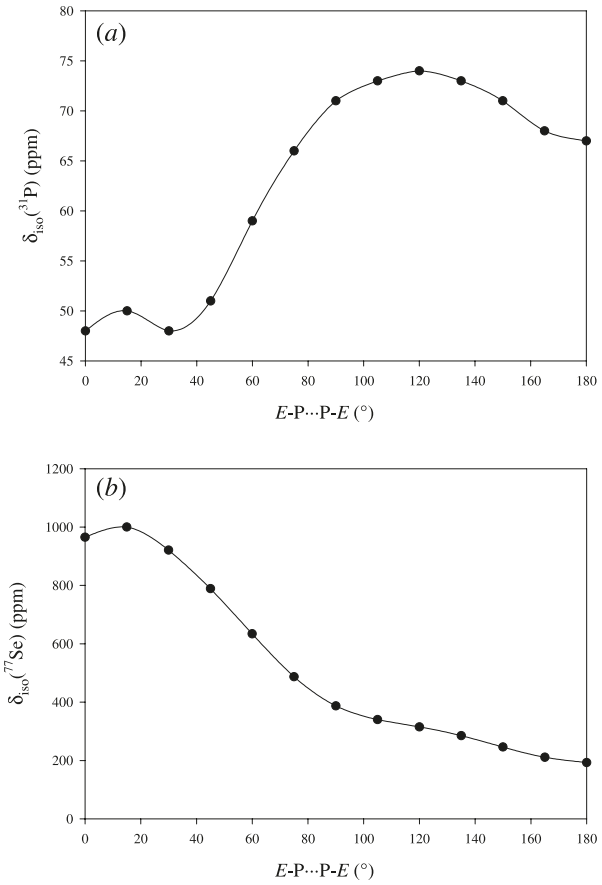

and selenium chemical shifts, the calculations predict the opposite effect to what was observed experimentally; that is, the *anti* structures of $HN(Me_2PSe)_2$ possess less shielded phosphorus and more shielded selenium environments than any of the *gauche* structures. The outcome of these calculations suggest that the electronic effect of the chosen *R* group dominates the impact of the *E*-P···P-*E* torsion angle, which is supported by the solution ^{31}P NMR reported for the mixed alkyl system $Ph_2P(S)NHP(S)^iPr_2$ (94). The isotropic phosphorus chemical shifts of $Ph_2P(S)NHP(S)^iPr_2$, 100.0 and 51.5 ppm, display an even larger separation than those found between the phenyl and isopropyl compounds studied herein, $HN(R_2PE)_2$ (*E* = O, S, Se) (Table 1). Rotation of the S-P···P-S angle in solution may effectively average the conformational impact on the phosphorus chemical shift present in the solid state. Thus, the electronic effect of *R* groups on the phosphorus shielding is not opposed to the same extent by the conformation of the *E*PNP*E* backbone and the isotropic phosphorus chemical shifts are found to be further apart.

Conclusions

The iminobis(diorganophosphine chalcogenide) systems, $HN(R_2PE)_2$ (*E* = O, S, Se; *R* = Ph, ^{i}Pr), have been investigated by solid-state ^{31}P and ^{77}Se NMR spectroscopy and DFT computational chemistry. The phosphorus environments of the $HN(Ph_2PE)_2$ (*E* = O, S, Se) systems are all more shielded, with larger spans and smaller skews than the corresponding $HN(^iPr_2PE)_2$ systems. Aside from $Ph_2P(OH)NP(O)Ph_2$, the calculated orientations of the two phosphorus chemical shift tensors in each $HN(R_2PE)_2$ system are essentially identical with δ_{33} oriented nearly parallel to the P-*E* vector as expected from tris-organophosphine chalcogenide systems (89). The experimental and theoretical selenium chemical shift tensors in $HN(Ph_2PSe)_2$ were found to be sensitive to the presence of hydrogen bonding in its solid state dimer structure, while those of $HN(^iPr_2PSe)_2$ were susceptible to the disorder found in its structure. The impact of the conformation of the *E*PNP*E* backbone via the *E*-P···P-*E* torsion angle was studied by DFT nuclear magnetic shielding calculations on a truncated system, $HN(Me_2PSe)_2$. The steric impact of the Se-P···P-Se angle on the computed phosphorus and selenium isotropic chemical shifts was found to have the opposite effect to what was observed experimentally, suggesting that the choice of phenyl or isopropyl group is more important than the conformational contributions to the phosphorus and selenium shielding in these systems.

Finally, this study further demonstrates the feasibility of the measurement of phosphorus and selenium chemical shift tensors for these important ligands. Furthermore, the sensitivity of these tensors to subtle structural effects is apparent.

Acknowledgements

We thank the Natural Sciences and Engineering Research Council of Canada, the Alberta Ingenuity Fund, and the University of Alberta for research grants and scholarships. REW is a Canada Research Chair in Physical Chemistry at the University of Alberta. The authors wish to thank Dr. Devin Sears for use of his computational resources.

References

1. R.C. Mehrotra, R. Bohra, and D.P. Gaur. Metal β-diketonates and allied derivatives. Academic Press, London, UK. 1978. p. 382.
2. K.-I. Itoh and O. Matsumoto. Thin Solid Films, **345**, 29 (1999).
3. S.I. Toroyanov, N.P. Kuzmina, I.E. Soboleva, and N.V. Chugarov. Electrochemical Society Proceedings, **97–25**, 886 (1997).
4. A.N. Gleizes. Chem. Vap. Deposition, **6**, 155 (2000).
5. M. Green and P. O'Brien. Chem. Commun. (Cambridge), 2235 (1999).
6. N.L. Pickett and P. O'Brien. Chem. Rec. **1**, 467 (2001).
7. J. Novosad, S.V. Lindeman, J. Marek, J.D. Woollins, and S. Husebye. Heteroat. Chem. **9**, 615 (1998).
8. L.M. Gilby and B. Piggott. Polyhedron, **18**, 1077 (1999).
9. V. Montiel-Palma, E. Huitrón-Rattinger, S. Cortés-Llamas, M.-Á. Muñoz-Hernández, V. García-Montalvo, E. López-Honorato, and C. Silvestru. Eur. J. Inorg. Chem. 3743 (2004).
10. P. Bhattacharyya, J. Novosad, J. Phillips, A.M.Z. Slawin, D.J. Williams, and J.D. Woollins. J. Chem. Soc. Dalton Trans. 1607 (1995).
11. A.N. Knyazeva, E.A. Shugam, and L.M. Shkol'nikova. Zh. Strukt. Khim. **11**, 938 (1970).
12. S. Onuma, K. Horioka, H. Inoue, and S. Shibata. Bull. Chem. Soc. Jpn. **53**, 2679 (1980).
13. J.D. Woollins. J. Chem. Soc. Dalton Trans. 2893 (1996).

© 2008 NRC Canada

14. M. Valderrama, R. Contreras, M.P. Lamata, F. Viguri, D. Carmona, F.J. Lahoz, S. Elipe, and L.A. Oro. J. Organomet. Chem. **607**, 3 (2000).
15. P. Bhattacharyya and J.D. Woollins. Polyhedron, **14**, 3367 (1995).
16. P. Bhattacharyya, A.M.Z. Slawin, and M.B. Smith. J. Chem. Soc. Dalton Trans. 2467 (1998).
17. V. García-Montalvo, J. Novosad, P. Kilian, J.D. Woollins, A.M.Z. Slawin, P. García y García, M. López-Cardoso, G. Espinosa-Pérez, and R. Cea-Olivares. J. Chem. Soc. Dalton Trans. 1025 (1997).
18. R. Cea-Olivares, V. García-Montalvo, J. Novosad, P. Kilian, J.D. Woollins, A.M.Z. Slawin, P. García y García, M. López-Cardoso, G. Espinosa-Pérez, R.A. Toscano, S. Hernández, G. Canseco-Melchor, L. Lima-Montaño, and C. Rodríguez-Narváez. Phosphorus Sulfur Silicon Relat. Elem. **124**, 347 (1997).
19. R. Cea-Olivares, M. Moya-Cabrera, V. García-Montalvo, R. Castro-Blanco, R.A. Toscano, and S. Hernández-Ortega. J. Chem. Soc. Dalton Trans. 1017 (2005).
20. M. Afzaal, D.J. Crouch, P. O'Brien, J. Raftery, P.J. Skabara, A.J.P. White, and D.J. Williams. J. Mater. Chem. **14**, 233 (2004).
21. I. Haiduc and I. Silaghi-Dumitrescu. Coord. Chem. Rev. **74**, 127 (1986).
22. T.Q. Ly and J.D. Woollins. Coord. Chem. Rev. **176**, 451 (1998).
23. M. Afzaal, D. Crouch, M.A. Malik, M. Motevalli, P. O'Brien, and J.-H. Park. J. Mater. Chem. **13**, 639 (2003).
24. D.J. Crouch, M. Helliwell, P. O'Brien, J.-H. Park, J. Waters, and D.J. Williams. J. Chem. Soc. Dalton Trans. 1500 (2003).
25. M. Afzaal, D. Crouch, M.A. Malik, M. Motevalli, P. O'Brien, J.-H. Park, and J.D. Woollins. Eur. J. Inorg. Chem. 171 (2004).
26. M. Afzaal, K. Ellwood, N.L. Pickett, P. O'Brien, J. Raftery, and J. Waters. J. Mater. Chem. **14**, 1310 (2004).
27. J.-H. Park, M. Afzaal, M. Helliwell, M.A. Malik, P. O'Brien, and J. Raftery. Chem. Mater. **15**, 4205 (2003).
28. A. Singhal, D.P. Dutta, S.K. Kulshreshtha, S.M. Mobin, and P. Mathur. J. Organomet. Chem. **691**, 4320 (2006).
29. J.S. Ritch, T. Chivers, M. Afzaal, and P. O'Brien. Chem. Soc. Rev. **36**, 1622 (2007).
30. C. Silvestru and J.E. Drake. Coord. Chem. Rev. **223**, 117 (2001).
31. D. Cupertino, D.J. Birdsall, A.M.Z. Slawin, and J.D. Woollins. Inorg. Chim. Acta, **290**, 1 (1999).
32. V. García-Montalvo, M.K. Zamora-Rosete, D. Gorostieta, R. Cea-Olivares, R.A. Toscano, and S. Hernández-Ortega. Eur. J. Inorg. Chem. 2279 (2001).
33. H. Rudler, B. Denise, J.R. Gregorio, and J. Vaissermann. Chem. Commun. (Cambridge), 2299 (1997).
34. M. Goyal, J. Novosad, M. Necas, H. Ishii, R. Nagahata, J.-I. Sugiyama, M. Asai, M. Ueda, and K. Takeuchi. Appl. Organomet. Chem. **14**, 629 (2000).
35. K.A. Chatziapostolou, K.A. Vallianatou, A. Grigoropoulos, C.P. Raptopoulou, A. Terzis, I.D. Kostas, P. Kyritsis, and G. Pneumatikakis. J. Organomet. Chem. **692**, 4129 (2007).
36. J.G. H. du Preez, K.U. Knabl, L. Krüger, and B.J.A.M. van Brecht. Solvent Extr. Ion Exch. **10**, 729 (1992).
37. O. Navrátil, M. Fofana, and J. Smola. Z. Chem. **24**, 30 (1984).
38. M.-Á. Muñoz-Hernández, A. Singer, D.A. Atwood, and R. Cea-Olivares. J. Organomet. Chem. **571**, 15 (1998).
39. Q.T.H. Le, S. Umetani, and M. Matsui. J. Chem. Soc. Dalton Trans. 3835 (1997).
40. N. Platzer, H. Rudler, C. Alvarez, L. Barkaoui, B. Denise, N. Goasdoué, M.-N. Rager, J. Vaissermann, and J.-C. Daran. Bull. Soc. Chim. Fr. **132**, 95 (1995).
41. L. Barkaoui, M. Charrouf, M.-N. Rager, B. Denise, N. Platzer, and H. Rudler. Bull. Soc. Chim. Fr. **134**, 167 (1997).
42. S. W. Magennis, S. Parsons, A. Corval, J.D. Woollins, and Z. Pikramenou. Chem. Commun. (Cambridge), 61 (1999).
43. R.D. Bereman, F.T. Wang, J. Najdzionek, and D.M. Braitsch. J. Am. Chem. Soc. **98**, 7266 (1976).
44. U. Sakaguchi and A.W. Addison. J. Am. Chem. Soc. **99**, 5189 (1977).
45. O. Siiman and J. Vetuskey. Inorg. Chem. **19**, 1672 (1980).
46. M. Hernández-Arganis, S. Hernández-Ortega, R.A. Toscano, V. García-Montalvo, and R. Cea-Olivares. Chem. Commun. (Cambridge), 310 (2004).
47. D. Cupertino, R. Keyte, A.M.Z. Slawin, D.J. Williams, and J.D. Woollins. Inorg. Chem. **35**, 2695 (1996).
48. V.V. Korshak, I.A. Gribova, T.V. Artamonova, and A.N. Bushmarina. Vysokomol. Soedin. **2**, 377 (1960).
49. C.D. Schmulbach. Prog. Inorg. Chem. **4**, 275 (1962).
50. H. Nöth. Z. Naturforsch. B, **37**, 1491 (1982).
51. S. Husebye and K. Maartmann-Moe. Acta Chem. Scand. Ser. A, **37**, 439 (1983).
52. P.B. Hitchcock, J.F. Nixon, I. Silaghi-Dumitrescu, and I. Haiduc. Inorg. Chim. Acta, **96**, 77 (1985).
53. C.G. Pernin and J.A. Ibers. Acta Crystallogr. C, **56**, 376 (2000).
54. A. Schmidpeter and H. Groeger. Z. Anorg. Allg. Chem. **345**, 106 (1966).
55. F.T. Wang, J. Najdzionek, K.L. Leneker, H. Wasserman, and D.M. Braitsch. Synth. React. Inorg. Metal-Org. Chem. **8**, 119 (1978).
56. G.P. McQuillan and I.A. Oxton. Inorg. Chim. Acta, **29**, 69 (1978).
57. R. Czernuszewicz, E. Maslowsky, and K. Nakamoto. Inorg. Chim. Acta, **40**, 199 (1980).
58. B. Wrackmeyer, E. Garcia-Baez, F. J. Zuno-Cruz, G. Sanchez-Cabrera, and M.J. Rosales. Z. Naturforsch. B, **55**, 185 (2000).
59. B.A. Demko and R.E. Wasylishen. J. Chem. Soc. Dalton Trans. 481 (2008).
60. B.A. Demko and R.E. Wasylishen. Inorg. Chem. **47**, 2786 (2008).
61. I. Haiduc. *In* Inorganic experiments. *Edited by* J.D. Woollins. VCH, New York, USA, Basel, Switzerland; Cambridge, UK; Tokyo, Japan. 1994. p. 145.
62. D.J. Williams. Inorg. Nucl. Chem. Lett. **16**, 189 (1980).
63. G. Metz, X. Wu, and S.O. Smith. J. Magn. Reson. A, **110**, 219 (1994).
64. A.E. Bennett, C.M. Rienstra, M. Auger, K.V. Lakshmi, and R.G. Griffin. J. Chem. Phys. **103**, 6951 (1995).
65. D.L. Bryce, G.M. Bernard, M. Gee, M. Lumsden, K. Eichele, and R.E. Wasylishen. Can. J. Anal. Sci. Spectrosc. **46**, 46 (2001).
66. M.J. Collins, C.I. Ratcliffe, and J.A. Ripmeester. J. Magn. Reson. **68**, 172 (1986).
67. M.M. Maricq and J.S. Waugh. J. Chem. Phys. **70**, 3300 (1979).
68. J. Herzfeld and A.E. Berger. J. Chem. Phys. **73**, 6021 (1980).
69. K. Eichele and R.E. Wasylishen. WSOLIDS. Verson 1.17.30 {computer program]. Dalhousie University, Halifax, N.S., Canada. 2001.
70. J. Mason. Solid State Nucl. Magn. Reson. **2**, 285 (1993).
71. G. Schreckenbach and T. Ziegler. J. Phys. Chem. **99**, 606 (1995).
72. G. Schreckenbach and T. Ziegler. Int. J. Quantum Chem. **61**, 899 (1997).
73. S.K. Wolff and T. Ziegler. J. Chem. Phys. **109**, 895 (1998).
74. E.J. Baerends, D.E. Ellis, and P. Ros. Chem. Phys. **2**, 41 (1973).
75. L. Versluis and T. Ziegler. J. Chem. Phys. **88**, 322 (1988).
76. G. te Velde and E.J. Baerends. J. Comput. Phys. **99**, 84 (1992).
77. C. Fonseca Guerra, J.G. Snijders, G. te Velde, and E.J. Baerends. Theor. Chem. Acc. **99**, 391 (1998).

© 2008 NRC Canada

78. E.J. Baerends. Theoretical chemistry. Vrije Universiteit, Amsterdam. Available from http://www.scm.com.
79. S.H. Vosko, L. Wilk, and M. Nusair. Can. J. Phys. **58**, 1200 (1980).
80. A.D. Becke. Phys. Rev. A, **38**, 3098 (1988).
81. J.P. Perdew. Phys. Rev. B, **33**, 8822 (1986).
82. J.P. Perdew. Phys. Rev. B, **34**, 7406 (1986).
83. C. Chang, M. Pelissier, and P. Durand. Phys. Scr. **34**, 394 (1986).
84. E. van Lenthe, E.J. Baerends, and J.G. Snijders. J. Chem. Phys. **99**, 4597 (1993).
85. E. van Lenthe, E.J. Baerends, and J.G. Snijders. J. Chem. Phys. **101**, 9783 (1994).
86. E. van Lenthe, R. van Leeuwen, E.J. Baerends, and J.G. Snijders. Int. J. Quantum Chem. **57**, 281 (1996).
87. C.J. Jameson, A. de Dios, and A.K. Jameson. Chem. Phys. Lett. **167**, 575 (1990).
88. B.A. Demko, K. Eichele, and R.E. Wasylishen. J. Phys. Chem. A, **110**, 13537 (2006).
89. J.B. Robert and L. Wiesenfeld. Mol. Phys. **44**, 319 (1981).
90. N.J. Clayden, C.M. Dobson, L.-Y. Lian, and D.J. Smith. J. Magn. Reson. **69**, 476 (1986).
91. M. Gee, R.E. Wasylishen, K. Eichele, and J.F. Britten. J. Phys. Chem. A, **104**, 4598 (2000).
92. H. Duddeck. Prog. Nucl. Magn. Reson. Spectrosc. **27**, 1 (1995).
93. H. Duddeck. Annu. Rep. NMR Spectrosc. **52**, 105 (2004).
94. D.J. Birdsall, A.M.Z. Slawin, and J.D. Woollins. Polyhedron, **20**, 125 (2001).
95. C.J. Jameson. *In* Multinuclear NMR. *Edited by* J. Mason. Plenum Press, New York. 1987. p. 89.
96. C.J. Jameson. *In* Phosphorus-31 NMR spectroscopy in stereochemical analysis. Organic compounds and metal complexes. Vol. 8. *Edited by* J.G. Verkade and L.D. Quin. VCH Publishers Inc., Deerfield Beach, Fla., USA. 1987. p. 205.

© 2008 NRC Canada

Dissecting out the effect of Ru-OAr bonding in a five-coordinate complex of ruthenium (II)[1]

Sebastien Monfette, João A. Duarte Silva, Serge I. Gorelsky, Scott J. Dalgarno, Eduardo N. dos Santos, Maria H. Araujo, and Deryn E. Fogg

Abstract: Blue Ru(*o*-cat)(PPh_3)$_3$ (**5**; *o*-cat = *ortho*-catecholate), obtained in 94% yield by reaction of $RuCl_2(PPh_3)_3$ (**4**) with dithallium catecholate, was characterized by NMR, MALDI-MS, IR, and single crystal X-ray analysis, and by a combined electronic spectroscopy and time-dependent density functional theory (TD-DFT) study. The frontier orbitals in **5** participate in a low-energy charge transfer excitation involving donation from the Ru-catecholate π bond (largely localized on catecholate) to a low-lying σ* orbital on Ru-$PPh_{3(apical)}$. The energy of this transition increases on binding a pyridine ligand in the sixth site.

Key words: ruthenium aryloxide, catecholate, phosphine, electronic spectroscopy, time-dependent DFT.

Résumé : Le Ru(*o*-cat)(PPh_3) bleu (**5**; *o*-cat = *ortho*-catécholate) qui est obtenu avec un rendement de 94% par réaction du $RuCl_2(PPh_3)_3$ (**4**) avec le catécholate de dithallium a été caractérisé par RMN, spectrométrie de masse "MALDI", spectroscopie IR et par diffraction des rayons X par un cristal unique ainsi que par une combinaison de spectroscopie électronique et d'une étude de théorie de la fonctionnelle de densité en fonction du temps. Les orbitales frontières du produit **5** participent dans une excitation par transfert de charge de basse énergie impliquant le don d'électron à partir de la liaison π du catécholate de ruthénium (principalement localisée sur le catécholate) vers une orbitale σ* de basse énergie du Ru-$PPh_{3(apical)}$. L'énergie de cette transition augmente lors de la fixation d'un ligand pyridine sur le sixième site.

Mots-clés : aryloxyde de ruthénium, catécholate, phosphine, spectroscopie électronique, théorie de la fonctionnelle de densité en fonction du temps.

[Traduit par la Rédaction]

Introduction

Olefin metathesis is now one of the most powerful methods in use for the construction of C=C bonds (1). Of the many well-defined catalysts developed for this versatile reaction, the Grubbs-class catalysts, $RuCl_2LL'$(=CHPh), have had the greatest impact in organic synthesis owing to their relative robustness and ease of handling. We have been engaged in a program of study focusing on the largely neglected (2) potential of the anionic sites to expand the modularity, tunability, and lifetime of the Ru-NHC catalysts (3) (NHC = *N*-heterocyclic carbene). Particular success has emerged for derivatives containing monodentate or κ^2-chelating aryloxide ligands (Fig. 1). These exhibit, inter alia, increased lifetime (for **1**), enhanced efficiency (**2** and **3**), and a high kinetic selectivity for cyclic vs. oligomeric products in macrocycle RCM (**2**, **3**; RCM = ring-closing metathesis) (3).

Emerging findings from our laboratory have focused our attention on the importance of the Ru-aryloxide electronic interactions in determining not merely catalyst activity, but also the kinetic bias toward RCM products. In the present work, we wished to evaluate the electronic interactions specific to the basal Ru-aryloxide moiety within the square pyramidal coordination geometry, unperturbed by the variety of additional bonding interactions present in the alkylidene complexes of Fig. 1. While five-coordinate Ru complexes containing monodentate phosphine and phenoxide ligands (e.g., $RuX(OPh)(PPh_3)_3$) would be suitable candidates for study, such species are unstable with respect to isomerization to piano-stool structures (Scheme 1) (4), unless the aryloxide ligand is stabilized by electron-withdrawing substituents that add to the complexity of our intended electronic analysis.

In earlier work, we established that σ–π isomerization of aryloxide donors in these labile, coordinatively unsaturated

Received 3 June 2008. Accepted 31 July 2008. Published on the NRC Research Press Web site at canjchem.nrc.ca on 25 November 2008.

This paper is dedicated to Professor Dick Puddephatt, in honour of his many contributions to chemistry and the Canadian chemistry community.

S. Monfette, S.I. Gorelsky, and D.E. Fogg.[2] Department of Chemistry, Center for Catalysis Research & Innovation, University of Ottawa, Ottawa ON K1N 6N5, Canada.
S.J. Dalgarno.[3] School of EPS-Chemistry, Heriot-Watt University, Edinburgh EH14 4AS Scotland.
J.A. Duarte Silva, E.N. dos Santos, and M.H. Araujo. Departamento de Química– ICEx, Universidade Federal de Minas Gerais, 31270–901 Belo Horizonte, Brazil.

[1]This article is part of a Special Issue dedicated to Professor R. Puddephatt.

[2]Corresponding author (e-mail: dfogg@uottawa.ca).

[3]Present address: Department of Chemistry, University of Missouri, 601 S. College Ave, Columbia, MO 65211, USA.

 doi:10.1139/V08-147 © 2008 NRC Canada

Fig. 1. Key Ru-aryloxide catalysts (3); one isomer shown for **2**. IMes = *N,N′*-bis(mesityl)imidazol-2-ylidene, py = pyridine.

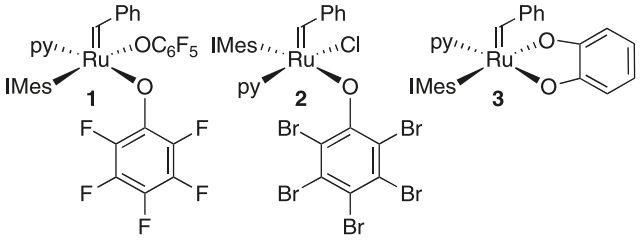

Scheme 1.

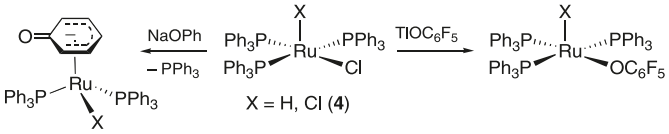

species is not inhibited by chelation within large (seven-membered) chelate rings (4*a*). The stability of the catecholate ligand in **3**, however, suggested that a smaller chelate might stabilize our target systems. We therefore sought to examine an alternative model complex, Ru(*o*-cat)(PPh_3)$_3$ (**5**, *o*-cat = *ortho*-catecholate). Here we describe the synthesis and structural characterization of **5** and an analysis of its frontier orbital interactions by electronic spectroscopy and time-dependent density functional theory (TD-DFT) calculations.

Results and discussion

Synthesis of Ru(*o*-cat)(PPh_3)$_3$ (5)

The addition of solid thallium catecholate to a homogeneous solution of $RuCl_2(PPh_3)_3$ **4** in THF caused a colour change from brown to deep blue within 1 h at room temperature, accompanied by precipitation of TlCl. ^{31}P NMR analysis of the crude reaction mixture indicated clean formation of a single Ru product, without liberation of PPh_3. The suspension was filtered through Celite, and the Ru product was isolated in 94% yield by precipitation from THF–hexanes. It was identified as Ru(κ^2-$O_2C_6H_4$)(PPh_3)$_3$ **5** (Scheme 2) on the basis of spectroscopic, crystallographic, and combustion analysis. This complex exhibits high air-sensitivity even in the solid state (possibly a function of the high-lying HOMO in this system; vide infra).

The anaerobic MALDI-TOF mass spectrum (5) of **5** revealed a well-defined isotope pattern for [M–PPh_3]$^{+\cdot}$ at *m*/*z* 734.4 Da. The facile elimination of one triphenylphosphine group in the gas phase probably reflects the steric pressure within the three approximately facial PPh_3 ligands. Retention of all three of these ligands in the solid state is confirmed by X-ray analysis, as discussed below; their retention in solution can be inferred from the ^{1}H NMR integration values as well as the absence of a signal for free PPh_3 in the ^{31}P NMR spectrum of the crude reaction mixture. Unexpectedly, however, a sharp ^{31}P{^{1}H} NMR *singlet* was observed at 55.1 ppm, rather than the A_2X pattern predicted on the basis of the square pyramidal geometry of Scheme 2. This singlet undergoes no change in multiplicity even on cooling to –90 °C. We confirmed that the square pyramidal

Scheme 2.

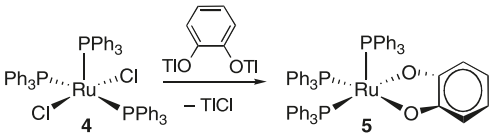

Scheme 3.

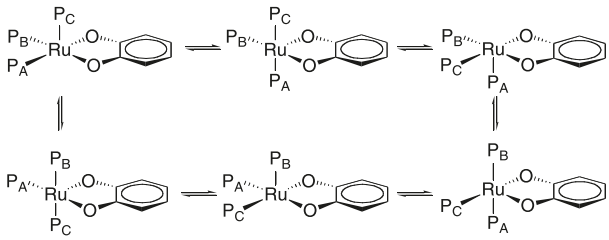

coordination geometry represents the energetic minimum by DFT optimization. The steric constraints in **5** may thus cause averaging of the ^{31}P environments in solution, via a series of equilibria such as those depicted in Scheme 3. Notably, no loss of PPh_3 in solution is evident by NMR analysis, despite this steric pressure, and in contrast to the behaviour of the corresponding dichloride complex **4** (6). This point is examined in more detail below.

Blocky blue crystals of **5** suitable for X-ray analysis were obtained by slow evaporation of a benzene solution. An ORTEP diagram is shown in Fig. 2 with crystal data in Table 1. Only one five-coordinate Ru-catecholate complex, Ru(o-cat)$_2$(≡N) **6** (7), has previously been structurally characterized. In contrast with the slightly distorted square pyramidal geometry of **6**, in which the nitrido ligand is only 0.6 Å above the basal plane, the structure of **5** exhibits significant deviations, though it remains closer to square pyramidal than trigonal bipyramidal at Ru. Two "basal" PPh_3 ligands lie trans to the catecholate oxygen donors (P(1)-Ru(1)-O(1) = 144.61(4)°; P(2)-Ru(1)-O(2) = 158.53(4)°), with the third phosphine approximately apical (P(3)-Ru(1)-P(1) = 97.766(17)°; P(3)-Ru(1)-P(2) = 99.561(17)°; P(3)-Ru(1)-O(1) = 116.13(4)°; P(3)-Ru(1)-O(2) = 98.45(4)°), trans to the vacant site. The extent of distortion is also evident from the 0.05 Å difference in length between the two Ru–P bonds in the basal plane (Ru(1)–P(1) 2.2954(5) Å; Ru(1)–P(2) 2.3496(5) Å). The apical Ru–P bond (Ru(1)–P(3) 2.2527(5) Å) is shorter by 0.04–0.09 Å. This is *not* due to population of the Ru-P(3) σ*-orbital (LUFO+1 of [$Ru(PPh_3)_3$]$^{2+}$): while there is indeed a 19% population of this orbital, the basal Ru–P bonds are likewise populated and to a greater extent (22% for LUFO; 11% for LUFO+2). Instead, the decreased bond length is due to the apical position of the phosphine ligand involved, and the consequent absence of a trans ligand that would give rise to a competing donor–acceptor interaction. A similar effect was found for the apical Ru–P bond in the dichloride analogue **4** (6).

The distorted geometry of **5** is unsurprising, given the rigidity and small bite angle of the catecholate ligand and the unfavourable steric interaction between the three cis-PPh_3 ligands. In comparison, the crystal structure of **4**, containing a meridional arrangement of these ligands, shows little distortion in the bond angles about ruthenium (6). Similarly,

© 2008 NRC Canada

Fig. 2. ORTEP diagram for Ru(*o*-cat)(PPh_3)$_3$ **5**·C_6H_6. Thermal ellipsoids at 50% probability; hydrogen atoms omitted for clarity.

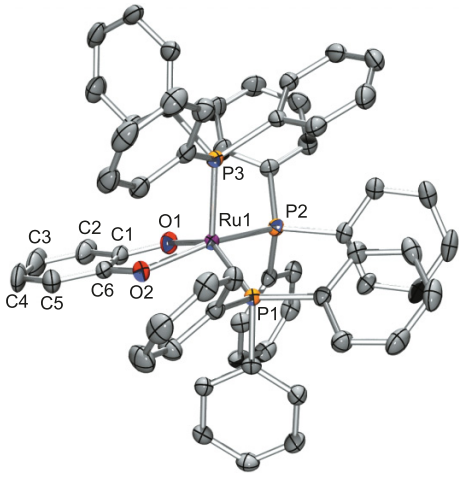

Table 1. Crystal data and structure refinement for **5**·C_6H_6

Formula	$C_{66}H_{55}O_2P_3Ru$
Formula mass	1074.08
Size (mm)	0.6 × 0.44 × 0.42
Colour, crystal morphology	Blue, block
Temperature (K)	173(2) K
Wavelength (Å)	0.710 73
Crystal system, space group	Monoclinic, $P2_1/c$
a (Å)	13.3727(13)
b (Å)	17.1572(18)
c (Å)	23.022(2)
α (°)	90
β (°)	94.653(3)
γ (°)	90
Volume (Å^3)	5264.7(9)
Z, calcd. density (mg/m^3)	4, 1.355
Absorption coefficient (mm^{-1})	0.435
F(000)	2224
Data collection range	1.48° ≤ θ ≤ 27.07°
Index ranges	–17 ≤ h ≤ 12, –17 ≤ k ≤ 21, –22 ≤ l ≤ 28
Reflections collected	21 831
Independent reflections	10 952 [R(int) = 0.0224]
Observed reflections	9287 [$I > 2\sigma(I)$]
Absorption correction	Multi-scan
Max. and min. transmission	0.8383 and 0.7802
Refinement method	Full
Data, restraints, parameters	10 952, 0, 649
Goodness of fit	1.032
Final R indices [$I > 2\sigma(I)$]	R_1 = 0.0286, wR_2 = 0.0716
R indices (all data)	R_1 = 0.0375, wR_2 = 0.075
Largest diff. peak and hole (e Å^{-3})	0.558 and –0.279

six-coordinate Ru(II)-catecholate complexes containing smaller neutral ligands such as PMe_3 (8) or pyridine (9) form reasonably regular octahedral complexes. The C–O bond

Fig. 3. Experimental and calculated electronic spectra for **5** (solid black and red lines, respectively) and calculated spectrum for **7** (dashed red line).

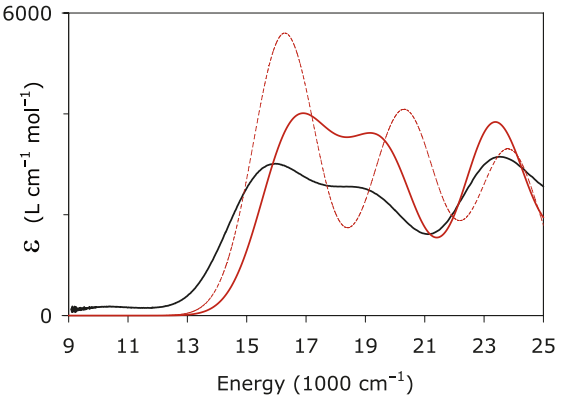

lengths within **5** (1.350(2) and 1.345(2) Å for C(1)–O(1) and C(6)–O(2), respectively) are within the range of 1.34–1.47 Å usual for Ru-catecholate complexes; benzoquinone complexes exhibit shorter C–O bond lengths (1.27–1.31 Å (10)). The magnitude and uniformity of C–C bond lengths within the $O_2C_6H_4^{2-}$ ligand (1.372(4)–1.407(4) Å) likewise support formulation of **5** as a Ru-catecholate complex, as does the presence of an IR band for $\nu_{C\text{-}O}$ at 1270 cm^{-1}, which is not observed for starting **4**, but is present in the IR spectra of the catecholate salts.

The electronic structure of **5** was analyzed experimentally by UV–vis spectroscopy and theoretically by use of TD-DFT calculations (11–13) to establish the key metal-ligand bonding contributions. Our interest was stimulated further by the unusual blue color of **5**, rare in Ru(II) complexes (for examples see refs. 14–21), which could provide added insight into its properties. A fragment molecular orbital (FMO) analysis enabled the quantification of charge donation. Orbital interactions were considered in terms of dative bonds between the lowest unoccupied fragment orbitals (LUFOs) of the metal fragment $[Ru(PPh_3)_3]^{2+}$ and the highest occupied fragment orbitals (HOFOs) of the $O_2C_6H_4^{2-}$ ligand.

The calculated electronic spectrum is in very good agreement with the experimental spectrum (Fig. 3). The latter, measured in THF, is comprised of three absorption maxima of near-identical intensity (16 000, 18 400, and 23 500 cm^{-1}), whereas TD-DFT predicts three principal bands (16 500, 19 700, and 23 200 cm^{-1}), of which the latter two overlap with two weaker bands at 18 000 and 23 600 cm^{-1}. The band energies thus correspond within ca. 500 cm^{-1} vs. the more typical agreement of 2 000 cm^{-1} (11–13, 22); a minor difference in intensity is also evident. The level of theory was therefore deemed appropriate for the analysis of the electronic transitions. Electron excitations contributing to each band are summarized in Table 2.

The FMO analysis indicates that the formation of **5** involves a significant (>2%) change in the electronic population for only three orbitals on the Ru fragment. We therefore confine our discussion of the metal-based orbital interactions to these three acceptor orbitals. Contributions from Ru are cited as the composite of s, p, and d contributions; those from PPh_3 are largely p in character (for individual constitu-

© 2008 NRC Canada

Table 2. Electron excitations contributing to bands in the visible region for **5**.

		(TD-DFT (B3LYP/DZVP))	
Exptl. energy[a]	Calcd. energy[a]	f[b]	Assignment[c]
16.0	16.5	0.0370	H→L (44%), H-2→L (29%), H-1→L (10%)
18.4	18.0	0.0190	H-1→L (57%), H→L (17%)
	19.7	0.0338	H-2→L (45%), H-3→L (24%)
			H→L (15%)
23.5	23.2	0.0272	H-3→L (31%), H-4→L (20%)
			H→L+1 (15%)
	23.6	0.0166	H→L+1 (47%)

[a]Band locations in 10^3 cm^{-1}.
[b]Oscillator strength.
[c]H = HOMO; L = LUMO. Only major (> 10%) parent one-electron excitations shown; percentage contributions to wavefunctions of excited states in parentheses.

Fig. 4. Lowest unoccupied fragment orbitals (LUFOs) of $[Ru(PPh_3)_3]^{2+}$ and their compositions (excluding phenyl ontributions). Isosurface contour value for orbital images 0.03 au.

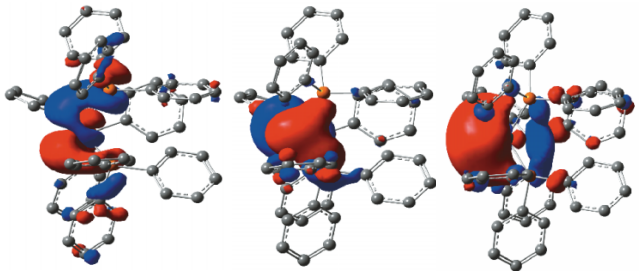

Table 3. Molecular orbital energies (E) and atomic contributions for **4** and **5**.

Orbital	$-E$ (eV)	Ru (%)	PPh_3 (%)	X-ligand (%)
4, LUMO	2.03	47.3	47.6	5.1
4, HOMO	5.10	55.6	5.9	38.5
5, LUMO +1	1.07	7.0	91.5	1.5
5, LUMO	1.81	38.5	49.1	12.4
5, HOMO	4.62	12.8	8.5	78.7
5, HOMO –1	5.26	34.3	7.9	57.8
5, HOMO –2	5.43	46.5	11.8	41.7
5, HOMO –3	5.80	53.3	16.9	29.8
5, HOMO –4	6.13	59.3	12.9	27.8

Note: Atomic contributions evaluated by Mulliken population analysis.

ents see Fig. 4). The LUFO is 62% Ru and 38% PPh_3 (of which 21% is contributed from the P atoms) in character; cf. relative contributions of 58% Ru + 42% PPh_3 for LUFO+1, and 59% Ru + 40% PPh_3 for LUFO+2. The population of each of these orbitals increases from its null value in the non-interacting fragment to 22%, 19%, and 11%, respectively, in **5**. LUFO and LUFO+2 participate in forming the two σ bonds with the ligand, while LUFO+1 forms a π bond (19% × 2 = 0.38 e^-). For the catecholate FMOs, turning on the bonding interaction with Ru results in a significant change in population for six occupied and one unoccupied orbital. These are the HOFO (–21%, i.e., 21% depopulation), HOFO–1 (–14%), HOFO–2 (–7%), HOFO–3 (–3%), HOFO–6 (–5%), HOFO–7 (–4%), and LUFO (+5% population). Thus, in addition to strong ligand-to-metal charge donation (0.94 e^-), formation of the complex involves significant polarization of the electron density on the catecholate ligand through 5% population of the LUFO. This charge distribution description is consistent with the Mulliken population analysis (23–26) and the NPA-derived charges assessed for the catecholate ligand in the complex (–1.06 and –1.20 au, respectively; NPA = natural population analysis).

The molecular orbitals that contribute to the visible spectrum of **5** are summarized in Table 3; visual depictions of all of these are given in the supporting information.[4] The LUMO is a σ* orbital for the apical Ru-PPh_3 bond (Fig. 5), while LUMO+1 consists principally of the aromatic π* orbitals of PPh_3 with a 7% contribution from the Ru 4d orbitals. The low energy of the LUMO of **5** derives from the contribution of a single (apical) phosphine ligand to this σ* orbital (p_z(P)–d_{z2}(Ru)); the other σ* orbital involves both basal PPh_3 ligands. The HOMO is a π bonding orbital between the catecholate and Ru. HOMO-1, HOMO-2, and HOMO-3 are also dominated by Ru-catecholate contributions: these are a largely non-bonding π orbital, a largely σ nonbonding orbital, and a σ–π hybrid, respectively. Finally, HOMO-4 is nonbonding, being composed of a Ru d orbital and the catecholate π orbital.

For four of the five visible bands calculated for **5**, the LUMO (σ* orbital of the apical Ru-PPh_3 bond) participates

[4]Supplementary data contains molecular orbitals implicated in the visible spectrum of **5**; tables of crystal data collection and refinement parameters, atomic coordinates, bond lengths, and angles, anisotropic displacement parameters and hydrogen coordinates, and NMR spectra for **5**. Supplementary data for this article are available on the journal Web site (canjchem.nrc.ca) or may be purchased from the Depository of Unpublished Data, Document Delivery, CISTI, National Research Council Canada, Ottawa, ON K1A 0R6, Canada. DUD 3854. For more information on obtaining material refer to cisti-icist.nrc-cnrc.gc.ca/cms/unpub_e.shtml. CCDC 689209 contains the crystallographic data for this manuscript. These data can be obtained, free of charge, via www.ccdc.cam.ac.uk/conts/retrieving.html (Or from the Cambridge Crystallographic Data Centre, 12 Union Road, Cambridge CB2 1EZ, UK; fax +44 1223 336033; or deposit@ccdc.cam.ac.uk).

© 2008 NRC Canada

Fig. 5. Frontier orbitals for (*a*) **4** and (*b*) **5**. Isosurface contour value for orbital images = 0.03 au.

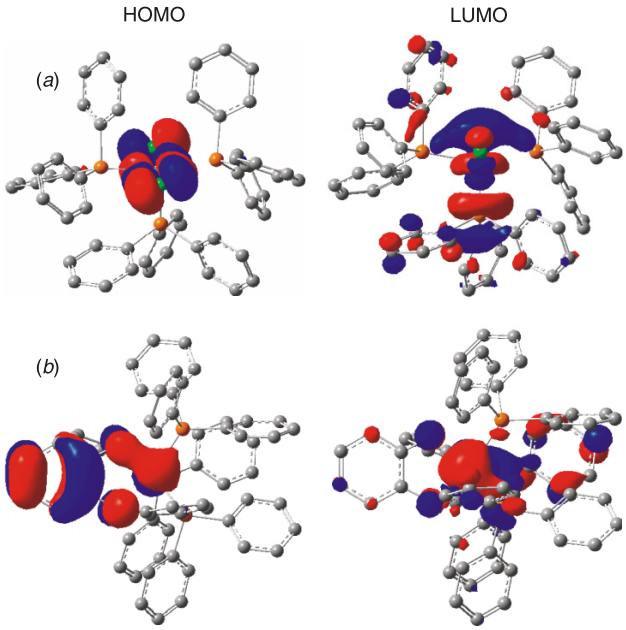

in the electronic excitations. However, the LUMO+1, composed of the π* orbitals of the aromatic rings of the PPh_3 ligands (Table 3), is also implicated in the absorption bands at 23 200 and 23 600 cm^{-1}. To determine whether this orbital plays a significant role in the electronic spectrum, we calculated the electronic spectrum of Ru(*o*-cat)$(PMe_3)_3$ (**7**), which contains no π*(Ph) orbitals. The calculated spectra for **5** and **7** are very similar, as shown in Fig. 3 (**7**: three absorption maxima at 16 300, 20 400, and 23 800 cm^{-1}; cf. the values for **5** noted above). We conclude that the LUMO is more critical to the spectroscopic features in the visible region than is LUMO+1. The intense blue colour of **5** (ε 3000 L $mol^{-1}cm^{-1}$) is thus due to charge transfer from the Ru-catecholate π bond (localized mostly on catecholate) to the low-lying σ* orbital on the apical Ru-PPh_3 bond.

Replacing the two chloride ligands in **4** by catecholate reduces the magnitude of the HOMO–LUMO gap, as evidenced by the change in colour from brown to blue. Consistent with this, the calculated values drop from –3.06 eV for **4** to –2.81 eV for **5**. The coordination number also affects the energy of the relevant electronic transitions, as noted above; Ru(*o*-cat)$(PMe_3)_4$ (8) and Ru(*o*-cat)$(py)_4$ (9), for example, are yellow in colour. While crystallographic analysis has demonstrated that a phenyl ring blocks the sixth coordination site in the solid state for **4**, the Ru–H distance (2.82 Å, corresponding to a bond order of 0.03) precludes the presence of an agostic C–H bond (27). We therefore exclude octahedral coordination as a potential explanation for the higher-energy visible transition for **4**. The smaller HOMO–LUMO gap in **5** is thus due principally to the higher energy of the HOMO, the Ru-P_{apical} σ* LUMO interaction being less affected, as shown in Fig. 5 and Table 3.

While the smaller HOMO–LUMO gap present in **5** might be expected to heighten reactivity, the resistance of this complex to loss of PPh_3 is in striking contrast to the behaviour of **4** (phosphine dissociation being the stepping-stone to the rich coordination chemistry of this classic ruthenium precursor (28)). The low lability of the PPh_3 ligand in **5**, evident by NMR analysis, is further supported by the unreactivity of the complex toward terminal alkynes, a facile, high-yield route to cumulenylidene products for **4** (29). The difference in behaviour lies in the stronger donation and back-donation involving the basal PPh_3 ligands in **5**, which result in a larger binding energy for Ru-$P_{(basal)}$ (–16.0 kcal mol^{-1} in **5** and –10.6 kcal mol^{-1} in **4**) (1 cal = 4.184 J). The weaker donation from the catechol ligand, relative to chloride, is anticipated on the basis of the higher electronegativity of oxygen vs. chlorine, reinforced by the capacity of the catecholate phenyl ring to delocalize negative charge. Consistent with this view, the NPA-derived charge for the catecholate ligand is –1.20 au, while for the chloride ligands the corresponding sum charge is –1.11 au.

Summary

The foregoing demonstrates that replacing chloride by catecholate in the simple model system $RuCl_2(PPh_3)_3$ raises the energy of the X-based HOMO. By analogy, replacing chloride by catecholate in Ru metathesis catalysts is expected to raise the energy of the corresponding Ru-X occupied molecular orbital(s). While the nature and energy of the frontier molecular orbitals in Ru metathesis catalysts has been surprisingly little examined (30), it is clear that the higher energy of the Ru-OAr HOMO will facilitate interaction with any LUMOs of appropriate symmetry present (which may include those for the alkylidene and bound olefin as well as the neutral donor that serves as a proxy for incoming olefin). These amplified interactions enhance the potential for modulating reactivity and selectivity by tuning the electronic properties of the anionic donors. Important steps in the catalytic cycle for olefin metathesis that may be affected range from dissociation of the neutral donor (in **3**, the pyridine ligand), to olefin binding and activation, and potentially, the key 2+2 cycloaddition step. Of additional interest is the extent to which the energy of the Ru-X (catecholate) HOMO is affected by the constrained bond geometry of the catecholate ligand. Future work will explore the specifics of these interactions, and their impact on the energy profile for metathesis in the $RuX_2(IMes)(py)(=CH_2)$ family of catalysts (X = Cl, *o*-cat, OC_6F_5).

Experimental

General procedures

Synthesis of **5** was carried out at room temperature (RT) (23 °C) under N_2 using standard drybox techniques. Dry, oxygen-free solvents, obtained using a Glass Contour solvent purification system, were stored over Linde 4 Å molecular sieves. Thallium catecholate (3*d*) and $RuCl_2(PPh_3)_3$ (31) were prepared by the methods reported.

^1H NMR (500 MHz), ^{13}C (125 MHz), and ^{31}P (121 MHz) spectra were recorded on a Bruker Avance-500 spectrometer. Chemical shifts are reported relative to TMS (^1H, ^{13}C) or 85% H_3PO_4 (^{31}P) at 0 ppm. X-ray data were collected on a Bruker SMART 1000 CCD diffractometer. IR spectra were measured on a Bomem MB100 IR spectrometer. Inert-atmosphere MALDI-MS analyses were carried out using a

© 2008 NRC Canada

Bruker OmniFlex MALDI-TOF mass spectrometer equipped with an N_2 laser (337 nm), interfaced to an MBraun glovebox (5). Data were collected in positive reflectron mode, with the accelerating voltage held at 20 kV. Matrix (pyrene) and analyte solutions were prepared in CH_2Cl_2 at concentrations of 20 and 1 mg/mL, respectively. Samples were mixed in a matrix/analyte ratio of 20:1. UV–vis spectra were measured on a Varian Cary-50 spectrophotometer at a scan rate of 600 nm/min. Samples were prepared under N_2 by filling a Hellma screw-top optical glass cell with 2 mL of a 0.24 mmol/L solution of **5** in THF and sealing prior to analysis. Microanalyses were carried out by Guelph Chemical Laboratories Ltd., Guelph, Ontario, Canada.

Note: The toxicity of thallium (particularly in the +1 oxidation state) is well-established (32). Care must be taken to prevent introduction into the body by inhalation, ingestion, or through the skin. All thallium reagents and wastes, including contaminated solvents, were handled using double-glove and secondary containment procedures, with separate disposal of all wastes in accordance with government regulations.

Synthesis of Ru(κ^2-*O,O′*-$O_2C_6H_4$)(PPh_3)$_3$ 5

Solid thallium catecholate (296 mg, 0.573 mmol) was added to a stirred solution of **4** (500 mg, 0.521 mmol) in 10 mL THF at RT. A colour change from brown to blue took place over 1 h, and the solution became cloudy. The suspension was filtered through Celite to remove TlCl, and the filtrate stripped to dryness. Precipitation from THF–hexanes and washing with hexanes (3 × 5 mL) afforded deep blue **5**. Yield 486 mg (94%). ^{1}H NMR (C_6D_6, 500 MHz) δ: 7.39 (m, 2H, catechol CO-C*H*), 7.30 (m, 18H, *o*-C*H* of PPh_3), 7.02 (m, 2H, catechol C*H*), 6.90 (m, 9H, *p*-C*H* of PPh_3), 6.74 (m, 18H, *m*-C*H* of PPh_3). ^{13}C{^{1}H} NMR (C_6D_6, 125 MHz) δ: 163.3 (s, catechol *C*-O), 137.4–137.1 (m, *i-C* of PPh_3), 135.3–135.2 (m, *o-C*H of PPh_3), 128.9 (s, *p-C*H of PPh_3), 127.5–127.4 (m, *m-C*H of PPh_3), 117.6 (s, catechol *C*H), 117.5 (s, catechol *C*H). ^{31}P{^{1}H} NMR (C_6D_6, 121 MHz) δ: 55.1 ppm (s); multiplicity unchanged down to –90 °C. IR (Nujol, cm^{-1}): $\nu_{C\text{-}O}$ 1270. Anal. calcd. for $C_{60}H_{49}O_2P_3Ru$: C 72.35, H 4.96%; found C 72.08, H 4.85%. MALDI-MS, *m/z* (pyrene matrix): calcd. for $[M\text{-}PPh_3]^{+\cdot}$: 734.1; found, 734.4.

Representative reaction of 5 and 3,3-dimethylbutyne

To a blue solution of **5** (14 mg, 0.014 mmol) in C_6D_6 (1 mL) was added 3,3-dimethylbutyne (10 μL, 0.084 mmol, 6 equiv). The reaction vessel was sealed and heated to 60 °C in an aluminum block for up to 72 h, after which NMR analysis showed only unreacted **5**.

Representative reaction of 5 with 1,1-diphenylprop-2-yn-1-ol

To a blue solution of **5** (25 mg, 0.025 mmol) in THF (2 mL) was added solid 1,1-diphenylprop-2-yn-1-ol (6 mg, 0.029 mmol, 1.2 equiv). No reaction was evident by NMR analysis at RT over a period of 24 h. Only the ^{31}P NMR signal for **5** was present after heating for 1 h in an oil bath set at 70 °C. Complex **5** remains a major species after heating for 17 h, but it is accompanied by multiple products, suggesting sample decomposition. Similar results were found on use of up to 5 equiv of the alkyne.

Structural determination

Blue, blocky crystals of **5** were grown by slow evaporation of a saturated benzene solution. Data were collected on a Bruker SMART 1000 CCD diffractometer with Mo Ka radiation using the ω-scan mode. A single crystal (0.6 mm × 0.44 mm × 0.42 mm) was mounted on a thin glass fiber using paraffin oil and cooled to the data collection temperature (173 K). Data were corrected using the SADABS program (Bruker). Structure solution in the space group $P2_1/c$ was performed with Patterson methods, completed with difference Fourier syntheses, and refined by full-matrix least-squares procedures based on F^2 using the SHELX-97 software package. All non-hydrogen atoms were refined anisotropically; hydrogen atoms were placed at geometrically calculated positions and allowed to ride on their parent atoms. Although the crystals were weakly diffracting, a satisfactory structural solution was obtained.

Computational details

DFT calculations were carried out using the Gaussian 03 package (33). The X-ray structures of **4** (27*b*) and **5** were used for these calculations, after adjusting all C–H distances to 1.08 Å, as only aromatic C–H bonds are present in the structure. All other interatomic distances were left unperturbed. That the square pyramidal structure represents a true energy minimum for **5** was confirmed by geometry optimization. DFT calculations utilized the B3LYP (34) exchange-correlation functional with the DZVP basis set (35) for all atoms. Tight SCF convergence criteria (10^{-8} au) were used for all calculations. The converged wave functions were tested to confirm that they correspond to the ground-state surface. Bond orders and the compositions and populations of molecular orbitals were calculated using the AOMix program (36). The energies and intensities of the lowest 30 singlet-singlet transitions were calculated by TD-DFT. Absorption profiles were calculated from TD-DFT bands by the method reported (22), assuming for all electronic transitions a bandwidth at half-height of 2500 cm^{-1} (a typical value for complexes of the type described). Pseudo-Voigt functions with 50% weights for contributing Gaussian and Lorentzian functions were used to simulate the absorption bands.

Acknowledgements

This work was supported by Natural Sciences and Engineering Research Council of Canada (NSERC) of Canada, the Canada Foundation for Innovation, and the Ontario Innovation Trust. NSERC and Coordenação de Aperfeiçoamento de Pessoal de Nível Superior (CAPES) and Conselho Nacional de Desenvolvimento Científico e Tecnológico (CNPq) of Brazil are acknowledged for fellowships to SM and JDS.

References

1. Please see these leading reviews: (*a*) R.H. Grubbs. Handbook of metathesis. Wiley-VCH, Weinheim, Germany. 2003; (*b*) K.C. Nicolaou, P.G. Bulger, and D. Sarlah. Angew. Chem. Int. Ed. **44**, 4490 (2005); (*c*) R.R. Schrock. Angew. Chem. Int.

© 2008 NRC Canada

Ed. **45**, 3748 (2006); (*d*) R.H. Grubbs. Angew. Chem. Int. Ed. **45**, 3760 (2006).
2. For exceptions, see: (*a*) R. Gawin, A. Makal, K. Wozniak, M. Mauduit, and K. Grela. Angew. Chem. Int. Ed. **46**, 7206 (2007); (*b*) N. Ledoux, R. Drozdzak, B. Allaert, A. Linden, P. Van Der Voort, and F. Verpoort. Dalton Trans. 5201 (2007); (*c*) J.O. Krause, O. Nuyken, K. Wurst, and M.R. Buchmeiser. Chem. Eur. J. **10**, 777 (2004); (*d*) M.S. Sanford, J.A. Love, and R.H. Grubbs. J. Am. Chem. Soc. **123**, 6543 (2001).
3. (*a*) J.C. Conrad, D. Amoroso, P. Czechura, G.P.A. Yap, and D.E. Fogg. Organometallics, **22**, 3634 (2003); (*b*) J.C. Conrad, H.H. Parnas, J.L. Snelgrove, and D.E. Fogg. J. Am. Chem. Soc. **127**, 11882 (2005); (*c*) J.C. Conrad, M.D. Eelman, J.A. Duarte Silva, S. Monfette, H.H. Parnas, J.L. Snelgrove, and D.E. Fogg. J. Am. Chem. Soc. **129**, 1024 (2007); (*d*) S. Monfette and D.E. Fogg. Organometallics, **25**, 1940 (2006).
4. (*a*) J.L. Snelgrove, J.C. Conrad, M.M. Moriarty, G.P.A. Yap, and D.E. Fogg. Organometallics, **24**, 103 (2005); (*b*) J.L. Snelgrove, J.C. Conrad, G.P.A. Yap, and D.E. Fogg. Inorg. Chim. Acta, **345**, 268 (2003), and refs. cited therein; (*c*) D.J. Cole-Hamilton, R.J. Young, and G. Wilkinson. J. Chem. Soc. Dalton Trans. 1995 (1976).
5. M.D. Eelman, J.M. Blacquiere, M.M. Moriarty, and D.E. Fogg. Angew. Chem. Int. Ed. **47**, 303 (2008).
6. P.R. Hoffman and K.G. Caulton. J. Am. Chem. Soc. **97**, 4221 (1975).
7. G.-S. Fang, J.-S. Huang, N. Zhu, and C.-M. Che. Eur. J. Inorg. Chem. 1341 (2004).
8. M. Hirano, H. Sato, N. Kurata, N. Komine, and S. Komiya. Organometallics, **26**, 2005 (2007).
9. H. Masui, A.B.P. Lever, and P.R. Auburn. Inorg. Chem. **30**, 2402 (1991).
10. O. Carugo, C.B. Castellani, K. Djinovic, and M. Rizzi. J. Chem. Soc. Dalton Trans. 837 (1992).
11. M.E. Casida. Recent Adv. Comput. Chem. **1**, 155 (1995).
12, M.E. Casida. Theor. Comput. Chem. **4**, 391 (1996).
13. R.E. Stratmann, G.E. Scuseria, and M.J. Frisch. J. Chem. Phys. **109**, 8218 (1998).
14. E.J. Derrah, D.A. Pantazis, R. McDonald, and L. Rosenberg. Organometallics, **26**, 1473 (2007).
15. P. Banerjee, S. Das, P.E. Fanwick, and S. Goswami. J. Organomet. Chem. **691**, 2915 (2006).
16. S. Jasimuddin, P. Byabartta, C. Sinha, G. Mostafa, and T.-H. Lu. Inorg. Chim. Acta **357**, 2015 (2004).
17. C. Das, A. Saha, C.-H. Hung, G.-H. Lee, S.-M. Peng, and S. Goswami. Inorg. Chem. **42**, 198 (2003).
18. P. Byabartta, S. Jasimuddin, B.K. Ghosh, C. Sinha, A.M.Z. Slawin, and J.D. Woollins. New J. Chem. **26**, 1415 (2002).
19. R.-A. Fallahpour and M. Neuburger. Helv. Chim. Acta, **84**, 715 (2001).
20. K. Mashima, H. Kaneyoshi, S.-i. Kaneko, A. Mikami, K. Tani, and A. Nakamura. Organometallics, **16**, 1016 (1997).
21. H. Tom Dieck, W. Kollvitz, and I. Kleinwaechter. Inorg. Chem. **23**, 2685 (1984).
22. S.I. Gorelsky and A.B.P. Lever. J. Organomet. Chem. **635**, 187 (2001).
23. R.S. Mulliken. J. Chem. Phys. **23**, 2343 (1955).
24. R.S. Mulliken. J. Chem. Phys. **23**, 2338 (1955).
25. R.S. Mulliken. J. Chem. Phys. **23**, 1841 (1955).
26. R.S. Mulliken. J. Chem. Phys. **23**, 1833 (1955).
27. (*a*) S.J. LaPlaca and J.A. Ibers. Inorg. Chem. **4**, 778 (1965); (*b*) CCDC file number 214959.
28. E.A. Seddon and K.R. Seddon. The chemistry of ruthenium. Elsevier, Amsterdam. 1984.
29. Please see these representative reports: (*a*) D. Touchard, S. Guesmi, M. Bouchaib, P. Haquette, A. Daridor, and P.H. Dixneuf. Organometallics, **15**, 2579 (1996); (*b*) Y. Wakatsuki, N. Koga, H. Yamazaki, and K. Morokuma. J. Am. Chem. Soc. **116**, 8105 (1994); (*c*) A. Keller, B. Jasionka, T. Glowiak, A. Ershov, and R. Matusiak. Inorg. Chim. Acta, **344**, 49 (2003); (*d*) K.J. Harlow, A.F. Hill, and J.D.E.T. Wilton-Ely. J. Chem. Soc. Dalton Trans. 285 (1999).
30. C.H. Suresh and N. Koga. Organometallics, **23**, 76 (2004).
31. P.S. Hallman, T.A. Stephenson, and G. Wilkinson. Inorg. Synth. **12**, 237 (1970).
32 S. Galvan-Arzate and A. Santamaria. Toxicol. Lett. **99**, 1 (1998).
33. M.J. Frisch, G.W. Trucks, H.B. Schlegel, G.E. Scuseria, M.A. Robb, J.R. Cheeseman, J.A. Montgomery, Jr., T. Vreven, K.N. Kudin, J.C. Burant, J.M. Millam, S.S. Iyengar, J. Tomasi, V. Barone, B. Mennucci, M. Cossi, G. Scalmani, N. Rega, G.A. Petersson, H. Nakatsuji, M. Hada, M. Ehara, K. Toyota, R. Fukuda, J. Hasegawa, M. Ishida, T. Nakajima, Y. Honda, O. Kitao, H. Nakai, M. Klene, X. Li, J. E. Knox, H.P. Hratchian, J.B. Cross, C. Adamo, J. Jaramillo, R. Gomperts, R.E. Stratmann, O. Yazyev, A.J. Austin, R. Cammi, C. Pomelli, J.W. Ochterski, P.Y. Ayala, K. Morokuma, G.A. Voth, P. Salvador, J.J. Dannenberg, V.G. Zakrzewski, S. Dapprich, A.D. Daniels, M.C. Strain, O. Farkas, D.K. Malick, A.D. Rabuck, K. Raghavachari, J.B. Foresman, J.V. Ortiz, Q. Cui, A.G. Baboul, S. Clifford, J. Cioslowski, B.B. Stefanov, G. Liu, A. Liashenko, P. Piskorz, L. Komaromi, R.L. Martin, D.J. Fox, T. Keith, M.A. Al-Laham, C.Y. Peng, A. Nanayakkara, M. Challacombe, P.M. W. Gill, B. Johnson, W. Chen, M.W. Wong, C. Gonzalez, J.A. Pople. Gaussian 03. Revision B.04 [computer program]. Gaussian, Inc., Pittsburgh, Penn., USA. 2003.
34. (*a*) A.D. Becke. J. Chem. Phys. **98**, 5648 (1993); (*b*) B. Miehlich, A. Savin, H. Stoll, and H. Preuss. Chem. Phys. Lett. **157**, 200 (1989); (*c*) C. Lee, W. Yang, and G. Parr. Phys. Rev. B, **37**, 785 (1988).
35. N. Godbout, D.R. Salahub, J. Andzelm, and E. Wimmer. Can. J. Chem. **70**, 560 (1992).
36. S.I. Gorelsky. AOMix: Program for molecular orbital analysis. Version 6.35. University of Ottawa, Ottawa, Ont., Canada. 2007.

© 2008 NRC Canada

Zinc halide oxazoline complexes — The quest for structural diversity[1]

Robert A. Gossage, Paras N. Yadav, Timothy D. MacInnis, J. Wilson Quail, and Andreas Decken

Abstract: The synthesis and characterization of 14 ZnX_2 (X = Cl or Br) complexes containing aryl-oxazoline (ox) ligands is reported. Eleven of these derivatives have been structurally elucidated in the solid state by single crystal X-ray diffraction methods. The ligands used are 2-(3-R-phenyl)-2-oxazoline (R = Cl or Me), 2-(4-R-phenyl)-2-oxazoline (R = Cl, F, Me or –OMe), and 2-(anisol-2-yl)-4,4-dimethyl-2-oxazoline (**7a**). All oxazolines, with the exception of **7a**, lead to the formation of materials identified as $ZnX_2(ox)_2$ upon reaction with ZnX_2. A distorted tetrahedral coordination motif around the Zn metal centre is displayed in nine examples that have been characterized by single crystal X-ray diffraction methods. In the case of ligand **7a**, an unusual dimeric species (X-ray) of formula $[ZnCl_2(\mathbf{7a})]_2$ (**7b**) is formed upon reaction with $ZnCl_2$. Compound **7b** displays a rare (formally neutral) μ-$(Cl)_2$-$(Zn[L]Cl)_2$ (L = neutral donor ligand) unit in addition to secondary bonding interactions between the Zn centres and the *O*-atom of the –OMe group (Zn···O distance of ~2.56 Å). In contrast, reactions of **7a** with $ZnBr_2$ lead to the formation of a monomeric species containing a chelating molecule of **7a** with binding through the oxazoline *N*-atom and the methoxy (Zn–O distance of ~2.14 Å) group, i.e., $ZnBr_2(\mathbf{7a}\text{-}\kappa^2 N,O_{OMe})$. These complexes are discussed in terms of structurally related Zn species and some comment is made as to the direction to be explored within this series of materials that may lead to further unusual structural diversity.

Key words: oxazoline, oxazole, zinc, X-ray crystal structure, coordination complex, Zn(II) halide.

Résumé : On rapporte la synthèse et la caractérisation de quatorze complexes de ZnX_2 (X = Cl ou Br) contenant des ligands aryloxazoline (ox). On a élucidé les structures de onze de ces dérivés en faisant appel à des méthodes de diffraction des rayons X à l'état solide. Les ligands utilisés comprennent des 2-(3-R-phényl)-2-oxazolines (R = Cl ou Me), des 2-(3-4-phényl)-2-oxazolines (R = Cl, F, Me ou OMe) et la 2-(anisoly-2-yl)-4,4-diméthyl-2-oxazoline (**7a**). Par réaction avec du ZnX_2, toutes les oxazolines, à l'exception du composé **7a**, conduisent à la formation de produits identifiés par la formule générale $ZnX_2(ox)_2$. Dans neuf exemples caractérisés par des méthodes de diffraction des rayons-X par un cristal unique présentent un motif de coordination de tétraèdre déformé autour du centre métallique Zn. Dans le cas du ligand **7a**, il se forme une espèce dimère inhabituelle (aux rayons X) de formule $[ZnCl_2(\mathbf{7a})]_2$ (**7b**). Le composé **7b** comporte une unité rare (formellement neutre) μ-(Cl_2)-$(Zn[L]Cl)_2$ (L = ligand donneur neutre) en plus des interactions de liaisons secondaires entre les centres Zn et l'atome d'oxygène du groupe –OMe (distance Zn···O de ~2,56 Å). Par opposition, les réactions du composé **7a** avec le $ZnBr_2$ conduit à la formation d'espèces monomères contenant une molécule chélatante de **7a** qui donne des liaisons par le biais de l'atome d'azote de l'oxazoline et du groupe méthoxy (distance Zn–O de ~2,14 Å), c'est-à-dire $ZnBr_2(\mathbf{7a}\text{-}\kappa^2 N,O_{OMe})$. On discute de ces complexes en fonction d'espèces de Zn reliées d'un point de vue structural et on fait quelques commentaires concernant la direction qui devrait être explorer dans cette série de produits qui pourrait conduire à une plus grande diversité structurale.

Received 7 April 2008. Accepted 7 October 2009. Published on the NRC Research Press Web site at canjchem.nrc.ca on 29 November 2008.

This manuscript is dedicated to Professor Richard J. Puddephatt in recognition of his outstanding contributions to Canadian science.

R.A. Gossage.[2] Department of Chemistry & Biology, Ryerson University, 350 Victoria Street, Toronto ON M5B 2K3 Canada.
P.N. Yadav[3] **and T.D. MacInnis.**[4] The David Upton Hill Laboratories of Inorganic Chemistry, Department of Chemistry, Acadia University, Wolfville NS B4P 2R6 Canada.
J.W. Quail.[5] Saskatchewan Structural Sciences Centre and Department of Chemistry, Thorvaldson Building, 110 Science Place, University of Saskatchewan, Saskatoon SK S7N 5C9 Canada.
A. Decken.[6] Department of Chemistry, University of New Brunswick, Fredericton NB E3B 6E2 Canada.

[1]Oxazoles XIX. This article is part of a Special Issue dedicated to Professor R. Puddephatt.
[2]Corresponding author (e-mail: gossage@ryerson.ca)
[3]Present address: Central Department of Chemistry, Tribhuvan University, Kirtipur, Kathmandu, Nepal.
[4]Present address: Department of Chemistry, University of Victoria, Victoria BC V8W 3V6 Canada.
[5]Correspondence regarding X-ray structure determinations of compounds **7b** and **7c** (e-mail: wilson.quail@usask.ca).
[6]Correspondence regarding X-ray structure determinations of compounds **1b–5b**, **2c–4c**, and **6c** (e-mail: adecken@unb.ca).

 doi:10.1139/V08-174 © 2008 NRC Canada

Mots-clés : oxazoline, oxazole, structure cristalline par diffusion des rayons X, complexe de coordination, halogénure de Zn(II).

[Traduit par la Rédaction]

Fig. 1. Some of the known structural motifs for $(ZnX_2[py–R]_n)_m$ complexes.

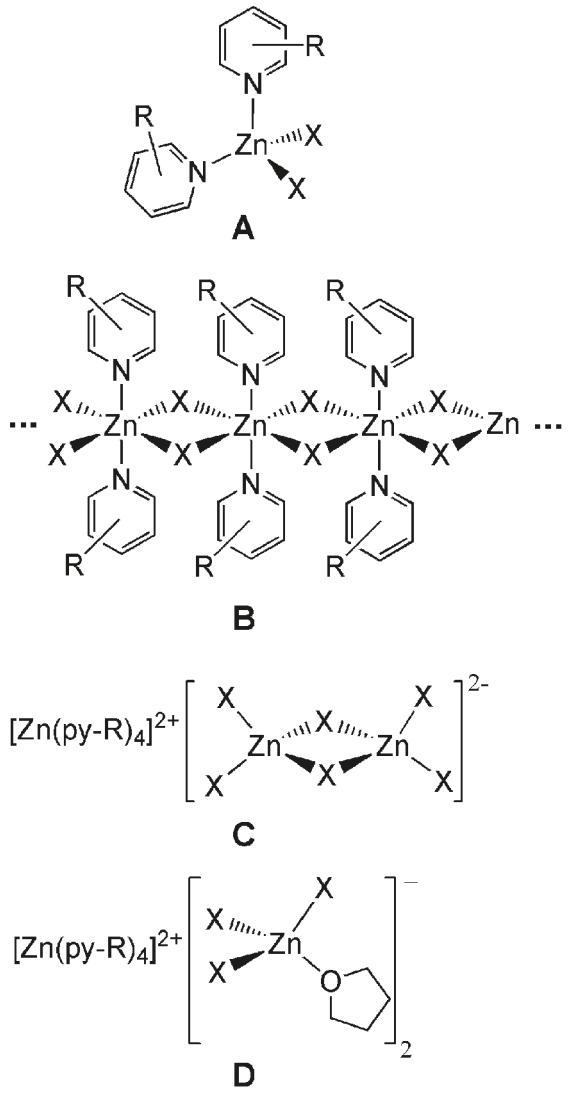

Introduction

Despite the stability of only a single cationic oxidation state, zinc displays rich and diverse coordination chemistry in both the natural and artificial (i.e., synthetic) settings (1). The formal Zn^{2+} ion binds with a large variety of ligands (1) including alkyl and aryl anions, halides, P-donor, O-donor, and N-donor fragments, etc. Many Zn materials have been isolated with heterocyclic ligands, with substituted pyridines (py–R) being a particularly noteworthy example. Several years ago, we reported our initial investigations into the coordination chemistry of the zinc(II) halides (i.e., ZnX_2) with heterocyclic bases containing a single oxazoline (i.e., 4,5-dihydro-1,3-oxazole) group. In this earlier work, we observed that the only structural motif observed (X-ray) was that of a neutral four-coordinate Zn species with a distorted tetrahedral coordination mode around the metal centre (2). Ligation to zinc in our case invariably consisted of two metal-bound halide atoms and two oxazolines, the latter of which was shown to bind through the N-atom, as expected (3). This is in sharp contrast to the complimentary py–R donor series (Fig. 1), in which tetrahedra4l (**A**), polymeric octahedral (**B**), Magnus type salts (**C**), multi-component salts (**D**), and a variety of five-coordinate structures have all been structurally characterized (4).

Fig. 2. Ligands employed in this study (**1a**–**7a**) and the structure of L-573,655 (**8**).

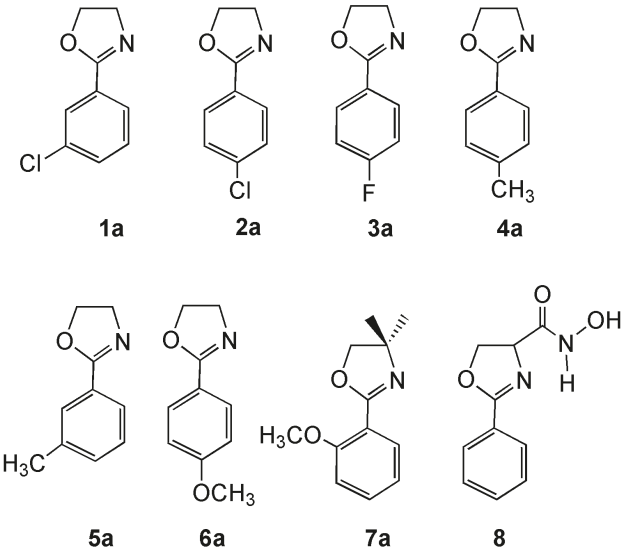

A secondary underlying theme of our research is the focus on biologically relevant metal complexes (5). In this regard, the lead drug candidate L-573,655 (**8**: Fig. 2) has been shown to inhibit *Lipid A* biosynthesis by selective binding to an enzyme-bound Zn^{2+} ion (6). This result emphasises the biological relevance and importance of the structure and variability in Zn-oxazoline complexes. In this report, we expand our fundamental investigations of the solid-state structure of Zn halide aryl-oxazoline complexes. This study reveals that although the tetrahedral coordination motif seems to dominate the coordination chemistry of ZnX_2 with oxazolines, unusual species can be produced from a simple ortho-substituted aryl oxazoline.

Results and discussion

Syntheses and spectroscopic characterization

The synthesis of the materials discussed here is quite straightforward. Treatment of diethylether solutions of ZnX_2 with an excess of oxazoline (ox) ligand (Fig. 2, **1a**–**7a**) typically leads to the rapid precipitation of a white coloured ma-

© 2008 NRC Canada

terial. This is essentially pure $(ZnX_2[ox]_n)_m$, which can then be readily recrystallized from a variety of organic solvents (e.g., CH_2Cl_2/petroleum ether mixtures, MeOH/Et_2O mixtures). Although most of the complexes reported here have quite low solubility in deuterochloroform, solubility is sufficient to obtain ^{1}H NMR spectra; attempts to obtain spectra in DMSO-d_6 or MeOH-d_4 resulted in ligand displacement by these solvents. These properties precluded ^{13}C NMR studies of these compounds. The observed spectroscopic properties (^{1}H NMR, IR, etc., see Experimental section) of these materials display the expected behaviour with respect to the free ligand form (2, 7, 8). Specifically, these data are characterized by a lowering of the IR stretching frequency assigned to the ν(C=N) absorption of the oxazoline ring system and the appearance of lower frequency bands attributed to Zn-ligand bonding vibrations (see Experimental section and refs. 8*d* and 8*e*). Other spectroscopic trends of this ligand class upon coordination to ZnX_2 have been discussed previously in some detail (2, 8*e*).

Examination of these materials by elemental analysis strongly suggests that chlorido compounds **1b**–**6b** and the bromo-containing **1c**–**6c** are characterized by the presence of two oxazolines per [ZnX_2] unit. Hence, a likely structural motif is that of the distorted tetrahedral array around the Zn atom, although polymeric materials (Fig. 1, cf., **B**) cannot be ruled out by these data. Compounds 7b and **7c**, however, analyse for a 1:1 ratio of the zinc halide unit per oxazoline. This is a situation that we did not encounter in our previous investigations (2). Thus, an examination of a number of these materials by X-ray diffraction methods was obviously in order (vide infra).

Solid-state crystal structures

Despite the widespread use of oxazolines (9) and their transition metal complexes (3*h*), there is surprisingly little structural information on Group 12 species containing mono-oxazolines (2, 3*a*, 3*h*). As stated earlier, our previous work (2) had revealed only mononuclear formally Zn^{2+} halide complexes with both alkyl- and aryl-oxazolines, all with similar bonding motifs. Unfortunately during this study, crystals suitable for X-ray diffraction of compounds **6b** and **1c** could not be obtained and therefore one can only assign a 2:1 ratio of the oxazolines to the ZnX_2 unit based on their respective elemental analyses. The rest of the compounds reported here yielded crystalline material from CH_2Cl_2 or $CHCl_3$ solutions that had been layered with excess Et_2O and (or) petroleum ether.

ZnX_2 Complexes possessing a 2:1 oxazoline/Zn ratio

The lack of suitable crystals of compounds **6b** and **1c** means that we are unable to comment any further with regards to the overall structural nature of these two complexes (Scheme 1). The crystalline material obtained of compound **5c** was invariably of only very poor quality in terms of the suitability of the crystals for X-ray diffraction analysis. As a result, the diffraction data could only be used to confirm the *global* structure of the molecule(s) in the unit cell. Although one can discern the general aspects of the atom connectivity, exact data on bond lengths, bond angles, etc. could not be obtained within acceptable experimental error. However, a mononuclear structure of this material was established that contains a Zn atom with a distorted tetrahedral array of bonded groups (comprising of two bromide atoms and two N-bonded oxazoline ligands: Fig.1, cf. **A**). This is similar to that observed (2) for ZnX_2(2-phenyl-2-oxazoline-κ$^1N)_2$ (X = Cl: **9** or Br: **10**). The other nine compounds of 2:1 oxazoline-to-metal stoichiometry reported herein (i.e., **1b**–**5b**, **2c**–**4c**, and **6c**) have all been fully characterized by single crystal X-ray diffraction. Tables 1 and 3 contain the data on the $ZnCl_2$ derivatives and Tables 2 and 3 report the results for the $ZnBr_2$ complexes. ORTEP representations of a molecule within the unit cell of each of complexes **1b**–**5b**, **2c**–**4c**, and **6c** appear in Figs. 3 to 11. Of this group, all are structural analogues of the previously reported parent materials **9** or **10** (2). This bonding motif involves two metal-bound halide atoms and two N-bound oxazolines forming a distorted tetrahedral coordination motif around the zinc atom (Scheme 1). There is little variability in the Zn–N bond lengths (Table 3), which all lie in the range of 2.03–2.08 Å and can be compared with similar bond distances of 2.026(2) and 2.050(2) Å reported for **9**, and 2.025(3) and 2.053(3) Å for **10** (2). In five of the nine novel complexes, the narrowest bond angle containing the Zn atom is the N-Zn-N angle, and perhaps not surprisingly, the larger halide atoms (vs. that of N) occupy the fragment with the larger E-Zn-E (E = donor atom) angle (Table 3 and Supplementary Data).[7] The exceptions to this trend are found with complexes **5b**, **2c**, and **3c**. All three of these compounds contain at least one N-Zn-X angle that is identical in magnitude (within experimental error) to that of the X-Zn-X angle. In contrast, compound **6c** displays an N-Zn-N angle that is larger than that of the Br-Zn-Br grouping (Table 3). This is similar to that observed in the complex $ZnBr_2$(4,4-dimethyl-2-phenyl-2-oxazoline-κ$^1N)_2$ reported previously (2). Further details on the structure of these materials can be found in the Supplementary Data.[7]

ZnX_2 Complexes possessing a 1:1 oxazoline/Zn ratio (ZnX_2 derivatives of 7a)

The analytical data of complexes **7b** and **7c** present the first examples of stoichiometric diversity within the $(ZnX_2[ox]_n)_m$ series thus far investigated. Both of these materials contain oxazoline **7a**. In terms of the ligand itself, the primary difference between this compound and other oxazolines (ref. 2 and this work) is the presence of a potentially donating substituent located on the ortho-position of the aromatic ring.[8] This leads to the formation of 1:1 complexes in both cases, regardless of the use of excess **7a** in the

[7] Supplementary data for this article are available on the journal Web site (canjchem.nrc.ca) or may be purchased from the Depository of Unpublished Data, Document Delivery, CISTI, National Research Council Canada, Ottawa, ON K1A 0R6, Canada. DUD 3867. For more information on obtaining material refer to cisti-icist.nrc-cnrc.gc.ca/cms/unpub_e.shtml. CCDC 684048–684058 contain the crystallographic data for this manuscript. These data can be obtained, free of charge, via www.ccdc.cam.ac.uk/conts/retrieving.html (Or from the Cambridge Crystallographic Data Centre, 12 Union Road, Cambridge CB2 1EZ, UK; fax +44 1223 336033; or deposit@ccdc.cam.ac.uk).

[8] Our previous work (2) included several examples of oxazoline ligands with methyl groups on oxazoline ring position-4, such as 4,4-dimethyl-2-phenyl-2-oxazoline and 2,4,4-trimethyl-2-oxazoline.

© 2008 NRC Canada

Table 1. General crystal data for the zinc chloride complexes reported herein.

Complex	**1b**	**2b**	**3b**	**4b**	**5b**	**7b**
Formula	$C_{18}H_{16}N_2O_2Cl_4Zn$	$C_{18}H_{16}N_2O_2Cl_4Zn$	$C_{18}H_{16}F_2N_2O_2Cl_2Zn$	$C_{20}H_{22}N_2O_2Cl_2Zn$	$C_{20}H_{22}N_2O_2Cl_2Zn$	$C_{24}H_{30}N_2O_4Cl_4Zn_2$
Formula mass	499.50	499.50	466.60	458.67	458.67	683.08
Crystal size (mm)	0.325 × 0.20 × 0.20	0.40 × 0.275 × 0.275	0.45 × 0.375 × 0.30	0.35 × 0.28 × 0.03	0.45 × 0.35 × 0.35	0.18 × 0.14 × 0.10
a (Å)	7.9936(19)	14.5843(7)	14.471(2)	7.746(3)	14.2616(7)	10.6836(2)
b (Å)	20.551(6)	10.2029(7)	10.151(2)	11.458(4)	10.2571(7)	13.5370(2)
c (Å)	12.445(3)	15.2384(10)	14.742(3)	12.186(4)	15.1165(9)	11.4155(3)
α (°)	90	90	90	89.477(5)	90	90
β (°)	92.456(4)	116.810(2)	118.540(5)	86.762(5)	113.168(2)	121.6680(10)
γ (°)	90	90	90	71.336(5)	90	90
V (Å^3)	2042.6(9)	2023.8(2)	1902.3(6)	1023.0(6)	2033.0(2)	1405.13(5)
D_{calc} (g/cm^3)	1.624	1.639	1.629	1.489	1.499	1.614
Crystal system, space group	Monoclinic, *C*2/*c*	Monoclinic, *C*2/*c*	Monoclinic, *C*2/*c*	Triclinic, *P*-1	Monoclinic, *C*2/*c*	Monoclinic, $P2_1/c$
Z	4	4	4	2	4	2
F(000)	1008	1008	944	472	944	696
T (K)	198(1)	213(1)	193(1)	173(1)	173(1)	173(2)
Absorption coefficient (mm^{-1})	1.742	1.758	1.607	1.479	1.488	2.120
2θ range (°)	1.98–27.50	2.54–27.49	2.57–27.49	1.67–27.49	2.52–27.49	2.58–30.04
Limiting indices	$-10 \le h \le 9$	$-18 \le h \le 18$	$-18 \le h \le 18$	$-9 \le h \le 9$	$-17 \le h \le 18$	$-15 \le h \le 13$
	$-26 \le k \le 26$	$-13 \le k \le 12$	$-13 \le k \le 13$	$-14 \le k \le 14$	$-13 \le k \le 13$	$-19 \le k \le 19$
	$-15 \le l \le 16$	$-19 \le l \le 19$	$-18 \le l \le 19$	$0 \le l \le 15$	$-19 \le l \le 19$	$-16 \le l \le 16$
Reflections collected	6 743	6 855	6 375	4 682	6 850	30 209
Reflections unique	2 273	2 279	2 115	4 682	2 273	4 101
Reflections $I > 2\sigma(I)$	2 273	2 279	2 115	4 682	2 273	4 101
Parameters	123	155	123	247	167	167
GOF on F^2	1.179	1.070	1.058	1.107	1.098	1.083
Final R indices $I > 2\sigma(I)$	R_1 = 0.0379,	R_1 = 0.0221,	R_1 = 0.0206,	R_1 = 0.0350,	R_1 = 0.0228,	R_1 = 0.0415,
	wR_2 = 0.1001	wR_2 = 0.0624	wR_2 = 0.0590	wR_2 = 0.0993	wR_2 = 0.0631	wR_2 = 0.0897
R indices (all data)	R_1 = 0.0443,	R_1 = 0.0249,	R_1 = 0.0217,	R_1 = 0.0411,	R_1 = 0.0239,	R_1 = 0.0613,
	wR_2 = 0.1020	wR_2 = 0.0640	wR_2 = 0.0597	wR_2 = 0.1015	wR_2 = 0.0637	wR_2 = 0.1014
$\rho_{min,max}$ (e Å^{-3})	1.063, –0.245	0.406, –0.146	0.337, –0.173	0.604, –0.355	0.399, –0.161	0.769, –0.745

© 2008 NRC Canada

Table 2. General crystal data for the zinc bromide complexes reported herein.

Complex	**2c**	**3c**	**4c**	**6c**	**7c**
Formula	$C_{18}H_{16}N_2O_2Cl_2ZnBr_2$	$C_{18}H_{16}F_2N_2O_2ZnBr_2$	$C_{20}H_{22}N_2O_2ZnBr_2$	$C_{20}H_{22}N_2O_4ZnBr_2$	$C_{12}H_{15}NO_2ZnBr_2$
Forumal mass	588.42	555.52	458.67	579.59	430.44
Crystal size (mm)	0.40 × 0.35 × 0.25	0.50 × 0.40 × 0.35	0.45 × 0.20 × 0.175	0.45 × 0.35 × 0.15	0.15 × 0.15 × 0.10
a (Å)	14.5424(10)	14.501(3)	14.4148(7)	10.5967(16)	6.9385(2)
b (Å)	10.3753(10)	10.360(3)	10.4163(7)	16.065(2)	20.2638(6)
c (Å)	15.4015(14)	14.918(4)	15.4021(10)	13.488(2)	12.1570(3)
α (°)	90	90	90	90	90
β (°)	117.283(2)	118.104(8)	114.098(2)	109.624(3)	118.756(2)
γ (°)	90	90	90	90	90
V (Å^3)	2065.3(3)	1976.8(9)	2111.1(2)	2162.7(6)	1498.48(8)
D_{calc} (g/cm^3)	1.892	1.867	1.723	1.780	1.908
Crystal sytem, space group	Monoclinic, *C*2/*c*	Monoclinic, *C*2/*c*	Monoclinic, *C*2/*c*	Monoclinic, $P2_1/c$	Monoclinic, $P2_1/c$
Z	4	4	4	4	4
F(000)	1152	1088	1088	1152	840
T (K)	173(1)	173(1)	213(1)	173(1)	173(2)
Absorption coefficient (mm^{-1})	5.333	5.318	4.966	4.859	6.965
2θ range (°)	2.52–27.49	2.53–27.49	2.49–27.49	2.04–27.49	2.77–27.56
Limiting indices	$-18 \le h \le 18$	$-17 \le h \le 18$	$-16 \le h \le 18$	$-13 \le h \le 12$	$-9 \le h \le 9$
	$-13 \le k \le 13$	$-13 \le k \le 13$	$-13 \le k \le 13$	$-20 \le k \le 20$	$-26 \le k \le 26$
	$-19 \le l \le 19$	$-18 \le l \le 16$	$-19 \le l \le 20$	$0 \le l \le 17$	$-15 \le l \le 15$
Reflections collected	6 961	6 624	7 203	9 531	21 620
Reflections unique	2 305	2 222	2 379	9 531	3 431
Reflections $I > 2\sigma(I)$	2 273	2 222	2 379	9 531	3 431
Parameters	155	123	124	265	168
GOF on F^2	1.057	1.066	1.055	0.972	1.083
Final *R* indices $I > 2\sigma(I)$	$R_1 = 0.0205$,	$R_1 = 0.0279$,	$R_1 = 0.0219$,	$R_1 = 0.0489$,	$R_1 = 0.0353$,
	$wR_2 = 0.0536$	$wR_2 = 0.0716$	$wR_2 = 0.0596$	$wR_2 = 0.1195$	$wR_2 = 0.0680$
R indices (all data)		$R_1 = 0.0231$,	$R_1 = 0.0330$,	$R_1 = 0.0251$,	$R_1 = 0.0658$,
		$wR_2 = 0.0536$	$wR_2 = 0.0738$	$wR_2 = 0.0609$	$wR_2 = 0.1238$
$\rho_{min,max}$ (e Å^{-3})	0.415, –0.414	0.937, –0.317	0.498, –0.338	1.014, –0.946	0.582, –0.707

Table 3. Selected bond lengths and angles for the ZnX_2 complexes reported herein (standard deviations are given in parentheses).

	Bond lengths (Å)		Bond angles (°)		Bond lengths (Å)
Complex	Zn–N	Zn–X (X = Cl or Br)	N-Zn-N	X-Zn-X (X = halogen)	C=N (oxazoline)
1b	2.039(2)	2.2298(9)	112.80(13)	116.82(6)	1.279(4)
2b	2.0489(12)	2.2371(4)	103.54(7)	115.01(3)	1.284(2)
3b	2.0408(11)	2.2350(5)	104.03(7)	113.11(3)	1.284(2)
4b	2.042(3)	2.2419(10)	109.09(11)	114.26(4)	1.284(4)
	2.041(3)	2.2317(10)			1.273(4)
5b	2.0433(11)	2.2425(4)	102.94(6)	112.51(2)	1.285(2)
2c	2.0397(14)	2.3766(3)	103.31(8)	112.42(2)	1.283(2)
3c	2.036(2)	2.3746(6)	103.96(10)	111.21(3)	1.282(3)
4c	2.0354(14)	2.3795(3)	103.59(8)	110.65(2)	1.288(2)
6c	2.045(3)	2.4039(6)	116.16(11)	113.77(2)	1.283(4)
	2.043(3)	2.4060(6)			1.276(5)
7b	2.009(2)	2.2201(7)[a]	n/a[b]	[c]	1.285(3)
		2.3152(7)[d]			
7c	1.991(3)	2.3348(6)	85.42(11)[e]	120.01(2)	1.285(5)
	2.141(3)[f]	2.3371(6)			

[a]Terminal Zn–Cl.
[b]n/a = not applicable.
[c]See Supplementary Data.[7]
[d]Bridging Zn–Cl.
[e]N-Zn-O bond angle.
[f]Zn–O bond length.

© 2008 NRC Canada

Fig. 3. ORTEP representation of a molecule of complex **1b**.

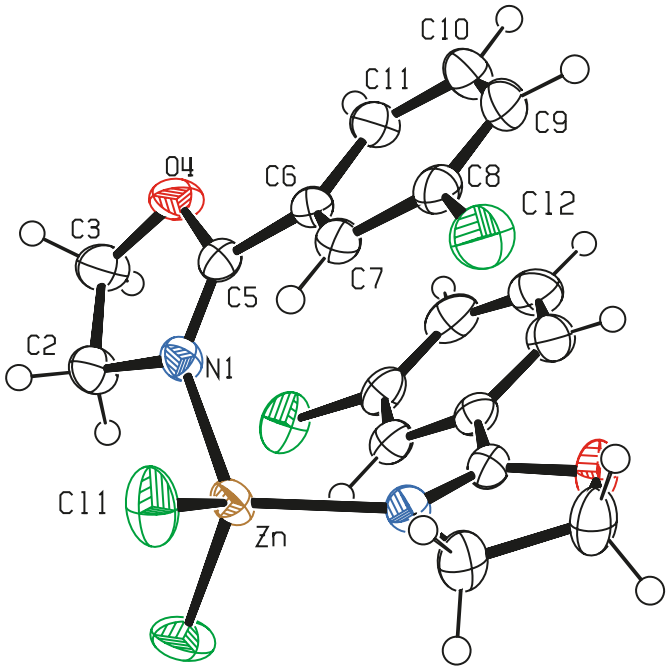

Fig. 4. ORTEP representation of a molecule of complex **2b**.

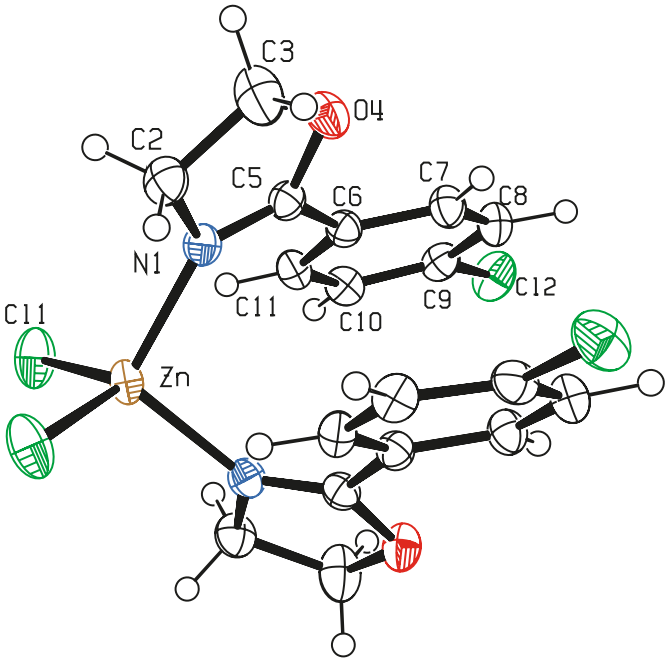

Fig. 5. ORTEP representation of a molecule of complex **3b**.

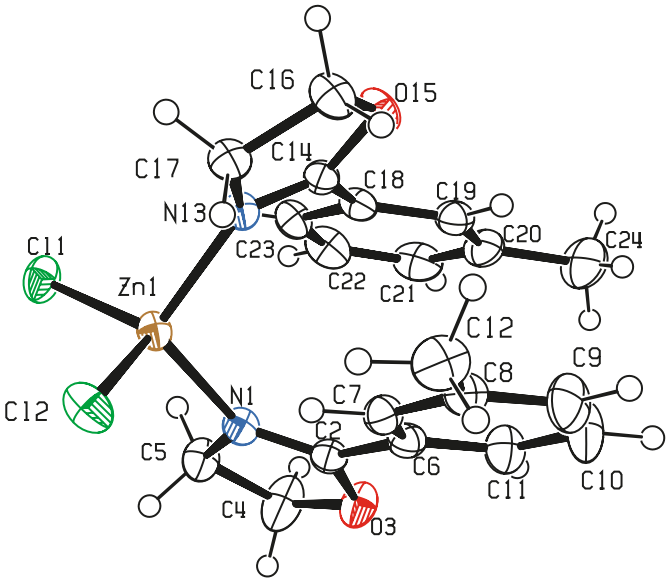

Fig. 7. ORTEP representation of a molecule of complex **5b**.

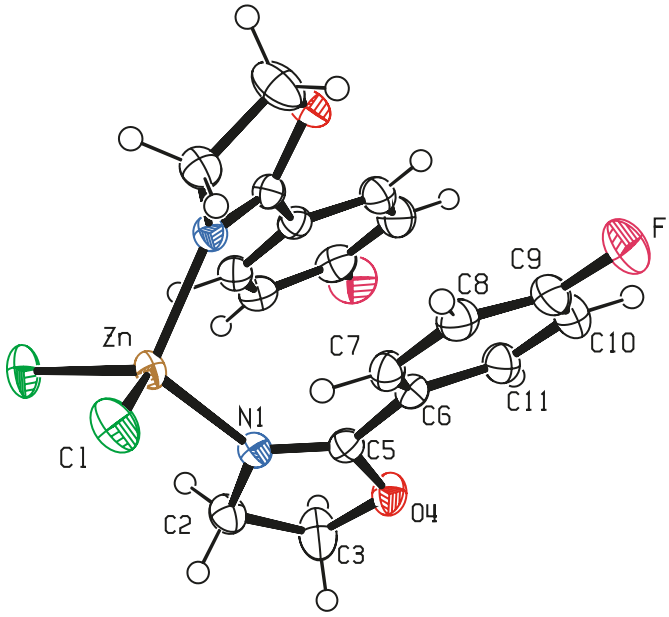

synthetic protocol. The chlorido case, complex **7b**, reveals itself (X-ray) to be a dinuclear species in which two Zn atoms are connected via two symmetry-related chloride bridges (Fig. 12). The residual coordination polyhedron around the Zn atom contains a second, albeit terminal, chloride atom. The terminal Zn–Cl bond is distinctly shorter than that found in the complimentary bridging halide (Table 3, ~2.22 vs. ~2.32 Å). In addition, a single N-bonded oxazoline is coordinated to each Zn atom. This latter ligand also displays secondary bonding interactions between the metal nucleus and the O-atom of the –OMe group contained on the aromatic ring. The Zn···O bond distance is a respectable 2.56 Å. Of particular interest in the structure of **7b** is the presence of a μ-$(X)_2$-$(M[L]X)_2$ unit (M = Group 12 element, X = halogen, L = neutral donor ligand).

Although this dimeric structure is well-known in the case of M = Cd or Hg, zinc derivatives with such a bridging motif are surprisingly rare.[9] Structurally characterized examples include the phosphine or arsine compounds μ-$(I)_2$-

[9] See the Cambridge structural database (CSD) at http://www.ccdc.cam.ac.uk/products/csd. Further information on Cd and Hg compounds containing the μ-$(X)_2$-$(M[L]X)_2$ structural unit can be found in Comprehensive coordination chemistry. Vol. 5. *Edited by* G. Wilkinson. Elsevier, Toronto, Ont., Canada, 1987. Chaps. 56.1–56.2 and Comprehensive coordination chemistry II. Vol. 6. *Edited by* J.A. McCleverty and T.J. Meyer. Elsevier, Toronto, Ont., Canada, 2003.

© 2008 NRC Canada

Fig. 6. ORTEP representation of a molecule of complex **4b**.

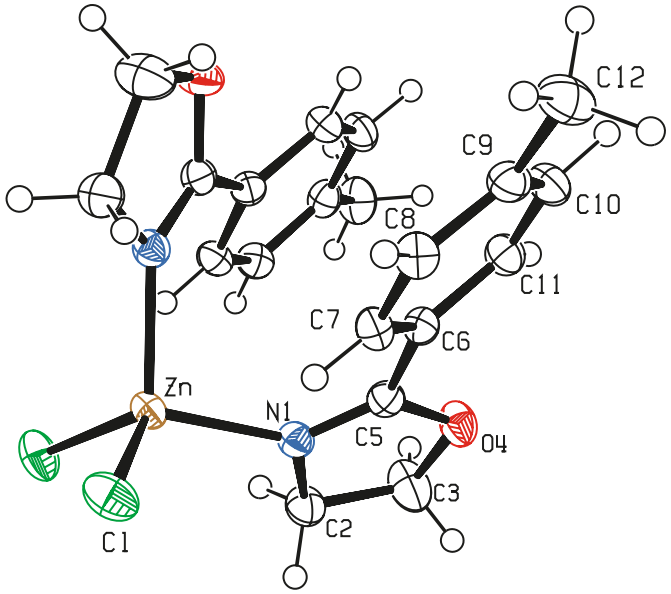

Fig. 8. ORTEP representation of a molecule of complex **2c**.

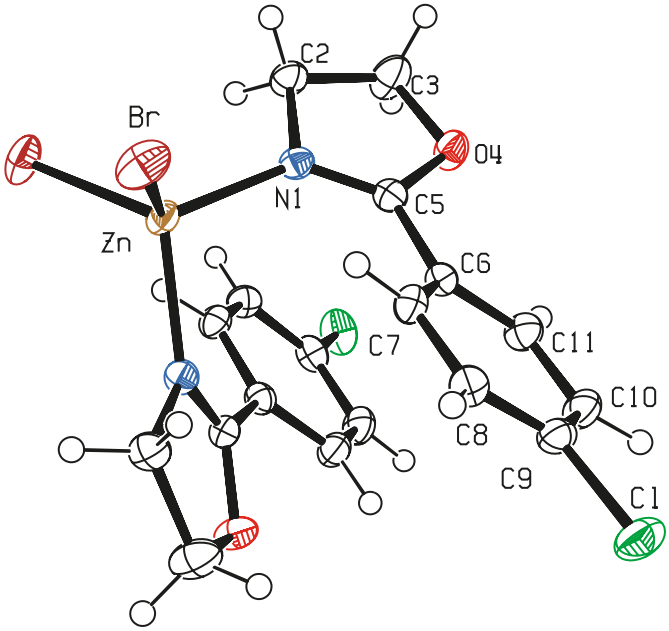

Fig. 9. ORTEP representation of a molecule of complex **3c**.

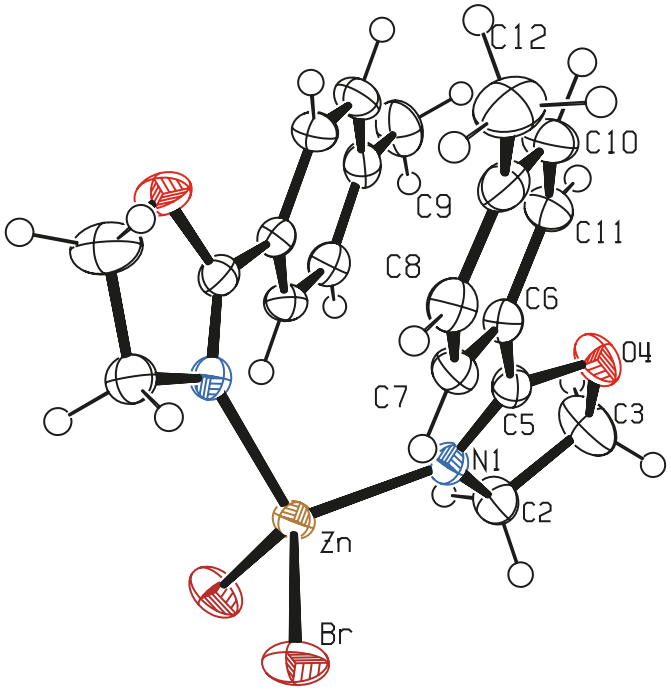

Fig. 10. ORTEP representation of a molecule of complex **4c**.

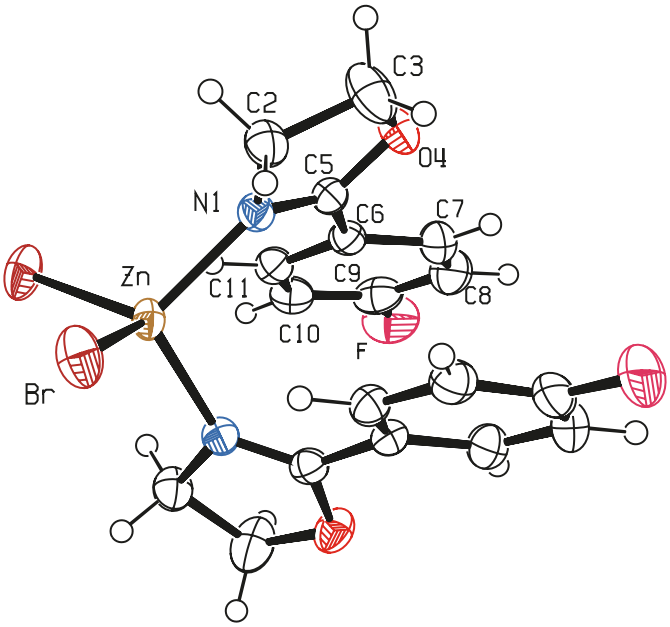

$(ZnI[P\{NMe_2\}_3])_2$ (10*a*), μ-$(I)_2$-$(ZnI[PEt_3])_2$ (10*b*), and μ-$(I)_2$-$(ZnI[AsEt_3])_2$ (10*c*), in addition to the tetranuclear nitrido complex **11** (10*d*), bridged oxo compound **12** (10*e*), tin-containing **13** (10*f*), the unusual iron carbonyl (10*g*) species **14** (Fig. 13), amongst others (10*h*, 10*i*). Hence, our material **7b** is the first oxazoline (and, in fact, imine) example of this structural motif in Zn chemistry.

The bromide analogue of complex **7b** (viz., complex **7c**) is not a structural relative of the chlorido congener (Fig. 14). With the heavier halogen, a mononuclear complex is revealed and as expected it contains only a single oxazoline ligand. This organic group is found to chelate to the $ZnBr_2$ fragment via bonding of the oxazoline N-atom and the O-atom of the –OMe group (i.e., a $\kappa^2 N,O_{OMe}$ bonding pattern). This is the only member of the series with a distinct chelate (Zn–O distance = ~2.14 Å) and the only one with an NOX_2 atomic composition of the Zn-binding set. Not surprisingly, compound **7c** displays a narrow N-Zn-O bond angle (~85°) to accommodate the chelating ligand; this is accompanied by a slightly shorter (with respect to **1b**–**5b**, **2c**–**4c**, **6c**, **9**, and **10**) Zn–N bond length (~1.99 Å). The Zn–Br bond lengths are also the shortest in this series (~2.33 Å). These data can be compared with another $ZnBr_2$ species with the NOX_2 Zn-

© 2008 NRC Canada

Fig. 11. ORTEP representation of a molecule of complex **6c**.

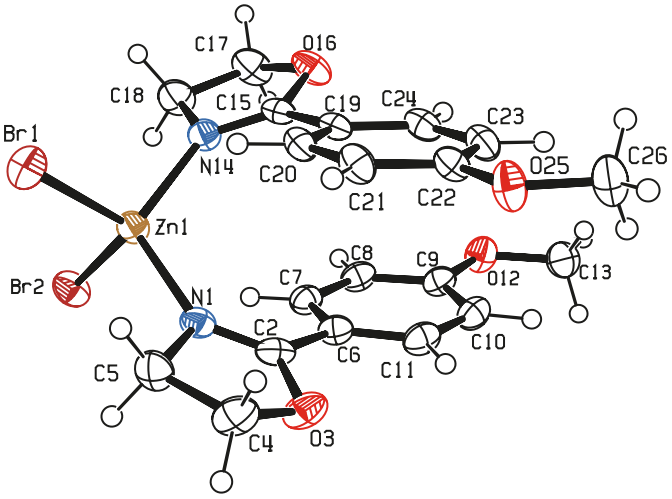

Fig. 12. ORTEP representation of a molecule of complex **7b**.

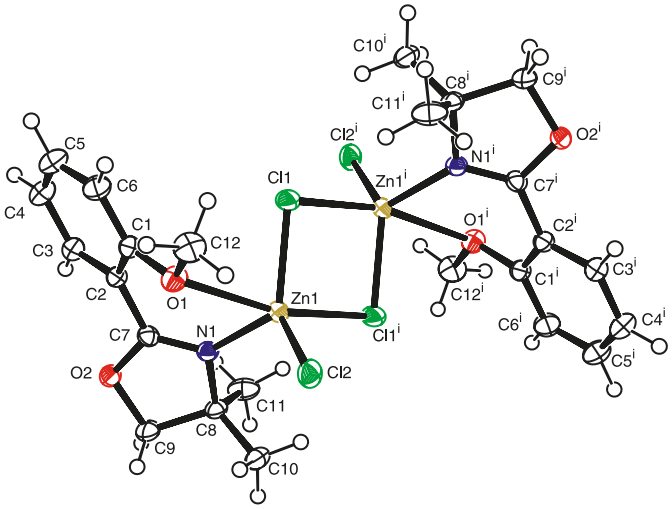

binding set, viz. 2-picoline-6-carbaldehyde-κ^2N,O zinc(II) bromide (**15**). As observed for **7c**, complex **15** (11) contains a six-membered chelate ring with a similarly narrow N-Zn-O bond angle (80.3(6)°) and similar metal-ligand bond lengths (Zn–N: 2.05(2) Å, Zn–O: 2.10(1) Å; Zn–Br: 2.314(3) and 2.334(4) Å).

In terms of potential future work in relation to the above investigations, the presence of a sterically bulky group on oxazoline ring position-2 seems to be a potential gateway for the discovery of other structural classes of Zn materials. Our intentions are to survey ligands such as 2-*t*-butyl-2-oxazoline in this regard. In terms of other bulky 2-aryl-2-oxazolines, the use of ortho-substituted aromatic groups may also lead to novel structural forms, especially if such substitution contains groups that are unlikely to form a stabilization interaction with Zn (e.g., Me, Ph, *t*-Bu, etc.). As a variety of nucleophiles are known to readily replace the –OMe group from **7a** (12), this is an obvious avenue for our continued investigations into ligand design strategies and coordination chemistry in general (13). Two further aspects that we have yet to vary are the effect of solvent(s) and the replacement of

Fig. 13. Some previously characterized relatives of complex **7b**

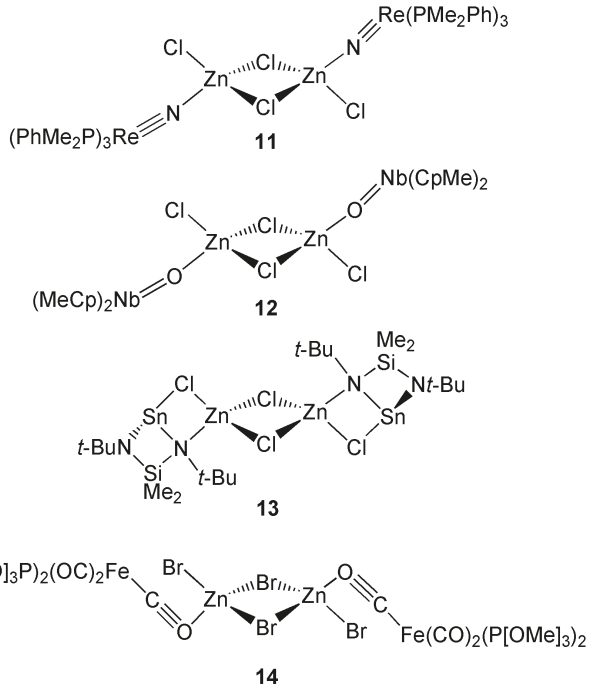

Fig. 14. ORTEP representation of a molecule of complex **7c**.

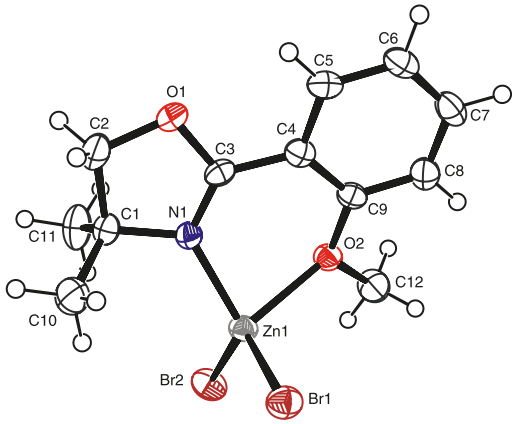

the halides for other anionic sources (e.g., NO_3^-, ClO_4^-, etc.) on the structural nature of the resulting products (Fig. 1, cf., **D**). These facets will also be included in some of our future synthetic endeavours.

Conclusions

The results reported herein greatly expand the number of structurally characterized ZnX_2 oxazoline complexes, although unfortunately the structural elucidation of compounds **6b** and **1c** has thus far eluded us. Generally speaking, 2-aryl-2-oxazoline ligands have demonstrated little structural diversity with the Zn(II) halides, regardless of the presence of electron-withdrawing (**1a**, **2a**, and (or) **3a**) or electron-donating groups (**4a**, **5a**, and (or) **6a**) located meta or para within the arene framework (Scheme 1). Although admittedly only represented here by ligand **7a**, the formation of novel binuclear Zn-imine complex **7b** or ligand chelation

© 2008 NRC Canada

Scheme 1. A summary of the products synthesized herein.

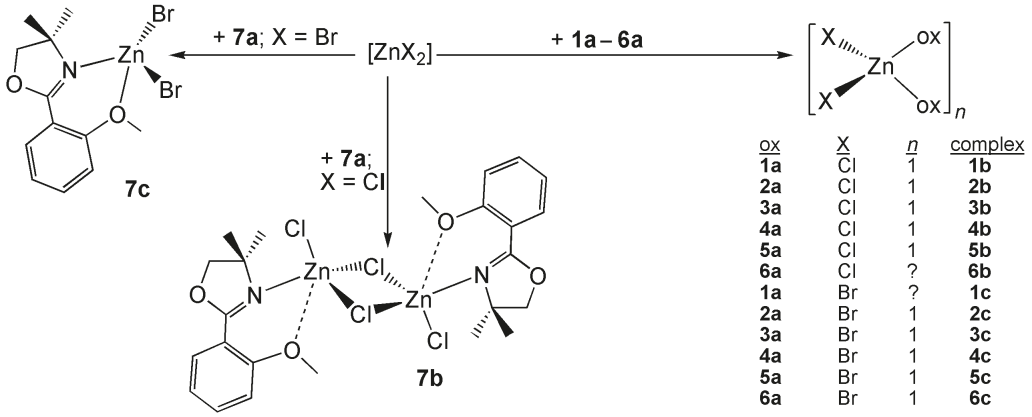

(**7c**) has been realised with an appropriately basic ortho-functionality (Scheme 1).

Experimental

General

All reactions were carried out using standard bench top techniques employing commercially available, reagent grade solvents. Zinc bromide and **7a** (Fig. 2) were purchased and used as received. Commercial zinc chloride was purified as detailed previously (2). Ligands **1a**–**6a** (Fig. 2) were synthesized using published protocols (7, 8, 14), and their purity checked by a combination of mp and ^{1}H NMR spectroscopy (7, 8). The ^{1}H NMR spectra (300 MHz) were recorded at room temperature (RT) using a Bruker Avance 300 NMR spectrometer using $CHCl_3$-*d* as solvent (except where noted); chemical shifts are reported vs. that of external $SiMe_4$ (δ_H = 0.00 ppm), which is, in turn, referenced to residual non-deuterated solvent resonance. IR data (CsCl or CsI plates) was recorded using a PerkinElmer 283B IR spectrometer and (or) a Nicolet Avatar 300 FT-IR spectrometer. Elemental analyses were carried out by the Analyst Centre (University of Toronto, Canada), the Analytical Services Department of the University of Saskatchewan, and by Lakehead University Centre for Analytical Services (Thunder Bay, Canada).

Synthesis of bis-(2-[*m*-chlorophenyl]-2-oxazoline-κ^1*N*) zinc(II) chloride (1b)

A sample of $ZnCl_2$ (0.068 g, 0.50 mmol) was dissolved in Et_2O (10 mL) and stirred at RT for 20 min. The mixture was filtered and a solution (10 mL of Et_2O) of **1a** (0.218 g, 1.20 mmol) was added. The product began to precipitate almost immediately. Stirring was continued for 24 h (RT) and the resulting solid was isolated by filtration and washed with Et_2O (15 mL) and then allowed to dry in open air. The yield of cream coloured product was 0.26 g (95%), mp 217–220 °C (decomp). IR (cm^{-1}): 1631 (s, ν[C=N]), Zn–L (L = ligand) vibrations: 295 (m) 230 (w). ^{1}H NMR δ: 4.39 (m, 2H, NCH_2), 4.57 (m, 2H, OCH_2), 7.33 (m, 1H, Ar*H*), 7.55 (m, 1H, Ar*H*), 7.62 (m, 1H, Ar*H*), 7.77 (s, 1H, Ar*H*). Anal. calcd. for $C_{18}H_{16}N_2O_2Cl_4Zn$ (%): C 43.28, H 3.23, N 5.61; found: C 43.32, H 3.12, N 5.43.

Synthesis of bis-(2-[*p*-chlorophenyl]-2-oxazoline-κ^1*N*) zinc chloride (2b)

Complex **2b** was produced in a manner similar to that of **1b** using of $ZnCl_2$ (0.068 g, 0.50 mmol) and oxazoline **2a** (0.218 g, 1.20 mmol). The yield of cream coloured product was 0.28 g (96%), mp 198–200 °C (decomp). IR (cm^{-1}): 1635 (s, ν[C=N]), Zn–L vibrations: 300 (s), 285 (s), 232 (m). ^{1}H NMR δ: 4.30 (t, *J* = 9.0 Hz, 2H, NCH_2), 4.50 (t, *J* = 9.0 Hz, 2H, OCH_2), 7.40 (d, *J* = 8.4 Hz, 2H, Ar*H*), 7.83 (d, 2H, Ar*H*). Anal. calcd. for $C_{18}H_{16}N_2O_2Cl_4Zn$ (%): C 43.28, H 3.23, N 5.61; found: C 43.30, H 3.37, N 5.24.

Synthesis of bis-(2-[*p*-fluorophenyl]-2-oxazoline-κ^1*N*) zinc(II) chloride (3b)

Complex **3b** was produced in a manner similar to that of **1b** using of $ZnCl_2$ (0.068 g, 0.50 mmol) and oxazoline **3a** (0.198 g, 1.20 mmol). The yield of cream coloured product was 0.18 g (78%), mp 229–231 °C (decomp). IR (cm^{-1}): 1633 (s, ν[C=N]), Zn–L vibrations: 296 (s), 286 (s), 232 (w). ^{1}H NMR δ: 4.33 (m, 2H, NCH_2), 4.48 (m, 2H, OCH_2), 7.10 (m, 2H, Ar*H*), 7.91 (m, 2H, Ar*H*). Anal. calcd. for $C_{18}H_{16}N_2F_2O_2Cl_2Zn$ (%): C 46.33, H 3.46, N 6.00; found: C 46.01, H 3.48, N 5.67.

Synthesis of bis-(2-[*p*-tolyl]-2-oxazoline-κ^1*N*) zinc(II) chloride (4b)

Complex **4b** was produced in a manner similar to that of **1b** using of $ZnCl_2$ (0.068 g, 0.50 mmol) and oxazoline **4a** (0.193 g, 1.20 mmol). The yield of cream coloured product was 0.18 g (79%), mp 206–209 °C (decomp). IR (cm^{-1}): 1628 (s, ν[C=N]), Zn–L vibrations: 296 (s), 288 (s). ^{1}H NMR δ: 2.44 (s, 3H, CH_3), 4.30 (m, 4H, CH_2CH_2), 7.21 (d, *J* = 8.1, 2H, Ar*H*), 7.71 (d, *J* = 8.1, 2H, Ar*H*). Anal. calcd. for $C_{20}H_{22}N_2O_2Cl_2Zn$ (%): C 52.37, H 4.83, N 6.11; found: C 51.94, H 4.88, N 6.06.

Synthesis of bis-(2-[*m*-tolyl]-2-oxazoline-κ^1*N*) zinc(II) chloride (5b)

Complex **5b** was produced in a manner similar to that of **1b** using of $ZnCl_2$ (0.068 g, 0.50 mmol) and oxazoline **5a** (0.193 g, 1.20 mmol). The yield of cream coloured product was 0.19 g (85%), mp 175–177 °C (decomp). IR (cm^{-1}): 1634 (s, ν[C=N]), Zn–L vibrations: 295 (m), 230 (w). ^{1}H

© 2008 NRC Canada

NMR δ: 2.41 (s, 3H, CH_3), 4.31 (m, 4H, NCH_2), 4.50 (t, J = 8.9, 2H, OCH_2), 7.28 (m, 1H, ArH), 7.31 (m, 1H, ArH), 7.57 (m, 2H, ArH). Anal. calcd. for $C_{20}H_{22}N_2O_2Cl_2Zn$ (%): C 52.37, H 4.83, N 6.11; found: C 51.67, H 4.82, N 6.03.

Synthesis of bis-(2-[*p*-anisolyl]-2-oxazoline-κ^1*N*) zinc(II) chloride (6b)

Complex **6b** was produced in a manner similar to that of **1b** using of $ZnCl_2$ (0.068 g, 0.50 mmol) and oxazoline **6a** (0.212 g, 1.20 mmol). The yield of cream coloured product was 0.24 g (99%), mp 230–232 °C (decomp). IR (cm^{-1}): 1626 (s, ν[C=N]), Zn–L vibrations: 300 (s), 284 (s), 234 (w). ^{1}H NMR δ: 3.89 (s, 3H, CH_3), 4.32 (m, 4H, CH_2CH_2), 6.89 (d, J = 8.7 Hz, 2H, ArH), 7.82 (d, J = 8.7 Hz, 2H, ArH). Anal. calcd. for $C_{20}H_{22}N_2O_4Cl_2Zn$ (%): C 48.96, H 4.52, N 5.71; found: C 48.21, H 4.39, N 5.52.

Synthesis of bis-(2-[*m*-chlorophenyl]-2-oxazoline-κ^1*N*) zinc(II) bromide (1c)

A sample of $ZnBr_2$ (0.112 g, 0.497 mmol) was dissolved in Et_2O and treated with **1a** (0.218 g, 1.20 mmol) dissolved in 10 mL of Et_2O. The cream coloured product (0.21 g, 82%) was isolated as for compound **1b**, mp 217–219 °C (decomp). IR (cm^{-1}): 1630 (s, ν[C=N]), Zn–L vibrations: 286 (s), 274 (m), 240 (m), 232 (m). ^{1}H NMR δ: 4.47 (m, 2H, NCH_2), 4.61 (m, 2H, OCH_2), 7.32 (m, 1H, ArH), 7.57 (m, 2H, ArH), 7.77 (s, 1H, ArH). Anal. calcd. for $C_{18}H_{16}N_2O_2Cl_2ZnBr_2$ (%): C 36.74, H 2.74, N 4.76; found: C 36.82, H 2.74, N 4.98.

Synthesis of bis-(2-[*p*-chlorophenyl]-2-oxazoline-κ^1*N*) zinc(II) bromide (2c)

Complex **2c** was produced in a manner similar to that of **1c**, using of $ZnBr_2$ (0.112 g, 0.497 mmol) and oxazoline **2a** (0.218 g, 1.20 mmol). The yield was 0.20 g (67%) of a cream coloured solid, mp 215–217 °C (decomp). IR (cm^{-1}): 1632 (s, ν[C=N]), Zn–L vibrations: 286 (m), 268 (m), 258 (m). ^{1}H NMR δ: 4.37 (t, J = 8.7 Hz; 2H, NCH_2), 4.49 (t, 2H, OCH_2), 7.39 (d, J = 8.4 Hz, 2H, ArH), 7.81 (d, 2H, ArH). Anal. calcd. for $C_{18}H_{16}N_2O_2Cl_2ZnBr_2$ (%): C 36.74, H 2.74, N 4.76; found: C 36.31, H 2.67, N 4.43.

Synthesis of bis-(2-[*p*-fluorophenyl]-2-oxazoline-κ^1*N*) zinc(II) bromide (3c)

Complex **3c** was produced in a manner similar to that of **1c**, using of $ZnBr_2$ (0.112 g, 0.497 mmol) and oxazoline **3a** (0.198 g, 1.20 mmol). The yield was 0.28 g (99%) of a cream coloured solid, mp 235–237 °C (decomp). IR (cm^{-1}): 1630 (s, ν[C=N]), Zn–L vibrations: 304 (m), 275 (w), 260 (w), 232 (w). ^{1}H NMR δ: 4.34 (m, 2H, NCH_2), 4.49 (m, 2H, OCH_2), 7.10 (m, 2H, ArH), 7.89 (m, 2H, ArH). Anal. calcd. for $C_{18}H_{16}N_2F_2O_2ZnBr_2$ (%): C 38.92, H 2.90, N 5.04; found: C 38.92, H 3.02, N 5.32.

Synthesis of bis-(2-[*p*-tolyl]-2-oxazoline-κ^1*N*) zinc(II) bromide (4c)

Complex **4c** was produced in a manner similar to that of **1c**, using of $ZnBr_2$ (0.112 g, 0.497 mmol) and oxazoline **4a** (0.193 g, 1.20 mmol). The yield was 0.27 g (99%) of a cream coloured solid, mp 224–226 °C (decomp). IR (cm^{-1}): 1624 (s, ν[C=N]), Zn–L vibrations: 304 (m), 282 (w), 270 (w). ^{1}H NMR δ: 2.44 (s, 3H, CH_3), 4.33 (m, 4H, CH_2CH_2), 7.19 (d, J = 8.1, 2H, ArH), 7.70 (d, J = 8.1, 2H, ArH). Anal. calcd. for $C_{20}H_{22}N_2O_2ZnBr_2$ (%): C 43.87, H 4.05, N 5.12; found: C 43.50, H 3.98, N 5.10.

Synthesis of bis-(2-[*m*-tolyl]-2-oxazoline-κ^1*N*) zinc(II) bromide (5c)

Complex **5c** was produced in a manner similar to that of **1c**, using of $ZnBr_2$ (0.112 g, 0.497 mmol) and oxazoline **5a** (0.193 g, 1.20 mmol). The yield was 0.22g (81%) of a cream coloured solid, mp 173–175 °C (decomp). IR (cm^{-1}): 1631 (s, ν[C=N]), Zn–L vibrations: 324 (w), 310 (w), 262 (m). ^{1}H NMR δ: 2.39 (s, 3H, CH_3), 4.36 (m, 4H, CH_2CH_2), 7.28 (m, 1H, ArH), 7.38 (m, 1H, ArH), 7.58 (m, 2H, ArH). Anal. calcd. for $C_{20}H_{22}N_2O_2ZnBr_2$ (%): C 43.87, H 4.05, N 5.12; found: C 43.24, H 3.88, N 5.02.

Synthesis of bis-(2-[*p*-anisolyl]-2-oxazoline-κ^{1}N) zinc(II) bromide (6c)

Complex **6c** was produced in a manner similar to that of **1c**, using of $ZnBr_2$ (0.112 g, 0.497 mmol) and oxazoline **6a** (0.212 g, 1.20 mmol). The yield was 0.20 g (69%) of a cream coloured solid, mp 222–224 °C (decomp). IR (cm^{-1}): 1621 (s, ν[C=N]), Zn–L vibrations: 296 (w), 286 (w), 270 (w), 232 (w). ^{1}H NMR δ: 3.89 (s, 3H, OCH_3), 4.37 (m, 4H, CH_2CH_2), 6.88 (d, J = 9.0 Hz, 2H, ArH), 7.82 (d, J = 9.0 Hz, 2H, ArH). Anal. calcd. for $C_{20}H_{22}N_2O_4ZnBr_2$ (%): C 41.45, H 3.83, N 4.83; found: C 41.81, H 3.56, N 4.76.

Synthesis of μ-bis-chloro-bis-([4,4-dimethyl-2-{*o*-anisolyl}-2-oxazoline-κ^1*N*]zinc monochloride) (7*b*)[10]

A 1.0 g sample of $ZnCl_2$ (7.3 mmol) was added to Et_2O (100 mL), and the mixture was stirred until virtually all of the zinc materials had dissolved. The mixture was then filtered and 1.52 g of **7a** (7.41 mmol) was added at RT with stirring. Within a few seconds, a white solid had precipitated from the solution. Stirring was continued for 1 h, and then the product was isolated by filtration and then washed with Et_2O (2 × 50 mL). The yield was 2.18 g (87%). IR (cm^{-1}): 1624 (s, ν[C=N]). ^{1}H NMR (acetone-d_6) δ: 1.49 (s, 6H, CH_3), 4.03 (s, 3H, OCH_3), 4.29 (s, 2H, OCH_2), 7.06 (m, 1H, ArH), 7.25 (d, 1H, J = 8.4 Hz, ArH)), 7.59 (m, 1H, ArH), 7.80 (m, 1H, ArH). Anal. calcd. for $C_{24}H_{30}N_2O_4Cl_4Zn_2$ (%): C 42.20, H 4.43, N 4.10; found: C 42.29, H 4.50, N 3.96.

Synthesis of 4,4-dimethyl-2-(*o*-anisolyl)-2-oxazoline-κ^2*N*,*O*$_{OMe}$ zinc(II) bromide (7*c*)[10]

To a sample of $ZnBr_2$ (1.0 g, 4.4 mmol) was added Et_2O (75 mL), and the mixture was stirred at RT until the Zn material had dissolved. This mixture was then filtered and oxazoline **7a** (1.13 g, 5.51 mmol) was added in a single portion. A white solid began to precipitate almost immediately. This material was isolated by filtration after 1 h of stirring at RT, and the product was then washed with Et_2O (50 mL). The yield was 1.75 g (92%). IR (cm^{-1}): 1626 (s, ν[C=N]). ^{1}H NMR δ: 1.69 (s, 6H, CH_3), 4.00 (s, 3H, OCH_3), 4.35 (*AB*-pattern, 2H, OCH_2), 7.25 (m, 2H, ArH), 7.69 (m, 1H,

[10]Optimized reaction conditions based on product stoichiometry.

© 2008 NRC Canada

Ar*H*), 7.99 (dd, J = 7.8; 1.8, 1H, Ar*H*). Anal. calcd. for $C_{12}H_{15}NO_2ZnBr_2$ (%): C 33.48, H 3.51, N 3.25; found C 33.53, H 2.96, N 3.15.

Single crystal X-ray structure determinations

X-ray structures of 1b–5b, 2c–4c, and 6c

Suitable crystals of complexes **1b**-**5b**, **2c**–**4c**, and **6c** were obtained from a CH_2Cl_2 solution of the compounds that had been layered with an equal volume of Et_2O or petroleum ether and then set aside for several days at RT. Single crystals were coated with Paratone-N oil, mounted using a glass fibre, and frozen in the cold nitrogen stream of the goniometer. A hemisphere of data was collected on a Bruker AXS P4/SMART 1000 diffractometer using ω and θ scans with a scan width of 0.3° and 10 s exposure times. The detector distance was 5 cm. The data were reduced (SAINT) (15) and corrected for absorption (SADABS) (16). The structure was solved by direct methods and refined by full-matrix least-squares on F^2 (SHELXTL). All non-hydrogen atoms were refined anisotropically. Hydrogen atoms were found in Fourier difference maps and refined isotropically (n.b., thermal ellipsoid plots are at the 30% probability level and pictorial representations are drawn at the 50% probability level) (17–20).

X-ray structures of 7b and 7c

Suitable crystals of complexes **7b** and **7c** were obtained from a CH_2Cl_2 solution of the compounds that had been layered with an equal volume of Et_2O, sealed with a rubber septum, and then set aside for several days at RT. Data was collected at –100 °C on a Nonius Kappa CCD diffractometer, using the COLLECT program (21). Cell refinement and data reductions used the programs DENZO and SCALEPACK (22). SIR97 (23) was used to solve the structure and SHELXL-97 (24) was used to refine the structure. ORTEP-3 for Windows (25) was used for molecular graphics, and PLATON (26) was used to prepare material for publication. H atoms were placed in calculated positions with U_{iso} constrained to be 1.5 times U_{eq} of the carrier atom for methyl protons and 1.2 times U_{eq} of the carrier atom for all other H atoms.

For complex **7b**, the only checkCIF ALERT is for a high Hirschfeld test (6.59 s.u.) for Zn1 Cl1A. The Cl1 atom is a bridge Cl, and this behaviour is commonly found for such atoms. For complex **7c**, the only checkCIF ALERT is at the C level. The centre of gravity of the molecule is claimed to be outside the unit cell. To us it appears inside the unit cell and PLATON does not give a new set of coordinates.

For the molecular representations found in Figs. 12 and 14, a general ORTEP (25) view of the molecule of the title compound is displayed with non-hydrogen displacement ellipsoids drawn at the 50% probability level.

Acknowledgements

The authors are indebted to the generous support of Natural Sciences and Engineering Research Council of Canada, Ryerson University, the Canadian Breast Cancer Foundation, and Acadia University. Laura Botelho is also thanked for her expert experimental assistance.

References

1. (*a*) F.A. Cotton and G. Wilkinson. Advanced inorganic chemistry. 4th ed. John Wiley and Sons, Toronto, Ont., Canada. 1980. Chap 19; (*b*) H. Vahrenkamp. Dalton Trans. 4751 (2007); (*c*) M.N. Hughes. The inorganic chemistry of biological processes. John Wiley and Sons, Toronto, Ont., Canada. 1974; (*d*) E.-I. Ochiai. Bioinorganic chemistry: An introduction. Allyn and Bacon, Toronto, Ont., Canada. 1977, Chap 13; (*e*) S.J. Archibald. Zinc. *In* Comprehensive coordination chemistry II. *Edited by* J.A. McCleverty and T.J. Meyer. Elsevier, Toronto, Ont., Canada. 2003. Chap 6.8.; (*f*) S. Aoki and E. Kimura. Zinc hydrolases. *In* Comprehensive coordination chemistry II. *Edited by* J.A. McCleverty and T.J. Meyer. Elesvier, Toronto, Ont., Canada. 2003. Chap 8.23; (*g*) R.A. Gossage. Curr. Org. Chem. **10**, 923 (2006).
2. T.M. Barclay, I. del Río, R.A. Gossage, and S.M. Jackson. Can. J. Chem. **81**, 1482 (2003).
3. (*a*) A. Decken, C.R. Eisnor, R.A. Gossage, and S.M. Jackson. Inorg. Chim. Acta, **359**, 1743 (2006); (*b*) B. Hajjem, A. Kallel, I. Svoboda, and J. Sakurai. Acta Crystallogr. Sect. C, **48**, 1002 (1992); (*c*) J.M. Atkins, S.A. Moteki, S.G. DiMagno, and J.M. Takacs. Org. Lett. **8**, 2759 (2006); (*d*) J.M. Takacs, P.M. Hrvatin, J.M. Atkins, D.S. Reddy, and J.L. Clark. New J. Chem. **29**, 263 (2005); (*e*) C. Capacchione, H. Wadepohl, and L.H. Gade. Z. Anorg. Allg. Chem. **633**, 2131 (2007); (*f*) J. Castro, S. Cabaleiro, P. Pérez-Lourido, J. Romero, J.A. García-Vázquez, and A. Sousa. Z. Anorg. Allg. Chem. **628**, 1210 (2002); (*g*) M. Seitz, M. Zabel, and O. Reiser. Acta Crystallogr. Sect E, **62**, m1517 (2006); (*h*) M. Gómez, G. Muller, and M. Rocamora. Coord. Chem. Rev. **193–195**, 769 (1999); (*i*) G. Desimoni, G. Faita, and K.A. Jørgensen. Chem. Rev. **106**, 3561 (2006); (*j*) R.A. Gossage and H.A. Jenkins. Anal. Sci. **24**, x155 (2008); (*k*) R.A. Gossage, H.A. Jenkins, N.D. Jones, R.C. Jones, and B.F. Yates. Dalton Trans. 3115 (2008); (*l*) P.N. Yadav, R.A. Gossage, and A. Decken. Anal. Sci. **24**, (2008) in press.
4. (*a*) B.K.S. Lundberg. Acta Crystallogr. **21**, 901 (1966); (*b*) R.E. Marsh and V. Schomaker. Inorg. Chem. **18**, 2331 (1979); (*c*) C. Hu and U. Englert. CrystEngComm, **23**, 1 (2001); (*d*) W.L. Steffen and G.J. Palenik. Inorg. Chem. **16**, 1119 (1977); (*e*) W.L. Steffen and G.J. Palenik. Acta Crystallogr. Sect. B, **32**, 298 (1976); (*f*) S. İde, A. Ataç, and Ş. Yurdakul. J. Mol. Struct. **605**, 103 (2002); (*g*) E. Şahin, S. İde, A. Ataç, and Ş. Yurdakul. J. Mol. Struct. **616**, 253 (2002); (*h*) H. Lynton and M.C. Sears. Can. J. Chem. **49**, 3418 (1971); (*i*) L. Fanfani, A. Nunzi, and P.F. Zanazzi. Acta Crystallogr. Sect. B, **28**, 323 (1972); (*j*) P.J.F. Le Querler, M.M. Borel, and A. Leclaire. Acta Crystallogr. Sect. B, **33**, 2299 (1977); (*k*) E.M. Cameron, W.E. Louch, T.S. Cameron, and O. Knop. Z. Anorg. Allg. Chem. **624**, 1629 (1998); (*l*) D.J. Darensbourg, S.J. Lewis, J.L. Rodgers, and J.C. Yarbrough. Inorg. Chem. **42**, 581 (2003); (*m*) I. del Río, R.A. Gossage, M.S. Hannu, M. Lutz, A.L. Spek, and G. van Koten. Can. J. Chem. **78**, 1620 (2000); (*n*) J. Qin, N. Su, C. Dai, C. Yang, D. Liu, M.W. Day, B. Wu, and C. Chen. Polyhedron, **18**, 3461 (1999); (*o*) Y. Li, Z. Liu, and H. Deng. Acta Crystallogr. Sect. E, **63**, m3065 (2007); (*p*) F.B. Panosyan, A.J. Lough, and J. Chin. Acta Crystallogr. Sect. E, **59**, m864 (2003).
5. For example see: A. Decken and R.A. Gossage. J. Inorg. Biochem. **99**, 664 (2005).
6. (*a*) C.H. Stammer, A.N. Wilson, C.F. Spencer, F.W. Bachelor, F.W. Holly, and K. Folkers. J. Am. Chem. Soc. **79**, 3236 (1957); (*b*) H.R. Onishi, B.A. Pelak, L.S. Gerckens, L.L. Sil-

© 2008 NRC Canada

ver, F.W. Kahan, M.-H. Chen, A.A. Patchett, S.M. Galloway, S.A. Hyland, M.S. Anderson, and C.R.H. Raetz. Science, **274**, 980 (1996); (*c*) T. Kline, N.H. Anderson, E.A. Hardwood, J. Bowman, A. Malada, S. Endsley, A.L. Erwin, M. Doyle, S. Fong, A.L. Harris, B. Mendelsohn, K. Mdluli, C.R.H. Raetz, C.K. Stover, P.R. White, A. Yabannavar, and S. Zhu. J. Med. Chem. **45**, 3112 (2002); (*d*) M.C. Rirrung, N. Tumey, A.L. McClerren, and C.R.H. Raetz. J. Am. Chem. Soc. **125**, 1575 (2003).

7. (*a*) A. Decken, L. Botelho, A.L. Sadowy, P.N. Yadav, and R.A. Gossage. Acta Crystallogr. Sect. E, **62**, o5414 (2006); (*b*) M. Lobert, U. Köhn, R. Hoogenboom, and U.S. Schubert. Chem. Commun. 1458 (2008).
8. (*a*) T.G. Bassiri, A. Levy, and M. Litt. Polym. Lett. **5**, 871 (1966); (*b*) S. Kobayashi, T. Tokuzawa, and T. Saegusa. Macromolecules, **15**, 707 (1982); (*c*) I. Mohammadpoor-Baltork, A.R. Khosropour, and S.F. Hojati. Synlett, 2747 (2005); (*d*) K. Nakamoto. Infrared and Raman spectra of inorganic and coordination compounds. Part B. 5th ed. John Wiley and Sons, Toronto, Ont., Canada. 1997; (*e*) E.J. Duff and M.N. Hughes. J. Chem. Soc. A, 2144 (1968).
9. For example see: (*a*) A.I. Meyers. J. Org. Chem. **70**, 6137 (2005); (*b*) K. Aoi and M. Okada. Prog. Polym. Sci. **21**, 151 (1996); (*c*) B.M. Culbertson. Prog. Polym. Sci. **27**, 579 (2002); (*d*) J.T. Banks, K.M. Button, R.A. Gossage, T.D. Hamilton, and K.E. Kershaw. Heterocycles, **55**, 2251 (2001); (*e*) A. Pfaltz. J. Heterocyclic Chem. **36**, 1437 (1999); (*f*) H.A. McManus and P.J. Guiry. Chem. Rev. **104**, 4151 (2004); (*g*) R. Rasappan, D. Laventine, and O. Reiser. Coord. Chem. Rev. **252**, 702 (2008).
10. (*a*) S.M. Godfrey, C.A. McAuliffe, R.G. Pritchard, and J.M. Sheffield. Inorg. Chim. Acta, **292**, 213 (1999); (*b*) N. Bricklebank, S.M. Godfrey, C.A. McAuliffe, A.G. Mackie, and R.G. Pritchard. J. Chem. Soc. Chem. Commun. 944 (1992); (*c*) S.M. Godfrey, C.A. McAuliffe, R.G. Pritchard, and J.M. Sheffield. J. Chem. Soc. Dalton Trans. 3309 (1996); (*d*) A. Hagenbach and J. Strähle. Z. Anorg. Allg. Chem. **625**, 1181 (1999); (*e*) P.-F. Fu, M.A. Khan, and K.M. Nicholas. Organometallics, **11**, 2607 (1992); (*f*) D.H. Gibson, J.O. Franco, B.A. Sleadd, W. Naing, M.S. Mashuta, and J.F. Richardson. Organometallics, **13**, 4570 (1994); (*g*) M. Veith, A. Müller, L. Stahl, M Nötzel, M. Jarczyk, and V. Huch. Inorg. Chem. **35**, 3848 (1996); (*h*) A. Eichhöfer, D. Fenske, and O. Fuhr. Z. Anorg. Allg. Chem. **623**, 762 (1997); (*i*) M. Krieger, K. Harms, J. Magull, and K. Dehnicke. Z. Naturforsch. **52b**, 243 (1997).
11. B. Müller and H. Vahrenkamp. Eur. J. Inorg. Chem. 137 (1999).
12. (*a*) A.I. Meyers and E.D. Mihelich. J. Am. Chem. Soc. **97**, 7383 (1975); (*b*) C.R. Ellefson, K.A. Prodan, L.R. Broughham, and A. Miller. J. Med. Chem. **23**, 977 (1980); (*c*) A.I. Meyers and W.B. Avila. J. Org. Chem. **46**, 3881 (1981); (*d*) H.W. Gschwend and A. Hamdan. J. Org. Chem. **47**, 3652 (1982); (*e*) J.W.H. Watthey, T. Gavin, M. Desai, B.M. Finn, R.K. Rodebaugh, and S.L. Patt. J. Med. Chem. **26**, 1116 (1983); (*f*) M.A. Rizzacasa and M.V. Sargent. J. Chem. Soc. Perkin Trans. 1, 2773 (1991); (*g*) M.F. Comber and M.V. Sargent. J. Chem. Soc. Perkin Trans. 1, 2783 (1991); (*h*) D.J. Carini, J.V. Duncia, P.E. Aldrich, A.T. Chiu, A.L. Johnson, M.E. Pierce, W.A. Price, J.B. Santella III, G.J. Wells, R.R. Wexler, P.C. Wong, S.-E. Yoo, and P.B.M.W.M. Timmermans. J. Med. Chem. **34**, 2525 (1991).
13. (*a*) A. Decken, R.A. Gossage, and P.N. Yadav. Can. J. Chem. **83**, 1185 (2005); (*b*) R.A. Gossage, H.A. Jenkins, and P.N. Yadav. Tetrahedron Lett. **45**, 7689 (2004) (Corrigendum: **46**, 5243 (2005)); (*c*) J.A. Cabeza, I. da Silva, I. del Río, R.A. Gossage, D. Miguel, and M. Suárez. Dalton Trans. 2450 (2006); (*d*) D. J. Berg, C. Zhou, T. Barclay, X. Fei, S. Feng, K.A. Ogilvie, R.A. Gossage, B. Twamley, and M. Wood. Can. J. Chem. **83**, 449 (2005); (*f*) J.A. Cabeza, I. da Silva, I. del Río, R.A. Gossage, L. Martínez-Méndez, and D. Miguel. J. Organomet. Chem. **692**, 4346 (2007); (*g*) K.M. Button, R.A. Gossage, and R.K.R. Phillips. Synth. Commun. **32**, 363 (2002).
14. B.F. Mundy and Y. Kim. J. Heterocyclic Chem. **19**, 1221 (1982).
15. SAINT. Version 6.45 [computer program]. Bruker AXS, Inc., Madison, Wisc., USA. 2003.
16. G.M. Sheldrick. SADABS. Version 2.10 [computer program]. Bruker AXS, Inc., Madison, Wisc., USA. 1997.
17. SHELXTL. Version 6.14 [computer program]. Bruker AXS, Inc., Madison, Wisc., USA. 2000.
18. GEMINI. Version 1.0 [computer program]. Bruker AXS, Inc., Madison, Wisc., USA. 1999.
19. RLATT. Version 2.72 [computer program]. Bruker AXS, Inc., Madison, Wisc., USA. 1999.
20. SMART. Version 5.054 [computer program]. Bruker AXS, Inc., Madison, Wisc., USA. 1999.
21. Nonius. COLLECT. Nonius BV, Delft, The Netherlands. 1998.
22. Z. Otwinowski and W. Minor. Macromolecular crystallography. Part A. *In* Methods in Enzymology. Vol. 276. Part A. *Edited by* C.W. Carter and R.M. Sweet. Academic Press, London, UK. 1997. pp. 307–326.
23. A. Altomare, M.C. Burla, M. Camalli, G. Cascarano, C. Giacovazzo, and A. Guagliardi. SHELXTL. Version 6.10 [computer program]. Bruker-AXS, Madison, WI. 2000.
24. G.M. Sheldrick. SHELXL-97. University of Göttingen. Germany. 1997.
25. L.J. Farrugia. J. Appl. Cryst. **30**, 565 (1997).
26. A.L. Spek. PLATON [computer program]. University of Utrecht, The Netherlands. 2001.

© 2008 NRC Canada

Phenylene-1,4- and biphenylene-4,4′-diselenolate bridged complexes of gold(I)[1]

Deeb Taher, Nicholas J. Taylor, and John F. Corrigan

Abstract: Homobimetallic gold-selenolate complexes of the type [(Ph_2R)PAuSe(C_6H_4)$_n$SeAuP(Ph_2R)] (**3a**, *R* = Et, *n* = 1; **3b**, *R* = Et, *n* = 2; **5a**, *R* = Ph, *n* = 1; **5b**, *R* = Ph, *n* = 2) are obtained by the reaction of [Ph_2RPAuCl] (**1**, *R* = Et; **4**, *R* = Ph) with 0.5 equiv. of $Me_3SiSe(C_6H_4)_nSeSiMe_3$ (**2a**, *n* = 1; **2b**, *n* = 2) in good yield. Complex [(Pr_3P)AuSe(C_6H_4)$_2$SeAu(PPr_3)] **7b** can be prepared in a two-step synthesis procedure: treatment of [AuCl(SMe_2)] **6** with 0.5 equiv. of $Me_3SiSe(C_6H_4)_2SeSiMe$**3 2b** gives [(Me_2S)AuSe(C_6H_4)$_2$SeAu(SMe_2)], which further reacts with PPr_3 to afford **7b**. The new gold-selenolate complexes have been characterized by multinuclear NMR (^{1}H, ^{31}P, ^{77}Se) and elemental analysis. The solid state structures of **3b**, **5a**, and **7b** were determined by single X-ray structure analysis.

Key words: gold, dimer, selenolate, biphenylene, phenylene.

Résumé : La réaction des produits de formule générale [Ph_2RPAuCl] (**1**, *R* = Et; **4**, *R* = Ph) avec 0,5 équivalents de $Me_3SiSe(C_6H_4)_nSeSiMe_3$ (**2a**, n = 1; **2b**, n = 2) conduit à la formation de complexes homobimétalliques sélénolate d'or du type [(Ph_2R)PAuSe(C_6H_4)$_n$SeAuP(Ph_2R)] (**3a**, *R* = Et, *n* = 1; **3b**, *R* = Et, *n* = 2; **5a**, *R* = Ph, *n* = 1; **5b**, *R* = Ph, *n* = 2) avec de bons rendements. On peut préparer le complexe [(Pr_3P)AuSe(C_6H_4)$_2$Au(PPr_3)] (**7b**) par une méthode de synthèse en deux étapes dans laquelle le traitement du [AuCl(SMe_2)] (**6**) avec 0,5 équivalents de $Me_3SiSe(C_6H_4)_2SeSiMe_3$ (**2b**) conduit à la formation du [(Me_2S)AuSe(C_6H_4)$_2$SeAu(SMe_2)] qui, par réaction subséquente avec du PPr_3, fournit le produit **7b**. Les nouveaux complexes sélénolates d'or ont été caractérisés par la RMN multinucléaire (^{1}H, ^{31}P et ^{77}Se) et par analyse élémentaire. Faisant appel à la diffraction des rayons X, on a déterminé les structures des produits **3b**, **5a** et **7b** à l'état solide.

Mots-clés : or, dimère, sélénolate, biphénylène, phénylène.

[Traduit par la Rédaction]

Introduction

The coordination chemistry of Au(I) is a most important branch of inorganic chemistry (1), and in particular there has been considerable interest in the study of gold(I) phosphine complexes of the type R_3PAuL (L = anionic ligand) in part because of the successful use of auranofin (a second-line, orally administered gold drug) for the treatment of rheumatoid arthritis (2, 3). Recent reviews by McKeage et al. (4) and Tiekink (5) also highlight that Et_3PAuCl and other gold(I) phosphine complexes can act as potential anti-tumor agents. With the rapid explosion of the ligand chemistry of the heavier chalcogen elements, it is somewhat surprising that the chemistry of gold selenolates has been the focus of less attention, despite the great possibilities that the compounds can offer regarding their structures (6). Gold(I) selenolates, including mononuclear gold(I) complexes of the type [Au(Se*R*)(PR_3)] (7, 8), have been prepared by the reaction of gold(I) chloride with selenols (9), or alkali metal selenolate salts (10, 11, 12), the coupling of stannyl diselenolate (13), the reaction with $PhSeSiMe_3$ (14, 15), as well as reactions between gold(I) chloride with organic selenolate ligands in the presence of $AgSbF_6$ (15). They have also been prepared by the reaction $Ph_3PAuN(SiMe_3)_2$ with selenols (16).

As part of our continued interest in developing the structural chemistry of metal–selenium interactions with conjugated diselenolate ligands (17), we report here a simple and efficient method for the synthesis and characterization of a small series of dimeric gold(I) selenolate complexes incorporating phosphines as ligands. These represent the first structures for gold selenolates of this type.

Results and discussion

When RPh_2PAuCl (**1**, *R* = Et; **4**, *R* = Ph) was reacted with 0.5 equimolar amounts of 1,4-bis(trimethylsilylseleno)-phenylene (**2a**) or biphenylene-4,4′-bis(trimethylsilylselenium)

Received 25 July 2008. Accepted 18 August 2008. Published on the NRC Research Press Web site at canjchem.nrc.ca on 3 December 2008.

Dedicated with thanks and admiration to Richard J. Puddephatt: a more magnanimous colleague will never be found.

D. Taher and J.F. Corrigan.[2] Department of Chemistry, The University of Western Ontario, London, ON N6A 5B7, Canada.
N.J. Taylor.[3] Department of Chemistry, University of Waterloo, Waterloo, ON N2L 3G1, Canada.

[1]This article is part of a Special Issue dedicated to Professor R. Puddephatt.
[2]Corresponding author (e-mail: corrigan@uwo.ca).
[3]Deceased.

 doi:10.1139/V08-159 © 2008 NRC Canada

Scheme 1.

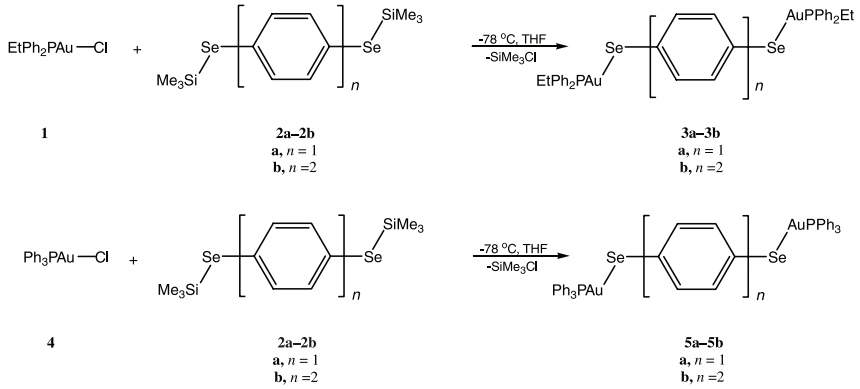

Table 1. Selected NMR spectroscopic data for **3a**, **3b**, **5a**, and **5b** in $CDCl_3$ and yield.

Compound	^{31}P	^{77}Se	Yield (%)
3a	38.9	148.6	72
3b	41.4	157.0	75
5a	39.9	148.2	71
5b	39.6	156.6	73
7b	32.5	143.7	75

Note: Chemical shifts are reported in ppm.

Table 2. A summary of the bond lengths and angles.

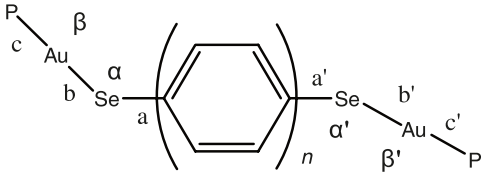

Compounds	**3b**	**5a**	**7b**
Bond lengths (Å)			
a	1.88(1)	1.93(1)	1.94(1)
a′	1.88(1)	1.90(1)	1.91(1)
b	2.409(1)	2.408(1)	2.407(1)
b′	2.409(1)	2.401(2)	2.407(2)
c	2.271(2)	2.264(3)	2.274(4)
c′	2.271(2)	2.263(4)	2.265(4)
Bond angles (°)			
α	105.5(3)	103.2(4)	102.1(4)
α′	105.5(3)	103.5(4)	105.2(4)
β	173.47(7)	178.95(8)	179.6(1)
β′	173.47(7)	175.26(9)	178.4(1)

(**2b**), the digold(I) selenolate complexes [(*R*Ph_2P)AuSe-(C_6H_4)$_n$SeAu(PPh_2*R*)] (**3a**, *R* = Et, *n* = 1; **3b**, *R* = Et, *n* = 2; **5a**, *R* = Ph, *n* = 1; **5b**, *R* = Ph, *n* = 2) are formed, with the elimination of Me_3SiCl (Scheme 1). After appropriate work-up, **3a**, **3b**, **5a**, and **5b** can be isolated in yields between 71% and 75% as pale yellow solids.

Air stable **3a**, **3b**, **5a**, and **5b** are soluble in common organic solvents, including dichloromethane and chloroform. They were characterized by ^1H, $^{31}P\{^1H\}$, and $^{77}Se\{^1H\}$ NMR spectroscopy. The results are summarized in Table 1.

The ^1H NMR spectrum of [($EtPh_2P$)AuSeC_6H_4SeAu(PPh_2Et)] **3a** displays, in addition to the aromatic and aliphatic resonances from the phosphine ligands, a singlet for the aryl protons of the 1,4-phenylene moiety at 7.41 ppm. The $^{31}P\{^1H\}$ NMR spectra of solutions of **3a** display one singlet for the two equivalent phosphorus atoms at 38.9 ppm with no evidence for satellites arising from $^2J_{PSe}$ coupling. The $^{77}Se\{^1H\}$ NMR spectrum consists of a singlet for the two equivalent selenium atoms at 148.6 ppm. Reactions with triphenylphosphine gold(I) chloride proceeded under similar conditions to yield 1,4-[(Ph_3P)AuSeC_6H_4SeAu(PPh_3)] **5a**. Small, single crystals of **5a** were obtained by diffusing *n*-pentane onto CH_2Cl_2 solutions, isolated as the CH_2Cl_2 solvate. The structural parameters are summarized in Table 2, and the crystallographic details are provided in the Experimental section (Table 3). The structure of **5a** (Fig. 1) confirms the expected, near liner coordination about the Au(I) centres (P-Au-Se = 178.95(8)° for Au1 and 175.26(9)° for Au2). The two Ph_3PAuSe units are nearly parallel (deviation = 1.1°), with each rotated out of the plane defined by the C_6 phenylene spacer by 99°.

Schmidbaur and co-workers (18) reported recently that treatment of phenylene-1,4-diol with [{(*p*-$CH_3C_6H_4$)$_3$PAu}$_3$O][BF_4] in a 1:1 ratio leads to the formation of the tetragold dicationic complex 1,4-[{(*p*-$CH_3C_6H_4$)$_3$PAu}$_2$$SC_6H_4$S{Au(P-*p*-$C_6H_4CH_3$)$_3$}$_2$][$BF_4$]$_2$. This also leads to short intramolecular (3.16–3.21 Å) and intermolecular (2.97–3.16 Å) Au–Au interactions and an infinite chain-like arrangement of the 1,4-[$(Au)_2SC_6H_4S(Au)_2]^{2+}$ repeat units (18). In **5a**, no significant Au···Au interactions are present, with distances (4.45 Å) significantly longer than the sum of the van der Waals radii (3.6 Å). A "head-to-tail" arrangement of adjacent Ph_3P-Au fragments leads to the crystallographic repeat observed in **5a**, with only weak interactions between adjacent 1,4-[(Ph_3P)AuSeC_6H_4SeAu(PPh_3)] (Au···Se = 3.37 and 3.54 Å) (Fig. 2).

The ^1H NMR spectra of biphenylene bridged 4,4′-[($EtPh_2P$)AuSe(C_6H_4)$_2$SeAu(PPh_2Et)] **3b** and 4,4′-[(Ph_3P)AuSe(C_6H_4)$_2$SeAu(PPh_3)] **5b** display two doublets at 7.68 and 7.24 ppm, and 7.73 and 7.24 ppm, respectively, for the equivalent protons of the biphenylene rings. Consistent with the proposed structures, the $^{31}P\{^1H\}$ NMR spectrum displays one signal for the equivalent phosphorus atoms (41.4 ppm for **3b** and 39.6 for **5b**), and the $^{77}Se\{^1H\}$ NMR spectrum shows the expected equivalence of the AuSe(C_6H_4)$_2$SeAu groups with one signal for each complex

© 2008 NRC Canada

Table 3. Crystallographic data summary for complexes **3b**, **5a**, and **7b**.

	3b	**5a**	**7b**
Empirical formula	$C_{40}H_{38}Au_2P_2Se_2$	$C_{43}H_{36}Au_2Cl_2P_2Se_2$	$C_{30}H_{50}Au_2P_2Se_2$
Wavelength		0.710 73	
Temp (K)	295	150	150
Radiation type		Mo Kα	
Space group	*P*2(1)/*n*	*P*2(1)/*c*	*P*-1
a (Å)	13.214(1)	19.045(2)	8.4172(3)
b (Å)	9.9501(9)	15.0517(6)	12.6614(5)
c (Å)	14.366(1)	15.583(1)	17.4832(8)
α (°)			110.580(2)
β (°)	95.403(3)	113.930(1)	99.271(3)
γ (°)			95.174(3)
μ (mm^{-1})	9.840	9.200	10.875
Diffractometer	Bruker APEX	Nonius Kappa CCD	Nonius Kappa CCD
F(000)	1068	2336	972
θ range (°)	2.00–26.37	2.34–27.55	2.48–27.70
Index ranges	$-13 \le h \le 16$	$-24 \le h \le 24$	$-10 \le h \le 10$
	$-12 \le h \le 11$	$-12 \le k \le 19$	$-16 \le k \le 16$
	$-17 \le k \le 16$	$-20 \le l \le 20$	$-22 \le l \le 22$
No. of reflns collected	8661	14974	14635
No. of ind. reflns	3843	9362	7776
R indices [$(I) > 2\sigma(I)$]	$R_1 = 0.0481$	$R_1 = 0.0657$	$R_1 = 0.0883$
	$wR_2 = 0.0591$	$wR_2 = 0.1521$	$wR_2 = 0.2332$
R indices (all data)	$R_1 = 0.0954$	$R_1 = 0.1612$	$R_1 = 0.1055$
	$wR_2 = 0.0654$	$wR_2 = 0.1976$	$wR_2 = 0.2485$
Refinement method	Full-matrix least-squares on F^2		
Refinement software	SHELXTL		

Note: $R_1 = \Sigma \left| |F_o| - |F_c| \right| / \Sigma |F_o|$; $wR_2 = \{\Sigma [w(F_o^2 - F_c^2)^2 / \Sigma [wF_o^2]^2]\}^{1/2}$.

Fig. 1. A perspective view of the molecular structure of 1,4-[$(Ph_3P)AuSeC_6H_4SeAu(PPh_3)$] **5a**. Thermal ellipsoids are drawn at the 40% probability level.

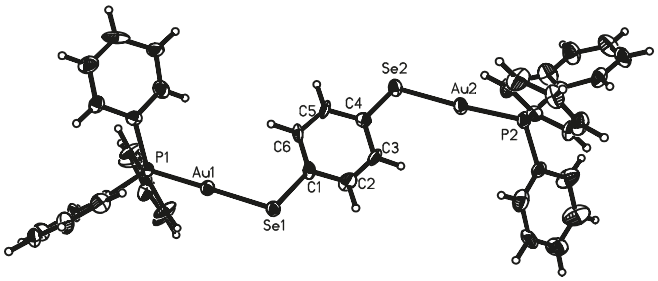

Fig. 2. The packing of 1,4-[$(Ph_3P)AuSeC_6H_4SeAu(PPh_3)$] **5a** in the crystal (hydrogen atoms omitted).

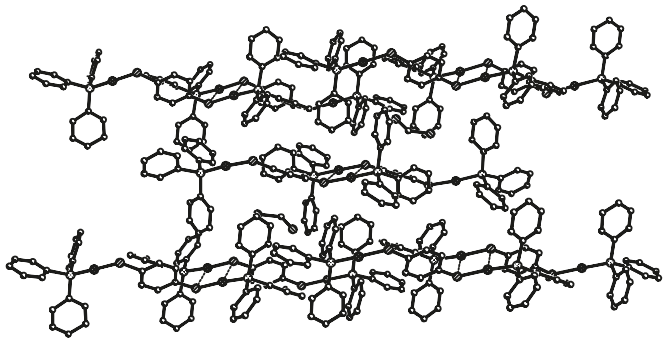

(**3b**: 157.0; **5b**: 156.6 ppm). The $^{31}P\{^1H\}$ NMR data are similar to those reported for related (triphenylphosphine)gold(I) thiolate and selenolate complexes (12, 19, 20, 21). The ^{77}Se NMR shifts of the biphenylene linked **3b** and **5b** resonate at higher field than their 1,4-phenylene linked counterparts **3a** and **5a**.

Crystals of 4,4′-[$(EtPh_2P)AuSe(C_6H_4)_2SeAu(PPh_2Et)$] **3b** were obtained from layering CH_2Cl_2 solutions with pentane. A summary of bond lengths and angles is provided in Table 2. Molecular **3b** resides about a crystallographic inversion centre (monoclinic space group $P2_1/n$), which bisects the atoms labelled C4-C4A (Fig. 3). The two C_6 rings are thus crystallographically co-planar and thus similar to the reported 4,4′-[$Cl(Bu_3P)_2PdSe(C_6H_4)_2SePd(PBu_3)_2Cl$] (17) and 4,4′-[$(Cy_3P)AuS(C_6H_4)_2SAu(PCy_3)$] (18). The Au centres in **3b** deviate from linearity (173.47(7)) sightly more than was oberved in **5a**. There are no significant intermolecular interactions.

Treatment of $(Me_2S)AuCl$ in THF solution with $Me_3SiSe(C_6H_4)_2SeSiMe_3$ (**2b**) at –78 °C produced an insoluble material ("$(Me_2S)AuSe(C_6H_4)_2SeAu(SMe_2)$") which can be used without isolation for the preparation of trialkylphosphine stabilized $(R_3P)AuSe(C_6H_4)_2SeAu(PR_3)$. The addition of two equivalents of PPr_3 to a suspension of $(Me_2S)AuSe(C_6H_4)_2SeAu(SMe_2)$ (at –78 °C) resulted in a clear solution from which weakly diffracting single crystals

© 2008 NRC Canada

Fig. 3. A perspective view of the molecular structure of 4,4′-[$(EtPh_2P)AuSe(C_6H_4)_2SeAu(PPh_2Et)$] **3b**. Thermal ellipsoids are drawn at the 40% probability level.

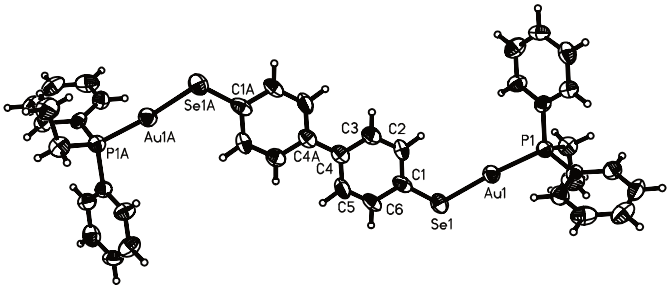

Fig. 4. The molecular structure of 4,4′-[$(Pr_3P)AuSe(C_6H_4)_2SeAu(PPr_3)$] **7b**. Thermal ellipsoids are drawn at the 40% probability level.

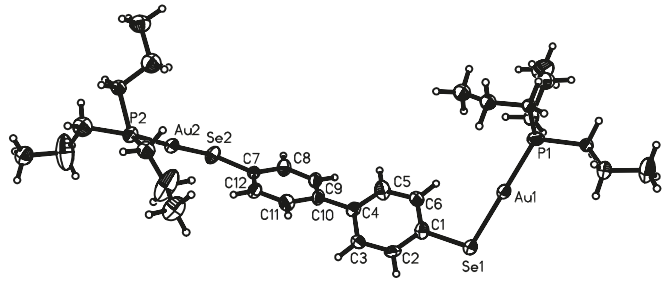

of 4,4′-[$(Pr_3P)AuSe(C_6H_4)_2SeAu(PPr_3)$] **7b** could be isolated. ^1H NMR spectra for **7b** display the expected signals for the equivalent propyl groups at 1.80, 1.58, 1.02 ppm with the aromatic resonances at 7.65 and 7.28 ppm, and in the $^{31}P\{^1H\}$ NMR spectrum the equivalent phosphorus units gives rise to single signal at 32.5 ppm. The $^{77}Se\{^1H\}$ shows a singlet at 143.7 ppm. Attempts to prepare 4,4′-[$(EtPh_2PAuSe(C_6H_4)_2SeAu(PPh_2Et)]$ **3b** and 4,4′-[$(Ph_3PAuSe(C_6H_4)_2SeAu(PPh_3)]$ **5b** from ("$(Me_2S)AuSe(C_6H_4)_2SeAu(SMe_2)$") via the addition of PPh_2Et were unsuccessful, as the suspended precipitate did not dissolve with the addition of the larger, less basic phosphine ligand in a variety of common organic solvents. Similarly, attempts to prepare 4,4′-[$(Pr_3P)AuSe(C_6H_4)_2SeAu(PPr_3)$] **7b** from 4,4′-$Me_3SiSe(C_6H_4)_2SeSiMe_3$ **2b** Pr_3PAu-Cl led to only poor yields of **7b**.

X-ray diffraction analysis of single crystals of **7b** illustrate that the molecular geometry in the solid state is markedly different than that oberved for **3b** (Fig. 4). Unlike the planar C_6-C_6 structure observed in **3b**, the two phenylene rings in **7b** are rotated such that there is a 35.9° angle between them, similar to what was reported in 4,4′-[{$(p$-$CH_3C_6H_4)_3PAuS(C_6H_4)_2S\{Au(P$-$p$-$C_6H_4CH_3)_3\}_2]^+$ (40.3°). Unlike in **3b**, the P-Au-Se moieties asymmetrically lie on the same side of the biphenylene spacer, with a 42.4° angle between the two Se-Au-P vectors (Fig. 5). The Au-Se and Au-P distances are, however, similar to those oberved in **3b** and **5a** (Table 2).

In summary, the facile preparation of **3**, **5**, and **7b** from ligated Au-Cl and silylated selenium reagents has led to the first examples of dinuclear AuSe-spacer-SeAu. The strategies employed herein lend themselves to facile adaptation using didentate ligands (e.g., [$ClAuPPh_2(CH_2)_xPh_2PAuCl$]),

Fig. 5. A projection along the inter-ring C–C bond in 4,4′-[$(Pr_3P)AuSe(C_6H_4)_2SeAu(PPr_3)$] **7b** illlustrating the orientation of the phenylene rings and the Au-Se-P moeities (propyl chains omitted).

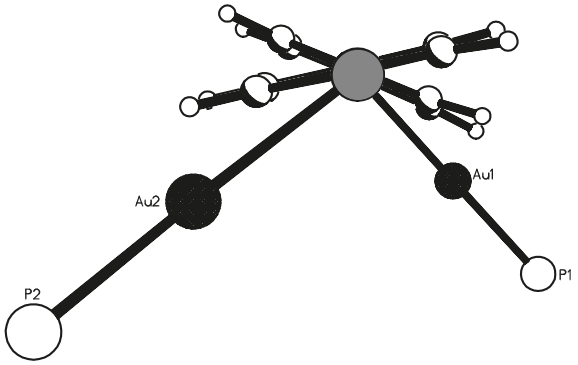

which would allow for the preparation of coordination polymers (23) of the type $[AuPPh_2(CH_2)_xPh_2PAuSe(C_6H_4)_2Se]_n$. We are currently developing these avenues of research.

Experimental section

All syntheses were carried out under an atmosphere of high-purity dried nitrogen using standard double-manifold Schlenk line techniques and nitrogen-filled gloveboxes. Solvents were dried and collected using an MBraun MB-SP Series solvent purification system. Chloroform-*d* was dried and distilled over P_2O_5. NMR spectra [^1H (399.763 MHz), $^{13}C\{^1H\}$ (100.522 MHz), $^{77}Se\{^1H\}$ (76.217 MHz)] were recorded on a Varian Inova 400 NMR spectrometer. ^1H and ^{13}C NMR chemical shifts were referenced internally to $SiMe_4$ using the residual proton and carbon signal of the deuterated solvent, respectively. ^{77}Se $\{^1H\}$ spectra were referenced to external standards $C_6H_5SeSiMe_3$ at +85.6 ppm, relative to Me_2Se at 0 ppm. Elemental analyses were performed by Guelph Chemical Laboratories (Guelph, Canada). Crystals of **3b** and **7b** were mounted immersed in cooled mineral oil and placed in a cold stream of N_2 during data collection. X-ray structural analyses were carried out on Bruker AXS (**3b**) and Enraf-Nonius Kappa CCD (**5a** and **7b**) single-crystal X-ray diffractometers. Data were corrected for Lorentz and polarization effects. The SHELXTL (G.M. Sheldrick, Madison, Wisconsin, USA) program package was used to solve (direct methods, Au, Se, and P) and refine the structures. The weighting scheme employed was of the form $w = 1/[\sigma^2(F_o^2) + (aP)^2 + bP]$ (a, b = refined variables, $P = 1/3\ \max(F_o^2, 0) + 2/3\ F_c^2$). All non-hydrogen atoms, with the exception of disordered carbon centers, were refined with anisotropic thermal parameters. Hydrogen atoms were included as riding on their respective carbon atoms. The structures solved and refined without complications, with the following exceptions: In **3b**, a solvent moleceule of crystallization (CH_2Cl_2) was refined as disordered over two sites with restrained geometries; in **7b**, many of the carbon atoms of the propyl chains were disordered over two sites. A satisfactory model with 50:50 occupancy was refined using mild restraints (SADI command). All non-hydrogen atoms, with the exception of disordered carbon centres, were refined with anisotropic thermal parameters.

© 2008 NRC Canada

Hydrogen atoms were included as riding on their respective carbon atoms.[4]

Materials

Phenylene-1,4-bis(trimethylsilylselenium) and biphenylene-4,4′-bis(trimethylsilylselenium) (17), [AuCl(SMe_2)] (22), and R_3PAuCl (23) were synthesized according to literature procedures.

Synthesis of $EtPh_2PAuSeC_6H_4SeAuPPh_2Et$ (3a)

$EtPh_2PAuCl$ (220.7 mg, 0.494 mmol) was added in one portion to 1,4-$C_6H_4(SeSiMe_3)_2$ (94.0 mg, 0.247 mmol) in tetrahydrofuran (30 mL) at –78 °C and warmed to room temperature (RT) after 15 min. After 2 h of stirring at RT, all volatiles were removed in vacuo, and the residue obtained was washed with *n*-pentane. Crystallization from *n*-pentane/dichloromethane (8:1) gave yellow crystals of **3a** in 72% yield (188 mg, 0.178 mmol). ^{1}H NMR ($CDCl_3$) δ: 7.65 (m, 12 H, C_5H_4), 7.46 (m, 8 H, C_5H_4), 7.41 (s, 4 H,, C_6H_4), 2.44 (dq, 4 H, J_{HH} = 8 Hz, J_{HP} = 16 Hz, CH_2), 1.23 (dt, 6 H, J_{HH} = 8 Hz, J_{HP} = 20 Hz, CH_2). ^{131}P{^{1}H} δ: 38.9. ^{77}Se{^{1}H} δ: 148.6. Anal. for $C_{34}H_{34}Au_2P_2Se_2$ (1056.43): found: C 37.75, H 3.43; calcd.: C 38.65, H 3.24.

Synthesis of $EtPh_2PAuSe(C_6H_4)_2SeAuPPh_2Et$ (3b)

One hundred mg of 4,4′-$(C_6H_4SeSiMe_3)_2$ (0.219 mmol) was reacted with 196 mg (0.438 mmol) of $EtPh_2PAuCl$ as described for the preparation of **3a** (above). After appropriate work-up, **3b** was isolated as yellow crystals in 75% yield (186 mg, 0.164 mmol). ^{1}H NMR ($CDCl_3$) δ: 7.68 (d, 4 H, J_{HH} = 8 Hz, C_6H_4), 7.65 (m, 12 H, C_5H_4), 7.45 (m, 8 H, C_5H_4), 7.24 (d, 4 H, J_{HH} = 8 Hz, C_6H_4), 2.45 (dq, 4 H, J_{HH} = 8 Hz, J_{HP} = 20 Hz, CH_2), 1.23 (dt, 6 H, J_{HH} = 8 Hz, J_{HP} = 20 Hz, CH_2). ^{131}P{^{1}H} δ: 41.4. ^{77}Se{^{1}H} δ: 157.0. Anal. for $C_{40}H_{38}Au_2P_2Se_2$ (1132.52): found: C 42.18, H 3.36; calcd.: C 42.42, H 3.38.

Synthesis of $Ph_3PAuSeC_6H_4SeAuPPh_3$ (5a)

One hundred mg of 1,4-$C_6H_4(SeSiMe_3)_2$ (0.263 mmol) was reacted with 260 mg (0.526 mmol) of Ph_3PAuCl as described for the preparation of **3a** (above). After appropriate work-up, **3b** was isolated as a yellow solid in 71% yield (216 mg, 0.187 mmol). ^{1}H NMR ($CDCl_3$) δ: 7.47 (m, 30 H, C_6H_5), 7.42 (s, 4 H, C_6H_4). ^{131}P{^{1}H} δ: 39.9. ^{77}Se{^{1}H} δ: 148.2. Anal. for $C_{42}H_{34}Au_2P_2Se_2$ (1152.52): found: C 43.49, H 2.93; calcd.: C 43.77, H 2.97.

Synthesis of $Ph_3PAuSe(C_6H_4)_2SeAuPPh_3$ (5b)

One hundred mg of 4,4′-$(C_6H_4SeSiMe_3)_2$ (0.219 mmol) was reacted with 217 mg (0.438 mmol) of Ph_3PAuCl as described for the preparation of **3a** (above). After appropriate work-up, **3b** was isolated as yellow solid in 73% yield (196 mg, 0.160 mmol). ^{1}H NMR ($CDCl_3$) δ: 7.73 (d, 4 H, J_{HH} = 8 Hz, C_6H_4), 7.53 (m, 18 H, C_6H_5), 7.43 (m, 12 H, C_6H_5), 7.24 (d, 4 H, J_{HH} = 8 Hz, C_6H_4). ^{131}P{^{1}H} δ: 39.6. ^{77}Se{^{1}H} δ: 156.6. Anal. for $C_{48}H_{38}Au_2P_2Se_2$ (1228.62): found: C 46.54, H 2.99; calcd.: C 46.92, H 3.12.

Synthesis of $Pr_3PAuSe(C_6H_4)_2SeAuPPr_3$ (7b)

[AuCl(SMe_2)] (65 mg, 0.221 mmol) was added in one portion to 4,4′-$(C_6H_4SeSiMe_3)_2$ (51 mg, 0.111 mmol) in tetrahydrofuran (30 mL) at –78 °C and warmed to RT after 15 min. After 2 h of stirring at RT, a yellow suspension formed. The reaction mixture was again cooled to –78 °C, and 0.43 mL of PPr_3 (35.4 mg, 0.221 mol) was added in one portion to the reaction mixture. After 2 h of stirring at RT, all volatiles were removed in vacuo from the clear yellow solution, and the residue obtained was washed with *n*-pentane. Crystallization from *n*-pentane/dichloromethane (8:1) gave colorless crystals of **7b** in 75% yield (79 mg, 0.083 mmol). ^{1}H NMR ($CDCl_3$) δ: 7.65 (d, 4 H, J_{HH} = 8 Hz, C_6H_4), 7.23 (d, 4 H, J_{HH} = 8 Hz, C_6H_4), 1.80 (m, 12 H, $CH_2CH_2CH_3$), 1.58 (m, 12 H, $CH_2CH_2CH_3$), 1.02 (m, 18H, $CH_2CH_2CH_3$). ^{131}P{^{1}H} δ: 32.5. ^{77}Se{^{1}H} δ: 143.7.

Acknowledgements

We gratefully acknowledge the financial support of the Natural Sciences and Engineering Research Council (NSERC) of Canada. *The* University *of* Western Ontario and the Canada Foundation for Innovation are thanked for equipment funding. DT thanks Tafila Technical University (Jordan) for travel support to Canada.

References

1. H.G. Raubenheimer and S. Cronje. *In* Gold, progress in chemistry, biochemistry and technology. *Edited by* H. Schmidbaur. Wiley, Chichester, NY, USA. 1999. p. 557.
2. C.F. Shaw III. Chem. Rev. **99**, 2589 (1999).
3. S.L. Best and P.J. Sadler. Gold Bull. **29**, 2987 (1996).
4. M.J. McKeage, L. Maharaj, and S.J. Berners-Price. Coord. Chem. Rev. **232**, 127 (2002).
5. E.R.T. Tiekink. Crit. Rev. Oncol/Hematol. **42**, 225 (2002).
6. S. Canales, O. Crespo, M.C. Gimeno, P.G. Jones, and A. Laguna,. Inorg. Chem. **43**, 7234 (2004).
7. P.G. Jones and C. Thöne. Chem. Ber. **123**, 1975 (1990).
8. W. Eikens, C. Kienitz, P.G. Jones, and C. Thöne. J. Chem. Soc. Dalton Trans. 83 (1994).
9. (*a*) R.J. Puddephatt and P.J. Thompson. J. Organomet. Chem. **117**, 396 (1976); (*b*) S. Canales, O. Crespo, M.-C.Gimeno, P.G. Jones, A. Laguna, and P. Romero. J. Chem. Dalton Trans. 4525 (2003).
10. A. Laromaine, F. Teixidor, R. Kivekäs, R. Sillanpää, M. Arca, V. Lippolis, E. Crespo, and C. Viñas. J. Chem. Soc. Dalton Trans. 5240 (2006).
11. P.J. Bonasia, D.E. Cindelberger, and J. Amold. Inorg. Chem. **32**, 5126 (1993).
12. I. Wagner and W.-W. du Mont,. J. Organomet. Chem. **395**, C23 (1990).
13. E. Cerrada, S. Elipe, M. Laguna, F. Lahoz, and A. Moreno. Synth. Met. **102**, 1759 (1999).

[4] Supplementary data for this article are available on the journal Web site (canjchem.nrc.ca) or may be purchased from the Depository of Unpublished Data, Document Delivery, CISTI, National Research Council Canada, Ottawa, ON K1A 0R6, Canada. DUD 3861. For more information on obtaining material refer to cisti-icist.nrc-cnrc.gc.ca/cms/unpub_e.shtml. CCDC 696168–696170 contain the crystallographic data for this manuscript. These data can be obtained, free of charge, via www.ccdc.cam.ac.uk/conts/retrieving.html (Or from the Cambridge Crystallographic Data Centre, 12 Union Road, Cambridge CB2 1EZ, UK; fax +44 1223 336033; or deposit@ccdc.cam.ac.uk).

© 2008 NRC Canada

14. S. Canales, O. Crespo, M.C. Gimeno, P.G. Jones, and A. Laguna. Inorg. Chem. **43**, 7234 (2004).
15. W. Eikens, C. Kienitz, P.G. Jones, and C. Thöne. J. Chem. Soc. Dalton Trans. 83 (2004).
16. P.J. Bonasia, D.E. Cindelberger, and J. Arnold. Inorg. Chem. **32**, 5126 (1993).
17. A.I. Wallbank, M.J. Brown, C. Nitschke, and J.F. Corrigan. Organometallics, **23**, 5648 (2004).
18. H. Ehlich, A. Schier, and H. Schmidbaur. Inorg. Chem. **41**, 3721 (2002).
19. P.G. Jones and C. Thöne. Chem. Ber. **123**, 1975 (1990).
20. P.G. Jones and C. Thöne. Chem. Ber. **124**, 2725 (1991).
21. P.G. Jones and C. Thöne. Inorg. Chim. Acru, **181**, 291 (1991).
22. M.-C. Brandys, M.C. Jennings, and R.J. Puddephatt. J. Chem. Soc. Dalton Trans. 4601 (2000).
23. A.A. Isab, M.B. Fettouhi, S. Ahmad, and L. Ouahab. Polyhedron, **22**, 1349 (2003).

© 2008 NRC Canada

Tunable electrogenerated chemiluminescence from CdSe nanocrystals[1]

Jigang Zhou, Jun Zhu, Jack Brzezinski, and Zhifeng Ding

Abstract: Electrochemical behavior and related optoelectronic properties of CdSe nanocrystals (NCs) in aprotic solutions have been investigated. NCs of 2.50 ± 0.50 nm diameter were synthesized using a modified procedure in which the temperatures at the time of Se precursor injection and NC growth were controlled. The electrochemical band gap was found to agree with those determined by UV–vis absorption spectroscopy and by the tunneling current-voltage spectrum in the literature. Electrogenerated chemiluminescence of the NCs with peak maxima at 1.90 eV (red, 653 nm) and 2.55 eV (blue, 486 nm) can be generated and altered by scanning the voltage between –1.60 and –1.80 V and between –2.00 and –2.20 V, respectively. The results demonstrate the potential capability of the NCs for light emission tuned by the applied potential.

Key words: CdSe nanocrystals, electrochemistry, electrogenerated chemiluminescence, UV–vis spectroscopy, photoluminescence.

Résumé : On a étudié le comportement électrochimique et les propriétés optoélectroniques apparentés de nanocristaux (NC) de CdSe dans des solutions aprotiques. On a effectué la synthèse des NC d'un diamètre de 2,50 ± 0,50 nm en utilisant une méthode modifiée dans laquelle les températures sont contrôlées tant au moment de l'injection du Se précurseur que de la croissance du NC. On a trouvé que l'intervalle de la bande électrochimique est en accord avec ceux déterminés dans la littérature par la spectroscopie d'absorption UV–visible et par les spectres de l'effet tunnel courant/voltage. La chimiluminescence électrogénérée de NC avec un pic maximal à 1,90 eV (rouge, 653 nm) et 2,55 eV (bleu, 486 nm) peut être générée et modifiée par un balayage du voltage respectivement entre –1,60 et –1,80 V et entre –2,00 et –2,20 V. Les résultats démontrent la capacité potentielle des NC d'émettre de la lumière de longueur d'onde modifiée par le potentiel appliqué.

Mots-clés : nanocristaux de CdSe, électrochimie, chimiluminescence électrogénérée, spectroscopie UV–visible, photoluminescence.

[Traduit par la Rédaction]

Introduction

Semiconductor nanocrystals (NCs), which have a direct band gap structure, strongly exhibit size dependent electronic, optical, and electrochemical properties (1) when their dimensions are smaller than 10 nm. Recently, active devices have been exploited that combine the diversity of organic materials with the high-performance electronic and optical properties of semiconductor NCs (2, 3). Any desired color emission can be varied by changing the NC size or the luminescent organic materials (4). However, reports concerning the optoelectronic properties of semiconductor NCs remain scarce (5, 6) because of limited investigation methods. Electrogenerated chemiluminescence (ECL) (7–9) of semiconductor NCs (10–15) can reveal information about their structure and about the electroluminescence mechanisms of the future devices.

Because of their photon-emitting properties, CdSe NCs are beginning to make an impact in light-emitting diode and photonics technology (2–4). However, light emission is known to be sensitive to the nature of the particle surface due to the large surface area and the possible presence of surface states caused by uncoordinated atoms (14). For instance, the peak position in the ECL spectrum of CdSe NCs capped with trioctyl phosphine oxide (TOPO) was red-shifted by hundreds of nanometers compared with the PL spectrum (11), while the ECL spectrum of CdSe NCs passivated with a shell of the wider band gap material, ZnSe, is similar to the PL spectrum (12).

Here we describe the ECL of small size CdSe NCs (2.50 ± 0.50 nm) capped with TOPO. Two colours of light emission (blue and red) were observed and could be altered by tuning the applied potential. This new observation may lead to potential tuned LEDs fabricated with the NCs.

Received 5 October 2008. Accepted 14 November 2008. Published on the NRC Research Press Web site at canjchem.nrc.ca on 5 December 2008.

Dedicated to Professor Richard J. Puddephat for his many years of pioneering research in inorganic chemistry.

J. Zhou, J. Zhu,[2] J. Brzezinski, and Z. Ding.[3] Department of Chemistry, The University of Western Ontario, London, Ontario N6A 5B7, Canada

[1]This article is part of a Special Issue dedicated to Professor R. Puddephatt.

[2]Present address: School of Chemical and Environmental Engineering, Beijing Technology and Business University, Beijing 100037, P.R. China

[3]Corresponding author (e-mail: zfding@uwo.ca).

 doi:10.1139/V08-180 © 2008 NRC Canada

Experimental section

Synthesis of CdSe NCs

CdSe NCs capped with TOPO were synthesized according to procedures reported by Peng's group (16) and Bard's group (12), with modifications to the temperatures at the time of the Se precursor injection and NC growth (17). Briefly, a Se solution was prepared by mixing 0.16 g of Se powder, 4 g of trioctylphosphine (TOP), and 80 μL of toluene. Approximately 12 g of technical grade trioctylphosphineoxide (TOPO) and 0.1 g of cadmium acetate hydrate were placed into a 3-neck round-bottomed flask and heated to ~140 °C. After degassing with argon for 1 hour at this temperature, the solution in the flask was heated to 280 °C. At this temperature, the heating mantle was removed immediately, and a cold Se solution was quickly injected into the reaction vessel through a rubber septum. The temperature decreased to 250 °C after the injection was done. With continuous stirring, the temperature further decreased to 180 °C. At this point, the flask was reheated to about 220 °C, and the first aliquot, the sample under investigation in this report, was removed from the flask. The sample solution was cooled to ~50 °C with cold tap water. After addition of 10 mL of $CHCl_3$, the solution was kept in the dark.

The NCs were precipitated with a copious amount of methanol and collected by centrifugation and decantation. The collected precipitate was dissolved in $CHCl_3$ and precipitated again with methanol. This cycle was repeated three times. The final product was dissolved in $CHCl_3$. NCs were obtained by evaporating the solvent and drying under vacuum. The resulting NCs were used for the electrochemistry and ECL experiments.

All chemicals were purchased from Sigma-Aldrich and used with no further purification.

Physical methods

A JEOL 2010F high-resolution transmission electron microscope (HRTEM), a Varian Cary 100 UV–vis absorption spectrometer, and a Spex Fluorolog 3–11 fluorimeter were employed to characterize the morphology, electronic structure, and photo-induced luminescence (PL) of the prepared NCs.

A specially designed photoelectrochemical cell was used for all the electrochemical and ECL measurements. The cell consisted of a Pt disk working electrode (0.07 cm^2), a Pt wire counter electrode, and an Ag wire quasi-reference electrode. CdSe NC solutions were prepared with 0.1 mol/L tetrabutylammonium perchlorate (TBAP) as the supporting electrolyte and with 2 mL CH_2Cl_2 as the solvent, freshly treated by a solvent purification system. The bottom of the cell has a flat Pyrex window for detection of the light generated from the working electrode (7, 18). The loaded cell was degassed with Ar and sealed with an air-tightening Teflon cap.

Differential pulse voltammograms (DPVs) were obtained using an electrochemical workstation, CHI 610A (CH instruments, Austin, Texas). The experimental parameters for DPVs were as follows: 0.05 V pulse height, 60 ms pulse width, 200 ms period, and 0.02 V/s scan rate. Voltammetric ECL curves were obtained using the electrochemical workstation coupled with a photomultiplier tube (PMT, R928, Hamamatsu, Japan) held at –750 V with a high-voltage power supply (7, 18). The ECL generated at the working electrode was collected by the PMT under the flat Pyrex window at the bottom of the cell. The photocurrent from the PMT was transformed into a voltage signal by an electrometer (Model 6517, Keithley, Cleveland, Ohio). This signal, along with the potential and current signals from the electrochemical workstation. was sent through a DAQ board (DAQ 6052E, National Instruments, Austin, Texas) to the computer where the dada acquisition system was controlled by a homemade LabVIEW (National Instruments, Austin, Texas) program.

ECL spectra (7, 18) were measured by employing a potential program with the electrochemical workstation. By collecting the ECL light through the Pyrex window of the cell in a spectrograph (Spectra Physics, Cornerstone 260M) and dispersing the emission with a grating, the output was recorded on a back-illuminated charge coupled device (CCD) camera (Andor 420BU), which was electrothermally cooled to below –56 °C.

The electrochemical potential was calibrated at the end of each experiment by the addition of ferrocene as an internal standard with the formal potential of Fc^+/Fc 0.400 V vs. SHE (19). ECL quantum yields were calculated by comparing the integrated ECL intensities and the current values (charge) of the NCs with the reference $Ru(bpy)_3^{2+}$ (Φ_{ECL} = 5%) (20). The quantum yield was calculated using the following equation:

$$[1] \qquad \Phi_{NC} = 100 \times \left(\frac{\int_a^b \mathrm{ECL}\, dt}{\int_a^b \mathrm{Current}\, dt} \right)_{NC} \Bigg/ \left(\frac{\int_a^b \mathrm{ECL}\, dt}{\int_a^b \mathrm{Current}\, dt} \right)_{St}$$

where Φ_{NC} is the quantum yield (%) relative to $Ru(bpy)_3^{2+}$, ECL is the ECL intensity, Current is the electrochemical current value, St is the standard, and NC is the nanocrystal sample.

Results and discussions

The temperature effect on NC growth

We believe that precursor concentration and temperature for injection and NC growth are two important factors that manipulate NC size in general. The NC growth was fast, and it was difficult to obtain desired NC sizes under reported temperature conditions (16). Temperature was therefore chosen as our major parameter to optimize. We decreased the reaction temperature of the Cd precursor solution in a flask by using a cold Se precursor solution and a fast injection speed, as well as by removing the heat mantle under the reaction flask before injection. Growth solution was cooled quickly with an ice bath once the desired size was achieved, which was monitored via absorption wavelength. With this method, we were able to control NC sizes undergoing different growth times. The emission colours of the obtained NCs covered almost the entire visible spectrum when excited by a UV lamp.

© 2008 NRC Canada

Fig. 1. (*a*) Room temperature absorption and emission spectra of CdSe nanocrystals dispersed in $CHCl_3$. Excitation wavelength: 370 nm. Inset is a typical TEM picture of an individual NC. (*b*) TEM of NCs.

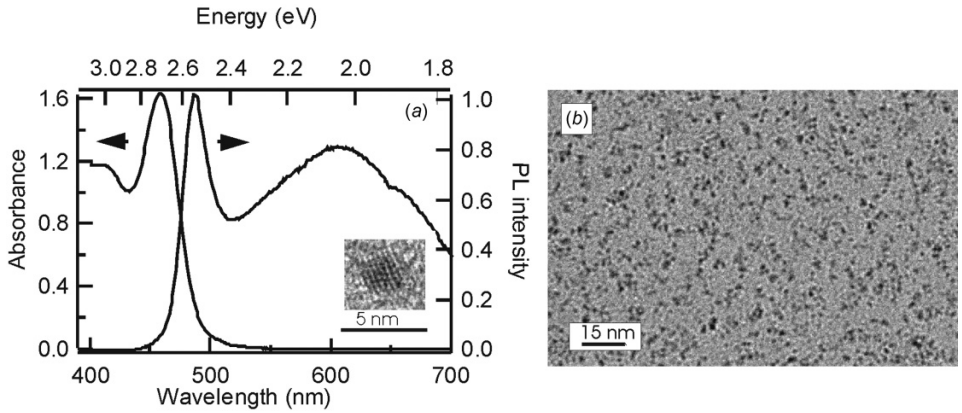

Characterization of CdSe NCs

One batch of small size NCs was selected for study, with the focus on probing their electronic structure by electrochemistry and ECL. As shown in Fig. 1, the NCs were characterized by TEM, high-resolution TEM, UV–vis absorption, and PL spectra (Fig. 1). TEM experiments showed a narrow size distribution, and NC size was determined to be 2.50 ± 0.50 nm, as demonstrated in Fig. 1*b*. According to the UV–vis absorption spectrum, the diameter of the NCs was estimated at about 2.0 nm (21, 22), and the sharp peak illustrated that the size distribution was narrow. From the PL spectrum, one sharp peak at 2.55 eV and a second broad peak at 2.03 eV were observed. The narrow absorption peak diminishes the possibility of wide size distribution, thus we can attribute the sharp PL peak to the core structure emission and the broad peak to the surface state emission. The NCs in question may produce strong PL emission from both core excitons and surface traps, as depicted by the energy diagram in Scheme 1*a*.

Scheme 1. Schematic mechanisms and energy diagrams describing (*a*) PL and (*b*) ECL occurring in CdSe core (hollow) and surface (shadow). Symbols ● and ○ represent electrons and holes.

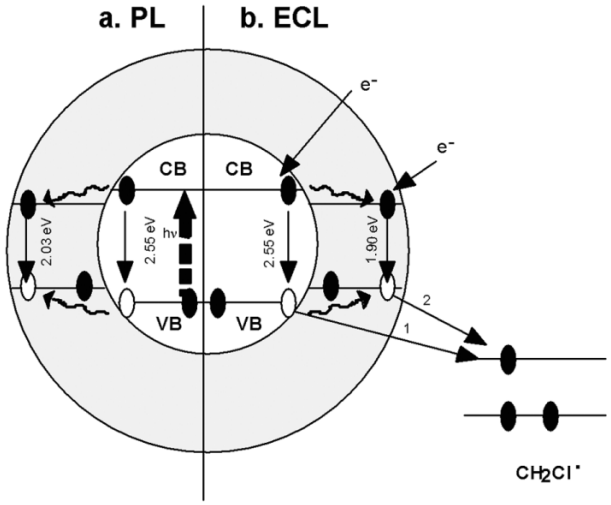

Electrochemistry

NC reduction (electron injection, whose mechanism is illustrated in Scheme 1*b*) in the negative bias region, as shown by the DPV in Fig. 2, was characterized by a doublet followed by a continuous increase in current, with the applied potential becoming more negative. This is indicative of two discrete charge transfers followed by multiple charge transfers. The various peak spacings in the DPV can be attributed to Coulomb charging into higher energy levels (10). The DPV responses in this region reveal information about the conduction levels and look very similar to the tunneling current-voltage spectrum (TCVS) of a similar size CdSe NC at 4.2 K, obtained by Alperson et al. (23). The doublet was attributed to the two consecutive electron injections to the first conduction band, $1S_e$ (s character) in the case of electrochemically prepared NCs (23). The energy difference between the first two peaks, i.e., the Coulomb charging, was 0.37 eV in DPV, which agrees well with the value in the TCVS (0.34 eV). Broader peaks were observed in DPV than those observed in the TCVS. While the CdSe NCs were monodisperse in size, the broadness of the peaks might be due to the surface states, which increased the complexity of the electronic structure. Furthermore, a continuous increase in current, instead of a Coulomb staircase for the electron injections to the second conduction band, was observed in DPV. However, up to six peaks spaced by values close to the Coulomb charging energy in TCVS for a single InAs dot were reported by Banin et al. (24). This might be caused by an overlap of core and shell (surface) electronic structures as well as an interplay between level spacing and single electron tunneling. Alternatively, two oxidation (hole injection) peaks were seen in the positive bias side of the DPV in Fig. 2. These peaks were broader, and the Coulomb charging energy was larger (0.48 eV) than that of the negative side. These results were expected because of the higher density of valence levels and the close proximity between Coulomb charging and level spacing as well as the multiplicity of electronic structures.

The electrochemical gap was determined to be 2.34 eV from the separation of the first oxidation and reduction peaks in the DPV (Fig. 2). This is in good agreement with the optical band gaps, 2.50 and 2.06 eV, estimated from the absorption onset and the broad PL peak of the NC, respectively (25). The zero current gap in TCVS, 2.88 to 3.13 eV, also provided a qualitative description of the band gap (23). The electrochemical gap is strongly affected by the presence

© 2008 NRC Canada

Fig. 2. Differential pulse voltammograms (DPVs) of a dichloromethane solution containing 0.1 mol/L tetrabutylammonium perchlorate (TBAP) as supporting electrolyte (dotted line) and 2.50 nm CdSe NCs (40 μmol/L) dispersed in the same solution (solid line) at a 0.07 cm^2 Pt disk working electrode. The lower lines are DPVs with a potential scan from positive to negative, while the upper lines from negative to positive. A potential increment of 4 mV, a sample width of 0.0167 s, a pulse period of 0.2 s, a pulse width of 0.05 s, and a pulse amplitude of 50 mV were used.

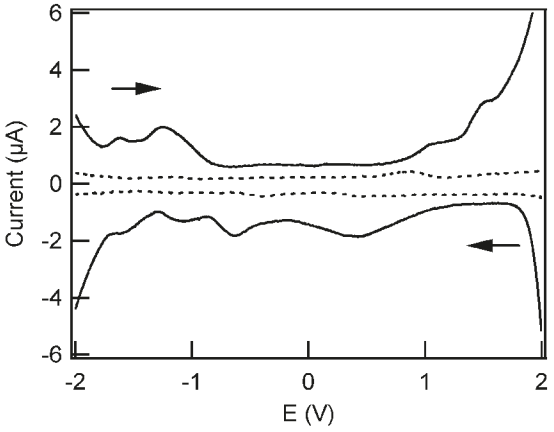

of surface states that can act as local traps for electrons and holes. Considering the small size of NCs studied here, a large part of the CdSe should be on the surface of the NCs (14, 17), which may be capped with TOPO or possibly a small amount of oxide. Very recently, Bard's group reported an electrochemical study of CdTe NCs (13). In comparison to CdTe NCs, CdSe NCs were assumed to be less passivated by TOPO in similar preparation conditions (11, 13). The CdSe NCs in question had even richer surface states than those reported previously (11). This is observed in an intense photoluminescence peak at a longer wavelength, i.e., surface state emission. Such evidence suggests that the above observed oxidation and reduction may reflect the properties of the NC surface. Electron and hole injections may first occur on the $1S_e$ and 1VB bands of surface CdSe, respectively (23). However, it is not clear from the DPV where further charge injections occur. In addition, forward and reverse DPV scans are relatively less symmetric than those of Si NCs (10), indicating that charge transfers are not very reversible.

Cyclic voltammograms (CVs) of the CdSe NCs dispersed in the same dichloromethane electrolyte solution are demonstrated in Fig. 3. As shown by the DPVs, the redox behavior of the NCs is dependent on the scan direction of the applied potential. The NC anions are more stable than the cations as illustrated by the CV in Fig. 3*a*: the anions generated at the negative potential can be re-oxidized in the forward scan, while the cations produced at the positive potential can barely be re-reduced in the backward scan. A new peak also appears at 0.11 V, probably due to the new species from the decomposed cations. In addition, the CV in the reversed order of forward and backward scans as above does not show evident reduction peaks and the following oxidation reaction due to the depletion of the NCs in the vicinity of the electrode (Fig. 3*b*).

Fig. 3. Cyclic voltammograms (CVs) of a dichloromethane solution containing 0.1 mol/L tetrabutylammonium perchlorate (TBAP) as supporting electrolyte (dotted line) and 2.50 nm CdSe NCs (40 μmol/L) dispersed in the same solution (solid line) at a 0.07 cm^2 Pt disk working electrode. (*a*) CV with a potential scan from –2.000 to 2.000 and back to –2.000 V. (*b*) CV with a potential scan from 2.000 to –2.000 and back to 2.000 V. A scan rate of 100 mV/s was used.

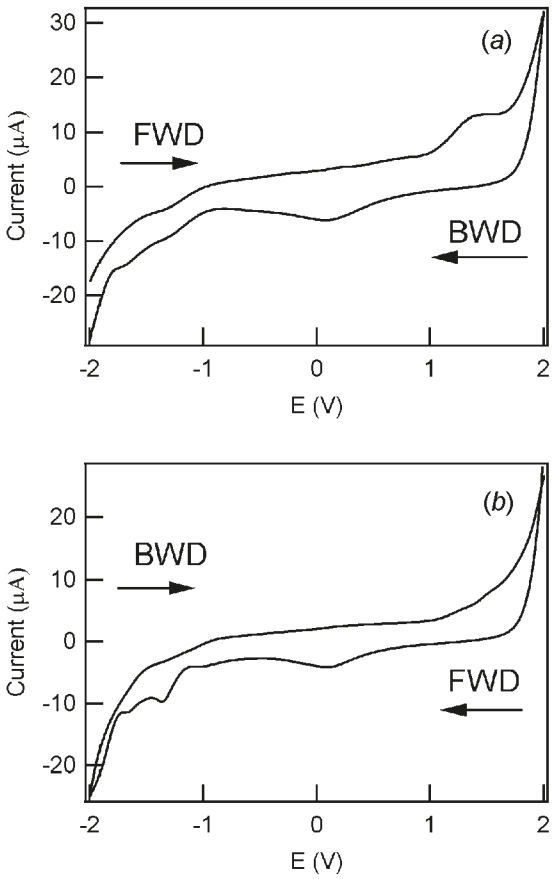

Electrogenerated chemiluminescence (ECL)

ECL of the same electrolyte solution used for electrochemical experiments was first investigated by recording voltammetric photocurrent with a photomultiplier tube (PMT) (10). ECL was observed under various stimulus conditions. We found that emission was produced in both negative and positive sides when the applied potential was swept between –2.30 and 2.30 V, though the ECL intensity is rather weak. An annihilation mechanism, i.e., electron transfer between reduced and oxidized NCs, was assumed in this light emission process (10, 11). More interestingly, a significant ECL signal was detected as the potential was scanned from 0.00 to –3.00 V, as shown in Fig. 4. The ECL-potential curve showed two overlapping peaks, which may correspond to two emission processes. ECL turn-on potential was at –1.30 V, which is slightly more negative than the first reduction peak in DPV. Stable ECL could be obtained even at pesudo constant potentials on the negative side, e.g., slowly scanning from –1.60 to –1.80 V or from –2.00 to –2.20 V. The second peak on the ECL-potential curve appeared at –2.12 V. Note that in these cases, only the reduced species

© 2008 NRC Canada

Fig. 4. Voltammetric ECL curves of at a 0.07 cm^2 Pt disk working electrode immersed in 0.1 mol/L TBAP CH_2Cl_2 electrolyte solution containing 2.50 nm CdSe NCs (40 μmol/L). Scan rate was at 0.5 V/s. Two cycles are overlapped in the figure.

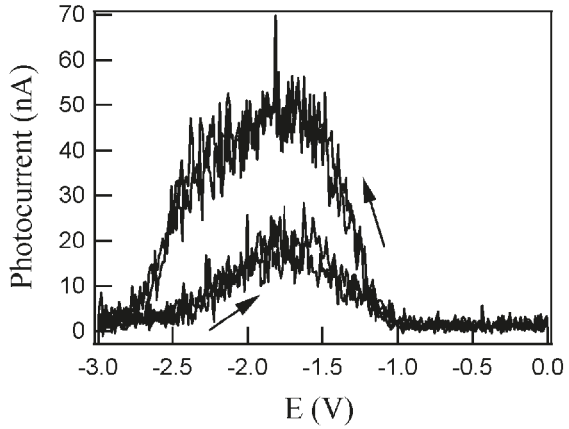

existed in the solution, and the above electrochemical study showed a higher stability of anions than that of cations. The annihilation leading to light emission in this situation could not occur. Therefore, there must be another oxidant that accepted an electron from the valance band of anion NC radicals to form excited states. Bard and co-workers (13) suggested that similar emission from CdTe NCs might occur through an electron transfer reaction between anion CdTe radicals and electrogenerated oxidant radicals, $CH_2Cl^{\bullet}$, from the dichloromethane used as the solvent. This is the so-called co-reactant emission mechanism (26). This mechanism explains well the ECL signal at more negative potential and is depicted in Scheme 1*b*, according to our observation. This mechanism is illustrated in Scheme 2. However, our ECL "turn-on voltage" of –1.30 V is not negative enough to generate the oxidant, and similar ECL was observed in dimethylformide (DMF) solution. Nevertheless, it was found that ECL was enhanced several times by introducing air to the electrolyte solution. Similar to the chemiluminescence of certain linear hydrazides, aldehydes, and ketones in dimethyl sulfoxide with potassium tert-butoxide and oxygen (27, 28), ECL might be emitted from the excited states formed by the reaction of the anion radicals with oxygen molecules,

$$(CdSe)_{NC} + e^- \rightarrow (CdSe)^{\bullet -}_{NC}$$

$$(CdSe)^{\bullet -}_{NC} \xrightarrow{O_2} (CdSe)^{*}_{NC}$$

$$(CdSe)^{*}_{NC} \rightarrow (CdSe)_{NC} + h\nu$$

It is unlikely that an oxygen molecule accepts an electron to form a superoxide ion ($O_2^{-\bullet}$), as in the case of hydrazides, aldehydes, and ketones, since the redox potential of O_2/O_2^- (–0.33 V) is too negative. Indeed, this redox couple acted as an electron donor in an alkaline solution to the CdSe NC packed film (6).

As demonstrated in Scheme 2, CdSe NCs were recycled with dichloromethane or oxygen molecules acting as a scavenger in this emission mechanism. ECL was therefore very stable with repetitive potential cycling over a long time period. Nearly constant ECL intensity was also measured periodically over several weeks. The ECL efficiency was found to be half that of $Ru(bpy)_3^{2+}$ under the same experimental conditions.

Scheme 2. Schematic mechanisms for ECL of the CdSe NCs with CH_2Cl_2 as the co-reactant.

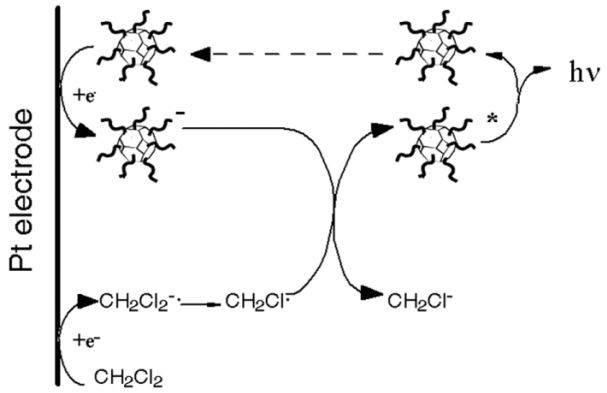

ECL spectra are presented in Fig. 5. The integration time for the spectra is 6 min. As the potential was scanned from 0 to –2.20 V, the ECL spectrum, consisting two peaks at 1.90 and 2.55 eV, was very broad and weak. However, strong ECL at 1.90 eV (red, 653 nm) was observed at potentials slowly scanned between –1.60 and –1.80 V. Even stronger ECL consisting of two peaks at 1.90 and 2.55 eV (blue, 486 nm) was emitted at more negative potentials (–2.00 to –2.20 V). We assume that ECL at 1.90 and 2.55 eV correspond to the surface state and core structure emission, respectively. These energies are in good agreement with band gaps from surface and core electronic structures as analyzed from our electrochemical and spectroscopic study above. Illustrative ECL mechanisms for the core and the surface are summarized in Scheme 1*b*. Emission at 2.55 eV implies that the current rise at very negative potentials in DPV resulted from the electron injections to the core conduction bands. Quantitatively, however, it is not clear why the NCs luminesced at 1.90 eV simultaneously when stimulated with higher energy. It is even more difficult to understand at this point why ECL was only observed at longer wavelength (1.70 eV) for 3.2 nm diameter CdSe NCs prepared using similar methods in a previous report (11). We can speculate that ECL from the core was not favorable in the absence of oxygen molecules in an airtight electrochemical cell. Another speculation is that we might obtain the NCs with different crystallinity from that of the NCs in the previous report (11), which lead to different crystal band structures. Bawendi and co-workers (21) found that simulated X-ray powder diffraction spectra for 3.5 nm diameter spherical nanocrystallites such as zincbende, wurtzite, and wurtzite with one stacking fault are very different. However, more detailed studies are needed to understand the relationship between the nanocrystallinity and the ECL.

Conclusion

In addition to size-tunable character, light emission is also potentially tunable for the CdSe NCs under investigation. This new phenomenon is rather remarkable as it provides a

© 2008 NRC Canada

Fig. 5. ECL spectra of 40 µmol/L CdSe NCs in CH_2Cl_2 containing 0.1 mol/L TBAP at a 0.07 cm^2 Pt working electrode, obtained by scanning applied potential between (*a*) –1.60 and –1.80 V, (*b*) –2.000 and –2.200 V, and (*c*) 0.000 and –2.200 V. All potentials are referred to Ag wire. Scan rates for (*a*), (*b*), and (*c*) were at 10, 10, and 500 mV/s. An integration time of 6 min was used to obtain the spectra. Dotted curves represent the responses of corresponding blank supporting electrolyte solutions recorded at the same conditions. Vertical lines are cosmic rays on the CCD camera.

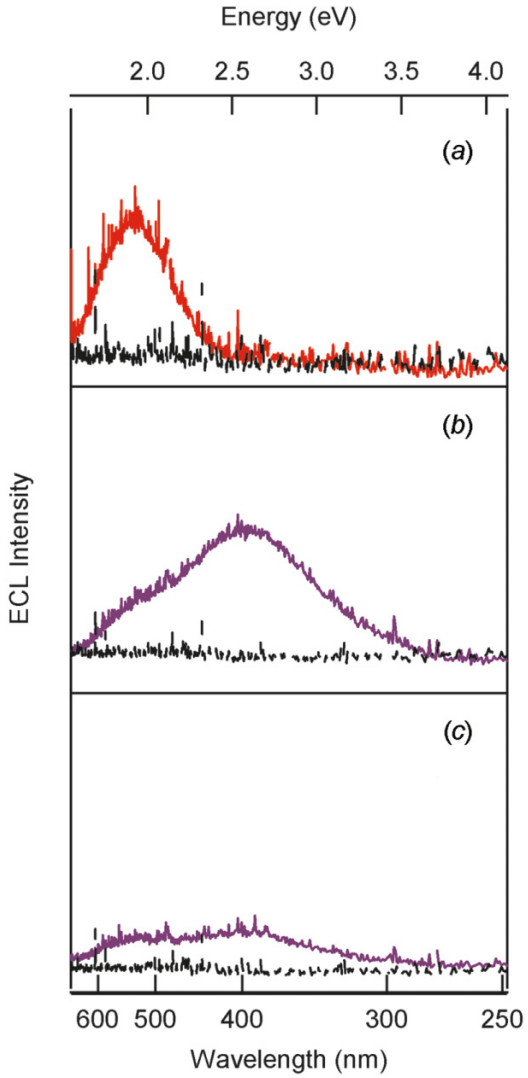

new avenue to tune colours of light emission from CdSe NCs simply by switching applied potentials. An impact to optoelectronics technology such as light-emitting diodes and color-display screens is anticipated.

Acknowledgements

We thank Hubert Girault, Bin Su, Xuhui Sun, Xingtai Zhou, Xueliang Sun, Gianluigi Botton, Fred Pearson, John Vanstone, Sherrie McPhee, Mary Lou Hart, and Marty Scheiring for discussions and technique supports. This work was supported by the Natural Sciences and Engineering Research Council of Canada (NSERC), Canada Foundation for Innovation, Ontario Innovation Trust, the Premier's Research Excellence Award, and the University of Western Ontario. ZFD was a visiting professor at the Swiss Federal Institute of Technology in Lausanne (EPFL) in the summer of 2003. JZ was an overseas scholar supported by Beijing City in 2004. JB was an NSERC summer student in 2004.

References

1. A.P. Alivisatos. J. Phys. Chem **100**, 13226 (1996).
2. S. Coe, W.-K. Woo, M. Bawendi, and V. Bulovic. Nature, **420,** 800 (2002).
3. K. Karrai, R.J. Warburton, C. Schulhauser, A. Hoegele, B. Urbaszek, E.J. McGhee, A.O. Govorov, J.M. Garcia, B.D. Gerardot, and P.M. Petroff. Nature, **427**, 135 (2004).
4. V.L. Colvin, M.C. Schlamp, and A.P. Allvisatos. Nature, **370**, 354 (1994).
5. C. Wang, M. Shim, and P. Guyot-Sionnest. Science, **291**, 2390 (2001).
6. S.K. Poznyak, D.V. Talapin, E.V. Shevchenko, and H. Weller. Nano Lett. **4**, 693 (2004).
7. C. Booker, X. Wang, S. Haroun, J. Zhou, M. Jennings, B.L. Pagenkopf, and Z. Ding. Angew. Chem. Int. Ed. **47**, 7731 (2008).
8. W. Miao. Chem. Rev. **108**, 2506 (2008).
9. M.M. Richter. Chem. Rev. **104**, 3003 (2004).
10. Z. Ding, B.M. Quinn, S.K. Haram, L.E. Pell, B.A. Korgel, and A.J. Bard. Science, **296**, 1293 (2002).
11. N. Myung, Z. Ding, and A.J. Bard. Nano Lett. **2**, 1315 (2002).
12. N. Myung, Y. Bae, and A.J. Bard. Nano Lett. **3**, 1053 (2003).
13. Y. Bae, N. Myung, and A.J. Bard. Nano Lett. **4**, 1153 (2004).
14. A.J. Bard, Z. Ding, and N. Myung. Structure and bonding (Berlin, Germany), **118**, 1 (2005).
15. Y. Bae, D.C. Lee, E.V. Rhogojina, D.C. Jurbergs, B.A. Korgel, and A.J. Bard. Nanotechnology, **17**, 3791 (2006).
16. J. Aldana, Y.A. Wang, and X. Peng. J. Am. Chem. Soc. **123**, 8844 (2001).
17. J. Zhou, X. Zhou, X. Sun, M. Murphy, F. Heigl, T.-K. Sham, and Z. Ding. Can. J. Chem. **85**, 756 (2007).
18. J. Zhou, J. Zhu, and Z. Ding. Proc. Electrochem. Soc. **2005–04**, 129 (2005).
19. D.R. Lide. CRC handbook of chemistry and physics. 84th ed. CRC Press LLC, Boca Raton, Fla., USA. 2003.
20. H.S. White and A.J. Bard. J. Am. Chem. Soc. **104**, 6891 (1982).
21. C.B. Murray, D.J. Norris, and M.G. Bawendi. J. Am. Chem. Soc. **115**, 8706 (1993).
22. W.W. Yu, L. Qu, W. Guo, and X. Peng. Chem. Mater. **15**, 2854 (2003).
23. B. Alperson, I. Rubinstein, G. Hodes, D. Porath, and O. Millo. Appl. Phys. Lett. **75**, 1751 (1999).
24. U. Banin, Y. Cao, D. Katz, and O. Millo. Nature, **400**, 542 (1999).
25. E. Kucur, J. Riegler, G.A. Urban, and T. Nann. J. Chem. Phys. **119**, 2333 (2003).
26. L.R. Faulkner and A.J. Bard. *In* Electroanalytical chemistry. Vol. 10. *Edited by* A.J. Bard. Dekker, New York. 1977. p. 1.
27. E. Rapaport, M.W. Cass, and E.H. White. J. Am. Chem. Soc. **94**, 3160 (1972).
28. E. Rapaport, M.W. Cass, and E.H. White. J. Am. Chem. Soc. **94**, 3153 (1972).

© 2008 NRC Canada

TRIBUTE/HOMMAGE

A Tribute to a Complete Academic: Dick Puddephatt

It is a privilege to be able to provide this biographical sketch of my colleague Richard J. (Dick) Puddephatt. It is well-known that Dick is a world-class organometallic and coordination chemist. Perhaps less appreciated are his immense contributions to teaching and service at the University of Western Ontario and beyond. His sustained record of excellence in all areas of university life allows me to state with complete conviction that Dick is the complete academic.

Dick was educated at University College, London, where he received his B.Sc. in 1965 and Ph.D. in 1968, working with A.G. Davies and R.J.H. Clark. He did postdoctoral research with H.C. Clark at the University of Western Ontario, took up a position as lecturer and then senior lecturer at the University of Liverpool, before coming back to the University of Western Ontario as a Professor in 1978. He currently holds the rank of Distinguished University Professor, Western's highest academic honour. He also held a Tier 1 Canada Research Chair in Materials Chemistry.

Dick's research has encompassed studies of reactivity and mechanism in organometallic chemistry related to catalysis, especially involving activation of normally inert bonds, in metallacyclobutane chemistry, the chemistry of binuclear and trinuclear complexes as models for reactions on metal surfaces, and the structure, bonding, and spectroscopy of organometallic compounds. In organometallic and coordination chemistry related to materials science, he has designed new precursors for chemical vapor deposition of thin films of metals and metal oxides, used dynamic coordination chemistry to make macrocycles, catenanes, polymers, and network materials, defined elegant examples of dynamic ring-opening polymerization, and shown how secondary bonding forces can be used to organize the higher-order structures of functional molecular materials. He has been particularly enamored with the chemistry of platinum and gold.

To date he has published over 550 papers, 3 books, and several reviews. The impact of his work can be gauged by a number of factors. With an h-index of 56, Dick is one of the top cited chemists in the world. The esteem in which Dick's work is held can be measured in part by the numerous awards he has received including the Florence Bucke Science Prize, a Distinguished Research Professorship, and the Hellmuth Research Award from the University of Western Ontario, the Alcan and Steacie Awards of the Canadian Society for Chemistry, the Noble Metal Chemistry award and Nyholm Lecture Award from the Royal Society of Chemistry, and the CIC Medal of the Canadian Institute of Chemistry. He is a Fellow of the Royal Society of Canada (FRSC) and the Royal Society, U.K. (FRS). The citation on his election as Officer of the Order of Canada in 2007 read, "For his contributions to the advancement of organometallic chemistry, as well as for his inspirational leadership of generations of researchers".

On research alone, Dick would be an obvious and worthy candidate for this special issue of the Canadian Journal of Chemistry. However, his talents and contributions don't end there. Dick is a gifted teacher. As a long time departmental Teaching Coordinator for Inorganic Chemistry at Western, Dick has been a leading advocate for, and developer and instructor of an inorganic curriculum that is both rigorous and innovative. Dick's record in graduate teaching is equally impressive. His average graduate teaching evaluations are among the highest in the department.

What is particularly noteworthy at the graduate level is Dick's record of graduate supervision. He has successfully supervised 52 Ph.D. students, 13 M.Sc. students and over 30 postdoctoral fellows during his career. Over the years, his group size was routinely 10–15 graduate students and postdocs. Visiting faculty members from around the world have also been guests in his research group while on sabbatical leave. I name below a list of some of his students and where they have ended up as an indicator of Dick's role as a mentor. This list is not meant to be exhaustive or exclusive. All of Dick's students have benefited from working in his group because as a supervisor Dick encourages students to work and think independently, creatively, and rigorously, and to take a broad view of science.

Some of his former students have made academic careers in Canada: Ross Hill, Patrick Monaghan, Brian Lloyd, Lucio Gelmini, Hilary Jenkins, Greg Spivak, Ernie Prokopchuk, Brian Sterenberg; USA: Craig Anderson, Chris Levy; UK: Jon Rourke, Jianliang Xiao; Germany: Fabian Mohr; Spain: Margarita Crespo; Australia: Lou Rendina; Hong Kong: Guochen Jia; Poland: Wanda Radecka-Paryzek; India: Sujit Roy; Bangladesh: Mohammed Quyser, Kazi Azam; Iraq: Jaafar Jawad; Iran: Mehdi Rashidi. They have made independent careers in diverse areas, using their training in organometallic chemistry but also applying their creativity to address new problems. For example, Ross Hill (Professor, Simon Fraser University) is expert in photochemical processing of materials for microelectronics and has successful patents as well as distinguished publications in that area. Jianliang Xiao (Reader, University of Liverpool) has built an independent reputation in environmental catalysis, especially using supercritical carbon dioxide or ionic liquids as recyclable, non-polluting solvents. Lou Rendina (Reader, University of Sydney) is a leading researcher in the developing field of bio-organometallic chemistry. Guochen Jia (Professor, Hong Kong University of Science and Technology) has made major contributions to dihydrogen chemistry and the chemistry of metal–carbon multiple bonds. Chris Levy (Assistant Professor, University of Kansas) is expert in metal complex catalysis and self-assembly of molecular materials.

Many former students have made successful careers in research and development and management in industry. For example, in Canada, senior R&D positions are held by Marie-Claude Brandys and Mike Irwin (3M Canada), John Scott (3M, Barrday), Gilles Arsenault (Wellington Laboratories, Bayer), Ian Jobe (Nova, Bayer), Geoff Hill (Bowater Canada), Tom Burton (ICI Canada). Sudhir Achar has been director of paint research for ICI India and food research for Unilever India, Zheng Yuan is a senior materials chemist in the microelectronics industry in the USA, and Guy Schoettel is a senior pharmaceutical chemist in Switzerland. Many have made the transition from R&D to management. For example, Ilse Treurnicht is CEO of MaRS (Toronto), and John Laws is Director of Sales for Proctor and Gamble in the USA.

Students who have flourished in government or professional careers include Paul Makin (scientific publishing, U.N.), Peter Hall (forensic scientist, UK), Maria Stalteri (medical research, UK), Sam Choi (environmental science, Hong Kong), Dave Elliot (research institute, Australia), Jan Hux (COO, Institute for

© 2009 NRC Canada

Clinical Evaluative Sciences and medical doctor, Canada), Mary-Ann MacDonald (dentist, Canada).

It was only fitting, given Dick's record in teaching and graduate supervision, that he was awarded Western's highest teaching accolade, the Edward G. Pleva Award for Excellence in Teaching in 2003-04.

Dick's service record is equally outstanding. He has been served on many NSERC committees including those for Discovery Grants, Collaborative Grants, Steacie Fellows, and the Gold Medal, the Polanyi Prize selection committee (including as its Chair), and on the Rutherford award selection committee of the Royal Society of Canada (including as its Chair). He is the past President of the Chemical Institute of Canada and the Canadian Society for Chemistry. He has also served on various subcommittees of these organizations. He is a past Senior Editor of the Canadian Journal of Chemistry and currently an Editor of Inorganica Chimica Acta. He is a member of several editorial advisory boards of other chemistry journals. His contributions to the Chemistry community were recognized by the Montreal Medal of the Chemical Institute of Canada in 2006.

On a personal note, Dick is a true gentleman. His experience and altruistic nature makes his opinions highly sought. I cannot recall a single instance where he had to raise his voice to get his point across, and that point is rarely ignored. He has been a leader in building up the Chemistry department at Western. On a further personal note, I will always be grateful for Dick's support and advice when I took over from him as Senior Editor of the Canadian Journal of Chemistry. The quality and quantity of the papers in this issue and the response of the community to this special issue shows that my thoughts regarding Dick are not unique. I congratulate him on this distinction and wish him all the best for the future.

Rob Lipson
Senior Editor

© 2009 NRC Canada

HOMMAGE/TRIBUTE

Hommage à un universitaire remarquable : Dick Puddephatt

C'est pour moi un privilège de pouvoir fournir un aperçu biographique de mon collègue Richard J. (Dick) Puddephatt. Reconnu mondialement en chimie organométallique et en chimie de coordination, Dick est peut-être moins bien reconnu pour sa remarquable contribution à l'enseignement et aux services à l'Université Western Ontario (UWO) et ailleurs. Ses grandes réalisations dans tous les domaines de la vie universitaire me permettent d'affirmer avec conviction que Dick est vraiment le parfait universitaire.

Formé à l'University College de Londres, Dick a obtenu un baccalauréat ès sciences en 1965 et un doctorat en 1968, en travaillant avec A.G. Davies et R.J.H. Clark. Chercheur postdoctoral sous la direction de H.C. Clark à l'UWO, Dick a par la suite accepté un poste de chargé de cours à l'Université de Liverpool, puis de chargé de cours principal, avant de revenir à l'UWO comme professeur en 1978. Il occupe maintenant le rang de professeur émérite à l'UWO. Ce rang constitue la plus haute distinction de cette institution. Enfin, il a été titulaire de la chaire de recherche du Canada sur la chimie des matériaux (niveau 1).

Les travaux de Dick ont porté sur l'étude de la réactivité et des mécanismes en chimie organométallique sur le plan de la catalyse, surtout en ce qui touche l'activation de liaisons normalement inertes en chimie des métallocyclobutanes, la chimie des complexes binucléaires et trinucléaires comme modèles de réaction sur des surfaces métalliques, ainsi que la structure, les liaisons et la spectroscopie des composés organométalliques. Dans le domaine de la science des matériaux lié à la chimie organométallique et à la chimie de coordination, Dick a conçu de nouveaux précurseurs pour le dépôt chimique en phase vapeur de feuils de métaux et d'oxydes métalliques, il a utilisé la chimie de coordination dynamique pour produire des macrocycles, des caténanes, des polymères et des matériaux de réseaux, il a décrit des exemples élégants de polymérisation dynamique par ouverture de cycle et il a montré comment les forces de liaison secondaire peuvent être utilisées pour organiser les structures d'ordre supérieur des matériaux moléculaires fonctionnels. Il était particulièrement friand de la chimie du platine et de l'or.

À ce jour, il a publié plus de 550 articles, trois livres et plusieurs synthèses. De nombreux facteurs permettent de mesurer l'impact de ses travaux. Avec un indice h de 56, Dick est un des chimistes les plus cités dans le monde. La considération pour les travaux des Dick se mesure en partie par les nombreux prix qu'il a reçus, dont le Florence Bucke Science Prize, le Distinguished Research Professorship et le prix Hellmuth de l'UWO, les prix Alcan et Steacie de la Société canadienne de chimie, les prix Noble Metal Chemistry et Nyholm Lecture de la Royal Society of Chemistry, et la médaille de l'Institut de chimie du Canada. Il est membre de la Société royale du Canada et de la Royal Society de Londres. La citation de sa nomination comme officier de l'Ordre du Canada en 2007 se lisait comme suit : « Pour sa contribution à l'avancement de la chimie organométallique, ainsi que pour son leadership qui est une source d'inspiration auprès de plusieurs générations de chercheurs. »

Les recherches de Dick suffisent amplement à faire de lui le candidat tout désigné pour ce numéro spécial de la *Revue canadienne de chimie*. Toutefois, ses talents et ses contributions ne se limitent pas à ses recherches. Dick est un enseignant doué. Sa longue expérience en qualité de coordonnateur de l'enseignement de la chimie inorganique à l'UWO a fait de lui un acteur de premier plan de la promotion, de l'établissement et de l'enseignement d'un programme de chimie inorganique rigoureux et novateur. Le bilan de Dick aux cycles supérieurs est tout aussi impressionnant, et les évaluations de son enseignement sont parmi les meilleures du département.

Ce qui est particulièrement remarquable en ce qui concerne les études de cycles supérieurs, c'est l'expérience de Dick en matière de supervision. Durant sa carrière, Dick a dirigé 52 étudiants de doctorat, 13 étudiants de maîtrise et plus de 30 boursiers postdoctoraux. Au fil des ans, il a dirigé des groupes de 10 à 15 étudiants des cycles supérieurs et boursiers postdoctoraux. Des professeurs des quatre coins du monde ont aussi été invités à se joindre à son groupe de recherche durant leur congé sabbatique. Vous trouverez ci-dessous une liste non exhaustive de certains des étudiants de Dick et de l'endroit où ils sont maintenant, laquelle liste illustre son rôle de mentor. Tous les étudiants ont bien profité de leur collaboration avec le groupe de Dick puisque ce dernier supervise ses étudiants en les incitant à travailler et à penser de façon indépendante, créative et rigoureuse, et à voir la science dans une vaste perspective.

Certains de ses anciens étudiants ont eu une carrière universitaire au Canada (Ross Hill, Patrick Monaghan, Brian Lloyd, Lucio Gelmini, Hilary Jenkins, Greg Spivak, Ernie Prokopchuk, Brian Sterenberg), aux États-Unis (Craig Anderson, Chris Levy), au Royaume-Uni (Jon Rourke, Jianliang Xiao), en Allemagne (Fabian Mohr), en Espagne (Margarita Crespo), en Australie (Lou Rendina), à Hong Kong (Guochen Jia), en Pologne (Wanda Radecka-Paryzek), en Inde (Sujit Roy), au Bangladesh (Mohammed Quyser, Kazi Azam), en Iraq (Jaafar Jawad) et en Iran (Mehdi Rashidi). Ils ont fait carrière indépendamment dans divers domaines, en utilisant leur formation en chimie organométallique, mais aussi en mettant leur créativité au service de la résolution de nouveaux problèmes. Par exemple, Ross Hill (professeur à l'Université Simon Fraser) est expert du traitement photochimique des matériaux en microélectronique. Il est détenteur de brevets fructueux dans ce domaine et auteur de publications reconnues. Jianliang Xiao (chargé de cours à l' Université de Liverpool) a forgé sa réputation dans le domaine de la catalyse écologique, particulièrement en utilisant du dioxyde de carbone supercritique ou des liquides ioniques comme solvants recyclables et non polluants. Lou Rendina (chargé de cours à l'Université de Sydney) est un éminent chercheur dans le domaine de la chimie bioorganométallique, en plein développement. Guochen Jia (professeur à l'Université de science et technologie de Hong Kong) a contribué de façon significative à la chimie du dihydrogène et des liaisons multiples métal-carbone. Chris Levy (professeur adjoint à l'Université du Kansas) est expert de la catalyse des complexes métalliques et de l'autoassemblage des matériaux moléculaires.

De nombreux anciens étudiants ont connu une brillante carrière en recherche et développement (R-D) et en gestion dans l'industrie. À titre d'exemple, au Canada, les personnes suivantes occupent des postes supérieurs en R-D : Marie-Claude Brandys et Mike Irwin (3M Canada), John Scott (3M, Barrday), Gilles Arsenault (Wellington Laboratories, Bayer), Ian Jobe (Nova, Bayer), Geoff Hill (Bowater Canada), Tom Burton (ICI Canada). Sudhir Achar a été directeur de la recherche sur la

© 2009 NRC Canada

peinture à Peintures ICI et directeur de la recherche sur les aliments à Unilever en Inde. Zheng Yuan est chimiste supérieur en microélectronique aux États-Unis. Guy Schoettel est pharmacochimiste supérieur en Suisse. De nombreux autres sont passés de la R-D à la gestion, notamment Ilse Treurnicht, directrice générale à MaRS (Toronto), et John Laws, directeur des ventes chez Proctor and Gamble aux États-Unis.

Parmi ceux et celles qui travaillent comme fonctionnaires ou qui exercent une profession libérale, mentionnons Paul Makin (édition scientifique, ONU), Peter Hall (expert judiciaire, R.-U.), Sam Choi (science de l'environnement, Hong Kong), Dave Elliot (institut de recherche, Australie), Jan Hux (directeur de l'exploitation à l'Institute for Clinical Evaluative Sciences et médecin, Canada) et Mary-Ann MacDonald (dentiste, Canada).

Compte tenu de ce bilan en enseignement et à la direction d'études supérieures, il n'est pas surprenant que l'UWO lui décerne sa plus haute récompense, le prix Edward G. Pleva pour l'excellence en enseignement en 2003-2004.

Le dossier de Dick est tout aussi exceptionnel sur le plan des services. Il a siégé à de nombreux comités du CRSNG, dont ceux des subventions à la découverte, des subventions de recherche et développement coopérative et des bourses Steacie, ainsi qu'aux comités de sélection de la médaille d'or et du prix Polanyi (y compris à titre de président). Il a aussi siégé au comité de sélection du prix Rutherford de la Société royale du Canada (y compris à titre de président). Il a présidé l'Institut de chimie du Canada et la Société canadienne de chimie, et siégé à divers sous-comités de ces organismes. Ancien rédacteur en chef de la *Revue canadienne de chimie*, il est maintenant corédacteur en chef d'*Inorganica Chimica Acta* et membre du comité de rédaction de plusieurs autres revues en chimie. En 2006, l'Institut de chimie du Canada lui a remis la médaille de Montréal pour souligner ses contributions au milieu de la chimie.

Sur un plan personnel, Dick est un vrai gentleman. Son opinion est très recherchée en raison de son expérience et de sa nature altruiste. Je ne peux me souvenir d'une seule occasion où il aurait élevé la voix pour convaincre ses interlocuteurs; ses arguments son généralement très convaincants. Il a été un des ténors de la création du Département de chimie à l'UWO. Pour ma part, je serai toujours reconnaissant envers Dick pour son appui et ses conseils quand je l'ai remplacé au poste de rédacteur en chef de la *Revue canadienne de chimie*. La qualité des articles publiés dans ce numéro spécial, leur quantité et la réponse du milieu de la chimie montrent bien que je ne suis pas seul à tenir Dick en très haute estime. Je le félicite pour cette distinction et lui souhaite bonne chance pour l'avenir.

Rob Lipson
Rédacteur en chef

© 2009 NRC Canada

A mild and efficient chemoselective *N*-benzyloxycarbonylation of amines using TBAB as a catalyst under solvent-free conditions

Kothamasu Suresh Babu, Vidadala Rama Subba Rao, Ravu Ranga Rao, Sakhamuri Sivaram Babu, and Janaswami Madhusudana Rao

Abstract: We describe a mild and efficient method for the chemoselective *N*-benzyloxycarbonylation of amines by treatment of amines and aminoesters with benzyloxycarbonyl chloride (Cbz-Cl) in the presence of TBAB under solvent-free conditions in excellent yields. The method is general for the preparation of a wide variety of *N*-Cbz derivatives of aliphatic, aromatic amines, and aminoesters.

Key words: amines, green chemistry, benzyloxycarbonyl chloride, TBAB, solvent-free conditions.

Résumé : On décrit une méthode douce et efficace de *N*-benzyloxycarbonylation chimio-sélective des amines par traitement des amines ou des aminoesters par du chlorure de benzyl-oxy-carbonyle (Cbz-Cl), en présence de TBAB, dans des conditions sans solvant et avec d'excellents rendements. La méthode est générale et elle s'applique à une grande variété de dérivés d'amines ou d'aminoesters aliphatiques ou aromatiques portant un groupe benzyloxycarbonyle (CBZ).

Mots-clés : amines, chimie verte, chlorure de benzyloxycarbonyle, TBAB, conditions sans solvant.

[Traduit par la Rédaction]

Introduction

The protection and deprotection of amines is a common event in multistep organic syntheses. Among protecting groups of amines, the *N*-benzyloxycarbonyl (Cbz) group is very important and provides a useful functionality for the protection of amines because *N*-Cbz is stable in the presence of a wide range of nucleophiles in alkaline and also in aqueous acidic conditions. It is easily removable by catalytic hydrogenation, without any side reactions, to get the parent amine. In addition, it also serves as a stable protecting group in peptide chemistry.[1] There are several methods available for the protection of amino groups as *N*-Cbz derivatives, with aryl and (or) alkyl amine and benzyloxycarbonyl chloride (Cbz-Cl) in the presence of 4-(dimethylamino)pyridine (DMAP) being the most commonly employed method.[1] Recently, LiHMDS in THF-HMPA[2] and β-cyclodextrin in aqueous medium have been reported for this transformation.[3,4] However, the utility of a catalyst having quaternaryammonium salt for the preparation of *N*-Cbz derivatives has not been thoroughly investigated.

Organic reactions using mild water tolerant catalysts have received much attention in recent years, as they can conveniently be handled and removed from the reaction mixture, making the experimental procedure simple and ecofriendly.[5] On the other hand, organic reactions carried out in the absence of solvent are also attracting the attention of chemists because of their ease of processing and environmentally friendly nature. Tetra-alkylammonium bromides $(NR_4)^+Br^-$ have a molecular structure similar to that of the cationic surfactants previously employed,[6] the main difference being the absence of the long hydrophobic tail that prevents the formation of any organised structure (micelle) and thereby the partition of the substrate. These salts are promising additives, as different alkyl residues in the $(R_4N)^+$ ammonium cation lead to different charge density and hydrophobicity. In continuation of our work to develop new organic transformations,[7] we have observed the *N*-benzyloxycarbonylation of amines and (or) aminoesters with Cbz-Cl using TBAB as a mild and efficient catalyst under solvent-free conditions at room temperature (RT) (Scheme 1).

Scheme 1.

Results and discussion

In the present method, we describe a mild, efficient, and high yielding protocol for the *N*-benzyloxycarbonylation of amines and (or) aminoesters. In general, all the reactions were carried out by the addition of amines and (or) aminoesters (1 mmol) to Cbz-Cl (1.2 mmol) in the presence of TBAB under solvent-free conditions at RT to give the corresponding *N*-benzyloxycarbamates in excellent yields (Table 1, 75%–99%). The times required for derivatization were comparatively very short (5–35 min). This method

Received 9 July 2008. Accepted 15 October 2008. Published on the NRC Research Press Web site at canjchem.nrc.ca on 17 December 2008.

K.S. Babu, V.R.S. Rao, R.R. Rao, S.S. Babu,[1] and J.M. Rao. Organic Chemistry Division-I, Indian Institute of Chemical Technology, Uppal Road, Hyderabad 500-007, India.

[1]Corresponding author (e-mail: sivarambabu_anu@yahoo.co.in).

Table 1. A mild and efficient chemoselective *N*-benzyloxycarbonylation of amines using TBAB as a catalyst.

S. No	Substrate	Product[a8–11]	Time (min)	Yield (%)[b]
1	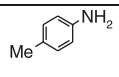	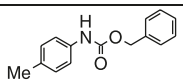	10	90
2		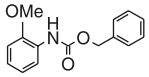	20	95
3	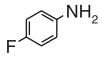	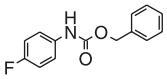	20	90
4		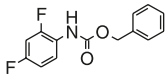	20	95
5		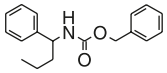	10	90
6		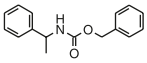	20	92
7		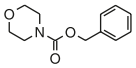	15	90
8		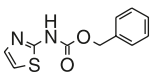	20	91
9		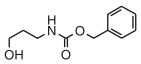	20	95
10		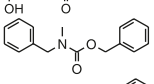	20	94
11	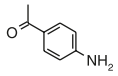	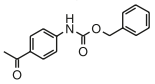	25	85
12		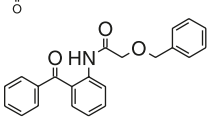	23	96
13		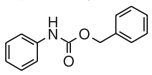	10	95
14	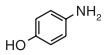	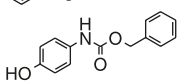	5	98
15	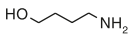	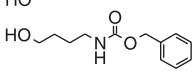	5	99
16		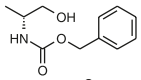	20	90
17	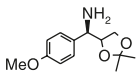	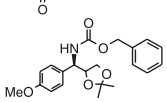	5	98
18		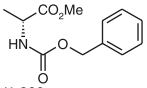	35	79
19	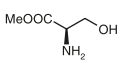	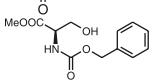	25	82
20	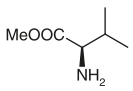	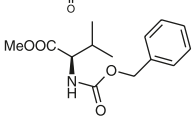	25	80

[a]All products were characterized by IR, ^{1}H NMR and mass spectral analysis.

[b]Yields refer to pure isolated products.

was compatible with various amines including aliphatic, aromatic, heteroaromatic, and some aminoesters. Amino groups with different chemical natures further demonstrated the chemoselectivity of the reaction. Similarly, in the cases of an amino phenol (Table 1, entry 14) and an amino alcohol (Table 1, entry 15), only the amino groups were protected. In the case of a mixture of aliphatic and aromatic amines (1 mmol), only the aliphatic amine was derivatized in the reaction with Cbz-Cl (1 mmol) in the presence of TBAB. Aromatic amines containing electron-withdrawing groups also gave the desired derivatives in good yields. Chiral substrates were resistant to racemization and labile functionalities, such as esters, were compatible in this conversion. The protocol is highly chemoselective, involves simple experimental procedures, mild reaction conditions, and gives excellent yields of Cbz-protected amines.

In conclusion, we have described a mild and efficient method for the protection of amines and (or) aminoesters as their *N*-benzyloxycarbonyl derivatives in the presence of catalytic amount of TBAB under solvent-free conditions at RT in excellent yields of the corresponding products. In the absence of TBAB, the reaction takes more time to complete and leads to a laborious process. The advantages of the method are reduced reaction times, simple experimental work-up procedures, and high product yields, making it a useful addition to the existing methodologies.

Experimental

IR spectra were recorded on a PerkinElmer FT-IR 240-c spectrometer using KBr optics. ^{1}H NMR spectra were recorded on a Gemini-200 spectrometer in $CDCl_3$ using TMS as internal standard. Mass spectra were recorded on an Agilent 1200 spectrometer. Starting materials were obtained commercially from Sigma-Aldrich and Lancaster, and were used without purification.

Typical experimental procedure

To a mixture of amine and (or) aminoesters (1 mmol) and benzyloxycarbonyl chloride (Cbz-Cl) (1.2 mmol) was added TBAB (5 mol %), and the reaction was stirred under solvent-free conditions at RT for an appropriate amount of time (Table 1). After completion of the reaction as monitored by TLC, saturated sodium bicarbonate was added to the reaction mixture, and the product was extracted into ethyl acetate (3 × 20 mL). The combined organic layer was washed with brine, dried over anhydrous sodium sulphate, and concentrated under reduced pressure to give a crude product that was purified by silica gel column chromatography to afford the corresponding *N*-benzyloxycarbonyl-protected amines or aminoesters. Spectral data for selected compounds are given below.

Entry 1

Mp and recrystallization in EtOH 70–71 °C. ^{1}H NMR (200 MHz, $CDCl_3$) δ: = 2.28 (s, 3H), 5.15 (s, 2H), 6.68 (br s, 1H), 7.08 (d, 2H, J = 8.55 and 2.80 Hz), 7.25 (d, 2H, J = 8.55 and 2.80 Hz), 7.30–7.40 (m, 5H). EIMS (M + 1) *m*/*z*: 242.

Entry 2

Mp and recrystallization in EtOH 72–74 °C. IR (KBr, cm^{-1}): 3425, 1733, 1529, 1461, 125, 1208, 1047, 745. ^{1}H NMR (200 MHz, $CDCl_3$) δ: = 3.98 (s, 3H), 5.21 (s, 2H), 6.80n (b s, 1H), 7.00 (m, 2H), 7.20 (dd, 1H, J = 8.50 and 2.81 Hz), 7.40 (m, 5H), 8.19 (dd, 1H, J = 8.00 and 2.80 Hz). EIMS (M + 1) *m*/*z*: 258.

Entry 3

Mp and recrystallization in EtOH 65–66 °C. IR (KBr, cm^{-1}): 3291, 3073, 2938, 1694, 1555, 1515, 1254, 1216, 1062, 834, 739, 694. ^{1}H NMR (200 MHz, $CDCl_3$). δ: = 5.18 (s, 2H), 6.60 (br s, 1H), 6.90–6.95 (m, 2H), 7.25–7.40 (m, 7H). EIMS (M + 1) *m*/*z*: 246.

Entry 4

Mp and recrystallization in EtOH 73–75 °C. IR (KBr, cm^{-1}): 3415, 1699, 1616, 1241, 1100, 1055, 619. ^{1}H NMR (200 MHz, $CDCl_3$) δ = 5.20 (s, 2H), 6.78 (br s, 1H), 6.85–7.00 (m, 2H), 7.35–7.40 (m, 5H), 8.10 (br s, 1H). EIMS (M + 1) *m*/*z*: 264.

Entry 5

Mp and recrystallization in EtOH 55–57 °C. IR (KBr, cm^{-1}): 3324, 3059, 3022, 2979, 1680, 1537, 1256, 1055, 1025, 756, 697. ^{1}H NMR (200 MHz, $CDCl_3$) δ: = 0.90 (t, 3H, J = 7.00 Hz), 1.20–1.40 (m, 2H) 1.60–1.80 (m, 2H), 4.60 (br s, 1H), 5.01 (d, 1H, J = 12.80), 5.03 (d, 1H, J = 12.80 Hz), 4.97 (m, 1H), 7.15–7.40 (m, 10H). EIMS (M + 1) *m*/*z*: 284.

Entry 6

Mp and recrystallization in EtOH 47–48 °C. ^{1}H NMR (200 MHz, $CDCl_3$) δ: = 1.50 (d, 3H, J = 6.60), 4.80 (m, 1H), 4.90 (br s, 1H), 5.10 (s, 2H), 7.20–7.40 (m, 10H). EIMS (M + 1) *m*/*z*: 256.

Entry 7

Mp and recrystallization in EtOH 47–50 °C. IR (KBr, cm^{-1}): 2859, 1702, 1427, 1241, 1119, 769. ^{1}H NMR (200 MHz, $CDCl_3$) δ: = 3.45 (t, 4H, J = 4.50 Hz), 3.65 (t, 4H, J = 4.00 Hz), 5.15 (s, 2H), 7.30–7.38 (m, 5H). ^{13}C NMR (75 MHz, CDCl3) δ: = 44.1, 66.5, 67.2, 128.0, 128.1, 128.5, 136.4, 155.2. EIMS (M + 1) *m*/*z*: 222.

Entry 8

Mp and recrystallization in EtOH 49–50 °C. IR (KBr, cm^{-1}): 3422, 2122, 2733, 1722, 1590, 1301, 1248, 1169, 1081, 1053, 695. ^{1}H NMR (200 MHz, $CDCl_3$) δ: = 5.32 (s, 2H), 6.80 (d, 1H, J = 4.30 Hz), 7.20 (d, 1H, J = 4.30 Hz), 7.38–7.40 (m, 5H). EIMS (M + 1) *m*/*z*: 235.

Entry 9

Mp and recrystallization in EtOH 41–43 °C. IR (KBr, cm^{-1}) 3431, 2929, 1692, 1405, 1260, 1208, 1147, 1058, 743, 697. ^{1}H NMR (200 MHz, $CDCl_3$) δ: = 1.65 (m, 2H), 3.28 (m, 2H), 3.65 (t, 2H, J = 5.20 Hz) 5.18 (s, 2H), 5.20 (br s, 1H), 7.28–7.38 (m, 5H). ^{13}C NMR (75 MHz, $CDCl_3$) δ: = 27.0, 29.0, 46.0, 62.0, 67.1, 127.3, 128.5, 136.1, 157.2. EIMS (M + 1) *m*/*z*: 210.

Entry 10

Mp and recrystallization in EtOH 52–53 °C. IR (KBr, cm^{-1}): 3031, 2930, 1702, 1453, 1402, 1219, 1140, 698; ^1H NMR (200 MHz, $CDCl_3$) δ: = 2.89 (s, 3H), 4.50 (s, 2H), 5.15 (s, 2H), 7.20–7.40 (m, 5H). EIMS (M + 1) *m*/*z*: 256.

Entry 13

Mp and recrystallization in EtOH 68–69 °C. IR (KBr, cm^{-1}): 3323, 3146, 3058, 3028, 2950, 1709, 1601, 1538, 1445, 1314, 1220, 1054, 754, 695. ^1H NMR (300 MHz, $CDCl_3$) δ: = 5.25 (s, 2H), 6.76 (br s, 1H), 7.08 (t, 1H, *J* = 8.0 Hz,), 7.20–7.45 (m, 9H). EIMS (M + 1) *m*/*z*: 228.

Entry 15

Mp and recrystallization in EtOH 75–76 °C. ^1H NMR (200 MHz, $CDCl_3$) δ: = 1.53–1.62 (m, 4H), 2.90 (br s, 1H, -OH), 3.13–3.25 (m, 2H), 3.60–3.66 (m, 2H), 4.99 (br s, NH),5.06 (s, 2H), 7.22–7.36 (m, 5H). ^{13}C NMR (75 MHz, $CDCl_3$) δ: = 29.7, 40.5, 62.1, 66.5, 127.6, 128.0, 135.7, 156.3. EIMS (M + 1) *m*/*z*: 224.

Entry 16

Mp and recrystallization in EtOH 79–81 °C. IR (KBr, cm^{-1}), 3315, 3065, 2975, 1687, 1540, 1452, 1255, 1073, 1040, 695. ^1H NMR (300 MHz, $CDCl_3$) δ: = 1.16 (d, 3H, *J* = 6.80 Hz), 2.44 (brs, 1H), 3.53 (dd, 1H, *J* = 5.3, 9.8 Hz), 3.66 (d, 1H, *J* = 9.8 Hz), 3.84 (m, 1H), 4.94 (br s, 1H), 5.07 (s, 2H), 7.39 –7.28 (m, 5H). EIMS (M + 1) *m*/*z*: 210.

Entry18

A pale yellow oil. ^1H NMR (300 MHz, $CDCl_3$) δ: = 1.40 (d, 3H, *J* = 7.17 Hz) 3.70 (s, 3H), 4.38 (m, 1H), 5.05 (s, 2H), 5.39 (br s, NH), 7.30–7.27 (m, 5H). ^{13}C NMR (75 MHz, $CDCl_3$) δ: = 18.7, 48.7, 52.5, 67.0, 128.5, 127.0, 136.2, 156.8, 174.8. EIMS (M + 1) *m*/*z*: 238.

Entry 19

A pale yellow oil. IR (KBr, cm^{-1}): 2955, 2888, 1714, 1456, 1380, 1345, 1214, 1064. ^1H NMR (300 MHz, $CDCl_3$) δ: = 3.47 (s, 1H), 3.65 (s, 3H), 3.83 (dq, 2H, *J* = 11.0 Hz, 3 Hz), 4.35 (br s, 1H), 5.04 (s, 2H), 6.08 (br s, 1H), 7.25 (m, 5H). ^{13}C NMR (75 MHz, $CDCl_3$) δ: = 52.4, 56.0, 68.0, 67.0, 128.0, 128.0, 128.3, 136.0, 156.3, 171.1. EIMS (M + 1) *m*/*z*: 254.

Entry 20

A pale yellow oil. ^1H NMR (300 MHz, $CDCl_3$) δ: = 0.89 (d, 3H, *J* = 6.79 Hz), 0.96 (d, 3H, *J* = 6.79 Hz), 2.19 (m, 1H), 3.66 (s, 3H), 4.34 (m, 1H), 5.08 (s, 2H), 5.68 (d, NH, *J* = 9.0 Hz), 7.31 (m, 5H). ^{13}C NMR (75 MHz, $CDCl_3$) δ: = 17.1, 18.7, 30.8, 58.7, 66.6, 127.8, 128.2, 135.9, 156.4, 175.3. EIMS (M + 1) *m*/*z*: 266.

Acknowledgement

The authors thank University Grants Commission, New Delhi, India, for the financial support and to the Director, Indian Institute of Chemical Technology, for his encouragement.

References

(1) Greene, T. W.; Wuts, P. G. M. *Protective groups in organic synthesis, 3rd ed.* John Wiley and Sons: New York, USA, 1999.
(2) Fieser, L. F.; Fieser, M. In *Reagents in organic synthesis.* John Wiley and Sons:New York, USA, 1967.
(3) Hernandez, J. N.; Martin, V. S. *J. Org. Chem.* **2004**, *69*, 3590. doi:10.1021/jo049759+. PMID:15132580.
(4) Pavan Kumar, V.; Reddy, M. S.; Narender, M.; Rama Rao, K. *Tetrahedron Lett.* **2006**, *47*, 6393. doi:10.1016/j.tetlet.2006.06.162.
(5) Green, T. W. *Protecting groups in organic synthesis.* Wiley: New York, USA, 1981.
(6) Viparelli, P.; Alfani, F.; Gallifuoco, A.; Cantarella, M. *J. Mol. Catal. B Enzym.* **2004**, *28*, 101. doi:10.1016/j.molcatb.2004.02.002.
(7) Suresh Babu, K.; Rao, V. R. S.; Sunitha, P.; Babu, S.; Rao, J. M. *Synth. Commun.* **2008**, *38*, 1784. doi:10.1080/00397910801989600.
(8) Mahesh, K. C.; Narasimhulu, M.; Reddy, T. S.; Suryakiran, N.; Venkateswarlu, Y. *Tetrahedron Lett.* **2001**, *48*, 55.
(9) Suryakiran, N.; Mahesh, K. C.; Ramesh, D.; Selvam, J. J. P.; Venkateswarlu, Y. *Tetrahedron Lett.* **2008**, *49*, 2607. doi:10.1016/j.tetlet.2008.02.108.
(10) Hernández, J. N.; Martin, V. S. *J. Org. Chem.* **2004**, *69*, 3591.
(11) Schlessinger, R. H.; Iwanowicz, E. J. *Tetrahedron Lett.* **1987**, *28*, 2083 and refs. cited therein. doi:10.1016/S0040-4039(00)96049-0.

Chemical constituents from the bark of *Anisopus mannii*

Apollinaire Tsopmo, Pierre Kamnaing, Jean Watchueng, Jin-Ming Gao, Yasuo Konishi, and Olov Sterner

Abstract: A minor novel 1,7-naphthyridine alkaloid with an unprecedented skeleton, named anisopusine (**1**), was isolated from the CH_2Cl_2 soluble materials of an acetone extract of the bark of *Anisopus mannii* (Asclepiadaceae) together with four known compounds 5α-hydroxy-lup-20(29)-en-3β-yl eicosanoate (**2**), [6]-gingerdione (**3**), [6]-dehydrogingerdione (**4**), and ferulic acid (**5**). Their structures were determined on the basis of spectroscopic data, including 1D and 2D NMR, HR-EI-MS. Compounds (**2–5**) were characterized for the first time from this genus.

Key words: Asclepiadaceae, *Anisopus mannii*, 1,7-naphthyridine alkaloid, anisopusine, gingerdione, 5α-hydroxy-lup-20(29)-en-3β-yl eicosanoate.

Résumé : Dans les matériaux solubles dans le CH_2Cl_2, obtenus à partir des produits solides obtenus par extraction de l'écorce d'*Anisopus mannii* (asclépiadacée) avec de l'acétone, on a isolé un nouvel alcaloïde mineur dont la structure comporte un squelette inconnu jusqu'à maintenant, une 1,7-naphtypyridine, et qui a été dénommé anisopusine (**1**); à ses côtés, on a aussi retrouvé quatre produits connus, l'eiconinate de 5α-hydroxylup-20(29)-én-3β-yle (**2**), la [6]-gingerdione (**3**), la [6]-déhydrogingerdione (**4**) et l'acide férulique (**5**). Les structures ont été déterminées sur la base de données spectroscopiques, dont la RMN en 1D et 2D et la spectrométrie de masse à ionisation électronique à haute résolution (SM-IE-HR). La caractérisation des composés **2** à **5** dans ce gène est une première.

Mots-clés : Asclépiadacée, *Anisopus mannii*, 1,7-naphtypyridine, alcaloïde, anisopusine, gingerdione, eiconinate de 5α-hydroxylup-20(29)-én-3β-yle.

[Traduit par la Rédaction]

Introduction

It is well-established that plant species, belonging to the botanical family of Asclepiadaceae contain cardenolides[1] and pregnane glycosides,[2–4] as well as pyrroloisoquinoline and phenanthroindolizidine alkaloids.[5,6] 7-Demethoxytylophorine from *Cynanchum komarovii*[5] inhibited tobacco mosaic virus (TMV) while cryptolepine, an indoloquinoline alkaloid from *Cryptolepis sanguinolenta*, showed antimalarial properties.[7,8] Several cytotoxic and antiviral activities have been reported for some glycosides.[9–11]

Some species within the Asclepiadaceae family have been used to prepare arrow poisons for fishing,[12] and some have been used traditionally to treat diseases like fevers,[13] rheumatism, and urinary diseases.[14] The genus *Anisopus* belongs to this important family with about six species and subspecies in Africa. Little is known about its chemistry and biology. A report of the use of *Anisopus larvae* to treat intestinal and urino-genital myiasis was published in 1966.[15] In Cameroon, *Anisopus mannii* N. E. Br. is a shrub indigenous to the Southwest province where it is used as a fish poisoning agent.[12] In our continuous search for secondary metabolites from the Cameroon medicinal plants,[16,17] an acetone extract of the bark of *A. mannii* was investigated, and we herein report the isolation and structure elucidation of a novel naphthyridine alkaloid with an unprecedented skeleton, named anisopusine (**1**), as well as four previously reported compounds (**2–5**).

Received 16 September 2008. Accepted 27 October 2008. Published on the NRC Research Press Web site at canjchem.nrc.ca on 7 January 2009.

A. Tsopmo and J. Gao.[1] Research Centre for Natural Medicinal Chemistry, College of Science, Northwest A & F University, Yangling, Shaanxi 712100, China.
P. Kamnaing. Department of Chemistry, Carleton University, 1125 Colonel By Drive, Ottawa, ON K1S 5B6, Canada.
J. Watchueng and Y. Konishi. Chemical Biology Group, Biotechnology Research Institute, 6100 Royalmount Av., Montreal, QC H4J 1P2, Canada.
O. Sterner. Department of Organic and Bioorganic chemistry, Lund University, Box 124, SE-221 00 Lund, Sweden.

[1]Corresponding author (e-mail: jinminggaocn@yahoo.com.cn).

Results and discussion

The CH_2Cl_2 -soluble materials of an acetone extract of the ground parts of *A. mannii* was subjected to repeated column chromatography on silica gel to afford a novel alkaloid (**1**) together with four known compounds (**2–5**) (Fig. 1). Their structures were elucidated by 1D and 2D NMR, HR-EI-MS, and by comparison with published data.

Compound **1** was obtained as red needles (yield: 0.0001% on dry wt. basis), and named anisopusine. The high resolution (HR) EI-MS of **1** showed a molecular ion peak at *m/z* 276.0910, corresponding to the molecular formula $C_{17}H_{12}N_2O_2$, with thirteen degrees of unsaturation. The IR spectrum of this molecule displayed absorption bands for a secondary amine group at 3308 cm^{-1}, two conjugated car-

Fig. 1. Molecular structures of compounds (**1–5**) from *A. mannii*.

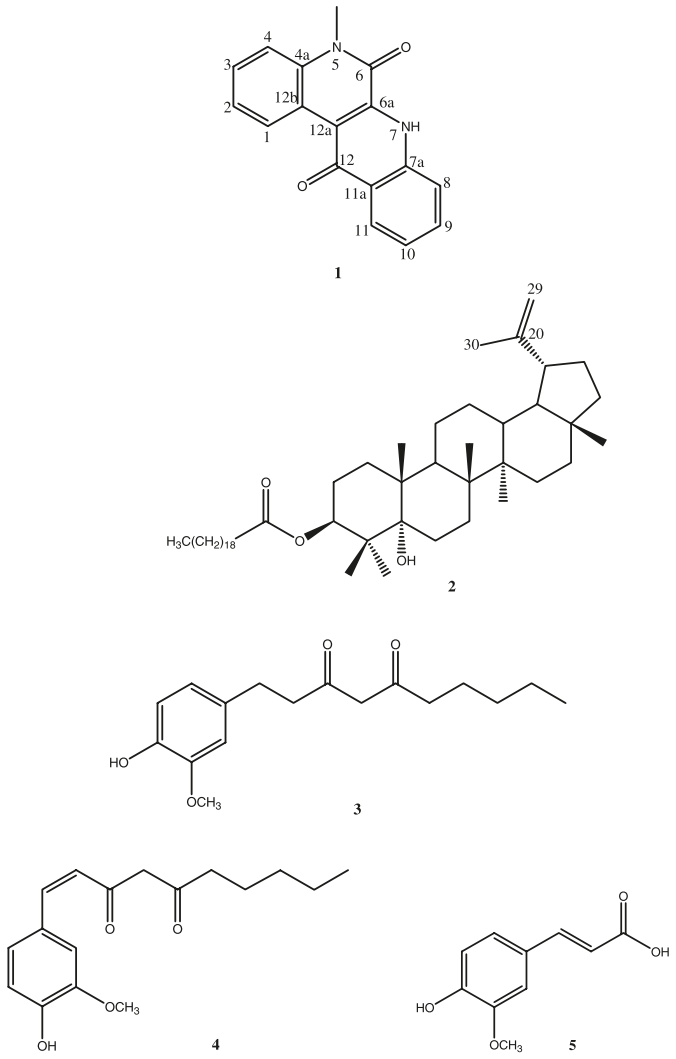

bonyl functionalities at 1692 and 1657 cm^{-1}, and a benzene ring backbone (s) at 1608, 1585, and 1481 cm^{-1}. This molecule could encompass a tertiary amide, since strong absorption bands are typically observed for tertiary amides between 1700 and 1650 cm^{-1}.[7] The ^1H and ^{13}C NMR data of **1** in $CDCl_3$ analyzed in conjunction with the HMQC spectrum showed the presence of 17 carbon signals attributed to an amide carbonyl, a ketone carbonyl, six sp^2 quaternary carbons, eight sp^2 methines, and one sp^3 methyl. Because 11 out of 13 unsaturation degrees were accounted for, **1** was inferred to possess two rings in the molecule.

The ^1H NMR spectrum of **1** exhibited eight aromatic proton signals in the downfield region of δ 6.8–9.0 and one nitrogen methyl group at δ 3.36. The ^1H NMR and ^1H–^1H COSY spectra of **1** showed two aromatic spin systems: δ 8.90 (d, J = 7.8 Hz, H-1), 7.16 (dt, J = 1.0, 7.8 Hz, H-2), 7.34 (dt, J = 1.0, 7.8 Hz, H-3), and 6.89 (d, J = 7.8 Hz, H-4), and δ 7.00 (d, J = 7.6 Hz, H-8), 7.52 (dt, J = 1.2, 7.6 Hz, H-9), 7.02 (t, J = 7.6 Hz, H-10), and 7.75 (d, J = 7.9 Hz, H-11). Two proton–proton connectivities from H-1 through H-4 and from H-8 through H-11 were revealed from the ^1H–^1H COSY spectrum (Fig. 2). This suggested the presence of two ortho-substituted aromatic rings in this molecule. The ^{13}C NMR spectrum showed two carbonyl carbon signals at δ 170.7 and 188.2; the former being characteristic of a tertiary amide function. This amide group was further confirmed on the basis of 2D NMR. Pertinent HMBC correlations were observed from the N-methyl group (δ 3.36) to an aromatic quaternary carbon C-4a (δ 142.9) and a carbonyl carbon C-6 (δ 170.7), indicating that it was linked to a nitrogen atom of the amide moiety. Further HMBC correlations were observed from H-8 to C-7a (δ 151.8), C-10 (δ 121.5), and C-11a (δ 120.0), as well as from H-11 to C-7a (δ 151.8), C-9 (δ 136.9), and C-12 (δ 188.2), which in turn suggested that the ketone carbon C-12 is attached to an aromatic quaternary carbon C-11a. The remaining amino group (–NH–) was connected between C-6a (δ 139.3) and C-7a (δ 151.8), since their chemical shifts appeared at lower field. Inspection of the HMBC spectrum (Fig. 2) enabled us to construct the skeleton of **1**, as depicted in Fig. 1. As a consequence, based on the above spectroscopic analysis, compound **1** was unambiguously characterized as a novel naphthyridine alkaloid, 7-methyl-5,7-dihydrodibenzo[b,*f*]-1,7-naphthyridine-4,8-dione, which has an unprecedented skeleton.

Fig. 2. H–H COSY and important HMBC correlations in anisopusine (**1**).

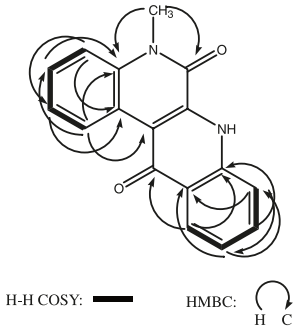

The four other known compounds obtained in the present investigation were identified as lup-20(29)-en-3-ol-3,5-dihydroxyeicosanoate,[18] [6]-gingerdione,[19] [6]-dehydrogingerdione[19], and ferulic acid[20] by comparison of their spectroscopic data with those reported in the literature.

It is worthwhile to point out that two pungent flavouring gingerdione derivatives, [6]-gingerdione (**3**) and [6]-dehydrogingerdione (**4**), are the major active components from the rhizomes of the spice and oriental herbal medicine ginger, *Zingiber officinale* Rosc (Zingiberaceae). These two products have been reported to possess many properties, such as anti-inflammatory and analgesic,[21–23] inhibition of cell proliferation in HL-60 cells,[24] and anti-feedant activities.[25,26] In this work, from the bark of *A. mannii*, we have isolated these two compounds in addition to a naphthyridine alkaloid anisopusine (**1**), which is a new secondary metabolite. This is the first reported occurrence of an alkaloid based on a 1,7-naphthyridine skeleton from plants. To the best of our knowledge, this is the first characterization of compounds (**2–5**) from this genus. Biogenetically, this existing alkaloid (**1**) may be formed from anthranilic acids and acetic acids via a sequence of condensation, decarboxylation, N-methylation, and oxidation coupling reactions.

Experimental

General

Melting points were measured with a Reichter microscope and are uncorrected. IR spectra were recorded with an FTIR Shimazu Hyper 1.51 spectrophotometer. ^{1}H NMR (500 MHz) and ^{13}C NMR (125 MHz) were taken in $CDCl_3$ using a Brucker ARX500 spectrometer with an inverse multinuclear 5 mm probe head equipped with a shielded gradient coil. The chemical shifts (δ) are reported in parts per million (ppm) relative to chloroform (7.26 ppm for $CHCl_3$ and 77.0 ppm for $CDCl_3$), while the coupling constants (*J*) are given in Hz. COSY, HMQC, and HMBC experiments were recorded with gradient enhancements using sine-shaped gradient pulses. For 2D heteronuclear correlation spectroscopy, the refocusing delays were optimized for $^1J_{CH}$ = 145 Hz and $^nJ_{CH}$ = 10 Hz. The raw data were transformed, and the spectra were evaluated with the standard Bruker UXNMR software. HR-EI-MS and EI-MS spectra (direct inlet at 70 eV) were recorded with a JEOL SX102 spectrometer. Column chromatography was run on Merck silica gel 60. TLC analyses were carried out on silica gel GF_{254} precoated plates with detection accomplished by spraying with 15% H_2SO_4 followed by heating at 100 °C or by visualizing under a UV lamp at 254 nm.

Plant material

The bark of *A. mannii* N. E. Br. was collected from the Southwest Province, Cameroon, in December 2006. Authentification was done at the Limbe botanic garden, and the voucher specimen (CM 0611068) was deposited at its Herbarium.

Extraction and isolation

The air-dried and powdered bark of *A. mannii* (3 kg) was extracted by percolation with acetone to yield a crude extract (79 g). The crude extract was dissolved in a mixture of 500 mL of MeOH/H_2O (1:1, *v*/*v*), and then extracted with CH_2Cl_2 (3 × 400 mL) to afford on evaporation 21 g of the CH_2Cl_2 soluble residue. The resulting residue was subjected to vacuum liquid chromatography on silica gel using hexane/EtOAc of increasing polarity (1:0–0:1) to provide three fractions (A–C). Fraction A (3 g) contained most fats and was not further investigated. Fraction B (2.5 g) was separated by flash chromatography on silica gel using hexane/ethyl acetate (85:15) to give 5α-hydroxy-lup-20(29)-en-3β-yl eicosanoate (500 mg, **2**) and a crude product containing **1**. The crude product was purified by flash chromatography on silica gel using hexane/EtOAc (85:15) to afford anisopusine (3 mg, yield: 0.0001% on dry wt. basis, **1**). Fraction C (3.7 g) after two successive flash chromatography columns using hexane/EtOAc gradient system gave five fraction Ca–e. Fraction Cb was subjected to flash chromatography on silica gel using hexane/acetone (90:10, 80:20, and 70:30) to afford [6]-gingerdione (15 mg, **3**) as a yellow oil and [6]-dehydrogingerdione (21 mg, **4**) as yellow needles. Fraction Cd was repeatedly separated by flash chromatography on silica gel using $CHCl_3$/MeOH (80:20) to give ferulic acid (150 mg, **5**).

7-Methyl-5,7-dihydrodibenzo[*b*,*f*]-1,7- naphthyridine-4,8-dione (anisopusine)

Red needles; mp 231–233 °C (acetone). IR ($CHCl_3$) ν_{max}: 3308 (NH), 1692 (ArC=O), 1657(ArNC=O), 1609, 1585, 1481, 1382, 1319, 1103, 1082, 939 cm^{-1}. ^{1}H NMR (500 MHz, $CDCl_3$) δ_H: 8.90 (1H, d, *J* = 7.8 Hz, H-1), 7.16 (1H, dt, *J* = 1.0, 7.8 Hz, H-2), 7.34 (1H, dt, *J* = 1.0, 7.8 Hz, H-3), 6.89 d (1H, d, *J* = 7.8 Hz, H-4), 7.00 (1H, d, *J* = 7.6 Hz, H-8), 7.52 (1H, dt, *J* = 1.2, 7.6 Hz, H-9), 7.02 t (1H, t, *J* = 7.6 Hz, H-10), 7.75 (1H, d, *J* = 7.9 Hz, H-11), 3.36 (3H, s, N–CH_3), 10.55 (1H, br s, NH). ^{13}C NMR (125 MHz, $CDCl_3$) δ_C: 125.5 (C-1), 122.7 (C-2), 129.2 (C-3), 107.9 (C-4), 142.9 (C-4a), 170.7 (C-6), 139.3 (C-6a), 151.8 (C-7a), 111.9 (C-8), 136.9 (C-9), 121.5 (C-10), 125.2 (C-11), 120.0 (C-11a), 188.2 (C-12), 106.8 (C-12a), 121.0 (C-12b), 26.0 (N–CH_3). EI-MS *m*/*z*: 276 $[M]^+$ (100), 248 [M – CO](22), 247(51), 220(11), 219(19), 205(15), 172(15), 143(15), 117(14), 104(9), 76(16). HR-EI-MS *m*/*z*: 276.0910 $[M]^+$ (calcd. for $C_{17}H_{12}N_2O_2$: 276.0899).

Acknowledgements

Financial support from Swedish Natural Science Research Council and the Program for New Century Excellent Talents in University (NCET-05-0852) are gratefully acknowledged.

References

(1) Srivastav, S.; Deepak, D.; Khare, A. *Tetrahedron* **1994**, *50*, 789. doi:10.1016/S0040-4020(01)80794-8.
(2) Sigler, P.; Saksna, R.; Deepak, D.; Khare, A. *Phytochemistry* **2000**, *54*, 983. doi:10.1016/S0031-9422(99)00611-1. PMID:11014302.
(3) Yoshikawa, K.; Matsuchika, K.; Takahashi, K.; Tanaka, M.; Arihara, S.; Chang, H. C.; Wang, J. D. *Chem. Pharm. Bull. (Tokyo)* **1999**, *47*, 798. PMID:10399837.
(4) Li, J.-Z.; Liu, H.-Y.; Lin, Y.-J.; Hao, X.-J.; Ni, W.; Chen, C.-X. *Steroids* **2008**, *73*, 594. doi:10.1016/j.steroids.2008.01.015. PMID:18328519.
(5) An, T.; Huang, R. Q.; Yang, Z.; Zhang, D. K.; Li, G. R.; Yao, Y. C.; Gao, J. *Phytochemistry* **2001**, *58*, 1267. doi:10.1016/S0031-9422(01)00382-X. PMID:11738420.
(6) Zhang, R.; Fang, S. D.; Chen, Y.; Lu, S. X. *Acta Bot. Sin.* **1991**, *33*, 870.
(7) Tackie, A. N.; Boye, G. L.; Sharaf, M. H. M.; Schiff, P. L., Jr.; Crouch, R. C.; Spitzer, T. D.; Johnson, R. L.; Dunn, J.; Minick, D.; Martin, G. E. *J. Nat. Prod.* **1993**, *56*, 653. doi:10.1021/np50095a001.
(8) Wright, C. W. *J. Pharm. Pharmacol.* **2007**, *59*, 899. doi:10.1211/jpp.59.6.0017. PMID:17637183.
(9) Itokawa, H.; Xu, J.; Takeya, K. *Chem. Pharm. Bull. (Tokyo)* **1988**, *36*, 4441. PMID:3246012.
(10) Zhang, X. H.; Zhu, H. L.; Yu, Q.; Xuan, L. J. *Chem. Biodivers.* **2007**, *4*, 998. doi:10.1002/cbdv.200790091. PMID:17510995.
(11) Li, Y.; Wang, L.; Li, S.; Chen, X.; Shen, Y.; Zhang, Z.; He, H.; Xu, W.; Shu, Y.; Liang, G.; Fang, R.; Hao, X. *Proc. Natl. Acad. Sci. U.S.A.* **2007**, *104*, 8083. doi:10.1073/pnas.0702398104. PMID:17470783.
(12) Neuwinger, H. D. *Toxicon* **2004**, *44*, 417. doi:10.1016/j.toxicon.2004.05.014. PMID:15302524.
(13) Boye, G. L.; Ampofo, O. *In* Proceedings of the first international symposium on Cryptolepine. University of Science and Tachnology, Kumasi, Ghana. 1983.

(14) Deepak, D.; Srivastav, S.; Khare, N. K.; Khare, A. *Progress in the Chemistry of Organic Natural Products* **1996**, *69*, 71. PMID:8981834.
(15) Smith, K. G. *Nature* **1966**, *210* (5038), 852. doi:10.1038/210852a0. PMID:5958461.
(16) Tsopmo, A.; Ayimele, G. A.; Tane, P.; Ayafor, J. F.; Connolly, J. D.; Sterner, O. *Tetrahedron* **2002**, *58*, 2725. doi:10.1016/S0040-4020(02)00183-7.
(17) Tomla, C.; Kamnaing, P.; Ayimele, G. A.; Tanifum, E. A.; Tsopmo, A.; Tane, P.; Ayafor, J. F.; Connolly, J. D. *Phytochemistry* **2002**, *60*, 197. doi:10.1016/S0031-9422(02)00075-4. PMID:12009324.
(18) Sobrinho, D. C.; Hauptli, M. B.; Braz-Filho, R. *J. Braz. Chem. Soc.* **1991**, *2*, 15.
(19) Kiuchi, F.; Shibuya, M.; Sankawa, U. *Chem. Pharm. Bull. (Tokyo)* **1982**, *30*, 754. PMID:7094159.
(20) Kelley, C. J.; Harruff, R. C.; Carmack, M. *J. Org. Chem.* **1976**, *41*, 449. doi:10.1021/jo00865a007.
(21) Kimura, I.; Pancho, L. R.; Koizumi, T.; Kimura, M. *J. Pharmacobio-Dyn.* **1989**, *12*, 220. PMID:2795431.
(22) Grzanna, R.; Lindmark, L.; Frondoza, C. G. *J. Med. Food.* **2005**, *8*, 125. doi:10.1089/jmf.2005.8.125. PMID:16117603.
(23) Flynn, D. L.; Rafferty, M. F.; Boctor, A. M. *Prostaglandins Leukot. Med.* **1986**, *24*, 195. doi:10.1016/0262-1746(86)90126-5. PMID:3467378.
(24) Hsu, M. H.; Kuo, S. C.; Chen, C. J.; Chung, J. G.; Lai, Y. Y.; Huang, L. J. *Leukemia Res.* **2005**, *29*, 1399. doi:10.1016/j.leukres.2005.04.014.
(25) Escoubas, P.; Lajide, L.; Mizutani, J. *Phytochemistry* **1995**, *40*, 1097. doi:10.1016/0031-9422(95)00154-Y.
(26) Rahuman, A. A.; Gopalakrishnan, G.; Venkatesan, P.; Geetha, K.; Bagavan, A. *Phytother. Res.* **2008**, *22*, 1035. doi:10.1002/ptr.2423. PMID:18618523.

One-pot synthesis of β-amido ketones using Brønsted acidic ionic liquid as an efficient and reusable catalyst

Krishna M. Deshmukh, Ziyauddin S. Qureshi, Nitin S. Nandurkar, and Bhalchandra M. Bhanage

Abstract: An efficient protocol was developed for one-pot condensation of an aldehyde, ketone, acetyl chloride, and nitriles catalyzed by a stable and reusable 1-methyl-imidazolium hydrogen sulfate ([Hmim][HSO_4]) as a Brønsted acidic ionic liquid. The system tolerated a variety of functional groups affording the corresponding β-amido ketones in moderate to good yields under milder operating conditions.

Key words: ionic liquids, multicomponent reactions, β-amido ketones, one-pot synthesis.

Résumé : On a développé un protocole efficace pour la condensation monotope d'un aldéhyde, d'une cétone, du chlorure d'acétyle et de nitriles, catalysée par un liquide ionique stable et réutilisable, le sulfate acide de 1-méthyl-imidazolium [Hmim][HSO_4] qui agit comme acide de Brønsted. Le système tolère une grande variété de groupements fonctionnels conduisant à la formation des β-amidocétones correspondantes avec des rendements allant de modérés à bons, dans les conditions d'opération les plus douces.

Mots-clés : liquides ioniques, réactions à plusieurs composantes, β-amidocétones, synthèse monotope.

[Traduit par la Rédaction]

Introduction

β-Amido ketones constitute an important class of compounds having biological and medicinal properties.[1,2] They are used as precursors for the synthesis of 1,3-amino alcohol present in antibiotic drug such as nikkomycines or neopolyoxines.[3,4] Traditionally, these compounds are synthesized by a Dakin–West reaction, which involves the condensation of an α-amino acid with acetic anhydride in the presence of a base.[5] Iqbal and co-workers proposed a multicomponent route for the synthesis of β-acetamido ketones via condensation of an aldehyde, enolizable ketones, acetyl chloride, and acetonitrile using $CoCl_2$[6] and Montmorillonite K10[7] as the catalysts. Subsequently, other groups extended these methodologies by exploring various Lewis or Brønsted acid catalysts such as $FeCl_3 \cdot 6H_2O$,[8] $ZrOCl_2 \cdot 8H_2O$,[9] silica sulfuric acid,[10,11] $SiCl_4$-$ZnCl_2$,[12] heteropoly acid,[13] ZnO,[14] and $BiCl_3$ generated from BiOCl.[15] Inspite of their potential applications, these methodologies face disadvantages like the requirement of harsh reaction conditions, use of expensive and moisture sensitive Lewis acid catalysts, and elevated temperatures.

Received 1 August 2008. Accepted 24 October 2008. Published on the NRC Research Press Web site at canjchem.nrc.ca on 18 December 2008.

K.M. Deshmukh, Z.S. Qureshi, N.S. Nandurkar, and B.M. Bhanage.[1] Department of Chemistry, Institute of Chemical Technology, University of Mumbai, N. Parekh Marg, Matunga, Mumbai 400 019, India.

[1]Corresponding author (e-mail: bhalchandra_bhanage@yahoo.com).

In recent years, application of ionic liquids have gained considerable interest in the context of green synthesis. Although ionic liquids were initially introduced as an alternative green reaction media, today they have marched far beyond this border for their significant role in controlling the reaction as a catalyst. Among various ionic liquids developed to date, Brønsted acidic ionic liquids have emerged as a most promising alternative for a wide variety of acid catalyzed reactions.[16–24]

Results and discussion

We herein report an efficient protocol for one-pot condensation of an aldehyde, ketone, acetyl chloride, and nitriles catalyzed by a stable and reusable Brønsted acidic ionic liquid, 1-methyl-imidazolium hydrogen sulfate ([Hmim][HSO_4]). The system tolerated a variety of functional groups affording corresponding β-amido ketones in moderate to good yields under milder operation conditions (Scheme 1).

Initially, condensation of benzaldehyde, acetophenone, acetyl chloride, and acetonitrile were chosen as model reaction and the role of the different ionic liquids as a catalyst and it's loading on the reaction system was investigated (Table 1, entries 1–4). The influence of various 1-methyl-imidazolium based ionic liquids, such as 1-butyl-3-methyl-imidazolium hydrogen sulfate ([C_4mim][HSO_4]), 1-methyl-imidazolium hydrogen sulfate ([Hmim][HSO_4]), 1-methyl-imidazolium tetraflouroacetate ([Hmim][Tfa]), and 1-methyl-imidazolium nitrate ([Hmim][NO_3]), were studied. Out of various ionic liquids screened, the [Hmim][HSO_4] ionic liquid was found to be the most effective, providing good yield of the desired product. The effect of catalyst

Scheme 1. Synthesis of β-amido ketones using ionic liquid as catalyst.

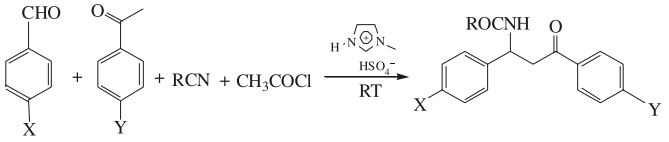

loading on the reaction system was also investigated and 40 mol% [Hmim][HSO_4] was found to be the most effective in providing a higher yield. (Table 1, entries 5–10).

Since [Hmim][HSO_4] was one of the most effective functional ionic liquids, it was selected to investigate the possibility of recyclability. After the completion of the reaction, the reaction mixture was evaporated under reduced pressure to obtain a residue. The residue was dissolved in ethyl acetate to obtain two phases; the ionic liquid phase was separated by decantation of ethyl acetate. The ionic liquid phase was then washed with diethyl ether (3 × 5 mL) and was evaporated under reduced pressure at 80 °C for 1 h to remove the redundant mixed solvent and it was then used for further recyclability test.

It can be seen from Table 1, entry 2, that there was no obvious change on the recovered catalyst (88%–95%) and excellent yield was obtained. After recycling three times, [Hmim][HSO_4] was still stable enough and had less impact on the catalytic activity. The purity of the recycled ionic liquid was confirmed using ^{1}H NMR and it was the same as that used for the first run. This indicated that [Hmim][HSO_4] was a highly efficient and recyclable catalyst for synthesis of β-amido ketones.

Thus, using [Hmim][HSO_4] as the best catalyst, the condensation of various aldehydes, ketones, and nitriles with different steric and electronic properties were investigated (Table 2, entries 1–22). The condensation of benzaldehyde, acetophenone, acetyl chloride, and nitriles provided a 75% yield of the desired product. Aldehydes with electron-donating (CH_3, OCH_3) and electron-withdrawing substituents (NO_2, Cl, Br, F) were also investigated and found to provide good yields (50%–84%) under the present conditions. Substituted acetophenones having activating and deactivating groups were found to be compatible and provided good yields of the desired products (Table 2, entries 2–4, 10–13, 16, 17, 21, 22). To show the generality of the protocol, the effect of aliphatic and aromatic nitriles, such as acetonitrile, benzonitrile, and phenylacetonitrile were also investigated. The reaction of benzonitrile require longer reaction times, up to 24 h and the probable reason for this may be the steric factor as well as low nucleophilicity of benzonitrile (Table 2, entries 14–17).

The reaction of acetonitrile and phenylacetonitrile were found to proceed smoothly under the present conditions, providing good yields of the desired products. Thus, the protocol is general in nature and tolerates a wide range of functional groups. A plausible reaction mechanism for the present reaction may proceed as depicted in Scheme 2. The yield of β-amido ketones depends upon the ionic liquid chosen, as shown in Table 1. It can be seen that [Hmim][NO_3] gives a lower yield of the product as compared to [Hmim][HSO_4] and [C_4mim][HSO_4], which suggests that the counter anion also plays a catalytic role in the reaction (Scheme 2). The counter anion protonates the ketone by a donating proton.

Table 1. Effect of catalysts and catalyst loading on the condensation of benzaldehyde, acetophenone, acetyl chloride, and acetonitrile.

Entry	Catalyst	Catalyst loading (mol %)	Yield (%)[a]
1	[C_4mim][HSO_4]	40	60
2[b]	[Hmim][HSO_4]	40	75, 73, 71
3	[Hmim][Tfa]	40	66
4	[Hmim][NO_3]	40	36
5	[Hmim][HSO_4]	10	50
6	[Hmim][HSO_4]	20	54
7	[Hmim]HSO_4]	30	63
8	[Hmim][HSO_4]	50	72
9	[Hmim][HSO_4]	60	70
10	[Hmim][HSO_4]	100	62

Note: Reaction conditions: benzaldehyde (1 mmol); acetophenone (1 mmol); acetyl chloride (0.3 mL); acetonitrile (4 mL); reaction time: 10 h at RT.

[a]Isolated yields.

[b]Recyclability of the catalyst tested up to three cycles.

Scheme 2. Mechanism for the synthesis of β-amido ketones.

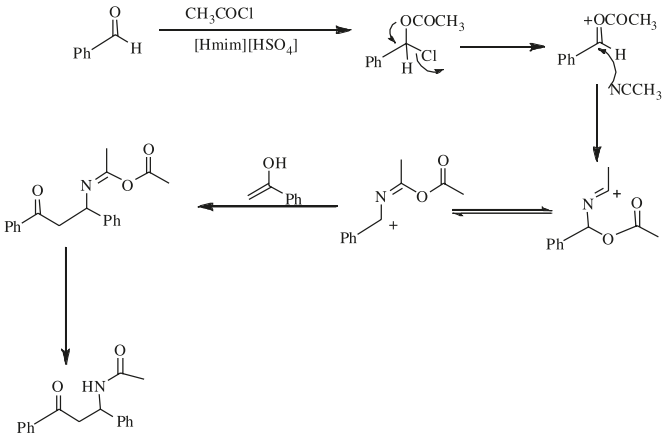

In summary, [Hmim][HSO_4] is a reusable and moisture stable Brønsted acidic ionic liquid, reported as an efficient catalyst for the synthesis of a wide range of β-amido ketone under mild operating conditions. The system tolerates a wide range of functional groups affording the desired products in good to excellent yields. Further work is in progress to broaden the scope of ionic liquids to various other organic transformations.

Experimental section

The chemicals and solvents were supplied by Sigma-Aldrich, Fluka, and S.D. Fine-chem Ltd. companies and used without further purification

Synthesis of ionic liquids

In this study, the ionic liquids used were synthesized according to the procedure reported in the literature[22–24] and were characterized by ^{1}H NMR.

Table 2. One-pot condensation of aldehyde, ketone, acetyl chloride, and nitriles to give the corresponding β-amido ketone catalyzed by [Hmim][HSO_4].

Entry	Aldehyde	Ketone	Product	Yield (%)[a]	Mp found (°C)	Mp reported (°C), Ref.
1	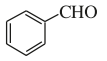		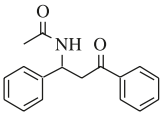	75	100–102	101–103, 13
2	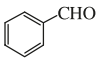	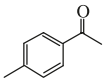	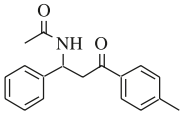	64	120–121	121–123, 11
3	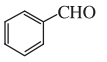	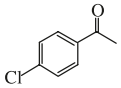	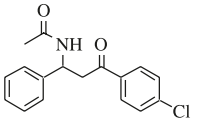	77	112–114	114–115, 11
4	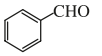	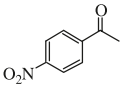	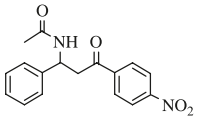	65	76–78	74–76, 13
5	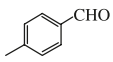		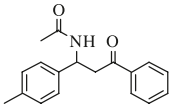	68	111–114	112, 6
6	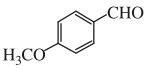		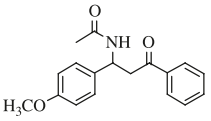	84	112–115	115–117, 13
7	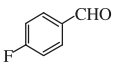		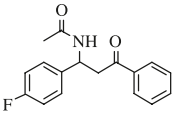	76	109–111	109–111, 11
8	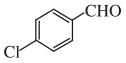		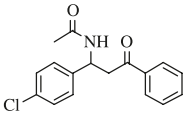	61	143–145	144–146, 13
9	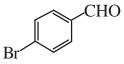		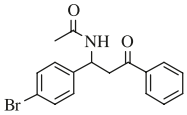	66	148–150	148–150, 8
10	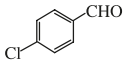	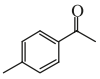	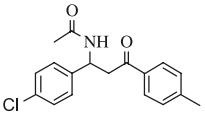	72	143–145	14
11	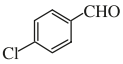	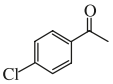	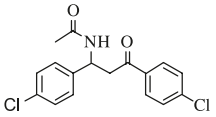	53	140–142	141–143, 10

Synthesis of β-amido ketones using [Hmim][HSO_4] as the catalyst

To a stirred suspension of [Hmim] [HSO_4] (40 mol %) in acetonitrile (4 mL) were added benzaldehyde (1 mmol), acetophenone (1 mmol), and acetyl chloride (0.3 mL). The reaction mixture was stirred at ambient temperature for 10 h. After the completion of the reaction, crushed ice (30 mL) was added to the reaction mixture and stirred thoroughly. On solidification, the products were filtered off and dried to get the corresponding β-amido ketone. The solid product obtained was recrystallized from the mixture of solvents (ethyl acetate–hexane) to get the pure product. All compounds are known compounds and were characterized by using IR and ^{1}H NMR.

Selected spectroscopic data

Characterization of ionic liquids using ^{1}H NMR

1-Butyl-3-methyl-imidazolium hydrogen sulfate ([C_4mim][HSO_4])

^{1}H NMR (400 MHz, $CDCl_3$, ppm) δ: 0.91 (t, J = 7.5 Hz,

Table 2 (*concluded*).

Entry	Aldehyde	Ketone	Product	Yield (%)[a]	Mp found (°C)	Mp reported (°C), Ref.
12	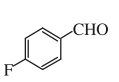	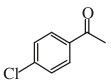	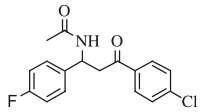	57	109–111	108–110, 11
13	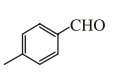	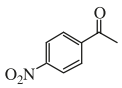	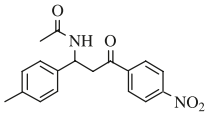	53	84–86	83–85, 13
14[b]	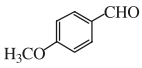		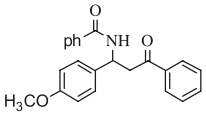	60	175–177	12
15[b]	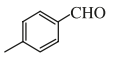		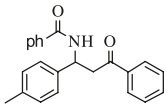	62	169–170	172–173, 12
16[b]	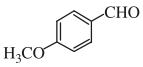		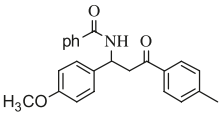	63	178–180	12
17[b]	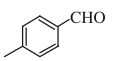		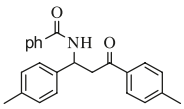	66	176–177	12
18	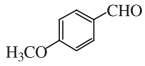		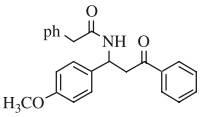	67	128–130	131–132, 12
19	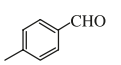		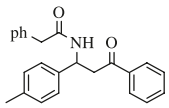	64	127–129	12
20	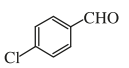		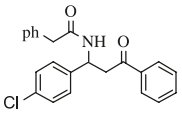	50	143–145	12
21	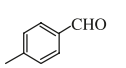		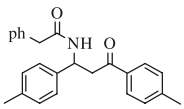	56	129–131	12
22	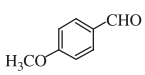		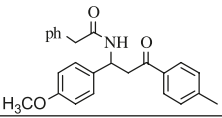	65	133–134	12

Note: Reaction conditions: aldehyde (1mmol), ketone (1mmol), acetyl chloride (0.3mL), nitriles (4 mL), [Hmim] [HSO_4] (40%), and reaction time 10 h at ambient temperature.
[a] Isolated yield.
[b] Reaction time 24 h.

3H), 1.25 (m, J = 7.4 Hz, 2H), 1.75 (m, J = 7.4 Hz, 2H), 2.5 (s, 3H), 4.18 (t, J = 7.0 Hz, 2H), 7.70 (m, 2H), 7.79 (s, 1H), 9.25 (s, 1H).

1-Methyl-imidazolium hydrogen sulfate ([Hmim][HSO_4])

IR (KBr, cm^{-1}) ν: 3265, 3145, 2846, 1550, 1480, 1186, 1058, 883, 618. ^{1}H NMR (400 MHz, $CDCl_3$, ppm) δ: 3.86 (s, 3H), 7.67 (m, 3H), 9.07 (s, 1H), 14.5 (br, s, 1H).

Characterization of β-amido ketones using ^{1}H NMR and FT-IR

N-*[3-Oxo-1,3-diphenyl-propyl] acetamide (Table 2, entry 1)*

IR (KBr, cm^{-1}) ν: 3284, 3058, 2925, 1690, 1646, 1540, 1225, 988, 618. ^{1}H NMR (200 MHz, $CDCl_3$, ppm) δ: 2.03 (s, 3H), 3.40 (dd, J = 6.0, 16.9 Hz, 1H), 3.76 (dd, J = 6.0, 16.9 Hz, 1H), 5.57 (m, 1H), 6.70 (br d, J = 7.5 Hz, 1H), 7.22–7.61 (m, 8H), 7.91 (d, J = 7.5 Hz, 2H).

N-*[1-(4-Fluorophenyl)-3-oxo-3-phenyl-propyl] acetamide (Table 2, entry 7)*

IR (KBr, cm^{-1}) ν: 3283, 3083, 1686, 1635, 1574, 1372, 1298, 990, 895. ^1H NMR (200 MHz, $CDCl_3$, ppm) δ: 2.01 (s, 3H), 3.45 (dd, J = 6.0, 16.9 Hz, 1H), 3.75 (dd, J = 6.0, 16.9 Hz, 1H), 5.50 (m, 1H), 6.72 (brs, 1H), 7.01 (t, 2H), 7.40 (m, 5H), 7.83 (d, J = 7.5 Hz, 2H).

N-*[1-(4-Methoxyphenyl)-3-oxo-3-(4-methylphenyl) propyl]-2-phenylacetamide (Table 2, entry 22)*

IR (KBr, cm^{-1}) ν: 3333, 2955, 1689, 1640, 1515, 1247, 1184, 1032, 822, 733. ^1H NMR (200 MHz, $CDCl_3$, ppm) δ: 2.32 (s, 3H), 3.22 (dd, J = 5.5, 16.6 Hz, 1H), 3.45 (dd, J = 5.5, 16.6 Hz, 1H), 3.51 (s, 2H), 3.68 (s, 3H), 5.39 (m, 1H), 6.49 (brs, 1H), 7.03 (d, J = 7.5 Hz, 2H), 7.13–7.28 (m, 9H), 7.69 (d, J = 7.8 Hz, 2H).

Acknowledgments

Financial assistance from the Indira Gandhi Center for Atomic Research (IGCAR) is kindly acknowledged.

References

(1) Casimir, J. R.; Turetta, C.; Ettouati, L.; Paris, J. *Tetrahedron Lett.* **1995**, *36*, 4797.
(2) Godfrey, A. G.; Brooks, D. A.; Hay, L. A.; Peters, M.; McCarthy, J. R.; Mitchell, D. *J. Org. Chem.* **2003**, *68*, 2623. doi:10.1021/jo026655v. PMID:12662031.
(3) Dahn, U.; Hagenmaier, H.; Hohne, H.; Konig, W. A.; Wolf, G.; Zahner, H. *Arch. Microbiol.* **1976**, *107*, 143. doi:10.1007/BF00446834. PMID:818968.
(4) Kobinata, K.; Uramoto, M.; Nishii, M.; Kusakabe, H.; Nakamura, G.; Isono, K. *Agric. Biol. Chem.* **1980**, *44*, 1709.
(5) Dakin, H. D.; West, R. *J. Biol. Chem.* **1928**, *78*, 745.
(6) Mukhopadhyay, M.; Bhatia, B.; Iqbal, J. *Tetrahedron Lett.* **1997**, *38*, 1083. doi:10.1016/S0040-4039(96)02474-4.
(7) Bahulayan, D.; Das, S. K.; Iqbal, J. *J. Org. Chem.* **2003**, *68*, 5735. doi:10.1021/jo020734p. PMID:12839472.
(8) Khan, A. T.; Parvin, T.; Choudhury, L. H. *Tetrahedron* **2007**, *63*, 5593. doi:10.1016/j.tet.2007.04.019.
(9) Ghosh, R.; Maiti, S.; Chakraborty, A.; Chakraborty, S.; Mukherjee, A. K. *Tetrahedron* **2006**, *62*, 4059. doi:10.1016/j.tet.2006.02.037.
(10) Khodaei, M. M.; Khosropour, A. R.; Fattahpour, P. *Tetrahedron Lett.* **2005**, *46*, 2105. doi:10.1016/j.tetlet.2005.01.149.
(11) Yakaiah, T.; Venkat Reddy, G.; Lingaiah, B. P. V.; Shanthan Rao, P. *Synth. Commun.* **2005**, *35*, 1307. doi:10.1081/SCC-200057240.
(12) Salama, T. A.; Elmorsy, S. S.; Abdel-Galel, M. K.; Ismail, M. A. *Tetrahedron Lett.* **2007**, *48*, 6199. doi:10.1016/j.tetlet.2007.06.128.
(13) (a) Rafiee, E.; Tork, F.; Joshaghani, M. *Bioorg. Med. Chem. Lett.* **2006**, *16*, 1221 doi:10.1016/j.bmcl.2005.11.080. PMID:16338236.; (b) Rafiee, E.; Shahbazi, F.; Joshaghani, M.; Tork, F. *J. Mol. Catal. Chem.* **2005**, *242*, 129. doi:10.1016/j.molcata.2005.08.005.
(14) Maghsoodlou, M. T.; Hassankhani, A.; Shaterian, H. R.; Habibi-Khorasani, S. M.; Mosaddegh, E. *Tetrahedron Lett.* **2007**, *48*, 1729. doi:10.1016/j.tetlet.2007.01.060.
(15) Ghosh, R.; Maiti, S.; Chakraborty, A. *Synlett* **2005**, 115. doi:10.1055/s-2004-836024.
(16) Cole, A. C.; Jensen, J. L.; Ntai, I.; Tran, K. L. T.; Weaver, K. J.; Forbes, D. C.; Davis, J. H., Jr. *J. Am. Chem. Soc.* **2002**, *124*, 5962. doi:10.1021/ja026290w. PMID:12022828.
(17) Arfan, A.; Bazureau, J. P. *Org. Process Res. Dev.* **2005**, *9*, 743. doi:10.1021/op058002x.
(18) Chowdhury, S.; Mohan, R. S.; Scott, J. L. *Tetrahedron* **2007**, *63*, 2363. doi:10.1016/j.tet.2006.11.001.
(19) Yadav, L. D. S.; Srivastava, V. P.; Patel, R. *Tetrahedron Lett.* **2008**, *49*, 3142. doi:10.1016/j.tetlet.2008.03.016.
(20) Sahoo, S.; Joseph, T.; Halligudi, S. B. *J. Mol. Catal. Chem.* **2006**, *244*, 179. doi:10.1016/j.molcata.2005.09.012.
(21) Palimkar, S. S.; Siddiqui, S. A.; Daniel, T.; Lahoti, R. J.; Srinivasan, K. V. *J. Org. Chem.* **2003**, *68*, 9371. doi:10.1021/jo035153u. PMID:14629159.
(22) Hajipour, A. R.; Khazdooz, L.; Ruoho, A. E. *Catal. Commun.* **2008**, *9*, 89. doi:10.1016/j.catcom.2007.05.003.
(23) Chiappe, C.; Leandri, E.; Tebano, M. *Green Chem.* **2006**, *8*, 742. doi:10.1039/b606258j.
(24) Zhao, G.; Jiang, T.; Gao, H.; Han, B.; Huang, J.; Sun, D. *Green Chem.* **2004**, *6*, 75. doi:10.1039/b309700p.

A DFT study of thymine and its tautomers

Dongsheng Jiao, Hongyan Wang, Yanlan Zhang, and Yu Tang

Abstract: The structures and the relative energies of six possible tautomers of the thymine base have been studied by density functional theory (DFT) using the B3LYP and BP86 functionals. The keto-thymine (T1) is predicted to be the most stable thymine tautomer, which is consistent with the other theoretical results and experimental data. The corresponding thymine cations and anions are studied using the same level of theory with double-ζ plus polarization and diffuse functions (DZP++) basis sets. The ionization potentials (IPs), the electron affinities (EAs), and proton affinities (PAs) for different protonation sites in thymine base are obtained. T1 has the largest ionization potential and the lowest proton affinity among all the considered thymine tautomers.

Key words: thymine, DFT, tautomer, IP, EA, PA.

Résumé : Faisant appel à la théorie de la fonctionnelle de la densité et utilisant des fonctions B3LP et BP86, on a étudié les structures et les énergies relatives de six tautomères potentiels de la thymine à l'été de base. Sur la base de ces calculs, il est prédit que la cétothymine (T1) est le tautomère le plus stable de la thymine; cette conclusion est en accord avec les autres calculs théoriques et avec les résultats expérimentaux. Les cations et anions correspondants à la thymine ont aussi été étudiés aux même niveaux de la théorie en utilisant comme ensembles de base des fonctions de polarisation double ζ plus et des fonctions diffuses (DZP++). On en a extrait les potentiels d'ionisation (PI), les affinités électroniques (AE) et les affinités protoniques (AP) pour les différents sites de protonation de la thymine. La cétothymine (T1) possède le potentiel d'ionisation le plus élevé et l'affinité protonique la plus faible parmi tous les tautomères considérés de la thymine.

Mots-clés : thymine, théorie de la fonctionnelle de la densité (TFD), tautomère, potentiel d'ionisation (PI), affinité électronique (AE), affinité protonique (AP).

[Traduit par la Rédaction]

Introduction

Recently, there has been increasing interest in the damage of DNA, which may cause various diseases such as cancer.[1–5] DNA is made of thymine (T), cytosine (C), guanine (G), and adenine (A). The nucleic-acid bases store the genetic information for cell replication and synthesis of proteins. Their physical chemistry has been extensively studied both experimentally and theoretically. In these bases, the thymine is the simplest pyrimidine base and only exists in DNA, not in RNA. It has been a highly frequent subject of theoretical studies because of its biochemical importance.[6,7] One of the possible molecular mechanisms for the formation of spontaneous mutations is conditioned by the tautomerism of DNA bases.[8–10]

Theoretically, M.J. Scanlan and I.H. Hillier researched the relative energies of the six tautomers of thymine using a 3–21G basis at an ab initio study in 1984.[11] J. Gu and J. Leszczynski studied the molecular geometries, energy properties, H-bonding patterns, and electrostatic potential characters of the thymine (T) and the role of the potassium cation in the formation of the T tetrad at the B3LYP/6–311G(d, p) and the HF/6–311G(d, p) levels of theory in 2001.[12] The tautomerism of the N_1-methylated derivatives of uracil, thymine, and 5-bromouracil has been studied to analyze its implications in the mutagenicity of 5-bromouridine by Michal Hanus in 2004.[7] The protonated keto-thymine (T1) have been predicted by A.K. Chandra et al.,[13] who predicted the interaction between thymine and water, compared with uracil. Their result indicates that O_8 is the preferred protonation site.

S.K. Kim et al. explored the gas-phase hydration of adenine, cytosine, thymine, and uracil in supersonic molecular beams by mass spectra and ionization potential measurements in 1996.[14] They researched the IP of hydrated thymine and obtained the IP of T1 (9.15 eV). S.L. Zhang et al. reported the vibration spectra and experiment assignments of thymine and nine of its isomers.[15] The IR and Raman spectra have been presented in their study. D.M. Close and coworkers studied the IPs of the DNA bases in gas phase and in aqueous solution in 2004.[16,17] The goal of their work is to explore methods to performe the IP calculations with DFT, and compare with the experiment and PMP2 method.

Recently, S. Yarasi et al. calculated the vibration properties of uracil and three of its isomers, thymine and nine of its isomers using DFT method at the B3LYP/6–311G(d, p) level.[18] In 2006, K. Mazurkiewicz et al. studied the thymine tautomers using MP2, CCSD, and B3LYP methods.[19] In their work, the energy ordering of thymine tautomers are

Received 28 April 2008. Accepted 23 October 2008. Published on the NRC Research Press Web site at canjchem.nrc.ca on 18 December 2008.

D. Jiao, Y. Zhang, and Y. Tang. Institute of Atomic and Molecular Physics, Sichuan University, Chengdu 610065, P.R. China.
H. Wang.[1] College of Sciences, Southwest Jiaotong University, Chengdu 610031, P.R. China.

[1]Corresponding author (e-mail: wanghyxx@yahoo.com).

Fig. 1. Geometries of thymine tautomers.

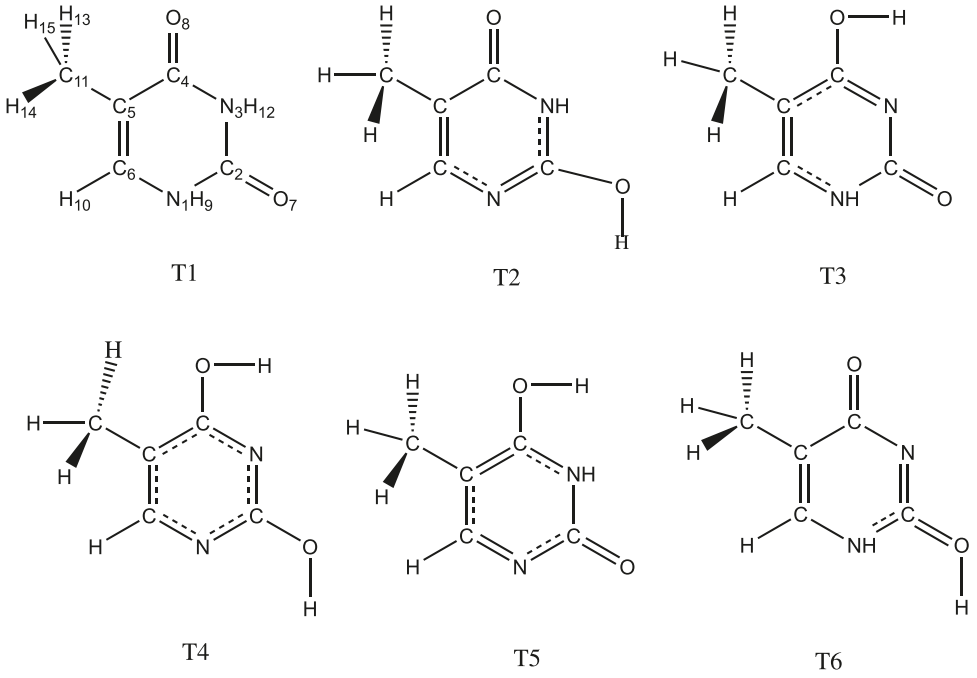

Table 1. Relative energies (kcal/mol) of neutral thymine tautomers.

	Relative energies (kcal/mol)		ZPE corrected relative energies (kcal/mol)	
Tautomers	B3LYP	BP86	B3LYP	BP86
T1	0	0	0	0
T2	10.6	10.7	10.4	10.3
T3	12.5	12.1	12.3	11.9
T4	12.7	13.2	12.5	13.0
T5	25.6	24.8	24.4	23.6
T6	29.0	28.8	27.8	27.5

predicted by different methods, and the anionic states of thymine are characterized using different methods.

The purpose of the research is to carry out a comprehensive theoretical investigation of all possible thymine tautomers using different DFT methods. All the anions and cations are considered to compare with K. Mazurkiewicz's paper.

Computational details

Two DFT methods were used to optimize the geometries of the thymine and its five tautomers. The first functional is the hybrid B3LYP method, which incorporates Becke's three-parameter exchange functional (B3) with the Lee, Yang, and Parr (LYP) correlation functional.[20,21] The second approach is the BP86 method, which marries Becke's 1988 exchange functional (B) with Perdew's 1986 correlation functional.[22,23] Double-ζ quality basis sets with polarization and diffuse functions (denoted DZP++) were used throughout structure optimizations and frequency analyses. The DZP++ basis sets were constructed by augmenting the Huzinaga–Dunning[24,25] set of contracted double-ζ Gaussian functions with one set of p-type polarization functions for each H atom and one set of five d-type polarization functions for each C, N, and O atom [α_p (H) = 0.75, α_d (C) = 0.75, α_d (N) = 0.80, α_d (O) = 0.85]. The B3LYP functional with the DZP++ basis sets has been previously reported to yield excellent predictions of the electron affinities of various chemical species.[26] The average absolute error for the computed electron affinities (EAs), compared with 91 species experiment EAs, was 0.14 eV (0.16 eV after ZPE corrections). The geometries of all cations and anions were fully optimized using both the B3LYP/DZP++ and BP86/DZP++ methods. All optimized structures were confirmed to be genuine local minima with no imaginary frequencies through vibration frequency analyses.

All computations were carried out with the Gaussian 03W program[27] in which the fine grid (75 302) is the default for evaluating integrals numerically, and the tight (10^{-8} Hartree) designation is the default for the energy convergence.[28]

To analyze the unpaired electron distributions, molecular orbital and spin density were constructed from the B3LYP/DZP++ method. Natural population atomic (NPA) charges were determined using the natural bond order (NBO) analysis of Reed and Weinhold.[29]

The electron affinities, the ionization potentials of the thymine and its tautomers were determined in the following manner. The adiabatic electron affinity (AEA) is defined as the energy difference between the neutral and corresponding anion species at their respective optimized geometries, AEA = $E_{(\text{optimized neutral})} - E_{(\text{optimized anion})}$. The vertical electron affinity (VEA) of the molecular is defined as VEA = $E_{(\text{optimized neutral})} - E_{(\text{anion at optimized neutral geometry})}$.

The ionization potential is defined as the amount of energy required to remove an electron from a neutral molecular. The adiabatic ionization potential is calculated employing the following formula: AIP = $E_{(\text{optimized cation})} - E_{(\text{optimized neutral})}$. The vertical ionization potential is defined as VIP = $E_{(\text{cation at optimized neutral geometry})} - E_{(\text{optimized neutral})}$.

Fig. 2. Optimized geometries of cations of thymine tautomers (the natural charges for C, N, and O are indicated).

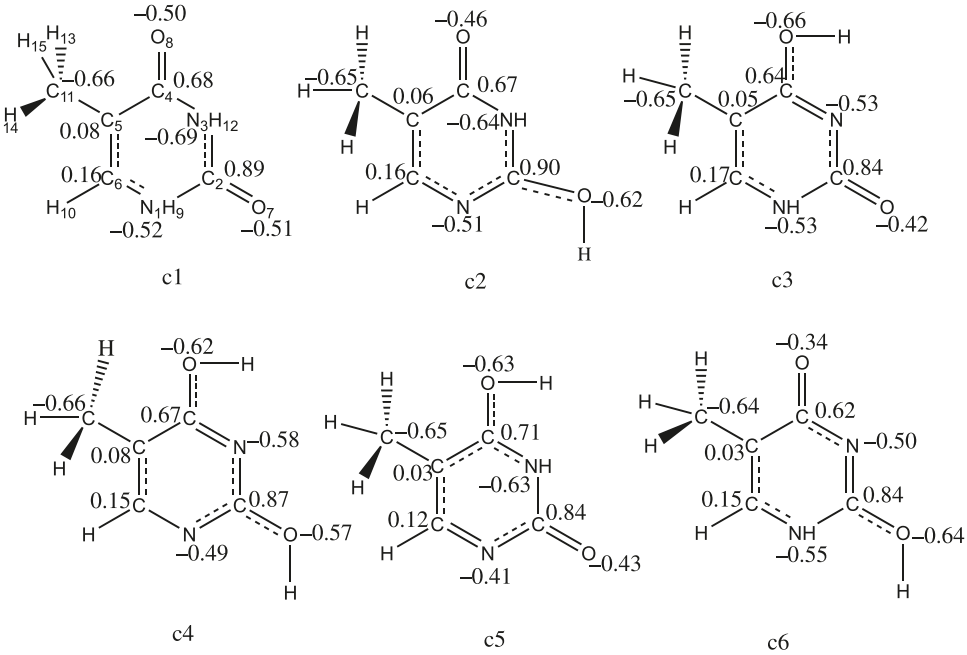

Fig. 3. Optimized geometries of anions of thymine tautomers (the natural charges for C, N, and O are indicated).

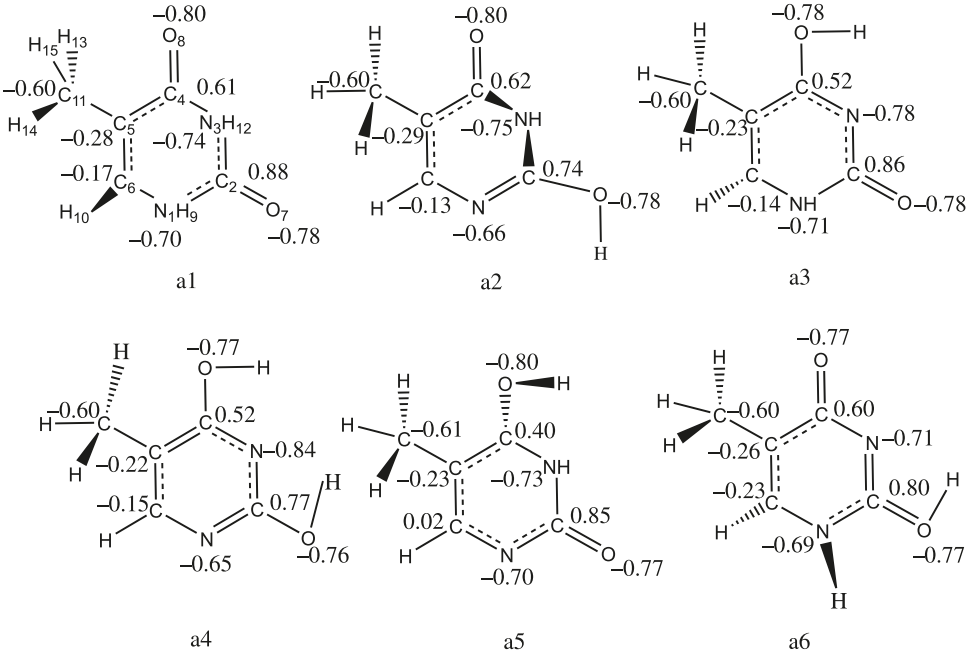

Results and discussion

Geometry

Thymine

We consider six thymine tautomers (Fig. 1). Geometries and atomic numberings of thymine tautomers are presented in Fig. 1 at the B3LYP/DZP++ level.

The relative energies (with ZPE corrections) of the six neutral structures at the B3LYP/DZP++ and BP86/DZP++ level of theory are presented in Table 1. T1 is the global minimum with the lowest total energy. T2 is obtained when a hydrogen atom is shift from N_1 site to O_7, which is about 10.6 kcal/mol (B3LYP) or 10.7 kcal/mol (BP86) above the global minimum. T3 with C_s symmetry is also derived from T1 when a hydrogen atom is moved from N_3 site to O_8, which lies 12.5 kcal/mol (B3LYP) or 12.1 kcal/mol (BP86) above the global minimum T1. T4 and T5 are predicted to lie 12.7 kcal/mol (B3LYP) and 25.6 kcal/mol (B3LYP) above the global minimum T1, respectively. T4 is obtained by moving a hydrogen atom from N_1 site to O_7 and moving hydrogen atom from N_3 site to O_8. T5 is obtained by moving

Table 2. Relative energies (kcal/mol) of tautomers of thymine anions and cations.

	Anions				Cations			
	Relative energy (kcal/mol)		ZPE corrected relative energy (kcal/mol)		Relative energy (kcal/mol)		ZPE corrected relative energy (kcal/mol)	
Tautomers	B3LYP	BP86	B3LYP	BP86	B3LYP	BP86	B3LYP	BP86
1	0	0	0	0	0	0	0	0
2	15.9	15.2	15.3	14.6	2.8	4.0	2.6	4.0
3	11.8	11.9	11.4	11.6	7.9	7.9	7.7	7.9
4	23.7	23.8	22.6	22.9	10.3	11.0	10.4	11.1
5	21.2	18.6	20.8	17.7	15.0	15.7	14.5	15.3
6	27.7	23.3	27.2	23.8	26.6	24.9	25.2	24.1

hydrogen atom from N_1 site to O_8. T6 is the isomer with the highest total energy, namely 29.0 kcal/mol (at B3LYP/DZP++ level of theory without ZPE) higher than T1. For T6, a hydrogen atom is moved from N_3 site to O_7, which causes the C_2–O_7 bond distance to increase significantly by 0.134 Å compared with T1. Thus, the order of the relative energy is T1< T2 < T3 < T4 < T5 < T6, which is different from the results of P.U. Civcir,[6] who predicted that T5 was the unstable by using AM1 and PM3 methods. R.D. Brown et al. predicted the microwave spectrum of thymine tautomers (T1, T2, and T3),[30] indicating that T1 is the most stable. M. Piacenza and S. Grimme studied the relative energies of the energetically low-lying tautomers of pyridine, cytosine, uracil, thymine, guanine, and *iso*-cytosine using a variety of different quantum chemical methods. They also predicted T1 was the most stable tautomer.[31] In Mazurkiewicz's study,[19] they consider four thymine tautomers (T1, T2, T3, and T4) utilizing CCSD(T)/aug-cc-pVDZ level of theory. They found that the energies order of thymine tautomer is T1 < T2 < T4 <T3, consistent with Grime's result.[31] While in most DFT study, the T3 is more stable than T4.[31] The energies of T3 and T4 are rather close (0.2 kcal/mol in our study), which suggests a highly fluxional system due to the localized orbital on the thymine ring.

Optimized geometries of thymine cations and anions, labeled as c1–c6 and a1–a6, are presented in Figs. 2 and 3 at the B3LYP/DZP++ level, in which the natural population analysis (NPA) charges for C, N, and O are indicated. The Mulliken spin density is contained in the Supplementary data. The relative energies of the six cations at B3LYP/DZP++ and BP86/DZP++ levels of theory are listed in Table 2, including the ZPE corrections. The cations keep the C_s symmetry except T6 and T2, for which the geometry shows minor difference from the neutral. Their relative stability agrees with the neutral. The cation of T1 has the lowest energy on the potential surface whose spin density is predicted to primarily on the C_5 (0.53) and N_1 (0.27) atoms. The energetic favourability of the c1 may be due to the conjugation between the centre N_1 and the neighbouring double bond $C_5 = C_6$, as shown in Fig. 2. It can be seen that in the gas phase of cations, C_2 and C_4 positions carry most positive charges (Table S5). Cation c2 lies 2.8 kcal/mol above the c1. The unpaired electron has significant contributions from C_5 (0.54), O_8 (0.26), and N_1 (0.22). Cation c3 lies 7.9 kcal/mol above the c1. The unpaired electron is mainly localized on the C_5, O_7, with spin densities 0.47 and 0.34, respectively. The positive charges are mainly focused on C_2 (0.84 e^-) and C_4 (0.64 e^-) atoms. Cation c4 is predicted to lie 10.3 kcal/mol higher than c1, whose spin density resides on C_5 (0.57). Cations c5 and c6 are predicted to lie 15.0 kcal/mol and 26.6 kcal/mol, respectively, above the c1.

Geometrical structures of six anions are predicted, and their relative energies are reported in Table 2. The energy order of the anions differs significantly from that of the neutrals and cations due to the significant geometrical alterations that accompany anion formation. The six-member ring in anion a3 is seriously distorted from plane compared with T3. These considerable structural changes of the neutrals and their related anions confirm that all anions have distinct covalent character. It is intriguing to compare the geometry alterations between a3 and T3. The bond distances change from T3 to a3 in the following way: C_4–O_8 1.35 to 1.39 Å, C_2–O_7 1.23 to 1.25 Å, C_2–N_3 1.38 to 1.36 Å, and C_4–C_5 1.44 to 1.39 Å. It is seen that longer bond lengths in the neutral become shorter in the anions, while some shorter distances become longer.

The energetic ordering of the anions is a1< a3 < a2 < a5 < a4 < a6. Anion a1 is the most favoured energetically. The unpaired electron is mainly delocalized to the C_6, C_4, with spin densities 0.66 and 0.15, respectively. The nitrogen and oxygen atom have higher negative charges in the NBO analysis (Table S6). A similar condition may occur for other anions. The anion a3 lies 11.8 kcal/mol above a1 without symmetry, whose hydrogen atom at C_6 site depart the plane. The spin density for a3 is predicted to reside on C_6 (0.73). The anion a2 lies above a1 15.9 kcal/mol. The unpaired electron for a2 is mainly localized on the C_6 (0.61). The anions a4, a5, and a6 are very close in the energy, i.e., 21–28 kcal/mol (B3LYP) above a1. However, the energy difference between a3 and a6 is larger than 15.9 kcal/mol (B3LYP). The unpaired electron for a4 and a6 has significant contributions from C_6 atom. For six anions, the C_{11} atom of methyl has a high negative charge (–0.60 e^-) from the NBO analysis.

T1

Bond lengths and bond angles for the most stable tautomers of thymine (T1) are listed in Table 3, compared with the crystalline monomer, which is obtained by X-ray coordinates.[32] Previous HF and MP2 calculations[33,34] predicted T1 to be the most stable. The calculated results are in good agreement with the available experimental data. The differences in the bond lengths hardly exceed 0.1 Å and those in the bond angles 1°. The value of the N_1–C_2–N_3 bond angle

Table 3. Structural parameters of thymine (T1), its cation, and anion at the BP86/DZP++ level of theory (bond lengths in angstroms and angles in degrees).

Bond	Neutral	Cation	Anion	Experimental[32]	Angle	Neutral	Cation	Anion	Experimental[32]
C_4C_5	1.48	1.50	1.42	1.48	$C_5C_4N_3$	114.4	115.1	114.4	114.3
C_4N_3	1.42	1.41	1.46	1.41	$C_5C_4O_8$	125.4	122.9	129.5	124.4
C_4O_8	1.24	1.23	1.27	1.19	$N_3C_4O_8$	120.2	122.0	116.0	121.2
C_5C_6	1.37	1.42	1.43	1.37	$C_4C_5C_6$	118.1	118.3	120.7	118.6
C_5C_{11}	1.51	1.48	1.51		$C_4C_5C_{11}$	118.2	118.8	118.9	
C_6N_1	1.39	1.34	1.43		$C_6C_5C_{11}$	123.7	122.9	120.3	
C_6H_{10}	1.10	1.10	1.10	1.08	$C_5C_6N_1$	122.6	120.7	117.9	
C_2N_1	1.40	1.45	1.38	1.31	$N_1C_2N_3$	112.4	113.0	113.7	117.8
C_2N_3	1.39	1.38	1.39	1.35	$N_1C_2O_7$	123.2	119.7	122.9	121.6
C_2O_7	1.23	1.22	1.26	1.25	$N_3C_2O_7$	124.5	127.3	123.4	120.5
N_1H_9	1.02	1.03	1.02	1.01	$C_6N_1C_2$	124.0	125.4	124.7	
N_3H_{12}	1.03	1.03	1.02	1.01	$C_4N_3C_2$	128.4	121.3	127.5	125.9

is slightly underestimated by the BP86 computations. In the crystal, the carbonyl moiety can be engaged in hydrogen bonds, and this effect could be even more important in hydrated crystals. This effect can probably explain at least part of the observed discrepancy between experimental and calculated geometries.

For T1 cation, C_1–N_3, C_4–O_8, C_5–C_{11}, C_6–N_1, C_2–N_3, C_2–O_7, C_5–C_6, C_6–N_1, and C_2–N_1 bonds undergo the largest (changed 0.05 Å) modifications. In particular, the C_6–N_1 bond length increases by 0.05 Å (from 1.34 to 1.39 Å at B3LYP/DZP++ level), while the C_5–C_6 bond shortens from 1.42 to 1.37 Å. The C_2–N_1 bond also shortens from 1.45 to 1.40 Å. The changes in the other bond lengths are less significantly. The lengths of both the C_6–H_{10} bond and the N_3–H_{12} bond are unchanged. The bond between C_5 and the methyl group (C_{11}) is increased by about 0.03 Å. Because of the rigid ring structure, the changes in the bond angles are generally negligible.

T1 anion has significant changes in the geometries compared with neutral T1. The bond distances change from T1 to a1 in the following way: the N_3–H_{12} bond is shortened from 1.03 to 1.02 Å, the C_2–N_1 bond also shortened from 1.40 to 1.38 Å, the C_4–C_5 bond from 1.48 to 1.42 Å. The C_4–N_3, C_4–0_8, C_5–C_6, C_6–C_1, and C_2–0_7 bonds are increased. The largest modification is the C_5–C_6 bond (changed 0.06 Å). The lengths of the C_5–C_{11}, C_2–N_3, N_1–H_9, and C_6–H_{10} bonds are unchanged. The differences in the bond angles almost exceed 1°. The biggest change is C_5–C_6–N_1 bond angle (5°). But the C_5–C_4–N_3, C_6–N_1–C_2, and C_4–C_5–C_{11} bond angles change a little.

The ionization potential of thymine tautomers

The formation of cationic centers plays an important role in the mechanism of radiation damage to DNA. These charged species are known to undergo protonation and deprotonation reactions that in turn can lead to a permanent alteration of the original bases and to an uncorrected transfer of genetic information.[38,39] Thus, the determination of ionization potentials (IPs) of DNA bases can assume a great significance, which has been a high frequent subject of theoretical and experimental studies.

The gas-phase adiabatic ionization potentials (AIPs) and vertical ionization potentials (VIPs) for thymine and its tautomers are presented in Table 4. There is good agreement between the calculated IP of thymine and the experimental data. In contrast to the anions, the geometries of the neutral and cationic species have C_s symmetry except T6, c2, and c6, and the formation of cation is achieved by only a bit change in geometry.

Thymine tautomers have been studied using semi-empirical AM1 and PM3 quantum-chemical calculations at the SCF level in the gas and aqueous phase by P.U.Civcir.[6] AM1 and PM3 calculations seem to overestimate the value of thymine (Table 4). Most IP calculations in the literature are given with the ZPE corrections.[40] The ZPE corrections for thymine at the B3LYP/DZP++ and BP86/DZP++ are listed in Table 4. In our work, it can be seen for the canonical bases at least that the corrections are very small for IPs (for T1, 8.69 eV without ZPE corrections and 8.63 eV with ZPE corrections). To T1, B3LYP calculations seem to underestimate the AIP by slightly less than 0.18 eV, com-

Table 4. IP (eV) of thymine (the value in the parentheses with ZPE corrected).

	AIP		VIP		(VIP)[6]		Expt.	
Tautomers	B3LYP	BP86	B3LYP	BP86	AM1	PM3	AIP	VIP
T1	8.77(8.63)	8.69(8.63)	9.00	12.63	9.60	9.44	8.95±0.10,[35] 8.87,[36] 8.80[37]	9.14±0.03[35]
T2	8.43(8.39)	8.40(8.36)	8.67	8.59	9.24	9.22		
T3	8.57(8.46)	8.50(8.46)	8.71	8.63	9.50	9.31		
T4	8.67(8.63)	8.59(8.55)	8.93	8.80	9.71	9.67		
T5	8.31(8.27)	8.29(8.27)	8.48	8.44	9.26	9.13		
T6	8.66(8.49)	8.51(8.49)	8.85	8.67	9.42	9.52		

Table 5. Electron affinities of thymine tautomers (the value of AEA in the parentheses with ZPE corrections).

	Electron affinity (eV)					
	AEA		VEA		Experimental	
Tautomers	B3LYP	BP86	B3LYP	BP86	AEA	VEA
T1	0.07(0.20)	–0.14(0.28)	–0.30	–0.17	0.79±0.05[41]	–0.29[42]
T2	–0.16(–0.02)	–0.05(0.09)	–0.47	–0.33		
T3	0.10(0.24)	0.15(0.29)	–0.24	–0.13		
T4	–0.41(–0.24)	–0.31(–0.15)	–0.66	–0.75		
T5	0.26(0.36)	0.41(0.53)	–0.19	–0.68		
T6	0.12(0.22)	0.38(0.44)	0.25	0.37		

pared with the result of W.G. Mallard et al. for BP86 computations is 0.26 eV.[35]

T1 is predicted to be the only species present in measurable abundance under the experimental conditions for IP. Comparing with the experimental data,[35] VIP is excellent agreement, and the maximum deviations are of about 0.14 eV (B3LYP). The BP86 computations overestimate the VIP by 3.49 eV, indicating that the results of the B3LYP are stable and good. The AIP 8.77 eV (B3LYP) is close to the experimental data (8.87 eV),[36] while S.K. Kim et al obtained 9.15 eV using ionization potential measurements.[14]

Other tautomers have no direct experimental measurement of the gas-phase AIPs and VIPs. T4 has the largest AIP in thymine tautomers (8.67 eV with B3LYP method without ZPE corrections), whereas T5 has the lowest values of AIP and VIP with B3LYP and BP86; it keeps the same results with PM3, different from AM1 (T2 has the lowest IP). T6 has 8.66 eV AIP from B3LYP. The AIP ordering of thymine tautomers is T1 > T4 > T6 > T3 > T2 > T5; it is different from the energies order of neutral and cation thymine tautomers. T3 followed T6 with 8.57 eV AIP. T3 is a controversial focus whose stability is not clear. Ab initio study predicted T3 is more unstable than T4, but most DFT study favoured the assumption that T4 is more stable than T3.[31] T2 has 8.43 eV AIP below T3. In our work, T5 has the lowest AIP (8.31 eV). T1 has the largest IP in all thymine tautomers, which shows that T1 is very difficult to form cation, and the other tautomers are more susceptible to radiation damage through the capture of an electron and more readily form cationic sites. T5 forms cation very easily owing to the lowest IP.

Electron affinities of thymine tautomers

There are two kinds of neutral–anion energy difference, namely the adiabatic electron affinity and the vertical electron affinities (VEA), which are shown in Table 5. The EA of T1 was concerned by several studies because it is the most stable of thymine tautomers. There are only a few recent direct experimental determinations on electron affinities.[43–48] S.D. Wetmore et al. computed the AEA (0.14 eV) using B3LYP method with 6–311+G(2df, p) basis set.[49] But N. Russo and co-workers obtained the small value (0.07 eV) using B3LYP method with TZVP basis.[50] In 2001, S. S. Wesolowski et al. calculated the electron affinities of DNA and RNA[24] using different methods. Their results are consistent with our conclusion.

The adiabatic electron affinities of T2 and T4 are negative because their anions are most destabilized with respect to their neutral species. This means that the extra electron interacts weakly with the LUMO of the neutral molecule, which confirmed by the small geometrics distortions from the neutral to the anion structure. On the other hand, T2 and T4 have dipole moments of 2.84 and 1.79 D, respectively, and should not form a dipole-bound anion that stabilizes the negative structure. The adiabatic electron affinities of other tautomers are positive by B3LYP method. The stabilization of their anions is accompanied by a distortion of the geometry, suggesting the entrance of the extra electron in the LUMO of their neutral. The dipole moments of T1, T3, T5, and T6 are 4.59, 5.51, 6.45, and 8.93 D, respectively.

T5 has the largest AEA (0.26 eV with B3LYP, 0.41 eV with BP86), whereas T1 has a nearly zero AEA value (0.07 eV at the B3LYP/DZP++ level of theory), indicating that T1 has a very low propensity to combine an electron. Compared with the experimental value, the results of BP86 are very fine, but the B3LYP method is often considered to be the most reliable.[25,26]

Table 6. Total energies (*E* in Hartree) and HOMO–LUMO gap (eV) for neutral thymine tautomers at the B3LYP/DZP++ level of theory without ZPE corrections.

Structure	T1	T2	T3	T4	T5	T6
-HOMO$^{\alpha}$	0.255	0.244	0.245	0.252	0.238	0.250
-LUMO$^{\alpha}$	0.058	0.052	0.061	0.045	0.064	0.052
Gap	5.36	5.22	5.01	5.63	4.73	5.39
-*E*	454.232894	454.215928	454.212929	454.212635	454.192157	454.186610

Fig. 4. The frontier orbitals for neutral thymine tautomers.

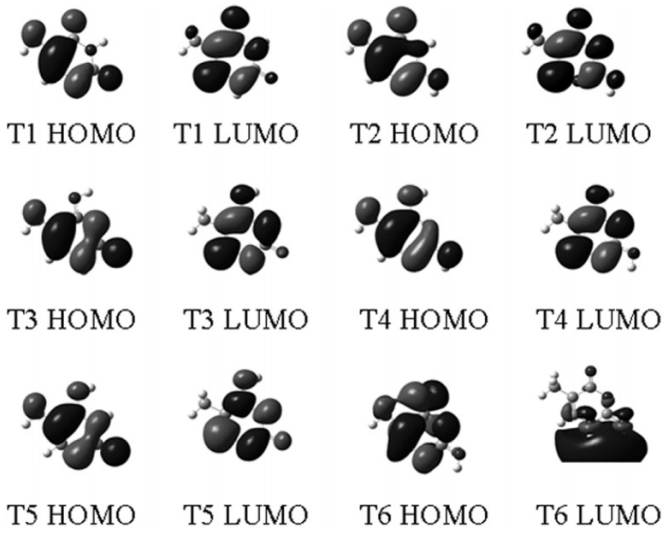

Fig. 5. The frontier orbitals for thymine anions.

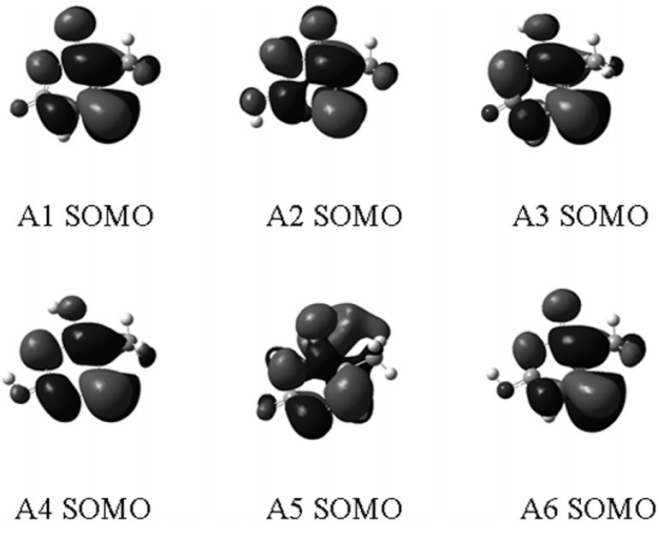

The VEA values of thymine tautomers are negative, except T6, which means that T6 can bind an electron at its equilibrium geometry, whereas others cannot. T1's VEA value (–0.30 eV) is in good agreement with the experimental value (–0.29 eV), which cannot bind an electron at its equilibrium geometry owing to the negative VEA value.

The theoretical VEA values are quite different from the AEA, owing to the considerable geometrical changes between the neutrals and the corresponding anions. Compared with the AEA value, the value of T5 is quite small (–0.68 eV from BP86), because the optimized neutral geometrical structure is significantly different from the optimized anionic structure.

Orbital analysis

Orbital analysis was performed for the thymine tautomers and their anions. The HOMO–LUMO energy gaps are shown in Table 6. The frontier molecular orbitals of thymine tautomers and anions are compared in Figs. 4 and 5. In thymine tautomers, the largest HOMO–LUMO gap, namely 5.63 eV, is found in T4, while the lowest HOMO–LUMO energy gap is in T5. From Fig. 4, for the neutral thymine tautomers, the highest occupied molecular orbital (HOMO) is completely localized on the thymine ring. The lowest unoccupied molecular orbitals (LUMO) of T3, T4, and T5 are mainly localized on the ring, except the methyl group. For T1 and T2, LUMOs are localized on the whole ring. For T6, the LUMO is localized on the methyl group, which leads that T6 is the most unstable. From Fig. 5, we obtain that the SOMOs of anions are completely localized on the ring. But SOMO of a3 and a6 are not localized on O_7 atom, while for a5, SOMOs are localized on the whole atoms except H_{15}. For a2 and a4, SOMO is not localized on the hydrogen atom at O_7 atom.

The proton affinities of thymine tautomers

Protonation reactions are among the most important in chemistry and biology. Protonation/deprotonation is the first step in many fundamental chemical rearrangements and in most enzymatic reactions. The gas-phase basicity and proton affinity are used to characterize the ability of a molecule in the gas phase to accept a proton. Experimental determination of these parameters is not easy; much attention has been given to the possibility of calculating these parameters by quantum methods with the growth in computer power. Ab initio approaches are very successful in providing reliable values of PAs and gas-phase basicities for small molecules; however, due to computational expense, application of Ab initio methods to the estimation of PAs is still impractical for larger molecules. The DFT methods are computationally less and include electron correlation energy via the correlation/exchange potential compared with ab initio approaches. Thus, they are used widely.

In our work, T1 is predicted to be the only species present in measurable abundance under the experimental conditions. There are three double bonds for T1 considered here. Thus, by attaching one hydrogen atom to break a double bond, six isomers can be generated from the thymine structure. The hydrogen could not add to C_4 and C_2 for the structure undergoing a big change. The proton attachment at N_6 implies a significant geometrical distortion of the ring. In a word, we consider five possible sites, which are O_8 (N_3), O_8 (C_5), O_7 (N_3), O_7 (N_1), C_5, and C_6. O_8 (N_3) denotes the proton at-

Table 7. The proton affinities of T1 (kcal/mol) at the B3LYP/DZP++ level of theory.

Structure	PA
$O_8(N_3)$	205.2
$O_8(C_5)$	207.9
$O_7(N_3)$	200.7
$O_7(N_1)$	199.5
C_5	187.1
C_6	157.3
Experimental	209.0±0.1[52]

Table 8. The proton affinities of thymine tautomers (kcal/mol) at the B3LYP/DZP++ level of theory.

Structure	T2	T3	T4	T5	T6
1	164.2	158.1	159.3	198.1	177.3
2	193.9	190.8	189.3	232.3	196.4
3	213.1	190.8	189.3	198.1	194.0
4	141.2	222.9	141.0	232.3	233.7
5	213.1	182.8	201.4	214.5	228.4
6	173.8	215.2	223.1	227.1	184.3
7	209.9	217.5		232.3	228.4

Fig. 6. Optimized geometries of the most stable protonation thymine tautomers.

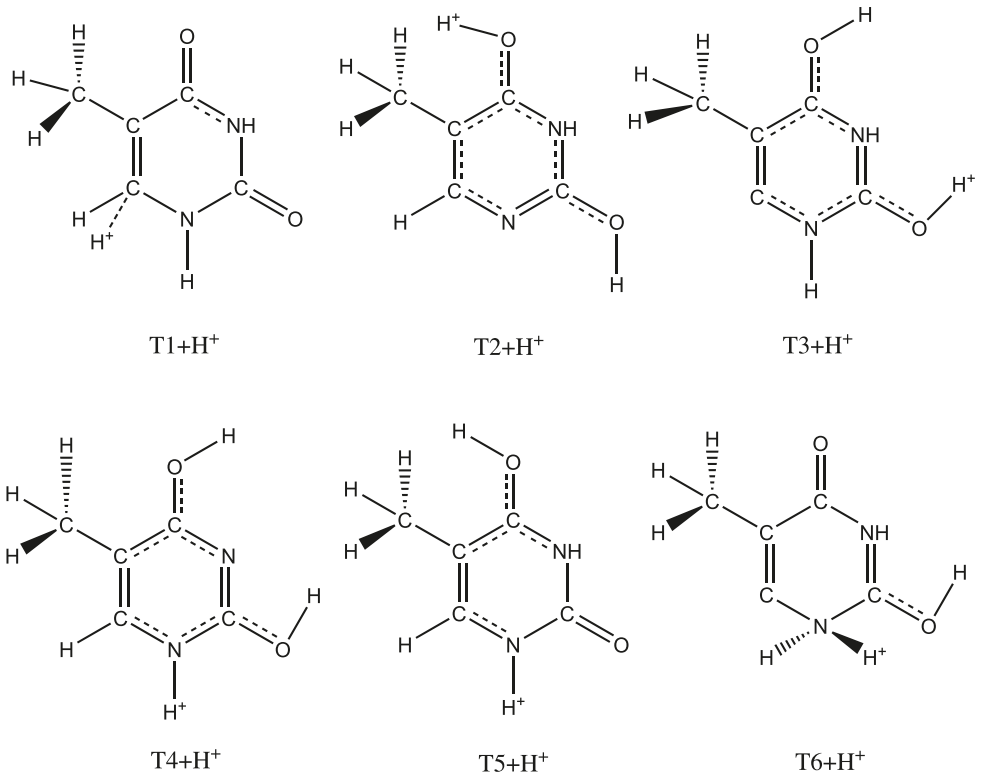

tached on the N_3 side of the C=O group. The results indicate that O_7 and O_8 are the preferred protonated sites, in good agreement with the N. Russo and A. K. Chandra's conclusions[13,51] and experimental data.[52] The proton affinities of T1 and thymine tautomers are summarized in Table 7 and Table 8, respectively. The six most stable protonated thymine tautomers are shown in Fig. 6.

For T2, the proton attachment sites possess seven possibilities: C_6, C_5, C_4, C_2, O_8, N_3, and N_1, whose order is consistent with the value of PAs. The results display that O_8 is the most preferred protonated site (Fig. 6). The proton added to N_1 site causes the ring rupture. The same value is found when adding the proton to C_4 and O_8 sites. The geometries of the protonated T2 have C_s symmetry except for adding proton to C_6, C_5, and C_2 sites, which have no symmetry.

For T3, there are also seven possibilities corresponding to C_6, C_5, C_4, C_2, N_1, O_7, and N_3. O_7 is the most preferred protonated site (Fig. 6). Adding the proton to C_4 and C_5 produces the same results. The proton added to N_3 site leads to the ring rupture. The geometries of the protonated T3 also have C_s symmetry except for adding proton to C_5, C_4, and C_2 sites, which have no symmetry.

For T4, the proton attachment sites have six possibilities: C_6, C_5, C_4, C_2, N_3, and N_1. The preferred one is N_1 site (Fig. 6). The geometries of the proton added to C_6, N_3, and N_1 sites have C_s symmetry, but adding to C_5, C_4, and C_2 sites have no symmetry.

T5 and T6 all have seven probabilities, namely T5, C_5, C_6, C_4, C_2, N_3, O_7, and N_1 sites and T6, C_6, C_5, C_4, O_8, C_2, N_1, and N_3 sites, respectively. The same value is obtained when adding the proton to C_6, C_2, and N_1 sites for T5.

For T6, the most preferred protonated site is the O_8 (Fig. 6). The geometries of the proton added to O_8, N_1, and N_3 sites have C_s symmetry, but adding to C_6, C_5, C_4, and C_2 sites have no symmetry.

For protonated thymine tautomers, T6 has the largest PA

(233.7 kcal/mol at O_8 site), T1 has the lowest PA (207.9 kcal/mol at O_8 site). The results show that O_8 is the preferred protonated site.

Conclusions

In this work, thymine tautomers and their corresponding cations and anions have been studied theoretically. The structures, energies, theoretical electron affinities, and proton affinities are predicted using the B3LYP and BP86 density functional methods in conjunction with DZP++ basis sets.

(1) The computational results for six neutral tautomers are compared with experiment and previous theoretical studies. T1 is predicted to be the global minimum on the potential energy surface. T6 has the highest energy, namely 29.0 kcal/mol (B3LYP) above the global minimum T1.

(2) The energies order for the anions differs significantly from that of the neutrals. The global minimum among all the anion structures is a1.

(3) The IPs calculated in this work indicate that T1 has the larger IP than other tautomers.

(4) Using the B3LYP and BP86 methods, adiabatic electron affinities are predicted for the thymine tautomers in the ranges of –0.41 to 0.26 eV (B3LYP) and –0.31 to 0.41 eV (BP86), respectively. The ZPE corrections are generally small. T5 has the largest AEA (0.26 eV from B3LYP computation), while T4 and T2 do not bind an electron (–0.41 and –0.16 eV, respectively). The theoretical VEA values are quite different from the adiabatic electron affinities, owing to the considerable geometrical changes between the neutrals and the corresponding anions.

(5) All protonated sites for thymine tautomers are considered, showing that O_8 is the preferred site.

Supplementary data

Supplementary data for this article are available on the journal Web site (canjchem.nrc.ca) or may be purchased from the Depository of Unpublished Data, Document Delivery, CISTI, National Research Council Canada, Ottawa, ON K1A 0R6, Canada. DUD 3863. For more information on obtaining material, refer to cisti-icist.nrc-cnrc.gc.ca/cms/unpub_e.shtml.

Acknowledgments

We are grateful to the Program for New Century Excellent Talents in University (NCET-07–0581), Sichuan Province Young Science and Technology Foundation (2008–20–360), and China National Science Foundation (Grants 10774104) for support of this work.

References

(1) Demple, B.; Harrison, L. *Annu. Rev. Biochem.* **1994**, *63*, 915. doi:10.1146/annurev.bi.63.070194.004411. PMID:7979257.

(2) Loft, S.; Poulsen, H. E. *J. Mol. Med.* **1996**, *74*, 297. doi:10.1007/BF00207507. PMID:8862511.

(3) Nakabeppu, Y.; Sakumi, K.; Sakamoto, K.; Tsuchimoto, D.; Tsuzuki, T.; Nakatsu, Y. *Biol. Chem.* **2006**, *387*, 373. doi:10.1515/BC.2006.050. PMID:16606334.

(4) Michael, B. D.; O'Neill, P. *Science* **2000**, *287*, 1603. doi:10.1126/science.287.5458.1603. PMID:10733428.

(5) Miller, J. H.; Wilson, W. W.; Ritchie, R. H. In *Computational Approaches in Molecular Radiation Biology*. Varma, M. N., Chatterjee, J., Eds. Plenum: New York, 1994; pp 65–76.

(6) Civcir, P. U. *J. Mol. Struct.* **2000**, *532*, 157.

(7) Orozco, M.; Hernandez, B.; Luque, F. J. *J. Phys. Chem. B* **1998**, *102*, 5228. doi:10.1021/jp981005+.

(8) Lowdin, P. O. *Rev. Mod. Phys.* **1963**, *35*, 724. doi:10.1103/RevModPhys.35.724.

(9) Gorb, L.; Podolyan, Y.; Dziekonski, P.; Sokalski, W.A.; Leszczynski, J. *J. Am. Chem. Soc.* **2004**, *126*, 10119. doi:10.1021/ja049155n. PMID:15303888.

(10) Noguera, M.; Sodupe, M.; Bertrán, J. *Theor. Chem. Acc.* **2007**, *118*, 113. doi:10.1007/s00214-007-0248-z.

(11) Scanlan, M. J.; Hillier, I. H. *J. Am. Chem. Soc.* **1984**, *106*, 3737. doi:10.1021/ja00325a005.

(12) Gu, J.; Leszczynski, J. *J. Phys. Chem. A* **2001**, *105*, 10366. doi:10.1021/jp004550v.

(13) Chandra, A.K.; Nguyen, M. T.; Zeegers-Huyskens, T.*J. Phys. Chem. A* **1998**, *102*, 6010. doi:10.1021/jp981259v.

(14) Kim, S. K.; Lee, W.; Herschbach, D. R. *J. Phys. Chem.* **1996**, *100*, 7933. doi:10.1021/jp960635d.

(15) Zhang, S. L.; Michaelian, K. H.; Loppnow, G. R. *J. Phys. Chem. A* **1998**, *102*, 461. doi:10.1021/jp972385m.

(16) Close, D. M. *J. Phys. Chem. A* **2004**, *108*, 10376. doi:10.1021/jp046660y.

(17) Crespo-Hernández, C. E.; Arce, R.; Ishikawa, Y. *J. Phys. Chem. A* **2004**, *108*, 6373. doi:10.1021/jp049270k.

(18) Yarasi, S.; Billinghurst, B. E.; Loppnow, G. R. *J. Raman Spectrosc.* **2007**, *38*, 1117. doi:10.1002/jrs.1722.

(19) Mazurkiewicz, K.; Bachorz, R. A.; Gutowski, M.; Rak, J. *J. Phys. Chem. B* **2006**, *110*, 24696. doi:10.1021/jp065666f. PMID:17134233.

(20) Becke, A. D. *J. Chem. Phys.* **1993**, *98*, 5648. doi:10.1063/1.464913.

(21) Lee, C.; Yang, W.; Parr, R. G. *Phys. Rev. B* **1988**, *37*, 785. doi:10.1103/PhysRevB.37.785.

(22) Becke, A. D. *Phys. Rev. A* **1988**, *38*, 3098. doi:10.1103/PhysRevA.38.3098. PMID:9900728.

(23) Perdew, J. P. *Phys. Rev. B* **1986**, *33*, 8822. doi:10.1103/PhysRevB.33.8822.

(24) Wesolowski, S. S.; Leininger, M. L.; Pentchev, P. N.; Schaefer, H. F., III. *J. Am. Chem. Soc.* **2001**, *123*, 4023. doi:10.1021/ja003814o. PMID:11457153.

(25) Smith, D. M. A.; Jalbout, A. F.; Smets, J.; Adamowicz, L. *Chem. Phys.* **2000**, *260*, 45. doi:10.1016/S0301-0104(00)00245-7.

(26) Rienstra-Kiracofe, J. C.; Tschumper, G. S.; Schaefer, H. F.; Nandi, S.; Ellison, G. B. *Chem. Rev.* **2002**, *102*, 231. doi:10.1021/cr990044u. PMID:11782134.

(27) Frisch, M. J.; Trucks, G. W.; Schlegel, H. B.; Scuseria, G. E.; Robb, M. A.; Cheeseman, J. R.; Zakrzewski, V. G.; Montgomery, J. A.; Stratmann, R. E.; Burant, J. C.; Dapprich, S.; Millam, J. M.; Daniels, A. D.; Kudin, K. N.; Strain, M. C.; Farkas, O.; Tomasi, J.; Barone, V.; Cossi, M.; Cammi, R.; Mennucci, B.; Pomelli, C.; Adamo, C.; Clifford, S.; Ochterski, J.; Petersson, G. A.; Ayala, P. A.; Cui, Q.; Morokuma, K.; Salvador, P.; Dannenberg, J. J.; Malick, D. K.; Rabuck, A. D.; Raghavachari, K.; Foresman, J. B.; Cioslowski, J.; Ortiz, J. V.; Baboul, A. G.; Stefanov, B. B.; Liu,

G.; Liashenko, A.; Piskorz, P.; Komaromi, I.; Gomperts, R.; Martin, R. L.; Fox, D. J.; Keith, T.; Al-Laham, M. A.; Peng, C. Y.; Nanayakkara, A.; Challacombe, M.; Gill, P. M. W.; Johnson, B. G.; Chen, W.; Wong, M. W.; Andres, J. L.; Gonzalez, C.; Head-Gordon, M.; Replogle, E. S.; Pople, J. A. *Gaussian03,* Revision B.02; Gaussian Inc.: Pittsburgh, PA, 2003 (used in Chengdu).

(28) Frisch, M. J.; Trucks, G. W.; Schlegel, H. B.; Gill, P. M. W.; Johnson, B. G.; Robb, M. A.; Cheeseman, J. R.; Keith, T.; Petersson, G. A.; Montgomery, J. A.; Raghavachari, K.; Al-Laham, M. A.; Zakrzewski, V. G.; Ortiz, J. V.; Foresman, J. B.; Peng, C. Y.; Ayala, P. Y.; Chen, W.; Wong, M. W.; Andres, J. L.; Replogle, E. S.; Gomperts, R.; Martin, R. L.; Fox, D. J.; Binkley, J. S.; Defrees, D. J.; Baker, J.; Stewart, J. P.; Head-Gordon, M.; Gonzalez, C.; Pople, J. A. *Gaussian 94*, Revision B.3; Gaussian Inc.: Pittsburgh, PA, 1995.

(29) Reed, A. E.; Weinstock, R. B.; Weinhold, F. *J. Chem. Phys.* **1985**, *83*, 735. doi:10.1063/1.449486.

(30) Brown, R. D.; Godfrey, P. D.; McNaughton, D.; Pierlot, A. P. *J. Chem. Soc. Chem. Commun.* **1989**, *1*, 37. doi:10.1039/c39890000037.

(31) Piacenza, M.; Grimme, S. *J. Comput. Chem.* **2004**, *25*, 83. doi:10.1002/jcc.10365.

(32) Mirzaei, M.; Hadipour, N. L.; Ahmadi, K. *Biophys. Chem.* **2007**, *125*, 411. doi:10.1016/j.bpc.2006.10.007. PMID:17175092.

(33) Ha, T.-K.; Gunthard, H. H. *J. Am. Chem. Soc.* **1993**, *115*, 11939. doi:10.1021/ja00078a036.

(34) Morsy, M. A.; Al-Somali, A. M.; Suwaiyan, A. *J. Phys. Chem. B* **1999**, *103*, 11205. doi:10.1021/jp990858e.

(35) Mallard, W. G.; Linstrom, P. J., (*Editors*). NIST Chemistry WebBook, NIST Standard. Reference Database, Number 69, February 2000. National Institute of Standards and Technology, Gaithersburg, MD. Available from http://webbook.nist.gov.

(36) Orlov, V. M.; Smirnov, A. N.; Varshavsky, Y. M. *Tetrahedron Lett.* **1976**, *48*, 4377. doi:10.1016/0040-4039(76)80120-7.

(37) Lias, S. G.; Bartmess, J. E.; Liebman, J. F.; Holmes, L. J.; Levin, R. D.; Mallard, W. G. *J. Phys. Chem. Ref. Data* **1988**, *17*.

(38) Sagstuen, E.; Hole, E. O.; Nelson, W. H.; Close, D. M. *Radiat. Res.* **1998**, *149*, 120. doi:10.2307/3579920. PMID:9457890.

(39) Sagstuen, E.; Hole, E. O.; Nelson, W. H.; Close, D. M. *Radiat. Res.* **1996**, *146*, 425. doi:10.2307/3579304. PMID:8927714.

(40) The vertical EA's of the bases cannot be appropriately corrected for ZPE's, since they are not in their relaxed states as anion radicals, see for example: Li, X.; Cai, Z.; Sevilla, M. D. J. Phys. Chem. A **2002**, *106*, 1596; Sevilla also noted that (private correspondence) the same should apply to IPs. While a ZPE correction to a vertical state does seem to be in the right direction, it does not provide a full correction.

(41) Chen, E. C. M.; Chen, E. S. *J. Phys. Chem. B* **2000**, *104*, 7835. doi:10.1021/jp001553z.

(42) Aflatooni, K.; Gallup, G. A.; Burrow, P. D. *J. Phys. Chem. A* **1998**, *102*, 6205. doi:10.1021/jp980865n.

(43) Desfrançois, C.; Abdoul-Carime, H.; Schermann, J. P. *J. Chem. Phys.* **1996**, *104*, 7792. doi:10.1063/1.471484.

(44) Hendricks, J. H.; Lyapustina, S. A.; de Clercq, H. L.; Snodgrass, J. T.; Bowen, K. H. *J. Chem. Phys.* **1996**, *104*, 7788. doi:10.1063/1.471482.

(45) Desfrançois, C.; Periquet, V.; Bouteiller, Y.; Schermann, J. P. *J. Phys. Chem.* **1998**, *102*, 1274.

(46) Compton, R. N.; Yoshioka, Y.; Jordan, K. D. *Theor. Chim. Acta* **1979**, *54*, 259. doi:10.1007/BF00578345.

(47) Schiedt, J.; Weinkauf, R.; Neumark, D. M.; Schlag, E. W. *Chem. Phys.* **1998**, *239*, 511. doi:10.1016/S0301-0104(98)00361-9.

(48) Periquet, V.; Moreau, A.; Carles, S.; Schermann, J. P.; Desfrançois, C. *J. Electron Spectrosc. Relat. Phenom.* **2000**, *106*, 141. doi:10.1016/S0368-2048(99)00072-9.

(49) Wetmore, S. D.; Boyd, R. J.; Eriksson, L. A. *Chem. Phys. Lett.* **2000**, *322*, 129. doi:10.1016/S0009-2614(00)00391-2.

(50) Russo, N.; Toscano, M.; Grand, A. *J. Comput. Chem.* **2000**, *21*, 1243. doi:10.1002/1096-987X(20001115)21:14<1243::AID-JCC3>3.0.CO;2-M.

(51) Russo, N.; Toscano, M.; Grand, A.; Jolibosi, F. *J. Comput. Chem.* **1998**, *19*, 989. doi:10.1002/(SICI)1096-987X(19980715)19:9<989::AID-JCC1>3.0.CO;2-F.

(52) Greco, F.; Liguori, A.; Sindona, G.; Uccella, N. *J. Am. Chem. Soc.* **1990**, *112*, 9092. doi:10.1021/ja00181a009.

A catalyst-free protocol for the green and efficient condensation of indoles with aldehydes in ionic liquids

Abdolkarim Zare, Abolfath Parhami, Ahmad Reza Moosavi-Zare, Alireza Hasaninejad, Ali Khalafi-Nezhad, and Mohammad Hassan Beyzavi

Abstract: Indoles are efficiently condensed with aromatic and aliphatic aldehydes in the absence of any catalyst in ionic liquid 1-butyl-3-methylimidazolium bromide {bmim]Br} under microwave irradiation to afford bis(indolyl)methanes in good to excellent yields and in short reaction times.

Key words: catalyst-free, indole, aldehyde, ionic liquid, microwave, bis(indolyl)methane.

Résumé : Les indoles se condensent d'une manière efficace avec les aldéhydes aliphatiques et aromatiques, sans nécessité de catalyseur, dans le liquide ionique bromure de 1-butyl-3-méthylimidazolium {[bmim]Br} et sous irradiation par des microondes et ces réactions conduisent, en un court laps de temps, à la formation de bis(indolyl)méthanes avec des rendements allant de bons à excellents.

Mots-clés : sans catalyseur, indole, aldéhyde, liquide ionique, micro-onde, bis(indolyl)méthane.

[Traduit par la Rédaction]

Introduction

In recent years, catalyst-free reactions have attracted increasing interest due to their ease of experimental procedure as well as work-up, low cost, possibility of using acid- or base-sensitive substrates, and their environmentally benign nature.[1–10] This useful technique has been used in several chemical transformations, such as self-assembly of carbon nanotubes, carbon nanowires, and carbon filaments,[1] synthesis of 2-aminothiazoles,[2] N-benzyloxycarbonylation of amines,[3] synthesis of benzoic esters and benzyl esters,[4] gem-bisallylation of carboxylic acid derivatives,[5] synthesis of polyorganosiloxanes,[6] synthesis of dithiocarbamates,[7] regioselective conversion of epoxides to vicinal-halohydrins,[8] transesterification of triglycerides,[9] and Michael-type addition of amines to electron-deficient alkenes.[10] As a part of our continuing interest in developing efficient synthetic methodologies in organic synthesis, we have initiated a program to study useful organic transformations in the absence of catalyst. Herein, we find that the condensation of indoles with aldehydes can be efficiently achieved without any catalyst in neutral ionic liquids under microwave irradiation.

Currently, ionic liquids have been the subject of considerable interest as benign reaction media in organic synthesis because of their unique properties such as non-volatility, non-flammability, recyclability, and ability to dissolve a wide range of materials.[11] During the past decade, a variety of ionic liquids have been demonstrated to be efficient and practical alternatives to volatile organic solvents for many important organic transformations.[11] Together with the substitution of common molecular solvents, non-conventional activation methods, mainly microwave irradiation, have emerged as powerful techniques to decrease reaction times and to enhance reaction rates.[12]

The condensation of indoles with carbonyl compounds is of importance, because this reaction provides a simple route to bis(indolyl)methanes synthesis.[13] For this class of compounds, different pharmacological and biological activities have been reported.[14] Several methods have been developed for the preparation of bis(indolyl)methanes from indoles and carbonyl compounds using catalysts such as silica sulfuric acid,[13a] Ru (III),[13b] $H_3PMo_{12}O_{40}{\cdot}xH_2O$,[13c] P_2O_5/SiO_2,[13d] silica chloride,[13e] $ZrOCl_2{\cdot}8H_2O$,[13f] PPh_3-$HClO_4$(TPP),[13g] $AlPW_{12}O_{40}$,[13h] $In(OTf)_3$,[13i] $Dy(OTf)_3$,[13j] and $La(PFO)_3$.[13k] This transformation has been also carried out in H_2O in the presence of sodium dodecyl sulfate.[13l] Moreover, in this report the same reaction has been performed in the absence of catalyst in MeOH.[13l] In the mentioned paper, the results obtained from a H_2O/sodium dodecyl sulfate system are good; however, the catalyst-free conditions have some drawbacks including low yields, long reaction times, and no generality.[13l] To the best of our knowledge, there is no other report on the condensation of indoles with aldehydes without catalyst.

Received 12 August 2008. Accepted 29 October 2008. Published on the NRC Research Press Web site at canjchem.nrc.ca on 19 December 2008.

A. Zare,[1] A. Parhami,[2] and A.R. Moosavi-Zare. Department of Chemistry, College of Sciences, Payame Noor University (PNU), Iran.
A. Hasaninejad. Department of Chemistry, Faculty of Sciences, Persian Gulf University, Bushehr 75169, Iran.
A. Khalafi-Nezhad and M.H. Beyzavi. Department of Chemistry, College of Sciences, Shiraz University, Shiraz 71454, Iran.

[1]Corresponding author (e-mail: abdolkarimzare@yahoo.com).
[2]Corresponding author (e-mail: rezaparhami@yahoo.com).

Scheme 1. The condensation of indole with benzaldehyde.

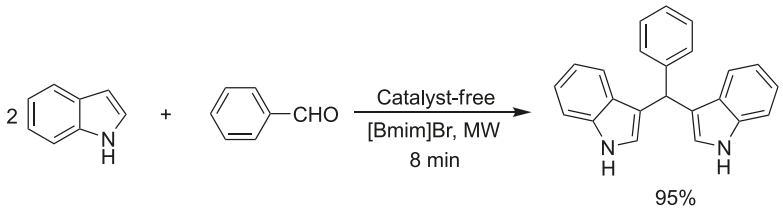

Table 1. The catalyst-free condensation of indole with benzaldehyde under solvent-free conditions as well as in ionic liquids promoted by microwave irradiation (400 W, max, 150 °C).

Entry	Solvent	Time (min)	Yield[a] (%)
1	Solvent-free	30	Trace
2	[bmim]Br	8	95
3	[bmim]Cl	8	69
4	[bmim]I	8	47

[a]Isolated yield.

In this study, we report a catalyst-free, efficient, green, and simple method for the condensation of indoles with aromatic and aliphatic aldehydes in [bmim]Br under microwave irradiation (Scheme 1).

Results and discussion

At first, we examined condensation of indole (2 mmol) with benzaldehyde (1 mmol) in the absence of any catalyst under solvent-free and microwave conditions at 400 W of microwave power; but these conditions afforded the corresponding bis(indolyl)methane **1** in trace yield after 30 min (Table 1). Increasing the reaction time or microwave power did not improve the yield. The yield increased to 95% when the reaction was performed in ionic liquid [bmim]Br (0.25 g) at 400 W (max 150 °C) (Table 1 and Scheme 1). Moreover, the reaction of indole with benzaldehyde was examined in ionic liquids [bmim]Cl and [bmim]I (Table 1). As Table 1 indicates, [bmim]Br afforded the best results.

The condensation of indole with benzaldehyde was also tested at different microwave powers (100–600 W, max. 150 °C). The reasonable results were obtained at 400 W.

To assess the generality and the scope of this catalyst-free protocol, indoles were reacted with structurally diverse aldehydes. The results are summarized in Table 2. As can be seen in Table 2, all reactions proceeded efficiently and the desired products were produced in good to excellent yields and in short reaction times. It must be mentioned that aliphatic and aromatic aldehydes possessing electron-releasing substituents gave the corresponding bis(indolyl)methanes in lower yields and in longer reaction times in comparison with the others (Table 2, entries 7–10 and 17).

One of the most interesting properties of ionic liquids is their ease of recycling. For the reaction of indole with benzaldehyde no significant loss of the product yield was observed when [bmim]Br was reused, even after three repeated uses.

It has long been studied that hydrogen bond formation can occur between the solute and cationic or anionic counterpart of ionic liquids.[15] Moreover, Deb et al. have suggested a mechanism for the condensation of indoles with aldehydes based on the activation of a carbonyl group of aldehydes via hydrogen bond formation with solvent.[13l] According to these observations, we suggest a mechanism for our reaction (Scheme 2). In this mechanism, the [bmim]-based ionic liquid has a dual activation role. Activation of the carbonyl group occurs via hydrogen bond between 2-H of the [bmim] moiety of the ionic liquid and oxygen of the carbonyl group. Moreover, indole is activated when the bromide ion of the ionic liquid removes the NH proton of the indole, since it increases the nucleophilicity of the indole. We suggest that firstly (3*H*-indol-3-yl)-phenyl-methanol (**I**) forms as a result of nucleophilic attack of activated indole to electrophilic carbon of activated carbonyl function of benzaldehyde. Then, intermediate **I** eliminates a water molecule to convert into 3-benzylidene-3*H*-indole (**II**). The electrophilicity of the exocyclic double bond of intermediate **II** increases through hydrogen bond formation between sp^2 nitrogen of intermediate **II** and 2-H of [bmim] moiety. Finally, the activated indole attacks the exocyclic double bond providing the bis(indolyl)methane **1**. Ionic liquids also stabilize charged intermediates and enhance reaction rates.[16] Moreover, these polar solvents absorbs microwave irradiation and increase reaction temperature rapidly.[12a,12j]

In summary, we have reported a new application of catalyst-free protocol in organic synthesis. In this study, bis(indolyl)methanes efficiently synthesized from indoles and aldehydes in a ionic liquid under microwave conditions.

Experimental

All chemicals were purchased from Merck or Fluka chemical companies. The ionic liquid was prepared according to the reported methods.[17] All reactions were carried out using a laboratory microwave oven (MicroSYNTH, Milestone Company, Italy). The ^{1}H NMR (250 MHz) and ^{13}C NMR (62.5 MHz) were run on a Bruker Avance DPX-250 FT-NMR spectrometer, δ in ppm. Mass spectra were recorded on a Shimadzu GC MS-QP 1000 EX apparatus. Microanalyses were performed on a PerkinElmer 240-B microanalyzer. Melting points were recorded on a Büchi B-545 apparatus in open capillary tubes.

General procedure for the catalyst-free condensation of indoles with aldehydes

To a mixture of indole (2 mmol, 0.234 g) and aldehyde (1 mmol) in a microwave vessel was added [bmim]Br (0.25 g), and the mixture was stirred carefully with a small rod. The resulting mixture was irradiated in a microwave oven at 400 W for the appropriate time (Table 2). The microwave was programmed to give a maximum internal temperature of 150 °C. Afterward, the reaction mixture was

Table 2. Catalyst-free condensation of indoles with aldehydes in [bmim]Br under microwave irradiation (400 W, max 150 °C).

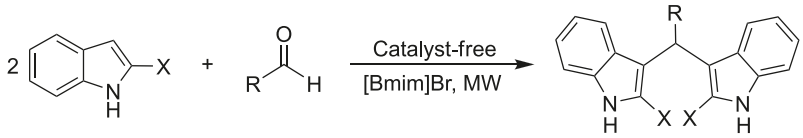

Entry	X	R	Product	Time (min)	Yield[a] (%)	Mp °C (Lit.)
1	H	C_6H_5	**1**	8	95	140–142 (140–142)[13d]
2	CH_3	C_6H_5	**2**	10	89	246–248 (245–247)[13e]
3[b]	H	*p*-$NO_2C_6H_4$	**3**	6	97	216–218 (217–220)[13l]
4[b]	H	*m*-$NO_2C_6H_4$	**4**	6	96	220–222 (220–222)[13d]
5	H	*m*-CNC_6H_4	**5**	7	96	99–101 (98–100)[13d]
6[b]	CH_3	*p*-$NO_2C_6H_4$	**6**	8	92	240–242 (241–243)[13e]
7	H	*p*-$CH_3C_6H_4$	**7**	17	88	94–96 (97–99)[13a]
8	H	*p*-$OMeC_6H_4$	**8**	18	85	185–187 (178–181)[13a]
9	H	*p*-OHC_6H_4	**9**	18	83	120–122 (119–121)[13d]
10	CH_3	*p*-$CH_3C_6H_4$	**10**	21	86	175–177 (174–175)[13l]
11	H	*p*-ClC_6H_4	**11**	8	97	77–79 (76–77)[13l]
12	H	*o*-ClC_6H_4	**12**	14	85	73–75 (70–71)[13l]
13	H	4-Pyridyl	**13**	7	90	160–162 (161–163)[13e]
14	H	2-Furyl	**14**	15	82	315–317 (>300)[13l]
15	H	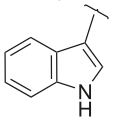	**15**	20	80	161, dec. (162, dec.)[13d]
16	H	E-C_6H_5CH=CH	**16**	15	88	99–101 (98–99)[13l]
17[c]	H	$CH_3(CH_2)_3CH_2$	**17**	20	81	70–72 (71–73)[13d]

[a]Isolated yield.
[b]This reaction was carried out at 300 W of microwave power (max 150 °C).
[c]This reaction was performed in a sealed vessel.

Scheme 2. Suggested mechanism for the condensation of indoles with aldehydes.

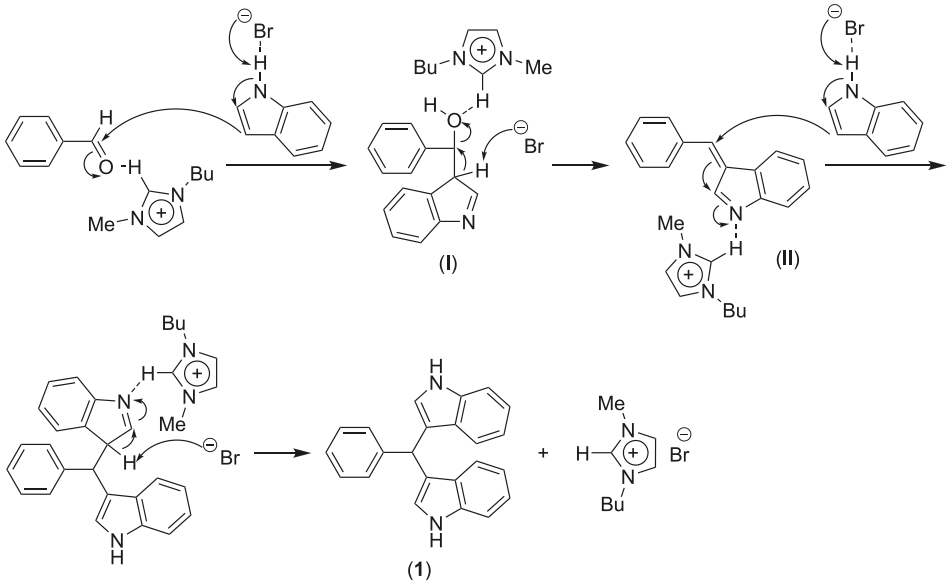

cooled to room temperature and was extracted with Et_2O (2 × 20 mL). The organic extracts were then combined and washed with saturated solution of $NaHSO_3$ (2 × 20 mL) to remove unreacted aldehyde and then with water (2 × 20 mL). The organic layer was separated and dried with $CaCl_2$. The solvent was evaporated and the crude product was purified by recrystallization from EtOAc/petroleum ether (1:2) or plate chromatography on silica gel eluted with EtOAc/petroleum ether (1:2). After isolation of the product, the remaining Et_2O in [bmim]Br was evaporated, and it was used for the next run under identical reaction conditions.

3-((1*H*-Indol-3-yl)(phenyl)methyl)-1*H*-indole (1)

Recrystallization from EtOAc/petroleum ether (1:2) gave pink solid; yield 0.306 g (95%); mp 140–142 °C (lit. 140–142 °C).[13d] ^{1}H NMR ($CDCl_3$, ppm) δ: 5.86 (s, 1H, ArCH), 6.66 (s, 2H), 7.11 (t, 2H, *J* = 6.9 Hz), 7.14–7.22 (m, 3H), 7.28–7.31 (m, 2H), 7.35–7.42 (m, 6H), 7.93 (br, 2H, NH). ^{13}C NMR ($CDCl_3$, ppm) δ: 31.6, 110.9, 111.9, 118.4, 119.5, 121.2, 124.0, 126.3, 127.1, 128.5, 128.6, 137.0, 145.2. MS *m*/*z*: 322 [M$^+$]. Anal. calcd. for $C_{23}H_{18}N_2$: C 85.68, H 5.63, N 8.69; found: C 85.87, H 5.79, N 8.46.

2-Methyl-3-((2-methyl-1*H*-indol-3-yl)(phenyl)methyl)-1*H*-indole (2)

Purification by plate chromatography on silica gel, eluted with EtOAc/petroleum ether (1:2), gave pink solid; yield 0.312 g (89%); mp 246–248 °C (lit. 245–247 °C).[13e] ^{1}H NMR ($CDCl_3$, ppm) δ: 2.05 (s, 6H), 5.88 (s, 1H, ArCH), 6.78–7.01 (m, 6H), 7.14–7.22 (m, 5H), 7.28–7.31 (m, 2H), 8.02 (br, 2H, NH). ^{13}C NMR ($CDCl_3$, ppm) δ: 13.4, 38.7, 109.6, 112.1, 118.9, 120.0, 121.4, 126.5, 128.4, 128.6, 129.1, 132.4, 135.7, 139.8. MS *m*/*z*: 350 [M$^+$]. Anal. calcd. for $C_{25}H_{22}N_2$: C 85.68, H 6.33, N 7.99; found: C 85.47, H 6.48, N 7.86.

3-((1*H*-Indol-3-yl)(4-nitrophenyl)methyl)-1*H*-indole (3)

Recrystallization from EtOAc/petroleum ether (1:2) gave yellow needles; yield 0.355 g (97%); mp 216–218 °C (lit. 217–220 °C).[13l] ^{1}H NMR ($CDCl_3$, ppm) δ: 6.01 (s, 1H, ArCH), 6.72 (s, 2H), 7.02–7.08 (m, 4H), 7.36 (d, 2H, *J* = 8.1 Hz), 7.41 (d, 2H, *J* = 8.1 Hz), 7.49 (d, 2H, *J* = 8.6 Hz), 8.05 (br, 2H, NH), 8.17 (d, 2H, *J* = 8.6 Hz). ^{13}C NMR ($CDCl_3$, ppm) δ: 40.2, 112.0, 113.1, 119.1, 120.4, 121.8, 122.1, 123.7, 127.4, 131.8, 136.1, 145.1, 153.5. MS *m*/*z*: 367 [M$^+$]. Anal. calcd. for $C_{23}H_{17}N_3O_2$: C 75.19, H 4.66, N 11.44; found: C 75.36, H 4.51, N 11.31.

3-((1*H*-Indol-3-yl)(3-nitrophenyl)methyl)-1*H*-indole (4)

Recrystallization from EtOAc/petroleum ether (1:2) gave yellow solid; yield 0.352 g (96%); mp 220–222 °C (lit. 220–222 °C).[13d] ^{1}H NMR ($CDCl_3$, ppm) δ: 6.23 (s, 1H, ArCH), 7.01 (t, 2H, *J* = 7.3 Hz), 7.06 (s, 2H), 7.22 (t, 2H, *J* = 7.0 Hz), 7.45 (d, 2H, *J* = 7.5 Hz), 7.53 (d, 2H, *J* = 8.0 Hz), 7.75 (m, 1H), 8.02 (d, 1H, *J* = 7.6 Hz), 8.26 (d, 1H, *J* = 7.7 Hz), 8.33 (s, 1H), 8.09 (br, 2H, NH). ^{13}C NMR ($CDCl_3$, ppm) δ: 38.7, 111.0, 112.6, 118.4, 119.0, 120.7, 121.9, 123.4, 125.3, 127.8, 129.5, 135.2, 136.8, 138.5, 148.0. MS *m*/*z*: 367 [M$^+$]. Anal. calcd. for $C_{23}H_{17}N_3O_2$: C 75.19, H 4.66, N 11.44; found: C 75.38, H 4.50, N 11.57.

3-(Di(1*H*-indol-3-yl)methyl)benzonitrile (5)

Recrystallization from EtOAc/petroleum ether (1:2) gave pink solid; yield 0.334 g (96%); mp 99–101 °C (lit. 98–100 °C).[13d] ^{1}H NMR ($CDCl_3$, ppm) δ: 6.09 (s, 1H, ArCH), 6.83 (s, 2H), 6.98–7.07 (m, 4H), 7.19 (d, 2H, *J* = 7.6 Hz), 7.42 (d, 2H, *J* = 7.6 Hz), 7.65–7.87 (m, 4H), 8.02 (br, 2H, NH). ^{13}C NMR ($CDCl_3$, ppm) δ: 39.2, 111.0, 111.9, 112.5, 116.8, 118.9, 119.4, 122.1, 123.7, 127.2, 129.7, 130.0, 133.8, 134.2, 136.2, 140.1. MS *m*/*z*: 347 [M$^+$]. Anal. calcd. for $C_{24}H_{17}N_3$: C 82.97, H 4.93, N 12.10; found: C 82.74, H 5.04, N 11.98.

2-Methyl-3-((2-methyl-1*H*-indol-3-yl)(4-nitrophenyl)methyl)-1*H*-indole (6)

Recrystallization from EtOAc/petroleum ether (1:2) gave yellow solid; yield 0.365 g (92%); mp 240–242 °C (lit. 241–243 °C).[13e] ^{1}H NMR ($CDCl_3$, ppm) δ: 2.13 (s, 6H), 5.96 (s, 1H), 6.71–6.96 (m, 6H), 7.21 (d, 2H, *J* = 8.0 Hz), 7.47 (d, 2H, *J* = 8.5 Hz), 8.00 (d, 2H, *J* = 8.5 Hz), 8.07 (br, 2H, NH). ^{13}C NMR ($CDCl_3$, ppm) δ: 12.1, 39.0, 109.8, 111.9, 118.7, 119.1, 119.5, 121.5, 128.2, 129.4, 132.0, 135.0, 144.1, 152.4. MS *m*/*z*: 395 [M$^+$]. Anal. calcd. for $C_{25}H_{21}N_3O_2$: C 75.93, H 5.35, N 10.63; found: C 75.69, H 5.46, N 10.48.

3-((1*H*-Indol-3-yl)(p-tolyl)methyl)-1*H*-indole (7)

Recrystallization from EtOAc/petroleum ether (1:2) gave pink solid; yield 0.297 g (88%); mp 94–96 °C (lit. 97–99 °C).[13a] ^{1}H NMR ($CDCl_3$, ppm) δ: 2.33 (s, 3H, $ArCH_3$), 5.87 (s, 1H, ArCH), 6.69 (s, 2H), 7.04 (t, 2H, *J* = 7.1 Hz), 7.12 (d, 2H, *J* = 7.1 Hz), 7.23–7.28 (m, 6H), 7.41 (d, 2H, *J* = 7.2 Hz), 7.94 (br, 2H, NH). ^{13}C NMR ($CDCl_3$, ppm) δ: 21.8, 39.4, 110.1, 111.8, 118.7, 119.6, 121.9, 123.4, 127.2, 129.4, 134.2, 135.1, 135.9. MS *m*/*z*: 336 [M$^+$]. Anal. calcd. for $C_{24}H_{20}N_2$: C 85.68, H 5.99, N 8.33; found: C 85.46, H 6.13, N 8.51.

3-((1*H*-Indol-3-yl)(4-methoxyphenyl)methyl)-1*H*-indole (8)

Purification by plate chromatography on silica gel, eluted with EtOAc/petroleum ether (1:2), gave brown solid; yield 0.298 g (85%); mp 185–187 °C (lit. 178–181 °C).[13a] ^{1}H NMR ($CDCl_3$, ppm) δ: 3.76 (s, 3H, OCH_3), 5.85, (s, 1H, ArCH), 6.68 (s, 2H), 6.91 (d, 2H, *J* = 8.2 Hz), 7.02 (t, 2H, *J* = 7.3 Hz), 7.16 (t, 2H, *J* = 7.3 Hz), 7.20 (m, 2H), 7.35–7.41 (m, 4H), 7.95 (br, 2H, NH). ^{13}C NMR ($CDCl_3$, ppm) δ: 38.6, 55.3, 110.6, 112.2, 115.0, 119.0, 119.8, 122.0, 123.9, 127.5, 130.2, 131.1, 136.4, 145.4. MS *m*/*z*: 352 [M$^+$]. Anal. calcd. for $C_{24}H_{20}N_2O$: C 81.79, H 5.72, N 7.95; found: C 81.98, H 5.63, N 7.79.

4-(Di(1*H*-indol-3-yl)methyl)phenol (9)

Purification by plate chromatography on silica gel, eluted with EtOAc/petroleum ether (1:2), gave pink solid; yield 0.282 g (83%); mp 120–122 °C (lit. 119–121 °C).[13d] ^{1}H NMR (DMSO-d_6, ppm) δ: 5.74 (s, 1H), 6.63 (m, 4H), 6.87 (t, 2H, *J* = 7.5 Hz), 7.03 (t, 2H, *J* = 7.6 Hz), 7.13 (d, 2H, *J* = 7.5 Hz), 7.34 (m, 4H), 8.58 (s, 1H, OH), 9.78 (br, 2H, NH). ^{13}C NMR (DMSO-d_6, ppm) δ: 43.6, 115.9, 119.6, 123.7, 124.8, 125.2, 126.9, 129.3, 131.9, 134.7, 140.5, 142.5, 160.2. MS *m*/*z*: 338 [M$^+$]. Anal. calcd. for $C_{23}H_{18}N_2O$: C 81.63, H 5.36, N 8.28; found: C 81.38, H 5.48, N 8.16.

2-Methyl-3-((2-methyl-1*H*-indol-3-yl)(p-tolyl)methyl)-1*H*-indole (10)

Purification by plate chromatography on silica gel, eluted with EtOAc/petroleum ether (1:2), gave pink solid; yield 0.312 g (86%); mp 175–177 °C (lit. 174–175 °C).[13l] ^{1}H NMR ($CDCl_3$, ppm) δ: 2.09 (s, 6H), 2.29 (s, 3H, $ArCH_3$), 5.92 (s, 1H, ArCH), 6.71–6.96 (m, 6H), 7.00–7.09 (m, 4H), 7.18 (d, 2H, *J* = 7.7 Hz), 7.98 (br, 2H, NH). ^{13}C NMR ($CDCl_3$, ppm) δ: 14.0, 20.9, 38.7, 109.8, 111.8, 118.6,

119.7, 121.5, 127.1, 129.3, 132.4, 133.8, 135.4, 136.1. MS *m/z*: 364 [M+]. Anal. calcd. for $C_{26}H_{24}N_2$: C 85.68, H 6.64, N 7.69; found: C 85.87, H 6.55, N 7.72.

3-((4-Chlorophenyl)(1*H*-indol-3-yl)methyl)-1*H*-indole (11)

Recrystallization from EtOAc/petroleum ether (1:2) gave pink solid; yield 0.345 g (97%); mp 77–79 °C (lit. 76–77 °C).[13l] ^{1}H NMR ($CDCl_3$, ppm) δ: 5.86 (s, 1H, ArCH), 6.65 (s, 2H), 6.85–7.96 (m, 12H), 8.00 (br, 2H, NH). ^{13}C NMR ($CDCl_3$, ppm) δ: 37.9, 110.7, 111.7, 118.5, 119.3, 121.6, 123.5, 126.9, 128.1, 129.8, 130.2, 135.2, 135.8. MS *m/z*: 356 [M+]. Anal. calcd. for $C_{23}H_{17}ClN_2$: C 77.41, H 4.80, N 7.85; found: C 77.58, H 4.68, N 8.01.

3-((2-Chlorophenyl)(1*H*-indol-3-yl)methyl)-1*H*-indole (12)

Purification by plate chromatography on silica gel, eluted with EtOAc/petroleum ether (1:2), gave pink solid; yield 0.305 g (85%); mp 73–75 °C (lit. 70–71 °C).[13l] ^{1}H NMR ($CDCl_3$, ppm) δ: 6.32 (s, 1H, ArCH), 6.67 (s, 2H), 7.02 (t, 2H, *J* = 7.8 Hz), 7.10–7.22 (m, 6H), 7.38–7.43 (m, 4H), 7.98 (br, 2H, NH). ^{13}C NMR ($CDCl_3$, ppm) δ: 37.1, 110.4, 111.6, 119.2, 120.0, 122.4, 123.9, 126.8, 127.3, 128.5, 130.5, 131.4, 135.6, 136.8, 141.5. MS *m/z*: 356 [M+]. Anal. calcd. for $C_{23}H_{17}ClN_2$: C 77.41, H 4.80, N 7.85; found: C 77.26, H 4.91, N 7.98.

3-((1*H*-Indol-3-yl)(pyridin-4-yl)methyl)-1*H*-indole (13)

Purification by plate chromatography on silica gel, eluted with EtOAc/petroleum ether (1:2), gave brown solid; yield 0.291 g (90%); mp 160–162 °C (lit. 161–163 °C).[13e] ^{1}H NMR ($CDCl_3$, ppm) δ: 5.96 (s, 1H, ArCH), 6.67 (s, 2H), 7.08–7.15 (m, 4H), 7.36 (d, 2H, *J* = 8.1 Hz), 7.43 (d, 2H, *J* = 8.1 Hz), 7.37 (d, 2H, *J* = 7.9 Hz), 7.99 (br, 2H, NH), 8.34 (d, 2H, *J* = 7.9 Hz). ^{13}C NMR ($CDCl_3$, ppm) δ: 40.1, 111.3, 112.2, 119.6, 120.8, 122.1, 122.7, 124.5, 126.7, 136.4, 148.7, 152.9. MS *m/z*: 323 [M+]. Anal. calcd. for $C_{22}H_{17}N_3$: C 81.71, H 5.30, N 12.99; found: C 81.49, H 5.17, N 12.86.

3-(Furan-2-yl(1*H*-indol-3-yl)methyl)-1*H*-indole (14)

Purification by plate chromatography on silica gel, eluted with EtOAc/petroleum ether (1:2), gave brown solid; yield 0.257 g (82%); mp 315–317 °C (lit. >300 °C).[13l] ^{1}H NMR ($CDCl_3$, ppm) δ: 5.97 (s, 1H, ArCH), 6.90 (s, 2H), 7.08–7.43 (m, 11H), 8.00 (br, 2H, NH). ^{13}C NMR ($CDCl_3$, ppm) δ: 34.8, 106.5, 110.2, 111.3, 112.2, 118.0, 119.3, 119.7, 121.7, 124.3, 126.3, 135.9, 142.0. MS *m/z*: 312 [M+]. Anal. calcd. for $C_{21}H_{16}N_2O$: C 80.75, H 5.16, N 8.97; found: C 80.95, H 5.26, N 9.11.

Tri(1*H*-indol-3-yl)methane (15)

Purification by plate chromatography on silica gel, eluted with EtOAc/petroleum ether (1:2), gave pale yellow solid; yield 0.290 g (80%); mp 161 °C (dec.) [lit. 162 °C (dec.)].[13d] ^{1}H NMR (DMSO-d_6, ppm) δ: 6.11 (s, 1H, ArCH), 6.86–6.91 (m, 6H), 7.05 (m, 3H), 7.35 (d, 3H, *J* = 7.9 Hz), 7.52 (d, 3H, *J* = 7.9 Hz), 10.59 (s, 3H, NH). ^{13}C NMR (DMSO-d_6, ppm) δ: 31.8, 111.6, 117.4, 118.0, 119.6, 121.2, 123.5, 127.2, 135.9. MS *m/z*: 361 [M+]. Anal. calcd. for $C_{25}H_{19}N_3$: C 83.08, H 5.30, N 11.63; found: C 82.85, H 5.19, N 11.75.

(*E*)-3-(1-(1*H*-Indol-3-yl)-3-phenylallyl)-1*H*-indole (16)

Purification by plate chromatography on silica gel, eluted with EtOAc/petroleum ether (1:2), gave pale yellow solid; yield 0.306 g (88%); mp 99–101 °C (lit. 98–99 °C).[13l] ^{1}H NMR ($CDCl_3$, ppm) δ: 5.22 (m, 1H), 6.19 (m, 1H), 6.57 (d, 1H, *J* = 15.4 Hz), 6.89 (s, 2H), 7.02–7.09 (m, 4H), 7.26–7.32 (m, 7H), 7.49 (d, 2H, *J* = 7.9 Hz), 7.92 (br, 2H, NH). ^{13}C NMR ($CDCl_3$, ppm) δ: 43.1, 111.3, 117.4, 118.7, 120.0, 121.8, 122.3, 123.6, 126.8, 127.2, 128.4, 128.9, 129.3, 134.3, 136.7. MS *m/z*: 348 [M+]. Anal. calcd. for $C_{25}H_{20}N_2$: C 86.17, H 5.79, N 8.04; found: C 86.03, H 5.88, N 7.93.

3-(1-(1*H*-Indol-3-yl)hexyl)-1*H*-indole (17)

Purification by plate chromatography on silica gel, eluted with EtOAc/petroleum ether (1:2), gave colorless solid; yield 0.257 g (81%); mp 70–72 °C (lit. 71–73 °C).[13d] ^{1}H NMR ($CDCl_3$, ppm) δ: 0.89 (t, 3H, *J* = 6.7 Hz), 1.27–1.33 (m, 6H), 1.52 (m, 2H), 4.79 (t, 1H, *J* = 6.6 Hz), 6.91 (s, 2H), 6.99–7.07 (m, 4H), 7.30 (d, 2H, *J* = 7.8 Hz), 7.55 (d, 2H, *J* = 7.8 Hz), 7.94 (br, 2H, NH). ^{13}C NMR ($CDCl_3$, ppm) δ: 13.8, 23.2, 25.9, 29.7, 31.5, 41.7, 110.8, 114.7, 118.6, 119.4, 121.9, 124.1, 127.5, 136.3. MS *m/z*: 316 [M+]. Anal. calcd. for $C_{22}H_{24}N_2$: C 83.50, H 7.64, N 8.85; found: C 83.69, H 7.54, N 8.99.

Acknowledgements

The authors appreciate Payame Noor University and Persian Gulf University Research Councils for the financial support of this work.

References

(1) (a) Schneider, J. J.; Maksimova, N. I.; Engstler, J.; Joshi, R.; Schierholz, R.; Feile, R. *Inorg. Chim. Acta* **2008**, *361*, 1770 doi:10.1016/j.ica.2006.10.025.; (b) Rantonen, N. J. K.; Toyabe, T.; Maekawa, T. *Carbon* **2008**, *46*, 1225. doi:10.1016/j.carbon.2008.04.025.

(2) Potewar, T. M.; Ingale, S. A.; Srinivasan, K. V. *Tetrahedron* **2008**, *64*, 5019. doi:10.1016/j.tet.2008.03.082.

(3) Shrikhande, J. J.; Gawande, M. B.; Jayaram, R. V. *Tetrahedron Lett.* **2008**, *49*, 4799. doi:10.1016/j.tetlet.2008.05.010.

(4) Li, X.; Eli, W.; Li, G. *Catal. Commun.* **2008**, *9*, 2264. doi:10.1016/j.catcom.2008.05.015.

(5) Wei, Y.; Ren, H.; Wang, J. *Tetrahedron Lett.* **2008**, *64*, 26.

(6) Ogawa, T.; Watanabe, J.; Oshima, Y. *Supercrit. Fluid* **2008**, *45*, 80. doi:10.1016/j.supflu.2007.11.010.

(7) Azizi, N.; Aryanasab, F.; Saidi, M. R. *Org. Lett.* **2006**, *8*, 5275. doi:10.1021/ol0620141. PMID:17078696.

(8) Ranu, B. C.; Banerjee, S. *J. Org. Chem.* **2005**, *70*, 4517. doi:10.1021/jo0500885. PMID:15903336.

(9) Geuens, J.; Kremsner, J. M.; Nebel, B. A.; Schober, S.; Dommisse, R. A.; Mittelbach, M.; Tavernier, S.; Kappe, C. O.; Maes, B. U. W. *Energy Fuels*, **2008**, *22*, 643. doi:10.1021/ef700617q.

(10) Ranu, B. C.; Dey, S. S.; Hajra, A. *ARKIVOC,* **2002**, *vii*, 76.

(11) (a) Wasserscheid, P.; Welton, T. Ionic liquids in synthesis. Wiley-VCH: Weinheim, Germany, 2003; (b) Welton, T. *Chem. Rev.* **1999**, *99*, 2071 doi:10.1021/cr980032t. PMID:11849019.; (c) Mikami, K. Green reaction media in organic synthesis. Blackwell Publishing: Oxford, UK, 2005; (d) Rogers, R. D. Ionic liquids as green solvents: Progress and prospects. An American Chemical Society Publication,

2005; (e) Rasalkar, M. S.; Bhilare, S. V.; Deorukhkar, A. R.; Darvatkar, N. B.; Salunkhe, M. M. *Can. J. Chem.* **2007**, *85*, 77 doi:10.1139/V06-176.; (f) Fan, X.; Li, Y.; Zhang, X.; Qu, G.; Wang, J. *Can. J. Chem.* **2006**, *84*, 794. doi:10.1139/V06-070.; (g) Karthikeyan, G.; Perumal, P. T. *Can. J. Chem.* **2005**, *83*, 1746. doi:10.1139/v05-186.

(12) (a) Loupy, A. Microwaves in organic synthesis. Wiley-VCH: Weinheim, Germany, 2006; (b) Varma, R. S. Advances in green chemistry: Chemical synthesis using microwave irradiation. Astra Zeneca Research Foundation, Kavitha Printers, Bangalore, India, 2002; (c) Tanaka, K. Solvent-free organic synthesis. Wiley-VCH: GmbH and KGaA, Weinheim, Germany, 2004; (d) Yin, J.; Li, X.; Wu, X.; Chen, B.; Liu, Z.; Song, Q. *Can. J. Chem.* **2005**, *83*, 2140 doi:10.1139/v05-251.; (e) Joshi, B. P.; Sharma, A.; Sinha, A. K. *Can. J. Chem.* **2005**, *83*, 1826 doi:10.1139/v05-185.; (f) Singh, S.; Ishar, M. P. S.; Singh, G.; Singh, R. *Can. J. Chem.* **2005**, *83*, 260 doi:10.1139/v05-049.; (g) Kidwai, M.; Mohan, R. *Can. J. Chem.* **2004**, *82*, 427 doi:10.1139/v03-191.; (h) Khalafi-Nezhad, A.; Zare, A.; Parhami, A.; Soltani Rad, M. N.; Nejabat, G. R. *Can. J. Chem.* **2006**, *84*, 979 doi:10.1139/V06-119.; (i) Zare, A.; Hasaninejad, A.; Moosavi Zare, A. R.; Parhami, A.; Sharghi, H.; Khalafi-Nezhad, A. *Can. J. Chem.* **2007**, *85*, 438 doi:10.1139/V07-050.; (j) Zare, A.; Hasaninejad, A.; Beyzavi, M. H.; Parhami, A.; Moosavi Zare, A. R.; Khalafi-Nezhad, A.; Sharghi, H. *Can. J. Chem.* **2008**, *86*, 317. doi:10.1139/V08-022.

(13) (a) Pore, D. M.; Desai, U. V.; Thopate, T. S.; Wadgaonkar, P. P. *ARKIVOC* **2006**, *xii*, 75; (b) Tabatabaeian, K.; Mamaghani, M.; Mahmoodi, N.; Khorshidi, A. *Can. J. Chem.* **2006**, *84*, 1541 doi:10.1139/V06-159.; (c) Zolfigol, M. A.; Salehi, P.; Shiri, M. *Phosphorus Sulfur Silicon* Relat. Elem. **2004**, *179*, 2273 doi:10.1080/10426500490484904.; (d) Hasaninejad, A.; Zare, A.; Sharghi, H.; Niknam, K.; Shekouhy, M. *ARKIVOC* **2007**, *xiv*, 39; (e) Hasaninejad, A.; Zare, A.; Sharghi, H.; Shekouhy, M.; Khalifeh, R.; Salimi Beni, A.; Moosavi Zare, A. R. *Can. J. Chem.* **2007**, *85*, 416 doi:10.1139/V07-051.; (f) Firouzabadi, H.; Iranpoor, N.; Jafarpour, M.; Ghadiri, A. *J. Mol. Cat. Chem. (Kyoto)* **2006**, *253*, 249 doi:10.1016/j.molcata.2006.03.043.; (g) Nagarajan, R.; Perumal, P. T. *Synth. Commun.* **2002**, *32*, 105 doi:10.1081/SCC-120001515.; (h) Firouzabadi, H.; Iranpoor, N.; Jafari, A. A. *Mol. Catal. Chem. (Kyoto)* **2006**, *244*, 168. doi:10.1016/j.molcata.2005.09.005.; (i) Nagarajan, R.; Perumal, P. T. *Tetrahedron* **2002**, *58*, 1229 doi:10.1016/S0040-4020(01)01227-3.; (j) Mi, X.; Luo, S.; He, J.; Cheng, J. P. *Tetrahedron Lett.* **2004**, *45*, 4567 doi:10.1016/j.tetlet.2004.04.039.; (k) Wang, L.; Han, J. H.; Sheng, T.; Fan, J. Z.; Tang, X. *Synlett* **2005**, 337 doi:10.1055/s-2004-837210.; (l) Deb, M. L.; Bhuyan, P. J. *Tetrahedron Lett.* **2006**, *47*, 1441. doi:10.1016/j.tetlet.2005.12.093.

(14) (a) Food phytochemicals for cancer prevention 1: Fruits and vegetables. Michnovicz, J. J.; Bradlow, H. L.; Huang, M. J.; Osawa, T.; Ho, C. T. Rosen, R. T., Eds.; American Chemical Society, Washington, DC, 1994; (b) Osawa, T.; Namiki, M. *Tetrahedron Lett.* **1983**, *24*, 4719 doi:10.1016/S0040-4039(00)86237-1.; (c) Bell, R.; Carmell, S.; Sar, N. *J. Nat. Prod.* **1994**, *57*, 1587 doi:10.1021/np50113a022. PMID:7853008.; (d) Bifulco, G.; Bruno, I.; Riccio, R.; Lavayre, J.; Bourdy, G. *J. Nat. Prod.* **1995**, *58*, 1254. doi:10.1021/np50122a017. PMID:7595591.; (e) Ramirez, A.; Garcia-Rubio, S. *Curr. Med. Chem.* **2003**, *10*, 1891 doi:10.2174/0929867033457016. PMID:12871110.; (f) Zhao, S.; Liao, X.; Cook, J. M. *Org. Lett.* **2002**, *4*, 687 doi:10.1021/ol010222h. PMID:11869102.; (g) Bell, M. C. *Gynecol. Oncol.* **2000**, *78*, 123. doi:10.1006/gyno.2000.5847. PMID:10926790.

(15) (a) Anderson, J. L.; Ding, J.; Welton, T.; Armstrong, D. W. *J. Am. Chem. Soc.* **2002**, *124*, 14248.; (b) Liu, Q.; Janssen, M. H. A.; Rantwijk, F.; Sheldon, R. A. *Green Chem.* **2005**, *7*, 39. doi:10.1039/b412848f.

(16) (a) Gordon, C. M. *Appl. Catal. A* **2001**, *222*, 101. doi:10.1016/S0926-860X(01)00834-1.; (b) Yadav, J. S.; Reddy, B. V. S.; Chetia, L.; Srinivasulu, G.; Kunwar, A. C. *Tetrahedron Lett.* **2005**, *46*, 1039. doi:10.1016/j.tetlet.2004.11.137.

(17) (a) Dupont, J.; Consorti, C. S.; Suarez, P. A. Z.; de Souza, R. F. *Org. Synth. Coll.* **2004**, *10*, 184; (b) Creary, X.; Willis, E. D. *Org. Synth.* **2005**, *82*, 166.

Photochemistry of 3-alkoxychromones I — Photocyclisation of 6-chloro-3-alkoxy-2-(furan-3-yl)-4*H*-chromen-4-ones

Ramesh C. Kamboj, Urmila Berar, Surinder Berar, Mandeep Thakur, Rita Arora, and Satish C. Gupta

Abstract: 3-Alkoxy/allyloxy-6-chloro-2-(furan-3-yl)-4*H*-chromen-4-ones yield angular tetracyclic products involving the 2-furyl group on photoirradiation through the intermediacy of 1,4-biradicals. The nature of the 3-alkoxy/allyloxy group influenced the photoproduct distribution. The stereochemical dispositions of the products have been established using the J/Φ relationship and were corroborated by MM2 calculations.

Key words: furylchromone, type-II reaction, 1,5-sigmatropic shift.

Résumé : La photoirradiation des 3-alkoxy/allyloxy-6-chloro-2-(furan-3-yl)-4*H*-chroménones conduit à des produits tétracycliques angulaires impliquant le groupe 2-furyle par l'intermédiaire de biradicaux-1,4. La nature du groupe 3-alkoxy/allyloxy influence la distribution des photoproduits. Les dispositions stéréochimiques des produits ont été déterminées à l'aide de la relation J/Φ et elles ont été corroborées par des calculs théoriques MM2.

Mots-clés : furylchromone, réaction de type II, déplacement sigmatropique 1,5.

[Traduit par la Rédaction]

Introduction

In photochemical transformations of 3-alkoxy-2-aryl-4*H*-chromen-4-one,[1] the products formed depend upon the nature of substituents at C-2 and C-3. The 2-methyl-3-methoxy derivatives produced dimeric oxetanols and underwent demethoxylation.[2] The photolysis of 3-alkoxy-2-(phenyl/furyl/thienyl)-4*H*-chromen-4-one[3] produced angular tetracyclics, whereas 2-styryl[4] derivatives provided linear tricyclics. The photochemical reaction in these substrates are basically γ-H abstractions[1,5] and have provided interesting mechanistic and structural studies as well as synthetic utility.[6] We now report the results of our investigations on the photoreactions of 3-alkoxy/allyloxy-6-chloro-2-(furan-3-yl)-4*H*-chromen-4-ones. The study was aimed at the effect of different 3-alkoxy groups on the product distribution and stereochemistry when the furyl group is tethered to the chromone through its 3-position instead of 2-position.[3]

Results and discussion

The targets, 2-(furan-3-yl)-4*H*-chromen-4-ones (**3a**–**3j**), were synthesized commencing with the condensation of 5-chloro-2-hydroxyacetophenone with furan-3-carbaldehyde as per Scheme 1.

Received 16 July 2008. Accepted 10 November 2008. Published on the NRC Research Press Web site at canjchem.nrc.ca on 7 January 2009.

R.C. Kamboj,[1] U. Berar, S. Berar, M. Thakur, R. Arora, and S.C. Gupta. Department of Chemistry, Kurukshetra University, Kurukshetra 136 119, India.

[1]Corresponding author (e-mail: rckamboj@rediffmail.com).

The structures of compounds **3a**–**3j** were found to be consistent with their spectral parameters (IR, ^{1}H-^{13}C NMR, Experimental secion).

The photolysis of the methanolic solution of **3a**–**3j** with pyrex filtered UV light, under nitrogen atmosphere produced the photoproducts **4a**–**4j**, **4b′**, **4h′**, **5g**, and **6g**. The structures of these photoproducts (Fig. 1) were confirmed by their spectral parameters(IR,^{1}H-^{13}C NMR) and elemental analysis.

Here, the interesting feature in the photoproducts isolated is the stereochemistry of ring C, which is in a half chair conformation (Fig. 2). In the photoproducts, **4a**–**4j**, **4b′**, **5g**, and **4h′**, the stereochemistry of the C/D ring junction is cis, as the trans-fusion of a five-membered ring will result in higher conformational strain as calculated by the MM2 energy minimizations program.[7] This is further borne out by the fact that $J_{3a,11b} = \sim 9.0$ Hz, which correlates with calculated values of $\Phi_{3a,11b}$ (karplus rule) with cis-fusion of these protons (Table 1) and also from literature references.[8] Now assuming the C/D ring fusion as cis, the orientation of H-4 can be cis to H-3a or trans to H-3a. Here again, regarding the relative stereochemical disposition of H-3a and H-4, the use of the J/Φ relationship[9] and MM2 program has been invoked. The correlation of $\Phi_{3a,4}$ values obtained from two possible MM2 energy minimized 3D conformations,[7] **A** (H-4 trans to H-3a) and **B** (H-4 cis to H-3a), with $J_{3a,4}$ observed from ^{1}H NMR is shown in Table 1. In compound **4a** and **4c** both conformation are equivalent as substituents at C-4 are the same. A look at Table 1 demonstrates the trans disposition of H-3a and H-4 in compounds **4b**, **4d**–**4f**, and **4h**, whereas it is a cis disposition in compounds **4g**, **4i**, **4j**, **4b′**, **4h′**, and **5g**, which are in accordance with karplus rule.[9] This has given the stereocentre at C-4 - a *R* configuration in compounds **4b**, **4d**–**4f**, and **4h** and a *S* configuration in com-

Scheme 1. Synthesis of furylchromones **3a**–**3j**.

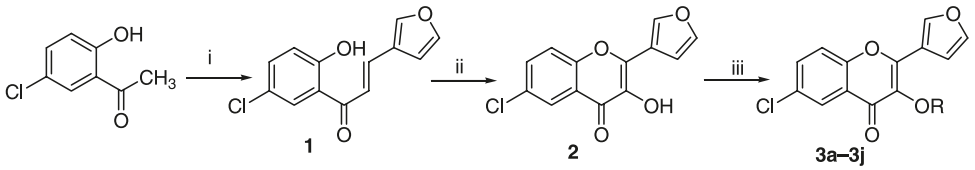

i: 3-Furaldehyde, C_2H_5OH, anhy·$Ba(OH)_2$, reflux
ii: KOH, H_2O_2(30%), 0°C
iii: K_2CO_3, CH_3COCH_3, $Bu_4N^+I^-$, RX

RX =			
CH_3I	**3a**, R = CH_3	80%
CH_3CH_2I	**3b**, R = CH_2CH_3	82%
$(CH_3)_2CHBr$	**3c**, R = $CH(CH_3)_2$	70%
H_2CCHCH_2Br	**3d**, R = CH_2CHCH_2	85%
$H_2CC(CH_3)CH_2Cl$	**3e**, R = $CH_2C(CH_3)CH_2$	72%
$(CH_3)_2CCHCH_2Br$	**3f**, R = $CH_2CHC(CH_3)_2$	70%
$C_6H_5CHCHCH_2Cl$	**3g**, R = $CH_2CHCHC_6H_5$	68%
$HCCCH_2Br$	**3h**, R = CH_2CCH	88%
$C_6H_5CH_2Cl$	**3i**, R = $CH_2C_6H_5$	70%
(*p*)$CH_3OC_6H_4CH_2Cl$	**3j**, R = $CH_2C_6H_4OCH_3$(*p*)	58%

Fig. 1. Structures of photoproducts.

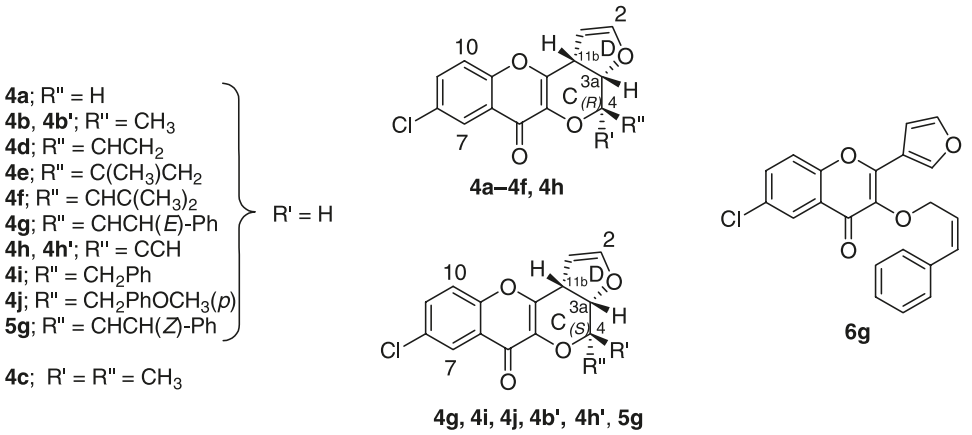

Fig. 2. MM2 energy minimized structures of compound **4h** and **4h**′.

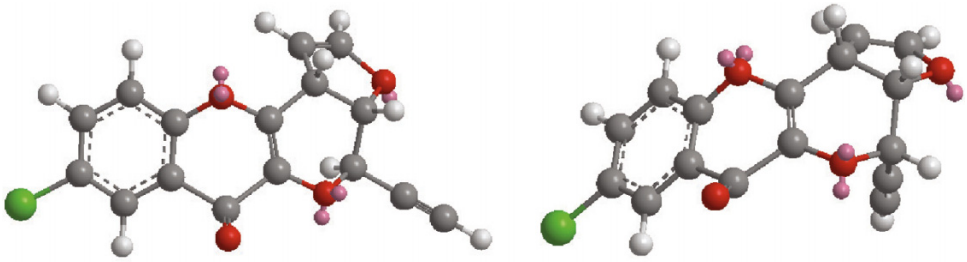

4h (conformation **A**) **4h'** (conformation **B**)

pounds **4g**, **4i**, **4j**, **4b**′, **4h**′, and **5g**. A correlation of steric energy (E_{kcal}) also shows that in most cases the lower energy conformations are the ones that explain the observed J/Φ relationship (Table 1).

Here it is worth mentioning that in photolysis of chromones **3b** and **3h**, both photoproducts with conformation **A** and **B** were isolated, whereas in all other chromones only one product was isolated (either conformation **A** or **B**). The reason for this behaviour could be from the steric influence of the C-4 substituent, where the second isomer is either not formed or formed in such low concentrations that it escaped isolation. The 3-cinnamyloxychromone, **3g**, along with cyclisation to yield **4g** also underwent isomerization of the cinnamyl double bond to yield two new products, **5g** and **6g**, where the cinnamyl double bond is cis (J = 11.7 Hz).

The phototransformations (Scheme 2) described above can be visualized as having occurred through the formation of the 1,4 biradical intermediate[1] **7**. The products have been expected to be formed through a bond formation between the -CH- and the C-2 atom of the furan ring, which

Table 1. J/Φ correlation of conformations of photoproducts.

Comp.	Coupling constant		Conformation **A**			Conformation **B**		
	$J_{3a,11b}$ (Hz)	$J_{3a,4}$ (Hz)	$\Phi_{3a,11b}$	$\Phi_{3a,4}$	E_{kcal}	$\Phi_{3a,11b}$	$\Phi_{3a,4}$	E_{kcal}
4a	10.2	9.0	16.84	167.0	11.40	16.84	167.0	11.40
4b*	7.8	8.4	15.00	167.0	11.66			
4b′	9.9	1.2				13.75	43.24	11.91
4c	9.3	—	13.77	—	12.38	13.77	—	12.38
4d	9.6	6.9	15.30	169.0	11.67	15.47	44.35	12.18
4e	9.3	7.5	19.36	175.0	12.90	8.12	32.63	13.56
4f	9.0	7.2	13.96	171.0	12.89	14.10	43.01	14.05
4g	9.6	7.2	1.90	90.50	13.93	13.81	14.28	14.24
4h*	9.9	6.9	16.33	167.0	11.13			
4h′	9.9	2.7				16.51	48.21	11.17
4i	9.6	8.1	3.97	85.59	15.87	3.60	19.70	15.19
4j	9.9	8.4	5.40	86.51	20.47	8.72	3.65	16.67
5g	9.0	7.2	19.97	66.97	13.88	15.98	8.0	14.44

*Isomeric compounds with both conformations were isolated.

is followed by ketonisation and H-migration to C-11b (1,5-H migration). The furyl group at C-2 also possesses a 5-carbon for clipping of the 3-alkoxy radical but here, the 1,5-sigmatropic shift is not feasible.

The secondary ring contraction products observed by cleavage of ring D, as isolated in our earlier work on 3-alkoxy-2-(2′-furyl) chromones,[3,10] are altogether absent here and were not even observed by further photolysis of pure photoproducts. The reason attributed to such diversity may be the difference in stabilization of radicals (Fig. 3) formed by the cleavage of ring D, which determines the ease of C–O bond cleavage.

The radical at C-11b in **8** (obtained in photolysis of 2′-furyl chromones) is stabilized by pyrone moiety and thus the C–O bond becomes prone to cleavage. There is no such stabilization available to the radical (at C-3a) in **9** for its formation and for the formation of ring contracted secondary photoproducts.

Fig. 3. Structures of proposed radicals.

8 **9**

Conclusion

3-Alkoxy/allyloxy-6-chloro-2-(furan-3-yl)-4*H*-chromen-4-ones upon photoirradiation yielded angular tetracyclic products through the 1,4-biradical furnished through γ-H abstraction. No ring contracted secondary photoproduct formation was observed.

Experimental

General

Melting points were determined in open capillaries and are thus uncorrected. ^{1}H NMR spectra were recorded on a 300 MHz Bruker spectrometer using TMS as the internal standard. IR spectra were recorded on a Buck Scientific 500 spectrophotometer using KBr pellets. Mass spectra were recorded at 70 eV. Elemental analysis was carried out on a Perkin Elmer 2400 instrument. TLC plates were coated with silica gel G (suspended in $CHCl_3$-MeOH) and iodine vapours were used as the visualizing agent. The columns for purification were packed with Silica gel 100–200 mesh in petroleum ether/benzene (9:1) and left overnight before use. The elution was carried out with increasing proportions of benzene in the petroleum ether–benzene mixture. The yields reported are based on the amount of isolated photoproducts and are calculated by excluding the recovered substrates.

Synthesis of chromones 3a–3j

1-(5-Chloro-2-hydroxyphenyl)-3-(furan-3-yl)prop-2-en-1-one (1)

A solution of 5-chloro-2-hydroxyacetophenone (17.0 g, 0.1 mol) and 3-furaldehyde (9.6 g, 0.1 mol) in absolute ethanol and dehydrated S-200 barium hydroxide (dried at 200 °C for 2 h, 20.0 g) were refluxed in a water bath for 20 min. The dark red mixture was cooled and poured on ice-HCl to obtain **1** (17.36 g, 70%) as a yellow solid, crystallized from EtOH, mp 110–113 °C. IR ν_{max} (cm^{-1}): 1648.0 (C=O), 3405(OH). ^{1}H NMR ($CDCl_3$) δ: 12.72 (1H, s, OH), 7.85 (1H, d, $J_{3,2}$ = 15.0 Hz, H-3), 7.80 (1H, d, J_m = 2.7 Hz, H-6′), 7.79 (1H, br s, H-2″), 7.49 (1H, d, $J_{5'',4''}$ = 2.4 Hz, H-5″), 7.42 (1H, dd, J_m = 2.7 Hz, J_o = 9.0 Hz, H-4′), 7.25 (1H, d, $J_{2,3}$ = 15.0 Hz, H-2), 6.96 (1H, d, J_o = 9.0 Hz, H-3′), 6.75 (1H, d, $J_{4'',5''}$ = 2.4 Hz, H-4″). Anal. calcd. for $C_{13}H_9ClO_3$: C 62.79, H 3.65; found: C 62.70, H 3.61.

6-Chloro-3-hydroxy-2-(furan-3-yl)-4H-chromen-4-one (2)

A solution of compound **1** (2.48 g, 0.01 mol) in EtOH at 0 °C was mixed with 12.0 mL 20% aq. NaOH by stirring. To this dark red solution was added H_2O_2 (30%) dropwise until the colour changed to yellow and the stirring was continued for 4 h. The reaction mixture was neutralized with ice-HCl to give creamy white precipitates, crystallized (chloroform-ethanol) to creamy white crystals (2.37 g, 90%), mp 206–208 °C. IR ν_{max} (cm^{-1}): 1615.0 (C=O), 3400(OH). ^{1}H NMR ($CDCl_3$) δ: 8.31 (1H, br s, H-2′), 8.21

Scheme 2. Cyclisation and 1,5-H shift of 1,4-biradical.

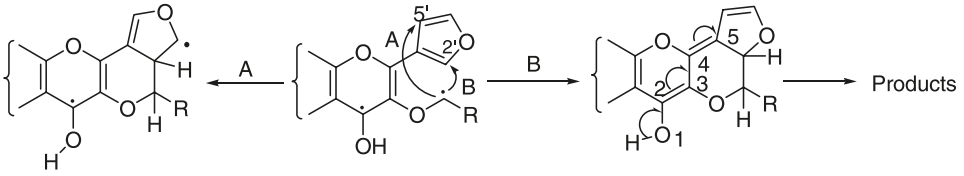

(1H, d, J_m = 2.4 Hz, H-5), 7.63 (1H, dd, J_m = 2.4 Hz, J_o = 9.0 Hz, H-7), 7.58 (1H, t, $J_{5',2'}$ = 1.5 Hz, $J_{5',4'}$ = 1.8 Hz, H-5′), 7.51 (1H, d, J_o = 9.0 Hz, H-8), 7.05 (1H, dd, $J_{4',2'}$ = 0.3 Hz, $J_{4',5'}$ = 1.8 Hz, H-4′). Anal. calcd. for $C_{13}H_7ClO_4$: C 59.45, H 2.69; found: C 59.31, H 2.69.

6-Chloro-3-methoxy-2-(furan-3-yl)-4H-chromen-4-one (3a)

The compound **2** (2.50 g, 0.01 mol), CH_3I (1.2 g, 0.01 mol), dry K_2CO_3 (1.0 g), and tetra-*n*-butylammonium iodide (100 mg) were refluxed in dry acetone (50 mL) for 2 h. Filtration, evaporation of the solvent, and crystallization of the residue (MeOH) gave **3a** (80%), a light brown solid, mp 114–117 °C. IR ν_{max} (cm^{-1}): 1655.0 (C=O). ^1H NMR ($CDCl_3$) δ: 8.30 (1H, br s, H-2′), 8.23 (1H, d, J_m = 2.4 Hz, H-5), 7.62 (1H, dd, J_m = 2.4 Hz, J_o = 9.0 Hz, H-7), 7.59 (1H, dd, $J_{5',2'}$ = 1.2 Hz, $J_{5',4'}$ = 1.5 Hz, H-5′), 7.48 (1H, d, J_o = 9.0 Hz, H-8), 7.02 (1H, dd, $J_{4',2'}$ = 0.3 Hz, $J_{4',5'}$ = 1.5 Hz, H-4′), 4.03 (3H, s, OCH_3). ^{13}C NMR ($CDCl_3$) δ: 172.83 (C-4), 153.24 (C-8a), 151.74 (C-2), 145.37 (C-5′), 143.75 (C-2′), 139.31 (C-4a), 133.44 (C-7), 130.67 (C-6), 125.33 (C-3), 125.15 (C-5), 119.50 (C-8), 117.71 (C-3′), 108.61 (C-4′), 59.53 (3-OCH_3). Anal. calcd. for $C_{14}H_9ClO_4$: C 60.78, H 3.28; found: C 63.65, H 3.31.

The other ethers (**3b**–**3j**) were synthesized by reacting 3-hydroxychromone (**2**) with ethyl iodide, isopropyl bromide, allyl bromide, methyl allyl chloride, dimethyl allyl bromide, cinnamyl chloride, propargyl bromide, benzyl chloride, and para methoxy benzyl chloride, respectively, by the procedure as described for compound **3a**.

6-Chloro-3-ethoxy-2-(furan-3-yl)-4H-chromen-4-one (3b)

Yield 82%, colourless solid; mp 104–106 °C (MeOH). IR ν_{max} (cm^{-1}): 1635.0 (C=O). ^1H NMR ($CDCl_3$) δ: 8.33 (1H, br s, H-2′), 8.20 (1H, d, J_m = 2.1 Hz, H-5), 7.60 (1H, dd, J_m = 2.1 Hz, J_o = 9.0 Hz, H-7), 7.57 (1H, t, $J_{5',2'}$ = 1.2 Hz, $J_{5',4'}$ = 1.5 Hz, H-5′), 7.46 (1H, d, J_o = 9.0 Hz, H-8), 7.02 (1H, dd, $J_{4',2'}$ = 0.3 Hz, $J_{4',5'}$ = 1.5 Hz, H-4′), 4.31 (2H, q, J_{vic} = 7.2 Hz, H-1″), 1.44 (3H, t, J_{vic} = 7.2 Hz, H-2″). ^{13}C NMR ($CDCl_3$) δ: 172.98 (C-4), 153.19 (C-8a), 151.70 (C-2), 145.27 (C-5′), 143.62 (C-2′), 139.09 (C-4a), 133.38 (C-7), 130.59 (C-6), 125.29 (C-3), 125.15 (C-5), 119.50 (C-8), 117.91 (C-1′), 108.71 (C-4′), 67.89 (C-1″), 15.71 (C-2″). Anal. calcd. for $C_{15}H_{11}ClO_4$: C 61.98, H 3.81; found: C 61.88, H 3.78.

6-Chloro-3-isopropyloxy-2-(furan-3-yl)-4H-chromen-4-one (3c)

Yield 70%, colourless solid; mp 95–97 °C (MeOH); IR ν_{max} (cm^{-1}): 1639.2 (C=O). ^1H NMR ($CDCl_3$) δ: 8.36 (1H, d, J = 0.9 Hz, H-2′), 8.19 (1H, d, J_m = 2.7 Hz, H-5), 7.59 (1H, dd, J_m = 2.7 Hz, J_o = 9.0 Hz, H-7), 7.55 (1H, t, $J_{5',2'}$ = 1.5 Hz, $J_{5',4'}$ = 1.8 Hz, H-5′), 7.46 (1H, d, J_o = 9.0 Hz, H-8), 7.04 (1H, d, $J_{4',5'}$ = 1.8 Hz, H-4′), 5.15 (1H, septet, J_{vic} = 6.3 Hz, H-1″), 1.32 (6H, d, J_{vic} = 6.3 Hz, $C_{1''}$-CH_3). ^{13}C NMR ($CDCl_3$) δ: 173.07 (C-4), 153.12 (C-8a), 151.79 (C-2), 145.73 (C-5′), 143.32 (C-2′), 137.00 (C-4a), 133.26 (C-7), 130.49 (C-6), 125.13 (C-5), 125.00 (C-3), 119.44 (C-8), 118.13 (C-1′), 108.92 (C-4′), 73.98 (C-1″), 22.49 ($C_{1''}$-CH_3). Anal. calcd. for $C_{16}H_{13}ClO_4$: C 63.06, H 4.30; found: C 62.97, H 4.27.

3-Allyloxy-6-chloro-2-(furan-3-yl)-4H-chromen-4-one (3d)

Yield 85%, light brown solid; mp 93–95 °C(MeOH). IR ν_{max} (cm^{-1}): 1641 (C=O), 1613 (C=C). ^1H NMR ($CDCl_3$) δ: 8.33 (1H, br s, H-2′), 8.20 (1H, d, J_m = 2.4 Hz, H-5), 7.60 (1H, dd, J_m = 2.4 Hz, J_o = 9.0 Hz, H-7), 7.56 (1H, dd, $J_{5',2'}$ = 0.9 Hz, $J_{5',4'}$ = 1.8 Hz, H-5′), 7.47 (1H, d, J_o = 9.0 Hz, H-8), 7.02 (1H, dd, $J_{4',2'}$ = 0.3 Hz, $J_{4',5'}$ = 1.8 Hz, H-4′), 6.08 (1H, tdd, J_{vic} = 6.3 Hz, J_{trans} = 17.4 Hz, J_{cis} = 10.2 Hz, H-2″), 5.39 (1H, td, J_{allyl} = 1.5 Hz, J_{trans} = 17.4 Hz, H-3″b), 5.26 (1H, d, J_{cis} = 10.2 Hz, H-3″a), 4.80 (2H, dd, J_{vic} = 6.3 Hz, J_{allyl} = 1.5 Hz, H-1″). ^{13}C NMR ($CDCl_3$) δ: 171.00 (C-4), 153.10 (C-8a), 153.00 (C-2), 145.50 (C-5′), 143.62 (C-2′), 139.09 (C-4a), 133.45 (C-7), 133.30(C-2″), 130.60 (C-6), 123.14 (C-3), 123.34 (C-5), 119.83(C-3″), 119.10 (C-8), 117.84 (C-3′), 108.70 (C-4′), 72.69 (C-1″). Anal. calcd. for $C_{16}H_{11}ClO_4$: C 63.48, H 3.66; found: C 63.33, H 3.65.

6-Chloro-2-(furan-3-yl)-3-(2-methylallyloxy)-4H-chromen-4-one (3e)

Yield 72%, creamy white solid; mp 90–92 °C (MeOH). IR ν_{max} (cm^{-1}): 1637 (C=O), 1619 (C=C). ^1H NMR ($CDCl_3$) δ: 8.32 (1H, dd, J_m = 0.9 Hz, H-2′), 8.20 (1H, d, J_m = 2.7 Hz, H-5), 7.59 (1H, dd, J_m = 2.7 Hz, J_o = 9.0 Hz, H-7), 7.56 (1H, t, $J_{5',2'}$ = 0.9 Hz, $J_{5',4'}$ = 1.8 Hz, H-5′), 7.46 (1H, d, J_o = 9.0 Hz, H-8), 7.01 (1H, dd, $J_{4',2'}$ = 0.9 Hz, $J_{4',5'}$ = 1.8 Hz, H-4′), 5.15 (1H, s, H-3″b), 5.01 (1H, s, H-3″a), 4.67 (2H, s, H-1″), 1.87 (3H, s, 2″-CH_3). ^{13}C NMR ($CDCl_3$) δ: 172.78 (C-4), 153.18 (C-8a), 151.65 (C-2), 145.44 (C-5′), 143.64 (C-2′),141.18 (C-2″), 138.80 (C-4a), 133.37 (C-7), 130.63 (C-6), 125.29 (C-3), 125.12 (C-5), 119.48 (C-8), 117.76 (C-1′),113.80 (C-3″), 108.68 (C-4′), 75.13 (C-1″), 19.79 (2″-CH_3). Anal. calcd. for $C_{17}H_{13}ClO_4$: C 64.46, H 4.14; found: C 64.30, H 4.11.

6-Chloro-2-(furan-3-yl)-3-(3-methylbut-2-enyloxy)-4H-chromen-4-one (3f)

Yield 70%, off-white solid; mp 81–84 °C (MeOH). IR ν_{max} (cm^{-1}): 1637.2 (C=O), 1608.6 (C=C). ^1H NMR ($CDCl_3$) δ: 8.33 (1H, d, $J_{2',5'}$ = 1.2 Hz, H-2′), 8.21 (1H, d, J_m = 2.4 Hz, H-5), 7.59 (1H, dd, J_m = 2.4 Hz, J_o = 9.0 Hz, H-7), 7.55 (1H, t, $J_{5',2'}$ = 1.2 Hz, $J_{5',4'}$ = 1.8 Hz, H-5′), 7.46 (1H, d, J_o = 9.0 Hz, H-8), 7.01 (1H, d, $J_{4',5'}$ = 1.8 Hz, H-4′), 5.53 (1H, tt, J_{vic} = 7.2 Hz, J_{allyl} = 1.5 Hz, H-2″), 4.78 (1H, d,

J_{vic} = 7.2 Hz, H-1″), 1.75 (3H, d, J_{allyl} = 1.5 Hz, H-4″), 1.73 (3H, s, $C_{3''}$-CH_3). ^{13}C NMR ($CDCl_3$) δ: 172.17 (C-4), 153.18 (C-8a), 152.79 (C-2), 145.63 (C-5′), 143.82 (C-2′), 137.90 (C-4a), 132.96 (C-7), 131.85 (C-3″), 130.42 (C-6), 124.23 (C-5), 123.50 (C-3), 120.80 (C-2″), 119.02 (C-8), 118.13 (C-3′), 108.62 (C-4′), 68.99 (C-1″), 18.05 (C-4″), 25.86 (3″-CH_3). Anal. calcd. for $C_{18}H_{15}ClO_4$: C 65.36, H 4.57; found: C 65.24, H 4.52.

*6-Chloro-2-(furan-3-yl)-3-(3-phenylallyloxy)-4*H*-chromen-4-one (3g)*

Yield 68%, light brown solid; mp 91–94 °C (EtOH). IR ν_{max} (cm^{-1}): 1648.4 (C=O), 1617(C=C). ^{1}H NMR ($CDCl_3$) δ: 8.36 (1H, t/dd, $J_{2',5'}$ = 1.5 Hz, $J_{2',4'}$ = 1.8 Hz, H-2′), 8.22 (1H, d, J_m = 2.4 Hz, H-5), 7.60 (1H, dd, J_m = 2.4 Hz, J_o = 9.0 Hz, H-7), 7.56 (1H, t, $J_{5',2'}$ = 1.5 Hz, $J_{5',4'}$ = 1.8 Hz, H-5′), 7.46 (1H, d, J_o = 9.0 Hz, H-8), 7.29–7.35 (5H, m, H-2‴-6‴), 7.03 (1H, t, $J_{4',2'}$ = 1.8 Hz, $J_{4',5'}$ = 1.8 Hz, H-4′), 6.70 (1H, d, $J_{3',2'}$ = 15.9 Hz, H-3″), 6.44 (1H, td, $J_{2',3'}$ = 15.9 Hz, $J_{2',1'}$ = 6.6 Hz, H-2″), 4.96 (2H, d, $J_{1',2'}$ = 6.6 Hz, H-1″). ^{13}C NMR ($CDCl_3$) δ: 172.94 (C-4), 153.21 (C-8a), 152.03 (C-2), 145.50 (C-5′), 143.67 (C-2′), 136.26 (C-1‴), 134.61 (C-7), 133.44 (C-3″), 130.66(C-4‴), 128.57 (C-2‴, C-6‴), 128.05 (C-3), 126.70 (C-3‴, C-5‴), 125.26 (C-6), 125.14 (C-2″), 125.14 (C-4a), 124.29 (C-5), 119.54 (C-8), 117.91 (C-1′), 108.77 (C-4′), 72.48 (C-1″). Anal. calcd. for $C_{22}H_{15}ClO_4$: C 69.75, H 3.99; found: C 69.68, H 3.97.

*6-Chloro-2-(furan-3-yl)-3-propargyloxy-4*H*-chromen-4-one (3h)*

Yield 88%, light brown solid; mp 121–123 °C (MeOH). IR ν_{max} (cm^{-1}): 1634.3 (C=O), 2135(C≡C). ^{1}H NMR ($CDCl_3$) δ: 8.40 (1H, dd/t, $J_{2',5'}$ = 1.2 Hz, $J_{2',4'}$ = 0.6 Hz, H-2′), 8.20 (1H, d, J_m = 2.4 Hz, H-5), 7.61 (1H, dd, J_m = 2.4 Hz, J_o = 9.0 Hz, H-7), 7.56 (1H, t, $J_{5',2'}$ = 1.2 Hz, $J_{5',4'}$ = 1.8 Hz, H-5′), 7.48 (1H, d, J_o = 9.0 Hz, H-8), 7.05 (1H, d, $J_{4',5'}$ = 1.8 Hz, $J_{4',2'}$ = 0.6 Hz, H-4′), 5.09 (2H, d, $J_{1',3'}$ = 2.4 Hz, H-1″), 2.44 (1H, d, $J_{3',1'}$ = 2.4 Hz, H-3″). ^{13}C NMR ($CDCl_3$) δ: 172.50 (C-4), 153.22 (C-2), 152.10 (C-8a), 145.96 (C-5′), 143.55 (C-2′), 138.50 (C-7), 133.60 (C-3), 130.82 (C-5), 128.42 (C-6), 125.11 (C-4a), 119.51 (C-8), 117.62 (C-1′), 108.83 (C-4′), 78.45 (C-2″), 76.27 (C-3″), 59.08 (C-1″). Anal. calcd. for $C_{16}H_9ClO_4$: C 63.91, H 3.02; found: C 63.72, H 3.00.

*3-Benzyloxy-6-chloro-2-(furan-3-yl)-4*H*-chromen-4-one (3i)*

Yield 70%, light yellow solid; mp 86–89 °C (MeOH). IR ν_{max} (cm^{-1}): 1643.3 (C=O). ^{1}H NMR ($CDCl_3$) δ: 8.23 (1H, d, J_m = 2.7 Hz, H-5), 8.20 (1H, d, $J_{2',5'}$ = 1.2 Hz, H-2′), 7.60 (1H, dd, J_m = 2.7 Hz, J_o = 9.0 Hz, H-7), 7.50 (1H, t, $J_{5',2'}$ = 1.2 Hz, $J_{5',4'}$ = 1.5 Hz, H-5′), 7.49 (1H, d, J_o = 9.0 Hz, H-8), 7.39–7.26 (5H, m, H-2″, 3″, 4″, 5″, 6″), 6.94 (1H, d, $J_{4',5'}$ = 1.5 Hz, H-4′), 5.30 (2H, s, -OCH_2-). ^{13}C NMR ($CDCl_3$) δ: 172.87 (C-4), 153.19 (C-2), 151.83 (C-8a), 145.57 (C-5′), 143.51 (C-2′), 138.74 (C-1″), 136.59 (C-7), 133.40 (C-3), 130.66 (C-4″), 128.85 (C-3″, C-5″), 128.50 (C-2″, C-6″), 128.42 (C-6), 125.28 (C-4a), 125.15 (C-5), 119.51 (C-8), 117.71 (C-1′), 108.69 (C-4′), 73.79 (-OCH_2-). Anal. calcd. for $C_{20}H_{13}ClO_4$: C 68.09, H 3.71; found: C 62.95, H 3.66.

*6-Chloro-2-(furan-3-yl)-3-(4-methoxybenzyloxy)-4*H*-chromen-4-one (3j)*

Yield 58%, light yellow solid; mp 89–92 °C (MeOH). IR ν_{max} (cm^{-1}): 1650.4 (C=O). ^{1}H NMR ($CDCl_3$) δ: 8.16 (1H, d, J_m = 2.7 Hz, H-5), 8.13 (1H, br s, H-2′), 7.52 (1H, dd, J_m = 2.7 Hz, J_o = 9.0 Hz, H-7), 7.44 (1H, t, $J_{5',2'}$ = 1.5 Hz, $J_{5',4'}$ = 1.8 Hz, H-5′), 7.38 (1H, d, J_o = 9.0 Hz, H-8), 7.33 (2H, d, J_o = 8.4 Hz, H-2″, H-6″), 6.87 (1H, d, $J_{4',5'}$ = 1.8 Hz, H-4′), 6.79 (2H, d, J_o = 8.4 Hz, H-3″, H-5″), 5.18 (2H, s, -OCH_2-), 3.73 (3H, s, $C_{4''}$-OCH_3). ^{13}C NMR($CDCl_3$) δ: 171.49 (C-4), 158.31 (C-4″), 151.71 (C-8a), 150.39 (C-2), 144.12 (C-5′), 142.00 (C-2′), 137.19 (C-1″), 131.90 (C-7), 129.19 (C-2″, C-6″), 129.00 (C-3), 126.26 (C-6), 123.79 (C-4a), 123.65 (C-5), 118.06 (C-8), 116.31 (C-1′), 112.39 (C-3″, C-5″), 107.25 (C-4′), 72.00 (OCH_2), 53.79 ($C_{4''}$-OCH_3). Anal. calcd. for $C_{21}H_{15}ClO_4$: C 65.89, H 3.95; found: C 65.68, H 3.91.

Photoirradiation of chromones 3a–3j

*Photolysis of 6-chloro-2-(furan-3-yl)-3-methoxy-4*H*-chromen-4-one (3a)*

A methanolic solution (150 mL) of chromone **3a** (200 mg, 0.72 mmol) was irradiated with light from a 125 W Hg vapor lamp in a pyrex reactor under nitrogen atmosphere for 45 min. The removal of the solvent left a gummy solid, which was chromatographed to yield **4a**.

*Compound **4a***

Yield 45%, white solid; mp 185–188 °C (EtOH). IR ν_{max} (cm^{-1}): 1649.7 (C=O). ^{1}H NMR ($CDCl_3$) δ: 8.23 (1H, d, J_m = 2.4 Hz, H-7), 7.58 (1H, dd, J_m = 2.4 Hz, J_o = 9.0 Hz, H-9), 7.40 (1H, d, J_o = 9.0 Hz, H-10), 6.46 (1H, dd/t, $J_{2,11b}$ = 2.1 Hz, $J_{2,1}$ = 2.4 Hz, H-2), 5.28 (1H, dd/t, $J_{1,2}$ = 2.4 Hz, $J_{1,11b}$ = 2.7 Hz, H-1), 5.10 (1H, d{dd}, $J_{3a,4a}$ = 2.4 Hz, $J_{3a,4b}$ = 9.0 Hz, $J_{3a,11b}$ = 10.2 Hz, H-3a), 4.34 (1H, dd, $J_{11b,1}$ = 2.7 Hz, $J_{11b,3a}$ = 10.2 Hz, H-11b), 4.14–4.07 (2H, m, H-4a, H-4b). ^{13}C NMR ($CDCl_3$) δ: 170.52 (C-6), 153.58 (C-10a), 151.94 (C-11a), 148.39 (C-2), 138.83 (C-6a), 133.47 (C-9), 130.57 (C-8), 125.45 (C-7), 124.73 (C-5a), 119.48 (C-10), 100.60 (C-1), 78.73 (C-4), 65.88 (C-3a), 40.83 (C-11b). Anal. calcd. for $C_{14}H_9ClO_4$: C 60.78, H 3.28; found: C 63.58, H 3.34. Mass (*m*/*z*): 276 (M^+, 100%).

*Photolysis of 6-chloro-3-ethoxy-2-(furan-3-yl)-4*H*-chromen-4-one (3b)*

A methanolic solution of **3b** (0.20 g, 0.7 mmol) on photolysis for 45 min furnished **4b** and **4b**′. These isomeric photoproducts were separated from the starting substrate **3b** by column chromatography. They were further separated from each other by preparative TLC.

*Compound **4b***

Yield 22%, white solid; mp 174–176 °C (EtOH). IR ν_{max} (cm^{-1}): 1651.0 (C=O). ^{1}H NMR ($CDCl_3$) δ: 8.24 (1H, d, J_m = 2.4 Hz, H-7), 7.58 (1H, dd, J_m = 2.4 Hz, J_o = 9.0 Hz, H-9), 7. 41 (1H, d, J_o = 9.0 Hz, H-10), 6.44 (1H, d, $J_{2,1}$ = 2.7 Hz, H-2), 5.36 (1H, dd/t, $J_{1,2}$ = 2.7 Hz, $J_{1,11b}$ = 2.7 Hz, H-1), 4.63 (1H, dd, $J_{3a,11b}$ = 7.8 Hz, $J_{3a,4}$ = 8.4 Hz, H-3a), 4.23 (1H, dd, $J_{11b,1}$ = 2.7 Hz, $J_{11b,3a}$ = 7.8 Hz, H-11b), 3.88 (1H, q{d}, J_{vic} = 6.6 Hz, $J_{4,3a}$ = 8.4 Hz, H-4), 1.65 (3H, d, J_{vic} = 6.6 Hz, C_4-CH_3). ^{13}C NMR ($CDCl_3$) δ: 171.10 (C-6),

153.63 (C-10a), 151.11 (C-11a), 147.27 (C-2), 138.22 (C-6a), 133.43 (C-9), 130.51 (C-8), 125.49 (C-7), 124.79 (C-5a), 119.46 (C-10), 100.69 (C-1), 80.69 (C-4), 71.72 (C-3a), 41.78 (C-11b), 17.69 (C_4-CH_3). Anal. calcd. for $C_{15}H_{11}ClO_4$: C 61.98, H 3.81; found: C 61.90, H 3.80. Mass (*m*/*z*): 290 (M^+, 100%).

*Compound **4b′***

Yield 11%, white solid; mp 160–162 °C (EtOH). IR $\nu_{max.}$ (cm^{-1}): 1652.0 (C=O). ^1H NMR ($CDCl_3$) δ: 8.22 (1H, d, J_m = 2.4 Hz, H-7), 7.56 (1H, dd, J_m = 2.4 Hz, J_o = 9.0 Hz, H-9), 7.38 (1H, d, J_o = 9.0 Hz, H-10), 6.44 (1H, d, $J_{2,1}$ = 2.7 Hz, H-2), 5.25 (1H, d, $J_{1,2}$ = 2.7 Hz, H-1), 4.91 (1H, d, $J_{3a,11b}$ = 9.9 Hz, H-3a), 4.15 (1H, q, J_{vic} = 6.3 Hz, H-4), 4.05 (1H, d, $J_{11b,3a}$ = 9.9 Hz, H-11b), 1.55 (3H, d, J_{vic} = 6.3 Hz, C_4-CH_3). Anal. calcd. for $C_{15}H_{11}ClO_4$: C 61.98, H 3.81; found: C 61.87, H 3.78. Mass (*m*/*z*): 290 (M^+, 100%).

Photolysis of 6-chloro-2-(furan-3-yl)-3-isopropyloxy-4H-chromen-4-one (3c)

A methanolic solution of **3c** (0.20 g, 0.66 mmol) on photolysis for 45 min furnished **4c**.

*Compound **4c***

Yield 48%, white solid; mp 165–167 °C ($CHCl_3$-EtOH). IR ν_{max} (cm^{-1}): 1655.8 (C=O). ^1H NMR ($CDCl_3$) δ: 8.23 (1H, d, J_m = 2.7 Hz, H-7), 7.56 (1H, dd, J_m = 2.7 Hz, J_o = 9.0 Hz, H-9), 7.38 (1H, d, J_o = 9.0 Hz, H-10), 6.43 (1H, dd, $J_{2,11b}$ = 1.8 Hz, $J_{2,1}$ = 3.0 Hz, H-2), 5.30 (1H, dd/t, $J_{1,2}$ = 3.0 Hz, $J_{1,11b}$ = 3.0 Hz, H-1), 4.64 (1H, d, $J_{3a,11b}$ = 9.3 Hz, H-3a), 3.95 (1H, dd{d}/m, $J_{11b,2}$ = 1.8 Hz, $J_{11b,1}$ = 3.0 Hz, $J_{11b,3a}$ = 9.3 Hz, H-11b), 1.62 (3H, s, C_4-CH_3b), 1.39 (3H, s, C_4-CH_3a). ^{13}C NMR ($CDCl_3$) δ: 173.00 (C-6), 159.00 (C-10a), 152.00 (C-11a), 148.20 (C-2), 135.00 (C-6a), 133.18 (C-9), 130.00 (C-8), 125.47 (C-7), 125.00 (C-5a), 119.39 (C-10), 100.49 (C-1), 85.99 (C-3a), 75.37 (C-4), 39.73 (C-11b), 23.94 (C_4-*C*H_3b), 23.38 (C_4-*C*H_3a). Anal. calcd. for $C_{16}H_{13}ClO_4$: C 63.06, H 4.30; found: C 63.01, H 4.25. Mass (*m*/*z*): 304/306 (M^+, 100%).

Photolysis of 3-allyloxy-6-chloro-2-(furan-3-yl)-4H-chromen-4-one (3d)

A methanolic solution of **3d** (0.20 g, 0.66 mmol) on photolysis for 45 min furnished **4d**.

*Compound **4d***

Yield 29%, white solid; mp 145–146 °C (EtOH). IR ν_{max} (cm^{-1}): 1637(C=O). ^1H NMR ($CDCl_3$) δ: 8.17 (1H, d, J_m = 2.4 Hz, H-7), 7.51 (1H, dd, J_m = 2.4 Hz, J_o = 9.0 Hz, H-9), 7.34 (1H, d, J_o = 9.0 Hz, H-10), 6.40 (1H, d, $J_{2,1}$ = 2.7 Hz, H-2), 5.93 (1H, ddd, J_{vic} = 5.1 Hz, J_{trans} = 17.4 Hz, J_{cis} = 10.8 Hz, H-1′), 5.47 (1H, d, J_{trans} = 17.4 Hz, H-2′b), 5.35 (1H, d, J_{cis} = 10.8 Hz, H-2′a), 5.30 (1H, t, $J_{1,2}$ = 2.7 Hz, $J_{1,11b}$ = 2.7 Hz, H-1), 4.77 (1H, dd $J_{3a,4}$ = 6.9 Hz, $J_{3a,11b}$ = 9.6 Hz, H-3a), 4.10 (1H, dd, $J_{11b,1}$ = 2.7 Hz, $J_{11b,3a}$ = 9.6 Hz, H-11b), 4.40 (1H, dd, $J_{4,3a}$= 6.9 Hz, $J_{4,1'}$ = 5.1 Hz, H-4). ^{13}C NMR ($CDCl_3$) δ: 172.00 (C-6), 151.61 (C-10a), 149.35 (C-11a), 145.57 (C-2), 135.47 (C-6a), 131.49 (C-9), 130.76 (C-1′), 128.59 (C-8), 123.51 (C-7), 122.79 (C-5a), 117.67 (C-10), 117.50 (C-2′), 98.77 (C-1), 77.91 (C-4), 73.23 (C-3a), 39.11 (C-11b). Anal. calcd. for $C_{16}H_{11}ClO_4$: C 63.48, H 3.66; Found: C 63.46, H 3.60. Mass (*m*/*z*): 302 (M^+, 100%).

Photolysis of 6-chloro-2-(furan-3-yl)-3-(2-methylallyloxy)-4H-chromen-4-one (3e)

A methanolic solution of **3e** (0.20 g, 0.63 mmol) on photolysis for 45 min furnished **4e**.

*Compound **4e***

Yield 24%, white solid; mp 196–200 °C ($CHCl_3$-EtOH). IR ν_{max} (cm^{-1}): 1641 (C=O). ^1H NMR ($CDCl_3$) δ: 8.22 (1H, d, J_m = 2.4 Hz, H-7), 7.59 (1H, dd, J_m = 2.4 Hz, J_o = 9.0 Hz, H-9), 7. 41 (1H, d, J_o = 9.0 Hz, H-10), 6.47 (1H, d, $J_{2,1}$ = 2.7 Hz, H-2), 5.37 (1H, s, H-2′b), 5.17 (1H, s, H-2′a), 5.13 (1H, dd/t, $J_{1,2}$ = 2.7 Hz, $J_{1,11b}$ = 2.7 Hz, H-1), 4.63 (1H, dd, $J_{3a,11b}$ = 9.3 Hz, $J_{3a,4}$ = 7.5 Hz, H-3a), 4.31 (1H, q{d}, J_{vic} = 6.6 Hz, $J_{4,3a}$ = 7.5 Hz, H-4), 3.88 (1H, dd, $J_{11b,1}$ = 2.7 Hz, $J_{11b,3a}$ = 9.3 Hz, H-11b), 1.85 (3H, s, $C_{1'}$-CH_3). ^{13}C NMR ($CDCl_3$) δ: 171.80 (C-6), 152.68 (C-10a), 149.05 (C-11a), 146.27 (C-2), 135.82 (C-6a), 133.40 (C-9), 140.28 (C-1′), 129.51 (C-8), 126.49 (C-7), 122.70 (C-5a), 118.06 (C-10), 108.45 (C-2′), 99.69 (C-1), 80.10 (C-4), 72.70 (C-3a), 40.15 (C-11b), 18.69 (1′-*C*H_3). Anal. calcd. for $C_{17}H_{13}ClO_4$: C 64.46, H 4.14; found: C 64.34, H 4.12. Mass (*m*/*z*): 316 (M^+, 100%).

Photolysis of 6-chloro-2-(furan-3-yl)-3-(3-methylbut-2-enyloxy)-4H-chromen-4-one (3f)

A methanolic solution of **3f** (0.20 g, 0.6 mmol) on photolysis for 45 min furnished **4f**.

*Compound **4f***

Yield 31%, light brown solid; mp 99–102 °C ($CHCl_3$-EtOH). IR ν_{max} (cm^{-1}): 1637.2 (C=O). ^1H NMR ($CDCl_3$) δ: 8.23 (1H, d, J_m = 2.4 Hz, H-7), 7.58 (1H, dd, J_m = 2.4 Hz, J_o = 9.0 Hz, H-9), 7.44 (1H, d, J_o = 9.0 Hz, H-10), 6.45 (1H, d, $J_{2,1}$ = 2.7 Hz, H-2), 5.49 (1H, dd/t, $J_{1,2}$ = 2.7 Hz, $J_{1,11b}$ = 3.0 Hz, H-1), 5.37 (1H, dd, $J_{1',4}$ = 5.7 Hz, J_{allyl} = 1.5 Hz, H-1′), 4.75 (1H, dd, $J_{3a,11b}$ = 9.0 Hz, $J_{3a,4}$ = 7.8 Hz, H-3a), 4.58 (1H, dd, $J_{4,3a}$ = 7.8 Hz, $J_{4,1'}$ = 5.7 Hz, H-4), 4.21 (1H, dd, $J_{11b,1}$ = 3.0 Hz, $J_{11b,3a}$ = 9.0 Hz, H-11b), 1.80 (3H, d, J_{allyl} = 1.5 Hz, $C_{2'}$-CH_3b), 1.76 (3H, s, $C_{2'}$-CH_3a). ^{13}C NMR ($CDCl_3$) δ: 172.50 (C-6), 153.41 (C-10a), 150.30 (C-11a), 144.28 (C-2), 135.00 (C-6a), 132.78 (C-9), 132.70 (C-2′), 128.00 (C-8), 123.20 (C-1′), 123.50 (C-7), 123.05 (C-5a), 119.19 (C-10), 101.79 (C-1), 79.80 (C-3a), 70.37 (C-4), 39.97 (C-11b), 25.20 (2′-*C*H_3b), 19.20 (2′-*C*H_3a). Anal. calcd. for $C_{18}H_{15}ClO_4$: C 65.36, H 4.57; found: C 65.28, H 4.51. Mass (*m*/*z*): 330 (M^+, 100%).

Photolysis of 6-chloro-2-(furan-3-yl)-3-(3-phenylallyloxy)-4H-chromen-4-one (3g)

A methanolic solution of **3g** (0.20 g, 0.53 mmol) on photolysis for 45 min furnished three photoproducts: **4g**, **5g**, and **6g**.

*Compound **4g***

Yield 16%, light yellow solid; mp 155–157 °C ($CHCl_3$-EtOH). IR ν_{max} (cm^{-1}): 1639.6 (C=O). ^1H NMR ($CDCl_3$) δ: 8.25 (1H, d, J_m = 2.7 Hz, H-7), 7.58 (1H, dd, J_m = 2.7 Hz, J_o = 9.0 Hz, H-9), 7.41 (1H, d, J_o = 9.0 Hz, H-10), 7.28–7.36 (5H, m, H-2″-6″), 6.85 (1H, d, $J_{2',1'}$ = 16.5 Hz, H-2′),

6.50 (1H, dd/t, $J_{2,11b}$ = 2.1 Hz, $J_{2,1}$ = 2.4 Hz, H-2), 6.33 (1H, dd, $J_{1',4}$ = 6.0 Hz, $J_{1',2'}$ = 16.5 Hz, H-1′), 5.40 (1H, dd/t, $J_{1,11b}$ = 2.4 Hz, $J_{1,2}$ = 2.4 Hz, H-1), 4.91 (1H, dd, $J_{3a,4}$ = 7.2 Hz, $J_{3a,11b}$ = 9.6 Hz, H-3a), 4.58 (1H, t, $J_{4,3a}$ = 7.2 Hz, $J_{4,1'}$ = 6.0 Hz, H-4), 4.25 (1H, t{d}, $J_{11b,2}$ = 2.1 Hz, $J_{11b,1}$ = 2.4 Hz, $J_{11b,3a}$ = 9.6 Hz, H-11b). ^{13}C NMR ($CDCl_3$) δ: 172.13 (C-6), 154.05 (C-10a), 151.91 (C-11a), 144.50 (C-2), 138.44 (C-6a), 137.20 (C-1″), 130.78 (C-2′), 129.65 (C-9), 129.06 (C-3″, C-5″), 128.00 (C-4″), 127.77 (C-2″, C-6″), 126.02 (C-1′), 125.81 (C-7), 125.54 (C-8), 124.37 (C-5a), 118.06 (C-10), 98.88 (C-1), 77.56 (C-3a), 75.00 (C-4), 38.75 (C-11b). Anal. calcd. for $C_{22}H_{15}ClO_4$: C 69.75, H 3.99; found: C 69.60, H 3.95. Mass (*m*/*z*): 378 (M^+, 100%).

Compound ***5g***

Yield 10%, light yellow solid; mp 181–182 °C ($CHCl_3$-EtOH). IR ν_{max} (cm^{-1}): 1642 (C=O). ^{1}H NMR ($CDCl_3$): 8.23 (1H, d, J_m = 2.7 Hz, H-7), 7.58 (1H, dd, J_m = 2.7 Hz, J_o = 9.0 Hz, H-9), 7.41 (1H, d, J_o = 9.0 Hz, H-10), 7.28–7.36 (5H, m, H-2″-6″), 6.93 (1H, d, $J_{2',1'}$ = 11.7 Hz, H-2′), 6.39 (1H, dd/t, $J_{2,11b}$ = 2.4 Hz, $J_{2,1}$ = 2.4 Hz, H-2), 5.83 (1H, dd, $J_{1',4}$ = 6.0 Hz, $J_{1',2'}$ = 11.7 Hz, H-1′), 5.35 (1H, dd/t, $J_{1,11b}$ = 2.4 Hz, $J_{1,2}$ = 2.4 Hz, H-1), 4.72 (1H, dd, $J_{3a,4}$ = 7.2 Hz, $J_{3a,11b}$ = 9.0 Hz, H-3a), 4.58 (1H, t, $J_{4,3a}$ = 7.2 Hz, $J_{4,1'}$ = 6.0 Hz, H-4), 4.25 (1H, t{d}, $J_{11b,2}$ = 2.4 Hz, $J_{11b,1}$ = 2.4 Hz, $J_{11b,3a}$ = 9.6 Hz, H-11b). ^{13}C NMR ($CDCl_3$) δ: 172.92 (C-6), 154.56 (C-10a), 151.21 (C-11a), 144.59 (C-2), 137.94 (C-6a), 138.88 (C-1″), 132.05 (C-2′), 129.42 (C-9), 129.86 (C-3″, C-5″), 128.05 (C-4″), 127.95 (C-2″, C-6″), 126.22 (C-1′), 126.01 (C-7), 125.54 (C-8), 124.72 (C-5a), 119.08 (C-10), 98.76 (C-1), 77.25 (C-3a), 75.84 (C-4), 39.08(C-11b). Anal. calcd. for $C_{22}H_{15}ClO_4$: C 69.75, H 3.99; found: C 69.65, H 3.93. Mass (*m*/*z*): 378 (M^+, 100%).

Compound ***6g*** *(data from a mixture of* ^{1}*H NMR/IR of* ***3g*** *and* ***6g****)*

Yield 25%. IR ν_{max} (cm^{-1}): 1653 (C=O). ^{1}H NMR ($CDCl_3$) δ: 8.32 (1H, t, $J_{2',5'}$ = 1.8 Hz, $J_{2',4'}$ = 1.8 Hz, H-2′), 8.23 (1H, d, J_m = 2.4 Hz, H-5), 7.55 (1H, dd, J_m = 2.4 Hz, J_o = 9.0 Hz, H-7), 7.55 (1H, t, $J_{5',2'}$ = 1.8 Hz, $J_{5',4'}$ = 1.8 Hz, H-5′), 7.44 (1H, d, J_o = 9.0 Hz, H-8), 7.20–7.28 (5H, m, H-2‴-6‴), 7.00 (1H, t, $J_{4',2'}$ = 1.8 Hz, $J_{4',5'}$ = 1.8 Hz, H-4′), 6.65 (1H, d, $J_{3',2'}$ = 11.4 Hz, H-3″), 6.35 (1H, td, $J_{2',3'}$ = 11.4 Hz, $J_{2',1'}$ = 6.6 Hz, H-2″), 4.93 (2H, d, $J_{1',2'}$ = 6.6 Hz, H-1″).

Photolysis of 6-chloro-2-(furan-3-yl)-3-propargyloxy-4H-chromen-4-one (3h)

A methanolic solution of **3h** (0.20 g, 0.66 mmol) on photolysis for 45 min furnished two isomeric products: **4h** and **4h′**. These photoproducts were separated from the starting substrate by column chromatography. They were further separated from each other by preparative TLC.

Compound ***4h***

Yield 21%, white solid; mp 140–145 °C ($CHCl_3$-EtOH). IR ν_{max} (cm^{-1}): 1641.2 (C=O), 2130 (C≡C). ^{1}H NMR ($CDCl_3$): 8.24 (1H, d, J_m = 2.4 Hz, H-7), 7.58 (1H, dd, J_m = 2.4 Hz, J_o = 9.0 Hz, H-9), 7.42 (1H, d, J_o = 9.0 Hz, H-10), 6.51 (1H, dd, $J_{2,11b}$ = 1.5 Hz, $J_{2,1}$ = 2.4 Hz, H-2), 5.31 (1H, t, $J_{1,11b}$ = 2.1 Hz, $J_{1,2}$ = 2.4 Hz, H-1), 5.17 (1H, dd, $J_{3a,4}$ = 2.7 Hz, $J_{3a,11b}$ = 9.9 Hz, H-3a), 5.06 (1H, t, $J_{4,3a}$ = 2.7 Hz, $J_{4,2'}$ = 2.1 Hz, H-4), 4.16 (1H, t, $J_{11b,1}$ = 2.1 Hz, $J_{11b,2}$ = 1.5 Hz, $J_{11b,3a}$ = 9.9 Hz, H-11b), 2.63 (1H, d, $J_{2',4}$ = 2.1 Hz, H-2′). ^{13}C NMR ($CDCl_3$) δ: 172.08 (C-6), 153.06 (C-10a), 151.22 (C-11a), 145.32 (C-2), 136.12 (C-6a), 134.02 (C-9), 130.11 (C-8), 127.24 (C-7), 124.30 (C-5a), 119.00 (C-10), 101.68 (C-1), 77.44 (C-1′), 74.50 (C-3a), 73.78 (C-2′), 68.98 (C-4), 40.45 (C-11b). Anal. calcd. for $C_{16}H_9ClO_4$: C 63.91, H 3.02; found: C 63.83, H 3.06. Mass (*m*/*z*): 300 (M^+, 100%).

Compound ***4h′***

Yield 20%, white solid; mp 121–122 °C ($CHCl_3$-EtOH). IR $\nu_{max.}$ (cm^{-1}): 1645 (C=O), 2128 (C≡C). ^{1}H NMR ($CDCl_3$) δ: 8.21 (1H, d, J_m = 2.4 Hz, H-7), 7.58 (1H, dd, J_m = 2.4 Hz, J_o = 9.0 Hz, H-9), 7.40 (1H, d, J_o = 9.0 Hz, H-10), 6.46 (1H, d, $J_{2,1}$ = 3.0 Hz, H-2), 5.31 (1H, d, $J_{1,2}$ = 3.0 Hz, H-1), 5.09 (1H, d, $J_{3a,11b}$ = 9.9 Hz, $J_{3a,4}$ = 6.9 Hz, H-3a), 4.86 (1H, q, $J_{4,3a}$ = 6.9 Hz, $J_{4,2'}$ = 2.1 Hz, H-4), 4.12 (1H, d, $J_{11b,3a}$ = 9.9 Hz, H-11b), 2.49 (1H, d, $J_{2',4}$ = 1.8 Hz, H-2′). ^{13}C NMR ($CDCl_3$) δ: 171.68 (C-6), 152.56 (C-10a), 152.92 (C-11a), 145.60 (C-2), 135.98 (C-6a), 134.44 (C-9), 130.19 (C-8), 127.22 (C-7), 124.54 (C-5a), 119.23 (C-10), 101.45 (C-1), 77.49 (C-1′), 74.67 (C-3a), 73.88 (C-2′), 68.38 (C-4), 40.15 (C-11b). Anal. calcd. for $C_{16}H_9ClO_4$: C 63.91, H 3.02; found: C 63.80, H 2.99. Mass (*m*/*z*): 300 (M^+, 100%).

Photolysis of 3-benzyloxy-6-chloro-2-(furan-3-yl)-4H-chromen-4-one (3i)

A methanolic solution of **3i** (0.20 g, 0.57 mmol) on photolysis for 45 min furnished **4i**.

Compound ***4i***

Yield 50%, white solid; mp 116–118 °C ($CHCl_3$-EtOH). IR ν_{max} (cm^{-1}): 1647.2 (C=O). ^{1}H NMR ($CDCl_3$) δ: 8.25 (1H, d, J_m = 2.4 Hz, H-7), 7.59 (1H, dd, J_m = 2.4 Hz, J_o = 9.0 Hz, H-9), 7.49–7.36 (6H, m, H-10, 2′, 3′, 4′, 5′, 6′), 6.51 (1H, dd, $J_{2,11b}$ = 1.8 Hz, $J_{2,1}$ = 2.4 Hz, H-2), 5.44 (1H, t, $J_{1,11b}$ = 2.1 Hz, $J_{1,2}$ = 2.4 Hz, H-1), 5.08 (1H, dd, $J_{3a,4}$ = 8.1 Hz, $J_{3a,11b}$ = 9.6 Hz, H-3a), 4.80 (1H, d, $J_{4,3a}$ = 8.1 Hz, H-4), 4.30 (1H, t, $J_{11b,1}$ = 2.1 Hz, $J_{11b,2}$ = 2.4 Hz, $J_{11b,3a}$ = 9.6 Hz, H-11b). ^{13}C NMR ($CDCl_3$) δ: 171.00 (C-6), 153.00 (C-10a), 150.78 (C-11a), 146.96 (C-2), 138.00 (C-6a), 136.42 (C-1′), 133.08 (C-9), 130.31 (C-8), 128.34 (C-4′), 128.20 (C-3′, C-5′), 126.83 (C-2′, C-6′) 125.14 (C-7), 124.00 (C-5a), 119.07 (C-10), 100.45 (C-1), 79.99 (C-4), 76.38 (C-3a), 41.75 (C-11b). Anal. calcd. for $C_{20}H_{13}ClO_4$: C 68.09, H 3.71; found: C 63.15, H 3.66. Mass (*m*/*z*): 352 (M^+, 100%).

Photolysis of 6-chloro-2-(furan-3-yl)-3-(4″-methoxybenzyloxy)-4H-chromen-4-one (3j)

A methanolic solution of **3j** (0.20 g, 0.52 mol) on photolysis for 45 min furnished **4j**.

Compound ***4j***

Yield 37%, white solid; mp 172–174 °C ($CHCl_3$-EtOH). IR ν_{max} (cm^{-1}): 1644.6 (C=O). ^{1}H NMR ($CDCl_3$) δ: 8.17 (1H, d, J_m = 2.4 Hz, H-7), 7.52 (1H, dd, J_m = 2.4 Hz, J_o = 9.0 Hz, H-9), 7.35 (1H, d, J_o = 9.0 Hz, H-10), 7.34 (2H, d, J_o = 8.7 Hz, H-2′, H-6′), 6.86 (2H, d, J_o = 8.7 Hz, H-3′, H-5′), 6.43 (1H, dd, $J_{2,11b}$ = 2.1 Hz, $J_{2,1}$ = 3.6 Hz, H-2), 5.36

(1H, dd, $J_{1,11b}$ = 2.4 Hz, $J_{1,2}$ = 3.6 Hz, H-1), 5.00 (1H, dd, $J_{3a,4}$ = 8.4 Hz, $J_{3a,11b}$ = 9.9 Hz, H-3a), 4.75 (1H, d, $J_{4,3a}$ = 8.4 Hz, H-4), 4.24 (1H, t{d}, $J_{11b,2}$ = 2.1 Hz, $J_{11b,1}$ = 2.4 Hz, $J_{11b,3a}$ = 9.9 Hz, H-11b), 3.74 (3H, s, $C_{4'}$-OCH_3). ^{13}C NMR ($CDCl_3$) δ: 171.00 (C-6), 156.96 (C-4′), 154.00 (C-10a), 151.00 (C-11a), 144.37 (C-2), 138.00 (C-6a), 135.55 (C-1′), 130.47 (C-9), 125.84 (C-8), 125.66 (C-2′, C-6′), 124.00 (C-5a), 122.54 (C-7), 116.49 (C-10), 111.06 (C-3′, C-5′), 97.83 (C-1), 77.29 (C-3a), 74.00 (C-4), 39.25(C-11b), 52.31 ($C_{4'}$-OCH_3). Anal. calcd. for $C_{21}H_{15}ClO_4$: C 65.89, H 3.95; found: C 65.93, H 3.96. Mass (*m*/*z*): 382 (M^+, 100%).

Acknowledgements

We thank the University Grants Commission (UGC) and the Council of Scientific and Industrial Research (CSIR), New Delhi, for generous financial support of this work.

References

(1) (a) Waiss, A. C.; Corse, J. *J. Am. Chem. Soc.* **1965**, *87*, 2068 doi:10.1021/ja01087a051.; (b) Waiss, A. C.; Lundin, R. E.; Lee, A.; Corse, J. *J. Am. Chem. Soc.* **1967**, *89*, 6213 doi:10.1021/ja01000a039.; (c) Matsuura, T.; Matsushima, H. *Tetrahedron* **1968**, *24*, 6615 doi:10.1016/S0040-4020(01)96876-0.; (d) Gupta, S. C.; Mukerjee, S. K. *Indian J. Chem.* **1973**, *11*, 1263.

(2) (a) Gupta, S. C.; Mukerjee, S. K. *Tetrahedron Lett.* **1973**, *14*, 5073 doi:10.1016/S0040-4039(01)87390-1.; (b) Mandal, P.; Nath, A.; Venkateswaran, R. V. *Tetrahedron* **1996**, *52*, 7855. doi:10.1016/0040-4020(96)00356-0.

(3) (a) Gupta, S. C.; Saini, A.; Kumar, D.; Yadav, N. S.; Chand, K.; Mor, S.; Dhawan, S. N. *J. Chem. Soc. Perkin Trans. I* **1995**, 177 doi:10.1039/p19950000177.; (b) Gupta, S. C.; Sharma, S.; Saini, A.; Dhawan, S. N. *J. Chem. Soc. Perkin Trans. I* **1999**, 2391. doi:10.1039/a901090d.

(4) (a) Gupta, S. C.; Yusuf, M.; Sharma, S.; Saini, A.; Arora, S.; Kamboj, R. C. *Tetrahedron* **2004**, *60*, 8445 doi:10.1016/j.tet.2004.07.003.; (b) Berar, S.; Berar, U.; Thakur, M.; Gupta, S. C.; Kamboj, R. C. *J. Indian Chem. Soc.* **2008**, *85*, 1.

(5) (a) Feigenbaum, A.; Fort, Y.; Pete, J. P.; Scholler, D. *J. Org. Chem.* **1986**, *51*, 4424 doi:10.1021/jo00373a015.; (b) Gupta, S. C.; Yadav, N. S.; Dhawan, S. N. *Indian J. Chem., Sect. B* **1991**, *30*, 790.

(6) (a) Gupta, S. C.; Saini, A.; Sharma, S.; Dhawan, S. N.; Kapoor, M. *Tetrahedron Lett.* **1996**, *37*, 8913 doi:10.1016/S0040-4039(96)02046-1.; (b) Gupta, S. C.; Thakur, M.; Berar, S.; Berar, U.; Kamboj, R. C. *Beilstein J. Org. Chem.* **2007**, *3*, 14 doi:10.1186/1860-5397-3-14. PMID:17374172.; (c) Gupta, S. C.; Yusuf, M.; Sharma, S.; Arora, S. *Tetrahedron Lett.* **2002**, *43*, 6875. doi:10.1016/S0040-4039(02)01366-7.

(7) Minimize energy to a minimum RMS gradient of 0.100 by MM2 incorporated in Chem office 8.0 Chem 3D ultra 8.0.

(8) (a) Pachler, K. G. R.; Underwood, W. G. E. *Tetrahedron* **1967**, *23*, 1817 doi:10.1016/S0040-4020(01)82581-3.; (b) Banks, S. W.; Steele, M. J.; Ward, D.; Dewick, P. M. *J. Chem. Soc. Chem. Commun.* **1982**, 156; (c) Chavdarian, C. G.; Seeman, J. I.; Wooten, J. B. *J. Org. Chem.* **1983**, *48*, 492 doi:10.1021/jo00152a016.; (d) Harper, S. H.; Kemp, A. D.; Underwood, W. G. E. *J. Chem. Soc. Chem. Commun.* **1965**, 309; (e) Perrin, D. R.; Bottomley, W. *J. Am. Chem. Soc.* **1962**, *84*, 1919. doi:10.1021/ja00869a030.

(9) (a) Jackman, L. M.; Sternhell, S. *Applications of NMR Spectroscopy in Organic Chemistry,* 2nd ed.; Pergamon Press: NewYork, 1969; p. 281; (b) Haasnoot, C. A. G.; de Leeuw, F. A. A. M.; Altona, C. *Tetrahedron* **1980**, *36*, 2783. doi:10.1016/0040-4020(80)80155-4.

(10) (a) Van Tamelen, E. E.; Whitesides, T. H. *J. Am. Chem. Soc.* **1971**, *93*, 6129 doi:10.1021/ja00752a025.; (b) Van Tamelen, E. E.; Whitesides, T. H. *J. Am. Chem. Soc.* **1968**, *90*, 3894. doi:10.1021/ja01016a071.

A chromatography-free synthesis of (2*S*,12*Z*)-2-acetoxy-12-heptadecene — The major sex pheromone component of the pistachio twig borer moth (*Kermania pistaciella*)

Robert Britton, Grigori Khaskin, and Gerhard Gries

Abstract: Recently, (2*S*,12*Z*)-2-acetoxy-12-heptadecene was identified as the major sex pheromone component of the pistachio twig borer moth, *Kermania pistaciella*, one of the most serious insect pests of pistachio plantations in Iran and Turkey. In field studies, an attract-and-kill formulation containing (2*S*,12*Z*)-2-acetoxy-12-heptadecene demonstrated efficacy in reducing damage caused by *K. pistaciella* and may become a widely-used, earth-friendly tactic for control of this insect in commercial pistachio production. To further develop this technology, a cost-effective, chromatography-free synthesis of (2*S*,12*Z*)-2-acetoxy-12-heptadecene was required and is described in this communication.

Key words: synthesis, pheromone, (2*S*,12*Z*)-2-acetoxy-12-heptadecene, chromatography-free.

Résumé : On a récemment identifié le (2*S*,12*Z*)-2-acétoxy-12-heptadécène comme le composant principal de la phéromone sexuelle de la pyrale du rameau de pistaches, *Kermania pistaciella*, un lépidoptère reconnu comme l'un des insectes les plus nuisibles pour les plantations de pistaches d'Iran et de Turquie. Dans des études sur le terrain, une formulation destinée à attirer et à tuer contenant du (2*S*,12*Z*)-2-acétoxy-12-heptadécène ont démontré son efficacité à réduire les dommages causés par *K. pistaciella*; il pourrait éventuellement être utilisé comme tactique écologiquement correcte et largement utilisée pour contrôler cet insecte dans la production commerciale de la pistache. Afin d'améliorer cette technologie, il était nécessaire de pouvoir accès à une méthode de synthèse du (2*S*,12*Z*)-2-acétoxy-12-heptadécène n'impliquant pas de chromatographie et efficace d'un point de vue coût et c'est ce qui est décrit dans ce travail.

Mots-clés : synthèse, phéromone, (2*S*,12*Z*)-2-acétoxy-12-heptadécène, sans chromatographie.

[Traduit par la Rédaction]

Introduction

The pistachio twig borer moth (*Kermania pistaciella*) is a major insect pest in pistachio plantations in Turkey and Iran.[1] Each year, female *K. pistaciella* lay up to 60 eggs near the shoot tips and fruit clusters on the pistachio tree and the larvae then bore into and feed upon terminal buds, twigs and shoots, resulting in serious economic damage by fruit wilt and twig weakening.[2] Recently, employing gas chromatographic-electroantennographic detection (GC-EAD) and GC-mass spectrometric analyses of extracts from the pheromone gland of female *K. pistaciella*, (2*S*,12*Z*)-2-acetoxy-12-heptadecene (**1**, Fig. 1) was identified as the major sex pheromone component.[2,3] Exploiting its inherent attractive ability, in a 75 ha field test, plots treated with an attract-and-kill[4] formulation containing **1** (approximately 0.6 mg/tree) had significantly fewer larvae-infested fruit branches than insecticide-treated plots or control plots.[2,5] One study[2] also revealed that the attractiveness of **1** was significantly reduced by the presence of the *R*-enantiomer ((–)-**1**) and consequently enantioselective syntheses of **1** were developed that relied on an enzymatic acetylation of (±)-(*Z*)-12-heptadecen-2-ol[2] or a hydrolytic kinetic resolution of (±)-1,2-epoxy-12-heptadecyne[3] to construct the desired antipode. While these processes provide access to (+)-**1** (15%–45% overall yield), necessary chromatography and loss of >50% of the material following enzymatic/kinetic resolution realistically preclude their application to large-scale production. Thus, further development of this attract-and-kill formulation will rely on an economic and scalable synthesis of optically pure **1**. With this in mind, we report a high-yielding, chromatography-free synthesis of **1** designed to support further field-testing, as well as the potential commercialization of this earth-friendly technology.

Fig. 1. (2*S*,12*Z*)-2-Acetoxy-12-heptadecene (**1**), the major sex pheromone component of the pistachio twig borer moth.

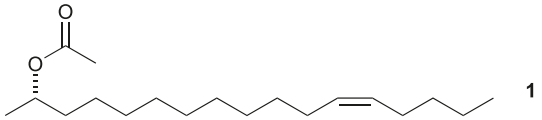

Received 4 September 2008. Accepted 7 October 2008. Published on the NRC Research Press Web site at canjchem.nrc.ca on 13 January 2009.

R. Britton.[1] Department of Chemistry, Simon Fraser University, 8888 University Drive, Burnaby, BC V5A 1S6, Canada.
G. Khaskin and G. Gries. Department of Biological Sciences, Simon Fraser University, 8888 University Drive, Burnaby, BC V5A 1S6, Canada.

[1]Corresponding author (e-mail: rbritton@sfu.ca).

Results and discussions

As detailed in Scheme 1, the synthesis of **1** initiated with the conversion of commercially available (*Z*)-9-tetradecen-1-ol (**2**)[6] into the corresponding alkyl bromide. Thus, treatment of **2** with *p*-TsCl and pyridine in reagent grade DCE provided a crude tosylate (not shown) that was subsequently reacted with LiBr in refluxing acetone to afford (*Z*)-1-bromotetradec-9-ene (**3**). Not surprisingly, the alkyl bromide produced via this route was contaminated with significant amounts of *p*-TsOH and derivatives of this substance. Even following repeated aqueous extractions (neutral, basic, or acidic) we were unable to isolate **3** in >60% purity (as determined by GC analysis). Unfortunately, the presence of these TsCl-derived impurities had a detrimental effect on subsequent Grignard formation from **3** and (or) coupling of the Grignard reagent with (*S*)-propylene oxide. Bearing in mind our ultimate objective, it became essential to develop a non-chromatographic method to remove *p*-TsOH-derived impurities from **3**. As indicated in Scheme 1, a straightforward solution to this problem was eventually discovered that exploits the immiscibility of hexane and MeCN.[7] Thus, extracting a solution of crude **3** in hexane with MeCN effectively removed these impurities and, following concentration of the hexane layer, provided a 14.5:1 mixture of **3** and the corresponding chlorotetradecene **4** with a combined purity of >97%. Formation of the corresponding Grignard reagents from this mixture of alkyl halides proceeded smoothly in refluxing degassed THF.[8] This mixture was subsequently cooled (–30 °C) and treated with a catalytic amount of CuI followed by (*S*)-propylene oxide,[9] while maintaining the reaction temperature between –23 and –15 °C. Following standard workup, the crude product **5**[10,11] was dissolved in pyridine and treated with acetic anhydride and a catalytic amount of DMAP to afford (+)-**1**. Final purification by vacuum distillation provided (2*S*,12*Z*)-2-acetoxy-12-heptadecene (**1**) as a colorless oil (>97% purity, >99% enantiomeric purity).[12]

Scheme 1. Synthesis of the *K. pistaciella* sex pheromone component **1**.

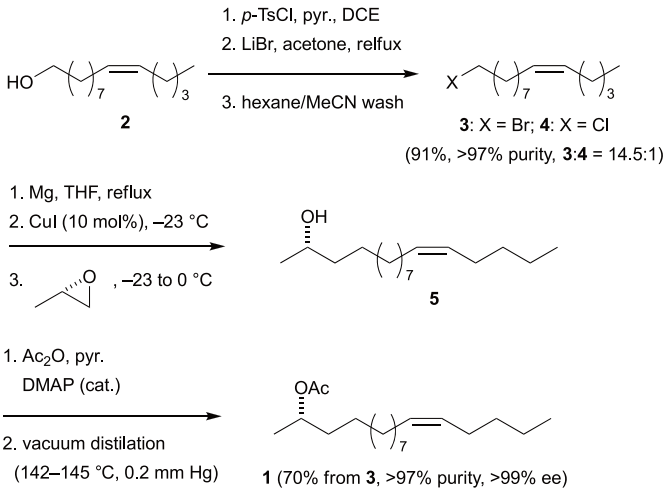

Conclusion

In summary, we have developed a chromatography-free, high yielding (63% overall yield) four-step synthesis of (+)-**1** from readily available chemicals. Of note is the practical method identified to remove organic impurities of divergent polarity on a large scale that exploits the immiscibility of MeCN and hexane, and proved crucial to the success of this process. Based on these efforts, sufficient amounts of **1** have been produced to support further development of earth-friendly pheromone-based tactics to control *K. pistaciella* populations in pistachio plantations in Turkey and Iran.[13]

Experimental

General methods

All reactions were performed in oven-dried glassware. THF was distilled from sodium/benzophenone. Commercial DCE, acetone, and pyridine (reagent grade) were used without further purification. All other reagents were used as supplied. NMR spectra were recorded using deuteriochloroform ($CDCl_3$) as the solvent. Signal positions (δ) are given in parts per million from tetramethylsilane (δ: 0) and were measured relative to the signal of $CDCl_3$ (^{1}H NMR δ: 7.26; ^{13}C NMR δ: 77.0). ^{1}H NMR spectra were recorded on a Varian Inova 500 (500 MHz) and ^{13}C NMR spectra were recorded on a Varian Inova 500 (125 MHz). Optical rotation was measured on a Perkin Elmer Polarimeter 341.

Synthesis of (*Z*)-1-bromotetradec-9-ene (3)

To a stirred solution of (*Z*)-9-tetradecen-1-ol (**2**) (25.0 g, 0.118 mol) in DCE (200 mL) at room temperature (RT) was added *p*-TsCl (29.1 g, 0.153 mol) followed by pyridine (14.3 mL, 0.177 mol), and the reaction mixture was stirred for 20 h. After this time, *p*-TsCl (8.9 g, 0.047 mol) and pyridine (4.7 mL, 0.058 mol) were added, and the reaction was stirred for an additional 20 h. The reaction mixture was filtered through a Büchner funnel to remove the precipitate, and the filtrate was concentrated. The crude residue was dissolved in hexanes (200 mL) and washed successively with 1 N HCl (100 mL), saturated aqueous $NaHCO_3$ (100 mL), and brine (100 mL) and concentrated at RT. The crude concentrate was dissolved in acetone (200 mL), LiBr (30.8 g, 0.354 mol) was added, and the resulting solution was heated at reflux for 3 h. After this time, the reaction mixture was filtered through a Büchner funnel, and the filtrate was concentrated to provide an oily residue that was dissolved in hexane (200 mL), washed with H_2O (100 mL) and MeCN (2 × 100 mL), and concentrated. The combined MeCN washes were extracted with hexane (2 × 50 mL) and these hexane extracts were combined, washed with acetonitrile (2 × 50 mL), and concentrated. Combination of the hexane concentrates afforded a 14.5:1 mixture of **3/4** (28.9 g, 91%) as a colorless oil. The purity of this material was determined to be >97% by GC analysis.[14]

Synthesis of (2*S*,12*Z*)-2-acetoxy-12-heptadecene (1)

A solution of a 14.5:1 mixture of **3/4** (13.7 g, 0.051 mol) in degassed THF (10 mL) was added to a vigorously stirred suspension of magnesium turnings (2.4 g, 0.099 mol, activated with a crystal of iodine) in degassed THF[8] (60 mL), and the resulting mixture was heated at reflux for 2.5 h. After this time, the reaction mixture was cooled to –30 °C, and CuI (93 mg, 4.9 mmol) was added in one portion and

the resulting mixture was warmed to –23 °C. (*S*)-Propylene oxide (4.8 mL, 0.069 mol) was then added dropwise, while maintaining the reaction temperature between –23 °C and –15 °C. After 0.5 h, the black mixture was warmed to 0 °C and treated with saturated aqueous NH_4Cl. After a further 1 h of stirring, the mixture was extracted with Et_2O/pentane (1:1, 60 mL). The organic layer was then washed with H_2O (25 mL) and brine (25 mL), dried ($MgSO_4$), and concentrated to afford 14.1 g of a crude mixture containing (2*S*,12*Z*)-12-heptadecen-2-ol.[10,11] To a solution of this crude mixture in pyridine (6.45 mL) and Ac_2O (6.60 mL) was added a catalytic amount of DMAP (2 mg) and the reaction mixture was stirred for 2 h at RT. After this time, H_2O (50 mL) and Et_2O/pentane (1:1, 60 mL) were added and the organic layer was removed and washed sequentially with 2 N HCl (25 mL), H_2O (25 mL), and saturated aqueous $NaHCO_3$ (25 mL), then dried (Na_2SO_4) and concentrated. Purification of the crude product by vacuum distillation (0.2–0.25 mm Hg) provided a 9.54 g fraction that boiled at 142–145 °C containing (2*S*,12*Z*)-2-acetoxy-12-heptadecene (**1**) (>97% purity, 66.5% yield from bromide).[15] $[\alpha]_D^{20}$ = +0.83° (*c* 4.5; $CHCl_3$). Anal. calcd. for $C_{19}H_{36}O_2$ (%): C 80.24, H 13.47; found: C 79.96, H 13.24.[12]

Acknowledgements

We thank the Natural Sciences and Engineering Research Council of Canada (NSERC) and Scentomos Research and Development Inc. for support. We thank Regine Gries (Simon Fraser University (SFU)) for carrying out chiral GC analysis and Dr. Andrew Lewis (SFU) for assistance with NMR spectroscopy.

References

(1) van Achterberg, C.; Mehrnejad, M. R. *Zool. Med. Leiden* **2002**, *76*, 27.

(2) Gries, R.; Khaskin, G.; Daroogheh, H.; Mart, C.; Karadag, S.; Kubilay Er, M.; Britton, R.; Gries, G. *J. Chem. Ecol.* **2006**, *32*, 2667. doi:10.1007/s10886-006-9190-0. PMID:17123172.

(3) Gries, R.; Khaskin, G.; Daroogheh, H.; Mart, C.; Britton, R.; Gries, G. International Patent WO 2007/079563 A1, July 19, 2007.

(4) Stetter, J.; Lieb, F. *Angew. Chem. Int. Ed.* **2000**, *39*, 1724. doi:10.1002/(SICI)1521-3773(20000515)39:10<1724::AID-ANIE1724>3.0.CO;2-5.

(5) Khaskin, G.; Gries, R.; Rozenberg, E.; Daroogheh, H.; Mircioiu, L.; Gries, G. International Patent Application Number PCT/CA2006/000594, April 13, 2006.

(6) (*Z*)-9-Tetradecen-1-ol is available from Bedoukian Research Inc.

(7) Ahmed, H.; Poole, C. F. *J. Chromatogr. A* **2006**, *1104*, 82. doi:10.1016/j.chroma.2005.11.065. PMID:16337209.

(8) When the THF was not degassed a significant amount (up to 13%) of (*Z*)-9-tetradecen-1-ol (**2**) was isolated from this reaction.

(9) (*S*)-Propylene oxide is commercially available from a number of suppliers or can be readily prepared on a multi-kg scale via Jacobsen hydrolytic kinetic resolution. For preparation see: Tokunaga, M.; Larrow, J. F.; Kakiuchi, F.; Jacobsen, E. N. *Science* **1997**, *277*, 936. doi:10.1126/science.277.5328.936. PMID:9252321.

(10) Analysis of the crude mixture by GC and ^{1}H NMR spectroscopy indicated the presence (and concentration) of the following compounds: (2*S*,12*Z*)-12-heptadecen-2-ol (73%), (*Z*)-9-tetradecen-1-ol (3%), (*Z*)-1,9-tetradecadiene (2%), (*Z*)-1-chloro-9-tetradecene (2%), (5*Z*,23*Z*)-5,23-octacosadiene (10%), (*Z*)-5-tetradecene (10%).

(11) While it proved possible to remove (*Z*)-1-chloro-9-tetradecene and (5*Z*,23*Z*)-5,23-octacosadiene from this mixture by extraction into pentane using a MeCN/CH_3OH/pentane (1:1:1) mixture, the presence of nonvolatiles (e.g., (5*Z*,23*Z*)-5,23-octacosadiene) proved beneficial in the final distillation of **1**.

(12) The enantiomeric purity of **1** was determined by chiral GC analysis following the procedure described in ref. 2.

(13) Following the reaction sequence described in Scheme 1, multi-kg amounts of **1** have been produced to support the commercialization of this technology.

(14) The spectral data derived from **3** were consistent with those reported in Yamagiwa, Y.; Ohashi, K.; Sakamoto, Y.; Hirakawa, S.; Kamikawa, T.; Kubo, I. *Tetrahedron* **1987**, *43*, 3387. doi:10.1016/S0040-4020(01)81629-X.

(15) A further 0.5 g of (2*S*,12*Z*)-2-acetoxy-12-heptadecene could be recovered by flash chromatography from a combination of lower and higher boiling fractions.

^{31}P NMR and ESI-MS studies of metal ion-phosphorus pesticide residue complexes

In Sun Koo, Dildar Ali, Kiyull Yang, Yong Park, Abdelhamid Esbata, Gary W. vanLoon, and Erwin Buncel

Abstract: ^{31}P NMR and ESI-MS structural studies have been carried out for *O*,*O*-dimethylphosphorothioate anion (PA^-) interacting with Ag^+, Hg^{2+}, and Na^+ cations. Evidence is presented for the formation of $PA^-\cdots Ag^+$ and $PA^-\cdots Hg^{2+}$ metal complexes and for ionic PA^-Na^+, with ^{31}P chemical shift values of 43, 40, and 65 ppm, respectively. The ^{31}P chemical shifts for $PA^-\cdots Ag^+$ and $PA^-\cdots Hg^{2+}$ complexes exhibit an initial sharp rise as the $[Ag^+]/[PA]$ and $[Hg^{2+}]/[PA]$ ratio increases from 0 to 1.0 and 0 to 0.5, respectively, and remain almost constant beyond these ratios. These results indicate the formation of 1:1 $PA^-\cdots Ag^+$ and 2:1 $(PA^-)_2\cdots Hg^{2+}$ complexes. Electrospray ionization mass spectroscopy (ESI-MS) revealed peaks corresponding to $[O\text{-}P(=S)(OCH_3)_2 + Ag + H]^+$ and $\{2[O\text{-}P(=S)(OCH_3)_2] + Hg + H\}^+$ for PAH interacting with Ag^+ and Hg^{2+}, supporting the 1:1 $PA^-\cdots Ag^+$ and 2:1 $(PA^-)_2\cdots Hg^{2+}$ stoichiometry. The experimental results support the predominance of species with greater P=O double bond and P–S single bond character, relative to P-O/P=S. Our results on ^{31}P NMR chemical shifts have a bearing on the use of ^{31}P chemical shifts as a tool for organophosphorus pesticide identification.

Key words: ^{31}P NMR, ESI-MS, metal ion-phosphorus pesticide residue complexes, *O*,*O*-dimethylphosphorothioate anion.

Résumé : Faisant appel à la RMN du ^{31}P et à la spectrométrie de masse avec ionisation par électronébulisation (SM-IEN), on a procédé à des études sur de structures de l'anion *O*,*O*-diméthophosphorothionate (PA^-) interagissant avec des cations Ag^+, Hg^{2+} et Na^+. On présente des données relatives à la formation de complexes métalliques $PA^-\cdots Ag^+$ et PA^-Hg^{2+} et du produit ionique PA^-Na^+ pour lesquels les valeurs des déplacements chimiques du ^{31}P sont respectivement de 43, 40 et 65 ppm. Les déplacements chimiques du ^{31}P pour les complexes métalliques $PA^-\cdots Ag^+$ et PA^-Hg^{2+} présentent une augmentation initiale abrupte lorsqu'on augmente les rapports de $[Ag^+]/[PA]$ et $[Hg^{2+}]/(PA)$ respectivement de 0 à 1,0 et de 0 à 0,5 alors que les valeurs deviennent constantes au-delà de ces rapports. Ces résultats indiquent qu'il y a formation de complexes 1:1 $PA^-\cdots Ag^+$ et 2:1 $(PA^-)_2\cdots Hg^{2+}$. Pour le PHA interagissant respectivement avec Ag^+ et Hg^{2+}, la spectrométrie de masse avec ionisation par électronébulisation comporte des pics correspondant aux espèces $[O\text{–}P(=S)(OCH_3)_2\text{+Ag+H}]^+$ et $[2\{O^-P(=S)(OCH_3)_2\}\text{+Hg+H}]$ qui supportent la stoechiométrie 1:1 $PA^-\cdots Ag^+$ et 2:1 $(PA^-)_2\cdots Hg^{2+}$. Les résultats expérimentaux sont en accord avec le fait que, par rapport au rapport P–O/P=S, il existe une prédominance d'espèces avec un caractère de double liaison P=O par rapport aux espèces avec un caractère de simple liaison P–S. Nos résultats sur les déplacements chimiques du ^{31}P en RMN pourraient avoir une incidence pour ceux qui voudraient utiliser les déplacements chimiques du ^{31}P comme outil pour identifier les pesticides du phosphore.

Mots-clés : RMN du ^{31}P, SM-IEN, ion métallique, complexes résiduels de pesticides à base de phosphore, anion *O*,*O*-diméthophosphorothionate.

[Traduit par la Rédaction]

Introduction

Due to their biological and environmental importance, the degradation of organophosphorus (OP) pesticides has been studied extensively over the past several decades.[1] In addition to investigation of the pathways and mechanisms of degradation, metal ion-promoted hydrolysis has also been of interest.[1e,1f] Organophosphorus esters are known to undergo a variety of hydrolysis mechanisms. At the phosphorus centre, three possible mechanisms have been identified: unimolecular nucleophilic substitution, $S_N1(P)$, formation of a pentacoordinate intermediate (addition-elimination), and bimolecular concerted nucleophilic substitution, $S_N2(P)$.[1,2] Equation [1] shows the general reaction for phosphoro-

Received 5 June 2008. Accepted 30 October 2008. Published on the NRC Research Press Web site at canjchem.nrc.ca on 13 January 2009.

I.S. Koo and K. Yang. Department of Chemistry Education and Research Institute of Natural Science, Gyeongsang National University, Gyeongsang, Jinju 660-701, Korea.
D. Ali,[1] Y. Park, A. Esbata,[2] G.W. vanLoon, and E. Buncel.[3] Department of Chemistry, Queen's University, Kingston, ON K7L 3N6, Canada.

[1]Present address: H.E.J. Research Institute of Chemistry, University of Karachi, Pakistan.
[2]Present address: Department of Chemistry, Misurata University, Misurata, Libya.
[3]Corresponding author (e-mail: buncele@chem.queensu.ca).

Table 1. ^{31}P NMR chemical shifts for various types of organophosphorus esters.[6,7,10–12]

OP ester structures	P=O and P=S pesticides (δ, ppm)		Average (δ, ppm)[a]
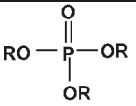	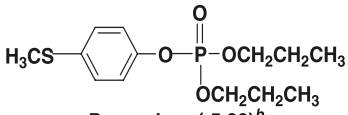 Propaphos (-5.28)[b]	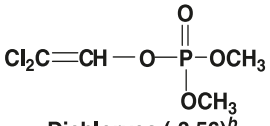 Dichlorvos (-3.56)[b]	-4.35 (±1.00)[c]
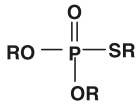	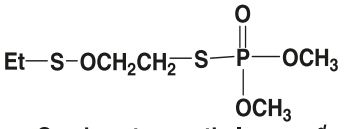 Oxydemeton-methyl (30.14)[d]	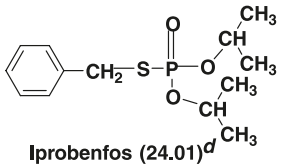 Iprobenfos (24.01)[d]	28.11 (±2.90)[c]
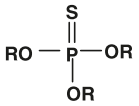	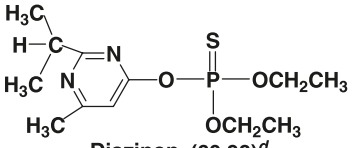 Diazinon (60.98)[d]	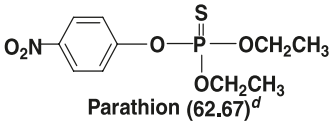 Parathion (62.67)[d]	64.58 (±2.21)[c]
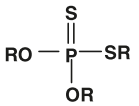	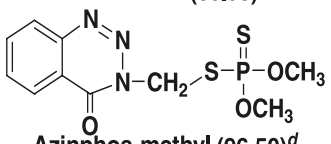 Azinphos-methyl (96.50)[d]	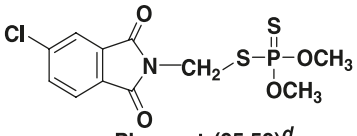 Phosmet (95.59)[d]	94.72 (±2.63)[c]

[a]Average values were taken from refs. 7, 8 and 13–17.
[b]Ref. 13.
[c]Standard deviation.
[d]Ref. 15.

thioate pesticides where L is a leaving group such as para-nitrophenolate, thiolate, etc.

[1] 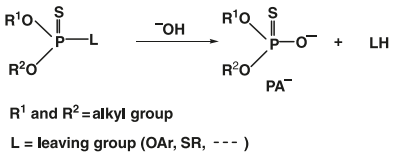

An example is the hydrolytic decomposition of the P=S pesticide, fenitrothion (FN), to give 3-methyl-4-nitrophenol (PNP) and *O*,*O*-dimethylphosphorothioate anion (PA$^-$), eq. [2]. Hydrolysis can readily be followed through UV–vis spectroscopy or ^{31}P NMR, hence the spectroscopic characterization of reactants and products.

[2] 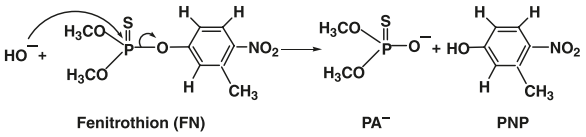

A number of studies of pesticide hydrolysis and alcoholysis have been reported from our laboratory; these have prompted the present ^{31}P NMR study of PA$^-$ and its interaction with metal ions with the view of clarifying some of the factors pertinent to variation of ^{31}P chemical shifts with structural variation among compounds with P=O, P=S, P-O, and P-S moieties.

^{31}P NMR chemical shift values afford insight into factors such as electronegativity (P=O/P-S vs P-O/P=S) and d_π-p_π orbital overlap.[3,4] Interestingly, ^{31}P NMR chemical shifts of

Scheme 1.

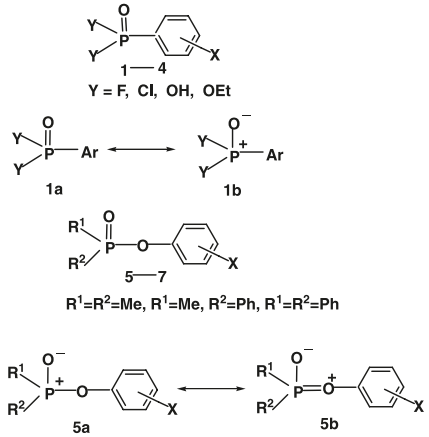

the series of compounds **1**–**4** show *upfield* shifts when electronegative atoms or groups X are attached, pointing to a shielding effect on the phosphorus atom.[3–6] Upfield shifts are also observed when transition metal ions are added.[7,8] However, contrastingly, Hoz et al.[3] found in a study of a series of meta- and para-substituted phenyl diphenylphosphinates (**5**–**7**) that $\delta^{31}P$ values exhibit an *increasing downfield* (i.e., normal) trend as the electron-withdrawing property of the substituent X becomes greater.[3,9–12] Buncel and co-workers[4] observed a good correlation between δ ^{31}P NMR chemical shifts in aryl phosphinates with Hammett substituent constants (σ or σ^0); i.e., electron-withdrawing substituents X act to deplete electron density on the aryl

Table 2. ^{31}P NMR chemical shifts of PA$^-$ (δ, ppm) in the absence and presence of varying Ag$^+$ concentrations in 25% D_2O-75% acetone-d_6.

[Ag$^+$] × 10^2 mol/L	[Ag$^+$]/[PA$^-$][a]	pH[b]	δ	Δδ[c]
0.00	0.00	—	65.94	0.00
0.265	0.25	6.55	57.17	8.77
0.655	0.62	6.33	51.94	14.00
1.05	0.99	6.27	42.96	22.98
1.31	1.24	6.21	43.30	22.68
2.63	2.48	5.95	42.96	22.98
5.25	4.95	5.65	42.54	23.40

[a][PA$^-$] = 1.06 × 10^{-2} mol/L.
[b]Unadjusted experimental pH values.
[c]Δδ = δ (PA$^-$) – δ (PA$^-$···Ag$^+$).

Table 3. ^{31}P NMR chemical shifts of PA$^-$ (δ, ppm) in the absence and presence of varying Hg^{2+} concentrations in 25% D_2O-75% acetone-d_6.

[Hg$^+$] × 10^3 mol/L	[Hg^{2+}]/[PA$^-$][a]	pH[b]	δ	Δδ[c]
0.00	0.00		65.94	0.00
0.655	0.063	6.80	64.04	1.90
1.31	0.12	6.59	56.31	9.63
2.63	0.25	6.34	49.64	16.30
5.25	0.50	6.09	40.54	25.40
10.5	1.00	5.60	39.75	26.19
21.0	2.00	5.38	38.19	27.75

[a][PA$^-$] = 1.05 × 10^{-2} mol/L.
[b]Unadjusted pH values.
[c]Δδ = δ (PA$^-$) – δ (PA$^-$···Hg^{2+}).

oxygen, via resonance structure **5b**, thereby weakening a p_π-d_π bonding interaction between the aryl oxygen and phosphorus (Scheme 1).[4]

Interestingly, a literature survey showed that the ^{31}P NMR chemical shifts of structurally modified OP pesticides, replacing (RO)P=O by (RS)P=O, (RO)P=S and (RS)P=S functionalities, resulted in ^{31}P chemical shift changes by up to 100 ppm (Table 1).[7,8,13–17] This finding emphasizes the need for a systematic investigation of ^{31}P chemical shifts in which experimental results complement theoretical approaches as one changes structure of the OP residues.

In this work, we report the preparation of a model OP compound, PAH, and experimental measurements of ^{31}P NMR chemical shifts of PA$^-$ in the absence and presence of Ag$^+$, Hg^{2+}, and Na$^+$ cations.

ESI-MS studies have also been carried out with the view of obtaining independent evidence on PA-metal ion complexes.

Results and discussion

Metal ion effects on ^{31}P chemical shifts (PA$^-$)

^{31}P chemical shifts, δ and Δδ, for PA$^-$ in the absence and presence of various Ag$^+$, Hg^{2+}, and Na$^+$ concentrations, in 25% D_2O-75% acetone-d_6 at nominal pH values varying between 1 and 10 are given in Tables 2, 3, and 4. In the absence of metal ions, the ^{31}P chemical shift of PA$^-$ occurs at 65.94 ppm. On addition of Ag$^+$, this undergoes an ~23 ppm upfield shift to 42.54 ppm as the [Ag$^+$]/[PA] ratio increases, Table 2. The plots for [Ag$^+$]/[PA] versus Δδ and [Hg^{2+}]/[PA] versus Δδ are shown in Figs. 1 and 2, respectively. As

Table 4. ^{31}P NMR chemical shifts of PA$^-$ (δ, ppm) in the absence and presence of varying Na$^+$ concentrations in 25% D_2O-75% acetone-d_6.

[Na$^+$] × 10^2 mol/L	[Na$^+$]/[PA$^-$][a]	pH[b]	δ	Δδ[c]
0.00	0.00	—	65.94	0.00
1.05	1.00	6.55	65.70	0.24
0.655	2.00	6.33	64.13	1.81
1.31	5.00	6.21	64.70	1.24
2.63	10.0	5.95	64.26	1.68

[a][PA$^-$] = 1.06 × 10^{-2} mol/L.
[b]Experimental unadjusted values.
[c]Δδ = δ (PA$^-$) – δ (PA$^-$···Na$^+$).

Fig. 1. Effect of varying [Ag$^+$]/PA] ratios on ^{31}P chemical shift of PA$^-$ and PA$^-$···Ag$^+$ metal complex.

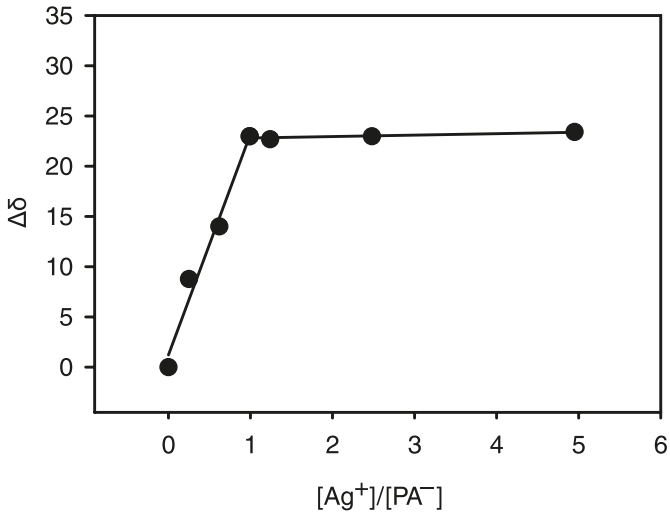

Fig. 2. Effect of varying [Hg^{2+}]/[PA$^-$] ratios on ^{31}P chemical shift of PA$^-$ and PA$^-$···Hg^{2+} metal complex.

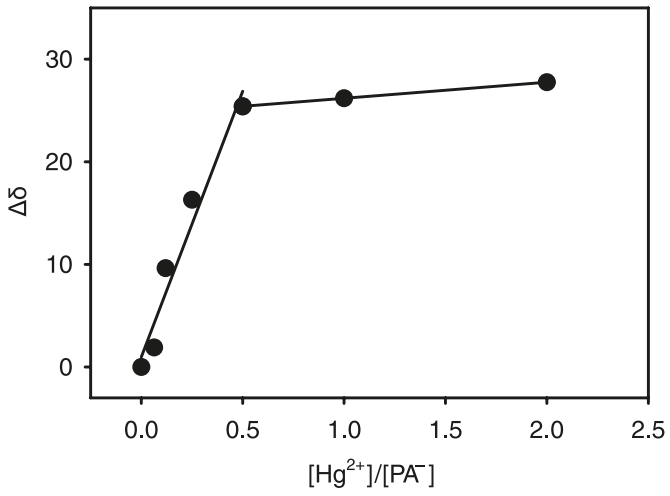

Scheme 2. Complexes of PA^- with Ag^+, Hg^{2+}, and Na^+ and chemical shifts.

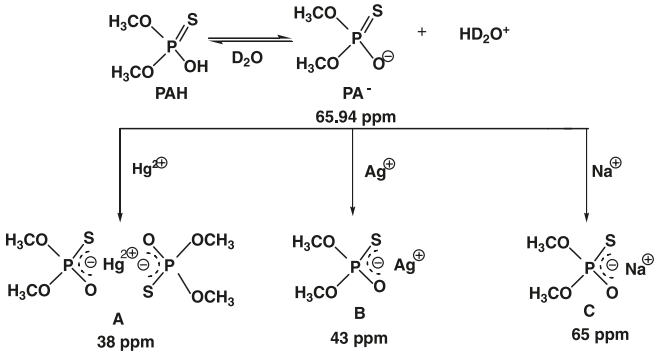

the $[Ag^+]/[PA]$ ratio increases from 0 to 1.0 and beyond, the chemical shift for the $PA^-\cdots Ag^+$ complex exhibits an initial sharp increase and then remains nearly constant (Fig. 1), indicating the formation of a 1:1 $PA^-\cdots Ag^+$ complex.

In the presence of Hg^{2+}, the ^{31}P chemical shift of PA^- undergoes an ~28 ppm upfield shift to 38 ppm as the $[Hg^{2+}]/[PA]$ ratio increases, Table 3. Now, the ^{31}P chemical shift for $PA^-\cdots Hg^{2+}$ complex exhibits an initial sharp increase as the $[Hg^{2+}]/[PA]$ ratio increases from 0 to 0.5 and beyond that remains nearly constant (Fig. 2), which indicates the formation of a 2:1 $(PA^-)_2\cdots Hg^{2+}$ complex.

We have considered the possibility of using the data shown diagrammatically in Figs. 1 and 2 to calculate stability constants. It is helpful in this regard to refer to the treatment by Popov.[18] The salient feature is that in the case of AgPA, virtually complete conversion to the 1:1 complex is seen when the ratio of added AgPA is exactly 1:1, i.e., no excess Ag is required to completely form the complex, indicating that the equilibrium

$$Ag^+ + PA^- = AgPA$$

lies far to the right, i.e., very large formation constant. The same applies to the reaction

$$Hg^{2+} + 2PA^- = \quad HgPA_2$$

For such strong complexes it is difficult to estimate an accurate K_f value. Our attempts at curve fitting yielded values in the order 10^{14}, however values greater than 10^5 must be considered to be highly inaccurate.[18] Thus, the NMR data are better fitted to the shown linear intersecting plots in Figs. 1 and 2 rather than to curved titration type plots.

^{31}P chemical shifts (δ and $\Delta\delta$) for PA^- in the absence and presence of various Na^+ concentrations in 25% D_2O–75% acetone-d_6 are given in Table 4. It is seen that the ^{31}P chemical shifts for PA^- with Na^+ remain almost constant (only ~1.5 ppm upfield shift) as Na^+ is added to PA^-. Thus, the chemical shift of PA^- is affected by Ag^+ and Hg^{2+}, but is unchanged on addition of Na^+. The above relationships of ^{31}P chemical shift changes on addition of metal ions can be represented by Scheme 2.

The observed trends in ^{31}P chemical shifts brought about by metal ions can be explained on the basis of the resonance structures for $PA^-\cdots Hg^{2+}$ (A) and $PA^-\cdots Ag^+$ (B) complexes

Scheme 3. Resonance structures of $PA^-\cdots Ag^+$ and $PA^-\cdots Hg^{2+}$ complexes.

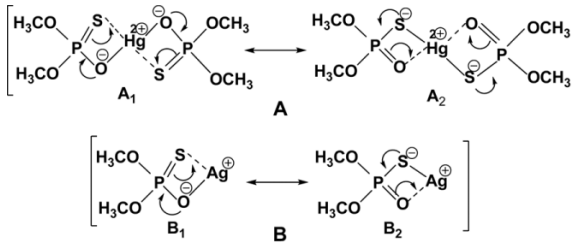

Scheme 4.

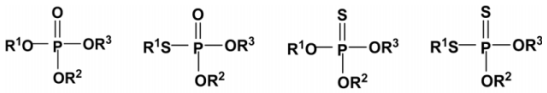

shown in Scheme 3. Complex A has two contributing resonance structures, A1 and A2, and similarly B has two contributing resonance structures, B1 and B2. Now, the contributing resonance structures A2 and B2 have greater P=O double bond character and P–S single bond character relative to PA^-. Concomitantly, the P=S double bond character decreases while the P–S single bond character increases. It follows that the A2 and B2 resonance structures are more dominant than A1 and B1. As shown in Table 1, the ^{31}P NMR chemical shift for RO-P(=S)$(OR)_2$ (64.58 ± 2.21 ppm) is larger than that for RS-P(=O)$(OR)_2$ (28.11 ± 2.90 ppm).[7,8,13–17] Thus, the ^{31}P chemical shift of structures with P–S single bond (and P=O double bond) is more upfield than that of compounds with P=S double bond (and P–O single bond) in similar structures.

Our results on ^{31}P NMR chemical shifts have a bearing on the use of ^{31}P chemical shifts as a tool for organophosphorus pesticide identification. Literature data show a marked variation of ^{31}P chemical shifts depending on structure. It is possible to classify the OP compounds largely on the basis of P=O versus P=S, and P-O versus P—S bonding shown in Scheme 4 as a subset of the phosphate/thiophosphate functionalities in Table 1.

It is also seen in Table 1 that there is much smaller variation of chemical shift as the nature of the substituents, R^1, R^2, R^3, is changed. This finding is in essential agreement with compilations found in texts and reviews.[5,6] Many factors are considered to contribute to these results; for example, nine important factors are cited in the text by Verkade and Quin.[6b] It is also of importance in the present context that metal ions have an influence on ^{31}P chemical shifts, apparently through influencing O=P-S/S=P-O bonding.

ESI-MS studies — PA^- in the presence of Ag^+ and Hg^{2+}

PAH has been chosen to study possible interaction with transition metals, Ag^+ and Hg^{2+}, utilizing the unshared electron pairs on the S atom. Ag^+ and Hg^{2+} ions have strong affinity for S-containing compounds on the basis of Pearson's hard-and-soft acid-base theory.[19]

The ESI-MS spectra for PAH in the absence and presence of Ag^+ and Hg^{2+} in aqueous methanol are shown in Figs. 3 and 4; data are given in Table 5. The protonated molecular ion peak at 143 (m/z) is attributed to $[PAH + H]^+$; silver has

Fig. 3. ESI-MS spectrum of PAH with Ag^+ in 50% aqueous methanol containing [PAH] = 1.0×10^{-5} mol/L and [Ag^+] = 5.0×10^{-4} mol/L.

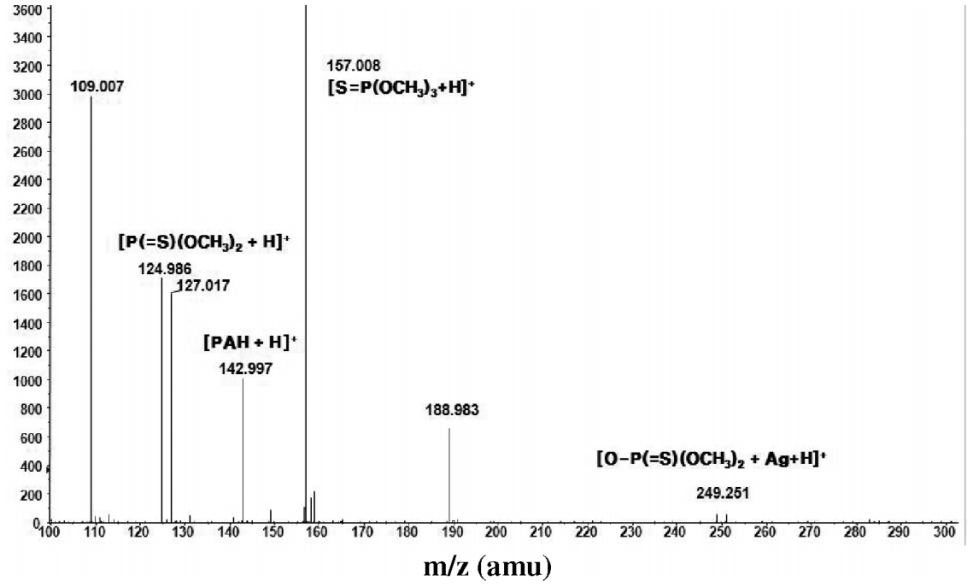

Fig. 4. ESI-MS spectrum of PAH with Hg^{2+} in 50% aqueous methanol containing [PAH] = 1.0×10^{-4} mol/L and [Hg^{2+}] = 5.0×10^{-4} mol/L.

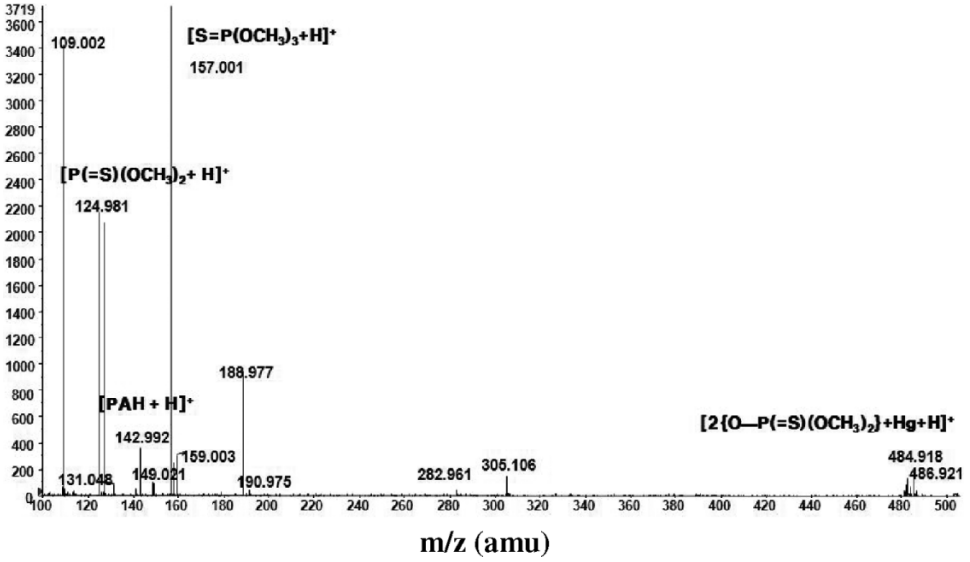

Table 5. ESI-MS data for the PAH in methanol and PAH with Ag^+ and Hg^{2+} in 50% DDW-50% methanol.

Metal salt added	Mode	Ions at *m/z*	Major species
No metal, H^+	MS	143	$[PAH+H]^+$
$AgNO_3$	MS	249, 251	$[O\text{-}P(=S)(OCH_3)_2 + Ag + H]^+$
		157	$[S=P(OCH_3)_3 + H]^+$
		143	$[PAH + H]^+$
		125	$[P(=S)(OCH_3)_2 + H]^+$
$Hg(NO_3)_2$	MS	481, 482, 483, 484, 485, 487	$\{2[S\text{-}P(=O)(OCH_3)_2] + Hg + H\}^+$
		157	$[S=P(OCH_3)_3 + H]^+$
		143	$[PAH + H]^+$
		125	$[P(=S)(OCH_3)_2 + H]^+$

two isotopes (^{107}Ag and ^{109}Ag) with a natural abundance ratio of 52:48.[20a] The major peaks in the PAH/Ag^+ spectrum correspond to $[O\text{-}P(=S)(OCH_3)_2 + Ag + H]^+$: *m/z* = 249, 251; $[S=P(OCH_3)_3 + H]^+$: *m/z* = 157, 143; $[PAH + H]^+$: *m/z* = 143; and $[P(=S)(OCH_3)_2 + H]^+$: *m/z* = 125. Thus, the peaks in the ESI-MS spectrum for $[O\text{-}P(=S)(OCH_3)_2 + Ag + H]^+$ are supportive of a 1:1 $PA^{-}\cdots Ag^+$ complex (discussed under NMR studies).

Peaks containing mercury ion can be recognized readily by the isotopic pattern of Hg: ^{196}Hg, ^{198}Hg,^{199}Hg, ^{200}Hg, ^{201}Hg, ^{202}Hg, and ^{204}Hg, with a natural abundance of 0.14, 10.02, 16.84, 23.13, 13.22, 29.80, and 6.85, respectively[20b]; all other isotopes would be detectable except ^{196}Hg. The major peaks in the PAH/Hg^{2+} spectrum are those of {2[S-P(=S)$(OCH_3)_2$] + Hg + H}$^+$: m/z = 481, 482, 483, 484, 485, 487, [S=P$(OCH_3)_3$ + H]$^+$: m/z = 157, [PAH + H]$^+$: m/z = 143, and [P(=S)$(OCH_3)_2$ + H]$^+$: m/z = 125. The peak in the spectrum for {2[O-P(=S)$(OCH_3)_2$] + Hg + H}$^+$ is supportive of a 2:1 $PA^-\cdots Hg^{2+}$ complex as discussed under NMR studies.

Experimental section

Materials

Methanol was procured from Sigma-Aldrich (HPLC grade) and D_2O, acetone-d_6, and dimethyl chlorothiophosphate from Sigma-Aldrich (GR grade). Fenitrothion was a gift from Sumitomo Chemicals (Japan) and was purified by column chromatography as previously described.[1b]

Preparation of *O*,*O*-dimethylphosphorothioic acid (PAH)

A mixture of 2 mL dimethyl chlorothiophosphate (2.64 g, 16.5 mmol) in 8 mL acetonitrile (MeCN) and 30 mL sodium hydroxide (NaOH, 1.60 g, 42.0 mmol) in 40% MeCN-60% water, was stirred magnetically overnight at 30 °C. After 12 h, the reaction mixture was acidified with HCl (6 mol/L). After thrice extraction with 30 mL CH_2Cl_2, the organic layer was collected and evaporated on rotary evaporator. The residue was dried under vacuum to a pale yellow oil (0.47g, 20%). The product was identified using ^{1}H, ^{13}C, and ^{31}P NMR spectroscopy (400 MHz Bruker). ^{1}H NMR (400 MHz, $CDCl_3$, ppm) δ: 3.80 (d, CH_3O, $^3J_{P\text{-}H}$ = 9.0 Hz, 6H), 6.8 (s, OH). ^{13}C NMR (400 MHz, $CDCl_3$, ppm) δ: 55.63. ^{31}P NMR (400 MHz, $CDCl_3$, relative to external 85% H_3PO_4, ppm) δ: 65.19. Aqueous solution of PAH generated the PA^- product.

[3] 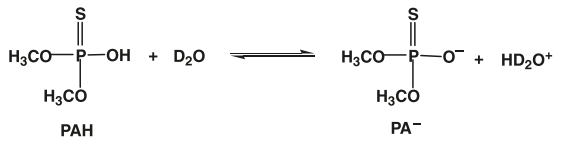

^{31}P NMR study

A PAH stock solution, 1.41×10^{-2} mol/L, was prepared by dissolving 0.01 g PAH in 5 mL acetone-d_6. Various concentrations of Ag^+, Hg^{2+}, and Na^+ stock solutions (Tables 2, 3, and 4) were prepared by dissolving $AgNO_3$, $HgCl_2$, and $NaNO_3$ in D_2O. For NMR analysis, 0.15 mL of metal ion (Ag^+, Hg^{2+}, and Na^+) 1.41×10^{-2} mol/L stock solution was added to 0.45 mL PAH stock solution in an NMR tube. The ^{31}P NMR experiments were carried out with PA^- in the absence and presence of metal ions. Changes in chemical shifts (Δδ) were calculated by subtracting the ^{31}P chemical shift values in the presence of each metal ion from those of metal free solutions. ^{31}P NMR experiments were carried out with PA^- in the absence and presence of metal ions, Ag^+, Hg^{2+}, and Na^+ using Bruker 400.302 MHz NMR spectrometer. ^{31}P NMR chemical shifts (δ) are reported in parts per million (ppm) with respect to 85% H_3PO_4 external reference. The spectra were acquired using 90° pulses with $1000 \approx 1500$ scans for ^{31}P nucleus.

Electrospray ionization mass spectrometry (ESI-MS)

A 1.0×10^{-4} mol/L PAH stock solution was prepared in HPLC grade methanol. $AgNO_3$ and $HgCl_2$ were dissolved in DDW for preparation of 5.0×10^{-4} mol/L Ag^+ and Hg^{2+} stock solutions. Low micromolar FN solution in methanol and aqueous Ag^+ and Hg^{2+} solutions were acidified to pH 4 using 0.01 mol/L nitric acid. Low micromolar FN solution in methanol (pH 4.0) was added with varying concentrations of aqueous Ag^+ and Hg^{2+} solutions (pH 4.0) and sprayed with a flow rate of 6.0 μL/min into a QSTAR XL QqTOF mass spectrometer (Applied Biosytems/MDS Sciex) employing a regular ESI source setup. Fragmentation of the transition metal-pesticide complex was achieved by two methods: first, in-source fragmentation by elevating the cone voltage, and second, low energy CID in the Q2 collision cell using nitrogen as collision gas. Combination of both methods allowed for pseudo-MS^3 analysis of the complexes. Accurate mass measurements enabled the correct assignment of molecular formulae for fragments in case of isobaric overlap of possible fragmentation products.

Acknowledgements

This work was supported by the Korea Research Foundation Grant (KRF-2006–013-C00119) and Gyeongsang National University (ISK) and the Natural Sciences and Engineering Research Council of Canada (EB).

References

(1) (a) Balakrishnan, V. K.; Han, X.; vanLoon, G. W.; Dust, J. M.; Toullec, J.; Buncel, E. *Langmuir* **2004**, *20*, 6586 doi:10.1021/la049572d. PMID:15274559.; (b) Balakrishnan, V. K.; Dust, J. M.; vanLoon, G. W.; Buncel, E. *Can. J. Chem.* **2001**, *79*, 157 doi:10.1139/cjc-79-2-157.; (c) Eneji, I. S.; Buncel, E.; vanLoon, G. W. J. *Agric. Food Chem.* **2002**, *50*, 5634 doi:10.1021/jf0203747.; (d) Balakrishnan, V. K.; Buncel, E.; vanLoon, G. W. *Environ. Sci. Technol.* **2005**, *39*, 5824 doi:10.1021/es050234o. PMID:16124321.; (e) Dunn, E. J.; Moir, R. Y.; Buncel, E.; Purdon, J. G.; Bannard, R. A. B. *Can. J. Chem.* **1990**, *68*, 1837 doi:10.1139/v90-286.; (f) Esbata, A. A. Ph.D. thesis, Queen's University, Department of Chemistry, Kingston, ON. 2005.

(2) Haake, P.; Ossip, P. S. J. *Am. Chem. Soc.* **1971**, *93*, 6924. doi:10.1021/ja00754a039.

(3) Hoz, S.; Dunn, E. J.; Buncel, E.; Bannard, R. A. B.; Purdon, J. G. *Phosphorus Sulfur* Silicon Relat. Elem. **1985**, *24*, 321. doi:10.1080/03086648508074244.

(4) Dunn, E. J.; Purdon, J. G.; Bannard, R. A. B.; Albright, K.; Buncel, E. *Can. J. Chem.* **1988**, *66*, 3137–3142. doi:10.1139/v88-484.

(5) Lechter, J. H.; Van Wazer, J. R. *Top. Phosphorus Chem.* **1967**, *5*, 75.

(6) (a) *Phosphorus-31 NMR;* Gorenstein, D. G. Ed.; Academic Press: New York, 1984; Chapter1;(b) *Phosphorus-31 NMR spectroscopy in stereochemical analysis;* Verkade, J. G.; Quin, L. D; VCH Publishers: New York, 1987.

(7) Kireev, A. F.; Rybal'chenko, I. V.; Khamidi, B. A.; Kholstov, V. I. J. *Anal. Chem.* **2001**, *56*, 421. doi:10.1023/A:1016666717557.

(8) Pehkonen, S. O.; Judeh, Z. M. A. *Environ. Sci. Technol.* **2005**, *39*, 2586. doi:10.1021/es0486869. PMID:15884353.
(9) Mitsch, C. C.; Freedman, L. D.; Morland, C. G. J. *Magnes. Res.* **1970**, *3*, 446.
(10) Szafraniec, L. L. *Org. Magn. Reson.* **1974**, *6*, 565. doi:10.1002/mrc.1270061102.
(11) Grabiak, R. C.; Miles, J. A.; Schwenger, G. M. *Phosphorus Sulfur* Silicon Relat. Elem. **1980**, *9*, 197. doi:10.1080/03086648008078240.
(12) Allen, D. W.; Hutley, B. G.; Mellor, M. T. J. J. *Chem. Soc. Perkin* Trans. 2 **1977**, 789. doi:10.1039/p29770000789.
(13) Mortimer, R. D.; Dawson, B. A. J. *Agric. Food Chem.* **1991**, *39*, 911. doi:10.1021/jf00005a022.
(14) Mahajna, M.; Quistad, G. B.; Casida, J. E. *Chem. Res. Toxicol.* **1996**, *9*, 1202. doi:10.1021/tx9600715. PMID:8902277.
(15) Miyata, Y.; Ando, H. *Jpn. J. Toxicol. Environ. Health* **1994**, *40*, 49.
(16) Greenhalgh, R.; Blackwell, B. A.; Preston, C. M.; Murray, W. J. J. *Agric. Food Chem.* **1983**, *31*, 710. doi:10.1021/jf00118a008.
(17) Kirk, K.; Kuchel, P. W. *Biochemistry* **1988**, *27*, 8803. doi:10.1021/bi00424a017. PMID:3242610.
(18) Popov, A. I. Equilibria Studies in Solutions. In *Modern NMR Techniques and Their Applications in Chemistry;* Popov, A. I.; Hallenga, K. Marcel Dekker, Inc.: New York, 1991; Chapter 8, Figure 8, p 509.
(19) (a) Pearson, R. G. J. *Am. Chem. Soc.* **1963**, *85*, 3533 doi:10.1021/ja00905a001.; (b) Pearson, R. G. *Science* **1966**, *151*, 172. doi:10.1126/science.151.3707.172. PMID:17746330.
(20) (a) Zeinali, M.; Torrents, A. *Environ. Sci. Technol.* **1988**, *32*, 2238; (b) Weast, R. C. *Handbook of Chemistry and Physics,* 50th ed. The Chemical Rubber Co: Cleveland, OH, 1969.

Synthesis of arylbromides from arenes and *N*-bromosuccinimide (NBS) in acetonitrile — A convenient method for aromatic bromination

Eli Zysman-Colman, Karla Arias, and Jay S. Siegel

Abstract: Regioselective and chemoselective electrophilic bromination of a wide series of activated arenes using *N*-bromosuccinimide (NBS) in acetonitrile occurs readily. Environmentally friendly conditions, large substrate scope, and ease of synthesis enhance the utility of this method over other electrophilic bromination conditions.

Key words: arylbromides, electrophilic aromatic bromination, *N*-bromosuccinimide.

Résumé : La bromation électrophile chimiosélective et régiosélective d'une grande variétés d'arènes activés, à l'aide de *N*-bromo-succinimide dans l'acétonitrile, se fait facilement. Des conditions expérimentales environnementalement correctes, un large éventail de substrats et la facilité de la synthèse augmentent l'utilité de cette méthode par comparaison avec celles nécessaires pour d'autres bromations électrophiles.

Mots-clés : bromures d'arènes, bromation aromatique, *N*-bromo-succinimide.

[Traduit par la Rédaction]

Introduction

Bromoarenes are important intermediates for synthesis, specifically as useful substrates in metal-mediated aryl-coupling chemistry.[1–3] Since the late 1950s,[4] there has been considerable interest in *N*-bromosuccinimide (NBS) as an electrophilic aromatic brominating reagent. A major advantage in the use of inexpensive NBS is that the succinimide byproduct can be easily recovered and rebrominated.[5] A number of NBS-based aromatic bromination methods have been reported, each with their own scope and conditions (e.g., NBS/Brønsted acids,[6] NBS/Brønsted bases,[7] NBS plus alkyl amines,[8] NBS in chlorinated solvents,[9] NBS in CS_2,[10] hexanes,[11] THF,[12] DMF,[13,14] propylene carbonate,[4] and MeOH,[15] NBS supported on silica gel,[16,17] NBS with Amberlyst® 15,[18] and NBS in ionic liquids[19]). Aromatic heterocycles can also be brominated by NBS in polar solvents.[20] Carreño and co-workers' reports using NBS in acetonitrile (ACN), for the efficient bromination of methoxy-substituted arenes[21] and naphthalenes,[22] drew our attention. Herein we document the substrate scope, regio-,[10] and chemo-selectivity of this relatively safe and user-friendly bromination procedure.

Received 24 July 2008. Accepted 21 October 2008. Published on the NRC Research Press Web site at canjchem.nrc.ca on 19 January 2009.

E. Zysman-Colman,[1] K. Arias, and J.S. Siegel.[2] Organisch-chemisches Institut, Universität Zürich, Winterthurerstrasse 190, Zurich 8057, Switzerland.

[1]Present address: Département de Chimie, Université de Sherbrooke, 2500 Boul. Université, D1-2133, Sherbrooke, QC, Canada, J1K 2R1.
[2]Corresponding author (e-mail: jss@oci.uzh.ch).

Results and discussion

Bromination of arenes with 1 equiv. of NBS in ACN at 0 °C proceeded readily over a wide range of substrates (Table 1) and was found to be highly para-selective with respect to the most activating substituent; in instances where the para position is blocked, bromination occurred ortho to the most activating group.[23]

Work-ups were trivial, frequently requiring only a water quench to dissolve the succinimide and an extraction using hexanes.[24] Some products even precipitated once water was added and thus were easily filtered off (Table 1, entries 27–28).

The chemoselectivity was also excellent, monobromination occurring at a faster rate than dibromination, even for electron-rich anisidines (Table 1, entries 18–20); additionally, no benzylic bromination was detected. In the vast majority of cases, yields of monobrominated products were excellent, without the use of any additive. In particular, NBS monobromination was possible with phenols (Table 1, entries 10–14)[25] as well as unalkylated anilines (Table 1, entries 16–20). Bromination of arenes bearing deactivating groups occurred in the presence of a strong activating group (Table 1, entries 5, 12, 17); however, bromination of the weakly activated alkyl arenes, toluene (Table 1, entry 21) or *t*-butylbenzene, was not possible even at reflux.

Polyalkylbenzenes spanned the gamut of affinities toward bromination. Ortho- and *p*-xylene (Table 1, entries 23–24) proved to be poor substrates and the conversion to the corresponding monobrominated product was diminutive even using excess NBS and with longer reaction times. Efficient bromination of *m*-xylene (Table 1, entry 22) was possible; however, a reaction time of five days was required to obtain complete conversion. Isomers of trimethylbenzene provide some insight to the reactivity issue. Whereas mesitylene (Table 1, entry 25) readily monobrominates with quantita-

Table 1. Scope of substrates for the bromination of arenes.

Entry	Educt	Product	Yield[a]	GC	Ortho	Para	Di
1		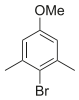	99	99	1	99	0
2		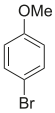	97	100	0	100	0
3		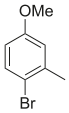	97	100	0	99	1
4	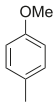	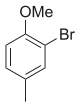	63	91	100	–	–
5		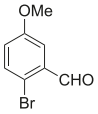	81	98	0	99	0
6		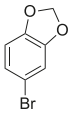	94	99	0	100	0
7	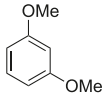	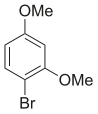	99	100	0	100	0
8	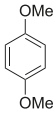	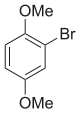	96	96	96	–	4
9[b]		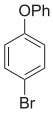	–	91	0	93	7
10		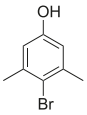	96	100	5	95	0
11		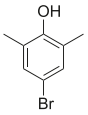	91	100	0	99	0
12	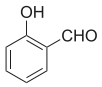	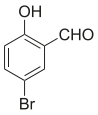	18	67	3	25	72
13	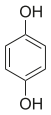	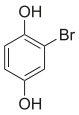	43	97	97	0	3
14		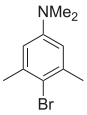	95	100	0	99	1
15		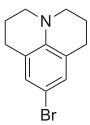	92	100	0	100	0

Table 1 (*concluded*).

Entry	Educt	Product	Yield[a]	GC	Ortho	Para	Di
16		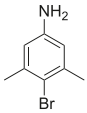	94	98	2	96	2
17		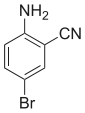	97	100	0	100	0
18	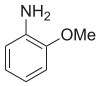	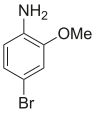	71	62	16	68	16
19	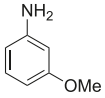	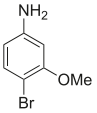	47	92	0	86	14
20	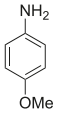	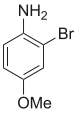	20	100	69	0	31
21		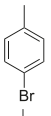	0	–	–	–	–
22[c]		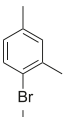	98	100	0	85	0
23		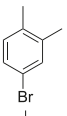	–	<3	–	–	–
24	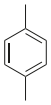	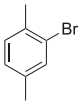	–	<3	–	–	–
25		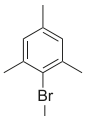	93	100	0	100	0
26		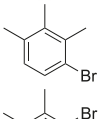	43	67	0	100	0
27	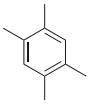	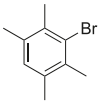	92	97	98	0	2
28		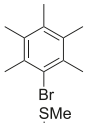	94	100	0	100	0
29[b,d]		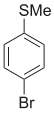	–	99	3	74	0

Note: Conditions: 5 mmol NBS in 5 mL dry ACN was added to 5 mmol substrate in 5 mL dry ACN at 0 °C. Solution stirred for 18 h (0 °C – RT). The products were characterized by ^{1}H NMR, ^{13}C NMR, Mp, and MS and quantified by GC. Brominations were repeated at least once per substrate and isolated yields and GC conversions were reproducible.

[a]Isolated yields (GC conversion).

[b]Product not isolated.

[c]Reaction stirred for five days.

[d]Side product: PhSSPh (see text).

Fig. 1. NBS bromination of (*a*) 0.41 mol/L 3,5-dimethylanisole in ACN and (*b*) 0.36 mol/L mesitylene in ACN. The progress of each of the reactions was monitored by GC-MS with *t*-butylbenzene as an internal standard.

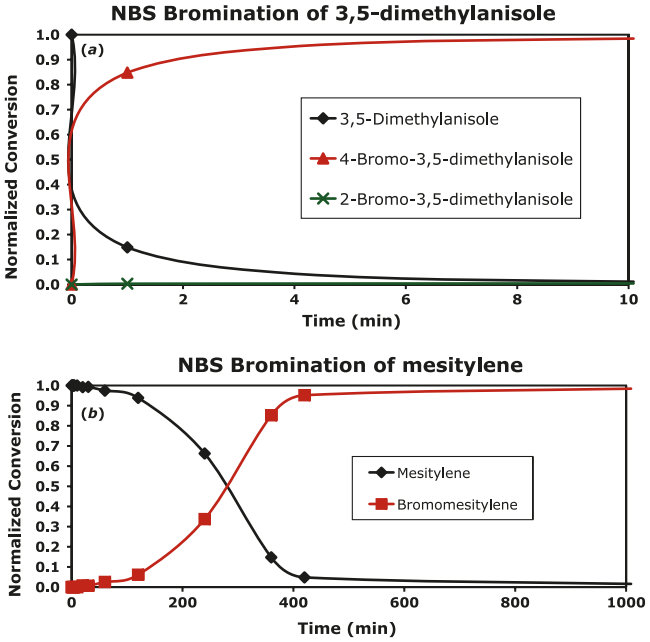

tive conversion, monobromination of 1,2,3-trimethylbenzene (Table 1, entry 26) proceeded much less readily, affording only one regioisomeric product in moderate yield.

Effective bromination by this method appears to require site activation equivalent to at least two (better three) *o*,*p* alkyl groups. Treating this as a linear free energy issue, one sees that phenols and anilines activate roughly equivalent to three methyl groups. After monobromination, the remaining possible sites of bromination are deactivated by being meta to bromine, thus favoring monobromination.

Though our standard protocol reflects a reaction time of 18 h, bromination can actually occur within minutes. For instance, the bromination of 3,5-dimethylanisole (Table 1, entry 1) proceeds smoothly, the reaction attaining completion in 20 min (Fig. 1*a*), as monitored by GC-MS. The bromination of isosteric mesitylene (Fig. 1*b*) is much slower, taking hours to go to completion. The rate of bromination is much faster than that observed in DMF (24 h) for similar substrates.[13]

Reactions are also easily amenable to scale-up; monobromination of 3,5-dimethylanisole, for instance, has been accomplished at a 200 g scale with no loss in yield or purity.

The bromination of thioanisole (Table 1, entry 29) did not proceed cleanly, with the observed formation of ca. 20% diphenyl disulfide as a byproduct, as observed by GC-MS and ^{1}H NMR and compared to an authentic sample. The oxidation of thiols with electrophilic bromine sources such as NBS is not unprecedented[17,25]; however, to our knowledge, the tandem demethylation–oxidation of thioanisoles to form disulfides is not known but can be rationalized (Scheme 1).

Bromination of deactivated aromatics such as halobenzenes and haloaldehydes did not occur under our conditions; bromination of 2-hydroxy-4-methylbenzoic acid also did not

Scheme 1. Formation of diphenyl disulfide.

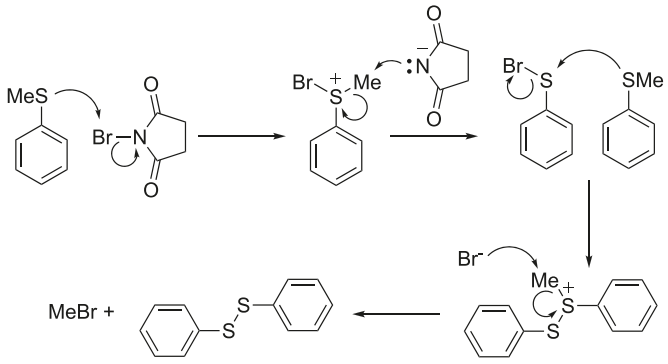

proceed, perhaps because of the sparing solubility of the substrate in ACN.

Recently, Chhattise et al.[26] reported the photochemically induced aromatic bromination of phenols using NBS in acetonitrile. In that report, alkyl species were avoided due to free radical bromination at the benzyllic positions (Table 2, entry 8 of their paper refers to the benyllic bromination of toluene). We find that light is not needed for the aromatic bromination and therefore our method is amenable to xylene and mesitylene bromination, whereas that of Chhatise et al.[26] is not. Indeed, even cresol derivatives, which undergo bromination rapidly and cleanly under our conditions, brominate less cleanly under their conditions, likely because of complications from light-induced free radical side reactions.

We have demonstrated the useful potential of NBS bromination of activated arenes in ACN. The advantages of our current procedure are simple work-ups, mild reaction conditions tolerant of diverse functionality, and high regio- and chemoselectivity, the products of which could usually be isolated by simple filtration or solvent extraction.

Experimental

All experiments were carried out under nitrogen in reagent grade acetonitrile. Commercial chemicals were used as supplied. Column chromatography was performed using silica gel (Merck 60 0.040–0.063 mm). Analytical thin layer chromatography (TLC) was performed with Mecherey-Nagel SIL N-H/UV$_{254}$ plates with aluminum backings. Compounds were visualized under UV light. GC-MS samples were run through a Zebron Zb5 column. ^{1}H and ^{13}C NMR spectra were recorded on a Brucker Avance (300 MHz) and a Brucker ARX 300 (75 MHz) spectrometer, respectively, with the solvent peak as an internal standard. The following abbreviations have been used for multipilicity assignments: "s" for singlet, "d" for doublet, "t" for triplet, "m" for multiplet, and "br" for broad.

The following is a sample procedure for the bromination of arenes using NBS in ACN.

Bromomanisole

To a 0 °C solution of 3,5-dimethylanisole (685 mg, 5 mmol, 1 equiv.) in 5 mL ACN was added a solution of NBS (890 mg, 5 mmol, 1 equiv.) in 5 mL ACN via addition funnel. The solution was allowed to come to room temperature (RT) and stirred for an additional period, typically between 0.1 and 20 h, depending on the activity of the ring (cf. Fig. 1). The reac-

tion was quenched with H_2O, hexanes were added, and the layers separated. The aqueous phase was extracted with 3 × hexanes. The organic phase was dried over $MgSO_4$, filtered under reduced pressure, and the organic phase concentrated under reduced pressure then under vacuum. A clear liquid (1.09 g) was obtained. Yield: 99%. GC conversion: 100%. ^{1}H NMR (300 MHz, $CDCl_3$) δ: 6.63 (s, 2H), 3.74 (s, 3H), 2.37 (s, 6H). ^{13}C NMR (75 MHz, $CDCl_3$) δ: 158.0, 139.0, 118.1, 113.7, 55.2, 23.9. GC-MS (6.56) $[M]^+$: 213.8. Anal. calcd. for $C_9H_{11}BrO$: C 50.26, H 5.15; found: C 50.37, H 4.95. This procedure could be scaled up to 100 g of 3,5-dimethylanisole with no measurable loss in yield or purity. ^{1}H NMR spectrum is in agreement with that previously reported.[27,28]

2-Bromo-5-methoxybenzaldehyde

White solid. Yield: 81%, mp 76–79 °C (lit.[29] mp 78–80 °C). GC conversion: 98%. ^{1}H NMR (300 MHz, $CDCl_3$) δ: 10.31 (s, 1H), 7.51 (d, J = 8.7 Hz, 1H), 7.40 (d, J = 3.3 Hz, 1H), 7.02 (dd, J = 3.0, 9.0 Hz, 1H), 3.82 (s, 3H). ^{13}C NMR (75 MHz, $CDCl_3$) δ: 191.7, 159.3, 134.5, 134.0, 123.1, 117.9, 112.7, 55.7. GC-MS (6.87) $[M]^+$: 216.0. Anal. calcd. for $C_8H_9BrO_3$: C 44.68, H 3.28; found: C 44.85, H 3.51. ^{1}H NMR and ^{13}C NMR spectra are in agreement with those previously reported.[29]

4-Bromo-3,5-dimethylaniline

White solid. The product was purified via flash chromatography (20% EtOAc/hexanes on silica, R_f: 0.15). Yield: 94%, mp 73–75 °C (lit.[29] mp 75–76 °C). GC conversion: 98% with 2% dibrominated side product. ^{1}H NMR (300 MHz, $CDCl_3$) δ: 6.39 (s, 2H), 3.55 (s, 2H), 2.30 (s, 6H). ^{13}C NMR (75 MHz, $CDCl_3$) δ: 144.9, 138.7, 115.8, 115.0, 23.7. GC-MS (7.40) $[M]^+$: 198.8. Anal. Calcd. for $C_8H_{10}BrN$: C 48.02, H 5.04, N 7.00; found: C 48.38, H 5.10, N 7.01. ^{1}H NMR spectrum is in agreement with that previously reported.[30]

1-Bromo-2,3,4,5,6-pentamethylbenzene

White solid. R_f: 0.43 (hexanes on silica). Yield: 94%, mp 160–161 °C (lit.[31,32] mp 159–161 °C; lit.[33] mp 163.5–164.5 °C). GC conversion: 100%. ^{1}H NMR (300 MHz, $CDCl_3$) δ: 2.43 (s, 6H), 2.25 (s, 6H), 2.12 (s, 3H). ^{13}C NMR (75 MHz, $CDCl_3$) δ: 133.8, 133.3, 126.7, 21.4, 17.7, 16.8. GC-MS (8.27) $[M]^+$: 225.9. Anal. calcd. for $C_{11}H_{15}Br$: C 58.17, H, 6.66; found: C 58.06, H 6.20.

2-Amino-5-bromobenzonitrile

White solid. R_f: 0.06 (20% EtOAc/hexanes on silica). Yield: 97%, mp 97–99 °C (lit.[34] mp 98 °C). GC conversion: 100%. ^{1}H NMR (300 MHz, $CDCl_3$) δ: 7.46 (dd, J = 2.1, 13.0 Hz, 1H), 7.37 (dd, J = 2.4, 9.0 Hz, 1H), 6.61 (d, J = 13.0 Hz, 1H), 4.43 (s, 2H). ^{13}C NMR (75 MHz, $CDCl_3$) δ: 148.6, 136.9, 134.0, 116.7, 116.2, 108.6, 97.5. GC-MS (7.78) $[M]^+$: 196.0. ^{1}H NMR spectrum is in agreement with that previously reported.[34]

Bromodurene

White solid. The product was purified via flash chromatography (hexanes on silica). R_f: 0.39 (hexanes on silica). Yield: 92%, mp 60–61 °C (lit.[35] mp 59–60 °C). GC conversion: 97%. ^{1}H NMR (300 MHz, $CDCl_3$) δ: 6.88 (s, 1H), 2.35 (s, 6H), 2.27 (s, 6H). ^{13}C NMR (75 MHz, $CDCl_3$) δ: 134.7, 133.8, 130.2, 128.9, 20.8, 20.1. GC-MS (6.76) $[M]^+$: 212.0. Anal. Calcd. for $C_{10}H_{13}Br$: C 56.36, H 6.15; found: C 55.93, H 6.15. ^{1}H NMR spectrum is in agreement with that previously reported.[35]

2-Bromomesitylene

Pale yellowish liquid. Yield: 93%. ^{1}H NMR (300 MHz, $CDCl_3$) δ: 6.92 (s, 2H), 2.41 (s, 6H), 2.27 (s, 3H). ^{13}C NMR (100 MHz, $CDCl_3$) δ: 137.9, 136.2, 129.2, 124.4, 24.1, 20.8. GC-MS (5.24) $[M]^+$: 197.8. ^{1}H NMR and ^{13}C NMR spectra are in agreement with those previously reported.[36]

1-Bromo-2,3,4-trimethylbenzene

Clear oil. The product was purified via flash chromatography (hexanes on silica). R_f: 0.40 (hexanes on silica). Yield: 43%. GC conversion: 66%. ^{1}H NMR (300 MHz, $CDCl_3$) δ: 7.30 (d, J = 8.1 Hz, 1H), 6.85 (d, J = 8.1 Hz, 1H), 2.41 (s, 3H), 2.47 (s, 6H). ^{13}C NMR (75 MHz, $CDCl_3$) δ: 136.9, 135.5, 129.3, 128.5, 122.8, 20.5, 19.9, 16.7. GC-MS (5.80) $[M]^+$: 197.9. ^{1}H NMR spectrum is not in agreement with that previously reported.[37]

Bromohydroquinone

White solid. The product was purified via flash chromatography (1:2:1 CH_2Cl_2/hexanes/Et_2O on silica). R_f: 0.19 (1:2:1 CH_2Cl_2/hexanes/Et_2O on silica). Yield: 42%, mp 110–112 °C (lit.[37] mp 106–109 °C). GC Conversion: 97%. ^{1}H NMR (300 MHz, $CDCl_3$) δ: 6.97 (d, J = 3.0 Hz, 1H), 6.87 (d, J = 8.7 Hz, 1H), 6.70 (dd, J = 3.0, 9.0 Hz, 1H), 5.10 (s, 1H), 4.74 (s, 1H). ^{13}C NMR (75 MHz, acetone-d_6) δ: 151.8, 147.8, 119.9, 117.6, 116.3, 110.1. GC-MS (6.69) $[M]^+$: 187.9. Anal. calcd. for $C_6H_5BrO_2$: C 38.13, H 2.67; found: C 38.10, H 2.90. ^{1}H NMR and ^{13}C NMR spectra are in agreement with those previously reported.[38]

4-Bromo-3,5-dimethylphenol

White solid. R_f: 0.13 (10% EtOAc/hexanes on silica). The product was purified via flash chromatography (33% CH_2Cl_2/hexanes on silica, R_f: 0.05). Yield: 96%, mp 116–117 °C (lit.[38] mp 114–115 °C). GC conversion: 100%. ^{1}H NMR (300 MHz, $CDCl_3$) δ: 6.57 (s, 2H), 4.99 (s, 1H), 2.34 (s, 6H). ^{13}C NMR (75 MHz, $CDCl_3$) δ: 153.7, 139.4, 118.3, 115.2, 23.7. GC-MS (7.20) $[M]^+$: 199.8. Anal. calcd. for C_8H_9BrO: C 47.79, H 4.51; found: C 47.71, H 4.57. ^{1}H NMR spectrum is in agreement with that previously reported.[39]

4-Bromo-2,6-dimethylphenol

Yellow-orange solid. Yield: 96%, mp 78–79 °C (lit.[40] mp 79–80 °C). GC conversion: 99%. ^{1}H NMR (300 MHz, $CDCl_3$) δ: 7.10 (s, 2H), 4.55 (s, 1H), 2.22 (s, 6H). ^{13}C NMR (75 MHz, $CDCl_3$) δ: 151.2, 130.9, 125.3, 112.0, 15.6. GC-MS (6.64) $[M]^+$: 199.8. ^{1}H NMR and ^{13}C NMR spectra are in agreement with those previously reported.[40]

5-Bromobenzo[d][1,3]dioxole

Brown oil. R_f: 0.10 (hexanes on silica). Yield: 94%. GC conversion: 99%. ^{1}H NMR (300 MHz, $CDCl_3$) δ: 6.91–6.88 (m, 2H), 6.63 (dd, J = 1.8, 8.1 Hz, 1H), 5.91 (d, J = 0.9 Hz,

2H). ^{13}C NMR (75 MHz, $CDCl_3$) δ: 148.5, 146.9, 124.2, 113.0, 112.4, 109.4, 101.6. GC-MS (5.42) $[M]^+$: 200.0. ^{1}H NMR and ^{13}C NMR spectra are in agreement with those previously reported.[41] The compound was reported as a colorless oil.

1-(4-Bromophenoxy)benzene

The reaction mixture was stirred for two days. Clear oil. R_f: 0.19 (hexanes on silica). GC conversion: 91% with 7% dibrominated side product. ^{1}H NMR (300 MHz, $CDCl_3$) δ: 7.41 (d, J = 9.0 Hz, 2H), 7.31 (t, J = 8.1 Hz, 2H), 7.11 (tt, J = 0.9, 6.9 Hz, 1H), 6.99 (dd, J = 1.2, 6.9 Hz, 2H), 6.87 (d, J = 9.0 Hz, 2H). ^{13}C NMR (75 MHz, $CDCl_3$) δ: 156.6, 132.6, 129.8, 123.6, 120.5, 120.3, 118.9, 115.5. GC-MS (8.81) $[M]^+$: 247.9. ^{1}H NMR and ^{13}C NMR spectra are in agreement with those previously reported.[42]

4-Bromoanisole

Clear oil. R_f: 0.18 (hexanes on silica). Yield: 97%. GC conversion: 100%. ^{1}H NMR (300 MHz, $CDCl_3$) δ: 7.36 (d, J = 8.4 Hz, 2H), 6.76 (d, J = 8.4 Hz, 2H), 3.77 (s, 3H). ^{13}C NMR (75 MHz, $CDCl_3$) δ: 158.6, 132.1, 115.6, 112.7, 55.3. GC-MS (4.61) $[M]^+$: 185.9. ^{1}H NMR and ^{13}C NMR spectra are in agreement with those previously reported.[20,40]

1-Bromo-2,4-dimethylbenzene

The reaction mixture was stirred for five days. Clear oil. R_f: 0.19 (hexanes on silica). Yield: 98%. GC conversion: 100% with 3% benzyl and other monobrominated side products. ^{1}H NMR (300 MHz, $CDCl_3$) δ: 7.36 (d, J = 8.1 Hz, 1H), 7.03 (m, 1H), 6.84 (dd, J = 2.4, 8.1 Hz, 1H), 2.34 (s, 3H), 2.25 (s, 3H). ^{13}C NMR (75 MHz, $CDCl_3$) δ: 137.0, 135.2, 132.0, 131.7, 127.7, 121.7, 22.8, 20.9. GC-MS (4.23) $[M]^+$: 183.7. ^{1}H NMR and ^{13}C NMR spectra are in agreement with those previously reported.[36]

1-Bromo-4-methoxy-2-methylbenzene

Clear oil, which solidified to a white solid under vacuum. R_f: 0.16 (hexanes on silica). Yield: 97%. ^{1}H NMR conversion: 100%. ^{1}H NMR (300 MHz, $CDCl_3$) δ: 7.40 (d, J = 8.7 Hz, 1H), 6.79 (d, J = 3.0 Hz, 1H), 6.61 (dd, J = 2.7, 8.7 Hz, 1H), 3.76 (s, 3H), 2.38 (s, 3H). ^{13}C NMR (75 MHz, $CDCl_3$) δ: 158.8, 138.7, 132.7, 116.5, 115.3, 112.9, 55.2, 23.0. GC-MS (5.63) $[M]^+$: 200.0. ^{1}H NMR spectrum is in agreement with that previously reported.[43,44]

2-Bromo-1-methoxy-4-methylbenzene

Clear oil. R_f: 0.30 (10% EtOAc/hexanes on silica). The product was purified via flash chromatography (10% EtOAc/hexanes on silica). Yield: 63%. ^{1}H NMR (300 MHz, $CDCl_3$) δ: 7.34 (d, J = 2.1 Hz, 1H), 7.04 (dd, J = 2.2, 8.1 Hz, 1H), 6.77 (d, J = 8.4 Hz, 1H), 3.84 (s, 3H), 2.26 (s, 3H). ^{13}C NMR (75 MHz, $CDCl_3$) δ: 153.7, 133.6, 131.4, 128.8, 111.8, 111.2, 56.2, 20.1. GC-MS (5.72) $[M]^+$: 200.0. ^{1}H NMR spectrum is in agreement with that previously reported.[43,45]

1-Bromo-2,4-dimethoxybenzene

Clear oil. R_f: 0.19 (20% EtOAc/hexanes on silica). Yield: 99%. ^{1}H NMR (300 MHz, $CDCl_3$) δ: 7.38 (d, J = 8.7 Hz, 1H), 6.46 (d, J = 2.7 Hz, 1H), 6.37 (dd, J = 2.7, 8.4 Hz, 1H), 3.84 (s, 3H), 3.77 (s, 3H). ^{13}C NMR (75 MHz, $CDCl_3$) δ: 158.7, 155.0, 131.6, 104.4, 100.9, 98.5, 54.6, 54.0. GC-MS (7.10) $[M]^+$: 217.8. Anal. calcd. for $C_8H_9BrO_2$: C 44.27, H 4.18; found: C 44.18, H 4.25. ^{1}H NMR and ^{13}C NMR spectra are in agreement with that previously reported.[46]

1-Bromo-2,5-dimethoxybenzene

Yellow oil. R_f: 0.06 (10% EtOAc/hexanes on silica). Yield: 99%. ^{1}H NMR (300 MHz, $CDCl_3$) δ: 7.10 (m, 1H), 6.82 (m, 2H), 3.82 (s, 3H), 3.74 (s, 3H). ^{13}C NMR (75 MHz, $CDCl_3$) δ: 154.0, 118.9, 114.6, 113.6, 112.9, 111.9, 56.9, 55.8. GC-MS (6.83) $[M]^+$: 217.8. ^{1}H NMR spectrum is in agreement with that previously reported.[47]

4-Bromo-2-methoxybenzenamine

Red liquid. R_f: 0.07 (20% EtOAc/hexanes on silica). The product was purified via flash chromatography (20% EtOAc/hexanes on silica). Mp 59–60 °C (liquid) (lit.[48] mp 60–61 °C). Yield: 71%. ^{1}H NMR (300 MHz, $CDCl_3$) δ: 6.86 (m, 2H), 6.55 (dd, J = 2.1, 8.7 Hz, 1H), 3.80 (s, 3H), 3.74 (s, 2H). ^{13}C NMR (75 MHz, $CDCl_3$) δ: 147.8, 135.3, 123.6, 115.6, 113.7, 109.4, 55.6. GC-MS (7.17) $[M]^+$: 202.9. ^{1}H NMR and ^{13}C NMR spectra are in agreement with those previously reported.[48] The compound was reported as a brown solid.

3,4-Dibromo-2-methoxybenzenamine

Red liquid, isolated as a side product in the monobromination reaction of *o*-anisidine. R_f: 0.25 (20% EtOAc/hexanes on silica). The product was purified via flash chromatography (20% EtOAc/hexanes on silica). Yield: 12%. ^{1}H NMR (300 MHz, $CDCl_3$) δ: 7.15 (d, J = 2.1 Hz, 1H), 6.80 (d, J = 2.1 Hz, 1H), 4.12 (s, 2H), 3.81 (s, 3H). ^{13}C NMR (75 MHz, $CDCl_3$) δ: 147.6, 134.1, 126.1, 112.5, 108.5, 108.1, 56.0. GC-MS (8.86) $[M]^+$: 278.9. ^{1}H NMR spectrum is in agreement with that previously reported.[48]

4-Bromo-3-methoxybenzenamine

White solid. R_f: 0.05 (30% EtOAc/hexanes on silica). The product was purified via flash chromatography (30% EtOAc/hexanes on silica). Yield: 47%, mp 94–95.5 °C (lit.[23,49] mp 93–94 °C). ^{1}H NMR (300 MHz, $CDCl_3$) δ: 7.19 (d, J = 8.4 Hz, 1H), 6.20 (d, J = 2.7 Hz, 1H), 6.14 (dd, J = 2.4, 8.4 Hz, 1H), 3.75 (s, 3H), 3.71 (s, 2H). ^{13}C NMR (75 MHz, $CDCl_3$) δ: 156.3, 147.3, 133.2, 108.4, 99.6, 99.2, 55.9. GC-MS (7.92) $[M]^+$: 201.0. Anal. calcd. for C_7H_8BrNO: C 41.61, H 3.99, N 6.93; found: C 41.80, H 4.21, N 6.80. ^{1}H NMR and ^{13}C NMR spectra are in agreement with those previously reported.[48]

2-Bromo-4-methoxybenzenamine

Red liquid. R_f: 0.13 (20% EtOAc/hexanes on silica). The product was purified via flash chromatography (20% EtOAc/hexanes on silica). Yield: 20%. ^{1}H NMR (300 MHz, $CDCl_3$) δ: 6.98 (dd, J = 0.9, 2.1 Hz, 1H), 6.70 (m, 2H), 3.79 (s, 2H), 3.70 (s, 3H). ^{13}C NMR (75 MHz, $CDCl_3$) δ: 153.3, 138.6, 118.1, 117.2, 115.6, 110.1, 56.5. GC-MS (6.94) $[M]^+$: 201.0. ^{1}H NMR and ^{13}C NMR spectra are in agreement with those previously reported.[48,49]

5-Bromo-2-hydroxybenzaldehyde

White solid. R_f: 0.37 (20% EtOAc/hexanes on silica). The product was purified via flash chromatography (20% EtOAc/hexanes on silica). Yield: 18%, mp 102–105 °C (lit.[50] mp 104–105 °C). ^{1}H NMR (300 MHz, $CDCl_3$) δ: 10.92 (s, 1H), 9.83 (s, 1H), 7.65 (d, J = 2.4 Hz, 1H), 7.58 (dd, J = 2.7, 9.0 Hz, 1H), 6.89 (d, J = 9.0 Hz, 1H). ^{13}C NMR (75 MHz, $CDCl_3$) δ: 196.1, 161.3, 140.5, 136.4, 122.5, 120.6, 112.1. GC-MS (5.53) $[M]^+$: 200.0. ^{1}H NMR and ^{13}C NMR spectra are in agreement with those previously reported.[50,51]

4-Bromo-3,5-dimethyl-*N*,*N*-dimethylaniline

Isolated as a thick colorless oil that solidified to a crystalline white substance after sitting under high vacuum for 16 h. R_f: 0.35 (50% CH_2Cl_2/hexanes on silica). The product was purified via flash chromatography (50% CH_2Cl_2/hexanes on silica). Yield: 95%, mp 25–26 °C. ^{1}H NMR (300 MHz, $CDCl_3$) δ: 6.51 (s, 2H), 2.81 (s, 6H), 2.41 (s, 6H). ^{13}C NMR (100 MHz, $CDCl_3$) δ: 149.2, 138.2, 114.5, 112.7, 40.6, 24.1. GC-MS (8.12) $[M]^+$: 227.0. ^{1}H NMR spectrum is in agreement with that previously reported.[52] The compound was reported as a colorless liquid.

Bromojulolidine (referred to as 9-bromojulolidine in the reference)

The product was extracted with CH_2Cl_2 to produce a dark red crystalline solid. Yield: 92%, mp 35–37 °C (lit[53] mp 36.5 °C). R_f: 0.30 (CH_2Cl_2 on silica). The product was purified via flash column chromatography (CH_2Cl_2 on silica). ^{1}H NMR (300 MHz, $CDCl_3$) δ: 6.93 (d, J = 0.6 Hz, 2H), 3.17 (t, J = 6.5 Hz, 4H), 2.76 (t, J = 5.7 Hz, 4H), 2.01 (m, 4H). ^{13}C NMR (100 MHz, $CDCl_3$) δ: 142.3, 129.6, 124.0, 107.5, 50.3, 28.0, 22.3, 28.0. GC-MS (10.85) $[M]^+$: 251.1.

4-Bromothioanisole

Clear oil. GC conversion: 75%. R_f: 0.21 (hexanes on silica). ^{1}H NMR (300 MHz, $CDCl_3$) δ: 7.37 (d, J = 8.7 Hz, 2H), 7.10 (d, J = 8.7 Hz, 2H), 2.46 (s, 3H). GC-MS (6.16) $[M]^+$: 201.9.

Acknowledgment

E.Z.-C. acknowledges le Fonds Québécois de la Recherche sur la Nature et les Technologies (FQRNT) for funding in the form of a post-doctoral scholarship.

References

(1) Garofalo, A. W.; Litvak, J.; Wang, L.; Dubenko, L. G.; Cooper, R.; Bierer, D. E. J. *Org. Chem.* **1999**, *64*, 3369. doi:10.1021/jo9822838.
(2) Pulley, S. R.; Czako, B. *Tetrahedron Lett.* **2004**, *45*, 5511. doi:10.1016/j.tetlet.2004.05.018.
(3) Alvarez-Manzaneda, E. J.; Diaz, C. G. *Synlett* **2000**, 1561.
(4) Ross, S. D.; Finkelstein, M.; Petersen, R. C. J. *Am. Chem. Soc.* **1958**, *80*, 4327. doi:10.1021/ja01549a053.
(5) Yadav, J. S.; Reddy, B. V. S.; Reddy, P. S. R.; Basak, A. K.; Narsaiah, A. V. *Adv. Synth. Catal.* **2004**, *346*, 77. doi:10.1002/adsc.200303229.
(6) (a) Lambert, F. L.; Ellis, W. D.; Parry, R. J. *J. Org. Chem.* **1965**, *30*, 304; Here, catalytic HCl was used in acetone. doi:10.1021/jo01012a512.; (b) Andersh, B.; Murphy, D. L.; Olson, R. J. *Synth. Commun.* **2000**, *30*, 2091 doi:10.1080/00397910008087387.; (c) Oberhauser, T. J. *Org. Chem.* **1997**, *62*, 4504. doi:10.1021/jo9622993.
(7) Auerbach, J.; Weissman, S. A.; Blacklock, T. J.; Angeles, M. R.; Hoogsteen, K. *Tetrahedron Lett.* **1993**, *34*, 931. doi:10.1016/S0040-4039(00)77457-0.
(8) This method affords predominantly orthobrominated arenes: Fujisaki, S.; Nishida, A. *Bull. Chem. Soc. Jpn.* **1993**, *66*, 1576. doi:10.1246/bcsj.66.1576.
(9) (a) Bromination in CCl_4: Djerassi, C. *Chem. Rev.* **1948**, *43*, 271 doi:10.1021/cr60135a004. PMID:18887958.; (b) Bromination in CH_2Cl_2: Mistry, A. G.; Smith, K.; Bye, M. R. *Tetrahedron Lett.* **1986**, *27*, 1051 doi:10.1016/S0040-4039(86)80045-4.; (c) Bloomer, J. L.; Zheng, W. *Synth. Commun.* **1998**, *28*, 2087 doi:10.1080/00397919808007185.; (d) Bromination in $CHCl_3$: Mitchell, R. H.; Chen, Y.; Zhang, J. *Org. Prep. Proced. Int.* **1997**, *29*, 715.
(10) Orthobromination of phenols predominates in CS2: Carreño, M. C.; Urbano, A. *Synlett* **1997**, 1241–1242.
(11) Goldberg, Y.; Alper, H. *J. Org. Chem.* **1993**, *58*, 3072. doi:10.1021/jo00063a028.
(12) This study only investigated the bromination of pyrroles: Gilow, H. M.; Burton, D. E. J. *Org. Chem.* **1981**, *46*, 2221. doi:10.1021/jo00324a005.
(13) Mitchell, R. H.; Lai, Y.-H.; Williams, R. V. *J. Org. Chem.* **1979**, *44*, 4733. doi:10.1021/jo00393a066.
(14) Dijkstra, P. J.; den Hertog, H. J., Jr.; van Eerden, J.; Harkema, S.; Reinhoudt, D. N. *J. Org. Chem.* **1988**, *53*, 374. doi:10.1021/jo00237a027.
(15) Catalytic Koser's reagent (HTIB) or TsOH was also added: Bovonsombat, P.; McNelis, E. *Synthesis* **1993**, *46*, 237.
(16) (a) Konishi, H.; Aritomi, K.; Okano, T.; Kiji, J. *Bull. Chem. Soc. Jpn.* **1989**, *62*, 591 doi:10.1246/bcsj.62.591.; (b) Here, the zeolite catalyst HZSM-5 (40:1 SiO_2/Al_2O_3) was used in CCl_4: Paul, V.; Sudalai, A.; Daniel, T.; Srinivasan, K. V. *Tetrahedron Lett.* **1994**, *35*, 7055. doi:10.1016/0040-4039(94)88224-X.
(17) Here, silica gel was mixed with LiClO4: Bagheri, M.; Saidi, M. R. *Can. J. Chem.* **2005**, *83*, 146. doi:10.1139/v05-001.
(18) Goldberg, Y.; Alper, H. *J. Mol. Catal.* **1994**, *88*, 377. doi:10.1016/0304-5102(93)E0278-O.
(19) (a) Ganguly, N. C.; De, P.; Dutta, S. *Synthesis* **2005**, 1103 doi:10.1055/s-2005-861866.; (b) Rajagopal, R.; Jarikote, D. V.; Lahoti, R. J.; Daniel, T.; Srinivasan, K. V. *Tetrahedron Lett.* **2003**, *44*, 1815. doi:10.1016/S0040-4039(03)00092-3.
(20) Cañibano, V.; Rodriguez, J. F.; Santos, M.; Sanz-Tejedor, A.; Carreño, M. C.; Gonzales, G.; García Ruano, J. L. *Synthesis* **2001**, 2175. doi:10.1055/s-2001-18070.
(21) Carreño, M. C.; García Ruano, J. L.; Sanz, G.; Toledo, M. A.; Urbano, A. J. *Org. Chem.* **1995**, *60*, 5328. doi:10.1021/jo00121a064.
(22) Using similar conditions, the bromination of alkylnapthalenes has also been investigated. See: Cammidge, A. N.; Fugier, M. *Synth. Commun.* **1997**, *27*, 4159. doi:10.1080/00397919708005463.
(23) The bromination of air sensitive julolidine (Table 1, entry 15) proceeded under a nitrogen atmosphere.
(24) For more polar products, such as 2-bromohydroquinone, CH_2Cl_2 could be used to extract the product. Additionally, unlike reactions in DMF,[13] no oxidation to *p*-benzoquinone was observed during the reaction.
(25) Olah, G. A.; Arvanaghi, M.; Vankar, Y. D. *Chem. Commun.* **1979**, 721.
(26) Chhattise, P. K.; Ramaswamy, A. V.; Waghmode, S. B. *Tetrahedron Lett.* **2008**, *49*, 189.

(27) Sprecher, M.; Kost, D. *J. Am. Chem. Soc.* **1994**, *116*, 1016. doi:10.1021/ja00082a024.
(28) Gruter, G.-J. M.; Akkerman, O. S.; Bickelhaupt, F. *J. Org. Chem.* **1994**, *59*, 4473. doi:10.1021/jo00095a023.
(29) Rosillo, M.; Dominguez, G.; Casarrubios, L.; Amador, U.; Perez-Castells, J. *J. Org. Chem.* **2004**, *69*, 2084. doi:10.1021/jo0356311. PMID:15058956.
(30) Glogowski, M. E.; Zumbulyadis, N.; Williams, J. L. R. *J. Organomet. Chem.* **1982**, *231*, 97. doi:10.1016/S0022-328X(00)81948-8.
(31) Smith, L. I.; Nichols, J. *J. Org. Chem.* **1941**, *6*, 489. doi:10.1021/jo01204a003.
(32) Keefer, R. M.; Andrews, L. J. *J. Am. Chem. Soc.* **1956**, *78*, 3637. doi:10.1021/ja01596a022.
(33) Kajigaeshi, S.; Kakinami, T.; Moriwaki, M.; Tanaka, T.; Fujisaki, S.; Okamoto, T. *Bull. Chem. Soc. Jpn.* **1989**, *62*, 439. doi:10.1246/bcsj.62.439.
(34) Insik, I.; Kim, S. Y. *Polymer (Guildf.)* **2006**, *47*, 4549. doi:10.1016/j.polymer.2006.04.052.
(35) Catalytic Koser's reagent (HTIB) or TsOH was also added: Bovonsombat, P.; McNelis, E. *Synthesis* **1993**, *46*, 237. doi:10.1055/s-1993-25839.
(36) Kikuchi, D.; Sakaguchi, S.; Ishii, Y. *J. Org. Chem.* **1998**, *63*, 6023. doi:10.1021/jo972263q. PMID:11672208.
(37) Mitchell, R. H.; Lai, Y.-H.; Williams, R. V. *J. Org. Chem.* **1979**, *44*, 4733. doi:10.1021/jo00393a066.
(38) Coumbarides, G. S.; Dingjan, M.; Eames, J.; Weerasooriya, N. *Bull. Chem. Soc. Jpn.* **2001**, *74*, 179. doi:10.1246/bcsj.74.179.
(39) Espenson, J. H.; Zhu, Z.; Zauche, T. H. *J. Org. Chem.* **1999**, *64*, 1191. doi:10.1021/jo9817164.
(40) Kavala, V.; Naik, S.; Patel, B. K. *J. Org. Chem. 70* (70), 4267.
(41) Braddock, D. C.; Cansell, G.; Hermitage, S. A. *Synlett* **2004**, 461. doi:10.1055/s-2004-815410.
(42) Rao, H.; Jin, Y.; Fu, H.; Jiang, Y.; Zhao, Y. *Chem. Eur. J.* **2006**, 3636. doi:10.1002/chem.200501473.
(43) De Almeida, L. S.; Esteves, P. M.; De Mattos, M. C. S. *Synthesis* **2006**, 21.
(44) Le, Z.-G.; Chen, Z.-C.; Hu, Y. *Chin. J. Chem.* **2005**, *23*, 1537. doi:10.1002/cjoc.200591537.
(45) Gupta, B. D.; Kumar, M.; Roy, S. *Inorg. Chem.* **1989**, *28*, 11. doi:10.1021/ic00300a006.
(46) Bovicelli, P.; Mincione, E.; Antonioletti, R.; Bernini, R.; Colombari, M. *Synth. Commun.* **2001**, *31*, 2955. doi:10.1081/SCC-100105667.
(47) Konishi, H.; Aritomi, K.; Okano, T.; Kiji, J. *Bull. Chem. Soc. Jpn.* **1989**, *62*, 591. doi:10.1246/bcsj.62.591.
(48) Chretien, J.-M.; Zammattio, F.; Le Grognec, E.; Paris, M.; Cahingt, B.; Montavon, G.; Quintard, J.-P. *J. Org. Chem.* **2005**, *70*, 2870. doi:10.1021/jo0480141. PMID:15787591.
(49) Tidwell, J. H.; Buchwald, S. L. *J. Am. Chem. Soc.* **1994**, *116*, 11797. doi:10.1021/ja00105a021.
(50) Yadav, J. S.; Reddy, B. V. S.; Reddy, P. S. R.; Basak, A. K.; Narsaiah, A. V. *Adv. Synth. Catal.* **2004**, *346*, 77. doi:10.1002/adsc.200303229.
(51) Bajwa, N.; Jennings, M. P. *J. Org. Chem.* **2006**, *71*, 3646. doi:10.1021/jo0601664. PMID:16626159.
(52) Kajiyama, K.; Yoshimune, M.; Kojima, S.; Akibe, K.-y. *Eur. J. Org. Chem.* **2006**, 2739. doi:10.1002/ejoc.200600031.
(53) Smith, P. A. S.; Yu, T.-Y. *J. Org. Chem.* **1952**, *17*, 1281. doi:10.1021/jo50009a015.

Investigations of the supramolecular host properties of a fluorescent bistren cage compound

Patricia G. Boland, Sara J. Accardi, Carrie A. Snow, and Brian D. Wagner

Abstract: The host properties of a bistren cage compound, previously reported to be an efficient anion sensor, are shown to include encapsulation of small aromatic guest molecules. It is also shown that the intrinsic fluorescence of this cage compound, arising from the anthracenyl moiety in its structure, is sensitive to the encapsulation of aromatic guests in aqueous solution and can be used to measure the binding constants for any such guest. This makes this bistren cage a rare example of a fluorescent host for aromatic guests, and suggests potential applications of this compound as a versatile fluorescent sensor for a variety of guests of interest. The binding of a number of benzene derivatives was studied; these were all found to form 1:2 host–guest inclusion complexes with a wide range in total binding constants (K_1K_2), from 6.4×10^3 to 3.5×10^7 $(mol/L)^{-2}$, indicating a significant degree of selectivity for different benzene derivatives. The binding strength was found to depend on both the guest polarity and aqueous solubility.

Key words: bistren cage, host–guest inclusion, fluorescent host, binding constants.

Résumé : Pour un composé bistrène en forme de cage qui, selon des études antérieures, serait un senseur anionique efficace, on démontre que ses propriétés hôtes incluent l'encapsulation de petites molécules aromatiques invitées. On démontre aussi que la fluorescence intrinsèque de ce composé en cage, qui tire son origine dans la portion anthracényle de sa structure, est sensible à l'encapsulation de molécules aromatiques hôtes dans la solution aqueuse et qu'elle peut être utilisée pour mesurer les constantes de fixation de telles molécules invitées. Cette propriété fait que bistrène en forme de cage est un rare exemple d'un hôte pour invités aromatiques et suggère des applications potentielles de ce composé comme senseur fluorescent versatile pour une variété de molécules invitées présentant des intérêts divers. On a étudié la fixation d'un certain nombre de dérivés aromatiques qui forment tous des complexes d'inclusion hôte:invité 1:2 pour lesquels les constantes de fixation totale (K_1K_2) s'étalent de $6{,}4 \times 10^3$ à $3{,}5 \times 10^7$ $(mol/L)^{-2}$, ce qui suggère un degré significatif de sélectivité pour les différents dérivés du benzène. On a noté que la force de la fixation dépend à la fois de la polarité de la molécule invitée et de la solubilité dans l'eau.

Mots-clés : cage bistrène, inclusion hôte-invité, hôte fluorescent, constantes de fixation.

[Traduit par la Rédaction]

Introduction

Supramolecular host–guest inclusion complexes, in which a small guest molecule becomes encapsulated within the internal cavity of a larger cage-like host molecule, have shown tremendous utility for molecular recognition, with a high degree of guest selectivity.[1] A wide range of applications of inclusion complexes have been reported, including chemical separations,[2] food and chemical industries,[3] drug delivery,[4] and fluorescence-based trace analysis.[5] Fluorescence spectroscopy has been shown to be an extremely sensitive and accurate experimental method for studying such inclusion systems, for example, extracting the binding constant K for the complex formation.[6,7] However, since most commonly used hosts, such as cyclodextrins[8] and cucurbiturils,[9] are non-fluorescent, the use of fluorescence to study their inclusion complexes is limited to the specific cases of polarity-sensitive fluorescent guests.[6,7]

Bistrens are an important class of cryptand ligands and were first prepared by J.-M. Lehn et al. over 30 years ago.[10] The simplest bistrens, *O*-bistren and *C*-bistren, consist of polyamine cages constructed from two tripodal tetramine "tren" (2,2′,2″-triaminetriethylamine) units, which have been joined through their terminal amines by three ether (*O*-bistren) or alkyl (*C*-bistren) spacer groups.[11] The resulting molecule has an ellipsoidal internal cavity, the size and rigidity of which depend on the type and length of the spacer groups.[11] These cages have been shown to be highly selective hosts for metal ions, tightly binding two metal cations.[10,12,13] In addition, the resulting di-metal cation complexes have been shown to be useful hosts for other guests: dicobalt-*O*-bistren as a molecular oxygen carrier[12] and di-copper-*O*- and *C*-bistren for OH^- and F^- anions as bridging "cascade" guests.[13]

Fabbrizzi and co-workers extended the versatility of bistren hosts by adding aromatic groups within the spacer linkages, including 1,4-xylyl[11] and 9,10-anthracenyl.[14] The structure of the latter bistren **1** is shown in Fig. 1; it contains

Received 5 November 2008. Accepted 18 November 2008. Published on the NRC Research Press Web site at canjchem.nrc.ca on 19 January 2009.

P.G. Boland, S.J. Accardi, C.A. Snow, and B.D. Wagner.[1] Department of Chemistry, University of Prince Edward Island, 550 University Ave, Charlottetown, PEI C1A 4P3, Canada.

[1]Corresponding author (e-mail: bwagner@upei.ca).

Fig. 1. Structure of the fluorescent bistren host compound **1**.

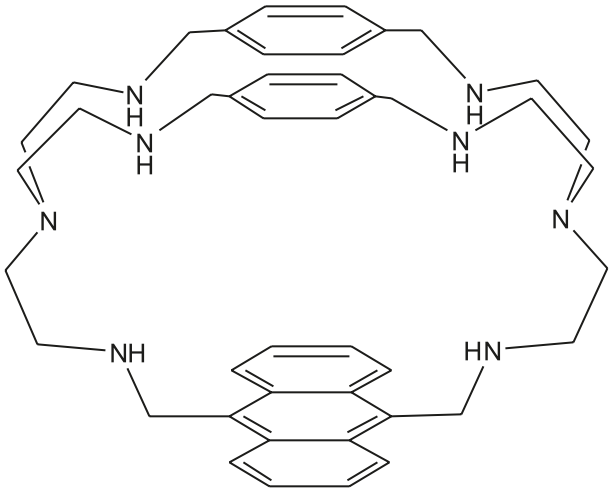

two 1,4-xylyl and one 9,10-anthracenyl group in the spacer arms. This incorporation of the strongly fluorescent 9,10-anthracenyl moiety within the cage architecture makes this bistren **1** a relatively rare example of an intrinsically fluorescent host. Its fluorescence properties were well characterized by Fabbrizzi et al.[14] and shown to be highly pH dependent. The strong fluorescence was found to be greatly reduced above pH 4–6; this was explained to be a result of efficient quenching of the anthracenyl fluorescence by the unprotonated amine groups in the cage structure. At low pH, the amine groups are protonated to the ammonium form, which does not quench anthracene fluorescence and thus the cage is highly fluorescent. At a high enough pH so that at least one adjacent nitrogen is in the amine form, the fluorescence is efficiently quenched. In the presence of two equivalents of Zn(II), however, the Zn cations enter the cage and engage the amines, greatly reducing the amine quenching and restoring the cage fluorescence. This fluorescence was also found to be quenched by the binding of certain anions, such as azide, via a photoinduced electron transfer. The authors proposed this dizinc(II)···**1** complex as an efficient and highly selective sensor for ambidentate anions.[14]

This host compound **1** has huge potential because it has been virtually unexplored as a fluorescent host. Although Fabbrizzi considered anion and metal cation binding, no inclusion complexes of this host with neutral guests have been reported, and in fact there have been no subsequent papers describing its host properties with any guest, since the original publication in 1998.

To explore the host abilities of this interesting cage compound **1**, its binding of a series of substituted benzenes was investigated. These guests were chosen for three reasons: (*i*) they are aromatic, so have the potential to undergo π–π interactions with the aromatic moieties of the cage walls, (*ii*) they absorb well below the host absorption band, so their addition will not interfere with the excitation of the fluorescent cage (this would not be the case for naphthalene derivatives, for example), and (*iii*) they are relatively small and expected to be a good size match for the bistren cavity.

Fig. 2. Normalized fluorescence spectra of the bistren cage compound **1** (—) and anthracene (- - -) in methanol.

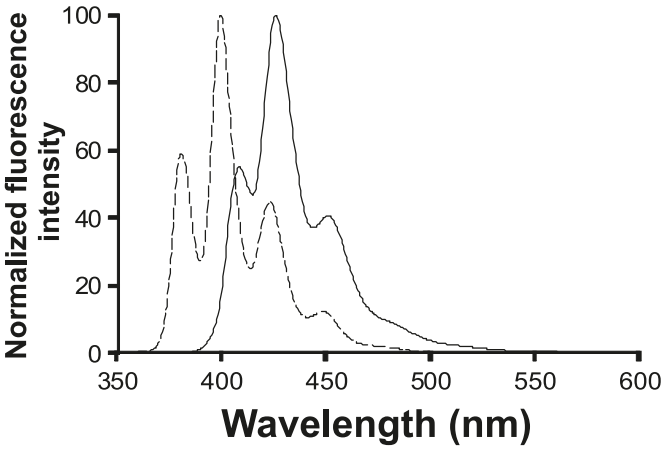

Experimental

The following compounds were obtained from the indicated sources and used as received: 9,10-bis(chloromethyl)anthracene (ABCR GmbH and Co. KG); tris(2-aminoethyl)amine, toluene, terephthalaldehyde, sodium borohydride, methanol, dichloromethane, sodium sulfate, phenol (Sigma-Aldrich); benzene (BDH); aniline and anisole (Fisher). The first eight compounds were all used in the synthesis of **1**, the final four were used as aromatic guests.

The bistren cage **1** was synthesized according to published methods[14,15] and purified by high-performance liquid chromatography (HPLC). According to the literature, the solid product is recovered as the hydrochloride salt **1**···8HCl.[14] The purified product was characterized by ^{1}H NMR (Bruker 300 MHz Ultra-Shield) and electrospray mass spectrometry, which reproduced the literature-reported mass spectrometry data with a *m*/*z* peak of 699. Furthermore, all of the fluorescence properties previously reported in the literature were able to be reproduced using this synthesized sample (see next section).

Bistren solutions were prepared in nanopure deionized water, with 5 min of sonication, to give an absorbance in the range of 0.20 to 0.25 at the excitation wavelength of 340 nm; these solutions had concentrations of ca. 2×10^{-5} mol/L. Fluorescence spectra were measured on a Photon Technology International LS-100 or a PerkinElmer LS 55 luminescence spectrophotometer.

Results and discussion

The bistren cage was successfully synthesized and purified, and its fluorescence emission was found to be in excellent agreement with that reported in the original literature paper.[14] All of the reported fluorescence properties were able to be reproduced, including the pH dependence, the effect of Zn(II) binding, and the effect of adding azide to the Zn(II)···**1** complex. However, no spectra were shown in Fabbrizzi's paper. Figure 2 shows the normalized fluorescence spectrum of the bistren cage **1**, as well as that of anthracene, the fluorophore of the cage, both in methanol for comparison. It is clear that the rest of the cage architecture

Fig. 3. Normalized absorption (- - -) and fluorescence (—) spectra of the bistren cage compound **1** in water.

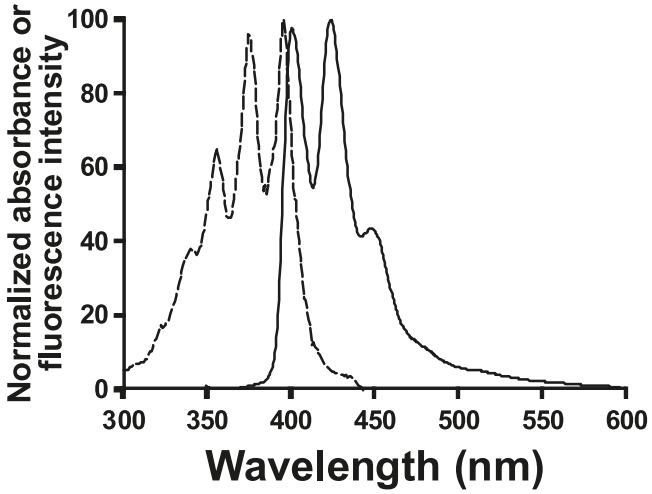

has a significant effect on the photophysics of the 9,10-anthracenyl fluorophore, as a significant red-shift is observed.

The fluorescence properties of **1** in nanopure water were then investigated to see if a strong fluorescence signal could be measured in unbuffered aqueous solution. This was done to avoid the effects of competitive binding of the metal cations (e.g., Na^+) present from the buffer salts used by Fabbrizzi et al.[14] The pH of the prepared bistren stock solution was found to be on the order of 4.0 (a result of the fact that the solid bistren is recovered as **1**···8HCl), so the bistren cage will be in its protonated form. Both the absorption and emission spectra of **1** in nanopure water are shown in Fig. 3. These spectra show a strong mirror image relationship, with a very small Stokes shift, indicating minimal displacement of the excited state energy surface relative to that of the ground state. The fluorescence observed at pH 4.0 is very strong, in agreement with the reported pH dependence.[14] It is thus clear that an intense fluorescence emission can be observed for **1** in unbuffered, slightly acidic aqueous solution, which has the potential to allow for the study of its ability to include guests.

The first guest tried was benzene. However, addition of up to 20 mmol/L of benzene (aqueous solubility = 23 mmol/L[16]) showed no effect on the bistren fluorescence. It was decided that a more polar guest would be more likely to bind (considering the fact that the only previous guests reported to bind were all ionic), so aniline was chosen. In this case, a very strong reduction of the bistren host fluorescence was observed upon addition of aniline, as shown in Fig. 4. To quantify this effect, the fluorescence suppression F/F_o was calculated as the ratio of the integrated bistren fluorescence spectrum in the presence (F) and absence (F_o) of added aniline.[6] In the experiment shown in Fig. 4, F/F_o was found to be 0.19, i.e., the bistren emission was reduced by a factor of over 5-fold in the presence of 10 mmol/L of aniline. This very large reduction in intensity was not accompanied by a significant spectral shift; the peak shifted by ≤1 nm.

An analogous set of experiments were performed by adding 10 mmol/L of aniline to solutions of 9,10-dichloromethylanthracene (the source of the 9,10-anthracenyl moiety in the bistren synthesis) and anthracene itself. In both cases, only a very small decrease in fluorescence (<10%) was observed. This indicates that the cage structure of the bistren is essential for this quenching to occur, and provides strong evidence that the aniline is being included within the bistren cage as a guest.

Fig. 4. The effect of added aniline on the fluorescence of the bistren host compound **1**: the relative fluorescence spectrum of bistren in the absence of guest (—) and in the presence of 10 mmol/L of aniline (- - -).

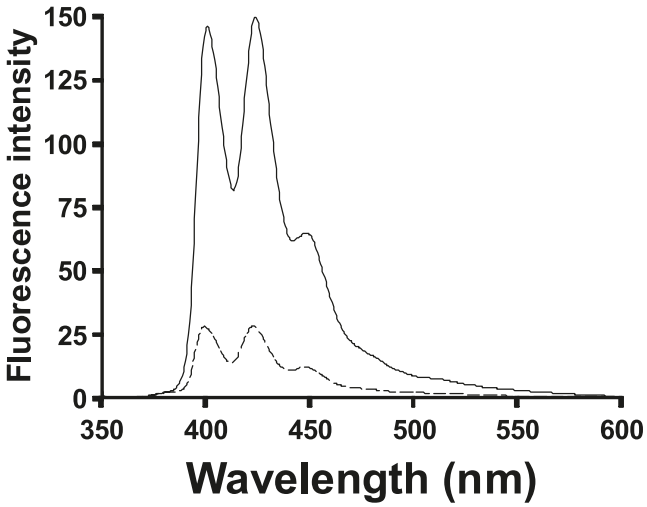

Fig. 5. Fluorescence titration of bistren fluorescence with aniline. The solid line is the best fit to eq. [1] for a 1:2 host–guest complex, with K_1 = 3900 mol/L^{-1}and K_2 = 11 000 mol/L^{-1} for this trial. The inset shows the double reciprocal plot.

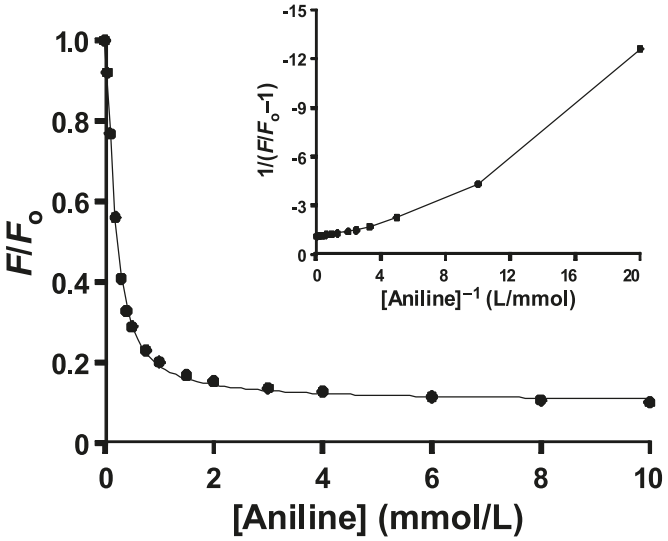

To determine the binding constant, a titration of the bistren fluorescence spectrum was performed in which F/F_o was measured as a function of added aniline concentration. The results are shown in Fig. 5.

To determine whether simple 1:1 host–guest complexation was occurring, a double reciprocal plot of $1/(F/F_o-1)$ versus 1/[aniline] was generated; this plot will be linear for 1:1 complexation but curved if higher-order complexes are

Table 1. Binding of substituted benzene guests by the bistren host (average of three trials).

Guest	Substituent	K_1 ((mol/L)$^{-1}$)	K_2 ((mol/L)$^{-1}$)	K_1K_2 ((mol/L)$^{-2}$)
Benzene	-H	<10	<10	<100
Aniline	-NH_2	$2.6\pm0.8\times10^3$	$1.4\pm0.2\times10^4$	$3.5\pm1.0\times10^7$
Anisole	-OCH_3	$3.2\pm0.6\times10^2$	$1.6\pm0.2\times10^2$	$5.1\pm1.5\times10^4$
Phenol	-OH	$3.5\pm0.5\times10^1$	$1.9\pm0.3\times10^2$	$6.4\pm0.4\times10^3$

being formed.[6] As can be clearly seen in the inset of Fig. 5, this plot was indeed highly curved, indicating that the bistren-aniline complexes are higher order than 1:1. Given the much larger size of the host compared with the guest, the most likely stoichiometry is 1:2 bitren-aniline. The equation for the dependence of the fluorescence of a guest on host concentration in the case of 2:1 host–guest complexes is well-established.[17] This equation is equally valid for the current case of the dependence of the fluorescence of a host as a function of guest concentration ([G]) for a 1:2 host–guest complex, as given below:

$$[1] \qquad \frac{F}{F_o} = \frac{1 + F_a K_1[G] + F_b K_1 K_2[G]^2}{1 + K_1[G] + K_1 K_2[G]^2}$$

In this equation, K_1 and K_2 are the equilibrium constants for the stepwise binding of the first, then the second guest, respectively, and F_a and F_b are the relative fluorescence upon complete 1:1, then 2:1 complexation, respectively. The solid line shows the excellent fit of the data to eq. [1], using a non-linear least-squares fitting program, confirming the 1:2 stoichiometry. In this particular experiment, the following fit values for eq. [1] were obtained: $F_a = 0.94$; $K_1 = 3900$ mol/L^{-1}; $F_b = 0.10$; $K_2 = 11\,000$ mol/L^{-1}. Three trials were performed; the average values of the binding constants obtained are shown in Table 1. These show that aniline is bound very strongly by the bistren cage, with an overall binding constant (K_1K_2) for the two aniline guests per cage of $3.5 \pm 1.0 \times 10^7$ (mol/L)$^{-2}$. The value of K_2 is found to be larger than that of K_1, indicating that once the first aniline is bound, the second binds even more strongly. This might be the result of the first aniline displacing bound solvent molecules, freeing up the cavity, or changing the shape of the cage, making it easier for the second guest to fit in. The strong binding is postulated to be at least partly a result of strong π–π interactions between the polar aromatic guest aniline and the anthracenyl moiety in the host wall; such interactions are found to be stronger for substituted benzenes than for benzene itself.[18]

Two other benzene derivatives were also studied as guests: anisole and phenol. The results averaged over three trials are also shown in Table 1. Both of these guests were also found to bind with the bistren as 1:2 host–guest complexes. It can be seen that in the case of anisole, the binding is much weaker than with aniline, with an overall binding constant K_1K_2 of $5.1 \pm 1.5 \times 10^4$ (mol/L)$^{-2}$. This is almost three orders of magnitude smaller than that in the case of aniline, and is attributed to the lower polarity of anisole relative to aniline, as indicated by either the dielectric constant ε for the liquid (4.30 versus 7.06[19]) or the dipole moment μ (1.26[20] versus 1.53 D[21]). It makes sense that the binding strength of anisole falls between that of benzene and that of aniline, in terms of the relative polarity. However in the case of phenol, which exhibits higher polarity than aniline,[22] the binding is unexpectedly found to be weaker than even anisole, with a K_1K_2 of $6.4 \pm 0.4 \times 10^3$ (mol/L)$^{-2}$. This surprising result is postulated to be a result of the relative aqueous solubility of these guests[16]: phenol is by far the most soluble of the three, with an aqueous solubility of 1 mol/L, compared with aniline (0.4 mol/L) and anisole (0.014 mol/L). Thus, in comparing phenol and anisole, the higher polarity of phenol would be expected to result in a stronger π–π and other interactions with the bistren cage, however its much higher solubility in the bulk water greatly reduces the hydrophobic effect,[23] reducing the driving force for inclusion into the less polar internal cavity. In the case of aniline, while the solubility is significantly higher than that of anisole, the much greater polarity is the dominant factor and results in a much stronger binding. The relative ability of these guests to form hydrogen bonds with the solvent may also play a role (as it does in the relative solubility), as formation of stronger hydrogen bonds with water would also decrease the driving force for inclusion into the host cavity (although hydrogen bonds with the host cage are also possible, which would strengthen the binding). This is a very interesting case of two co-existing driving forces for inclusion that have opposing dependence on the polarity (which is indirectly related to the aqueous solubility) of the guest. This makes it very difficult to predict the strength of binding for benzene derivatives based solely on polarity considerations; the solubility and hydrogen bonding to water also need to be taken into account in this case. This is an excellent illustration of the complexity and variability of the driving forces for host–guest inclusion as a phenomenon and the difficulty in predicting which host–guest partners will bind most strongly.

It is interesting that the bistren fluorescence decreases upon complexation of these aromatic guests. This observation of a decrease in fluorescence of a host with an aromatic fluorophore upon inclusion of an aromatic guest has been observed previously by our group, in the case of a fluorescent analogue of cucurbit[6]uril containing aromatic bisphthalhydrazide walls.[24,25] In that case, the fluorescence was seen to decrease significantly upon binding of both benzene and the aromatic fluorescent dye Nile Red, and there was also no accompanying spectral shift.[24] This effect was explained as a result of conformational changes in the host upon binding of the aromatic guest through strong π–π interactions, resulting in increased non-radiative decay pathways for the host excited state.[24] A similar effect of π–π interaction resulting in significant bistren conformational change, with a concomitant increase in nonradiative decay rate, is also likely for this case of the bistren binding of these benzene derivatives. This proposal will be further investigated by performing a full photophysical study, measuring fluorescence lifetimes and quantum yields to determine the rate

constants for the radiative and non-radiative decay pathways in the absence and presence of bound aromatic guests.

Conclusions

The bistren cage **1** has been shown to be a versatile and extremely useful host for neutral aromatic guests in addition to the ionic guests reported previously. In addition, the intrinsic fluorescence of this host has been shown to be highly sensitive to the presence of included aromatic guests, which makes the study of its inclusion complexes and measurement of binding constants very simple, using fluorescence spectroscopy.

In the case of the simple benzene derivatives studied, 1:2 host–guest complexes were formed, with two substituted benzene rings included in the large, oval-shaped host cavity. Very large total binding constants K_1K_2 were measured, ranging from 6.4×10^3 $(mol/L)^{-2}$ in the case of phenol to 3.5×10^7 $(mol/L)^{-2}$ in the case of aniline. The strength of the binding was found to depend in an interesting manner on two competing guest properties, namely the polarity and aqueous solubility. Strong binding was found to require the presence of strongly electron-donating substituents such as NH_2 in aniline (benzene itself was not found to bind) to strengthen $\pi-\pi$ interactions. Such substituents also allow for hydrogen bonding with the ammonium groups of the cage. However in the case of the relatively polar phenol, binding was much weaker than expected, presumably due to its much higher aqueous solubility, resulting in a decreased hydrophobic driving force for inclusion.

The results obtained in this study using some simple benzene derivatives should be extendable to other aromatic guests. The range of binding constants obtained indicates a good potential for guest selectivity, and this combined with its guest-sensitive intrinsic fluorescence makes this cage compound potentially useful as a versatile fluorescent sensor (for guests that do not absorb at 340 nm). Furthermore, the fact that this bistren cage **1** strongly binds two aniline guests means that there is the potential to form 1-dimensional chains by using 4,4′-diaminobiphenyl as a bridging guest. In this way, it is predicted that nanostructures consisting of long, one-dimensional architectures could be built by self-assembly of the bistren cage compound **1** and 4,4′-diaminobiphenyl in aqueous solution. Such a structure would be an organic supramolecular analogue of one-dimensional coordination polymers based on 4,4′-bipyridine and metal ion nodes.[26]

Acknowledgement

The authors acknowledge financial support from the Natural Sciences and Engineering Research Council of Canada (NSERC) through a Discovery Grant (BDW), Canada PGS Grants (PGB and CAS), and a Summer Undergraduate Research Award (SJA), as well as the Reactive Intermediates Student Exchange (RISE) program for providing a RISE Scholarship (SJA).

References

(1) Schneider, H.-J.; Yatsimirsky, A. K. *Chem. Soc. Rev.* **2008**, *37*, 263. doi:10.1039/b612543n. PMID:18197343.

(2) Li, S.; Purdy, W. C. *Chem. Rev.* **1992**, *92*, 1457. doi:10.1021/cr00014a009.

(3) Hedges, A. R. *Chem. Rev.* **1998**, *98*, 2035. doi:10.1021/cr970014w. PMID:11848958.

(4) Uekama, K.; Hirayama, F.; Irie, T. *Chem. Rev.* **1998**, *98*, 2045. doi:10.1021/cr970025p. PMID:11848959.

(5) Wagner, B. D. *Current Analytical Chemistry* **2007**, *3*, 183. doi:10.2174/157341107781023839.

(6) Wagner, B. D. Fluorescence studies of supramolecular host–guest inclusion complexes. In *Handbook of photochemistry and photobiology*; Nalwa, H. S., Ed.; American Scientific Publishers: New York, 2003; pp. 1–57.

(7) Wagner, B. D. In *The effects of cyclodextrins on guest fluorescence in cyclodextrin materials photochemistry, photophysics and photobiology*; Douhal, A., Ed.; Elsevier B.V.; 2006; pp. 27–59.

(8) Szejtli, J. *Chem. Rev.* **1998**, *98*, 1743. doi:10.1021/cr970022c. PMID:11848947.

(9) Lagona, J.; Mukhopadhyay, P.; Chakrabarti, S.; Isaacs, L. *Angew. Chem. Int. Ed.* **2005**, *44*, 4844. doi:10.1002/anie.200460675.

(10) Lehn, J.-M.; Pine, S. H.; Watanabe, E.; Willard, A. K. *J. Am. Chem. Soc.* **1977**, *99*, 6766. doi:10.1021/ja00462a055.

(11) De Santis, G.; Fabbrizzi, L.; Perotti, A.; Sardone, N.; Taglietti, A. *Inorg. Chem.* **1997**, *36*, 1998. doi:10.1021/ic960933p. PMID:11669814.

(12) Motekaitis, R. J.; Martell, A. E. *J. Am. Chem. Soc.* **1988**, *110*, 7715. doi:10.1021/ja00231a021.

(13) Martell, A. E. *J. Incl. Phenom. Macrocycl. Chem.* **1989**, *7*, 99. doi:10.1007/BF01112787.

(14) Fabbrizzi, L.; Faravelli, I.; Francese, G.; Licchelli, M.; Perotti, A.; Taglietti, A. *Chem. Commun. (Cambridge)* **1998**, 971. doi:10.1039/a800851e.

(15) Fabbrizzi, L.; Francese, G.; Licchelli, M.; Perotti, A.; Taglietti, A. *Chem. Commun. (Cambridge)* **1997**, 581. doi:10.1039/a608531h.

(16) Jorgensen, W. L.; Duffy, E. M. *Bioorg. Med. Chem. Lett.* **2000**, *10*, 1155. doi:10.1016/S0960-894X(00)00172-4. PMID:7525921.

(17) Nigam, S.; Durocher, G. *J. Phys. Chem.* **1996**, *100*, 7135. doi:10.1021/jp952855h.

(18) Sinnokrot, M. O.; Sherrill, C. D. *J. Am. Chem. Soc.* **2004**, *126*, 7690. doi:10.1021/ja049434a. PMID:15198617.

(19) Lide, D. R. (*Editor*). CRC Handbook of chemistry and physics. 85th ed. CRC Press: Boca Raton, Fla., USA, 2004.

(20) Desyatnyk, O.; Pszczółkowski, L.; Thorwirth, S.; Krygowski, T. M.; Kisiel, Z. *Phys. Chem. Chem. Phys.* **2005**, *7*, 1708. doi:10.1039/b501041a.

(21) Kawski, A.; Kukliński, B.; Bojarski, P. *Chem. Phys. Lett.* **2005**, *415*, 251. doi:10.1016/j.cplett.2005.09.008.

(22) Ko, C. H.; Fan, C.; Chiang, P. N.; Wang, M. K.; Lin, K. C. *J. Hazard. Mater.* **2007**, *149*, 275. doi:10.1016/j.jhazmat.2007.03.075. PMID:17478038.

(23) Liu, L.; Guo, Q.-X. *J. Incl. Phenom. Macrocycl. Chem.* **2002**, *42*, 1. doi:10.1023/A:1014520830813.

(24) Wagner, B. D.; Boland, P. G.; Lagona, J.; Isaacs, L. *J. Phys. Chem. B* **2005**, *109*, 7686. doi:10.1021/jp044369c. PMID:16851892.

(25) Lagona, J.; Wagner, B. D.; Isaacs, L. *J. Org. Chem.* **2006**, *71*, 1181. doi:10.1021/jo052294i. PMID:16438536.

(26) Moulton, B.; Zaworotko, M. J. From molecules to crystals: supramolecular synthesis of solids. In *Advances in supramolecular chemistry*; Gokel, G., Ed.; JAI Press; 2000; Vol. 7, pp. 235–283.

Comparing the fragmentation chemistry of gas-phase adducts of poly(dimethylsiloxane) oligomers with metal and organic ions

Justin Renaud, Abdulhrahman M. Alhazmi, and Paul M. Mayer

Abstract: Gas-phase ions of poly(dimethylsiloxane) oligomers were formed by electrospray ionization either by protonating them in solution with formic acid or by generating adducts of the oligomers with the metal ions Li^+, Na^+, K^+, and Ag^+ as well as with the organic cations NH_4^+, $CH_3CH_2NH_3^+$, and protonated glycine, aspartic acid, and 1,2-diphenylethylamine. The collision-induced fragmentation of the oligomeric ions was strongly dependent on the nature of the charging species. Ag^+ adducts dissociated in a manner previously observed in secondary ion mass spectrometry experiments generating a series of linear and cyclic fragment ions, while Li^+ adducts fragmented to form two ions: an adduct of the metal ion with the oligomer end-group and one with the remaining oligomer. Na^+ and K^+ adducts simply dissociate to form the bare metal ion. The organic species, to varying extents, transfer the proton to the oligomer to form a protonated poly(siloxane) ion. These protonated oligomers then dissociate at very low laboratory-frame collision energy along the siloxane backbone by loss of a silanol. These backbone fragments can then lose a methyl group to form a second series of fragment ions. Suggestions for probable mechanistic pathways for these processes are presented.

Key words: PDMS oligomers, amino acid, bases, metal ions, CID, mass spectrometry, fragmentation pathways.

Résumé : On a observé la formation en phase gazeuse d'ions d'oligomères poly(diméthylsiloxane) lors de l'ionisation par électronébulisation d'oligomères protonés en solution avec de l'acide formique ou par la génération d'adduits des oligomères avec les ions métalliques Li^+, Na^+, K^+ et Ag^+, les cations organiques NH_4^+, $CH_3CH_2NH_2^+$, ou les formes protonées de la glycine, de l'acide aspartique et de la 1,2-diphényléthylamine. La fragmentation induite par des collisions des ions oligomères dépend fortement de la nature des espèces utilisées pour les charger. Les adduits avec le Ag^+ se dissocient de la façon observée antérieurement lors d'expériences de spectrométrie de masse d'ions secondaires pour une série de fragments ioniques linéaires et cycliques alors que les adduits avec le Li^+ se fragmentent pour donner deux ions, un adduit de l'ion métallique avec la partie terminale de l'oligomère et un avec le reste de l'oligomère. Les adduits du Na^+ et du K^+ se dissocient simplement pour donner un ion métallique nu. Les espèces organiques transfèrent à des degrés variables le proton vers l'oligomère pour former un ion poly(siloxane) protoné. Sous l'influence d'énergie de collisions très faibles dans le cadre d'un laboratoire, les oligomères protonés se dissocient alors le long du squelette siloxane pour conduire à des pertes de silanol. Ces fragments de squelette peuvent alors perdre un groupe méthyle pour conduire à la formation d'une deuxième série de fragments ioniques. On présente des suggestions concernant les voies mécanistiques probables pour ces processus.

Mots-clés : oligomères poly(diméthylsiloxane), acide aminé, bases, ions métalliques, spectrométrie de masse, dissociation induite par des collisions, voies de fragmentations.

[Traduit par la Rédaction]

Introduction

Mass spectrometry (MS) has found increasing use in studying polymers because unlike other classical methods that provide a bulk characterization of polymers and (or) require a calibration standard, MS is able to examine individual oligomers.[1] Mass spectrometry is also capable of detecting contamination of the polymer sample, identifying endgroups, co-polymer characterization, and examining the fragmentation processes. Secondary ion mass spectrometry using time of flight has also proved to be a valuable tool in studying polymer surfaces and the fragmentation process. The fragmentation of specific polymers can be affected by numerous factors, including conformation in the gas phase.[2]

Polysiloxanes find significant use in a wide range of applications. Poly(dimethylsiloxane) (PDMS) is nontoxic to proteins and cells[3] and has a high thermal and chemical inertness making it ideal for industrial uses such as lubricants, sealants, caulking, water repellents, and resins as well as biomedical and biochemical applications including fabrication of microfluidic devices.[4]

Because of its importance, many studies have examined PDMS, including thermal degradation and mass spectrometry studies into the effects of functional group substitution and endgroup substitution[5] on the fragmentation process. Chen, using ab initio calculations and fourier transform ion cyclotron resonance (FT-ICR) mass spectrometry, has proposed that certain functionalized endgroups can be directly

Received 15 September 2008. Accepted 10 December 2008. Published on the NRC Research Press Web site at canjchem.nrc.ca on 23 January 2009.

J. Renaud, A.M. Alhazmi, and P.M. Mayer.[1] Department of Chemistry, University of Ottawa, 10 Marie-Curie, Ottawa, ON K1N 6N5, Canada.

[1]Corresponding author (e-mail: pmmayer@uottawa.ca).

involved in assisting in the cleavage of the siloxane bond through a backbiting mechanism.[6]

The most industrially relevant endgroup of PDMS is trimethylsilyl because of its increased stability compared with hydroxyl-terminated oligomers.[7] The disadvantage of studying PDMS terminated with this endgroup is that trimethylsilyl cannot be directly protonated such as amine-containing endgroups like (aminopropyl)dimethylsiloxane and (amidopropyl)dimethylsiloxane. Mass spectra of PDMS have been obtained for smaller mass ranges using electron ionization (EI)[8] and pyrolysis[9] methods. Much higher molecular weight samples have been analyzed using secondary ion time of flight mass spectrometry (SIMS-TOF), which has evaluated the molecular weight[10] and fragmentation pathway of PDMS[11] and other polysiloxanes.[12] In the examples above that used SIMS, silver was used as a substrate and so several Ag^+ adducts were observed. The predominant low mass fragment ions observed in the mass spectra were linear and cyclic PDMS oligomers. Dong et al. proposed a mechanism for the formation of the cyclic fragment ions in which the silver ion does not play a role (Scheme 1). However, because of the nature of the SIMS process, it is often difficult to ascertain the origin of the observed fragment ions and the effects the silver ion has on the fragmentation processes. As studies involving other polymers have shown, the complexing agent can directly impact the observed fragmentation patterns.[13]

Depending on the polymer, it is possible for it to be directly protonated or cationized by certain metal ions such as Li^+, K^+, or Ag^+. In addition to metals, it has recently been shown that some organic molecules, including amino acids and small peptides, can be used to form proton-bound complexes with oligomers of poly(methylmethacrylate) and poly(butylacrylate) using electrospray ionization mass spectrometry (ESI-MS), and that these complexes fragment in a complimentary way to their metal ion adduct analogues.[14] The aim of this study was to explore a range of conventional and nonconventional ionizing agents capable of forming a complex with PDMS oligomers and to identify and compare their major fragmentation pathways.

Experimental procedures

Poly(dimethylsiloxane), terminated by trimethylsilyl having an average molecular weight of 800 Da, was obtained from Sigma-Aldrich. PDMS concentrations of 0.1 mgL^{-1} were mixed in a 1:1 ratio with a metal salt (LiCl, NaCl, KOH, or $AgNO_3$) or organic molecule (ammonium acetate, ethylamine, 1,2-diphenylethylamine, glycine, and aspartic acid) of concentration of 0.1 mgL^{-1} in a solvent of 1:1 methanol/iso-propanol. One drop of 5% formic acid was added to the organic solutions to protonate the amine. Protonated PDMS was obtained by adding only 1 drop of 5% formic acid directly to the PDMS solution.

A Micromass Quattro LC (Waters Micromass, Manchester, UK) triple quadrupole mass spectrometer was used to carry out the low-resolution electrospray ionization mass spectrometry (ESI-MS) and tandem mass spectrometry (ESI-MS/MS). Sample solutions were introduced by syringe pump at a flow rate of 40 μL/min. The sample cone voltage was set between 20 and 130V. Collision-induced dissociation was carried out with argon at a gas pressure of 1×10^{-3} mbar (1 bar = 100 kPa), and laboratory frame collision energies ranging from 0 to 100 eV (specific settings are included in each figure caption). All collision energies reported are in the laboratory frame. The resolution of the first quadrupole was set to unit mass resolution (15 in the Masslynx software) for all experiments. The resolution of the final quadrupole was held constant at 12 to increase the sensitivity of the ESI-MS/MS experiments. A Micromass Q-TOF 1 was used for the accurate mass CID experiments with a resolution of 6 000 and mass accuracy of 15 ppm. The calibration ion was the doubly charged molecular ion of [glu[1]]-Fibrinopeptide B.

Scheme 1.

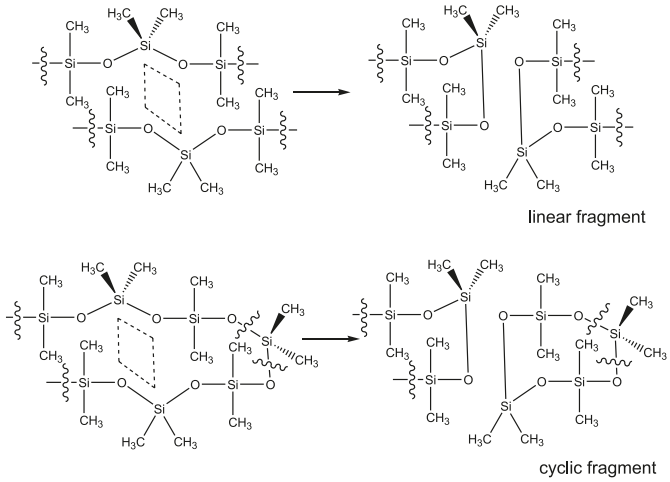

Results and discussion

Table 1 summarizes the masses for the PDMS oligomers and assorted ions used to form adducts in ESI-MS.

Electrospray ionization mass spectrometry

While it is straightforward to create protonated PDMS (Fig. 1*a*), any of the metal ion adducts (Fig. 1*b* and Fig. S1 in the Suplementary data) and adducts with any of the organic species listed in Table 1 (Fig. 1*c* and Fig. S2 in the Supplementary data), those with the proton and aspartic acid exhibited a low intensity to the point that the ion series due to $(PDMS)H^+$ and $(PDMS)(Asp)H^+$ were less abundant than those due to $(PDMS)Na^+$ arising from contamination of the glassware use to prepare the samples. A similar oligomer distribution was observed in each case, corresponding to linear trimethylsilyl terminated PDMS. No evidence for the presence of cyclic oligomers could be detected in the mass spectra in the mass range studied (Fig. 1). SIMS-TOF studies of PDMS using a silver substrate observed both cyclic and linear oligomer fragments in the same *m/z* range as this study.[11,12] This illustrates that the cyclic ions proposed in the SIMS work were indeed due to the fragmentation of higher molecular weight oligomers in the ionization–desorption process.

A sample containing equimolar amounts of $AgNO_3$, LiCl, and glycine (0.0018 mmol/L each) was mixed with 0.3 mg/mL of PDMS, and the dependence on cone voltage of the formation of oligomer adducts was examined (Fig. 2).

Table 1. Summary of masses for PDMS oligomers and ionizing agents.

Species	Mass (Da)
$(CH_3)_3Si$-$[OSi(CH_3)_2]_n$-CH_3	
$OSi(CH_3)_2$	74
$(CH_3)_3Si$	73
CH_3	15
Li^+	7
Na^+	23
K^+	39
Ag^+	107, 109
NH_4^+	18
$CH_3CH_2NH_3^+$	46
(Glycine)H^+	76
(Aspartic acid)H^+	134
(1,2-diphenylethylamine)H^+	198

Lower voltages (20 V) favoured adducts with glycine, with the relative abundance of these adducts decreasing with increasing voltage. Moderate cone voltages (> 50 V) completely disrupt the proton-bound complex with glycine, while Li^+ exhibits a tendency to prefer the shorter oligomers and Ag^+ the longer oligomers.

Tandem mass spectrometry

In the following discussion, "R" represents the number of monomers (dimethylsiloxyl) in a fragment ion, while "M" will be used to represent the number of monomers left in a neutral, trimethylsilyl-terminated oligomer.

Lithium

Lithium ion adducts of PDMS exhibit unique fragmentation chemistry upon collision activation. At laboratory-frame collision energies of 50 eV, two dominant fragment ion peaks are observed (Fig. 3*a*), *m*/*z* 81 and a peak resulting from the precursor ion losing 74 Da retaining the lithium. Accurate mass measurements of *m*/*z* 613 and the molecular ion peak in Fig. 3*a* give *m*/*z* 613.287 and 687.262. The accurate mass of the neutral loss between the precursor ion and *m*/*z* 613 in Fig. 3*a* is 73.975 Da, which is closer to that expected for $(CH_3)_2SiO$, 74.018 Da, than for $(CH_3)_3SiH$, 74.0549 Da. The observed fragment ion with *m*/*z* 81 (which lies outside the calibration mass range of the GFP standard and whose accurate mass cannot be used for elemental composition) suggests a mechanism similar to that proposed for the fragmentation of poly(methyl methacrylate) oligomers ionized with sodium.[15] The oligomer ion adopts a cyclic structure, with Li^+ binding near the two terminal ends. Charge-induced methyl group transfer and cleavage near one end would result in the lithium ion departing with one of the $(CH_3)_2SiO$ groups at the end of the oligomer (Scheme 2). If the Li^+ remains with the rest of the oligomer, *m*/*z* 613 results. Fragmentation along the lines of that shown in Scheme 1 should result in a wide distribution of $(R_n)Li^+$ fragment ions and almost never $((CH_3)_2SiO)Li^+$.

Sodium and potassium

CID of the sodiated or potassiated adducts resulted primarily in the dissociation of the complex giving the bare metal ion; increasing collision energy resulted in an increase in the Na^+ or K^+ peak intensity and a decrease in precursor ion intensity. In the case of K^+, weak fragment ions appearing to contain potassium were observed with *m*/*z* 200–400 but could not be reliably identified (Fig. 3*b*). The results of the CID experiments for Li^+, Na^+, and K^+ adducts appear to confirm the binding energy order $Li^+ > Na^+ > K^+$ noted by Gidden et al.[15]

Fig. 1. ESI mass spectra of PDMS oligomers complexed with (*a*) H^+, (*b*) Li^+, and (*c*) NH_4^+.

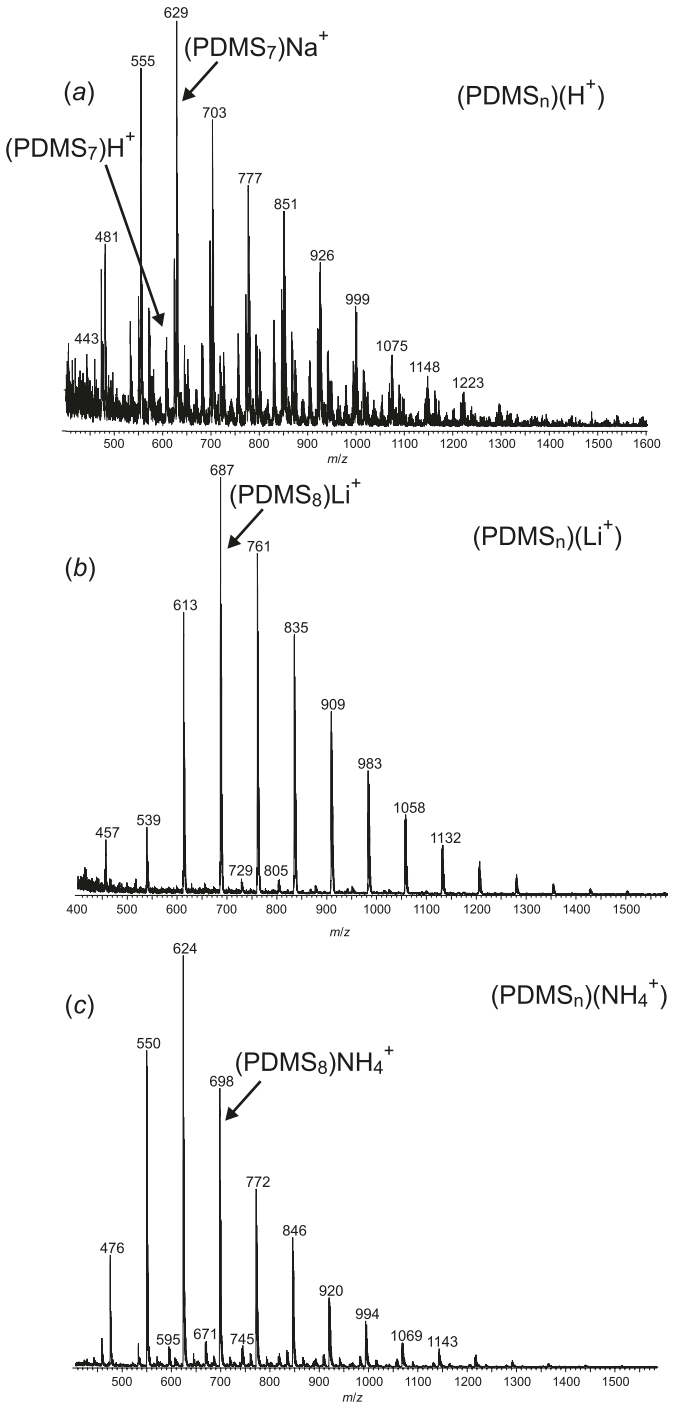

Fig. 2. ESI mass spectra of PDMS oligomers mixed with equimolar amounts of LiCl, $AgNO_3$, and glycine at a cone voltage of (*a*) 20 V and (*b*) 130 V. In each mass spectrum G, L, and A denote the adducts formed with protonated glycine, lithium ions, and silver ions, respectively.

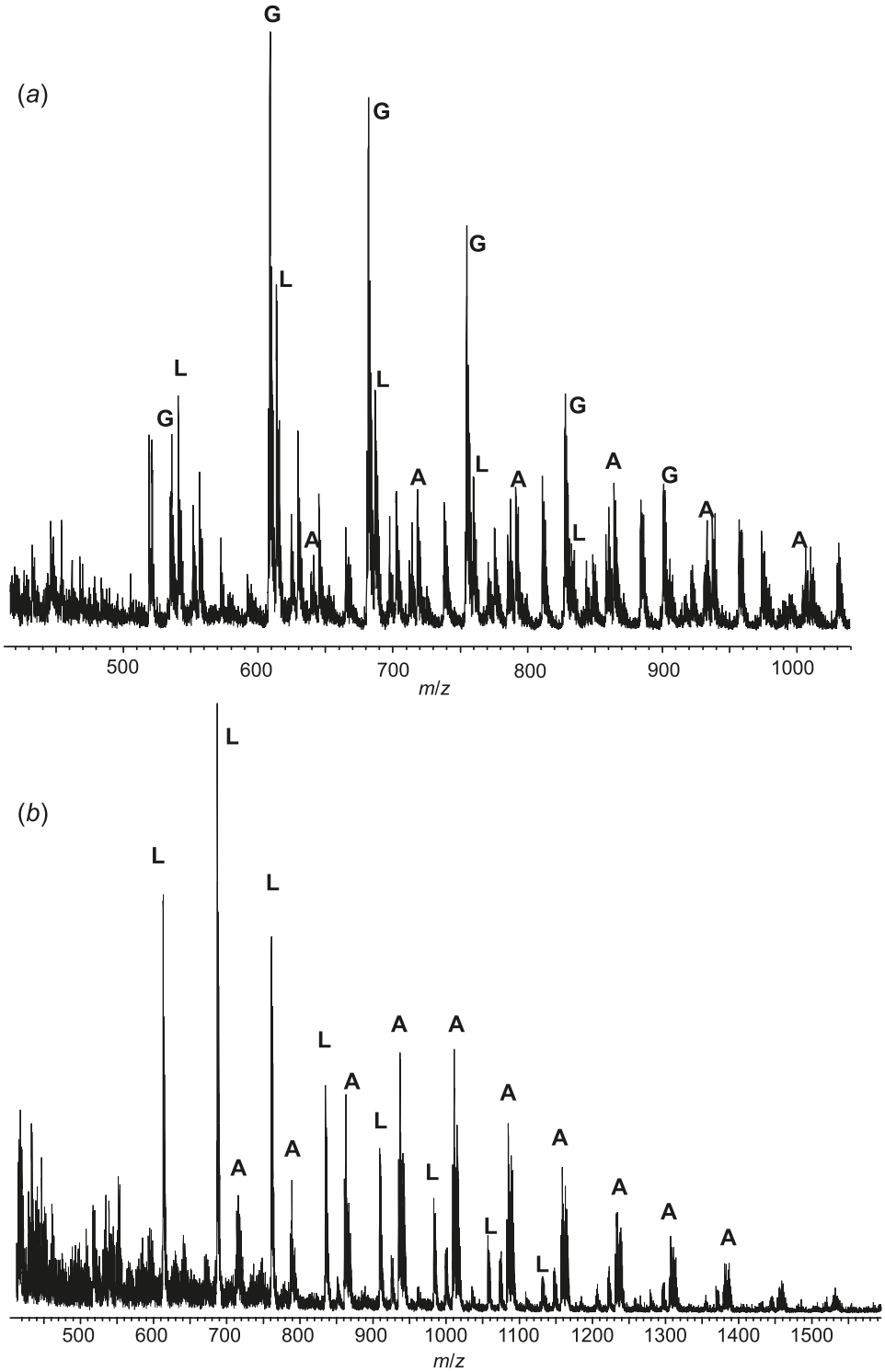

Silver

Two major series of fragment ions are observed above collision energies of 25 eV: $(R_n+73)^+$ and $(R_n+58)^+$ (Fig. 3*c*). Both are due to the initial charge transfer from Ag^+ to the oligomer, followed by fragmentation of the resulting radical cation. The series denoted $(R_n+58)^+$ nominally are due to the loss of a methyl radical and are consistent with the "cyclic" ions observed in the SIMS studies of these complexes. The collision energy dependence of the CID mass spectra shows that $(R_n+73)^+$ and $(R_n+58)^+$ arise simultaneously at a collision energy of 30 eV (Fig. 4*a*), supporting the proposed scheme whereby a four-member siloxane ring is formed, yielding linear and cyclic fragments in the same process (Scheme 1, after charge trans-

Fig. 3. CID mass spectra for PDMS oligomers complexed with (*a*) Li^+ (50 eV), (*b*) K^+ (25 eV), and (*c*) $^{109}Ag^+$ (40 eV).

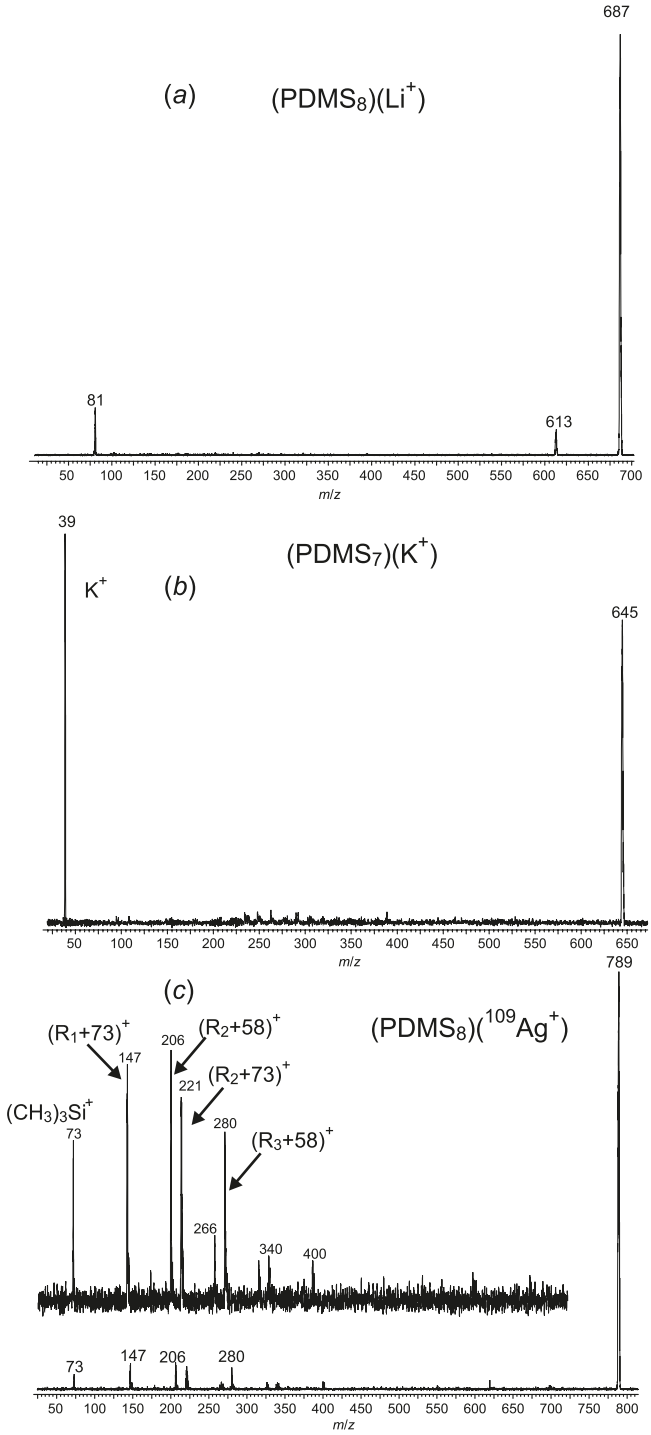

Fig. 4. Collision energy resolved breakdown diagrams for the formation of the $(R_2+73)^+$ and $(R_2+58)^+$ fragment ions from (*a*) $(PDMS_7)(Ag^+)$ and (*b*) $(PDMS_7)(NH_4^+)$ complexes.

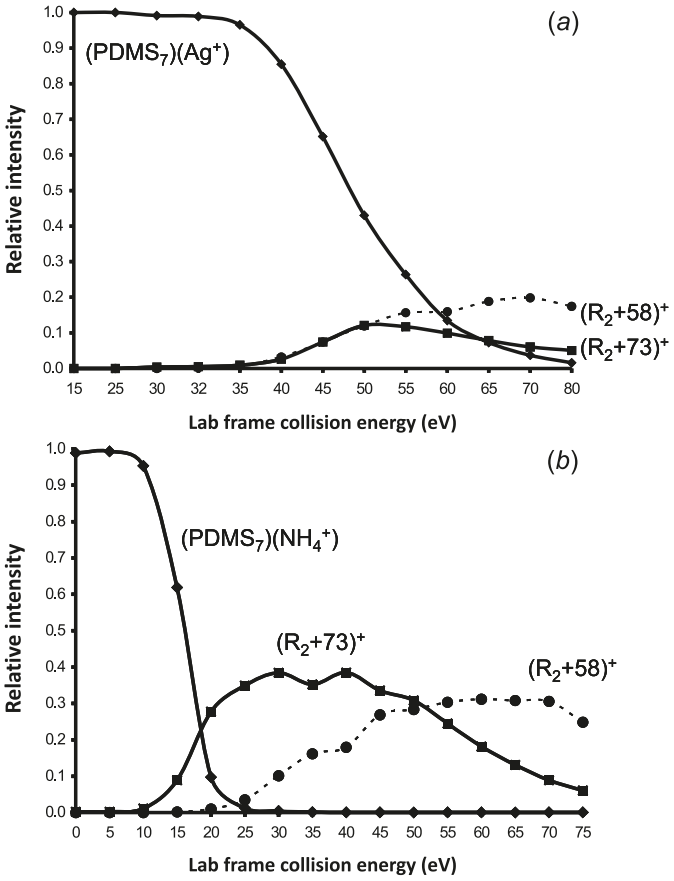

Fig. 5. CID mass spectrum of $(PDMS_7)(NH_4^+)$ (5 eV). Molecular ion at *m/z* 624 not shown.

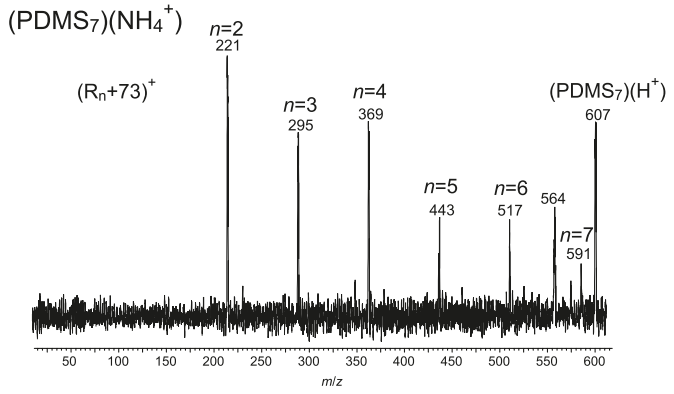

fer to the oligomer). At higher collision energies, the cyclic $(R_2+58)^+$ ions become dominant over the linear $(R_2+73)^+$. The low *m/z* fragment ions are almost the same as those reported in previous SIMS studies, with the exception that the Ag^+ ion peak is not very intense.[11,12]

Protonation, ammonia, ethylamine and glycine

CID of the proton-bound oligomer–ethylamine complex results only in the formation of protonated ethylamine, indicating that the gas-phase basicities of the PDMS oligomers are significantly less than that of ethylamine (878 kJ mol^{-1}).[16] In contrast, CID of $(PDMS)H^+$, $(PDMS)NH_4^+$, and $(PDMS)(Gly)H^+$ complexes result in the formation of $(R_n+73)^+$ fragment ions at very low collision energies (Fig. 5). Upon dissociation of the proton-bound complex, the proton may be associated with any of the oxygen atoms along the oligomer backbone, driving cleavage to form the $(R_n+73)^+$ series of ions (Scheme 3). As the length of the oligomers in-

Scheme 2.

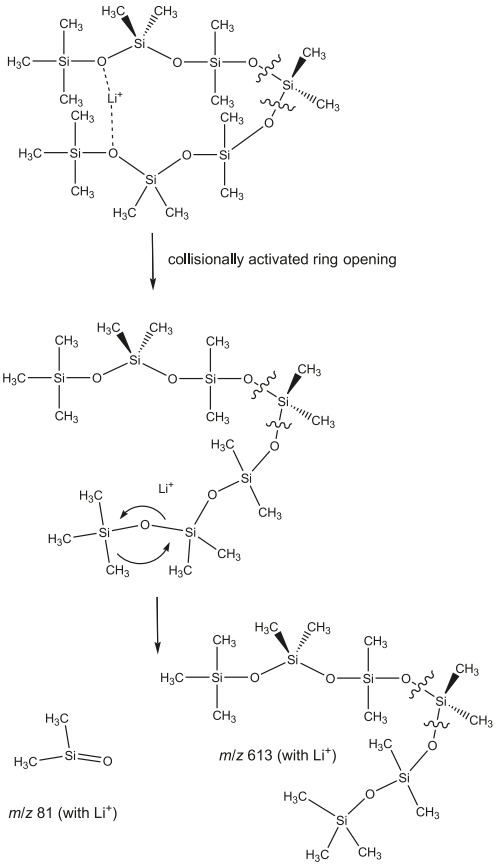

Scheme 3.

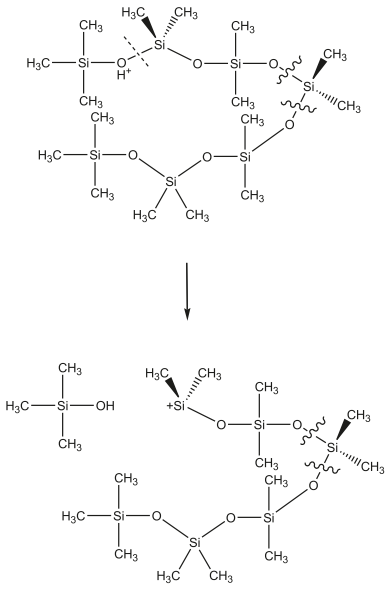

creases, the same series is observed, but fragment ions above $(R_6+73)^+$ are not as prominent as those with $2 \leq n \leq 6$. The trimethylsilyl fragment (*m/z* 73) and the $(R_1+73)^+$ fragment ions only appear at higher collision energies. $(R_n+58)^+$ fragment ions do appear with low abundance in the CID mass spectra, but the collision energy dependence clearly shows them to be formed sequentially from the $(R_n+73)^+$ ions by methyl radical loss (Fig. 4*b*). It is therefore unlikely that they have the cyclic structure previously proposed, as this would be an entropically unfavourable pathway.

1,2 diphenylethylamine

CID of the (PDMS)(DPEA)H^+ complex results predominantly in the formation of protonated DPEA. Although a small signal due to the protonated oligomer is observed, it does not undergo the same degree of fragmentation observed in the case of H^+, NH_4^+, or $GlyH^+$. One explanation is if the deposited collision energy is statistically distributed among all the degrees of freedom of the complex, relatively less will land up in the protonated oligomer than was the case when the adduct was formed with a smaller molecule.

Conclusion

Changing the complexing agent from a metal ion to a protonated organic base facilitates the formation of a gas-phase protonated PDMS oligomer upon collisional activation. This protonated oligomer undergoes a well-defined cleavage along the Si-O backbone, which is quite distinct from that observed for the metal ion adducts. This approach may be useful for sequencing co-polymers containing dimethylsiloxane or for locating branching sites in more complex samples.

Supplementary data

Supplementary data for this article are available on the journal Web site (canjchem.nrc.ca) or may be purchased from the Depository of Unpublished Data, Document Delivery, CISTI, National Research Council Canada, Ottawa, ON K1A 0R6, Canada. DUD 3876. For more information on obtaining material refer to cisti-icist.nrc-cnrc.gc.ca/cms/unpub_e.shtml.

Acknowledgements

PMM thanks the Natural Sciences and Engineering Research Council of Canada for continuing financial support. JR thanks the same agency for a summer USRA during which this work was completed. The authors thank Waters Micromass for the generous donation of the Q-TOF 1 mass spectrometer.

References

(1) Vergne, M. J.; Hercules, D. M.; Lattimer, R. P. *J. Chem. Educ.* **2007**, *84*, 81.
(2) Casey, J.; Alhazmi, A.; Mayer, P. M. *Eur. J. Mass Spectrom. (Chichester, Eng.)* **2005**, *11*, 557. doi:10.1255/ejms.779.
(3) Ng, J. M. K.; Gitlin, I.; Stroock, A. D.; Whitesides, G. M. *Electrophoresis* **2002**, *23*, 3461. doi:10.1002/1522-2683(200210)23:20<3461::AID-ELPS3461>3.0.CO;2-8. PMID:12412113.
(4) Duffy, D. C.; McDonald, J. C.; Schueller, O. J. A.; Whitesides, G. M. *Anal. Chem.* **1998**, *70*, 4974. doi:10.1021/ac980656z.
(5) Maziarz, E. P.; Baker, G. A.; Wood, T. D. *Macromolecules* **1999**, *32*, 4411. doi:10.1021/ma981877+.
(6) Chen, H. *J. Am. Soc. Mass Spectrom.* **2003**, *14*, 1039. doi:10.1016/S1044-0305(03)00400-8.
(7) Lauprêtre, N.; Monnerie, L. *Eur. Polym. J.* **1978**, *14*, 415. doi:10.1016/0014-3057(78)90061-7.

(8) Pickering, G. R.; Olliff, C. J.; Rutt, K. J. *Org. Mass Spectrom.* **1975**, *10*, 1035. doi:10.1002/oms.1210101114.
(9) Ballistreri, A.; Garozzo, D.; Montaudo, G. *Macromolecules* **1984**, *17*, 1312. doi:10.1021/ma00137a003.
(10) Inoue, M.; Murase, A. *Anal. Sci.* **2004**, *20*, 1623. doi:10.2116/analsci.20.1623. PMID:15636505.
(11) Dong, X.; Proctor, A.; Hercules, D. M. *Macromolecules* **1997**, *30*, 63. doi:10.1021/ma961018q.
(12) Dong, X.; Gusev, A.; Hercules, D. M. *J. Am. Soc. Mass Spectrom.* **1998**, *9*, 292. doi:10.1016/S1044-0305(98)00003-8.
(13) Selby, T. L.; Wesdemiotis, C.; Lattimer, R. P. *J. Am. Soc. Mass Spectrom.* **1994**, *5*, 1081. doi:10.1016/1044-0305(94)85069-0.
(14) Alhazmi, A. M.; Mayer, P. M. *J. Am. Soc. Mass Spectrom.* **2009**, *20*, 60. doi:10.1016/j.jasms.2008.09.014.
(15) Gidden, J.; Jackson, A. T.; Scrivens, J. H.; Bowers, M. T. *Int. J. Mass Spectrom.* **1999**, *188*, 121. doi:10.1016/S1387-3806(98)14287-2.
(16) Hunter, E. P.; Lias, S. G. *Proton affinity evaluation. NIST Chemistry WebBook, NIST Standard Reference Database Number 69.* Linstrom, P. J., and Mallard, W. G., Eds.; National Institute of Standards and Technology: Gaithersburg, Md., USA. Available from http://webbook.nist.gov [accessed September 2008].

Syntheses, X-ray structures, and redox behaviour of the group 14 bis-boraamidinates M[PhB(μ-*N*-*t*-Bu)$_2$]$_2$ (M = Ge, Sn) and Li$_2$M[PhB(μ-*N*-*t*-Bu)$_2$]$_2$ (M = Sn, Pb)

Jari Konu, Heikki M. Tuononen, and Tristram Chivers

Abstract: The solid-state structures of the complexes M[PhB(μ-*N*-*t*-Bu)$_2$]$_2$ (**1a,** M= Ge; **1b**, M = Sn) were determined to be spirocyclic with two orthogonal boraamidinate (*bam*) ligands N,N′-chelated to the group 14 centre. Oxidation of **1b** with SO_2Cl_2 afforded the thermally unstable, blue radical cation {Sn[PhB(μ-*N*-*t*-Bu)$_2$]$_2$}$^{\bullet+}$, identified by electron paramagnetic resonance (EPR) spectroscopy supported by density functional theory (DFT) calculations, whereas the germanium analogue **1a** was inert towards SO_2Cl_2. The reaction between Li$_2$[PhB(μ-*N*-*t*-Bu)$_2$]$_2$ and $SnCl_2$ or PbI_2 in 2:1 molar ratio in diethyl ether produced the novel heterotrimetallic complexes Li$_2$Sn[PhB(μ-*N*-*t*-Bu)$_2$]$_2$ (**2b**) and (Et$_2$O·Li)LiPb[PhB(μ-*N*-*t*-Bu)$_2$]$_2$ (**2c**·OEt$_2$), respectively. By contrast, treatment of Li$_2$[PhB(μ-*N*-*t*-Bu)$_2$]$_2$ with $C_4H_8O_2$·$GeCl_2$ yielded the germanium(IV) complex **1a** via a redox process. The X-ray structures of **2b** and **2c**·THF revealed polycyclic arrangements in which one *bam* ligand is N,N′-chelated to the Sn(II) or Pb(II) atom and one of the Li$^+$ cations, while the second *bam* ligand exhibits a unique bonding mode, bridging all three metal centres. The fluctional behaviour of **2b** was investigated by variable temperature, multinuclear NMR spectroscopy.

Key words: germanium, tin, lead, boraamidinate, cation radical.

Résumé : On a déterminé que les structures à l'état solide des complexes M[PhB(μ-*N*-*t*-Bu)$_2$]$_2$ (**1a**, M = Ge; **1b**, M = Sn) sont spirocycliques avec deux ligands orthogonaux boraamidinate (bam) avec une chélation N,N′ avec le centre du groupe 14. L'oxydation du produit **1b** à l'aide de SO_2Cl_2 conduit à la formation du cation radical bleu, thermiquement instable {Sn[PhB(μ-*N*-*t*-Bu)$_2$]$_2$}$^{\bullet+}$ identifié par spectroscopie RPE supportée par des calculs à base de la théorie de la fonctionnelle de la densité; l'analogue germanié 1a est inerte vis-à-vis du SO_2Cl_2. La réaction du Li$_2$[PhB(μ-*N*-*t*-Bu)$_2$]$_2$ avec le $SnCl_2$ ou le PbI_2, dans un rapport molaire de 2:1, dans l'éther éthylique, conduit à la formation de nouveaux complexes hétérométalliques Li$_2$Sn[PhB(μ-*N*-*t*-Bu)$_2$]$_2$ (**2b**) et (Et$_2$O·Li)LiPb[PhB(μ-*N*-*t*-Bu)$_2$]$_2$ (**2c**·OEt2). Toutefois, le traitement du Li$_2$[PhB(μ-*N*-*t*-Bu)$_2$]$_2$ par du $C_4H_8O_2$·$GeCl_2$ fournit le complexe de germanium(IV) (**1a**) par le biais d'un processus redox. Les structures des produits **2b** et **2c**·THF, déterminées par diffraction des rayons X, révèlent la présence d'arrangements polycycliques dans lesquels un ligand bam est soumis à une chélation en N,N′ par rapport à l'atome de Sn(II) ou Pb(II) et un des cations Li$^+$ alors que le second ligand bam donne lieu à un mode unique de liaison et qu'il crée un pont pour les trois centres métalliques. On a étudié le comportement fluxionnel du produit en faisant appel à la spectroscopie RMN multinucléaire à température variable.

Mots-clés : germanium, étain, plomb, boraamidinate, cation radical.

[Traduit par la Rédaction]

Introduction

The dianionic boraamidinate (*bam*) ligand, [RB(NR′)$_2$]$^{2-}$ (**B**), is formally isoelectronic with the extensively studied monoanionic amidinate (*am*) ligand, [RC(NR′)$_2$]$^-$ (**A**). A wide range of main-group element and transition-metal complexes have been structurally characterized and a variety of bonding modes have been established for the *bam* ligand.[1–4]

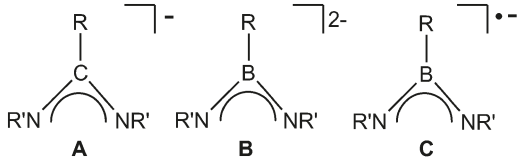

The most intriguing consequence of the 2– charge is the facile tendency for redox transformations to occur in which the dianion **B** is oxidized to the corresponding monoanion radical [*bam*]$^{\bullet-}$ (**C**). This paramagnetic ligand can be stabilized through chelation, e.g., to early main-group metals.[5,6] In the case of group 13 metals it has been possible to isolate *stable* neutral radicals. For example, the intensely coloured paramagnetic species {M[PhB(μ-*N*-*t*-Bu)$_2$]$_2$}$^{\bullet}$ (M = Al, dark red; M = Ga, dark green) are produced by one-electron oxidation of the corresponding anions with iodine, and the X-

Received 17 October 2008. Accepted 1 December 2008. Published on the NRC Research Press Web site at canjchem.nrc.ca on 27 January 2009.

J. Konu and T. Chivers.[1] Department of Chemistry, University of Calgary, Calgary, AB T2N 1N4, Canada.
H.M. Tuononen. Department of Chemistry, University of Jyväskylä, P.O. Box 35, FI-40014 Jyväskylä, Finland.

[1]Corresponding author (e-mail: chivers@ucalgary.ca).

ray structures of these spirocyclic complexes have been determined (Scheme 1).[5] The singly occupied molecular orbital (SOMO) of these neutral radicals is located primarily and equally in p-orbitals on the four nitrogen atoms of the two *bam* ligands; there is very little electron density on the group 13 centres. The corresponding boron and indium-containing radicals $\{M[PhB(\mu\text{-}N\text{-}t\text{-}Bu)_2]_2\}^\bullet$ (M = B, In) were characterized only in solution by electron paramagnetic resonance (EPR) spectroscopy.[6]

The synthesis and characterization of the group 13 complexes $\{M[PhB(\mu\text{-}N\text{-}t\text{-}Bu)_2]_2\}^\bullet$ (M = Al, Ga, In) raises the question of whether the isoelectronic group 14 cation radicals $\{M[PhB(\mu\text{-}N\text{-}t\text{-}Bu)_2]_2\}^{\bullet+}$ (M = Si, Ge, Sn) will be accessible by mild oxidation of the corresponding neutral precursors. Several *bam* complexes of group 14 elements (Si, Ge, Sn, Pb) have been reported.[1] Although the metathesis reactions of two equivalents of Li_2*bam* reagents with MCl_4 (M = Ge, Sn) afford the corresponding M(*bam*)$_2$ complexes,[7,8] the synthesis of a silicon analogue (M = Si) by this method has not been reported. The known silicon complexes have only one *bam* ligand chelated to silicon in complexes of the type RR′Si(*bam*); they were prepared by indirect approaches rather than metathesis.[9,10] The solid-state structures of M(*bam*)$_2$ complexes (M = Ge, Sn) have not been determined. Interestingly, the reaction of $Li_2[PhB(\mu\text{-}N\text{-}t\text{-}Bu)_2]$ with $PbCl_4$ produces the dimeric lead(II) complex $\{Pb[PhB(\mu_3\text{-}N\text{-}t\text{-}Bu)_2]\}_2$, which is preferably prepared by using $PbCl_2$ as a source of lead(II).[11] There are no reports of complexes in which two *bam* ligands are chelated to a group 14 metal in the formal +2 oxidation state, i.e., $[M(bam)_2]^{2-}$ (M = Ge, Sn, Pb). These dianions are isoelectronic with the corresponding group 15 monoanions of the type $[M(bam)_2]^-$ (M = As, Sb, Bi), which exhibit interesting polycyclic structures in the solid state and fluctional behaviour in solution.[12] The synthesis of dilithio derivatives of the group 14 dianions $[M(bam)_2]^{2-}$ (M = Ge, Sn, Pb) is, therefore, of interest for comparison with their group 15 analogues.

In this contribution we report (*a*) the X-ray structures of the complexes $M[PhB(\mu\text{-}N\text{-}t\text{-}Bu)_2]_2$ (**1a**, M = Ge; **1b**, M = Sn), (*b*) oxidation of **1b** with SO_2Cl_2 to give the radical cation $\{Sn[PhB(\mu\text{-}N\text{-}t\text{-}Bu)_2]_2\}^{\bullet+}$, which was identified by EPR spectroscopy supported by density functional theory (DFT) calculations, (*c*) the synthesis and X-ray structures of the new heterotrimetallic complexes $Li_2Sn[PhB(\mu\text{-}N\text{-}t\text{-}Bu)_2]_2$ (**2b**) and (THF·Li)LiPb$[PhB(\mu\text{-}N\text{-}t\text{-}Bu)_2]_2$ (**2c**·THF), and (*d*) variable temperature, multinuclear (^{1}H, ^{13}C, ^{7}Li, ^{11}B, and ^{119}Sn) NMR investigations of the fluctional behaviour of **2b**.

Experimental section

Reagents and general procedures

All reactions and the manipulations of products were performed under an argon atmosphere by using standard Schlenk techniques or an inert atmosphere glove box. The compounds $PhBCl_2$ (Sigma-Aldrich, 97%), $GeCl_4$ (Strem, 99.99%), $C_4H_8O_2{\cdot}GeCl_2$ (Sigma-Aldrich, 99%), $SnCl_4$ (Sigma-Aldrich, 1.0 mol/L soln. in heptane), $SnCl_2$ (Sigma-Aldrich, 98%), PbI_2 (Strem, 99.999%), and *t*-$BuNH_2$ (Sigma-Aldrich, 98%) were used as received. SO_2Cl_2 (Sigma-Aldrich, 97%) was distilled prior to use. LiN(H)-*t*-Bu was prepared by the addition of *n*-BuLi to a solution of anhydrous *t*-$BuNH_2$ in *n*-hexane at –10 °C and its purity was checked by ^{1}H NMR spectroscopy. The compounds $PhB[N(H)\text{-}t\text{-}Bu]_2$ and $Li_2[PhB(\mu\text{-}N\text{-}t\text{-}Bu)_2]$ were prepared as described earlier.[13] The solvents *n*-hexane, toluene, Et_2O, and THF were dried by distillation over Na/benzophenone under an argon atmosphere prior to use. Elemental analyses were performed by Analytical Services, Department of Chemistry, University of Calgary (Calgary, Alberta).

Scheme 1. Synthesis of spirocyclic $\{M[PhB(\mu\text{-}N\text{-}t\text{-}Bu)_2]_2\}^\bullet$ radicals.

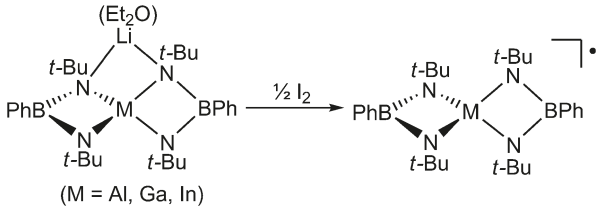

Spectroscopic methods

The ^{1}H, ^{7}Li, ^{11}B, ^{13}C, and ^{119}Sn NMR spectra were obtained in d_8-toluene at 23 °C on a Bruker DRX 400 spectrometer operating at 399.59, 155.30, 128.20, 100.49, and 149.00 MHz, respectively. ^{1}H and ^{13}C spectra are referenced to the solvent signal and the chemical shifts are reported relative to $(CH_3)_4Si$. ^{7}Li and ^{11}B NMR spectra are referenced externally and the chemical shifts are reported relative to a 1.0 mol/L solution of LiCl in D_2O and to a solution of $BF_3{\cdot}Et_2O$ in C_6D_6, respectively. Similarly, the ^{119}Sn NMR spectra are referenced externally and the chemical shifts are reported relative to $(CH_3)_4Sn$.

The X-band EPR spectra were recorded on a Bruker EMX 113 spectrometer equipped with a variable-temperature accessory. EPR spectral simulations were carried out by using WINEPR SimFonia (version 1.25, 1996) and PEST WinSim (version 0.98, 2002) softwares.[14]

X-ray crystallography

Crystallographic data for **1a**, **1b**, **2b**, and **2c**·THF are summarized in Table 1 (also see the Supplementary data). Crystals of $Ge[PhB(\mu\text{-}N\text{-}t\text{-}Bu)_2]_2$ (**1a**), $Sn[PhB(\mu\text{-}N\text{-}t\text{-}Bu)_2]_2$ (**1b**), $Li_2Sn[PhB(\mu\text{-}N\text{-}t\text{-}Bu)_2]_2$ (**2b**), and (THF·Li)LiPb$[PhB(\mu\text{-}N\text{-}t\text{-}Bu)_2]_2$ (**2c**·THF) were coated with Paratone 8277 oil and mounted on a glass fibre. Diffraction data were collected on a Nonius Kappa CCD diffractometer using monochromated Mo Kα radiation (λ = 0.71073 Å) at –100 °C. The data sets were corrected for Lorentz and polarization effects, and empirical absorption correction was applied to the net intensities. The structures were solved by direct methods using SHELXS-97[15] and refined using SHELXL-97.[16] After full-matrix least-squares refinement of the nonhydrogen atoms with anisotropic thermal parameters, the hydrogen atoms were placed in calculated positions [C-H = 0.98 Å for $C(CH_3)_3$ and 0.95 Å for phenyl hydrogens]. The isotropic thermal parameters of the hydrogen atoms were fixed at 1.2 times to that of the corresponding carbon for phenyl hydrogens and 1.5 times for $C(CH_3)_3$. In the final refinement the hydrogen atoms were riding on their respective carbon atoms.

In the structure of **2b**, the Li2 and Sn1 atoms were disordered with the atoms statistically distributed over the two

Table 1. Crystallographic data for **1a**, **1b**, **2b,** and **2c**·THF.

Compound	**1a**	**1b**	**2b**	**2c**·THF
Empirical formula	$C_{28}H_{46}B_2N_4Ge$	$C_{28}H_{46}B_2N_4Sn$	$C_{28}H_{46}B_2Li_2N_4Sn$	$C_{32}H_{54}B_2Li_2N_4OPb$
Formula weight	532.90	579.00	592.88	753.48
Crystal system	Orthorhombic	Monoclinic	Monoclinic	Triclinic
Space group	*Pbcn*	*C*2/*c*	$P2_1/c$	*P*-1
a (Å)	17.259(4)	24.846(5)	13.544(3)	9.188(2)
b (Å)	8.917(2)	8.738(2)	11.828(2)	10.201(2)
c (Å)	20.256(4)	18.065(4)	20.059(4)	20.649(4)
α (°)	90.00	90.00	90.00	79.05(3)
β (°)	90.00	128.29(3)	104.72(3)	84.95(4)
γ (°)	90.00	90.00	90.00	71.49(3)
V (Å^3)	3117(1)	3078(2)	3108(1)	1801.1(7)
Z	4	4	4	2
T (°C)	–100	–100	–100	–100
$\rho_{calcd.}$ (g/cm^3)	1.135	1.249	1.267	1.389
μ(Mo Kα) (mm^{-1})	1.004	0.851	0.844	4.712
Crystal size (mm^3)	0.20 × 0.16 × 0.12	0.44 × 0.36 × 0.06	0.40 × 0.06 × 0.02	0.24 × 0.20 × 0.08
F(000)	1136	1208	1232	760
θ range (°)	2.57–25.02	3.23–25.02	3.38–25.03	3.57–25.03
Reflns. collected	5083	5103	9846	12174
Unique reflns.	2732	2709	5430	6335
R_{int}	0.0213	0.0236	0.0457	0.0282
Reflns. [$I > 2\sigma(I)$]	2066	2449	4020	5945
R_1 [$I > 2\sigma(I)$][a]	0.0360	0.0311	0.0468	0.0234
wR_2 (all data)[b]	0.0901	0.0808	0.0993	0.0555
GoF on F^2	1.059	1.033	1.103	1.032
Completeness	0.990	0.996	0.991	0.996

Note: λ (MoKα) = 0.71073 Å.

[a] $R_1 = \Sigma||F_o| - |F_c|| / \Sigma|F_o|$.

[b] $wR_2 = [\Sigma w(F_o^2 - F_c^2)^2 / \Sigma wF_o^4]^{1/2}$.

atomic sites. The two atoms were constrained to be located in the same position and the anisotropic thermal parameters were restricted to be equal. In the final refinement, the site occupation factors were ca. 93% and 7%, respectively. The scattering factors for the neutral atoms were those incorporated with the programmes.

Computational details

All calculations were done with the Gaussian 03 program using density functional theory.[17] Molecular structures were optimized using the hybrid PBE1PBE exchange-correlation functional[18] together with the Ahlrichs' TZVP basis sets[19]; an effective core potential basis set of similar valence quality was used for the heavy tin nuclei.[20] Hyperfine coupling constants were then calculated by single-point calculations employing the optimized geometries and the basis set combination used for optimizations. The orbital plot was obtained by the program gOpenMol.[21]

Synthesis of Ge[PhB(μ-*N*-*t*-Bu)$_2$]$_2$ (1a)

A solution of Li_2[PhB(μ-*N*-*t*-Bu)$_2$] (0.366 g, 1.50 mmol) in 30 mL of diethyl ether was added to a solution of $GeCl_4$ (0.161 g, 0.75 mmol) in 30 mL of diethyl ether at –80 °C. The reaction mixture was allowed to reach room temperature in 30 min and it was then heated to 35 °C for 15 h. The precipitate of LiCl was removed by filtration and the solvent was evaporated under vacuum giving Ge[PhB(μ-*N*-*t*-Bu)$_2$]$_2$ (**1a**) as a white powder (0.442 g, 83%). The ^{1}H, ^{11}B, and ^{13}C NMR spectra were in good agreement with the literature values.[7] Anal. calcd. for $C_{28}H_{46}B_2N_4Ge$: C 63.10, H 8.70, N 10.51; found: C 62.85, H 8.94, N 10.71. Crystallization from *n*-hexane afforded colourless X-ray quality crystals of Ge[PhB(μ-*N*-*t*-Bu)$_2$]$_2$ (**1a**).

Synthesis of Sn[PhB(μ-*N*-*t*-Bu)$_2$]$_2$ (1b)

A solution of Li_2[PhB(μ-*N*-*t*-Bu)$_2$] (0.244 g, 1.00 mmol) in 25 mL of diethyl ether was added to a solution of $SnCl_4$ (0.5 mL of a 1.0 mol/L solution in heptane, 0.50 mmol) in 25 mL of diethyl ether at –80 °C. The reaction mixture was stirred for 30 min at –80 °C and 6 h at 23 °C. The precipitate of LiCl was removed by filtration and the solvent was evaporated under vacuum giving Sn[PhB(μ-*N*-*t*-Bu)$_2$]$_2$ (**1b**) as a white powder (0.257 g, 87%). The ^{1}H, ^{11}B, and ^{13}C NMR spectra were in excellent agreement with the literature values.[7] ^{119}Sn NMR δ: –83.0 (cf. –117.8 ppm for Sn[(2,4,6-^{i}Pr$_3$C$_6$H$_2$)B(μ-*N*-*t*-Bu)$_2$]$_2$ in $CDCl_3$).[8] Anal. calcd. for $C_{28}H_{46}B_2N_4Sn$: C 58.08, H 8.01, N 9.68; found: C 58.30, H 7.93, N 9.03. Crystallization from *n*-hexane afforded colourless X-ray quality crystals of Sn[PhB(μ-*N*-*t*-Bu)$_2$]$_2$ (**1b**).

Oxidation of Sn[PhB(μ-*N*-*t*-Bu)$_2$]$_2$ (1b) with SO_2Cl_2

A solution of SO_2Cl_2 (0.040 mL, 0.067 g, 0.50 mmol) was dissolved in 10.0 mL of diethyl ether; 1.0 mL (0.05 mmol) of this solution was added to a solution of **1b**

(0.058 g, 0.10 mmol) in 80 mL of diethyl ether at –80 °C. The reaction mixture was allowed to warm up to ca. –40 °C at which point the colourless solution became bright blue and a small amount of white powder (LiCl) appeared. An aliquot of the reaction solution was used for EPR spectroscopic measurements. The remaining reaction solution was allowed to reach room temperature, which resulted in the decomposition of the paramagnetic species at ca. 0 °C as indicated by disappearance of the blue colour.

Synthesis of $Li_2Sn[PhB(\mu\text{-}N\text{-}t\text{-}Bu)_2]_2$ (2b)

A solution of $Li_2[PhB(\mu\text{-}N\text{-}t\text{-}Bu)_2]$ (0.366 g, 1.50 mmol) in 25 mL of diethyl ether was added to a suspension of $SnCl_2$ (0.142 g, 0.75 mmol) in 25 mL of diethyl ether at –80 °C. The reaction mixture was stirred for 30 min at –80 °C and 5 h at 23 °C. The precipitate of LiCl was removed by filtration and the solvent was evaporated under vacuum. The product was then washed with cold *n*-hexane (ca. 10 mL) to give **2b** as a white powder (0.364 g, 75%). ^{1}H NMR (d_8-toluene, 23 °C) δ: 6.98–7.72 (m, 10H, C_6H_5), 1.39 (shoulder, br, 9H, $C(CH_3)_3$), 1.19 (s, br, 27H, $C(CH_3)_3$). ^{1}H NMR (0 °C) δ: 6.96–7.72 (m, 10H, C_6H_5), 1.44 (s, 9H, $C(CH_3)_3$), 1.21 (s, 27H, $C(CH_3)_3$). ^{1}H NMR (–20 °C) δ: 6.92–7.70 (m, 10H, C_6H_5), 1.46 (s, 9H, $C(CH_3)_3$), 1.24 (s, 9H, $C(CH_3)_3$), 1.21 (s, 18H, $C(CH_3)_3$). ^{13}C NMR (–20 °C) δ: 133.9–125.8 (C_6H_5), 54.4 (s, $C(CH_3)_3$), 52.1 (s, $C(CH_3)_3$), 51.1 (s, $C(CH_3)_3$), 37.0 (s, $C(CH_3)_3$), 36.6 (s, $C(CH_3)_3$), 36.1 (s, $C(CH_3)_3$). ^{11}B NMR (–20 °C) δ: 36.6. ^{7}Li NMR (–20 °C) δ: 1.10. ^{119}Sn NMR (d_8-toluene, 23 °C, ppm) δ: –167.9. Anal. calcd. for $C_{32}H_{56}B_2Li_2N_4Sn$: C 56.72, H 7.82, N 9.45; found: C 55.45, H 7.99, N 9.18. X-ray quality crystals of **2b** were obtained by dissolving the white powder in boiling *n*-hexane and then allowing the solution to cool down to room temperature in ca. 3 h.

Synthesis of $(Et_2O{\cdot}Li)LiPb[PhB(\mu\text{-}N\text{-}t\text{-}Bu)_2]_2$ (2c·OEt_2)

Method A

A solution of $Li_2[PhB(\mu\text{-}N\text{-}t\text{-}Bu)_2]$ (0.244 g, 1.00 mmol) in 30 mL of diethyl ether was added to a suspension of PbI_2 (0.231 g, 0.50 mmol) in 30 mL of diethyl ether at –80 °C. The reaction mixture was allowed to reach room temperature in 30 min and it was then heated to 35 °C for 12 h. The precipitate of LiI was removed by filtration and the solvent was evaporated under vacuum giving a pale yellow, amorphous powder (0.294 g). ^{1}H NMR spectroscopy revealed a mixture of products among which the lead(II) complex, $\{Pb[PhB(\mu\text{-}N\text{-}t\text{-}Bu)_2]\}_2$, was identified (δ: 1.15 ppm, d_8-toluene, 23 °C; lit. value[11] δ: 1.19 in C_6D_6) in addition to the resonances of **2c**·OEt_2 (see discussion of the VT NMR experiments). **2c**·OEt_2: ^{1}H NMR (d_8-toluene, 23 °C) δ: 7.02–7.78 (m, C_6H_5), 3.40 (q, 6H, $(CH_3CH_2)_2O$), 1.27 (s, br, 36H, $C(CH_3)_3$), 1.00 (t, 6H, $(CH_3CH_2)_2O$). ^{1}H NMR (0 °C): δ: 7.08–7.82 (m, C_6H_5), 3.34 (q, 6H, $(CH_3CH_2)_2O$), 1.35 (shoulder, 9H, $C(CH_3)_3$), 1.29 (s, 18H, $C(CH_3)_3$), 1.25 (shoulder, 9H, $C(CH_3)_3$), 0.97 (t, 6H, $(CH_3CH_2)_2O$). ^{1}H NMR (–10 °C) δ: 7.10–7.83 (m, C_6H_5), 3.34 (q, 6H, $(CH_3CH_2)_2O$), 1.36 (s, 9H, $C(CH_3)_3$), 1.30 (s, 18H, $C(CH_3)_3$), 1.25 (s, 9H, $C(CH_3)_3$), 0.96 (t, 6H, $(CH_3CH_2)_2O$). ^{7}Li NMR (–20 °C) δ: 0.87. Crystallization from THF afforded a few colourless crystals of $(THF{\cdot}Li)LiPb[PhB(\mu\text{-}N\text{-}t\text{-}Bu)_2]_2$ (**2c**·THF).

Method B

The Pb(II) complex $\{Pb[PhB(\mu_3\text{-}N\text{-}t\text{-}Bu)_2]\}_2$ was prepared by a modification of the procedure reported earlier[11] from the reaction of PbI_2 (0.461 g, 1.00 mmol) and $Li_2[PhB(\mu\text{-}N\text{-}t\text{-}Bu)_2]$ (0.244 g, 1.00 mmol) in diethyl ether. The purity of the compound was checked by ^{1}H NMR spectroscopy. A solution of $Li_2[PhB(\mu\text{-}N\text{-}t\text{-}Bu)_2]$ (0.244 g, 1.00 mmol) in 30 mL of diethyl ether was added to a solution of $\{Pb[PhB(\mu_3\text{-}N\text{-}t\text{-}Bu)_2]\}_2$ (0.437 g, 0.50 mmol) in 30 mL of diethyl ether at –80 °C. The reaction mixture was allowed to reach room temperature in 30 min and it was then heated to 35 °C for 18 h. The precipitate of LiI was removed by filtration and the solvent was evaporated under vacuum giving a pale yellow, amorphous powder (0.546 g). The ^{1}H NMR spectrum of this powder in d_8-toluene revealed a complex mixture of products. The reactions described in methods **A** and **B** were also carried out in THF at 55 °C without significant improvement in the yield of **2c.**

Reaction of $Li_2[PhB(\mu\text{-}N\text{-}t\text{-}Bu)_2]$ with $C_4H_8O_2{\cdot}GeCl_2$

A solution of $Li_2[PhB(\mu\text{-}N\text{-}t\text{-}Bu)_2]$ (0.183 g, 0.75 mmol) in 25 mL of diethyl ether was added to a solution of $C_4H_8O_2{\cdot}GeCl_2$ (0.174 g, 0.75 mmol) in 25 mL of diethyl ether at –80 °C. The reaction mixture was stirred for 30 min at –80 °C and 16 h at 23 °C. The precipitate of LiCl was removed by filtration and the solvent was evaporated under vacuum giving a pale yellow, amorphous powder (0.185 g, 78% calculated as a 1:2 mixture of **1a** and $\{Ge[PhB(\mu\text{-}N\text{-}t\text{-}Bu)_2]\}_2$, see discussion). ^{1}H NMR (d_8-toluene, 23 °C) δ: 7.02–7.96 (m, 30H, C_6H_5), 1.41 (s, 36H, $C(CH_3)_3$), 1.39 (s, 36H, $C(CH_3)_3$), 1.30 (s, 36H, $C(CH_3)_3$). ^{11}B NMR (–20 °C) δ: ca. 36.5 (br). Crystallization from *n*-hexane afforded a few colourless crystals of $Ge[PhB(\mu\text{-}N\text{-}t\text{-}Bu)_2]_2$ (**1a**).

Results and discussion

X-ray structures of $M[PhB(\mu\text{-}N\text{-}t\text{-}Bu)_2]_2$ (1a, M = Ge; 1b, M = Sn)

The germanium(IV) and tin(IV) complexes **1a** and **1b** were obtained by a modification of the literature synthesis[7] in which the dilithium reagent $Li_2[PhB(\mu\text{-}N\text{-}t\text{-}Bu)_2]$ was isolated and purified prior to reaction with MCl_4 (M = Ge, Sn) in a 2:1 molar ratio in diethyl ether. This new procedure afforded analytically pure **1a** and **1b** in ca. 85% yields, cf. lit. **1a** (31%) and **1b** (44%).[7] Attempts to make the silicon analogue $Si[PhB(\mu\text{-}N\text{-}t\text{-}Bu)_2]_2$ by a similar procedure were unsuccessful.

The X-ray structural determinations of **1a** and **1b** confirmed the expected spirocyclic structures with two orthogonal *bam* ligands *N*,*N*′-chelated to the distorted tetrahedral metal centres (Fig. 1). In both complexes the molecule lies on a crystallographic twofold axis that imposes equivalence on the two *bam* ligands. The diamagnetic complexes **1a** and **1b** are isostructural with the paramagnetic group 13 analogues $\{M[PhB(\mu\text{-}N\text{-}t\text{-}Bu)_2]_2\}^\bullet$ (M = Al, Ga).[5] The centrosymmetric germanium(IV) complex **1a** represents the first structurally characterized germanium *bam* complex.[1]

Selected bond lengths and bond angles for **1a** and **1b** are summarized in Table 2. The distorted tetrahedral germanium centre in **1a** exhibits equal Ge–N bond lengths, which are

Fig. 1. Molecular structure of Ge[PhB(μ-*N*-*t*-Bu)$_2$]$_2$ (**1a**) with the atomic numbering scheme. Hydrogen atoms have been omitted for clarity. The tin complex **1b** is isostructural with **1a**. Symmetry operation: [a] –*x*, *y*, 0.5 – *z* (E = Ge); 1 – *x*, *y*, 1.5 – *z* (E = Sn).

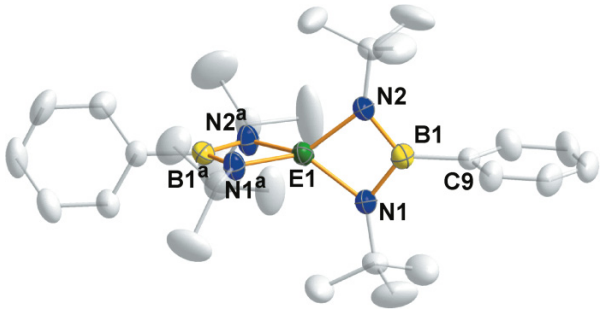

noticeably shorter (by ca. 0.20 Å) than the corresponding M–N bonds in the heavier tin analogue **1b**. Somewhat surprisingly, the Ge–N bonds in **1a** are also significantly shorter than the Ga–N bond lengths of 1.922(2) Å observed in the neutral radical Ga[PhB(μ-*N*-*t*-Bu)$_2$]$_2$•,[5] despite the difference of only one electron between the two centres (Ge and Ga). The Ge–N bond lengths are, however, equal within estimated standard deviation with the Al–N bond lengths of 1.842(2) and 1.852(2) Å reported for {Al[PhB(μ-*N*-*t*-Bu)$_2$]$_2$}•,[5] for which the difference between the two metal centres (Ge and Al) is nine electrons. These trends in bond lengths may be attributed to the weaker Coulomb interaction in the paramagnetic group 13 complexes where the total charge on the ligands is formally 3– compared to the diamagnetic group 14 complexes for which the formal charge is 4–. Interestingly, the Ge–N bonds in **1a** are also ca. 0.04 Å longer than the As–N bond lengths of 1.797(4)–1.811(4) Å observed in the isostructural, and *isoelectronic*, group 15 cation As[PhB(μ-*N*-*t*-Bu)$_2$]$_2^+$ (in the $GaCl_4^-$ salt).[22] Since the single bond covalent radius is the same for Ge and As (1.22 Å),[23] the shorter As–N bonds are probably due to the stronger electrostatic interaction between the positively charged arsenic centre and the two dianionic *bam* ligands. In the tin(IV) complex **1b** the Sn–N bonds within each *bam* ligand are equal in length and are close to the values of 2.043(3)–2.066(3) Å observed in the eight-membered rings {Me$_2$Sn[μ-N(Me)B(R)NMe]$_2$SnMe$_2$} (*R* = 2,4,6-*i*-Pr$_3$C$_6$H$_2$, 2,4,6-*t*-Bu$_3$C$_6$H$_2$), which also involve Sn(IV) centres,[8,24] but they are somewhat shorter than the value of 2.105(1) Å found for the Sn–N bond involving a three-coordinate nitrogen atom in the dimeric Sn(II) complex, {Sn[MeB(μ-NSiMe$_3$)$_2$]}$_2$.[25] The B–N bond lengths in both **1a** and **1b** are equal and represent typical values for the *bam* ligand.[1]

The M-N-B angles in **1a** and **1b** are close to 90° and the geometry about boron atom is trigonal planar as indicated by the sum of bond angles (360°). The N-B-N and all N-Ge-N angles in **1a** are close to the corresponding bond angles observed in {Al[PhB(μ-*N*-*t*-Bu)$_2$]$_2$}•[5] due to the identical Ge-N/Al-N and B–N bond lengths, whereas the longer Sn–N bonds result in a narrower N-Sn-N angle by ca. 7° and 3° within the *bam* ligands in **1b**. The GeBN$_2$ four-membered rings in **1a** are planar with torsion angles of 0.5(2)° and 0.6(2)° for ∠ N2-Ge1-N1-B1 and Ge1-N1-B1-N2, respectively, while the corresponding torsion angles for the slightly puckered SnBN$_2$ four-membered rings in **1b** are 4.6(2)° and 6.5(3)°.

Although all four isostructural compounds (**1a**, **1b**, and M[PhB(μ-*N*-*t*-Bu)$_2$]$_2$• (M = Al, Ga)) exhibit a centre of symmetry at the group 13 or 14 atom, the tin complex **1b** exhibits different crystal packing from the other three complexes as indicated by the crystal system and space group [monoclinic *C*2/*c* for **1b** vs orthorhombic *Pbcn* for **1a** and M[PhB(μ-*N*-*t*-Bu)$_2$]$_2$• (M = Al, Ga)].

EPR spectra and DFT calculations of the radical cation {Sn[PhB(μ-*N*-*t*-Bu)$_2$]$_2$}•+

The intensely coloured spirocyclic group 13 radicals {M[PhB(μ-*N*-*t*-Bu)$_2$]$_2$}• (M = Al, Ga) (Scheme 1) are stable in the solid state,[5] while the indium analogue {In[PhB(μ-*N*-*t*-Bu)$_2$]$_2$}• has only been characterized in solution by EPR spectroscopy.[6] In an attempt to generate the isoelectronic radical cations with a group 14 metal centre, {M[PhB(μ-*N*-*t*-Bu)$_2$]$_2$}•+ (M = Ge, Sn), we have investigated the reactions of **1a** and **1b** with various oxidizing agents (Scheme 2).

The attempted one-electron oxidation of **1a** or **1b** to the corresponding radical cation by one-half equivalent of I_2 in diethyl ether or THF resulted in no reaction even at elevated temperatures. The tin(IV) complex **1b** was also inert towards [NO][SbF_6] and, surprisingly, the germanium(IV) complex **1a** showed no indication of a reaction with SO_2Cl_2. However, the treatment of **1b** with one-half equivalent of SO_2Cl_2 in diethyl ether at low temperatures produced a bright blue solution of {Sn[PhB(μ-*N*-*t*-Bu)$_2$]$_2$}•+ (vide infra), which was persistent below –40 °C, but decomposed above 0 °C, cf. the thermal instability of the isoelectronic indium-containing neutral radical {In[PhB(μ-*N*-*t*-Bu)$_2$]$_2$}•.[6]

The EPR spectrum of the blue solution in diethyl ether displays an eight-line pattern and a highly broadened lineshape (Fig. 2); the g-value of this radical is 2.0055. Several attempts to resolve additional fine structure in the EPR spectrum by variations in the solvent, concentration of the solution, and temperature, as well as changes in the measurement parameters, were unsuccessful. A reasonable simulation of the observed spectrum is obtained by using a line width of 2.85 G (95% Gaussian shape) and by including hyperfine coupling constants to one boron atom (^{11}B, *I* = 3/2, 9.88 G) and two equivalent nitrogen centres (^{14}N, *I* = 1, 9.18 G) (Fig. 2) thus suggesting localization of the unpaired electron in only one of the *bam* units, in contrast to the delocalization over both *bam* ligands observed for the neutral group 13 radicals {M[PhB(μ-*N*-*t*-Bu)$_2$]$_2$}• (M = Al, Ga, In).[5,6] This electron distribution is, however, reminiscent of the behaviour noted for the persistent radicals {(Et$_2$O)Li[PhB(μ-*N*-*t*-Bu)$_2$]$_2$M}• (M = Mg, Zn), which exhibit localization of the unpaired electron on the spin-active nuclei in only one of the *bam* ligands as a consequence of the coordination of the additional lithium counter-cation to the second *bam* unit.[6]

The apparent localization of the unpaired electron in only one of the *bam* ligands, and the strong coordinating nature of the Cl^- counter-anion, raised the possibility of the formation of neutral radicals, {Sn[PhB(μ-*N*-*t*-Bu)$_2$]$_2$Cl}•, comprising a Sn-Cl or B-Cl contact instead of the ion-separated radical cation, {Sn[PhB(μ-*N*-*t*-Bu)$_2$]$_2$}•+ (Scheme 3), cf. the Zwitterionic arsenic(V) complex, {[PhB(μ-*N*-*t*-Bu)$_2$]As[(μ-*N*-*t*-Bu)$_2$B(Cl)Ph]}, with a covalent B–Cl bond.[22] Conse-

Table 2. Selected bond lengths (Å) and angles (°) in **1a** and **1b**.

	1a[a]	**1b**[b]		**1a**[a]	**1b**[b]
Bond lengths (Å)					
M1–N1	1.846(2)	2.047(2)	B1–N1	1.438(3)	1.436(4)
M1–N2	1.842(2)	2.047(2)	B1–N2	1.439(4)	1.438(4)
Bond angles (°)					
N1-M1-N2	75.9(1)	69.2(1)	M1-N2-B1	90.2(2)	91.1(2)
N1-M1-N1'	128.6(1)[c]	129.2(2)[d]	N1-B1-N2	104.0(2)	107.9(2)
N1-M1-N2'	127.8(1)[c]	132.8(1)[d]	N1-B1-C9	127.3(2)	126.5(3)
N2'-M1-N2'	129.8(1)[c]	135.5(1)[d]	N2-B1-C9	128.7(2)	125.6(3)
M1-N1-B1	90.0(2)	91.2(2)			

[a]M = Ge.
[b]M = Sn. Symmetry operation for the atoms marked with a single quote (').
[c]–*x*, *y*, 0.5 – *z*.
[d]1 – *x*, *y*, 1.5 – *z*.

Scheme 2. One-electron oxidation of {M[PhB(μ-*N*-*t*-Bu)$_2$]$_2$} (M = Ge, Sn).

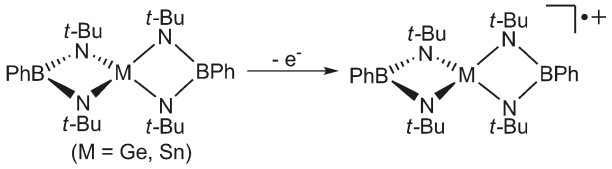

Scheme 3. Possible structures of the product of one-electron oxidation of **1b** with SO_2Cl_2.

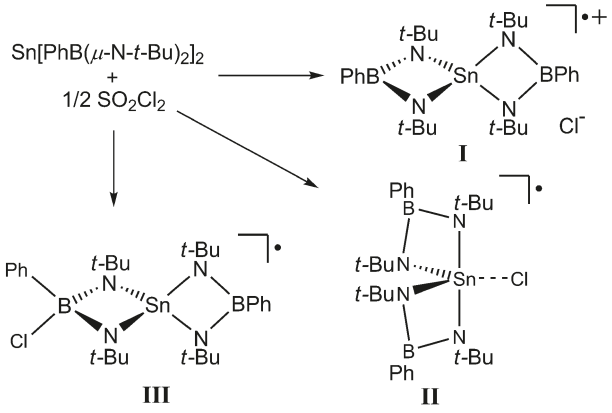

Fig. 2. (*a*) Simulated and (*b*) experimental EPR spectra of {Sn[PhB(μ-*N*-*t*-Bu)$_2$]$_2$}$^{\bullet+}$Cl$^-$ measured in diethyl ether at –20 °C.

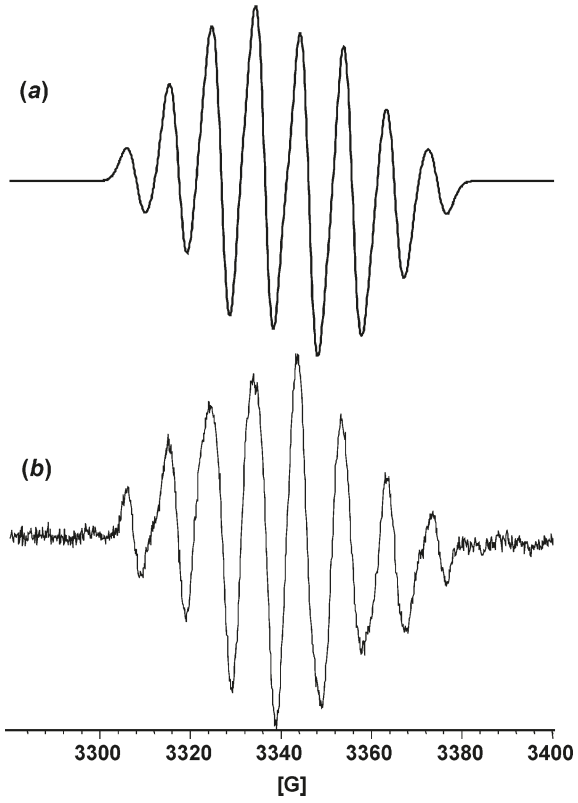

quently, the replacement of the Cl^- anion by the weakly coordinating SbF_6^- was performed by an in situ reaction with $AgSbF_6$. The thermal stability of the radical cation was not improved, but a colour change from blue to purple was observed along with the formation of AgCl. The EPR spectrum of the purple solution, however, was unaffected by the change of the counter-anion, suggesting that the one-electron oxidation product of **1b** is present *in very dilute diethyl ether solutions as the ion-separated radical cation **I*** rather than the "contact ion-pairs" **II** or **III**.

Density functional theory calculations conducted for the cation radical {Sn[PhB(μ-*N*-*t*-Bu)$_2$]$_2$}$^{\bullet+}$ predict a C_{2v}-symmetric minimum structure and localized spin density on only one *bam* ligand (Fig. 3). A D_{2d}-symmetric structure, analogous to that observed for the neutral group 13 radicals {M[PhB(μ-*N*-*t*-Bu)$_2$]$_2$}$^{\bullet}$ (M = Al, Ga) (Scheme 1), is a transition state with respect to Sn-N stretching vibrations and only 5 kJ mol^{-1} higher in energy. Hence, it appears that the spiroconjugative interactions in **1b** are not sufficiently strong to give rise to a fully delocalized electron distribution in the corresponding cation,[26] and the system adopts a structure with the two *bam* ligands bearing different formal charges, i.e., Sn(IV)(*bam*)$^{2-}$(*bam*)$^{-\bullet}$. This is consistent with the finding that optimizations carried out for the lighter group 14 congeners of {M[PhB(μ-*N*-*t*-Bu)$_2$]$_2$}$^{\bullet+}$ (M = Si, Ge) give minima with significantly shorter N···N

Fig. 3. SOMO of the radical cation $\{Sn[PhB(\mu\text{-}N\text{-}t\text{-}Bu)_2]_2\}^{\bullet+}$ (±0.05 isodensity surfaces).

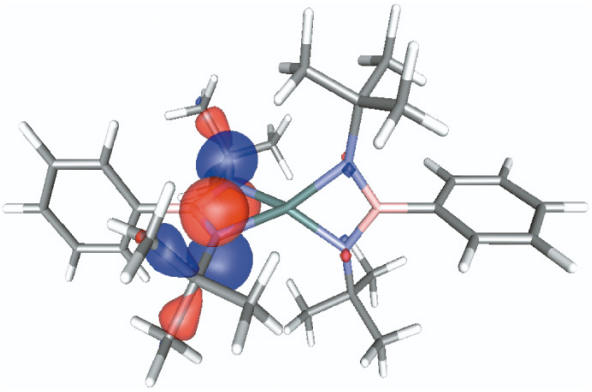

separations and, consequently, only D_{2d}-symmetric structures are found.

The hyperfine coupling constants calculated for $Sn[PhB(\mu\text{-}N\text{-}t\text{-}Bu)_2]_2\}^{\bullet+}$ ($2 \times {}^{14}N$, 7.35 G; $2 \times {}^{14}N$, 0.05 G; ^{11}B, –10.96 G; ^{11}B, –0.32 G) are in good agreement with the values determined from the experimental spectrum. Similar to the previous observations for the persistent radicals $\{(Et_2O)Li[PhB(\mu\text{-}N\text{-}t\text{-}Bu)_2]_2M\}^{\bullet}$ (M = Mg, Zn),[6] the calculated nitrogen couplings are too small, whereas the coupling to the boron nuclei is slightly larger than the value inferred from the simulation; there is an apparent tendency of this functional basis set combination to underestimate couplings that result from the spin density of the unpaired electron while overestimating those that arise from spin-polarization effects.[5,6] The undulating baseline of the EPR spectrum and the low intensity humps visible at both ends of the spectrum most likely arise from the presence of small amounts of isotopomers, which contain the spin-active tin nuclei (^{117}Sn, I = 1/2, 7.6%; ^{119}Sn, I = 1/2, 8.6%). The magnitudes of the two Sn couplings cannot, however, be obtained with the current computational method due to the indirect treatment of relativistic effects via effective core potential basis sets. The observed broad lineshape can, at least in part, be attributed to the numerous smaller couplings to the hydrogen atoms of the *t*-Bu groups.[27]

Synthesis of $Li_2Sn[PhB(\mu\text{-}N\text{-}t\text{-}Bu)_2]_2$ (2b) and $(THF{\cdot}Li)LiPb[PhB(\mu\text{-}N\text{-}t\text{-}Bu)_2]_2$ (2c·THF)

The reactions of $Li_2[PhB(\mu\text{-}N\text{-}t\text{-}Bu)_2]$ with group 14 dihalides in a 2:1 molar ratio were investigated with a view to isolating and structurally characterizing complexes of the type $Li_2M[PhB(\mu\text{-}N\text{-}t\text{-}Bu)_2]_2$ in which the dianions $M[PhB(\mu\text{-}N\text{-}t\text{-}Bu)_2]_2^{2-}$ (M = Ge, Sn, Pb) are isoelectronic with the previously reported group 15 anions $M[PhB(\mu\text{-}N\text{-}t\text{-}Bu)_2]_2^{-}$ (M = As, Sb, Bi), which were obtained as monolithium derivatives.[12] The outcome of these reactions was markedly dependent on the nature of the group 14 metal.

The reaction between $Li_2[PhB(\mu\text{-}N\text{-}t\text{-}Bu)_2]$ and $SnCl_2$ in a 2:1 molar ratio in diethyl ether proceeded cleanly to produce $Li_2Sn[PhB(\mu\text{-}N\text{-}t\text{-}Bu)_2]_2$ (**2b**) in 75% yield (eq. [1]). The unsolvated heterotrinuclear complex **2b** was characterized in solution by multinuclear NMR spectroscopy and in the solid state by single crystal X-ray crystallography.

$$[1]\quad 2Li_2[PhB(\mu\text{-}N\text{-}t\text{-}Bu)_2] + SnCl_2 \rightarrow Li_2Sn[PhB(\mu\text{-}N\text{-}t\text{-}Bu)_2]_2 + 2LiCl \quad (\mathbf{2b})$$

The reaction of $Li_2[PhB(\mu\text{-}N\text{-}t\text{-}Bu)_2]$ with PbI_2 in 2:1 molar ratio was conducted under various conditions in an effort to produce the analogous lead(II) complex $Li_2Pb[PhB(\mu\text{-}N\text{-}t\text{-}Bu)_2]_2$ (**2c**). The ^1H NMR spectrum of the reaction mixture, however, revealed several products, one of which was identified as the previously reported mononuclear lead(II) complex, $\{Pb[PhB(\mu_3\text{-}N\text{-}t\text{-}Bu)_2]\}_2$.[11] In an alternative synthetic approach, this dimeric Pb(II) complex was prepared and isolated prior to treatment with two equivalents of $Li_2[PhB(\mu\text{-}N\text{-}t\text{-}Bu)_2]$. However, this two-step method also afforded a mixture of products from which only a few crystals of **2c** were isolated as the tetrahydrofuran solvate, (THF·Li)-$LiPb[PhB(\mu\text{-}N\text{-}t\text{-}Bu)_2]_2$ (**2c**·THF).

The reaction of $Li_2[PhB(\mu\text{-}N\text{-}t\text{-}Bu)_2]$ with $C_4H_8O_2{\cdot}GeCl_2$ in 2:1 molar ratio in diethyl ether produced several products (^1H NMR). Consequently, the reaction was repeated in 1:1 molar ratio in an attempt to form the unknown germanium(II) complex, $Ge[PhB(\mu\text{-}N\text{-}t\text{-}Bu)_2]$, for subsequent reaction with $Li_2[PhB(\mu\text{-}N\text{-}t\text{-}Bu)_2]$; this two-step approach was previously found to be necessary for the successful synthesis of the aluminum complex $(Et_2O{\cdot}Li)Al[PhB(\mu\text{-}N\text{-}t\text{-}Bu)_2]_2$.[5] The ^1H NMR spectrum of the product(s) showed three equally intense resonances for *N*-*t*-Bu groups at 1.41, 1.39, and 1.30 ppm (d_8-toluene, 23 °C). The chemical shift of 1.30 ppm is identical with the value observed for the *t*-Bu groups in the germanium(IV) complex $Ge[PhB(\mu\text{-}N\text{-}t\text{-}Bu)_2]_2$ (**1a**),[8] suggesting that a redox process has occurred. The resonances at 1.41 and 1.39 are tentatively assigned to the *t*-Bu groups attached to the three- and four-coordinate nitrogen atoms of the dimeric complex germanium(II) complex $\{Ge[PhB(\mu\text{-}N\text{-}t\text{-}Bu)_2]\}_2$; however, attempts to isolate this second product were unsuccessful.

X-ray structures of $Li_2Sn[PhB(\mu\text{-}N\text{-}t\text{-}Bu)_2]_2$ (2b) and $(THF{\cdot}Li)LiPb[PhB(\mu\text{-}N\text{-}t\text{-}Bu)_2]_2$ (2c·THF)

Crystals of **2b** and **2c**·THF were obtained by recrystallization from boiling *n*-hexane and THF, respectively.[28] The crystal structures of **2b** and **2c**·THF with the atomic numbering scheme are depicted in Fig. 4 and the pertinent bond parameters are summarized in Table 3. The structures reveal novel polycyclic arrangements, which bear a close similarity with each other despite the introduction of a solvent molecule in **2c**·THF. In both frameworks one of the *bam* ligands is *N*,*N*′-chelated to both the M(II) atom (M = Sn, Pb) and one of the Li^+ ions while the second *bam* ligand exhibits a unique bonding motif by bridging all three metal centres.[1] While one of the Li^+ ions (Li1) in both structures is coordinated to three nitrogens, the second lithium in **2c**·THF is coordinated to two nitrogen atoms and the solvent molecule. The absence of the solvent molecule in **2b** affords a third, albeit relatively weak, Li···N close contact [2.557(6) Å] for the second lithium cation that results in a formal coordination number of five for the N4 atom (Fig. 4*a*).

Lithium salts of the group 15 monoanions $M[PhB(\mu\text{-}N\text{-}t\text{-}Bu)_2]_2^{-}$ (**3**, M = Sb; **4**, M = Bi),[12] which are isoelectronic with the group 14 dianions $M[PhB(\mu\text{-}N\text{-}t\text{-}Bu)_2]_2^{2-}$ (M = Sn,

Fig. 4. Crystal structures of (*a*) $Li_2Sn[PhB(\mu\text{-}N\text{-}t\text{-}Bu)_2]_2$ (**2b**) and (*b*) (THF·Li)LiPb[PhB(μ-*N*-*t*-Bu)$_2$]$_2$ (**2c**·THF) with the atomic numbering scheme. Hydrogen atoms have been omitted for clarity.

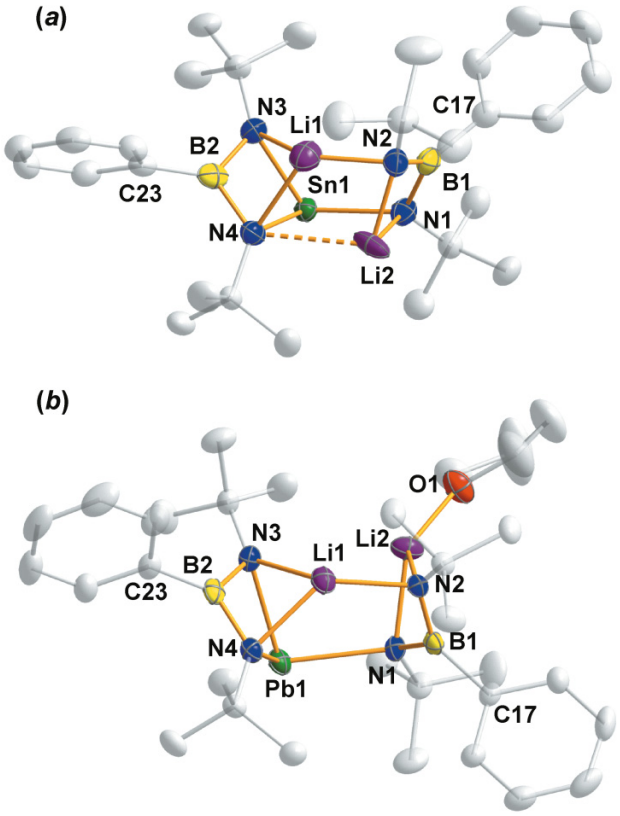

Pb), provide an interesting benchmark for comparison with the structures of **2b** and **2c**·THF (Scheme 4). Curiously, the lighter complexes in both group 14 (M = Sn) and group 15 (M = Sb) seem to favour unsolvated structures, whereas solvation of the Li^+ cation is observed for the heavier congeners (M = Pb, Bi). The molecular structure of the antimony complex **3** is comprised of two four-membered rings, BN_2Li and BN_2Sb, connected by Li–N and Sb–N bonds to form a tricyclic compound with both three- and four-coordinate nitrogens.[12] The introduction of a second Li^+ ion in **2b** has a surprisingly small effect on the overall structure; the molecule retains the ladder-like backbone and cisoid arrangement of the PhBN-*t*-Bu units. Most significantly, however, the Li2···N4 contact in **2b** (Fig. 4*a*, dashed line in Scheme 4) is elongated by ca. 0.28 Å compared to the analogous bond in the antimony complex due to the pseudo-five-coordination of the nitrogen atom. The lithium cation in the bismuth complex **4**·OEt_2 (Scheme 4) is four-coordinate, being *N*,*N*′-chelated by one *bam* ligand and bonded to one nitrogen of the second *bam* ligand; the fourth coordination site is occupied by an Et_2O molecule.[12] The introduction of a second Li^+ ion in **2c**·THF ruptures the bond between the solvated Li^+ ion and the second *bam* ligand, and cleaves the fourth M–N bond (M = Bi) that exists in the structure of **4**·OEt_2, although it is elongated compared to the other three Bi–N bonds (by ca. 0.18 Å).[12] As a result, both Li^+ ions are three-coordinate and all four nitrogen atoms are four-coordinate in **2c**·THF.

The average Sn–N bond length of 2.187(4) Å in **2b** (Fig. 4*a*, Table 3) is significantly longer than the values of 2.043(3)–2.066(3) Å observed in **1b** and in the Sn(IV) complexes $\{Me_2Sn[\mu\text{-}N(Me)B(R)NMe]_2SnMe_2\}$ (R = 2,4,6-*i*-$Pr_3C_6H_2$, 2,4,6-*t*-$Bu_3C_6H_2$),[8,24] but slightly shorter than the distance of 2.254(13) Å found for the Sn–N bonds involving four-coordinate nitrogen atoms in the dimeric Sn(II) complex $\{Sn[MeB(\mu_3\text{-}NSiMe_3)_2]\}_2$.[25] Expectedly, the Sn–N bond lengths are also close to the values of 2.145(5) and 2.198(5) Å observed for the Sb–N bonds to the four-coordinate nitrogens in **3** (the single bond covalent radii for Sn and Sb are 1.40 and 1.43 Å, respectively).[23] The Li1–N distance to the bridging *bam* ligand is ca. 0.18 Å shorter than the two Li1–N bonds to the chelating *bam* ligand. To compensate for the long Li2···N4 contact, the two Li2–N bonds of 1.869(5) and 1.884(5) Å are among the shortest lithium–nitrogen bonds observed for this ligand system.[1]

The introduction of a second Li^+ ion in **2b** results in opening the angle between BN_2Sn and LiN_2Sn four-membered rings as illustrated by the N1-Sn1-N3 and Li2-N4-B2 angles, which are ca. 4° and 9° wider, respectively, than the corresponding angles in the related antimony complex, **3**.[12] Widening of these angles and elongation of the Sn1-N1 and Li2-N4 contacts in **2b** compared to the analogous Sb–N and Li–N bonds, however, allows B1 and N2 atoms to incline towards the central $SnLiN_2$ four-membered ring and, consequently, the Sn1-N1-B1 and N4-Li2-N2 angles are ca. 4° and 5° narrower than the comparable angles in **3**. The N-Sn-N angle within the chelating *bam* ligand in **2b** is ca. 5.7° smaller than the corresponding angle in **1b** owing to the slightly longer Sn–N bonds in **2b**.

The average Pb–N bond length in **2c**·THF (Fig. 4*b*, Table 3) of 2.330(3) Å is identical to the value of 2.329(6) Å observed for the Pb–N bond involving a four-coordinate nitrogen atom in the dimeric lead(II) complex $\{Pb[PhB(\mu_3\text{-}N\text{-}t\text{-}Bu)_2]\}_2$.[10] The Pb–N bonds are ca. 0.06 Å longer than the three Bi–N bonds in **4**·OEt_2 (cf. the single bond covalent radii of 1.54 and 1.52 Å for Pb and Bi, respectively),[23] but they are ca. 0.11 Å shorter than the fourth, elongated, Bi–N bond in the bismuth complex.[12] The Li-N distances to the N2 atom in the bridging ligand in **2c**·THF are somewhat shorter than the remaining three Li-N interactions (ca. 0.12 and 0.07 Å for Li1-N2 and Li2-N2, respectively). All these distances are consistent with, for example, those in the group 13 and 15 complexes $(Et_2O\cdot Li)M[PhB(\mu\text{-}N\text{-}t\text{-}Bu)_2]_2$, which show two (M = Ga, In, As) or three (M = Bi) Li-N interactions.[4,12] The N-Pb-N angle in the chelating ligand is ca. 10° narrower than the N-Li-N angle at the unsolvated Li^+ ion due to the longer Pb–N bonds.

The bridging *bam* ligand in both **2b** and **2c**·THF exhibits a significant disparity in the B–N bond lengths (ca. 0.12 and 0.08 Å, respectively), presumably as a result of the different environments of N1 and N2, whereas the equality of the B–N bonds in the chelating *bam* ligand is not significantly perturbed by the weak Li2···N4 contact. The N-B-N angle in the chelating ligand in both **2b** and **2c**·THF is somewhat smaller (by 7.1° and 6.4°, respectively) than the analogous bond angle in the bridging *bam* ligand. Nevertheless, the boron atom assumes trigonal planar geometry in the *bam* ligands in both complexes. The bond angles at the nitrogen atoms in the chelating ligand are close to 90°, whereas the loss of

Table 3. Selected bond lengths (Å) and angles (°) in **2b** and **2c**·THF.

	2b[a]	**2c**·THF[b]		**2b**[a]	**2c**·THF[b]
Bond lengths (Å)					
M1–N1	2.194(4)	2.346(3)	Li2–N2	1.884(5)	1.974(6)
M1–N3	2.189(3)	2.335(3)	Li2–N4	2.557(6)	—
M1–N4	2.179(4)	2.309(2)	B1–N1	1.520(6)	1.490(4)
Li1–N2	1.915(9)	1.921(6)	B1–N2	1.408(7)	1.412(4)
Li1–N3	2.075(9)	2.039(6)	B2–N3	1.434(7)	1.447(5)
Li1–N4	2.115(9)	2.030(6)	B2–N4	1.466(6)	1.444(5)
Li2–N1	1.869(5)	2.055(6)			
Bond angles (°)					
N1-M1-N3	108.3(1)	99.5(1)	Li1-N3-B2	76.4(4)	77.7(2)
N1-M1-N4	99.1(1)	105.2(1)	M1-N3-Li1	84.7(3)	81.5(2)
N3-M1-N4	63.5(1)	59.8(1)	M1-N4-B2	89.7(3)	89.9(2)
N1-B1-N2	112.0(4)	112.9(3)	M1-N4-Li1	84.0(3)	82.3(2)
N3-B2-N4	104.9(4)	106.5(3)	Li1-N4-B2	74.5(3)	78.1(2)
M1-N1-B1	122.3(3)	120.1(2)	Li2-N4-B2	131.3(3)	—
Li2-N1-B1	80.5(3)	77.5(2)	N2-Li1-N3	132.7(5)	131.1(3)
M1-N1-Li2	89.5(2)	103.1(2)	N2-Li1-N4	121.9(4)	132.3(3)
Li1-N2-B1	108.2(4)	109.5(3)	N3-Li1-N4	66.5(3)	69.4(2)
Li2-N2-B1	82.8(3)	102.6(2)	N1-Li2-N2	80.6(2)	73.8(2)
Li1-N2-Li2	75.2(3)	88.7(3)	N4-Li2-N2	104.0(2)	—
M1-N3-B2	90.1(3)	88.8(2)			

[a]M = Sn.
[b]M = Pb.

Scheme 4. Comparison of the structures of $Li_2M[PhB(\mu\text{-}N\text{-}t\text{-}Bu)_2]_2$ (M = Sn, Pb) and $LiM[PhB(\mu\text{-}N\text{-}t\text{-}Bu)_2]_2$ (M = Sb, Bi).

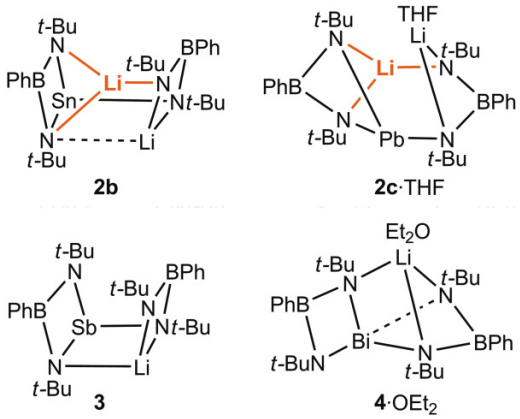

the fourth M–N bond results in a wider M1-N1-B1 angle by ca. 32° (M = Sn) and 30° (M = Pb).

NMR spectra and fluctional behaviour of $Li_2Sn[PhB(\mu\text{-}N\text{-}t\text{-}Bu)_2]_2$ (2b)

The ^{1}H NMR spectrum of **2b** in d_8-toluene at 23 °C exhibits a broad, poorly resolved signal for *t*-Bu groups, in addition to typical resonances for the phenyl groups. When the temperature is lowered to 0 °C, this broad resonance resolves into two well-separated signals at 1.44 and 1.21 ppm in a 1:3 intensity ratio. Cooling the solution to –20 °C results in resolution of the latter resonance to give three singlets at 1.46, 1.24, and 1.21 ppm in a 1:1:2 intensity ratio.[29] No further changes are apparent at lower temperatures. Consistently, the ^{13}C NMR spectrum of **2b** at –20 °C exhibits three singlets at 54.4, 52.1, and 51.1 ppm for the α-carbon atoms of the *t*-Bu groups; three singlets are also observed for the methyl carbons at 37.0, 36.6, and 36.1 ppm, in addition to the phenyl resonances. Throughout the temperature range (from –80 to +23 °C) only one broad singlet is observed in both the ^{11}B and ^{7}Li NMR spectrum (at 36.6 and 1.10 ppm, respectively, at –20 °C in d_8-toluene). The ^{119}Sn NMR spectrum of **2b** shows a single resonance at –167.9 ppm, which exhibits a significant shift to higher field from the value of 120 ppm reported for the dimeric tin(II) complex, $\{Sn[MeB(\mu_3\text{-}NSiMe_3)_2]\}_2$.[25] However, chemical shift values of –151.8 to –158.1 ppm have been reported for the related tin(II) complexes $\{Sn[RSi(\mu_3\text{-}N\text{-}t\text{-}Bu)_2]\}_2$ (R = C_3H_6, C_4H_6, C_4H_8 and C_5H_{10}),[30] which exhibit a coordination environment around the tin(II) centres similar to that in **2b**. The three resonances with a 1:1:2 intensity ratio observed at –20 °C in the ^{1}H NMR spectrum of **2b** are assigned to the *tert*-butyl groups attached to N1, N2, and N3/N4, respectively (Fig. 4*a*). The observation of only one broad resonance for the inequivalent boron and lithium atoms in the structure of **2b** even at low temperatures is attributed to overlap of these resonances.

The fluctional behaviour observed for **2b** is reminiscent of the exchange processes exhibited by the related group 15 complexes, **3** and **4**·OEt_2, which both showed only a single *t*-Bu resonance at room temperature.[12] These types of fluctional processes in lithium derivatives of polyimido anions of p-block elements are known to have low activation energies.[31] In the case of **3** and **4**·OEt_2, the fluctionality was determined to originate from a Berry pseudorotation.[12] In a similar manner, the single resonance observed at room temperature in the ^{1}H NMR spectra of **2b** can be attributed to a rapid exchange in which each of the four nitrogens, in turn, occupy the site that is not coordinated to the tin centre.

Conclusions

Comparison of the properties of the cation radicals $\{M[PhB(\mu\text{-}N\text{-}t\text{-}Bu)_2]_2\}^{\bullet+}$ (M = Si, Ge, Sn) with those of the isoelectronic neutral radicals $M[PhB(\mu\text{-}N\text{-}t\text{-}Bu)_2]_2^{\bullet}$ (M = Al, Ga, In) was limited to the tin derivative as a result of the inertness of $Ge[PhB(\mu\text{-}N\text{-}t\text{-}Bu)_2]_2$ towards oxidizing agents and the inaccessibility of $Si[PhB(\mu\text{-}N\text{-}t\text{-}Bu)_2]_2$. The blue radical cation $\{Sn[PhB(\mu\text{-}N\text{-}t\text{-}Bu)_2]_2\}^{\bullet+}$, which exhibits thermal instability similar to that of the neutral group 13 analogue $In[PhB(\mu\text{-}N\text{-}t\text{-}Bu)_2]_2^{\bullet}$, was characterized at low temperatures by EPR spectroscopy. In contrast to the isoelectronic, D_{2d}-symmetric indium bis-*bam* radical, DFT calculations predict a C_{2v} symmetry for the radical cation $\{Sn[PhB(\mu\text{-}N\text{-}t\text{-}Bu)_2]_2\}^{\bullet+}$ with spin density localized on only one of the *bam* ligands owing to the weak spiroconjugative N···N interactions that, presumably, prevent the delocalization of the unpaired electron over both ligands.

In the heterotrimetallic complexes $Li_2M[PhB(\mu\text{-}N\text{-}t\text{-}Bu)_2]_2$ [M = Sn, Pb (THF omitted)], one of the *bam* ligands exhibits a novel bonding mode in which it bridges all three metal centres.[1] The solid-state structures of these group 14 complexes are comparable with those of the previously reported group 15 complexes $LiM[PhB(\mu\text{-}N\text{-}t\text{-}Bu)_2]_2$ [M = Sb, Bi (OEt_2 omitted)].[12] Despite the introduction of a second Li^+ ion, the tin complex maintains the ladder-like backbone and cisoid arrangement of the *bam* ligands found in the antimony analogue. The intrusion of a second Li^+ ion in the lead complex results in rupture of the bond between the solvated Li^+ ion and one of the *bam* ligands, as well as cleavage of the fourth M–N bond (M = Bi, Pb) that exists in the structure of $(Et_2O{\cdot}Li)Bi[PhB(\mu\text{-}N\text{-}t\text{-}Bu)_2]_2$. In view of these structural similarities it is, perhaps, not surprising that the variable temperature NMR spectra of $Li_2Sn[PhB(\mu\text{-}N\text{-}t\text{-}Bu)_2]_2$ show trends comparable to those previously observed for the group 15 complex $LiSb[PhB(\mu\text{-}N\text{-}t\text{-}Bu)_2]_2$,[12] implying that the fluctional processes are also similar.

Supplementary data

Supplementary data for this article are available on the journal Web site (canjchem.nrc.ca) or may be purchased from the Depository of Unpublished Data, Document Delivery, CISTI, National Research Council Canada, Ottawa, ON K1A 0R6, Canada. DUD 3875. For more information on obtaining material refer to cisti-icist.nrc-cnrc.gc.ca/cms/unpub_e.shtml. CCDC 705641–705644 contain the crystallographic data for this manuscript. These data can be obtained, free of charge, via www.ccdc.cam.ac.uk/conts/retrieving.html (Or from the Cambridge Crystallographic Data Centre, 12 Union Road, Cambridge CB2 1EZ, UK; fax +44 1223 336033; or deposit@ccdc.cam.ac.uk).

Acknowledgements

The authors gratefully acknowledge financial support from the Natural Sciences and Engineering Research Council of Canada and the Academy of Finland. Professor M. Balakrishna carried out a preliminary reaction of PbI_2 with $Li_2[PhB(\mu\text{-}N\text{-}t\text{-}Bu)_2]$, which produced the crystals that were used in the X-ray structural determination of **2c**·THF.

References

(1) For a recent review see: Fedorchuk, C.; Copsey, M. C.; Chivers, T. *Coord. Chem. Rev.* **2007**, *251*, 897. doi:10.1016/j.ccr.2006.06.010.
(2) Manke, D. R.; Nocera, D. G. *Inorg. Chem.* **2003**, *42*, 4431. doi:10.1021/ic0340478. PMID:12844317.
(3) Manke, D. R.; Loh, Z.-H.; Nocera, D. G. *Inorg. Chem.* **2004**, *43*, 3618. doi:10.1021/ic049795r. PMID:15180415.
(4) Chivers, T.; Fedorchuk, C.; Schatte, G.; Parvez, M. *Inorg. Chem.* **2003**, *42*, 2084. doi:10.1021/ic0206286. PMID:12639145.
(5) Chivers, T.; Eisler, D. J.; Fedorchuk, C.; Schatte, G.; Tuononen, H. M.; Boeré, R. T. *Chem. Commun. (Camb.)* **2005**, 3930. doi:10.1039/b506253e. PMID:16075075.
(6) Chivers, T.; Eisler, D. J.; Fedorchuk, C.; Schatte, G.; Tuononen, H. M. *Inorg. Chem.* **2006**, *45*, 2119. doi:10.1021/ic0520014.
(7) Fest, D.; Habben, C. D.; Meller, A.; Sheldrick, G. M.; Stalke, D.; Pauer, F. *Chem. Ber.* **1990**, *123*, 703. doi:10.1002/cber.19901230409.
(8) Albrecht, T.; Elter, G.; Noltemeyer, M.; Meller, A. *Z. Anorg. Allg. Chem.* **1998**, *624*, 1514. doi:10.1002/(SICI)1521-3749(199809)624:9<1514::AID-ZAAC1514>3.0.CO;2-5.
(9) Paetzold, P.; Hahnfeld, D.; Englert, U.; Wojnowski, W.; Dreczewski, B.; Pawelec, Z.; Walz, L. *Chem. Ber.* **1992**, *125*, 1073. doi:10.1002/cber.19921250514.
(10) Luthin, W.; Stratmann, J.-G.; Elter, G.; Meller, A.; Heine, A.; Gornitzka, H. *Z. Anorg. Allg. Chem.* **1995**, *621*, 1995. doi:10.1002/zaac.19956211204.
(11) Heine, A.; Fest, D. *J. Chem. Soc. Chem. Commun.* **1990**, 742. doi:10.1039/c39900000742.
(12) Konu, J.; Balakrishna, M. S.; Chivers, T.; Swaddle, T. W. *Inorg. Chem.* **2007**, *46*, 2627. doi:10.1021/ic0622757. PMID:17326629.
(13) Chivers, T.; Fedorchuk, C.; Schatte, G.; Brask, J. K. *Can. J. Chem.* **2002**, *80*, 821. doi:10.1139/v02-111.
(14) (a) *WINEPR SimFonia,* version 1.25; Bruker Analytische: Messtechnik, Germany, 1996; (b) Duling, D. R. *J. Mag. Res. Ser. B* **1994**, *104*, 105. doi:10.1006/jmrb.1994.1062.
(15) Sheldrick, G. M. *SHELXS-97: Program for Crystal Structure Determination;* University of Göttingen: Göttingen, Germany, 1997.
(16) Sheldrick, G. M. *SHELXL-97: Program for Crystal Structure Refinement;* University of Göttingen: Göttingen, Germany, 1997.
(17) Frisch, M. J.; Trucks, G. W.; Schlegel, H. B.; Scuseria, G. E.; Robb, M. A.; Cheeseman, J. R.; Montgomery, J. A., Jr.; Vreven, T.; Kudin, K. N.; Burant, J. C.; Millam, J. M.; Iyengar, S. S.; Tomasi, J.; Barone, V.; Mennucci, B.; Cossi, M.; Scalmani, G.; Rega, N.; Petersson, G. A.; Nakatsuji, H.; Hada, M.; Ehara, M.; Toyota, K.; Fukuda, R.; Hasegawa, J.; Ishida, M.; Nakajima, T.; Honda, Y.; Kitao, O.; Nakai, H.; Klene, M.; Li, X.; Knox, J. E.; Hratchian, H. P.; Cross, J. B.; Bakken, V.; Adamo, C.; Jaramillo, J.; Gomperts, R.; Stratmann, R. E.; Yazyev, O.; Austin, A. J.; Cammi, R.; Pomelli, C.; Ochterski, J. W.; Ayala, P. Y.; Morokuma, K.; Voth, G. A.; Salvador, P.; Dannenberg, J. J.; Zakrzewski, V. G.; Dapprich, S.; Daniels, A. D.; Strain, M. C.; Farkas, O.; Malick, D. K.; Rabuck, A. D.; Raghavachari, K.; Foresman, J. B.; Ortiz, J. V.; Cui, Q.; Baboul, A. G.; Clifford, S.; Cioslowski, J.; Stefanov, B. B.; Liu, G.; Liashenko, A.; Piskorz, P.; Komaromi, I.; Martin, R. L.; Fox, D. J.; Keith, T.; Al-Laham, M. A.; Peng, C. Y.; Nanayakkara, A.; Challacombe, M.; Gill, P. M. W.;

Johnson, B.; Chen, W.; Wong, M. W.; Gonzalez, C.; Pople, J. A. *Gaussian 03,* revision C.02; Gaussian, Inc.: Wallingford, CT, 2004.

(18) (a) Perdew, J. P.; Burke, K.; Ernzerhof, M. *Phys. Rev. Lett.* **1996**, *77*, 3865 doi:10.1103/PhysRevLett.77.3865.; (b) Perdew, J. P.; Burke, K.; Ernzerhof, M. *Phys. Rev. Lett.* **1997**, *78*, 1396 doi:10.1103/PhysRevLett.78.1396.; (c) Perdew, J. P.; Burke, K.; Ernzerhof, M. J. *Chem. Phys.* **1996**, *105*, 9982; (d) Ernzerhof, M.; Scuseria, G. E. J. *Chem. Phys.* **1999**, *110*, 5029.

(19) (a) Schäfer, A.; Huber, C.; Ahlrichs, R. J. *Chem. Phys.* **1994**, *100*, 5829; (b) Eichkorn, K.; Weigend, F.; Treutler, O.; Ahlrichs, R. *Theor. Chem. Acc.* **1997**, *97*, 119.

(20) Andrae, D.; Haeussermann, U.; Dolg, M.; Stoll, H.; Preuss, H. *Theor. Chim. Acta* **1990**, *77*, 123. doi:10.1007/BF01114537.

(21) (a) Laaksonen, L. J. *Mol. Graph.* **1992**, *33*, 10; (b) Bergman, D. L.; Laaksonen, L.; Laaksonen, A. *J. Mol. Graph. Model.* **1997**, *15*, 301. doi:10.1016/S1093-3263(98)00003-5.

(22) Konu, J.; Tuononen, H. M.; Chivers, T.; Corrente, A. M.; Boeré, R. T.; Roemmele, T. *Inorg. Chem.* **2008**, *47*, 3823. doi:10.1021/ic702435e.

(23) (a) Pauling, L. *The Nature of the Chemical Bond,* 3rd ed.; Cornell University Press: Ithaca, NY, 1960; (b) Housecroft, C. E.; Sharpe, A. G. *Inorganic Chemistry,* 2nd ed.; Pearson Education Ltd.: Harlow, UK. 2005.

(24) Geschwentner, M.; Noltemeyer, M.; Elter, G.; Meller, A. *Z. Anorg. Allg. Chem.* **1994**, *620*, 1403. doi:10.1002/zaac.19946200813.

(25) Fusstetter, H.; Nöth, H. *Chem. Ber.* **1979**, *112*, 3672. doi:10.1002/cber.19791121115.

(26) Spiroconjugation is thought to contribute to the stability of the neutral group 13 radicals $\{M[PhB(\mu\text{-}N\text{-}t\text{-}Bu)_2]_2\}^{\bullet}$ (M = Al, Ga) (see ref. 5 and refs. cited therein).

(27) DFT calculations were also performed for the neutral (C_1 symmetric) systems **II** and **III** (Scheme 3), which comprise a Sn–Cl or a B–Cl bond, respectively. The paramagnetic species **II** is ca. 80 kJ mol^{-1} lower in energy, but the calculated hyperfine coupling constants for **II** and **III** are in poor agreement with those obtained from the experimental spectrum. The Sn–Cl bonded radical **II** exhibits a large (–11.56 G) coupling to the ^{11}B centre but, due to the lack of symmetry, the hfc couplings to the two nitrogen atoms are not equal (9.15 G and 5.56 G). The B–Cl bonded system **III** displays a coupling of –7.37 G to the ^{11}B isotope, and two inequivalent couplings of 11.24 and 2.26 G to the ^{14}N nuclei.

(28) Crystals of **2b** could not be obtained from diethyl ether. The attempted recrystallization of **2b** from THF resulted in a yellow solution, which contained the tin(IV) complex **1b** [^{1}H NMR spectrum (in d_8-THF)] as one component.

(29) The variable temperature ^{1}H NMR spectra of the lead complex **2c** exhibit similar trends; the broad singlet observed for *t*-Bu groups at 1.27 ppm at 23 °C resolves into three resonances at 1.36, 1.30, and 1.25 ppm (with a 1:2:1 intensity ratio) at –10 °C. However, these and other NMR data for **2c** were obtained on a reaction mixture and, consequently, any conclusions are necessarily tentative.

(30) Kim, S.-J.; Lee, Y.-J.; Kim, S. H.; Ko, J.; Cho, S.; Kang, S. O. *Organometallics* **2002**, *21*, 5358. doi:10.1021/om020587l.

(31) Brask, J. K.; Chivers, T. *Angew. Chem. Int. Ed. Engl.* **2001**, *40*, 3960. doi:10.1002/1521-3773(20011105)40:21<3960::AID-ANIE3960>3.0.CO;2-U.

Concise strategy for the synthesis of eleven-membered and ansa-bridged thirteen-membered lactone macrolides by ring-closing metathesis reaction

Krishna C. Majumdar, Buddhadeb Chattopadhyay, and Inul Ansary

Abstract: The eleven-membered macrolides and thirteen-membered ansa-bridged macrolides have been synthesized successfully by ring-closing metathesis reaction in the absence of the additive $Ti(OiPr)_4$, which is essential for the metathesis reaction of the ester precursors.

Key words: ring-closing metathesis, Grubbs catalyst, macrolide, eleven- and thirteen-membered lactone.

Résumé : On a réalisé la synthèse de macrolides à onze chaînons et de macrolides à pont ansa à treize chaînons par le biais d'une réaction de fermeture de cycle impliquant une métathèse, en l'absence du catalyseur $Ti(OiPr)_4$ qui est essentiel aux réactions de métathèse dans lesquelles les précurseurs sont des esters.

Mots-clés : fermeture de cycle impliquant une métathèse, catalyseur de Grubbs, macrolide, lactones à 11 et 13 chaînons.

[Traduit par la Rédaction]

Introduction

Recently, Singh et al. have reported[1] the isolation of two natural products, aspercyclides (Fig. 1, **a** and **b**), from the fungal metabolites and claimed that these natural products (**a** and **b**) possess several important biological activities.[2] The natural products aspercyclides consist of an eleven-membered lactone moiety that is flanked by differently substituted diaryl ether lactone. Subsequently, Furstner and Muller[3] achieved the total synthesis of "aspercyclide C" (Fig. 1, **a**) to explore its biological activity.

Moreover, numerous natural products possess a macrolactone subunit and exhibit important biological and cytotoxic activities.[4] *Pondaplin* D,[5] an ansa-bridged thirteen-membered macrolide isolated from *Annoa glabra* is known to be cytotoxic against six different human tumor cell lines (Fig. 2).[5] This thirteen-membered ansa-bridged macrolide framework confers strong rigidity to the whole structure. Therefore, all these factors made its synthesis a challenging purpose.

With the discovery of useful as well as air-stable catalysts, ring-closing metathesis (RCM) is now a practical and beneficial method of choice for the synthesis of cyclic compounds from highly functionalized molecules.[6] This protocol has been tremendously applied for the synthesis of macrolactones of different ring sizes.[7] The synthesis of ansa-bridged macrolides by ring-closing metathesis has been developed only in few cases.[3,8] This has prompted us to undertake a study of the synthesis of new lactone macrolides[9] for possible evaluation as biologically active compounds or any other useful compounds by the application of the ring-closing metathesis reaction of less studied ester precursors. Additional interest is derived from our interest in the synthesis of heterocycles by transition metal-mediated[10] heterocyclization.

Received 21 July 2008. Accepted 27 October 2008. Published on the NRC Research Press Web site at canjchem.nrc.ca on 28 January 2009.

K.C. Majumdar,[1] B. Chattopadhyay, and I. Ansary. Department of Chemistry, University of Kalyani, Kalyani 741235, W.B. India.

[1]Corresponding author (e-mail: kcm_ku@yahoo.co.in).

Results and discussion

The preparation of starting materials **6a**–**6f** is depicted on Scheme 1. Commercially available 2-hydroxy ethyl benzoate **1a** was conveniently allylated in dry acetone in the presence of anhyd. K_2CO_3 with allyl bromide for 15 h in refluxing condition to give *O*-allylated compound **2a**. Compound **2a** under saponification condition yielded the corresponding acid **3a**, which was finally converted to acid chloride **4a** by treatment with $SOCl_2$ in the presence of a catalytic amount of DMF. 2-Hydroxyl-1-allyl naphthalene **5a** was prepared according to the earlier reported procedure.[10a] The starting material **6a** was obtained by coupling of two partners **5a** and **4a** in dry DCM–Et_3N solvent in the presence of a catalytic amount of DMAP at 0 °C –RT for 12 h. Similarly, other starting materials **6b, 6c**, and **6d**–**6f** were prepared.

Attempts to carry out the metathesis reaction of the substrate **6a** with Grubbs first-generation catalyst in dichloromethane at RT proved unsuccessful. The entire starting material remained unchanged in the reaction mixture. When the reaction was conducted in refluxing condition for two days, only the decomposition of the catalyst was observed, leaving the starting material unchanged. However, when the substrate **6a** was refluxed with 5 mol% Grubbs second-generation catalyst in dry dichloromethane solution under nitrogen atmosphere for two days, the eleven-membered macrolide **7a** was obtained in 62% yield (Scheme 2). We have obtained only the *E*-olefin as evidenced by the *J* values (17.6 Hz) for the

Fig. 1. Naturally occurring aspercyclides, eleven-membered macrolides.

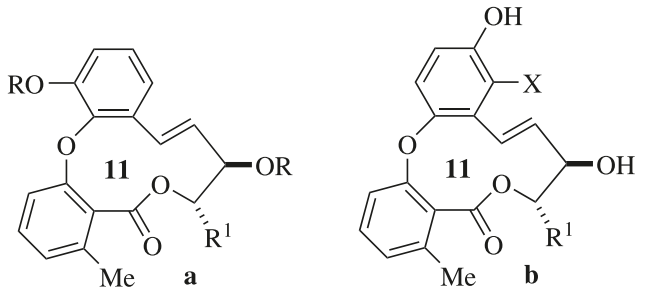

Fig. 2. Pondaplin, ansa-bridged thirteen-membered macrolide.

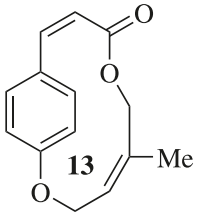

olefinic protons. To test the generality of this macrolization, the substrates **6b** and **6c** were treated under similar reaction conditions as above to afford the macrolides **7b** and **7c** in 59% and 63% yields, respectively.

We then extended the reaction to the synthesis of the thirteen-membered macrolides. Initially, we attempted the reaction of **6d** using Grubbs first-generation catalyst in dry dichloromethane solution under nitrogen atmosphere for 2–3 day without any success. No cyclized product was obtained even at the refluxing conditions. We then tried to carry out the same reaction by changing the solvent DCM with benzene, toluene, or xylene, but no macrolization was observed. Finally, we have succeeded in obtaining the thirteen-membered macrolide **7d** in 63% yield from **6d** by treatment with Grubbs second-generation catalyst in refluxing dichloromethane solution under nitrogen atmosphere for 4 days.

Here, the preparations of both the eleven- and thirteen-membered macrolides were achieved under high dilution.[11] The macrolides **7e** and **7f** were also prepared accordingly.

We have also attempted to extend the reaction by changing the allyl part of the compound **4** by crotyl and propargyl moieties. Unfortunately, we failed to obtain any cyclized product. The reaction conditions are summarized in Table 1.

Recently, Furstner[12] reported that the substrates possessing carboxylate moiety in one of the diene partners of the metathesis precursors cannot undergo the metathesis reaction with the Grubbs catalyst in the absence of additive $Ti(OiPr)_4$ in the reaction mixture. The reaction does not proceed because of the fact that the ruthenium carbene complex coordinates on to the ester by chelation with the ester carbonyl moiety and the olefin (Fig. 3).

When the reaction is conducted in the presence of $Ti(OiPr)_4$ along with the Grubbs catalyst, $Ti(OiPr)_4$ probably acts because of factors such as (*i*) $Ti(OiPr)_4$ is weakly Lewis acidic additive and consequently avoids the formation of unreactive chelate complex by coordination with the ester carbonyl moiety, (*ii*) $Ti(OiPr)_4$ may abstract one of the basic PCy_3 ligands from the Grubbs catalyst and thereby enhancing the catalytic activity of the Grubbs catalyst.

Conclusion

In conclusion, we have successfully synthesized the eleven-membered macrolides that are present in many natural-product core moieties such as aspercyclide C and thirteen-membered ansa-bridged macrolides that are the core structure of the natural product "pondaplin" by the implementation of ring-closing metathesis reaction without $Ti(OiPr)_4$ additive.[12] We believe that the methodology is simple and straightforward and will be useful to the synthetic community.

Experimental

General remarks

Melting points were determined in open capillaries and are uncorrected. IR spectra were run for KBr discs (and neat for liquid samples), and NMR spectra were determined for solutions in $CDCl_3$ with TMS as internal standard. Silica gel (60–120 mesh) was used for chromatographic separation. Silica gel-G was used for TLC. Petroleum ether refers to the fraction between 60 and 80 °C.

General methods for the preparation of compounds 6a–6f

A mixture of 2-hydroxy ethyl benzoate **1a** (4.0 g, 24.07 mmol), allyl bromide (3.49 g, 28.88 mmol), anhyd. potassium carbonate (13.30 g, 96.28 mmol), and catalytic amount of sodium iodide in dry acetone (100 mL) was refluxed for 15 h. The reaction mixture was cooled, filtered, and acetone was evaporated to give the corresponding *O*-allylated compound **2a** (4.9 g). Compound **2a** (4.9 g) was hydrolyzed with potassium hydroxide (3.3 g, 59.41 mmol) in ethanolic solution (50 mL) for 4 h at refluxing condition. Excess ethanol was removed by distillation, and the reaction mixture was cooled and was made acidic by adding 6 N HCl to give the corresponding acid **3a** (4.0 g, 95%).

The acid **3a** (0.425 g, 2.38 mmol) was then refluxed with $SOCl_2$ (1.5 mL) in the presence of DMF (catalytic amount) for 1 h, and excess $SOCl_2$ was removed under reduced pressure to give the acid chloride (0.47 g, 100%) **4a**. Finally, the acid chloride **4a** (0.47 g, 2.39 mmol) in dry dichloromethane (15 mL) was added dropwise to a mixture of 1-allyl-2-naphthol **5a** (440 mg, 2.39 mmol), triethylamine (2 mL), and a catalytic amount of DMAP in dry dichloromethane solution (30 mL) at ice-cold temperature. The reaction mixture was stirred at RT for 12 h to afford the esterified compound **6a** (0.69 g, 82%). Similarly, other starting materials **6b–6f** were prepared. Compounds **6a–6f** were recrystallized from dichloromethane–petroleum ether (60–80 °C).

Compound 6a

Yield: 82%; colourless solid; mp 53–54 °C (dichloromethane–petroleum ether). IR (KBr, cm^{-1}): 1744, 2853, 2923. ^1H NMR ($CDCl_3$, 400 MHz) δ_H: 3.85 (d, 2H, J = 5.9 Hz, CH_2), 4.68 (d, 2H, J = 5.0 Hz, OCH_2), 4.99–5.03 (m, 2H, $=CH_2$), 5.25 (dd, 1H, J = 10.6 Hz, J = 1.4 Hz, $=CH_aH_b$), 5.49 (dd, 1H, J = 17.2 Hz, J = 1.4 Hz, $=CH_aH_b$), 5.96–6.08 (m, 2H, =CH), 7.04 (d, 1H, J = 8.2 Hz, ArH), 7.08 (d, 1H, J = 7.7 Hz, ArH), 7.34 (d, 1H, J = 8.8 Hz, ArH), 7.45

Scheme 1. Reagents and conditions: (i) Acetone, K_2CO_3, allyl bromide, reflux, 15 h. (ii) EtOH, KOH, reflux, 4 h. 6 N HCl. (iii) $SOCl_2$, DMF, reflux, 1 h. (iv) dry DCM, **4a**, Et_3N, DMAP, 0 °C –RT, stirring, 12 h. (v) dry DCM, **4b**, Et_3N, DMAP, 0 °C–RT, stirring, 12 h.

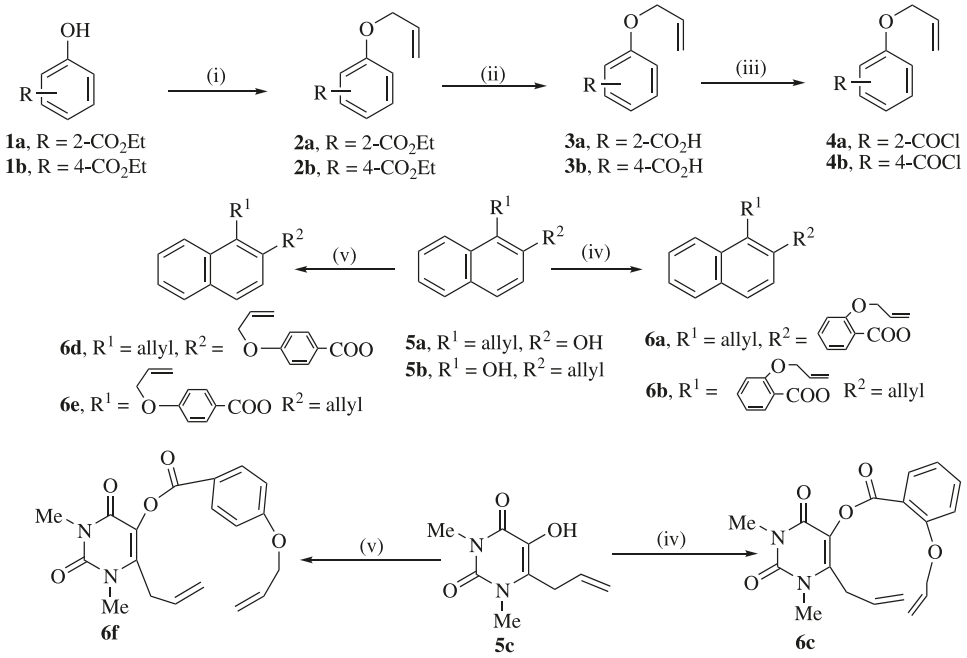

Scheme 2.

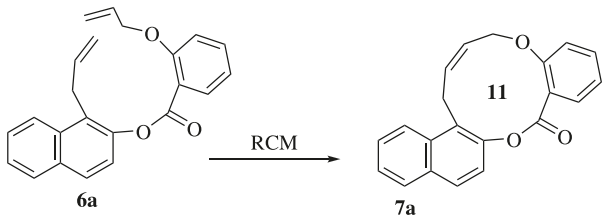

(d, 1H, *J* = 6.9 Hz, ArH), 7.48–7.55 (m, 2H, ArH), 7.79 (d, 1H, *J* = 8.8 Hz, ArH), 7.86 (d, 1H, *J* = 7.9 Hz, ArH), 8.03 (d, 1H, *J* = 8.0 Hz, ArH), 8.06 (d, 1H, *J* = 1.6 Hz, ArH). ^{13}C NMR ($CDCl_3$, 100 MHz) δ_C: 30.2, 69.4, 113.6, 115.9, 117.7, 119.5, 120.5, 122.0, 124.3, 125.2, 126.2, 126.3, 128.0, 128.6, 132.1, 132.3, 132.5, 132.8, 134.1, 135.8, 146.7, 158.7, 164.9. HRMS: Calcd. for $C_{23}H_{20}O_3$: 367.1318 (M + Na). Found: 367.1310 (M + Na).

Compound 6b

Yield: 88%; colourless solid; mp 56–57 °C (dichloromethane–petroleum ether). IR (KBr, cm^{-1}): 1744, 2868, 2921. ^{1}H NMR ($CDCl_3$, 400 MHz) δ_H: 3.51 (d, 2H, *J* = 6.4 Hz, CH_2), 4.71 (d, 2H, *J* = 5.0 Hz, OCH_2), 5.11–5.16 (m, 2H, $=CH_2$), 5.39 (dd, 1H, *J* = 10.6 Hz, *J* = 1.1 Hz, $=CH_aH_b$), 5.58 (dd, 1H, *J* = 17.2 Hz, *J* = 1.1 Hz, $=CH_aH_b$), 5.99–6.19 (m, 2H, =CH), 7.05 (d, 2H, *J* = 7.9 Hz, ArH), 7.41–7.55 (m, 3H, ArH), 7.78 (d, 1H, *J* = 8.4 Hz, ArH), 7.89 (dd, 1H, *J* = 8.8 Hz, *J* = 1.7 Hz, ArH), 7.93 (dd, 1H, *J* = 7.6 Hz, *J* = 1.7 Hz, ArH), 8.13 (d, 2H, *J* = 8.8 Hz, ArH). MS *m*/*z*: 344 (M$^+$). Anal. calcd. for $C_{23}H_{20}O_3$: C, 80.21; H, 5.85. Found: C, 80.43; H, 6.01.

Compound 6c

Yield: 79%; colourless solid; mp 94–95 °C (dichloromethane–petroleum ether). IR (KBr, cm^{-1}): 1664, 1706, 1753, 2853, 2923. ^{1}H NMR ($CDCl_3$, 400 MHz) δ_H: 3.39 (s, 3H, $-NCH_3$), 3.40 (d, 3H, *J* = 6.3 Hz, $-CH_2$), 3.44 (s, 3H, $-NCH_3$), 4.62 (d, 2H, *J* = 5.0 Hz, OCH_2), 5.18–5.23 (m, 2H, $=CH_2$), 5.25 (dd, 1H, *J* = 10.6 Hz, *J* = 1.3 Hz, $=CH_aH_b$), 5.44 (dd, 1H, *J* = 17.9 Hz, *J* = 1.3 Hz, $=CH_aH_b$), 5.79–5.86 (m, 1H, =CH), 5.98–6.08 (m, 1H, =CH), 6.97–7.04 (m, 2H, ArH), 7.50 (dd, 1H, *J* = 8.6 Hz, *J* = 1.5 Hz, ArH), 8.00 (dd, 1H, *J* = 7.7 Hz, *J* = 1.4 Hz, ArH). MS *m*/*z*: 356 (M$^+$). Anal. calcd. for $C_{19}H_{20}N_2O_5$: C, 64.04; H, 5.66; N, 7.86. Found: C, 63.91; H, 5.88; N, 8.03.

Compound 6d

Yield: 84%; colourless solid; mp 84–85 °C (dichloromethane–petroleum ether). IR (KBr, cm^{-1}): 1730, 2849, 2917. ^{1}H NMR ($CDCl_3$, 400 MHz) δ_H: 3.80 (d, 2H, *J* = 5.9 Hz, CH_2), 4.63 (d, 2H, *J* = 5.2 Hz, OCH_2), 4.96–5.01 (m, 2H, $=CH_2$), 5.34 (dd, 1H, *J* = 10.5 Hz, *J* = 1.1 Hz, $=CH_aH_b$), 5.44 (dd, 1H, *J* = 16.3 Hz, *J* = 1.1 Hz, $=CH_aH_b$), 5.93–6.12 (m, 2H, =CH), 7.01 (d, 2H, *J* = 8.8 Hz, ArH), 7.31 (d, 1H, *J* = 8.8 Hz, ArH), 7.45–7.59 (m, 3H, ArH), 7.79 (d, 1H, *J* = 8.8 Hz, ArH), 7.86 (d, 1H, *J* = 7.9 Hz, ArH), 8.02 (d, 1H, *J* = 8.4 Hz, ArH), 8.19 (d, 1H, *J* = 8.8 Hz, ArH). MS *m*/*z*: 344 (M$^+$). Anal. calcd. for $C_{23}H_{20}O_3$: C, 80.21; H, 5.85. Found: C, 79.99; H, 5.63.

Compound 6e

Yield: 86%; colourless solid; mp 72–73 °C (dichloromethane–petroleum ether). IR (KBr, cm^{-1}): 1732, 2858, 2919. ^{1}H NMR ($CDCl_3$, 400 MHz) δ_H: 3.46 (d, 2H, *J* = 6.4 Hz, CH_2), 4.65 (d, 2H, *J* = 5.0 Hz, OCH_2), 5.04–5.09 (m, 2H, $=CH_2$), 5.34 (dd, 1H, *J* = 10.6 Hz, *J* = 1.1 Hz, $=CH_aH_b$), 5.44 (dd, 1H, *J* = 17.2 Hz, *J* = 1.1 Hz, $=CH_aH_b$), 5.91–5.99 (m, 2H, =CH), 7.05 (d, 2H, *J* = 8.8 Hz, ArH), 7.40 (d, 1H, *J* = 8.3 Hz, ArH), 7.42–7.46 (m, 2H, ArH), 7.73 (d, 1H, *J* = 8.5 Hz, ArH), 7.77 (t, 1H, *J* = 5.7 Hz, ArH), 7.84 (dd, 1H,

Table 1. Summarized results of the macrolization by ring-closing metathesis reaction.

Entry	Substrates	Conditions	Products	Yield (%)
1	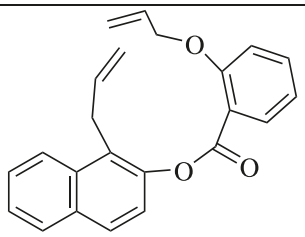 **6a**	Cat: 5 mol%; DCM, reflux, 2 day	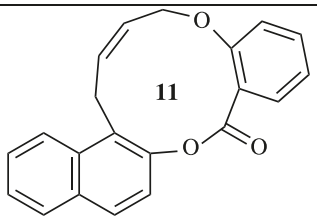 **7a**	62
2	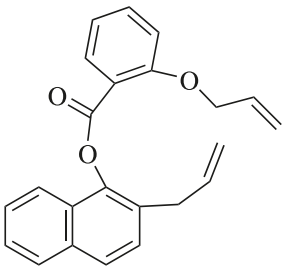 **6b**	Cat: 5 mol%; DCM, reflux, 2 day	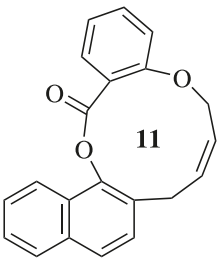 **7b**	59
3	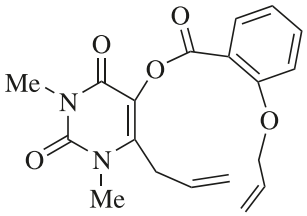 **6c**	Cat: 5 mol%; DCM, reflux, 2 day	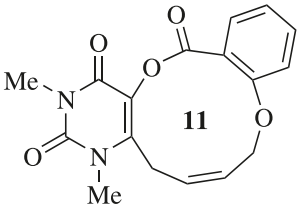 **7c**	64
4	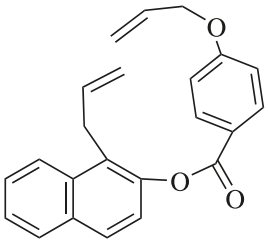 **6d**	Cat: 10 mol%; DCM, reflux, 4 day	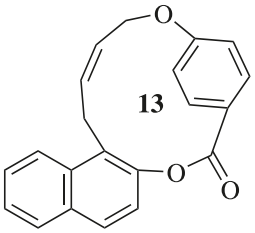 **7d**	63
5	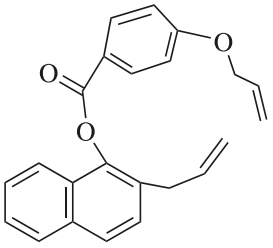 **6e**	Cat: 10 mol%; DCM, reflux, 4 day	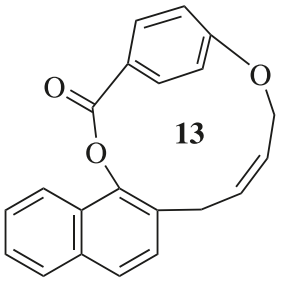	57
6	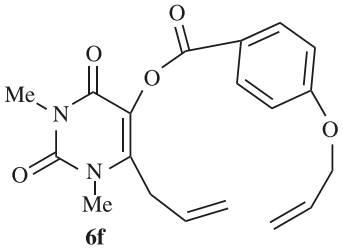 **6f**	Cat: 10 mol%; DCM, reflux, 4 day	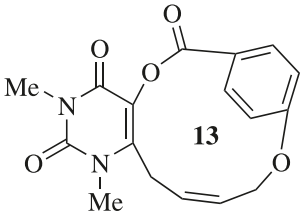 **7f**	59

Fig. 3. Unreactive chelate complex of Ru with esterified double bond.

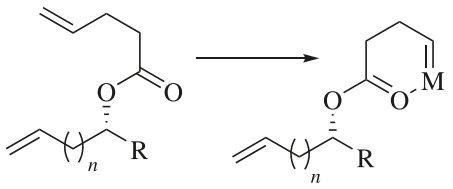

J = 7.7 Hz, J = 1.3 Hz, ArH), 8.27 (d, 2H, J = 8.8 Hz, ArH). MS *m/z*: 344 (M^+). Anal. calcd. for $C_{23}H_{20}O_3$: C, 80.21; H, 5.85. Found: C, 80.29; H, 6.11.

Compound 6f

Yield: 85%; colourless solid; mp 109–110 °C (dichloromethane–petroleum ether). IR (KBr, cm^{-1}): 1663, 1704, 1741, 2851, 2918. ^1H NMR ($CDCl_3$, 400 MHz) δ_H: 3.39 (s, 3H, $-NCH_3$), 3.40 (d, 2H, J = 6.3 Hz, $-CH_2$), 3.43 (s, 3H, $-NCH_3$), 4.59 (d, 2H, J = 5.0 Hz, $-OCH_2$), 5.08–5.16 (m, 2H, $=CH_2$), 5.19 (dd, 1H, J = 10.6 Hz, J = 1.3 Hz, $=CH_aH_b$), 5.39 (dd, 1H, J = 17.9 Hz, J = 1.3 Hz, $=CH_aH_b$), 5.77–5.81 (m, 1H, =CH), 5.98–6.04 (m, 1H, =CH), 6.99 (d, 2H, J = 8.1 Hz, ArH), 7.41 (dd, 1H, J = 7.7 Hz, J = 1.9 Hz, ArH), 7.99 (dd, 1H, J = 8.2 Hz, J = 1.9 Hz, ArH). MS *m/z*: 356 (M^+). Anal. calcd. for $C_{19}H_{20}N_2O_5$: C, 64.04; H, 5.66; N, 7.86. Found: C, 64.23; H, 5.83; N, 7.68.

General methods for the synthesis of macrolides 7a–7f

To a solution of the substrate **6a** (30 mg, 0.16 mmol) in dry degassed dichloromethane (40 mL) under nitrogen atmosphere was added Grubbs second-generation catalyst (5 mol%, 17 mg) and the reaction was stirred at rt for 1 h. The mixture was then refluxed for 2 days. The solvent was distilled off and the residue was purified by flash column chromatography on silica gel using 10% ethyl acetate-petroleum ether to afford the compound **7a**. Accordingly compounds **7b-7f** were synthesized. Compounds **7a-7f** were recrystallized from dichloromethane-petroleum ether (60–80 °C).

Compound 7a

Yield: 62%; colourless solid; mp 104–105 °C (dichloromethane–petroleum ether). IR (KBr, cm^{-1}): 1740, 2851, 2957. ^1H NMR ($CDCl_3$, 400 MHz) δ_H: 4.04 (d, 2H, J = 5.0 Hz, CH_2), 4.59 (d, 2H, J = 5.0 Hz, OCH_2), 5.96 (dt, 1H, J = 17.6 Hz, J = 5.0 Hz, =CH), 6.09 (dt, 1H, J = 17.6 Hz, J = 5.0 Hz, =CH), 6.94 (d, 1H, J = 6.8 Hz, ArH), 7.02 (dt, 1H, J = 6.0 Hz, J = 3.1 Hz, ArH), 7.30 (d, 1H, J = 7.1 Hz, ArH), 7.45–7.55 (m, 3H, ArH), 7.76 (d, 1H, J = 7.1 Hz, ArH), 7.84 (dd, 1H, J = 7.1 Hz, J = 1.4 Hz, ArH), 7.89 (d, 1H, J = 6.6 Hz, ArH), 8.07 (d, 1H, J = 7.3 Hz, ArH). ^{13}C NMR ($CDCl_3$, 100 MHz) δ_C: 29.1, 70.1, 112.9, 120.4, 120.7, 121.9, 124.2, 125.2, 125.3, 125.9, 126.4, 128.0, 128.7, 131.8, 132.1, 132.8, 133.6, 133.9, 146.5, 157.6, 166.9. HRMS: Calcd. for $C_{21}H_{16}O_3$: 339.0997 (M + Na). Found: 339.0990 (M + Na).

Compound 7b

Yield: 59%; colourless solid; mp 96–97 °C (dichloromethane–petroleum ether). IR (KBr, cm^{-1}): 1742, 2850, 2921. ^1H NMR ($CDCl_3$, 400 MHz) δ_H: 3.49 (d, 2H, J = 5.0 Hz, CH_2), 4.63 (d, 2H, J = 5.0 Hz, OCH_2), 5.85 (dt, 1H, J = 17.6 Hz, J = 5.0 Hz, =CH), 6.06 (dt, 1H, J = 17.6 Hz, J = 5.0 Hz, =CH), 6.98 (dd, 1H, J = 7.9 Hz, J = 1.7 Hz, ArH), 7.40 (d, 1H, J = 6.9 Hz, ArH), 7.44 (m, 2H, ArH), 7.49 (dt, 1H, J = 7.1 Hz, J = 3.0 Hz, ArH), 7.53 (d, 1H, J = 8.1 Hz, ArH), 7.63 (dd, 1H, J = 6.7 Hz, J = 1.0 Hz, ArH), 7.72 (dt, 1H, J = 7.7 Hz, J = 3.0 Hz, ArH), 7.80 (t, 1H, J = 7.0 Hz, ArH), 8.04 (dt, 1H, J = 7.4 Hz, J = 2.3 Hz, ArH). MS *m/z*: 316 (M^+). Anal. calcd. for $C_{21}H_{16}O_3$: C, 79.73; H, 5.10. Found: C, 79.61; H, 5.23.

Compound 7c

Yield: 64%; colourless solid; mp 149–150 °C (dichloromethane–petroleum ether). IR (KBr, cm^{-1}): 1649, 1701, 1739, 2849, 2920. ^1H NMR ($CDCl_3$, 400 MHz) δ_H: 3.37 (s, 6H, -NCH_3), 3.41 (d, 2H, J = 5.4 Hz, CH_2), 5.09 (d, 2H, J = 5.4 Hz, OCH_2), 5.77 (dt, 1H, J = 17.6 Hz, J = 5.0 Hz, =CH), 5.92 (dt, 1H, J = 17.6 Hz, J = 5.0 Hz, =CH), 6.90–7.04 (m, 2H, ArH), 7.47 (dd, 1H, J = 8.5 Hz, J = 1.7 Hz, ArH), 7.99 (dd, 1H, J = 7.5 Hz, J = 1.7 Hz, ArH). MS *m/z*: 328 (M^+). Anal. calcd. for $C_{17}H_{16}N_2O_5$: C, 62.19; H, 4.91; N, 8.53. Found: C, 62.33; H, 5.09; N, 8.66.

Compound 7d

Yield: 63%; colourless solid; mp 120–121 °C (dichloromethane–petroleum ether. IR (KBr, cm^{-1}): 1730, 2850, 2920. ^1H NMR ($CDCl_3$, 400 MHz) δ_H: 3.79 (d, 2H, J = 5.0 Hz, CH_2), 4.61 (d, 2H, J = 5.0 Hz, OCH_2), 5.88 (dt, 1H, J = 17.6, J = 5.0 Hz, =CH), 6.03 (dt, 1H, J = 17.6 Hz, J = 5.0 Hz, =CH), 7.08 (d, 1H, J = 7.5 Hz, ArH), 7.29–7.33 (m, 2H, ArH), 7.49 (dt, 2H, J = 7.9 Hz, J = 3.0 Hz, ArH), 7.69 (dd, 1H, J = 6.9 Hz, J = 1.1 Hz, ArH), 7.79 (t, 1H, J = 8.0 Hz, ArH), 7.81 (dd, 1H, J = 6.8 Hz, J = 1.2 Hz, ArH), 8.01 (d, 1H, J = 8.8 Hz, ArH), 8.11 (d, 1H, J = 7.9 Hz, ArH). MS *m/z*: 316 (M^+). Anal. calcd. for $C_{21}H_{16}O_3$: C, 79.73; H, 5.10. Found: C, 79.86; H, 4.89.

Compound 7e

Yield: 57%; colourless solid; mp 113–114 °C (dichloromethane–petroleum ether). IR (KBr, cm^{-1}): 1731, 2851, 2921. ^1H NMR ($CDCl_3$, 400 MHz) δ_H: 3.47 (dd, 2H, J = 5.7 Hz, J = 1.0 Hz, CH_2), 4.62 (dd, 2H, J = 7.3 Hz, J = 1.0 Hz, OCH_2), 6.00 (dt, 1H, J = 17.6 Hz, J = 5.0 Hz, =CH), 6.09 (dt, 1H, J = 17.6 Hz, J = 5.0 Hz, =CH), 7.00 (d, 1H, J = 6.8 Hz, ArH) 7.08 (d, 1H, J = 7.3 Hz, ArH), 7.38–7.43 (m, 3H, ArH), 7.51 (dd, 2H, J = 8.8 Hz, J = 1.7 Hz, ArH), 7.85 (dt, 1H, J = 7.1 Hz, J = 3.0 Hz, ArH), 8.14 (d, 2H, J = 8.0 Hz, ArH). MS *m/z*: 316 (M^+). Anal. calcd. for $C_{21}H_{16}O_3$: C, 79.73; H, 5.10. Found: C, 79.69; H, 5.33.

Compound 7f

Yield: 59%; colourless solid; mp 157–158 °C (dichloromethane–petroleum ether). IR (KBr, cm^{-1}): 1650, 1705, 1734, 2851, 2921. ^1H NMR ($CDCl_3$, 400 MHz) δ_H: 3.36 (d, 2H, J = 5.6 Hz, CH_2), 3.38 (s, 3H, $-NCH_3$), 3.45 (s, 3H, $-NCH_3$), 5.17 (d, 2H, J = 5.6 Hz, OCH_2), 5.80 (dt, 1H, J = 17.6 Hz, J = 5.0 Hz, =CH), 6.03 (dt, 1H, J = 17.6 Hz, J = 5.0 Hz, =CH), 6.95 (d, 2H, J = 7.7 Hz, J = 1.7 Hz, ArH), 8.09 (dd, 2H, J = 8.9 Hz, J = 3.0 Hz, ArH). MS *m/z*: 328 (M^+). Anal. calcd. for $C_{17}H_{16}N_2O_5$: C, 62.19; H, 4.91; N, 8.53. Found: C, 61.97; H, 5.11; N, 8.69.

Acknowledgements

We thank the DST (New Delhi) and the CSIR (New Delhi) for financial assistance. Two of us (BC and IA) are grateful to the CSIR (New Delhi) and UGC (New Delhi) for a senior and a junior research fellowships, respectively.

References

(1) Singh, S. B.; Jayasuriya, H.; Zink, D. L.; Polishook, J. D.; Dombrowski, A. W.; Zweerink, H. *Tetrahedron Lett.* **2004**, *45*, 7605. doi:10.1016/j.tetlet.2004.08.116.

(2) (a) Kinet, J.-P. *Annu. Rev. Immunol.* **1999**, *17*, 931 doi:10.1146/annurev.immunol.17.1.931. PMID:10358778.; (b) Jardieu, P. *Curr. Opin. Immunol.* **1995**, *7*, 779 doi:10.1016/0952-7915(95)80047-6. PMID:8679119.; (c) For the structure of the human high-affinity IgE receptor, see: Garman, S. C.; Kinet, J.-P.; Jardetzky, T. S. *Annu. Rev. Immunol.* **1999**, *17*, 973 doi:10.1146/annurev.immunol.17.1.973. PMID:10358779.; (d) For peptidic antagonists of the high-affinity IgE receptor, see: Nakamura, G. R.; Reynolds, M. E.; Chen, Y. M.; Starovasnik, M. A.; Lowman, H. B. *Proc. Natl. Acad. Sci. U.S.A.* **2002**, *99*, 1303; and refs. cited therein. doi:10.1073/pnas.022635599. PMID:11830661.

(3) Furstner, A.; Muller, C. *Chem. Commun.* **2005**, 5583. doi:10.1039/b512877c. PMID:16358071.

(4) (a) Norcross, R. D.; Paterson, I. *Chem. Rev.* **1995**, *95*, 2041 doi:10.1021/cr00038a012.; (b) Ishibashi, M.; Kobayashi, J. *Heterocycles*, **1997**, *44*, 543.

(5) Liu, X.-X.; Pilarinou, E.; McLaughlin, J. L. *Tetrahedron Lett.* **1999**, *40*, 399. doi:10.1016/S0040-4039(98)02401-0.

(6) (a) Trnka, T. M.; Grubbs, R. H. *Acc. Chem. Res.* **2001**, *34*, 18 doi:10.1021/ar000114f.; (b) Furstner, A. *Angew. Chem. Int. Ed.* **2000**, *39*, 3012 doi:10.1002/1521-3773(20000901)39:17<3012::AID-ANIE3012>3.0.CO;2-G.; (c) Grubbs, R. H.; Chang, S. *Tetrahedron,* **1998**, *54*, 4413 doi:10.1016/S0040-4020(97)10427-6.; (d) Armstrong, S. K. *J. Chem. Soc. Perkin Trans.* **1998**, *1*, 371 doi:10.1039/a703881j.; (e) Schuster, M.; Blechert, S. *Angew. Chem. Int. Ed. Engl.* **1997**, *36*, 2036 doi:10.1002/anie.199720361.; (f) Bressy, C.; Piva, O. *Synlett,* **2003**, 87.

(7) (a) Fürstner, A.; Langemann, K. *J. Org. Chem.* **1996**, *61*, 3942 doi:10.1021/jo960733v. PMID:11667264.; (b) Goldring, W. P. D.; Hodder, A. S.; Weiler, L. *Tetrahedron Lett.* **1998**, *39*, 4955 doi:10.1016/S0040-4039(98)00966-6.; (c) Fürstner, A.; Thiel, O. R.; Ackermann, L. *Org. Lett.* **2001**, *3*, 449 doi:10.1021/ol0069554. PMID:11428036.; (d) Fürstner, A.; Dierkes, T.; Thiel, O. R.; Blanda, G. *Chem. Eur. J.* **2001**, *7*, 5286. doi:10.1002/1521-3765(20011217)7:24<5286::AID-CHEM5286>3.0.CO;2-G.

(8) (a) Boger, D. L.; Hong, J.-Y. *J. Am. Chem. Soc.* **2001**, *123*, 8515 doi:10.1021/ja011271s. PMID:11525659.; (b) Fürstner, A.; Gastner, T.; Weintritt, H. *J. Org. Chem.* **1999**, *64*, 2361 doi:10.1021/jo982088t.; (c) Martin, S. F. J.; Humphrey, M.; Ali, A.; Hillier, M. C. *J. Am. Chem. Soc.* **1999**, *121*, 866 doi:10.1021/ja9829259.; (d) Nicolaou, K. C.; Vassilikogiannakis, G.; Montagnon, T. *Angew. Chem. Int. Ed.* **2002**, *41*, 3276 doi:10.1002/1521-3773(20020902)41:17<3276::AID-ANIE3276>3.0.CO;2-P.; (e) Bach, T.; Lemarchand, A. *Synlett*, **2002**, 1302. doi:10.1055/s-2002-32958.

(9) (a) For eleven- and thirteen-membered rings by RCM strategy, see: Bressy, C.; Piva, O. *Synlett,* **2003**, 87; (b) Ramana, C. V.; Mondal, M. A.; Puranik, V. G.; Gurjar, M. K. *Tetrahedron Lett.* **2007**, *48*, 7524 doi:10.1016/j.tetlet.2007.08.050.; (c) For other examples of macrolization reactions via RCM using various catalysts, see: Miller, S. J.; Grubbs, R. H. *J. Am. Chem. Soc.* **1995**, *117*, 5855 doi:10.1021/ja00126a027.; (d) Miller, S. J.; Blackwell, H. E.; Grubbs, R. H. *J. Am. Chem. Soc.* **1996**, *118*, 9606 doi:10.1021/ja961626l.; (e) Clark, T. D.; Ghadiri, M. R. *J. Am. Chem. Soc.* **1995**, *117*, 12364 doi:10.1021/ja00154a051.; (f) Konig, B.; Horn, C. *Synlett*, **1996**, 1013. doi:10.1055/s-1996-5643.

(10) (a) Majumdar, K. C.; Chattopadhyay, B.; Sinha, B. *Tetrahedron Lett.* **2008**, *49*, 1319 doi:10.1016/j.tetlet.2007.12.096.; (b) Majumdar, K. C.; Chattopadhyay, B.; Nath, S. *Tetrahedron Lett.* **2008**, *49*, 1609 doi:10.1016/j.tetlet.2008.01.035.; (c) Majumdar, K. C.; Chattopadhyay, B. *Synlett,* **2008**, 979 doi:10.1055/s-2008-1072510.; (d) Majumdar, K. C.; Chattopadhyay, B.; Ray, K. *Tetrahedron Lett.* **2007**, *48*, 7633 doi:10.1016/j.tetlet.2007.08.121.; (e) Majumdar, K. C.; Chattopadhyay, B.; Taher, A. *Synthesis,* **2007**, 3647 doi:10.1055/s-2007-990846.; (f) Majumdar, K. C.; Pal, A. K.; Taher, A.; Debnath, P. *Synthesis*, **2007**, 1707. doi:10.1055/s-2007-966052.; (g) Majumdar, K. C.; Muhuri, S.; Rahaman, H.; Islam, R.; Roy, B. *Chem. Lett.* **2006**, *35*, 1430 doi:10.1246/cl.2006.1430.; (h) Majumdar, K. C.; Rahaman, H.; Islam, R.; Roy, B. *Tetrahedron Lett.* **2006**, *47*, 2111 doi:10.1016/j.tetlet.2006.01.132.; (i) Majumdar, K. C.; Islam, R.; Rahaman, H.; Roy, B. *Org. Biomol. Chem.* **2006**, *4*, 2393 doi:10.1039/b603125k. PMID:16763684.; (j) Majumdar, K. C.; Rahaman, H.; Roy, B. *Synlett*, **2006**, 0466 doi:10.1055/s-2006-926238.; (k) Majumdar, K. C.; Rahaman, H.; Roy, B. *Lett. Org. Chem.* **2006**, *3*, 526 doi:10.2174/157017806778341816.; (l) Majumdar, K. C.; Maji, P. K.; Rahaman, H.; Roy, B. *Lett. Org. Chem.* **2006**, *3*, 845 doi:10.2174/157017806779117094.; (m) Majumdar, K. C.; Rahaman, H.; Roy, B. *Curr. Org. Chem.* **2007**, 1339. doi:10.2174/138527207782023166.

(11) Illuminati, G.; Mandolini, L. *Acc. Chem. Res.* **1981**, *14*, 95. doi:10.1021/ar00064a001.

(12) (a) Furstner, A. *J. Am. Che. Soc.* **1997**, *119*, 9130 doi:10.1021/ja9719945.; (b) Furstner, A.; Langemann, K. *Synthesis*, **1997**, 792 doi:10.1055/s-1997-4472.; (c) Furstner, A. *Angew. Chem. Int. Ed.* **2000**, *39*, 3012. doi:10.1002/1521-3773(20000901)39:17<3012::AID-ANIE3012>3.0.CO;2-G.

Radioisotopic study of ^{11}C-labelling methanol decomposition on iron oxide modified mesoporous MCM-41 silica

Eva Sarkadi-Pribóczki, Tanya Tsoncheva, and Ljubomira Ivanova

Abstract: Novel ^{11}C-radiolabelling method was applied for the investigation of methanol conversion on iron oxide modified mesoporous MCM-41. Changes in the selectivity were observed varying the state of the loaded iron species or the degree of the surface coverage with ^{11}C-radiolabelling methanol. Combining the Moessbauer spectroscopy, X-ray diffraction (XRD), N_2-physisorption, and temperature-programmed reduction- thermogravimetric (TPR-TG) techniques with the high sensitive ^{11}C-radioisotopic catalytic analysis, the contribution of the different reaction pathways of methanol conversion was discussed.

Key words: ^{11}C-radiolabelling technique, methanol conversion, iron oxide modified MCM-41.

Résumé : On a utilisé une nouvelle méthode de radiomarquage du ^{11}C pour étudier la conversion du méthanol sur du MCM-41 mésoporeux modifié avec de l'oxyde de fer. On a observé les changements de sélectivité résultant d'un changement de l'état des espèces de fer ajoutées ou le degré de couverture de la surface avec du méthanol radiomarqué au ^{11}C. En se basant sur une combinaison de la spectroscopie de Mössbauer, de la de physisorption du N_2 et des techniques de TPR-TG avec l'analyse catalytique radioisotopique du ^{11}C à haute sensibilité, on discute de la contribution des diverses voies réactionnelles dans la conversion du méthanol.

Mots-clés : technique de radiomarquage du ^{11}C, conversion du méthanol, MCM-41 modifié avec de l'oxyde de fer.

[Traduit par la Rédaction]

Introduction

Nanosized iron-containing materials are well known for their potential application in the fields of electronic, nonlinear optics medicine, and catalysis because of their unusual magnetic and optical properties and superior catalytic activity.[1–4] It was well established that their behaviour could be successfully tuned, hosting the iron species in various porous materials[5–7] and much of our previous results in this aspect are summarized by Tsoncheva and co-workers.[8–17] Recently, we reported some initial data on a new approach for the characterization of the state of iron and iron oxide species, hosted in MCM-41, via the combination of a conventional catalytic method and high sensitivity ^{11}C-radiolabelling technique.[18] In the current investigation we expand our results with catalytic experiments using different coverage of the solid surface with ^{11}C-labelling methanol. The aim of the study is to elucidate the contribution of various reaction pathways of methanol conversion on iron-modified MCM-41 materials depending on the state of the iron species in them. For this purpose, samples prepared by impregnation of MCM-41 silica with iron nitrate or acetylacetonate precursors are compared.

Received 16 October 2008. Accepted 9 December 2008. Published on the NRC Research Press Web site at canjchem.nrc.ca on 5 February 2009.

E. Sarkadi-Pribóczki. Institute of Nuclear Research, Hungarian Academy of Science, Debrecen, Hungary.
T. Tsoncheva[1] and L. Ivanova. Institute of Organic Chemistry with Centre of Phytochemistry, Bulgarian Academy of Science, Sofia, Bulgaria.

[1]Corresponding author (e-mail: tsoncheva@orgchm.bas.bg).

Experimental

Materials

Iron-modified mesoporous silicas were obtained by impregnation of MCM-41[19] with iron nitrate or acetylacetonate precursors as described by Tsoncheva et al.[9,17] Typically, 1 g of template free silica support was impregnated with 40 mL 0.0286 mol/L aqueous or toluene solution of $Fe(NO_3)_3$ or Fe(III) acetylacetonate, respectively, for 2 h at room temperature. After the impregnation the samples were dried in a rotary evaporator for 1 h at 313 K. The precursor was decomposed in a flow of air at 773 K for 2 h. Materials containing 6% wt. of iron were obtained and denoted as Fe/MCM-41(N) and Fe/MCM-41(A) for the nitrate and acetylacetonate precursor, respectively.

Methods of investigations

Powder X-ray diffraction was carried out on a Bruker AXS D8 Advance diffractometer equipped with a secondary monochromator and automatic divergence slits (filtered Cu Kα radiation, 40 kV, 40 mA). Nitrogen physisorption was conducted at 77 K on a Quantochrome Autosorb 6. The specific surface area was elucidated using the standard BET method. Pore volumes and pore size distribution were calculated by Autosorb 1 for Windows 1.25 software (Quantachrome Instruments) using the Barret–Joyner–Halenda (BJH) method. The temperature-programmed reduction thermogravimetric (TPR-TG) investigations were performed in a Setaram TG92 instrument in a flow of 50 vol% H_2 in Ar (100 cm^3/min) up to 873 K at 5 K/min and a final hold-up of 1 h. Prior to the TPR experiments, the samples were treated in situ in a flow of air (10 K/min) up to 773 K,

followed by a hold-up of 1 h. The Mössbauer spectra were obtained in air at room temperature with a Wissel (Wissenschaftliche Elektronik GmbH, Germany) electromechanical spectrometer working in a constant acceleration mode. A ^{57}Co/Cr (activity $\cong$10 mCi) source and α-Fe standard were used. The experimentally obtained spectra were fitted by the least-squares method.

The catalytic experiments were performed in a fixed-bed reactor (0.055 g catalyst) at a methanol partial pressure of 1.57 kPa and a weight hourly space velocity (WHSV) of 1.5 h^{-1}, argon being used as a carrier gas. On-line gas chromatographic analysis was performed on a Porapak Q column using an absolute calibration method.

The radio-experiments were applied for monitoring of radiolabelled methanol behaviour using a GM (Geiger–Müller) radiodetector as well as FID-radio gas chromatograph.[20–22] About 370 MBq ^{11}C-methanol was formed by a radiochemical process at cyclotron ($T_{1/2}$ = 20.4 min). Catalytic experiments were started, introducing ^{11}C-methanol by He gas flow into a closed static mode reactor. After the ^{11}C-methanol adsorption, the sample was heated up to the required temperature. During desorption, He gas was used to remove and trap the gas phase ^{11}C-methanol into the P_2O_5 trap for radioactivity measuring by a dose calibrator before the further temperature increase. Above 473 K the ^{11}C-labelled gas products were analyzed by GC with FID coupled on-line with a radioactivity detector.

Results and discussion

Physicochemical characterization of the samples

Small angle X-ray diffraction (XRD) patterns (Fig. 1) of parent and differently iron-modified silica materials represent all reflections typical of *p6mm* hexagonal pore symmetry of MCM-41 mesophase.[19] This indicates a high quality of mesoporous silica support and its preservation after the modification procedure. The observed decrease in the intensity of the small angle reflections after the modification could be assigned to an overall decrease in the electron density contrast between the silica walls and the mesopore due to the location of iron oxide species inside the mesopores of the silica support.[23] At the same time, no or very slight reflections are registered in a wide-angle region of the XRD patterns (Fig. 1, inset), which could be assigned to the formation of finely dispersed iron containing species.

N_2-physisorption isotherms and the corresponding calculated parameters are presented in Fig. 2 and Table 1, respectively. The isotherms of parent and iron modified samples are type IV (IUPAC classification) with a well-pronounced capillary condensation step at 0.3–0.4 relative pressure, which is characteristic of mesoporous materials with uniform cylindrical pores and diameters of about 2.9 nm. This confirms the data from the XRD measurements for the preservation of the silica host structure during the iron loading procedure. The observed decrease in the BET surface area and total pore volume after the silica modification (Table 1) could both be from the mass increase or pore filling after the modification. When the correction for the mass of the modified samples was done, a higher degree of iron particles located in the mesoporous volume could be assumed for Fe/MCM-41(A).

Fig. 1. XRD patterns of parent and iron modified MCM-41 materials.

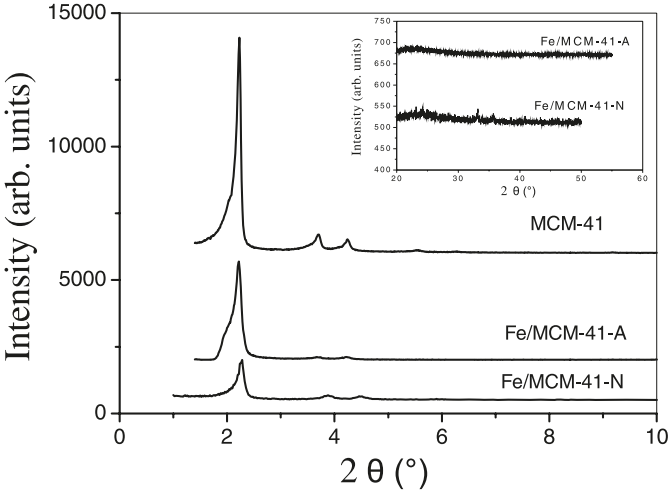

Fig. 2. Nitrogen physisorption isotherms of parent and iron modified MCM-41 materials.

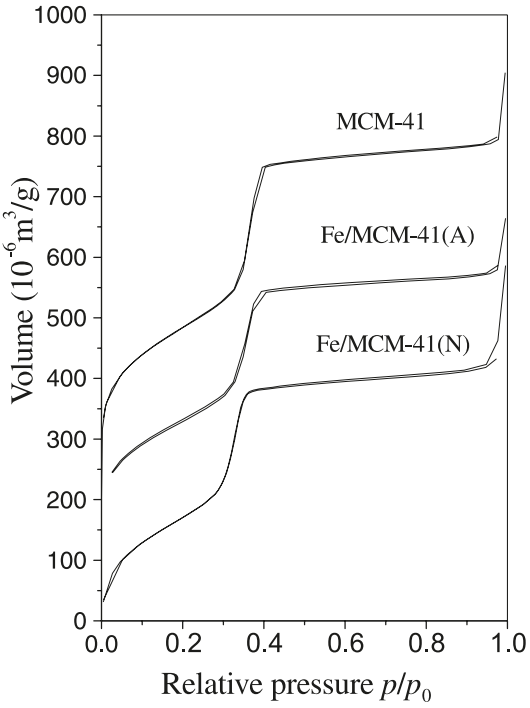

Table 1. Nitrogen physisorption parameters of parent and iron modified silicas: BET - specific surface area (BJH), V_p - total pore volume, ΔBET - relative decrease in the samples specific surface area compared to that of the parent silica material, and ΔV_p - relative decrease in the samples pore volume compared to that of the parent silica material.

Sample	BET (m^2/g)	V_p (cc/g)	ΔBET (m^2/g)	ΔV_p (cc/g)
MCM-41	1023	0.88	—	—
Fe/M41(N)	980	0.81	43	0.07
Fe/M41(A)	902	0.74	121	0.14

Table 2. Mössbauer parameters of MCM-41 iron modifications: isomer shift (IS), quadrupole splitting (QS), effective internal magnetic field (H_{eff}), line widths (FWHM), and relative weight of the partial components in the spectra (G).

Sample	Compounds	IS (mm/s)	QS (mm/s)	H_{eff} (kOe)	FWHM (mm/s)	G (%)
Fe/M41 (N)	Dbl 1 Fe^{3+}, SPM Fe_2O_3, core	0.34	0.59	—	0.39	52
	Dbl 2 Fe^{3+}, SPM Fe_2O_3, shell	0.32	1.02	—	0.47	48
Fe/M41 (A)	Dbl 1 Fe^{3+}, SPM Fe_2O_3, core	0.33	0.81	—	0.39	48
	Dbl 2 Fe^{3+}, SPM Fe_2O_3, shell	0.34	1.29	—	0.50	52

The main parameters from the Mössbauer spectra of the samples are listed in Table 2 and selected spectra are illustrated in Fig. 3. An idealized core/shell model was applied to distinguish the particles with different sizes more precisely. The spectra of both materials represent only doublets with parameters typical of high spin Fe^{3+} ions in octahedral coordination. The existence of finely dispersed hematite-like species (up to 6 nm) with superparamagnetic behaviour could be assumed,[24,25] and this is in agreement with the data obtained from XRD analysis. The core/shell ratio for Fe/MCM-41(N) is slightly higher, which could be associated with the presence of larger iron oxide species in this sample in comparison with Fe/MCM-41(A). Under the temperature of liquid nitrogen, Mössbauer spectra of both materials preserved their doublet character and no changes in the core/shell ratio were observed, which could be an indication for the presence of ultra finely dispersed iron oxide particles, probably less then 4 nm.

To determine the state of the iron species in both materials more precisely, TPR-TG analyses were also carried out (Table 3, Fig. 4). Total reduction degree for both materials does not exceed 100% up to 870 K, which confirms the formation of finely dispersed iron oxide species. The TPR profiles represent two distinct reductive effects in the 450–660 K and 700–870 K regions. The low temperature (LT) peak could be ascribed to the reduction of bulk hematite (Fe_2O_3) nanoparticles.[26,27] The higher T_{max} in this stage, which is registered for Fe/MCM-41(A), could be evidence for the presence of relatively smaller particles in it, and this assumption is in accordance with the Mössbauer data (see above). The second, high-temperature (HT) TPR peak probably arose from the reduction of the strongly interacting iron supported oxide species with lower degrees of crystallinity.[28] They could be two-dimensional FeO_x patches or even isolated iron ions, grafted to the silica surface. Their relative part seems to be much larger in the case of Fe/MCM-41(N) and this is proved by the lower LT/HT ratio in this case (Table 3).

Fig. 3. Mössbauer spectra of selected samples: initial Fe/MCM-41(A), the same material after reduction Fe/MCM-41(A)-r and after the catalytic test Fe/MCM-41(A)-c.

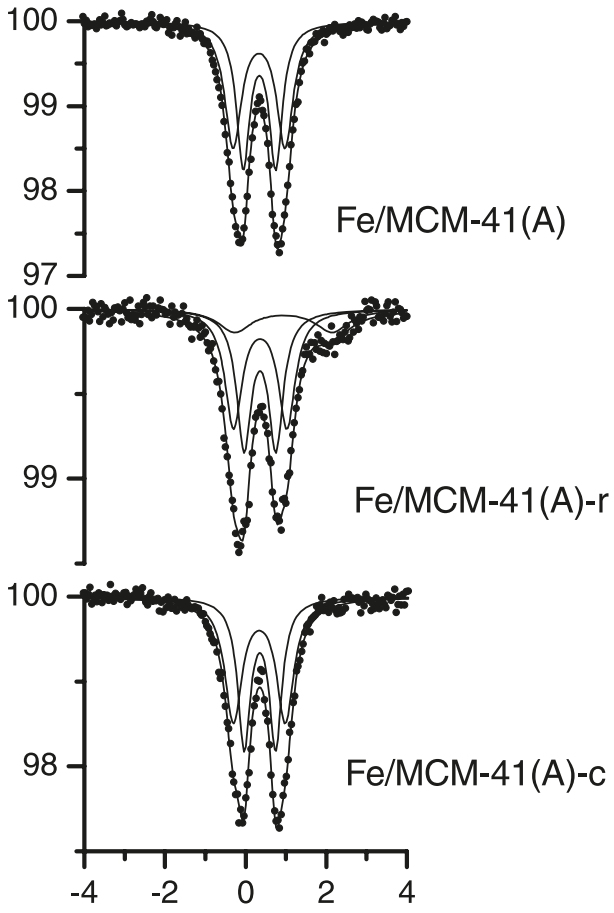

Catalytic test

In Fig. 5, the kinetic curves of methanol conversion for both iron modified materials at different temperatures are compared. Methanol decomposition to CO and methane as well as its dehydration to dimethyl ether (DME) are observed in all cases. The selectivity to DME is higher for Fe/MCM-41(N), while higher methane selectivity is registered for Fe/MCM-41(A). The catalytic activity of the samples decreases with time on stream, the effect being more pronounced for Fe/MCM-41(N) in comparison with Fe/MCM-41(A). Changes in the products distribution under isothermal conditions are also registered (Fig. 3). At the same time, the Mössbauer spectra of the materials used in the catalytic experiment show the appearance of a new doublet component, with a significantly higher IS value (about 0.97 mm/s), attributable to the presence of Fe^{2+} containing clusters (Fig. 3). These reduction phase transformations, occurring because of the influence of the reaction medium, could be considered as possible reasons for the changes in the catalytic behaviour of the samples under the isothermal conditions (Fig. 5). A higher initial catalytic activity is registered for Fe/MCM-41(N) and this observation is confirmed by the calculated values of the activation energy, which are 7.7 and 14.1 kcal/mol (1 cal = 4.184 J) for Fe/MCM-41(N) and Fe/MCM-41(A), respectively.

Table 3. TPR-TG parameters for the various iron modified materials.

Sample	Tmax (K)*	Weight loss (mg)		Reduction degree (%)†	LT/HT weight loss
		LT stage	HT stage		
Fe/M41(N)	563	0.22	0.43	76	0.51
Fe/M41(A)	572	0.24	0.28	66	0.86

*Temperature of the low-temperature reduction maximum in the DTG curves.
†Total weight loss during the low-temperature (LT) and high-temperature (HT) stages referenced to the calculated theoretical weight loss for the reduction of Fe^{3+} to Fe^0.

Fig. 4. TPR-TG profiles of Fe/MCM-41(A) and Fe/MCM-41(N).

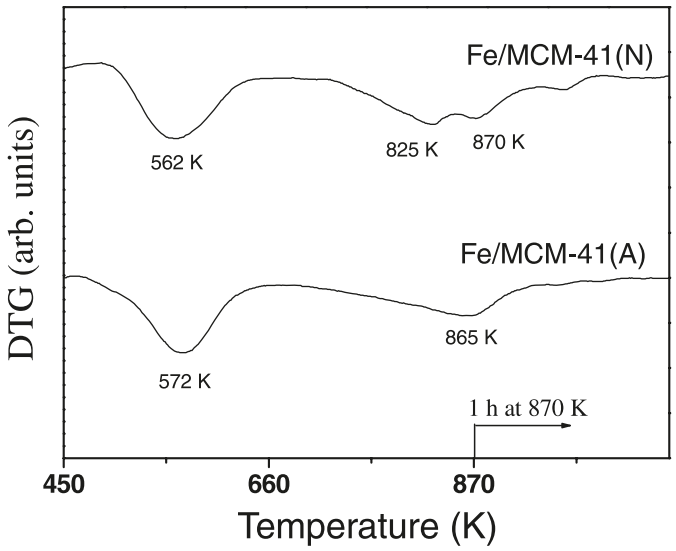

^{11}C-radiolabelling measurements

In Fig. 6, ^{11}C-methanol desorption measurements for both iron modified materials are presented. The experiments were carried out after methanol trapping at ambient temperature and further heating of the samples, up to 463 K. No products of methanol conversion are registered in a whole temperature interval. The sharp decrease in the radioactivity rate above 383 K indicates the start of the desorption process. It could be seen that the desorption curve of Fe/MCM-41(A) is shifted to higher temperatures in comparison with Fe/MCM-41(N). For the former sample, a higher level of radioactivity rate at the final desorption temperature is also found, which could be assigned to the larger amount of non-desorbed methanol in it. These observations point to the differences in the state of the iron species in both materials and it is in accordance with the data discussed above (see the sections titled physicochemical characterization of the samples and catalytic test).

In Fig. 7, some typical ^{11}C labelling radiochromatograms for both iron modifications are presented . The evolution of the process with the temperature confirms the data from the conventional catalytic test for the higher catalytic activity and better dehydration selectivity to DME for Fe/MCM-41(N) in comparison to Fe/MCM-41(A). Formaldehyde (FA) and CO_2 were also registered as products of methanol decomposition. In the case of Fe/MCM-41(N), significant yields of methylal (DMM) are also observed.

Taking into account the data from the physicochemical and catalytic measurements, we could ascribe the higher DME selectivity, which is registered for Fe/MCM-41(N), to the presence of a higher amount of Lewis acidic centres in this sample. According to the literature data,[29] they could be isolated iron ions or FeO_x species in a low degree of coordination, and their reduction probably corresponds to the larger HT reduction effect in the TPR profile of this sample. We could also point out that methanol dehydrogenation to CO, CO_2, and CH_4 seems to be facilitated for the iron oxide species with higher degrees of crystallinity.[30,31] They are in a weaker interaction with the silica support and probably reducible in the LT region. The formation of DMM, which is clearly shown only in the case of Fe/MCM-41(N), indicates the activity of centres with dual redox and Lewis acidic activity.[29,32] In this aspect, the observed differences in the dehydration and dehydrogenation selectivity of the iron modified materials could be a test for variations in the state of iron species in them.

Critical remarks on the mechanism of methanol conversion on iron modified MCM-41 materials

In Fig. 8*a*, radiochromatograms are presented of methanol conversion on Fe/MCM-41(N) when the catalytic experiment was carried out after consecutive adsorption of methanol at room temperature, followed by its partial desorption and removal from the reactor at 473 K. We could expect that under this preliminary treatment, the surface coverage of the solid with methanol is very low and its molecules occupy predominantly the strongest adsorption sites. Under these conditions, only formaldehyde (FA) and small amounts of DME are registered, and in this aspect they could be considered as the primary products of methanol conversion (Fig. 8*a*). The formation of methoxy species as intermediates (Scheme 1, routes 1–2) and their further transformation to FA (Scheme 1, route 3) or DME (Scheme 1, route 4) with the participation of the strongest Fe-O acidic-basic pairs of the hematite species could be proposed.[29–35] Because of the low surface coverage with the predominant engagement of the strongest adsorption sites with methanol, a mechanism of DME formation via dimerization of two non-decomposed methanol molecules seems to be less probable.

In Figs. 8*b*–8*d*, radiochromatograms are presented of methanol conversion with a step by step increase of the surface coverage with methanol. For this purpose, a preliminary adsorption of various amounts of ^{11}C-methanol (a few nanomols, 10 μmol, and 100 μmol, respectively) was carried out at ambient temperature. Obviously, under this adsorption procedure catalytic sites with different adsorption strengths are expected to be occupied. We should stress some variations in the selectivity, which were observed in these cases. At lower methanol loading (Fig. 8*b*), hemimethylal (HM) is

Fig. 5. Total conversion (C) and selectivity to methane (CH_4) and dimethyl ether (DME) vs time on stream on Fe/MCM-41(N) (full circles) and Fe/MCM-41(A) (empty circles) at (*a*) 630 K, (*b*) 650 K, (*c*) 680 K, and (*d*) 700 K.

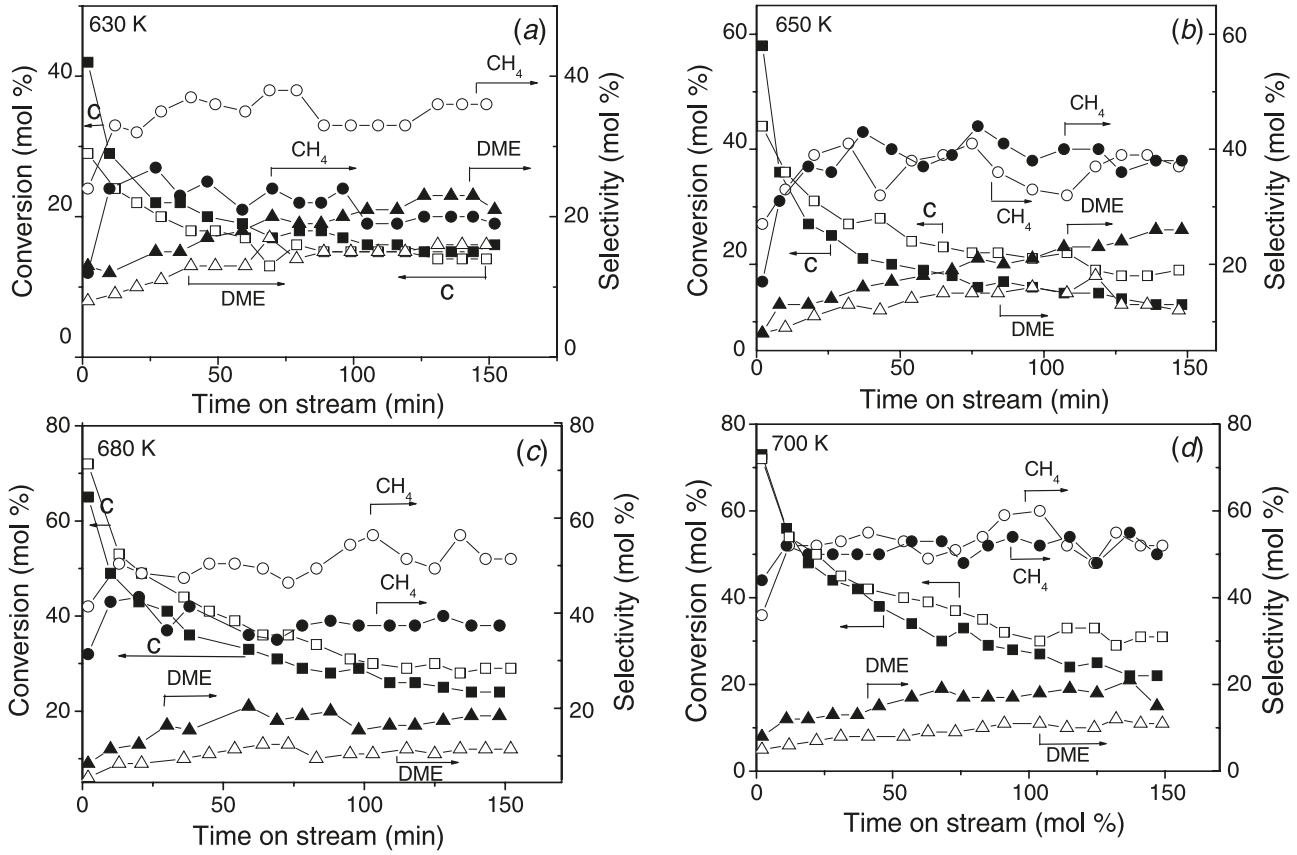

Fig. 6. Radioactivity rates on Fe/MCM-41(A) and Fe/MCM-41(N) (in Geiger-Müller radiation counts) vs temperature of desorption.

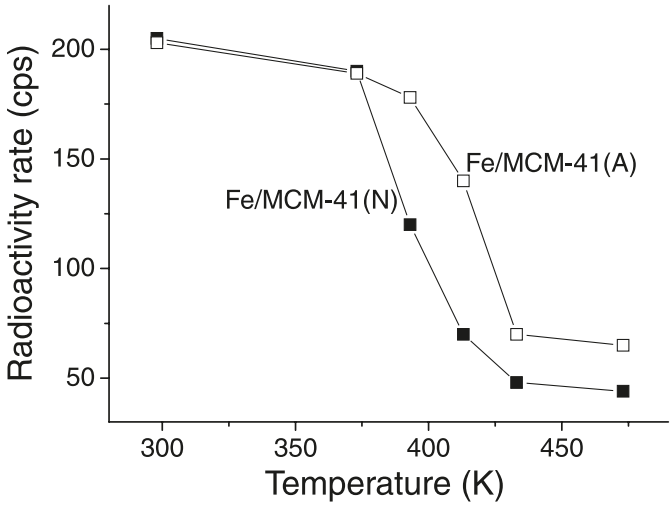

the only registered product at 523 K, which could be produced via interaction of the formed FA with nondecomposed methanol molecules, situated on the close weaker redox or acidic catalytic sites (Scheme 1, route 12). A further temperature increase, up to 573 K ,leads to the formation of CH_4, CO, and CO_2 probably via decomposition of HM and FA (Scheme 1, routes 6–8) or partial oxidation of methoxy intermediates to formic acid with the insertion of oxygen from the solid (Scheme 1, routes 5, 9, 10).[30,36] We suggest that the progressive reduction of the iron oxide species during the experiment, which is confirmed by the Mössbauer spectra of the materials used in the catalytic test (see above), results in the lower contribution of the latter reaction route. With the increase in the amount of the pre-adsorbed methanol, methylformate (MF) is also registered (Fig. 8*c*). Several mechanisms of its formation propose higher surface coverage with methanol or its intermediates could be assumed (Scheme 1, routes 7, 11, 13).[34,37] Further increase in the temperature results in the formation of significant amounts of FA, CH_3OH, CO, and CO_2 (Fig. 8*c*), probably due to the MF conversion via different reaction routes (Scheme 1, route 14). The formation of DMM under these conditions could be assumed as a further interaction of HM with methanol molecules on the Lewis acidic sites, situated in the vicinity of the redox ones (Scheme 1, Route 15). The proposed reaction scheme is also confirmed at higher surface methanol loading (Fig. 8*d*), where MF, HM, and DMM are registered in a much higher extent.

Conclusion

Summarizing the physicochemical data, the results from the conventional catalytic test, and the data from the ^{11}C-labelling measurements, it could be concluded that the impregnation of MCM-41 silica with acetylacetonate and nitrate precursors leads to a simultaneous formation of well-

Fig. 7. Radio-gas chromatograms of ^{11}C- methanol conversion at different temperatures for (*a*) Fe/MCM-41(N) and (*b*) Fe/MCM-41(A) with methanol pre-adsorption at 473 K. MeOH - methanol, FA - formaldehyde, DME - dimethyl ether, HM - hemimethilal, DMM - methylal (dimethoxymethan), and MF - methylformate.

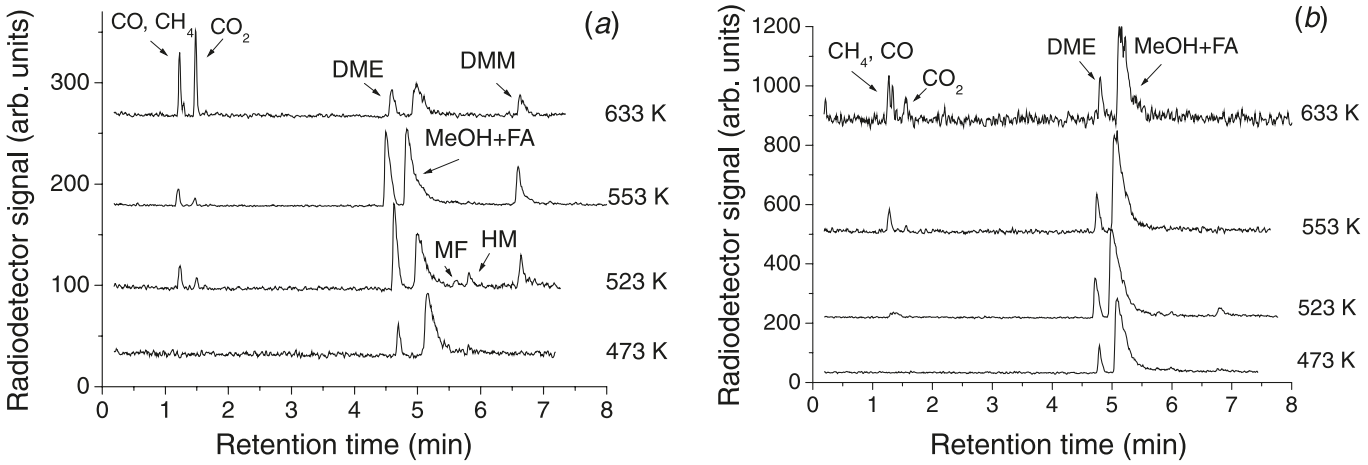

Fig. 8. Radio-gas chromatograms of ^{11}C- methanol conversion at different temperatures on Fe/MCM-41(N) under (*a*) methanol pre-adsorption at 298 K and further methanol removal at 543 K before the catalytic test, (*b*) methanol pre-adsorption at 298 K with a few nanomols of methanol loading, (*c*) 10 μmol methanol loading, and (*d*) 100 μmol methanol loading. MeOH - methanol, FA - formaldehyde, DME - dimethyl ether, HM - hemimethilal, DMM - methylal (dimethoximethane), and MF - methylformate.

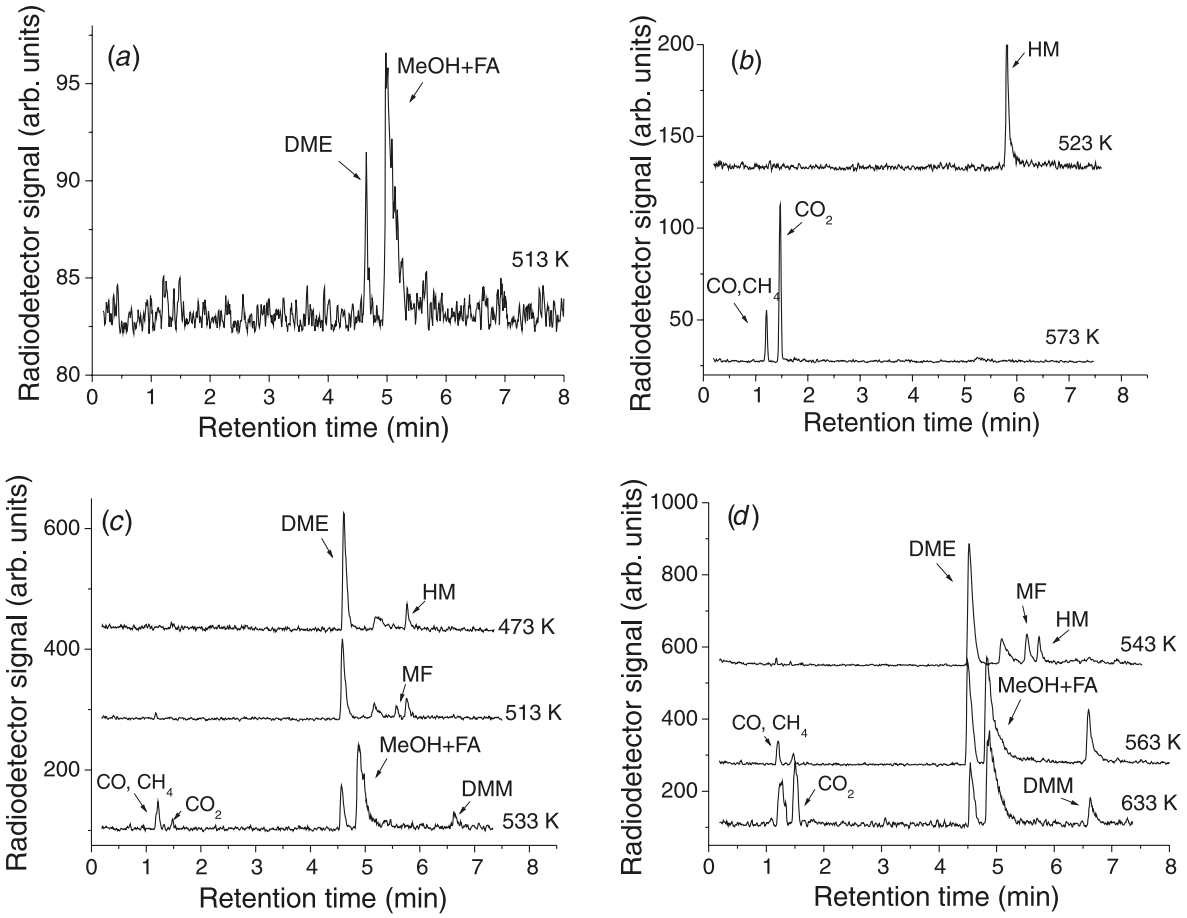

crystallized hematite particles and a relatively large fraction of isolated, strongly interacting support iron ions or FeO_x patches. The different iron species could be easily determined by the nature of the iron precursor. The first type of iron species seems to exhibit high catalytic activity in methanol decomposition to CO and methane. The second one also possesses acidic functionality and facilitates the dehydration of methanol to DME. The formation of HM and

Scheme 1.

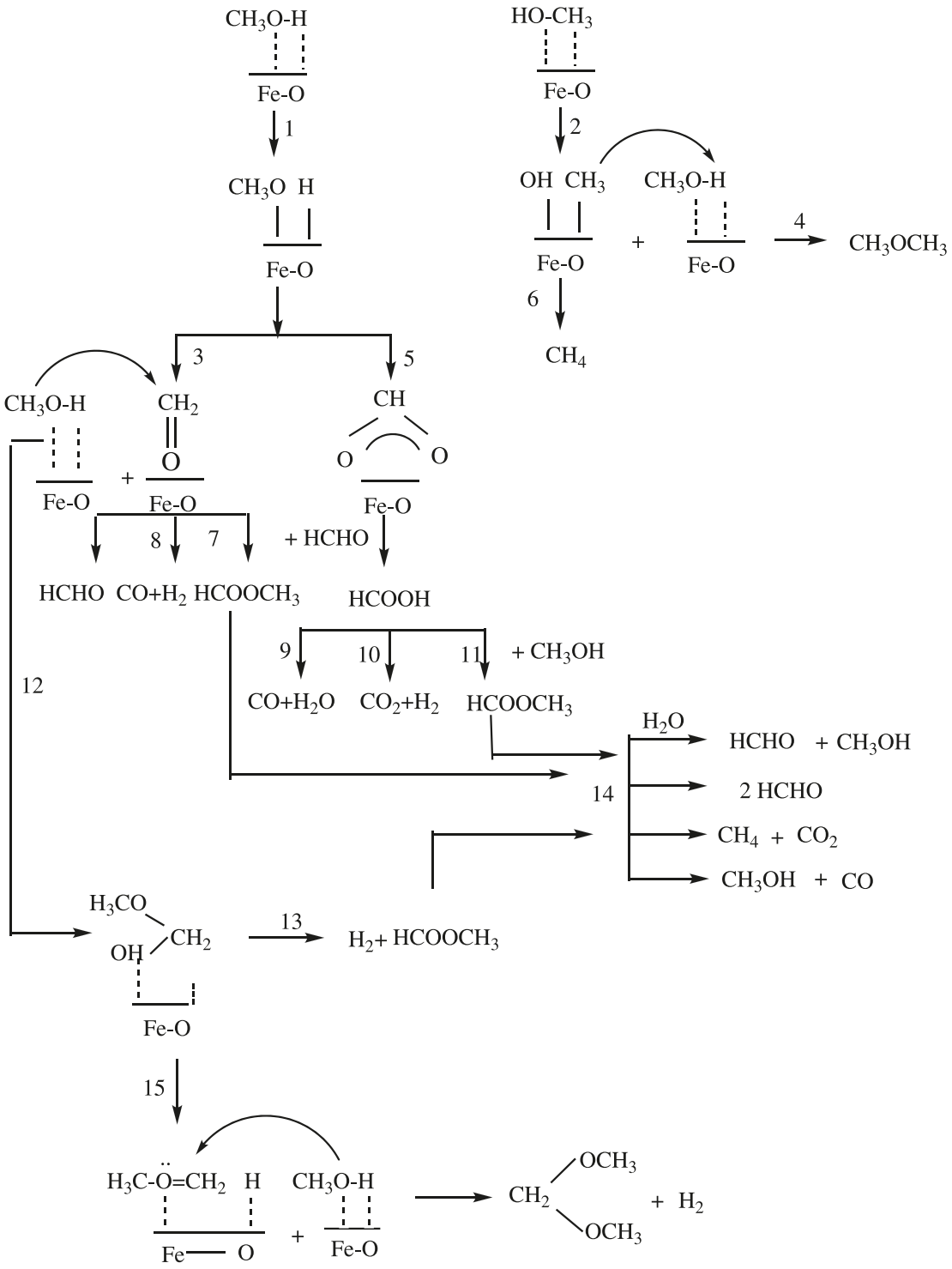

DMM could be assigned to the simultaneous activity of sites with dual redox and acidic properties.

Acknowledgements

Financial support from the Bulgarian Academy of Sciences, the Bulgarian-Hungary interacademic exchange, and by the Hungarian Scientific Research Fund No. T 048345 is gratefully acknowledged. We thank Dr. M. Dimitrov for the samples. Acknowledgements are made to Professor Mitov and Dr. Paneva for the Mössbauer spectra.

References

(1) Johnson, B. F. G. *Top. Catal.* **2003**, *24*, 147. doi:10.1023/B:TOCA.0000003086.83434.b6.

(2) Zhang, X.; Jenekhe, S. A.; Perlstein, H. *J. Chem. Mater.* **1996**, *8*, 1571.

(3) Fendler, J. H. *Chem. Mater.* **1996**, *8*, 1616. doi:10.1021/cm960116n.
(4) Daniel, M.-C.; Astruc, D. *Chem. Rev.* **2004**, *104*, 293. doi:10.1021/cr030698+. PMID:14719978.
(5) Taguchi, A.; Schüth, F. *Microporous Mesoporous Mater.* **2005**, *77*, 1. doi:10.1016/j.micromeso.2004.06.030.
(6) Van Der Voort, P.; Mitchell, M. B.; Vansant, E. F.; White, M. G. *Interface Sci.* **1997**, *5*, 169. doi:10.1023/A:1008669528505.
(7) Kuśtowski, P.; Chmielarz, L.; Dziembaj, R.; Cool, P.; Vansant, E. F. *J. Phys. Chem. B* **2005**, *109*, 11552. doi:10.1021/jp050696o. PMID:16852417.
(8) Köhn, R.; Paneva, D.; Dimitrov, M.; Tsoncheva, T.; Mitov, I.; Minchev, C.; Fröba, M. *Microporous Mesoporous Mater.* **2003**, *63*, 125. doi:10.1016/S1387-1811(03)00457-8.
(9) Tsoncheva, T.; Rosenholm, J.; Teixeira, C. V.; Dimitrov, M.; Linden, M.; Minchev, C. *Microporous Mesoporous Mater.* **2006**, *89*, 209. doi:10.1016/j.micromeso.2005.10.028.
(10) Tsoncheva, T.; Rosenholm, J.; Linden, M.; Ivanova, L.; Minchev, C. *Appl. Catal. Gen.* **2007**, *318*, 234. doi:10.1016/j.apcata.2006.11.008.
(11) Tsoncheva, T.; Tiemann, M.; Roggenbuck, J.; Ivanova, L.; Paneva, D.; Mitov, I.; Minchev, C. *Microporous Mesoporous Mater.* **2008**, *110*, 339. doi:10.1016/j.micromeso.2007.06.021.
(12) Tsoncheva, T.; Linden, M.; Areva, S.; Minchev, C. *Catal. Commun.* **2006**, *7*, 357. doi:10.1016/j.catcom.2005.12.001.
(13) Tsoncheva, T.; Areva, S.; Dimitrov, M.; Paneva, D.; Mitov, I.; Linden, M.; Minchev, C. *J. Mol. Catal. Chem. (Kyoto)* **2006**, *246*, 118. doi:10.1016/j.molcata.2005.10.028.
(14) Minchev, C.; Huwe, H.; Tsoncheva, T.; Paneva, D.; Dimitrov, M.; Mitov, I.; Fröba, M. *Microporous Mesoporous Mater.* **2005**, *81*, 333.
(15) Tsoncheva, T.; Venkov, Tz.; Dimitrov, M.; Minchev, C.; Hadjiivanov, K. *J. Mol. Catal. Chem.* **2004**, *209*, 125. doi:10.1016/j.molcata.2003.08.008.
(16) Tsoncheva, T.; Ivanova, L.; Paneva, D.; Dimitrov, M.; Mitov, I.; Stavrev, S.; Minchev, C. *J. Colloid Interface Sci.* **2006**, *302*, 492. doi:10.1016/j.jcis.2006.06.041. PMID:16876813.
(17) Tsoncheva, T.; Rosenholm, J.; Linden, M.; Kleitz, F.; Tiemann, M.; Ivanova, L.; Dimitrov, M.; Paneva, D.; Mitov, I.; Minchev, C. *Microporous Mesoporous Mater.* **2008**, *112*, 327. doi:10.1016/j.micromeso.2007.10.005.
(18) Sarkadi-Pribóczki, E.; Ivanova, L. *Catal. Commun.* **2008**, *9*, 1932. doi:10.1016/j.catcom.2008.03.034.
(19) Fröba, M.; Köhn, R.; Bouffaund, G.; Richard, O.; van Tendeloo, G. *Chem. Mater.* **1999**, *11*, 2858. doi:10.1021/cm991048i.
(20) Sarkadi-Pribóczki, E.; Szelecsényi, F. *Radiochim. Acta* **1997**, *76*, 197.
(21) Sarkadi-Pribóczki, E.; Murzin, D. Yu. *Catal. Lett.* **2007**, *114*, 17. doi:10.1007/s10562-007-9035-7.
(22) Sarkadi-Pribóczki, E.; Murzin, D. Yu. *Catal. Lett.* **2004**, *93*, 101. doi:10.1023/B:CATL.0000016956.04114.22.
(23) Marler, B.; Oberhagemann, U.; Vortmann, S.; Gies, H. *Microporous Mater.* **1996**, *6*, 375. doi:10.1016/0927-6513(96)00016-8.
(24) Tuel, A.; Arcon, I.; Millet, J. M. M. *J. Am. Chem. Soc. Faraday Trans.* **1998**, *94*, 3501. doi:10.1039/a806912c.
(25) Selvam, P.; Dapurkar, S. E.; Badamali, S. K.; Murugasan, M.; Kuwano, H. *Catal. Today* **2001**, *68*, 69. doi:10.1016/S0920-5861(01)00292-9.
(26) Liu, S.; Cool, P.; Lu, L.; Beyers, E.; Van der Voort, P.; Vansant, E. F.; Jiang, M. *Microporous Mesoporous Mater.* **2005**, *79*, 299. doi:10.1016/j.micromeso.2004.11.020.
(27) Gao, X.; Shen, J.; Hsia, Y.; Chen, Y. *J. Chem. Soc. Faraday Trans.* **1993**, *89*, 1079. doi:10.1039/ft9938901079.
(28) Arena, F.; Gatti, G.; Stievano, L.; Martra, G.; Coluccia, S.; Frusteri, F.; Spadaro, L.; Parmaliana, A. *Catal. Today* **2006**, *117*, 75. doi:10.1016/j.cattod.2006.05.047.
(29) Trejda, M.; Kujawa, J.; Ziolek, M. *Catal. Lett.* **2006**, *108*, 141. doi:10.1007/s10562-006-0035-9.
(30) Mavrikakis, M.; Barteau, M. A. *J. Mol. Catal. Chem. (Kyoto)* **1998**, *131*, 135. doi:10.1016/S1381-1169(97)00261-6.
(31) Levis, R. J.; Zhicheng, J.; Winograd, N. *J. Am. Chem. Soc.* **1989**, *111*, 4605. doi:10.1021/ja00195a013.
(32) Liu, H.; Iglesia, E. *J. Phys. Chem. B* **2003**, *107*, 10840. doi:10.1021/jp0301554.
(33) Ziolek, M.; Kujawa, J.; Saur, O.; Lavalley, J. C. *J. Phys. Chem.* **1993**, *97*, 9761. doi:10.1021/j100140a037.
(34) Ballarini, N.; Cavani, F.; Maselli, L.; Montaletti, A.; Passeri, S.; Scagliarini, D.; Flego, C.; Perego, C. *J. Catal.* **2007**, *251*, 423. doi:10.1016/j.jcat.2007.07.033.
(35) Burcham, L. J.; Briand, L. E.; Wachs, I. E. *Langmuir* **2001**, *17*, 6164. doi:10.1021/la010009u.
(36) Barteau, M. A. *Chem. Rev.* **1996**, *96*, 1413. doi:10.1021/cr950222t. PMID:11848796.
(37) Chung, M. J.; Park, K. Y.; Lee, B. G.; Ihm, S. K. *Korean J. Chem. Eng.* **1993**, *10*, 188. doi:10.1007/BF02705142.

Deoxy-cytochalasins from a marine-derived fungus *Spicaria elegans*

Zhen-Jian Lin, Tian-Jiao Zhu, Guo-Jian Zhang, Hong-Juan Wei, and Qian-Qun Gu

Abstract: Treatment of *Spicaria elegans* with cytochrome P-450 inhibitor resulted in two new deoxy-cytochalasins, 7-deoxy-cytochalasin Z_7 (**1**) and 7-deoxy-cytochalasin Z_9 (**2**), which were recognized as plausible precursors of cytochalasins Z_7 and Z_9, respectively. Their structures were elucidated by spectroscopic methods and the absolute configuration of **1** was determined by the conventional Mosher ester method. Their cytotoxicities against two cancer cell lines were evaluated.

Key words: cytochalasin, *Spicaria elegans*, cytochrome P-450 inhibitor, cytotoxicity.

Résumé : Le traitement du *Spicaria elegans* par l'inhibiteur du cytochrome P-450 conduit à la formation de deux nouvelles désoxycytochalasines, le 7-désoxycytochalasine Z_7 (**1**) et 7-désoxycytochalasine Z_9 (**2**) qui ont été reconnues comme des précurseurs plausibles respectivement pour les cytochalasines Z_7 et cytochalsaines Z_9. Les structures des composés **1** et **2** ont été élucidées par des méthodes spectroscopiques et la configuration absolue du produit **1** a été déterminée par la méthode conventionnelle de l'ester de Mosher. On a évalué leurs cytotoxicités contre deux séries de cellules cancéreuses.

Mots-clés : cytochalasine, *Spicaria elegans*, inhibiteur de cytochrome P-450, cytotoxicité.

[Traduit par la Rédaction]

Introduction

In our ongoing search for new bioactive secondary metabolites from marine fungi, a series of cytochalasins has been isolated from the marine-derived fungus *Spicaria elegans*, some of which exhibited interesting cytotoxicities against the A-549 cell line,[1,2] which attracted our continuous attentions. Given that P450 mono-oxygenases are believed to catalyze the oxidative polyketide tailoring reactions of cytochalasins,[3] it is possible to use the inhibitors to obtain various biosynthetic precursor products. The achievement of this was realized by the discovery of 7-deoxy-cytochalasin Z_7 (**1**) and 7-deoxy-cytochalasin Z_9 (**2**) by the addition of metyrapone, an inhibitor of P-450 dependent monooxygenases, in the culture of fungus *S. elegans*. We describe herein the isolation, structure elucidation, and biological activities of **1** and **2**.

Results and discussion

Previous study had shown that the strain *S. elegans* produced 10 phenyl-cytochalasins (Z_7–Z_{15})[1,2] as the major components, which were all oxidized at the 7-position. Metyrapone (1 mmol/L), a cytochrome P-450 inhibitor, was added on the sixth day after inoculation to the culture of *S. elegans*. After an additional 14 days of static fermentation, the metabolites were extracted from the mycelium. Compared with nontreated samples, two new 7-deoxy-cytochalasins (**1** and **2**) were recognized by HPLC-MS analysis and isolated by semiprepared HPLC.

Received 14 November 2008. Accepted 10 December 2008. Published on the NRC Research Press Web site at canjchem.nrc.ca on 11 February 2009.

Z. Lin, T. Zhu, G. Zhang, H. Wei, and Q. Gu.[1] Key Laboratory of Marine Drugs, Chinese Ministry of Education, Institute of Marine Drugs and Food, Ocean University of China, Qingdao 266003, PR China.

[1]Corresponding author (e-mail: guqianq@ouc.edu.cn).

7-Deoxy-cytochalasin Z_7 (**1**) was isolated as a white powder. Its molecular formula was established as $C_{28}H_{35}NO_4$ by HR-ESI-MS (*m/z* 450.2652 $[M + H]^+$, anal. calcd. for $C_{28}H_{36}NO_4$: 450.2644) and indicated twelve degrees of unsaturation. The IR spectrum had bands due to NH and (or) OH (3392 cm^{-1}), an α,β-unsaturated ester/lactone carbonyl (1698 cm^{-1}), and an amide carbonyl (1680 cm^{-1}). The ^1H NMR spectrum (Table 1) showed the presence of an amide NH (δ_H: 5.79), three methyl doublets (δ_H: 0.97, 1.05, and 1.17), a methyl singlet (δ_H: 1.72), and 11 methine and (or) methylene protons. Ten olefinic protons (δ_H: 5.10, 5.34, 5.66, 5.96, and 7.16–7.33), suggesting a monosubstituted benzene ring, were also observed. The ^{13}C NMR spectrum of **1** displayed signals for 28 carbon atoms and confirmed the presence of an α,β-unsaturated ester/lactone carbonyl (δ_C: 167.4) and an amide carbonyl (δ_C: 172.5) (Table 1). Analysis of the DEPT spectrum revealed the presence of four methyl, two methylene, 17 methine, and three quaternary carbons, in addition to the two carbonyls. All of these 1D NMR features of **1** suggested it was closely related to an analog of cytochalasins. Accurate inspection of its 1D NMR spectra revealed, with respect to that of cytochalasin Z_7, the absence of exocyclic olefinic methylene (12-CH_2). Whereas a trisubstituted double bond (δ_H: 5.34, δ_C: 123.9, 140.0) and a methyl goup (12-Me, δ_H: 1.72, δ_C: 19.8) was present. These findings indicated that the 7-OH and the exocyclic olefinic methylene were missing, instead, a trisubstituted double bond was located between C-6 and C-7. The structure of **1** was further supported by its molecular formula ($C_{28}H_{35}NO_4$), with one fewer oxygen than cytochalasin Z_7. Compound **1** possessed a 12-membered macrocyclic ring, the same as that in cytochalasin Z_7. Accurate inspection of the ^1H and ^{13}C NMR data, including ^1H NMR coupling con-

Table 1. ^{1}H (600 MHz) and ^{13}C (150 MHz) NMR spectroscopic data for **1** and **2** in $CDCl_3$

Compound position	**1**		**2**	
	δ_H (J in Hz)	δ_C	δ_H (J in Hz)	δ_C
1		172.5 (s)		172.1 (s)
2-NH	5.79 (brs)		5.89 (brs)	
3	3.22 (m)	55.9 (d)	3.20 (m)	55.9 (d)
4	3.04 (m)	50.8 (d)	2.91 (m)	51.5 (d)
5	3.04 (m)	33.8 (d)	2.91 (m)	34.1 (d)
6		140.0 (s)		139.9 (s)
7	5.34 (brs)	123.9 (d)	5.36 (brs)	123.8 (d)
8	3.47 (m)	45.4 (d)	3.38 (m)	46.7 (d)
9		88.0 (s)		87.7 (s)
10	2.89 (dd, J = 13.2, 4.1), 2.70 (d, J = 13.7)	45.1 (t)	2.89 (m), 2.85 (m)	44.8 (t)
11	1.17 (d, J = 6.8)	13.8 (q)	1.14 (d, J = 6.6)	13.8 (q)
12	1.72 (brs)	19.8 (q)	1.74 (brs)	19.8 (q)
13	5.96 (ddd, J = 15.1, 10.0, 2.0)	125.9 (d)	5.91 (ddd, J = 15.1, 10.0, 2.7)	126.3 (d)
14	5.10 (ddd, J = 15.1, 10.1, 4.6)	137.2 (d)	5.28 (ddd, J = 15.1, 10.1, 2.7)	137.1 (d)
15	2.08 (m)	42.0 (t)	2.10 (brd, J = 14.3), 1.97 (ddd, J = 14.3, 10.4, 10.4)	43.5 (t)
16	1.62 (m)	32.5 (d)	1.39 (m)	32.5 (d)
16-CH_3	0.97 (d, J = 7.3)	18.4 (q)	1.05 (d, J = 7.1)	22.2 (q)
17	3.87 (dd, J = 3.2, 4.1)	77.3 (d)	1.77 (dd, J = 13.6, 5.5), 1.64 (dd, J = 13.6, 2.2)	53.2 (d)
18	2.72 (m)	42.8 (d)		72.8 (s)
18-CH_3	1.05 (d, J = 6.4)	8.7 (q)	1.34 (s)	27.1 (q)
19	7.16–7.33 (m)	157.5 (d)	7.45 (d, J = 16.0)	159.5 (d)
20	5.66 (dd, J = 16.0, 1.9)	120.5 (d)	5.75 (d, J = 16.0)	118.4 (d)
21		167.4 (s)		167.4 (s)
1′		137.4 (s)		137.7 (s)
2′	7.16–7.33 (m)	128.8 (d)	7.18–7.33 (m)	128.9 (d)
3′	7.16–7.33 (m)	129.0 (d)	7.18–7.33 (m)	129.0 (d)
4′	7.16–7.33 (m)	127.0 (d)	7.18–7.33 (m)	126.9 (d)
5′	7.16–7.33 (m)	129.0 (d)	7.18–7.33 (m)	129.0 (d)
6′	7.16–7.33 (m)	128.8 (d)	7.18–7.33 (m)	128.9 (d)

Fig. 1. Structures of compounds **1** and **2**.

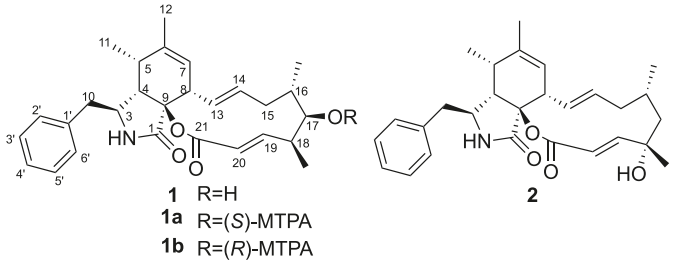

Fig. 2. The key $\Delta\delta$ values [$\Delta\delta$ (in ppm) = $\delta_S - \delta_R$] obtained for (*S*)- and (*R*)-MTPA esters of compound **1**.

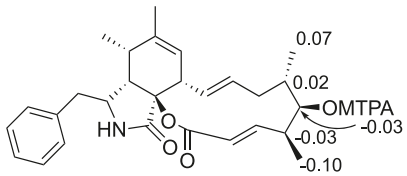

stants, for compound **1** and cytochalasin Z_7 should have the most coincident relative configuration (structure from C-15 to C-19). The absolute configuration of the 17 position in **1** was established by a conventional Mosher ester method using the (*S*)- and (*R*)-α-methoxy-α-trifluoromethyl-α-phenylacetic acid (MTPA) esters (**1a** and **1b**, respectively) (Fig. 1), where the positive values of $\Delta\delta^{S-R}$ for H-16 and 16-CH_3 and negative values of $\Delta\delta^{S-R}$ for H-18 and 18-CH_3 (Fig. 2) suggested a 17-(*R*) configuration in **1**, which was the same as that of cytochalasin Z_7. Therefore, the absolute configurations of **1** could be deduced as shown in Fig. 1.

7-Deoxy-cytochalasis Z_9 (**2**) was isolated as a white powder. Its HR-ESI-MS (*m*/*z* 450.2638 $[M + H]^+$, anal. calcd. for $C_{28}H_{36}NO_4$: 450.2644) suggested that it might be a deoxy-derivative of cytochalasin Z_9, with a molecular formula of $C_{28}H_{35}NO_4$ showing one fewer oxygen atom than cytochalasin Z_9. This assumption could be confirmed by its 1D NMR spectra. Analysis of its 1D NMR spectra, with respect to that of cytochalasin Z_9, revealed that the singlet of 11-CH_3 in cytochalasis Z_9 was upfiled shifted to δ_H: 1.14 and changed to a doublet, which suggested the double bond at C-5,6 was missing in **2**. Most similarly to **1**, the 1D NMR spectra of **2** (Table 1) also showed the absence of the oxygenated methine group at C-7, whereas there was the appearance of a trisubstituted double bond (δ_H: 5.36, δ_C: 123.8, 139.9) assigned between C-6 and C-7. On the basis of these 1D NMR spectra features, the structure of **2** was elucidated as 7-deoxy-cytochalasis Z_9.

Compounds **1**and **2** were evaluated for their cytotoxicities against the A-549 and P-388 cell lines by the MTT [3-

(4,5-dimethylthiazol-2-yl)-2,5-diphenyltetrazolium bromide] method. Compound **1** showed moderate cytotoxicity against the A-549 cell line with an IC_{50} value of 15.0 μmol/L, while **2** was inactive. In comparison to that of cytochalasins Z_7 and Z_9, the double bond (C-6,7) in **1** and **2** resulted in a much weaker cytotoxicity.

A new generation of plausible precursors of chaetoglobosin A[4] and epoxycytochalasin H[5] had been obtained by treatment fungi with cytochrome P-450 inhibitors. Those results, as well as the experiments in this paper, indicated that the biosynthetic oxidation at the 7 position of cytochalasins was exactly due to the cytochrome P-450. More frequently, the cytochalasins, likewise cytochalasins Z_7 and Z_9, have an oxidation at the C-9 position, which was believed to be formed from the acetate-derived polyketide chain by an enzymatic 'Baeyer–Villager'-like oxidation.[6] Even though a cytochrome P-450 monooxygenase CYP85A2 had been reported to have a Baeyer–Villiger oxidation activity,[7] it was still unknown whether the Baeyer–Villager-like oxidation in cytochalasins was related to the cytochrome P-450. In our experiments, no more deoxy-cytochalasin was detected except for **1** and **2** when *S. elegans* was treated with metyrapone, therefore, the P-450 enzyme inhibitor can't block the Baeyer–Villager-like oxidation in this strain. Maybe it is not the P-450 enzyme that catalyzed the Baeyer–Villager-like oxidation in the biosynthetic pathway of cytochalasins. This warrants further investigations.

Experimental section

General

Optical rotations were obtained on a JASCO P-1020 digital polarimeter. UV spectra were recorded on Beckman DU® 640 spectrophotometer. IR spectra were taken on a NICOLET NEXUS 470 spectrophotometer in KBr discs. ^1H, ^{13}C NMR and DEPT, and 2D NMR spectra were recorded on a JEOL JNM-ECP 600 spectrometer using TMS as an internal standard and chemical shifts were recorded as δ values. NOESY experiments were carried out using a mixing time of 0.5 s. ESI-MS was measured on a Q-TOF ULTIMA GLOBAL GAA076 LC mass spectrometer. Semiprepartive HPLC was performed using an ODS column (Shin-pak ODS $_H$, 10 mm × 250 mm, 5 μm, 4 mL/min).

Fungal material

The fungus *Spicaria elegans* was isolated from the marine sediments collected in Jiaozhou Bay, China. It was preserved in the China Center for Type Culture Collection (patent depositary number: KLA03 CCTCC M 205049). Working stocks were prepared on potato dextrose agar slants stored at 4 °C.

Fermentation and extraction

The fungus was incubated at 28 °C under static conditions in 30 1000 mL conical flasks containing the liquid medium (300 mL/flask) composed of glucose (20 g/L), peptone (5 g/L), malt extract (3 g/L), yeast extract (3 g/L), and sea-water after adjusting its pH to 7.0. The inhibitor metyrapone (1 mmol/L) was added on the sixth day after inoculation to the culture of *S. elegans*. After an additional 14 days of static fermentation, the fermented whole broth (9 L) was extracted three times with EtOAc to give an EtOAc solution, which was concentrated under reduced pressure to give a crude extract (5.5 g).

Purification

The crude extract (5.5 g) was separated into four fractions (Fr. 1–4) on a Si gel column using a gradient elution of $CHCl_3$:MeOH. Fr. 2 was eluted with $CHCl_3$:MeOH (100:1, 0.4 g) and was purified into 8 subfractions (Fr. 2-1 ~ Fr. 2-8) by Si gel column using stable elution of $CHCl_3$:MeOH (200:1). Subfraction Fr. 2-6 was further purified by reverse-phase column using stable elution of MeOH:H_2O (7: 3) to give 4 subfractions (Fr. 2-6-1 ~ Fr. 2-6-4), respectively. Further purification of subfraction Fr. 2-6-4 by extensive HPLC (75% MeOH, 4.0 mL/min) gave compounds **1** (3 mg) and **2** (2 mg).

7-Deoxy-cytochalasin Z_7 (1)

White powder. $[\alpha]_D^{25}$ +94.8 (*c* 0.1, MeOH). UV (MeOH) λ_{max} (nm) (log ε): 233 (2.43). IR (KBr, cm^{-1}) ν_{max}: 3368, 2937, 1700, 1444, 1214, 1076, 990. ^1H and ^{13}C NMR (see Table 1). HR-ESI-MS *m/z*: 450.2652 $[M + H]^+$. Anal. calcd. for $C_{28}H_{36}NO_4$: 450.2644.

7-Deoxy-cytochalasin Z_9 (2)

White powder. $[\alpha]_D^{25}$ +12.8 (*c* 0.1, MeOH). UV (MeOH) λ_{max} (nm) (log ε): 230 (2.00). IR (KBr, cm^{-1}) ν_{max}: 3298, 2900, 1694, 1321 1201, 999. ^1H and ^{13}C NMR (see Table 1). HR-ESI-MS *m/z*: 450.2638 $[M + H]^+$. Anal. calcd. for $C_{28}H_{36}NO_4$: 450.2644.

Preparation of the (*S*)- and (*R*)-MTPA ester derivatives of 1

Compound **1** (2.0 mg) was divided into two aliquots and transferred into two clean reaction bottles and was dried completely under vacuum. Each solubilized in 0.5 mL of pyridine. The two samples were treated with (*R*)- and (*S*)-α-methoxy-α-trifluoromethylphenylacetyl chloride (1 equiv.) under a N_2 gas stream, and then stirred for 24 h at room temperature. The organic layer was then washed with water, HCl (1 mol/L), water, $NaHCO_3$(satd.), and water, then dried (Na_2SO_4) and concentrated under reduced pressure to obtain the ester. Final purification achieved by HPLC gave **1a** and **1b**, respectively. ^1H NMR data for the (*S*)-MTPA ester derivative (**1a**) of **1** (600 MHz, $CDCl_3$) δ: 5.76 (1H, brs, 2-NH), 3.24 (1H, m, H-3), 3.05 (1H, m, H-4), 3.05 (1H, m, H-5), 5.35 (1H, brs, H-7), 3.48 (1H, m, H-8), 2.90 (1H, dd, *J* = 4.1, 13.8 Hz, H-10a), 2.69 (1H, dd, *J* = 9.6, 13.8 Hz, H-10b), 1.20 (3H, d, *J* = 6.9 Hz, H-11), 1.73 (3H, brs, H-12), 6.04 (1H, ddd, *J* = 13.0, 10.6, 1.8 Hz, H-13), 5.07 (1H, m, H-14), 2.30 (1H, ddd, m, H-15a), 2.09 (1H, brd, *J* = 14.6 Hz, H-15b), 1.80 (1H, m, H-16), 0.88 (3H, d, *J* = 6.4 Hz, 16-CH_3), 5.09 (1H, m, H-17), 2.80 (1H, m, H-18), 0.97 (3H, d, *J* = 7.3 Hz, 18-CH_3), 5.68 (1H, dd, *J* = 15.5, 2.3 Hz, H-19), 7.15 ~ 7.56 (11H, m, H-20 and Ph-H). ^1H NMR data for the (*R*)-MTPA ester derivative (**1b**) of **1** (600 MHz, $CDCl_3$) δ: 5.82 (1H, brs, 2-NH), 3.24 (1H, m, H-3), 3.05 (1H, m, H-4), 3.05 (1H, m, H-5), 5.35 (1H, brs, H-7), 3.48 (1H, m, H-8), 2.90 (1H, dd, *J* = 4.1, 13.8 Hz, H-10a), 2.69 (1H, dd, *J* = 9.6, 13.8 Hz, H-10b), 1.20 (3H, d, *J* = 6.9 Hz, H-11), 1.73 (3H, brs, H-12), 6.04 (1H, ddd, *J* =

13.0, 10.6, 1.8 Hz, H-13), 5.07 (1H, m, H-14), 2.34 (1H, ddd, m, H-15a), 2.05 (1H, brd, J = 14.6 Hz, H-15b), 1.78 (1H, m, H-16), 0.81 (3H, d, J = 6.4 Hz, 16-CH_3), 5.12 (1H, m, H-17), 2.83 (1H, m, H-18), 1.07 (3H, d, J = 7.3 Hz, 18-CH_3), 5.71 (1H, dd, J = 15.5, 2.3 Hz, H-19), 7.15 ~ 7.56 (11H, m, H-20 and Ph-H).

Biological assays

Cytotoxic activity was evaluated by the MTT method using A-549 and H-L60 cell lines. The cell lines were grown in RPMI-1640 supplemented with 10% FBS under a humidified atmosphere of 5% CO_2 and 95% air at 37 °C (tsFT210 cell line at 32 °C). An aliquot (200 μL) of those cell suspensions at a density of 5×10^4 cell mL^{-1} was plated in 96 well microtiter plates and incubated for 24 h at the above condition. Then 2 μL of the test compound solutions (in DMSO) at different concentrations was added to each well and further incubated for 72 h in the same condition. MTT solution (20 μL of 5 mg/mL in IPMI-1640 medium) was added to each well and incubated for 4 h. Old medium containing MTT (150 μL) was then gently replaced by DMSO and pipetted to dissolve any formazan crystals that had formed. Absorbance was then determined on a SPECTRA MAX PLUS plate reader at 570 nm.

Acknowledgements

This work was financially supported by the Chinese National Natural Science Fund (No. 30772640) and the Shandong Province (No. Z2006C13). The antitumor assay was performed at the Shanghai Institute of Materia Medica, Chinese Academy of Sciences.

References

(1) Liu, R.; Gu, Q. Q.; Zhu, W. M.; Cui, C. B.; Fan, G. T.; Fang, Y. C.; Zhu, T. J.; Liu, H. B. *J. Nat. Prod.* **2006**, *69*, 871. doi:10.1021/np050201m. PMID:16792402.

(2) Liu, R.; Lin, Z. J.; Zhu, T. J.; Fang, Y. C.; Gu, Q. Q.; Zhu, W. M. *J. Nat. Prod.* **2008**, *71*, 1127. doi:10.1021/np070539b. PMID:18507474.

(3) Schümann, J.; Hertweck, C. *J. Am. Chem. Soc.* **2007**, *129*, 9564. doi:10.1021/ja072884t. PMID:17636916.

(4) Oikawa, H.; Murakami, Y.; Ichihara, A. *J. Chem. Soc. Perkin Trans. 1,* **1992**, 2949. doi:10.1039/p19920002949.

(5) Kakeya, H.; Morishita, M.; Onozawa, C.; Usami, R.; Horikoshi, K.; Kimura, K.; Yoshihama, M.; Osada, H. *J. Nat. Prod.* **1997**, *60*, 669. doi:10.1021/np970151o. PMID:9249969.

(6) Binder, M.; Tamm, C. *Helv. Chim. Acta*, **1973**, *56*, 966. doi:10.1002/hlca.19730560312. PMID:4733353.

(7) Nomura, T.; Kushiro, T.; Yokota, T.; Kamiya, Y.; Bishop, G. J.; Yamaguchi, S. J. *Biol. Chem.* **2005**, *280*, 17873.

Novel pressure control in supercritical fluid chromatography using a resistively heated restrictor

Jian Jun Li and Kevin B. Thurbide

Abstract: An alternative means of independently controlling column pressure in supercritical fluid chromatography (SFC) by resistively heating the post-column restrictor is demonstrated. Compared to conventional block heating methods, resistive restrictor heating provides at least four times greater pressure programming rates and allows for much faster cooling times in between runs, thereby increasing sample throughput. When applying resistive restrictor heating in proximity to a flame ionization detector, the chromatographic baseline noise increases substantially and obscures peaks. However, adding about 100 mL/min of nitrogen into the flame burner essentially removes this noise and returns the detector response to normal. The analyte retention time in consecutive pressure gradient trials reproduces well with a minimal relative standard deviation of 0.36% (n = 3). The resistive restrictor heating technique presented is also found to be equally effective for either capillary or packed SFC operating modes. Results suggest that this method can potentially provide a simple, inexpensive, and convenient alternative to limited passive restrictors or more costly and complex backpressure regulators that are often used to maintain system pressure in supercritical fluid chromatography.

Key words: supercritical fluid chromatography, pressure control, resistive heating, rapid.

Résumé : On a mis au point une méthode alternative qui permet de contrler la pression de la colonne en chromatographie avec des fluides supercritiques et qui fait appel à un chauffage à l'aide d'une résistance après le point de restriction de la colonne. Par comparaison avec les méthodes de chauffage par bloc, la nouvelle méthode permet d'obtenir des taux de programmation quatre fois plus grands et elle permet de bénéficier des temps de refroidissement beaucoup plus courts entre les divers essais, augmentant du coup l'encours. Lorsqu'on applique un chauffage par résistivité à proximité d'un détecteur par ionisation à flamme, le bruit de fond chromatographique augmente considérablement et obscurcit les pics. Toutefois, l'addition d'environ 100 mL/min d'azote dans la flamme du brûleur élimine pratiquement tout ce bruit et permet de retourner à une réponse normale du détecteur. Les temps de rétention de l'analyse dans des essais successifs consécutifs de gradients de pression se reproduisent bien, avec une déviation standard relative minimale de 0,36 % (n = 3). On a aussi observé que la technique de chauffage par résistivité présentée est aussi efficace pour les chromatographies avec des fluides supercritiques en mode capillaire ou remplie. Les résultats suggèrent que cette méthode pourrait éventuellement fournir une alternative simple, peu coûteuse et facile aux processus de restriction passifs ou à ceux plus coûteux et plus complexes faisant appel à des régulateurs de rétropression qui sont souvent utilisés pour maintenir la pression du système en chromatographie avec des fluides supercritiques.

Mots-clés : chromatographie avec des fluides supercritiques, contrôle de la pression, chauffage à l'aide d'une résistance, rapide.

[Traduit par la Rédaction]

Introduction

Supercritical fluid chromatography (SFC) is an established method that provides separation properties that are complimentary to those of conventional high-performance liquid chromatography and gas chromatography.[1,2] The most widely used mobile phase in SFC is supercritical carbon dioxide. In addition to being relatively inert, nontoxic, inexpensive, and environmentally compatible compared with conventional organic solvents, supercritical carbon dioxide is also a significantly compressible fluid.[3,4] As such, its density and ability to solvate analytes can be directly manipulated through the pressure applied to the chromatographic system. Thus, pressure control is a very important operational parameter in SFC.[1–5]

For SFC employing capillary columns (cSFC) and low flows, system pressure is most commonly maintained by using a length of narrow bore fused silica tubing as a restrictor at the end of the column.[6] Such restrictors have the advantage of being reasonably simple and inexpensive to fabricate and use. However, because they are passive devices, any change in the pressure (or flow rate) setting at the CO_2 pump, will also change the corresponding flow rate (or pressure) in the system. This often complicates cSFC method development since the effects of column pressure and flow rate become convoluted.[5,6]

Received 30 June 2008. Accepted 9 December 2008. Published on the NRC Research Press Web site at canjchem.nrc.ca on 11 February 2009.

J.J. Li and K.B. Thurbide.[1] Department of Chemistry, University of Calgary, 2500 University Drive, NW, Calgary, AB T2N 1N4, Canada.

[1]Corresponding author (e-mail: thurbide@ucalgary.ca).

For SFC employing larger packed columns (pSFC) and flows, system pressure is normally maintained by a backpressure regulator. Through external electronic control, this post-column device variably restricts the quantity of fluid traversing a tiny orifice. In this way it can manage system pressure downstream while an upstream pump maintains column flow. The significant clear advantage of using a backpressure regulator is that column flow and system pressure can each be actively and independently controlled. However, disadvantages include its relatively large cost, limited lifespan, and its incompatibility with narrow bore/capillary columns due to the considerable dead volume it adds to the system.[5,6]

Over the years, a number of interesting alternative methods to control pressure in SFC have also appeared. Many of these involve the addition of a pressure regulating fluid at the column outlet in both cSFC[7–10] and pSFC applications.[11] This approach successfully provides independent control of column flow and pressure. However, several of the designs can be relatively complex, require the use of an extra pump, and (or) may possibly lead to problems in interfacing with flame-based detection systems due to the very large extra gas flows that normally stream from such backpressure devices.[5]

An especially useful alternate means of controlling pressure in SFC involves heating the outlet restrictor as earlier introduced by Greibrokk et al.,[12] Berger and Toney,[13] and Berger.[14] This method essentially houses the restrictor in a heated metal block (e.g., detector heating block), where the applied temperature causes thermal expansion of the tubing material and restriction of the flow. Thus, in conjunction with a constant pressure or flow pump upstream, independent control of column flow and pressure can be attained by this method. Further advantages of this approach are that it is readily achieved with simple apparatus, it does not add dead volume to the system, and it does not require extreme auxiliary gas flows that might interfere with downstream detector operation. However, despite its potential advantages, no separations demonstrating the method are found in these early reports. In fact, to date, extremely few actual chromatographic applications of this approach have been reported.[15,16] One potential reason for this limited activity may concern the relatively large thermal mass of the heating block, which prevents rapid changes in temperature (and hence system pressure).[5] For example, this factor can directly limit the rate of system pressure gradients that can be achieved by this method. As well, it can also seriously impact the sample throughput capacity of the technique due to the considerably long times required for the heating block to cool in between runs. Thus overall, while this approach has great potential for SFC pressure control, it remains much less used relative to conventional methods.

Recently, we developed a method for offsetting efficiency losses due to large pressure drops across the column used in pSFC.[17] This technique involved, in part, the use of a low thermal mass resistively heated wire to gently heat the column outlet area. Overall, the method was found to be rapid, straightforward, rugged, and inexpensive to operate. Given its relative simplicity, it appeared that it could also potentially be effective as a direct restrictor heating device that might act as an alternative approach to the conventional heating block method reported earlier. If so, it could potentially allow for greater sample throughput in this mode and provide a relatively easy means of independently controlling pressure and flow in SFC. This paper explores the use of a resistively heated wire to control the restrictor temperature and hence column pressure in SFC. The characteristics and operating parameters of the method are presented and compared against a conventional heating block apparatus. The approach is also subsequently demonstrated as a pressure control method in cSFC separations and for the first time pSFC separations as well.

Experimental

Instrumentation

A Gilson SF3 (Gilson, Villiers-le-Bel, France) reciprocating pump was usually employed to deliver the CO_2 mobile phase through the system. However, in certain instances, specified in the text, an Isco Model 260D (Isco, Lincoln, Nebraska, USA) syringe pump was also explored for this purpose. All pressure measurements were taken at the pump used. A Rheodyne Model 7520 injection valve with a 0.2 μL sample loop (Alltech, Deerfield, Illinois, USA) was used to introduce samples to the column. A Shimadzu GC 9A (Shimadzu, Kyoto, Japan) gas chromatograph equipped with a flame ionization detector (FID) was used to maintain column temperature and provide detection. The column oven temperature was normally set between 50 and 100 °C. A DB-1 capillary column (30 m × 0.25 mm; 0.25 μm dimethylpolysiloxane coating; J & W Scientific, Folsom, California, USA) was used in cSFC experiments. For pSFC applications, a PRP-1 packed column (50 mm × 4.1 mm; 5 μm particles; Hamilton, Reno, Nevada, USA) with a polystyrene divinylbenzene stationary phase was used. The column outlet was connected to the detector by a restrictor made from a 35 cm length of deactivated fused silica capillary tubing (0.05 mm i.d.). This tubing had a taper on the end, which was achieved by drawing the capillary through a Bunsen burner.[6]

Restrictor heating method

For experiments testing the conventional restrictor heating method, the restrictor typically terminated inside the detector heating block about 1–2 mm below the surface. For experiments testing the resistive heating method proposed here, the restrictor terminated about 3 cm below the surface of a glass burner used for the FID flame. The burner resembles one used earlier in our laboratory[18] and was made of a quartz tube with two bores. The burner end was 55 mm long with an inner diameter of 4 mm, and the connecting end was 25 mm long with an inner diameter of 2 mm. This burner configuration easily allowed stable, sensitive FID flame operation at typical decompressed CO_2 gas flow rates of about 40 mL/min or larger. The resistive heating coil was made of Ni-Cr wire (0.5 mm diameter). A 10 cm length of wire was wrapped around the burner and powered by a standard laboratory variable transformer (120 V supply, 10 A max; model 3PN 1010, Staco Inc., Dayton, OH, USA) to heat the coil and restrictor. The coil was comprised of 20 turns over a distance of 1.5 cm and was centered about the end of the restrictor. Voltages applied to the heating coils were typically up to 10% of the full-scale settings, which provided respective temperatures up to about 600 °C. During these experiments, the detector heating block was turned off.

Chemicals and reagents

Instrument-grade CO_2 (99.99%; Praxair, Calgary, Alberta, Canada) was used as the mobile phase. High purity hydrogen and oxygen (Praxair) were used as the flame gases. High purity nitrogen (Praxair) was used in certain experiments as an auxiliary gas. Linear *n*-alkanes (99%; Sigma-Aldrich, Oakville, Ontario, Canada) were used as standards. Paraffin wax (Sigma-Aldrich) was also used in some demonstrations. All samples were prepared by dissolving the solutes in hexane or carbon disulfide to a final concentration between 2 and 4 μg/μL.

Results and discussion

Detector heating block mode

Initial experiments were performed using the GC detector heating block to control the restrictor temperature similar to the original method described earlier.[12,13,15] Since the restrictor was situated inside the heating block, changes in the detector block temperature were therefore directly used to constrict flow at the outlet and alter the system pressure. Upon applying this approach with a constant flow pump upstream it was found that the system pressure indeed varied as a function of the block (i.e., restrictor) temperature. Of note, at a flow rate of 200 μL/min, as the restrictor temperature increased from 50 to 250 °C the corresponding system pressure increased from 12 to 24 MPa, which is similar to that reported earlier.[12] Figure 1 shows how these restrictor temperature and system pressure changes can impact the separation of some test solutes in pSFC. As seen at a restrictor temperature of 50 °C, the decane and undecane separation is over in 12 min. Subsequently, as the restrictor temperature is increased up to 200 °C and the system pressure rises accordingly, elution time is continually reduced (at the expense of resolution) until the decane and solvent peaks co-elute and undecane emerges around 6 min. This clearly demonstrates that the block restrictor heating method can control column pressure (and hence analyte retention) independent of column flow rate. Somewhat surprisingly, however, only a few cSFC applications of this technique exist,[15,16] and to our knowledge, this is its first demonstration in pSFC.

Perhaps related to this is that pressure programs are often used in SFC to increase analysis speed. To achieve such programs here, the detector heating block temperature was systematically raised. However, in doing so it was observed that the column pressure increased at a relatively small rate. In our experience, a maximum value near only 0.2 MPa/min could be obtained because of the relatively large thermal mass of the heating block and the time required (often 20 min or more) to significantly raise its temperature. Of even greater concern, though, the heating block needed a much longer time to cool down. For example, usually 90 min or more was required for it to fall from about 250 to 50 °C. Therefore, this long cycle time can very negatively impact sample throughput when attempting to use this method. As such, an alternative approach that allows rapid heating and cooling of the restrictor could potentially improve upon this otherwise very useful technique of pressure control and facilitate its broader application in SFC. To investigate this, a resistively heated coil wrapped around the restrictor outlet was explored.

Fig. 1. The effect of detector block restrictor heating on pSFC elution. Conditions are a column temperature of 45 °C and a constant flow rate of 200 μL/min (reciprocating pump) using the PRP-1 column. The peaks in order of elution are solvent (CS_2), *n*-decane, and *n*-undecane. The restrictor temperature is labelled on each run.

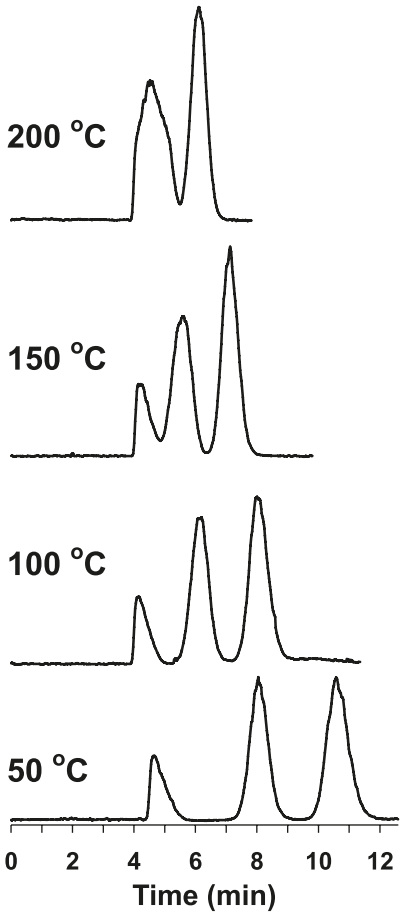

Resistive heating mode

An immediate advantage noted in using the resistive heating method was that the restrictor temperature could be raised relatively much more rapidly. For example, only 1–2 min was required to increase the restrictor temperature from 25 to 450 °C. As well, after the heating was stopped, the restrictor also rapidly cooled from such high temperatures (normally <3 min to achieve 25 °C). This is a direct result of the lower thermal mass of the apparatus, which enormously reduces the cycle time of this method by comparison. Subsequently, the system pressure was also observed to change faster when the restrictor was resistively heated. For instance, pressure programming rates of 0.8 MPa/min could be readily attained by this method. Further, this rate of change could be altered depending on factors such as the mobile phase flow rate, the column used, and how the heating was applied.

Figure 2 displays some pressure-time curves demonstrating the different rates of pressure change obtained when the heating coil was operated at different temperatures. As seen in each trial of Fig. 2, after the selected temperature is applied to the restrictor at 0 min the system pressure steadily rises before it plateaus at the corresponding final value. While closer contact between the heating coil and the re-

Fig. 2. Pressure change over time with the resistively heated restrictor. Conditions are a column temperature of 50 °C and a constant flow rate of 200 μL/min (reciprocating pump) using the DB-1 column. The restrictor temperatures employed are 350 °C (▲), 450 °C (■), and 600 °C (●). In each case the restrictor heating begins at 0 min.

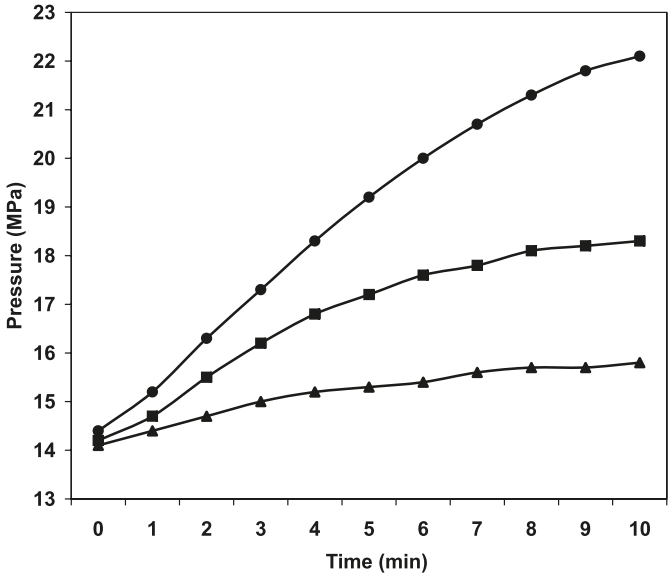

strictor (e.g., a smaller FID flame burner design) or greater voltages applied to appropriate wire coils could potentially translate into even greater rates of pressure increase, these parameters were not further optimized in the current study.

When subsequently exploring the use of the resistive heating method in SFC separations, initial results surprisingly indicated that a relatively excessive amount of noise was generated during the heating period. This, in turn, seriously obscured chromatographic peaks. A possible reason for the increased noise observed was that it might be due to an increase in the burner surface temperature, which caused the adjacent FID polarizer to overheat and induce fluctuations in the detector response. To potentially offset this problem, a flow of nitrogen was added as an auxiliary cooling gas into the bottom of the burner. Consequently, the noise generated by rapid heating was dramatically reduced. Ultimately, a flow of about 100 mL/min of nitrogen essentially removed the noise and peak appearance returned to normal. Figure 3 demonstrates this for the cSFC separation of some test solutes. As shown, the initial separation obtained without heating the restrictor (Fig. 3*a*) is seriously eroded after 450 °C of heat is applied (Fig. 3*b*). However upon adding 100 mL/min of nitrogen, the peak appearance without and with restrictor heating applied (Figs. 3*c* and 3*d*, respectively) is of similar quality to that originally presented in Fig. 3*a*. As such, nitrogen was used in all subsequent trials.

It is worth noting that the separations shown in Fig. 3 were generated using a syringe pump in the constant pressure mode to propel mobile phase through the capillary column. This is a standard arrangement in typical cSFC separations.[6] As such, in contrast to the variable pressure separations shown in Fig. 1, when heating is applied to the restrictor in this case, the flow rate is reduced from about 200 to 100 μL/min and

Fig. 3. The effect of resistive restrictor heating on peak appearance with and without nitrogen present. The cSFC conditions are a column temperature of 70 °C and a constant CO_2 pressure of 12.7 MPa (syringe pump) using the DB-1 column. The *n*-alkane solutes in order of elution are C_{20}, C_{22}, and C_{26}. The chromatograms shown have (*a*) no restrictor heating applied and no nitrogen flow, (*b*) 450 °C applied to the restrictor upon injection and no nitrogen flow, (*c*) no restrictor heating applied and 100 mL/min nitrogen, and (*d*) 450 °C applied to the restrictor upon injection and 100 mL/min nitrogen.

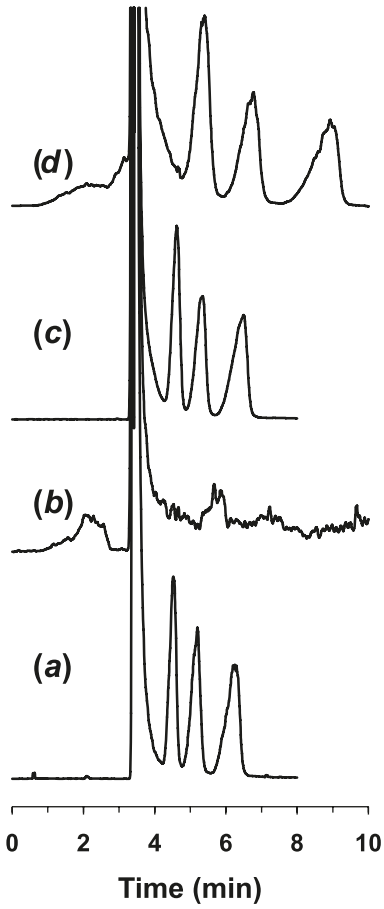

analyte retention increases accordingly (Fig. 3*d*). This marks an important difference between typical cSFC and pSFC runs given that the former often uses a syringe pump in constant pressure mode to drive the mobile phase, whereas the latter often uses a reciprocating pump in constant flow mode for this purpose (e.g., as in Fig. 1). Regardless, in our experience this operational difference was inconsequential since the resistive heating method worked equally well in either mode and with either style of pump or column. Still, due to the convenience of continuous mobile phase delivery from the reciprocating pump, it was often preferable in many experiments. As such, it delivered a constant flow of mobile phase while downstream restrictor heating acted to control the system pressure as desired.

To demonstrate the utility of this resistive restrictor heating approach, the method was applied to the analysis of a wax sample. Figure 4 demonstrates the effect of using various restrictor heating (i.e., pressure) programs on the separation of this sample in the pSFC mode. As seen, the rapid

Fig. 4. The impact of restrictor heating pressure programs on analyte elution in pSFC. Conditions are a column temperature of 80 °C, a constant flow rate of 400 μL/min (reciprocating pump) using the PRP-1 column, and 100 mL/min of nitrogen. Analyte: C_{20}–C_{33} wax sample in CS_2. The pressure programs invoked are (*a*) 25–35 MPa within the first 10 min, (*b*) 25–35 MPa within the first 15 min, (*c*) 25 MPa for the first 5 min then increasing to 35 MPa within the next 10 min, and (*d*) held isobarically at 25 MPa for the entire run.

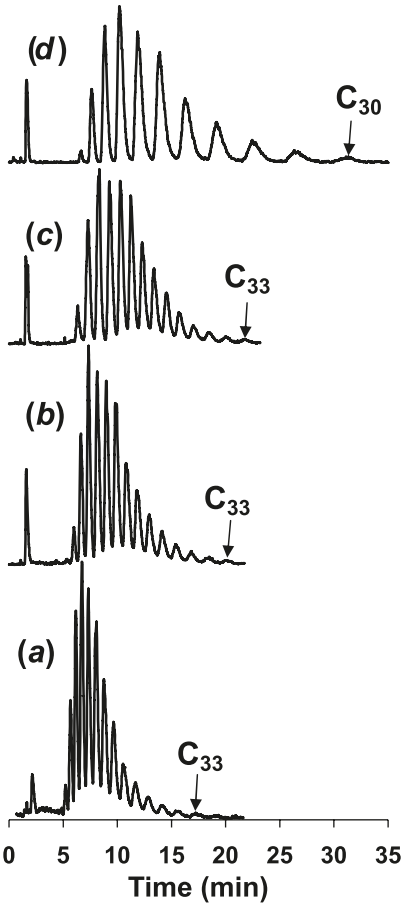

heating method provides effective control of column pressure and analyte retention in pSFC. Figure 4*a* shows a relatively fast elution of the sample, which was obtained by heating the restrictor such that the pressure changed from 25 to 35 MPa in the first 10 min. Conversely, Fig. 4*b* spans this same pressure change over 15 min and the resulting separation time and resolution both increase. The separation shown in Fig. 4*c* was obtained by maintaining the column pressure at 25 MPa for the first 5 min and then increasing it to 35 MPa over the next 10 min. This also affords increased resolution and analysis time. For comparison, Fig. 4*d* shows how the same separation appears when pressure programming is not applied and conditions are held isobarically at 25 MPa for the whole run. As seen, this results in a weaker elution strength and only C_{30} being one of the last distinguishable peaks. Thus, as shown, analyte elution profiles and analysis times can be directly manipulated through carefully planning the restrictor heating (i.e., pressure program) strategy. As would be expected, it should also be mentioned that these effects are not analyte dependant and similar results were also obtained for fatty acids and alcohols in addition to the alkane trials shown here.

Fig. 5. Reproducibility of column pressure as a function of time in three consecutive trials spanning about an hour. Conditions are a column temperature of 70 °C and a flow rate of 180 μL/min (reciprocating pump) using the PRP-1 column. The pressure program applied is 12.4 MPa at time zero to 16.0 MPa within 14 min.

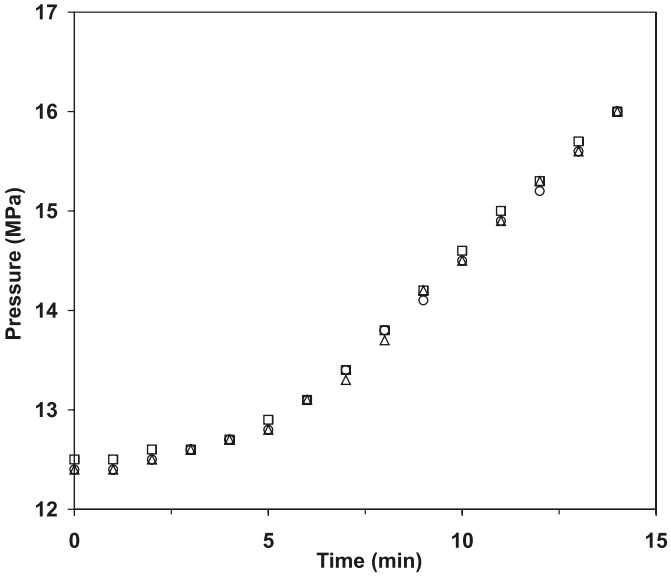

An important feature in any chromatographic gradient method is its reproducibility. For instance, the ability to precisely recreate pressure programs in SFC can directly impact the precision of analyte retention times. As such, it was essential to probe this aspect of the resistively heated restrictor method. Figure 5 displays the pressure versus time curves obtained from three consecutive runs of the same pressure program performed within about an hour. As can be seen, the plotted values from each pressure program agree very well with each other over the course of time. As a result, a C_{28} alkane test analyte also chromatographed under these conditions eluted quite reproducibly. Of note, the triplicate experiments performed yielded a relative standard deviation of 0.36% for the retention time of this analyte. Thus, no method difficulties appear in this regard.

It should be noted that if the restrictor was not compromised, then the day to day reproducibility of the method gave much the same results as that displayed in Fig. 5. However, restrictor lifetime is limited in SFC. In our experience, this amounted to nearly two months of regular restrictor usage before it required replacement. To minimize dimensional variations in the new tapered restrictor created, we carefully trimmed the taper tip until a similar flow of carbon dioxide streamed through it at set pressure and temperature. Typically this value could be achieved within about 4 mL/min, which resulted in restrictor to restrictor trials of the method agreeing within about 1 MPa of achieved pressure for the same set temperature. Therefore, some fine tuning of the pressure and temperature calibration is expected when changing restrictors, however this is found to be minimal. As such, the method is generally quite robust and reproducible.

Conclusions

The ability to independently control system flow rate and pressure in SFC using a resistively heated restrictor has been demonstrated. The method is inexpensive, convenient, and efficient. Of note, it allows the restrictor to be heated and subsequently cooled much more rapidly than conventional heating block methods, allowing for improved sample cycling times. A significantly increased FID detector noise was noted when using resistive heating. However, this was successfully eliminated by simultaneously introducing an auxiliary nitrogen flow into the flame burner. The method was equally effective when using syringe or reciprocating pumps to deliver the mobile phase and also when using capillary or packed columns as the separation medium. Results indicate that this technique could provide a useful alternative to passive restrictors normally used to maintain pressure in cSFC and also to much more expensive and complex backpressure regulators frequently used to control pressure in pSFC. Further, this method may also be useful in other modes of capillary chromatography (e.g., subcritical fluid methods) where dead volume issues are of concern and independent pressure control is desirable.

Acknowledgements

The authors are grateful to the Natural Sciences and Engineering Research Council of Canada for a Discovery Grant in support of this research.

References

(1) Chester, T. L.; Pinkston, J. D. *Anal. Chem.* **2004**, *76*, 4606. doi:10.1021/ac040088p. PMID:15307769.
(2) Chester, T. L.; Pinkston, J. D. *Anal. Chem.* **2002**, *74*, 2801. doi:10.1021/ac020226f. PMID:12090666.
(3) Ventura, M. C.; Farrell, W. P.; Aurigemma, C. M.; Greig, M. J. *Anal. Chem.* **1999**, *71*, 2410. doi:10.1021/ac981372h.
(4) Ventura, M. C.; Farrell, W. P.; Aurigemma, C. M.; Greig, M. J. *Anal. Chem.* **1999**, *71*, 4223. doi:10.1021/ac9902906.
(5) Olesik, S. V.; Pekay, L. A. *Chromatographia* **1990**, *29*, 69. doi:10.1007/BF02261142.
(6) Chester, T. L. In *Analytical Instrumentation Handbook;* Ewing, G. W., Ed.; Marcel Dekker: New York, 1997; Chapter 24.
(7) Raynie, D. E.; Markides, K. E.; Lee, M. L.; Goates, S. R. *Anal. Chem.* **1989**, *61*, 1178. doi:10.1021/ac00185a027.
(8) Janssen, H.-G.; Rijks, J. A.; Cramers, C. A. *J. Microcol.* **1990**, *2*, 26. doi:10.1002/mcs.1220020107.
(9) Hirata, Y.; Nakata, F. *Chromatographia* **1986**, *21*, 627. doi:10.1007/BF02311916.
(10) Pyo, D. *Chromatographia* **1993**, *37*, 635. doi:10.1007/BF02274115.
(11) Chester, T. L.; Pinkston, J. D. *J. Chromatogr. A* **1998**, *807*, 265. doi:10.1016/S0021-9673(98)00082-X.
(12) Greibrokk, T.; Berg, B. E.; Blilie, A. L.; Doehl, J.; Farbrot, A.; Lundanes, E. *J. Chromatogr.* **1987**, *394*, 429. doi:10.1016/S0021-9673(01)83810-3.
(13) Berger, T. A.; Toney, C. *J. Chromatogr.* **1989**, *465*, 157. doi:10.1016/S0021-9673(01)92654-8.
(14) Berger, T. A. Supercritical Fluid Chromatography. U.S. Patent 4 845 985, 1989.
(15) Pyo, D. *Analyst (Lond.)* **1994**, *119*, 1315. doi:10.1039/an9941901315.
(16) Pyo, D. *Bull. Korean Chem. Soc.* **2006**, *27*, 1429.
(17) Li, J.; Thurbide, K. B. *Can. J. Anal. Sci. Spectrosc.* **2006**, *51*, 187.
(18) Thurbide, K. B.; Gilbert, S. *Can. J. Chem.* **2004**, *82*, 479. doi:10.1139/v04-008.

On the relationship between free energy difference calculations by thermodynamic integration and harmonic frequency analysis

Jason Jechow and Tom Ziegler

Abstract: Harmonic frequency analysis (HFA), based on statistical mechanics, is a widely used and powerful tool for evaluating free energy changes between molecular states. It has, as such, been employed extensively to evaluate the free energy of reaction and activation for chemical processes. Alternatively, free energy differences can be calculated using thermodynamic integration (TI). In TI, the force on a constrained reaction coordinate is calculated, and this force from *a* to *b* is integrated to obtain the Helmholtz free energy change ΔA_{ab}. Although HFA and TI clearly are related from a fundamental statistical mechanics point-of-view, the relationship is not immediately obvious when one considers the quite different procedures applied in the two methods. This article provides a detailed analysis and proof of the relation between HFA and TI.

Key words: thermodynamic integration, free energy, harmonic approximation.

Résumé : L'analyse de fréquence harmonique (AFH), basée sur la mécanique statistique, est fréquemment utilisée et elle s'avère un outil puissant pour évaluer les changements d'énergie libre entre des états moléculaires. Elle a été couramment utilisée de la sorte pour évaluer l'énergie libre de réaction et l'activation de processus chimiques. D'une façon alternative, on peut calculer des différences d'énergie libre en utilisant l'intégration thermodynamique (IT). Dans cette méthode, on calcule la force sur une coordonnée réactionnelle contrainte et on intègre cette force de a à b pour obtenir le changement d'énergie libre d'Helmholtz, ΔA_{ab}. Même si l'AFH et l'IT sont clairement apparentées d'un point de vue de la mécanique statistique fondamentale, la relation n'est toutefois pas immédiatement évidente lorsqu'on considère les méthodes très différentes appliquées dans les deux méthodes. Dans cet article, on présente une analyse détaillée et une preuve de la relation entre l'AFH et l'IT.

Mots-clés : intégration thermodynamique, énergie libre, approximation harmonique.

[Traduit par la Rédaction]

1. Introduction

Thermodynamic integration (TI) calculates changes in free energy along a predefined reaction path.[1–3] This involves defining the reaction path (the change in a bond length, bond angle, or some other quantity), constraining the molecular system at various points along this reaction path, and performing a molecular dynamics simulation at each of these points. As the molecular system vibrates, a force to hold the constraint is determined, and the derivative of the free energy, with respect to the constraint, can be calculated from this force. Subsequently, the Helmholz free energy change between the molecular states *a* and *b* can be calculated by integrating the force along the reaction coordinate from *a* to *b*.

For a linear constraint, the average force along the constraint in a molecular dynamics simulation is known to be the negative of the derivative of the free energy along the constraint.[4] This derivation is determined by examining the Lagrangian for a constrained molecular system and the Lagrangian for the corresponding unconstrained molecular system, and by observing how the motion would be different in the two systems. Then, by assuming a linear constraint, the formula for the derivative of the free energy simplifies to the negative of the force along the linear constraint.

It is also possible to calculate the Helmholtz free energy change ΔA_{ab} by harmonic frequency analysis (HFA).[5] In HFA we calculate *A* at *a* and *b* based on the well-known formula from statistical mechanics containing atomic masses, geometrical parameters, and harmonic frequencies. We subsequently calculate ΔA_{ab} as the simple difference $A_b - A_a$ without integration.

This article shows how these two seemingly different procedures (TI and HFA) for the determination of ΔA_{ab} are related, and under what condition they will afford the same free energy difference ΔA_{ab}. It is organized as follows: in Sects. 2,3, and 4 we determine the time average force on a constraint that is coupled to a number of harmonic degrees of freedom, and in Sect. 5 we determine the derivative of the free energy from the HFA.

Received 3 September 2008. Accepted 19 November 2008. Published on the NRC Research Press Web site at canjchem.nrc.ca on 13 February 2009.

J. Jechow and T. Ziegler.[1] Department of Chemistry, University of Calgary, 2500 University Drive, Calgary AB T2N 1N4, Canada.

[1]Corresponding author (e-mail: ziegler@ucalgary.ca).

2. Approximating the potential energy near a given conformation

An intrinsic reaction path (IRP) is the minimum energy path that lies along the potential energy surface of a given

chemical reaction.[6] The IRP is a set of conformations for a molecular system that represent the reaction path. The first conformation may be a reactant geometry, a middle conformation may be a transition-state geometry, and the the last conformation may be a product geometry.

The IRP will be represented by ξ. $\xi = a$ could represent a reactant conformation, while $\xi = b$ could represent a product conformation. Any value of ξ will produce a conformation $\vec{x}(\xi)$ of the molecular system. Performing a Taylor expansion of the potential energy surface[7] about a given conformation yields,

$$[1] \qquad V(\vec{x}) = \sum_{i=1}^{n}\left(\frac{\partial V}{\partial x_i}\right)_{\xi^*} x_i + \sum_{i,j=1}^{n}\frac{1}{2}\left(\frac{\partial^2 V}{\partial x_i \partial x_j}\right)_{\xi^*} x_i x_j + \sum_{i,j,k=1}^{n}\frac{1}{6}\left(\frac{\partial^3 V}{\partial x_i \partial x_j \partial x_k}\right)_{\xi^*} x_i x_j x_k$$

This is an approximation of the potential energy surface near a given conformation ξ* on the IRP. The coordinates (x_i) given are with respect to a particular conformation along the IRP, i.e., x_i implies $x_i - x_i(\xi^*)$. The reference energy for eq. [1] is zero. Therefore, $V_{\xi^*} = V(\vec{x}_{\xi^*}) = 0$. Next, the coordinates are converted into mass-weighted coordinates. This ensures that the gradient of the potential energy is parallel to the forces acting on the atoms. Equation [2] shows the conversion between standard coordinates and mass-weighted coordinates,

$$[2] \qquad \left(\frac{\partial V}{\partial x_i}\right)_{\xi^*} x_i = \left(\frac{\partial V}{\sqrt{m_i}\partial x_i}\right)_{\xi^*} \sqrt{m_i} x_i = \left(\frac{\partial V}{\partial x_i'}\right)_{\xi^*} x_i'$$

where x_i prime, x_i', indicates mass-weighted coordinates. Later, a third coordinate system will be introduced and labeled x_i double prime, x_i''. The potential energy function in mass-weighted coordinates is,

$$[3] \qquad V(\vec{x}') = \sum_{i=1}^{n}\left(\frac{\partial V}{\partial x_i'}\right)_{\xi^*} x_i' + \sum_{i,j=1}^{n}\frac{1}{2}\left(\frac{\partial^2 V}{\partial x_i' \partial x_j'}\right)_{\xi^*} x_i' x_j' + \sum_{i,j,k=1}^{n}\frac{1}{6}\left(\frac{\partial^3 V}{\partial x_i' \partial x_j' \partial x_k'}\right)_{\xi^*} x_i' x_j' x_k'$$

To simplify eq. [3], the coordinate system is rotated such that x_1 is parallel to the gradient of the potential energy. This makes coordinate one tangent to the IRP,

$$[4] \qquad V(\vec{x}') = \left(\frac{\partial V}{\partial x_1'}\right)_{\xi^*} x_1' + \sum_{i,j=1}^{n}\frac{1}{2}\left(\frac{\partial^2 V}{\partial x_i' \partial x_j'}\right)_{\xi^*} x_i' x_j' + \sum_{i,j,k=1}^{n}\frac{1}{6}\left(\frac{\partial^3 V}{\partial x_i' \partial x_j' \partial x_k'}\right)_{\xi^*} x_i' x_j' x_k'$$

3. The force along the IRP as a function of time

For mass-weighted coordinates, the force along the IRP is,

$$[5] \qquad F_1' = -\frac{\partial V}{\partial x_1'}$$

Inserting the Taylor-expanded potential (eq. [4]) into eq. [5] yields,

$$[6] \qquad F_1' = -\left(\frac{\partial V}{\partial x_1'}\right)_{\xi^*} - \sum_{i=1}^{n}\left(\frac{\partial^2 V}{\partial x_i' \partial x_1'}\right)_{\xi^*} x_i' - \sum_{i,j=1}^{n}\frac{1}{2}\left(\frac{\partial^3 V}{\partial x_1' \partial x_i' \partial x_j'}\right)_{\xi^*} x_i' x_j'$$

The goal is to determine how the force along coordinate one at $x_1 = 0$ is affected by the other coordinates of the molecular system. Setting $x_1 = 0$ yields,

$$[7] \qquad F_1'(x_1' = 0) = -\left(\frac{\partial V}{\partial x_1'}\right)_{\xi^*} - \sum_{i=2}^{n}\left(\frac{\partial^2 V}{\partial x_1' \partial x_i'}\right)_{\xi^*} x_i' - \sum_{i,j=2}^{n}\frac{1}{2}\left(\frac{\partial^3 V}{\partial x_1' \partial x_i' \partial x_j'}\right)_{\xi^*} x_i' x_j'$$

Coordinate one is parallel to the gradient of the potential energy surface. Therefore,

$$[8] \qquad \left(\frac{\partial V}{\partial x_{i\neq 1}'}\right)_{\xi^*} = 0$$

This means that the force to maintain $x'_1 = 0$ is linearly independent of the other coordinates, i.e., the second term in eq. [7] is zero,

$$[9] \qquad \sum_{i=2}^{n}\left(\frac{\partial^2 V}{\partial x'_1 \partial x'_i}\right)_{\xi^*} x'_i = 0$$

and the force to maintain the constraint $x'_1 = 0$ simplifies to,

$$[10] \qquad F'_1(x'_1 = 0) = -\left(\frac{\partial V}{\partial x'_1}\right)_{\xi^*} - \sum_{i,j=2}^{n}\frac{1}{2}\left(\frac{\partial^3 V}{\partial x'_1 \partial x'_i \partial x'_j}\right)_{\xi^*} x'_i x'_j$$

Equation [10] shows how the force to maintain the constraint $x'_1 = 0$ varies with respect to the other coordinates, namely x'_i and x'_j. Note that the second term on the right-hand side is the change in the energy Hessian $\partial^2 V/\partial x'_i \partial x'_j$ over the harmonic degrees of freedom perpendicular to the reaction coordinate. As the Hessian is related to the vibrational frequencies, the force in eq. [10] is related to the change in the frequencies along the reaction coordinate. In Sect. 5, this force will prove to be identical to the one obtained by differentiating the free energy expression from a Harmonic frequency analysis with respect to the reaction coordinate.

The equations of motion must now be constructed for the other degrees of freedom. To obtain these equations of motion, the force for each degree of freedom needs to be evaluated. The force along coordinate $i \neq 1$ is,

$$[11] \qquad F'_{i\neq 1}(x'_1 = 0) = -\frac{\partial V}{\partial x'_i} = -\sum_{j=2}^{n}\left(\frac{\partial^2 V}{\partial x'_i \partial x'_j}\right)_{\xi^*} x'_j - \sum_{j,k,=2}^{n}\frac{1}{2}\left(\frac{\partial^3 V}{\partial x'_i \partial x'_j \partial x'_k}\right)_{\xi^*} x'_j x'_k$$

The force along $x_{i\neq 1}$ is dominated by linear terms (see eq. [11], whereas the force along x_1 had the quadratic terms as the largest correction (see eq. [10]). The force along $x_{i\neq 1}$ can be simplified by ignoring the quadratic terms. Hence,

$$[12] \qquad F'_{i\neq 1}(x'_1 = 0) = -\sum_{j=2}^{n}\left(\frac{\partial^2 V}{\partial x'_i \partial x'_j}\right)_{\xi^*} x'_j$$

The equation that relates force and change in position is $F = ma$. In mass-weighted coordinates this equation is,

$$[13] \qquad F'_i = \frac{\partial^2 x'_i}{\partial^2 t}$$

Inserting eq. [12] into eq. [13] yields,

$$[14] \qquad \frac{\partial^2 x'_i}{\partial^2 t} = -\sum_{j=2}^{n}\left(\frac{\partial^2 V}{\partial x'_i \partial x'_j}\right)_{\xi^*} x'_j$$

or in matrix form,

$$[15] \qquad \frac{\partial^2}{\partial^2 t}\vec{x}' = -\mathbf{A}'\vec{x}'$$

where,

$$[16] \qquad A'_{ij} = \left(\frac{\partial^2 V}{\partial x'_i \partial x'_j}\right)_{\xi^*}$$

There exists a unitary matrix $\mathbf{U}$ that makes $\mathbf{A}'$ diagonal. Performing this unitary transformation gives,

$$[17] \qquad \frac{\partial^2}{\partial^2 t}\mathbf{U}\vec{x}' = -\mathbf{U}\mathbf{A}'\mathbf{U}^{\mathrm{T}}\mathbf{U}\vec{x}'$$
$$\frac{\partial^2}{\partial^2 t}\vec{x}'' = -\mathbf{A}''\vec{x}''$$

This decouples each vibrational degree of freedom from all other vibrational degrees of freedom. Now, differential equations can be applied to obtain the equations of motion for each individual degree of freedom,

$$[18] \qquad \frac{\partial^2}{\partial^2 t}x''_{i\neq 1}(t) = -A''_{ii}x''_i(t)$$
$$x''_{i\neq 1}(t) = a_i\cos\left(\sqrt{A''_{ii}}t\right) + b_i\sin\left(\sqrt{A''_{ii}}t\right)$$

Equation [18] is the equation of motion for coordinate i, and constants a_i and b_i are determined from the initial conditions. The initial position is chosen to be $x_i(0) = 0$, and the initial velocity is determined from the temperature of the system. Using this choice of initial conditions, the equation of motion becomes,

$$[19] \qquad x''_{i\neq 1}(t) = b_i(T)\sin\left(\sqrt{A''_{ii}}t\right)$$

Equation [19] must be inserted into eq. [10] to obtain the force along coordinate 1 as a function of time, but eq. [10] needs to be transformed into the double prime basis. Simplifying eq. [10] gives,

$$[20] \qquad F'_1 = -\left(\frac{\partial V}{\partial x'_1}\right)_{\xi^*} - \sum_{i,j=2}^{n}\frac{1}{2}\left(\frac{\partial^3 V}{\partial x'_1 \partial x'_i \partial x'_j}\right)_{\xi^*} x'_i x'_j$$
$$= -\left(\frac{\partial V}{\partial x'_1}\right)_{\xi^*} - \sum_{i,j=2}^{n}\frac{1}{2}\left(\frac{\partial}{\partial x'_1}A'_{ij}\right)x'_i x'_j$$
$$= -\left(\frac{\partial V}{\partial x'_1}\right)_{\xi^*} - \sum_{i,j=2}^{n}\frac{1}{2}B'_{ij}x'_i x'_j$$

To convert coordinates from the prime basis ($'$) to the double prime basis ($''$) and vice versa, the unitary transformation is used (eq. [17],

$$[21]\qquad \vec{x}'' = \mathbf{U}\vec{x}' \qquad \vec{x}' = \mathbf{U}^{\mathrm{T}}\vec{x}'' \qquad x_i' = \sum_{k=2}^{n} U_{ki} x_k''$$

Inserting eq. [21] into eq. [20] yields the force along coordinate one as a function of other degrees of freedom in the double prime basis,

$$[22]\qquad F_1' = -\left(\frac{\partial V}{\partial x_1'}\right)_{\xi^*} - \sum_{i,j=2}^{n}\sum_{k,l=2}^{n}\frac{1}{2}B_{ij}' U_{ki} x_k' U_{lj} x_1'$$

Inserting the explicit time dependence of each degree of freedom (eq. [19]) into the force equation of coordinate one (eq. [22]) gives,

$$[23]\qquad F_1'(t) = -\left(\frac{\partial V}{\partial x_1'}\right)_{\xi^*} - \sum_{i,j=2}^{n}\sum_{k,l=2}^{n}\frac{1}{2}B_{ij}' U_{ki} U_{lj} b_k(T)\sin\left(\sqrt{A_{kk}''}t\right) b_l(T)\sin\left(\sqrt{A_{ll}''}t\right)$$

Equation [23] is the force along the IRP (coordinate one) as a function of time.

4. Average force along the Intrinsic Reaction Path (IRP)

The time average for the force along the IRP is,

$$[24]\qquad \begin{aligned} F_{1-\mathrm{ave}}' &= \lim_{\tau\to\infty}\frac{1}{\tau}\int_0^{\tau} F_1'(t)\,dt \\ &= -\left(\frac{\partial V}{\partial x_1'}\right)_{\xi^*} - \sum_{i,j=2}^{n}\sum_{k,l=2}^{n}\frac{1}{4}B_{ij}' U_{ki} U_{lj} b_k(T) b_l(T)\delta_{kl} \\ &= -\left(\frac{\partial V}{\partial x_1'}\right)_{\xi^*} - \sum_{i,j,l=2}^{n}\frac{1}{4}B_{ij}' U_{li} U_{lj} b_l(T)^2 \end{aligned}$$

Next, the functional form of the $b_i(T)$ coefficients needs to be defined. The internal energy of each degree of freedom at a given temperature is,

$$[25]\qquad U_i(T) = k\theta_i\left(\frac{1}{2} + \frac{\exp\left(-\theta_i/T\right)}{1-\exp\left(-\theta_i/T\right)}\right)$$

Taking the high temperature limit, the internal energy is,

$$[26]\qquad U_i(T) = kT$$

At $t = 0$, the kinetic energy of the system is the internal energy because the potential energy of each degree of freedom is chosen to be zero at $t = 0$ ($x_i(t = 0) = 0$, so $V = 0$). The initial kinetic energy of all degrees of freedom in the double prime basis is,

$$[27]\qquad \mathrm{KE}_{\mathrm{tot}} = \frac{1}{2}\left(\left(\frac{\partial x_1''}{\partial t}\right)^2 + \left(\frac{\partial x_2''}{\partial t}\right)^2 + \ldots + \left(\frac{\partial x_n''}{\partial t}\right)^2\right)$$

Equating the initial kinetic energy of each mode (eq. [27]) with the internal energy for each mode (eq. [26]) yields,

$$[28]\qquad \frac{1}{2}\left(\frac{\partial x_i'' x_{i''}}{\partial t}\right)_{t=0}^2 = kT$$

Inserting eq. [19] into eq. [28] yields,

$$[29]\qquad \frac{1}{2}\left(\frac{\partial}{\partial t} b_i(T)\sin\left(\sqrt{A_{ii}''}t\right)\right)_{t=0}^2 = kT$$

Differentiating and solving for the b coefficients:

$$[30]\qquad \frac{1}{2}\left(b_i(T)\ \sqrt{A_{ii}''}\right)^2 = kT$$

$$[31] \qquad b_i(T) = \sqrt{\frac{2kT}{A''_{ii}}}$$

Inserting the amplitude of each vibrational degree of freedom (b coefficients in eq. [31]) into the expression for the average force along the IRP (eq. [24]) yields,

$$[32] \qquad F'_{1-\text{ave}} = -\left(\frac{\partial V}{\partial x'_1}\right)_{\xi^*} - \sum_{i,j,l=2}^{n} \frac{1}{4} B'_{ij} U_{li} U_{lj} b_l(T)^2$$
$$= -\left(\frac{\partial V}{\partial x'_1}\right)_{\xi^*} - \frac{kT}{2} \sum_{i,j,l=2}^{n} \left(\frac{\partial}{\partial x'_1} A'_{ij}\right) U_{li} (\mathbf{A}'')^{-1}_{ll} U_{lj}$$

The unitary matrix remains constant for small changes in x'_1. Simplifying eq. [32],

$$[33] \qquad F'_{1-\text{ave}} = -\left(\frac{\partial V}{\partial x'_1}\right)_{\xi^*} - \frac{kT}{2} \sum_{i,j,l=2}^{n} \left(\frac{\partial}{\partial x_{1'}} U_{li} A'_{ij} U_{lj}\right) (A''_{ll})^{-1}$$
$$= -\left(\frac{\partial V}{\partial x'_1}\right)_{\xi^*} - \frac{kT}{2} \sum_{i=2}^{n} \frac{1}{A''_{ii}} \left(\frac{\partial A''_{ii}}{\partial x'_1}\right)$$

Equation [33] is the average force along the IRP (coordinate 1) for a molecular dynamics simulation where all motion perpendicular to the IRP is harmonic.

5. Derivative of the free energy

It is also possible to calculate the Helmholtz free energy along the IRP. This involves calculating the partition function for all degrees of freedom perpendicular to the IRP, and then applying the following formula,

$$[34] \qquad A_{\xi^*} = -kT \ln\left(Q_{\xi^*}\right) + C$$

where C is a reference energy and Q_{ξ^*} is the partition function. Inserting the partition function for all the vibrational degrees of freedom orthogonal to the IRC gives,

$$[35] \qquad A_{\xi^*} = -kT \sum_{i=2}^{n} \ln\left(q_{i,\xi^*}\right) = -kT \sum_{i=2}^{n} \left(\frac{-\theta_{i,\xi^*}}{2T} - \ln\left(1 - \exp\left(\frac{-\theta_{i,\xi^*}}{T}\right)\right)\right) + C_{\xi^*}$$

where θ_i is the vibrational temperature, which is related to the vibrational frequency, for each vibrational mode. Taking the derivative of the free energy with respect to coordinate 1 (parallel to the IRP) yields,

$$[36] \qquad \left(\frac{\partial A}{\partial x'_1}\right)_{\xi^*} = kT \sum_{i=2}^{n} \left(\frac{1}{2T} \frac{\partial \theta_{i,\xi^*}}{\partial x'_1} + \frac{\exp\left(-\theta_{i,\xi^*}/T\right)}{1 - \exp\left(-\theta_{i,\xi^*}/T\right)} \frac{1}{T} \frac{\partial \theta_{i,\xi^*}}{\partial x'_1}\right) + \left(\frac{\partial C}{\partial x'_1}\right)_{\xi^*}$$
$$= k \sum_{i=2}^{n} \left(\frac{1}{2} + \frac{\exp\left(-\theta_{i,\xi^*}/T\right)}{1 - \exp\left(-\theta_{i,\xi^*}/T\right)}\right) \frac{\partial \theta_{i,\xi^*}}{\partial x'_1} + \left(\frac{\partial C}{\partial x'_1}\right)_{\xi^*}$$

Assuming that T (the temperature) is much greater than θ_i then,

$$[37] \qquad \left(\frac{1}{2} + \frac{\exp\left(-\theta_{i,\xi^*}/T\right)}{1 - \exp\left(-\theta_{i,\xi^*}/T\right)}\right) = \frac{T}{\theta_{i,\xi^*}}$$

where this high temperature simplification is identical to the high temperature simplification done for internal energy (eqs. [25] and [26]). Inserting eq. [37] into eq. [36] yields,

$$[38] \qquad \frac{\partial A}{\partial x'_1} = k \sum_{i=2}^{n} \frac{T}{\theta_{i,\xi^*}} \left(\frac{\partial \theta_i}{\partial x'_1}\right)_{\xi^*} + \left(\frac{\partial C}{\partial x'_1}\right)_{\xi^*}$$

In these derivations, all motion perpendicular to the IRP is harmonic, and the reference energy is at the bottom of the potential well. Therefore, the reference energy is the potential energy along the IRP,

$$[39] \qquad \left(\frac{\partial C}{\partial x'_1}\right)_{\xi^*} = \left(\frac{\partial V}{\partial x'_1}\right)_{\xi^*}$$

Inserting eq. [39] into eq. [38] yields,

$$[40] \qquad \frac{\partial A}{\partial x'_1} = \left(\frac{\partial V}{\partial x'_1}\right)_{\xi^*} + kT \sum_{i=2}^{n} \frac{1}{\theta_{i,\xi^*}} \left(\frac{\partial \theta_i}{\partial x'_1}\right)_{\xi^*}$$

The vibrational temperature of one vibrational degree of freedom is,

$$[41] \qquad \theta_i = \frac{h}{2\pi k} \sqrt{A''_{ii}}$$

The vibrational temperature shown in eq. [41] is identical to the vibrational temperature seen in statistical mechanics texts,[5] namely,

$$[42] \qquad \theta_i = \frac{h}{2\pi k_B}\sqrt{\frac{k}{\mu_i}}$$

One can see that A_{ii}'' is the force constant of a vibrational mode divided by the reduced mass of that vibrational mode. Inserting the vibrational temperature (eq. [41]) into eq. [40] yields,

$$[43] \qquad \frac{\partial A}{\partial x_1'} = \left(\frac{\partial V}{\partial x_1'}\right)_{\xi^*} + kT\sum_{i=2}^{n}\frac{1}{\sqrt{A_{ii}''}}\left(\frac{\partial\sqrt{A_{ii}''}}{\partial x_1'}\right) = \left(\frac{\partial V}{\partial x_1'}\right)_{\xi^*} + \frac{kT}{2}\sum_{i=2}^{n}\frac{1}{A_{ii}''}\left(\frac{\partial A_{ii}''}{\partial x_1'}\right)$$

Equation [43] is the derivative of the free energy along the IRP (coordinate 1), derived by calculating the partition function of harmonic motion perpendicular to the IRP.

6. Summary

The potential energy surface can be Taylor expanded for a particular point along the IRP, to third order along the IRP, and to second order for all other coordinates. The equations of motion, given suitable initial conditions, can be used to determine how the force along the IRP will vary with respect to time at a given temperature. Averaging the force for a long period of time will yield the average force along the IRP as a function of temperature (eq. [33]). This average force is the average force that is expected in a molecular dynamics simulation.

The derivative of the free energy along the IRP can be calculated by using the vibrational partition function (eq. [42]).

Examining eqs. [33] and [43], it is evident that the right-hand side of eq. [33] is the negative of the right-hand side of eq. [43],

$$[44] \qquad F_{1-\mathrm{ave}}' = -\frac{\partial A}{\partial x_1'}$$

Therefore, the average force along the IRP, calculated in a molecular dynamics simulation, is the negative of the derivative of the free energy. Integrating the average force from state *a* to state *b*, as done in TI, yields the free energy change between state *a* and state *b*. This free energy change is identical to the free energy change calculated using HFA.

This derivation reinforces the methodology behind thermodynamic integration. It is common, when verifying the results of thermodynamic integration, to compare the results with the corresponding frequency analysis.[1,8] As shown above, when motion perpendicular to the reaction path is harmonic, the free energy change calculated using thermodynamic integration proves to be identical to the free energy change calculated using frequency analysis.

References

(1) Kelly, E.; Seth, M.; Ziegler, T. *J. Phys. Chem. A.*, **2004**, *108*, 2167. doi:10.1021/jp036007v.

(2) Yang, S.; Fleurat-Lessard, P.; Hristov, I.; Ziegler, T. *J. Phys. Chem. A,* **2004**, *108*, 9461. doi:10.1021/jp046954j.

(3) Straatsma, T. P.; McCammon, J. A. *J. Phys. Chem. A*, **1991**, *95*, 1175.

(4) Fleurat-Lessard, P.; Ziegler, T. *J. Chem. Phys.* **2005**, *123*, 084101. doi:10.1063/1.1948367.

(5) McQuarrie, D. A. *Statistical thermodynamics*; Harper and Row: New York, 1973.

(6) Deng, L. Q.; Ziegler, T. *Int. J. Quantum Chem.* **1994**, *52*, 731. doi:10.1002/qua.560520406.

(7) Slater, J. C.; Frank, N. H. *Mechanics*; McGraw-Hill Book Company Inc.: New York and London, 1947; pp. 122–142.

(8) Jechow, J.; Ziegler, T. *Mol. Phys.* **2007**, *105*, 2919. doi:10.1080/00268970701797418.

Magnetic separable PSA@Fe_3O_4/Ag composites — Fabrication and catalytic properties

Cuifeng Jiang, Mingwei Chen, Shouhu Xuan, Wanquan Jiang, Xinglong Gong, and Zhong Zhang

Abstract: A novel PSA@Fe_3O_4/Ag composite, with high efficiency in the degradation of Rhodamine B, was synthesized through a simple wet-chemistry method. The results showed that the rate of the catalytic reaction was significantly concentration-dependent. Furthermore, there was no significant loss in the catalytic activity of the recycled catalysts, even after being recycled nine times (average 83%), from which one can deduce that almost all the nanosilver were regathered due to the super-paramagnetic Fe_3O_4 nanoparticles.

Key words: recyclable catalysts, magnetite, silver, rhodamine B.

Résumé : Faisant appel à une méthode simple de chimie humide, on a synthétisé un nouveau composite PDA@Fe_3O_4/Ag très efficace pour la dégradation de la Rhodamine B. Les résultats montrent que la vitesse de la réaction catalytique dépend fortement de la concentration. De plus, il n'y a pas de perte significative de l'activité des catalyseurs recyclés, même après neuf recyclages (moyenne de 83%); ces résultats permettent de déduire que pratiquement tout le nanoargent est récupéré en raison des nanoparticules de Fe_3O_4 superparamagnétiques.

Mots-clés : catalyseurs recyclables, magnétite, argent, rhodamine B.

[Traduit par la Rédaction]

Introduction

Recently, metal nanoparticles have become a hotspot in various fields,[1–3] not only because of their particular properties,[4,5] which are obviously different from their bulk materials, but also for their widespread applications in the practical world.[6] It has been extensively demonstrated that metal nanoparticles have high catalytic activities for NO reduction, CO oxidation, and degradation of organic dyes[7–9] because of their very large surface-to-volume ratio.

However, metal-nanoparticle catalysts have proved to be of somewhat limited use owing to the difficulties in separating the products and residual catalysts using traditional methods such as filtration or centrifugation.[10] The immobilization of metal-nanoparticle catalysts has therefore attracted a lot of attention. Among various support materials, magnetic-nanoparticle supports are now frequently used just because they allow the catalysts to be recovered conveniently through applying an external magnetic field.[11] Many efforts have been made to develop this kind of recyclable catalyst. For example, T.J. Yoon and co-workers considered magnetic nanoparticles as a catalyst vehicle for simple and easy recycling.[12] Unfortunately, since magnetic nanoparticles themselves have strong magnetic properties and could easily aggregate together, the preparation of magnetic recyclable catalysts with better dispersion is rather challenging.

Generally, to obtain better dispersion, the magnetic components are modified with layers of rigid materials (SiO_2, carbon, and so forth) and (or) functional organic agents (amines, oleate, and so forth) in advance.[4,11,13,14] PSA (poly(styrene-*o*-acrylic acid)), an important and versatile polymer, is the expected template for composites, especially for those needed to be modified. Though various modified metal nanoparticles catalysts have been obtained,[15–17] to the best of our knowledge no PSA-based recyclable metal catalysts have been reported so far. In this report, a novel magnetically recycled PSA@Fe_3O_4/Ag composite catalysts have been successfully synthesized by a simple wet-chemistry method. Consequently, the catalysts cannot only be recovered easily, but also be dispersed homogeneously without an excess amount of surface active agent.

Received 6 October 2008. Accepted 11 January 2009. Published on the NRC Research Press Web site at canjchem.nrc.ca on 20 February 2009.

C. Jiang, M. Chen, S. Xuan, and W. Jiang.[1] Department of Chemistry, University of Science and Technology of China, Hefei 230026, P.R. China.
X. Gong.[2] CAS Key Laboratory of Mechanical Behaviour and Design of Materials, Department of Modern Mechanics, University of Science and Technology of China, Hefei 230027, P.R. China.
Z. Zhang. National Center for Nanoscience and Technology, Beijing 100080, P.R. China.

[1]Corresponding author (e-mail: jiangwq@ustc.edu.cn).
[2]Corresponding author (e-mail: gongxl@ustc.edu.cn).

Experimental

Reagents

Ferric chloride hexahydrate ($FeCl_3 \cdot 6H_2O$, AR), sodium sulfite anhydrous (Na_2SO_3, AR), sodium borohydride ($NaBH_4$), hexamethylene tetramine (AR), and rhodamine B (RhB, AR) were obtained from Sinopharm Chemical Reagent Co. Ltd. Silver nitrate ($AgNO_3$) and ammonium hydroxide ($NH_3 \cdot H_2O$, 25%–28%) were obtained from Lingfeng Chemical Reagent Co. Ltd. of Shanghai. All reagents were used as received without further purification.

Fig. 1. TEM micrographs of (*a*) PSA@ Fe_3O_4 and silver nanoparticles supported on PSA@ Fe_3O_4 before (*b*) and after (*c*) the catalytic reaction.

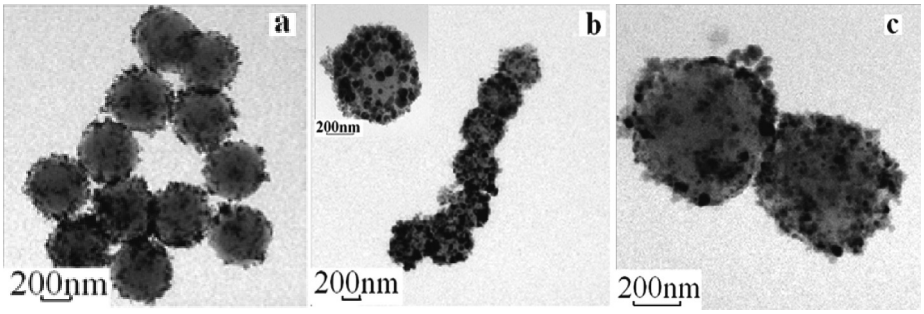

Fig. 2. X-ray diffraction patterns of PSA@Fe_3O_4/Ag before (*a*) and after (*b*) catalytic reaction.

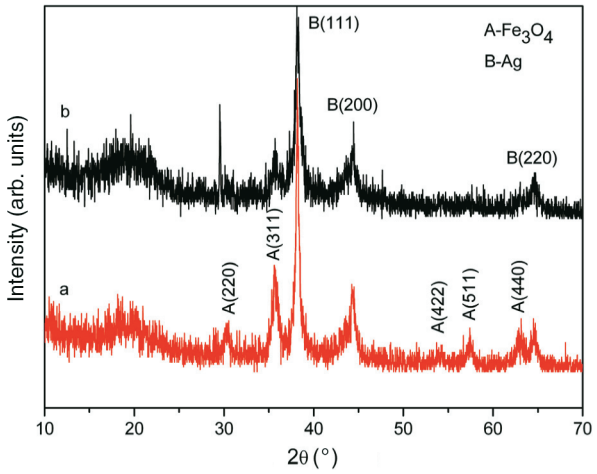

Fig. 3. Magnetization curve of PSA@Fe_3O_4/Ag.

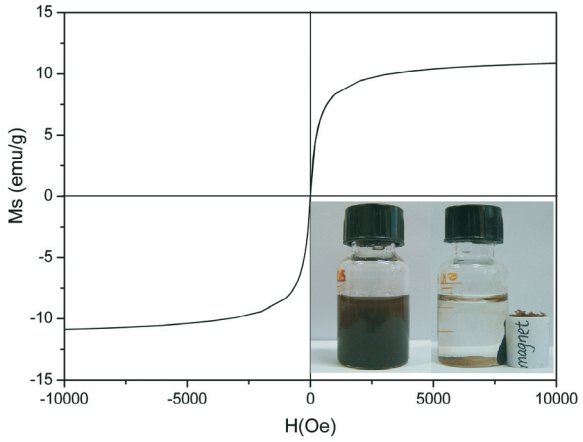

Preparation of PSA@Fe_3O_4/Ag

Uniform PSA microspheres with an average diameter of 400 nm were synthesized by a method reported previously.[18] In a typical synthesis, PSA was dispersed in a blend solution with volume ratio of 2:1 ($v_{ethanol}/v_{water}$ = 2:1), and 50 mL of $FeCl_3 \cdot 6H_2O$ (0.006 mol/L), which has been purged with nitrogen for 20 min to remove all traces of oxygen, was added. After stirring for 20 min, Na_2SO_3 (0.001 mol/L) aqueous solution was gradually added under stirring, followed by a dropwise addition of $NH_3 \cdot H_2O$ to adjust the pH value to 8. The mixture was stirred for 3 h at 65 °C under nitrogen atmosphere and then placed in a magnetic field (B = 300 mT) for separation. After that, the PSA@Fe_3O_4 precipitate was obtained.

The magnetic catalysts were prepared as follows: First, 0.05 g of $AgNO_3$ was added to an ethanol solution containing 0.1 g of PVP and 0.05 g of PSA@Fe_3O_4 as described above, and the mixture solution was sonicated for dispersion. Then, 20 mL of ethanol solution containing 0.2 g of hexamethylene tetramine was gradually dropped into the above-mentioned mixture suspension under stirring, and the resulting solution was vigorously stirred for 1 h. Then, the reaction system was allowed to stand for 10 h under circumfluence at 85 °C. After being separated by magnetic field, the resulting samples were washed with water and ethanol, then dried at 50 °C under vacuum. Finally, the PSA@Fe_3O_4/Ag composites were obtained.

The catalytic properties of the obtained PSA@Fe_3O_4/Ag composites

A given amount of PSA@Fe_3O_4/Ag composite was well-dispersed in an aqueous solution containing RhB, and the volume of the mixture was adjusted to 30 mL with distilled water. After that, 10 mL of $NaBH_4$ solution were rapidly injected under stirring. The colour of the mixture gradually vanished, indicating the reduction of the dye. Changes in the concentration of RhB were monitored by examining the variations in maximal absorption in UV–vis spectra at 553 nm.

Catalyst-recycling experiments were examined to find the recycle efficiency. 1.5 mL of PSA@Fe_3O_4/Ag solution were used to catalyze RhB ([RhB] = 2×10^{-5} mol/L, [$NaBH_4$] = 1×10^{-2} mol/L). After the reaction was completed, the catalysts were separated by a magnetic field, then followed by another "repeat". The recycle catalytic efficiency was determined by measuring the absorption value of RhB at the end of the catalytic reaction.

Characterization

Transmission electron microscopy (TEM) photographs were taken on a Hitachi model H-800 transmission electron microscope at an accelerating voltage of 200 kV. X-ray powder diffraction (XRD) patterns of the products were obtained on a Japan Rigaku D/Max-γA rotation anode X-ray diffractometer equipped with graphite monochromatized Cu Kα radiation (λ = 0.154 178 nm). The magnetization curves

Fig. 4. UV–vis spectra of RhB during the degradation catalyzed by PSA@Fe_3O_4/Ag, [RhB] = 4 × 10^{-5}mol/L.The arrows mark the increase of the reaction time. (*a*) 1 mL PSA@ Fe_3O_4/Ag; (*b*) 1.4 mL PSA@ Fe_3O_4/Ag; (*c*) 2 mL PSA@ Fe_3O_4/Ag, (*d*) curves of absorption vs. time at different concentrations of the catalyst (a: 1 mL, b: 1.4 mL, c:2 mL PSA@ Fe_3O_4/Ag solution).

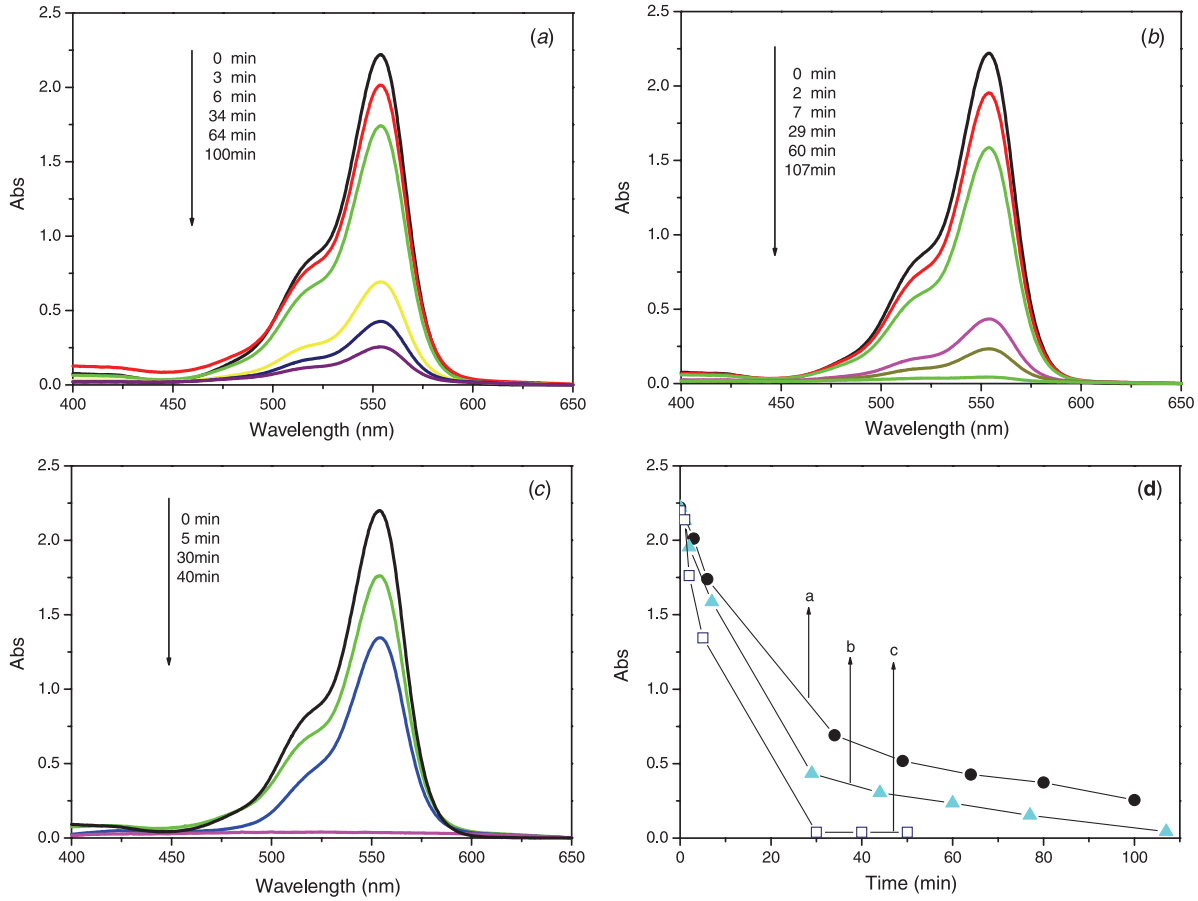

(M–H curve) of the samples were recorded on a MPMS XL-7 magnetometer made by Quantum Design Corp. The optical absorption was recorded on an ultraviolet–visible (UV)-2401(PC)S made by Shimadzu Corporation.

Results and discussion

The characterization of PSA@Fe_3O_4/Ag composites

As mentioned above, the PSA@Fe_3O_4/Ag composites were prepared by a simple and rapid method. The formation of the composites was confirmed by TEM as presented in Fig. 1, from which monodisperse composites can be seen. TEM analysis on both PSA@Fe_3O_4 and PSA@Fe_3O_4/Ag reveal that silver and magnetite nanoparticles decorated the PSA substrate with a diameter of 400 nm. It is evident that the darker dots represent the silver nanoparticls while the others are Fe_3O_4 nanoparticles. The absorption function is strong enough so that the silver nanoparticles remain attached to the PSA@Fe_3O_4 during the catalytic reaction, which was verified by the TEM images of the silver particles supported on PSA@Fe_3O_4 before and after catalytic reactions (Fig. 1*b* and 1*c*).

To study the stability of the composite catalysts, the sample was subjected to XRD. As shown in Fig. 2, all of the diffraction peaks match well with Ag crystal and Fe_3O_4 crystal.[19,20] As one can see, peaks of both Ag and Fe_3O_4 become a little weaker in Fig. 2*b* compared with Fig. 2*a*, which means that a portion of the crystal has been lost during the catalytic reaction. That is why in the recycle experiments, the composite catalysts deactivated more or less during the degradation reaction.

The magnetic properties of the composites have been elucidated in Fig. 3. The saturation magnetization of the composites is 11 emu/g at an external field of 10 kOe at room temperature. Obviously, it is much lower than the reported saturation magnetization of Fe_3O_4 (68.7 emu/g).[21] The emerging of this phenomenon is because of the existence of silver in very small size. On one hand, this feature allows catalysts separation under relatively low external magnetic field. On the other hand, the negligible coercivity indicates the superparamagnetic property of the sample, which is available for redispersion of the catalysts in solution without the occurrence of severe assembly or aggregation usually appearing in ferromagnetic nanoparticles.[22–25] That is why Fe_3O_4 rather than Fe serves as the magnetic support.

The inset of Fig. 3 illuminates the effective model of catalysts separation and redispersion under an external magnetic field. Before applying an external field, the catalysts were homogeneously dispersed to show their high catalytic activity.[26] After applying an external field, the intact catalysts were separated from the mixture suspension for reusage. Thus, the PSA@Fe_3O_4 composites are very appropriate

Fig. 5. The change of RhB's colour under the catalysis of PSA@Fe_3O_4/Ag.

Table 1. Catalytic efficiency at different concentrations of the catalyst.

	Catalytic efficiency (%)									
(mL)	0	1	2	6	30	45	50	60	80	100 (min)
1.0	0	2.54	9.4	21.7	68.8	75.5	76.8	80.6	83.2	88.5
1.4	0	3.96	12.0	28.6	80.5	86.3	87.6	89.5	93.1	98.0
2.0	0	2.74	19.8	38.8	98.2	98.2	98.2	98.2	98.2	98.2

as catalyst supports for separation and redispersion[4] because of superparamagnetic Fe_3O_4 nanocrystals.

The catalytic properties of as-prepared PSA@Fe_3O_4/Ag catalysts

Previous results[6,27,28] demonstrated that silver nanoparticles exhibit catalysis on organic dyes, such as rhodamine B (RhB), methylene blue (MB), and eosin (EO). In this paper, catalysis experiments were conducted to study the catalytic properties of the nanosilver. Figure 4 shows the evolution of the UV–vis spectra of RhB during catalytic reductions at the PSA@Fe_3O_4/Ag solution. Evidently, the absorbance at λ_{max} = 553 nm of the RhB gradually decreased with reaction time, which is indicative of the reduction of RhB. As expected, the catalytic reduction of RhB proceeded successfully, and no deactivation or poisoning of the catalysts was observed. Changing of RhB's colour in the process of catalysis reaction (Fig. 5) further affirms the degradation. With time, the colour of RhB became lighter and lighter. As one can see, the pure RhB was carmine; after 20 min reaction, the solution became peachblow; and then at the end of the reaction (50 min), the colour almost disappeared. It was observed that the reduction of RhB by PSA or PSA@Fe_3O_4 did not occur to an appreciable extent in the absence of the Ag nanoparticles. This indicates that silver nanoparticles play the key role of the catalysts for the reduction of RhB, while PSA supports the catalyst, and Fe_3O_4 makes it possible to be reused. According to earlier work,[7] the catalytic process can be explained by an electrochemical mechanism, where PSA@Fe_3O_4/Ag serve as an electron relay for an oxidant and a reductant, and electron transfer occurs via the supported silver particles. Dyes are electrophilic, while BH_4^- ions are nucleophilic in nature with respect to silver nanoparicles.

Reactions with various concentrations of catalysts were examined to find the optimal conditions for the reaction. The rate of the catalytic reaction proved to be significantly concentration-dependent.

It is apparent that the rate of the catalyzed reduction of RhB increased with the increase of the concentration of the PSA@Fe_3O_4/Ag as displayed in Table 1. It is obviously observed that after 30 min reaction, the degradation of RhB for three volumes of PSA@Fe_3O_4/Ag solution (1 mL, 1.4 mL, and 2 mL) was 60%, 83%, and almost 100%, respectively. Therefore, to improve catalytic efficiency, increasing the mass of catalysts is effective.

Fig. 6. Recycle experiments of the degradation reaction of RhB catalyzed by PSA@Fe_3O_4/Ag.

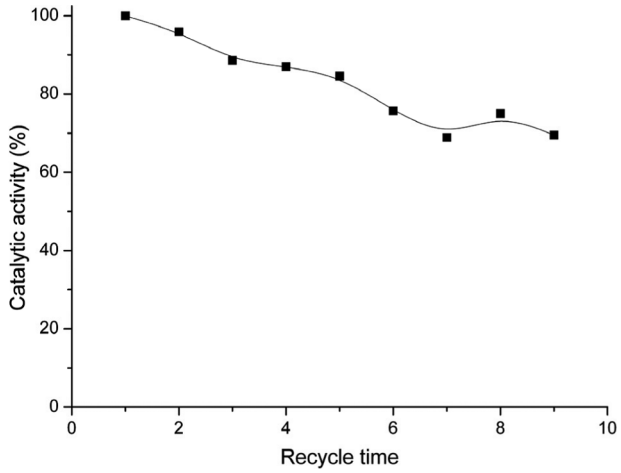

Recycleability of the catalysts was examined to evaluate the role of PSA@Fe_3O_4. The hybrid composite catalysts, doped with magnetic particles, can be isolated by a magnetic device and reused for consecutive reactions. When the external magnetic field was applied after the reaction was accomplished, the magnetic composites were regathered (B = 300 mT), and the rest of the solution became clean within 5 min. Under these reaction conditions, the degradation of RhB was carried out nine times with the recycled catalysts. As shown in Fig. 6, there was no significant change in the catalytic activity of the recycled magnetic composite even after being recycled nine times (average 83%). Consequently, the small decrease of the catalytic activity can result from incomplete separation of catalysts or the loss of catalysts during the degradation reduction. All these results showed that the PSA@Fe_3O_4 substrate played an important role in the catalytic process. One is to avoid the aggregation

of the metal nanoparticles during the catalytic process, which ensures the catalyzed reduction of RhB.[6] The other is to facilitate separation of catalysts from the solution system. This fascinating property of magnetic catalysts is expected to be applied in many other important industrial processes.

Conclusion

With the assistance of PSA, a novel magnetically recyclable Ag-based catalyst was synthesized. Results showed the obtained magnetic catalysts exhibited good catalytic activity and could be recycled for several times by magnetic separation without major loss of activity. The significance of PSA@Fe_3O_4 lies in avoiding the aggregation of the silver nanoparticles during the catalytic process and offering an easy separation approach after catalysis. Furthermore, the overall synthetic process for the composites is simple and rapid, and it is anticipated that this synthetic approach may be readily extended to recyclable catalysts that contain catalytically active metals instead of Ag.

Acknowledgements

Financial support from National Basic Research Program of China (973 Program, Grant No. 2007CB936800) is gratefully acknowledged.

References

(1) Henglein, A. *Chem. Mater.* **1998**, *10*, 444. doi:10.1021/cm970613j.
(2) Grass, M. E.; Yue, Y.; Habas, S. E.; Rioux, R. M.; Teall, C. I.; Yang, P.; Somorjai, G. A. *J. Phys. Chem. Comm. C,* **2008**, *112*, 4797. doi:10.1021/jp7097679.
(3) Patel, A. C.; Li, S. X.; Wang, C.; Zhang, W. J.; Wei, Y. *Chem. Mater.* **2007**, *19*, 1231. doi:10.1021/cm061331z.
(4) Jiang, Y. J.; Jiang, J. H.; Gao, Q. M.; Ruan, M. L.; Yu, H. M.; Qi, L. J. *Nanotechnology*, **2008**, *19*, 075714. doi:10.1088/0957-4484/19/7/075714.
(5) Cui, K.; Song, Y. H.; Yao, Y.; Huang, Z. Z.; Wang, L. *Electrochem. Commun.* **2008**, *10*, 663. doi:10.1016/j.elecom.2008.02.016.
(6) Pal, T.; Sau, T. K.; Jana, N. R. *Langmuir*, **1997**, *13*, 1481. doi:10.1021/la960834o.
(7) Lu, Q.; Yang, B.; Zhuang, L.; Lu, J. *J. Phys. Chem. B*, **2005**, *109*, 1715. doi:10.1021/jp0461652. PMID:16851149.
(8) Li, J. H.; Zhu, Y. Q.; Ke, R.; Hao, J. M. *Appl. Catal. B Environ.* **2008**, *80*, 202. doi:10.1016/j.apcatb.2007.08.016.
(9) Bokhimi, X.; Zanella, R.; Morales, A. J. *Phys. Chem. Comm.* **2007**, *111*, 15210.
(10) Shokouhimehr, M.; Piao, Y. Z.; Kim, J.; Jang, Y. J.; Hyeon, T. *Angew. Chem. Int. Ed.* **2007**, *46*, 7039. doi:10.1002/anie.200702386.
(11) Zhang, D. H.; Li, G. D.; Li, J. X.; Chen, J. S. *Chem. Commun.* **2008**, 3414. doi:10.1039/b805737k. PMID:18633507.
(12) Yoon, T. J.; Lee, W.; Oh, Y. S.; Lee, J. K. *N. J. Chem.* **2003**, *27*, 227. doi:10.1039/b209391j.
(13) Yi, D. K.; Lee, S. S.; Ying, J. Y. *Chem. Mater.* **2006**, *18*, 2459. doi:10.1021/cm052885p.
(14) Stevens, P. D.; Fan, J. D.; Gardimalla, H. M. R.; Yen, M.; Gao, Y. *Org. Lett.* **2005**, *7*, 2085. doi:10.1021/ol050218w. PMID:15901140.
(15) Chimentão, R. J.; Medina, F.; Fierro, J. L. G.; Sueiras, J. E.; Cesteros, Y.; Salagre, P. *J. Mol. Catal. Chem. (Kyoto)*, **2006**, *258*, 346. doi:10.1016/j.molcata.2006.07.028.
(16) Williams, F. J.; Bird, D. P. C.; Palermo, A.; Santra, A. K.; Lambert, R. M. *J. Am. Chem. Soc.* **2004**, *126*, 8509. doi:10.1021/ja039378y. PMID:15238008.
(17) Chimentão, R. J.; Kirm, I.; Medina, F.; Rodríguez, X.; Cesteros, Y.; Salagre, P.; Sueiras, J. E.; Fierro, J. L. G. *Appl. Surf. Sci.* **2005**, *252*, 793. doi:10.1016/j.apsusc.2005.02.064.
(18) Chen, C. N.; Zhu, C. L.; Hao, L. Y.; Hu, Y.; Chen, Z. Y. *Inorg. Chem. Commun.* **2004**, *7*, 322. doi:10.1016/j.inoche.2003.11.021.
(19) Lu, Y.; Mei, Y.; Schrinner, M.; Ballauff, M.; Mller, M. W.; Breu, J. J. *Phys. Chem. Comm.* **2007**, *111*, 7676.
(20) Chen, M.; Kim, Y. N.; Lee, H. M.; Li, C.; Cho, S. O. J. *Phys. Chem. Comm.* **2008**, *112*, 8870.
(21) Deng, H.; Li, X. L.; Peng, Q.; Wang, X.; Chen, J. P.; Li, Y. D. *Angew. Chem. Int. Ed.* **2005**, *44*, 2782. doi:10.1002/anie.200462551.
(22) Ajjou, A. N.; Alper, H. *J. Am. Chem. Soc.* **1998**, *120*, 1466. doi:10.1021/ja973048u.
(23) Chung, Y. M.; Kang, K. K.; Ahn, W. S.; Lim, P. K. *J. Mol. Catal. Chem. (Kyoto)*, **1999**, *137*, 23. doi:10.1016/S1381-1169(98)00080-6.
(24) Chen, J. H.; Alper, H. *J. Am. Chem. Soc.* **1997**, *119*, 893. doi:10.1021/ja9623875.
(25) Yavuz, C. T.; Mayo, J. T.; Yu, W. W.; Prakash, A.; Falkner, J. C.; Yean, S.; Cong, L. L.; Shipley, H. J.; Kan, A.; Tomson, M.; Natelson, D.; Colvin, V. L. *Science*, **2006**, *314*, 964. doi:10.1126/science.1131475. PMID:17095696.
(26) Wang, Y. H.; Lee, J. K. *J. Mol. Catal. Chem. (Kyoto)*, **2007**, *263*, 163. doi:10.1016/j.molcata.2006.08.069.
(27) Jana, N. R.; Sau, T. K.; Pal, T. *J. Phys. Chem. B,* **1999**, *103*, 115. doi:10.1021/jp982731f.
(28) Pal, T.; Sau, T. K.; Jana, N. R. *J. Colloid Interface Sci.* **1998**, *202*, 30. doi:10.1006/jcis.1997.5353.

Scaled quantum mechanical force fields for trifluoromethyl selenium derivatives. II. The $(CF_3)_2Se$ and $(CF_3Se)_2$ molecules.

L.E. Fernández and E.L. Varetti

Abstract: Force fields and vibrational properties of bis(trifluoromethyl)selenide, $(CF_3)_2Se$, and bis(trifluoromethyl)diselenide, $(CF_3Se)_2$, were calculated using density functional theory (DFT) techniques. The previously available experimental data and assignments for these molecules were confirmed by the theoretical results. These data were subsequently used in the definition of the corresponding scaled quantum mechanical (SQM) force fields. The obtained internal force constants are compared with results previously published for related selenium compounds.

Key words: trifluoromethyl selenium, force constants, structure, DFT calculation.

Résumé : Faisant appel à des calculs à base de la théorie de la fonctionnelle de la densité (TFD), on a calculé les propriétés de champs de force et vibrationnelles du bis(trifluorométhyl)séléniure, $(CF_2)_2Se$, et du bis(trifluorométhyl)diséléniure, $(CF_2)_2Se_2$. Les résultats théoriques ont permis de confirmer les données expérimentales disponibles antérieurement ainsi que les attributions faites pour ces molécules. On a subséquemment utilisé ces données dans la définition des champs de forces correspondants en mécanique quantique . On a comparé les constantes de force internes ainsi obtenues avec les résultats publiés antérieurement pour des composés séléniés apparentés.

Mots-clés : trifluorométhylsélénium, constantes de force, structure, calculs selon la théorie fonctionnelle de la densité (TFD).

[Traduit par la Rédaction]

Introduction

Theoretical studies on the vibrational properties of the selenium compounds, CF_3SeX (X = H, D, Cl, or Br) and two simple CF_3Se derivatives, i.e., CF_3SeCN and CF_3SeCH_3, were recently performed in our laboratory.[1,2] Now, we turn our attention to the vibrational studies of other two selenium compounds, i.e., $(CF_3)_2Se$ and $(CF_3Se)_2$.

These molecules were prepared by Dale, Emeléus, and Haszeldine[3] and by Emeléus and Dunn.[4] The molecular structures were obtained by Marsden and Sheldrick by means of electron diffraction techniques.[5,6] The vibrational spectra and assignments were reported for these two molecules by Marsden[7] and Clase et al.[8]

In the present work, the vibrational characteristics of the above-mentioned molecules were calculated using the methods of quantum chemistry to check the published normal mode frequencies and their assignments and to obtain the corresponding force constants, which were scaled to reproduce the experimental frequencies. Such adjustment was made using the formalism of the scaled quantum mechanical (SQM) force field, as defined by Pulay et al.[9]

Received 24 July 2008. Accepted 29 October 2008. Published on the NRC Research Press Web site at canjchem.nrc.ca on 27 February 2009.

L.E. Fernández. Instituto de Química Física, Facultad de Bioquímica, Química y Farmacia, Universidad Nacional de Tucumán, San Lorenzo 456, 4000 S.M. de Tucumán, República Argentina.
E.L. Varetti.[1] Centro de Química Inorgánica (CEQUINOR, CONICET-UNLP), Departamento de Química, Facultad de Ciencias Exactas, Universidad Nacional de La Plata, C.Correo 962, 1900 La Plata, República Argentina.

[1]Corresponding author (e-mail: varetti@quimica.unlp.edu.ar).

Calculation procedure

Optimized structures, force constants, and vibrational frequencies for the $(CF_3)_2Se$ and $(CF_3Se)_2$ molecules were obtained with density functional theory (DFT) methods using the B3LYP functional[10,11] together with the 6–311G* basis set. These theoretical data allowed a good reproduction of the experimental frequencies and facilitated the comparison of the results with those obtained in previous studies[1,2] in which the same combination of functional and basis set was used. All calculations were made for the isolated molecules using the Gaussian 03 set of programs.[12]

The harmonic force field in Cartesian coordinates given by the theoretical calculation was transformed to natural (local symmetry) coordinates[13] through the corresponding **B** matrix,[14] calculated with a standard program. The resulting force field was subsequently scaled using the scheme of Pulay et al.,[9] in which the diagonal force constants are multiplied by scale factors f_i, f_j, and so forth, and the corresponding interaction constants are multiplied by $(f_i \cdot f_j)^{1/2}$, adjusting the scaled factors by a least-squares procedure to reproduce as well as possible the experimental frequencies. No anharmonicity corrections of these frequencies were made because of the lack of the necessary experimental data. The potential-energy distribution (PED), which gives the participation of each defined coordinate to each

Table 1. Calculated energy of the conformations with C_2 and C_{2v} symmetries of the $(CF_3)_2Se$ molecule at different level of theory.

Method	C_2 conformation	C_{2v} conformation	
	E (Hartree)	E (Hartree)	ΔE (kJ mol^{-1})
B3LYP			
6–31G*	–3074.617261	–3074.617220	0.109
6–311G*	–3076.993702	–3076.993676	0.067
6–311+G*	–3077.016765	–3077.016745	0.054
B3PW91			
6–31G*	–3074.356303	–3074.356261	0.109
6–311G*	–3076.723494	–3076.723470	0.063
6–311+G*	–3076.742751	–3076.742728	0.058

normal mode of vibration, was calculated with the resulting SQM force field.

The force field transformation, scaling, and PED calculation were performed with the program FCARTP.[15]

Structural results

The molecular conformations of $(CF_3)_2Se$ were investigated starting with an initial, staggered structure having FCSeC dihedral angles of 180° (C_{2v} symmetry). The CF_3 groups were both rotated around the Se–C bonds in opposite directions, so that the C_2 symmetry was preserved. The twist angles were varied from 0° to 60°, in steps of 5°, and the structure was optimized with that dihedral angle frozen. These calculations showed that only a single conformer exists for this molecule for a twist angle of ~5°. This structure was fully optimized at the B3LYP/6-311G* level to obtain the real position of the minimum, which was located for a twist angle of 6° and FCSeC dihedral angles of 174°. The starting C_{2v} conformation turned out to be a transition state characterized by an imaginary frequency associated with the CF_3 torsion, as expected. However, the difference in energy between both conformations (0.067 kJ mol^{-1} at B3LYP/6–311G* level) is very small. The relative energies of the two forms are listed in Table 1 at various levels of theory; at all investigated approximations, the C_2 conformation was the most stable, always very close in energy to C_{2V}. These theoretical results do not agree completely with the electron diffraction data; in fact, Marsden and Sheldrick[5] found two possible structures in good agreement with the data having CF_3 twist angles of 4° and 33°, respectively.

A similar analysis was performed for the $(CF_3Se)_2$ molecule starting with an initial structure in which the CF_3 groups are in an exactly staggered position in relation to the Se–Se bond. This conformation has CSeSeC and FCSeSe dihedral angles of 91° and 180°, respectively. The CF_3 groups were rotated simultaneously in steps of 5°, preserving always the C_2 symmetry and the mentioned CSeSeC angle. A single minimum in the potential energy curve was found, corresponding to the conformation in which the twist angle was equal to 10° for both CF_3 groups. Subsequently, this structure was fully optimized to a dihedral angle of 9.2°. On the other hand, the potential energy curve was also explored varying the CSeSeC dihedral angle in steps of 5°. These calculations confirmed the existence of only one minimum in the potential energy surface for this molecule. The optimized molecular structure for $(CF_3Se)_2$ agrees with the electron diffraction study.[6]

Fig. 1. The calculated structures for the molecules $(CF_3)_2Se$ and $(CF_3Se)_2$.

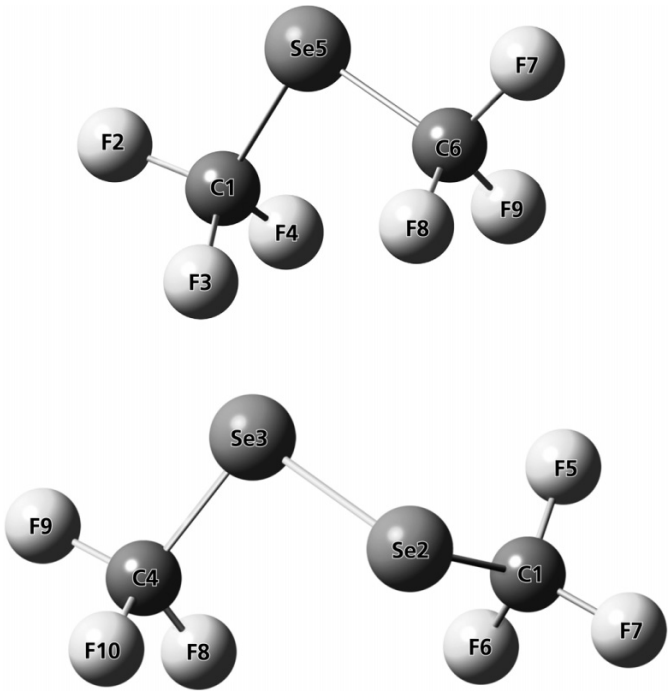

The structures of the most stable conformations predicted for $(CF_3)_2Se$ and $(CF_3Se)_2$ molecules are shown in Fig. 1. The corresponding calculated geometric parameters and experimental values appear in Table 2. The (mean) calculated and experimental distances and angles do not differ in more than 0.045 Å (for the Se–Se distance) and 6.5° (for the CSeSeC dihedral angle), respectively. The theoretical tilt angles, existing between the C–Se bonds and the ideal symmetry axis of the CF_3 group, also appear in Table 2; this angle was calculated for the CF_3 groups as $1/3[2\alpha(F_{3,4}CSe)–2\alpha(F_2CSe)]$.[16]

Vibrational results

Marsden[7] and Clase et al.[8] have reported and assigned the vibrational spectra of the two molecules studied. Clase et al checked Marsden's assignments and performed some changes, particularly in the CF_3 stretching region. A revision of the published assignments for both molecules was made by comparison between the existing experimental data and our theoretical results. The computed atomic displacement vectors for each vibrational mode served to understand qualitatively the nature of the molecular vibrations and were used also for such revision. This analysis showed that the assignments proposed by Clase et al. were correct.

The bands observed in the IR spectra of $(CF_3)_2Se$ at 1142 and 1065 cm^{-1} correspond to the CF_3 symmetric stretching modes (ν_3 and ν_{14}, respectively), whereas the bands at 1152, 1193, and 1200 cm^{-1} are assigned to the CF_3 antisymmetric stretching modes (ν_{13}, ν_{12}, and ν_1, respectively). The calculated band at 1162 cm^{-1}, which seems to be too weak to appear in the experimental spectra, is attributed to the

Table 2. Optimized and experimental geometric parameters for the molecules $(CF_3)_2Se$ and $(CF_3Se)_2$.

	$(CF_3)_2Se$		$(CF_3Se)_2$	
	Calculated	Experimental[5]	Calculated	Experimental[6]
Bonds lengths (Å)				
C–F[a]	1.338	1.332	1.338	1.326
C–Se	1.986	1.980	2.000	2.018
Se–Se	—	—	2.337	2.292
Bond angles (°)				
F-C-F[a]	108.3	108.9	108.3	109.9
F-C-Se[a]	110.6	—	110.6	109.1
C-Se-Se	—	—	99.8	98.0
C-Se-C	96.4	94.1	—	—
Dihedral angles (°)				
F-C-Se-C	174.0	—	—	—
C-Se-Se-C	—	—	91.0	84.5
F-C-Se-Se	—	—	175.4	—
Twist angle	6.0	4.2	9.2	11.8
Tilt angle	4.1	2.0 (fixed)	4.3	—

[a]Mean of the calculated values.

CF_3 antisymmetric stretching mode (ν_2), unless it corresponds to the very weak band at 1178 cm^{-1} only reported by Clase et al.

Concerning the $(CF_3Se)_2$ molecule, the IR band at 1188 cm^{-1} corresponds to the CF_3 antisymmetric stretching modes (ν_1 and ν_2, respectively), whereas the band located at 1144 cm^{-1} seems to be spurious, since our theoretical calculations did not predict bands near that frequency.

The assignments adopted in this work for the $(CF_3)_2Se$ molecule are based on the C_2 symmetry, assuming local C_{3v} symmetry for the CF_3Se group. That agrees with Marsden's proposition and the present theoretical results, whereas Clase et al. assumed a C_{2v} symmetry for this molecule.

The normal vibrational modes of the studied molecules are classified as 11A + 10B for $(CF_3)_2Se$ and 13A + 11B for $(CF_3Se)_2$, respectively, in accordance with their C_2 symmetry.

There is a fair agreement between the simulated spectra and the experimental data[8] for both molecules. The calculated frequencies and IR and Raman intensities as well as the corresponding experimental values are shown in Tables 3 and 4. The agreement between measured and calculated frequencies was evaluated by means of the root-mean-square deviation (RMSD), which was equal to 12 cm^{-1} for $(CF_3)_2Se$ and 13 cm^{-1} for $(CF_3Se)_2$. After the force-field scaling procedure, these values fell to 5 and 7 cm^{-1}, respectively.

Force constants

The harmonic force fields in Cartesian coordinates, as generated by the Gaussian programs for the two molecules, were transformed to the set of coordinates defined in Tables 5 and 6. Such coordinates consider the local symmetry of the CF_3 groups and follow the proposals of Fogarasi et al.[13] The resulting force constants were subsequently scaled according to the methodology proposed by Pulay et al.,[9] as mentioned before (in the Calculation procedure Section), to reproduce as well as possible the experimental frequencies.

The final scaling factors, corresponding to each force constant for the studied molecules, appear in Table 7. It can be seen that most of these factors are greater than one; this is the case when heavy atoms (after the second row of the Periodic Table) appear in the molecule. This fact has been reported for many molecules containing nonmetallic heavy atoms[17] as well as for several CF_3SO_2X molecules[18] and CF_3SeX species.[1,2] The scaling factors previously obtained for common coordinates of other selenium compounds[1,2] were similar to those calculated for $(CF_3)_2Se$ and $(CF_3Se)_2$ molecules in this work. The resulting SQM force-constant matrices are available as Supplementary data for this work.

The internal force constants for the two molecules, appearing in Table 8, were also calculated from the corresponding SQM force fields. These force constants are compared with the values previously obtained for other selenium derivates using the same calculation procedure.[2]

The SQM force fields were used to calculate the potential energy distribution (PED) for each molecule. These values appear in Tables 3 and 4, and show that the coordinates corresponding to ν CF_3 symm., δ CF_3 symm., and ν C–Se are strongly mixed, as expected and observed also for other CF_3SeX molecules.[1,2]

Supplementary data

Supplementary data for this article are available on the journal Web site (canjchem.nrc.ca) or may be purchased from the Depository of Unpublished Data, Document Delivery, CISTI, National Research Council Canada, Ottawa, ON K1A 0R6, Canada. DUD 3874. For more information on obtaining material, refer to cisti-icist.nrc-cnrc.gc.ca/cms/unpub_e.shtml.

Acknowledgements

Research grants from the following institutions from R. Argentina are gratefully acknowledged: CONICET (Consejo Nacional de Investigaciones Científicas y Técnicas), ANP-

Table 3. Experimental and calculated frequencies, IR and Raman intensities, and potential energy distribution (PED) for $(CF_3)_2Se$.

Mode	Experimental[a]	Calculated[b]	Calculated SQM[c]	IR intensity (km mol^{-1})	Raman intensity (Å^4 amu^{-1})	PED (contributions ≥ 10%)	Main coordinate
A							
ν_1	1200 vs	1202	1210	432.53	0.79	90 S_1 + 17 S_5	ν (CF_3) antisymm.
ν_2	?	1162	1166	0.36	0.08	101 S_2 + 18 S_6	ν (CF_3) antisymm.
ν_3	1142 vs (vw)	1126	1138	143.00	1.63	64 S_3 + 46 S_4 + 21 S_7	ν (CF_3) symm.
ν_4	749 (vs)*	743	751	11.38	8.35	42 S_4 + 37 S_3 + 12 S_7	δ (CF_3) symm.
ν_5	553 (vvw)*	551	554	0.17	1.69	65 S_5	δ (CF_3) antisymm.
ν_6	538	532	534	0.00	0.24	74 S_6	δ (CF_3) antisymm.
ν_7	363 s (m)	358	364	4.57	4.50	32 S_7 + 30 S_8 + 13 S_5 + 10 S_{10}	ν (C–Se)
ν_8	278 vw (vs)	268	275	0.01	5.94	39 S_8 + 41 S_7	ρ (CF_3)
ν_9	267 (vw)*	259	252	0.00	1.51	99 S_9 + 12 S_6	ρ (CF_3)
ν_{10}	109 (w)*	96	100	0.71	0.30	86 S_{10} + 36 S_8	δ (CSeC)
ν_{11}	?	25	25	0.00	0.05	107 S_{11}	Torsion (CF_3)
B							
ν_{12}	1193 vs	1188	1192	512.57	1.35	101 S_{12} + 17 S_{17}	ν (CF_3) antisymm.
ν_{13}	1152 vs	1148	1153	246.39	0.65	104 S_{13} + 19 S_{16}	ν (CF_3) antisymm.
ν_{14}	1065 vs (vw)	1050	1060	598.80	3.25	81 S_{14} + 50 S_{15} + 24 S_{18}	ν (CF_3) symm.
ν_{15}	746 s	738	747	43.77	0.14	47 S_{15} + 28 S_{14} + 15 S_{18}	δ (CF_3) symm.
ν_{16}	535 w (w)	531	533	0.62	0.69	78 S_{16}	δ (CF_3) antisymm.
ν_{17}	535 w (w)	527	529	2.30	1.64	74 S_{17}	δ (CF_3) antisymm.
ν_{18}	340 m (w)	323	339	0.56	3.47	68 S_{18} + 15 S_{15}	ν (C–Se)
ν_{19}	258 (w)*	294	286	0.03	0.87	96 S_{19} + 11 S_{17}	ρ (CF_3)
ν_{20}	253 vw	252	245	0.42	0.90	98 S_{20}	ρ (CF_3)
ν_{21}	?	49	48	0.10	0.07	101 S_{21}	Torsion (CF_3)
RMSD (cm^{-1})		12	5				

[a]From Ref. [8]. Starred frequencies were measured in the Raman spectrum of the liquid substance; other frequencies are from the infrared gas spectrum. Qualitative intensities for observed bands in IR and Raman (in parentheses): w, weak; m, medium; s, strong; v, very.

[b]B3LYP/6–311G* calculations.

[c]From scaled quantum mechanics force field.

Table 4. Experimental and calculated frequencies, IR and Raman intensities, and potential energy distribution (PED) for $(CF_3Se)_2$.

Mode	Experimental[a]	Calculated[b]	Calculated SQM[c]	IR intensity (km mol^{-1})	Raman intensity (Å^4 amu^{-1})	PED (contributions ≥ 10%)	Main coordinate
A							
ν_1	1188 vs	1194	1175	329.68	0.70	79 S_1 + 21 S_2 + 15 S_5	ν (CF_3) antisymm.
ν_2	1188 vs	1170	1198	0.11	1.76	78 S_2 + 18 S_1 + 14 S_6	ν (CF_3) antisymm.
ν_3	1115 vs (vvw)	1098	1107	282.79	2.39	71 S_3 + 48 S_4 + 20 S_7	ν (CF_3) symm.
ν_4	742 (s)*	738	744	17.38	11.00	45 S_4 + 33 S_3 + 12 S_7	δ (CF_3) symm.
ν_5	531 mw (w)	540	541	0.03	2.74	74 S_5	δ (CF_3) antisymm.
ν_6	531 mw (w)	530	530	0.83	1.27	75 S_6	δ (CF_3) antisymm.
ν_7	333 (m)*	328	333	1.13	5.44	27 S_7 + 22 S_9 + 20 S_8 + 10 S_{11}	ν (C–Se)
ν_8	318 (mw)*	304	318	0.63	3.24	57 S_8 + 39 S_7	ν (Se–Se)
ν_9	245 (vs)*	285	239	0.07	2.31	57 S_9 + 27 S_8	ρ (CF_3)
ν_{10}	245 (vs)*	239	273	0.02	7.42	92 S_{10} + 12 S_6	ρ (CF_3)
ν_{11}	101 (s)*	90	94	0.01	2.02	98 S_{11} + 19 S_9	δ (CSeSe)
ν_{12}	?	53	53	0.17	0.43	92 S_{12}	Torsion skeletal
ν_{13}	?	27	27	0.01	0.06	98 S_{13} + 13 S_{12}	Torsion (CF_3)
B							
ν_{14}	1169 vs (vvw)	1172	1163	397.70	0.17	57 S_{14} + 47 S_{15} + 11 S_{18}	ν (CF_3) antisymm.
ν_{15}	1169 vs (vvw)	1158	1176	246.21	0.64	55 S_{15} + 45 S_{14}	ν (CF_3) antisymm.
ν_{16}	1090 vs (vvw)	1069	1078	653.29	3.78	77 S_{16} + 49 S_{17} + 22 S_{20}	ν (CF_3) symm.
ν_{17}	741 vs	736	743	33.39	0.29	46 S_{17} + 30 S_{16} + 13 S_{20}	δ (CF_3) symm.
ν_{18}	531 mw (w)	540	542	0.10	0.22	74 S_{18}	δ (CF_3) antisymm.
ν_{19}	531 mw (w)	526	527	1.19	0.38	78 S_{19}	δ (CF_3) antisymm.
ν_{20}	321 ms (mw)	319	328	1.75	3.69	56 S_{20} + 12 S_{17}	ν (C–Se)
ν_{21}	280 m (w)	279	275	1.64	1.35	65 S_{21} + 16 S_{20}	ρ (CF_3)
ν_{22}	280 m (w)	272	260	0.14	0.39	95 S_{22}	ρ (CF_3)
ν_{23}	101 (s)*	96	99	1.34	1.28	89 S_{23} + 30 S_{21}	δ (CSeSe)
ν_{24}	?	28	29	0.02	0.04	101 S_{24}	Torsion (CF_3)
RMSD (cm^{-1})		13	7				

[a]From Ref. [8]. Starred frequencies were measured in the Raman spectrum of the liquid substance; other frequencies are from the infrared gas spectrum. Qualitative intensities for observed bands in IR and Raman (in parentheses): w, weak; m, medium; s, strong; v, very.

[b]B3LYP/6–311G* calculations.

[c]From scaled quantum mechanics force field.

Table 5. Natural internal (local symmetry) coordinates for $(CF_3)_2Se$.

Definition (according to Fig. 1)	Description[a]
A	
S_1 = 2d (1-2) – d (1-3) – d (1-4) + 2d (6-7) – d (6-9) – d (6-8)	ν (CF_3) antisymm.
S_2 = d (1-3) – d (1-4) + d (6-9) – d (6-8)	ν (CF_3) antisymm.
S_3 = d (1-2) + d (1-3) + d (1-4) + d (6-7) + d (6-9) + d (6-8)	ν (CF_3) symm.
S_4 = α (2-1-3) + α (2-1-4) + α (3-1-4) – β (2-1-5) – β (3-1-5) – β (4-1-5) + α (9-6-7) + α (9-6-8) + α (7-6-8) – β (9-6-5) – β (7-6-5) – β (8-6-5)	δ (CF_3) symm.
S_5 = 2α (3-1-4) – α (2-1-3) – α (2-1-4) + 2α (9-6-8) – α (9-6-7) – α (7-6-8)	δ (CF_3) antisymm.
S_6 = α (2-1-3) – α (2-1-4) + α (9-6-7) – α (7-6-8)	δ (CF_3) antisymm.
S_7 = t (1-5) + t (6-5)	ν (C–Se)
S_8 = 2β (2-1-5) – β (3-1-5) – β (4-1-5) + 2β (7-6-5) – β (9-6-5) – β (8-6-5)	ρ (CF_3)
S_9 = β (3-1-5) – β (4-1-5) + β (9-6-5) – β (8-6-5)	ρ (CF_3)
S_{10} = δ (1-5-6)	δ (CSeC)
S_{11} = Σ τ [F_i-C_1-Se_5-C_6] + Σ τ [F_i-C_6-Se_5-C_1]	Torsion (CF_3)
B	
S_{12} = d (1-3) – d (1-4) – d (6-9) + d (6-8)	ν (CF_3) antisymm.
S_{13} = 2d (1-2) – d (1-3) – d (1-4) – 2d (6-7) + d (6-9) + d (6-8)	ν (CF_3) antisymm.
S_{14} = d (1-2) + d (1-3) + d (1-4) – d (6-7) – d (6-9) – d (6-8)	ν (CF_3) symm.
S_{15} = α (2-1-3) + α (2-1-4) + α (3-1-4) – β (2-1-5) – β (3-1-5) – β (4-1-5) – α (9-6-7) – α (9-6-8) – α (7-6-8) + β (9-6-5) + β (7-6-5) + β (8-6-5)	δ (CF_3) symm.
S_{16} = 2α (3-1-4) – α (2-1-3) – α (2-1-4) – 2α (9-6-8) + α (9-6-7) + α (7-6-8)	δ (CF_3) antisymm.
S_{17} = α (2-1-3) – α (2-1-4)– α (9-6-7) + α (7-6-8)	δ (CF_3) antisymm.
S_{18} = t (1-5) – t (6–5)	ν (C–Se)
S_{19} = β (3-1-5) – β (4-1-5) – β (9-6-5) + β (8-6-5)	ρ (CF_3)
S_{20} = 2β (2-1-5) – β (3-1-5)– β (4-1-5) – 2β (7-6-5) + β (9-6-5) + β (8-6-5)	ρ (CF_3)
S_{21} = Σ τ [F_i-C_1-Se_5-C_6] – Σ τ [F_i-C_6-Se_5-C_1]	Torsion (CF_3)

[a]ν, stretching; δ, deformation; ρ, rocking.

Table 6. Natural internal (local symmetry) coordinates for $(CF_3Se)_2$.

Definition (according to Fig. 1)	Description[a]
A	
S_1 = 2d (1-7) – d (1-5) – d (1-6) + 2d (4-9) – d (4-10) – d (4-8)	ν (CF_3) antisymm.
S_2 = d (1-5) – d (1-6) + d (4-10) – d (4-8)	ν (CF_3) antisymm.
S_3 = d (1-7) + d (1-5) + d (1-6) + d (4-9) + d (4-10) + d (4-8)	ν (CF_3) symm.
S_4 = α (5-1-7) + α (5-1-6) + α (6-1-7) – β (5-1-2) – β (6-1-2) – β (7-1-2) + α (10-4-8) + α (10-4-9) + α (8-4-9) – β (10-4-3) – β (8-4-3) – β (9-4-3)	δ (CF_3) symm.
S_5 = 2α (5-1-6) – α (5-1-7) – α (6-1-7) + 2α (10-4-8) – α (10-4-9) – α (8-4-9)	δ (CF_3) antisymm.
S_6 = α (5-1-7) – α (6-1-7) + α (10-4-9) – α (8-4-9)	δ (CF_3) antisymm.
S_7 = t (1-2) + t (4-3)	ν (C–Se)
S_8 = r (2-3)	ν (Se–Se)
S_9 = 2β (7-1-2) – β (6-1-2) – β (5-1-2) + 2β (9-4-3) – β (8-4-3) – β (10-4-3)	ρ (CF_3)
S_{10} = β (6-1-2) – β (5-1-2) + β (8-4-3) – β (10-4-3)	ρ (CF_3)
S_{11} = δ (1-2-3) + δ (2-3-4)	δ (CSeSe)
S_{12} = τ (1-2-3-4)	Torsion skeletal
S_{13} = Σ τ [F_i-C_1-Se_2-C_3] + Σ τ [F_i-C_4-Se_3-C_2]	Torsion (CF_3)
B	
S_{14} = 2d (1-7) – d (1-5) – d (1-6) – 2d (4-9) + d (4-10) + d (4-8)	ν (CF_3) antisymm.
S_{15} = d (1-5) – d (1-6) – d (4-10) + d (4-8)	ν (CF_3) antisymm.
S_{16} = d (1-7) + d (1-5) + d (1-6) – d (4-9) – d (4-10) – d (4-8)	ν (CF_3) symm.
S_{17} = α (5-1-7) + α (5-1-6) + α (6-1-7) – β (5-1-2) – β (6-1-2) – β (7-1-2) – α (10-4-8) – α (10-4-9) – α (8-4-9) + β (10-4-3) + β (8-4-3) + β (9-4-3)	δ (CF_3) symm.
S_{18} = 2α (5-1-6) – α (5-1-7) – α (6-1-7) – 2α (10-4-8) + α (10-4-9) + α (8-4-9)	δ (CF_3) antisymm.
S_{19} = α (5-1-7) – α (6-1-7) – α (10-4-9) + α (8-4-9)	δ (CF_3) antisymm.
S_{20} = t (1-2) – t (4-3)	ν (C–Se)
S_{21} = 2β (7-1-2) – β (6-1-2) – β (5-1-2) – 2β (9-4-3) + β (8-4-3) + β (10-4-3)	ρ (CF_3)
S_{22} = β (6-1-2) – β (5-1-2) – β (8-4-3) + β (10-4-3)	ρ (CF_3)
S_{23} = δ (1-2-3) – δ (2-3-4)	δ (CSeSe)
S_{24} = Σ τ [F_i-C_1-Se_2-C_3] – Σ τ [F_i-C_4-Se_3-C_2]	Torsion (CF_3)

[a]ν, stretching; δ, deformation; ρ, rocking.

Table 7. Scaling factors for the force field of the molecules $(CF_3)_2Se$ and $(CF_3Se)_2$.

Coordinates[a]	$(CF_3)_2Se$	$(CF_3Se)_2$
ν (CF_3), δ (CF_3), Torsion (CF_3)	1.009	1.008
δ (CSeC), ν (C–Se)	1.136	1.115
δ (CSeSe), ν (Se–Se)	—	1.115
ρ (CF_3)	0.935	0.907

[a]ν, stretching; δ, deformation; ρ, rocking.

Table 8. Internal force constants for $(CF_3)_2Se$, $(CF_3Se)_2$, and the related molecules CF_3SeX.

	This work		(2)	
Force constant[a]	$(CF_3)_2Se$	$(CF_3Se)_2$	CF_3SeCN	CF_3SeCH_3
Bond stretchings				
f (C–F)[b]	6.047	5.982	6.167	5.841
f (C–Se)	2.730	2.502	2.583	2.742
f (Se–Se)	—	2.273		
f (C–F/C–F)[b]	0.824	0.809	0.802	0.789
f (C–F/C–Se)	0.390	0.338	0.390	0.362
Deformations				
f (F–C–F)[b]	1.287	1.278	1.269	1.304
f (F–C–Se)[b]	0.818	0.788	0.854	0.874
f (C–Se–Se)	—	1.064		
f (C–Se–C)	1.254	—	0.973	0.916

[a]Units are mdyn $Å^{-1}$ for stretchings and stretch–stretch interactions and mdyn Å rad^{-2} for angular deformations.
[b]Mean values.

CYT (Agencia Nacional de Promoción Científica y Tecnológica, BID 1728/OC-AR, PICT 11127), UNLP (Universidad Nacional de La Plata), and CIUNT (Consejo de Investigaciones de la Universidad Nacional de Tucumán). We also thank Dr. G. Arteca, Laurentian University, Canada, for providing access to some published articles.

References

(1) Fernández, L. E.; Varetti, E. L. *J. Mol. Struct. (Theochem.)* **2006**, *761*, 217. doi:10.1016/j.theochem.2005.12.016.
(2) Fernández, L. E.; Varetti, E. L. *Can. J. Chem.* **2006**, *84*, 1626. doi:10.1139/V06-171.
(3) Dale, J. W.; Emeleus, H. J.; Haszeldine, R. N. *J. Chem. Soc.* **1958**, 2939. doi:10.1039/jr9580002939.
(4) Emeléus, H. J.; Dunn, M. J. *J. Inorg. Nucl. Chem.* **1965**, *27*, 752. doi:10.1016/0022-1902(65)80289-5.
(5) Marsden, C. J.; Sheldrick, G. M. *J. Mol. Struct.* **1971**, *10*, 405. doi:10.1016/0022-2860(71)85063-9.
(6) Marsden, C. J.; Sheldrick, G. M. *J. Mol. Struct.* **1971**, *10*, 419. doi:10.1016/0022-2860(71)85065-2.
(7) Marsden, C. J. *J. Fluor. Chem.* **1975**, *5*, 401. doi:10.1016/S0022-1139(00)82499-9.
(8) Clase, H. J.; Wahi, P. K.; Bomford, D. R. L. *Can. J. Spectros.* **1977**, *22*, 92.
(9) Pulay, P.; Fogarasi, G.; Pongor, G.; Boggs, J. E.; Vargha, A. *J. Am. Chem. Soc.* **1983**, *105*, 7037. doi:10.1021/ja00362a005.
(10) Becke, A. D. *J. Chem. Phys.* **1993**, *98*, 5648. doi:10.1063/1.464913.
(11) Lee, C.; Yang, W.; Parr, R. G. *Phys. Rev.* **1988**, *B37*, 785.
(12) Frisch, M. J.; Trucks, G. W.; Schlegel, H. B.; Scuseria, G. E.; Robb, M. A.; Cheeseman, J. R.; Montgomery, J. A., Jr.; Vreven, T.; Kudin, K. N.; Burant, J. C.; Millam, J. M.; Iyengar, S. S.; Tomasi, J.; Barone, V.; Mennucci, B.; Cossi, M.; Scalmani, G.; Rega, N.; Petersson, G. A.; Nakatsuji, H.; Hada, M.; Ehara, M.; Toyota, K.; Fukuda, R.; Hasegawa, J.; Ishida, M.; Nakajima, T.; Honda, Y.; Kitao, O.; Nakai, H.; Klene, M.; Li, X.; Knox, J. E.; Hratchian, H. P.; Cross, J. B.; Adamo, C.; Jaramillo, J.; Gomperts, R.; Stratmann, E.; Yazyev, O.; Austin, A. J.; Cammi, R.; Pomelli, C.; Ochterski, J. W.; Ayala, P. Y.; Morokuma, K.; Voth, G. A.; Salvador, P.; Dannenberg, J. J.; Zakrzewski, V. G.; Dapprich, S.; Daniels, A. D.; Strain, M. C.; Farkas, O.; Malick, D. K.; Rabuck, A. D.; Raghavachari, K.; Foresman, J. B.; Ortiz, J. V.; Cui, Q.; Baboul, A. G.; Clifford, S.; Cioslowski, J.; Stefanov, B. B.; Liu, G.; Liashenko, A.; Piskorz, P.; Komaromi, I.; Martin, R. L.; Fox, D. J.; Keith, T.; Al-Laham, M. A.; Peng, C. Y.; Nanayakkara, A.; Challacombe, M.; Gill, P. M. W.; Johnson, B.; Chen, W.; Wong, M. W.; Gonzalez, C.; Pople, J. A. *GAUSSIAN 03 [computer program]*; Gaussian, Inc.: Pittsburgh, Penn., USA, 2003.
(13) Fogarasi, G.; Zhou, X.; Taylor, P. W.; Pulay, P. *J. Am. Chem. Soc.* **1992**, *114*, 8191. doi:10.1021/ja00047a032.
(14) Wilson, E. B.; Decius, J. C.; Cross, P. C. *Molecular vibrations*; MacGraw-Hill: New York, USA, 1955.
(15) Collier, W. B. Program FCARTP (QCPE #631). Department of Chemistry. Oral Roberts University, Tulsa, OK. 1992.
(16) Francisco, J. S. *Spectrochim. Acta [A]*, **1984**, *40*, 923.
(17) Kalincsák, F.; Pongor, G. *Spectrochim. Acta [A]*, **2002**, *58*, 999. doi:10.1016/S1386-1425(01)00572-8.
(18) Fernández, L. E.; Ben Altabef, A.; Varetti, E. L. *J. Mol. Struct.* **2002**, *612*, 1. doi:10.1016/S0022-2860(01)00940-1.

Morphology of potassium chloride in aqueous and in formamide solution — An experimental and computational investigation

Ajeet Singh, T. Selvamani, Indrajit Mukhopadhyay, and Bishwajit Ganguly

Abstract: The morphology of potassium chloride grown in pure water as well as in water–formamide solution was investigated. Surface morphology of the crystals was examined by using scanning electron microscopy. It has been observed that the potassium chloride crystals are largely grown with {100} face at different concentrations in pure water, which contradicts earlier reports. Experimental results show that the potassium chloride crystals grown in formamide are also cubic in nature. However, it has been found that the sodium chloride crystals are octahedrons under similar conditions. The difference in the morphological behavior of these two alkali halides with formamide was investigated with computational methods. The calculated results revealed that formamide is largely preferred to adsorb on the {111} surface of NaCl, which can lead to octahedrons. However, the energetics is not substantially different for the adsorption of additives to the important surfaces of potassium chloride and results in the formation of a competing stable {100} surface.

Key words: density functional theory (DFT), crystal morphology, growth from solution, additive.

Résumé : On a étudié la morphologie du chlorure de potassium qui a cristallisé dans de l'eau pure ainsi que d'autre qui a cristallisé à partir d'une solution d'eau et de formamide. On a examiné la morphologie de la surface des cristaux à l'aide de la microscopie électronique à balayage. On a observé que les cristaux de chlorure de potassium croissent principalement avec la face {110} à diverses concentrations dans de l'eau pure et que cette observation est en contradiction avec des rapports antérieurs. Les résultats expérimentaux montrent que les cristaux de chlorure de potassium qui ont cru dans le formamide sont aussi de nature cubique. Toutefois, on a trouvé que, dans les mêmes conditions, les cristaux de chlorure de sodium sont octaédriques. On a étudié la différence de comportement morphologique de ces deux halogénures alcalins avec le formamide en faisant appel à des calculs théoriques. Les résultats calculés révèlent que le formamide s'adsorbe d'une façon préférentielle marquée sur la surface {111} du NaCl qui conduit à la formation d'octaèdres. Toutefois, les niveaux d'énergies impliqués ne sont pas très différents pour l'adsorption d'additifs sur les surfaces importantes du chlorure de potassium, ce qui conduit à la formation d'une surface {100} compétitive stable.

Mots-clés : théorie de la fonctionne de densité, morphologie cristalline, croissance à partir d'une solution, additif.

[Traduit par la Rédaction]

Introduction

The nucleation, growth, and morphology of crystals can be significantly altered by the presence of low concentrations of impurities. These impurities may be reaction by-products or impurities present in the reactants or they may be additives purposely added to alter the crystallization process. The effect of impurities and additives on crystallization are summarized in some recent reviews.[1,2] Additives can reduce crystal growth rate and alter morphology by binding to crystal faces and interfering with propagation steps.[3,4] The control of crystal morphology by use of additives is a subject of great interest, which has been studied experimentally and theoretically employing molecular modeling techniques.[5–7] The crystallization of common salt has been a subject of many studies of crystal growth in aqueous solution.[8,9] In particular, the influence of additives on its crystal habit has received considerable attention. Rome de 1'Isle[10] showed that octahedrons instead of normal cubes are formed, if rocksalt is grown in the presence of urine. Many authors have since reported the cube-octahedron shape transition under various experimental conditions. In this regard, earlier work reported that octahedron crystals can also be obtained from pure water solution.[11–13] It was observed that crystals with rocksalt structure were octahedrons, if they were grown at high supersaturation conditions. On the other hand, if they were grown at low supersaturation, cubic crystals were formed. Recently, Enckevort and co-workers[14] have shown that the {111} face of sodium chloride, which has the appearance of octahedrons at high

Received 13 April 2008. Accepted 21 November 2008. Published on the NRC Research Press Web site at canjchem.nrc.ca on 21 February 2009.

A. Singh, T. Selvamani, I. Mukhopadhyay,[1] and B. Ganguly.[2] Central Salt & Marine Chemicals Research Institute (CSIR), Bhavnagar-364002, Gujarat, India.

[1]Corresponding author (e-mail: indrajit@csmcri.org).
[2]Corresponding author (e-mail: ganguly@csmcri.org).

Scheme 1. Progressive change of an alkali halide crystal from cube to octahedron.

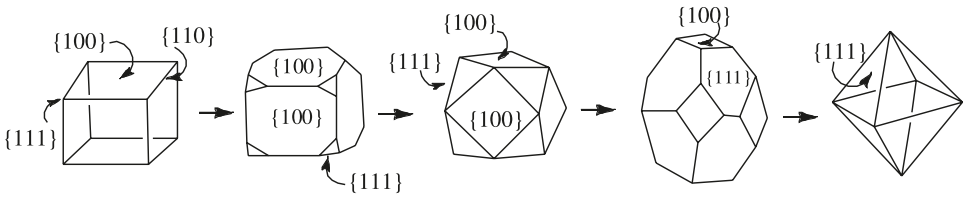

supersaturation, is most likely an artifact and in aqueous solutions only the {100} faces are stable. In the experiment of Bienfait et al.,[13] microcrystals of KCl grown from solutions of relatively low supersaturations were mainly cubic. However, when the supersaturation ratio defined by $\beta = c/c_o$ (where c and c_o are the actual and equilibrium solution concentrations, respectively) was greater than the critical supersaturation ratio, $\beta_c = 1.25$ at 293.15 K, microcrystals were cubo-octahedral, and with a further increase in c they were octahedral.[2,13] The conclusion of cubic crystals in supersaturated solutions for sodium chloride being contrary to earlier reports[11–14] prompted us to examine the results reported for the morphology of KCl crystals grown at different concentrations. We have extended the morphological study of KCl with impurity as well. The morphology of KCl crystals has been examined in formamide–water solutions. Earlier reports on the growth of NaCl crystals from water–formamide solutions showed that the crystals were octahedrons in nature.[14,15] Therefore, it is of interest to see whether the similar morphology of KCl crystals can be obtained in formamide–water solutions. Recently, there have been some efforts to crystallize KCl in carbon nanotubes.[16] A schematic diagram for the change in the shape of an alkali halide crystal from cubic to octahedron was shown in Scheme 1.

The observed changes in the morphology of NaCl crystals with additives were rationalized on the basis of charge distributions and strong interactions between the more exposed carbonyl oxygen of amides like formamide and urea with the sodium ions of the {111} surface of sodium chloride.[15] In earlier observations, Speidel[17], Cabrera and Vermilyea,[18] and Bunn[19] have also considered that an additive strongly interacts with certain crystal faces to influence the morphology of the crystal. Bunn[19] explained that the habit modification of NaCl by urea in aqueous solutions is due to adsorption of the impurity on certain crystal faces during crystal growth. Though there are many proposals reported to explain the habit of alkali halides, the studies towards the importance of interactions at the molecular level are limited. There are some efforts to understand the mechanism of growth kinetics and the bulk crystal habit with molecular modeling techniques in the light of additive-step specific interactions in calcite and calcium oxalate crystals.[20–22] The results emphasized the mechanism underlying crystal modification through organic molecules by considering both stereochemical recognition and the effects of binding on the interfacial energies of the growing crystal. These studies shed light on the possible interactions of additives with the surfaces of crystals and the reasons for the growth of specific faces. Therefore, it would be interesting to investigate the influence of formamide on shaping the crystals of sodium chloride and potassium chloride using computational techniques. We report the density functional study on the interaction of formamide with the relevant surfaces of sodium chloride and potassium chloride to understand the difference in the morphology of these two alkali halides in the presence of formamide as an impurity.

Experimental

Materials

The NaCl suprapur (99.99%) and KCl suprapur (99.99%) were obtained from Merck and formamide was obtained from Sigma-Aldrich Chemicals. All chemicals were used without any further purification. For crystallization, mili-Q water was used.

Methods

Batch crystallization

The test samples of KCl and NaCl crystals were obtained by crystallizing them from aqueous solution at different levels of supersaturations under controlled temperature (25 °C ± 2 °C), pressure (atmospheric), and relative humidity (50% ± 10%) conditions. The crystallizations were carried out in glass beakers of 20 mL capacity in the laboratory for facilitating free evaporation. The effect of pH on the crystallization process was studied by controlling the pH of the supersaturated solution during the initial phase of the crystallization process to two limiting values, 3 and 10, by using suitable acid/base. In this study, the supersaturation (β) has been defined as the ratio of the actual concentration to the equilibrium concentration of the halides, where, the equilibrium concentration of NaCl and KCl are 6.14 mol/L and 4.17 mol/L, respectively, at room temperature.[23] For batch crystallization, saturated alkali halide solutions of desired concentration were made using mili-Q water. Potassium chloride crystallizations were carried out with aqueous solution and formamide solution. Different batch crystallization were carried out: (*a*) In the first crystallization experiment, 5 mL of 4.2 mol/L KCl solution were taken in the glass beaker and kept for crystallization. (*b*) In the second batch, the concentration of KCl was increased to 5.5 mol/L (5 mL) and was taken in a glass beaker for crystallization. (*c*) In the third batch, the concentration of KCl was further increased up to 5.8 mol/L (5 mL) and was taken in a glass beaker for crystallization. In this third batch, the dissolution of solute was carried out by heating the mixture temporarily to an elevated temperature (~50 °C). Once the clear solution formed it was decanted to a glass beaker and 5 mL of the solution was taken in another glass beaker for crystallization.

To examine the influence of formamide on the morphology of KCl, separate sets of crystallization experiments were carried out at different concentrations: (*d*) In a beaker,

Table 1. Experimental details showing the effect of halide concentration, additive concentration, and pH on the crystallite size and morphology of alkali halides.

Serial No.	Conc. of the halides	Formamide conc. (wt%)	pH	Crystallite size (μm)	Remarks
a	4.2 mol/L KCl	—	7.0	1.7	Cubic
b	5.5 mol/L KCl	—	7.0	1.8	Cubic
c	5.8 mol/L KCl	—	7.0	1.8	Cubic
d	4.2 mol/L KCl	20	7.0	0.9	Cubic
e	5.5 mol/L KCl	20	7.0	0.7	Cubic
f	5.8 mol/L KCl	20	7.0	0.7	Cubic
g	6.14 mol/L NaCl	20	7.0	0.23	Octahedron

5 mL of 4.2 mol/L KCl solution was taken and 20 wt% (with respect to the net weight of the solute KCl) formamide solution was added. This impurity content KCl solution was kept for crystallization. (*e*) The crystallization of KCl at 5.5 mol/L with 20 wt% of formamide was also kept for crystallization. (*f*) The formamide impurity (20 wt%) was added to increase the concentration of the KCl (5.8 mol/L) and kept for crystallization. (*g*) Finally, for a comparative study, crystals were grown from a saturated 6.14 mol/L NaCl solution contaminated with 20 wt% formamide (with respect to the solute) under similar conditions.[14,15] The study was also performed with other concentrations of formamide, such as 5, 10, 15, 25, and 30 wt% (*w*/*w*) for the above mentioned (i.e., 4.2, 5.5, and 5.8 mol/L) concentrations of KCl (Fig. S3 in the Supplementary data). The representative formamide concentrations are shown for KCl and NaCl in Table 1.

Instrumentation

The surface structure of the grown crystals was observed by scanning electron microscopy (SEM). The samples for the SEM studies were prepared on cleaned and mirror-polished brass stubs by spreading 100 μL of the dispersion and evaporating the solvent in air. A LEO SEM model 1430 VP was used for this purpose. The crystallographic planes were further characterized by recording the X-ray powder diffraction (XRPD) pattern of finely grinded homogeneous alkali halides using Cu Kα radiation (λ = 1.540 56 Å). Optical microscopic images were taken by normal light microscopy (AXIO IMAGER, Carl Zeiss). The statistical distribution of the crystals was observed in the crystallization bath (10 mL volumetric glass beaker). Individual crystals were examined by putting them on glass slides.

Computational

The interaction study of formamide with three-dimensional (3D) slabs of sodium chloride and potassium chloride has been performed employing the density functional program DMol^3 in Material Studio (version 4.1) of Accelrys Inc.; the physical wave functions are expanded in terms of numerical basis sets.[24–26] We used DND double numerical basis set, which is comparable to the 6-31G* basis set. Local spin density approximation with Perdew–Wang correlational (LDA/PWC) and generalized gradient corrected functional (GGA/PW91) has been employed for the adsorption study of formamide on the {100}, {110}, and {111} surface of sodium chloride.[24–28] 3D-slabs of sodium chloride and potassium chloride [{100}, {110}, and {111}] were generated employing periodic boundary conditions. The Perdew–Wang correlational (LDA/PWC) functional with DND basis set was used to optimize the {100} NaCl slab structure. The optimized {100} slab contains seven layers of sodium chloride (112 ions) with a vaccum thickness of 12 Å. The corresponding k-points used were medium and the k-point separations were 0.051/Å. For {110} and {111}, the optimized slabs contain eight layers of sodium and chloride ions (128 ions) with a vaccum thickness of 18 and 14 Å, respectively. For KCl, the {100} slab was optimized with Perdew–Wang correlational (LDA/PWC) functional contains seven layers of KCl (112 ions) and a vaccum thickness of 12 Å, however, {110} and {111} contain eight and seven layers with a vaccum thickness of 12 Å, respectively. To estimate the relaxation effects on additive interaction energies, the top first and second layers of slabs were relaxed, while keeping the bottom layers fixed at a bulk position. The tolerances of energy, gradient, and displacement convergence were 2×10^{-5} Ha, 4×10^{-3} Ha/Å, and 5×10^{-3} Å, respectively. For additive and crystal surface interactions, formamide has been placed at the midpoint of the NaCl and KCl surface in each case and optimized at the LDA/PWC/DND level of theory. The maximum gradient for most of the optimized structures was less than 2×10^{-3} Ha/Å. Adsorption energies were computed by subtracting the energies of the gas and solvent phase additive molecules and surface from the energy of the adsorption system as shown in eq. [1].

$$[1] \qquad E_{ad} = E(\text{additive/surface}) - E(\text{additive}) - E(\text{surface})$$

To examine the effective interaction of formamide with specific surfaces of sodium and potassium chloride, the approach similar to surface docking developed to predict the influence of additives on the crystal morphology was employed.[29–37] The basis of this approach is to analyze the effect of additives on the individual crystal faces, which are cleaved from a crystal. If the additive has a strong interaction on a specific face, the growth of this face will be slower, as a result, the other fast growing surfaces will disappear and eventually, the slow growing surface will control the morphology. In this way, the additive influences the morphology of crystals. The stable {100} surfaces of sodium and potassium chloride were modeled with an alternating arrangement of cations and anions. However, the {111} polar surfaces have a very high divergent electrostatic energy, which makes them theoretically highly unstable.[38–40] In the {111} polar surface, the bulk structure consists of alternating cations and anionic sheets stacked along the <111> directions. It has been shown in earlier studies that the adsorption of additives would be preferred with the positive

ions on the top of the surface of alkali halides.[14,15] Therefore, in the present study, the polar {111} surface has been modeled with Na^+ and K^+ ions on the top of the surface. The {110} surface was modeled with alternating rows of cations and anions in each case. It is important to note that the morphological change in the alkali halide crystals generally takes place in the presence of a higher concentration of organic additives.[14,15] Davey and Mullin[41] have rationalized the theoretical implications of adsorption at sites in relation to experimental observations. A very low impurity level affected the kink site adsorption, whereas, more impurity is required to adsorb to the step sites, while a much higher level may be required if adsorption only occurs on a ledge or face site.[2]

Results and discussion

Experimental observations

In the experiment of Bienfait et al.[13] with crystallization of alkali halides from aqueous solutions it was observed that the geometrical forms of microcrystals depend on solution concentration. KCl crystals grown under supersaturated conditions were cubo-octahedrons or octahedrons. These experimental results were further corroborated by Polak and Sangwal[42] in their theoretical study. Experimental results on crystallization contradicts with their reports as KCl crystals grown from supersaturated solution of KCl at a concentration, c, of 4.2 mol/L in mili-Q water were cubic (Table 1). The scanning electron microscope image of the grown KCl crystals is shown in Fig. 1. This observation is similar to that reported by Bienfait et al.[13] in their study. At a concentration of $c > 5.3$ mol/L, it was reported that the KCl crystals grown in pure water were octahedrons.[13] To examine that, we have performed the experiments at concentration c = 5.5 mol/L in pure water (Table 1). The crystals' appearance under this condition were cubic in contrast to the octahedrons reported (Fig. 2*a*). Further, the KCl crystals grown at an even higher concentration, c = 5.8 mol/L, showed the formation of cubic crystals (Fig. 2*b* and Table 1) and we have not observed the island formation as reported by Bienfait et al.[13] at this concentration. However, the crystals were found to have a lot of defects, such as holes and steps on the surface.

To further confirm the predominant planes in the resulting crystals, we have examined these crystals by XRPD technique. The powder XRD pattern of the KCl crystals, grown from its aqueous solution (concentration of 5.5 mol/L) at room temperature is shown in Fig. 3. The pattern clearly indicates preferential growth of the {100} planes with normal FCC unit cell. The relative ratio of the intensity of {111} to {100} planes is found to be 0.1. We have also performed the growth of KCl crystals at different pH conditions. The concentration of KCl solution was kept at $c \sim 4.2$ mol/L. Under acidic and basic pH 3 and 10, adjusted before initiation of crystallization, KCl crystals were cubic with {100} planes (Fig. S1 in the Supplementary data). Our observation of KCl crystals grown from aqueous solution distinctively shows that, independent of saturation conditions, {100} faces are the only faces that appear. We did not observe the appearance of octahedral faces at the mentioned concentration in the literature. In an earlier report, the experiments carried out with sodium chloride in aqueous solution also showed that the solvent does not work as a habit modifier for NaCl.[15] The earlier claims of octahedral NaCl growth suffered the problem of cubes resting on the {111} face.[15] Such claims were based on the optical microscopic image of the crystals grown in aqueous solutions. These visual disparities were overcome by using SEM in the present study. The three-dimensional image generated with SEM clearly showed the morphology of NaCl and KCl crystals grown in pure water. Figure 4 represents the SEM image of KCl crystals grown in formamide–water solution. In this study, the concentration of KCl solution was varied from c = 4.2 mol/L to 5.8 mol/L. The KCl crystals at 4.2 mol/L grown in the presence of 20 wt% formamide were cubic in nature (Table 1). Some of the grown KCl crystals appeared to be hollowed and broken. The contours of the holes have steps descending from the sides of the cube (Fig. 4*b*).

Continuing the similar study with a KCl saturation composition of c = 5.5 and 5.8 mol/L, we have found the growth of cubic crystals from a bath contaminated with formamide solution (Table 1). The crystals predominantly exhibited the growth of {100} planes (Fig. 5). The variation in concentrations of formamide from 5 to 30 wt% (*w*/*w*) does not show any change in the habit of potassium chloride (Fig. S3 in the Supplementary data, Table 1). These results suggest that the habit remains unaffected, even unchanged, even in the presence of formamide–water solutions. For comparison, we have performed the similar experiment with sodium chloride crystals in formamide–water solutions. The NaCl crystals grown in the presence of 20 wt% (*w*/*w*) formamide solution

Fig. 1. Scanning electron microscopy (SEM) images of KCl crystals obtained from a 4.2 mol/L solution in pure water.

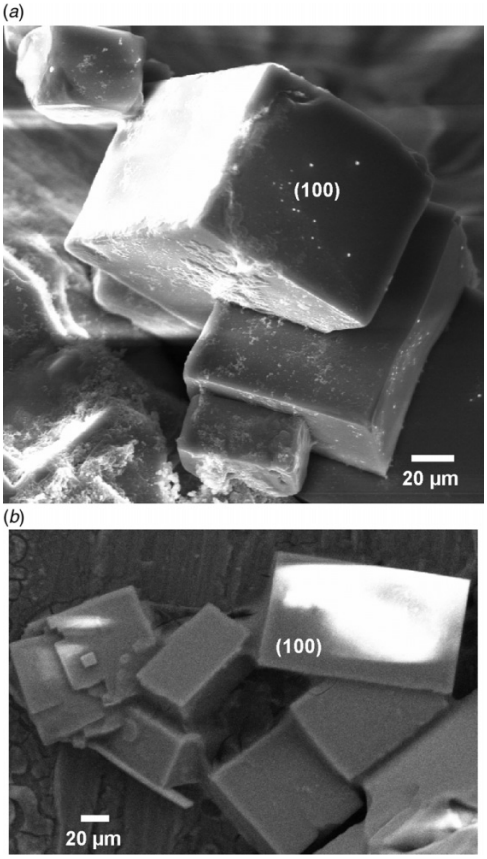

Fig. 2. Scanning electron microscopy (SEM) images of KCl crystals obtained from 5.5 and 5.8 mol/L solutions in pure water.

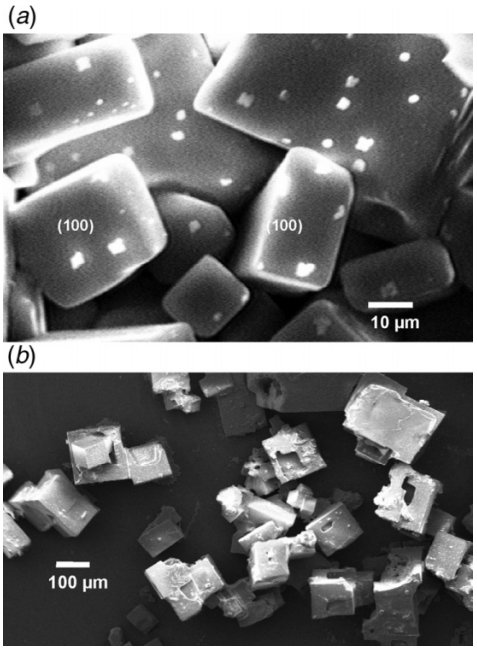

Fig. 3. X-ray powder diffraction (XRPD) pattern of homogeneously grinded KCl crystals obtained by crystallization from aqueous solution.

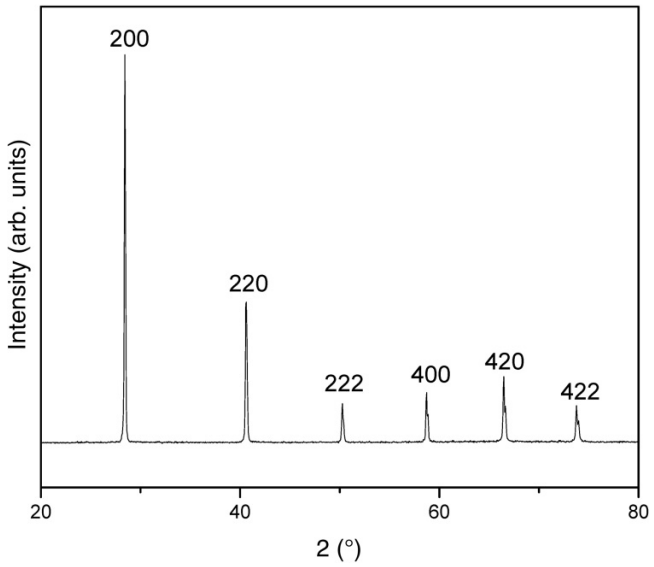

were octahedron in nature. The appearance of the {111} face is visible in the crystals of NaCl (Figs. 6*a* and 6*b*). This observation is in agreement with the earlier reports.[10,14,15]

We have further established the planes of the growing crystals for NaCl and KCl in the presence of formamide by XRPD. Figure 7 shows that both the crystals grown from a formamide contaminated solution at a concentration of 5.5 mol/L have FCC unit cell. However, the ratio of the intensity of the {111} to {100} planes for KCl grown from formamide solution is 0.05 where as the same ratio for NaCl is 0.1, which is enhanced nearly by an order of magnitude from the corresponding XRPD pattern of the NaCl

Fig. 4. Scanning electron microscopy (SEM) images of 4.2 mol/L KCl crystals grown in 20 wt% formamide–water solutions.

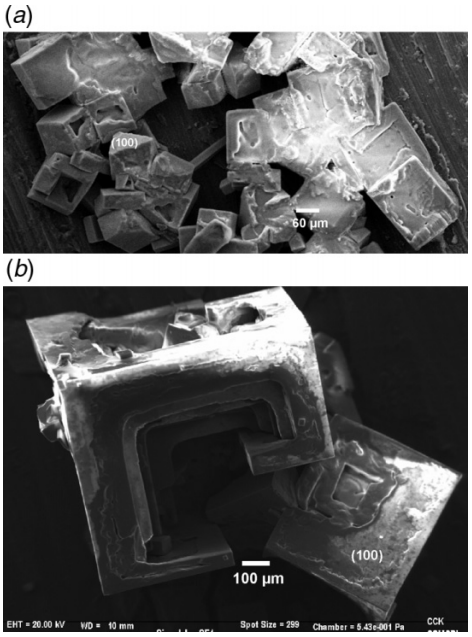

Fig. 5. Scanning electron microscopy (SEM) images of KCl crystals obtained from 5.5 and 5.8 mol/L solutions in 20 wt% formamide–water solutions.

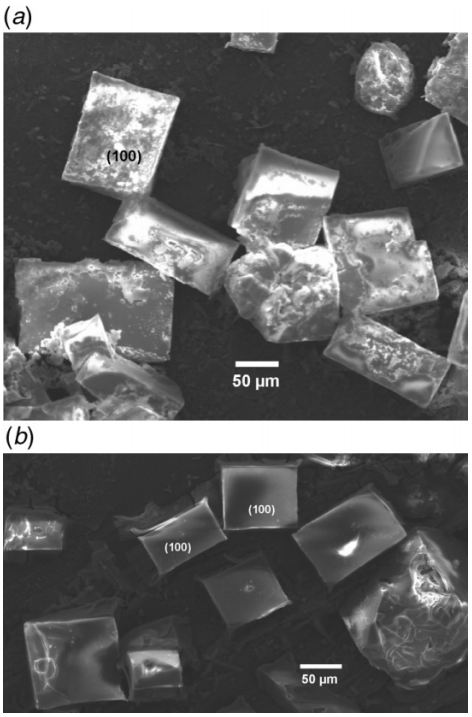

crystals obtained from NaCl aqueous solution. This clearly supports the SEM results that the presence of formamide in KCl aqueous solution does not facilitate the growth of unstable surfaces like {110} and {111} planes. These results showed that the influence of formamide was more pronounced in the solutions of sodium chloride towards the change in morphology. Therefore, it appears that the effective interaction of formamide with the {111} surface of

Fig. 6. Scanning electron microscopy (SEM) images of NaCl crystals obtained from 6.14 mol/L NaCl crystals grown in 20 wt% formamide–water solutions.

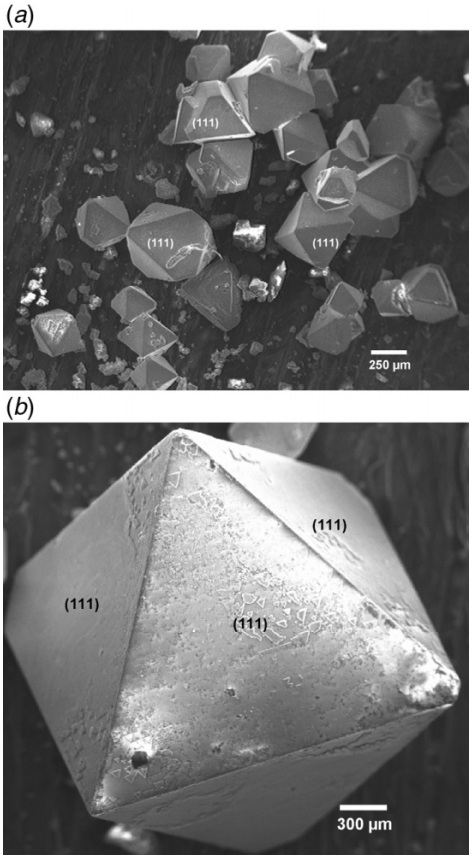

Fig. 7. X-ray powder diffraction (XRPD) patterns of the homogeneous halide crystals obtained by crystallization from (*a*) 20 wt% formamide contaminated 5.5 mol/L KCl solution and (*b*) 20 wt% formamide contaminated 6.14 mol/L NaCl solution. (*c*) 6.14 mol/L NaCl solution.

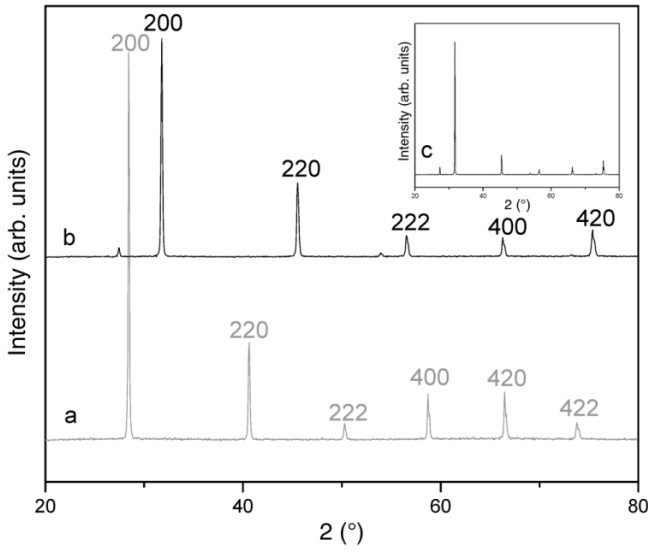

NaCl will be more dominant than that of the more stable {100} surface, as a result, the growth rate of the {111} surface will be slowed down, and this face will become relatively larger than the other faces.[2] Further, one can presume that the effect of an additive is not as pronounced for developing other planes [{110} and {111}] of KCl; as a result, no decisive influence can be seen for this alkali halide. Moreover, it can be noticed from Table 1 that the overall growth rate of the crystals decreases in the presence of formamide impurity.

Density functional theory (DFT) calculations

In the first set of calculations, formamide was fully optimized on the surfaces of sodium and potassium chloride keeping the surface ions fixed. In another set of calculations, the first and second layers of NaCl and KCl surfaces were relaxed, while optimizing formamide on the surfaces to examine the effect of relaxation on the binding energy of an additive at the respective surfaces.[30–36] In this case, the rest of the bottom layers were kept fixed in the bulk position. The interaction energies calculated for formamide with sodium and potassium chloride surfaces are shown in Table 2. The computed results suggest that the interaction of formamide is energetically preferred with the polar {111} surface by $\sim$13.0 kcal/mol than with the {100} surface of sodium chloride. The interaction of formamide with the {110} surface is weaker compared to the {111} surface of sodium chloride.

The amide functionality (-$CONH_2$) of formamide interacts with the {100} and {110} planes of sodium chloride (Figs. 8*a* and 8*b*), whereas, the carbonyl group of the additive interacts with the {111} surface of NaCl (Fig. 8*c*). Formamide fits in a similar fashion to the relaxed sodium chloride surfaces (Fig. S2 in the Supplementary data). The relaxation of layers does not seem to affect the trend of formamide interaction energies with NaCl surfaces (Table 2).

These results corroborate the earlier rationalizations[15,17] that the preferential adsorption of formamide on the {111} plane would reduce the growth of this plane of NaCl compared to the other {100} and {110} planes, consequently, octahedron crystals would form for sodium chloride. In the case of KCl, the interaction energies computed for formamide with a {100}, {110}, and {111} surface suggests that the {110} is slightly energetically preferred, $\sim$3.0 kcal/mol, over {100} and {111} surfaces (Table 2). Relaxation in the surfaces of KCl didn't show much perturbation in the layers and (or) in the geometry of the additive on the surface[30–37,43] (Fig. S2 in the Supplementary data). The amide functionality (-$CONH_2$) of formamide interacts with the {100} and {110} planes of potassium chloride (Figs. 8*d* and 8*e*), whereas, the carbonyl group of the additive interacts with the {111} surface of KCl (Fig. 8*f*). Other orientations of formamide with the {100} plane were also examined, which, however, were found to be higher in energy compared to the one shown in Fig. 8*a* (Table S1 in the Supplementary data). It is important to note that the mode of interaction of formamide with the {111} surface of NaCl and KCl is different (Fig. 8*c* and 8*f*). This presumably arises due to the difference in the distance of ions in the {111} lattice planes of NaCl and KCl. The distance between the neighboring potassium ions in the {111} plane is 4.426 Å, whereas, the corresponding distance for NaCl is 4.06 Å. Formamide maximizes the interaction while tilting on the {111} surface of KCl, whereas, the relatively smaller lattice distance does not allow

Table 2. Interaction energies calculated at the GGA/PW91/DND level using LDA/PWC/DND optimized geometries for formamide with {100}, {110}, and {111} surfaces of NaCl and KCl slab models in kcal/mol.

	NaCl			KCl		
Surface	{100}	{110}	{111}	{100}	{110}	{111}
Fixed layer	–15.0	–17.8	–28.4	–14.1	–17.6	–16.6
One layer relaxed	–15.5	–17.0	–28.7	–13.5	–18.9	–15.3
Two layers relaxed	–16.2	–19.4	–28.8	–14.4	–18.2	–15.5

Fig. 8. LDA/PWC/DND calculated geometries of formamide with {100}, {110}, and {111} surfaces of sodium chloride and potassium chloride in slab models (purple: sodium, green: chlorine, red: oxygen, blue: nitrogen, and white: hydrogen). (*a*) {100}NaCl:formamide; (*b*) {110}NaCl:formamide; (*c*) {111}NaCl:formamide; (*d*) {100}KCl:formamide; (*e*) {110}KCl:formamide; (*f*) {111} KCl:formamide.

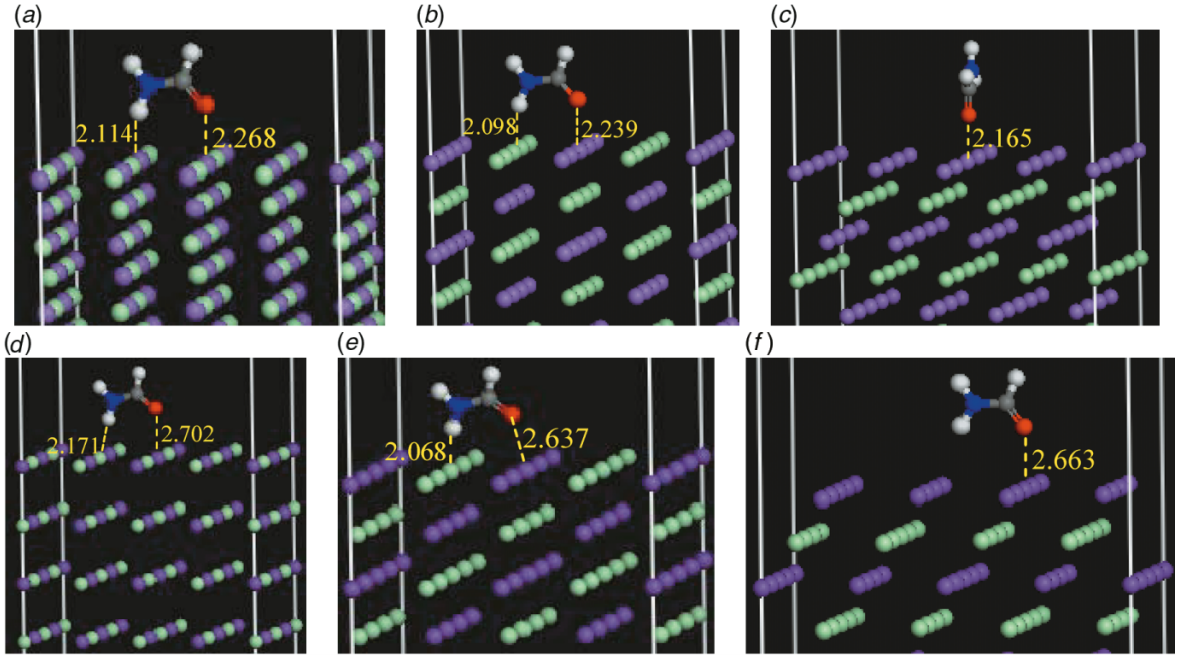

Table 3. Interaction energies calculated at GGA/PW91/DND using LDA/PWC/DND optimized geometries for one water molecule with {100}, {110}, and (111) surfaces of NaCl and KCl slab models in kcal/mol.

Surface	NaCl			KCl		
	{100}	{110}	{111}	{100}	{110}	{111}
GGA/PW91/DND	–13.1	–15.8	–15.7	–12.0	–16.0	–16.1

the additive to tilt on the {111} plane of NaCl. Attempts to achieve the interaction of formamide with the {111} surface of KCl similar to that of NaCl failed and converged to the orientation shown in Fig. 8*f*. The slight preference of formamide towards the {110} face of KCl was not observed in our experiments as the obtained KCl crystals were cubic. It appears that the small interaction energy difference between the planes of KCl with formamide is not sufficient to inhibit growing unstable faces and the competing stable {100} surface appears in the formamide solution.

It has been reported that the habit of alkali halides changes in an aqueous solution with impurities like formamide, hence the competing interaction of formamide with water molecules on these surfaces[44–49] can be important to govern the morphology, besides the effective interaction with additives. It is important to note that the water as a solvent does not influence the habit of alkali halides.[15] Therefore, it can be envisaged that if formamide interaction is stronger compared to water molecules with the unstable growing surfaces, such as {111} of these halides, then such interactions can retard the growth of that particular plane and hence can influence the habit.

We have investigated the competition between the water molecule and formamide by comparing the interaction energies with surfaces of NaCl and KCl. The interaction of a water molecule with different surfaces of NaCl and KCl is shown in Table 3. By comparing the interaction energies for water and formamide with NaCl surfaces, it appears that formamide binds more strongly to the {100}, {110}, and {111} surfaces than the water molecule (Tables 2 and 3). In particular, the interaction of formamide is significantly larger for the {111} NaCl surface compared to that of a water mole-

cule and suggests that the formation of octahedron crystals can take place for NaCl in formamide solution.[15] However, the energetic preferences were found to be comparable for formamide and water with KCl surfaces (Tables 2 and 3). Formamide may not be able to stabilize the {111} surface of KCl sufficiently, and hence, cannot lead to the change in morphology of this alkali halide.

Conclusion

A systematic study of the growth of potassium chloride crystals from pure water and formamide contaminated water at different concentrations and pH conditions was studied. Potassium chloride at c = 4.2 mol/L, only cubic crystals were found to grow from pure water as well as a 20 wt% formamide contaminated solution. At a concentration of $c >$ 5.3 mol/L of KCl (5.5 mol/L) in pure water, we have observed the growth of {100} planes in contrary to earlier reports. At an even higher concentration (5.8 mol/L), the cubic crystals were found with defects, holes and steps on the {100} planes. The effects of the pH of the crystallizing bath on the morphology of KCl crystals are not significant. The calculated results predicted the preferential interaction of formamide with {111} by ~13.0 kcal/mol compared to the stable {100} surface of sodium chloride and is in agreement with the formation of octahedron crystals. However, the interaction energies calculated for formamide with potassium chloride {110} and {111} surfaces are not substantially lower (~1–3 kcal/mol) compared to {100} to stabilize those unstable planes and that was reflected in the crystallization experiments. Further, the competing effect with water on the surfaces of these alkali halides suggest that formamide can displace the water molecules from the surface NaCl, however, this may not be possible with KCl surfaces.

Supplementary data

Supplementary data for this article are available on the journal Web site (canjchem.nrc.ca) or may be purchased from the Depository of Unpublished Data, Document Delivery, CISTI, National Research Council Canada, Ottawa, ON K1A 0R6, Canada. DUD 3879. For more information on obtaining material refer to cisti-icist.nrc-cnrc.gc.ca/cms/unpub_e.shtml.

Acknowledgements

We thank the Department of Science & Technology (DST), New Delhi, India for financial support. We thank the reviewers for their comments and suggestions that have helped us to improve the paper.

References

(1) Klug, D. L. In *Handbook of Industrial Crystallization;* Myerson, A. S., Ed.; Butterworth: Montvale, MA, 1993; p 65.
(2) Mullin, J. W. *Crystallization,* 3rd ed.; Butterworth: London, 1993; p 238.
(3) Doremus, R. H.; Roberts, B. W.; Turnbull, D. *Growth and Perfection of Crystals;* Wiley: New York, 1958; p 393.
(4) van der Eerden, J. P.; Muller-Krumbhaar, H. *Electrochim. Acta* **1986**, *31*, 1007. doi:10.1016/0013-4686(86)80016-0.
(5) Chen, B. D.; Garside, J.; Davey, R. J.; Maginn, S. J.; Matsuoka, M. *J. Phys. Chem.* **1994**, *98*, 3215. doi:10.1021/j100063a027.
(6) Meenan, P.; Roberts, R. J.; Sherwood, J. N. *Powder Technol.* **1991**, *65*, 219. doi:10.1016/0032-5910(91)80184-K.
(7) Geertman, R. M.; van der Heijden, A. E. D. M. *J. Cryst. Growth.* **1992**, *125*, 363. doi:10.1016/0022-0248(92)90349-N.
(8) Rumford, F.; Bain, J. *Trans. Inst. Chem. Eng.* **1960**, *38*, 10.
(9) Rodriguez-Clemente, R. In *Industrial Crystallization;* Mullin, J. W., Ed.; Plenum: New York, 1976; p 157.
(10) Rome de l'Isle, B. *Crystallographie;* L'impremerie de Monsieur: Paris, 1783; p. 379.
(11) Kern, R. *Bull. Soc. Fr. Mineral. Cristallogr.* **1953**, *76*, 391.
(12) Johnsen, A. *Wachstum und Auflösung der Kristallen;* Engelmann: Leipzig, Germany, 1910.
(13) Beinfait, M.; Boistelle, R.; Kern, R. In *Adsorption et Croissance Cristalline;* Kern, R., Ed.; Centre National de la Recherche Scientifique: Paris, 1965; pp 152, 515.
(14) Radenović, N.; Enckevort, W.; van VerwerVlieg, P. E. *Surf. Sci.* **2003**, *523*, 307. doi:10.1016/S0039-6028(02)02463-9.
(15) Radenović, N.; Enckevort, W.; van Vlieg, E. J. *Cryst. Growth* **2004**, *263*, 544.
(16) Hsu, W. K.; Li, W. Z.; Zhu, Y. Q.; Grobert, N.; Terrones, M.; Terrones, H.; Yao, N.; Zhang, J. P.; Firth, S.; Clark, R. J. H.; Cheetham, A. K.; Hare, J. P.; Kroto, H. W.; Walton, D. R. M. *Chem. Phys. Lett.* **2000**, *317*, 77. doi:10.1016/S0009-2614(99)01347-0.
(17) Speidel, R. *Neues Jahrbuch fur Mineralogie, Part 4* **1961**, *4*, 81.
(18) Cabrera, N.; Vermilyea, D. A. *Growth and Perfection of Crystals;* John Wiley & Sons Inc.: New York, 1958; p 393.
(19) Bunn, C. W. *Proc. R. Soc. A* **1933**, *141*, 567. doi:10.1098/rspa.1933.0140.
(20) Orme, C. A.; Noy, A.; Wierzbicki, A.; McBride, M. T.; Grantham, M.; Teng, H. H.; Dove, P. M.; DeYoreo, J. J. *Nature* **2001**, *411*, 775. doi:10.1038/35081034. PMID:11459051.
(21) Qiu, S. R.; Wierzbicki, A.; Salter, E. A.; Zepeda, S.; Orme, C. A.; Hoyer, J. R.; Nancollas, G. H.; Cody, A. M.; De Yoreo, J. J. *J. Am. Chem. Soc.* **2005**, *127*, 9036. doi:10.1021/ja043591s. PMID:15969581.
(22) Elhadj, S.; Salter, E. A.; Wierzbicki, A.; De Yoreo, J. J.; Han, N.; Dove, P. M. *Cryst. Growth Des.* **2006**, *6*, 197. doi:10.1021/cg050288+.
(23) Lide, D. R., Ed. *CRC Handbook of Chemistry and Physics,* 85th ed.; CRC Press: Boca Raton, FL, 2004.
(24) Delley, B. J. *Chem. Phys.* **1990**, *92*, 508.
(25) Delley, B. J. *Chem. Phys.* **1996**, *100*, 6107. doi:10.1021/jp952713n.
(26) Delley, B. J. *Chem. Phys.* **2000**, *113*, 7756.
(27) Perdew, J. P.; Wang, Y. *Phys. Rev. B* **1986**, *33*, 8800. doi:10.1103/PhysRevB.33.8800.
(28) Perdew, J. P.; Wang, Y. *Phys. Rev. B* **1992**, *45*, 13244. doi:10.1103/PhysRevB.45.13244.
(29) Coveney, P. C.; Humphries, W. *J. Chem. Soc. Faraday Trans.* **1996**, *92*, 831. doi:10.1039/ft9969200831.
(30) Coveney, P. C.; Davey, R.; Griffin, J. L. W.; He, Y.; Hamlin, J. D.; Stackhouse, S.; Whiting, A. *J. Am. Chem. Soc.* **2000**, *122*, 11557. doi:10.1021/ja990885i.
(31) Wierzbicki, A.; Cheung, H. S. *J. Mol. Struct. (THEOCHEM)* **1998**, *454*, 287.
(32) Coveney, P. V.; Davey, R. J.; Griffin, J. L. W.; Whiting, A. *Chem. Commun. (Cambridge)* **1998**, 1476.
(33) Wierzbicki, A.; Sikes, C. S.; Sallis, J. D.; Madura, J. D.; Stevens, E. D.; Martin, K. L. *Calcif. Tissue Int.* **1995**, *56*, 297. doi:10.1007/BF00318050. PMID:7767841.

(34) Wierzbicki, A.; Sikes, C. S.; Sallis, J. D.; Madura, J. D.; Drakee, B. *Calcif. Tissue Int.* **1994**, *54*, 133. doi:10.1007/BF00296064. PMID:8012868.
(35) Lu, J. J.; Ulrich, J. *Cryst. Res. Technol.* **2003**, *38*, 63. doi:10.1002/crat.200310008.
(36) Singh, A.; Chakraborty, S.; Ganguly, B. *Langmuir* **2007**, *23*, 5406. doi:10.1021/la062405o. PMID:17429985.
(37) Deak, P. *Phys. Status Solidi* **2000**, *9*, 217.
(38) Tasker, P. W. *Philos. Mag. A* **1979**, *39*, 119. doi:10.1080/01418617908236887.
(39) Tasker, P. W. *J. Phys. C Solid State Phys.* **1979**, *12*, 4977. doi:10.1088/0022-3719/12/22/036.
(40) Radenovic, N.; Kaminski, D.; van Enckevort, W.; Graswinckel, S.; Shah, I.; Alga, M.; Vlieg, E. J. *Chem. Phys.* **2006**, *124*,o. 164706.
(41) Davey, R. J.; Mullin, J. W. *Kristall und Technik* **1976**, *11*, 229. doi:10.1002/crat.19760110303.
(42) Polak, W.; Sangwal, K. *Cryst. Res. Technol.* **1999**, *34*, 655. doi:10.1002/(SICI)1521-4079(199906)34:5/6<655::AID-CRAT655>3.0.CO;2-X.
(43) Shih, H. D.; Jone, F.; Jepin, D. W.; Marais, D. *Phys. Rev. Lett.* **1976**, *37*, 1622. doi:10.1103/PhysRevLett.37.1622.
(44) Davey, R. J.; Mullin, J. W.; Whiting, M. J. L. *J. Cryst. Growth* **1982**, *58*, 304. doi:10.1016/0022-0248(82)90277-9.
(45) Stoica, C.; Verwer, P.; Meekes, H.; van Hoof, P. J. C. M.; Kaspersen, F. M.; Vlieg, E. *Cryst. Growth Des.* **2004**, *4*, 765. doi:10.1021/cg0342314.
(46) Hurley, L. A.; Jones, A. G.; Hammond, R. B. *Cryst. Growth Des.* **2004**, *4*, 711. doi:10.1021/cg034046q.
(47) Khoshkhoo, S.; Anwar, J. *J. Chem. Soc. Faraday Trans.* **1996**, *92*, 1023. doi:10.1039/ft9969201023.
(48) de Leeuw, N. H.; Parker, S. C.; Rao, K. H. *Langmuir* **1998**, *14*, 5900. doi:10.1021/la980269k.
(49) Kundu, T. K.; Rao, K. H.; Parker, S. C. *J. Phys. Chem. B.* **2005**, *109*, 11286. doi:10.1021/jp0580367. PMID:16852378.

Synthesis and binding characteristics of novel calix[4]arene(amidocrown) diquinones

Har Mohindra Chawla, Satya Narayan Sahu, and Rahul Shrivastava

Abstract: A series of new calix[4]arene(amidocrown) diquinones (**3a**–**3d**) have been synthesized, characterized, and evaluated for cation recognition. It has been observed that **3b** interacts with alkali metal ions (Li^+, Na^+, and K^+) and ammonium ions to induce an unprecedented downfield shift in the NH proton resonance, which can be attributed to polarization of the amidocrown ring of the calix[4]arene diquinone receptor. The observation has been confirmed by a significant anodic shift ($Li^+ > NH_4^+ > Na^+ > K^+$) of the corresponding amidocrown-diquinone redox couple in cyclic and square wave voltammetric experiments. Both NMR and electrochemical studies of the binding characteristics of **3b** with alkali metal cations and ammonium ions revealed a 1:1 binding stoichiometry for all and exhibited the highest association constant for lithium ions. This indicated that the receptor **3b** selectively binds the lithium ion in preference to other alkali metal cations and ammonium ions.

Key words: calix[4]arene diquinones, amidocrowns, cation-induced polarization.

Résumé : Une série de nouvelles calix[4]arène(amidocouronne)diquinones (**3a**–**3d**) a été synthétisée, caractérisée et évaluée pour la reconnaissance des cations. On a observé que le composé **3b** interagit avec les métaux alcalins (Li^+, Na^+ et K^+) et les ions ammonium et induit un déplacement chimique sans précédent vers les bas champs dans la résonance du proton NH qui est attribué à une polarisation du noyau amidocouronne du récepteur calix[4]arènediquinone. L'observation a été confirmée par un déplacement anodique significatif ($Li^+ > NH_4 > Na^+ > K^+$) du couple redox correspondant amidocouronnediquinone dans des expériences de voltampérométrie cycle et à onde carrée. Tant les études de RMN que celles d'électrochimie relatives aux caractéristiques de fixation du composé **3b** avec les cations alcalins et les ions ammonium ont mis en évidence dans tous les cas une stoechiométrie de fixation 1:1 alors que la constante d'association avec le lithium est la plus élevée, ce qui indiquerait que le récepteur **3b** fixe sélectivement le lithium de préférence aux autres cations métalliques alcalins et des ions ammonium.

Mots-clés : calix[4]arènediquinones, amidocouronnes, polarisation induite par les cations.

[Traduit par la Rédaction]

Introduction

Macrocyclic compounds have been widely used as molecular receptors for recognition of ionic and molecular species of biological and environmental importance.[1] In this context, calix[*n*]arene molecular architecture with distinct hydrophobic upper and hydrophilic lower rims has emerged strongly as a building block for obtaining plausible receptors.[2,3] Amongst various functionalized calix[*n*]arenes, the calix[*n*]arene quinones have also been viewed as molecules of considerable inherent potential to develop into electrochemical sensor materials, devices, and models for charge transfer in biological systems.[4] The synthesis and electrochemical behaviour of various calix[4]arene quinones possessing diverse functionalities have been published by many workers.[5–8] Consequently, we envisaged that calix[4]arene(amidocrown) diquinones possessing amidocrown and quinone units in a single molecular framework would possibly offer additional multiple binding options through soft nitrogen and oxygen donors in the pre-organised calixarene cavity (Fig. 1).

Such abiotic receptors would hopefully shed light on the nature of the interaction of cyclic amidocrown calixquinones with different metal ions. The additional amide functionalities in such receptors would be expected to be flexible enough to define a pseudocavity through convergent orientation of >C=O and -NH binding sites for interaction and recognition of guest species through hydrogen bond and electrostatic forces.[9,10] Accordingly, we have synthesized a series of calix[4]arene(amidocrown) diquinones (**3a**–**3d**) with a variable ring size from calix[4]arene derivatives (**2a**–**2d**)[11] through chlorine dioxide oxidation and have examined their interaction with alkali metal and ammonium ions by ^{1}H NMR and electrochemical measurements. It has been observed that calix[4]arene(amidocrown) diquinones on interaction with alkali metal and ammonium ions exhibit a downfield shift in the NH proton resonance, which has not been reported earlier in calixquinone systems.[12] This NH downfield shift is possibly due to cation induced NH polarization within the amidocrown ring, which has been confirmed by cyclic and square wave voltammetric experiments.

Received 16 September 2008. Accepted 10 December 2008. Published on the NRC Research Press Web site at canjchem.nrc.ca on 4 March 2009.

H.M. Chawla,[1] S.N. Sahu, and R. Shrivastava. Department of Chemistry, Indian Institute of Technology, Hauz Khas, New Delhi 110 016, India.

[1]Corresponding author (e-mail: hmchawla@chemistry.iitd.ernet.in).

Results and discussion

Synthesis and characterization of products

25,27-Di(ethoxycarbonylmethoxy)-26,28-dihydroxy-calix[4]arene (**1**) was obtained from the reaction of calix[4]arene with ethyl bromoacetate in the presence of K_2CO_3/acetonitrile for 15 h.[13] It could be envisaged that **3a–3d** could be synthesized either by conversion of **1** to amidocrown calix[4]arenes followed by oxidation or oxidation of **1** followed by aminolysis to give the target compounds. When **1** was treated with different diamines in a mixture of toluene and methanol for 24–48 h, as reported by Bitter et al.,[11a] it gave **2a–2b** and **2d**. Preparation of **2c** was done by the method recently reported by us.[11b] When **2a–2d** were subjected to oxidation with chlorine dioxide (ClO_2) in the presence of phosphate-buffer in acetone, they gave calix[4]arene(amidocrown) diquinones (**3a–3d**) as yellow powders (Scheme 1). Application of the mentioned alternative strategy involving the oxidation of 25,27-di(ethoxycarbonylmethoxy)-26,28-dihydroxy-calix[4]arene (**1**) followed by aminolysis, resulted in a mixture of products that resisted facile separation to provide useful yields of amidocrown diquinones (**3a–3d**).

The structures of **3a–3d** were established by analysis of their ^{1}H NMR, ^{13}C NMR, and FT-IR spectra. For instance, the molecular structure of **3b** could be confirmed by the analysis of its ^{1}H NMR spectrum (in $CDCl_3$), which revealed a prominent D_2O exchangeable singlet at δ 8.74 for amidic protons while a broad signal for aromatic protons and a singlet for quinonoid protons appeared at δ 6.92 and 6.64, respectively. The ArOCH_2- protons appeared at δ 4.27, while a pair of doublets at δ 3.98 and 3.17 could be assigned to the Ar-CH_2-Q protons. The -NHCH_2 and -NHCH_2CH_2- protons appeared as broad singlets at δ 3.50 and 2.09, respectively.

The presence of a pair of AB-type doublets for Ar-CH_2-Q protons in the ^{1}H NMR spectrum of **3b** suggested that the molecule possessed a symmetrical cone conformation in its solution state, which was further confirmed by the appearance of a distinct signal at δ 30.7 for the methylene carbons in the ^{13}C NMR spectrum.[14] Similarly, other derivatives of the series (**3a**, **3c**, and **3d**) could be characterized by their ^{1}H NMR and ^{13}C NMR spectra. A sharp peak for **3a–3d** was shown at around 1656–1659 cm^{-1} in their FT-IR spectra that indicated the presence of quinonoid groups (Table 1).

Recognition characteristics of calix[4]arene(amidocrown) diquinones (3a–3d) for alkali metal and ammonium cations

NMR studies

The proton NMR spectrum of **3a–3d**, when recorded in three different deuterated solvents (e.g., $CDCl_3$, CD_3CN, and acetone-d_6), exhibited different chemical shifts for the amidic NH proton resonance as depicted in Table 2. This difference in chemical shift of the NH proton is possibly due to a different solvation of NH fragments in aprotic solvents. The VT NMR experiments on **3b** revealed an upfield shift of NH resonance at higher temperatures and the shifts were found to be larger in $CDCl_3$ than in CD_3CN.

These observations indicated that the amido groups of **3b** favour the formation of stronger intramolecular hydrogen bonds in $CDCl_3$[15] than in CD_3CN indicating that CD_3CN should be the preferred solvent for studying the recognition of ions by **3b**. Accordingly, the binding of alkali (Li^+, Na^+, and K^+) perchlorates and ammonium hexafluorophosphate with receptor **3b** were examined in deuterated acetonitrile. It was observed that the addition of alkali metal and ammonium ions to a 10 mmol/L solution of receptor **3b** exhibited a significant downfield shift of NH resonance at δ 8.33 in the proton NMR spectrum. That this downfield shift was due to the cations and not due to counter anions (perchlorate or hexafluorophosphate) was unequivocally confirmed by examining the effect of the addition of tetrabutylammonium perchlorate (TBA.ClO_4) and tetrabutylammonium hexafluorophosphate (TBA.PF_6) to **3b** (in CD_3CN) when no downfield shift in the NH proton resonance was observed. The observed cation-induced downfield shift of NH resonance was found to be more significant in the case of **3b** in comparison to the other receptors (Table 3).

The effect of the addition of Li^+, Na^+, K^+, and NH_4^+cations to **3b** gave different downfield shifts for the NH proton resonance as shown in Fig. 2. For instance, the Li^+ ion exhibited the maximum downfield shift followed by sodium and ammonium ions. The addition of potassium ions exhibited the lowest downfield shift in the NH proton resonance (Table 3).

It was also observed that gradual addition of lithium cation to **3b** (in CD_3CN) exhibited a regular increase in the chemi-

Fig. 1. Calix[4]arene(amidocrown) diquinone possessing multiple binding options (X = bridged substitutent).

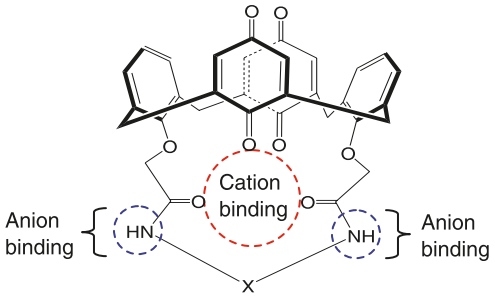

Scheme 1. Synthesis of calix[4]arene(amidocrown) diquinones (**3a–3d**). Reagents and conditions: (*a*) diamine (H_2N-X-NH_2), 20 equiv., toluene/MeOH (1:1), refluxing, 24–48 h; (*b*) ClO_2, phosphate-buffer (pH = 7), acetone, RT, 48–60 h.

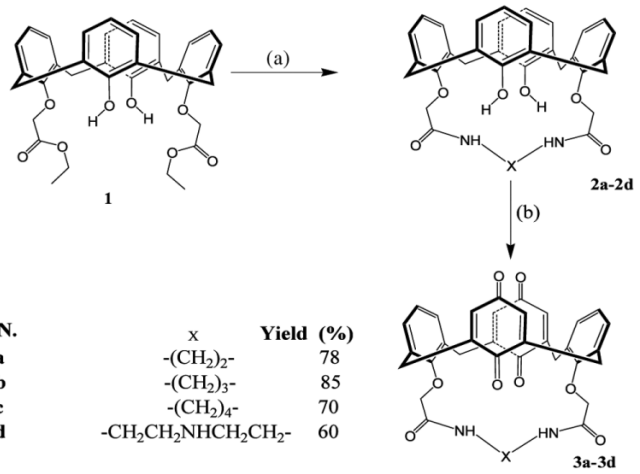

S.N.	X	Yield (%)
3a	-$(CH_2)_2$-	78
3b	-$(CH_2)_3$-	85
3c	-$(CH_2)_4$-	70
3d	-$CH_2CH_2NHCH_2CH_2$-	60

Table 1. ^{1}H NMR spectral data (300 MHz, 298 K, $CDCl_3$) and FT-IR stretching frequency for C=O of quinonoid units of the calix[4]arene(amidocrown) diquinone receptors (**3a**–**3d**).

	^{1}H NMR values and splitting patterns, δ (ppm)				
Comp. No.	NH(CO)	Aromatic protons	Quinone protons	Methylene bridge protons (8 H) Ar-CH_2-Q	FT-IR, $\nu_{c=o}$ (cm^{-1})
3a	8.75 (s, 2H)	6.91 (m, 6H)	6.64 (br s, 4H)	3.97 (d, 4H), 3.14 (d, 4H)	1656
3b	8.74 (s, 2H)	6.92 (m, 6H)	6.64 (br s, 4H)	3.98 (d, 4H), 3.17 (d, 4H)	1658
3c	8.71 (s, 2H)	6.89 (m, 6H)	6.54 (br s, 4H)	4.10 (d, 4H), 3.44 (d, 4H)	1659
3d	8.73 (s, 2H)	6.91 (m, 4H), 6.74 (m, 2H)	6.51 (br s, 4H)	4.15 (d, 4H), 3.45 (br s, 4H)	1657

Table 2. Chemical shifts of the NH protons of an uncomplexed (**3b**) and complexed (**3b** + Li^+) receptor in various solvents.

	NH chemical shift, δ (ppm)		
Solvents	Uncomplexed	Complexed	Δδ
$CDCl_3$	8.74	—	—
CD_3CN	8.33	8.78	+0.45
Acetone-d_6	8.34	8.75	+0.41

Table 3. Change in chemical shift values (Δδ, ppm) for NH proton resonance in **3a**, **3b**, and **3c** upon addition of 10 equiv. of cations in CD_3CN (300 MHz and 298 K).

Cation	**3a** Δδ	**3b** Δδ	**3c** Δδ
Li	0.15	0.45	0.06
Na	0.13	0.25	0.02
NH_4	—	0.25	—
K	—	0.12	—

cal shift of NH protons till it finally attained a saturation point at 1 equiv. of Li^+ addition revealing a 1:1 binding stoichiometry for the **3b**-Li^+ complex (Fig. 3*a*). A Job's plot experiment of **3b** with Li^+ ions further confirmed the 1:1 binding stoichiometry with maximum complexation at 0.5 mol fraction of cation as shown in Fig. 3*c*. Similarly, gradual addition of Na^+, K^+, and NH_4^+ ions to **3b** also led to a change in the chemical shift of NH proton resonance, indicating a 1:1 binding stoichiometry for all the cations studied. Analysis of the saturation data of **3b**:cation interactions with a nonlinear regression curve-fitting programme WinEQNMR[16] further confirmed the 1:1 binding stoichiometry with an association constant of $2.7(\pm0.6) \times 10^3$ $(mol/L)^{-1}$ and $1.9(\pm0.7) \times 10^3$ $(mol/L)^{-1}$, respectively, for lithium and ammonium ions (Figs. 3*a* and 3*b*). This observation indicated that the receptor **3b** shows high selectivity to the lithium ion in preference to other alkali metal cations. The findings revealed a higher binding constant for lithium cation in comparison to the case of previously reported crown ether and calix[4]arene systems.[8c,17]

The addition of lithium ion to **3b** also led to a change in the chemical shift of aromatic, quinone, and methylene bridged protons of the calix[4]arene unit (Fig. 4).

The downfield shifts observed for quinone (ArH_Q) and ester methylene (-O-CH_2-CO) protons on addition of Li^+ to **3b** suggested that the cation was possibly bound by the calix[4]arene cavity utilizing the lower rim oxygen atoms and amido carbonyl groups. This was further confirmed by the ^{13}C NMR signals of **3b**, which exhibited a downfield

Fig. 2. The partial ^{1}H NMR spectra of **3b** in the presence of various cations in CD_3CN at 298 K and 300 MHz. (*a*) **3b**, (*b*) **3b** + K^+, (*c*) **3b** + Na^+, (*d*) **3b** + NH_4^+, (*e*) **3b** + Li^+.

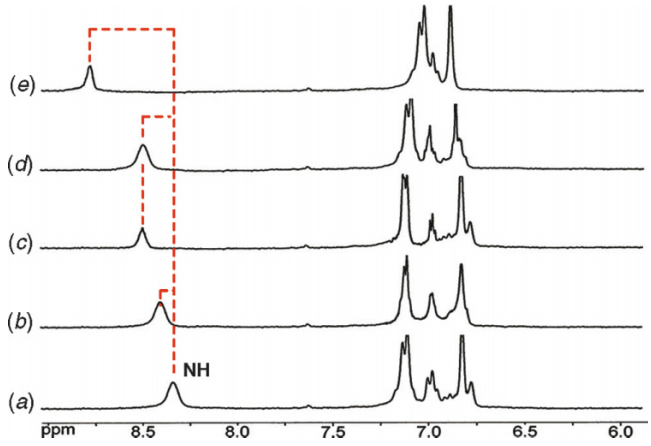

Scheme 2. Possible model structure for the cation complex of calix[4]arene(amidocrown) diquinone receptor **3b** and the cation induced polarization on the amidoring NH protons.

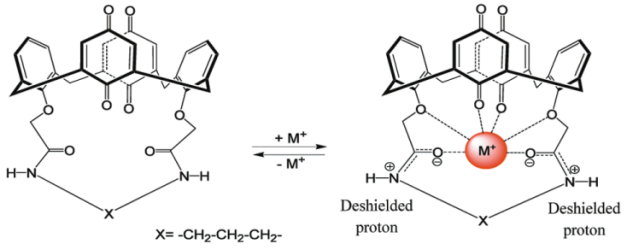

shift (Δδ ≈ 2 ppm) for the amido and quinone carbonyl carbons in the presence of lithium cation.

The observed downfield shift of NH proton resonance in **3b** on interaction with lithium ion is interesting as earlier groups[18] have proposed an upfield shift in NH signals of noncyclic amido-calix[4]arenes when complexed with alkali cations. The observed downfield shift in the NH resonance could possibly be ascribed to the cation induced polarization of the amido carbonyl group, which decreases the electron density over the nitrogen atom to deshield the NH proton (Scheme 2) when it is present in a cyclic amidocrown ring.

A study on the influence of different cations indicated an increase in the chemical shift of the NH signal in the expected order of $K^+ < NH_4^+ \approx Na^+ < Li^+$ (Fig. 2 and Table 3). This could be ascribed to the increased electron-withdrawing character of amido carbonyl groups upon cation complexation, which seemed to follow the order of charge density of cations. However, the greater downfield shift exhibited by am-

Fig. 3. The titration isotherm for the NH proton within **3b** upon addition of (*a*) Li^+ and (*b*) NH_4^+ ions. (*c*) Job's plot for the titration of 0.01 mol/L $LiClO_4$ with 10^{-2} mol/L solution of receptor **3b** in CD_3CN.

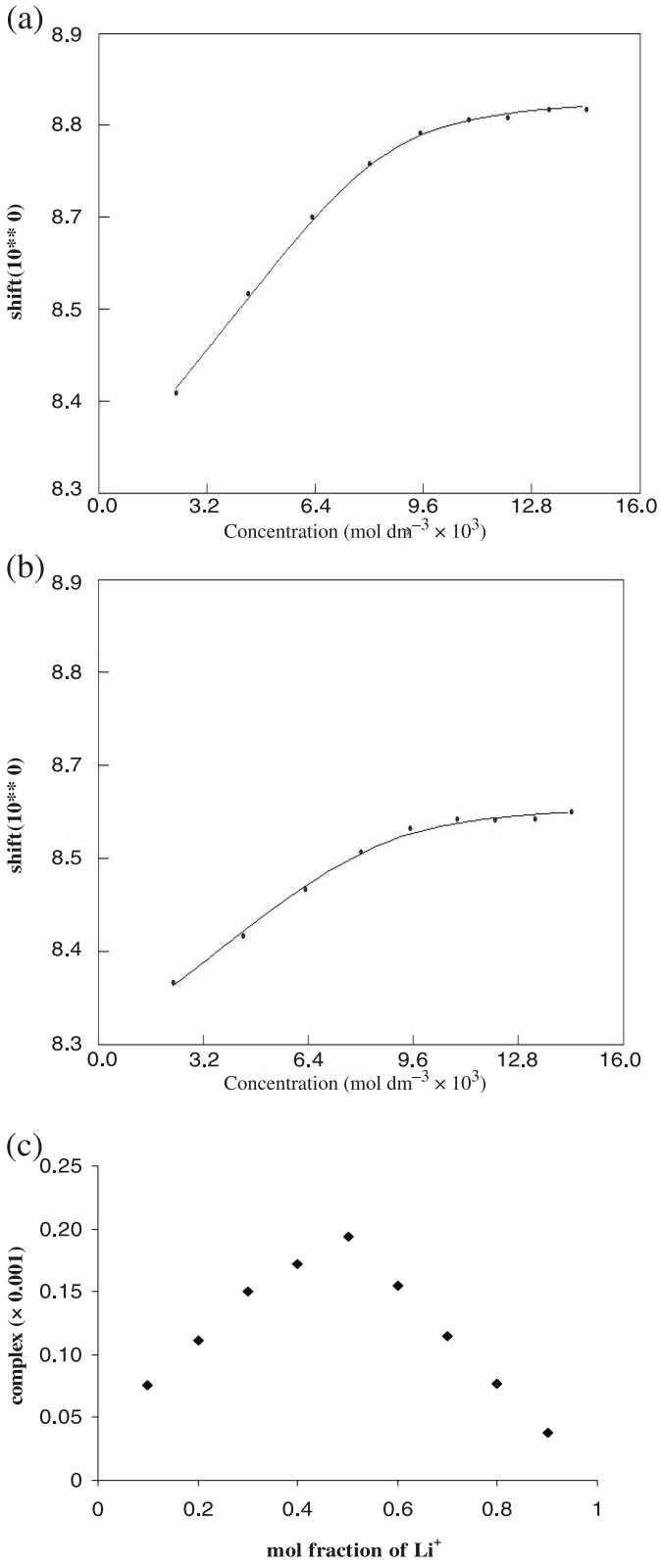

monium ions on interaction with **3b** over potassium ion could possibly be ascribed to extra stabilization of ammonium cation through hydrogen bond interactions with the amido carbonyl groups of the receptor molecule in consonance with literature precedents.[19] This was further corroborated from the association constant observed for **3b** with ammonium ions.

Fig. 4. Partial ^{1}H NMR spectrum in CD_3CN at 298 K and 300 MHz. (*a*) **3b** and (*b*) **3b** + 1.0 equiv. $LiClO_4$.

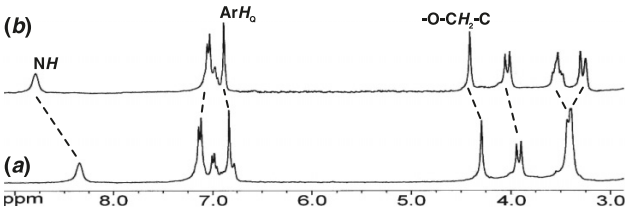

Fig. 5. Cyclic voltammograms of (*a*) free **3b**, (*b*) **3b** + 1.0 equiv. of NH_4^+, and (*c*) **3b** + 1.0 equiv. of Li^+.

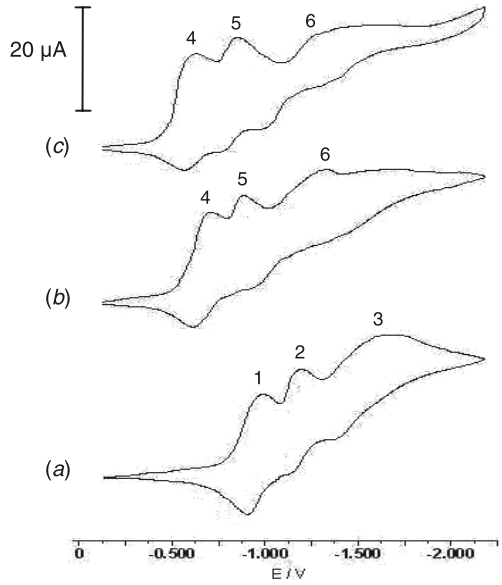

Electrochemical studies

The electrochemical behavior of **3a–3d** was investigated by cyclic voltammetry and square wave voltammetry with a glassy carbon electrode using 0.1 mol/L tetrabutylammonium hexafluorophosphate ($TBAPF_6$) in acetonitrile solution. A solution of 1 mmol/L concentration of **3b,** when examined voltammetrically, gave three redox waves in the potential range of 0 to –2.0 V (Fig. 5*a*), which could be attributed to different reduction processes in quinone units as reported in previous electrochemical studies on calix[4]arene diquinones.[6c]

The two cathodic waves observed at –969 mV and –1188 mV (Fig. 5*a*) could be described as 1/1′ and 2/2′, respectively, for two one-electron reduction processes for each quinone unit, while the third more negative wave 3 at –1594 mV could be ascribed to the two-electron irreversible reduction process.[20] Likewise, **3a**, **3c**, and **3d** exhibited three redox waves in their voltammograms for couples 1/1′, 2/2′, and wave 3 in the presence of 0.1 mol/L $TBAPF_6$ in acetonitrile (Table 4).

When examined by cyclic and square wave voltammetry in the presence of 0.1 mol/L $TBAPF_6$ as the supporting electrolyte, **3b** exhibited a decrease in peak intensity of the cathodic waves 1/1′, 2/2′, and 3 on gradual addition of lithium ions to its electrochemical solution (10^{-3} mol/L in acetonitrile). A new set of redox waves at more positive potentials were observed during the cation binding process. The addition of 1 equiv. of lithium ion results in a complete disappearance of the original redox waves at –969, –1188, and –1594 mV with a corresponding increase in the intensities of the new waves observed at –624, –833, and –1266 mV for the couples 4/4′, 5/5′, and wave 6, respectively (Fig. 5*c* and Table 5). This observation again indicated that the lithium ion is possibly bound to **3b** through a 1:1 binding stoichiometry.

Similarly, the cyclic voltammograms recorded after the addition of 1 equiv. of Na^+, K^+, and NH_4^+ ions to the electrochemical solution of **3b** led to a change in the cathodic peak potentials as summarized in Table 5. Square wave voltammetry measurement of **3b** in the presence of 1 equiv.of Li^+ ion also exhibited the new anodically shifted peaks 4, 5, and 6 at –624, –833, and –1266 mV, respectively, in the square wave voltammograms (Fig. 6).

The change in cathodic current of **3b** when examined in the presence of alkali cations indicated that the addition of lithium ions leads to a large decrease in cathodic current while the addition of potassium ions exhibited the least effect. The decrease in cathodic current of the redox waves 1/1′ and 2/2″ was found to follow the order $Li^+ > NH_4^+ > Na^+ > K^+$, which is in consonance with the order of potential shift ($\Delta E_{(1/1')} = E^{complex} - E^{3b}$; Li^+ 345, NH_4^+ 267, Na^+ 32, K^+ 18 mV) observed for wave 1/1′ (Table 5). This indicated that the receptor **3b** binds the lithium ion more strongly than the other cations. Incremental addition of alkali cations to an electrochemical solution of **3b** revealed that the addition of 1 equiv. of lithium ion leads to a complete disappearance of the original redox couples, 1/1′ and 2/2′, while even a fivefold excess of Na^+ and K^+ ions to **3b** could not induce a similar effect (Table 5). On the other hand, addition of 1 equiv. of NH_4^+ ion to **3b** led to the disappearance of the redox couples 1/1′ and 2/2′ (which was not observed in the case of Na^+ and K^+ ions) as depicted in Fig. 5*b*.

The anodic shifts observed in the redox couples of **3b** on addition of Li^+, Na^+, K^+, and NH_4^+ ions could possibly be ascribed to the easier reduction of diquinone units through extra stabilization of the reduced quinone species in the presence of positively charged metal ions. This stabilization was found to be maximum in the case of lithium ion due to its higher charge density. This was evidenced by the observed large decrease in cathodic current of waves 1/1′ and 2/2′ and larger anodic shifts in the new redox waves 4/4′ and 5/5′ of **3b** obtained in the presence of lithium ions (Fig. 5*c* and Table 5). The anodic shift exhibited by NH_4^+ ions was larger than that of Na^+ and K^+ ions ostensibly due to stronger hydrogen bond interactions of ammonium cations with the quinone units in **3b**.[19] This observation was further confirmed by ^{1}H NMR, which revealed a greater downfield shift in δ NH on addition of NH_4^+ ions. The binding enhancement[8c,21] of **3b** on interaction with cationic guests was calculated from the shift in half wave potentials ($E_{1/2}$) of the bound and free **3b**. It was observed that a lithium ion binding with **3b** is roughly ten times stronger than with an ammonium ion (Table 5). These observations are in consonance with the NMR measurements, which show a higher binding affinity of **3b** towards lithium ions amongst the other tested alkali metal cations.

In conclusion, a series of new calix[4]arene(amidocrown) diquinones (**3a–3d**) have been synthesized in good yields. The NMR studies on the interaction of **3b** with alkali metals and ammonium ions exhibited a significant downfield shift

Table 4. Electrochemical data of the synthesized calix[4]arene(amidocrown) diquinone receptors (**3a**–**3d**) in acetonitrile.

Redox couple or wave (mV)	3a	3b	3c	3d
$E_{1/2}$ (1/1′)	–969	–969	–968	–970
$E_{1/2}$ (2/2′)	–1189	–1188	–1187	–1190
E_{pc} (3)	–1596	–1594	–1598	–1601

Note: $E_{1/2}$ values are the cathodic peak potentials of the described couple referenced to an Ag/Ag^+ electrode at 298 K. E_{pc} is the cathodic peak potential of wave 3, which is irreversible.

Table 5. Redox couples and waves of **3b** upon addition of 1 equiv. of Li^+, Na^+, K^+, and NH_4^+ cations.

	Redox couple or wave (mV)							
Comp.	(1/1′)	(2/2′)	(3)	(4/4′)	(5/5′)	(6)	Binding enhancement[a]	
Free **3b**	–969	–1188	–1594				K_2/K_1	K_3/K_2
3b + Li^+				–624	–833	–1266	6.7×10^5	9.8×10^5
3b + NH_4^+				–702	–892	–1328	3.2×10^4	9.9×10^4
3b + Na^+[b]	–970	–1192	–1596	–937	–1125	–1502		
3b + K^+[b]	–973	–1191	–1592	–951	–1158	–1532		

Note: Experiments were carried out in acetonitrile using Ag/Ag^+ as the reference electrode and $TBA.PF_6$ as the supporting electrolyte.

[a] K_2/K_1 and K_3/K_2 are the calculated binding enhancements in the presence of metal ions.

[b] The original waves appeared even in the presence of 5 equiv. of metal ions.

Fig. 6. Square wave voltammograms (10 Hz) of free **3b** (black) and in the presence of 1.0 equiv. of Li^+ cations (red) in acetonitrile.

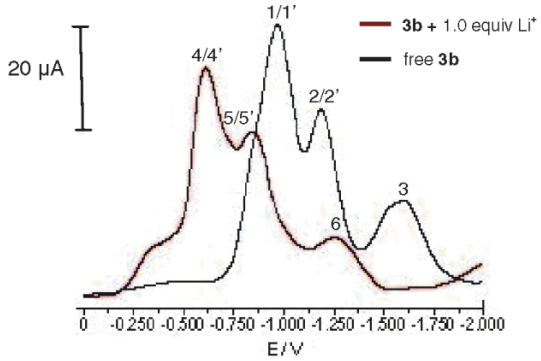

in the NH proton resonance, which could possibly be ascribed to cation-induced polarization of the amidocrown ring. The cyclic voltammetry of **3b** in the presence of lithium ions gives a larger anodic shift in the original redox waves. Both NMR and electrochemical studies revealed a 1:1 binding stoichiometry for the interaction of **3b** with alkali metal and ammonium ions and exhibited the highest binding constant for lithium ions, which indicated that **3b** shows high selectivity for lithium ions in preference to other alkali metal cations and ammonium ions. These studies may be helpful in the development of novel ion-selective electrodes, electrochemical sensors, and molecular devices. Further work in this area is in progress.

Experimental section

Instruments

All the reagents used in the study were purchased from Sigma-Aldrich or Merck and were chemically pure. Solvents used were predried and purified by distillation. Column chromatography was performed on silica gel (60–120 mesh) obtained from Merck. Melting points were recorded on an electric melting point apparatus (Toshniwal, India) and are uncorrected. FT-IR spectra were recorded on a Nicolet Protege 460 spectrometer using KBr discs while CHN analyses were taken on a Perkin-Elmer 240C elemental analyzer. ^1H NMR spectra were recorded on a 300 MHz Bruker DPX 300 instrument at room temperature (RT) using tetramethylsilane (TMS) as an internal standard. The electrochemical measurements were carried out using an AUTOLAB PGSTAT 100 cyclic voltammeter obtained from Metrohm Ltd., Switzerland. The ESI mass spectra were recorded on a MICROMASS QUATTRO II triple quadrupole mass spectrometer setting the ESI capillary at 3.5 kV and the cone voltage at 40 V.

Preparation of starting materials

Debutylated-calix[4]arene and 25,27-di(ethoxycarbonylmethoxy)-26,28-dihydroxy-calix[4]arene (**1**) were synthesized by the methods reported earlier.[13] The amidocrown calix[4]arene derivatives (**2a**–**2d**) were prepared as previously reported.[11]

General procedure for the synthesis of calix[4]arene(amidocrown) diquinones (3a–3d)

A slurry of compound **2a**–**2d** (2.0 g) was dissolved in acetone (170 mL) and phosphate buffer[22] (70 mL) was added to it. A portion of yellowish chlorine dioxide solution[22] (150 mL) was then added and the reaction mixture was stirred at RT for 48–60 h. The reaction was evaporated in vacuo on completion of the reaction to obtain a yellowish precipitate. The precipitate was extracted with chloroform (3 × 50 mL) and washed three times with water. The com-

bined organic layer was dried over anhydrous Na_2SO_4, filtered, and concentrated on a rotary evaporator to obtain a sticky yellow product, which on trituration with methanol gave yellowish solids. The crude products were purified by silica gel chromatography ($CHCl_3$-EtOAc 90:10 *v*/*v*) to give **3a**–**3d** as bright yellow powders.

Compound 3a

Yellow solid; yield: 1.63 g (78%); mp 268 °C (decomp.). IR (KBr, cm^{-1}) ν_{max}: 3345, 1679, 1656. ^1H NMR (300 MHz, $CDCl_3$, ppm) δ: 8.75 (2H, br s, N*H*), 6.91 (6H, m, Ar*H*), 6.64 (4H, br s, ArQ*H*), 4.26 (4H, s, OCH_2), 3.97 (4H, d, *J* = 12.5 Hz, ArCH_2Q), 3.61 (4H, br s, NCH_2), 3.14 (4H, d, *J* = 12.5 Hz, ArCH_2Q). ^{13}C NMR (75 MHz, $CDCl_3$, ppm) δ: 188.1, 185.9, 169.2, 148.5, 147.2, 133.4, 132.6, 129.5, 125.3, 72.7, 37.7, 31.2. ESI mass (*m*/*z*): 593 $(M + 1)^+$. Anal. calcd. for $C_{34}H_{28}N_2O_8$ (%): C 68.91, H 4.76, N 4.73; found: C 68.68, H 4.75, N 4.76.

Compound 3b

Yellow solid; yield: 1.77 g (85%); mp 260 °C (decomp.). IR (KBr, cm^{-1}) ν_{max}: 3354, 1682, 1658. ^1H NMR (300 MHz, $CDCl_3$, ppm) δ: 8.74 (2H, br s, N*H*), 6.92 (6H, m, Ar*H*), 6.64 (4H, br s, ArQ*H*), 4.27 (4H, br s, OCH_2), 3.98 (4H, d, *J* = 12.7 Hz, ArCH_2Q), 3.50 (4H, br s, NCH_2), 3.17 (4H, d, *J* = 12.7 Hz, ArCH_2Q), 2.09 (2H, br s, NCH_2CH_2). ^{13}C NMR (75 MHz, $CDCl_3$, ppm) δ: 187.3, 185.9, 168.6, 148.0, 144.5, 132.3, 130.6, 127.5, 124.3, 71.7, 36.7, 30.7, 25.7. ESI mass (*m*/*z*): 607 $(M + 1)^+$. Anal. calcd. for $C_{35}H_{30}N_2O_8$ (%): C 69.30, H 4.98, N 4.62; found: C 69.48, H 4.96, N 4.61.

Compound 3c

Yellow solid; yield: 1.46 g (70%); mp 264 °C (decomp.). IR (KBr, cm^{-1}) ν_{max}: 3359, 1681, 1659. ^1H NMR (300 MHz, $CDCl_3$, ppm) δ: 8.71 (2H, br s, N*H*), 6.89 (6H, m, Ar*H*), 6.54 (4H, br s, ArQ*H*), 4.54 (4H, s, OCH_2), 4.10 (4H, d, *J* = 13.5 Hz, ArCH_2Q), 3.54 (4H, br s, NCH_2), 3.44 (4H, d, *J* = 13.5 Hz, ArCH_2Q), 2.58 (4H, br s, NCH_2CH_2). ^{13}C NMR (75 MHz, $CDCl_3$, ppm) δ: 188.6, 187.2, 168.8, 148.9, 146.3, 135.4, 133.3, 129.9, 125.2, 74.2, 38.9, 31.4, 24.7. ESI mass (*m*/*z*): 621 $(M + 1)^+$. Anal. calcd. for $C_{36}H_{32}N_2O_8$ (%): C 69.67, H 5.20, N 4.51; found: C 69.54, H 5.23, N 4.50.

Compound 3d

Yellow solid; yield: 1.25 g (60%); mp 265 °C (decomp.). IR (KBr, cm^{-1}) ν_{max}: 3350, 1680, 1657. ^1H NMR (300 MHz, $CDCl_3$, ppm) δ: 8.73 (2H, br s, CON*H*), 6.91 (4H, m, Ar*H*), 6.74 (2H, m, Ar*H*), 6.51 (4H, br s, ArQ*H*), 6.19 (1H, br s, N*H*), 4.42 (4H, s, OCH_2), 4.15 (4H, d, *J* = 12.8 Hz, ArCH_2Q), 3.45 (8H, br s, CONHCH_2 + ArCH_2Q), 2.90 (4H, br s, $CONHCH_2CH_2$). ^{13}C NMR (75 MHz, $CDCl_3$, ppm) δ:187.6, 186.3, 168.9, 148.3, 143.8, 137.4, 136.3, 126.9, 123.2, 74.9, 46.9, 36.1, 30.8. ESI mass (*m*/*z*): 636 $(M + 1)^+$. Anal. calcd. for $C_{36}H_{33}N_3O_8$ (%): C 68.02, H 5.23, N 6.61; found: C 68.15, H 5.20, N 6.66.

Analytical procedures for electrochemical and NMR experiments

Cyclic (CV) and square wave voltammetric (SWV) analysis were performed using an AUTOLAB PG-STAT 100 cyclic voltammeter (Metrohm Ltd., Switzerland) fitted with three electrodes consisting of a glassy carbon working electrode (conducting area of 3 mm diameter), a platinum wire counter electrode, and an Ag/Ag^+ reference electrode. Analysis of the cyclic and square wave voltammetric data were performed using the GPES software (version 4.9.005).[23] All the electrochemical measurements were carried out in an electrolyte solution of 0.1 mol/L tetrabutylammonium hexafluorophosphate ($TBA.PF_6$) in acetonitrile, unless otherwise indicated. The electrolytic solutions were sonicated for 20 min and then bubbled with nitrogen for 5–7 min before each measurement to minimize the oxygen interference. A 0.001 mol/L solution (5 mL) of molecular receptor **3b** (5×10^{-6} mol) and tetrabutylammonium hexafluorophosphate (5×10^{-4} mol) was prepared in acetonitrile and the metal salt solution containing a mixture of metal salt (5×10^{-4} mol) and tetrabutylammonium hexafluorophosphate (5×10^{-4} mol) was added directly to the cell through a microsyringe to have the desired cation/ligand ratios. Redox currents were determined from CV scans of the complex solutions at a scan rate of 50 mVs^{-1}.

^1H NMR titration: A 10 mmol/L solution of the receptor **3b** was prepared in CD_3CN. To 0.5 mL of **3b** solution, 0.0–2.5 equiv. of cations (Li^+, Na^+, K^+, and NH_4^+ of 40 mmol/L in CD_3CN) were added to an NMR tube and the spectra were recorded. The chemical shifts of the NH protons were followed after each addition and plotted against the equivalents of cations added.

Job's plot experiments: Stock solutions of the receptor **3b** (10 mmol/L) and $LiClO_4$ (10 mmol/L) were prepared in CD_3CN. A total volume of 500 μL of **3b** and $LiClO_4$ were added to nine NMR tubes in the following volume ratios 50:450, 100:400, 150:350, 200:300, 250:250, 200:300, 150:350, 100:400, and 50:450.

Acknowledgements

The authors thank the financial assistance received from the Department of Science and Technology (DST), the Department of Biotechnology (DBT), the Ministry of Environment and Forests (MOEF), the Ministry of Food Processing Industries (MFPI), and the Ministry of Rural Development (MRD) (Government of India). The award of Senior Research Fellowship (SRF) to SNS and RS by the Council of Scientific and Industrial Research, New Delhi is thankfully acknowledged. Assistance received from the Sophisticated Analytical Instrument Facility (Central Drug Research Institute, Lucknow, India) for recording the ESI-MS spectra reported in this paper is gratefully acknowledged.

References

(1) (a) Izatt, R. M.; Bradshaw, J. S.; Nielsen, S. A.; Lamb, J. D.; Christensen, J. J.; Sen, D. *Chem. Rev.* **1985**, *85*, 271 doi:10.1021/cr00068a003.; (b) Izatt, R. M.; Pawlak, K.; Bradshaw, J. S.; Bruening, R. L. *Chem. Rev.* **1995**, *95*, 2529 doi:10.1021/cr00039a010.; (c) Ikeda, A.; Shinkai, S. *Chem. Rev.* **1997**, *97*, 1713 doi:10.1021/cr960385x. PMID:11851464.; (d) Ogoshi, H.; Mizutani, T. *Curr. Opin. Chem. Biol.* **1999**, *3*, 736. doi:10.1016/S1367-5931(99)00033-2. PMID:10600717.

(2) (a) Gutsche, C. D. In *Calixarenes: Monographs in Supramolecular Chemistry;* Stoddart, J. F., Ed.; The Royal Society of Chemistry: Cambridge, UK, 1989; (b) Gutsche, C. D. In *Calixarenes Revisited: Monographs in Supramolecular Chemistry;* Stoddart, J. F., Ed.; The Royal Society of Chemistry: Cambridge, UK, 1998; (c) Asfari, Z.; Bohmer, V.; Harrow-

field, J.; Vicens, J. *Calixarenes: 2001;* Kluwer Academic Publishers: Dordrecht, 2001.

(3) (a) Chawla, H. M.; Pant, N.; Srivastava, B.; Upreti, S. *Org. Lett.* **2006**, *8*, 2237 doi:10.1021/ol0605124. PMID:16706495.; (b) Chawla, H. M.; Singh, S. P.; Sahu, S. N.; Upreti, S. *Tetrahedron* **2006**, *62*, 7854 doi:10.1016/j.tet.2006.05.040.; (c) Chawla, H. M.; Sahu, S. N.; Shrivastava, R. *Tetrahedron Lett.* **2007**, *48*, 6054 doi:10.1016/j.tetlet.2007.06.075.; (d) Chawla, H. M.; Singh, S. P.; Upreti, S. *Tetrahedron* **2007**, *63*, 5636 doi:10.1016/j.tet.2007.04.012.; (e) Chawla, H. M.; Singh, S. P. *Tetrahedron* **2008**, *64*, 741 doi:10.1016/j.tet.2007.11.010.; (f) Chawla, H. M.; Shrivastava, R.; Sahu, S. N. *New. J. Chem.* **2008**, *32*, 1999. doi:10.1039/b800502h.

(4) (a) Webber, P. R. A.; Cowley, A.; Beer, P. D. *J. Chem. Soc. Dalton Trans.* **2003**, 3922; (b) Chung, T. D.; Park, J.; Kim, J.; Lim, H.; Choi, M. J.; Kim, J. R.; Chang, S. K.; Kim, H. *Anal. Chem.* **2001**, *73*, 3975 doi:10.1021/ac001050p. PMID:11534725.; (c) Aviram, A.; Seiden, P. E. In *Molecular Electronic Devices;* Carter, F. L., Ed.; Marcel Dekker: New York, 1982; p 5; (d) Pressman, B. C. *Annu. Rev. Biochem.* **1976**, *45*, 501. doi:10.1146/annurev.bi.45.070176.002441. PMID:786156.

(5) (a) Morita, Y.; Agawa, T.; Nomura, E.; Taniguchi, H. *J. Org. Chem.* **1992**, *57*, 3658 doi:10.1021/jo00039a027.; (b) Morita, Y.; Agawa, T.; Kai, Y.; Kanehisa, N.; Kasai, N.; Nomura, E.; Taniguchi, H. *Chem. Lett.* **1989**, 1349. doi:10.1246/cl.1989.1349.

(6) (a) Reddy, P. A.; Kashyap, R. P.; Watson, W. M.; Gutsche, C. D. *Isr. J. Chem.* **1992**, *32*, 89; (b) Reddy, P. A.; Gutsche, C. D. *J. Org. Chem.* **1993**, *58*, 3245 doi:10.1021/jo00064a009.; (c) Gomez-Kaifer, M.; Reddy, P. A.; Gutsche, C. D.; Echegoyen, L. *J. Am. Chem. Soc.* **1994**, *116*, 3580 doi:10.1021/ja00087a051.; (d) Gomez-Kaifer, M.; Reddy, P. A.; Gutsche, C. D.; Echegoyen, L. *J. Am. Chem. Soc.* **1997**, *119*, 5222. doi:10.1021/ja963601s.

(7) (a) Webber, P. R. A.; Beer, P. D.; Chen, G. Z.; Felix, V.; Drew, M. G. B. *J. Am. Chem. Soc.* **2003**, *125*, 5774 doi:10.1021/ja029740t. PMID:12733918.; (b) Webber, P. R. A.; Chen, G. Z.; Drew, M. G. B.; Beer, P. D. *Angew. Chem. Int. Ed.* **2001**, *40*, 2265. doi:10.1002/1521-3773(20010618)40:12<2265::AID-ANIE2265>3.0.CO;2-1.

(8) (a) Chung, T. D.; Choi, D.; Kang, S. K.; Lee, S. K.; Chang, S. K.; Kim, H. *J. Electroanal. Chem. (Kyoto)* **1995**, *396*, 431 doi:10.1016/0022-0728(95)04112-2.; (b) Chung, T. D.; Kim, H. *J. Incl. Phenom. Mol. Recog. Chem.* **1998**, *32*, 179 doi:10.1023/A:1008059326436.; (c) Kerdpaiboon, N.; Tomapatanaget, B.; Chailapakul, O.; Tuntulani, T. *J. Org. Chem.* **2005**, *70*, 4797. doi:10.1021/jo050324b. PMID:15932320.

(9) (a) Beer, P. D.; Chen, Z.; Gale, P. A.; Heath, J. A.; Knubley, R. J.; Ogden, M. I. *J. Incl. Phenom. Mol. Recog. Chem.* **1994**, *19*, 343 doi:10.1007/BF00708992.; (b) Rudkevich, D. M.; Verboom, W.; Reinhoudt, D. N. *J. Org. Chem.* **1994**, *59*, 3683 doi:10.1021/jo00092a031.; (c) Scheerder, J.; Vreekamp, R. H.; Engbersen, J. F. J.; Verboom, W.; van Duynhoven, J. P. M.; Reinhoudt, D. N. *J. Org. Chem.* **1996**, *61*, 3476. doi:10.1021/jo9600262.

(10) (a) Liu, S. Y.; He, Y. B.; Wu, J. L.; Wei, L. H.; Qin, H. J.; Meng, L. Z.; Hu, L. *Org. Biomol. Chem.* **2004**, *2*, 1582 doi:10.1039/b400140k. PMID:15162208.; (b) Zlatuskova, P.; Stibor, I.; Tkadlecova, M.; Lhotak, P. *Tetrahedron* **2004**, *60*, 11383 doi:10.1016/j.tet.2004.09.088.; (c) Beer, P. D.; Cooper, J. B.; *J. Chem. Soc. Chem. Commun.* **1998**, 129. doi:10.1039/c39940002207.; (d) Pelizzi, N.; Casnati, A.; Friggeri, A.; Ungaro, R. *J. Chem. Soc. Perkin Trans. 2,* **1998**, , 1307.

(11) (a) Bitter, I.; Grun, A.; Toth, G.; Balazs, B.; Toke, L. *Tetrahedron* **1997**, *53*, 9799 doi:10.1016/S0040-4020(97)00627-3.; (b) Chawla, H. M.; Singh, S. P.; Upreti, S. *Tetrahedron* **2006**, *62*, 9758. doi:10.1016/j.tet.2006.07.047.

(12) (a) Chen, Z.; Gale, P. A.; Heath, J. A.; Beer, P. D. *J. Chem. Soc. Faraday Trans.* **1994**, *90*, 2931 doi:10.1039/ft9949002931.; (b) Beer, P. D.; Chen, Z.; Drew, M. G. B.; Gale, P. A. *J. Chem. Soc. Chem. Commun.* **1994**, 2207. doi:10.1039/c39940002207.; (c) Beer, P. D.; Gale, P. A.; Chen, Z.; Drew, M. G. B.; Heath, J. A.; Ogden, M. I.; Powell, H. R. *Inorg. Chem.* **1997**, *36*, 5880 doi:10.1021/ic9704851. PMID:11670211.; (d) Choi, D.; Chung, T. D.; Kang, S. K.; Lee, S. K.; Kim, T.; Chang, S. K.; Kim, H. *J. Electroanal. Chem. (Kyoto)* **1995**, *387*, 133. doi:10.1016/0022-0728(95)03946-E.

(13) (a) Gutsche, C. D. *Org. Synth.* **1990**, *68*, 234; (b) Gutsche, C. D.; Iqbal, M.; Steward, D. *J. Org. Chem.* **1986**, *51*, 742 doi:10.1021/jo00355a033.; (c) Creaven, B. S.; Deasy, M.; Gallagher, J. F.; Mcginley, J.; Murry, B. A. *Tetrahedron* **2001**, *57*, 8883. doi:10.1016/S0040-4020(01)00872-9.

(14) Jaime, C.; De Mendoza, J.; Prados, P.; Nieto, P. M.; Sanchez, C. *J. Org. Chem.* **1991**, *56*, 3372. doi:10.1021/jo00010a036.

(15) (a) Reichardt, C. *Solvent and Solvent Effects in Organic Chemistry,* 2nd ed.; VCH: Weinheim, Germany, 1988; pp 13–27; (b) Shimizu, K. D.; Rebek, J., Jr. *Proc. Natl. Acad. Sci. U.S.A.* **1995**, *92*, 12403 doi:10.1073/pnas.92.26.12403. PMID:8618910.; (c) Mogck, O.; Bohmer, V.; Vogt, W. *Tetrahedron* **1996**, *52*, 8489 doi:10.1016/0040-4020(96)00404-8.; (d) Frkanec, L.; Visnjevac, A.; Kojic-Prodic, B.; Zinic, M. *Chem. Eur. J.* **2000**, *6*, 442. doi:10.1002/(SICI)1521-3765(20000204)6:3<442::AID-CHEM442>3.0.CO;2-1.

(16) (a) Hynes, M. J. *Chem. Soc. Dalton Trans.* **1993**, 311 doi:10.1039/DT9930000311.; (b) WinEQNMR: A computer program for the calculation of stability constants from nuclear magnetic resonance chemical shift data. This program was kindly gifted by the developer, Michael J. Hynes, Department of Chemistry, National University of Ireland, Galway, Ireland on our request. Available from michael.j.hynes@nuigalway.ie.

(17) (a) Fakhari, A. R.; Shamsipur, M. *J. Incl. Phenom. Mol. Recog. Chem.* **1996**, *26*, 243 doi:10.1007/BF01053542.; (b) Costa, J. M. C.; Rodrigues, P. M. S. *Port. Electrochim. Acta* **2002**, *20*, 167; (c) Asfari, Z.; Abidi, R.; Arnaud, F.; Vicens, J. *J. Incl. Phenom. Mol. Recog. Chem.* **1992**, *13*, 163. doi:10.1007/BF01053640.

(18) (a) Nomura, E.; Takagaki, M.; Nakaoka, C.; Uchida, M.; Taniguchi, H. *J. Org. Chem.* **1999**, *64*, 3151 doi:10.1021/jo982251k. PMID:11674414.; (b) Murakami, H.; Shinkai, S. *Tetrahedron Lett.* **1993**, *34*, 4237 doi:10.1016/S0040-4039(00)60537-3.; (c) Mareque Rivas, J. C.; Schwalbe, H.; Lippard, S. J. *Proc. Natl. Acad. Sci. U.S.A.* **2001**, *98*, 9478. doi:10.1073/pnas.161257798. PMID:11504936.

(19) (a) Beer, P. D.; Chen, Z.; Gale, P. A. *Tetrahedron* **1994**, *50*, 931 doi:10.1016/S0040-4020(01)80807-3.; (b) Chung, T. D.; Kang, S. K.; Kim, J.; Kim, H. S.; Kim, H. *J. Electroanal. Chem. (Kyoto)* **1997**, *438*, 71. doi:10.1016/S0022-0728(97)00100-9.

(20) (a) Casnati, A.; Comelli, E.; Fabbi, M.; Bocchi, V.; Mori, G.; Ugozzoli, F.; Lanfredi, A. M. M.; Pochini, A.; Ungaro, R. *Recl. Trav. Chim. Pays Bas* **1993**, *112*, 384; (b) Suga, K.; Fujihara, M.; Morita, Y.; Agawa, T. *J. Chem. Soc. Faraday Trans.* **1991**, *87*, 1575 doi:10.1039/ft9918701575.; (c) Jeong, H.; Choi, E. M.; Kang, S. O.; Nam, K. C.; Jeon, S. *J. Electroanal. Chem. (Kyoto)* **2000**, *485*, 154. doi:10.1016/S0022-0728(00)00108-X.

(21) (a) Gustowski, D. A.; Delgado, M.; Gatto, V. J.; Echegoyen, L.; Gokel, G. W. *J. Am. Chem. Soc.* **1986**, *108*, 7553 doi:10.1021/ja00284a019.; (b) Delgado, M.; Gustowski, D. A.; Yoo, H. K.; Gatto, V. J.; Gokel, G. W.; Echegoyen, L. *J. Am. Chem. Soc.* **1988**, *110*, 119 doi:10.1021/ja00209a019.; (c) Echegoyen, L.; Hafez, Y.; Lawson, R. C.; De Mendoza, J.; Torres, T. *J. Org. Chem.* **1993**, *58*, 2009. doi:10.1021/jo00060a010.

(22) A concentrated aqueous buffer solution was prepared by dissolving 4.36 g of $Na_2HPO_4 \cdot 2H_2O$ and 2.42 g of $NaH_2PO_4 \cdot 2H_2O$ in 100 mL of Milli-Q water. A pH ~ 7.0 buffer solution was obtained when the concentrated solution was diluted five times in volume. Chlorine dioxide (ClO_2) solution was obtained by mixing equal volumes of $NaClO_2 \cdot 2H_2O$ solution (31.60 g in 500 mL Milli-Q water) and $Na_2S_2O_8$ solution (29.70 g in 500 mL Milli-Q water). The mixed solution was then stored in a dark coloured bottle at 0 °C overnight to get the yellowish chlorine dioxide solution.

(23) *GPES for Windows*, version 4.9.005; Supplied with the equipment from Eco Chemie, Netherlands.

Preparation and properties of thienyl and 2,2′-bithienyl substituted cobalt-bis(semiquinone) valence tautomers

Thomas J. O'Sullivan, Brandon Djukic, Paul A. Dube, and Martin T. Lemaire

Abstract: The synthesis and characterization of two new 2,2′-bipyridine ligands containing 3-ethynylthiophene and 3,3′-diethynyl-2,2′-bithiophene substituents is presented, along with the preparation, electronic, and magnetic properties of mono- and bimetallic cobalt-semiquinone valence tautomers containing these ligands.

Key words: cobalt complexes, valence tautomerism, semiquinone radical anions, magnetic switches.

Résumé : On a réalisé la synthèse et effectué la caractérisation de deux nouveaux ligands 2,2′-bipyridine portant des substituants 3-éthynylthiophène et 3,3′-diéthynyl-2,2′-bithiophène; on rapporte aussi la préparation ainsi que les propriétés électroniques et magnétiques des tautomères de valence cobalt-semiquinone mono- et bimétalliques contenant ces ligands.

Mots-clés : complexes de cobalt, tautomérie de valence, anions radicaux semiquinones, interrupteurs magnétiques.

[Traduit par la Rédaction]

Introduction

Valence tautomerism (VT) in cobalt(II) coordination complexes containing 2,2′-bipyridine and semiquinone anion-radical ligands was discovered in 1980 by Pierpont and Buchanan.[1] These fascinating molecular materials feature dynamic electronic structures that can switch between different electronic states as a result of a similarity in the frontier orbital energies of cobalt(II) and the coordinated semiquinone. In particular, an intramolecular electron transfer reaction results in the formation of cobalt(III)-catecholate species, and accompanying the cobalt(II)-to-semiquinone electron transfer is a change in spin state of the cobalt ion from high to low. These changes are manifested as observable changes to the structural, electronic, and in particular, the magnetic properties of the complexes over a range of temperatures, even upon application of pressure or light irradiation.[2]

Since the discovery of Pierpont and Buchanan,[1] a number of related VT complexes have been reported, some exhibiting thermal hysteresis in magnetic properties and others exhibiting interesting light induced VT.[3] The vast majority of these complexes are monometallic and the number of these reports dwarfs the number of reported bimetallic VT complexes, and to our knowledge there are no reported VT complexes containing more than two cobalt ions (this does not include two VT *coordination polymers* reported by Pierpont and co-workers[4b] and Shultz and co-workers,[4a] and recently reported VT metal-organic nanoparticles).[4] We are interested in the preparation of new variants of polymetallic VT materials leading to, among other things, new *multistate molecular switches*. We reasoned that a conjugated organic backbone based on the thiophene heterocycle should serve as a nice platform to construct polymetallic VT complexes, and as an added advantage, the synthetic aspects of oligothiophene chemistry are well documented. Herein we report the synthesis and magnetic properties of two new mono- and bimetallic VT complexes (**3** and **4**, respectively) containing new 2,2′-bipyridine derivatives bearing thiophene **1**, or a bridgining 2,2′-bithiophene **2**, substituents. Complexes **3** and **4** serve as models to study the effect of thiophene substitution on the electronic or magnetic properties of cobalt-bis(semiquinone) VT complexes.

Received 29 October 2008. Accepted 5 January 2009. Published on the NRC Research Press Web site at canjchem.nrc.ca on 7 March 2009.

T.J. O'Sullivan, B. Djukic, and M.T. Lemaire.[1] Department of Chemistry, Brock University, 500 Glenridge Avenue, St. Catharines, ON L2S 3A1, Canada.
P.A. Dube. Brockhouse Institute for Materials Research, McMaster University, 1280 Main Street West, Hamilton, ON L8S 4M1, Canada.

[1]Corresponding author (e-mail: mlemaire@brocku.ca).

Experimental

General procedures

All reagents were commercially available and used as received unless otherwise stated. Deaerated and anhydrous solvents were obtained from a Puresolve PS MD-4 solvent purification system, and all air and (or) moisture sensitive reactions were carried out using standard Schlenk techniques. FT-IR spectra were recorded on a ThermoMattson RS-1 spectrometer as KBr discs. EI and FAB mass spectra were obtained using a Kratos Concept 1S High Resolution E/B mass spectrometer. UV–vis spectra were recorded on a Shimadzu 3600 UV-Vis-NIR spectrophotometer as solutions in ethanol at room temperature. Spectra at 77 K were obtained as frozen ethanol glasses in 5 mm NMR tubes immersed in a liquid N_2 dewar. Elemental analyses were carried out by Guelph Chemical Laboratories Ltd., Guelph, ON, Canada.

Electrochemical measurements

Cyclic voltammetry (CV) experiments were performed with a Bioanalytical Systems Inc. Epsilon electrochemical workstation. Compounds were dissolved in anhydrous solvent (CH_2Cl_2, CH_3CN, or DMF) and deareated by sparging with dinitrogen gas for 20 min. Solution concentrations were approximately 10^{-3} mol/L in analyte containing 0.1 mol/L supporting electrolyte (Et_4NPF_6). A typical three-electrode setup was used, including a platinum working electrode, Ag wire pseudoreference electrode, and a platinum wire auxiliary electrode. Ferrocene was used in all cases as an internal standard in our setup and was oxidized at potentials of +0.50, +0.54, and +0.70 V in CH_2Cl_2, CH_3CN, and DMF, respectively; all potentials quoted are versus the ferrocene oxidation potential. Scan rates for CV experiments were 100 mV/s.

Variable temperature magnetic susceptibility measurements

Variable temperature magnetic susceptibility measurements were recorded on a superconducting quantum interference device (SQUID) magnetometer (Quantum Design MPMS) with a 5.5 T magnet (temperature range from 2 to 300 K) in an external field of 1000 Oe. Samples were carefully weighed into gelatin capsules, with empty gelatin capsules above and below to eliminate background contributions from the gelatin, which were loaded into plastic straws and attached to the sample transport rod. Diamagnetic corrections were made using Pascal's constants.

Synthesis

5-(Trimethylsilylethynyl)-2,2′-bipyridine

The following is a modified version of the procedure reported by Ziessel and co-workers.[5] 5-Bromo-2,2′-bipyridine (1.00 g, 4.385 mmol), $PdCl_2(PPh_3)_2$ (92 mg, 0.131 mmol, 3 mol%), PPh_3 (69 mg, 0.263 mmol, 6 mol%), and CuI (83 mg, 0.438 mmol, 10 mol%) were added successively to a two-necked round-bottomed flask, which was flushed with N_2. Anhydrous *N*,*N*-diisopropylamine (90 mL) was syringed into the flask, and the mixture was stirred and deareated for 30 min. Lastly, ethynyltrimethylsilane (0.579 g, 6.577 mmol, 0.82 mL) was added, and the reaction mixture was refluxed for 20 h. The solvent was evaporated, and the residue was dissolved in chloroform; pentane was used to precipitate impurities that were removed by gravity filtration. The filtrate was passed through a Celite pad and concentrated. The residue was dissolved in acetone, filtered, and concentrated to afford 1.067 g (96%) yield of the product. Spectroscopic properties are consistent with those reported by Ziessel and co-workers.[5] ^{1}H NMR (300 MHz, $CDCl_3$, ppm) δ: 8.75 (d, 1H, J = 2 Hz), 8.70 (d, 1H, J = 5 Hz), 8.40 (m, 2H), 7.84 (m, 2H), 7.33 (m, 1H), 0.29 (s, 9H). MS (EI+) *m*/*z* (%): 252 (M^+, 100).

5-(3-Ethynylthienyl)-2,2′-bipyridine (1)

A solution of 3-bromothiophene (0.100 mL, 1.063 mmol) in anyhydrous *N*,*N*-diisopropylamine (20 mL) was deaerated by sparging with N_2 gas for 30 min. Five mol% of each of the following were successively added to the flask: $PdCl_2(PPh_3)_2$ (0.037 g, 0.053 mmol), PPh_3 (0.014 g, 0.053 mmol), and CuI (0.010 g, 0.053 mmol), followed by 5-ethynyl-2,2′-bipyridine (0.230 g, 1.276 mol). The reaction mixture was refluxed overnight until starting materials had been consumed, as verified by TLC. The crude product was passed through a pad of Celite, and the filtrate was washed with brine (3 × 50 mL), and then dried with sodium sulfate. After concentration, the crude product was recrystallized from acetone(hot)/water (5:1) to yield 0.258 g of a yellow solid (92% yield). Mp 141 °C. FT-IR (KBr, cm^{-1}): 3405 (m, br), 3072 (m), 2920 (w), 2205 (m), 1717 (w), 1586 (m), 1541 (m), 1457 (s), 1433 (m), 1366 (m), 1126 (w), 1090 (w), 1019 (m), 854 (m), 784 (s), 739 (w), 623 (m). ^{1}H NMR (300 MHz, $CDCl_3$, ppm) δ: 8.82 (s, 1H), 8.71 (d, 1H, J = 2 Hz), 8.43 (t, 2H, J = 3.4 Hz), 7.94 (dd, 1H, J = 4, 1 Hz), 7.85 (td, 1H, J = 4, 1 Hz), 7.62 (d, 1H, J = 1 Hz), 7.35 (m, 2H), 7.26 (d, 1H, J = 2 Hz). ^{13}C NMR (600 MHz, $CDCl_3$, ppm) δ: 155.5, 154.7, 151.5, 149.3, 139.2, 137.0, 129.8, 129.4, 125.6, 123.9, 121.7, 121.3, 120.3, 120.3, 88.6, 85.9. MS (FAB+) *m*/*z* (%): 262 (M^+, 100). Anal. calcd. for $C_{16}H_{10}N_2S$ (%): C 73.27, H 3.85, N 10.69; found: C 72.96, H 4.07, N 10.35.

3,3′-Bis(5-ethynyl-2,2′-bipyridine)-2,2′-bithiophene (2)

In a Schlenk flask anhydrous *N*,*N*-diisopropylamine (60 mL) was deaerated by N_2 sparging for 30 min, followed by the successive addition of 5-ethynyl-2,2′-bipyridine (0.500 g, 2.775 mmol), 3,3′-dibromo-2,2′-bithiophene (0.408 g, 1.261 mmol), and 3 mol% each of $PdCl_2(PPh_3)_2$ (0.58 g, 0.083 mmol) and CuI (0.015 g, 0.083 mmol). The reaction mixture was refluxed overnight under N_2. Following consumption of starting materials (TLC), the reaction mixture was concentrated and then passed through a Celite pad. The filtrate was concentrated under reduced pressure, and the residue was pre-absorbed onto neutral alumina, and then loaded onto a plug of neutral alumina. Impurities were separated by elution with hexanes, and the product was eluted with copious amounts of dichloromethane. The residue was recrystallized from 4:1 hot chloroform/hexanes to produce 0.434 g (66%) of a bright yellow solid. Mp >200 °C. FT-IR (KBr, cm^{-1}): 3428 (s, br), 3052 (w), 2994 (w), 2918 (w), 2849 (w), 2192 (w), 1630 (w), 1572 (m), 1540 (w), 1458 (s), 1433 (s), 1364 (m), 1243 (w), 1092 (w), 1018 (m), 829 (w), 795 (s), 719 (s), 640 (m). ^{1}H NMR (300 MHz, $CDCl_3$, ppm) δ: 8.89 (s, 2H), 8.72 (d, 2H, J = 2 Hz), 8.45 (t, 4H, J = 4 Hz), 7.99 (dd, 2H, J = 4, 1 Hz), 7.86 (t, 2H, J = 4 Hz), 7.35 (d, 4H, J = 3 Hz), 7.25 (d, 2H, J = 3 Hz). ^{13}C NMR (600 MHz, $CDCl_3$, ppm) δ: 155.4, 154.9, 151.4, 149.3, 139.0, 138.6, 137.0, 130.4, 124.8, 124.0, 121.3, 120.4, 120.3, 119.1, 92.4, 89.8. MS (EI+) *m*/*z* (%): 183 [$(M - C_{20}H_{11}N_2S_2)^+$, 50)], 262 [$(M - C_{16}H_9N_2S)^+$, 100], 522 ($M^+$, 100). Anal. calcd. for $C_{32}H_{18}N_4S_2$ (%): C 73.55, H 3.47, N 10.73; found: C 73.27, H 3.69, N 10.68.

(1)Co(DBSQ)$_2$ (3)

A dry Schlenk flask was charged with $Co_4(DBSQ)_8$ (0.114 g, 0.057 mmol) and flushed with N_2 gas. Anhydrous toluene (20 mL) was added to the flask, which was deareated for 20 min by sparging with N_2 gas. Solid **1** (0.060 g, 0.229 mmol) was added to the toluene solution of

$Co_4(DBSQ)_8$, and the mixture was stirred for 5 h at room temperature under N_2. The dark green solution was concentrated to about half-volume under a stream of N_2, and the precipitated complex was isolated by vacuum filtration, and washed with small portions of cold toluene to afford 0.125 g (71%) of purple crystals. UV–vis (MeOH, nm) λ_{max}: 389. FT-IR (KBr, cm^{-1}): 3447 (m, br), 3042 (w), 2955 (s), 2902 (m), 2864 (m), 2361 (w), 2210 (m), 1570 (m), 1464 (s), 1440 (s), 1356 (m), 1283 (s), 1242 (s), 1204 (w), 984 (m), 841 (m) 791 (m). MS (FAB+) *m/z* (%): 541 [(M –DBSQ)$^+$, 100], 321 [(M – 2DBSQ)$^+$, 55]. Anal. calcd. for $C_{44}H_{50}N_2SO_4Co$ (%): C 69.36, H 6.62, N 3.68, S 4.20; found: C 69.02, H 6.80, N 3.73, S 3.95.

(2)[Co(DBSQ)$_2$]$_2$ (4)

To a solution of $Co_4(DBSQ)_8$ (0.172 g, 0.086 mmol) in anhydrous and deaerated toluene (25 mL) was added solid **2** (0.090 g, 0.172 mmol), and the mixture was stirred overnight under N_2 at room temperature. The dark green precipitate was isolated by vacuum filtration, washed with cold toluene, and dried to afford 0.177 g (68%) of **4**. UV–vis (MeOH, nm) λ_{max}: 404. FT-IR (KBr, cm^{-1}): 3448 (s, br), 2955 (s), 2904 (m), 2866 (m), 2364 (w), 2201 (w), 1625 (m), 1578 (m), 1467 (s), 1356 (m), 1243 (m), 1164 (w), 1094 (w), 1029 (w), 984 (m), 903 (w), 790 (w), 728 (w), 637 (w), 485 (w). MS (FAB+) *m/z* (%): 1080 [(M – 2DBSQ)$^+$, 15], 860 [(M – 3DBSQ)$^+$, 20], 581 [(M – 4DBSQ + Co)$^+$, 55]. Anal. calcd. for $C_{88}H_{98}N_4S_2O_8Co_2$ (%): C 69.45, H 6.50, N 3.68, S 4.21; found: C 69.19, H 6.79, N 3.74, S 3.83.

Results and discussion

Ligand synthesis and coordination chemistry

Our general synthetic strategy toward multimetallic VT materials is based upon the structural modification of the prototypical VT system, (2,2′-bipyridine)Co(DBSQ)$_2$ (DBSQ = 3,5-di-*tert*-butyl-1,2-semiquinone), to enable covalent attachment to a conjugated backbone. Our first target ligand contains a 3-ethynyl-thienyl substituent joined to the 2,2′-bipyridine structure (**1**) as a model to probe the effect of thiophene substitution on the VT properties of (2,2′-bipyridine)Co(DBSQ)$_2$, and to ensure that this substitution has not altered the electronic properties of the cobalt ion so much that VT is no longer observed. The ethynyl spacer fixed between the thiophene heterocycle and 2,2′-bipyridine is to prevent undesirable steric congestion in future complexes containing oligo- or poly-thiophene backbones. Methodology for preparing monohalogenated derivatives of 2,2′-bipyridine is known, and our first target **1** was prepared as shown (Scheme 1). We followed Fang and Hanan's[6] procedure to obtain 5-bromo-2,2′-bipyridine via a palladium catalyzed Neigishi cross-coupling of 2-pyridylzinc bromide with 2,5-dibromopyridine, and we modified Ziessel and co-worker's[5] procedure, which utilizes Sonogashira methodology, to generate 5-trimethylsilyl-2,2′-bipyridine. Fluoride ion deprotection generated 5-ethynyl-2,2′-bipyridine, which was reacted with 3-bromothiophene in another Sonogashira cross-coupling reaction to afford **1** as a yellow solid. In the FT-IR spectrum of **1**, the acetylene stretch is observed at 2205 cm^{-1}.

Bis(bidentate) bridging ligand **2** was prepared in three steps from commercially available 2,2′-bithiophene (Scheme 1).

Scheme 1. Preparation of **1** and **2**. Reagents and conditions: (a) 5 mol% $Pd(PPh_3)_4$, THF, RT, 24 h; (b) ethynyltrimethylsilane, 10 mol% CuI, 3 mol% $Pd(PPh_3)_2Cl_2$, $^iPr_2NH$, followed by deprotection with KF in MeOH; (c) 3 mol% CuI and $Pd(PPh_3)_2Cl_2$, $^iPr_2NH$, reflux 24 h; (d) 3 mol% CuI and $Pd(PPh_3)_2Cl_2$, $^iPr_2NH$, reflux 24 h.

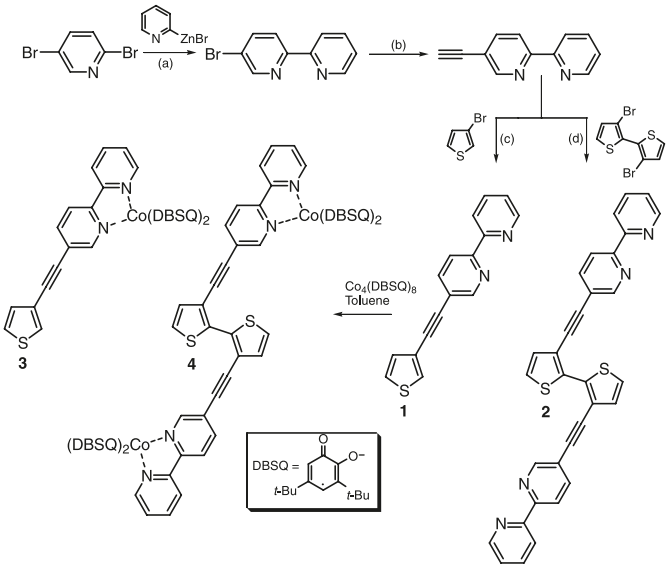

3,3′,5,5′-Tetrabromo-2,2′-bithiophene is obtained by bromination of 2,2′-bithiophene with aq. HBr and Br_2, and reductive dehalogenation with zinc dust afforded 3,3′-dibromo-2,2′-bithiophene, which was reacted with 2 equiv. of 5-ethynyl-2,2'-bipyridine to provide **2** as a canary yellow powder following chromatography and recrystallization.[7] The spectroscopic properties of **2** are very similar to **1**, with the exception of one missing singlet resonance in the ^1H NMR spectrum of **2**, corresponding to the H atom on C2 of the thiophene ring in **1**.

Complexes **3** or **4** were prepared by combination of stoichiometrically appropriate amounts of **1** or **2** with Pierpont's "tetramer" $Co_4(3,5\text{-}DBSQ)_8$ in toluene solution (Scheme 1).[8] These reactions generated analytically pure powders of complexes; unfortunately, repeated attempts to grow crystals suitable for X-ray diffraction were unsuccessful in all cases. As solids, these complexes are indefinitely stable, even under ambient conditions; however, solutions of these complexes are quite unstable, even under inert conditions. In any event, our analytical data (C, H, N, and S) is in good agreement with theoretical values, and these results in conjunction with FT-IR and other spectrometric data (FAB mass spectrometry) strongly support that the anticipated formulations have been obtained.

Electronic spectroscopy

The electronic absorption properties of **3** and **4** were measured in ethanol solution at 298 K, and as a frozen ethanol glass at 77 K. The vis-NIR spectrum obtained from **3** at each temperature is shown in Fig. 1 (the spectrum of **4** is included in the Supplementary data).

As is typical of cobalt-bis(semiquinone) valence tautomers, changing temperature results in a significant change to the electronic spectrum.[9] At 298 K, the spectrum of **3** fea-

Fig. 1. Vis-NIR spectrum of **3** at 298 and 77 K (bold trace) in ethanol.

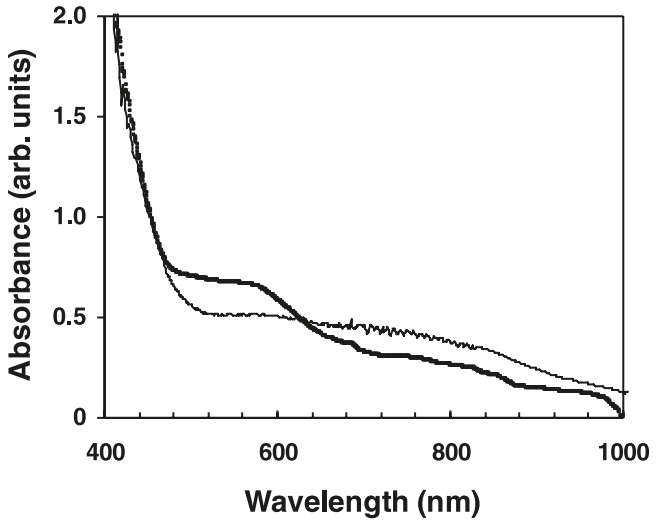

Fig. 2. Cyclic voltammogram of **4** recorded in deareated DMF, containing 0.1 mol/L Et_4NPF_6.

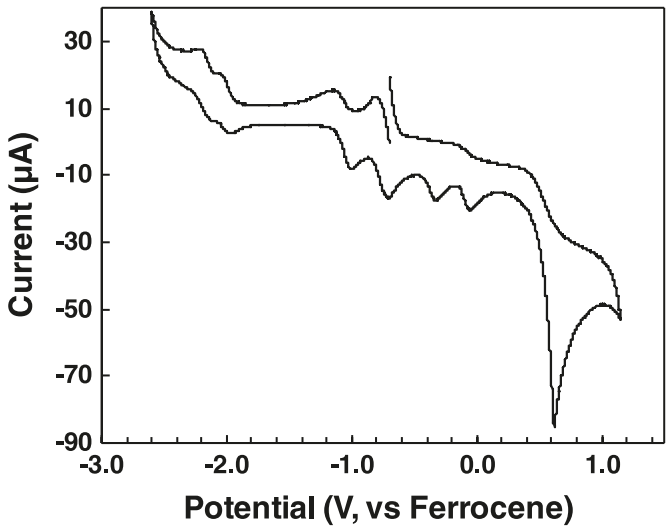

tures broad absorptions across the visible region into the NIR. Typically, the higher temperature tautomer features a cobalt(II)-to-semiquinone charge transfer absorption centered at approximately 800 nm.[10] We observe a decrease in the absorption of this band at 77 K, and an increase in absorption between 500 and 600 nm, consistent with optical changes that have been observed for other reported valence tautomers. The new, more strongly absorbing feature, having a maximum absorbance at 580 nm is consistent with a catecholate-to-cobalt(III) charge transfer band, which is typical for the lower temperature tautomer. Similar features are observed in the electronic spectra of **4** at 298 and 77 K (Supplementary data). All of the observed optical changes are completely consistent with valence tautomerism in **3** and **4**.

Electrochemical properties

The electrochemical properties of compounds **1**–**4** were studied by cyclic voltammetry. Because of solubility differences between the ligands and coordination complexes, voltammograms of **1** and **2** were run in CH_2Cl_2 and complexes **3** and **4** were run in DMF. In all cases, quoted potentials are referenced to the Fc/Fc^+ couple in the particular solvent noted. As an example, the voltammogram of **4** is presented in Fig. 2; voltammograms of **1**, **2**, and **3** can be found in the Supplementary data. Electrochemical data for all compounds is listed in Table 1.

Table 1. Electrochemical data for compounds **1**–**4** (irr = irreversible).

Compound	E'_{ox} (V) (peak separation, mV)	E'_{red} (V) (peak separation, mV)
1	+0.8 (irr)	–1.3 (180)
2	+0.8 (irr), +0.98 (irr)	–1.3 (200)
3	+0.7 (irr) (CH_3CN)	–2.3 (200), –1.0 (irr), –0.7 (170), –0.3 (irr), –0.05 (irr) (DMF)
4	+0.7 (irr), +0.92 (irr) (CH_3CN)	–2.2 (120), –2.0 (120), –1.1 (200), –0.8 (146), –0.3 (irr), –0.04 (irr) (DMF)

Fig. 3. Temperature dependence of the magnetic moment (μ) for **3** (■) and **4** (▲). External field of 1000 Oe.

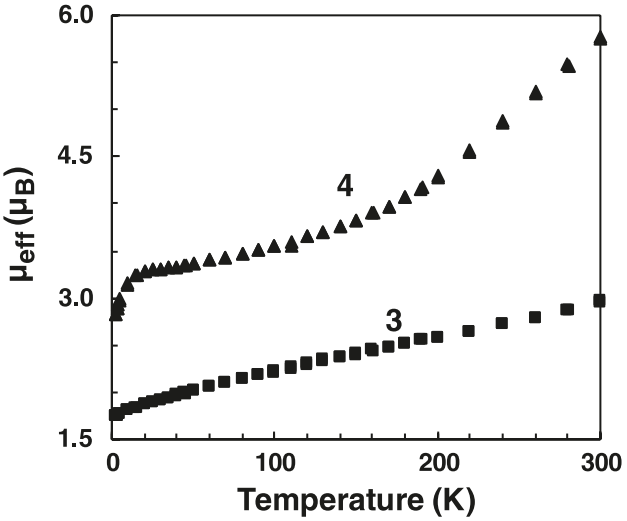

Ligands **1** and **2** exhibit very similar voltammograms. In each case, one pseudoreversible cathodic wave is present (–1.3 V), assigned to the reduction of the 2,2′-bipyridine substituent. Over anodic potentials, **1** features an irreversible wave at +0.8 V, likely due to oxidation of the thiophene ring; a similar wave is observed in **2**, with a second irreversible wave noted at a slightly higher potential (+0.98 V). These are assigned to successive oxidations of the 2,2′-bithienyl substituent, producing first a radical-cation and then dication.

In the voltammograms of **3** and **4**, all waves are cathodic versus ferrocene, and a complex series of reduction processes are observed (Fig. 2). Two closely spaced and pseudoreversible waves are present at the most negative potentials (–2.2 and –2.0 V), and represent reduction of 2,2′-bipyridine. These potentials are much more negative than those observed in uncoordinated **1** and **2**, which is typical for electronic changes that occur upon metal ion coordination. Another set of pseudoreversible waves are observed at –1.1 and –0.8 V, followed by two irreversible processes

at –0.3 and –0.04 V. These likely represent DBSQ/DBCAT and cobalt(III)/(II) reduction events.

Presumably, anodic processes that were observed for the thiophene and 2,2′-bithiophene substituents in **1** and **2** fall at higher positive potentials than the solvent (DMF) window will allow measurement of, and so these waves were not observed in the anodic scans of **3** or **4**. We ran anodic scans of **3** and **4** in acetonitrile solution, which is known to exhibit a wider anodic window than DMF. Oxidation of the thiophene ring occurred at +0.7 V in **3**; 2,2′-bithophene oxidation was observed at +0.7 and +0.9 V in **4**. These potentials are only slightly less positive than those observed for the same processes in uncoordinated **1** and **2**, suggesting, as anticipated, that metal coordination has little effect on the electronic structure of the remote heterocyclic substituents.

Repeated cycles (5 to 10 scans) between 0 and 1.5 V in acetonitrile solutions of **3** and **4** did not result in electropolymerization of these complexes. An increase in peak current with increasing scan number was not observed, nor was a deposited electroactive film observed on the working electrode following the experiment. It is likely that the steric bulk of the cobalt(DBSQ)$_2$ substituent prevented electropolymerization.

Variable temperature magnetic properties

Magnetic susceptibility measurements were carried out with a SQUID magnetometer over the temperature range 2–300 K from complexes **3** and **4**. The data are displayed as plots of effective magnetic moment (μ_{eff}) versus temperature in Fig. 3.

The profile of the data clearly suggests that valence tautomerism is operative within each complex. The magnetic moment of **3** at 2 K is 1.74 μ_B, which is equal to the expected value for one unpaired electron residing in the lone coordinated DBSQ ligand of the low temperature tautomer. Increasing the temperature results in a steady increase in magnetic moment, which approaches 3.0 μ_B at 300 K. This value is less than expected for noninteracting S = 3/2 cobalt(II) with two coordinated S = 1/2 DBSQ radicals (4.98 μ_B). The reduced moment results from a combination of antiferromagnetic coupling between cobalt and coordinated DBSQ and the presence of some proportion of the cobalt(III)(DBSQ)(DBCAT) tautomer at this temperature.

At 2 K the magnetic moment of bimetallic **4** is equal to 2.8 μ_B, which is a touch higher than the expected value for two noninteracting unpaired electrons (2.45 μ_B). Between 20 and 200 K, the moment increases very gradually from approximately 3.5 to 4 u_B, but between 200 and 300 K the rate of increase in moment is much faster. At 300 K the moment, which is clearly still ascending, is 5.76 μ_B, which is less than the expected value for two nonintereacting cobalt(II) ions and four semiquinone radical anions (6.95 μ_B), likely a result of cobalt-semiquinone antiferromagnetic coupling and the presence of lower spin tautomers. It is interesting to speculate on the possibility of a high-spin/low-spin intermediate state, in between the expected fully low- and high-spin tautomers in **4**, possibly within the 20 to 200 K regime, where the moment changes gradually. We are currently probing this hypothesis. Whatever the case, our data clearly indicates the presence of valence tautomerism in **3** and **4**.

Conclusions

We have described the synthesis of two new derivatives of 2,2′-bipyridine containing thiophene and a bridging 2,2′-bithiophene substituents. Reaction of these ligands with $Co_4(DBSQ)_8$ resulted in mono- and bimetallic coordination complexes that exhibited valence tautomerism in solution (demonstrated optically) and the solid state (demonstrated by variable temperature magnetic susceptibility experiments). Unfortunately, these complexes did not undergo electropolymerization, and we are actively pursuing the synthesis of other derivatives that should be more amenable to electropolymerization. We are also synthesizing larger 2,2′-bipyridine-substituted oligothiophene backbones for the generation of tri-, tetra-, and penta-metallic VT complexes. These efforts will be reported in due course.

Supplementary data

Supplementary data for this article are available on the journal Web site (canjchem.nrc.ca) or may be purchased from the Depository of Unpublished Data, Document Delivery, CISTI, National Research Council Canada, Ottawa, ON K1A 0R6, Canada. DUD 3891. For more information on obtaining material refer to cisti-icist.nrc-cnrc.gc.ca/cms/unpub_e.shtml.

Acknowledgement

MTL thanks the Research Corporation for a Cottrell grant (No. CC6686), the Natural Sciences and Engineering Research Council of Canada (NSERC) for Research Tools and Instruments (RTI) funding, Professor Melanie Pilkington for use of electrochemistry equipment, and Professor Fereidoon Razavi for assistance with SQUID experiments.

References

(1) Buchanan, R. M.; Pierpont, C. G. *J. Am. Chem. Soc.* **1980**, *102*, 4951. doi:10.1021/ja00535a021.

(2) (a) Beni, A.; Dei, A.; Rizzitano, M.; Sorace, L. *Chem. Commun. (Camb.)* **2007**, 2160 doi:10.1039/b702932b. PMID: 17520122.; (b) Sato, O.; Cui, A.; Matsuda, R.; Tao, J.; Hayami, S. *Acc. Chem. Res.* **2007**, *40*, 361 doi:10.1021/ar600014m. PMID:17451224.; (c) Caneschi, A.; Dei, A.; Fabrizi de Biani, F.; Gutlich, P.; Ksenofontov, V.; Levchenko, G.; Hoefer, A.; Renz, F. *Chem. Eur. J.* **2001**, *7*, 3926. doi:10.1002/1521-3765(20010917)7:18<3926::AID-CHEM3926>3.0.CO;2-6.

(3) (a) Evangelio, E.; Ruiz-Molina, D. *Eur. J. Inorg. Chem.* **2005**, 2957 doi:10.1002/ejic.200500323.; (b) Sato, O.; Tao, J.; Zhang, Y.-Z. *Angew. Chem. Int. Ed. Engl.* **2007**, *46*, 2152. doi:10.1002/anie.200602205. PMID:17348074.

(4) (a) Jung, O.-S.; Pierpont, C. G. *J. Am. Chem. Soc.* **1994**, *116*, 2229 doi:10.1021/ja00084a107.; (b) Bodnar, S. H.; Caneschi, A.; Dei, A.; Shultz, D. A.; Sorace, L. *Chem. Commun. (Camb.)* **2001**, 2151; (c) Carbonera, C.; Dei, A.; Létard, J.-F.; Sangregorio, C.; Sorace, L. *Angew. Chem. Int. Ed. Engl.* **2004**, *43*, 3136 doi:10.1002/anie.200453944.; (d) Tao, J.; Maruyama, H.; Sato, O. *J. Am. Chem. Soc.* **2006**, *128*, 1790 doi:10.1021/ja057488u. PMID:16464068.; (e) Bin-Salamon, S.; Brewer, S. H.; Depperman, E. C.; Franzen, S.; Kampf, J. W.; Kirk, M. L.; Kumar, R. K.; Lappi, S.; Peariso, K.; Preuss, K. E.; Shultz, D. A. *Inorg. Chem.* **2006**, *45*, 4461 doi:10.

1021/ic060170y. PMID:16711696.; (f) Hearns, N. G. R.; Korčok, J. L.; Paquette, M. M.; Preuss, K. E. *Inorg. Chem.* **2006**, *45*, 8817 doi:10.1021/ic0608997. PMID:17054329.; (g) Bin-Salamon, S.; Brewer, S.; Franzen, S.; Feldheim, D. L.; Lappi, S.; Shultz, D. A. *J. Am. Chem. Soc.* **2005**, *127*, 5328 doi:10.1021/ja042520q. PMID:15826164.; (h) Imaz, I.; Maspoch, D.; Rodríquez-Blanco, C.; Pérez-Falcón, J. M.; Campo, J.; Ruiz-Molina, D. *Angew. Chem. Int. Ed. Engl.* **2008**, *47*, 1857. doi:10.1002/anie.200705263. PMID:18228233.

(5) Grosshenny, V.; Romero, F. M.; Ziessel, R. *J. Org. Chem.* **1997**, *62*, 1491. doi:10.1021/jo962068w.

(6) Fang, Y.-Q.; Hanan, G. S. *Synlett*, **2003**, 852.

(7) Liao, L.; Cirpan, A.; Chu, Q.; Karasz, F. E.; Pang, Y. *J. Polym. Sci. Part A Polym. Chem. (Kyoto),* **2007**, *45*, 2048. doi:10.1002/pola.21970.

(8) Buchanan, R. M.; Fitzgerald, B. J.; Pierpont, C. G. *Inorg. Chem.* **1979**, *18*, 3439. doi:10.1021/ic50202a030.

(9) Adams, D. M.; Hendrickson, D. N. *J. Am. Chem. Soc.* **1996**, *118*, 11515. doi:10.1021/ja9619566.

(10) Adams, D. M.; Noodleman, L.; Hendrickson, D. N. *Inorg. Chem.* **1997**, *36*, 3966. doi:10.1021/ic9611812.

The neutral hydrolysis of methyl acetate — Part 1. Kinetic experiments

Yih-Huang Hsieh, Noham Weinberg, and Saul Wolfe

Abstract: The neutral hydrolysis of methyl acetate and catalysis of the reaction by the acetic acid product have been studied in the temperature range 90–110 °C. Extrapolated to 25 °C, the rate constants are 0.17×10^{-8} s^{-1} for the uncatalyzed reaction and 1.4×10^{-4} $(mol/L)^{-1}s^{-1}$ for the catalyzed reaction. The acid catalysis is specific not general: at 90 °C the rate constants for hydrochloric acid catalysis and catalysis by ionized acetic acid are the same as the rate constant, $k_H = 1.4 \times 10^{-2}$ $(mol/L)^{-1}s^{-1}$, determined in the neutral reaction.

Key words: specific acid catalysis, general acid catalysis, cooperative mechanism.

Résumé : Opérant à des températures allant de 90 à 110 °C, on a étudié l'hydrolyse neutre de l'acétate de méthyle et la catalyse de la réaction par l'acide acétique produit. Extrapolées à 25 °C, les constantes de vitesse sont égales à 0,17 x 10^{-8} s^{-1} pour la réaction non catalysée et à 1,4 x 10^{-4} $(mol/L)^{-1}$ s^{-1} pour la réaction catalysée. La catalyse acide n'est pas générale; à 90 °C, les constantes de vitesse pour la catalyse par l'acide chlorhydrique et pour la catalyse par l'acide acétique ionisé sont les mêmes que la constante de vitesse, k_H = 1,4 x 10^{-2} $(mol/L)^{-1}$ s^{-1}, déterminée pour la réaction en milieu neutre.

Mots-clés : catalyse acide spécifique, catalyse acide générale, mécanisme coopératif.

[Traduit par la Rédaction]

Introduction

In recent publications,[1–4] we have reported that the neutral, acetic acid-catalyzed and 2-hydroxypyridine(2-pyridone) catalyzed aqueous hydrations of carbonyl compounds are paradigms of cooperativity,[5,6] by which we mean that C–O bond formation and proton transfer to oxygen take place in each case through an uncharged bridge of solvent and (or) catalyst molecules. This mechanism provides a preferred neutral alternative to multistep ionic processes in which charged intermediates would be undergoing continuous solvation and desolvation as they appear and disappear.[5]

The series of studies of which the present article is Part 1 was undertaken to determine if a neutral ester hydrolysis, whether via a one-step (Scheme 1) or two-step (Scheme 2) pathway, can also proceed via a cooperative mechanism.

The issue is complicated experimentally because neutral ester hydrolysis produces a carboxylic acid, which can affect kinetics by a combination of general and specific acid catalysis, i.e.,

$$[1] \qquad k_{obs} = k_o + k_{HA}[HA] + k_H[H^+]$$

where k_o is the rate constant of the neutral reaction of interest, k_{HA} is the rate constant resulting from general acid catalysis by the product, and k_H is the rate constant resulting from specific acid catalysis by the product. Our interest is in k_o, but k_{HA}, if important, may also involve cooperativity. The specific objective of the present work is to obtain the experimental values of k_o and k_{HA} or k_H for the hydrolysis of methyl acetate in water solvent, for comparison with the values of k_o and k_{HA} calculated[7] assuming cooperative mechanisms. Prior to this work, it had been reported that ethyl acetate exhibits $k_o = 2.47 \times 10^{-10}$ s^{-1} [8] and ethyl formate exhibits $k_o = 5.0 \times 10^{-6}$ s^{-1} at 298 K.[9]

Received 27 August 2008. Accepted 23 October 2008. Published on the NRC Research Press Web site at canjchem.nrc.ca on 12 March 2009.

Y. Hsieh,[1] N. Weinberg,[2] and S. Wolfe.[2,3] Department of Chemistry, Simon Fraser University, Burnaby, BC V5A 1S6, Canada.

[1]Present address: Ningbo Smart Pharmaceutical Co. Inc. 315803 Ningbo, China.
[2]Present address: Department of Chemistry, University of the Fraser Valley, Abbotsford BC V2S 7MA, Canada.
[3]Corresponding author (e-mail: swolfe@sfu.ca).

Experimental

Materials

Methyl acetate was dried over anhyd. copper sulfate, distilled under nitrogen, and stored over 4 Å molecular sieves. $H_2{}^{16}O$ was obtained from an Easypure UV/UF ultrapure water system. Acetic acid (1.000 mol/L, Aldrich) was standardized by titration with 0.1 mol/L sodium hydroxide.

Neutral hydrolyses

Experiments were performed in sealed tubes, which had been washed sequentially with chromic acid and water, and dried at 110 °C. During reactions, all tubes were completely immersed in a stirred, temperature-controlled oil bath for the required time. Temperature control was achieved with a Model 51 Thermotronic temperature controller. To stop reactions, tubes were removed, cooled in ice, and maintained at –20 °C. Kinetics were monitored by measurement of the integrals of the methoxy peaks of methyl acetate and methanol. For reactions at 90 ± 0.5 °C, methyl acetate (4.80 mL, 4.473 g, 60.3 mmol) was added to water (60.0 mL) to give a 1.00 mol/L solution, and this solution was transferred to 60 × 1 cm tubes, which were sealed and frozen until used. For reactions at 100 ± 0.8 °C and 110 ± 0.8 °C, methyl acetate (3.60 mL, 3.355 g, 45.3 mmol) was added to water

Scheme 1.

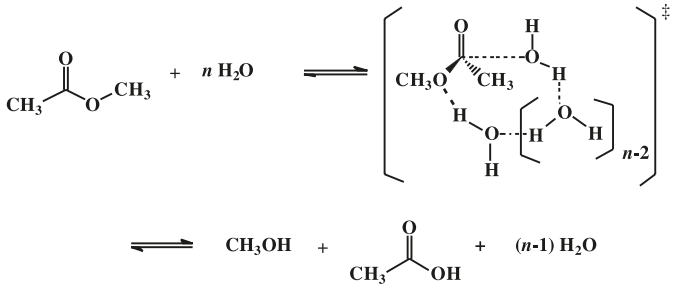

Scheme 2.

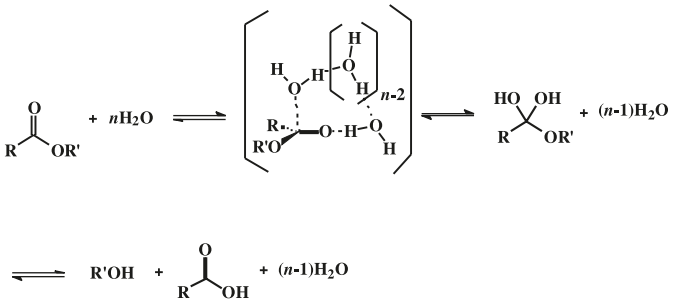

(45.0 mL) to give a 1.00 mol/L solution, and this solution was transferred to two sets of 45 × 1 cm tubes, which were sealed and frozen until used.

Catalysis by hydrochloric acid at 90 °C

0.93 mmol/L HCl

Methyl acetate (2.40 mL, 2.239 g, 30.2 mmol) and hydrochloric acid (0.30 mL, 0.100 mol/L) were added to water (30.0 mL) to give a solution (1.00 mol/L in methyl acetate and 0.93 mmol/L in hydrochloric acid). This solution was transferred to 33 × 1 cm tubes, which were sealed and frozen until needed.

4.8 mmol/L HCl

Methyl acetate (1.60 mL, 1.491 g, 20.1 mmol) and hydrochloric acid (1.0 mL, 0.100 mol/L) were added to water (20.0 mL) to give a solution (1.00 mol/L in methyl acetate and 4.8 mmol/L in hydrochloric acid). This solution was transferred to 22 × 1 cm tubes, which were sealed and frozen until needed.

6.5 mmol/L HCl

Methyl acetate (2.40 mL, 2.239 g, 30.2 mmol) and hydrochloric acid (2.1 mL, 0.100 mol/L) were added to water (30.0 mL) to give a solution (1.00 mol/L in methyl acetate and 6.5 mmol/L in hydrochloric acid), and this solution was transferred to 33 × 1 cm tubes, which were sealed and frozen until needed.

9.1 mmol/L HCl

Methyl acetate (2.40 mL, 2.239 g, 30.2 mmol) and hydrochloric acid (3.0 mL, 0.100 mol/L) were added to water (30.0 mL) to give a solution (1.00 mol/L in methyl acetate and 9.1 mmol/L in hydrochloric acid). This solution was transferred to 33 × 1 cm tubes, which were sealed and frozen until needed.

Catalysis by acetic acid at 90 °C

Methyl acetate (0.168 mL, 0.1562 g, 2.11 mmol) was added to acetic acid (21.0 mL, 1.00 mol/L) to give a solution (0.10 mol/L in methyl acetate and 1.00 mol/L in acetic acid). This solution was transferred to 21 × 1 cm tubes, which were sealed and frozen until needed.

Analysis of kinetic data

Kinetic data for the neutral hydrolyses were treated using Scheme 3 and eq. [2],

$$[2] \qquad v = -\frac{dC_E}{dt} = k_1 C_E - k_{-1} C_A C_B$$

where C_E, C_A, and C_B are the concentrations of ester, acetic acid, and methanol. Since the process is catalyzed by the product,

$$[3] \qquad k_1 = k_1^0 + k_1^H[H^+]$$

and

$$[4] \qquad k_{-1} = k_{-1}^0 + k_{-1}^H[H^+]$$

where k_1^0 and k_{-1}^0 are the neutral rate constants and k_1^H and k_{-1}^H are the specific acid-catalyzed rate constants of the forward and reverse reactions. The contribution of k_{-1}^0 can be neglected because in the initial stages of the reaction there is no reverse reaction, and as hydrolysis proceeds, the acid-catalyzed reverse reaction becomes dominant. Since C_A and C_B are stoichiometrically related to C_E and its initial value C_{E0}, eq. [2] becomes

$$[5] \qquad v = -\frac{dC_E}{dt} = (k_1^0 + k_1^H)C_E - k_{-1}^H(C_{E_0} - C_E)^2$$

The required specific acid concentration $[H^+]$ can be found from eq. [6],

$$[6] \qquad [H^+] = \frac{-(H_o + K_a) + \sqrt{(H_o + K_a)^2 + 4(C_{E_0} - C_E)K_a}}{2}$$

where H_o is 10^{-7} mol/L and K_a is the dissociation constant of acetic acid, $1.7 \pm 0.2 \times 10^{-5}$.[10]

The Verlet algorithm[11] was employed to integrate eq. [5] with a time step δt for a given set of the parameters k_1^0, k_{-1}^0, and k_{-1}^H

$$[7] \qquad C_E(t + \delta t) = C_E(t) + v(t)\delta t + \frac{1}{2}a(t)\delta t^2$$

The required acceleration of the reaction, $a(t)$, was found by differentiation of eq. [5] with respect to time

$$[8] \qquad a(t) = \frac{dv}{dt} = \{2k_{-1}^H[(C_{E_0} - C_E) - (k_1^0 + k_1^H)][H^+]v(t) + k_{-1}^H[(C_{E_0} - C_E)^2 - (k_1^0 + k_1^H)C_E]\} \times \left[\frac{-K_a}{\sqrt{(H_o + K_a)^2 + 4K_a(C_{E_0} - C_E)}}\right] v(t)$$

Scheme 3.

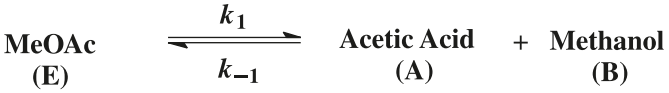

Fig. 1. Hydrolysis of methyl acetate at different temperatures.

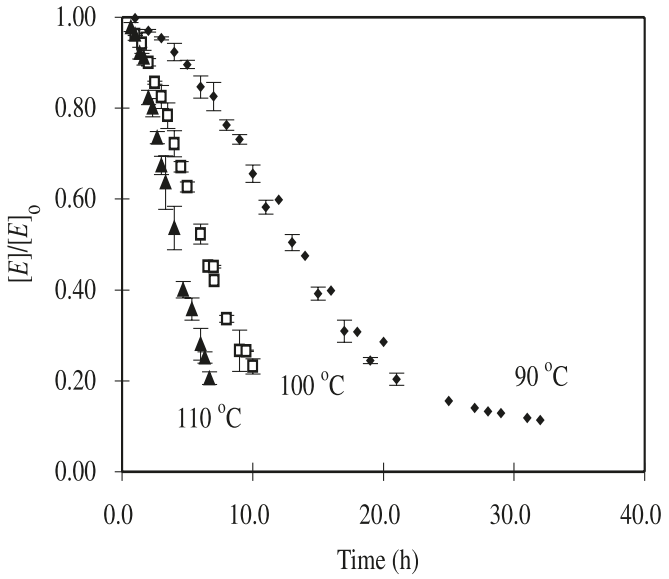

Fig. 2. Hydrolysis of methyl acetate at 90 °C.

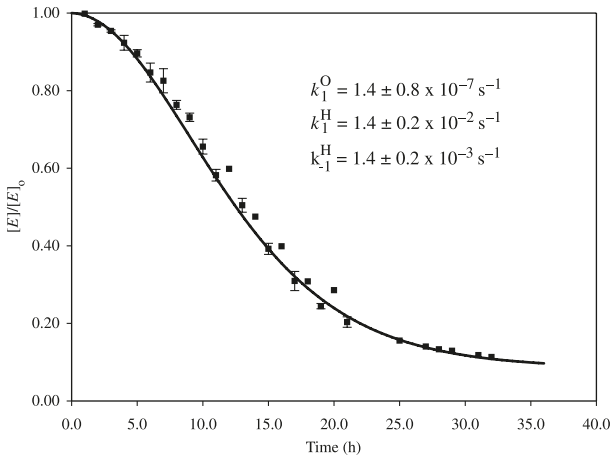

Results

Tables 1–3 of the Supplementary data and Fig. 1 provide the primary data for the hydrolysis of methyl acetate in water at 90°, 100°, and 110 °C.

The rate constants k_1^0, k_1^H, and k_{-1}^H were obtained by the best root-mean-square fit of the integrated $C(t)$ to these data (Figs. 2–4).

Figures 5 and 6 are the Arrhenius plots for k_1^0 and k_1^H, and Table 4 summarizes the results. At 25 °C, the extrapolated neutral hydrolysis rate constant k_1^0 is $1.7 \pm 1.1 \times 10^{-9}$ s^{-1}.

Catalysis by HCl

Catalysis of the hydrolysis by HCl was examined to obtain an independent determination of k_1^H and k_{-1}^H. Reactions

Fig. 3. Hydrolysis of methyl acetate at 100 °C.

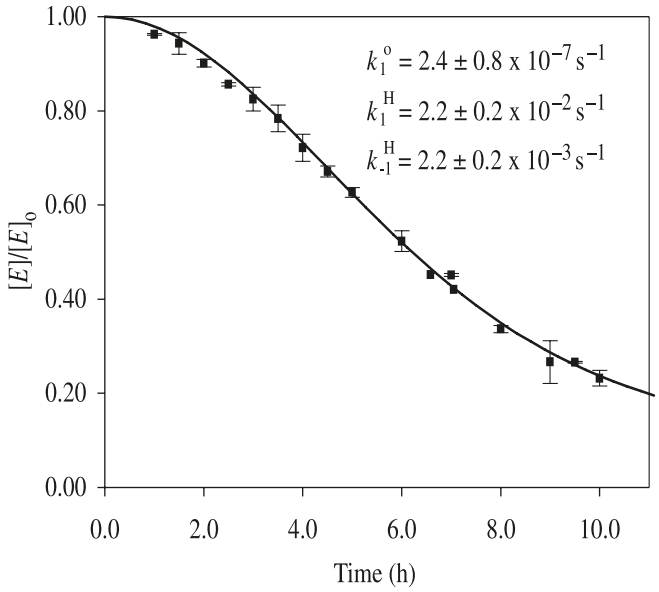

Fig. 4. Hydrolysis of methyl acetate at 110 °C.

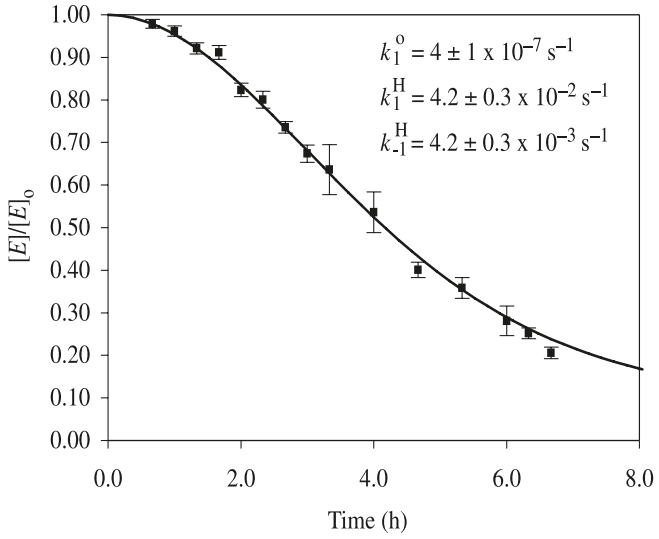

Fig. 5. Arrhenius plot of k_1^0.

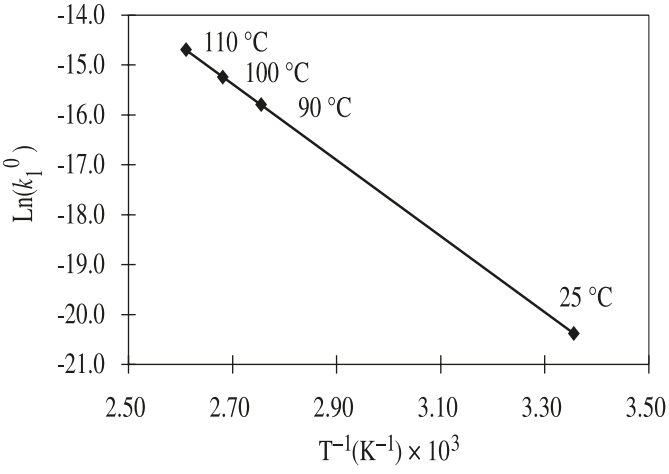

Fig. 6. Arrhenius plot of k_1^H.

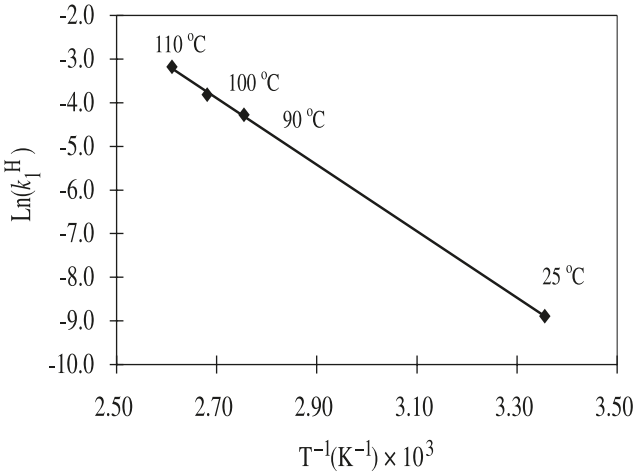

Table 4. Hydrolysis of methyl acetate at different temperatures.

Temperature (°C)	k_1^0 (s^{-1})	k_1^H (s^{-1})
110 ± 0.8	4 ± 1 × 10^{-7}	4.2 ± 0.3 × 10^{-2}
100 ± 0.8	2.4 ± 0.8 × 10^{-7}	2.2 ± 0.2 × 10^{-2}
90 ± 0.5	1.4 ± 0.8 × 10^{-7}	1.4 ± 0.2 × 10^{-2}
25	0.17 ± 0.11 × 10^{-8}[a]	1.4 ± 0.3 × 10–4[a]

[a]Extrapolated value.

Fig. 7. Hydrochloric acid catalysis of the hydrolysis of 1.0 mol/L ethyl acetate at 90 °C.

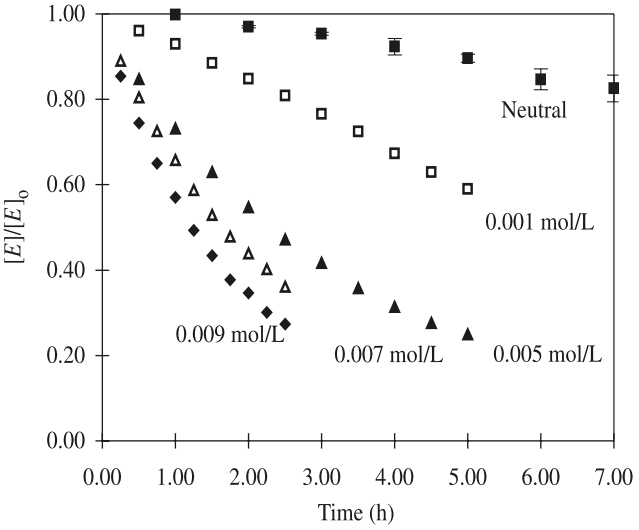

were performed at 90 °C using 1.0 mol/L methyl acetate and 1, 5, 7, and 9 mmol/L HCl. Tables 5–8 of the Supplementary data and Fig. 7 summarize the results.

The data of Fig. 7 were fitted to theoretical curves obtained by numerical integration of the rate equation, using the Verlet algorithm as before, with the results shown in Fig. 8. The values of $k_1^H = 1.4 \pm 0.2 \times 10^{-2}$ s^{-1}(mol/L)$^{-1}$ and $k_{-1}^H = 1.4 \pm 0.2 \times 10^{-3}$ s^{-1}(mol/L)$^{-2}$ are the same as in Fig. 2.

Catalysis by acetic acid

Table 9 of the Supplementary data summarizes the hydrolysis of 0.10 mol/L methyl acetate in the presence of

Fig. 8. Analysis of hydrochloric acid catalysis of the hydrolysis of 1.0 mol/L methyl acetate at 90 °C.

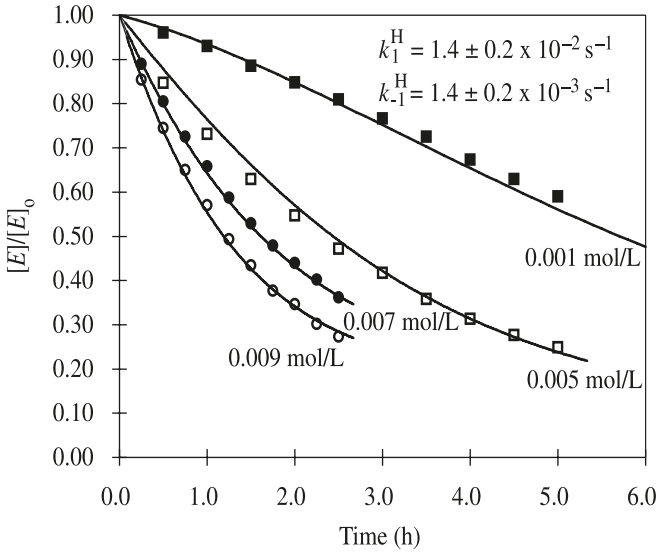

Fig. 9. Pseudo-first-order plot of the hydrolysis of 0.10 mol/L methyl acetate in the presence of 1.0 mol/L acetic acid.

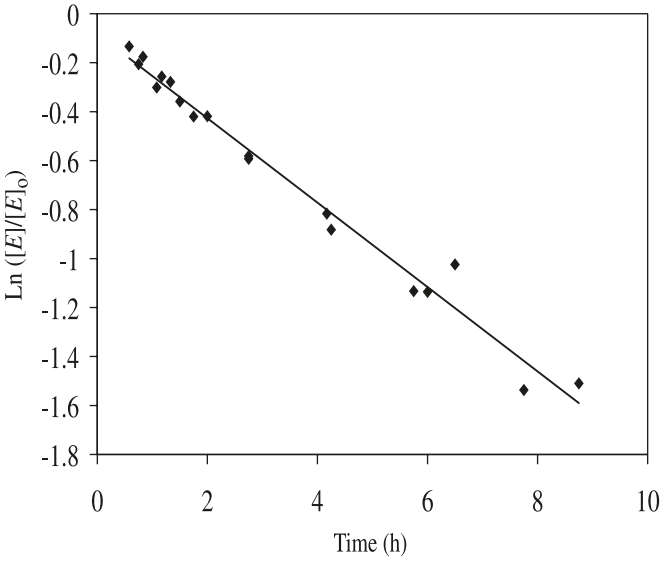

1.00 mol/L acetic acid at 90 °C, and Fig. 9 is a pseudo-first-order plot of the data, giving $k_{obs} = 5.2 \pm 0.5 \times 10^{-5}$ s^{-1}.

From eq. [6] and the dissociation constant of acetic acid, the specific hydrogen-ion concentration of 1.0 mol/L acetic acid is 4.16 × 10^{-3} mol/L. If acetic acid functions by specific acid catalysis, i.e., $k_{obs} = k_H[H^+]$, k_H is calculated to be $1.3 \pm 0.1 \times 10^{-2}$ s^{-1}, identical to the value found in catalysis by HCl and in the analysis of neutral hydrolysis. It can be concluded that the hydrolysis of methyl acetate does not proceed with general acid catalysis by the product.

Supplementary data

Supplementary data for this article are available on the journal Web site (canjchem.nrc.ca) or may be purchased from the Depository of Unpublished Data, Document Delivery, CISTI, National Research Council Canada, Ottawa, ON

K1A 0R6, Canada. DUD 3882. For more information on obtaining material, refer to cisti-icist.nrc-cnrc.gc.ca/cms/unpub_e.shtml.

Acknowledgement

This research was supported financially by a Discovery Grant from the Natural Sciences and Engineering Research Council of Canada (NSERC).

References

(1) Wolfe, S.; Kim, C.-K.; Yang, K.; Weinberg, N.; Shi, Z. *J. Am. Chem. Soc.* **1995**, *117*, 4240. doi:10.1021/ja00120a005.
(2) Wolfe, S.; Shi, Z.; Yang, K.; Ro, S.; Weinberg, N.; Kim, C.-K. *Can. J. Chem.* **1998**, *76*, 114. doi:10.1139/cjc-76-1-114.
(3) Hsieh, Y.-H.; Weinberg, N.; Yang, K.; Kim, C.-K.; Shi, Z.; Wolfe, S. *Can. J. Chem.* **2005**, *83*, 769. doi:10.1139/v05-027.
(4) Hsieh, Y.-H.; Weinberg, N.; Wolfe, S. *Can. J. Chem.* **2008**, *86*, 81. doi:10.1139/V07-074.
(5) Eigen, M. *Discuss. Faraday Soc.* **1965**, *39*, 7. doi:10.1039/df9653900007.
(6) Huang, H. H.; Robinson, R. R.; Long, F. A. *J. Am. Chem. Soc.* **1966**, *88*, 1866. doi:10.1021/ja00961a003.
(7) Shi, Z.; Hsieh, Y.-H.; Weinberg, N.; Wolfe, S. *Can. J. Chem.* **2009**, *87*, 544. doi:10.1139/v09-011.
(8) Skrabal, A.; Zahorka, A. *Monatsh. Chem.* **1929**, *53–54*, 562. doi:10.1007/BF01521817.
(9) Mata-Segreda, J. F. *Int. J. Chem. Kinet.* **2000**, *32*, 67. doi:10.1002/(SICI)1097-4601(2000)32:1<67::AID-JCK8>3.0.CO;2-M.
(10) Sue, K.; Usami, T.; Arai, K. J. *J. Chem. Eng. Data*, **2003**, *48*, 1081. doi:10.1021/je030142j.
(11) (a) Verlet, L. *Phys. Rev.* **1967**, *159*, 98. doi:10.1103/PhysRev.159.98.; (b) The dissociation constants of carboxylic acids show little temperature dependence. Please see: Lee, I.-J.; Kang, G.-S.; Kim, K. *J. Solut. Chem.* **1994**, *23*, 1283. doi:10.1007/BF00974181.

The neutral hydrolysis of methyl acetate — Part 2. Is there a tetrahedral intermediate?

Zheng Shi, Yih-huang Hsieh, Noham Weinberg, and Saul Wolfe

Abstract: A computational strategy that reproduces the experimental rates of hydration of formaldehyde, acetaldehyde, acetone, and cyclohexanone and the rates of acetic acid and 2-hydroxypyridine-catalyzed hydration of acetone has been extended to the results of the neutral hydrolysis of methyl acetate reported in Part 1. Calculations have been performed for one-step and two-step mechanisms, with cooperative assistance from one to three additional water molecules in the presence and absence of the acetic acid product. The calculations predict that, for the neutral reaction, a one-step mechanism will be favoured if tetrahedral intermediates have a short lifetime and do not interconvert prior to breakdown (case A), and a two-step mechanism will be operative if tetrahedral intermediates are allowed to interconvert prior to breakdown (case B). The experimental results are consistent with the predictions of case A. In the presence of acetic acid, case A predicts that the acid will contribute only 1.6% to the overall rate, a negligible acceleration over the noncatalytic process, and case B predicts general acid catalysis to be an order of magnitude greater than the experimental result. It is concluded that the neutral hydrolysis of methyl acetate is mainly a cooperative one-step process, and that general acid catalysis by the acetic acid product does not occur.

Key words: cooperative mechanism, one-step mechanism, tetrahedral intermediate.

Résumé : Une stratégie théorique permettant de reproduire les vitesses expérimentales d'hydratation du formaldéhyde, de l'acétaldéhyde, de l'acétone et de la cyclohexanone ainsi que les vitesses d'hydratation de l'acétone catalysée par l'acide acétique et la 2-hydroxypyridine a été étendue aux résultats de l'hydrolyse neutre de l'acétate de méthyle rapportée dans la partie 1. Les calculs ont été effectués pour les mécanismes à une et à deux étapes, avec l'assistance coopérative d'une, deux ou trois molécules d'eau, en présence et en absence d'acide acétique produit. Les calculs permettent de prédire que, pour la réaction neutre, le mécanisme en une étape sera favorisé si les intermédiaires tétraédriques sont de courte vie et qu'ils ne donnent pas lieu à une interconversion avec leur rupture (cas A) et un mécanisme en deux étapes qui opérera si les intermédiaires peuvent subir une interconversion avant leur rupture (cas B). Les résultats expérimentaux sont en accord avec les prédictions du cas A. En présence d'acide acétique, le cas A prédit que l'acide ne contribuera qu'à 1,6% de la vitesse globale, une accélération négligeable par rapport au processus non catalytique; le cas B prédit une catalyse acide générale qui serait d'un ordre de grandeur plus important que le résultat expérimental. On peut donc en conclure que l'hydrolyse neutre de l'acétate de méthyle est principalement en processus coopératif en une étape et que la catalyse par l'acide acétique produit n'a pas lieu.

Mots-clés : mécanisme coopératif, mécanisme en une étape, intermédiaire tétraédrique.

[Traduit par la Rédaction]

Introduction

Background

In recent publications, we have discussed the neutral,[1,2] acetic acid-catalyzed,[3] and 2-hydroxypyridine-catalyzed[4] aqueous hydrations of acetone as exemplars of cooperativity, by which we mean that in each case concurrent C–O bond formation and proton transfer to oxygen take place through a bridge of solvent and (or) catalyst molecules (eq [1]). As originally posited by Eigen[5] and by Long and co-workers,[6] the cooperative mechanism offers a preferred neutral alternative to a multistep ionic mechanism in which charged intermediates are subjected to continuous solvation and desolvation as they appear and disappear.

[1] 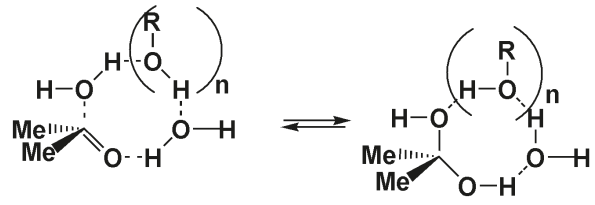

Received 27 August 2008.. Accepted 25 November 2008 Published on the NRC Research Press Web site at canjchem.nrc.ca on 12 March 2009.

Z. Shi,[1] Y. Hsieh,[2] N. Weinberg,[3] and S. Wolfe.[4] Department of Chemistry, Simon Fraser University, Burnaby, BC V5A 1S61, Canada.

[1]Present address: Institute for Fuel Cell Innovation, National Research Council, 3250 East Mall, Vancouver, BC V6T 1W5, Canada.
[2]Present address: Ningbo Smart Pharmaceutical Co. Ltd., Ningbo, 315803, China.
[3]Present address: Department of Chemistry, University of the Fraser Valley, Abbotsford, BC V2S 7MA, Canada.
[4]Corresponding author (e-mail: swolfe@sfu.ca).

In the work of ref. 1, we found that experimental hydration rates in water solvent can be reproduced by a computational strategy that affords the free energy barriers exhibited by different reaction complexes as well as the concentrations of these complexes. This is achieved by HF/3–21G calculations,[7,8] in conjunction with the self-consistent reaction field (SCRF, Onsager) model[9,10] with a dielectric constant of 78.5. The previously optimized gas-phase structures were used to estimate the radius of the cavity for SCRF calculations. Transition structures were located by the reaction coordinate method.

Free energies of complexes, corrected for loss of translational and rotational degrees of freedom, are calculated using eq. [2].[1,2]

$$[2]\qquad \Delta G = \Delta H - T\Delta S_{\text{vib}} - 6RT\left\{\frac{\hbar\omega/kT}{\exp\left(\hbar\omega/kT\right)-1} - \ln\left[1-\exp\left(-\frac{\hbar\omega}{kT}\right)\right]\right\}$$

The first term on the right-hand side of eq. [2] is the enthalpy change calculated using the 3–21G basis set[8] and augmented by correction for the basis set superposition error (BSSE).[1,11] The second term on the right-hand side accounts for the intramolecular vibration entropy change, and it is also calculated by the Gaussian programme.[8] The third term on the right-hand side refers to the entropy change resulting from the loss of six low-frequency vibration modes representing rotational and translational motions in solution. These vibrations are described by a mass-dependent effective frequency ω, scaled as a root of molecular mass[2] and defined in terms of a single adjustable parameter ω_0, which is estimated numerically for water monomer (m_0 = 18 au) to be 20 cm^{-1}.[1]

At 298 K, the neutral hydration of acetone exhibits k_{obs} = 8.9 × 10^{-6} s^{-1}.[2] The calculated rate is k_{calc} = 19.6 × 10^{-6} s^{-1}, and the principal channel, comprising 97% of the overall reaction, proceeds via the four-water molecule complex **1**, whose free energy barrier and concentration are 11.34 kcal/mol (1 cal = 4.184 J) and 1.63 × 10^{-10} mol/L, respectively.

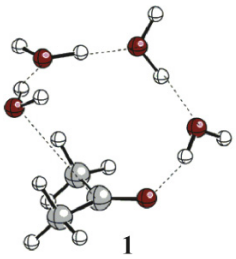

1

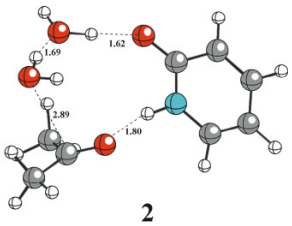

2

Addition of 1 mmol/L 2-hydroxypyridine to a 1 mol/L acetone solution leads to k_{obs} = 1.3 × 10^{-3} s^{-1} at 298 K, a catalytic effect of 150.[4] The calculated rate is k_{calc} = 2.1 × 10^{-3} s^{-1}, and 96% of the reaction, with a free energy barrier of 11.97 kcal/mol, proceeds via the 2-*pyridone* dihydrate **2**, whose concentration of 1.08 × 10^{-7} mol/L is almost 700 times greater than that of **1**. The "bifunctional catalysis"[12] exhibited by 2-hydroxypyridine therefore resides in the exceptional stability of **2**.

Neutral ester hydrolysis

The present work was undertaken to determine whether an appropriate extension of the cooperative mechanism,

Scheme 1.

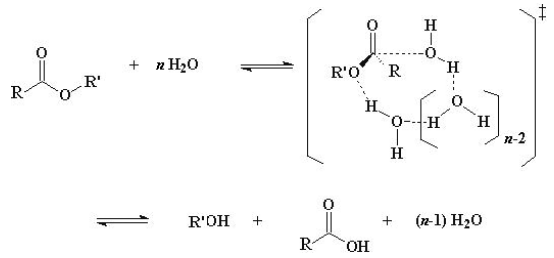

Scheme 2.

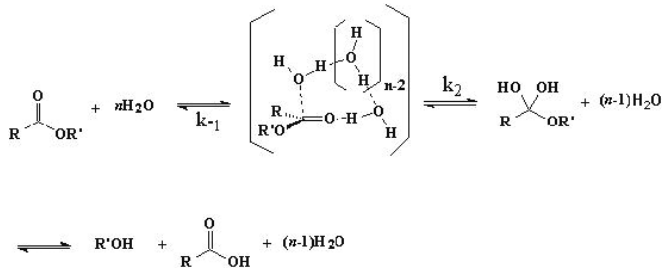

e.g., Scheme 1 or 2, could be relevant in neutral ester hydrolysis in water solvent. It will be noticed that Scheme 1 suggests the possibility of a one-step process that bypasses the tetrahedral intermediate of Scheme 2,[13] which is well established for acid-catalyzed (**3a**) and base-catalyzed (**3b**) ester hydrolysis.

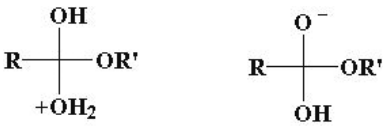

3a **3b**

In contrast to the extensive literature on acid- and base-catalyzed ester hydrolysis,[13–15] there has been only sporadic interest in neutral hydrolysis (Table 1). At 298 K (Table1, entry 1) the hydrolysis of ethyl acetate proceeds with a first-order rate constant of 2.47 × 10^{-10} s^{-1} ($\Delta G^{\ddagger}$ = 30.6 kcal/mol[21]).

Temperature dependence studies of the hydrolyses of alkyl- and aryl-substituted trifluoroacetates in aqueous acetone lead to rate constants of 1.67–5.67 × 10^{-8} s^{-1} at 25 °C (Table 1, entry 2). For the hydrolysis of chloromethyl chloroacetate (Table 1, entry 3), $\Delta H^{\ddagger}$ = 11.8 kcal/mol and $\Delta S^{\ddagger}$ = –37 cal mol^{-1} K^{-1} at 25 °C. From the rates of hydrolysis of ethyl trifluorothiolacetate in the presence of potassium acetate – acetic acid buffers, and extrapolation to zero buffer concentration, a neutral rate constant of 5.02 × 10^{-3} s^{-1} at 25 °C is obtained (Table 1, entry 4), and proton inventory experiments suggest that there are two to three hydrons in flight. The kinetics and activation parameters for the hydrolysis of ethyl formate in the temperature range 30–50 °C provide a rate constant of 5.0 × 10^{-6} s^{-1} at 298 K (Table 1, entry 5).

The theoretical treatment of neutral ester hydrolysis is even less well-advanced than the limited number of experi-

Table 1. Experimental studies of neutral ester hydrolysis.

Entry	Reactant	Solvent	Rate (s^{-1})[a]	$\Delta H^{\ddagger}$[b] or Ea[b]	$\Delta S^{\ddagger}$[c]	Ref.
1	$MeCO_2Et$	H_2O	2.47×10^{-10}			16
2	CF_3CO_2R	Me_2CO/H_2O				17
	R = C_3H_7		5.67×10^{-8}	9.8	–51.7	
	R = C_4H_9		3.50×10^{-8}	10.9	–49.1	
2	R = C_6H_5		1.67×10^{-8}	6.85	–45.9	
3	$ClCH_2CO_2CH_2Cl$	H_2O	2.29×10^{-5}	11.8	–37	18
4	CF_3COSEt	H_2O	5.02×10^{-3}			19
5	HCO_2Et	H_2O	5.0×10^{-6}[d]	22	–11	20

[a]At 298 K.
[b]In kcal/mol.
[c]In cal mol^{-1} K^{-1}.
[d]Extrapolated value.

mental studies just cited. For the hydrolysis of methyl formate via Schemes 1 and 2, with n = 3, gas-phase B3LYP/6–31G* geometry optimizations, followed by single-point calculations with a polarized continuum model of bulk water, give free energy barriers of 45.66 and 48.05 kcal/mol, respectively, for two-step and one-step mechanisms.[22]

For a two-step gas-phase hydrolysis of ethyl acetate with n = 2 (Scheme 2), 6–31+G* calculations afford a free energy barrier of 64.3 kcal/mol.[21] In the B3LYP/6–31G*/SCRF calculations of Yamabe et al. on the aqueous hydrolysis of ethyl acetate in the presence of different numbers of active water molecules,[23] the concerted (one-step) free energy barrier ranges between 42.9 and 47.9 kcal/mol, much higher than the experimental $\Delta G^{\ddagger}$ of Skrabal and Zahorka.[16] A two-step mechanism with $k_{-1} \approx k_2$ gives free energy barriers close to the experimental $\Delta G^{\ddagger}$, the reaction via a four-water molecule complex being favoured.

Each of the theoretical studies just cited has focused on the magnitudes of calculated barriers. However, as in the hydration studies discussed earlier, we presume that the calculation of hydrolysis *rates* will require that the *concentrations* of reaction complexes also be taken into account.

Present work

In the present work, of which this is Part 2, we have applied our computational strategy[1,2] to study the neutral hydrolysis of methyl acetate. Since the acetic acid product of hydrolysis catalyzes the reaction,[24] the notion of cooperativity has also been extended to this reaction. The kinetic experiments designed to test the predictions of Part 2 are found in Part 1.[24]

Neutral hydrolysis

One-step mechanism

In Scheme 1, the addition of a water molecule to the carbonyl group takes place in concert with proton transfer to the methoxy group. Calculations were performed for n = 1–4 to obtain the free energies of the stationary structures of Scheme 3 in water solvent, where $\mathbf{W}_n\mathbf{E}$ is a cyclic reactant complex of methyl acetate (**E**) with n water molecules (**W**; n = 1–4), **TS***n*′ is a cyclic transition structure derived from $\mathbf{W}_n\mathbf{E}$, and **PC***n* is a product complex of methanol, acetic acid, and (n – 1) water molecules.

Scheme 3.

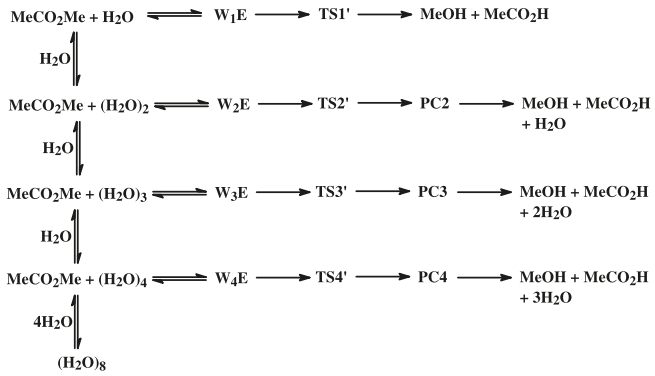

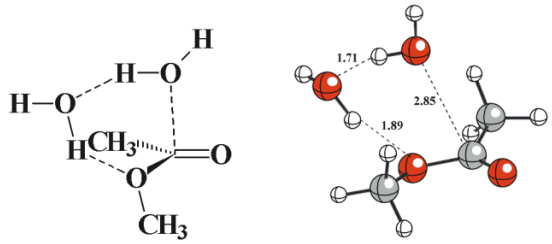

4b

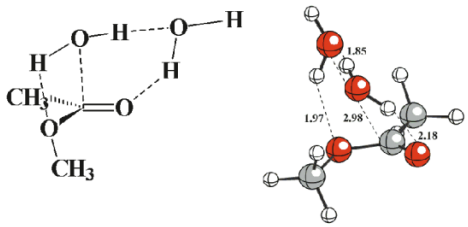

4c

More than one $\mathbf{W}_n\mathbf{E}$ complex is possible when n > 1, e.g., **4b** and **4c** for n = 2. All conceivable topologies of reactant complexes of Scheme 3 were taken into account.

Table 2 lists the ΔG and $\Delta G^{\ddagger}$ calculated at 298 K. Structures **4a**, **4b–4c**, **4d–4f**, and **4g–4k** are, respectively, one-water, two-water, three-water, and four-water $\mathbf{W}_n\mathbf{E}$, and structures **5a–5k** are the **TS***n*′ derived from these complexes. (Structures not shown in the text and full Tables 2–9 are available in the Supplementary data below.)

Table 2. Calculated Gibbs free energies for the neutral hydrolysis of methyl acetate at 298 K via Scheme 3.

Complex	ΔG (kcal/mol)
W_1E 4a	4.04
W_2E 4b	8.57
W_2E 4c	10.27
W_3E 4d	8.28
W_3E 4e	8.31
W_3E 4f	4.74
W_4E 4g	12.06
W_4E 4h	14.35
W_4E 4i	10.94
W_4E 4j	13.83
W_4E 4k	16.33
Transition structure	$\Delta G^{\ddagger}$ (kcal/mol)
TS1′ 5a	47.62
TS2′ 5b	29.31
TS2′ 5c	50.07
TS3′ 5d	22.27
TS3′ 5e	31.20
TS3′ 5f	36.62
TS4′ 5g	15.28
TS4′ 5h	17.43
TS4′ 5i	37.45
TS4′ 5j	37.70
TS4′ 5k	34.33

Scheme 4.

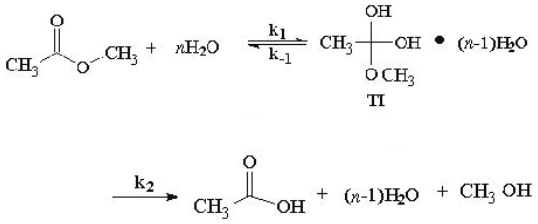

Two-step mechanism

Scheme 4 describes a two-step neutral ester hydrolysis via **TI**, a tetrahedral intermediate. In the network of reactions shown in Scheme 5, the hydrolysis proceeds from the reactant complexes $\mathbf{W}_n\mathbf{E}$, via a first transition structure $\mathbf{TS}n''$ to the tetrahedral intermediates $\mathbf{TI}n$, and then via a second transition structure $\mathbf{TS}n'''$ to the product complexes $\mathbf{PC}n$. As before, more than one $\mathbf{W}_n\mathbf{E}$ complex is possible for $n > 1$. All conceivable topologies of reactant complexes of Scheme 5 were taken into account.

Tables 3 and 4 list the ΔG and $\Delta G^{\ddagger}$ calculated at 298 K. Structures **6a**, **6b–6c**, **6d–6g**, and **6h–6o** are, respectively, one-water, two-water, three-water, and four-water $\mathbf{W}_n\mathbf{E}$, structures **7a–7o** refer to $\mathbf{TS}n''$, the transition structures connecting $\mathbf{W}_n\mathbf{E}$ to the tetrahedral intermediates **8a–8o**, and structures **9a–9o** refer to $\mathbf{TS}n'''$, the transition structures connecting the tetrahedral intermediates to the products.

The theoretical rate constant

As in our previous works,[1–4] the hydrolysis rate constant can be calculated by taking into account pre-equilibrium

Table 3. Calculated Gibbs free energies of the reactant complexes $\mathbf{W}_n\mathbf{E}$ and transition states $\mathbf{TS}n''$ for the neutral hydrolysis of methyl acetate at 298 K via Scheme 5.

Complex	ΔG (kcal/mol)
W_1E 6a	2.54
W_2E 6b	4.95
W_2E 6c	8.14
W_3E 6d	4.78
W_3E 6e	13.79
W_3E 6f	13.82
W_3E 6g	8.77
W_4E 6h	16.49
W_4E 6i	12.16
W_4E 6j	23.24
W_4E 6k	19.16
W_4E 6l	21.10
W_4E 6m	11.97
W_4E 6n	20.55
W_4E 6o	11.67
TSn″	$\Delta G^{\ddagger}$ (kcal/mol)
TS1″ 7a	48.66
TS2″ 7b	21.64
TS2″ 7c	41.56
TS3″ 7d	14.36
TS3″ 7e	14.95
TS3″ 7f	14.38
TS3″ 7g	38.93
TS4″ 7h	14.34
TS4″ 7i	13.17
TS4″ 7j	8.06
TS4″ 7k	10.30
TS4″ 7l	9.49
TS4″ 7m	34.12
TS4″ 7n	17.87
TS4″ 7o	18.44

Scheme 5.

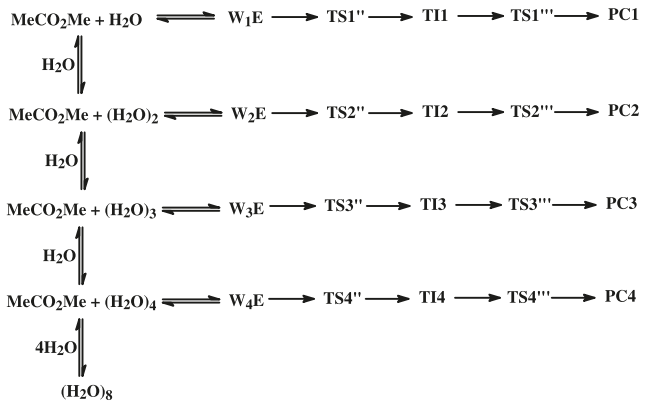

Table 4. Calculated Gibbs free energies of the intermediates **TI*n*** and transition states **TS*n*‴** for the neutral hydrolysis of methyl acetate at 298 K via Scheme 5.

TI*n*	ΔG (kcal/mol)
TI1 8a	5.79
TI2 8b	3.96
TI2 8c	1.03
TI3 8d	9.01
TI3 8e	–2.25
TI3 8f	–3.45
TI3 8g	–1.39
TI4 8h	0.39
TI4 8i	0.11
TI4 8j	–5.11
TI4 8k	–6.16
TI4 8l	–6.97
TI4 8m	–4.56
TI4 8n	–4.15
TI4 8o	4.63
TSn‴	$\Delta G^{\ddagger}$ (kcal/mol)
TS1‴ 9a	46.27
TS2‴ 9a	39.04
TS2‴ 9c	20.56
TS3‴ 9d	34.74
TS3‴ 9e	15.82
TS3‴ 9f	14.95
TS3‴ 9g	14.59
TS4‴ 9h	37.95
TS4‴ 9i	15.77
TS4‴ 9j	11.20
TS4‴ 9k	7.41
TS4‴ 9l	5.82
TS4‴ 9m	12.57
TS4‴ 9n	18.11
TS4‴ 9o	25.94

Scheme 6.

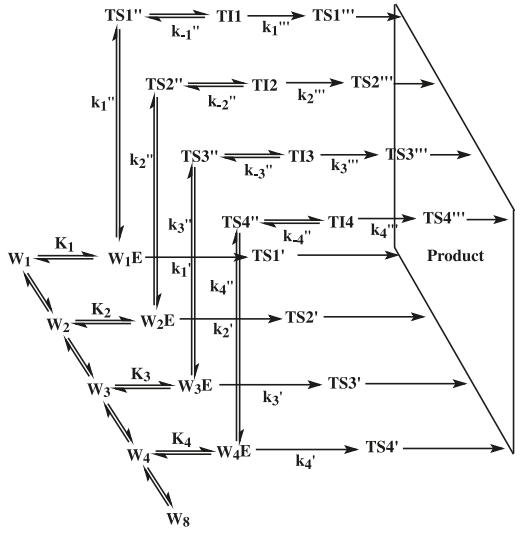

Scheme 7.

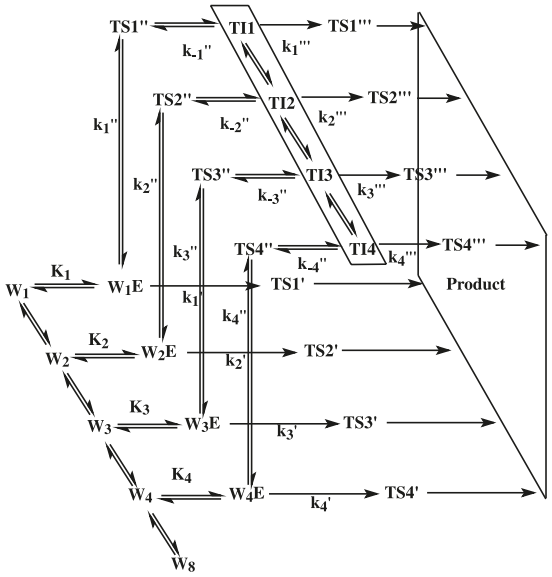

among water clusters and reactant complexes, as shown in Scheme 6, combining one- and two-step channels of Schemes 3 and 5. There is, however, an additional complication here because **TI**–water complexes may interconvert. To treat this possibility, two limiting cases were considered: in case (A) the **TI** are short-lived and do not undergo exchange with the solvent (Scheme 6); in case (B) the **TI** are sufficiently stable to allow equilibration among complexes containing different numbers of water molecules (Scheme 7). In either case, $\mathbf{W}_n$ refers to n-mers of water, **E** is the ester, $\mathbf{K}_n$ is the equilibrium constant for the formation of $\mathbf{W}_n\mathbf{E}$, k'_n is the rate constant of a reaction channel of the one-step mechanism, and k''_n, k''_{-n}, and k'''_n are the rate constants of the two-step mechanism.

As already noted, more than one $\mathbf{W}_n\mathbf{E}$ complex is possible for $n > 1$. Those that interconvert through a single step mechanism are labelled $\mathbf{W}_n\mathbf{E}'$, and those that interconvert through a two-step mechanism are labelled $\mathbf{W}_n\mathbf{E}''$. The overall concentration $[\mathbf{W}_n\mathbf{E}]$ is,

$$[\mathrm{W}_n\mathrm{E}] = \sum[\mathrm{W}_n\mathrm{E}'] + \sum[\mathrm{W}_n\mathrm{E}'']$$

and the independent relationships among the concentrations of $\mathbf{W}_n$ and $\mathbf{W}_n\mathbf{E}$ are,

$$[\mathrm{W}_n] = K_n^w[\mathrm{W}_1]^n$$
$$[\mathrm{W}_n\mathrm{E}'] = K'_n[\mathrm{W}_n][\mathrm{E}] = K'_nK_n^w[\mathrm{W}_1]^n[\mathrm{E}]$$
$$[\mathrm{W}_n\mathrm{E}''] = K''_n[\mathrm{W}_n][\mathrm{E}] = K''_nK_n^w[\mathrm{W}_1]^n[\mathrm{E}]$$

In addition, the following two equations of material balance apply to these concentrations,

$$[3] \qquad C_{\mathrm{W}} = \sum_n n[\mathrm{W}_n] + \sum_n n[\mathrm{W}_n\mathrm{E}]$$

$$[4] \qquad C_{\mathrm{E}} = [\mathrm{E}] + \sum_n [\mathrm{W}_n\mathrm{E}]$$

where C_{W} and C_{E} are the analytical concentrations of water (55.5 mol/L) and ester, respectively.

Table 5. Complexes providing major contributions to the rate of hydrolysis of 1.0 mol/L methyl acetate (limiting case A).

Species	Concentration (mol/L)	Rate constant (s^{-1})	Partial rate (mol/L s^{-1})	Contribution (%)[a]
One-step				
W_4E' 4g	1.21×10^{-10}	79.0	9.58×10^{-9}	71.68
All **W_4E'**	—	—	9.58×10^{-9}	71.72
Two-step				
W_4E'' 6i	1.02×10^{-10}	3.42×10	3.48×10^{-9}	26.02
All **W_4E''**	—	—	3.78×10^{-9}	28.28
Total rate (s^{-1})			1.34×10^{-8}	

[a]Contribution to the overall rate of reaction.

Table 6. Complexes providing major contributions to the rate of hydrolysis of 1.0 mol/L methyl acetate (limiting case B).

Species	Concentration (mol/L)	Rate constant (s^{-1})	Partial rate (mol/L s^{-1})	Contribution (%)[a]
One-step				
W_4E' 4g	1.21×10^{-10}	7.90×10	9.58×10^{-9}	2.67
All **W_4E'**	—	—	9.58×10^{-9}	2.67
Two-step: **$W_nE \rightleftharpoons TSn''$**				
W_2E'' 6b	4.61×10^{-5}	1.72×10^{-3}[b]		
		1.36[c]	7.93×10^{-8}	22.70
W_3E'' 6d	2.40×10^{-10}	3.69×10^{2}[b]		
		1.48×10^{9}[c]	4.88×10^{-8}	13.97
W_3E'' 6e	5.99×10^{-17}	1.38×10^{2}[b]		
		3.07[c]	-1.48×10^{-8}[d]	–4.25
W_3E'' 6f	5.67×10^{-17}	3.61×10^{2}[b]		
		1.06[c]	-3.89×10^{-8}[d]	–11.15
W_4E'' 6i	1.02×10^{-10}	2.77×10^{3}[b]		
		3.36×10^{3}[c]	2.82×10^{-7}	80.66
Two-step: **$TIn \rightarrow TSn'''$**				
TI3 8f	3.66×10^{-8}	4.03×10^{-1}	1.47×10^{-8}	4.22
TI3 8g	1.12×10^{-9}	24.1	2.70×10^{-8}	7.72
TI4 8k	1.39×10^{-11}	1.40×10^{3}	1.95×10^{-8}	5.57
TI4 8l	5.41×10^{-11}	5.27×10^{3}	2.85×10^{-7}	81.50
All **TIn**	—	—	3.49×10^{-7}	97.33
Total rate (s^{-1})			35.9×10^{-8}	

[a]Contribution to the overall rate of reaction.
[b]Rate constant for **$W_nE \rightarrow TSn''$**, the forward reaction.
[c]Rate constant for **$TIn \rightarrow TSn''$**, the reverse reaction.
[d]The reverse process dominates.

Limiting case A: No interconversion between TI*n* (Scheme 6)

In this case, all two-step channels are considered to be independent of each other. Application of the steady-state approximation leads to a set of effective rate constants,

$$[5] \qquad k_{\text{eff},\,n} = \frac{k''_n k'''_n}{(k''_{-n} + k'''_n)}$$

resulting in eqs. [6] and [7] for the overall rate of hydrolysis and its pseudo first-order rate constant k.

$$[6] \qquad v = kC_E = \sum k'_n[W_nE'] + \sum k_{\text{eff},\,n}[W_nE''']$$

$$[7] \qquad k = \frac{\sum k'_n K'_n[W_n] + \sum k''_n K''_n[W_n]}{1 + \sum K'_n[W_n] + \sum K''_n[W_n]}$$

Table 5 summarizes the results for the hydrolysis of a 1.00 mol/L methyl acetate solution at 298 K. According to this analysis, at 298 K the rate of hydrolysis is 1.34×10^{-8} s^{-1}, 72% of the reaction proceeds by a one-step mechanism from the four-water complex **4g** (Fig. 1) and 26% by a two-step mechanism from the four-water complex **6i** (Fig. 2).

Table 7. Calculated Gibbs free energies at 298 K for species involved in the acetic acid-catalyzed hydrolysis of methyl acetate via Scheme 8.

W_nEA'	ΔG (kcal/mol)	$TSAn'$	$\Delta G^{\ddagger}$ (kcal/mol)
W_1EA' 12a	–2.14	**TSA1′ 13a**	22.61
W_1EA' 12b	–4.24	**TSA1′ 13b**	36.78
W_2EA' 12c	32.14	**TSA2′ 13c**	25.12
W_2EA' 12d	34.65	**TSA2′ 13d**	26.74
W_2EA' 12e	29.09	**TSA2′ 13e**	19.95
W_2EA' 12f	33.49	**TSA2′ 13f**	13.51
W_nEA''		**$TSAn''$**	
W_1EA'' 14a	0.57	**TSA1″ 15a**	7.12
W_1EA'' 14b	–7.01	**TSA1″ 15b**	25.28
W_1EA'' 14c	–2.80	**TSA1″ 15c**	40.30
W_1EA'' 14d	5.56	**TSA1″ 15d**	43.35
W_2EA'' 14e	4.09	**TSA2″ 15e**	11.76
W_2EA'' 14f	–1.57	**TSA2″ 15f**	10.29
W_2EA'' 14g	1.18	**TSA2″ 15g**	14.87
W_2EA'' 14h	7.36	**TSA2″ 15h**	6.27
W_2EA'' 14i	8.24	**TSA2″ 15i**	17.79
W_2EA'' 14j	4.72	**TSA2″ 15j**	12.23
W_2EA'' 14k	1.80	**TSA2″ 15k**	39.67
W_2EA'' 14l	–0.08	**TSA2″ 15l**	36.25
W_3EA'' 14m	9.75	**TSA3″ 15m**	4.87
W_3EA'' 14n	7.29	**TSA3″ 15n**	7.48
W_3EA'' 14o	9.90	**TSA3″ 15o**	7.75
W_3EA'' 14p	3.89	**TSA3″ 15p**	5.09
TIA*n*		**$TSAn'''$**	
TIA1 16a	–4.93	**TSA1‴ 17a**	27.81
TIA1 16b	8.20	**TSA1‴ 17b**	40.79
TIA1 16c	–1.85	**TSA1‴ 17c**	10.44
TIA1 16d	–0.41	**TSA1‴ 17d**	12.32
TIA2 16e	–0.92	**TSA2‴ 17e**	31.44
TIA2 16f	–0.67	**TSA2‴ 17f**	36.83
TIA2 16g	1.37	**TSA2‴ 17g**	15.21
TIA2 16h	–6.06	**TSA2‴ 17h**	9.33
TIA2 16i	–0.77	**TSA2‴ 17i**	12.88
TIA2 16j	–5.58	**TSA2‴ 17j**	5.39
TIA2 16k	–0.36	**TSA2‴ 17k**	13.42
TIA2 16l	–4.50	**TSA2‴ 17l**	9.67
TIA3 16m	–6.86	**TSA3‴ 17m**	13.04
TIA3 16n	–8.77	**TSA3‴ 17n**	3.09
TIA3 16o	–8.98	**TSA3‴ 17o**	4.35
TIA3 16p	–7.65	**TSA3‴ 17p**	1.58

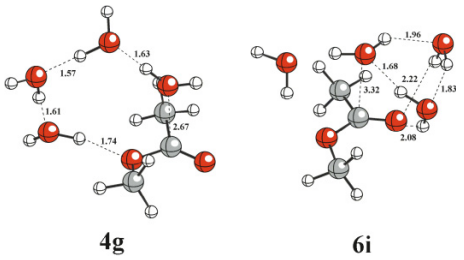

Limiting case B: Fast equilibrium among TI*n*

If equilibrium among **TI**′s is taken into account, Scheme 6 is modified to Scheme 7, and the rate of the reversible reac-

Fig. 1. Reaction coordinate of the major hydrolysis channel of limiting case A.

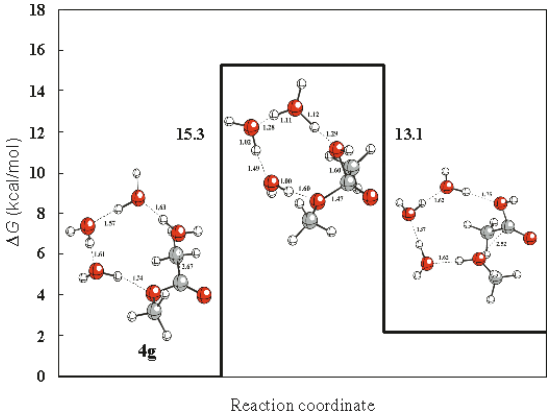

Fig. 2. Reaction coordinate of the minor hydrolysis channel of limiting case A.

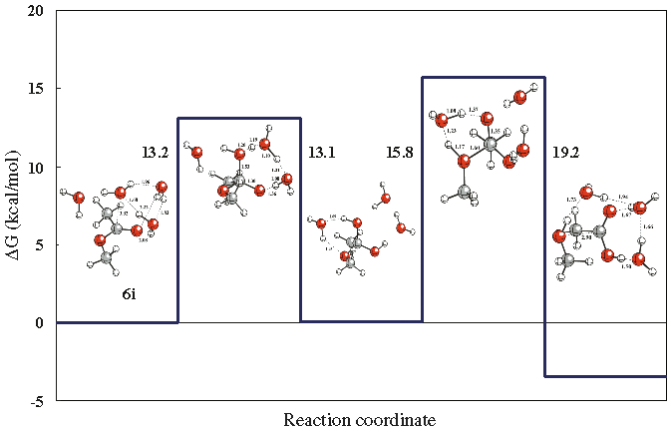

Scheme 8.

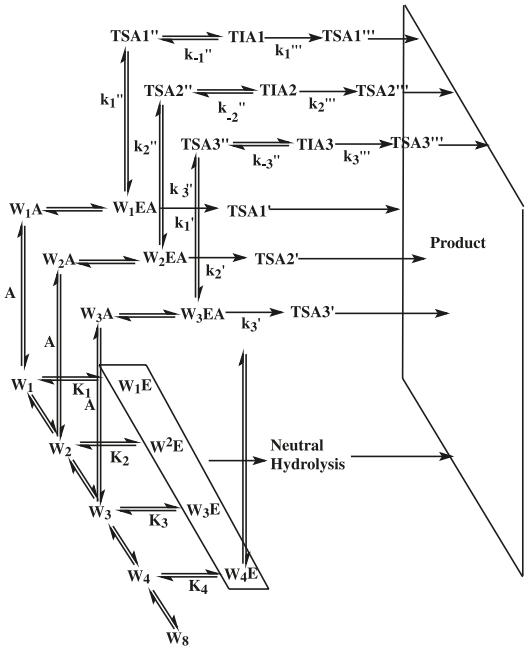

Table 8. Complexes providing major contributions to the rate of hydrolysis of 1.0 mol/L methyl acetate in 1.00 mol/L in acetic acid (limiting case A).

Species	Concentration (mol/L)	Rate constant (s^{-1})	Partial rate (mol/L s^{-1})	Contribution to overall rate (%)
W_4E' 4g	1.19×10^{-10}	79.0	9.40×10^{-9}	70.53
Neutral: 1-step (all **W_nE'**)	—	—	9.41×10^{-9}	70.57
W_4E'' 6i	9.97×10^{-11}	3.42×10	3.41×10^{-9}	25.60
Neutral: 2-step (all **W_nE''**)	—	—	3.71×10^{-9}	27.83
Acetic acid: 1-step (all **W_nEA'**)	—	—	1.43×10^{-14}	0.00
Acetic acid: 2-step (all **W_nEA''**)	—	—	2.14×10^{-10}	1.60
Total rate (s^{-1})			1.34×10^{-8}	
Neutral			1.31×10^{-8}	98.40
Acid			2.14×10^{-10}	1.60

Table 9. Complexes providing major contributions to the rate of hydrolysis of 1.0 mol/L methyl acetate in 1.00 mol/L in acetic acid (limiting case B)

Species	Concentration (mol/L)	Rate constant (s^{-1})	Partial rate (mol/L s^{-1})	Contribution (%)[a]
Neutral: 1-step				
All **W_nE'**	—	—	9.41×10^{-9}	0.00
Neutral, 2-step: **$W_nE \rightleftharpoons TSn''$**				
W_2E'' 6b	4.57×10^{-5}	1.72×10^{-3}[b] 1.36[c]	7.86×10^{-8}	22.88
W_3E'' 6d	2.37×10^{-10}	3.69×10^{2}[b] 1.48×10^{9}[c]	4.81×10^{-8}	13.99
W_3E'' 6e	5.91×10^{-17}	1.38×10^{2}[b] 3.07[c]	-1.47×10^{-8}[d]	–4.27
W_3E'' 6f	5.59×10^{-17}	3.61×10^{2}[b] 1.06[c]	-3.85×10^{-8}[d]	–11.19
W_4E'' 6i	9.97×10^{-11}	2.77×10^{3}[b] 3.36×10^{3}[c]	2.77×10^{-7}	80.53
Neutral, 2-step: **$TIn \rightarrow TSn'''$**				
All **TIn**	—	—	3.44×10^{-7}	0.02
Acid: 1-step				
All **W_nEA'**	—	—	1.43×10^{-14}	0.00
Acid, 2-step: **$W_nEA \rightleftharpoons TSAn''$**				
W_1EA" 14a	4.44×10^{-13}	$7.49\times10^{7}b$ 1.84×10^{4}[c]	3.24×10^{-5}	60.69
W_2EA'' 14f	9.28×10^{-11}	3.59×10^{5}[b] 1.15×10^{5}[c]	3.33×10^{-5}	62.24
W_3EA'' 14m	1.82×10^{-24}	3.34×10^{9}[b] 3.15×10^{4}[c]	-7.09×10^{-6}[d]	–13.26
W_3EA'' 14p	3.63×10^{-20}	2.32×10^{9}[b] 5.71×10^{3}[c]	-4.91×10^{-6}[d]	–9.19
Acid, 2-step: **$TIA \rightarrow TSA'''$**				
TIA				
TIA3 16n	5.69×10^{-9}	2.53×10^{4}	1.44×10^{-4}	7.21
TIA3 16p	8.60×10^{-10}	2.14×10^{6}	1.84×10^{-3}	91.90
Sum	-	-	2.00×10^{-3}	99.98
Total rate (s^{-1})			2.00×10^{-3}	
Neutral			3.53×10^{-7}	0.02
Acid			2.00×10^{-3}	99.98

[a]Contribution to the reaction.
[b]Rate constant for **$W_nE \rightarrow TSn''$**, the forward reaction.
[c]Rate constant for **$TIn \rightarrow TSn''$**, the reverse reaction.
[d]The reverse process dominates.

Fig. 3. Reaction coordinate of the major hydrolysis channel of limiting case B.

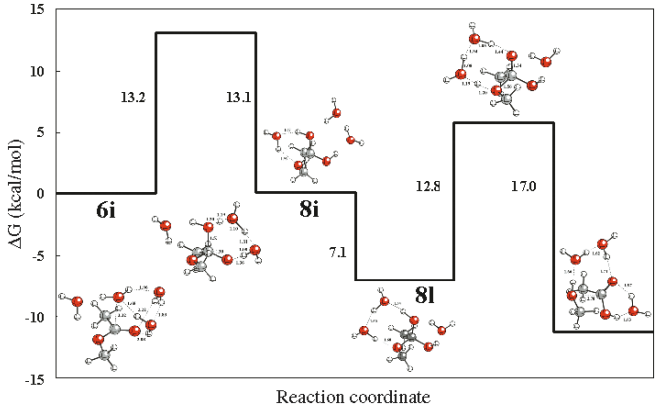

tion from $\mathbf{W}_n\mathbf{E}''$ to $\mathbf{TI}n$, given by eq. [8], can be negative if the reverse process dominates.

$$[8] \qquad v''_n = k'_n[\mathrm{W}_n\mathrm{E}''] - k''_{-n}[\mathrm{TI}n]$$

The overall rate of the first step of the two-step process is

$$[9] \qquad v'' = \sum v_n = \sum k''_n[\mathrm{W}_n\mathrm{E}'] - \sum k''_{-n}[\mathrm{TI}n]$$

and the rate of the second step is

$$[10] \qquad v''' = \sum v'''_n = \sum k'''_n[\mathrm{TI}n]$$

Applying the steady-state approximation to the overall concentration of TI gives

$$[11] \qquad \frac{\mathrm{d}[\mathrm{TI}]}{\mathrm{d}t} = \sum k''_n[\mathrm{W}_n\mathrm{E}''] - \sum (k''_{-n} + k'''_n)[\mathrm{TI}n] = 0$$

leading to

$$[12] \qquad \sum k''_n[\mathrm{W}_n\mathrm{E}''] = \sum (k''_{-n} + k'''_n)[\mathrm{TI}n]$$

Since $[\mathrm{TI}n] = K_{\mathrm{TI}n}[\mathrm{TI}_1][\mathrm{W}_1]^{n-1}$ where **TI**1 is unsolvated **TI**, and $K_{\mathrm{TI}n}$ are equilibrium constants relating $[\mathrm{TI}n]$ to [TI1], eq. [12] can be converted to,

$$[13] \qquad \sum k''_n[\mathrm{W}_n\mathrm{E}''] = \{\sum (k''_{-n} + k'''_n)K_{\mathrm{TI}n}[\mathrm{W}_1]^{n-1}\}[\mathrm{TI}1]$$

which gives

$$[14] \qquad [\mathrm{TI}1] = \frac{\sum k''_n[\mathrm{W}_n\mathrm{E}'']}{\sum (k''_{-n} + k'''_n)K_{\mathrm{TI}n}[\mathrm{W}_1]^{n-1}}$$

Since the tetrahedral intermediate hydrates **TI***n* are no longer short-lived, their contributions to C_{W} and C_{E} have to be taken into account comparable to the reactant complexes $\mathbf{W}_n\mathbf{E}$, which expands eqs. [3] and [4] to,

$$[15] \qquad C_{\mathrm{W}} = \sum_n n[\mathrm{W}_n] + \sum_n n[\mathrm{W}_n\mathrm{E}] + \sum_n (n-1)[\mathrm{TI}n]$$

$$[16] \qquad C_{\mathrm{E}} = [\mathrm{E}] + \sum_n [\mathrm{W}_n\mathrm{E}] + \sum_n [\mathrm{TI}n]$$

The overall rate of hydrolysis and its pseudo first-order rate constant k can then be found from eqs. [17] and [18].

$$[17] \qquad v = kC_{\mathrm{E}} = \sum k'_n[\mathrm{W}_n\mathrm{E}'] + \sum k'''_n[\mathrm{TI}n]$$

$$[18] \qquad k = \frac{\sum k'_n K'_n[\mathrm{W}_n] + \sum k'''_n[\mathrm{TI}n]}{1 + \sum K'_n[\mathrm{W}_n] + \sum K''_n[\mathrm{W}_n] + \sum [\mathrm{TI}n]}$$

Table 6 summarizes the results for the hydrolysis of a 1.00 mol/L methyl acetate solution at 298 K. In the limiting case B, the rate of hydrolysis is 35.9×10^{-8} s^{-1}, 27 times faster than the rate calculated for the limiting case A, and over 97% of the reaction proceeds by a two–step mechanism via **8f**, **8g**, **8k**, and **8l**, the **TI** having the lowest second-step barrier.

The situation is summarized in the schematic reaction profile of Fig. 3, according to which the four-water complex **6i** is converted to **8i**, which equilibrates with **8l**, which proceeds to the products.

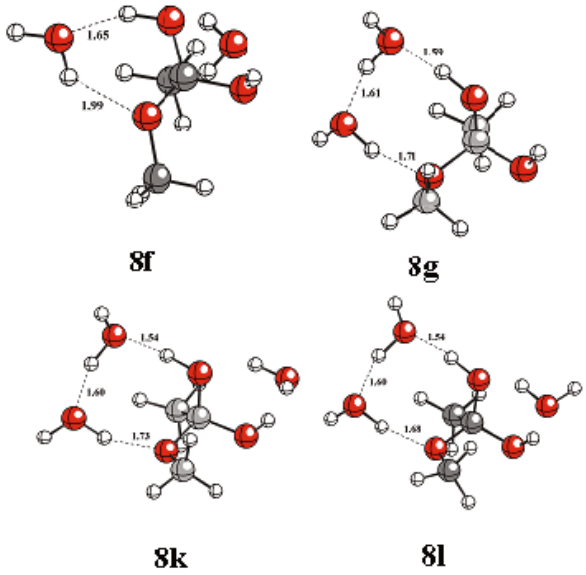

Limiting cases A and B are distinguishable

The calculated reaction rates, 1.34×10^{-8} s^{-1} for case A, in which a one-step four-water mechanism is preferred, and 35.9×10^{-8} s^{-1} for case B, in which a two-step four-water mechanism predominates, would appear to be sufficiently different for the two methods to be distinguishable. The observed rate is 0.17×10^{-8} s^{-1}.[24] It can be concluded that the neutral hydrolysis of methyl acetate mainly proceeds by a one-step cooperative mechanism, as described by limiting case A.

General acid catalysis by acetic acid

Acetic acid provides cooperative *general* acid catalysis of the aqueous hydration of acetone, mainly via complexes **10** and **11**.[3] However, despite the fact that spontaneous hydrolysis of methyl acetate is an autocatalytic process, subject to *specific* acid catalysis by the acetic acid product,[24] no general acid catalysis was experimentally observed in that case. To examine this situation theoretically, we augmented Schemes 6 and 7 by incorporating in them the acetic acid-containing species. The resultant kinetic networks are shown in Schemes 8 and 9 for limiting cases A and B, respectively.

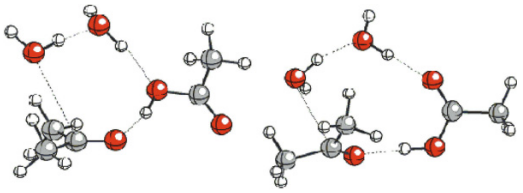

10 11

In these Schemes $\mathbf{W}_n\mathbf{A}$ are complexes of acetic acid with n water molecules and $\mathbf{W}_n\mathbf{EA}$ are cyclic complexes of methyl acetate with one molecule of acetic acid and n water molecules. There is more than one complex for each $\mathbf{W}_n\mathbf{EA}$. For example, **12a** and **12b** are possibilities for n = 1. All conceivable topologies of reactant complexes for n = 1–3 were taken into account.[25]

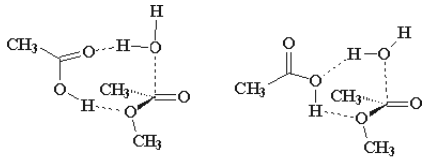

12a 12b

Cyclic transition states **TSA*n***′ (structures **13a–13f**) are derived from $\mathbf{W}_n\mathbf{EA}'$ (structures **12a–12f**). Tetrahedral intermediates **TIA*n*** (structures **16**) are obtained from $\mathbf{W}_n\mathbf{EA}''$ (structures **14**) via transition states **TSA*n***″ (structures **15**) and further transform into product compexes via transition states **TSA*n***‴ (structures **17**).

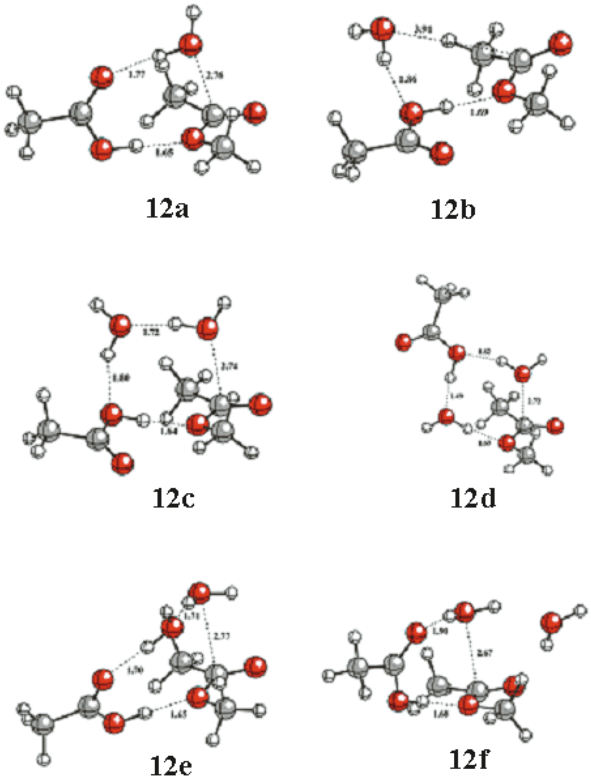

12a 12b 12c 12d 12e 12f

Scheme 9.

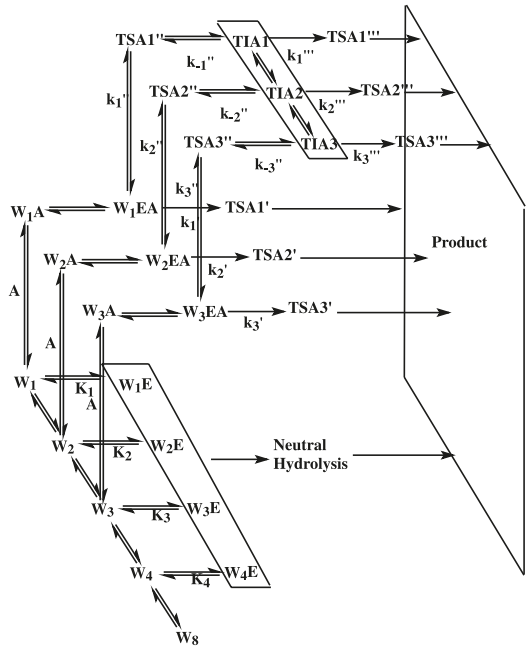

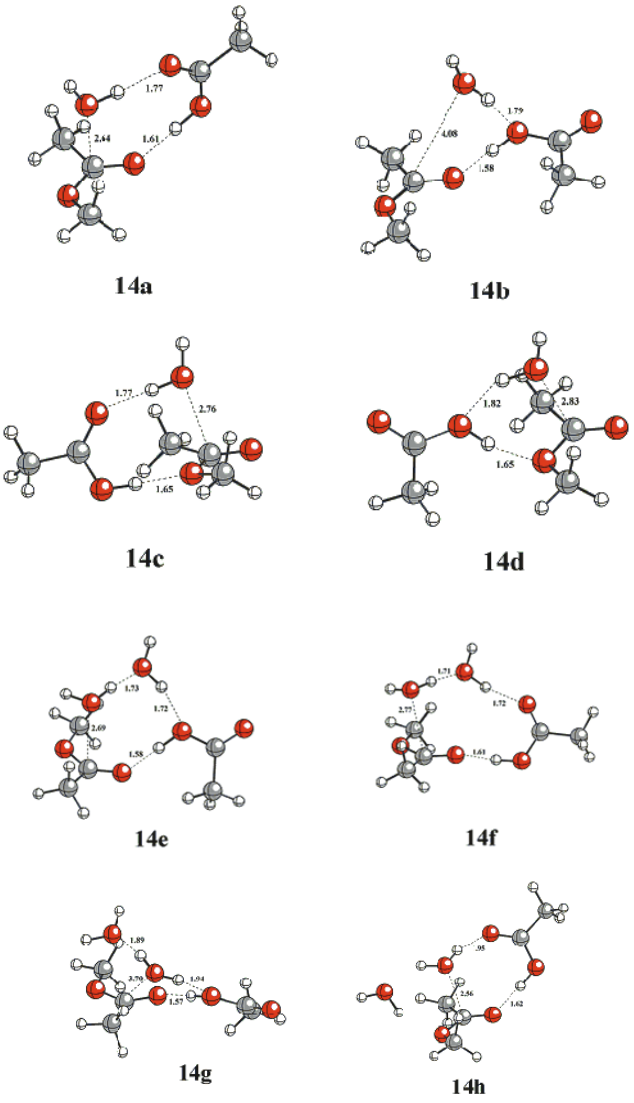

14a 14b 14c 14d 14e 14f 14g 14h

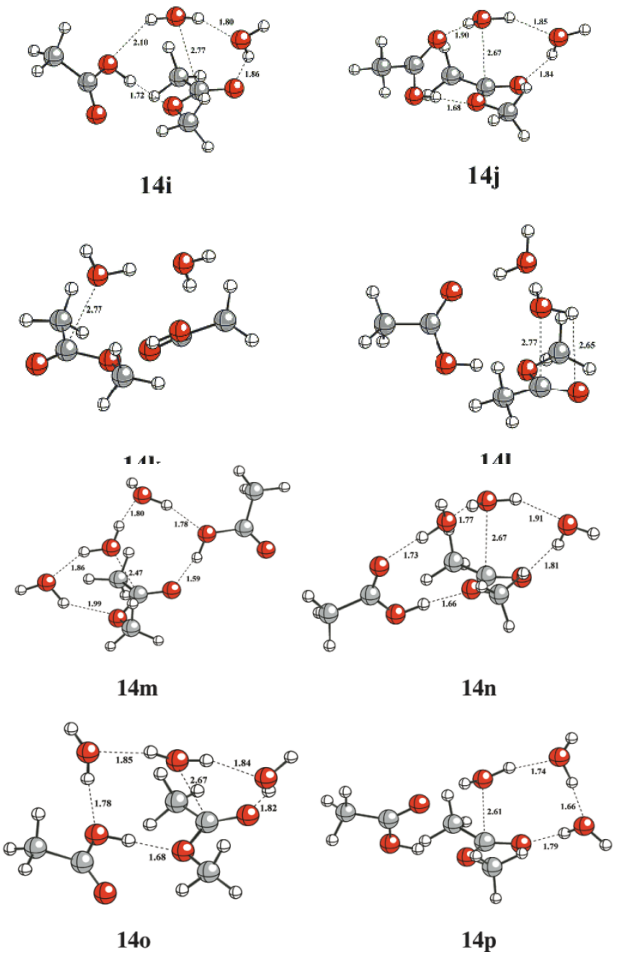

Table 7 lists the ΔG and $\Delta G^{\ddagger}$ at 298 K calculated for species involved in Scheme 8, which were then used to calculate the partial and overall rate constants of hydrolysis of 1 mol/L methyl acetate in the presence of 1 mol/L acetic acid by a trivial extension of the method described in the previous section. The results are summarized in Table 8 (for the limiting case A) and Table 9 (for the limiting case B).

The analysis of these results reveals that on the assumption that tetrahedral intermediates are short-lived and do not interconvert (case A), the acetic-acid-involving channels contribute only 1.6% to the overall rate through non-ionic processes and thus produce a negligible acceleration over the non-catalytic process. This is consistent with the conclusion of Part 1[24] that the catalysis by acetic acid is entirely *specific*.

On the other hand in case B, the computations predict a strong (four orders of magnitude) effect of *general* catalysis by acetic acid, inconsistent with experiment. We therefore conclude that, with and without acetic acid, the non-ionic hydrolysis of methyl acetate predominantly proceeds by a concerted one-step mechanism.

Supplementary data

Supplementary data for this article are available on the journal Web site (canjchem.nrc.ca) or may be purchased from the Depository of Unpublished Data, Document Delivery, CISTI, National Research Council Canada, Ottawa, ON K1A 0R6, Canada. DUD 3888. For more information on obtaining material refer to cisti-icist.nrc-cnrc.gc.ca/cms/unpub_e.shtml.

Acknowledgements

The authors thank the Natural Sciences and Engineering Research Council of Canada (NSERC) for financial support of this research. The authors are also grateful to Ms. Elna Deglint for assistance in formatting the final draft of the paper.

References

(1) Wolfe, S.; Kim, C.-K.; Yang, K.; Weinberg, N.; Shi, Z. *J. Am. Chem. Soc.* **1995**, *117*, 4240. doi:10.1021/ja00120a005.
(2) Wolfe, S.; Shi, Z.; Yang, K.; Ro, S.; Weinberg, N.; Kim, C.-K. *Can. J. Chem.* **1998**, *76*, 114. doi:10.1139/cjc-76-1-114.
(3) Hsieh, Y.-H.; Weinberg, N.; Yang, K.; Kim, C.-K.; Shi, Z.; Wolfe, S. *Can. J. Chem.* **2005**, *83*, 769. doi:10.1139/v05-027.
(4) Hsieh, Y.-H.; Weinberg, N.; Wolfe, S. *Can. J. Chem.* **2008**, *86*, 81. doi:10.1139/V07-074.
(5) Eigen, M. *Discuss. Faraday Soc.* **1965**, *39*, 7. doi:10.1039/df9653900007.
(6) Huang, H. H.; Robinson, R. R.; Long, F. A. *J. Am. Chem. Soc.* **1966**, *88*, 1866. doi:10.1021/ja00961a003.
(7) Hehre, W. J.; Radom, L.; v Schleyer, P. R.; Pople, J.A. *Ab initio molecular orbital theory*; Wiley: New York. 1986.
(8) Frisch, M. J.; Trucks, G. W.; Schlegel, H. B.; Scuseria, G. E.; Robb, M. A.; Cheeseman, J. R.; Zakrzewski, V. G.; Montgomery, J. A., Jr.; Stratmann, R. E.; Burant, J. C.; Dapprich, S.; Millam, J. M.; Daniels, A. D.; Kudin, K. N.; Strain, M. C.; Farkas, O.; Tomasi, J.; Barone, V.; Cossi, M.; Cammi, R.; Mennucci, B.; Pomelli, C.; Adamo, C.; Clifford, S.; Ochterski, J.; Petersson, G. A.; Ayala, P. Y.; Cui, Q.; Morokuma, K.; Malick, D. K.; Rabuck, A. D.; Raghavachari, K.; Foresman, J. B.; Cioslowski, J.; Ortiz, J. V.; Stefanov, B. B.; Liu, G.; Liashenko, A.; Piskorz, P.; Komaromi, I.; Gomperts, R.; Martin, R. L.; Fox, D. J.; Keith, T.; Al-Laham, M. A.; Peng, C. Y.; Nanayakkara, A.; Gonzalez, C.; Challacombe, M.; Gill, P. M. W.; Johnson, B.; Chen, W.; Wong, M. W.; Andres, J. L.; Head-Gordon, M.; Replogle, E. S.; Pople, J. A. *Gaussian 98*, revision A.6. Gaussian, Inc.: Pittsburgh, Penn., USA, 1998.
(9) (a) Tapia, O.; Goscinski, O. *Mol. Phys.* **1975**, *29*, 1653 doi:10.1080/00268977500101461.; (b) Mierts, S.; Scrocco, E.; Tomasi, J. *Chem. Phys.* **1981**, *55*, 117 doi:10.1016/0301-0104(81)85090-2.; (c) Pascual-Ahuir, J. L.; Silla, E.; Tomasi, J.; Bonaccorsi, R. J. *Comput. Chem.* **1987**, *8*, 778 doi:10.1002/jcc.540080605.; (d) Milne, G. W. A.; Nicklaus, M. C.; Hodošček, M. J. *J. Mol. Struct.* **1993**, *291*, 89 doi:10.1016/0022-2860(93)80255-T.; (e) del Valle, F. J. O.; Aguilar, M. A.; Contador, J. C. *Chem. Phys.* **1993**, *170*, 161 doi:10.1016/0301-0104(93)80060-M.; (f) Aguilar, M.; Bianco, R.; Miertus, S.; Persico, M.; Tomasi, J. *Chem. Phys.* **1993**, *174*, 397 doi:10.1016/0301-0104(93)80006-U.; (g) Mingos, D. M. P.; Rohl, A. L.; Burgess, J. J. Chem. Soc. Dalton Trans. 1993, 423; (h) Honig, B.; Sharp, K.; Yang, A.-S. *J. Phys. Chem.* **1993**, *97*, 1101 doi:10.1021/j100108a002.; (i) Kim, H. J.; Bianco, R.; Gertner, B. J.; Hynes, J. T. *J. Phys. Chem.* **1993**, *97*, 1723 doi:10.1021/j100111a001.; (j) Bachs, M.; Luque, F. J.; Orozco, M. J. *Comput. Chem.* **1994**, *15*, 446. doi:10.1002/jcc.540150408.

(10) (a) Wong, M. W.; Wiberg, K. B.; Frisch, M. J. J. *Chem. Phys.* **1991**, *95*, 8991; (b) Wong, M. W.; Frisch, M. J.; Wiberg, K. B. *J. Am. Chem. Soc.* **1991**, *113*, 4776. doi:10.1021/ja00013a010.

(11) (a) Boys, S. F.; Bernardi, F. *Mol. Phys.* **1970**, *19*, 553 doi:10.1080/00268977000101561.; (b) Ventura, O. N.; Coitino, E. L.; Irving, K.; Iglesias, A.; Lledós, A. *J. Mol. Struct. (Theochem.)* **1990**, *210*, 427. doi:10.1016/0166-1280(90)80066-W.; (c) Cook, D. B.; Sordo, T. L.; Sordo, J. A. J. Chem. Soc. Chem. Comm. 1990, 185; (d) Aastrand, P. O.; Wallqvist, A.; Karlström, G. J. *J. Phys. Chem.* **1991**, *95*, 6395 doi:10.1021/j100169a058.; (e) Eggenberger, R.; Gerber, S.; Huber, H.; Searles, D. *Phys. Lett.* **1991**, *183*, 223; (f) Valiron, P.; Vibók, A.; Mayer, I. J. *Comput. Chem.* **1993**, *14*, 401 doi:10.1002/jcc.540140404.; (g) Turi, L.; Dannenberg, J. J. *J. Phys. Chem.* **1993**, *97*, 2488 doi:10.1021/j100113a002.; (h) Dobado, J. A.; Molina, J. M. *J. Phys. Chem.* **1993**, *97*, 7499 doi:10.1021/j100131a018.; (i) Davidson, E. R.; Chakravorty, S. J. *Chem. Phys. Lett.* **1994**, *217*, 48 doi:10.1016/0009-2614(93)E1356-L.; (j) Mayer, I.; Vibók, A.; Valiron, P. *Chem. Phys. Lett.* **1994**, *224*, 166 doi:10.1016/0009-2614(94)00523-0.; (k) Neuheuser, T.; Hess, B. A.; Reutel, C.; Weber, E. *J. Phys. Chem.* **1994**, *98*, 6459 doi:10.1021/j100077a007.; (l) Kieninger, M.; Suhai, S.; Mayer, I. *Chem. Phys. Lett.* **1994**, *230*, 485. doi:10.1016/0009-2614(94)01201-6.

(12) (a) Swain, C. G.; Brown, J. F., Jr. *J. Am. Chem. Soc.* **1952**, *74*, 2538 doi:10.1021/ja01130a024.; (b) Rony, P. R.; McCormack, W. E.; Wunderly, S. W. *J. Am. Chem. Soc.* **1969**, *91*, 4244 doi:10.1021/ja01043a037.; (c) Rony, P. R. *J. Am. Chem. Soc.* **1969**, *91*, 6090 doi:10.1021/ja01050a027.; (d) Rony, P. R.; Neff, R. O. *J. Am. Chem. Soc.* **1973**, *95*, 2896 doi:10.1021/ja00790a028.; (e) Engdahl, K.-A.; Bivehed, H.; Ahlberg, P.; Saunders, W. H., Jr. *J. Am. Chem. Soc.* **1983**, *105*, 4767 doi:10.1021/ja00352a040.; (f) Morpurgo, S.; Bossa, M. *Phys. Chem. Chem. Phys.* **2003**, *5*, 1181 doi:10.1039/b210328c.; (g) Lee, Y.-N.; Schmir, G. L. *J. Am. Chem. Soc.* **1979**, *101*, 3026[, and references cited therein.]. doi:10.1021/ja00505a033.

(13) (a) Day, J. N. E.; Ingold, C. K. *Trans. Faraday Soc.* **1941**, *37*, 686 doi:10.1039/tf9413700686.; (b) Jencks, W. P.; Carriuolo, J. *J. Am. Chem. Soc.* **1961**, *83*, 1743 doi:10.1021/ja01468a044.; (c) Johnson, S. L. *Adv. Phys. Org. Chem.* **1967**, *5*, 237 doi:10.1016/S0065-3160(08)60312-3.; (d) Patai, S. *The chemistry of carboxylic acids and esters*; John Wiley and Sons: London, UK, 1969; (e) Jencks, W. P. *Catalysis in chemistry and enzymology*; Dover Publications Inc.: New York, USA, 1987; (f) Stefanidis, D.; Jencks, W. P. *J. Am. Chem. Soc.* **1993**, *115*, 6045. doi:10.1021/ja00067a020.

(14) (a) Bender, M. L. *J. Am. Chem. Soc.* **1951**, *73*, 1626 doi:10.1021/ja01148a063.; (b) Bender, M. L. *Chem. Rev.* **1960**, *60*, 53. doi:10.1021/cr60203a005.

(15) Kellogg, B. A.; Tse, J. E.; Brown, R. S. *J. Am. Chem. Soc.* **1995**, *117*, 1731. doi:10.1021/ja00111a009.

(16) (a) Skrabal, A.; Zahorka, A. *Monatshefte*, **1929**, *53-54*, 562 doi:10.1007/BF01521817.; (b) Poethke, W. *Chem. Ber.* **1935**, 1031.

(17) Moffat, A.; Hunt, H. *J. Am. Chem. Soc.* **1959**, *81*, 2082. doi:10.1021/ja01518a014.

(18) (a) Euranto, E.; Cleve, N. J. *Acta Chem. Scand.* **1963**, *17*, 1584 doi:10.3891/acta.chem.scand.17-1584.; (b) Cleve, N. J.; Euranto, E. K. *Suomen Kemistilehti B,* **1964**, *37*, 126; (c) Euranto, E. K. *Suomen Kemistilehti A*, **1965**, *38*, 25; (d) Euranto, E. K.; Cleve, N. J. *Suomen Kemistilehti B,* **1970**, *43*, 147; (e) Cleve, N. J. *Suomen Kemistilehti B,* **1973**, *46*, 5; (f) Cleve, N. J. *Suomen Kemistilehti B,* **1973**, *46*, 232; (g) Cleve, N. J.; Euranto, E. K. Finn. Chem. Lett. 1974, 82.

(19) Venkatasubban, K. S.; Davis, K. R.; Hogg, J. L. *J. Am. Chem. Soc.* **1978**, *100*, 6125. doi:10.1021/ja00487a026.

(20) Mata-Segreda, J. F. *Int. J. Chem. Kinet.* **2000**, *32*, 67. doi:10.1002/(SICI)1097-4601(2000)32:1<67::AID-JCK8>3.0.CO;2-M.

(21) Schmeer, G.; Sturm, P. *Phys. Chem. Chem. Phys.* **1999**, *1*, 1025. doi:10.1039/a808558g.

(22) Kallies, B.; Mitzner, R. *J. Mol. Model.* **1998**, *4*, 183. doi:10.1007/s0089480040183.

(23) Yamabe, S.; Tsuchida, N.; Hayashida, Y. *J. Phys. Chem. A* **2005**, *109*, 7216. doi:10.1021/jp058029i. PMID:16834086.

(24) Hsieh, Y.-H.; Weinberg, N.; Wolfe, S. **2009**, *Can. J. Chem.* **2009**, *87*, 539. doi:10.1139/v09-003.

(25) Inclusion of additional water molecules does not alter the calculated rate.

Mapping the sirodesmin PL biosynthetic pathway — A remarkable intrinsic steric deuterium isotope effect on a ^{1}H NMR chemical shift determines β-proton exchange in tyrosine

M. Soledade C. Pedras and Yang Yu

Abstract: Sirodesmin PL is both an antibiotic and a phytotoxin produced by a fungal plant pathogen (*Leptosphaeria maculans,* asexual stage *Phoma lingam*) that causes blackleg disease on crucifers. To determine potential biosynthetic precursors of sirodesmin PL, deuterated compounds were synthesized and incubated with cultures of *L. maculans*. Incorporations of deuterium into sirodesmin PL (**7**) and its precursor phomamide (**4**) were determined using ^{1}H and ^{13}C NMR spectroscopy, LC-HRMS-ESI and HRMS-EI spectrometry. Spectroscopic analyses established that [3,3-$^2H_2$]L-tyrosine (**1a**), [3,3-$^2H_2$]*O*-prenyl-L-tyrosine (**9a**), [3,3,5′,5′,5′-$^2H_5$]*O*-prenyl-L-tyrosine (**9b**), and [5,5-$^2H_2$]phomamide (**4a**) were incorporated efficiently into sirodesmin PL (**7**). Interestingly, an unexpected "twist" revealed that one of the β-deuteria (*pro-R*) of [3,3-$^2H_2$]L-tyrosine (**1a**) was exchanged stereospecifically before incorporation into sirodesmin PL (**7**). As well, our studies revealed that *O*-prenyl-L-tyrosine is likely to be the first committed precursor en route to sirodesmin PL (**7**).

Key words: biosynthesis, isotope effect, deuterium incorporation, *Leptosphaeria maculans*, phytotoxin, sirodesminbiosynthèse, effet isotopique, incorporation de deutérium, , *Leptosphaeria maculans*, phytotoxine, sirodesmine.

Résumé : La sirodesmine PL est à la fois un antibiotique et une phytotoxine produite par un champignon pathogène (*Leptosphaeria maculans*, stade asexuel du Phoma lingam) qui provoque la maladie de la jambe noire chez les crucifères. Dans le but de déterminer la nature des précurseurs biosynthétiques potentiels de la sirodesmine PL, on a effectué la synthèse de produits deutériés qui ont été incubés avec des cultures de *L. maculans*. L'incorporation du deutérium dans la sirodesmine PL (7) et dans son précurseur, la phomamide (**4**), a été déterminé en faisant appel à la RMN du ^{1}H et du ^{13}C ainsi que par chromatographie liquide liée à la spectrométrie de masse à haute résolution avec ionisation par impact électronébulisation (CL-SMHR-IEN) et par spectrométrie de masse à haute résolution avec ionisation par impact électronique (SMHR-IE). Les analyses spectroscopiques ont permis de déterminer que la [3,3-$^2H_2$]L-tyrosine (**1a**), la [3,3-$^2H_2$]*O*-prényl-l-tyrosine (**9a**), la [3,3,5′,5′,5′-$^2H_5$]*O*-prényl-l-tyrosine (**9b**) et la [5,5-$^2H_2$]phomamide (**4a**) s'incorporent d'une façon efficace dans la sirodesmine PL (**7**). Un fait intéressant à été noté, à savoir celui qu'un des atomes de deutérium en β, le *pro-R*, de la [3,3-$^2H_2$]L-tyrosine (**1a**) s'échange d'une façon stéréospécifique avant l'incorporation dans la sirodesmine PL (**7**). Des plus, nos études ont révélé que la *O*-prényl-l-tyrosine est probablement le premier précurseur dédié en route vers la sirodesmine PL (**7**).

[Traduit par la Rédaction]

Introduction

Mapping biosynthetic pathways used by living organisms to assemble complex libraries of natural products is generally accomplished using isotopically labeled precursors. The choice of isotope depends on the chemical structure of the natural product and hypothetical precursors. Currently, the use of stable isotopes is common due to the availability of highly sensitive analytical tools, while a few decades ago only radioactive isotopes were thinkable.[1] Nonetheless, great challenges remain, particularly for unusual and complex pathways assembled by nonribosomal peptide synthases, such as those producing sirodesmins.[2] Sirodesmins are epipolythio-2,5-dioxopiperazines (ETPs) produced by two unrelated fungal species, *Sirodesmium diversum* (sirodesmins A–G)[3] and *Leptosphaeria maculans* (asexual stage *Phoma lingam*, sirodesmin PL, deacetylsirodesmin PL,[4] and sirodesmins H,[5] J, and K[6]). Sirodesmin PL (**7**) is both an antibiotic and a phytotoxin, i.e., toxic to plant cells. Interest in ETPs has increased over the past years because of their biological activity[7] and potential ecological roles. The current focus on sirodesmin PL (**7**) is motivated by its potential involvement in the interaction of the plant pathogen *L. maculans* with its host plants.[8,9]

The primary biosynthetic precursors of sirodesmin PL (**7**) together with its biosynthetic pathway were proposed based on results of experiments using radiolabeled (^{3}H and ^{14}C) and stable (^{13}C) isotopes,[10] and later on confirmed by Bu'Lock and Clough.[11] The proposed pathway involved dioxopiperazine formation between L-tyrosine (**1**) and L-serine (**2**), isoprenylation with dimethylallylpyrophosphate (DMAPP) to form phomamide (**4**), followed by a number of oxidative rearrangements. As well, the isolation of a toxin structurally related to sirodesmin PL (**7**), phomalirazine (**6**), led us to propose a modification of the Curtis–Férézou pathway.[12]

Received 12 November 2008. Accepted 24 December 2008. Published on the NRC Research Press Web site at canjchem.nrc.ca on 17 March 2009.

M.S.C. Pedras[1] and Y. Yu. Department of Chemistry, University of Saskatchewan, 110 Science Place, Saskatoon, SK S7N 5C9, Canada.

[1]Corresponding author (e-mail: s.pedras@usask.ca).

Scheme 1. Biosynthetic pathway of sirodesmin PL (**7**): precursors L-tyrosine (**1**), L-serine (**2**), and DMAPP (dimethylallylpyrophosphate) and potential intermediates **3**–**6**.

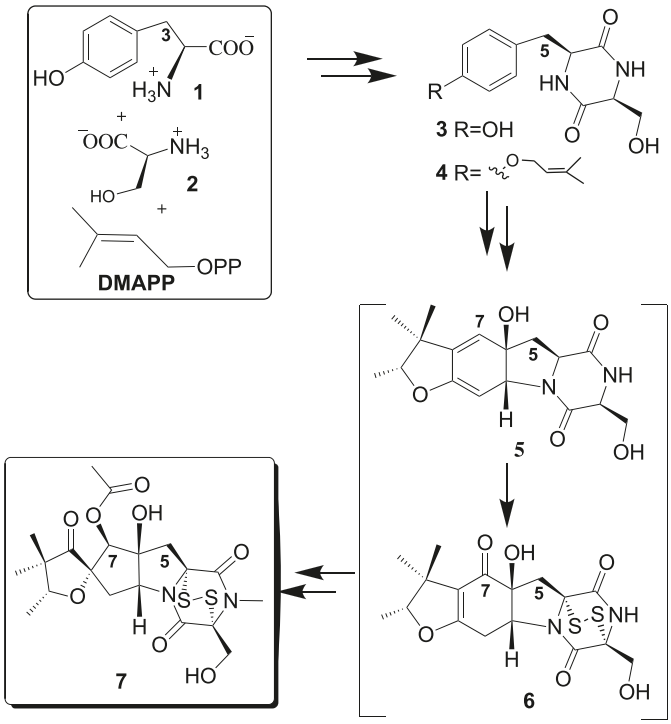

The recent cloning of a gene cluster involved in the biosynthesis of sirodesmin PL (**7**) suggested a more detailed pathway that took into account the ascribed functions of the cloned genes.[8] A simplified pathway showing relevant potential intermediates is depicted in Scheme 1.

These recent developments reawakened our interest in the sirodesmin PL (**7**) biosynthetic pathway. Specific goals to uncover the structure(s) of intermediate(s) immediately preceding insertion of the disulfide bridge and to determine the stage at which prenylation occurred directed our experimental design. Based on the structures of metabolites recently isolated,[13] we hypothesized that a compound containing a bis-ylidine 2,5-dioxopiperazine moiety (**8**) might be a plausible substrate for enzymatic introduction of the disulfide bridge into sirodesmin PL (**7**). If **8** was a precursor, then incorporation of dideuterated [3,3-$^2H_2$]L-tyrosine (**1a**) or [5,5-$^2H_2$]phomamide (**4a**) would lead to the incorporation of only one deuterium into sirodesmin PL (**7**, ^{2}H–C-5, Scheme 2). Alternatively, the presence of two deuteria in sirodesmin PL would eliminate **8** from this biosynthetic map (Scheme 2). Toward this end, we describe work to establish biosynthetic precursors of phomamide (**4**) and sirodesmin PL (**7**).

Results and discussion

The deuterated compounds [3,3-$^2H_2$]*O*-prenyl-L-tyrosine (**9a**),[14] [3,3,5′,5′,5′-$^2H_5$]*O*-prenyl-L-tyrosine (**9b**), [5,5-$^2H_2$]cyclo-L-Tyr-L-Ser (**3a**), and [5,5-$^2H_2$]phomamide (**4a**)[15] were prepared from [3,3-$^2H_2$]L-tyrosine (**1a**) following modifications of previously reported methods, as described in the Supplementary data. HRMS-EI analyses indicated that the percentage of deuterium in the synthetic deuterated compounds was higher than 98%.

Scheme 2. Hypothetical intermediate **8** for introduction of sulfur into sirodesmin PL (**7**).

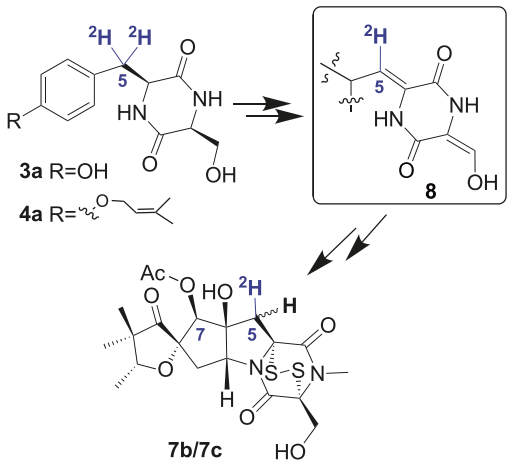

Incorporation experiments using deuterated compounds [3,3-$^2H_2$]L-tyrosine (**1a**), [3,3-$^2H_2$]*O*-prenyl-L-tyrosine (**9a**), [3,3,5′,5′,5′-$^2H_5$]*O*-prenyl-L-tyrosine (**9b**), [2,3,3-$^2H_3$]L-serine (**2a**), [5,5-$^2H_2$]phomamide (**4a**), and [5,5-$^2H_2$]cyclo-L-Tyr-L-Ser (**3a**) were carried out using a wild type isolate of *L. maculans*. After incubation of the fungal cultures with deuterated compounds, cultures were extracted and phomamide (**4**) and sirodesmin PL (**7**) were purified as described in the experimental. Similar conditions were used for control experiments in which the corresponding natural abundance compounds were administered to fungal cultures. Incorporation of deuterium, or lack of it, was determined using ^{1}H and ^{13}C NMR spectroscopy, LC-HRMS-ESI and HRMS-EI spectrometry.

First analysis of HRMS data established that (*i*) [3,3-$^2H_2$]L-tyrosine (**1a**), [3,3-$^2H_2$]*O*-prenyl-L-tyrosine (**9a**), [3,3,5′,5′,5′-$^2H_5$]*O*-prenyl-L-tyrosine (**9b**), and [5,5-$^2H_2$]phomamide (**4a**) were incorporated efficiently (>10%) into sirodesmin PL (**7**); (*ii*) [3,3-$^2H_2$]L-tyrosine (**1a**), [3,3-$^2H_2$]*O*-prenyl-L-tyrosine (**9a**), and [3,3,5′,5′,5′-$^2H_5$]*O*-prenyl-L-tyrosine (**9b**) were incorporated efficiently (>20%) into phomamide (**4**); (*iii*) [5,5-$^2H_2$]cyclo-L-Tyr-L-Ser (**3a**) and [2,3,3-$^2H_3$]L-serine (**2a**) were incorporated poorly (<5%) into either phomamide (**4**) or sirodesmin PL (**7**) (Table 1). Detailed analyses of spectroscopic data obtained for phomamide (**4**) and sirodesmin PL (**7**) isolated from fungal cultures incubated with deuterated compounds (summarized in Table 1 and Fig. 1) provided important additional information, as described below.

The HRMS-EI data of purified phomamide (**4**) isolated from cultures incubated with [3,3-$^2H_2$]L-tyrosine (**1a**) indicated that its $[M + 1]^+$ and $[M + 2]^+$ were about 20% and 12% higher, respectively, than those of control samples, suggesting that 20% of phomamide (**4**) was monodeuterated (equation for calculation is shown in Table 1) and 12% was dideuterated, i.e., 32% of phomamide (**4**) resulted from incorporation of [3,3-$^2H_2$]L-tyrosine (**1a**) (Table 1, entry 1). The ^{1}H NMR spectrum (provided in the Supplementary data) of phomamide (**4**) showed that the protons H-5a (δ_H 3.30, dd, J = 14.0, 3.5 Hz) and H-5b (δ_H 2.99, J = 14.0, 8.9 Hz) integrated for ca. 0.7 and 0.9, respectively, whereas control samples showed the expected integration of ca. 1 for H-5a and H-5b (H-5a (δ_H 3.30) / H-5b (δ_H 2.99) = 1.0). The

Table 1. Percentages of incorporation of deuterated compounds into phomamide (**4**) and sirodesmin PL (**7**) in cultures of *Leptosphaeria maculans.*

Entry	Deuterated compound	Phomamide (**4**) (% of ^2H, analytical method)	Sirodesmin PL (**7**) (% of ^2H, analytical method)
1	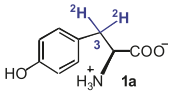 **1a**	32 (HRMS-EI: monodeuterated = 20; dideuterated = 12)[a]; 30 (^1H NMR, H_2-5a,5b)	32 (HRMS-EI: monodeuterated = 19; dideuterated = 13)[a]; 30 (^1H NMR, H-7)[b]
2	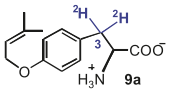 **9a**	41 (HRMS-EI: monodeuterated = 24; dideuterated = 17)[a]; 39 (^1H NMR, H_2-5a,5b)	35 (HRMS-EI: monodeuterated = 21; dideuterated = 15)[a]; 32 (^1H NMR, H-7)[b]
3	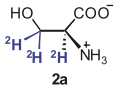 **2a**	3 (HRMS-EI)[a]	4 (HRMS-EI)[a]
4	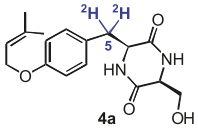 **4a**	—	30 (HRMS-EI: monodeuterated = 4; dideuterated = 26)[a]; 27 (^1H NMR, H-7)[b]
5	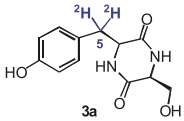 **3a**	3 (HRMS-EI: monodeuterated = 1; dideuterated = 2)[a]	2 (HRMS-EI: monodeuterated = 0; dideuterated = 2)[a]
6	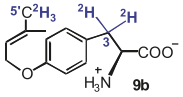 **9b**	23 (HRMS-ESI: tetradeuterated = 16; pentadeuterated = 7)[c]; 26 (^1H NMR, H_2-5a,5b)	13 (HRMS-ESI: tetradeuterated = 9; pentadeuterated = 4)[c]; 23 (^1H NMR, H-7)[b]

[a]The percentage of incorporation (*I*) was determined by HRMS-EI and was calculated using the formula $I = \{([M + n]^+ - [M + n]^+_{Ctl}) / ([M]^+ + [M + 1]^+ + [M + 2]^+)\} \times 100$; $n = 1, 2$; $[M + n]^+$ = intensity of deuterated molecular ion; $[M + n]^+_{Ctl}$ = intensity of molecular ion of control samples (natural abundance).

[b]Resolution of signals was enhanced through a Lorentz–Gaussian lineshape transformation (gb = 0.3, lb = –1).

[c]The percentage of incorporation (*I*) was determined by HRMS-ESI (positive mode) and was calculated using the formula $I = \{([M + 1 + n]^+ - [M + 1 + n]^+_{Ctl}) / ([M + 1]^+ + [M + 2]^+ + [M + 5]^+ + [M + 6]^+)\} \times 100$; $n = 4, 5$; $[M + n]^+$ = intensity of deuterated molecular ion; $[M + n]^+_{Ctl}$ = intensity of molecular ion of control samples (natural abundance).

percentage of deuterium at the C-5 of phomamide resulting from feeding [3,3-$^2H_2$]L-tyrosine (**1a**) was calculated to be 30% for H-5a (δ_H 3.30) and 11% for H-5b (δ_H 2.99). These ^1H NMR data indicated that about 11% of phomamide (**4**) was dideuterated, whereas the remaining 19% of phomamide was monodeuterated (Table 1, entry 1), in complete agreement with the HRMS data. Similar results were obtained when cultures were incubated with [3,3-$^2H_2$]*O*-prenyl-L-tyrosine (**9a**, Table 1, entry 2).

Similarly, the HRMS-EI spectroscopic data of purified sirodesmin PL (**7**) isolated from cultures fed with [3,3-$^2H_2$]L-tyrosine (**1a**) provided percentages of deuterium incorporation. Because the $[M]^+$ of sirodesmin PL (**7**) observed in the HRMS-EI spectrum was very weak, the base peak $[M - S_2]^+$ was used to calculate the percentage of deuterium incorporation, as follows. The intensity of the $[M - S_2 + 1]^+$ of sirodesmin PL was ca. 19% higher than that of control samples, whereas that of $[M - S_2 + 2]^+$ was ca. 13% higher than that of control samples. These results indicated that both monodeuterated (19%) and dideuterated (13%) sirodesmin PL (**7**) were biosynthesized from **1a** (Table 1, entry 1). Therefore, the total amount of deuterated **7** (mono plus di) calculated from the HRMS-EI data was ca. 32%.

The ^1H NMR spectrum of sirodesmin PL (**7**) was less informative (provided in the Supplementary data) than that of phomamide (**4**) because the signals due to protons H_2-5 (δ_H 3.27) appeared as a broad AB quartet; this signal integrated for ca. 2 in natural abundance samples of **7** and for <2 (1.4–1.6) in samples resulting from incorporation of [3,3-$^2H_2$]L-tyrosine (**1a**). Unexpectedly, a closer inspection of the signal due to H-7 (δ_H 5.56) in the ^1H NMR spectrum of sirodesmin PL (**7**) isolated from feeding experiments using [3,3-$^2H_2$]L-tyrosine (**1a**) showed two partially overlapping peaks attributable to H-7 (δ_H 5.56) that were not apparent in nondeuterated samples (i.e., natural abundance samples of **7**). Integration of these signals (δ_H 5.56) using resolution enhancement (Lorentz–Gaussian lineshape transformations and baseline corrections) showed resonances at δ_H 5.556 and δ_H 5.550 in a 2:1 ratio (Figs. 1*a* and 1*b*). The presence of both peaks suggested that replacement of H_2-5 of sirodesmin PL (**7**) with deuterium affected the chemical shift of H-7, i.e., the new peak at δ_H 5.550 was caused by the isotope shift effect of $^2H_2$-5 on H-7. The integrated area of this peak (δ_H 5.550) in conjunction with the HRMS-EI data (Table 1, entry 1) indicated that it accounted for the total amount of monodeuterated and dideuterated **7** (ca. 33%). Nonetheless, detection of a deuterium isotope shift effect over four covalent bonds was not expected.[1,16] To further understand this result, the proton decoupled ^{13}C NMR spectrum of this deuterated sample of sirodesmin PL (**7**) was obtained and analyzed. The signal of C-5 (single plus multiplet) had low intensity due to the presence of deuterium; as well, C-4 (δ_C 75.46, 75.40, 75.32) and C-6 (δ_C 82.44, 82.38, 82.34, Figs. 1*c* and 1*d*) displayed the expected two additional peaks

Fig. 1. Sections of NMR spectra of sirodesmin PL: (*a*) ^{1}H NMR, H-7 signal of natural abundance **7**; (*b*) ^{1}H NMR, H-7 signal (peaks 1 at δ 5.556 and 2 at δ 5.550) of **7** due to partial deuteration at C-5; (*c*) ^{13}C NMR, peak 3: C-6 signal of natural abundance **7**; (*d*) ^{13}C NMR, peak 3: C-6 signal of **7**, peak 4: C-6 signal of **7b**, and peak 5: C-6 signal of **7a** due to partial deuteration at C-5 (full ^{1}H NMR spectra of isolated deuterated phomamides and sirodesmins PL are provided in the Supplementary data).

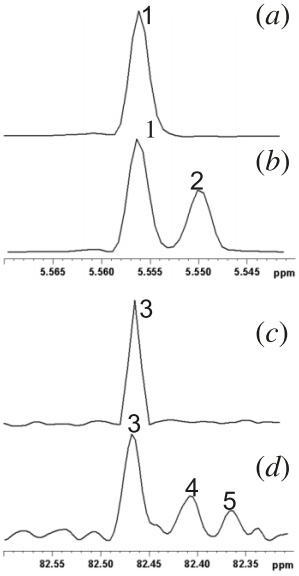

due to the β-isotope shift.[1,16] Importantly, only one ^{13}C NMR peak was observed for C-7 (δ_C 79.2), indicating that the deuterium at C-5 caused no isotope shift effect on C-7, as expected due to the additional bond separation. Similar results were obtained when cultures were incubated with [3,3-$^{2}H_2$]*O*-prenyl-L-tyrosine (**9a**) (Table 1, entry 2). Furthermore, feeding [2,3,3-$^{2}H_3$]L-serine (**2a**) and [5,5-$^{2}H_2$]cyclo-L-Tyr-L-Ser (**3a**) led to very low incorporation of deuterium into sirodesmin PL (**7**) (Table 1, entries 3 and 5, respectively).

The results described above and summarized in entries 1 and 2 of Table 1 demonstrated that 30%–35% of both monodeuterated (**7b**) and dideuterated (**7a**) sirodesmin PL (**7**) was obtained from incorporation experiments with dideuterated precursors **1a** and **9a**, whereas mostly dideuterated **7a** was obtained from incorporation of **4a** (full ^{1}H NMR spectra of isolated deuterated phomamides and sirodesmins PL are provided in the Supplementary data). Consequently, these results indicated that deuterium exchange took place before the final step of phomamide (**4**) biosynthesis and thus the proposed bis-ylidine 2,5-dioxopiperazine (**8**) is not a likely intermediate of the biosynthetic pathway.

Further data analysis and additional calculations clarified the specific nature of this deuterium exchange, as follows. The HRMS-EI data (Table 1, entry 1) showed that the total amount of monodeuterated (19%) and dideuterated (13%) molecules of **7** was 32% (19% + 13%, relative to natural abundance compound), whereas the two ^{1}H NMR peaks due to H-7 at δ_H 5.556 and 5.550 (2:1, Figs. 1*a* and 1*b*) were due to the total amount of **7**, i.e., natural abundance, monodeuterated, and dideuterated. Since integration of both H-7 NMR peaks showed that the signal at δ_H 5.550 represented ca. 33% of H-7 and this amount corresponded to the total amount of deuterated **7** determined by HRMS-EI (19:13 ratio), the 33% accounted by ^{1}H NMR must necessarily represent a mixture of dideuterated (**7a**) and monodeuterated (**7b**) compound in a 19:13 ratio, respectively. This unexpected isotope shift effect (higher field signal of H-7, δ_H 5.550) could be explained by a through space intrinsic deuterium isotope effect on H-7.

Isotope effects on proton and (or) carbon chemical shifts in compounds where deuterium and the observed proton(s)/carbon(s) were separated by four or more covalent bonds but where the nuclei were close together in space, termed "intrinsic steric isotope effects", have been reported and characterized.[17] The dideuterated sirodesmin molecules had both *pro-R* and *pro-S* deuteria at C-5 (13%), whereas the monodeuterated molecules (19%) in principle could have either the *pro-R* or the *pro-S* deuterium (corresponding to the *pro-R* or the *pro-S* hydrogens) or a mixture of *pro-R* and *pro-S* (e.g., a 1:1 ratio). However, considering the nature of intrinsic steric deuterium isotope effects, it would be expected that only the deuterated molecules having the deuterium close to H-7 (ca. <3 Å) would display this effect. Molecular mechanics calculations[18] showed that structure **7b** has the *pro-S* hydrogen at C-5 in closer proximity of H-7 (2.47 Å) than the *pro-R* hydrogen (3.59 Å). Therefore, these interatomic distances are in close agreement with previous reports[17] on intrinsic steric deuterium isotope effects on proton(s).

From the overall analysis it was concluded that only the monodeuterated structure **7b** was formed (but not **7c**), in addition to the dideuterated **7a**. Finally, extrapolation of this conclusion to the precursor [3,3-$^{2}H_2$]L-tyrosine (**1a**) indicated that its $^{2}H_R$ was partially and stereospecifically exchanged before incorporation into phomamide (**4**), which in turn was incorporated without further deuterium exchange into sirodesmin PL. Furthermore, considering that feeding either [3,3-$^{2}H_2$]L-tyrosine (**1a**) or [3,3-$^{2}H_2$]*O*-prenyl-L-tyrosine (**9a**) yielded monodeuterated products as well, it is surmised that deuterium exchange occurred before formation of phomamide, i.e., either in L-tyrosine or *O*-prenyl-L-tyrosine or both (Scheme 3).

Comparable results in which dideuterated (**11a**) and monodeuterated (**11b**) gliotoxin were obtained from feeding experiments using [3,3-$^{2}H_2$]D,L-phenylalanine (**8a**) were reported previously;[19] however, stereospecific exchange of the *pro-S* deuterium of deuterated phenylalanine (Scheme 4) was established using stereospecifically monodeuterated phenylalanines **10b** and **10c**.

Finally, to clarify the stage at which prenylation occurred (i.e., amino acid or dioxopiperazine), incorporation of [3,3,5′,5′,5′-$^{2}H_5$]*O*-prenyl-L-tyrosine (**9b**) was investigated. The ^{1}H NMR spectra of both phomamide (**4**) and sirodesmin PL (**7**) isolated from cultures incubated with [3,3,5′,5′,5′-$^{2}H_5$]*O*-prenyl-L-tyrosine (**9b**) showed that integration of the peak area of protons H-5a, H-5b, and H_3-5′ of phomamide (**4**) and H_2-5 and H_3-17 of sirodesmin PL (**7**) were lower than those of control samples. That is, both pentadeuterated and tetradeuterated phomamide (**4c**, 7%; **4d**, 16%) and sirodesmin PL (**7d**, 4%; **7e**, 9%) were produced in cultures incubated with pentadeuterated prenyl tyrosine **9b** (Table 1, entry 6). These amounts of deuterium incorporation and the

Scheme 3. Incorporation of [3,3-$^2H_2$]L-tyrosine (**1a**), [3,3-$^2H_2$]*O*-prenyl-L-tyrosine (**9a**), and [5,5-$^2H_2$]phomamide (**4a**) into sirodesmin PL showing partial structures of dideuterated (**7a**) and monodeuterated (**7b**) sirodesmin PL; **7c** is not formed; **7d** and **7e** result from incorporation of [3,3,5′,5′,5′-$^2H_5$]*O*-prenyl-L-tyrosine (**9b**). The curved arrow indicates an intrinsic steric deuterium isotope (ISDI) effect (ca. 3 Hz) of ^2H_S-5 on the ^1H NMR chemical shift of H-7.

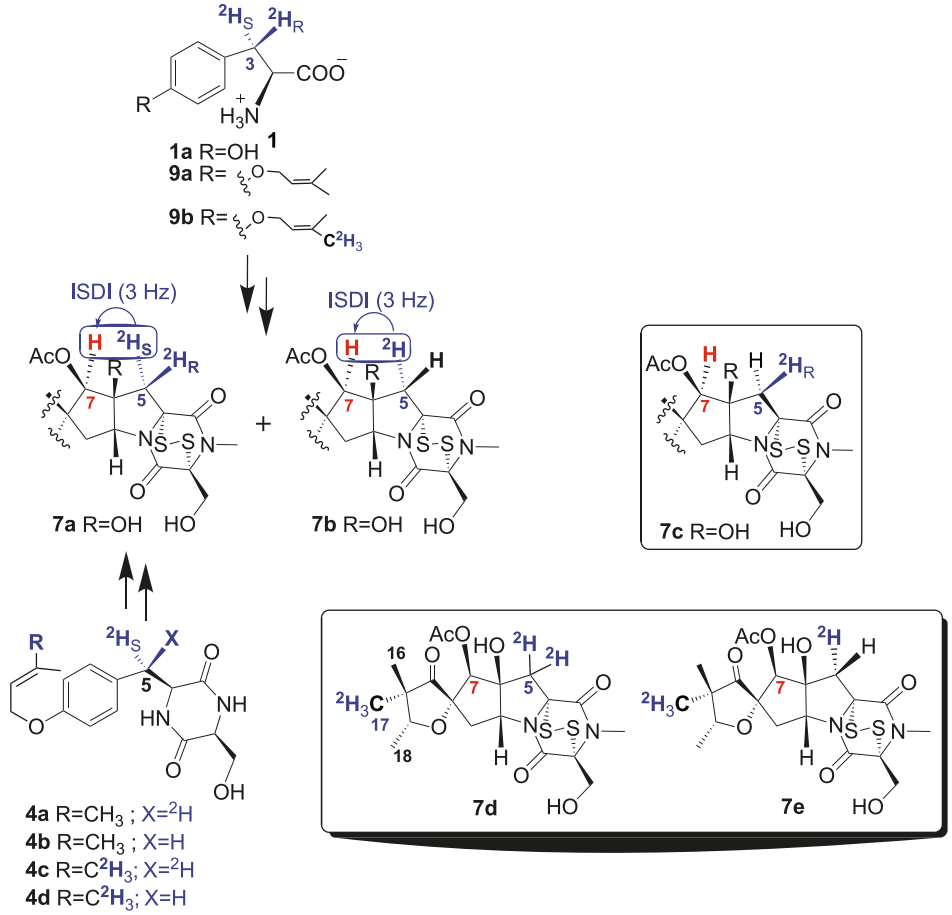

Scheme 4. Incorporation of [3,3-$^2H_2$]D,L-phenylalanine (**10a**) into dideuterogliotoxin (**11a**) and monodeuterogliotoxin (**11b**).[19]

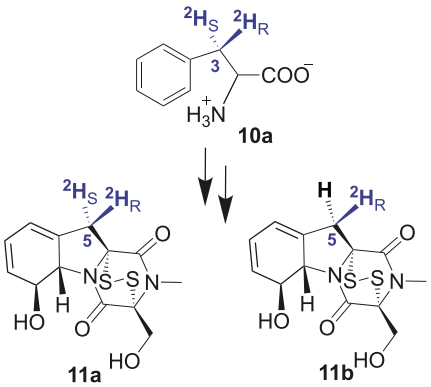

much lower incorporation of **3a** (≤2%) relative to compounds **1a**, **9a**, and **4a** indicated that **3** was not a likely intermediate in the sirodesmin PL (**7**) pathway. In addition, the incorporation of specifically deuterated prenyl derivative demonstrated clearly that CH_3-17 is derived from the deuterated methyl of substituted tyrosine **9b**, which agrees with previous data.[10] Substantially lower incorporations of serine than tyrosine may reflect a faster deployment of serine into other primary pathways (e.g., synthesis of proteins and tryptophan and (or) degradation to pyruvate and glycine). Previous results using radiolabeled serine and tyrosine reported a rather low incorporation of both amino acids into phomamide (**4**) and sirodesmin PL (**7**).[10]

Conclusion

In summary, this work demonstrated that both dideuterated and monodeuterated sirodesmin PL (**7a** and **7b**) and phomamide (**4a** and **4b**) were produced when the precursors [3,3-$^2H_2$]L-tyrosine (**1a**) and [3,3-$^2H_2$]*O*-prenyl-L-tyrosine (**9a**) were incubated with cultures of *L. maculans*. Importantly, a remarkable intrinsic steric deuterium isotope effect detected on the NMR chemical shift of H-7 of monodeuterated sirodesmin PL (**7b**) revealed that the *pro-R* deuterium of sirodesmin PL exchanged stereospecifically. This stereospecific exchange occurred before incorporation of tyrosine (**1a**) into phomamide (**4**), thus the proposed bis-ylidine 2,5-dioxopiperazine (**8**) is not a likely intermediate of the sirodesmin pathway. That is, a percentage of [3,3-$^2H_2$]L-tyrosine (**1a**) is directly channelled into sirodesmin biosynthesis and another fraction rechannelled after diverging into a pathway(s) where a β-deuterium is exchanged stereospecifically. Such a pathway(s) might involve transamination via pyri-

doxal phosphate with concomitant stereospecific exchange of the *pro-R* β-deuterium with a proton.[20] A fraction of the resulting monodeuterated tyrosine ([3-^2H_S]L-tyrosine) could eventually be redirected into the sirodesmin pathway. In addition, our results strongly suggested that prenylation occurred before dioxopiperazine formation and thus *O*-prenyl-L-tyrosine is a likely intermediate of phomamide (**4**) en route to sirodesmin PL (**7**). Therefore, prenylation of tyrosine by the prenylase sirD appears to be the first committed step in the biosynthetic pathway to sirodesmin PL (**7**).

As a final point, it is of interest to highlight that, in general, demonstration of stereospecific isotope exchange observed in biological pathways[20,21] require feeding experiments with stereospecifically labeled substrates, e.g., phenylalanine (**10b** and **10c**) → gliotoxin (**11** and **11b**) (Scheme 4). By contrast, in this work, the detection and substantiation of an intrinsic steric deuterium isotope shift effect revealed clearly a stereospecific deuterium exchange (**7b** and **7e**) in the biosynthetic pathway to sirodesmin PL (**7**).

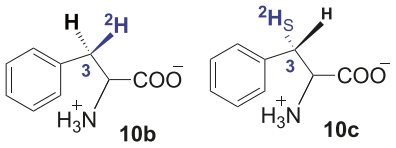

Materials and methods

General experimental procedures

All solvents were HPLC grade and used as such. Organic extracts were dried with Na_2SO_4 and solvents removed under reduced pressure in a rotary evaporator. Preparative thin layer chromatography was carried out on silica gel plates, Kieselgel 60 F_{254} (20 cm × 20 cm × 0.25 mm), compounds were visualized under UV light. NMR spectra were recorded on Bruker Avance 500 series spectrometers; for ^1H (500 MHz), δ values were referenced as follows for ^1H to $CHCl_3$ (7.27 ppm) and for ^{13}C to $CDCl_3$ (77.23 ppm). Mass spectra (MS) were obtained on a mass spectrometer using a solids probe.

Synthesis of labeled precursors

The deuterated materials [3,3-$^2H_2$]*O*-prenyl-L-tyrosine (**9a**), [3,3,5′,5′,5′-$^2H_5$]*O*-prenyl-L-tyrosine (**9b**), [5,5-$^2H_2$]cyclo-L-Tyr-L-Ser (**3a**), and [5,5-$^2H_2$]phomamide (**4a**) were prepared following modifications of previously reported methods, as described in the Supplementary data. All compounds gave satisfactory spectroscopic data; in each case the percentage of deuterated synthetic compound was ≥98% (HRMS-EI).

Incorporation of labeled precursors

Fungal cultures of *L. maculans* isolate BJ 125 were obtained from the IBCN collection, Agriculture and Agri-Food Canada Research Station, Saskatoon, SK. Cultures were handled as described previously.[22] Isolate BJ 125 was grown in 250 mL Erlenmeyer flasks containing 100 mL minimal media inoculated with fungal spores at 1×10^9 cells per flask. The cultures were incubated on a shaker at 130 rpm, at 24 ± 2 °C for 3 d, then deuterated compounds (dissolved in sterile distilled water, 5.0 mmol/L) were added to cultures. At the 5th day, the broth of each flask was extracted with EtOAc (100 mL × 3) and concentrated to dryness. The residue was separated by preparative TLC (MeOH–CH_2Cl_2, 10:90) to give sirodesmin PL (**7**) (R_f = 0.75, ca. 90 mg/L) and phomamide (**4**) (R_f = 0.25, ca. 10 mg/L).

Supplementary data

Supplementary data for this article are available on the journal Web site (canjchem.nrc.ca) or may be purchased from the Depository of Unpublished Data, Document Delivery, CISTI, National Research Council Canada, Ottawa, ON K1A 0R6, Canada. DUD 3898. For more information on obtaining material refer to cisti-icist.nrc-cnrc.gc.ca/cms/unpub_e.shtml.

Acknowledgments

Support for the authors' work was obtained from the Natural Sciences and Engineering Research Council of Canada (Discovery grant to MSCP), Canada Foundation for Innovation, Canada Research Chairs (MSCP), and the University of Saskatchewan (teaching assistantship to YY). We acknowledge the technical assistance of K. Brown (NMR), G. Schatte (NMR), and K. Thoms (MS) for data acquisition.

References

(1) For a relevant review see: Schneider, B. *Prog. Nucl. Magn. Reson. Spectrosc.* **2007**, *51*, 155. doi:10.1016/j.pnmrs.2007.02.006.

(2) For a recent review on ETPs see: Gardiner, D. M.; Howlett, B. J. *Microbiology* **2005**, *151*, 1021. doi:10.1099/mic.0.27847-0. PMID:15817772.

(3) Curtis, P. J.; Greatbanks, D.; Hesp, B.; Forbes, C. A.; Freer, A. A. *J. Chem. Soc. Perkin Trans.* **1977**, *2*, 180. doi:10.1039/p19770000180.

(4) Quesneau-Thierry, A.; Boudart, G. *Nouv. J. Chim.* **1977**, *1*, 327.

(5) Pedras, M. S. C.; Abrams, S. R.; Séguin-Swartz, G. *Tetrahedron Lett.* **1988**, *29*, 3471. doi:10.1016/0040-4039(88)85192-X.

(6) Pedras, M. S. C.; Taylor, J. L.; Nakashima, T. T. *J. Org. Chem.* **1993**, *58*, 4778. doi:10.1021/jo00070a002.

(7) Kupfahl, C.; Heinekamp, T.; Geginat, G.; Ruppert, T.; Haertl, A.; Hof, H.; Brakhage, A. A. *Mol. Microbiol.* **2006**, *62*, 292. doi:10.1111/j.1365-2958.2006.05373.x. PMID:16956378.

(8) Gardiner, D. M.; Cozijnsen, A. J.; Wilson, L. M.; Pedras, M. S. C.; Howlett, B. J. *Mol. Microbiol.* **2004**, *53*, 1307. doi:10.1111/j.1365-2958.2004.04215.x. PMID:15387811.

(9) Elliot, C. E.; Gardiner, D. M.; Thomas, G.; Cozijnsen, A.; Van de Wouw, A.; Howlett, B. J. *Molecular Plant Pathology* **2007**, *8*, 791. doi:10.1111/j.1364-3703.2007.00433.x.

(10) Ferezou, J.-P.; Quesneau-Thierry, A.; Servy, C.; Zissmann , E.; Barbier, M. *J. Chem. Soc. Perkin Trans. 1* **1980**, 1739. doi:1.1039/P19800001739.

(11) Bu'Lock, J. D.; Clough, L. E. *Aust. J. Chem.* **1992**, *45*, 39. doi:10.1071/CH9920039.

(12) Pedras, M. S. C.; Abrams, S. R.; Séguin-Swartz, G.; Quail, J. W.; Jia, Z. *J. Am. Chem. Soc.* **1989**, *111*, 1904. doi:10.1021/ja00187a068.

(13) Pedras, M. S. C.; Yu, Y. *Bioorg. Med. Chem.* **2008**, *16*, 8063. doi:10.1016/j.bmc.2008.07.060. PMID:18701303.

(14) Fraile, J. M.; Garcia, J. I.; Mayoral, J. A.; Royo, A. J. *Tetrahedron Asymmetry* **1996**, *7*, 2263. doi:10.1016/0957-4166(96)00281-9.
(15) (a) Férézou, J. P.; Quesneau-Thierry, A.; Barbier, M.; Kollmann, A.; Bousquet, J. F. *J. Chem. Soc. Perkin Trans.* **1980**, *1*, 113. doi:10.1039/p19800000113.; (b) Mancilla, T.; Carrillo, L.; Zamudio-Rivera, L. S.; Beltran, H. I.; Farfan, N. *Org. Prep. Proced. Int.* **2001**, *33*, 34; (c) Nitecki, D. E.; Halpern, B.; Westley, J. W. *J. Org. Chem.* **1968**, *33*, 864. doi:10.1021/jo01266a091.
(16) Jurlina, J. L.; Stothers, J. B. *J. Am. Chem. Soc.* **1982**, *104*, 4677. doi:10.1021/ja00381a030.
(17) (a) Anet, F. A. L.; Dekmezian, H. J. *J. Am. Chem. Soc.* **1979**, *101*, 5449 doi:10.1021/ja00512a073.; (b) Ernst, L.; Eltamany, S.; Hopf, H. *J. Am. Chem. Soc.* **1982**, *104*, 299 doi:10.1021/ja00365a060.; (c) Saunders, M.; Wolfsberg, M.; Anet, F. A. L.; Kronja, O. J. *J. Am. Chem. Soc.* **2007**, *129*, 10276. doi:10.1021/ja072375r. PMID:17655301.
(18) Computational calculations of the interatomic distances in sirodesmin PL (**7**) were carried out using the Spartan 06 software package, method MMFF94.
(19) Bu'Lock, J. D.; Ryles, A. P.; Johns, N.; Kirby, G. W. *J. Chem. Soc. Chem. Comm.* **1972**, 100. doi:10.1039/c39720000100.
(20) Sawada, S.; Kumagai, H.; Yamada, H.; Hill, R. K. *J. Am. Chem. Soc.* **1975**, *97*, 4334. doi:10.1021/ja00848a033. PMID:1141596.
(21) Hanson, K. R. *Annu. Rev. Biochem.* **1976**, *45*, 307. doi:10.1146/annurev.bi.45.070176.001515. PMID:786152.
(22) Pedras, M. S. C.; Khan, A. Q. *J. Agr. Food Chem.* **1996**, *44*, 3403. doi:10.1021/jf960098u.

Measurement and calculation of ^{13}C and ^{15}N NMR chemical-shift tensors of a push–pull ethylene

Saeed K. Amini, Mohsen Tafazzoli, Hilary A. Jenkins, Gillian R. Goward, and Alex D. Bain

Abstract: Methyl 3-dimethylamino-2-cyanocrotonate (MDACC) has a remarkably weak carbon–carbon double bond. It has strong electron-withdrawing groups on one end and electron-donating groups on the other: a so-called push–pull ethylene. To investigate this unusual electronic structure, we have determined the crystal structure and measured both the ^{13}C and ^{15}N NMR chemical-shift tensors. These measurements are supplemented by shielding-tensor calculations done with density functional methods. The large difference (approximately 100 ppm) between isotropic chemical shifts of the two alkenyl carbons reflects a large charge release from the electron-donating side of C=C double bond to the electron-withdrawing groups. Comparison of the calculated orientations of the principal components of the alkenyl carbons obtained from ab initio calculations shows that the primary changes in charge density occur in the molecular plane. On the other hand, smaller charge density changes above and below the plane of the C=C double bond establish the conjugation of donor and acceptor groups with π^* and π molecular orbitals of the central double bond, respectively, which lowers the barrier to rotation about this bond.

Key words: density functional methods, NMR, shielding anisotropy, CSA, push–pull ethylenes, crystal structure.

Résumé : La double liaison carbone-carbone du 3-diméthylamino-2-cyanocrotonate de méthyle (DMACCM) est extrêmement faible. Il porte des groupes électroattracteurs à une extrémité et des groupes électrodonneurs à l'autre, un éthylène de type « push-pull ». Dans le but d'étudier ce type de structure électronique inhabituelle, on a déterminé sa structure électronique et on a aussi mesuré les tenseurs des déplacements chimiques en RMN tant du ^{13}C que du ^{15}N. Pour ajouter à ces mesures, on a aussi fait des calculs de tenseur de blindage à l'aide de méthodes de la fonctionnelle de la densité. Une différence importante (d'environ 100 ppm) entre les déplacements chimiques isotropes des deux atomes de carbone du groupe alcényle est un reflet d'un dont important de charge à partir du çté électrodonneur de la double liaison C=C vers les groupes électroattracteurs. Une comparaison des valeurs calculées pour les orientations des principaux composants des carbones alcényles obtenues par des calculs ab initio montre que les changements primaires dans la densité de charge se produisent dans le plan moléculaire. Par ailleurs, des changements plus faibles dans la densité de la charge, au-dessus et au-dessous du plan de la double liaison C=C, permettent d'établir la conjugaison des groupes donneurs et accepteurs respectivement avec les orbitales moléculaires π^* et π de la double liaison centrale qui abaisse la barrière à la rotation autour de cette liaison.

Mots-clés : méthodes de la fonctionnelle de la densité, RMN, anisotropie de blindage, ASC, éthylènes « push-pull », structure cristalline..

[Traduit par la Rédaction]

Introduction

Push–pull alkenes are special derivatives of ethylene in which hydrogen nuclei are substituted with electron-donating and electron-withdrawing functional groups at opposite ends of a double bond.[1–9] The π electrons of the central C=C double bond are strongly delocalized so that push–pull alkenes are extremely polarized along this bond. It is clear from extensive investigations that this interaction depends on the individual combination of donor and acceptor substituents in a non-additive manner.[10,11] This effect has been described by some parameters, such as bond length and π-bond order of the central double bond. A further manifestation is a much lower barrier to rotation in comparison to ordinary C=C double bonds.

Evaluation of the barrier to rotation about this bond by NMR methods[12–14] has been a major part of studies of push–pull alkenes. In most cases, either dynamic NMR lineshapes or 2D EXSY NMR experiments were employed to study this barrier.[4,15–17] These studies include the use of both the barrier to rotation about the double bond and the chemical-shift difference between two alkenyl carbons to quantify the push–pull effect. However, corresponding barriers to rotation have been correlated poorly to bond length and π-bond order of the central partial double bond. This may be due to steric hindrance, hydrogen bonding, or stabilization and destabilization effects of donor and acceptor groups in both the ground state and the transition state of

Received 3 September 2008. Accepted 14 January 2009. Published on the NRC Research Press Web site at canjchem.nrc.ca on 17 March 2009.

S.K. Amini. Department of Chemistry, McMaster University, Hamilton, ON L8S 4M1, Canada; Department of Chemistry, Sharif University of Technology, P.O. Box 11365-9516 Tehran, Iran.
M. Tafazzoli. Department of Chemistry, Sharif University of Technology, P.O. Box 11365-9516 Tehran, Iran.
H.A. Jenkins, G.R. Goward, and A.D. Bain.[1] Department of Chemistry, McMaster University, Hamilton, ON L8S 4M1, Canada.

[1]Corresponding author (e-mail: bain@mcmaster.ca).

Table 1. Bond lengths and angles for MDACC.

Bond lengths (Å)	
C(1)—O(12)	1.219(2)
C(1)—O(9)	1.349(2)
C(1)—C(2)	1.453(2)
C(2)—C(3)	1.405(2)
C(2)—C(10)	1.423(2)
C(3)—N(4)	1.333(2)
C(3)—C(7)	1.498(2)
N(4)—C(5)	1.460(2)
N(4)—C(6)	1.468(2)
C(8)—O(9)	1.426(2)
C(10)—N(11)	1.1464(18)
Bond angles (°)	
O(12)–C(1)–O(9)	121.41(15)
O(12)–C(1)–C(2)	127.50(15)
O(9)–C(1)–C(2)	111.05(13)
C(3)–C(2)–C(10)	120.42(14)
C(3)–C(2)–C(1)	123.65(13)
C(10)–C(2)–C(1)	115.64(14)
N(4)–C(3)–C(2)	122.46(12)
N(4)–C(3)–C(7)	117.10(14)
C(2)–C(3)–C(7)	120.40(15)
C(3)–N(4)–C(5)	123.12(13)
C(3)–N(4)–C(6)	122.45(13)
C(5)–N(4)–C(6)	114.34(14)
C(1)–O(9)–C(8)	116.79(12)
N(11)–C(10)–C(2)	176.93(16)

Fig. 1. Structure and numbering scheme for MDACC. Carbon 3 (called C+ in the text) is much less shielded than carbon 2 (C–).

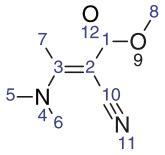

Fig. 2. View of the crystal structure of MDACC, looking down the carbon-–carbon double bond. Carbons are grey, nitrogens are blue, oxygens are red, and hydrogens are white.

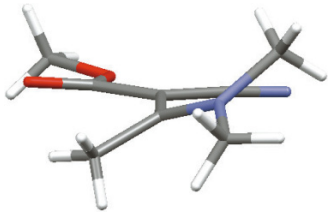

the restricted rotation. So, not only the π-bond order of the central C=C double bond, but also the total π-charge density along the central C=C double bond affect these stabilization and destabilization processes.[15]

This encouraged us to quantify the push–pull effect by measuring the full chemical-shift tensors of a typical push–pull ethylene, methyl 3-dimethylamino-2-cyanocrotonate (MDACC),[17–19] in the solid state. As well, the crystal structure of this molecule is reported here. This compound, which has a small barrier to rotation, has been the subject of both 2D EXSY studies in solution and some ab initio calculations.[17] Such calculations can give insight into the way that NMR parameters are affected by a multiple bond.[20–26] The literature contains many calculations of isotropic chemical shifts, but relatively few take it to the level of comparing individual shielding-tensor elements with experimental values. In the present paper, we determine the principal components of the ^{13}C and ^{15}N shift tensors and compare them to those calculated using high-level density functional theory.[27–37] The combination of accurate structure determination with calculated and observed shift tensors[38–42] gives a very detailed picture of the unusual electronic structure of this molecule.

Experimental

MDACC was prepared by reacting 24 mL (0.18 mol) of *N*,*N*-dimethylacetamide dimethyl acetal with 14.2 mL (0.16 mol) of methyl cyanoacetate and stirring for 30 min.[17,19] Both reagents were purchased from Sigma-Aldrich and used without further purification. The resultant crude product was purified using a cold-finger sublimation apparatus operating at 140 °C under vacuum conditions to yield a pale brown solid.

The molecule exists as an equilibrium mixture of *E* and *Z* conformations in solution, but it crystallizes in the *E* structure. For the crystallography, a colourless rod (0.20 × 0.40 × 0.60 mm) was mounted on the end of a glass fibre. Data were collected on a Bruker Smart 6000 CCD three-circle D8 diffractometer with a Cu RA (Rigaku) X-ray source at 295 K. Cross-coupled parallel focusing mirrors were used to monochromate the X-ray radiation. The data were collected using 60 s frames for the detector at –40° (2θ) and using 120 s frames for the detector at –100° (2θ). Data were integrated using SAINT, corrected for absorption (empirical correction) using SADABS and then solved using the BRUKER SHELXTL Suite 6.14. All non-hydrogen atoms were treated as anisotropic thermal ellipsoids; hydrogen atoms were placed in calculated positions based on the framework of the molecule. Final *R* values were R_1 = 2.96%, wR_2 = 8.64%. Selected bond lengths and angles are given in Table 1, and the full set of crystallographic data and derived bond lengths and angles are given in Tables S1–S6 in the Supplementary data. Figures 1 and 2 show the structure of MDACC (also see Supplementary data).

Slow-spinning magic-angle (MAS) NMR experiments were carried out to measure the intensities of spinning sidebands. The experiments were done on Bruker AVANCE instruments operating at 7.1 and 11.7 T. A 4 mm solid state MAS probe was used, spinning at 3.7, 4.2, 4.5, and 5.8 kHz for the ^{13}C data and 2.0 and 3.5 kHz for the ^{15}N data. All experiments were done at room temperature and spectra were acquired using a ramped cross polarization, with a 7 ms contact time and TPPM decoupling. Spinning sideband patterns were analyzed using the DMFIT program.[43]

^{13}C chemical shifts were referenced to the carbonyl carbon of glycine at 176.14 ppm with respect to TMS at 0 ppm (absolute shielding of 188.1 ppm[30,44]). The ^{15}N values were set relative to the amide nitrogen of glycine, which was calibrated at –347.5 ppm relative to liquid CH_3NO_2 at

Table 2. Summary of experimental chemical shifts of ^{13}C and ^{15}N nuclei of MDACC at 11.7 T.

Spin rate(Hz)	δ_{iso}	δ_{11}	δ_{22}	δ_{33}
C+ nucleus				
5800	172.6	57.3	210.1	250.4
4500	172.7	58.2	207.1	252.9
4200	172.6	55.7	210.6	251.5
3700	172.7	57.9	204.2	255.9
COO nucleus				
5800	168.9	104.8	144.3	256.0
4500	168.4	106.2	144.3	254.3
4200	168.3	105.7	147.5	251.9
3700	168.4	106.5	145.0	253.8
^{13}CN nucleus				
5800	120.2	–77.8	199.5	239.2
4500	120.3	–80.0	220.5	220.5
4200	120.2	–80.1	210.3	230.4
3700	120.2	–79.8	205.2	235.3
C- nucleus				
5800	70.1	35.5	58.6	116.3
4500	70.2	40.0	53.9	116.7
4200	70.1	38.5	54.9	116.9
3700	70.1	38.1	58.0	114.3
C^{15}N nucleus				
2000	–117.4	–334.6	–46.8	29.2
3500	–117.4	–345.4	–37.6	30.8

Fig. 3. Spinning sideband pattern of some of the carbon atoms in the region from 65 ppm to 265 ppm. The C+ nucleus is represented by red circles, the carboxyl by green triangles us, the cyano nucleus by cyan triangles down, and the C– nucleus by dark green squares. Centrebands are denoted by large symbols, and sidebands by smaller symbols.

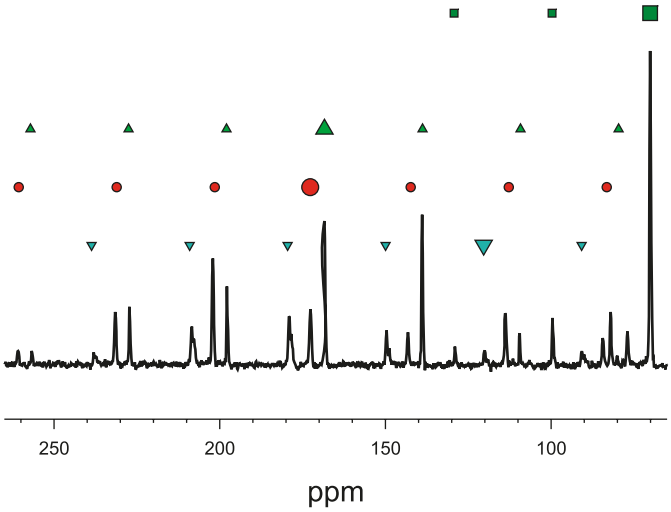

0 ppm (absolute shielding of –135.8 ppm[30,45]). Chemical shifts can also be calculated by performing a calculation on the chemical-shift reference at the same level of theory. Such calculations were done on both TMS and CH_3NO_2, as well as on benzene, which is also used as a reference compound for ^{13}C chemical shifts.[46,47]

Both ab initio geometry optimization and chemical-shielding calculations were performed using the G03 package from Gaussian, Inc.[48] on an Intel Pentium-4 based computer operating at 1.6 GHz with 512 megabytes of RAM. The chemical shielding calculations used the gauge invariant atomic orbital (GIAO) method. Since both basis set size and method can have large effects on chemical-shielding calculations, different methods were used: B3LYP, MPW1PW91, and MPWLYP, with different basis sets: 6–31++G(d,p), 6–311++G(d,p), and 6–311++G(3df,p). Three different geometries were used for each basis set/functional combination. One was the molecular structure optimized using the same level of theory used in the NMR calculations, and the second was the measured crystal structure. The third was based on the crystal structure, but the hydrogen positions were optimized using the MPW1PW91 functional and the 6–311++G(d,p) basis set.

Results

The measured structure, summarized in Table 1, corresponds closely to the structure calculated at various levels of theory with various functionals. The geometry around the C=C double bond is not planar, but this appears to be a steric effect. Calculations on a similar molecule with the *N*,*N*-dimethyl group replaced by an NH_2 group show a planar structure around the central double bond. The carbon-—carbon bond length at 1.405 Å is intermediate between a standard double bond and a single bond, and is similar to reported values in similar molecules.[49–52]

Measured chemical-shift values of ^{13}C and ^{15}N nuclei and their principal components obtained from spectra at different

Fig. 4. Calculated absolute NMR shielding tensor elements for C+ (carbon 3, shown with arrow in diagram) of MDACC, for different geometries, basis sets and functionals. Data are from Table S7 in the Supplementary data. The two basis sets are denoted by the heights of the bars, and the three geometries by different colours and slightly different vertical positions. The large bar at the bottom represents the experimentally determined value. Functional 1 is B3LYP, functional 2 is MPW1PW91, and functional 3 is MPWLYP. The two different basis sets used were 6–311++G(d,p) (shorter bars) and 6–311++G(3df,p) (taller bars). The black bars represent calculations using the experimental crystal structure, the red bars represent a geometry in which the hydrogen positions of the crystal structure were optimized at the level of MPW1PW91/6–311++G(d,p), and the green bars represent a fully optimized geometry with the same basis set and functional as that used for the shielding calculation.

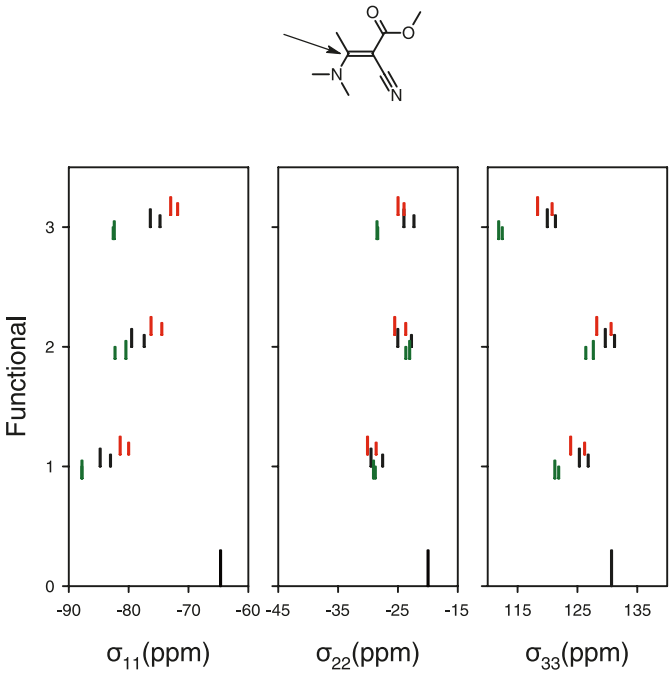

spin rates using the 11.7 T instrument are collected in Table 2. Figure 3 presents the ^{13}C spectra at 4.5 kHz spin rate acquired at 11.7 T. The results of different spinning rates were similar and their differences are in error regimes of experimental and fitting processes.

In the calculations, it was found that in many cases, the basis set 6–31++G(d,p) gave substantially (up to 20 ppm) different results from the higher basis sets, so only the results based on 6–311++G(d,p) and 6–311++G(3df,p) are reported here. The experimentally measured chemical shifts were converted to absolute shieldings using the absolute shielding of carbon in TMS as 188.1 ppm[44] and absolute shielding of –135.8 ppm[45] for the ^{15}N in CH_3NO_2. The results are presented graphically in Figs. 4 through 8 and Tables S7–S11 in the Supplementary data. They give the calculated absolute shieldings for the carboxyl carbon, the two carbons connected by the double bond, the cyano carbon, and the cyano nitrogen, in the order of the isotropic shifts. Figure 9 plots the calculated isotropic shifts of the shift reference standards (TMS, benzene, and CH_3NO_2) using the same levels of theory.

Fig. 5. Calculated absolute NMR shielding tensor elements for the designated carboxyl carbon in MDACC, for different geometries, basis sets, and functionals. Data from Table S8 (see Supplementary data). Symbols and scales as in Fig. 4.

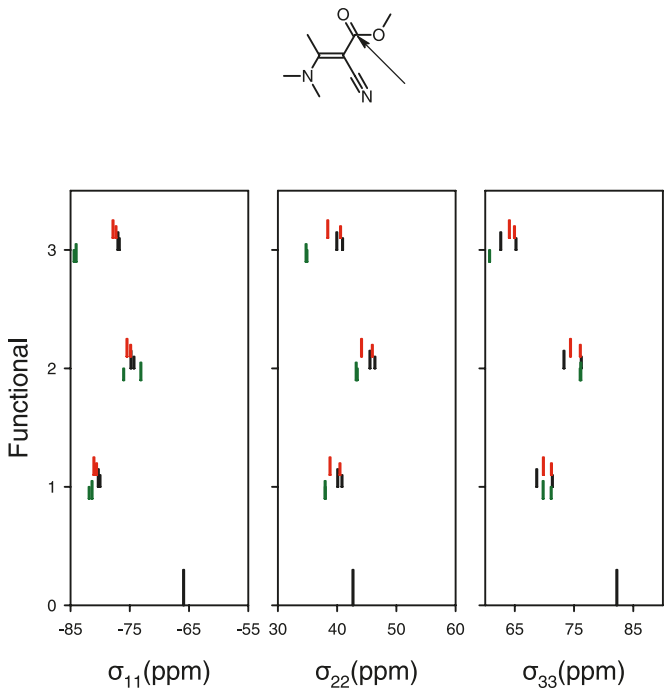

Fig. 6. Calculated absolute NMR shielding tensor elements for the cyano carbon of MDACC, for different geometries, basis sets, and functionals. Data from Table S9 (see Supplementary data). Symbols and scales as in Fig. 4.

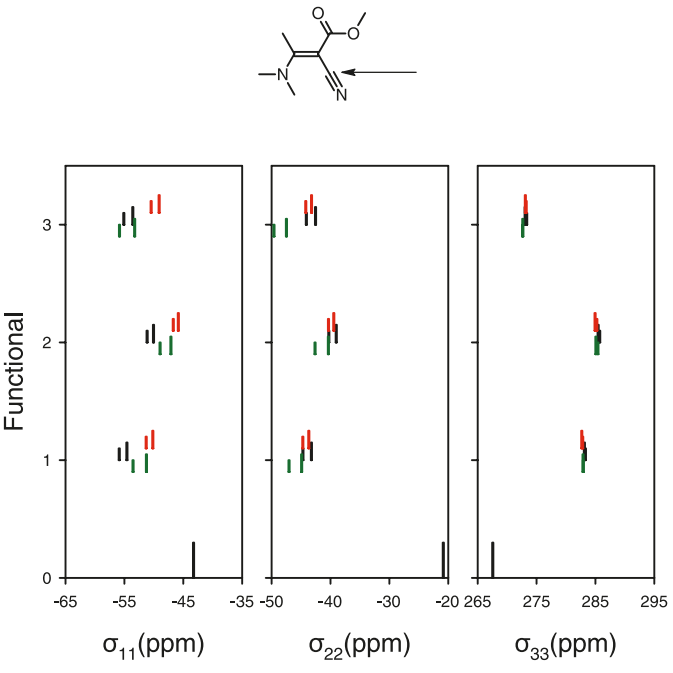

Fig. 7. Calculated absolute NMR shielding tensor elements for the designated C– carbon of MDACC at the other end of the formal double bond from Fig. 4, for different geometries, basis sets, and functionals. Data from Table S10 (see Supplementary data). Symbols and scales as in Fig. 4.

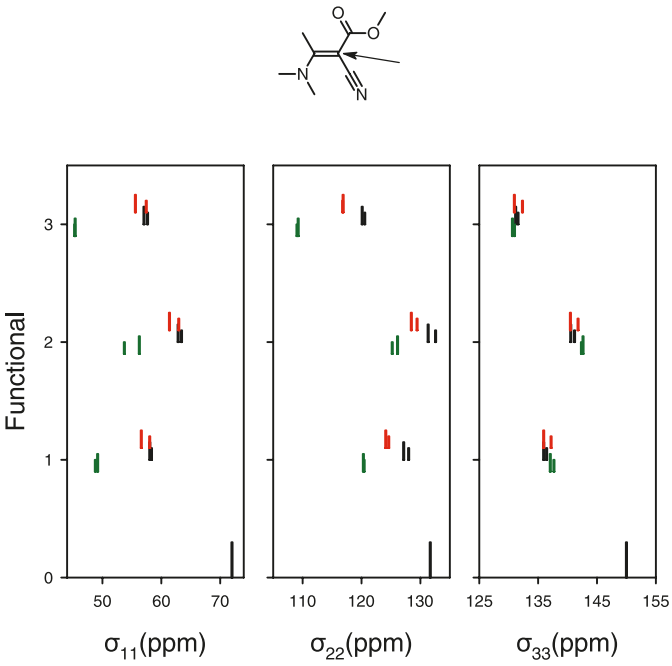

Fig. 8. Calculated absolute NMR shielding tensor elements for the cyano nitrogen of MDACC, for different geometries, basis sets, and functionals. Data from Table S11 (see Supplementary data). Symbols are the same as previous figures, but the horizontal scale (in ppm/cm) is twice the previous value.

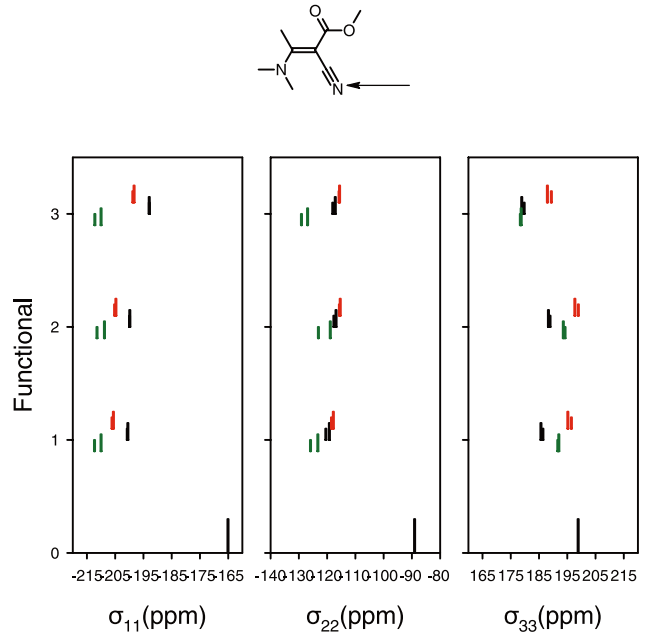

Discussion

Figures 4 through 8 and the numerical values in the Supplementary data show the effects of basis set, functional, and geometry on the calculated shielding-tensor elements. The

Fig. 9. Calculated absolute NMR isotropic shieldings for the chemical-shift reference materials, for different basis sets and functionals. The two basis sets are denoted by the heights of the bars. The large bar at the bottom represents the experimentally determined value.[44,45] Functional 1 is B3LYP, functional 2 is MPW1PW91, and functional 3 is MPWLYP. The two different basis sets used were 6–311++G(d,p) (shorter bars) and 6–311++G(3df,p) (taller bars). In each case, the geometry used is a fully optimized geometry with the same basis set and functional as that used for the shielding calculation.

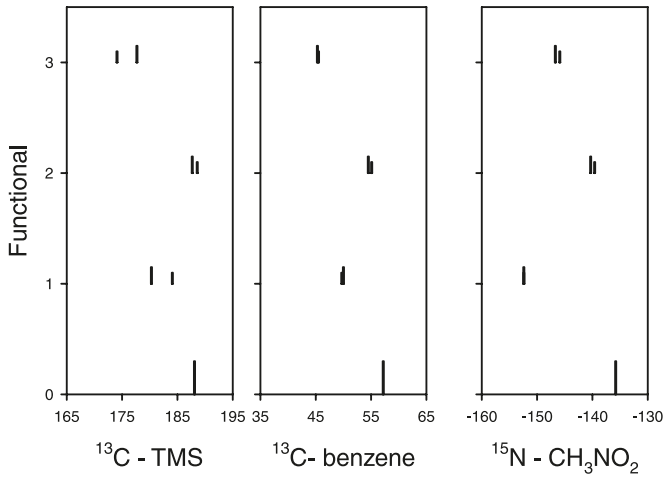

two basis sets, 6–311++G(d,p) and 6–311++G(3df,p), give substantially the same numbers for all cases, so these basis sets and higher should be sufficient for a molecule with this unusual electronic structure. However, as mentioned previously, the basis set 6–31++G(d,p) gave significantly worse results, and they are not shown. The carbon shieldings (Figs. 4–7) are more accurate than the nitrogen in the cyano group (Fig. 8, note the change of horizontal scale from the previous figures).

Geometry and functional lead to most of the variation, but no clear pattern emerges. There are also significant differences in the reproducibility of numbers between the various tensor elements: some patterns in the figures are very tight, whereas others are spread out. In almost all cases, the calculated shielding is less than the measured value. The functional MPWLYP often leads to less shielding in all the tensor elements, but this is also true in calculations of the standards, so chemical shifts relative to a calculated standard will be better.

The ethylene molecule is the prototype for these discussions. It has the following absolute shieldings[53,54] (Table 3): in-plane, perpendicular to the carbon–carbon bond (+164 ppm); in-plane, parallel to the carbon–carbon bond (+68 ppm); and perpendicular to the molecular plane (–46 ppm). This pattern of the out-of-plane direction being the most de-shielded, the in-plane, perpendicular to the bond, being the most shielded, and the direction along the bond being the intermediate value is confirmed in similar olefins.[55,56] The experiments on powders do not give the orientations of the tensors, but estimates are available from the calculations.

Table 3 gives the experimental eigenvalues of the shielding tensors and the calculated associated direction cosines

Table 3. Direction cosines of the shielding tensor elements for ethylene[45,46] and for the double-bond carbons in MDACC.

Ethylene	**X** (out of plane)	**Y** (in plane, ⊥ bond)	**Z** (along bond)
168	1.0	0.0	0.0
–121	0.0	1.0	0.0
48	0.0	0.0	1.0
MDACC C+			
121.2	0.93	–0.35	0.01
–87.8	0.34	0.93	0.06
–29.0	0.2	0.05	–0.99
MDACC C–			
137.1	0.98	–0.20	0.06
49.2	0.19	0.96	0.16
120.3	0.09	0.14	–0.98

Table 4. Selected coefficients of the atomic contributions to the frontier orbitals.

	MO	HOMO-1	HOMO	LUMO	LUMO+1
Atom	Energy (au)	–0.2622	–0.218	–0.0404	0.03704
C-2	2s	0.04	–0.01	–0.02	0.01
	$2p_z$	0.14	0.00	0.03	0.03
	$2p_y$	–0.07	0.07	–0.02	–0.01
	$2p_x$	0.01	0.37	–0.17	–0.10
C-3	2s	–0.02	0.00	–0.01	0.01
	$2p_z$	–0.03	0.00	0.04	0.04
	$2p_y$	–0.01	–0.05	–0.07	–0.02
	$2p_x$	–0.01	0.12	0.45	0.09
C10	2s	–0.03	0.00	0.02	0.01
	$2p_z$	–0.11	–0.01	0.01	0.12
	$2p_y$	0.05	–0.02	–0.05	–0.06
	$2p_x$	0.00	–0.07	–0.07	–0.25
N-11	2s	–0.01	0.00	–0.01	0.00
	$2p_z$	–0.17	0.01	–0.04	–0.13
	$2p_y$	–0.04	–0.05	0.05	0.05
	$2p_x$	0.02	–0.26	0.13	0.27
N-4	2s	0.02	–0.01	0.02	0.03
	$2p_z$	0.04	–0.01	0.02	0.00
	$2p_y$	0.01	0.15	0.12	0.04
	$2p_x$	–0.04	–0.30	–0.24	–0.03
C-1	2s	0.03	0.00	–0.02	–0.03
	$2p_z$	–0.06	0.00	0.03	0.02
	$2p_y$	0.02	0.01	–0.04	0.05
	$2p_x$	0.00	0.04	–0.23	0.44
O-12	2s	–0.01	0.00	0.01	0.01
	$2p_z$	0.53	0.01	–0.02	–0.01
	$2p_y$	0.13	–0.03	0.03	–0.03
	$2p_x$	0.02	–0.18	0.18	–0.29
O9	2s	–0.01	0.00	0.00	–0.01
	$2p_z$	0.07	0.01	–0.01	0.00
	$2p_y$	0.24	–0.02	0.01	–0.04
	$2p_x$	–0.04	–0.09	0.14	–0.16

(eigenvectors). The planar ethylene molecules lies exactly in the *yz* plane, with the double bond along *z*. MDACC is not planar, but we have oriented the molecule so the carbon–carbon double bond lies along the *z* axis and the cyano carbon lies in the *yz* plane. In other words, the carbons of the double bond and the cyano carbon define the *yz* plane. These results show that the out-of-plane component of the shielding tensor is not strongly affected by the push–pull interactions. The component along the double bond of the two carbons (the *z* axis) is shielded and deshielded relative to ethylene. The in-plane component perpendicular to the bond (along *y*) is shielded (relative to ethylene) for both carbons of the double bond; one dramatically more so than the other.

The cyano group shows some interesting phenomena. In the case of carbon, the largest calculated tensor component, σ_{33}, is larger than the experimental value, whereas for almost all the other components, the calculated values are smaller (less shielded) than the experimental values. In experimental terms, this means the shielding anisotropy of the cyano carbon is significantly overestimated by the calculations.[57] Furthermore, the shielding tensor is close to cylindrical, in contrast to the cyano nitrogen.

The cyano nitrogen isotropic shielding is close to typical values,[58] but the three tensor elements are quite different, as shown in Fig. 8. A good deal of the study of cyano nitrogens has been based on more ionic cyanide-ion species,[30,59,60] where the electronic environment is more cylindrical. As well, there is a good deal of work on nitrogens in sp^2 hybridization[61] and the important amide nitrogen tensors in proteins.[62–66] In the case of MDACC, the asymmetry of the nitrogen-shift tensor reflects the overall planar nature of the molecule much more than the carbon tensor of the cyano group.

The frontier orbitals can help us understand the mechanism behind these large shifts. Detailed lists of coefficients are difficult to read, so Table 4 presents the coefficients of just the 2s and the three 2p orbitals in the HOMO and the orbital below it in energy, and the two lowest unoccupied MO's (LUMO and LUMO+1). We ignore the hydrogen atoms and the methyl groups on the nitrogen. The molecule lies approximately in the *xz* plane with the double bond along *z*. The coefficients suggest that HOMO-1 is mainly the in-plane lone pair of the carbonyl oxygen. The HOMO has significant density in the out-of-plane p orbitals on both the nitrogens, but on only one of the carbons of the formal double bond. This is carbon 2 in Fig. 1, which we have called C–, the more shielded carbon. By contrast, the LUMO has a large coefficient on other carbon, C+, of the double bond.

Only an in-plane magnetic field will strongly mix the HOMO and LUMO, as in the rationalization of the ethylene shifts. In particular, a field perpendicular to the bond, but in the same plane will have the biggest mixing of the HOMO (polarized one way along the double bond) and the LUMO (polarized the other way). This is exactly what we see in the measurements.

Conclusions

This powerful combination of structural methods and theoretical calculations gives a very detailed view of the electronic structure of this class of molecules. In particular, the experimental and theoretical resolutions of the components of the shielding tensors give us further information, since most of the push–pull effect is due to in-plane elements of the shielding tensors. Conjugation with the rest of the π system in the molecule appears to maintain the out-of-plane values. In general, the elements of the shift tensor are always available from a calculation, and the experimental values are readily obtained with a modern solid-state NMR instruments and current software. All these methods are well within the capabilities of many laboratories, so we hope that many future studies will be done at this or higher levels.

Supplementary data

Supplementary data for this article are available on the journal Web site (canjchem.nrc.ca) or may be purchased from the Depository of Unpublished Data, Document Delivery, CISTI, National Research Council Canada, Ottawa, ON K1A 0R6, Canada. DUD 3897. For more information on obtaining material, refer to cisti-icist.nrc-cnrc.gc.ca/cms/unpub_e.shtml. CCDC 717038 contains the crystallographic data for this manuscript. These data can be obtained, free of charge, via www.ccdc.cam.ac.uk/conts/retrieving.html (Or from the Cambridge Crystallographic Data Centre, 12 Union Road, Cambridge CB2 1EZ, UK; fax +44 1223 336033; or deposit@ccdc.cam.ac.uk).

Acknowledgements

We would like to thank the Natural Sciences and Engineering Research Council of Canada (NSERC) for financial support, and Dr. Bob Berno and Mr. Jason Traer for their help in acquiring the spectra.

References

(1) Sandstrom, J. *Top. Stereochem.* **1983**, *14*, 83. doi:10.1002/9780470147238.ch2.
(2) Wennerbeck, I.; Sandstrom, J. *Org. Magn. Reson.* **1972**, *4*, 783. doi:10.1002/mrc.1270040604.
(3) Dreir, C.; Henriksen, L.; Karlsson, S.; Sandstrom, J. *Acta Chem. Scand. A,* **1978**, *B32*, 282.
(4) Kleinpeter, E.; Klod, S.; Rudorf, W. D. *J. Org. Chem.* **2004**, *69*, 4317. doi:10.1021/jo0496345. PMID:15202885.
(5) Kleinpeter, E.; Heyndenreich, M.; Chatterjee, S. K.; Rudorf, W. D. *Magn. Reson. Chem.* **1994**, *32*, 473. doi:10.1002/mrc.1260320808.
(6) Kleinpeter, E.; Thomas, St.; Uhlig, G.; Rudorf, W.-D. *Magn. Reson. Chem.* **1993**, *31*, 714. doi:10.1002/mrc.1260310805.
(7) Pappalardo, R. R.; Marcos, E. S.; Ruiz-Lopez, M. F.; Rinaldi, D.; Rivail, J.-L. *J. Am. Chem. Soc.* **1993**, *115*, 3722. doi:10.1021/ja00062a043.
(8) Alkorta, I.; Wentrup, C.; Elguero, J. *J. Mol. Struct. (Theochem.)*, **2002**, *585*, 27. doi:10.1016/S0166-1280(02)00036-2.
(9) Bernhardt, P. V.; Koch, R.; Moloney, D. W. J.; Shtaiwi, M.; Wentrup, C. *J. Chem. Soc. Perkin Trans.* **2002**, *2*, 515.
(10) McDaniel, D. H.; Brown, H. C. *J. Org. Chem.* **1958**, *23*, 420. doi:10.1021/jo01097a026.
(11) Kleinpeter, E.; Schulenburg, A. *Tetrahedron Lett.* **2005**, *46*, 5995. doi:10.1016/j.tetlet.2005.07.030.
(12) Jackman, L. M.; Cotton, F. A. Dynamic nuclear magnetic resonance spectroscopy. Academic Press, New York. 1975.
(13) Sandstrom, J. Dynamic NMR spectroscopy. Academic Press, London. 1982.
(14) Bain, A. D. *Prog. Nucl. Magn. Reson. Spectrosc.* **2003**, *43*, 63. doi:10.1016/j.pnmrs.2003.08.001.
(15) Fischer, G.; Kleinpeter, E. *Magn. Reson. Chem.* **1991**, *29*, 204. doi:10.1002/mrc.1260290303.
(16) Fischer, G.; Rudorf, W. D.; Kleinpeter, E. *Magn. Reson. Chem.* **1991**, *29*, 212. doi:10.1002/mrc.1260290305.
(17) Dwyer, T.; Norman, J. E.; Jasien, P. G. *J. Chem. Educ.* **1998**, *75*, 1635.
(18) Perrin, C. L.; Dwyer, T. *Chem. Rev.* **1990**, *90*, 935. doi:10.1021/cr00104a002.
(19) Shvo, Y.; Shanan-Atidi, H. *J. Am. Chem. Soc.* **1969**, *91*, 6689. doi:10.1021/ja01052a026.

(20) Beeler, A. J.; Orendt, A. M.; Grant, D. M.; Cutts, P. W.; Michl, J.; Zilm, K. W.; Downing, J. W.; Facelli, J. C.; Schindler, M. S.; Kutzelnigg, W. *J. Am. Chem. Soc.* **1984**, *106*, 7672. doi:10.1021/ja00337a003.
(21) Sherwood, M. H.; Facelli, J. C.; Alderman, D. W.; Grant, D. M. *J. Am. Chem. Soc.* **1991**, *113*, 750. doi:10.1021/ja00003a003.
(22) Baaden, M.; Granger, P.; Strich, A. *Mol. Phys.* **2000**, *98*, 329. doi:10.1080/002689700162478.
(23) Strohmeier, M.; Barich, D. H.; Grant, D. M.; Miller, J. S.; Pugmire, R. J.; Simons, J. *J. Phys. Chem. A* **2006**, *110*, 7962. doi:10.1021/jp061920s.
(24) Dahn, H. J. Chem. Ed. 2000, **77,** 905.
(25) Miller, J. S.; Novoa, J. J. *Acc. Chem. Res.* **2007**, *40*, 189. doi:10.1021/ar068175m. PMID:17370990.
(26) Garcia-Yoldi, I.; Miller, J. S.; Novoa, J. J. *Phys. Chem. Chem. Phys.* **2008**, *10*, 4106. doi:10.1039/b806900j. PMID: 18612512.
(27) deDios, A. C. *Prog. Nucl. Magn. Reson. Spectrosc.* **1996**, *29*, 229. doi:10.1016/S0079-6565(96)01029-1.
(28) Helgaker, T.; Jaszunski, M.; Ruud, K. *Chem. Rev.* **1999**, *99*, 293. doi:10.1021/cr960017t.
(29) Schreckenbach, G.; Ziegler, T. *Theor. Chem. Acc.* **1998**, *99*, 71. doi:10.1007/s002140050306.
(30) Jackowski, K.; Molchanov, S.; Gryff-Keller, A. M. *J. Mol. Struct. (Theochem.)*, **2000**, *497*, 189. doi:10.1016/S0166-1280(99)00309-7.
(31) Kaupp, M.; Buhl, M.; Malkin, V. G. Calculation of NMR and EPR parameters. Wiley-VCH, Weinheim. 2004.
(32) Mothana, B.; Ban, F.; Boyd, R. *J. Chem. Phys. Lett.* **2005**, *401*, 7. doi:10.1016/j.cplett.2004.10.145.
(33) Mothana, B.; Ban, F.; Boyd, R. J.; Thompson, A.; Haddon, C. E. *Mol. Phys.* **2005**, *103*, 1113. doi:10.1080/00268970412331333519.
(34) Sefzik, T. H.; Turco, D.; Iuliucci, R. J.; Facelli, J. C. *J. Phys. Chem. A* **2005**, *109*, 1180. doi:10.1021/jp0455780.
(35) Tafazzoli, M.; Shaghaghi, H.; Jalali-Heravi, M. *Concepts Magn. Reson.* **2008**, *32A*, 157. doi:10.1002/cmr.a.20111.
(36) Siehl, H. *Adv. Phys. Org. Chem.* **2007**, *42*, 125. doi:10.1016/S0065-3160(07)42003-2.
(37) Blanco, F.; Alkorta, I.; Elguero, J. *Magn. Reson. Chem.* **2007**, *45*, 797. doi:10.1002/mrc.2053. PMID:17661432.
(38) Brouwer, D. H.; Enright, G. D. *J. Am. Chem. Soc.* **2008**, *130*, 3095. doi:10.1021/ja077430a. PMID:18281985.
(39) Brouwer, D. H. *J. Magn. Reson.* **2008**, *194*, 136. doi:10.1016/j.jmr.2008.06.020. PMID:18656402.
(40) Harris, R. K.; Hodgkinson, P.; Pickard, C. J.; Yates, J. R.; Zorin, V. *Magn. Reson. Chem.* **2007**, *45*, S174. doi:10.1002/mrc.2132. PMID:18157842.
(41) Facelli, J. C.; Grant, D. M.; Michl, J. *Acc. Chem. Res.* **1987**, *20*, 152. doi:10.1021/ar00136a005.
(42) Carter, C. M.; Alderman, D. W.; Facelli, J. C.; Grant, D. M. *J. Am. Chem. Soc.* **1987**, *109*, 2639. doi:10.1021/ja00243a015.
(43) Massiot, D.; Fayon, F.; Capron, M.; King, I.; LeCalve, S.; Alonso, B.; Durand, J. O.; Bujoli, B.; Gan, Z.; Hoatson, G. L. *Magn. Reson. Chem.* **2002**, *40*, 70. doi:10.1002/mrc.984.
(44) Jameson, A. K.; Jameson, C. *J. Chem. Phys. Lett.* **1987**, *134*, 461. doi:10.1016/0009-2614(87)87173-7.
(45) Jameson, C. J.; Jameson, A. K.; Oppusunggu, D.; Wille, S.; Burrell, P. M.; Mason, J. *J. Chem. Phys.* **1981**, *74*, 81. doi:10.1063/1.440797.
(46) Buhl, M.; Sassmanshausen, J *J. Chem. Soc. Dalton Trans.* **2001**, 79.
(47) Marques, M. A. L.; d'Avezac, M.; Mauri, F. *Phys. Rev. B*, **2006**, *73*,o. 125433. doi:10.1103/PhysRevB.73.125433.
(48) Frisch, M. J.; Trucks, G. W.; Schlegel, H. B.; Scuseria, G. E.; Robb, M. A.; Cheeseman, J. R.; Montgomery, J. A.; Vreven, T.; Kudin, K. N.; Burant, J. C.; Millam, J. M.; Iyengar, S. S.; Tomasi, J.; Barone, V.; Mennucci, B.; Cossi, M.; Scalmani, G.; Rega, N.; Petersson, G. A.; Nakatsuji, H.; Hada, M.; Ehara, M.; Toyota, K.; Fukuda, R.; Hasegawa, J.; Ishida, M.; Nakajima, T.; Honda, Y.; Kitao, O.; Nakai, H.; Klene, M.; Li, X.; Knox, J. E.; Hratchian, H. P.; Cross, J. B.; Adamo, C.; Jaramillo, J.; Gomperts, R.; Stratmann, R. E.; Yazyev, O.; Austin, A. J.; Cammi, R.; Pomelli, C.; Ochterski, J. W.; Ayala, P. Y.; Morokuma, K.; Voth, G. A.; Salvadori, P.; Dannenberg, J. J.; Zakrzewski, V. G.; Dapprich, S.; Daniels, A. D.; Strain, M. C.; Farkas, O.; Malik, D. K.; Rabuck, A. D.; Raghavachari, K.; Foresman, J. B.; Ortiz, J. V.; Cui, Q.; Baboul, A. G.; Clifford, S.; Cioslowski, J.; Stefanov, B. B.; Liu, G.; Liashenko, A.; Piskorz, P.; Komaromi, I.; Martin, R. L.; Fox, D. J.; Keith, T. A.; Al-Laham, M. A.; Peng, C. Y.; Nanayakkara, A.; Challacombe, M.; Gill, P. M. W.; Johnson, B.; Chen, W.; Wong, M. W.; Gonzalez, C.; Pople, J. A. Gaussian 03 [computer program], Revison B.02. Gaussian Inc., Pittsburg, PA. 2003.
(49) Mittelbach, M.; Sterk, H.; Junek, H.; Wagner, U. *Liebigs Ann. Chem.* **1987**, (12): 1131. doi:10.1002/jlac.198719870888.
(50) O'Callaghan, C. N.; Conlon, C. M. A.; Cardin, C. J. *J. Chem. Res. (S)* **1988**, 248.
(51) Szulzewsky, K.; Schulz, B.; Kulpe, S.; Kreutzmann, J. *Acta Crystallogr. C* **1984**, *40*, 280. doi:10.1107/S0108270184003826.
(52) Depree, G. J.; Main, L.; Nicholson, B. K. *J.Organomet. Chem.* **1998**, *551*, 281. doi:10.1016/S0022-328X(97)00474-9.
(53) Zilm, K. W.; Conlin, R. T.; Grant, D. M.; Michl, J. *J. Am. Chem. Soc.* **1980**, *102*, 6672. doi:10.1021/ja00542a003.
(54) Zilm, K. W.; Grant, D. M. *J. Am. Chem. Soc.* **1981**, *103*, 2913. doi:10.1021/ja00401a001.
(55) Bernard, G. M.; Wu, G.; Wasylishen, R. E. *J. Phys. Chem. A* **1998**, *102*, 3184. doi:10.1021/jp980558h.
(56) Ma, Z.; Facelli, J. C.; Pugmire, R. J.; Dunn, B. C.; Turpin, G. C.; Eyring, E. M.; Ernst, R. D. *Magn. Reson. Chem.* **2007**, *45*, 393. doi:10.1002/mrc.1981. PMID:17394221.
(57) Mahwhinney, R. C.; Peslherbe, G. H.; Muchall, H. M. *J. Phys. Chem.* **2008**, *112B*, 650.
(58) Witanowski, M.; Webb, G. A. Nitrogen NMR. Plenum Press, London. 1973.
(59) Bernard, G. M.; Eichele, K.; Wu, G.; Kirby, C. W.; Wasylishen, R. E. *Can. J. Chem.* **2000**, *78*, 614. doi:10.1139/cjc-78-5-614.
(60) Kroeker, S.; Wasylishen, R. E.; Hanna, J. V. *J. Am. Chem. Soc.* **1999**, *121*, 1582. doi:10.1021/ja983253p.
(61) Leppert, J.; Heise, B.; Ramchandran, R. *J. Magn. Reson.* **2000**, *145*, 307. doi:10.1006/jmre.2000.2087. PMID:10910699.
(62) Cornilescu, G.; Bax, A. *J. Am. Chem. Soc.* **2000**, *122*, 10143. doi:10.1021/ja0016194.
(63) Brender, J. R.; Taylor, D. M.; Ramamoorthy, A. *J. Am. Chem. Soc.* **2001**, *123*, 914. doi:10.1021/ja001980q. PMID: 11456625.
(64) Bernard, G. M.; Miskolzie, M.; Kotovych, G.; Wasylishen, R. E. *Can. J. Chem.* **2004**, *82*, 1554. doi:10.1139/v04-131.
(65) Heise, B.; Leppert, J.; Ramachandran, R. *Solid State Nucl. Magn. Reson.* **2000**, *16*, 177. doi:10.1016/S0926-2040(00)00073-4. PMID:10868570.
(66) Lee, D. K.; Wei, Y. F.; Ramamoorthy, A. *J. Phys. Chem. B* **2001**, *105*, 4752. doi:10.1021/jp002902s.

Effect of surface heterogeneity steps-terraces in a mean field model for the catalytic CO-NO reaction

Joaquín Cortés and Eliana Valencia

Abstract: Based on a model proposed by Olsson et al. (*Surf. Sci.* **2003**, *529*, 338), a study is made through a mean field scheme of the effect of steps-terraces superficial heterogeneity, whose energy differences have been determined recently by means of density functional theory (DFT), in the catalytic reduction reaction of NO by CO over palladium. Several aspects are seen, such as the relation between the activities produced in both sectors of the surface as a function of temperature and the energy difference between them, the activity and coverage versus the temperature and the gas phase concentration curves, and the effect on these variables of the activation energy values on the steps of some stages of the kinetic mechanism. The system shows a reaction order with respect to CO and NO that changes sign between low and high temperatures, from negative to positive in the case of CO and the opposite for NO.

Key words: mean field model in a superficial reaction, catalytic CO-NO reaction, surface heterogeneity in a superficial reaction, superficial catalytic reaction, CO-NO reaction over palladium, steps-terraces superficial heterogeneity.

Résumé : En se basant sur un modèle proposé par Olsson et al. (*Surf. Sci.* **2003**, *529*, 338), on a effectué une étude à l'aide d'un schéma de champ moyen de l'effet de l'hétérogénéité superficielle en paliers et en terrasses dont les différences d'énergie ont récemment été déterminées à l'aide de la théorie de la fonctionnelle de densité, dans la réaction de réduction catalytique du NO par le CO sur le palladium. On a observé plusieurs aspects, telle la relation entre les activités produites dans les deux secteurs de la surface en fonction de la température et la différence d'énergie entre elles, l'activité et la couverture en fonction de la température et des courbes de concentration en phase gazeuse ainsi que l'effet de ces variables sur les valeurs de l'énergie d'activation sur les paliers de certaines étapes du mécanisme cinétique. Le système présente un ordre de réaction qui varie par rapport au CO et au NO avec des changements de signe entre les basses et les hautes températures et qui vont de négatif à positif dans le cas du CO et l'inverse dans le cas du NO.

Mots-clés : modèle de champ moyen dans une réaction superficielle, réaction catalytique CO-NO, hétérogénéité de la surface dans une réaction superficielle, réaction catalytique superficielle, réaction CO-NO sur du palladium, hétérogénéité superficielle en paliers et terrasses.

[Traduit par la Rédaction]

Introduction

Over the last decades great progress has been made in the knowledge of superficial catalytic reactions, partly due to modern laboratory techniques and partly to the greater understanding of the behavior of irreversible dynamic systems of which superficial reactions are an example. These kinds of systems have attracted the joint attention of chemists, because of their applications in catalysis, and of physicists, because they are good examples of nonequilibrium models that show interesting complex phenomena like oscillations, kinetic phase transitions, hysteresis, chaos, dissipative structures, etc.[1]

Because of the complexity of the kinetics of these superficial reactions, the interpretation of experimental data by theoretical models is generally poor, as has been discussed by our laboratory[2] and analyzed in detail in an interesting article by Zhdanov and Kasemo,[3] and for that reason usually the mechanisms proposed by experimenters are only used to carry out qualitative observations of the data obtained. This is due to the simplifications introduced in the models because of the difficulties in interpreting the adequate stages of the kinetic mechanism, the various kinds of lateral interactions of the reactants that occur at moderately high pressures (0.1–30 torr (1 torr = 133.322 4 Pa)), and the unavoidable heterogeneity of the surface of the catalyst corresponding to actual experimental situations.

In general, the theoretical models used are, in one way or another, mean field schemes. This introduces an inevitable difficulty in the interpretation of all forms of heterogeneity of the real system, which has been partially overcome by using simulations, generally Monte Carlo. Both kinds of techniques have been widely used in the study of superficial reactions that have been reviewed in some excellent monographs by Evans,[4] Albano et al.,[5] and Zhdanov and Kasemo.[6]

For quite some time at our laboratory we have been interested in studying the kinetics of some systems that are also of practical importance in the catalytic control of motor ve-

Received 28 April 2008. Accepted 10 December 2008. Published on the NRC Research Press Web site at canjchem.nrc.ca on 24 March 2009.

J. Cortés[1] and E. Valencia. Facultad de Ciencias Físicas y Matemáticas, Universidad de Chile, P.O Box 2777, Santiago, Chile.

[1]Corresponding author (e-mail: jcortes@dqb.uchile.cl).

hicle exhaust emissions, like the CO-O_2 and CO-NO reactions, which we have used as prototypes to relate various mean field models and Monte Carlo simulations with experimental results.[7,8] Our interest in introducing the heterogeneity factor in a mean field model, which goes back to our work in the field of adsorption on heterogeneous surfaces[9] commented in the monograph of Rudzinski and Everett,[9] led us to later propose a mean field theory of a superficial reaction on a disordered substrate.[10] In that paper, we proposed a sites as well as a pairs approximation, characterizing the substrate through the set $\{q_i\}$ of probabilities that the superficial site has i neighbors that belong to the substrate in the model. A different approach has been considered recently by Olsson, Zhdanov, and Kasemo (OZK model),[11] in an interesting paper that, by taking into account the existence of terraces and steps in the catalyst's surface, introduces the heterogeneity of the substrate in a mean field model that analyzes the kinetics of the CO-NO reaction. That paper also takes into account recent advances that use the density functional theory (DFT) approximation[11–13] to determine the role of the steps in the study of heterogeneous catalytic reactions.

In this paper we have used the OZK model, together with some recent studies made by our laboratory on the CO-NO reaction, to analyze various aspects of the heterogeneity of the catalytic substrate from the standpoint of a mean field theory of a superficial reaction. This paper has the purpose of promoting the use of mean field kinetics equations that take into account the existence of simple surface heterogeneities that occur in real systems, as suggested by models like that of OZK, in experimental catalysis research, where use is commonly made of kinetics equations that assume uniform surfaces to interpret the data. This line of research is currently under way in our laboratory.

The kinetic sheme of the CO-NO reaction

The reduction reaction of NO by CO (CO-NO reaction) over rhodium has been studied extensively in the last decades, particularly because of its applications in catalytic converters of automobiles.[14] Recently, however, there has been increasing interest in the study of palladium catalysts, moved by economic reasons for its possible use in converters, since the latest progress in the purification of gasoline avoids the poisoning of these catalysts with lead.[15]

The determination of the kinetic mechanism of the CO-NO reaction over rhodium has a long and controversial history, since the first work of Hecker and Bell,[16] followed by, among others, the studies of Oh et al.,[17] Cho,[18] Chiang and Tan,[19] Peden et al.,[20] and Permana et al.,[21] and those from our laboratory,[22] in the latter case considering recent experiments carried out by Zaera's group.[23] In the case of palladium, however, as admitted by some authors,[15] no adequate mechanism has been established for the CO-NO reaction, largely because of the scant information on adequate experimental data. In a recent paper,[8] we have used the kinetic mechanism proposed by Peden et al.[20] and Permana et al.,[21] which appears most frequently in the literature and is shown in Scheme 1, to interpret some experiments that we have made with the CO-NO reaction over palladium. Table 1 shows the parameters that we used in the paper, some of them belonging to a previous paper by Nakao et al.[25] for

Scheme 1. Mechanism of the CO-NO reaction used in the paper.

$$CO + S \underset{}{\overset{k_1}{\rightleftarrows}} CO_{(a)} \qquad (M1)$$

$$CO_{(a)} \xrightarrow{k_2} CO + S \qquad (M2)$$

$$NO + S \xrightarrow{k_3} NO_{(a)} \qquad (M3)$$

$$NO_{(a)} \xrightarrow{k_4} NO + S \qquad (M4)$$

$$NO_{(a)} + S \xrightarrow{k_5} N_{(a)} + O_{(a)} \qquad (M5)$$

$$2N_{(a)} \xrightarrow{k_6} N_2 + 2S \qquad (M6)$$

$$CO_{(a)} + O_{(a)} \xrightarrow{k_7} CO_2 + 2S \qquad (M7)$$

$$NO_{(a)} + N_{(a)} \xrightarrow{k_8} N_2O + 2S \qquad (M8)$$

the same system in the low pressure zone, adjusting other parameters to our experimental data, and considering for the adsorption constants ka_j of gas j, the kinetic theory of gases expression

$$[1] \qquad k_{aj(\mathrm{ads})} = S_j \sigma (2\pi M_j RT)^{-1/2}$$

where M_j is the molecular mass of j, S_j is the corresponding sticking coefficient, and σ is the area occupied by one mole of metal atoms on the catalyst's surface.

The system described by Scheme 1 and Table 1 will be used as the basis for the discussion presented in this paper. The OZK model proposed originally considered a simplified mechanism for the CO-NO reaction, and the activation energies calculated by Hammer[13] according to the DFT for a palladium surface were used. In these calculations Hammer[13] determined the differences between the activation energies of different stages of the mechanism of the CO-NO reaction over Pd(111) and Pd-step. His results show that there is practically no variation in the desorption stages. On the other hand, it is seen that for various stages the activation energy on the steps is lower than its values on the terraces (Pd(111)): 70% in stage M5 of NO dissociation, 65% in stage M6 of N_2 production, and 71% in stage M7 of CO_2 production. No calculations were made for stage M8 of N_2O production, and adsorption usually takes place without activation energy.

In this paper, a qualitative analysis of the OZK model will be made, however, considering the complete mechanism, which includes stage M8 and the existence of oxygen adsorbed on the surface. The latest DFT calculations,[13] on the other hand, show the existence of a lower activation energy in the steps for certain stages, and that has encouraged us to analyze the influence of different variations of that energy.

Table 1 shows the kinetics parameters used in the paper. For the activation energy, except for stage M8 of N_2O production, use has been made of the values published by Nakao et al.[25] obtained under ultra high vaccum (UHV) conditions. The use of UHV parameters to interpret experiments in higher pressure zones leads to interpretation errors because, in general, the kinetic parameters depend on the coverage. This problem, which has been called the "pressure gap problem", has been studied in the literature by Zdanov

Table 1. Kinetics parameters of Nakao et al.[24] and the fitting parameters used in the paper.

Events	Activation energy, *Ei* (kcal/mol)	Frequency factor, *νi* (sec^{-1})
CO desorption (k_2)	35.5[a]	(1.0×10^{17})[a]
NO desorption (k_4)	36.0[b]	(1.0×10^{17})[c]
NO dissociation (k_5)	34.2[d]	(7.9×10^{21})[c]
N_2 production (k_6)	29.0[e]	(6.5×10^{13})[e]
N_2O production (k_8)	32.7[f]	(5.3×10^{16})[c]
CO_2 production (k_7)	33.6[g]	(1.2×10^{16})[c]
S_{CO}= 0.93[h], S_{NO} = 0.9[h]		

[a](Behm et al. 1980; Guo and Yates 1989).[25]

[b](Ramsier et al. 1994).[26]

[c]Values of *νi* in parentheses correspond to a fit with experimental data from Fig. 1 of Cortés et al. (2007).[8]

[d](Nakao et al. 2005).[24]

[e](Olsson et al. 2003; Sellers and Anderson 2001).[11,27]

[f](Walker et al. 1997).[29]

[g](Olsson et al. 2003).[11]

[h](Hirsimaki and Valden 2001).[28]

and Kasemo,[3] with discouraging results. With the purpose of partially overcoming that situation, in our calculations we have used some frequency factors from a previous paper[8] obtained by fitting experiments made at the same medium pressures used in this paper. Taking that set of parameters for the (Pd(111)) terraces, we have considered that the steps in the M5, M6 and M7 stages have activation energies lower than those by the percentages given in the previous paragraph, corresponding to the variations found by Hammer[13] in his DFT calculations. Since the corresponding frequency factors have not been determined theoretically, we have assumed that they are equal for the steps and the terraces, considering implicitly that the activation energies absorb the total differences between the various zones of the surface.

In the calculations we will define the relation KK(*i*) between the activation energy of stage *Mi* in the steps (*s*) and terraces (*t*) by the expression $E^s(i) = KK(i)E^t(i)$, so that the set of KK(*i*) values describe completely the analyzed case. In all cases KK(*i*) = 1 was considered for desorption stages M2 and M4 and stage M8 of N_2O formation.

The mean field model

Appendix A shows the details of the analytical solution of a mean field model that we had published earlier[8,22] for the mechanism of Scheme 1. It represents the development of the corresponding kinetic equations if it is assumed that the catalyst's surface is uniform and that the adsorbates $CO_{(a)}$ and $NO_{(a)}$ remain in equilibrium with the gas phase during the process. This means that the adsorption–desorption stages are considered to be sufficiently fast, as has been done in the literature.[11] Below we will extend this development to the analysis of the OZK model using the parameters given in Table 1.

The study of the OZK model is very interesting because it allows the application of a mean field scheme to a catalytic surface with simple heterogeneity, made of few sectors with different energy characteristics. The most obvious examples are surfaces formed by different crystal faces or that have step sites of different activity, presumably more active, than the terrace sites of the rest of the surface. The latter was the case studied by OZK, motivated by the quantum studies that use DFT to investigate the role of the steps in the heterogeneous catalysis phenomenon.[12,13] On the other hand, there have been reports of experimental information of systems in which activity differences have been observed between steps and terraces,[30] as well as cases in which these differences have apparently not been found.[31]

The OZK model analyzes two situations. In the first it is assumed that the terraces and the steps operate independently, and the second case considers that they are interconnected due to the fast diffusion of the adsorbates.[32]

The first case can be treated by simply applying independently the kinetic equations of the uniform case developed in Appendix A to each of the sectors of the surface. If n^t and n^s are the numbers of site terraces and steps, respectively, then $f = n^s/(n^s + n^t)$ is the fraction of sites belonging to the steps. The total production R_i of species (*i*) will be equal to the weighted sum of productions R^t and R^s of terraces and steps, respectively, so

$$[2] \qquad R_{N_2} = (1-f)k_6^t(\theta_N^t)^2 + fk_6^s(\theta_N^s)^2$$

$$[3] \qquad R_{CO_2} = (1-f)k_7^t\theta_{CO}^t\theta_O^t + fk_7^s\theta_{CO}^s\theta_O^s$$

$$[4] \qquad R_{N_2O} = (1-f)k_8^t\theta_{NO}^t\theta_N^t + fk_8^s\theta_{NO}^s\theta_N^s$$

where θ_i^t and θ_i^s are the fractions of covered surface of species (*i*) in terraces and steps.

The second case assumes that the steps and terraces are interconnected. Let us consider also the situation in which the kinetic constants of CO and NO desorption are identical in the terraces and in the steps, approximately in agreement with the data published by Hammer[13] for the CO-NO reaction over palladium, which is the system that will be used as a prototype in this analysis, as we comment in greater detail below. Since eq. [1] also assumes adsorption without activation energy, it means that eqs. [A1]–[A4] in Appendix A are valid for this case. The conservation eqs. [A5] and [A6], however, which represent steady states for the superficial species $N_{(a)}$ and $O_{(a)}$ ($d\theta_N/dt = 0$ and $d\theta_O/dt = 0$), now have the following form

$$[5] \qquad n^tk_5^t\theta_{NO}^t\theta_S^t + n^sk_5^s\theta_{NO}^s\theta_S^s = 2n^tk_6^t(\theta_N^t)^2 + 2n^sk_6^s(\theta_N^s)^2 + n^tk_8^t\theta_{NO}^t\theta_N^t + n^sk_8^s\theta_{NO}^s\theta_N^s$$

$$[6] \qquad n^tk_5^t\theta_{NO}^t\theta_S^t + n^sk_5^s\theta_{NO}^s\theta_S^s = n^tk_7^t\theta_{CO}^t\theta_O^t + n^sk_7^s\theta_{CO}^s\theta_O^s$$

In the development of the model we will assume a rapid diffusion of all the superficial species according to the OZK model.[11,32] As those authors point out, the values published[32] for the activation energies for the diffusion of superficial species, even atomic ones like N and O, are in general smaller than for the other stages *Mi* of the mechanism of Scheme 1. This leads to considering, as a fundamental assumption of the model, that the fraction of covered surface of species (*i*) is the same for all the heterogeneous surface S12, i.e., θ_i^t is equal to θ_i^s for each species (*i*) if the sectors

are interconnected. Introducing eq. [A4] into expressions eqs. [5] and [6], using the definition $y = n^s/n^t$, and recalling that $\theta_i^t = \theta_i^s = \theta_i$, we get

$$[7] \quad k_5^t AB\theta_{CO}^2 + yk_5^s AB\theta_{CO}^2 = 2k_6^t\theta_N^2 + 2yk_6^s\theta_N^2 + k_8^t A\theta_N\theta_{CO} + yk_8^s A\theta_N\theta_{CO}$$

$$[8] \quad k_5^t AB\theta_{CO}^2 + yABk_5^s\theta_{CO}^2 = k_7^t\theta_{CO}\theta_O + yk_7^s\theta_{CO}\theta_O$$

from which it is possible to obtain eq. [9] for the covered fraction of $O_{(a)}$

$$[9] \quad \theta_O = E\theta_{CO}$$

where

$$[10] \quad E = AB(k_5^t + yk_5^s)/(k_7^t + yk_7^s)$$

If we also define for θ_N, the coverage $N_{(a)}$, $\theta_N = F\theta_{CO}$, from eq. [7] we get that

$$[11] \quad F = \left[(-A(k_8^t + yk_8^s) + (A^2(k_8^t + yk_8^s)^2 + 8AB(k_6^t + yk_6^s)(k_5^t + yk_5^s))^{1/2}\right]/4(k_6^t + yk_6^S)$$

and using conservation eq. [A7] we obtain for the coverage of $CO_{(a)}$

$$[12] \quad \theta_{CO} = 1/(1 + A + B + E + F)$$

The production expressions are similar to eqs. [2]–[4] of the previous case, in which now $\theta_i^t = \theta_i^s = \theta_i$.

Relative contribution of terraces and steps to the activity of the CO-NO reaction

The first aspect of interest is the relative importance of both sectors of the surface on the activity of the catalytic process. In this analysis we will take into account the case of R_{CO2}, the production of CO_2, defining RTS as the fraction of the contribution of the terraces sector to the total production of CO_2 by

$$[13] \quad RTS = R_{CO_2}^t/(R_{CO_2}^t + R_{CO_2}^s)$$

In general terms, surface heterogeneity is manifested only in intermediate situations of the values of RTS, where 1 >> RTS >> 0. In the extreme cases the system becomes uniform, because when RTS = 0 the phenomenon only occurs in the steps, and if RTS = 1 only in the terraces.

If we assume that the rate constants can be expressed by Arrhenius' equation

$$[14] \quad k_i^j = \nu_i^j \exp(-E_{ai}^j/RT)$$

where ν_i^j and E_{ai}^j are, respectively, the frequency factor and the activation energy of terraces and steps ($j = t,s$), then we have

$$[15] \quad RTS = \frac{(1-f)\nu_{CO_2}^t\theta_{CO}^t\theta_O^t\exp(-E_{CO_2}^t/RT)}{((1-f)\nu_{CO_2}^t\theta_{CO}^t\theta_O^t\exp(-E_{CO_2}^t/RT) + f\nu_{CO_2}^s\theta_{CO}^s\theta_O^s\exp(-E_{CO_2}^s/RT))}$$

In the later calculations we will assume that the frequency factors are equal in terraces and steps, so that they only differ in the value of the corresponding activation energies that characterize them. If $\Delta E = E_{CO_2}^t - E_{CO_2}^s$ expresses that difference, from eq. [15] we can write the following expressions for RTS in the cases of independent sectors, RTS_{ind}, and interconnected sectors RTS_{int}, respectively

$$[16] \quad RTS_{int} = \frac{1}{\left(1 + \left(\frac{f}{1-f}\right)\right)\exp(\Delta E/RT)}$$

$$[17] \quad RTS_{ind} = \frac{1}{\left(1 + \left(\frac{f}{1-f}\right)\right)\left(\frac{\theta_{CO}^s\theta_O^s}{\theta_{CO}^t\theta_O^t}\right)\exp(\Delta E/RT)}$$

Figure 1 shows the changes of RTS at different temperatures in both cases. The first aspect of interest that arises from the above expressions is that the RTS of the interconnected case does not depend on the configuration of the adsorbed phase, but only on ΔE and temperature. In that case it is seen that RTS always increases with temperature according to eq. [16], as shown by the examples of Fig. 1*a*.

On the other hand, Figs. 1*b* and 1*c* show that when the sectors are independent RTS can increase or decrease with temperature due to the influence of the relations between the different coverages in the steps or the terraces as shown in eq. [17]. In these cases RTS depends on the values chosen for KK(*i*), which are kept constant in both figures. Since $\Delta E = (1 - KK_{(CO2)})E^t(_{CO2})$ and the value of $KK_{(CO2)}$ is kept constant, the various values of ΔE can be assumed to be generated by the variation of $E_{CO_2}^t$, leading to a set of ΔE values for constant $E_{CO_2}^s/E_{CO_2}^t$. Alternatively, the energy of steps or terraces can be fixed and the energy difference, ΔE, can be varied. On the other hand, it is seen that in all the cases of Fig. 1 a value of RTS = 1 is obtained for ΔE = 0, and in the last two figures (Fig. 1*b* and 1*c*) it would correspond to the case of $KK_{(CO2)} = 1$.

Figure 2*a* shows some examples of changes of RTS with temperature when ΔE is constant, where two situations have been chosen for each case. When the sectors are interconnected an increase with temperature occurs, while that happens in only one of the examples chosen when the sectors are independent. In Figs. 2*b* and 2*c* we have graphed, for the independent sectors examples, the changes of RTS and of the CO and O coverages with temperature in the steps and in the terraces, because the latter appeared in eq. [17]. This makes it possible to see how the interrelations of the coverages in terraces and steps are the cause of the different behavior of RTS. For example, in the case in which RTS decreases at low temperatures the phenomenon occurs mainly in the terraces, since coverage with oxygen in the steps has significant values only at high temperatures, in contrast with

Fig. 1. RTS (fraction of CO_2 production in terraces). Equation [13] versus ΔE (energy difference between terraces and steps) at different temperatures, P_{CO} = 20.52 torr; P_{NO} = 39.52 torr and y = 0.01: ○ (450 K); ● (500 K); △ (550 K); ▲ (600 K); □ (650 K); ■(700 K). (*a*) Interconnected sectors. (*b*) Independent sectors $KK_{(CO2)}$ = 0.71; $KK_{(NO)}$ = 0.70; $KK_{(N2)}$ = 0.65. (*c*) Independent sectors $KK_{(CO2)}$ = 0.71; $KK_{(NO)}$ = $KK_{(N2)}$ = 1.

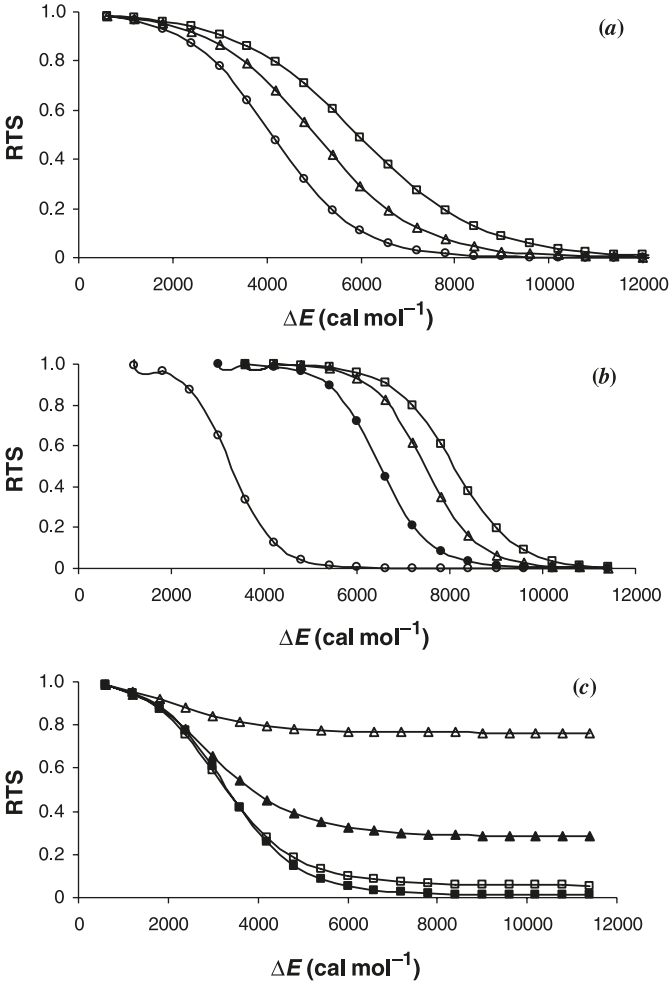

Fig. 2. (*a*) RTS versus temperature, P_{CO} = 20.52 torr; P_{NO} = 39.52 torr; y = 0.01; ΔE = 6000 cal mol^{-1}. ○ Interconnected sectors $KK_{(CO2)}$ = 0.71; $KK_{(NO)}$ = 0.7; $KK_{(N2)}$ = 0.65; ● The same as above for $KK_{(CO2)}$ = 0.82. △ Independent sectors $KK_{(CO2)}$ = $KK_{(NO)}$ = $KK_{(N2)}$ = 1. ▲ Independent sectors $KK_{(CO2)}$ = 0.71; $KK_{(NO)}$ = 0.7; $KK_{(N2)}$ = 0.65. (*b*) RTS and superficial coverage θ_i versus T; Independent sectors $KK_{(CO2)}$ = 0.71; $KK_{(NO)}$ = 0.7; $KK_{(N2)}$ = 0.65. X(RTS); △ (θ^t_{CO}); ○ (θ^t_O); ▲ (θ^s_{CO}); ● (θ^s_O). (*c*) The same as (*b*) for $KK_{(CO2)}$ = 0.82; $KK_{(NO)}$ = $KK_{(N2)}$ = 1.

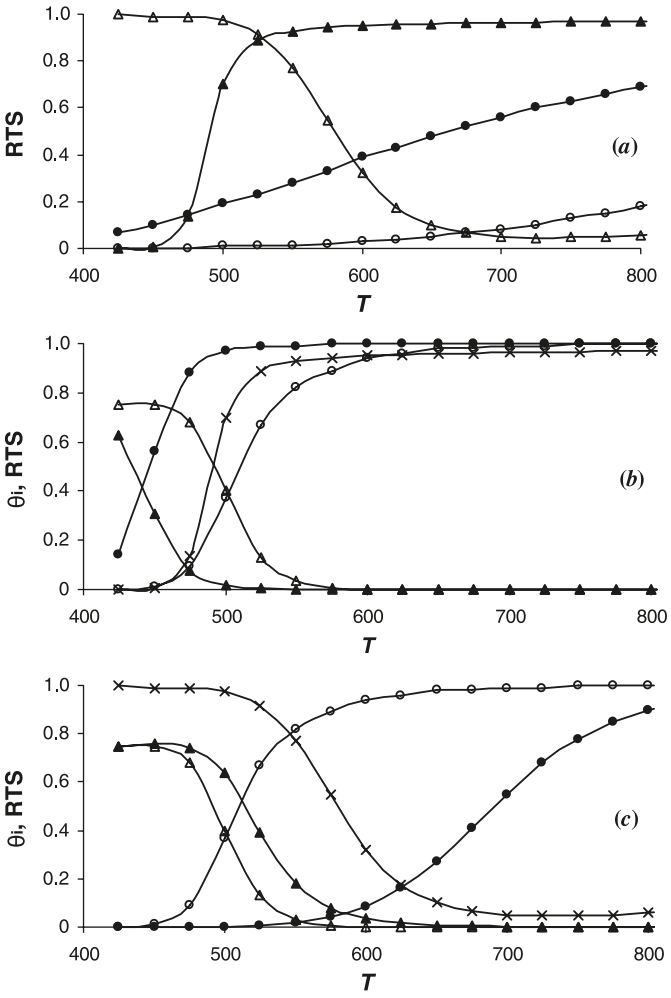

the case in which RTS increases. Finally, it must be kept in mind that in all cases RTS is independent of the pressure or concentration of the gas phase.

Effect of temperature on the activity of the system and Arrhenius behavior

In general, a maximum of activity, R_i, with temperature is seen in all cases, the same as in the situation of a uniform surface that we have reported recently.[8] This is shown in Fig. 3 for systems having interconnected systems in the cases in which RTS has an intermediate value, when the system is heterogeneous with a similar influence of the terraces and the steps, and when it has a small value and the phenomenon occurs only in the steps, except at high temperatures. The maximum of R_i, which in general coincides with the maximum found for coverage with nitrogen, occurs because at low temperatures oxygen coverage is very low, while at high temperatures the fraction covered with CO is small. The maximum then occurs at intermediate temperatures where both coverages show a substantial value. The above can be visualized in the corresponding figures (Fig. 3) of coverage versus temperature for the three cases chosen. In the first of them (Fig. 3*a*) the selectivity (SE) curve for N_2 defined by $R_{N_2}/(R_{N_2} + R_{N_2})$ has been added, which in the second case (Fig. 3*b*) has always been equal to one.

The changes of the superficial configuration commented in the previous paragraph, which lead to the formation of a maximum in the graph of CO_2 production versus temperature has as a consequence a similar behavior in the $\ln R_i$ versus $1/T$ Arrhenius curves, distinguishing two zones around the maximum where only one of them allows the calculation of an apparent positive activation energy that has physical meaning. This maximum between production and tempera-

Fig. 3. Production (R_i) and superficial coverage (θ_i) versus T for interconnected sectors, P_{CO} = 20.52 torr; P_{NO} = 39.52 torr and y = 0.01. ♦ (R_{CO2}); ◊ (R_{N2}); □ (R_{N2O}); △ (θ_{CO}); ■ (θ_O); ○ (θ_N); ▲ (θ_{NO}). (*a*) R_i versus T. $KK_{(CO2)}$ = 0.82; $KK_{(NO)}$ = $KK_{(N2)}$ = 1. (*b*) θ_i versus T. $KK_{(i)}$ the same as (*a*) —— (SE (selectivity)); ----- (RTS). (*c*) Arrhenius behavior corresponding to (*a*). (*d*) The same as (*a*) with $KK_{(CO2)}$ = 0.71; $KK_{(NO)}$ = 0.7; $KK_{(N2)}$ = 0.65. (*e*) The same as (*b*) with $KK_{(i)}$ the same as (*d*) —— (RTS), SE = 1. (*f*) The same as (*c*) with $KK_{(i)}$ the same as (*d*).

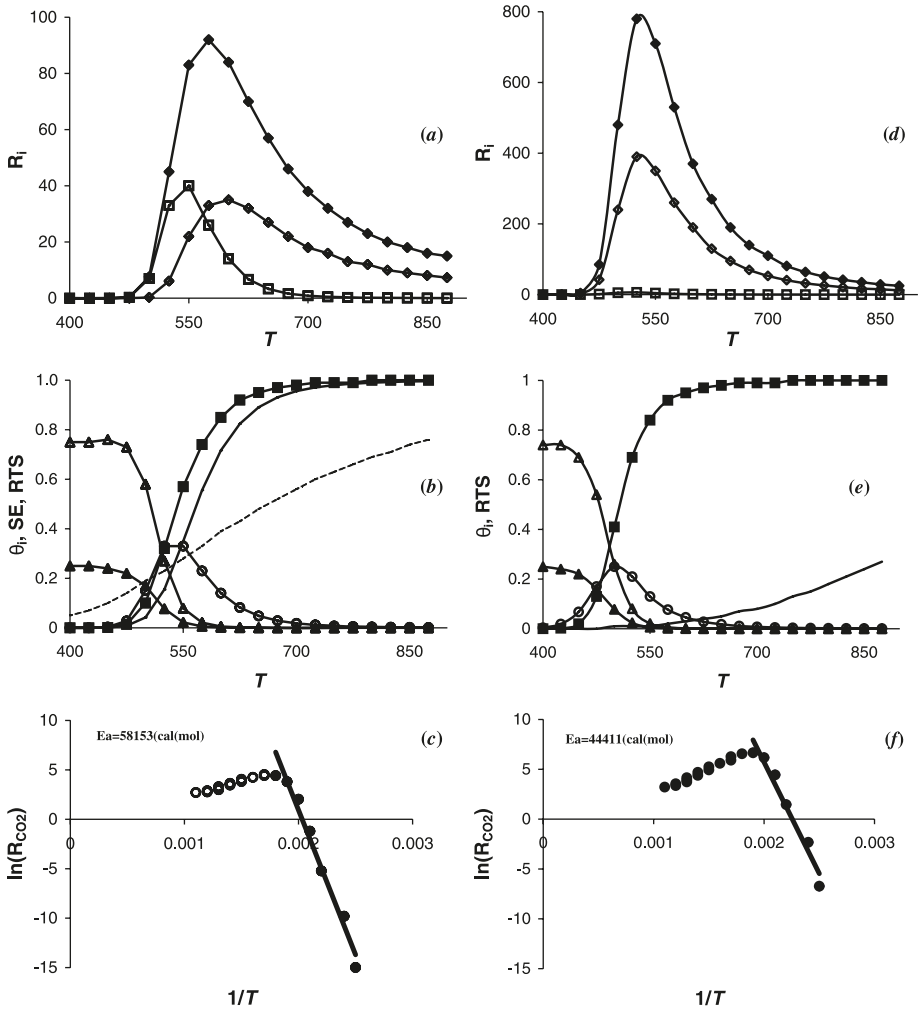

ture has been observed experimentally for this system over single-crystal Pd catalysts that presumably have steps and terraces zones on the surface[33] and on supported Pd in UHV zones.[15] The energy obtained in this way is only apparent and its value, although of a reasonable size, is sufficiently high compared to that of the steps in Table 1 to indicate that in the corresponding zone in which the energy has been calculated, the phenomenon does not occur through a controlling step like those that were considered in Scheme 1. In general, this kinetic process is complex, and it has been reported in the case of single crystals of Pd, for example, that the dissociation of NO is the rate limiting stage at low temperatures, while CO adsorption is rate-limiting at high temperatures.[34]

Effect of gas phase concentration, phase and activity diagrams, and reaction order

Figure 4 shows the phase and concentration diagrams at three different temperatures in the case of interconnected step and terrace zones, for systems that show a substantial degree of heterogeneity with RTS values higher than 10%. The types of activity diagrams (R_i, y_{CO}) are a direct consequence of the behavior of the phase diagrams (θ_i, y_{CO}). At a low temperature, for example, it is seen only at low CO concentrations, y_{CO} in the gas phase, that there is sufficient oxygen adsorbed on the surface for production to exist. At a high temperature, on the other hand, production is seen only in the zone of high CO concentration in the gas phase, because only then is there sufficient CO adsorbed on the surface. Finally, for intermediate temperatures the activity curve presents a maximum, because production decreases at low y_{CO} concentrations where there is little superficial CO, and at high y_{CO} concentrations because coverage with oxygen decreases.

Figure 5 shows how, in the case of interconnected sectors, the model has a reaction order m with respect to CO and n with respect to NO, if we assume that the following empirical expression, with which experimenters often describe their data, is valid

$$[18] \qquad R_i = k_i P_{CO}^m P_{NO}^n$$

Fig. 4. Production (R_i, y_{CO}) and phase (θ_i, y_{CO}) diagrams versus CO concentration in the gas (y_{CO}) interconnected sectors $KK_{(CO2)} = 0.71$; $KK_{(NO)} = KK_{(N2)} = 1$; $P_{CO} = 20.52$ torr; $P_{NO} = 39.52$ torr; $y = 0.01$. ♦ (R_{CO2}); ◊ (R_{N2}); □ (R_{N2O}); —— (SE (selectivity)); △ (θ_{CO}); ▲ (θ_{NO}); ○ (θ_O); ● (θ_N); ■ (θ_S). (*a*) and (*b*) $T = 450$ K; RTS = 0.10. (*c*) and (*d*) $T = 550$ K; RTS = 0.28. (*e*) and (*f*) $T = 650$ K; RTS = 0.48.

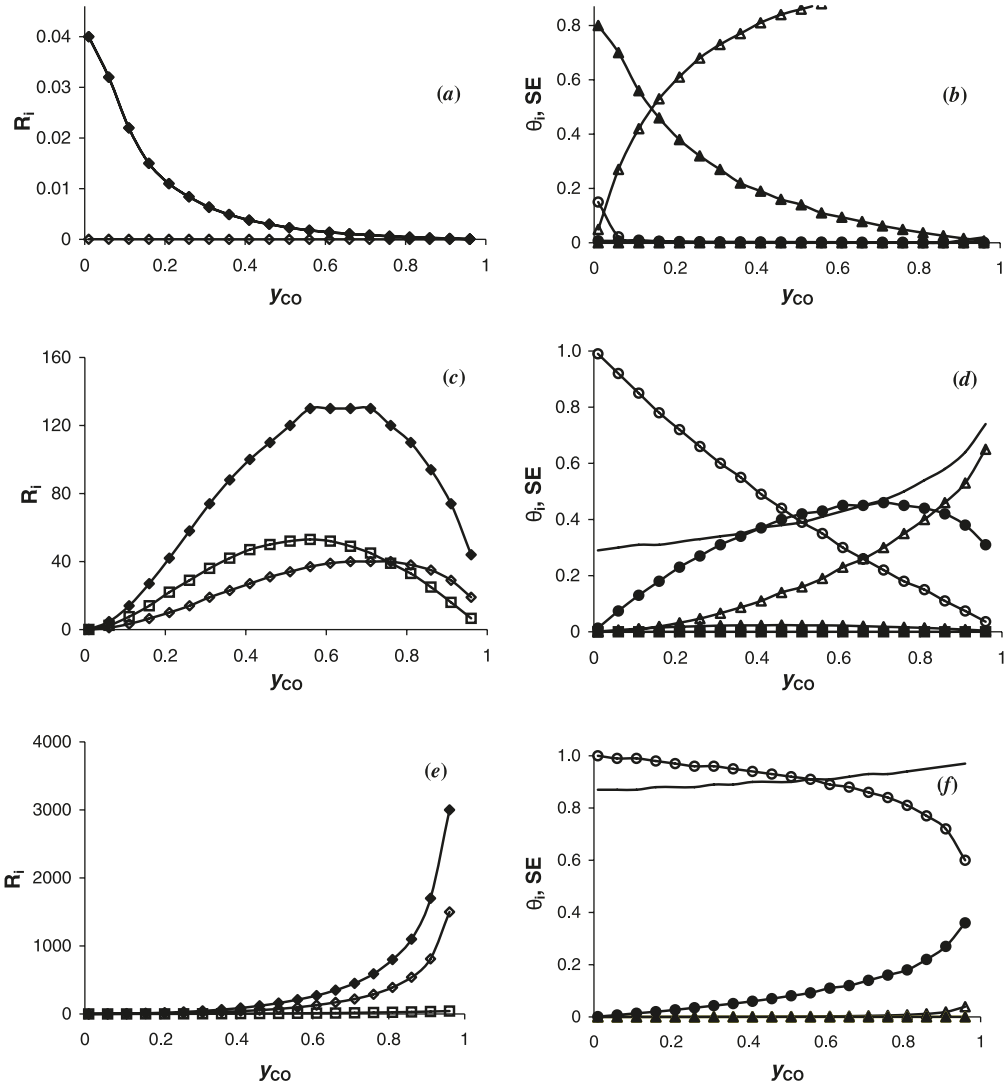

The figures (Fig. 5) show straight lines with a high correlation if the logarithm of production is graphed versus the logarithm of the corresponding pressure, keeping the other pressure constant, allowing for the determination of the respective *m* and *n* parameters. In all the cases studied a change of sign of the order with temperature was seen. In the case of CO, *m* was negative at low temperatures and positive at high temperatures, while the opposite occurred with *n* for NO. This behavior of the reaction order has been reported in experiments made in the low temperature zone on supported Pd with values similar to those of Fig. 5 by Rainer et al.[35] On the other hand, Holles et al.[36] reported experimental results for a series of supported Pd catalysts having different characteristics at relatively low temperatures, getting various positive values for the order of NO and negative values for CO. Holles et al.,[37] on the other hand, made interesting experiments on a bimetallic Pd/Rh supported catalyst, finding that it behaved in a manner similar to the Rh catalyst, showing orders close to zero for NO, in both cases at temperatures around 550 K. The catalysts in all these experiments must be considered in some way heterogeneous, with zones of the steps and terraces or similar types on the surface.

Effect of the variation of the activation energy of the steps for different stages of the kinetic mechanism

Considering the interest caused by the recent DFT studies, which have shown the catalytic importance of the energy differences between the step and terrace sites, it may be significant to visualize the behavior of the system for different values of the activation energy of various stages corresponding to step sites if the energy of the terrace sites is kept constant. Figure 6 shows the activity and surface coverage curves versus the activation energy of the steps for stage M5 of NO dissociation, stage M6 of N_2 production, and stage M7 of CO_2 production.

Fig. 5. Reaction order (eq. [18]). $y = 0.01$. (*a*) CO_2 production as a function of CO pressure with a fixed NO pressure of 39.52 torr at 450 K in the steady state for $KK_{(CO2)} = 0.82$; $KK_{(NO)} = KK_{(N2)} = 1$. (*b*) The same as (*a*) at 650 K. (*c*) The same as (*a*) as a function of NO pressure with a fixed CO pressure of 20.53 torr. (*d*) The same as (*c*) at 650 K.

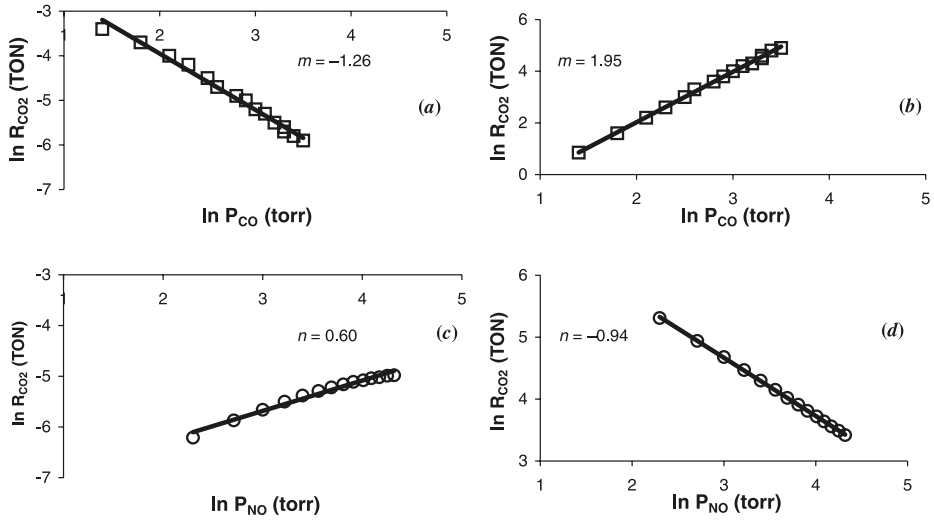

Fig. 6. Production (R_i), superficial coverage (θ_i), and selectivity (SE) versus the variation of the activation energy of stages M5 (E^s_{EDINO}), M6 (E^s_{N2}), M7 (E^s_{RCO}); interconnected sectors; $T = 500$ K; $P_{CO} = 20.52$ torr; $P_{NO} = 39.52$ torr; $y = 0.01$. Symbols R_i and θ_i are the same as in Fig. 4, and ---- RTS; (*a*) and (*b*) $KK_{(CO2)} = 0.71$; $KK_{(N2)} = 0.65$; (*c*) and (*d*) $KK_{(CO2)} = 0.71$; $KK_{(NO)} = 0.7$; (*e*) and (*f*) $KK_{(NO)} = 0.70$; $KK_{(N2)} = 0.65$.

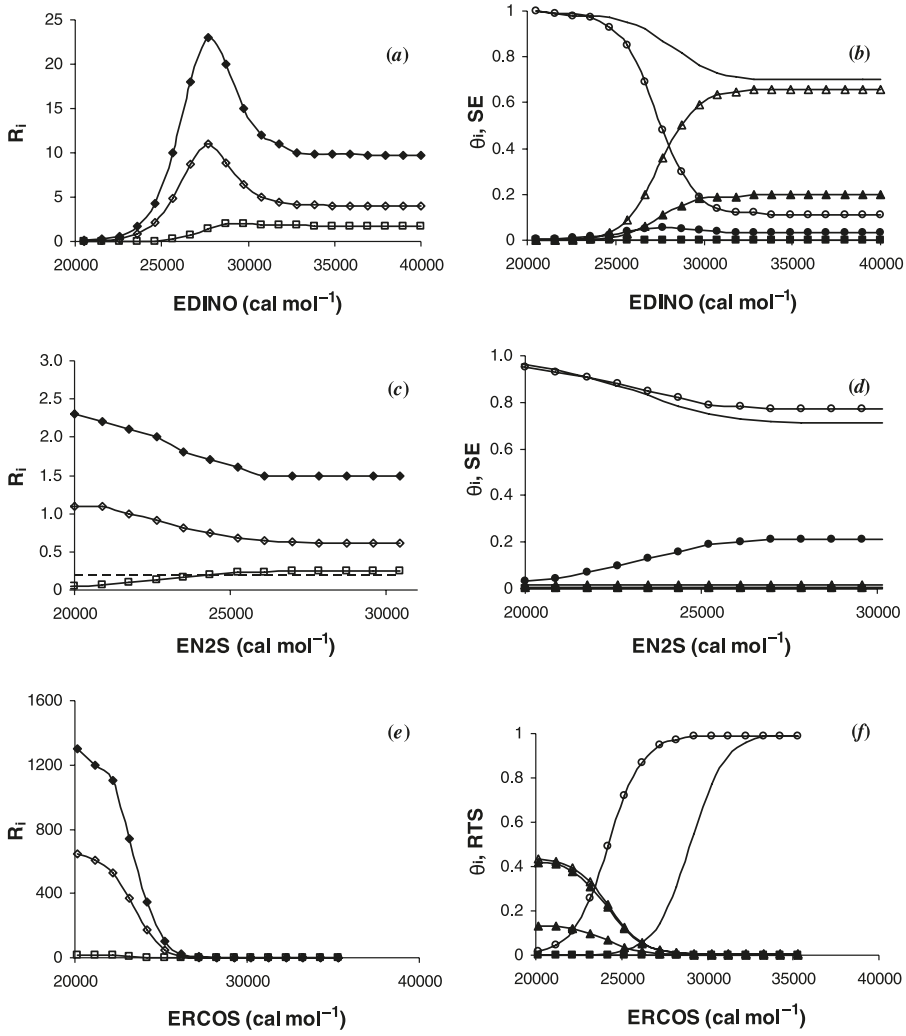

The maximum seen in Fig. 6*a* for the system's productions when the dissociation energy of the steps is varied is explained because all low values of this energy has the high dissociation of NO producing an excess of adsorbed oxygen, because superficial CO remains constant, leaving few vacant sites where the process can take place. The opposite effect occurs in the case of a high activation energy for dissociation, where there will be a deficiency of superficial nitrogen and oxygen that leads to decreased production. In a manner similar to the phase and production diagrams versus gas phase concentration, the production maximum coincides with the maximum nitrogen coverage and the intersection of the O and CO surface coverage curves.

The diagrams corresponding to the N_2 and CO_2 production stages have a similar behavior, because in both cases the decrease in production due to the increase in activation energy causes poisoning of the surface with the corresponding surperficial element produced by the dissociation of NO that does not react, like nitrogen with the increased production energy of N_2, and oxygen in the case of the production energy of CO_2.

Conclusions

The study of a mean field model, based on a previous formulation by Olsson et al.,[11] for the case of the CO-NO reaction on a heterogeneous catalytic surface formed by steps and terraces has been developed in the paper. Also, from the analysis of the behavior of the model in terms of various parameters of the system, its formulation is validated, contrasting some of its results with experiments in the literature carried out with the same reaction on heterogeneous substrates, stressing the interest of using a mean field heterogeneous model of catalysis to interpret the experimental data. Some of the most important results are stated below.

The relative importance of both sectors of the surface (steps and terraces) depends only on the energy difference between the sectors and the temperature if interconnected steps and terraces are assumed. If they are assumed to be independent, this relation also depends on the relation between the coverages of the different zones of the surface. This implies, for example, that the fraction of the process that occurs in the terraces always increases with temperature in the interconnected case, while it can increase or decrease in the case of independent sectors.

In all the cases maximum production with temperature is seen, in agreement with what happens in the superficial configuration, and it accounts for the Arrhenius behavior shown by the phenomenon. This behavior has been reported in the literature in experiments with the CO-NO reaction on heterogeneous substrates.

The activity versus concentration curves of the gas phase in contact with the surface show various behaviors that can be explained by what happens to the configuration of the adsorbed surface.

The system shows a reaction order with respect to CO and NO. In the case of CO, it is negative at low temperatures and positive at higher temperatures. In the case of NO, the opposite is true. These results interpret reasonably well, qualitatively and quantitatively, with some experimental data from the literature obtained at relatively low temperatures for the CO-NO reaction on heterogeneous substrates.

The activity of the process versus the value of the activation energy of the dissociation of NO in the steps has a maximum that can be accounted for by the behavior of the configuration of the adsorbed phase. An increase of the activation energy of N_2 or CO_2 production in the steps causes a decrease of the system's activity, with the consequent increase of surface poisoning with nitrogen or oxygen.

Acknowledgements

The authors acknowledge the financial support of this work by FONDECYT (Fondo Nacional de Desarrollo Científico y Tecnológico) under Project No. 1070351.

References

(1) (a) Nicolis, G.; Prigogine, I. *Self-Organization in Nonequilibrium Systems;* Wiley Interscience: New York, 1977; (b) Haken, H. *Synergetics;* Springer-Verlag: New York, 1977; (c) Marro, J.; Dickman, R. *Nonequilibrium Phase Transitens in Lattice Models;* University Press: Cambridge, 1999.

(2) Cortés, J.; Valencia, E. *J. Phys. Chem. B* **2004**, *108*, 2979. doi:10.1021/jp030803j.

(3) Zhdanov, V. P.; Kasemo, B. *Surf. Sci. Rep.* **1997**, *29*, 31. doi:10.1016/S0167-5729(97)00009-5.

(4) Evans, J. W. *Langmuir* **1991**, *7*, 2514. doi:10.1021/la00059a020.

(5) (a) Albano, E. V. *Heterog. Chem. Rev.* **1996**, *3*, 389 doi:10.1002/(SICI)1234-985X(199612)3:4<389::AID-HCR68>3.0.CO;2-2.; (b) Albano, E. V.; Borowko, M. *Computational methods in surface and colloid science;* Marcel Dekker: New York, 2000; Chapter 8, pp 387–437.

(6) Zhdanov, V. P.; Kasemo, B. *Surf. Sci. Rep.* **1994**, *20*, 111. doi:10.1016/0167-5729(94)90009-4.

(7) (a) Cortés, J.; Puschmann, H.; Valencia, E. *J. Chem. Phys.* **1996**, *105*, 6026 doi:10.1063/1.472438.; (b) Cortés, J.; Puschmann, H.; Valencia, E. *J. Chem. Phys.* **1998**, *109*, 6086 doi:10.1063/1.477235.; (c) Valencia, E.; Cortés, J. J. *Surf. Sci.* **2000**, *470*, L109 doi:10.1016/S0039-6028(00)00859-1.; (d) Cortés, J.; Valencia, E. *Physica A* **2002**, *309*, 26 doi:10.1016/S0378-4371(02)00610-6.; (e) Cortés, J.; Valencia, E. *J. Phys. Chem. B* **2004**, *108*, 2979. doi:10.1021/jp030803j.

(8) Cortés, J.; Valencia, E.; Herrera, J.; Araya, P. *J. Phys. Chem. C* **2007**, *111*, 7063. doi:10.1021/jp070697b.

(9) (a) Cortés, J. *J. Chem. Phys.* **1989**, *91*, 1932 doi:10.1063/1.457099.; (b) Cortés, J. *Surf. Sci.* **1989**, *218*, L461 doi:10.1016/0039-6028(89)90615-8.; (c) Cortés, J.; Araya, P. *J. Colloid Interface Sci.* **1987**, *115*, 271 doi:10.1016/0021-9797(87)90033-6.; (d) Cortés, J.; Araya, P. *J. Chem. Phys.* **1991**, *95*, 7741 doi:10.1063/1.461347.; (e) Rudzinski, W.; Everett, D. H. *Adsorption of Gases on Heterogeneous Surfaces;* Academic Press: London, 1992.

(10) Cortés, J.; Narváez, A.; Puschmann, H.; Valencia, E. *Chem. Phys.* **2003**, *288*, 77. doi:10.1016/S0301-0104(02)01052-2.

(11) Olsson, L.; Zhdanov, V. P.; Kasemo, B. *Surf. Sci.* **2003**, *529*, 338. doi:10.1016/S0039-6028(03)00275-9.

(12) (a) Ge, Q. F.; Kose, R.; King, D. A. *Adv. Catal.* **2000**, *45*, 207 doi:10.1016/S0360-0564(02)45015-8.; (b) Norskov, J. K.; Bligaard, T.; Logadottir, A.; Bahn, S.; Hansen, L. B.; Bollinger, M.; Bengaard, H.; Hammaer, B.; Sljivancanin, Z.;

Mavrikakis, M.; Xu, Y.; Dahl, S.; Jacobsen, C. J. H. *J. Catal.* **2002**, *209*, 275. doi:10.1006/jcat.2002.3615.
(13) Hammer, B. *J. Catal.* **2001**, *199*, 171. doi:10.1006/jcat.2000.3147.
(14) (a) Taylor, K. C. *Catal. Rev., Sci. Eng.* **1993**, *457*, 35; (b) Shelef, M.; Graham, G. *Catal. Rev., Sci. Eng.* **1994**, *36*, 433. doi:10.1080/01614949408009468.
(15) (a) Prévot, G.; Henry, C. *J. Phys. Chem. B* **2002**, *106*, 12191 doi:10.1021/jp0257451.; (b) Thirunavukkarasu, K.; Thirumoorthy, K.; Libuda, J.; Gopinath, Ch. *J. Phys. Chem. B* **2005**, *109*, 13272. doi:10.1021/jp050478v. PMID:16852655.
(16) Hecker, W. C.; Bell, A. T. *J. Catal.* **1983**, *84*, 200. doi:10.1016/0021-9517(83)90098-2.
(17) (a) Oh, S. H.; Fisher, G. B.; Carpenter, J. E.; Wayne, D. J. *J. Catal.* **1986**, *100*, 360 doi:10.1016/0021-9517(86)90103-X.; (b) Oh, S. H.; Eickel, C. C. *J. Catal.* **1991**, *128*, 526. doi:10.1016/0021-9517(91)90310-Z.
(18) (a) Cho, B. K. *J. Catal.* **1992**, *138*, 255 doi:10.1016/0021-9517(92)90021-9.; (b) Cho, B. K. *J. Catal.* **1994**, *148*, 697. doi:10.1006/jcat.1994.1256.
(19) Chuang, S.; Tan, C. *J. Catal.* **1998**, *173*, 95. doi:10.1006/jcat.1997.1922.
(20) Peden, C.; Belton, D.; Schmieg, S. J. *J. Catal.* **1995**, *155*, 204. doi:10.1006/jcat.1995.1204.
(21) (a) Permana, H.; Simon, K.; Peden, C.; Schmieg, S. J.; Belton, D. J. *J. Phys. Chem.* **1995**, *99*, 16344 doi:10.1021/j100044a022.; (b) Permana, H.; Simon, K.; Peden, C.; Schmieg, S. J.; Lambert, D. K.; Belton, D. J. *J. Catal.* **1996**, *164*, 194. doi:10.1006/jcat.1996.0375.
(22) (a) Cortés, J.; Valencia, E. *J. Phys. Chem. B* **2004**, *108*, 2979 doi:10.1021/jp030803j.; (b) Cortés, J.; Valencia, E. *J. Phys. Chem. B* **2006**, *110*, 7887. doi:10.1021/jp052885c. PMID:16610887.
(23) (a) Zaera, F.; Gopinath, Ch. S. J. *J. Chem. Phys.* **1999**, *111*, 8088 doi:10.1063/1.480142 .; (b) Zaera, F.; Gopinath, Ch. S. *Chem. Phys. Lett.* **2000**, *332*, 209 doi:10.1016/S0009-2614(00)01247-1.; (c) Zaera, F.; Gopinath, Ch. S. *J. Chem. Phys.* **2002**, *116*, 1128. doi:10.1063/1.1426381.
(24) Nakao, K.; Ito, S.; Tomishige, K.; Kunimori, K. *J. Phys. Chem. B* **2005**, *109*, 17579. doi:10.1021/jp052895d. PMID:16853249.
(25) (a) Behm, R. J.; Christmann, K.; Ertl, G.; Van Hove, M. A. *J. Chem. Phys.* **1980**, *73*, 2984 doi:10.1063/1.440430.; (b) Guo, X.; Yates, J. T., Jr. *J. Chem. Phys.* **1989**, *90*, 6761. doi:10.1063/1.456294.
(26) Ramsier, R. D.; Gao, Q.; Waltenburg, H. N.; Lee, K. W.; Nooij, O. W.; Lefferts, L.; Yates, J. T., Jr. *Surf. Sci.* **1994**, *320*, 209. doi:10.1016/0039-6028(94)90310-7.
(27) Sellers, H.; Anderson, J. *Surf. Sci.* **2001**, *475*, 11. doi:10.1016/S0039-6028(00)00969-9.
(28) Hirsimaki, M.; Valden, M. *J. Chem. Phys.* **2001**, *114*, 2345. doi:10.1063/1.1335816.
(29) Walker, A. V.; Gruyters, M.; King, D. A. *Surf. Sci.* **1997**, *384*, L791. doi:10.1016/S0039-6028(97)00244-6.
(30) (a) Sprunger, P. T.; Okawa, Y.; Besenbacher, F.; Stensgaard, I.; Tanaka, K. *Surf. Sci.* **1995**, *344*, 98 doi:10.1016/0039-6028(95)00852-7.; (b) Rocca, M.; Savio, L.; Vattuone, L. *Surf. Sci.* **2002**, *502–503*, 331 doi:10.1016/S0039-6028(01)01972-0.; (c) Somorjai, G. A. *Introduction to Surface Chemistry and Catalysis;* Wiley: New York, 1994; (d) Zambelli, T.; Wintterlin, J.; Trost, J.; Ertl, J. *Science* **1996**, *273*, 1688. doi:10.1126/science.273.5282.1688.
(31) Ford, L. P.; Blowers, P.; Masel, R. I. *J. Vac. Sci. Technol. A* **1999**, *17*, 1705. doi:10.1116/1.581877.
(32) Barth, J. V. *Surf. Sci. Rep.* **2000**, *40*, 75. doi:10.1016/S0167-5729(00)00002-9.
(33) Thirunavukkarasu, K.; Thirumoorthy, K.; Lipuda, J.; Gopinath, Ch. S. *J. Phys. Chem. B* **2005**, *109*, 13272. doi:10.1021/jp050478v. PMID:16852655.
(34) Piccolo, L.; Henry, C. R. *J. Mol. Catal. A* **2001**, *167*, 181. doi:10.1016/S1381-1169(00)00505-7.
(35) Rainer, D. R.; Koranne, M.; Vesecky, S. M.; Goodman, D. W. *J. Phys. Chem. B* **1997**, *101*, 10769. doi:10.1021/jp971262z.
(36) Holles, J. H.; Davis, R. J.; Murray, T. M.; Howe, J. M. *J. Catal.* **2000**, *195*, 193. doi:10.1006/jcat.2000.2985.
(37) Holles, J. H.; Switzer, M. A., Davis, R. J. *J. Catal.* **2000**, *190*, 247. doi:10.1006/jcat.1999.2780.

Appendix A. Analytical solution of the reaction model used in the paper

In a manner similar to the development shown in one of our previous papers,[1,2] we will synthetize the equations used in this paper for the mechanism of Scheme A1. Since it is assumed that the $CO_{(a)}$ and $NO_{(a)}$ adsorbates are in equilibrium with the gas phase, it is possible to write the relations

$$[A1] \qquad \frac{k_1}{k_2} = K_{CO} = \frac{\theta_{CO}}{\theta_S P_{CO}}, \quad \frac{k_3}{k_4} = K_{NO} = \frac{\theta_{NO}}{\theta_S P_{NO}}$$

where the equilibrium constants are expressed as functions of the coverages (θ_{CO} and θ_{NO}), and the partial pressures (P_{CO} and P_{NO}) of the gas phase, and θ_s represents the coverage of the vacant surface sites. The procedure used consists in expressing the coverages (θ_i) as functions of θ_{CO}, for which, if we define

$$[A2] \qquad A = \frac{P_{NO}K_{NO}}{P_{CO}K_{CO}}$$

$$[A3] \qquad B = \frac{1}{P_{CO}K_{CO}}$$

it is possible to write the relations

$$[A4] \qquad \theta_{NO} = A\theta_{CO} \quad \theta_S = B\theta_{CO}$$

The following conservation equations can be written, where the first two represent the steady state for the surface species $N_{(a)}$ and $O_{(a)}$ $\left(\frac{d\theta_N}{dt} = 0 \quad \text{and} \quad \frac{d\theta_O}{dt} = 0\right)$

$$[A5] \qquad k_5\theta_{NO}\theta_S - 2k_6\theta_N^2 - k_8\theta_{NO}\theta_N = 0$$

$$[A6] \qquad k_5\theta_{NO}\theta_S - k_7\theta_{CO}\theta_O = 0$$

$$[A7] \qquad \theta_S + \theta_{CO} + \theta_{NO} + \theta_N + \theta_O = 1$$

If we define the relations

$$[A8] \qquad C = (-k_8A + ((k_8A)^2 + 8k_5k_6AB)^{1/2})/4k_6$$

Scheme A1. Mechanism of the CO-NO reaction used in the paper.

$$CO + S \overset{k_1}{\underset{}{\rightleftarrows}} CO_{(a)} \quad \text{(M1)}$$

$$CO_{(a)} \xrightarrow{k_2} CO + S \quad \text{(M2)}$$

$$NO + S \xrightarrow{k_3} NO_{(a)} \quad \text{(M3)}$$

$$NO_{(a)} \xrightarrow{k_4} NO + S \quad \text{(M4)}$$

$$NO_{(a)} + S \xrightarrow{k_5} N_{(a)} + O_{(a)} \quad \text{(M5)}$$

$$2N_{(a)} \xrightarrow{k_6} N_2 + 2S \quad \text{(M6)}$$

$$CO_{(a)} + O_{(a)} \xrightarrow{k_7} CO_2 + 2S \quad \text{(M7)}$$

$$NO_{(a)} + N_{(a)} \xrightarrow{k_8} N_2O + 2S \quad \text{(M8)}$$

$$[A9] \qquad D = k_5AB/k_7$$

it is possible to write

$$[A10] \qquad \theta_N = C\theta_{CO}, \quad \theta_O = D\theta_{CO}$$

so that from eq. [A7] we have

$$[A11] \qquad \theta_{CO} = 1/(1 + A + B + C + D)$$

Therefore, the productions R_i are the following

$$[A12] \qquad R_{CO_2} = k_7\theta_{CO}\theta_O, R_{N_2} = k_6\theta_N^2, R_{N_2O} = k_8\theta_{NO}\theta_N$$

and the selectivity (SE) for the nitrogen is defined by

$$[A13] \qquad SE = R_{N_2}/(R_{N_2} + R_{N_2O})$$

References

(1) Cortés, J.; Valencia, E.; Herrera, J.; Araya, P. *J. Phys. Chem. C* **2007**, *111*, 7063. doi:10.1021/jp070697b.

(2) (a) Cortés, J.; Valencia, E. *J. Phys. Chem. B* **2004**, *108*, 2979 doi:10.1021/jp030803j.; (b) Cortés, J.; Valencia, E. *J. Phys. Chem. B* **2006**, *110*, 7887. doi:10.1021/jp052885c. PMID: 16610887.

Reversible decomposition of mono(α-hydroxy)-phosphines and their reaction with α,β-unsaturated aldehydes

Dmitry V. Moiseev, Paolo Marcazzan, and Brian R. James

Abstract: The mono(α-hydroxy)phosphines $R_2PCH(OH)R'$ (R = Ph, R′ = H, Et, CH_2Ph, Ph, *p*-X-C_6H_4; R = cyclohexyl, R′ = Ph) are prepared under solvent-free conditions by a 1:1 reaction of Ph_2PH with the appropriate aldehyde, and their stabilities (with respect to reversible dissociation into reactants), studied in DMSO, Et_2O, and MeOH, increase with decreased basicity of the hydroxyphosphine; for example, for the $Ph_2PCH(OH)C_6H_4$-*p*-X phosphines, stability decreases in the order: X = CN > Cl > F > H > Me > OMe. A 1:1 room-temperature reaction of the (α-hydroxy)phosphines (except for R′ = H) with cinnamaldehyde in DMSO slowly yields the known mono- and di-phosphines $Ph_2PCH(Ph)CH_2CHO$ (**4a**) and $Ph_2PCH(Ph)CH_2CH(PPh_2)OH$ (**10a**), and the corresponding R′CHO aldehyde. In MeOH, the sequentially formed intermediates, $PhCH{=}CHCH(OH)PPh_2$, $PhCH(OH)CH{=}CHPPh_2$, and $Ph_2PCH(Ph)CH{=}CHOH$, were detected en route to **4a** and **10a**. Reaction of cinnamaldehyde with Ph_2PCH_2OH gives **4a** and the hemiacetal $Ph_2PCH_2OCH_2OH$ formed from the reactant hydroxyphosphine with the co-product formaldehyde. Reactions carried out in MeOH are faster because of the formation of hemiacetals from the phosphine-containing aldehyde products; thus, **4a** is seen as $Ph_2PCH(Ph)CH_2CH(OMe)(OH)$, which on dissolution in Et_2O, reverts to the aldehyde. The reaction rates and equilibrium concentrations of the various species depend on the R′ group of the reactant phosphine; the rates of consumption of the hydroxyphosphines in the reactions with cinnamaldehyde decrease in the order: $Ph_2PCH(OH)Ph > Ph_2PCH(OH)Et > Ph_2PCH(OH)CH_2Ph >> Ph_2PCH_2OH$. The reactivity pattern of $Ph_2PCH(OH)Ph$ with sinapaldehyde [3,5-$(OMe)_2$-4-OH-cinnamaldehyde] in DMSO follows that seen for cinnamaldehyde. Reaction of Ph_2PH with cinnamaldehyde in DMSO affords **4a** and **10a** via the same intermediates seen with the $Ph_2PCH(OH)R'$ reagents, but these latter reactions are thought to occur via direct attack on cinnamaldehyde by the hydroxyphosphine rather than via Ph_2PH.

Key words: (α-hydroxy)phosphines, α,β-unsaturated aldehydes, diphenylphosphine, hydrophosphination.

Résumé : On a préparé des mono(α-hydroxy)phosphines $R_2CH(OH)R'$ [R = Ph, R′ H, Et, CH_2Ph, Ph, *p*-X-C_6H_4; R = cyclohexyle; R′ = Ph] dans des conditions sans solvant, en faisant réagir des quantités équimoléculaires (1:1) de Ph_2PH et de l'aldéhyde approprié. On a de plus étudié leurs stabilités par rapport à leur dissociation en réactifs dans le DMSO, Et_2O et MeOH qui augmente avec une diminution de la basicité de l'hydroxyphosphine; par exemple, pour les phosphines $Ph_2PCH(OH)C_6H_4$-*p*-X, la stabilité diminue dans l'ordre X = CN > Cl > F > H > Me > OMe. Une réaction de quantités équimoléculaires des (α-hydroxy)phosphines (à l'exception de celle dans laquelle R′ = H) et de cinnamaldéhyde, dans le DMSO, conduit lentement à la formation des mono- et diphosphines connues, $Ph_2PCH(Ph)CH_2CHO$ (**4a**) et $Ph_2PCH(Ph)CH_2CH(PPh_2)OH$ (**10a**), ainsi qu'à l'aldéhyde correspondant, R′CHO. Dans le méthanol, les produits $PhCH{=}CH(OH)PPh_2$, $PhCH(OH){=}CHPPh_2$ et $Ph_2PCH(Ph)CH{=}CHOH$, qui se forment successivement comme intermédiaires entre **4a** et **10a**. La réaction du cinnamaldéhyde avec le Ph_2PCH_2OH conduit à la formation du produit **4a** et de l'hémiacétal, $Ph_2PCH_2OCH_2OH$, qui résulte de la réaction du réactif hydroxyphosphine avec le formaldéhyde obtenu comme coproduit. Les réactions effectuées dans le MeOH sont plus rapides en raison de la formation d'hémiacétals à partir des produits aldéhydiques contenant une phosphine; ainsi, le produit **4a** observé sous la forme de $Ph_2PCH(Ph)CH_2CH(OMe)(OH)$ qui, par dissolution dans Et_2O se retransforme en aldéhyde. Les vitesses de réaction et les concentrations à l'équilibre des diverses espèces dépendent de la nature du groupe R′ présent sur la phosphine; les vitesses de consommation des hydroxyphosphines dans les réactions avec le cinnamaldéhyde diminuent dans l'ordre $Ph_2PCH(OH)Ph > Ph_2PCH(OH)Et > Ph_2PCH(OH)Ph > Ph_2PCH(OH)CH_2Ph > Ph_2PCH_2OH$. Le patron de réactivité du $Ph_2PCH(OH)Ph$ avec le sinapaldéhde [3,5-(Ome)2-4-OH-cinnamaldéhyde], dans le DMSO, est similaire à celui du cinnamaldéhyde. La réaction du Ph_2PH avec le cinnamaldéhyde, dans le DMSO, conduit à la formation des produits **4a** et **10a** par le biais des mêmes intermédiaires que ceux observés avec les réactifs $Ph_2PCH(OH)R'$; on croit toutefois que ces dernières réactions se produisent par le biais d'une attaque directe de l'hydroxyphosphine sur le cinnamaldéhyde pluṭt que par le biais d'une attaque via Ph_2PH.

Received 27 October 2008. Accepted 13 January 2009. Published on the NRC Research Press Web site at canjchem.nrc.ca on 30 March 2009.

D.V. Moiseev, P. Marcazzan, and B.R. James.[1] Department of Chemistry, The University of British Columbia, Vancouver, BC V6T 1Z1, Canada.

[1]Corresponding author (e-mail: brj@chem.ubc.ca).

Mots-clés : (α-hydroxy)phosphines, aldéhydes α,β-insaturés, diphénylphosphine, hydrophosphination.

[Traduit par la Rédaction]

Introduction

Collaborative research involving our group has revealed that (hydroxymethyl)phosphines, particularly $P(CH_2OH)_3$ (abbreviated THP), are excellent bleaching and brightness stabilization agents for pulps, and interaction of such phosphines with conjugated carbonyl components of lignin is important in the bleaching process.[1] A current, widely used pulp-bleaching agent is sodium dithionite ($Na_2S_2O_4$), industrially called "hydrosulfite", and the collaborative studies revealed a remarkable synergistic effect in the use of a combination of THP and $Na_2S_2O_4$ for the bleaching;[2] this led us to study the complicated interaction between these two chemicals in aqueous solution, where some bis(hydroxymethyl)phosphine $PH(CH_2OH)_2$ was observed.[3] This encouraged us to study the reaction of secondary phosphines with lignin-model compounds, exemplified by cinnamaldehyde, where use of neat reagents gave isolable products from hydrophosphination of first the C=C and subsequently the C=O bonds (Scheme 1).[4] The isolated (α-hydroxy)phosphine **II** was found in solution to decompose reversibly to **I** and Ph_2PH with rates that were highly solvent-dependent.[4] The analogous reversible decomposition of $Ph_2PCH(OH)Et$ to propionaldehyde and Ph_2PH was also demonstrated,[4] and this confirmed the generality of such a process, which was first noted for the benzaldehyde/Ph_2PH system;[5] a more recent study with phenolic aldehydes has also demonstrated such equilibria.[6] This chemistry was clearly relevant for our studies involving THP, a tris(α-hydroxy)phosphine, and we decided to investigate reactivity between cinnamaldehyde and mono(α-hydroxy)phosphines, which could well be present in the bleaching systems formed via addition of PH of the observed $PH(CH_2OH)_2$ across carbonyl and (or) olefinic functionalities. This paper presents our findings on these systems, studied in organic solvents. The studies complement those of our recent papers, which describe the interactions in aqueous solution between cinnamaldehyde and $P[(CH_2)_2OH]_3$,[7] and between substituted cinnamaldehydes and non-functionalized tertiary phosphines.[8]

There is literature describing reactivity of (α-hydroxy)phosphines (mostly THP) with α,β-unsaturated carbonyl-containing compounds in organic solvents, where the phosphorus atom attacks the activated C=C bond followed by loss of an aldehyde; e.g., THP with acrylonitrile gives $P(CH_2CH_2CN)_3$ with loss of formaldehyde, the net reaction being addition of P–H across the C=C bond (eq. [1]).[9,10] Similarly, reaction of the bis(α-hydroxy)phosphines $RP(CH_2OH)_2$ (R = Me, Et) with acrylonitrile can lead to formation of $RP(CH_2CH_2CN)_2$.[11] Reaction of THP with methyl acrylate in organic solvents generates the phosphine oxide $O=P(CH_2CH_2CO_2Me)_3$ formed because of the presence of trace water,[12] while THP (formed from the tetrakis(hydroxy)phosphonium salt $[P(CH_2OH)_4]Cl$ and base) reacts with acrylamide to give a mixture of $[(HOCH_2)P(CH_2CH_2NHCH_2OH)_3]OH$ and $O=P(CH_2CH_2NHCH_2OH)_3$, and with acrylic acid to yield a phosphobetaine (eq. [2]).[10] In this relatively early literature work, studied during the early days of ^{31}P NMR, the products, although likely correct, were not always well-characterized.

Scheme 1. 1:1 and 2:1 reactions of Ph_2PH with cinnamaldehyde; * indicates a chiral centre (ref. 4).

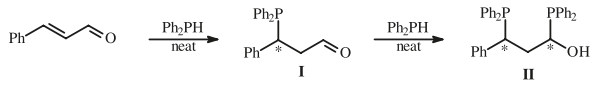

$$[1]\quad P(CH_2OH)_3 + 3CH_2{=}CHCN \rightarrow P(CH_2CH_2CN)_3 + 3CH_2O$$

$$[2]\quad [P(CH_2OH)_4]Cl + NaOH + CH_2{=}CHCO_2H \rightarrow (HOCH_2)_3P^+CH_2CH_2CO_2^- + CH_2O + H_2O + NaCl$$

Our studies reported here describe mainly reactions of cinnamaldehyde with the hydroxyphosphines $R_2PCH(OH)R'$ (R = Ph, R′ = H, Et, CH_2Ph, Ph, or *p*-substituted-Ph) in DMSO and in MeOH, as well as reversible decomposition of the hydroxyphosphines.

Experimental section

Cinnamaldehyde, sinapaldehyde [3,5-$(OMe)_2$-4-OH-cinnamaldehyde], PhCHO, and 4-X-C_6H_4CHO (X = CN, Cl, F, Me, and MeO), all Aldrich products, were distilled under reduced pressure or recrystallized, and stored under Ar before use. Ph_2PH and Cy_2PH (Cy = cyclohexyl) from Strem Chemicals were used as received. Ph_2PCH_2OH was prepared as reported from Ph_2PH and paraformaldehyde,[13] but purified by trituration using hexane/$CHCl_3$ (6:1), while $Ph_2PCH(OH)Et$, $Ph_2PCH(OH)CH_2Ph$, $Ph_2PCH(OH)Ph$, and $Cy_2PCH(OH)Ph$ were prepared from the appropriate secondary phosphine and aldehyde by our recently described procedure under Ar using Schlenk glassware or a glovebox.[4] ^1H, $^1H\{^{31}P\}$, and $^{13}C\{^1H\}$ NMR data for a DMSO-d_6 solution, and elemental analyses, of the new (α-hydroxy)phosphines are given in Table S1 (see Supplementary data). The $^{31}P\{^1H\}$ singlets for these phosphines in different solvents are listed in Table S2 (see Supplementary data). Organic solvents were dried over the appropriate reagents, and then distilled under Ar, while CD_3OD and DMSO-d_6 (Cambridge Isotope Laboratory) were used as received. $^{31}P\{^1H\}$ NMR spectra were recorded on a Bruker AV300 spectrometer (121 MHz) at 300 K unless otherwise stated; ^1H and ^{13}C NMR spectra were similarly recorded on an AV400 instrument (400 MHz for ^1H, 100 MHz for $^{13}C\{^1H\}$). A residual deuterated solvent proton (relative to external $SiMe_4$) and external 85% aq. H_3PO_4 were used as references: br = broad, s = singlet, d = doublet, t = triplet, p = pentet, and m = multiplet. *J* values are given in Hertz. When necessary, atom assignments were made by means of ^1H–^1H, ^1H–$^{13}C\{^1H\}$ (HMQC and HMBC) and ^1H–$^{31}P\{^1H\}$ NMR correlation spectroscopies.

Stability (with respect to reversible dissociation) of mono(α-hydroxy)phosphines in organic solvents

In a glovebox, the phosphine (0.05 mmol) was dissolved in 1 mL of a selected solvent, and a sample (~0.7 mL) of the solution was placed under Ar in a J-Young NMR tube; $^{31}P\{^{1}H\}$ NMR spectral changes were then monitored as a function of time at 300 K.

Reactions of Ph_2PH with aromatic aldehydes in MeOH

In a glovebox, Ph_2PH (18.6 mg, 0.1 mmol) was added to a MeOH solution of the aldehyde (0.1 mmol in 1 mL), and $^{31}P\{^{1}H\}$ NMR spectral changes of a sample were then monitored as described above.

Reactions of Ph_2PH or a mono(α-hydroxy)phosphine with an α,β-unsaturated aldehyde

As above, the phosphine (0.1 mmol) was added under Ar to a solution of the aldehyde (0.1 mmol) in air-free DMSO/DMSO-d_6 or MeOH/CD_3OD (1 mL), and a sample was monitored by NMR spectroscopy at 300 K.

Results and discussion

Synthesis and decomposition of (α-hydroxy)phosphines

The (α-hydroxy)phosphines **2a**–**2e** were prepared quantitatively as white solids by reaction of Ph_2PH (**1a**) or Cy_2PH (**1b**) with the corresponding aldehydes under solvent-free conditions at room temperature (Scheme 2), following the procedure reported earlier for **2b**;[4] the ^{1}H, $^{1}H\{^{31}P\}$, and $^{13}C\{^{1}H\}$ NMR data in DMSO-d_6 (Table S1 of the Supplementary data) are assigned as done previously for **2b**.[4] We have shown[4] that **2b** in solution at ambient conditions reversibly decomposes into Ph_2PH and propionaldehyde, greater stability being seen generally in higher donor number (DN) solvents such as DMSO, DMF, and pyridine,[14] and for this reason, the NMR data obtained in DMSO-d_6 are listed. The $^{31}P\{^{1}H\}$ data in four solvents (Table S2 of the Supplementary data) reveal a qualitative decomposition trend, and semiquantitative studies on **2a**–**2e** were undertaken in DMSO, Et_2O, and MeOH by monitoring the $^{31}P\{^{1}H\}$ singlet; decomposition in $CHCl_3$ and CH_2Cl_2 was significantly faster.

In DMSO (DN = 29.8), **2a**–**2d** are stable, with only trace amounts of **1a** being detected even after several hours, while **2e** essentially decomposes completely over 12 h (Fig. S1). In Et_2O (DN = 19.2), **2e** fully decomposes within 5 min, while Fig. S2 shows decomposition curves for **2b**–**2d** in this solvent, where the rates and degree of decomposition of **2d** are the highest, an equilibrium with ~90% conversion being set up with $t_{1/2} \approx 5$ h; for **2c**, an equilibrium is established with ~45% conversion ($t_{1/2} \approx 12$ h), while for **2b**, there is only ~60% conversion after 10 days, and no decomposition is evident for **2a**.

In MeOH, although a good donor (DN = 30.0), all the (hydroxy)phosphines show some instability, because they now decompose to the secondary phosphine and some hemiacetal formed from the aldehyde and MeOH; data in Fig. S3 show that the rates and the degree of decomposition decrease in the order: **2e >> 2b > 2d > 2c > 2a** (with **2e,** the $^{31}P\{^{1}H\}$ spectrum after 5 min showed only the resonance of **1b**). Rapid removal of the aldehyde as hemiacetal impedes regeneration of the (hydroxy)phosphines. Methanol is the only solvent studied where decomposition of **2a** was observed (~15% equilibrium, with $t_{1/2} \approx 3$ h). Establishing overall equilibria requires that measureable equilibria exist also between the aldehyde and its methanol hemiacetal, which is consistent with literature data, for example, in the case of **2d**, for benzaldehyde[15] (see below). The decompositions of **2a**–**2d** occur faster and to a greater extent in MeOH than in Et_2O, and hemiacetal formation must be one factor, although the presence of trace water in the MeOH possibly plays a role by favouring formation of a phosphonium intermediate. We have suggested previously[4] that decomposition of (α-hydroxy)phosphines could occur via an acid–base interaction between the OH proton and phosphine lone pair to give a phosphonium intermediate that re-arranges to the aldehyde and secondary phosphine (Scheme 5 in ref. 4); this implies also that a more electron-rich P atom gives a less stable (α-hydroxy)phosphine, and the above data for $Ph_2PCH(OH)Ph$ (**2d**) versus those for $Cy_2PCH(OH)Ph$ (**2e**) support such a premise. Of note, the tertiary phosphines $P[(CH_2)_nOH]_3$ (n = 1, 3) react quite differently with benzaldehyde in aqueous solution at ~90 °C via a redox reaction to give benzyl alcohol and the corresponding phosphine oxide.[16]

Scheme 2. Preparation and reversible decomposition of (α-hydroxy)phosphines.

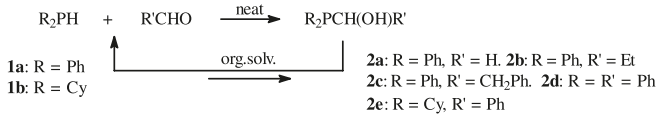

We then investigated, by NMR-scale reactions in MeOH (see Experimental section), the effect of a *p*-substituent (X) in a series of benzaldehydes on the stability of the (α-hydroxy)phosphines derived from Ph_2PH (eq. [3]). The data are summarized in Fig. S4, which shows that the rates and degrees of formation of the (α-hydroxy)phosphines decrease in the order: CN > Cl > F > H > Me > OMe; an excellently linear Hammett relationship results from plotting the relative equilibrium concentration vs. σ (Fig. S5). Thus, similar to the effect of the nature of the secondary phosphine, electron-withdrawing groups of the aldehyde favour the formation of the (α-hydroxy)phosphines and, consistent with this, the pentafluorophenyl derivative $Ph_2PCH(OH)C_6F_5$ is known to be stable.[5] It should be pointed out that the linearity of the Hammett plot may be fortuitous in that the presence of the aldehyde ⇌ hemiacetal equilibria is ignored, while the degree of formation of the hemiacetal is reported to be favoured with increasing electron-withdrawing nature of X.[15] Indeed, experimental NMR and enthalpy data[15] imply relatively little hemiacetal formation for the benzaldehydes that we studied, although there are significant discrepancies between some of the measured and calculated values;[15] one set of data is X = OMe (1.5% formation of hemiacetal), Me (2.1%), H (3.7%), and Cl (13%). The data of Figs. S4 and S5 must reflect the effect of X on (α-hydroxy)phosphine stability because the effect of X on the hemiacetal equilibria would itself give an apparent decrease in formation of the hydroxyphosphines by removal of the aldehyde.

[3] 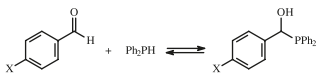

Fig. 1. The in situ $^{31}P\{^{1}H\}$ spectrum during reaction of cinnamaldehyde (**3a**) with Ph_2PCH_2OH (**2a**) (1:1, Ar, 300 K, DMSO-d_6): (A) after 2 days and (B) 22 days.

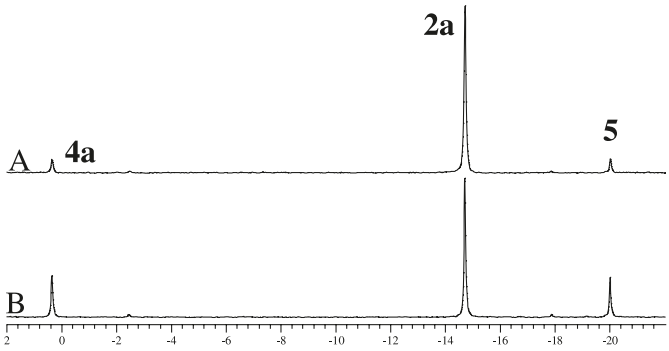

Fig. 2. The in situ $^{31}P\{^{1}H\}$ spectrum of the reaction of cinnamaldehyde (**3a**) with Ph_2PCH_2OH (**2a**) (1:1, Ar, 300 K, MeOH): (A) after 25 min, (B) 50 min, (C) 2 h, (D) 4 h, (E) 8 h, (F) 22 h, and (G) 48 h.

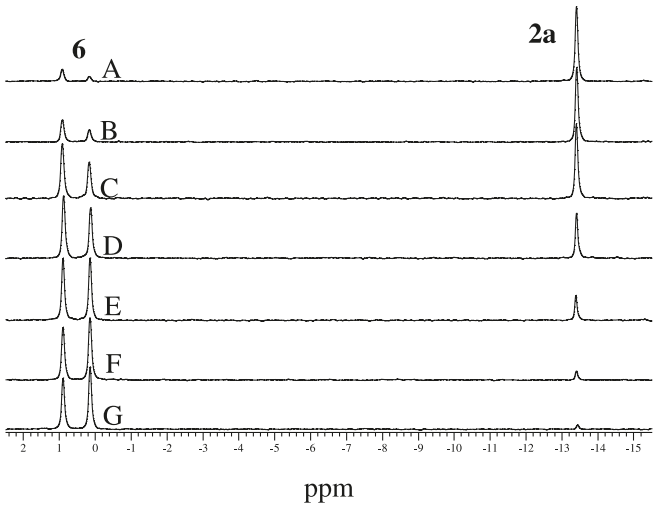

Reactions of (α-hydroxy)phosphines with α,β-unsaturated compounds

On a 1:1 reaction of Ph_2PCH_2OH (**2a**) with cinnamaldehyde (**3a**) in DMSO-d_6, the $^{31}P\{^{1}H\}$ resonance of **2a** (δ_P –14.7) was very slowly displaced by two almost equal intensity singlets at δ_P 0.4 and –20.0 (Fig. 1A); ^{1}H–^{1}H COSY and ^{1}H–$^{31}P\{^{1}H\}$ HMQC data (Figs. S6 and S7) show that the singlets are associated, respectively, with the known phosphine **4a** (**I** in Scheme 1)[4] and the phosphinated hemiacetal co-product **5** (eq. [4]). The net reaction would seem to be the formation of **4a** by nucleophilic attack of **2a** at the C=C bond of **3a** (but see below), with concomitant liberation of formaldehyde, which is not detected because it interacts via the OH group of **2a** to afford **5**. The P–CH_2 protons of **5** appear in the ^{1}H spectrum as a doublet at δ_H 4.27 ($^{2}J_{PH}$ = 5.0 Hz), which collapses to a singlet in the $^{1}H\{^{31}P\}$ spectrum. The corresponding protons of **2a** appear at δ_H 4.25 as a doublet of doublets due to extra coupling to the OH proton ($^{2}J_{PH}$ = 6.8, $^{3}J_{HH}$ = 5.5 Hz), and this reduces to a doublet in the $^{1}H\{^{31}P\}$ spectrum. The CH_2OH protons of **5** appear as a doublet at δ_H 4.67 both in the ^{1}H and $^{1}H\{^{31}P\}$ spectra ($^{3}J_{HH}$ = 7.9 Hz), and the OH proton is seen as a triplet at δ_H 6.45. After 22 days, integration of the $^{31}P\{^{1}H\}$ signals (Fig. 1B) shows that **4a** and **5** are each formed in ~20% yield (based on **2a**). Attempts to isolate pure **5** from reaction of CH_2O with **2a**, which itself is prepared from the reversible reaction of CH_2O with Ph_2PH,[13] have thus far been unsuccessful. Phosphines of this type have been synthesized previously from CH_2O and the (α-hydroxy)phosphine $P(CH_2OH)_3$.[17] There is no evidence for hemiacetal formation from **4a** and **2a**, consistent with higher reactivity (electrophilicity) of CH_2O versus that of **4a**.

[4] 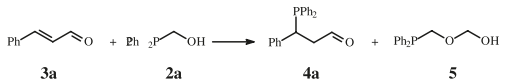

The reaction of **2a** with **3a** in MeOH is much faster than that in DMSO, the products now being the hemiacetal **6** (formed from **4a** and MeOH) and formaldehyde–hemiacetal (seen in CD_3OD as CD_3OCH_2OD, δ_H 4.65). Compound **6** is formed as a mixture of diastereomers (eq. [5]), observed in the $^{31}P\{^{1}H\}$ spectrum as two singlets δ_P 0.9 and 0.1 (Fig. 2), the diastereomeric ratio (d.r.) of a presumed mixture of *S*,*S*/*R*,*R*- and *S*,*R*/*R*,*S*-enantiomers changing from 0.37 (after 25 min) to 1.25 (after 2 days). The phosphine **4a** is almost insoluble in MeOH, but slowly dissolves as the hemiacetal **6**, when the δ_P 0.9 diastereomer is again initially preferred, the d.r. changing from 0.65 (90 min) to 1.25 (5 days) (Fig. S8). The same d.r. values result from integration of the ^{1}H signals, where the C*H*(OD)-protons appear as ddd

[5] 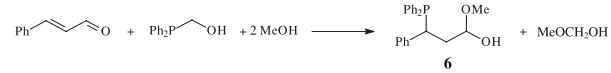

patterns at δ_H 4.17 and 4.09 with similar coupling constants ($^{3}J_{HH}$ = 8.9, $^{3}J_{HH}$ = 2.7, and $^{4}J_{PH}$ = 0.8 Hz), and the PhC*H*-protons are seen as overlapping ddd patterns at δ_H 3.76 and 3.73 ($^{3}J_{HH}$ = 12.0, $^{3}J_{HH}$ = 3.4, and $^{2}J_{PH}$ = 6.7 Hz). $^{13}C\{^{1}H\}$ NMR data for **6** are as follows: δ 142–127 (s and d, Ph groups), δ 97.9 (s, *C*HOMe), 42.2 (d, $^{1}J_{PC}$ = 11.0, Ph*C*H), and 41.7 (d, $^{2}J_{PC}$ = 20.6, *C*H_2) for one diastereomer; δ 97.8 (s, C*H*OMe), 42.1 (d, $^{1}J_{PC}$ = 11.3, Ph*C*H), and 41.0 (d, $^{2}J_{PC}$ = 20.6, *C*H_2) for the second diastereomer; the assignments for the Ph*C*H and *C*H_2 carbons, although unusual in that $^{2}J_{PC} > {}^{1}J_{PC}$, are based on definitive correlation NMR data for the corresponding C atoms of **4a**, which have such δ and *J* values.[4]

Of note, we have previously synthesized **4a** by the reaction of **3a** with Ph_2PH using neat reagents[4] (Scheme 1 in the Introduction), and it is plausible that the formation of **4a** illustrated in eq. [4] might involve the same chemistry, Ph_2PH being formed by decomposition of **2a** with formaldehyde as co-product (Scheme 2). This will be discussed later when data from reactions of cinnamaldehydes with the other (hydroxy)phosphines **2b**–**2d** have been considered (here, a different set of products and intermediates were observed). For example, a 1:1 reaction of $Ph_2PCH(OH)Et$ (**2b**) with cinnamaldehyde (**3a**) in DMSO-d_6 generates after 30 min two new singlets at δ_P –3.5 and 2.6 in the $^{31}P\{^{1}H\}$ spectrum

Fig. 3. The in situ $^{31}P\{^{1}H\}$ spectrum of the reaction of cinnamaldehyde (**3a**) with $Ph_2PCH(OH)Et$ (**2b**) (1:1, Ar, 300 K, DMSO): (A) after 30 min, (B) 6 h, (C) 22 h, (D) 46 h, and (E) 12 days; **10a** is a mixture of diastereomers (**α-I** and **β-I**) and (**α-II** and **β-II**) (Ref. 4).

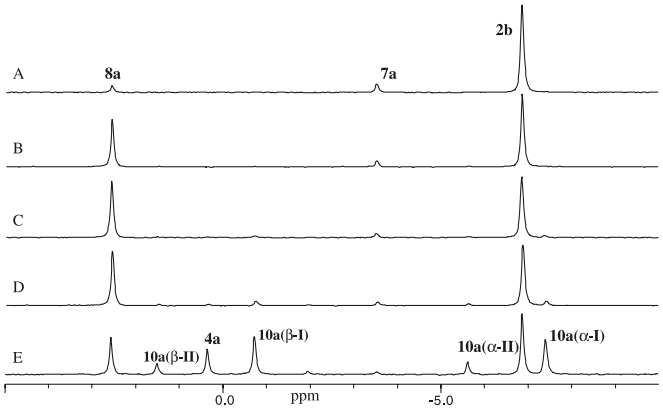

Scheme 3. Formation of intermediates in reactions of (α-hydroxy)-phosphines with α,β-unsaturated compounds.

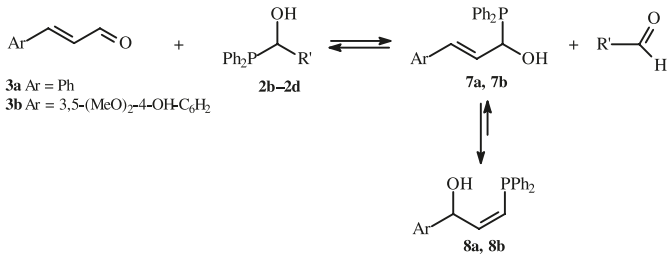

(Fig. 3A), which are assigned to the racemates of the phosphines species **7a** and **8a**, respectively (Scheme 3). A kinetic intermediate, (α-hydroxy)phosphine **7a**, is formed by nucleophilic attack of the P atom at the aldehyde C atom. In the ^{1}H spectrum (Fig. S9), the γ- and β-vinyl protons (δ_H 6.43 and 6.19, respectively) give dd and ddd patterns, which collapse to a doublet and a doublet of doublets in the $^{1}H\{^{31}P\}$ spectrum, respectively (Fig. S10) [$^{3}J_{HH}$ (trans H atoms) = 16.0, $^{4}J_{PH}$ = 3.3, $^{3}J_{PH}$ = 4.6 Hz]; the α-H appears as a broad doublet centered at δ_H 5.21 both in the ^{1}H and in the $^{1}H\{^{31}P\}$ spectrum, and the broad singlet of the OH proton is seen at δ_H 5.73. Intramolecular re-arrangement within **7a**, involving OH migration from the α- to the γ-C, affords **8a**. The downfield shift of the ^{31}P resonance (compared to that for **7a**) is consistent with the relative positions of the C=C moiety. The β- and α-vinyl ^{1}H proton signals are upfield-shifted (dd and ddd at δ_H 4.78 and 4.48, respectively) versus those for **7a**, the $^{3}J_{HH}$ value of 10.8 Hz implying a cis conformation ($^{2}J_{PH}$ = 6.5, $^{3}J_{PH}$ = 6.6 Hz), while the γ-H signal appears at δ_H 6.23 and overlaps with the β-H resonance of **7a**; the $^{1}H\{^{31}P\}$ spectra support the assignments (Figs. S9 and S10). The cis conformation might entail hydrogen-bonding between the OH proton and the P atom. The $^{1}H–^{31}P\{^{1}H\}$ correlation spectra of **7a** and **8a** are shown in Fig. S11. The eventual higher concentration of **8a** (vs. that of **7a**) implies a higher thermodynamic stability of the former (Figs. 3A–3D).

The hydroxyphosphines (**2c**–**2d**) also react with cinnamaldehyde (**3a**) according to Scheme 3. Figure 4 shows the rate of consumption of **2b**–**2d** in the reaction with **3a** under iden-

Fig. 4. The consumption of the starting phosphine in the reactions: (A) **2c** + **3a**, (B) **2b** + **3a**, (C) **2d** + **3b**, (D) **2d** + **3a**, and (E) **1a** + **3a**. Reactions were carried out under standard conditions (1:1, Ar, 300 K, DMSO).

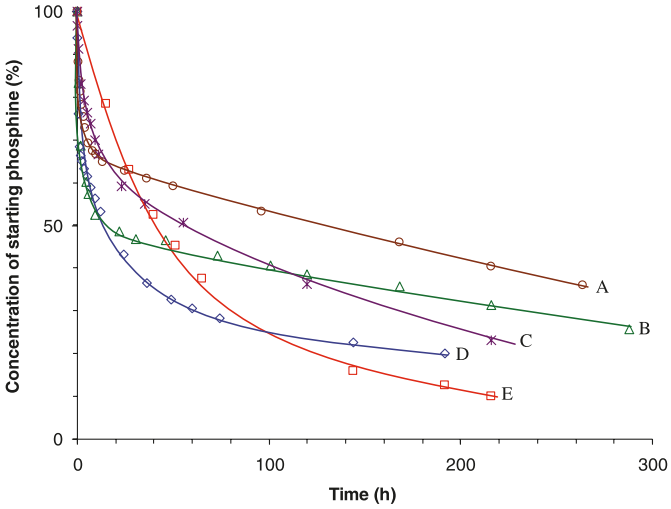

Fig. 5. The relative concentration of the intermediate **7** in the reactions: (A) **2c** + **3a**, (B) **2b** + **3a,** (C) **2d** + **3b,** (D) **2d** + **3a, and** (E) **1a** + **3a**. Reactions were carried out under standard conditions (1:1, Ar, 300 K, DMSO).

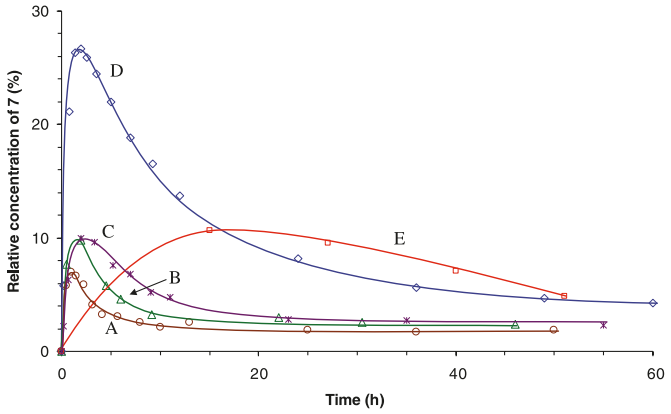

Fig. 6. The relative concentration of the intermediate **8** in the reactions: (A) **2c** + **3a**, (B) **2b** + **3a,** (C) **2d** + **3b,** (D) **2d** + **3a,** and (E) **1a** + **3a**. Reactions were carried out under standard conditions (1:1, Ar, 300 K, DMSO).

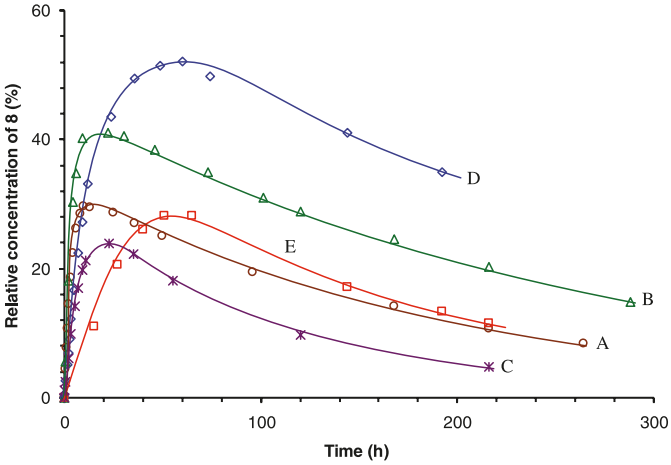

Fig. 7. The relative concentration of the diphosphine **10** in the reactions: (A) **2c** + **3a**, (B) **2b** + **3a,** (C) **2d** + **3b,** (D) **2d** + **3a,** and (E) **1a** + **3a**. All reactions were carried out under standard conditions (1:1, Ar, 300 K, DMSO).

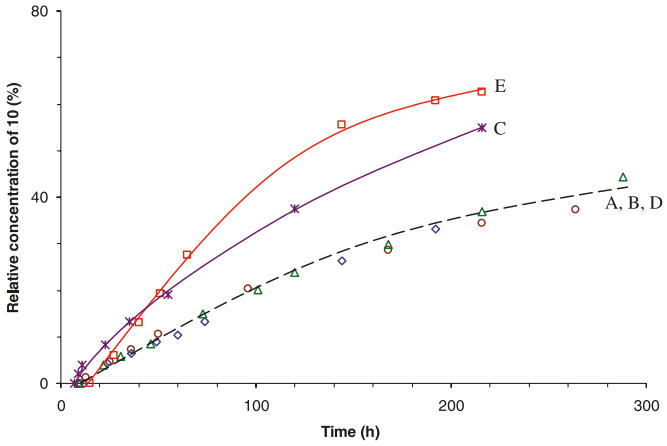

Fig. 8. The relative concentration of the phosphine **4a** or **4b** in the reactions: (A) **2c** + **3a,** (B) **2b** + **3a,** (C) **2d** + **3b,** (D) **2d** + **3a,** and (E) **1a** + **3a**. All reactions were carried out under standard conditions (1:1, Ar, 300 K, DMSO).

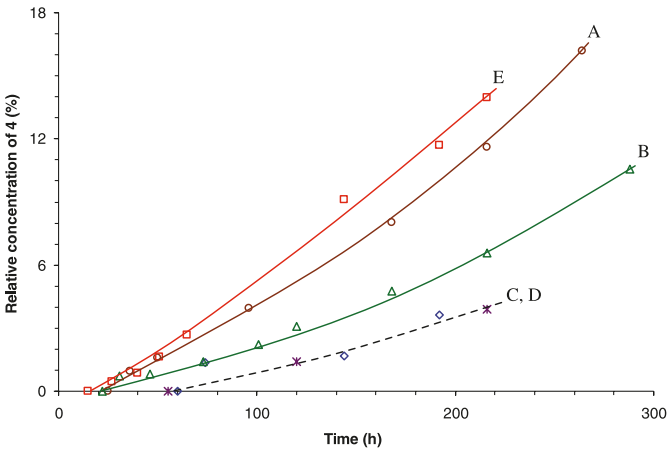

tical conditions (1:1, DMSO, 300 K, Ar), while Figs. 5 and 6 show the relative concentrations of the corresponding intermediates **7** and **8**, respectively. The degree of the consumption of **2b**–**2d** in their reaction with **3a** to form **7a/8a** (Scheme 3) decreases in the order: **2d** > **2b** > **2c** (Fig. 4), and also the extents of generation of **7a** (Fig. 5) and of **8a** (Fig. 6) decrease in the same order. This means that within the upper reaction of Scheme 3, benzaldehyde is a better "leaving group" than propionaldehyde, which is better than phenylacetaldehyde; with a more electrophilic aldehyde component of the reactant hydroxyphosphine, this equilibrium will be shifted to the left, and recall that in the reaction of **2a** (involving CH_2O, the most electrophilic of aldehydes) with **3a**, intermediates of the type **7** or **8** were not detected, and **4a** and **5** were the products (see above).

With the **2b**–**2d** systems, the concentrations of **7a** and **8a** do decrease slowly with formation of **4a** (Figs. 3, 5, and 6). However, **4a** can also then react with the starting phosphine **2b**–**2d** to generate the known diphosphine **10a** as a mixture of diastereomers, which is seen in the $^{31}P\{^1H\}$ spectrum as two sets of two equal intensity singlets (δ_P 1.5, –5.6 and –0.7, –7.4) (Figs. 3C-3E); eqs. [6] and [7] summarize the later stages of the chemistry (**9a** was detected in MeOH, see below). In recent work, we have characterized **10a**, where it was isolated from reaction of cinnamaldehyde with Ph_2PH via intermediate formation of **4a**[4] (see Scheme 1 in the Introduction) where **4a** and **10a** are labelled **I** and **II**, respectively.

Of note, the concentration of **10a** generated is independent of the reactant phosphine (**2b**–**2d**) used (Fig. 7), while the rate of formation of **4a** depends on the starting phosphine and decreases in the order: **2c** > **2b** > **2d** (Fig. 8). These findings can be rationalized qualitatively by considering the reverse reactions of the aldehydes with the diphosphine **10a** (eq. [7], Figs. 4 and 8), where again a more reactive aldehyde will shift the equilibrium to the left. The concentrations of **2b** and **8a** decrease simultaneously after the relatively fast stage (10 h), while the concentration of **7a** remains constant (Figs. 4–6), and this requires the upper reaction of Scheme 3 to be an equilibrium. This was confirmed by addition of EtCHO (the precursor to **2b**) to a solution containing **7a** and **8a** such as the one used to measure spectrum A in Fig. 3: the **7a**:**2b** ratio decreased rapidly from 0.15 to 0.02 on addition of two equiv. of EtCHO to the solution, while the **8a**:**2b** ratio increased from 0.15 to 0.30. The final product in these systems is **4a** (evident after 2 months!), and this requires also the reaction of eq. [7] to be reversible, and this was confirmed by addition of EtCHO to a DMSO solution of **10a**, when production of **2b** and **4a** was seen by using $^{31}P\{^1H\}$ NMR spectroscopy.

Evidence that **4a** likely derives from **7a** via the enol intermediate **9a** (formed from **7a** by migration of the Ph_2P group from the α- to γ- position) (eq. [6] was obtained by carrying out 1:1 reactions of **2b**–**2d** with cinnamaldehyde in MeOH/CD_3OD, which are much faster than the reaction in DMSO. Figure 9 shows a $^{31}P\{^1H\}$ NMR profile of the reaction for **2d** in MeOH, which is complete in 1 h. The final products of the reaction are the diastereomeric mixture of the hemiacetal **6** formed from **4a** (eq. [5], Fig. 9) and traces of the diastereomers of diphosphine **10a**. The 1:1 stoichiometry determines that **6** is essentially the sole product, while the observed intermediacy of **10a** again reveals the reversibility of the eq. [7] reaction. The **10a** diastereomers are detected at δ_P 2.6, –4.5, and 0.3, –6.6 (Fig. 9C). Figure 10 shows the ^1H–$^{31}P\{^1H\}$ HMQC correlation spectrum of this system in CD_3OD recorded after ~10 min, when the intermediates **7a,** **8a**, and **9a** are readily identified. The ^{31}P signals of **7a** (δ_P –2.3) and **8a** (δ_P 3.9) are downfield-shifted from those seen in DMSO, while the associated α-, β-, and γ-proton signals are at chemical shifts similar to those observed in DMSO-d_6 (see above) but are better resolved; e.g., the α-H of **7a** appears at δ_H 5.17 as a pseudo-doublet of triplets ($^2J_{PH}$ = $^4J_{HH}$ = 1.5, $^3J_{HH}$ = 6.5 Hz). Three ^1H resonances correlating with the $^{31}P\{^1H\}$ resonance at δ_P –0.7 in the ^1H–$^{31}P\{^1H\}$ HMQC spectrum (Fig. 10) are assigned to the enol species **9a**: the vinyl α- and β-protons appear at δ_H 4.10 and 5.02, respectively, as dd and ddd patterns ($^4J_{PH}$ = 6.8, $^3J_{PH}$ = 7.1, $^3J_{HH}$ = 9.1 Hz), the $^3J_{HH}$ value again implying a cis conformation at the olefinic bond, while the γ-H appears as a dd pattern centered at δ_H 6.15 and overlaps with the γ-H of **7a**; the $^3J_{HH}$ coupling constant to the β-H is 12.3 Hz ($^2J_{PH}$ is diffi-

Fig. 9. The in situ $^{31}P\{^{1}H\}$ spectrum of the reaction of cinnamaldehyde (**3a**) with $Ph_2PCH(OH)Ph$ (**2d**) (1:1, Ar, 300 K, MeOH): (A) after 8 min, (B) 11 min, (C) 20 min, (D) 30 min, (E), and (F) 50 min; **10a** is a mixture of diastereomers (**α-I** and **β-I**) and (**α-II** and **β-II**) (Ref. 4).

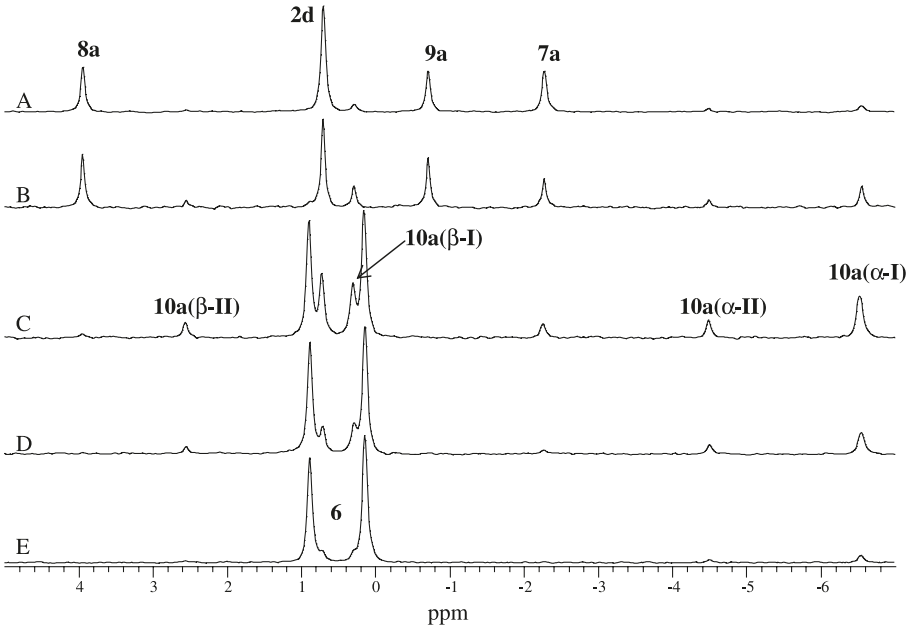

Fig. 10. The in situ ^{1}H–$^{31}P\{^{1}H\}$ HMQC spectrum of the reaction of cinnamaldehyde (**3a**) with **2d** (1:1, Ar, 300 K, CD_3OD) after ~10 min.

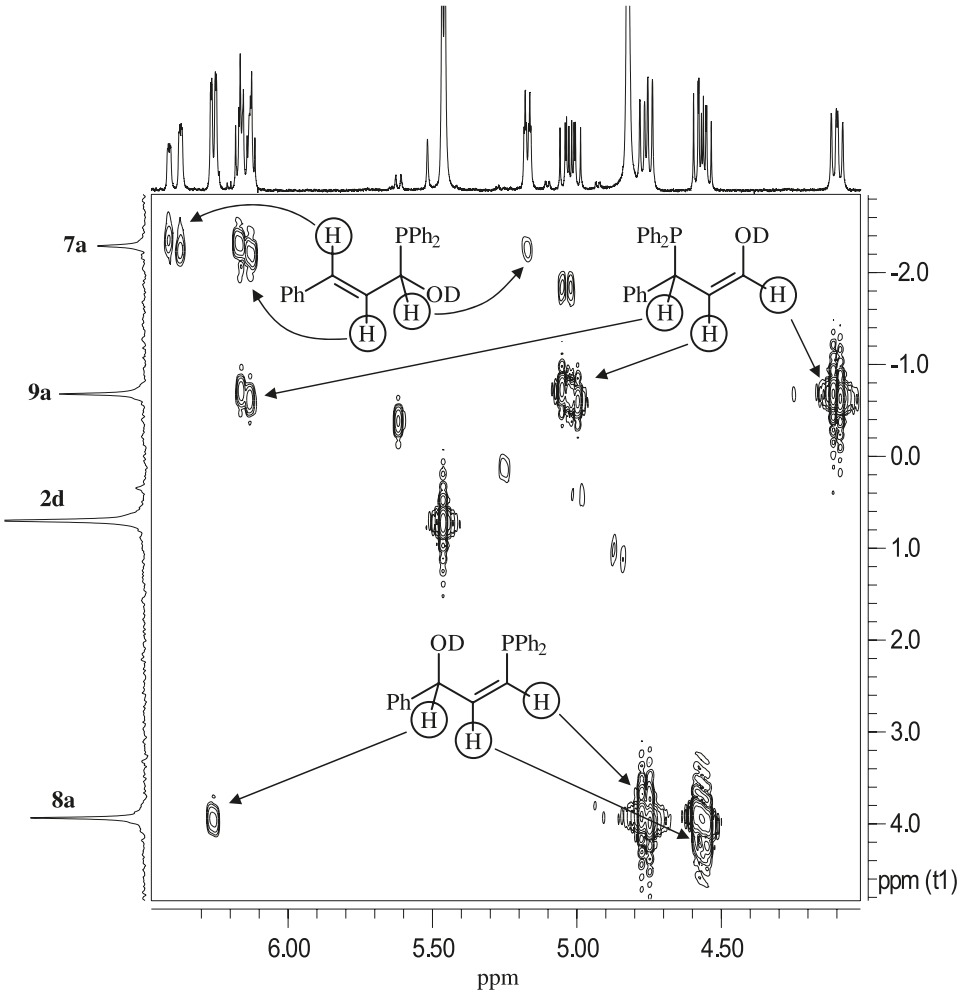

Fig. 11. The in situ $^{31}P\{^{1}H\}$ spectrum of the reaction of sinapaldehyde (**3b**) with $Ph_2PCH(OH)Ph$ (**2d**) (1:1, Ar, 300 K, DMSO): (A) after 40 min, (B) 3 h, (C) 7 h, (D) 24 h, (E) 5 days, and (F) 12 days; **10a** is a mixture of diastereomers (**α-I** and **β-I**) and (**α-II** and **β-II**) (Ref. 4).

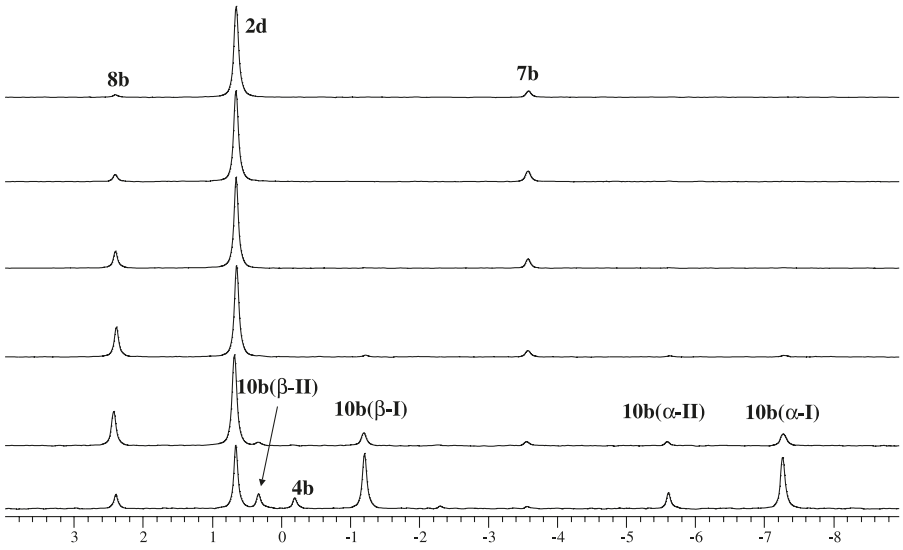

cult to determine). In CD_3OD, the product **6** is monodeuterated in the β-position, consistent with an enol-OD intermediate being involved in the formation of **4a**.

[6] 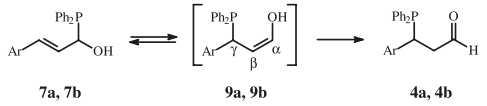

7a, 7b **9a, 9b** **4a, 4b**

[7] 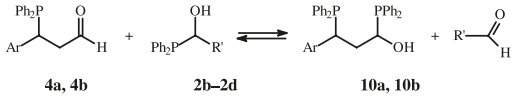

4a, 4b **2b–2d** **10a, 10b**

Sinapaldehyde (**3b**), a lignin-type aldehyde,[18] was also reacted with $Ph_2PCH(OH)Ph$ (**2d**) in DMSO to compare its reactivity with that of cinnamaldehyde (**3a**). The reason for this study was that the presence of an OH group para to the unsaturated aliphatic chain of **3a** has been shown to change significantly in aqueous solution the interaction of such aldehydes with PR_3 phosphines, where R does not contain an α-OH group.[8] However, in DMSO, the reactivity of **2d** with **3b** is found to be similar to that with **3a**, with corresponding intermediates and products (**4b**, **7b, 8b**, and **10b**) being detected by NMR (Fig. 11). Data in Figs. 4–6 (C curves) show that the consumption of **2d** is slower in the reaction with **3b**, leading to lower concentrations of **7b** and **8b** at a selected reaction time; the resulting higher concentration of **2d** leads to a higher concentration of **10b** (Fig. 7, eqs. [6] and [7]), although the rate of the generation of phosphine product **4b** is the same as for **4a** (Fig. 8).

It cannot be completely ruled out that **4a** and **4b** derive via **9a** and **9b**, respectively, formed at least partially by initial direct nucleophilic attack of a hydroxyphosphine at the C=C bond of the α,β-unsaturated aldehyde (eq. [6]). Further, **10a/10b**, which are hydroxyphosphines, could react with the cinnamaldehydes to form **4a/4b** giving intermediates **7a/7b** as co-products (cf. Scheme 3, upper equilibrium). However, the NMR studies support strongly the overall chemistry as presented in Scheme 3 and eqs. [6] and [7], and, although complicated because of the various equilibria involved, the reaction pathways are considered substantiated.

Because Ph_2PH (**1a**) is a decomposition product of the (α-hydroxy)phosphines (**2a**–**2d**) in organic media (Scheme 2), **1a** was always detected by $^{31}P\{^{1}H\}$ and ^{1}H NMR in small amounts (<6%) in all the reactions discussed above (δ_P –39.7 in DMSO, δ_P –39.8 in MeOH; δ_H 5.22, d, $^{1}J_{PH}$ = 222 Hz; see Figs. S9 and S12), and further, since **1a** is known to react with **3a** to give **4a**,[4] we thus studied the reaction of **3a** with **1a** in DMSO to see the plausibility of whether **4a** was being formed by this "decomposition" route. The expected intermediates and product discussed above (**7a**, **8a**, and **4a**) were detected; the consumption rate of Ph_2PH was slower than in the case of the hydroxyphosphines **2c** and **2d** (Fig. 4), presumably due to the lower nucleophilicity of the secondary phosphine compared with that of the tertiary phosphines and, as a result, the generation of **7a** and **8a** is also slower (Figs. 5 and 6). The formations of monophosphine **4a** (Fig. 8) and diphosphine (**10a**) (Fig. 7) are faster because no aldehyde is present in the reaction mixture (see the reversible reactions involving R′CHO shown in Scheme 3 and eq. [7]). The slower reactions seen with Ph_2PH (vs. **2c** and **2d**) are consistent with reaction pathways for the hydroxyphosphines via their direct attack on the unsaturated aldehydes rather than via Ph_2PH, although this latter route might contribute also; direct attack is expected to form (via nucleophilic attack of the phosphine at the C=O moiety) an (α-hydroxy)phosphonium intermediate such as $PhCH{=}CHCH(OH){-}R_2P^{+}CH(O^{-})R'$,[8,17b,19] which subsequently forms **7a** with release of R′CHO (Scheme 3). When Ph_2PH was reacted with **3a** (1:1) in MeOH, intermediates **7a**–**10a** were seen, while the only final product was hemiacetal **6** (see eq. [5]) formed from **4a** (see Scheme 1, where **I** ≡ **4a**); removal of the MeOH yielded **6** as a pink, viscous liquid, which could be dissolved in Et_2O and then removal of the Et_2O regenerated **4a** (see also the discussion on eq. [5]). From an experimental point of view, the solid mono(α-hydroxy)phosphines are useful storage agents for Ph_2PH, a foul smelling, easily oxidizable liquid.

Conclusions

Several synthesized mono(α-hydroxy)phosphines, $R_2PCH(OH)R'$, are confirmed to be generally reversibly unstable in organic solvents to give R_2PH and R′CHO, the degree of decomposition depending on the following: (a) the solvent, where stability typically increases with solvent donor number, except in the case of MeOH for which hemiacetal formation promotes decomposition, and (b) the nature of substituents R and R′, where more basic phosphines promote decomposition. Reactions of the phosphines with cinnamaldehyde in DMSO and in MeOH yield the known phosphine $Ph_2PCH(Ph)CH_2CHO$ (**4a**) and, depending on R′, the known diphosphine $Ph_2PCH(Ph)CH_2CH(PPh_2)OH$ (**10a**), as well as the liberated R′CHO aldehyde and hemiacetal co-products that result from interactions between aldehyde and alcohol functionalities. A series of sequential intermediates, more readily detected in MeOH, includes $PhCH=CHCH(OH)PPh_2$, $PhCH(OH)CH=CHPPh_2$, and $Ph_2PCH(Ph)CH=CHOH$; relative rates of formation of **4a**, **10a**, and the intermediates as a function of R′ in various equilibria are described. The reactions are thought not to proceed via Ph_2PH, which is formed by decomposition of the $Ph_2PCH(OH)R'$ compounds, although the secondary phosphine reacts with cinnamaldehyde to give the same products and intermediates.

Supplementary data

Supplementary data for this article are available on the journal Web site (canjchem.nrc.ca) or may be purchased from the Depository of Unpublished Data, Document Delivery, CISTI, National Research Council Canada, Ottawa, ON K1A 0R6, Canada. DUD 3905. For more information on obtaining material, refer to cisti-icist.nrc-cnrc.gc.ca/cms/unpub_e.shtml.

References

(1) (a) Hu, T. Q.; James, B. R.; Yawalata, D.; Ezhova, M. B. World Patent. PCT WO 2004 070110 A1. 2004.; (b) Chandra, R.; Hu, T. Q.; James, B. R.; Ezhova, M. B.; Moiseev, D. V. *J. Pulp Paper Sci.* **2007**, *33*, 15, and refs. cited therein.
(2) Hu, T. Q.; James, B. R.; Williams, T.; Schmidt, J. A.; Moiseev, D. V. World Patent. PCT WO 2007 016769 A1. 2007.
(3) Moiseev, D. V.; James, B. R.; Hu, T. Q. Unpublished work.
(4) Moiseev, D. V.; Patrick, B. O.; James, B. R. *Inorg. Chem.* **2007**, *46*, 11467. doi:10.1021/ic701597g. PMID:17990874.
(5) Evangelidou-Tsolis, E.; Ramirez, F.; Pilot, J. F.; Smith, C. P. *Phosphorus, Sulfur Silicon Relat. Elem.* **1974**, *4*, 109.
(6) Chikkali, C.; Gudat, D. *Eur. J. Inorg. Chem.* **2006**, 3005. doi:10.1002/ejic.200600330.
(7) Moiseev, D. V.; James, B. R.; Hu, T. Q. *Inorg. Chem.* **2007**, *46*, 4704. doi:10.1021/ic0701559. PMID:17432851.
(8) Moiseev, D. V.; Patrick, B. O.; James, B. R.; Hu, T. Q. *Inorg. Chem.* **2007**, *46*, 9389. doi:10.1021/ic7007478. PMID: 17914858.
(9) Valetdinov, R. K.; Kuznetsov, E. V.; Komissarova, S. L. *Zh. Obshch. Khim.* **1969**, *39*, 1744.
(10) Vullo, W. J. *Ind. Eng. Chem. Prod. Res. Dev.* **1966**, *5*, 346. doi:10.1021/i360020a011.
(11) Komissarova, S. L.; Valetdinov, R. K.; Kuznetsov, E. *Zhur. Obshch. Khim.* **1971**, *41*, 322.
(12) Valetdinov, R. K.; Zuikova, A. N. *Zh. Obshch. Khim.* **1978**, *48*, 1726.
(13) Kühl, O.; Blaurock, S.; Sieler, J.; Hey-Hawkins, E. *Polyhedron*, **2001**, *20*, 2171. doi:10.1016/S0277-5387(01)00811-7.
(14) Marcus, Y. *J. Sol. Chem.* **1984**, *13*, 599. doi:10.1007/BF00650369.
(15) Fuchs, R.; Young, T. M.; Rodewald, R. F. *Can. J. Chem.* **1973**, *51*, 4122. doi:10.1139/v73-616.
(16) Moiseev, D. V.; Patrick, B. O.; James, B. R.; Hu, T. Q. *Inorg. Chem.* **2006**, *45*, 10338. doi:10.1021/ic0613560. PMID: 17140243.
(17) (a) Vullo, W. J. *J. Org. Chem.* **1968**, *33*, 3665 doi:10.1021/jo01273a080.; (b) Ellzey, S. E., Jr.; Connick, W. J., Jr.; Boudreaux, G. J. *J. Org. Chem.* **1972**, *37*, 3453 doi:10.1021/jo00795a015.; (c) Valetdinov, R. K.; Zuikova, A. N.; Zyablikova, T. A.; Il'yasov, A. V. *Zh. Obshch. Khim.* **1978**, *48*, 97; (d) Valetdinov, R. K.; Zuikova, A. N.; Yakiminskaya, N. Sh.; Zyablikova, T. A.; Ofitserov, E. N.; Il'yasov, A. V. *Zh. Obshch. Khim.* **1978**, *48*, 2653; (e) Kisanga, P.; Verkade, J. *Heteroatom Chem.* **2001**, *12*, 114. doi:10.1002/hc.8.
(18) Pew, J. C.; Connors, W. J. *Tappi J.* **1971**, *54*, 245.
(19) Grayson, M. *J. Am. Chem. Soc.* **1963**, *85*, 79. doi:10.1021/ja00884a016.

Activation of the *N*C–H bond of Morita–Baylis–Hillman adducts of *N*-substituted isatins with cerium ammonium nitrate (CAN) and alcohol (ROH)

Ponnusamy Shanmugam and Vadivel Vaithiyanathan

Abstract: A study on the activation of the *N*C–H bond of Morita–Baylis–Hillman adducts of *N*-substituted isatin with cerium ammonium nitrate (CAN) and saturated and unsaturated alcohols have been carried out. The choice of a Morita–Baylis–Hillman adduct for this study is screened with a number of adducts. A comparative and reactivity pattern study on *N*C-H activation of Morita–Baylis–Hillman adducts of *N*-substituted isatin derivatives viz. *N*-methyl, *N*-ethyl, *N*-methyl acetate, *N*-benzyl, *N*-propargyl, and *N*-isopropyl isatins have been carried out. Effect of aryl ring substitution has also been investigated. A plausible mechanism for the formation of the ether products has been outlined.

Key words: cerium ammonium nitrate (CAN), Morita–Baylis–Hillman adduct, *N*-CH activation, functionalised ethers, nitration.

Résumé : On a effectué une étude sur l'activation, par le nitrate d'ammonium cérique (NAC), de la liaison *N*C-H d'adduits Morita–Baylis–Hillman d'isatine *N*-substituée et d'alcools saturés et non saturés. Le choix de l'adduit Morita–Baylis–Hillman pour cette étude est évalué avec un certain nombre d'adduits. On a aussi réalisé une étude comparative et une étude de patron de réactivité sur l'activation *N*C-H d'adduits Morita–Baylis–Hillman d'isatines *N*-substituées, entre autre par des groupes *N*-méthyle, *N*-éthyle, *N*-méthylacétate, *N*-benzyle, *N*-propargyle et *N*-isopropyle. On a aussi étudié l'effet de la substitution sur les groupes aryles. On propose un mécanisme plausible pour la formation d'éthers comme produits.

Mots-clés : NAC, adduit de Morita–Baylis–Hillman, activation *N*C-H, éthers fonctionnalisés, nitration.

[Traduit par la Rédaction]

Introduction

The C–H bond activation method is one of the challenging synthetic routes in organic synthesis.[1–12] Activation of C–H bonds particularly by oxidative processes[1–5] and by organometallic reagents[6–12] has been of great interest to organic chemists in recent years. Cerium(IV) ammonium nitrate (CAN) has emerged as a versatile reagent for a number of synthetic transformations.[13,14] The synthetic flexibility of isatin and its derivatives has led to the extensive use of this compound in synthetic organic chemistry.[15] Recently, the Morita–Baylis–Hillman (MBH) reaction has emerged as an important carbon–carbon bond, forming reactions that, in general, afford densely functionalized molecular frame works and the reaction is considered as atom economic.[16–19] As part of our ongoing research in the area of novel synthetic methodologies based on MBH adducts,[20–26] we have reported the preliminary results on activation of the *N*C–H bond of MBH adducts of *N*-methylisatin with CAN/ROH (alcohol).[27] In continuation of the work, a detailed study on *N*C-H activation of various MBH derivatives of *N*-substituted isatins with CAN as a one electron oxidant and with a number of alcohols as reagents was carried out. The details of this study are the subject matter of this paper.

Received 22 August 2008. Accepted 12 January 2009. Published on the NRC Research Press Web site at canjchem.nrc.ca on 31 March 2009.

P. Shanmugam[1,2] and V. Vaithiyanathan. Chemical Sciences and Technology Division, National Institute for Interdisciplinary Science and Technology, Trivandrum 695019, Kerala, India.

[1]Corresponding author (e-mail: shanmu196@rediffmail.com).
[2]Present address: Organic Chemistry Division, Central Leather Research Institute (CLRI), Adyar, Chennai 600 020, India.

Results and discussion

Optimization of the *N*C-H activation and choice of MBH adducts of isatin

The optimization studies were initiated using the MBH adduct of *N*-methylisatin (**1**) as a model substrate. The preliminary study and results are shown in Table 1. Initially, adduct **1** was treated with 2 equiv. of CAN and excess methanol (10 mL) to afford the *N*C-H activated product **2** in trace amount (5%) (Table 1, entry 1). Repeating the reaction with 3 equiv. of CAN and MeOH (5 mL) for 12 h afforded **2** in a slightly improved yield (10%, Table 1, entry 2). Fine-tuning of the reaction conditions is shown in Table 1. Thus, the optimum condition was found as 4 equiv. of CAN and MeOH (1.6 mL, 40 equiv.) and CH_3CN (0.5 mL) and at room temperature (RT) for 24 h (Table 1, entry 4).

Further, to examine the selectivity and structural requirements of *N*-methyl isatin derivatives for *N*C-H activation, we chose different isatin derivatives (**1, 4–9**), as shown in Fig. 1.

Under the optimized condition, MBH adducts **1, 4**, and **5** of *N*-methyl isatin afforded the ether products **2, 10**, and **12** in 24%–66% yields and the nitrated compound **3, 11**, and **13** in trace-30% yields, respectively (Table 2, entries 1–3). In-

Table 1. Optimization of the *N*C-H activation of 1 with CAN/MeOH.

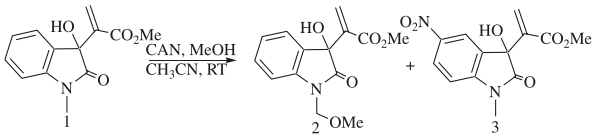

Entry	MeOH (mL)	CH_3CN (mL)	CAN (equiv.)	Time (h)	Yield (%) 2	3
1	10.0	—	2.0	12	5	—
2	5.0	—	3.0	12	10	—
3	3.0	3.0	4.0	24	20	35
4	1.6	0.5	4.0	24	66	30

Fig. 1. A Choice of different isatin derivatives (1, 4–9) for C-H activation.

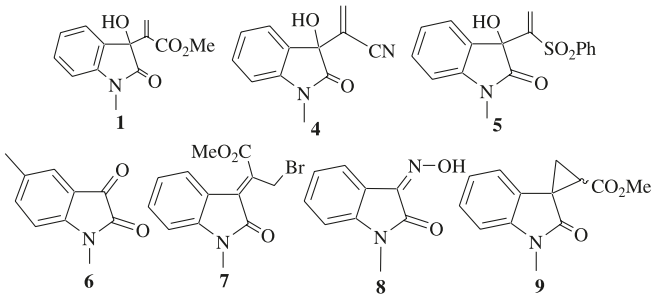

terestingly, the simple *N*-methyl isatin **6** yielded only the nitrated product **14** in 15% yields. Other *N*-methylisatin derivatives such as the bromo-derived adduct (**7**), oxime derivative of *N*-methyl isatin (**8**), and *N*-methyl-3-spirocyclopropyl-2-indolone (**9**) did not yield any *N*C-H activated ether product or nitrated product. The results of the preliminary investigation are summarized in Table 2. Hence, the study showed that the MBH adduct of *N*-methyl isatin was the most suitable substrate for *N*C-H activation reaction.

Excellent preliminary results on *N*C-H activation of MBH adduct of *N*-methyl isatin prompted us to investigate a systematic activation study of various *N*-substituted MBH adducts of isatin derivatives. Thus, we chose various MBH adducts with different *N*-alkyl substitutions such as methyl, methylene, and methine, which in principle generate 1•, 2•, and 3• radical cation intermediates during the *N*C-H activation process (Fig. 2).

*N*C-H activation study of primary methyl radical sources

To investigate the *N*C-H activation via primary radical cation intermediates, MBH adducts **1, 3, 4**, and **15** were chosen (Fig. 3.) and the details are discussed in the following section.

NC-*H activation of MBH adducts of* N-*methyl isatin 1 and 4*

As discussed earlier, during the optimization study the MBH adduct **1** with CAN/MeOH afforded the products **2** (ether) and **3** (nitrate). This observation prompted us to further explore the study using adducts **1** and **4** with various saturated and unsaturated 1• alcohols (R^4OH)/CAN. The reactions afforded the *N*C-H activated ethers **10** and **16–23** along with nitrated products **3** and **11** in moderate yield (Table 3, entries 1–9). Notably, the reaction of MBH adduct **1** with 2•- and 3•-alcohols (isopropanol and *t*-butanol) did not yield any *N*C-H activated product and only the nitrated product **3** was obtained in good yields (Table 3, entries 10 and 11). However, the reactions with allyl alcohol/CAN and cinnamyl alcohol/CAN did not afford the *N*C-H activated product. Only alcohol oxidation was observed during the course of the reaction (Table 3, entries 12 and 13). All the new compounds were characterized by spectroscopic (IR, ^1H, and ^{13}C NMR) and HRMS data. The results are summarized in Table 3.

Table 2. *N*C-H activation reactions of isatin derivatives.

Entry	Substrate	Products Ether (A)	Nitrates (B)	Yield (%) A	B
1	**1**	**2**	**3**	66	30
2	**4**	**10**	**11**	50	30
3	**5**	**12**	**13**	24	Trace
4	**6**	—	**14**	—	15
5	**7**	—	—	—	—
6	**8**	—	—	—	—
7	**9**	—	—	—	—

Fig. 2. Choice of different sources of MBH adduct of isatin derivatives for *N*C-H activation.

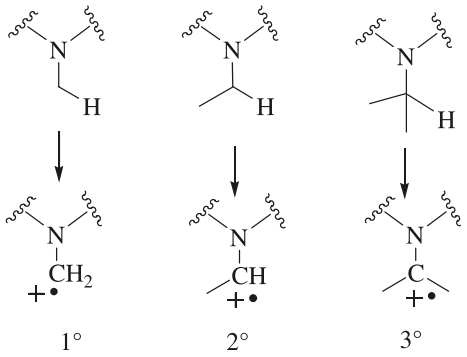

Fig. 3. Choice of different MBH adducts having a methyl *N*C-H source.

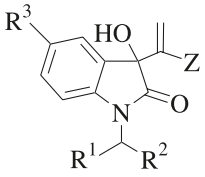

R^1 = H; R^2 =H; R^3=H; Z =CO_2Me **1**
R^1 = H; R^2 =H; R^3 =NO_2; Z =CO_2Me **3**
R^1 = H; R^2 =H; R^3 =H; Z =CN **4**
R^1 = H; R^2 =H; R^3 =Br; Z =CO_2Me **15**

Effect of aryl ring substitution on NC-*H activation of MBH adducts 15 and 3*

To circumvent nitration and to check the effect of substitution at the aryl ring, we examined the activation study with MBH adduct **15** with CAN and alcohols such as methanol, ethanol, homopropargyl alcohol, and *t*-butanol. The reactions underwent smoothly at an enhanced rate (1.5–2 h) and afforded the *N*C-H activated compounds (**24–27**) in good yields (Table 3, entries 14–17). Investigation on the effect of substitution and to understand the reactivity pattern

Table 3. Results of *N*C-H activation study of primary methyl radical sources.

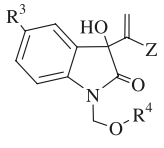

R^3 = H; R^4 = Et; Z = CO_2Me **16**
R^3 = H; R^4 = H_2C—≡; Z = CO_2Me **17**
R^3 = H; R^4 = H_2C ; Z = CO_2Me **18**
R^3 = H; R^4 = H_2C OH; Z = CO_2Me **19**
R^3 = H; R^4 = H_2C OH ; Z = CO_2Me **20**
R^3 = H; R^4 = CH_2Ph; Z = CO_2Me **21**
R^3 = H; R^4 = Me; Z = CN **10**
R^3 = H; R^4 = Et; Z = CN **22**
R^3 = H; R^4 = H_2C—≡; Z = CN **23**
R^3 = Br; R^4 = Me; Z = CO_2Me **24**
R^3 = Br; R^4 = Et; Z = CO_2Me **25**
R^3 = Br; R^4 = H_2C ; Z = CO_2Me **26**
R^3 = Br; R^4 = ^{t}Bu; Z = CO_2Me **27**

				Products		Yield (%)	
Entry	MBHA	Alcohol (R^4)	Time (h)	*N*C-H activation (A)	Nitration (B)	A	B
1	**1**	EtOH	24	**16**	—	52	—
2	**1**	Propargyl	24	**17**	—	51	—
3	**1**	Homopropargyl	24	**18**	**3**	58	25
4	**1**	Ethane-1,2-diol	24	**19**	—	55	—
5	**1**	Propane-1,3-diol	24	**20**	—	67	—
6	**1**	Benzyl alcohol	24	**21**	—	59	—
7	**4**	MeOH	24	**10**	**11**	50	30
8	**4**	EtOH	24	**22**	**11**	53	27
9	**4**	Propargyl	24	**23**	**11**	57	35
10	**1**	Isopropanol	24	—	**3**	—	54
11	**1**	*t*-Butanol	24	—	**3**	—	65
12	**1**	Allyl alcohol	24	—	—	—	—
13	**1**	Cinnamyl	24	—	—	—	—
14	**15**	MeOH	2.0	**24**	—	52	—
15	**15**	EtOH	2.0	**25**	—	51	—
16	**15**	Homopropargyl	1.0	**26**	—	58	—
17	**15**	*t*-BuOH	1.5	**27**	—	55	—
18	**3**	EtOH	48	—	—	—	—
19	**3**	MeOH	48	—	—	—	—

of adducts due to electron withdrawing substitution, the reactions with 5-nitro substituted adduct **3** in methanol and ethanol were tested (Table 3, entries 18 and 19). No *N*C-H activation was found even after allowing the reaction to proceed for a longer period of time (48 h) and with an excess of CAN (6 equiv.); only starting material was recovered quantitatively.

*N*C-H activation study of secondary methylene radical sources

To inspect and understand the *N*C-H activation reaction, which proceeded through a secondary radical intermediate, MBH adducts **28**–**35** were chosen (Fig. 4).

A general synthesis of MBH adducts **28–35** is shown in Scheme 1. Accordingly, *N*-alkylation of isatin was carried out with CaH_2 and alkyl halide in DMF at 60 °C to afford *N*-alkyl isatins in excellent yield. The MBH adducts formation of *N*-alkyl isatins with methyl acrylate and DABCO (1,4-diazabicyclo[2.2.2]octane) in methanol afforded the desired MBH adducts (**28–35**) in excellent yield.

Activation study of MBH adducts 28 and 29 of N-*ethyl isatin*

Activation reaction of adduct **28** with CAN/MeOH in CH_3CN for 24 h provided only the nitrated compound **36**

Fig. 4. Choice of different MBH adducts having a methylene *N*C-H source.

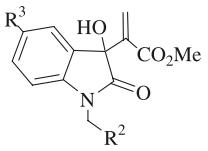

R^2 = CH_3; R^3 = H **28;** R^2 = CH_3; R^3 = Br **29;**
R^2 = CO_2Me; R^3 = H **30;** R^2 = CO_2Et; R^3 = H **31;**
R^2 = Ph; R^3 = H **32;** R^2 = Ph; R^3 = Br **33;**
R^2 = CCH; R^3 = H **34;** R^2 = CCH; R^3 = Br **35**

Scheme 1. Synthesis of MBH adducts 28–35.

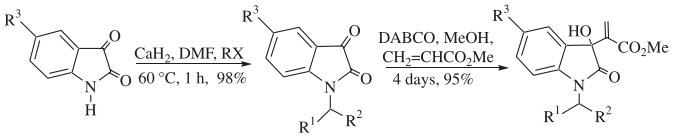

and no *N*C-H activated product was observed (Table 4, entry 1). Experiments with other alcohols such as ethanol, propargyl alcohol, and propane-1,3-diol provided only nitrated compound **36** and no *N*C-H activated product was observed in all the cases (Table 4, entries 2–4). The structure of nitrated compound **36** was analyzed by spectroscopic studies. The number of aromatic protons and chemical shifts were the tool for detection of nitration. Accordingly, in the aromatic region, a doublet at δ 6.97 due to ortho coupling (J = 8.6 Hz, 1H), meta coupled doublet at δ 8.04 (J =

Table 4. Results of the *N*C-H activation study of secondary methylene radical sources.

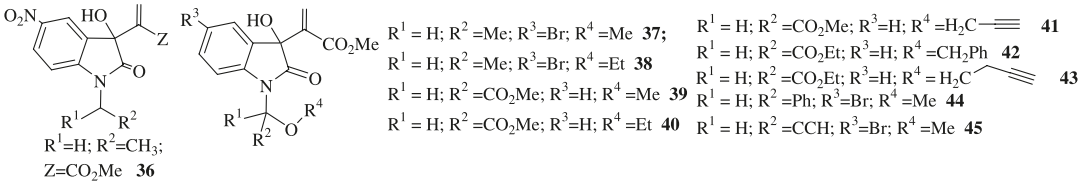

				Products		Yield (%)	
Entry	MBHA	Alcohol (R^4)	Time (h)	*N*C-H activation (A)	Nitration (B)	A	B
1	**28**	MeOH	24	—	**3**	—	56
2	**28**	EtOH	24	—	**36**	—	49
3	**28**	Propargyl alcohol	24	—	**36**	—	45
4	**28**	Propane-1,3-diol	24	—	**36**	—	55
5	**29**	MeOH	48	**37**	—	Trace	—
6	**29**	EtOH	48	**38**	—	Trace	—
7	**30**	MeOH	24	**39**	—	58	—
8	**30**	EtOH	24	**40**	—	49	—
9	**30**	Propargylol	24	**41**	—	55	—
10	**31**	Benzylol	24	**42**	—	47	—
11	**31**	Homopropargylol	24	**43**	—	54	—
12	**32**	MeOH	24	—	—	—	—
13	**32**	EtOH	24	—	—	—	—
14	**33**	MeOH	24	**44**	—	47	—
15	**34**	EtOH	24	—	—	—	—
16	**34**	MeOH	24	—	—	—	—
17	**35**	MeOH	2	**45**	—	85	—

2.3 Hz, 1H), and one doublet of doublet at δ 8.31 (J = 8.6, 2.3 Hz, 1H) due to ortho and meta couplings appeared. The alkyl and olefin region were similar to that of starting material **28**. To demonstrate and to check the effect of electron donating substitution at the aryl ring on *N*C-H activation, another adduct (**29**) was selected. Reactions in methanol and ethanol were carried out (Table 4, entries 5 and 6). To our surprise, we found only a trace of *N*C-H activated product formation (**37**, **38**) as evidenced from its ^{1}H NMR of crude reaction mixture at regular intervals for 48 h.

Activation study of MBH adduct of N-*methyl/ethyl acetate isatin 30 and 31*

Since, the compound **28** with electron releasing substitution at α to the *N*C-H bond did not yield any C-H activation products, we considered checking electron withdrawing substitution at α to the *N*C-H bond for *N*C-H activation of MBH adduct such as **30**. In contrast to the substrates **28** and **29**, activation of adduct **30** with CAN/methanol under optimized reaction condition provided a good yield of *N*C-H activated product **39** (Table 4, entry 7). The presence of -OMe group due to *N*C-H activation in the product **39** was confirmed from its ^{1}H NMR spectrum. Thus, the methoxy protons were observed at δ 3.63 as a singlet and the methine proton was observed as a singlet at δ 5.96. The reactions with ethanol and propargyl alcohol were also tested and the respective *N*C-H activated products (**40** and **41**) were isolated in moderate to good yields (Table 4, entries 8 and 9). Similarly, reactions of adduct **31** with benzyl alcohol and homopropargyl alcohol afforded the corresponding *N*C-H activated products **42** and **43**, respectively (Table 4, entries 10 and 11).

Activation study on MBH adduct of N-*benzyl and propargyl derivatives of isatin 32–35*

Having surprising results obtained from adducts **30** and **31**, we were interested in surveying the *N*C-H activation of highly functionalized MBH adducts **32–33** and **34–35** of *N*-benzyl and *N*-propargyl isatins, respectively. The desired adducts **32–33** and **34–35** were synthesized using standard procedure described earlier (Scheme 1).

The adduct **32** with CAN/methanol and CAN/ethanol under optimized reaction conditions yielded neither *N*C-H activated product nor nitrated derivative and the starting material was recovered quantitatively (Table 4, entries 12 and 13). However, the 5-bromo MBH adduct **33** afforded the desired *N*C-H activated product (**44**) in good yield (Table 4, entry 14). In the case of adduct (**34**), the reaction mixture became complex (TLC) with CAN/methanol and CAN/ethanol mixture and no *N*C-H activated and nitrated product was obtained (Table 4, entries 15 and 16), while the adduct **35** provided an excellent yield of *N*C-H activated product **45** in 2 h (Table 4, entry 17).

*N*C-H activation study of tertiary methine radical source *N*-isopropyl isatin (46)

For a comparative study on *N*-alkyl series of isatin derivatives, we chose the MBH adduct of *N*-isopropyl isatin (**46**) as substrate, which is believed to precede the *N*C-H activation via a tertiary radical intermediate (Fig. 5). Adduct **46** was prepared under standard procedure described earlier.

The *N*C-H activation of adduct **46** with CAN/MeOH, under optimized condition did not yield any *N*C-H activated product, instead only a moderate yield of nitrated product **47**

Fig. 5. Choice of MBH adducts having methine *N*C-H source.

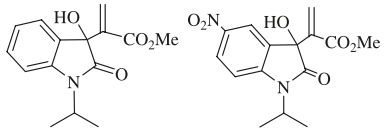

Scheme 2. A plausible mechanism for ether formation.

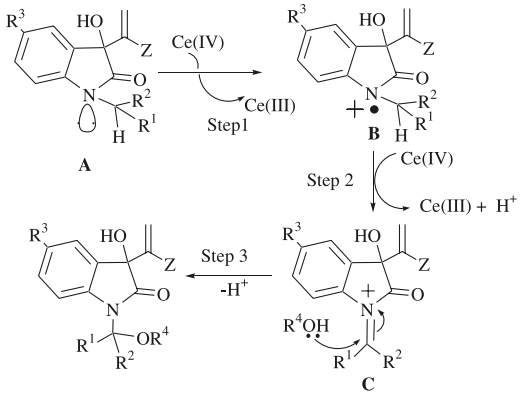

was obtained. Similarly, reactions with ethanol, propargyl alcohol, and propane-1,3-diol furnished only nitrated compound **47**. The results are collected in Tables 2 and 3. The structure of nitrated compound **47** was confirmed from its proton NMR data. Thus, the aromatic protons in **47** showed an ortho coupled doublet at δ 7.10 (J = 8.7 Hz, 1H), a meta coupled doublet at δ 8.03 (J = 2.3 Hz, 1H), and ortho-meta coupled doublet of doublet at δ 8.28 (J = 2.3, 8.7 Hz, 1H). The alkyl and olefin region were similar to that of starting material **46**.

A plausible mechanism of *N*-CH activation/nitration

A plausible mechanism for the formation of the ether products is delineated in Scheme 2. In the first step, the MBH adduct **A** is oxidized by CAN to form a radical cation[28–30] **B**. Further oxidation of radical cation **B** and liberation of H^+ by CAN produce a cation intermediate **C**, which is quenched by alcohol to afford the *N*C-H activated ether product. The proposed mechanism is supported from the results obtained in the studies. It should be noted that for comparison among MBH adducts **1**, **15**, and **3,** only adduct **15** underwent *N*C-H activation in 1.5–2.0 h whilst adduct **1** took 24 h for *N*C-H activation and adduct **3** did not provide any *N*C-H activation product with a clear indication of direct involvement of the nitrogen lone pair in the reaction mechanism.

The reactivity nature of MBH adducts **28**–**35** and **46** towards *N*C-H activation can be explained based on the effect of bulky substitution, which reduces the availability of lone pair on the nitrogen atom, which prevents the first step oxidation and less approach possibility by bulky reagent Ce(IV) towards nitrogen in adducts **28**, **32**, **34**, and **46**. The 5-bromo substitution, which increases the electron density on nitrogen, is clearly found from the reactivity of adducts **29** (trace of *N*C-H activation, 48 h), **33** (47% *N*C-H activation, 24 h), and **35** (85% *N*C-H activation, 2 h). However, quite the opposite occurs; the nitro substituent, having direct resonance

Fig. 6. Effect of substitution and magnitude of lone pair availability on nitrogen.

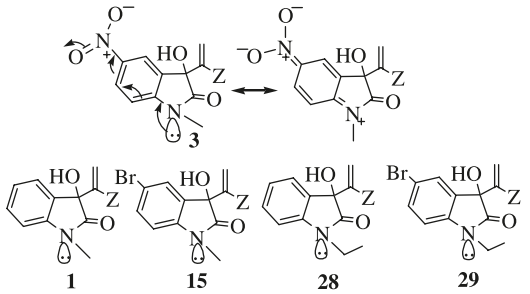

Fig. 7. Selectivity reason for *N*C-H activation towards MBH adducts alone.

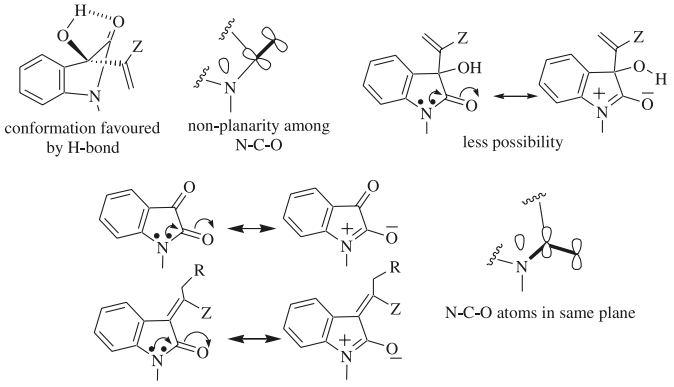

with nitrogen lone pair, averts the reactivity of the adduct **3**. A pictorial representation for substitution effect and magnitude of nitrogen lone pair is shown in Fig. 6. The nitration mechanism of the aromatic ring with CAN is well known in the literature.[31]

The selectivity reason for *N*C-H activation towards MBH adducts alone may be due to the conformation favoured by H-bonding in the adduct structure, which brings more availability of lone pair on nitrogen atom and avoids resonance with the adjacent carbonyl group. However, the highly planar structure in the compounds **6**–**9** allows the nitrogen lone pair to be in resonance with the adjacent carbonyl group. Hence, no *N*C-H activation happened with simple isatin derivatives (Fig. 7).

Conclusion

In conclusion, we have carried out a novel study on *N*C-H activation of various Morita–Baylis–Hillman adducts of *N*-substituted isatin with a number of alcohols using CAN as a single electron oxidizing agent. A plausible mechanism of the reaction is proposed. It is noteworthy that the compounds obtained here are highly functionalized and can be used for further synthetic manipulations. Further studies using the reagent system for novel synthetic methods are in progress in our laboratory.

Experimental

General consideration

Analytical thin layer chromatography was performed on silica gel TLC plates. Purification by gravity column chro-

matography was carried out using silica gel (100–200 mesh). Mixture of ethyl acetate and hexane and pure ethyl acetate were used as eluent as required. IR spectra were run on a Nicolet (impact 400D FT-IR) spectrophotometer. NMR spectra were obtained using chloroform-d as solvent on Bruker DPX 300 MHz NMR spectrometer. Chemical shifts are given in δ scale with TMS as the internal reference. HRMS were measured on the JMS 600 JEOL mass spectrometer. Yields refer to quantities obtained after chromatography. Solvents used are reagent grade and were purified before use according to the literature procedure.[32]

General experimental procedure for alkylation of isatin

A mixture of isatin (1 mmol), alkyl bromide/iodide (1.5 mmol), and calcium hydride (3 mmol) in DMF was stirred at 60 °C for 1 h. After completion of the reaction (monitored by TLC), the crude mixture was diluted with water, neutralized with 2 N HCl and extracted using ethyl acetate. The organic layer was separated, dried (Na_2SO_4), and concentrated in vacuo. The crude product obtained was purified by silica gel chromatography using EtOAc–hexane (20:80) as eluent to afford the desired *N*-alkylisatin derivatives.

General procedure for the preparation of MBH adducts

A mixture of *N*-alkyl isatin (1 mmol), methyl acrylate (1.5 mmol), and DABCO (0.02 mmol) in MeOH (5 mL) was stirred at RT for 3–4 d. After completion of the reaction (monitored by TLC), the reaction mixture was diluted with ethyl acetate. The organic layer was washed successively with 0.2 N HCl, water, and brine. The organic layer was separated, dried (Na_2SO_4), and concentrated in vacuo. The crude product obtained was purified by silica gel column chromatography using EtOAc–hexane (20:80) as eluent to afford the desired MBH adducts of *N*-alkyl isatin.

Spectral data of MBH adducts 28, 30, 34, and 46

Methyl 2-(1-ethyl-3-hydroxy-2-oxoindolin-3-yl)acrylate (28)

Colourless solid. Mp 148–150 °C. R_f = 0.48 (25% EtOAc–Hexanes). ν_{max} (CH_2Cl_2, cm^{-1}): 3341, 1723, 1615. ^1H NMR ($CDCl_3$) δ_H: 1.32 (3H, t, J = 7.2 Hz), 2.45 (1H, brs), 3.62 (3H, s), 3.74 (2H, q, J = 7.2 Hz), 6.41 (1H, s), 6.56 (1H, s), 6.88 (1H, d, J = 7.8 Hz), 7.05 (1H, t, J = 6.7 Hz), 7.19 (1H, d, J = 6.4 Hz), 7.32 (1H, t, J = 7.7 Hz). ^{13}C NMR ($CDCl_3$) δ_C: 12.4, 52.3, 64.5, 70.5, 110.4, 123.6, 124.1, 128.0, 129.1, 130.72, 139.2, 143.3, 165.3, 176.5. Anal. calcd. for $C_{14}H_{15}NO_4$: 261.1001; found: 261.1000.

Methyl 2-(1-methylene carbomethoxy-3-hydroxy-2-oxoindolin-3-yl)acrylate (30)

Colourless waxy solid. R_f = 0.29 (25% EtOAc–Hexanes). ν_{max} (CH_2Cl_2, cm^{-1}): 3350, 1716, 1615, 1087, 1063. ^1H NMR ($CDCl_3$) δ_H: 3.64 (3H, s), 3.78 (3H, s), 4.41 (1H, brs), 4. 41 (1H, d, J = 17.6 Hz), 4.61 (1H, d, J = 17.6 Hz), 6.44 (1H, s), 6.59 (1H, s), 6.74 (1H, d, J = 7.8 Hz), 7.06 (1H, t, J = 7.4 Hz), 7.06–7.34 (2H, m). ^{13}C NMR ($CDCl_3$) δ_C: 41.4, 52.1, 52.7, 76.0, 108.6, 123.4, 124.1, 128.3, 129.4, 130.3, 138.5, 142.9, 165.2, 168.2, 176.0. Anal calcd. for $C_{15}H_{15}NO_6$: 305.0899; found: 305.0896.

Methyl 2-(3-hydroxy-2-oxo-1-(prop-2-ynyl) indolin-3-yl)acrylate (34)

Colourless waxy solid. R_f = 0.34 (25% EtOAc–Hexanes). ν_{max}(CH_2Cl_2, cm^{-1}): 3425, 2131, 1718, 1611. ^1H NMR ($CDCl_3$) δ_H: 2.28 (1H, t, J = 2.2 Hz), 3.59 (3H, s), 4.07 (1H, s), 4.51–4.58 (2H, m), 6.44 (1H, s), 6.57 (1H, s), 7.04–7.09 (2H, m), 7.18 (1H, d, J = 6.48 Hz), 7.35 (1H, t, J = 7.6 Hz). ^{13}C NMR ($CDCl_3$) δ_C: 29.5, 52.1, 72.6, 76.1, 76.6, 109.6, 123.3, 123.9, 128.1, 129.2, 130.2, 138.9, 142.5, 164.9, 175.4. Anal. calcd. for $C_{15}H_{13}NO_4$: 271.0845; found: 271.0841.

Methyl 2-(3-hydroxy-1-isopropyl-2-oxoindolin-3-yl)acrylate (46)

Colourless waxy solid. R_f = 0.42 (25% EtOAc–Hexanes). ν_{max} (CH_2Cl_2, cm^{-1}): 3353, 1699, 1611. ^1H NMR ($CDCl_3$) δ_H: 1.52 (6H, d, J = 8.15 Hz), 3.55 (1H, br s), 3.61 (3H, s), 4.58 (1H, sept, J = 7.0 Hz), 6.42 (1H, s), 6.56 (1H, s), 7.02 (2H, d, J = 7.7 Hz), 7.17 (1H, d, J = 6.6 Hz), 7.30 (1H, t, J = 6.8 Hz). ^{13}C NMR ($CDCl_3$) δ_C: 19.1 (2C), 43.3, 51.8, 75.8, 109.7, 122.3, 124.0, 127.6, 129.8 (2C), 139.3, 143.1, 164.8, 176.1. Anal. calcd. for $C_{15}H_{17}NO_4$: 275.1158; found: 275.1152.

General experimental procedure for *N*C-H activation

A mixture of MBH adduct (1 mmol), 4 equiv. of cerium ammonium nitrate (4 mmol), and 40 equiv. of ROH (1.6 mL) in CH_3CN (0.5 mL) was allowed to stir at RT for 2–48 h. The progress of reaction was monitored by TLC. After completion of the reaction, the solvent was removed under reduced pressure. The crude reaction mixture was extracted with dichloromethane and washed with water and brine. The organic layer was separated, dried (Na_2SO_4), and concentrated in vacuo. The crude mixture was purified by silica gel column chromatography using gradient elution with hexane and hexane and EtOAc to afford pure functionalized ethers and aromatic nitrated products.

Spectral data for *N*C-H activated compounds

Methyl 2-(3-hydroxy-1-(methoxy methyl)-2-oxoindolin-3-yl)acrylate (2)

Waxy solid. R_f = 0.35 (20% EtOAc–Hexanes). ν_{max} (CH_2Cl_2, cm^{-1}): 3386, 1716, 1085, 1063. ^1H NMR ($CDCl_3$) δ_H: 2.57 (1H, bs), 3.41 (3H, s), 3.65 (3H, s), 5.13 (1H, d, J = 11.1 Hz), 5.17 (1H, d, J = 11.1 Hz), 6.42 (1H, s), 6.59 (1H, s), 7.06–7.10 (2H, m), 7.20 (1H, d, J = 7.5 Hz), 7.32 (1H, t, J = 7.5 Hz). ^{13}C NMR ($CDCl_3$) δ_C: 52.5, 53.2, 70.5, 76.6, 110.4, 123.7, 124.1, 127.8, 129.1, 130.6, 139.5, 143.3, 164.8, 176.9. Anal. calcd. for $C_{14}H_{15}NO_5$: 277.0950; found: 277.0947.

2-(3-Hydroxy-1-(methoxymethyl)-2-oxoindolin-3-yl)acrylonitrile (10)

Waxy solid. R_f = 0.44 (20% EtOAc–Hexanes). ν_{max} (CH_2Cl_2, cm^{-1}): 3376, 2209, 1726, 1614, 1087. ^1H NMR ($CDCl_3$) δ_H: 3.36 (3H, s), 4.07 (1H, s), 5.10 (1H, d, J = 10.9 Hz), 5.19 (1H, d, J = 10.9 Hz), 6.21 (1H, s), 6.39 (1H, s), 7.12 (1H, d, J = 7.7 Hz), 7.17 (1H, t, J = 8.1 Hz), 7.41 (2H, d, J = 7.5 Hz). ^{13}C NMR ($CDCl_3$) δ_C: 52.1, 70.7, 76.7, 110.8,

115.5, 123.2, 123.9, 124.8, 126.8, 128.1, 131.5, 142.5, 176.3. Anal. calcd. for $C_{13}H_{12}N_2O_3$: 244.0848; found: 244.0836.

Methyl 2-(1-(ethoxymethyl)-3-hydroxy-2-oxoindolin-3-yl)acrylate (16)

Waxy solid. R_f = 0.43 (20% EtOAc–Hexanes). ν_{max} (CH_2Cl_2, cm^{-1}): 3382, 1716, 1089, 1053. ^1H NMR ($CDCl_3$) δ_H: 1.20 (3H, t, J = 6.9 Hz), 2.67 (1H, bs), 3.65 (5H, m), 5.17 (1H, d, J = 11.1 Hz), 5.22 (1H, d, J = 11.1 Hz), 6.43 (1H, s), 6.58 (1H, s), 7.05–7.13 (2H, m), 7.20 (1H, d, J = 7.2 Hz), 7.35 (1H, t, J = 7.2 Hz). ^{13}C NMR ($CDCl_3$) δ_C: 15.1, 52.3, 64.6, 70.5, 76.6, 110.4, 123.6, 124.1, 128.0, 128.9, 130.6, 139.2, 143.2, 165.2, 176.9. Anal. calcd. for $C_{15}H_{17}NO_5$: 291.1107; found: 291.1088.

Methyl 2-(3-hydroxy-2-oxo-1-((prop-2-ynyloxy)methyl) indolin-3-yl)acrylate (17)

Waxy solid. R_f = 0.37 (20% EtOAc–Hexanes). ν_{max} (CH_2Cl_2, cm^{-1}): 3390, 2210, 1716, 1615, 1087, 1064. ^1H NMR ($CDCl_3$) δ_H: 2.48 (1H, t, J = 2.4 Hz), 2.67 (1H, bs), 3.63 (3H, s), 4.28 (2H, d, J = 2.4 Hz), 5.20 (1H, d, J = 11.2 Hz), 5.37 (1H, d, J = 11.2 Hz), 6.48 (1H, s), 6.59 (1H, s), 7.05–7.20 (3H, m), 7.35 (1H, t, J = 7.6 Hz). ^{13}C NMR ($CDCl_3$) δ_C: 30.5, 52.3, 56.3, 70.3, 75.5, 78.6, 110.7, 123.6, 124.2, 128.1, 129.1, 130.5, 139.3, 143.2, 165.3, 176.9. Anal. calcd. for $C_{16}H_{15}NO_5$: 301.0950; found: 301.0941.

Methyl 2-(1-[(but-3-ynyloxy)methyl]-3-hydroxy-2-oxoindolin-3-yl)acrylate (18)

Waxy solid. R_f = 0.47 (20% EtOAc–Hexanes). ν_{max} (CH_2Cl_2, cm^{-1}): 3406, 1716, 1614, 1089, 1050. ^1H NMR ($CDCl_3$) δ_H: 1.80 (1H, bs), 1.95 (1H, t, J = 2.4 Hz), 2.46 (2H, td, J = 6.6, 2.4 Hz), 3.63 (3H, s), 3.66 (2H, t, J = 6.6 Hz), 5.20 (1H, d, J = 11.1 Hz), 5.28 (1H, d, J = 11.1 Hz), 6.46 (1H, s), 6.59 (1H, s), 7.05–7.20 (3H, m), 7.35 (1H, t, J = 7.8 Hz). ^{13}C NMR ($CDCl_3$) δ_C: 19.8, 30.4, 52.3, 66.9, 69.5, 70.6, 81.3, 110.5, 123.7, 124.1, 126.2, 127.9, 130.7, 139.2, 143.1, 165.2, 176.9. Anal. calcd. for $C_{17}H_{17}NO_5$:315.1107; found: 315.1101.

Methyl 2-(1-((2-hydroxyethoxy)methyl)-3-hydroxy-2-oxoindolin-3-yl)acrylate (19)

Waxy solid. R_f = 0.23 (20% EtOAc–Hexanes). ν_{max} (CH_2Cl_2, cm^{-1}): 3416, 1716, 1614, 1085, 1065. ^1H NMR ($CDCl_3$) δ_H: 2.67 (2H, bs), 3.62 (3H, s), 3.69–3.75 (4H, m), 5.21 (1H, d, J = 11.1 Hz), 5.28 (1H, d, J = 11.1 Hz), 6.50 (1H, s), 6.60 (1H, s), 7.05–7.26 (3H, m), 7.34 (1H, t, J = 6.6 Hz). ^{13}C NMR ($CDCl_3$) δ_C: 52.4, 59.7, 66.1, 70.5, 76.3, 110.1, 123.5, 123.9, 128.3, 129.4, 130.6, 139.0, 143.2, 165.3, 175.6. Anal. calcd. for $C_{15}H_{17}NO_6$: 307.1056; found: 307.1047.

Methyl 2-(1-[(3-hydroxypropoxy)methyl]-3-hydroxy-2-oxoindolin-3-yl)acrylate (20)

Waxy solid. R_f = 0.28 (20% EtOAc-Hexanes). ν_{max} (CH_2Cl_2, cm^{-1}): 3418, 1716, 1613, 1086, 1055. ^1H NMR ($CDCl_3$) δ_H: 1.73 (2H, quintet, J = 7.2 Hz), 3.11 (2H, bs), 3.48–3.80 (7H, m), 5.14 (1H, d, J = 11.4 Hz), 5.21 (1H, d, J = 11.4 Hz), 6.55 (1H, s), 6.60 (1H, s), 7.03–7.16 (3H, m),7.33 (1H, t, J = 7.5 Hz). ^{13}C NMR ($CDCl_3$) δ_C: 32.6, 52.4, 59.8, 66.2, 70.5, 76.3, 110.1, 123.6, 123.9, 128.4, 129.4, 130.5, 139.0, 143.1, 165.4, 177.2. Anal. calcd. for $C_{16}H_{19}NO_6$: 321.1212; found: 321.1205.

Methyl 2-(1-((benzyloxy)methyl)-3-hydroxy-2-oxoindolin-3-yl)acrylate (21)

Waxy solid. R_f = 0.29 (20% EtOAc–Hexanes). ν_{max} (CH_2Cl_2, cm^{-1}): 3314, 1716, 1617, 1083, 1055. ^1H NMR ($CDCl_3$) δ_H: 2.67 (1H, bs), 3.62 (3H, s), 4.36 (1H, d, J = 11.6 Hz), 4.72 (1H, d, J = 11.6 Hz), 5.24 (1H, d, J = 11.1 Hz), 5.32 (1H, d, J = 11.1 Hz), 6.47 (1H, s), 6.59 (1H, s), 7.08–7.35 (9H, m). ^{13}C NMR ($CDCl_3$) δ_C: 52.1, 70.1, 70.7, 76.4, 110.3, 123.5, 123.8, 127.8 (2C), 128.2(2C), 128.3 (2C), 128.7, 130.5, 137.5, 138.9, 143.0, 165.0, 176.6. Anal. calcd. for $C_{20}H_{19}NO_5$: 353.1263; found: 353.1254.

2-(1-(Ethoxymethyl)-3-hydroxy-2-oxoindolin-3-yl) acrylonitrile (22)

Waxy solid. R_f = 0.34 (20% EtOAc–Hexanes). ν_{max} (CH_2Cl_2, cm^{-1}): 3378, 2917, 2185, 1732, 1613, 1487, 1097. ^1H NMR ($CDCl_3$) δ_H: 1.19 (3H, t, J = 7.2 Hz), 1.90 (1H, bs), 3.57 (2H, q, J = 7.2 Hz), 5.15 (1H, d, J = 11.1 Hz), 5.25 (1H, d, J = 11.1 Hz), 6.21 (1H, s), 6.36 (1H, s), 7.14–7.22 (2H, m), 7.40–7.45 (2H, m). ^{13}C NMR ($CDCl_3$) δ_C: 15.0, 64.8, 70.7, 76.8, 111.1, 115. 6, 123.3, 124.6, 124.9, 126.5, 128.6, 131.6, 142.0, 175.5. Anal. calcd. for $C_{14}H_{14}N_2O_3$: 258.1004; found: 258.0992.

2-(3-Hydroxy-2-oxo-1-[(prop-2-yloxy)methyl] indolin-3-yl)acrylonitrile (23)

Waxy solid. R_f 0.42 = (20% EtOAc–Hexanes). ν_{max} (CH_2Cl_2, cm^{-1}): 3390, 2305, 1733, 1614, 1073. ^1H NMR ($CDCl_3$) δ_H: 1.80 (1H, bs), 2.48 (1H, t, J = 2.4 Hz), 4.21 (2H, d, J = 2.4 Hz), 5.24 (1H, d, J = 11.1 Hz), 5.36 (1H, d, J = 11.1 Hz), 6.21 (1H, s), 6.37 (1H, s), 7.10–7.29 (2H, m), 7.42 (2H, d, J = 7.5 Hz). ^{13}C NMR ($CDCl_3$) δ_C: 30.6, 56.4, 69.5, 75.8, 78.7, 110.9, 115.7, 123.1, 125.0, 126.9, 128.8, 131.6, 132.6, 141.9, 174.9. Anal. calcd. for $C_{15}H_{12}N_2O_3$: 268.0848; found: 268.0840.

Methyl 2-(5-bromo-3-hydroxy-1-(methoxymethyl)-2-oxoindolin-3-yl)acrylate (24)

Waxy solid. R_f = 0.47 (20% EtOAc–Hexanes). ν_{max} (CH_2Cl_2, cm^{-1}): 3376, 1710, 1079, 1060. ^1H NMR ($CDCl_3$) δ_H: 3.40 (3H, s), 3.58 (1H, s), 3.65 (3H, s), 5.09 (1H, d, J = 11.0 Hz), 5.16 (1H, d, J = 11.0 Hz), 6.47 (1H, s), 6.62 (1H, s), 6.97 (1H, d, J = 8.3 Hz), 7.30 (1H, d, J = 1.8 Hz), 7.46 (1H, dd, J = 8.3, 1.8 Hz). ^{13}C NMR ($CDCl_3$) δ_C: 52.5, 53.1, 70.6, 76.7, 111.8, 116.1, 126.8, 128.3, 130.8, 133.2, 138.6, 142.1, 164.7, 174.4. Anal. calcd. for $C_{14}H_{14}BrNO_5$: 355.0055; found: 355.0051.

Methyl 2-(5-bromo-1-(ethoxymethyl)-3-hydroxy-2-oxoindolin-3-yl)acrylate (25)

Waxy solid. R_f = 0.45 (20% EtOAc–Hexanes). ν_{max} (CH_2Cl_2, cm^{-1}): 3379, 1715, 1084, 1062. ^1H NMR ($CDCl_3$) δ_H: 1.19 (3H, t, J = 7.8 Hz), 1.89 (1H, bs), 3.45–3.63 (5H, m), 5.13 (1H, d, J = 11.1 Hz), 5.19 (1H, d, J = 11.1 Hz), 6.47 (1H, s), 6.60 (1H, s), 7.00 (1H, d, J = 8.3 Hz), 7.28 (1H, d, J = 1.9 Hz), 7.46 (1H, dd, J = 8.3, 1.9 Hz). ^{13}C NMR ($CDCl_3$) δ_C: 14.8, 52.1, 64.4, 70.4, 76.2, 111.8, 116.0, 127.1, 128.3, 130.8, 133.2, 138.6, 142.1, 164.7, 174.3. Anal. calcd. for $C_{15}H_{16}BrNO_5$: 369.0212; found: 369.0201.

Methyl 2-(5-bromo-1-((but-3-ynyloxy)methyl)-3-hydroxy-2-oxoindolin-3-yl)acrylate (26)

Waxy solid. R_f = 0.39 (20% EtOAc–Hexanes). ν_{max} (CH_2Cl_2, cm^{-1}): 3390, 2210, 1716, 1085, 1063. ^1H NMR ($CDCl_3$) δ_H: 1.94 (1H, t, J = 2.4 Hz), 2.46 (2H, td, J = 6.7, 2.4 Hz), 3.61–3.76 (5H, m), 5.18 (1H, d, J = 11.2 Hz), 5.18 (1H, d, J = 11.2 Hz), 5.25 (1H, d, J = 11.2 Hz), 6.48 (1H, s), 6.62 (1H, s), 7.01 (1H, d, J = 8.3 Hz), 7.29 (1H, d, J = 1.7 Hz), 7.46 (1H, dd, J = 8.3, 1.7 Hz). ^{13}C NMR ($CDCl_3$) δ_C: 19.3, 30.4, 52.5, 67.3, 69.5, 70.5, 81.1, 110.9, 116.2, 127.1, 128.3, 130.7, 133.2, 138.5, 143.0, 164.8, 176.3. Anal. calcd. for $C_{17}H_{16}BrNO_5$: 393.0212; found: 393.0203.

Methyl 2-(1-(t-butoxymethyl)-5-bromo-3-hydroxy-2-oxoindolin-3-yl)acrylate (27)

Waxy solid. R_f = 0.47 (20% EtOAc–Hexanes). ν_{max} (CH_2Cl_2, cm^{-1}): 3376, 1710, 1079, 1060. ^1H NMR ($CDCl_3$) δ_H: 1.23 (9H, s), 3.58 (1H s), 3.65 (3H, s), 5.07 (1H, d, J = 10.8 Hz), 5.30 (1H, d, J = 10.8 Hz), 6.38 (1H, s), 6.58 (1H, s), 7.02 (1H, d, J = 8.3 Hz), 7.29 (1H, d, J = 1.9 Hz), 7.46 (1H, dd, J = 8.3, 1.9 Hz). ^{13}C NMR ($CDCl_3$) δ_C: 28.4, 29.7, 65.3, 75.1, 76.3, 109.8, 114.3, 117.1, 121.5, 127.1, 128.3, 133.1, 138.4, 159.0, 164.9. Anal. calcd. for $C_{17}H_{20}BrNO_5$: 397.0525; found: 397.0523.

Methyl 2-(3-hydroxy-1-(methyl 2-methoxyacetate)-2-oxoindolin-3-yl)acrylate (39)

Waxy solid. R_f = 0.44 (20% EtOAc–Hexanes). ν_{max} (CH_2Cl_2, cm^{-1}): 3420, 1718, 1606, 1051. ^1H NMR ($CDCl_3$) δ_H: 1.90 (1H, bs), 3.59 (3H, s), 3.63 (3H, s), 3.79 (3H, s), 5.96 (1H, s), 6.55 (1H, s), 6.63 (1H, s), 7.04–7.10 (2H, m), 7.17–7.32 (2H, m). ^{13}C NMR ($CDCl_3$) δ_C: 46.9, 52.1, 56.9, 76.0, 79.7, 111.4, 123.6, 123.8, 128.1, 128.7, 130.5, 138.6, 140.8, 164.7, 166.9, 176.3. Anal. calcd. for $C_{16}H_{17}NO_7$: 335.1005; found: 335.1001.

Methyl 2-(3-hydroxy-1-(methyl 2-ethoxyacetate)-2-oxoindolin-3-yl)acrylate (40)

Waxy solid. R_f = 0.42 (20% EtOAc–Hexanes). ν_{max} (CH_2Cl_2, cm^{-1}): 3421, 1727, 1615, 1056. ^1H NMR ($CDCl_3$) δ_H: 1.28 (3H, t, J = 7.2 Hz), 3.97 (1H, bs), 3.65 (3H, s), 3.79 (3H, s), 4.25 (2H, q, J = 7.2 Hz), 6.02 (1H, s), 6.44(1H, s), 6.59 (1H, s), 7.06–7.31 (4H, m). ^{13}C NMR ($CDCl_3$) δ_C: 14.8, 52.1, 53.7, 62.4, 76.0, 79.7, 110.6, 123.6, 123.8, 127.8, 128.7, 130.4, 137.9, 141.5, 165.5, 166.9, 176.2. Anal. calcd. for $C_{17}H_{19}NO_7$: 349.1162; found: 349.1155.

Methyl 2-(3-hydroxy-1-(methyl 2-(prop-2-ynyloxy)acetate)-2-oxoindolin-3-yl)acrylate (41)

Waxy solid. R_f = 0.48 (20% EtOAc–Hexanes). ν_{max} (CH_2Cl_2, cm^{-1}): 3294, 2120, 1712, 1610, 1051. ^1H NMR ($CDCl_3$) δ_H: 2.54 (1H, t, J = 2.4 Hz), 3.57 (1H, bs), 3.63 (3H, s), 3.81 (3H, s), 4.46 (2H, d, J = 2.4 Hz), 6.24 (1H, s), 6.57 (1H, s), 6.62 (1H, s), 7.07–7.13 (2H, m), 7.19–7.34 (2H, m). ^{13}C NMR ($CDCl_3$) δ_C: 22.3, 41.5, 52.2, 55.9, 62.7, 75.9, 77.9, 109.3, 111.5, 123.7, 124.1, 128.1, 130.3, 138.7, 140.8, 165.9, 176.1, 176.5. Anal. calcd. for $C_{18}H_{17}NO_7$: 359.1005; found: 359.0996.

Methyl 2-(3-hydroxy-1-(methyl 2-(benzyloxy)acetate)-2-oxoindolin-3-yl)acrylate (42)

Waxy solid. R_f = 0.43 (20% EtOAc–Hexanes). ν_{max} (CH_2Cl_2, cm^{-1}): 3396, 1717, 1084, 1065. ^1H NMR ($CDCl_3$) δ_H: 1.19 (3H, t, J = 7.17 Hz), 3.51 (1H, s), 3.64 (3H, s), 4.24 (2H, q, J = 7.17 Hz), 4.72 (1H, d, J = 11.8 Hz), 4.91 (1H, d, J = 11.8 Hz), 6.03 (1H, s), 6.44 (1H, s), 6.64 (1H, s), 7.01 (1H, t, J = 7.5 Hz), 7.18 (2H, t, J = 7.6 Hz), 7.27–7.39 (6H, m). ^{13}C NMR ($CDCl_3$) δ_C: 14.4, 52.6, 62.9, 70.7, 76.5, 112.3, 114.6, 124.4, 128.7 (2C), 128.8 (2C), 129.3 (2C), 130.7 (2C), 136.7, 141.5, 165.6, 167.2, 177.8. Anal. calcd. for $C_{21}H_{20}NO_5$: 366.1341; found: 366.1326.

Methyl 2-(3-hydroxy-1-(methyl 2-(but-3-ynyloxy)acetate)-2-oxoindolin-3-yl)acrylate (43)

Waxy solid. R_f = 0.46 (20% EtOAc–Hexanes). ν_{max} (CH_2Cl_2, cm^{-1}): 3388, 2210, 1718, 1615, 1087, 1064. ^1H NMR ($CDCl_3$) δ_H: 1.24 (3H, t, J = 7.20 Hz), 1.90 (1H, t, J = 2.5 Hz), 3.56 (1H, s), 3.63 (3H, s), 4.13–4.28 (4H, m), 6.01 (1H, s), 6.54 (1H, s), 6.62 (1H, s), 7.06–7.29 (4H, m). ^{13}C NMR ($CDCl_3$) δ_C: 13.9, 19.3, 31.6, 62.5, 66.9, 69.7, 76.0, 78.2, 80.2, 111.7, 123.6, 124.0, 128.1, 128.8, 130.3, 138.4, 140.9, 164.7, 165.9, 176.2. Anal. calcd. for $C_{18}H_{18}NO_5$: 328.1185; found: 328.1183.

Methyl 2-(5-bromo-3-hydroxy-1-(methoxy(phenyl) methyl)-2-oxoindolin-3-yl)acrylate (44)

Waxy solid. R_f = 0.39 (20% EtOAc–Hexanes). ν_{max} (CH_2Cl_2, cm^{-1}): 3382, 1717, 1085, 1057. ^1H NMR ($CDCl_3$) δ_H: 2.15 (1H, s), 3.45 (3H, s), 3.66 (3H, s), 6.48 (1H, s), 6.53 (1H, s), 6.58 (1H, s), 7.19–7.45 (8H, m). ^{13}C NMR ($CDCl_3$) δ_C: 52.1, 53.4, 65.4, 76.4, 110.3, 123.5, 124.3, 127.8 (2C), 128.1 (2C), 128.2 (2C), 128.7, 131.3, 137.4, 139.0, 143.0, 164.5, 175.5. Anal. calcd. for $C_{20}H_{18}BrNO_5$: 431.0368; found: 431.0357.

Methyl 2-(5-bromo-3-hydroxy-1-(1-methoxyprop-2-ynyl)-2-oxoindolin-3-yl)acrylate (45)

Waxy solid. R_f = 0.48 (20% EtOAc–Hexanes). ν_{max} (CH_2Cl_2, cm^{-1}): 3396, 2212, 1714, 1089, 1055. ^1H NMR ($CDCl_3$) δ_H: 2.61 (1H, d, J = 2.1 Hz), 3.48 (3H, s), 3.61 (3H, s), 3.79 (1H, s), 6.12 (1H, d, J = 2.1 Hz), 6.38 (1H, s), 6.43(1H, s), 7.27 (1H, d, J = 8.3 Hz), 7.32 (1H, d, J = 1.9 Hz), 7.46 (1H, dd, J = 8.3, 1.9 Hz). ^{13}C NMR ($CDCl_3$) δ_C: 52.3, 55.9, 56.4, 72.3, 75.1, 75.8, 114.1, 116.4, 126.9, 128.6, 130.9, 132.9, 138.3, 139.5, 164.5, 175.3. Anal. calcd. for $C_{16}H_{14}BrNO_5$: 379.0055; found: 379.0043.

Spectral data for nitrated derivatives

Methyl 2-(1-ethyl-3-hydroxy-5-nitro-2-oxoindolin-3-yl)acrylate (36)

Waxy solid. R_f = 0.48 (25% EtOAc–Hexanes). ν_{max} (CH_2Cl_2, cm^{-1}): 3348, 1706, 1611. ^1H NMR ($CDCl_3$) δ_H: 1.32 (3H, t, J = 7.23 Hz), 2.2 (1H, bs), 3.62 (3H, s), 3.77–3.9 (2H, m), 6.58 (1H, s), 6.67 (1H, s), 6.97 (1H, d, J = 8.6 Hz), 8.04 (1H, d, J = 2.3 Hz), 8.31 (1H, dd, J = 2.3 Hz, J = 8.6 Hz). ^{13}C NMR ($CDCl_3$) δ_C: 12.1, 43.6, 52.3, 76.1, 109.6, 120.32, 122.3, 123.1, 128.7, 129.9, 144.4, 144.7, 164.8, 176.1. Anal. calcd. for $C_{14}H_{14}N_2O_6$: 306.0852; found: 306.0841.

Methyl 2-(3-hydroxy-1-isopropyl-5-nitro-2-oxoindolin-3-yl)acrylate (47)

Waxy solid. R_f = 0.49 (25% EtOAc–Hexanes). ν_{max} (CH_2Cl_2, cm^{-1}): 3351, 1709, 1612. ^1H NMR ($CDCl_3$) δ_H:

1.55 (6H, d, J = 8.1 Hz), 3.47 (1H, s), 3.63 (3H, s), 4.58–4.63 (1H, m), 6.56 (1H, s), 6.67 (1H, s), 7.1 (1H, d, J = 8.7 Hz), 8.03 (1H, d, J = 2.3 Hz), 8.28 (1H, dd, J = 2.3, J = 8.7 Hz). ^{13}C NMR ($CDCl_3$) δ_C: 19.1 (2C), 43.3, 51.8, 75.8, 109.7, 122.3, 124.0, 127.6, 129.8 (2C), 140.4, 143.2, 164.8, 176.1. Anal. calcd. for $C_{15}H_{16}N_2O_6$: 320.1008; found: 320.1008.

Acknowledgements

The authors thank Professor T. K. Chandrashekar, Director, for providing infrastructure facilities. Financial support (SR/S1/OC-38/2005) from the Department of Science Technology (DST, New Delhi) is gratefully acknowledged. V.V. thanks the Council of Scientific and Industrial Research (CSIR, New Delhi) for the award of Senior Research Fellowship (SRF). Thanks are due to Mrs. Viji and Mrs. Soumini Mathew for providing HRMS and NMR data, respectively.

References

(1) Shilov, A. E.; Shul'pin, G. B. *Chem. Rev.* **1997**, *97*, 2879. doi:10.1021/cr9411886. PMID:11851481.
(2) Sen, A. *Acc. Chem. Res.* **1998**, *31*, 550. doi:10.1021/ar970290x.
(3) Barluenga, J.; Bobes, F. G.; Gonzales, J. M. *Angew. Chem.* **2002**, *114*, 2668. doi:10.1002/1521-3757(20020715)114:14<2668::AID-ANGE2668>3.0.CO;2-V.
(4) Sakaguchi, S.; Nishiwaki, Y.; Kitamura, T.; Ishii, Y. *Angew. Chem.* **2001**, *113*, 228. doi:10.1002/1521-3757(20010105)113:1<228::AID-ANGE228>3.0.CO;2-R.
(5) (a) Lee, S.; Fuchs, P. L. *Org. Lett.* **2004**, *6*, 1437 doi:10.1021/ol049712a. PMID:15101761.; (b) Yu, X. Q.; Huang, J. S.; Zhou, X. G.; Che, C. M. *Org. Lett.* **2000**, *2*, 2233. doi:10.1021/ol000107r. PMID:10930251.
(6) Crabtree, R. H. *J. Organomet. Chem.* **2004**, *689*, 4083. doi:10.1016/j.jorganchem.2004.07.034.
(7) Periana, R. A.; Bhalla, G.; Tenn, W. J., III; Young, K. J. H.; Liu, X. Y.; Mironov, O.; Jones, C. J.; Ziatdinov, V. R. *J. Mol. Catal. Chem. (Kyoto)* **2004**, *220*, 7. doi:10.1016/j.molcata.2004.05.036.
(8) Erker, G. *Coord. Chem. Rev.* **2006**, *250*, 1056. doi:10.1016/j.ccr.2005.10.008.
(9) Ahrens, S.; Strassner, T. *Inorg. Chim. Acta* **2006**, *359*, 4789. doi:10.1016/j.ica.2006.05.042.
(10) Sydora, O. L.; Goldsmith, J. I.; Vaid, T. P.; Millar, A. E.; Wolczanski, P. T.; Abruna, H. D. *Polyhedron* **2004**, *23*, 2841. doi:10.1016/j.poly.2004.08.006.
(11) Corkey, B. K.; Taw, F. L.; Bergman, R. G.; Brookhart, M. *Polyhedron* **2004**, *23*, 2943. doi:10.1016/j.poly.2004.09.005.
(12) Volpe, E. C.; Chadeayne, A. R.; Wolczanski, P. T.; Lobkovsky, E. B. J. *Organomet. Chem.* **2007**, *692*, 4774. doi:10.1016/j.jorganchem.2007.06.047.
(13) Nair, V.; Deepthi, A. *Chem. Rev.* **2007**, *107*, 1862. doi:10.1021/cr068408n. PMID:17432919.
(14) Nair, V.; Balagopal, L.; Rajan, R.; Mathew, J. *Acc. Chem. Res.* **2004**, *37*, 21; and refs. cited therein. doi:10.1021/ar030002z. PMID:14730991.
(15) da Silva, J. F. M.; Garden, S. J.; Pinto, A. C. *J. Braz. Chem. Soc.* **2001**, *12*, 273.
(16) Basavaiah, D.; Rao, A. J.; Satyanarayana, T. *Chem. Rev.* **2003**, *103*, 811. doi:10.1021/cr010043d. PMID:12630854.
(17) Drewes, S. E.; Roos, G. H. P. *Tetrahedron* **1988**, *44*, 4653. doi:10.1016/S0040-4020(01)86168-8.
(18) Lee, K. Y.; Gowrisankar, S.; Kim, J. N. *Bull. Korean Chem. Soc.* **2005**, *26*, 1481.
(19) Basavaiah, D.; Rao, K. P.; Reddy, R. J. *Chem. Soc. Rev.* **2007**, *36*, 1581. doi:10.1039/b613741p. PMID:17721583.
(20) Shanmugam, P.; Vaithiyanathan, V.; Viswambharan, B. *Tetrahedron* **2006**, *62*, 4342. doi:10.1016/j.tet.2006.02.072.
(21) Shanmugam, P.; Vaithiyanathan, V.; Viswambharan, B. *Aust. J. Chem.* **2007**, *60*, 296. doi:10.1071/CH07020.
(22) Shanmugam, P.; Vaithiyanathan, V.; Viswambharan, B.; Madhavan, S. *Tetrahedron Lett.* **2007**, *48*, 9190. doi:10.1016/j.tetlet.2007.10.103.
(23) Shanmugam, P.; Viswambharan, B.; Vaithiyanathan, V. *Aust. J. Chem.* **2007**, *60*, 850. doi:10.1071/CH07123.
(24) Shanmugam, P.; Viswambharan, B.; Madhavan, S. *Org. Lett.* **2007**, *9*, 4095. doi:10.1021/ol701533d. PMID:17877359.
(25) Shanmugam, P.; Vaithiyanathan, V. *Tetrahedron* **2008**, *64*, 3322. doi:10.1016/j.tet.2008.02.002.
(26) Shanmugam, P.; Vaithiyanathan, V.; Selvakumar, K. *Tetrahedron Lett.* **2008**, *49*, 2119. doi:10.1016/j.tetlet.2008.01.119.
(27) Shanmugam, P.; Vaithiyanathan, V.; Viswambharan, B. *Tetrahedron Lett.* **2006**, *47*, 6851. doi:10.1016/j.tetlet.2006.07.070.
(28) Fletton, R. A.; Humber, D. C.; Roberts, S. M.; Wright, J. L. *J. Chem. Soc. Perkin Trans. 1* **1985**, 1523. doi:10.1039/p19850001523.
(29) Dallaeort, A. D.; Barbera, A. L.; Mandolini, L. *J. Chem. Res. (S)* **1983**, *44*.
(30) Chang, M.-Y.; Lin, C.-Y.; Pai, C.-L. *Tetrahedron Lett.* **2006**, *47*, 2565. doi:10.1016/j.tetlet.2006.02.039.
(31) Yang, X.; Xi, C.; Jiang, Y. *Tetrahedron Lett.* **2005**, *46*, 8781. doi:10.1016/j.tetlet.2005.10.028.
(32) Perrin, D. D.; Armearego, W. F. L. *Purification of Laboratory Chemicals*, 3rd ed.; Pergamon Press: New York. 1988.

X-ray absorption spectroscopy of aqueous solutions in the X-ray energy region from 1800 to 3700 eV

Astrid Jürgensen

Abstract: A methodology for the X-ray XANES and EXAFS analyses of aqueous solutions was developed for the Double Crystal Monochromator (DCM) beamline of the Canadian Synchrotron Radiation Facility (CSRF). The technique is based on the implementation of a liquid cell, which is compatible with the standard solid-state sample holding mechanism used at the beamlines of CSRF and the Canadian Light Source (CLS). Aluminized Mylar film with a thickness of 5 μm has been thoroughly investigated for use as a window material for the cell, and found acceptable for the collection of the S, Cl, and K K-edge spectra of ions in aqueous solution, but not for P K-edge or Rb $L_{2,3}$-edge spectra. Some of the limitations of this methodology, such as diffusion of the solution through the window and the detection limit at low ion concentration, are investigated and discussed.

Key words: XANES, EXAFS, aqueous solutions, X-ray region from 1800 to 3700 eV.

Résumé : Une méthodologie était développée pour analyser les solutions aqueuses avec la spectroscopie XANES et EXAFS en la région des rayons-X à la Double Crystal Monochromator (DCM) beamline de la Canadian Synchrotron Radiation Facility (CSRF). Cette technique est basée sur la mise en oeuvre d'une cellule des liquides, qui est compatible avec la mécanisme du cadre support des spécimens solides à les beamlines de CSRF et aussi à certaines beamlines de la Canadian Light Source (CLS). Une pellicule Mylar aluminisée avec une épaisseur de 5 μm était examinée pour l'utilisation comme matériel de la fenêtre de la cellule. On a trouvé que cette matériel est acceptable pour mesurer les spectres d'absorption pour les discontinuités K de S, Cl et K des ions en solution aqueuse, mais pas pour les spectres de la discontinuité K de P et la discontinuité $L_{2,3}$ de Rb. Quelques limitations de cette méthodologie (la diffusion de la solution par la fenêtre et la limite de détection a concentration base) sont analysée et examinée.

Mots-clés : XANES EXAFS, solutions aqueuses, rayons X de 1800 à 3700 eV.

[Traduit par la Rédaction]

Introduction

Many chemical and biochemical reactions involving metal ions occur in aqueous solutions. The kinetics of these reactions depend upon the stability of the region around the solute species, the hydration shell. This very narrow region, typically ~5 Å for monatomic ions,[1] represents the transition region between the solute species and the bulk structure of liquid water. Molecular dynamics simulations suggest that the structure of the hydration shell depends on electrostatic interactions between ions and water molecules[1] and the formation of hydrogen bonds.[1–5] The formation of short-lived (a few ps) ionic clusters is predicted to become more common at higher concentrations (≥1.0 mol/L), even for alkali halide solutions.[6–8] Both charge and size of the ion can have significant effects on the structure[1–4] and stability[9] of the hydration shell, which, in turn, can affect the properties of the solute ion, such as the luminescence intensity[10,11] and the permeability through cell membranes.[9–12]

X-ray absorption spectroscopy can be used to study the local structure and chemical bonding of ions in aqueous solution. The X-ray absorption near edge structure (XANES) spectrum provides information about the oxidation state of the absorbing atom and the electronic interactions between it and its neighbours. The identity, interatomic distance, and coordination geometry of the neighbouring atoms can be determined from the extended X-ray absorption fine structure (EXAFS) spectrum. For ions in aqueous solution, this information represents a time-averaged structure of the hydration shell.

These spectroscopic methods have been used to study the structure of transition-metal aquo complexes, $TM(H_2O)_6^{n+}$ (n = 2, 3), and its correlation with the water-exchange rate, the electron exchange reactions of transition-metal complexes, and structural differences of metal complexes in solids compared to aqueous solutions.[13] More recent applications include the characterization of arsenite in water,[12] the study of the $Pb^{2+}_{(aq)}$ adsorption mechanisms at the calcite–water interface,[14] and the hydration structure of Ca^{2+} in aqueous solution.[15] The structural information about the hydration shell obtained from X-ray spectroscopy data

Received 9 October 2008. Accepted 20 January 2009. Published on the NRC Research Press Web site at canjchem.nrc.ca on 3 April 2009.

A. Jürgensen.[1] Canadian Synchrotron Radiation Facility, Synchrotron Radiation Center, 3731 Schneider Drive, Stoughton, WI 53589, USA.

[1]Present address: Fachbereich für Anorganische Chemie, Technische Universität Berlin, Berlin, Germany.

can also be used to test and improve the theoretical molecular dynamics models, and thus provide us with a better understanding of solute–solvent interactions.

These spectroscopies are, furthermore, element-specific and relatively non-destructive. The analysis can be performed on samples without prior chemical treatments. Thus, XANES and EXAFS are now widely used to study the elemental composition and chemical speciation of various environmental samples, including bacteria, manure, meteorites, plants, sediments, and soils.[16–23] These substances often contain water, and thus, ions in aqueous solution. Upon dissolving in water, the local environment of a molecular species changes compared to the solid state. The crystal structure of the solid breaks down, and isolated ions or molecules surrounded by water molecules are formed. These structural changes lead to modifications in the observed fine structure of the XANES and EXAFS spectra. To identify the features observed in the XANES spectra properly, the set of standard compounds used to analyze the spectra of environmental samples should therefore include aqueous solutions. Furthermore, with minor adaption, the methodology for the XANES and EXAFS measurement of aqueous solutions can also be used to analyze environmental samples in their natural wet state, eliminating the need for freeze-drying them and, thus, avoiding possible changes in chemical speciation caused by the freeze-drying process.

In the X-ray energy region from 1800 to 3700 eV, the mean free path of photons in air at atmospheric pressure is ≤11 cm.[24] Thus, the XANES spectra need to be collected in vacuo ($P \leq 2 \times 10^{-6}$ torr) (1 torr = 133.322 Pa). At such pressures and room temperature, water is not stable in the liquid phase (at 20 °C, the vapour pressure of water is 17.51 torr[25]). Solutions need to be contained in a sample holder that isolates them from the vacuum but, at the same time, allows the X-rays to reach the sample. Alternatively, the experimental station could be put under a helium atmosphere.[26–28] Here too, a sample holder is required, which minimizes exposure of the solution to the dry helium surrounding it; and a windowed barrier is required to separate the experimental station (P ~760 torr) from the ultra-high-vacuum ($P < 1 \times 10^{-9}$ torr) in the rest of the beamline.

This paper describes a technique for the XANES and EXAFS study of aqueous solutions in the X-ray region from 1800 to 3700 eV. It is based on the implementation of a liquid cell, which isolates the solution from the vacuum in the absorption chamber while allowing the X-rays to reach the sample. The design aspects of the cell and the resulting experimental limitations for the XANES spectroscopy of solutions are discussed, and the first experimental data at the S, Cl, and K K-edges are shown. This methodology is currently used at the Double Crystal Monochromator (DCM) beamline of the Canadian Synchrotron Radiation Facility (CSRF). By adapting the cell design to the solid-state sample holding mechanism actually used, it could be implemented at other beamlines.

Experimental

Cell design

For convenience, the liquid cell was designed to be compatible with the standard solid-state sample holding mechanism used at the CSRF beamlines. This determined the shape and size of the cell, as shown in Fig. 1. The stainless steel cell body is hollow in the centre, and the volume of this cavity is 0.6 mL. Liquids are trapped inside this cavity using o-ring seals. The plate attached to the back of the cell is an aluminum disk with a diameter of 1.897 cm and a thickness of 0.152 cm. The front plate consists of two doughnut-shaped disks, each with an outer diameter of 2.223 cm and a thickness of 0.076 cm. The centre hole of each disk has a diameter of 0.953 cm. A thin film, sandwiched between the disks, covers the hole. It is glued to the disks with VACSEAL® (Trademark of Space Environment Laboratories) to hold it in place and to provide a proper seal. This creates a window that allows X-rays to pass through while keeping the liquid trapped inside the cell. The material chosen for this window has to meet two stringent requirements. It has to withstand the pressure differential between the liquid on the inside and the vacuum on the outside; and it has to be transparent to both the incident X-rays and the lower-energy fluorescence X-rays. These impose opposing requirements on the film thickness. The former needs the film to be as thick as possible, while a very thin film would be ideal for the latter. Furthermore, the film must not contain an element that has an absorption edge in the energy region of interest, and it must not react with the liquid inside the cell.

Fig. 1. The sample holder for liquids. The protrusions (three in total) on the cell body are bayonets used to attach the cell to the sample holder support in the vacuum chamber. The front plate is composed of two doughnut-shaped disks, each with a thickness of 0.076 cm. The window is sandwiched between them.

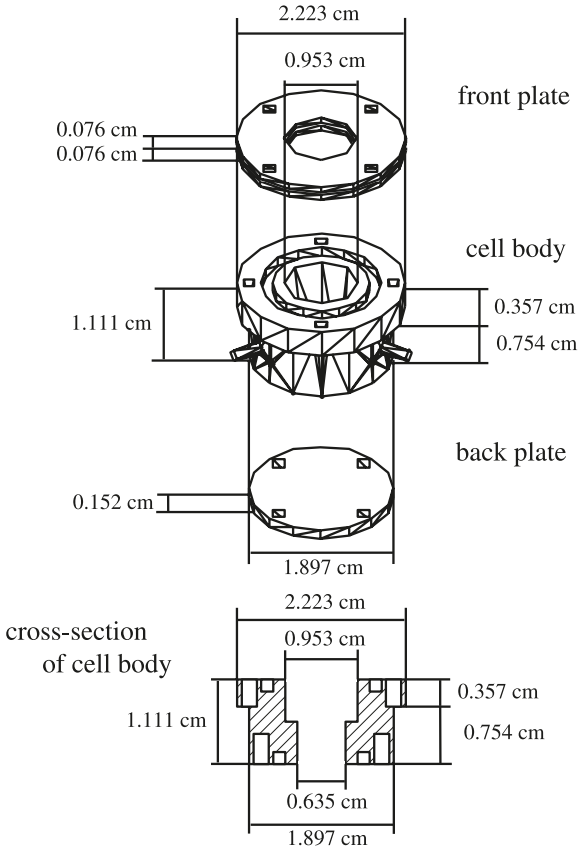

Fig. 2. The theoretical X-ray transmission of a 5 μm aluminized Mylar (Al-Mylar) film, assuming the following thickness: Mylar = 5 μm, Al = 0.15 μm, total = 5.15 μm, and assuming that the total transmission of the film is the product of the transmission of the individual layers. The data for the 5 μm Mylar and 0.15 μm Al layers were obtained from the Web site of the Center for X-Ray Optics (CXRO) at Berkeley Lab, using the routine for calculating the X-ray transmission of a solid.[29]

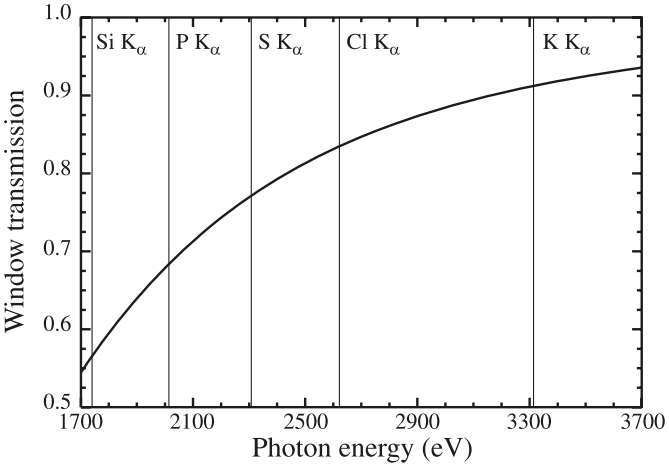

The material chosen, aluminized Mylar® (Trademark of DuPont Teijin Films) (Al-Mylar) with a thickness of 5 μm, is an adequate compromise to meet these conditions. It is relatively inert, it can withstand the pressure differential, and it is fairly transparent to X-rays with energies between 1700 and 3700 eV (Fig. 2). The transmission of the window is, however, not uniform over this energy range. It increases from ~54% at 1700 eV to ~94% at 3700 eV.[29] This variation in the window transmission can distort the relative peak intensities of the measured spectra, especially for long-range EXAFS scans. Corrections for this can be made readily by dividing the measured spectrum by the theoretical transmission of the window material.

This cell design does not permit data collection in the transmission mode, because the back plate (a solid aluminum disk) is not transparent to the X-rays. Also, the present path length through the cell is 1.1 cm (11000 μm), and all of the incident photon flux is absorbed by the solvent (water)[30] over this distance. It might be possible to make the cell suitable for transmission by using a windowed back plate. However, a reduction of the path length through the cell to < 100 μm is also required to make the measurement of transmission spectra feasible, a major design challenge. Thus, it is preferable to use the fluorescence-yield-detection method for the XANES measurement of aqueous solutions.

Method of filling the cell

First, the window is attached to the front of the cell. If necessary, the window is conveniently assembled simultaneously. The cell is then filled from the back. The liquid is added dropwise with the aid of a pipette, and the cell is filled to slightly above capacity, so that the meniscus forms a convex surface. Then, the back plate is screwed tightly onto the cell body, forming an o-ring seal. If the closed cell is filled properly, the window should have a smooth convex surface.

Collection of XANES spectra

The liquid cell is loaded into the sample chamber using the standard procedure employed for solid samples. With the liquid cell in the chamber, the pressure is typically between 5×10^{-7} and 3×10^{-6} torr. XANES spectra of a variety of different aqueous solutions were collected at the Rb $L_{2,3}$-edge and the P, S, Cl, and K K-edges. They were measured by fluorescence yield (FY) using an Ortec nine-element solid-state photon detector. Specific X-ray fluorescence energies, for example the sulfur K_α-line, can be selected for measurement, while all others are excluded. This enhances the detectability of the XANES spectra of elements present in low concentration in the sample, and eliminates the background fluorescence signal from the window material. The FY detector was attached to the absorption chamber at a port that is at 90° to the incident photon beam. To maximize the fluorescence photons reaching the detector, the sample holder was oriented so that the angle between the incident photon beam and the window surface was ~60° (The sample surface was not exactly on the rotation axis, causing the beam spot to move horizontally upon rotation. The 60° angle kept the beam spot approximately centred on the cell window while maximizing the FY signal).

The XANES spectra were normalized with respect to the incident photon flux (I_0) using the total-electron-yield (TEY) spectrum from an in-line ion chamber with ~1.5 torr air that is located upstream from the main absorption chamber. Energy calibration was achieved by measurement of the K-edge XANES spectra of standards (powders of SiO_2, $Na_4P_2O_7$, $ZnSO_4$, KCl, and $CaCO_3$) and then adjusting the energy scale using a fourth-order polynomial calibration function obtained from these standard spectra. Effects of the variable window transmission on the peak intensities were removed by dividing the XANES spectra by the theoretical transmission (Fig. 2) of the window material for the incident X-rays. Solutions of RbCl, Na_3PO_4, $Na_2S_2O_3$, Na_2SO_4, NaCl, $NaClO_4$, and KCl were used in this study. The salts were obtained commercially from Sigma-Aldrich and used without further purification.

Results and discussion

Background signal from the window and the solution

The measured FY signal is a combination of the signal from the solution and the signal from the window. The window material, Al-Mylar, contains the elements hydrogen, carbon, oxygen, and aluminum. None of these chemical elements has an absorption edge in the 1700–3700 eV energy region, and thus, the FY signal from them will only contribute to the overall scattered light background signal. Furthermore, most of this background signal is effectively eliminated from the FY spectrum by using the nine-element Ortec detector. Figure 2 shows the transmission of the Al-Mylar film to X-rays from 1700 to 3700 eV. This transmission increases with increasing photon energy, from ~57% for the Si K_α-line to ~91% for the K K_α-line, increasing the detection efficiency at higher photon energies. This, however, is partially offset by the reduction in overall photon flux from the beamline at higher energies.

Impurities in the window material could contain chemical elements that have absorption edges in the 1700–3700 eV

Fig. 3. Impurities in the Al-Mylar window.

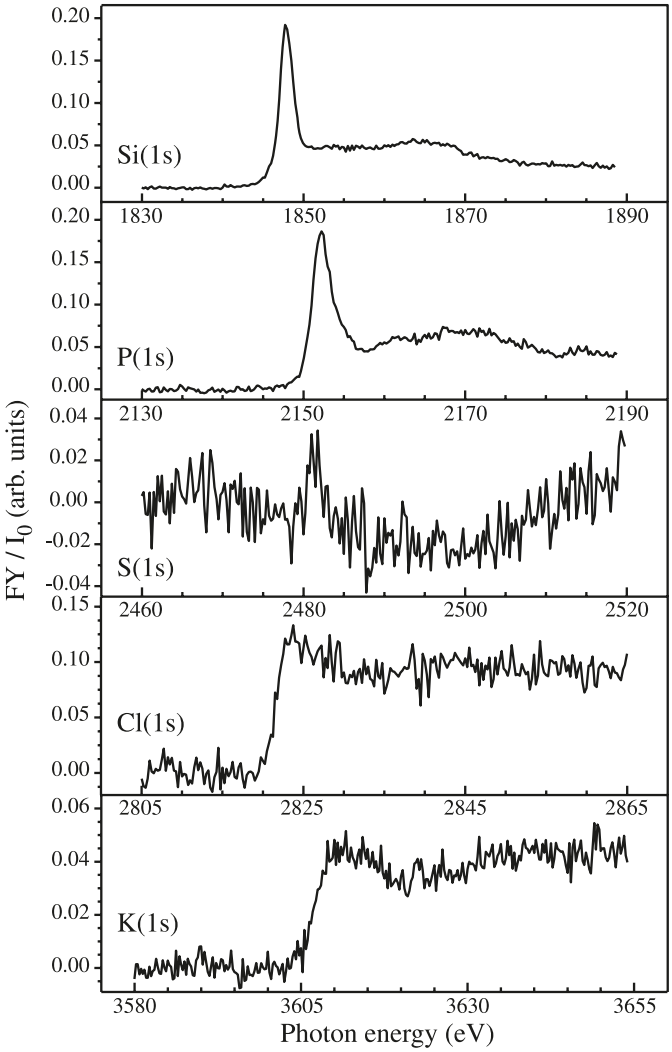

Fig. 4. The effect of window impurities on the XANES spectra of solutions: (*a*) Comparison of the P K-edge spectra from the window and from a 0.268 mol/L Na_3PO_4 solution, (*b*) Comparison of the Cl K-edge spectra from the window and from a 0.0024 mol/L NaCl solution, and (*c*) The Rb $L_{2,3}$-edge XANES spectrum of RbCl, solid powder, and a 1.005 mol/L aqueous solution.

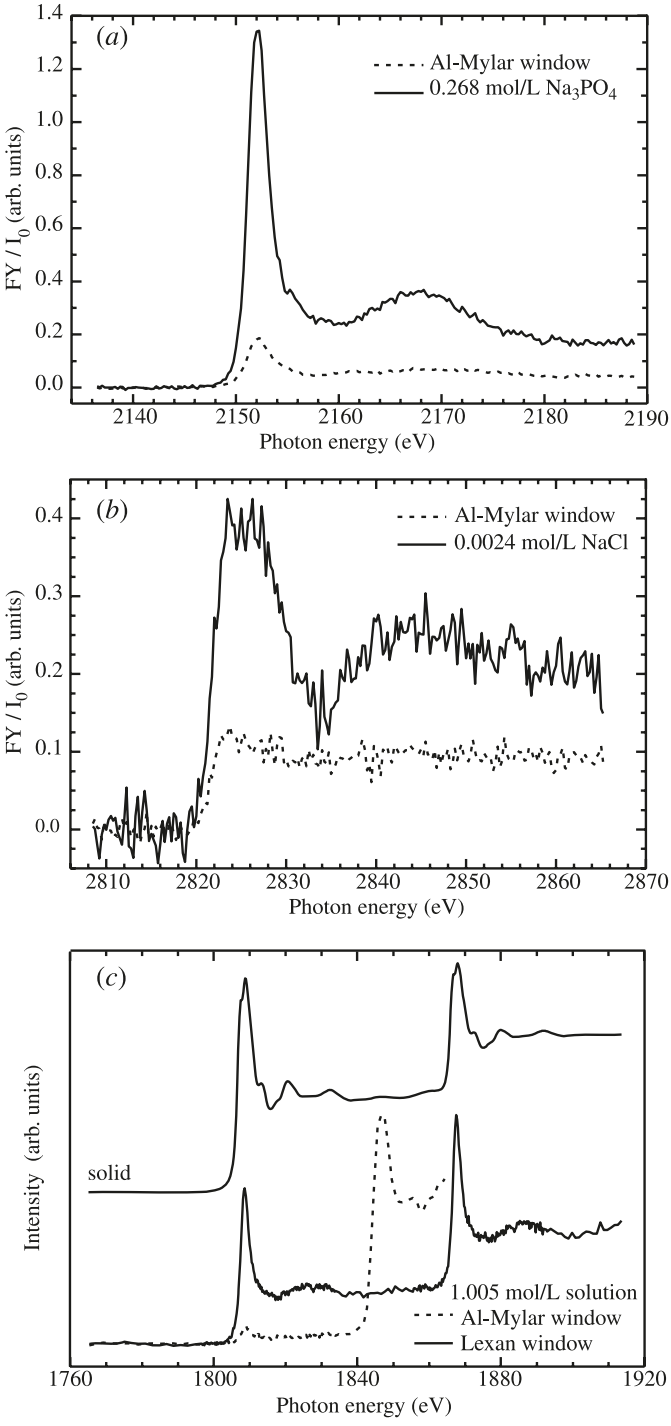

energy region. If these overlap with the absorption edge of the ion of interest, the FY signal from these impurities can contribute to the measured XANES spectrum. To check for possible Si, P, S, Cl, or K impurities, K-edge XANES spectra for these elements were collected from the empty cell, with a clean unused window at the front, and the back being open. The collection time for each data point was 15 s/pt. Four scans were collected at each edge and averaged. The resulting spectra (Fig. 3) show that the window contains silicate and phosphate impurities. Small amounts of chloride and potassium are present as well.

The integrated intensity (area under the curve) of the phosphate XANES spectrum of the window is ~20% of the integrated intensity obtained for a 0.268 mol/L PO_4^{3-} solution (Fig. 4*a*). Hence, there is a significant contribution from the window to the observed XANES spectrum, even for fairly concentrated solutions. The intensity of the Si K-edge of the window is of similar magnitude as that of the P K-edge. While the feasibility of the cell for Si in solution has not been tested, it is expected that the signal from the window would make at least a similar contribution to the overall Si K-edge as it does for the P K-edge. Furthermore, it is not possible to completely resolve the Al-K_α (1487 eV) and Si-K_α (1740 eV) lines with the nine-element Ortec detector, so that the Si K-edge always has some extra background signal from the Al in the window. The window transmission is also lowest at the Si K-edge, ~61% for the incident photons at 1840 eV and ~57% for the Si-K_α fluo-

rescence at 1740 eV (Fig. 2), further increasing the intensity of the signal from the window impurity relative to the signal from the solution.

The Cl K-edge XANES signal from the window has much lower integrated intensity, only ~39% of the signal obtained from a 0.0024 mol/L Cl^- solution (Fig. 4*b*). While it does limit the detectability of Cl^- at low concentration, it does not contribute significantly to the measured XANES spectrum of concentrated Cl^- solutions. The intensity of the K K-edge from the window is of similar magnitude as the Cl K-edge signal (Fig. 3), ~12% of the signal from a 0.0024 mol/L K^+ solution. Furthermore, the K-impurity can be removed from the window by rinsing it with deionized water. Hence, the K K-edge spectrum of the window can be eliminated, and it does not limit the detectability of K^+ at low concentration.

This window material is thus suitable for the study of S, Cl, and K K-edges in aqueous solution, but less desirable for the K-edges of Si and P. XANES spectra of elements with absorption edges and fluorescence lines close to those of Si and P, for example, Rb ($L_{3,2}$-edges: 1804 and 1864 eV, L_α-line: 1694 eV), also cannot be adequately measured using the 5 μm Al-Mylar window. An investigation into the suitability of other window materials is in progress. Initial results have shown that a 6 μm Lexan® (Trademark of General Electric Company) window is a better choice for the measurement of Rb $L_{2,3}$-edge (Fig. 4*c*) and P K-edge XANES spectra in aqueous solution. However, it is not as resistant to radiation damage. The resulting development of pinholes necessitates frequent window replacement, making Lexan an inferior choice for the S, Cl, and K K-edges compared to Al-Mylar. A third window material, 3 μm Mylar, could potentially be a better choice than the 5 μm Al-Mylar for the S, Cl, and K K-edges. It has a higher X-ray transmission (~77% at the Si-K_α line and ~96% at the K-K_α line) than the 5 μm Al-Mylar, it is strong enough to withstand the pressure differential between the liquid and the vacuum, and it is resistant to radiation damage. However, the diffusion rate through the window and the low concentration detection limit of solute species have not yet been tested. Other window materials[31] were also considered for this cell, but found to be unsuitable. Kapton, Mica, Al-foil, and Si_3N_4 all have insufficient transmission, and Be-foil might be too reactive with solvent or solute.

The FY signal from the solution is the combined signal resulting from interactions of the incident X-rays with the solvent and all solute species. In the specific case of aqueous solutions, the solvent (water) does not have an absorption edge in the 1700–3700 eV energy region, and thus absorption by the solvent only generates a background FY signal, which is effectively eliminated from the FY spectrum by using the nine-element Ortec detector. The change in X-ray transmission of the solvent with increasing photon energy leads to a change in the penetration depth of the incident X-rays, but the energy and thus the escape depth of the fluorescence X-rays remain constant. As long as the former exceeds the latter, the actual sampling depth of the FY detection method remains constant, and the change in X-ray transmission has minimal effect on the measured spectrum. However, at absorption edges of the solvent or of solutes in high concentration, the penetration depth of the incident X-rays could decrease to values below the escape depth of the fluorescence X-rays. This leads to a dependence of the sampling depth on the incident X-ray energy, and thus to distortions in the spectrum (the self-absorption effect often detected for solid samples). The correction techniques for solids[32–35] can also be applied to the spectra of aqueous solutions.

Diffusion of the liquid through the window

With the liquid cell in the chamber, the base pressure is relatively high (5×10^{-7} to 3×10^{-6} torr), compared with when the cell is absent ($\leq 5 \times 10^{-8}$ torr). This indicates that the cell is not perfectly sealed, and some liquid slowly leaks out of the cell. This is supported by the observation that after long stays (~14 h or more) in vacuum, the cell window is no longer smooth and convex. Leakage of liquid out of the cell could occur through the o-ring seals or, more likely, through the window. Diffusion of the solution through the window, followed by the deposition of solids on the outside window surface, could possibly affect the measured FY spectrum of the solution.

The possibility of diffusion through the window and its potential effect on the XANES spectrum were investigated for the S K-edge by collecting 18 successive spectra of a 0.001 mol/L $S_2O_3^{2-}{}_{(aq)}$ solution over a time period of about 9.5 h with a collection time of 12 s/pt. There are two observations (Fig. 5*a*): (*i*) the overall intensity of the sulfur signal increased with time, and (*ii*) the spectral features changed with time. The early spectra (Nos.1–4) resemble that of a more concentrated $S_2O_3^{2-}{}_{(aq)}$ solution (Fig. 5*b*). The peaks are, however, not as well-resolved owing to the low ion concentration and the corresponding decrease in *S/N* in the spectrum. A gradual increase in the overall signal intensity is observed starting with scan No. 5. Relative to scan No. 1, the integrated intensity (area) has increased by a factor of 2.28 for scan No. 8, a factor of 2.94 for scan No. 9 and a factor of 4.80 for scan No. 18. This gradual intensity increase over time can be explained by the deposition of solid-state sulfur compounds on the outside surface of the window following diffusion of the solution through the window and evaporation of the solvent. In addition, changes in the spectral features are observed. Starting with scan No. 5, the sulfide peak increases relative to the sulfate peak and, starting with scan No. 9, a shift in the sulfide peak position toward lower energy is observed. This indicates the gradual formation of new sulfur species, probably the products of various redox reactions. Least-squares fitting of scan No. 18 with the XANES spectra of various standards suggests that the most abundant forms of sulfur are Al_2S_3 (50%), S_8 (25%), $S_2O_3^{2-}{}_{(aq)}$ (15%), and $Al_2(SO_4)_3$ (1.2%) (Fig. 6). Possible reactions that could produce these compounds include

[1] $$S{-}SO_3^{2-} + 2H_2O + h\nu \rightarrow S + H_2SO_3 + 2OH^-$$

[2] $$H_2SO_3 + 2\,OH^- + S \rightarrow SO_4^{2-} + H_2S + H_2O$$

[3] $$H_2SO_3 + H_2O + S \rightarrow SO_4^{2-} + 2H^+ + H_2S$$

[4] $$8S \rightarrow S_8$$

Fig. 5. (*a*) The effect of diffusion through the window on the S K-edge XANES of a 0.001 mol/L $Na_2S_2O_3$ solution and (*b*) The S(1s) XANES of a 0.0916 mol/L $Na_2S_2O_3$ solution.

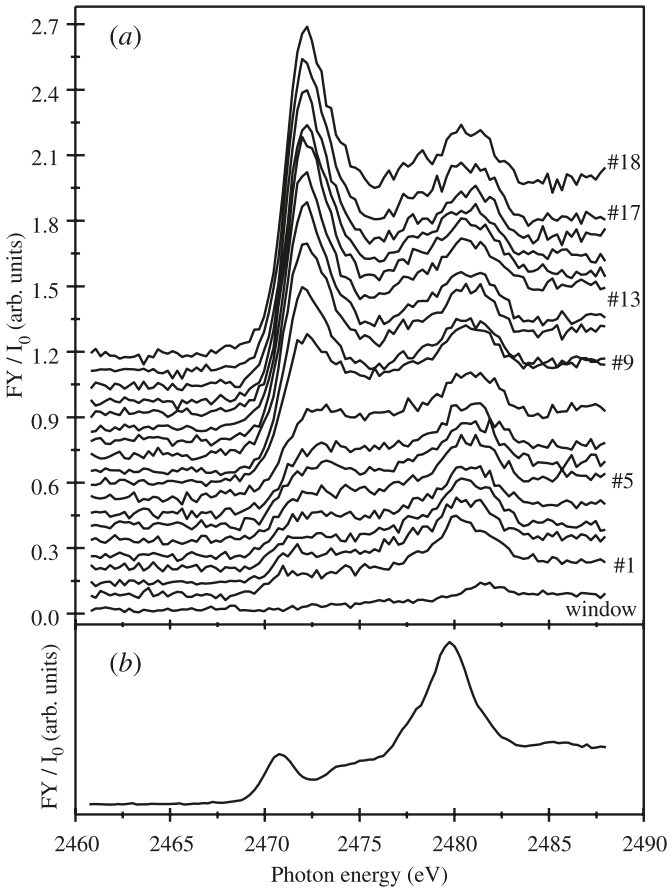

Fig. 6. Least-squares fit of the 18th scan of the 0.001 mol/L $S_2O_3^{2-}{}_{(aq)}$ solution (Fig. 5). The individual-component spectra of standards are also shown with their intensities adjusted according to their contribution to the overall fit.

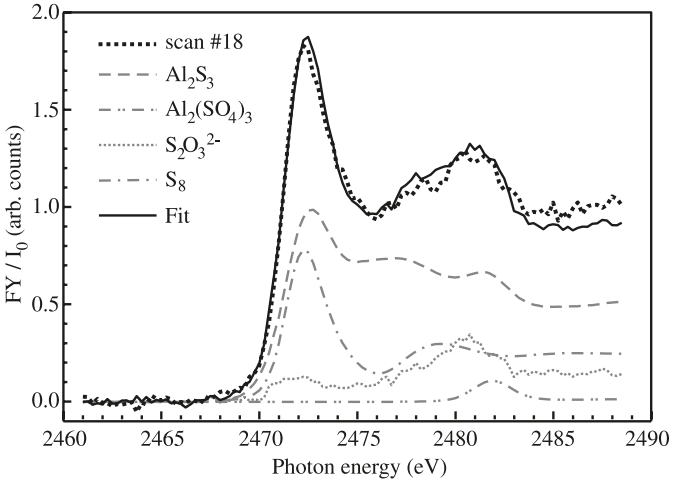

[5] $2\,Al + 3\,S \rightarrow Al_2S_3$

[6] $6H^+ + 2\,Al + 3\,SO_4{}^{2-} \rightarrow 3H_2 + Al_2(SO_4)_3$

The slow formation rate of the new compounds coupled with the overall intensity increase suggest that they are formed in the vicinity of the outside window surface. They could also be products of photochemical reactions that occur in the solution.

The results of this study suggest that window diffusion is a relatively slow process occurring over several hours. It is therefore possible to measure reliable XANES spectra with minimal contribution from the window, if the experiment is conducted in a timely manner (e.g., < 1 h). The measurement of good quality EXAFS spectra typically takes more than 1 h. Thus, the signal resulting from solids deposited on the outside window surface could contribute significantly to the overall spectrum. Corrections for this can be made through the application of the following procedure:

i) The EXAFS spectrum of the solution of interest is collected.

ii) The inside of the cell is rinsed repeatedly with deionized water, and then dried with a Kimwipe® (Trademark of Kimberly-Clark Worldwide Inc.).

iii) The EXAFS spectrum is collected from the empty cell, with the used window at the front, and the back being open. Alternatively, the cell is filled with deionized H_2O and the EXAFS spectrum of the window plus the solvent is measured. The scan parameters are kept the same as for the spectrum of the solution.

iv) After normalization with respect to I_0, the spectrum of the window is subtracted from the spectrum of the solution.

The effectiveness of this procedure is illustrated in Fig. 7 for the Cl K-edge EXAFS spectrum of a 1.003 mol/L $NaClO_4$ solution, where the contribution to the spectrum due to diffusion through the window is minor.

It should be noted that this diffusion-rate study was done for $S_2O_3^{2-}{}_{(aq)}$ at low concentration, and the results are not universally applicable. Further studies are needed to investigate the effects of ion concentration and ion identity on the diffusion rate. The above procedure for the removal of the signal from solids on the outside window surface can be applied to XANES spectra as well.

The loss of liquid caused by the diffusion through the window represents a flaw of the cell that might not be easily eliminated. To allow the X-rays to pass through with sufficient intensity for meaningful measurement, the window needs to be very thin. However, such a very thin window is also more permeable than a thicker window, increasing the diffusion rate. It might be possible to use another less permeable window material, but only if it is also transparent to the X-rays. However, the present study suggests that diffusion through the window is a relatively slow process that does not affect the measurements significantly. Hence, this flaw of the cell can be tolerated.

XANES spectra: solid state vs. solution

Upon dissolution in water, the local environment of a molecular species changes compared with the solid state. The crystal structure of the solid breaks down and isolated ions and molecules are formed that are surrounded by water molecules, forming the hydration shell. The structure of this hydration shell depends on the type and size of the solute ion

Fig. 7. Elimination of the window spectrum from the Cl K-edge EXAFS spectrum of $ClO_{4(aq)}^-$: (*a*) The spectrum of a 1.003 mol/L $NaClO_4$ solution and the 5 μm Al-Mylar window. (*b*) The spectrum of the 5 μm Al-Mylar window after the measurement of the $NaClO_4$ solution. (*c*) The spectrum of $ClO_{4(aq)}^-$, obtained by subtracting the spectrum of the window (*b*) from the combined spectrum (*a*).

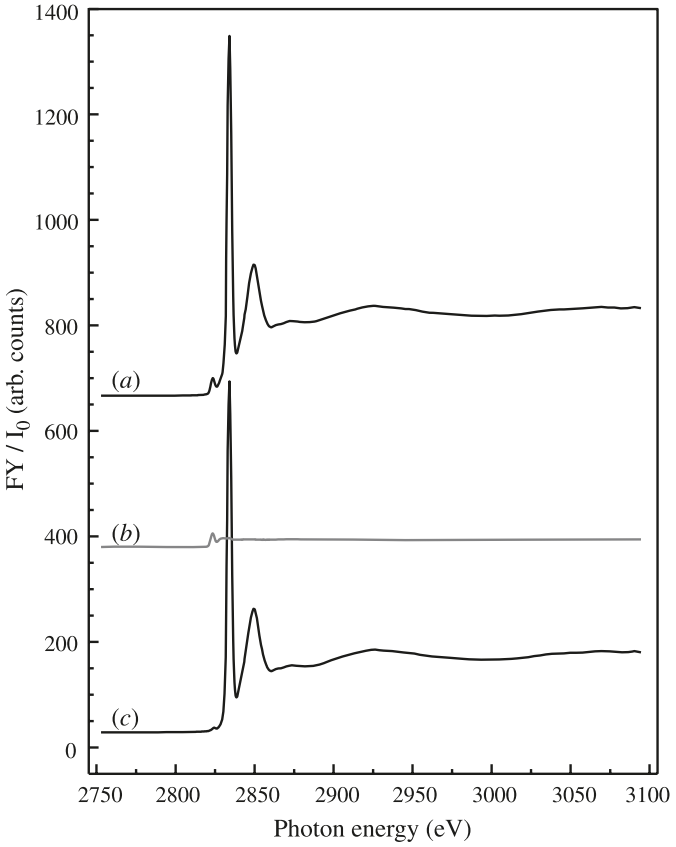

and the concentration of the solute. These structural changes between the solid and the solution lead to modifications in the observed structure of the XANES spectrum. In particular, the long-range crystal structure of the solid is lost upon solvation, leading to alterations in the scattering pattern of photoelectrons and, thus, to changes in the spectrum following the main absorption peak. The overall extent of the spectral changes depends upon the species involved, as illustrated for Na_2SO_4 vs. $SO_{4(aq)}^{2-}$ and NaCl vs. $Cl_{(aq)}^-$ (Fig. 8).

In the case of Na_2SO_4, the anion (SO_4^{2-}) is a tetrahedral polyatomic anion with the sulfur atom at the centre. The first coordination shell of the S atom, four oxygen atoms, remains the same in solution as in the solid, except for minor perturbations. The water molecules of the hydration shell form the 2nd and 3rd coordination shells of the S atom. In consequence, there are only minor changes to the electronic structure and chemical bonding of the sulfur upon solvation of Na_2SO_4. This is reflected in the XANES spectra (Fig. 8*a*). The position and intensity of the main absorption peak are the same in both spectra. The fine structure following the main peak, however, is caused by scattering of the photoelectrons by atoms in the first few coordination shells of sulfur. The structural differences in the 2nd and higher coordination shells between the solid and the solution lead to significant differences in the spectra: two peaks at 2490.3

Fig. 8. K-edge XANES spectra (solid state vs. aqueous solution): (*a*) $Na_2SO_{4(s)}$ vs. $SO_{4(aq)}^{2-}$ and (*b*) $NaCl_{(s)}$ vs. $Cl_{(aq)}^-$.

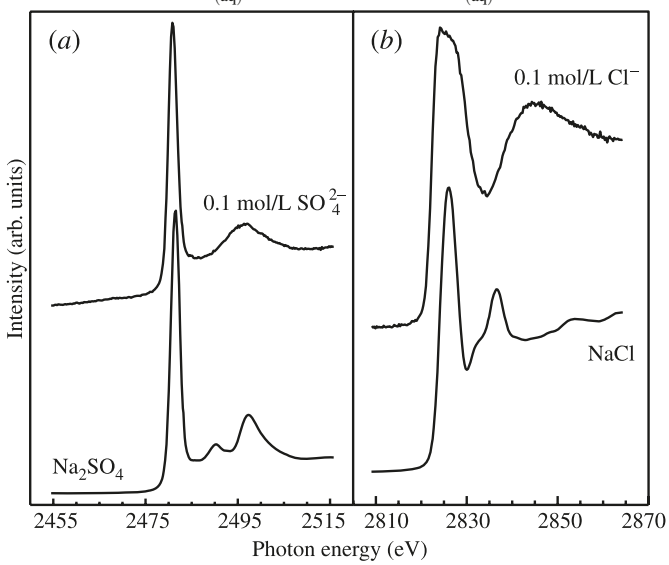

and 2497.4 eV for the solid vs. one peak at 2496.5 eV for the solution.

In contrast, the anion of NaCl, Cl^-, is a monatomic ion with eight Na^+ ions as nearest neighbours. Upon solvation, these Na^+ cations are replaced by water molecules, causing significant changes to the electronic structure and chemical bonding of the Cl^- ion. This is reflected in the XANES spectra (Fig. 8*b*). There are changes to the main absorption peak as well as to the fine structure. The absorption edge shifts down by ~1.7 eV, and the main peak (much broader than for solid-state NaCl) is composed of two partially resolved peaks. They could possibly result from the presence of $Cl_{(aq)}^-$ ions in two different chemical environments, i.e., the first coordination shell of the $Cl_{(aq)}^-$ ion has two distinct structures. The position and relative intensity of these peaks are not dependent on the ion concentration (Fig. 9*b*), and a dependence on the pH of the solution still needs to be investigated.

A similar effect on the XANES spectrum of the cation can be seen in Fig. 4*c*, where the fine structure in the Rb $L_{2,3}$-edge XANES of RbCl is not observed in the spectrum of a 1.005 mol/L RbCl solution. In all three cases ($SO_{4(aq)}^{2-}$, $Cl_{(aq)}^-$, and $Rb_{(aq)}^+$), the lack of fine structure following the main peak can be attributed to a lack of long-range order in the solution.

XANES spectra: effect of ion concentration

Liquid environmental samples, for example, lake water, probably contain the ions of interest in fairly low concentrations. Thus, the sensitivity of the experimental apparatus in detecting ions at low concentration was investigated. The dependence of the signal intensity on the ion concentration was tested for the S, Cl, and K K-edges by measurement of the XANES spectra of solutions with different ion concentrations. Solutions of $Na_2S_2O_3$, NaCl, and KCl were used for the S, Cl, and K K-edge spectra, respectively. Their concentrations are listed in Table 1. The XANES spectra obtained for these solutions show that measurement is possible

Fig. 9. K-edge XANES spectra as a function of the concentration of the solution. The intensity (FY/I_0) of the signal decreases with decreasing ion concentration, as listed. For clarity, the spectra of the solutions were multiplied by a constant scaling factor given next to the corresponding XANES spectrum: (*a*) $S_2O_3^{2-}_{(aq)}$, (*b*) $Cl^-_{(aq)}$, and (*c*) $K^+_{(aq)}$.

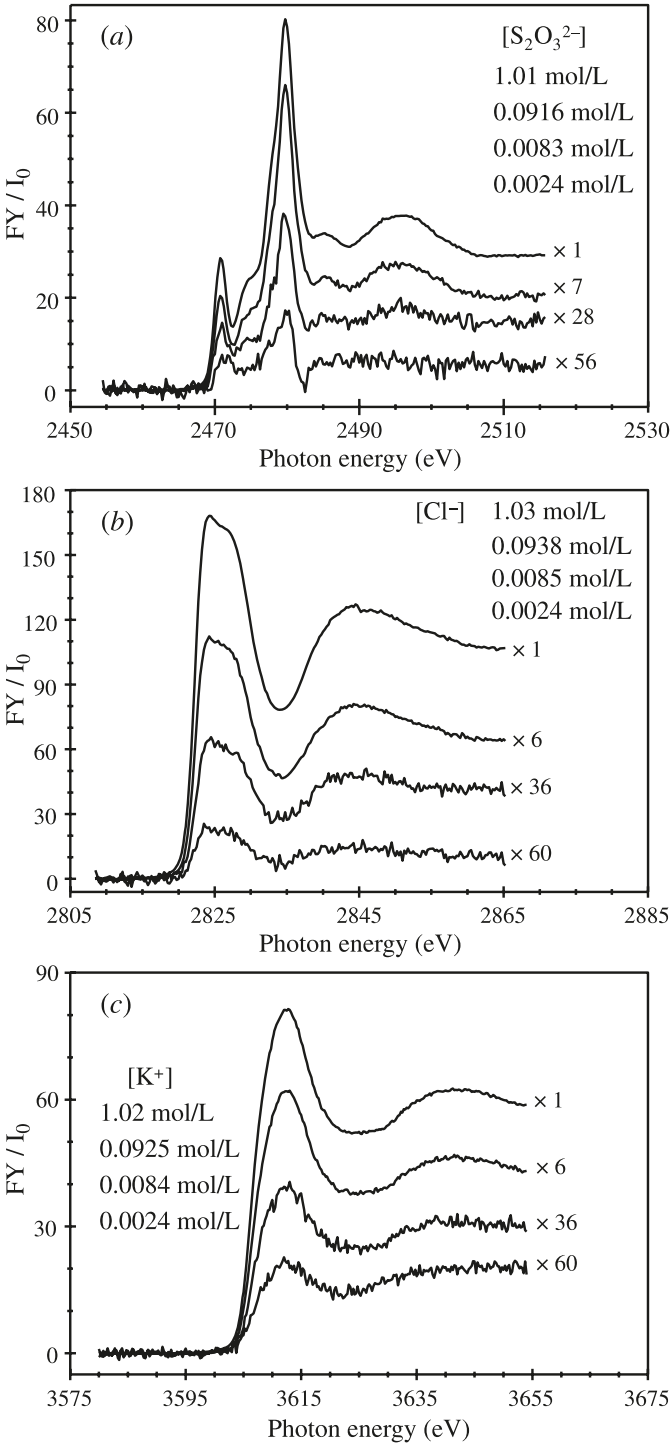

for concentrations as low as 0.0024 mol/L (Fig. 9). All 12 spectra were collected with the synchrotron ring energy at 800 MeV. With the ring energy at 1 GeV, the incident photon flux increases by a factor of 4 to 12, depending on the photon energy, which would probably enable the XANES measurement of ions at even lower concentration.

As seen in Fig. 9, the intensity of the signal increases with increasing ion concentration. For both the maximum of the main absorption peak and the integrated intensity, this increase with respect to ion concentration is approximately linear for the concentration range investigated (Fig. 10). XANES spectroscopy can thus be used to quantitatively determine the concentration of ions in liquid environmental samples. However, for the concentration range (~three orders of magnitude) studied here, it would be desirable to have a few additional calibration points to establish a suitable conversion formula between the FY signal intensity and the ion concentration.

Vacuum vs. helium atmosphere

In other XANES studies of aqueous solutions using X-rays below 3000 eV,[26–28] the sample was put in a helium atmosphere (P ~760 torr), while in the present study a vacuum (5×10^{-7} torr $\leq P \leq 3 \times 10^{-6}$ torr) was used. The solutions investigated in those studies had ion concentrations of comparable magnitude to the ones studied here, and the XANES spectra obtained were of comparable quality.

A clear advantage of using a helium atmosphere is that there is a lower risk of the sample cell window breaking because of the pressure differential between the inside and the outside of the cell. It is even possible to dispense with a windowed sample cell and use a straw with a small slit instead.[28] However, the use of a helium atmosphere also comes with a few challenges. The most difficult of these is how to effectively isolate the experimental station (P ~760 torr He) from the beamline ($P < 1 \times 10^{-9}$ torr), unless the beamline itself is also filled with helium.[26] One possibility is to attach a Si_3N_4 membrane at the end of the beamline.[28] This works well for the Al K-edge at 1560 eV (attenuation length = 4.33 μm[30]), but the membrane becomes opaque at the Si K-edge (attenuation length = 1.28 μm[30]). At the S K-edge, the absorption length has increased to 2.69 μm,[30] which might be sufficient for the measurement of S(1s) XANES spectra. A second possibility is to use a 3 μm Mylar film window supported by a capillary array, which has ~50% transmission at the S K-edge.[27] This represents a significant loss of photon flux, and in conjunction with the loss at the sample cell window, it could limit the measurement of XANES spectra to solutions with high ion concentration. Both barriers require fast acting gate valves interlocked with ion gauges to prevent beamline venting in case that the window breaks.

Use of the liquid cell in vacuum has the same requirements as a gas-phase experiment: a barrier window of sufficient strength between the sample and the vacuum and fast-acting gate valves interlocked with ion gauges to protect the beamline from venting. The use of a helium atmosphere does not eliminate these requirements. Instead, it adds the extra complexity of a high-pressure gas-phase experiment (typical pressures for gas-phase experiments are between 1×10^{-5} and 2 torr, depending on the experimental set-up). In addition, the helium atmosphere does not improve the X-ray transmission: at 2472 eV, the attenuation length of 3×10^{-6} torr H_2O (the vacuum) is 9.953×10^8 cm compared with 1959 cm for 760 torr He.[36] For a reasonable path length, e.g., 15 cm, the difference in X-ray transmission is

Table 1. The concentrations of the sensitivity-test solutions.

		Concentration (mol/L)			
Edge	Compound	Solution I	Solution II	Solution III	Solution IV
S K-edge	$Na_2S_2O_3$	1.01	9.16×10^{-2}	8.3×10^{-3}	2.4×10^{-3}
Cl K-edge	NaCl	1.03	9.38×10^{-2}	8.5×10^{-3}	2.4×10^{-3}
K K-edge	KCl	1.02	9.25×10^{-2}	8.4×10^{-3}	2.4×10^{-3}

Fig. 10. The effect of ion concentration on the intensity of the XANES signal: (*a*) the height of the main absorption peak vs. ion concentration (best fits: $S_2O_3^{2-}$ peak at 2471 eV, log(height) = 1.43 + 0.86 log([$S_2O_3^{2-}$]); $S_2O_3^{2-}$ peak at 2480 eV, log(height)=1.92 + 0.90 log([$S_2O_3^{2-}$]); Cl^- peak, log(height) = 2.24 + 0.98 log([Cl^-]); K^+ peak, log(height) = 1.92 + 0.89 log([K^+])) and (*b*) the integrated intensity (area) of the XANES spectrum vs. ion concentration (best fits: $S_2O_3^{2-}$, log(area) = 3.20 + 0.91 log([$S_2O_3^{2-}$]); Cl^-, log(area) = 3.74 + 1.02 log([Cl^-]); K^+, log(area) = 3.46 + 0.88 log([K^+])). Note that in Fig. 10*a* the K^+ peak intensity was shifted down by a factor of $10^{0.2}$ for clarity.

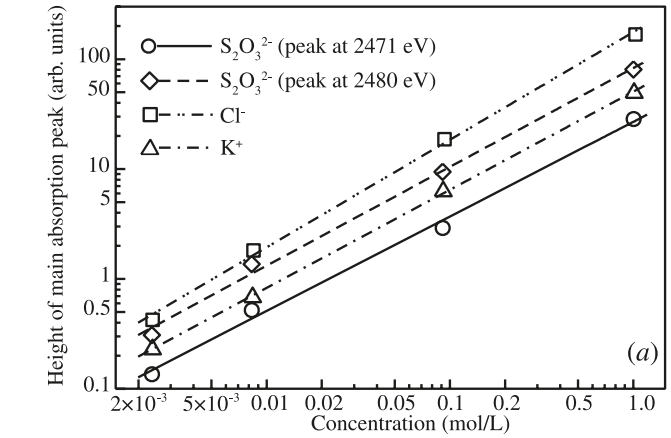

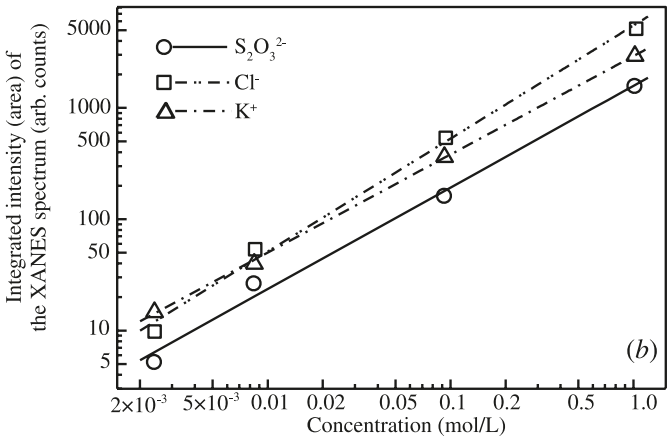

negligible in the 1700 to 3700 eV region (100% for 3×10^{-6} torr H_2O and 97%–100% for 760 torr He[36]), but at lower energies, the loss of flux to the He atmosphere can become significant (e.g., at 600 eV with a 15 cm path length: 100% transmission for 3×10^{-6} torr H_2O and 48% for 760 torr He[36]).

The DCM beamline of CSRF was designed to permit the XANES measurement of corrosive gases, for example, PF_3. Thus, it has a built-in barrier section between the ultra-high-vacuum of the beamline and the experimental station. This barrier consists of the gas cell used for the I_0 measurement (12.5 cm long with a 12.5 μm Be window at each end and filled with ~1.5 torr air) followed by a differential pumping section. A gate valve, set to close automatically at $P > 1 \times 10^{-4}$ torr, separates the latter from the experimental station. It is thus possible to conduct the XANES measurement under a helium atmosphere. Only two steps are needed to set it up: (*i*) adding another 12.5 μm Be window between the differential pumping section and the solid-state chamber and (*ii*) filling the solid-state chamber with ~760 torr He.

The present study, however, has demonstrated that the extra complexity of a helium atmosphere is not required for the XANES measurement of aqueous solutions. The standard vacuum conditions used for solid samples were sufficient, simplifying the experimental procedure. Using a vacuum rather than a helium atmosphere also makes it easier to extend the XANES analysis of solutions to even lower energy X-ray photons. A vacuum in the experimental station will allow the use of very thin (e.g., 1.5 μm Mylar) windows between it and the beamline, thus maximizing the transmission of the incident X-rays. If an effective differential pumping station is present, it might even be possible to run the experiment without the barrier window. Under these conditions and with a 3 μm Mylar window, the liquid cell could probably be used to study the L-edges of first-row transition-metal ions.

Summary

A methodology for the XANES and EXAFS study of aqueous solutions in the 1800–3700 eV energy region has been implemented successfully at the DCM beamline of CSRF. The design of the required sample holder for liquids is compatible with the standard solid-state sample holding mechanism used at the CSRF beamlines, thus allowing for easy loading of solution samples into the vacuum chamber. An aliquot of 0.6 mL can be contained in this liquid cell, and a 5 μm Al-Mylar film proved sufficient as a window material. An investigation into the impurity components of this window material, however, revealed that it cannot be employed for the measurement of P K-edge and Rb $L_{2,3}$-edge spectra of, for example, $PO_{4(aq)}^{3-}$ and $Rb_{(aq)}^{+}$ ions.

The measurement of XANES spectra at the S, Cl, and K K-edges is limited to solutions with ion concentrations of ~0.0025 mol/L or higher, owing to the dependence of signal intensity on ion concentration. It might be possible to decrease the lower concentration limit by increasing the incident photon flux or by using a window material with higher transmission of the X-rays. Diffusion of the solution through the window followed by the deposition of solids on the outside window surface was investigated. The results suggest that this is a relatively slow process, and that for concentrated solutions, the signal from these solids has low inten-

sity compared with the signal from the solution. Thus, window diffusion effects play only a minor role in limiting the measurement of reliable XANES and EXAFS spectra of aqueous solutions.

Investigations to use this methodology to study electron-transfer reactions in aqueous solutions with X-ray excitation optical luminescence (XEOL) spectroscopy are in progress. Future development of this methodology will include ways to adapt the cell design to allow the study of solid–solution interfaces, wet environmental samples (e.g., leaves), and solvents other than water. By adapting the cell design to the solid-state sample holding mechanism actually used, this methodology could be implemented at other beamlines.

Acknowledgements

CSRF is funded by the National Research Council of Canada (NRC-CRNC) and the Natural Sciences and Engineering Research Council of Canada (NSERC-CRSNG). It is located at the Synchrotron Radiation Center (SRC), which is operated by the University of Wisconsin, Madison and funded by the National Science Foundation (NSF) of the USA under grant No. DMR-05–37588.

References

(1) Degrève, L.; de Pauli, V. M.; Duarte, M. A. *J. Chem. Phys.* **1997**, *106*, 655. doi:10.1063/1.473403.

(2) Chandrasekhar, J.; Spellmeyer, D. C.; Jorgensen, W. L. *J. Am. Chem.Soc.* **1984**, *106*, 903. doi:10.1021/ja00316a012.

(3) Cannon, W. R.; Pettitt, B. M.; McCammon, J. A. *J. Phys. Chem.* **1994**, *98*, 6225. doi:10.1021/j100075a027.

(4) Jorgensen, W. L.; Gao, J. *J. Phys. Chem.* **1986**, *90*, 2174. doi:10.1021/j100401a037.

(5) Jorgensen, W. L.; Briggs, J. M. *J. Am. Chem.Soc.* **1989**, *111*, 4190. doi:10.1021/ja00194a007.

(6) Degrève, L.; da Silva, F. L. B. *J. Chem. Phys.* **1999**, *111*, 5150. doi:10.1063/1.479783.

(7) Vieira, D. S.; Degrève, L. *J. Mol. Struct. (Theochem.),* **2002**, *580*, 127. doi:10.1016/S0166-1280(01)00607-8.

(8) Degrève, L.; Mazzé, F. M. *Mol. Phys.* **2003**, *101*, 1443. doi:10.1080/0026897031000092256.

(9) Degrève, L.; Vechi, S. M.; Quintale, C., Jr. *Biochim. Biophys. Acta,* **1996**, *1274*, 149. doi:10.1016/0005-2728(96)00019-9.

(10) van Veggel, F. C. J. M.; Reinhoudt, D. N. *Chem. Eur. J.* **1999**, *5*, 90. doi:10.1002/(SICI)1521-3765(19990104)5:1<90::AID-CHEM90>3.0.CO;2-8.

(11) Kulmala, S.; Hakanen, A.; Laine, E.; Haapakka, K. *J. Alloys Compd.* **1995**, *225*, 279. doi:10.1016/0925-8388(94)07141-1.

(12) Ramírez-Solís, A.; Mukopadhyay, R.; Rosen, B. P.; Stemmler, T. L. *Inorg. Chem.* **2004**, *43*, 2954. doi:10.1021/ic0351592. PMID:15106984.

(13) Sham, T.-K. X-ray absorption studies of liquids: Structure and reactivity of metal complexes in solution and X-ray photoconductivity of hydrocarbon solutions of organometallics. In *Topics in current chemistry: Synchrotron radiation in chemistry and biology I*. Mandelkow, E, Ed.; Springer-Verlag: Berlin/Heidelberg. 1988. Vol. 45. Chapter 4. pp. 81–106.

(14) Rouff, A. A.; Elzinga, E. J.; Reeder, R. J.; Fisher, N. S. *Environ. Sci. Technol.* **2004**, *38*, 1700. doi:10.1021/es0345625. PMID:15074678.

(15) Fulton, J. L.; Heald, S. M.; Badyal, Y. S.; Simonson, J. M. *J. Phys. Chem. A*, **2003**, *107*, 4688. doi:10.1021/jp0272264.

(16) Rompel, A.; Cinco, R. M.; Latimer, M. J.; McDermott, A. E.; Guiles, R. D.; Quintanilha, A.; Krauss, R. M.; Sauer, K.; Yachandra, V. K.; Klein, M. P. *Proc. Natl. Acad. Sci. U.S.A.* **1998**, *95*, 6122. doi:10.1073/pnas.95.11.6122. PMID: 9600928.

(17) Villalobos, M.; Toner, B.; Bargar, J.; Sposito, G. *Geochim. Cosmochim. Acta,* **2003**, *67*, 2649. doi:10.1016/S0016-7037(03)00217-5.

(18) Toor, G. S.; Peak, J. D.; Sims, J. T. *J. Environ. Qual.* **2005**, *34*, 1380. doi:10.2134/jeq2004.0232. PMID:15758121.

(19) Jürgensen, A.; Widmeyer, J. R.; Gordon, R. A.; Bendell-Young, L. I.; Moore, M. M.; Crozier, E. D. *Am. Mineral.* **2004**, *89*, 1110.

(20) Pickering, I. J.; Prince, R. C.; Divers, T.; George, G. N. *FEBS Lett.* **1998**, *441*, 11. doi:10.1016/S0014-5793(98)01402-1. PMID:9877155.

(21) Sneeden, E. Y.; Harris, H. H.; Pickering, I. J.; Prince, R. C.; Johnson, S.; Li, X.; Block, E.; George, G. N. *J. Am. Chem. Soc.* **2004**, *126*, 458. doi:10.1021/ja039239g. PMID:14719930.

(22) Yu, E. Y.; Pickering, I. J.; George, G. N.; Prince, R. C. *Biochim. Biophys. Acta*, **2001**, *1527*, 156. PMID:11479032.

(23) Cavell, R. G.; Barnes, E. M.; Arboleda, P. H.; Cavell, P. A.; Feng, R.; Gordon, R. A.; Webb, M. A. *Am. Mineral.* **2004**, *89*, 519.

(24) Gullikson, E. X-ray transmission of a gas, part of X-ray interactions with matter [online]; Center for X-Ray Optics (CXRO). Available from www.cxro.lbl.gov (accessed April 29, 2008). Parameters: Air ($N_{1.562}$ $O_{0.420}$ $C_{0.0003}$ $Ar_{0.0094}$) → P = 760 torr, T = 295 K, Path length = 11 cm, Energy = 1700–4200 eV, 500 steps.

(25) Forsythe, W. Smithsonian physical tables. 9th revised ed. Knovel. 2003. pp. 168–178.

(26) Hedman, B.; Frank, P.; Penner-Hahn, J. E.; Roe, A. L.; Hodgson, K. O.; Carlson, R. M. K.; Brown, G.; Cerino, J.; Hettel, R.; Troxel, T.; Winick, H.; Yang, J. *Nucl. Instrum. Methods Phys. Res. Sect. A*, **1986**, *246*, 797. doi:10.1016/0168-9002(86)90196-8.

(27) Roper, M. D.; van der Laan, G.; Flaherty, J. V.; Padmore, H. A. *Rev. Sci. Instrum.* **1992**, *63*, 1482. doi:10.1063/1.1143048.

(28) Nachimuthu, P.; Matsuo, S.; Farangis, B.; Lindle, D. W.; Wakita, H.; Perera, R. C. C. *J. Alloys Compd.* **2004**, *362*, 124. doi:10.1016/S0925-8388(03)00572-3.

(29) Gullikson, E. X-ray transmission of a solid, part of X-ray interactions with matter [online]; Center for X-ray Optics (CXRO). Available from http://www.cxro.lbl.gov (accessed April 29, 2008). Parameters: Mylar = 3.0 and 5.0 μm, Al = 0.15 μm, and Lexan = 6.0 μm, T = 295 K, Energy: 1700–3700 eV, 500 steps.

(30) Gullikson, E. The X-ray attenuation length of a solid, part of X-ray interactions with matter [online]; Center for X-Ray Optics (CXRO). Available from http://www.cxro.lbl.gov (accessed April 29, 2008). Parameters: Si_3N_4 → Density = 3.44 g/cm^3, Angle = 90°, Energy: 1800–2600 eV, 400 steps and 1500–1600 eV, 100 steps. H_2O → Density = 1.00 g/cm^3, Angle = 90°, Energy: 1600–4000 eV, 480 steps.

(31) Lurio, L.; Mulders, N.; Paetkau, M.; Jemian, P. R.; Narayanan, S.; Sandy, A. *J. Synchrotron Rad.* **2007**, *14*, 527. doi:10.1107/S0909049507042409.

(32) Booth, C. H.; Bridges, F. *Phys. Scr.* **2005**, *T115*, 202. doi:10.1238/Physica.Topical.115a00202.

(33) Haskel, D. *FLUO: Correcting XANES for self-absorption in fluorescence measurements*, Computer program and documentation [online]. Available from http://www.aps.anl.gov/xfd/people/haskel/fluo.html (accessed January 4, 2009).

(34) Pfalzer, P.; Urbach, J.-P.; Klemm, M.; Horn, S.; denBoer, M. L.; Frenkel, A. I.; Kirkland, J. P. *Phys. Rev. B*, **1999**, *60*, 9335. doi:10.1103/PhysRevB.60.9335.
(35) Tröger, L.; Arvanitis, D.; Baberschke, K.; Michaelis, H.; Grimm, U.; Zschech, E. *Phys. Rev. B,* **1992**, *46*, 3283. doi:10.1103/PhysRevB.46.3283.
(36) Gullikson, E. X-ray transmission of a gas, part of X-ray interactions with matter [online]; Center for X-ray Optics (CXRO). Available from http://www.cxro.lbl.gov (accessed May 1, 2008. Parameters: He → P = 760 torr, T = 295 K, Path length = 1959.25 cm, Energy: 2440–2500 eV, 30 steps. H_2O → $P = 3 \times 10^{-6}$ torr, T = 295 K, Path length = 9.953×10^8 cm, Energy: 2440–2500 eV, 30 steps. He → P = 760 torr, T = 295 K, Path length = 15 cm, Energy: 1700–3700 eV, 500 steps and 600–1800 eV, 500 steps. H_2O → $P = 3 \times 10^{-6}$ torr, T = 295 K, Path length = 15 cm, Energy: 1700–3700 eV, 500 steps and 600–1800 eV, 500 steps.

8-Isocyanoamphilecta-11(20),15-diene, a new antimalarial isonitrile diterpene from the sponge *Ciocalapata* sp.

Chatchai Wattanapiromsakul, Naphatson Chanthathamrongsiri, Somchai Bussarawit, Supreeya Yuenyongsawad, Anuchit Plubrukarn, and Khanit Suwanborirux

Abstract: A new isonitrile diterpene of the amphilectane family, 8-isocyanoamphilecta-11(20),15-diene (**4**), was isolated from the sponge *Ciocalapata* sp., along with three known isonitriles, 8,15-diisocyano-11(20)-amphilectene (**1**), 7-isocyanoamphilecta-11(20),15-diene (**2**), and 8-isocyanoamphilecta-11(20),14-diene (**3**), and two steroidal peroxides, ergosterol peroxide (**5**) and 5α,9α-epidioxy-8α,14α-epoxy-(22*E*)-ergosta-6,22-dien-3β-ol (**6**). The structure of the new isonitrile was elucidated spectroscopically. In addition, anomalous multiplicities in the NMR spectra of some isolated isonitriles were observed and are reported here. The four isonitriles were strongly active against *Plasmodium falciparum* K1 with IC_{50} in a range of 0.09–1.07 μmol/L. Except for **1**, which was cytotoxic against both MCF-7 and fibroblast cell lines, the other three diterpenes showed no significant cytotoxicity against either targeted cell lines. On the other hand, the steroidal peroxides **5** and **6**, which were less active in the antimalarial bioassay (IC_{50} values of 6.28 and 7.13 μmol/L, respectively), were strongly cytotoxic against MCF-7 (IC_{50} values of 0.025 and 0.003 μmol/L, respectively), with very little toxicity against human fibroblasts.

Key words: isonitrile diterpenes, antimalarial, *Ciocalapata*, steroidal peroxides, *Plasmodium falciparum*.

Résumé : À partir de l'éponge *Ciocalapata* sp., on a isolé un nouvel isonitrile diterpénique de la famille des amphilectanes le 8-isocyanatoamphilecta-11(20)-15-diène (**4**), ainsi que cinq produits déjà connus dont trois isonitriles, le 8,15-diisocyanoamphilect-11(20)-ène (**1**), le 7-isocyanoamphilect-11(20),15-diène (**2**) et le 8-isocyanoamphilect-11(20),14-diène (**3**) ainsi que deux peroxydes stéroïdaux, le peroxyde d'ergostérol (**5**) et le 5α,9α-épidioxo-8α14α-épidioxo-(22E)-ergosta-6,22-diène-3β-ol (**6**). On a élucidé les structures des deux nouveaux isonitriles sur la base de la spectroscopie. De plus, on a observé des multiplicités anormales dans les spectres RMN de certains isonitriles isolés et elles sont rapportées ici. Les quatre isonitriles sont fortement actifs contre *Plasmodium falciparum* K1 avec des concentrations inhibant 50% de l'effet observé, CI_{50}, de l'ordre de 0,09 à 107 μmol/L. à l'exception du composé **1** qui est cytotoxique contre les lignées cellulaires MCF-7 et fibroblaste, les deux autres diterpènes ne présentent pas de cytotoxicité significative contre l'une ou l'autre des lignées cellulaires visées. Par ailleurs, les peroxydes stéroïdaux **5** et **6** qui étaient moins actifs dans les essais biologiques antipaludéens (CI_{50} de 6,28 et 7,13 μmol/L respectivement) sont fortement cytotoxiques contre MCF-7 (CI_{50} de 0,025 et 0,003 μmol/L respectivement), mais très peu toxiques contre les fibroblastes humains.

Mots-clés : diterpène isonitrile, antipaludéen, *Ciocalapata*, peroxydes stéroîdaux, *Plasmodium falciparum*.

[Traduit par la Rédaction]

Introduction

Malaria is one of the deadliest infectious diseases troubling the global healthcare system. Despite the severity and high mortality of the disease, to date only two classes of antimalarial drugs, antimalarial quinolines and endoperoxides, are available for clinical use. Whereas the precise mechanisms of the two classes of drugs are still debated, it

Received 25 December 2008. Accepted 18 February 2009. Published on the NRC Research Press Web site at canjchem.nrc.ca on 3 April 2009.

C. Wattanapiromsakul[1] and A. Plubrukarn.[2] Marine Natural Products Research Unit, Department of Pharmacognosy and Pharmaceutical Botany, Faculty of Pharmaceutical Sciences, Prince of Songkla University, Hat-Yai, Songkhla 90112, Thailand; Center of Bioactive Natural Products from Marine Organisms and Endophytic Fungi (BNPME), Department of Pharmacognosy, Chulalongkorn University, Patumwan, Bangkok 10330, Thailand.
N. Chanthathamrongsiri and S. Yuenyongsawad. Marine Natural Products Research Unit, Department of Pharmacognosy and Pharmaceutical Botany, Faculty of Pharmaceutical Sciences, Prince of Songkla University, Hat-Yai, Songkhla 90112, Thailand.
S. Bussarawit. Marine Biology Research Center, Cape Panwa, Phuket 93000, Thailand.
K. Suwanborirux. Center of Bioactive Natural Products from Marine Organisms and Endophytic Fungi (BNPME), Department of Pharmacognosy, Chulalongkorn University, Patumwan, Bangkok 10330, Thailand.

[1]Corresponding author (e-mail: chatchai.w@psu.ac.th).
[2]Corresponding author (e-mail: anuchit.pl@psu.ac.th).

is widely accepted that both classes antagonize hemozoin biocrystallization in the malarial parasites by means of heme-drug complex formation.[1,2] Such complexes cause a blockade in the sequestration of heme in such a way that the parasites are unable to polymerize heme into hemazoin, resulting in the toxic monomeric heme that causes damage to the parasites via oxidative stresses.[3] Using heme as an antimalarial drug target is therefore a reasonable approach for antimalarial drug design, since heme detoxification is a distinctive metabolic pathway found specifically in *Plasmodium* and a few other blood parasites and not in mammal cells.

Apart from the quinolines and endoperoxides, several classes of bioactive natural products have been reported to be active against various species and strains of *Plasmodium*. These include sponge-derived terpenoids bearing isonitrile and related functionalities. Despite a wide variety in the core terpenoid skeletons, ranging from sesquiterpenes of the spiroaxanes, cadinanes, eudesmanes, and guaianes,[4] to diterpenes of the bifloranes, amphilectanes, and cycloamphilectanes,[4g–4i,5] it was the nitrogen-bearing functionalities, i.e., isonitrile, isocyanate, and isothiocyanate, that were proposed to be important in imparting antimalarial activity. In fact, a recent report on pseudoreceptor modeling of isonitrile terpenoids suggested that the complex formation between the axial isonitrile functionality and Fe(III) of protoporphyrin could be crucial in the inhibition of heme detoxification in the parasites.[6]

As part of a research project aimed towards the isolation of bioactive metabolites from Thai marine invertebrates against certain tropical disease pathogens, we found that an extract from a sponge of the genus *Ciocalapata* showed strong antimalarial activity against *Plasmodium falciparum* K1. Further investigation led to the isolation of four antimalarial isonitrile diterpenes, **1**–**4**, among which **4** was a new derivative. In addition, two known steroidal peroxides, **5** and **6**, were also isolated. Here, the isolation and structure elucidation of the new compounds are discussed, and the biological activities of all the isolated compounds are reported.

Results and discussion

The sponge *Ciocalapata* sp. was collected from the vicinity of Koh-Tao, Surat-Thani Province, Thailand, in April 2002. The freeze-dried sponge (279 g) was crushed and extracted consecutively and exhaustively with hexane, CH_2Cl_2, and MeOH. The hexane extract, which showed strong antimalarial activity (IC_{50} 0.05 μg/mL), was subjected to a chromatographic separation to yield **1** (101 mg) after repeated crystallization in hexane. Two other major active fractions pooled from the first chromatographic step were also selected for further separation. The less polar fraction of the two (IC_{50} 0.27 μg/mL) was chromatographed to yield **2**, **3**, and **4** (4, 7, and 6 mg, respectively). Successive chromatography of another main active fraction (IC_{50} 0.45 μg/mL) led to the isolation of **5** and **6** (3 and 4 mg, respectively).

The identification of the isolated compounds was carried out by means of spectroscopic analysis and data comparison with published reports. Compounds **1**, **2**, and **3** were identified to be the known isonitrile diterpenes: 8,15-diisocyano-11(20)-amphilectene, 7-isocyanoamphilecta-11(20),15-diene, and 8-isocyanoamphilecta-11(20),14-diene.[4g,5d,5e] The structures of **5** and **6**, elucidated in the same manner as discussed above, were identified as two known steroidal peroxides: ergosterol peroxide and 5α,9α-epidioxy-8α,14α-epoxy-(22*E*)-ergosta-6,22-dien-3β-ol.[7]

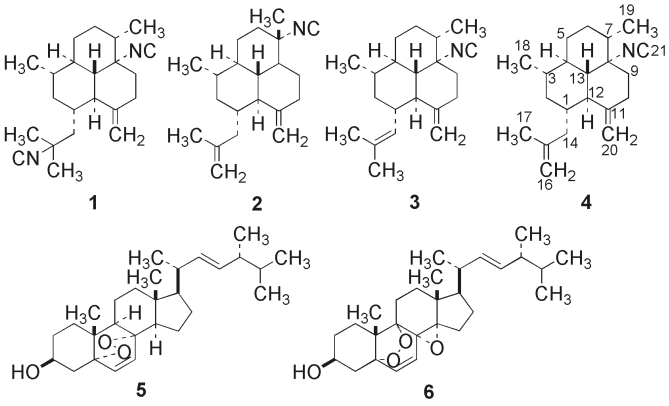

Compound **4**, which was obtained from the same chromatographic step as for **2** and **3**, possesses a molecular formula of $C_{21}H_{31}N$, according to the pseudomolecular ion peak $[M + Na]^+$ at *m/z* 320.2338 in the HR-ESI mass spectrum (calcd. for $C_{21}H_{31}NNa$ 320.2348). The proposed molecular formula yields an unsaturation degree of 7, belonging to two olefinic and one isonitrile functional groups, and three ring systems.

The presence of the isonitrile functionality in **4** was easily recognized from the characteristic IR absorption band at 2150 cm^{-1} and from two triplets (from ^{13}C–^{14}N coupling) carbon resonances at δ 159.9 ($^1J_{CN}$ = 4.2 Hz; C-21) and 66.6 ($^1J_{CN}$ = 4.2 Hz; C-8). The ^1H and ^{13}C NMR spectra (Table 1, 500 MHz for ^1H, C_6D_6) of **4** also showed downfield resonances of two methylidene moieties at δ_H 4.66 (d, *J* = 1.1 Hz; H-20pro-*Z*), 4.77 (br s, 2H; overlapping H-16pro-*Z* and H-20pro-*E*), and 4.85 (br s; H-16pro-*E*), and at δ_C 105.8 (C-20), 111.5 (C-16), 144.2 (C-15), and 150.1 (C-11). The remaining signals in the ^1H NMR spectrum of **4** were found clustered in the highfield region, and the elucidation of all the signals relied heavily on the analysis of the ^1H–^1H COSY spectrum, which led to the proposed amphilectane skeleton of **4** (Fig. 1). The connection of the quaternary carbons via the HMBC correlations (Fig. 1), especially from C-8 to H-9 (δ 1.90 and 0.86), H-12 (δ 1.93, br t, *J* = 11.0 Hz), H-13 (δ 0.64, tt, *J* = 11.0, 3.2 Hz), and H-19 (δ 0.82, br s, 3H); from C-11 to H-10 (δ 2.34, td, *J* = 13.1, 4.4 Hz; and 2.00, ddd, *J* = 13.0, 4.3, 2.3 Hz), H-12, and H-20; and from C-15 to H-1 (δ 1.67), H-16, and H-17 (δ 1.66, s, 3H), confirmed the proposed structure of **4** as a new amphilectane-type isonitrile diterpene, 8-isocyanoamphilecta-11(20),15-diene.

The relative configuration of **4** was determined on the basis of nOe-ds experiments and on that of coupling constant analysis. Six methine protons, i.e., H-1, H-3, H-4, H-7, H-12, and H-13, adopt the axial orientation according to their ^1H–^1H coupling constants (Table 1, 500 MHz, $CDCl_3$). Based on the dipolar couplings among H-1, H-3, H-7, and H-13, and between H-4 and H-12, the first four protons reside on the same plane (i.e., β plane) whereas the latter two reside on the other (i.e., α plane). The close similarity of the ^1H chemical shifts and coupling constants among **1, 3** and **4**, both from the published data[4g,5d,5e] and from our observa-

Table 1. NMR spectral data of **4** (500 MHz for ^{1}H).

Position	δ_H (C_6D_6, mult., J in Hz)[a]	δ_H ($CDCl_3$, mult., J in Hz)[a]	δ_C (C_6D_6, mult.)
1	1.67[b]	1.72[b]	33.9 (CH)
2a	1.78[b]	1.77[b]	39.8 (CH_2)
2b	0.58 (dt; 13.2, 11.7)	0.67 (td; 12.0, 11.5)	
3	0.79[b]	1.00[b]	35.9 (CH)
4	1.13 (br dt; 11.0, 11.0)	1.07 (tdd; 11.0, 10.0, 3.3)	43.0 (CH)
5a	1.78[b]	1.96 (dddd; 12.8, 6.6, 3.3, 3.1)	30.0 (CH_2)
5b	0.48 (qd; 11.0, 4.4)	0.81 (tdd; 12.8, 11.0, 4.3)	
6a	1.46[b]	1.52[b]	30.1 (CH_2)
6b	1.28 (br d; 13.4)	1.42 (ddd; 13.4, 12.5, 3.9)	
7	0.83[b]	1.36[b]	10.8 (CH)
8	—	—	66.6 (C)[d]
9a	1.90[b]	2.27[b]	39.4 (CH_2)
9b	0.86[b]	1.28[b]	
10a	2.34 (td; 13.1, 4.4)	2.32 (td; 13.9, 4.2)	33.6 (CH_2)
10b	2.00 (ddd; 13.1, 4.4, 2.3)	2.24[b]	
11	—	—	150.1 (C)
12	1.93 (br t; 11.0)	1.82 (dd; 10.6, 10.4)	46.1 (CH)
13	0.64 (tt; 11.0, 3.2[c])	0.98[b]	55.5 (CH)
14a	2.66 (br d; 14.7)	2.57 (d; 14.3)	43.0 (CH_2)
14b	1.43[b]	1.50[b]	
15	—	—	144.2 (C)
16 (pro-*E*)	4.85 (br s)	4.73 (br s)	111.5 (CH_2)
16 (pro-Z)	4.77 (br s)	4.64 (br s)	
17	1.66 (s; 3H)	1.70 (s; 3H)	22.7 (CH_3)
18	0.75 (s; 3H)	0.86 (d; 6.1; 3H)	19.7 (CH_3)
19	0.82 (s; 3H)	0.96 (d; 6.4; 3H)	15.7 (CH_3)
20 (pro-*E*)	4.77 (br s)	4.82 (br s)	105.8 (CH_2)
20 (pro-Z)	4.66 (d; 1.1)	4.61 (br s)	
21	—	—	159.9 (C)[d]

[a]Unless stated otherwise, each proton signal was integrated to 1H.
[b]The multiplicities could not be elucidated because of overlapping signals.
[c]1:1:1 triplet of $^3J_{HN}$.
[d]t; $^1J_{CN}$ = 4.2 Hz.

Fig. 1. ^{1}H–^{1}H COSY (bold lines) and HMBC (C → H) correlations of **4.**

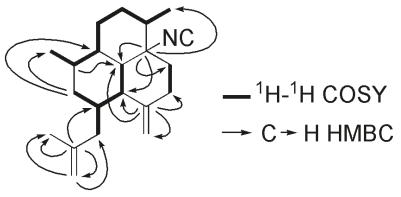

4

tions, indicated that the three compounds held the same relative configurations at all chiral centers. Regarding the absolute stereochemistry, the close observation suggested that for the 8-axial isonitrile amphilectane-type diterpenes with all *trans* ring junctions and with no endocyclic olefinic functionality (i.e., as of **1**, **3**, and **4**), an analog with 8*S* configuration generally corresponds with a levorotatory optical rotation.[4g,5d,5e] The configurations of all seven asymmetric carbons of **4** are therefore arbitrarily proposed here to be identical to those of **3** as the following: 1*S*, 3*S*, 4*R*, 7*S*, 8*S*, 12*S*, and 13*S*.

During the course of the NMR spectral analysis of **1**, **2**, and **4**, we noticed unconventional multiplicities in their ^{1}H NMR spectra. In spite of the fact that all spectral data of each isonitrile strongly indicated the substitutions of the methyl-18 on the secondary carbon C-3 (for **1**, **2**, and **4**) and of methyl-19 on C-7 (for **1** and **4**), the NMR signals of both methyls obtained from C_6D_6 did not resolve into the conventional doublets. Instead, singlet resonances were observed for H-18 for all three isonitriles and for H-19 of **4** (Table 1). The typical doublet methyl resonances resumed when $CDCl_3$ was used as an operating NMR solvent. For instance, H-18 and H-19 of **4** (Table 1, 500 MHz, $CDCl_3$) resonated as doublets at δ 0.86 (J = 6.1 Hz) and 0.96 (J = 6.4 Hz), respectively. It is noteworthy to mention that H-19 of **1**, on the other hand, resonates as a theoretical doublet in C_6D_6 (J = 6.4 Hz).

It can be argued that such unresolved multiplicity had resulted either from the operating concentrations or from intrinsic factors of the spectrometer itself (for example, the homogeneity in the magnetic field). However, similar phenomena were also observable when the re-dissolved samples in C_6D_6 were re-analyzed on other NMR spectrometers (Bruker 300 and 500 MHz spectrometers, data not shown). It could also be argued that such singlets were in fact parts of second-order spectra caused by the strong coupling between each methyl and its vicinal proton (e.g., for **4**, esti-

Table 2. Antimalarial and cytotoxic activities of **1–6.**

Compounds	Antimalarial activity(IC_{50}, μmol/L)	Cytotoxicity (IC_{50}, μmol/L)	
		MCF-7	Fibroblast
1	0.09	9.0	13.9
2	1.07	Inactive[a]	Inactive[a]
3	0.44	NA[b]	Inactive[a]
4	0.98	Inactive[a]	Inactive[a]
5	6.28	0.025	Inactive[a]
6	7.13	0.003	Inactive[a]
Artemisinin	0.01	12.1	21.1
Dihydroartemisinin	0.004	—	—
Camptothecin	—	0.002	0.5

[a]No inhibition was observed or cell viability was higher than 80% at the highest concentration of 5 μg/mL.

[b]The IC_{50} could not be calculated because of inconsistent statistical results.

mated $\Delta\nu/J$ between H-3 and H-18 ca. 2.5; between H-7 and H-19 ca. 2.0; 500 MHz, C_6D_6); nevertheless, this argument was not applicable to the singlet signals of methyl-18 of **1** and **2** (estimated $\Delta\nu/J$ between H-3 and H-18 of **1** ca. 23; of **2** ca. 25; 500 MHz, C_6D_6). The solvent effects on the NMR chemical shifts are widely acknowledged. Also, the effect of the concentration upon the proton chemical shifts of the methyl groups on steroid nucleus when operated in C_6D_6 were reported.[8] Nonetheless, to our knowledge, such unresolved multiplicity and coupling constants due to the changes in operating solvents have never been documented. At the moment, we are yet unable to account for such abnormalities, although it could be speculated that the stacking interaction between the molecules of each sample and C_6D_6, facilitated by the rigid and planar amphilectane skeleton, might exert its role to a certain extent. To make a generalized statement on this solvent effect, however, a larger compound dataset with a wider variety of operating solvents, structural features, and field strengths, is required. This extensive investigation is currently underway.

All the isolated compounds were subjected to biological activity determination, namely antimalarial activity against *P. falciparum* K1 and cytotoxicity against MCF-7 and fibroblasts, respectively, representing cancer and normal cell lines (Table 2). Except **2**, which was previously reported to be active against *P. falciparum* D2 and W2 (IC_{50} 1.7 and 0.8 μmol/L, respectively)[9], the antimalarial activity of all the isolated compounds is reported here for the first time. With the IC_{50} values in a range of 0.04–1.07 μmol/L (Table 2), albeit 10–100 times less active than the standards artemisinin and dihydroartemisinin, the antimalarial activity of **1–4** is nonetheless considerably strong. The range of the antimalarial activity of the isolated isonitriles was also in a range similar to that of other related isonitriles and isothiocyanates, whose IC_{50} values were reported to be in a range of 0.01–10 μmol/L.[9,10] In addition, the dramatic contrast between the antimalarial and cytotoxic activities (against both cancer and normal cell lines) suggested their potential as promising leads for the development of new class of antimalarial agents.

The steroidal peroxides **5** and **6**, on the other hand, although less active as antimalarial agents, were rather interesting as cytotoxic agents. Their strong cytotoxicity against the MCF-7 cancer cell line and undetectable toxicity against human fibroblasts are also reported here for the first time. Such selectivity suggests their possible applications in anticancer drug development programs in the future.

Conclusion

A new amphilectane-type isonitrile diterpene, 8-isocyanoamphilecta-11(20),15-diene (**4**), along with its three known isonitrile analogs and two known steroidal peroxides, were isolated from the Thai sponge *Ciocalapata* sp. The antimalarial and cytotoxic activities of all the isolated compounds were assessed to show strong activities with promising selectivity for two bioassays. Regarding the possible targets and mechanisms of actions, especially for the diterpenes, it has been long known that the isonitrile functionality can bind specifically to Fe(III) in heme, and that such binding causes conformation distortions in the heme molecule.[11] The influence of complex formation between isonitrile terpenoids and Fe(III) in protoporphyrin on the inhibition of heme detoxification in *Plasmodium* parasites based on the modeled pseudoreceptor of isonitriles has also been reported.[6] Our findings therefore support previous postulations and extend the possibility of the isonitrile terpenoids as a potential source of future antimalarial agents. In addition, the selective cytotoxicity of the steroidal peroxides **5** and **6** suggests that these may be of use in anticancer drug development programs.

Experimental

General

Specific rotations were recorded on a PerkinElmer 341 polarimeter. IR spectra were obtained using a Jasco IR-810 infrared spectrometer. UV spectra were measured on a Hewlett Peckard 8452 diode array spectrophotometer. Mass spectra, both low- and high-resolution ones, were obtained on an MAT 95 XL mass spectrometer. All NMR experiments were performed on an FT-NMR Varian Unity Inova 500 spectrometer (500 MHz for ^1H), referencing solvent signals as stated accordingly. For the chromatographic separation, the chromatographic supporting materials were Scharlau SiO_2 (230–400 mesh) for flash chromatography and GE Health-

care Sephadex LH-20 for size exclusion chromatography. HPLC separations were performed on a Water 600E multisolvent delivery system, equipped with a Water 484 UV tunable detector and a Rheodyne 7125 injector port.

Animal material

The sponge *Ciocalapata* sp. (family Halichondriidae)[12] was collected in April 2002, at a depth of 15–20 m in the vicinity of Koh-Tao, Surat-Thani Province, Thailand (10° 7.569′ N, 99° 48.665′ E). Upon surfacing, the specimen appeared as a lumpy mass with porous texture and rough external surface. The outer color was pale khaki with dark brown to green spots. Taxonomic identification was carried out by one of us (SB),[12] and a voucher specimen (PMBC24607) was deposited at Phuket Marine Biological Center, Phuket, Thailand.

Extraction and isolation

The freeze-dried sponge (279 g) was consecutively and exhaustively macerated in a series of solvents to yield hexane, CH_2Cl_2, and MeOH extracts (7, 6, and 63 g, respectively). In this report, only the hexane extract, which showed the most potent antimalarial activity (IC_{50} 0.05 μg/mL), was studied further. The chemical investigations of the less active CH_2Cl_2 and MeOH extracts, which are now underway, will be reported elsewhere. The hexane extract was subjected to a SiO_2 vacuum chromatography (stepped gradient from hexane to MeOH/CH_2Cl_2 1:1). The fractions containing the major constituent were combined and recrystallized repeatedly in hexane to yield **1** as white needles (101 mg, 1.4% of hexane extract). Two additional major fractions from subsequent fractional pools were also selected for the separation based on their potent antimalarial activity. The first fraction was subjected to the following chromatographies: SiO_2 flash chromatography (EtOAc/hexane 1:49), then C-18 reverse-phase HPLC (Phenomenex 250 × 10 mm, 10 μm particle size; H_2O/MeCN 1:9, 4.5 mL/min), and **2**, **3**, and **4** (4, 7, and 6 mg; 0.06%, 0.1%, and 0.09% of hexane extract, respectively) were obtained (t_Rs 20.8, 22.6, and 24.0 min, respectively). The second fraction was subjected to the following: Sephadex LH-20 chromatography (EtOAc/hexane 1:1), SiO_2 flash chromatographies (EtOAc/hexane 1:1 and THF/EtOAc/hexane 9:18:73), and C-18 reverse-phase HPLC (Phenomenex 250 × 10 mm, 10 μm particle size; H_2O/MeCN 1:19, 3 mL/min), and **5** and **6** (3 and 4 mg; 0.04% and 0.06% of hexane extract, respectively) were obtained (t_Rs 21.1 and 33.8 min, respectively).

8,15-Diisocyano-11(20)-amphilectene (1)

White needles. $[\alpha]_D$ –56 (c = 0.28, $CHCl_3$). UV ($CHCl_3$, nm) λ_{max} (log ε) 244 (2.41). IR (thin film, cm^{-1}) ν_{max} 2925, 2150. ^1H NMR (500 MHz, C_6D_6) δ: (mult., J in Hz) 4.77 (br s; H-20a), 4.71 (br s; H-20b), 2.25 (ddd, 13.2, 12.8, 4.1; H-10a), 2.08 (br d, 13.2; H-2a), 2.00 (ddd, 12.8, 4.1, 2.7; H-10b), 1.93 (br d, 13.3; H-9a), 1.81 (overlapped; H-14a), 1.80 (overlapped; H-1), 1.78 (overlapped; H-12), 1.76 (overlapped; H-6a), 1.41 (dddd, 13.7, 13.2, 12.4, 3.7; H-6b), 1.25 (dddd, 13.2, 3.7, 3.2, 3.2; H-5a), 1.05 (br s; 6H; H-16 & H-17), 1.04 (overlapped; H-3), 0.88 (overlapped; H-9b), 0.84 (overlapped; H-7), 0.82 (d, 6.4; 3H; H-19), 0.71 (overlapped; H-14b), 0.76 (br s; 3H; H-18), 0.76 (overlapped; H-4), 0.67 (overlapped; H-13), 0.62 (overlapped; H-2b), 0.50 (dddd, 13.2, 13.2, 11.9, 3.2; H-5b). ^{13}C NMR (125 MHz, C_6D_6) δ: 159.7 (t, $^1J_{CN}$ = 3.7 Hz; C-22), 157.8 (t, $^1J_{CN}$ = 5.0 Hz; C-21), 149.8 (C-11), 106.5 (C-20), 66.7 (t, $^1J_{CN}$ = 3.7 Hz; C-8), 56.3 (t, $^1J_{CN}$ = 5.0 Hz; C-15), 55.2 (C-13), 46.1 (C-12), 45.5 (C-14), 42.7 (C-4), 41.0 (C-2), 40.7 (C-7), 39.5 (C-9), 35.4 (C-3), 33.7 (C-10), 33.3 (C-1), 31.4 (C-17), 30.2 (C-16), 30.0 (C-6), 29.8 (C-5), 19.8 (C-18), 15.7 (C-19). ESI-MS m/z (% relative intensity): 347 ($[M + Na]^+$, 8), 271 (30), 212 (100).

7-Isocyanoamphilecta-11(20),15-diene (2)

White glass. $[\alpha]_D$ +63 (c = 0.25, $CHCl_3$). UV ($CHCl_3$, nm) λ_{max} (log ε) 244 (2.70). IR (thin film, cm^{-1}) ν_{max} 2950, 2125, 880. ^1H NMR (500 MHz, C_6D_6) δ: (mult., J in Hz) 4.86 (br s; 2H; H-16a & H-20a), 4.80 (br s; H-16b), 4.67 (br s; H-20b), 2.72 (br d, 13.7; H-14a), 2.24 (ddd, 15.1, 5.9, 1.6; H-10a), 2.02 (dt, 15.1, 9.5; H-10b), 1.84 (ddd, 13.5, 3.4, 3.4; H-2a), 1.74 (br ddd, 15.5, 7.1, 7.1; H-5a), 1.68 (br s; 3H; H-17), 1.66 (overlapped; H-9a), 1.64 (overlapped; H-9b), 1.58 (m; H-1), 1.44 (overlapped; H-14b), 1.43 (overlapped; H-6a), 1.42 (overlapped; H-4), 1.35 (t, 10.5; H-12), 1.19 (m; H-8), 1.08 (overlapped; H-3), 1.06 (overlapped; H-6b), 0.98 (t, $^3J_{HN}$ = 1.8 Hz; 3H; H-19), 0.87 (br dd, 10.8, 10.6; H-13), 0.77 (br s; 3H; H-18), 0.66 (dtd, 15.5, 8.1, 7.9; H-5b), 0.50 (ddd, 13.5, 11.4, 11.4; H-2b). ^{13}C NMR (125 MHz, C_6D_6) δ: 158.5 (t, $^1J_{CN}$ = 5.0 Hz; C-21), 148.8 (C-11), 144.3 (C-15), 111.7 (C-16), 106.6 (C-20), 59.3 (t, $^1J_{CN}$ = 5.0 Hz; C-7), 49.2 (C-12), 45.5 (C-13), 42.3 (C-8 & C-14), 41.3 (C-2), 39.9 (C-3 & C-4), 34.9 (C-1), 33.9 (C-10), 33.6 (C-6), 28.7 (C-19), 24.7 (C-5), 22.5 (C-17), 21.8 (C-9), 19.4 (C-18). ESI MS m/z (% relative intensity): 320 ($[M + Na]^+$, 100), 271 (9).

8-Isocyanoamphilecta-11(20),14-diene (3)

White glass. $[\alpha]_D$ –27 (c = 0.38, $CHCl_3$). IR (thin film, cm^{-1}) ν_{max} 2925, 2125. UV ($CHCl_3$, nm) λ_{max} (log ε) 244 (2.57). ^1H NMR (500 MHz, C_6D_6) δ: (mult., J in Hz) 4.88 (br d, 8.5; H-14), 4.79 (br s; H-20a), 4.68 (br d, 1.3; H-20b), 2.43 (br t, 13.2; H-9a), 2.32 (br dd, 10.7, 10.0; H-1), 2.07 (t, 10.7; H-12), 2.00 (dddt; 13.2, 2.0, 2.0, 2.0; H-9b), 1.90 (br d, 13.2; H-10a), 1.78 (br d, 13.0; H-5a), 1.62 (br s; 3H; H-17), 1.57 (br s; 3H; H-16), 1.47 (overlapped; H-2a), 1.47 (overlapped; H-6a), 1.25 (dd, 13.7, 13.0; H-6b), 1.16 (br dd, 10.5, 10.2; H-4), 0.88 (overlapped; H-3), 0.87 (overlapped; H-2b), 0.85 (overlapped; H-10b), 0.83 (br d, 6.4; 3H; H-19), 0.83 (overlapped; H-7), 0.75 (dd, 6.0, 1.3; 3H; H-18), 0.64 (ddt, 10.7, 10.2, 2.0; H-13), 0.52 (dddd, 13.5, 13.0, 10.5, 4.1; H-5b). ^{13}C NMR (125 MHz, C_6D_6) δ: 159.9 (t, $^1J_{CN}$ = 3.7 Hz; C-21), 149.3 (C-11), 131.8 (C-14), 128.5 (C-15), 107.7 (C-20), 66.5 (t, $^1J_{CN}$ = 3.7 Hz; C-8), 54.3 (C-13), 46.1 (C-12), 42.9 (C-4), 41.2 (C-2), 40.7 (C-7), 38.6 (C-10), 37.7 (C-1), 36.3 (C-3), 33.1 (C-9), 30.1 (C-6 & C-5), 25.6 (C-17), 19.6 (C-18), 17.8 (C-16), 15.7 (C-19). ESI-MS m/z (% relative intensity): 320 ($[M + Na]^+$, 100), 271 (18).

8-Isocyanoamphilecta-11(20),15-diene (4)

White glass. $[\alpha]_D$ –51 (c = 0.33, $CHCl_3$). UV ($CHCl_3$, nm) λ_{max} (log ε) 244 (2.38). IR (thin film, cm^{-1}) ν_{max} 2950, 2150, 895. For ^1H and ^{13}C NMR, see Table 1. HR ESI-MS m/z: 320.2338 (calcd. for $C_{21}H_{31}NNa$: 320.2348). ESI-MS m/z (% relative intensity): 320 ($[M + Na]^+$, 100).

Antimalarial activity determination

The antimalarial bioassay was serviced by BIOTEC Central Research Unit, BIOTEC, Thailand, according to the microculture radioisotope technique.[13] The targeted parasite was *P. falciparum* K1 (chloroquine- and pyrimethamine-resistant strain), and the potency was assessed using artemisinin and dihydroartemisinin as standard reference drugs.

Cytoxicity determination

The cytotoxicity bioassay was performed in-house using the sulforhodamine B assay protocol.[14] The targeted cell lines were MCF-7 breast adenocarcinoma and human oral fibroblasts, representing cancer and normal cell lines, respectively. The cytotoxicity was assessed using camptothecin as a standard reference.

Supplementary data

Supplementary data for this article are available on the journal Web site (canjchem.nrc.ca) or may be purchased from the Depository of Unpublished Data, Document Delivery, CISTI, National Research Council Canada, Ottawa, ON K1A 0R6, Canada. DUD 3911. For more information on obtaining material refer to cisti-icist.nrc-cnrc.gc.ca/cms/unpub_e.shtml.

Acknowledgements

This work is supported by Prince of Songkla University Research Supporting Grant, and the joint grant from the Thailand Research Fund and Commission on Higher Education (MRG5080190). BNPME is supported by a grant for the Center of Excellence, Commission on Higher Education, Thailand. NC thanks the TRF/BIOTEC Special Program for Biodiversity Research and Training Grant (BRT T_650008) and the Academic Excellence Enhancing Program in Pharmaceutical Sciences for her thesis supporting grants. We also thank Professor L.A. Damani, Faculty of Pharmaceutical Sciences, Prince of Songkla University, for his scientific and editorial comments.

References

(1) Sullivan, D. J., Jr.; Gluzman, I. Y.; Russell, D. G.; Goldberg, D. E. *Proc. Natl. Acad. Sci. U.S.A.* **1996**, *93*, 11865. doi:10.1073/pnas.93.21.11865. PMID:8876229.

(2) Shukla, K. L.; Gund, T. M.; Meshnick, S. R. *J. Mol. Graph.* **1995**, *13*, 215. doi:10.1016/0263-7855(94)00001-9.

(3) (a) Sullivan, D. J., Jr.; Matile, H.; Ridley, R. G.; Goldberg, D. E. *J. Biol. Chem.* **1998**, *273*, 31103 doi:10.1074/jbc.273.47.31103.; (b) Pandey, A. V.; Tekwanis, B. L.; Singh, R. L.; Chauhan, V. S. *J. Biol. Chem.* **1999**, *274*, 19383 doi:10.1074/jbc.274.27.19383.; (c) Kannan, R.; Sahal, D.; Chauhan, V. S. *Chem. Biol.* **2002**, *9*, 321. doi:10.1016/S1074-5521(02)00117-5. PMID:11927257.

(4) (a) Cafieri, F.; Fattorusso, E.; Magno, S.; Santacroce, C.; Sica, D. *Tetrahedron* **1973**, *29*, 4259 doi:10.1016/0040-4020(73)80267-4.; (b) Fattorusso, E.; Magno, S.; Mayol, L.; Santacroce, C.; Sica, D. *Tetrahedron* **1974**, *30*, 3911 doi:10.1016/S0040-4020(01)97082-6.; (c) Di Blasio, D.; Fattorusso, E.; Magno, S.; Mayol, L.; Pedone, C.; Santacroce, C.; Sica, D. *Tetrahedron* **1976**, *32*, 473 doi:10.1016/0040-4020(76)80065-8.; (d) Braekman, J. C.; Daloze, D.; Moussiaux, B.; Stoller, C.; Deneubourg, F. *Pure Appl. Chem.* **1989**, *61*, 509 doi:10.1351/pac198961030509.; (e) Angerhofer, C. K.; Pezzuto, J. M.; König, G. M.; Wright, A. D.; Sticher, O. *J. Nat. Prod.* **1992**, *55*, 1787 doi:10.1021/np50090a014. PMID:1294700.; (f) Burgoyne, D. L.; Dumdei, E. J.; Anderson, R. J. *Tetrahedron* **1993**, *49*, 4503 doi:10.1016/S0040-4020(01)81280-1.; (g) Mitome, H.; Shirato, N.; Miyaoka, H.; Yamada, Y.; van Soest, R. W. M. *J. Nat. Prod.* **2004**, *67*, 833 doi:10.1021/np030458p. PMID:15165146.; (h) Manzo, E.; Ciavatta, M. L.; Gavagnin, M.; Mollo, E.; Guo, Y.; Cimino, G. *J. Nat. Prod.* **2004**, *67*, 1701 doi:10.1021/np0400961. PMID:15497943.; (i) Yan, X. H.; Zhu, X. Z.; Yu, J. L.; Jin, D. Z.; Guo, Y. W.; Mollo, E.; Cimino, G. *J. Asian Nat. Prod. Res.* **2006**, *8*, 579. doi:10.1080/10286020410001721096. PMID:16931436.

(5) (a) Chang, C. W. J.; Patra, A.; Roll, D. M.; Scheuer, P. J.; Matsumoto, G. K.; Clady, J. *J. Am. Chem. Soc.* **1984**, *106*, 4644 doi:10.1021/ja00328a073.; (b) König, G. M.; Wright, A. D.; Angerhofer, C. K. *J. Org. Chem.* **1996**, *61*, 3259 doi:10.1021/jo952015z.; (c) Linden, A.; König, G. M.; Wright, A. D. *Acta Crystallogr. C* **1996**, *52*, 2601 doi:10.1107/S010827019600515X.; (d) Ciavatta, M. L.; Fontana, A.; Puliti, R.; Scognamiglio, G.; Cimino, G. *Tetrahedron* **1999**, *55*, 12629 doi:10.1016/S0040-4020(99)00737-1.; (e) Ciavatta, M. L.; Gavagnin, M.; Manzo, E.; Puliti, R.; Mattia, C. A.; Mazzarella, L.; Cimino, G.; Simpson, J. S.; Garson, M. J. *Tetrahedron* **2005**, *61*, 8049. doi:10.1016/j.tet.2005.05.102.

(6) Wright, A. D.; Wang, H.; Gurrath, M.; König, G. M.; Kocak, G.; Newman, G.; Loria, P.; Foley, M.; Tilley, L. *J. Med. Chem.* **2001**, *44*, 873. doi:10.1021/jm0010724.

(7) (a) da Graça Sgarbi, D. B.; da Silva, A. J.; Carlos, I. Z.; Silva, C. L.; Angluster, J.; Alviano, C. S. *Mycopathologia* **1997**, *139*, 9 doi:10.1023/A:1006803832164. PMID:9511231.; (b) Bok, J. W.; Lermer, L.; Chilton, J.; Klingeman, H. G.; Towers, G. H. *Phytochemistry* **1999**, *51*, 891 doi:10.1016/S0031-9422(99)00128-4. PMID:10423860.; (c) Nam, K. S.; Jo, Y. S.; Kim, Y. H.; Hyun, J. W.; Kim, H. W. *Life Sci.* **2001**, *69*, 229 doi:10.1016/S0024-3205(01)01125-0. PMID:11441913.; (d) Wang, J.; Huang, Y.; Fang, M.; Xie, W.; Su, W.; Zhao, Y. *Acta Crystallogr. E* **2004**, *60*, o764 doi:10.1107/S160053680400813X.; (e) Yaoita, Y.; Yoshihara, Y.; Kakuda, R.; Machida, K.; Kikuchi, M. *Chem. Pharm. Bull. (Tokyo)* **2002**, *50*, 551. doi:10.1248/cpb.50.551. PMID:11964010.

(8) Gunatilaka, A. A. L.; Gopichand, Y.; Schmitz, F. J.; Djerassi, C. *J. Org. Chem.* **1981**, *46*, 3860. doi:10.1021/jo00332a020.

(9) Wright, A. D.; König, G. M.; Angerhofer, C. K.; Greenidge, P.; Linden, A.; Desqueyroux-Faúndez, R. *J. Nat. Prod.* **1996**, *59*, 710. doi:10.1021/np9602325. PMID:8759172.

(10) (a) Singh, C.; Srivastav, N. C.; Puri, S. K. *Bioorg. Med. Chem. Lett.* **2002**, *12*, 2277 doi:10.1016/S0960-894X(02)00457-2. PMID:12161115.; (b) Laurent, D.; Pietra, F. *Mar. Biotechnol.* **2006**, *8*, 433. doi:10.1007/s10126-006-6100-y. PMID:16565802.

(11) (a) Reisberg, P. I.; Olsen, J. S. *J. Biol. Chem.* **1980**, *255*, 4144; (b) Robberecht, P.; De Neef, P.; Buscail, L.; Christophe, J. *Biochem. J.* **1989**, *261*, 959. PMID:2552994.

(12) Hooper, J. N. A. *Sponge guide: Guide to sponge collection and identification*; Queensland Museum, Queensland, 2000; pp. 70–71.

(13) (a) Desjardins, R. E.; Canfield, C. J.; Haynes, J. D.; Chulay, J. D. *Antimicrob. Agents Chemother.* **1979**, *16*, 710 PMID:

394674.; (b) Jongrungruangchok, S.; Kittakoop, P.; Yongsmith, B.; Bavovada, R.; Tanasupawat, S.; Lartpornmatulee, N.; Thebtaranonth, Y. *Phytochemistry* **2004**, *65*, 2569. doi:10.1016/j.phytochem.2004.08.032. PMID:15451319.

(14) Skehan, P.; Storeng, R.; Scudiero, D.; Monks, A.; McMahon, J.; Vistica, D.; Warren, J. T.; Bokesch, H.; Kenney, S.; Boyd, M. R. *J. Natl. Cancer Inst.* **1990**, *82*, 1107. doi:10.1093/jnci/82.13.1107. PMID:2359136.

Controlling the regioselectivity of the di-π-methane rearrangements of 1,2-naphtho-annelated barrelene derivatives — Solution versus solid-state photochemistry

Jia Luo, Heiko Ihmels, Hans-Jörg Deiseroth, and Marc Schlosser

Abstract: The synthesis of 1,2-naphtho-annelated barrelene derivatives, namely dimethyl-7,12-dihydro-7,12-ethenobenzo[*a*]anthracene-13,14-dicarboxylate (**4a**) and dimethyl-7,14-dihydro-7,14-ethenodibenzo[*a,j*]-anthracene-15,16-dicarboxylate (**4b**), and the investigation of their photoreactivity in solution and in the solid state is reported. The irradiation of **4a** and **4b** resulted in regioselective di-π-methane rearrangements to give semibullvalene products; however, the product distribution is inverted upon changing the reaction medium from solution to the solid state. In solution, an α-naphtho–vinyl bridging predominates as the initial photochemical step because of the selective stabilization of the corresponding transition state, as discussed on the basis of the structures of the related biradical intermediates, whereas the solid-state photoreaction is significantly influenced by the steric constraints within the crystal lattice that only allow a β-naphtho–vinyl bridging.

Key words: di-π-methane rearrangement, barrelene derivatives, solid-state photochemistry.

Résumé : On a réalisé la synthèse de dérivés condensés 1,2-naphtobarrèlènes, à savoir le 7,12-dihydro-7,12-éthénobenzo[*a*]anthracène-13,14-dicarboxylate de diméthyle (**4a**) et le 7,14-dihydro-7,14-éthénobenzo[*a,j*]anthracène-15,16-dicarboxylate de diméthyle (**4b**), et on a étudié leur photoréactivité en solution et à l'état solide. L'irradiation des composés **4a** et **4b** conduit à des réarrangements di-π-méthane régiosélectifs et à la formation de produits semibullvalènes; toutefois, la distribution des produits est inversée lorsque le milieu réactionnel passe de la solution à l'état solide. En solution, un pont α-naphtovinyle prédomine comme étape photochimique initiale en raison de la stabilisation sélective de l'état de transition correspondant, tel que discuté sur la base des structures des intermédiaires biradicalaires apparentés, alors que la photoréaction à l'état solide est fortement influencée par des contraintes stériques dans le réseau cristallin qui ne permettent que la formation d'un pont β-naphtovinyle.

Mots-clés : réarrangement di-π-méthane, dérivés du barrèlène, photochimie à l'état solide.

[Traduit par la Rédaction]

Introduction

The di-π-methane rearrangement[1] of benzo-annelated derivatives of barrelene (bicyclo[2.2.2]octatriene)[2] and norbornadiene (bicyclo[2.2.1]heptadiene)[3] has been shown to be an appropriate model reaction for the assessment of the substituent effects on the selectivity of organic photoreactions. In particular, the structural features that govern the type-selectivity, the regioselectivity, and the stereoselectivity of dibenzobarrelene photoreactions in solution[1c–1f] and in constrained media have been evaluated in detail.[4] Thus, in a pivotal paper,[2a] Zimmerman et al. have shown that the irradiation of dibenzobarrelene **1a** leads to the selective formation of the dibenzosemibullvalene **2a** (Scheme 1), and this remarkable regioselectivity has been rationalized in terms of the selective stabilization of one of the four possible biradicals by the electron-accepting substituent on the benzene ring. In addition, it has been shown that the nature and the position of the substituents at the benzene rings of dibenzobarrelene derivatives **1b**–**1f** have a strong influence on the regioselectivity of the di-π-methane rearrangement (Scheme 1).[2b,2c] Notably, both donor and acceptor substituents were shown to influence the regioselectivity of the photorearrangement of dibenzobarrelenes. At the same time, there are only a few studies with a focus on the influence of an annelated naphthalene unit on the regioselectivity of the di-π-methane rearrangement of barrelene derivatives.[5] In particular, the competition between vinyl–naphtho and vinyl–vinyl bridging in the initial step of the di-π-methane rearrangement of naphthobarrelenes was examined, and the following order of reactivity was deduced: α-naphtho–vinyl > vinyl–vinyl > β-naphtho–vinyl > benzo-vinyl. Nevertheless, no studies have been reported on the direct competition between photoinduced benzo–vinyl and α-naphtho–vinyl bridging in annelated barrelene derivatives. To fill this gap, we synthesized the naphtho-annelated

Received 18 December 2008. Accepted 29 January 2008. Published on the NRC Research Press Web site at canjchem.nrc.ca on 8 April 2009.

J. Luo and H. Ihmels.[1] University of Siegen, Organic Chemistry II, Adolf-Reichwein-Str. 2, 57068 Siegen, Germany. **H.-J. Deiseroth and M. Schlosser.** University of Siegen, Inorganic Chemistry I, Adolf-Reichwein-Str. 2, 57068 Siegen, Germany.

[1]Corresponding author (e-mail: ihmels@chemie.uni-siegen.de).

Scheme 1. Substituent effects on the di-π-methane rearrangement of dibenzobarrelene derivatives.

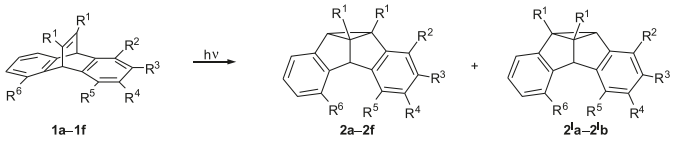

	R^1	R^2	R^3	R^4	R^5	R^6	**2** : **2ᴵ**
a:	D	H	H	CN	H	H	>99 : <1
b:	CO_2Me	CN	H	H	H	CN	80 : 20
c:	CO_2Me	OMe	H	H	H	OMe	86 : 14
d:	CO_2Me	H	CO_2Me	CO_2Me	H	H	83 : 17
e:	CO_2Me	H	OMe	OMe	H	H	42 : 58
f:	CO_2Me	OMe	H	H	OMe	H	80 : 20

Scheme 2. Synthesis of 1,2-naphthobarrelene derivatives **4a**–**4c**.

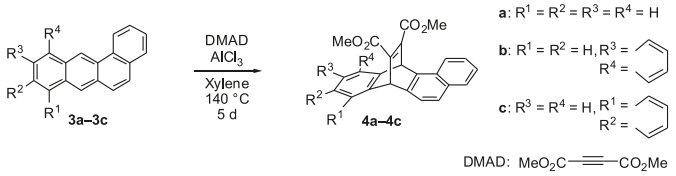

barrelene derivatives **4a** and **4b** and investigated their photochemical behavior. Herein, we show that the photoinduced di-π-methane rearrangements of these compounds proceed with high regioselectivity in solution and in the solid state, notably with inverse selectivities.

Results

Synthesis

The benzonaphthobarrelene **4a** was obtained in 68% yield by a Diels–Alder reaction of dimethyl acetylenedicarboxylate (DMAD) with benzo[*a*]anthracene (**3a**) (Scheme 2).[6] For the analogous synthesis of dinaphthobarrelene derivatives **4b** and **4c**, a mixture of the two isomeric dibenzoanthracene derivatives **3b** and **3c** was employed. The latter were obtained from the reaction of 1-bromonaphthalene with *N*-lithio-2,2,6,6-tetramethylpiperidine in THF in a ratio of 72:28, as determined by ^{1}H NMR spectroscopic analysis.[7] Since the dibenzoanthracene derivatives are air and light sensitive, the product mixture was immediately made to react with DMAD to give the dinaphthobarrelenes **4b** and **4c** in 30% overall yield in a ratio of 71:29 (Scheme 2). Attempts to separate the two isomers **4b** and **4c** by column chromatography failed; however, the dinaphthobarrelene **4b** was isolated by crystallization in 6% yield. At the same time, we observed a strong tendency of the two isomers **4b** and **4c** to co-crystallize in a 1:1 ratio.

It should be noted that all chiral products are formed without enantioselectivity. Thus, all presented chiral compounds are actually racemic mixtures.

Photoreactions

In acetone solution, the naphthobenzobarrelene **4a** (long-wavelength absorption: $\lambda_{abs,max}$ = 292 nm) underwent an essentially clean di-π-methane rearrangement upon irradiation (λ_{ex} > 254 nm) to give the two semibullvalene derivatives **5a^{I}** and **5a^{II}** in a 87:13 ratio, as determined by ^{1}H NMR spectroscopic analysis (Scheme 3). Although it was impossible to separate the two semibullvalenes **5a^{I}** and **5a^{II}** by

Scheme 3. Photoreaction of benzonaphthobarrelene **4a**.

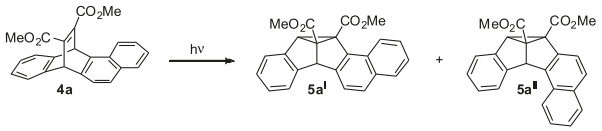

column chromatography, the major photoproduct **5a^{I}** was isolated in 61% yield by crystallization directly from the reaction mixture. The preferential formation of the photoproduct **5a^{I}** in solution was also observed in MeCN and benzene solution, however, with slightly lower selectivity (Table 1). Thus, as commonly observed for free-radical reactions, there is no pronounced solvent effect on the selectivity.[8] Moreover in all employed solvents, the product distribution did not change with varying irradiation wavelength, i.e., from λ > 254 nm (quartz glass) to λ > 310 nm (Pyrex glass). Nevertheless in MeCN and benzene, the reactions were significantly slower when the light was filtered through Pyrex glass, most likely because the Pyrex glass cuts off a significant area of the chromophore absorption.

The irradiation of crystalline samples of benzonaphthobarrelene **4a** resulted in the formation of the same two semibullvalenes **5a^{I}** and **5a^{II}**, but the selectivity was reversed compared with the photoreaction in solution, i.e., the semibullvalene **5a^{II}** was formed predominantly upon solid-state photolysis (Table 1). The direct irradiation of crystals of barrelene **4a**, obtained by crystallization from methanol, gave the photoproducts **5a^{I}** and **5a^{II}** in 22:78 ratio at 10% conversion. The conversion was improved to 41% with only a slight decrease of selectivity (25:75) by the irradiation of ground crystals, which were placed between quartz slides, i.e., by increasing the surface area exposed to the UV light. Prolonged irradiation times did not increase the conversion further, probably because of an inner-filter effect that protects the inside of the solid sample towards the light. On the other hand, the selectivity was improved to 16:84 by using ground *single crystals* of **4a**.

The low conversion and small scale of the solid-state photoreactions often limits their potential application in synthetic organic chemistry;[7] however, this drawback may be overcome by the performance of the photoreaction with a suspension of the finely ground substrate in a solvent in which it is insoluble.[9] To test this approach, thoroughly stirred suspensions of the benzonaphthobarrelene **4a** in hexane or water were irradiated. Thus, on the scale of 60.0 mg (0.16 mmol) of compound **4a**, the photoreaction in hexane resulted in 90% conversion with a ratio of 33:67 between the semibullvalenes **5a^{I}** and **5a^{II}**. In water suspension, the irradiation proceeded with lower conversion of 67%, but the selectivity was much better (**5a^{I}**:**5a^{II}** = 14:86). From each reaction mixture, the semibullvalene **5a^{II}** was isolated in yields as high as 37% as colorless cubes, by crystallization of the photolysate.

The product structures were identified on the basis of ^{1}H and ^{13}C NMR spectroscopy and elemental analysis. The annelated semibullvalene structure in compounds **5a^{I}** and **5a^{II}** was indicated by the characteristic shifts of the cyclopropane methine protons (**5a^{I}**: δ 5.21 ppm; **5a^{II}**: δ 5.59 ppm) and the proton in the benzylic position (δ 4.64 ppm for both **5a^{I}** and **5a^{II}**). In particular, the unambiguous structure assignment of

Table 1. Medium-dependent regioselectivity of the di-π-methane rearrangements of benzonaphthobarrelene **4a**.

Medium	mb[a,b] (%)	Convn[a,c] (%)	Ratio **5a^{I}/5a^{II}** [a,d]
Acetone solution	>97	>97	87:13
Acetonitrile solution	>97	>97	80:20
Benzene solution	89	>97[e]	71:29
Bulk crystals[f]	97	10	22:78
Ground crystals[f,g]	95	41	25:75
Single crystal[f]	95	32	16:84
Hexane suspension	92	90	33:67
Water suspension	94	65[h]	14:86

[a]Determined by ^{1}H NMR spectroscopic analysis directly on the crude product mixture relative to *m*-dimethyl isophthalate as internal standard; error limits: ±3% of the given value.

[b]Mass balance.

[c]Conversion.

[d]If not stated otherwise, **5a^{I}** and **5a^{II}** were the only detectable products.

[e]Approx. 10% of unidentified byproducts were formed.

[f]Crystallized from methanol solution.

[g]Ground crystals crushed between quartz slides.

[h]Approx. 3% of unidentified byproducts were formed.

Fig. 1. Structural assignment of the benzonaphthosemibullvalene derivatives **5a^{I}** and **5a^{II}** by NOE (arrows indicate NOEs between the corresponding protons).

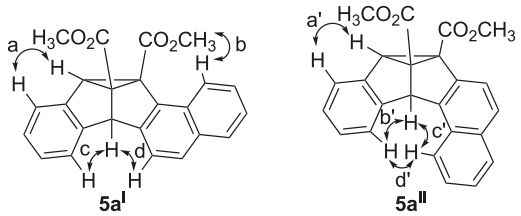

the two isomers **5a^{I}** and **5a^{II}** was made by NOESY NMR experiments (Fig. 1). In both cases, the substitution pattern of the cyclopropane ring, i.e., the position of the ester groups, was indicated by the NOE between the methine proton of the cyclopropane and the *ortho*-proton of the annelated benzene part (arrow a and a′). The assignment of the benzene protons was confirmed by additional NOE data, in particular by the NOE between the benzylic proton and the benzene and naphthalene protons (arrows c,d and b′–d′) . Moreover, the orientation of the naphthalene unit in compounds **5a^{I}** and **5a^{II}** was determined by the NOE between the protons of the methyl substituent and the aromatic proton (8′-H) of the naphthalene part in isomer **5a^{I}** (arrow b).

The photoreactivity of dinaphthobarrelene **4b** resembles the one of barrelene derivative **4a** (Scheme 4). In acetone solution, the irradiation of **4b** led to a mixture of semibullvalenes **5b^{I}** and **5b^{II}** in a ratio of 87:13, whereas the regioselectivity is reversed to 18:82 upon irradiation in the solid state. The product **5b^{I}** was obtained by crystallization in 55% yield and fully characterized by ^{1}H and ^{13}C NMR spectroscopy and elemental analysis. Additional NOESY NMR experiments confirmed the structure of the semibullvalene derivative **5b^{I}** by characteristic NOE signals between an 8′-H proton of naphthalene and the cyclopropane methine proton, as well as between the benzyl proton and the 8′-H proton of naphthalene (Scheme 4). The isomer **5b^{II}** could not be isolated, but its structure was identified by NMR spectroscopic analysis directly from the product mixture.

Scheme 4. Photoinduced di-π-methane rearrangement of dinaphthbarrelene **4b** (arrows indicate NOEs between the corresponding protons).

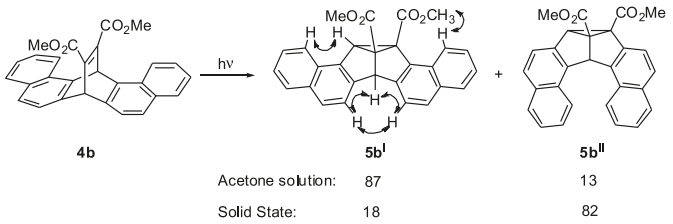

Scheme 5. Reaction mechanism of the di-π-methane rearrangement of dibenzobarrlene (**1g**).

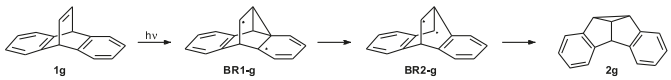

Discussion

The photoinduced di-π-methane rearrangement of annelated barrelenes, e.g., the parent dibenzobarrelene **2g**, is initiated by a carbon–carbon bond formation between the etheno unit and an *ipso* carbon of the annelated aromatic ring to form a 1,4-biradical intermediate **BR1-g** (Scheme 5), followed by rearomatization to afford the biradical **BR2-g**, and subsequent radical recombination to the semibullvalene **2g**.[1a,1d] Depending on the substitution pattern of the substrate, up to four different regioisomeric products may be formed, and it was demonstrated that the selectivity of the initial reaction step determines the selectivity of the overall reaction (Scheme 1).[1c] It should be noted, however, that the selectivity of a chemical reaction, in particular the di-π-methane rearrangement, is mainly governed by the different reaction rates, i.e., by the energies of the different transition states rather than the ones of the corresponding reaction intermediates. Nevertheless, it is assumed that factors that stabilize one particular 1,4-biradical intermediate also stabilize the preceding transition state and thus lead to the preferen-

Scheme 6. Reaction pathways of the di-π-methane rearrangement of barrelene derivative **4a**.

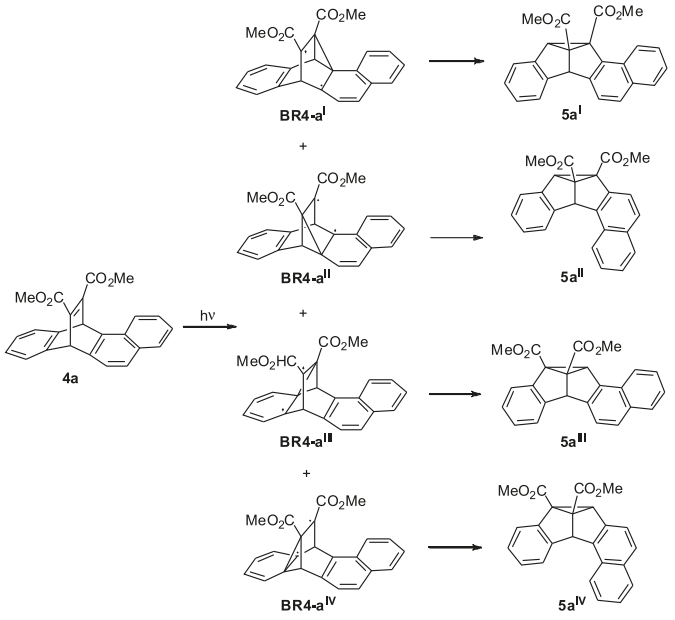

Scheme 7. Resonance stabilization in biradicals **BR4-a^{I}** and **BR4-b^{I}**.

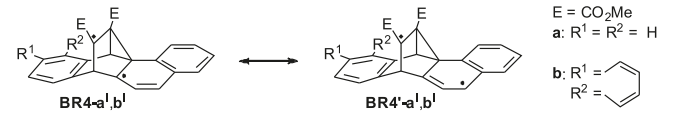

tial formation of the corresponding semibullvalene isomer. According to these considerations, the regioselectivity observed in the photoreactions of the barrelene derivatives **4a** and **4b** may be discussed in terms of the relative stability of the possible biradical intermediates. Thus, during the di-π-methane rearrangemenent of the barrelene derivative **4a**, the four regioisomeric biradicals **BR4-a^{I}**–**BR4-a^{IV}** may be formed initially, which lead to the four isomeric benzonaphthosemibullvalenes **5a^{I}**–**5a^{IV}** (Scheme 6). Nevertheless, the products **5a^{III}** and **5a^{IV}** are not formed in detectable amounts, indicating that the intermediates **BR4-a^{III}** and **BR4-a^{IV}** are only generated to negligible extents. We propose that the high preference for the photoinduced vinyl–naphtho bridging is governed by the significantly higher stabilization of the intermediate radicals in the naphthalene unit, compared with the stabilization in the cyclohexadienyl radical part in **BR4-a^{III}** and **BR4-a^{IV}**. Moreover, the biradicals **BR4-a^{I}** and **BR4-a^{II}** still contain two intact benzene rings, whose resonance energy contributes more to the overall stabilization than the one of the single naphthalene ring in **BR4-a^{III}** and **BR4-a^{IV}**.[10]

It was demonstrated that the di-π-methane rearrangemenent of the unsubstituted 1,2-naphthobarrelene is introduced by a highly selective vinyl–naphtho bridging that takes place *exclusively* between a vinyl carbon atom and the C1 position (α position) of the naphthalene.[3] These observations have been explained by a higher extent of delocalization within the aromatic part of the corresponding 1,4-biradical. The same argument may be employed to rationalize the enhanced formation of the products **5a^{I}** and **5b^{I}** resulting from initial bridging to the C1 carbon upon irradiation of annelated barrelene derivatives **4a** and **4b**. In contrast to the intermediate **BR4-a^{II}**, the biradicals **BR4-a^{I}** and **BR4-b^{I}** exhibit two resonance structures with a complete benzene ring providing additional aromatic stabilization. Moreover, one of the resonance forms, indicated as **BR4′**, reveals a particular stabilization as the radical is located both in allylic and benzylic position (Scheme 7).

Notably, the solid-state photoreaction of the annelated barrelene derivatives **4a** and **4b** yields the semibullvalene derivative **5a^{II}** and **5b^{II}** as the main products. Apparently, the stereoelectronic factors that determine the regioselectivity of the di-π-methane rearrangement of **4a** and **4b** in solution are no longer effective in the solid state. Since it has been demonstrated that solid-state photoreactions often proceed on a reaction pathway that avoids steric interactions with neighboring molecules,[11] it may be assumed that inter- or intra-molecular steric factors determine the solid-state reactivity of **4a** and **4b** rather than electronic effects. To investigate this aspect, an X-ray diffraction analysis was performed with single crystals of compound **4a**. The benzonaphthobarrelene **4a** crystallizes in the monoclinic space group of $P2_1/c$ (a = 11.3159 Å, b = 11.8742 Å, c = 14.586 Å; β = 104.55°), with each unit cell containing two pairs of enantiomers of the barrelene molecules. Most notably, significant close contacts between two molecules were detected. The two different views of the molecular arrangement in the solid state given in Fig. 2 reveal that the benzene unit of one molecule (black in Fig. 2) is partially positioned between the vinyl unit and the naphthalene part of a neighboring molecule (Fig. 2, white, red, blue, respectively). In this arrangement, the closest contacts between the two molecules were identified between one carbonyl carbon atom of an ester group (Fig. 2, red) and an *ortho*-hydrogen atom of the benzene ring (Fig. 2*a*, C···H: 289 pm), and between the carbonyl oxygen atom of the same ester functionality and the bridgehead hydrogen atom (Fig. 2*a*, O···H: 262 pm). These distances correspond essentially to the sum of the van der Waals radii of the respective atoms (C···H: 290 pm, O···H: 272 pm)[12] and may thus result in significant intermolecular steric repulsion during the solid-state rearrangement of compound **4a**. In particular, the movement of one of the ester functionalities, namely the one at the C16 position (Fig. 2, red), in the course of a di-π-methane rearrangement appears to be significantly hindered. To achieve the vinyl–naphtho bridging to give **BR4-a^{I}**, this ester group needs to pass the proximate benzene unit of the neighboring molecule, and the close contacts described above clearly indicate that this pathway is essentially blocked. At the same time, the other ester group (Fig. 2, blue) is free to move as there are no significant contacts with the proximate molecule (>350 pm; not shown), so that an almost unhindered vinyl–naphtho bridging is possible in the solid state to afford biradical **BR4-a^{II}**. Notably, both vinyl–benzo bridging pathways leading to the semibullvalene products **5a^{III}** and **5a^{IV}** are not sterically hindered in the crystal. Thus, in the absence of steric constraints in the crystal, the solid-state photoreaction is determined by the same electronic factors as in isotropic solution.

Fig. 2. Structure of the benzonaphthobarrelene **4a** in the solid state (dashed lines indicate closest contacts between two neighboring molecules).

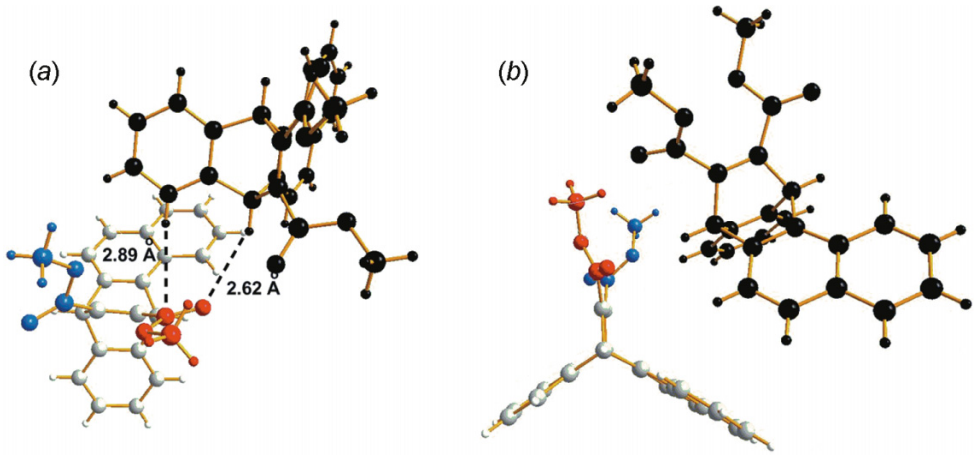

Table 2. Crystallographic data and details of the structure determination for **4a**.

Parameter	Value
Molecular formula	$C_{24}H_{18}O_4$
Formula mass	M = 370.38 g/mol
Colour	Colourless
Crystal system	Monoclinic
Space group	$P2_1/c$ (No. 14)
Unit cell dimensions	a = 11.3159(9) Å, b = 11.8742(7) Å, c = 14.586(1) Å, β = 104.55(1)°
Volume	V = 1897.0(3) Å^3
Formula units/unit cell	Z = 4
Calculated density	ρ = 1.297 g/cm^3
Diffractometer	IPDS (STOE)
Wave length	λ = 0.710 73 (Mo-Kα)
Monochromator	Graphite
Crystal size	0.29 mm × 0.28 mm × 0.17 mm
Measuring temperature	T = 296(2) K
Scan type	φ - scan
Measured θ-range	2.24° ≤ θ ≤ 28.14°
Index ranges	–15≤ h ≤ 14, –15 ≤ k ≤ 15, –19 ≤ l ≤ 19
Reflections collected	20 010
Independent reflections	4 614
Observed reflections	21 51 [I>2σ(I)]
Data averaging[a]	R_{int} = 0.0664, R_σ = 0.0739
Completeness to θ_{max}	99.5%
Absorption coefficient	μ = 0.088 mm^{-1}
Extinction coefficient	ε = 0.0079(9)
Structure solution	Direct methods (ref. 12)
Structure refinement	Full-matrix least-squares on F^2 (ref. 12)
Number of parameters	256
Number of restraints	0
GooF on F^2	0.794
F(000)	776
Weighting scheme[b]	A = 0.0458, B = 0
Fig. of merit[a] [I>2σ(I)]	R_1 = 0.0396, wR_2 = 0.0791
Fig. of Merit[a] [all data]	R_1 = 0.1071, wR_2 = 0.0936
Residual electron density	–0.143 ≤ ρ ≤ 0.194 e/Å^3

[a]Definition of R factors see ref.13
[b]$w = 1/[\sigma^2(F_0^2) + (AP)^2 + BP)]$, $P = (F_0^2 + 2F_c^2)/3$

Summary and conclusion

In summary, we have shown that the di-π-methane rearrangement of 1,2-naphtho annelated barrelene derivatives **4a** and **4b** proceeds with high regioselectivity. Most notably, a drastic change of the selectivity was observed upon changing from isotropic solution to the solid state. Whereas in solution, the course of the reaction is mainly governed by the selective stabilization of the corresponding transition states, which lead to the primary biradical intermediates **BR4**, the solid-state photoreaction is significantly influenced by the steric constraints within the crystal lattice. To be stressed is the fact that in the case of **4a**, the major products from both reactions, i.e., in solution and in the solid state, could be isolated in reasonable yields. Considering the importance of the annelated semibullvalene derivatives as synthons in organic synthesis,[1f] the presented systems may be employed along these lines as a useful source for the selective synthesis of complex 1,2-naphtho-annelated polycyclic aromatic compounds.[1f]

Experimental section

General

NMR spectra: Bruker Avance 400 (^{1}H NMR: 400 MHz; ^{13}C NMR: 100 MHz) and a Varian NMR System 600 (^{1}H NMR: 600 MHz; ^{13}C NMR: 150 MHz). ^{1}H NMR chemical shifts refer to δ_{TMS} 0.0 ppm. ^{13}C NMR chemical shifts refer to solvent signals ($CDCl_3$: δ 77.0 ppm). Melting points: Büchi 510K apparatus (uncorrected). Mass spectra: Hewlett-Packard HP 5968 (EI, 70 eV). Elemental analyses: KEKA-tech EuroEA combustion analyzer by Mr. H. Bodenstedt, Organic Chemistry I, University of Siegen. Benzo[*a*]anthracene[5] and benzotetracenes[6] were prepared according to literature procedures. All the other reagents and solvents were obtained from Acros Organics and Sigma-Aldrich and used as received.

*Dimethyl-7,12-dihydro-7,12-ethenobenzo[**a**]anthracene-13,14-dicarboxylate (4a)*

Under nitrogen-gas atmosphere, a suspension of benzo[*a*]anthracene (5.89 g, 25.8 mmol), DMAD (9.18 mL, 75.0 mmol), and $AlCl_3$ (0.2 g) in xylene (15 mL) was heated at 140 °C for 5 days. The mixture was cooled to room temperature (RT) and diluted with ethyl acetate (100 mL). The organic phase was extracted with 2N aq. HCl (50 mL) and brine (50 mL), and subsequently separated, dried with Na_2SO_4. The solvent was removed in vacuo and the residue was purified by column chromatography (SiO_2; EtOAc/hexane = 1:2, *v*/*v*; R_f = 0.45) to give an orange oil, which was solidified upon treatment with methanol to give dimethyl-7,12-dihydro-7,12-ethenobenzo[*a*]anthracene-13,14-dicarboxylate (**4a**) as ^{1}H NMR spectroscopically pure light yellow granules (6.47 g, 17.5 mmol, 68%). An analytical sample was prepared by recrystallization from methanol as clusters of colorless prisms, mp 142–144 °C. UV ($CHCl_3$): λ_{max} (log ε) = 245 (4.40), 270 (3.85), 281 (3.90), 292 (3.92), 329 (3.27). ^{1}H NMR (400 MHz, $CDCl_3$) δ: 3.79 (s, 3H, OCH_3), 3.80 (s, 3H, OCH_3), 5.64 (s, 1H, CH), 6.32 (s, 1H, CH), 6.98–7.01 (m, 2H, ar-CH), 7.39–7.47 (m, 3H, ar-CH), 7.53–7.61 (m, 3H, ar-CH), 7.81 (d, *J* = 8 Hz, ar-CH), 8.27 (d, *J* = 8 Hz, ar-CH). ^{13}C NMR (100 MHz, $CDCl_3$) δ: 48.2 (CH_3), 52.4 (overlapped CH_3 and CH), 53.6 (CH), 122.0 (ar-CH), 122.5 (6,11-CH), 123.7 (ar-CH), 123.8 (ar-CH), 125.1 (ar-CH), 125.2 (two ar-CH overlapped), 125.6 (ar-CH), 126.4 (ar-CH), 128.7 (ar-CH), 129.0 (C_q), 131.7 (C_q), 141.2 (C_q), 142.6 (C_q), 144.0 (C_q), 144.8 (C_q), 146.8 (C_q), 149.0 (C_q), 165.8 (C=O), 166.2 (C=O). EI-MS (70 eV): 370 [M^+]. Elemental analysis calcd. (%) for $C_{24}H_{18}O_4$ (370.40): C 77.82, H 4.90; found C 77.62, H 4.86.

*Dimethyl-7,14-dihydro-7,14-ethenodibenzo[**a**,**j**]-anthracene-15,16-dicarboxylate (4b)*

Under argon protection, a mixture of dibenzo[*a,h*]- and dibenzo[*a,j*]anthracene (28:72, 690 mg, 2.48 mmol), DMAD (0.50 mL, 4.1 mmol), and $AlCl_3$ (20 mg) in xylene (15 mL) was heated at 140 °C for 5 days. After cooling RT, the mixture was diluted with EtOAc (70 mL). The organic phase was extracted with 2N aq. HCl (20 mL) and brine (50 mL), and subsequently separated, dried with Na_2SO_4. The solvent was removed in vacuo and the residue was purified by column chromatography (SiO_2; EtOAc/hexane = 1:4, *v*/*v*; R_f = 0.31) to give a mixture of the two dinaphthobarrelenes **4b** and **4c** (**4b**/**4c** 71:29, 312 mg, 0.74 mmol, 30%). Two-fold recrystallization from EtOAc/hexane gave pure **4b** as colorless needles (42 mg, 6%), mp 223–225 °C. ^{1}H NMR (400 MHz, $CDCl_3$) δ: 3.79 (s, 3H, CH_3), 3.82 (s, 3H, CH_3), 5.80 (s, 1H, CH), 7.23 (s, 1H, CH), 7.39 (d, *J* = 8 Hz, 2H, ar-CH), 7.55–7.59 (m, 4H, ar-CH), 7.65 (d, *J* = 8 Hz, 2H, ar-CH), 7.80 (d, *J* = 8 Hz, 2H, ar-CH). ^{13}C NMR (100 MHz, $CDCl_3$) δ: 44.0 (CH), 52.5 (CH_3), 52.5 (CH_3), 54.8 (CH), 122.1 (ar-CH), 122.5 (ar-CH), 125.2 (ar-CH), 125.3 (ar-CH), 126.6 (ar-CH), 128.8 (ar-CH), 129.2 (C_q), 131.6 (C_q), 141.7 (C_q), 144.1 (C_q), 146.8 (C_q), 151.0 (C_q), 165.7 (C=O), 166.4 (C=O). MS (*m*/*z*): 420 [M^+]. Elemental analysis calcd. (%) for $C_{28}H_{20}O_4$ (420.46): C 79.98, H 4.79; found C 79.60, H 4.67.

Photoreactions

Irradiations were performed with a TQ150 middle-pressure mercury lamp (Heraeus, UV-Consulting Peschl), which was placed in a quartz cooling tube. The sample container was placed 10–15 cm in front of the lamp. The solution contained one molar equivalent of *m*-dimethyl isophthalate as internal standard for the quantitative ^{1}H NMR spectroscopic analysis of the photolysate.

Photolysis in solution

Solutions (10^{-3} to 10^{-2} mol/L) were placed in a 200 mL Pyrex tube (acetone) or a 50 mL quartz tube (other solvents) and purged with argon for at least 20 min. The stirred solution was irradiated for 6–13 h until the starting material was fully consumed as determined by ^{1}H NMR analysis. After evaporation of the solvent in vacuo, the photolysate was analyzed by ^{1}H NMR spectroscopy, or, in preparative experiments, recrystallized from EtOAc/hexane to obtain the major photoproduct.

Photolysis in crystalline state

15–25 μmol of the crystalline starting material were placed in an argon-purged and sealed quartz test tube and irradiated. Afterwards, the stock solution of *m*-dimethyl iso-

phthalate was added as internal standard, and the mixture was dissolved in dichloromethane. The solvent was removed and the mixture was analyzed by ^{1}H NMR analysis.

Alternatively, the crystalline solids were ground to powders and sandwiched between a pair of quartz slides, which were sealed in an argon-purged polyethylene bag and irradiated. The photolysate was dissolved in dichloromethane and the stock solution of *m*-dimethyl isophthalate was added as internal standard. After the removal of solvent, the mixture was analyzed by ^{1}H NMR analysis.

Photolysis in suspensions

In a 20 mL quartz tube, 0.05–0.16 mmol of starting material and 10 mL of hexane or water were added. The mixture was sonicated for 10 min to destroy the larger crystals and purged with argon for 20 min. After irradiation, dichloromethane was used to dissolve (hexane) or extract (water) the photolysate. After evaporation of the solvent in vacuo the product mixture was subjected to ^{1}H NMR spectroscopic analysis, or redissolved in acetone/methanol to crystallize the major photoproduct.

Dimethyl-4b,10b-dihydro-benzo[5,6]cyclopropa[3,4]pentaleno[1,2-a]naphthalene-4c,10d-dicarboxylate (5a^I)

Prepared by photoreaction in acetone solution. Yield 61%, colorless needles, mp 177–179 °C. UV ($CHCl_3$): λ_{max} (log ε) = 246 (4.44), 281 (3.73), 328 (2.97). ^{1}H NMR (400 MHz, $CDCl_3$) δ: 3.76 (s, 3H, CH_3), 3.83 (s, 3H, CH_3), 4.64 (s, 1H, CH), 5.21 (s, 1H, CH), 7.00–7.08 (m, 2H, ar-CH), 7.17 (d, *J* = 7 Hz, 1H, ar-CH), 7.33–7.44 (m, 4H, ar-CH), 7.64–7.68 (m, 2H, ar-CH), 7.75 (d, *J* = 8 Hz, 1H, ar-CH). ^{13}C NMR (100 MHz, $CDCl_3$) δ: 49.7 (CH_3), 52.4 (CH), 52.9 (CH), 55.5 (CH_3), 58.4 (C_q), 66.8 (C_q), 120.2 (ar-CH), 121.3 (ar-CH), 123.5 (ar-CH), 125.0 (ar-CH), 125.7 (ar-CH), 126.6 (ar-CH), 126.8 (ar-CH), 127.4 (ar-CH), 127.7 (C_q), 128.8 (ar-CH), 129.5 (ar-CH), 130.3 (C_q), 133.1 (C_q), 134.8 (C_q), 147.8 (C_q), 150.0 (C_q), 169.6 (C=O), 169.6 (C=O). MS (*m*/*z*): 370 [M$^+$]. Elemental analysis calcd. (%) for $C_{24}H_{18}O_4$ (370.40): C 77.82, H 4.90; found C 77.74, H 4.81.

Dimethyl-4b,10c-dihydro-benzo[5,6]cyclopropa[1,2-h]naphthalene-4c,10e-dicarboxylate (5a^{II})

Prepared by photoreaction in water suspension. Yield 37%, colorless cuboids, mp 173–175 °C. ^{1}H NMR (600 MHz, CD_3Cl) δ: 3.75 (s, 3H, CH_3), 3.91 (s, 3H, CH_3), 4.64 (s, 1H, CH), 5.59 (s, 1H, CH), 6.98–7.04 (m, 2H, ar-CH), 7.28 (d, *J* = 8 Hz, 1H, ar-CH), 7.34 (d, *J* = 8 Hz, 1H, ar-CH), 7.38 (d, *J* = 9 Hz, 1H, ar-CH), 7.34 (d, *J* = 8 Hz, 1H, ar-CH), 7.44 (dd, *J* = 7 Hz, 1H, ar-CH), 7.59 (dd, *J* = 7 Hz, 1H, ar-CH), 7.62 (d, *J* = 8 Hz, 1H, ar-CH), 7.62 (d, *J* = 8 Hz, 1H, ar-CH), 7.78 (d, *J* = 8 Hz, 1H, ar-CH), 8.14 (d, *J* = 8 Hz, 1H, ar-CH). ^{13}C NMR (150 MHz, CD_3Cl) δ: 50.1 (CH_3), 52.4 (CH), 52.9 (CH), 53.7 (CH_3), 67.8 (C_q), 68.7 (C_q), 121.4 (ar-CH), 123.3 (ar-CH), 123.7 (ar-CH), 125.7 (two overlapped ar-CH), 126.7 (ar-CH), 127.0 (ar-CH), 127.3 (ar-CH), 127.8 (ar-CH), 128.8 (ar-CH), 129.8 (C_q), 133.2 (C_q), 134.9 (C_q), 145.3 (C_q), 148.9 (C_q), 168.6 (C=O), 169.4 (C=O), one C_q signal is overlapped. MS (*m*/*z*): 370 [M$^+$]. Elemental analysis calcd. (%) for $C_{24}H_{18}O_4$ (370.40): C 77.82, H 4.90; found C 77.98, H 4.81.

Dimethyl-6d,12b-dihydro-cyclopropa[3,4]pentaleno-[1,2-a;6,5-c′]dinaphthalene-6c,12d-dicarboxylate (5b^I)

Prepared by photoreaction in acetone solution. Yield 55%, white granules, mp 217–218 °C. ^{1}H NMR (600 MHz, $CDCl_3$) δ: 3.78 (s, 3H, CH_3), 3.89 (s, 3H, CH_3), 5.13 (s, 1H, CH), 5.34 (s, 1H, CH), 7.30–7.38 (m, 4H, ar-CH), 7.41 (d, *J* = 8 Hz, 1H, ar-CH), 7.46 (dd, *J* = 7 Hz, 1H, ar-CH), 7.59 (d, *J* = 8 Hz, 1H, ar-CH), 7.64 (two overlapped doublet, *J* = 8 Hz, 2H, ar-CH), 7.68–7.71 (m, 2H, ar-CH), 8.10 (d, *J* = 8 Hz, 1H, ar-CH). ^{13}C NMR (100 MHz, $CDCl_3$) δ: 48.5 (CH), 52.4 (CH_3), 53.0 (CH_3), 56.3 (CH_3), 58.8 (C_q), 67.4 (C_q), 120.0 (ar-CH), 120.1 (ar-CH), 123.5 (ar-CH), 124.3 (ar-CH), 125.0 (ar-CH), 125.3 (ar-CH), 126.6 (ar-CH), 126.6 (ar-CH), 127.5 (C_q), 128.3 (ar-CH), 128.4 (ar-CH), 128.8 (ar-CH), 129.4 (ar-CH), 129.8 (C_q), 130.5 (C_q), 130.7 (C_q), 132.5 (C_q), 133.1 (C_q), 146.9 (C_q), 148.0 (C_q), 169.6 (C=O), 169.7 (C=O). MS (*m*/*z*): 420 [M$^+$]. Elemental analysis calcd. (%) for $C_{28}H_{20}O_4$ (420.46): C 79.98, H 4.79; found C 79.47, H 4.71.

X-ray diffraction analysis of compound 4a

The conditions and parameters adopted for the determination of crystallographic data of compound **4a** are listed in Table 2.

Supplementary data

Supplementary data for this article are available on the journal Web site (canjchem.nrc.ca) or may be purchased from the Depository of Unpublished Data, Document Delivery, CISTI, National Research Council Canada, Ottawa, ON K1A 0R6, Canada. DUD 3912. For more information on obtaining material refer to cisti-icist.nrc-cnrc.gc.ca/cms/unpub_e.shtml. CCDC 720890 contains the crystallographic data for this manuscript. These data can be obtained, free of charge, via www.ccdc.cam.ac.uk/conts/retrieving.html (Or from the Cambridge Crystallographic Data Centre, 12 Union Road, Cambridge CB2 1EZ, UK; fax +44 1223 336033; or deposit@ccdc.cam.ac.uk).

Acknowledgement

This paper is dedicated to Trevor Linden on the occasion of his retirement and in appreciation of his exemplary behavior on and off the ice. We thank Dr. Thomas Paululat for carrying out the NOESY experiments and for helpful discussions on spectra analysis.

References

(1) (a) Zimmerman, H. E. In *Rearrangements in ground and excited states*; de Mayo, P., Ed.; Academic Press: New York, USA, 1980; chap. 16; (b) Liao, C.-C.; Yang, P.-H. In *Handbook of Photochemistry and Photobiology*; Horspool, W. M., Song, P.-S., Eds.; CRC Press: Boca Raton, Fla., USA, 1995; chap. 15; (c) Scheffer, J. R.; Yang, J. In *Handbook of Photochemistry and Photobiology*; Horspool, W. M., Song, P.-S., Eds.; CRC Press: Boca Raton, Fla., USA, 1995; chap. 16; (d) Zimmerman, H. E.; Armesto, D. *Chem. Rev.* **1996**, *96*, 3065 doi:10.1021/cr910109c. PMID:11848853.; (e) Liao, C.-

C.; Peddinti, R. K. In *Handbook of Photochemistry and Photobiology*; Horspool, W. M., Lenci, F., Eds.; CRC Press: Boca Raton, Fla., USA, 2003; chap. 32; (f) Ramaiah, D.; Sajimon, M. C.; Joseph, J.; George, M. V. *Chem. Soc. Rev.* **2005**, *34*, 48. doi:10.1039/b300843f. PMID:15643489.

(2) (a) Zimmerman, H. E.; Sulzbach, H. M.; Tollefson, M. B. *J. Am. Chem. Soc.* **1993**, *115*, 6548 doi:10.1021/ja00068a011.; (b) Ihmels, H.; Mohrschladt, C. J.; Grimme, J. W.; Quast, H. *Synthesis* **2001**, *8*, 1175 doi:10.1055/s-2001-15064.;(c) Rattray, G.; Yang, J.; Gudmundsdottir, A. D.; Scheffer, J. R. *Tetradedron Lett.* **1993**, *34*, 35. doi:10.1016/S0040-4039(00)60051-5.

(3) Snow, R. A.; Cottrell, D. M.; Paquette, L. A. *J. Am. Chem. Soc.* **1977**, *99*, 3734. doi:10.1021/ja00453a036.

(4) (a) Garcia-Garibay, M.; Scheffer, J. R.; Watson, D. G. *J. Chem. Soc. Chem. Commun.* **1989**, 600. doi:10.1039/c39890000600.; (b) Garcia-Garibay, M.; Omkaram, N.; Schffer, J. R.; Trotter, J.; Wirenko, F. *J. Am. Chem. Soc.* **1989**, *111*, 4985 doi:10.1021/ja00195a066.; (c) Chen, J.; Scheffer, J. R.; Trotter, J. *Tetrahedron* **1992**, *48*, 3251 doi:10.1016/0040-4020(92)85002-V.; (d) Benitez, M.; Bringmann, G.; Dreyer, M.; Garcia, H.; Ihmels, H.; Waidelich, M.; Wissel, K. *J. Org. Chem* **2005**, *70*, 2315 doi:10.1021/jo047878j.; (e) Ding, J.; Desikan, V.; Han, X. X.; Xiao, T. L.; Ding, R. F.; Jenks, W. S.; Armstrong, D. W. *Org. Lett.* **2005**, *7*, 335. doi:10.1021/ol047599i. PMID:15646991.

(5) (a) Zimmerman, H. E.; Bender, C. O. *J. Am. Chem. Soc.* **1969**, *91*, 7516 doi:10.1021/ja01054a053.; (b) Zimmerman, H. E.; Bender, C. O. *J. Am. Chem. Soc.* **1970**, *92*, 4366. doi:10.1021/ja00717a038.

(6) Platt, K. L.; Oesch, F. *J. Org. Chem.* **1981**, *46*, 2601. doi:10.1021/jo00325a041.

(7) *Photochemistry in organized and constrained media*; Ramamurthy, V., Ed.; VCH: NY, USA, 1991.

(8) Reichardt, C. *Solvents and solvent effects on organic chemistry*; Wiley-VCH: Weinheim, Germany, 2003; chap. 5.

(9) (a) Toda, F. *Top. Curr. Chem.* **2005**, *254*, 1 doi:10.1007/b98357.; (b) Scheffer, J. R.; Wang, K. *Synthesis* **2001**, *8*, 1253. doi:10.1055/s-2001-15056.

(10) Dewar, M. I. S.; de Liano, C. *J. Am. Chem. Soc.* **1969**, *91*, 789. doi:10.1021/ja01032a001.

(11) Ramamurthy, V.; Venkatesan, K. *Chem. Rev.* **1987**, *87*, 433. doi:10.1021/cr00078a009.

(12) Bondi, A. *J. Phys. Chem.* **1964**, *68*, 441. doi:10.1021/j100785a001.

(13) Sheldrick, G. M. *SHELX-97* [computer program]; University of Göttingen, Göttingen, Germany, 1997.

Hydrogen-bond self-assembly of DNA-base analogues — Experimental results

Felaniaina Rakotondradany, Hanadi Sleiman, and M.A. Whitehead

Can. J. Chem. Downloaded from www.nrcresearchpress.com by Sichuan Normal University on 09/14/12
For personal use only.

Abstract: A novel biomimetic DNA analogue with fluorescence has been synthesized to generate functional supramolecular architectures. Experimental studies show that triaminopyrimidine nucleoside (**2**) undergoes a sterically controlled self-assembly into hydrogen-bonded linear tapes and hexameric rosettes. Self-association of the hydrogen-bonded triaminopyrimidine–cyanuric acid complex into elongated, rodlike nanostructures was shown by dynamic light scattering and transmission electron microscopy, suggesting hierarchical formation of higher-order, π-stacked assemblies. The hydrogen-bond self-assembly of the DNA analogue decreased the fluorescence of the nucleosides. This guest-induced fluorescence quenching can be used to develop DNA-hybridization probes. MM^+ molecular modelling and semi-empirical molecular orbital PM3 calculations (**1**) predicted the incorporation of triaminopyrimidine nucleoside into new types of artificial DNA strands and triplex formation with natural, complementary DNA strands containing thymine (**1**).

Key words: hydrogen bond, self-assembly, DNA analogues.

Résumé : Dans le but de générer des architectures supramoléculaires fonctionnelles, on a synthétiser un nouvel analogue biomimétique de l'ARN fluorescent. Les études expérimentales montrent que le nucléoside de la triaminopyrimidine (**2**) donne lieu à un autoassemblage sous contrôle cinétique qui conduit à des bandes linéaires ou des rosettes hexamères reliées par liaisons hydrogènes. Faisant appel à la diffusion dynamique de la lumière et à la microscopie électronique de transmission, on a pu démontrer que l'autoassociation du complexe triaminopyrimidine–acide cyanurique par des liaisons hydrogènes conduit à des nanostructures allongées, en forme de baguettes, suggérant qu'il y a une formation hiérarchique d'un ordre élevé d'assemblages par empilement π. L'autoassemblage par liaisons hydrogènes de l'analogue de l'ADN diminue la fluorescence des nucléosides. Cette extinction de la fluorescence induite par l'hôte pourrait être utilisée pour développer des sondes d'hybridation de l'ADN. Des calculs de modelage moléculaire, MM+, et des calculs d'orbitales moléculaires semi-empiriques, PM3 (**1**), permettent de prédire qu'il y aura incorporation du nucléoside de la triaminopyrimidine dans les nouveaux types de brins artificiels d'ADN et formation de triplex des brins naturels complémentaires d'ADN contenant de la thymine (**1**).

Mots-clés : liaison hydrogène, autoassemblage, analogues de l'ADN.

[Traduit par la Rédaction]

Introduction

Hierarchical assembly of low molecular weight building blocks has generated functional supramolecular architectures with high predictability.[1] Molecularly self-assembled photoresponsive systems were constructed by combining strong, directional, hydrogen bonds or metal coordination, with weak isotropic, intramolecular π-stacking and van der Waals interactions. These supramolecular structures have been investigated theoretically[1] and now experimentally, stressing the use of light-induced isomerization on self-organization. Theory[1] and the present experiments were intimately connected to characterize the hierarchical assemblies and improve the binding selectivity and strength. Theoretical calculations[1] predicted the noncovalently bound oligomeric geometries and thermodynamic properties for the experimentally designed and synthesized monomeric species.

To identify these monomers and their self-assembly behaviour, which were found to agree with theoretical predictions, it was essential to combine molecular and bulk characterization techniques. These theoretical methods were consequently extended to novel biologically interesting systems based on deoxyribonucleoside DNA analogues.

Engineering materials with controlled physical and chemical properties at the nanoscale have proved attractive to researchers. Supramolecular chemistry is a powerful method to achieve this goal because of its ability to efficiently generate well-defined, functional architectures.[2] In particular, hydrogen-bond self-assembly has successfully exploited the specificity of Watson–Crick pairing between complementary DNA bases to create cages,[2] helical,[3] linear,[4] and macro-cyclic structures[5,6] with controlled functionality from DNA building blocks.

Incorporating novel nucleosides in DNA[7] gave new artificial hydrogen-bonded,[7a–7e] π-stacked,[7] or metal-coordinated[7] DNA base pairs, which were enzymatically replicated to perform biological tasks. DNA[8,9] forms higher-order aggre-

Received 22 July 2008. Accepted 22 December 2008. Published on the NRC Research Press Web site at canjchem.nrc.ca on 15 April 2009.

F. Rakotondradany. Imperial Oil Resources, Oil Sands Development and Research, 3535 Research Road NW, Calgary, AB T2L 2K8, Canada.
H. Sleiman and M. Whitehead.[1] Department of Chemistry, McGill University, Otto Maass Chemistry Building, 801 Sherbrooke St. West, Montreal, QC H3A 2K6, Canada.

[1]Corresponding author (e-mail: tony.whitehead@mcgill.ca).

Can. J. Chem. Downloaded from www.nrcresearchpress.com by Sichuan Normal University on 09/14/12
For personal use only.

gates in vitro by hydrogen bonding. Among these DNA aggregates, triple helices[10] and G-quadruplexes,[11] are interesting because of their well-defined morphologies, biological properties, and therapeutic applications.[12,13] A DNA *iso*-guanosine pentaplex has been generated using metal-assisted hydrogen bonding.[14]

Procedure

The design and self-assembly of artificial nucleosides to create new DNA motifs, and to expand the repertoire of DNA assemblies, from pentaplexes to hexameric architectures, is reported.

This approach integrates knowledge from chemical biology with organo-supramolecular chemistry. The newly synthesized DNA-base analogues are used to generate new hydrogen-bonded supramolecular structures. The synthesis and characterization of a DNA-base analogue (**2**) (Fig. 1), which undergoes hydrogen-bond self-assembly with natural and artificial DNA bases and with small molecules, is described theoretically and experimentally by its hydrogen-bonding and π-stacking: self-assembly of (**2**) by hydrogen-bonding and π-stacking leads to rodlike nanostructures.

DNA-base analogue (**2**) is a triaminopyrimidine base attached to a 3′,5′-disiloxane protected ribofuranose (Fig. 1), providing two donor–acceptor–donor (DAD) type hydrogen-bonding sites. The spatial orientation of these hydrogen-bonding groups is similar to the relative position of the carboxylic acid groups in isophthalic acid; therefore, a 120° angle is expected between the DAD faces. Nucleoside (**2**) can thus be associated with two complementary thymine residues to form DNA-based triple helices and with barbituric acid derivatives like (**1**) and cyanuric acid derivatives like (**3**) to give linear tapes or hexameric rosettes (Fig. 1 and Scheme 1).

Results and discussion

Synthesis of DNA-base analogues (2) and (3)

Synthesis of triaminopyrimidine DNA-base analogue (2)

Several approaches were considered to synthesize triaminopyrimidine DNA-base analogue (**2**). The first synthetic route involved coupling of tosyl-activated 2-deoxy-D-ribose (**6**) with the lithiated *t*-BOC-protected 1,3,5-triaminopyrimidine, generated through transmetallation of the brominated triaminopyrimidine (**7**) using *n*-BuLi (Scheme 2). However, instead of producing the desired protected nucleoside (**8**), this method lead to a mixture of *t*-BOC-protected 1,3,5-triaminopyrimidine and 3′,5′-protected sugar (**5**), suggesting unfavourable steric hindrance between the disiloxane and *t*-butoxycarbonyl protecting group, or amine deprotonation before halogen–metal exchange.

A second synthetic method used two main coupling steps (Scheme 3). First, the tosylated sugar (**6**) was allowed to undergo nucleophilic attack of malononitril, under basic conditions, to give the dicyano derivative, which was then reacted with guanidine to obtain the desired triaminopyrimidine (**2**). Although the first coupling reaction successfully led to malonate (**9**), the isolated yield was disappointingly low (<10%). Mass spectrometry analysis of the reaction products revealed formation of dimeric species and deprotected sugar derivatives, suggesting the instability of tosylated sugar to basic reaction conditions, possibly because of the labile tosyl leaving group or because of a base-sensitivty of the protecting group.

Fig. 1. Diethylbarbituric acid (**1**), triaminopyridine (**2**), and cyanuric acid nucleosides (**3**).

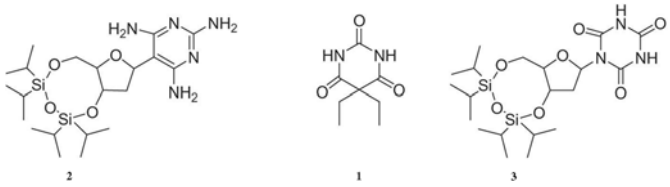

Direct reaction of malononitrile with the 3′,5′-protected sugar under similar conditions (Scheme 4),[15,16] through nucleophilic attack of the *keto* form of the 2-deoxyribofuranose derivative (**10**), improved the coupling yield, allowing synthesis of (**2**) with neutralized guanidinium hydrochloride. Reduction of the basicity of the reaction mixture, by decreasing the NaH/malononitrile ratio, or even by using catalytic amounts of K_2CO_3, resulted in isomer (**11**), as detected by mass spectrometry and ^{1}H NMR (Scheme 4). ^{1}H NMR spectroscopy suggested the presence of both α- and β-anomeric sugars in solutions of the triaminopyrimidine nucleoside (**2**), which was used in the same way as in the self-assembly studies.

A third approach used the palladium-mediated cross-coupling reaction[17] of 3′,5′-diprotected ribofuranoid glycal (**12**) with iodinated benzoyl-protected triaminopyrimidine to improve the overall yield (Scheme 5). Preliminary synthetic attempts at the first elimination step gave the glycal in low yields (ca. 10%).

Synthesis of cyanuric acid DNA-base analogue (3)

Scheme 6 outlines the synthesis of DNA-base analogue (**3**), derived from a previously published procedure where a toluyl-protected 2-deoxyribofuranosylchloride is used as a starting material.[18] The tosyl derivative of the 3′,5′-disiloxane protected sugar was formed and coupled with in situ protected cyanuric acid, under basic conditions, to yield the cyanuric acid DNA-base analogue (**3**). Nucleoside (**3**) was obtained as a mixture of α- and β-sugar anomers, as shown by the ^{1}H NMR data; it was not purified further for the self-assembly studies.

Self-assembly of triaminopyrimidine (15) with diethylbarbituric acid (1)

^{1}H NMR titration of DNA-base analogue (2) by diethylbarbituric acid (1)

The hydrogen-bonded self-assembly of DNA-base analogue (**2**), with diethylbarbituric acid (**1**), was investigated by doing an ^{1}H NMR titration experiment (Fig. 2). The ^{1}H NMR of the triaminopyrimidine (**2**) in CD_2Cl_2 showed broad peaks in the three main regions corresponding to the amino groups (ca. 6.9 ppm), to the sugar protons (3.0–5.0 ppm), and to the disiloxane protecting groups (ca. 1.1 ppm). These broad peaks suggest the presence of oligomeric aggregates that arise from the self-association of individual triaminopyrimidine units in solution. Progressive addition of a diethylbarbituric acid solution in deuterated dichloromethane induced a downfield shift

Can. J. Chem. Downloaded from www.nrcresearchpress.com by Sichuan Normal University on 09/14/12
For personal use only.

Scheme 1. Hydrogen-bond self-assembly of nucleoside (**2**) with thymine (T), barbituric acid (**1**), and cyanuric acid (**3**).

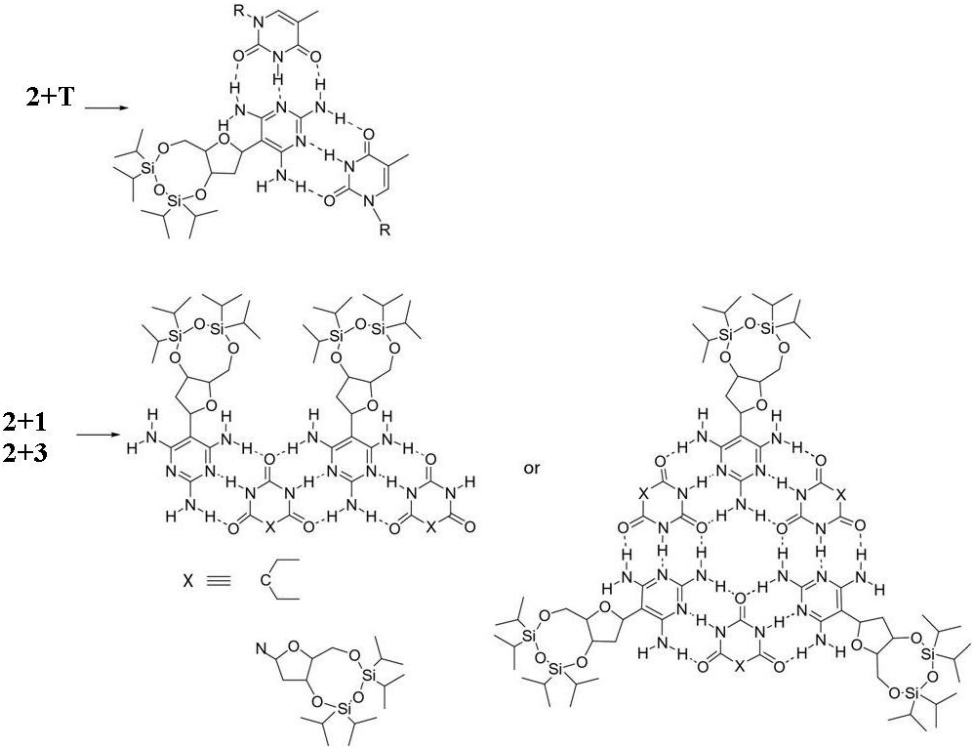

Scheme 2. Attempted synthesis of protected nucleoside (**8**). (*a*) 1,1′,3,3′-tetraisopropyldisiloxane, pyridine, 40 °C, 2 h, 69%; (*b*) *p*-toluenesulfonyl chloride, Et_3N, CH_2Cl_2, 97%; (*c*) 7, *n*-BuLi (1.2 equiv.), –78 °C → RT, 4 h then 20 h.

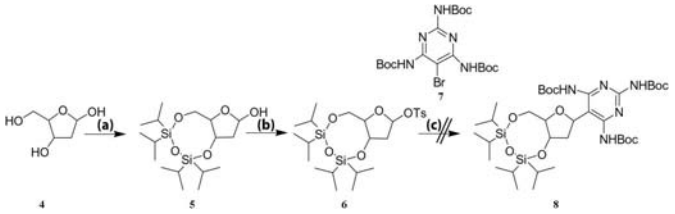

Scheme 3. Attempted synthesis of triaminopyrimidine (**2**). (*a*) Malononitrile (3 equiv.), 95% NaH (3 equiv.), THF, 0 °C → RT, 12 h, 5%–10%; (*b*) guanidine hydrochloride, Na, EtOH, reflux, 8 h, 29%.

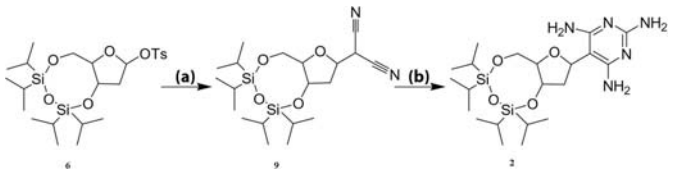

of the NH_2 protons from 6.96 to 8.71 ppm, characteristic of hydrogen-bond formation. However, the ^{1}H NMR of the triaminopyrimidine/diethylbarbituric acid equimolar mixture did not display improved peak widths even after 2 days of ultrasonication. This suggests the formation of hydrogen-bonded polydisperse, oligomeric structures from DNA-base analogue (**2**) and diethylbarbituric acid (**1**).[5,6]

Electrospray ionization mass spectrometry of DNA-base analogue (2) and diethylbarbituric acid (1) mixture

The ^{1}H NMR titration experiment suggested that the self-assembly of triaminopyrimidine nucleoside (**2**) with diethylbarbituric acid (**1**) had resulted in hydrogen-bonded oligomers. However, these ^{1}H NMR experiments do not provide quantitative information about the size of these hydrogen-bonded aggregates. Electrospray ionization mass spectrometry (ESI-MS) analysis was therefore used to quantify the number of monomers involved in the hydrogen bonding of triaminopyrimidine nucleoside (**2**) with diethylbarbituric acid (**1**).

Scheme 4. Synthesis of triaminopyrimidine (**2**). (*a*) Malononitrile (3 equiv.), 95% NaH (3 equiv.), THF, 0 °C → RT, 2 h, 33%; (*b*) guanidine hydrochloride, Na, EtOH, reflux, 5 h, 29%; (*c*) malononitrile (3 equic.), 95% NaH (1 equiv.), THF, 0 °C → RT, 24 h or malononitrile (1 equiv.), K_2CO_3 (0.1 equiv.), MeOH, 24 h, 13%.

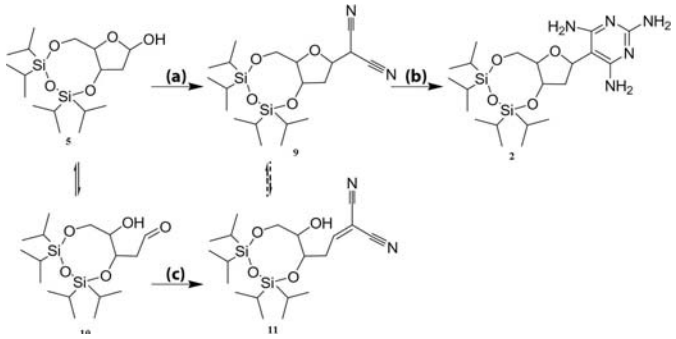

Figure 3 shows the ESI mass spectrum of equimolar mixtures of triaminopyrimidine nucleoside (**2**) and diethylbarbituric acid (**1**). Using M_1 and M_2 for the monomer molecular weights (M_1 for (**2**) = 483, M_2 for (**1**) = 184), *m*/*z* molecular ions detected can be listed as ($M_1+M_2+Na^+ +Li^+$), $2(M_1+M_2+Na^+ +Li^+)$, $(2M_1+M_2+2H^+)$, $2(M_1+Na^+ +H^+)$. However, no peak corresponding to the hexameric rosette ex-

Scheme 5. Attempted synthesis of triaminopyrimidine (**2**) from glycals. (*a*) Methanesulfonyl chloride, Et_3N, CH_2Cl_2, –40 °C to –50 °C → 50 °C, 3h → 15 h, 10%; (*b*) PdOAc, $AsPh_3$, MeCN, reflux, 4 h.

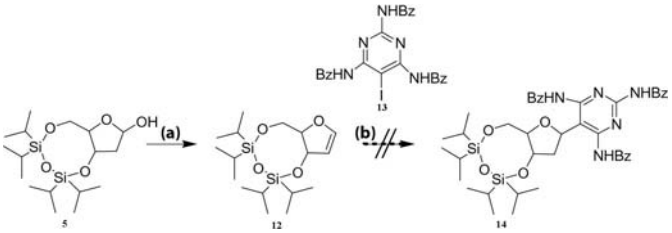

Scheme 6. Synthesis of cyanuric acid (**3**) (*a*) Cyanuric acid, potassium nonafluorobutanesulfonate, hexamethyldisilazane, $(CH_3)_3SiCl$, reflux, 16 h, 37%.

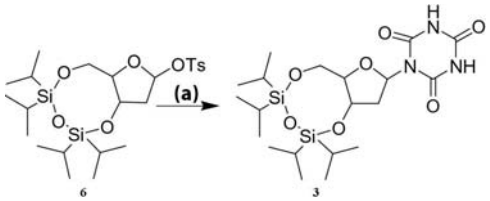

Fig. 2. ^{1}H NMR titration of DNA-base analogue (**2**) using diethylbarbituric acid (**1**) in CD_2Cl_2. (*a*) Before titration; (*b*) after adding 0.5 equiv. of diethylbarbituric acid (**1**); (*c*) after adding 1.0 equiv. of diethylbarbituric acid (**1**).

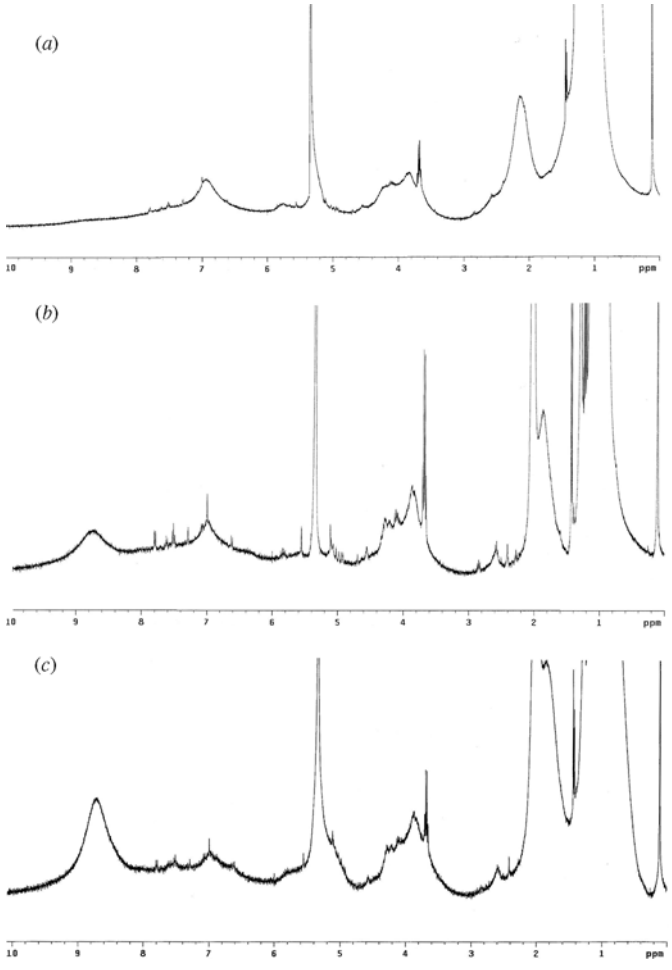

pected molecular weight (M = 2004) was detected, consistent with the absence of discrete supramolecular structures from triaminopyrimidine (**2**) and diethylbarbituric acid (**1**).

Self-assembly of triaminopyrimidine (2) with DNA-base analogue (3)

^{1}H NMR titration of DNA-base analogue (2) by cyanuric acid (3)

Similar ^{1}H NMR titration experiments showed the hydrogen-bonded self-assembly of triaminopyrimidine DNA-analogue (**2**) (Fig. 4*a*) with cyanuric acid DNA-analogue (**3**) (Fig. 4*b*) to differ dramatically from its assembly with diethylbarbituric acid (**1**) (Fig. 5). Addition of cyanuric acid (**3**) caused the same 1.75 ppm downfield shift of the NH_2 protons as for diethylbarbituric acid guest molecules, caused by intermolecular hydrogen-bonding between the two DNA-base analogues. However, addition of 1 equiv. of a CD_2Cl_2 solution of cyanuric acid (**3**) resulted in the immediate emergence of a finer structure for complementary molecules (Fig. 5), suggesting the creation of discrete, macrocyclic structures from (**2**) and (**3**) in solution. Despite a significant gain in peak resolution, the NMR peaks were still slightly broad. This is probably caused by the presence of two anomers for each of the triaminopyrimidine (**2**) and cyanuric acid (**3**), which result in a less selective self-assembly for the system.

Electrospray ionization mass spectrometry of DNA-base analogue (2) and cyanuric acid (3) mixtures

For the triaminopyrimidine nucleoside (**2**)–diethylbarbituric acid (**1**) system, ESI-MS analysis was used to evaluate the size of the discrete supramolecular structures formed from DNA-base analogues (**2**) and (**3**).

The hydrogen-bonded aggregates seen for equimolar mixture of nucleosides (**2**) and (**3**) correspond to highly charged hexameric rosettes containing sodium or potassium ions in the 1700–2000 Da mass range (Fig. 6). Using M_1 and M_2 for the monomer molecular weights (M_1 for (**2**) = 483, M_2 for (**3**) = 486), R_6 for the hexameric rosette expected molecular weights (R_6 = 2907), *m*/*z* molecular ions detected can be listed as $[3(R_6–6H^+{+}6Na^+){+}5H^+]/5$, $[3R_6{+}2Na^+{+}Li^+{+}2H^+]/5$, $[R_6{+}2H^+{+}MeOH]/2$, $[3R_6{+}2H^+]/6$, $M_1{+}M_2$, and $M_1{+}Na^+$. Many other possible structures were tried and were inconsistent with the observed peaks. These molecular ions suggest the possible presence of monomeric, dimeric, and hexameric hydrogen-bonded species in the equimolar mixture of (**2**) and (**3**). Consequently, our preliminary ^{1}H NMRspectroscopy and ESI-MS studies, as well as theoretical MM+ and PM3 calculations are all consistent with the probable self-assembly of triaminopyrimidine DNA-analogue (**2**) with cyanuric acid DNA-analogue (**3**) into cyclic hexamers by hydrogen bonding. Whereas, the data suggest that oligomeric linear tapes were obtained from triaminopyrimidine nucleoside (**2**) and diethylbarbituric acid (**1**).

Absorbance and fluorescence properties of DNA-base analogue (2)

DNA-strand hybridization has usually been assayed by absorbance. Fluorescence spectroscopy has been used to evaluate DNA-hybridization using fluorophore labelled-

Can. J. Chem. Downloaded from www.nrcresearchpress.com by Sichuan Normal University on 09/14/12
For personal use only.

Can. J. Chem. Downloaded from www.nrcresearchpress.com by Sichuan Normal University on 09/14/12
For personal use only.

Fig. 3. Electrospray ionization mass spectrum of equimolar triaminopyrimidine nucleoside (**2**) and diethylbarbituric acid (**1**) mixture.

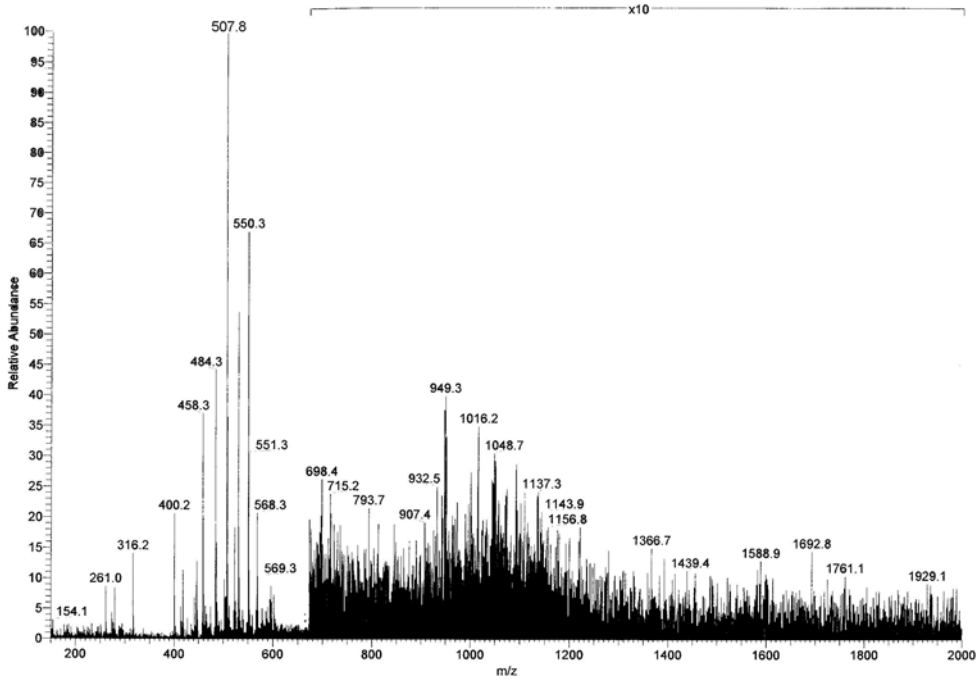

oligonucleotides, which can be attached to microarrays.[18] Substituted pyrimidines, including a few 2,4,6-triaminopyrimidine derivatives,[19] have shown fluorescence properties. Triaminopyrimidine nucleoside (**2**) was strongly fluorescent under UV–vis light.[16] The fluorescence of triaminopyrimidine (**2**) solutions, in chloroform, was measured using its UV–vis absorbance spectra (Figs. 7 and 8).

The UV–vis absorbance spectra gave a principal absorbance at λ_{max} = 254 nm, corresponding to a $\pi \rightarrow \pi^*$ transition of the triaminopyrimidine (**2**), along with a shoulder around 350 nm (Fig. 8). Preliminary fluorescence measurements monitored the self-assembly between triaminopyrimidine (**2**) and its complementary cyanuric acid building block (**3**) and probed the potential abilities of nucleoside analogue (**2**) to detect hybridization, which reflects the combined effects of hydrogen-bonding and π-stacking interactions. Addition of 1 equiv. of cyanuric acid (**2**) solution, in chloroform, induced a 1.4-fold fluorescence quenching along with a 3 nm bathochromic shift. These fluorescence experiments suggest that π-stacking might be involved in the hydrogen-bond assembly of triaminopyrimidine (**2**) and cyanuric acid (**3**) and generate higher-order structures from these complementary units.

Transmission electron microscopy and dynamic light scattering studies of triaminopyrimidine (2)/diethylbarbituric acid (1) and triaminopyrimidine (2)/cyanuric acid (3) mixtures

Transmission electron microscopy (TEM) studies of triaminopyrimidine (**2**)/diethylbarbituric acid (**1**), and triaminopyrimidine (**2**)/cyanuric acid (**3**) mixtures, allowed direct visualization of the second level of self-organisation of these molecules, as well as their different self-assembly behaviour. Figures 9 and 10 show transmission electron micrographs of carbon-coated grids, prepared from deposited solutions of triaminopyrimidine (**2**)/diethylbarbituric acid (**1**) and triaminopyrimidine(**2**)/cyanuric acid (**3**) mixtures, in dichloromethane. On the micrographs, the uranyl acetate appears dark gray and the carbon light gray. The error on the measurements is estimated to be ±1 nm.

Large, sheetlike aggregates are observed for triaminopyrimidine (**2**)/diethylbarbituric acid (**1**) (Fig. 10). Similar electron micrographs were generated from hydrogen-bonded linear tapes of *trans*-azobenzoic acid derivatives. No fine structure was detected at higher magnification, consistent with the absence of rodlike nanostructures from the triaminopyrimidine (**15**)/diethylbarbiturate (**14**) mixture.

On the other hand, the TEM of samples of triaminopyrimidine (**2**)/cyanuric acid (**3**) mixtures showed formation of significantly different supramolecular structures. In contrast with triaminopyrimidine (**2**)/diethylbarbituric acid[1] mixture, elongated aggregates, with lengths as great as 170 nm, arise from the triaminopyrimidine (**2**)/cyanuric acid (**3**) pair (Fig. 10). The outer hydrodynamic diameter of these elongated aggregates was determined from the intensity profile of the electron micrograph (Figs. 10*c* and 10*d*), which measures the contrast across the rodlike structures, hence the topography. The outer hydrodynamic diameter of these rodlike structures was measured as ca. 4.2 ± 1.0 nm, in close agreement with the estimated diameter of the self-assembled hexameric macrocycles of triaminopyrimidine (**2**) and cyanuric acid (**3**) (3.2 nm). This diameter was observed on freshly purified samples of triaminopyrimidine (**2**) and cyanuric acid (**3**) mixtures and for various direct deposition conditions, with and without staining; unstained samples of equimolar triaminopyrimidined (**15**)/cyanuric acid (**16**) mixtures showed rodlike structures by electron microscopy, but staining was needed to give a good contrast (Experimental section). The fluorescence measurements confirm further interaction of the hydrogen-bonded structures from triaminopyrimidine (**2**) and cyanuric acid (**3**) equimolar mixtures by π–π stacking and (or) alkyl–alkyl interactions.

Dynamic light scattering (DLS) studies for equimolar

Fig. 4. (*a*) ^{1}H NMR spectrum of DNA-base analogue (**2**) in MeOD; (*b*) ^{1}H NMR spectrum of DNA-base analogue (**3**) in $CDCl_3$.

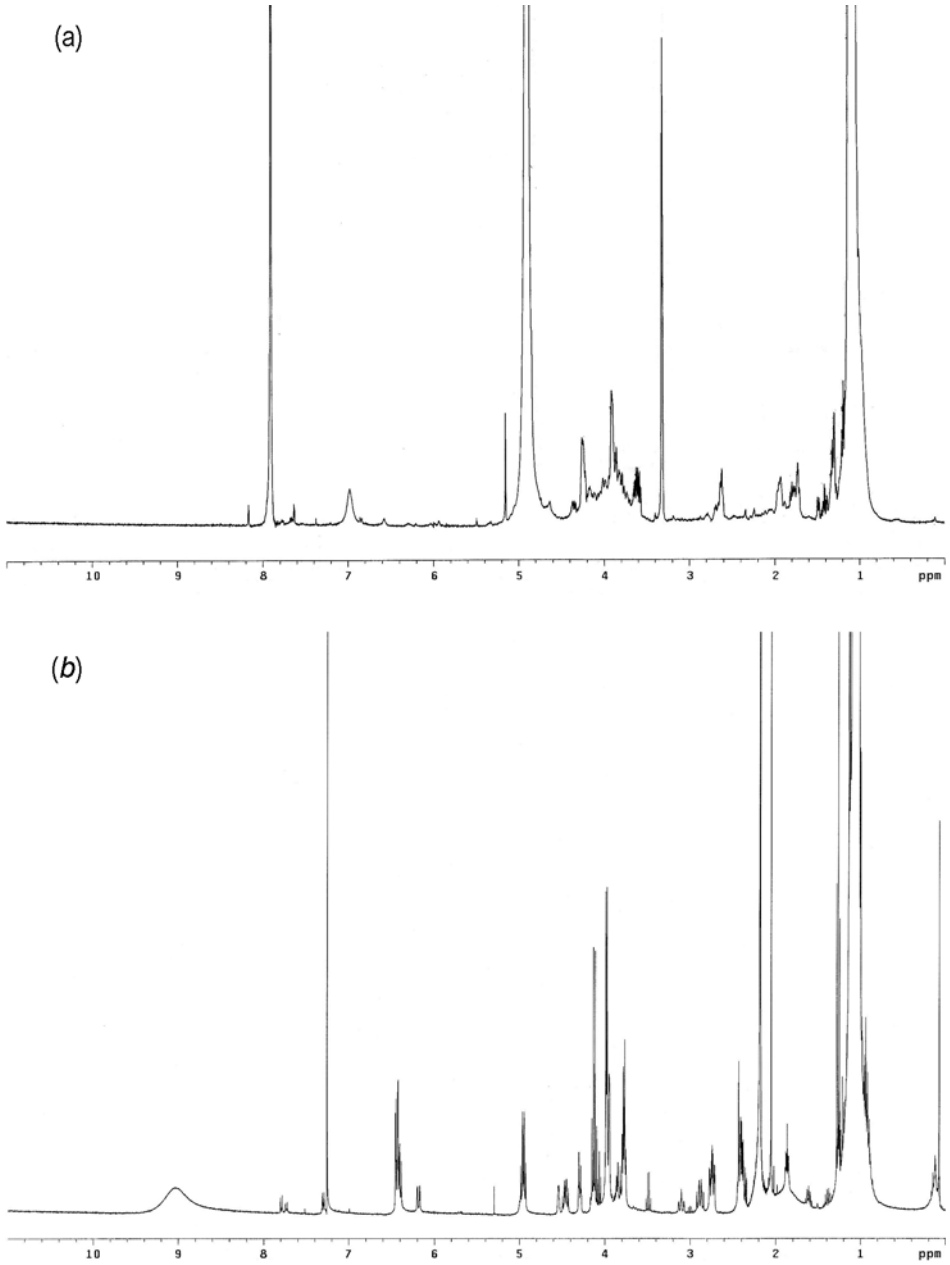

Can. J. Chem. Downloaded from www.nrcresearchpress.com by Sichuan Normal University on 09/14/12
For personal use only.

mixtures of triaminopyrimidine (**2**) and cyanuric acid (**3**) in dichloromethane, at scattering angles of 45°, 90°, and 135°, confirmed the presence of elongated aggregates in solution. The hydrodynamic diameters obtained for these angles were significantly different from one angle to the other, e.g., 165.1 nm at 45° and 93.8 nm at 135°, consistent with the presence of elongated, rather than spherical aggregates in solution.

Therefore, the molecules (**2**) and (**3**) undergo self-assembly into elongated aggregates both in solution (DLS) and in the solid state (TEM).

Conclusion

A novel biomimetic DNA analogue with interesting fluorescence properties has been successfully synthesized to generate functional supramolecular architectures. These preliminary experimental studies suggest that triaminopyrimidine nucleoside (**2**) might undergo sterically controlled self-assembly into hydrogen-bonded linear tapes and hexameric rosettes. Self-association of the hydrogen-bonded triaminopyrimidine–cyanuric acid complex into elongated, rodlike nanostructures was shown using DLS and TEM and suggested the possible hierarchical formation of higher-order, π–π stacked assemblies. The hydrogen-bond self-assembly of the DNA analogue significantly decreased the fluorescence of the nucleosides, and this guest-induced fluorescence quenching can be used to develop DNA-hybridization probes. Preliminary MM^+ molecular modelling and semi-empirical molecular orbital PM3 calculations[1] predicted the possible incorporation of the triaminopyrimidine nucleoside into new types of artificial DNA strands and triplex forma-

Fig. 5. ^{1}H NMR titration of DNA-base analogue (**2**) using cyanuric acid (**3**) in CD_2Cl_2. (*a*) Before titration; (*b*) after adding 0. 5 equiv. of cyanuric acid (**3**); (*c*) after adding 1.0 equiv. of cyanuric acid (**3**).

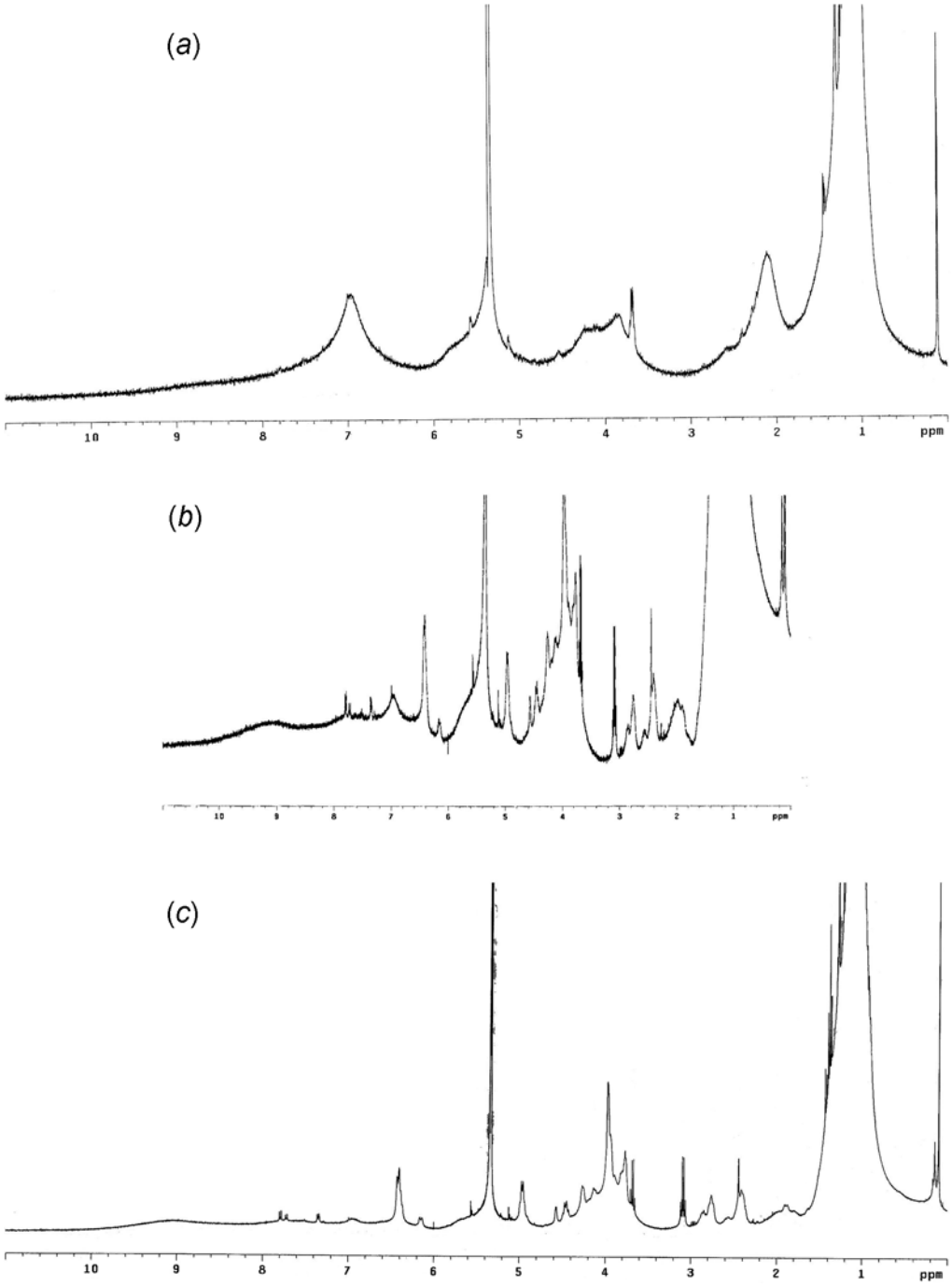

Can. J. Chem. Downloaded from www.nrcresearchpress.com by Sichuan Normal University on 09/14/12
For personal use only.

tion with natural, complementary DNA strands containing thymine, extending the application of this monomer of DNA analogues to antisense–antigene technologue.[2]

Experimental section

Materials

All reagents were purchased from the Sigma-Aldrich Chemical Co. The structures of the intermediates and the final products were confirmed by NMR spectroscopy and mass spectrometry.

Equipment

^{1}H and ^{13}C NMR spectra were acquired on Varian Mercury 400 and Varian Unity 500 spectrometers and 2D-COSY NMR spectra were acquired on a Varian Unity 500 spectrometer. Electrospray ionization (ESI) and atmospheric pressure chemical ionization (APCI) mass spectra were acquired by direct infusion into a Quattro II triple quadrupole (Micromass, Manchester, UK) with the spray voltage set to 3.5 kV, the source temperature 150–200 °C, sample infusion rate 5° μl/min using a syringe pump (Harvard Apparatus). UV–vis spectra were measured on a Varian CARY 1 UV–

Fig. 6. Electrospray ionization mass spectrum of equimolar triaminopyrimidine (**2**) and cyanuric acid (**3**) mixture.

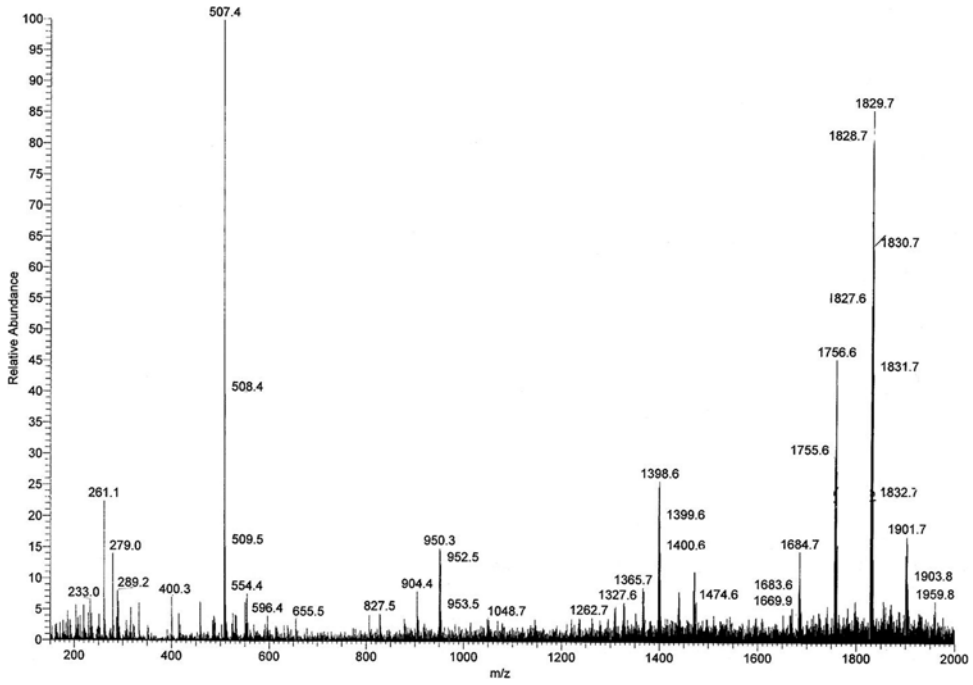

vis spectrophotometer equipped with a Peltier temperature controller. Fluorescence data was acquired using a PTI (Photon Technology International) TimeMaster model C-720F spectrofluorimeter. TEM was conducted on a JEOL-2000 FX instrument by using the direct method with and without uranyl staining.

Experimental synthesis

*2-deoxy-3,5-bis-*O*-(tetraisopropylsiloxyl)-*D*-ribofuranose (5)*

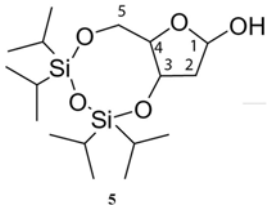

5

2-Deoxy-D-ribose (1 g, 7.41 mmol) in freshly distilled pyridine (9.26 mL) was stirred under N_2 atmosphere at 40 °C in presence of 1,3-dichloro-1,1′,3,3′-tetraisopropyldisiloxane (2.6 mL, 8.89 mmol). After 2 h, the reaction mixture was neutralized using 1 mol/L HCl (3 mL) and diluted with diethyl ether (50 mL). The organic layer was washed with saturated $NaHCO_3$ (50 mL) and water (2 × 50 mL), then dried over $MgSO_4$. The solvent was evaporated under reduced pressure to give a colourless oil. The desired compound (**5**) was isolated by column chromatography on silica gel using ethyl acetate/hexanes (20:90) as the eluent. (**5**) (1.922 g, 69%). ^{1}H NMR (400 MHz, $CDCl_3$) δ: 5.46 (dd, H_1, 4.8 Hz), 4.45 (m, H_4), 4.06 (dd, H_3, 7.6 Hz), 3.85 (d, H_5, 7.2 Hz), 3.68 (dd, H_5, 8.4 Hz, 15.8), 2.31 (m, H_2), 2.02–2.12 (m, H_2), 1.07 (s, 28 H). ESI-MS (neg): 376.

Fig. 7. UV–vis absorbance spectra of triaminopyrimidine (**2**) alone and in equimolar mixtures of cyanuric acid (**3**) in chloroform.

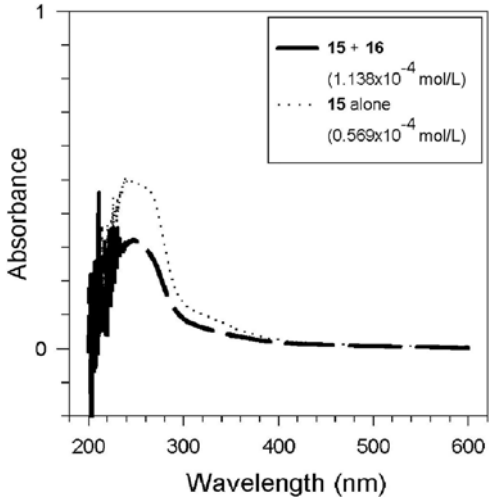

*1-*O*-(*p*-toluenesulfonyl)-2-deoxy-3,5-bis-*O*-(tetraisopropylsiloxyl)-ribofuranose (6)*

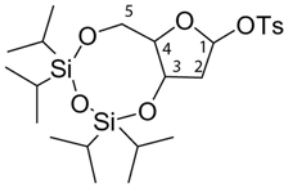

6

A solution of compound (**5**) (250 mg, 0.66 mmol) in dry CH_2Cl_2 (5 mL) was stirred with *p*-toluenesulfonyl chloride (150.0 mg, 0.66 mmol) under N_2 atmosphere in presence of

Can. J. Chem. Downloaded from www.nrcresearchpress.com by Sichuan Normal University on 09/14/12
For personal use only.

Can. J. Chem. Downloaded from www.nrcresearchpress.com by Sichuan Normal University on 09/14/12
For personal use only.

Fig. 8. Steady-state emission fluorescence spectra of triaminopyrimidine (**2**) alone and in equimolar mixtures of cyanuric acid (**3**) at λ_{exc} = 365 nm in chloroform.

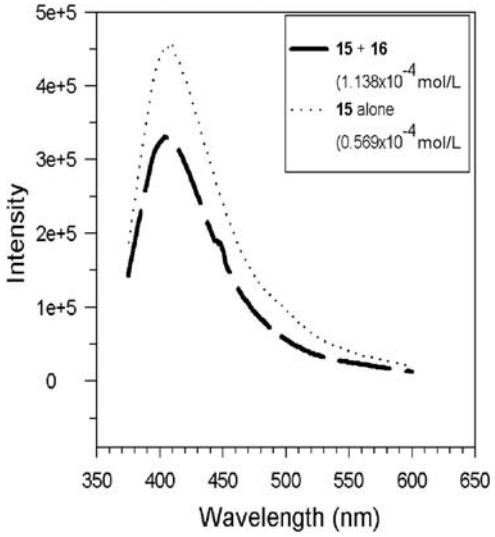

Fig. 9. Electron micrographs prepared from deposited solutions of triaminopyrimidine (**2**)/diethylbarbituric acid (**1**).

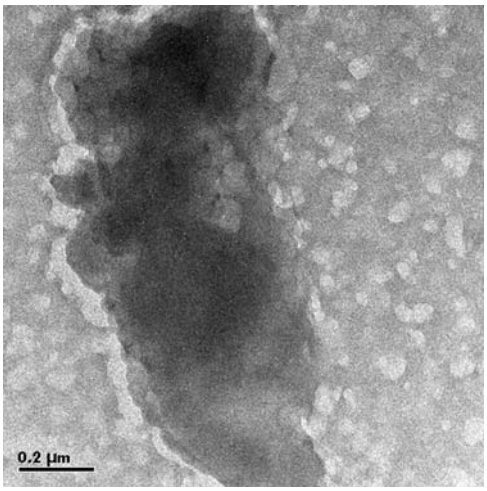

Et_3N (0.1 µL) for 2 h. The reaction was diluted with CH_2Cl_2 (10 mL) and quenched by adding water (10 mL). The organic layer was washed with saturated $NaHCO_3$ (2 × 10 mL) and water (10 mL), then dried over $MgSO_4$. The solvents were evaporated under reduced pressure. The formation of the *p*-toluenesulfonyl derivative (**6**) was verified by ^1H NMR in $CDCl_3$, which showed two sets of doublets in the aromatic region and two singlets corresponding to the methyl protons, consistent with the presence of two anomers α and β. The compound was used without further purification (341.7 mg, crude yield 97%). ^1H NMR (400 MHz, $CDCl_3$) δ: 7.92 (d, Ar-H_1, 8.0 Hz), 7.78 (d, Ar-H_1', 8.0 Hz), 7.40 (d, Ar-H_2, 8.0 Hz), 7.12 (d, Ar-H_2', 8.0 Hz), 5.56 (t, H_1, 7.2 Hz), 4.57 (dd, H_4, 7.2 Hz), 4.12–3.84 (m, H_3, $2H_5$), 3.17 (dd, H_2, 6.8 Hz, 11.6 Hz), 3.00 (m, H_2), 2.50 (s, $1CH_3$), 2.50 (s, $1CH_3$), 2.33 (s, $1CH_3$), 1.04 (s, 28 H).

(Tri-*N*-tert-butoxycarbonyl)-2,4,6-triamine-5-bromopyrimidine (7)

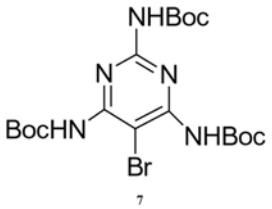

7

2,4,6-Triamino-5-bromopyrimidine was synthesized from 2,4,6-triaminopyrimidine using a protocol in the literature (29) The brominated pyrimidine (721.9 mg, 3.52 mmol), di(-*tert*-butoxy)carbonate (5.096 g, 24.79 mmol), and dimethylaminopyridine (310.4 mg, 2.48 mmol) were dissolved, in the presence of Et_3N (4.04 mL, 28.34 mmol), in freshly distilled THF (45 mL). The reaction mixture was stirred under N_2 atmosphere at RT for 15 h resulting in an orange brown suspension. The reaction was quenched using aqueous 5% $NaHCO_3$ (1.5 mL), and the solvents evaporated under reduced pressure. The residue was dissolved in diethyl ether (25 mL), and the organic layer washed with aqueous 5% $NaHCO_3$ (2 × 25 mL), water (25 mL) and brine (25 mL). The organic layer was dried over anhydrous $MgSO_4$, filtered, and the solvents evaporated under reduced pressure. The desired compound **7** (972.7 mg, 54%) was isolated by column chromatography on silica gel. using ethyl acetate/hexanes (40:60) as the eluent. R_f ~0.75. ^1H NMR (400 MHz, $CDCl_3$, ppm) δ: 1.10–1.90 (27 H).

1-(2′-deoxy-5′,3′-bis-*O*-(tetraisopropylsiloxyl)-ribofuranosyl) propanedinitrile (9)

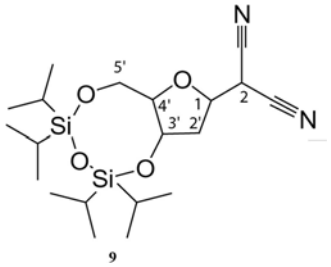

9

Method A

Malononitrile (149.0 mg, 2.26 mmol) in freshly distilled THF (1 mL) was added dropwise to a suspension of 95% NaOH (54 mg, 2.26 mmol) in THF (0.25 mL) at 0 °C. Tosylate (**6**) (400 mg, 0.75 mmol) in THF (0.5 mL) was added dropwise, and the reaction mixture stirred at RT overnight under N_2 atmosphere. The reaction was quenched with 5% aqueous NH_4Cl (6 mL). The reaction mixture was diluted with ethyl acetate, or dichloromethane (25 mL), and washed with water (2 × 25 mL) and brine (25 mL). The organic layer was dried over anhydrous $MgSO_4$, filtered, and the solvents evaporated under reduced pressure. Compound (**9**) (20 mg, 5%) was obtained as an off-white oil, after silica gel chromatography, using ether/hexanes (60:40) as eluent.

Fig. 10. (*a*) and (*b*) Electron micrographs prepared from deposited solutions of triaminopyrimidine (**2**)/cyanuric acid (**3**) using uranyl acetate as a staining agent; (*c*) and (*d*) profile analysis of the TEM images. Insets: magnified profile analysis to single rodlike structures (see text).

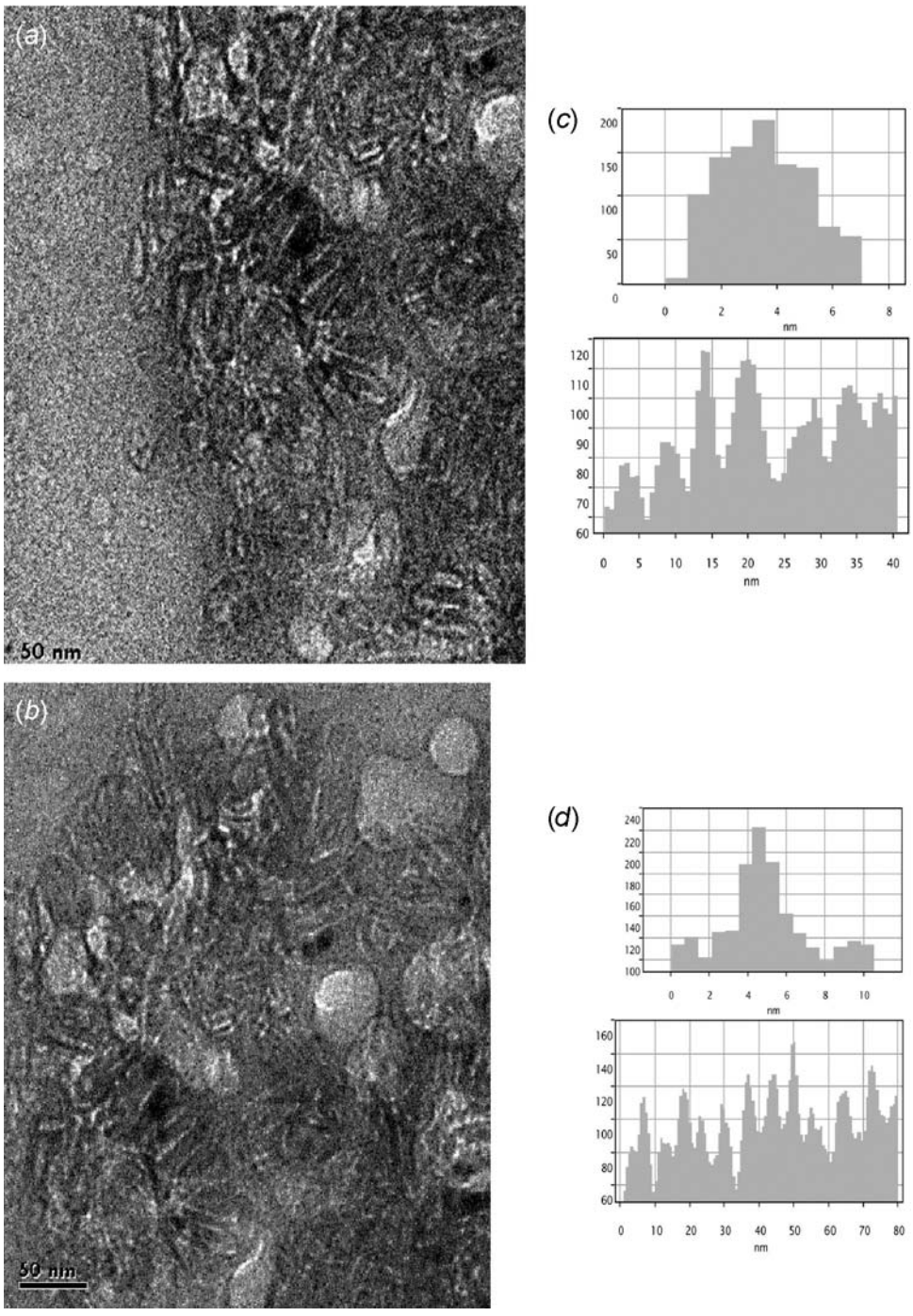

Can. J. Chem. Downloaded from www.nrcresearchpress.com by Sichuan Normal University on 09/14/12
For personal use only.

Method B

Malononitrile (52.7 mg, 0.80 mmol) in freshly distilled THF (0.5 mL) was added dropwise to a suspension of 95% NaOH (19.2 mg, 0.80 mmol) in THF (0.25 mL) at 0 °C. Protected sugar (**5**) (100 mg, 0.26 mmol) in THF (0.5 mL) was added dropwise, and the reaction mixture stirred at RT under N_2 atmosphere. The reaction was monitored by TLC until the disappearance of the starting material (1 h), then quenched with saturated NH_4Cl (6 mL). The reaction mixture was diluted with dichloromethane (25 mL) and washed with water (2 × 25 mL) and brine (25 mL). The organic layer was dried over anhydrous $MgSO_4$, filtered, and the solvents evaporated under reduced pressure. Compound (**9**) (37.7 mg, 33%) was obtained as an off-white oil after silica gel chromatography using ether/hexanes (60:40) as eluent. R_f ~0.25. ^{1}H NMR (400 MHz, $CDCl_3$) δ: 4.38 (dd, H_4', 8.0 Hz, 2.4 Hz), 4.13–3.98 (m, H_1', H_3', H_5'), 3.77 (dd, H_5', 6.0 Hz, 9.6 Hz), 3.13–3.18 (m, H_2'), 2.55–2.22 (m, H_2'), 1.06 (s, 28 H). APCI-MS *m/z*: calcd. 425.0 (M + 1), 849.0 (2M + 1); found: 425.4 (M + 1), 849.1 (2M + 1).

Can. J. Chem. Downloaded from www.nrcresearchpress.com by Sichuan Normal University on 09/14/12
For personal use only.

1-(2′-deoxy-5′,3′-bis-O-(tetraisopropylsiloxyl)-ribofuranosyl) propylidene dinitrile (11)

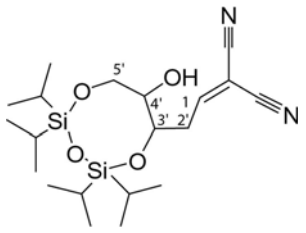

11

Method A

Malononitrile (17.6 mg, 0.26 mmol) in freshly distilled MeOH (1 mL) was added to a suspension of K_2CO_3 (3.7 mg, 0.026 mmol) in MeOH (0.5 mL) at RT. Protected sugar (**5**) (50 mg, 0.13 mmol) in THF (0.5 mL) was added dropwise, and the reaction mixture stirred at RT overnight under N_2 atmosphere. The reaction was quenched with saturated NH_4Cl (6 mL). The reaction mixture was diluted with dichloromethane (25 mL) and washed with water (2 × 25 mL) and brine (25 mL). The organic layer was dried over anhydrous $MgSO_4$, filtered, and the solvents evaporated under reduced pressure. Compound (**11**) (8.3 mg, 15%) was obtained as an off-white oil after silica gel chromatography, using ether/hexanes (60:40) as eluent. $R_f \sim 0.5$.

Method B

Malononitrile (17.8 mg, 0.27 mmol) in freshly distilled THF (0.5 mL) was added dropwise to a suspension of 95% NaOH (12.2 mg, 0.53 mmol) in THF (0.25 mL) at 0 °C. Protected sugar (**5**) (200 mg, 0.53 mmol) in THF (0.5 mL) was added dropwise, and the reaction mixture stirred at RT under N_2 atmosphere. The reaction was monitored by TLC until the disappearance of the starting material (1 h), then quenched with saturated NH_4Cl (6 mL). The reaction mixture was diluted with dichloromethane (25 mL) and washed with water (2 × 25 mL) and brine (25 mL). The organic layer was dried over anhydrous $MgSO_4$, filtered, and the solvents evaporated under reduced pressure. Compound (**11**) (29.1 mg, 13%) was an off-white oil after silica gel chromatography, using ether/hexanes (60:40) as eluent. $R_f \sim 0.5$. ^{1}H NMR (400 MHz, $CDCl_3$) δ: 4.53 (d, H_1), 4.14 (dd, H_4'), 4.04 (dd, H_5'), 3.97 (dd, H_3'), 3.82 (dd, H_1'), 3.77 (dd, H_5'), 3.04 (m, H_2'), 2.40–2.19 (m, H_2'), 1.06 (s, 28 H).

1,4-anhydro-(5′,3′-bis-O-(tetraisopropylsiloxyl))- 2′-deoxy-D-erythro-pent-1-enitol (12)

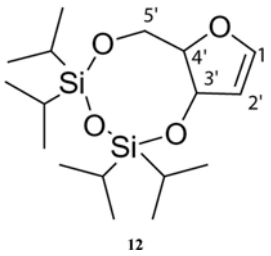

12

The 3,5-diprotected sugar (**5**) (100 mg, 0.265 mmol) was placed under vacuum in a flame-dried three-necked flask, equipped with a condenser. Dichloromethane (2 mL) was added under N_2 atmosphere with Et_3N (139 μL, 1.006 mmol). The resulting solution was cooled to –40 to –50 °C, and then mesyl chloride (25.5 μL, 0.331 mmol) was added dropwise. The reaction mixture was maintained at –40 to –50 °C for 3 h, then warmed to RT, and heated to reflux (50–60 °C) for 15 h. The solution was cooled to RT and filtered through a short silica gel column. The filtrate evaporated under reduced pressure to give a clear oil, which was purified by silica gel chromatography using diethyl ether/petroleum ether (2:98) as eluent, to give (**12**) (9.5 mg, 10%). ^{1}H NMR (400 MHz, $CDCl_3$) δ: 6.40 (dd, H_1'), 4.84 (t, H_2'), 4.44 (t, H_3'), 4.12 (dt, H_4'), 3.89 (dd, H_5'), 3.78 (m, H_5'), 1.07 (s, 28 H). ^{13}C NMR (100 MHz, $CDCl_3$) δ: 146.16, 100.90, 70.56, 64.75, 64.63, 18.14, 17.99, 17.95, 17.90, 17.83, 17.65, 17.56, 17.54, 14.60, 13.70, 13.63, 13.05.

1-(2′-deoxy-3′,5′-bis-O-(tetraisopropylsiloxyl)-ribofuranosyl)pyrimidine-2,4,6-triamine (2)

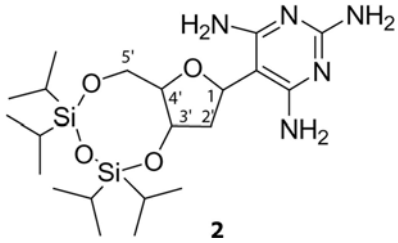

2

Sodium (15.05 mg, 0.65 mmol) and guanidine hydrochloride (62.5 mg 0.65 mmol) were stirred in freshly distilled EtOH (1.5 mL), under N_2 atmosphere until a solution was obtained. A solution of (**22**) (185.0 mg, 0.44 mmol) in freshly distilled EtOH was added dropwise to the mixture, which was heated to reflux for 5 h. The reaction mixture was cooled to RT and the solvents evaporated under reduced pressure. The compound (60.9 mg, 29%) was isolated as a mixture of α and β anomers by column chromatography on silica gel, using dichloromethane/ethanol (0:100 to 40:60 gradient). $R_f \sim 0.1$ (10:90 dichloromethane/ethanol). ^{1}H NMR (400 MHz, CD_3OD) δ: 6.98 (s, NH_2), 4.25 (m, H_1'), 3.82–4.01 (dd, H_3', H_4'), 3.61 (m, H_5'), 2.63 (m, H_5'), 2.01–1.71 (m, $2H_2'$), 1.06 (s, 28 H). ^{13}C NMR (100 MHz, CD_3OD) δ: 159.34, 158.65, 118.69, 77.52, 77.16, 76.41, 69.27, 68.85, 44.85, 38.29, 36.06, 24.43, 23.82, 16.98, 13.00. ESI-MS *m/z*: calcd. 484 (M + 1), 507 (M + Na + 1); found 484.3 (M + 1), 507.3 (M + Na + 1).

1-(2-deoxy-3,5-bis-O-(tetraisopropylsiloxyl)-ribofuranosyl)cyanuric acid (3)

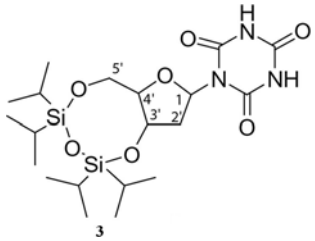

3

A mixture of the tosyl derivative (**6**) (353 mg, 0.67 mmol), cyanuric acid (85.2 mg, 0.67 mmol), potassium nonafluorobutanesulfonate (539.6 mg, 1.75 mmol), hexamethyldisilazane (98 μL, 0.54 mmol), and trimethylsilyl chlor-

Can. J. Chem. Downloaded from www.nrcresearchpress.com by Sichuan Normal University on 09/14/12
For personal use only.

ide (261 μL, 2.08 mmol) was heated to reflux, in freshly distilled acetonitrile (6.66 mL) under N_2 atmosphere. The reaction proceeded for 16 h and then cooled to RT. The solvents evaporated under reduced pressure and the residue was dissolved in $CHCl_3$ (25 mL), washed with saturated $NaHCO_3$ (25 mL) and water (25 mL), dried over $MgSO_4$. After solvent evaporation, the compound (119.2 mg, 37%) was isolated by two consecutive column chromatographies on silica gel, using dichloromethane, and then ethyl acetate/hexanes 1:1 as the eluents. ^{1}H NMR (400 MHz, $CDCl_3$) δ: 6.44 (m, H_1'), 4.96 (dd, H_4'), 4.55–4.28 (m, H_3'), 3.98 (dd, H_5'), 3.78 (dd, H_5'), 2.75 (m, H_2'), 2.40 (m, H_2'), 1.07 (s, 28 H). ^{13}C NMR (100 MHz, $CDCl_3$) δ: 148.53, 148.16, 147.91, 85.79, 83.60, 81.75, 72.74, 70.42, 63.58, 38.87, 17.86, 13.69.

Characterization of the self-assembly of nucleoside (2) with barbituric acid (1) and cyanuric acid (3)

Electrospray ionization mass spectrometry (ESI) measurements

An equimolar solution of triaminopyrimidine (**2**) with diethylbarbituric acid (**1**) or cyanuric acid (**3**) in a 10% $MeOH/CH_2Cl_2$ mixture was directly infused into a Quattro II triple quadrupole (Micromass, Manchester, UK), configured for positive product ion analysis and used with a spray voltage of 3.5 kV, a source temperature of 100–200 °C, a sample infusion rate of 5° μl/min, using a syringe pump (Harvard Apparatus). For molecular weight determination, the spectrometer was programmed to scan for product ions from *m/z* 150 to 2000, in the multichannel acquisition mode (MCA) showing *m/z* for the monomers and the hexamer.

Sample preparation for TEM measurements by the direct method

A solution of cyanuric acid and 2,4,6-triaminopyrimidine (1:1) was prepared by dissolving the sample in dichloromethane. A carbon-coated 400 mesh copper grid, prewashed with chloroform for 12 h, was dipped into the solution for approximately 1 min and dried on a filter paper.

Sample preparation for TEM measurements by staining

A solution of cyanuric acid and 2,4,6-triaminopyrimidine (1:1) was prepared by dissolving the sample in dichloromethane. The solution (10 μL) was deposited on a carbon-coated 400 mesh copper grid, prewashed with chloroform for 12 h, and blotted. A drop of aqueous 2% uranyl acetate was deposited on the air-dried copper grid, blotted, rinsed with a drop of water after 30 s, and then dried on paper filter.

Dynamic light scattering (DLS) measurements

Dynamic light scattering measurements were performed using a 532 nm laser equipped photo-multiplier detector. The autocorrelation functions were acquired for θ values of 45°, 90°, and 135° for prefiltered equimolar solutions of triaminopyrimidine (**2**) and cyanuric acid (**3**) in dichloromethane. Data acquisition was carried out at 20 °C within a few hours to get a better particle size distribution. Inverse Laplace transforms of the data were performed using Provencher's FORTRAN programme CONTIN,[20] and diffusion coefficients were determined from the slope of the relaxation frequencies (Γ) versus q^2. Assuming a spherical behaviour for the particles and using the translational coefficient DTr and the Stokes–Einstein equation, the hydrodynamic diameters were calculated for each scattering angle.

References

(1) Rakotondradany, F.; Sleiman, H.; Whitehead, M. A. *Can. J. Chem.* **2009**, *87*, in press.

(2) (a) Lehn, J.-M. *Supramolecular chemistry: Concepts and perspectives;* VCH: Weinheim, Germany, 1995; (b) *Comprehensive supramolecular chemistry*; Atwood, J. L.; Davies, J. E. D.; MacNicol, D. D.; Vögtle, F.; Lehn, J.-M., Eds.; Pergamon: Oxford, UK, 1996; (c) Whitesides, G. M.; Simanek, E. E.; Mathias, J. P.; Seto, C. T.; Chin, D. N.; Mammen, M.; Gordon, D. M. *Acc. Chem. Res.* **1995**, *28*, 37 doi:10.1021/ar00049a006.; (d) Lawrence, D. S.; Jiang, T.; Levett, M. *Chem. Rev.* **1995**, *95*, 2229 doi:10.1021/cr00038a018.; (e) Conn, M. M.; Rebek, J., Jr. *Chem. Rev.* **1997**, *97*, 1647 doi:10.1021/cr9603800. PMID:11851461.; (f) Prins, L. J.; Reinhoudt, D. N.; Timmerman, P. *Angew. Chem. Int. Ed.* **2001**, *40*, 2382 doi:10.1002/1521-3773(20010702)40:13<2382::AID-ANIE2382>3.0.CO;2-G.; (g) Archer, E. A.; Gong, H.; Krische, M. J. *Tetrahedron* **2001**, *57*, 1139. doi:10.1016/S0040-4020(00)00986-8.; (h) Meléndez, R. E.; Hamilton, A. D. *Top. Curr. Chem.* **1998**, *198*, 97. doi:10.1007/3-540-69178-2_3.

(3) Drain, C. M.; Fischer, R.; Nolen, E. G.; Lehn, J.-M. *J. Chem. Soc. Chem. Commun.* **1993**, 243. doi:10.1039/c39930000243.

(4) (a) Forman, S. L.; Fettinger, J. C.; Pieraccini, S.; Gottarelli, G.; Davis, J. T. *J. Am. Chem. Soc.* **2000**, *122*, 4060 doi:10.1021/ja9925148.; (b) Giorgi, T.; Lena, S.; Mariani, P.; Cremoni, M. A.; Masiero, S.; Pieraccini, S.; Rabe, J. P.; Samori, P.; Piero, G.; Spada, G. P.; Gottarelli, G. *J. Am. Chem. Soc.* **2003**, *125*, 14741. doi:10.1021/ja0364827. PMID:14640649.

(5) (a) Sessler, J. L.; Sathiosatham, M.; Doerr, K.; Lynch, V.; Abboud, K. A. *Angew. Chem. Int. Ed.* **2000**, *39*, 1300 doi:10.1002/(SICI)1521-3773(20000403)39:7<1300::AID-ANIE1300>3.0.CO;2-I.; (b) Sessler, J. L.; Wang, R. *Angew. Chem. Int. Ed.* **1998**, *37*, 1726 doi:10.1002/(SICI)1521-3773(19980703)37:12<1726::AID-ANIE1726>3.0.CO;2-X.; (c) Sessler, J. L.; Wang, R. *J. Org. Chem.* **1998**, *63*, 4079 doi:10.1021/jo980194p.; (d) Mezzina, E.; Mariani, P.; Itri, R.; Masiero, S.; Pieraccini, S.; Spada, G. S.; Spinozzi, F.; Davis, J. T.; Gottarelli, G. *Chem. Eur. J.* **2001**, *7*, 388. doi:10.1002/1521-3765(20010119)7:2<388::AID-CHEM388>3.0.CO;2-V.

(6) (a) [Trimers:] Zimmerman, S. C.; Duerr, B. F. *J. Org. Chem.* **1992**, *57*, 2215 doi:10.1021/jo00034a005.; (b) Boucher, E.; Simard, M.; Wuest, J. D. *J. Org. Chem.* **1995**, *60*, 1408 doi:10.1021/jo00110a050.; (c) Sessler, J. L.; Jayawickramarajah, J.; Sathiosatham, M.; Sherman, C. L.; Brodbelt, J. S. *Org. Lett.* **2003**, *5*, 2627 doi:10.1021/ol034765y. PMID:12868875.; (d) [2 + 2 Tetramer:] Yang, J.; Fan, E.; Geib, S. J.; Hamilton, A. D. *J. Am. Chem. Soc.* **1993**, *115*, 5314 doi:10.1021/ja00065a061.; (e) [Isoguanine tetramers:] Tirumala, S.; Davis, J. T. *J. Am. Chem. Soc.* **1997**, *119*, 2769 doi:10.1021/ja963213q.; (f) [Isoguanine pentamer-cesium complex:] Shi, X.; Fettinger, J. C.; Cai, M.; Davis, J. T. *Angew. Chem. Int. Ed.* **2000**, *39*, 3124 doi:10.1002/1521-3773(20000901)39:17<3124::AID-ANIE3124>3.0.CO;2-X.; (g) [3 + 3 Hexamer:] Zerkowski, J. A.; Seto, C. T.; Whitesides, G. M. *J. Am. Chem. Soc.* **1992**, *114*, 5473 doi:10.1021/ja00039a096.; (h) Vreekamp, R. H.; van Duynhoven,

Can. J. Chem. Downloaded from www.nrcresearchpress.com by Sichuan Normal University on 09/14/12
For personal use only.

J. P. M.; Hubert, M.; Verboom, W.; Reinhoudt, D. N. *Angew. Chem. Int. Ed. Engl.* **1996**, *35*, 1215. doi:10.1002/anie.199612151.

(7) (a) [For hexamers using GC-like hydrogen-bonding:] Marsh, A.; Silvestri, M.; Lehn, J.-M. *Chem. Commun. (Camb.)* **1996**, 1527 doi:10.1039/cc9960001527.; (b) Mascal, M.; Hext, N. M.; Warmuth, R.; Arnall-Culliford, J. R.; Moore, M. H.; Turkenburg, J. P. *J. Org. Chem.* **1999**, *64*, 8479 doi:10.1021/jo990719t.; (c) Ma, Y.; Kolotuchin, S. V.; Zimmerman, S. C. *J. Am. Chem. Soc.* **2002**, *124*, 13757 doi:10.1021/ja0202006. PMID:12431106.; (d) Fenniri, H.; Mathivanan, P.; Vidale, K. L.; Sherman, D. M.; Hallenga, K.; Wood, K. V.; Stowell, J. G. *J. Am. Chem. Soc.* **2001**, *123*, 3854 doi:10.1021/ja005886l. PMID:11457132.; (e) Fenniri, H.; Deng, B.; Ribbe, A. E. *J. Am. Chem. Soc.* **2002**, *124*, 11064. doi:10.1021/ja026164s. PMID:12224954.

(8) (a) Piccirilli, J. A.; Krauch, T.; Moroney, S. E.; Benner, S. A. *Nature* **1990**, *343*, 33 doi:10.1038/343033a0. PMID:1688644.; (b) Switzer, C. Y.; Moroney, S. E.; Benner, S. A. *Biochemistry* **1993**, *32*, 10489 doi:10.1021/bi00090a027. PMID:7691174.; (c) McMinn, D. L.; Ogawa, A. K.; Wu, Y.; Liu, J.; Schultz, P. G.; Romesberg, F. E. *J. Am. Chem. Soc.* **1999**, *121*, 11585 doi:10.1021/ja9925150.; (d) Tae, E. L.; Wu, Y.; Xia, G.; Schultz, P. G.; Romesberg, F. E. *J. Am. Chem. Soc.* **2001**, *123*, 7439 doi:10.1021/ja010731e. PMID:11472182.;

(9) (a) Wu, Y.; Ogawa, A. K.; Berger, M.; McMinn, D. L.; Schultz, P. G.; Romesberg, F. E. *J. Am. Chem. Soc.* **2000**, *122*, 7621 doi:10.1021/ja0009931.; (b) Kool, E. T. *J. Am. Chem. Soc.* **1991**, *113*, 6265 doi:10.1021/ja00016a050.; (c) Vo, T.; Wang, S.; Kool, E. T. *Nucleic Acids Res.* **1995**, *23*, 2937 doi:10.1093/nar/23.15.2937. PMID:7544889.; (d) Weizman, H.; Tor, Y. *J. Am. Chem. Soc.* **2001**, *123*, 3375 doi:10.1021/ja005785n. PMID:11457077.; (e) Tanaka, K.; Tengeiji, A.; Kato, T.; Toyama, N.; Shiro, M.; Shionoya, M. *J. Am. Chem. Soc.* **2002**, *124*, 12494 doi:10.1021/ja027175o. PMID:12381191.; (f) Zimmermann, N.; Meggers, E.; Schultz, P. G. *J. Am. Chem. Soc.* **2002**, *124*, 13684 doi:10.1021/ja0279951. PMID:12431092.; (g) Atwell, S.; Meggers, E.; Spraggon, G.; Schultz, P. G. *J. Am. Chem. Soc.* **2001**, *123*, 12364 doi:10.1021/ja011822e. PMID:11734038.; (h) Thum, O.; Jäger, S.; Famulok, M. *Angew. Chem. Int. Ed.* **2001**, *40*, 3990. doi:10.1002/1521-3773(20011105)40:21<3990::AID-ANIE3990>3.0.CO;2-O.

(10) (a) Franklin, R. E.; Gossling, R. G. *Nature* **1953**, *171*, 740 doi:10.1038/171740a0. PMID:13054694.; (b) Watson, J. D.; Crick, F. H. C. *Nature* **1953**, *171*, 737. doi:10.1038/171737a0. PMID:13054692.

(11) (a) Giovannangeli, C.; Hélène, C. *Curr. Opin. Mol. Ther.* **2000**, *2*, 288 PMID:11249623.; (b) Praseuth, D.; Guieysse, A. L.; Hélène, C. *Biochim. Biophys. Acta* **1999**, *1489*, 181 PMID:10807007.; (c) Vasquez, K. M.; Wilson, J. H. *Trends Biochem. Sci.* **1998**, *23*, 4 doi:10.1016/S0968-0004(97)01158-4. PMID:9478127.; (d) Knauert, M. P.; Glazer, P. M. *Hum. Mol. Genet.* **2001**, *10*, 2243 doi:10.1093/hmg/10.20.2243. PMID:11673407.; (e) Guntaka, R. V.; Varma, B. R.; Weber, K. T. *Int. J. Biochem. Cell Biol.* **2003**, *35*, 22. doi:10.1016/S1357-2725(02)00165-6. PMID:12467644.

(12) (a) Keniry, M. A. *Biopolymers* **2000**, *56*, 123 doi:10.1002/1097-0282(2000/2001)56:3<123::AID-BIP10010>3.0.CO;2-3.; (b) Rhodes, D.; Giraldo, R. *Curr. Opin. Struct. Biol.* **1995**, *5*, 311 doi:10.1016/0959-440X(95)80092-1. PMID:7583629.; (c) Pilch, D. S.; Plum, G. E.; Breslauer, K. J. *Curr. Opin. Struct. Biol.* **1995**, *5*, 334 doi:10.1016/0959-440X(95)80095-6. PMID:7583632.; (d) Feigon, J.; Koshlap, K. M.; Smith, F. W. *Methods Enzymol.* **1995**, *261*, 225. doi:10.1016/S0076-6879(95)61012-X. PMID:8569497.

(13) (a) [For DNA-triple helices:] Sun, J. S.; Garestier, T.; Hélène, C. *Curr. Opin. Struct. Biol.* **1996**, *6*, 327 doi:10.1016/S0959-440X(96)80051-0. PMID:8804836.; (b) Thuong, N. T.; Hélène, C. *Angew. Chem. Int. Ed. Engl.* **1993**, *32*, 666. doi:10.1002/anie.199306661.

(14) (a) [For G-quartets:] Blackburn, E. H. *Cell* **1994**, *77*, 621 doi:10.1016/0092-8674(94)90046-9. PMID:8205611.; (b) Sen, D.; Gilbert, W. *Nature* **1988**, *334*, 364 doi:10.1038/334364a0. PMID:3393228.; (c) Sundquist, W. I.; Klug, A. *Nature* **1989**, *342*, 825 doi:10.1038/342825a0. PMID:2601741.; (d) Williamson, J. R.; Raghuraman, M. K.; Cech, T. R. *Cell* **1989**, *59*, 871. doi:10.1016/0092-8674(89)90610-7. PMID:2590943.; (e) Neidle, S.; Parkinson, G. *Nat. Rev. Drug Res.* **2002**, *1*, 383. doi:10.1038/nrd793.

(15) Rakotondradany, F.; Palmer, A.; Toader, V.; Chen, B.; Whitehead, M. A.; Sleiman, H. F. *Chem. Commun.* **2005**, *43*, 5441. doi:10.1039/b511984g.

(16) (a) Chaput, J. C.; Switzer, C. *Proc. Natl. Acad. Sci. U.S.A.* **1999**, *96*, 10614. doi:10.1073/pnas.96.19.10614.; (b) Davis, J. T. *Angew. Chem. Int. Ed.* **2000**, *39*, 3649. doi:10.1002/1521-3773(20001016)39:20<3649::AID-ANIE3649>3.0.CO;2-8.

(17) (a) Germain, F.; Chapleur, Y.; Castro, B. *Tetrahedron* **1982**, *38*, 3593 doi:10.1016/0040-4020(82)80065-3.; (b) Germain, F.; Chapleur, Y.; Castro, B. *Synthesis* **1983**, 119.

(18) Gasparutto, D.; Da Cruz, S.; Bourdat, A. G.; Jaquinod, M.; Cadet, J. *Chem. Res. Toxicol.* **1999**, *12*, 630. doi:10.1021/tx980255e. PMID:10409403.

(19) [Blue fluorescence could be qualitatively observed on TLC plates or in solutions of nucleoside **2** using a hand-held UV lamp (λ_1 = 254 nm, λ_2 = 365 nm)].

(20) (a) Provencher, S. W. *Comput. Phys.* **1982**, *27*, 213 doi:10.1016/0010-4655(82)90173-4.; (b) Provencher, S. W. *Comput. Phys.* **1982**, *27*, 229 doi:10.1016/0010-4655(82)90174-6.; (c) Schmitz, K. S. *An introduction to dynamic light scattering by mcromolecules.* Academic Press Inc.: San Diego, Calif., USA, 1990.

Cleavage of models for RNA mediated by a diZn(II) complex of bis[1,4-N_1,N_1'(1,5,9-triazacyclododecanyl)]butane in methanol and ethanol

C. Tony Liu, Stephanie A. Melnychuk, Chaomin Liu, Alexei A. Neverov, and R. Stan Brown

Abstract: The cleavage of seven RNA model 2-hydroxypropyl aryl phosphates (**1**) catalyzed by a dinuclear Zn(II) complex of bis[1,4-N_1,N_1'(1,5,9-triazacyclododecanyl)]butane (**4**) was studied in methanol and ethanol at 25 °C under pH controlled conditions. The results are compared with what was reported earlier for the dinuclear Zn(II) complex of the lower homologue bis[1,3-N_1,N_1'(1,5,9-triazacyclododecanyl)]propane (**3**). In methanol, the higher homologue exhibits saturation binding with substrates having poor aryloxy leaving groups. With good leaving groups there is an observed linear dependence of k_{obs} versus complex concentration without saturation binding over the catalyst concentration range investigated. In ethanol, strong saturation binding between the active form of the catalyst ((RO^-):$Zn(II)_2$:**4**) and all substrates is observed, the results observed in both solvents being similar to what was reported for the lower (RO^-):$Zn(II)_2$:**3** homologue. Energetics calculations are presented for the (RO^-):$Zn(II)_2$:**4**-catalyzed cleavage of each substrate in both solvents to assess the catalytic efficiency via the $\Delta\Delta G^{\ddagger}$ for catalyst binding a transition state comprising $[RO^-$:**1**$]^{\ddagger}$ or its kinetic equivalent.

Key words: dinuclear Zn(II) catalyst, RNA model cleavage, methanolysis, ethanolysis, kinetics, mechanism.

Résumé : Opérant dans des conditions de pH contrôlé, à 25 °C, en solution dans le méthanol et l'éthanol, on a étudié la réaction de clivage de sept phosphates d'aryle et de 2-hydroxypropyle (**1**), des modèles de l'ARN, catalysé par un complexe dinucléaire du Zn(II) et le bis[1,4-N_1,N_1'(1,5,9-triazacyclododécanyl)]butane (**4**). On compare les résultats avec ceux rapportés antérieurement pour le complexe dinucléaire du Zn(II) l'homologue inférieur bis[1,3-N_1,N_1'(1,5,9-triazacyclododécanyl)]propane (**3**). Dans le méthanol, l'homologue supérieur on observe qu'il y a saturation du site de fixation avec les substrats pour lesquels l'habilité à partir des groupes aryloxy est faible. Avec de bons groupes partant, pour toute la plage de concentration de catalyseur utilisée dans ce travail, on observe une dépendance linéaire de k_{obs} en fonction de la concentration du complexe. Dans l'éthanol, on observe une forte saturation des sites de fixation entre tous les substrats et la forme active du catalyseur [(RO^-):$Zn(II)_2$:**4**]; dans les deux solvants, les résultats sont similaires à ceux rapportés pour l'homologue inférieur [(RO^-):$Zn(II)_2$:**3**]. Afin d'évaluer l'efficacité catalytique par le biais du $\Delta\Delta G^{\ddagger}$ de la fixation par le catalyseur d'un état d'activation comportant $[RO^-$:**1**$]^{\ddagger}$ ou son équivalent cinétique, on a effectué des calculs d'énergie pour le clivage de chacun des substrats, catalysés par [(RO^-):$Zn(II)_2$:**4**].

Mots-clés : catalyseur de Zn(II) dinucléaire, clivage d'un modèle d'ARN, méthanolyse, éthanolyse, cinétique, mécanisme.

[Traduit par la Rédaction]

Introduction

Phosphate diesters that form the backbone of RNA and DNA are highly stable toward hydrolytic cleavage under physiological conditions in the absence of enzymes or specific catalysts.[1,2] However, with the assistance of enzymes, the cleavage of these sorts of phosphate diesters can be accelerated by up to 10^{15}–10^{17}.[1] Many naturally occurring phosphodiesterases have active sites containing two or more metal ions such as Zn(II), Ca(II), Mg(II), Fe(III), and Mn(II) in close proximity (3–4 Å apart).[3] In an effort to understand the origins of this exalted catalysis numerous researchers have studied mono- and di-nuclear metal ion catalysts for cleaving selected phosphate diesters.[4–7] We have reported the rapid cleavage of a series of activated RNA (**1**)[8,9] and DNA (**2**)[8,10] models catalyzed by the dinuclear **3**:$Zn(II)_2$:($^-$OR) complex in methanol and ethanol under ^S_SpH controlled conditions.[11] As shown in Scheme 1, the catalyzed cleavage of **1** involves intramolecular participation of the 2-hydroxylpropyl group to form a cyclic phosphate intermediate (**5**), which rapidly opens up to the two isomeric products, **6** and **7**.[12]

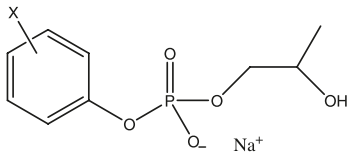

1

1a. X = 4-NO_2
1b. X = 4-NO_2-3-CH_3
1c. X = 3-NO_2
1d. X = 4-Cl
1e. X = 3-OCH_3
1f. X = H
1g. X = 4-OCH_3

Received 16 December 2008. Accepted 13 February 2009. Published on the NRC Research Press Web site at canjchem.nrc.ca on 23 April 2009.

C.T. Liu, S.A. Melnychuk, C. Liu, A.A. Neverov, and R.S. Brown.[1] Department of Chemistry, Queen's University, 90 Bader Lane, Kingston, ON K7L 3N6, Canada.

[1]Corresponding author (e-mail: rsbrown@chem.queensu.ca).

Scheme 1.

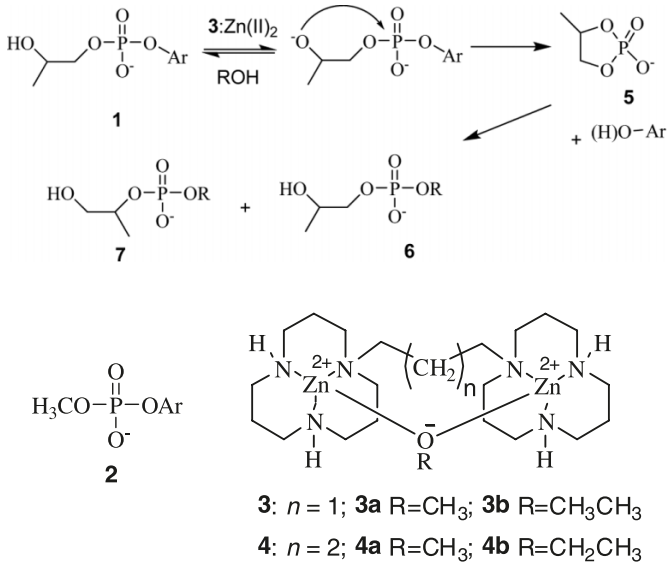

Although **3**:$Zn(II)_2$ is reported to exhibit poor catalysis of the cleavage of bis-*p*-nitrophenyl phosphate in water,[13] it is dramatically different in methanol[9] and ethanol[14] where, as an alkoxy form (**3a**, **3b**), it accelerates the cleavages of **1a**–**1g** by 10^{11} to 10^{14} relative to the background alkoxide-facilitated reactions at near neutral $^{S}_{S}$pH values and 25 °C. The origin of the very large enhancement of activity obtained by an apparently simple change in solvent is uncertain at this time, but is probably related to a variety of factors including a reduced polarity and dielectric constant (dielectric constant, ϵ = 78, 31.5, and 24.3 for water, methanol, and ethanol, respectively[15]) and overall solvation changes that enhance the interaction between the oppositely charged catalyst and substrate in the ground state and increasingly so in the transition state for the catalyzed reaction.

Herein, we report on a slightly more flexible $Zn(II)_2$ complex of ligand **4**, which is the C_4 higher homologue of **3**. To shed light on how the additional flexibility of the higher homologue might affect the catalysis under $^{S}_{S}$pH controlled conditions, studies of the **4**:$Zn(II)_2$-catalyzed transesterification of **1a**–**1g** in methanol and ethanol were undertaken to compare with what was seen earlier with **3**:$Zn(II)_2$. As will be shown, **4**:$Zn(II)_2$ accelerates the cleavage reactions of **1a**–**1g** by around 10^{11} to 10^{12} (at $^{S}_{S}$pH [11] 9.5 and 25 °C) in methanol and a factor of 10^{15} to 10^{16} (at $^{S}_{S}$pH 9.0 and 25 °C) in ethanol relative to the background alkoxide-promoted reactions in the respective solvents.[16]

Experimental

Materials

Anhydrous methanol (99.8%), sodium methoxide (0.50 mol/L solution in methanol, titrated against N/50 certified standard aqueous HCl solution and found to be 0.49 mol/L), sodium ethoxide (21 wt. % solution in denatured ethanol, titrated against N/50 standard aqueous HCl solution and found to be 2.68 mol/L), $Zn(CF_3SO_3)_2$, and tetrabutylammonium trifluoromethanesulfonate (99%) were used without further purification. $HClO_4$ (70% aqueous solution, titrated to be 11.40 mol/L) was used as supplied as was Paraoxon® (diethyl *p*-nitrophenyl phosphate, 99.5%), methanol-d_4 (D, 99.8%) and absolute ethanol which was then de-gassed by bubbling Ar through it for 1h prior to storing it under Ar. Freshly dispensed degassed ethanol ([H_2O], determined to be 0.028 ± 0.007 mol/L[14,17] by Karl Fischer titration) was used for conducting kinetic experiments. The sodium salts of the 2-hydroxylpropyl aryl phosphates (**1a**–**1g**) were prepared as described in earlier reports[9,18,19] where the characterizations of the compounds can be found. The dinuclear catalyst was prepared as 2.5 mmol/L stock solutions by sequential addition of aliquots of stock solutions of sodium alkoxide, **4**, and $Zn(CF_3SO_3)_2$ such that the relative ratios were 1:1:2 in either solvent at 25 °C. The complete formation of the complexes required 25 and 80 min in methanol and ethanol (as monitored by the changed in catalytic activity over time).

Bis[1,4-N_1,N_1'(1,5,9-triazacyclododecanyl)]butane (4)

To a solution of 1,5,7-triazabicyclo[4,4,0]dec-5-ene[20] (2.50 g, 13.8 mmol) in 50 mL of dry acetonitrile, 1.48 g (6.9 mmol) of 1,4-dibromobutane was added. The reaction mixture was heated at reflux for 3 d and the resulting off-white solid was filtered and washed with dry acetonitrile. The crude product was then mixed with 6 N aqueous HCl (20 mL) and heated to reflux for 48 h before the majority of the solvent was removed in vacuo. Absolute ethanol was added to the residue to induce precipitation. The white precipitates were washed four times with 8 mL portions of absolute ethanol and then dried in vacuo after which they were recrystallized from 1:9 aqueous ethanol to afford the HCl salt of **4** as a white solid in 67% overall yield. Conversion of the HCl salt into the free amine (**4**) was accomplished by stirring 897 mg (1.48 mmol) in 30 mL of water along with excess 5 N NaOH for 2 h at ambient temperature, followed by extracting the solution with four 25 mL portions of $CHCl_3$. The combined $CHCl_3$ extracts were dried over $MgSO_4$ and filtered before the solvent was removed in vacuo affording pure **4** as a nearly colorless oil in 78% yield (456 mg). ^{1}H NMR (400 MHz, CD_3OD, 25 °C) δ: 2.80 (t, 8H, J = 6.0 Hz, $HNCH_2CH_2CH_2NH$), 2.75 (t, 8H, J = 6.0 Hz, $HNCH_2(CH_2)_2N(CH_2)_2$), 2.59 (t, 8H, J = 6.0 Hz, $N(CH_2)_2CH_2$), 2.46 (m, 4H, $N(CH_2)_2CH_2$), 1.70 (m, 12H, $HNCH_2CH_2CH_2N$), 1.49 (m, 4H, $CH_2CH_2CH_2CH_2$). ^{13}C NMR (100 MHz, D_2O, 25 °C) δ: 53.2, 51.8, 48.8, 47.3, 25.4, 25.2, 23.2. HRMS (EI-TOF) *m/z*: calcd. for ($C_{22}H_{48}N_6$): 396.3940; found: 396.3943 (M^+).

Methods

^{1}H NMR and ^{31}P NMR spectra were determined at 400 and 162.04 MHz. The $CH_3OH_2^+$ and $CH_3CH_2OH_2^+$ concentrations were determined potentiometrically with a combination glass electrode (Radiometer model # XC100-111-120-161) calibrated with standard aqueous buffers (pH = 4.00 and 10.00) as described previously.[11] The $^{S}_{S}$pH values in methanol and ethanol were determined by subtracting the correction constants of –2.24[11a,11b] and –2.54,[11c] respectively, from the electrode readings. The autoprotolysis constants are $10^{-16.77}$ $(mol/L)^2$ for methanol and $10^{-19.1}$ $(mol/L)^2$ for ethanol. The kinetic experiments were conducted under buffer-free conditions of low but variable ionic strength determined by the catalyst concentration since the presence of buffer and excess salts that might be used to keep ionic strength

constant is observed to inhibit the catalysis, probably due to binding of the anions.

Stopped-flow kinetics

The rates for the catalyzed transesterification of **1a**–**1g** were determined by following the appearance of the phenolic products using a stopped-flow reaction analyzer thermostatted at 25.0 ± 0.1 °C. The production of the phenol was monitored at the following wavelengths: **1a**, 320 nm; **1b**, 323 nm; **1c**, 340 nm; **1d**, 284 nm; **1e**, 282 nm; **1f**, 280 nm; and **1g**, 292 nm. Stock solutions (2.5 mmol/L) of **4**:$Zn(II)_2$:($^-OCH_3$) in methanol and **4**:$Zn(II)_2$:($^-OCH_2CH_3$) in ethanol were prepared in oven-dried vials that were capped and sealed with Parafilm®. These were used to prepare catalyst solutions of concentrations ranging from 0.34 mmol/L ≤ **4**:$Zn(II)_2$:($^-OCH_3$) ≤ 2.06 mmol/L in methanol and 0.06 mmol/L ≤ **4**:$Zn(II)_2$:($^-OCH_2CH_3$) ≤ 0.28 mmol/L in ethanol. The catalyst solutions were loaded into one of the two syringes in the stopped-flow analyzer while a solution containing 0.1 mmol/L of substrate **1a**–**1g** in either methanol or ethanol was loaded into the other. The final concentrations of catalyst after mixing in the cell of the stopped-flow analyzer were 0.17 mmol/L ≤ **4**:$Zn(II)_2$:($^-OCH_3$) ≤ 1.03 mmol/L in methanol and 0.03 mmol/L ≤ **4**:$Zn(II)_2$:($^-OCH_2CH_3$) ≤ 0.14 mmol/L in ethanol while the final concentration of **1a**–**1g** was 0.05 mmol/L in either alcohol. At each catalyst concentration at least five kinetic runs were recorded and the average values were used for the k_{obs} for the appearance of the product. The $^S_Sp K_a$ values of the corresponding phenol leaving groups of **1a**–**1g** in methanol[9] and ethanol[14] have been reported.

The degree of triflate inhibition on the catalysis in methanol was determined from a kinetic experiment that involved monitoring the cleavage of paraoxon (0.05 mmol/L) mediated by 0.43 mmol/L of **4**:$Zn(II)_2$:($^-OCH_3$) in the presence of added tetrabutylammonium triflate so that the final $[\text{triflate anion}]_{total}$ ranged between 2.0 and 8.0 mmol/L. The effect of [triflate anion] on the catalyzed reactions in ethanol was determined by following the change in reactivity of 0.08 mmol/L **4**:$Zn(II)_2$:($^-OCH_2CH_3$) mediating the cleavage of **1a** (0.05 mmol/L) in ethanol with varying tetrabutylammonium triflate concentration so that the final $[CF_3SO_3^-]_{total}$ ranged between 0.3 and 3.4 mmol/L.

Kinetic titration of 4:$Zn(II)_2$ for reactions of 1g in methanol and 1b in ethanol

Ethanol

Varying amounts of $NaOCH_2CH_3$ or $HClO_4$ stock solutions (5 mmol/L) in ethanol were added to solutions containing 1.6×10^{-4} mol/L of a preformed **4**:$Zn(II)_2$:($^-OCH_2CH_3$) complex in ethanol, which had been prepared 80 min in advance to allow for complete formation of the complex. After the introduction of the additional acid or base, the mixture was allowed to stand for 15 min to equilibrate (independent experiments showed that this time was optimum to stabilize the kinetic activity) and then loaded into one syringe of the stopped-flow analyzer while a 1.0×10^{-4} mol/L solution of **1b** in ethanol was loaded into the other. The final concentrations after mixing were 8×10^{-5} mol/L of **4**:$Zn(II)_2$ and 5×10^{-5} mol/L of **1b** in ethanol. The ^S_SpH values were measured at the end of the reactions and assumed to have been set immediately on mixing. The ^S_SpH/log rate constant profile plot is presented in Fig. 1 with the line through the data being derived from a fit of the solid squares data to a process that depended on two ionizable groups having $^S_Sp K_a$ values of 8.48 and 10.38 (see the Supplementary data).

Fig. 1. Two ^S_SpH/log $k_{obs}^{max\ corr}$ profiles for the reaction of **4**:$Zn(II)_2$:($^-OCH_2CH_3$) and **1b**, as well as **4**:$Zn(II)_2$:($^-OCH_3$) with **1g** conducted at 25 °C in ethanol and methanol. The lines through the data points in the indicated boxes are computed on the basis of a bell-shaped ^S_SpH/rate profile. (See text and ref. 14).

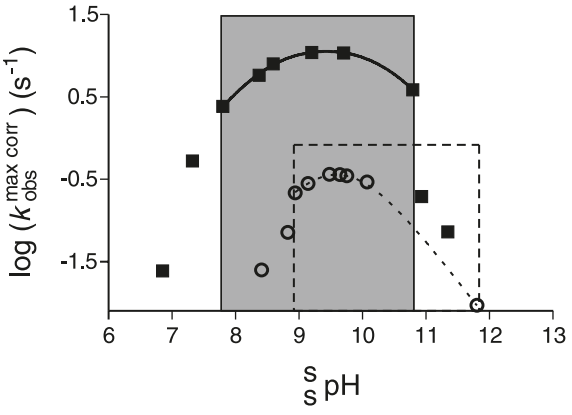

Methanol

The ^S_SpH/log rate constant profile for the cleavage of **1g** catalyzed by **4**:$Zn(II)_2$ in methanol was conducted as described above. The final concentrations of triflate-free **4**:$Zn(II)_2$ and **1g** after mixing in the reaction chamber of the stopped-flow analyzer were 6.4×10^{-4} mol/L (after triflate correction) and 5×10^{-5} mol/L, respectively. The kinetic data, shown in Fig. 1, were fitted to a process depending on two ionizable groups having $^S_Sp K_a$ values of 9.38 and 9.80.

Results

4:$Zn(II)_2$:($^-OCH_3$)-catalyzed cyclization of 1a–1g in methanol

As is the case with **3**:$Zn(II)_2$-catalyzed methanolysis reactions, triflate anion inhibits the catalysis afforded by **4**:$Zn(II)_2$ (inhibition constant, K_i = 7.2 ± 0.9 mmol/L; see the Supplementary data). The raw kinetic data are accordingly corrected for triflate inhibition to determine the concentration of free catalyst, $[\mathbf{4}:Zn(II)_2:(^-OCH_3)]_{free}$. The detailed methodology for these treatments can be found in earlier publications[8,9] and is applied specifically to this system in the Supplementary data.

Unfortunately, the kinetic data we have for the catalyzed reactions with substrates **1** are available only over a 0.2 mmol/L < $[\mathbf{4}:Zn(II)_2:(^-OCH_3)]_{free}$ < 0.75 mmol/L range due to the limited solubility of the catalyst (2.3 mmol/L in one drive syringe of the stopped-flow reaction analyzer is diluted by a factor of 2 on mixing) and to its relatively high triflate inhibition constant. Due to these limitations, fitting of the data to any given model has a larger error than was the case with $[\mathbf{3}:Zn(II)_2:(^-OCH_3)]_{free}$.[8–10] Nevertheless, the following limited observations and analysis can be made.

Fig.2. A plot of k_{obs} vs [**4**:Zn(II)$_2$:($^-$OCH$_3$)]$_{free}$ for the catalyzed methanolysis of **1a** (5×10^{-5} mol/L) determined from the rate of appearance of product phenol at 320 nm, ^S_SpH 9.5 ± 0.2, and 25.0 ± 0.1 °C. Linear regression of the data gives a second order rate constant (k_2) of (2.08 ± 0.04) $\times 10^4$ (mol/L)$^{-1}$s^{-1} with an intercept of A = 0.12 ± 0.02 mmol/L, r^2 = 0.998.

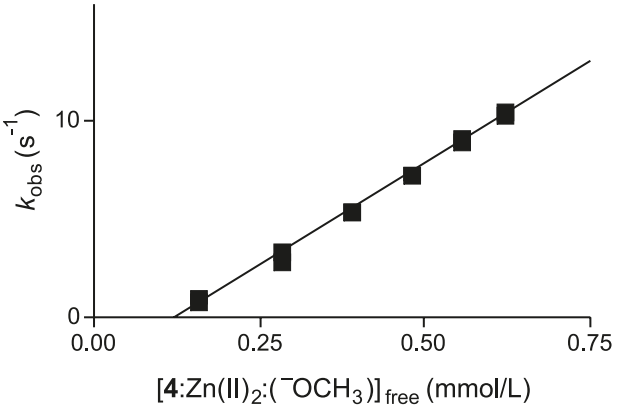

Fig.3. A plot of k_{obs} vs [**4**:Zn(II)$_2$:($^-$OCH$_3$)]$_{free}$ for the catalyzed methanolysis of **1g** (5×10^{-5} mol/L) determined from the rate of appearance of product phenol at 295 nm, ^S_SpH 9.5 ± 0.2, and 25.0 ± 0.1 °C. Fitting the data to the expression given in eq. [S1] of the Supplementary data gives k_{cat}^{max} = (5.2 ± 0.4) $\times 10^{-1}$ s^{-1}, K_M = (1.9 ± 0.3) $\times 10^{-4}$ mol/L, and an x-intercept of A = 0.20 ± 0.01 mmol/L, r^2 = 0.986.

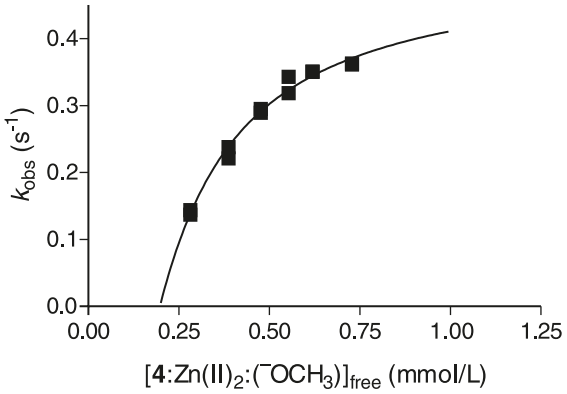

The more reactive substrates (**1a**–**1d**) exhibited a linear relationship between k_{obs} versus [**4**:Zn(II)$_2$:($^-$OCH$_3$)]$_{free}$ for the catalyzed reactions, whereas the less reactive ones (**1e**–**1g**) showed apparent saturation over that same concentration range. Shown in Figs. 2 and 3 are k_{obs} versus [**4**:Zn(II)$_2$:($^-$OCH$_3$)]$_{free}$ plots for the catalyzed transesterifications of **1a** and **1g**. It was earlier observed that the k_{obs} versus [**3**:Zn(II)$_2$:($^-$OCH$_3$)]$_{free}$ plots displayed a prominent x-intercept that was attributed to a dissociation of Zn(II) away from the catalytic complex at very low concentrations,[8–10] and the data in Figs. 2 and 3 show the same trend with [**4**:Zn(II)$_2$:($^-$OCH$_3$)]$_{free}$. The kinetic k_{obs} versus catalyst concentration data for substrates **1a**–**1c** are linear (as are those for **1d**, which may have a perceptible downward curvature but are analyzed as being linear) over the concentration range investigated. However, these data for **1e**–**1g** show a definite downward curvature suggestive of saturation binding.

The saturation kinetics observed for each of **1e**–**1g** were fit by nonlinear least-squares (NLLSQ) treatment to a universal binding equation presented in earlier reports,[8–10,14] which is applicable to both weak and strong binding cases (this is given as eq. [S1] of the Supplementary data, which also describes the mathematical treatment to account for the x-intercept). In Table 1, the best fit K_M and k_{cat}^{max} constants for the [**4**:Zn(II)$_2$:($^-$OCH$_3$)]$_{free}$ catalyzed transesterification of **1e**–**1g** are presented, along with the experimentally observed second order rate constants (k_2^{cat}) for substrates **1a**–**1d** derived from the linear regression of the rate constant versus [**4**:Zn(II)$_2$:($^-$OCH$_3$)]$_{free}$ data.

4:Zn(II)$_2$:($^-$OCH$_2$CH$_3$)-catalyzed cyclization of 1a–1g in ethanol

The rates of the reactions of **1a**–**1g** as a function of increasing [**4**:Zn(II)$_2$:($^-$OCH$_2$CH$_3$)] exhibit saturation kinetics with very strong binding (see the Supplementary data), similar to what was observed previously with **3**:Zn(II)$_2$ in ethanol.[14] A few key points are notable. First, a kinetic study where the [$^-$OCH$_2$CH$_3$] is varied shows that the rate for the cyclization of **1a** is highest when the ratio of [**4**:Zn(II)$_2$]/[$^-$OCH$_2$CH$_3$] is in unity (see the Supplementary data). Second, the inhibition constant of triflate anion on the catalysis afforded by **4**:Zn(II)$_2$:($^-$OCH$_2$CH$_3$) in ethanol is found to be K_i = 1.21 mmol/L (see the Supplementary data) suggesting that triflate inhibition is even stronger in ethanol than in methanol. However, the triflate inhibition observed with **4**:Zn(II)$_2$:($^-$OCH$_2$CH$_3$) is not as significant as that for the **3**:Zn(II)$_2$:($^-$OCH$_2$CH$_3$) system in ethanol (K_i = 0.36 ± 0.02 mmol/L).[14] Third, as is the case with the **3**:Zn(II)$_2$ system in ethanol,[14] triflate is an uncompetitive[21] inhibitor of the **4**:Zn(II)$_2$:($^-$OCH$_2$CH$_3$)-catalyzed reactions. Thus, the raw kinetic data (k_{obs}^{uncorr}) were corrected for triflate inhibition using eqs. [1] and [2] as described[14] to yield k_{obs}^{corr} values.

$$[1] \qquad [\mathbf{4}\text{:Zn(II)}_2\text{:}(^-\text{OCH}_2\text{CH}_3)]_{free} = \frac{(K_i)[\mathbf{4}\text{:Zn(II)}_2\text{:}(^-\text{OCH}_2\text{CH}_3)]_{total}}{K_i + [^-\text{OTf}]}$$

$$[2] \qquad k_{obs}^{corr} = \frac{k_{obs}^{uncorr}(K_i + [^-\text{OTf}])}{K_i}$$

The k_{obs}^{corr} values obtained as a function of [**4**:Zn(II)$_2$:($^-$OCH$_2$CH$_3$)] in ethanol follow saturation behaviour with a strong binding for the entire series of **1a**–**1g** as is exemplified by the plot shown in Fig. 4 for **1a**. We have not used buffers due to the inhibitory effect of their associated anions, so it is important to note that the solution ^S_SpH decreases slightly as the ratio of catalyst concentration/[**1**] increases up to the point where it finally stabilizes at a reasonably constant value of 9.0 ± 0.3 (measured after the stopped-flow reaction) at the plateau region, where the first order rate constant of the catalyzed reaction, corrected for triflate inhibition is defined as $k_{cat}^{max\ corr}$.

Fitting of the kinetic data to the universal binding equation and iteratively varying the **4**:Zn(II)$_2$:($^-$OCH$_2$CH$_3$):**1** dissociation constant (K_M) until the goodness-of-fit is maximized[14] allows estimation of upper limits for the K_M ($10^{-7.5}$ mol/L (3.2×10^{-8} mol/L)) and $k_{cat}^{max\ corr}$ values for catalytic cleavage of the bound substrates given in Table 2.

Table 1. Kinetic constants (maximum rate constants (k_{cat}^{max}), Michaelis–Menten constants (K_M), and second-order rate constants (k_2 or k_{cat}^{max}/K_M)) for the cleavage of **1a**–**1g** mediated by [**4**:Zn(II)$_2$:($^-$OCH$_3$)]$_{free}$ in anhydrous methanol at ^S_SpH 9.5 ± 0.2 and 25.0 ± 0.1 °C.

Subs	Phenol ^S_SpK_a	k_2^{cat} ((mol/L)$^{-1}$s^{-1} × 10^{-3})	k_{cat}^{max} (s^{-1} × 10)[a]	K_M (mol/L) (×10^4)[a]	Accel. ^S_SpH 9.5 (×10^{-11})
1a	11.30	20.8±0.4	NA	NA	1.5[b]
1b	11.50	15.1±0.7	NA	NA	5.3[b]
1c	12.49	13.8±0.8	NA	NA	3.8[b]
1d	13.59	2.6±0.1	NA	NA	9.4[c]
1e	13.93	*2.3±1.3*[d]	9.5±1.9	4.8±3.1	10.5[c]
1f	14.33	*4.0±1.0*[d]	7.2±0.7	1.8±0.4	11.1[c]
1g	14.77	*2.7±0.5*[d]	5.2±0.4	1.9±0.3	16.2[c]

[a]K_M and k_{cat}^{max} values were not determined for the faster reacting substrates (**1a**–**1d**).

[b]Acceleration in terms of 1 mmol/L catalyst reacting with the observed second order rate constant relative to the methoxide reaction at ^S_SpH 9.5.

[c]Acceleration in terms of k_{cat}^{max} relative to the methoxide reaction at ^S_SpH 9.5 where [$^-$OCH$_3$] = 5.37 × 10^{-8} mol/L.

[d]The k_2 values for **1a**–**1d** are the experimentally observed values from the slopes of the k_{obs} versus [**4**:Zn(II)$_2$:($^-$OCH$_3$)]$_{free}$ plots. The k_2 values in italics are computed from k_{cat}^{max}/K_M.

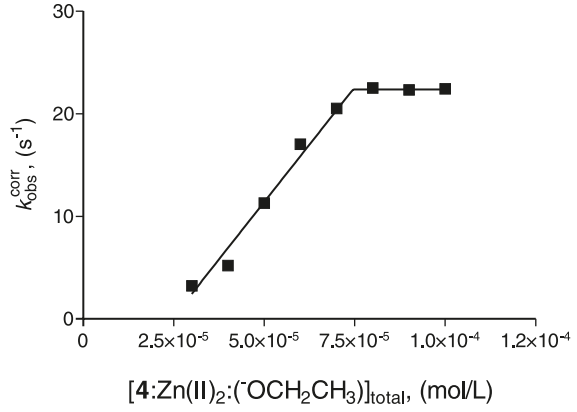

Fig. 4. A plot of k_{obs} versus [**4**:Zn(II)$_2$:($^-$OCH$_2$CH$_3$)]$_{total}$ for the catalyzed cleavage of **1a** (5 × 10^{-5} mol/L) at 323 nm, ^S_SpH 9.0 ± 0.3, and 25.0 ± 0.1 °C. Fitting of the data to the universal binding expression given in the Supplementary data gives k_{cat}^{max} = 22.4 ± 0.5 s^{-1} and an intercept, A = (2.5 ± 0.1) × 10^{-5} mol/L. The raw kinetic data have been corrected for $^-$OTf inhibition as described in the text.

Shown in Fig. 5 is a Brønsted plot of log ($k_{cat}^{max\ corr}$) for the catalyzed reactions versus the ^S_SpK_a values[14] of the corresponding phenols in ethanol. The two lines through the data are from a linear regression and a nonlinear regression as described in the legend of Fig. 5.

Determination of kinetic ^S_SpK_a values for formation of 4:Zn(II)$_2$:($^-$OR) in methanol and ethanol

In the absence of any buffer, the ^S_SpH values depend on the catalytic system itself and were generally found to be 9.0 ± 0.3 in the plateau region of the k_{obs}^{corr} versus [**4**:Zn(II)$_2$:($^-$OCH$_2$CH$_3$)]$_{total}$ plots. Unfortunately, as was the case with **3**:Zn(II)$_2$, the complexes with **4**:Zn(II)$_2$ require re-equilibration when the ^S_SpH is altered so it is not possible to undertake potentiometric titrations of the complexes in either methanol or ethanol due to the time required for the catalyst to reach equilibrium following addition of each aliquot of acid or base. However, the kinetic ^S_SpH/$k_{obs}^{max\ corr}$ profile shown in Fig. 1 for the cleavage of **1b** catalyzed by **4**:Zn(II)$_2$ in ethanol can be constructed as described in the Experimental above. The plot exhibits a broad plateau from ^S_SpH 7.9–10 and a precipitous drop in rate constant at higher and lower values. The line through the data was derived from a fit of the solid squares data to a kinetic process that depended on two ionizable groups[14] having first and second ^S_SpK_a values of 8.48 ± 0.02 and 10.38 ± 0.03. Only the data in the shaded box were used for the fitting because of the rapid fall-off in the rate constant at lower and higher ^S_SpH values, where the **4**:Zn(II)$_2$ complex that is substantially devoid of alkoxide or has more than one alkoxide apparently decomposes during the timescale of the experiment.

In an analogous way, the kinetic ^S_SpK_a values were determined for **4**:Zn(II)$_2$ in methanol from the reaction of **4**:Zn(II)$_2$:($^-$OCH$_3$) with **1g** conducted at 25 °C in methanol as described in the Experimental above. The fit of the bell-shaped data set enclosed in the dotted box of Fig. 1 gave two ^S_SpK_a values of 9.38 ± 0.07 and 9.80 ± 0.06.

Discussion

General considerations

Earlier studies of the cyclization of **1a**–**1g** promoted by **3**:Zn(II)$_2$($^-$OR) in methanol[9] and ethanol[14] were interpreted in terms of the general process illustrated in Scheme 1 involving at least two binding events, followed by one or more chemical steps that released the observed phenol product of the reaction. The binding steps were proposed to involve phosphate diester association with one metal followed by a rearrangement where it becomes doubly activated via binding to the second metal ion. The chemical step was considered to involve internal deprotonation of the 2-hydroxyl group followed by cyclization with expulsion of the aryloxy leaving group. The major difference between methanol and ethanol was the very much stronger binding of the anionic alkoxide and substrate to the complex in ethanol. Thus, for the process in Scheme 2, the first substrate binding step (k_1/k_{-1}) is very much larger in ethanol. The findings with **4**:Zn(II)$_2$ in the present study are consistent with this general scheme.

Table 2. Maximum catalytic rate constant ($k_{cat}^{max\ corr}$), for the **4**:Zn(II)$_2$:($^-$OCH$_2$CH$_3$)-catalyzed reactions, second order rate constants for the ethoxide-promoted reactions (k_2^{OEt}),[14] and accelerations of cleavage provided for bound **1a–1g** at ^S_SpH 9.0 in ethanol at 25 ± 0.1 °C.

Subs	$^S_S p K_a$ phenol	$k_{cat}^{max\ corr}$ (s^{-1}) for the catalyzed reactions [a]	k_2^{OEt} ((mol/L)$^{-1}s^{-1}$) for the ethoxide reactions	Acceleration by catalyst at ^S_SpH 9.0[b]
1a	12.05	22.4±0.5	(2.43±0.09)×10^{-4}	1.2×10^{15}
1b	12.39	10.9±0.2	(8.3±0.4)×10^{-5}	1.7×10^{15}
1c	13.60	7.3±0.3	(9.7±0.7)×10^{-6}	9.5×10^{15}
1d	14.83	1.60±0.05	(6.3±0.3)×10^{-7}	3.2×10^{16}
1e	15.15	0.50±0.02	3.7×10^{-7} [c]	1.7×10^{16}
1f	15.60	0.31±0.01	1.4×10^{-7} [c]	2.8×10^{16}
1g	15.92	0.25±0.01	7.4×10^{-8} [c]	4.2×10^{16}

[a] k_{cat}^{max} values are determined as described in text by fitting the k_{cat}^{corr} vs [**4**:Zn(II)$_2$:($^-$OCH$_2$CH$_3$)] data to eq. [S1], Supplementary data.

[b] Acceleration was calculated at ^S_SpH 9.0 in ethanol, which corresponds to $10^{(-19.1+9.0)}$ mol/L of ethoxide. For example, for substrate **1c** the acceleration = 7.3 s^{-1}/[($10^{-10.1}$ mol/L) × (9.7 × 10^{-6} (mol/L)$^{-1}$ s^{-1})] = 9.5 × 10^{15}.

[c] k_2^{OEt} values for the base promoted reactions of the less reactive substrates (**1e–1g**) were estimated from the linear regression equation for the Brønsted plot in Fig. 1 of ref. 14.

Fig. 5. Brønsted plot of log ($k_{cat}^{max\ corr}$) vs the $^S_S pK_a$ values of the corresponding phenol leaving groups for the **4**:Zn(II)$_2$:($^-$OCH$_2$CH$_3$)-catalyzed cleavage of **1a–1g** in absolute ethanol at 25 °C. The line was constructed by NLLSQ fitting all the data to an expression $k_{cat}^{max\ corr} = k_1k_2 / (k_{-1} + k_2) = C_1C_2 10^{(\beta 1+\beta 2)pK_a}/(C_{-1}10^{\beta -1 pK_a} + C_2 10^{\beta 2 pK_a})$.[22] The two fitted β values are –0.76 and –0.10, r^2 = 0.9768, with a point of transition at $^S_S pK_a$ = 14.3. The linear regression of the data (dotted line) has a gradient of –0.50 ± 0.05, r^2 = 0.9537 (7 data).

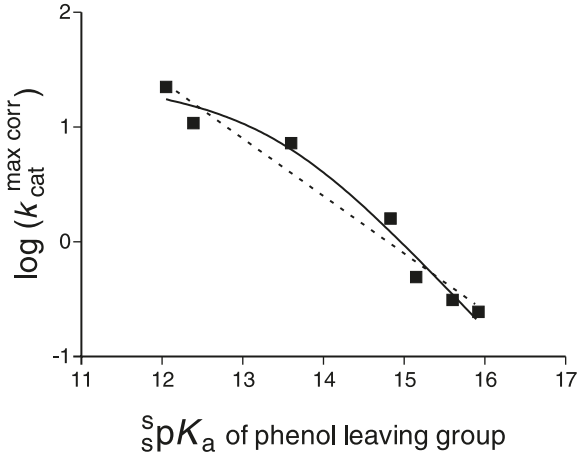

Scheme 2. R′ = CH$_3$ or CH$_2$CH$_3$

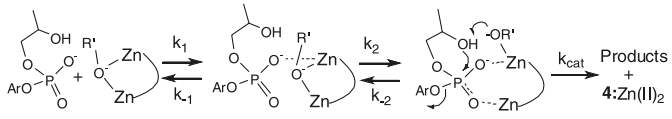

4:Zn(II)$_2$:($^-$OCH$_3$)-promoted cleavage of 1a–1g in methanol

The k_{obs} versus catalyst concentration profiles for catalyzed cleavage of phosphates **1a–1g** of both **3**:Zn(II)$_2$ and **4**:Zn(II)$_2$ complexes show the same trend of being linear for substrates containing good leaving groups (**1a–1c**, e.g., Fig. 2) and downward curved for substrates with poorer leaving groups (**1e–1g**, e.g., Fig. 3). Unfortunately, due to the combination of poorer solubility and a greater triflate inhibition

Scheme 3. Thermodynamic cycle for assessing the binding energy of catalyst **4**:Zn(II)$_2$ to a hypothetical transition state comprising alkoxide and substrate.

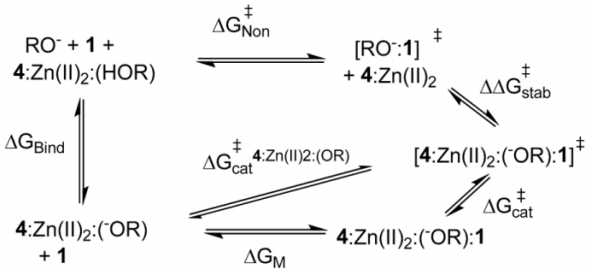

for **4**:Zn(II)$_2$ than **3**:Zn(II)$_2$, the concentration range over which the former's catalytic activity could be investigated was limited, which introduces considerable error into the calculated k_{cat}^{max} and K_M values given in Table 1. Nevertheless, it appears that **4**:Zn(II)$_2$:($^-$OCH$_3$) is slightly less catalytically active than its lower homologue and binds slightly weaker with phosphates **1e–1g** than does **3**:Zn(II)$_2$:($^-$OCH$_3$) in methanol, although the differences for substrates where saturation behaviour is observed are not large. When comparing the maximum rate constants (k_{cat}^{max}) for the bound substrates **1e–1g**, a given reaction promoted by **3**:Zn(II)$_2$ is about 3–5 times faster than that with **4**:Zn(II)$_2$. In this case, the shift from a rate-limiting binding process (for **1a–1c**) to a rate-limiting chemical process (for **1e–1g**) seems to occur around substrate **1d** (see the Supplementary data).

The Brønsted plot (not shown) of the observed k_2 or computed k_{cat}^{max}/K_M values for the entire series of substrates gives a poorly defined linear regression, log(k_2) = –(0.28 ± 0.05) $^S_S pK_a$ + (7.41 ± 0.70) (r^2 = 0.84, 7 data). This can be compared with what was found for the **3**:Zn(II)$_2$:($^-$OCH$_3$) reaction, log k_{cat}^{max} = (–0.97 ± 0.05) $^S_S pK_a$ + (14.36 ± 0.57), and with the regression of the CH$_3$O$^-$-promoted reaction, log(k_2^-OMe) = (–0.72 ± 0.08) $^S_S pK_a$ + (5.36 ± 1.08).[9] In the case of the C$_3$ catalyst, the larger negative β_{lg} is consistent with a rate limiting step where there substantial cleavage of the P–OAr bond. The apparent reduced value of the β_{lg} observed for the catalyzed reaction promoted by **4**:Zn(II)$_2$:($^-$OCH$_3$) indicates a more modest dependence on

Table 3. Summary of the ($k_{cat}^{max}/K_M/k_2^{-OR}$ constants and the computed free energies for the formation of catalytic complexes ($\Delta G_{Bind} - \Delta G_M$), the free energies of activation for k_{cat}^{max} ($\Delta G_{cat}^{\ddagger}$), and the free energies of stabilization of the RO^-:**1** transition state through its binding to **4**:Zn(II)$_2$ ($\Delta\Delta G_{stab}^{\ddagger}$) as in the reaction of **4**:Zn(II)$_2$:($^-$OR) with substrates **1a**–**1g** at 25 °C in methanol (M) and ethanol (E).

Subs	$k_{cat}^{max}/K_M/k_2^{-OR}$	$\Delta G_{Bind} - \Delta G_M$ (kcal/mol)[b]	$\Delta G_{cat}^{\ddagger}$ (kcal/mol)[c]	$\Delta G_{Non}^{\ddagger}$ (kcal/mol)[c]	$\Delta\Delta G_{stab}^{\ddagger}$ (kcal/mol)
1a (M)[d]	8.0×10^{6}			20.9	–19.5[e]
1a (E)	2.9×10^{12}	–24.7	15.6	22.3	–31.5
1b (M)[d]	2.8×10^{7}			21.9	–20.2[e]
1b (E)	4.2×10^{12}	–24.7	16.0	23.0	–31.7
1c (M)[d]	2.1×10^{7}			21.7	–20.0[e]
1c (E)	2.4×10^{13}	–24.7	16.2	24.2	–32.7
1d (M)[d]	5.0×10^{7}			23.3	–20.6[e]
1d (E)	8.0×10^{13}	–24.7	17.1	25.9	–33.4
1e (M)	1.4×10^{8}	–14.6	17.4	23.9	–21.1
1e (E)	4.3×10^{13}	–24.7	17.8	26.2	–33.1
1f (M)	3.3×10^{8}	–15.1	17.6	24.1	–21.7
1f (E)	7.1×10^{13}	–24.7	18.1	26.8	–33.3
1g M)	4.5×10^{8}	–15.1	17.8	24.5	–21.9
1g (E)	1.1×10^{14}	–24.7	18.2	27.1	–33.6

[a]Kinetic first $^{S}_{S}pK_a$ in methanol determined as in the Experimental section to be $10^{-9.38}$; $K_W^{methanol} = 10^{-16.77}$; $(K_a/K_w)^M = 2.5 \times 10^7$; $\Delta G_{Bind}^{MeOH} = -10.1$ kcal/mol. Kinetic first $^{S}_{S}pK_a$ in ethanol is $10^{-8.48}$; $K_W^{ethanol} = 10^{-19.1}$; $(K_a/K_w)^E = 4.16 \times 10^{10}$; $\Delta G_{Bind}^{EtOH} = -14.5$ kcal/mol.

[b]Computed as $(\Delta G_{Bind} - \Delta G_M) = -RT\ln((K_a/K_w)/K_M)$.

[c]Computed from $\Delta G_{cat}^{\ddagger} = -RT\ln(k_{cat}^{max}/(kT/h))$ or $\Delta G_{Non}^{\ddagger} = -RT\ln(k_2^{-OR}/(kT/h))$ from the Eyring equation where $(kT/h) = 6 \times 10^{12}$ s^{-1} at 298 K.

[d]k_{cat}^{max} and K_M values for substrates **1e**–**1g** from Table 1 and 2; k_2 values for substrates **1a**–**1d** from Table 1 determined as gradients of the k_{obs} vs [**4**:Zn(II)$_2$:($^-$OCH$_3$)]$_{free}$ plots. k_2^{-OMe} and k_2^{-OEt} values from refs. 9 and 14.

[e]$\Delta\Delta G_{stab}^{\ddagger}$ computed from application of kinetic and equilibrium constants to eqs. [3] and [4].

the nature of the leaving group, and is consistent with the mechanism shown in Scheme 1 where there is relatively little cleavage of the P–OAr bond in the cases where the chemical steps are rate limiting. This could be indicative of a stepwise cleavage reaction where there is little change in the P–OAr bonding in a rate limiting cyclization step forming a phosphorane intermediate or alternatively to a concerted process with an early transition state having a component of the intramolecular rearrangement. Possibly due to the increased flexibility of the longer linker chain, this rearrangement process is slower for **4**:Zn(II)$_2$:($^-$OCH$_3$) than **3**:Zn(II)$_2$:($^-$OCH$_3$) as evidenced by the k_2 values (Table 1) for **1a** and **1b** of 21 000 and 15 000 (mol/L)$^{-1}$s^{-1}, respectively, which are 13 times lower than observed for those same substrates when reacted with **3**:Zn(II)$_2$:($^-$OCH$_3$) (275 000 and 194 000 (mol/L)$^{-1}$s^{-1}, respectively[9]).

4:Zn(II)$_2$:($^-$OCH$_2$CH$_3$)-promoted cleavage of 1a–1g in ethanol

The findings for **4**:Zn(II)$_2$-promoted cleavage of **1a**–**1g** in ethanol are very similar to those found for **3**:Zn(II)$_2$ in ethanol.[14] Following correction of the kinetic data for triflate inhibition (as described in ref. 14) the plots of k_{obs}^{corr} versus [**4**:Zn(II)$_2$:($^-$OCH$_2$CH$_3$)]$_{total}$ for all substrates showed very strong binding behavior illustrated in Fig. 4. Due to the strong binding, exact determination of the K_M values is not possible, so an iterative procedure was used[14] where the K_M was held constant, but varied until the goodness-of-fit was optimized. This upper limit for the K_M value for all substrates, defined as the dissociation constant for the **4**:Zn(II)$_2$:($^-$OCH$_2$CH$_3$):**1** Michaelis complex, is $\sim 10^{-7.5}$ mol/L (3.2×10^{-8} mol/L).

The Brønsted plot of log($k_{cat}^{max\ corr}$) versus the $^{S}_{S}pK_a$ of the corresponding phenols of **1a**–**1g** is shown in Fig. 5. Due to the rather scattered nature of the $k_{cat}^{max\ corr}$ data, we cannot distinguish with certainty whether the plot is linear (dotted line suggestive of a single step being rate limiting with $\beta_{lg} = 0.5$) or a downward curving line suggestive of a change in rate limiting step for the $k_{cat}^{max\ corr}$ term. The latter would be consistent with what was proposed for the **3**:Zn(II)$_2$:($^-$OCH$_2$CH$_3$) system in ethanol where there was a transition from substrate binding being rate limiting for substrates with good leaving groups, and chemical cleavage being rate limiting for substrates with poorer leaving groups.[14] The line through the data in Fig. 5 is obtained by NLLSQ fitting to the equation given in the caption[22] depending on the two β values of –0.76 ± 0.33 for poor leaving groups, and –0.1 ± 0.69 for good leaving groups. Although the parameters, particularly the latter one, are poorly defined in the fit, the β_{lg} value of –0.1 suggests that the rate limiting step for this process does not involve much change in the POAr bonding as would expected for a process such as depicted in Scheme 1 involving a rate limiting rearrangement step.[14] The data also support the contention that the rearrangement process for **4**:Zn(II)$_2$:($^-$OCH$_2$CH$_3$) is about 10 times slower than that for **3**:Zn(II)$_2$:($^-$OCH$_2$CH$_3$) since the respective $k_{cat}^{max\ corr}$ values of substrates **1a** and **1b** are 22 and 11 s^{-1} for the C$_4$ catalyst and 168 and 133 s^{-1} with the C$_3$ catalyst, respectively.

Energetics of 4:Zn(II)$_2$:($^-$OR) catalyzed cleavages of 1a–1g in methanol and ethanol

One can quantify the catalytic efficiency by calculating the difference in energy of a transition state containing only [RO$^-$:**1**], and one where the latter is bound to the catalyst[23] to form a hypothetical transition state [**4**:Zn(II)$_2$:($^-$OR):**1**]‡ or its kinetic equivalent [**4**:Zn(II)$_2$:($^-$**1**)]‡. Presented in Scheme 3 is a thermodynamic cycle involving both the alkoxide reaction and the **4**:Zn(II)$_2$:($^-$OR) promoted reactions of **1a–1g**. Equation [3] provides the free energy difference ($\Delta\Delta G^{‡}_{stab}$) between [**4**:Zn(II)$_2$:($^-$OR):**1**]‡ relative to [RO$^-$:**1**]‡. In Scheme 2, ΔG_{Bind}, $\Delta G^{‡}_{cat}$ and $\Delta G^{‡}_{Non}$ are the respective free energies for (1)

$$[3]\qquad \Delta\Delta G^{\neq}_{stab} = (\Delta G_{Bind} - \Delta G_M + \Delta G^{\neq}_{cat}) - \Delta G^{\neq}_{Non} = -RT\ln\left[\frac{(k_{cat}/K_M)(K_a/K_w)}{k_2^{-OR}}\right]$$

$$[4]\qquad \Delta\Delta G^{\neq}_{stab} = \left(\Delta G_{Bind} + \Delta G^{\neq \mathbf{4}:Zn(II)_2:(-OR)}_{cat}\right) - \Delta G^{\neq}_{Non} = -RT\ln\left[\frac{(k_2^{obs})(K_a/K_w)}{k_2^{-OR}}\right]$$

methoxide binding to **4**:Zn(II)$_2$, (2) the free energy of activation for unimolecular reaction of the **4**:Zn(II)$_2$:($^-$OR):**1** complex or its kinetic equivalent, and (3) the free energy of activation for the reaction of alkoxide with **1**. ΔG_M is the free energy for association of **1** and **4**:Zn(II)$_2$:($^-$OR) computed from the Michealis constant for each substrate in either solvent. In eq. [4] is the free energy calculation specific for the reactions with **1a–1d** in methanol that show only a first order dependence on [**4**:Zn(II)$_2$:($^-$OCH$_3$)]$_{free}$ throughout the concentration range investigated. The various terms in eqs. [3] and [4] are described in earlier publications.[9,14] K_a/K_w can be readily shown to be formally equivalent to the binding constant of alkoxide to the dinuclear complex **4**:Zn(II)$_2$ to form **4**:Zn(II)$_2$:($^-$OR). K_a refers to the first acid dissociation constant of **4**:Zn(II)$_2$:(HOR), determined from the kinetic $^{S}_{SP}K_a$ studies above as $10^{-8.48}$ in ethanol and $10^{-9.38}$ in methanol, and K_w is the autoprotolysis constant for ethanol ($10^{-19.1}$) and methanol ($10^{-16.77}$). Finally, k_2^{-OR} is the second order rate constant for the methoxide[9] and ethoxide[14] reactions of each substrate.

Listed in Table 3 are the $k_{cat}/K_M/k_2^{-OR}$ (or $k_2^{\mathbf{4}:Zn(II)_2:OMe}/k_2^{-OR}$) constants and computed ΔG_{Bind}, ΔG_M, ΔG_{cat}, ΔG_{Non}, and $\Delta\Delta G^{‡}_{stab}$ values for the various processes described in Scheme 2 for the complex and alkoxide catalyzed and reactions of **1**; all values were computed at the standard state of 1 mol/L and 25 °C. The first ratio provides the acceleration in second order rate constant for the complex catalyzed reactions relative to the alkoxide reactions, while the various ΔG values, when inserted into eqs. [3] and [4], provide the free energy of stabilization ($\Delta\Delta G^{‡}_{stab}$) of the complex catalyzed reaction relative to the methoxide reaction. Of these constants, the K_a/K_w terms contributes –10.1 and –14.5 kcal/mol while the ($\Delta G_{Bind} - \Delta G_M$) term contributes approximately –15 and –24.5 kcal/mol in methanol and ethanol, respectively, to the $\Delta\Delta G^{‡}_{stab}$ for the series. This means that in the less polar solvent, the binding of both alkoxide and substrate to the **4**:Zn(II)$_2$ complex is more exergonic. In the two solvents, the $k_{cat}/K_M/k_2^{-OMe}$ term contributes –11.0 to –13.2 kcal/mol in methanol and approximately –17 to –19 kcal/mol in ethanol, with the slowest reacting substrates having the more negative values. These numbers give the energetic reduction of the catalyzed apparent second order rate constant for the **4**:Zn(II)$_2$ promoted reactions relative to the alkoxide reactions.

Conclusions

The rate constants and energetics for the cyclizations of **1a–1g** promoted by **4**:Zn(II)$_2$ found in this study invite comparison with what was found recently for the same cyclization reactions catalyzed by **3**:Zn(II)$_2$ in both methanol[9] and ethanol.[14] In methanol, **4**:Zn(II)$_2$ is somewhat more fragile than **3**:Zn(II)$_2$ as is judged from the kinetic stability as a function of time. Whereas **3**:Zn(II)$_2$ retains good activity for nearly one day, the activity of **4**:Zn(II)$_2$ diminishes after about 10 h. Additionally, **4**:Zn(II)$_2$ suffers from a somewhat reduced solubility in methanol and a larger triflate ion inhibition, which reduces the overall concentration range over which the study can be conducted. Although we have determined that **4**:Zn(II)$_2$ can promote cleavage of the DNA models **2** with appreciable rate accelerations, the above technical factors prevent determination of meaningful binding and k_{cat} constants for the entire series that was investigated with **3**:Zn(II)$_2$ in methanol.[8,10]

In spite of these difficulties, it appears that the overall mechanism by which **4**:Zn(II)$_2$ cleaves **1** is similar to what we proposed to be operative for **3**:Zn(II)$_2$. From the available data in Table 1 above and the comparable data in Table 4 of ref. 9, the k^{max}_{cat} and K_M terms for both catalysts are similar for substrates where the chemical steps are rate limiting (**1e–1g**), although the binding of the C_4 catalyst for these slower reacting substrates is slightly weaker. On the other hand, the apparent second order rate constants for those substrates that do not show saturation kinetics, and where the rate limiting step is proposed to be a nonchemical one, such as substrate binding and translocation (**1a–1d**), is about one order of magnitude less than was seen for **3**:Zn(II)$_2$. Perhaps this is a consequence of the flexibility of the system, which resists the putative intramolecular rearrangement to reposition the first bound substrate complex into a doubly-activated complex as shown in Scheme 1.

In ethanol, both catalysts display very strong binding for which only upper limits can be set for the dissociation of the Michaelis complex ($10^{-7.5}$ and $10^{-6.5}$ mol/L, respectively, for **4**:Zn(II)$_2$ and **3**:Zn(II)$_2$). The apparent greater binding constant for the C_4 complex relative to the C_3 complex probably cannot be considered significant given that the determination of the K_M values in each case gave only an upper limit for the dissociation constant. When comparing the data obtained with the C_4 catalyst in this study with that disclosed in Table 3 of ref.14 for the C_3 catalyst, the ($\Delta G_{Bind} - \Delta G_M$) term, which refers to the composite energy of binding of the ethoxide and substrate to the catalyst, is nearly the same for each catalyst (only about ~0.4 kcal/mol less for the C_3 complex than the C_4 complex). This results from an apparent stronger binding of the phosphate substrate to the C_4 catalyst compensated by weaker binding of ethoxide. What is interesting is the k^{max}_{cat} values for the various substrates are about 5–20 times less for the C_4 complex relative to the C_3 com-

plex, which translates into about 1 to 1.6 kcal/mol increase in the ΔG_{cat} activation energy for the C_4 catalyst. It is likely that this stems from a less tightly bound substrate/catalyst complex at the transition state for the C_4 catalyzed process, perhaps suggesting that flexibility, while required for the initial strong catalyst:substrate binding, has a deleterious effect on the transition state for the catalyzed reaction.

Supplementary data

Tables of original pseudofirst order rate constants for the cleavage of **1a**–**1g** as a function of [**4**:$Zn(II)_2$:($^-$OR)] in methanol and ethanol; Figures plotting the latter; information concerning the modeling of the ${}^{S}_{S}pH/\log k^{max}_{obs}$ profiles to determine the kinetic first and second ${}^{S}_{S}pK_a$ values for the complex in both solvents. Supplementary data for this article are available on the journal Web site (canjchem.nrc.ca) or may be purchased from the Depository of Unpublished Data, Document Delivery, CISTI, National Research Council Canada, Ottawa, ON K1A 0R6, Canada. DUD 3908. For more information on obtaining material, refer to cisti-icist.nrc-cnrc.gc.ca/cms/unpub_e.shtml.

Acknowledgements

The authors gratefully acknowledge the financial assistance of the Natural Sciences and Engineering Research Council of Canada (NSERC), the Canada Council of the Arts through the award of a Killam Research fellowship to RSB, and the Canada Foundation for Innovation (CFI). This project received support from the Defense Threat Reduction Agency - Joint Science and Technology Office, Basic and Supporting Science Division, Grant # HDTRA-08-1-0046. In addition, CTL thanks NSERC for a Postgraduate Scholarship (PGS D-2).

References

(1) (a) Wolfenden, R. *Chem. Rev.* **2006**, *106*, 3379 doi:10.1021/cr050311y. PMID:16895333.; (b) Wolfenden, R.; Snider, M. J. *Acc. Chem. Res.* **2001**, *34*, 938 doi:10.1021/ar000058i.; (c) Schroeder, G. K.; Lad, C.; Wyman, P.; Williams, N. H.; Wolfenden, R. *Proc. Natl. Acad. Sci. U.S.A.* **2006**, *103*, 4052. doi:10.1073/pnas.0510879103. PMID:16537483.

(2) (a) Williams, N. H.; Wyman, P. *Chem. Commun. (Camb.)* **2001**, 1268 doi:10.1039/b103317b.; (b) Haake, P. C.; Westheimer, F. H. *J. Am. Chem. Soc.* **1961**, *83*, 1102 doi:10.1021/ja01466a025.; (c) Guthrie, J. P. *J. Am. Chem. Soc.* **1977**, *99*, 3991 doi:10.1021/ja00454a018.; (d) Bunton, C. A.; Mhala, M. M.; Oldham, K. G.; Vernon, C. A. *J. Chem. Soc.* **1960**, 3293. doi:10.1039/jr9600003293.

(3) (a) Cowan, J. A. *Chem. Rev.* **1998**, *98*, 1067 doi:10.1021/cr960436q. PMID:11848925.; (b) Weston, J. *Chem. Rev.* **2005**, *105*, 2151 doi:10.1021/cr020057z. PMID:15941211.; (c) Wilcox, D. E. *Chem. Rev.* **1996**, *96*, 2435 doi:10.1021/cr950043b. PMID:11848832.; (d) Sträter, N.; Lipscomb, W. N.; Klabunde, T.; Krebs, B. *Angew. Chem. Int. Ed. Engl.* **1996**, *35*, 2024 doi:10.1002/anie.199620241.; (e) Lipscomb, W. N.; Sträter, N. *Chem. Rev.* **1996**, *96*, 2375 doi:10.1021/cr950042j. PMID:11848831.; (f) Cleland, W. W.; Hengge, A. C. *Chem. Rev.* **2006**, *106*, 3252. doi:10.1021/cr050287o. PMID:16895327.

(4) (a) Mancin, F.; Tecillia, P. *N. J. Chem.* **2007**, *31*, 800 doi:10.1039/b703556j.; (b) Mancin, F.; Scrimin, P.; Tecilla, P.; Tonellato, U. *Chem. Commun. (Camb.)* **2006**, 2540; (c) Morrow, J. R.; Iranzo, O. *Curr. Opin. Chem. Biol.* **2004**, *8*, 192 doi:10.1016/j.cbpa.2004.02.006. PMID:15062781.; (d) Williams, N. H. *Biochim. Biophys. Acta* **2004**, *279*, 1697; (e) Livieri, M.; Mancin, F.; Saielli, G.; Chin, J.; Tonellato, U. *Chem. Eur. J.* **2007**, *13*, 2246 doi:10.1002/chem.200600672.; (f) Webb, S. *J. Ann. Rep. Prog. Chem. Sect. B* **2007**, *103*, 392. doi:10.1039/b614416k.

(5) (a) Yang, M.-Y.; Morrow, J. R.; Richard, J. P. *Bioorg. Chem.* **2007**, *35*, 366 doi:10.1016/j.bioorg.2007.02.003. PMID:17434205.; (b) Iranzo, O.; Kovalevsky, A. Y.; Morrow, J. R.; Richard, J. P. *J. Am. Chem. Soc.* **2003**, *125*, 1988. doi:10.1021/ja027728v. PMID:12580627.

(6) Yatsimirsky, A. K. *Coord. Chem. Rev.* **2005**, *249*, 1997. doi:10.1016/j.ccr.2005.04.016.

(7) (a) Feng, G.; Natale, D.; Prabaharan, R.; Mareque-Rivas, J. C.; Williams, N. H. *Angew. Chem. Int. Ed.* **2006**, *45*, 7056 doi:10.1002/anie.200602532.; (b) Feng, G.; Mareque-Rivas, J. C.; Williams, N. H. *Chem. Commun. (Camb.)* **2006**, 1845. doi:10.1039/b514328d. PMID:16622503.

(8) Neverov, A. A.; Lu, Z.-L.; Maxwell, C.; Mohamed, M. F.; White, C. J.; Tsang, J. S. W.; Brown, R. S. *J. Am. Chem. Soc.* **2006**, *128*, 16398. doi:10.1021/ja0651714. PMID:17165797.

(9) Bunn, S. E.; Liu, C. T.; Lu, Z.-L.; Neverov, A. A.; Brown, R. S. *J. Am. Chem. Soc.* **2007**, *129*, 16238. doi:10.1021/ja076847d.

(10) Neverov, A. A.; Liu, C. T.; Bunn, S. E.; Edwards, D.; White, C. J.; Melnychuk, S. A.; Brown, R. S. *J. Am. Chem. Soc.* **2008**, *130*, 6639. doi:10.1021/ja8006963. PMID:18479083.

(11) (a) For the definitions and measurement of ${}_{S}^{S}pH$ in methanol and ethanol see: Bosch, E.; Rived, F.; Rosés, M.; Sales, J. *J. Chem. Soc. Perkin Trans. I* **1999**, *2*, 1953; (b) Gibson, G.; Neverov, A. A.; Brown, R. S. *Can. J. Chem.* **2003**, *81*, 495 doi:10.1139/v03-035.; (c) Gibson, G. T. T.; Mohamed, M. F.; Neverov, A. A.; Brown, R. S. *Inorg. Chem.* **2006**, *45*, 7891. doi:10.1021/ic060517x. PMID:16961382.

(12) Tsang, W. Y.; Edwards, D. R.; Melnychuk, S. A.; Liu, C. T.; Liu, C.; Neverov, A. A.; Brown, R. S. *J. Am. Chem. Soc.* **2009**, *131*, 4158.

(13) Kim, J.; Lim, H. *Bull. Korean Chem. Soc.* **1999**, *20*, 491.

(14) Liu, C. T.; Neverov, A. A.; Brown, R. S. *J. Am. Chem. Soc.* **2008**, *130*, 16711. doi:10.1021/ja806462x.

(15) Harned, H. S.; Owen, B. B. *The Physical Chemistry of Electrolytic Solution,* 3rd ed.; ACS Monograph Series 137; Reinhold Publishing: New York, NY, 1957; p 161.

(16) For the designation of pH in nonaqueous solvents we use the forms recommended by: IUPAC (International Union of Pure and Applied Chemistry). *Compendium of Analytical Nomenclature. Definitive Rules 1997,* 3rd ed.; Blackwell: Oxford, UK, 1998. If one calibrates the measuring electrode with aqueous buffers and then measures the pH of an aqueous buffer solution, the term ${}^{W}_{W}pH$ is used; if the electrode is calibrated in water and the pH of the neat buffered alcohol solution measured, the meter reading gives ${}^{S}_{W}pH$; if the electrode is calibrated in the same solvent and the pH reading is made, then the term ${}^{S}_{S}pH$ is used. Since the autoprotolysis constant of methanol and ethanol are $10^{-16.77}$ and $10^{-19.1}$, neutral ${}^{S}_{S}pH$ is 8.38 and 9.55, respectively.

(17) Liu, C. T.; Neverov, A. A.; Brown, R. S. *J. Am. Chem. Soc.* **2008**, *130*, 13870. doi:10.1021/ja805801j. PMID:18821763.

(18) Tsang, J. S.; Neverov, A. A.; Brown, R. S. *J. Am. Chem. Soc.* **2003**, *125*, 1559. doi:10.1021/ja021176z. PMID:12568616.

(19) Brown, D. M.; Usher, D. A. *J. Chem. Soc.* **1965**, 6558. doi:10.1039/jr9650006558.

(20) Alder, R.; Mowlam, R. W.; Vachon, D. J.; Weisman, D. R. J. *Chem. Soc. Chem. Commun.* **1992**, 507. doi:10.1039/c39920000507.
(21) Nelson, D. L.; Cox, M. M. *Lehninger Principles of Biochemistry,* 3rd ed.; Worth Publishers: New York, 2000; pp 266–268.
(22) Neverov, A. A.; Sunderland, N. E.; Brown, R. S. *Org. Biomol. Chem.* **2005**, *3*, 65. doi:10.1039/b414763d. PMID:15602600.
(23) Wolfenden, R. *Nature* **1969**, *223*, 704. doi:10.1038/223704a0. PMID:4979456.

Chiral α-substituted allylboronates in a one-pot three-component asymmetric allylic alkylation/carbonyl allylation reaction sequence — Applications to the syntheses of (+)-(3*R*,5*R*)-3-hydroxy-5-decanolide and (–)-massoialactone

Lisa Carosi and Dennis G. Hall

Can. J. Chem. Downloaded from www.nrcresearchpress.com by Sichuan Normal University on 09/14/12
For personal use only.

Abstract: The use of different organomagnesium reagents in the copper-catalyzed allylic alkylation of 3-chloropropenyl boronates with chiral phosphoramidite ligands produces the desired α-substituted allylic boronate reagents in high regioselectivity and with modest to high enantioselectivities (up to 96% ee). The size of the incoming alkyl substituent from the organomagnesium reagent was found to impact the yield and selectivity of the allylic alkylation. A one-pot procedure for the preparation of these chiral allylic boronates followed by a Lewis acid (BF_3) catalyzed addition to aldehydes delivers the desired allylboration products, homoallylic secondary alcohols, in good yields and very high diastereoselectivity. This three-component reaction methodology was applied to the syntheses of two lactone-containing natural products, (–)-massoialactone and (+)-(3*R*,5*R*)-3-hydroxy-5-decanolide. The key step of these syntheses involved the one-pot enantioselective copper-catalyzed allylic alkylation/allylboration reaction with a benzylic aldehyde, and afforded the desired product in 87% yield, 92% ee, and high *E*/*Z* selectivity in a ratio of 22:1. Remarkably, the allylic alkylation step of this sequential reaction was performed with a low catalyst loading of 2 mol% on a scale of >15 mmol that can provide multiple grams of the three-component product.

Key words: allylboration, allylic alkylation, boronic esters, carbonyl allylation, copper catalysis.

Résumé : L'utilisation de divers réactifs organomagnésiens dans une réaction d'alkylation allylique des boronates 3-chloropropénylés catalysée par le cuivre et un ligand chiral de type phosphoramidite produit les réactifs boronates allyliques α-substitués avec une haute régiosélectivité et une enantiosélectivité variant de modeste à élevée (jusqu'à 96 % ee). Il fut observé que la grosseur du substituant alkyle sur le réactif organomagnésien joue un rôle déterminant sur le rendement chimique et la sélectivité de l'alkylation allylique. Une procédure réactionnelle de type « one-pot » pour la préparation des boronates allyliques chiraux est suivie d'une addition sur les aldéhydes catalysée par un acide de Lewis (BF_3) qui mena aux produits désirés d'allylboration, les alcools secondaires homoallyliques, avec un bon rendement chimique et une diastereoselectivité très élevée. Cette réaction à trois-composants fut par la suite appliquée à une synthèse de deux produits naturels, la (–)-massoialactone and la (+)-(3*R*,5*R*)-3-hydroxy-5-decanolide. L'étape-clé de ces synthèses impliqua la réaction « one-pot » catalytique énantioselective d'alkylation allylique/allylboration avec un aldehyde benzylique, produisant le produit désiré dans un rendement chimique de 87 %, avec un ee de 92 % et une sélectivité *E*/*Z* élevée dans un ratio de 22 :1. Il est remarquable de constater que l'étape d'alkylation allylique de cette réaction séquentielle fut réalisée avec une faible charge catalytique de 2 mol% sur une échelle supérieure a 15 mmol qui permet d'isoler plusieurs grammes du produit de réaction à trois-composants.

Mots-clés : alkylation allylique, allylation de composés carbonylés, allylboration, catalyse du cuivre, esters boroniques.

Introduction

Over the past three decades, additions of allylic boron reagents have undergone tremendous developments and have emerged as one of the most powerful methods for stereoselective C–C bond formation.[1] In additions of allylic boron reagents to achiral aldehydes, three strategies were set forth to provide control of the enantiofacial selectivity of the reaction: (1) the use of "B-chiral" allylic boranes and boronates where the two nonallylic substituents on the boron are chiral directors such as terpene units,[2] a chiral diol,[3] or a chiral diamine;[4] (2) the use of a chiral Lewis or Brønsted acid catalyst with achiral reagents;[5] and (3) the use of optically pure α-substituted allylboronates of type **1**,[6] also called "C-chiral" or "α-chiral" allylboronates. Amongst these methods, the use of B-chiral allylic boron reagents has been in use for a long time and is still the method of choice even though it is far from ideal, as it uses a stoichiometric amount of chiral directors. Nevertheless, this class of reagents has been widely

Received 7 January 2009. Accepted 25 February 2009. Published on the NRC Research Press Web site at canjchem.nrc.ca on 24 April 2009.

L. Carosi and D.G. Hall.[1] Department of Chemistry, University of Alberta, Edmonton, AB T6G 2G2, Canada.

[1]Corresponding author (e-mail: dennis.hall@ualberta.ca).

Can. J. Chem. Downloaded from www.nrcresearchpress.com by Sichuan Normal University on 09/14/12
For personal use only.

Fig. 1. Possible transition structures in additions of α-substituted allylboronates **1** to aldehydes.

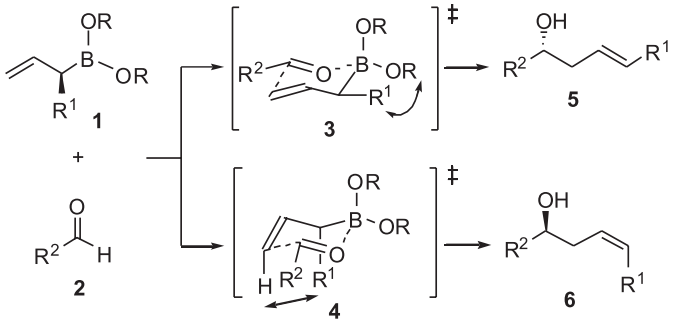

used in the synthesis of acetate and propionate units found in numerous polyketide natural products.[1b] In contrast, chiral α-substituted allylboronate reagents of type **1** have undergone modest development and applications, which is likely due to their stepwise preparation and the difficulty to control the enantiofacial selectivity of their additions to carbonyl compounds.

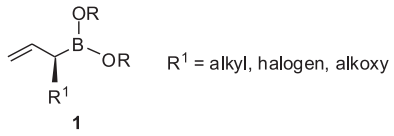

Selectivity with α-substituted allylboronates

Hoffmann and co-workers[6] have demonstrated that the reagent-controlled additions of optically enriched α-substituted allylboronates (**1**) to achiral aldehydes (**2**) proceed with near perfect transfer of chirality from the chiral reagent to the allylic alcohol product. As seen in Fig. 1, the two possible transition states lead to diastereomeric homoallylic alcohol products, **5** and **6**, which have opposite stereochemistry at the alcohol center and opposite alkene geometry. Hence, the *E*/*Z* proportion in the reaction products mirrors the enantioselectivity of the reaction process.[6] The proportion of *E* and *Z* diastereomers is dependent on the nature of the α-substituent and on the structure of the boronic ester. The selectivity between transition states **3** and **4** can be explained in terms of dipolar effects and steric effects. With a nonpolar α-substituent (R^1) such as an alkyl group, steric effects are dominant. It is known that the use of a nonpolar α-substituent leads to mixtures of products **5** and **6** with a modest selectivity for product **5**. In fact, there are unfavorable interactions in both transition states. In the chairlike transition structure, **3**, the unfavorable nonbonding interactions between the boronic ester and the pseudo-equatorial α-substituent (R^1) can be aggravated by the use of a large boronic ester or a bulky α-substituent.[7] In contrast, transition structure **4**, with the α-substituent at the pseudo-axial position, suffers from 1,3-allylic strain between the α-substituent and the pseudo-axial olefinic hydrogen. One transition state can be favored over the other by changing the size of the boronic ester.[7] Hence, the use of the bulky pinacol boronic ester will provide a modest selectivity for transition state **4** leading to the *Z* isomer **6**. On the other hand, the use of the smaller 2,2-dimethyl-1,3-propanediol boronic ester provides selectivity for transition state **3** leading to the *E* isomer **5**.[7] Furthermore, the use of Lewis or Brønsted acid catalysis can provide improved selectivity for the *E* isomer.[8] Recent density functional theory (DFT) calculations by Sakata and Fujimoto[9] have shown that under Lewis acid activation, the transition state displays a shorter B–O bond and a longer B–C bond with the aldehyde. Compared to the uncatalyzed reaction, this longer B–C bond alleviates the unfavorable steric interactions between the boronic ester and the α-substituent in transition state **3**. As a result, the use of Lewis acid catalysis can afford high selectivity for the *E* isomer even with the bulky pinacol boronic ester.[8]

Scheme 1. Optimal conditions for the one-pot three-component allylic alkylation/aldehyde allylation with substrate **7** and exemplified with benzaldehyde.

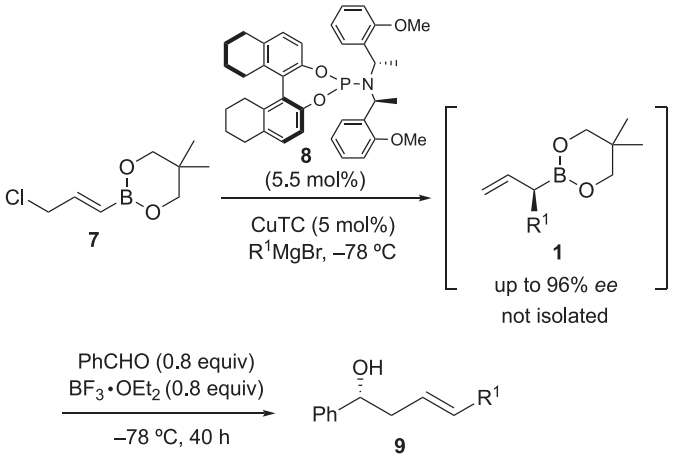

Enantioselective approaches to α-substituted allylboronates

The preparation of α-substituted allylboron reagents is limited to the more stable allylic boronic esters because allylic dialkyl boranes undergo a rapid 1,3-borotropic shift at and below ambient temperatures.[1e,10] Hoffmann and co-workers[6] pioneered the preparation and applications of acyclic optically enriched α-substituted allylboronates. Equations [1]–[4] show examples of preparative methods for chiral α-substituted allylic boronates (pin = $OCMe_2CMe_2O$). Until the mid-1990s, methods to access these reagents were limited to the asymmetric Matteson homologation reaction using a stoichiometric chiral directing group,[11] which may subsequently be exchanged through a transesterification reaction (eq. [1]). Recently, additional methods to access chiral α-substituted allylboronates were reported. For example, a [3,3] sigmatropic rearrangement reaction of chiral 3-hydroxy propenyl boronates was developed (eq. [2]).[12] The ideal approach would be catalytic and would avoid the use of stoichiometric chiral directors. Such methods were also reported and include the use of a palladium-catalyzed enantioselective diboration of allenes (eq. [3]),[13] and the use of a copper-catalyzed enantioselective allylic substitution of allylic carbonates with diboron reagents (eq. [4]),[14a,14b] or an iridium-catalyzed variant.[14c]

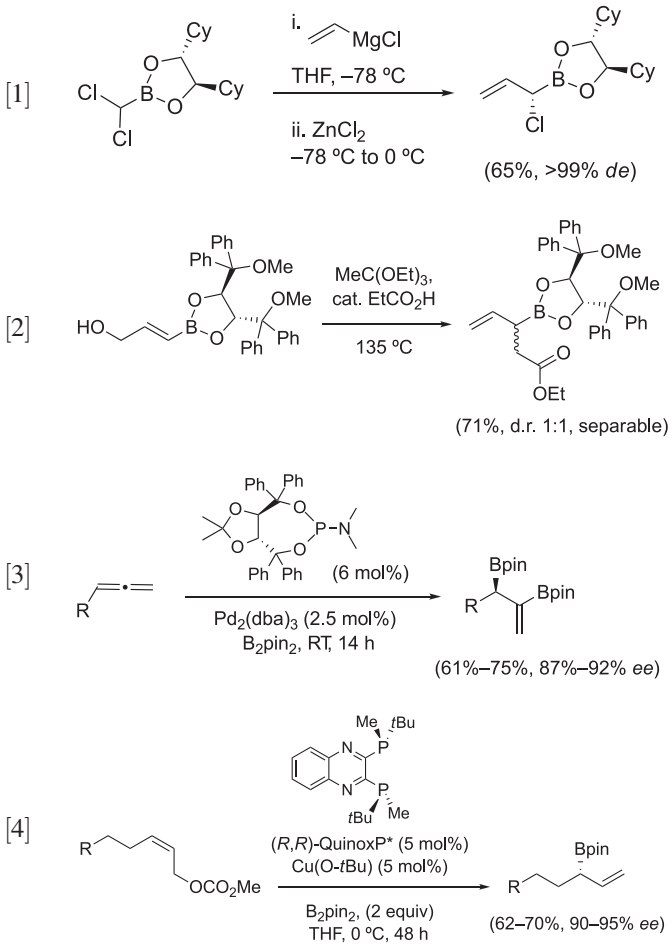

Table 1. Exploration of the scope of the Grignard reagent with **7** under the optimal conditions of Scheme 1.

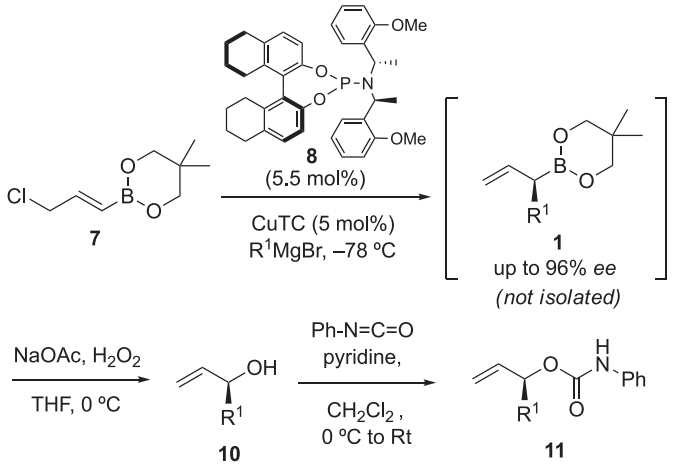

Entry	R^1MgX^a	Product	S_N2'/S_N2 ratio[b]	ee (%)[c]
1	EtMgBr	**1a**	7:1	96
2	*n*-BuMgBr	**1b**	11:1	86
3	(4-Pentenyl)MgBr	**1c**	17:1	88
4	(Cyclohexyl)MgBr	**1d**	12:1	69

Note: Reaction conditions: ligand **8** and CuTC were premixed at RT, then **7** was added, followed by R^1MgX at –78 °C. Typical reaction scale: 1.0 mmol at 0.3 mol/L concentration.

[a]From halide-free 3 mol/L solutions in Et_2O.

[b]Measured by ^1H NMR spectroscopy of an aliquot of the crude reaction mixtures.

[c]Measured by chiral HPLC of isocyanate derivatives (**11**) of oxidation products (**10**) of boronates (**1**) as shown in the above scheme.

In 2007, we reported a new preparative method based on a copper-catalyzed enantioselective allylic substitution reaction (Scheme 1).[15] We were able to employ the resulting chiral α-substituted allylboronates (**1**) in a one-pot sequential protocol initiated by the enantioselective copper-catalyzed allylic alkylation and followed by an aldehyde allylation. The optimal combination of alkenylboronate (**7**) and chiral phosphoramidite (**8**)[16] led to reagent **1** with up to 96% ee.

This protocol resulted in a new enantioselective multicomponent route to homoallylic alcohols. Even though the preliminary communication included the scope and limitations of the three-component reaction sequence with regards to the aldehyde, it provided little information on the scope of the alkyl α-substituent (i.e., the organomagnesium reagent). Herein we report on the scope of the reaction with regards to the alkyl α-substituent, and on the application of this methodology to the synthesis of two small α-lactone natural products.

Results and discussion

Reaction scope

Our preliminary results on the nature of the Grignard reagent had indicated that the size of the organomagnesium alkyl group had an important effect on the enantioselectivity of the allylic substitution reaction.[15] To further investigate this trend, we prepared aliphatic Grignard reagents with various size and length. We then used these reagents in the allylic substitution reaction with the 3-chloropropenyl boronate (**7**) using our previously optimized reaction conditions. The outcome of this study is summarized in Table 1. In this initial study, the enantioselectivity was measured on carbamate derivatives (**11**), which were obtained from the boronate oxidation products (**10**). It is well-established that this oxidation process occurs with near perfect retention of stereochemistry.[17] Because of the volatility of alcohols **10**, no yields were compiled for this derivatization process.

We found that the use of linear organomagnesium reagents allow for a higher level of enantioselectivity. The length of the alkyl chain also affects the S_N2'/S_N2 regioselectivity and the level of enantioselectivity. The short ethylmagnesium bromide reagent afforded the best enantioselectivity, giving **1a** with 96% ee (Table 1, entry 1), whereas the longer butylmagnesium or pentenylmagnesium bromide provided very good, albeit lower enantioselectivity (Table 1, entries 2–3). On the other hand, the bulkier cyclohexylmagnesium bromide gave a much lower level of enantioselectivity (Table 1, entry 4). With this data in hand, we set out to gain information on the behavior of the chiral α-substituted allylboronates in their additions to aldehydes. Performing the one-pot allylic alkylation/aldehyde allylation protocol with our previously optimized reaction conditions allowed us to verify the efficiency of the chirality transfer

Can. J. Chem. Downloaded from www.nrcresearchpress.com by Sichuan Normal University on 09/14/12
For personal use only.

Can. J. Chem. Downloaded from www.nrcresearchpress.com by Sichuan Normal University on 09/14/12
For personal use only.

Table 2. Exploration of the scope of α-substituted allylboronates **1a**–**1d** in the one-pot three-component reaction from **7** under the optimal conditions of Scheme 1.

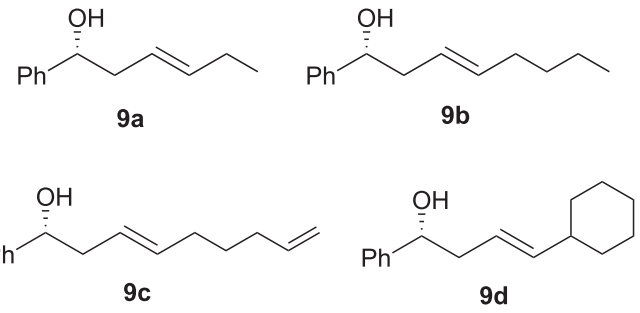

Entry	R^1MgX^a	Product	*E*/*Z* ratio[b]	Yield (%)[c]	ee (%)[d]
1	EtMgBr	**9a**	18:1	75	92
2	*n*-BuMgBr	**9b**	99:1	52	85
3	(4-Pentenyl)MgBr	**9c**	98:2	40	83
4	(Cyclohexyl)MgBr	**9d**	99:1	41	68

Note: Reaction conditions: ligand **8** and CuTC were premixed at RT, then **7** was added, followed by R^1MgX at –78 °C. Typical reaction scale: 1.0 mmol at 0.3 mol/L concentration.

[a]From halide-free 3 mol/L solutions in Et_2O.
[b]Measured by HPLC-MS of crude reaction mixtures.
[c]Isolated yields.
[d]Measured by chiral HPLC of pure products (**9**).

from reagents **1a**–**1d** to the homoallylic alcohol products **9a**–**9d**. Indeed, the enantioselectivity level found in the chiral α-substituted allylboronates (Table 1) was representative of that found in the benzaldehyde allylation products (Table 2). Larger α-substituents proved to be favorable in providing high selectivity for the *E* isomer. Unfortunately, the overall efficiency of the transformation was negatively affected by the use of larger α-substituents as lower yields were obtained with the butylmagnesium, pentenylmagnesium, and cyclohexylmagnesium bromides (respective products are **9b**–**9d** in Table 2, entries 2–4). Small amounts of the undesired allylic alcohol products resulting from the 1,3-borotropic shift of the allylboronates, followed by aldehyde allylboration, were found in these cases. Trombini and co-workers[18] had found that with α-substituted allylboronates, the nature of the boronic ester has a big influence on the propensity of the 1,3-borotropic shift to take place. For instance, the 2,2-dimethyl-1,3-propanediol boronic ester is known to undergo this shift more easily than the corresponding pinacol ester. Nevertheless, as demonstrated with the preparation of **9a** from reagent **1a** (Table 2, entry 1), our approach to homoallylic alcohols via a one-pot enantioselective copper-catalyzed allylic alkylation/aldehyde allylation reaction sequence allows for high selectivity of the desired products (**9**) in good yield from two steps.

Application to the synthesis of lactone natural products

Our next objective was to demonstrate the versatility of this methodology with an application in target-oriented synthesis. As targets, we selected two naturally occurring δ-lactones: (+)-(3*R*,5*R*)-3-hydroxy-5-decanolide

Scheme 2. Retrosynthesis of (–)-massoialactone from (+)-(3*R*,5*R*)-3-hydroxy-5-decanolide using the one-pot three component allylic alkylation/aldehyde allylation.

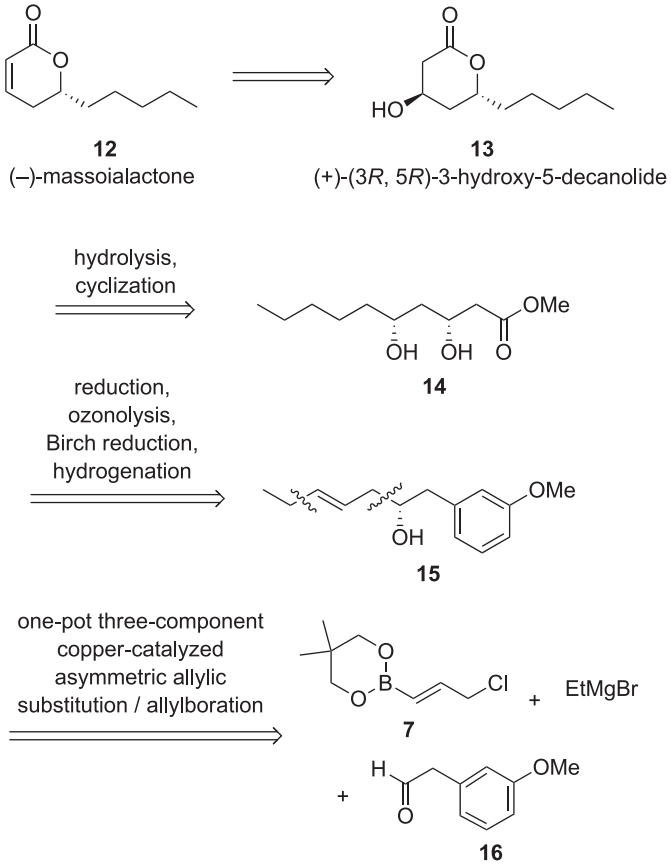

and (–)-massoialactone (**13** and **12** in Scheme 2). (+)-(3*R*,5*R*)-3-Hydroxy-5-decanolide was isolated in 1971 from the culture liquor of the fungus *Cephalosporium recifei* NRRL 5161.[19] This metabolite is part of the *trans*-β-hydroxy-δ-lactone family, which is known to inhibit the enzyme HMG-CoA reductase, thus it is potentially a cholesterol-lowering agent.[20] (–)-Massoialactone's structure is related to (+)-(3*R*,5*R*)-3-hydroxy-5-decanolide's structure as it lacks the 3-hydroxy group, which is replaced by the α,β-unsaturation. (–)-Massoialactone has antibacterial and antifungal activity,[21] it is a skin irritant, and can be isolated from many different natural sources. Abe[22] first isolated (–)-massoialactone in 1937 from the bark oil of *Cryptocarya massoia*, an oil used for centuries in native medicine. It was found to be the defense secretion of two species of formicin ants of the genus *Camponotus* found in western Australia.[23] Numerous syntheses of both (+)-(3*R*,5*R*)-3-hydroxy-5-decanolide and (–)-massoialactone have been reported.[24] As well, separate syntheses for (+)-(3*R*,5*R*)-3-hydroxy-5-decanolide[25] or for (–)-massoialactone[26] have been published. Various strategies were used to introduce chirality, including stereoselective reduction with Baker's yeast,[24a,24b,25a] enzymatic lactonization,[24d] dynamic kinetic resolution of starting material,[26c] metal-catalyzed enantioselective reduction,[26e] allylboration with a chiral auxiliary,[26a] and simply using the chiral pool.[24c, 24e, 24f, 26b, 26d, 26f] Amongst all those strategies, the most efficient synthesis

Can. J. Chem. Downloaded from www.nrcresearchpress.com by Sichuan Normal University on 09/14/12
For personal use only.

of (–)-massoialactone to date features the chiral auxiliary directed allylboration reaction as the key initial step followed by esterification and ring closing metathesis providing (–)-massoialactone with an overall yield of 49%.[26a]

Retrosynthetically, we first planned to access (–)-massoialactone, **12**, from (+)-(3*R*,5*R*)-3-hydroxy-5-decanolide (**13**) through a dehydration reaction (Scheme 2). Our strategy to access (+)-(3*R*,5*R*)-3-hydroxy-5-decanolide was to perform the lactonization reaction from the open chain intermediate **14**. This intermediate could be accessed through a Birch reduction followed by ozonolysis of the aromatic precursor **15**, which in turn could be synthesized from our key enantioselective copper-catalyzed allylic alkylation/aldehyde allylation one-pot reaction sequence with benzylic aldehyde **16**. The use of reagent **1a**, assembled from **7** and EtMgBr, will provide the requisite pentyl side chain of **12** and **13** following hydrogenation of the disubstituted alkene of **15**.

Even though aldehyde **16** is commercially available, its prohibitive price prompted us to find a more affordable source. Therefore, it was synthesized in two steps: reduction of the inexpensive (3-methoxyphenyl)acetic acid, **17**, followed by Dess–Martin periodinane oxidation. This sequence provided aldehyde **16** in high yield (eq. [5]).[27]

[5] 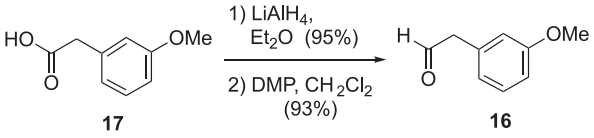

From **16**, the key step of one-pot enantioselective copper-catalyzed allylic substitution/allylboration reaction afforded the desired product **15** in 87% yield, 92% ee, and high *E*/*Z* selectivity with a ratio of 22:1 (Scheme 3). Furthermore, scale-up of this key step was straightforward: the catalyst loading had to be lowered to 2 mol% to provide a constantly high *E* selectivity and the allylboration reaction had to be performed at –30 °C to ensure reaction completion. Additionally, the reaction was performed on up to 16 mmol of starting material **7** resulting in over 2 g of pure product **15**.

Hydrogenation of **15** was first attempted with palladium on charcoal but when this reaction was performed on a larger scale, isomerization of the alcohol's stereogenic center was observed, providing product **18** with only 76% ee. In this event, hydrogenation of the double bond was performed with Adams catalyst to afford the desired product **18** in 98% yield with 88% ee. The decrease in enantiomeric excess observed under these conditions, from 92% ee for the starting material **15** to 88% ee for the product **18**, is expected. This decrease is due to the diastereomeric nature of the inseparable *E* and *Z* mixture of **15** obtained after the allylboration step. From **18**, the carbonyl and the 1,3-diol moieties of **14** were introduced in a three-step sequence. First, a Birch reduction with in situ protection of the alcohol with DIBAL-H provided diene **19** in moderate yield with recoverable unreacted starting material. A longer reaction time, a higher reaction temperature, or the addition of more lithium did not provide a better conversion. On the other hand, Birch reduction without in situ protection of the alcohol afforded a full, but messy conversion of the starting material with a lower yield. Therefore, we chose to use the Birch reduction with in situ protection of the alcohol. Following this sequence, ozonolysis of diene **19** and immediate stereoselective 1,3-syn reduction of the ketone afforded compound **14** in 44% yield for the two steps. Hydrolysis of the methyl ester was performed with sodium hydroxide in methanol and water. Letting acid **20** stand at room temperature for 6 d formed the desired natural product in 71% yield (eq. [6]).

Scheme 3. Synthesis of (–)-massoialactone and (+)-(3*R*,5*R*)-3-hydroxy-5-decanolide.

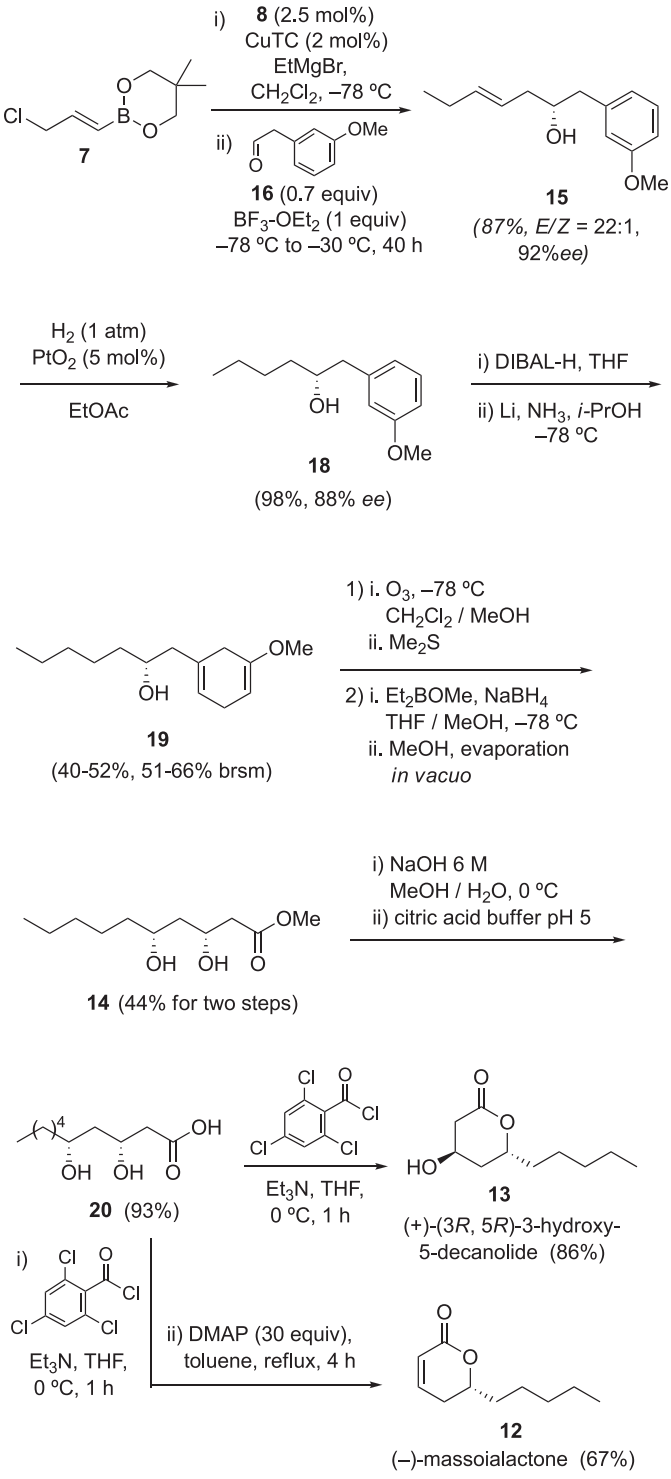

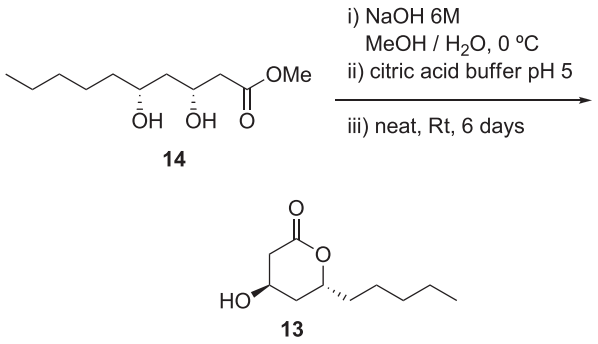

[6]

(+)-(3*R*, 5*R*)-3-hydroxy-5-decanolide (71%)

Alternatively, (+)-(3*R*,5*R*)-3-hydroxy-5-decanolide (**13**) could be accessed from **20** by forming the mixed anhydride, which self-cyclized immediately in 86% yield.[28] Thus, the synthesis of (+)-(3*R*,5*R*)-3-hydroxy-5-decanolide was completed in five or six steps with an overall yield of 15%. Optical rotation for pure (+)-(3*R*,5*R*)-3-hydroxy-5-decanolide (**13**) ($[\alpha]_D^{20}$: +25.5° (*c* 1.2, $CHCl_3$)) matched that from its natural source (lit.[20] $[\alpha]_D^{25}$: +27.4° (*c* 11.7, $CHCl_3$)).

On the other hand, (–)-massoialactone (**12**) was also formed from intermediate **20** by performing the cyclization, which was immediately followed by dehydration with DMAP in refluxing toluene. This sequence provided (–)-massoialactone in six steps with an overall yield of 13%. The optical rotation of synthetic (–)-massoialactone ($[\alpha]_D^{20}$: –74.2° (*c* 1.0, $CHCl_3$)) was lower than that of its natural source (lit.[23] $[\alpha]_D^{25}$: –91° (*c* 1.0, $CHCl_3$)), but all other analytical data for the sample of synthetic (–)-massoialactone agreed to that reported in the literature. It is interesting to note that the high-dilution Yamaguchi lactonization of **20** has been alleged to provide the macrocyclic dimeric lactone verbalactone,[29] which is also a natural substance.[30] However, under several conditions and after numerous attempts, in our hands verbalactone was never isolated, and the only products observed were **12** and **13**.

Conclusion

In summary, the one-pot three-component enantioselective copper-catalyzed allylic substitution/allylation reaction sequence proved to be efficient with regards to various chiral α-alkyl allylboronate reagents. The α-substituent was used in a productive way for the short syntheses of two natural products: (+)-(3*R*,5*R*)-3-hydroxy-5-decanolide and (–)-massoialactone.

Experimental

Unless otherwise noted, all reactions were performed under an argon atmosphere using flame-dried glassware. Toluene, hexanes, and dichloromethane were distilled over CaH_2. THF and Et_2O were distilled over sodium/benzophenone ketyl. Ethylmagnesium bromide was purchased from Sigma-Aldrich as a 3.0 mol/L solution in Et_2O and titrated using a literature procedure.[31] Other Grignard reagents were prepared[32] and titrated using literature procedures. Alkenylboronate **7** was prepared according to refs. 15 and 17. Ligand **8** was prepared according to refs. 15 and 16a. Thin layer chromatography (TLC) was performed on Merck Silica Gel 60 F_{254} plates and was visualized with UV light and 5% phosphomolybdic acid in EtOH (PMA); or 1% potassium permanganate in water ($KMnO_4$); or 5% vanillin, 4% concentrated sulfuric acid in ethanol (vanillin); or 4% ammonium molybdate, 0.08% cerium (IV) sulfate in 10% aqueous sulfuric acid. Flash chromatography was performed on Silicycle SiliaFlash® F60 ultra pure silica gel 230–400 mesh or on a Teledyne Isco Combiflash® Companion® automated flash instrument. NMR spectra were recorded on Varian INOVA-300, INOVA-400, or INOVA-500 MHz instruments. The residual solvent protons (^1H) or the solvent carbons (^{13}C) were used as internal standards. ^1H NMR data are presented as follows: chemical shift in ppm downfield from tetramethylsilane (multiplicity, integration, coupling constant). The accuracy of coupling constants is deemed to be ±0.4 Hz. High-resolution mass spectra were recorded by the University of Alberta Mass Spectrometry Services Laboratory using either electron impact (EI) or electrospray (ES). Infrared spectra were obtained on a Nicolet Magna-IR 760 instrument equipped with a Nic-Plan microscope. Elemental analyses were performed on a Carlo Erba EA1108 system. Optical rotations were obtained with a PerkinElmer 241 polarimeter. Infrared spectra, elemental analyses, and optical rotations were recorded by the University of Alberta Analytical and Instrumentation Laboratory.

General procedure for the synthesis and characterization of chiral α-substituted allylboronates (1a–1d)

Copper thiophene carboxylate (CuTC) (9.5 mg, 0.050 mmol) and ligand **8** (0.054 mmol) were charged in a 25 mL round-bottom flask equipped with a magnetic stirrer. The flask was purged three times with a light vacuum and argon sequence. Dichloromethane (1.5 mL) was added and the mixture was stirred for 30 min at room temperature. In the meantime, a solution of boronic ester **7** (0.19 g, 1.0 mmol) in dichloromethane (0.5 mL) was prepared. The solution of **7** was added dropwise and the reaction mixture was stirred another 5 min at room temperature before cooling to –78 °C (the reaction turned to a blue-green color). The Grignard reagent (3.0 mol/L in Et_2O, 1.2 mmol) diluted with dichloromethane (0.6 mL) was added at –78 °C over 4 h using a syringe pump, keeping the needle immersed in the reaction mixture. The reaction mixture turned to a bright yellow color after about 3.5 h of addition. Once the addition was complete, the mixture was stirred for another 1.5–2 h at –78 °C. At that point a small aliquot was taken to verify for completion of reaction and for S_N2/S_N2' ratio measurement by ^1H NMR of chiral α-substituted allylboronates (**1a**–**1d**). In situ oxidation to alcohols **10a**–**10d** was performed using the following sequence: water (0.5 mL) and tetrahydrofuran (2 mL) were added and the reaction mixture was brought to 0 °C. An aqueous 3 mol/L solution of sodium acetate (1 mL, 3 mmol) was added followed by 30% aqueous hydrogen peroxide (0.6 mL, 5 mmol). The mixture was stirred overnight while being allowed to reach room temperature. After this time, an aqueous saturated solution of sodium sulfite (1.5 mL) was added and the mixture was stirred for 15 min at room temperature. The mixture was then extracted three times with Et_2O. The combined organic phases were washed once with a saturated aqueous solution of ammonium chloride and once with brine. It was dried over anhydrous sodium sulfate, filtered, and partially con-

Can. J. Chem. Downloaded from www.nrcresearchpress.com by Sichuan Normal University on 09/14/12
For personal use only.

Can. J. Chem. Downloaded from www.nrcresearchpress.com by Sichuan Normal University on 09/14/12
For personal use only.

centrated in vacuo due to high volatility of the allylic alcohol product. The isocyanate derivative was synthesized as follows: the allylic alcohol solution was cooled to 0 °C, dichloromethane (1 mL) was added followed by pyridine (0.17 mL, 2.0 mmol) and phenylisocyanate (0.17 mL, 1.5 mmol). The mixture was stirred overnight while being allowed to reach room temperature. It was quenched with water and the water layer was extracted three times with dichloromethane. The combined organic phases were dried over anhydrous magnesium sulfate, filtered, and concentrated in vacuo to afford the crude isocyanate derivatives **11a**–**11d**. Although yields for these products were not compiled due to the high volatility of alcohols (**10a**–**10d**), analytical samples were characterized as follows.

(3S)-3-[Phenylcarbamic ester] 1-pentene (11a) for chiral α-substituted allylboronate (1a)

Flash chromatography (5% Et_2O–pentane) yielded a colorless oil (52 mg, 25% yield), which had satisfactory analytical data (NMR, MS) as reported in the literature.[15] TLC (30% Et_2O–pentane, UV, PMA): 0.53. HPLC followed a literature procedure: Chiralcel OD, 25 °C, 20% *i*-PrOH hexanes, 0.60 mL/min, UV detection at 280 nm, major peak at 9.8 min, minor peak at 11.6 min, 96% ee.

(3S)-3-[Phenylcarbamic ester] hept-1-ene (11b) for chiral α-substituted allylboronate (1b)

Flash chromatography (100% hexane to 2% EtOAc–hexane) yielded a colorless oil (82 mg, 34% yield). TLC (25% EtOAc–hexane, UV, PMA): 0.53. $[\alpha]_D^{20}$: +5.7° (*c* 1.2, $CHCl_3$). IR (neat, cm^{-1}): 3322, 3061, 2957, 2872, 1700, 1601, 1539, 1444, 1313, 1228, 1120, 752, 692. ^1H NMR (500 MHz, $CDCl_3$) δ: 7.39–7.29 (m, 4H), 7.06 (dd, 1H, *J* = 7.4, 7.4 Hz), 6.58 (br s, 1H), 5.83 (ddd, 1H, *J* = 17.3, 10.7, 6.6 Hz), 5.31 (ddd, 1H, *J* = 17.3, 1.3, 1.3 Hz), 5.23 (ddd, 1H, *J* = 6.6, 6.6, 6.6 Hz), 5.20 (ddd, 1H, *J* = 10.6, 1.3, 1.3 Hz), 1.75–1.68 (m, 1H), 1.67–1.60 (m, 1H), 1.40–1.32 (m, 4H), 0.91 (t, 3H, *J* = 7.1 Hz). ^{13}C NMR (100 MHz, $CDCl_3$) δ: 153.06, 138.00, 136.81, 129.01, 123.30, 118.56, 116.64, 75.82, 34.11, 27.23, 22.50, 14.0. HRMS (EI, *m*/*z*) calcd. for $C_{14}H_{19}O_2N$: 233.1416; found: 233.1414. HPLC: Chiralcel OD, 25 °C, 5% *i*-PrOH hexanes, 0.60 mL/min, UV detection at 280 nm, major peak at 16.3 min, minor peak at 19.8 min, 86% ee.

(3S)-3-[Phenylcarbamic ester] 1,7-octadiene (11c) for chiral α-substituted allylboronate (1c)

Flash chromatography (100% hexane to 2% EtOAc–hexane) yielded a colorless oil (62 mg, 25% yield). TLC (25% EtOAc–hexane, UV, PMA): 0.52. $[\alpha]_D^{20}$: +9.6° (*c* 1.0, $CHCl_3$). IR ($CHCl_3$ cast film, cm^{-1}): 3322, 3078, 2940, 1705, 1602, 1537, 1445, 1313, 1226, 1052, 915, 753. ^1H NMR (500 MHz, $CDCl_3$) δ: 7.37–7.35 (m, 2H), 7.30–7.26 (m, 2H), 7.03 (dd, 1H, *J* = 7.3, 7.3, Hz), 6.58 (br s, 1H), 5.84–5.74 (m, 2H), 5.29 (ddd, 1H, *J* = 17.2, 1.3, 1.3 Hz), 5.24 (ddd, 1H, *J* = 6.2, 6.2, 6.2 Hz), 5.18 (ddd, 1H, *J* = 10.5, 1.3, 1.3 Hz), 5.03–4.98 (m, 1H), 4.97–4.94 (m, 1H), 2.12–2.07 (m, 2H), 1.75–1.61 (m, 2H), 1.52–1.44 (m, 2H). ^{13}C NMR (100 MHz, $CDCl_3$) δ: 152.9, 138.3, 137.9, 136.6, 129.0, 123.3, 118.6, 116.8, 114.9, 75.6, 33.8, 33.4, 24.3. HRMS (EI, *m*/*z*) calcd. for $C_{15}H_{19}O_2N$: 245.1416; found: 245.1414. HPLC: Chiralcel OD, 25 °C, 5% *i*-PrOH hexanes, 0.60 mL/min, UV detection at 280 nm, major peak at 18.4 min, minor peak at 26.7 min, 88% ee.

(3S)-3-[Phenylcarbamic ester]-3-cyclohexyl-1-propene (11d) for chiral α-substituted allylboronate (1d)

Flash chromatography (100% hexane to 2% EtOAc–hexane) yielded a white solid (136 mg, 53% yield). TLC (25% EtOAc–hexane, UV, PMA): 0.56. $[\alpha]_D^{20}$: +18.7° (*c* 1.0, $CHCl_3$). IR ($CHCl_3$ cast film, cm^{-1}): 3319, 3061, 2928, 2854, 1704, 1602, 1542, 1444, 1230, 1050, 751. ^1H NMR (500 MHz, $CDCl_3$) δ: 7.39–7.36 (m, 2H), 7.30–7.26 (m, 2H), 7.03 (dd, 1H, *J* = 7.4, 7.4 Hz), 6.58 (br s, 1H), 5.79 (ddd, 1H, *J* = 17.4, 10.5, 7.0 Hz), 5.27 (ddd, 1H, *J* = 17.2, 1.5, 1.5 Hz), 5.21 (ddd, 1H, *J* = 10.5, 1.5, 1.5 Hz), 5.03 (dd, 1H, *J* = 6.8, 6.8 Hz), 1.83–1.57 (m, 6H), 1.28–1.01 (m, 5H). ^{13}C NMR (100 MHz, $CDCl_3$) δ: 153.03, 137.96, 135.17, 128.93, 123.20, 118.53, 117.45, 79.82, 41.66, 28.53, 28.34, 26.30, 25.90, 25.88. HRMS (EI, *m*/*z*) calcd. for $C_{16}H_{21}O_2N$: 259.1572; found: 259.1575. HPLC: Chiralcel OD, 25 °C, 5% *i*-PrOH hexanes, 0.60 mL/min, UV detection at 280 nm, major peak at 14.9 min, minor peak at 16.4 min, 69% ee.

General procedure for the one-pot protocol of enantioselective copper-catalyzed allylic substitution/aldehyde allylation — Preparation of homoallylic alcohols (9a–9d)

Copper thiophene carboxylate (CuTC) (9.5 mg, 0.050 mmol) and ligand **8** (33 mg, 0.054 mmol) were charged in a flame-dried 25 mL round-bottom flask equipped with a magnetic stirrer. The flask was purged three times with a light vacuum and argon sequence. Dichloromethane (1.5 mL) was added and the mixture was stirred for 30 min at room temperature. In the meantime, a solution of boronic ester **7** (188 mg, 1.0 mmol) in dichloromethane (0.5 mL) was prepared. The solution of **7** was added dropwise to the reaction mixture and stirred for 5 min at room temperature (the reaction mixture turned to a blue-green color) before cooling to –78 °C. The Grignard reagent (3.0 mol/L in Et_2O, 1.2 mmol) diluted with dichloromethane (0.6 mL) was added at –78 °C over 4 h using a syringe pump, keeping the needle immersed in the reaction mixture. The reaction mixture turned to a bright yellow color after about 3.5 h of addition. Once the addition was complete, the mixture was stirred another 1.5–2 h at –78 °C. The aldehyde (0.7–0.8 mmol) was added at –78 °C immediately followed by boron trifluoride diethyl etherate (BF_3-OEt_2) (0.10 mL, 0.80 mmol). The reaction mixture was stirred approximately 24 h at –78 °C and 16 h at –30 °C. The reaction was cooled back to –78 °C and was quenched with the addition of a saturated aqueous solution of sodium bicarbonate (1.5 mL). The mixture was then warmed up to room temperature over 3 h and stirred for an additional 30 min at room temperature. The phases were separated and the aqueous phase was extracted three times using dichloromethane. The combined organic extracts were dried over anhydrous sodium sulfate, filtered, and concentrated in vacuo.

(3E,1R)-1-Phenyl-3-hexen-1-ol (9a)

Flash chromatography (100% hexanes to 5% EtOAc–

Can. J. Chem. Downloaded from www.nrcresearchpress.com by Sichuan Normal University on 09/14/12
For personal use only.

hexanes) yielded a colorless oil (108 mg, 75%), which gave satisfactory analytical data (NMR, MS) as reported in the literature.[15,33] TLC: (20% EtOAc–hexanes, UV, PMA) 0.34. $[\alpha]_D^{20}$: +57.4° (*c* 1.0, $CHCl_3$). HPLC for *E*/*Z* ratio measurement on the crude product: Zorbax SB-C18 4.6 mm × 150 mm, 5 μm, 40 °C, mobile phase A: 0.05% formic acid – H_2O, mobile phase B: 0.05% formic acid – MeOH, program: 70:30 at 0 min, 64.5% of B at 55 min, 80% of B at 58 min, 30% of B at 58.01 min, 1 mL/min, UV detection at 220 nm, retention times: (3*Z*)-1-phenyl-3-hexen-1-ol, 44.5 min; (3*E*)-1-phenyl-3-hexen-1-ol, 45.8 min. HPLC for enantiomeric excess measurement on purified product is based on a literature procedure:[15] Chiralcel OD, 10 °C, 5% *i*-PrOH hexane, 0.3 mL/min, UV detection at 220 nm, retention times: (3*E*,1*R*)-1-phenyl-3-hexen-1-ol, 25.8 min; (3*Z*,1*R* or 1*S*)-1-phenyl-3-hexen-1-ol, 29.4 min; (3*E*,1*S*)-1-phenyl-3-hexen-1-ol, 32.0 min; (3*Z*,1*R* or 1*S*)-1-phenyl-3-hexen-1-ol, 35.2 min; 92% ee.

*(3*E*,1*R*)-1-Phenyl-3-octen-1-ol (9b)*

Flash chromatography using an automated flash system (4 g SiO_2 column, 10 column volumes (CV) 100% petroleum ether, 20 CV 100% petroleum ether to 5% EtOAc, 30 CV 5% EtOAc, 10 CV 5% EtOAc to 50% EtOAc) yielded a colorless oil (84 mg, 52%), which gave satisfactory analytical data (NMR, MS) as reported in the literature.[34] Note: 34 mg (21%) of the borotropic shift/allylation product was also isolated. TLC (10% EtOAc–petroleum ether, PMA): 0.28. $[\alpha]_D^{20}$: +32.2° (*c* 1.0, $CHCl_3$). HPLC for *E*/*Z* ratio measurement on crude product: Zorbax SB-C18 4.6 mm × 150 mm, 5 μm, 40 °C, mobile phase A: 0.05% formic acid – H_2O, mobile phase B: 0.05% formic acid – MeOH, program: 70:30 at 0 min, 64.5% of B at 110 min, 30% of B at 110.01 min, 1 mL/min, UV detection at 210 nm, retention times: (3*Z*)-1-phenyl-3-octen-1-ol, 104.4 min; (3*E*)-1-phenyl-3-octen-3-ol, 106.9 min. HPLC for enantiomeric excess measurement on purified product: Chiralcel OD, 10 °C, 2% *i*-PrOH hexane, 0.5 mL/min, UV detection at 254 nm, retention times: (3*E*,1*R*)-1-phenyl-3-octen-1-ol, 22.7 min; (3*E*,1*S*)-1-phenyl-3-octen-1-ol, 26.5 min; 85% ee.

*(3*E*,1*R*)-1-Phenyl-3,8-nonadien-1-ol (9c)*

Flash chromatography using an automated flash system (4 g SiO_2 column, 10 column volumes (CV) 100% petroleum ether, 20 CV 100% petroleum ether to 5% EtOAc, 30 CV 5% EtOAc, 10 CV 5% EtOAc to 50% EtOAc) yielded a colorless oil (68 mg, 40%). Note: 41 mg (24%) of the borotropic shift/allylation product was also isolated. TLC (10% EtOAc–petroleum ether, PMA): 0.24. $[\alpha]_D^{20}$: +30.9° (*c* 1.0, $CHCl_3$). IR ($CHCl_3$ cast film, cm^{-1}): 3378, 3030, 2927, 2855, 1640, 1454, 970, 911. ^1H NMR (500 MHz, $CDCl_3$) δ: 7.36–7.35 (m, 4H), 7.29–7.27 (m, 1H), 5.78 (dddd, 1H, *J* = 17.0, 10.3, 6.7, 6.7 Hz), 5.55 (dm, 1H, *J* = 15.1 Hz), 5.39 (dm, 1H, *J* = 15.5 Hz), 4.98 (dm, 1H, *J* = 17.1 Hz), 4.93 (dm, 1H, *J* = 10.2 Hz), 4.67 (ddd, 1H, *J* = 8.0, 4.9, 3.2 Hz), 2.50–2.38 (m, 2H), 2.06–2.00 (m, 5H), 1.48–1.42 (m, 2H). ^{13}C NMR (100 MHz, $CDCl_3$) δ: 144.0, 138.7, 134.6, 128.3, 127.4, 125.8 (2C), 114.5, 73.5, 42.8, 33.2, 32.0, 28.5. HRMS (EI, *m*/*z*) calcd. for $C_{15}H_{20}O$: 216.1514; found: 216.1520. HPLC for *E*/*Z* ratio measurement on crude product: Zorbax SB-C18 4.6 mm × 150 mm, 5 μm, 40 °C, mobile phase A: 0.05% formic acid – H_2O, mobile phase B: 0.05% formic acid – MeOH, program: 70:30 at 0 min, 64.5% of B at 110 min, 30% of B at 110.01 min, 1 mL/min, UV detection at 210 nm, retention times: (3*Z*)-1-phenyl-3,8-nonadien-1-ol, 104.4 min; (3*E*)-1-phenyl-3,8-nonadien-1-ol, 106.7 min. HPLC for enantiomeric excess measurement on purified product: Chiralcel OD, 10 °C, 2% *i*-PrOH hexane, 0.5 mL/min, UV detection at 270 nm, retention times: (3*E*,1*R*)-1-phenyl-3,8-nonadien-1-ol, 25.6 min; (3*E*,1*S*)-1-phenyl-3,8-nonadien-1-ol, 33.2 min; 83% ee.

*(3*E*,1*R*)-4-Cyclohexyl-1-phenyl-3-buten-1-ol (9d)*

Flash chromatography using an automated flash system (4 g SiO_2 column, 10 column volumes (CV) 100% petroleum ether, 20 CV 100% petroleum ether to 5% EtOAc, 30 CV 5% EtOAc, 10 CV 5% EtOAc to 50% EtOAc) yielded a colorless oil (74 mg, 41%), which gave satisfactory analytical data (NMR, MS) as reported in the literature.[35] Note: 46 mg (23%) of the borotropic shift/allylation product was also isolated. TLC (10% EtOAc–petroleum ether, PMA): 0.28. $[\alpha]_D^{20}$: +23.2° (*c* 1.0 $CHCl_3$). HPLC for *E*/*Z* ratio measurement on crude product: Zorbax SB-C18 4.6 mm × 150 mm, 5 μm, 40 °C, mobile phase A: 0.05% formic acid – H_2O, mobile phase B: 0.05% formic acid – acetonitrile, program: 50:50 at 0 min, 95% of B at 25 min, 50% of B at 25.01 min, 1 mL/min, UV detection at 210 nm, retention times: (3*Z*)-4-cyclohexyl-1-phenyl-3-buten-1-ol, 12.6 min; (3*E*)-4-cyclohexyl-1-phenyl-3-buten-1-ol, 13.2 min. HPLC for enantiomeric excess measurement on purified product: Chiralcel OD, 10 °C, 2% *i*-PrOH hexane, 0.5 mL/min, UV detection at 220 nm, retention times: (3*E*,1*R*)-4-cyclohexyl-1-phenyl-3-buten-1-ol, 23.4 min; (3*E*,1*S*)-4-cyclohexyl-1-phenyl-3-buten-1-ol, 33.4 min; 68% ee.

Experimental procedures in the syntheses of (+)-(3*R*,5*R*)-3-hydroxy-5-decanolide (13) and (–)-massoialactone (12)

2-(3-Methoxyphenyl) ethanol

This compound was synthesized following a literature procedure[27a] and yielded a colorless oil (4.33 g, 95%), which gave satisfactory analytical data (NMR, MS), as reported in the literature,[27b] and was used without further purification.

(3-Methoxyphenyl) acetaldehyde (16)

This compound was synthesized following a published procedure.[27c] Flash chromatography (5% Et_2O–dichloromethane) yielded a light yellow oil (1.74 g, 93%). TLC (50% Et_2O–dichloromethane, UV, $KMnO_4$): 0.38. IR (CH_2Cl_2 cast film, cm^{-1}): 3004, 2941, 2837, 2728, 1723, 1602, 1492, 1258, 1152, 1042, 782, 697. ^1H NMR (400 MHz, $CDCl_3$) δ: 9.74 (t, 1H, *J* = 2.4 Hz), 7.30 (dd, 1H, *J* = 7.9, 7.9 Hz), 6.88–6.76 (m, 3H), 3.82 (s, 3H), 3.66 (d, 2H, *J* = 2.4 Hz). ^{13}C NMR (100 MHz, $CDCl_3$) δ: 199.3, 160.1, 133.2, 130.0, 121.9, 115.3, 112.8, 55.2, 50.6. HRMS (EI, *m*/*z*) calcd. for $C_9H_{10}O_2$: 150.0681; found: 150.0683. Anal. calcd. for $C_9H_{10}O_2$: C 71.98, H 6.71; found: C 71.78, H 6.71.

*(4*E*,2*R*)-1-(3-Methoxyphenyl)-4-heptene-2-ol (15)*

Copper thiophene carboxylate (CuTC) (61 mg, 0.32 mmol) and ligand **8** (240 mg, 0.39 mmol) were charged in a flame-dried 100 mL round-bottom flask equipped with a

Can. J. Chem. Downloaded from www.nrcresearchpress.com by Sichuan Normal University on 09/14/12
For personal use only.

magnetic stirrer. The flask was purged three times with a light vacuum and argon sequence. Dichloromethane (24 mL) was added and the mixture was stirred for 30 min at room temperature. In the meantime, a solution of boronic ester **7** (3.01 g, 16.0 mmol) in dichloromethane (8 mL) was prepared. The solution of **7** was added dropwise to the reaction mixture and stirred for 5 min at room temperature (the reaction mixture turned to a blue-green color) before cooling to –78 °C. Ethylmagnesium bromide (3.0 mol/L in Et_2O, 19 mmol) diluted with dichloromethane (10 mL) was added at –78 °C over 4 h using a syringe pump, keeping the needle immersed in the reaction mixture. The reaction mixture turned to a bright yellow color after about 3.5 h of addition. Once the addition was complete, the mixture was stirred for another 2 h at –78 °C. Boron trifluoride diethyl etherate (BF_3-OEt_2) (2.0 mL, 16 mmol) was added immediately followed by (3-methoxyphenyl) acetaldehyde (**16**) (1.65 g, 11.0 mmol) at –78 °C. The reaction mixture was stirred for approximately 24 h at –78 °C and 16 h at –30 °C. The reaction was quenched at –78 °C via the addition of a saturated aqueous solution of sodium bicarbonate (20 mL). The mixture was then warmed up to room temperature over 3 h and stirred for an additional 30 min at room temperature. The phases were separated and the aqueous phase was extracted three times using dichloromethane. The combined organic extracts were dried over anhydrous sodium sulfate, filtered, and concentrated in vacuo.

Flash chromatography (100% hexanes to 20% Et_2O–hexanes) yielded a colorless oil as an inseparable mixture of *E*/*Z* isomers **15** in a 22:1 ratio (2.12 g, 87%). TLC (50% Et_2O–hexanes, UV, PMA): 0.27. $[\alpha]_D^{20}$: –2.9° (*c* 1.0, $CHCl_3$). IR ($CHCl_3$ cast film, cm^{-1}): 3421, 2961, 2934, 1602, 1585, 1489, 1261, 1046. ^1H NMR (400 MHz, $CDCl_3$) δ: 7.23, (dd, 1H, *J* = 8.9, 7.5 Hz), 6.79–6.76 (m, 3H), 5.62 (dm, 1H, *J* = 15.1 Hz), 5.45 (dm, 1H, *J* = 15.5 Hz), 3.88–3.81 (m, 1H), 3.81 (s, 3H), 2.79 (dd, 1H, *J* = 13.6, 5.1 Hz), 2.70 (dd, 1H, *J* = 13.6, 7.9 Hz), 2.29–2.27 (m, 1H), 2.17–2.15 (m, 1H), 2.10–2.02 (m, 2H), 1.71 (d, 1H, *J* = 3.2 Hz), 1.00 (t, 3H, *J* = 7.4 Hz). ^{13}C NMR (100 MHz, $CDCl_3$) δ: 159.6, 140.1, 136.1, 129.3, 124.5, 121.7, 115.0, 111.7, 71.8, 55.0, 43.2, 39.9, 25.6, 13.7. HRMS (EI, *m*/*z*) calcd. for $C_{14}H_{20}O_2$: 220.1463; found: 220.1461. HPLC for enantiomeric excess: Chiralcel OD, 10 °C, 2% *i*-PrOH hexane, 0.7 mL/min, UV detection at 280 nm, retention times: (4*E*,2*S*)-1-(3-methoxyphenyl)-4-heptene-2-ol, 20.8 min; (4*Z*,2*R* or 2*S*)-1-(3-methoxyphenyl)-4-heptene-2-ol, 22.7 min; (4*E*,2*R*)-1-(3-methoxyphenyl)-4-heptene-2-ol, 28.2 min; (4*Z*,2*R* or 2*S*)-1-(3-methoxyphenyl)-4-heptene-2-ol, 30.2 min; 92% ee.

*(2**R**)-1-(3-Methoxyphenyl)-2-heptanol (18)*

(4*E*,2*R*)-1-(3-Methoxyphenyl)-4-heptene-2-ol (**15**) (2.12 g, 9.6 mmol) was charged in a flame-dried flask under argon. Ethyl acetate (100 mL) and Adams's catalyst (PtO_2) (108 mg, 0.48 mmol) were added and the flask was purged three times with a light vacuum and argon sequence and three times with a light vacuum and H_2 sequence. The reaction mixture was stirred for 1.5 h at room temperature under an atmospheric pressure of H_2 (using a H_2 balloon). The reaction mixture was then purged with a light vacuum and argon sequence before being filtered on celite and rinsed with EtOAc. The filtrate was concentrated in vacuo. Flash chromatography on a short column (30% Et_2O–hexanes) yielded a yellow oil (2.10 g, 98%). TLC: (50% Et_2O–hexanes, UV, $KMnO_4$, vanillin (blue stain)) 0.33. Note: even though the product and the starting material have the same R_f, the product took longer to stain with $KMnO_4$. $[\alpha]_D^{20}$: –10.4° (*c* 1.0, $CHCl_3$). IR ($CHCl_3$ cast film, cm^{-1}): 3407, 2931, 2858, 1602, 1489, 1465, 1259, 1154, 1046. ^1H NMR (400 MHz, $CDCl_3$) δ: 7.24 (ddd, 1H, *J* = 7.4, 7.4, 1.2 Hz), 6.83–6.78 (m, 3H), 3.82–3.81 (m, 1H), 3.81 (s, 3H), 2.82 (dd, 1H, *J* = 13.5, 4.2 Hz), 2.63 (dd, 1H, *J* = 13.6, 8.5 Hz), 1.57–1.51 (m, 4H), 1.34–1.31 (m, 5H), 0.91 (t, 3H, *J* = 6.9 Hz). ^{13}C NMR (100 MHz, $CDCl_3$) δ: 159.7, 140.2, 129.4, 121.6, 115.0, 111.7, 72.5, 55.0, 44.0, 36.7, 31.8, 25.3, 22.6, 13.9. HRMS (EI, *m*/*z*) calcd. for $C_{14}H_{22}O_2$: 222.1620; found: 222.1621. Anal. calcd. for $C_9H_{10}O_2$: C 71.98, H 6.71; found: C 71.78, H 6.71. HPLC for enantiomeric excess: Chiralcel OD, 10 °C, 2% *i*-PrOH hexane, 0.7 mL/min, UV detection at 280 nm, retention times: (2*S*)-1-(3-methoxyphenyl)-2-heptanol, 21.0 min; (2*R*)-1-(3-methoxyphenyl)-2-heptanol, 28.8 min; 88% ee.

*(2**R**)-1-(5-Methoxy cyclohexadienyl)-2-heptanol (19)*

This compound was synthesized following a literature procedure performed on a different substrate.[36] Flash chromatography (100% petroleum ether to 6% EtOAc–petroleum ether) yielded a colorless oil (239 mg, 46%) along with starting material (152 mg, 65% yield brsm). TLC: (20% EtOAc–petroleum ether, vanillin (red stain)): 0.38. $[\alpha]_D^{20}$: –8.1° (*c* 1.0, $CHCl_3$). IR (microscope, cm^{-1}): 3418, 2930, 1695, 1665, 1467, 1390, 1222, 1136, 1024, 776. ^1H NMR (400 MHz, $CDCl_3$) δ: 5.56 (brs, 1H), 4.64 (dd, 1H, *J* = 3.6, 3.6 Hz), 3.80–3.69 (m, 1H), 3.56 (s, 3H), 2.87–2.81 (m, 2H), 2.78–2.68 (m, 1H), 2.66–2.56 (m, 1H), 2.19 (br d, 1H, *J* =13.8 Hz), 2.09 (dd, 1H, *J* = 13.8, 9.1 Hz), 1.63 (br s, 1H), 1.49–1.43 (m, 3H), 1.37–1.27 (m, 5H), 0.90 (t, 3H, *J* = 6.9 Hz). ^{13}C NMR (100 MHz, $CDCl_3$) δ: 152.7, 131.3, 122.1, 90.2, 68.5, 53.9, 45.3, 37.0, 31.9, 31.6, 26.8, 25.4, 22.6, 14.0. HRMS (EI, *m*/*z*) calcd. for $C_{14}H_{24}O_2$: 224.1776; found: 224.1781. Anal. calcd. for $C_{14}H_{24}O_2$: C 74.95, H 10.78; found: C 74.94, H 10.81.

*(3**R**,5**R**)-Methyl 3,5-dihydroxydecanoate (14)*

Ozonolysis was performed following modified literature procedures performed on different substrates.[36,37] In a three-neck flask equipped with a $CaCl_2$ drying tube, a solution of (2*R*)-1-(5-methoxy cyclohexadienyl)-2-heptanol (**19**) (0.22 g, 1.0 mmol) in dichloromethane (4.2 mL) and methanol (1.8 mL) was prepared and pyridine (90 mL, 1.1 mmol) was added. The solution was cooled to –78 °C and a light stream of ozone was bubbled through until the reaction was saturated at which point the reaction mixture turned blue and the color persisted. Ozone was removed with oxygen until the blue color disappeared. Dimethyl sulfide (3 mL) was added at –78 °C and the reaction mixture was stirred for 1 h at room temperature. A saturated sodium chloride solution was added, the layers were separated, and the aqueous layer was extracted four times with dichloromethane. The combined organic extracts were dried over anhydrous sodium sulfate, filtered, and concentrated in vacuo. The unstable crude material was immediately used in the following step.

Can. J. Chem. Downloaded from www.nrcresearchpress.com by Sichuan Normal University on 09/14/12
For personal use only.

The ketone reduction was performed following a modification of a literature procedure.[37,38] Crude (5*R*)-methyl-5-hydroxy-3-oxodecanoate was charged in a flame-dried flask under argon. It was diluted with THF (12 mL) and methanol (3 mL) and cooled to –78 °C for dropwise addition of diethylmethoxyborane (1.1 mL, 1.1 mmol) as a 1.0 mol/L solution in THF. The reaction mixture was stirred for 15 min at –78 °C and sodium borohydride (0.19 g, 5.1 mmol) was added in one portion. The reaction mixture was stirred for 3 h at –78 °C and was quenched with the addition of a saturated aqueous solution of ammonium chloride. The reaction flask was brought carefully to room temperature as gas evolution occurred. The reaction was stirred at room temperature until no more gas evolution was observed. The phases were separated and the aqueous phase was extracted three times with Et_2O. The combined organic extracts were dried over anhydrous sodium sulfate, filtered, and concentrated in vacuo. The resulting boronate was purified on a short pad of silica (1% MeOH, 50% Et_2O–hexanes) and the diol was freed by performing the following cycle four times: addition of MeOH and evaporation in vacuo. The resulting oil (96 mg, 44% for two steps) was used without further purification as flash chromatography on the free diol resulted in decomposition. TLC (80% EtOAc–hexanes, 0.08% cerium (IV) sulfate in 10% aqueous sulfuric acid): 0.40. $[\alpha]_D^{20}$: –17.7° (*c* 1.1, $CHCl_3$). IR (neat, cm^{-1}): 3406, 2932, 1738, 1439, 1164. ^1H NMR (400 MHz, $CDCl_3$) δ: 4.30–4.23 (m, 1H), 3.86 (br s, 1H), 3.70 (s, 3H), 3.30 (br s, 1H), 2.49–2.48 (m, 2H), 1.61–1.53 (m, 2H), 1.50–1.37 (m, 3H), 1.34–1.24 (m, 6H), 0.87 (t, 3H, *J* = 6.8 Hz). ^{13}C NMR (100 MHz, $CDCl_3$) δ: 172.8, 72.2, 69.0, 51.8, 42.2, 41.6, 37.8, 31.8, 25.0, 22.6, 14.0. HRMS (ES, *m/z*) calcd. for $C_{11}H_{22}O_4$ (M + Na): 241.1410; found: 241.1410.

(3R,5R)- 3,5-Dihydroxydecanoic acid (20)

(3*R*,5*R*)-Methyl 3,5-dihydroxydecanoate (**14**) (0.20 g, 0.92 mmol) was diluted with MeOH (20 mL) and water (3 mL). The reaction flask was cooled to 0 °C and sodium hydroxide (3 mL, 18 mmol) as a 6 mol/L aqueous solution was added. The reaction was stirred at 0 °C for 1 h, and a sodium hydroxide/citric acid pH 5 buffer was added followed by a 1 mol/L aqueous citric acid solution until pH 5 was reached (measured with a pH meter). The aqueous phase was extracted three times with EtOAc. The combined organic extracts were washed once with brine, dried over anhydrous sodium sulfate, filtered, and concentrated in vacuo to afford a colorless oil (175 mg, 93%) containing 13% of cyclized product. This compound was used immediately, without purification, in subsequent reactions since it rapidly cyclized upon standing.

(–)-Massoialactone (12)

This compound was prepared following a modification of a literature procedure.[28b,29] In a flame-dried flask under argon, (3*R*,5*R*)-3,5-dihydroxydecanoic acid (**20**) (56 mg, 0.27 mmol) was added, then diluted with THF (27 mL) and cooled to 0 °C. Freshly distilled triethylamine (0.23 mL, 1.6 mmol) was added followed by freshly distilled 2,4,6-trichlorobenzoyl chloride (65 μL, 0.41 mmol). The reaction was stirred at 0 °C for 1 h. In the meantime, a three-neck flask equipped with a condenser in one neck, a 25 cm Vigreux column in the other, and a rubber septum in the third neck, was charged with DMAP (0.99 g, 8.1 mmol) and toluene (27 mL) and was heated at reflux so that 15 cm of the Vigreux column (isolated with cotton) would be heated with the refluxing toluene. The first reaction mixture, containing the mixed anhydride, was transferred to a syringe and added over 2 h using a syringe pump, at the top of the Vigreux column to the DMAP solution in refluxing toluene. Once the addition was complete the reaction mixture was refluxed for another 2 h. The reaction mixture was cooled to room temperature and the solvents were evaporated in vacuo. Flash chromatography (30% EtOAc–hexanes to 80% EtOAc–hexanes) afforded (–)-massoialactone (**12**) (30 mg, 67%) as a light yellow oil with a strong coconut fragrance. TLC (40% EtOAc–hexanes, 0.08% cerium (IV) sulfate in 10% aqueous sulfuric acid): 0.44. $[\alpha]_D^{20}$: –74.2° (*c* 1.0, $CHCl_3$) (lit.[23] $[\alpha]_D^{25}$: –91° (*c* 1.0, $CHCl_3$)). IR (neat, cm^{-1}): 3056, 2955, 2862, 1725, 1389, 1251, 1040, 816. ^1H NMR (300 MHz, $CDCl_3$) δ: 6.88 (ddd, 1H, *J* = 9.7, 3.6, 3.6 Hz), 6.03 (ddd, 1H, *J* = 9.7, 1.5, 1.5 Hz), 4.47–4.38 (m, 1H), 2.36–2.31 (m, 2H), 1.87–1.27 (m, 8H), 0.90 (t, 3H, *J* = 6.9 Hz). ^{13}C NMR (100 MHz, $CDCl_3$) δ: 164.6, 145.0, 121.5, 78.1, 34.9, 31.6, 29.4, 24.5, 22.5, 14.0. HRMS (EI, *m/z*) calcd. for $C_{10}H_{16}O_2$: 168.1150; found: 168.1150.

(+)-(3R,5R)-3-Hydroxy-5-decanolide (13)

In a flame-dried flask under argon, (3*R*,5*R*)-3,5-dihydroxydecanoic acid (**20**) (25 mg, 0.12 mmol) was charged, diluted with THF (1 mL), and cooled to 0 °C. Freshly distilled triethylamine (0.10 mL, 0.72 mmol) was added followed by freshly distilled 2,4,6-trichlorobenzoyl chloride (30 μL, 0.18 mmol). The reaction was stirred at 0 °C for 1 h and solvents were removed in vacuo. Flash chromatography (30% EtOAc-hexanes to 50% EtOAc-hexanes) afforded (+)-(3*R*,5*R*)-3-Hydroxy-5-decanolide **13** (19 mg, 86%) as a colorless oil. TLC (80% EtOAc–hexanes, 0.08% cerium (IV) sulfate in 10% aqueous sulfuric acid): 0.31. $[\alpha]_D^{20}$: +25.48° (*c* 1.2, $CHCl_3$) (lit.[19] $[\alpha]_D^{20}$: +27.4° (*c* 11.7, $CHCl_3$)). IR ($CHCl_3$ cast film, cm^{-1}): 3415, 2932, 2861, 1713, 1256, 1069. ^1H NMR (500 MHz, $CDCl_3$) δ: 4.69 (dm, 1H, *J* = 11.0 Hz), 4.41–4.40 (m, 1H), 2.75 (1H, dd, *J* = 17.6, 5.1 Hz), 2.62 (ddd, 1H, *J* = 17.6, 3.7, 1.7 Hz), 1.96 (dm, 1H, *J* = 14.5 Hz), 1.75 (ddd, 1H, *J* = 14.6, 11.4, 3.4 Hz), 1.73–1.69 (m, 1H), 1.63–1.49 (m, 2H), 1.45–1.38 (m, 2H), 1.34–1.29 (m, 4H), 0.90 (t, 3H, *J* = 6.4 Hz). ^{13}C NMR (100 MHz, $CDCl_3$) δ: 170.8, 76.0, 62.7, 38.6, 35.9, 31.5, 24.5, 22.5, 13.9. HRMS (ES, *m/z*) calcd. for $C_{10}H_{18}O_3$ (M + Na): 209.1148, found: 209.1150.

Supplementary data

Supplementary data for this article are available on the journal Web site (canjchem.nrc.ca) or may be purchased from the Depository of Unpublished Data, Document Delivery, CISTI, National Research Council Canada, Ottawa, ON K1A 0R6, Canada. DUD 3915. For more information on obtaining material refer to cisti-icist.nrc-cnrc.gc.ca/cms/unpub_e.shtml.

Can. J. Chem. Downloaded from www.nrcresearchpress.com by Sichuan Normal University on 09/14/12
For personal use only.

Aknowledgements

This work was funded by the Natural Sciences and Engineering Research Council (NSERC) of Canada and the University of Alberta. LC thanks NSERC for a postgraduate scholarship and Novartis pharmaceuticals of Canada for a graduate scholarship. We thank Dr. Klaus Ditrich (BASF) for the generous gift of (*S*)-1-(2-methoxyphenyl) ethylamine and Mr. Eric Pelletier (University of Alberta) and Supelco Analytical for help with HPLC analyses.

References

(1) (a) Denmark, S. E.; Almstead, N. G. In *Modern Carbonyl Chemistry;* Otera, J., Ed.; Wiley-VCH: Weinheim, Germany, 2000; Chapter 10, pp. 299–402; (b) Chemler, S. R.; Roush, W. R. In *Modern Carbonyl Chemistry;* Otera, J., Ed.; Wiley-VCH: Weinheim, Germany, 2000; Chapter 11, pp. 403–490; (c) Ramachandran, P. V. *Aldrichim Acta* **2002**, *35*, 23; (d) Kennedy, J. W. J.; Hall, D. G. In *Boronic Acids;* Hall, D. G., Ed.; Wiley-VCH: Weinheim, Germany, 2005; Chapter 6, pp. 241–277; (e) Lachance, H.; Hall, D. G. In *Organic Reactions;* Denmark, S. E., Ed.; Wiley: Hoboken, NJ, 2009; Vol. 73, pp. 1–624.

(2) (a) Brown, H. C.; Jadhav, P. K. *J. Am. Chem. Soc.* **1983**, *105*, 2092 doi:10.1021/ja00345a085.; (b) Brown, H. C.; Bhat, K. S. *J. Am. Chem. Soc.* **1986**, *108*, 293 doi:10.1021/ja00262a017.; (c) Garcia, J.; Kim, B.; Masamune, S. *J. Org. Chem.* **1987**, *52*, 4831 doi:10.1021/jo00230a043.; (d) Short, R. P.; Masamune, S. *J. Am. Chem. Soc.* **1989**, *111*, 1892 doi:10.1021/ja00187a061.; (e) Burgos, C. H.; Canales, E.; Matos, K.; Soderquist, J. A. *J. Am. Chem. Soc.* **2005**, *127*, 8044. doi:10.1021/ja043612i. PMID:15926828.

(3) (a) Hoffmann, R. W.; Ladner, W. *Tetrahedron Lett.* **1979**, *20*, 4653 doi:10.1016/S0040-4039(01)86674-0.; (b) Hoffmann, R. W.; Zeiss, H.-J. *Angew. Chem. Int. Ed. Engl.* **1979**, *18*, 306 doi:10.1002/anie.197903061.; (c) Roush, W. R.; Ando, K.; Powers, D. B.; Palkowitz, A. D.; Halterman, R. L. *J. Am. Chem. Soc.* **1990**, *112*, 6339 doi:10.1021/ja00173a023.; (d) Lachance, H.; Lu, X.; Gravel, M.; Hall, D. G. *J. Am. Chem. Soc.* **2003**, *125*, 10160 doi:10.1021/ja036807j. PMID:12926924.; (e) Gravel, M.; Lachance, H.; Lu, X.; Hall, D. G. *Synthesis* **2004**, 1290 doi:10.1055/s-2004-822359.; (f) Wu, T. R.; Shen, L.; Chong, J. M. *Org. Lett.* **2004**, *6*, 2701. doi:10.1021/ol0490882.

(4) (a) Corey, E. J.; Yu, C.-M.; Kim, S. S. *J. Am. Chem. Soc.* **1989**, *111*, 5495 doi:10.1021/ja00196a082.; (b) Corey, E. J.; Yu, C.-M.; Lee, D.-H. *J. Am. Chem. Soc.* **1990**, *112*, 878. doi:10.1021/ja00158a064.

(5) (a) Ishiyama, T.; Ahiko, T.-a.; Miyaura, N. *J. Am. Chem. Soc.* **2002**, *124*, 12414 doi:10.1021/ja0210345. PMID:12381174.; (b) Rauniyar, V.; Hall, D. G. *Angew. Chem. Int. Ed.* **2006**, *45*, 2426 doi:10.1002/anie.200504432.; (c) Rauniyar, V.; Zhai, H.; Hall, D. G. *J. Am. Chem. Soc.* **2008**, *130*, 8481. doi:10.1021/ja8016076. PMID:18540580.

(6) (a) Hoffmann, R. W. *Pure Appl. Chem.* **1988**, *60*, 123 doi:10.1351/pac198860010123.; (b) Hoffmann, R. W.; Neil, G.; Schlapbach, A. *Pure Appl. Chem.* **1990**, *62*, 1993. doi:10.1351/pac199062101993.

(7) Hoffman, R. W.; Weidmann, U. *J. Organomet. Chem.* **1980**, *195*, 137. doi:10.1016/S0022-328X(00)89998-2.

(8) Carosi, L.; Lachance, H.; Hall, D. G. *Tetrahedron Lett.* **2005**, *46*, 8981. doi:10.1016/j.tetlet.2005.10.115.

(9) Sakata, K.; Fujimoto, H. *J. Am. Chem. Soc.* **2008**, *130*, 12519. doi:10.1021/ja804168z. PMID:18712868.

(10) Brown, H. C.; Rangaishenvi, M. V.; Jayaraman, S. *Organometallics* **1992**, *11*, 1948. doi:10.1021/om00041a029.

(11) Matteson, D. S. *Tetrahedron* **1998**, *54*, 10555. doi:10.1016/S0040-4020(98)00321-4.

(12) (a) Pietruszka, J.; Schöne, N. *Angew. Chem. Int. Ed.* **2003**, *42*, 5638 doi:10.1002/anie.200352210.; (b) Pietruszka, J.; Schöne, N. *Eur. J. Org. Chem.* **2004**, 5011. doi:10.1002/ejoc.200400572.

(13) Pelz, N. F.; Woodward, A. R.; Burks, H. E.; Sieber, J. D.; Morken, J. P. *J. Am. Chem. Soc.* **2004**, *126*, 16328. doi:10.1021/ja044167u. PMID:15600327.

(14) (a) Ito, H.; Kawakami, C.; Sawamura, M. *J. Am. Chem. Soc.* **2005**, *127*, 16034 doi:10.1021/ja056099x. PMID:16287284.; (b) Ito, H.; Ito, S.; Sasaki, Y.; Matsuura, K.; Sawamura, M. *J. Am. Chem. Soc.* **2007**, *129*, 14856.(c) Peng, F.; Hall, D. G. *Tetrahedron Lett.* **2007**, *48*, 3305. doi:10.1016/j.tetlet.2007.02.124.

(15) Carosi, L.; Hall, D. G. *Angew. Chem. Int. Ed.* **2007**, *46*, 5913. doi:10.1002/anie.200700975.

(16) (a) Tissot-Croset, K.; Polet, D.; Alexakis, A. *Angew. Chem. Int. Ed.* **2004**, *43*, 2426 doi:10.1002/anie.200353744.; (b) Malda, H.; van Zijl, A. W.; Arnold, L. A.; Feringa, B. *Org. Lett.* **2001**, *3*, 1169. doi:10.1021/ol0156289. PMID:11348186.

(17) Tripathy, P. B.; Matteson, D. S. *Synthesis* **1990**, 200. doi:10.1055/s-1990-26829.

(18) Lombardo, M.; Morganti, S.; Tozzi, M.; Trombini, L. *Eur. J. Org. Chem.* **2002**, 2823. doi:10.1002/1099-0690(200208)2002:16<2823::AID-EJOC2823>3.0.CO;2-J.

(19) Vesonder, R. F.; Stodola, F. H.; Rohwedder, W. K. *Can. J. Biochem.* **1972**, *50*, 363. PMID:4337565.

(20) Endo, A. *J. Med. Chem.* **1985**, *28*, 401. doi:10.1021/jm00382a001. PMID:3981532.

(21) (a) Simionatto, E.; Porto, C.; Stüker, C. Z.; Dalcol, I. I.; da Silva, U. F. *Quim. Nova* **2007**, *30*, 1923; (b) Parker, S. R.; Cutler, H. G.; Jacyno, J. M.; Hill, R. A. *J. Agric. Food Chem.* **1997**, *45*, 2774 doi:10.1021/jf960681a.; (c) Kishimoto, N.; Sugihara, S.; Mochida, K.; Fujita, T. *Biocontrol Sci.* **2005**, *10*, 31.

(22) Abe, S. *J. Chem. Soc. Jpn.* **1937**, *58*, 246.

(23) Cavill, G. W. K.; Clark, D. V.; Whitfiel, F. B. *Aust. J. Chem.* **1968**, *21*, 2819.

(24) (a) Bennett, F.; Knight, D. W. *Heterocycles* **1989**, *29*, 639 doi:10.3987/COM-89-4853.; (b) Bennett, F.; Knight, D. W.; Fenton, G. *J. Chem. Soc., Perkin Trans. 1* **1991**, 1543 doi:10.1039/p19910001543.; (c) Romeyke, Y.; Keller, M.; Kluge, H.; Grabley, S.; Hammann, P. *Tetrahedron* **1991**, *47*, 3335 doi:10.1016/S0040-4020(01)86398-5.; (d) Bonini, C.; Pucci, P.; Racioppi, R.; Viggiani, L. *Tetrahedron Asymmetry* **1992**, *3*, 29 doi:10.1016/S0957-4166(00)82308-3.; (e) Takano, S.; Setoh, M.; Ogasawara, K. *Tetrahedron Asymmetry* **1992**, *3*, 533 doi:10.1016/S0957-4166(00)80259-1.; (f) Sabitha, G.; Bhaskar, V.; Yadav, J. S. *Synth. Commun.* **2008**, *38*, 3129. doi:10.1080/00397910802055294.

(25) (a) Satõ, T. *Can. J. Chem.* **1987**, *65*, 2732 doi:10.1139/v87-454.; (b) Miyazawa, M.; Matsuoka, E.; Sasaki, S.; Oonuma, S.; Maruyama, K.; Miyashita, M. *Chem. Lett.* **1998**, 109. doi:10.1246/cl.1998.109.

(26) (a) For selected recent enantioselective syntheses see: Ramachandran, P. V.; Reddy, M. V. R.; Brown, H. C. *Tetrahedron Lett.* **2000**, *41*, 583 doi:10.1016/S0040-4039(99)02130-9.; (b) Ishikawa, M.; Amaike, M.; Itoh, M.; Warita, Y.; Kitahara, T. *Biosci. Biotechnol. Biochem.* **2003**, *67*, 2210 doi:10.1271/bbb.67.2210. PMID:14586110.; (c) Gupta, P.; Naidu, S. V.; Kumar, P. *Tetrahedron Lett.* **2004**, *45*, 849 doi:10.1016/j.tetlet.2003.11.032.; (d) Fournier, L.; Kocienski,

P.; Pons, J. M. *Tetrahedron* **2004**, *60*, 1659 doi:10.1016/j.tet.2003.11.094.; (e) Touati, R.; Ratovelomanana-Vidal, V.; Ben Hassine, B.; Genet, J. P. *Tetrahedron Asymmetry* **2006**, *17*, 3400 doi:10.1016/j.tetasy.2006.11.048.; (f) Sabitha, G.; Gopal, P.; Yadav, J. S. *Synth. Commun.* **2007**, *37*, 1495. doi:10.1080/00397910701229107.

(27) (a) Hunter, J. H.; Hogg, J. A. *J. Am. Chem. Soc.* **1949**, *71*, 1922 doi:10.1021/ja01174a007.; (b) Gómez, C.; Maciá, B.; Lillo, V. J.; Yus, M. *Tetrahedron* **2006**, *62*, 9832 doi:10.1016/j.tet.2006.08.028.; (c) Bold, G.; Floersheimer, A.; Furet, P.; Guagnano, V.; Masuya, K.; Vaupel, A.; Schoepfer, J. *PCT Int. Appl.* **2005**, WO 2005/047273 A047271.

(28) (a) Inanaga, J.; Hirata, K.; Saeki, H.; Katsuki, T.; Yamaguchi, M. *Bull. Chem. Soc. Jpn.* **1979**, *52*, 1989 doi:10.1246/bcsj.52.1989.; (b) Mulzer, J.; Mareski, P. A.; Buschmann, J.; Luger, P. *Synthesis* **1992**, 215. doi:10.1055/s-1992-34154.

(29) (a) Gogoi, S.; Barua, N. C.; Kalita, B. *Tetrahedron Lett.* **2004**, *45*, 5577.(b) Allais, F.; Louvel, M. C.; Cossy, J. *Synlett* **2007**, 451.

(30) Magiatis, P.; Spanakis, D.; Mitaku, S.; Tsitsa, E.; Mentis, A.; Harvala, C. *J. Nat. Prod.* **2001**, *64*, 1093. doi:10.1021/np010025r. PMID:11520236.

(31) Love, B. E.; Jones, E. G. *J. Org. Chem.* **1999**, *64*, 3755. doi:10.1021/jo982433e. PMID:11674512.

(32) Tissot-Croset, K.; Polet, D.; Gille, S.; Hawner, C.; Alexakis, A. *Synthesis* **2004**, *15*, 2586. doi:10.1055/s-2004-829188.

(33) Nokami, J.; Nomiyama, K.; Matsuda, S.; Imai, N.; Kataoka, K. *Angew. Chem. Int. Ed.* **2003**, *42*, 1273. doi:10.1002/anie.200390327.

(34) Jones, P.; Knochel, P. *J. Org. Chem.* **1999**, *64*, 186. doi:10.1021/jo981623m. PMID:11674102.

(35) Takahara, J. P.; Masuyama, Y.; Kurusu, Y. *J. Am. Chem. Soc.* **1992**, *114*, 2577. doi:10.1021/ja00033a034.

(36) Evans, D. A.; Gauchet-Prunet, J. A.; Carreira, E. M.; Charette, A. B. *J. Org. Chem.* **1991**, *56*, 741. doi:10.1021/jo00002a048.

(37) Aggarwal, V. K.; Bae, I.; Lee, H. Y. *Tetrahedron* **2004**, *60*, 9725. doi:10.1016/j.tet.2004.07.044.

(38) Chen, K. M.; Hardtmann, G. E.; Prasad, K.; Repic, O.; Shapiro, M. J. *Tetrahedron Lett.* **1987**, *28*, 155. doi:10.1016/S0040-4039(00)95673-9.

Can. J. Chem. Downloaded from www.nrcresearchpress.com by Sichuan Normal University on 09/14/12
For personal use only.

Matrix effects on mass spectrometric determinations of four pharmaceuticals and personal care products in water, sediments, and biota

Ève B. Dussault, Vimal K. Balakrishnan, Keith R. Solomon, and Paul K. Sibley

Abstract: Simple analytical methods were developed for the extraction and determination of four pharmaceuticals and personal care products (PPCPs) from water, sediments, and biota. PPCPs were determined using tandem LC–MS in electrospray ionization mode, and interactions with matrix co-eluents were investigated. Extractions of water samples were performed using solid-phase extraction (SPE), sediments were extracted by pressurized liquid extraction (PLE), and biota was extracted by liquid extraction. The selected analytical methods yielded recoveries ≥ 61% in all matrixes. Matrix interactions were investigated throughout the linear range of quantification of each compound, revealing that dissolved salts had relatively minor effects on ionization (between 14% suppression to 12% enhancement), but that sediment and biota extracts caused significant matrix effects (ranging from 56% suppression to 25% enhancement). The direction and magnitude of matrix interactions reflected the physico-chemical properties of each analyte, particularly their pK_a. Among the compounds analyzed in electrospray positive mode, carbamazepine was insensitive to matrix interactions, because it is a strong proton acceptor (pK_a = 14.0). In contrast, atorvastatin (pK_a = 4.5), a weaker proton acceptor, was particularly sensitive to matrix effects. For those compounds analyzed in negative-ion mode, sample alkalinity was found to be important. With a pK_a of 10.4, 17α-ethinylestradiol generally exhibited matrix enhancement with increased sample alkalinity. However, the presence of acidic co-eluents contributed to matrix suppression. Lastly, TCS was particularly sensitive to matrix suppression, as its circumneutral pK_a (7.9) caused even slight changes in sample pH to considerably impact ionization. We conclude that while different matrixes have clear impacts on ionization of these PPCPs, matrix effects can be quantified and overcome.

Key words: pharmaceuticals and personal care products, matrix effects, LC–MS/MS, sediments, biota.

Résumé : On a développé des méthodes analytiques simples pour l'extraction et la détermination de quatre produits pharmaceutiques et de soins personnels (PPSP) à partir de solutions aqueuses, de sédiments et du biote. On a déterminé les PPSP en faisant appel à la chromatographie liquide opérant en tandem avec spectrométrie de masse en mode d'ionisation par électronébulisation (CL–SM) et on a étudié les interactions avec les coéluants de la matrice. Les extractions à partir de solutions aqueuses ont été effectuées en utilisant l'extraction en phase solide (EPS) alors que les sédiments ont été soumis à une extraction avec un liquide pressurisé (ELP) et que le biote a été soumis à une extraction liquide. Dans l'ensemble des matrices, les méthodes analytiques choisies ont permis d'obtenir des taux de récupération d'au moins 61 %. On a étudié les interactions avec la matrice pour la plage entière de quantification de chaque composé et ces études ont révélé que les sels dissous n'ont que des effets mineurs sur l'ionisation (allant de 14 % de suppression à 12 % de renforcement); toutefois, dans les cas des extractions des sédiments et du biote, on observe des effets de matrice importants allant de 56 % de suppression à 25 % de renforcement. La direction et l'amplitude des interactions de matrice sont des reflets des propriétés physico-chimiques de chaque analyte, en particulier de leur pK_a. Parmi les composés analysés en mode d'électronébulisation positive, la carbamazépine est insensible aux interactions de matrice dû au fait qu'il s'agit d'un produit fortement accepteur de proton (pK_a = 14,0). À l'opposé, l'atorvastatine (pK_a = 4,5), un accepteur de proton beaucoup plus faible, est particulièrement sensible aux effets de matrice. Pour les composés analysés en mode d'ion négatif, on a trouvé que l'alcalinité de l'échantillon est importante. Avec un pK_a de 10,4, le 17α-éthinylestradiol présente généralement un renforcement de matrice avec une augmentation de l'alcalinité de l'échantillon. Toutefois, la présence de coéluants acides contribue à la suppression de l'effet de matrice. Enfin, le « TCS » est particulièrement sensible à la suppression de la matrice dû au fait que son pK_a pratiquement neutre (7,9) provoque des changements considérables dans l'ionisation même pour de faibles changements dans le pH des échantillons. On en conclut que même si les diverses matrices ont une influence certaine sur

Received 11 September 2008. Published on the NRC Research Press Web site at canjchem.nrc.ca on 30 April 2009.

È.B. Dussault.[1] Department of Environmental Biology, University of Guelph, Guelph, ON N1G 2W1, Canada; Water Science and Technology Directorate, Aquatic Ecosystem Protection Research Division, Environment Canada, Burlington, ON, L7R 4A6, Canada.
V.K. Balakrishnan. Water Science and Technology Directorate, Aquatic Ecosystem Protection Research Division, Environment Canada, Burlington, ON, L7R 4A6, Canada.
K.R. Solomon and P.K. Sibley. Department of Environmental Biology, University of Guelph, Guelph, ON N1G 2W1, Canada.

[1]Corresponding author (e-mail: Eve.Dussault@ec.gc.ca).

l'ionisation de ces PPSP, les effets de matrice peuvent être quantifiés et surmontés.

Mots-clés : produits pharmaceutiques et de soins personnels, effets de matrice, CL–SM/SM, sédiments, biote.

[Traduit par la Rédaction]

Introduction

Environmental contamination of aquatic systems by pharmaceuticals and personal care products (PPCPs) has been of increasing concern in the last decade. However, limited availability of adequate analytical tools, mass spectral libraries, and analytical standards had, until the 1990s, significantly hindered investigations.[1,2] Since then, hundreds of products have been detected in wastewater effluents and surface water, including lipid regulators, analgesics, antimicrobials, and endocrine disruptors.[2–4] In addition, as the fate, effects, and environmental risks posed by the presence of PPCPs in aquatic systems are evaluated, there is an increasing demand for reliable analytical methods permitting their quantification in various matrixes.

Monitoring studies have generally detected PPCPs at low concentrations. However, some compounds are relatively persistent, due to their continuous usage and release into aquatic environments.[1–3] Consequently, aquatic organisms may be exposed to a multitude of these bioactive compounds at sublethal concentrations over the duration of their life cycle.

Despite the important role they play in aquatic food webs, potential effects of PPCPs on aquatic invertebrates, such as the midge *Chironomus tentans* and the freshwater amphipod *Hyalella azteca*, have been less frequently investigated than vertebrate species (e.g., fish). To execute studies into the effects of PPCPs on these aquatic organisms, it is critical to first establish and validate analytical methods for their extraction and determination in environmental matrixes.

PPCPs differ from many other pollutants in that they are specifically designed to elicit responses from target species with the potential for unintended consequences on non-target species. Accordingly, these compounds are generally moderately water-soluble, non-volatile, and thermally labile, hindering analysis by GC–MS without prior derivatization.[1] In contrast, analysis by LC–MS provides a more facile alternative to GC–MS analysis. However, a complication associated with LC–MS analysis is the potential for interactions with other matrix co-eluents, believed to arise from competition between the analyte ions and co-eluents for gas-phase emission in the electrospray ionization source.[5,6] As the number of co-eluents increases, their interactions with the target analytes interferes with adequate quantification, thereby hindering investigations.[5,7,8]

Several approaches have been suggested for the resolution of matrix effects. Quantification via matrix-matched calibration has been suggested, but the availability of non-contaminated material is problematic when studying contaminated sites. Another method consists of the addition of an internal standard (typically isotopically labelled) to each sample prior to analysis to correct for variations in ionization efficiency brought about by interactions with matrix co-eluents. Although widely accepted, this technique is most effective when the co-eluents have an identical effect on both the internal standard and the target analyte(s).[7] However, in their study of matrix effects on sulfonamide antibiotics, Balakrishnan et al.[9] recently showed that such an assumption is not necessarily valid, even in comparing $^{13}C_6$-sulfamethazine with unlabelled sulfamethazine. In cases where the internal standard interacts with matrix components in a different manner than do the target analytes, the use of this approach would incorporate a non-systematic bias into calculations, resulting in quantification errors.

The objectives of this study were two-fold: to develop separate extraction and analytical methods for the determination of four PPCPs in water, sediment, and biota, and to investigate the impact of these matrixes (water, sediment, and biota) on compound ionization. First, various extraction techniques were explored for each PPCP of interest, via extraction of samples spiked with known concentrations of analytical standards, and for which the recovery of each compound was calculated. Once satisfactory extraction methods were established, the matrix interactions of these extracts were individually assessed and quantified for each target analyte.

Experimental

Materials

Compound selection

The four compounds of interest were selected based on various criteria, including usage in Canada, persistence, and previous work in our laboratory, as described in Dussault et al.,[10] and included the lipid-regulator atorvastatin, the antiepileptic drug carbamazepine, the synthetic hormone 17α-ethinylestradiol, and the antimicrobial triclosan. The structures are shown in Table 1.

Chemicals

Atorvastatin (ATO, ≥99%) was obtained from Rugao Foreign Trade Corp. (Shanghai, China), carbamazepine (CBZ, ≥99%) was purchased from China Jiangsu Textiles (Nanjiing, China), and 17α-ethinylestradiol (EE2, ≥98%) and triclosan (TCS, ≥97%) were acquired from Sigma-Aldrich (Oakville, ON, Canada).

Calcium chloride ($CaCl_2$), calcium sulfate dihydrate ($CaSO_4{\cdot}2H_2O$), magnesium sulfate ($MgSO_4$), potassium chloride (KCl), sodium bicarbonate ($NaHCO_3$), and sodium bromide (NaBr), were purchased from Fisher Scientific (Whitby, ON, Canada). Ammonium carbonate was obtained from Caledon Laboratories (Georgetown, ON, Canada).

Acetonitrile (MeCN, HPLC grade), methanol (MeOH, HPLC grade), and acetone ($(CH_3)_2CO$, distilled in glass) were acquired from Caledon Laboratories (Georgetown, ON, Canada). Deionized water was obtained by Milli-Q (Millipore) filtration.

Isotopically labelled $^{13}C_5$-atorvastatin ($^{13}C_5$-ATO, ≥98%) was purchased from Toronto Research Chemicals (North

Table 1. Chemical structures and pK_a of the four pharmaceuticals and personal care products used in this study.

	Atorvastatin (ATO)	Carbamazepine (CBZ)	17α-Ethinylestradiol (EE2)	Triclosan (TCS)
Molecular structure	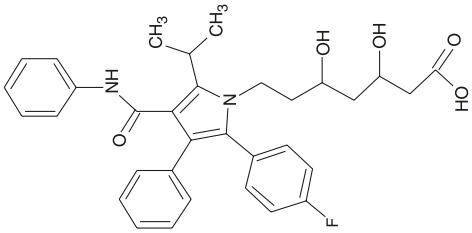	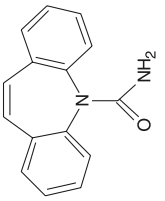	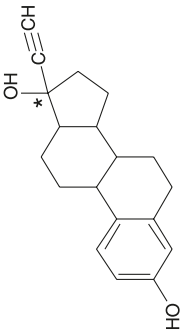	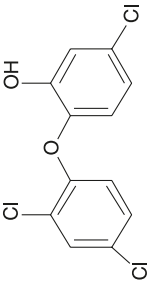
CAS reference number	134523–00–5	298–46–4	57–63–6	3380–34–5
pK_a	4.46[11]	14.0[12]	10.4[13]	7.9[11]

*denotes C-17.

York, ON, Canada), $^2H_{10}$-carbamazepine ($^2H_{10}$-CBZ, ≥98%) was purchased from Cambridge Isotope Laboratories (Andover, MA, USA), and $^2H_2$-17β-estradiol ($^2H_2$-E2, atomic purity 98%) was obtained from Sigma-Aldrich (Oakville, ON, Canada). $^{13}C_6$-Triclosan ($^{13}C_6$-TCS, ≥99%) was purchased from Wellington Laboratories (Guelph, ON, Canada).

Standard solutions

A 10 mg/L stock solution of each analyte was prepared in 1:1 MeOH/H_2O. Calibration standards corresponding to the linear range of detection (10–5000 μg/L) were prepared by dilution in MeOH/H_2O. To correct for instrumental variability, an internal standard was added to each vial prior to analysis, by addition of 50 μL of either 10 mg/L $^{13}C_5$-ATO or $^2D_2$-E2, 5 mg/L $^2D_{10}$-CBZ or 1 mg/L $^{13}C_6$-TCS, as appropriate, to 250 μL of sample. Standards and QC samples were stored at –20 °C until analysis. QC samples were analyzed with the study samples; the results of which formed the basis of accepting or rejecting a run.

Reconstituted water

Two types of reconstituted water for standard toxicity testing were selected and prepared, representing the range of variability commonly found in southern Ontario waters. Recon A represented Lake Ontario water (Ontario, Canada; pH 7.7, conductivity 395 mS/cm, alkalinity 0.11 mequiv., hardness 0.13 mmol), and contained 147 mg $CaCl_2$, 84 mg $NaHCO_3$, 1 mg NaBr, 3.7 mg KCl, and 30.1 mg $MgSO_4$ per litre of distilled water.[14] Recon B was selected to represent the water hardness of the Grand River watershed (Ontario, Canada; pH 8.4, conductivity 606 mS/cm, alkalinity 0.35 mequiv., hardness 0.25 mmol), and contained 192 mg of $NaHCO_3$, 120 mg of $CaSO_4{\cdot}2H_2O$, 120 mg of $MgSO_4$, and 8 mg of KCl in 1 L of distilled water.[15]

Analytical methods

Separation

Individual isocratic liquid chromatographic methods were developed for each PPCP, using an Acquity UPLC (Waters, Milford, MA, USA). Ten microlitre aliquots were injected into an Xterra MS-C8 column (particle size 3.5 μm, 2.1 id × 100 mm) fitted with a column guard, kept at 35 °C. For all compounds, HPLC separation involved the use of two solvents: H_2O (A) and MeCN (B), at a flow rate of 300 μL/min, with the exception of TCS, for which a flow rate of 200 μL/min was used. For ATO, an isocratic mixture of 20% A: 80% B was used, where A and B both contained 0.1 formic acid (*v*/*v*). The CBZ and EE2 solvent mixture was 40% A: 60% B, and the TCS solvent mixture was 10% A: 90% B. EE2 required the post-column infusion of 0.5% ammonium carbonate, at a rate of 10 μL/min.

Detection

Analyses were performed using a Quatro Ultima tandem LC triple quadrupole mass spectrometer (Micromass, Manchester, UK) equipped with a Z-Spray electrospray ionization (ESI) source. A positive-ionization mode was used for the determination of ATO and CBZ, while a negative-ionization mode was used for analysis of EE2 and TCS. Nitrogen was used as both drying and nebulizing gas, at flow

rates of 500 and 70 L/h, respectively. Argon was used as the collision gas, at a pressure of 2.5×10^{-3} mbar (1 bar = 100 kPa), with the exception of TCS, where the pressure was lowered to 2.5×10^{-4} mbar. Source and desolvation temperatures were 120 and 350 °C, respectively.

For the detection of TCS, ion fragmentation did not provide satisfactory quantifiable transitions, even at low ion energy, a phenomenon that has been observed in other studies.[6,16] Quantification was therefore performed using precursor-to-precursor transitions (i.e., both quadrupoles were set to select the $[M - H]^-$ mass) for the TCS ions (*m/z* 288.8 and 286.8, found in proportion to the isotopic ratio of chlorine) and internal standard (*m/z* 299.1 and 301.1). Tandem LC–MS conditions are summarized in Table 2.

Extraction procedures: development and validation

Water extractions

For each solid-phase extraction (SPE) cartridge tested, triplicate 500 mL aliquots of ultrapure water were spiked with a known quantity of each individual PPCP, using 100 μL of either a 5 or 10 mg/L solution of ATO, CBZ, EE2, or TCS in MeOH. Samples were acidified to pH 2 using 50% sulfuric acid, after which they were extracted through a SPE cartridge. For comparison purposes, SPE cartridges used were Supelco ENVI-18 (Sigma-Aldrich, Oakville, ON, Canada), OASIS MAX and OASIS HLB (Waters, Mississauga, ON, Canada). Cartridges were first conditioned with 6 mL of $(CH_3)_2CO$, followed by 6 mL of MeOH, and 12 mL of deionized water, adjusted to pH 2 with 50% H_2SO_4. Cartridges were loaded at a rate of approximately 10 mL/min, and eluted with 3 × 2 mL MeOH. Samples were then evaporated to 1 mL, and reconstituted to 2 mL with ultrapure water. Samples were frozen at –20 °C until analysis, usually performed within 2 weeks (with the exception of EE2 samples, which were analyzed after 9 weeks).

Sediment extractions

For each compound investigated, triplicate samples of 10–15 g of wet sediment from Environment Canada Reference site No. 112, pH 8.17, alkalinity 89 mg/L, 36% clay, 55% silt, 9% sand, 1.9% total organic carbon,[17] was added to pressurized liquid extraction (PLE) cells previously filled with 10–15 g of Ottawa sand reference material (Fisher Scientific, Whitby, ON, Canada). The sediments were then spiked with 1 μg of ATO, CBZ, EE2, or TCS, by adding 100 μL of 10 mg/L in MeOH of the analyte to the sediments. The remaining volume of the cells was filled with Ottawa sand, and samples were extracted in MeOH by PLE (ASE 300 Accelerated Solvent Extraction System; Dionex, Oakville, ON, Canada) at a temperature of 100 °C and pressure of 1500 psig. The extraction procedures included four cycles of 15 min (static), using a solvent delivery of 60% of cell volume. The extracts were evaporated to 1–5 mL, after which an equal volume (1–5 mL) of $CaCl_2$ (0.5 mol/L) was added to facilitate the precipitation of suspended solids.[18] Samples were vortexed and centrifuged at 1000*g* for 30 min at 4 °C. The supernatant was collected, filtered through 0.45 μm syringe filters (Chromatographic Specialties, Brockville, ON, Canada), and stored at –20 °C pending analysis, which typically took place within 2 months of extraction (however, due to unforeseen complications, the EE2 samples were stored for 12 months prior to analysis).

To compare the results of the PLE of ATO and in the absence of data from the literature, a triplicate Soxhlet extraction was performed using MeOH. Approximately 2 g of sediments were spiked with 0.1 μg of ATO by addition of 1 mL of a 0.1 mg/L ATO solution in MeOH, after which the sediments were extracted for 24 h using a Soxhlet extraction apparatus. The extracts were then evaporated following the same procedures as with the PLE extractions.

Biota extractions

Extractions were performed on two benthic invertebrates, the midge *Chironomus tentans* and the freshwater amphipod *Hyalella azteca*. For each organism and compound investigated, the extraction consisted of the addition of 9–12 animals to 2 mL of $(CH_3)_2CO$ ($n = 6$), into which 10 μL of a 10 mg/L solution of ATO, CBZ, EE2, or TCS in MeOH was added. Samples were thoroughly mixed and sonicated for 30 min (Branson Ultrasonic, Danbury, CT, USA). After additional mixing, samples were centrifuged at 1000*g* for 30 min at 4 °C, and the supernatant was collected and evaporated to dryness. Samples were reconstituted in 1 mL of 50:50 MeOH/H_2O, filtered through 0.45 μm syringe filters, and stored at –20 °C pending analysis that was performed within 5 days.

Precision and accuracy

Method precision was determined using replicate extractions ($n = 3$) of spiked samples in all matrixes investigated in the present study. For biota (*C. tentans* and *H. azteca*), six replicate sample extractions were performed ($n = 6$) because of the expected greater matrix complexity. The linearity of all standard curves was verified in each matrix by plotting the peak area of the analyte versus its concentration, and the Response (R) of the analyte against concentration was calculated using the equation

$$[1] \qquad R = \frac{\text{Peak area}_{\text{Std}} \times \text{Concn}_{\text{IS}}}{\text{Peak area}_{\text{IS}}}$$

The accuracy of the method was estimated using the standard error of the mean and the relative standard deviation. The standard error of the mean was calculated using the equation

$$[2] \qquad \text{SEM} = \frac{\text{SD}}{\sqrt{n}}$$

where SD is the standard deviation, and n is the number of replicates. The relative standard deviation (RSD) was calculated using the equation

$$[3] \qquad \text{RSD}(\%) = \frac{\text{SD}_\text{A}}{\text{Concn}_\text{A}} \times 100\%$$

where SD_A is the standard deviation of the analyte, and $Concn_A$ is the average concentration of the analyte.

Method selectivity

For each PPCP, the selectivity (susceptibility to cross-contamination) of the LC–MS/MS methods employed in the

Table 2. Optimized LC–MS/MS conditions for the analysis of four pharmaceuticals and personal care products and their internal standards in water and sediments. Argon served as the collision gas, at a pressure of 2.5×10^{-3} mbar.

Analyte	ES mode (+/–)	Retention time (min)	Parent ion (*m/z*)	Daughter ions		Cone voltage (kV)	Collision energy (eV)
				Quantitation (*m/z*)	Confirmation (*m/z*)		
Atorvastatin	ES+	1.10	559.2	440.3	292.3	44	19
$^{13}C_5$-Atorvastatin[a]		1.08	564.2	445.2	297.2	65	18
Carbamazepine	ES+	1.22	237.1	194.2	179.1	39	27
$^{2}D_{10}$-Carbamazepine[a]		1.20	247.2	204.2	186.0		32
17α-Ethinylestradiol	ES–	1.47	295.1	145.0	159.0	20	37
$^{2}D_2$-17β-Estradiol[a]		1.44	273.1	147.0	185.0	20	36
Triclosan[b]	ES–	1.60	288.8	288.8	—	20	0
			286.8	286.8	—	20	0
$^{13}C_{10}$-Triclosan[a]		1.59	299.1	299.1	—	20	0
			301.1	301.1	—	20	0

Note: Collision-gas pressure for triclosan was 2.5×10^{-4} mbar to avoid excessive fragmentation.

[a]Internal standard.

[b]Quantification of triclosan was performed using only the precursor-to-precursor transition.

present study was investigated by analyzing solutions that contained the individual PPCP, or its internal standard, across all MRM channels. For all PPCPs, a solution concentration of 5000 μg/L was used, while the internal standards were used at concentrations of 1667 (ATO, EE2), 833 (CBZ), or 167 (TCS) μg/L, corresponding to the final concentrations of each internal standard to be employed during sample analysis. The extent of cross-contamination was calculated using the equation

$$[4] \qquad \text{CC}\ (\%) = \left[\frac{\text{Area}_\text{A}}{\text{Area}_\text{C}}\right] \times 100\%$$

where Area_A is the peak area for the analyte quantitation ion, and Area_C is the peak area for the quantitation ion of the suspected cross-contaminant.

Matrix effects

Given the well-established susceptibility of LC–MS/MS techniques to matrix effects,[5,7,8] the impact of reconstituted water, sediments, and biota on the MS/MS ionization responses of the four PPCPs was carefully assessed in each extracted matrix as follows. Spiked samples were frozen at –20 °C and analyzed within 1 week.

Water

For each analyte, matrix interactions were investigated by spiking the target analyte in 50:50 MeOH/Recon (A or B) at concentrations corresponding to those of the standard curve prepared in MeOH/Milli-Q water (10–5000 μg/L). Each series of spikes was prepared in duplicate. The appropriate internal standard (see standard solutions Section) was added to each vial prior to analysis.

Sediments

A 13 g sample of wet sediment was extracted by PLE, as outlined above. The sediment extracts were used to spike various concentrations of the target analyte (10–5000 μg/L) for comparison with the standard curve prepared in Milli-Q water. For each PPCP, each series of spikes was prepared in duplicate. The suitable internal standard was added to each sample prior to analysis.

Biota

A pooled sample of 10–15 animals each of *Chironomus tentans* or *Hyalella azteca* was extracted following the procedures outlined above. Twelve biota extracts were pooled in two groups of six, to provide duplicates of 6 mL, for biota tissue concentrations of 10.5 mg/mL (*C. tentans*) and 1.9 mg/mL (*H. azteca*). A series of spiked samples (10–5000 μg/L) were prepared from both duplicates, for each PPCP investigated, and the appropriate internal standard was added to each vial prior to analysis.

Calculations

For each solution sample (in 50:50 MeOH/Milli-Q) and corresponding spiked matrix sample, the matrix effect was calculated at each concentration as

$$[5] \qquad M_x(\%) = \left[\frac{\left(\frac{\text{Area}_\text{A}}{\text{Area}_\text{IS}}\right)_\text{matrix}}{\left(\frac{\text{Area}_\text{A}}{\text{Area}_\text{IS}}\right)_\text{standard}} - 1\right] \times 100\%$$

where M_x is the matrix effect at concentration x (%); $M_x > 0$ corresponds to matrix enhancement and $M_x < 0$ corresponds to matrix suppression. According to this calculation, the standard solvent, by definition, produces no matrix effects. In addition, if the internal standard fully corrects for the variation in ionization efficiency, the ratio $\frac{\text{Area}_\text{A}}{\text{Area}_\text{IS}}$ will be the same, regardless of the matrix, and the matrix effect will be zero ($M_x = 0$). This approach resembles the method proposed by Matuszewski et al.,[19] which is calculated using the equation

$$[6] \qquad M_x(\%) = \left[\frac{\text{Area}_\text{matrix}}{\text{Area}_\text{MilliQ}} - 1\right] \times 100\%$$

with the exception that we have chosen to include an internal standard (IS) in our calculations, thus permitting differentiation between those effects caused by actual matrix

components from effects arising from simple variations in the ionization efficiency of the mass spectrometer.

Statistical analyses

For each analyte, differences between concentrations and matrixes were determined using a multiple factor Analysis of Variance and Tukey's adjustment for multiple comparisons.[20] The interactions of the following factors were analyzed: concentration, matrix, and concentration × matrix, the results of which are presented in the Matrix effects Section (below). All statistical computations were performed using SAS® (Version 9.1, Cary, NC, USA).

Results and discussion

Extraction procedures: development and validation

The calibration curves for each matrix extract are presented in the Supplementary data, Fig. S1 (peak area vs. concentration) and Fig. S2 (response vs. concentration). All calibration curves exhibited satisfactory linearity throughout the range of concentrations examined (limit of quantification: 5000 μg/L), with R^2 values of 0.9881–0.9999 (Table 3). 3). The limit of detection (LOD) and limit of quantification (LOQ), calculated for each matrix investigated, are also presented in Table 3.

Water extractions

The use of solid-phase extraction for the determination of PPCPs in aqueous environmental samples has been investigated in several studies.[21–23] In the present study, the recovery of PPCPs after SPE varied with cartridge selection (Table 4). The Supelco ENVI-18 yielded the most satisfactory accuracy for the extraction of CBZ, EE2, and TCS with average recoveries of 91%, 87%, and 84%, respectively. Given the better accuracy and precision provided by the Oasis HLB cartridge, the latter was selected for the recovery of ATO (71%; Table 4), a finding in agreement with those of Miao and Metcalfe.[24] Our recoveries are consistent with those obtained in similar studies, where recoveries for ATO ranged from 77% to 86%,[24,25] CBZ varied between 57% and 100%,[4,21,26–29] EE2 ranged from 76% to 96%,[30] and TCS varied between 36% and 95%.[16,22,31,32] Satisfactory linearity was obtained, with R^2 values of 0.9964 to 0.9999 (Table 3).The limit of detection for each analyte in Milli-Q water was 1.12, 1.12, 3.45, and 4.33 μg/L for ATO, CBZ, EE2, and TCS, respectively, while the limit of quantification was 3.76, 3.76, 11.50, and 14.42 μg/L, respectively (Table 3). For Recon A, the limit of detection was 0.65, 0.82, 6.29, and 5.37 μg/L, and the limit of quantitation was 2.18, 2.74, 20.97, and 17.91 μg/L for ATO, CBZ, EE2, and TCS, respectively (Table 3). For Recon B, the limit of detection was 0.61, 1.00, 5.41, and 3.03 for ATO, CBZ, EE2, and TCS, while the limit of quantitation was 2.03, 3.35, 18.06, and 10.10 μg/L, respectively (Table 3).

Sediment extractions

PLE proved to be a straightforward and reliable technique for the extraction and determination of PPCPs in sediments, with recovery rates varying between 70% (ATO) and 116% (EE2) (Table 5). The recovery of ATO following Soxhlet extraction was 42 ± 9.3% (mean ± SEM, n = 3), considerably lower than that obtained via PLE. Although PLE is a widely used technique for the analysis of several organic contaminants (e.g., PAHs, PCBs, surfactants, and pesticides),[33,34] there are notably fewer studies using this method for the extraction of PPCPs. Miao et. al.[35] successfully used PLE for the extraction of CBZ from biosolids, and had similar recoveries, while another study reported EE2 recovery of 87% from sediments.[36] Lastly, three studies successfully extracted TCS by PLE, and obtained 100%–120% recovery in sediments,[16,32,37] which is consistent with our values. To our knowledge, this study is the first to report extraction of ATO by PLE. Linearity varied between 0.9918 and 0.9997 (Table 3). The limit of detection of each analyte in sediment extracts was 4.72, 7.99, 7.62, and 17.76 μg/L for ATO, CBZ, EE2, and TCS, respectively. The limit of quantification was 15.72, 26.63, 25.39, and 59.19 μg/L, respectively (Table 3).

Biota extractions

Although the use of PLE presents clear advantages for the analysis of sediments and biota, the large sample sizes required (e.g., several grams) preclude its use with very small animals, such as benthic invertebrates, due to limitations in the availability of animal tissue. The liquid extraction we present here is a simple and flexible technique, which could be adapted to various sample sizes. All compounds exhibited satisfactory recoveries, ranging from 61% to 129% (Table 6). 6). Few studies to date have investigated the extraction of PPCPs from non-target organisms. Liquid–liquid extraction methods have been proposed for the analysis of estrogens in algae,[38] and for a wide variety of PPCPs and triclosan in fish,[39,40] with recoveries varying between 40% and 119%. Recently, a study proposed the extraction of selective serotonin re-uptake inhibitors from fish by PLE.[39] It is noteworthy that the studies reporting methods for estrogens and triclosan proposed GC–MS analyses, which involved preliminary derivatization of the target analytes. To the best of our knowledge, this study is also the first to propose extraction procedures for both ATO and CBZ in biota. In addition, the quantification we propose by tandem LC–MS represents an alternative to the derivatization processes involved in the analysis of PPCPs by GC–MS. Linearity (R^2 values) varied between 0.9881 and 0.9993 (*C. tentans*) and 0.9888 and 0.9998 (*H. azteca*; Table 3). For the *C. tentans* extracts, the limit of detection for ATO, CBZ, EE2, and TCS was 0.34, 1.12, 3.74, and 7.67 μg/L, respectively; the limit of quantification of each analyte was 1.12, 2.87, 12.47, and 25.58 μg/L (Table 3). For the *H. azteca* extracts, the limit of detection was 1.29, 1.10, 6.50, and 7.99 μg/L for ATO, CBZ, EE2, and TCS, respectively, while the limit of quantification was 4.31, 3.66, 21.68, and 26.65 μg/L, respectively (Table 3).

Method selectivity

Cross-talk between the MRM channels of each analyte and internal standard was investigated using individual solutions of each PPCP and its internal standard, the results of which are presented in Supplementary data Figs. S3–S10. We observed negligible cross-talk between each analyte and their respective internal standard. For ATO, a cross-talk of 0.05% was calculated (S3), representing the percentage of

Table 3. Limit of detection (LOD; μg/L), limit of quantification (LOQ; μg/L), and linearity (R^2; 5–5000 μg/L) for four pharmaceuticals and personal care products in various matrixes.

	Atorvastatin			Carbamazepine			17α-Ethinylestradiol			Triclosan		
	LOD[a]	LOQ	R^2	LOD	LOQ[b]	R^2	LOD	LOQ	R^2	LOD	LOQ	R^2
Milli-Q	1.13	3.76	0.9996	1.13	3.76	0.9999	3.45	11.50	0.9999	4.33	14.41	0.9989
Recon A	0.65	2.18	0.9996	0.82	2.74	0.9965	6.29	20.97	0.9999	5.37	17.91	0.9985
Recon B	0.60	2.03	0.9999	1.01	3.35	0.9975	5.42	18.06	0.9999	3.03	10.10	0.9964
Sediment	4.72	15.72	0.9997	7.99	26.63	0.9918	7.62	25.39	0.9994	17.76	59.19	0.9964
Biota A (*Chironomus tentans*)	0.34	1.12	0.9881	0.86	2.87	0.9988	3.74	12.47	0.9993	7.67	25.58	0.9926
Biota B (*Hyalella azteca*)	1.29	4.31	0.9990	1.10	3.66	0.9993	6.50	21.68	0.9998	7.99	26.65	0.9888

[a]The LOD was calculated as 3σ, where σ is the relative standard deviation of 6–7 analyses of a low-concentration standard in the matrix of interest.
[b]The LOQ was calculated as 10σ, where σ is the relative standard deviation of 6–7 analyses of a low-concentration standard in the matrix of interest.

the peak area detected in the quantitation MRM channel of its internal standard. For $^{13}C_5$-ATO, a cross-talk of 0.03% was calculated; in other words, the peak area detected in the quantitation MRM channel of ATO was 0.03% of that detected for the quantitation ion of $^{13}C_5$-ATO (Fig. S4). This level of cross-talk is neglible in comparison with the purity of the internal standard, which was ≥98%. CBZ exhibited a cross-talk of 0.01% (Fig. S5), while that of $^2H_{10}$-CBZ was 0.05% (Fig. S6), both are also negligible compared with the purity of the chemical (≥98%). For EE2 and $^2D_2$-E2, no cross-talk was detected (Figs. S7–S8), because the analyte and its internal standard were different compounds. For TCS, the cross-talk was calculated for both precursor transitions; the cross-talk of TCS was 0.4% for both transitions (Fig. S9), but that of $^{13}C_6$-TCS was 6.1% and 3.1% for the heavier and lighter precursors, respectively (Fig. S10). While these values are greater than those expected based on the purity of the internal standard (≥99%), they remain well under the RSD (precision) associated with the various extractions (9.2%–21.8%), and thus further correction against the impact of cross-talk was deemed unnecessary.

Matrix effects

To further minimize the potential impact of matrix interactions, we selected an internal standard that closely resembled the properties of each target analyte. For ATO, CBZ, and TCS, an isotopically labelled version of the compound of interest was used, while for EE2, a deuterated estradiol standard was selected, from which the target analyte differs only by the presence of an ethinyl group on C-17 (Table 1). The physico-chemical properties of both compounds are relatively similar, and they exhibited nearly identical elution times (Table 2). The impact of various matrixes on each analyte was investigated at concentrations ranging from 10 to 5000 μg/L. The greatest matrix effects were generally detected at lower concentrations of analyte, since the co-eluents (i.e., matrix) are present in a greater proportion relative to the analyte. The calibration curves for each analyte and matrix prior to correction for variations in ionization efficiency are presented in Fig. S1, while the calibration curves corrected for each analyte using their respective internal standard are presented in Fig. S2.

To illustrate the benefits of integrating an internal standard into the calculation of matrix interactions, the absolute matrix effects, calculated using the approach of Matuszewski et al.,[19] are represented in Fig. S11 for comparison with the approach used in the present study (Fig. 1). Although the differences are minimal for the two aqueous matrixes, the absolute matrix effects calculated using the approach of Matuszewski et al.[19] were greater than those calculated using our method, especially with complex matrixes such as sediment and biota, (note the change in *y* axis, increased to 250%–400% in Figs. S11C–S11E). In the absence of internal standards, the variation in ionization efficiency brought about by the presence of matrix co-eluents is incorporated into the absolute matrix effect, thus increasing its intensity. These data are in agreement with the calibration curves presented in Fig. S1, where, for example, a significant matrix enhancement was associated with the presence of sediment or biota with TCS (see Fig. S1D).

Table 4. Recovery (accuracy ± SEM (precision)) of four pharmaceuticals and personal care products in aqueous samples, and cartridge selected for each PPCP investigated. In each case, $n = 3$ and optimum recoveries are denoted in bold font.

	Recovery[a] (%)			
	ENVI-18	MAX	HLB	Cartridge selected
Atorvastatin	62±1.3 (3.6)	71±4.9 (11.9)	**71±1.9 (4.7)**	HLB
Carbamazepine	**95±3.4 (6.1)**	82±1.2 (1.5)	75±4.5 (6.0)	ENVI-18
17α-Ethinylestradiol	**92±7.9 (14.7)**	79±5.2 (11.4)	86±8.1 (16.3)	ENVI-18
Triclosan	**103±5.5 (9.2)**	96±13.2 (33.5)	43±3.8 (8.9)	ENVI-18

Note: Precision was expressed as RSD × 100.

[a]Cartridges selected for recovery experiment were Supelco ENVI-18, Waters Oasis MAX, and Waters Oasis HLB.

Table 5. Recovery (% ± SEM (precision)) of four pharmaceuticals and personal care products in sediments by pressurized liquid extraction (PLE). In each case, $n = 3$.

Compound	Recovery (%)
Atorvastatin	70±2.5 (6.2)
Carbamazepine	89±2.7 (5.2)
17α-Ethinylestradiol	116±4.0 (6.0)
Triclosan	109±6.2 (9.9)

Note: Precision was expressed as RSD × 100.

Table 6. Recovery (% ± SEM (precision)) of four pharmaceuticals and personal care products in biota, after sonication. In each case, $n = 6$.

	Compound	Recovery (%)
Chironomus tentans	Atorvastatin	61±2.8 (11.0)
	Carbamazepine	118±2.2 (4.5)
	17α-Ethinylestradiol	98±5.7 (14.3)
	Triclosan	69±7.0 (21.8)
Hyalella azteca	Atorvastatin	108±2.8 (6.3)
	Carbamazepine	129±1.4 (2.6)
	17α-Ethinylestradiol	95±2.9 (7.4)
	Triclosan	81±3.3 (17.0)

Note: Precision was expressed as RSD × 100.

Water

When the compounds of interest were dissolved in reconstituted water, the presence of salts generally had minor effects on compound ionization, which were usually adequately corrected by the selected internal standards (Fig. 1). CBZ was generally insensitive to either Recon A or B, as reflected by the low amplitude of matrix effects (5% enhancement) and the absence of differences in matrix interactions between the two water types. With a pK_a of 14, CBZ is a very strong proton acceptor compared with other bases in solution, such as HCO_3^- (pK_a 6.1). Consequently, CBZ will be preferentially protonated, regardless of the differences in the composition of Recon A or B. In contrast, the presence of salts in the softer water (Recon A) caused, on average, 4% and 8% suppression with TCS and ATO, respectively (Fig. 1). This interaction is not surprising, given the known ability of sulfates and phosphates to cause matrix suppression.[8] However, effects were more noticeable with EE2, where the addition of salts caused, on average, 12% matrix enhancement, which was most pronounced at lower concentrations (Fig. 1). The addition of further salts, as found in Recon B, did not appear to significantly affect CBZ and EE2, leaving matrix effects relatively unchanged. Meanwhile, Recon B yielded greater matrix suppression (14% on average) of ATO than did Recon A (Fig. 1). Matrix suppression was not dependent on ATO concentration ($p = 0.99$), suggesting that the increased suppression is attributable to differences between the two matrixes (Recon A and B). The main difference in these two systems lies in their relative alkalinity and buffering capacity, with Recon A having an alkalinity of 0.11 mequiv. (compared with 0.35 mequiv. for Recon B), and a buffering capacity of 84 mg $NaHCO_3$ (vs. 192 mg $NaHCO_3$ for Recon B). In effect, the higher alkalinity and buffering capacity of Recon B would serve as a "proton sponge", steadily reducing the protonation of ATO, regardless of concentration. The reduced protonation of ATO in solution would thus lead to a greater suppression in Recon B than in Recon A, due to the presence of a larger quantity of a stronger base (HCO_3^-).

Addition of 0.5 mol/L ammonium carbonate base post-injection facilitated the ionization of EE2 in ES^- mode, resulting from the increased alkalinity of the mobile phase. The presence of carbonate (via HCO_3^-) in Recon A and B likely further increased the alkalinity of the mobile phase, thus facilitating the ionization of the target analyte even further, and resulting in matrix enhancement. In the case of TCS (pK_a 7.9), it is suspected that the alkalinity in Recon B (pH 8.4) may have facilitated ionization, thus causing a slight matrix enhancement (3%), whereas Recon A (pH 7.7) may not have been sufficiently alkaline to fully ionize a compound of comparable pK_a (as expected under the Henderson–Hasselback equation), as seen by the overall 6% matrix suppression.

Sediments

In contrast with the generally minor matrix effects in water, the presence of sediment extracts had a noticeable impact on compound ionization, especially with ATO, where the signal amplitude was reduced 10 fold in comparison with Milli-Q water (see Fig. S1). This is also reflected in the higher limits of detection and quantitation associated with analyses in sediment extracts, which increased by a factor of 2–8 compared with the standards prepared in Milli-Q water (Table 3). When the appropriate internal standards were used to correct for these variations in ionization efficiency, the matrix effects varied, on average, be-

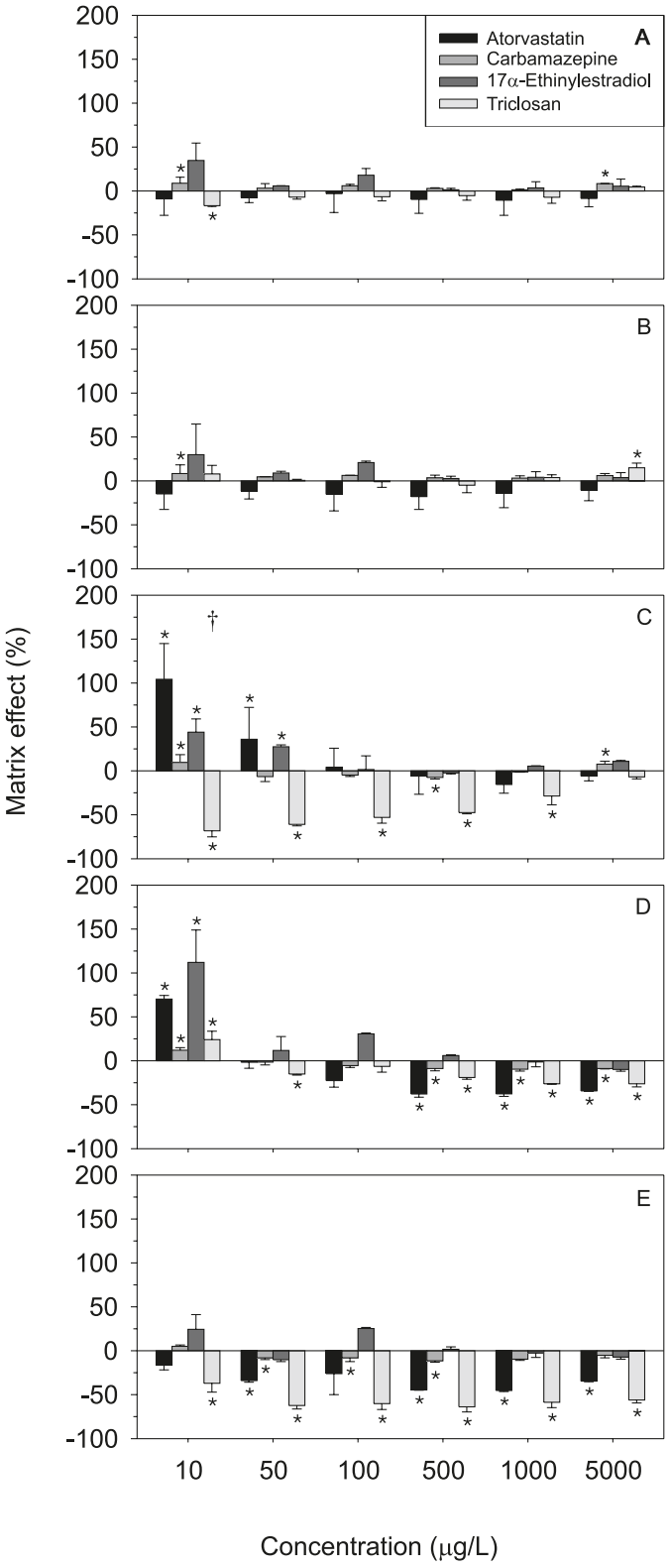

Fig. 1. Matrix effects (mean ± SEM; $n = 2$) in two types of reconstituted water (A, B), sediment extracts (C), and biota extracts (D, *Chironomus tentans*; E, *Hyalella azteca*) with increasing standard concentration on four pharmaceuticals and personal care products. The matrix effect signifies the compound is *X*% more or less recoverable than in the absence of the matrix of interest. * denotes values significantly different from zero ($p < 0.05$). †denotes concentrations below the limit of detection (LOD) and should be interpreted with caution.

tween 39% suppression (TCS) and 19% enhancement (ATO). There were negligible matrix effects associated with CBZ (no overall matrix effect), while EE2 showed, on average, a 15% enhancement (Fig. 1). All effects were concentration-dependent, with most significant interactions at the lowest concentration investigated (10 μg/L, $p \leq 0.012$), where the relative amount of matrix constituents to target analytes were highest. The presence of humic and fulvic acids have been reported to cause matrix suppression in the LC–MS analysis of the pesticide dichlorvos, as well as naphthenic acids,[41,42] and may have been responsible for the matrix interactions observed in the present study. Given the comparatively low pK_a of ATO, the addition of such acidic components to the ionization matrix would increase the protonation of ATO, leading to the observed matrix enhancement. At low concentrations of ATO, the higher [acid]:[ATO] ratio would lead to proportionately greater ATO protonation than would be seen at higher ATO concentrations. In contrast, because of its high pK_a, the presence of additional acids had no impact on CBZ ion formation. Lastly, suppression was observed at all but the highest TCS concentration (Fig. 1). The pK_a (7.9) of TCS was closest to the pH of the sediments (8.17), and was the compound most affected by the presence of dissolved acids.

Biota

Matrix interactions in the presence of biota extracts were remarkably similar to observations made with other matrixes. The presence of *C. tentans* extracts had neglible effects on the analysis of CBZ, with an overall matrix suppression of 4% (Fig. 1). A 25% matrix enhancement was observed with EE2, while an average matrix suppression of 11% and 14% was observed with ATO and TCS, respectively (Fig. 1). However, these values were mainly due to a significant matrix enhancement observed at the lowest concentration with all analytes in *C. tentans* extracts: CBZ (15%), TCS (24%), ATO (70%), and EE2 (112%; $p \leq 0.0024$). The effects then became of lower magnitude with increasing concentrations (Fig. 1), as the relative ratio of matrix:analyte decreased. Note that while the lowest concentrations used for EE2 and TCS with *C. tentans* were below the LOQ, the concentrations exceeded the LOD. Since the compounds could be detected, the impact of the matrix on the ionization response could thus be determined.

Given the smaller animal size, and hence, lower biomass extracted, we expected the magnitude of effects in *H. azteca* extracts to be lower than in *C. tentans*. Indeed, matrix effects of low magnitude were observed with CBZ (6% suppression) and EE2 (5% enhancement; Fig. 1). However, greater matrix suppression was observed with ATO and TCS, throughout the range of concentrations investigated, with average suppressions of 33% and 56%, respectively, indicating that the composition of the matrix plays a greater role than its quantity. Given the wide variety of possible co-eluents associated with each species (particularly ionizable groups, such as amines from amino acids or phenolic moieties found in lipids, which are present in greater relative abundance in *H. azteca*, 6%,[43] than in *C. tentans*, 1%[44]), we

recommend that further investigations be conducted to identify the origin of this matrix suppression.

Recent studies dedicated to the extraction of PPCPs from fish tissues have reported the presence of significant matrix effects.[39,45] While investigating the extraction of the selective serotonine re-uptake inhibitors from fish tissue, Chu and Metcalfe[45] reported matrix suppression of 19%, 35%, and 39% for paroxetine, fluoxetine, and norfluoxetine, respectively. Another study also describing analytical methods for the extraction of PPCPs from fish tissue reported matrix effects varying between –95% for miconazole and +867% for erythromycin.[39]

In some respects, the observation of matrix effects in the presence of isotopically labelled analogues of the target analytes themselves may appear somewhat surprising. After all, it has been posited that the structural similarity of isotopically labelled substrates to their unlabelled analogues should lead to both compounds exhibiting similar behaviour, and hence, similar matrix effects. However, it has been well-established that acid dissociation constants (much like kinetic rate constants) are subject to often significant isotope effects. For example, laccase has been shown to have a pK_a of 8.98 in water, whereas in deuterated water, the pK_a becomes 9.24.[46] Meanwhile, the pK_a of chloracetic acid differs from that of ^{2}H-chloracetic acid labelled in the alpha position.[47] If the labelled and unlabelled compounds have different susceptibilities to ionization (as suggested by their differing pK_a values), then matrixes that can affect ionization in the mass spectrometer will have different impacts on the labelled and unlabelled compounds; hence, differing matrix effects will be observed.[9]

Conclusions

This study aimed to develop simple and straightforward methods for the extraction of four PPCPs from water, sediments, and biota, with the objective of subsequently applying these techniques to toxicological studies. The four compounds of interest were successfully extracted from water by solid-phase extraction with recoveries of at least 71%. Meanwhile, the pressurized liquid extraction method, developed to extract PPCPs from sediments, yielded recoveries > 70%. Lastly, the liquid extraction method, developed specifically to accommodate small tissue samples, yielded recoveries for the four compounds ranging from 61% to 129%.

Despite the use of carefully chosen internal standards to appropriately correct for variation in the ionization efficiency of each analyte, matrix effects of variable direction and amplitude were detected in the four PPCPs investigated. Although matrix suppression of greater amplitude has been observed in more polar compounds,[7] we found that physicochemical properties of each analyte, especially pH–pK_a interactions, could explain the direction and even magnitude of the matrix effect. For example, because of its high pK_a of 14.0, CBZ was not particularly sensitive to matrix effects at circumneutral pH. Meanwhile, matrix suppression was generally observed in ATO, which had the lowest pK_a (4.46), and for which the addition of alkaline salts likely caused significant matrix suppression. On the other hand, sediments having low concentrations of ATO were subject to matrix enhancement, presumably due to the additive effect of acidic co-eluents, such as humic and fulvic acids. Conversely, EE2 was generally susceptible to matrix enhancement in the presence of alkaline salts, which improved the ionization efficiency in negative electrospray mode. However, the presence of sediment co-eluents (presumably of acidic nature) had suppressive effects at low analyte concentrations. Lastly, TCS was the analyte most susceptible to matrix effects, exhibiting considerable matrix suppression in sediment and biota matrixes. We believe that its circumneutral pK_a (7.9) makes this compound more sensitive to pH-related changes. Overall, we have shown that matrix effects exist and may not be fully corrected using isotopically labelled analogues of target analytes. Our results demonstrate that potential matrix interactions should be taken in consideration during the development and application of analytical methods for pharmaceuticals and personal care products in environmental and biological matrixes, since failure to do so could drastically bias quantification and undermine study validity.

Supplementary data

Supplementary data for this article are available on the journal Web site (canjchem.nrc.ca) or may be purchased from the Depository of Unpublished Data, Document Delivery, CISTI, National Research Council Canada, Ottawa, ON K1A 0R6, Canada. DUD 3925. For more information on obtaining material, refer to cisti-icist.nrc-cnrc.gc.ca/cms/unpub_e.shtml.

Acknowledgements

The authors wish to thank John Toito for his valuable assistance, and Dr. Bill Lee, for kindly providing the $^2D_2$-17β-estradiol for our analyses. This study was funded by the Ontario Ministry of Agriculture, Food and Rural Affairs and the Livestock Environment Initiative (PKS), and the Canadian Environmental Protection Act (VKB). Additional financial support was provided by the Natural Sciences and Engineering Research Council of Canada (NSERC) and Ontario Graduate Scholarship (OGS) (ÈBD).

References

(1) Daughton, C. G.; Ternes, T. A. *Environ. Health Perspect.* **1999**, *107*, 907. doi:10.2307/3434573. PMID:10592150.

(2) Kolpin, D. W.; Furlong, E. T.; Meyer, M. T.; Thurman, E. M.; Zaugg, S. D.; Barber, L. B.; Buxton, H. T. *Environ. Sci. Technol.* **2002**, *36*, 1202. doi:10.1021/es011055j. PMID:11944670.

(3) Hirsch, R.; Ternes, T.; Haberer, K.; Kratz, K. L. *Sci. Total Environ.* **1999**, *225*, 109. doi:10.1016/S0048-9697(98)00337-4. PMID:10028708.

(4) Metcalfe, C. D.; Koenig, B. G.; Bennie, D. T.; Servos, M. R.; Ternes, T. A.; Hirsch, R. *Environ. Toxicol. Chem.* **2003**, *22*, 2872. doi:10.1897/02-469. PMID:14713026.

(5) Pascoe, R.; Foley, J. P.; Gusev, A. I. *Anal. Chem.* **2001**, *73*, 6014. doi:10.1021/ac0106694. PMID:11791574.

(6) Quintana, J. B.; Reemtsma, T. *Rapid Commun. Mass Spectrom.* **2004**, *18*, 765. doi:10.1002/rcm.1403. PMID: 15052558.

(7) Bonfiglio, R.; King, R. C.; Olah, T. V.; Merkle, K. *Rapid Commun. Mass Spectrom.* **1999**, *13*, 1175. doi:10.1002/(SICI)1097-0231(19990630)13:12<1175::AID-RCM639>3.0.CO;2-0. PMID:10407294.

(8) King, R.; Bonfiglio, R.; Fernandez-Metler, C.; Miller-Stein, C.; Olah, T. *J. Am. Soc. Mass Spectrom.* **2000**, *11*, 942. doi:10.1016/S1044-0305(00)00163-X. PMID:11073257.
(9) Balakrishnan, V. K.; Terry, K. A.; Toito, J. *J. Chromatog. A* **2006**, *1131*, 1. doi:10.1016/j.chroma.2006.07.011.
(10) Dussault, È. B.; Balakrishnan, V. K.; Sverko, E.; Solomon, K. R.; Sibley, P. K. *Environ. Toxicol. Chem.* **2008**, *27*, 425. doi:10.1897/07-354R.1. PMID:18348646.
(11) MERCK. The Merck index: An encyclopedia of chemicals, drugs, and biologicals. Merck & Co., Inc., Whitehouse Station, NJ. 2006.
(12) Scheytt, T.; Mersmann, P.; Lindstãdt, R.; Heberer, T. *Water Air Soil Pollut.* **2005**, *165*, 3. doi:10.1007/s11270-005-3539-9.
(13) Clara, M.; Strenn, B.; Saracevic, E.; Kreuzinger, N. *Chemosphere* **2004**, *56*, 843. doi:10.1016/j.chemosphere.2004.04.048. PMID:15261530.
(14) Borgmann, U. Toxicity test methods and observations using the freshwater amphipod. *In* Hyalella, NWRI 02–332. National Water Research Institute, Burlington, ON. 2002.
(15) ASTM. Annual book of ASTM Standards. E729–96. ASTM International, West Conshohocken, PA. 2004.
(16) Agüera, A.; Fernández-Alba, A. R.; Piedra, L.; Mézcua, M.; Gómez, M. J. *Anal. Chim. Acta* **2003**, *480*, 193. doi:10.1016/S0003-2670(03)00040-0.
(17) Grapentine, L. Personal communication. Environment Canada, Burlington, ON. 2007.
(18) USEPA. Nitroaromatics and nitramines by high performance liquid chromatography (HPLC). USEPA, WA. 1997.
(19) Matuszewski, B. K.; Constanzer, M. L.; Chavez-Eng, C. M. *Anal. Chem.* **2003**, *75*, 3019. doi:10.1021/ac020361s. PMID:12964746.
(20) Sokal, R. R.; Rohlf, F. J. Biometry: The principles and practice of statistics in biological research. 3rd Ed. W.H. Freeman and Company, New York, NY. 1995.
(21) Ternes, T. A.; Hirsch, R.; Mueller, J.; Haberer, K. *Fresenius J. Anal. Chem.* **1998**, *362*, 329. doi:10.1007/s002160051083.
(22) Lee, H. B.; Peart, T. E.; Svoboda, M. L. *J. Chromatog. A* **2005**, *1094*, 122. doi:10.1016/j.chroma.2005.07.070.
(23) Peck, A. M. *Anal. Bioanal. Chem.* **2006**, *386*, 907. doi:10.1007/s00216-006-0728-3. PMID:17047946.
(24) Miao, X.-S.; Metcalfe, C. D. *J. Chromatog. A* **2003**, *998*, 133. doi:10.1016/S0021-9673(03)00645-9.
(25) Lam, M. W.; Young, C. J.; Brain, R. A.; Johnson, D. J.; Hanson, M. A.; Wilson, C. J.; Richards, S. M.; Solomon, K. R.; Mabury, S. A. *Environ. Toxicol. Chem.* **2004**, *23*, 1431. doi:10.1897/03-421. PMID:15376529.
(26) Farré, M.; Ferrer, I.; Ginebreda, A.; Figueras, M.; Olivella, L.; Tirapu, L.; Vilanova, M.; Barceló, D. *J. Chromatog. A* **2001**, *938*, 187. doi:10.1016/S0021-9673(01)01154-2.
(27) Öllers, S.; Singer, H. P.; Fässler, P.; Müller, S. R. *J. Chromatog. A* **2001**, *911*, 225. doi:10.1016/S0021-9673(01)00514-3.
(28) Miao, X.-S.; Metcalfe, C. D. *Anal. Chem.* **2003**, *75*, 3738.
(29) Hao, C.; Lissemore, L.; Nguyen, B.; Kleywegt, S.; Yang, P.; Solomon, K. *Anal. Bioanal. Chem.* **2006**, *384*, 505. doi:10.1007/s00216-005-0199-y. PMID:16365778.
(30) Ternes, T. A.; Stumpf, M.; Mueller, J.; Haberer, K.; Wilken, R. D.; Servos, M. R. *Sci. Total Environ.* **1999**, *225*, 81. doi:10.1016/S0048-9697(98)00334-9. PMID:10028705.
(31) McAvoy, D. C.; Schatowitz, B.; Jacob, M.; Hauk, A.; Eckhoff, W. S. *Environ. Toxicol. Chem.* **2002**, *21*, 1323. doi:10.1897/1551-5028(2002)021<1323:MOTIWT>2.0.CO;2. PMID:12109730.
(32) Singer, H.; Müller, S.; Tixier, C.; Pillonel, L. *Environ. Sci. Technol.* **2002**, *36*, 4998. doi:10.1021/es025750i. PMID:12523412.
(33) Schantz, M. M. *Anal. Bioanal. Chem.* **2006**, *386*, 1043. doi:10.1007/s00216-006-0648-2. PMID:16896622.
(34) Carabias-Martínez, R.; Rodríguez-Gonzalo, E.; Hernández-Méndez, J. *J. Chromatog. A* **2005**, *1089*, 1. doi:10.1016/j.chroma.2005.06.072.
(35) Miao, X.-S.; Yang, J.-J.; Metcalfe, C. D. *Environ. Sci. Technol.* **2005**, *39*, 7469. doi:10.1021/es050261e. PMID: 16245817.
(36) Céspedes, R.; Petrovic, M.; Raldúa, D.; Saura, Ú.; Piña, B.; Lacorte, S.; Viana, P.; Barceló, D. *Anal. Bioanal. Chem.* **2004**, *378*, 697. doi:10.1007/s00216-003-2303-5. PMID: 14658021.
(37) Morales-Muñoz, S.; Luque-García, J. L.; Ramos, M. J.; Fernández-Alba, A.; Luque de Castro, M. D. *Anal. Chim. Acta* **2005**, *552*, 50. doi:10.1016/j.aca.2005.07.042.
(38) Lai, K. M.; Johnson, K. L.; Scrimshaw, M. D.; Lester, J. N. *Environ. Sci. Technol.* **2000**, *34*, 3890. doi:10.1021/es9912729.
(39) Ramirez, A. J.; Mottaleb, M. A.; Brooks, B. W.; Chambliss, C. K. *Anal. Chem.* **2007**, *79*, 3155. doi:10.1021/ac062215i. PMID:17348635.
(40) Okumura, T.; Nishikawa, Y. *Anal. Chim. Acta* **1996**, *325*, 175. doi:10.1016/0003-2670(96)00027-X.
(41) Yang, L.; Liu, Y. H.; Zhe, L.; Li, Y.; Liq, J. *Chromatog. Rel. Technol.* **2006**, *29*, 2943. doi:10.1080/10826070600981025.
(42) Ohlenbusch, G.; Zwiener, C.; Meckenstock, R. U.; Frimmel, F. H. *J. Chromatog. A* **2002**, *967*, 201. doi:10.1016/S0021-9673(02)00785-9.
(43) Driscoll, S. K.; Landrum, P. F. *Environ. Toxicol. Chem.* **1997**, *16*, 2179. doi:10.1897/1551-5028(1997)016<2179:ACOEPA>2.3.CO;2.
(44) West, C. W.; Ankley, G. T.; Nichols, J. W.; Elonen, G. E.; Nessa, D. E. *Environ. Toxicol. Chem.* **1997**, *16*, 1287. doi:10.1897/1551-5028(1997)016<1287:TABOTP>2.3.CO;2.
(45) Chu, S.; Metcalfe, C. D. *J. Chromatog. A* **2007**, *1163*, 112. doi:10.1016/j.chroma.2007.06.014.
(46) Koudelka, G. B.; Hansen, F. B.; Ettinger, M. J. J. *Biol. Chem.* **1985**, *29*, 15561.
(47) Barnes, K. K.; Christenson, S. C.; Kolpin, D. W.; Focazio, M. J.; Furlong, E. T.; Zaugg, S. D.; Meyer, M. T.; Barber, L. B. *Ground Water Monit. Remediat.* **2004**, *24*, 119. doi:10.1111/j.1745-6592.2004.tb00720.x.

NanoMORALs — Metal nanoparticles doped with organic molecules

Giovanni Palmisano, Vincenzo Augugliaro, Rosaria Ciriminna, and Mario Pagliaro

Abstract: A new class of nanosized metal–organic alloys (MORALs) has been synthesized for the first time. Silver nanoparticles doped with Cu(II) and Fe(III) phthalocyanines were thus synthesized in the presence of sodium dodecyl sulfate (SDS). The resulting materials were characterized by means of XRD, SEM, TEM coupled to energy dispersive X-ray analysis, and thermogravimetric analysis. No leaching of the photoactive dopant species was observed in water or in common organic solvents.

Key words: hybrid, alloy, nanoparticle, metal–organic.

Résumé : On a synthétisé pour la première fois une nouvelle classe d'alliages métallo-organiques « MORALs » à l'échelle nano. On a ainsi synthétisé des nanoparticules d'argent dopées avec des phtalocyanines de Cu(II) et de Fe(III) en présence de sulfate de dodécyle et de sodium. Les produits obtenus ont été caractérisés par les techniques de diffraction des rayons X (DRX), de microscopie électronique à balayage (MEB) et de microscopie électronique à transmission (MET) couplées à des analyses de rayons X à dispersion d'énergie et d'analyse thermogravimétrique. On n'a observé aucune lixiviation des espèces dopantes photoréactives, que ce soit dans l'eau ou dans les solvants organiques communs.

Mots-clés : hybride, alliage, nanoparticule, métallo-organique.

[Traduit par la Rédaction]

Introduction

Metal–organic alloys (MORALs) are new materials with a variety of potential applications in different fields. Organic molecules as diverse as dyes[1] and polymers,[2] both water-soluble and not, have been efficiently incorporated within Ag, Au, and Cu either by simple homogeneous reduction of the corresponding metal cations in the presence of the desired organic species, or by heterogeneous reduction by a sacrificial reducing metal in solution.[3] In general, the encapsulated organic dopant is not affected by the mild encapsulation process, and once entrapped, it remains accessible to reactants in solution. As expected, however, the physicochemical properties of the doped metal species are largely altered. For example, various functional applications were readily proved, such as the use of Nafion@Ag as acid catalyst,[4] and the improvement of Ag catalytic performance upon encapsulation of Congo Red for oxidation of methanol to formaldehyde.[5] Clearly, considering the immense variety of organic molecules and the abundance of metals in the periodic table, these findings have opened the route to a new, and large, chemistry of doped metals.[1–5]

Entrapment is markedly distinct from adsorption and confers interesting new properties to the resulting hybrid composites. For example, although a water-soluble species such as Congo Red readily leaches out in water when adsorbed at the surface of Ag,[1] no leaching is observed from the corresponding MORAL (with DMSO being the only solvent capable to extract the organic dopant molecules).[3] Moreover, a one-to-two orders of magnitude larger amount of organics can be entrapped in metal compared with simple surface adsorption. Such first-generation MORALs consist of macro-mesoporous materials.

Herein, we report the first preparation of Ag-based MORAL nanoparticles made of silver doped with Cu(II) and Fe(III) phthalocyanines (CuPc and FePc, respectively). We demonstrate that carrying out the reductive encapsulation in the presence of micellar sodium dodecyl sulfate (SDS) makes it possible to obtain particles with diameters as small as the nanometer fraction. The method is general and opens the way to the practically viable synthesis of a new class of nanostructured hybrid metals of large applicative potential.

Experimental

Silver nanoparticles doped with metal phthalocyanines (MPc) were prepared by reducing Ag(I) ions with NaH_2PO_2 in the presence of SDS micelles (Scheme 1).

A solution of SDS (6.92 mmol) and NaH_2PO_2 (34.1 mmol) in H_2O (0.5 L) was left under agitation at

Received 9 September 2008. Published on the NRC Research Press Web site at canjchem.nrc.ca on 30 April 2009.

G. Palmisano. "Schiavello-Grillone" Photocatalysis Group, Dipartimento di Ingegneria Chimica dei Processi e dei Materiali, Università degli Studi di Palermo, viale delle Scienze, 90128 Palermo, Italy; Istituto per lo Studio dei Materiali Nanostrutturati, CNR, via Ugo La Malfa 153, 90146 Palermo, Italy.
V. Augugliaro. "Schiavello-Grillone" Photocatalysis Group, Dipartimento di Ingegneria Chimica dei Processi e dei Materiali, Università degli Studi di Palermo, viale delle Scienze, 90128 Palermo, Italy.
R. Ciriminna and M. Pagliaro.[1] Istituto per lo Studio dei Materiali Nanostrutturati, CNR, via Ugo La Malfa 153, 90146 Palermo, Italy.

[1]Corresponding author (e-mail: mario.pagliaro@ismn.cnr.it).

Scheme 1. Reaction scheme describing the synthesis of MORALs nanoparticles.

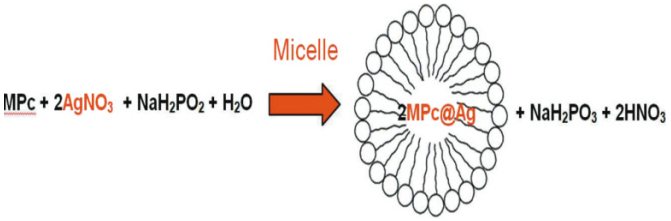

room temperature for 5 min, after which $AgNO_3$ (712 μmol) was added. Both doped and pure Ag samples were prepared. In the case of doped silver, 6.46 μmol CuPc or FePc were added to the starting solution, sonicating the reaction mixture (Bandelin Sonorex Digitec instrument) for 1 h to ensure complete solubility of the phthalocyanines. The solution thereby obtained was kept under slow agitation (300 rpm) for 4 days, after which it was centrifuged at 5 °C to separate the doped nanoparticles, which segregate from the micelles. The resulting silver MORAL particles were characterized by X-ray diffraction on Bruker D8 Advance instrument (40 kV, 35 mA, Cu Kα 1.542 Å). A Zeiss DSM-950 instrument operating at 80 kV was used for scanning electron microscopy images. Tablets of MORALs and pure silver powders were prepared applying uniaxial pressure (2.26 t/cm^2) and metallizing with gold before the analysis. Transmission electron microscopes JEOL mod. JEM-2000 FX and LEO 910 were employed for TEM analyses at 200 kV. Samples for TEM were prepared by sonicating a diluted suspension of MORAL in water (~10 mg MORAL in 1 L H_2O) for 10 min . A drop of this suspension was deposited on the Cu grid support used for analysis. Eventually, water was evaporated at 50 °C for 2 days. EDAX analyses were carried out with an energy dispersive X-ray analysis system connected to TEM. Thermogravimetric analysis (TGA) was performed on a SEIKO TG/ATD 320U, SSC 5200 (Seiko Instruments) from 25 to 900 °C at a heating rate of 10 °C/min in flowing dry air (100 mL/min). UV spectra were recorded on a UV–vis Shimadzu UV2401 spectrometer.

Results and discussion

Phosphite is a mild reducing agent, which does not react with the MPc (as shown in blank experiments). The SDS surfactant, in its turn, does not interfere with the efficiency of the molecular entrapment in the metal particles. The resulting nanoparticles of doped silver in the aqueous phase, in which the inorganic salts are dissolved, are thus readily sequestered in the hydrophobic core of the micelle as their formation takes place. Silver nanoparticles, indeed, are highly hydrophobic, and this property has been exploited, for example, in the synthesis of elegant nanostructures.[6]

The by-products together with SDS were easily washed off with EtOH and after a mild thermal treatment powders with the classical shine of silver (in the case of the undoped metal) or coloured in green (FePc@Ag) and blue (for the CuPc@Ag) were eventually isolated. No leaching was observed by keeping the metal–organic composite particles in contact with water or with common organic solvents, such as ethanol, acetone, and toluene, for prolonged time (as shown by the UV spectra of the filtered suspension, which showed no presence of organics even after 4 weeks). Ag nanocrystals slowly form and agglomerate within the structure of the SDS micelles. The crystallinity of silver is revealed by XRD diffractogram (Fig. 1) that showed the absence of silver oxides or salts.

Fig. 1. XRD spectrum of undoped silver.

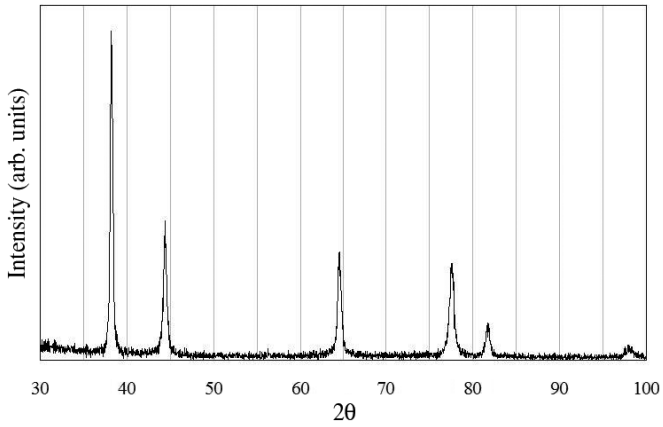

It may be noted that all the peaks are attributable to the metal. The presence of entrapped phthalocyanines does not influence the position and shape of typical lines in the diffractogram (2θ = 38.2°, 44.4°, 64.6°, 77.6°, 81.8°, 97.9°). Thus, similar patterns were obtained for both the doped and undoped metal. The primary particle size by the Scherrer's equation[7] applied to all the six peaks gave results ranging from 9 to 13 nm, with an average value of 11 nm, both for doped and undoped silver. The presence of smaller particle sizes, however, is evident from TEM images (Fig. 2), coupled with EDAX (Fig. 3), that show how MORALs nanoparticles ranging from ~30 nm down to fraction of nanometers are actually obtained by carrying out the synthesis in the presence of the micelle (the particles are not mono-disperse, as the synthesis protocol was not optimized for that purpose).

It is also worth noting that the principal Ag peak in the EDAX spectrum was present (at ~3 keV) even in the case of particles with dimensions less than 1 nm (Fig. 3*b*). Peaks of Cu, Si, and O atoms in the same spectra were all due to the support used for the analysis, whereas the signal of C can be ascribed to the organic moiety of Pc and partly to the support.

Moving observation at a larger scale, the morphology of the powders appeared to be the same for both doped MORALs and undoped silver (Fig. 4) with aggregates of hundreds of nanometers up to few micrometers being clearly visible in SEM images.

Successful encapsulation of phthalocyanines was verified by means of thermogravimetric analysis. Figure 5 indeed shows that, although the very close peaks for the free and encapsulated phthalocyanine point to the presence of the organic dopant inside the metal bulk, quite different thermal degradations occurred for CuPc@Ag and FePc@Ag.

Fig. 2. TEM images of CuPc@Ag (*a*) and FePc@Ag (*b*, *c*). Magnifications: (*a*) × 400 000, (*b*) and (*c*) × 300 000.

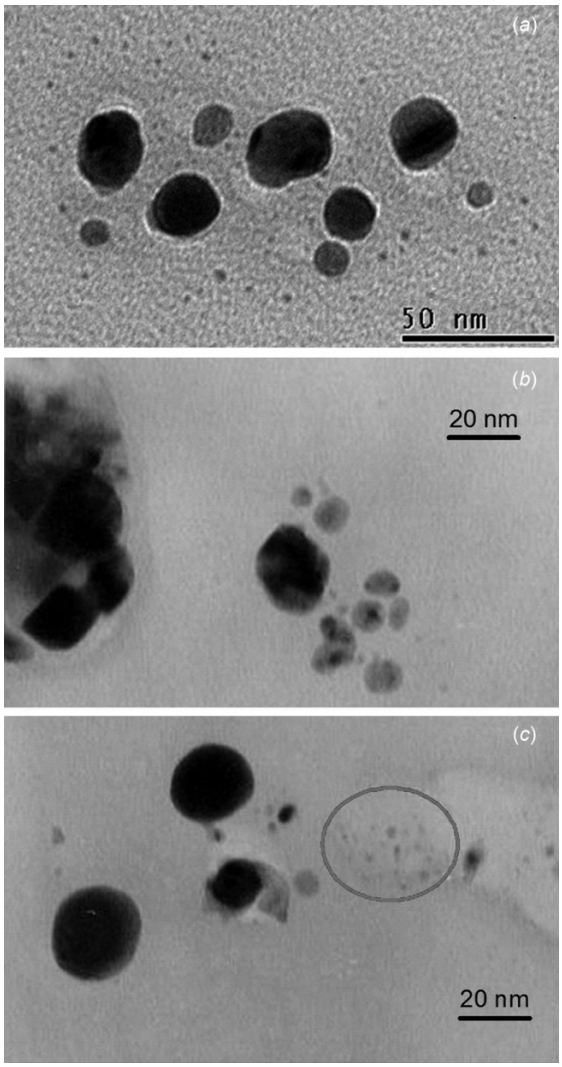

Fig. 3. EDAX spectra corresponding to images of (*a*) Fig. 2*a* and (*b*) circle in Fig. 2*c*.

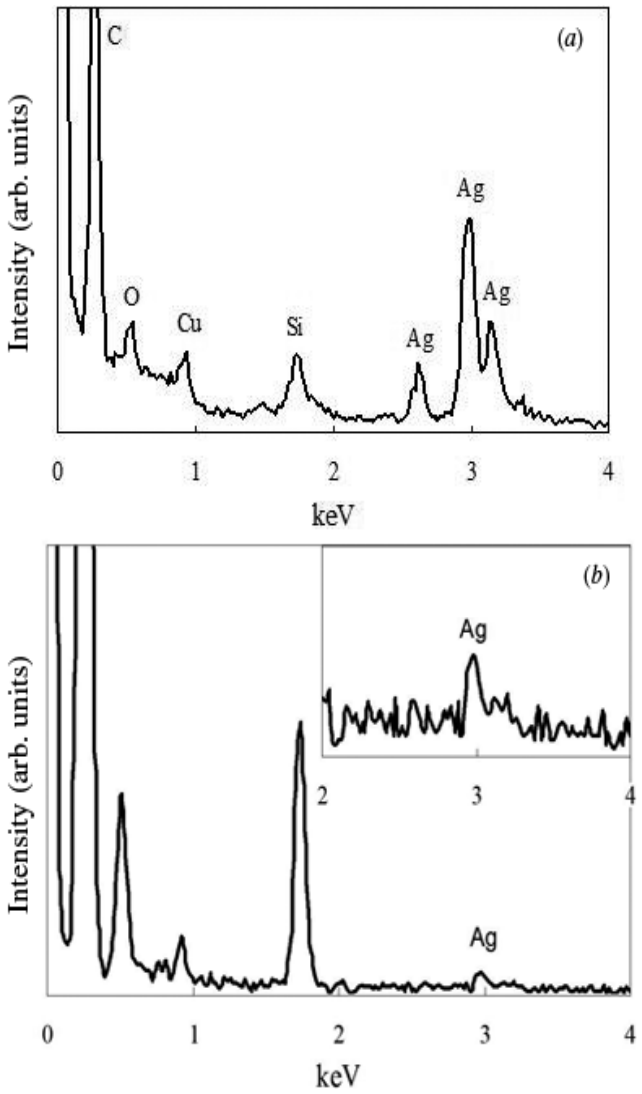

In fact, a clear degradation peak was obtained at 438 °C for the free phthalocyanine (Fig. 5*a*), whereas in the CuPc@Ag MORAL, concomitant narrowing of the decomposition temperature range and enhancement in thermal stability are noticed upon entrapment (ΔT = 24 °C between the degradation temperature of the free and encapsulated CuPc, Fig. 5*b*). The first effect may be due to the known catalytic action of Ag in thermal oxidative degradation processes,[5] as well as to being a clue to material's homogeneity; whereas the second effect is in accord with the behaviour previously observed for the polyacid Nafion entrapped in silver.[4]

Free FePc degrades between 320 °C and 410 °C (Fig. 5*c*) in a two-step process resulting in a main peak at 376 °C and a lower signal at 349 °C. On the other hand, in the case of FePc entrapped in silver, a broad peak is observed at 359 °C with degradation of the organic species occurring over a rather large temperature range in which the material apparently reacts with oxygen. Indeed, the increase in mass shown by the TGA profile of FePc@Ag after the decomposition points to oxygen fixation and shows how markedly the reactivity of the metal is changed upon its doping with the iron phthalocyanine.

The shown TGA analyses are in some ways similar to those previously reported of similar materials, and the lack of organics' stability with temperature can be ascribed to the catalytic effect of silver.[4]

Finally, the TGA data, along with observation of (*i*) complete segregation of the metallocomplexes from the starting solution and (*ii*) lack of leaching in most common solvents, indirectly prove that MPc are located into the metallic particle, namely incorporated into the regular periodic structure of Ag nanoparticle as MPc and not as metal ions (Cu and Fe) left after washing or loose adsorbed complexes at the surface. In the latter case, in fact, water easily washes away the adsorbed molecules, while the TGA spectra should point to inhomogeneous materials when, to the opposite, data in Fig. 5 clearly point to materials' homogeneity.

It is still an open question whether, in the case of Nano-MORALs, entrapment takes place inside or outside the

Fig. 4. SEM images of tablets made of CuPc@Ag (*a*) and undoped Ag (*b*). Magnifications and bars: (*a*) × 5000, 5 μm; (*b*) × 10 000, 2 μm.

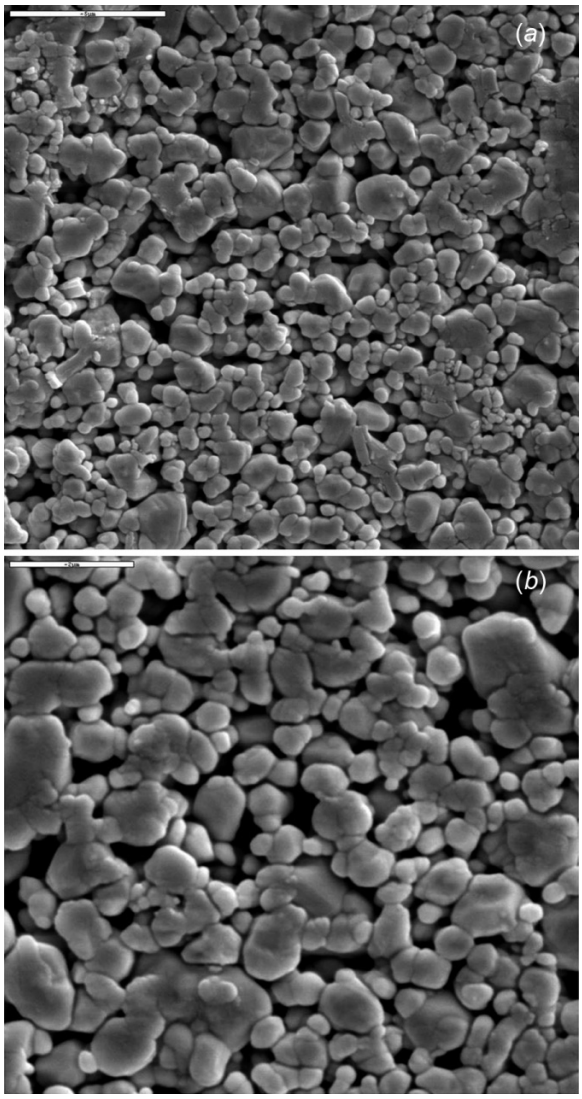

Fig. 5. TGA and DTA (in dry air) of CuPc (*a*), CuPc@Ag (*b*), FePc (*c*), and FePc@Ag (*d*).

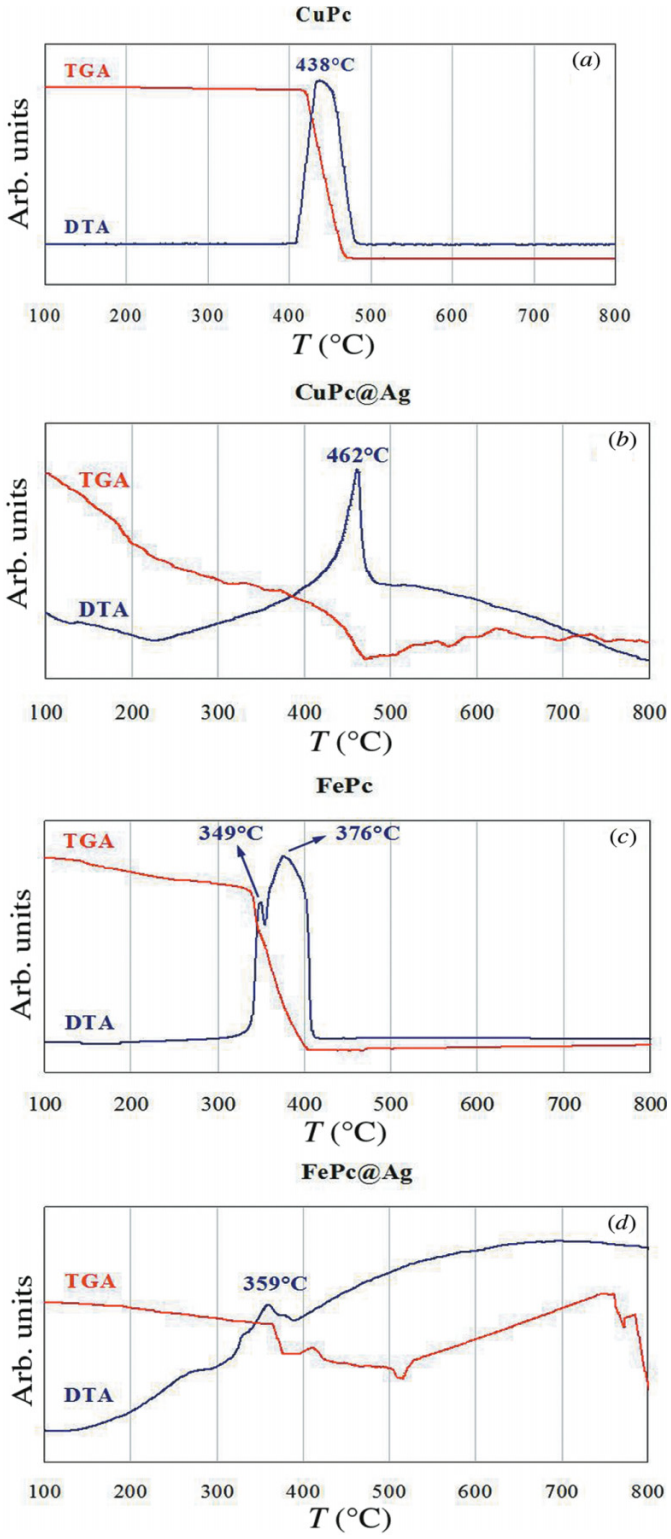

metal particle, making shells. Further structural studies on related materials are in course. In conclusion, we have developed the synthesis of nanosized metal–organic composites by employing a straightforward micelle-assisted synthesis. Silver nanoparticles[8] and metal phthalocyanines[9] have many functional applications, and soon these new nanomaterials might find practical use. From a fundamental viewpoint, however, the method described in this report is general and opens the route to the synthesis of a new class of metal–organic nanocomposites, termed NanoMORALs, whose forthcoming applications may indeed go beyond those, remarkable, being discovered in the case of the corresponding MORAL materials.

Acknowledgements

This work is dedicated to Loretta Napoleoni in memory of her splendid seminar on the "Rogue Economics" on the occasion of the 5th Seminar "Marcello Carapezza" (Bagheria, February 20, 2008). G. P. is grateful to a University of Palermo's grant enabling his stay at Madrid's Consejo Superior de Investigaciones Científicas (CSIC).

References

(1) Behar-Levy, H.; Avnir, D. *Chem. Mater.* **2002**, *14*, 1736. doi:10.1021/cm011558o.

(2) Behar-Levy, H.; Shter, G. E.; Grader, G. S.; Avnir, D. *Chem. Mater.* **2004**, *16*, 3197. doi:10.1021/cm049824w.

(3) Yosef, I.; Avnir, D. *Chem. Mater.* **2006**, *18*, 5890. doi:10.1021/cm0615368.

(4) Behar-Levy, H.; Avnir, D. *Adv. Funct. Mater.* **2005**, *15*, 1141. doi:10.1002/adfm.200400370.

(5) Shter, G. E.; Behar-Levy, H.; Gelman, V.; Grader, G. S.; Avnir, D. *Adv. Funct. Mater.* **2007**, *17*, 913. doi:10.1002/adfm.200600482.

(6) Pasricha, R.; Swami, A.; Sastry, M. *J. Phys. Chem. B* **2005**, *109*, 19620. doi:10.1021/jp0530552. PMID:16853537.

(7) We recall here that the particle size of silver nanoparticles calculated by XRD pattern is an average value, whereas the larger particles observed from TEM are only a fraction of the total.

(8) (a) Mafuné, F.; Kohno, J.; Takeda, Y.; Kondow, T.; Sawabe, H. *J. Phys. Chem. B* **2000**, *104*, 9111 doi:10.1021/jp001336y.; (b) Sun, J.; Ma, D.; Zhang, H.; Liu, X.; Han, X.; Bao, X.; Weinberg, G.; Pfänder, N.; Su, D. *J. Am. Chem. Soc.* **2006**, *128*, 15756 doi:10.1021/ja064884j. PMID:17147385.; (c) Sun, Y.; Xia, Y. *Science* **2002**, *298*, 2176. doi:10.1126/science.1077229. PMID:12481134.

(9) For an overview on phthalocyanines industrial applications, see: Gregory, P. *J. Porphyrins Phthalocyanines* **2000**, *4*, 432. doi:10.1002/(SICI)1099-1409(200006/07)4:4<432::AID-JPP254>3.0.CO;2-N.

On the reactivity of indium(III) benzenechalcogenolates (chalcogen = sulfur and selenium) towards organyl halides for the synthesis of organyl phenyl chalcogenides

Clovis Peppe and Liérson Borges de Castro

Abstract: The reactivity of indium(III) benzenechalcogenolates (chalcogen = sulfur, selenium) towards organyl halides (organyl = alkyl, allyl, benzyl, acyl) was examined. A practical one-pot method to prepare organyl phenyl chalcogenides from indium metal and diphenyl dichalcogenide was found. The coupling is fairly broad in scope and generally works better for organyl halides capable to produce stable carbocations.

Key words: diphenyl diselenide, diphenyl disulfide, indium(III) benzenechalcogenolates, organyl phenyl chalcogenides.

Résumé : On a étudié la réactivité des benzènechalcogénolates d'indium(III) (chalcogène = soufre, sélénium) vis-à-vis des halogénures d'organyles (organyle = alkyle, allyle, benzyle, acyle). On a mis au point une méthode monotope pratique de préparer des chalcogénures d'organyle et de phényle à partir de l'indium métallique et du dichalcogénure de diphényle. La portée de la réaction de couplage est assez large et elle fonctionne généralement mieux avec les halogénures d'organyle susceptibles de donner naissance à des carbocations stables.

Mots-clés : diséléniure de diphényle, disulfure de diphényle, benzènechalcogénolates d'indium(III), chalcogénures d'organyle et de phényle.

[Traduit par la Rédaction]

Introduction

Indium(III) arylchalcogenolates, $In(EAr)_3$ (E = S, Se), were prepared by methathetical reactions,[1,2] redox processes,[3,4] and electrochemically by sacrificing indium electrodes.[5] Heteroleptic compounds bearing a halide ligand, $XIn(EPh)_2$ (X = Cl, Br, I; E = S, Se), were prepared by the oxidative insertion of the corresponding indium monohalide into the dichalcogenides.[6] $In(SePh)_3$ was found polymeric by X-ray means, crystallizing in two polymorfic forms: a triclinic containing five-coordinated indium centers with asymmetrical bridging benzeneselenolate ligands[7] and a monoclinic containing six-coordinated indium atoms with symmetrical bridging benzeneselenolate ligands.[8] The sulfur analogue, $In(SPh)_3$, is also believed to be polymeric,[2] but its X-ray structure was not established until now. However, the sterically hindered arylthiolate complex $(2,4,6\text{-}t\text{-}Bu_3C_6H_2S)_3In$, soluble in organic solvents, was crystallized and had its distorted trigonal planar structure determined by X-ray methods.[9] A common property relating both the homoleptic $In(EPh)_3$ and the heteroleptic $XIn(EPh)_2$ compounds is that they act as Lewis acids, forming stable molecular adducts with several nitrogen,[1–3,6,8] phosphorus,[1,3,4] sulfoxide,[1] and halide[1,3] ligands.

Received 6 November 2008. Published on the NRC Research Press Web site at canjchem.nrc.ca on 1 May 2009.

C. Peppe[1] and L. Borges deCastro. Laboratório de Materiais Inorgânicos, Departamento de Quimica, Universidade Federal de Santa Maria, Santa Maria – RS 97105-900, Brazil.

[1]Corresponding author (e-mail: peppe@quimica.ufsm.br).

Indium(III) chalcogenolates contain indium–chalcogen bonds made of a hard In(III) cation[10] and a soft thiolate and (or) selenolate anions.[11,12] Hard acids – soft bases complexes possess intrinsic thermodynamic unstability, suggesting that the chalcogenolate anion could effectively be used as a nucleophile in organic reactions to produce new carbon–chalcogen bonds. Our group and other groups have introduced the heteroleptic $XIn(EPh)_2$ compounds as sources of the benzenechalcogenolate nucleophiles to produce organic chemicals of interest in reactions, such as ring opening of epoxides to β–hydroxyselenides[13] and sulfides,[14] ring opening of aziridines to selenocysteine and selenotreonine,[15] hydrochalcogenation of alkynes[16–18] to vinyl chalcogenides, also obtained through Pd(0)-catalyzed coupling of $IIn(SePh)_2$ with vinyl bromides[19], and finally for coupling with organyl halides to organyl phenyl chalcogenides.[20,21]

Recently, while trying to hydrochalcogenate aminoalkines with the heteroleptic compounds, $XIn(EPh)_2$, we observed ineffectiveness.[22] The task was accomplished with the indium(III) benzenechalcogenolate complexes, $In(EPh)_3$ (E = S, Se) generated by refluxing a 2:3 molar ratio of the metallic element and the corresponding diphenyl dichalcogenide in dichloroethane (DCE). The cleavage of the chalcogen–chalcogen bond by indium metal in mild conditions to the $In(EPh)_3$ compounds capable to deliver the benzenechalcogenolate nucleophiles is very attractive to the synthetic chemist because of the nontoxic nature and the stability of indium towards air and moisture. Furthermore, to replace the air-sensitive indium(I) halides to promote the cleavage of the chalcogen–chalcogen bonds is also desirable because it will allow to conduct one-pot

preparations directly from the stable metal. To gain a better understanding on the reactivity pattern of the $In(EPh)_3$ compounds generated by this method, we have examined their reactions with organyl halides (Scheme 1). We also compared the new results with the ones obtained using earlier similar procedures leading to PhER compounds involving the cleavage of the dichalcogenides by InI[20,21] and In metal.[23] A striking difference in reactivity, depending on the organyl halides, was observed; this was interpreted in terms of the polymeric nature of the $In(EPh)_3$ compounds and allowed to design experiments to the chemoselective production of a desired PhER compound.

Scheme 1. One-pot preparation of organyl phenyl chalcogenides.

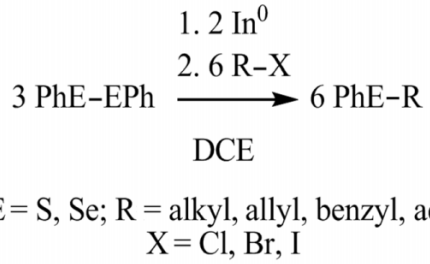

Results and discussion

The $In(EPh)_3$ (E = S, Se) compounds were easily prepared by refluxing 2:3 molar quantities of elemental indium and the dichalcogenide in DCE. Typically, the metal was consumed after 1–2 h, but sonication of a suspension of the metal in DCE for 10 min prior to heating accelerated the process. The selenium product remained in solution, while the sulfur analogue precipitated as a white powder. Addition of 3 equiv. of the organyl halides depicted in Table 1 afforded the corresponding organyl phenyl chalcogenides products with condensation of up to three benzenechalcogenolate ligands from the $In(EPh)_3$ reagents. The nucleophilic substitution is easily followed by TLC chromatography, and in the case of the sulfur complex, reaction completeness is verified just by observing the dissolution of the reagent in the reaction media; in most cases, optimum yields were obtained as soon as the white precipitate dissolved.

The reactivity trends of the organyl halides in condensations with the benzenechalcogenolate nucleophiles from the $IIn(EPh)_2$ (E = S, Se) compounds in dichloromethane was investigated by Ranu and co-workers, who demonstrated that primary, secondary, benzylic, and allylic chlorides, bromides, and iodides as well as acid chlorides readily participated in the reaction to form the desired organyl phenyl chalcogenides.[20,21] Jang and co-workers examined the problem through a one-pot reaction involving metallic indium, diphenyl diselenide, and organyl halides; in that work, they found that the reaction is initiated by organyl radicals generated by a one-electron reduction of the R–X substrate by metallic indium. Accordingly, a relative I > Br > Cl reactivity order was established for the organyl halides.[23]

There are remarkable differences in the reactivity of the $In(EPh)_3$ compounds towards organyl halides compared with the reagents discussed above. In the present work, we have verified that the nature of the organyl moiety of the halide controls the efficiency of the process. Tertiary, benzylic, allylic (leading exclusively to the α-coupling product), and acyl halides (Table 1, entries 22–39) instantaneously reacted with the $In(EPh)_3$ compounds at room temperature to produce good yields of the desired product. Reactions involving primary halides (Table 1, entries 1–17 and 40–42), on the other hand, took several hours for completion even with heating at 83 °C or completely resisted the transformation as observed for the chlorides (Table 1, entries 1 and 2). We further note that only the higher members of the series of bis(phenyl chalcogen)alkanes $PhE(CH_2)_nEPh$ (n = 1, 2, 3, 5, or 10) were efficiently obtained from the corresponding

Scheme 2. Proposed pathway for reaction of $In(EPh)_3$ and RX.

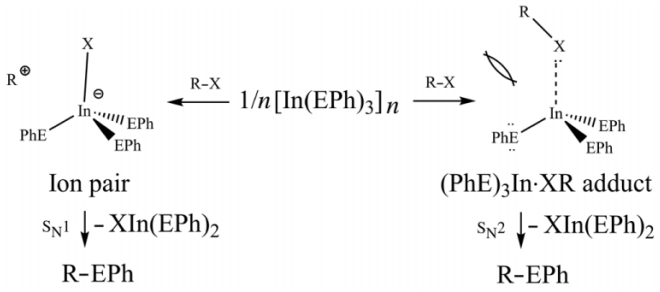

dibromo substrates (Table 1, entries 9–17). Secondary alkyl halides (Table 1, entries 18–21) failed to undergo efficient condensations, and surprisingly, from these reactions with $In(SePh)_3$ (Table 1, entries 19 and 21), we have isolated 1,4-bis(phenyl selanyl)butane, $PhSe(CH_2)_4SePh$ (0.83 mmol per 1 mmol of $In(SePh)_3$), fully characterized by elemental analysis, mass spectrometry, and ^1H and ^{13}C NMR spectroscopy; the actual course of the reaction leading to the butane derivative is still undetermined, but it is important to notice that we did not observe any direct reaction between $In(SePh)_3$ and the DCE solvent under these experimental conditions, except perhaps in these two cases for which it is reasonable to assume solvent participation in the process.

The experimental observations made above seem to indicate that the polymeric nature of the $In(EPh)_3$ compounds is an important aspect ruling their reactivity pattern towards organyl halides, and that allows one to understand the differences when compared with reactions involving the $IIn(EPh)_2$ compounds[20,21] and the proposed free-radical process initiated by metallic indium.[23] The polymeric nature involving bridging benzenechalcogenolate ligands together with the ability of the $In(EPh)_3$ complexes to act as Lewis acids strongly suggest that depolymerization to reactive monomeric intermediates is achieved by halide coordination to the indium centers replacing the bridging chalcogenolate ligands responsible for holding the polymeric structures. Thus, it is expected that organyl halides capable to produce stable tertiary, benzylic, allylic, and acyl carbocations would be the most reactive substrates and that these will react according to an S_N1 path, possibly through an ion-pair intermediate. The instantaneous reactions at room temperature involving these substrates together with the deep colouration, typical of carbocations, developed in the DCE solutions particularly in reactions with benzylic and allylic halides, are in agreement with this picture (Scheme 2). The enormous difference in reactivity presented by primary alkyl

Table 1. One-pot preparation of organyl phenyl chalcogenides.

Entry	R–X	E	*T* (°C)	Time	Yield (%)[a]	Reference
1	*n*-$C_6H_{13}Cl$	S	83	20 h	NR[b]	—
2	*n*-$C_6H_{13}Cl$	Se	83	20 h	NR	—
3	*n*-C_4H_9Br	S	83	20 h	65	24
4	*n*-C_4H_9Br	Se	83	12 h	54	25
5	*n*-C_4H_9I	S	83	20 h	56	24
6	*n*-C_4H_9I	Se	83	12 h	55	—
7	*n*-$C_8H_{17}Br$	S	83	20 h	83	26
8	*n*-$C_8H_{17}Br$	Se	83	6 h	78	27
9	$Br(CH_2)_{10}Br$	S	83	16 h	80	28
10	$Br(CH_2)_{10}Br$	Se	83	6 h	80	—
11	$Br(CH_2)_5Br$	S	83	20 h	52	29
12	$Br(CH_2)_5Br$	Se	83	6 h	57	30
13	$I(CH_2)_3I$	S	83	48 h	NR	—
14	$I(CH_2)_3I$	Se	83	18 h	60	31
15	$Br(CH_2)_2Br$	S	83	48 h	NR	—
16	$Br(CH_2)_2Br$	Se	83	48 h	NR	—
17	CH_2I_2	S	83	48 h	NR	—
18	$CH_3CH(Br)C_2H_5$	S	83	24 h	Traces	—
19	$CH_3CH(Br)C_2H_5$	Se	83	6 h	25[c]	27
20	$C_6H_{11}Br$[d]	S	83	20 h	Traces	—
21	$C_6H_{11}Br$[d]	Se	83	18 h	Traces[c]	—
22	$(CH_3)_3CBr$	S	25	3 min	44	20
23	$(CH_3)_3CBr$	Se	25	3 min	68	27
24	$PhCH_2Br$	S	25	3 min	90	26
25	$PhCH_2Br$	Se	25	3 min	87	27
26	$PhCH(CH_3)Br$	S	25	3 min	95	32
27	$PhCH(CH_3)Br$	Se	25	3 min	87	20
28	$H_2C{=}CHCH_2Br$	S	25	3 min	75	26
29	$H_2C{=}CHCH_2Br$	Se	25	3 min	80	33
30	(*Z*+*E*)-$CH_3HC{=}CHCH_2Br$	S	25	3 min	66	20
31	(*Z*+*E*)-$CH_3HC{=}CHCH_2Br$	Se	25	3 min	94	33
32	(*E*)-$PhHC{=}CHCH_2Br$	S	25	3 min	54	20
33	(*E*)-$PhHC{=}CHCH_2Br$	Se	25	3 min	48	20
34	$H_2C{=}C(CH_3)CH_2Br$	S	25	3 min	73	26
35	$H_2C{=}C(CH_3)CH_2Br$	Se	25	3 min	88	—
36	CH_3COCl	S	25	3 min	66	34
37	CH_3COCl	Se	25	3 min	62	20
38	PhCOCl	S	25	3 min	89	34
39	PhCOCl	Se	25	3 min	87	33
40	$C_2H_5OC(O)CH_2Br$	S	83	24 h	50	20
41	$C_2H_5OC(O)CH_2Br$	Se	83	24 h	80	20
42	$PhC(O)CH_2Br$	S	83	24 h	78	26

[a]Isolated yield of analytically pure product.
[b]NR = No reaction.
[c]Plus 0.83 mmol of $PhSeCH_2(CH_2)_2CH_2SePh$ per 1.00 mmol of indium.
[d]Cyclohexyl bromide.

halides, which only reacted after prolonged refluxing in DCE (83 °C), and the lack of reactivity of secondary alkyl halides suggest an alternative pathway. We propose for these cases that depolymerization to reactive monomeric intermediates is achieved by formation of $(PhE)_3In{\cdot}X{-}R$ adducts by coordination of the halogen atom of the organyl halide to the indium centers. This description accommodates well the failure of secondary alkyl halides to react efficiently due to stereo-hindrance during adduct formation (Scheme 2). Together with the product of the coupling between the first equivalent of the phenyl chalcogenolate nucleophile with the organyl halide leading to the first equivalent of the non-symmetric PhE–R chalcogenide, occurs the simultaneous production of the indium(III) heteroleptic product $XIn(EPh)_2$ used by Ranu and co-workers in their earlier work,[20,21] a compound responsible for formation of the two extra equivalents of the PhE–R final product. Considering these ideas, one can understand the higher reactivity of the $IIn(EPh)_2$ compared with the indium(III) benzenechalcogenolate reagents with primary and secondary alkyl halides in terms of the degree of polymerization of the $XIn(EPh)_2$ and the $In(EPh)_3$ reagents. Although $In(EPh)_3$ are polymeric, there

must not be significant association of the $XIn(EPh)_2$ compounds in solutions.

The milder reactivity of the $In(EPh)_3$, compared with the $XIn(EPh)_2$ reagents[20,21] and with the radical species generated from the in situ reaction involving indium metal and diphenyl diselenide,[23] suggests that the indium(III) benzenechalcogenolates can chemoselectively produce R–EPh (R = ^{t}alkyl, allyl, or benzyl) in the presence of primary or secondary alkyl halides. Accordingly, a competitive experiment involving $In(SePh)_3$ with 3 mol of allyl bromide and *n*-bromobutane produced C_3H_5–SePh exclusively with no signs of ^{n}Bu–SePh being detected.

Conclusion

The development of a one-pot efficient synthesis of organyl phenyl chalcogenides from alkyl halides and diphenyl dichalcogenides with the cleavage of the chalcogen–chalcogen bond performed by metallic indium is very attractive to the synthetic chemists because of the easy handling and accentuated stability of the metallic element towards moisture and air. We have interpreted this process as being intermediated by $[In(EPh)_3]_n$ polymers whose association must be broken to monomeric complexes by coordination and (or) interaction with the halide atom of the organyl halide. The degree of this coordination or interaction determines the reactivity of these reagents towards the organyl halide. Organyl halides, giving stable carbocations, react promptly following an S_N1-type reaction pathway leading to high yields of the nonsymmetrical chalcogenides, while primary alkyl halides require long periods of continuous heating, possibly following an S_N2-type process. The striking difference in reactivity, depending on the nature of the organyl halide, allows selective condensations as we have demonstrated with the experiment involving allyl bromide and bromobutane, which produced exclusively the allyl selenide.

Experimental

General

Indium powder and diphenyl disulfide were commercial products from Aldrich. Diphenyl diselenide was prepared from phenylmagnesium bromide and elemental selenium.[35] DCE was dried over CaH_2 and distilled before use. All the organyl halides were obtained from commercial suppliers and distilled, when necessary, before use. ^{1}H and ^{13}C NMR spectra were acquired on a Bruker DPX 200 and (or) Bruker DPX 400 spectrometers.

Preparation of organyl phenyl chalcogenides

To a Schlenk tube truly dried (flame) was sequentially added DCE (2 mL), diphenyl dichalcogenide (0.52 mmol), and indium powder (0.35 mmol). The mixture was sonicated for 10 min and then heated under reflux for 1–2 h. After all the metal being consumed, a yellow solution is obtained for the selenium derivative and a white precipitate for the sulfur case. At this point, the reaction was brought to room temperature, and the organyl halide (1 mmol) was added. The substrates corresponding to entries 22–39 (Table 1) were immediately (1–3 min) consumed as verified by TLC, while the remaining were consumed after heating for the periods specified in Table 1. The reactions were quenched with distilled water (10 mL), the organics extracted with dichloromethane (3 × 10 mL), the extracts were sequentially dried over sodium sulfate, evaporated to dryness (vaccum), and the organyl phenyl chalcogenides purified by column chromatography over silica gel using hexanes/ ethyl acetate mixtures. The sulfur derivatives are colourless oils or solids, while the selenium products are yellow compounds. All products are known compounds, and they were identified by comparison of their spectral data (^{1}H and ^{13}C NMR) with those reported in the literature (see Table 1 for references).

n-*Butyl phenyl sulfide (Table 1, entries 3 and 5)*

^{1}H NMR ($CDCl_3$) δ: 7.25–7.04 (m, 5H), 2.81 (t, *J* = 7.5 Hz, 2H), 1.53 (qui, *J* = 7.5 Hz, 2H), 1.34 (sex, *J* = 7.5 Hz, 2H), 0.81 (t, *J* = 7.5 Hz, 3H). ^{13}C NMR ($CDCl_3$) δ: 136.96, 128.70, 128.67, 125.48, 33.10, 31.11, 21.87, 13.57.

n-*Butyl phenyl selenide (Table 1, entries 4 and 6)*

^{1}H NMR ($CDCl_3$) δ: 7.42–7.38 (m, 2H), 7.18–7.10 (m, 3H), 2.83 (t, *J* = 7.6 Hz, 2H), 1.61 (qui, *J* = 7.6 Hz, 2H), 1.34 (sex, *J* = 7.6 Hz, 2 H), 0.82 (t, *J* = 7.3 Hz, 3H). ^{13}C NMR ($CDCl_3$) δ: 132.29, 130.66, 128.90, 126.50, 32.19, 27.55, 22.89, 13.50.

n-*Octyl phenyl sulfide (Table 1, entry 7)*

^{1}H NMR ($CDCl_3$) δ: 7.28–7.04 (m, 5H), 2.84 (t, *J* = 7.5 Hz, 2H), 1.58 (qui, *J* = 7.5 Hz, 2H), 1.32–1.16 (broad, 10H), 0.82 (t, *J* = 6.6 Hz, 3H). ^{13}C NMR ($CDCl_3$) δ: 137.04, 128.94, 128.68, 125.46, 33.44, 31.73, 29.10, 29.06, 28.78, 22.58, 14.03.

n-*Octyl phenyl selenide (Table 1, entry 8)*

^{1}H NMR ($CDCl_3$) δ: 7.44–7.39 (m, 2H), 7.20–7.12 (m, 3H), 2.84 (t, *J* = 7.3 Hz, 2H), 1.64 (qui, *J* = 7.3 Hz, 2H), 1.33–1.16 (broad, 10H), 0.82 (t, *J* = 6.6 Hz, 3H). ^{13}C NMR ($CDCl_3$) δ: 132.28, 130.70, 128.86, 126.46, 31.74, 30.09, 29.78, 29.11, 28.99, 27.87, 22.58, 14.03.

1,10-Bis(phenylthio)decane (Table 1, entry 9)

Mp 64–65 °C. ^{1}H NMR ($CDCl_3$) δ: 7.25–7.10 (m, 10H), 2.82 (t, *J* = 7.4 Hz, 4H), 1.56 (qui, *J* = 7.3 Hz, 4H), 1.36–1.15 (broad, 12H). ^{13}C NMR ($CDCl_3$) δ: 136.98, 128.97, 128.73, 125.53, 33.46, 33.28, 29.31, 29.04, 28.72.

1,10-Bis(phenyl selanyl)decane (Table 1, entry 10)

Mp 67–68 °C. ^{1}H NMR ($CDCl_3$) δ: 7.41–7.35 (m, 4H), 7.18–7.10 (m, 6H), 2.81 (t, *J* = 7.4 Hz, 4H), 1.60 (qui, *J* = 7.2 Hz, 4H), 1.32–1.14 (broad, 12H). ^{13}C NMR ($CDCl_3$) δ: 132.23, 130.63, 128.86, 126.46, 30.03, 29.70, 29.30, 28.94, 27.81.

1,5-Bis(phenylthio)pentane 7 (Table 1, entry 11)

^{1}H NMR ($CDCl_3$) δ: 7.24–7.06 (m, 10H), 2.80 (t, *J* = 6.9 Hz, 4H), 1.61–1.41(m, 6H). ^{13}C NMR ($CDCl_3$) δ: 136.62, 128.93, 128.77, 125.69, 33.33, 28.56, 27.78.

1,5-Bis(phenyl selanyl)pentane (Table 1, entry 12)

^{1}H NMR ($CDCl_3$) δ: 7.38–7.34 (m, 4H), 7.15–7.08 (m, 6H), 2.76 (t, *J* = 7.3 Hz, 4H), 1.58 (qui, *J* = 7.6 Hz, 4H), 1.40 (m, 2H). ^{13}C NMR ($CDCl_3$) δ: 132.34, 130.32, 128.86, 126.54, 29.72, 29.41, 27.49.

1,3-Bis(phenyl selanyl)propane (Table 1, entry 14)

^{1}H NMR ($CDCl_3$) δ: 7.38–7.34 (m, 4H), 7.16–7.11 (m, 6H), 2.89 (t, J = 7.3 Hz, 4H), 1.95 (qui, J = 7.3 Hz, 2H). ^{13}C NMR ($CDCl_3$) δ: 132.59, 129.81, 128.95, 126.77, 30.10, 27.34.

sec-*Butyl phenyl selenide (Table 1, entry 19)*

^{1}H NMR ($CDCl_3$) δ: 7.51–7.44 (m, 2H), 7.19–7.15 (m, 3H), 3.16 (sex, J = 6.8 Hz, 1H), 1.57 (m, 2H), 1.31 (d, J = 6.9 Hz, 3H), 0.92 (t, J = 7.3 Hz, 3H). ^{13}C NMR ($CDCl_3$) δ: 134.78, 129.12, 128.77, 127.18, 41.44, 30.37, 21.53, 12.25.

tert-*Butyl phenyl sulfide (Table 1, entry 22)*

^{1}H NMR ($CDCl_3$) δ: 7.48–7.41 (m, 2H), 7.28–7.19 (m, 3H), 1.22 (s, 9H). ^{13}C NMR ($CDCl_3$) δ: 137.47, 128.62, 128.41, 127.13, 45.82, 30.92.

tert-*Butyl phenyl selenide (Table 1, entry 23)*

^{1}H NMR ($CDCl_3$) δ: 7.59–7.53 (m, 2H), 7.29–7.17 (m, 3H), 1.33 (s, 9H). ^{13}C NMR ($CDCl_3$) δ: 138.11, 128.52, 128.36, 128.28, 43.00, 32.12.

Benzyl phenyl sulfide (Table 1, entry 24)

Mp 39–40 °C. ^{1}H NMR ($CDCl_3$) δ: 7.25–7.08 (m, 10H), 4.02 (s, 2H). ^{13}C NMR ($CDCl_3$) δ: 137.37, 136.32, 129.71, 128.76, 128.74, 128.41, 127.09, 126.24, 38.93.

Benzyl phenyl selenide (Table 1, entry 25)

Mp 32–33 °C. ^{1}H NMR ($CDCl_3$) δ: 7.35–7.31 (m, 2H), 7.14–7.05 (m, 8H), 3.98 (s, 2H). ^{13}C NMR ($CDCl_3$) δ: 138.48, 133.37, 130.33, 128.85, 128.72, 128.29, 127.14, 126.73, 32.07.

1-Phenylethyl phenyl sulfide (Table 1, entry 26)

^{1}H NMR ($CDCl_3$) δ: 7.29–7.15 (m, 10H), 4.32 (q, J = 7.0 Hz, 1H), 1.61 (d, J = 7.0 Hz, 3H). ^{13}C NMR ($CDCl_3$) δ: 143.14, 135.07, 132.40, 128.60, 128.31, 127.20, 127.05, 127.02, 47.91, 22.27.

1-Phenylethyl phenyl selenide (Table 1, entry 27)

^{1}H NMR ($CDCl_3$) δ: 7.44–7.38 (m, 2H), 7.23–7.12 (m, 8H), 4.42 (q, J = 7.0 Hz, 1H), 1.72 (d, J = 7.0 Hz, 3H). ^{13}C NMR ($CDCl_3$) δ: 143.48, 135.32, 129.76, 128.68, 128.19, 127.65, 127.12, 126.80, 42.33, 22.09.

Allyl phenyl sulfide (Table 1, entry 28)

^{1}H NMR ($CDCl_3$) δ: 7.27–7.07 (m, 5H), 5.79 (d of sex, J = 6.8 Hz, 3.0 Hz, 1H), 5.01 (m, 2H), 3.45 (d of t, J = 6.7 Hz, 0.9 Hz, 2H).

Allyl phenyl selenide (Table 1, entry 29)

^{1}H NMR ($CDCl_3$) δ: 7.51–7.46 (m, 2H), 7.28–7.20 (m, 3H), 5.94 (d of sex, J = 7.0 Hz, 2.3 Hz, 1H), 4.95 (m, 2H), 3.51 (d, J = 7.4 Hz, 2H). ^{13}C NMR ($CDCl_3$) δ: 134.35, 133.31, 129.15, 128.91, 127.10, 116.81, 30.65.

Crotyl phenyl sulfide, mixture of isomers, cis:trans = 1:4 (Table 1, entry 30)

^{1}H NMR ($CDCl_3$) δ: 7.26–7.04 (m, 5H), 5.53–5.39 (m, 2H), 3.48–3.44 (m, 1.6H), 3.22–3.18 (m, 0.4H), 1.59 (t, J = 4.8 Hz, 3H). ^{13}C NMR ($CDCl_3$) δ: 130.22, 129.55, 129.25, 129.05, 128.90, 128.70, 127.46, 127.13, 126.03, 126.03, 125.96, 125.92, 36.79, 36.34, 17.95, 17.73.

Crotyl phenyl selenide, mixture of isomers, cis:trans = 1:4 + traces of 3-benzenoselanyl-butene-1 (Table 1, entry 31)

^{1}H NMR ($CDCl_3$) δ: 7.52–7.41 (m, 2H), 7.24–7.20 (m, 3H), 5.67–5.31 (m, 2H), 3.55(d, J = 7.8 Hz, 0.4H), 3.48 (dd, J = 7.0 Hz, 1.1 Hz, 1.6H), 1.61 (dd, J = 6.0 Hz, 1.1 Hz, 2.4H), 1.47 (dd, J = 5.2 Hz, 1.3 Hz, 0.6H). ^{13}C NMR ($CDCl_3$) δ: 133.53, 133.15, 131.39, 130.31, 129.07, 128.76, 128.74, 128.22, 127.59, 127.00, 126.92, 126.88, 126.82, 126.01, 29.99, 24.29, 17.60, 12.27.

trans-*Cinnamyl phenyl sulfide (Table 1, entry 32)*

Mp 74–75 °C. ^{1}H NMR ($CDCl_3$) δ: 7.39–7.11 (m, 10H), 6.40 (d, J = 15.8 Hz, 1H), 6.21 (d of t, J = 15.8 Hz, 6.9 Hz, 1H), 3.67 (d, J = 6.9 Hz, 2H). ^{13}C NMR ($CDCl_3$) δ: 136.59, 135.36, 132.65, 130.05, 128.75, 128.42, 127.47, 126.27, 126.23, 124.91, 36.93.

trans-*Cinnamyl phenyl selenide (Table 1, entry 33)*

Mp 61–62 °C. ^{1}H NMR ($CDCl_3$) δ: 7.45–7.37 (m, 2H), 7.18–7.09 (m, 8H), 6.30–6.07 (m, 2H), 3.57 (d, J = 6.6 Hz, 2H). ^{13}C NMR ($CDCl_3$) δ: 136.72, 133.81, 131.97, 129.77, 128.87, 128.41, 127.34, 127.23, 126.17, 125.79, 30.63.

2-Methylallyl phenyl sulfide (Table 1, entry 34)

^{1}H NMR ($CDCl_3$) δ: 7.34–7.15 (m, 5H), 4.81 (dd, J = 0.7 Hz, 2H), 3.51 (s, 2H), 1.84 (d, J = 0.7 Hz, 3H). ^{13}C NMR ($CDCl_3$) δ: 140.75, 136.40, 129.92, 128.66, 126.13, 113.90, 41.85, 21.09.

2-Methylallyl phenyl selenide (Table 1, entry 35)

^{1}H NMR ($CDCl_3$) δ: 7.42–7.38 (m, 2H), 7.18–7.13 (m, 3H), 4.63 (m, 1H), 4.61 (m, 1H), 3.42 (d, J = 0.8 Hz, 2H), 1.77 (dd, J = 0.8 Hz, 0.5 Hz, 3H). ^{13}C NMR ($CDCl_3$) δ: 141.70, 133.42, 130.47, 128.80, 127.04, 113.38, 35.95, 21.26.

S-*Phenyl ethanethioate (Table 1, entry 36)*

^{1}H NMR ($CDCl_3$) δ: 7.31 (s, 5H), 2.30 (s, 3H). ^{13}C NMR ($CDCl_3$) δ: 193.76, 134.29, 129.26, 129.04, 127.83, 30.01.

Se-*Phenyl ethaneselenoate (Table 1, entry 37)*

^{1}H NMR ($CDCl_3$) δ: 7.44–7.40 (m, 2H), 7.29–7.25 (m, 3H), 2.34 (s, 3H). ^{13}C NMR ($CDCl_3$) δ: 196.55, 135.58, 129.24, 128.81, 126.54, 33.90.

S-*Phenyl benzothioate (Table 1, entry 38)*

^{1}H NMR ($CDCl_3$) δ: 8.06 (m, 2H), 7.64–7.46 (m, 8H). ^{13}C NMR ($CDCl_3$) δ: 190.07, 136.54, 135.04, 133.60, 129.47, 129.19, 128.69, 127.42, 127.26.

S-*Phenyl benzoselenoate (Table 1, entry 39)*

^{1}H NMR ($CDCl_3$) δ: 7.96 (m, 2H), 7.65–7.60 (m, 3H), 7.52–7.42 (m, 5H). ^{13}C NMR ($CDCl_3$) δ: 193.33, 138.44, 136.28, 133.84, 129.32, 129.02, 128.89, 127.28, 125.71.

Ethyl 2-(phenylthio)acetate (Table 1, entry 40)

^{1}H NMR ($CDCl_3$) δ: 7.43–7.18 (m, 5H), 4.16 (q, J = 7.2 Hz, 2H), 3.63 (s, 2H), 1.22 (t, J = 7.2 Hz, 3H). ^{13}C

NMR ($CDCl_3$) δ: 169.61, 134.94, 129.94, 128.93, 126.88, 61.45, 36.65, 14.00.

Ethyl 2-(phenylseleno)acetate (Table 1, entry 41)

^1H NMR ($CDCl_3$) δ: 7.59–7.55 (m, 2H), 7.30–7.23 (m, 3H), 4.10 (q, J = 7.2 Hz, 2H), 3.49 (s, 2H), 1.18 (t, J = 7.2 Hz, 3H). ^{13}C NMR ($CDCl_3$) δ: 170.65, 133.23, 129.05, 128.97, 127.63, 61.08, 27.39, 13.86.

2-(Phenylthio)acetophenone (Table 1, entry 42)

^1H NMR ($CDCl_3$) δ: 7.76 (m, 2H), 7.41–7.01 (m, 8H), 4.09 (s, 2H). ^{13}C NMR ($CDCl_3$) δ: 193.72, 135.01, 134.59, 133.18, 129.95, 128.77, 128.38, 128.35, 126.68, 40.80.

1,4-Bis(phenylselanyl)butane[30] (Table 1, entries 19 and 21)

^1H NMR ($CDCl_3$) δ: 7.37–7.34 (m, 4H), 7.16–7.10 (m, 6H), 2.77 (t, 4H), 1.70 (t, 4H). ^{13}C NMR ($CDCl_3$) δ: 132.43, 130.13, 128.87, 126.61, 29.95, 27.01. Calculated for $C_{16}H_{18}Se_2$ (%): C, 52.18; H, 4.93. Found (%): C, 52.23; H, 4.77. MS (70 eV, EI, for ^{80}Se) m/z (%): 369[4] [M –1], 210 (100), 157,[15] 155 (64), 77.[24]

Acknowledgements

We thank the Conselho Nacional de Desenvolvimento Científico e Tecnológico (CNPq) for operating grants (to C.P.) and for the award of a scholarship (to L.B.D.).

References

(1) Chadha, R. K.; Hayes, P. C.; Mabrouk, H. E.; Tuck, D. G. *Can. J. Chem.* **1987**, *65*, 804. doi:10.1139/v87-136.
(2) Suh, S.; Hoffman, D. M. *Inorg. Chem.* **1998**, *37*, 5823. doi:10.1021/ic980671m.
(3) Kumar, R.; Mabrouk, H. E.; Tuck, D. G. *J. Chem. Soc., Dalton Trans.* **1988**, 1045. doi:10.1039/dt9880001045.
(4) Briand, G. G.; Davidson, R. J.; Decken, A. *Inorg. Chem.* **2005**, *44*, 9914. doi:10.1021/ic051138r. PMID:16363862.
(5) Green, J. H.; Kumar, R.; Seudeal, N.; Tuck, D. G. *Inorg. Chem.* **1989**, *28*, 123. doi:10.1021/ic00300a028.
(6) Peppe, C.; Tuck, D. G. *Can. J. Chem.* **1984**, *62*, 2798. doi:10.1139/v84-474.
(7) Kuchta, M. C.; Rheingold, A. L.; Parkin, G. *N. J. Chem.* **1999**, *23*, 957. doi:10.1039/a905250j.
(8) Annan, T. A.; Kumar, R.; Mabrouk, H. E.; Tuck, D. G.; Chadha, R. K. *Polyhedron* **1989**, *8*, 865. doi:10.1016/S0277-5387(00)86436-0.
(9) Ruhlandt-Senge, K.; Power, P. P. *Inorg. Chem.* **1993**, *32*, 3478. doi:10.1021/ic00068a016.
(10) Harris, W. R.; Messori, L. *Coord. Chem. Rev.* **2002**, *228*, 237. doi:10.1016/S0010-8545(02)00037-1.
(11) Ho, T.-L. *Chem. Rev.* **1975**, *75*, 1. doi:10.1021/cr60293a001.
(12) Leverd, P. C.; Ephritikhine, M.; Lance, M.; Vigner, J.; Nierlich, M. *J. Organomet. Chem.* **1996**, *507*, 229. doi:10.1016/0022-328X(95)05773-I.
(13) Barros, O. S. D.; de Carvalho, A. B.; Lang, E. S.; Peppe, C. *Lett. Org. Chem.* **2004**, *1*, 43. doi:10.2174/1570178043488671.
(14) Ranu, B. C.; Mandal, T. *Can. J. Chem.* **2006**, *84*, 762. doi:10.1139/V06-065.
(15) Braga, A. L.; Schneider, P. H.; Paixão, M. W.; Deobald, A. M.; Peppe, C.; Bottega, D. P. *J. Org. Chem.* **2006**, *71*, 4305. doi:10.1021/jo060286b. PMID:16709076.
(16) Peppe, C.; Lang, E. S.; Ledesma, G. N.; de Castro, L. B.; Barros, O. S. D.; Mello, P. D. *Synlett* **2005**, 3091. doi:10.1055/s-2005-921931.
(17) For hydroselenation of alkynols with $IIn(SePh)_2$, see: Barros, O. S. D.; Lang, E. S.; de Oliveira, C. A. F.; Peppe, C.; Zeni, G. *Tetrahedron Lett.* **2002**, *43*, 7921. doi:10.1016/S0040-4039(02)01904-4.
(18) Barros, O. S. D.; Lang, E. S.; Peppe, C.; Zeni, G. *Synlett* **2003,** 1725. doi:10.1055/s-2003-41006.
(19) Ranu, B. C.; Chattopadhyay, K.; Banerjee, S. *J. Org. Chem.* **2006**, *71*, 423. doi:10.1021/jo052087i. PMID:16388676.
(20) Ranu, B. C.; Mandal, T. *J. Org. Chem.* **2004**, *69*, 5793. doi:10.1021/jo0493727. PMID:15307762.
(21) Ranu, B. C.; Mandal, T.; Samanta, S. *Org. Lett.* **2003**, *5*, 1439. doi:10.1021/ol034178c. PMID:12713293.
(22) Peppe, C.; de Castro, L. B.; Mello, M. D.; Barros, O. S. D. *Synlett* **2008**, 1165. doi:10.1055/s-2008-1072725.
(23) Munbunjong, W.; Lee, E. H.; Chavasiri, W.; Jang, D. O. *Tetrahedron Lett.* **2005**, *46*, 8769. doi:10.1016/j.tetlet.2005.10.025.
(24) Bates, C. G.; Gujadhur, R. K.; Venkataraman, D. *Org. Lett.* **2002**, *4*, 2803. doi:10.1021/ol0264105. PMID:12153239.
(25) Krief, A.; Dumont, W.; Gillin, F. *Arkivoc* **2007**, 51.
(26) Yoon, N. M.; Choi, J.; Ahn, J. H. *J. Org. Chem.* **1994**, *59*, 3490. doi:10.1021/jo00091a047.
(27) Cohen, R. J.; Fox, D. L.; Salvatore, R. N. *J. Org. Chem.* **2004**, *69*, 4265. doi:10.1021/jo0401265. PMID:15176857.
(28) Awaleh, M. O.; Badia, A.; Brisse, F.; Bu, X. H. *Inorg. Chem.* **2006**, *45*, 1560. doi:10.1021/ic051357c. PMID:16471967.
(29) Abou, A.; Foubelo, F.; Yus, M. *Arkivoc* **2007**, 196.
(30) Duddeck, H.; Wagner, P.; Rys, B. *Magn. Reson. Chem.* **1993**, *31*, 736. doi:10.1002/mrc.1260310809.
(31) Gulliver, D. J.; Hope, E. G.; Levason, W.; Murray, S. G.; Potter, D. M.; Marshall, G. L. *J. Chem. Soc., Perkin Trans.* **1984**, *2*, 429.
(32) Ranu, B. C.; Samanta, S.; Hajra, A. *Synlett* **2002**, 0987. doi:10.1055/s-2002-31911.
(33) Nishino, T.; Okada, M.; Kuroki, T.; Watanabe, T.; Nishiyama, Y.; Sonoda, N. *J. Org. Chem.* **2002**, *67*, 8696. doi:10.1021/jo026032h. PMID:12444664.
(34) Grieco, P. A.; Yokoyama, Y.; Williams, E. *J. Org. Chem.* **1978**, *43*, 1283. doi:10.1021/jo00400a070.
(35) Clive, D. L. J. *Tetrahedron* **1978**, *34*, 1049. doi:10.1016/0040-4020(78)80135-5.

Theoretical study on the scattering resonance state and isotope effect of the F + HD(H_2) → HF + D(H) reactive system

Hong Yue, Xi Lu, Zhengting Cai, and Xiaomin Sun

Abstract: The scattering resonance state of the F + H_2 reactive system has been the focus of the reactive resonance or Feshbach resonance, since the reaction can generate infrared laser. The partial potential-energy surface is constructed with the ab initio method, and the formation mechanism of the scattering resonance is studied. The resonance energy is given, and the first resonance life is estimated. The F + H_2 and F + HD reactive systems are investigated simultaneously to study the isotope effect, and some valuable results are achieved.

Key words: F + H_2 system, the partial potential-energy surface, isotope effect, scattering resonance state.

Résumé : Compte tenu du fait que la réaction associée à l'état de résonance de diffusion du système réactif F + H_2 peut générer un laser infrarouge, elle a fait l'objet d'attentions particulières de la résonance réactive et de la résonance de Feshbach. La surface d'énergie potentielle partielle a été construite à l'aide de méthodes théoriques ab initio et on a étudié le mécanisme de formation de la résonance de diffusion. On rapporte l'énergie de résonance et on a évalué la vie de la première résonance. On a étudié d'une façon simultanée les systèmes réactifs F + H_2 et F + HD afin d'évaluer l'effet isotopique et on a obtenu quelques résultats utiles.

Mots-clés : système F + H_2, surface d'énergie potentielle partielle, effet isotopique, état de résonance de diffusion.

[Traduit par la Rédaction]

Introduction

In 1970, Kuppermann[1] predicted the existence of the scattering resonance phenomenon in elementary chemical reactions based on the calculation of quantum-scattering theory. The reactive resonance, or Feshbach resonance, is one of the most fascinating phenomena in chemical reaction dynamics.[2] The term "resonance state" in this context refers to a metastable or quasi-bound state, also called scattering resonance state. The scattering resonance state of the F + H_2 reactive system has been the focus of study. As an important infrared pump source, more attention has been paid to it.

Schatz and Kuppermann[3] calculated the reaction probability of the F + H_2 → HF + H system on the semi-experience potential-energy surface, discovered the oscillation behaviour of reaction probability with the collision energy, and predicted the scattering resonance state in the chemical reaction, which promoted the cross-beam molecular detection of the reactive resonance of the F + H_2 system. Using the crossed-beam scattering experiment, Lee[4] measured the curve of the differential cross section with the collision energy, $\sigma(E, \theta) \sim E$, and verified the prediction of Schatz and Kuppermann. However, after the average of scattering angle θ, the peak on the curve of integral cross section with collision energy (also known as excitation function) $\sigma(E) \sim E$ is no longer apparent. Therefore, it has been a controversial issue whether the resonance phenomenon exists in chemical reaction or not. Liu[5] measured the curve of $\sigma(E) \sim E$ using the crossed molecular-beam experiment in his study of the F + HD → HF + D (H + DF) reaction in 2000. Yang and Zhang[6,7] observed the Feshbach resonance in the F + H_2 → HF + H reaction. Both studies confirmed the existence of the resonance. This discovery is of great importance in both the academic field and the application area. Schatz[8] and Zare[9] ever highly praised it as an important advance in the field of chemical reaction dynamics and called for more theoretical and experimental chemists to study the scattering resonance state. However, the formation mechanism of the resonance state and the lifetime of the resonance state have been rarely investigated.

The partial potential-energy surface (PPES) is constructed with the ab initio method. Then, the formation mechanism of scattering resonance state is discussed using the PPES, which can also provide many important dynamic quantities, such as the resonance energy, the lifetime of resonance, and so on. The vibrational dynamic behaviour in the strong interaction region can be shown clearly on the PPES. The results obtained using the PPES are in good agreement with previous theoretical and experimental work.

Received 11 December 2008. Accepted 6 March 2009. Published on the NRC Research Press Web site at canjchem.nrc.ca on 1 May 2009.

H. Yue, X. Lu, and Z. Cai. Institute of Theoretical Chemistry, Shandong University, Jinan 250100, P.R. China.
X. Sun.[1] Environment Research Institute, Shandong University, Jinan 250100, P.R. China.

[1]Corresponding author (e-mail: sxmwch@sdu.edu.cn).

Fig. 1. The PPES of the F + HD → HF + D reaction system.

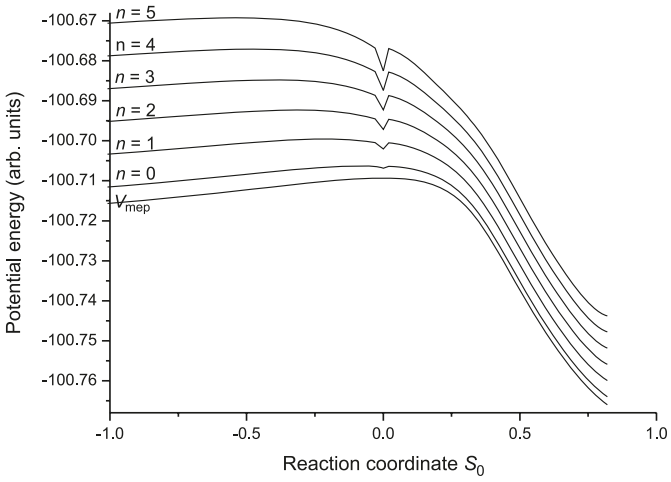

Fig. 2. The PPES of the F + H_2 → HF + H reaction system.

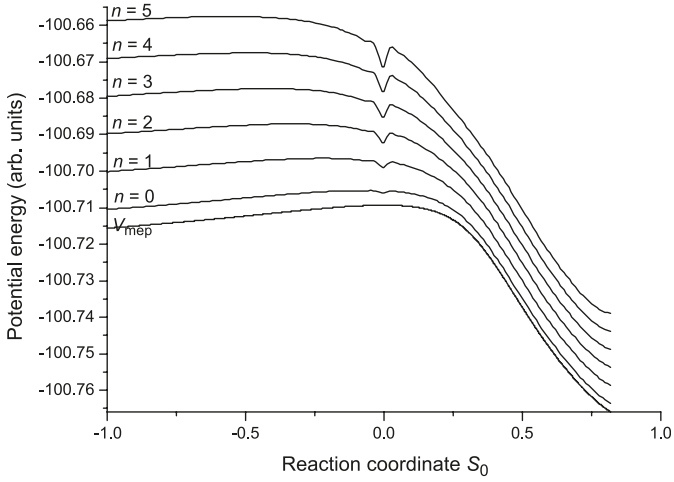

In this paper, the F + H_2[10] and F + HD reactive systems are investigated simultaneously, and the isotope effect is discussed. Some valuable results are achieved.

The theoretical method

For the sake of convenience, the construction of the partial potential-energy surface is briefly introduced as follows. According to the literature,[11] the scattering equation in the natural collision coordinate of the A + BC → AB + C exchange reaction can be written as

$$[1] \qquad \widehat{H}\psi(s,\rho) = E\psi(s,\rho)$$

and Hamiltonian operator is as follows:

$$[2] \qquad \widehat{H} = -\left(\frac{\hbar^2}{2\mu}\eta^{-1}\frac{\partial}{\partial s}\eta^{-1}\frac{\partial}{\partial s}\right) - \left(\sum_{i=1}^{f}\frac{\hbar^2}{2\mu}\eta\frac{\partial}{\partial \rho_{\mathrm{i}}}\eta^{-1}\frac{\partial}{\partial \rho_{\mathrm{i}}}\right) + V(s,\rho)$$

Full-dimensional potential-energy surface $V(s, \rho)$ is expanded by Taylor series expansion

$$[3] \qquad V(s,\rho) = V_{\mathrm{o}}(s) + \sum_{n=2}\sum_{i=1}\left(\frac{1}{n!}\frac{\partial^n V(s,\rho)}{\partial \rho_i^n}|\rho = 0\right)\rho_i^n$$

where s is the reaction coordinate, $\rho = \rho_1, \rho_2, \ldots, \rho_f$ is the normal vibration coordinates, and f is the freedom degree of the normal vibration. The whole wave function of the reaction system can be spread as follows:

$$[4] \qquad \psi(s,\rho) = \sum_{n_1,\, n_2,\, \ldots,\, n_f} \xi_{n_1,\, n_2,\, \ldots,\, n_f}(s)\ \varphi_{n_1,\, n_2,\, \ldots,\, n_f}(s,\rho)$$

where $\xi_{n_1,\, n_2,\, \ldots,\, n_f}(s)$ is the translation wave function. $\varphi_{n_1,\, n_2,\, \ldots,\, n_f}(s,\rho)$ is the orthogonal normalized complete set, and given by the solutions of the following equation:

$$[5] \qquad \left[-\sum\frac{\hbar^2}{2\mu}\eta\frac{\partial}{\partial \rho_i}\eta^{-1}\frac{\partial}{\partial \rho_i} + V(s,\rho)\right]\varphi_{n_1,\, n_2,\, \ldots,\, n_f}(s,\rho) = \varepsilon_{n_1,\, n_2,\, \ldots,\, n_f}(s)\varphi_{n_1,\, n_2,\, \ldots,\, n_f}(s,\rho)$$

The $\varepsilon_{n_1,\, n_2,\, \ldots,\, n_f}(s)$ can be called as the PPES. First, $V(s, \rho)$ is full-dimensional potential function, while $\varepsilon_{n_1,\, n_2,\, \ldots,\, n_f}(s)$ is only a function of reaction coordinate s. Second, $\varepsilon_{n_1,\, n_2,\, \ldots,\, n_f}(s)$ provides a potential field for the translation of the scattering system. The latter can be seen clearly from the following derivation.

Equation [4] is substituted into the eq. [1], left-multiplied by $\varphi^*_{n_1',\, n_2',\, \ldots,\, n_f'}(s,\rho)$, integrated to ρ, and then associated with eq. [5], the Schrödinger eq. [6] can be obtained which is satisfied by $\varepsilon_{n_1,\, n_2,\, \ldots,\, n_f}(s)$.

$$[6] \qquad \left[\left(-\frac{\hbar^2}{2\mu}\eta^{-1}\frac{\partial}{\partial s}\eta^{-1}\frac{\partial}{\partial s}\right) + \varepsilon_{n_1,\, n_2,\, \ldots,\, n_f}(s) - E\right]\xi_{n_1,\, n_2,\, \ldots,\, n_f}(s) = \sum_{n_1',\, n_2',\, \ldots,\, n_f'} G_{n_1',\, n_2',\, \ldots,\, n_f';\, n_1,\, n_2,\, \ldots,\, n_f}(s)\xi_{n_1',\, n_2',\, \ldots,\, n_f'}(s)$$

Fig. 3. The structure of the transition state of the F + HD(H_2) → HF + H(D) reaction system.

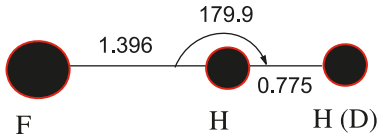

In the equation, $G_{n'_1, n'_2, ..., n'_f; n_1, n_2, ..., n_f}(s)$ is the non-adiabatic coupling mode of vibration, and can be presented by the following equation:

$$[7] \quad G_{n'_1, n'_2, ..., n'_f; n_1, n_2, ..., n_f}(s) = \left\langle \varphi_{n'_1, n'_2, ..., n'_f}(s,\rho) \left| -\frac{\hbar^2}{2\mu}\eta^{-1}\frac{\partial}{\partial s}\eta^{-1}\frac{\partial}{\partial s} \right| \varphi_{n_1, n_2, ..., n_f}(s,\rho) \right\rangle_\rho$$

When there is only one degree of freedom of vibration (for example, the exchange reaction of three atoms in line) and Taylor equation spreads for two grade (i.e., harmonic oscillator model), eq. [8] can be obtained.

$$[8] \quad \varepsilon_n(s) = V_o(s) + (n + \frac{1}{2})\hbar\omega(s)$$

and

$$[9] \quad \omega^2(s) = \frac{1}{\mu}\left[\frac{\partial^2 V(s,\rho)}{\partial\rho^2}\right]_{\rho=0}$$

Obviously, $\omega(s)$ can be calculated according to the Hessian matrix, and can be used to calculate the potential-energy surface. In the PPES, $V_{mep}(s)$ is the so-called minimum-energy reaction pathway (MEP). It is worth emphasizing that the construction of the PPES need not build full-dimensional potential-energy surface $V(s, \vec{\rho})$, but could solve the vibration equation of scattering system to get the potential-energy surface and obtain the basis set of the spreading of $\psi(s, \vec{\rho})$.

In this paper, we optimize the structure of the transition state of the F + H_2 → HF + H using MP2 method with the 6–311++G** basis set. The PPESs of the F + HD and F + H_2 systems (Figs. 1 and 2) are constructed using the above methods, which have been applied to some typical heavy-light-heavy systems.[12–19] The transient collision complex state structures of the two systems are shown in Fig. 3.

Results and discussions

According to the curves on the PPES (Figs. 1 and 2), it can be seen that the curves of V_{mep} have no shallow well, which is difficult to satisfy the existence of the scattering resonance state. However, if $n \geq 1$, the well will appear obviously in the neighbourhood of $s = 0$ (the strong interaction region on the PPES or transition region), which is called dynamic shallow well[20] in the literature. The existence of reactive resonance can be conceptually traced back to dynamic trapping in wells on the vibrationally adiabatic PES, even when there is no potential well on the Born–Oppenheimer PES. It is the dynamic shallow well that traps the reactive system to form the so-called quasi-bound or scattering resonance state, which means the formation of resonance state.

From Figs. 1 and 2, the first resonance energy of the two reactions is 43.82 kJ/mol and 50.13 kJ/mol, respectively. Evidently, the resonance energy is reduced comparing the F + HD → HF + D reaction with the F + H_2 → HF + H reaction.

Comparing Fig. 1 with Fig. 2, the potential well in F + HD → HF + D reaction is a little deeper than that of the F + H_2 → HF + H reaction. Therefore, the former scattering resonance state has longer lifetime than that of the latter.

The geometry structure of transition collision complex is drawn in Fig. 3. According to the Born–Oppenheimer approximation, adopting different isotopes has no impact on the optimization of the geometric and the calculation of the electronic structure of the transient collision complex. Therefore, the transition collision complex structures of two reactions are identical. The calculation of the frequency of the constant matrix (Hessian matrix) is unchanged, but reduced mass changes, so the frequencies in the two reactions are different form each other. The frequencies of the two reactions, F + HD → HF + D and F + H_2 → HF + H, are 1120.37(i), 135.50, 2640.61; 1231.96(i), 146.42, and 3316.32.

According to the uncertainty principle $\Delta E\ \Delta\tau \sim \hbar$, the lifetime of the first reactive resonance state of the F + HD → HF + D reaction is about 21 *fs*, which is very close to Neumark's result[10] obtained from the high-resolution threshold photo detachment spectroscopy, 19 *fs*. ΔE is the first resonance energy. Compared with the experimental result, the relative error is only 10%. As for the F + H_2 system, the first scattering resonance state lifetime is 14 *fs*. It is obvious that the lifetime of the first scattering resonance state of the F + HD system is longer than that of the F + H_2 system. After D atom replaces H atom, it is reasonable that the reduced mass of the system increases, and the force constant of the symmetrical stretching vibration decreases. The force constant of the symmetrical stretching vibration in F + HD system and F + H_2 system is 0.9857 and 1.0279, respectively. Then, the vibration frequency decreases, which results in the decrease of the resonance energy and the increase of the resonance lifetime.

Conclusions

There is no potential wells on the minimum-energy reaction pathway (V_{mep}) of the F + H_2 and F + HD reactions, but the dynamical wells exist near the transition-state region of PPES. It is the dynamical wells that trap the system to form the scattering resonance state. After D replaces H, the reduced mass of the system becomes a little larger, the resonance energy decreases, and the resonance lifetime increases. There is also slight difference in the location of dynamical well. It can be seen that the isotope effect is obvious.

It is convenient to study the resonance energy, the resonance lifetime, and the isotope effect using the partial potential-energy surface.

Acknowledgement

This work is supported by National Natural Science Foundation of China (No. 20873074 and No. 20603030), 973 project of the Ministry of Science and Technology of China (No. 2009CB930103), and Natural Science Foundation of Shandong Province (No. Q2008B07).

References

(1) Kuppermann, A. Potential energy surface and dynamics calculations. *Edited by* D.G. Truhlar. Plenum Publishing Corp. Vol. 375. 1981.

(2) Shiu, W.; Lin, J. J.; Liu, K. *Phys. Rev. Lett.* **2004**, *92*, 103201. doi:10.1103/PhysRevLett.92.103201. PMID:15089205.

(3) Schatz, G. C.; Kuppermann, A. *J. Chem. Phys.* **1973**, *59*, 964. doi:10.1063/1.1680122.

(4) Lee, Y. T.; Shen, Y. R. *Phys. Today* **1980**, *33*, 52.

(5) Skodje, R. T.; Skouteris, D.; Manolopoulos, D. E.; Lee, S. H.; Dong, F.; Liu, K. *J. Chem. Phys.* **2000**, *112*, 4536. doi:10.1063/1.481041.

(6) Qiu, M.; Ren, Z.; Che, L.; Dai, D.; Harich, S. A.; Wang, X.; Yang, X.; Xu, C.; Xie, D.; Gustafsson, M.; Skodje, R. T.; Sun, Z.; Zhang, D. H. *Science* **2006**, *311*, 1440. doi:10.1126/science.1123452.

(7) Zhang, D. H.; Xie, D.; Yang, M.; Lee, S. Y. *Phys. Rev. Lett.* **2002**, *89*, 283203. doi:10.1103/PhysRevLett.89.283203. PMID:12513143.

(8) Schatz, G. C. *Science* **2000**, *288*, 1599. doi:10.1126/science.288.5471.1599.

(9) Zare, R. N. *Science* **2006**, *311*, 1383. doi:10.1126/science.1124421. PMID:16527958.

(10) Hayes, M.; Gustafsson, M.; Mebel, A. M.; Skodje, R. T. *Chem. Phys.* **2005**, *308*, 259. doi:10.1016/j.chemphys.2004.05.028.

(11) Wang, Q.; Cai, Z. T.; Feng, D. C. *J. Mol. Struct. (Theochem.)* **2006**, *759*, 31. doi:10.1016/j.theochem.2005.11.009.

(12) Sun, X. M.; Wang, H. Y.; Cai, Z. T.; Feng, D. C. *Acta Chimi. Sin.* **2005**, *5*, 372.

(13) Sun, X. M.; Wang, H. Y.; Cai, Z. T.; Feng, D. C.; Bian, W. S. *Chem. Res. Chin. Univ.* **2005**, *21*, 569.

(14) Wang, H. Y.; Sun, X. M.; Cai, Z. T.; Feng, D. C. *J. Theor. Comp. Chem.* **2006**, *5*, 307. doi:10.1142/S0219633606002271.

(15) Wang, H. Y.; Sun, X. M.; Cai, Z. T.; Feng, D. C. *Chin. J. Chem. Phys.* **2006**, *19*, 411.

(16) Sun, X. M.; Wang, H. Y.; Cai, Z. T.; Feng, D. C. *J. Theor. Comput. Chem.* **2004**, *3*, 543. doi:10.1142/S0219633604001197.

(17) Wang, H.; Lu, X.; Sun, X.; Cai, Z.; Feng, D. *Chem. Phys. Lett.* **2007**, *443*, 369. doi:10.1016/j.cplett.2007.06.005.

(18) Lu, X.; Wang, H.; Cai, Z.; Feng, D. *J. Theor. Comp. Chem.* **2007**, *6*, 575. doi:10.1142/S0219633607003234.

(19) Lu, X.; Wang, H.; Cai, Z.; Feng, D. *Int. J. Quantum Chem.* **2008**, *108*, 334. doi:10.1002/qua.21505.

(20) Ma, W. Y.; Cai, Z. T.; Feng, D. C. *Chem. Phys. Lett.* **1999**, *304*, 121. doi:10.1016/S0009-2614(99)00274-2.

Oxyhalogen–sulfur chemistry — Kinetics and mechanism of oxidation of methionine by aqueous iodine and acidified iodate

Edward Chikwana, Bradley Davis, Moshood K. Morakinyo, and Reuben H. Simoyi

Abstract: The oxidation of methionine (Met) by acidic iodate and aqueous iodine was studied. Though the reaction is a simple two-electron oxidation to give methionine sulfoxide (Met–S=O), the dynamics of the reaction are, however, very complex, characterized by clock reaction characteristics and transient formation of iodine. In excess methionine conditions, the stoichiometry of the reaction was deduced to be $IO_3^- + 3Met \rightarrow I^- + 3Met–S=O$. In excess iodate, the iodide product reacts with iodate to give a final product of molecular iodine and a 2:5 stoichiometry: $2IO_3^- + 5Met + 2H^+ \rightarrow I_2 + 5Met–S=O + H_2O$. The direct reaction of iodine and methionine is slow and mildly autoinhibitory, which explains the transient formation of iodine, even in conditions of excess methionine in which iodine is not a final product. The whole reaction scheme could be simulated by a simple network of 11 reactions.

Key words: methionine, organosulfur, iodine, antioxidant, nonlinear dynamics, methionine sulfoxide.

Résumé : On a étudié la réaction d'oxydation de la méthionine (Met) par l'ion iodate, en milieu acide et en présence d'iode aqueux. Même si la réaction d'une simple oxydation à deux électrons pour conduire au sulfoxyde de méthionine (Met–S=O), la dynamique de la réaction est toutefois fort complexe ayant les caractéristiques d'une réaction horloge et comportant la formation transitoire d'iode. Dans des conditions où la méthionine est en excès, on a déduit que la stoechiométrie de la réaction est $IO_3^- + 3Met \rightarrow I^- + 3Met–S=O$. Dans des conditions où l'iodate est en excès, l'iodure produit réagit avec l'iodate pour donner de l'iode moléculaire comme produit final avec une stoechiométrie 2:5: $2IO_3^- + 5Met + 2H^+ \rightarrow I_2 + 5Met–S=O + H_2O$. La réaction directe de l'iode avec la méthionine est très lente et donne lieu à une légère autoinhibition qui explique la formation transitoire d'iode, même dans des conditions d'excès de méthionine dans lesquelles l'iode n'est pas un produit final. L'ensemble des réactions peut être simulé par un réseau simple de onze réactions.

Mots-clés : méthionine, organosulfuré, iode, antioxydant, dynamique non linéaire, sulfoxyde de méthionine.

[Traduit par la Rédaction]

Introduction

Methionine is an essential amino acid, obtained only from dietary sources and found mainly in animal protein. In addition to its role as a precursor in protein synthesis, L-methionine participates in a wide range of biochemical reactions, including the production of *S*-adenosyl methionine, homocysteine, L-cysteine, taurine, and sulfate. It is believed to be the major methyl donor for methylation of DNA, RNA, proteins, and other molecules.[1,2] Methionine is also thought to keep fat from building up in the liver, and it is often included in liver-detoxifying products called lipotropic combinations.[3] These formulations are believed to accelerate the flow of bile and cell-damaging toxins away from the liver.

Depletion of methionine is strongly linked to inhibited growth, apoptotic death, and necrosis of cancerous cells, especially in combination with chemotherapy.[4] On the other hand, high levels of methionine in the physiological system are associated with several metabolic disorders such as homocystinuria, which is characterized by increased levels of homocysteine in the serum.[5] Homocystine is one of the products of methionine metabolism and its accumulation has been linked to atherosclerosis and arteriosclerosis.[1,5] Atherosclerosis is characterized by the development of lesions within and around blood vessels.[5,6] While atherosclerosis provides the plaque that narrows the artery, arteriosclerosis stiffens the arteries so that they cannot expand with each heart beat to compensate for the blockage caused by plaque formation.[6,7] In most cases of myocardial infarction, both atherosclerosis and arteriosclerosis have been shown to be present.

It has been proposed that methionine residues in proteins serve as an antioxidant defense system for the protection of proteins from oxidation under conditions of oxidative stress.[8,9] Various biological oxidants, such as hydrogen peroxide, hydroxyl radicals, ozone, peroxynitrite, and hypochlorite, have been shown to mediate the oxidation of methionine.[9,10] Methionine has been shown to be effective in radical scavenging processes, such as those involving reactive nitrogen species, to form methionine sulfoxide and ethylene.[9] In the physiological environment, oxidation of methionine residues to methionine sulfoxide is easily re-

Received 24 October 2008. Accepted 24 December 2008. Published on the NRC Research Press Web site at canjchem.nrc.ca on 7 May 2009.

E. Chikwana,[1] B. Davis, M.K. Morakinyo, and R.H. Simoyi.[2] Department of Chemistry, Portland State University, Portland, OR 97207-0751, USA.

[1]Present address: Department of Chemistry, Franklin College, Franklin, IN 46131-2623, USA.
[2]Corresponding author (e-mail: rsimoyi@pdx.edu).

Fig. 1. Titration results for the oxidation of methionine in excess iodate conditions. The *x*-intercept strongly suggest a 1:3 (iodate:methionine) stoichiometric ratio. $[Met]_0 = 3.0 \times 10^{-3}$ mol/L, $[H^+]_0 = 6 \times 10^{-3}$ mol/L.

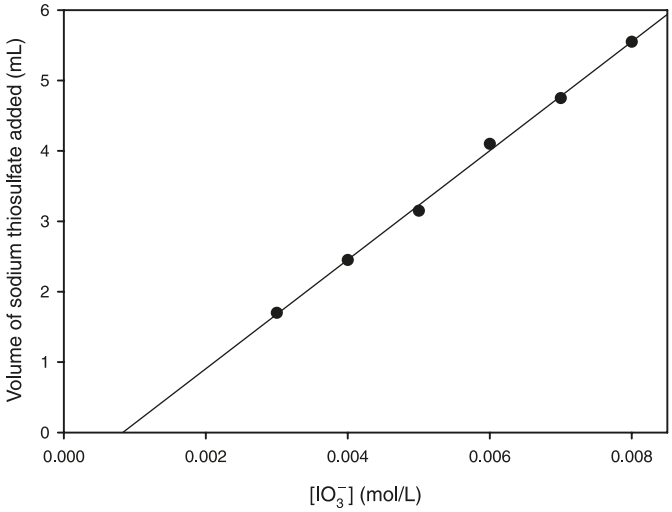

Fig. 2. (A) NMR spectrum for the product of the DL-methionine oxidation by acidic iodate/iodine solution showing the *S*-methyl peak at 2.79 ppm. (B) Spectrum of DL-methionine shows the peak initially at 2.12 ppm. Spectra for reagent grade methionine sulfoxide (C) and methionine sulfone (D) shows the shifting in the *S*-methyl group as expected from the oxidation of the sulfur center. The product solution in this case shows strong similarity to the spectrum of the sulfoxide as predicted from the stoichiometric determination.

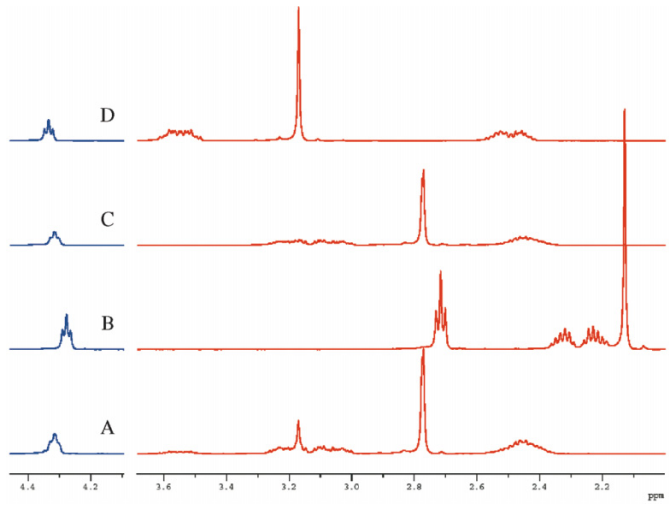

versed by the action of the enzyme methionine sulfoxide reductase.[9] Even though methionine has three coordinating centers (O, N, and S), studies have shown that the sulfur center is the most susceptible to oxidative attack.[9,11–13]

The key to understanding the physiological role of methionine requires an understanding of its specialized function, its reactive intermediates, and oxidation products. Even though most of the methionine is believed to be metabolized in the liver via the transmethylation and transsulfuration pathways,[1] alternative pathways cannot be excluded. Its interaction with different oxidants in the physiological

Fig. 3. Iodate variation shows transient iodine formation below the stoichiometry (traces a–c). In excess iodate conditions, the final iodine amount reaches a maximum determined by the methionine concentration as shown by traces e–h. The relation between iodate concentration and induction time is also apparent. $[Met]_0$ = 0.005 mol/L, $[H^+]_0$ = 0.02 mol/L, $[IO_3^-]_0$ = (a) 0.001, (b) 0.00125, (c) 0.0015, (d) 0.00175, (e) 0.002, (f) 0.0025, (g) 0.003, (h) 0.004 mol/L.

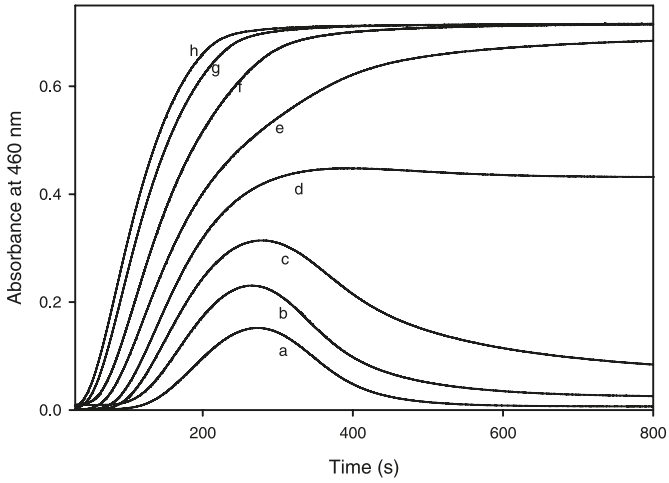

system, such as the oxygen radical species, hydrogen peroxide, hypobromous acid, hypochlorous acid, and iodine, can go a long way in providing data on the depletion of excessive dietary methionine in tissues that, unlike the liver, do not contain the complete methionine cycle.

Methionine has also been shown to inhibit in vivo thyroid peroxidase (TPO) iodide oxidation and iodination activities.[11,14] Its reaction with iodine is expected to play a major role in its interaction with the thyroid enzymes. Several organosulfur compounds are well-known goitrogenics whose actions are based on their ability to abstract the active iodine cation from the thyroid, thereby reducing its hyperactivity.[15–19] We report, in this manuscript, on a detailed kinetics and mechanistic study of the oxidation by iodate/iodine of DL-methionine. This simple oxidation reaction was surprisingly complex, characterized by nonlinear exotic kinetics behavior.

Experimental

Materials

Iodine, potassium iodide (Sigma-Aldrich), sodium perchlorate (98%) (Acros Organics), potassium iodate, DL-methionine (99%), DL-methionine sulfone (99%), DL-methionine sulfoxide, perchloric acid (72%), soluble starch, sodium thiosulfate, and hydrochloric acid (Fisher Scientific) were used without further purification. The concentration of iodine was determined by standardization against thiosulfate with starch as the indicator. Spectrophotometry was also utilized by measuring iodine absorbance at its isosbestic point with triiodide at 460 nm where the extinction coefficient had been deduced to be 770 $(mol/L)^{-1}$ cm^{-1}. This standardization was carried out before each series of kinetics experiments due to the volatile nature of iodine. Methionine solutions were prepared just before use and not kept for more than

Fig. 4. (*a*) The effect of varying acid concentrations for reactions run in excess iodate. Acid is not a reactant in the reaction but strongly catalyzes the reaction by reducing the induction period. $[Met]_0$ = 0.003 mol/L, $[IO_3^-]_0$ = 0.03 mol/L, $[H^+]_0$ = (a) 0.003, (b) 0.004, (c) 0.0045, (d) 0.005, (e) 0.006, (f) 0.007, (g) 0.008 mol/L. (b) The effect of acid variation in excess methionine. The effect of increasing acid can be seen in the form of a shorter induction period and a higher maximum transient iodine concentration. $[Met]_0$ = 0.005 mol/L, $[IO_3^-]_0$ = 0.001 mol/L, $[H^+]_0$ = (a) 0.0125, (b) 0.015, (c) 0.0175, (d) 0.02, (e) 0.025, (f) 0.03 mol/L.

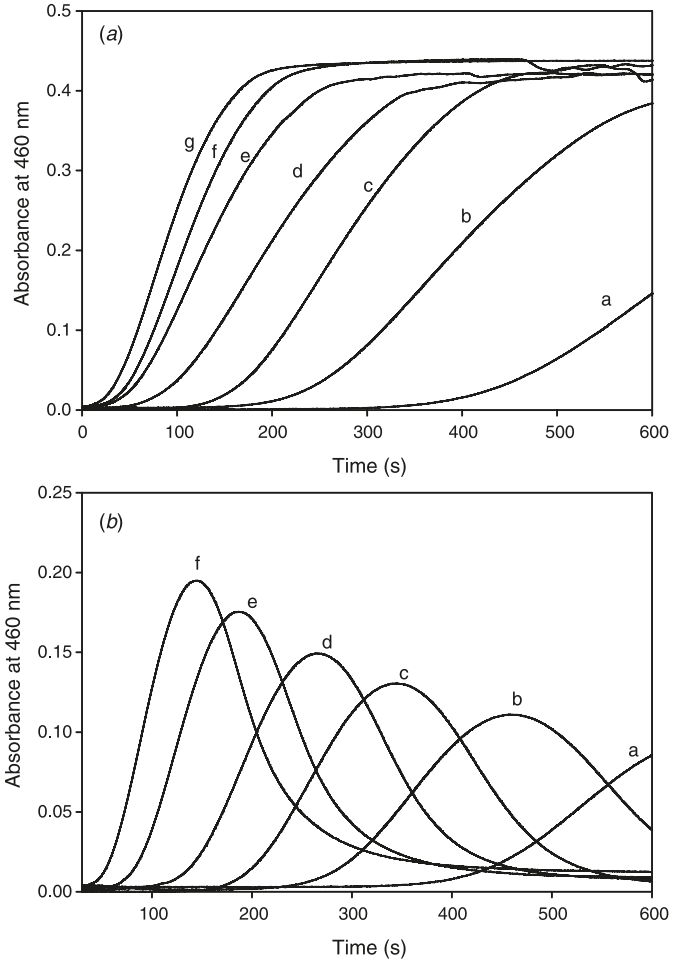

24 h. All solutions were prepared using distilled water from a Barnstead Sybron Corporation water purification unit. Inductively coupled plasma mass spectrometry (ICPMS) was used to show that our reaction medium did not contain enough copper ions to affect the overall reaction kinetics and mechanism.[20]

Methods

All experiments were carried out at 25.0 ± 0.1 °C and with a constant ionic strength of 1.0 mol/L ($NaClO_4$). Methionine, sodium perchlorate, and perchloric acid solutions were mixed in one vessel and iodate (or iodine) solutions in another. Kinetics measurements for the slower reactions and spectrophotometric determinations were performed on a PerkinElmer Lambda 25 UV–vis Spectrophotometer. The faster reactions, especially those involving iodine oxidations were monitored on a Hi-Tech Scientific SF-61 stopped-flow spectrophotometer as well as on a Hi-Tech Scientific SF-DX2 double-mixing stopped-flow spectrophotometer.

Fig. 5. Absorbance traces for methionine variation in its oxidation by iodate. Initially, the final iodine absorbances increase (a–d) but as the stoichiometric point is approached they start to decrease and show transient iodine formation (e). $[IO_3^-]_0$ = 0.003 mol/L, $[H^+]_0$ = 0.0045 mol/L, $[Met]_0$ = (a) 0.003, (b) 0.004, (c) 0.005, (d) 0.006, (e) 0.007 mol/L.

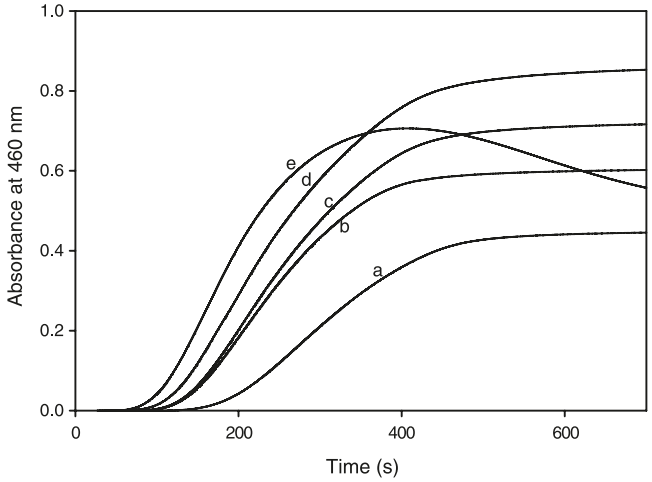

Fig. 6. Iodide effect on the iodate oxidation of methionine. The effect of iodide can be seen on the reduced induction period and increased final absorbance of iodine as iodide concentration is increased. $[Met]_0$ = 0.003 mol/L, $[H^+]$ = 0.0045 mol/L, $[IO_3^-]$ = 0.0275 mol/L, $[I^-]$ = (a) no iodide, (b) 6×10^{-6}, (c) 9×10^{-6}, (d) 5×10^{-5}, (e) 1×10^{-4} mol/L.

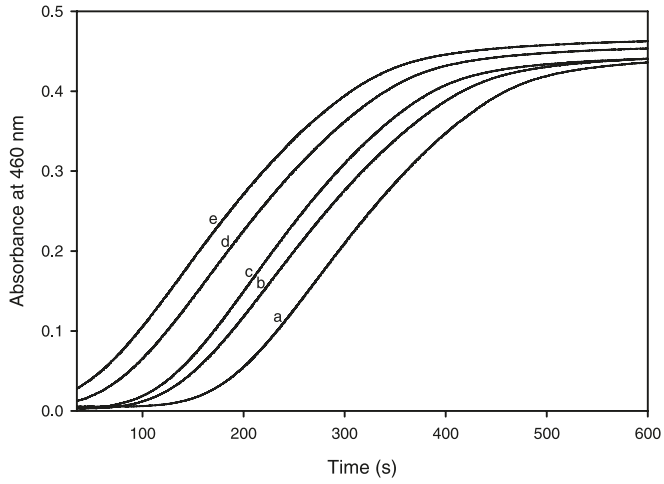

Stoichiometric determinations

The stoichiometry for the methionine–IO_3^- reaction was determined both in excess iodate and excess methionine conditions. In excess iodate the total excess oxidizing power was determined by titration. Excess acidified iodide was added to the reaction solution and the released iodine was titrated against standard thiosulfate. Spectrophotometric measurements were also used to determine the amount of iodine formed in excess iodate by its absorbance at 460 nm. In the I_2–methionine reaction, the stoichiometry was determined by titrating standardized iodine solution from a bu-

Fig. 7. (*a*) Traces showing variation of Methionine concentration with constant iodine concentration. As the methionine is increased, the reaction takes a much shorter time to reach completion. $[I_2]_0$ = 0.0003 mol/L; $[Met]_0$ = (a) 0.01, (b) 0.015, (c) 0.02, (d) 0.025, (e) 0.03, (f) 0.04, (g) 0.045, (h) 0.05 mol/L. (*b*) The data shown in Fig. 7*a* shows a linear dependence between initial rate of reaction and methionine concentration.

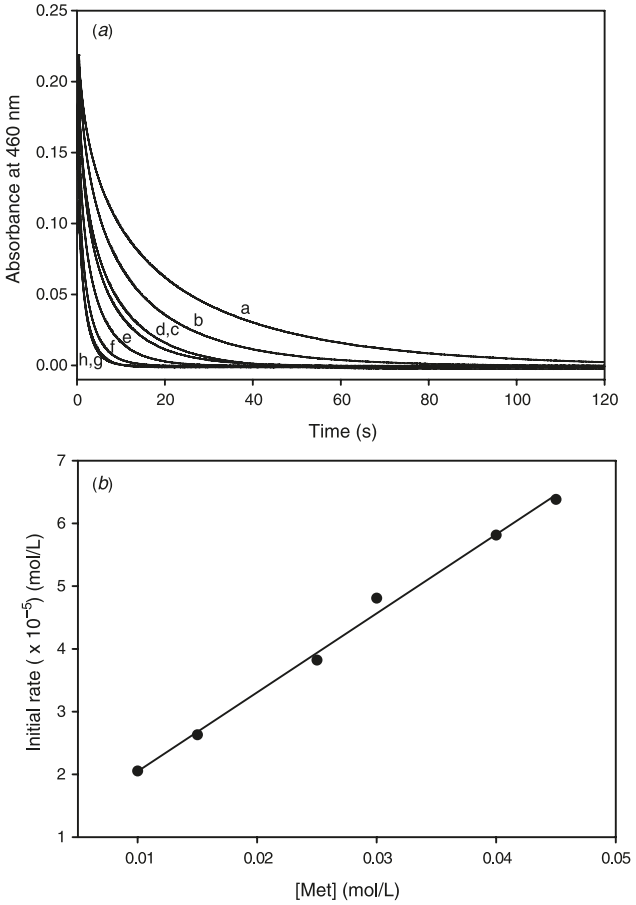

Fig. 8. (*a*) Effect of deliberately added iodide (product of the reaction) on the rate of reaction. [Met] = 5.0×10^{-3} mol/L; $[I_2] = 2.2 \times 10^{-4}$ mol/L ; $[I^-]$ = (a) no added iodide; (b) 5.0×10^{-5}; (c) 1.0×10^{-4}; (d) 2.0×10^{-4}; (e) 3.0×10^{-4}; (f) 4.0×10^{-4}; (g) 5.0×10^{-4} mol/L. (*b*) The inverse plot of initial rate and iodide concentrations for the data in Fig. 8*a*. Plot assumes I_3^- is inert. The inability of these data to reproduce the rate constant and K_{eq} indicates that the I_3^- is not inert.

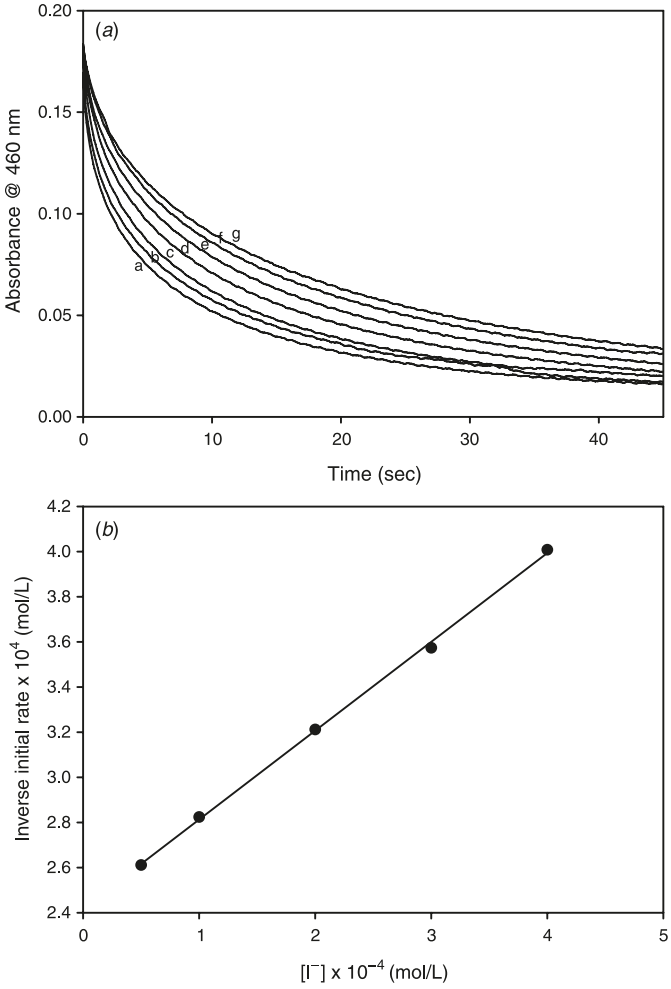

rette into a solution of methionine of known strength. The end point, which was enhanced by the starch indicator, was detected as the point where the blue-black color lingers. In excess iodine conditions, spectrophotometric determinations were used to complement the titrimetric techniques.

Results

Stoichiometry

Solutions with varying ratios of iodate to methionine were prepared and their excess oxidizing power determined by iodometric titrations. Excess oxidant was acidified and mixed with excess iodide to generate iodine according to the Dushman reaction, eq. [R1].

$$[R1] \qquad IO_3^- + 5I^- + 6H^+ \rightarrow 3I_2 + 3H_2O$$

The iodine was titrated against standard sodium thiosulfate and a plot of thiosulfate titer required versus initial iodate concentration was made and is shown in Fig. 1. The number of moles of iodate that were required to react with methionine without formation of iodine (from excess iodate) can be determined from extrapolation to the methionine concentration axis.[21] The data in Fig. 1, which were derived using a constant concentration of 0.003 mol/L methionine, show that there is no excess oxidizing power when $[IO_3^-]_0 = 0.001$ mol/L, which simplifies to a ratio of 1:3. In excess methionine, the stoichiometry for the reaction involved 1 mol of iodate reacting with 3 moles of methionine. This suggests a two-electron oxidation of the sulfur center, with methionine sulfoxide as the most likely product. Titrimetric and spectrometric techniques were both used to verify the following stoichiometry

$$[R2] \qquad IO_3^- + 3\ \text{Methionine (Met)} \rightarrow I^- + 3\ \text{Methionine sulfoxide(Met-S=O)}$$

In stoichiometric excess of iodate, in addition to MetS=O, iodine is also produced with an overall reaction stoichiometry of

Scheme 1. Mechanism of reaction of methionine with iodic acid.

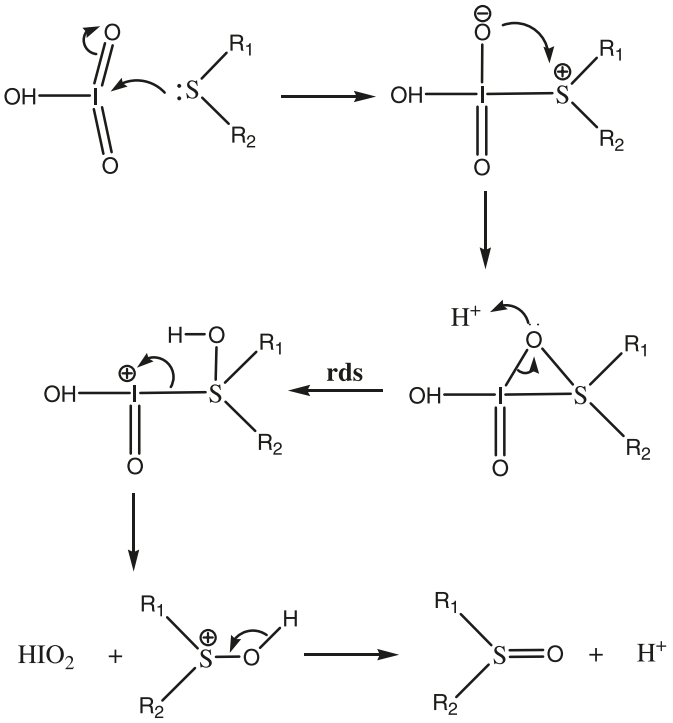

$$[R3] \quad 2IO_3^- + 5Met + 2H^+ \rightarrow I_2 + 5Met{-}S{=}O + H_2O$$

Essentially, stoichiometry eq. [R3] is a linear combination of stoichiometry eqs. [R1] and [R2]: [R1] + 5[R2]. Iodide produced in stoichiometry eq. [R1] is consumed by the excess iodate to produce iodine, and the end of reaction is determined by a complete consumption of iodide for as long as there is still excess iodate to fuel the Dushman reaction, eq. [R1]. Initially there is an increase in the amount of iodine produced as the iodate to substrate ratio, $R = [IO_3^-]_0/[Met]_0$, is increased from 0.333 (stoichiometry eq. [R2]), until a saturation point is reached where the methionine becomes limiting at a ratio of 0.400. In this short range of ratios, the final iodine amount was reproducibly determined spectrophotometrically to be 0.2 times the amount of methionine used as predicted by stoichiometry eq. [R3].

The direct reaction of methionine with iodine was rapid enough for the stoichiometry to be determined by direct titration of an iodine solution with methionine and vice-versa. The detection of the end point was aided by the starch indicator and the stoichiometry was determined to be

$$[R4] \quad Met + I_2 + H_2O \rightarrow Met{-}S{=}O + 2I^- + 2H^+$$

Stoichiometry eq. [R4] could also be obtained spectrophotometrically in excess iodine conditions by observing the absorbance of the excess iodine at 460 nm (at the end of the reaction).

Confirmation of products

The two major products that could possibly be obtained from the oxyhalogen oxidation of the sulfur center in methionine are the sulfoxide and the sulfone. Due to the lack of $BaSO_4$ precipitation, there was no evidence to suggest further oxidation resulting in cleavage to the C–S bond. Proton NMR spectroscopy was used to confirm the products as predicted from the stoichiometry. In Fig. 2, spectrum A is of the product of reaction between acidic iodate and methionine. Spectrum B is pure DL-methionine, which shows the expected strong singlet for the *S*-methyl group at 2.12 ppm. These protons appear as a singlet due to the presence of the sulfur, which acts as a shield from the splitting effects of the other protons on adjacent carbon atoms. Spectrum C shown is of reagent grade DL-methionine sulfoxide, showing a downfield shift of the methyl protons (2.79 ppm) due to the presence of the oxygen on the sulfur center. Addition of another oxygen to form the sulfone results in a further downfield shift of these protons to 3.20 ppm. Spectrum D is reagent grade methionine sulfone. Spectrum A, the reaction product, is similar to the spectrum for the reagent grade sulfoxide (C). Solutions to obtain spectra B–D were prepared in neutral conditions while DCl was used to acidify the solution used to obtain spectrum A. The difference in pH between these solutions accounts for the small difference between spectra A and C. The spectrum of oxidation of methionine by acidified iodate shows that there is a small amount of sulfone formed as a minor product, but this could not be detected iodometrically due to the oxidation of iodide by the sulfone to iodine and the sulfoxide. To further confirm the sulfoxide as the major product, reagent grade sulfoxide was mixed with acidified iodate solution and no further reaction was observed.

Reaction dynamics

The reaction exhibited clock behavior[22] with transient iodine formation. Figure 3 shows both aspects of this dynamical behavior. When the oxidant-to-reductant ratio, $R = [IO_3^-]_0/[Met]_0$, is less than 0.333, no iodine is expected to be formed at the end of the reaction as predicted by stoichiometry eq. [R2]. Traces a–c in Fig. 3 are derived from reaction solutions in which $R < 0.333$, but, however, show transient iodine formation, which is an indication of the dominance of the reactions that form iodine over those that consume it during the initial stages of the reaction. As the reaction proceeds, iodine consumption reactions later become dominant. Clock reaction characteristics, in which there is an initial quiescent period followed by formation of iodine, are also exhibited for all values of *R*, as shown by traces a–h (Fig. 3). In stoichiometric excess of oxidant, which gives stoichiometry eq. [R3], i.e., $R \geq 0.333$, the final iodine formation is determined by the concentration of methionine. When $R > 0.4$, however, the amount of iodine formed becomes invariant to further increases in iodate concentrations. The increase in final iodine concentration between traces d and e (Fig. 3) is justified based on the fact that stoichiometry eq. [R3] is a step wise linear combination of eqs. [R1] and [R2].

Figure 3 also shows that as the iodate concentration is increased, the rate of iodine formation increases while the quiescent time before iodine formation commences (induction period), decreases.[23] Formation of iodine, in all traces (Fig. 3), is not sharp, but gradual. Thus the induction period was estimated to be the point where rapid formation of iodine commenced.

Figure 4*a* shows that not only does an increase in acid decrease the induction period, but it also increases the rate of

Table 1. Iodate–Iodine–Methionine reaction network.

Number	Reaction	K_f; k_r
M1	$IO_3^- + I^- + 2H^+ \rightleftharpoons HIO_2 + HOI$	2.8; 1.44×10^3
M2	$HIO_2 + I^- + H^+ \rightleftharpoons 2HOI$	2.1×10^8; 90
M3	$HOI + I^- + H^+ \rightleftharpoons I_2 + H_2O$	3.1×10^{12}; 2.2
M4	$IO_3^- + HOI + H^+ \rightleftharpoons 2HIO_2$	8.6×10^2; 2.00
M5	$I_2 + I^- \rightleftharpoons I_3^-$	6.2×10^9; 8.5×10^6
M6	$IO_3^- + H^+ \rightleftharpoons HIO_3$	5.0×10^9; 1.25×10^9
M7	$HIO_3 + Met + H^+ \rightarrow HIO_2 + Met{-}SO + H^+$	50
M8	$HIO_2 + Met \rightarrow HOI + Met{-}SO$	125
M9	$HOI + Met \rightarrow Met{-}SO + I^- + H^+$	165
M10	$I_2 + Met + H_2O \rightarrow Met{-}SO + 2H^+ + 2I^-$	72
M11	$I_3^- + Met + H_2O \rightarrow Met{-}SO + 2H^+ + 3I^-$	16

Fig. 9. Computer modeling: traces showing the simulated results (circles) and the experimental data (solid line) for trace g shown in Fig. 4*a*. $[Met]_0 = 0.003$ mol/L, $[IO_3^-]_0 = 0.03$ mol/L, $[H^+] = 0.008$ mol/L.

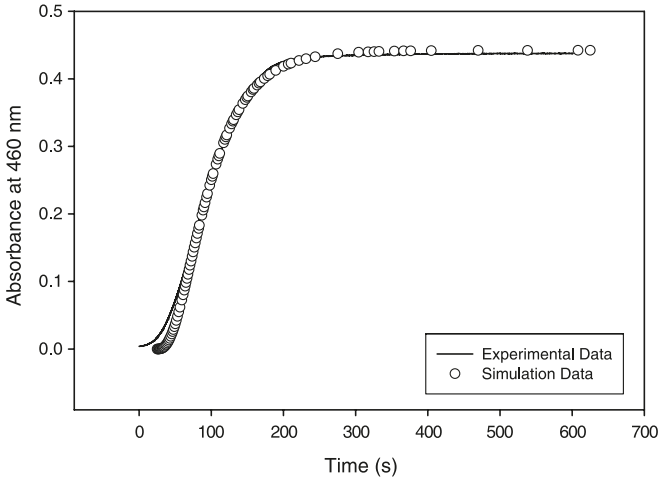

formation of iodine. The catalytic effect of acid on the Dushman[24–27] reaction (eq. [R1]) is responsible for the increase in rate of formation of iodine in conditions where $R > 0.4$. Since the final amount of iodine does not change with an increase in acid, acid influences only the overall rate of formation of iodine, which in turn affects the induction period. The effect of acid for low R values ($R < 0.33$), however, is more complex as shown in Fig. 4*b*. Figure 4*b* shows traces in excess methionine conditions where no final iodine accumulation is expected. As the acid is increased from a to f (Fig. 4*b*), the induction period is shortened while the maximum amount of transient iodine is increased. This indicates acid catalysis in formation of iodine, resulting in rapid accumulation of iodine and shorter induction periods as acid concentrations are increased. Higher acid traces in Fig. 4*b* also show a narrower "excursion" indicating that an increase in acid also increases the rate of consumption of iodine. Given that the general shape of the traces is not symmetrical, it would also appear that acid catalyzes the formation of iodine to a greater extent than it catalyzes its consumption.

The oxidant-to-reductant ratio, R, plays an important role in determining the dynamics of the reaction as can be seen in Fig. 5, which shows the effect of progressively increasing the methionine concentration at constant iodate and acid concentration. As R is reduced from a–d (Fig. 5), the final iodine amount increases to a final concentration that is determined by stoichiometry eq. [R3]. As reaction stoichiometry eq. [R2] is approached, the monotonic formation of iodine gives way to transient formation of iodine as shown in trace e (Fig. 5).

In excess oxidant conditions, the effect of iodide can easily be seen by the increase in final iodine concentration. This is expected in conditions where $R > 0.4$, in which the iodide ions initially added to the reaction mixture combine with those produced by the reaction in eq. [R2] to fuel the Dushman reaction,[24,26] eq. [R1]. This is clearly evident in Fig. 6 where an increase in iodide concentrations increases the final iodine concentration as well as reducing the induction time.

The direct reaction of iodine and methionine plays a crucial role in this mechanism. The rate at which iodine oxidizes methionine determines whether methionine can coexist with iodine. If this reaction is fast, then final iodine formation would mean that all the methionine has been consumed. Figure 7*a* shows the iodine consumption of methionine in high excess of methionine. Despite this high excess, no pseudo-first-order kinetics are observed, indicating that this is not a simple electrophilic attack of iodine on the thioether group. There is a linear dependence between the initial rate of reaction with both methionine and iodine concentrations. Figure 7*b* shows the methionine dependence. Figure 8*a* shows that iodide is inhibitory to the oxidation of methionine by iodine. Figure 8*b* shows that there is an inverse dependence relationship between the initial rate of reaction and iodide concentrations. Iodide is a product of the iodine–methionine reaction, and thus its effect is autoinhibitory. This explains why no pseudo-first-order kinetics were observed in the data shown in Fig. 7*a*.

Mechanism

The bulk of iodate-based oxidations are borne by the reactive oxyiodine species HIO_2, IO_2, and HOI as well as molecular iodine, I_2. These species can be generated in acidic iodate conditions, and the rate of iodate oxidations are usually controlled by the rate at which these reactive species are generated.[28,29] There is some debate as to the exact initiation sequence of iodate oxidations, but a nucleophilic attack on a protonated iodate species (see reaction eq. [R7]) appears to be the most widely accepted initiation to produce iodous and hypoiodous acids.

Scheme 2. Schematic representation of all possible reactions, intermediates, and products in the oxidation of methionine by acidic iodate and aqueous iodine.

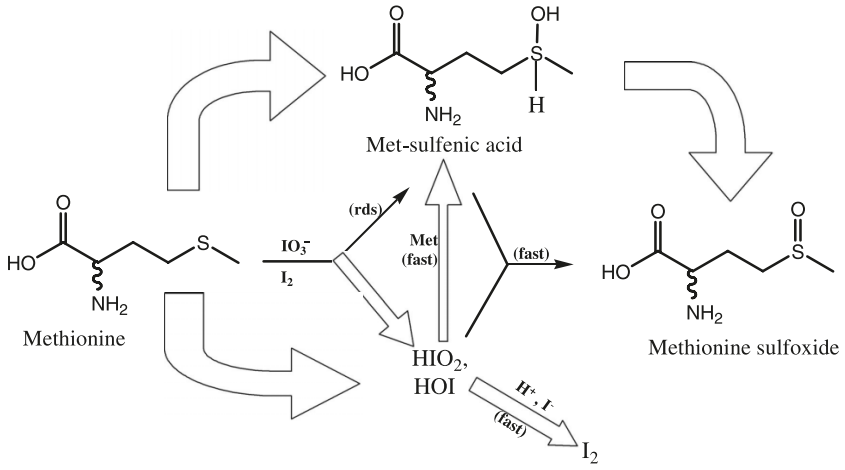

$$[R5] \quad IO_3^- + H^+ \rightleftharpoons IO_3H$$

Investigators of the Briggs–Rauscher[30,31] and Bray–Liebhafsky[25,32] reactions have suggested that this nucleophilic species is the trace amount of iodide ions that are contained in normal iodate solutions.

$$[R6] \quad IO_3H + H^+ \rightleftharpoons {}^+IO(OH)_2$$

$$[R7] \quad {}^+IO(OH)_2 + I^- \rightleftharpoons I{-}IO(OH)_2$$

The $H_2I_2O_3$ species formed in eq. [R7] can then break down in a rate-determining step to produce the reactive species, HIO_2 and HOI.[29]

$$[R8] \quad I{-}IO(OH)_2 \rightarrow HIO_2 + HOI$$

HOI is extremely reactive as an oxidizing species, and will rapidly react with the substrate, methionine, to produce iodide and the oxidation product, methionine sulfoxide.

$$[R9] \quad HOI + :SR_1R_2 \rightarrow R_1R_2S{=}O + H^+ + I^-$$

The iodide produced in eq. [R9] feeds back into reaction eq. [R7] to facilitate further oxidation of the reactive species. While we may accept iodous acid as a viable oxidant, it, however, rapidly reacts with iodide to produce more hypoiodous acid:

$$[R10] \quad HIO_2 + H^+ + I^- \rightleftharpoons 2HOI$$

Addition of the reactions leading to the oxidation of methionine in the initial stages shows that the reaction's initial activity is the build-up of iodide, which is autocatalytically produced in these early stages of the reaction of eqs. [R5] + [R6] + [R7] + [R8] + 3[R9] + [R10];

$$[R11] \quad IO_3^- + 2I^- + 3MetS \rightarrow 3I^- + 3MetSO$$

The iodide material balance for the initial stages suggests a mechanism that is based on cubic autocatalysis in iodide.

There are, however, two major flaws with the eqs. [R5]–[R10] sequence. The first flaw is from pure mass action kinetics. The expected iodide concentrations, which exist in these iodate solutions, should be approximately 5.0×10^{-7} mol/L. Assuming eqs. [R9] and [R10] are relatively rapid, one can utilize reaction eq. [R8] to determine the rate of formation of iodide and subsequently the rate of oxidation of methionine. A simple integration gives a sigmoidal curve for iodide generation. Literature values give the composite forward rate constant of reaction eq. [R8] as 2.2 $(mol/L)^{-3}$ s^{-1}. Using these values, one generates a very slow rate of iodide formation and subsequent rate of reaction, giving reaction times in the order of hours instead of the observed 2–10 min. This suggests that iodide formation is not solely through the composite reaction eq. [R11]. The next flaw arises from the effect of iodide observed in Fig. 6. With cubic autocatalysis, as profiled in reaction eq. [R11], addition of minute amounts of iodide should result in a greatly enhanced rate of reaction. Figure 6 shows that, while iodide is catalytic, it is not as strong as would have been expected from an autocatalyst.

It appears then, that initial formation of iodide should be derived from the substrate itself acting as a nucleophile on either the iodic acid or the protonated iodic acid. Both scenarios would produce kinetically indistinguishable reaction profiles and mechanisms. In Scheme 1, methionine is represented as R_1SR_2.

The iodous acid produced in Scheme 1 can be further reduced successively by methionine to hypoiodous acid and iodide. Reaction eq. [R9] is a rapid oxygen transfer reaction, and thus, the overall rate of reaction should be the rate of formation of HOI.

Accumulation of iodide will then transfer the rate of reaction to standard Dushman reaction kinetics with the composite rate-determining step eq. [R12]:

$$[R12] \quad IO_3^- + I^- + 2H^+ \rightleftharpoons HIO_2 + HOI$$

Iodine is formed from the reverse of its hydrolysis reaction:

$$[R13] \quad HOI + I^- + H^+ \rightleftharpoons I_2(aq) + H_2O$$

Through relaxation spectroscopy, reaction eq. [R13] is known to be very rapid and acid-catalyzed.[33] Basic condi-

tions catalyze and support the hydrolysis reaction. Our experiments, however, were carried out in acidic conditions since iodate is essentially inert in basic environments. A summary of all possible reactions, intermediates, and products in the oxidation of methionine by acidic iodate and its oxidative derivatives is shown in Scheme 2.

The methionine–iodine reaction

The direct reaction of methionine with aqueous iodine is very important in determining the overall global dynamics observed with respect to iodine formation. Transient iodine formation, as observed in Fig. 4*b*, is derived from the coupling of the reaction that forms iodine, eq. [R13],[33] with those that consume iodine. If the methionine-iodine reaction is extremely rapid (e.g., diffusion controlled), no transient iodine formation would be observed and the end of the induction period would be very sharp, and would signify complete consumption of methionine. The nonlinear kinetics observed indicate that the reactions involved in the formation and consumption of iodine are comparable in magnitude and each set asserts itself based on the availability of the relevant reagents and mass action kinetics.

The reaction commences with an electrophilic attack by aqueous iodine on the electron-rich sulfur center of methionine:

$$[R14] \qquad R_1R_2S: + I{-}I \rightleftharpoons [R_1R_2S{-}I]^+ + I^-$$

followed by the standard hydrolysis:

$$[R15] \qquad [R_1R_2S{-}I]^+ + H_2O \rightarrow R_1R_2S{=}O + 2H^+ + I^-$$

Addition of eqs. [R14] and [R15] gives the 1:1 experimentally observed stoichiometry for this reaction. Initial rate data, before accumulation of iodide, was used to evaluate $k_{14} = 72 \pm 1.4$ (mol/L)$^{-1}$ s^{-1}.

Although the reaction is autoinhibitory, the autoinhibition is not as strong as the one observed with the iodine–thiocyanate[34,35] and iodine–thiourea reactions.[36] In these systems, it was assumed that iodine reacts with the product, iodide, to produce an inert product, triiodide:

$$[R16] \qquad I_2 + I^- \rightleftharpoons I_3^-; K_{eq}$$

If one assumes that the triiodide anion is inert, then the following rate law emerges:

$$[1] \qquad \left|\frac{1}{\text{Rate}}\right| = \frac{1}{k_{14}[\text{Met}]_0[I_2]_0}(1 + K_{eq}[I^-])$$

A plot of the inverse of the rate versus iodide concentrations on the basis of eq. [1] should give a straight line, which should allow for the calculation of k_{14} and a confirmation of the well known value of $K_{eq} = 770$ (mol/L)$^{-1}$. This plot is shown in Fig. 8*b* where the data gave a value of k_{14} that was much lower than that derived from initial rate data, and also gave a much lower K_{eq} value that was an order of magnitude lower than the literature value.[37] This suggests that I_3^- is not inert, and that the autoinhibition observed is derived from the sluggish kinetics obtained with I_3^- when it predominates in concentrations as iodide accumulates.

$$[R17] \qquad R_1R_2S: + I_3^- + H_2O \rightarrow R_1R_2S{=}O + 3I^- + 2H^+$$

Combining reaction eqs. [R14] and [R17] gives a rate law of the form

$$[2] \qquad \text{Rate} = \frac{[\text{Met}]_0[I_2]_0}{1 + K_{eq}[I^-]}[k_{14} + k_{17}K_{eq}[I^-]]$$

In the initial stages, before iodide accumulates, rate law eq. [2] simplifies to a simple bimolecular rate law. In the limit of high initial iodide concentrations, in which one can assume constant iodide concentrations, an upper limit rate constant for k_{17} was derived as 16.0 (mol/L)$^{-1}$ s^{-1}.

Computer simulation

The reaction scheme was modeled using the Kintecus software generated by James Ianni.[41] The full mechanism, which takes into account the formation and consumption of iodine, is shown in Table 1. It is a very simple mechanism made up of 11 reactions with the most important reactions being M1 and M7 (Table 1), which are responsible for initiating the reaction. Since iodate oxidations only proceed at reasonable rates in highly acidic media, the simulations could be simplified by assuming that acid concentrations were buffered throughout the duration of the reaction. By using a constant acid concentration, reactions M2–M4 and M7 (Table 1) could be reduced to the simpler bimolecular kinetics. Reactions M1–M4 (Table 1) are the standard oxyiodine reactions whose rate constants are well-known and were derived from literature.[24–27] These were not altered during the modeling exercises. Reaction M5 (Table 1) was studied by laser-Raman techniques and the forward and reverse rate constants and subsequent equilibrium constant were also derived from literature and also not varied.[37,38] Reaction M6 (Table 1) is a rapid protolytic process in which the only relevant parameter was the assumed K_a of iodic acid. Literature reports a wide range of values for this K_a.[39] The K_a value is apparently heavily dependent on the reaction medium, especially acid concentrations.[29] Elegant experimental work done by Naidich and Ricci[40] in 1939 established that concentrations of iodic acid become significant in acidic iodate solutions at a pH of less than 2.00. All our reactions were run at pH conditions lower than this value. The final adopted value of 0.400 was extrapolated from the barium iodate solubility data of Naidichi and Ricci.[40] The simulations were insensitive to the adopted values of the forward and reverse rate constants for M6 (Table 1) for as long as they were both rapid and linked by K_a. More realistic diffusion-controlled rate constants for M6 (Table 1) stiffened the simulations considerably and slowed the calculations but without affecting the resulting simulations. Reactions M7–M9 (Table 1) represent the initiation reactions in the absence of initially added iodide. Reactions M8 and M9 (Table 1) are not important in determining the observed reaction dynamics for as long as they are faster than M7 (Table 1). Rate constants for reactions M10 and M11 (Table 1) were determined from this study. Effectively, since half of the reactions' parameters were obtained from literature values, the only parameters that could be altered for best fit to the data were K_a for iodic acid and k_{M7}. Figure 9 shows that this simple mechanism gave a reasonably good fit of the experimental data for the case involving excess io-

date concentrations, resulting in a monotonic formation of iodine. The transient iodine formation traces (Figs. 3 and 4*b*) were more difficult to reproduce with this abbreviated mechanism. It was easier to fit the initial formation of iodine but much more difficult to fit its consumption, even though the model could easily reproduce the trivial iodine consumption traces shown in Fig. 7*a*. The inability to correctly simulate Figs. 3 and 4*b* lay in our inability to correctly ascribe the correct activity of aqueous iodine in these highly acidic solutions. Literature does not contain reliable data on these solutions, especially when spiked with iodide.

Conclusion

Our short study has shown that iodine oxidizes the simple biologically important thioether, methionine, to just the sulfoxide. Organosulfur compounds are the most effective goitrogenics available, and their reaction rate and mechanism with iodine would be a significant physiological interaction.

Acknowledgements

This work was supported by grant number CHE 0614924 from the National Science Foundation.

References

(1) Boers, G. H.; Smals, A. G.; Trihbels, J. F.; Leermakers, A. I.; Kloppenborg, P. W. *J. Clin. Invest.* **1983**, *72*, 1971. doi:10.1172/JCI111161. PMID:6643682.
(2) Epner, D. E. *J. Am. Coll. Nutr.* **2001**, *20*, 443S. PMID: 11603655.
(3) Finkelstein, J. D.; Martin, J. J. *J. Biol. Chem.* **1986**, *261*, 1582. PMID:3080429.
(4) Yang, Z.; Wang, J.; Yoshioka, T.; Li, B.; Lu, Q.; Li, S.; Sun, X.; Tan, Y.; Yagi, S.; Frenkel, E. P.; Hoffman, R. M. *Clin. Cancer Res.* **2004**, *10*, 2131. doi:10.1158/1078-0432.CCR-03-0068. PMID:15041734.
(5) Wilcken, D. E.; Wilcken, B. *J. Clin. Invest.* **1976**, *57*, 1079. doi:10.1172/JCI108350. PMID:947949.
(6) Wasan, K. M.; Cassidy, S. M.; Kennedy, A. L.; Peteherych, K. D. *Atherosclerosis: Experimental Methods and Protocols;* Humana Press: Clifton, NJ, 1995; pp 27–35.
(7) Zieman, S. J.; Melenovsky, V.; Kass, D. A. *Arterioscler. Thromb. Vasc. Biol.* **2005**, *25*, 932. doi:10.1161/01.ATV.0000160548.78317.29. PMID:15731494.
(8) Moskovitz, J.; Berlett, B. S.; Poston, J. M.; Stadtman, E. R. *Proc. Natl. Acad. Sci. U.S.A.* **1997**, *94*, 9585. doi:10.1073/pnas.94.18.9585. PMID:9275166.
(9) Stadtman, E. R.; Moskovitz, J.; Berlett, B. S.; Levine, R. L. *Mol. Cell. Biochem.* **2002**, *234–235*, 3. doi:10.1023/A:1015916831583.
(10) Moskovitz, J.; Berlett, B. S.; Poston, J. M.; Stadtman, E. R. *Proc. Natl. Acad. Sci. U.S.A.* **1997**, *94*, 9585. doi:10.1073/pnas.94.18.9585. PMID:9275166.
(11) Carvalho, D. P.; Ferreira, A. C. F.; Coelho, S. M.; Moraes, J. M.; Camacho, M. A. S.; Rosenthal, D. *Braz. J. Med. Biol. Res.* **2000**, *33*, 355. PMID:10719389.
(12) Levine, R.; Mosoni, L.; Berlett, B.; Stadtman, E. *Proc. Natl. Acad. Sci. U.S.A.* **1996**, *93*, 15036. doi:10.1073/pnas.93.26.15036. PMID:8986759.
(13) Meenakshisundaram, S.; Vinothini, R. *Croat. Chem. Acta* **2003**, *76*, 75.
(14) Sato, K.; Robbins, J. *Endocrinology* **1981**, *109*, 844. PMID: 6790265.
(15) Miller, W. H.; Roblin, R. O.; Astwood, E. B. *J. Am. Chem. Soc.* **1945**, *67*, 2201. doi:10.1021/ja01228a043.
(16) Doniach, I. *Monogr. Neoplast. Dis. Var. Sites* **1970**, *6*, 73. PMID:4950336.
(17) Lindsay, R. H.; Hulsey, B. S.; Aboul-Enein, H. Y. *Biochem. Pharmacol.* **1975**, *24*, 463. doi:10.1016/0006-2952(75)90129-X. PMID:46147.
(18) Kabadi, U.; Cech, R. *Thyroidology* **1994**, *6*, 87. PMID: 7545000.
(19) Oren, R.; Dotan, I.; Papa, M.; Marravi, Y.; Aeed, H.; Barg, J.; Zeidel, L.; Bruck, R.; Halpern, Z. *Hepatology* **1996**, *24*, 419. doi:10.1002/hep.510240221. PMID:8690414.
(20) Darkwa, J.; Olojo, R.; Chikwana, E.; Simoyi, R. H. *J. Phys. Chem. A* **2004**, *108*, 5576. doi:10.1021/jp049748k.
(21) Chikwana, E.; Otoikhian, A.; Simoyi, R. H. *J. Phys. Chem. A* **2004**, *108*, 11591. doi:10.1021/jp045897r.
(22) Oliveira, A. P.; Faria, R. B. *J. Am. Chem. Soc.* **2005**, *127*, 18022. doi:10.1021/ja0570537. PMID:16366551.
(23) Chanakira, A.; Chikwana, E.; Peyton, D.; Simoyi, R. *Can. J. Chem.* **2006**, *84*, 49. doi:10.1139/v05-263.
(24) Liebhafsky, H. A.; Roe, G. M. *Int. J. Chem. Kinet.* **1979**, *11*, 693. doi:10.1002/kin.550110703.
(25) Kolaranic, L.; Schmitz, G. *J. Chem. Soc., Faraday Trans.* **1992**, *88*, 2343. doi:10.1039/ft9928802343.
(26) Schmitz, G. *Phys. Chem. Chem. Phys.* **1999**, *1*, 1909. doi:10.1039/a809291e.
(27) Schmitz, G. *Phys. Chem. Chem. Phys.* **2000**, *2*, 4041. doi:10.1039/b003606o.
(28) Mambo, E.; Simoyi, R. H. *J. Phys. Chem.* **1993**, *97*, 13662. doi:10.1021/j100153a039.
(29) Xie, Y.; McDonald, M. R.; Margerum, D. W. *Inorg. Chem.* **1999**, *38*, 3938. doi:10.1021/ic9807442.
(30) Tiktonova, L. P.; Kovalenko, A. S.; Labunskaya, I. F.; Ivashchenko, T. S. *Teoreticheskaya I Eksperimentalnaya Khimiya* **1991**, *27*, 737.
(31) Lalitha, P. V. N.; Ramaswamy, R. *Collect. Czech. Chem. Commun.* **1992**, *57*, 2235. doi:10.1135/cccc19922235.
(32) Agreda B, J. A.; Field, R. J.; Lyons, N. J. *J. Phys. Chem. A* **2000**, *104*, 5269. doi:10.1021/jp000271w.
(33) Eigen, M.; Kustin, K. *J. Am. Chem. Soc.* **1962**, *84*, 1355. doi:10.1021/ja00867a005.
(34) Simoyi, R. H.; Manyonda, M.; Masere, J.; Mtambo, M.; Ncube, I.; Patel, H.; Epstein, I. R.; Kustin, K. *J. Phys. Chem.* **1991**, *95*, 770. doi:10.1021/j100155a052.
(35) Simoyi, R. H.; Epstein, I. R.; Kustin, K. *J. Phys. Chem.* **1989**, *93*, 2792. doi:10.1021/j100344a019.
(36) Rabai, G.; Beck, M. T. *J. Chem. Soc. Dalton Trans.* **1985**, 1669. doi:10.1039/dt9850001669.
(37) Turner, D. H.; Flynn, G. W.; Sutin, N.; Beitz, J. V. *J. Am. Chem. Soc.* **1972**, *94*, 1554. doi:10.1021/ja00760a020.
(38) Ruasse, M. F.; Aubard, J.; Galland, B.; Adenir, A. *J. Phys. Chem.* **1986**, *90*, 4382. doi:10.1021/j100409a034.
(39) Kraus, C. A.; Parker, H. C. *J. Am. Chem. Soc.* **1922**, *44*, 2429. doi:10.1021/ja01432a011.
(40) Naidich, S.; Ricci, J. E. *J. Am. Chem. Soc.* **1939**, *61*, 3268. doi:10.1021/ja01267a010.
(41) Ianni, J. C. Kintecus, Windows Version 3.95, 2008, http://www.kintecus.com/.

Cerium(IV) sulfate catalyzed one-pot three-component diastereo selective synthesis of 4-amidotetrahydropyrans

Nagarajan Panneer Selvam and Paramasivan T. Perumal

Abstract: A convenient and diastereoselective one-pot synthesis of *cis*-4-amidotetrahydropyrans is described. This simple protocol involves Prins cyclization of homoallylic alcohol and aldehydes, followed by Ritter reaction of acetonitrile leading to the formation of *cis*-4-acetamidopyrans in good yields.

Key words: cerium(IV) sulfate, diastereoselective, tetrahydroamidopyrans, Prins–Ritter reaction.

Résumé : On décrit une méthode de synthèse monotope commode et diastéréosélective des *cis*-4-amidotétrahydropyranes. Ce protocole simple implique des réactions de cyclisation de Prins entre l'alcool homoallylique et divers aldéhydes, suivies d'une réaction de Ritter avec de l'acétonitrile qui conduit à la formation des *cis*-4-acétamidopyranes avec de bons rendements.

Mots-clés : sulfate de cérium(IV), diastéréosélective, tétrahydroamidopyranes, réaction de Prins–Ritter.

[Traduit par la Rédaction]

Introduction

Multicomponent one-pot syntheses are highly important because of their wide range of applications in pharmaceutical chemistry for the production of structural scaffolds and combinatorial libraries for drug discovery.[1] The tetrahydropyran ring has attracted significant attention in recent years, as it is part of the backbone of many natural products.[2] It is featured widely in many natural products, such as phorboxazole A, psymberin, and (–)-centrolobine. The 4-amino tetrahydropyran ring system is a core unit in a number of natural products, such as ambruticin VS, glycamino acid, and others[3] (Fig. 1). Because of their prevalence, there are multiple strategies for the construction of these six-membered ring systems, including Prins cyclization,[4] hetero Diels–Alder reactions,[5] and intramolecular nucleophilic reactions.[6] Among the several methods available, Prins cyclization[7] offers one of the most versatile methods for the construction of the tetrahydropyran ring. A few reports on the use of the Ritter reaction to terminate Prins cyclizations;[8] the scope of this process has not been explored extensively. Recently, Yadav et al. described the synthesis of substituted tetrahydroamidopyran derivatives using $CeCl_3 \cdot 7H_2O$/acetyl chloride,[9] phosphomolybdic acid[10] catalyst. Because of the unique pharmacological, biological, and industrial importance, simple and efficient protocols for the synthesis of these compounds are highly desirable.

Received 18 November 2008. Published on the NRC Research Press Web site at canjchem.nrc.ca on 8 May 2009.

N.P. Selvam and P.T. Perumal.[1] Organic Chemistry Division, Central Leather Research Institute, Chennai 600 020, India.

[1]Corresponding author (e-mail: ptperumal@gmail.com).

Results and discussion

In continuation of our work on the development of useful synthetic methodologies using cerium(IV) sulfate,[11] we herein describe an efficient Prins–Ritter reaction sequence for the direct synthesis of 4-acetamidotetrahydropyrans from homoallylic alcohols, carbonyl compounds, and acetonitrile. First, we carried out a three-component coupling reaction of 4-chlorobenzaldehyde with but-3-en-1-ol in acetonitrile in the presence of 20 mol% $Ce(SO_4)_2$ at room temperature. The reaction proceeded to completion in 6.5 h, and the product, 4-acetamidotetrahydropyran (**3a**), was obtained in 93% yield with cis-selectivity (Scheme 1).

Other Lewis acid catalysts, such as zinc(II) chloride, ferric chloride hexahydrate, stannous chloride dihydrate, potassium hydrogen sulfate, cerium(IV) sulfate, and phosphotungstic acid, were tested, but $Ce(SO_4)_2$ was found to be the most efficient in terms of conversion.

Thus encouraged, we examined various substituted aryl aldehydes and homoallylic alcohols for the synthesis of 4-acetamidotetrahydropyrans under optimized reaction conditions. 4-Chlorobenzaldehyde, 2,4-dichlorobenzaldehyde, 4-nitrobenzaldehyde, 3-nitrobenzaldehyde, 4-methylbenzaldehyde, 4-bromobenzaldehyde, and 4-methoxybenzaldehyde reacted well with 3-buten-1-ol and acetonitrile to produce the corresponding 4-acetamidotetrahydropyrans in high yields (Table 1, entries 1–8). An aliphatic aldehyde (propionaldehyde) also reacted with 3-buten-1-ol and acetonitrile to afford the product in 82% yield (Table 1, entry 9). Furthermore, substituted homoallylic alcohols, such as 1-phenyl-but-3-en-1-ol, 1-(3-nitrophenyl)-but-3-en-1-ol, 1-(4-chlorophenyl)but-3-en-1-ol, and 1-(2,4-dichlorophenyl)-but-3-en-1-ol also participated in this transformation (Table 1, entries 10–15). Ketones, such as cyclohexanone and cyclopentanone, reacted comparably

Scheme 1. Synthesis of 4-acetamidotetrahydropyran derivatives.

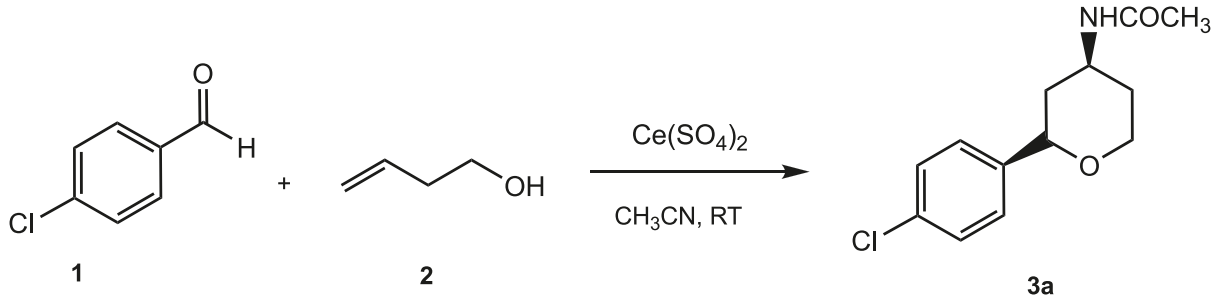

Scheme 2. Synthesis of spirocyclic 4-acetamidotetrahydropyrans.

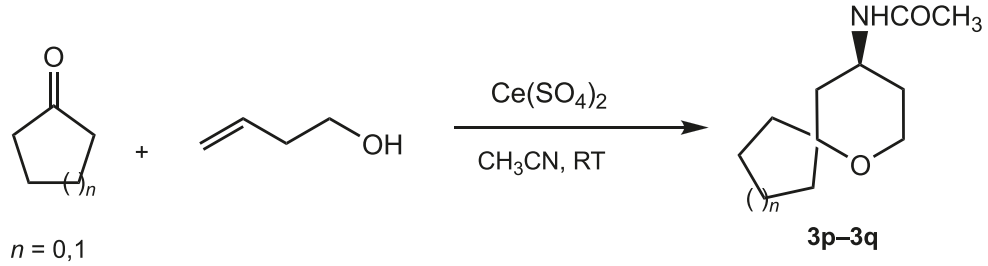

Fig. 1. Examples of tetrahydropyran derivatives.

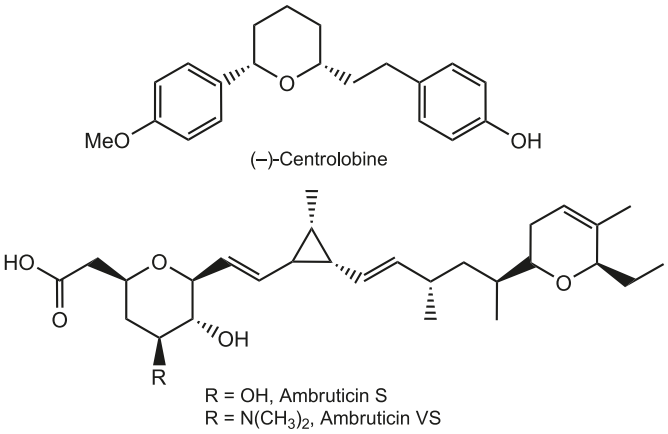

giving spirocyclic 4-acetamidotetrahydropyrans in good yields (Table 1, entries 16 and 17; Scheme 2).

The reactions were clean, and the products were obtained in excellent yields with high diastereoselectivity as determined from the NMR spectra of the products. In all cases, cis-isomer were obtained exclusively, and the structure of which was confirmed by NOE experiments. The formation of the products can be explained by hemi-acetal formation followed by Prins cyclization and subsequent Ritter amidation (Scheme 3).

The structures of compounds **3a**–**3q** were characterized by spectral and elemental analyses. Compound **3j** showed peaks at 3282, 3071, 1638, and 1114 cm^{-1}, indicating the presence of –NH–, –CH, –CO, and –C–O–C– groups in the IR spectrum. A singlet at δ 1.96 and a doublet at 5.49 (D_2O exchangeable) in the ^1H NMR and signals at δ 22.7 and 168.5 in the ^{13}C NMR spectrum confirmed the presence of acetamido group in the molecule. The mass spectral data and elemental analysis also supported the structural assignments. The structure of **3j** was also established by NOE experiments (Fig. 2).

A rationale for the cis selectivity could be explained by assuming the formation of an (*E*)-oxocarbenium ion via a chair-like transition state, which has an increased stability relative to the open oxocarbenium ion due to delocalization. The optimal geometry for this delocalization places the hydrogen atom at C4 in a pseudo-axial position, which favours equatorial attack of the nucleophiles.[12]

The structure **3j** shown in Fig. 2 was deduced from the NMR data, where the two substituents were shown to be cis to each other. The H2 and H6 protons have a large coupling of J = 10.0 Hz. Presence of the large coupling indicates that it is in axial position, with large diaxial coupling with H3a and H5a, which implies an equatorial position for the aromatic group at C2. Similarly, the equatorial orientation of the substituent at C4 is suggested by the multiplicities of H3a and H5a protons. The equatorial orientation of the substituents at C2 and C4 was also confirmed by NOESY cross peaks for H2 with H4 and H6. This structure was further confirmed by NOESY cross peaks for NH/H3a, NH/H3e, NH/H5a, NH/H5e, Ar/H3a, and Ar/H3e.

In summary, we have described an efficient Prins–Ritter reaction to produce highly substituted 4-acetamidotetrahydropyrans in high yields with all cis selectivity. The use of inexpensive and readily available cerium(IV) sulfate makes this procedure simple, convenient, and practical. In addition to its simplicity, efficiency, and milder reaction conditions, this method provides an easy access for 4-acetamidotetrahydropyran derivatives with diverse chemical structures.

Experimental

Materials and methods

Zinc(II) chloride, ferric chloride hexahydrate, stannous chloride dihydrate, and potassium hydrogen sulfate were ob-

Table 1. Synthesis of 4-acetamidotetrahydropyrans via Prins–Ritter reaction.

Entry	Homoallyl alcohol (**1**)	Carbonyl compound (**2**)	Product[a] (**3**)	Time (h)	Yield (%)[b]
1	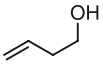	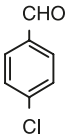	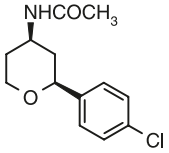 **3a**	6.5	93
2	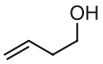	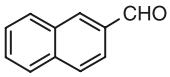	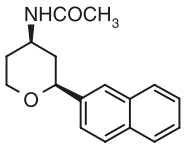 **3b**	7.0	90
3	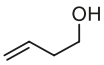	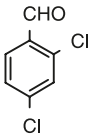	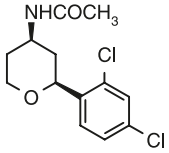 **3c**	6.5	94
4	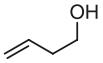	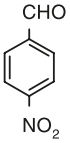	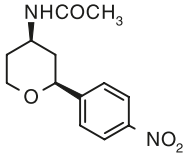 **3d**	6.0	92
5	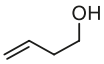	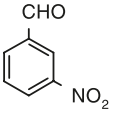	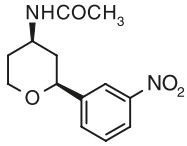 **3e**	6.0	92
6	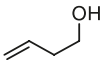	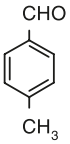	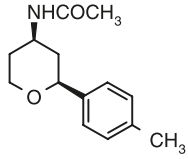 **3f**	7.5	88
7	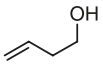	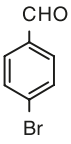	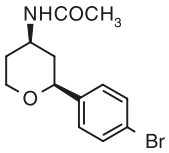 **3g**	7.0	90
8	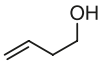	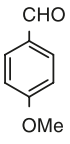	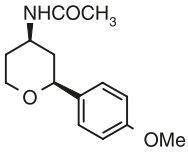 **3h**	7.5	88
9	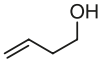		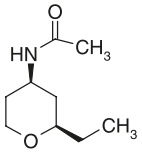 **3i**	7.5	82

Table 1. *Concluded.*

Entry	Homoallyl alcohol (**1**)	Carbonyl compound (**2**)	Product[a] (**3**)		Time (h)	Yield (%)[b]
10	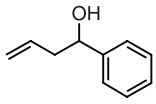	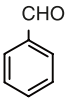	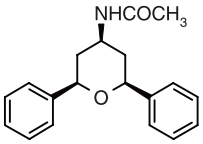	**3j**	6.5	85
11	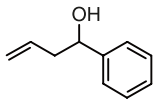	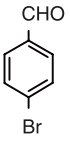	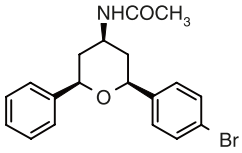	**3k**	6.0	87
12	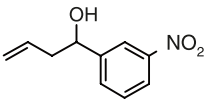	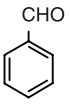	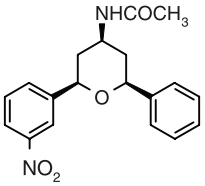	**3l**	6.5	87
13	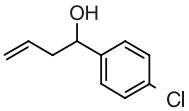	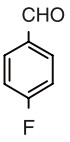	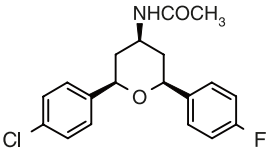	**3m**	6.0	86
14	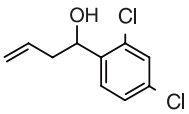	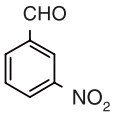	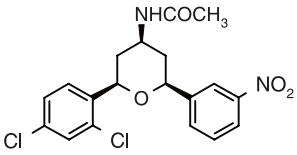	**3n**	6.0	88
15	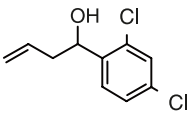	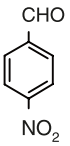	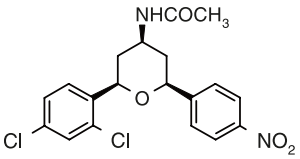	**3o**	6.0	86
16	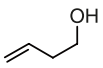		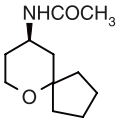	**3p**	7.0	85
17	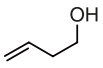	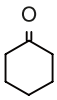	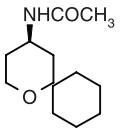	**3q**	7.0	83

[a] All the products were characterized by ^{1}H NMR, ^{13}C NMR, IR, MS, and elemental analysis.
[b] Isolated yield.

Scheme 3. Plausible mechanism.

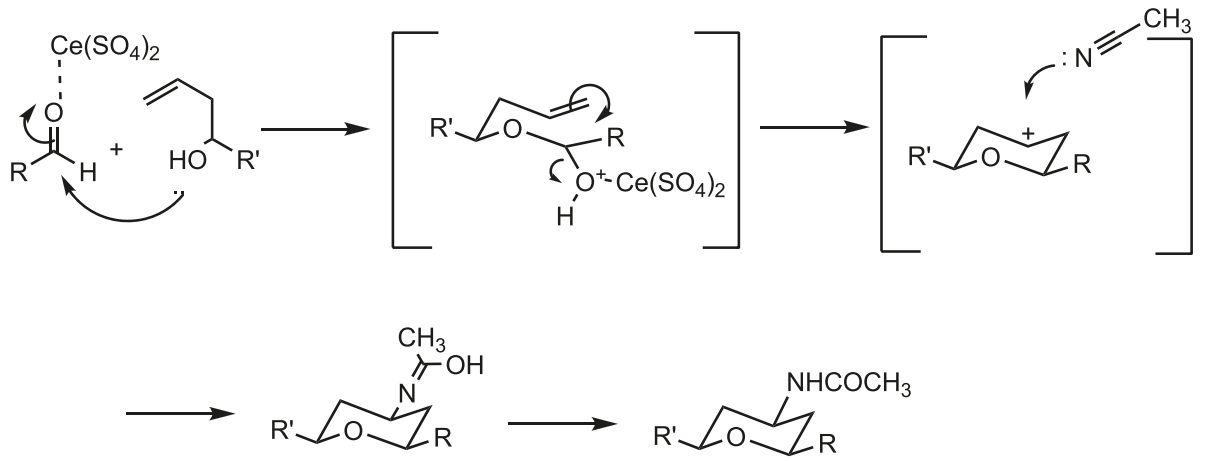

Fig. 2. Characteristic NOE of **3j**.

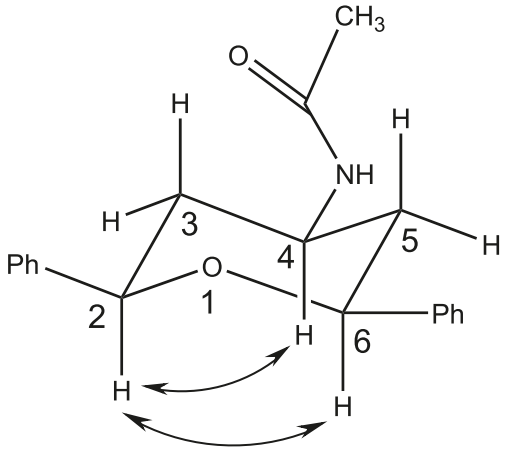

tained from S.D. Fine Chemicals. Cerium(IV) sulfate and phosphotungstic acid were purchased from Aldrich. Reagent-grade acetonitrile was used. All melting points are uncorrected. IR spectra were recorded on a PerkinElmer FTIR spectrophotometer. ^{1}H and ^{13}C NMR spectra were recorded in DMSO-d_6 and $CDCl_3$ using TMS as an internal standard on a JEOL and Bruker spectrometers at 500 MHz and 125 MHz, respectively. Mass spectra were recorded on a Thermo Fennign mass spectrometer using electrospray ionization method. Elemental analyses were recorded using a Thermo Finnigan FLASH EA 1112 CHN analyzer. Column chromatography was performed on silica gel (100–200 mesh, SRL, India). Analytical TLC was performed on precoated plastic sheets of silica gel G/UV-254 of 0.2 mm thickness (Macherey-Nagel, Germany).

General procedure for the synthesis of 4-acetamidotetrahydropyrans (3a–3q)

A mixture of homoallylic alcohol (1.0 mmol), carbonyl compound (1.0 mmol), and cerium(IV) sulfate (20 mol%) in acetonitrile (5 mL, used as a solvent) was stirred at room temperature for a specified time (Table 1). After completion of the reaction as indicated by TLC, the reaction mixture was quenched with ice water (10 mL) and extracted with ethyl acetate (2 × 15 mL). The combined organic layers were dried over anhydrous Na_2SO_4. Removal of solvent followed by purification on silica gel (Merck, 100–200 mesh, ethyl acetate – hexane, 4:6) gave pure 4-acetamidotetrahydropyran.

N-[2-(4-Chlorophenyl)tetrahydropyran-4-yl]acetamide 3a (Table 1, entry 1)

White solid. Isolated yield: 93%, mp 177–179 °C. ^{1}H NMR (500 MHz, DMSO-d_6) δ: 1.16 (q, 1H, J = 11.5 Hz), 1.37 (m, 1H), 1.70 (m, 4H), 1.91 (d, 1H, J = 13.0 Hz), 3.49 (t, 1H, J = 12.3 Hz), 3.89 (m, 2H), 4.34 (d, 1H, J = 10.7 Hz), 7.28 (m, 4H), 7.84 (d, 1H, J = 7.65 Hz, D_2O exchangeable). ^{13}C NMR (125 MHz, DMSO-d_6) δ: 23.2, 32.6, 42.0, 46.0, 66.8, 77.4, 122.7, 128.6, 132.1, 142.1, 168.9. IR ν_{max} (KBr): 3287, 2930, 2845, 1643, 1563, 1362, 1148, 1090, 830 cm^{-1}. Mass (ESI): 254 (M + 1). Anal. calcd. for $C_{13}H_{16}NO_2Cl$: C, 61.54; H, 6.36; N, 5.52%. Found: C, 61.75; H, 6.40; N, 5.58%.

N-(2-Naphthalen-2-yl-tetrahydropyran-4-yl)acetamide 3b (Table 1, entry 2)

Pale yellow solid. Yield: 90%, mp 154–156 °C. ^{1}H NMR (500 MHz, $CDCl_3$) δ: 1.52 (m, 2H), 1.89 (s, 3H), 2.03 (m, 1H), 2.32 (m, 1H), 3.76 (m, 1H), 4.23 (m, 1H), 4.24 (m, 1H), 4.56 (dd, 1H, J_1 = 3.4 Hz, J_2 = 13.0 Hz), 5.46 (d, 1H, J = 8.4 Hz, D_2O exchangeable), 7.47 (m, 3H), 7.59 (m, 4H).^{13}C NMR (125 MHz, $CDCl_3$) δ: 23.2, 32.9, 40.3, 47.1, 67.4, 78.7, 124.1, 124.6, 125.9, 126.8, 127.4, 128.3, 133.0, 134.1, 139.8, 169.9. IR ν_{max} (KBr): 3276, 3048, 2943, 1639, 1550, 1372, 1250, 1145, 1089, 964 cm^{-1}. Mass (ESI): 270 (M + 1). Anal. calcd. for $C_{17}H_{19}NO_2$: C, 75.81; H, 7.11; N, 5.20%. Found: C, 76.09; H, 7.16; N, 5.17%.

N-[2-(2,4-Dichlorophenyl)tetrahydropyran-4-yl]acetamide 3c (Table 1, entry 3)

White solid. Isolated yield: 94%, mp 153–155 °C. ^{1}H NMR (500 MHz, DMSO-d_6) δ: 1.07 (q, 1H, J = 12.2 Hz), 1.41 (m, 1H), 1.72 (m, 4H), 1.99 (m, 1H), 3.54 (t, 1H, J = 11.5 Hz), 3.91 (m, 1H), 4.01 (m, 1H), 4.56 (d, 1H, J = 10.7 Hz), 7.38 (d, 1H, J = 8.4 Hz), 7.44 (d, 1H, J = 8.4 Hz), 7.51 (s, 1H), 7.86 (d, 1H, J = 6.9 Hz, D_2O exchangeable). ^{13}C NMR (125 MHz, DMSO-d_6) δ: 23.7, 32.5, 39.0, 45.77, 67.1, 74.8, 127.5, 128.4, 129.7, 131.8, 133.1, 139.3, 169.1. IR ν_{max} (KBr): 3299, 2934, 2864, 1642, 1540,

1366, 1145, 1086, 817, 714 cm^{-1}. Mass (ESI): 288 (M + 1). Anal. calcd. for $C_{13}H_{15}NO_2Cl_2$: C, 54.18; H, 5.25%; N, 4.86. Found: C, 54.39; H, 5.29; N, 4.81%.

_N_-[2-(4-Nitrophenyl)tetrahydropyran-4-yl]acetamide 3d (Table 1, entry 4)

White solid. Isolated yield: 92%, mp 164–166 °C. ^{1}H NMR (500 MHz, DMSO-d_6) δ: 1.14 (q, 1H, J = 11.5 Hz), 1.40 (m, 1H), 1.71 (m, 4H), 1.99 (d, 1H, J = 12.2 Hz), 3.52 (t, 1H, J = 12.2 Hz), 3.93 (m, 1H), 4.02 (dd, 1H, J_1 = 3.85 Hz, J_2 = 11.5 Hz), 4.52 (d, 1H, J = 10.0 Hz), 7.55 (d, 2H, J = 8.4 Hz) 7.97 (d, 1H, J = 7.7 Hz), 8.14 (d, 2H, J = 8.4 Hz, D_2O exchangeable). ^{13}C NMR (125 MHz, DMSO-d_6) δ: 23.8, 32.6, 39.3, 44.8, 68.4, 74.3, 126.8, 129.7, 132.9, 139.6, 168.4. IR ν_{max} (KBr): 3288, 2922, 2858, 1672, 1519, 1425, 1345, 1148, 1084, 854 cm^{-1}. Mass (ESI): 265 (M + 1). Anal. calcd. for $C_{13}H_{16}N_2O_4$: C, 59.08; H, 6.10; N, 10.60%. Found: C, 58.87; H, 6.16; N, 10.56%.

_N_-[2-(3-Nitrophenyl)-tetrahydropyran-4-yl]acetamide 3e (Table 1, entry 5)

White solid. Isolated yield: 92%, mp 186–188 °C. ^{1}H NMR (500 MHz, DMSO-d_6) δ: 1.17 (q, 1H, J = 12.3 Hz), 1.41 (m, 1H), 1.73 (m, 4H), 2.03 (m, 1H), 3.54 (t, 1H, J = 11.5 Hz), 3.92 (m, 1H), 4.03 (m, 1H), 4.52 (d, 1H, J = 11.5 Hz), 7.57 (t, 1H, J = 8.4 Hz) 7.73 (d, 1H, J = 7.7 Hz), 7.86 (d, 1H, J = 7.7 Hz), 8.07 (d, 1H, J = 8.4 Hz, D_2O exchangeable), 8.11 (s, 1H). ^{13}C NMR (125 MHz, DMSO-d_6) δ: 23.2, 32.5, 41.6, 45.9, 66.9, 76.8, 120.5, 122.6, 130.3, 133.5, 145.3, 148.2, 169.2. IR ν_{max} (KBr): 3288, 2930, 2855, 1635, 1536, 1345, 1148, 1090, 735 cm^{-1}. Mass (ESI): 265 (M + 1). Anal. calcd. for $C_{13}H_{16}N_2O_4$: C, 59.08; H, 6.10; N, 10.60%. Found: C, 59.31; H, 6.16; N, 10.58%.

_N_-(2-_p_-Tolyltetrahydropyran-4-yl)acetamide 3f (Table 1, entry 6)

White solid. Yield: 88%, mp 163–165 °C. ^{1}H NMR (500 MHz, $CDCl_3$) δ: 1.43 (m, 2H), 1.90 (s, 3H), 1.98 (m, 1H), 2.21 (m, 1H), 2.36 (s, 3H), 3.65 (m, 1H), 4.17 (m, 2H), 4.37 (dd, 1H, J_1 = 3.1 Hz, J_2 = 12.6 Hz), 5.46 (d, 1H, J = 8.4 Hz, D_2O exchangeable), 7.73 (m, 4H). ^{13}C NMR (125 MHz, $CDCl_3$) δ: 21.6, 21.9, 23.4, 26.1, 34.0, 40.6, 42.8, 126.3, 128.3, 134.8, 136.3, 169.3. IR ν_{max} (KBr): 3286, 2957, 2938, 1651, 1556, 1371, 1096, 1042, 871, 730 cm^{-1}. Mass (ESI): 256 (M + Na). Anal. calcd. for $C_{14}H_{19}NO_2$: C, 72.07; H, 8.21; N, 6.00%. Found: C, 72.37; H, 8.26; N, 6.02%.

_N_-[2-(4-Bromophenyl)tetrahydropyran-4-yl]acetamide 3g (Table 1, entry 7)

White solid. Yield: 90%, mp 176–178 °C. ^{1}H NMR (500 MHz, $CDCl_3$) δ: 0.96 (t, 3H, J = 7.5 Hz), 1.61 (m, 4H), 2.19 (m, 4H), 3.69 (m, 1H), 4.10 (m, 2H), 4.36 (dd, 1H, J_1 = 2.2 Hz, J_2 = 11.6 Hz), 5.21 (d, 1H, J = 7.7 Hz, D_2O exchangeable), 7.19 (d, 2H, J = 8.4 Hz), 7.49 (d, 2H, J = 8.4 Hz).^{13}C NMR (125 MHz, $CDCl_3$) δ: 22.7, 32.8, 39.6, 47.1, 69.1, 77.9, 122.3, 128.4, 132.6, 142.1, 173.2. IR ν_{max} (KBr): 3296, 2956, 2849, 1648, 1560, 1268, 1096, 741 cm^{-1}. Mass (ESI): 327 (M + 1). Anal. calcd. for $C_{15}H_{20}BrNO_2$: C, 55.23; H, 6.18; N, 4.29%. Found: C, 55.46; H, 6.23; N, 4.32%.

_N_-[2-(4-Methoxyphenyl)tetrahydropyran-4-yl]acetamide 3h (Table 1, entry 8)

Pale green solid. Yield: 88%, mp 182–184 °C. ^{1}H NMR (500 MHz, $CDCl_3$) δ: 1.36 (q, 1H, J = 12.5 Hz), 1.39 (m, 1H), 1.98 (s, 3H), 2.10 (m, 1H), 2.16 (m, 1H), 3.69 (m, 1H), 3.78 (s, 3H), 4.17 (m, 2H), 4.33 (dd, 1H, J_1 = 2.2 Hz, J_2 = 11.8 Hz), 5.36 (d, 1H, J = 7.7 Hz, D_2O exchangeable), 6.96 (d, 2H, J = 8.4 Hz), 7.18 (m, 2H). ^{13}C NMR (125 MHz, $CDCl_3$) δ: 23.1, 41.4, 43.1, 46.7, 54.7, 59.6, 74.1, 114.8, 129.1, 134.3, 156.8, 169.4. IR ν_{max} (KBr): 3341, 2956, 2937, 1649, 1561, 1371, 1079, 1043, 814, 733 cm^{-1}. Mass (ESI): 250 (M + 1). Anal. calcd. for $C_{14}H_{19}NO_3$: C, 67.45; H, 7.68; N, 5.62%. Found: C,67.63; H,7.71; N, 5.66%.

_N_-(2-Ethyltetrahydropyran-4-yl)acetamide 3i (Table 1, entry 9)

White solid, Isolated yield: 82%, mp 80–83 °C. ^{1}H NMR (500 MHz, $CDCl_3$) δ: 0.96 (t, 3H, J = 7.5 Hz), 1.26 (m, 4H), 1.86 (m, 2H), 1.97 (s, 3H), 3.28 (m, 1H), 3.47 (m, 1H), 3.96 (m, 2H), 5.46 (d, 1H, J = 8.4 Hz, D_2O exchangeable) . ^{13}C NMR (125 MHz, $CDCl_3$) δ: 9.9, 23.6, 29.3, 33.1, 39.3, 47.3, 68.9, 77.7, 169.3. IR ν_{max} (KBr): 3288, 3097, 2956, 2936, 2847, 1648, 1560, 1439, 1374, 1156, 1096, 978, 738 cm^{-1}. Mass (ESI): 194 (M + Na). Anal. calcd. for $C_9H_{17}NO_2$: C, 63.13; H, 10.01; N, 8.18%. Found: C, 63.37; H, 10.08; N, 8.21%.

_N_-(2,6-Diphenyltetrahydropyran-4-yl)acetamide 3j (Table 1, entry 10)

Pale yellow solid. Isolated yield: 85%, mp: 220–222 °C. ^{1}H NMR (500 MHz, $CDCl_3$) δ: 1.38 (q, 2H, J = 12.2 Hz), 1.96 (s, 3H), 2.26 (m, 2H), 4.35 (m, 1H), 4.64 (d, 2H, J = 10.0 Hz), 5.49 (d, 1H, J = 8.4 Hz, D_2O exchangeable), 7.27 (m, 2H), 7.32 (t, 4H, J = 6.9 Hz), 7.40 (d, 4H, J = 6.9 Hz). ^{13}C NMR (125 MHz, DMSO-d_6) δ: 22.7, 45.8, 77.3, 125.6, 127.2, 128.2, 142.5, 168.5. IR ν_{max} (KBr): 3282, 3071, 2832, 1638, 1547, 1438, 1290, 1114, 738 cm^{-1}. Mass (ESI): 296 (M + 1). Anal. calcd. for $C_{19}H_{21}NO_2$: C, 77.26; H, 7.17; N, 4.74%. Found: C, 77.47; H, 7.21; N, 4.69%.

_N_-[2-(4-Bromophenyl)-6-phenyltetrahydropyran-4-yl]acetamide 3k (Table 1, entry 11)

Pale yellow solid. Yield: 87%, mp 169–172 °C. ^{1}H NMR (500 MHz, $CDCl_3$) δ: 1.30 (m, 2H), 1.79 (s, 3H), 2.36 (m, 2H), 4.39 (m, 1H), 4.62 (m, 2H), 5.39 (d, 1H, J = 7.7 Hz, D_2O exchangeable), 7.30 (m, 5H), 7.46 (m, 2H), 7.52 (m, 2H). ^{13}C NMR (125 MHz, $CDCl_3$) δ: 23.2, 40.8, 42.6, 47.8, 77.9, 79.3, 125.8, 128.3, 129.6, 130.6, 132.1, 141.6, 142.9, 143.2, 169.3. IR ν_{max} (KBr): 3321, 2956, 2846, 1656, 1548, 1363, 1078, 946, 813, 736 cm^{-1}. Mass (ESI): 375 (M + 1). Anal. calcd. for $C_{19}H_{20}BrNO_2$: C, 60.97; H, 5.39; N, 3.74%. Found: C, 61.10; H, 5.40; N, 3.76%.

_N_-[2-(3-Nitrophenyl)-6-phenyltetrahydropyran-4-yl]acetamide 3l (Table 1, entry 12)

Off-white solid. Isolated yield: 87%, mp 178–180 °C. ^{1}H NMR (500 MHz, DMSO-d_6) δ: 1.35 (m, 2H), 1.89 (s, 3H), 2.09 (m, 2H), 4.15 (m, 1H), 4.65 (m, 2H), 7.23 (m, 9H), 8.74 (d, 1H, J = 7.5 Hz, D_2O exchangeable). ^{13}C NMR

(125 MHz, DMSO-d_6) δ: 22.7, 24.0, 33.4, 45.6, 56.9, 77.5, 120.1, 120.8, 122.3, 125.6, 127.2, 129.9, 132.3, 142.1, 144.6, 147.8, 168.9. IR ν_{max} (KBr): 3301, 1663, 1533, 1347, 1096, 698 cm^{-1}. Mass (ESI): 341 (M + 1). Anal. calcd. for $C_{19}H_{20}N_2O_4$: C, 67.05; H, 5.92; N, 8.23%. Found: C, 67.29; H, 5.98; N, 8.27%.

***N*-[2-(4-Chlorophenyl)-6-(4-fluorophenyl)-tetrahydropyran-4-yl]acetamide 3m (Table 1, entry 13)**

Pale brown solid. Yield: 86%, mp 108–111 °C. ^{1}H NMR (500 MHz, $CDCl_3$) δ: 1.35 (m, 2H), 1.96 (s, 3H), 2.23 (m, 2H), 4.35 (m, 1H), 4.59 (d, 2H, J = 10.7 Hz), 5.61 (d, 1H, J = 7.7 Hz, D_2O exchangeable), 6.99 (t, 2H, J = 8.4 Hz), 7.30 (m, 6H). ^{13}C NMR (125 MHz, $CDCl_3$) δ: 24.0, 36.3, 40.3, 46.2, 62.4, 78.3, 115.6, 126.5, 127.9, 129.3, 133.3, 137.7, 140.4, 162.7 (J_{C-F} = 210.2 Hz), 169.6. IR ν_{max} (KBr): 3314, 2924, 1639, 1545, 1372, 1219, 1075, 828, 579 cm^{-1}. Mass (ESI): 348 (M + 1). Anal. calcd. for $C_{19}H_{19}NO_4FCl$: C, 65.61; H, 5.51; N, 4.03%. Found: C, 65.73; H, 5.52; N, 4.06%.

***N*-[2-(2,4-Dichlorophenyl)-6-(3-nitrophenyl)tetrahydropyran-4-yl]acetamide 3n (Table 1, entry 14)**

White solid. Yield: 88%, mp 128–131 °C. ^{1}H NMR (500 MHz, DMSO-d_6) δ: 1.24 (q, 1H, J = 11.5 Hz), 1.37 (q, 1H, J = 11.5 Hz), 1.76 (s, 3H), 2.09 (t, 2H, J = 13.8 Hz), 4.17 (m, 1H), 4.88 (t, 2H, J = 10.0 Hz), 7.46 (d, 1H, J = 8.4 Hz), 7.57 (s, 1H), 7.62 (m, 2H), 7.85 (d, 1H, J = 7.7 Hz), 7.91 (d, 1H, J = 7.7 Hz), 8.11 (d, 1H, J = 8.4 Hz, D_2O exchangeable), 8.20 (s, 1H). ^{13}C NMR (125 MHz, $CDCl_3$) δ: 23.2, 38.6,, 40.3, 45.8, 74.7, 77.1, 121.1, 122.1, 123.6, 128.1, 129.1, 129.9, 131.2, 132.2, 133.6, 138.9, 144.7, 148.3, 169.1. IR ν_{max}: 3277, 2926, 2849, 1634, 1535, 1473, 1346, 1128, 1098, 815 cm^{-1}. Mass (ESI): 409 (M + 1). Anal. calcd. for $C_{19}H_{18}N_2O_4Cl_2$: C, 55.76; H, 4.43; N, 6.84. Found: C, 55.96; H, 4.46; N, 6.80%.

***N*-[2-(2,4-Dichlorophenyl)-6-(4-nitrophenyl)tetrahydropyran-4-yl]acetamide 3o (Table 1, entry 15)**

White solid. Yield: 86%, mp 118–120 °C. ^{1}H NMR (500 MHz, DMSO-d_6) δ: 1.30 (q, 2H, J = 12.3 Hz), 1.79 (s, 3H), 2.02 (m, 2H), 4.12 (m, 1H), 4.94 (m, 2H), 7.23 (m, 3H), 7.40 (m, 4H), 8.23 (d, 1H, J = 8.4 Hz, D_2O exchangeable). ^{13}C NMR (125 MHz, $CDCl_3$) δ: 23.2, 36.8, 42.7, 48.7, 63.1, 74.6, 122.3, 126.9, 129.6, 132.1, 133.9, 134.3, 137.1, 138.2, 139.3, 147.6, 169.4. IR ν_{max} (KBr): 3291, 3066, 2929, 2854, 1648, 1520, 1348, 1079, 848, 746, 699 cm^{-1}. Mass (ESI): 431 (M + Na). Anal. calcd. for $C_{19}H_{18}N_2O_4Cl_2$: C, 55.76; H, 4.43; N, 6.84%. Found: C, 55.99; H, 4.47; N, 6.81%.

***N*-(6-Oxaspiro[4.5]dec-9-yl)acetamide 3p (Table 1, entry 16)**

Pale yellow solid. Yield: 85%, mp 148–150 °C. ^{1}H NMR (500 MHz, $CDCl_3$) δ: 1.26 (m, 12H), 1.89 (s, 3H), 3.47 (m, 2H), 3.97 (m, 1H), 5.80 (d, 1H, J = 8.4 Hz, D_2O exchangeable). ^{13}C NMR (125 MHz, $CDCl_3$) δ: 23.2, 24.6, 33.6, 42.9, 43.4, 45.7, 63.1, 85.2, 169.8. IR ν_{max} (KBr): 3353, 3041, 2976, 1638, 1600, 1563, 1367, 1145, 994, 746 cm^{-1}. Mass (ESI): 198 (M + 1). Anal. calcd. for $C_{11}H_{19}NO_2$: C, 66.97; H, 9.71; N, 7.10%. Found: C, 67.21; H, 9.77; N, 7.06%.

***N*-(1-Oxaspiro[5.5]undec-4-yl)acetamide 3q (Table 1, entry 17)**

White solid. Yield: 83%, mp 146–148 °C. ^{1}H NMR (500 MHz, $CDCl_3$) δ: 1.27 (m, 12H), 1.87 (m, 1H), 1.98 (s, 3H), 2.00 (m, 1H), 3.71 (m, 1H), 3.69 (m, 1H), 4.16 (m, 1H), 5.21 (d, 1H, J = 7.2 Hz, D_2O exchangeable). ^{13}C NMR (125 MHz, $CDCl_3$) δ: 21.3, 23.8, 27.6, 33.4, 36.4, 41.8, 47.9, 68.4, 79.8, 169.4. IR ν_{max} (KBr): 3346, 2958, 2931, 2847, 1648, 1536, 1349, 1208, 1098, 746 cm^{-1}. Mass (ESI): 234 (M + Na). Anal. calcd. for $C_{12}H_{21}NO_2$: C, 68.21; H, 10.02; N, 6.63%. Found: C, 68.43; H, 10.07; N, 6.59%.

Supplementary data

Supplementary data for this article are available on the journal Web site (canjchem.nrc.ca) or may be purchased from the Depository of Unpublished Data, Document Delivery, CISTI, National Research Council Canada, Ottawa, ON K1A 0R6, Canada. DUD 3929. For more information on obtaining material, refer to cisti-icist.nrc-cnrc.gc.ca/cms/unpub_e.shtml.

Acknowledgement

One of the authors, N.P., thanks the Council of Scientific and Industrial Research, New Delhi, for the research fellowship.

References

(1) (a) Armstrong, R. W.; Combs, A. P.; Tempest, P. A.; Brown, S. D.; Keating, T. A. *Acc. Chem. Res.* **1996**, *29*, 123 doi:10.1021/ar9502083.; (b) Terrett, N. K.; Gardner, M.; Gordon, D. W.; Kobylecki, R. J.; Steel, J. *Tetrahedron* **1995**, *51*, 8135. doi:10.1016/0040-4020(95)00467-M.

(2) (a) Bahnck, K. B.; Rychnovsky, S. D. *Chem. Commun.* **2006**, 2388 PMID:16733589.; (b) Yang, X.-F.; Wang, M.; Zhang, Y.; Li, C.-J. *Synlett* **2005**, 1912; (c) Aubele, D. L.; Wan, S.; Floreancig, P. E. *Angew. Chem., Int. Ed.* **2005**, *44*, 3485. doi:10.1002/anie.200500564.

(3) (a) Michelet, V.; Genet, J.-P. *Curr. Org. Chem.* **2005**, *9*, 405; (b) Suhara, Y.; Yamaguchi, Y.; Collins, B.; Schnaar, R. L.; Yanagishita, M.; Hildreth, J. E. K.; Shimada, I.; Ichikawa, Y. *Bioorg. Med. Chem.* **2002**, *10*, 1999. doi:10.1016/S0968-0896(02)00020-2. PMID:11937360.

(4) (a) Hart, D. J.; Bennett, C. E. *Org. Lett.* **2003**, *5*, 1499 doi:10.1021/ol0342756. PMID:12713308.; (b) Jasti, R.; Vitale, J.; Rychnovsky, S. D. *J. Am. Chem. Soc.* **2004**, *126*, 9904. doi:10.1021/ja046972e. PMID:15303848.

(5) (a) Waldmann, H. *Synthesis* **1994**, 535 doi:10.1055/s-1994-25519.; (b) Dossetter, A. G.; Jamison, T. F.; Jacobsen, E. N. *Angew. Chem., Int. Ed.* **1999**, *38*, 2398. doi:10.1002/(SICI)1521-3773(19990816)38:16<2398::AID-ANIE2398>3.0.CO;2-E.

(6) (a) Hilli, F.; White, J. M.; Rizzacasa, M. A. *Org. Lett.* **2004**, *6*, 1289 doi:10.1021/ol0497943. PMID:15070319.; (b) Takahashi, S.; Kubota, A.; Nakata, T. *Tetrahedron* **2003**, *59*, 1627. doi:10.1016/S0040-4020(03)00135-2.

(7) (a) Yadav, J. S.; Reddy, B. V. S.; Reddy, M. S.; Niranjan, N.; Prasad, A. R. *Eur. J. Org. Chem.* **2003**, 1779 doi:10.1002/ejoc.200210638.; (b) Yadav, J. S.; Reddy, B. V. S.;

Gupta, M. K.; Biswas, S. K. *Synthesis* **2004**, 2711 doi:10.1055/s-2004-831220.; (c) Bach, T.; Löbel, J. *Synthesis* **2002**, 2521 doi:10.1055/s-2002-35645.; (d) Tian, G.-Q.; Shi, M. *Org. Lett.* **2007**, *9*, 2405. doi:10.1021/ol0709026. PMID: 17503842.

(8) (a) Epstein, O. L.; Rovis, T. J. *J. Am. Chem. Soc.* **2006**, *128*, 16480 doi:10.1021/ja066794k. PMID:17177379.; (b) Perron, F.; Albizati, K. F. *J. Org. Chem.* **1987**, *52*, 4128 doi:10.1021/jo00227a037.; (c) Al-Mutairi, E. H.; Crosby, S. R.; Darzi, J.; Harding, J. R.; Hughes, R. A.; King, C. D.; Simpson, T. J.; Smith, R. W.; Willis, C. L. *Chem. Commun. (Camb.)* **2001**, 835. doi:10.1039/b101414p.

(9) Yadav, J. S.; Reddy, B. V. S.; Aravind, S.; Kumar, G. G. K. S. N.; Madhavi, C.; Kunwar, A. C. *Tetrahedron* **2008**, *64*, 3025. doi:10.1016/j.tet.2008.01.038.

(10) Yadav, J. S.; Reddy, B. V. S.; Kumar, G. G. K. S. N.; Reddy, G. M. *Tetrahedron Lett.* **2007**, *48*, 4903. doi:10.1016/j.tetlet.2007.05.056.

(11) (a) Selvam, N. P.; Perumal, P. T. *Can. J. Chem.* **2007**, *85*, 989 doi:10.1139/V07-116.; (b) Selvam, N. P.; Perumal, P. T. *Tetrahedron Lett.* **2006**, *47*, 7481. doi:10.1016/j.tetlet.2006.08.038.

(12) (a) Alder, R. W.; Harvey, J. N.; Oakley, M. T. *J. Am. Chem. Soc.* **2002**, *124*, 4960 doi:10.1021/ja025902+. PMID: 11982351.; (b) Jasti, R.; Rychnovsky, S. D. *Org. Lett.* **2006**, *8*, 2175. doi:10.1021/ol0606738. PMID:16671810.

Effet des cations extra-réseau de la zéolithe Y sur l'activité catalytique du palladium dans la réaction de combustion du méthane

Mongia Saïd Zina, Lobna Bassalah et Abdelhamid Ghorbel

Can. J. Chem. Downloaded from www.nrcresearchpress.com by Sichuan Normal University on 09/14/12
For personal use only.

Résumé : Les cations compensateurs alcalins et alcalino-terreux sont introduits dans les supports à base de zéolithe pour étudier l'influence de leurs basicités sur l'activité du palladium supporté dans la réaction de combustion totale du méthane. Cette étude a aussi pour objectif de montrer que les propriétés acido-base du support peuvent affecter la structure et l'état d'oxydation du palladium. Les résultats montrent que tous les échantillons s'activent légèrement avec le temps. De plus, à une température inférieure à 430 °C, PdLiNaY semble être le catalyseur le plus actif, tandis qu'à des températures plus élevées, PdHY est l'échantillon le plus actif. À l'exception de PdHY, tous les catalyseurs au palladium ont une énergie d'activation (E_a) dans la gamme entre 79 et 97 kJ mol^{-1}.

Mots-clés : zeolithe NaY, basicité, palladium, combustion de méthane.

Abstract: Alkali and alkaline earth metal cations were introduced into zeolite to explore their influence on the activity of supported palladium in the total combustion of methane and to study how the acido-basic properties of the support affected the structure and the oxidation state of Pd. The results show that all samples exhibit a slight activation with time. Moreover, at temperatures below 430 °C, PdLiNaY seems to be the most active catalyst, while PdHY is the most active sample at higher temperatures. Except for PdHY, all Pd catalysts lead to an activation energy (E_a) value in the range of 79–97 kJ mol^{-1}.

Key words: NaY zeolite, basicity, palladium, methane combustion.

Introduction

La réaction de combustion du méthane étudiée sur les catalyseurs à base de palladium ou de platine a été considérée sensible à la structure.[1–4] La nature de la phase active dans l'oxydation complète du méthane sur du palladium supporté demeure l'objet de discussions. En effet, la nature des sites catalytiques évoqués dans la littérature sont : le palladium métallique Pd^0, l'oxyde de palladium PdO et une phase mixte de Pd^0/PdO,[4] cependant plusieurs travaux de recherches ont affirmé que la palladium métallique est inactif dans l'oxydation du méthane.

Parmi les supports utilisés dans la réaction d'oxydation du méthane, les zéolithes ont fait l'objet également de plusieurs études. En vue d'obtenir un catalyseur performant à basse température et thermiquement stable, Li et Armor[5] ont étudié l'échange cationique du palladium dans les zéolithes ZSM-5, mordenite et ferrite pour l'oxydation du méthane. Ils ont conclu que l'activité élevée enregistrée pour ces catalyseurs par rapport à celle de Pd/Al_2O_3 est due à la haute dispersion du palladium sur les supports zéolithiques.

Certes les catalyseurs basiques ont eu de l'intérêt mais pas autant que les catalyseurs acides. Cependant, il s'est avéré que ce type de catalyseur possède une activité considérable dans plusieurs réactions telles que la déshydrogénation du 2-propanol, l'alkylation du toluène,[6] l'isomérisation, la condensation, l'addition et la polymérisation.[7] Des chercheurs ont mené des travaux sur des zéolithes échangées aux cations alcalins dans la réaction de condensation du benzaldéhyde et l'éthyle cyanoacétate, et ils ont remarqué que l'activité du catalyseur étudié augmente quand le rapport Si/Al diminue et le rayon cationique de l'ion compensateur augmente.[8] U.D. Joshi et al.[9] ont étudié la corrélation entre l'activité et la basicité des zéolithes. Ils ont montré, également, que l'activité catalytique de la zéolithe NaX échangée aux cations alcalins dans une réaction de condensation croît lorsque la taille du cation échangé augmente selon la séquence CsX > RbX > KX > NaX. D'autres travaux[8] ont suggéré que la cristallinité du support peut influer son activité catalytique.

Notre étude consiste en la modification des supports zéolithiques NaY par échange ionique des cations Na^+ par des cations alcalins Li^+, K^+, Cs^+, des cations alcalino-terreux Ca^{2+} et Mg^{2+} et par les ions ammonium NH_4^+ et la préparation de catalyseurs monométalliques à base de palladium supporté sur la zéolithe modifiée. Nous avons étudié, en premier lieu, l'effet de la nature du cation compensateur sur les propriétés structurales et texturales. En second lieu, nous avons testé l'activité catalytique du palladium supporté dans la réaction d'oxydation totale du méthane.

Reçu le 11 novembre 2008. Acceptée le 2 mars 2009. Publié sur le site Web des Presses scientifiques du CNRC, à revcanchim.cnrc.ca le 19 mai 2009.

M.S. Zina,[1] L. Bassalah et A. Ghorbel. Université El Manar, Faculté des sciences de Tunis, Département de chimie, Laboratoire de chimie des matériaux et catalyse, 2092 Campus Universitaire, Tunis, Tunisie.

1. Auteure correspondante (courriel : mongiasaid@gmail.com).

Partie expérimentale

Préparation et traitement des échantillons

La zéolithe, objet de notre étude, est la faujasite NaY (SK40) de formule $Na_{56}(AlO_2)_{56}(SiO_2)_{136}\cdot x H_2O$ et de rap-

Can. J. Chem. Downloaded from www.nrcresearchpress.com by Sichuan Normal University on 09/14/12
For personal use only.

port Si/Al = 2,4. Elle est fournie par la firme Union Cabride Linde Division (New York, USA). Dans le but de varier la basicité du support zéolithique, nous avons procédé à une opération d'échange en solutions aqueuses de sels de cations alcalins Li, K, Ca (LiCl : VWR Prolabo (Fontenay sous Bois, France), KCl : VWR Prolabo; $CaCl_2$: Acros Organics (Paris, France)) et alcalino-terreux Mg et Cs ($MgCl_2$: Acros Organics; $CsNO_3$: Acros Organics). La forme NH_4Y utilisée dans ce travail est obtenue par des échanges ioniques répétés de la forme NaY dans une solution de NH_4Cl.[10]

Expérimentalement, 2 g de zéolithe NaY sont mis en contact avec 100 mL de la solution à 0,1 mol L^{-1} de l'un des sels de cations alcalins et alcalino-terreux à 80 °C pendant 6 h,[11] la suspension est maintenue ensuite sous agitation à la température ambiante pendant une nuit. Une fois l'opération d'échange achevée, l'échantillon obtenu est filtré et lavé abondamment à l'eau distillée afin d'éliminer les ions NO_3^-, Cl^- et Na^+ libres dans les différentes solutions. Le produit final est enfin séché à l'étuve à 80 °C pendant 24 h. Les matériaux obtenus sont notés MY avec M = Li, K, Ca, Mg ou Cs.

Le protocole d'échange du palladium dans les zéolithes modifiés est inspiré de la méthode décrite dans la littérature,[10] qui consiste à diluer la solution commerciale de chlorure de palladium tétrammine $Pd(NH_3)_4Cl_2$ (Pallic Soc., Engelhart) (à pH 10,0) puis l'ajouter à la zéolithe NaY. Le mélange est gardé sous agitation pendant 24 h à la température ambiante. Après filtration, le produit est lavé abondamment à l'eau distillée puis séché à 90 °C à l'étuve.

Les différents catalyseurs préparés précédemment PdMY (M = Na, H, Li, K, Ca, Mg ou Cs) sont soumis à un prétraitement thermique sous atmosphère oxydante. Les échantillons sont calcinés sous débit d'oxygène de 1,5 L h^{-1} en montée lente de température (1 °C min^{-1}) jusqu'à la température de 500 °C. La calcination à 500 °C est maintenue pendant 12 h.

Caractérisation des échantillons

Les analyses chimiques sont effectuées à l'aide d'un spectromètre d'absorption atomique de type PerkinElmer modèle 3300. Le taux de palladium dans tous les échantillons est d'environ 1 % en masse. L'analyse du sodium dans les différents échantillons montre que les taux d'échange sont inférieurs à 100 % pour tous les cations étudiés (tableau 1). Par ailleurs, on remarque que les différents cations n'ont pas la même facilité de s'échanger. En effet, d'après les résultats, et pour le même mode opératoire d'échange, l'ion Li^+ est le cation le plus difficile à échanger.

Les échantillons calcinés ont été caractérisés par diffraction des rayons X (DRX) au moyen d'un diffractomètre automatisé modèle Philips Panaletical équipé d'un détecteur de type Celator. La radiation utilisée est celle du cuivre Kα, sous une tension accélératrice de 40 kV et d'un courant de 30 mA. L'angle de balayage 2θ pour les diffractogrammes se situe entre 2° et 50°. Les paramètres de maille ont été déterminés à l'aide du programme d'affinement « CELREF/ERACEL ».

Les surfaces spécifiques « BET » des échantillons sont évaluées à partir des isothermes d'adsorption–désorption de l'azote à 77 K, utilisant un appareil volumétrique. Les mesures du volume d'azote adsorbé en fonction de la pression relative P/P° sont déterminées à l'aide d'un appareil Micromeritics de type ASAP 2000.

Tableau 1. Taux d'échange en cations.

Supports	mmol g^{-1} de Na	% de Na échangé
NaY	3,39	0
HY	1,65	51,3
LiY	2,52	25,7
KY	1,09	67,8
CsY	1,13	66,7
MgY	1,30	61,7
CaY	0,96	71,7

Test catalytique

Les catalyseurs ont été réactivés sous atmosphère oxydante et en montée de température de 5 °C min^{-1} jusqu'à 500 °C, puis maintenus sous O_2 pendant 1 h à 500 °C. La réaction de combustion du méthane est réalisée sous pression atmosphérique dans un réacteur à lit fixe traversé par le mélange réactionnel constitué de méthane et d'oxygène dilués dans l'hélium. Les débits volumiques pour le méthane, l'oxygène et l'hélium sont, respectivement, de 1, 4 et 95 mL min^{-1}, et le débit volumique global du mélange est de 6 L h^{-1} (mélange riche en oxygène $O_2/CH_4 = 4$ et masse du catalyseur de 50 mg).

L'analyse des effluents est effectuée à l'aide d'un chromatographe de type Intersmat IGC équipé d'un détecteur à conductivité thermique (catharomètre).

Résultats expérimentaux

Caractérisation des catalyseurs

Étude par DRX

La pureté et la cristallinité des phases cristallines des échantillons traités ont été étudiées par diffraction des rayons X. La zéolithe NaY brute ainsi que les zéolithes échangées ont été analysées dans les mêmes conditions. Le diffractogramme représenté par la figure 1A est celui de la zéolithe NaY, produit de départ des catalyseurs préparés dans ce travail; ce diffractogramme montre essentiellement les pics de diffraction caractéristiques de la zéolithe de type faujasite qui appartient au groupe d'espace Fd3m et est de structure cubique.

À partir des diffractogrammes obtenus des différents échantillons (fig. 1), aucun pic, autre que ceux caractéristiques de la zéolithe Y, lié à des impuretés dues à la préparation ou au traitement des échantillons n'a été détecté. Néanmoins, les diffractogrammes de certains échantillons montrent un léger fond lié à une phase amorphe aux alentours de $2\theta \approx 30°$. En effet, la figure 1 montre que le diffractogramme relatif au catalyseur PdHY présente une phase amorphe détectée vers $2\theta = 29°$ due à une destruction partielle du réseau zéolithique. Ceci est confirmé par la valeur obtenue de la cristallinité de cet échantillon évaluée à 85 %. On observe aussi qu'après échange de la zéolithe, les intensités des pics caractéristiques (111), (220), (311) et (331) diminuent considérablement par rapport à la zéolithe NaY

Can. J. Chem. Downloaded from www.nrcresearchpress.com by Sichuan Normal University on 09/14/12
For personal use only.

Fig. 1. Diffractogrammes des échantillons traités : (A) NaY, PdNaY et PdHY; (B) PdNaY, PdLiY et PdCsY; (C) PdNaY, PdCaY et PdMgY.

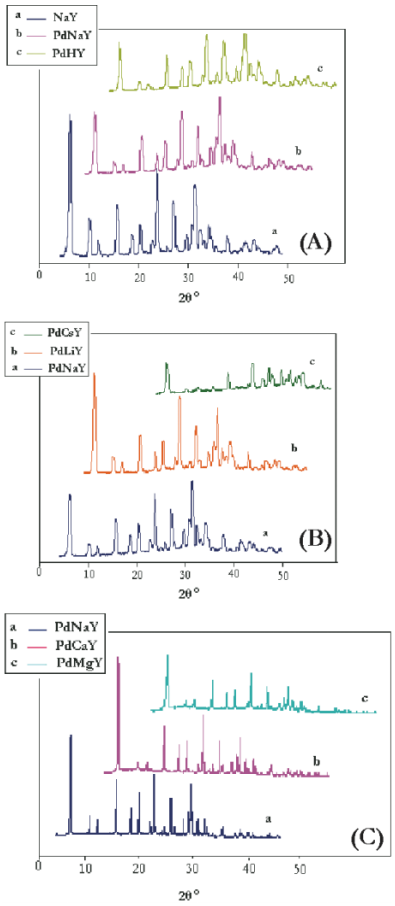

brute. Le diffractogramme relatif au catalyseur PdNaY montre une diminution des intensités des raies de diffraction caractéristiques par rapport à la zéolithe NaY. Toutefois, la cristallinité n'a pas été affectée puisqu'elle vaut 96 %.

Plusieurs études[9,12,13] ont montré que la procédure d'échange ionique n'affecte ni la structure zéolithique ni la nature des phases cristallines. En revanche, dans notre cas, les deux échantillons PdHY et PdCsY ont révélé une légère baisse de la cristallinité générée par une désalumination partielle du support. Le tableau 2 regroupe les valeurs des paramètres de la maille et des rapports Si/Al obtenus à partir de la relation de Breck.[14]

Caractérisation texturale des catalyseurs par la méthode volumétrique

Les isothermes d'adsorption et de désorption de l'azote à 77 K des échantillons permettent d'accéder à la surface spécifique de l'échantillon déterminée selon la méthode « BET ». Les isothermes d'adsorption obtenues sont du type I selon la classification BDDT.[15] Les solides examinés contiennent donc essentiellement des micropores de diamètre inférieur à 20 Å. Le tableau 3 regroupe les résultats obtenus de la caractérisation texturale des échantillons après calcination.

Les zéolithes de type faujasite NaY montrent une surface spécifique élevée dérivant de leur structure microporeuse. Les modifications et les traitements réalisés sur ces supports

Tableau 2. Rapport Si/Al et paramètres de la maille.

Échantillons	*a* (Å)	Si/Al
NaY	24,612	2,96
PdNaY	24,648	2,65
PdHY	24,538	3,80
PdLiY	24,628	2,81
PdKY	24,667	2,50
PdCsY	24,602	3,05
PdCaY	24,668	2,49
PdMgY	24,668	2,49

entraînent des variations dans les paramètres caractéristiques de leur texture qui dépendent de la nature de l'ion échangé.

L'introduction du palladium dans la structure zéolithique a entraîné une légère diminution de la surface spécifique par rapport à la zéolithe de départ, probablement due à l'occupation des ions Pd^{2+} dans les cavités internes de la zéolithe. Par ailleurs, le volume microporeux est presque constant après l'échange.

Le tableau 3 montre également que la surface spécifique S_{BET} ainsi que le volume microporeux accusent une baisse appréciable lorsque les ions Na^+ sont remplacés par les cations monovalents K^+ ou Cs^+ (fig. 2). Dans le cas de la zéolithe échangée au césium (PdCsY), on a noté une réduction d'environ 23 % de la surface spécifique et de 22 % du volume microporeux par rapport à la zéolithe sodique en raison de la taille importante du cation Cs^+.

Cette diminution résulte probablement de l'augmentation de la taille des cations échangés. En effet, plus le cation est volumineux moins la S_{BET} et le volume microporeux sont développés. Ce résultat est confirmé par l'étude obtenue par DRX qui a montré que la cristallinité de ces deux échantillons a été affectée. En revanche, la surface spécifique S_{BET} des échantillons échangés au cations moins volumineux est légèrement affectée, contrairement à celle correspondante aux échantillons échangés par des cations de plus grande taille.

Comme il a été suggéré par Langmi et al.,[16] l'accessibilité des molécules d'azote aux pores dans le cas où le support a subi un échange cationique est limitée, et la présence de cations de large taille affecte le volume poreux disponible. Par ailleurs, pour les échantillons échangés aux cations bivalents Mg^{2+} et Ca^{2+}, une légère diminution de la surface S_{BET} et du volume poreux par rapport à la zéolithe NaY est enregistrée.

Des études antérieures[17] ont montré que la surface spécifique du catalyseur PdHY est légèrement plus élevée que celle du catalyseur PdNaY en raison du remplacement des ions sodium par les protons moins volumineux. Toutefois, les résultats obtenus, dans le cadre de nos travaux, montrent une diminution du volume des micropores ainsi que de la surface spécifique de l'échantillon PdHY, ceci est dû à la destruction partielle de la structure causée par une désalumination du support. Cette suggestion est appuyée par les résultats de l'analyse par diffraction des rayons X.

Test catalytique

Dans ce travail, nous avons suivi la combustion catalytique du méthane en CO_2 et H_2O en fonction du temps et contrôlé la variation de l'activité des catalyseurs en fonction

Tableau 3. Résultats de l'étude texturale des catalyseurs.

	NaY	PdHY	PdLiY	PdNaY	PdKY	PdCsY	PdMgY	PdCaY
S_{BET} (m^2 g^{-1})	607	556	606	601	544	462	580	581
$S_{Langmuir}$ (m^2 g^{-1})	960	885	953	958	864	735	911	928
$S_{\mu poreuse}$ (m^2 g^{-1})	567	494	581	564	519	440	535	521
$V_{t\ des\ pores}$ (cm^3 g^{-1})	0,36	0,33	0,35	0,36	0,32	0,27	0,35	0,36
$i_{micropores}$ (cm^3 g^{-1})	0,32	0,28	0,32	0,32	0,29	0,25	0,30	0,30
$Ø_{micropores}$ (Å)	15,0	15,0	14,8	15,0	14,8	14,8	15,2	15,3

Fig. 2. Évolution de la surface spécifique en fonction du rayon ionique des ions alcalins échangés.

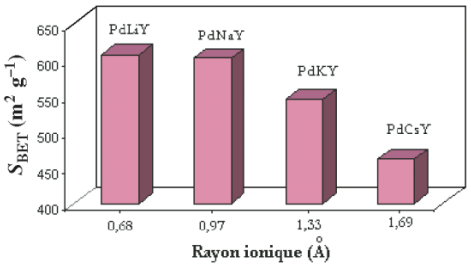

de la température. Les chromatogrammes obtenus nous ont permis de déterminer les taux de transformations globales de la réaction considérée.

Variation du taux de conversion en fonction du temps

La réaction de combustion du méthane en présence des différents catalyseurs a été étudiée pendant 180 min. L'activité propre du support zéolithique a été testée dans les mêmes conditions des catalyseurs préparés, et il s'est avéré que le support a une activité négligeable par rapport à celle du palladium supporté. Par ailleurs, seuls le dioxyde de carbone et l'eau sont obtenus, et aucune trace de monoxyde de carbone n'a été détectée lors de ce travail. De plus, nous signalons que les bilans en carbone sont respectés.

Les figures 3A et 3B représentent les variations du taux de transformation globale en fonction du temps à 500 °C pour les catalyseurs dont le support à été modifié par échange cationique avec H^+ ou des cations alcalins (fig. 3A). Ces courbes montrent que tous les échantillons s'activent légèrement au cours du temps et évoluent d'une manière pratiquement similaire. Cependant, les catalyseurs PdNaY et PdKY se stabilisent après 30 min, alors que PdHY, PdLiY et PdCsY atteignent leur régime quasi-stationnaire après une période relativement plus longue. Signalons aussi que l'activité initiale de PdNaY est la plus élevée et se stabilise rapidement, alors que celle de PdHY est plus faible mais augmente et devient supérieure à celle de PdNaY après 30 min de réaction.

Par ailleurs, pour le catalyseur PdKY, la conversion du méthane est faible par rapport à l'échantillon de référence PdNaY et évolue légèrement en fonction du temps. Lorsqu'on observe le comportement du catalyseur PdCsY, on remarque que son activité est la plus faible par rapport aux autres catalyseurs et que le taux de conversion augmente légèrement au cours du temps et atteint un état quasi-stationnaire après plus de 2,5 h de réaction.

La figure 3B regroupe les résultats des tests catalytiques correspondant aux catalyseurs au palladium supportés sur zéolithes échangées aux cations Ca^{2+} et Mg^{2+} ainsi que le catalyseur de référence PdNaY. La courbe relative à l'échantillon PdCaY révèle une activité initiale légèrement plus faible que celle de PdNaY, mais les taux de conversions de ces deux catalyseurs sont quasi égaux après 90 min de réaction. De plus, l'activité de PdCaY atteint l'état stationnaire au bout d'1 h. En revanche le catalyseur déposé sur MgY révèle une faible activité initiale qui augmente et atteint son régime stationnaire après 2 h de réaction. Quant au taux de conversion, il est nettement inférieur à celui de PdCaY mais comparable à celui de PdKY.

Variation du taux de conversion en fonction de la température

Nous avons étudié l'évolution de la conversion du méthane en fonction de la température de la réaction entre 300 et 500 °C pour les catalyseurs dont les supports ont été échangés par les cations monovalents et bivalents. Les courbes obtenues révèlent que tous les catalyseurs étudiés sont quasiment inactifs à une température inférieure à 300 °C (fig. 4) et montrent qu'à des températures inférieures à 400 °C, le catalyseur PdLiY est le plus actif, alors qu'à des températures plus élevées c'est le catalyseur PdHY qui devient le plus actif. Cependant, dans ce domaine de température, le catalyseur PdCsY présente l'activité catalytique la plus faible.

L'analyse de l'évolution de l'activité en fonction de la température montre que le catalyseur supporté sur la zéolithe sodique est le plus sensible à la température du fait qu'aux alentours de 500 °C, la variation du taux de conversion du méthane est la plus élevée. En effet, en évaluant la pente de la tangente de chaque courbe à 500 °C et les températures relevées pour des taux de conversion du méthane de 10 %, 30 % et 60 %, on trouve les valeurs rassemblées dans le tableau 4. Les valeurs déterminées T_{10} et T_{30} montrent que l'échantillon PdNaY est légèrement plus actif que PdCaY dans les régions de basses températures.

On remarque que la valeur de T_{30} pour le catalyseur PdHY est comparable à celle rapportée par Ishihara et al.[18] En ce qui concerne le catalyseur PdNaY, les valeurs déterminées (tableau 4) sont proches que celles trouvées dans la littérature.[19,20]

Les résultats du tableau 4 montrent que pour les échantillons PdKY et PdCsY, une conversion du méthane de 60 % est obtenue à des températures supérieures à 600 °C, alors que pour le catalyseur PdLiY, ce taux de conversion est obtenu à une température de l'ordre de 495 °C. Ce catalyseur s'active donc à des températures plus basses que celles des échantillons PdKY et PdCsY.

En effet, l'évolution de l'activité catalytique en fonction de la température montre que les catalyseurs supportés sur les zéolithes échangées aux cations moins volumineux s'activent à des températures plus basses que celles relatives aux échantillons échangées par des cations de taille plus élevée

Can. J. Chem. Downloaded from www.nrcresearchpress.com by Sichuan Normal University on 09/14/12
For personal use only.

Fig. 3. Variation de la conversion du méthane en fonction du temps pour les catalyseurs échangés aux cations alcalins (A) ou aux cations alcalino-terreux (B).

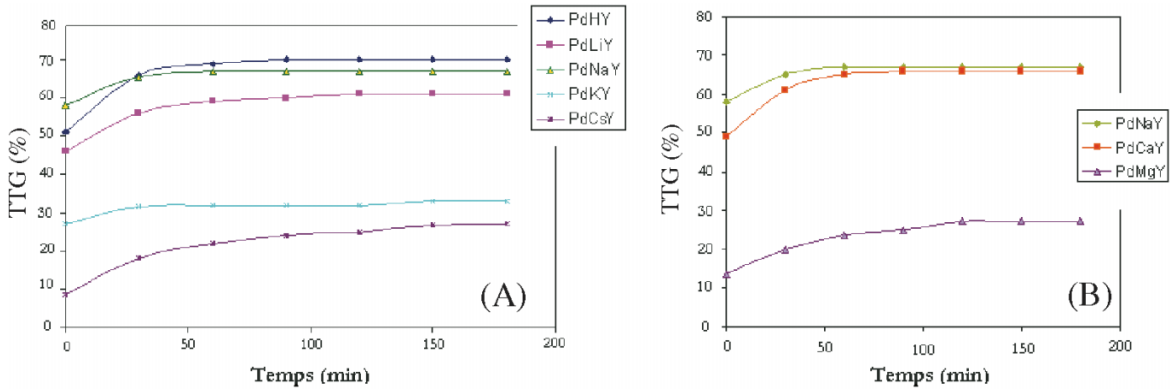

Fig. 4. Variation de la conversion du méthane en fonction de la température pour les catalyseurs échangés aux : (A) cations alcalins et (B) alcalino-terreux; comparé à l'échantillon PdNaY et PdHY.

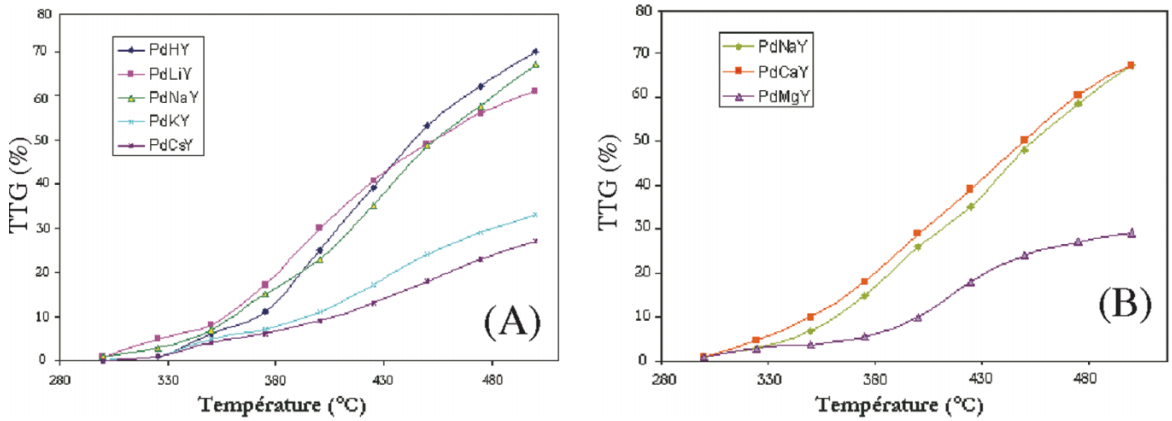

Tableau 4. Températures correspondant aux taux de conversion 10 %, 30 % et 60 % et valeurs des pentes des tangentes aux courbes TTG = f(*T*) à 500 °C.

	PdHY	PdNaY	PdLiY	PdKY	PdCsY	PdMgY	PdCaY
T_{10} (°C)	372	361	357	395	406	400	350
T_{30} (°C)	409	415	400	480	514*	682*	430
T_{60} (°C)	469	480	495	666*	698*	—	475
Pente	0,34	0,36	0,24	0,18	0,18	0,12	0,32

*Valeur déterminée par extrapolation des courbes représentatives de la conversion en fonction de la température.

(K^+ et Cs^+). Les courbes représentées par la figure 4B révèlent que le catalyseur supporté sur zéolithe échangée au calcium (PdCaY) est plus actif à des températures inférieures à 500 °C, alors que l'échantillon PdMgY est nettement moins actif dans ce domaine de température. Il est à préciser également, que ces catalyseurs sont pratiquement inactifs à des températures inférieures à 300 °C.

L'allure des courbes présentant le taux de conversion en fonction de la température montre qu'au voisinage de 500 °C, l'activité de PdCaY semble s'égaliser à celle de PdNaY, seulement la pente de la courbe à cette température pour l'échantillon PdNaY est supérieure à celle de PdCaY (tableau 4). Quant à l'échantillon PdMgY, il est beaucoup moins actif que PdNaY ou PdCaY et ne semble pas voir son activité catalytique augmenter à des températures supérieures à 500 °C, puisque la pente de la courbe correspondante en ce point est plus faible.

Les énergies apparentes d'activation E_a sont déterminées dans le domaine de température variant de 350 C à 425 °C correspondant à des taux de conversion de méthane inférieures à 50 % pour lesquels les limitations diffusionnelles sont minimisées. Le tableau 5 présente les valeurs de E_a obtenues en présence des différents catalyseurs.

Discussions

L'activité des catalyseurs au palladium supporté sur zéolithe modifiée par échange cationique de cations alcalins et alcalino-terreux dans la réaction d'oxydation totale du méthane dépend de la nature du cation compensateur et varie selon les séquences suivantes :

$$\text{PdHY} \approx \text{PdNaY} > \text{PdLiY} > \text{PdKY} > \text{PdCsY et PdCaY} \approx \text{PdNaY} > \text{PdMgY}$$

Can. J. Chem. Downloaded from www.nrcresearchpress.com by Sichuan Normal University on 09/14/12
For personal use only.

Tableau 5. Résultats des énergies apparentes d'activation E_a.

	PdHY	PdNaY	PdLiY	PdKY	PdCsY	PdCaY	PdMgY
E_a (kJ mol^{-1})	124	97	82	102	97	79	91

Schéma 1. Activation du méthane sur une surface de particule composée de deux sites adjacents formés d'une paire Pd–PdO.

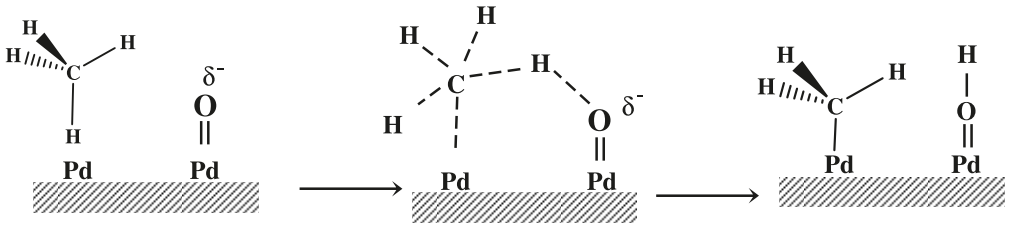

En se basant sur les résultats obtenus de la caractérisation physicochimique des catalyseurs supportés sur zéolithe échangée aux cations alcalins, on peut déduire que l'activité du palladium supporté est sensible à la structure et la texture du support. En effet, la caractérisation texturale par la méthode volumétrique a montré que la porosité et la surface spécifique sont affectées par la nature et la taille du cation compensateur. En effet, plus le cation est volumineux, moins la S_{BET} et le volume microporeux sont développés, et l'activité des catalyseurs PdNaY, PdKY et PdCsY augmente quand la taille du cation diminue, excepté pour PdLiY qui révèle une activité légèrement moins élevée que celle de PdNaY. Le catalyseur PdHY a montré l'activité la plus importante dans cette réaction, toutefois il présente une surface spécifique réduite, probablement en raison de la destruction partielle due à une désalumination du support qui conduit à un rapport Si/Al plus élevé, donc une activité plus importante. Ce résultat rejoint celui de Okumara et al.[21] qui ont trouvé que l'activité du palladium dans la réaction de combustion du méthane augmente lorsque le rapport Si/Al croît.

Les travaux de la littérature ont relié l'activité relativement élevée de certains catalyseurs, sur le support sodique, à la présence des ions Na^+ qui conduisent à un enrichissement électronique de la surface des particules de palladium et par conséquent de celle des espèces PdO, supposées être les sites actifs qui assurent la rupture de la liaison C—H dans la réaction de combustion du méthane[22] (schéma 1). Par conséquent, en rapportant le taux de conversion du méthane par mole d'atome de sodium dans une maille (fig. 5), on constate alors qu'à 500 °C le catalyseur PdCaY est le plus actif. Par ailleurs, il est probable que l'augmentation du taux d'échange du support en Ca pourrait améliorer le taux de conversion du méthane.

Par ailleurs, des études[23,24] ont montré que suite à une calcination sous atmosphère oxydante à 500 °C, les complexes $Pd(NH_3)_4^{2+}$ se désaminent, et les ions Pd^{2+} migrent dans les sites de positions S_I et $S_{I'}$ situés près des prismes hexagonaux et les cages sodalites qui sont des sites inaccessibles aux molécules réactives. Néanmoins, dans le cas du catalyseur supporté sur zéolithe échangée au calcium qui montre une activité importante dans la combustion du méthane, les cations Ca^{2+} ont une grande affinité pour le site de position S_I, où ils s'y situent préférentiellement. De ce fait, les ions Pd^{2+} migrent pour occuper des sites plus accessibles qui sont les sites S_{II} et $S_{II'}$ situés dans la supercage et

Fig. 5. Taux de conversion du méthane par atome de sodium dans une maille élémentaire de la zéolithe.

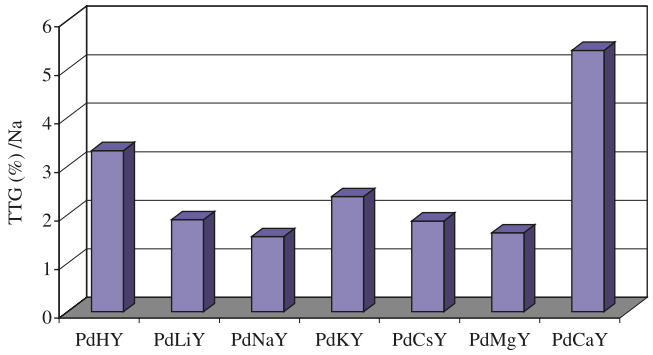

la cavité sodalite. Ceci est prouvé par les études de Michalik et al.[25] portant sur la réactivité des catalyseurs à base de palladium supporté sur des zéolithes X échangées aux ions Ca^{2+}, Mg^{2+} et K^+ dans la réaction de dimérisation de l'éthylène, mais aussi, par les travaux de Ghosh et al.[26] et ceux de Z. Zhang et al.[27]

La faible activité enregistrée pour le catalyseur PdCsY peut être attribuée à la localisation des cations Cs^+ qui occupent principalement les sites $S_{II'}$ situés dans les cages sodalites, et les sites S_{II} et S_{III}, situés dans la supercage,[28] ces cations ne peuvent pas en effet accéder aux sites de position localisés à proximité des prismes hexagonaux (S_I), et bloquent ainsi la migration des ions Pd^{2+} vers des sites plus accessibles.

Des travaux antérieurs[29] ont montré que la basicité de la structure zéolithique est liée à la charge partielle négative des atomes d'oxygène. Cette charge peut être augmentée par un échange ionique du cation compensateur moins électronégatif que Na^+ (schéma 2). En effet, les travaux de Breysse[29] sur la zéolithe NaX échangée par les cations des métaux alcalins K, Rb et Cs ont montré que la charge négative (δ^-) de l'oxygène du réseau croît selon la séquence suivante : $Na_{100}X < K_{98,5}Na_{1,5}X < Rb_{64}Na_{36}X < Cs_{68}Na_{32}X$.

Il a été aussi établi[30] pendant longtemps que l'échange cationique des zéolithes X induit une force de basicité du support qui dépend de la nature du cation échangé et qui croît dans l'ordre suivant : Li < Na < K < Rb < Cs. De plus d'après Chatterjee,[31] l'énergie de stabilisation des cations dans les sites S_I suit l'ordre suivant : $Mg^{2+} > Ca^{2+} > Li^+ >$

Can. J. Chem. Downloaded from www.nrcresearchpress.com by Sichuan Normal University on 09/14/12
For personal use only.

Schéma 2. Influence de l'échange cationique dans la zéolithe sur la charge négative des oxygènes du réseau.

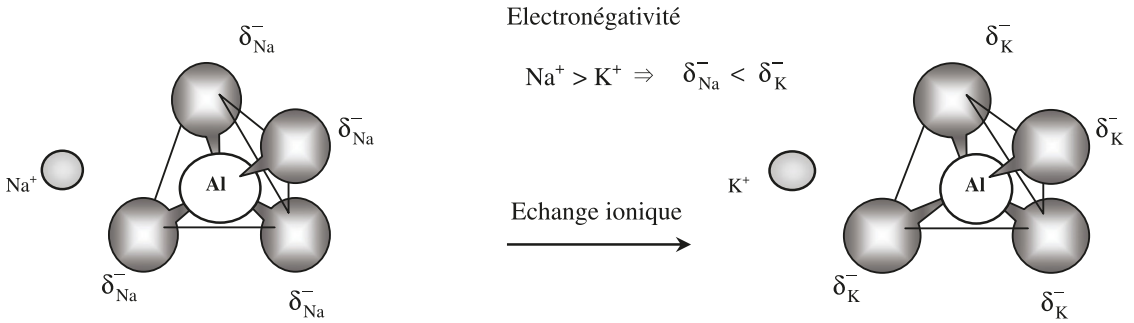

$$\delta^-_{Li} < \delta^-_{Na} < \delta^-_K < \delta^-_{Cs} \quad \text{et} \quad \delta^-_{Na} < \delta^-_{Ca} < \delta^-_{Mg}$$

$K^+ > Na^+$, alors que dans les sites S_{II}, l'énergie de stabilisation des cations varie selon la séquence $Mg^{2+} < Ca^{2+} < Na^+ < K^+ < Li^+$. Par conséquent, Na^+ est le moins stable en site S_I, alors que Li^+ se trouve le plus stable en site S_{II}.

Toutefois, des résultats expérimentaux[32] ont mis en évidence la migration de ces cations en présence d'un réactif et ont montré par RMN et DRX une interaction entre Na^+ et le réactif. Ces travaux ont été poursuivis plus tard[33] pour montrer que les liaisons de la molécule de réactif avec le support sont contrôlées par des interactions électrostatiques locales incluant la combinaison de H–R (réactif) avec la charpente zéolithique et le cation compensateur.

De ce qui précède, on peut alors avancer que les ions alcalins et alcalino-terreux modifient l'activité intrinsèque du palladium suite au changement de la densité de charge du site actif. Par ailleurs, la basicité ou l'aptitude de l'électrodonnation des additifs joue un rôle important dans les performances des catalyseurs au palladium. Si on adopte le schéma proposé par Fujimoto[34] montrant l'adsorption du méthane sur une paire de sites adjacents composés de Pd et PdO, où le méthane est adsorbé dans une lacune d'oxygène et est en interaction avec PdO (schéma 1), la densité électronique de la lacune d'oxygène responsable de l'activité catalytique dépend de son environnement, donc du caractère acido-basique du support, de la nature du cation compensateur et de sa localisation.

Conclusion

Le présent travail a montré que les propriétés basiques des zéolithes ont une influence sur l'interaction métal–support et donc sur l'activité catalytique du palladium. En effet la basicité de la zéolithe varie, entre autre, avec la nature des cations alcalins extra-réseau compensateurs de charge qui jouent un rôle très important dans la localisation des espèces catalytiques actives et leur migration dans les sites accessibles aux molécules réactives.

De ce fait, la modification du support par échange des cations compensateurs a un effet sur le taux de conversion du méthane. En effet, la nature et la taille du cation agissent sur le comportement du catalyseur dans la réaction d'oxydation du méthane, de plus l'acidité du support est un paramètre influant sur l'activité du palladium dans cette réaction.

Bibliographie

(1) Otto, K. *Langmuir* **1989**, *5*, 1364. doi:10.1021/la00090a018.
(2) Briot, P.; Primet, M. *Appl. Catal. B* **1991**, *68*, 301. doi:10.1016/S0166-9834(00)84110-X.
(3) Hicks, R.F.; Qi, H.; Young, M.L.; Lee, R.G.*J. Catal.* **1990**, *122*, 280. doi:10.1016/0021-9517(90)90282-O.
(4) Okumura, K.; Matsumoto, S.; Nishiaki, N.; Niwa, M. *Appl. Catal. B* **2003**, *40*, 151. doi:10.1016/S0926-3373(02)00149-2.
(5) Li, Y.; Armor, J.N. *Appl. Catal. B* **1994**, *3*, 275. doi:10.1016/0926-3373(94)0006Z-H.
(6) Yagi, F.; Kanuka, N.; Kita, H.; Hattori, H. *Stud. Surf. Sci. Catal.* **1994**, *90*, 349. doi:10.1016/S0167-2991(08)61845-5.
(7) McKetta, J.J., Ed. *Chemical processing handbook*; Marcel Dekker, 1993.
(8) Sheldon, R.A.; van Bekkum, H., Eds.. *Fine chemicals through heterogeneous catalysis*. Wiley-VCH, 2001.
(9) Joshi, U.D.; Joshi, P.N.; Tamhankar, S.S.; Joshi, V.V.; Rode, C.V.; Shiralkar, V.P. *Appl. Catal. A* **2003**, *239*, 209. doi:10.1016/S0926-860X(02)00391-5.
(10) Saïd Zina, M.; Ghorbel, A. *Solid State Sci.* **2004**, *6*, 973. doi:10.1016/j.solidstatesciences.2004.04.013.
(11) Hasegawa, Y.; Watanabe, K.; Kusakabe, K.; Morooka, S. *Separ. Purif. Tech.* **2001**, *22-23*, 319. doi:10.1016/S1383-5866(00)00154-4.
(12) Coker, E.N.; Rees, L.V.C. *Microporous Mesoporous Mater.* **2005**, *84*, 171. doi:10.1016/j.micromeso.2005.05.028.
(13) Breysse, E.; Fajula, F.; Finiels, A.; Fremy, G.; Tichit, D.; Moreau, C. *J. Catal.* **2005**, *233*, 288. doi:10.1016/j.jcat.2005.05.002.
(14) Breck, D.W. Zeolite molecular sieves. Éditions Wiley Interscience, New York. 1974.
(15) Brunauer, S.; Deming, L.; Deming, W.; Teller, E.J. *J. Am. Chem. Soc.* **1940**, *62*, 1723. doi:10.1021/ja01864a025.
(16) Langmi, H.W.; Book, D.; Walton, A.; Johnson, S.R.; Al-Mamouri, M.M.; Speight, J.D.; Edwards, P.P.; Harris, I.R.; Anderson, P.A. *J. Alloys Compd.* **2005**, *404-406*, 637. doi:10.1016/j.jallcom.2004.12.193.
(17) Saïd Zina, M.; Ghorbel, A. *Ann. Chim. Sci. Mat.* **2008**, *33* (2), 111. doi:10.3166/acsm.33.111-122.
(18) Ishihara, T.; Sumi, H.; Takita, Y. *Chem. Lett.* **1994**, *23* (8), 1499. doi:10.1246/cl.1994.1499.
(19) Gélin, P.; Primet, M. *Appl. Catal. B* **2002**, *39*, 1. doi:10.1016/S0926-3373(02)00076-0.
(20) Yamaoka, K.; Takata, N. *Chem. Lett.* **1994**, *8*, 1503. doi:10.1246/cl.1994.1503.

Can. J. Chem. Downloaded from www.nrcresearchpress.com by Sichuan Normal University on 09/14/12
For personal use only.

(21) Okumura, K.; Matsumoto, S.; Nishiaki, N.; Niwa, M. *App. Catal. B* **2003**, *40*, 151. doi:10.1016/S0926-3373(02)00149-2.
(22) Broclawik, E.; Haber, J.; Endou, A.; Stirling, A.; Yamauchi, R.; Kubo, M.; Miyamoto, A. *J. Mol. Catal. A* **1997**, *119*, 35. doi:10.1016/S1381-1169(97)80042-8.
(23) Sachtler, W.M.H.; Cavalcanti, F.A.p., Zhang, Z. *Catal. Lett.* **1991**, *9*, 261. doi:10.1007/BF00773184.
(24) Imelik, B.; Védrine, J.C. Les techniques physiques d'étude des catalyseurs. Éditions Technip, Paris. 1988.
(25) Michalik, J.; Lee, H.; Kevan, L.*J. Phys. Chem.* **1985**, *89*, 4282. doi:10.1021/j100266a028.
(26) Ghosh, A.K.; Kevan, L.*J. Phys. Chem.* **1988**, *92*, 4439. doi:10.1021/j100326a039.
(27) Zhang, Z.; Wong, T.T.; Sachtler, W.M.H. *J. Catal.* **1991**, *128*, 13. doi:10.1016/0021-9517(91)90062-9.
(28) Norby, P.; Poshni, F.I.; Gualtieri, A.F.; Hanson, J.C.; Grey, C.P. *J. Phys. Chem. B* **1998**, *102*, 839. doi:10.1021/jp9730398.
(29) Breysse, E.; Fajula, F.; Finiels, A.; Fremy, G.; Tichit, D.; Moreau, C.*J. Catal.* **2005**, *233*, 288. doi:10.1016/j.jcat.2005.05.002.
(30) Sanderson, R. T. Chemical bonds and bond energy. 2e éd. Academic Press, New York. Vol. 126. 1976.
(31) Chatterjee, A.; Mizukami, F. *Chem. Phys. Lett.* **2004**, *385*, 20. doi:10.1016/j.cplett.2003.12.035.
(32) Grey, C.P.; Poshini, F.I.; Gualtieri, A.F.; Norby, P.; Hansen, J.; Corbin, D.R. *J. Am. Chem. Soc.* **1997**, *119*, 1981. doi:10.1021/ja963565x.
(33) Lim, L.H.; Jouse, F.; Auerbach, S.M.; Grey, C.P. *J. Phys. Chem. B* **2001**, *105*, 9918. doi:10.1021/jp0045989.
(34) Fujimoto, K.; Ribeiro, F.H.; Avalos-Borja, M.; Iglesia, E.*J. Catal.* **1998**, *179*, 431. doi:10.1006/jcat.1998.2178.

Can. J. Chem. Downloaded from www.nrcresearchpress.com by Sichuan Normal University on 09/14/12
For personal use only.

A simple and facile synthesis of amidoalkyl naphthols catalyzed by $Yb(OTf)_3$ in ionic liquids

Anil Kumar, M. Sudershan Rao, Israr Ahmad, and Bharti Khungar

Can. J. Chem. Downloaded from www.nrcresearchpress.com by Sichuan Normal University on 09/14/12
For personal use only.

Abstract: An improved, simple, and facile synthesis of amidoalkyl naphthols by employing three-component one-pot condensation reaction of β-naphthol, aromatic aldehydes, and amides in ionic liquids using ytterbium triflate as a mild Lewis acid catalyst is described. Advantageously, amidoalkyl naphthols were obtained in high yield under eco-friendly, economical, and non-corrosive conditions, and the catalyst was recycled.

Key words: amidoalkyl naphthols, ytterbium triflate, ionic liquid, β-naphthol, three-component condensation.

Résumé : On a mis au point une méthode simple, facile et améliorée de synthèse d'amidoalkylnaphtols impliquant une réaction de condensation monotope à trois composants, dont le β-naphtol, des aldéhydes et des amides aromatiques dans des liquides ioniques et faisant appel au triflate d'ytterbium comme catalyseur acide de Lewis doux. L'avantage de la méthode est que les amidoalkylnaphtols sont obtenus avec des rendements élevés, dans de bonnes conditions écologiques, économiques et non corrosives et que le catalyseur peut être recyclé.

Mots-clés : amidoalkylnaphtols, triflate d'ytterbium, liquide ionique, condensation à trois composants.

[Traduit par la Rédaction]

Introduction

Multicomponent reactions (MCRs) are of increasing importance in organic and medicinal chemistry and have emerged as a powerful strategy in the preparation of structurally diverse libraries of drug-like molecules.[1] MCRs constitute an especially attractive synthetic strategy, since they provide easy and rapid access to large libraries of drug-like organic compounds with diverse substitution patterns.[2] As MCRs are one-pot reactions, they are easier to carry out and offer significant advantages over conventional linear-type syntheses.

The amidoalkyl naphthols are important precursors for the synthesis of 1,3-amino oxygenated compounds. The 1,3-amino oxygenated functionality is present in various biologically important natural products and drug molecules.[3] The amidoalkyl naphthols have been prepared by multi-component condensation of aldehydes, 2-naphthol, and acetonitrile or amide in the presence of Lewis[4–6] or Brønsted acid[7] catalysts. However, some of these catalysts require prolonged reaction times and suffer from low yields, toxicity, and recovery and reusability of the catalyst. Therefore, there is great need of an eco-friendly and green catalysts, which can be recycled at the end of reactions and give high yields of amidoalkyl naphthols under mild reaction conditions.

Recently, rare-earth metal triflates have enjoyed extensive applications in a variety of Lewis acid catalyzed organic reactions.[8] The growing interest in use of these salts is due to their ease of handling, non-corrosiveness, reusability, and unique reactivity and selectivity. Among all rare-earth metal triflates, ytterbium triflate has high acidity due to its small ionic radii.[8b] It was first used by Forsberg et al.,[9] and since then, it has found a wide utility in deprotection,[10] cycloaddition reactions,[11] aldol-Grob reaction,[12] imino-ene reaction,[13] electrophilic substitutionn, cyclization,[14] and synthesis of heterocyclic[15] and natural products.[16]

The ionic liquids, especially those based on 1,3-dialkylimidazolium cations, have gained considerable interest as green alternative to volatile organic solvents.[17] Various reactions have been reported with the immobilization of metal triflates in ionic liquids with increased catalytic activity along with their easy reuse.[18] During the course of our recent studies directed towards the development of eco-friendly procedures for various organic transformations,[19] we wish to report three-component, one-pot condensation of β-naphthol, aromatic aldehydes, and amides to amidoalkyl naphthols using $Yb(OTf)_3$ as a catalyst in ionic liquids (Scheme 1). To the best of our knowledge, there is no report on the use of lanthanide triflates and ionic liquids for the synthesis of amidoalkyl naphthols.

Results and discussion

First, we studied the three-component condensation reaction of 4-chlorobenzaldehyde, 2-naphthol, and acetamide in the presence of catalytic amount of several Lewis acids in [bmim][BF_4] ionic liquid (Table 1). In the absence of the catalyst, no product formation was observed even after 48 h at 80 °C (Table 1, entry 1). Ytterbium triflate was found to be the most useful catalyst among all the used catalysts under these conditions, giving highest yield of product (92%) (Table 1, entry 7). The high activity of $Yb(OTf)_3$ compared with the metal triflates used may be attributed to its high acidity.

Received 8 December 2008. Accepted 5 February 2009. Published on the NRC Research Press Web site at canjchem.nrc.ca on 23 May 2009.

A. Kumar,[1] M.S. Rao, I. Ahmad, and B. Khungar. Department of Chemistry, Birla Institute of Technology and Science, Pilani 333 031 Rajasthan, India.

[1]Corresponding author (e-mail: anilkadian@gmail.com).

Scheme 1. Synthesis of amidoalkyl naphthols in ionic liquid.

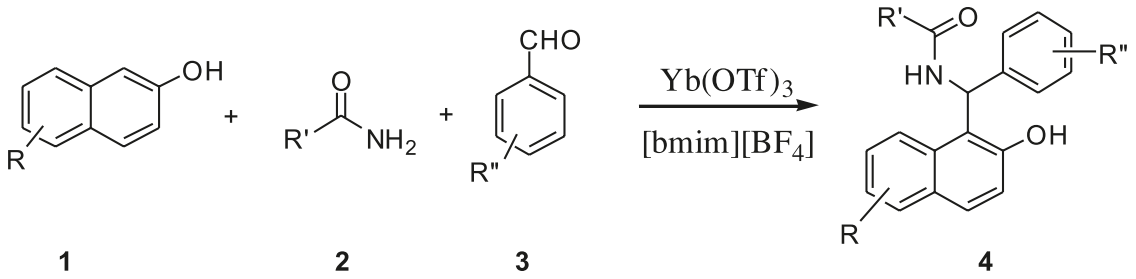

Table 1. Effect of different Lewis acid catalyst on the synthesis of **4a** in ionic liquid at 80 °C.

Entry	Catalyst	Time (h)	Yield (%)[a]
1	—	48	—[b]
2	$CoCl_2$	12	20
3	$BF_3{\cdot}Et_2O$	12	30
4	$ZrOCl_2{\cdot}8H_2O$	12	50
5	$In(OTf)_3$	8	55
6	$Y(OTf)_3$	8	50
7	$Yb(OTf)_3$	4	92
8	$La(OTf)_3$	8	60
9	$Sc(OTf)_3$	12	35
10	$Zn(OTf)_2$	12	Trace
11	$Ba(OTf)_3$	12	Trace

Note: In each case, 20 mol% catalyst was used.

[a]Isolated yield.

[b]No product formation observed.

The condensation of 4-chlorobenzaldehyde (**1**), 2-naphthol (**2**), and acetamide (**3**) at 80 °C in ionic liquid, [bmim][BF_4], containing 20 mol% $Yb(OTf)_3$, gave 92% of **4a** (Table 2, entry 1). After extraction from ionic liquid, the product was purified by recrystallization with ethanol and characterized by IR, MS, ^{1}H NMR, and ^{13}C NMR spectroscopy. Presence of a doublet at δ 8.53 ppm in ^{1}H NMR spectrum for –CH–NH group along with other aromatic protons, peak at δ 169.45 ppm for C=O group in ^{13}C NMR, and a strong peak at 1663 cm^{-1} for –$NHCOCH_3$ group in IR confirms the structure of **4a**.

Next, we examined the effect of different solvents, such as [bmim][BF_4], toluene, DMSO, DMF, Ethanol, H_2O, PEG-400, 1,2-dichloroethane, $CHCl_3$, and DCM, as model reaction using $Yb(OTf)_3$ as catalyst. All the reactions were run using 20 mol% of the catalyst. As shown in Table 3, **4a** was obtained in excellent yield (92%) in the ionic liquid [bmim][BF_4]. Therefore, we chose [bmim][BF_4] as the solvent of choice for further reactions. These results point towards the need of the proper catalyst and solvent system, which play the key role for the success of the reaction. As shown in Table 3, no product formation was observed in polar organic solvents, such as DMSO, DMF, and ethanol, as well as aqueous solvent. It may be due to the interaction of these solvents with the catalyst.

Encouraged by our results for the one-pot condensation of 2-naphthol and acetamide with 4-chlorobenzaldehyde in ionic liquid, we next examined the generality of this methodology for the synthesis of various amidoalkyl naphthols by condensation of substituted β-naphthols, aldehydes, and amides. The results are shown in Table 2. Several functionalities present in the aldehydes and 2-naphthols, such as halogen, methoxy, and nitro groups, were tolerated. In all cases, the corresponding amidoalkyl naphthols were obtained in good to excellent yields (Table 2). When benzamide was used instead of acetamide in the one-pot condensation of 2-naphthol with benzaldehyde in ionic liquid, it resulted only in 35% yield of **4p** (Table 2, entry p). Similarly, when we used *N*-methylacetamide, we found that the reaction is slower compared with acetamide, and the yield of the corresponding product was only 61% after 12 h.

A plausible mechanism for the formation of amidoalkyl naphthols by the reaction of 2-naphthol with aldehydes in presence of ytterbium triflate is shown in Scheme 2. As reported in the literature, in situ generation of *ortho*-quinone methides (*o*-QMs) is expected to take place.[7a,7b] These *o*-QMs, generated in situ, react with amides via conjugate addition to form the amidoalkyl naphthols. The aromatic aldehydes with electron-withdrawing groups reacted faster than the aromatic aldehydes with electron-donating groups, which is in agreement with the reaction mechanism. The rate of conjugate addition is higher to *o*-QMs as the lowest unoccupied molecular orbital (LUMO) of alkene in *o*-QMs is at lower energy in the presence of electron-withdrawing groups compared with electron-donating groups.[20] The role of the ionic liquid is not yet clear, but it is expected that the noncoordinating nature and high dielectric constant of the ionic liquid may help in the generation of *o*-QMs and enhance the rate of nucleophilic conjugate addition. Such effect of ionic liquid on the rate of nucleophilic substitution reaction is reported in literature.[21] The lower reactivity of

Can. J. Chem. Downloaded from www.nrcresearchpress.com by Sichuan Normal University on 09/14/12
For personal use only.

Can. J. Chem. Downloaded from www.nrcresearchpress.com by Sichuan Normal University on 09/14/12
For personal use only.

Table 2. Synthesis of different amidoalkyl naphthols catalyzed by $Yb(OTf)_3$ in ionic liquid.

Entry	Product	Time (h)	Mp (°C)	Yield[a, b] (%)
a	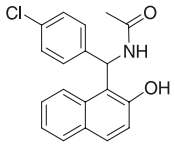	4	218	92[c]
b	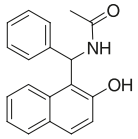	6	234	90
c	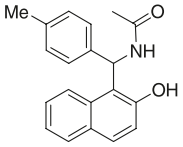	6	220	87
d	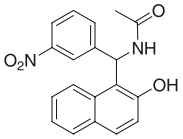	4	245	88
e	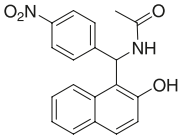	4	237	89
f	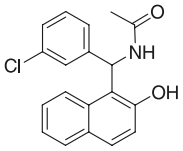	4	235	91
g	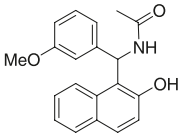	8	228	88
h	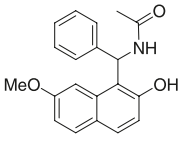	6	168	89
i	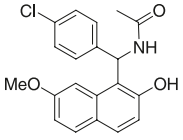	4	120	90

Table 2. *Concluded.*

Entry	Product	Time (h)	Mp (°C)	Yield[a, b] (%)
j	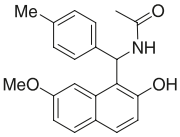	6	180	85
k	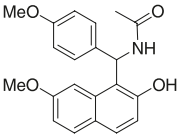	6	192	88
l	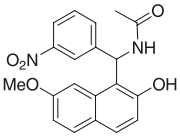	5	205	85
m	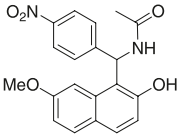	4	217	89
n	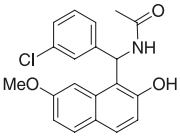	4	186	89
o	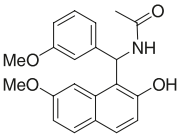	8	177	88
p	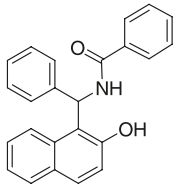	10	181	35
q	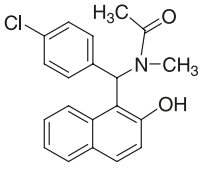	12	—	61

[a] Isolated yield by column chromatography on silica gel.

[b] All products were characterized by IR, MS, ^{1}H NMR, and ^{13}C NMR.

[c] Yields for recycling of catalyst were 92, 91, 87, 85, and 86, respectively for five cycles.

benzamide compared with acetamide may be attributed to the difference in acidity constants of these weakly basic substrates in acidic media. The reported pK_a values of acetamide and benzamide are –0.73 and –1.54, respectively.[22]

From an environmental point of view, it is desirable to minimize the amount of waste for each organic transformation. In this context, we recycled the catalyst solution for subsequent runs. To study the reusability, $Yb(OTf)_3$ immobi-

Can. J. Chem. Downloaded from www.nrcresearchpress.com by Sichuan Normal University on 09/14/12
For personal use only.

Table 3. Effect of different solvents on the synthesis of **4a** catalyzed by $Yb(OTf)_3$.

Entry	Solvent	Temperature (°C)	Time (h)	Yield (%)[a]
1	[bmim][BF_4]	80	4	92
2	Toluene	100	12	Trace
3	DMSO	100	12	—[b]
4	DMF	100	12	—[b]
5	Ethanol	Reflux	12	—[b]
6	H_2O	100	12	—[b]
7	PEG-400	100	12	<10
8	$ClCH_2CH_2Cl$	80	12	35
9	$CHCl_3$	Reflux	12	20
10	DCM	Reflux	12	20

Note: $Yb(OTf)_3$, 20 mol%.

[a]Isolated yield.

[b]No product formation observed.

Scheme 2. Probable mechanism for the synthesis of amidoalkyl naphthols catalyzed by $Yb(OTf)_3$.

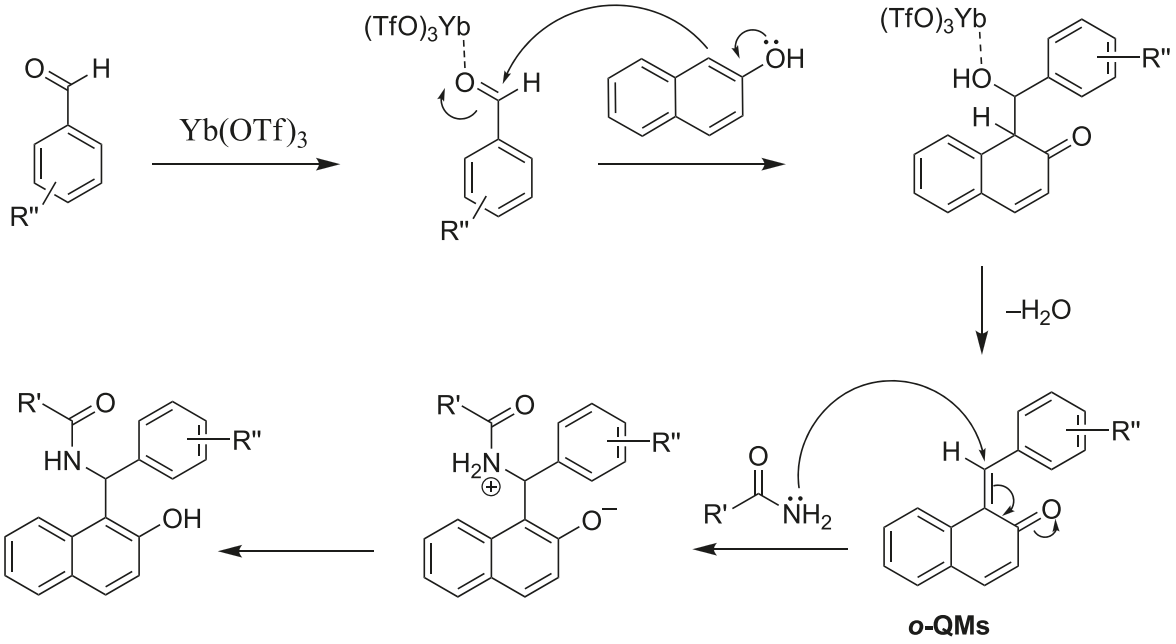

lized in ionic liquid, [bmim][BF_4], was reused for the synthesis of amidoalkyl naphthol **4a**. After extraction of amidoalkyl naphthols from ionic liquid with ethyl acetate – hexane mixture, the ionic liquid containing $Yb(OTf)_3$ was concentrated on rotatory evaporator under reduced pressure to remove the organic solvent for 30 min. To this dried ionic liquid containing $Yb(OTf)_3$, β-naphthol, 4-chlorobenzaldehyde, and acetamide were added and stirred at room temperature for 4 h. The reaction mixture was extracted by ethyl acetate – hexane mixture, and the combined organic layer was evaporated to give amidoalkyl naphthols **4a**. This cycle was repeated for five times. The catalysts showed good reactivity and yield even after five cycles with little deterioration in catalytic activity (Table 2, entry a).

Conclusion

In conclusion, an efficient, simple, and eco-friendly method has been described for the synthesis of amidoalkyl naphthols by employing three-component one-pot condensation reaction of β-naphthol, aromatic aldehydes, and amides in ionic liquids using ytterbium triflate as a mild Lewis acid catalyst. The catalyst was recovered and recycled in successive reaction cycles.

Experimental section

All chemicals and reagents were of analytical grade. β-Naphthol, acetamide, aldehydes, and acetyl chloride were purchased form S. D. Fine and Spectrochem, India. Sodium tetrafluoroborate and 1-methylimidazole were purchased from Aldrich. Ionic liquid, [bmim][BF_4], was prepared according to earlier reported procedure.[19a,19b] The ^1H NMR spectra were recorded on a Brucker Heaven Avance 11 400 (400 MHz) spectrophotometer using TMS as internal standard and $CDCl_3$ as solvent, and the chemical shifts were expressed in ppm. The IR spectra were recorded using KBr pellets on Shimadzu Prestige-21 FTIR spectrophotometer and ν_{max} was expressed in cm^{-1}. Mass spectra were recorded on a KC455 Waters TOF MS spectrometer. TLC was run on the silica-gel-coated aluminium sheets (Silica gel 60 F_{254}, E. Merck, Germany) and visualized in UV light (254 nm).

Can. J. Chem. Downloaded from www.nrcresearchpress.com by Sichuan Normal University on 09/14/12
For personal use only.

General procedure for the synthesis of amidoalkyl naphthols catalyzed by $Yb(OTf)_3$ in ionic liquid

4-Chlorobenzaldehyde (103 μL, 1.49 mmol), β-naphthol (110 μL, 1.49 mmol), acetamide (1.79 mmol), and $Yb(OTf)_3$ (20 mol%, 46.2 mg) were added to a 10 mL round-bottom flask containing the ionic liquid, $[bmim][BF_4]$ (3.0 mL). The reaction mixture was stirred at 80 °C for 4 h in oil bath. After completion of the reaction as indicated by TLC, the reaction mixture was cooled to room temperature and extracted with ethyl acetate – hexane (2 × 5 mL, 4:1, *v*/*v*). The ionic liquid, containing ytterbium triflate, was recovered and dried under vacuum. The combined organic layer was evaporated under reduced pressure. The product was recrystallized from ethanol to give pure **4a** (450 mg, 92%). The product was characterized by ^1H and ^{13}C NMR, IR, and mass spectroscopic data.

Spectral data of selected amidoalkyl naphthols

N-*((4-Chlorophenyl)(2-hydroxynaphthalen-1-yl)-methyl)acetamide (4a)*

^1H NMR (Me_4Si; 400 MHz, DMSO-d_6) δ: 2.02 (s, 3H), 7.14–7.32 (m, 7H), 7.39 (brs, 1H), 7.77–7.82 (m, 3H), 8.53 (s, 1H), 10.02 (s, 1H). ^{13}C NMR (100 MHz, DMSO-d_6) δ: 22.61, 47.42, 117.67, 118.42, 122.42, 123.16, 124.62, 126.47, 127.03, 127.89, 128.45, 129.47, 130.64, 133.23, 141.78, 153.22, 169.45. HR-MS-EI: *m*/*z* calcd. for $C_{19}H_{16}ClNO_2$ 325.0870; found: 326.1458 $[M + H]^+$.

N-*((2-Hydroxynaphthalen-1-yl)(phenyl)methyl)-acetamide (4b)*

^1H NMR (Me_4Si; 400 MHz, DMSO-d_6) δ: 2.01 (s, 3H), 7.15–7.26 (m, 8H), 7.36 (t, J = 7.56 Hz, 1H), 7.79 (dd, J = 8.0 Hz, 2H), 7.87 (brs, 1H), 8.58 (s, 1H), 10.02 (s, 1H). ^{13}C NMR (100 MHz, DMSO-d_6) δ: 22.68, 47.97, 118.67, 118.77, 122.17, 123.09, 126.05, 126.08, 126.25, 127.94, 128.25, 128.51, 129.14, 132.38, 142.73, 153.75, 169.19. HR-MS (EI): *m*/*z* calcd. for $C_{19}H_{17}NO_2$ 291.1259; found: 292.1458 $[M + H]^+$.

N-*((2-Hydroxynaphthalen-1-yl)(p-tolyl)methyl)-acetamide (4c)*

^1H NMR (Me_4Si; 400 MHz, DMSO-d_6) δ: 2.04 (s, 3H), 2.24 (s, 3H), 7.08 (d, J = 7.81 Hz, 2H), 7.14 (d, J = 7.84 Hz, 2H), 7.21–7.39 (m, 3H), 7.39 (t, J = 8.0 Hz, 1H), 7.70 (dd, J = 8.0 Hz, 2H), 7.94 (brs, 1H), 8.52 (d, J = 8.0 Hz, 1H), 10.08 (s, 1H). ^{13}C NMR (100 MHz, DMSO-d_6) δ: 20.54, 22.70, 47.74, 118.55, 119.05, 122.37, 123.34, 126.05, 126.27, 128.56, 129.16, 132.38, 135.07, 139.59, 153.17, 169.27. HR-MS (EI): *m*/*z* calcd. for $C_{20}H_{19}NO_2$ 305.1416; found: 306.2213 $[M + H]^+$.

N-*((2-Hydroxynaphthalen-1-yl)(3-nitrophenyl)-methyl)acetamide (4d)*

^1H NMR (Me_4Si; 400 MHz, DMSO-d_6) δ: 2.07 (s, 3H), 7.27–7.30 (m, 3H), 7.43–7.45 (m, 1H), 7.51–7.56 (m, 1H), 7.61–7.63 (m, 1H), 7.82–7.84 (m, 2H), 7.95 (brs, 1H), 8.06–8.10 (m, 2H), 8.71 (s, 1H), 10.22 (d, J = 8.6 Hz, 1H). ^{13}C NMR (100 MHz, DMSO-d_6) δ: 22.54, 47.67, 117.84, 118.47, 120.47, 121.21, 122.61, 122.78, 126.77, 128.41, 128.69, 129.50, 129.90, 132.18, 132.85, 145.41, 147.72, 153.38, 169.79. HR-MS (EI): *m*/*z* calcd. for $C_{19}H_{16}N_2O_4$ 336.1110; found: 337.1523 $[M + H]^+$.

N-*((2-Hydroxynaphthalen-1-yl)(4-nitrophenyl)-methyl)acetamide (4e)*

^1H NMR (Me_4Si; 400 MHz, DMSO-d_6) δ: 2.09 (s, 3H), 7.25–7.32 (m, 3H), 7.43 (t, J = 8.0 Hz, 1H), 7.46–7.49 (m, 3H), 7.82 (d, J = 8.0 Hz, 1H), 7.89 (brs, 1H), 8.16 (d, J = 8.0 Hz, 2H), 8.67 (d, J = 8.0 Hz, 1H), 10.22 (s, 1H). ^{13}C NMR (100 MHz, DMSO-d_6) δ: 22.53, 47.96, 117.91, 118.45, 122.58, 122.87, 123.19, 126.72, 127.13, 128.45, 128.67, 129.88, 132.23, 145.90, 151.22, 153.43, 169.84. HR-MS (EI): *m*/*z* calcd. for $C_{19}H_{16}N_2O_4$ 336.1110; found: 337.1476 $[M + H]^+$.

Acknowledgement

This work was supported by Department of Science and Technology, New Delhi (SR-FTP-CS-34–2007) and Council of Scientific and Industrial Research (CSIR), New Delhi (01(2214)/08/EMR-II). The author, IA, is thankful to Birla Institute of Technology and Science, Pilani, for institutional research fellowship.

References

(1) (a) Ugi, I.; Dömling, A.; Hörl, W. *Endeavour* **1994**, *18*, 115 doi:10.1016/S0160-9327(05)80086-9.; (b) Ugi, I. *Pure Appl. Chem.* **2001**, *73*, 187 doi:10.1351/pac200173010187.; (c) Armstrong, R. W.; Combs, A. P.; Tempest, P. A.; Brown, S. D.; Keating, T. A. *Acc. Chem. Res.* **1996**, *29*, 123 doi:10.1021/ar9502083.; (d) Ugi, I.; Dömling, A.; Werner, B. *J. Heterocyclic Chem.* **2000**, *37*, 647; (e) Orru, R. V. A.; de Greef, M. *Synthesis* **2003**, 1471 doi:10.1055/s-2003-40507.; (f) Zhu, J.; Bienaymé, H.; Eds. Multicomponent reactions. Wiley-VCH, Weinheim. 2005.

(2) (a) Weber, L. *Drug Discov. Today* **2002**, *7*, 143 PMID: 11790626.; (b) Dömling, A. *Curr. Opin. Chem. Biol.* **2002**, *6*, 306 doi:10.1016/S1367-5931(02)00328-9. PMID: 12023110.; (c) Tietze, L. F.; Modi, A. *Med. Res. Rev.* **2000**, *20*, 304. doi:10.1002/1098-1128(200007)20:4<304::AID-MED3>3.0.CO;2-8. PMID:10861729.

(3) (a) Knapp, S. *Chem. Rev.* **1995**, *95*, 1859 doi:10.1021/cr00038a006.; (b) Seebach, D.; Matthews, J. L. *Chem. Commun.* **1997**, 2015. doi:10.1039/a704933a.

(4) (a) Shaterian, H. R.; Yarahmadi, H. *Tetrahedron Lett.* **2008**, *49*, 1297 doi:10.1016/j.tetlet.2007.12.093.; (b) Shaterian, H. R.; Hosseinian, A.; Yarahmadi, H.; Ghashang, M. *Lett. Org. Chem.* **2008**, *5*, 290. doi:10.2174/157017808784049524.

(5) (a) Nagawade, R. N.; Shinde, D. B. *Acta Chim. Slov.* **2007**, *54*, 642; (b) Nagawade, R. N.; Shinde, D. B. *Chin. J. Chem.* **2007**, *25*, 1710 doi:10.1002/cjoc.200790316.; (c) Su, W.; Tang, W.; Li, J. *J. Chem. Res.* **2008**, 123.

(6) (a) Srihari, G.; Nagaraju, M.; Murthy, M. M. *Helv. Chim. Acta* **2007**, *90*, 1497 doi:10.1002/hlca.200790156.; (b) Patil, S. B.; Singh, P. R.; Surpur, M. P.; Samant, S. D. *Synth. Commun.* **2007**, *37*, 1659 doi:10.1080/00397910701263858.; (c) Kantevari, S.; Vuppalapati, S. V. N.; Nagarapu, L. *Catal. Commun.* **2007**, *8*, 1857. doi:10.1016/j.catcom.2007.02.022.

(7) (a) Khosropour, A. R.; Khodaei, M. M.; Moghanian, H. *Synlett* **2006**, 916; (b) Das, B.; Laxminarayana, K.; Ravikanth, B.; Rao, B. R. *J. Mol. Catal. Chem. (Kyoto)* **2007**, *261*, 180 doi:10.1016/j.molcata.2006.07.077.; (c) Patil, S. B.; Singh, P.

Can. J. Chem. Downloaded from www.nrcresearchpress.com by Sichuan Normal University on 09/14/12
For personal use only.

R.; Surpur, M. P.; Samant, S. D. *Ultrason. Sonochem.* **2007**, *14*, 515 doi:10.1016/j.ultsonch.2006.09.006. PMID: 17145194.; (d) Selvam, N. P.; Perumal, P. T. *Tetrahedron Lett.* **2006**, *47*, 7481; (e) Das, B.; Laxminarayana, K.; Thirupathi, P.; Rao, B. R. *Synlett* **2007**, 3103. doi:10.1016/j.tetlet.2006.08.038.

(8) (a) Kobayashi, S. *Synlett* **1994**, 413; (b) Kobayashi, S.; Sugiura, M.; Kitagawa, H.; Lam, W. W. L. *Chem. Rev.* **2002**, *102*, 2227 doi:10.1021/cr010289i. PMID:12059268.; (c) Kishida, T.; Yamauchi, T.; Kubota, Y.; Sugi, Y. *Green Chem.* **2004**, *6*, 57. doi:10.1039/b308227j.

(9) (a) Forsberg, J. H.; Balasuramanian, T. M.; Spaziano, V. T. *J. Chem. Soc., Chem. Commun.* **1976**, 1060b doi:10.1039/c3976001060b.; (b) Forsberg, J. H.; Spaziano, V. T.; Balasubramanian, T. M.; Liu, G. K.; Kinsley, S. A.; Duckworth, C. A.; Poteruca, J. J.; Brown, P. S.; Miller, J. L. *J. Org. Chem.* **1987**, *52*, 1017. doi:10.1021/jo00382a009.

(10) (a) Sharma, G. V. M.; Ilangovan, A. *Synlett.* **1999**, 1963. doi:10.1055/s-1999-2975.; (b) Lu, R. J.; Liu, D.; Giese, R. W. *Tetrahedron Lett.* **2000**, *41*, 2817 doi:10.1016/S0040-4039(00)00270-7.; (c) Kotsuki, H.; Ohishi, T.; Araki, T.; Arimura, K. *Tetrahedron Lett.* **1998**, *39*, 4869. doi:10.1016/S0040-4039(98)00950-2.

(11) (a) Kobayashi, S.; Hachiya, I.; Takahori, T.; Araki, M.; Ishitani, H. *Tetrahedron Lett.* **1992**, *33*, 6815 doi:10.1016/S0040-4039(00)61783-5.; (b) Keller, E.; Feringa, B. L. *Synlett* **1997**, 842. doi:10.1055/s-1997-5761.

(12) Curini, M.; Epifano, F.; Maltese, F.; Marcotullio, M. C. *Eur. J. Org. Chem.* **2003**, 1631. doi:10.1002/ejoc.200300076.

(13) (a) Yamanaka, M.; Nishida, A.; Nakagawa, M. *J. Org. Chem.* **2003**, *68*, 3112 doi:10.1021/jo0268153. PMID: 12688780.; (b) Yamanaka, M.; Nishida, A.; Nakagawa, M. *Org. Lett.* **2000**, *2*, 159. doi:10.1021/ol991260s. PMID: 10814271.

(14) (a) Janczuk, A.; Zhang, W.; Xie, W.; Lou, S.; Cheng, J.; Wang, P. G. *Tetrahedron Lett.* **2002**, *43*, 4271 doi:10.1016/S0040-4039(02)00736-0.; (b) Jia, Q.; Xie, W.; Zhang, W.; Janczuk, A.; Lou, S.; Zhang, B.; Cheng, J. P.; Ksebati, M. B.; Wang, P. G. *Tetrahedron Lett.* **2002**, *43*, 2339. doi:10.1016/S0040-4039(02)00262-9.

(15) (a) Wang, L.; Xia, J.; Qin, F.; Qian, C.; Sun, J. *Synthesis* **2003**, 1241 doi:10.1055/s-2003-39397.; (b) Kiselyov, A. S.; Smith, L.; Armstrong, R. W. *Tetrahedron* **1998**, *54*, 5089 doi:10.1016/S0040-4020(98)00248-8.; (c) Su, W.; Yang, D.; Jin, C.; Zhang, B. *Tetrahedron Lett.* **2008**, *49*, 3391. doi:10.1016/j.tetlet.2008.03.124.

(16) Lee, Y. R.; Kweon, H. I.; Koh, W. S.; Min, K. R.; Kim, Y.; Lee, S. H. *Synthesis* **2001**, 1851. doi:10.1055/s-2001-17516.

(17) (a) van Rantwijk, F.; Sheldon, R. A. *Chem. Rev.* **2007**, *107*, 2757 doi:10.1021/cr050946x. PMID:17564484.; (b) Parvulescu, V. I.; Hardacre, C. *Chem. Rev.* **2007**, *107*, 2615 doi:10.1021/cr050948h. PMID:17518502.; (c) Jain, N.; Kumar, A.; Chauhan, S.; Chauhan, S. M. S. *Tetrahedron* **2005**, *61*, 1015 doi:10.1016/j.tet.2004.10.070.; (d) Song, C. E. *Chem. Commun.* **2004**, 1033 doi:10.1039/b309027b. PMID: 15116175.; (e) Dupont, J.; DeSouza, R. F.; Suarez, P. A. Z. *Chem. Rev.* **2002**, *102*, 3667 doi:10.1021/cr010338r. PMID: 12371898.; (f) Wasserscheid, P.; Keim, W. *Angew. Chem., Int. Ed.* **2000**, *39*, 3772 doi:10.1002/1521-3773(20001103)39:21<3772::AID-ANIE3772>3.0.CO;2-5.; (g) Welton, T. *Chem. Rev.* **1999**, *99*, 2071 doi:10.1021/cr980032t. PMID: 11849019.; (h) Wasserscheid, P.; Welton, T. Ionic liquids in synthesis. 2nd ed. Wiley-VCH, Weinheim. 2007.

(18) Binnemans, K. *Chem. Rev.* **2007**, *107*, 2592; and references cited therein. doi:10.1021/cr050979c. PMID:17518503.

(19) (a) Kumar, A.; Ahmad, I.; Rao, M. S. *Can. J. Chem.* **2008**, *86*, 899 doi:10.1139/V08-121.; (b) Kumar, A.; Ahmad, I.; Rao, M. S.; Patel, G.; Kumar, D. *Indian J. Chem.* **2009**, *48B*, 611; (c) Kumar, A. *Catal. Commun.* **2007**, *8*, 913 doi:10.1016/j.catcom.2006.08.052.; (d) Kumar, A.; Jain, N.; Chauhan, S. M. S. *Synlett* **2007**, 0411 doi:10.1055/s-2007-967951.; (e) Chauhan, S. M. S.; Kumar, A.; Srinivas, K. A. *Chem. Commun.* **2003**, 2348 doi:10.1039/b305888c. PMID: 14518908.; (f) Srinivas, K. A.; Kumar, A.; Chauhan, S. M. S. *Chem. Commun.* **2002**, 2456 doi:10.1039/b207072n. PMID:12430488.; (g) Kumar, A.; Jain, N.; Chauhan, S. M. S. *Synth. Commun.* **2004**, *34*, 2835 doi:10.1081/SCC-200026242.; (h) Kumar, A.; Jain, N.; Rana, S.; Chauhan, S. M. S. *Synlett* **2004**, 2785.

(20) Anslyn, E. V.; Dougherty, D. A. *In* Modern physical organic chemistry. University Science Books, Sausalito, CA. 2006.

(21) (a) Kim, D. W.; Song, C. E.; Chi, D. Y. *J. Org. Chem.* **2003**, *68*, 4281 doi:10.1021/jo034109b. PMID:12762727.; (b) Wheeler, C.; West, K. N.; Liotta, C. L. C.; Eckert, A. *Chem. Commun.* **2001**, 887. doi:10.1039/b101202a.

(22) Cox, R. A.; Druet, L. M.; Klausnert, A. E.; Modro, T. A.; Wan, P.; Yates, K. *Can. J. Chem.* **1981**, *59*, 1568. doi:10.1139/v81-231.

Chemical-bond properties and hardness of nonlinear optical crystals LiB_3O_5 and β-BaB_2O_4

Guangping Zhao and Bingjie Yu

Abstract: The chemical-bond parameters of LiB_3O_5 (LBO) and β-BaB_2O_4 (BBO) nonlinear optical crystals have been calculated using the chemical-bond theory of complex crystals. Their hardnesses have been predicted by the chemical-bond definition of hardness. The calculated results indicate that their hardnesses are determined only by Li–O and Ba–O bonds. The BO_3 anionic clusters do not contribute to their hardness. The calculation of hardness indicates that all of the compounds possess good mechanical properties.

Key words: nonlinear optical crystal, chemical bond, hardness, borate.

Résumé : Faisant appel à la théorie de la liaison chimique des cristaux complexes, on a calculé les paramètres des liaisons chimiques des cristaux optiques non linéaires de borate de lithium (LBO) et de borate de baryum (BBO). Leur dureté a été prédite par la définition de la dureté en fonction de la liaison chimique. Les résultats calculés indiquent que leurs duretés ne sont déterminées que par la liaison Li–O, Ba–O. Les agrégats anioniques de BO_3 ne contribuent pas à ces duretés. Le calcul de la dureté indique que tous les composés possèdent de bonnes propriétés mécaniques.

Mots-clés : cristal optique non linéaire, liaison chimique, dureté, borate.

[Traduit par la Rédaction]

The materials exhibiting nonlinear optical (NLO) properties have become objects of an extensive recent interest. Lithium triborate (LBO) and β-BaB_2O_4 (BBO) are the relatively new nonlinear optical borate material. They possess distinguished NLO properties and high optical-damage resistance. These unique properties, combined with high mechanical stability and nonhygroscopic behaviour, make LBO and BBO the suitable candidates for high-power lasers and optical parametric processes.[1,2] Therefore, the studies of properties governing the applicability of LBO and BBO single crystals are important. A number of papers focused on their optical properties, electrical conductivity, thermal properties, and dielectric constants.[3–7] However, the mechanical properties of LBO and BBO are little investigated, although they are obviously important for all kinds of device applications. The theoretical study on the mechanical properties of novel materials is of interest.[8–13] Therefore, this paper gives a theoretical prediction of hardness values of these crystals by using the chemical-bond theory of complex crystals[14–17] and hardness theory.[18–21] It helps to understand further the other mechanical properties. The calculations of the chemical-bond parameters may obtain some useful information concerning the modification of NLO responses of borate crystals. It is also interesting to study the effect of the BO_3^{-3} clusters on the hardness of borate crystals.

Received 14 January 2009. Accepted 24 March 2009. Published on the NRC Research Press Web site at canjchem.nrc.ca on 26 May 2009.

G. Zhao[1] and B. Yu.[1,2] College of Environment and Chemical Engineering, Yanshan University, Qinhuangdao 066004, P.R. China.

[1]Present address: Lab of Physics, 9th School of QHD, Qinhuangdao 066000, P.R. China.
[2]Corresponding author (e-mail: ysdx139140@sina.com).

A theory describing the chemical bond of complex crystals has been developed by Zhang et al.[14–17,22,23] It has been successfully applied to the optical properties.[24–26] Zhang[14] has pointed out that the properties of a crystal can be described by chemical-bond parameters, and any complex crystal can be decomposed into different kinds of pseudo-binary crystals. In theory, the "crystal formula" is a combination of sub-formulae for a chemical bond. The sub-formula for any kind of chemical bond A–B in the multibond crystal A_aB_b can be expressed by the following formula:

$$[1] \qquad \left[\frac{N(\mathrm{B}-\mathrm{A})a}{N_{\mathrm{CA}}}\right]\mathrm{A}\left[\frac{N(\mathrm{A}-\mathrm{B})b}{N_{\mathrm{CB}}}\right]\mathrm{B}$$

where A, B represent different elements or different sites of the same element in the crystal formula; a, b represent numbers of the corresponding element; N(B–A) represents the number of B ions in the A ion coordination group, and N_{CA} represents the nearest coordination number of an A ion. After decomposing the complex crystal into different kinds of pseudo-binary crystals, which form an isotropic system, and then introducing an effective charge to the valence electron by the Pauling bond-valence method, P–V–L theory[22,23] can be used directly to calculate the chemical-bond parameters in the complex crystal compound.

The average energy gap E_g^μ for every μ bond can be separated into homopolar E_h^μ and heteropolar C^μ parts

$$[2] \qquad (E_g^\mu)^2 = (E_h^\mu)^2 + (C^\mu)^2$$

The ionicity f_i^μ and covalency f_c^μ of any type of chemical bond is defined as follows

$$[3] \qquad f_i^\mu = (C^\mu)^2/(E_g^\mu)^2$$

Table 1. Chemical-bond parameters and calculated hardnesses of LBO crystals, where H_ν^μ is the hardness of a psuedo-binary compound composed of μ-type bonds, $H_{avg.}$ and $H_{v\ exptl.}$ are calculated average value and experimental microhardness, respectively.

Bond	d^μ(Å)	f_c	v_b^μ (Å^3)	N_a (Å^{-2})	H_ν^μ	$H_{avg.}$ (GPa)	$H_{v\ exptl.}$ (GPa)[27]
LiO	2.00	0.63	10.19	0.21	13.55	11.97	10–15
LiO	2.02	0.63	10.48	0.21	12.95	—	—
LiO	2.01	0.63	10.36	0.21	13.20	—	—
LiO	2.18	0.61	13.27	0.18	8.87	—	—
BO	1.39	0.54	3.41	0.44	62.22	—	—
BO	1.35	0.54	3.13	0.47	71.42	—	—
BO	1.34	0.55	3.04	0.48	74.87	—	—
BO	1.45	0.35	3.92	0.40	40.45	—	—
BO	1.48	0.17	4.14	0.39	30.03	—	—
BO	1.45	0.35	3.92	0.40	40.57	—	—
BO	1.50	0.34	4.35	0.38	34.30	—	—
BO	1.36	0.54	3.21	0.46	68.69	—	—
BO	1.34	0.27	3.06	0.47	53.55	—	—
BO	1.41	0.63	3.56	0.43	65.10	—	—

$$[4]\qquad f_c^\mu = (E_h^\mu)^2/(E_g^\mu)^2$$

where

$$[5]\qquad E_h^\mu\ (\mathrm{eV}) = 39.74/(d^\mu)^{2.48}$$

where d^μ is the bond length. For any binary crystal AB_n-type compounds, the heteropolar C^μ part is defined as

$$[6]\qquad C^\mu\ \ (\mathrm{eV}) = \{14.4b^\mu[(Z_A^\mu)^* + \Delta Z_A^\mu - n(Z_B^\mu)^*]e^{-k_s^\mu r_0^\mu}\}/r_0^\mu$$

$$[7]\qquad r_0^\mu = d^\mu/2$$

$$[8]\qquad k_s^\mu = (4k_F^\mu/\pi a_B)^{1/2}$$

$$[9]\qquad (k_F^\mu)^3 = 3\pi^2 N_e^\mu$$

where $(Z_A^\mu)^*$ is the number of effective valence electrons of A ion, ΔZ_A^μ is correction factors from d electron effects, such as the crystal field stable energy and Jahn–Teller effect,[15] n is the ratio of element B to element A in the subformula, k_s^μ is Thomas–Fermi screening wave number of valence electron in binary crystal composed of only one type of bond μ, a_B is the Bohr radius, k_F^μ is Fermi wave number of valence electron in binary crystal composed of only one type of bond μ, N_e^μ is the number of valence electrons of type μ bond per cubic angstroms, b^μ is proportional to the square of the average coordination number N_c^μ

$$[10]\qquad \begin{aligned} b^\mu &= \beta(N_c^\mu)^2 \\ N_c^\mu &= [N_{CA}^\mu/(1+n)] + [nN_{CB}^\mu/(1+n)] \end{aligned}$$

where b^μ depends on a given crystal structure.

The hardness of a pseudo-binary compound composed of μ-type bonds can be calculated as follows[18–21]

$$[11]\qquad H_v\ (\mathrm{GPa}) = 556\left[\frac{N_a e^{-1.191 f_i}}{d^{2.5}}\right] = 350\left[\frac{(N_e)^{2/3} e^{-1.191 f_i}}{d^{2.5}}\right]$$

where N_a is the number of bonds per unit area, N_e^μ is expressed as follows

$$[12]\qquad N_e^\mu = (n_e^\mu)^*/v_b^\mu$$

$$[13]\qquad (n_e^\mu)^* = [(Z_A^\mu)^*/N_{CA}^\mu] + [(Z_B^\mu)^*/N_{CB}^\mu]$$

$$[14]\qquad v_b^\mu = (d^\mu)^3/\sum_\nu [(d^\nu)^3 N_b^\nu]$$

where $(n_e^\mu)^*$ is the number of effective valence electrons per μ bond, v_b^μ is the bond volume.

The hardness of a multicomponent compound system can be expressed as an average of the hardnesses of all binary systems in the solid. Hardness surely involves the cooperative softening of many bonds. When there are differences in the strength among different types of bonds, the trend of breaking the bonds will start from a softer one. Therefore, the hardness H_v of complex crystals should be calculated by a geometric average of all bonds as follow

$$[15]\qquad H_v = \left[\prod_\mu^\mu (H_\nu^\mu)^{n^\mu}\right]^{1/\Sigma n^\mu}$$

where n^μ is the number of bonds of type μ composing the actual complex crystal.

Lithium triborate, LiB_3O_5 (LBO), is characterized by orthorhombic structure (space group: (33) $Pna2_1$; unit-cell parameters: a = 8.444 Å, b = 7.378 Å, c = 5.146 Å[1] at ambient conditions). The space group of BBO is $R3$, and its unit-cell parameters are a = 12.532 Å, c = 12.717 Å.[2] Theoretically,[14] LBO and BBO can be decomposed into the sum of pseudo-binary crystals as follows

$$\begin{aligned}[16]\qquad LiB_3O_5 = {} & 1/4LiO(1)_{4/3} + 1/4LiO(3)_{4/3} + + 1/4LiO(3)_{4/3} + 1/4LiO(4)_{4/3} + 1/3B(1)O(3) + + 1/3B(1)O(4) \\ & + 1/3B(1)O(5) + 1/4B(2)O(3)_{4/3} + 1/4B(2)O(3)_2 + 1/4B(2)O(4)_{4/3} + 1/4B(2)O(5)_{4/3} + 1/3B(3)O(1) \\ & + 1/3B(3)O(2)_{3/2} + 1/3B(3)O(3)\end{aligned}$$

Table 2. Chemical-bond parameters and calculated hardnesses of BBO crystals, where H_v^μ is the hardness of a psuedo-binary compound composed of μ-type bonds, $H_{avg.}$ and $H_{v\ exptl.}$ are calculated average value and experimental microhardness, respectively.

Bond	d^μ(Å)	f_c	v_b^μ (Å^3)	N_a (Å^{-2})	H_v^μ	$H_{avg.}$ (GPa)
BaO	2.80	0.04	10.81	0.20	2.77	2.86
BaO	2.74	0.10	10.12	0.21	3.30	—
BaO	3.05	0.10	14.03	0.17	2.01	—
BaO	2.80	0.10	10.86	0.20	2.96	—
BaO	2.89	0.10	11.95	0.19	2.56	—
BaO	2.63	0.11	8.94	0.23	3.98	—
BaO	2.83	0.10	11.13	0.20	2.85	—
BaO	2.75	0.04	10.20	0.21	3.03	—
BaO	2.81	0.04	10.88	0.20	2.75	—
BaO	2.80	0.10	10.82	0.20	2.97	—
BaO	2.73	0.10	10.05	0.21	3.32	—
BaO	3.04	0.10	13.80	0.17	2.06	—
BaO	2.61	0.11	8.79	0.23	4.08	—
BaO	2.86	0.10	11.48	0.20	2.72	—
BaO	2.93	0.10	12.41	0.19	2.42	—
BaO	2.78	0.04	10.63	0.21	2.85	—
BO	1.40	0.32	1.35	0.82	87.28	—
BO	1.36	0.32	1.25	0.86	98.61	—
BO	1.33	0.09	1.17	0.90	83.26	—
BO	1.37	0.32	1.26	0.85	96.68	—
BO	1.36	0.32	1.24	0.87	99.26	—
BO	1.36	0.09	1.23	0.87	76.74	—
BO	1.28	0.10	1.03	0.98	99.84	—
BO	1.39	0.32	1.33	0.83	89.67	—
BO	1.41	0.32	1.37	0.81	85.61	—
BO	1.31	0.09	1.10	0.94	90.78	—
BO	1.39	0.32	1.33	0.83	89.09	—
BO	1.41	0.32	1.38	0.81	84.69	—

$$\begin{aligned}\beta\text{-}BaB_2O_4 = {} & 1/16Ba(1)O(1)_{8/3} + 1/16Ba(1)O(3)_2 + 1/16Ba(1)O(3)_2 + 1/16Ba(1)O(4)_2 + 1/16Ba(1)O(5)_2 \\ & + 1/16Ba(1)O(6)_2 + 1/16Ba(1)O(6)_2 + 1/16Ba(1)O(8)_{8/3} + 1/16Ba(2)O(2)_{8/3} + 1/16Ba(2)O(3)_2 \\ & + 1/16Ba(2)O(4)_2 + 1/16Ba(2)O(4)_2 + 1/16Ba(2)O(5)_2 + 1/16Ba(2)O(5)_2 + 1/16Ba(2)O(6)_2 \\ & + 1/16Ba(2)O(7)_{8/3} + 1/6B(1)O(1) ++ 1/6B(1)O(1) + 1/6B(1)O(5)_{4/3} + 1/6B(2)O(2)++1/6B(2)O(2) \\ & + 1/6B(2)O(6)_{4/3}++1/6B(3)O(7)++1/6B(3)O(7)+1/6B(3)O(3)_{4/3}+1/6B(4)O(8)++1/6B(4)O(8) \\ & + 1/6B(4)O(4)_{4/3}\end{aligned} \quad [17]$$

By using the above theories, the chemical-bond covalency of each type of the constituent chemical bonds and the hardness of pseudo-binary crystals composed of the corresponding constituent bonds can be calculated. Results are listed in Tables 1 and 2. Since BO_3 is an anionic cluster, its B–O bond may not break in hardness test. In other words, the hardness of LBO results only from the breaking of the other bonds, including Li–O bond. The hardness of BBO results only from the breaking of the other bonds, including Ba–O bond. Our calculated values of the average hardness for LBO, taking only Li–O bond, 11 GPa, is in good agreement with the available experimental one. Therefore, we can conclude that the anionic cluster, BO_3, does not contribute to the hardness of LBO and BBO; it would slip in one unit under indenter. The calculated hardness of BBO in Table 2 is lower than that of LBO.

According to eq. [11], the ionicity plays an important role in the hardness calculation. The hardness of ionic crystals is far lower than that of covalent crystals. Hence, the hardness resulting from a covalent component plays a determining role in partially covalent ionic crystals. Although the electronegativity of Li, 1.0, is less than that of B, 2.0, our chemical-bond calculations show that the covalencies of Li–O bonds are greater than those of B–O bonds. Pauling's empirical electronegativity scale is derived from thermochemical bond-energy data. Although decreasing Pauling's electronegativity differences within each binary compound of a series can usually be taken as an indication for increasing covalency, this is not necessarily the case for a series of binary oxides, i.e., for P_2O_5, SiO_2, $A1_2O_3$, MgO, and Na_2O, the electronegativity difference, $X_o - X_M$, decreases gradually from MgO to P_2O_5 in accordance with the expected increasing covalency, but for Na_2O, the difference is approximately equal to that for SiO_2. From the point of view of chemical bond, it is expected that the bonding in SiO_2 is significantly

Fig. 1. Structure of LiB_4O_7.

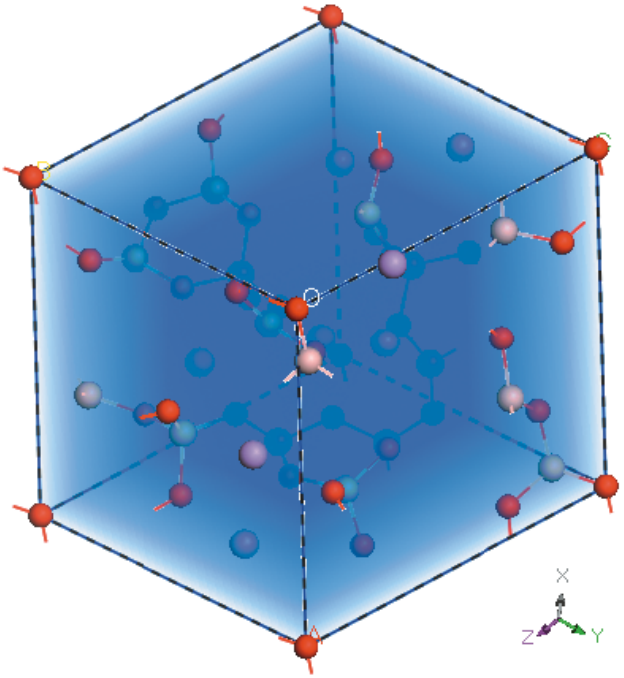

more covalent than that in Na_2O. Therefore, it is acceptable that the calculated covalency of Li–O bond is slightly larger than that of B–O bond. It is because of the larger covalency of Li–O bonds that the hardness of LBO crystal is up to about 11 GPa, comparable to that of SiO_2 quartz.

Using the above-mentioned method, the hardness of another nonlinear optical crystal LiB_4O_7, its crystal structure is shown in Fig. 1, is also estimated at 9.1 GPa, which is in agreement with the measured value.[28] Results indicate that the Li–O bonds play the key role in determining the hardness of the nonlinear optical crystal LiB_4O_7.

For BBO crystal, the covalency of the Ba–O bonds is remarkably smaller than that of the BO bonds, leading to the lower-hardness BBO crystal.

In summary, the chemical-bond parameters of LBO and BBO compounds have been calculated using the chemical-bond theory of complex crystals. Their hardnesses have been predicted by the chemical-bond definition of hardness. The calculated results indicate that their hardnesses are determined only by Li–O and Ba–O bonds. The BO_3 anionic cluster does not contribute to their hardness.

References

(1) Chen, C.; Wu, B.; Jiang, A.; You, G. *Sci. Sin. B* **1985**, *28*, 235.

(2) Chen, C.; Wu, Y.; Jiang, A.; Wu, B.; You, G.; Li, R.; Lin, S. *J. Opt. Soc. Am. B* **1989**, *6*, 616. doi:10.1364/JOSAB.6.000616.

(3) (a) Raja, C. R.; Gobinathan, R.; Gnanan, F. D. *Cryst. Res. Technol.* **1993**, *28*, 453 doi:10.1002/crat.2170280405.; (b) Mori, Y.; Kuroda, I.; Nakajima, S.; Sasaki, T.; Nakai, S. *Appl. Phys. Lett.* **1995**, *67*, 1818. doi:10.1063/1.115413.

(4) Aka, G.; Kahn-Harari, A.; Vivien, D.; Benitez, J.-M.; Salin, F.; Godard, J. *Eur. J. Solid State Inorg. Chem.* **1996**, *33*, 727.

(5) Kannan, C. V.; Kimura, H.; Miyazaki, A.; Ramasamy, P. *J. Cryst. Growth* **2005**, *275*, e769. doi:10.1016/j.jcrysgro.2004.11.091.

(6) Guo, R.; Markgraf, S. A.; Furukawa, Y.; Sato, M.; Bhalla, A. S. *J. Appl. Phys. (Berl.)* **1995**, *78*, 7234.

(7) Lin, Z.; Xu, L. F.; Li, R. K.; Wang, Z.; Chen, C.; Lee, M.-H.; Wang, E. G.; Wang, D.-S. *Phys. Rev. B* **2004**, *70*, 233104. doi:10.1103/PhysRevB.70.233104.

(8) Gou, H. Y.; Hou, L.; Zhang, J. W.; Gao, F. *Appl. Phys. Lett.* **2008**, *92*, 241901. doi:10.1063/1.2938031.

(9) Gou, H. Y.; Hou, L.; Zhang, J. W.; Wang, Z. B.; Gao, L. H.; Gao, F. M. *Appl. Phys. Lett.* **2007**, *90*, 191905. doi:10.1063/1.2737130.

(10) Tse, J. S.; Klug, D. D.; Gao, F. *Phys. Rev. B* **2006**, *73*, 140102. doi:10.1103/PhysRevB.73.140102.

(11) Gou, H.; Hou, L.; Zhang, J.; Li, H.; Sun, G.; Gao, F. *Appl. Phys. Lett.* **2006**, *88*,o. 221904. doi:10.1063/1.2208367.

(12) Gou, H. Y.; Hou, L.; Zhang, J. W. *Appl. Phys. Lett.* **2006**, *89*,o. 141910. doi:10.1063/1.2359434.

(13) Gou, H. Y.; Hou, L.; Zhang, J. W.; Sun, G. F.; Gao, L. H.; Gao, F. M. *Physica Status Solidi B* **2008**, *245*, 58. doi:10.1002/pssb.200743241.

(14) Zhang, S. Y.; Gao, F. M.; Wu, C. X. *J. Alloys Compd.* **1998**, *835*, 275.

(15) Gao, F. M.; Li, D. C.; Zhang, S. Y. *J. Phys. Condens. Matter.* **2003**, *15*, 5079. doi:10.1088/0953-8984/15/29/319.

(16) Wu, Z.; Meng, Q.; Zhang, S. *Phys. Rev. B* **1998**, *58*, 958. doi:10.1103/PhysRevB.58.958.

(17) Xue, D.; Zhang, S. *Appl. Phys. Lett.* **1997**, *70*, 943. doi:10.1063/1.118448.

(18) Gao, F. M. *Phys. Rev. B* **2004**, *69*, 094113. doi:10.1103/PhysRevB.69.094113.

(19) Gao, F. M.; Xu, R.; Liu, K. *Phys. Rev. B* **2005**, *71*,o. 052103. doi:10.1103/PhysRevB.71.052103.

(20) Gao, F. M.; Hou, L.; He, Y. H. *J. Phys. Chem. B* **2004**, *108*, 13069. doi:10.1021/jp047627e.

(21) Gao, F. M.; Qin, X. J.; Wang, L. Q.; He, Y.; Sun, G.; Hou, L.; Wang, W. *J. Phys. Chem. B* **2005**, *109*, 14892. doi:10.1021/jp052547b. PMID:16852886.

(22) Phillips, J. C. *Rev. Mod. Phys.* **1970**, *42*, 317. doi:10.1103/RevModPhys.42.317.

(23) Levine, B. F. *J. Chem. Phys.* **1973**, *59*, 1463.

(24) Gao, F. M.; Zhang, S. Y. *J. Phys. Chem. Solids* **1997**, *58*, 1991. doi:10.1016/S0022-3697(96)00139-4.

(25) Gao, F. M. *J. Phys. Condens. Matter* **2003**, *15*, L637. doi:10.1088/0953-8984/15/41/L02.

(26) Gao, F. M.; Zhang, S. Y. *J. Chin. Rare Earth Soc.* **1993**, *11*, 186.

(27) Shakhverdova, I. P.; Paufler, P.; Bubnova, R. S.; Filatov, S. K.; Meyer, D. C. *Cryst. Res. Technol.* **2008**, *43*, 339. doi:10.1002/crat.200711104.

(28) Kar, S.; Verma, S.; Bartwal, K. S. *Cryst. Res. Technol.* **2008**, *43*, 438. doi:10.1002/crat.200710992.

Synthesis of a new heterocyclic system — Fluoreno[1,2-*d*]imidazol-10-one

Mohammad Rahimizadeh, Mehdi Pordel, Mehdi Bakavoli, Shima Rezaeian, and Hossein Eshghi

Can. J. Chem. Downloaded from www.nrcresearchpress.com by Sichuan Normal University on 09/14/12
For personal use only.

Abstract: Synthesis of various substituted fluoreno[1,2-*d*]imidazol-10-ones (**5a**–**5g**) has been accomplished by the cyclization of diazotized 1-substituted 4-benzoyl-5- aminobenzimidazoles (**4a**–**4g**). Compounds **4a**–**4g** were prepared by reductive ring opening of 3*H*-imidazo[4′,5′:3,4]benzo[*c*]isoxazoles (**3a**–**3g**) with zinc dust in EtOH/NaOH solution.

Key words: fluoreno[1,2-*d*]imidazol-10-ones, diazotation, imidazo[4′,5′:3,4]benzo[*c*]isoxazoles, reductive ring opening.

Résumé : On a réalisé la synthèse de diverses fluoréno[1,2-*d*]imidazol-10-ones substituées, **5a**–**5g**, en procédant à la cyclisation de 4-benzoyl-5-aminobenzimidazoles diazotés, substitués en position 1, **4a**–**4g**. Les produits **4a**–**4g** ont été obtenus par l'ouverture réductrice de cycle de 3*H*-imidazo[4′,5′:3,4]benzo[*c*]isoxazoles, **3a**–**3g**, avec de la poudre de zinc dans une solution EtOH/NaOH.

Mots-clés : fluoréno[1,2-*d*]imidazol-10-ones, diazotation, imidazo[4′,5′:3,4]benzo[*c*]isoxazoles, ouverture réductrice de cycle.

[Traduit par la Rédaction]

Introduction

Fluorenones (fluorine-9-ones) are among the oldest classes of bioactive compounds, which are widely used as antiviral[1–3] and anticancer[4,5] agents and act as the key synthetic intermediates in many reactions.[6,7] Also, fluorenones with a suitable functionality can be used as a fluorescent electrophilic reagent.[8] Recently, they have mainly been considered as an important unit in polymer chemistry.[9–12] The fluorenone structural unit provides both rigidly planarized biphenyl units within the polymer backbone and the possibility of remote functionalization at C-9, the latter offer the prospect of improving both polymer processibility and mediating potential interchain interactions in films.[13]

There are several methods for the synthesis of these useful compounds, including the Friedel–Crafts ring closures of biarylcarboxylic acid derivatives,[14,15] intramolecular [4+2] cycloaddition reactions of conjugated enynes,[16] oxidation of fluorenes,[17] remote metalation of *m*-teraryl and biaryl amides[18] or combined directed ortho metalation-directed remote metalation,[19] palladium-catalyzed cyclocarbonylation of ortho halobiaryls,[20] and several other new methods.[21–23] Intramolecular reaction of diazotized 2-aminobenzophenones is one of the oldest methods for the preparation of fluorenones with relatively well-clarified mechanistic features.[24] A literature survey disclosed that the diazotized 4-benzoyl-5-aminobenzimidazoles have not been converted to fluoreno[1,2-*d*]imidazol-10-ones. Owing to our growing interest in the synthesis of bioactive heterocycles,[25] we became interested in examining the cyclization of diazotized compounds **4a**–**4g** to new fluoreno[1,2-*d*]imidazol-10-ones (**5a**–**5g**).

Received 17 September 2008. Accepted 6 January 2009. Published on the NRC Research Press Web site at canjchem.nrc.ca on 23 May 2009.

M. Rahimizadeh,[1] M. Pordel, M. Bakavoli, S. Rezaeian, and H. Eshghi. Department of Chemistry, School of Sciences, Ferdowsi University of Mashhad, Mashhad 91775-1436, Iran.

[1]Corresponding author (e-mail: rahimizh@yahoo.com).

Results and discussion

The new 3*H*-imidazo[4′,5′:3,4]benzo[*c*]isoxazoles (**3a**–**3g**) were obtained via the nucleophilic substitution of hydrogen of 1-alkyl-5-nitrobenzimidazoles (**1a**–**1c**) with arylacetonitriles (**2a**–**2d**) in basic MeOH solution[26] (Scheme 1). The reaction does not occur when R_2 is an electron-withdrawing group, since the conjugated base of **2d** is a weak nucleophile.

The reductive ring opening of benzo[*c*]isoxazoles has been reported with Fe/HOAC[27] and Raney Ni/$N_2H_4{\cdot}H_2O$[28] methods. Herein, we introduce the reduction of benzo[*c*]isoxazoles with zinc dust in EtOH and 20% NaOH solution as a highly efficient route to the synthesis of new key intermediates **4a**–**4g** in excellent yields and short reaction times (Scheme 2).

Diazotized compounds **4a**–**4g** underwent cyclization in moderate-to-high yields to new fluoreno[1,2-*d*]imidazol-10-ones (**5a**–**5g**) at 70 °C (Scheme 3). The yield of reaction varies with the nature of the substituent on the benzoyl ring and is better with electron-donating groups (EDGs), since with EDGs, the electron density of the aromatic ring is higher, and it can act as a better nucleophile.

The structural assignments of compounds **5a**–**5g** were based on the analytical and spectral data. For example, in the ^{1}H NMR spectrum of **5c**, the signal at δ 4.16 ppm, assignable to exchangeable protons (NH_2 group), and two doublet signals at δ 6.78 ppm and δ 7.36 ppm, attributed to four aromatic protons of *p*-methoxyphenyl ring of compound **4c**, are not present. Instead, there are the doublet of doublet signal at δ 6.64 ppm (J = 8.1 Hz and J' = 2.1 Hz), the doublet signal at δ 7.03 ppm with meta J (2.1 Hz), and the doublet signal at δ 7.66 ppm with ortho J (8.1 Hz), assignable to three aromatic protons of methoxyphenyl ring. Moreover,

Can. J. Chem. Downloaded from www.nrcresearchpress.com by Sichuan Normal University on 09/14/12
For personal use only.

Scheme 1.

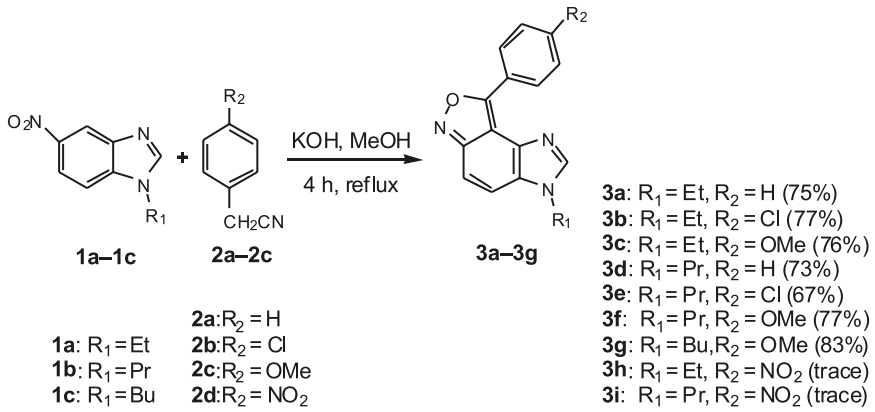

Scheme 2.

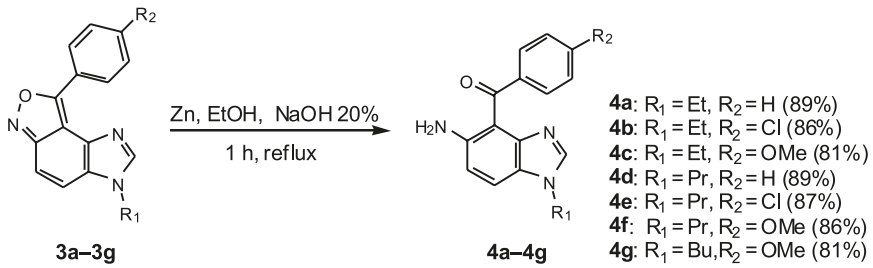

Scheme 3.

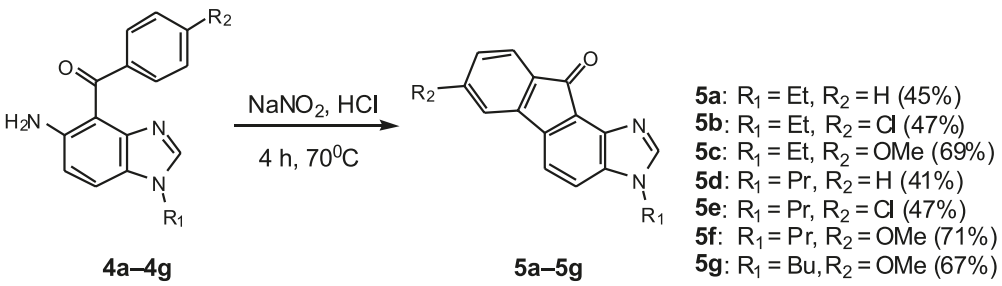

the FTIR spectrum of **5c** in KBr did not show the absorption band at 3320 cm^{-1}, corresponding to NH_2 group. All these evidences plus the molecular-ion peak at *m/z* 278 and micro-analytical data strongly support the tetracyclic structure of compound **5c**.

Conclusion

In summary, this research has demonstrated that the cyclization of diazotized *o*-amino-ketones is a reliable work, which can be extended to the synthesis of other new heterocyclic compounds.

Experimental

CH_2Cl_2 and MeOH were distilled from CaH_2. Silica gel 60 (0.040–0.063 mm, Merck) was used for column chromatography. Compounds **1a**–**1c** were obtained according to the published methods.[29] Other reagents were commercially available. Melting points were recorded on an Electrothermal type-9100 melting-point apparatus and are uncorrected. The IR spectra were obtained on a 4300 Shimadzu spectrometer, and only noteworthy absorptions are listed. The ^1H NMR (100 MHz) spectra were recorded on a Bruker AC 100 spectrometer. Chemical shifts are reported in ppm downfield from TMS as internal standard; coupling constance *J* are given in Hz. The mass spectra were recorded on a Varian Mat. CH-7 at 70 eV. Elemental analysis was performed on a Thermo Finnigan Flash EA microanalyzer.

Synthesis of imidazo[4′,5′:3,4]benzo[*c*]isoxazoles (3a–3g)

General procedure

Compounds **1a**–**1c** (10 mmol) and **2a**–**2c** (12 mmol) were added with stirring to a solution of KOH (20 g, 357 mmol) in methanol (80 mL). The mixture was refluxed with stirring for 4 h, and then poured into water. The precipitate was collected by filtration, washed with water, and air-dried to give **3a**–**3g**.

*3-Ethyl-8-phenyl-3*H*-imidazo[4′,5′:3,4]benzo[*c*]isoxazole (3a)*

Compound **3a** was obtained as colourless needles (EtOH). Yield (75%); mp 99–101 °C. ^1H NMR ($CDCl_3$) δ: 1.56 (t, *J* = 7.0 Hz, 3H), 4.25 (q, *J* = 7.0 Hz, 2H), 7.44–7.66 (m, 5H), 7.88

Can. J. Chem. Downloaded from www.nrcresearchpress.com by Sichuan Normal University on 09/14/12
For personal use only.

(s, 1H), 8.88 (dd, J = 8.0 Hz, J' = 2.0 Hz, 2H). MS (*m*/*z*): 263 (M^+). Anal. calcd. for $C_{16}H_{13}N_3O$ (263.3): C, 72.99; H, 4.98; N, 15.96. Found: C, 72.75; H, 4.83; N, 15.88.

8-(4-Chlorophenyl)-3-ethyl-3*H-*imidazo[4′,5′:3,4]benzo[c]isoxazole (3b)

Compound **3b** was obtained as colourless needles (EtOH). Yield (77%); mp 186–188 °C. ^{1}H NMR ($CDCl_3$) δ: 1.59 (t, J = 7.0 Hz, 3H), 4.27 (q, J = 7.0 Hz, 2H), 7.43 (d, J = 9.5 Hz, 1H), 7.59 (d, J = 9.5 Hz, 1H), 7.65 (d, J = 8.6 Hz, 2H), 7.89 (s, 1H), 8.91 (d, J = 8.6 Hz, 2H). MS (*m*/*z*): 299 (M^+ + 2). Anal. calcd. for $C_{16}H_{12}ClN_3O$ (297.7): C, 64.54; H, 4.06; N, 14.11. Found: C, 64.34; H, 3.97; N, 13.86.

3-Ethyl-8-(4-methoxyphenyl)-3*H-*imidazo[4′,5′:3,4]benzo[c]isoxazole (3c)

Compound **3c** was obtained as colourless needles (EtOH). Yield (76%); mp 173–174 °C. ^{1}H NMR ($CDCl_3$) δ: 1.62 (t, J = 7.3 Hz, 3H), 3.89 (s, 3H), 4.28 (q, J = 7.3 Hz, 2H), 7.17 (d, J = 9.0 Hz, 2H), 7.38 (d, J = 9.5 Hz, 1H), 7.55 (d, J = 9.5 Hz, 1H), 7.88 (s, 1H), 8.84 (d, J = 9.0 Hz, 2H). MS (*m*/*z*): 293 (M^+). Anal. calcd. for $C_{17}H_{15}N_3O_2$ (293.3): C, 69.61; H, 5.15; N, 14.33. Found: C, 69.55; H, 5.12; N, 14.44.

8-Phenyl-3-propyl-3*H-*imidazo[4′,5′:3,4]benzo[c]isoxazole (3d)

Compound **3d** was obtained as colourless needles (EtOH). Yield (73%); mp 119–122 °C. ^{1}H NMR ($CDCl_3$) δ: 0.99 (t, J = 7.0 Hz, 3H), 1.77–2.12 (m, 2H), 4.21 (t, J = 7.0 Hz, 2H), 7.47–7.69 (m, 5H), 7.89 (s, 1H), 8.89 (dd, J = 8.0 Hz, J' = 2.0 Hz, 2H). MS (*m*/*z*): 277 (M^+). Anal. calcd. for $C_{17}H_{15}N_3O$ (277.3): C, 73.63; H, 5.45; N, 15.15. Found: C, 73.87; H, 5.51; N, 15.47.

8-(4-Chlorophenyl)-3-propyl-3*H-*imidazo[4′,5′:3,4]benzo[c]isoxazole (3e)

Compound **3e** was obtained as colourless needles (EtOH). Yield (67%); mp 158–160 °C. ^{1}H NMR ($CDCl_3$) δ: 1.05 (t, J = 7.3 Hz, 3H), 1.85–2.21 (m, 2H), 4.18 (t, J = 7.3 Hz, 2H), 7.40 (d, J = 9.5 Hz, 1H), 7.56 (d, J = 9.5 Hz, 1H), 7.62 (d, J = 8.6 Hz, 2H), 7.86 (s, 1H), 8.89 (d, J = 8.6 Hz, 2H). MS (*m*/*z*): 313 (M^+ + 2). Anal. calcd. for $C_{17}H_{14}ClN_3O$ (311.8): C, 65.49; H, 4.53; N, 13.48. Found: C, 65.25; H, 4.41; N, 13.55.

8-(4-Methoxyphenyl)-3-propyl-3*H-*imidazo[4′,5′:3,4]benzo[c]isoxazole (3f)

Compound **3f** was obtained as colourless needles (EtOH). Yield (77%); mp 155–157 °C. ^{1}H NMR ($CDCl_3$) δ: 0.97 (t, J = 7.3 Hz, 3H), 1.83–2.19 (m, 2H), 3.90 (s, 3H), 4.17 (t, J = 7.3 Hz, 2H), 7.12 (d, J = 9.0 Hz, 2H), 7.40 (d, J = 9.5 Hz, 1H), 7.57 (d, J = 9.5 Hz, 1H), 7.85 (s, 1H), 8.85 (d, J = 9.0 Hz, 2H). MS (*m*/*z*): 307 (M^+). Anal. calcd. for $C_{18}H_{17}N_3O_2$ (307.3): C, 70.34; H, 5.58; N, 13.67. Found: C, 70.25; H, 5.62; N, 13.55.

3-Butyl-8-(4-methoxyphenyl)-3*H-*imidazo[4′,5′:3,4]benzo[c]isoxazole (3g)

Compound **3g** was obtained as colourless needles (EtOH). Yield (83%); mp 139–141 °C. ^{1}H NMR ($CDCl_3$) δ: 0.98 (t, J = 7.0 Hz, 3H), 1.23–1.58 (m, 2H), 1.82–2.10 (m, 2H), 3.90 (s, 3H), 4.18 (t, J = 7.0 Hz, 2H), 7.11 (d, J = 9.0 Hz, 2H), 7.39 (d, J = 9.5 Hz, 1H), 7.57 (d, J = 9.5 Hz, 1H), 7.87 (s, 1H), 8.84 (d, J = 9.0 Hz, 2H). MS (*m*/*z*): 321 (M^+). Anal. calcd. for $C_{19}H_{19}N_3O_2$ (321.4): C, 71.01; H, 5.96; N, 13.08. Found: C, 70.75; H, 5.82; N, 13.45.

Synthesis of *o*-amino-ketones (4a–4g)

General procedure

Zinc dust (1 g, 15.3 mmol) was added with stirring over 5 h period to a solution of **3a**–**3g** (4 mmol) in EtOH (30 mL) and 20% NaOH (20 mL). After the addition was completed, the mixture was refluxed for 1 h and then poured into water. The product was extracted with $CHCl_3$ (2 × 30 mL). The extract was washed with water (2 × 30 mL), and then it was dried and evaporated to give pure **4a**–**4g**.

(5-Amino-1-ethyl-1*H-*benzo[d]imidazol-4-yl)(phenyl)methanone (4a)

Compound **4a** was obtained as colourless needles. Yield (89%); mp 185–187 °C. IR (KBr): 3315 cm^{-1} (NH_2), 1635 cm^{-1} (C=O).^{1}H NMR ($CDCl_3$) δ: 1.51 (t, J = 7.3 Hz, 3H), 3.75 (br s, 2H), 4.13 (q, J = 7.3 Hz, 2H), 6.67 (d, J = 8.5 Hz, 1H), 7.09 (d, J = 8.5 Hz, 1H), 7.19–7.60 (m, 5H), 7.78 (s, 1H). MS (*m*/*z*) 265 (M^+). Anal. calcd. for $C_{16}H_{15}N_3O$ (265.3): C, 72.43; H, 5.70; N, 15.84. Found: C, 72.21; H, 5.65; N, 15.76.

(5-Amino-1-ethyl-1*H-*benzo[d]imidazol-4-yl)(4-chlorophenyl)methanone (4b)

Compound **4b** was obtained as colourless needles. Yield (86%); mp 174–176 °C. IR (KBr): 3320 cm^{-1} (NH_2), 1635 cm^{-1} (C=O).^{1}H NMR ($CDCl_3$) δ: 1.51 (t, J = 7.3 Hz, 3H), 3.86 (br s, 2H), 4.12 (q, J = 7.3 Hz, 2H), 6.63 (d, J = 8.5 Hz, 1H), 7.11 (d, J = 8.5 Hz, 1H), 7.22 (d, J = 10.5 Hz, 2H), 7.42 (d, J = 10.5 Hz, 2H), 7.77 (s, 1H). MS (*m*/*z*): 301 (M^+ + 2). Anal. calcd. for $C_{16}H_{14}ClN_3O$ (299.8): C, 64.11; H, 4.71; N, 14.02. Found: C, 63.96; H, 4.61; N, 13.83.

(5-Amino-1-ethyl-1*H-*benzo[d]imidazol-4-yl)(4-methoxyphenyl)methanone (4c)

Compound **4c** was obtained as colourless needles. Yield (81%); mp 142–144 °C. IR (KBr): 3320 cm^{-1} (NH_2), 1635 cm^{-1} (C=O). ^{1}H NMR ($CDCl_3$) δ: 1.50 (t, J = 7.3 Hz, 3H), 3.74 (s, 3H), 4.13 (q, J = 7.3 Hz, 2H), 4.16 (br s, 2H), 6.65 (d, J = 8.5 Hz, 1H), 6.78 (d, J = 10.0 Hz, 2H), 7.09 (d, J = 8.5 Hz, 1H), 7.36 (d, J = 10.0 Hz, 2H), 7.77 (s, 1H). MS (*m*/*z*): 295 (M^+). Anal. calcd. for $C_{17}H_{17}N_3O_2$ (295.3): C, 69.14; H, 5.80; N, 14.23. Found: C, 68.83; H, 5.71; N, 13.99.

(5-Amino-1-propyl-1*H-*benzo[d]imidazol-4-yl)(phenyl)methanone (4d)

Compound **4d** was obtained as colourless needles. Yield (89%); mp 168–169 °C. IR (KBr): 3315 cm^{-1} (NH_2), 1635 cm^{-1} (C=O). ^{1}H NMR ($CDCl_3$) δ: 0.94 (t, J = 7.5 Hz, 3H), 1.75–2.10 (m, 2H), 4.04 (t, J = 7.5 Hz, 2H), 4.12 (br s, 2H), 6.62 (d, J = 8.5 Hz, 1H), 7.03 (d, J = 8.5 Hz, 1H), 7.11–7.52 (m, 5H), 7.75 (s, 1H). MS (*m*/*z*): 279 (M^+). Anal. calcd. for $C_{17}H_{17}N_3O$ (279.3): C, 73.10; H, 6.13; N, 15.04. Found: C, 72.86; H, 6.01; N, 14.83.

(5-Amino-1-propyl-1*H-*benzo[d]imidazol-4-yl)(4-chlorophenyl)methanone (4e)

Compound **4e** was obtained as colourless needles. Yield

Can. J. Chem. Downloaded from www.nrcresearchpress.com by Sichuan Normal University on 09/14/12
For personal use only.

(87%); mp 150–152 °C. IR (KBr): 3315 cm^{-1} (NH_2), 1635 cm^{-1} (C=O). ^1H NMR ($CDCl_3$) δ: 0.94 (t, *J* = 7.4 Hz, 3H), 1.67–2.05 (m, 2H), 3.76 (br s, 2H), 4.05 (t, *J* = 7.4 Hz, 2H), 6.66 (d, *J* = 8.5 Hz, 1H), 7.13 (d, *J* = 8.5 Hz, 1H), 7.21 (d, *J* = 9.0 Hz, 2H), 7.41 (d, *J* = 9.0 Hz, 2H), 7.75 (s, 1H). MS (*m*/*z*): 315 (M^+ + 2). Anal. calcd. for $C_{17}H_{16}ClN_3O$ (313.8): C, 65.07; H, 5.14; N, 13.39. Found: C, 64.89; H, 5.03; N, 13.20.

(5-Amino-1-propyl-1*H*-benzo[*d*]imidazol-4-yl)(4-methoxyphenyl)methanone (4f)

Compound **4f** was obtained as colourless needles. Yield (87%); mp 122–124 °C. IR (KBr): 3315 cm^{-1} (NH_2), 1635 cm^{-1} (C=O). ^1H NMR ($CDCl_3$) δ: 1.11 (t, *J* = 7.3 Hz, 3H), 1.87–2.23 (m, 2H), 3.92 (s, 3H), 4.22 (t, *J* = 7.3 Hz, 2H), 4.25 (br s, 2H), 6.79 (d, *J* = 8.5 Hz, 1H), 6.92 (d, *J* = 9.5 Hz, 2H), 7.28 (d, *J* = 8.5 Hz, 1H), 7.51 (d, *J* = 9.5 Hz, 2H), 7.91 (s, 1H). MS (*m*/*z*): 309 (M^+). Anal. calcd. for $C_{18}H_{19}N_3O_2$ (309.4): C, 69.88; H, 6.19; N, 13.58. Found: C, 69.69; H, 6.02; N, 13.41.

(5-Amino-1-butyl-1*H*-benzo[*d*]imidazol-4-yl)(4-methoxyphenyl)methanone (4g)

Compound **4g** was obtained as colourless needles. Yield (81%), mp 142–143 °C. IR (KBr): 3315 cm^{-1} (NH_2), 1635 cm^{-1} (C=O).^1H NMR ($CDCl_3$) δ: 1.11 (t, *J* = 7.0 Hz, 3H), 1.31–1.69 (m, 2H), 1.81–2.11 (m, 2H), 3.91 (s, 3H), 4.23 (t, *J* = 7.0 Hz, 2H), 4.27 (br s, 2H), 6.78 (d, *J* = 8.5 Hz, 1H), 6.93 (d, *J* = 9.5 Hz, 2H), 7.24 (d, *J* = 8.5 Hz, 1H), 7.52 (d, *J* = 9.5 Hz, 2H), 7.91 (s, 1H). MS (*m*/*z*): 323 (M^+). Anal. calcd. for $C_{19}H_{21}N_3O_2$ (323.4): C, 70.57; H, 6.54; N, 12.99. Found: C, 70.44; H, 6.41; N, 12.86.

Synthesis of fluoreno[1,2-*d*]imidazol-10-one (5a–5g)

General procedure

To a solution of **4a**–**4f** (2 mmol) in 3 N HCl (4 mL) maintained at 0–5 °C, a solution of sodium nitrite (0.2 g, 6 mmol) in water (2 mL) was added with stirring over a 5 min period. After the addition was completed, the mixture was stirred at 0–5 °C for 15 min, and then it was maintained at 70 °C in a water bath for 4 h. After pouring this mixture into crushed ice and water (50 mL), the precipitated solid was removed by filtration, washed with water, and dried to give crude **5a**–**5f**.

3-Ethyl-3,10-dihydrofluoreno[1,2-*d*]imidazol-10-one (5a)

Compound **5a** was passed through silica-gel column ($CHCl_3$/MeOH 30:1) to give **5a** as yellow crystals. Yield (45%); mp 160–162 °C. IR (KBr): 1660 cm^{-1} (C=O).^1H NMR ($CDCl_3$) δ: 1.56 (t, *J* = 7.2 Hz, 3H), 4.24 (q, *J* = 7.2 Hz, 2H), 7.09–7.55 (m, 5H), 7.63 (d, *J* = 9.0 Hz, 1H), 8.01 (s, 1H). MS (*m*/*z*): 248 (M^+). Anal. calcd. for $C_{16}H_{12}N_2O$ (248.3): C, 77.40; H, 4.87; N, 11.28. Found: C, 77.23; H, 4.73; N, 11.12.

7-Chloro-3-ethyl-3,10-dihydrofluoreno[1,2-*d*]imidazol-10-one (5b)

Compound **5b** was passed through silica-gel column ($CHCl_3$/MeOH 20: 1) to give **5b** as yellow crystals. Yield (47%); mp 170–172 °C. IR (KBr): 1660 cm^{-1} (C=O). ^1H NMR ($CDCl_3$) δ: 1.50 (t, *J* = 7.1 Hz, 3H), 4.12 (q, *J* = 7.1 Hz, 2H), 7.38 (dd, *J* = 9.0 Hz, *J*′ = 2.1 Hz, 1H), 7.58 (d, *J* = 9.0 Hz, 1H), 8.02 (d, *J* = 8.4 Hz, 1H), 8.12 (d, *J* = 2.1 Hz, 1H), 8.25 (d, *J* = 8.4 Hz, 1H), 8.02 (s, 1H). MS (*m*/*z*): 284 (M^+ + 2). Anal. calcd. for $C_{16}H_{11}ClN_2O$ (282.7): C, 67.97; H, 3.92; N, 9.91. Found: C, 67.65; H, 3.81; N, 9.70.

3-Ethyl-7-methoxy-3,10-dihydrofluoreno[1,2-*d*]imidazol-10-one (5c)

Compound **5c** was passed through silica-gel column ($CHCl_3$/MeOH 20:1) to give **5c** as yellow crystals. Yield (69%); mp 165–167 °C. IR (KBr): 1660 cm^{-1} (C=O). ^1H NMR ($CDCl_3$) δ: 1.56 (t, *J* = 7.3 Hz, 3H), 3.90 (s, 3H), 4.23 (q, *J* = 7.3 Hz, 2H), 6.64 (dd, *J* = 8.1 Hz, *J*′ = 2.1 Hz, 1H), 7.03 (d, *J* = 2.1 Hz, 1H), 7.40 (d, *J* = 8.6 Hz, 1H), 7.49 (d, *J* = 8.6 Hz, 1H), 7.66 (d, *J* = 8.1 Hz, 1H), 8.01 (s, 1H). MS (*m*/*z*): 278 (M^+). Anal. calcd. for $C_{17}H_{14}N_2O_2$ (278.3): C, 73.37; H, 5.07; N, 10.07. Found: C, 73.56; H, 5.21; N, 9.83.

3-Propyl-3,10-dihydrofluoreno[1,2-*d*]imidazol-10-one (5d)

Compound **5d** was passed through silica-gel column ($CHCl_3$/MeOH 30:1) to give **5d** as yellow crystals. Yield (41%); mp 135–137 °C. IR (KBr): 1660 cm^{-1} (C=O). ^1H NMR ($CDCl_3$) δ: 0.97 (t, *J* = 7.3 Hz, 3H), 1.77–2.12 (m, 2H), 4.13 (t, *J* = 7.3 Hz, 2H), 7.08–7.54 (m, 5H), 7.65 (d, *J* = 9.0 Hz, 1H), 8.00 (s, 1H). MS (*m*/*z*): 262 (M^+). Anal. calcd. for $C_{17}H_{14}N_2O$ (262.3): C, 77.84; H, 5.38; N, 10.68. Found: C, 78.05; H, 5.41; N, 10.50.

7-Chloro-3-propyl-3,10-dihydrofluoreno[1,2-*d*]imidazol-10-one (5e)

Compound **5e** was passed through silica-gel column ($CHCl_3$/MeOH 30:1) to give **5e** as yellow crystals. Yield (47%); mp 159–161 °C. IR (KBr): 1660 cm^{-1} (C=O).^1H NMR ($CDCl_3$) δ: 1.01 (t, *J* = 7.3 Hz, 3H), 1.77–2.15 (m, 2H), 4.22 (t, *J* = 7.3 Hz, 2H), 7.43 (dd, *J* = 9.0 Hz, *J*′ = 2.1 Hz, 1H), 7.56 (d, *J* = 9.0 Hz, 1H), 8.03 (d, *J* = 8.4 Hz, 1H), 8.12 (d, *J* = 2.1 Hz, 1H), 8.23 (d, *J* = 8.4 Hz, 1H), 8.02 (s, 1H). MS (*m*/*z*): 298 (M^+ + 2). Anal. calcd. for $C_{17}H_{13}ClN_2O$ (296.8): C, 68.81; H, 4.42; N, 9.44. Found: C, 68.60; H, 4.31; N, 9.31.

7-Methoxy-3-propyl-3,10-dihydrofluoreno[1,2-*d*]imidazol-10-one (5f)

Compound **5f** was passed through silica-gel column ($CHCl_3$/MeOH 30:1) to give **5f** as yellow crystals. Yield (71%); mp 140–142 °C. IR (KBr): 1660 cm^{-1} (C=O). ^1H NMR ($CDCl_3$) δ: 0.98 (t, *J* = 7.2 Hz, 3H), 1.77–2.13 (m, 2H), 3.91 (s, 3H), 4.14 (t, *J* = 7.2 Hz, 2H), 6.66 (dd, *J* = 8.1 Hz, *J*′ = 2.1 Hz, 1H), 6.98 (d, *J* = 2.1 Hz, 1H), 7.38 (d, *J* = 8.6 Hz, 1H), 7.47 (d, *J* = 8.6 Hz, 1H), 7.62 (d, *J* = 8.1 Hz, 1H), 8.03 (s, 1H). MS (*m*/*z*): 292 (M^+). Anal. calcd. for $C_{18}H_{16}N_2O_2$ (292.3): C, 73.95; H, 5.52; N, 9.58. Found: C, 74.12; H, 5.69; N, 9.31.

3-Butyl-7-methoxy-3,10-dihydrofluoreno[1,2-*d*]imidazol-10-one (5g)

Compound **5g** was passed through silica-gel column ($CHCl_3$/MeOH 30:1) to give **5g** as yellow crystals. Yield (67%); mp 120–122 °C. IR (KBr): 1660 cm^{-1} (C=O). ^1H NMR ($CDCl_3$) δ: 0.91 (t, *J* = 7.0 Hz, 3H), 1.15–1.55 (m, 2H), 1.71–2.01 (m, 2H), 3.88 (s, 3H), 4.14 (t, *J* = 7.0 Hz, 2H), 6.65 (dd, *J* = 8.1 Hz, *J*′ = 2.1 Hz, 1H), 6.96 (d, *J* =

2.1 Hz, 1H), 7.39 (d, J = 8.6 Hz, 1H), 7.46 (d, J = 8.6 Hz, 1H), 7.66 (d, J = 8.1 Hz, 1H), 7.98 (s, 1H). MS (m/z): 306 (M^+). Anal. calcd. for $C_{19}H_{18}N_2O_2$ (306.4): C, 74.49; H, 5.92; N, 9.14. Found: C, 74.21; H, 5.79; N, 8.86.

References

(1) Alcaro, S.; Arena, A.; Di Bella, R.; Neri, S.; Ottanà, R.; Ortuso, F.; Pavone, B.; Trincone, A.; Vigorita, M. G. *Bioorg. Med. Chem.* **2005**, *13* (10), 3371–3378. doi:10.1016/j.bmc.2005.03.016. PMID:15848749.

(2) Lyakhov, S. A.; Lyakhova, E. A.; Karpenko, A. S.; Mal′tsev, G. V.; Vel'cheva, I. V.; Litvinova, L. A.; Lebedyuk, M. N.; Khorokhorina, G. A.; Fedchuk, V. P. *Pharm. Chem. J.* **2004**, *38* (3), 128–131. doi:10.1023/B:PHAC.0000034300.89484.b1.

(3) Sill, A. D.; Albrecht, W. L.; Andrews, E. R.; Fleming, R. W.; Horgan, S. W.; Roberts, E. M.; Sweet, F. W. *J. Med. Chem.* **1973**, *16* (3), 240–245. doi:10.1021/jm00261a016. PMID:4354693.

(4) Samanta, S.; Pain, A.; Ghosh, M.; Dutta, S.; Sanyal, U. *Exp. Oncol.* **2005**, *27* (4), 279–285. PMID:16404347.

(5) Perry, P. J.; Read, M. A.; Davies, R. T.; Gowan, S. M.; Reszka, A. P.; Wood, A. A.; Kelland, L. R.; Neidle, S. *J. Med. Chem.* **1999**, *42* (14), 2679–2684. doi:10.1021/jm990084q. PMID:10411488.

(6) Koyama, H.; Kamikawa, T. *Tetrahedron Lett.* **1997**, *38* (22), 3973–3976. doi:10.1016/S0040-4039(97)00793-4.

(7) Gould, S. J.; Melville, C. R.; Cone, M. C.; Chen, J.; Carney, J. R. *J. Org. Chem.* **1997**, *62* (2), 320–324. doi:10.1021/jo961486y. PMID:11671405.

(8) Enoch, I. V. M. V.; Swaminathan, M. *J. Fluoresc.* **2006**, *16* (4), 501–510. doi:10.1007/s10895-006-0074-z. PMID:16794872.

(9) Nie, G.; Cai, T.; Qu, L.; Xu, J.; Wei, Q.; Zhang, S. *J. Electroanal. Chem.* **2008**, *612* (2), 191–200. doi:10.1016/j.jelechem.2007.09.025.

(10) Kono, S.; Sinananwanich, W.; Shibasaki, Y.; Ando, S.; Ueda, M. *Polym. J.* **2007**, *39* (11), 1150–1156. doi:10.1295/polymj.PJ2007090.

(11) Yang, G.-Z.; Wu, M.; Lu, S.; Wang, M.; Liu, T.; Huang, W. *Polymer (Guildf.)* **2006**, *47* (13), 4816–4823. doi:10.1016/j.polymer.2006.04.056.

(12) Uckert, F.; Setayesh, S.; Mullen, K. *Macromolecules* **1999**, *32* (14), 4519–4524. doi:10.1021/ma990157f.

(13) Lemmer, U.; Heun, S.; Mahrt, R.; Scherf, U.; Hopmeier, M.; Siegner, U.; Gobel, E.; Mullen, K.; Bassler, H. *Chem. Phys. Lett.* **1995**, *240* (4), 373–378. doi:10.1016/0009-2614(95)00512-3.

(14) Olah, G. A.; Mathew, T.; Farnia, M.; Prakash, S. *Synlett* **1999**, *1999* (7), 1067–1068. doi:10.1055/s-1999-2770.

(15) Yu, Z.; Velasco, D. *Tetrahedron Lett.* **1999**, *40* (16), 3229–3232. doi:10.1016/S0040-4039(99)00370-6.

(16) Danheiser, R. L.; Gould, A. E.; de la Pradilla, R. F.; Helgason, A. L. *J. Org. Chem.* **1994**, *59* (19), 5514–5515. doi:10.1021/jo00098a002.

(17) Hashemi, M.; Beni, Y. *J. Chem. Res. Synop.* **1999**, (7): 434–435. doi:10.1039/a807641c.

(18) Fu, J.-M.; Zhao, B.-P.; Sharp, M. J.; Snieckus, V. *J. Org. Chem.* **1991**, *56* (5), 1683–1685. doi:10.1021/jo00005a004.

(19) McCubbin, J. A.; Tong, X.; Wang, R.; Zhao, Y.; Snieckus, V.; Lemieux, R. P. *J. Am. Chem. Soc.* **2004**, *126* (4), 1161–1167. doi:10.1021/ja038920f. PMID:14746485.

(20) Campo, M. A.; Larock, R. C. *J. Org. Chem.* **2002**, *67* (16), 5616–5620. doi:10.1021/jo020140m. PMID:12153259.

(21) Yawer, M. A.; Hussain, I.; Reim, S.; Ahmed, Z.; Ullah, E.; Iqbal, I.; Fischer, C.; Reinke, H.; Görls, H.; Langer, P. *Tetrahedron* **2007**, *63* (51), 12562–12575. doi:10.1016/j.tet.2007.10.027.

(22) Tu, S.; Jiang, B.; Jiang, H.; Zhang, Y.; Jia, R.; Zhang, J.; Shao, Q.; Li, C.; Zhou, D.; Cao, L. *Tetrahedron* **2007**, *63* (25), 5406–5414. doi:10.1016/j.tet.2007.04.053.

(23) Fillion, E.; Dumas, A. M.; Hogg, S. A. *J. Org. Chem.* **2006**, *71* (26), 9899–9902. doi:10.1021/jo0618876. PMID:17168619.

(24) DeTar, D. F.; Relyea, D. I. *J. Am. Chem. Soc.* **1954**, *76* (6), 1680–1685. doi:10.1021/ja01635a066.

(25) (a) Bakavoli, M.; Feizyzadeh, B.; Rahimizadeh, M. *Tetrahedron Lett.* **2006**, *47* (50), 8965–8968. doi:10.1016/j.tetlet.2006.10.037.; (b) Bakavoli, M.; Nikpour, M.; Rahimizadeh, M. *J. Heterocycl. Chem.* **2006**, *43* (5), 1327–1329. doi:10.1002/jhet.5570430527.; (c) Bakavoli, M.; Davoodnia, A.; Vahedinia, A.; Rahimizadeh, M.; Roshani, M. *Heterocycles* **2006**, *68* (4), 801. doi:10.3987/COM-06-10669.; (d) Bakavoli, M.; Bakavoli, M.; Davoodnia, A.; Heravi, M. M.; Rahimizadeh, M.; Heravi, M. M. *Mendeleev Commun.* **2006**, *16* (1), 29. doi:10.1070/MC2006v016n01ABEH002177.; (e) Bakavoli, M.; Nikpour, M.; Rahimizadeh, M.; Saberi, M. R.; Sadeghian, H. *Bioorg. Med. Chem.* **2007**, *15* (5), 2120–2126. doi:10.1016/j.bmc.2006.12.022. PMID:17210254.; (f) Bakavoli, M.; Pordel, M.; Rahimizadeh, M.; Jahandari, P.; Rezaei Seresht, E. *Heterocycles* **2008**, *75* (1), 165. doi:10.3987/COM-07-11148.

(26) Davis, R. B.; Pizzini, L. C. *J. Org. Chem.* **1960**, *25* (11), 1884–1888. doi:10.1021/jo01081a015.

(27) Simpson, J. C. E.; Stephenson, O. *J. Chem. Soc.* **1942**, 353. doi:10.1039/jr9420000353.

(28) Pechenia, V. M.; Mukhina, N. A.; Klimenko, V. G.; Granik, V. G. *Chem. Heterocycl. Compd.* **1986**, *8*, 1082.

(29) Aliprandi, B.; Cacace, F.; Possagno, E. *Ann. Chim. (Italy)* **1958**, *48*, 1349.

Can. J. Chem. Downloaded from www.nrcresearchpress.com by Sichuan Normal University on 09/14/12
For personal use only.

Synthesis, characterization, and surface studies of conjugated polymers possessing 2,2′-biimidazole moieties

D.T. Walker, C.D. Douglas, and B.J. MacLean

Abstract: Two novel 2,2′-biimidazole-thiophene structures, 5,5′-bis(2,2′-bithiophene-5-yl)-1,1′-dimethyl-2,2′-biimidazole and 5,5′-bis(3,4-ethylenedioxythiophene-2-yl)-1,1′-dimethyl-2,2′-biimidazole, have been synthesized and electrochemically polymerized. These materials underwent facile oxidation on Pt and ITO surfaces in CH_2Cl_2/Bu_4NPF_6 to yield conjugated, electroactive polymer films. The films were characterized with cyclic voltammetry, electronic absorption spectroscopy, and atomic force microscopy.

Key words: imidazole, conjugated polymer, electropolymerization.

Résumé : On a effectué la synthèse de deux nouvelles structures de 2,2′-biimidazole-thiophène, le 5,5-bis(2,2′-bithiophén-5-yl)-1,1′-diméthyl-2,2′-biimidazole et le 5,5′-bis(3,4-éthylènedioxythiophén-2-yl)-1,1′-diméthyl-2,2′-biimidazole, et on a réalisé leur polymérisation par voie électrochimique. En solution dans un mélange de CH_2Cl_2/Bu_4NPF_6, sur des surfaces de Pt et d′ITO, ces produits donnent facilement lieu à des réactions d'oxydation qui conduisent à la formation de films de polymères conjugués électroactifs. On a caractérisé ces films par voltampérométrie cyclique, spectroscopie d'absorption électronique et par microscopie des forces atomiques.

Mots-clés : imidazole, polymère conjugué, électropolymérisation.

[Traduit par la Rédaction]

Introduction

Although published reports of electroactive heterocyclic polymers appeared as early as 1876,[1] these structures became more interesting to materials scientists around the time the first reports of highly conductive conjugated polymers emerged.[2–4] Since this event, homopolymers consisting of pyridine (**1**), pyrrole (**2**), thiophene (**3**), and other heterocyclic structures (Chart 1) have abounded and have found applications in electronics, corrosion inhibition, sensing, actuators, and energy technology, to name just a few of the more popular areas.[5] Several of these heterocycles may be polymerized electrochemically (e.g., aniline, pyrrole, and thiophene).[6–9] Electrochemical polymerization offers several advantages over chemical polymerization routes.[10] This collection of techniques comprises methods which allow controlled oxidation and (or) reduction of redox-active species at an electrode–solution interface, and thus the methods enable a degree of control over polymerization rate and provide a means of producing polymer films of a desired thickness (and perhaps, quality). Often, the most important advantage provided by electrochemical polymerization, however, is that problems which accompany low polymer solubilities (i.e., difficulties in polymer processing) can be circumvented. For structures which are unable to be polymerized via electrochemical methods (e.g., pyridine), it is usually possible to achieve this goal through the incorporation of polymerizable substituents. The most popular substituent in this application appears to be thiophene and its derivatives. Thienyl substituents have been used in the polymerization of a wide variety of heterocyclic compounds and in many cases, metal complexes.[11–15]

Imidazole (**4**) (Chart 1) has been the topic of relatively few investigations concerning conjugated polymers. This may seem surprising at first, since imidazole possesses pyrrole-like and pyridine-like nitrogens, which should make it an attractive candidate for chemical studies of this sort. The imine centers on imidazole enable derivatives like 2,2′-biimidazole (**5a**) (Chart 1) and others to be utilized as ligands in metal complexes.[16,17] Such assemblies have been shown to display pH-dependent properties and are thus intriguing in sensory applications.[18,19] Benzimidazole polymers and metallopolymers have also been reported to exhibit pH-responsive electrochemistry, which influences electronic communication between metal centers in these materials.[20]

There appear to be two reasons why imidazoles are not as widely studied as other heterocycles. Importantly, protecting groups are required when chemistry is to be carried out at any of the carbon centers on the ring, which adds to preparation time and cost.[21] Furthermore, when bicyclic **5a** is considered, low solubilities in most common organic solvents, due to strong self-association (hydrogen bonding and π-stacking), is a real problem.[22] Here, the use of protecting groups (e.g., benzyl, trimethylsilylethoxymethyl substituents) has been shown to greatly enhance solubility.[23,24]

Received 20 November 2008. Accepted 6 March 2009. Published on the NRC Research Press Web site at canjchem.nrc.ca on 27 May 2009.

D. Walker, C. Douglas, and B. MacLean.[1] Department of Chemistry, St. Francis Xavier University, P.O. Box 5000, Antigonish, NS B2G-2W5, Canada.

[1]Corresponding author (e-mail: bjmaclea@stfx.ca).

Chart 1.

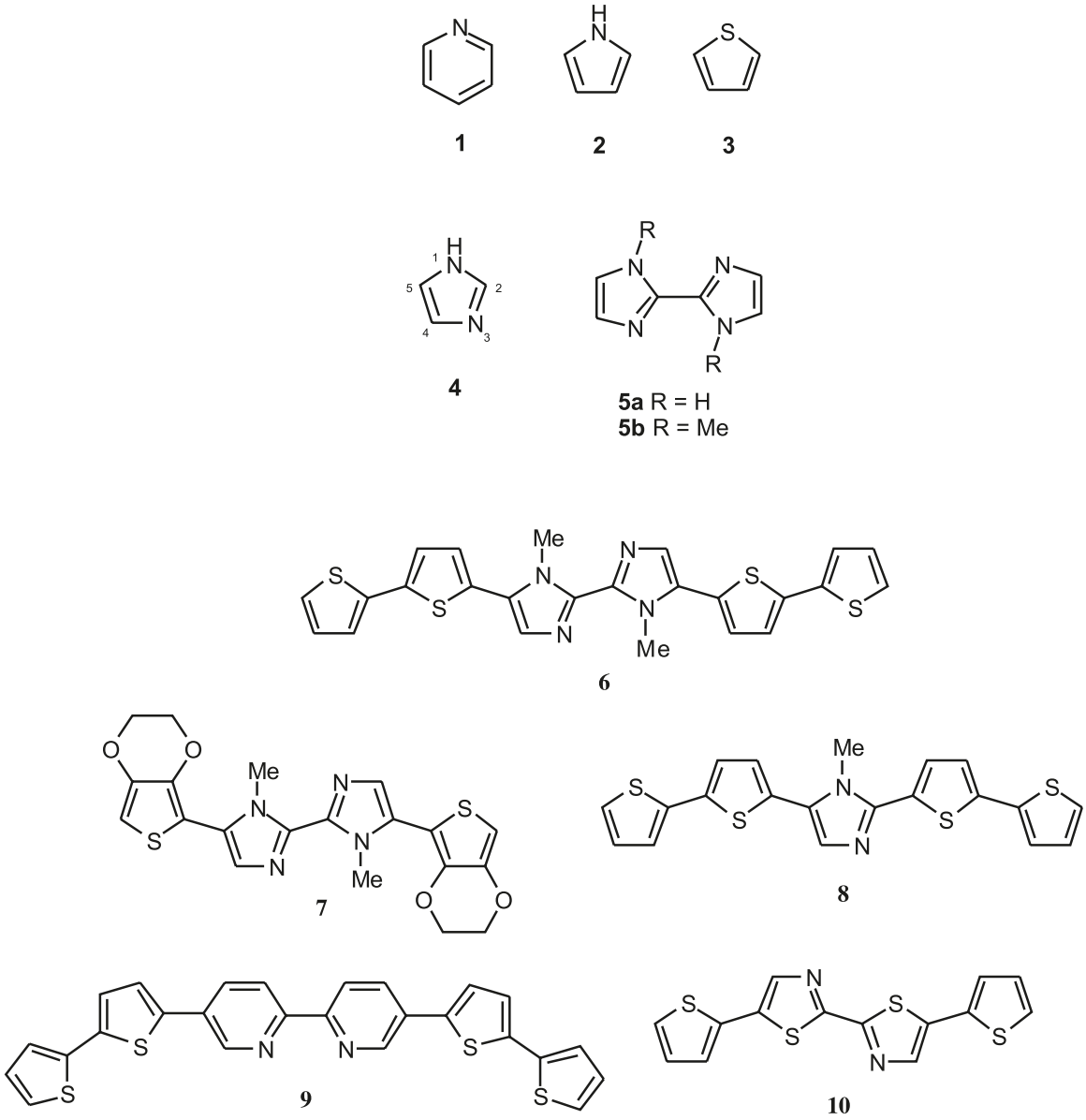

Chemically polymerized 1,1′-diprotected-2,2′-biimidazoles have been detailed by Yamamoto et al.[25,26] In these studies, a range of biimidazoles that were 1,1′-difunctionalized with either alkyl (e.g., **5b**) (Chart 1) or methoxymethyl (MOM) substituents were polymerized via chemical polycondensation reactions. In the case of poly(1,1′-dimethoxymethyl-2,2′-biimidazole), 90% deprotection of the MOM-protected biimidazole sites was possible, yielding a polymer with H-functionalized 2,2′-biimidazole units. Electropolymerizable models, such as 5,5′-bis(2,2′-bithiophene-5-yl)-1,1′-dimethyl-2,2′-biimidazole (**6**) (Chart 1) and 5,5′-bis(3,4-ethylenedioxythiophene-2-yl)-1,1′-dimethyl-2,2′-biimidazole (**7**) (Chart 1), would enable the synthesis of thiophene–imidazole copolymers through convenient electrochemical polymerization experiments. Structures possessing 1,1′-disubstituted biimidazole moieties would be interesting because they would be soluble in organic solvents and because the facile chemistry that yields 1,1′-disubstitution could be varied to provide a means of tuning the electronic properties of such compounds and their polymers. Additionally, as noted earlier, it should be possible to tune their chemical behavior through judicious choice of solution pH. In fact, such a study has recently been reported for a related structure, 2,5-bis(2,2′-bithiophene-5-yl)-1-methylimidazole (**8**) (Chart 1), for which significant blue-shifts in the p-doping potentials of its polymerized form, poly-**8,** were observed upon the addition of trifuoroacetic acid to test solutions.[27]

A promising avenue of research for conjugated polymers containing 2,2′-biimidazole units would be heterogeneous catalysis, since these compounds would be capable of coordinating metal ions, and may thus be interesting for their potential as catalyst supports.[28] The ability to tune the electronic and chemical properties of such complexes would be of paramount importance in this application. Towards this end, we have synthesized the electropolymerizable 2,2′-biimidazole structures **6** and **7**.

Experimental section

Equipment

Cyclic voltammetry experiments were carried out with a PC-interfaced CH Instruments 750C bipotentiostat. Data acquisition was accomplished using CH Instruments software (version 6.24). Voltammetry experiments were conducted on platinum-button electrodes (CH Instruments, 1 mm diameter) in a three-compartment glass cell. Pt electrodes were cleaned prior to each experiment by polishing with an Al_2O_3 dispersion (0.05 μm). Potentials are referenced to an Analytical Sensors, Inc. calomel electrode having a 4 mol L^{-1} KCl internal solution. A platinum wire served as a counter electrode. A scan rate of 0.100 V s^{-1} was used in each experiment, unless otherwise noted. Polymers obtained from electropolymerization experiments were washed with acetone and air-dried before subsequent experiments were carried out on them. Electrochemical solutions were purged for 10 min with nitrogen gas before experiments were carried out. A flow of nitrogen was maintained over the surface of each solution for the duration of these studies. All cyclic voltammetry experiments were carried out at 25 °C.

Electronic absorption spectrophotometry experiments were conducted with a JASCO J-815 instrument running in absorbance mode, employing baseline correction. Data acquisition was accomplished with Spectra Manager software (JASCO, version 1.54.03). The energies of π–π* transitions for the monomers in solution were determined from the onset of absorption by extrapolation of the low-energy side of these peaks and the baseline. Scans were conducted at a rate of 1 nm s^{-1} with data collection at 2 nm intervals. Indium – tin oxide coated glass electrodes for experiments on polymer films were purchased from Delta Technologies (R_s = 8–12 Ω).

Nuclear magnetic resonance (NMR) experiments were carried out on a Bruker Avance II 400 MHz instrument at room temperature. Chemical shifts are referenced to a TMS peak, which was assigned a value of 0 ppm. Elemental analyses were performed by Canadian Microanalytical Services Ltd., Delta, BC. Atomic force microscopy (AFM) was used to investigate polymer-film topology using a XE-120 Park Systems Inc. instrument in contact mode under ambient conditions. Melting points were carried out in air using an Electrothermal Mel-Temp capillary tube apparatus and are not corrected.

AM1 calculations were performed with Gaussian 03 and Gaussview 3.09 software.[29,30]

Materials

All chemicals employed in this study were of reagent-grade or better and were used as received unless otherwise noted. Syntheses of biimidazole monomers were carried out under an atmosphere of UHP-grade argon using standard Schlenk-line techniques. Acetonitrile (CH_3CN) and *N*,*N*-dimethylformamide (DMF) were both anhydrous and purchased from Caledon Laboratories Ltd. These solvents were delivered from an MBraun solvent purification system onto type 4 Å molecular sieves and stored under argon before use. Dichloromethane (CH_2Cl_2, VWR) for cyclic voltammetry experiments was purified by distillation from P_2O_5 and stored on type 4 Å molecular sieves prior to use. CH_3CN for electrochemical experiments was stored on activated alumina under a blanket of argon until use. Tetraethylammonium perchlorate (Et_4NClO_4) was synthesized from perchloric acid and tetraethylammonium bromide, recrystallized three times from water, and dried in a vacuum oven at 110 °C. Tetrabutylammonium hexafluorophosphate (Bu_4NPF_6) was synthesized from hexafluorophosphoric acid and tetrabutylammonium bromide, recrystallized three times from ethanol, and dried in a vacuum oven at 110 °C.

Synthesis of 2,2′-biimidazole, 5a

Ammonium hydroxide (300 mL, 18 mol L^{-1}) was added dropwise over a 30 min period to an ice-cooled conical flask that contained a solution of 40% *w*/*w* glyoxal (170 mL). The opening between the funnel and flask was covered with a wax film to prevent leakage of NH_3(g). The resulting, dark brown mixture was stirred overnight and then filtered. The residue was dissolved with 0.1 mol L^{-1} HCl and heated to boiling. It was then treated with activated charcoal, filtered, and neutralized with a saturated K_2CO_3(aq) solution, precipitating a tan coloured solid. The product was collected by filtration and air-dried. ^{1}H NMR data were in agreement with those reported.[23] Yield: 21.22g (32%). Mp > 300 °C (Lit.[31] 307 °C). ^{1}H NMR (400 MHz, DMSO-d_6) δ (ppm): 12.65 (s (br), 2H), 7.06 (s, 4H).

Synthesis of 1,1′-dimethyl- 2,2′-biimidazole, 5b

A method reported by Logemann and co-workers.[32] was followed: 2,2′-biimidazole (2.00 g, 1.49 mmol) was refluxed in a solution of 11.5 mL of 20% NaOH in 40 mL of ethanol. Dimethyl sulfate (8.66 g, 69 mmol) was added dropwise over a 30 min period. Refluxing was continued overnight. By the next day, the mixture had changed from a deep brown solution to an opaque, golden mixture. The reaction flask was cooled to room temperature and neutralized with aqueous $NaHCO_3$. It was then filtered and extracted with $CHCl_3$ (3 × 50 mL). The organic layer was washed with aqueous NaOH (2.4 g in 30 mL of H_2O) and dried over $MgSO_4$. It was then filtered and evaporated to dryness to yield an orange solid. This was recrystallized from heptane to yield pale-yellow needles. ^{1}H NMR signals were in agreement with those published for this structure.[33] Yield: 1.84g (76%). ^{1}H NMR (400 MHz, $CDCl_3$) δ (ppm): 7.11 (s, 2H, *J* = 1.0 Hz), 6.95 (s, 2H, 1.0 Hz), 4.04 (s, 6H). ^{13}C NMR (400 MHz, $CDCl_3$) δ (ppm): 138.74, 127.88, 122.64, 35.37.

Synthesis of 5,5′-dibromo-1,1′-dimethyl-2,2′-biimidazole

N-Bromosuccinimide (0.764 g, 4.3 mmol) was added portionwise via a powder-addition funnel to a solution of 1,1′-dimethyl-2,2′-biimidazole (0.349 g, 2.15 mmol) in $CHCl_3$ (25 mL). The solution immediately turned green before gradually becoming a brown–orange colour. The mixture was stirred overnight. The following day, the solution was washed with $NaHCO_3$(aq) and then water. The organic solution was then dried over $MgSO_4$, filtered, and evaporated to yield a beige solid, which was dried in vacuo. The product was recrystallized from heptane to yield pale yellow needles. ^{1}H NMR results were in agreement with the results reported by Yamamoto et al.[26] Yield: 0.524g (76%). Mp 155–156 °C. ^{1}H NMR (400 MHz, $CDCl_3$) δ (ppm): 7.12 (s, 2H), 3.96 (s, 6H).

Synthesis of 5,5′-bis(2,2′-bithiophene-5-yl)-1,1′-dimethyl-2,2′-biimidazole, 6

5,5′-Dibromo-1,1′-dimethyl-2,2′-biimidazole (0.678 g, 2.12 mmol) was stirred in a solution of $Pd(PPh_3)_2Cl_2$ (0.149 g, 0.212 mmol) in anhydrous DMF (50 mL). 5-Tributyltin-2,2′-bithiophene (2.41 g, 5.29 mmol)[34] was added through a syringe, and the mixture was refluxed, causing a gradual colour change from pale yellow to dark brown. After removal of the solvent, the residue was washed with CH_2Cl_2 using a Soxhlet extractor. The organic effluent was then washed with brine solution (25 mL), water (3 × 25 mL), and dried over $MgSO_4$. The solution was then filtered and treated with petroleum ether. Dropwise addition of the ether caused precipitation of a bright yellow solid, which was filtered and dried in vacuo. Yield: 0.675 g (65%). Mp 205–208 °C. ^{1}H NMR (400 MHz, $CDCl_3$) δ (ppm): 7.31 (s, 2H), 7.26 (d, 2H), 7.22 (d, J = 2.7 Hz, 2H), 7.20 (d, J = 3.7 Hz, 2H), 7.08 (d, J = 3.5 Hz, 2H), 7.05 (m, 2H), 4.10 (s, 6H). ^{13}C NMR (400 MHz, $CDCl_3$) δ (ppm): 140.0, 138.3, 136.7, 129.3, 128.6, 128.4, 128.0, 127.5, 124.9, 124.2, 124.1, 33.9. Elemental analysis: Calculated for $C_{24}H_{18}N_4S_4$: C 58.75%, H 3.70%, N 11.42%. Found: C 58.98%, H 3.93%, N 12.18%.

Synthesis of 5,5′-bis(3,4-ethylenedioxythiophene-2-yl)-1,1′-dimethyl-2,2′-biimidazole, 7

5,5′-Dibromo-1,1′-dimethyl-2,2′-biimidazole (0.185g; 0.58 mmol) was dissolved in a solution of $Pd(PPh_3)_2Cl_2$ (0.041 g, 0.058 mmol) in dry DMF (50 mL). 5-Tributyltin-3,4-ethylenedioxythiophene (0.623 g, 1.44 mmol)[35] was added through a syringe, and the resulting mixture was refluxed. The appearance of the mixture changed from a pale yellow to a deep brown overnight. Following removal of the solvent, the product was extracted from the residue with CH_2Cl_2, using a Soxhlet extractor. The resulting solution was dried over $MgSO_4$, filtered, and concentrated on a rotary evaporator. The residue was redissolved in CH_2Cl_2 and precipitated by dropwise addition of petroleum ether. A pale, yellow product obtained, and was dried in vacuo. Yield: 0.241 g (94%). Mp 238–240 °C ^{1}H NMR (400 MHz, $CDCl_3$) δ (ppm): 7.25 (s, 2H), 6.44 (s, 2H), 4.26 (s, 8H), 2.98 (s, 6H). ^{13}C NMR (400 MHz, $CDCl_3$) δ (ppm): 141.6, 139.6, 139.4, 129.1, 126.1, 104.5, 100.1, 68.8, 68.5, 33.6. Elemental analysis: Calculated for $C_{20}H_{18}N_4O_4S_2$: C 54.29%, H 4.10%, N 12.66%. Found: C 54.89%, H 4.25%, N 12.29%.

Results and discussion

Synthesis

An early report concerning the synthesis of 2,2′-biimidazole involved bubbling ammonia gas into a solution of glyoxal to obtain the product as a light brown powder after purification.[36] Other preparations have emerged since this time[37]; however, we chose to use a modified version of the above route, since the reactants for this approach were readily available and because of the route's simplicity. We obtained better yields through a slow addition of NH_4OH(aq) to a cooled, covered glyoxal solution. The product could be recrystallized from DMF to yield small, pale-yellow crystals; however, even without recrystallization, the product was pure enough to proceed with the next step. 1,1′-Dimethyl-2,2′-biimidazole was produced following a literature method.[32] On each occasion, the preparation was carried out in our hands, the reaction of dimethyl sulfate with deprotonated 2,2′-biimidazole yielded an acidic solution, unlike the mixture described by Logemann and co-workers.[32] Neutralization was thus accomplished with a bicarbonate salt rather than HCl, as described. A Stille coupling reaction involving 5,5′-dibromo-1,1′-dimethyl-2,2′-biimidazole was used to attach 2,2′-bithiophene and 3,4-ethylenedioxythiophene (EDOT) groups to the 2,2′-biimidazole moiety. Because of overlap with the solvent peak for **6** in $CDCl_3$, a coupling constant for the signal at 7.26 ppm could not be determined. Both **6** and **7** were soluble in chloroform and dichloromethane, and insoluble in hexanes and petroleum ether, which permitted their precipitation from a mixed solvent system. The carbon content in the elemental analysis data for **7** is slightly high, a result of residual grease used in the preparation of this compound, which could not be removed after repeated washing with petroleum ether (Weak signals at 0.93 and 1.26 ppm could be seen in the ^{1}H NMR spectrum for this compound).

Electrochemistry

Both **6** and **7** were able to be electrochemically polymerized using cyclic voltammetry from 1 mmol L^{-1} monomer solutions in CH_2Cl_2/0.1 mol $L^{-1}Bu_4NPF_6$. Cyclic voltammtery is often utilized in electrochemical polymerization experiments because it provides real-time "evidence" of electrochemical coupling. During potential cycling, electroactive polymer films deposited onto the electrode sufaces. With each potential cycle, as more electroactive polymer material is formed, a greater amount of charge is stored in the immobilized film. As a consequence of this, greater currents will be observed with each scan (Fig. 1). Films prepared by anodic electropolymerization are typically grown by recurrent cycling of the working electrode potential between a low limit (0 V vs. calomel electrode in this study), at which the monomer is not involved in an electron-transfer reaction, and a potential just above the monomer's peak oxidation potential. Poly-**6** and poly-**7** films were also able to be grown at constant applied potentials; however, no significant differences were observed in the cyclic voltammograms grown by potentiostatic polymerization versus potentiodynamic polymerization. Oxidation of **6** yielded a peak at ~0.90 V and a following wave centered at ~1.05 V. It was necessary to cycle the working electrode potential as high as 1.30 V to produce poly-**6**-coated modified electrodes having good coverage. Poly-**6** films were grown by cycling the working electrode potential 10 times, and were obtained as dark yellow films on platinum and ITO-coated glass substrates. These films were dark green in the oxidized state. For **7**, an oxidation peak is observed at ~0.84 V on the first scan; this peak decayed on subsequent scans. Repetitive potential cycling between 0 V and 0.90 V suggested sustained polymerization of the monomer; however, visual inspection of the electrode surface following these experiments indicated that the surface coverage of the film was quite poor, even after 20 potential cycles. Scanning through a second oxidation peak at ~1.15 V permitted polymer-film deposition. Thus, poly-**7** films were deposited by potential cycling within a 0 V to 1.20 V window. The films produced in this manner were dark green.

Fig. 1. Anodic polymerization of (*a*) **6** and (*b*) **7** from 1 mmol L^{-1} solutions of each monomer in CH_2Cl_2/0.1 mol L^{-1} Bu_4NPF_6.

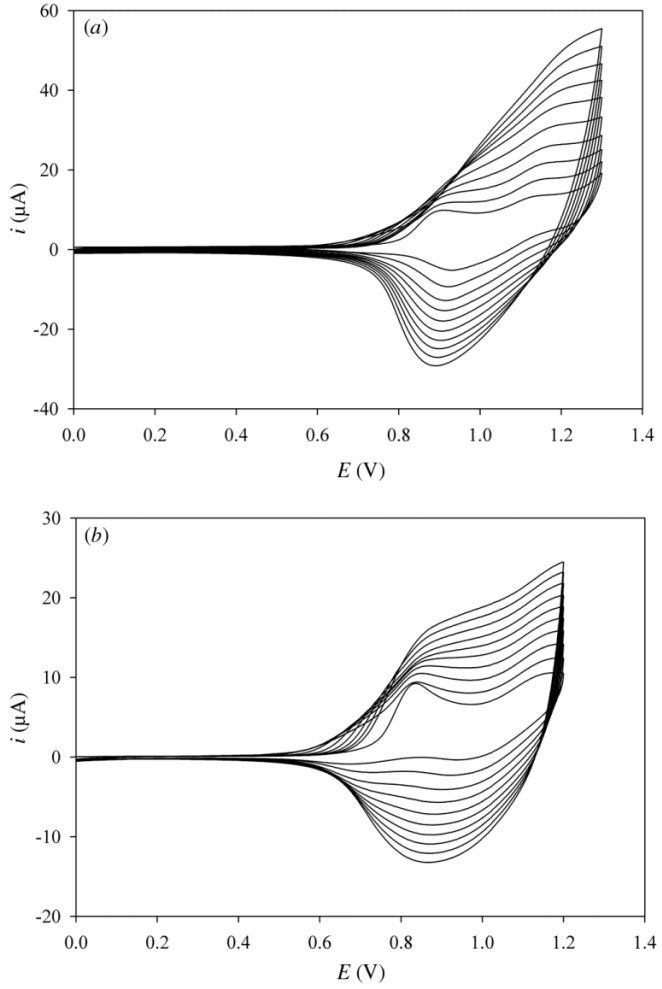

Fig. 2. P-doping and n-doping experiments for (*a*) poly-**6** and (*b*) poly-**7** in CH_3CN/0.1 mol L^{-1} Et_4NClO_4.

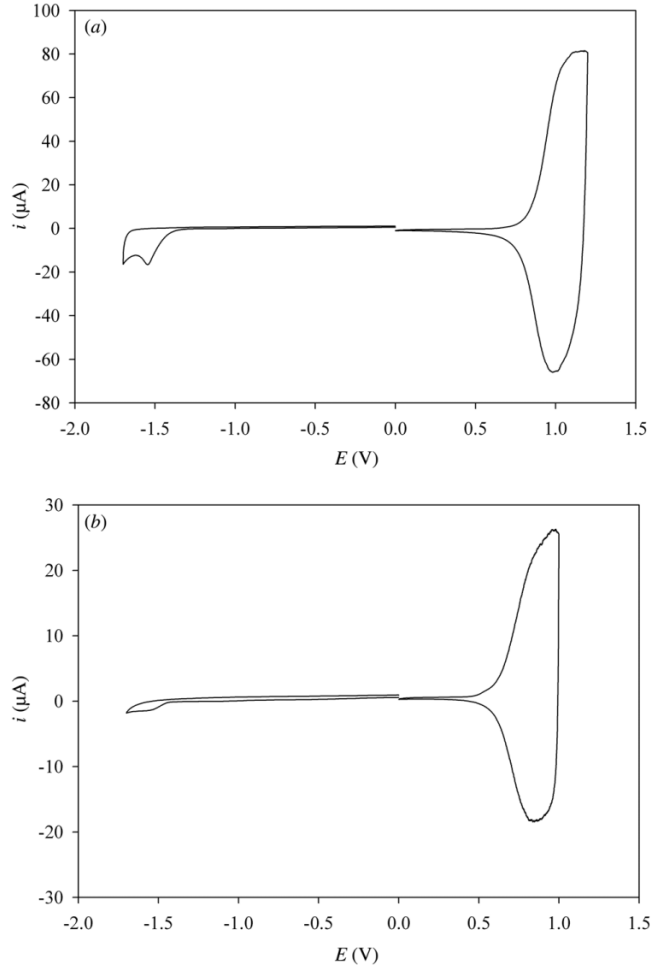

While distinct oxidation processes were observable for both monomers **6** and **7**, it was found that reduction peaks for neither monomer were observed within the electrochemical window provided by the CH_2Cl_2/Bu_4NPF_6 medium.

Immediately following their preparations, the polymer films were studied in monomer-free CH_3CN/0.01 mol L^{-1} Et_4NClO_4 solutions (Fig. 2). The voltammograms shown in this figure illustrate the films' redox behavior after two complete cycles of the working electrode potential (0 V → λ → 0 V; λ = 1.20 V for poly-**6** and 1.00 V for poly-**7**). It was found that the appearance of the voltammograms did not change significantly in subsequent cycles. Oxidation of the polymers yields their p-doping, while reduction yields n-doped polymers. Poly-**6** films were stable when p-doped; however, at potentials above 1.20 V, significant decreases in doping/undoping currents were observed, suggesting deactivation of the poly-**6** conjugated backbone under these conditions. This outcome is likely due to attack of oxidized sites in the p-doped polymer by trace nucleophiles present in the solvent–electrolyte system. It is expected that such reactions would occur at electron-rich tetrathiophene segments of poly-**6**, rather than at dimethybiimidazole segments. Oxidation of thiophene at potentials that yield its polymerization is known to result in decreased conjugation lengths in the resulting polymers.[38] For poly-**6**, the p-doping and undoping peaks are centered around 1.05 V. Interestingly, a small reduction peak for poly-**6** was found at ~ –1.65 V, which was not present in subsequent scans. This observation, as well as the magnitude of the peak (compared with the peak observed for p-doping) suggests that n-doped poly-**6** is less stable than its p-doped form. Poly-**7** films were stable at applied potentials of up to 1.00 V. The p-doping/undoping peak for poly-**7** is centered at ~0.88 V, a significantly lower potential than what was found for poly-**6** films. Polymerized 3,4-ethylenedioxythiophene (PEDOT) films have been shown to undergo oxidation at low potentials to produce very stable p-doped materials.[39] The fused, electron-donating dioxyethylene component in EDOT facilitates oxidation in this structure and also enhances stereoregularity in polymers by preventing α–β′ coupling. A slight reduction wave for this polymer was evident at ~ –1.60 V, which was absent on following scans. Cyclic voltammograms collected at varying scan rates for these polymers indicate that the electrochemical reactions observed during p-doping/undoping cycles are surface-confined, and not due to reactions involving a solution species (i_p is proportional to the square root of the scan rate). Figure 3 illustrates the scan-rate-dependence behavior of a poly-**6** film.

Fig. 3. Cyclic voltammograms for poly-**6** film at scan rates = 0.025, 0.050, 0.075, 0.100, 0.125, and 0.150 V s^{-1}. Scan rate increases in the direction indicated by the arrow.

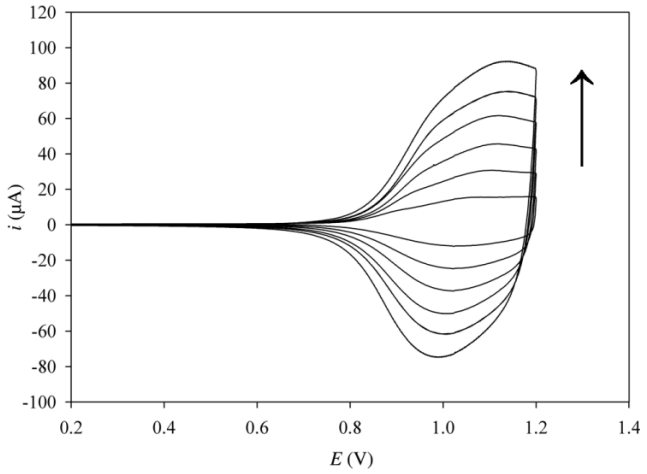

Table 1 presents a comparison of data for **6**, **7**, poly-**6,** and poly-**7** films with the related systems, 5,5′-bis(2,2′-bithiophene-5-yl)-1,1′-dimethyl-2,2′-bipyridine (**9**) and 5,5′-bis(2-thienyl)-2,2′-bithiazole (**10**) (Chart 1), from cyclic voltammetry and electronic absorption spectroscopy experiments.[34,35,40] Data in Table 2 present AM1 energies for the highest occupied molecular orbital (HOMO) and lowest unoccupied molecular orbital (LUMO) in each of these same systems. The 2,2′-bipyridine-containing system, **9**, displays the lowest HOMO energy in the series, while **7** possesses the highest LUMO energy. Since oxidation involves the HOMO, it should be expected that oxidation will be observed at a higher potential for poly-**9** than for poly-**6** and poly-**7**. Likewise, reduction of poly-**9** should occur at higher (less negative) potentials as compared with poly-**6** and poly-**7**. Experimentally, oxidation is found to occur at higher potentials for poly-**9**, and a distinct reduction process is observable for this polymer.[34] On the basis of the calculated energies, it should be easier to reduce poly-**6** than poly-**7**; however, the above experiments demonstrate that both poly-**6** and poly-**7** are unstable when n-doped. The higher HOMO energy in **7** supports the notion of the greater electron-donating capacity of the EDOT groups in this compound, as compared with the bithiophene substituents of **6**. Poly-**10** incorporates bithiophene segments in its conductive backbone, unlike the tetrathiophene links present in poly-**6**, poly-**7**, and poly-**9**. Poly-**10** would thus be expected to undergo p-doping at the highest potential, and this is confirmed by the data presented in Table 1.

Electronic absorption spectrophotometry

Polymer-coated ITO electrodes for electronic absorption studies could be grown as described above, through cyclic voltammetry experiments. However, more uniform films could be grown on ITO-coated glass electrodes by application of a constant potential, and so this approach was used to coat electrodes for electronic absorption studies. The best results were found for poly-**6** films grown at 1.25 V and poly-**7** films grown at 1.00 V.

Table 1. Comparison of electrochemical data (formal potential for oxidation, $E^{\circ\prime}$) and spectroscopic data (λ_{max}, λ_{onset}) for poly-**6** and poly-**7** with related 2,2′-bipyridine and 2,2′-bithiazole systems. The data for poly-**9** were reported in MeCN/0.1 mol L^{-1} Bu_4NPF_6 vs. Ag wire (ferrocene internal reference) and poly-**10** data in MeCN/0.1 mol L^{-1} Et_4NClO_4 vs. SSCE. Polymer absorption data are presented for solid films deposited onto ITO-glass slides, while the monomer data are presented for CH_2Cl_2 solutions.

Compound	$E^{\circ\prime}$	λ_{max} (nm)	λ_{onset} (nm)
6	—	364	430
7	—	316	370
9	—	400	442
10	—	404	—
Poly-**6**	1.05	402	532
Poly-**7**	0.88	326	418
Poly-**9**	1.12	—	—
Poly-**10**	1.24	—	—

Table 2. Semi-empirical AM1 HOMO and LUMO energies for **6**, **7**, **9**, and **10**.

Compound	HOMO (eV)	LUMO (eV)
6	–7.957	–0.936
7	–7.807	–0.657
9	–8.363	–1.169
10	–8.464	–1.375

Data obtained in electronic absorption studies are summarized in Table 1. Absorption peaks (λ_{max}) for **6** and **7** were found at 364 nm and 316 nm, respectively. For the polymer films, absorption peaks were broader, and red-shifted (Fig. 4). The peak absorption for poly-**6** was shifted by about 38 nm, and was considerably broader. Conversely, λ_{max} for poly-**7** was found to be red-shifted by only 10 nm. These red shifts can be explained by an enhanced degree of conjugation in the longer polymer structures relative to what exists in the monomers. It is also acknowledged here that absorption data obtained for monomers will be influenced by solvents, and that absorption data for solid polymers will be influenced by counter-ions to a small degree. The broader polymer absorption profiles can be attributed to the polydispersity of poly-**6** and poly-**7,** as well as non-uniform (α–α′, α–β′) links between thiophenes in poly-**6** chains. The absorption peak observed for poly-**7** was less broad than for poly-**6**, likely a consequence of the greater stereoregularity provided by the EDOT substituents of **7**. HOMO–LUMO energy differences for **6** and **7** can be estimated using the low energy wavelength edge (λ_{onset} in Table 1) for π–π* absorptions. These energies are 2.88 eV for **6** and 3.35 eV for **7**. Optical bandgaps for the polymer films, estimated from λ_{onset} values, are found to be 2.33 eV for poly-**6** and 2.97 eV for poly-**7**.

A comparison of the absorption data shows that **9** displays a smaller optical bandgap than the other systems considered here. Since both **6** and **7** undergo oxidation at comparatively

Fig. 4. Normalized electronic absorption spectra for monomers and polymers. Monomer spectra collected on CH_2Cl_2 solutions. Polymer spectra collected for poly-**6**- and poly-**7**-coated ITO-glass electrodes with a bare ITO electrode used for baseline correction.

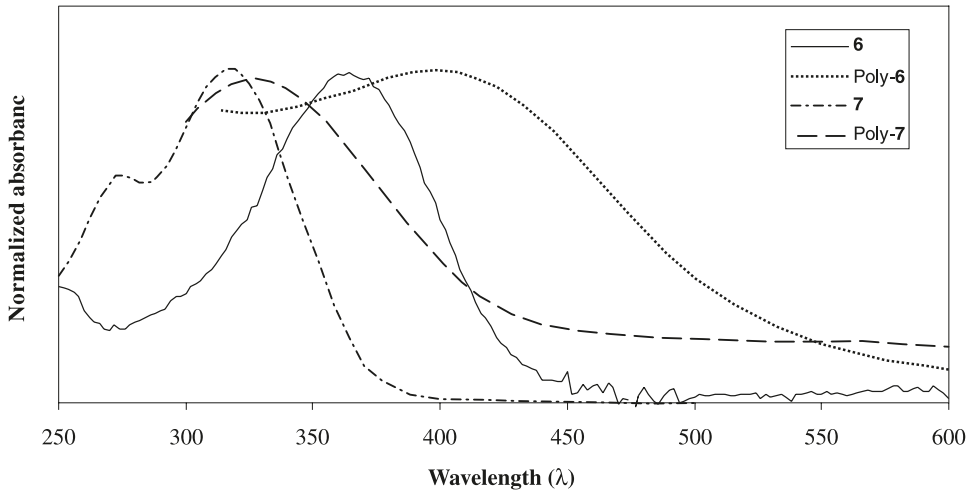

Fig. 5. Atomic force microscopy images of top: poly-**6**; middle: poly-**7**; and bottom: a bare ITO-coated glass slide. Images are presented as 3-D surfaces (left) and 1st derivatives (right).

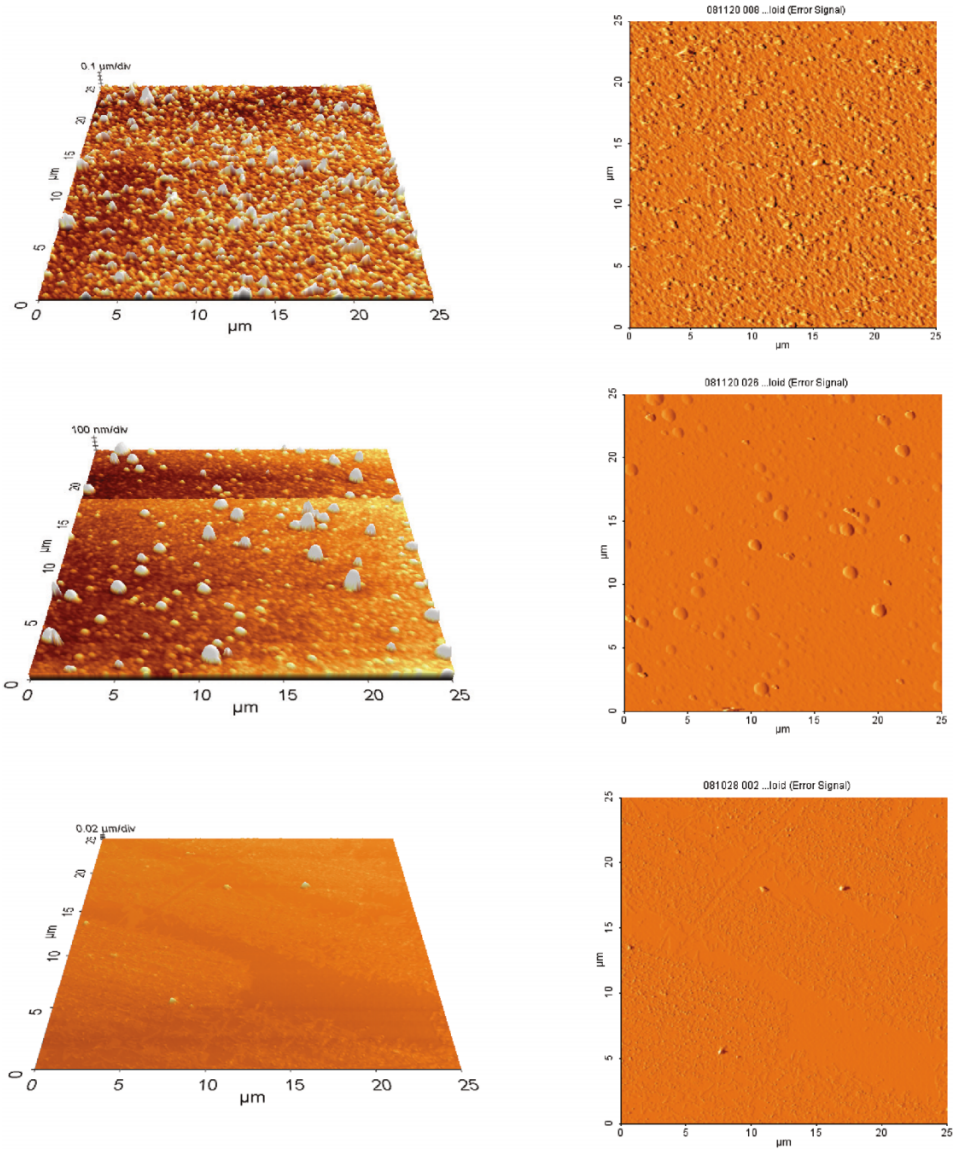

low, positive potentials, it would be expected that reduction of both of these monomers must require quite negative potentials, presumably a consequence of the greater electron-donating nature of the dimethylbiimidazole center. Indeed, we were unable to observe these processes in our experiments.

Atomic force microscopy

Atomic force microscopy (AFM) was used to investigate the topography of poly-**6** and poly-**7** films deposited onto ITO-coated glass electrodes (Fig. 5). These films appeared smooth to the naked eye. The 25 μm × 25 μm images of poly-**6** show a fairly homogeneous polymer surface, with polymer particles of roughly 1 μm diameter distributed on the electrode surfaces. Note that the vertical scale in this image is roughly one-tenth the *x*- and *y*-axis scales. The poly-**7** surface looks smooth in most areas, but also shows regions where larger grains have deposited, of approximately 1 μm diameter, on average.

Conclusions

Two novel thiophene–imidazole structures have been synthesized, and their electrochemical and electronic properties were investigated. Polymer films of 5,5′-bis(2,2′-bithiophene-5-yl)-1,1′-dimethyl-2,2′-biimidazole and 5,5′-bis(3,4-ethylenedioxythiophene-2-yl)-1,1′-dimethyl-2,2′-biimidazole were grown on platinum and indium-tin oxide-coated glass through electrochemical polymerization. The films deposited were fairly homogeneous, as indicated by AFM studies. The facile polymerization of these materials and the potential to vary the identity of the substituent on N_1 makes these materials promising candidates for further studies aimed at creating supports for tunable heteogeneous electrocatalysts.

Acknowledgements

We gratefully acknowledge the Natural Sciences and Engineering Research Council of Canada (NSERC) and St. Francis Xavier University for funding this work. We would also like to express our gratitude to the Canada Foundation for Innovation (CFI) for a Leaders Opportunity Fund award, which permitted the purchase of instruments used in this study.

References

(1) Goppelsroeder, F. *Bull Soc. Ind.* **1876**, *82*, 1392.
(2) Shirakawa, H.; Louis, E. J.; MacDiarmid, A. G.; Chiang, C. J.; Heeger, A. J. *J. Chem. Soc, Chem. Commun.* **1977**, 59.
(3) Chiang, C. K.; Fincher, C. R.; Park, Y. W.; Heeger, A. J. *Phys. Rev. Lett.* **1977**, *39* (17), 1098–1101. doi:10.1103/PhysRevLett.39.1098.
(4) Chiang, C. K.; Druy, M. A.; Gau, S. C.; Heeger, A. J.; Louis, E. J.; MacDiarmid, A. G.; Park, Y. W.; Shirakawa, H. *J. Am. Chem. Soc.* **1978**, *100* (3), 1013–1015. doi:10.1021/ja00471a081.
(5) Skotheim, T. A.; Elsebaumer, R. L.; Reynolds, J. R., Eds,; In *Handbook of conducting polymers,* 2nd ed, revised and expanded; Marcel Dekker: New York. 1998.
(6) Guiseppi-Elie, A.; Pradhan, S. R.; Wilson, A. M.; Allara, D. L.; Zhang, P.; Collins, R. W.; Kim, Y. T. *Chem. Mater.* **1993**, *5* (10), 1474–1480. doi:10.1021/cm00034a017.
(7) Guiseppi-Elie, A.; Wilson, A. M.; Tour, J. M.; Brockmann, T. W.; Zhang, P.; Allara, D. L. *Langmuir* **1995**, *11* (5), 1768–1776. doi:10.1021/la00005a055.
(8) Barbarella, G.; Bongini, A.; Zambianchi, M. *Macromolecules* **1994**, *27* (11), 3039–3045. doi:10.1021/ma00089a022.
(9) Zhang, W.; Plieth, W.; Koßmehl, G. *Electrochim. Acta* **1997**, *42* (11), 1653–1661. doi:10.1016/S0013-4686(96)00301-5.
(10) Roncali, J. *J. Mater. Chem.* **1999**, *9* (9), 1875–1893. doi:10.1039/a902747e.
(11) Demeter, D.; Blanchard, P.; Allain, M.; Grosu, I.; Roncali, J. *J. Org. Chem.* **2007**, *40*, 4481.
(12) Cebeci, F. Ç.; Sezer, E.; Sarac, A. S. *Electrochim. Acta* **2007**, *52* (5), 2158–2165. doi:10.1016/j.electacta.2006.08.033.
(13) Albano, V. G.; Bandini, M.; Moorlag, C.; Piccinelli, F.; Pietrangelo, A.; Tommasi, S.; Umani-Ronchi, A.; Wolf, M. O. *Organnometallics* **2007**, *26* (18), 4373–4375. doi:10.1021/om070210l.
(14) McQuade, D. T.; Pullen, A. E.; Swager, T. M. *Chem. Rev.* **2000**, *100* (7), 2537–2574. doi:10.1021/cr9801014. PMID: 11749295.
(15) Li, G.; Wang, T.; Schulz, A.; Bhosale, S.; Lauer, M.; Espindola, P.; Heinze, J.; Fuhrhop, J. H. *Chem. Commun. (Camb.)* **2004**, (5): 552–553. doi:10.1039/b313415f. PMID:14973603.
(16) Derossi, S.; Adams, H.; Ward, M. D. *Dalton Trans.* **2006**, (1): 33–36. doi:10.1039/b614346f. PMID:17160171.
(17) Majumdar, P.; Peng, S.-M.; Goswami, S. *J. Chem. Soc., Dalton Trans.* **1998**, (10): 1569–1574. doi:10.1039/a801071d.
(18) Haga, M.; Ali, M. M.; Arakawa, R. *Angew. Chem., Int. Ed. Engl.* **1996**, *35* (1), 76–78. doi:10.1002/anie.199600761.
(19) Carina, R. F.; Verzegnassi, L.; Williams, A. F.; Bernardinelli, G. *Chem. Commun. (Camb.)* **1998**, (24): 2681–2682. doi:10.1039/a807321j.
(20) Cameron, C. G.; Pittman, T. J.; Pickup, P. G. *J. Phys. Chem. B* **2001**, *105* (37), 8838–8844. doi:10.1021/jp0109325.
(21) Chadwick, D.; Ngochindo, R. I. *J. Chem. Soc., Perkin Trans. 1* **1984**, 481. doi:10.1039/p19840000481.
(22) Cromer, D. T.; Ryan, R. R.; Storm, C. B. *Acta Crystallogr.* **1987**, *43*, 1435.
(23) Sánchez-García, D.; Borrós, S.; Nonell, S.; Borrell, J. I.; Colominas, C.; Teixidó, J. *J. Heterocycl. Chem.* **2002**, *39* (4), 733–735. doi:10.1002/jhet.5570390418.
(24) Matthews, D. P.; Whitten, J. P.; Mccarthy, J. R. *J. Heterocycl. Chem.* **1987**, *24* (3), 689–692. doi:10.1002/jhet.5570240328.
(25) Yamamoto, T.; Uemura, T. *J. Polym. Sci. Part Polym. Chem.* **2002**, *40* (15), 2686–2688. doi:10.1002/pola.10354.
(26) Yamamoto, T.; Uemura, T.; Tanimoto, A.; Sasaki, S. *Macromolecules* **2003**, *36* (4), 1047–1053. doi:10.1021/ma0211232.
(27) Toba, M.; Terashima, T.; Nakashima, T.; Kawai, T. *Jpn. J. Appl. Phys.* **2008**, *47* (2), 1371–1373. doi:10.1143/JJAP.47.1371.
(28) Ochmanska, J.; Pickup, P. G. *Can. J. Chem.* **1991**, *69* (4), 653–660. doi:10.1139/v91-099.
(29) Frisch, M. J.; Trucks, G. W.; Schlegel, H. B.; Scuseria, G. E.; Robb, M. A.; Cheeseman, J. R.; Montgomery, J. A., Jr.; Vreven, T.; Kudin, K. N.; Burant, J. C.; Millam, J. M.; Iyengar, S. S.; Tomasi, J.; Barone, V.; Mennucci, B.; Cossi, M.; Scalmani, G.; Rega, N.; Petersson, G. A.; Nakatsuji, H.; Hada, M.; Ehara, M.; Toyota, K.; Fukuda, R.; Hasegawa, J.; Ishida, M.; Nakajima, T.; Honda, Y.; Kitao, O.; Nakai, H.; Klene, M.; Li, X.; Knox, J. E.; Hratchian, H. P.; Cross, J. B.; Bakken, V.; Adamo, C.; Jaramillo, J.; Gomperts, R.; Stratmann, R. E.; Yazyev, O.; Austin, A. J.; Cammi, R.; Po-

melli, C.; Ochterski, J. W.; Ayala, P. Y.; Morokuma, K.; Voth, G. A.; Salvador, P.; Dannenberg, J. J.; Zakrzewski, V. G.; Dapprich, S.; Daniels, A. D.; Strain, M. C.; Farkas, O.; Malick, D. K.; Rabuck, A. D.; Raghavachari, K.; Foresman, J. B.; Ortiz, J. V.; Cui, Q.; Baboul, A. G.; Clifford, S.; Cioslowski, J.; Stefanov, B. B.; Liu, G.; Liashenko, A.; Piskorz, P.; Komaromi, I.; Martin, R. L.; Fox, D. J.; Keith, T.; Al-Laham, M. A.; Peng, C. Y.; Nanayakkara, A.; Challacombe, M.; Gill, P. M. W.; Johnson, B.; Chen, W.; Wong, M. W.; Gonzalez, C.; Pople, J. A. *Gaussian 03*, Revision C.02; Gaussian, Inc.: Wallingford, CT; 2004.

(30) Dennington, R., II; Keith, T.; Millam, J.; Eppinnett, K.; Hovell, W. L.; Gilliland, R. *GaussView*, Version 3.09; Semichem, Inc.: Shawnee Mission, KS; 2003.

(31) Matthews, D. P.; Whitten, J. P.; McCarthy, J. R. *Synthesis* **1986**, *1986* (04), 336–337. doi:10.1055/s-1986-31607.

(32) Melloni, P.; Dradi, E.; Logemann, W.; De Carneri, I.; Trane, F. *J. Med. Chem.* **1972**, *15* (9), 926–930. doi:10.1021/jm00279a012. PMID:4340569.

(33) Casas, J. S.; Castiñeiras, A.; Parajó, Y.; Sánchez, A.; Sánchez-González, Á.; Sordo, J. *Polyhedron* **2005**, *24* (10), 1196–1202. doi:10.1016/j.poly.2005.04.008.

(34) Zhu, S. S.; Swager, T. M. *Adv. Mater.* **1996**, *8* (6), 497–500. doi:10.1002/adma.19960080609.

(35) Zhu, S. S.; Swager, T. M. *J. Am. Chem. Soc.* **1997**, *119* (51), 12568–12577. doi:10.1021/ja972794w.

(36) Kuhn, R.; Blau, W. *Justus Liebigs Ann. Chem.* **1957**, *605* (1), 32–35. doi:10.1002/jlac.19576050106.

(37) Matthews, D. P.; Whitten, J. P.; MacArthy, J. R. *Synthesis* **1986**, 337.

(38) Krische, B.; Zagorska, M. *Synth. Met.* **1989**, *28* (1-2), 263–268. doi:10.1016/0379-6779(89)90531-6.

(39) Dietrich, M.; Heinze, J. *J. Electroanal. Chem.* **1994**, *369* (1-2), 87–92. doi:10.1016/0022-0728(94)87085-3.

(40) MacLean, B. J.; Pickup, P. G. *J. Mater. Chem.* **2001**, *11* (5), 1357–1363. doi:10.1039/b009568k.

Stable phenylene- and biphenylene-bis(isobenzofuran)s related to diphenylisobenzofuran

Sheri A. Klassen, Richard Boehme, Sean D. Derrick, Klaus Moock, A. Elizabeth Baker, Deryn E. Fogg, René T. Boeré, and Peter W. Dibble

Abstract: A series of phenyl-substituted bis(isobenzofuran)s in which the furan moieties are linked by 1,3-phenylene, 1,4-phenylene, or 4,4′-biphenylene linkers have been prepared in only two steps. They are comparable to diphenylisobenzofuran in their absorption and luminescent properties, their electrochemistry, and their reactivity. Their degree of similarity to diphenylisobenzofuran was found to depend significantly on the nature of the linking group. Diels–Alder reaction of the title compounds and subsequent aromatization gave very rapid access to penta- or hexa-aryl products.

Key words: isobenzofuran, diphenylisobenzofuran, fluorescence, UV spectroscopy, electrochemistry, pentaphenyl, hexaphenyl.

Résumé : On a préparé, par des réactions n'impliquant que deux étapes, une série de bis(isobenzofuranes) substitués par un groupe phényle dans lesquels les portions furanes sont liées par des tronçons 1,3-phénylène, 1,4-phénylène ou 4,4′-biphénylène. Par leurs propriétés d'absorption et de luminescence, d'électrochimie et de réactivité, ces produits se comparent au diphénylisobenzofurane. On a observé que leur degré de similarité avec le diphénylisobenzofurane dépend beaucoup de la nature du groupe qui les relie. La réaction de Diels–Alder des composés mentionnés dans le titre et l'aromatisation subséquente des produits obtenus donne un accès très rapide aux produits penta- ou hexarylés.

Mots-clés : isobenzofurane, diphénylisobenzofurane, fluorescence, spectroscopie UV, électrochimie, pentaphényle, hexaphényle.

[Traduit par la Rédaction]

Commercially available 1,3-diphenylisobenzofuran (**1**, Fig. 1) has found wide application in the identification of reactive olefins, as an analytical tool for measuring the rate of singlet-oxygen generation and is of interest for its fluorescence, electrochemical, chemi-, and electro-luminescent properties.[1,2] Examples have also been used as electron-transport materials.[3] The chemistry of the parent hydrocarbon isobenzofuran (IBF, **2**) and its derivatives continues to be of significant interest and has been reviewed regularly.[1,2,4–8]

In view of the many useful properties of **1**, we now wish to report the efficient synthesis of several compounds (**3a**–**3c**, Fig. 1) closely related to **1** but bearing two isobenzofuran moieties linked via one or two aromatic rings. Subsequent elaboration of these compounds into penta- and hexa-aryls is also described. Most preparations of diarylisobenzofurans are based on the addition of Grignard reagents to anhydrides or phthalides.[1,9] This work extends that of a report describing the preparation of teraryls via adducts of phenylenebis(isobenzofuran)s in which the furan species is generated transiently[10] from hemiaminal precursors.[11]

The title compounds were prepared in only two steps (Scheme 1) using an extension of methodology previously developed.[11] Phenyllithium was added to 2-bromobenzaldehyde, and the resulting addition product was metalated with *n*-BuLi. Addition of the appropriate dicyanoaryl gave, after hydrolysis, hemiaminal **4** as a mixture of diastereomers. The ^{1}H NMR spectrum of **4** contained singlets between 6.2 and 6.5 ppm corresponding to the methine protons on the furan ring of diastereomeric products. The oily hemiaminal product was refluxed with *p*-toluenesulfonic acid (TsOH) to form the stable IBFs (**3**) in approximately 50% yield (based on dinitrile).

A second method could also be used to prepare 4,4′-biphenylenebis(3-phenylisobenzofuran) (**3c**) (Scheme 2). Metalation of 4,4′-dibromobiphenyl and reaction of the dianion with 2 equiv. of bromobenzaldehyde was followed by metalation with *n*-butyllithium. Subsequent reaction with benzonitrile followed by hydrolysis gave hemiaminal **5**, confirmed by the appearance of two peaks at 6.24 ppm and 6.42 ppm in the ^{1}H NMR spectrum as for compound **4**. The hemiaminal and a catalytic amount of TsOH were refluxed in methanol to form the stable IBF (**3c**) in 39% yield (from 4,4′-dibromobiphenyl).

The three title compounds are all highly coloured: **3a** is a beautiful blood red, **3b** is orange, and **3c** is yellow. Solutions

Received 21 October 2008. Accepted 18 March 2009. Published on the NRC Research Press Web site at canjchem.nrc.ca on 1 June 2009.

S.A. Klassen, R. Boehme, S.D. Derrick, K. Moock, A.E. Baker, R.T. Boeré, and P.W. Dibble.[1] Department of Chemistry and Biochemistry, University of Lethbridge, Lethbridge, AB T1K 3M4, Canada.
D.E. Fogg. Department of Chemistry, University of Ottawa, Ottawa, ON K1N 6N5, Canada.

[1]Corresponding author (e-mail: Dibble@uleth.ca).

Fig. 1. Stable phenylenebis(isobenzofuran)s.

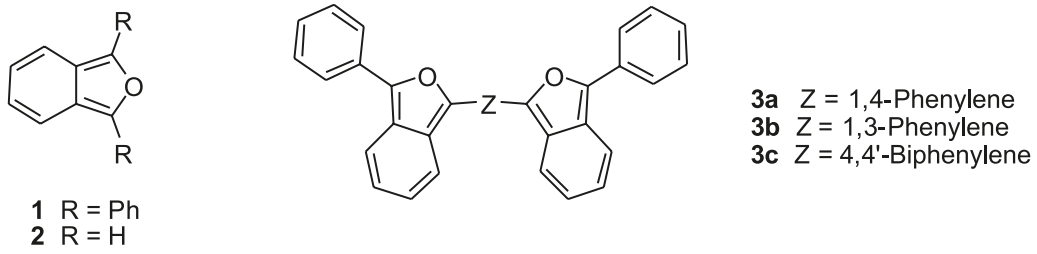

Scheme 1. Synthesis of **3a**–**3c.**

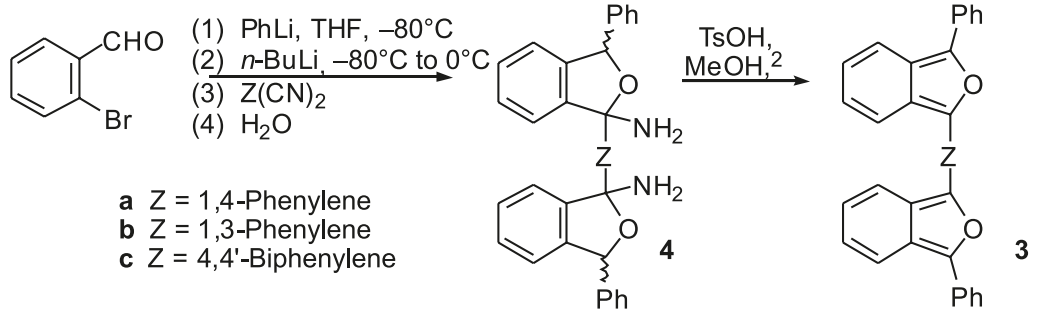

Scheme 2. Alternative synthesis of **3c**.

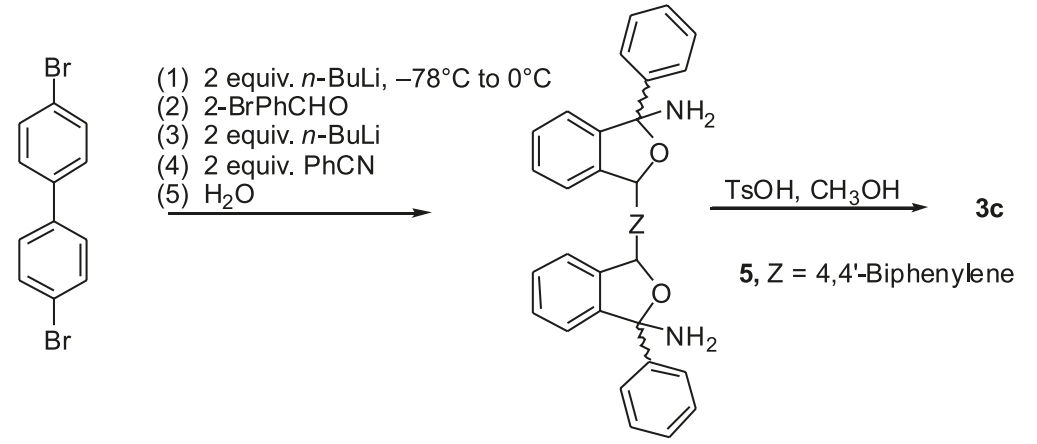

of all three compounds are also highly coloured and show the same fluorescent character as **1**, especially when irradiated with long-wavelength UV radiation. Example **3b** resembles **1** most closely in its visible fluorescence in solution.

The NMR spectra of **3** were largely unremarkable. The presence of a ring current in isobenzofurans is well-established, and all of the protons and carbon resonances were found in the aromatic region. In the carbon spectra, the quaternary carbons next to oxygen were found downfield in the 140 ppm region, typical for carbons of this type. In the proton NMR spectra, the typical AA′BB′ patterns of the isobenzofuran rings were obscured by the resonances of the phenyl substituents. Some protons of the central aromatic linker all experience significant downfield shifts: in **3b**, there is a singlet at 8.49 ppm (the proton between the two isobenzofurans); in **3a**, a four-proton singlet appears at 8.10 ppm; in **3c**, the biphenyl protons appear as an AB quartet centered at 7.80 ppm and 8.04 ppm. In **1**, the protons on the phenyl substituents ortho to the isobenzofuran appear at 7.9 ppm. These shifts are likely the result of steric-contact deshielding,[12,13] additive in the downfield signal of **3b**.

The UV absorbances for **1** and **3a**–**3c** are given in Table 1. For **1**, there are two principal bands at 415 and 261 nm. The latter band is common to all of **3a**–**3c** and is likely due to the phenyl substituents. The longer wavelength band of **1**, attributed to a π–π^* transition[1] is matched by one in **3b**, while in **3c** and **3a**, this band is found at progressively longer wavelength. These, and other data, make it clear that of **3a**–**3c**, it is the meta-substituted **3b** that most closely resembles **1**. Its high-wavelength band is found in the same position as **1**, while the other two examples exhibit significant red shifts expected of extended conjugation. Interestingly, of **3a** and **3c**, it is the smaller π-system of **3a** that exhibits the greatest red shift. We attribute this to steric hindrance about the biphenyl linkage that inhibits coplanarity of the π-systems, a structural feature that is absent in **3a**.

Emission data for this series of compounds are presented in Table 2. The luminescence properties of diarylisobenzo-

Table 1. UV–vis spectral data (λ_{max}, nm, $c = 10^{-5}$mol/L).

1 (Ether)[1]	**3a** (MeOH)	**3b** (Dioxane)	**3c** (Dioxane)
275 (4.5)	261 (4.7)	256 (4.6)	270 (4.3)
310 (3.95)	313 (4.3)	321 (3.8)	—
415 (4.45)	473 (4.4)	413 (4.1)	447 (3.9)

Table 2. Emission data for **1** and **3a–3c** (λ_{max}, nm, $c = 10^{-5}$ mol/L).

	1 (Hexane)[14]	**3a** (MeOH)	**3b** (MeOH)	**3c** (MeOH)
Excit. wavelength	—	476	416	270
	—	—	—	333
	458	566	461	507
	480	—	480	540
Stokes shift	43	93	48	60

Table 3. Electrochemical data for **1** and **3**.

	0/+ (V)	0/– (V)	–/2– (V)	2–/3– (V)	3–/4– (V)
1	0.75	–1.98	–2.52	—	—
3a	0.81	–1.69	–1.85	–2.43	–2.73
3b	—[a]	–2.06	–2.24	–2.68	–2.87[b]
3c	—[a]	–2.33	–2.73	–3.01	—

Note: Data were collected in THF solution containing 2 mmol/L NBu_4PF_6, referenced to internal ferrocene, and corrected to the SCE scale.

[a]Not observed (outside of solvent range).

[b]Observed only at –30 °C.

furans have been summarized.[1] The emission spectrum of **3b** is almost identical to that observed for **1**, exhibiting two bands at equal intensity at 461 and 480 nm. The trends for this series of compounds observed in the UV spectra are repeated here. Example **3a** has its fluorescence band shifted to higher wavelength to the greatest extent and appears as a single broad band. Compound **3c** is intermediate between the other two in terms of the position of its principal bands. Its spectrum differs in that it has an additional band at 333 nm (a band corresponding to the fluorescence band of biphenyl) and a shoulder at 470 nm.

The electrochemistry of **1** has been investigated, and we compared its behavior with **3a–3c** (Table 3). Compound **3a** shows four reduction processes and one oxidation process. Compounds **3b** and **3c** show four and three reductions, respectively, while **1** has two reductions and one oxidation. The data indicate **3a** is more easily reduced than **1**, but **3b** and **3c** are more difficult to reduce. The mechanism of reduction of **3a** and **3b** can be speculated by comparison with **1**. It can be estimated that the difference between the first reduction potential and the second reduction potential of **1** is in general the potential required to form a doubly reduced IBF dianion from the anion radical. For **1**, the second reduction requires an additional 0.54 V from the anion radical. The difference in potential for $[\mathbf{3a}]^{0/-}$ and $[\mathbf{3a}]^{-/2-}$ is 0.16 V, which is less than that required to form a doubly reduced IBF. This suggests that each IBF in **3a** has been reduced once. The next reduction requires an additional 0.58 V, which corresponds to the potential required to form a doubly reduced IBF. The magnitude of the potential of $[\mathbf{3a}]^{3-/4-}$ is comparable to the second reduction for **1**. A similar comparison can be made for **3b**. The data obtained for **3c** are not consistent with that of the other examples but may be compromised due to poor solubility in THF. The anions produced, excluding the anion formed from the last reduction, are stable under the conditions of the electrochemical experiment and may or may not be stable outside the conditions of the experiment.

The physical appearance, UV–visible spectra, and electrochemical data all show that it is meta-substituted **3b** that most closely resembles **1**. The other examples indicate that the through-conjugated connecting rings offer a better electronic interaction between the IBF moieties. This is seen in the shift of the 415 nm UV band of **1** to lower wavelengths in **3a** and **3c**. It is also consistent with the relative ease of reduction of **3a** in comparison to **3b**. We are interested in preparing polymeric versions of these molecules with alternating phenylene or biphenylene and isobenzofuran rings. These examples suggest that if one desires a polymeric form of **1**, then meta-phenylene linkages will serve to electronically insulate the IBF rings such that they retain the character of **1**. If it is desirable to tune the electronic properties of the IBF rings conjugatively, then through-conjugative linkages will work best.

Not surprisingly, **3a–3c** react in a fashion identical to **1**. When refluxed with an excess of dimethyl acetylene dicarboxylate (DMAD), Diels–Alder adducts **6** (Scheme 3) were isolated in yields of 67% to 75%, as mixtures of diastereomers. The presence of a mixture was clear in the case of **4c** where there were many methyl peaks evident in the proton NMR. In the case of **3a** and **3c**, the spectra showed only the number of peaks expected of a single diastereomer.

Scheme 3. Diels–Alder reactions.

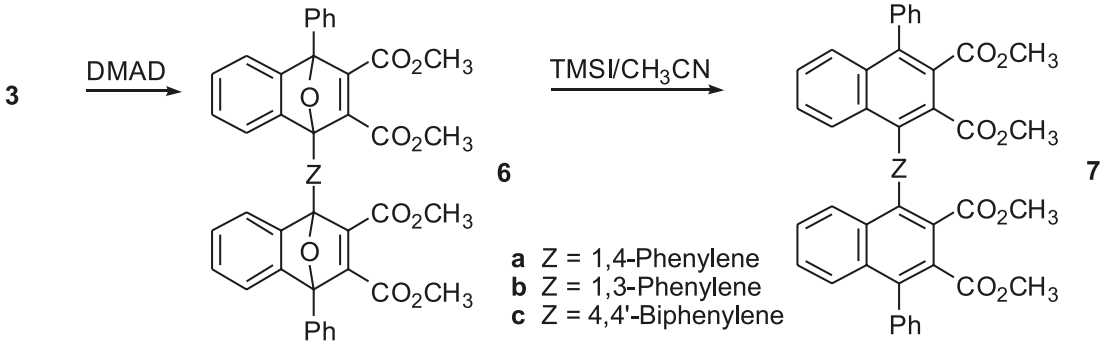

There is no reason to expect any diastereoselectivity in this reaction, however, so we conclude that the diastereomers formed in this reaction have identical NMR spectra. The adducts were deoxygenated by treatment with trimethylsilyl iodide[15,16] to form polyaryls **7**. This represents a very efficient synthesis of such molecules in only four steps from commercially available materials.

We did not anticipate, nor did we observe, any difference in reactivity between **3a**–**3c** and their DMAD monoadducts. Significant rate differences in fused difuran systems have been observed.[17] Reaction of **3a** with 1 equiv. of DMAD gave a mixture of monoadduct, bisadduct, and starting material. The presence of the monoadduct during reaction could be observed visually during the Diels–Alder reactions by the presence of the characteristic yellow-green colour of the diphenylisobenzofuran chromophore.

In summary, we have prepared and characterized a series of novel bis(isobenzofuran)s with properties similar to 1,3-diphenylisobenzofuran. The syntheses are efficient and should be easily generalized to other substituted examples. Reaction with DMAD and subsequent aromatization gives rapid access to penta- or hexa-aryl systems.

We have begun to explore the possibilities of preparing polymeric versions of **3** as well as preparing Diels–Alder polymers by reaction of **3** with quinone, DMAD and bis(maleimide) dienophiles. Furan/maleimide polymers have been reported to be self-mending.[18] Other examples of monomers based on diarylisobenzofurans have been reported.[19,20]

Experimental section

Cyclic voltammetric (CV) studies (scan rates N = 20–5000 mV/s) were made with a PAR 173 potentiostat, 175 Universal Programmer and recorded on a Houston Graphics 2000 XY plotter. Electrochemical experiments were performed on a platinum three-electrode system with the platinum working electrode either a 0.5 mm Pt wire or a 0.5 mm diameter Pt micro-tip. A positive feedback circuitry was employed to minimize iR drop losses. The vacuum-tight all glass electrochemical cell has been described in detail elsewhere.[21] The cell was charged with the supporting electrolyte NBu_4PF_6 with solvent THF. Compounds under investigation and ferrocene acting as an internal reference compound were added to the cell using break-seal techniques. Ferrocene was sublimed prior to use.

NMR spectra were recorded on a Bruker AC250 MHz spectrometer unless otherwise indicated. Melting points were performed in open capillaries and are uncorrected. Mass spectra were obtained from the Mass Spectroscopy Lab at the University of Alberta or the Centre for Molecular Architecture, Central Queensland University. Combustion analyses were performed by MHW Labs in Phoenix, Arizona.

1,4-Phenylenebis(1,3-dihydro-3-phenyl-1-isobenzofuranamine), 4a

In 300 mL of dry THF was dissolved 2-bromobenzaldehyde (3.5 g, 19 mmol), purged with N_2, and cooled to –80 °C. Phenyllithium (11 mL of a 1.8 mol/L solution in cyclohexane/ether, 20 mmol) was added by syringe. After 10 min, the reaction was warmed to room temperature. A small aliquot analyzed by proton NMR showed the presence of aldehyde, so an additional 1 mL of phenyllithium was added. After 5 min, the reaction was cooled to –80 °C, and 8.0 mL of 2.5 mol/L *n*-BuLi (in hexanes, 20 mmol) was added. After 15 min, the reaction was warmed to 0 °C, and stirring was continued for 20 min. An aliquot, quenched with water, was analyzed by proton NMR and indicated the loss of bromine. 1,4-Dicyanobenzene (1.09 g, 9.1 mmol) was added to the solution in a single portion, and the solution went dark. The reaction was allowed to warm to room temperature and stirred for 10 h. Water (300 mL) was added, and the reaction mixture was then extracted with diethyl ether (250 mL). The organic phase was separated and dried over $MgSO_4$. After filtration, the solvent was removed under reduced pressure and the residue recrystallized in methanol to give 2.0 g **4a** (63%) as a mixture of diastereomers: mp 90 °C (dec.). ^{1}H NMR (250 MHz, $CDCl_3$) δ: 2.50 (s, 4H, exchanges with D_2O), 6.14 and 6.33 (s, 2H), 6.91–7.51 (m, 18H), 7.72 (s, 4H). ^{13}C NMR (62.5 MHz, $CDCl_3$) δ: 82.9, 83.6, 98.59, 98.62, 98.71, 98.77, 122.28, 122.32, 122.37, 123.08, 123.12, 123.15, 123.3, 125.45, 125.6, 126.3, 126.4, 126.5, 127.2, 128.1, 128.25, 128.31, 128.37, 128.57, 128.64, 128.7, 140.7, 141.1, 141.75, 141.84, 141.86, 143.3, 143.9, 144.11, 144.17, 144.20. IR (KBr): 3391 and 3320, 1264, 1032, 1015, 953, 743 cm^{-1}. MS (EI) *m/e*: 478 (4), 462 (100), 295 (23), 231 (23), 165 (22), 154 (39), 85 (51), 83 (78). Analysis calcd. for $C_{34}H_{28}N_2O_2$: C, 82.23; H, 5.68; N, 5.64. Found: C, 82.00; H, 5.40; N, 5.66.

1,4-Phenylenebis(3-phenyl-1-isobenzofuran), 3a

To 120 mL of methanol were added 315 mg (0.64 mmol) of bishemiaminal (**4a**). The solution was brought to reflux,

and a total of 240 mg (1.26 mmol) TsOH was added over 5 h. After a further two hours at reflux, the solution was cooled and filtered of a bright red solid. Recrystallization from $CHCl_3/CH_3OH$ gave 222 mg of **3a** (76%). Use of crude hemiaminal **4a** gave a 63% yield from 1,4-dicyanobenzene: mp 216–218 °C. ^{1}H NMR (250 MHz, CD_2Cl_2) δ: 7.06–7.14 (m, 4H), 7.33 (t, J = 7.4 Hz, 2H), 7.53 (t, J = 7.8 Hz, 4H), 7.88–8.03 (m, 8H), 8.10 (s, 4H). ^{13}C NMR (62.5 MHz, $CDCl_3$) δ: 120.3, 122.4, 122.5, 124.9, 125.0 125.29, 125.35, 127.0, 129.0, 129.7, 131.6, 143.6, 144.0. IR (KBr): 1618, 1493, 829, 760, 683, 657 cm^{-1}. UV–vis (c = 1.0 × 10^{-5}, MeOH) ν_{max}: 261 (4.7), 313 (4.3), 473 (4.4) nm. MS (EI) *m/e*: 463 (M^+ + 1, 36), 462 (M^+, 100), 385 (2), 231 (20), 209 (51), 165 (6), 105 (10), 77 (11). Analysis calcd. for $C_{34}H_{22}O_2$: C, 88.29; H, 4.79. Found: C, 88.16; H, 4.96.

1,3-Phenylenebis(3-phenyl-1-isobenzofuran), 3b

A solution of 150 mL of dry THF and 1.943 g of 2-bromobenzaldehyde (10.50 mmol) was purged with N_2 and cooled to –80 °C with stirring. After 11.2 mL (15.75 mmol) of 1.4 mol/L Ph-Li was added via syringe, the mixture was warmed to 0 °C and allowed to react for 40 min. At –75 °C, 4.4 mL of *n*-butyllithium was added, and after 15 min, the reaction was warmed to 0 °C and allowed to react for 1 h. 1,3-Dicyanobenzene (0.6727 g, 5.25 mmol) was dissolved in dry THF and added very slowly by syringe, and the mixture was warmed to room temperature, reacting for 16 h. After treatment with H_2O, the mixture was extracted three times with ether, separating and collecting the organic phase. The ether was dried over $MgSO_4$, and then removed by vacuum to leave a brown oil. The oil was dissolved in methanol with TsOH (an equivalent amount) and brought to reflux for 4 h. The orange solid that precipitated out of the reaction mixture was recrystallized in methanol/acetone. The mother liquor was washed with 10% NaOH and extracted three times with chloroform. The organic phase was collected, and the solvent was dried over $MgSO_4$ and removed by vacuum leaving a brown oil. The oil was dissolved in acetone/methanol to give crystalline product **3b** (50%): mp 179–182 °C. ^{1}H NMR (250 MHz, $CDCl_3$) δ: 7.03–7.12 (m, 4H), 7.26–7.35 (m, 2H), 7.48–7.62 (m, 5H), 7.84–8.00 (m, 10H), 8.49 (s, 1H). ^{13}C NMR (250 MHz, $CDCl_3$) δ: 120.0, 120.7, 120.9, 122.2, 122.4, 123.1, 124.8, 125.2, 125.1, 127.0, 129.0, 129.4, 131.6, 132.2, 143.4, 144.0. IR (Nujol): 652.07, 676.35, 732.9, 763.81, 775.46, 1207.81, 1498.57, 1593.2 cm^{-1}. UV–vis (c = 1.0 × 10^{-5}, dioxane) ν_{max}: 256 (4.6), 321 (3.8), 413 (4.1) nm. MS (EI) *m/e*: 462 (M^+, 100), 446 (**3c**), 385 (5), 357 (2), 326 (2), 269 (2), 231 (2). Analysis calcd. for $C_{34}H_{22}O_2$: C, 88.29; H, 4.79. Found: C, 88.10; H, 5.00.

4,4′-Biphenylbis(3-phenyl-1-isobenzofuran), 3c from 4,4′-dibromobiphenyl

In a two-necked round-bottom flask, equipped with a stir bar and stoppers, a mixture of 4,4′-dibromobiphenyl (0.50 g, 1.60 mmol) and dry THF was purged with N_2 and cooled to –80 °C. After *n*-butyllithium (2.5 mol/L, 1.41 mL, 3.53 mmol) was added via syringe, the mixture was warmed to 0 °C and allowed to react for 40 min. At –75 °C, 2-bromobenzaldehyde (0.35 mL, 3.2 mmol) was added dropwise. The mixture was warmed to 0 °C, then to room temperature, and stirred for 16 h. After *n*-butyllithium (2.5 mol/L, 1.4 mL, 3.5 mmol) was added at –75 °C, the mixture was warmed to 0 °C and allowed to react for 40 min. At 0 °C, 0.36 mL (3.53 mmol) of benzonitrile was added. The mixture was warmed to room temperature and allowed to react for 1.5 h leaving a bright red-orange, fluorescent solution. The reaction was quenched with H_2O (120 mL) and extracted three times with ether. The organic phases were collected, dried over $MgSO_4$, and removed under vacuum to leave an orange oil. The yellow oil was dissolved in methanol, with a catalytic amount of PPTS and was brought to reflux with stirring. After 16 h, the reaction showed no change, and TsOH monohydrate was added and the mixture immediately turned from pale green to orange with solid precipitating out of solution. Recrystallization from DMF gave **3c** (39%): mp 296 °C (darkens, dec.). ^{1}H NMR (250 MHz, CD_2Cl_2) δ: 7.00–7.04 (m, 4H), 7.26 (t, J = 7 Hz, 2H), 7.45 (t, J = 7 Hz, 4H), 7.77–8.04 (m, 16H). IR (KBr): 657.8, 692.5, 742.6, 761.9, 821.7, 1491.1, 1595.2, 1676.2 cm^{-1}. UV–vis (c = 9.5 × 10^{-6}, dioxane) ν_{max}: 270 (4.3), 447 (3.9) nm. MS (EI) *m/e*: 538 (M^+, 100), 346 (35), 269 (14), 239 (16), 209 (17), 105 (25), 77 (20), 73 (57). Analysis calcd. for $C_{40}H_{26}O_2$: C, 89.19; H, 4.87. Found: C, 88.92; H, 4.98.

4,4′-Biphenylenebis(3-phenyl-1-isobenzofuran), 3c from 4,4′-dicyanobiphenyl

In 125 mL of dry THF was dissolved 2-bromobenzaldehyde (2.0 g, 10.8 mmol), and the solution cooled to –80 °C under nitrogen. Phenyllithium (6.0 mL of 1.8 mol/L in cyclohexane, 10.8 mmol) was added by syringe and the mixture warmed to 0 °C for 10 min. *n*-Butyllithium (4.7 mL of 2.5 mol/L in hexanes, 11.8 mmol) was then added. After 10 min, 0.99 g of 4,4′-dicyanobiphenyl was added as a solid in one portion. The solution was allowed to warm to room temperature overnight. Water (100 mL) and diethyl ether (150 mL) were added. The ether phase was separated, dried over anhydrous $MgSO_4$, filtered, and the solvent removed under reduced pressure. The resulting yellow oil (**4c**) had ^{1}H NMR (250 MHz, $CDCl_3$) δ: 2.4 (br s, 4H), s (5.88, 6.23, and 6.38 in a 1:2.4:1.3 ratio, total 2H), 7.0–7.9 m (26 H). It was not characterized further but was treated with TsOH to form **3c** as described in the preceding paragraph.

Dimethyl 1,4-phenylenebis(1,4-epoxy-1,4-dihydro-4-phenyl-1-naphthalene-2,3-dicarboxylate), 6a

In a 50 mL RBF were placed 67 mg of **3a**, 15 drops of DMAD, and a stirring bar. Dioxane (30 mL) was added, the flask wrapped in foil, and purged with nitrogen. The mixture was stirred for 10 h at which point it was colourless. The solvent was removed by rotary evaporation and the residue crystallized from $CHCl_3/CH_3OH$ to give 72 mg of adduct **6a** (67%): mp 284–287 °C (dec.). ^{1}H NMR (250 MHz, $CDCl_3$) δ: 3.68 (s, 6H), 3.69 (s, 6H), 7.15–7.17 (m, 4H), 7.47–7.53 (m, 10H), 7.73–7.76 (m, 4H), 7.85 (s, 4H). ^{13}C NMR (62.5 MHz, $CDCl_3$) δ: 52.6, 93.9, 93.9, 94.4, 122.3, 122.5, 126.26, 126.29, 128.23, 128.39, 128.44, 128.8, 129.4, 133.2, 134.2, 149.08, 149.18, 153.95, 154.06, 164.2. IR (Nujol): 1721, 1314, 1262, 1128, 752 cm^{-1}. MS (EI) *m/e*

calcd. for $C_{46}H_{34}O_{10}$: 746.21521, found: 746.21162; 746 (M^+, 2), 670 (51), 604 3b, 462 (38), 439 (50), 297 (38), 231 (18), 105 (100). Analysis calcd. for $C_{46}H_{34}O_{10}$: C, 73.99; H, 4.59. Found: C, 74.06; H, 4.66.

Dimethyl 1,3-phenylenebis(1,4-epoxy-1,4-dihydro-4-phenyl-1-naphthalene-2,3-dicarboxylate), 6b

In a round-bottom flask, **3c** (0.053 g, 0.115 mmol) and DMAD (0.082 g, 0.573 mmol) were dissolved in toluene. As the mixture was allowed to reflux (with stirring) for 2 h, the solution turned from bright yellow to clear. The solvent was removed by rotary evaporation to leave a pale yellow oil. The oil was crystallized in ethyl acetate / petroleum ether to give a 67% yield of **6b**, a white solid: mp 162–170 °C. ^{1}H NMR (250 MHz, $CDCl_3$) δ: 3.65–3.68 (m, 12H), 7.14–7.18 (m, 4H), 7.44–7.61 (m, 11H), 7.72–7.84 (m, 6H), 8.11 (s, 1H). ^{13}C NMR (62.5 MHz, $CDCl_3$) δ: 52.53, 52.56, 94.05, 94.08, 94.21, 94.24, 122.28, 122.36, 126.3, 127.7, 128.2, 128.8, 129.0, 129.1, 129.3, 133.3, 133.9. IR (KBr pellet): 702.08, 755.37, 793.51, 976.44, 1003.12, 1122.84, 1255.91, 1309.09, 1434.14, 1452.68, 1630.93, 1727.95, 2951.15 cm^{-1}. MS (EI) *m/e* calcd. for $C_{46}H_{34}O_{10}$: 746.2152, found: 746.2173; 746 (M^+, 0.3), 604 (27), 463 (14), 462 (38), 439 (41), 269 (18), 111 (12), 105 (100). Analysis calcd. for $C_{46}H_{34}O_{10}$: C, 73.99; H, 4.59. Found: C, 74.16; H, 4.70.

Dimethyl 4,4′-biphenylenebis(1,4-epoxy-1,4-dihydro-4-phenyl-1-naphthalene-2,3-dicarboxylate), 6c

In a round-bottom flask, 47.5 mg (0.088 mmol) of **3c** and 0.108 mL (0.882 mmol) of DMAD were dissolved in toluene. The mixture was allowed to reflux with stirring for 0.5 h as the solution turned from orange to lime green to clear. The solvent was removed, and the resulting yellow oil was dissolved in methanol to crystallize. Adduct **6c**, a white solid was obtained in 75% yield: mp 224–228 °C (melt/dec.). ^{1}H NMR (250 MHz, CDCl3) δ: 3.71 (s, 6H), 3.72 (s, 6H), 7.17–7.20 (m, 4H), 7.47–7.56 (m, 10H), 7.72–7.75 (m, 8H), 7.82–7.85 (m, 4H). ^{13}C NMR (250 MHz, $CDCl_3$) δ: 52.58, 52.62, 94.1, 94.3, 122.43, 122.46, 126.3, 127.6, 128.2, 128.8, 129.3, 132.7, 133.3, 141.5, 149.27, 149.33, 153.6, 154.5, 164.3, 164.4. IR (Nujol): 752.3, 1255.7, 1311.7, 1454.4, 1722.5 cm^{-1}. MS (FAB) *m/e*: 823 (MH^+, 0.9), 791 (2.4), 680 (2.1), 538 (2.5), 515 (2.9), 309 (5.1), 155 (39.7), 135 (48.7), 119 (100), 105 (73.1). Analysis calcd. for $C_{52}H_{38}O_{10}$: C, 75.90; H, 4.65. Found: C, 75.89; H, 4.86.

Dimethyl 1,4-phenylenebis(4-phenyl-1-naphthalene-2,3-dicarboxylate), 7a

Adduct **6a** (0.23 g, 0.32 mmol) and NaI (0.29 g, 1.9 mmol) were dissolved in 30 mL of dry acetonitrile. Trimethylsilyl chloride (0.25 mL, 1.9 mmol) was added by syringe and the mixture refluxed for 2 days. An equal volume of water was added and the mixture extracted twice with 50 mL of chloroform. The combined chloroform extracts were washed with 10% $NaHSO_3$ solution and dried over $MgSO_4$. The solvent was removed and the residue columned on 4 inches of silica eluting with chloroform graded to 1% ethyl acetate in chloroform. The fractions containing the product were stripped of solvent, and the product was precipitated by the addition of methanol. Filtration gave 0.17 g of **7a** (78%): ^{1}H NMR (250 MHz, $CDCl_3$) δ: 3.45 (6), 3.58 (6), 7.4–7.8 (m, 22H). ^{13}C NMR (75 MHz, $CDCl_3$) δ: 52.5, 53.5, 127.4, 127.7, 128.0, 128.1, 128.3, 129.0, 129.3, 129.97, 130.01, 132.8, 133.0, 137.45, 137.53, 137.7, 138.7, 139.5, 168.8, 168.9. IR (KBr): 1741 and 1726, 1436, 1241, 1221, 1130, 773, 702 cm^{-1}. MS (EI) *m/e* calcd. for $C_{46}H_{34}O_8$: 714.2253, found: 714.2267; 714 (M^+, 100), 651 (18), 326 (10), 87 (5).

Dimethyl 1,3-phenylenebis(4-phenyl-1-naphthalene-2,3-dicarboxylate), 7b

Adduct **6b** (0.43 g, 0.58 mmol) and NaI (0.43 g, 2.9 mmol) were dissolved in 50 mL of dry acetonitrile under nitrogen. The solution was cooled to 0 °C and TMSCl (0.37 mL, 2.9 mmol) added by syringe. The solution was then stirred at room temperature for 24 h. Saturated $NaHSO_3$ was added, and the solution was extracted twice with 50 mL portions of chloroform. The organic phase was separated, dried over $MgSO_4$, and stripped of solvent. The residue solidified and was recrystallized from methanol to give, in several crops, a total of 0.32 g (78%): mp 214–215 °C. ^{1}H NMR (250 MHz, $CDCl_3$) δ: 3.52 (3.67 and 3.68, J = 3s Hz, 12H), 7.33–7.78 (m, 22H). ^{13}C NMR (62.5 MHz, $CDCl_3$) δ: 52.32, 52.35, 52.5, 52.6, 127.3, 127.5, 127.6, 127.7, 127.8, 127.95, 127.98, 128.90, 128.08, 128.13, 128.18, 128.24, 128.27, 128.33, 128.4, 128.8, 129.01, 129.07, 129.21, 129.5, 129.98, 130.13, 130.2, 130.3, 131.7, 132.2, 132.89, 132.95, 133.00, 137.72, 137.74, 137.80, 138.88, 139.4, 139.5, 168.86, 168.89, 168.97. IR (KBr): 1741 and 1726 (C=O), 1436, 1241, 1221, 1130, 773, 702 cm^{-1}. Analysis calcd. for $C_{46}H_{34}O_8$: C, 77.30; H, 4.79. Found: C, 77.33; H, 5.00.

Dimethyl 4,4′-biphenylenebis(4-phenyl-1-naphthalene-2,3-dicarboxylate), 7c

Difuran **3c** (0.30 g, 0.56 mmol) and 240 mg DMAD (1.7 mmol) were refluxed in 150 mL dioxane for 8 h. The solvent was removed by rotary evaporation and evacuation under high vacuum. Acetonitrile (30 mL) and sodium iodide (0.54 g, 3.4 mmol) were added, the flask purged with nitrogen, and cooled to 0 °C. Chlorotrimethylsilane (0.50 mL, 3.9 mmol) was added by syringe and the reaction stirred for 6 h. The mixture was filtered and the solid material recrystallized from $CHCl_3$/MeOH to give 246 mg of **7c**, (57%): mp 368–370 °C. ^{1}H NMR (250 MHz, $CDCl_3$) δ: 3.54 (s, 6H), 3.60 (s, 6H), 7.40–7.55 (m, 18H), 7.68–7.79 (m, 4H), 7.87 (d, J = 7 Hz, 4H). ^{13}C NMR (62.5 MHz, $CDCl_3$) δ: 52.4, 52.6, 126.9, 127.6, 127.7, 127.96, 127.98, 128.1, 128.3, 129.0, 130.2, 130.8, 133.0, 137.1, 137.8, 138.9, 139.4, 140.1, 169.0. IR (Nujol): 1742, 1227, 1163, 1130, 774, 721, 700 cm^{-1}. MS (EI) *m/e*: 790 (M^+, 22), 744 (5), 552 (21), 457 (44), 456 (100), 207 (20), 126 (9), 78 (11).

Acknowledgements

The authors wish to thank the Natural Sciences and Engineering Research Council of Canada (NSERC) and the University of Lethbridge for funding (RTB and PWD) and the Centre for Molecular Architecture, Central Queensland, Australia for analytical support.

References

(1) Friedrichsen, W. *Adv. Heterocycl. Chem.* **1980**, *26*, 135–241. doi:10.1016/S0065-2725(08)60141-5.

(2) Friedrichsen, W. *Adv. Heterocycl. Chem.* **1999**, *73*, 1–96. doi:10.1016/S0065-2725(08)60940-X.

(3) Maindron, T.; Dodelet, J. P.; Lu, J.; Hlil, A. R.; Hay, A. S.; D'Iorio, M. *Synth. Met.* **2002**, *130* (3), 247–255. doi:10.1016/S0379-6779(02)00139-X.

(4) Rickborn, B. In *Advances in theoretically interesting molecules*; Thummel, R. P., Ed.; J.A.I. Press: Greenwich, CT, 1989; Vol. 1.

(5) Rodrigo, R. *Tetrahedron* **1988**, *44* (8), 2093–2135. doi:10.1016/S0040-4020(01)81720-8.

(6) Wiersum, U. E. *Aldrichim Acta* **1981**, *14*, 53.

(7) Friedrichsen, W. In *Houben-Weyl, Methoden der organischen chemie*; Kreher, R., Ed.; Thieme Verlag: Stuttgart, 1994; Vol. E6b, , pp. 163–216.

(8) Wege, D. In *Advances in theoretically interesting molecules*; Thummel, R. P., Ed.; J.A.I. Press: Greenwich, CT, 1998; Vol. 4, pp. 1–52.

(9) Mohanakrishnan, A. K.; Amaladass, P. *Tetrahedron Lett.* **2005**, *46* (42), 7201–7204. doi:10.1016/j.tetlet.2005.08.069.

(10) Leong-Neumann, S.; Derrick, S. D.; Dibble, P. W. *Tetrahedron Lett.* **1995**, *36* (24), 4181–4184. doi:10.1016/0040-4039(95)00777-A.

(11) Smith, J. G.; Dibble, P. W.; Sandborn, R. E. *J. Org. Chem.* **1986**, *51* (20), 3762–3768. doi:10.1021/jo00370a004.

(12) Barfield, M.; Grant, D. M.; Ikenberry, D. *J. Am. Chem. Soc.* **1975**, *97* (24), 6956–6961. doi:10.1021/ja00857a003.

(13) Cheney, B. V. *J. Am. Chem. Soc.* **1968**, *90* (20), 5386–5390. doi:10.1021/ja01022a009.

(14) Stevens, B.; Ors, J. A.; Christy, C. N. *J. Phys. Chem.* **1981**, *85* (2), 210–214. doi:10.1021/j150602a019.

(15) Smith, J. W.; Dibble, P. W. *J. Org. Chem.* **1988**, *53* (9), 1841–1848. doi:10.1021/jo00244a001.

(16) Jung, K. Y.; Koreeda, M. *J. Org. Chem.* **1989**, *54* (24), 5667–5675. doi:10.1021/jo00285a011.

(17) Thibault, M. E.; Closson, T. L. L.; Manning, S. C.; Dibble, P. W. *J. Org. Chem.* **2003**, *68* (22), 8373–8378. doi:10.1021/jo034777x. PMID:14575460.

(18) Chen, X.; Dam, M. A.; Ono, K.; Mal, A.; Shen, H.; Nutt, S. R.; Sheran, K.; Wudl, F. *Science* **2002**, *295* (5560), 1698–1702. doi:10.1126/science.1065879. PMID:11872836.

(19) Watson, K. A.; Bass, R. G. *High Perform. Polym* **2000**, *12* (2), 299–314. doi:10.1088/0954-0083/12/2/305.

(20) Godschalx, J. P.; Pechacek, J. T.; Arndt, K. E. Dow Chemical Company; International Patent WO073824, 2006.

(21) Moock, K. H.; Rock, M. H. *J. Chem. Soc., Dalton Trans.* **1993**, (16): 2459. doi:10.1039/dt9930002459.

γ-Silylated α,β-unsaturated amides — Preparation by [1,5]-sigmatropic rearrangement and use as masked dienolate equivalents in carbonyl condensations[1]

James R. Green, Babajide I. Alo, Marek Majewski, and Victor Snieckus

Can. J. Chem. Downloaded from www.nrcresearchpress.com by Sichuan Normal University on 09/14/12
For personal use only.

Abstract: The reaction of lithium dienolates derived from *N*,*N*-dialkylsenecioamides (**1a**–**1c**) with triorganosilyl electrophiles occurs initially at the oxygen atom predominantly, and is followed by an O → C silicon migration to afford the γ-silylated senecioamides (**4a**–**4h**). The γ-silylated senecioamide ***Z*-4a** undergoes fluoride-ion-mediated condensations with aromatic aldehydes to give kinetic α-(**6**) and thermodynamic γ-(**5**) condensation product patterns comparable to lithium dienolates. The $TiCl_4$-mediated reactions with aldehydes gives α-products (**6**) in a highly syn-selective manner. Possible transition-state models for the syn-selective condensations are discussed and a chair-like transition state featuring bidentate coordination to titanium (**11**) is proposed.

Key words: silicon migration, amide dienolate, allylsilane, Hosomi–Sakurai reaction, stereoselective.

Résumé : La réaction des diénolates de lithium dérivés des *N*,*N*-dialkylsénécioamides (**1a**–**1c**) avec des électrophiles triorganosilyles se produit dans un premier temps par le biais de l'atome d'oxygène et l'intermédiaire subit une migration O → C de l'atome de silicium qui conduit éventuellement aux sénécioamides γ-silylés (**4a**–**4h**). Le sénécioamide γ-silylé ***Z*-4a** donne des réactions de condensation avec les aldéhydes aromatiques, catalysées par l'ion fluorure, qui conduisent à la formation des produits de condensation cinétique, α-(**6**), et thermodynamique, γ-(**5**) avec des patrons similaires à ceux observés pour les diénolates de lithium. Les réactions des aldéhydes, catalysées par le $TiCl_4$, conduisent aux produits α-(**6**) avec une haute sélectivité syn. On discute de divers modèles d'états de transition qui pourraient expliquer la sélectivité syn des condensations et on suggère que la meilleure explication est un état de transition en forme de chaise comportant une coordination bidentate vers le titane (**11**).

Mots-clés : migration du silicium, diénolate amide, allylsilane, réaction de Hosomi–Sakurai, stéréosélective.

[Traduit par la Rédaction]

Introduction

From the considerable body of literature on dienolates derived from α,β-unsaturated acid derivatives,[2] including our work on α,β-unsaturated amides,[3] a clear pattern of reactivity has emerged, especially for carbon-based electrophiles. In the absence of additional heteroatom substitution, predominant to exclusive α-carbonyl substitution is observed, with preferential γ-substitution products arising under thermodynamic conditions. Conversely, the seminal work of Casey[4] demonstrated that dienolates derived from esters undergo kinetic O-silylation to give vinyl ketene *O*,*O*-acetals,[5] which then experience a [1,5]-sigmatropic O → C silicon migration to γ-silylated products. An analogous migration has been observed in β-pyrrolidino vinyl ketene *O*,*N*-acetals,[6] and O → C or C → O silicon migrations have been observed on related systems,[7–9] for many cases after our initial report in this area.[10] These combined results prompted the present systematic study on tertiary amide dienolate silylation and the potential rearrangement of the resulting vinyl ketene *N*,*O*-acetals to γ-silylated α,β-unsaturated amides (Scheme 1).

An additional incentive for the present study was the consideration that, with few exceptions, the reactivity of γ-silylated alkenoic acid derivatives has been restricted to electrophilic cyclizations on alkenes and epoxides.[11,12] Given the rich chemistry of allylsilanes,[13] such γ-silylated carbonyl compounds may be considered as storable dienolate equivalents. This is particularly relevant in the 3-methyl-2-butenamide (senecioamide) case, as the lithio dienolates give modest to poor α- kinetic aldol selectivity. Consequently, we set as a goal to test the functionalized allylsilane dienolate equivalent in fluoride- and Lewis acid mediated aldol chemistry to provide a contribution to the area of diastereoselective C–C bond formation.[10,14] The results of

Received 21 January 2009. Accepted 31 March 2009. Published on the NRC Research Press Web site at canjchem.nrc.ca on 2 June 2009.

J.R. Green.[1] Department of Chemistry, University of Windsor, Windsor, ON N9B 3P4, Canada.
B.I. Alo. Department of Chemistry, University of Lagos, Akoka, Lagos, Nigeria.
M. Majewski. Department of Chemistry, University of Saskatchewan, Saskatoon, SK S7N 5C9, Canada.
V. Snieckus.[2,3] Department of Chemistry, University of Waterloo, Waterloo, ON N21 3G1, Canada.

[1]Corresponding author (e-mail: jgreen@uwindsor.ca).
[2]Corresponding author (e-mail: snieckus@queensu.ca).
[3]Present address: Department of Chemistry, Queen's University, Kingston, ON K7L 3N6, Canada.

Scheme 1. Reagents and conditions: (a) Me_3SiCl; (b) Δ, THF.

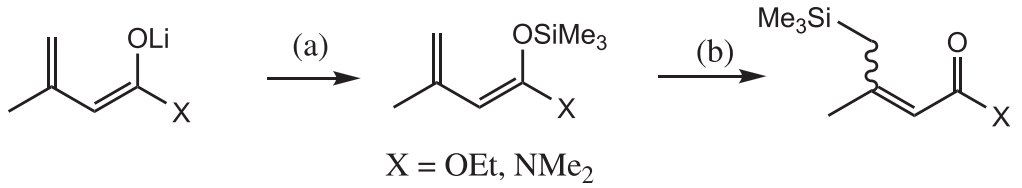

Scheme 2. Reagents and conditions: (a) (*i*) LDA, THF, –78 °C; (*ii*) R^1_3 SiCl, –78 °C to RT; (b) THF, Δ.

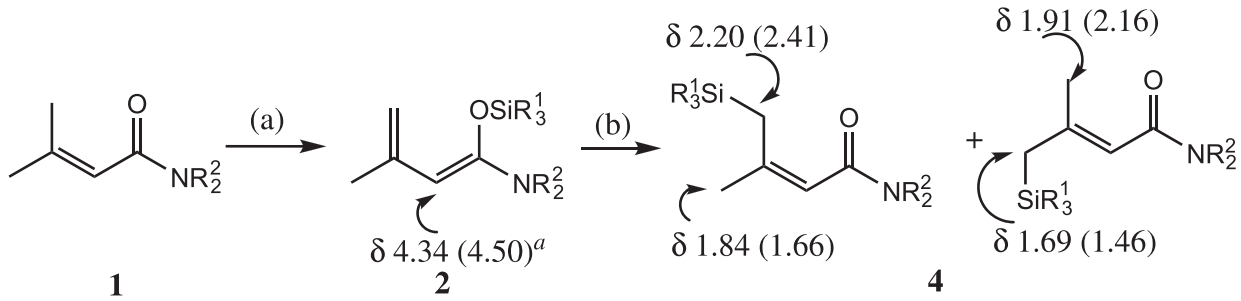

a, R^2 = Me
b, R^2 = Et
c, R^2 = *i*-Pr

a, R^1 = Me, R^2 = Me
b, R^1 = Et, R^2 = Me
c, R^1 = *i*-Pr, R^2 = Me
d, R^1_3 = Me_2Ph, R^2 = Me

e, R^1 = Me, R^2 = Et
f, R^1 = Et, R^2 = Et
g, R^1 = Me, R^2 = *i*-Pr
h, R^1_3 = Me_2Ph, R^2 = *i*-Pr

[a] Chemical shift data in $CDCl_3$ (C_6D_6) are for compounds **2a** and **4a**.

Scheme 3. Reagents and conditions: (a) DMAD, benzene, 0 °C.

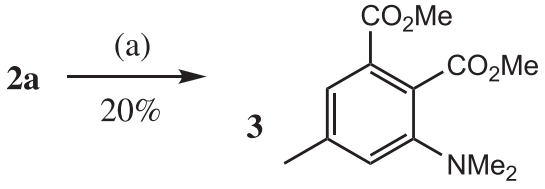

our studies concerning lithium dienolates derived from *N*,*N*-dialkylsenecioamides and their γ-silylated reaction products are presented herein.

Enolate silylation and silicon migration reactions of senecioamides

N,*N*,3-Trimethyl-2-butenamide (*N*,*N*-dimethylsenecioamide) (**1a**) was deprotonated with LDA under the established conditions,[3a] and the resultant dienolate underwent silylation with Me_3SiCl to afford the vinylketene *O*,*N*-acetal (**2a**) (Scheme 2). Compound **2a** was found not to be stable to an aqueous workup or chromatographic purification, but was identified by ^{1}H NMR spectroscopy; its characterization as the *Z*-isomer was supported by NOE difference experiments showing an enhancement of the vinyl CH resonance (δ 4.48) upon irradiation of the N-substituted methyl resonances (δ 2.26).[15] Furthermore, **2a** was trapped by Diels–Alder reaction with dimethyl acetylene dicarboxylate to give the phthalate ester **3** in low yield (Scheme 3) (see Supplementary data).[8] In normal practice, however, **2a** was heated at reflux in THF for 18 h to afford two isomeric 4-trimethylsilylated-2-butenamides, ***Z*-4a** and ***E*-4a**, in 74% and 2% yields, respectively. The stereochemistry of the two compounds was determined on the basis of the downfield ^{1}H NMR chemical shifts of the protons γ and cis to the amide function relative to those γ and trans to the carbonyl, and the expected aromatic solvent induced shift (ASIS)[16] of the γ,cis- and γ,trans-protons observed in their ^{1}H NMR spectra in C_6D_6 (Scheme 2).

Table 1. γ-Silylation results for senecioamides **1a**, **1b**, and **1c**.

Entry	R^1_3	R^2	Product	Yield (%)	*Z*:*E*
1	Me_3	Me	**4a**	75	91:9
2	Et_3	Me	**4b**	74	77:23
3	*i*-Pr_3	Me	**4c**	35	63:37
4	$MePh_2$	Me	**4d**	92[a]	36:64
5	Me_3	Et	**4e**	74	53:47
6	Et_3	Et	**4f**	67	31:69
7	Me_3	*i*-Pr	**4g**	65	35:65
8	$MePh_2$	*i*-Pr	**4h**	92[a]	59:41

[a]The THF at reflux step was not carried out.

The basic protocol outlined above was extended to other chlorosilanes (chlorotriethylsilane, chlorotriisopropylsilane, and chloromethyldiphenylsilane) and other senecioamides (**1b**, **1c**), and the combined results are presented in Table 1. For reaction of the dienolates with $MePh_2SiCl$, C-silylation did not require the heating-to-reflux step, and it was therefore omitted in these cases (Table 1, entries 4 and 8). In the isolated γ-silylated products (**4**) other than **4a**, the most noteworthy feature was the increased relative amounts of

Can. J. Chem. Downloaded from www.nrcresearchpress.com by Sichuan Normal University on 09/14/12
For personal use only.

Can. J. Chem. Downloaded from www.nrcresearchpress.com by Sichuan Normal University on 09/14/12
For personal use only.

Scheme 4. Reagents and conditions: (a) R^1_3SiCl, –78 °C to RT; (b) THF, Δ.

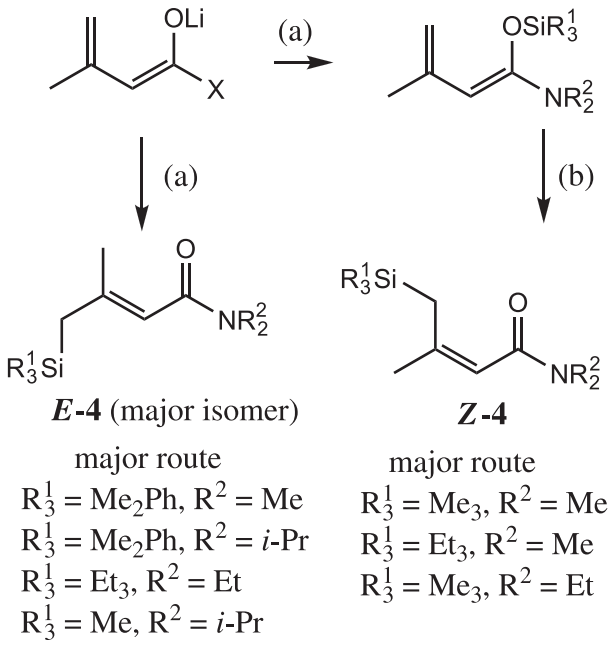

the *E*-isomer to the point where the *E*-isomer predominated in several instances (Table 1, entries 4, 6, and 7).

To further clarify the source of the γ,*E*-isomer silylation products, the reaction of the dienolate of **1a** with Et_3SiCl was examined more closely prior to the reflux step by subjecting an aliquot of the product to an anhydrous workup and the remainder to a conventional aqueous workup. For the former aliquot, integration of the respective vinyl proton resonances in the ^1H NMR spectrum showed a 23:77 ratio for γ-silylated products (***Z*- + *E*-4b**) and the ketene *O*,*N*-acetal (**2b**). Conversely, the material subjected to aqueous workup gave ***Z*-4b** and ***E*-4b** in 4% and 16% yields, respectively. Comparing this to entry 2 in Table 1 (***Z*-4b**, 58%; ***E*-4b**, 18%), it is apparent that most of the γ,*Z*-silylated product arose from the O- to C-[1,5]-silicon migration of the vinylketene *O*,*N*-acetal (**2b**), whereas the corresponding γ,*E*-silylated product most likely resulted from direct attack on the dienolate (Scheme 4). In the cases with $MePh_2SiCl$ as the electrophile, it is likely that both isomers of γ-silylation products result from direct silylation, in keeping with the relatively greater HSAB "softness" of $MePh_2SiCl$,[17] and in the fact that **2d** and **2h** are not actually formed in significant amounts.

The variation of *E/Z* ratios in these γ-silylated amides is worthy of further comment. In the *N*,*N*-dimethyl amide series, increasing amounts of *E*-isomers may reflect increasing direct γ-silylation due to a greater reactivity with bulkier chlorotrialkylsilanes when the dienolate is in the s-trans form. This proposal breaks down for the *N*,*N*-diisopropyl amide series, as $MePh_2SiCl$ undergoes reaction by direct γ-attack and yet gives predominantly ***Z*-4h.** The regiochemistry for direct γ-attack is clearly a more complex process in these cases.

To establish the inter- or intra-molecularity of the [1,5]-silicon migration, a crossover experiment was performed. The lithium dienolates of **1a** and **1b** were allowed to react

Scheme 5. Reagents and conditions: (a) THF, Δ, 19h.

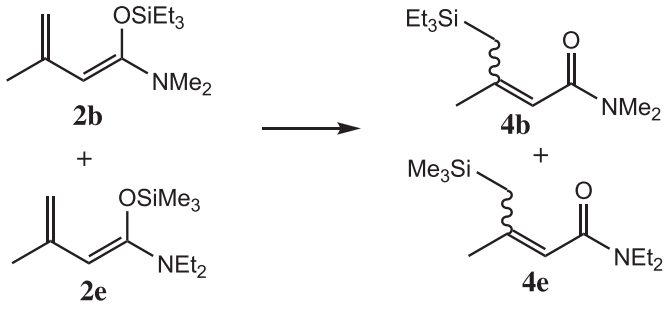

at –78 °C with Et_3SiCl and Me_3SiCl, respectively, and, after warming to room temperature, the respective solutions of the two reactions were mixed in a 1:1 ratio and heated to reflux (19 h). Analytical HPLC of the resultant mixture revealed the presence of γ-silylation products ***Z*-4b**, ***E*-4b**, ***Z*-4e**, and ***E*-4e,** but not crossover products ***Z*-4a**, ***E*-4a**, ***Z*-4f**, or ***E*-4f** (Scheme 5) (see Supplementary data).[8] This constitutes strong evidence for the intramolecular nature of the [1,5]-silicon migrations of these silylated vinylketene *O*,*N*-acetals.

With a facile method for generating γ-silylated-α,β-unsaturated amides in hand, attention was turned to the condensation chemistry of these compounds. Since ***Z*-4a** was obtained with the highest stereoselectivity and possesses the most widely employed silyl group, the reactivity of this compound with carbonyl derivatives was pursued. As described below, fluoride- and Lewis acid mediated condensation reactions were investigated.

Fluoride-mediated condensations of *Z*-4a

The reaction of ***Z*-4a** with benzaldehyde was induced by subjecting its THF solution to a catalytic amount of *n*-Bu_4NF (5 mol%) at RT to afford a mixture of γ-hydroxyalkylated compounds ***Z*-5a** and ***E*-5a** in 58% and 14% yields, respectively (Scheme 6). This process was extended to other aromatic aldehydes, and gave some interesting differences in the reaction products (Table 2). Aromatic aldehydes bearing strong electron-withdrawing groups (EWGs) gave mixtures of γ-(**5**) and α-hydroxyalkylation products (**6**) (Table 2, entries 4 and 5); conversely, substrates not possessing these EWGs gave only γ-hydroxyalkylated products (Table 2, entries 1–3). Reaction with benzophenone resulted in the formation of the γ-condensation products, but unless the reaction was performed at low temperature (–45 °C), these underwent elimination to give **7** (Table 2, entries 6 and 7). By contrast, attempted reaction with aliphatic aldehydes resulted in desilylation of ***Z*-4a** and isolation of only trace amounts of condensation products.

These condensations, if effected at lower temperatures (–45 °C) for short periods of time, required the use of stoichiometric amounts of fluoride ion. Under such conditions, however, α-condensation products predominated as separable syn/anti diastereomeric mixtures, together with small amounts of the γ,*Z*-condensation products (Scheme 6, Table 3).

The identities of the condensation products were readily established from their ^1H NMR spectra. The α-products (**6**)

Scheme 6. Reagents and conditions: (a) (*i*) ArCRO, 5 mol% *n*-BuNF, THF, –78 °C to RT; (*ii*) NH_4Cl(aq); (b) (*i*) ArCHO, 100 mol% *n*-BuNF, THF, –45 °C, 2 min; (*ii*) $NH_4Cl_{(aq)}$.

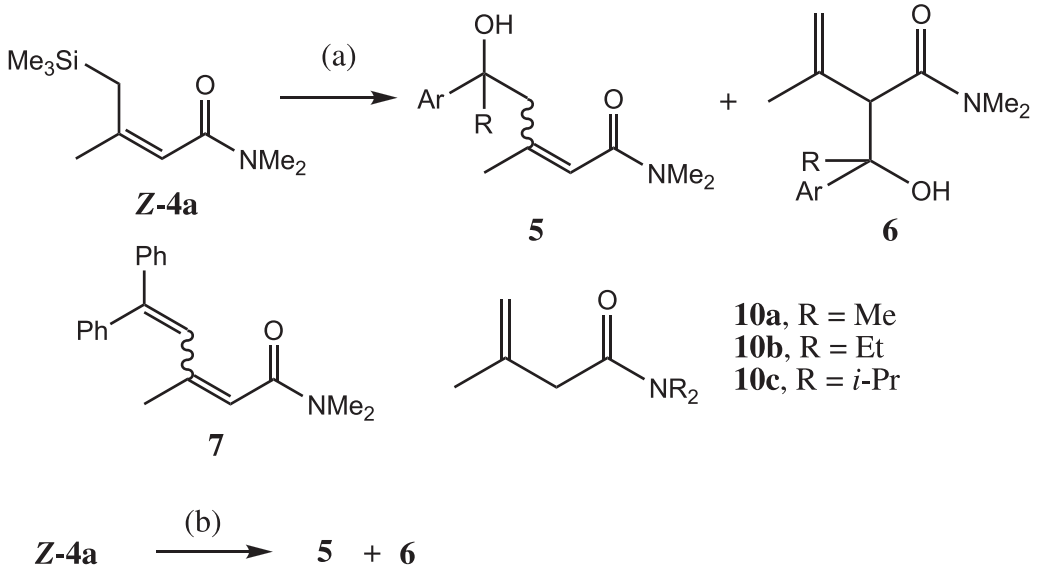

Table 2. Fluoride-catalyzed condensations of ***Z*-4a** with aromatic aldehydes and benzophenone.

Entry	ArCRO	γ-Product	Yield (%), (*Z*:*E*)	α-Product	Yield (%), (syn:anti)
1	PhCHO	**5a**	72, (80:20)		—
2	3,4-$(MeO)_2$ C_6H_3CHO	**5b**	75, (65:35)		—
3	Pyridine-3-CHO	**5c**	70, (81:19)		—
4	Pyridine-4-CHO	**5d**	42, (100:0)	**6d**	37 (56:44)
5	4-$O_2NC_6H_4CHO$	**5e**	31, (100:0)	**6e**	48 (45:55)
6	Ph_2CO[a]	**5g, 5f**[b]	68, (30:70)		—
7	Ph_2CO	**7**	29, (33:67)		—

[a]Reaction conducted at –45 °C.
[b]Isolated as the trimethylsilyl ether.

Table 3. Low-temperature stoichiometric fluoride-mediated condensations of ***Z*-4a** with aromatic aldehydes.

Entry	ArCHO	α-Product	α- (%), (syn:anti)	γ- (%)
1	PhCHO	**6a**	64, (48:52)	6
2	3,4-$(MeO)_2$ C_6H_3CHO	**6b**	52, (48:52)	6
3	Pyridine-4-CHO	**6d**	61, (44:56)	13
4	4-$O_2NC_6H_4CHO$	**6e**	57, (45:55)	30

were distinguished by virtue of the larger vicinal coupling constant of the α-methine proton in the anti-diastereomer (J = 6–7 Hz) relative to the syn-diastereomer (J = 4–5 Hz).[18] The *Z*- and *E*-isomers of the γ-condensation products (**5**) were most readily discriminated by the downfield ASIS of the allylic methyl groups of the *Z*-isomers, versus the upfield ASIS of the corresponding group in the *E*-isomers (Fig. 1).

The observation of predominant α-condensation products at low temperatures and short reaction times but γ-condensation products at higher temperatures and longer reaction times is a clear kinetic (α-) versus thermodynamic (γ-) product control situation similar to that observed for analogous lithium dienolate condensation chemistry.[3a] In the cases of 4-nitrobenzaldehyde and pyridine-4-carboxaldehyde, the EWGs render the initial kinetic condensation favourable to

Fig. 1. Stereochemical assignments of aldol adducts.

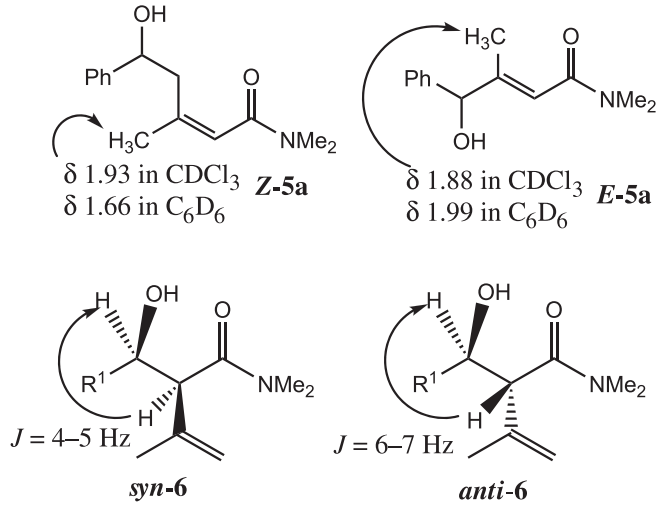

such a degree that reversibility is suppressed completely (4-nitrobenzaldehyde) or partially (pyridine-4-carboxaldehyde). We note that the amount of γ-product with 4-nitrobenzaldehyde under kinetic conditions is relatively high, although it is still the minor product. We attribute the nearly non-existent diastereoselectivity of the α-condensation in all cases to the re-

Can. J. Chem. Downloaded from www.nrcresearchpress.com by Sichuan Normal University on 09/14/12
For personal use only.

Scheme 7. Competitive transition states for kinetic fluoride-mediated condensations

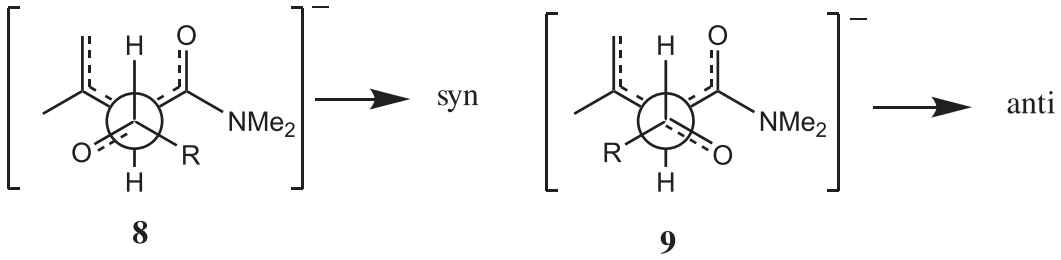

Scheme 8. Reagents and conditions: (a) (*i*) R^1R^2CO, $TiCl_4$, CH_2Cl_2, RT; (*ii*) $NH_4Cl_{(aq)}$.

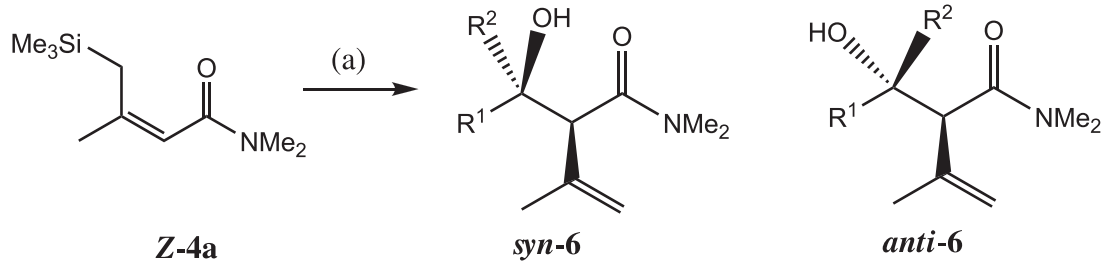

Table 4. $TiCl_4$-mediated condensations of **4a** with aldehydes and benzophenone.

Entry	R^1R^2CO	α-Product	Yield	syn:anti
1	PhCHO	**6a**	62	>97 : <3
2	4-$O_2NC_6H_4CHO$	**6e**	73	97:3
3	*n*-PrCHO	**6h**	64	96:4
4	*i*-PrCHO	**6i**	68	59:41
5	EtCHO	**6j**	52	87:13
6	Ph_2CO	**6g**	72	—

action proceeding via the nearly equal in energy acyclic transition states **8** and **9** (Scheme 7). While the pattern of reactivity is consistent with a reaction proceeding via a free enolate, we do not consider this as an unambiguous proof. Attempts to induce fluoride-ion-catalyzed reactions of silyl ketene acetal (**2a**) with benzaldehyde afforded only hydrolysis products.[19]

$TiCl_4$-mediated condensations of *Z*-4a with aromatic and aliphatic aldehydes and benzophenone

The condensation reaction of the γ-silylated amide ***Z*-4a** with benzaldehyde could also be initiated by a Mukaiyama-type process, often referred to as the Hosomi–Sakurai reaction,[14d] in the presence of stoichiometric amounts of $TiCl_4$ under mild conditions. The condensation was found to occur with exclusive α selectivity and nearly complete syn-diastereoselectivity to give product **6a** in reasonable yield (Scheme 8, Table 4). This process was extended to other aromatic and aliphatic aldehydes (**6e**–**6j**), with some caveats: aldehydes with Lewis basic sites (4-methoxybenzaldehyde and 3,4-dimethoxybenzaldehyde) gave only desilylation, without condensation, while branched aliphatic aldehyde (2-methylpropanal) gave much lower levels of diastereoselection (syn/anti **6h** = 59:41).

Alteration of this basic protocol was much less successful in obtaining condensation products stereoselectively. The use of a monodentate Lewis acid ($BF_3{\cdot}OEt_2$) and benzaldehyde under otherwise identical conditions resulted only in minimal conversion (<10%) of ***Z*-4a** to ***syn*-6a**; even excesses of $BF_3{\cdot}OEt_2$ (4.4 equiv.) and PhCHO (4.8 equiv.) afforded ***syn*-6a** in only 7% yield (see Supplementary data). Similarly, allylsilane ***E*-4a** was much less reactive than ***Z*-4a** under identical conditions. Even at higher temperature, attempted reaction of ***E*-4a** with benzaldehyde in the presence of $TiCl_4$ resulted mainly in the isolation of recovered starting material, along with only trace amounts of condensation product ***syn*-6a** and desilylation product **10a** (see Supplementary data). In the alternative obvious approach,[20] reaction of the lithium dienolate of **1a** with $TiCl_4$, followed by treatment with benzaldehyde, resulted only in the formation of oligomeric materials (see Supplementary data).

The observed high syn diastereoselectivity in the $TiCl_4$-mediated reactions of ***Z*-4a** with aromatic and linear aliphatic aldehydes is striking, particularly in light of the related condensation reactions of γ-stannyl- and γ-germylsenecioic "esters" reported by Yamamoto[21] and Hudlicky,[22] and indium-mediated Reformatsky reactions of γ-bromocrotonates,[23] which generally show high anti diastereoselectivity.[24] While experimentally the results are nicely complementary, clearly our results cannot be rationalized in terms of an acyclic transition state with an anti-periplanar relationship between the allylsilane and aldehyde functions, as advanced by Yamamoto.[25] A more plausible explanation is based on the ability for bidentate coordination to $TiCl_4$, and the greater basicity of the amide relative to the ester function.[26] Working on the assumption that the predominant s-cis-conformation of the unsaturated tertiary amide[27] is maintained, we envisage a cyclic transition state featuring coordination of both the amide and aldehyde carbonyls to Ti, with the allylsilane function positioned in an exocylic mode. Formulating this transition state as a chair, with the aldehyde R group pseudoequatorial and a synclinal orientation of the allylsilane and aldehyde (**11**), allows rationalization of the observed syn-

Can. J. Chem. Downloaded from www.nrcresearchpress.com by Sichuan Normal University on 09/14/12
For personal use only.

Scheme 9.

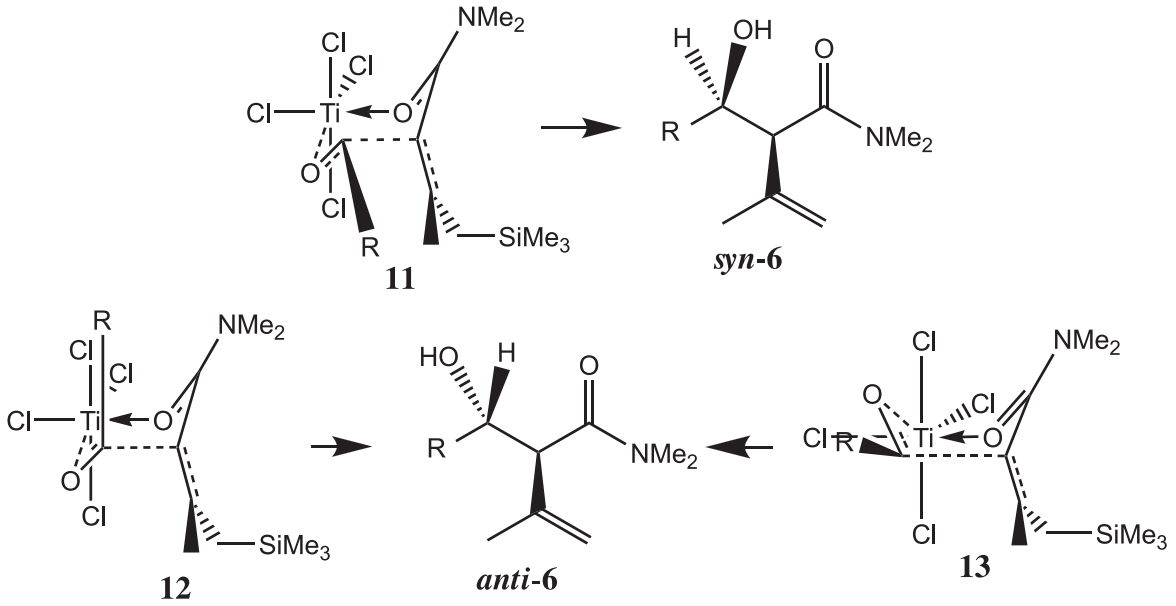

diastereomeric product (Scheme 9).[28] Formation of the anti-diastereomer would require either a pseudoaxial aldehyde R group (**12**), or boat transition state (**13**). In context of this proposal, the analogous $TiCl_4$-mediated condensations of γ-stannyl-/germyl-senecioic esters[21,22] lead to reduced anti-diastereoselection, which may indicate destructive competition of analogous bidentate coordination in these cases. In addition, it has been demonstrated that chiral senecioyl oxazolidinones undergo *n*-Bu_2BOTf-mediated reactions with aldehydes with high syn-selectivity and high diastereofacial selectivity.[29] For esters, however, the selectivity profile appears complementary to our work in that there is an apparent requirement for branching in aliphatic aldehydes to achieve high diastereoselectivity.[30]

The greater reactivity of ***Z*-4a** relative to ***E*-4a** may be rationalized in two possible ways. In a chair transition state for ***Z*-4a**, the depicted orientation (**14**) of the C–Si bond suggests potential intramolecular transfer of an apically ligated chloride to a syn-oriented silicon (Scheme 10), an analogous possibility does not exist for ***E*-4a**. This possibility has been advanced on occasion in Hosomi–Sakurai reactions,[10,31] and in silyl ketene acetal-aldehyde and allylsilane-enone condensation chemistry,[32] and has received computational support at the DFT level.[33] In contrast, careful experiments on intramolecular condensations of aldehydes with chiral allylsilanes and allylstannanes are not consistent with the stereochemical outcome for such a syn-S'_E orientation.[34]

The alternate plausible source of the greater reactivity of ***Z*-4a** stems from the possibility of a stabilizing secondary orbital overlap of the allylsilane (HOMO) with the aldehyde (LUMO) (**15**), which would not be available in the reaction path of ***E*-4a**. Originally proposed for aldol condensation chemistry,[35] this rationalization has been invoked in support of synclinal orientations in allylstannane-aldehyde condensations,[28d,36] and should, in principle, be capable of extension to Lewis acid mediated allylsilane-aldehyde condensations.

Pursuant to this question, transition states approximating **14** and **15** were calculated at the DFT level. An "outside" trimethylsilyl transition state corresponding to **11/15** was located (**16**, Scheme 11); it features a relatively short forming bond (1.81 Å), a significantly lengthened senecioamide C4–Si bond (2.00 Å), and nearly equal amide C2–C3 and C3–C4 bonds (1.44 and 1.44 Å). Furthermore, a senecioamide C4 – aldehyde oxygen distance (3.17 Å) shorter than the sum of the van der Waals radii is found, consistent with a weak bonding interaction between the two atoms. In contrast, an "inside" trimethylsilyl transition state corresponding to **14** was found to be 2.9 kcal mol^{-1} higher in energy (**17**). The nearest Cl–Si contact (3.85 Å) is larger than the sum of the van der Waals radii. Consequently, the intramolecular transfer of chloride transition state **14** is not supported in our system at this level of calculation.

Scheme 10.

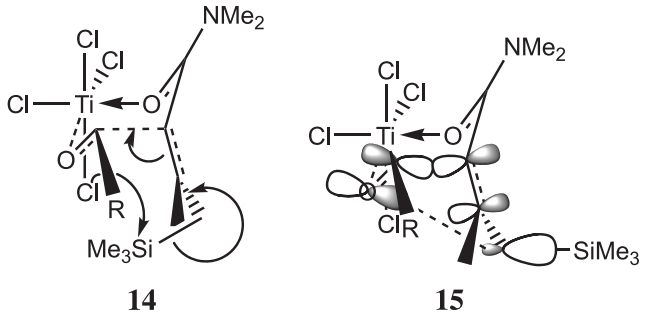

In summary, we have shown that γ-silylated senecioamides **4a**–**4h** are easily obtained by [1,5] O→C silicon migration or direct silylation of the corresponding enolates, depending upon the softness of silyl groups. The isomeric γ-(*Z*)-silylsenecioamides ***Z*-4a** – ***Z*-4c**, ***Z*-4e** – ***Z*-4g** are obtained by the O→C silicon migration but also are formed from the direct silylation reactions, whereas the corresponding *E*-isomers are exclusively or near-exclusively formed from the direct silylation process. The simplest γ-silylseneciomamide serves as a stable and easily stored (>1 year at –20 °C) senecioamide dienolate equivalent. Fluoride-catalyzed reactivity of ***Z*-4a** with aromatic aldehydes or

Can. J. Chem. Downloaded from www.nrcresearchpress.com by Sichuan Normal University on 09/14/12
For personal use only.

Can. J. Chem. Downloaded from www.nrcresearchpress.com by Sichuan Normal University on 09/14/12
For personal use only.

Scheme 11. DFT-minimized transition states of **15**, **14**, R = CH_3.

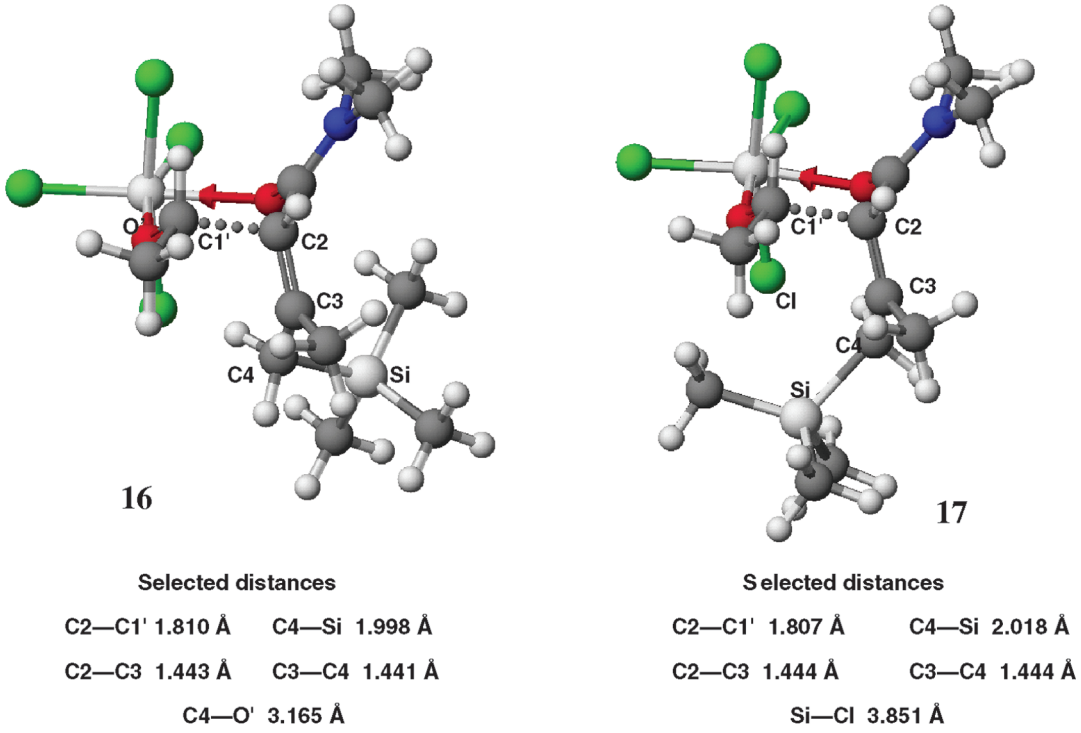

benzophenone shows product patterns analogous to those observed in dienolate chemistry, [2,3a] which is therefore consistent with, but not proof of, reaction via free enolates. The reaction of ***Z*-4a** with aromatic and aliphatic aldehydes mediated by $TiCl_4$ gives syn-α-condensation products **6a**–**6h**, and is proposed to proceed by a chair-like transition state featuring bidentate coordination to titanium (**11**). Further refinement by DFT calculations suggest involvement of the "outside TMS" **15** over the "inside TMS" **14** transition state. Although limited in scope, the diastereoselectivity observed for the $TiCl_4$-mediated reactions of α,β-unsaturated amides is complementary to that observed on analogous stannyl- and germyl-senecioates.[21,22]

The utility of the reported chemistry for the construction of diasteriomerically pure functionalized amides, especially in view of the recent availability of a mild method for amide to aldehyde conversion using the Schwartz reagent,[37] and adaption to enantioinduction modes of reaction may create further opportunities in synthetic chemistry.

Experimental section

General methods

Elemental analyses were performed by M-H-W Laboratories, Phoenix, Arizona. Melting points were determined on a Buchi SMP-20 instrument and are uncorrected. Infrared spectra were determined on a PerkinElmer 983 spectrophotometer. ^{1}H NMR spectra were determined with Bruker WP-80, Bruker AM-250, and Bruker Avance-500 spectrometers. The spectra were recorded at 80 MHz in $CDCl_3$ with tetramethylsilane as an internal standard unless otherwise stated. Spectral features are tabulated in the following order: chemical shift (δ, ppm), number of protons; multiplicity (s: singlet, d: doublet, t: triplet, q: quartet, sept: septet, m: multiplet, br: broad), coupling constant (*J*, Hz), number of protons; assignment. Low-resolution mass spectra were determined on a VG 7070F instrument at 20 eV unless otherwise stated. High-resolution mass spectra were determined on a VG ZAB-E spectrometer. Analytical gas chromatography (GC) was performed on either a Hewlett Packard 5840 A instrument or a Varian 6500 instrument using commercially available 10% SE-30 packed or capillary columns, respectively. Analytical thin layer chromatography (TLC) was performed using Merck precoated silica gel 60F-254 or aluminum oxide 150F-254 neutral (type T) sheets. Preparative TLC was performed using Merck silica gel 60GF-254 with a plate thickness of 1 mm. Column chromatography was carried out using silica gel 60 (0.063–0.20 mm and 0.04–0.063 mm). "Flash chromatography" refers to the method reported by Still.[38] Liquid chromatography was performed on a Varian 5000 Liquid Chromatography employing a reverse phase (C-18) column, and preparative HPLC was done on a Waters PREP-500 with a SiO_2 column.

All dry solvents were employed after distilling from the appropriate drying agent.[39] Diethyl ether (Et_2O), benzene, and tetrahydrofuran (THF) were distilled from benzophenone-ketyl immediately prior to use. Solutions of *n*-BuLi were titrated with 2,5-dimethoxybenzyl alcohol as a standard.[40] Diisopropylamine was dried and distillated over CaH_2 and stored in brown bottles over 4 Å molecular sieves in a dessicator containing $CaCl_2$. All other reagents were purified according to literature procedures. All lithiation reactions, and fluoride- or Lewis acid mediated reactions of ***Z*-4a** were carried out under high purity nitrogen or argon (Linde). Tetra(*n*-butylammonium) fluoride (TBAF, 1 mol/L in THF) was allowed to sit over 4 Å molecular sieves for approxi-

Can. J. Chem. Downloaded from www.nrcresearchpress.com by Sichuan Normal University on 09/14/12
For personal use only.

mately 15 min prior to use. Amides **1a** and **1c** were prepared by literature procedures.[3a]

The term "–78 °C" refers to the temperature of a CO_2 – acetone bath (normally –75 to –78 °C). The term "at –45 °C" refers to a reaction done in an acetonitrile–CO_2 slush bath (normally –45 to –50 °C). The term "at 0 °C" refers to a reaction done in an ice bath.

The phrase "workup in the usual manner" or "standard workup" refers to addition of saturated aqueous NH_4Cl to the reaction mixture, followed by evaporation of the organic solvent under reduced pressure, extraction of the residue with CH_2Cl_2 or diethyl ether (Et_2O), drying of the organic extract over $MgSO_4$, followed by filtration, and subsequent evaporation to dryness under reduced pressure to afford the crude product. Subsequent chromatography and (or) recrystallization and (or) distillation of the crude material afforded pure products.

DFT calculations were carried out using the B88-PW91 method, and a DZVP basis set, using CAChe® version 6.1.12.33 (see Supplementary data). All stationary points were confirmed via frequency calculations.

General procedure for the formation of lithium dienolates

Preparation of LDA

Diisopropylamine (5 mmol, 0.70 mL) was dissolved in THF (25 mL) and cooled to 0 °C. To this solution, *n*-BuLi (5 mmol) was added by syringe injection over a period of ~30 s. The solution was then stirred for a further 0.5 h at 0 °C.

Lithiation with LDA

Procedure A — The amide in question was added by syringe to 1.05 equiv. of LDA in THF at –78 °C such that the concentration in solution was roughly 0.2 mol/L. This solution was stirred at –78 °C for 1 h prior to electrophile addition.

Procedure B — The amide in question was added by syringe to 1.05 equiv. of LDA in THF at 0 °C such that the concentration in solution was roughly 0.2 mol/L. This solution was stirred at 0 °C for 0.5 h prior to electrophile addition.

Procedure C — The amide in question was added by syringe to 1.05 equiv. of LDA in THF at RT such that the concentration of the amide or amide dienolate in solution was roughly 0.2 mol/L. This solution was stirred at RT for 1 h prior to electrophile addition.

Silylations of lithium dienolates

To the solution of the lithium dienolate in THF at –78 °C was added, by syringe, 1.1 equiv. of the chlorosilane. The resulting solution was stirred at –78 °C for 0.5 h before the low temperature bath was removed and the reaction mixture allowed to warm to RT. Unless the silylating reagent was diphenylmethylsilyl chloride, the reaction mixture was then heated to reflux for the indicated amount of time, after which a standard workup was performed. In the case of chloromethyldiphenylsilane, the reaction mixture was subjected to a standard workup without prior heating.

N,N-*diethylsenecioamide*(N,N-*diethyl-3-methyl-Z-butenamide) 1b*

To a solution of senecioic acid (5.72 g, 57.1 mmol) in benzene (60 mL) under a drying tube was added thionyl chloride (9 mL, 123 mmol). The solution was allowed to stir overnight. The benzene and excess thionyl chloride were removed by evaporation under reduced pressure, and the resulting senecioyl chloride was slowly added to diethylamine (20 mL, 193 mmol) in diethyl ether (75 mL). The resulting mixture was subjected to filtration, and the filtrate was successively washed with H_2O (50 mL), 10% aqueous NaOH (2 × 50 mL), and H_2O (50 mL). The ethereal layer was dried over $MgSO_4$, subjected to filtration, and the filtrate was concentrated in vacuo. Distillation of the crude product gave 6.19 g (70%) of **1b**, bp 37.5–38.5 °C at 0.02 torr (1 torr = 133.322 Pa). IR (neat) ν_{max}: 1653, 1624 cm^{-1}. ^1H NMR, δ: 1.14 (t, *J* = 7, 6H), 1.84 (s, 3H), 1.93 (s, 3H), 3.37 (2 q, overlapping, *J* = 7, 4H), 5.81 (br s, 1H). MS *m/e* (rel. intensity): 155 (M^+, 25), 140(27), 83(100). Anal. calcd. for for $C_9H_{17}NO$: C, 69.63; H, 11.04; N. 9.02. Found: C, 69.70; H, 11.21; N, 9.18.

Z*-N,N,*3-trimethyl-1-trimethylsiloxyl-3-butadienamine 2a

N,*N*-Dimethylsenecioamide **1a** (1.916 g, 15.1 mmol) was lithiated according to procedure C. Chlorotrimethylsilane (1.91 mL, 15.1 mmol) was then added to the solution at 0 °C. After stirring for 20 min, the solvent was evaporated under reduced pressure, and hexane (20 mL) was added. This mixture was subjected to filtration through glass wool, and the hexane filtrate was evaporated under reduced pressure. An NMR spectrum of the crude product revealed the presence of **2a**. ^1H NMR (C_6D_6) δ: 0.18 (s, 9H), 2.06 (s, 3H), 2.26 (s, 6H), 4.48 (s, 1H), 4.67, 5.16 (2 m, 2H). Irradiation of the resonance at 2.26 ppm gave rise to a 7% integrated enhancement of the 4.48 ppm peak. ^{13}C NMR (C_6D_6): 0.4, 24.6, 40.6, 92.0, 109.3, 140.7, 155.1.

Z- and* E-N,N,*3-Methyl-4-trimethylsilyl-2-butenamide Z-4a and* E-*4a

N,*N*-Dimethylsenecioamide **1a** (8.2 mL, 60 mmol) was lithiated according to procedure A and silylated with chlorotrimethylsilane (8.4 mL, 66 mmol) in the normal manner for silylation (reflux 18 h) followed by a standard workup. Preparative HPLC (5:2 hexane – ethyl acetate) gave, in order of elution: ***Z*-4a** (8.9 g, 74%), bp 50–53 °C at 0.01 torr. IR (neat) ν_{max}: 1646 cm^{-1}. ^1H NMR (C_6D_6) δ: 0.11 (s, 9H), 1.66 (d, *J* = 1.4, 3H), 2.41 (d, *J* = 0,6, 2H), 2.54 (br s, 6H), 5.62 (br s, 1H). ^{13}C (125 MHz) δ: –1.0, 25.9, 27.4, 34.9, 37.5, 113.3, 152.1, 168.4. MS *m/e* (rel. intensity): 199 (M^+, 3), 184(100), 157(10), 58(20). Anal. calcd. for $C_{10}H_{21}NOSi$: C, 60.30; H, 10.55; N 7.04. Found: C, 60.22; H, 10.51; N, 7.01. ***E*-4a** (0.1915 g, 2%), bp 61–63 °C at 0.17 torr. IR (neat) ν_{max}: 1610 cm^{-1}. ^1H NMR (C_6D_6) δ: –0.05 (s, 9H), 1.46 (d, *J* = 0.7, 2H), 2.16 (d, *J* = 1.2, 3H), 2.51, 2.70 (2 br s, 6H), 5.60 (br s, 1H). MS *m/e* (rel. intensity): 199 (M^+, 18), 184(100), 155(25), 73(100). Anal. calcd. for $C_{10}H_{21}NOSi$: C, 60.30; H, 10.55; N 7.04. Found: C, 60.27; H, 10.61; N, 7.04. A third frac-

Can. J. Chem. Downloaded from www.nrcresearchpress.com by Sichuan Normal University on 09/14/12
For personal use only.

tion (0.9631 g, 13%) proved to be a mixture of the starting material **1a** and its deconjugated isomer **10a**.[3a]

Z- and E-N,N,*3-Trimethyl-4-triethylsilyl-2-butenamide Z-4b and* E-*4b*

N,*N*-Dimethylsenecioamide, **1a** (0.70 mL, 5.0 mmol), was lithiated according to procedure A, and the resulting dienolate was silylated with 0.92 mL (5.5 mmol) of chlorotriethylsilane in the normal manner. After a standard workup, column chromatography gave, in order of elution: ***Z*-4b** (0.71 g, 58%), bp 83–84 °C at 0.17 torr. IR (neat) ν_{max}: 1642 cm^{-1}. ^{1}H NMR (C_6D_6) δ: 0.5–1.2 (A_2B_3 spin system, 15H), 1.69 (d, *J* = 1.2, 3H), 2.46 (s, 2H), 2.56 (br s, 6H), 5.63 (br s, 1H). MS *m/e* (rel. intensity): 241 (M^+, 4), 226(93), 212(100), 198(45), 115(10), 87(27). HR-MS calcd. for $C_{13}H_{27}NOSi$: 241.1863. Found: 241.1847. ***E*-4b** (0.21 g, 18%), bp 94–96 °C at 0.15 torr. IR (neat) ν_{max}: 1642, 1618 cm^{-1}. ^{1}H NMR (C_6D_6) δ: 0.4–1.0 (A_2B_3 spin system, 15H), 1.54 (d, *J* = 1.0, 2H), 2.19 (d, *J* = 1.5, 3H), 2.51, 2.73 (2 br s, 6H), 5.68 (br s, 1H). MS *m/e* (rel. intensity): 241 (M^+, 8), 226(100), 212(76), 198(93). Anal. calcd. for $C_{13}H_{27}NOSi$: C, 64.67; H, 11.27; N 5.80. Found: C, 64.49; H, 11.11; N, 6.01.

N,*N*-Dimethylsenecioamide, **1a** (0.67 mL, 4.9 mmol) was lithiated according to procedure A. To the resulting dienolate, at –78 °C, was added chlorotriethylsilane (0.92 mL, 5.5 mmol). After stirring the solution for 0.5 h at –78 °C, the solution was allowed to warm to RT, and the solvents were removed under reduced pressure. A small amount of the residual material was removed; the ^{1}H NMR spectrum (C_6D_6) of this sample showed δ 4.35 (s, vinyl CH of **2b**) and δ 5.62 (br s, vinyl CH of ***Z*-** and ***E*-4b**) with rel.ative integrals of 77:23. The rest of the material was worked up in the usual manner, and the resultant crude product subjected to preparative HPLC. Three fractions were isolated. The first fraction (0.048 g, 4%) contained ***Z*-4b** (see above for spectral data). The second fraction (0.20 g, 16%) was shown to be ***E*-4b** (see above for spectral data). The third fraction (0.34 g, 53%) was found to contain a mixture of the starting **1a** and its β,γ-unsaturated isomer **10a**.

Z- and E-N,N,*3-Trimethyl-4-triisopropylsilyl-2-butenamide Z- and* E-*4c*

N,*N*-Dimethylsenecioamide, **1a** (0.66 mL, 4.8 mmol), was lithiated according to procedure A, and the resulting dienolate was silylated with 1.2 mL of chlorotriisopropylsilane (5.5 mmol) in the normal manner (reflux 40 h). Following standard workup, the crude mixture was subjected to preparative HPLC (ethyl acetate – hexane) to give, in order of elution: ***Z*-4c** (0.31 g, 23% bp 80–85 °C at 0.005 torr. IR (neat) ν_{max}: 1641 cm^{-1}. ^{1}H NMR (C_6D_6, 250 MHz) δ: 1.1–1.3 (AB, spin system, 21H), 1.76 (d, *J* = 1.2, 3H), 2.40, 2.71 (2 br s, 6H), 2.59 (s, 2H), 5.64 (s, 1H). MS *m/e* (rel. intensity): 283 (M^+, 1), 268(6), 240(100), 226(18). HR-MS calcd. for $C_{16}H_{33}NOSi$: 283.2333. Found: 283.2314. ***E*-4c** (0.18 g, 14%), bp 70–4 °C at 0.005 torr. IR (neat) ν_{max}: 1641 cm^{-1}. ^{1}H NMR (C_6D_6) δ: 1.05–1.2 (AB_6 spin system, 21H), 1.76 (d, *J* = 1.0, 3H), 2.51 (br s, 6H), 2.57 (s, 2H), 5.64 (br s, 1H). MS *m/e* (rel. intensity): 283 (M^+, 3), 268(7), 240(100), 226(22). Anal. calcd. for $C_{16}H_{33}NOSi$: C, 67.78; H, 11.73; N, 4.94. Found: C, 67.58; H, 11.96; N; 5.18. A mixture of the starting material and its deconjugated double bond isomer **10a** (0.140 g, 23%).

Z- and E-N,N,*3-Trimethyl-3-methyl-4-methyldiphenylsilyl-2-butenamide Z- and* E-*4d*

N,*N*-Dimethylsenecioamide, **1a** (0.275 mL, 2.0 mmol), was lithiated according to procedure A, and the resulting dienolate was silylated with diphenylmethylsilyl chloride (0.46 mL, 2.2 mmol) in the normal manner (no reflux). The crude reaction mixture was subjected to preparative TLC (3:1 hexane – ethyl acetate) to give two fractions, in order of elution: ***Z*-4d** (0.214 g, 33%), mp 56–58 °C (petroleum ether). IR (CCl_4) ν_{max}: 1633, 1610 cm^{-1}. ^{1}H NMR δ: 0.58 (s, 3H), 1.64 (s, 3H), 2.83 (2 s, overlapping, 8H), 5.69 (s, 1H), 7.2–7.7 (m, 10H). MS *m/e* (rel. intensity): 323 (M^+, 12), 308(100), 246(18), 232(22), 197(100). Anal. calcd. for $C_{20}H_{25}NOSi$: C, 74.25; H, 7.79; N, 4.33. Found: C, 74.48; H, 7.87; N, 4.38. ***E*-4d** (0.380 g, 59%), mp 50.5–51.5 °C (petroleum ether). IR (neat) ν_{max}: 1639, 1613 cm^{-1}. ^{1}H NMR δ: 0.63 (s, 3H), 1.87 (d, *J* = 1.0, 3H), 2.20 (s, 2H), 2.64, 2.87 (2s, 6H), 5.55 (br s, 1H). MS *m/e* (rel. intensity): 323 (M^+, 4), 308(45), 232(12), 197(100). Anal. calcd. for $C_{20}H_{25}NOSi$: C, 74.25; H, 7.79; N, 4.33. Found: C, 74.07; H, 7.83; N, 4.33.

Z- and E-N,N-*Diethyl-3-methyl-4-trimethylsilyl-2-butenamide Z- and* E-*4e*

N,*N*-Diethylsenecioamide, **1b** (0.780 g, 5.02 mmol), was lithiated according to procedure A, and the resulting dienolate was silylated with chlorotrimethylsilane (0.7 mL, 5.5 mmol) in the normal manner (reflux 17 h). The crude reaction mixture was subjected to preparative HPLC (3:1 hexane – ethyl acetate) to give, in order of elution: ***Z*-4e** (0.446 g, 39%), bp 90–95 °C at 0.6 torr. IR (neat) ν_{max}: 1637, 1612 cm^{-1}. ^{1}H NMR (C_6D_6) δ: 0.15 (s, 9H), 0.90 (br, 12H), 1.68 (d, *J* = 1.5, H), 5.51 (s, 2H), 3.10 (br, 2H), 5.70 (br s, 1H). MS *m/e* (rel. intensity): 227(2), 212(100), 73(30). Anal. calcd. for $C_{12}H_{25}NOSi$: C, 63.38; H, 11.08; N, 6.16. Found: C, 63.19; H, 10.92; N, 6.20. ***E*-4e** (0.395 g, 35%), bp 65–70 °C at 0.005 torr. IR (neat) ν_{max}: 1641, 1617 cm^{-1}. ^{1}H NMR (C_6D_6) δ: –0.05 (s, 9H), 0.93 (br, 12H), 1.47 (d, *J* = 1.0, 2H), 2.18 (d, *J* = 1.5, 3H), 3.16 (br, 2H), 5.66 (br s, 1H). MS *m/e* (rel. intensity): 227 (M^+, 8), 212(100), 155(26), 73(113). Anal. calcd. for $C_{12}H_{25}NOSi$: C, 63.38; H, 11.08; N, 6.16. Found: C, 63.64; H, 11.43; N, 6.57. A mixture of the starting material ***Z*-4e** and its deconjugated double bond isomer **10b** (0.0912 g, 12%).

Z- and E-N,N-*Diethyl-3-nethyl-4-triethylsilyl-2-butenamide Z- and* E-*4f*

N,*N*-Diethylsenecioamide, **1b** (0.6606 g, 5.03 mmol) was lithiated according to procedure A, and the resulting dienolate was silylated with chlorotriethylsilane (0.88 mL, 5.5 mmol) in the usual manner (reflux, 18 h). After a standard workup, flash chromatography (fine silica, 8:l hexane – ethyl acetate) yielded, in order of elution, two significant fractions: ***Z*-4f** (0.2805 g, 21%), bp 95–100 °C at 0.01 torr. IR (neat) ν_{max}: 1637, 1614 cm^{-1}. ^{1}H NMR (C_6D_6) δ: 0.5–1.2 (m, 21H), 1.71 (d, *J* = 1.2, 3H), 2.54 (s, 2H), 3.05 (br, 4H), 5.69 (br s, 1H). MS *m/e* (rel. intensity): 269 (M^+, 3), 254(100), 240(88), 226(22), HR-MS calcd. for $C_{15}H_{31}NOSi$:

Can. J. Chem. Downloaded from www.nrcresearchpress.com by Sichuan Normal University on 09/14/12
For personal use only.

269.2176. Found: 269.2152. ***E*-4f** (0.6270 g, 47%), bp 79–83 °C at 0.01 torr. IR (neat) ν_{max}: 1641, 1616 cm^{-1}. ^{1}H NMR (C_6D_6) δ: 0.3–1.1 (m, 21H), 1.55 (s, 2H), 2.22 (d, J = 1.2, 3H), 3.15 (br, 4H), 5.73 (br s, 1H). MS *m/e* (rel. intensity): 269 (M$^+$, 6), 254(100), 240(31), 226(23). Anal. calcd. for $C_{15}H_{31}NOSi$: C, 66.85; H, 11.59; N, 5.28. Found: C, 67.04; H, 11.35; N, 5.28.

Z- and E-N,N-*Diisopropyl-3-methyl-4-trimethylsilyl-2-butenamide* Z- *and* E-*4g*

N,*N*-Diisopropylsenecioamide **1c** (1.03 mL, 5 mmol) was lithiated according to procedure A. To the resulting solution of the dienolate was added, at –78 °C, 0.70 mL (5.5 mmol) of chlorotrimethylsilane. The mixture was allowed to stir at –78 °C for 15 min before warming to RT, and subsequent heating to 40 °C for 36 h. After a standard workup, the crude product was subjected to preparative HPLC (5:1 hexane – ethyl acetate), resulting, in order of elution, in two fractions: ***Z*-4g** (0.290 g, 23%), bp 57–60 °C at 0.02 torr. IR (neat) ν_{max}: 1649, 1632 cm^{-1}. ^{1}H NMR (C_6D_6) δ: 0.13 (s, 9H), 1.15 (br, 12H), 1.67 (d, J = 1.4, 3H), 2.33 (s, 2H), 3.54 (br, 2H), 5.64 (br s, 1H). MS *m/e* (rel. intensity): 255 (M$^+$, 4), 240(100), 212(66), 198(22), 171(25), 155(32), 73(145). Anal. calcd. for $C_{14}H_{29}NOSi$: C, 65.82; H, 11.44; N, 5.48. Found: C, 66.00; H, 11.46; N, 5.58. ***E*-4g**, bp 64–66 °C at 0.02 torr. IR (neat) ν_{max}: 1626 cm^{-1}. ^{1}H NMR (C_6D_6) δ: –0.04 (s, 9H), 1.21 (br, 12H), 1.45 (s, 2H), 2.00 (d, J = 1.2, 2H), 3.62 (br, 2H), 5.59 (br s, 1H). MS *m/e* (rel. intensity): 255 (M$^+$, 11), 240(36), 212(38), 155(100), 73(144). Anal. calcd. for $C_{14}H_{29}NOSi$: C, 65.82; H, 11.44; N, 5.48. Found: C, 65.66; H, 11:22; N, 5.49.

Z- and E-N,N-*Diisopropyl-3-methyl-4-methyldiphenylsilyl-2-butenamide* Z- *and* E-*4h*

N,*N*-Diisopropylsenecioamide (0.9223 g, 5.03 mmol) was lithiated according to procedure A, and the resulting dienolate was treated with chloromethyldiphenylsilane (1.16 mL, 5.5 mmol) in the normal manner (no subsequent heating). After a standard workup, the crude product was subjected to column chromatography (4:1 hexane – ethyl acetate), yielding, in order of elution, two fractions: ***Z*-4h** (1.025 g, 54%), mp 56–58 °C (hexane). IR (neat) ν_{max}: 1636, 1615 cm^{-1}. ^{1}H NMR δ: 0.58 (s, 3H), 1.26 (br, 12H), 1.56 (d, J = 1.5, 3H), 2.80 (s, 2H), 3.78 (br, 2H), 5.68 (br s, 1H), 7.2–7.7 (m, 10H). MS *m/e* (rel. intensity): 379 (M$^+$, 7), 364(61), 336(35), 295(23), 197(100). Anal. calcd. for $C_{24}H_{33}NOSi$: C, 75.60; H, 8.76; N, 3.69. Found: C, 75.72; H, 8.67; N, 3.64. ***E*-4h** (0.7200 g, 38%), bp 170–175 °C at 0.005 torr. IR (neat) ν_{max}: 1644, 1620 cm^{-1}. ^{1}H NMR δ: 0.63 (s, 3H), 1.12 (br, 12H), 1.77 (d, J = 1.2, 3H), 2.17 (s, 2H), 3.47 (br, 2H), 5.46 (br s, 1H), 7.2–7.7 (m, 10H, $2C_6H_5$). MS *m/e* (rel. intensity): 379 (M$^+$, 7), 364(58), 336(34), 295(22), 197(100). Anal. calcd. for $C_{24}H_{33}NOSi$: C, 75.93; H, 8.76; N, 3;69; Found: C, 75.60; H, 8.53; N, 3.96.

TBAF-mediated aldol condensations of Z-4a

Thermodynamic conditions

To a 0.3–0.4 mol/L solution of ***Z*-4a** in THF under an inert atmosphere was added 1.2 equiv. of the aldehyde or ketone in question. Five mol% of a 1 mol/L solution of tetra(*n*-butylammonium) fluoride (in THF) was then added by syringe. The resulting brown solution was stirred at ambient temperature for 16 h and worked up in the usual manner.

Kinetic conditions

To a 0.3–0.4 mol/L solution of ***Z*-4a** in THF under an inert atmosphere was added 1.2 equiv. of the aldehyde or ketone in question. The solution was cooled to –45 °C before a 1 mol/L solution of TBAF (in THF) was added by syringe. The resulting solution was stirred at –45 °C for 2 min before saturated aqueous NH_4Cl was added (at –45 °C), and a standard workup was performed.

$TiCl_4$-mediated aldol condensations of Z-4a

To 1.2 equiv. of the aldehyde in question under an inert atmosphere was added CH_2Cl_2 such that the eventual concentration of ***Z*-4a** was 0.3 mol/L. This solution was cooled to 0 °C, 1.1 equiv. of $TiCl_4$ was added by syringe, and the mixture was allowed to stir for 5 min. At this point, a solution of ***Z*-4a**, in a minimum amount of CH_2Cl_2, was added by syringe. The ice-bath was immediately removed, and the reaction mixture was allowed to stir for 3 h during which time it reached ambient temperature. A standard workup was then performed.

syn- *and* anti-Z-*Hydroxyphenylmethyl-N,N,3-trimethyl-3-butenamide* syn- *and* anti-*6a*

$TiCl_4$-mediated reaction

A mixture of compound ***Z*-4a** (0.3247 g, 1.63 mmol) and benzaldehyde (0.20 mL) in the presence of $TiC1_4$ (0.20 mL) was allowed to react in the manner described earlier. After a standard workup, column chromatography (1:l hexane – ethyl acetate) gave one fraction, 0.2763 g, which proved to be a 90:10 mixture (by ^{1}H NMR integration) of ***syn*-6a** (67%) and starting material ***Z*-4a** (7%). Recrystallization gave pure ***syn*-6a**, mp 59.5–61 °C (Et_2O – petroleum ether) (Lit.[3a] 59–61 °C (Et_2O – hexane)) whose ^{1}H NMR spectral data were identical to those reported.[3a]

TBAF-mediated reaction

A mixture of compound ***Z*-4a** (0.3217 g, 1.61 mmol) and benzaldehyde (0.20 mL) in the presence of TBAF (1.61 mL of a 1 mol/L solution) was allowed to react under the previously described kinetic control conditions. After a standard workup, the crude reaction mixture was subjected to preparative TLC (5:2 ethyl acetate – hexane) to give, in order of elution: ***syn*-6a** (0.1145 g, 30%), and 72:16:12 mixture (by ^{1}H NMR integration) (0.1610 g) of ***anti*-6a** (33%), ***Z*-4a** (6%), and desilylated material (7%). ***anti*-6a** was purified by recrystallization, mp 113–114 °C (CH_2Cl_2 – hexane) (Lit.[3a] 114–114.5 °C (Et_2O)) and showed ^{1}H NMR spectral data consistent with those reported.[3a]

Z- *and* E-*5-Hydroxy*-N,N,*3-trimethyl-5-phenyl-2-pentenamide* Z- *and* E-*5a*

A mixture of compound ***Z*-4a** (0.3770 g, 1.89 mmol) and benzaldehyde (0.23 mL) in the presence of TBAF (0.1 mL of a 1 mol/L solution) was allowed to react under the previously described thermodynamic control conditions. Following a workup in the usual manner, separation by flash chromatography (fine silica, 4:l ethyl acetate – hexane) gave, in order of elution: ***Z*-5a** (0.2564 g, 58%), mp 75–

Can. J. Chem. Downloaded from www.nrcresearchpress.com by Sichuan Normal University on 09/14/12
For personal use only.

77 °C (CH_2Cl_2 – hexane) (Lit.[3a] 76–76.5 °C (CH_2Cl_2 – hexane)), and ***E*-5a** (0.0625 g, 14%) as an undistillable viscous oil. IR (neat) ν_{max}: 1647, 1606 cm^{-1}. ^1H NMR δ: 1.89 (d, *J* = 1.2, 3H), 2.49 (d, *J* = 7, 2H), 2.81, 2.90 (2s, 6H), 3.51 (br, 1H, exchangeable), 4.85 (t, *J* = 7, 1H), 5.76 (br s, 1H), 7.32 (s, 5H). MS *m/e* (rel. intensity): 234 (M^+ + l, 3), 215(11), 127(100), 112(25). HR-MS calcd. for $C_{14}H_{19}NO_2$ + H: 234.1495. Found: 234.1492.

syn- *and* anti-*2-(3,4-Dimethoxy)phenylhydroxyethyl*-N,N,*3-trimethyl-3-butenamide* syn- *and* anti-*6b*

A mixture of compound ***Z*-4a** (0.2752 g, 1.38 mmol) and veratraldehyde (0.3238 g) in the presence of TBAF (1.38 mL of a 1 mol/L solution) was allowed to react under the previously described kinetic control conditions. After a standard workup, the crude reaction mixture was subjected to preparative TLC (5:2 ethyl acetate – hexane) yielding two fractions. The first fraction (0.123 g) was identified by ^1H NMR spectroscopy as a 79:21 mixture of ***syn*-6b** (25%) and desilylated starting material (7%) from which ***syn*-6b** was obtained by recrystallization, mp 102–103 °C (Et_2O – hexane) (Lit.[3a] 100–1.5 °C (Et_2O – hexane)). The second fraction (0.1197 g) was shown to be 81:19 mixture (by ^1H NMR spectroscopy) of ***anti*-6b** (27%) and ***Z*-5b** (6%) from which ***anti*-6b** was obtained by recrystallization, mp 120–12l °C (Et_2O) (Lit.[3a] 118 °C (CH_2C1_2 – hexane)). Products ***syn*-6b** and ***anti*-6b** showed ^1H NMR spectral data consistent with those reported.[3a]

Z- and E-*5-(3,4-Dimethoxy)phenyl-5-hydroxy*-N,N,*3-trimethyl-2-pentenamide Z- and E-5b*

A mixture of compound ***Z*-4a** (0.4695 g, 2.36 mmol) and veratraldehyde (0.4695 g) in the presence of a catalytic amount of TBAF (0.12 mL of a 1 mol/L solution) was allowed to react under the previously described thermodynamic control conditions, followed by workup under the usual conditions. The crude mixture was subjected to column chromatography, yielding three fractions. Fraction 1 (0.067 g, 12%) was shown to be desilylated starting material **1a/10a**. Fraction 2 (0.3520 g, 49%) was shown to be ***Z*-5b**, mp 78–80 °C (CH_2C1_2 – hexane) (Lit.[3a] 78–80 °C (CH_2Cl_2 – hexane)) by comparison with its ^1H NMR spectra with that reported.[3a] Fraction 3 (0.1880 g, 26%) proved to be ***E*-5b** as an undistillable viscous oil. IR (neat) ν_{max}: 3378, 1646, 1608 cm^{-1}. ^1H NMR δ: 1.93 (d, *J* = 1.2, 3H), 2.50 (d, *J* = 7, 2H), 2.90, 2.94 (2s, 6H), 3.87, 3.89 (2s, 6H), 4.83 (t, *J* = 7, 1H), 5.82 (br s, 1H), 6.8–7.0 (m, 3H), OH not observed. MS *m/e* (rel. intensity): 293 (M^+, 3), 127(100), 112(27). HR-MS calcd. for $C_{16}H_{23}NO_4$: 293.1628. Found: 293.1629.

Z- and E-*5-Hydroxy-5-(3-pyridyl)*-N,N,*3-trimethyl-2-pentenamide Z- and E-5c*

A mixture of compound ***Z*-4a** (0.3428 g, 1.72 mmol) and 3-pyridinecarboxaldehyde (0.18 mL) in the presence of a catalytic amount of TBAF (0.17 mL of a 1 mol/L solution) was allowed to react under the previously described thermodynamic control conditions. Following a standard workup, the crude product was subjected to column chromatography (100% acetone) yielding two fractions. Fraction 1 was shown to contain ***Z*-5c** (0.2289 g, 57%) as an undistillable, viscous oil. IR (neat) ν_{max}: 3223, 1648, 1598 cm^{-1}. ^1H NMR δ: 1.96 (d, *J* = 1.4, 3H, CH_3), 2.32 (dd, *J* = 13 and 3.5, 1H), 3.01, 3.05 (2s, 6H), 3.0 (obscured, 1H), 4.89 (dd, *J* = 10 and 3, 1H), 6.16 (br s, 1H), 6.2 (br, 1H, exchangeable), 7.27 (m, 1H), 7.87 (m, 1H), 8.4–8.7 (m, 2H). MS *m/e* (rel. intensity): 235 (M^+ + l, 4), 189(44), 162(29), 144(86), 112(100). HR-MS calcd. for $C_{13}H_{18}N_2O_2$ + H: 235.1448. Found: 235.1452. Fraction 2 was shown to be ***E*-5c** (0.0536 g, 13%) as an undistillable, viscous oil. IR (neat) ν_{max}: 3344, 1646, 1607 cm^{-1}. ^1H NMR δ: 1.92 (s, 3H), 2.49 (d, *J* = 7, 2H), 2.87, 2.91 (2s, 6H), 4.6 (br, 1H, exchangeable), 4.92 (t, *J* = 7, 1H), 5.81 (br s, lH), 7.28 (m, 1H), 7.73 (m, 1H), 8.52 (m, 2H). MS *m/e* (rel. intensity): 234 (M^+, 2), 216(40), 171(44), 144(63), 127(100), 109(63). HR-MS calcd. for $C_{13}H_{18}N_2O_2$: 234.1369. Found: 234.1362.

syn- *and* anti-*2-Hydroxy(4-pyridyl)methyl*-N,N,*3-trimethyl-3-butenamide* syn- *and* anti-*6d and Z-5-Hydroxy-5-(4-pyridyl)*-N,N,*3-trimethyl-2-pentenamide Z-5d*

TBAF-mediated reaction

A mixture of compound ***Z*-4a** (0.2720 g, 1.36 mmol) and 4-pyridinecarboxaldehyde (1.9 mL) in the presence of TBAF (1.37 mL of a 1 mol/L solution) was allowed to react under kinetic control conditions. After a standard workup, the resulting crude product was subjected to preparative TLC (in 1: 1 ethyl acetate – acetone) to give, in order of elution, three fractions identified by ^1H NMR spectroscopy: Fraction 1 (0.0364 g, 13%) was shown to be starting ***Z*-4a**. Fraction 2 was identified as a 1:l mixture of ***syn*-** and ***anti*-6d** (0.1718 g), while fraction 3 was shown to be a 35:65 mixture of ***anti*-6d** and ***Z*- 5d** (0.0646 g). The individual isomers of **6d** were purified by recrystallization: ***syn*-6d** (27%), mp 111–113 °C (CH_2Cl_2 – Et_2O – hexane) (Lit.[3a] 98–99 °C (CH_2Cl_2 – hexane)), mixture mp 109–116 °C. ***anti*-6d** (34%), mp 125 °C (CH_2Cl_2 – hexane) (Lit.[3a] 128–129 °C (CH_2Cl_2 – hexane)). Compounds ***syn*-6d** and ***anti*-6d** showed ^1H NMR spectral data consistent with those reported.[3a] Compound ***Z*-5d** (13%) was identified by its ^1H NMR spectrum (see below).

A mixture of compound ***Z*-4a** (0.3804 g, 1.908 mmol) and 4-pyridinecarboxaldehyde in the presence of TBAF (0.10 mL of a 1 mol/L solution) was allowed to react under thermodynamic control conditions. After a standard workup, chromatography on aluminum oxide (activity III, 5:2 ethyl acetate – hexane) gave two fractions. Fraction 1 (0.2813 g) was identified as a 2:l mixture of ***Z*-5d** (42%) and ***syn*-6d** (21%). Fraction 2 proved to be ***anti*-6d** (0.0743 g, 17%). Compound ***Z*- 5d** was further purified by repeated preparative TLC, but remained a viscous, undistillable oil. IR (neat) ν_{max}: 3229, 1637, 1598 cm^{-1}. ^1H NMR δ: 1.95 (s, 3H), 2.33 (d, *J* = 13 and 3, 1H), 3.00, 3.05 (2s, 6H), 3.0 (obscured, 1H), 4.85 (br d, *J* = 10, 1H), 6.17 (br s, 1H), 7.35, 8.55 (AA′BB′ spin system, *J* = 6, 4H), OH not observed. MS *m/e* (rel. intensity): 235 (M^+ + l, 2), 216(33), 127(100), 112(68), 83(30). HR-MS calcd. for $C_{13}H_{18}N_2O_2$ + H: 235.1448. Found: 235.1454.

syn- *and* anti-*2-Hydroxy(4-nitro)phenylmethyl*-N,N,*3-trimethyl-3-butenamide* syn- *and* anti-*6e and Z-5-Hydroxy-5-(4-nitro)phenyl*-N,N,*3-trimethyl-2-pentenamide Z-5e*

$TiCl_4$-mediated reaction

A mixture of compound ***Z*-4a** (0.3766 g, 1.89 mmol) and

Can. J. Chem. Downloaded from www.nrcresearchpress.com by Sichuan Normal University on 09/14/12
For personal use only.

4-nitrobenzaldehyde (0.3429 g) in the presence of $TiC1_4$ (0.23 mL) was allowed to react under the previously described conditions. After a standard workup, the crude reaction product was subjected to column chromatography (3:2 ethyl acetate – hexane) to give in order of elution: ***syn*-6e** (0.3578 9, 73%), mp 119.5–121 °C (Et_2O – hexane). IR ($CHCl_3$) ν_{max}: 3404, 1624 cm^{-1}. ^1H NMR δ: 1.64 (s, 3H), 2.96 (s, 6H), 3.42 (d, J = 3.7, 1H), 4.51, 4.96 (2s, 2H), 5.26 (s, 1H, exchangeable), 5.36 (d, J = 3.7, 1H), 7.54 and 8.18 (AA′BB′ spin system, J = 9, 4H). MS *m/e* (rel. intensity): 278 (M^+, 1), 127(100), 112(90), 83(100). Anal. calcd. for $C_{14}H_{18}N_2O_4$: C, 60.42; H, 6.52; N, 10.07. Found: C, 60.66; H, 6.51; N, 10.21. ***anti*-6e** (0.0047 g, 1%), mp 177–178 °C (CH_2Cl_2 – hexane). IR ($CHCl_3$) ν_{max}: 3443, 1626 cm^{-1}. ^1H NMR δ, 1.69 (s, 3H),. 2.91, 2.94 (2s, 6H), 3.41 (d, J = 6, 1H), 4.65–5.25 (m, 4H; on addition of D_2O gives 4.73 (s, 1H), 4.96 (s, 1H), 5.11 (d, J = 6, 1H)), 7.53, 8.19 (AA′BB′ spin system, J = 8, 4H). MS *m/e* (rel. intensity): 278 (M^+, 1), 127(100), 112(38), 83(89). Anal. calcd.. for $C_{14}H_{18}N_2O_4$: C, 60.42; H, 6.52; N, 10.07. Found: C, 60.54; H, 6.45; N, 10.06.

TBAF-mediated reaction

A mixture of compound ***Z*-4a** (0.3061 g, 1.54 mmol) and 4-nitrobenzaldehyde (0.3139 g) in the presence of TBAF (1.55 mL of a 1 mol/L solution) was allowed to reaction under the previously described kinetic control conditions. Following a standard workup, preparative (5:2 ethyl acetate – hexane) TLC of the crude product gave, in order of elution: recovered ***Z*-4a** (0.0096 g, 3%), ***syn*-6e** (0.1082 g, 25%), and a 51:49 mixture (by ^1H NMR spectroscopy) of ***anti*-6e** (31%) and ***Z*-5e** (30%) (0.2631 g). Compound ***Z*-5e** was obtained by crystallization, mp 113–115 °C (CH_2Cl_2 – Et_2O – hexane). IR ($CHCl_3$) ν_{max}: 3194, 1650, 1598 cm^{-1}. ^1H NMR δ: 1.95 (s, 3H), 2.33 (dd, J = 13 and 3), 3.0 (obscured, 1H), 3.01, 3.06 (2 s, 6H), 4.94 (m, 1H; on addition of D_2O becomes dd, J = 10 and 3), 6.18 (br s, 1H), 7.19 (d, J = 6, 1H, exchangeable), 7.63, 8.20 (AA′BB′ spin system, J = 9, 4H). MS *m/e* (rel. intensity): 278 (M^+, 2), 260(37), 216(39), 127(100), 112(97), 83(100). Anal. calcd. for $C_{14}H_{18}N_2O_4$: C, 60.42; H, 6.52; N, 10.07. Found: C, 60.35; H, 6.44; N, 9.93.

A mixture of compound ***Z*-4a** (0.3053 g, 1.53 mmol) and 4-nitrobenzaldehyde (0.2905 g) in the presence of TBAF (0.08 mL of a 1 mol/L solution) was allowed to reaction under the previously described thermodynamic control conditions. After a standard workup, the crude product was subjected to column chromatography (2:1 – 4:1 ethyl acetate – hexane) to give, in order of elution, two fractions: ***syn*-6e** (0.0926 g, 22%) and a 46:54 mixture of ***anti*-6e** (27%) and ***Z*-5e** (31%) (0.2468 g).

Z-5-Hydroxy-N,N,*3-trimethyl-5,5-diphenyl-2-pentenamide Z-5g and Z- and* E-N,N,*3-trimethyl-5,5-diphenyl-5-trimethylsiloxy-2-pentenamide Z- and* E-*5f*

TBAF-mediated reaction

To a solution of ***Z*-4a** (0.4794 g, 2.40 mmol) and benzophenone (0.5461 g, 1.24 equiv.) in 5 mL of THF cooled to –45 °C was added TBAF (0.12 mL of a 1 mol/L solution in THF, 5 mol%). After stirring for 1 h at –45 °C, the reaction mixture was quenched with saturated aqueous NH_4Cl (at –45 °C) and was worked up in the usual manner. The resultant crude product was subjected to flash chromatography (fine silica, 3:1 – 9:1 ethyl acetate – hexane), to give, in order of elution: ***Z*-5f** (0.1872 g, 20%). IR (neat) ν_{max}: 1623 cm^{-1}. ^1H NMR (C_6D_6) δ: –0.13 (s, 9H), 1.92 (s, 3H), 2.34, 2.78 (2s, 6H), 3.76 (s, 2H), 5.57 (br s, 1H), 7.36 (apparent s, 10H). This compound slowly underwent desilylation on standing to give ***Z*-5g**, mp 143–145 °C (Et_2O – petroleum ether). IR ($CHCl_3$) ν_{max}: 3191, 1643, 1598. cm^{-1}. ^1H NMR δ: 1.25 (s, 3H), 2.96, 3.03 (2 s, 6H), 3.42 (s, 2H), 6.08 (br s, 1H), 7.1–7.7 (m, 10H), 7.41 (s, 1H, exchangeable). MS *m/e* (rel. intensity): 291 (M^+ –18, 8), 182(49), 128(41), 105(100), 84(24), 77(48), 72(32). Anal. calcd. for C_{20} $H_{23}NO_2$: C, 77.64; H, 7.49; N, 4.53. Found: C, 77.16; H, 7.46; N, 4.62. ***E*-5f** (0.4418 g, 48%), mp 65–67 °C (Et_2O – petroleum ether). IR ($CHCl_3$) ν_{max}: 1646, 1610 cm^{-1}. ^1H NMR (C_6D_6) δ: –0.12 (s, 9H), 1.71 (s, 3H), 2.36, 2.81 (2s, 6H), 3.18 (s, 2H), 5.45 (br s, 1H), 7.25 (s, 10H). MS *m/e* (rel. intensity): 366 (M^+ – 15, 2), 291(6), 255(100), 199(28), 73(100). Anal. calcd. for $C_{22}H_{31}NO_2Si$: C, 72.39; H, 8.19; N, 3.67. Found: C, 72.62; H, 8.25; N, 3.80.

$TiCl_4$-mediated reaction

A mixture of compound ***Z*-4a** (0.211 g, 1.06 mmol) and benzophenone (0.273 g) in the presence of $TiC1_4$ (0.23 mL) was allowed to react under the previously described conditions. After a standard workup, the crude reaction product was subjected to column chromatography (3:1 ethyl acetate – hexane) to afford **6g** (0.236 g, 72%), whose spectroscopic data was shown to be identical with those reported.[3a]

Z- and* E-N,N,*3-Trimethyl-5,5-diphenyl-2,4-butadienamide Z- and* E-*7

A mixture of compound ***Z*-4a** (0.5210 g, 2.61 mmol) and benzophenone (1.6385 g, 3 equiv.) in the presence of TBAF (0.13 mL of a 1 mol/L solution) was allowed to react under thermodynamic conditions. After a standard workup, the crude product was subjected to flash chromatography (4:1 – 9:1 ethyl acetate – hexane) to give a mixture of ***Z*-** and ***E*-7** (0.2815 g, 29%), bp 145–150 °C at 0.01 torr. IR (neat) ν_{max}: 1630 cm^{-1}. ^1H NMR δ: 1.56 and 1.81 (s, 3H), 2.65 and 2.89 (s, 6H), 5.89 (br s, 1H), 6.55 and 7.24 (obscured) (br s, 1H), 7.24 (s, 10H). The relative integrals of the 1.8 and 1.56 peaks established the ratio of ***E*-7:*Z*-7** as 65:35. MS *m/e* (rel. intensity): 291 (M^+, 38), 219(100), 214(25), 204(49). HR-MS calcd. for $C_{20}H_{21}NO$: 291.1624. Found: 291.1631.

syn- *and* anti-*2-(1-Hydroxy-l-propyl)*-N,N,*3-trimethyl-3-butenamide* syn- *and* anti-*6h***

A mixture of compound ***Z*-4a** (0.4114 g, 2.06 mmol) and butanal (0.22 mL) in the presence of $TiCl_4$ (0.25 mL) was allowed to react under the previously described conditions. Following standard workup, the crude reaction product was subjected to column chromatography (2:l hexane – ethyl acetate) to give, in order of elution: ***syn*-6h** (0.2552 g, 62%), mp 44–45 °C (Et_2O – hexane) (Lit.[3a] 44–46 °C (Et_2O – hexane)). ***anti*-6h** (0.0097 g, 2%), mp 68–70 °C (CH_2Cl_2 – hexane) (Lit.[3a] 70 °C (CH_2Cl_2 – hexane)) both of which were shown to exhibit ^1H NMR spectral data consistent with their structures,[3a] and a mixture of desilylated 2- and 3-butenamides (0.0391 g, 14%).

Can. J. Chem. Downloaded from www.nrcresearchpress.com by Sichuan Normal University on 09/14/12
For personal use only.

syn- ***and*** **anti-*2-(1-Hydroxy-2-propyl)*-N,N,*3-trimethyl-3-butenamide* syn-** ***and*** **anti-*6i***

A mixture of compound ***Z*-4a** (0.3818 g, 1.92 mmol) and 2-methylpropanal (0.21 mL) in the presence of $TiC1_4$ (0.23 mL) was allowed to react under the previously described conditions. After workup in the usual manner, the crude reaction product was subjected to column chromatography (1:1 – 2:1 ethyl acetate – hexane) to give, in order of elution, two fractions: ***syn*-6i** (0.1520 g, 40%), mp 74–74.5 °C (hexane). IR (neat) ν_{max}: 3373, 1619 cm^{-1}. ^1H NMR δ: 0.96 (m, 6), 1.83 (obscured, 1), 1.83 (s, 3H), 2.95, 3.03 (2s, 6H), 3.41 (d, J = 4.4, 1H), 3.63 (m, 1H), 4.01 (br s, 1H, exchangeable), 4.01, 4.08 (2 s, 2H). MS *m/e* (rel. intensity): 199, (M^+, 2), 156(31), 127(11)0), 112(95), 83(100), 72(100) . Anal. calcd. for $C_{11}H_{21}NO$,: C, 66.30; H, 10.62; N, 7.03. Found: C, 66.34; H, 10.62; N, 7.05. ***anti*-6i** (0.1062 g, 28%), mp 111.5–112.5 °C (hexane). IR ($CHCl_3$) ν_{max}: 3400, 1624 cm^{-1}. ^1H NMR δ: 0.96 (d, J = 7, 6H), 1.77 (obscured, 1H), 1.77 (s, 3H), 2.96, 3.00 (2s, 6H), 3.34 (d, J = 5.9, 1H), 3.72 (m, 1H), 3.94 (0.5 of ABq, J = 7, 1H, exchangeable), 4.86, 4.99 (2s, 2H). MS *m/e* (rel. intensity): 199 (M^+, 4), 156(37), 127(100), 112(41), 83(98), 72(82). Anal. calcd. for $C_{11}H_{21}NO_2$: C, 66.30; H, 10.62; N, 7.03. Found: C, 66.46; H, 10.61; N, 7.08.

syn- ***and*** **anti-*2-(1-Hydroxy-2-ethyl)*-N,N,*3-trimethyl-3-butenamide* syn-** ***and*** **anti-*6j***

A mixture of compound ***Z*-4a** (0.1075 g, 0.539 mmol) and propanal (58 μL) in the presence of $TiC1_4$ (65 μL) was allowed to react under the previously described conditions. After workup in the usual manner, the crude reaction product was subjected to preparative TLC (3:2 ethyl acetate–hexane) to yield, in order of elution, two fractions: ***syn*-6j** (0.0450 g, 45% yield), bp 72–77 °C at 0.1 torr. IR (neat) ν_{max} 3440, 1634 cm^{-1}. ^1H NMR (500 MHz) δ: 0.96 (t, J = 7.2, 3H), 1.40–1.55 (m, 2H), 1.81 (s, 3H), 2.94, 3.00 (2s, 6H), 3.20 (d, J = 4.0, 1H), 3.93 (m, 1H), 4.28 (br s, 1H, exchangeable), 4.83 (s, 1H), 5.08 (t, J = 1.5, 1H), ^{13}C NMR: 10.5, 21.9, 27.0, 35.6, 37.3, 54.0, 73.0, 116.8, 139.7, 173.5. MS *m/e* (rel. intensity): 185 (M^+, 14), 126 (100), 111 (29), 83 (31). HR-MS calcd. for $C_{10}H_{19}NO_2$: 185.1405 (M^+), 167.1312 ($M^+ - H_2O$). Found: 185.1416, 167.1310. A 53:47 mixture of ***anti*-6j** (7%) and desilylated butenamides (6%) (0.0111g)**;** pure ***anti*-6j** was obtained by recrystallization, mp 80–82 °C (hexane). IR (neat) ν_{max}: 3415, 1623 cm^{-1}. ^1H NMR (500 Mz) δ: 0.96 (t, J = 7.3), 1.43 (m, 1H), 1.54 (m, 1H), 1.73 (s, 3H), 2.94, 2.97 (2s, 6H), 3.16 (d, J = 6.8, 1H), 3.85 (m, 1H), 4.84 (s, 1H), 4.97 (m, 1H). ^{13}C NMR: 10.2, 20.8, 21.2, 35.6, 37.2, 56.1, 72.8, 115.4, 140.5, 172.8. MS *m/e*: 185 (M^+, 13), 127 (75), 125 (100), 111(24). HR-MS calcd.. for $C_{10}H_{19}NO_2$: 185.1405 (M^+). Found: 185.1416.

Supplementary data

The experimental procedures and spectral data for the preparation of **3,** the crossover experiment of **1a** and **1b**, the attempted $TiCl_4$ mediated reaction of ***E*-4a** with benzaldehyde, the $BF_3{\cdot}OEt_2$ mediated reaction of ***Z*-4a** with benzaldehyde, the attempted generation of the titanium dienolate of **1a**, the attempted fluoride mediated reaction of **2a** with benzaldehyde, and the minimized structures and final Cartesian coordinates and energies for the calculated transition states **16** and **17,** have been deposited as Supplementary data for this article available on the journal Web site (canjchem.nrc.ca) or may be purchased from the Depository of Unpublished Data, Document Delivery, CISTI, National Research Council Canada, Ottawa, ON K1A 0R6, Canada. DUD 3932. For more information on obtaining material, refer to cisti-icist.nrc-cnrc.gc.ca/cms/unpub_e.shtml.

Acknowledgements

We are grateful to the Natural Sciences and Engineering Research Council of Canada (NSERC) for support of our synthetic programs. We also wish to thank Prof. James Gauld, Dr. Haining Liu, and Prof. Charles MacDonald (University of Windsor) for assistance with the DFT calculations on the allylsilane – aldehyde transition states.

References

(1) Dedicated to Peter Beak, in recognition of a career of rigorous physical organic studies, which enduringly enriched the field of carbanionic chemistry.

(2) (a) Casiraghi, G.; Zanardi, F.; Appendino, G.; Rassu, G. *Chem. Rev.* **2000**, *100*, 1929 doi:10.1021/cr990247i. PMID: 11749280.; (b) Denmark, S. E.; Heemstra, J. R., Jr.; Beutner, G. L. *Angew. Chem., Int. Ed.* **2005**, *44*, 4682 doi:10.1002/anie.200462338.; (c) Green, J. R. In *Science of synthesis*; Majewski, M. and Snieckus, V., Eds; Georg Thieme Verlag: Stuttgart, 2006; Vol. 8, pp. 427–486; (d) Casinos, I.; Mestres, R. *J. Chem. Soc., Perkin Trans* **1978**, *1*, 1651 doi:10.1039/p19780001651.; (e) Dugger, R. W.; Heathcock, C. H. *J. Org. Chem.* **1980**, *45*, 1181. doi:10.1021/jo01295a002.

(3) (a) Majewski, M.; Mpango, G. B.; Thomas, M. T.; Wu, A.; Snieckus, V. *J. Org. Chem.* **1981**, *46*, 2029 doi:10.1021/jo00323a012.; (b) Majewski, M.; Green, J. R.; Snieckus, V. *Tetrahedron Lett.* **1986**, *27*, 531 doi:10.1016/S0040-4039(00)84032-0.; (c) Green, J. R.; Majewski, M.; Snieckus, V. *Can. J. Chem.* **2006**, *84*, 1397. doi:10.1139/V06-112.

(4) Casey, C. P.; Jones, C. R.; Tukada, H. *J. Org. Chem.* **1981**, *46*, 2089. doi:10.1021/jo00323a022.

(5) (a) For reviews on ketene acetals, see: Schneider, C. In *Science of synthesis*; de Meijere, A., Ed.; Georg Thieme Verlag: Stuttgart, 2005; Vol. 24, pp. 293–322; (b) Mahrwald, R. *Chem. Rev.* **1999**, *99*, 1095 doi:10.1021/cr980415r. PMID:11749441.; (c) For a review on ketene *O*,*N*-acetals, see: Kantlehner, W. In *Science of synthesis*; de Meijere, A., Ed.; Georg Thieme Verlag: Stuttgart, 2005; Vol. 24, pp. 337–446; (d) For reviews on the chemistry of vinyl ketene acetals, see: Kalesse, M. *Top. Curr. Chem.* **2005**, *244*, 43; (e) Casiraghi, G.; Zanardi, F.; Appendino, G.; Rassu, G. *Chem. Rev.* **2000**, *100*, 1929. doi:10.1021/cr990247i. PMID: 11749280.

(6) Williard, P. G.; Tata, J. R.; Schlessinger, R. H.; Adams, A. D.; Iwanowicz, E. J. *J. Am. Chem. Soc.* **1988**, *110*, 7901. doi:10.1021/ja00231a065.

(7) (a) In esters, see: Kang, G. J.; Chan, T. H. *Can. J. Chem.* **1985**, *63*, 3102 doi:10.1139/v85-512.; (b) Barton, T. J.; Goure, W. F.; Witiak, J. L.; Wulff, W. D. *J. Organomet. Chem.* **1982**, *225*, 87 doi:10.1016/S0022-328X(00)86813-8.; (c) Bellassoued, M.; Ennigrou, R.; Gaudemar, M. *J. Organomet. Chem.* **1988**, *338*, 149 doi:10.1016/0022-328X(88)80497-2.; (d) Asakura, T.; Kojima, T.; Miura, T.; Iwasawa, N. *Angew. Chem., Int. Ed.* **2006**, *45*, 6874. doi:10.1002/anie.200602188.

(8) (a) In ketones and aldehydes, see: Shih, C.; Swenton, J. S. *J.*

Can. J. Chem. Downloaded from www.nrcresearchpress.com by Sichuan Normal University on 09/14/12
For personal use only.

Org. Chem. **1982**, *47*, 2668 doi:10.1021/jo00134a032.; (b) Fish, P. V. *Synth. Commun.* **1996**, *26*, 433 doi:10.1080/00397919608003634.; (c) Bartoli, G.; Bosco, M.; Dalpozzo, R.; De Nino, A.; Iantorno, E.; Tagarelli, A.; Palmieri, G. *Tetrahedron* **1996**, *52*, 9179 doi:10.1016/0040-4020(96)00468-1.; (d) Pirrung, M. C.; Fallon, L.; Zhu, J.; Lee, Y. R. *J. Am. Chem. Soc.* **2001**, *123*, 3638 doi:10.1021/ja002370t. PMID:11457095.; (e) Asakura, T.; Kojima, T.; Miura, T.; Iwasawa, N. *Angew. Chem., Int. Ed.* **2006**, *45*, 6874. doi:10.1002/anie.200602188.

(9) For a review of silicon migrations, see: Mitsuo, K.; Iwamoto, T. In *Chemistry of organic silicon compounds*; Rappoport, Z., Apeloig, Y., Eds.; Wiley: Chichester, 2001; Vol. 3, pp. 853–948.

(10) For the preliminary report, see: Green, J. R.; Snieckus, V. *Tetrahedron Lett.* **1986**, *27*, 535. doi:10.1016/S0040-4039(00)84033-2.

(11) (a) Armstrong, R. J.; Weiler, L. *Can. J. Chem.* **1983**, *61*, 2530 doi:10.1139/v83-436.; (b) Pettersson, L.; Magnuson, G.; Frejd, T. *Acta Chem. Scand.* **1993**, *47*, 196 doi:10.3891/acta.chem.scand.47-0196.; (c) Wennerberg, J.; Polla, M.; Frejd, T. *J. Org. Chem.* **1997**, *62*, 8735 doi:10.1021/jo971082l.; (d) Nakada, M.; Kojima, E.-i.; Iwata, Y. *Tetrahedron Lett.* **1998**, *39*, 313 doi:10.1016/S0040-4039(97)10554-8.; (e) Aggarwal, V. K.; Bethel, P. A.; Giles, R. *J. Chem. Soc., Perkin Trans* **1999**, *1*, 3315 doi:10.1039/a906589j.; (f) Beszant, S.; Giannini, E.; Zanoni, G.; Vidari, G. *Tetrahedron Asymmetry* **2002**, *13*, 1245 doi:10.1016/S0957-4166(02)00335-X.; (g) Pettersson, L.; Frejd, T. *J. Chem. Soc., Perkin Trans.* **2001**, *1*, 789 doi:10.1039/b010101j.; (h) Beszant, S.; Giannini, E.; Zononi, G.; Vidari, G. *Eur. J. Org. Chem.* **2003**, 3958. doi:10.1002/ejoc.200300276.

(12) (a) For broader study of electrophilic reactivity with alkenoates, see: Yamamoto, Y.; Hatsuya, S.; Yamada, J.-i. *J. Org. Chem.* **1990**, *55*, 3118 doi:10.1021/jo00297a030.; (b) Fan, R.; Hudlicky, T. *Tetrahedron Lett.* **1989**, *30*, 5533 doi:10.1016/S0040-4039(01)93792-X.; (c) For amination reactions, see: Loreto, M. A.; Pompei, F.; Tardella, P. A.; Tofavi, D. *Tetrahedron* **1997**, *53*, 15853. doi:10.1016/S0040-4020(97)10045-X.

(13) (a) Chabaud, L.; James, P.; Landais, Y. *Eur. J. Org. Chem.* **2004**, 3173 doi:10.1002/ejoc.200300789.; (b) Sarkar, T. K. In *Science of synthesis*; Fleming, I., Ed.; Georg Thieme Verlag: Stuttgart, 2002; Vol. 4, pp. 837–926; (c) Brook, M. A. *Silicon in organic, organometallic, and polymer chemistry*; Wiley: New York, 2000; Chap. 16; (d) Luh, T.-Y.; Liu, S.-T. In *Chemistry of organic silicon compounds*; Rappoport, Z., Apeloig, Y., Eds.; Wiley: Chichester, 1998; Vol. 2, Pt. 3, pp. 1793–1868; (e) Fleming, I.; Barbero, A.; Walter, D. *Chem. Rev.* **1997**, *97*, 2063 doi:10.1021/cr941074u. PMID:11848898.; (f) Langkopf, E.; Schinzer, D. *Chem. Rev.* **1995**, *95*, 1375 doi:10.1021/cr00037a011.; (g) Fleming, I.; Dunogues, J.; Smithers, R. *Org. React.* **1989**, *37*, 57; (h) Majetich, G. In *Organic synthesis: theory and applications*; Hudlicky, T, Ed.; JAI: Greenwich, 1989; Vol. 1, pp. 173–240.

(14) (a) Denmark, S. E.; Lee, W. *Chem. Asian J.* **2008**, *3*, 327 doi:10.1002/asia.200700300. PMID:18022982.; (b) Kalese, M.; Hassfeld, J. In *Asymmetric synthesis: the essentials*; Christmann, M., Bräse, S., Eds.; Wiley-VCH: Weinheim, 2007; pp. 105–109; (c) Hosokawa, S.; Tatsuta, K. *Mini Rev. Org. Chem.* **2008**, *5*, 1 doi:10.2174/157019308783498197.; (d) Jacques, T.; Markó, I. E.; Popisil, J. In *Multicomponent reactions*; Zhu, J, Bienaymé, H., Eds.; Wiley-VCH, 2005; pp. 398–452.

(15) (a) For an analogous NOE-based assignment of the alkene stereochemistry of vinylketene acetals, see: Bell, S. H.; Cameron, D. W.; Feutrill, G. I.; Skelton, B. W.; White, A. H. *Tetrahedron Lett.* **1985**, *26*, 6519 doi:10.1016/S0040-4039(00)99042-7.; (b) Adams, A. D.; Schlessinger, R. H.; Tata, J. R.; Venit, J. J. *J. Org. Chem.* **1986**, *51*, 3068. doi:10.1021/jo00365a045.

(16) Berger, S.; Braun, S. *200 and more NMR experiments: A practical course*, Wiley-VCH: Weinheim, 2004; pp. 277–279.

(17) (a) For examples of the influence of phenyl groups in silyl halides on O- versus C-silylation, see: Larson, G. L.; Fuentes, L. M. *J. Am. Chem. Soc.* **1981**, *103*, 2418 doi:10.1021/ja00399a052.; (b) Akai, S.; Kitagaki, S.; Naka, T.; Yamamoto, K.; Tsuzuki, Y.; Matsumoto, K.; Kita, Y. *J. Chem. Soc., Perkin Trans.* **1996**, *1*, 1705. doi:10.1039/p19960001705.

(18) (a) House, H. O.; Crumrine, D.; Teranishi, A. Y.; Olmstead, H. D. *J. Am. Chem. Soc.* **1973**, *95*, 3310 doi:10.1021/ja00791a039.; (b) Heathcock, C. In *Asymmetric synthesis*; Morrison, J. D., Ed.; Academic Press: New York, 1983; Vol. 3, pp. 111–212.

(19) (a) For support of an ion-paired enolate intermediate, see: Biddle, M. M.; Reich, H. J. *J. Org. Chem.* **2006**, *71*, 4031 doi:10.1021/jo0522409. PMID:16709041.; (b) For examples of results strongly implicating a pentacoordinated siliconate ion in a similar pKa range, see: Takahashi, O.; Maeda, T.; Mikami, K.; Nakai, T. *Chem. Lett.* **1986**, 1355. doi:10.1246/cl.1986.1355.

(20) (a) Reetz, M.; Peter, R. *Tetrahedron Lett.* **1981**, *22*, 4691 doi:10.1016/S0040-4039(01)83014-8.; (b) Evans, D. A.; Urpi, F.; Somers, T. C.; Clark, J. S.; Bilodeau, M. T. *J. Am. Chem. Soc.* **1990**, *112*, 8215 doi:10.1021/ja00178a082.; (c) Ghosh, A. K.; Shevlin, M. In *Modern aldol reactions*; Mahrwald, R., Ed.; Wiley-VCH: Weinhein, 2004; pp. 60–125.

(21) Yamamoto, Y.; Hatsuya, S.; Yamada, J.-i. *J. Org. Chem.* **1990**, *55*, 3118. doi:10.1021/jo00297a030.

(22) Fan, R.; Hudlicky, T. *Tetrahedron Lett.* **1989**, *30*, 5533. doi:10.1016/S0040-4039(01)93792-X.

(23) (a) Kaur, P.; Singh, P.; Kumar, S. *Tetrahedron* **2005**, *61*, 8231 doi:10.1016/j.tet.2005.06.045.; (b) Hansen, F. G.; Bundgaard, E.; Madsen, R. *J. Org. Chem.* **2005**, *70*, 10139. doi:10.1021/jo051645q. PMID:16292857.

(24) We and Hudlicky have chosen to define diastereomer nomenclature by the more conventional consideration of the carbonyl function as part of the main chain. Consequently, the syn- and anti-diastereomers of our work correspond to the anti- and syn-diastereomers, respectively, of theYamamoto and Kumar reports.

(25) (a) Yamamoto, Y.; Yitagai, Y.; Naruta, Y.; Maruyama, K. *J. Am. Chem. Soc.* **1980**, *102*, 7107 doi:10.1021/ja00543a040.; (b) For a more complete discussion of the possible open transition states in Hosomi–Sakurai reactions, see: Tietze, L. F.; Kinzel, T.; Schmatz, S. *J. Am. Chem. Soc.* **2006**, *128*, 11483 doi:10.1021/ja062528v. PMID:16939272.; (c) For a review on diastereoselection in Mukaiyama aldol reactions, see: Mahrwald, R. *Chem. Rev.* **1999**, *99*, 1095. doi:10.1021/cr980415r. PMID:11749441.

(26) Maria, P.-C.; Gal, J.-F. *J. Phys. Chem.* **1985**, *89*, 1296. doi:10.1021/j100253a048.

(27) (a) Montaudo, G.; Librando, V.; Caccamese, S.; Maravigna, P. *J. Am. Chem. Soc.* **1973**, *95*, 6365 doi:10.1021/ja00800a033.; (b) Kruk, C.; Spaargaren, K. *Spectrochim. Acta [A]* **1971**, *27*, 77.

(28) (a) For synclinal transition-state proposals in allylsilane carbonyl condensations, cyclic, see: Denmark, S. E.; Weber, E. J. *Helv. Chim. Acta* **1983**, *66*, 1655 doi:10.1002/hlca.19830660604.; (b) For acyclic, see: Jain, N. F.; Takenaka, N.; Panek, J. S. *J. Am. Chem. Soc.* **1996**, *118*, 12475 doi:10.1021/ja962877x.; (c) For allylstannanes, cyclic, see: Denmark, S. E.; Weber, E. J. *J. Am. Chem. Soc.* **1984**, *106*, 7970 doi:10.1021/ja00337a053.; (d) For allylstannanes, acyclic, see: Keck, G. E.; Savin, K. A.; Cressman, E. N. K.; Abbott, D. E. *J. Org. Chem.* **1994**, *59*, 7889. doi:10.1021/jo00104a054.

(29) (a) Evans, D. A.; Sjogren, E. B.; Bartroli, J.; Dow, R. L. *Tetrahedron Lett.* **1986**, *27*, 4957 doi:10.1016/S0040-4039(00)85106-0.; (b) Galatsis, P.; Millan, S. D.; Ferguson, G. *J. Org. Chem.* **1997**, *62*, 5048. doi:10.1021/jo961904z.

(30) Moreau, B.; Ginisty, M.; Alberico, D.; Charette, A. B. *J. Org. Chem.* **2007**, *72*, 1235. doi:10.1021/jo062099j. PMID: 17256906.

(31) (a) Gevorgyan, V.; Kadota, I.; Yamamoto, Y. *Tetrahedron Lett.* **1993**, *34*, 1313 doi:10.1016/S0040-4039(00)91783-0.; (b) Nishigaichi, Y.; Takuwa, A. *Tetrahedron Lett.* **2002**, *43*, 3045 doi:10.1016/S0040-4039(02)00409-4.; (c) Nishigaichi, Y.; Takuwa, A. *Tetrahedron Lett.* **2003**, *44*, 1405. doi:10.1016/S0040-4039(02)02867-8.

(32) (a) Goasdoue, G.; Goasdoue, N.; Gaudemar, M. *J. Organomet. Chem.* **1984**, *263*, 273 doi:10.1016/0022-328X(84)85032-9.; (b) Chan, T. H.; Aida, T.; Lau, P. W. K.; Gorys, V.; Harpp, D. N. *Tetrahedron Lett.* **1979**, 4029 doi:10.1016/S0040-4039(01)86495-9.; (c) Schinzer, D.; Solyom, S.; Becker, M. *Tetrahedron Lett.* **1985**, *26*, 1831. doi:10.1016/S0040-4039(00)94749-X.

(33) Bottoni, A.; Costa, A. L.; Di Tommaso, D.; Rossi, I.; Tagliavini, E. *J. Am. Chem. Soc.* **1997**, *119*, 12131. doi:10.1021/ja9723693.

(34) (a) Denmark, S. E.; Almstead, N. G. *J. Org. Chem.* **1994**, *59*, 5130 doi:10.1021/jo00097a008.; (b) Denmark, S. E.; Hosoi, S. *J. Org. Chem.* **1994**, *59*, 5133 doi:10.1021/jo00097a009.; (c) [see also:] Schlosser, M.; Franzini, L.; Bauer, C.; Leroux, F. *Chem. Eur. J.* **2001**, *7*, 1909. doi:10.1002/1521-3765(20010504)7:9<1909::AID-CHEM1909>3.0.CO;2-H.

(35) (a) Mulzer, J.; Brüntrup, G.; Finke, J.; Zippel, M. *J. Am. Chem. Soc.* **1979**, *101*, 7723 doi:10.1021/ja00520a020.; (b) Mulzer, J.; Zippel, M.; Brüntrup, G.; Segner, J.; Finke, J. *Liebigs Ann. Chem.* **1980**, 1108. doi:10.1002/jlac.198019800710.

(36) (a) Young, D.; Kitching, W. *Aust. J. Chem.* **1985**, *38*, 1767; (b) Denmark, S.; Weber, E. J.; Wilson, T. M.; Willson, T. M. *Tetrahedron* **1989**, *45*, 1053; (d) [Review:] Gung, B. W. *Org. React.* **2004**, *64*, 1.

(37) (a) White, J. M.; Tunoori, A. R.; Georg, G. I. *J. Am. Chem. Soc.* **2000**, *122*, 11995 doi:10.1021/ja002149g.; (b) Zhao, Y.; Snieckus, V. Unpublished results.

(38) Still, W. C.; Kahn, M.; Mitra, A. *J. Org. Chem.* **1978**, *43*, 2923. doi:10.1021/jo00408a041.

(39) Perrin, D. D.; Amarego, W. L.; Mitra, A. *Purification of laboratory chemicals*, 2nd ed; Pergamon: Oxford, 1980.

(40) Winkle, M. R.; Lansinger, J. M.; Ronald, R. C. *J. Chem. Soc., Chem. Commun.* **1980**, 87. doi:10.1039/c39800000087.

Can. J. Chem. Downloaded from www.nrcresearchpress.com by Sichuan Normal University on 09/14/12
For personal use only.

Novel formation of isoxazoline *N*-oxide in addition to Michael adduct from the reaction of β-nitrostyrenes with 2-methoxyfuran — Experimental and theoretical studies

Kuniaki Itoh, Shigehisa Kishimoto, and Kazuo Sagi

Can. J. Chem. Downloaded from www.nrcresearchpress.com by Sichuan Normal University on 09/14/12
For personal use only.

Abstract: 2-Methoxyfuran reacts with β-nitrostyrenes to give Michael adducts. Interestingly, isoxazoline *N*-oxides were obtained in the reactions with β-nitrostyrenes possessing additional electron-withdrawing groups [COPh (**2f**) and CO_2Et (**2g**)]. (*Z*)-Nitrostyrene (**2g**) gives *trans*-isoxazoline (**4g**) and (*E*)-nitrostyrene (**2f**) leads to the *cis*-form product **4f**. We have used theoretical methods to investigate the mechanism and to probe the regio- and stereo-selectivity observed in the rearrangement and the Michael reactions. To account for the selectivity observed in these reactions, we examined the Fukui functions and located the transition states (TS) using density functional theory (DFT) calculations at the B3LYP/6–31G* level. The first step involves a nucleophilic attack by the α-carbon atom (C4) of the furan ring on the vinyl C-atom (C5) of the nitrostyrene part to give a zwitterionic intermediate (IN1). Fission of the C–O bond of the furan ring in the intermediate and ring closure via the oxygen atom (endo-O atom) of the nitro group gives the isoxazoline *N*-oxide. Alternatively, the intermediate (IN1) may be transformed into the Michael adduct by an intramolecular proton transfer mediated by the formation of a four-membered transition-state structure. The potential-energy barriers for these reactions had the following values: 5.1 kcal/mol for **2f** and 17.0 kcal/mol for **2g′** (CO_2Me) at the rearrangement step, and 41–49 kcal/mol for the proton-transfer step. The solvent effect in $CHCl_3$ stabilized the electrophilic attack by 1–14 kcal/mol. DFT analysis of these reactions is in good agreement with the experimental results.

Key words: reaction mechanisms, nitrogen heterocycles, zwitterions, rearrangement, density functional calculations.

Résumé : Le 2-méthoxyfurane réagit avec les β-nitrostyrènes pour conduire à la formation d'adduits de Michael. À notre grande surprise, les réactions avec des β-nitrostyrènes possédant des groupes électro-attracteurs supplémentaires [COP (**2f**) et CO_2Et (**2g**)] conduisent à la formation de *N*-oxydes d'isoxazoline. Le (*Z*)-nitrostyrène (**2g**) conduit à la *trans*-isoxazoline (**4g**) alors que le (*E*)-nitrostyrène (**2f**) conduit à la *cis*-isoxazoline (**4g**). On a fait appel à des méthodes théoriques pour étudier le mécanisme et pour chercher à expliquer la régio- et la stéréo-sélectivité observée dans les réactions de réarrangement et de Michael. Pour expliquer la sélectivté observée dans ces réactions, on a examiné les fonctions de Fukui et localisé les états de transition (ET) en faisant des calculs au niveau B3LYP/6-31G* de la théorie de la fonctionnelle de la densité (TFD). La première étape implique une attaque nucléophile par l'atome de carbone C4 du noyau furane sur l'atome de carbone C5 vinylique de la partie nitrostyrène qui conduit à la formation d'un intermédiaire zwitterionique (IN1). La fission de la liaison C–O du cycle du furane intermédiaire et la cyclisation par le biais de l'atome d'oxygène (atome d'oxygène endo) du groupe nitro conduit à la formation du *N*-oxyde d'isoxazoline. D'une façon alternative, il est possible que l'intermédiaire IN1 se transforme en adduit de Michael par le biais d'un transfert de proton intramoléculaire catalysé par la formation d'un état de transition de structure à quatre chaînons. On a calculé que les barrières d'énergie potentielle de ces réactions sont les suivantes: 5,1 kcal/mol pour **2f** et 17,0 kcal/mol pour **2g′** (CO_2Me) au niveau de l'étape de réarrangement et de 41 à 49 kcal/mol pour l'étape de transfert de proton. L'effet de solvant dans le $CHCl_3$ stabilise l'attaque électrophile par 1 à 14 kcal/mole. Les résultats de l'analyse par la théorie de la fonctionnelle de la densité de ces réactions sont en bon accord avec les résultats expériementaux.

Mots-clés : mécanismes réactionnels, hétérocycles azotés, zwitterions, réarrangement, calculs suivant la théorie de la fonctionnelle de la densité.

[Traduit par la Rédaction]

Introduction

We have been studying the Diels–Alder reactions of furan derivatives with various types of electron-deficient dienophiles[1] for some time, with a view to synthesizing *C*-nucleosides via the Diels–Alder reaction of furan with methyl 3-nitroacrylate.[1b] Furans have been condensed with a wide variety of dienophiles, but they are known to be rather unreactive dienes because of their stabilized aromatic electronic configuration.[2] In some instances, Lewis acids or high-pressure conditions[3]

Received 8 October 2008. Accepted 20 March 2009. Published on the NRC Research Press Web site at canjchem.nrc.ca on 2 June 2009.

K. Itoh,[1] S. Kishimoto, and K. Sagi. Department of Chemistry, Faculty of Science, Kobe University, Nada-ku, Kobe 657-8501, Japan.

[1]Corresponding author (e-mail: kuitoh@kobe-u.ac.jp).

Can. J. Chem. Downloaded from www.nrcresearchpress.com by Sichuan Normal University on 09/14/12
For personal use only.

were employed in the reactions with less-reactive dienophiles. Sometimes, the incorporation of an electron-donating group into the 2-position of furan has been used as a means to enhance the reactivity of the heteroaromatic ring function.[4]

It appears therefore that Diels–Alder reactions of furans require the use of more reactive dienophiles. Nitro-olefins are powerful and versatile reagents,[5] which have found ample application in organic synthesis. Because of the strong electron-withdrawing property of the nitro group, conjugated nitroalkenes are excellent Michael acceptors and dienophiles in Diels–Alder reactions. Furthermore, the nitro group can be further transformed into a wide variety of functionalities.[6] In Diels–Alder reactions, nitroalkenes react not only with dienes to give nitrocycloalkenes,[7] but also with electron-deficient alkenes to afford cyclic alkyl nitronates.[8] The use of nitrostyrene derivatives in combination with cyclohexadiene or cyclopentadiene in the presence of $SnCl_4$ affords exclusively a nitronate. These compounds are biologically important intermediates in the synthesis of isoxazolines and many five-membered heterocyclic systems via 1,3-dipolar cycloaddition reactions.[9] Recently, we described some reactions of β-nitrostyrenes with 2-methoxyfurans.[10] In the present paper, our purpose is to use a computational approach to contribute to a better understanding of the mechanistic features of these processes, especially by locating and characterizing all the stationary points along the reaction coordinate involved in these types of addition and rearrangement reactions.

The Diels–Alder reaction may occur via either a synchronous concerted mechanism or a stepwise mechanism with zwitterionic intermediates.[11,12] In the case considered here, the presence of an electron-releasing group on the furan, the electron-withdrawing NO_2 group on the dienophile, and also the presence of the Ph group allows for an effective stabilization of developing electronic charge, which favors a stepwise mechanism via a zwitterionic intermediate.

Although the mechanism of the Diels–Alder reaction with furans has long been settled through a quantum chemistry approach,[1e,13] there is little agreement as to that of the Michael reaction.[14] We find that the Michael addition of furans with activated dienophiles proceeds via a two-step process by formation of a zwitterionic intermediate and an intermolecular proton transfer mediated by the formation of a four-membered structure, similar to the reaction of 1-methylpyrrole with dimethyl acetylenedicarboxylate reported by Domingo and co-workers[13] and by us.[1e]

Computational details

The density functional method computations for the gas-phase calculations were performed with the Spartan 04 for Windows package.[15] The reactant, product, and transition-state (TS) geometries for the above reactions were optimized by DFT calculations at the B3LYP/6–31G* level.[16] After the optimization of all transitional structures, we carried out vibrational analyses to check the nature of the stationary points. The transition states are defined by exactly one imaginary frequency. Unless otherwise indicated, all energies in the B3LYP/6–31G* optimizations reported in this paper include zero-point energies without scaling. To calculate the free energies of solvation needed to understand the effect of the solvent on the stereoselectivity,[17] we used the Gaussian 03 program.[18] To evaluate the solvent effect, we carried out a B3LYP/6–31G* single-point calculation, using the method based on the polarized continuum model (PCM).[19] The solvent used in the experimental work was chloroform; therefore, we employed the dielectric constant, $\varepsilon = 4.81$ and the solute radius, $\alpha = 3.92$. To reduce the time of the calculation, we used the β-methoxycarbonyl nitrostyrene (**2g′**) in the calculation instead of the β-ethoxycarbonyl nitrostyrene (**2g**) used in the experiments. Electrophilic and nucleophilic Fukui functions condensed to atoms were evaluated from single-point calculations performed in the ground state of molecules at the same level of theory.[20] This method evaluated Fukui functions using the gross charges of the Mulliken's population analysis.

Results and discussion

Experimental results

No reaction of nitrostyrenes with furan or 2-methylfuran took place under the reaction conditions defined below; therefore, in the present study, we used 2-methoxyfuran as a more reactive diene.[21]

A typical experimental procedure was as follows: to a stirred solution of 2-methoxyfuran (**1**) (1.5 mmol) in $CHCl_3$ (3 mL) was added β-bromo-β-nitrostyrene (**2d**) (1.1 mmol) at room temperature under N_2 atmosphere. After stirring for 3 days, the resultant solution was evaporated under reduced pressure leaving an oil, which was separated by column chromatography on silica gel (eluate mixture: AcOEt/hexane = 1/9) to give a mixture of Michael adducts **3d** (34%) (Scheme 1). An NMR analysis showed that the mixture was composed of a 1:1 mixture of two diastereoisomers (**I**, **II**), which showed different signals for furyl and alkyl H-atoms (**I**: 6.40 ppm (d, J = 10.7), 6.20 ppm (d, J = 3.3), 5.07 ppm (d, J = 3.3), 4.66 ppm (d, J = 10.7); **II**: 6.36 ppm (d, J = 10.7), 6.06 ppm (d, J = 3.3), 5.00 ppm (d, J = 3.3), 4.71 ppm (d, J = 10.7)). Results of reactions with other β-nitrostyrenes are given in Table 1. In general, β-nitrostyrenes **2a**–**2d** reacted with **1** to yield the corresponding Michael adducts (Table 1, entries 1–4). However, β-methyl-β-nitrostyrene (**2e**) gave no adduct and was recovered almost totally even after 4 days, presumably due to the presence of the electron-donating methyl group at the β-position.

Hence, the reaction of a more electron-deficient β-nitrostyrene, (*E*)-β-benzoyl-β-nitrostyrene (**2f**), with **1** was examined in the hope that the Diels–Alder reaction would occur,[22] but gave neither Michael adducts nor Diels–Alder adducts. Instead, an unexpected compound (**4f**, 27%) was obtained that showed no evidence of furan-ring signals in its ^1H and ^{13}C NMR spectra. The ^1H and ^{13}C NMR spectra of the main adduct indicated the presence of a methyl ester group (CO_2Me: 3.61 ppm, s, 3H (Me), and 53.4 (Me), 165.7 (CO_2) ppm) and an ethen-1,2-diyl group (CH=CH, (*Z*)-configuration: 6.05 ppm, dd, J = 1.5, 11.6 and 6.57 ppm, ddd, J = 1.5, 7.5, 11.6). Furthermore, the (*Z*)-configuration was confirmed by NOE experiments. The observed signals showed that scission of the furan ring had occurred. In addition, the two H-signals at higher field (4.70 ppm, d, J = 4.1, 1H, and 6.18 ppm, ddd, J = 1.5, 4.1, 7.5, 1H) are correlated

Scheme 1.

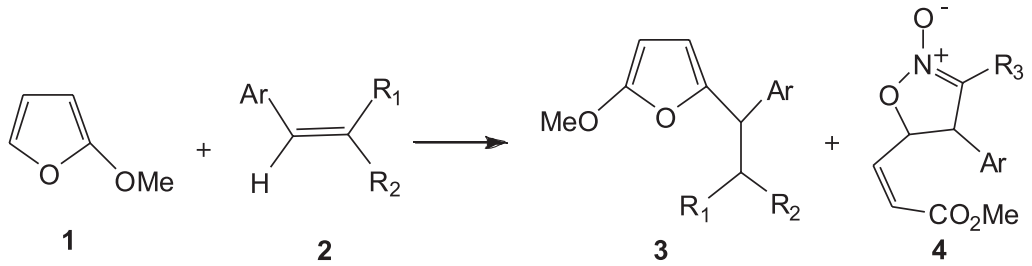

1 2 3 4

Compound	Ar	R_1	R_2	R_3
2a, 3a	Ph	H	NO_2	—
2b, 3b	*p*-MeOPh	H	NO_2	—
2c, 3c	*p*-ClPh	H	NO_2	—
2d, 3d	Ph	Br	NO_2	—
2e, 3e	Ph	Me	NO_2	—
2f, 3f	Ph	COPh	NO_2	—
2g, 3g	Ph	NO_2	CO_2Et	—
2h, 3h	*p*-MeOPh	COPh	NO_2	—
2i, 3i	*p*-MeOPh	NO_2	COPh	—
4f	Ph	—	—	COPh
4g	Ph	—	—	CO_2Et
4h	*p*-MeOPh	—	—	COPh
4i	*p*-MeOPh	—	—	COPh

Table 1. Reactions of β-nitrostyrenes (**2**) with 2-methoxyfuran (**1**).

		Product[a]			
Entry	Nitrostyrene	Michael adduct	Yield	isoxazoline	Yield
1	**2a**	**3a**	23%	—	—
2	**2b**	**3b**	31%	—	—
3	**2c**	**3c**	36%	—	—
4	**2d**	**3d**[b]	34%	—	—
5	**2e**	**3e**	0%	—	—
6	**2f**	—	—	**4f**[c]	27%
7	**2g**	**3g**[d]	8%	**4g**[e]	68%[e]
8	**2h**	**3h**	A small %	**4h**	31%
9	**2i**	**3i**	A small %	**4i**	36%

[a]The products were isolated using column chromatography, and the recovery was 70%–80%, except for the furan (**1**).
[b]Both isomers in a ratio of 1:1.
[c]Minor isomer (2%).
[d]Both isomers in a ratio of 3:1.
[e]See ref. 23.

with an H-atom of the ethen-1,2-diyl group (δ = 6.57 ppm). Finally, the structure of the main adduct was determined to be an isoxazoline *N*-oxide derivative by a single-crystal X-ray diffraction analysis (Fig. 1, X-ray crystallographic analysis, and Supplementary data).

The product **4f** showed a cis relation between the Ph and (*Z*)-MeOCOCH=CH groups. We also obtained a minor product (**4f′**, 2%). Since the product was isolated in a small amount, we could not fully clarify its structure. However, the ^{1}H NMR spectrum of **4f′** was similar to that of **4f**. The coupling constant between H–C(3) and H–C(4) amounts to 3.2, in agreement with the structure of the trans isomer of the main product. To confirm this stereoselectivity, (*Z*)-β-ethoxycarbonyl-β-nitrostyrene (**2g**) was reacted with **1**. The isoxazoline *N*-oxide derivative (**4g,** 68%) was the major product, and a Michael adduct occurred in lower yield (**3g**, 8%) in this reaction. The H-signals of the isoxazoline ring showed up at 4.41 (d, *J* = 2.4) and 6.03 ppm (ddd, *J* = 1.7, 2.4, 7.5). The signal pattern indicated a trans arrangement between the Ph and the (*Z*)-MeOCOCH=CH group. The structure of the adduct **4g** was confirmed by a single-crystal X-ray diffraction analysis (Fig. 2, X-ray crystallographic analysis, and Supplementary data). These results are informative and imply that the product formation involves a sterically controlled inter- or intra-molecular reaction. In addition, the sterically controlled nature of the reaction was confirmed by the

Can. J. Chem. Downloaded from www.nrcresearchpress.com by Sichuan Normal University on 09/14/12
For personal use only.

Can. J. Chem. Downloaded from www.nrcresearchpress.com by Sichuan Normal University on 09/14/12
For personal use only.

Fig. 1. Structure (ORTEP) of isoxazoline *N*-oxide (**4f**).

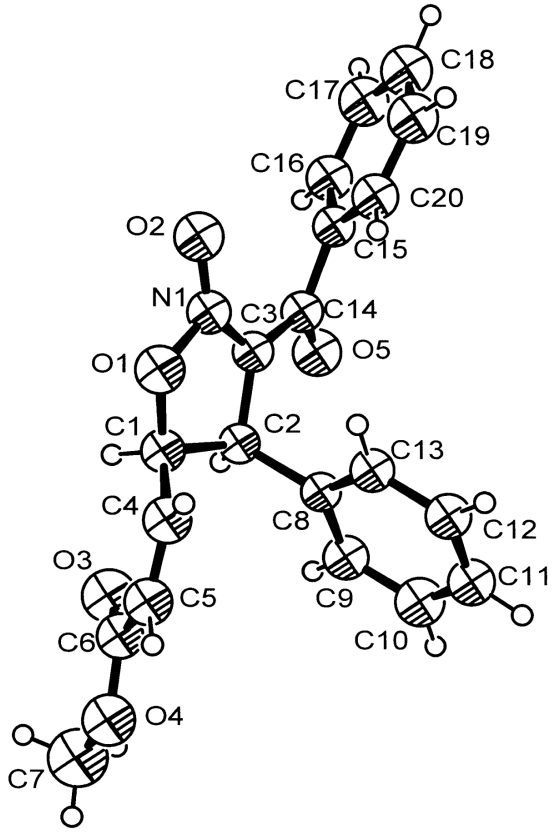

Fig. 2. Structure (ORTEP) of isoxazoline *N*-oxide (**4g**).

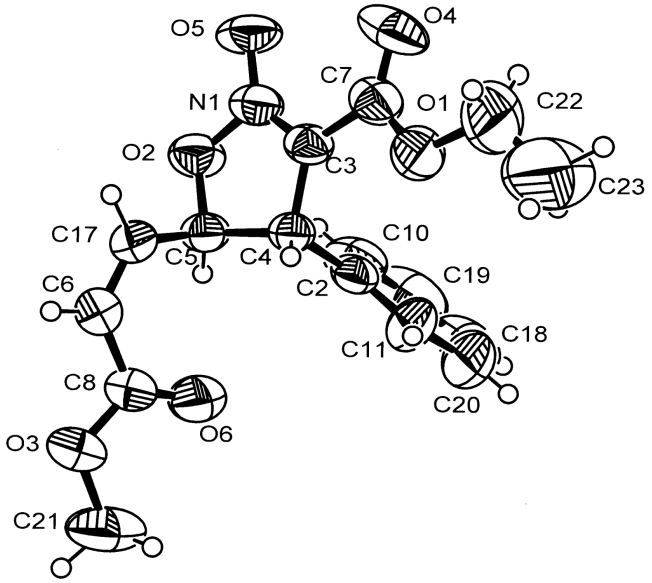

reaction of (*E*)- and (*Z*)-β-*p*-methoxybenzoyl-β-nitrostyrene (**2h** and **2i**, respectively).

Interestingly, the isoxazoline *N*-oxide was not formed via a Michael intermediate, as no trace of the isoxazoline *N*-oxide was detected after allowing the authentic Michael adduct to stand in $CHCl_3$ solution at room temperature for 2 weeks.

Concerning the formation of isoxazoline *N*-oxides, it is of interest to note that these products are mainly obtained from nitroacetate with aldehydes[24] or nitromethane with sulfonium salts[25] in the presence of an inorganic salt. They are also obtained from the decomposition of the Ag^+ salt of an aryldinitromethane in the presence of diarylethylene.[26] However, the reaction of β-nitrostyrene with alkenes in the presence of "Lewis" acids gave the corresponding nitronates (4*H*-[1,2]oxazine 2-oxides),[27] which is a quite different process in comparison with the present isoxazoline *N*-oxide-forming reaction. Therefore, it appears that the formation of isoxazoline *N*-oxides described here represents a new approach in comparison with the reactions conventionally employed.

Two processes may account for the formation of the isoxazoline *N*-oxide ring together with Michael adduct. In the first (Scheme 2), **1** and **2** react in one of their polarized mesomeric forms, **1**′ and **2**′, to give the intermediate IN1. It may then be transformed into the Michael adduct **3** by ordinary H^+-transfer. On the other hand, it could undergo ring formation to give an isoxazoline *N*-oxide **4** accompanied by C–O bond fission of the furan ring induced by an intramolecular nucleophilic attack by the nitronate part.

In an alternative route, the cycloaddition of the furan **1** and the β-nitrostyrene (**2**) yields a Diels–Alder adduct (DA).[28] This adduct may be transformed into the Michael adduct **3** by cleavage of the cyclohexenyl ring, promoted by the steric interaction between the phenyl group and the nitro group. On the other hand, cleavage of the cyclohexenyl ring, attributable to the stability of the mesomeric form of the methoxy group and steric effect, followed by intramolecular attack of the nitronate anion and cleavage of the oxygen bridge resulted in the formation of the isoxazoline *N*-oxide (**4**).

The regioselectivity for the addition reaction is predicted easily from the values of the orbital coefficients of the olefinic C-atoms found from a frontier molecular orbital model.[13] Consequently, we found that the C-atom bearing the Ph group of the olefin adds to the furyl C(4)-atom. However, by this means, we could not determine clearly which mechanism best satisfies the stereoselectivity. Therefore, we sought to predict the selectivity from the values of the potential energy at the transition states and the intermediates determined from DFT calculations at the B3LYP/6–31G* level.

Geometries and energies

Figure 3 and 4 display schematic representations of the energy profiles and the locations of the stationary points for the reactions. Figures 5, 6, and 7 present the geometry of these transition-state structures, including selected distances, while Tables 2 and 3 show the relative energies and thermodynamic parameters of the stationary points. In Table 4, the corresponding geometric parameters are reported for the INs and the TSs. For comparison, Tables 5 and 6 show some parameters for the Michael addition reactions.

The present reactions take place by a stepwise mechanism, which is initiated by the nucleophilic attack of the unsubstituted C(4)-atom of **1** on the C(5)-atom (the C-atom that bears the Ph group) of **2** to give a zwitterionic intermediate (IN1) (see Scheme 2). Bond formation between **1** and **2** can take place via an *re, re* and *re, si* approach of the involved C-atoms of the reactants. The resulting zwitterions, IN1-ax and IN1-eq are diastereoisomers with erythro- and threo-configuration at C(4) and C(5), respectively. The reactive nitronate ion part O(2) then attacks the electrophilic C(4) position of the

Scheme 2.

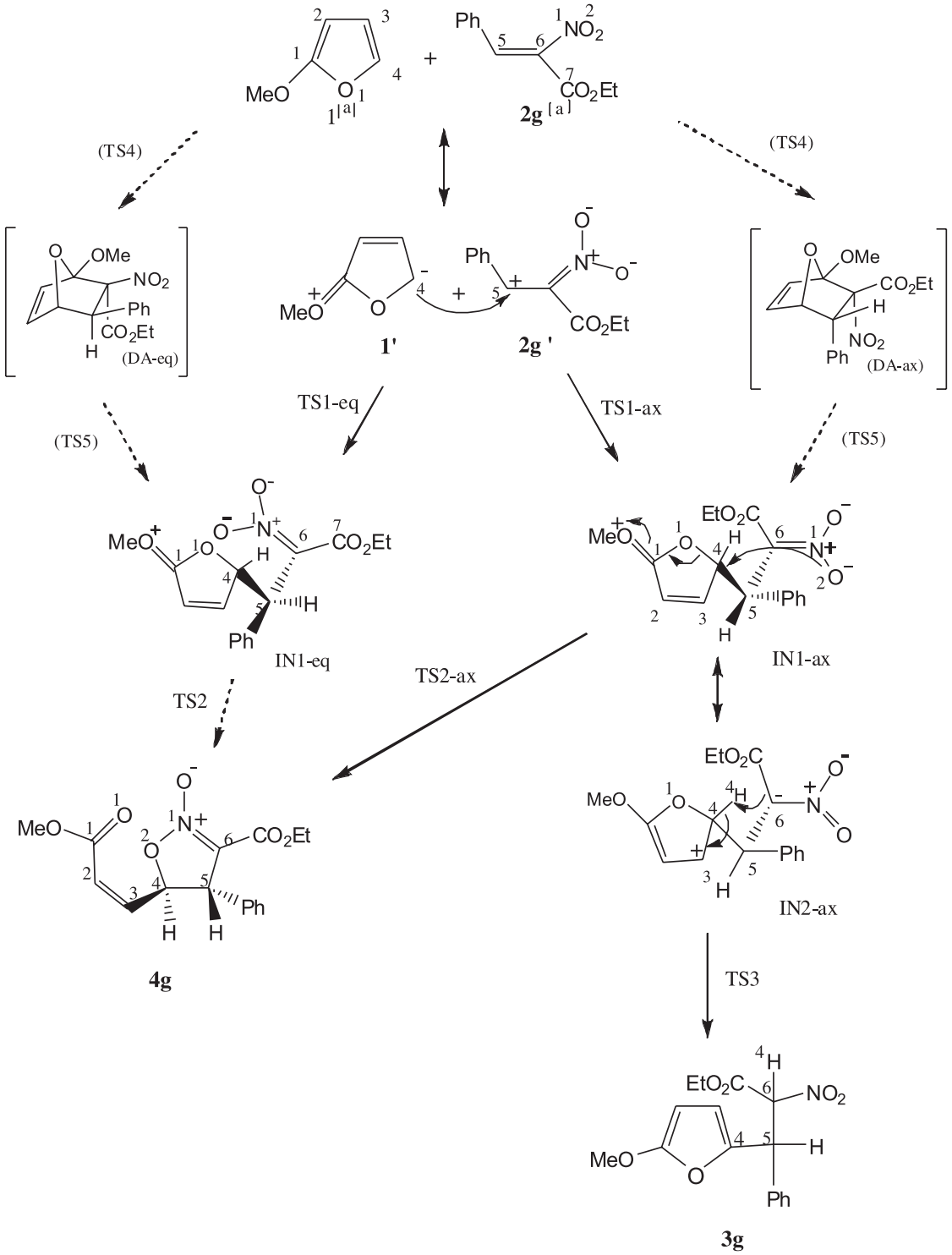

Can. J. Chem. Downloaded from www.nrcresearchpress.com by Sichuan Normal University on 09/14/12
For personal use only.

methoxyfuran accompanied by the C(4)–O(1) bond fission of the furan ring to give the isoxazoline *N*-oxide (**4**). Furthermore, in the case of the β-methoxycarbonyl-β-nitrostyrene (**2g**′), the intermediate (IN1) may be transformed into the Michael adducts **3g**′ by deprotonation reaction.

The reaction of 2-methoxyfuran (1) and β-benzoyl-β-nitrostyrene (2f)

At the first transition state of the attack of **1** on **2**, the potential-energy barriers associated with TS1-ax and TS1-eq are 31.9 and 18.8 kcal/mol, respectively, which indicates that the latter is 13.1 kcal/mol more favorable than TS1-ax (see Table 2 and Fig. 3). In the structure of TS1-ax, the NO_2 group is located on the face of the furan ring. Thus, the favorable Coulomb interaction that appears between the donor 2-methoxyfuran, positively charged from the O-atom, and the acceptor styrene, negatively charged from the N-atom of the NO_2 group, are responsible for the "axial"

Can. J. Chem. Downloaded from www.nrcresearchpress.com by Sichuan Normal University on 09/14/12
For personal use only.

Fig. 3. Potential-energy profiles for the reaction between **1** and **2f** and **2g′**.

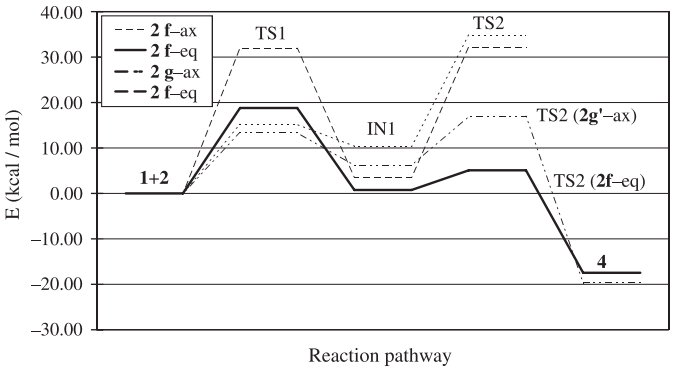

Fig. 4. Potential-energy profiles for the reaction between **1** and **2a**, **2d**, and **2g′**.

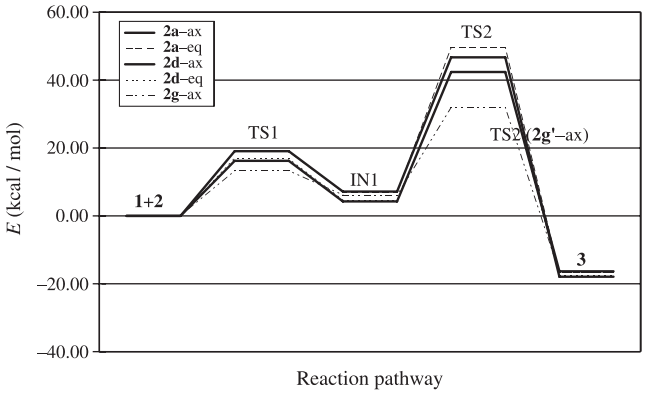

Fig. 5. Transition structure (TS2-ax) of **1** and **2g′.** O(1)–C(4)–O(2) bond in angstroms.

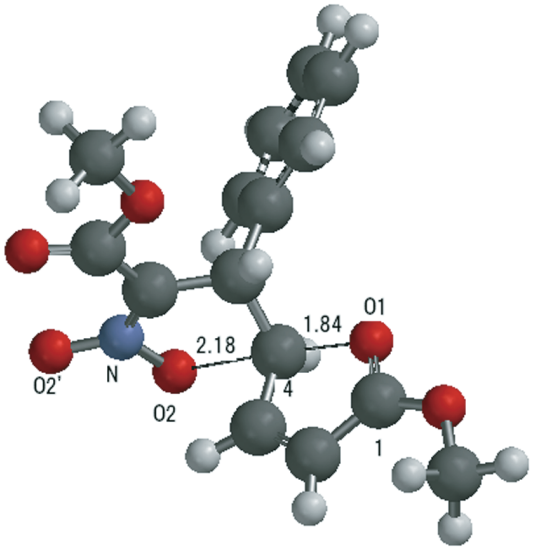

Fig. 6. Transition structure (TS2-eq) of **1** and **2g′.** O(1)–C(4)–O(2) bond in angstroms.

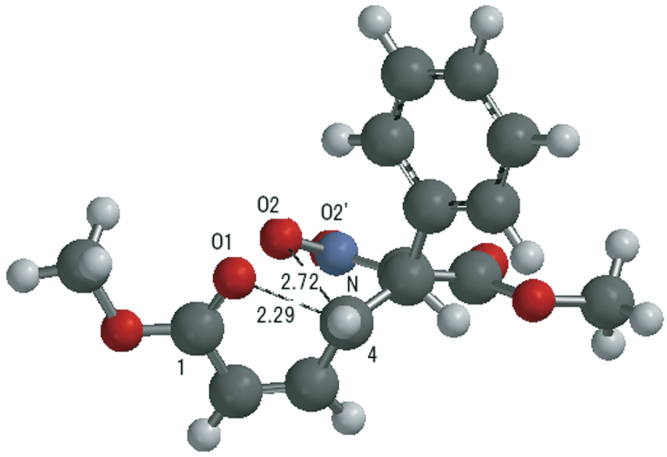

Fig. 7. Transition structure (TS3) of **1** and **2g′.** C(4)–H(4)–C(6) bonds in angstroms.

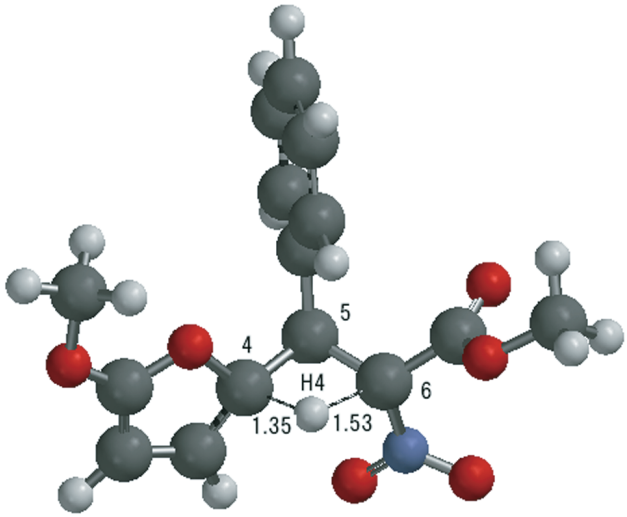

stereoselectivity found in those additions. On the other hand, at TS1-eq, the NO_2 group is located on the face of the furan ring, but the group is situated far away (C1–N1: 3.48 Å) because of the steric repulsion between the benzoyl group and the methoxy group of the furan ring (see Table 4). The lengths of the C4–C5 bond being formed in TS1-ax and TS1-eq are 1.55 Å and 1.63 Å, respectively, whereas the distances between C(1) and C(6) are 2.70 Å and 3.48 Å. In these transition structures of TS1, the NO_2 group at C(6) is in the plane of the C5–C6 bond, and the carbonyl group at C(6) is also in the plane of the C5–C6 bond. The values of the C5–C6–N1, C5–C6–C7 bond angles in TS1-ax are 117.04°, 120.93°, respectively, and those of TS1-eq are 114.71°, 119.91°, respectively. These bond angles show that there is sp^2 hybridization at C(6) in the transition structure (TS1). This arrangement allows for the effective delocalization of the negative charge being formed at C(6).

The zwitterionic intermediates (IN1-ax and IN1-eq) are diastereomers as shown before (threo conformer). The potential energy for the intermediate (IN1-eq) has a value of 0.8 kcal/mol and is lower than that of IN1-ax (3.6 kcal/mol) due to a favorable arrangement. In the intermediate (IN1-ax), the C1–C4–C6–N1 dihedral angle (3.06°) indicated that the furan ring and the C6=N1 double bond of the NO_2 group are parallel to each other. Further, the distance between the C(4) and O(2) atoms of the NO_2 group (2.82 Å) indicates

Can. J. Chem. Downloaded from www.nrcresearchpress.com by Sichuan Normal University on 09/14/12
For personal use only.

Table 2. Total energies (au), relative energies (kcal/mol, in parentheses) and entropies (ΔS, cal/mol K) for the stationary points corresponding to the reaction between 2-methoxyfuran (**1**) and β-nitrostyrenes (**2f**) and (**2g**′).

	4f-ax			**4f**-eq			**4g**′-ax			**4g**′-eq		
		ΔE	ΔS		ΔE	ΔS		ΔE	ΔS		ΔE	ΔS
1 + 2	–1203.067493	0.00	0.00	–1203.067493	0.00	0.00	–1086.557216	0.00	0.00	–1086.557216	0.00	0.00
TS1	–1203.016608	(31.93)	–60.66	–1203.037532	(18.80)	–65.10	–1086.535961	(13.37)	–57.63	–1086.533090	(15.18)	–62.86
IN1	–1203.061781	(3.58)	–58.57	–1203.066278	(0.76)	–54.65	–1086.547471	(6.15)	–59.62	–1086.540675	(10.39)	–55.31
TS2	–1203.016161	(32.21)	–55.10	–1203.059377	(5.09)	–61.45	–1086.530167	(16.97)	–57.35	–1086.501673	(34.86)	–54.66
4	—	—	—	–1203.095317	(–17.46)	–53.17	–1086.588520	(–19.61)	–51.95	—	—	—

Table 3. Total energies (au) and relative energies (kcal/mol, in parentheses) for the stationary points corresponding to the reaction between 2-methoxyfuran (**1**) and β-nitrostyrenes (**2f**) and (**2g**′), including solvent effects.

	4f-eq		**4g**′-ax	
Compound	ΔE		ΔE	
1 + 2	–1203.092036	0.00	–1086.577207	0.00
TS1	–1203.078286	(8.63)	–1086.568913	(5.20)
IN1	–1203.096609	(–2.87)	–1086.570987	(3.90)
TS2	–1203.084933	(4.46)	–1086.556981	(12.69)
3	–1203.121686	(–18.61)	–1086.613408	(–22.72)

that separation of these atoms is near to the van der Waals distance. On the other hand, for the IN1-eq intermediate, the dihedral angle of C1–C4–C6–C7 (–132.70°) indicates that the C1–C4 axis and the C6–C7 bond are approximately perpendicular, and the angle of C1–C4–C6–N1 (0.09°) suggests that the C1–C4 axis is located parallel to the C6–N1 bond. This arrangement, which is present in intermediates (IN1), allows to a smooth promotion of the next rearrangement reaction.

It is also possible that the intermediates (IN1) may occur via the scission of a (4+2) cycloadduct (Diels–Alder adduct) (TS4 and TS5 in Scheme 2) as observed in our paper concerning the reaction of the furan.[1,11,12,28] The potential-energy barrier of the transition state for the concerted (4+2) addition reaction are 22.9 kcal/mol (for the "axial" form) and 23.6 kcal/mol (for the "equatorial" form), values that are over 4 kcal/mol higher than the energy of TS1-ax (18.8 kcal/mol). They are due to the steric repulsion between the methoxy group of the furan ring and the benzoyl group or the NO_2 group of the styrene. Furthermore, not only the higher energy barrier but also the large electrophilic gaps on the reaction sites (see the next section) should inhibit this pathway.

The final step of these reactions corresponds to a rearrangement of the zwitterionic intermediate (IN1-eq) to give the final isoxazoline *N*-oxide (**4f**). This rearrangement process can take place by the nucleophilic attack of the O(2)-atom of the NO_2 group on the C(4)-atom of the furan ring with formation of the C–N bond, together with the fission process in the plane of the C4–O1 bond of the furan ring to produce of the CO_2 group. In the TS2-ax transition structure for this process, the bond angle O1–C4–O2 is only 64.71°, which makes this transformation very unlikely. The length of the C4–O2 bond being formed is 2.93 Å and the length of the C4–O1 bond being cleaved is 2.08 Å. The value of the H4–C4–C5–H5 dihedral angle (20.35°) is consistent with the formation of the cis-form product (**4f**).

On the other hand, the process involving TS2-eq has a low potential-energy barrier (5.1 kcal/mol). In the transition structure (see Fig. 5), the center tetrahedral carbon C4 (C3–C4–C5: 109.09°, C3–C4–H4: 112.49°, C5–C4–H4: 111.17°, C5–C4–O1: 111.41°) is located between the O(2)-atom of the NO_2 group and O(1)-atom of the furan. The O1–C4–O2 bond angle is 117.72°, that is, the O(1)-atom, the C(4)-atom, and the O(2)-atom are arranged almost on a single straight line. The value of this bond angle indicates that the C(4) center presents an sp hybridization, in which the charge lo-

Can. J. Chem. Downloaded from www.nrcresearchpress.com by Sichuan Normal University on 09/14/12
For personal use only.

Table 4. The selected geometric parameters for TSs and intermediate of the reactions between 2-methoxyfuran (**1**) and β-nitrostyrenes (**2f**) and (**2g′**).

	4f-ax	**4f**-eq	**4g′**-ax	**4g′**-eq
TS1				
Distance (Å) C1—C6	2.70	3.48	2.64	3.32
Distance (Å) C4—C5	1.55	1.63	1.59	1.58
Bond angle (°) C5–C6–N1	117.04	114.71	119.13	118.12
Bond angle (°) C5–C6–C7	120.93	119.91	115.60	116.81
Dihedral angle (°) C5–C6–C7–O3	–17.56	–4.02	57.36	5.69
Dihedral angle (°) C5–C6–N1–O2	3.56	–13.18	–7.76	5.03
IN1				
Distance (Å) C1—N1	2.51	2.49	2.52	2.55
Distance (Å) C4—C6	2.61	2.56	2.60	2.56
Distance (Å) C4—O2	2.82	2.83	2.81	3.01
Bond angle (°) C3–C4–H4	112.59	115.84	112.63	114.75
Bond angle (°) C5–C4–O1	109.54	109.26	109.50	109.75
Dihedral angle (°) C1–C4–C6–C7	142.83	–132.70	147.49	–158.62
Dihedral angle (°) C1–C4–C6–N1	3.06	0.02	–1.95	3.43
TS2				
Distance (Å) C4—O1	2.08	1.46	1.84	2.29
Distance (Å) C4—O2	2.93	2.49	2.18	2.72
Bond angle (°) C3–C4–H4	118.22	112.49	117.69	118.92
Bond angle (°) C3–C4–C5	123.12	109.09	120.54	121.46
Bond angle (°) C5–C4–H4	115.05	111.17	119.49	116.91
Bond angle (°) C5–C4–O1	116.54	111.41	100.10	125.49
Bond angle (°) O1–C4–O2	64.71	117.72	170.89	67.54
Dihedral angle (°) H4–C4–C5–H5	20.35	–68.18	139.12	78.18

Table 5. Relative energies (kcal/mol) in the gas phase and in $CHCl_3$ (kcal/mol, in parentheses) for the stationary points, and entropies (ΔS, cal/mol K) for the Michael addition reactions between 2-methoxyfuran (**1**) and β-nitrostyrenes (**2a**), (**2d**), and (**2g′**).

	3a-ax	**3a**-eq	**3d**-ax	**3d′-ax**	**3d**-eq	**3d′**-eq	**3g′**-ax
TS1	19.07	19.02	16.22	—	16.91	—	13.37
ΔS	–59.41	–59.30	–55.83	—	–57.07	—	–59.71
IN1	7.16	6.96	4.27	—	4.58	—	6.15
TS3	46.71	49.53	42.40	40.68	42.46	43.64	31.83
In $CHCl_3$	(35.29)	(35.00)	(29.62)	—	(28.62)	—	(19.49)
ΔS	–39.73	–44.56	–50.53	—	–50.00	—	–54.61
3	–17.93	–16.81	–16.33	—	–17.46	—	–16.66

cated at C(4) occupies a p atomic orbital. The length of the C4–O2 bond being formed is 2.49 Å and the length of the C4–O1 bond being cleaved is 1.46 Å. The value of the H4–C4–C5–H5 dihedral angle is –68.18°. These angles are consistent with the formation of the cis-form product (**4f**) in accords with the experimental results. The potential-energy gaps of the transformation process (TS2) are 32.2 kcal/mol for the ax conformer and 5.1 kcal/mol for the eq former. The latter is 27.1 kcal/mol more favorable than TS2-ax due to a favorable arrangement.

We have also computed relative entropies at 25 °C for the different stationary points (Table 2). At TS1, the large negative entropy change (61–65 cal/mol K) due to the restricted geometry associated with the intermolecular nature of the process is similar to that seen in Diels–Alder reaction.[29] However, for the second step (TS2), the activation entropy change is very small (–2.1 cal/mol K for ax form and –10.4 cal/mol K for eq form) due to the smooth intramolecular nature of the rearrangement process. Moreover, the formation of the *cis*-isoxazoline *N*-oxide (**4f**) is exothermic by –17.5 kcal/mol.

Thus, the formation of the isoxazoline via the eq form is kinetically and sterically more favorable than formation via the ax form. As a consequence, there is a large "equatorial" stereoselectivity along the path of nucleophilic attack of **1** on **2** in this stepwise mechanism in agreement with the experimental outcome.

The value of the H4–C4–C5–H5 dihedral angle in **4f** from the B3LYP/6–31G* calculation is 20.35°, which is in reasonable agreement with the value of 18.6(2)° found from the X-ray analysis (see Table 7). The other geometrical parameters obtained for the isoxazoline *N*-oxide (**4f**) from the calculation are in agreement with the experimental analysis of the structure of **4f**. The bond distances in the hetero-

Can. J. Chem. Downloaded from www.nrcresearchpress.com by Sichuan Normal University on 09/14/12
For personal use only.

Table 6. The selected geometric parameters for the Michael reactions between 2-methoxyfuran (**1**) and β-nitrostyrenes (**2a**), (**2d**), and (**2g′**).

	3a-eq	**3a**-ax	**3d**-eq	**3d′**-eq	**3d**-ax	**3d′**-ax	**3g′**
TS1							
Distance (Å) C1—C6	2.73	2.77	2.44	—	2.40	—	2.64
Distance (Å) C4—C5	1.69	1.68	1.63	—	1.58	—	1.56
Dihedral angle (°) C1–C4–C5–C6	15.46	9.71	9.92	—	8.72	—	0.37
IN1, IN2							
Distance (Å) C1—C6	3.48	3.54	3.45	3.19	3.48	3.52	3.36
Distance (Å) C4—C5	1.54	1.54	1.54	1.55	1.53	1.55	1.54
Dihedral angle (°) C1–C4–C5–C6	35.56	–39.54	30.53	54.26	–40.25	–38.51	27.98
TS3							
Distance (Å) C4—H4	1.25	1.29	1.28	1.35	1.32	1.35	1.34
Distance (Å) C6—H4	1.71	1.59	1.65	1.55	1.55	1.57	1.57
Bond angle (°) C4–H4–C6	100.82	105.01	103.08	106.07	106.28	106.98	106.94
Bond angle (°) C4–C5–C6	97.76	97.17	97.02	97.74	96.78	98.48	98.75
Bond angle (°) C3–C4–C5	128.49	128.11	130.87	130.97	130.62	126.75	133.28
Bond angle (°) H4–C4–C5	85.68	80.53	83.14	79.56	79.33	79.48	109.89

Table 7. Selected bond lengths, bond angles, and dihedral angles of **4f**, **4g**, and **4g′** from X-ray analysis and calculation.

Compound	**4f**	**4f**	**4g**	**4g′**
Parameters	X-ray	Calculated	X-ray	Calculated
N1—O2 (Å)	1.426(2)	1.446	1.415(7)	1.453
N1—C6 (Å)	1.313(2)	1.320	1.316(8)	1.324
C6—C5 (Å)	1.493(3)	1.480	1.494(8)	1.501
C4—C5 (Å)	1.547(3)	1.573	1.533(8)	1.566
C4—O2 (Å)	1.454(2)	1.439	1.458(7)	1.448
O2–N1–C6 (°)	111.1(2)	111.65	111.9(5)	109.95
N1–C6–C5 (°)	111.2(2)	111.46	110.6(6)	111.90
C6–C5–C4 (°)	101.5(2)	101.16	101.2(5)	99.76
C5–C4–O2 (°)	105.8(2)	105.77	105.0(5)	104.74
C4–O2–N1 (°)	106.6(1)	108.04	106.5(5)	106.03
H4–C4–C5–H5 (°)	18.6(2)	20.35	105.4(4)	102.07

cyclic ring for the calculated structure are slightly longer than those found by experiment (0.02 Å is the highest difference for the C4–C5 bond) with the sole exception of the C4–O2 bond distance, which is 0.015 Å shorter.

The reaction of 2-methoxyfuran (1) and β-methoxycarbonyl-β-nitrostyrene (2g′)

For these reactants, the potential-energy barriers associated with TS1-ax and TS1-eq are 13.4 and 15.2 kcal/mol, respectively, and the latter is disfavored by 2 kcal/mol relative to TS1-ax (see Table 2 and Fig. 3). In the structure of TS1-ax, the NO_2 group is located on the face of the furan ring. On the other hand, the NO_2 group is located out of the furan ring in TS1-eq. In these TS1 transition structures, the nitro group at C(6) is in the plane of the C5–C6 bond from C5–C6–N1–O2 dihedral angles (–7.76°, 5.03°), whereas the carbonyl group at C6 is also in the plane of C5–C6 bond from C5–C6–C7–O3 dihedral angles (57.36°, 5.69°) (see Table 4). This arrangement allows for the effective delocalization of the negative charge being formed at C(6) as in the case of **2f**.

In the zwitterionic intermediates (IN1-ax), the distance between C1 and N1 (2.6 Å), C4 and C6 (2.6 Å), and the dihedral angle of C1–C4–C6–N1 (–1.95°) all indicate that the nitro group is parallel to the plane of the furan ring and that of the C5=N1 double bond being attacked. On the other hand, the distance (2.8 Å) between the C(4) and O(2) atoms indicates that these atoms are positioned close to the sum of their van der Waals radii. The values of the C5–C4–O1 bond angles are ~110° and those of C3–C4–H4 are 113°, which show that C(4) is sp^3-hybridized. The intermediate (IN1-ax) has a potential energy that is 4.2 kcal/mol lower than IN1-eq due to a favorable electronic interaction between the furan ring and the NO_2 group.

With **2g′** as a reactant, the intermediates (IN1) can also undergo two transformations. One of them corresponds to the rearrangement process of the zwitterionic intermediate to give the final isoxazoline *N*-oxide (**4g′**). The other process (TS3) gives the Michael adducts. In the transition structure for this process (TS2) (see Figs. 5 and 6), the center tetrahedral carbon C4 (C3–C4–C5: 121°, C3–C4–H4: 118°, C5–C4–H4: 119°) is located between the O(2)-atom of the NO_2

Fig. 8. Fukui functions for the furan (**1**), the styrenes (**2f** and **2g′**), and the intermediates (IN1-**4f**, IN1-**4g′**).

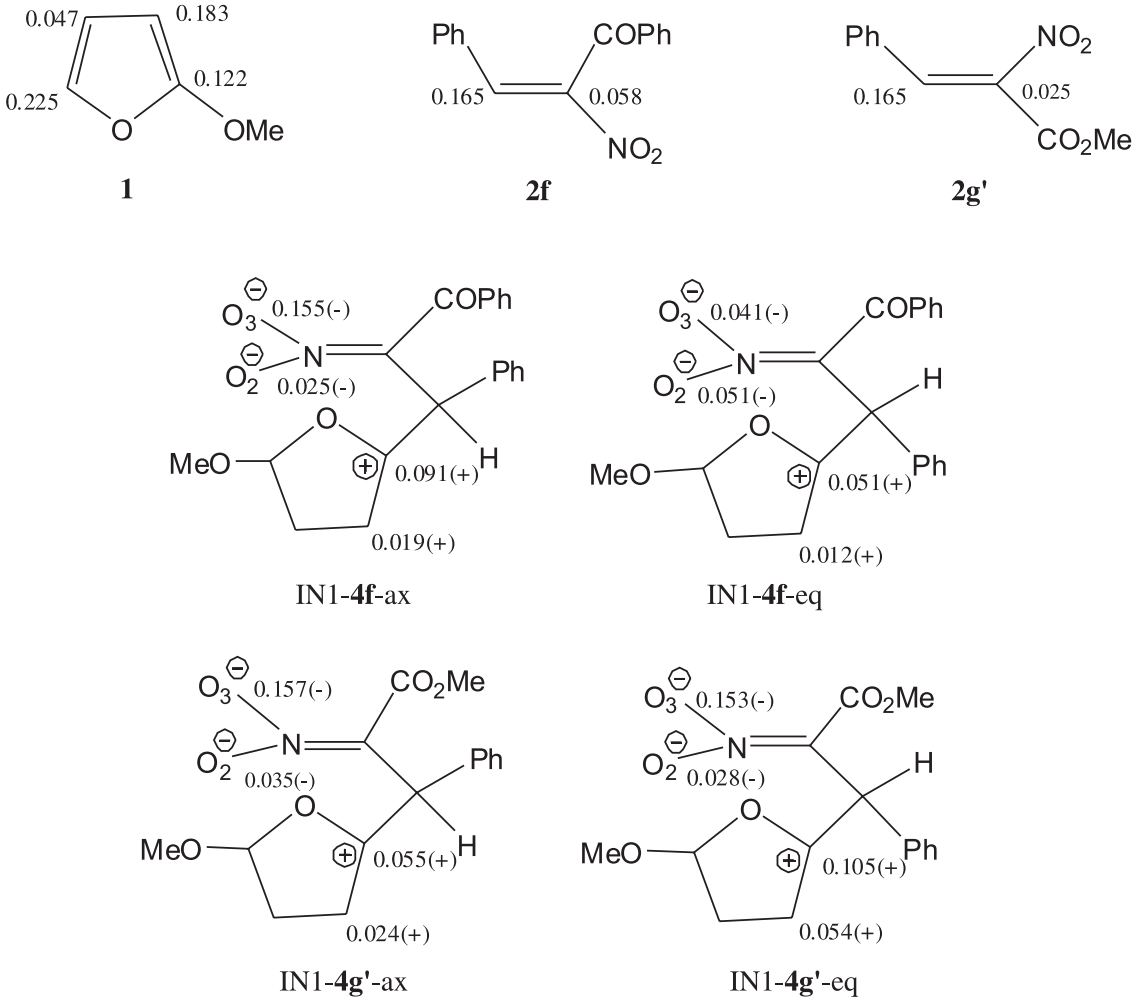

group and O(1)-atom of the furan. In TS2-ax, the O1–C4–O2 bond angle is 170.89°, that is, the O(1), C(4), and O(2) atoms are aligned in a single straight line. The length of the C4–O2 bond being formed is 2.18 Å and the length of the C4–O1 bond being cleaved is 1.84 Å. The value of the H4–C4–C5–H5 dihedral angle is 139.12°. These angles indicate that the reaction proceeds smoothly to the trans-form product (**4g′**). On the other hand, in TS2-eq, the O(1), C(4), and O(2) atoms are not arranged on a single straight line because the O1–C4–O2 bond angle is only 67.54°, which make this transformation unlikely. Furthermore, the value of the H4–C4–C5–H5 dihedral angle (78.18°) is consistent with the formation of the cis-form product, which is not consistent with the experimental results. The potential-energy gaps for the TS2 transformation process are 17.0 kcal/mol for the ax former and 34.9 kcal/mol for the eq former. The latter is 17.9 kcal/mol more disfavorable than TS2-ax.

As before, we have computed the relative entropies (see Table 2). At TS1, the large negative entropy change (58–63 cal/mol K) is due to the intermolecular nature of the process. However, for the second process (TS2), the difference of the negative activation entropy change is only 2–8 cal/mol K, the small value being due to the smooth intramolecular nature of the rearrangement process. Again, we find that the formation of the *trans*-isoxazoline *N*-oxide (**4g′**) is exothermic by –19.6 kcal/mol.

Thus, the formation of the isoxazoline from the ax form is kinetically more favorable than the formation from the eq form. As a consequence, there is a large axial stereoselectivity along the nucleophilic attack path of **1** on **2** in this stepwise mechanism in agreement with the experimental outcome.

The calculated geometrical parameters for the **4g** product are in good agreement with experiment. The value of the H4–C4–C5–H5 dihedral angle from the B3LYP/6–31G* calculation is –102.07°, which is in good agreement with the X-ray analysis for **4g** (–105.4(4)°) (see Table 7). The other geometrical parameters obtained for the isoxazoline *N*-oxide (**4g′**) from the calculation are in agreement with the experimental analysis of the structure of **4g**. The bond distances in the heterocyclic ring for the calculated structure are slightly longer than those from experiment, and the calculated bond angles only differ slightly from the experimental values (less than 1.5%).

Solvent effect on the rearrangement reactions

Solvent effects on cycloaddition are well-known[30] and have received considerable attention. Table 3 shows the relative energies of the stationary points corresponding to the

Can. J. Chem. Downloaded from www.nrcresearchpress.com by Sichuan Normal University on 09/14/12
For personal use only.

Can. J. Chem. Downloaded from www.nrcresearchpress.com by Sichuan Normal University on 09/14/12
For personal use only.

reaction in the $CHCl_3$ used as the experimental solvent. The energy differences of the transition state TS1 in this solvent are stabilized by 8–10 kcal/mol over that in the gas phase. The transition structure involving nucleophilic attack is preferentially stabilized relative to the reactants due to the large charge transfer that is developed along this polar transfer path. The solvent-effect increases for TS1 are more dramatic than those of TS2. Thus, inclusion of the solvent effect may accelerate this polar reaction, thanks to a larger stabilization of the transition state corresponding to nucleophilic attack, and decrease the energies. However, the data on IN1 do not show a definite difference between the gas phase and in-solvent. These results are due to the low variation of the dipole moments along the reactive channels and are related to the effective delocalization of the charge. Also, in the reaction of **2g′** at TS2, the transition structures in solvent are stabilized over the gas phase by 7 kcal/mol. This difference of TS energies in the solvent and in the gas phase is related to localization of the charge around the ester group. The low energy barrier found for the reaction is in good agreement with the fact that, experimentally, this reaction can be carried out at room temperature.

The formation process of the Michael adduct

The intermediate IN1 in the reaction of β-methoxycarbonyl-β-nitrostyrene (**2g′**) may also undergo an alternative process pathway that leads to the formation of a Michael adduct. Also, the reaction of **2a**–**2e** with **1** gave the Michael adducts.[31]

The canonical structure showed as IN1 at the zwitterionic intermediate formed in the previous process (TS1) takes to the other canonical structure (IN2) by the cation transfer from the O-atom of the furan to the atom of C(3) (see Scheme 2).[32] The intermediate IN2 may lead to the formation of the Michael adducts (**3**) via a four-membered transition structure in which the intramolecular proton (H4) transfers from the C(4) to the anionic C(6) center with furan ring (TS 3) (see Fig. 7). The energy barriers associated with TS3 together with TS1 and IN2, and the geometric parameters are shown in Tables 5 and 6 and Fig. 4.

This process (TS3) presents a high potential-energy barrier (46.7, 49.5 kcal/mol for **2a**; 42.4, 42.5 kcal/mol for **2d**) relative to the former addition steps (TS1), and the energies of the two stereoisomers do not show a definite difference. However, the potential energy (31.8 kcal/mol at the B3LYP/6–31G* level) for **2g′**-ax is significantly lower than those of **2a** and **2d**, but is unfavorable compared with that of the competitive pathway (TS2-ax: 17.0 kcal/mol). The larger potential-energy barrier in TS3 for **2g′** relative to TS2 is responsible for the lower reactivity seen in the former experiment.[33]

In the transition state TS3, the length of the C4–H4 bond being broken is 1.25–1.35 Å and the C6–H4 bond being formed is 1.55–1.71 Å. These lengths suggest a concerted bond-breaking and -formation process for the intramolecular proton transformation. One of the causes of the high potential energy of TS3 relative to TS1 is the angular strain associated with the formation of this transition structure. The C3–C4–C5 bond angle is 128°–133° (~110° at TS1) and the H4–C4–C5 bond angle is 79°–86° for **3a** and **3d** and 110° for **3g′**. These values show that the C(4) center is far from being sp^3-hybridized. In addition, the C4–C5–C6 bond angle (~98°) is associated with the strain that appears during the formation of this four-membered transition structure. In contrast, the TS1 route has a lower energy due to a favorable π–π electric interaction between the furan (**1**) and the nitrostyrene (**2**) taking a syn-periplanar conformation. However, for the intramolecular process, the negative activation entropy is lower by 15–20 cal/mol K for **2a**, 5–7 cal/mol K for **2d,** and 5 cal/mol K for **2g′**, compared with the more entropically favorable value for the asymmetrical addition reaction (TS1). In addition, the computed free energy of activation is found to be 5–8 kcal/mol. These cooperative factors permit the intramolecular process to occur with the smooth motion of the H(4) atom from the C(4) to the C(6) center. In addition, the energy differences of the transition state TS3 in solvent are stabilized by 11–15 kcal/mol over that in the gas phase. The transition structure involving proton transfer is preferentially stabilized relative to the reactants due to the large charge transfer that is developed along this polar transfer path.

Two Michael adducts (**3d** and **3d′**) are obtained from the reaction of **2d**. The new intermediates (IN2′), which corresponded to the anti conformation between the Ph and Br groups, have been found. The rotational barrier around the C5–C6 single bond may allow the easy equilibration between the two conformers (IN2 and IN2′); therefore, two isomers of the products (**3d** and **3d′**) are obtained in equivalent yields. In IN2′, the bond distances C4–C5 (1.55, 1.55 Å) and C1–C6 (3.52, 3.19 Å) and the C1–C4–C6–C5 angle (–38.5° and 54.3°) are similar to those of IN2. Also, the potential-energy barriers (40.7, 43.6 kcal/mol) at TS3′ are similar to those of TS3, and the geometrical parameters for TS3′ show similar values to those of TS3. They indicate that the Michael adduct from the IN2 and IN2′ may produce equivalent yields; the former gives the threo product and the latter gives the erythro product.

This transition structure presents a very high imaginary frequency (1500–2000i cm^{-1}), indicating that this process is associated mainly with the motion of the H4 atom from C4 to C6 centers.

Local electrophilicity/nucleophilicity analysis

Recent studies of cycloaddition reactions with a polar character have used an analysis of the electrophilic and nucleophilic Fukui functions to explain the observed experimental region-selectivities.[34] The local functions for our case are summarized in Fig. 8. The 2-methoxyfuran (**1**) has the largest nucleophilic activation at the nonsubstituted C4 position (f^- = 0.225); hence, this is the more reactive site for the electrophilic attack. On the other hand, for the styrene systems **2f** and **2g′**, there are two electrophilic sites (at the C5 and C6 carbon atoms). Analysis of the electrophilic Fukui functions for **2f** and **2g′** indicate that the C5 position has the lower electrophilic activity (f^+ = 0.165 > 0.058 for **2f**, 0.165 > 0.025 for **2g′**). Thus, the most favorable interaction will take place between the C4 carbon atom of **1** and the C5 carbon atom of **2**, in agreement with the regioselectivity observed.

The second step in the reaction is the rearrangement reaction of the zwitterionic intermediates IN1-ax and IN1-eq to give the isoxazoline **4**. This process involves the nucleophilic attack of the O(2)-atom of the NO_2 group at the styrene **2** side to the electron-poor furan residue (C4). As a conse-

Can. J. Chem. Downloaded from www.nrcresearchpress.com by Sichuan Normal University on 09/14/12
For personal use only.

quence, for IN1-ax and IN1-eq, the site analysis must be carried out at the electrophilic positions (C4) of the furan residues, the C4 (f^+ = 0.091(+), 0.051(+) for IN1-**4f**, and f^+ = 0.055(+), 0.105(+) for IN1-**4g′**, respectively) center, and the nucleophilic position of the styrene, O2 center (f^- = 0.025(–), 0.051(–) for IN1-**4f** and f^- = 0.035(–), 0.028(–) for IN1-**4g′**, respectively)[35] (see Fig. 8). These local Fukui functions show that the more favorable interaction along the addition reaction process corresponds to the attack of the nucleophilic C4 center on the electrophilic O2 and lead to formation of isoxazoline. Moreover, comparison of the nucleophilic function for the both isomers at **4f** and **4g′** indicate an activity at O2, but a quite large difference is found between the isomers, the value exhibiting an opposite tendency. The function has a larger value for the eq form at **4f** (0.025 < 0.051), but on the other hand, shows a larger value (0.035 > 0.028) for the ax form at **4g′**. These contrasting results allow us to explain the predominant isomer products, the more reactive nucleophilic attack for the eq form at **4f**, and the more reactive attack for the ax form at **4g′**. Thus, this local analysis is in agreement with the experimental results.

Experimental

IR spectra were recoreded in KBr bellets using *Hitachi I-2000*r instrument in cm^{-1}. ^1H and ^{13}C NMR Spectra were recorded on a Bruker *AC-250* and *GX-400* spectrometers in $CDCl_3$ solutions; δ in ppm; relative to $SiMe_4$ as the internal reference; *J* in Hz. Mass spectra (MS) were recorded on a *GCMS-QP2000A* instrument in *m/z*. Melting points were recorded using a *Yanaco* micro hot-plate apparatus and are uncorrected.

Materials

β-Nitrostyrene derivatives (**2a**–**2i**) were prepared according to the Knoevenagel condensation of benzaldehyde with nitroalkenes reported by either Dornow et al.[36] or Yamamura and co-workers.[37]

1-(2-Methoxyfuran-5-yl)-1-phenyl-2-nitroethane, (3a)

Oil. IR: 3028, 2944, 1620, 1588, 1556, 1456, 1378, 1260, 752, 704. ^1H NMR (250 MHz) δ: 3.80 (H, s), 4.75 (1H, dd, *J* = 6.0, 15.5), 4.78 (1H, dd, *J* = 6.0, 11.1), 4.95 (1H, dd, *J* = 11.1, 15.5), 5.05 (1H, d, *J* = 3.2), 5.97 (1H, d, *J* = 3.2), 7.30 (5H, m). ^{13}C NMR (67.8 MHz) δ: 43.6, 57.8, 80.1, 108.8, 127.9, 128.1, 129.1, 136.9, 141.6, 161.6. MS: 247(M^+), 188, 187, 150, 115, 104. Anal. calcd. for $C_{13}H_{13}NO_4$: C 63.15, H 5.30, N 5.67; found: C 63.08, H 5.38, N 5.48.

1-(2-Methoxyfuran-5-yl)-1-(*p*-methoxyphenyl)-2-nitroethane, (3b)

Oil. IR: 3108, 2944, 2840, 1558, 1380, 1176. ^1H NMR (250 MHz) δ: 3.68 (3H, s), 3.70 (3H, s), 4.72 (1H, dd, *J* = 7.5, 15.1), 4.74 (1H, dd, *J* = 7.5, 10.8), 4.94 (1H, dd, *J* = 10.8, 15.1), 5.03 (1H, d, *J* = 3.2), 5.94 (1H, d, *J* = 3.2), 6.87 (2H, d, *J* = 8.7), 7.21 (2H, d, *J* = 8.7). ^{13}C NMR (67.8 MHz) δ: 43.0, 55.4, 57.8, 80.0, 108.7, 114.5, 128.9, 129.1, 130.1, 142.0, 161.6. MS: 281(M^+), 135, 134, 115, 91, 77, 75, 59, 55. Anal. calcd. for $C_{14}H_{15}NO_4$: C 59.18, H 5.58, N 4.94; found: C 59.35, H 5.61, N 5.18.

1-(*p*-Chlorophenyl)-1-(2-methoxyfuran-5-yl)-2-nitroethane, (3c)

Oil. IR: 3024, 2940, 1620, 1556, 1092. ^1H NMR (250 MHz) δ: 3.80 (3H, s), 4.74 (1H, d, *J* = 8.0, 16.1), 4.76 (1H, d, *J* = 8.0, 11.1), 4.94 (1H, d, *J* = 11.1, 16.1), 5.04 (1H, d, *J* = 3.4), 5.96 (1H, d, *J* = 3.4), 7.27 (4H, m). ^{13}C NMR (67.8 MHz) δ: 43.0, 57.9, 80.1, 109.1, 114.7, 128.9, 129.3, 134.1, 135.4, 141.0, 161.7. MS: 138, 115, 77, 75, 55. Anal.calcd. for $C_{13}H_{12}NO_4Cl$: C 55.43, H 4.29, N 4.97; found: C 55.19, H 4.42, N 4.82.

2-Bromo-1-(2-methoxyfuran-5-yl)-1-phenyl)-2-nitroethane, (3d-I)

Oil. IR: 3028, 2988, 1570, 1356, 752, 700. ^1H NMR (250 MHz,) δ: 3.82 (3H, s), 4.66 (1H, d, *J* = 10.7), 5.07 (1H, d, *J* = 3.3), 6.20 (1H, d, *J* = 3.3), 6.40 (1H, d, *J* = 10.7), 7.36 (5H, m). ^{13}C NMR (67.8 MHz) δ: 51.8, 57.8, 80.4, 81.0, 110.8, 128.1, 129.0, 129.7, 135.2, 139.4, 161.9. MS: 297, 295, 217, 185, 183, 155, 115, 102, 77. Anal. calcd. for $C_{13}H_{12}NO_3Br$: C 56.14, H 4.35, N 5.04; found: C 56.10, H 4.66, N 4.82.

2-Bromo-1-(2-methoxyfuran-5-yl)-1-phenyl-2-nitroethane, (3d-II)

Oil. IR: 3108, 2960, 1570, 1346, 772, 702. ^1H NMR (250 MHz) δ: 3.77 (3H, s), 4.71 (1H, d, *J* = 10.7), 5.00 (1H, d, *J* = 3.3), 6.06 (1H, d, *J* = 3.3), 6.36 (1H, d, *J* = 10.7), 7.36 (5H, m). ^{13}C NMR (67.8 MHz) δ: 51.4, 57.8, 80.1, 80.8, 110.7, 128.0, 128.5, 129.2, 135.1, 138.7, 161.8. Anal. calcd. for $C_{13}H_{12}NO_3Br$: C 56.14, H 4.35, N 5.04; found: C 56.44, H 4.25, N 5.08.

Methyl-(2*z*)-3-(*N*-oxy-3-benzoyl-*cis*-(4-phenyl-4,5-dihydroisoxazol-5-yl))-propyl-2-enolate, (4f)

Mp 169.0–170.3 °C. IR: 3064, 2956, 1722, 1652, 1602, 1450, 1374, 1256, 1228, 1204, 798, 702. ^1H NMR (400 MHz) δ: 3.61 (3H, s), 4.70 (1H, d, *J* = 4.10), 6.05 (1H, dd, *J* = 1.47, 11.64), 6.18 (1H, ddd, *J* = 1.47, 4.10, 7.54), 6.57 (1H, ddd, *J* = 1.47, 7.54, 11.64), 7.18 (2H, m), 7.27 (3H, m), 7.42 (2H, m), 7.52 (1H, m), 7.72 (2H, m). ^{13}C NMR (67.8 MHz) δ: 52.0, 53.4, 85.6, 118.8, 123.1, 127.4, 128.1, 128.4, 128.5, 128.9, 129.1, 131.7, 133.4, 141.6, 159.2, 165.7, 184.9. MS: 351, 292, 171, 114, 105, 77. Anal. calcd. for $C_{20}H_{17}NO_5$: C 68.37, H 4.88, N 3.99; found: C 68.25, H 5.06, N 3.91.

Methyl-(2*z*)-3-(*N*-oxy-3-benzoyl-*trans*-(4-phenyl-4,5-dihydroisoxazol-5-yl))propyl-2-enolate, (4f′)

Mp 71.3–72.5 °C. IR: 1730, 1652, 1602, 1452, 1374, 1200, 798, 700. ^1H NMR (250 MHz) δ: 3.58 (3H, s), 4.75 (1H, d, *J* = 3.2), 6.04 (1H, dd, *J* = 1.4, 11.5), 6.21 (1H, ddd, *J* = 1.4, 3.2, 7.5), 6.56 (1H, dd, *J* = 7.5, 11.5), 7.50 (10H, m).

Ethyl 3-(5-methoxy(2-furyl))-2-nitro-3-phenylpropanoate, (3g)

Oil. ^1H NMR (250 MHz) δ: 1.22 (3H, t, *J* = 7.1), 3.79 (3H, s), 4.00 (2H, q, *J* = 7.1), 4.92 (1H, d, *J* = 11.5), 5.02 (1H, d, *J* = 3.2), 5.73 (1H, d, *J* = 11.1), 6.09 (1H, d, *J* = 3.2), 7.33 (5H, s). ^{13}C NMR (67.8 MHz) δ: 13.3, 48.2, 57.6, 62.9, 80.0, 90.0, 109.6, 128.0, 128.4, 135.7, 140.0, 161.0.

Anal. calcd. for $C_{16}H_{17}NO_4$: C 60.18, H 5.37, N 4.39; found: C 59.06, H 5.33, N 4.16.

2-Ethoxycarbonyl-1-(2-methoxyfuran-5-yl)-1-phenyl-2-nitroethane, (3g′)

Oil. ^{1}H NMR (250 MHz) δ: 0.96 (3H, t, J = 7.2), 3.79 (3H, s), 4.21 (2H, q, J = 7.2), 4.90 (1H, d, J = 11.4), 5.02 (1H, d, J = 3.2), 5.76 (1H, d, J = 11.4), 6.03 (1H, d, J = 3.2), 7.33 (5H, s).

Methyl-(2*z*)-3-(*N*-oxy-3-ethoxycarbonyl-*trans*-(4-phenyl-4,5-dihydro-isoxazol-5-yl))propyl-2-enolate, (4g)

Mp 63–64 °C. IR: 1732, 1728, 1626, 1442, 1382, 1354, 1286, 1230, 1200, 1198, 1026, 754. ^{1}H NMR (400 MHz) δ: 1.17 (3H, t, J = 3.7), 3.61 (3H, s), 4.18 (2H, q, J = 3.7), 4.41 (1H, d, J = 2.4), 6.01 (1H, dd, J = 1.7, 11.5), 6.03 (1H, ddd, J = 1.7, 2.4, 7.5), 6.51 (1H, dd, J = 7.5, 11.5), 7.36 (5H, m) . ^{13}C NMR (67.8 MHz) δ: 13.8, 51.7, 55.9, 61.6, 79.6, 111.2, 122.5, 127.4, 128.8, 129.1, 138.2, 145.2, 158.3, 165.8. MS: 319 (M^+), 197, 171, 147, 131, 117, 106. Anal. calcd. for $C_{16}H_{17}NO_4$: C 60.18, H 5.37, N 4.39; found: C 60.03, H 5.22, N 4.30.

Methyl-(2*z*)-3-(*N*-oxy-3-benzoyl-*cis*-(4-*p*-methoxyphenyl-4,5-dihydro-isoxazol-5-yl))-propyl-2-enolate, (4h)

Mp 164–165 °C. ^{1}H NMR (400 MHz) δ: 3.60 (3H, s), 3.80 (3H, s), 4.47 (1H, d, J = 3.7), 6.02 (1H, dd, J = 1.5, 11.6), 6.17 (1H, ddd, J = 1.5, 3.7, 7.8), 6.49 (1H, ddd, J = 1.5, 7.8, 11.6), 6.92 (2H, d, J = 7.7), 7.31 (2H, d, J = 7.7), 7.58 (5H, m). ^{13}C NMR (67.8 MHz) δ: 51.80, 54.58, 55.24, 85.83, 114.25, 122.27, 127.44, 128.16, 128.91, 129.92, 131.73, 132.36, 144.94, 159.16, 165.22, 184.80. MS: 381, 364, 350, 335, 322, 303, 275, 265, 239, 202, 146, 105. Anal. calcd. for $C_{20}H_{19}NO_6$: C 65.04, H 5.19, N 3.79; found: C 65.16, H 5.07, N 3.67.

Methyl-(2*z*)-3-(*N*-oxy-3-benzoyl-*trans*-(4-*p*-methoxyphenyl-4,5-dihydro-isoxazol-5-yl))-propyl-2-enolate, (4i)

Mp 67.5–69.0 °C. ^{1}H NMR (400 MHz) δ: 3.60 (3H, s), 3.78 (3H, s), 4.70 (1H, d, J = 4.1), 6.05 (1H, d, J = 11.6), 6.18 (1H, dd, J = 4.1, 7.5), 6.57 (1H, d, J = 7.5, 11.6), 6.90 (2H, d, J = 8.7), 7.34 (2H, d, J = 8.7), 7.57 (5H, m). ^{13}C NMR (67.8 MHz) δ: 51.84, 55.23, 56.21, 80.23, 114.54, 123.06, 128.39, 128.41, 128.91, 128.91, 129.59, 133.54, 135.15, 144.48, 159.52, 165.19, 184.93. MS: 381, 364, 350, 335, 322, 306, 265, 239, 238, 217, 202, 146, 105. Anal. calcd. for $C_{20}H_{19}NO_6$: C 65.04, H 5.19, N 3.79; found: C 65.13, H 5.12, N 3.70.

X-ray crystallographic analysis

X-ray crystallographic analysis was carried out on Rigaku AFC5R diffractometer. The diffraction data were collected by using Mo Kα radiation, and 4350 independent reflections were used for solving the structure by the teXsan program.[38] All non-H atoms were located by directed methods using SIR92[39] and were refined anisotropically.

Crystal data for the $C_{20}H_{17}NO_5$: formular weight = 339.35; monoclinic, space group $P2_1/C$; a = 15.197(1), b = 5.808(2), c = 19.563(1) Å; β = 95.321(5)°; V = 1719.2(6) Å^3; Z = 4; $d_{calcd.}$ = 1.31g cm^{-1}; R = 0.055 (R_w = 0.045) for 4509 reflection data with $I > \sigma$ and 2823 valuables.

Crystal data for the $C_{16}H_{17}NO_6$: formular weight = 319.31; triclinic, space group P-1; a = 9.753(7), b = 10.28(1), c = 9.25(1) Å; α = 106.0(2)°, β = 109.3(1)°, γ = 94.13(8)°; V = 828(1) Å^3; Z = 2; $d_{calcd.}$= 1.28 gcm^{-1}; R = 0.068 (R_w = 0.045) for 1389 reflection data with $I > 3\sigma$ and 208 valuables.

Summary

This study examined the reaction of 2-methoxyfuran with β-nitrostyrenes and the nature of the mechanism of the isoxazoline *N*-oxide and the Michael adduct produced using quantum mechanical calculations. Experimental data showed that by the reaction with the β–nitrostyrenes (**2f** and **2g′**), with electron-withdrawing groups, the isoxazoline is obtained and the *Z*-form of the nitrostyrene (**2g′**) gives the trans-product and the *E*-form (**2f**) gives the cis-product. We have shown the following:

(*i*) An analysis of the results of the calculation shows that the reaction takes place via a polar stepwise mechanism. The first step (TS1) corresponds to the nucleophilic attack of the furan ring on the nitrostyrene to give two zwitterionic intermediates (IN-ax and IN-eq). For the second step (TS2), an intramolecular substitution in the intermediate (IN) gives the formation of the isoxazoline (**4g′** and **4f**) together with fission of the furan ring. Alternatively, the intermediate (IN) is transformed into the Michael adduct (**3g′**) by an intramolecular proton transfer.

(*ii*) The isoxaszolines (**4g′** and **4f**) come from the ring closure via the oxygen atom (endo-O atom) of the nitro group of the intermediate (IN).

(*iii*) The Michael adduct, also, comes from the similar intermediate (IN-ax′).

(*iv*) From the theoretical results, the selectivity of the reaction is determined by the difference between the ax-form and the eq-form energies at TS1 and TS2.

(*v*) The solvent-effect increase for TS1 is more dramatic than that of TS2 owing to the localization of the charge.

(*vi*) The formation process of the Michael adducts (TS3) show a high potential energy, but that of **2g′**-ax is significantly higher than that of the competitive pathway (TS2).

(*vii*) The high potential energy of TS3 is due to the angular strain associated with the formation of the four-membered transition structure.

(*viii*) The local Fukui function analysis gave the good suggestion for the reaction site.

(*iv*) The calculation analysis obtained in this paper offered the reasonable explanation for the experimental results.

Supplementary data

Supplementary data for this article are available on the journal Web site (canjchem.nrc.ca) or may be purchased from the Depository of Unpublished Data, Document Delivery, CISTI, National Research Council Canada, Ottawa, ON K1A 0R6, Canada. DUD 3948. For more information on obtaining material, refer to cisti-icist.nrc-cnrc.gc.ca/cms/unpub_e.shtml. CCDC 440/175 and 291612 contain the X-

Can. J. Chem. Downloaded from www.nrcresearchpress.com by Sichuan Normal University on 09/14/12
For personal use only.

ray data in CIF format for $C_{20}H_{17}NO_5$ and $C_{16}H_{17}NO_6$, respectively, for this manuscript. These data can be obtained, free of charge, via www.ccdc.cam.ac.uk/conts/retrieving.html (Or from the Cambridge Crystallographic Data Centre, 12 Union Road, Cambridge CB2 1EZ, UK; fax +44 1223 336033; or deposit@ccdc.cam.ac.uk).

Acknowledgements

The authors are grateful to Professor K. Yamamura (Kobe university) for the gift of β-nitrostyrenes.

References

(1) (a) Itoh, K.; Kitoh, K.; Sera, A. *Heterocycles* **1999**, *51* (2), 243. doi:10.3987/COM-98-8398.; (b) Sera, A.; Itoh, K.; Yamaguchi, H. *Tetrahedron Lett.* **1990**, *31* (45), 6547–6548. doi:10.1016/S0040-4039(00)97113-2.; (c) Sera, A.; Ohara, M.; Kubo, T.; Itoh, K.; Yamada, H.; Mikata, Y.; Kaneko, C.; Katagiri, N. *J. Org. Chem.* **1988**, *53* (23), 5460–5464. doi:10.1021/jo00258a012.; (d) Itoh, K.; Iwata, S.; Kishimoto, S. *Heterocycles* **2006**, *68* (2), 395. doi:10.3987/COM-05-10656.; (e) Itoh, K.; Kitoh, K.; Kishimoto, S. *Can. J. Chem.* **2006**, *84* (3), 392–406. doi:10.1139/V06-013.

(2) (a) Lipshutz, B. H. *Chem. Rev.* **1986**, *86* (5), 795–819. doi:10.1021/cr00075a005.; (b) Woo, S.; Keay, B. A. *Synthesis* **1996**, *1996* (06), 669–686; and refs. cited therein. doi:10.1055/s-1996-4295.; (c) Lautens, M.; Fillion, E. *J. Org. Chem.* **1996**, *61* (23), 7994–7995. doi:10.1021/jo961635c. PMID:11667775.; (d) Sargent, M. V.; Dean, F. M. In *Comprehensive heterocyclic chemistry*; Pergamon: Oxford; 1984.

(3) (a) Kappe, C. O.; Murphree, S. S.; Padwa, A. *Tetrahedron* **1997**, *53* (42), 14179–14233. doi:10.1016/S0040-4020(97)00747-3.; (b) Tsuda, T.; Sugiyama, S.; Mori, A.; Takeshita, H. *Bull. Chem. Soc. Jpn.* **1987**, *60* (7), 2695–2697. doi:10.1246/bcsj.60.2695.; (c) Dauben, W. G.; Lam, J. Y. L.; Guo, Z. R. *J. Org. Chem.* **1996**, *61* (14), 4816–4819. doi:10.1021/jo960210n. PMID:11667419.; (d) Lipshutz, B. H. *Chem. Rev.* **1986**, *86* (5), 795–819. doi:10.1021/cr00075a005.

(4) (a) Potts, K. T.; Walsh, E. B. *J. Org. Chem.* **1988**, *53* (6), 1199–1202. doi:10.1021/jo00241a014.; (b) Padwa, A.; Dimitroff, M.; Waterson, A. G.; Wu, T. *J. Org. Chem.* **1997**, *62* (12), 4088–4096. doi:10.1021/jo9702599.

(5) (a) Barrett, A. G. M.; Graboski, G. G. *Chem. Rev.* **1986**, *86* (5), 751–762. doi:10.1021/cr00075a002.; (b) Barrett, A. G. M. *Chem. Soc. Rev.* **1991**, *20* (1), 95. doi:10.1039/cs9912000095.; (c) Feuer, H.; Nielsen, A. T. In *Nitro compounds: recent advances in synthesis and chemistry*; John Willey & Sons: New York. 1992; (d) Adams, J. P.; Box, D. S. *J. Chem. Soc., Perk. Tran.* 1, **1999**, (7), 749–764. doi:10.1039/a801494i.

(6) (a) Denmark, S. E.; Dixon, J. A. *J. Org. Chem.* **1998**, *63* (18), 6167–6177; and refs. cited therein. doi:10.1021/jo9802168. PMID:11672247.; (b) Denmark, S. E.; Thorarensen, A. *Chem. Rev.* **1996**, *96* (1), 137–166. doi:10.1021/cr940277f. PMID:11848747.

(7) (a) Carruthers, W. In *Cycloaddition reactions in organic synthesis*; Pergamon: Oxford. 1990; (b) Oppolzer, W. In *Comprehensive organic synthesis*; Trost, B. M., Fleming, I., Paquentte, L. A., Eds.; Pergamon: Oxford, Vol. 5, 1991; p. 315; (c) Perekalin, V. V.; Lipina, E. S.; Berestovitskaya, V. M.; Efremov, D. A. In *Nitroalkene: conjugated nitro compounds*; Wiley: New York, 1994; p. 131.

(8) (a) Torsell, K. B. G. In *Nitrile oxides, nitrones and nitrones in organic synthesis*; VCH: New York; 1988; (b) Gottlieb, L.; Hassner, A. *J. Org. Chem.* **1995**, *60* (12), 3759–3763. doi:10.1021/jo00117a030.; (c) Dehaen, W.; Hassner, A. *Tetrahedron Lett.* **1990**, *31* (52), 743–746. doi:10.1016/S0040-4039(00)94618-5.

(9) (a) Padwa, A. In *1,3-Dipolar cycloaddition chemistry;* Vol. 2. Padwa, A, Ed.; Wiley-Interscience: New York; 1984; (b) Curran, D. P. In *Advance in cycloaddition*; Vol. 1; JA/Press: Greenwich CT; 1988; p. 129.(c) Padwa, A. In *Synthetic applications of 1,3-dipolar cycloaddition chemistry toward heterocycles and natural products*; Person, W. H., Padwa, A, Eds.; Wiley & Sons: Hoboken, NY; 2003.

(10) (a) Itoh, K.; Kishimoto, S. *N. J. Chem.* **2000**, *24* (6), 347–349. doi:10.1039/b001049i.; (b) Itoh, K.; Kishimoto, S. *N. J. Chem.* **2009**, *33* (5), 1127–1138.

(11) (a) Loncharich, R. J.; Brown, F. K.; Houk, K. N. *J. Org. Chem.* **1989**, *54* (5), 1129–1134. doi:10.1021/jo00266a026.; (b) Houk, K. N.; Loncharich, R. J.; Blake, J. F.; Jorgensen, W. L. *J. Am. Chem. Soc.* **1989**, *111* (26), 9172–9176. doi:10.1021/ja00208a006.; (c) Birney, D. M.; Houk, K. N. *J. Am. Chem. Soc.* **1990**, *112* (11), 4127–4138. doi:10.1021/ja00167a005.; (d) Houk, K. N.; Gonzalez, J.; Li, Y. *Acc. Chem. Res.* **1995**, *28* (2), 81–90. doi:10.1021/ar00050a004.

(12) (a) Sustmann, R.; Tappanchai, S.; Bandmann, H. *J. Am. Chem. Soc.* **1996**, *118* (50), 12555–12561. doi:10.1021/ja961390l.; (b) Sustmann, R.; Sicking, W. *J. Am. Chem. Soc.* **1996**, *118* (50), 12562–12571. doi:10.1021/ja961391d.

(13) Domingo, L.; Jones, R.; Picher, M.; Sepulvedaarques, J. *Tetrahedron* **1995**, *51* (32), 8739–8748. doi:10.1016/0040-4020(95)00490-Y.

(14) (a) Fringuelli, F.; Taticchi, A. In *Dienes in the Diels–Alder reaction*; John Wiley & Sons, Inc.: New York; 1990; (b) Beno, B. R.; Wilsey, S.; Houk, K. N. *J. Am. Chem. Soc.* **1999**, *121* (20), 4816–4826. doi:10.1021/ja9818250.; (c) Marshall, J. A.; Jiang, H. *J. Org. Chem.* **1999**, *64* (3), 971–983. doi:10.1021/jo982057y. PMID:11674171.

(15) Doppmeier, B. J.; Driessen, A. J.; Hehre, T. S.; Hehre, W. J.; Johnson, J. A.; Khunzinger, P. E.; Leonard, J. M.; Pham, I. N.; Pietro, W. J.; Yu, J. *Spartan 02*, Version 1.5a, and *Spartan 04*, Version 1.0.0; Wavefunction, Inc.: Irvine, CA; 1988.

(16) (a) Lee, C.; Yang, W.; Parr, R. G. *Phys. Rev. B* **1988**, *37* (2), 785–789. doi:10.1103/PhysRevB.37.785.; (b) Becke, A. D. *J. Chem. Phys.* **1993**, *98* (7), 5648. doi:10.1063/1.464913.

(17) Chambers, C. C.; Hawkins, G. D.; Cramer, C. J.; Truhlar, D. G. *J. Phys. Chem.* **1996**, *100* (40), 16385–16398. doi:10.1021/jp9610776.

(18) Frisch, M. J.; Trucks, G. W.; Schlegel, H. B.; Scuseria, G. E.; Robb, M. A.; Cheeseman, J. R.; Montgomery, J. A., Jr.; Vreven, T.; Kudin, K. N.; Burant, J. C.; Millam, J. M.; Iyengar, S. S.; Tomasi, J.; Barone, V.; Mennucci, B.; Cossi, M.; Scalmani, G.; Rega, N.; Petersson, G. A.; Nakatsuji, H.; Hada, M.; Ehara, M.; Toyota, K.; Fukuda, R.; Hasegawa, J.; Ishida, M.; Nakajima, T.; Honda, Y.; Kitao, O.; Nakai, H.; Klene, M.; Li, X.; Knox, J. E.; Hratchian, H. P.; Cross, J. B.; Bakken, V.; Adamo, C.; Jaramillo, J.; Gomperts, R.; Stratmann, R. E.; Yazyev, O.; Austin, A. J.; Cammi, R.; Pomelli, C.; Ochterski, J. W.; Ayala, P. Y.; Morokuma, K.; Voth, G. A.; Salvador, P.; Dannenberg, J. J.; Zakrzewski, V. G.; Dapprich, S.; Daniels, A. D.; Strain, M. C.; Farkas, O.; Malick, D. K.; Rabuck, A. D.; Raghavachari, K.; Foresman, J. B.; Ortiz, J. V.; Cui, Q.; Baboul, A. G.; Clifford, S.; Cioslowski, J.; Stefanov, B. B.; Liu, G.; Liashenko, A.; Piskorz, P.; Komaromi, I.; Martin, R. L.; Fox, D. J.; Keith, T.; Al-Laham, M. A.; Peng, C. Y.; Nanayakkara, A.; Challacombe,

Can. J. Chem. Downloaded from www.nrcresearchpress.com by Sichuan Normal University on 09/14/12
For personal use only.

M.; Gill, P. M. W.; Johnson, B.; Chen, W.; Wong, M. W.; Gonzalez, C.; Pople, J. A. *Gaussian 03*, Revision C.02; Gaussian, Inc.: Wallingford, CT; 2004.

(19) (a) Mennucci, B.; Cances, E.; Tomasi, J. *J. Phys. Chem. B* **1997**, *101* (49), 10506–10517. doi:10.1021/jp971959k.; (b) Mennucci, B.; Tomasi, J. *J. Chem. Phys.* **1997**, *106* (12), 5151. doi:10.1063/1.473558.; (c) Cossi, M.; Rega, N.; Scalmani, G.; Barone, V. *J. Chem. Phys.* **2001**, *114* (13), 5691. doi:10.1063/1.1354187.; (d) Cossi, M.; Scalmani, G.; Rega, N.; Barone, V. *J. Chem. Phys.* **2002**, *117* (1), 43. doi:10.1063/1.1480445.; (e) Cossi, M.; Rega, N.; Scalmani, G.; Barone, V. *J. Comput. Chem.* **2003**, *24* (6), 669–681. doi:10.1002/jcc.10189. PMID:12666158.; (f) Scalmani, G.; Barone, V.; Kudin, K. N.; Pomelli, C. S.; Scuseria, G. E.; Frisch, M. *J. Theor. Chem. Acc.* **2003**, *111*, 90.

(20) (a) Arulmozhiraja, S.; Kolandaivel, P. *Mol. Phys.* **1997**, *90*, 55 doi:10.1080/002689797172868.; (b) Contreras, R. R.; Fuentealba, P.; Galvan, M.; Perez, P. *Chem. Phys. Lett.* **1999**, *304* (5-6), 405–413. doi:10.1016/S0009-2614(99)00325-5.; (c) Fuentealba, P.; Pérez, P.; Contreras, R. *J. Chem. Phys.* **2000**, *113* (7), 2544. doi:10.1063/1.1305879.

(21) (a) Kappe, C. O.; Murphree, S. S.; Padwa, A. *Tetrahedron* **1997**, *53* (42), 14179–14233. doi:10.1016/S0040-4020(97)00747-3.; (b) Oda, K.; Machida, M. *J. Chem. Soc., Chem. Commun.* **1994**, (12): 1477. doi:10.1039/c39940001477.; (c) Casiraghi, G.; Rassu, G. *Synthesis* **1995**, *1995* (6), 607–626. doi:10.1055/s-1995-3983.

(22) Diels, O.; Alder, K. *Justus Liebigs Ann. Chem.* **1928**, *460* (1), 98–122. doi:10.1002/jlac.19284600106.

(23) The calculation results presented up to now confirm in the experimental results. We can observe that the yield (68%) of the isoxazoline (**4g**) in chloroform decreased to 22% in benzene solvent.

(24) Harada, H.; Kaji, E.; Sasaki, K.; Zen, S. *Heterocycles* **1996**, *42* (1), 289. doi:10.3987/COM-95-S26.

(25) Chow, Y. L.; Shu, Y. Y.; Bakker, R. H.; Pillay, K. S. *Heterocycles* **1989**, *29*, 2245. doi:10.3987/COM-88-S17-1.

(26) Coutouli-Argyropoulou, E.; Alexandrou, N. E. *J. Org. Chem.* **1980**, *45* (21), 4158–4162. doi:10.1021/jo01309a018.

(27) Denmark, S. E.; Thorarensen, A. *Chem. Rev.* **1996**, *96* (1), 137–166. doi:10.1021/cr940277f. PMID:11848747.

(28) Ranganathan, D.; Rao, C. B.; Ranganathan, S.; Mehrotra, A. K.; Iyengar, R. *J. Org. Chem.* **1980**, *45* (7), 1185–1189. doi:10.1021/jo01295a003.

(29) (a) Schmidt, G. M. J. *Pure Appl. Chem.* **1971**, *27*, 647; (b) Schmidt, G. M. J. *J. Chem. Soc.* **1964**, 2000–2013.

(30) (a) Sustmann, R.; Sicking, W.; Schelkens, H.-L.; Ghosez, L. *Tetrahedron Lett.* **1991**, *32* (11), 1401–1404. doi:10.1016/0040-4039(91)80341-3.; (b) Sustmann, R.; Sicking, W. *Tetrahedron* **1992**, *48* (47), 10293–10300. doi:10.1016/S0040-4020(01)88334-4.; (c) Pindur, U.; Lutz, G.; Otto, C. *Chem. Rev.* **1993**, *93* (2), 741–761. doi:10.1021/cr00018a006.; (d) Li, C.-J. *Chem. Rev.* **1993**, *93* (6), 2023–2035. doi:10.1021/cr00022a004.

(31) Fringuelli, F.; Taticchi, A. In *The Diels–Alder reaction, selected practical methods*; John Wiley & Sons, Ltd.: West Surrex, England; 2002.

(32) Ranganathan et al. (ref. 27) reported that furan and nitroethylene gave 2-(β-nitromethyl)-furan and proposed that the Michael product yielded from a Diels–Alder adduct.

(33) The yields were calculated from the products isolated after column chromatography. For the isoxazoline, the separation was difficult; therefore, a small percentage loss may result.

(34) Mulliken and natural population analysis atomic charge indicate that the C1 center has the largest degree of electrophilic activation. Thus, the most favorable interaction takes place between the C1 and C6 atoms with the formation of the (4+2) cycloadduct, which is at odds with the experimental results. Thus, these rearrangement reactions cannot be successfully analyzed using these population analysis methods.

(35) The other O3-atom of the NO_2 group has the higher electrophilic activity, but the length from the nucleophilic center C4 is over 4.5 Å, so the O3-atom should not take part in bond formation.

(36) (a) Dornow, A.; Menzel, H. *Liebigs Ann. Chem.* **1954**, *588* (1), 40–44. doi:10.1002/jlac.19545880105.; (b) Dornow, A.; Müller, A.; Lüpfer, S. *Liebigs Ann. Chem.* **1955**, *594* (3), 191–198. doi:10.1002/jlac.19555940304.

(37) (a) Watarai, S.; Yamamura, K.; Kinugasa, T. *Bull. Chem. Soc. Jpn.* **1967**, *40* (6), 1448–1452. doi:10.1246/bcsj.40.1448.; (b) Yamamura, K.; Watarai, S.; Kinugasa, T. *Bull. Chem. Soc. Jpn.* **1971**, *44* (9), 2440–2443. doi:10.1246/bcsj.44.2440.

(38) Molecular Structure Corporation; *TEXSAN single crystal structure analysis software*; MSC: TX; 1982.

(39) Burla, M. C.; Camalli, M.; Cascarano, G.; Giacovazzo, C.; Polidori, G.; Spagna, R.; Viterbo, D. *J. Appl. Cryst.* **1989**, *22* (4), 389–393. doi:10.1107/S0021889889004103.

Can. J. Chem. Downloaded from www.nrcresearchpress.com by Sichuan Normal University on 09/14/12
For personal use only.

Combined tight-binding/DFT investigation of the electronic structure of triimine-platinum(II)/TCNQ extended stacks[1,2]

Hassan Rabaâ, Thomas R. Cundari, and Mohammad A. Omary

Abstract: . The [Pt(tbtrpy)(X)][TCNQ] (X = OH or SH) complexes form sandwich stacks with nitrile acceptors leading to extended-chain supramolecular assemblies, tbtrpy = 4,4′,4″-*tert*-Bu_3-2,2′:6′,2″-terpyridine. Calculations with the extended Hückel tight-binding (EHTB) method are performed upon crystalline {[Pt (tbtrpy)(X)][TCNQ]}$_\infty$ species to analyze their electronic structure and consequent properties, TCNQ = 7,7,8,8-tetracyanoquinodimethane. The donor/acceptor extended chains in the solid state are predicted to exhibit metallic behavior with a large contribution from π and π* bands of TCNQ to the valence and conduction bands, respectively. Moreover, the valence band moves upward (i.e., to a less negative energy) for X = SH as compared to X = OH. Density functional theory (DFT) calculations suggest that this is due to large thiolate character in the HOMO of the square-planar donor complex, which also supports the experimental assignment of the electronic absorption bands and redox potentials. Calculations of infrared (ν_{CN} bands of TCNQ) and structural (CC bond lengths within TCNQ) data explain the metallic behavior of the stacks in terms of charge delocalization, leading to fractionally-charged species of the form $[Pt(tbtrpy)X]^{(1+\delta)+}[TCNQ]^{(1+\delta)-}$ with $\delta > 0$ and a greater δ value for X = SH vs OH.

Key words: DFT, TCNQ, platinum complexes, solid-state calculations.

Résumé : Les complexes [Pt(tbtrpy)(X)][TCNQ], {tbtrpy = 4,4′,4″-*tert*-Bu_3-2,2′:6′,2″-terpyridine; X = OH, SH; TCNQ = 7,7,8,8-tétracyanoquinodiméthane} forment des empilements sandwiches avec des accepteurs nitriles qui conduisent à la formation d'assemblages supramoléculaires à chaînes étendues. Des calculs en utilisant la méthode de Hückel étendue à liaisons fortes ("EHTB") ont été faits sur les espèces cristallines{[Pt(tbtrpy)(X)][TCNQ]}$_\infty$ afin d'analyser leur structure électronique et les propriétés qui en découlent. Les calculs permettent de prédire que les chaînes étendues de donneur-accepteur devraient présenter un comportement métallique avec une contribution importante des bandes π et π* du TCNQ aux bandes de valence et de conduction respectivement. De plus, la bande de valence se déplace vers le haut (c'est-à-dire vers une énergie moins négative) avec X = SH par rapport à X = OH. Des calculs selon la théorie de la fonctionnelle de la densité (TFD) suggèrent que cette situation est due au caractère thiolate important dans l'orbitale moléculaire haute occupée du complexe donneur plan carré et ils supportent l'attribution expérimentale des bandes d'absorption électronique et des potentiels redox. Des calculs infrarouges (bandes ν_{CN} du TCNQ) et des données structurales (longueurs des liaisons CC dans le TNCQ) expliquent le comportement des empilements en fonction de la délocalisation de la charge, conduisant à des espèces à charge fractionnaire de la forme $[Pt(tbtrpy)(X)]^{(1+\delta)+}[TCNQ]^{(1+\delta)-}$ dans lesquelles $\delta > 0$ alors que la valeur de δ pour X = SH est plus grande que celle pour X = OH.

Mots-clés : TFD, TCNQ, complexe du platine, calculs à l'état solide.

[Traduit par la Rédaction]

Introduction

The Pt(II)-polyimine class of square-planar complexes has become an interesting series of targets in inorganic spectroscopy.[3,4] Much work has been done to demonstrate the ability to modify the spectroscopic and electrochemical properties of such complexes upon variation of ligands and their substituents, as well as on their relevance for applications that include solar energy conversion, nonlinear optics, optical sensing, DNA intercalation, protein probing, and photoinduced electron transfer for hydrogen production.[5,6]

Dunbar, Omary, and co-workers have reported that neutral (diimine)(dithiolato) Pt^{II} and Pd^{II} complexes form supramolecular stacks with nitrile acceptors (see Fig. 1).[7a] The crystal structure of [Pt(tbtrpy)(OH)]TCNQ with (tbtrpy = 4,4′,4″-*tert*-Bu_3-2,2′;6′,2″-terpyridine, TCNQ = 7,7,8,8-tetracyanoquinodimethane) exhibits a distorted square planar coordination (tbtrpy bite angles of 80.8° and N_{tbtrpy}-Pt-O angles of 97.7° and 100.4°). The mean metal-ligand distances are Pt–N = 1.98 ± 0.02 Å and Pt–O = 2.24 Å. The material crystallizes in the *Pbcn* space group with a = 13.84(3) Å, b = 23.17(4) Å, and c = 23.38(4) Å, within Z = 8. The 1:1 stacking motif between [Pt(tbtrpy)(OH)] and TCNQ shows an in-

Received 28 July 2008. Accepted 28 October 2008. Published on the NRC Research Press Web site at canjchem.nrc.ca on 13 January 2009.

H. Rabaâ. Department of Chemistry, E. S. C. T. M, Ibn Tofail University, P.O. Box 133, Kenitra, 14000, Morocco.
T.R. Cundari[1] and M.A. Omary. Department of Chemistry, Center for Advanced Scientific Computing and Modeling (CASCaM), University of North Texas, Box 305070, Denton, TX 76203-5070.

[1]Corresponding author (e-mail: tomc@unt.edu).

Fig. 1. Plot showing a single [Pt(tbtrpy)(OH)]TCNQ stack. The atoms are colored as follows: Pt (violet), O (red), N (blue), and C (grey).

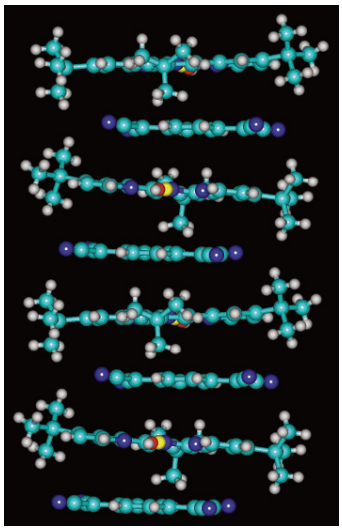

ter-planar separation between the respective centroids of ~3.5 Å. Within a stack the Pt···Pt distances are 7.7 Å, while intra-stack distances are 12 Å or longer.[7a]

These stacks exhibit favorable properties for solar cell applications, including strong absorptions across a wide spectral range. In subsequent work by the same researchers, the electronic absorption spectra were obtained for selected [Pt(tbtrpy)X]Y complexes (X = Cl, NCS, OH, or arylthiolates (SAr); Y^- = Cl^-, BF_4^-, or $TCNQ^-$ = 7,7,8,8,-tetracyanoquinodimethane radical anion).[7b] It was shown that varying the anionic ligand X to arythiolate leads to red shifts of charge transfer bands to the visible region, which can be red- or blue-shifted CT absorptions by using electron-donating or -withdrawing substituents, respectively.[7b] Additionally, varying the counterion to $TCNQ^-$ radical anion gives rise to additional absorptions in the near-infrared (NIR) region, thus rendering a recipe to attain "black absorbers", which might be suitable for solar energy conversion due to their continuous and strong absorptions across a wide spectral range in the UV–vis and NIR regions.

In this paper we examine the electronic structure of the [Pt(trpy)X]Y class of materials via quantum mechanical computations based on density functional theory (DFT) and semi-empirical (extended Hückel) methods. One important aspect in this research pertains to investigating the conducting behavior of metal compounds with $TCNQ^-$ as counterion. This present research is inspired by the experimental observations reported in ref. 5b that suggested possible charge delocalization in [Pt(tbtrpy)(X)]TCNQ, as inferred by electronic absorption features near 490 nm, characteristic of the $TCNQ^{2-}$ dianion as well as ν_{CN} infrared frequencies (~2175–2180 cm^{-1}) that were lower than those reported for both neutral TCNQ (2227 cm^{-1}) and $TCNQ^-$ (2195 cm^{-1}, Na^+ salt).[8] Similar charge delocalization has been reported for tetrathiafulvalene (TTF)–/TCNQ binary donor–/acceptor complexes. Related organic[9] and inorganic[10] complexes have also been reported to exhibit anisotropic, one-dimensional crystal structures with conducting properties.[11] Thus, we undertook a computational investigation of the bonding and structure of [Pt(trpy)X]TCNQ materials using two levels of theory. Extended Hückel tight binding (EHTB)[12] calculations of crystalline [Pt(tbtrpy)(X)]TCNQ (X = OH or SH) are used to provide insights regarding the possible solid-state electronic structure of this class of materials. We also scrutinize whether charge delocalization occurs by which the donor complex is partially oxidized to $[Pt(tbtrpy)X]^{(1+\delta)+}$, while the acceptor is accordingly reduced to $TCNQ^{(1+\delta)-}$; this is done via DFT computations that evaluate the ν_{CN} IR frequencies in model complexes compared with isolated TCNQ species. Both computational methods are also used to examine the electronic structure of $[Pt(trpy)X]^+$ complexes as a function of X.

Computational methods

The solid-state calculations described in this work are performed within the framework of the extended Hückel tight binding (EHTB) method[12], for which standard parameters are used within the YAeHMOP[13] software package. The off-diagonal elements of the Hamiltonian are evaluated with the Wolfsberg–Helmholtz formula.[14] Numerical integrations over the symmetry unique section of the Brillouin zone of the three-dimensional structure of [Pt(tbtrpy)(X)]TCNQ (X = OH or SH) were performed using a set of 40 k-points.[12,13] The EHTB approach has been used to describe or predict conductivity from band structure. For example, this method was used to describe the superconductivity of Chevrel phases.[14c] In another application, Lopes et al. used the EHTB method to study the 1-D conductor $(TTDM\text{-}TTF)_2[Au(mnt)_2]$[14d] (mnt = bis-maleonitriledithiolate, TTDM = thiophenothio-dimethylene).

The Gaussian 03 program is used for all density functional calculations described herein.[15] The valence basis sets (augmented with a d polarization function for main group atoms) and compact effective potentials of Stevens et al. are employed in conjunction with the B3LYP hybrid functional.[16,17] All geometries are optimized with restricted Kohn–Sham methods for singlets and unrestricted Kohn–Sham methods for higher multiplicities. Vibrational frequencies are calculated at all stationary points to characterize them as minima (no imaginary frequencies).

Results and discussion

Solid-state electronic structure of [Pt(tbtrpy)(X)]TCNQ

Figure 2 shows a plot of the total EHTB density of states (DOS) for [Pt(tbtrpy)(OH)]TCNQ plus DOS projections for Pt, tbtrpy, and TCNQ. The Fermi level is found to lie in the region of high DOS at –11.9 eV. *Therefore, [Pt(tbtrpy)(OH)]TCNQ is predicted to be metallic by the EHTB calculations.* Figure 2 indicates the role of the Pt(II) complex as a donor and TCNQ as an acceptor, as shown by the Pt projection in the valence band containing the Fermi level (top right) and the TCNQ projection in the band immediately above the Fermi level (bottom right). The substantial electron affinity of TCNQ[9k,11c] is consistent with the predicted metallic behavior of this solid, as TCNQ can readily accept electrons from the Pt complex via the low energy unoccupied π* orbitals of the former, which dominate the bands immediately above the Fermi level. Figure 2 also shows that the filled π orbitals of the terpyridyl ligand lie

Fig. 2. Plot of the density of states (DOS) for the crystal structure of [Pt(tbtrpy)(OH)]TCNQ showing the total DOS (top left), platinum projection (top right), tbtrpy projection (bottom left), and TCNQ projection (bottom right). The horizontal dashed line corresponds to the Fermi level.

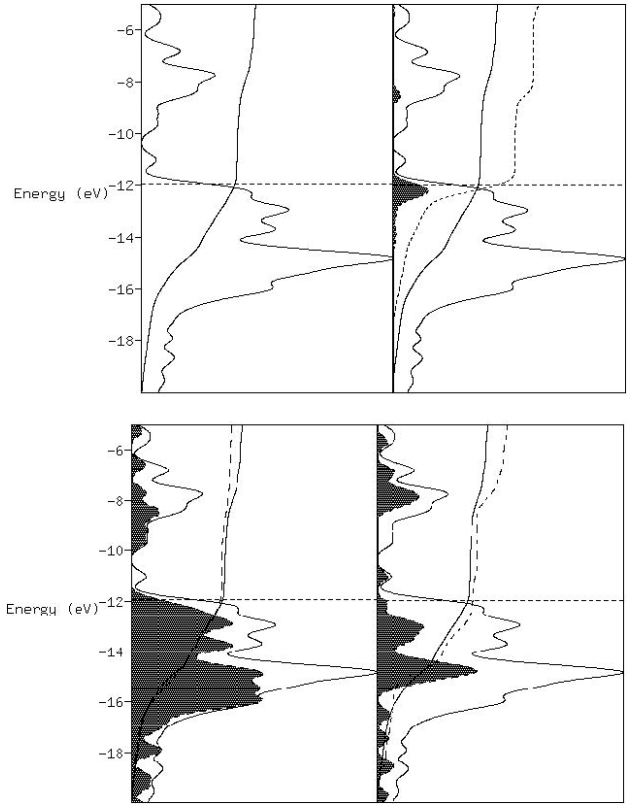

Fig. 3. View of the DOS of $[Pt(tbtrpy)(OH)]^+$ (left) and TCNQ (right) units in the crystal structure of [Pt(tbtrpy)(OH)]TCNQ. Note the nonmetallic behavior shown by the band gap in absence of interaction of these units with one another. The top of each band located around –11 eV corresponds to the Fermi level (horizontal dashed line).

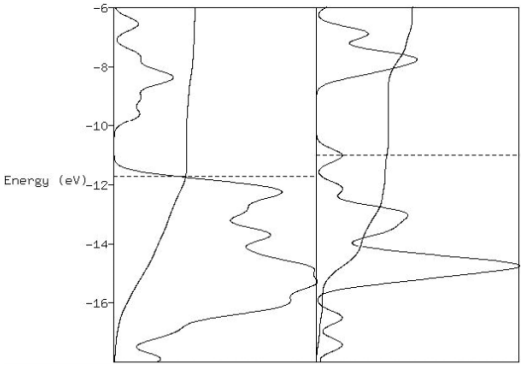

below both the Pt d_π orbitals and the TCNQ π orbitals, while the vacant π* orbitals of the terpyridyl ligand lie above the TCNQ π* orbitals. The results from the solid-state EHTB calculations are thus consistent with the electronic structure proposed in ref. 7b and are further assessed below for molecular models using DFT computations.

In solid [Pt(tbtrpy)(OH)]TCNQ, the interaction of the square planar Pt(II) complex with TCNQ results in an almost

Fig. 4. Density of states for [Pt(tbtrpy)(X)]TCNQ with projection for X = OH (left) and X = SH (right). The horizontal dashed line corresponds to the Fermi level.

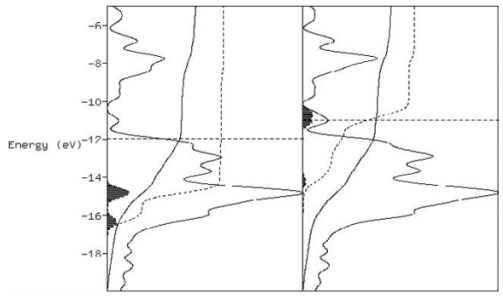

completely occupied valence band centered at –11.9 eV (Fig. 2). The critical role of donor–acceptor interaction in the conducting behavior can be seen by contrasting the results in Fig. 2 with those in Fig. 3, which illustrate nonmetallic behavior for both the solid-state arrangement of the metal donor species (Fig. 3, left) and the TCNQ acceptor (Fig. 3, right) in isolation. A pronounced band gap is seen for both situations (Fig. 3). In other words, the band structure changes drastically from an insulator (isolated TCNQ and [Pt(tbtrpy)(X)]) to that of a conductor ([Pt(tbtrpy)(X)]TCNQ). We further note that the band structure is flat (no sign of interaction) in the inter-stack direction because the overlap is very small.

Figure 4 presents DOS plots for the thiolate complex, [Pt(tbtrpy)(SH)]TCNQ. This model complex, which has yet to be synthesized experimentally, was constructed by assuming the same crystallographic structure of [Pt(tbtrpy)(OH)]TCNQ after adjusting the Pt–S and S–H distances with reasonable values based on reported structures of Pt(II)-thiolate complexes. While thiolate is expected to be a good electronic model for an arylthiolate, it must be kept in mind that the larger steric bulk of the latter may affect the separation between donor and acceptor moieties within the stack. *Significantly, the data in Fig. 4 suggest that [Pt(tbtrpy)(SH)]TCNQ is predicted to also be metallic with an improved conducting behavior versus [Pt(tbtrpy)(OH)]TCNQ.* Thus, the Fermi level shifts from –11.9 (X = OH) to –10.7 eV (X = SH), and the valence band becomes more dispersed in the case of X = SH. Figure 4 (right) also shows that the valence band has strong SH character for [Pt(tbtrpy)(SH)]TCNQ, as the SH projection occupies nearly half of this band. This is in sharp contrast to the analogous situation for [Pt(tbtrpy)(OH)]TCNQ, in which the OH ligand contributes only to bands that are well below the valence band (Fig. 4, left). One reason for the different Fermi level behavior is the relative energy of S_{3p} and O_{2p} orbitals ($\sim$1.2 eV difference in H_{ii} with sulfur higher in energy). The EHTB results are also consistent with the electronic structure proposed in ref. 7b, which predicted a significant thiolate character in the HOMO of $[Pt(tbtrpy)(thiolate)]^+$ complexes, based on an analysis of spectral and electrochemical data; further discussion of the electronic structure of the molecular units is provided in the DFT sections below.

We conclude from the EHTB calculations that sulfur incorporation in the donor–acceptor stacks that have X = SH can generate a more dispersed band compared with the DOS of the stacks that have X = OH. Consequently, this

Fig. 5. Contour plots of the Kohn–Sham HOMO (bottom) and LUMO (top) orbitals of $[Pt(tbtrpy)(X)]^+$ with different X ligands, based on DFT computations. The HOMO orbital energy is computed to be –0.343, –0.346, –0.330, –0.305, and –0.271 eV (left to right, respectively).

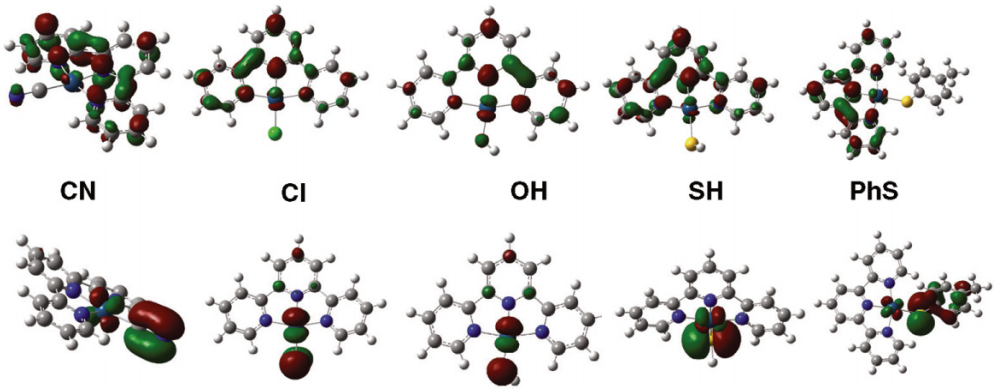

Fig. 6. Top: Singly-occupied molecular orbital (SOMO) for $TCNQ^-$ monoanion, which corresponds to the LUMO of neutral TCNQ. Bottom: Average crystallographic CC bond lengths (Å) reported in the CSD for different oxidation states of TCNQ. Given in parentheses are the sample standard deviations.

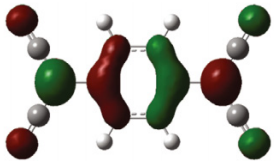

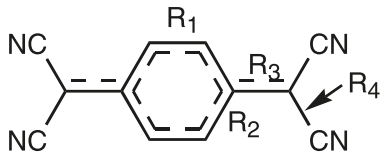

	R_1	R_2	R_3	R_4
neutral	1.346(14)	1.436(14)	1.384(22)	1.430(13)
anion	1.361(8)	1.419(12)	1.414(11)	1.419(10)

energy shift enhances the overlap between the bands of the $[Pt(tbtrpy)(SH)]^+$ and $TCNQ^-$ fragments. Any electronic excitation or CT effects are expected to involve this zone, which implies a great sensitivity of the spectroscopic and electrical properties of [Pt(tbtrpy)X]TCNQ to a judicious choice of X. Thus, using S-donor ligands as X is predicted to lead to better conductivity than that for [Pt(tbtrpy)(OH)]TCNQ because the lower ionization potential (inferred from a less negative Fermi level), the significant thiolate character, and the greater dispersion of the valence bands of [Pt(tbtrpy)(thiolate)]TCNQ solids suggest an easier partial oxidation and thus greater charge mobility in such binary stacks.

Density functional calculations for donor and acceptor units

Density functional calculations were carried out on molecular $[Pt(tbtrpy)(X)]^+$ and [Pt(tbtrpy)(X)][TCNQ] complexes, as well as free TCNQ models in neutral, anionic, and dianionic states. The modeling of a single link in the solid-state chains (and a better understanding of the donor–acceptor properties of TCNQ in their ground and excited states) can be useful when studying the optoelectronic properties of the crystalline materials.

Table 1. Calculated metrics (Å) for $TCNQ^{0,-,2-}$ optimized with the B3LYP functional and different basis sets.

	6–31G(d)	6–31G(3d,p)	6–311++G(d,p)
R_1			
Neutral	1.352	1.351	1.353
Anion	1.372	1.370	1.373
Dianion	1.392	1.391	1.392
R_2			
Neutral	1.446	1.445	1.446
Anion	1.424	1.421	1.424
Dianion	1.411	1.408	1.140
R_3			
Neutral	1.386	1.384	1.386
Anion	1.430	1.427	1.429
Dianion	1.473	1.471	1.473
R_4			
Neutral	1.427	1.421	1.427
Anion	1.416	1.413	1.412
Dianion	1.415	1.410	1.401

Table 2. Computed ν_{CN} frequencies (cm^{-1}) for TCNQ using (6–311++G(d,p)

TCNQ	Exptl.	DFT	DFT
	ν_{CN}	ν_{CN} (b_{1u})	ν_{CN} (b_{2u})
Neutral	2227	2327 (2227)	2310 (2194)
Anion	2185	2272 (2158)	2240 (2128)
Dianion	2164	2222 (2110)	2175 (2066)

Note: Values in parentheses are scaled by 0.95 to incorporate anharmonic, basis set, and electron correlation effects.

Electronic structure assignment of Pt donor complexes

It is worthwhile to start this section with a summary of the electronic absorption bands and their assignment for [Pt(tbtrpy)(X)]Y complexes based on the experimental study in ref. [7b]. The high-energy region of the electronic spectrum at $\lambda < 350$ nm is dominated by $\pi \rightarrow \pi^*$ transitions localized on the terpyridyl ligand, which are generally insensitive to X

Fig. 7. Computed (B3LYP/6-311+G(d,p)) IR spectra of (top) TCNQ neutral, (middle) anion, and (bottom) dianion. Unscaled frequencies (see Table 2) were used to generate these figures.

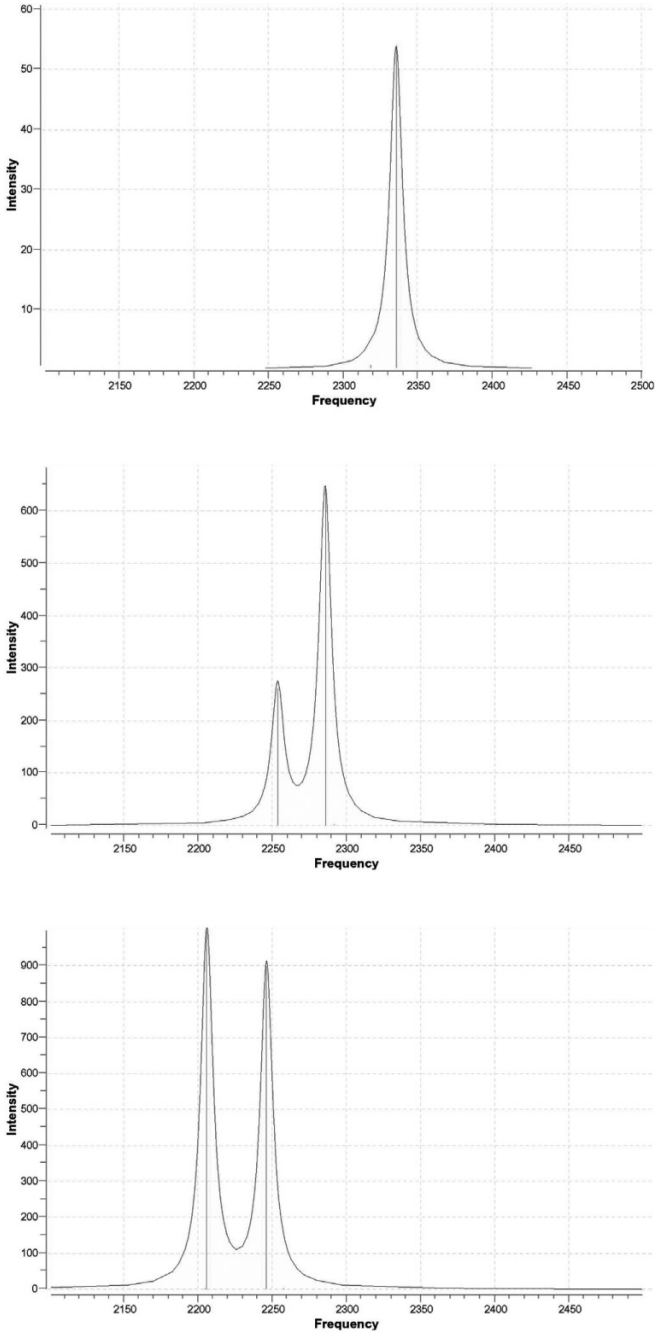

and Y modification.[7b] Longer-wavelength regions represent charge transfer (CT) transitions. The CT bands are presumed to be MLCT (metal-to-ligand CT) transitions in the near UV region for X = Cl^-, NCS^-, or OH^-, whereas changing the anionic ligand to SAr^- leads to a drastic red shift to the visible region because of a mixed thiolate-Pt HOMO.[7b] Figure 5 shows contour plots of the Kohn–Sham frontier orbitals of $[Pt(tbtrpy)(X)]^+$ with different X ligands, based on DFT computations. These computational results bear out both the aforementioned experimental assignment and the EHTB solid-state computations above because a greater thiolate

Fig. 8. B3LYP/SBKJC(*d*) optimized structure of [Pt(trpy)OH]TCNQ.

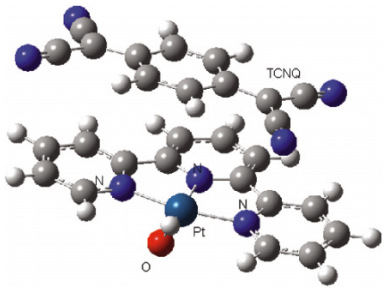

contribution as well as higher orbital energy have been obtained for the HOMO of the models that contain X = SH or PhS instead of other anionic ligands. The LUMO and other low-lying virtual orbitals, on the other hand, have a terpyridyl π* character regardless of X.

Molecular structure of TCNQ species

Considerable efforts have been devoted to the synthesis and study of TCNQ derivatives with enhanced materials characteristics.[7–9,11] The electron-accepting ability of TCNQ plays a fundamental role in the charge transfer process. Thus, several investigations into the structure and spectra of TCNQ, $TCNQ^-$, and $TCNQ^{2-}$ have been reported.[7–9,11] Different carbon–carbon bond lengths are observed for TCNQ in the solid state because its structure depends on the nature of the counterion (if TCNQ is not neutral) and the total charge of TCNQ (typically between 0 and 2–).

Figure 6 summarizes the results of an analysis of the Cambridge Structural Database (CSD).[18] In Fig. 6 are presented the averages and sample standard deviations (given in parentheses; the sample size is 154 for neutral TCNQ and 31 for $TCNQ^-$) for CC bonds as a function of the reported charge of the TCNQ. Systems whose TCNQ charge is obfuscated due to the presence in the unit cell of multiple TCNQ moieties with different assigned charges are ignored to isolate only the most reliable oxidation state assignments. For clarity in the text, the CC bonds are labeled R_1, R_2, R_3, and R_4 (Fig. 6). The endocyclic CC (R_1 and R_2) bonds and the CC bond to the cyano group (R_4) show changes upon reduction of TCNQ that are commensurate with the sample standard deviations. However, the CC exocyclic bonds (R_3) change more substantially, going from 1.384(22) Å in neutral TCNQ to 1.414(11) Å for $TCNQ^-$. Hence, reduction of TCNQ weakens R_3, which is consistent with the orbital character of the LUMO of TCNQ that is populated upon reduction (Fig. 6). *Thus, simple orbital arguments and analysis of extant crystallographic data suggest that the exocyclic CC bond length (R_3) is the most reliable structural indicator of TCNQ charge.*

The only TCNQ complex that we have been able to identify within the CSD that is designated as a dianion is the $[Cp^*_2Co]_2(TCNQ)\cdot 1/2^*(CH_3CN)$ complex reported by Miller et al.[9i] The exocyclic CC bonds lengths are 1.45(1) and 1.43(1) Å. The exocyclic CC bond, R_3, thus does continue the lengthening trend seen upon going from neutral to anionic TCNQ, as expected on the basis of calculations reported by Miller et al.[9i] Such a structural result is reasonable as the second reducing equivalent would go into the SOMO

Table 3. Critical distances (Å) in [Pt(triimine)(X)][TCNQ].

	X = OH (Calcd.)	X = SH (Calcd.)	X = OH (Exptl.)
R_1	1.38	1.40	1.35
R_2	1.43	1.45	1.43
R_3	1.44	1.45	1.43
R_4	1.17	1.17	1.13
Pt-N_{cis}	1.97	1.99	1.96
Pt-N_{trans}	2.05	2.05	2.02
Pt-N_{trans}	2.04	2.06	2.04
Pt-X	2.01	2.41	2.24
Interplanar (Pt-C)[a]	3.99	3.87	3.71

Note: For the computational models, triimine = trpy; for the experimental system, triimine = tbtrpy.

[a]Interplanar distances correspond to the closest platinum–carbon (on TCNQ counterion) distance.

Fig. 9. (Bottom) Kohn–Sham HOMO and (top) LUMO orbitals of [Pt(trpy)(OH)]TCNQ.

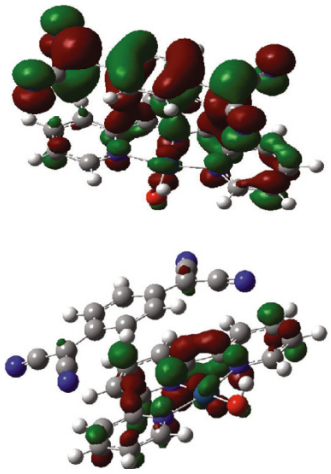

of the TCNQ radical anion, which a priori is expected to be very similar to the LUMO of neutral TCNQ.

DFT computations have been carried out for isolated TCNQ neutral, radical anion, and dianion to calibrate the experimental results for neutral and anionic TCNQ and to extend them to $TCNQ^{2-}$. All geometry optimizations have been performed under D_{2h} symmetry, and calculation of the energy Hessian has indicated each species to be at a potential energy minimum. Several basis sets have been utilized: modest (6-31G(d)), large (6-31G(3d,p)), and extended (6-311++G(d,p)) (Table 1). Little difference has been found in the computed CC bonds with different basis sets, and both the large and extended basis sets have shown good agreement with experimental averages.

IR spectra of TCNQ species

Theoretical computation of the IR spectra of TCNQ species is undertaken herein, as motivated by the experimental use of the cyano groups as "reporter" groups (through their CN stretching frequencies), for assessing the state of reduction of the TCNQ counterion.[8] The vibrational spectra for various TCNQ species have been studied experimentally.[7–9,11] The measurement of the IR spectra of Na_xTCNQ, prepared by a solvent-free vapor codeposition method, show a decrease in ν_{CN} from 2227 cm^{-1} in the neutral, to 2185 cm^{-1} in the anion, and to 2164 cm^{-1} for the dianion.[8] A theoretical investigation of the IR frequencies of TCNQ was undertaken using the B3LYP functional, and the same basis sets were used for geometry optimization tests. Similar calculations on Li_xTCNQ and K_xTCNQ (x = 1, 2) were also performed and show nearly identical trends. In this section we will focus on isolated TCNQ species in different oxidation states to minimize ancillary effects due to counterion and will likewise focus on the results with the extended 6-311++G(d,p) basis set. The b_{1u} and b_{2u} modes in the point group D_{2h} are the most intense in the IR and thus are the most reliable in terms of experimental assignments. The b_{1u} and b_{2u} modes correspond to symmetric and asymmetric stretching of all four CN bonds, respectively. Inspection of the data in Table 2 confirms the shift to lower ν_{CN} upon going from TCNQ to $TCNQ^{-}$ to $TCNQ^{2-}$. The anion to dianion differences in ν_{CN} are 48 cm^{-1} for b_{1u} and 56 cm^{-1} for b_{2u} using the scaled frequencies.

In Fig. 6, the calculated IR spectra are plotted in the range 2000–2500 cm^{-1}, the region that encompasses the ν_{CN} of TCNQ. Inspection of Fig. 7 shows the expected shift to lower frequencies upon reduction of TCNQ. What is more interesting is the change in IR peak shapes (Fig. 7, top). The neutral TCNQ displays a single ν_{CN} peak, due to the very low intensity of the b_{1u} stretch at 2310 cm^{-1}. Two peaks in this region are observed for the anion and dianion with intensity ratios (b_{1u}/b_{2u}) of $\sim$3:1 for the anion and $\sim$1:1 for the anion. While the comparison of calculated and experimental IR spectra is complicated by medium effects and the nature of the counterions (for charged species), the present results imply that IR peak shape analysis may be a useful tool for quickly gauging the reduction state of TCNQ in conducting materials.

Disproportionation of TCNQ species

The utility of TCNQ in solid-state applications is, in large part, due to its electronic "flexibility." As seen above for the hydroxo and thiolate complexes in the solid state, electron transfer to and from TCNQ can be easily (although perhaps not yet systematically) varied through modification of its chemical environment. To address this issue, we investigated the disproportionation of TCNQ anion (eq. [1]).

Table 4. CN Stretching Frequencies in [Pt(triimine)(XR)][TCNQ].

	XR = OH[a] (Calcd.)	XR = SH[a](Calcd.)	XR = SAr[b](Exptl.)
ν_1	2187	2187	2180 SPh
l_1	112	118	
ν_2	2190	2190	2178 DMBT[b] (KBr)
l_2	90	102	2179 DMBT (Nujol)
ν_3	2221	2222	2185 DMeOBT[b] (KBr)
l_3	553	519	2183 DMeOBT (Nujol)
ν_4	2228	2228	
l_4	10	8	

Note: For the computational models, triimine = trpy; for the experimental system, triimine = tbtrpy.

[a]These are the unscaled CN stretching frequencies (ν_n, cm^{-1}) and intensities (I_n, KM/Mole) calculated at the B3LYP/CEP-31G(d) level of theory.

$$[1] \qquad 2\,TCNQ^{-} \leftrightarrow TCNQ + TCNQ^{2-}$$

The disproportionation reaction provides insight into the ease with which TCNQ can accept and (or) donate electrons in response to chemical variations. The free energy of eq. [1] is calculated to be +97 kcal/mol (1 cal = 4.184 J) in the gas phase at the B3LYP/6-311++G(d,p) level of theory. However, this disproportionation is expected to become substantially more thermodynamically feasible when environmental factors such as solvation or the stabilization of counterions in the crystalline state are incorporated. To incorporate environmental effects, polarizable continuum model[19] calculations were carried using a solvent of moderate dielectric constant (acetonitrile, $\varepsilon = 37.5$). While reaction 1 remained endergonic, preferential stabilization of the dianion product yielded a ΔG_{rxn} of +19 kcal/mol in a polar acetonitrile environment. This change is due to the more substantial solvation of $TCNQ^{2-}$ (ΔG_{solv}(PCM,acetonitrile) = –145 kcal/mol) vs that for the anion (ΔG_{solv}(PCM,acetonitrile) = –44 kcal/mol) and neutral (ΔG_{solv}(PCM,acetonitrile) = –20 kcal/mol) TCNQ. The sensitivity of charge transfer to and from TCNQ in the solid state, with respect to changes in the polarity of the environment, lends further credence to the observed changes in the solid-state EHTB structure of [Pt(tbtrpy)(X)]TCNQ and further highlights the ability to fine-tune the properties of this family of complexes via modification of the chemical environment.

Density functional calculations on [Pt(tbtrpy)(X)][TCNQ]

In this part of the research, a molecular model is constructed representing a single [Pt(trpy)(X)]TCNQ link from the solid-state chain. In our model, the tbtrpy ligand is substituted by the parent trpy (trpy - 2,2′:6′,2″-terpyridine) ligand to reduce computational costs for the DFT simulations.

Molecular structure of [Pt(trpy)(X)][TCNQ]

We note that while direct calculation of atomic charges (and indeed other properties such as spin densities) is obviously possible via population analyses such as those of Mulliken, Löwdin, or the natural population method, such atomic charges are not only sensitive to the method utilized as well as the basis set and level of theory, they also do not yield an observable property that can be correlated with an experimental value. Hence, we focus on bond length metrics that may serve as an indicator of the extent of charge transfer, and which, once established, could be interrogated via techniques such as X-ray crystallography. In Fig. 8, the optimized structure of [Pt(trpy)OH]TCNQ obtained via DFT calculation (B3LYP/SBKJC(d)) is shown. A pseudopotential method was employed because of the presence of the heavy element platinum; test calculations indicated that the utilization of pseudopotentials had only a negligible effect on the calculated structural (Table 1) and vibrational (Table 2) data for TCNQ and its anionic forms, with changes of $\sim$1% and less than 10 cm^{-1}, respectively, for comparable all-electron and pseudopotential calculations. Table 3 lists the computed bond lengths of [Pt(trpy)(X)][TCNQ]. For clarity, the same CC bond labels in Fig. 6 (R_1, R_2, R_3, and R_4) were used. Recall from the previous discussion of the crystallographic data and DFT calculations on TCNQ ions that the R_3 bond is deemed to be the most reliable structural indicator of TCNQ oxidation state. Thus, it is very interesting that the calculated exocyclic CC bond length (R_3) is 1.438 Å (X = OH) and further lengthens to 1.451 Å for the thiolate (X = SH) congener. These calculated values compare quite favorably with the experimental value of R_3 for [Pt(tbtrpy)(OH)]TCNQ, which is 1.433 Å. Moreover, the R_3 bond lengths in Miller's $TCNQ^{2-}$ complex $[Cp^*_2Co]_2(TCNQ)\cdot 1/2^*(CH_3CN)$ complex are 1.45(1) and 1.43(1) Å.[9i] *Taken together, the present calculated and reported experimental values of R_3, when compared to the exemplars in Table 1, imply that the oxidation state of TCNQ in [Pt(triimine)(X)][TCNQ] complexes is between 1– and 2–, consistent with the hypothesized charge in ref. 7b.* Moreover, for the analysis and design of related materials, the data suggest that the degree of charge transfer between the platinum donor and TCNQ acceptor is quite sensitive to X.

In Fig. 9, the Kohn–Sham HOMO and LUMO are plotted for the optimized geometry of the [Pt(trpy)(OH)]TCNQ complex. *The figure clearly illustrates the localization of the electron density on the platinum donor complex in the HOMO and on the $TCNQ^{-}$ acceptor in the LUMO, thus providing further theoretical support for the contention that the Pt(II) complex acts as donor despite being a cation and the $TCNQ^{-}$ acts as an acceptor despite being an anion.*

IR spectra of [Pt(trpy)(X)][TCNQ]

The CN stretching frequencies of [Pt(trpy)(X)]TCNQ are calculated and organized in Table 4. The calculated CN stretching frequency for the most intense IR peak (~b_{1u} of

Table 2) are 2221 cm^{-1} for the hydroxo complex and 2222 cm^{-1} for the thiolate complex. Scaling these ν_{CN} by 0.95 yields estimated ν_{CN} of 2111 and 2110 cm^{-1}, respectively. Comparing the computed CN stretching frequencies for [Pt(trpy)(X)][TCNQ] with those calculated for isolated TCNQ ions (Table 2), the scaled ν_{CN} are much closer to the b_{1u} stretch of $TCNQ^{2-}$ (2110 cm^{-1}) than $TCNQ^{-}$ (2158 cm^{-1}). Of course, the effects of medium, counterions, and anharmonicity will certainly play a role in any comparison of theoretical and experimental IR frequencies. Reported experimental values are thus also organized in Table 4, along with the medium in which the IR experiment (KBr pellet or Nujol mull) was performed; the experimental values for the most intense peak range from 2178 to 2185 cm^{-1} for a variety of aryl-thiolates with differing substituents, [Pt(tbtrpy)(SAr)][TCNQ][7b] (Table 4). For NaTCNQ, ν_{CN} = 2185 cm^{-1} and 2164 cm^{-1} for Na_2TCNQ. The experimental values of ν_{CN} for the platinum complexes[7b] are intermediate ν_{CN} for NaTCNQ and Na_2TCNQ.[8] *Thus, the calculated and experimental CN stretching frequencies support a proposed charge distribution of* $[Pt(tbtrpy)X]^{(1+\delta)+}$ *complexed with* $TCNQ^{(1+\delta)-}$ where $0 < \delta < 1$.

Summary and conclusions

Several important conclusions have emerged from this computational analysis of solid-state and molecular Pt-TCNQ complexes. The most important among these are summarized here.

Tight-binding analyses of crystalline [Pt(tbtrpy)(X)][TCNQ] (X = OH or HS) and density functional calculations on molecular models of these materials indicate that they display conductor behavior. The valence-conduction band in solid-state [Pt(tbtrpy)(X)][TCNQ] has a Pt(II) donor character and TCNQ π^* acceptor character. The calculations suggest substantial changes in the transfer energy and the conduction properties of crystalline [Pt(tbtrpy)(X)][TCNQ] upon modification of X from OH to SH. For example, from the widening of the band gap in the thiolate complex, it is anticipated that electron excitation from the valence to the conduction band is more facile for this material. Additionally, the thiolate is predicted to be a better conductor and its UV–vis absorption peak should be red-shifted compared with the hydroxyl complex, which is consistent with experimental observations.[7b]

Density functional theory calculations are performed to probe the electronic, molecular, vibrational, and spectral properties of TCNQ (neutral, anion, and dianion) and the molecular complex [Pt(tbtrpy)(X)][TCNQ] (X = OH and SH). Of particular interest is the response of these properties in the TCNQ fragment to its oxidation level, i.e., δ in $[Pt(tbtrpy)X]^{(1+\delta)+}TCNQ^{(1+\delta)-}$. Orbital arguments and analysis of extant structural data suggest that the exocyclic CC bond length (R_3) is the most reliable structural indicator of TCNQ oxidation level and thus δ. Two major peaks in the ν_{CN} region are calculated for the anion and dianion states of TCNQ with intensity ratios of $\sim$3:1 and $\sim$1:1, respectively. Hence, in addition to analysis of shifts in ν_{CN}, IR peak shape analysis may be a useful experimental tool for quickly gauging the exact oxidation state of TCNQ in conducting and luminescent materials and thus the response of this important parameter to chemical modification.

The calculated and experimental bond lengths and IR spectra for [Pt(tbtrpy)(X)][TCNQ], support a proposed charge distribution of $[Pt(tbtrpy)X]^{(1+\delta)+}$ complexed with $TCNQ^{(1+\delta)-}$ where $0 < \delta < 1$, i.e., the TCNQ counterion possesses an oxidation state between 1– and 2– in these Pt(triimine) materials. In terms of the design of new and improved materials, the data suggest that the degree of charge transfer between the platinum donor and TCNQ acceptor is quite sensitive to X, which is perhaps the most easily modifiable chemical group.

Acknowledgements

HR acknowledges the University of North Texas (UNT), Department of Chemistry, and the Moroccan government for support of his contribution and travel expenses. TRC acknowledges the USA Departments of Education and Energy for their support of the CASCaM facility. Calculations employed the UNT computational chemistry resource, which is supported by the NSF through grant CHE-0741936. MAO acknowledges partial support of his contribution by the Robert A. Welch Foundation (Grant B-1542) and NSF (CAREER Award, CHE-0349313). TRC and MAO acknowledge the Texas Advanced Research Program (009741–0089–2007 for their support of this research.

References

(1) This article is part of a Special Issue dedicated to Professor T. Ziegler.
(2) Dedicated to Professor Tom Ziegler, in recognition of his many excellent contributions to the modeling of inorganic and organometallic chemistry.
(3) McMillin, D. R.; Moore, J. J. *Coord. Chem. Rev.* **2002**, *229*, 113. doi:10.1016/S0010-8545(02)00041-3.
(4) Fleeman, W. L.; Connick, W. B. *Comments Inorg. Chem.* **2002**, *23*, 205. doi:10.1080/02603590212096.
(5) (a) For representative examples for Pt(II)-triimines please see: Lippard, S. J. *Acc. Chem. Res.* **1978**, *11*, 211 doi:10.1021/ar50125a006.; (b) McFadyen, W. D.; Wakelin, L. P. G.; Roos, I. A. G.; Leopold, V. A. *J. Med. Chem.* **1985**, *28*, 1113 doi:10.1021/jm00146a026. PMID:4020833.; (c) Aldridge, T. K.; Stacy, E. M.; McMillin, D. R. *Inorg. Chem.* **1994**, *33*, 722 doi:10.1021/ic00082a017.; (d) Peyratout, C. S.; Aldridge, T. K.; Crites, D. K.; McMillin, D. R. *Inorg. Chem.* **1995**, *34*, 4484 doi:10.1021/ic00121a029.; (e) Lai, S. W.; Chan, M. C. W.; Cheung, K. K.; Che, C.-M. *Inorg. Chem.* **1999**, *38*, 4262 doi:10.1021/ic990446k.; (f) Rakhimov, R. D.; Weinstein, Y. A.; Lileeva, E. V.; Zheligovskaya, N. N.; Mel'nikov, M. Y.; Butin, K. P. *Russ. Chem. Bull.* **2003**, *52*, 1150 doi:10.1023/A:1024909325619.; (g) Zhang, D.; Wu, L.-Z.; Zhou, L.; Han, X.; Yang, Q.-Z.; Zhang, L.-P.; Tung, C.-H. *J. Am. Chem. Soc.* **2004**, *126*, 3440 doi:10.1021/ja037631o. PMID:15025468.; (h) Willison, S. A.; Jude, H.; Antonelli, R. M.; Rennekamp, J. M.; Eckret, N. A.; Bauer, J. A. K.; Connick, W. B. *Inorg. Chem.* **2004**, *43*, 2548 doi:10.1021/ic035066k. PMID:15074972.; (i) Du, P.; Schneider, J.; Jarosz, P.; Eisenberg, R. *J. Am. Chem. Soc.* **2006**, *128*, 7726. doi:10.1021/ja0610683. PMID:16771472.
(6) (a) For representative examples for Pt(II)-diimines please see: Cummings, S. D.; Eisenberg, R. *J. Am. Chem. Soc.* **1996**, *118*, 1949 doi:10.1021/ja951345y.; (b) Connick, W. B.; Gray, H. B. *J. Am. Chem. Soc.* **1997**, *119*, 11620 doi:10.1021/ja9723803 and refs. cited therein.; (c) Cocker, T. M.;

Bachman, R. E. *Inorg. Chem.* **2001**, *40*, 1550 doi:10.1021/ic000884n. PMID:11261963.; (d) Islam, A.; Sugihara, H.; Hara, K.; Singh, L. P.; Katoh, R.; Yanagida, M.; Takahashi, Y.; Murata, S.; Arakawa, H.; Fujihashi, G. *Inorg. Chem.* **2001**, *40*, 5371. doi:10.1021/ic010391y. PMID:11578182.; (e) Geary, E. A. M.; Hirata, N.; Clifford, J.; Durrant, J. R.; Parsons, S.; Dawson, A.; Yellowlees, L. J.; Robertson, N. *Dalton Trans.* **2003**, 3757 doi:10.1039/b306241d.; (f) Makedonas, C.; Mitsopoulou, C. A.; Lahoz, F. J.; Balana, A. I. *Inorg. Chem.* **2003**, *42*, 8853 doi:10.1021/ic034978j. PMID:14686867.; (g) Jude, H.; Krause-Bauer, J. A.; Connick, W. B. *J. Am. Chem. Soc.* **2003**, *125*, 3446 doi:10.1021/ja034003y. PMID:12643703.; (h) Grey, J. K.; Butler, I. S.; Reber, C. *J. Am. Chem. Soc.* **2002**, *124*, 9384 doi:10.1021/ja026629e. PMID:12167028.; (i) Zhang, J.; Du, P.; Schneider, J.; Jarosz, P.; Eisenberg, R. *J. Am. Chem. Soc.* **2007**, *129*, 7726. doi:10.1021/ja071789h. PMID:17547407.

(7) (a) Smucker, B. W.; Hudson, J. M.; Omary, M. A.; Dunbar, K. R. *Inorg. Chem.* **2003**, *42*, 4714 doi:10.1021/ic0259585. PMID:12870963.; (b) Chen, W.-H.; Reinheimer, E. W.; Dunbar, K. R.; Omary, M. A. *Inorg. Chem.* **2006**, *45*, 2770. doi:10.1021/ic051518c. PMID:16562930.

(8) (a) Khatkale, M. S.; Devlin, J. P. *J. Chem. Phys.* **1979**, *70*, 1851 doi:10.1063/1.437662.; (b) Chappell, J. S.; Bloch, A. N.; Bryden, W. A.; Maxifield, M.; Poehler, T. O.; Cowan, D. O. J. *Am. Chem. Soc.* **1981**, *103*, 2442. doi:10.1021/ja00399a066.

(9) (a) McConnell, H. M.; Hoffman, B. M.; Metzger, R. M. *Proc. Natl. Acad. Sci. U.S.A.* **1965**, *53*, 46 doi:10.1073/pnas.53.1.46. PMID:16578588.; (b) Long, R. E.; Sparks, R. A.; Trueblood, K. N. *Acta Crystallogr.* **1965**, *18*, 932 doi:10.1107/S0365110X65002256.; (c) Jonkman, H. T.; Kommandeur, J. *Chem. Phys. Lett.* **1972**, *15*, 496 doi:10.1016/0009-2614(72)80357-9.; (d) Konno, M.; Saito, Y. *Acta Crystallogr.* **1974**, *B30*, 1294; (e) Konno, M.; Saito, Y. *Acta Crystallogr.* **1975**, *B31*, 2007; (f) Konno, M.; Ishii, T.; Saito, Y. *Acta Crystallogr.* **1977**, *B33*, 763; (g) Shaik, S. S. *J. Am. Chem. Soc.* **1982**, *104*, 5328 doi:10.1021/ja00384a013.; (h) Miller, J. S.; Epstein, A. J. *J. Am. Chem. Soc.* **1987**, *109*, 3850 doi:10.1021/ja00247a006.; (i) Miller, J. S.; Zhang, J. H.; Reiff, W. M.; Dixon, D. A.; Preston, L. D.; Reis, E.; Gebert, A. H.; Extine, M.; Troup, J.; Epstein, A. J.; Ward, M. D. *J. Phys. Chem.* **1987**, *91*, 4344 doi:10.1021/j100300a028.; (j) Andruniow, T.; Pawlikowski, M.; Sterzel, M. *Vib. Spectrosc.* **1999**, *21*, 45 doi:10.1016/S0924-2031(99)00045-4.; (k) Milian, B.; Pou-Amerigo, R.; Viruela, R.; Orti, E. *J. Mol. Struct. THEOCHEM* **2004**, *709*, 97. doi:10.1016/j.theochem.2003.09.011.

(10) (a) Coomber, A. T.; Beljonne, D.; Friend, R. H.; Brédas, J. K.; Charlton, A.; Robertson, N.; Underhill, A. E.; Kurmoo, M.; Day, P. *Nature* **1996**, *380*, 144 doi:10.1038/380144a0.; (b) Tanaka, H.; Okano, Y.; Kobayashi, H.; Suzuki, W.; Kobayashi, A. *Science* **2001**, *291*, 285 doi:10.1126/science.291.5502.285. PMID:11209074.; (c) Kisch, H.; Eisen, B.; Dinnebier, R.; Shankland, K.; David, W. I. F.; Knoch, F. *Chem. Eur. J.* **2001**, *7*, 738 doi:10.1002/1521-3765(20010202)7:3<738::AID-CHEM738>3.0.CO;2-6.; (d) Rawashdeh-Omary, M.; Omary, M. A.; Fackler, M. A.; Galassi, J. P., Jr.; Pietroni, R.; Burini, B. R. *J. Am. Chem. Soc.* **2001**, *123*, 9689 doi:10.1021/ja016279g. PMID:11572697.; (e) Bigoli, F.; Deplano, P.; Mercuri, M. L.; Pellinghelli, M. A.; Pilia, L.; Pintus, G.; Serpe, A.; Trogu, E. F. *Inorg. Chem.* **2002**, *41*, 5241 doi:10.1021/ic025788w. PMID:12354058.; (f) Alonso, C.; Ballester, L.; Gutiérrez, A.; Perpinan, M. F.; Sanchez, M. A. E.; Azcondo, M. T. *Eur. J. Inorg. Chem.* **2005**, 486. doi:10.1002/ejic.200400540.

(11) (a) For reviews, please see: Kisch, H. *Comments. Inorg. Chem.* **1994**, *16*, 113 doi:10.1080/02603599408035855.; (b) Cassoux, P.; Valade, L. In *Inorganic Materials. 2nd ed.* Bruce, D. W. and O'Hare, D., Eds.; John Wiley and Sons, Chichester: UK; 1996; (c) *Handbook of organic conductive molecules and polymers. Vol. 1*. Halwa, H. S., Ed. Wiley, Chichester: UK;1997; pp. 200–310.(d) Robertson, N.; Cronin, L. *Coord. Chem. Rev.* **2002**, *227*, 93 doi:10.1016/S0010-8545(01)00457-X.; (e) Kobayashi, A.; Fujiwara, E.; Kobayashi, H. *Chem. Rev.* **2004**, *104*, 5243. doi:10.1021/cr030656l. PMID:15535649.

(12) (a) Hoffmann, R.; Lipscomb, W. N. *J. Chem. Phys.* **1962**, *36*, 2179 doi:10.1063/1.1732849.; (b) Hoffmann, R.; Lipscomb, W. N. *J. Chem. Phys.* **1962**, *36*, 3489. doi:10.1063/1.1732484.; (c) Hoffmann, R.; Lipscomb, W. N. *J. Chem. Phys.* **1963**, *37*, 590; (d) Hoffmann, R. *J. Chem. Phys.* **1963**, *39*, 1397 doi:10.1063/1.1734456.; (e) Hoffmann, R. *Solids and surfaces: A chemist's view of bonding in extended structures*. Wiley-VCH: New York; 1988; (f) Whangbo, M.-H.; Hoffmann, R. *J. Am. Chem. Soc.* **1978**, *100*, 6093 doi:10.1021/ja00487a020.; (g) Whangbo, M.-H.; Hoffmann, R.; Woodward, R. B. *Proc. R. Soc. A* **1979**, *366*, 23. doi:10.1098/rspa.1979.0037.

(13) Landrum, G. A.; Glassey, W. V. YAeHMOP, version 3.0. Available from *http://yaehmop.sourceforge.net*.

(14) (a) Ammeter, J. H.; Elian, M.; Summerville, R. H.; Hoffmann, R. *J. Am. Chem. Soc.* **1978**, *100*, 3686 doi:10.1021/ja00480a005.; (b) Whangbo, M.-H.; Hoffmann, R. *J. Am. Chem. Soc.* **1978**, *100*, 6093 doi:10.1021/ja00487a020.; (c) Cai, S.-H.; Liu, C.-W. *J. Chem. Soc. Faraday* Trans. **1995**, *91*, 479 doi:10.1039/ft9959100479.; (d) Lopes, E. B.; Alves, H.; Ribera, E.; Mas-Torrent, M.; Auban-Senzier, P.; Canadell, E.; Henriques, R. T.; Almeida, M.; Molins, E.; Veciana, J.; Rovira, C.; Jerome, D. *Eur. Phys. J. B* **2002**, *29*, 27. doi:10.1140/epjb/e2002-00258-x.

(15) Frisch, M. J.; Trucks, G. W.; Schlegel, H. B.; Scuseria, G. E.; Robb, M. A.; Cheeseman, J. R.; Montgomery, Jr., J. A.; Vreven, T.; Kudin, K. N.; Burant, J. C.; Millam, J. M.; Iyengar, S. S.; Tomasi, J.; Barone, V.; Mennucci, B.; Cossi, M.; Scalmani, G.; Rega, N.; Petersson, G. A.; Nakatsuji, H.; Hada, M.; Ehara, M.; Toyota, K.; Fukuda, R.; Hasegawa, J.; Ishida, M.; Nakajima, T.; Honda, Y.; Kitao, O.; Nakai, H.; Klene, M.; Li, X.; Knox, J. E.; Hratchian, H. P.; Cross, J. B.; Bakken, V.; Adamo, C.; Jaramillo, J.; Gomperts, R.; Stratmann, R. E.; Yazyev, O.; Austin, A. J.; Cammi, R.; Pomelli, C.; Ochterski, J. W.; Ayala, P. Y.; Morokuma, K.; Voth, G. A.; Salvador, P.; Dannenberg, J. J.; Zakrzewski, V. G.; Dapprich, S.; Daniels, A. D.; Strain, M. C.; Farkas, O.; Malick, D. K.; Rabuck, A. D.; Raghavachari, K.; Foresman, J. B.; Ortiz, J. V.; Cui, Q.; Baboul, A. G.; Clifford, S.; Cioslowski, J.; Stefanov, B. B.; Liu, G.; Liashenko, A.; Piskorz, P.; Komaromi, I.; Martin, R. L.; Fox, D. J.; Keith, T.; Al-Laham, M. A.; Peng, C. Y.; Nanayakkara, A.; Challacombe, M.; Gill, P. M. W.; Johnson, B.; Chen, W.; Wong, M. W.; Gonzalez, C.; and Pople, J. A.. *Gaussian 03*, revision C.02. Gaussian Inc.: Wallingford, CT. 2004.

(16) Stevens, W. J.; Basch, H.; Krauss, M. *J. Chem. Phys.* **1984**, *81*, 6026. doi:10.1063/1.447604.

(17) (a) Becke, A. D. *J. Chem. Phys.* **1993**, *98*, 1372 doi:10.1063/1.464304.; (b) Lee, C.; Yang, W.; Parr, R. G. *Phys. Rev.* **1998**, *B37*, 785.

(18) Allen, F. H. *Acta Crystallogr.* **2002**, *B58*, 380.

(19) Tomasi, J.; Mennucci, B.; Cammi, R. *Chem. Rev.* **2005**, *105*, 2999. doi:10.1021/cr9904009. PMID:16092826.

Moshinsky atom and density functional theory — A phase space view[1]

Jens Peder Dahl

Abstract: The problem of two particles in a common harmonic oscillator potential interacting through harmonic oscillator forces is discussed in the Weyl–Wigner phase-space representation. The Wigner function of the system is an ordinary function of the phase-space constants of the motion. The density functional description of the system is touched upon. The functional that determines the confining harmonic potential from the particle density is also an ordinary function.

Key words: harmonium, Hooke's atom, phase space, Wigner function, DFT.

Résumé : Le problème de deux particules dans un potentiel d'oscillateur harmonique commun interagissant par le biais de forces d'oscillateur harmonique est discuté dans la représentation phase-espace de Weyl–Wigner. La fonction de Wigner du système est une fonction ordinaire des constantes phase-espace du mouvement. On aborde la question de la description de la fonctionnelle de densité du système. La fonctionnelle qui détermine le potentiel harmonique confinant de la densité de particule est aussi une fonction ordinaire.

Mots-clés : harmonium, atome de Hooke, fonction de Wigner, phase-espace, théorie de la fonctionnelle de densité (TFD).

[Traduit par la Rédaction]

1. Introduction

Tom Ziegler's first article, from 1970, was written while he was a student under Professor Carl J. Ballhausen in the Department of Physical Chemistry at the University of Copenhagen. The department was an international center in theoretical chemistry, with many foreign postdocs and other visitors. Several bright Danish students also contributed to the scientific achievements of the department. I held a position as lecturer in valence theory and co-supervised many of Ballhausen's students, among them Tom Ziegler.

A major effort at the Department was the study of the electronic structure of molecules, in particular transition-metal complexes. We applied crystal-field theory, ligand-field theory, semiempirical and semiquantitative molecular-orbital theory, and ab initio theory. We discussed the various theoretical methods and their basis in seminars and group discussions. I found the standard derivation of the Hartree–Fock (HF) equations, with its emphasis on Lagrangian multipliers, rather cumbersome. I had therefore constructed an alternative derivation (reproduced in Dahl's *Introduction to the Quantum World of Atoms and Molecules*, 2001[2]), which was easier to handle and gave a more direct understanding of the role played by the off-diagonal multipliers. Tom took interest in this derivation, as did the Canadian postdoc D. Rodney Truax.

An article in the current literature caught the interest of Tom and Rodney. In the article, the assertion was made that the method of Lagrangian multipliers leads to incomplete conditions on the HF orbitals. We all set down over the weekend and were able to show that this was a false assertion, caused by certain logical imprecisions in the standard discussion of open-shell HF theory. We immediately wrote an article with our conclusions and published it in the fairly new Chemical Physics Letters.[3]

Studying the basics of HF theory was one thing. Applying the theory was something else. Transition-metal complexes contain many electrons, and to describe the chemical bond in these compounds it is necessary to include not only s- and p-orbitals, but also d-orbitals. In fact, we could only get through the calculations on these compounds by introducing serious approximations, such as neglecting small overlap integrals, etc. These approximations were tied to acronyms like ZDO, CNDO, INDO, etc. Tom was also interested in such methods and later included them in several calculations.

All of these approximations are, however, of little practical interest today. Another approximation has had a different history. This is the local density approximation (LDA) that evolved into density functional theory (DFT). We also discussed this kind of theory in our group, and in 1982 John Avery and I arranged the first major international symposium on *Local Density Approximations in Quantum Chemistry and Solid State Physics*, in Copenhagen. In the meantime, Tom had acquired his Master's degree at the University of Copenhagen in 1972, left Denmark, and earned a Ph.D. at the University of Calgary in 1978. He contributed to the multi-author book[4] that we edited on the occasion of the symposium with the article *On the Extension of the Statistical Energy Expression to Multi-Determinantal Wave Functions*.

Tom is a prominent international figure in the area of theoretical inorganic chemistry. He is a member of the Royal Danish Academy of Sciences and Letters. It is a pleasure to have worked with him when we were both quite young, and

Received 2 November 2008. Accepted 9 December 2008. Published on the NRC Research Press Web site at canjchem.nrc.ca on 21 February 2009.

J.P. Dahl.[1] Chemical Physics, Department of Chemistry, Technical University of Denmark, Kemitorvet 207, DK-2800 Kgs. Lyngby, Denmark (e-mail: dahlhome@webspeed.dk).

[1]Present address: Institut für Quantenphysik, Universität Ulm, D-89069 Ulm, Germany.

I am happy to be given the opportunity to contribute to this special issue of the Canadian Journal of Chemistry.

My contribution has the form of an essay in which I discuss one of the simplest model analogues to a two-electron atom, i.e., Moshinsky's harmonium atom, using the Weyl–Wigner formulation of quantum mechanics. The model is sufficiently simple that some implicitly given functionals become ordinary functions. Thus the Wigner function is a function of the constants of the motion as expressed in phase space. Also, the Hohenberg–Kohn relation[5] between the confining potential and the particle density is expressed by an explicit function.

The following section contains a few introductory and partly personal remarks on density functional theory. The discussion of the Moshinsky atom is given is Section 3 and its subsections. Section 4 is the summary.

2. Approximate density functional theory

One of Tom's key publications is his 1991 review article in Chemical Reviews, entitled *Approximate Density Functional Theory as a Practical Tool in Molecular Energetics and Dynamics*.[6] It is written with a clear understanding of the science on which it builds. And the author chooses his words with care. He uses the familiar acronym DFT for density functional theory in general, but always refers to the computational work as approximate density functional theory. I think this calls for a specific acronym for the latter. Hence, I shall refer to approximate density functional theory through the acronym ADFT.

My own relation to ADFT goes back to the mid-1960s when I worked as a postdoc in Professor John C. Slater's Solid-State and Molecular Theory Group (SSMTG) at MIT. Among other things, I studied electronic band structures by means of augmented plane wave (APW) calculations.[7] To make such calculations at all possible, it was necessary to approximate the non-local exchange potential with a local one, and the way this was done at the time was by invoking Slater's $\rho^{1/3}$ approximation,[8] in which the exchange potential, measured in Hartree units, is written

$$[1] \qquad V_{\mathrm{XS}}(\boldsymbol{r}) = -3\left[\frac{3}{4\pi}\rho\prime(\boldsymbol{r})\right]^{1/3}$$

where $\rho'(\boldsymbol{r})$ is the same-spin particle density at the point $\boldsymbol{r}$. This expression may be obtained by replacing the HF exchange potential by the average exchange potential in a free-electron gas, as described elsewhere.[9] This replacement takes place after the HF equations have been derived by applying the variational principle to the HF energy expression. If, instead, one approximates the energy expression before the variation, then one obtains an expression only two-thirds as great, as shown by Gaspar in 1954[10] and Kohn and Sham in 1965.[11] Both exchange potentials are contained in the expression

$$[2] \qquad V_{\mathrm{X}\alpha}(\boldsymbol{r}) = -3\alpha\left[\frac{3}{4\pi}\rho\prime(\boldsymbol{r})\right]^{1/3}$$

with $\alpha = 1$ for Slater's expression and $\alpha = 2/3$ for the Gaspar–Kohn–Sham expression. In the Xα method, one allows α to vary to also include some correlation beyond HF. In ADFT, the Xα expression is much refined and merged into the exchange-correlation potential. At the same time, the HF equations get replaced by the Kohn–Sham equations.

The exchange-correlation potential is in general a complicated functional of the spin-up and spin-down particle densities. When it happens that the functional takes on a simple form like that of eq. [2], it is in fact an ordinary function.

As is well known, the HF description approximates the many-electron wave function for a closed-shell system by a single Slater determinant, whereas ADFT puts focus on the particle density. Both HF theory and ADFT have led to an enormous progress in our understanding of the structure of atoms, molecules, and solids. Tom has given us a solid impression of some of these advances in the review article mentioned above.

ADFT is based on the (first) Hohenberg–Kohn theorem[5], which applies to a non-degenerate ground state of a system of N identical and interacting particles, moving in an external potential $v(\boldsymbol{r})$. It states that $v(\mathbf{r})$, and hence the total energy, is a unique functional of the particle density $\rho(\boldsymbol{r})$. The form of the functional is not known. To determine it may well be compared with the task of determining the wave function of the universe. Yet, the study of particular cases and simple models do give us some insight. Many such studies now exist. In the following I shall add a simple study, in which I invoke the phase-space representation of quantum mechanics.

3. The Moshinsky atom

The original proof of the theorem that $v(\boldsymbol{r})$ is a functional of $\rho(\boldsymbol{r})$ is formally quite simple.[2,5] Yet, some delicate objections have been raised (See for instance, Kryachko 2006[12] and Szczepanik et al. 2007[13] for a quite recent discussion). We shall not focus on the proof here. It proceeds by reductio ad absurdum and is accordingly implicit by nature. My goal is to present an explicit example of how to go from $\rho(\hat{\boldsymbol{r}})$ to $v(\hat{\boldsymbol{r}})$. This example is represented by a model atom consisting of two identical interacting particles moving in a confining harmonic potential. This is the so-called harmonium atom or Hooke's atom. It has been much studied in the literature. The interaction between the two particles has usually been taken to be Coulombic,[14] but some studies also exist in which it has been assumed to be harmonic. The first such study was performed by Moshinsky.[15] Lately, his study has been extended by March and co-workers[16,17] Independent investigations have been performed by Neal[18] and Schindlmayr.[19] I shall limit myself to the harmonic version of the harmonium atom, and following March et al., refer to it as the Moshinsky model atom or just the Moshinsky atom.

3.1. Hamiltonian and ground-state wave function

The Moshinsky atom is defined by the Hamiltonian,

$$[3] \qquad \hat{H}_{\mathrm{D}} = \frac{\hat{\boldsymbol{p}}_1^2}{2m} + \frac{\hat{\boldsymbol{p}}_2^2}{2m} + \frac{1}{2}m\omega^2\hat{\boldsymbol{x}}_1^2 + \frac{1}{2}m\omega^2\hat{\boldsymbol{x}}_2^2 + \frac{1}{2}m\omega^2\kappa|\hat{\boldsymbol{x}}_1 - \hat{\boldsymbol{x}}_2|^2$$

where $(\hat{\boldsymbol{x}}_1, \hat{\boldsymbol{p}}_1)$ are the position and momentum vectors of particle 1, and $(\hat{\boldsymbol{x}}_2, \hat{\boldsymbol{p}}_2)$ are the position and momentum vectors of particle 2. With the position and momentum vectors ex-

pressed in the usual Cartesian coordinates, the Hamiltonian becomes a sum of independent but equivalent sub-Hamiltonians, one for each of the D coordinate directions. It is therefore sufficient to consider the one-dimensional problem defined by the Hamiltonian,

$$[4] \qquad \hat{H} = \frac{\hat{p}_1^2}{2m} + \frac{\hat{p}_2^2}{2m} + \frac{1}{2}m\omega^2\hat{x}_1^2 + \frac{1}{2}m\omega^2\hat{x}_2^2 + \frac{1}{2}m\omega^2\kappa(\hat{x}_1 - \hat{x}_2)^2$$

Unlike Moshinsky who took $D = 3$, we shall therefore work in a single dimension.

In eqs. [3] and [4], m is the mass of a particle, ω^2 determines the strength of the potential in which the particles move, while $\omega^2\kappa$ determines the strength of the particle–particle interaction. This interaction is an attraction when κ is positive and a repulsion when κ is negative.

The Hamiltonian of eq. [4] may be separated into a center-of-mass or extracule part and a relative-distance or intracule part by introducing the new position variables,

$$[5] \qquad \hat{X} = \frac{1}{2}(\hat{x}_1 + \hat{x}_2), \quad \hat{x} = \hat{x}_1 - \hat{x}_2$$

and the corresponding momentum variables

$$[6] \qquad \hat{P} = \hat{p}_1 + \hat{p}_2, \quad \hat{p} = \frac{1}{2}(\hat{p}_1 - \hat{p}_2)$$

Thus, we get

$$[7] \qquad \hat{H} = \hat{H}_{\mathrm{cm}} + \hat{H}_{\mathrm{rel}}$$

where

$$[8] \qquad \hat{H}_{\mathrm{cm}} = \frac{\hat{P}^2}{4m} + m\omega^2\hat{X}^2$$

and

$$[9] \qquad \hat{H}_{\mathrm{rel}} = \frac{\hat{p}^2}{m} + \frac{1}{4}m\omega^2(1 + 2\kappa)\hat{x}^2$$

Equation [7] shows that $\hat{H}$ is the Hamiltonian for two uncoupled harmonic oscillators, provided $-1/2 < \kappa < \infty$. We restrict the values of κ to this interval.

Drawing on the textbook treatment of the harmonic oscillator,[2] we find that the ground state $|\Psi_0>$ of the Moshinsky atom has the energy,

$$[10] \qquad E_0 = \frac{1}{2}\hbar(1 + \sqrt{1 + 2\kappa})\omega$$

and the position-space wave function

$$[11] \qquad \Psi_0(x_1, x_2) = (1 + 2\kappa)^{1/8}\frac{\alpha}{\sqrt{\pi}}e^{-\alpha^2X^2}e^{-\frac{1}{4}\sqrt{1+2\kappa}\,\alpha^2x^2}$$

where $\alpha = \sqrt{m\omega/\hbar}$.

Accepting a slightly different notation, these results agree with those of Moshinsky[15] and March and co-worlers.[16,17] Those authors went on to study the Hartree–Fock description and the correlation problem. The results are also in accordance with those of Neal[18] and Schindlmayr[19] who went on to discuss the Kohn–Sham description.

Here, we shall continue by transforming the description into phase space. In so doing, we follow the general outline given in Dahl and Schleich[20].

3.2. Liouville space

To begin with, we go from Hilbert space where the ket $|\Psi_0>$ belongs, to operator space or Liouville space where the Hamiltonian lives together with other operators, in particular the state operator, or density matrix.

$$[12] \qquad \hat{\rho}_0 = |\Psi_0\rangle\langle\Psi_0|$$

For a non-degenerate ground state, the state operator is a function of the Hamiltonian. To see this, we introduce the orthonormal set of eigenkets of $\hat{H}$, that is, $|\Psi_0>$, $|\Psi_1>$, $|\Psi_2>$, ... and verify the well-known fact that $\hat{\rho}_0$ is a projection operator,

$$[13] \qquad \hat{\rho}_0\sum_{j=0}^{\infty}c_j|\Psi_j\rangle = c_0|\Psi_0\rangle, \quad \hat{\rho}_0^2 = \hat{\rho}_0$$

According to the general theory of projection operators,[21,22] we may therefore write,

$$[14] \qquad \hat{\rho}_0 = \prod_{j\neq 0}\frac{\hat{H} - E_j}{E_0 - E_j}$$

This expression shows indeed that $\hat{\rho}_0$ is a function of the Hamiltonian, that is,

$$[15] \qquad \hat{\rho}_0 = F(\hat{H})$$

To proceed, we move from Liouville space to phase space.

3.3. Phase space. The Weyl–Wigner representation

Among the different phase-space representations of quantum mechanics, the Weyl–Wigner representation[23–26] may be considered the canonical representation because of its simplicity.[28,29] It is a representation of quantum mechanics in its own right,[30–33] but may also be considered a mapping from Liouville space to phase space. Adopting the latter point of view, it maps Liouville-space operators $\hat{A}$ into phase-space functions $a(\mathbf{x}, \mathbf{p})$. The mapping may be expressed by the transformation,

$$[16] \qquad a(\boldsymbol{x}, \boldsymbol{p}) = \int_{-\infty}^{\infty}\mathrm{d}\boldsymbol{y}\langle\boldsymbol{x} + \boldsymbol{y}/2|\hat{A}\,|\boldsymbol{x} - \boldsymbol{y}/2\rangle e^{-\mathrm{i}\boldsymbol{p}\cdot\boldsymbol{y}/\hbar}$$

where the integration is over D-dimensional y-space. Equation [16] transforms operators of the form $G_1(\hat{\boldsymbol{x}}) + G_2(\hat{\boldsymbol{p}})$ into phase-space functions of the similar form $G_1(\boldsymbol{x}) + G_2(\boldsymbol{p})$. For operators containing products of position and momentum variables, there will be extra $\hbar$-dependent contributions.[28] Choosing $\hat{A}$ to be $\hat{\rho}/h^{\mathrm{D}}$, where $\hat{\rho}$ is a state operator, gives a Wigner function,

$$[17] \qquad W(\boldsymbol{x}, \boldsymbol{p}) = \frac{1}{(2\pi\hbar)^D} \times \int_{-\infty}^{\infty}\mathrm{d}\boldsymbol{y}\ \Psi^*(\boldsymbol{x} - \boldsymbol{y}/2)\Psi(\boldsymbol{x} + \boldsymbol{y}/2)e^{-\mathrm{i}\boldsymbol{p}\cdot\boldsymbol{y}/\hbar}$$

Now, let $a(\boldsymbol{x}, \boldsymbol{p})$ and $b(\boldsymbol{x}, \boldsymbol{p})$ be the phase-space images of the operators $\hat{A}$ and $\hat{B}$, respectively. The phase-space function $c(\boldsymbol{x}, \boldsymbol{p})$ corresponding to the operator $\hat{C} = \hat{A}\hat{B}$ is then

$$[18] \qquad c(\boldsymbol{x}, \boldsymbol{p}) = a(\boldsymbol{x}, \boldsymbol{p}) * b(\boldsymbol{x}, \boldsymbol{p})$$

This is a non-commutative binary operation known as a star multiplication. Explicitly, the star product may be written in the following form,[25]

$$[19] \qquad c(\boldsymbol{x}, \boldsymbol{p}) = \exp\left[\frac{i\hbar}{2}\left(\frac{\partial}{\partial \boldsymbol{x}_1}\cdot\frac{\partial}{\partial \boldsymbol{p}_2} - \frac{\partial}{\partial \boldsymbol{p}_1}\cdot\frac{\partial}{\partial \boldsymbol{x}_2}\right)\right] a(\boldsymbol{x}, \boldsymbol{p})b(\boldsymbol{x}, \boldsymbol{p})$$

The subscript 1 on a differential operator indicates that this operator acts only on the first function in the product $a(\boldsymbol{x}, \boldsymbol{p})b(\boldsymbol{x}, \boldsymbol{p})$. Similarly, the subscript 2 is used with operators that only act on the second function in the product. Alternative expressions for $c(\boldsymbol{x}, \boldsymbol{p})$ are,

$$[20] \qquad c(\boldsymbol{x}, \boldsymbol{p}) = a(\hat{\mathbf{X}}, \hat{\mathbf{P}})b(\boldsymbol{x}, \boldsymbol{p})$$

and

$$[21] \qquad c(\boldsymbol{x}, \boldsymbol{p}) = b(\hat{\mathbf{X}}^*, \hat{\mathbf{P}}^*)a(\boldsymbol{x}, \boldsymbol{p})$$

where we have introduced the Bopp operators,[32,34]

$$[22] \qquad \hat{\mathbf{X}} = \boldsymbol{x} + \frac{i\hbar}{2}\frac{\partial}{\partial \boldsymbol{p}}, \quad \hat{\mathbf{P}} = \boldsymbol{p} - \frac{i\hbar}{2}\frac{\partial}{\partial \boldsymbol{x}}$$

and

$$[23] \qquad \hat{\mathbf{X}}^* = \boldsymbol{x} - \frac{i\hbar}{2}\frac{\partial}{\partial \boldsymbol{p}}, \quad \hat{\mathbf{P}}^* = \boldsymbol{p} + \frac{i\hbar}{2}\frac{\partial}{\partial \boldsymbol{x}}$$

For yet other expressions, see the literature.[28]

By means of the above expressions it is easily seen that for combinations like $a(\boldsymbol{x}) * b(\boldsymbol{x})$ and $a(\boldsymbol{p}) * b(\boldsymbol{p})$, star multiplication is the same as ordinary multiplication. On the other hand, the star product $a(\boldsymbol{x}, \boldsymbol{p}) * a(\boldsymbol{x}, \boldsymbol{p})$ will in general be different from $a(\boldsymbol{x}, \boldsymbol{p})^2$. As far as the operators listed in Sect. 3.1 are concerned, each may be transformed into the corresponding phase-space function by simply removing the operator symbol for every variable. Thus for example, $H(x, p)$ becomes the phase-space function corresponding to the operator $\hat{H}(\hat{x}, \hat{p})$.

To determine the Wigner function $W_0(x_1, x_2, p_1, p_2)$ corresponding to the state operator $\hat{\rho}_0$, we first consider the one-dimensional oscillator with the Hamiltonian,

$$[24] \qquad \hat{H} = \frac{\hat{p}^2}{2m} + \frac{1}{2}m\omega^2\hat{x}^2$$

The ground-state wave function is

$$[25] \qquad \psi_0(x) = \left(\frac{\alpha^2}{\pi}\right)^{\frac{1}{4}} e^{-\frac{1}{2}\alpha^2 x^2}$$

Inserting this expression into the right-hand side of eq. [17] gives the ground-state Wigner function,

$$[26] \qquad W_0(x, p) = \frac{1}{\pi\hbar}\exp(-2H(x, p)/\hbar\omega)$$

This is a special case of the general expression,[20,25]

$$[27] \qquad W_n(x, p) = \frac{(-1)^n}{\pi\hbar}L_n(4H(x, p)/\hbar\omega) \times \exp(-2H(x, p)/\hbar\omega), \quad n = 0, 1, 2, \ldots$$

where L_n is a Laguerre polynomial.[27]

When applied to the one-dimensional oscillator, eq. [15] says that the state operator $\hat{\rho}_0$ is a function of $\hat{H}(\hat{x}, \hat{p})$. On the other hand, the Wigner function and $H(x, p)$ are the phase-space images of $\hat{\rho}_0$ and $\hat{H}(\hat{x}, \hat{p})$, respectively. Hence, we may in principle determine the form of the Wigner function by replacing the $\hat{H}$ on the right-hand side of eq. [14] by $H(x, p)$ and treating all multiplications as star products. We see that the result is an explicit function of $H(x, p)$ in the present case. This is a quite remarkable result. As we have discussed in Dahl and Schleich,[20] such a situation can only hold if $(H(x, p)^*)^n$ is a function of $H(x, p)$ for arbitrary n. We found that this condition is fulfilled whenever the Hamiltonian contains the position and momentum variables in a polynomial not higher than quadratic. In particular, it holds for the harmonic oscillator, and this is the reason why the Wigner function of eq. [27] merely depends upon x and p through $H(x, p)$.

Similar results hold in several dimensions, but here more than one constant of the motion may be present, and they may all enter into the expression for the Wigner function, This is in fact the case for the Moshinsky atom.

3.4. Densities and energies

The sub-Hamiltonians (eqs. [8] and [9]) both commute with the total Hamiltonian (eq. [7]), that is, they are constants of the motion. Both operators are of the type (eq. [24]) and define Wigner functions of the form (eq. [26]). The total ground-state Wigner function therefore becomes,

$$[28] \qquad W(x_1, x_2, p_1, p_2) = \frac{1}{(\pi\hbar)^2} \times \exp\left(-\frac{2H_{\mathrm{cm}}(X, P)}{\hbar\omega} - \frac{2H_{\mathrm{rel}}(x, p)}{\hbar\omega\sqrt{1+2\kappa}}\right)$$

It is the product of an extracule and an intracule phase-space density.

By integrating $W(x_1,x_2,p_1,p_2)$ over some of its variables we obtain reduced phase-space densities. Thus, integration over x_2 and p_2 followed by multiplication with 2 leads to the single-particle phase-space density,

$$[29] \qquad w(x_1, p_1) = \frac{2}{\pi\hbar}\sqrt{a(\kappa)b(\kappa)} \times \exp\left[-\alpha^2 a(\kappa)x_1^2 - \frac{b(\kappa)}{(\alpha\hbar)^2}p_1^2\right]$$

with α as defined earlier and

$$[30] \qquad a(\kappa) = \frac{2\kappa + 1 - \sqrt{2\kappa + 1}}{\kappa}$$
$$b(\kappa) = \frac{\sqrt{2\kappa + 1} - 1}{\kappa}$$

By further integration over p_1 we get the particle density in position space,

$$[31] \qquad \rho(x_1) = 2\alpha\sqrt{\frac{a(\kappa)}{\pi}}\exp[-\alpha^2 a(\kappa)x_1^2].$$

If instead, we integrate over x_1, we get the particle density in momentum space,

$$[32] \qquad \Pi(p_1) = \frac{2}{\alpha\hbar}\sqrt{\frac{b(\kappa)}{\pi}}\exp\left[-\frac{b(\kappa)}{(\alpha\hbar)^2}\, p_1^2\right]$$

By means of these densities we may evaluate the expectation values of symmetric operators. In this way, we find for instance the different contributions to the energy E_0 of our two-particle system,

$$[33] \qquad E_0 = \frac{\sqrt{2\kappa + 1} + 1}{4}\,\hbar\omega + \frac{\kappa}{2(2\kappa + 1 - \sqrt{2\kappa + 1})}\,\hbar\omega \quad + \frac{\kappa}{2\sqrt{2\kappa + 1}}\,\hbar\omega$$

Here, the first term is the kinetic energy, the second term is the confinement energy, and the last term is the interaction energy. The sum of the three terms is $E_0 = \frac{1}{2}(\sqrt{2\kappa + 1} + 1)\hbar\omega$, in accordance with the value given in eq. [10]. We note that the kinetic energy is just half the total energy, as expected from the virial theorem as applied to a harmonic system.[2,22]

The expectation values above could, of course, also have been evaluated by means of reduced density matrices in position space together with differential expressions for the momentum operators. The reduced density matrices would then have to be derived from the position-space wave function of eq. [11] in the usual way. However, the present procedure treats position and momentum symmetrically. We shall now consider the relation between the external potential and the particle density in position space.

3.5. The confining potential as a function of the particle density

According to the (first) Hohenberg–Kohn theorem,[5] the ground-state particle density in position space determines the external potential (the confining potential), that is, $v(x)$ is a functional of $\rho(x)$. Each type of interaction (Coulomb, harmonic, etc.) has its own branch of this functional. Here we consider the branch corrresponding to the harmonic interaction. When we also take the confining potential to be harmonic, we realize that we have to do with a lobe of that branch in which the functional simplifies to an ordinary function.

The $\rho(x)$ of eq. [31] has been determined by the direct method, namely, by solving the Schrödinger equation with the external potential $v(x) = \frac{1}{2}m\omega^2x^2$. We would, of course, have obtained the same $\rho(x)$ if we had taken $v(x)$ to be $v(x) = v_0 + \frac{1}{2}m\omega^2x^2$, where v_0 is an arbitrary constant. Let us therefore adopt this general form. We must then determine $v(x)$ by the inverse method, namely, from $\rho(x)$. To this end, we simply note that eq. [31] may be written,

$$[34] \qquad \rho(x) = 2\alpha\sqrt{\frac{a(\kappa)}{\pi}}\exp\left[\frac{2a(\kappa)}{\hbar\omega}v_0\right]\exp\left[-\frac{2a(\kappa)}{\hbar\omega}v(x)\right]$$

Inverting this relation gives,

$$[35] \qquad v(x) = -\frac{\hbar\omega}{2a(\kappa)}\ln\rho(x) + \tilde{v}_0$$

where $\tilde{v}_0$ is an arbitrary additive constant. This relation certainly gives us $v(x)$ if we know $a(\kappa)$ and ω.

To relate this result to density functional theory, we lock the strength of the particle–particle interaction, but include all strengths of the confining potential. We therefore rewrite eq. [4] in the form,

$$[36] \qquad \hat{H} = \frac{\hat{p}_1^2}{2m} + \frac{\hat{p}_2^2}{2m} + \frac{1}{2}m\omega^2\hat{x}_1^2 + \frac{1}{2}m\omega^2\hat{x}_2^2 + \frac{1}{2}m\eta(\hat{x}_1 - \hat{x}_2)^2$$

The fixed strength η now defines the particle type, and the free ω defines the class of confining potentials.

We have put $\kappa = \eta/\omega^2$. The $a(\kappa)$ of eq. [30] becomes therefore,

$$[37] \qquad a(\omega, \eta) = \frac{\omega^2 + 2\eta - \omega\sqrt{\omega^2 + 2\eta}}{\eta}$$

and eq. [35] reads

$$[38] \qquad v(x) = -\frac{\hbar\omega}{2a(\omega, \eta)}\ln\rho(x) + \tilde{v}_0$$

The determination of $v(x)$ from $\rho(x)$ now proceeds via the following arguments. We study a specific kind of interacting particle. Hence, η is fixed and known to us. We also know that a harmonic confining potential must produce a maximum in $\rho(x)$, at $x = x_0$ say, and according to eq. [31] we must at this point have,

$$[39] \qquad \rho''(x_0)/\rho(x_0) = -2a(\omega, \eta)m\omega/\hbar$$

The mass m we know, and measuring $\rho''(x_0)/\rho(x_0)$ therefore gives us ω. Thus, we have determined the external potential from the density.

This topological procedure is similar to the topological procedure used for interacting electrons in a nuclear framework. To fix η is similar to specifying the electronic charge. The determination of ω corresponds to exploiting the cusp condition at the nuclei.The difference is that in our case we have an explicit function instead of an implicit functional.

This is as far as we shall take the discussion of the Moshinsky atom. I refer the reader to the earlier cited literature[15–19] for discussions of, inter alia, the Hartree–Fock description, the correlation problem, and the Kohn–Sham description.

4. Summary

In this contribution I have discussed the ground state of Moshinsky's harmonium atom, which consists of two harmonically confined particles interacting through a harmonic force. The discussion has been tied to the phase-space representation of quantum mechanics in the Weyl–Wigner formulation. Explicit expressions and relations have been derived both for two-particle densities and one-particle densities. Special attention has been paid to the (first) Hohenberg–Kohn theorem and its relation between particle density and the external potential. In a general system, this relation is expressed by an implicit functional. In the simple case of the Moshinsky atom, the functional becomes an ordinary function. We have found the explicit form of this function and thus fulfilled an old desiderate[35]: *Could it be possible, for example, to obtain this functional for the oscillator model of the hydrogen atom, where all the Coulomb type potentials are replaced by their oscillator analogues?*

The Moshinsky atom is obviously an unrealistic substitute for a real atom. Its value as a model lies in the relative ease with which explicit expressions can be derived for most of its properties and in the way that some, generally intricate, relations simplify to ordinary functions.

5. Acknowledgments

I acknowledge fruitful conversations with W.P. Schleich, M. Springborg, and J.M. Gracia-Bondia. I am grateful to the Alexander von Humboldt Foundation for its support and to the Institut für Quantenphysik for its great hospitality. Finally, I thank the referee for the reference to the desiderate mentioned in the summary.

References

(1) This article is part of a Special Issue dedicated to Professor T. Ziegler.
(2) See, for instance: Dahl, J. P. *Introduction to the quantum world of atoms and molecules*. World Scientific: Singapore, 2001.
(3) Dahl, J. P.; Johansen, H.; Truax, D. R.; Ziegler, T. *Chem. Phys. Lett.* **1970**, *6*, 64. doi:10.1016/0009-2614(70)80132-4.
(4) *Local density approximations in quantum chemistry and solid state physics*; Dahl, J. P. and Avery, J. Eds.; Plenum: New York, 1984.
(5) Hohenberg, P.; Kohn, W. *Phys. Rev.* **1964**, *136*, B864. doi:10.1103/PhysRev.136.B864.
(6) Ziegler, T. *Chem. Rev.* **1991**, *91*, 651. doi:10.1021/cr00005a001.
(7) Dahl, J. P.; Switendick, A. C. J. *Phys. Chem. Solids,* **1966**, *27*, 931. doi:10.1016/0022-3697(66)90064-3.
(8) Slater, J. C. *Phys. Rev.* **1951**, *81*, 385. doi:10.1103/PhysRev.81.385.
(9) See, for instance: Slater, J. C. *Quantum theory of atomic structure*; McGraw-Hill: New York, 1960; Vol. 2.
(10) Gaspar, R. *Acta Phys. Acad. Sci. Hung.* **1954**, *3*, 263.
(11) Kohn, W.; Sham, L. J. *Phys. Rev.* **1965**, *140*, A1133. doi:10.1103/PhysRev.140.A1133.
(12) (a) Kryachko, E. S. *Int. J. Quantum Chem.* **2005**, *103*, 818 doi:10.1002/qua.20539.; (b) Kryachko, E. S. *Int. J. Quantum Chem.* **2006**, *106*, 1795. doi:10.1002/qua.20970.
(13) Szczepanik, W.; Dulak, M.; Wesolowski, T. A. *Int. J. Quantum Chem.* **2007**, *107*, 762. doi:10.1002/qua.21102.
(14) See, for instance: Cioslowski, J.; Pernal, K. J. *Chem. Phys.* **2000**, *113*, 8434 and refs. cited therein.
(15) Moshinsky, M. *Am. J. Phys.* **1968**, *36*, 52. doi:10.1119/1.1974410.
(16) Amovilli, C.; March, N. H. *Phys. Rev. A,* **2003**, *67*, 022509. doi:10.1103/PhysRevA.67.022509.
(17) March, N. H.; Cabo, A.; Claro, F.; Angilella, G. G. N. *Phys. Rev. A*, **2008**, *77*, 042504. doi:10.1103/PhysRevA.77.042504.
(18) Neal, H. L. *Am. J. Phys.* **1998**, *66*, 512. doi:10.1119/1.18892.
(19) Schindlmayr, A. *Am. J. Phys.* **1999**, *67*, 933. doi:10.1119/1.19156.
(20) Dahl, J. P.; Schleich, W. P. *Phys. Rev. A* **2009**, *79*, 024101. doi:10.1103/PhysRevA.79.024101.
(21) Löwdin, P. O. *Rev. Mod. Phys.* **1962**, *34*, 520. doi:10.1103/RevModPhys.34.520.
(22) Schiff, L. I. *Quantum mechanics*; 3rd ed. McGraw-Hill: New York, 1968; p. 167.
(23) Weyl, H. *The theory of groups and quantum mechanics*; Methuen, 1931.
(24) Wigner, E. *Phys. Rev.* **1932**, *40*, 749. doi:10.1103/PhysRev.40.749.
(25) Groenewold, H. J. *Physica* **1946**, *12*, 405. doi:10.1016/S0031-8914(46)80059-4.
(26) Moyal, J. E. *Proc. Camb. Philos. Soc.* **1949**, *45*, 99. doi:10.1017/S0305004100000487.
(27) *Handbook of mathematical functions*; Abramowitz, M.; Stegun, I. A.. Eds.; National Bureau of Standards: Washington, D.C., 1964.
(28) Dahl, J. P. A phase space essay. In *Conceptual Trends in Quantum Chemistry*; Kryachko, E. S.; Calais J. L. Eds.; Kluwer: Dortrecht, the Netherlands, 1994; p. 199.
(29) Wlodarz, J. J. *Phys. Lett. A,* **2001**, *286*, 97. doi:10.1016/S0375-9601(01)00402-9.
(30) Dahl, J. P. Dynamical equations for the Wigner functions. In *Energy Storage and Redistribution in Molecules*; Hinze. J. Ed.; Plenum: New York, 1983; p. 557.
(31) Hug, M.; Menke, C.; Schleich, W. P. *Phys. Rev. A*, **1998**, *57*, 3188, 3206. doi:10.1103/PhysRevA.57.3188.
(32) Schleich, W. P. *Quantum optics in phase space*; Wiley-VCH: Weinheim, Germany, 2001.
(33) Zachos, C.; Fairlie, D.; Curtright, T. *Quantum mechanics in phase space: An overview with selected papers*; World Scientific: Singapore, 2005.
(34) Bopp, F. Werner Heisenberg und die Physik unserer Zeit; Vieweg: Braunschweig, Germany,1961; p. 128.
(35) Kryachko, E. S.; Ludeña, E. V. *Energy density functional theory of many-electron systems*; Kluwer: Dordrecht, Nerthelands, 1990; p.413.

An implementation of the conductor-like screening model of solvation within the Amsterdam density functional package — Part II. COSMO for real solvents[1]

Cory C. Pye, Tom Ziegler, Erik van Lenthe, and Jaap N. Louwen

Abstract: The conductor-like screening model for real solvents (COSMO-RS) has been implemented in the Amsterdam density functional program. The surface building routines now allow for finer discretization of the GEPOL-based surfaces, and an additional surface due to Delley has been incorporated. One problem identified is the need for accurate density fitting in the region of the surface points. Another difficulty is the need to explicitly state for which atoms the hydrogen-bonding term applies. We present some vapour–liquid equilibrium curves of binary solvent systems to demonstrate the utility of the method.

Key words: Amsterdam density functional package, conductor-like screening model for real solvents, solvation, thermodynamics, chemical potential, chemical engineering.

Résumé : On a appliqué le modèle de triage apparenté aux conducteurs pour des solvants réels [« COSMO-RS »] dans le programme de la fonctionnelle de la densité d'Amsterdam. Les méthodes de construction des surfaces permettent maintenant d'obtenir des surfaces à base GEPOL beaucoup plus distinctes et on y a incorporé une surface additionnelle de Delley. La nécessité d'avoir des ajustements précis de densité dans la région des points de surface a été identifiée comme un problème. Une autre difficulté est la nécessité de spécifier explicitement à quels atomes le terme de liaison hydrogène s'applique. On présente quelques courbes d'équilibre vapeur–liquide de systèmes de solvants binaires pour démontrer l'utilité de la méthode.

Mots-clés : méthode de la fonctionnelle de la densité d'Amsterdam, modèle de triage apparenté aux conducteurs pour des solvants réels, solvatation, thermodynamique, potentiel chimique, génie chimique.

[Traduit par la Rédaction]

Introduction

The modelling of solvent effects in complex systems of technological, geochemical, and biological significance is an important field of study. In the past several years, the conductor-like screening model by Klamt[2] has emerged as a promising tool for efficiently treating these effects. We have implemented this method[3] into the Amsterdam density functional package (ADF).[4,5] Since the original implementation of the conductor-like screening model (COSMO), Klamt has subsequently developed the COSMO method for real solvents, COSMO-RS, which goes beyond the dielectric approximation and is very successful at predicting free energies of hydration, vapor pressure, and partition coefficients[6,7] as well as activity coefficients for use in chemical engineering.[8] In this paper, our implementation of the COSMO-RS method in the ADF package is described.

Since the publication of the original 1998 version of COSMO-RS, several variants have been published,[9–13] while in the commercial implementation COSMOtherm the method has been further developed, although precise details have not been published.[14] In this study we have restricted ourselves to the original 1998 version (with some necessary exceptions to be discussed later). This is because one of our purposes is to show that the implementation of COSMO-RS in a Slater orbital based quantum mechanical program like ADF leads to results similar to those obtained with non-Slater based programs. The 1998 COSMO-RS training data was published as supplementary material[7] including the deviations between observed and modeled data. This enables a detailed comparison between the original DMol and the ADF implementation.

Received 26 October 2008. Accepted 10 December 2008. Published on the NRC Research Press Web site at canjchem.nrc.ca on 21 February 2009.

C.C. Pye.[1] Department of Chemistry, Saint Mary's University, 923 Robie Street, Halifax, NS B3H 3C3 Canada.
T. Ziegler. Department of Chemistry, University of Calgary, 2500 University Drive NW, Calgary, AB T2N 1N4, Canada.
E. van Lenthe. Scientific Computing and Modelling NV,Vrije Universiteit, Theoretical Chemistry, De Boelelaan 1083, 1081 HV Amsterdam, The Netherlands.
J.N. Louwen.[2] Albemarle Corporation, Catalysts Research, PO Box 37650, 1030 BE Amsterdam, The Netherlands.

[1]Corresponding author (e-mail: cory.pye@smu.ca).
[2]Corresponding author (e-mail: jaap.louwen@albemarle.com).

Theory and implementation

Changes between ADF 2.3 and ADF99 COSMO

Several minor changes were made as part of the overall improvement of the software before general release in ADF99.[15]

(1) The GEPOL93 algorithm for constructing surfaces[16] was converted from Fortran 77 to Fortran 90 to take advantage of dynamic memory allocation. In addition, the original tessellation of 60 triangles per sphere was recently generalized to $60*4^{FDIV-1}$, where FDIV is a user-specified parameter.
(2) The fitted potential (default) method for calculating the C-matrix was incompatible with the disk potential smearing technique used for avoiding singularities in evaluating C-matrix and Fock matrix elements. One can now use the disk potential for the Fock matrix and the fitted potential for the C-matrix. Although the result is not fully variational, the effect is usually small (10^{-5} au).
(3) COSMO now works with both the Pauli and ZORA relativistic Hamiltonians in both scalar and spin-orbit forms for all C-matrix options.
(4) A more flexible input format for solute atomic radii was added for ease of use.

Theory of COSMO-RS

We briefly outline the COSMO-RS method of Klamt. For full details, including the derivation of the statistical mechanical expressions, the reader is referred to the description of the original DMol implementation of Klamt.[7] We keep the same notation to avoid confusion.

COSMO-RS is quite different from the underlying COSMO method in treating interactions between molecules in full detail. It achieves this in a fraction of the time required for traditional molecular simulations by making use of two essential features:

(1) By taking the molecule in the conductor as the reference state, instead of working out the long-range electrostatic forces between molecules, COSMO-RS deals only with charge mismatches at the cavity surface, thereby replacing the computationally very expensive evaluation of long-range intermolecular forces by the much more tractable computation of only local interactions.
(2) Segments of the molecular cavity are considered to be independent of each other. Although this leads to loss of information (i.e., on steric hindering and the multipolar nature of the electric field of a molecule), in practice this does not appear to create grave artefacts.

In the underlying COSMO method, the ideal net screening energy of molecule X can be written,

$$[1] \qquad \Delta^X = E^X_{\mathrm{COSMO}} - E^X_{\mathrm{gas}}$$

where the two terms on the right are the expectation values of the COSMO and gas-phase Hamiltonian, respectively. The dielectric component of this energy is,

$$[2] \qquad E^X_{\mathrm{diel}} = \frac{1}{2}\sum_{\nu} \Phi^X_{\nu} q^*_{\nu} = \frac{1}{2}\sum_{\nu} \Phi^X_{\nu} s_{\nu} \sigma^*_{\nu}$$

where each tessera ν is associated with a molecular electrostatic potential Φ^X_{ν}, and screening charge q^*_{ν}, which is equal to the product of the surface area s_{ν} and charge density σ^*_{ν}. The remainder accounts for the response of the wave function to the charges. In the original implementation of COSMO-RS, the two energies are linearly correlated and

$$[3] \qquad \Delta^X \approx \lambda_{\mathrm{reg}} E^X_{\mathrm{diel}}$$

with the regression coefficient $\lambda_{\mathrm{reg}} \approx 0.8$. We consider λ_{reg} as being variable and possibly a function of the theoretical level employed and the total molecular charge.

We consider the ideal reference state as that of the ideally screened molecule within a conductor. In condensed media with several molecules, this conductor must be removed to obtain the real system, and the molecular cavities touch each other over a surface patch of effective area a_{eff}. To regain the reference state for each molecule, imaginary charge densities need to be placed between the surface patches of the individual molecules that in general lead to a residual screening charge density over this area.

The residual screening charge density equals the negative of the sum of the screening charge densities of the two patches $\sigma + \sigma'$ as computed in the conductor, and the cost of introducing this imaginary charge density (due to the self-interaction of the residual charge density) is called the misfit energy and is a quadratic function of this residual.

To relate the average patch screening charge density to the charge density on the (generally much smaller) tessera used in the COSMO calculation, averaging formulae are employed

$$[4] \qquad \sigma_{\nu} = \frac{\sum_{\mu} \sigma^*_{\mu} \mathrm{I}_{\mu\nu}}{\sum_{\mu} \mathrm{I}_{\mu\nu}}$$

where

$$[5] \qquad I_{\mu\nu} = \frac{r^2_{\mu} r^2_{\mathrm{av}}}{r^2_{\mu} + r^2_{\mathrm{av}}} \exp\left\{ -\frac{d^2_{\mu\nu}}{r^2_{\mu} + r^2_{\mathrm{av}}} \right\}$$

and where r_{μ} is the mean radius of tessera μ, r_{av} is the mean radius of a patch, and $d_{\mu\nu}$ is the distance between the centers of tesserae μ and ν. Note that the charges obtained from multiplying the averaged charge density by the area of every segment do not in general add up to zero. This, however, does not appear to be a problem in practice.

The charge densities obtained after averaging determine the actual reference state. To be consistent in the comparison between gas-phase and condensed states, an expression for the gas-phase potential to the true reference state needs to be derived.

To that end, we define an average ideal screening energy,

$$[6] \qquad \Delta'^X = \Delta^X - \lambda_{\mathrm{reg}}(E'^X_{\mathrm{diel}} - E^X_{\mathrm{diel}})$$

in which E'^X_{diel} stands for the dielectric energy recomputed according to eq. [2], with the charge densities averaged as in eqs. [4] and [5].

The chemical potential of the gas-phase molecule with respect to the ideally screened state (albeit with averaged charges) can now be written as,

$$[7] \qquad \mu = -\Delta'^X - \sum_k \gamma_k A^X_k - \omega n^X_{\mathrm{ring}} + \eta RT$$

The second term is the dispersion energy of exposed surface area A^X_k of atom k with surface tension γ_k; the third term is a ring correction possibly related to entropy differences, as solvation should result in a larger entropy loss for

molecules without rings (n_{ring} is the number of atoms of X that are part of a ring, ω is a model parameter); the fourth term corrects for the gas-phase entropy as well as the different reference states (η is another model parameter).

We now turn to the chemical potential in the condensed phase. In the statistical mechanical treatment to follow, it is assumed that the surface patches are independent (i.e., there is no correlation between them). However, we will account for short-range correlation between surface patches so we can form a new screening charge density σ_ν° by averaging over a distance $2r_{av}$, instead of r_{av} in eqs. [4] and [5] and then orthogonalizing them over the entire data set to form a second descriptor of the surface patches,

$$[8] \qquad \sigma_\nu^\perp = \sigma_\nu^\circ - \lambda_{orth}\sigma_\nu$$

where $\lambda_{orth} = 0.816$ was estimated in the original implementation. In this work we will treat it as a free parameter.

The interaction energy between two surface patches is comprised of two terms, the misfit energy

$$[9] \qquad E_{misfit}(d,d') = \frac{\alpha'}{2}(\sigma+\sigma')[(\sigma+\sigma') + \lambda_{reg}(\sigma^\perp + \sigma^{\perp\prime})]$$

(introducing d as a general descriptor for the surface patch) and the hydrogen-bond energy

$$[10] \qquad \begin{cases} E_{hb}(d,\ d') = c_{hb}\max(0,\ \sigma_{acc} - \sigma_{hb})\min(0,\ \sigma_{don} + \sigma_{hb}) \\ \sigma_{acc} = \max[\sigma, \sigma'] \\ \sigma_{don} = \min[\sigma, \sigma'] \end{cases}$$

With these expressions in place, we now proceed to the computation of the pseudochemical potential of a component X of a mixture S. The pseudochemical potential was defined by Ben-Naim[17] as the chemical potential of a molecule at a fixed position in the mixture.

The pseudochemical potential of a surface patch with descriptor d is defined as,

$$[11] \qquad \tilde{\mu}_S(d) = -\ln\left[W^{-1}\sum_{X\in S} x_X \sum_{\nu\in X} s_\nu \exp\{-\beta^{-1}E(d,\ d_\nu^i) + \tilde{\mu}_S(d_\nu^i)\}\right]$$

where

$$[12] \qquad W = \sum_{X\in S} x_X \sum_{\nu\in X} s_\nu$$

and $\beta = RT/a_{eff}$. This equation is iterated to self-consistency. The residual part of the pseudochemical potential of solute X in solvent S is then written as

$$[13] \qquad \mu_{S,res}^{*X} = \beta\sum_{\nu\in X} s_\nu \tilde{\mu}_S(d_\nu)$$

To obtain the full pseudochemical potential, a cavitation–combinatorial term has to be added. In the original COSMO-RS scheme this term was chosen to be,

$$[14] \qquad \mu_{S,comb}^{*X} = -\lambda RT \ln A^{av}$$

where A^{av} is the mole fraction weighted average of the cavity surface of the individual components of the mixture.

It was later recognized that use of expression eq. [14] for the combinatorial part of the chemical potential leads to thermodynamic inconsistency (violation of the Gibbs–Duhem relation). Therefore, Klamt[14] introduced the following alternative expression,

$$[15] \qquad \mu_{S,comb}^{*X} = RT\left[\lambda_0 \ln\ V^X + \lambda_1\left(1 - \frac{V^X}{V^{av}} - \ln\ V^{av}\right) + \lambda_2\left(1 - \frac{A^X}{A^{av}} - \ln\ A^{av}\right)\right]$$

where A^X is the cavity surface area of component X in the mixture, and A^{av} the average as defined above. V^X and V^{av} are correspondingly defined for the cavity volume. We note that the areas and volumes are divided by 1 Å^2 and 1 Å^3, respectively, to render them dimensionless.

Despite our intention to remain true to the 1998 COSMO-RS implementation, we chose not to work with a combinatorial term that has been recognized as thermodynamically inconsistent (eq. [14]) and instead chose eq. [15]. Since, according to Klamt,[14] the estimated values for λ_0, λ_1, and λ_2 are usually of similar magnitude, we simply set: $\lambda = \lambda_0 = \lambda_1 = \lambda_2$ and thus replace one single parameter expression with another. We obtained a slightly better fit with eq. [15], which demonstrates its superiority. Note that for a pure liquid, the two expressions are identical if $\lambda = \lambda_0 = \lambda_1 = \lambda_2$.

Once the pseudochemical potential is defined, the other thermodynamic functions can be obtained through standard formulae.

Validation and fitting

To test the code as well as the viability of doing COSMO-RS modeling with ADF generated COSMO charge densities, the set of 217 molecules from the supplementary material of Klamt et al. [7] was recreated and optimized at the TZP level with the Becke–Perdew GGA density functional. COSMO calculations were then done on these molecules at the same level of theory to generate the σ-profiles. In contrast to the procedure advocated in the original COSMO-RS paper,[7] we did not optimize the molecular geometry in the conductor. Our COSMO calculations are all based on gas-phase optimized molecular geometries. We chose to do so for three reasons. Firstly, we obtained a slightly better fit this way. Secondly, the value of optimizing the molecular geometry in the conductor is, in general, of doubtful value. It biases the molecular geometry to environments of high dielectric constant. This bias may not have seemed unreasonable in the 1998 COSMO-RS implementation, which was aimed primarily at water-based properties, but since then COSMO-RS has increasingly been applied to engineering problems, e.g., to the solubility of solutes in apolar solvents. A final, more mundane reason for not doing geometry optimization in the conductor is that these are time consuming, in particular since convergence is often poor because changes in the cavity are not accounted for smoothly in the energy gradients.

The COSMO-RS parameters were then optimized to reduce the sum-of-squares error over the fit set. The radii used were initially fixed at the values published by Klamt. When we later tried to optimize the value for the radii, we found the values were already optimal to within 0.01 Å for the Becke–Perdew functional but not necessarily for other functionals. We did not fully optimize the radii for other functionals. Apparently, the optimal shape of the COSMO cavity depends on the density functional used, much more than on the type of basis set (Slater orbitals in our case, numerical atomic orbitals in the original DMol implementation).

In the initial stages of parameter estimation, a great deal of computer time was saved by replacing the exponential function with an approximation devised by Schraudolph and Cawley for use in neural networks.[18,19]

Exact versus fitted density — A caveat

In the early stages of estimating the COSMO-RS parameters using the default COSMO settings, it was noted that compounds containing aromatic rings seemed to dominate the set of outliers, and the σ-profile was broader than expected (Fig. 1). Because of the delocalized π-systems of these molecules, the electron density is more diffuse than that of comparable σ-only systems. Use of the **C-Matrix Exact** option (instead of the default **C-Matrix Potential** option), which details how the surface charge – electron density interaction is calculated[3], remedies this, which implies that the fitted density is less accurate than the exact density in the region of the surface points. Another option is to use the defaults, but to add the line **AddDiffuseFit** to improve the fitted density (or potential) in the region of the surface

Fig. 1. The σ-profile $\rho_S(\sigma^*)$ as a function of program and C-matrix evaluation scheme for (*a*) styrene: reference DMol.[20] ADF potential (default), and ADF exact (*b*) benzene: ADF potential (default), ADF exact, ADF potential with diffuse fit functions added.

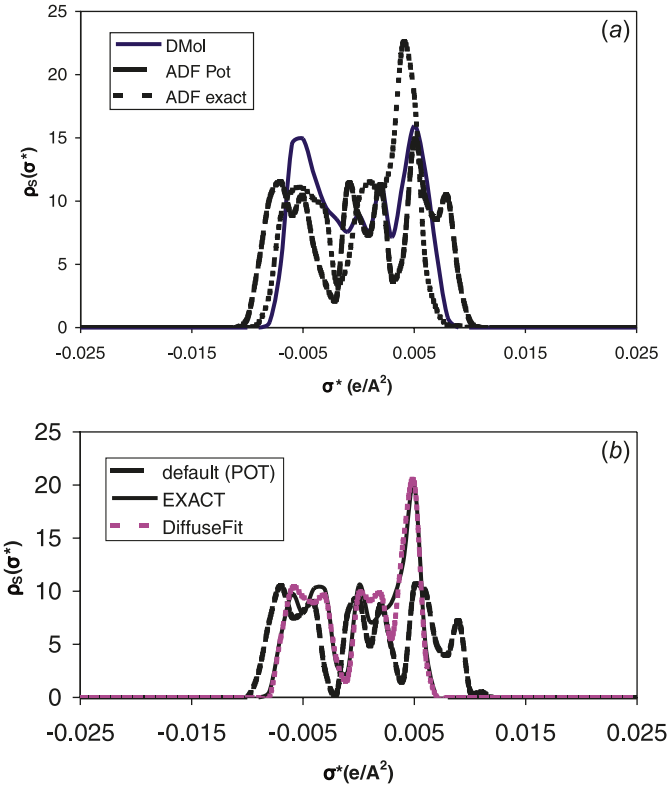

points. In Table 6 of the original ADF COSMO paper,[3] we noted that the energies calculated for ions using the **Potential** and **Fitted** methods are closer to each other for the most part than to the **Exact** method, which is probably a manifestation of this problem.

Surface construction

While pondering ways to improve the agreement between experimentally and theoretically derived quantities as part of our fitting procedure, we were curious whether our use of GEPOL, which tessellates each atom with 60 triangles, is introducing more error compared with the standard Klamt construction of 92 points per atom. One would expect that increasing the number of surface points per atom would increase the stability of the calculated σ-profiles with respect to small changes in the structure or orientation of the molecule. We decided to introduce the surface of Delley[21] to see if the tessellation scheme improves the results. This is specified by using **Surf Delley** in the Solvation block, and additional parameters **Leb1**, **Leb2**, and **Rleb** control the discretization per atom (i.e., if the radius of the atom is less than Rleb, use the Lebedev l-value Leb1, if it is greater, use the Lebedev l-value Leb2, maximum value 29). No significant overall improvement was noted in the comparison with experiment for Leb1 = 11 (60 points per atom) and Leb2 = 17 (110 points per atom), with some values getting better and some getting worse. The Delley surface area was only slightly smaller than the solvent-excluding surface area (Fig. 2).

Fig. 2. A plot of the solvent excluding surface area versus the Delley surface area for the test set of 217 molecules.

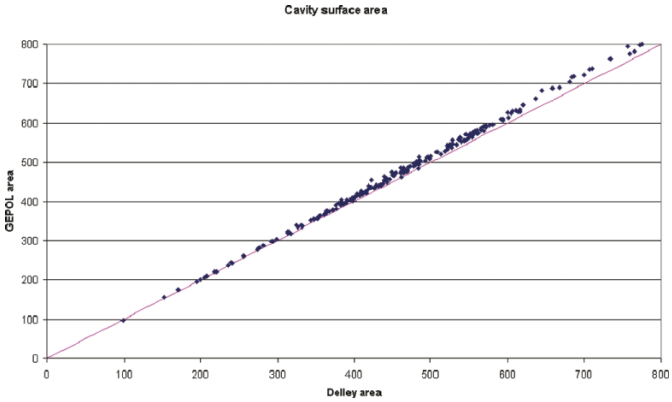

Hydrogen bonding term

In the initial phases of parameter estimation, we found most of the chlorinated molecules among the outliers. The issue with chlorinated molecules is demonstrated by considering the binary vapour–liquid equilibrium (VLE) diagram of chloroform and methanol predicted by an early version of our COSMO-RS implementation (see Fig. 3*a*). A strong negative deviation from Raoult's Law is predicted, whereas the observed deviation is positive. This indicates that experimentally the cohesive forces between like molecules are larger than between unlike, but we predict the reverse. It seemed plausible that the source of the poor agreement with experiment was due to the inappropriate use of the "hydrogen-bonding" term (eq. [10]). The hydrogen atom on chloroform is very electron-deficient, and therefore the magnitude of charge density on the associated surface patches is greater than the tolerance used to turn on the hydrogen-bonding term. In the case of the phase diagram with methanol, this hydrogen atom will form a hydrogen bond with the oxygen atom of methanol. By explicitly turning this interaction off for chloroform, considerably improved results were obtained. The residual error in the parameter estimation decreased markedly. As can be seen from the VLE diagram of chloroform and methanol, switching off the hydrogen bonding term for C-H hydrogen atoms on chlorinated molecules leads to a much more realistic account of the intermolecular interactions (Fig. 3*b*). It is not made clear in Klamt's paper describing the DMol implementation[7] whether or not such modifications are done. We chose to follow Lin et al.[10] and stipulate that only "classical" hydrogen bonds should be treated by the hydrogen bond term (i.e., the hydrogen must be bonded to an O, N, or F and be interacting with another O, N, or F).

Fitting

As object function in our fitting we have simply used the sum of squares between the numerical values of fitted and observed quantities, as given in the original fit set. The final result is expressed as kcal/mol (1 cal = 4.184 J). Klamt was able to achieve a rms value of 0.40 kcal/mol in his fitting, using the DMol implementation. Our various fitting attempts are chronicled in Tables 1 and 2. It is clear that the optimized parameters within each of the options that we explored was very self-consistent, which suggests that we are not overfitting our data.

Fig. 3. The vapor liquid equilibrium diagram (322.45 K) of methanol and chloroform (*a*) with, and (*b*) without explicit hydrogen bonding terms turned on. The triangles represent the experimental vapor pressure of the liquid with the specified composition, and the diamond at the same pressure indicates the composition of the resulting vapor. The lines represent the theoretical prediction.

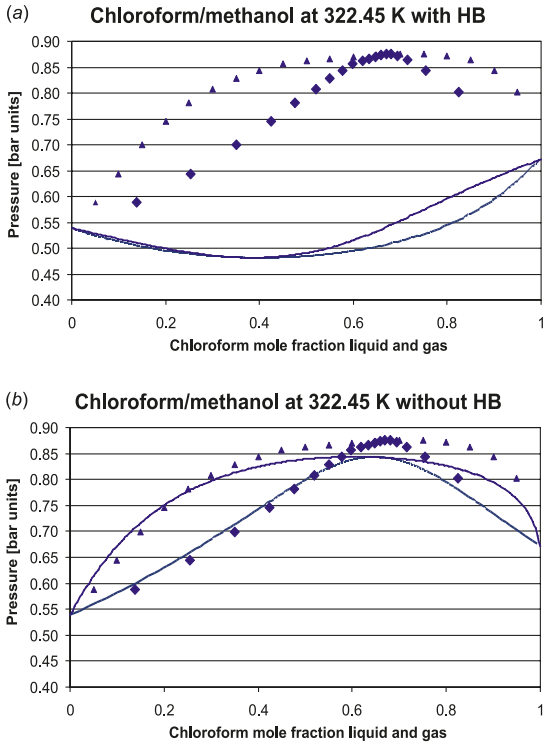

Examples

Though not originally developed for that purpose, COSMO-RS is increasingly being used in chemical engineering where the prediction of activity coefficients is the dominant application.[8] The activity coefficient of a component X in a mixture S is given by,

$$[16] \qquad \gamma_S^X = \exp\left(\frac{\mu_S^{*X} - \mu_{\text{pure}}^{*X}}{RT}\right)$$

where μ_S^{*X} and μ_{pure}^{*X} are the pseudochemical potential of component X in the mixture and its pure state, respectively.

Neiman et al. investigated the potential of COSMO-RS for predicting activity coefficients.[22] They used simulations of vapor–liquid equilibria of binary mixtures as a test case, since experimental VLE data of high quality is available. They concluded that COSMO-RS is capable of semiquantitatively correct predictions. Here, we have taken some examples from their paper to evaluate our ADF COSMO-RS implementation.

In generating the isothermal VLE diagrams, we assumed ideal gas behavior for the vapor phase, as did Neiman et al. That is, the total pressure in equilibrium with a binary liquid mixture is computed as,

Table 1. COSMO-RS general parameters and their final optimized values.

Functional	BP86	BP86	BP86	BP86	BPW91
Basis Set	TZP	TZP	TZP	TZP	DNP
Surface	SES	SES	Delley	Delley	Klamt
Combinatorial	Klamt98	Klamt98	Klamt98	Klamt05	Klamt98
H-bond	All	NOF	NOF	NOF	(NOF?)
r_{av} (Å)	0.337	0.334	0.415	0.400	0.5
α' (kcal/mol)(Å^2/e^2)	1430.0	1428.3	1515	1510	1288
f_{corr}	2.714	2.784	2.812	2.802	2.4
c_{hb} (kcal/mol)(Å^2/e^2)	8350	8800	8850	8850	7400
σ_{hb} (e/Å^2)	0.00871	0.00869	0.00849	0.00854	0.0082
a_{eff} (Å^2)	7.835	7.79	7.62	6.94	7.1
λ	0.131	0.130	0.129	0.130	0.14
ω (kcal/mol)	–0.221	–0.216	–0.217	–0.212	–0.21
η	–9.98	–10.05	–9.91	–9.65	–9.15
λ_{reg}	0.563	0.611	0.67	0.67	0.8
λ_{orth}	0.820	0.820	0.816	0.816	0.816
RMS (kcal/mol)	0.426	0.410	0.417	0.402	0.40

Table 2. COSMO-RS dispersion parameters (kcal/mol)(1/Å^2) and their final optimized values.

	BP86/SES/K98/All	BP86/SES/K98/NOF	BP86/Del/K98/NOF	BP86/Del/K05/NOF	Klamt
H	–0.0368	–0.0359	–0.0346	–0.0340	–0.041
C	–0.0330	–0.0347	–0.0356	–0.0356	–0.037
N	–0.0234	–0.0226	–0.0225	–0.0224	–0.027
O	–0.0304	–0.0317	–0.0322	–0.0333	–0.042
Cl	–0.0495	–0.0500	–0.0487	–0.0485	–0.052

Fig. 4. Some vapor liquid equilibrium diagrams for alcohol/water systems.

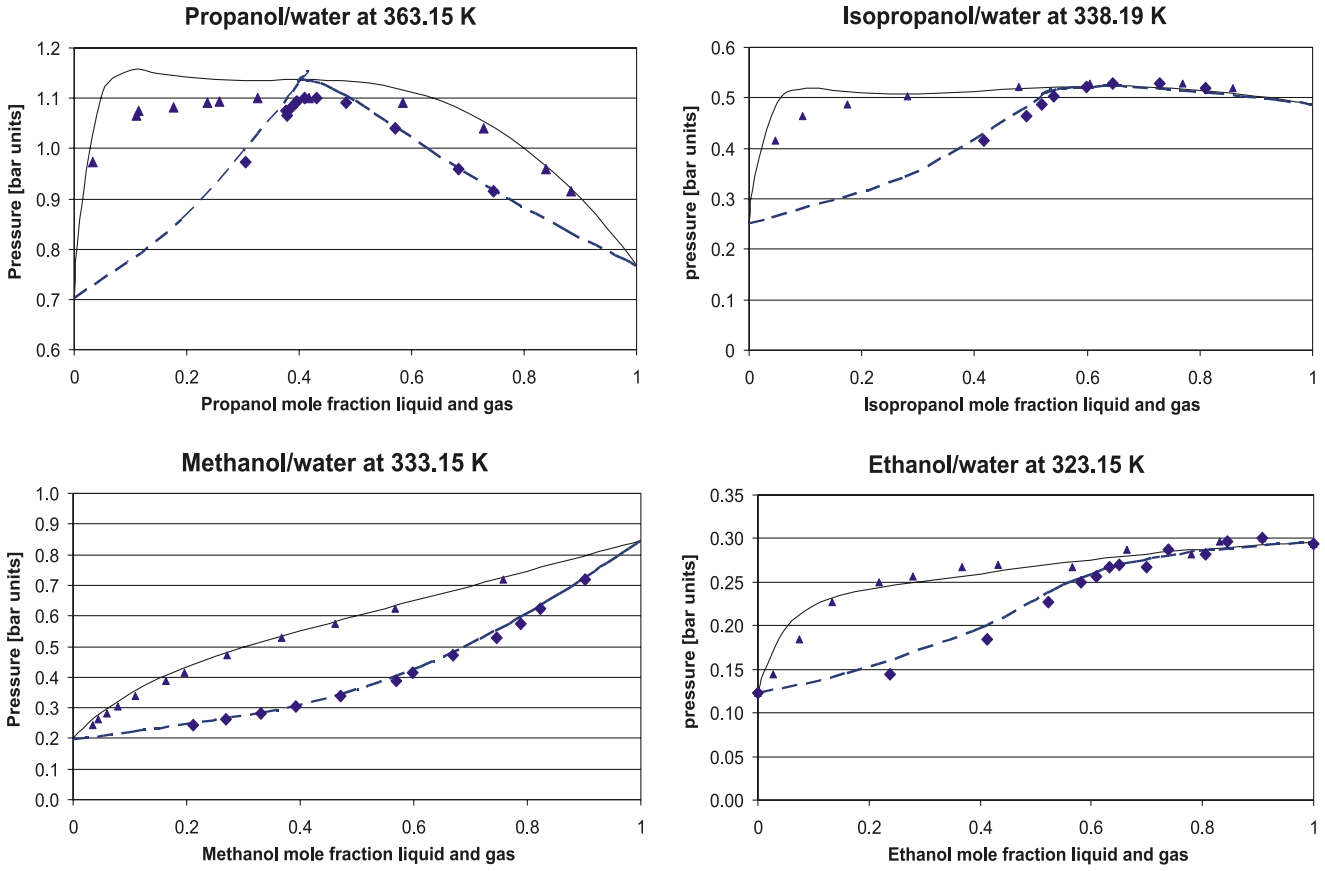

Fig. 5. Some vapor liquid equilibrium diagrams for acetone/methanol systems.

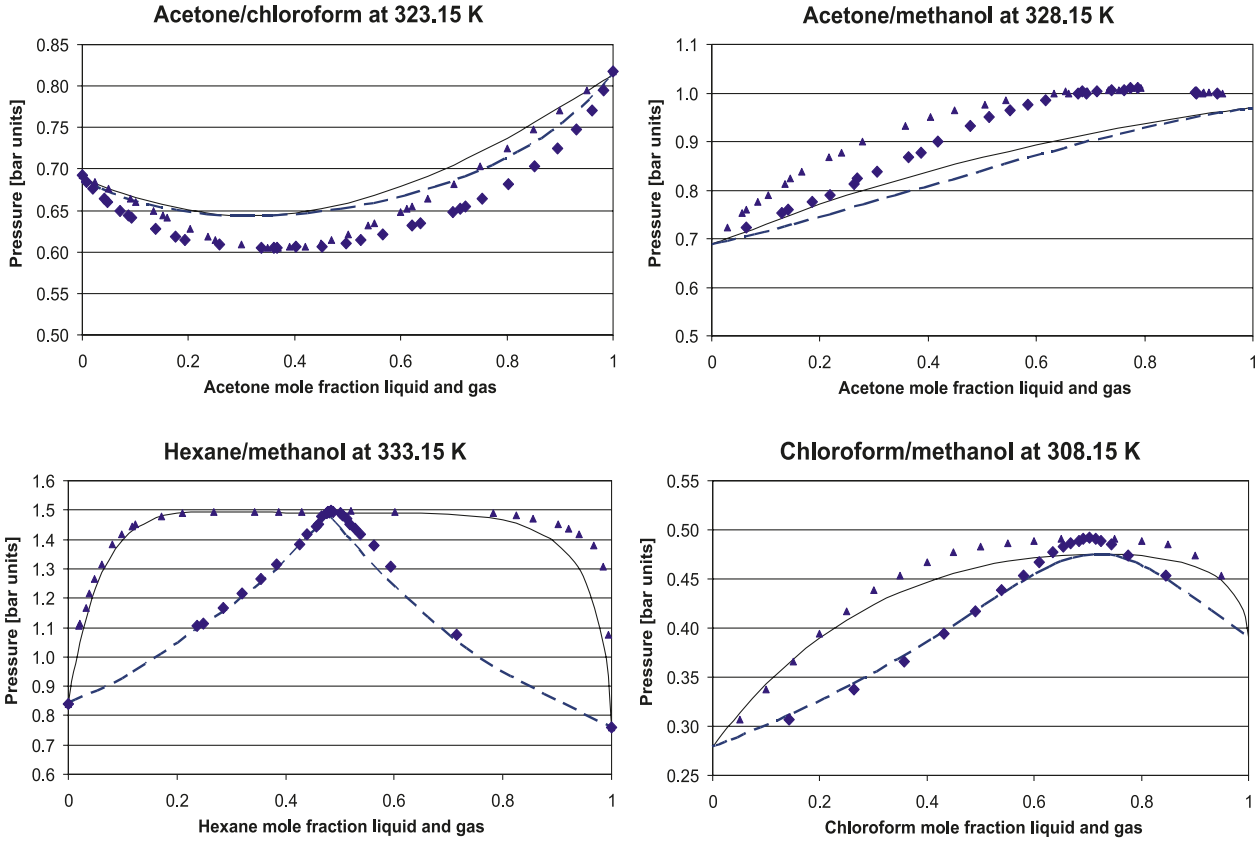

$$[17] \qquad p_{tot} = x_1\gamma_1 p_1 + x_2\gamma_2 p_2$$

where p_1 and p_2 are the vapor pressures of the pure liquids 1 and 2 at the operative pressure, x_1 and x_2 (= 1 – x_1) are the mole fractions for components 1 and 2, and γ_1 and γ_2 are the respective activity coefficients that we compute.

Subsequently, we compute the mole fraction of component 1 in the vapor phase as,

$$[18] \qquad y_1 = \frac{x_1\gamma_1 p_1}{p_{tot}}$$

Although the COSMO-RS method is capable of predicting the vapor pressure of the pure components, the accuracy of such predictions is limited and we used either experimental values or values derived from the Antoine equation for the pure component vapor pressures,[23] since our primary concern here is the prediction of the activity coefficients. Experimental data were taken from the literature.[24–29]

We reach the same conclusion as Neiman et al. for the VLE predictions of the ADF COSMO-RS implementation. In most cases, the results are quite good (see Fig. 4). The azeotrope point of isopropanol and water is correctly predicted, but COSMO-RS has difficulty predicting the azeotrope for ethanol and water. Note, however, that for both the propanol/water and isopropanol/water systems, a heterogeneous azeotrope is predicted contrary to experimental observations. There appear to be problems with acetone (see Fig. 5). The results for the acetone/chloroform mixture are rather poor, whereas the acetone/methanol prediction is quite bad. Other VLE diagrams involving methanol and chloroform are reasonably described. COSMO-RS significantly underestimates the activity coefficients and predicts pressures that are closer to linear interpolation than to the truth. Note, however, that the experimentally determined activity coefficients for this mixture are rather small (between 1 and 2), and small deviations have a relatively large effect. Probably, for this associating system a more detailed account of the interactions than offered by the empirical hydrogen bonding term is required.

Comparing our results to those reported by Neiman et al.[22] for the DMol implementation of COSMO-RS, we can see that the results are on par, with neither consistently superior to the other.

Conclusions

A COSMO-RS (1998 version) in ADF has been achieved that performs on par with the earlier DFT implementations. Although we are aware of several published and unpublished revisions to the original COSMO-RS, here we have chosen to retain the original procedure to be able to separate the effect of a different DFT scheme from proposed embellishments. Based on the current implementation, we foresee future developments, in particular for associating systems, where the current hydrogen-bond term in the segment interaction energy can provide only a crude account of the true physical interactions.

Acknowledgements

The assistance of a fellowship (PDF) granted by the Natural Sciences and Engineering Research Council of Canada (NSERC) is gratefully acknowleged by CCP. TZ thanks the Canadian government for a Canada Research Chair.

References

(1) This article is part of a Special Issue dedicated to Professor T. Ziegler.
(2) Klamt, A.; Schüürmann, G. *J. Chem. Soc. Perkin Trans. 2,* **1993**, 799.
(3) Pye, C. C.; Ziegler, T. *Theor. Chem. Acc.* **1999**, *101*, 396.
(4) te Velde, G.; Bickelhaupt, F. M.; Baerends, E. J.; Fonseca Guerra, C.; van Gisbergen, S. J. A.; Snijders, J. G.; Ziegler, T. *J. Comput. Chem.* **2001**, *22*, 931. doi:10.1002/jcc.1056.
(5) Pye, C. C.; Ziegler, T. *COSMO module within ADF* [computer program], version 2.3: Amsterdam, Netherlands,1998.
(6) Klamt, A. *J. Phys. Chem.* **1995**, *99*, 2224. doi:10.1021/j100007a062.
(7) Klamt, A.; Jonas, V.; Burger, T.; Lohrenz, J. C. W. *J. Phys. Chem. A,* **1998**, *102*, 5074. doi:10.1021/jp980017s.
(8) Klamt, A.; Eckert, F. *Fluid Phase Equil*ib. **2000**, *172*, 43. doi:10.1016/S0378-3812(00)00357-5.
(9) For COSMO-SAC-I please see: (a) Lin, S.-T.; Sandler, S. I. *Ind. Eng. Chem. Res.* **2002**, *41*, 899 doi:10.1021/ie001047w.; (b) Klamt, A. *Ind. Eng. Chem. Res.* **2002**, *41*, 2330 doi:10.1021/ie011031l.; (c) Lin, S.-T.; Sandler, S. I. *Ind. Eng. Chem. Res.* **2002**, *41*, 2332 doi:10.1021/ie020090b.; (d) Lin, S.-T.; Sandler, S. I. *Ind. Eng. Chem. Res.* **2004**, *43*, 1322. doi:10.1021/ie0308689.
(10) For COSMO-SAC-BP please see: (a) Lin, S.-T.; Chang, J.; Wang, S.; Goddard, W. A., III; Sandler, S. I. *J. Phys. Chem. A,* **2004**, *108*, 7429 doi:10.1021/jp048813n.; (b) Wang, S.; Lin, S. T.; Chang, J.; Goddard, W. A., III; Sandler, S. I. *Ind. Eng. Chem. Res.* **2006**, *45*, 5426 doi:10.1021/ie050352k.; (c) Klamt, A.; Eckert, F. *Ind. Eng. Chem. Res.* **2006**, *45*, 3766 doi:10.1021/ie0600083.; (d) Wang, S.; Lin, S.-T.; Chang, J.; Goddard, W. A., III; Sandler, S. I. *Ind. Eng. Chem. Res.* **2006**, *45*, 3767. doi:10.1021/ie060279d.
(11) For COSMO-SAC-II please see: (a) Wang, S.; Sandler, S. I.; Chen, C.-C. *Ind. Eng. Chem. Res.* **2007**, *46*, 7275 doi:10.1021/ie070465z.; (b) Klamt, A.; Eckert, F. *Ind. Eng. Chem. Res.* **2008**, *47*, 1351 doi:10.1021/ie071383d.; (c) Sandler, S. I.; Wang, S.; Lin, S. T.; Goddard, W. A., III. *Ind. Eng. Chem. Res.* **2008**, *47*, 1353. doi:10.1021/ie071600a.
(12) For COSMO-RS(Ol) please see: (a) Grensemann, H.; Gmehling, J. *Ind. Eng. Chem. Res.* **2005**, *44*, 1610 doi:10.1021/ie049139z.; (b) Klamt, A. *Ind. Eng. Chem. Res.* **2005**, *44*, 7042 doi:10.1021/ie050347g.; (c) Grensemann, H.; Gmehling, J. *Ind. Eng. Chem. Res.* **2005**, *44*, 7043. doi:10.1021/ie050523l.
(13) Banerjee, T.; Singh, M. K.; Khanna, A. *Ind. Eng. Chem. Res.* **2006**, *45*, 3207. doi:10.1021/ie051116c.
(14) Klamt, A. *COSMO-RS: Quantum Chemistry to Fluid Phase Thermodynamics and Drug Design*; Elsevier: Amsterdam, Netherlands, 2005.
(15) Pye, C. C.; Ziegler, T. *COSMO module within ADF* [computer program], version 99: Amsterdam, Netherlands, 1999.
(16) Pascual-Ahuir, J. L.; Silla, E.; Tuñon, I. J. *Comput. Chem.* **1994**, *15*, 1127. doi:10.1002/jcc.540151009.
(17) Ben-Naim, A. *Solvation Thermodynamics*; Plenum: New York, 1987.
(18) Schraudolph, N. N. *Neural Comput.* **1999**, *11*, 853. doi:10.1162/089976699300016467. PMID:10226185.
(19) Cawley, G. C. *Neural Comput.* **2000**, *12*, 2009. doi:10.1162/089976600300015033. PMID:10976136.
(20) Mullins, E.; Oldland, R.; Liu, Y.A.; Wang, S.; Sandler, S.I.; Chen, C.C.; Zwolak, M.; Seavey, K.C. *Ind. Eng. Chem. Res.* **2006**, *45*, 4389. doi:10.1021/ie060370h.
(21) Delley, B. *Mol. Simul.* **2006**, *32*, 117. doi:10.1080/08927020600589684.
(22) (a) Neiman, M.; Cheng, H.; Parekh, V.; Peterson, B.; Klier, K. *Phys. Chem. Chem. Phys.* **2004**, *6*, 3474 doi:10.1039/b400322e.; (b) Klamt, A. *Phys. Chem. Chem. Phys.* **2004**, *6*, 5081 doi:10.1039/b411213j.; (c) Cheng, H.; Parekh, V.; Peterson, B. *Phys. Chem. Chem. Phys.* **2004**, *6*, 5082. doi:10.1039/b411972j.
(23) Reid, R. C.; Prausnitz, J. M.; Sherwood, T. K. *The properties of liquids and gases*. McGraw-Hill: New York,1977; 3rd ed. .
(24) Gmehling, J.; Onken, U. *Chemistry data series. Vol. 1: Vapor-Liquid Equilibrium Data Collection, Part 1: Aqueous-Organic Systems*; Dechema: Frankfurt, Germany. 1977.
(25) Gmehling, J.; Onken, U. *Chemistry data series. Vol. 1: Vapor-Liquid Equilibrium Data Collection, Part 2a: Organic Hydroxy Compounds: Alcohols*; Dechema: Frankfurt, Germany. 1977.
(26) Gmehling, J.; Onken, U.; Arlt, W. *Chemistry data series. Vol. 1: Vapor-Liquid Equilibrium Data Collection, Parts 3+4: Aldehydes, Ketones, Ethers*; Dechema: Frankfurt, Germany. 1979.
(27) Gmehling, J.; Onken, U.; Arlt, W. *Chemistry data series. Vol. 1: Vapor-Liquid Equilibrium Data Collection, Part 1a: Aqueous-Organic Systems*; Dechema: Frankfurt, Germany. 1981.
(28) Gmehling, J.; Onken, U.; Arlt, W. *Chemistry data series. Vol. 1: Vapor-Liquid Equilibrium Data Collection, Part 2c: Organic Hydroxy Compounds*: *Alcohol*; Dechema: Frankfurt, Germany. 1982.
(29) Gmehling, J.; Onken, U.; Rarey-Nies, J. R. *Chemistry data series. Vol. 1: Vapor-Liquid Equilibrium Data Collection, Part 1b: Aqueous Systems*; Dechema: Frankfurt, Germany. 1988.

Bonding analysis for sterically uncongested simple aurocarbons C_nAu_m[1]

Patryk Zaleski-Ejgierd and Pekka Pyykkö

Abstract: The title series of simple model aurocarbons, CAu_4, C_2Au_2, C_2Au_4, C_2Au_6, and C_6Au_6, is investigated using density functional theory with TPSS and B3LYP functionals and the second-order Møller–Plesset perturbation theory, with the latest Karlsruhe basis sets. The vibrational frequencies and the 0 K thermodynamical properties are calculated. The bonding mechanism is also investigated. For C_2Au_n the calculated MP2 formation energy suggests increased stabilization with increasing n, due to the Au–Au aurophilic pair interactions.

Key words: aurocarbons, aurides, aurophilicity, metallophilicity, clusters, DFT, MP2.

Résumé : La série d'aurocarbones modèles simples mentionnés dans le titre, CAu_4, $C2Au_2$, C_2Au_4, C_2Au_6 et C_6Au_6, a été étudiée à l'aide de la théorie de la fonctionnelle de la densité, en faisant appel à des fonctions TPSS et B3LYP, ainsi qu'à l'aide de la théorie perturbationnelle de Møller–Plesset en faisant appel aux derniers ensembles de base de Karlsruhe. On a calculé les fréquences vibrationnelles et les propriétés thermodynamiques à 0 K. On a aussi étudié le mécanisme de liaison. Pour le C_2Au_n, l'énergie de formation MP2 calculée suggère que la stabilisation augmente avec une augmentation de n en raison d'interactions dans la paire aurophile Au–Au.

Mots-clés : aurocarbones, aurures, caractère aurophile, caractère métallophile, agrégats, théorie de la fonctionnelle de densité (TFD), MP2.

[Traduit par la Rédaction]

Introduction

Gold chemistry is fascinatingly rich. One of the conceptual tools in predicting new possible components is the chemical analogy between H and Au (or -$AuPR_3$). This was used to discuss CAu_4[2] or $SiAu_4$.[3] Interestingly, the attempts to completely aurate methane resulted in the C_{4v} system $[HC(AuPR_3)_4]^+$,[4] theoretically found to have a large proton binding energy.[5]

We furthermore note the existence of gold acetylides. A solid C_2Au_2 has been reported to be highly explosive.[6] For other examples on gold–acetylide bonds, see Puddephatt.[7] Recently, Naumkin[8] considered the possibility of completely aurating neopentane, $C(CH_3)_4$. The triple-bonded CAu^+ was predicted by Barysz and Pyykkö[9] and produced in the gas phase by Aquirre et al.[10] The dication CAu_2^{2+} was observed by Gibson by mass spectroscopy.[11] Its electronic structure was interpreted by Pyykkö et al.[12] as $[Au{=}C{=}Au]^{2+}$, with bonding, similar to that of O=C=O. They also considered the D_{3h} CAu_3^+, observed by Gibson,[11] and the C_2Au_2 that could be compared to either HCCH or $OCCO^{2-}$.

Against this background, we felt that a study of the aurated analogs of the simplest sp-, sp^2-, and sp^3-hybridized hydrocarbons would be interesting. The same uncongested conformations, as for their hydrocarbon analogs, are given preferential treatment.

Received 22 October 2008. Accepted 9 December 2008. Published on the NRC Research Press Web site at canjchem.nrc.ca on 6 March 2009.

P. Zaleski-Ejgierd and P. Pyykkö.[1] Department of Chemistry, University of Helsinki, P.O. BOX 55 (A. I. Virtasen aukio 1), Helsinki 00014, Finland.

[1]Corresponding author (e-mail: pekka.pyykko@helsinki.fi).

Computational procedure

All the reported calculations were performed using the TURBOMOLE (version 5.10) program package.[13] Because of the expected presence of the aurophilic interactions, the results were calculated with both density functional theory (DFT),[14,15] and the second-order Møller-Plesset perturbation theory (MP2)[16] using the resolution of identity (RI) approximation, as implemented in TURBOMOLE.[17] The recent, Karlsruhe quadruple-zeta (def2-QZVPP) basis sets were employed for all elements. In the case of gold, the 19-VE "small-core" effective core potential (ECP) of Andrae et al.[18] was introduced to account for scalar relativistic effects. For carbon and nitrogen, we used the corresponding all-electron basis sets. The currently applied combination of bases and ECPs was found to be suitable for calculations involving weak Au–Au interactions.[19]

The vibrational analysis was performed within the harmonic approximation at both DFT and RIMP2 levels of theory. The DFT/TPSS results are depicted in Fig. 1.

In case of the DFT approach, two exchange-correlation functionals were used, namely, the B3LYP hybrid functional[20,21] and the meta-generalized gradient approximation TPSS functional.[22] We used the small sized grid (434 grid-points) for numerical integration.

For the RI-assisted MP2, the corresponding auxiliary basis sets were applied,[23] and all the explicitly treated electrons were correlated.

Fig. 1. The DFT/TPSS harmonic frequency spectra (cm^{-1}) calculated for the family of aurocarbons.

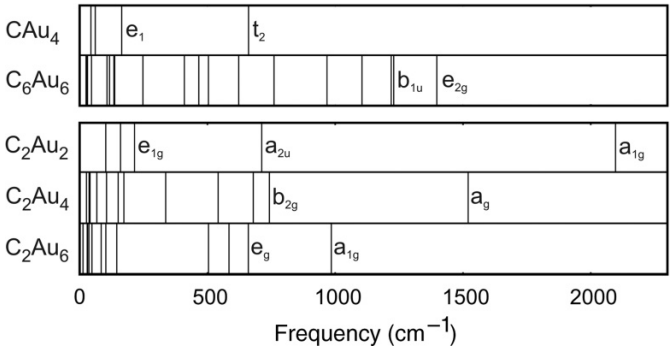

The spin–orbit interactions were neglected. For an s-element such as gold, and closed-shell species, this is expected to be reasonable.

The partial atomic charges were estimated using the Mulliken population analysis scheme, as implemented in the TURBOMOLE package. The molecular orbital (MO) contours were generated using Molden (version 4.6) package.[24]

Each of the six model compounds was optimized with the specific symmetry constrains: CAu_4 (C_1, effectively T_d), C_2Au_2 (C_{2v}, effectively $D_{\infty h}$), C_2Au_4 (D_{2h}), C_2Au_6 (D_{3d}), C_6Au_6 (D_{6h}), and $[CNAu_2]^+$ (C_{2v}, effectively $C_{\infty v}$). The resulting equilibrium structures were subjected to numerical vibration analysis. We did not find any imaginary frequencies.

Results and discussion

The geometry trends

We first note that although the investigated structures exhibit only real vibrational frequencies, the presented structures do not necessarily correspond to the global energy minima. It is possible that planar structures may be favored; for instance, 2D "flakes" are known to be exceptionally stable up to a certain number of gold atoms, depending on the electrical charge.[25,26]

In this work, we did not try to identify such energetically lowest isomers. Instead, we rather investigated the general trends of a new family of aurocarbons. The digold monocyanide cation, $[AuCNAu]^+$, was added as a potential isoelectronic species to C_2Au_2 for cation experiments.

The calculated equilibrium structures are depicted in Fig.2, while the corresponding geometrical parameters are presented in Table 1.

The DFT results obtained with the two different functionals (B3LYP and TPSS) agree. The average C–C bond length difference is $\sim$0.93 pm, and the Au–C difference is $\sim$2.15 pm. The discrepancy rises with the saturation of C–C bond.

The RIMP2 and DFT structures differ slightly. Two clear trends can be observed. In case of the Au–C and Au–Au/Au′–Au′ bonds, the RIMP2 distances are always the shortest, followed by TPSS and B3LYP. The opposite trend is observed in case of the C–C bond, with the notable exception of C_6Au_6.

The calculated Au–C and C–C bond lengths in C_2Au_2 are in good agreement with the experimental data obtained by Puddephatt et al. for species containing similar bonding patterns.[27]

Fig. 2. The aurocarbons, including the isoelectronic $[AuCNAu]^+$. The Au–Au and Au′–Au′ notations denote the shorter and longer aurophilic distances, respectively.

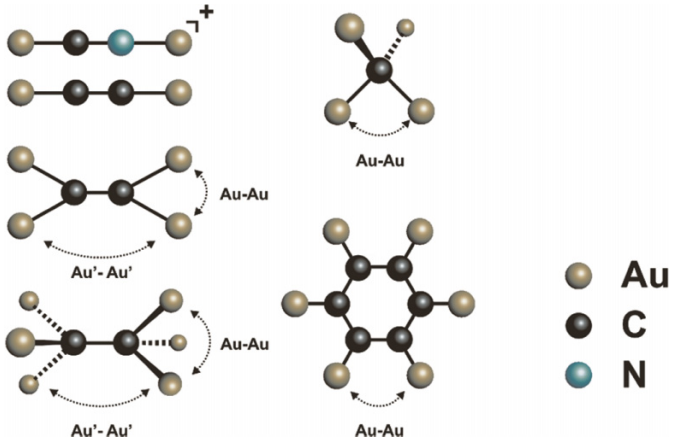

Table 1. The calculated bond distances for aurocarbons in Fig. 2. All values in pm.

Case	Method	C–C	Au–C	Au–Au	Au′–Au′
CAu_4	B3LYP	—	198.74	324.55	—
	TPSS	—	196.54	320.94	—
	RI-MP2	—	190.21	310.62	—
C_2Au_2	B3LYP	121.50	191.87	—	—
	TPSS	122.49	190.13	—	—
	RI-MP2	122.51	184.99	—	—
C_2Au_4	B3LYP	131.60	199.13	326.50	359.88
	TPSS	132.99	196.78	325.59	354.06
	RI-MP2	133.14	189.92	314.26	346.48
C_2Au_6	B3LYP	147.94	203.32	317.38	372.35
	TPSS	148.83	200.31	314.12	365.67
	RI-MP2	146.66	193.15	304.66	353.19
	HF	148.57	207.99	322.15	382.96
C_6Au_6	B3LYP	139.68	200.07	339.75	—
	TPSS	140.13	197.85	337.98	—
	RI-MP2	138.84	190.99	329.80	—

The C–C distances in the C_2Au_2, C_2Au_4, and C_2Au_6 are closely comparable with the corresponding hydrocarbons, suggesting analogous bonding. Interestingly, the C–C bond in C_2Au_6 is shorter than in C_2H_6 by $\leq$10 pm.

The Au–C distance varies from one molecule to the other by up to $\sim$12 pm and depends strongly on the type of the C–C bond. It lengthens with the level of substitution (or shortens with the hybridization as $sp < sp^2 < sp^3$, like the C–H bonds do).

While the Au′–Au′ distances only yield weak aurophilic interactions, the Au–Au distances are expected to have stronger ones. The Au-C-C angles remain practically constant for different methods: 124.18°, 124.96°, and 124.17° for C_2Au_4 and 115.12°, 115.68°, and 114.40° for C_2Au_6 at the B3LYP, TPSS, and RIMP2 levels of theory, respectively.

Vibrations

The harmonic frequencies were calculated at three levels of theory: DFT with the B3LYP, the TPSS exchange-correlation functionals, and the RIMP2.

Table 2. The thermochemical cycles.

	Total ΔE (kJ mol^{-1})			ΔE per Au–C pair (kJ mol^{-1})		
Case	B3LYP	TPSS	RIMP2	B3LYP	TPSS	RIMP2
1. $C + 2Au_2 \rightarrow CAu_4$	–545	–763	–829	—	—	—
2. $2C + Au_2 \rightarrow C_2Au_2$	–1068	–1168	–1189	—	—	—
3. $C_2Au_2 + Au_2 \rightarrow C_2Au_4$	–58	–174	–229	—	—	—
4. $C_2Au_4 + Au_2 \rightarrow C_2Au_6$	+24	–105	–254	—	—	—
5. $3C_2Au_2 \rightarrow C_6Au_6$	–512	–583	–850	—	—	—
6. $C_2H_2 + Au_2 \rightarrow C_2Au_2 + H_2$	+154	+55	+107	+77	+27	+54
7. $C_2H_4 + 2Au_2 \rightarrow C_2Au_4 + 2H_2$	+303	+88	+78	+76	+22	+19
8. $C_2H_6 + 3Au_2 \rightarrow C_2Au_6 + 3H_2$	+486	+144	–3	+81	+23	–0.5
9. $C_6H_6 + 3Au_2 \rightarrow C_6Au_6 + 3H_2$	+581	+242	+143	+97	+40	+24
10. $CH_4 + 2Au_2 \rightarrow CAu_4 + 2H_2$	+291	+70	+43	+73	+17	+11

Fig. 3. (Color online) The 37 highest occupied Kohn–Sham (TPSS) molecular orbitals of C_2Au_6 (D_{3d}). The LUMO orbital energy is –0.130 a.u., resulting in a gap of 0.048 a.u. or +1.31 eV. (HO-n stands for HOMO-n).

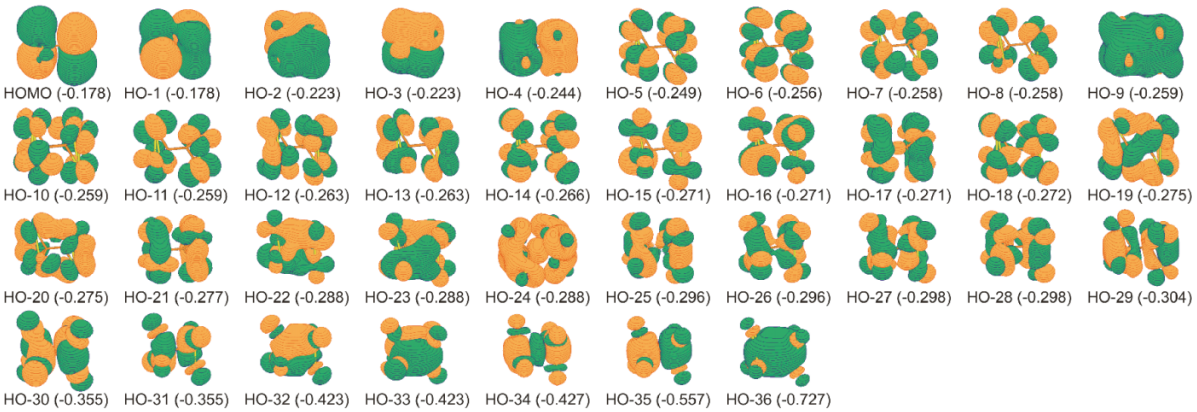

The TPSS frequencies are depicted in Fig. 1. The B3LYP results are similar, while the RIMP2 tend to give slightly higher values. The fact can be related to the M-C overbinding typical for MP2 method. The highest frequencies correspond to C–C stretch, while the lowest, to the out-of-plane deformations and the rotations with respect to the C–C axis. In the unlikely case of quantum dynamics for the gold nuclear motions, six gold atoms could still occupy the same special quantum state, with nuclear spin M_I from –5/2 to +5/2.[28]

Thermochemistry

The thermochemical analysis for a series of reactions listed in Table 2 was performed with respect to the isolated Au_2 and the $C(^3P_j)$ atoms. The CAu_4 and C_2Au_2 formation energy from pure elements (Table 2, cases 1–2) was found to be strongly negative for all methods. The energy of Au_2 addition in a C_2Au_2, C_2Au_4 series (Table 2, cases 3–4) varies with method. It remains negative for TPSS and RIMP2 but changes sign in case of B3LYP results. The trimerization energy of C_2Au_2 units (Table 2, case 5) is strongly exothermic. Since the accuracy of such estimates might be questionable, we applied an isodesmic approach (Table 2, cases 6–10) to make sure that the broken chemical bonds are of the same type as the type of bonds formed in the reaction. The DFT formation energy calculated per one Au–C bond is approximately constant for a given functional. Interestingly, the same energy calculated at RIMP2 level decreases systematically in the C_2Au_n (n = 2, 4, 6) series and became thermoneutral for C_2Au_6, most likely because of aurophilic stabilization. It is known that this attraction is exaggerated at the MP2 level.[29]

Bonding

The TPSS Kohn–Sham orbitals are given in the Supplementary data. They all correspond to the combinations expected from the existing C–C and Au–C local bonding orbitals. A fair amount of hybridization is also seen in the Au 5d band. An example on C_2Au_6 is depicted in Fig. 3. The simplest way to understand the bonding orbitals of C_2Au_6 (D_{3d}) in Fig. 3 is to classify the bonding orbitals HOMO to HOMO-4, and HOMO-9, as the e_g (2x), t_{1u} (3x), and a_{1g} combinations of the six Au–C local bonding orbitals under octahedral, quasi-O_h symmetry. The corresponding nodal structures are conspicuous in Fig. 3. The Mulliken charges are shown in Table 3. The C atoms are negative and the Au atoms positive.

Possible extensions

The present ideas can be extended by considering ionic isoelectronic analogs (BAu_4^-, CAu_4, NAu_4^{+1}) or by introducing other rows of the periodic table (CAu_4, $SiAu_4$, etc.). Another possibility is to replace the plain -Au by -$AuPR_3$.[5] The latter proposition is more realistic for bulk compounds. Many such monocentric compounds already exist, while the bicentric (C_2Au_6, etc.) gold compounds are more rare.

Table 3. The partial Mulliken charges, δ, for structures considered in Fig. 2.

Case	Method	δC	δAu(C)/δAu(N)	δN
$[AuCNAu]^+$	B3LYP	–0.25	+0.79/+0.79	–0.30
	TPSS	–0.27	+0.76/+0.83	–0.33
	HF	–0.30	+0.88/+0.92	–0.50
CAu_4	B3LYP	–1.27	+0.32/—	—
	TPSS	–1.30	+0.33/—	—
	HF	–1.52	+0.38/—	—
C_2Au_2	B3LYP	–0.31	+0.31/—	—
	TPSS	–0.34	+0.34/—	—
	HF	–0.47	+0.47/—	—
C_2Au_6	B3LYP	–1.31	+0.44/—	—
	TPSS	–1.43	+0.48/—	—
	HF	–1.43	+0.48/—	—
C_6Au_6	B3LYP	–0.61	+0.61/—	—
	TPSS	–0.64	+0.64/—	—
	HF	–0.42	+0.42/—	—

Conclusions

We have considered the H→Au analogs of the simplest hydrocarbons CH_4, C_2H_2, C_2H_4, C_2H_6, and C_6H_6. All are found to be local minima, but their Au–C bonding energies are smaller than the corresponding C–H ones.

The C_2Au_6 system possesses increased stability at the MP2 level and has in its D_{3d} structure altogether twelve aurophilic Au^I–Au^I attractions.

Supplementary data

Supplementary data for this article are available on the journal Web site (canjchem.nrc.ca) or may be purchased from the Depository of Unpublished Data, Document Delivery, CISTI, National Research Council Canada, Ottawa, ON K1A 0R6, Canada. DUD 3895. For more information on obtaining material refer to cisti-icist.nrc-cnrc.gc.ca/cms/unpub_e.shtml.

Acknowledgement

We belong to the Finnish Centre of Excellence (CoE) in Computational Molecular Science (CMS, 2006–2011). The Magnus Ehrnrooth Foundation is acknowledged for providing financial support for PZE and the Centre of Scientific Computing (CSC) Espoo, Finland for providing computer resources.

References

(1) This article is part of a Special Issue dedicated to Professor T. Ziegler.
(2) Pyykkö, P.; Zhao, Y.-F. *Chem. Phys. Lett.* **1991**, *177*, 103. doi:10.1016/0009-2614(91)90183-A.
(3) Kiran, B.; Li, X.; Zhai, H.-J.; Cui, L.-F.; Wang, L.-S. *Angew. Chem. Int. Ed. Engl.* **2004**, *43*, 2125. doi:10.1002/anie.200353602. PMID:15083462.
(4) Schmidbaur, H.; Gabbaï, F. P.; Schier, A.; Riede, J. *Organometallics* **1995**, *14*, 4969. doi:10.1021/om00011a001.
(5) Pyykkö, P.; Tamm, T. *Organometallics* **1998**, *17*, 4842. doi:10.1021/om980255+.
(6) Sneed, M. C.; Maynard, J. L.; Brasted, R. C. *Comprehensive inorganic chemistry*; D. van Nostrand Co. Inc.: Princeton, N.J., USA, 1954; Vol. 2, p. 238.
(7) Puddephatt, R. J. *Chem. Soc. Rev.* **2008**, *37*, 2012. doi:10.1039/b708622a. PMID:18762844.
(8) Naumkin, F. *Phys. Chem. Chem. Phys.* **2006**, *8*, 2539. doi:10.1039/b601415a.
(9) Barysz, M.; Pyykkö, P. *Chem. Phys. Lett.* **1998**, *285*, 398. doi:10.1016/S0009-2614(98)00025-6.
(10) Aguirre, F.; Husband, J.; Thompson, C. J.; Metz, R. B. *Chem. Phys. Lett.* **2000**, *318*, 466. doi:10.1016/S0009-2614(00)00044-0.
(11) Gibson, J. K. *J. Vac. Sci. Technol. A* **1998**, *16*, 653. doi:10.1116/1.581099.
(12) Pyykkö, P.; Patzschke, M.; Suurpere, J. *Chem. Phys. Lett.* **2003**, *381*, 45. doi:10.1016/j.cplett.2003.09.045.
(13) Ahlrichs, R.; Bär, M.; Häser, M.; Horn, H.; Kölmel, C. *Chem. Phys. Lett.* **1989**, *162*, 165. doi:10.1016/0009-2614(89)85118-8.
(14) Hohenberg, P.; Kohn, W. *Phys. Rev.* **1964**, *136*, B864. doi:10.1103/PhysRev.136.B864.
(15) Kohn, W.; Sham, L. J. *Phys. Rev.* **1965**, *140*, A1133. doi:10.1103/PhysRev.140.A1133.
(16) Møller, C.; Plesset, M. S. *Phys. Rev.* **1934**, *46*, 618. doi:10.1103/PhysRev.46.618.
(17) Weigend, F.; Köhn, A.; Hättig, C. J. *Chem. Phys.* **2001**, *116*, 3175.
(18) Andrae, D.; Häeussermann, U.; Dolg, M.; Stoll, H.; Preuss, H. *Theor. Chim. Acta* **1990**, *77*, 123. doi:10.1007/BF01114537.
(19) Pyykkö, P.; Zaleski-Ejgierd, P. J. *Chem. Phys.* **2008**, *128*, 124309.
(20) Becke, A. D. J. *Chem. Phys.* **1993**, *98*, 1372.
(21) Stephens, P. J.; Devlin, F. J.; Chabalowski, C. F.; Frisch, M. J. *J. Phys. Chem.* **1994**, *98*, 11623. doi:10.1021/j100096a001.
(22) Tao, J.; Perdew, J. P.; Staroverov, V. N.; Scuseria, G. E. *Phys. Rev. Lett.* **2003**, *91*,o. 146401. doi:10.1103/PhysRevLett.91.146401. PMID:14611541.
(23) Weigend, F.; Häser, M.; Patzelt, H.; Ahlrichs, R. *Chem. Phys. Lett.* **1998**, *294*, 143. doi:10.1016/S0009-2614(98)00862-8.
(24) Schaftenaar, G.; Noordik, J. H. J. *Comput.-Aided Mol. Design* **2000**, *14*, 123. doi:10.1023/A:1008193805436.
(25) Häkkinen, H. *Chem. Soc. Rev.* **2008**, *37*, 1847. doi:10.1039/b717686b. PMID:18762834.
(26) Pyykkö, P. *Chem. Soc. Rev.* **2008**, *37*, 1967. doi:10.1039/b708613j. PMID:18762842.
(27) Payne, N. C.; Ramachandran, R.; Puddephatt, R. J. *Can. J. Chem.* **1995**, *73*, 6. doi:10.1139/v95-002.
(28) Autschbach, J.; Hess, B. A.; Johansson, M. P.; Neugebauer, J.; Patzschke, M.; Pyykkö, P.; Reiher, M.; Sundholm, D. *Phys. Chem. Chem. Phys.* **2004**, *6*, 11. doi:10.1039/b310395a.
(29) Pyykkö, P.; Runeberg, N.; Mendizabal, F. *Chem. Eur. J.* **1997**, *3*, 1451. doi:10.1002/chem.19970030911.

The nuclear quadrupole moment of ^{69}Ga and ^{115}In[1]

Hana Yakobi, Ephraim Eliav, and Uzi Kaldor

Abstract: Electric field gradients at the nuclei of gallim and indium are determined by finite field calculations of the atomic energies as functions of the nuclear quadrupole moments. The four-component Dirac–Coulomb–Gaunt Hamiltonian serves as framework, and all electrons are correlated by Fock-space coupled cluster with single and double excitations or by single reference coupled cluster with approximate triples. Large, converged basis sets (e.g., 28s24p20d13f5g4h for In) and virtual spaces are used. Together with experimental nuclear quadrupole coupling constants, known with high precision, the calculated electric field gradients yield the nuclear quadrupole moments. For ^{69}Ga, we get Q = 174(3) mb, in agreement with the earlier 171(2) mb obtained from molecular calculations. The ^{115}In moment is Q = 772(5) mb, considerably lower than the previously accepted 810 mb, and in good agreement with the recent molecular value of 770(8) mb.

Key words: nuclear quadrupole moments, gallium, indium, relativity, coupled cluster method.

Résumé : En faisant appel à des calculs de champ fini des énergies atomiques en fonction des moments nucléaires quadripolaires, on a calculé les gradients de champs électriques des noyaux de gallium et d'indium. L'hamiltonien à quatre composants de Dirac–Coulom–Gaunt sert de référence et on a établi une corrélation entre tous les électrons à l'aide de l'agrégat couplé dans un espace de Fock avec des excitations simples ou doubles ou par l'agrégat couplé par référence simple avec des approximations de triplets. On a utilisé de grands ensembles de bases convergents (tels 28s24p20d13f5h4h pour l'indium) et des espaces virtuels. En se basant sur les constantes de couplage quadripolaire nucléaire expérimentales qui sont connues avec une grande précision, les gradients de champs électriques calculés ont permis de calculer les moments nucléaires quadripolaires. Pour le ^{69}GA, on a obtenu une valeur de Q = 174(3) mb, en accord avec la valeur de 171(2) mb obtenue antérieurement par calculs moléculaires. Pour le ^{115}In, le moment est de Q = 772(5) mb, une valeur beaucoup plus basse que celle acceptée antérieurement, 810 mb, mais en bon accord avec la valeur moléculaire de 770(8) mb obtenue récemment.

Mots-clés : moments quadripolaires nucléaires, gallium, indium, relativité, méthode de l'agrégat couplé.

[Traduit par la Rédaction]

Introduction

The nuclear quadrupole moment (NQM) of ^{115}In listed in Pyykkö's 2001 compilation[2] is 810 mb (with 7% uncertainty), obtained by Belfrage et al.[3] from the observed hyperfine structure of the 5s, 7p, and 8p ^{2}P states of the atom and the empirically derived $\langle r^{-3} \rangle$ value. A lower value of 760 mb (with 6% uncertainty) was later proposed,[4] based on X-ray data and calculations on the muonic atom.[5] DFT calculations on metallic indium[6] gave values of 760(20) and 780(20) mb, depending on the density functional used. The best effort to date involved relativistic coupled cluster calculations on several In-including molecules,[7] yielding a moment of 770(8) mb. The accepted value of the Ga NQM has been more stable. The reference value of 171(2) mb[2,8] is in agreement with the earlier 173(3) mb.[9]

An approach of potentially high accuracy combines experimentally observed nuclear quadrupole coupling constants of the atom, B, with calculated electric field gradients (EFG) at the nucleus, q. The NQM value Q (in barns) may be obtained from the equation

$$[1] \qquad Q[\mathrm{b}] = \frac{B[\mathrm{MHz}]}{234.9647q[\mathrm{au}]}$$

Since B is usually known with high accuracy, the quality of the calculated NQM depends solely on that of the EFG. This "atomic" approach has recently been applied to the halogen atoms[10] and to gold.[11] Here we apply it to Ga and In, for which accurate measurements of the coupling constants are available,[12,13] and compare the results to recent "molecular" values.[7,8]

Methodology

The relativistic Fock-space coupled cluster method with single and double excitations (FSCCSD) used here has been described earlier,[10,11,14] and only a few pertinent points will be discussed below. The inclusion of triple excitations in FSCC has been reported recently.[15]

Atomic and molecular properties are usually observed via the energy shifts generated by coupling to an external field. The desired property is the derivative of the energy with respect to the external field. The derivative may be calculated analytically by the Z-vector or Λ-operator method[16]; alternatively, the finite field approach[17] may be used, whereby an external field is added to the Hamiltonian and the derivative is obtained numerically. Early FSCC calculations were carried out for the EFG of several light elements, up to Mg.[18] Note that the analytic evaluation of general properties by FSCC is

Received 22 October 2008. Accepted 14 January 2009. Published on the NRC Research Press Web site at canjchem.nrc.ca on 17 March 2009.

H. Yakobi, E. Eliav, and U. Kaldor.[1] School of Chemistry, Tel Aviv University, 69978 Tel Aviv, Israel.

[1]Corresponding author (e-mail: kaldor@tau.ac.il).

Table 1. EFG at Ga nucleus as function of the basis set and number n_c of correlated electrons. The numbers indicate the n values used in the well tempered series of Huzinaga and Klobukowski.[23]

Basis	s	p	d	f	g	h	EFG(au)	n_c
26s22p17d10f7g2h	1–26	5–26	9–25	13–22	15–21	19–20	1.50544	21
27s22p17d10f7g2h	1–27	5–26	9–25	13–22	15–21	19–20	1.50544	21
26s23p17d10f7g2h	1–26	4–26	9–25	13–22	15–21	19–20	1.50547	21
26s23p17d10f7g2h	1–26	5–27	9–25	13–22	15–21	19–20	1.50502	21
26s22p18d10f7g2h	1–26	5–26	8–25	13–22	15–21	19–20	1.50546	21
26s22p18d10f7g2h	1–26	5–26	9–26	13–22	15–21	19–20	1.50539	21
26s22p17d11f7g2h	1–26	5–26	9–25	12–22	15–21	19–20	1.50538	21
26s22p17d11f7g2h	1–26	5–26	9–25	13–23	15–21	19–20	1.50454	21
26s22p17d10f8g2h	1–26	5–26	9–25	13–22	14–21	19–20	1.50552	21
26s22p17d10f8g2h	1–26	5–26	9–25	13–22	15–22	19–20	1.50662	21
26s22p17d10f7g3h	1–26	5–26	9–25	13–22	15–21	18–20	1.50534	21
26s22p17d10f7g3h	1–26	5–26	9–25	13–22	15–21	19–21	1.50687	21
26s22p17d10f7g4h	1–26	5–26	9–25	13–22	15–21	19–22	1.50729	29
26s22p17d10f7g4h	1–26	5–26	9–25	13–22	15–21	19–22	1.50723	31
26s22p17d11f8g3h	1–26	5–26	9–25	13–23	15–22	19–21	1.50900	31

still an open problem, although some progress has been made.[19] The finite field scheme circumvents this difficulty.

The finite field approach is used here to calculate the electric field gradient at the In and Ga nuclei. The Hamiltonian is modified to include the interaction with an (arbitrary) nuclear electric quadrupole Q,

$$[2] \qquad \hat{H}(Q) = \hat{H}_0 - eqQ/h$$

where e is the electron charge. The energy, which is the expectation value of $\hat{H}(Q)$, may be expanded as

$$[3] \qquad E(Q) = \langle \Psi(Q)|\hat{H}(Q)|\Psi(Q)\rangle = E_0 + Q\left(\frac{dE(Q)}{dQ}\right)_0 + \frac{Q^2}{2}\left(\frac{d^2E(Q)}{dQ^2}\right)_0 + \cdots$$

Differentiating and invoking the Hellmann–Feynman theorem, one obtains

$$[4] \qquad \frac{dE(Q)}{dQ}|_{Q=0} = -\frac{e}{h}\langle \Psi_0|\hat{q}_{ZZ}|\Psi_0\rangle$$

neglecting higher-order derivatives. The first derivative of the energy with respect to the nuclear quadrupole moment gives the required expectation value of the electric field gradient (multiplied by some constants).

Conflicting considerations determine the value of Q used in the calculations, which is *not* the physical NQM. The perturbation must be large enough for the energy change not to disappear in the precision of the calculations, yet small enough to stay in the linear regime. The linearity must be monitored by using several values of Q.

The four-component Dirac–Coulomb–Gaunt (DCG) Hamiltonian is used. In the presence of the electric field Q,

$$[5] \qquad H = \sum_i h_D(i) + \sum_{i<j}(1/r_{ij} + G_{ij}) - eqQ$$

where h_D is the one-electron Dirac operator with a Gaussian finite nucleus, and G_{ij} is the Gaunt operator.[20] Interaction with the external field is thus included from the start. The DIRAC relativistic ab initio electronic structure program[21] is used in all calculations, and the symmetry of the system is taken as $D_{\infty h}$. The Gaunt interaction is included fully at the HF stage; at the correlation stage it is taken using the atomic mean-field integral (AMFI) approximation.[22]

Electron correlation must be included at a high level to obtain accurate results. The FSCCSD method was applied here to the ns^2np states of In and Ga. Starting with the ionic state ns^2 as reference, an electron was added in the np orbitals, and the correlated energies in the presence of the field were obtained. In addition, the single reference coupled cluster method (SRCC) was applied to the $ns^2np_{3/2}$ $^2P_{3/2}$ state, which (for M_J=3/2) may be described by a single determinant. There is a major difference between the two approaches: The SRCC scheme gives the energy shift of the probed state with Q, while the FSCCSD method also yields the splitting between the $P_{3/2,3/2}$ and $P_{3/2,1/2}$ levels, which is the source of the experimental coupling constant B. In previous calculations,[10,11] we observed that the splittings remain linear for Q values as high as 10^{-5} au, whereas shifts start to show nonlinearity even at Q=10^{-8} au On the other hand, available programs make possible the approximate inclusion of triple excitations for the SRCC approach only.

Calculations and results

The uncontracted, well-tempered basis sets of Huzinaga and Klobukowski[23] were employed. The basis sets were increased to obtain convergence of the EFG, and all electrons were correlated at the final stage. Virtual orbitals with energies above 130 au were discarded at the CC stage. Raising the cutoff from 100 to 130 au changed the value of Q by less than 0.1 mb for Ga and 0.3 mb for In. The convergence of the calculated EFG with respect to the basis is demonstrated in Tables 1 and 2 for Ga and In, respectively. Basis functions with both higher and lower exponents were added for each l until the EFG converged. The values in these tables were obtained by the FSCCSD method, with virtual orbital cutoffs of 100 au and Q values of 0 and 5.0×10^{-6} au The basis functions giving convergence in the different l sectors were combined to give the basis sets shown in the

Table 2. EFG at In nucleus as function of the basis set and number n_c of correlated electrons.

Basis	s	p	d	f	g	h	EFG(au)	n_c
28s24p20d10f5g2h	1–28	5–28	8–27	17–26	21–25	23–24	2.45121	39
29s24p20d10f5g2h	1–29	5–28	8–27	17–26	21–25	23–24	2.45121	39
28s25p20d10f5g2h	1–28	4–28	8–27	17–26	21–25	23–24	2.45146	39
28s25p20d10f5g2h	1–28	5–29	8–27	17–26	21–25	23–24	2.45103	39
28s24p21d10f5g2h	1–28	5–28	7–27	17–26	21–25	23–24	2.45129	39
28s24p21d10f5g2h	1–28	5–28	8–28	17–26	21–25	23–24	2.45119	39
28s24p20d11f5g2h	1–28	5–28	8–27	16–26	21–25	23–24	2.44898	39
28s24p20d12f5g2h	1–28	5–28	8–27	15–26	21–25	23–24	2.44688	39
28s24p20d13f5g2h	1–28	5–28	8–27	14–26	21–25	23–24	2.44566	39
28s24p20d11f5g2h	1–28	5–28	8–27	17–27	21–25	23–24	2.45118	39
28s24p20d10f6g2h	1–28	5–28	8–27	17–26	20–25	23–24	2.45174	39
28s24p20d10f6g2h	1–28	5–28	8–27	17–26	21–26	23–24	2.45115	39
28s24p20d10f5g3h	1–28	5–28	8–27	17–26	21–25	22–24	2.45355	39
28s24p20d10f5g4h	1–28	5–28	8–27	17–26	21–25	21–24	2.45172	39
28s24p20d10f5g3h	1–28	5–28	8–27	17–26	21–25	23–25	2.45133	39
28s24p20d10f5g2h	1–28	5–28	8–27	17–26	21–25	23–24	2.46769	47
28s24p20d10f5g2h	1–28	5–28	8–27	17–26	21–25	23–24	2.46767	49
28s24p20d13f5g4h	1–28	5–28	8–27	14–26	21–25	21–24	2.46261	49

Table 3. Calculated EFG values at the gallium and indium nuclei (au).

Method	Ga	In
HF	1.49	2.45
MP2	1.60	2.53
SRCCSD	1.55	2.51
FSCCSD	1.51	2.47
SRCCSD+T	1.54	2.48
SRCCSD(T)	1.54	2.48
SRCCSD-T	1.54	2.49

Table 4. Nuclear quadrupole moments calculated from the EFGs of Table 3 (mb).

Method	Ga	In
HF	179	782
MP2	167	756
SRCCSD	172	762
FSCCSD	176	776
SRCCSD+T	173	771
SRCCSD(T)	173	770
SRCCSD-T	173	770

last row of Tables 1 and 2, which served in subsequent calculations.

As linearity of the energy change vs. Q is crucial to the precision of the calculations, it was carefully monitored. For the single reference methods, where the shift of one level is calculated, we used the differences between energies obtained for Q and $-Q$, thus eliminating the quadratic term in eq. [3]. This was not necessary in the multi-reference FSCCSD calculations, where the splitting of the two sublevels (see above) makes this elimination automatic. In both cases, a calculation with $2Q$ was carried out to test the linearity. For single reference methods it was necessary to take $Q = 2.5 \times 10^{-9}$ au to reduce nonlinearity below 0.2%, whereas FSCCSD gave this result for $Q = 2.5 \times 10^{-6}$ au

The EFG values at the Ga and In nuclei, calculated in the framework of the DCG Hamiltonian by the Hartree–Fock (HF), MP2, and single-reference and Fock-space CCSD methods, are collected in Table 3. Perturbative triple excitations were added to the SRCCSD values by the +T, (T), and –T schemes. Q values giving linearity of 0.2% or better were used, 2.5×10^{-6} au for FSCCSD and $\pm 2.5 \times 10^{-9}$ au for all other methods. The virtual orbital energy cutoff was 130 au The calculated EFG values and experimental nuclear quadrupole coupling constants[12,13] were inserted in eq. [1] to give the nuclear quadrupole moments, which are shown in Table 4. The Gaunt contribution to the final NQM is 0.5 mb for Ga and 1 mb for In.

Discussion

Considerable effort has been made to minimize the errors in the calculated EFGs, both systematic and numerical. The basis sets used are nearly complete, and deviations from linearity and other problems involving the extraction of the EFG from the energy data are small. The largest error comes from truncating the coupled cluster expansions at the SD or SD(T) level. Note that the definition of triple excitations may differ for the Fock space and single reference approaches, since they use different atomic orbitals and model spaces. In the present application, the SR approach is more accurate, as it uses AOs of the neutral atom (vs. the cation for FSCC) and includes approximate triples. The difference between these two schemes at the SD level may provide an indication of the triples contribution. Taking all these factors into account, our final NQMs are 174(3) mb for ^{69}Ga and 772(5) mb for ^{115}In. The gallium NQM agrees with the molecular value 171(2) mb.[2,8] The ^{115}In result is significantly lower than the previously accepted[2] 810 mb, and agrees with the value of 770(8) mb obtained in recent molecular calculations.[7]

References

(1) This article is part of a Special Issue dedicated to Professor T. Ziegler.

(2) Pyykkö, P. *Mol. Phys.* **2001**, *99*, 1617. doi:10.1080/00268970110069010.

(3) Belfrage, C.; Hörbäck, S.; Levinson, C.; Lindgren, I.; Lundberg, H.; Svanberg, S. *Z. Physica A* **1984**, *316*, 15. doi:10.1007/BF01415655.

(4) Leiberich, R.; Schmidt, P. C. Z. *Naturforsch. A Phys. Sci.* **1990**, *45*, 368.

(5) Lee, W. Y.; Bernow, S.; Chen, M. Y.; Cheng, S. C.; Hitlin, D.; Kast, J. W.; Macagno, E. R.; Rushton, A. M.; Wu, C. S.; Budick, B. *Phys. Rev. Lett.* **1969**, *23*, 648. doi:10.1103/PhysRevLett.23.648.

(6) Errico, L. A.; Rentería, M. *Phys. Rev. B* **2006**, *73*, 115125. doi:10.1103/PhysRevB.73.115125.

(7) van Stralen, J. N. P.; Visscher, L. *J. Chem. Phys.* **2002**, *117*, 3103. doi:10.1063/1.1492799.

(8) Pernpointner, M.; Visscher, L. *J. Chem. Phys.* **2001**, *114*, 10389.

(9) Tokman, M.; Sundholm, D.; Pyykkö, P. *Chem. Phys. Lett.* **1998**, *291*, 414. doi:10.1016/S0009-2614(98)00608-3.

(10) Yakobi, H.; Eliav, E.; Visscher, L.; Kaldor, U. *J. Chem. Phys.* **2007**, *126*,o. 054301. doi:10.1063/1.2431645.

(11) Yakobi, H.; Eliav, E.; Kaldor, U. *J. Chem. Phys.* **2007**, *126*, 184305. doi:10.1063/1.2735298.

(12) Daly, R. T., Jr.; Holloway, J. H. *Phys. Rev.* **1954**, *96*, 539. doi:10.1103/PhysRev.96.539.

(13) Eberz, J.; Dinger, U.; Huber, G.; Lochmann, H.; Menges, R.; Neugart, R.; Kirchner, R.; Klepper, O.; Kühl, T.; Marx, D.; Ulm, G.; Wendt, K.; and the ISOLDE Collaboration. *Nucl. Phys. A.* **1987**, *464*, 9. doi:10.1016/0375-9474(87)90419-2.

(14) (a) Eliav, E.; Kaldor, U.; Ishikawa, Y. *Phys. Rev. A* **1994**, *49*, 1724. doi:10.1103/PhysRevA.49.1724.; (b) Eliav, E.; Kaldor, U.; Ishikawa, Y. *Phys. Rev. A* **1994**, *50*, 1121. doi:10.1103/PhysRevA.50.1121.; (c) Kaldor, U.; Eliav, E. *Adv. Quantum Chem.* **1998**, *31*, 313.

(15) (a) Musial, M.; Bartlett, R. J. *J. Chem. Phys.* **2004**, *121*, 1670 doi:10.1063/1.1765096.; (b) Musial, M.; Bartlett, R. J. *J. Chem. Phys.* **2008**, *129*, 044101. doi:10.1063/1.2952521.

(16) (a) Goddard, J. D.; Handy, N. C.; Schaefer, H. F. *J. Chem. Phys.* **1979**, *71*, 1525 doi:10.1063/1.438494.; (b) Salter, E. A.; Trucks, G. W.; Bartlett, R. *J. Chem. Phys.* **1989**, *90*, 1752. doi:10.1063/1.456069.

(17) (a) Kaldor, U. *J. Phys. B* **1973**, *6*, 71 doi:10.1088/0022-3700/6/1/009.; (b) Monkhorst, H. J. *Int. J. Quantum Chem.* **1977**, *11*, 421.

(18) Bartlett, R. J. In *Modern Electronic Structure Theory*; Yarkony, D. R., Ed.; World Scientific: Singapore; 1995; Part II, p. 1047.

(19) (a) Ajitha, D.; Vaval, N.; Pal, S. *J. Chem. Phys.* **1999**, *110*, 2316; (b) Manohar, P. U.; Pal, S. *AIP Conf. Proc.* **2007**, *963*, 337.

(20) Gaunt, J. A. *Proc. R. Soc. A* **1929**, *122*, 513.

(21) Jensen, J. Aa.; Saue, T.; Visscher, L. *DIRAC (a relativistic ab initio electronic structure program)*, DIRAC04 version. With contributions from V. Bakken, E. Eliav, T. Enevoldsen, T. Fleig, O. Fossgaard, T. Helgaker, J. Laerdahl, C. V. Larsen, P. Norman, J. Olsen, M. Pernpointner, J. K. Pedersen, K. Ruud, P. Salek, J. N. P. van Stralen, J. Thyssen, O. Visser, and T. Winther. 2004. Available from http://dirac.chem.sdu.dk.

(22) Schimmelpfennig, B.; Maron, L.; Wahlgren, C.; Teichteil, H.; Fagerli, H.; Gropen, O. *Chem. Phys. Lett.* **1998**, *286*, 267[L. Visscher coded the Gaunt-AMFI interface in DIRAC]. doi:10.1016/S0009-2614(98)00121-3.

(23) Huzinaga, S.; Klobukowski, M. *Chem. Phys. Lett.* **1993**, *212*, 260. doi:10.1016/0009-2614(93)89323-A.

Bond activation by group-11 transition-metal cations[1]

G. Theodoor de Jong and F. Matthias Bickelhaupt

Abstract: We have computationally explored C–X bond activation by the group-11 transition-metal cations Cu^+, Ag^+, and Au^+, and, for comparison, Pd, using relativistic density functional theory (DFT) at ZORA-BLYP/TZ2P. Oxidative insertion of the second-row transition-metal species Ag^+ and Pd leads, for a given bond, to the highest overall reaction barriers. On the other hand, if we compare the different bonds oxidative insertion into the C–F bond is associated with (one of the) highest overall barriers whereas insertion into the C–Cl bond leads to the lowest overall barrier for any transition metal. The main trends in reactivity are rationalized using the activation strain model of chemical reactivity, which is an extension of the fragment approach to reaction profiles. In this model, the shape of the reaction profile $\Delta E(\zeta)$ and the height of the overall reaction barrier $\Delta E^{\neq} = \Delta E(\zeta=\zeta^{TS})$ are interpreted in terms of the strain energy $\Delta E_{strain}(\zeta)$ associated with deforming the reactants along the reaction coordinate ζ plus the interaction energy $\Delta E_{int}(\zeta)$ between these deformed reactants: $\Delta E(\zeta) = \Delta E_{strain}(\zeta) + \Delta E_{int}(\zeta)$.

Key words: activation strain model, catalysis, density functional calculations, oxidative addition, palladium, ligand effects, reaction mechanisms.

Résumé : Faisant appel à la théorie de la fonctionnelle de densité (TFD) relativiste au niveau ZORA-BLYP/TZ2P, on a évalué l'activation de la liaison C–X par les cations des métaux de transition du groupe 11, Cu^+, Ag^+ et Au^+ et, pour fins de comparaison, par le Pd. L'insertion oxydante d'espèces métalliques de transition de la deuxième rangée, Ag^+ et Pd, conduit pour une liaison donnée barrières réactionnelles globales les plus élevées. Par ailleurs, si on compare les diverses liaisons, l'insertion oxydante dans la liaison C–F est associée avec une des barrières globales les plus élevées alors que l'insertion dans une liaison C–Cl, pour n'importe lequel des métaux de transition, conduit à la barrière globale la plus faible. Les tendances principales dans la réactivité sont rationalisées à l'aide du modèle de la contrainte d'activation de la réactivité chimique qui est une extension de l'approche fragmentaire aux profils de réaction. Dans ce modèle, la forme du profil réactionnel $\Delta E(\zeta)$ et la hauteur de la barrière réactionnelle globale $\Delta E^{\neq} = \Delta E(\zeta=\zeta^{TS})$ sont interprétées en fonction de l'énergie de contrainte, $\Delta E_{contrainte}(\zeta)$, associée avec la déformation des réactifs le long de la coordonnée de réaction ζ plus l'énergie d'interaction, $\Delta E_{int}(\zeta)$, entre ces réactifs déformés: $\Delta E(\zeta)= \Delta E_{contrainte}(\zeta) + \Delta E_{int}(\zeta)$.

Mots-clés : modèle de contrainte d'activation, catalyse, calculs de la fonctionnelle de densité, addition oxydante, palladium, effets de ligand, mécanismes réactionnels.

[Traduit par la Rédaction]

Introduction

Oxidative addition and reductive elimination are ubiquitous as elementary reaction steps in homogeneous catalysis[2–4] (Scheme 1) and have been intensively investigated both experimentally[4–6] and theoretically.[6–12] A well-known class of processes involving oxidative addition is catalytic C–X bond activation.[2,13] The catalytically active species in these processes are in general coordination complexes of palladium or another transition metal. Oxidative addition is an efficient tool for selectively converting simple educts, via C–C bond formation, into more complex compounds, and it is therefore of major importance for synthetic chemistry. The most intensively used substrates for such C–C coupling reactions are aryl halides, whereas it is more difficult in this context to exploit alkyl halides.[14]

In a previous study, we investigated the activation of the C–H and C–C bonds by Pd compared with main group metals (Be, Mg, and Ca) and group-12 transition metals (Zn and Cd).[11] It was shown that Pd is able to activate these bonds better than the other metals, i.e., with lower reaction barriers, because it has both good electron-donating and good electron-accepting capacities due to the small gap between its occupied 4d and unfilled 5s atomic orbitals (AOs). In other studies, the profound effect of anion assistance in the case of the $PdCl^-$ complex (compared with uncoordinated Pd) on the activation barriers and the selectivity of reaction pathway was demonstrated and explained.[12]

In the present study, we extend these investigations to the cations of the group-11 transition-metal triad (Cu^+, Ag^+, and Au^+), which are also of interest for C–X bond activation processes.[15] To this end, we have investigated the oxidative insertion of the three d^{10} transition-metal cations and, for

Received 19 November 2008. Accepted 19 December 2008. Published on the NRC Research Press Web site at canjchem.nrc.ca on 7 March 2009.

G. Th. deJong and F.M. Bickelhaupt.[1] Department of Theoretical Chemistry and Amsterdam Center for Multiscale Modeling, Scheikundig Laboratorium der Vrije Universiteit, De Boelelaan 1083, NL-1081 HV Amsterdam, The Netherlands.

[1]Corresponding author (e-mail: fm.bickelhaupt@few.vu.nl).

Scheme 1. Catalytic cycle with oxidative addition and reductive elimination steps.

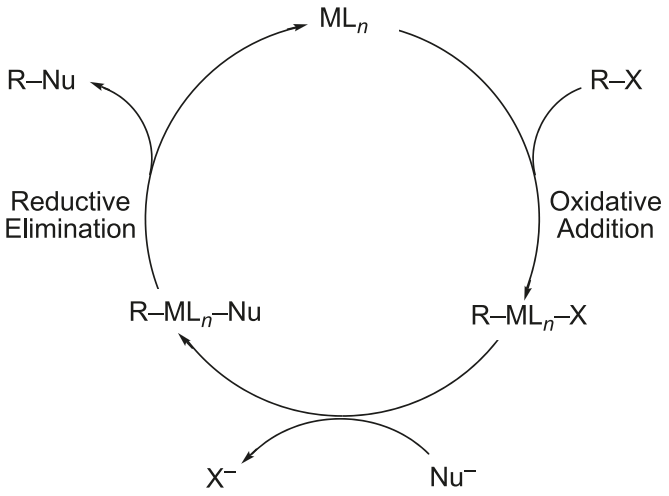

Fig. 1. Illustration of the activation strain model in case of oxidative insertion of a metal into a C–X bond.

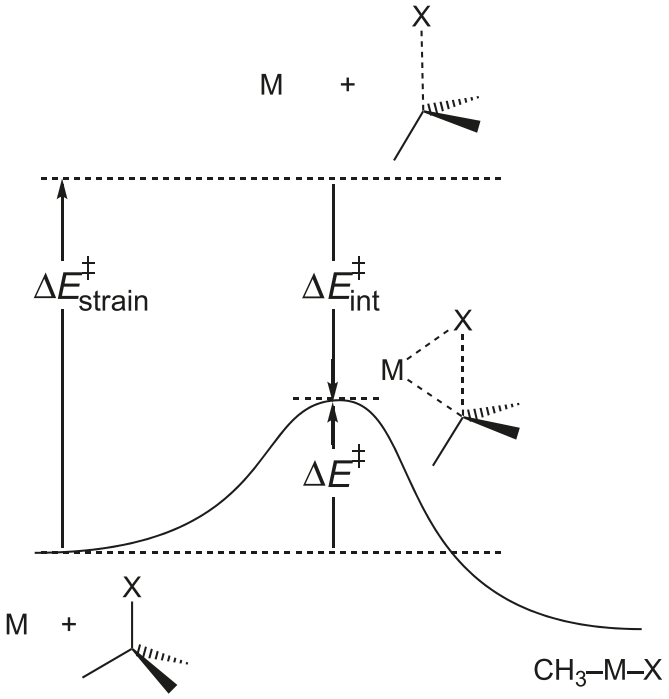

comparison, palladium into the C–H, C–C, C–F, and C–Cl bonds of methane, ethane, fluoromethane, and chloromethane, respectively (see eq. [1]: M = Pd, Cu^+, Ag^+, Au^+; X = H, CH_3, F, Cl), using density functional theory (DFT) at ZORA-BLYP/TZ2P, as implemented in the ADF program (see Methods section below).

$$[1] \qquad M + CH_3X \rightarrow CH_3 - M - X$$

To obtain a better understanding of the major trends in reaction barriers, we have analyzed our model reactions in terms of the activation strain model of chemical reactivity.[8,12,16] In this model, the energy of the reaction system $\Delta E(\zeta)$ is decomposed along the reaction coordinate ζ into the strain $\Delta E_{strain}(\zeta)$ within the increasingly deformed reactants plus the stabilizing interaction between these reactants $\Delta E_{int}(\zeta)$: $\Delta E(\zeta) = \Delta E_{strain}(\zeta) + \Delta E_{int}(\zeta)$.

Table 1. Energies of stationary points relative to reactants (in kcal/mol, 1 cal = 4.184 J) for the oxidative insertion reactions of Pd, Cu^+, Ag^+, and Au^+ with CH_4, C_2H_6, CH_3F, and CH_3Cl.

Metal	Activated bond	RC	TS	P
Pd	C–H	–6.7	3.9	–3.4
	C–C	–6.8	18.3	–9.3
	C–F	–5.5	17.7	–15.8
	C–Cl	–12.9	–0.6	–33.1
Cu^+	C–H	–30.7	[a]	(–3.1)[a,b]
	C–C	–34.9	–18.5	–25.7
	C–F	–35.4	–3.0	–5.9
	C–Cl	–49.4	–26.3	–27.1
Ag^+	C–H	–15.8	[a]	(27.6)[a,b]
	C–C	–19.1	12.9	7.9
	C–F	–22.6	31.7	31.6
	C–Cl	–32.1	[a]	(9.2)[a,b]
Au^+	C–H	–28.2	–21.3	–27.5
	C–C	–34.2	–12.8	–44.9
	C–F	–28.5	8.2	–4.9
	C–Cl	–49.8	–21.4	–33.6

Note: Computed at ZORA-BLYP/TZ2P (see also Figs. 2–5).

[a]Stationary point does not exist.

[b]The value in parentheses is estimated for the product, which is modeled by the labile structure with the C-M-X angle frozen to the value in the corresponding Pd product **1c** and all other internal coordinates fully optimized.

Methods

Computational details

All calculations are based on density functional theory (DFT),[17] using the Amsterdam Density Functional (ADF) program.[18,19] The BLYP density functional was used,[20] in combination with a large uncontracted set of Slater-type orbitals (STOs) containing diffuse functions. This basis set is designated TZ2P: it is of triple-ζ quality and has been augmented with two sets of polarization functions, 2p and 3d on H, 3d and 4f on C, F, and Cl, 4p and 4f on Cu, 5p and 4f on Pd and Ag, 6p and 5f on Pd. The core shells of carbon (1s), fluorine (1s), chlorine (1s2s2p), copper (1s2s2p), palladium (1s2s2p3s3p3d), silver (1s2s2p3s3p3d), and gold (1s2s2p3s3p3d4s4p4d) were treated by the frozen-core approximation.[18] An auxiliary set of s, p, d, f, and g STOs was used to fit the molecular density and to represent the Coulomb and exchange potentials accurately in each SCF cycle.[18] Relativistic effects were accounted for using the zeroth-order regular approximation (ZORA).[21] Recently, it has been shown that our approach is in good agreement with high-level ab initio calculations for oxidative addition reactions to Pd.[9,10]

Equilibrium and transition-state geometries were fully optimized using analytical gradient techniques. All structures were verified by frequency calculations: for minima all normal modes have real frequencies, whereas transition states have one normal mode with an imaginary frequency. The

Fig. 2. Geometries (Å, °) of stationary points along the potential energy surface for oxidative insertion of Pd into the C–X bond of CH_3X, computed at ZORA-BLYP/TZ2P.

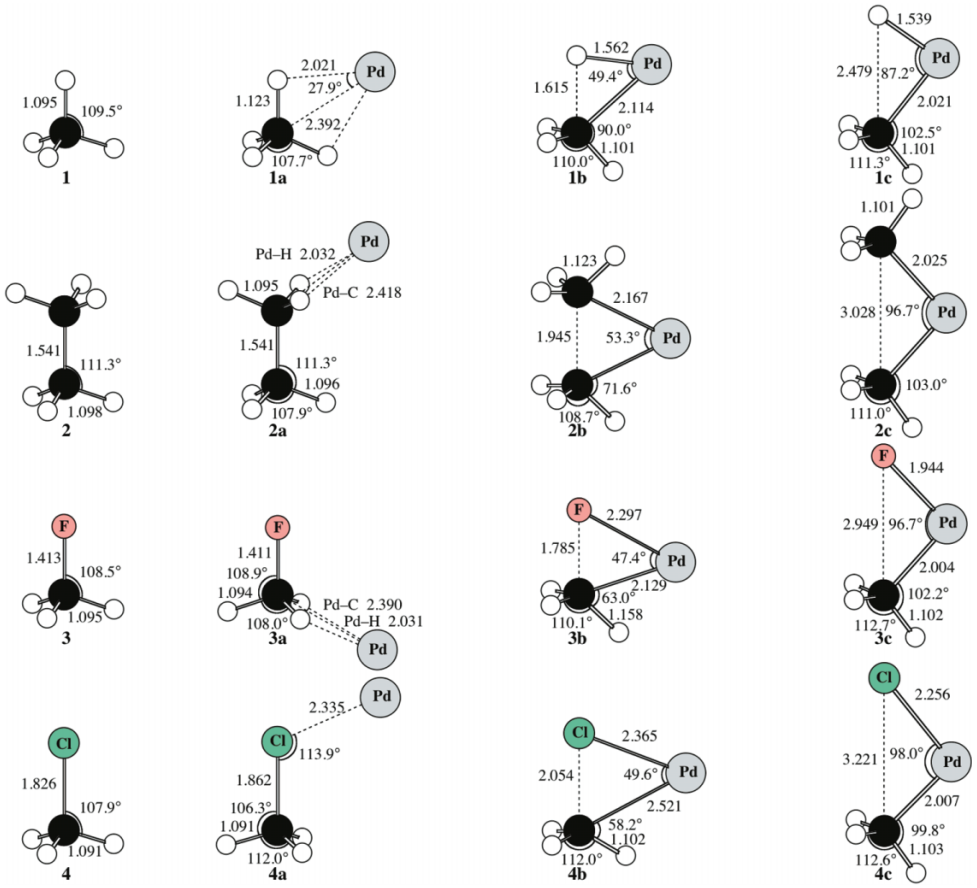

character of the normal mode associated with the imaginary frequency was analyzed to ensure that the correct transition state was found.

Activation strain analyses

Insight into how the reaction barriers arise is obtained through activation strain analyses of the various C–X bond activation processes.[8,12,16] The activation strain model is a systematic extension of the fragment approach (first introduced in the ADF program and in the context of DFT by Ziegler and Rauk[19]) from equilibrium structures to transition states as well as *nonstationary* points, e.g., points along a reaction coordinate. It is a fragment approach to understanding chemical reactions in which the height of reaction barriers is described and understood in terms of the original reactants. Thus, the potential energy surface $\Delta E(\zeta)$ is decomposed along the reaction coordinate ζ into the strain $\Delta E_{\text{strain}}(\zeta)$ associated with deforming the individual reactants plus the actual interaction $\Delta E_{\text{int}}(\zeta)$ between the deformed reactants,

$$[2] \qquad \Delta E(\zeta) = \Delta E_{\text{strain}}(\zeta) + \Delta E_{\text{int}}(\zeta)$$

The strain $\Delta E_{\text{strain}}(\zeta)$ is determined by the rigidity of the reactants and by the extent to which groups must reorganize in a particular reaction mechanism, whereas the interaction $\Delta E_{\text{int}}(\zeta)$ between the reactants depends on their electronic structure and on how they are mutually oriented as they approach each other. It is the interplay between $\Delta E_{\text{strain}}(\zeta)$ and $\Delta E_{\text{int}}(\zeta)$ that determines if and at which point along ζ a barrier arises. The activation energy of a reaction $\Delta E^{\neq} = \Delta E(\zeta^{\text{TS}})$ consists of the activation strain $\Delta E^{\neq}_{\text{strain}} = \Delta E_{\text{strain}}(\zeta^{\text{TS}})$ plus the TS interaction $\Delta E^{\neq}_{\text{int}} = \Delta E_{\text{int}}(\zeta^{\text{TS}})$,

$$[3] \qquad \Delta E^{\neq} = \Delta E^{\neq}_{\text{strain}} + \Delta E^{\neq}_{\text{int}}$$

This is illustrated in Fig. 1.

The reaction coordinate ζ is defined here as the path of steepest descent from the transition state down to the local energy minima on the educt and product side, connected by this transition state. This path is determined through the intrinsic reaction coordinate (IRC) method.[22] In the graphical representations shown hereafter, ζ is then projected onto the stretch of the C–X bond that is being activated. This C–X stretch is generally the dominant component of the reaction coordinate in our model systems and undergoes a well-defined change from an intact to a dissociated bond.

Results and discussion

Reaction profiles and geometries

Our ZORA-BLYP/TZ2P results for the 16 oxidative insertion (OxIn) reactions are collected in Table 1 (energies) and Figs. 2–5 (geometries). All model reactions (eq. [1]) involve the formation of a stable reactant complex (RC) between the

Fig. 3. Geometries (Å, °) of stationary points along the potential energy surface for oxidative insertion of Cu^+ into the C–X bond of CH_3X, computed at ZORA-BLYP/TZ2P. Structures **5b** and **5c** do not exist as stationary points; **5c** is modeled by the labile structure with the C-M-X angle frozen to the value in the corresponding Pd product **1c** and all other internal coordinates fully optimized.

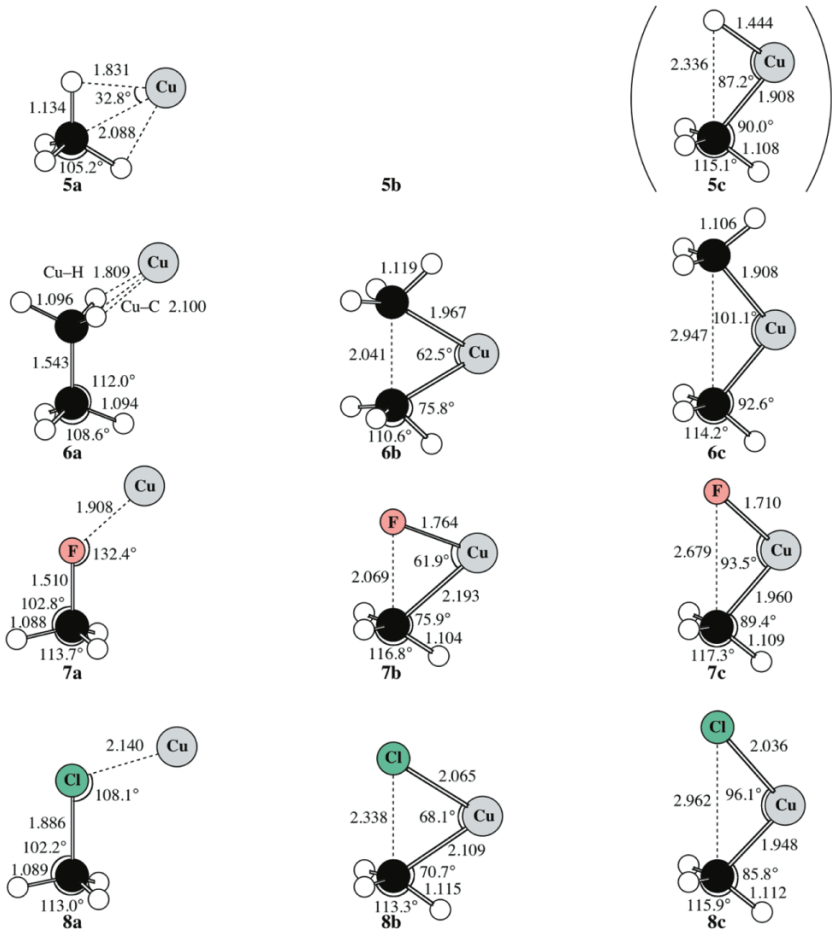

reactants (R) in which the substrate coordinates to the metal or metal cation, either via the hydrogen atoms or via the halogen atom. Coordination via hydrogen, M···H-C, occurs for all reactions of methane and ethane, and if M = Pd, also in the case of fluoromethane (see **1a**, **2a**, **3a**, **5a**, **6a**, **9a**, **10a**, **13a**, and **14a** in Figs. 2–5). Coordination via halogen, M···X-C, occurs in all other reactions with the substrates fluoromethane and chloromethane (see **4a**, **7a**, **8a**, **11a**, **12a**, **15a**, and **16a**). Most of the model reactions then proceed from the RC via the transition state (TS, see **1b**–**16b**) to the insertion product (P, see **1c**–**16c**).

Note, however, that OxIn of Cu^+ and Ag^+ into the methane C–H bond and OxIn of Ag^+ into the chloromethane C–Cl bond have no reverse barrier, that is, there are no stationary points corresponding to a TS or a stable product P. In other words, the conceivable OxIn product CH_3MX undergoes spontaneous reductive elimination. For these three model reactions, we have computed labile (i.e., nonstationary) model-product structures (see **5c**, **9c**, and **12c** in Figs. 3 and 4) by optimizing the geometries under the constraint that the C-M-X angle is frozen to its value in the corresponding OxIn product of Pd (see **1c** in Fig. 2). These structures are used as an estimate of the effective OxIn reaction barrier and also as starting points for exploring the reaction coordinate and profile through IRC calculations.

The formation of the RC is substantially more exothermic for the transition-metal cations (–16 to –50 kcal/mol) than for the neutral Pd (–6 to –13 kcal/mol), as can be seen in Table 1. The larger complexation energy of the cations has been traced to their increased ability to accept electronic charge from the substrate. This is reflected by the lowest unoccupied "molecular" orbitals (LUMOs) of Cu^+, Ag^+, and Au^+, i.e., the 4s, 5s and 6s atomic orbitals (AOs), respectively, which are consistently at much lower energy than the corresponding 5s acceptor orbital on Pd. This is illustrated in Fig. 6, which compares the energy levels of the four metal species and the four substrates on scale. We wish to point out, however, that in terms of HOMO–LUMO interactions with the substrate orbitals, the picture in Fig. 6 suggests an exaggerated stabilization of the AOs in the transition-metal cations compared with Pd. This is because in the vicinity of the metal cation the substrate orbitals also experience stabilization due to the net positive charge, although less so than the metal AOs, and are therefore effectively at lower energies than in the vicinity of the neutral Pd or in the isolated substrates shown in the figure.

All reactions are exothermic by –3 to –45 kcal/mol, except those involving Ag^+, which are all endothermic by 8 to 28 kcal/mol (see Table 1). The overall reaction barriers (TS relative to reactants) are graphically represented in the two-

Fig. 4. Geometries (Å, °) at ZORA-BLYP/TZ2P of stationary points along the potential energy surface for oxidative insertion of Ag^+ into the C–X bond of CH_3X. Structures **9b**, **9c**, **12b**, and **12c** do not exist as stationary points; **9c** and **12c** are modeled by the labile structures with the C-M-X angle frozen to the value in the corresponding Pd product **1c** and all other internal coordinates fully optimized.

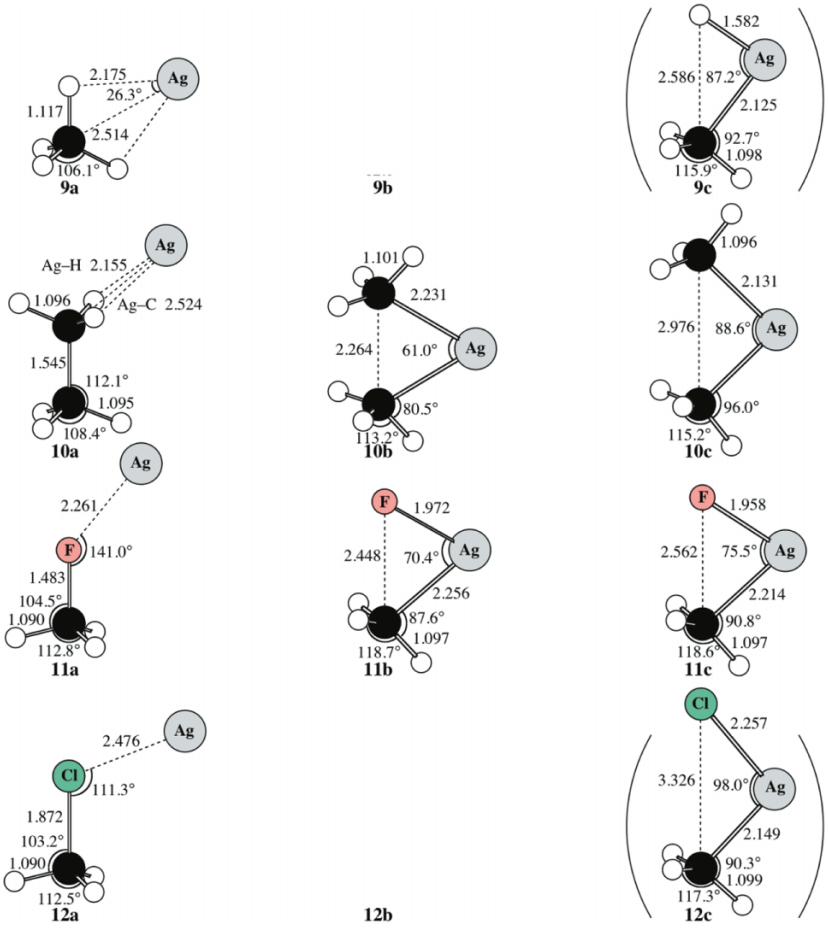

dimensional bar diagram of Fig. 7. As already pointed out above, oxidative insertion of Cu^+ and Ag^+ into the methane C–H bond and OxIn of Ag^+ into the chloromethane C–Cl bond have no reverse barriers, and the effective reaction barrier corresponds to the endothermicity associated with forming the OxIn product (which is labile with respect to reductive elimination, the reverse reaction).

Figure 7 shows that oxidative insertion of the second-row transition-metal species Ag^+ and Pd leads, for a given bond, to the highest overall reaction barriers. For example, the overall barrier for M + CH_3F is –3 (Cu^+), +8 (Au^+), +18 (Pd), and +32 kcal/mol (Ag^+). On the other hand, if we compare the different bonds, oxidative insertion into the C–F bond is associated with (one of the) highest overall barriers, whereas insertion into the C–Cl bond leads for any transition metal to the lowest overall barrier. For example, the overall barrier for Ag^+ + CH_3X is +9 (C–Cl), +13 (C–C), +28 (C–H), and +32 kcal/mol (C–F).

Apart from these global trends, there are also interesting changes in selectivity along the metal species for C–H versus C–C activation. Thus, Cu^+ favors the activation of C–C over C–H with overall barriers of –19 versus –3 kcal/mol whereas, on the other hand, Au^+ favors C–H over C–C activation with overall barriers of –34 versus –28 kcal/mol (see Table 1).

Activation strain analyses of reactions with Pd

The results of our activation strain analyses are shown in Fig. 8 in which they are collected, both per C–X bond reacting with each of the four metal species (Fig. 8*a*) and also per metal species M inserting into each of the four bonds (Fig. 8*b*). As a starting point for our discussion, we take the OxIn reactions of palladium that have been analyzed and discussed previously.[12] Here, we focus on the main trends of the Pd + CH_3X model systems.

The low reaction barrier for palladium-induced C–Cl bond activation compared with the other bonds is straightforwardly explained by the lower C–Cl bond strength, which manifests itself in a less destabilizing ΔE_{strain} curve (green in Fig. 8*b*, Pd). The bond dissociation energy (BDE) increases in the order C–Cl < C–C << C–H ≤ C–F from 82 to 90 to 110 to 115 kcal/mol, respectively, as computed at ZORA-BLYP/TZ2P.[12] The other bonds, i.e., C–H, C–F, and C–C, have more destabilizing ΔE_{strain} curves, which mutually differ comparatively little (see Fig. 8*b*, Pd). As far as the C–H and C–F bonds are concerned, this reflects again the relative bond strengths of these bonds that increase only slightly in the order C–H ≤ C–F. The fact that the ΔE_{strain} curve for the C–C bond also practically coincides here with those of the much stronger C–H and C–F bonds is not what

Fig. 5. Geometries (Å, °) of stationary points along the potential energy surface for oxidative insertion of Au^+ into the C–X bond of CH_3X, computed at ZORA-BLYP/TZ2P.

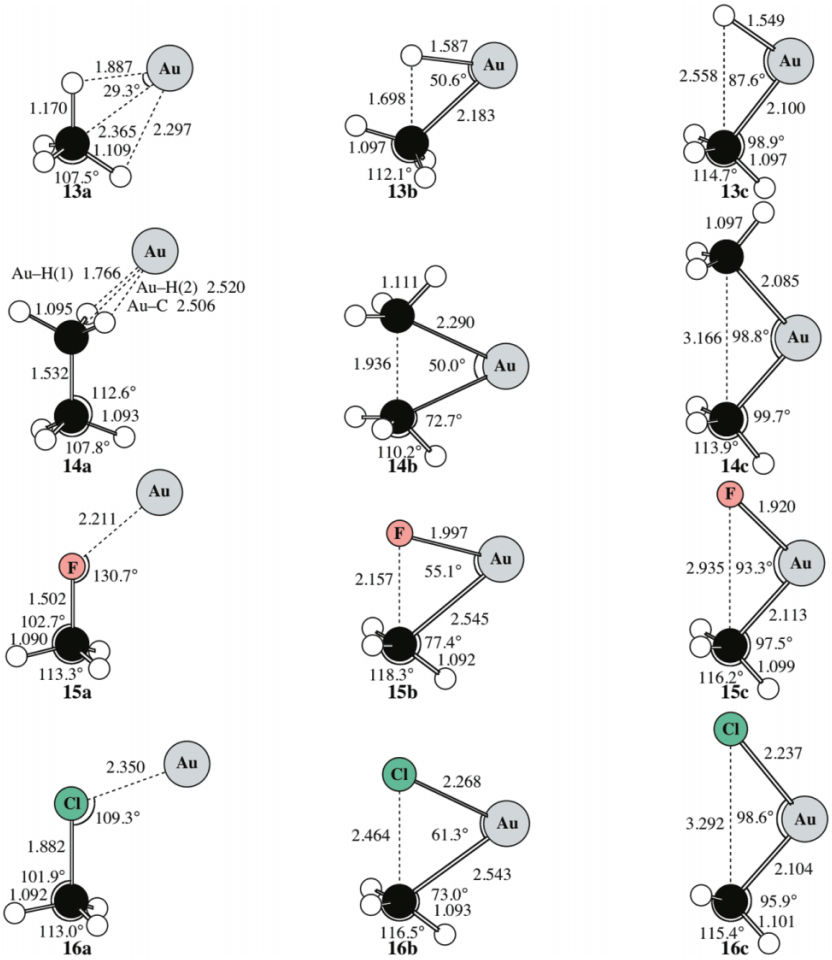

one would expect on the basis of the relative bond strengths. We will return to this issue later on.

Thus, the reaction barrier for C–H activation is higher than that for C–Cl activation because the C–H bond is stronger. However, the further increase of the barrier along C–H, C–C, and C–F appears to have its origin in the metal–substrate interaction ΔE_{int}. In Fig. 8*b* (Pd), it can be seen that initially the ΔE_{int} curves of the C–C and C–F bonds, and to a lesser extent also that of the C–Cl bond, lag behind that of the C–H bond, while later on they catch up. This initial lagging behind of the ΔE_{int} curves has the effect of pushing up the net energy profile ΔE, which causes the C–F and C–C barrier to be higher than that of C–H activation. The catching up in a somewhat later stage along the reaction coordinate ζ causes an increased (negative) slope in the ΔE_{int} curves. Compared with the situation for C–H, this shifts the stationary point (i.e., the TS) on the net potential energy surface $\Delta E(\zeta) = \Delta E_{strain}(\zeta) + \Delta E_{int}(\zeta)$ towards the left.

The origin of the lagging behind of the ΔE_{int} curves of C–C, C–F, and C–Cl compared with C–H is diverse.[12] One factor that the former three bonds have in common derives from the dependence of the metal 5s-substrate σ^*_{C-X} overlap on the progress along the reaction coordinate. The interaction of palladium with the C–H bond has, from the beginning, a relatively favorable overlap between a metal 4d AO and the σ^*_{C-H} acceptor orbital of the substrate with its large nodeless 1s lobe at hydrogen. This overlap situation is shown schematically below in **A** (the red dashed line indicates the nodal surface of the carbon 2p component of the σ^*_{C-H} MO, which contributes especially when the C–H bond begins to be stretched).

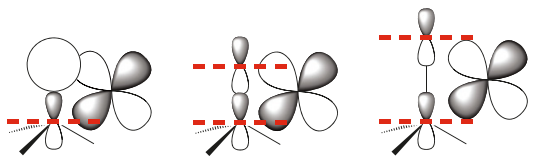

A **B** **C**

The corresponding overlap with the σ^*_{C-X} acceptor orbital of C–X bonds in which X is a main group atom (i.e., C–C, C–F, C–Cl) is less favorable, in the beginning, because now there is also a nodal surface at X that cuts through the metal 4d lobe, resulting in cancellation of overlap (see **B** above). However, the overlap soon catches up as the reaction proceeds and the C–X bond expands, because this causes the nodal surfaces of the substrates σ^*_{C-X} MO to move out of the way of the metal 4d AO (see **C** above). The ΔE_{int} curve for C–Cl activation benefits, in addition, from being already

Fig. 6. Orbital energies (eV) of the frontier orbitals of Pd, Cu^+, Ag^+, Au^+, CH_4, C_2H_6, CH_3F, and CH_3Cl, computed at ZORA-BLYP/TZ2P. All metals have closed $(nd)^{10}$ shells.

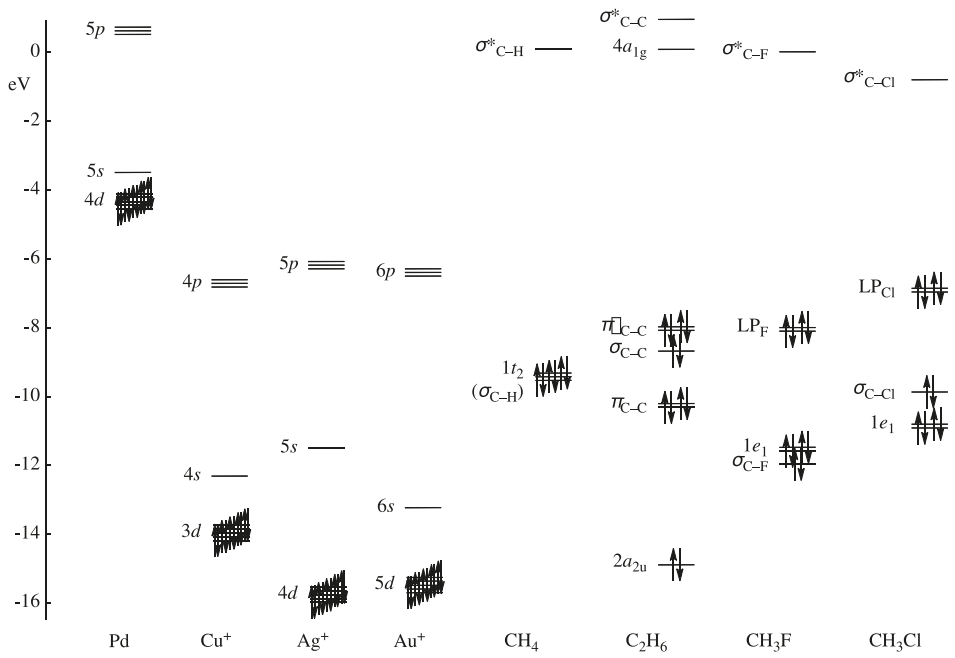

Fig. 7. Trends in overall activation energies relative to that of $Cu^+ + CH_3Cl$ ($\Delta E^{\neq}[M + CH_3X] - \Delta E^{\neq}[Cu^+ + CH_3Cl]$ in kcal/mol) for the oxidative insertion of Cu^+, Au^+, Pd, and Ag^+ into the C–Cl, C–C, C–H, and C–F bonds of CH_3X, computed at ZORA-BLYP/TZ2P.

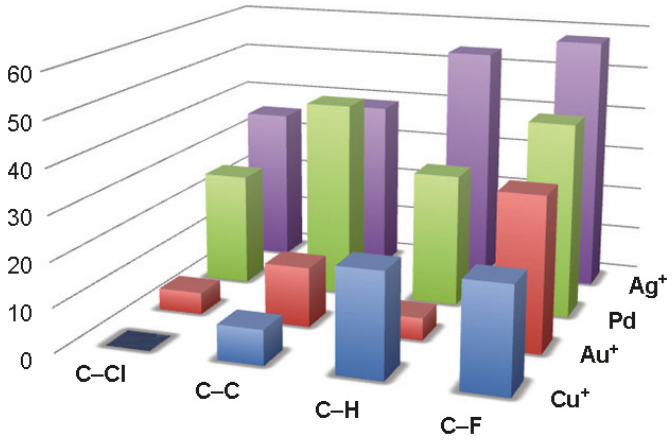

longer and thus closer to situation **C** in the RC, if compared with the C–F and C–C bonds (see Fig. 2).

The ethane C–C bond activation is special in the sense that yet another important mechanism is at work, namely, sterical shielding by the surrounding C–H bonds. Before palladium can achieve direct contact with the C–C bond, the C–H bonds have to be pushed away. This is achieved by C–C bond stretching and, importantly, the well-known tilting of the methyl groups along the reaction path, in particular, in the transition state **2b** (Fig. 2). The most eye-catching effect of this "first making room for the metal" is again a delay in the ΔE_{int} curve (compare blue C–C with black C–H curves in Fig. 8*b*, Pd).

The tilting of the methyl groups in ethane also represents an additional geometrical deformation that is the reason behind the unexpectedly high substrate strain that was mentioned above. Thus, the methyl tilting causes the ΔE_{strain} curve of C–C activation to be raised to the same level as that of C–H, even though the former (BDE = 90 kcal/mol) is 20 kcal mol^{-1} *weaker* than the latter bond (BDE = 110 kcal/mol). Note however that despite the tilting, the strain curve of C–C is not more destabilizing than that of C–H. Therefore, without the delay in interaction between metal and the initially sterically shielded C–C bond, the activation of the latter would not have a higher reaction barrier than C–H bond activation.

Activation strain analyses of reactions with Cu^+, Ag^+, and Au^+

Next, we consider how and why OxIn reactivity changes if the metal species is varied from Pd to the metal cations Cu^+, Ag^+, and Au^+. We begin with the oxidative insertion into the methane C–H bond (see Fig. 8*a*, C–H). Three striking observations can be made if one goes from Pd to the three metal cations: (*i*) the strain curves hardly change; (*ii*) the interaction curves all become more shallow; and (*iii*) as a result, the transition states all shift to a later, more product-like position along the reaction coordinate.

The reason for the more shallow interaction curves is easy to understand. At the beginning of the reaction, to the left in the activation strain plots in Fig. 8*a* (C–H), the transition-metal cations bind more strongly to the substrate than Pd because their low-energy ns AOs are better charge acceptors (see Fig. 6). On the other hand, towards the end of the reaction, at the right in the plots of Fig. 8*a*, (C–H), back-donation from the metal to the substrate σ^*_{C-X} becomes relatively more important. And this is something at which the metal cations are less good, because the low energy of

Fig. 8. Activation strain analysis for oxidative insertion of transition metals M into $H_3C–X$ bonds, along the IRC reaction coordinate ζ projected onto the C–X bond stretch, (*a*) grouped per C–X bond; (*b*) grouped per metal M (dots indicate TS).

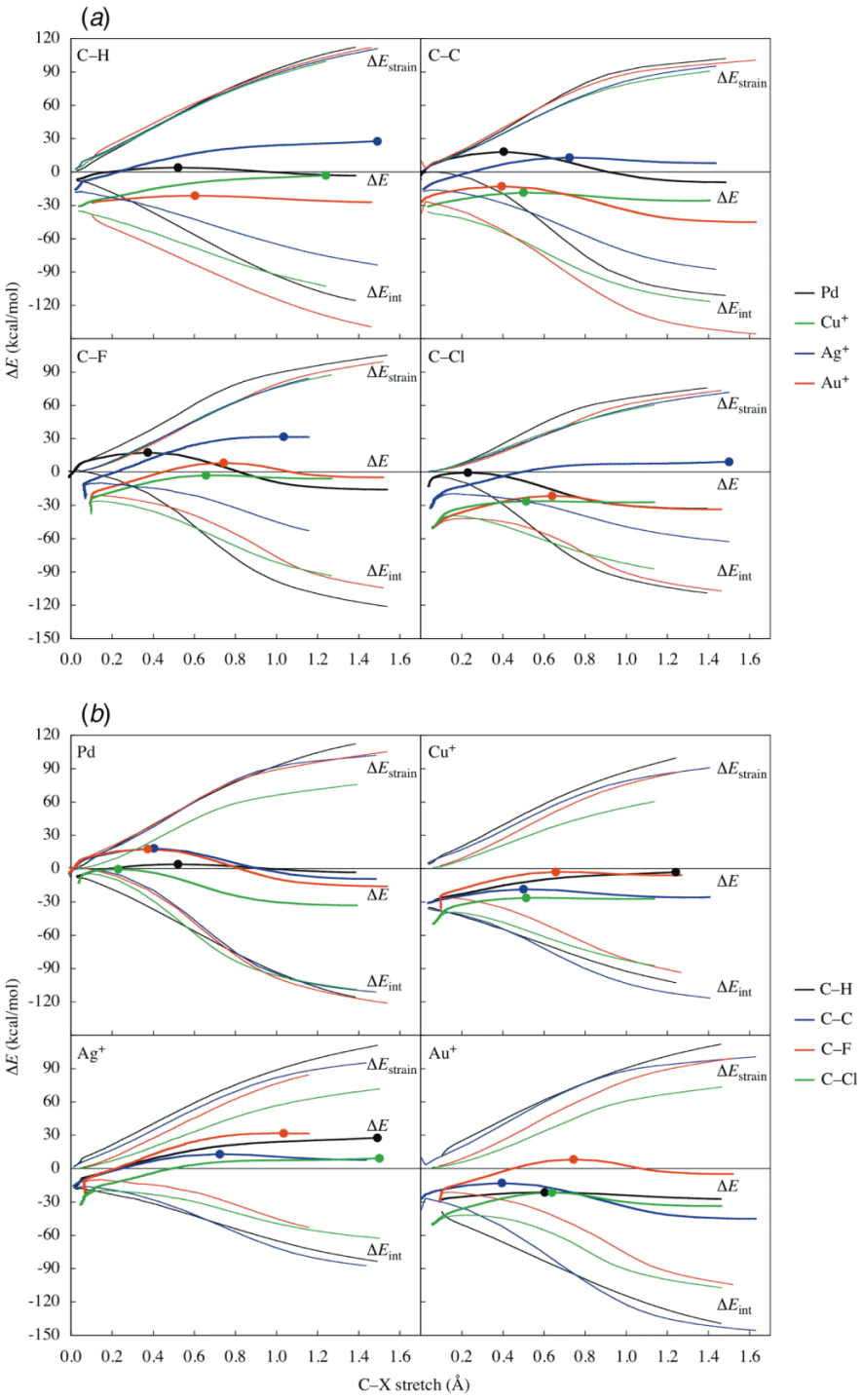

their nd AOs makes them less favorable donor orbitals in donor–acceptor interactions with the substrate $\sigma^*_{C–X}$.

This is nicely illustrated by Fig. 9, which shows the gross populations of the Pd 5s, the Cu^+ 4s, the Ag^+ 5s, and the Au^+ 6s acceptor AOs as well as the methane $\sigma^*_{C–X}$ acceptor orbital. At small C–H stretch, the population in the $\sigma^*_{C–H}$ orbital is small, which corresponds to little back-donation of electronic charge from metal to substrate. The population in the metal ns orbital is larger, which corresponds to a more important contribution of donation of electronic charge from substrate to metal in the interaction energy in the RC. The population in the Pd 5s AO is smaller than in the metal-cation ns AOs. The magnitude of the ns orbital populations decreases in the order Au^+ 6s > Cu^+ 4s > Ag^+ 5s, in line with the corresponding orbital energies that increase in the same order, i.e., –13.2, –12.3, and –11.5 eV (compare Figs. 6 and 9).

As the reaction proceeds, i.e., with increasing C–H stretch, the populations of all fragment LUMOs increase,

Fig. 9. Populations of the transition-metal ns orbital (solid lines: Pd 5s, Cu^+ 4s, Ag^+ 5s, or Au^+ 6s) and the methane substrate σ^*_{C-H} orbital (dashed lines), along the IRC reaction coordinate ζ for oxidative insertion projected onto the C–H bond stretch.

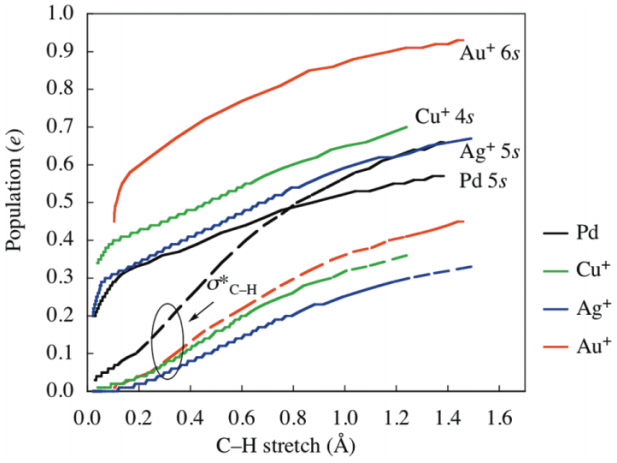

but most importantly the population in the σ^*_{C-H} orbital in the case of Pd insertion increases the most. Thus, back-donation from Pd to methane becomes larger than donation from methane to Pd. This large increase of back-donation is directly connected to the large increase in interaction energy in the case of Pd insertion. And it is the poor capability of the metal cations to back-donate electronic charge into the methane substrate that results in the less-pronounced stabilization of the interaction-energy curve in the corresponding OxIn reactions.

The effect of shifting the TS to the right is illustrated by a generic activation strain diagram in Fig. 10*a*. The additional stabilization at the beginning of the reaction makes the ΔE_{int} curve shallower. Consequently, the transition state, which is the point where $d[\Delta E_{int}(\zeta)]/d\zeta = -d[\Delta E_{strain}(\zeta)]/d\zeta$, is reached at a later stage, i.e., at larger ζ.

Note that the above effect leads to a different result than reinforcing an interaction mechanism that begins to play a role later on along the reaction coordinate, such as strengthening back-donation or diminishing Pauli repulsion (both play a role in situations of advanced C–H stretch and short metal-substrate distances).[12] Such a situation leads consistently to a stabilization and a shift of the TS "to the left", as is illustrated by the generic activation strain diagram in Fig. 10*b*.

Activation strain analyses of M + H_3C – X

There is a striking contrast between the systematic effect that the step from palladium to the metal cations has on the *position* of the TS along the reaction coordinate (nearly always a shift towards the product side) and the seemingly chaotic behavior of the *energy* of the TS, i.e., the overall reaction barrier, which in some cases is reduced whereas in other cases it goes up (see Table 1 and Fig. 8*a*). This is so, not only for OxIn reactions with the C–H bond but also for the other C–X bonds. Only the insertion of Au^+ into the C–C bond has a TS at a similar (in fact, a slightly smaller) elongation of the activated bond compared with the insertion of Pd (see Fig. 8*a*, C–C).

Seemingly chaotic, this behavior has a simple cause that can be easily recognized in terms of the activation strain model. Thus, the stabilization of the interaction curve $\Delta E_{int}(\zeta)$ at the reactant side also causes the net energy curve $\Delta E(\zeta)$ (the reaction profile) to be stabilized at that early stage of the reaction. But, because of the concomitant shift of the TS to the right, the latter occurs at a point at which the strain $\Delta E_{strain}(\zeta)$ is higher. If the shift of the TS to the right is not too pronounced (i.e., if the interaction curve does not become too shallow), the TS occurs at a point at which the additional stabilization of the interaction curve at the reactant side still outweighs the "shift-induced" increase in strain. Such a situation leads to a reduction of the barrier height as observed, for example, for the reactions of $Cu^+ + CH_4$ and C_2H_6. This is the situation that is schematically illustrated by the idealized activation strain diagram in Fig. 10*a*.

However, the shift of the TS to the right can also become so pronounced (i.e., if the interaction curve does become very shallow) that the TS, in a sense, merges into the product, which makes both of them disappear as stable stationary points. Such a situation leads to a high effective barrier, as observed for example, for the reactions of $Ag^+ + CH_4$ and CH_3Cl (see Fig. 8*b*, Ag^+). This situation is schematically illustrated by the idealized activation strain diagram in Fig. 10*c*.

Finally, we return to the strain curves which, as we already noticed, vary much less than the interaction curves if one changes the metal species (see Fig. 8*a*). This is because the dominant factor that determines the strain curves is the strength of the activated C–X bond. Nevertheless, the metal species also has a certain indirect, more subtle effect on the precise shape of the strain curve, as the exact geometrical deformation of the substrate depends also on the metal–substrate interaction. We wish to point out the two most prominent effects: (*i*) methyl-group tilting and (*ii*) methyl-group pyramidalization. The methyl groups, in particular in ethane, have to tilt away to make room for the approaching Pd atom, as discussed earlier (sub-section on activation strain analyses of reactions with Pd). This causes the C–C strain curve to be higher than one would expect on the basis of the C–C bond strength, namely, always close to the strain curve of the stronger C–H bond. This phenomenon is encountered also for the metal cations Cu^+, Ag^+, and Au^+, as can be seen in Fig. 8*b*.

Furthermore, as the metal cations are poor back-donation agents (vide supra), their OxIn reactions proceed with reduced charge transfer to the substrate compared with the reactions of palladium. In particular in the reactions with CH_3F and CH_3Cl, in which most of the back-donated charge goes into the halogen, this leads to methyl moieties with lower effective electron populations and thus less pyramidalization.[23] For example, the H-C-H angle in the OxIn product of M + CH_3F increases from 112.7° for Pd (see **3c** in Fig. 2) to 117.3°, 118.6°, and 116.2° for Cu^+, Ag^+, and Au^+ (see **7c**, **11c**, and **15c** in Figs. 3, 4, and 5, respectively). The relatively planar configuration of the methyl moieties in the reactions of the metal cations resembles more closely the intrinsic behavior of dissociating CH_3X. Furthermore, the partially positively charged methyl moiety tends to orient somewhat more towards the partially negatively charged

Fig. 10. Generic activation strain diagrams for qualitatively illustrating the effect on the black OxIn reaction profile ΔE of (*a*) stabilizing the ΔE_{int} curve at the reactant side, blue curves; (*b*) stabilizing the ΔE_{int} curve at the product side, green curves; (*c*) stabilizing the ΔE_{int} curve at the reactant side and destabilizing it at the product side, red curves. In (*d*) the four situations are combined, with black curves for the reference situation. Note that the ΔE_{strain} curves are identical in *a*–*d*, corresponding to a variation of the metal species inserting into one and the same model substrate.

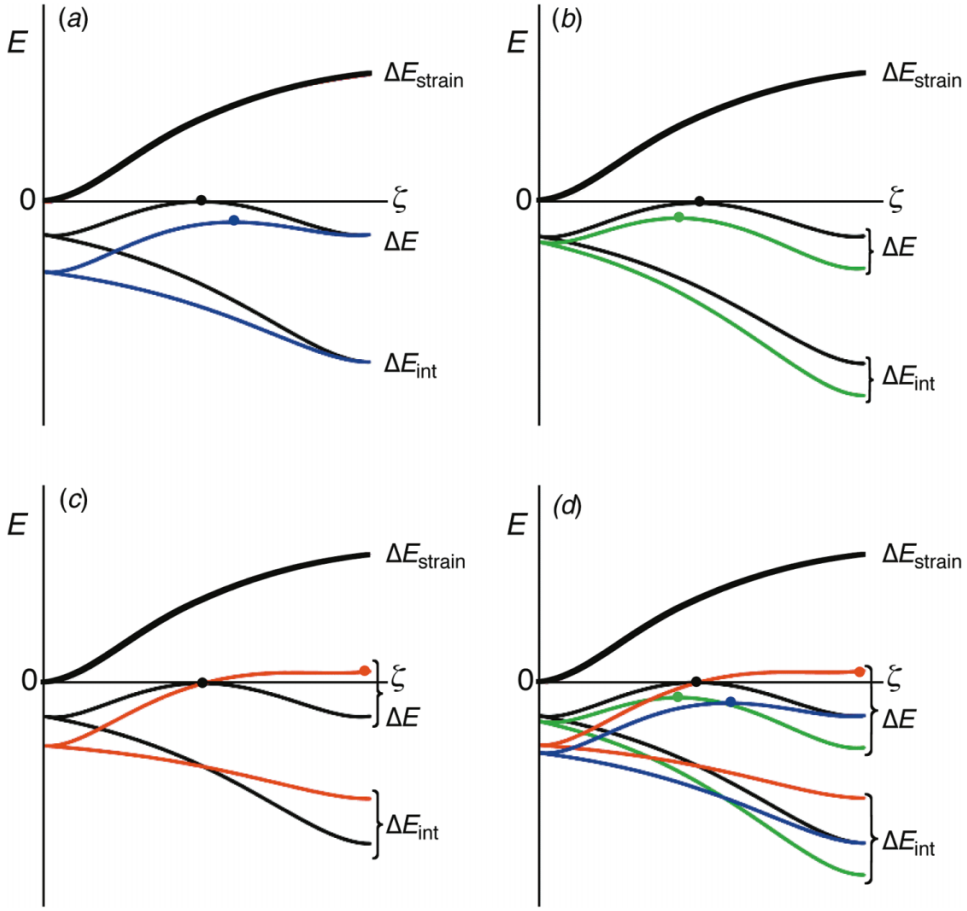

halogen, which corresponds to less tilting (compare Figs. 2–5). Together, these effects translate into a lowering of the corresponding strain curves for the reactions of the metal cations with fluoromethane and chloromethane compared with those with palladium (see Fig. 8*a*, C–F and C–Cl).

Conclusions

We have computationally explored C–X bond activation by the group-11 transition-metal cations Cu^+, Ag^+, and Au^+, and, for comparison, Pd, using relativistic density functional theory (DFT) at ZORA-BLYP/TZ2P. The main trends in reactivity are rationalized using the activation strain model in which the shape of the reaction profile $\Delta E(\zeta)$ and the height of the overall reaction barrier $\Delta E^{\neq} = \Delta E(\zeta{=}\zeta^{TS})$ is interpreted in terms of the strain energy $\Delta E_{strain}(\zeta)$ associated with deforming the reactants along the reaction coordinate ζ plus the interaction energy $\Delta E_{int}(\zeta)$ between these deformed reactants: $\Delta E(\zeta) = \Delta E_{strain}(\zeta) + \Delta E_{int}(\zeta)$.[12,16]

Oxidative insertion of the second-row transition-metal species Ag^+ and Pd leads, for a given bond, to the highest overall reaction barriers. On the other hand, if we compare the different bonds, oxidative insertion into the C–F bond is associated with (one of the) highest overall barriers, whereas insertion into the C–Cl bond leads for any transition metal to the lowest overall barrier.

It is tempting, but incorrect, to attribute the similar barrier heights for Ag^+ and Pd to a presumed similarity in the metal–substrate interaction of these isolelectronic second-row transition metal species. In fact, the difference in net charge translates into completely different bonding capabilities of the three metal cations on one hand and the neutral palladium on the other hand. The former have more shallow interaction curves (because of favorable substrate → metal ns donation in early stages of the reaction and reduced metal → substrate back-donation from the (n – 1)d AOs at later stages of the reaction), which causes the transition state (TS) to shift towards the product side where the strain curves are more destabilizing. The final position along the reaction coordinate depends in a subtle manner on the shape and balance between $\Delta E_{strain}(\zeta)$ and $\Delta E_{int}(\zeta)$ and may yield a stabilized (Cu^+, Au^+) but also a destabilized TS, as in the case of Ag^+. On the other hand, the low barrier for C–Cl activation originates straightforwardly from the low bond strength of this bond and thus the low strain curves along the reaction coordinate.

The above insights can, in principle, be used to more rationally design catalytically active and selective metal complexes, for example, by amplifying or attenuating the metal–substrate interaction in an early or late stage along the reaction coordinate. However, we stress once more that the precise point of balance between strain and interaction curves depends delicately on their exact shape. A quantitative verification of the activity of such a qualitatively designed catalyst is therefore still required.

Acknowledgements

We thank the Nederlandse Organisatie voor Wetenschappelijk Onderzoek (NWO-CW and NWO-NCF) for financial support.

References

(1) This article is part of a Special Issue dedicated to Professor T. Ziegler.

(2) (a) Collman, J. P.; Hegedus, L. S.; Norton, J. R.; Finke, R. G. *Principles and applications of organotransition metal chemistry*; University Science Books: Mill Valley, Calif., USA, 1987; (b) Elschenbroich, C. *Organometallics*; Wiley-VCH: Weinheim, Germany, 2006.

(3) (a) Grushin, V. V.; Alper, H. *Chem. Rev.* **1994**, *94*, 1047 doi:10.1021/cr00028a008.; (b) Amatore, C.; Jutand, A. *Acc. Chem. Res.* **2000**, *33*, 314 doi:10.1021/ar980063a. PMID: 10813876.; (c) Tsuji, J. *Palladium reagents and catalysts*; Wiley: Chichester, NY, USA, 1995.

(4) Luh, T.-Y.; Leung, M.-k.; Wong, K. T. *Chem. Rev.* **2000**, *100*, 3187. doi:10.1021/cr990272o. PMID:11749317.

(5) (a) Ritter, D.; Weisshaar, J. C. *J. Am. Chem. Soc.* **1990**, *112*, 6425 doi:10.1021/ja00173a056.; (b) Fayet, P.; Kaldor, A.; Cox, D. M. *J. Chem. Phys.* **1990**, *92*, 254 doi:10.1063/1.458472.; (c) Carroll, J. J.; Weisshaar, J. C. *J. Am. Chem. Soc.* **1993**, *115*, 800 doi:10.1021/ja00055a068.; (d) Casado, A. L.; Espinet, P. *Organometallics*, **1998**, *17*, 954 doi:10.1021/om9709502.; (e) Stürmer, R. *Angew. Chem.* **1999**, *111*, 3509 doi:10.1002/(SICI)1521-3757(19991115)111:22<3509::AID-ANGE3509>3.0.CO;2-A.; (f) Hinrichs, R. Z.; Schroden, J. J.; Davis, H. F. *J. Am. Chem. Soc.* **2003**, *125*, 860 doi:10.1021/ja0278842. PMID:12537471.; (g) de Pater, B. C.; Zijp, E. J.; Frühauf, H.-W.; Ernsting, J. M.; Elsevier, C. J.; Vrieze, K. *Organometallics* **2004**, *23*, 269 doi:10.1021/om0305418.; (h) Espinet, P.; Echavarren, A. *Angew. Chem.* **2004**, *116*, 4808; (i) Wang, G.; Chen, M.; Zhou, M. *Chem. Phys. Lett.* **2005**, *412*, 46 doi:10.1016/j.cplett.2005.05.115.; (j) Lersch, M.; Tilset, M. *Chem. Rev.* **2005**, *105*, 2471. doi:10.1021/cr030710y. PMID:15941220.

(6) (a) Weisshaar, J. C. *Acc. Chem. Res.* **1993**, *26*, 213 doi:10.1021/ar00028a012.; (b) Carroll, J. J.; Haug, K. L.; Weisshaar, J. C.; Blomberg, M. R. A.; Siegbahn, P. E. M.; Svensson, M. *J. Phys. Chem.* **1995**, *99*, 13955 doi:10.1021/j100038a030.; (c) Porembski, M.; Weisshaar, J. C. *J. Phys. Chem. A*, **2000**, *104*, 1524 doi:10.1021/jp993082q.; (d) Haynes, A.; Maitlis, P. M.; Morris, G. E.; Sunley, G. J.; Adams, H.; Badger, P. W.; Bowers, C. M.; Cook, D. B.; Elliott, P. I. P.; Ghaffar, T.; Green, H.; Griffin, T. R.; Payne, M.; Pearson, J. M.; Taylor, M. J.; Vickers, P. W.; Watt, R. J. *J. Am. Chem. Soc.* **2004**, *126*, 2847. doi:10.1021/ja039464y. PMID:14995202.

(7) (a) Siegbahn, P. E. M.; Blomberg, M. R. A.; Svensson, M. *J. Am. Chem. Soc.* **1993**, *115*, 1952 doi:10.1021/ja00058a048.; (b) Bickelhaupt, F. M.; Ziegler, T.; Schleyer, P. v. R. *Organometallics*, **1995**, *14*, 2288 doi:10.1021/om00005a030.; (c) Griffin, T. R.; Cook, D. B.; Haynes, A.; Pearson, J. M.; Monti, D.; Morris, G. E. *J. Am. Chem. Soc.* **1996**, *118*, 3029 doi:10.1021/ja952952o.; (d) Siegbahn, P. E. M. *J. Am. Chem. Soc.* **1996**, *118*, 1487 doi:10.1021/ja952338c.; (e) Wittborn, A. M. C.; Costas, M.; Blomberg, M. R. A.; Siegbahn, P. E. M. *J. Chem. Phys.* **1997**, *107*, 4318 doi:10.1063/1.474772.; (f) Cui, Q.; Musaev, D. G.; Morokuma, K. *J. Chem. Phys.* **1998**, *108*, 8418 doi:10.1063/1.476269.; (g) Torrent, M.; Solà, M.; Frenking, G. *Chem. Rev.* **2000**, *100*, 439 doi:10.1021/cr980452i. PMID:11749243.; (h) Senn, H. M.; Ziegler, T. *Organometallics*, **2004**, *23*, 2980 doi:10.1021/om049963n.; (i) Gooβen, L. J.; Koley, D.; Hermann, H.; Thiel, W. *Chem. Commun. (Cambridge, UK)* **2004**, 2141. PMID:15467842.; (j) Kozuch, S.; Shaik, S.; Jutand, A.; Amatore, C. *Chem. Eur. J.* **2004**, *10*, 3072 doi:10.1002/chem.200306056.; (k) Diefenbach, A.; Bickelhaupt, F. M. *J. Phys. Chem. A*, **2004**, *108*, 8460 doi:10.1021/jp047986+.; (l) Diefenbach, A.; Bickelhaupt, F. M. *J. Organomet. Chem.* **2005**, *690*, 2191 doi:10.1016/j.jorganchem.2005.02.013.; (m) de Jong, G. Th.; Kovács, A.; Bickelhaupt, F. M. *J. Phys. Chem. A,* **2006**, *110*, 7943. doi:10.1021/jp061501v. PMID:16789784.

(8) (a) Diefenbach, A.; Bickelhaupt, F. M. *J. Chem. Phys.* **2001**, *115*, 4030 doi:10.1063/1.1388040.; (b) Diefenbach, A.; de Jong, G. Th.; Bickelhaupt, F. M. *Mol. Phys.* **2005**, *103*, 995 doi:10.1080/00268970412331333546.; (c) Diefenbach, A.; de Jong, G. Th.; Bickelhaupt, F. M. *J. Chem. Theory Comput.* **2005**, *1*, 286. doi:10.1021/ct0499478.

(9) de Jong, G. Th.; Solà, M.; Visscher, L.; Bickelhaupt, F. M. *J. Chem. Phys.* **2004**, *121*, 9982. doi:10.1063/1.1792151. PMID:15549873.

(10) (a) de Jong, G. Th.; Geerke, D. P.; Diefenbach, A.; Bickelhaupt, F. M. *Chem. Phys.* **2005**, *313*, 261 doi:10.1016/j.chemphys.2005.01.017.; (b) de Jong, G. Th.; Geerke, D. P.; Diefenbach, A.; Solà, M.; Bickelhaupt, F. M. *J. Comput. Chem.* **2005**, *26*, 1006 doi:10.1002/jcc.20233. PMID:15880815.; (c) de Jong, G. Th.; Bickelhaupt, F. M. *J. Phys. Chem. A,* **2005**, *109*, 9685 doi:10.1021/jp053587i. PMID:16866421.; (d) de Jong, G. Th.; Bickelhaupt, F. M. *J. Chem. Theory Comput.* **2006**, *2*, 322. doi:10.1021/ct050254g.

(11) de Jong, G. Th.; Visser, R.; Bickelhaupt, F. M. *J. Organomet. Chem.* **2006**, *691*, 4341. doi:10.1016/j.jorganchem.2006.03.006.

(12) de Jong, G. Th.; Bickelhaupt, F. M. *Chem. Phys. Chem.* **2007**, *8*, 1170. doi:10.1002/cphc.200700092. PMID:17469091.

(13) (a) Smith, M. B.; March, J. *March's advanced organic chemistry: Reactions, mechanisms, and structure*; Wiley: New York, USA, 2007; (b) Dedieu, A. *Chem. Rev.* **2000**, *100*, 543 doi:10.1021/cr980407a. PMID:11749245.; (c) Nicolaou, K. C.; Bulger, P. G.; Sarlah, D. *Angew. Chem.* **2005**, *117*, 4516. doi:10.1002/ange.200500368.

(14) Frisch, A. C.; Beller, M. *Angew. Chem.* **2005**, *117*, 680. doi:10.1002/ange.200461432.

(15) (a) See, for example: Eller, K.; Schwarz, H. *Chem. Rev.* **1991**, *91*, 1121 doi:10.1021/cr00006a002.; (b) Weisshaar, J. C. *Acc. Chem. Res.* **1993**, *26*, 213 doi:10.1021/ar00028a012.; (c) *Organometallic ion Chemistry*; Freiser, B. S., Ed.; Kluwer Academic Publishers: Dordrecht, Netherlands, 1996; (d) Wei, C.; Li, C. J. *J. Am. Chem. Soc.* **2003**, *125*, 9584 doi:10.1021/ja0359299. PMID:12904013.; (e) De Vos, D. E.; Sels, B. F. *Angew. Chem.* **2005**, *117*, 30 doi:10.1002/ange.200461561.; (f) Hashmi, A. S. K. *Angew.*

Chem. **2005**, *117*, 7150 doi:10.1002/ange.200502735.; (g) Böhme, D. K.; Schwarz, H. *Angew. Chem. Int. Ed.* **2005**, *44*, 2336 doi:10.1002/anie.200461698.; (h) Mazurek, U.; Schwarz, H. *Chem. Commun. (Cambridge, UK),* **2003**, 1321. doi:10.1039/b211850e. PMID:12841225.

(16) (a) For early work on the activation strain model, see: Bickelhaupt, F. M. *J. Comput. Chem.* **1999**, *20*, 114 doi:10.1002/(SICI)1096-987X(19990115)20:1<114::AID-JCC12>3.0.CO;2-L.; (b) Bickelhaupt, F. M.; Nibbering, N. M. M.; Baerends, E. J.; Ziegler, T. *J. Am. Chem. Soc.* **1993**, *115*, 9160 doi:10.1021/ja00073a035.; (c) Other studies in which the reactant strain or distortion energy have been separated from the interaction energy for understanding chemical reactions are, for example: Mitchell, D. J.; Schlegel, H. B.; Shaik, S. S.; Wolfe, S. *Can. J. Chem.* **1985**, *63*, 1642 doi:10.1139/v85-276.; (d) Legault, C. Y.; Garcia, Y.; Merlic, C. A.; Houk, K. N. *J. Am. Chem. Soc.* **2007**, *129*, 12664. doi:10.1021/ja075785o. PMID:17914827.

(17) (a) Hohenberg, P.; Kohn, W. *Phys. Rev.* **1964**, *136*, B864 doi:10.1103/PhysRev.136.B864.; (b) Kohn, W.; Sham, L. J. *Phys. Rev.* **1965**, *140*, A1133(c) Parr, R. G.; Yang, W. *Density-functional theory of atoms and molecules*; Oxford University Press: New York, USA, 1989.

(18) (a) Baerends, E. J.; Ellis, D. E.; Ros, P. *Chem. Phys.* **1973**, *2*, 41 doi:10.1016/0301-0104(73)80059-X.; (b) te Velde, G.; Bickelhaupt, F. M.; Baerends, E. J.; Fonseca Guerra, C.; van Gisbergen, S. J. A.; Snijders, J. G.; Ziegler, T. *J. Comput. Chem.* **2001**, *22*, 931 doi:10.1002/jcc.1056.; (c) Baerends, E. J.; Autschbach, J.; Berces, A.; Bo, C.; Boerrigter, P. M.; Cavallo, L.; Chong, D. P.; Deng, L.; Dickson, R. M.; Ellis, D. E.; van Faassen, M.; Fan, L.; Fischer, T. H.; Fonseca Guerra, C.; van Gisbergen, S. J. A.; Groeneveld, J. A.; Gritsenko, O. V.; Grüning, M.; Harris, F. E.; van den Hoek, P.; Jacobsen, H.; Jensen, L.; van Kessel, G.; Kootstra, F.; van Lenthe, E.; McCormack, D. A.; Michalak, A.; Osinga, V. P.; Patchkovskii, S.; Philipsen, P. H. T.; Post, D.; Pye, C. C.; Ravenek, W.; Ros, P.; Schipper, P. R. T.; Schreckenbach, G.; Snijders, J. G.; Sola, M.; Swart, M.; Swerhone, D.; te Velde, G.; Vernooijs, P.; Versluis, L.; Visser, O.; Wang, F.; van Wezenbeek, E.; Wiesenekker, G.; Wolff, S. K.; Woo, T. K.; Yakovlev, A. L.; Ziegler, T. *Computer code ADF2005.01. SCM, Theoretical Chemistry*; Vrije Universiteit: Amsterdam, The Netherlands, 2005.

(19) (a) Ziegler, T.; Rauk, A. *Theor. Chim. Acta*, **1977**, *46*, 1; (b) Ziegler, T.; Rauk, A. *Inorg. Chem.* **1979**, *18*, 1558 doi:10.1021/ic50196a034.; (c) Ziegler, T.; Rauk, A. *Inorg. Chem.* **1979**, *18*, 1755. doi:10.1021/ic50197a006.

(20) (a) Becke, A. D. *Phys. Rev. A,* **1988**, *38*, 3098 doi:10.1103/PhysRevA.38.3098. PMID:9900728.; (b) Lee, C.; Yang, W.; Parr, R. G. *Phys. Rev. B,* **1988**, *37*, 785. doi:10.1103/PhysRevB.37.785.

(21) van Lenthe, E.; Baerends, E. J.; Snijders, J. G. *J. Chem. Phys.* **1994**, *101*, 9783. doi:10.1063/1.467943.

(22) Deng, L.; Ziegler, T.; Fan, L. *J. Chem. Phys.* **1993**, *99*, 3823. doi:10.1063/1.466129.

(23) Pierrefixe, S. C. A. H.; Poater, J.; Im, C.; Bickelhaupt, F. M. *Chem. Eur. J.* **2008**, *14*, 6901. doi:10.1002/chem.200800013.

Structure and stability of aquotetrafluorouranyl(VI) in the solid state — Density functional study of $[UO_2F_4(H_2O)][NMe_4]_2 \cdot 2H_2O$[1,2]

Michael Bühl

Abstract: Periodic density functional computations have been performed for solid $[UO_2F_4(H_2O)][NMe_4]_2 \cdot 2H_2O$ at the BLYP level. A model with disordered fluoro and aquo ligands in the uranyl anion is significantly lower in energy than one with a symmetrical assignment of these sites, which was favored in the original X-ray crystallography study. According to optimized energies and Car–Parrinello molecular dynamics (CPMD) simulations, the $[UO_2F_4(H_2O)]^{2-}$ ion in the solid is stable with respect to loss of the coordinated water molecule. In contrast, CPMD simulations had found this ligand to be unbound in aqueous solution. The role of the counterions in stabilizing the higher coordination number in the crystal is discussed.

Key words: uranyl complexes, density functional computations, molecular dynamics, simulations, counterion effects.

Résumé : Opérant au niveau BLYP, on a effectué des calculs de fonctionnelle de la densité périodique sur le solide $[UO_2F_4(H_2O)][NMe_4] \cdot 2H_2O$. L'énergie d'un modèle comportant des ligands fluoro et aquo dans l'anion uranyle est beaucoup plus faible que celle d'un modèle comportant une attribution symétrique de ces sites qui était favorisé dans l'étude originale par diffraction des rayons X. Sur la base d'énergies optimisées et de simulations de dynamique moléculaire Car-Parrinello (DMPC), l'ion $[UO_2F_4(H_2O)]^{2-}$ à l'état solide est stable par rapport à la perte de la molécule d'eau coordonnée. Par opposition, des simulations DMPC avaient suggéré que ce ligand se détache en solution aqueuse. On discute le rôle des contre-ions dans la stabilisation du nombre de coordination plus élevé dans le cristal.

Mots-clés : complexes d'uranyle, calculs de la fonctionnelle de densité, dynamique moléculaire, simulations, effets des contre-ions.

[Traduit par la Rédaction]

Introduction

Approximate density functional theory (DFT) has fertilized computational transition-metal chemistry tremendously,[3] especially since relativistic methods have been implemented that allow the proper treatment of heavy metals.[4] Complexes of the heaviest metals, actinides, have been early challenging targets for DFT[5,6] and are important benchmarks for calculations of spectroscopic properties such as NMR parameters.[7] DFT-based molecular dynamics simulations, long established as powerful tools to study elementary reaction steps at transition-metal centers,[8,9] are now also being applied to actinide chemistry.[10–13]

We have been applying Car–Parrinello molecular dynamics (CPMD) simulations to study structure,[11,12] speciation,[14] reactivities,[15] and NMR chemical shifts of uranyl(VI) complexes in aqueous solution. A protocol based on constrained CPMD and pointwise thermodynamic integration (PTI) has been shown to capture salient structural and energetic features reasonably well. With the possibility of evaluating changes in free energies under realistic conditions (i.e., taking temperature and solvation effects explicitly into account), this approach often surpasses static quantum-chemical computations with simpler solvation models. For instance, the acidity constant[16] and ligand-exchange barrier[15] in uranyl hydrate, $[UO_2(H_2O)_5]^{2+}$, as well as the free binding energies between the latter and ligands such as nitrate,[14] chloride,[17] and fluoride[18] have all been reproduced within ca. ±2.5 kcal/mol (1 cal = 4.184 J) of experiment, a rather respectable accuracy for present-day DFT.

In our recent study on mixed aquo fluoro uranyl species,[18] an apparent inconsistency between DFT and experiment was noted for the tetrafluoro complex. In two salts with organic counterions, this anion had been characterized as $[UO_2F_4(H_2O)]^{2-}$ (**1a**) by X-ray crystallography,[19,20] and evidence for its presence in aqueous solution had been given by EXAFS.[21] In CPMD simulations of pristine **1a**, in contrast, the water ligand turned out to be unbound both in gaseous and aqueous phases, where it spontaneously detaches, affording four-coordinate $[UO_2F_4]^{2-}$ (**1b**).[18] Employing the PTI technique and the U–O(water) distance as reaction coordinate, a shallow minimum corresponding to **1a** was found in water, but the driving force for dissociation of the aqua ligand from **1a** into the bulk was indicated to be substantial, $\Delta A = -7.2 \pm 1.5$ kcal/mol (1 cal = 4.184 J). Even when allowing for the general tendency of DFT to underestimate metal–ligand bond strengths,[22,23] this result appeared to be at odds with the observation of **1a** in the EXAFS experiment. No experimental value for this dissociation energy is

Received 31 October 2008. Accepted 21 November 2008. Published on the NRC Research Press Web site at canjchem.nrc.ca on 7 March 2009.

M. Bühl. School of Chemistry, North Haugh, University of St. Andrews, St. Andrews, KY16 9ST Fife, UK (e-mail: buehl@st-andrews.ac.uk).

known, but the EXAFS data furnished strong evidence for the presence of two shells in the equatorial plane of the tetrafluoride, corresponding to F and O atoms. Because it was difficult to refine the precise number of coordinated water ligands, in the adopted model this number was fixed to one (as observed in the solid),[21] implying rather strong binding of water (with a positive free energy for dissociation, and, possibly, zero as its lower limit[24]).

The BLYP density functional was used in the simulations. Rather well suited to describing the properties of liquid water and aqueous solutions,[25,26] it is not the first choice for geometries of transition-metal complexes in general.[27] BLYP is a typical member of the GGA family, i.e., pure, gradient-corrected functionals, which are sometimes outperformed by hybrid variants when it comes to reaction energies involving actinides.[28] As mentioned above, in the CPMD–PTI studies of aqueous uranyl complexes BLYP has performed quite well so far, but if it turns out to fail for the aquo tetrafluoro complex, the predictive power of this approach may be at stake. An utter failure would for instance be the incorrect prediction that **1a** should also be unstable in the environment of a known, stable crystal. In the present paper, initial investigations to that effect are reported, including, to the best of my knowledge, the first CPMD simulations of a uranyl complex in the solid state.

Of the two solids containing **1a**, $[UO_2F_4(H_2O)][NMe_4]_2{\cdot}2H_2O$ (**2**)[20] was chosen as the target, because it has the smaller unit cell. In addition, an ambiguity in the assignment of the atomic positions had been noted during analysis of the crystal structure, which will be addressed as well.

Computational details

All computations used the CPMD program[29] and the same settings as in the previous gas-phase and solution studies (BLYP functional,[30,31] Troullier–Martins pseudopotentials,[32,33] 80Ry plane-wave cutoff). The heavy-atom coordinates as deposited in the Cambridge Structure Database (refcode DAPWUM)[20] were used as the starting point. A simple orthorhombic cell with lattice constants fixed to the experimental values (a = 7.006 Å, b = 8.938 Å, c = 13.619 Å) and two formula units in the unit cell were used (affording a total of 100 atoms). Unfortunately, the current version of the CPMD program does not allow optimization of lattice constants for systems containing f-electrons. Hydrogen atoms were placed on the water oxygen atoms (pointing toward potential H-bond acceptors, but otherwise arbitrarily) and their positions relaxed both at the Γ-point and using 2, 2, and 1 k-points along the reciprocal a, b, and c axes, respectively.[34] Attempts to use more k-points resulted in severe convergence problems or, where wave functions could be converged, in relatively minor changes in total energies. Unless otherwise noted, results from the 2 × 2 × 1 k-point calculations are discussed in the following section. CPMD simulations were performed at the Γ-point, however (see discussion below), using a fictitious electronic mass of 600 au, a time step of 0.121 fs, and the deuterium mass for H atoms. Starting from the Γ-point optimized coordinates, the system was equilibrated for 0.5 ps, during which a temperature of 320 ± 50 K was maintained via velocity rescaling, and then propagated for 3 ps without constraints in the NVE ensemble. For population analysis, the orbitals represented in plane waves were projected onto suitable atomic orbitals, which were taken from the pseudo wave functions involved in construction of the pseudopotentials, except for hydrogen where a standard Slater function was used.[35]

Results and discussion

In the refinements of the X-ray data of **2**, an ambiguity concerning the location of F and O atoms was noted, and the simplest model had been adopted (denoted Model 1 here), in which an O atom of the coordinated water ligand (O2 in Fig. 1) resides on a symmetry plane.[20] Because the resulting U–O2 distance would be exceptionally short, however, this assignment was later questioned[21] and it was suggested that this O2 position would rather be occupied by an F atom, and that the O atom would be disordered over the F1 and F1^a sites, a possibility that was already mentioned in the X-ray study. This alternative assignment would be more consistent with the rather long bond distances between uranium and the F1 and F1^a sites. A corresponding model (denoted Model 2) was constructed by exchanging F and O in the F1^a and O2 sites in both uranyl moieties of the unit cell.

After relaxation of the H positions, Model 2 is lower in energy than Model 1 by ca. 125 kcal/mol; after full optimization (with fixed lattice constants), it is still favored by 13.4 kcal/mol. This result is thus in complete accord with the suggested revision of the atomic positions in the crystal and the concomitant disorder.[36]

In the following, only results for Model 2 will be discussed. Figure 2 shows perspective drawings of solid **2** after H-relaxation (top) and full optimization (bottom). To illustrate the packing more clearly, 8-fold unit cells with doubled lattice constants are displayed. The most notable change upon full optimization is that the O atoms of the two crystal water molecules move somewhat above and below the equatorial uranyl plane (which is a plane of symmetry in the point group of the crystal), and that the uranyl fluoride moieties rotate somewhat about the O=U=O axis. This can be seen in Fig. 3, an overlay of X-ray and optimized coordinates (both sets of coordinates are supplied in the Supplementary data for 3D visualization).

These changes could to some extent be due to the initial choice of the location of the H atoms, which would induce a bias for a particular H-bond pattern. An exhaustive search of all possible such patterns would be very involved and was not conducted at this point. It is rather noted that the overall features of the observed solid-state structure are reasonably well preserved in the DFT-optimized crystal, in particular if one allows for disorder in the former. Observed and correspondingly averaged computed bond distances are found to be in good accord, except for the U–F(O2) distance, the experimental value of which appears to be rather short also for an U–F bond (compare Expt. and CP-opt values in italics in Table 1).

In CPMD simulations of a single $[UO_2F_4(H_2O)]^{2-}$ anion, both in gaseous and aqueous phases, the water ligand has detached spontaneously from the complex.[18] To test if the same would happen in the crystal, CPMD simulations were performed for solid **2**. Unfortunately, CPMD simulations are not possible using k-point integration. The usual procedure

Fig. 1. Labeling of atoms in the original X-ray crystallography study (reference [20]; W denotes O atoms of crystal water).

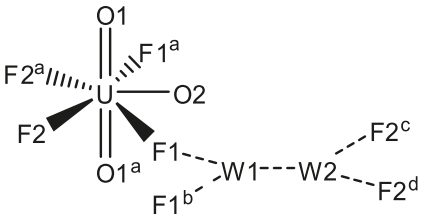

Fig. 2. Stereoviews of the solid after H-relaxation (top) and full optimization (bottom), showing 8 unit cells (over doubled lattice parameters).

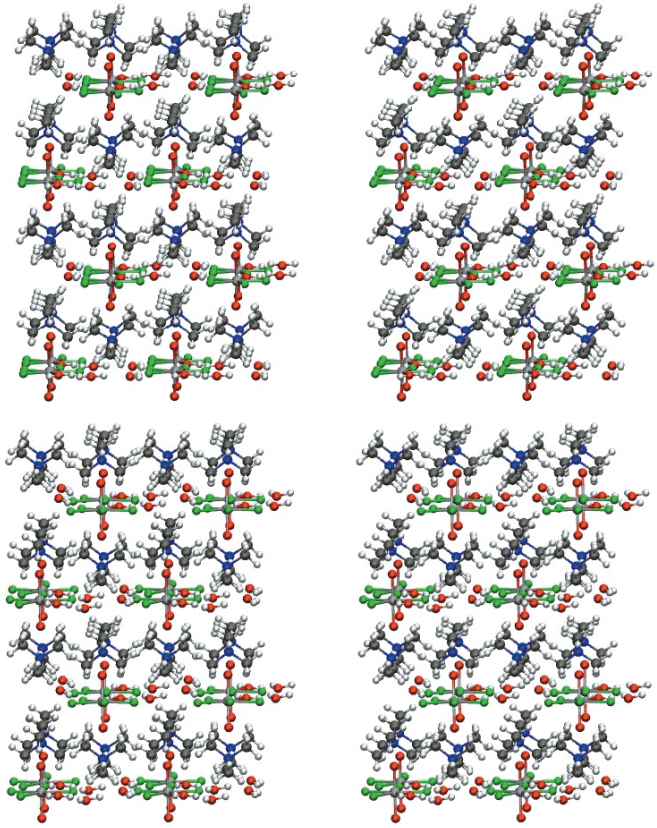

is to use supercells large enough that calculations at the Γ-point are sufficient. In the present case, this would mean that the lattice constants *a* and *b* would have to be doubled, which would render the simulations rather expensive. On the other hand, the structural parameters of the uranyl complex are very similar whether the solid is optimized using k-points or at the Γ-point only (compare CP-opt and Γ-opt entries in Table 1). It is thus to be expected that the artifacts of just using the Γ-point would not be too severe. In fact, if anything, neglect of the k-points appears to weaken the U–O(water) interaction, as evidenced by the increase of the U–O(F1[a]) distance on going from the CP-opt to the Γ-opt value (by 0.02 Å, Table 1). CPMD simulations were therefore performed at the Γ-point for the regular unit cell, bearing in mind that this procedure might artificially weaken the binding of the water ligands. Nonetheless, the five-coordinated uranyl complexes remain stable during a total simulation time of 3.5 ps (including equilibration) at a mean temperature of 314 K. Except for the U–O(water) distance, which increases noticeably by 0.04 Å, only minor changes are found on going from equilibrium to thermal-averaged bond distances (compare Γ-opt and CPMD values in Table 1).

Table 1. Observed and simulated uranium-ligand distances in the uranyl aquo fluoro anion **1a** [in Å]. For labeling see Fig. S1, with F(O2) and O(F1[a]) indicating the atoms that have been switched in model 2.

Bond	Expt.[a]	CP-opt	Γ-opt[b]	CPMD[b,c]
U–O(F1[a])	—	2.52	2.54	2.58(10)
U–F1	—	2.26	2.26	2.27(9)
mean	*2.39(1)*	*2.39*	*2.40*	*2.42(10)*
U–F(O2)	*2.11(2)*	*2.28*	*2.28*	*2.28(8)*
U–F2	—	2.28	2.28	2.27(7)
U–F2[a]	—	2.29	2.29	2.29(7)
mean	*2.28(1)*	*2.29*	*2.29*	*2.28(7)*

Note: Note: Figures in italics give theaverage of the denoted bonds assuming disorder of the O atom over F1 and F1[a] sites (see text).

[a]From ref. [20].

[b]Using Γ-point integration only (see Computational details).

[c]Mean values (in parentheses: standard deviations) over 3 ps of unconstrained MD.

Of course, the apparent stability of five-coordination in the solid during the CPMD simulations might just be caused by the confines of the fixed unit cell. To estimate how strongly the aquo ligand would be bound in the solid, a coordinated water molecule was removed from one of the optimized uranyl complexes in the unit cell (the other complex retaining five-coordination). The combined total energies of the fragments, i.e., that of the unit cell without one water and that of the water molecule in the same empty box, is 23.2 kcal/mol above that of the full, optimized solid (k-point results). Upon relaxation of these fragments, in the course of which the four-coordinated $[UO_2F_4]^{2-}$ moiety with its vacant coordination site optimizes to the usual approximately square-bipyramidal conformation of **1b**, this energy difference reduces to 7.9 kcal/mol. Thus, a substantial binding energy is indicated for the water ligand in the solid. Because the lattice constants were fixed throughout, this value is only to be used as a rough guide. It is quite possible that the "dehydrated" crystal would have a slightly smaller unit cell than the intact one or, more likely, that it would adopt a different, more stable morphology altogether. In particular, the latter question is impossible to address at present because the sheer size of the system precludes a true ab initio prediction of its crystal structure.

In any event, the estimated water dissociation energy of ca. +8 kcal/mol within the constraints of the solid is noteworthy, as it contrasts with the results obtained for free **1a** in the gas phase or in solution, where the water ligand is indicated to be unbound, with a computed dissociation energy of ca. –7 kcal/mol (ΔE at the BLYP/SDD(+)/PCM level or ΔA from constrained CPMD and PTI).[37] To shed more light on the possible reasons for the apparent stabilization of $[UO_2F_4(H_2O)]^{2-}$ in the solid,[38] a single such anion was retained in the fully optimized crystal and all other atoms deleted. The resulting slabs of $[UO_2F_4(H_2O)]^{2-}$ moieties approaching each other with their equatorial ligands are

Fig. 3. Overlay of X-ray derived (red) and optimized (blue) positions of the non-hydrogen atoms, viewed along the *a*-, *b*-, and *c*-axes (from left to right).

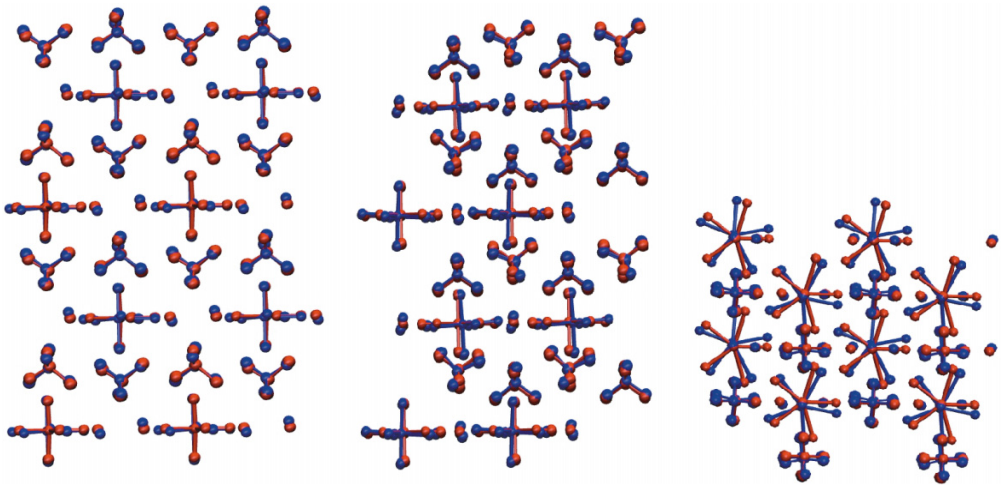

highly unphysical because of the strong Coulomb repulsion between them, but are an instructive model for comparison with the estimated water binding energy discussed above for the full crystal. When this "pristine" $[UO_2F_4(H_2O)]^{2-}$ moiety is further separated into $[UO_2F_4]^{2-}$ and H_2O fragments (again with the same unrelaxed structures in the otherwise empty cell), the combined energies of these fragments are 9.7 kcal/mol above that of the $[UO_2F_4(H_2O)]^{2-}$ slabs. When the fragments are relaxed, their combined energies drop below that of the complex (in its structure adopted in the full crystal), namely to –12.8 kcal/mol. In other words, it costs more energy (ca. 13 kcal/mol) to distort the separated fragments, **1b** and water, into the structures they adopt in the complex than is released upon binding between these distorted fragments (ca. –10 kcal/mol). Without the counterions (and the crystal water), the water ligand in **1a** is thus indicated to be unbound. Apparently, the interactions with the counterions are instrumental to the stability of **1a** in the solid, where each of these complexes is surrounded by eight NMe_4^+ ions (forming two "crowns" above and below the equatorial plane, see Fig. 2).

To assess the effect of this polar environment on the overall charge distribution, Mulliken population analysis was performed for the whole crystal and for the periodic $[UO_2F_4(H_2O)]^{2-}$ slabs cut out therefrom. The results are summarized in Table 2. While the absolute numbers should not be over-interpreted,[39] the general trend is interesting: When the neighbors around **1a** are removed, the overall charge density on the UO_2F_4 unit increases significantly, i.e., this fragment becomes more negative (by more than a fourth electronic charge unit, see last entry in Table 2). This additional negative charge is shared roughly equally between terminal oxo and equatorial fluoride ligands, but the U atom also becomes slightly less positive. Apparently, this increased negative charge makes the uranyl moiety less electrophilic toward the fifth water ligand, consistent with the computed drop in dissociation energy of the latter (from ca. 23 kcal/mol to 10 kcal/mol using the unrelaxed fragments, see above). Similarly, the Mayer bond orders between U and the water O atom decrease from 0.19 in the full crystal **2** to 0.15 in the slabs of **1a**.

Table 2. Mulliken charges in the uranyl aquo fluoro anion **1a**.

Atoms	Full crystal (**2**)	only **1a**[a]
U	2.32	2.29
$O(H_2O)$	–0.90	–0.90
F (mean)	–0.64	–0.67
O(uranyl)	–0.63	–0.69
$\Sigma\ UO_2F_4$[b]	–1.48	–1.75

Note: Note: At the Γ-point, CP-opt geometry for Model 2.

[a] $[UO_2F_4(H_2O)]^{2-}$ slabs from single **1a** unit retained in the unit cell (not relaxed).

[b] Total charge of this fragment.

Apparently, when pristine **1a** is immersed in water, the environment is not polar enough to increase the electrophilic character of the uranyl center to the same extent as the counterions do in the crystal. At this point it is tempting to speculate if counterions in solution, which were not included in the CPMD simulations so far, could be more efficient in that respect. In the EXAFS experiments, a considerable excess of NaF (ca. 9-fold) had been used to produce solutions that contain **1a** as major uranyl component.[21] It is possible that the notable concentration of Na^+ ions about **1a** in water (or the increased ionic strength) could result in an increased affinity between the tetrafluoro uranyl complex and the water ligand, which could eventually help to reconcile the apparent discrepancy between the DFT and EXAFS results. More work should be directed toward this question.

Conclusion

According to periodic DFT/BLYP computations for solid $[UO_2F_4(H_2O)][NMe_4]_2{\cdot}2H_2O$, a model with disordered fluoro and aquo ligands in the uranyl anion is significantly lower in energy than the originally adopted symmetrical assignment of these sites. This result supports the proposed revision of this structural detail that was based on a critical analysis of the refined bond distances. Thus, DFT computa-

tions akin to those presented here can be helpful in X-ray crystallography of uranyl complexes, when, as in the present case, competing structural models cannot be proved or disproved based on the diffraction data alone.

In these static model computations and in dynamic (CPMD) simulations, the water ligand in the $[UO_2F_4(H_2O)]^{2-}$ anion (**1a**) is indicated to be bound. There is no evidence that the DFT-based approach employed, including the BLYP functional, would fail utterly for **1a** in the sense that it would incorrectly predict an unbound water ligand in the solid state. This finding therefore does not invalidate our previous results for gaseous and aqueous phases, according to which the free tetrafluoride does not bind this fifth water ligand and should be formulated as four-coordinated $[UO_2F_4]^{2-}$ (**1b**), in apparent contrast to EXAFS experiments, which favor the formulation as five-coordinated **1a** in solution. Computational evidence has been presented suggesting that it is the crystal environment that stabilizes the higher coordination number in the solid. Studies are underway to explore if counterions in the aqueous solution, so far neglected in the simulations, could also increase the propensity of free **1b** to bind an additional water ligand, which would help to resolve the apparent discrepancy between theory and experiment on the structure of uranyl tetrafluoride in water.

Supplementary data

Supplementary data for this article are available on the journal Web site (canjchem.nrc.ca) or may be purchased from the Depository of Unpublished Data, Document Delivery, CISTI, National Research Council Canada, Ottawa, ON K1A 0R6, Canada. DUD 3881. For more information on obtaining material refer to cisti-icist.nrc-cnrc.gc.ca/cms/unpub_e.shtml.

Acknowledgments

M.B. wishes to thank EaStChem for support, H. Früchtl for technical assistance, and G. Wipff for helpful comments. Computations were performed on a local Opteron PC cluster.

References

(1) This article is part of a Special Issue dedicated to Professor T. Ziegler.
(2) Dedicated to Prof. Dr. Tom Ziegler on the occasion of his 65th birthday.
(3) Ziegler, T. *Chem. Rev.* **1991**, *91*, 651. doi:10.1021/cr00005a001.
(4) Ziegler, T. *Can. J. Chem.* **1995**, *73*, 743. doi:10.1139/v95-095.
(5) Wezenbeek, E. M.; Baerends, E. J.; Ziegler, T. *Inorg. Chem.* **1995**, *34*, 238. doi:10.1021/ic00105a039.
(6) Denning, R. G. J. *Phys. Chem. A* **2007**, *111*, 4125. doi:10.1021/jp071061n.
(7) Schreckenbach, G.; Wolff, S. K.; Ziegler, T. *J. Phys. Chem. A* **2000**, *104*, 8244. doi:10.1021/jp001143a.
(8) Woo, T. K.; Margl, P. M.; Lohrenz, J. C. W.; Blöchl, P. E.; Ziegler, T. *J. Am. Chem. Soc.* **1996**, *118*, 13021. doi:10.1021/ja962525q.
(9) De Angelis, F.; Fantacci, S.; Sgamellotti, A. *Coord. Chem. Rev.* **2006**, *250*, 1497. doi:10.1016/j.ccr.2006.02.008.
(10) Infante, I.; Visscher, L. J. *Comput. Chem.* **2003**, *25*, 386.
(11) Bühl, M.; Diss, R.; Wipff, G. *J. Am. Chem. Soc.* **2005**, *127*, 13506. doi:10.1021/ja054186j. PMID:16190708.
(12) Bühl, M.; Kabrede, H.; Diss, R.; Wipff, G. *J. Am. Chem. Soc.* **2006**, *128*, 6357. doi:10.1021/ja057301z. PMID:16683800.
(13) Nichols, P.; Bylaska, E. J.; Schenter, G. K.; de Jong, W. J. *Chem. Phys.* **2008**, *128*,o. 124507.
(14) Bühl, M.; Golubnychiy, V. *Inorg. Chem.* **2007**, *46*, 8129. doi:10.1021/ic701431u. PMID:17784755.
(15) Bühl, M.; Kabrede, H. *Inorg. Chem.* **2006**, *45*, 3834. doi:10.1021/ic060156l. PMID:16676935.
(16) Bühl, M.; Kabrede, H. *Chem. Phys. Chem.* **2006**, *7*, 2290. doi:10.1002/cphc.200600347. PMID:17051575.
(17) Bühl, M.; Sieffert, N.; Golubnichiy, V.; Wipff, G. *J. Chem. Phys. A* **2008**, *112*, 2428. doi:10.1021/jp710093w.
(18) Bühl, M.; Sieffert, N.; Wipff, G. *Chem. Phys. Lett.* **2009**, *467*, 287. doi:10.1016/j.cplett.2008.11.015.
(19) Ivanov, S. B.; Davidovich, R. L.; Mikhailov, Y. N.; Shchelokov, R. N. *Koord. Khim.* **1982**, *8*, 211.
(20) Mak, T. C. W.; Yip, W.-H. *Inorg. Chim. Acta* **1985**, *109*, 131. doi:10.1016/S0020-1693(00)84553-3.
(21) Vallet, V.; Wahlgren, U.; Schimmelpfennig, B.; Moll, H.; Szabó, Z.; Grenthe, I. *Inorg. Chem.* **2001**, *40*, 3516. doi:10.1021/ic001405n.
(22) Rotzinger, F. R. *J. Phys. Chem. B* **2005**, *109*, 1510. doi:10.1021/jp045407v. PMID:16851123.
(23) (a) For recent validation studies in context with associative vs. dissociative water exchange in uranyl hydrate see ref. 13 and Gutowski, K. W.; Dixon, D. A. *J. Phys. Chem. A* **2006**, *110*, 8840 doi:10.1021/jp061851h. PMID:16836448.; (b) Rotzinger, F. P. *Chem. Eur. J.* **2007**, *13*, 800 doi:10.1002/chem.200501472.; (c) Tsushima, S. *J. Phys. Chem. A* **2007**, *111*, 3613. doi:10.1021/jp070433p. PMID:17439107.
(24) Grenthe, I. (KTH Royal Institute of Technology, Stockholm, Sweden), private communication, August 2008.
(25) See for instance: Sprik, M.; Parrinello, M. J. *Chem. Phys.* **1996**, *105*, 1142.
(26) [See however:] VandeVondele, J.; Parrinello, M. J. *Chem. Phys.* **2005**, *122*, 014515[and references cited therein.].
(27) Bühl, M.; Reimann, C.; Pantazis, D. A.; Bredow, T.; Neese, F. *J. Chem. Theory Comput.* **2008**, *4*, 1449. doi:10.1021/ct800172j.
(28) Shamov, G. A.; Schreckenbach, G.; Vo, T. N. *Chem. Eur. J.* **2007**, *13*, 4932. doi:10.1002/chem.200601244.
(29) [CPMD Version 3.13.1 [computer program]. Copyright IBM Corp. 1990–2008, Copyright MPI für Festkörperforschung Stuttgart 1997–2001].
(30) Becke, A. D. *Phys. Rev. A* **1988**, *38*, 3098. doi:10.1103/PhysRevA.38.3098. PMID:9900728.
(31) Lee, C.; Yang, W.; Parr, R. G. *Phys. Rev. B* **1988**, *37*, 785. doi:10.1103/PhysRevB.37.785.
(32) Troullier, N.; Martins, J. L. *Phys. Rev. B* **1991**, *43*, 1993. doi:10.1103/PhysRevB.43.1993.
(33) Kleinman, L.; Bylander, D. M. *Phys. Rev. Lett.* **1982**, *48*, 1425. doi:10.1103/PhysRevLett.48.1425.
(34) k-Points are special integration points used to sample the first Brillouin zone in reciprocal space. When the unit cell is large enough, that zone is small and integration using just its center (the Γ-point) is sufficient.
(35) We note in passing that this type of Mulliken population analysis in a plane-wave basis is plagued by an incomplete partitioning of the total electron density onto the atomic pseudo-orbitals. The total amount of this "unassigned charge" is on the order of ca. 1% of the total number of

electrons (similar to findings in other ionic solids, see for example, Haiber, M.; Parrinello, M. *Am. Mineral.* **1997**, *82*, 913), which is most probably contained in regions of a more diffuse density shared by all atoms.

(36) To model the actual disorder, larger supercells with a 50:50 distribution of water molecules over the F1 and F1a sites would have to be employed. This was not pursued, because the concomitant effect on structural parameters and energies are expected to be too small to affect the qualitative conclusions.

(37) According to the relative energies at the SDD(+)–PCM level, water dissociation from **1a** is less endothermic with B3LYP than with the BLYP functional, but only by 2 kcal/mol (Table 3 in ref. 16).

(38) Quantitatively, a "water sublimation energy" from the crystal of ca. 8 kcal/mol (which should be close to the corresponding enthalpy of sublimation) does not indicate a particularly high stability, as it is slightly smaller than the enthalpy of desolvation of a single water molecule from the bulk liquid, 10.0 kcal/mol at 25 °C (cf. Ben-Naim, A.; Marcus, Y. J. *Chem. Phys.* **1984**, *81*, 2016).

(39) Wiberg, K. B.; Rablen, P. R. J. *Comput. Chem.* **1993**, *14*, 1504. doi:10.1002/jcc.540141213.

Theoretical investigation of CO adsorption on Rh_n (n = 3–13) clusters[1]

Sharan Shetty, Sebastian Strych, A.P.J. Jansen, and Rutger A. van Santen

Abstract: The adsorption of CO onto Rh_n (n = 3–13) clusters has been investigated using the density functional approach. Stable active sites for CO adsorption such as top, bridge, and hollow have been identified on these clusters. Our results show that CO mostly prefers the bridge or top site, except on the Rh_4 and Rh_{11} clusters where it prefers hollow sites. Rh_6 demonstrates two different active sites of almost equal energies for CO adsorption. Highly stable clusters show weak CO adsorption behavior. We also observe that the magnetic moment of the clusters is usually reduced after the CO adsorption. The preference of the active sites for CO adsorption has been analyzed using the charge density difference plots.

Key words: rhodium, clusters, carbon monoxide, adsorption, catalysis.

Résumé : Faisant appel à l'approche de la fonctionnelle de la densité, on a étudié l'adsorption du CO sur le Rh_n (n =3 à 13). On a identifié les sites actifs stables pour l'adsorption du CO sur ces agrégats, tels les sommets, les ponts et les trous. Nos résultats montrent que le CO s'adsorbe préférentiellement sur les ponts ou les sommets, à l'exception des agrégats Rh_4 et du Rh_{11} dans lesquels les trous sont privilégiés. Dans le Rh_6, il existe deux sites actifs différents d'énergies pratiquement égales pour l'adsorption du CO. Les agrégats très stables présentent des comportements d'adsorption faibles. On a aussi observé que le moment magnétique des agrégats est considérablement réduit après l'adsorption du CO. On a analysé la préférence des sites actifs pour l'adsorption du CO en faisant appel à des courbes de différence de densité de charge.

Mots-clés : rhodium, agrégats, monoxyde de carbone, adsorption, catalyse.

[Traduit par la Rédaction]

Introduction

CO dissociation on transition metal surfaces is considered to be the initial step for several important catalytic reactions.[2–4] This has led to a fundamental understanding of the catalytic reactivity of several transition metal surfaces. One of the important reactions is the Fischer–Tropsch (F–T) synthesis where the initial step is the dissociation of the adsorbed CO molecule on the surface.[5,6] Later reactions involve the synthesis of alcohols, ketones, etc.[3] The formation of these hydrocarbons depends on the activation of the CO molecule on the surface. The factors that decide chemisorption interactions are the unsaturation of the surface atoms, the coordination of the C–O bond, the electronic effect, and the change in the C–O bond energy.[7] The weakening of the C–O bond due to the adsorption at the low coordinated metal atoms was originally explained through the bonding and back-bonding concept proposed by Blyholder.[8] In contrast to this, Bagus et al. proposed that the CO adsorption on metals such as Na, Mg, and Al is through backdonation and σ repulsion between the filled 5σ orbital (HOMO) of CO and filled states at the metal center.[9] This was also confirmed on the transition metal clusters such as Ni, Cu, Ru, Rh, Pd, Ag, Ir, Pt, and Au using the density functional approach.[10] They showed that an increase of the d-shell occupancy and the principal quantum number cause an increase in the vibrational frequency of CO. Föhlisch et al. showed that the weakening of the CO bond on the metal surface is due to the rehybridization of the 1π and 2π* orbitals.[11] The weakening of the C–O bond is also correlated to the decrease in the C–O stretching frequency.[12] Several experimental and theoretical studies have been carried out to examine the reactivity of the metal surfaces towards CO adsorption.[7,12,13] These studies reveal that some transition metals such as Pt, Pd, and Rh have low reactivity for CO adsorption, wherease other transition metals such as Fe, Co, and Ru have the ability to adsorb CO strongly. Recent studies mainly focus on the reactivity of the metal surfaces having low coordinated atoms, such as the steps, kinks, or open surfaces. Recently Mongeot et al. showed that CO dissociation takes place on the faceted Rh(110) surface, which was not possible otherwise.[14] Ciobica and van Santen showed that the CO dissociation on the stepped Ru(1015) surface requires 130 kJ/mol less energy than on the flat Ru(0001) surface.[15] This was also confirmed by the experimental study by Zubkov et al.[16] Recently, Ge and Neurock have shown that the barrier required for CO dissociation on Co steps is less than on the flat Co(0001) surface.[17]

Correlation between the adsorption of CO and the coordination of the metal atoms on the surface has recently raised the possibility of using small metal particles for catalytic

Received 6 October 2008. Accepted 8 December 2008. Published on the NRC Research Press Web site at canjchem.nrc.ca on 18 March 2009.

S. Shetty,[1] S. Strych,[2] A. Jansen, and R.A. vanSanten. Schuit Institute of Catalysis, Eindhoven University of Technology, P.O. Box 513, 5600 MB Eindhoven, The Netherlands.

[1]Corresponding author (e-mail: s.g.shetty@tue.nl).
[2]Present address: Department of Chemistry and Biochemistry, Ludwig-Maxmilians Universitat München, Buteunandtstrasse 5-13, 81377 Munich, Germany.

purposes.[18] Xiao et al. observed aqueous phase F–T synthesis on small Ru clusters with dimensions of 2.0 to 2.5 nm.[19] The same synthesis was also carried out on Co clusters supported on carbon nanotubes.[20] Finely dispersed Au nanoparticles have been shown to be highly active in CO oxidation, H oxidation, and alkene epoxidation.[21] Izumi amd Iwasawa experimentally showed that the flexibility of small Ru and Rh clusters is crucial for the adsorption of CO molecules.[22] These studies reveal that there is a strong relationship between the size of the particle and its activity for a certain reaction. As a consequence, the activity of the reaction on small particles goes through a maximum as a function of particle size.[7]

Recent developments in experimental techniques have made it possible to study the adsorption of CO and NO molecules on small transition metal clusters consisting of less than 13 atoms. Knickelbein has used molecular beam deflection for analyzing the influence of the adsorbate on the magnetic moments of the Ni clusters.[23] This study showed that the adsorption of CO and H quench the magnetization on the Ni clusters. Anderson et al. studied the decomposition of NO on Rh_n ($n \leq 13$) charged clusters using cyclotron resonance mass spectrometry.[24] Their results revealed the size-dependent effect of the Rh clusters on N_2 formation. Hanmura et al. showed that NO reacts strongly with Co cations in the presence of H.[25] Andersson et al. have demonstrated the dissociation of CO on Rh clusters deposited on alumina substrates.[26] They showed that the CO dissociation highly depends on the structure of the adsorption site. Weber et al.. experimentally showed that Ir_4 and Rh_6 clusters supported in NaY zeolite have high catalytic activity.[27] Vayssilov et al. have studied the role of the Rh_6 cluster in the hydrogen spillover in zeolite.[28,29] There are several theoretical studies on CO adsorption on small Rh clusters. However, these studies were restricted to small clusters of two to five Rh atoms.[30,31] Guillermina and Zerner have investigated the bonding of CO on linear and two dimensional Rh clusters.[32] They showed that the CO binds to sites such as top and bridge through donation and back-donation. Nayak et al. studied the influence of the H-bonding on the magnetic and structural effects of Rh clusters.[33] A similar study was also made by Kumar and Kawazoe on Pd, Rh, and Ru clusters.[34] The other theoretical studies have mostly focused on the structural and magnetic properties of the bare Rh clusters.[35] These studies indicate that the structural, magnetic, and electronic properties of small transition metal clusters such as Pd, Rh, Ni, and Ru can influence the catalytic activity.

The present theoretical study follows a recent experimental work on the adsorption of CO on Rh_n clusters. The experimental work was carried out using IR multiple photon dissociation spectroscopy by Fielicke et al.[36] They analyzed the active sites for the adsorption of CO on the Rh clusters on the basis of the stretching frequency of C–O. Their study demonstrated that the CO binds to more than one Rh atom on clusters with $n \leq 4$ atoms such as the bridge and hollow sites. This was also supported by density functional calculations. The theoretical study was only confined to CO adsorption on Rh_3 and Rh_4. The clusters with more than five atoms exhibit either top or bridge sites. Moreover, other experimental studies have also explained the catalytic activity of the Rh clusters for CO adsorption on supported alumina.[37] Several issues still remain unanswered as mentioned in the experimental work: (1) Does a single cluster exhibit two or more adsorbing sites for CO? (2) Why do some of the sites show strong adsorbing behavior compared to others? (3) Is the magnetic moment suppressed after the CO adsorption? (4) How does the bonding of CO take place on these clusters? (5) Does strong adsorption of CO imply a dissociation? These issues will be investigated in the present theoretical work.

Computational details

The calculations were performed using a density functional approach with a plane wave basis set in conjunction with ultra-soft pseudopotential as implemented in the VASP code.[38] We made spin polarized calculations using generalized gradient approximation (GGA) with the PW-91 functional for the exchange correlation.[39] The bare and the CO-adsorbed Rh clusters were placed in a cubic supercell maintaining a vacuum gap of 10 Å between the neighboring images. The calculations were restricted to the gamma point in the Brillouin zone sampling. The energy cutoff used for the plane wave was 400 eV. The energy was converged till the forces on the atoms were less than 0.03 eV/Å. The structures were optimized using the conjugate gradient technique.

Results

Structure and energetics

In this section, we discuss the structure and stability of the bare Rh clusters and the CO adsorbed on different sites of these clusters. Several isomers were generated by changing the symmetry of the clusters and optimized to confirm the most stable structures of the bare Rh clusters. The CO adsorption was studied only on the most stable state Rh clusters. All the possible adsorption sites were explored on these clusters, and the most stable top, bridge, and hollow sites were analyzed.

Bare Rh clusters

The most stable structures and the first low-lying isomers of Rh_3 to Rh_6 are shown in Fig. 1. The stability and the magnetization of the Rh clusters are represented by the binding energy (B.E.) per atom (B.E./atom) and magnetic moment per atom (μ/atom), respectively, and are given in Table 1. These are defined as follows

$$[1] \qquad \text{B.E./atom} = \frac{(E(\text{cluster}) - nE(\text{atom}))}{n}$$

$$[2] \qquad \mu/\text{atom} = \frac{S_\alpha - S_\beta}{n}$$

The parameters defined in eqs. [1] and [2] are as follows: E(cluster), E(atom), and n are the energy of the Rh cluster, the energy of single Rh atom, and the number of Rh atoms in the cluster, respectively. S_α and S_β are the number of electrons with alpha and beta spins, respectively. The calculated B.E./atom of the bulk Rh is –5.59 eV/atom, in good agreement with the experimental value of –5.75 eV/atom.[40]

The most stable structure for Rh_3 is triangular. This is about 0.21 eV/atom more stable than the linear Rh_3 struc-

Fig. 1. (*a*) Most stable and (*b*) first low-lying isomers of Rh_n (n = 3,4,5,6).

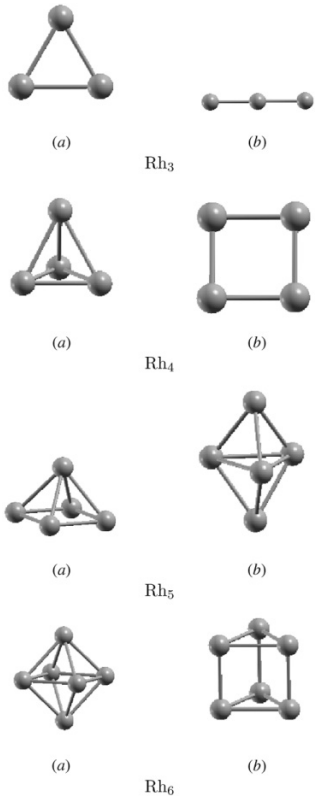

Table 1. Binding energy and magnetic moment of the (*a*) most stable and (*b*) first low-lying isomer of Rh_n (n = 3–13) clusters.

Rh_n	Binding energy (eV) / atom	Magnetic moment (μ) / atom)
3(a)	–2.13	1.0
3(b)	–1.92	0.3
4(a)	–2.57	1.5
4(b)	–2.55	1.0
5(a)	–2.84	1.0
5(b)	–2.78	1.4
6(a)	–3.01	1.0
6(b)	–2.99	1.4
7(a)	–3.13	1.8
7(b)	–3.09	1.0
8(a)	–3.36	1.5
8(b)	–3.25	1.3
9(a)	–3.374	1.4
9(b)	–3.371	1.4
10(a)	–3.447	0.7
10(b)	–3.442	1.4
11(a)	–3.517	1.4
11(b)	–3.512	0.8
12(a)	–3.65	0.7
12(b)	–3.48	1.2
13(a)	–3.66	0.7
13(b)	–3.63	1.9

Fig. 2. (*a*) Most stable and the (*b*) first low-lying isomers of Rh_n (n = 7,8,9,10).

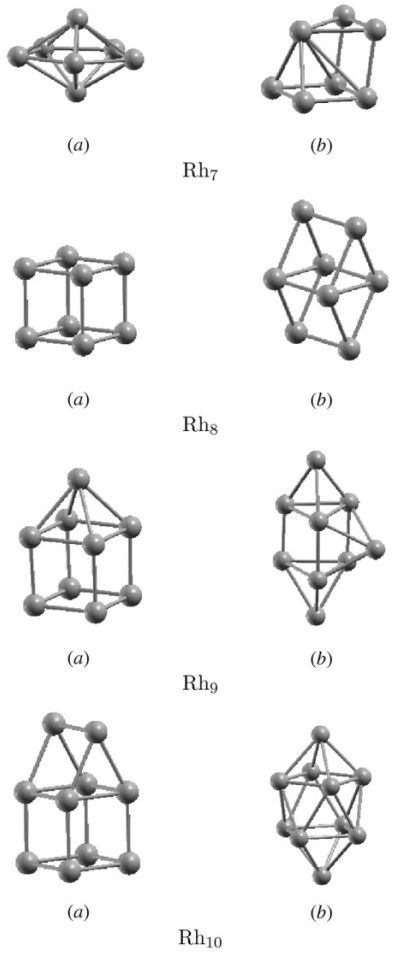

ture. The triangular structure has a magnetic moment of 1.0 μ/atom in contrast to 0.3 μ/atom for the linear isomer. The Rh–Rh distance is 2.40 Å. Rh_4 is a distorted tetrahedral structure with bond lengths between 2.4 and 2.8 Å and a magnetic moment of 1.5 μ/atom. The three-dimensional Rh_4 structure is only 0.02 eV/atom more stable than the square isomer. The geometry of the most stable Rh_5 is a square pyramid (Fig. 1) and is 0.06 eV/atom more stable than the triangular bipyramid. The stability and the geometries of the above clusters are in agreement with the earlier theoretical studies.[41,42] However, Rh_6 and Rh_7 clusters show a different trend. Rh_6 is a square bipyramid that is 0.02 eV/atom more stable than the triangular bi-prism isomer (Fig. 1) in contrast to the recent study by Bae et al.[41] Interestingly, the stable geometry of the Rh_6 cluster is in agreement with the study of Vayssilov et al.[29] They used a linear combination of Gaussian-type orbitals fitting functions density functional method (LCGTO-FF-DF) with a Becke–Perdew (BP) exchange correlation function. The average Rh–Rh distance of the stable square bipyramid and the triangular bi-prism isomer (Fig. 1) of the Rh_6 cluster corresponds to 2.54 and 2.48 Å, respectively, which are in agreement with the study of Vayssilov et al.

Moreover, Rh_7 (Fig. 2) shows the pentagonal bi-pyramid to be more stable than the bi-capped distorted pyramidal

Table 2. Adsorption energies (eV) and the magnetic moment (μ/atom) of the (*a*) most stable, (*b*) second most stable, and (*c*) third most stable sites of CO on Rh_n (n = 3–13) clusters.

Rh_n	Adsorption energy (eV)	Magnetic moment (μ) / atom
3(a)	–2.67	1.0
3(b)	–2.48	0.0
3(c)	–1.78	0.3
4(a)	–2.53	1.0
4(b)	–2.45	0.0
4(c)	–2.00	0.5
5(a)	–2.17	1.4
5(b)	–2.07	1.0
5(c)	–2.05	0.6
6(a)	–2.25	1.0
6(b)	–2.21	0.7
6(c)	–	–
7(a)	–2.22	1.6
7(b)	–2.06	1.6
7(c)	–2.05	1.3
8(a)	–1.98	1.3
8(b)	–1.60	1.3
8(c)	–0.80	1.3
9(a)	–2.55	1.2
9(b)	–2.29	1.2
9(c)	–2.05	1.0
10(a)	–2.50	1.0
10(b)	–2.30	0.8
10(c)	–1.93	0.6
11(a)	–2.01	1.2
11(b)	–1.97	1.2
11(c)	–1.93	1.2
12(a)	–2.08	0.5
12(b)	–1.65	0.5
12(c)	–0.91	0.7
13(a)	–2.34	0.4
13(b)	–2.16	0.5
13(c)	–2.14	0.5

structure. The difference between our calculations and the earlier results by Bae et al. is probably due to the high energy cutoff (400 eV) used in our calculations compared to the earlier studies (205.5 eV).[41] The magnetic moment of Rh_6 and Rh_7 are 1.0 and 1.8 μ/atom, respectively (Table 1). The most stable structure of Rh_8 is a cubic structure. This structure is 0.11 eV/atom more stable than its rhomboidal isomer (Fig. 2). The cubic Rh_8 cluster has a high magnetic moment of 1.5 μ/atom (Table 2) compared to the other clusters. This shows that it contains unpaired d-electrons which remain non-bonded and give rise to high magnetic moment.

The most stable and the isomeric structures of the Rh_9 cluster (Fig. 2) are degenerate with a difference of only 0.003 eV/atom. Consequently, they correspond to the same magnetic moment of 1.4 μ/atom (Table 2). Rh_{10} is a bi-capped cubic structure which is 0.005 eV/atom more stable than the bi-capped square anti-prism (Fig. 2). However, the magnetic moments are different. Interestingly, Rh_{11} is also

Fig. 3. (*a*) Most stable and (*b*) first low-lying isomers of Rh_n (n = 11,12,13)).

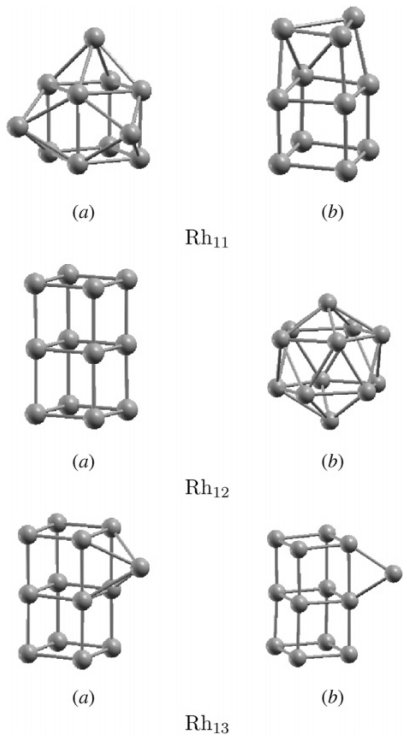

0.005 eV/atom more stable than the triangular capped cubic structure. This clearly shows that there exist low lying isomers as predicted by the experimental study.[36] Interestingly, we can see that the growth from Rh_9 to Rh_{11} is over the Rh_8 cubic core (Figs. 2 and 3). The most stable Rh_{12} cluster has a cuboid geometry, similar to the Rh_8 structure (Fig. 3). This structure is about 0.17 eV/atom more stable than the icosahedral structure. The magnetic moment of the stable Rh_{12} cluster is 0.67 μ/atom. Although, the structure has a similar symmetry to Rh_8 the magnetic moment is less than for Rh_8 (Table 1). This would be due to the number of bonding and non-bonding electrons involved in these systems. Rh_{13} consists of a single atom attached to the fourfold hollow site of the Rh_{12} cubic structure. This results in a slightly higher magnetic moment than for the Rh_{12} cluster. The isomeric Rh_{13} cluster is an Rh atom attached to the twofold bridge site (Fig. 3). The stability of the Rh_{12} is almost equal to the Rh_{13} cluster.

CO adsorption on Rh_n clusters

We now discuss the structure and stability of CO adsorption on the different stable sites such as the top, bridged, and hollow sites of the most stable Rh_n clusters discussed earlier. Figure 4 shows the CO adsorption on Rh_3 to Rh_6 clusters at different sites. The adsorption energies and corresponding magnetic moments of the CO adsorbed Rh clusters are given in Table 2. The adsorption energies (A.E.) are calculated as follows

$$[3] \qquad \text{A.E.} = E(\text{Rh}_n\text{CO}) - (E(\text{Rh}_n) + E(\text{CO}))$$

The most stable site for the adsorption on Rh_3 is the bridge site with an adsorption energy of –2.67 eV. This adsorption is 0.19 and 0.89 eV more stable than the threefold hollow and

Fig. 4. (*a*) Most stable, (*b*) second most stable, and (*c*) third most stable sites for the CO adsorption on the most stable Rh_n (n = 3,4,5,6) cluster. The grey, yellow, and red spheres indicate the Rh, C and O atoms, respectively.

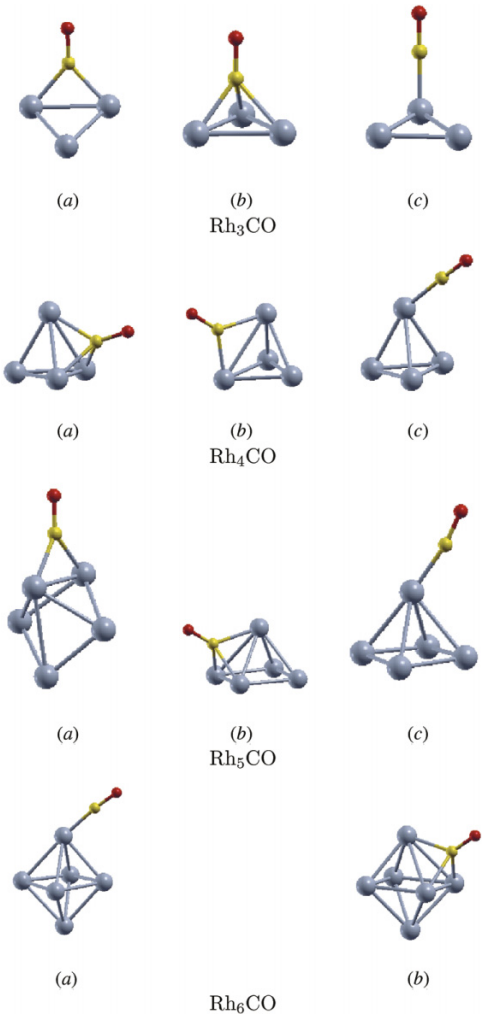

Fig. 5. (*a*) Most stable, (*b*) second most stable, and (*c*) third most stable sites for the CO adsorption on the most stable Rh_n (n = 7,8,9,10) cluster. The grey, yellow (light grey), and red spheres (dark) indicate the Rh, C, and O atoms, respectively (shades in parentheses refer to the printed version).

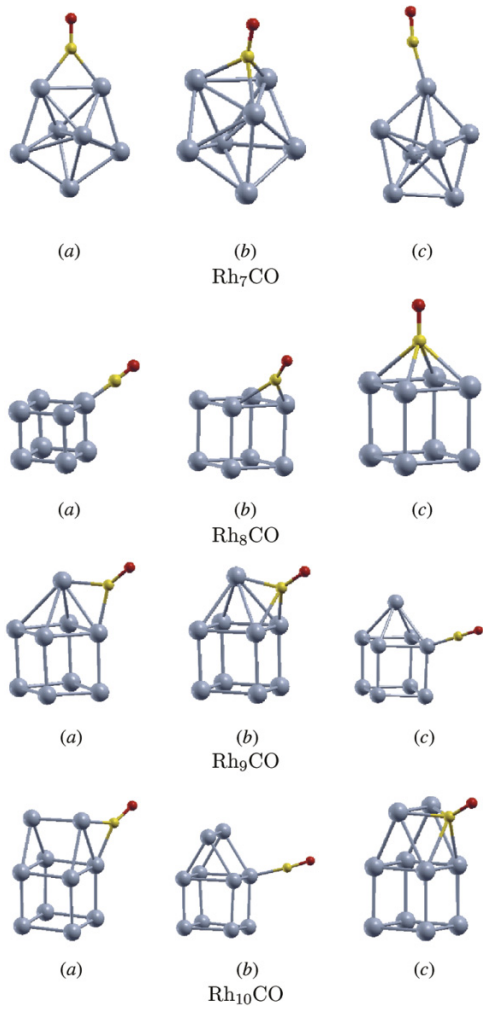

the top site, respectively. The bond length of the Rh–C in the bridge site is 1.93 Å. The C–O bond is stretched to 1.21 Å. CO adsorption on the bridge site does not affect the magnetic moment in Rh_3 . However, there is a considerable decrease in the magnetic moment with CO adsorbed in the other two stable sites (Table 2). The CO on the Rh_4 prefers a hollow site with an adsorption energy of –2.53 eV, as shown in the Fig. 4. Here the C–O is stretched to 1.22 Å. We can see that the CO adsorption energy on Rh_4 is decreased compared to that of Rh_3. This can be understood from the high stability of Rh_4 cluster compared to that of Rh_3 cluster. The CO adsorption on the Rh_4 cluster reduces the magnetic moment in all the three stable sites. This kind of reduced magnetic effect due to the CO adsorption on the Ni clusters has been experimentally observed.[23] The above trend on active sites for CO adsorption on Rh_3 and Rh_4 are in agreement with the earlier theoretical results obtained from all-electron calculations with localized basis set.[36]

The most stable adsorption site on Rh_5 is the bridge site with an energy of –2.17 eV. The other two sites, viz. the hollow and top sites, are almost equal in energy with a difference of 0.02 eV. Surprisingly, the magnetic moment has been increased from 1.0 to 1.4 μ/atom. This may be due to more non-bonding electrons available on the cluster due to back-donation from the Rh atoms to the $2\pi^*$ of the CO molecule. Only two adsorption states were found for the Rh_6 cluster. The top site is more stable than the hollow site by only 0.04 eV. The CO adsorbed in the bridge site moves into either a hollow or top site during the optimization. This indicates that there exist more than one binding site for the CO molecule on Rh_5 and Rh_6 clusters. This kind of behavior has been suggested by the experimental study.[36] Hence, the presence of more than one frequency band observed in the experiments can be attributed to the possibility of CO adsorbing in two different stable sites with degenerate adsorption energies. CO adsorbs strongly at the bridge site of the Rh_7 cluster with an adsorption energy of –2.22 eV. The hollow and the top sites have similar adsorption energies. CO adsorption on the cubic Rh_8 cluster is mostly stable on the top site. The magnetic moment is also reduced due to the adsorption. One can see that the adsorption energy of CO on the Rh_8 cluster is small compared to the other clusters.

Fig. 6. (*a*) Most stable, (*b*) second most stable and (*c*) third most stable sites for the CO adsorption on the most stable Rh_n (n = 11,12,13) cluster. The grey, yellow (light grey), and red (dark) spheres indicate the Rh, C, and O atoms, respectively (shades in parentheses refer to the printed version)

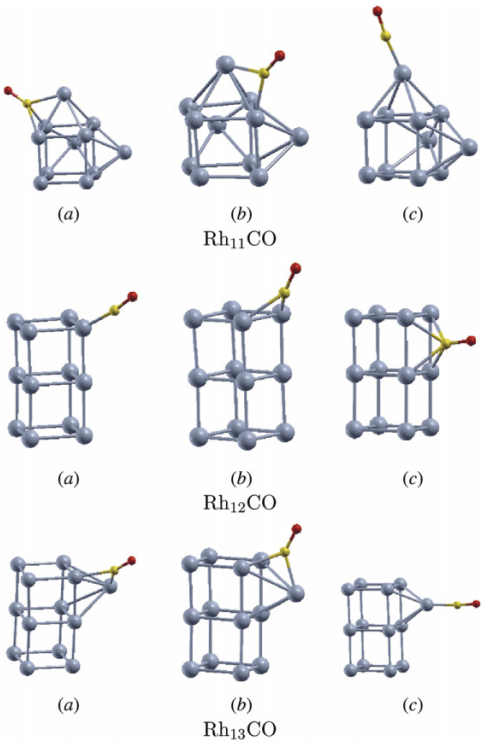

This is due to the high stability of the Rh_8 cluster. In the next section we will give a bonding analysis to explain how CO adsorbs in different sites.

On the Rh_9 cluster, bridge is the most stable site with an energy of –2.55 eV (Fig. 5). This pattern is also observed on the Rh_{10} cluster. As with CO adsorption on the Rh_5 cluster, CO adsorption on the Rh_{10} cluster increases the magnetic moment compared to the bare cluster. CO strongly adsorbs in a threefold hollow site on the Rh_{11} cluster. The stable adsorption site on Rh_{12} is the top site with an adsorption energy of –2.01 eV (Fig. 6). This site is similar to that of the cubic Rh_8 cluster. The adsorption at the bridge and fourfold hollow sites are –1.65 and –0.91 eV, respectively. Rh_{13} shows the bridge site as the most stable for the CO adsorption. The average stretching of the C–O bond on the above clusters is observed between 1.17 to 1.22 Å. Although, some of the Rh clusters adsorb CO strongly, one cannot deduce from this that the CO would easily decompose on these clusters as suggested by the experimental study.[36]

Bonding

In this section, we explain how the CO molecule adsorbs in different sites on the clusters through donation and back-donation. We use the charge density difference analysis to explain this behavior on some selected clusters with different adsorbing sites. Figure 7 shows the charge density difference of the CO adsorbed on the Rh_3 and Rh_4 cluster at the bridge, top, and hollow sites. The red and blue regions represent the charge depleted and gained, respectively. Let us

Fig. 7. Difference charge densities of the (*a*) most stable, (*b*) second most stable, and (*c*) third most stable sites for CO adsorption on the most stable Rh_n (n = 3 and 4) cluster. The blue (light) and red (dark) regions show the charge gained and lost, respectively (shades in parentheses refer to the printed version).

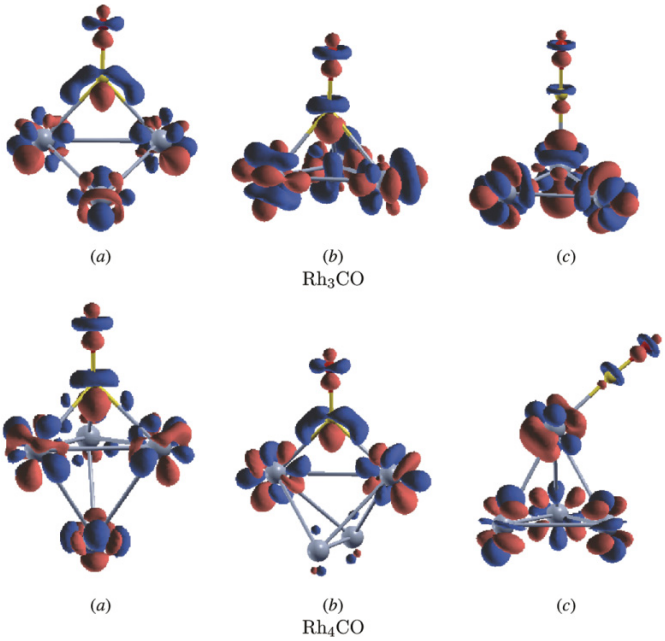

Fig. 8. Difference charge densities of the (*a*) most stable, (*b*) second most stable, and (*c*) third most stable sites for CO adsorption on the most stable Rh_n (n = 6 and 8) clusters. The blue (light) and red (dark) regions show the charge gained and lost, respectively (shades in parentheses refer to the printed version).

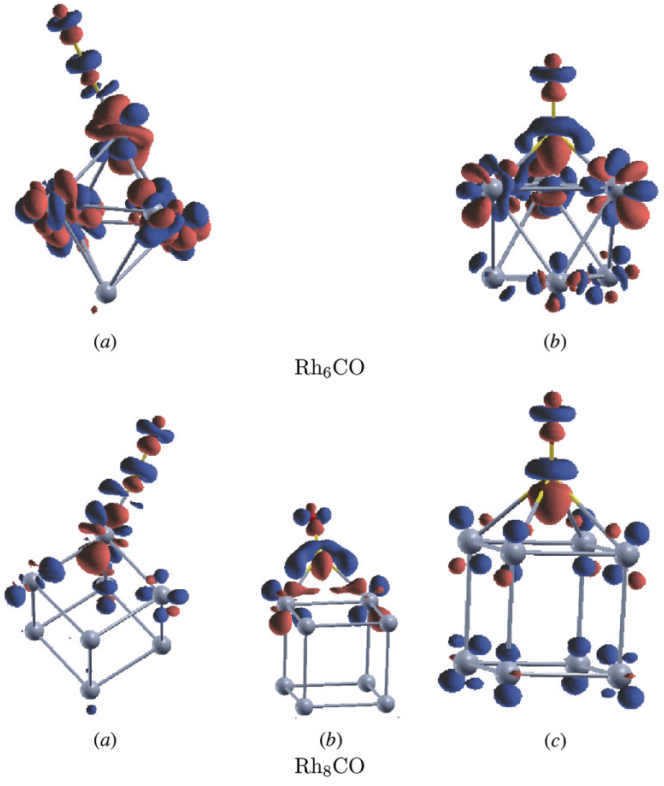

first consider the CO adsorption on Rh_3 at the most stable bridge site. We can clearly see that density from the bonding 5σ orbital of CO is lost and the anti-bonding 2π* has gained charge. It can be seen that there is a considerable change in the orbitals on the metal clusters. The Rh atoms involved in bonding with the CO have lost charge from one orbital and gained in another. This reflects back-donation in the 2π* orbitals of CO and donation from the 5σ orbital of CO to d orbitals corresponding to different symmetry. This agrees very well with the Blyholder model.[8] However, the decrease in the density of the bonding 5σ orbital of CO does not agree with the Bagus model.[9] This is also the reason that the C–O bond is stretched after the adsorption. This kind of picture is also observed on the other sites, viz. top and hollow sites. The important point to note is that in the bridge site there is strong build-up of the density between the C–Rh bond which is not the case in the top and the hollow sites. This is the reason for the strong adsorption of CO in the bridge site of Rh_3 cluster. In the case of Rh_4 we see a similar build-up of the density when the CO molecule adsorbs in the hollow site which is also the most stable site compared to the bridge and top sites. The rearrangement of the d-orbitals on the Rh atoms which are not involved in bonding are due to the relaxation of the cluster as a result of strong CO adsorption. This relaxation rearranges the d-orbitals on these atoms resulting in the flow of electron density from the occupied d-orbitals to the unoccupied d-orbitals of different symmetry.

In Rh_6 the top site and the hollow sites have very similar CO adsorption energies as discussed earlier. The charge density difference isosurface of the CO at the top site and hollow site of Rh_6 is shown in Fig. 8. We can clearly see that in both cases density is similarly built up between the Rh–C bond. This is the reason for a comparable bond strengths of Rh–C bond on the top and hollow sites resulting in near degenerate adsorption energies. It also explains the experimental predictions for the single cluster exhibiting two binding sites. The CO adsorbs more strongly on the top site of Rh_8 which is justified by the density lying between the Rh–C bond as seen the Fig. 8. CO adsorbed in the hollow site does not show much of the density build-up between the Rh–C bonds and this decreases the adsorption energy of CO in the hollow site of Rh_8. The other clusters also show a similar bonding nature for the top, bridge, and hollow sites as discussed above.

Conclusion

The present theoretical work follows a recent experimental study on the CO adsorption on small Rh_n clusters. Our study gives an insight into the different kinds of stable adsorption sites, viz. top, bridge, and hollow, on the Rh clusters. The important findings of the present investigation are as follows.

(1) The analysis of the bare Rh clusters reveal that some of the clusters are energetically degenerate and could result in cluster isomerism.

(2) The CO molecule predominantly prefers the bridge or the top site for adsorption on the cluster. The Rh_4 and Rh_{11} clusters show hollow as the stable adsorbing site. The bridge and the top site on the Rh_6 cluster have very close adsorption energies. This is consistent with the fact that two binding sites are predicted by the experimental study.

(3) We notice that the adsorption of CO reduces the magnetic moment of the cluster. This we predict due to the smaller number of unpaired electrons because of the donation and back-donation.

(4) The bonding analysis reveals that the CO prefers an active site where a strong build-up of the density is seen between the Rh–C bond. This is also the reason why the CO molecule prefers a particular adsorption site. It should be noted that in the case of degenerate isomers the density build-up will not be too different resulting in close adsorption energies as in the case of Rh_6.

(5) Although the CO molecule is strongly adsorpted on these clusters and the stretching of the C–O bond is observed between 1.17 and 1.22 Å, we don't see the dissociation of the adsorbed CO molecule. Our investigation indicates that the adsorption of CO on small Rh clusters is a combined effect of different binding sites of identical energies and metal cluster isomerism.

References

(1) This article is part of a Special Issue dedicated to Professor T. Ziegler.

(2) Vannice, M. A. *J. Catal.* **1977**, *50*, 228. doi:10.1016/0021-9517(77)90031-8.

(3) Olah, G. A.; Molnar, A. *Hydrocarbon chemistry*; Wiley-Interscience: New York, USA, 2003, 2nd ed.

(4) Thomas, J. M.; Thomas, W. J. *Principles and practice of heterogeneous catalysis*; VCH: Weinheim, Germany. 1997.

(5) Somorjai, G. A. *Introduction to surface chemistry and catalysis*; Wiley: New York, USA. 1994.

(6) Goodman, D. W. *The chemical physics of solid surface and heterogeneous catalysis*; Elsevier: Amsterdam, Netherlands. 1982.

(7) van Santen, R. A.; Neurock, M. *Molecular heterogeneous catalysis*; Wiley-VCH: Weinheim, Germany. 2006.

(8) Blyholder, G. *J. Phys. Chem.* **1964**, *68*, 2772. doi:10.1021/j100792a006.

(9) Bagus, P. S.; Nelin, C. J.; Bauschlicher, C. W. *Phys. Rev. B,* **1983**, *28*, 5423. doi:10.1103/PhysRevB.28.5423.

(10) Zeinalipour-Yazdi, C. D.; Efstathiou, A. M. *Surf. Sci.* **2008**, *602*, 1858. doi:10.1016/j.susc.2008.03.024.

(11) Föhlisch, A.; Nyberg, M.; Hasselström, J.; Karis, O.; Petterson, L. G. M.; Nilsson, A. *Phys. Rev. Lett.* **2000**, *85*, 3309. doi:10.1103/PhysRevLett.85.3309. PMID:11019328.

(12) Gajdo, M.; Eichler, A.; Hafner, J. *J. Phys. Condens. Matter.* **2004**, *16*, 1141. doi:10.1088/0953-8984/16/8/001.

(13) Liu, Z.-P.; Hu, P. J. *Chem. Phys.* **2001**, *114*, 8244. doi:10.1063/1.1372512 .

(14) de Mongeot, F. B.; Toma, A.; Molle, A.; Lizzit, S.; Petaccia, L.; Baraldi, A. *Phys. Rev. Lett.* **2006**, *97*, 056103. doi:10.1103/PhysRevLett.97.056103. PMID:17026119.

(15) Ciobica, I. M.; van Santen, R. A. *J. Phys. Chem. B* **2003**, *107*, 3808. doi:10.1021/jp030010x.

(16) Zubkov, T.; Morgan, G. A., Jr.; Yates, J. T., Jr.; Kühlert, O.; Lisowski, M.; Schillinger, R.; Fick, D.; Jänsch, H. J. *Surf. Sci.* **2003**, *57*, 526.

(17) Ge, Q.; Neurock, M. *J. Phys. Chem.* **2006**, *110*, 15368. doi:10.1021/jp060477i.

(18) Bell, A. T. *Science* **2003**, *299*, 1688. doi:10.1126/science.1083671. PMID:12637733.

(19) Botana, C.-x.; Cai, Z.-p.; Wang, T.; Kou, Y.; Ning, Y. *An-*

gew. Chem. Int. Ed. Engl. **2007**, *46*, 1. doi:10.1002/anie.200690172.
(20) Bezemer, G. L.; Bitter, J. H.; Herman, P. C.; Kuipers, C. E.; Oosterbeek, H.; Holewijn, J. E.; Xu, X.; Kapteijn, F.; van Dillen, J. A.; de Jong, K. P. *J. Am. Chem. Soc.* **2006**, *128*, 3956. doi:10.1021/ja058282w. PMID:16551103.
(21) Valden, M.; Lai, X.; Goodman, D. W. *Science* **1998**, *281*, 1647. doi:10.1126/science.281.5383.1647. PMID:9733505.
(22) Izumi, Y.; Iwasawa, Y. *Chemtech* **1994**, 20.
(23) Knickelbein, M. B. *J. Chem. Phys.* **2001**, *115*, 1983. doi:10.1063/1.1388542 .
(24) Anderson, M. L.; Ford, M. S.; Derrick, P. J.; Drewello, T.; Woodruff, D. P.; Mackenzie, S. R. *J. Phys. Chem. A*, **2006**, *110*, 10992. doi:10.1021/jp062178z. PMID:16986831.
(25) Hanmura, T.; Ichihashi, M.; Watanabe, Y.; Isomura, N.; Kondow, T. *J. Phys. Chem. A,* **2007**, *111*, 422. doi:10.1021/jp063273a. PMID:17228890.
(26) Andersson, S.; Frank, M.; Sandell, A. *J. Chem. Phys.* **1998**, *108*, 2967. doi:10.1063/1.475684 .
(27) Weber, W. A.; Zhao, A.; Gates, B. C. *J. Catal.* **1999**, *182*, 13. doi:10.1006/jcat.1998.2306.
(28) Vayssilov, G. N.; Gates, B.; Rösch, N. *Angew. Chem. Int. Ed. Engl.* **2003**, *42*, 1391. doi:10.1002/anie.200390357. PMID:12671977.
(29) Vayssilov, G. N.; Rösch, N. *J. Phys. Chem. B* **2004**, *108*, 180. doi:10.1021/jp036241l.
(30) Goursot, A.; Papai, I.; Salahub, D. R. *J. Am. Chem. Soc.* **1992**, *114*, 7452. doi:10.1021/ja00045a017.
(31) Mineva, T.; Russo, N.; Freund, H.-J. *J. Phys. Chem.* **2001**, *105*, 10723 doi:10.1021/jp0116398.
(32) Guillermina, E. L.; Zerner, M. C. *Int. J. Quantum Chem.* **2004**, *44*, 587.
(33) Nayak, S. K.; Weber, S. E.; Jena, P.; Wildberger, K.; Zeller, R.; Dederichs, P. H.; Stepanyuk, V. S.; Hergert, W. *Phys. Rev. B* **1997**, *56*, 8849. doi:10.1103/PhysRevB.56.8849.
(34) Kumar, V.; Kawazoe, Y. *Eur. Phys. J. D* **2003**, *24*, 81. doi:10.1140/epjd/e2003-00193-6.
(35) Futschek, T.; Marsman, M.; Hafner, J. *J. Phys. Condens. Matter.* **2005**, *17*, 5927. doi:10.1088/0953-8984/17/38/001.
(36) Fielicke, A.; von Helden, G.; Meijer, G.; Pedersen, D. B.; Simard, B.; Rayner, D. M. *J. Phys. Chem. B* **2004**, *108*, 14591. doi:10.1021/jp049214j.
(37) (a) Yates, J. T., Jr.; Duncan, T. M.; Worley, S. D.; Vaughan, R. W. *J. Chem. Phys.* **1979**, *70*, 1219. doi:DOI:10.1063/1.437603.(b) Cavanagh, R. R.; Yates, J. T., Jr. *J. Chem. Phys.* **1981**, *74*, 4150. doi:10.1063/1.441544.; (c) Zeinalipour-Yazdi, C. D.; Cooksy, A. L.; Efstathiou, A. M.*J. Phys. Chem. C*. **2007**, *111*, 13872. doi:10.1021/jp074549x.
(38) Kresse, G.; Hafner, J. *Phys. Rev. B,* **1994**, *49*, 14251. doi:10.1103/PhysRevB.49.14251.
(39) Perdew, J. P.; Wang, Y. *Phys. Rev. B*, **1992**, *45*, 13244. doi:10.1103/PhysRevB.45.13244.
(40) Kittel, C. *Introduction to solid state physics*; John Wiley and Sons Inc.: New York, London, Sydney. 1966; 3rd ed., Chap. 3.
(41) Bae, Y.-C.; Osanai, H.; Kumar, V.; Kawazoe, Y. *Phys. Rev. B,* **2004**, *70*,o. 195413. doi:10.1103/PhysRevB.70.195413.
(42) Bae, Y.-C.; Kumar, V.; Osanai, H.; Kawazoe, Y. *Phys. Rev. B,* **2005**, *72*,o. 125427. doi:10.1103/PhysRevB.72.125427.

Ethene trimerization at Cr^{I}/Cr^{III} — A density functional theory (DFT) study[1]

Peter H.M. Budzelaar

Abstract: Catalytic ethene trimerization at a chromium(I) indolate-AlR_2Cl centre has been studied by density functional theory (DFT) methods. The reaction is found to follow the standard metallacycle mechanism. At most stages of the reaction, coordination of Cr to the pyrrole ring of the indolate is preferred. In all 13-*e* intermediates, coordination of the Al-bound chloride to Cr provides additional stabilization: the chloride behaves as a hemilabile ligand. Benzene is found to compete with ethene for coordination to Cr^{I}. The final hexene-forming step involves direct Cβ → Cα′ hydrogen transfer; reductive elimination from a possible (hydride)(hexenyl) intermediate is more difficult. The kinetic isotope effect calculated for the direct hydrogen transfer (4.1) agrees well with the experimental value for a bis(phosphino)amide chromium catalyst. Side products obtained in such systems (methylenecyclopentane, methylcyclopentane) can plausibly be explained through routes not involving any (hydride)(alkyl) reductive elimination. Our results indicate that a Cr^{I}/Cr^{III} trimerization cycle is possible for some chromium trimerization catalysts, and also suggest that direct hydrogen transfer is most likely a general feature of trimerization at Cr centres.

Key words: trimerization, density functional theory (DFT), hydrogen transfer, mechanism.

Résumé : Faisant appel aux méthodes de la théorie de la fonctionnelle de densité (TFD), on a étudié la trimérisation catalytique de l'éthène au niveau du de l'indolate-AlR_2Cl de chrome(I). On a trouvé que la réaction se produit par un mécanisme impliquant un métallacycle standard. À la plupart des stades de la réaction, il y a une préférence pour la coordination du Cr avec le noyau pyrrole de l'indolate. Dans tous les intermédiaires 13-*e*, la coordination du chlorure lié à l'aluminium avec le Cr fournit une stabilisation additionnelle: le chlorure se comporte comme un ligand semilabile. On a observé que le benzène est en compétition avec l'éthène pour établir une coordination avec le Cr(I). L'étape finale de formation de l'hexène implique un transfert direct d'hydrogène Cβ → Cα′; l'élimination réductrice à partir d'un intermédiaire potentiel (hydrure)(hexényle) est plus difficile. L'effet isotopique cinétique calculé pour le transfert direct d'hydrogène (4,1) est en accord avec la valeur expérimentale obtenue avec un catalyseur de bis(phosphino)amide chrome. Les produits secondaires obtenus dans de tels systèmes (méthylènecyclopentane et méthylcyclopentane) peuvent facilement être expliqués par des voies n'impliquant aucune élimination réductrice à partir d'un intermédiaire potentiel (hydrure)(hexényle). Les résultats présentés ici indiquent qu'un cycle de trimérisation Cr(I)/Cr(III) est possible pour certains catalyseurs de trimérisation au chrome et ils suggèrent aussi que le transfert d'hydrogène direct est probablement la caractéristique générale des trimérisations à des centres de Cr.

Mots-clés : trimérisation, théorie de la fonctionnelle de densité (TFD), transfert d'hydrogène, mécanisme.

[Traduit par la Rédaction]

Introduction

Ethene dimerization, oligomerization, and polymerization are catalyzed by a wide range of transition metal complexes. These reactions generally follow a common propagation mechanism (migratory olefin insertion) and only differ in the relative rates of propagation and chain transfer, resulting in a Schulz–Flory distribution of molecular weights. There is, however, a small group of catalysts (mostly based on chromium,[2] although titanium[3] and tantalum[4] variations are known) that show a surprisingly high selectivity to the *trimer* 1-hexene. Since selective 1-hexene formation is commercially much more attractive than isolating the trimer from a Schulz–Flory distribution of products, this select group of catalysts has received considerable attention.

Trimerization generally follows a metallacycle mechanism[5] quite distinct from that of polymerization (Scheme 1). The most important fundamental difference is that two different oxidation states of the metal are involved. A common feature of most catalysts reported to date is the presence of hemilabile ligands, which presumably help to balance the energies of the two oxidation states.

While the general features of the metallacycle mechanism have been accepted for some time, the computational study by Yu and Houk[6] (for the Ta system[4]) was the first to point out that conversion of metallacycloheptane intermediate **D** to 1-hexene complex **E** occurs by direct Cβ → Cα′ hydrogen transfer rather than through discrete (hydride)(hexenyl) intermediate **F**.

Received 30 October 2008. Accepted 8 January 2009. Published on the NRC Research Press Web site at canjchem.nrc.ca on 25 March 2009.

P.H.M. Budzelaar. Department of Chemistry, University of Manitoba, Fort Garry Campus, Winnipeg, MB R3T 2N2, Canada (e-mail: budzelaa@cc.umanitoba.ca).

Scheme 1. Basic metallacycle mechanism for 1-hexene formation.

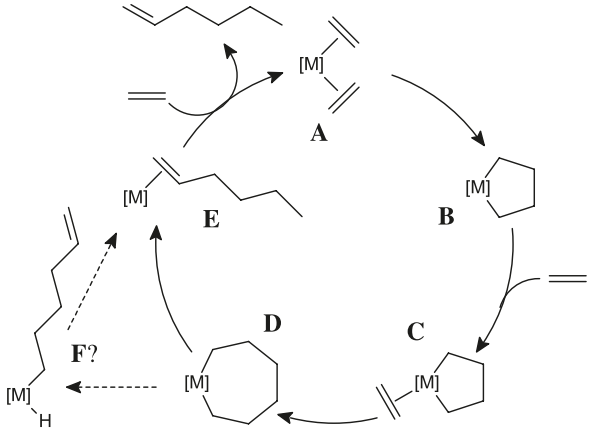

The Cp/arene Ti system described by Hessen and co-workers[3] is probably the "cleanest" trimerization system known to date, in the sense that little uncertainty remains about the nature of the active species. As a consequence, it has been the subject of a number of computational studies,[7–9] which all confirm the mechanism shown in Scheme 1. In addition, these studies revealed the importance of the hemilabile arene ligand in balancing the energies of the Ti^{II} and Ti^{IV} oxidation states.

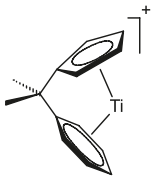

In contrast, knowledge of the commercially more important[10] chromium systems is limited. The system patented by Phillips Petroleum Company[11] uses chromium(III) alkanoates as precursors, pyrroles as co-catalysts, and aluminium alkyls as activators. Neither the structure of the active species nor even its oxidation state have been firmly established. A computational study of this system by van Rensburg and Steynberg[12] assumed a Cr^{II}/Cr^{IV} mechanism and obtained a viable catalytic cycle. "Hemilability" in that case showed up as η^5/σ flipping of a pyrrolate ligand and modulation of the interaction with the Et_3AlCl^- counterion. BP Chemical Ltd. has patented[13] Cr systems based on bis(phosphino)amide (PNP) ligands. These systems have been studied extensively by Bercaw and co-workers.[14] They concluded that the active species is most likely cationic and switches between Cr^{I} and Cr^{III}. However, even their well-defined precursors show an induction period for the catalysis, indicating that formation of the active species may not be straightforward. Some of the side products characterized by Bercaw and co-workers, most notable methylenecyclopentane and methylcyclopentane,[14b] appear to be derived from a (hydride)(hexenyl) intermediate, suggesting that perhaps this Cr system differs from others in not following a direct $C\beta \rightarrow C\alpha'$ hydrogen transfer path. However, it remains possible that these side products are not related to the main catalytic cycle. Van Rensburg and Steynberg[15] have reported calculations on the possible role of MAO in the PNP chromium system but not on the catalytic cycle itself.

Gambarotta and co-workers[16] recently described the preparation of two well-defined Cr/Al trinuclear compounds that, *without further activation*, are active in trimerization (complex **1**, Cr^{I}) or polymerization (complex **2**, Cr^{II}). Since complex **1** contains Cr^{I}, and no obvious oxidant is added, a $Cr^{II/IV}$ cycle seems unlikely for this system. In the present work, we analyze a possible $Cr^{I/III}$ cycle for the trimerizing species and discuss the implications for other chromium systems.

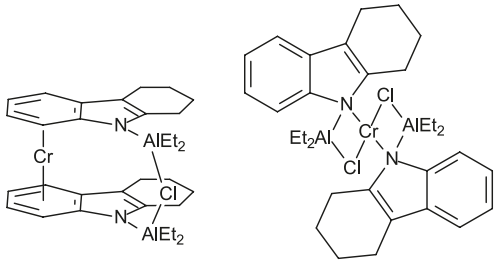

1 **2**

Methods

All geometry optimizations were done using the Turbomole program[17] coupled to PQS OPTIMIZE[18] as an external optimizer. All geometries were optimized at the unrestricted b3-lyp[19] level using the SV(P)[20] basis set. Vibrational analyses were carried out to check the nature of all stationary points, and also to calculate thermal corrections (enthalpy and entropy) for 273 K, 1 bar (1 bar = 100 kPa), gas phase. Improved single-point energies were calculated at the b3-lyp/TZVPP[21] level, and combined with the SV(P) thermal corrections to produce the final free energy values mentioned in the text. For lists of total energies and optimized geometries, see the Supplementary data.

Results and discussion

The $Cr^{I/III}$ trimerization cycle

The assumed mechanism corresponds to that in Scheme 1. To simplify calculations, we used an indolyl ligand as a model for the tetrahydrocarbazolyl ligand used by Gambarotta and co-workers,[16] and replaced the Al-bound ethyl groups by methyl groups. At all stages, the $AlMe_2Cl$ group stays coordinated to the indolate nitrogen, which means that the Cr atom must be π-coordinated to either the pyrrolate or the arene ring of the indolate ligand,[22] leading to models **3** and **4** for the Cr fragment in the active species.

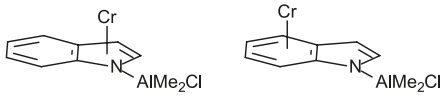

3 **4**

Both possibilities were explored; pyrrolate coordination was preferred by a modest margin (0–10 kcal/mol, 1 cal = 4.184 J) at most stages of the reaction, but slippage of the chromium fragment over the aromatic system was found to be very easy. The dangling $AlMe_2Cl$ group has the possibility of orienting its chloride towards Cr, thus constituting a hemilabile group. Indeed, we found Cl coordination to Cr in all 13-*e* Cr^{III} intermediates (in both **3** and **4**), but not in the

Fig. 1. Calculated structures for S = 3/2 states of 3B, 3C, 4B, and 4C, illustrating hemilabile behaviour of the AlR_2Cl group.

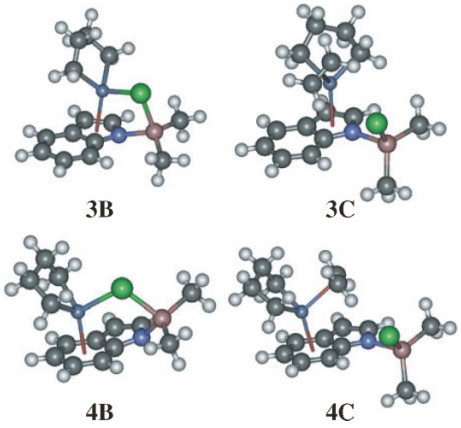

Scheme 2. Reactions studied computationally in this work.[24]

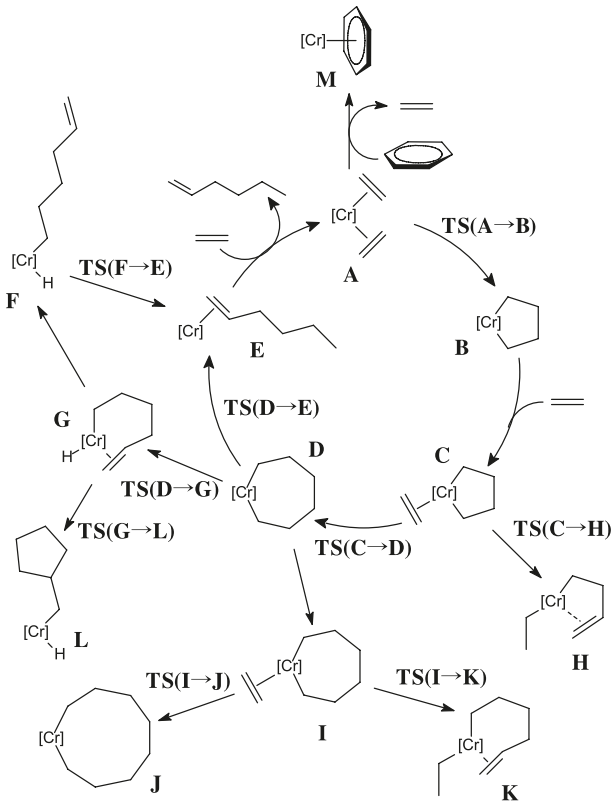

15-*e* intermediates, as illustrated in Fig. 1. The full catalytic cycle was investigated for both S = 3/2 and S = 1/2 states. The S = 3/2 state was consistently preferred by a significant margin (5–25 kcal/mol) for all species within the proposed catalytic cycle.[23] In the remainder of this work we only use the energies for the lowest-energy spin state (S = 3/2 or 1/2) and for the preferred ligand coordination (**3** or **4**) of each intermediate or transition state. The final cycle, including the various excursions and side reactions studied, is shown in Scheme 2. Figure 2 shows the corresponding free energy profile, and Table 1 lists the energies for all relevant species.

As in the cycles proposed earlier for Ta,[6] Ti,[7–9] and Cr[12] we find reductive coupling of two ethenes to a metallacyclopentane, ring expansion to a metallacycloheptane, and direct Cβ → Cα′ hydrogen transfer to form a 1-hexene complex.[25] The initial reductive coupling step (**A** → **B**) is very easy ($\Delta G^{\ddagger}$ = 7.7 kcal/mol, ΔG_{rxn} = –9.9 kcal/mol), reflecting the ease of oxidation of Cr^{I} to Cr^{III}; on the other hand, the final H transfer that reduces Cr^{III} back to Cr^{I} (**D** → **E**) has a high activation free energy of 18.4 kcal/mol.

The results reported by van Rensburg and Steynberg[12] for $Cr^{II/IV}$ [11] imply a somewhat less facile initial step ($\Delta G^{\ddagger}$ = 9.5 kcal/mol, ΔG_{rxn} = –2.1 kcal/mol) and a much easier final H transfer ($\Delta G^{\ddagger}$ = 10.0 kcal/mol).[26] The most common oxidation states of Cr in alkylchromium complexes are Cr^{II} and Cr^{III}. Thus, it makes sense that in a $Cr^{II/IV}$ cycle formation of the unusually *high* oxidation state Cr^{IV} from Cr^{II} is more difficult, and its subsequent reduction back to Cr^{II} is correspondingly easier. In our $Cr^{I/III}$ cycle, on the other hand, Cr starts out in the unusually *low* oxidation state Cr^{I}, so its oxidation to Cr^{III} (**B**) is easier but later reduction back to Cr^{I} (**F**) is more difficult.

However, the rate-limiting step for both types of cycles appears to be the insertion of the third olefin to form metallacycloheptane **D**. In the present system, this is calculated to have an effective free-energy barrier $\Delta G_{eff} = \Delta G$[**TS**(**C** → **D**)] – ΔG[**B**] of 28.1 kcal/mol. The height of this barrier is caused not so much by the insertion itself (which requires only 12.5 kcal/mol) but rather by the strong stabilization of metallacyclopentane **B** through coordination of the Al-bound chloride, which opposes coordination of the incoming ethene molecule.

Interestingly, the coordination of the hemilabile chloride in **D** doesn't assist the reductive Cβ → Cα′ hydrogen transfer, because it selectively stabilizes *high* oxidation states of the metal. Thus, the role of the hemilability in this system appears to be subtly different from that in other trimerization systems studied by DFT. Since the final H transfer is relatively difficult in this $Cr^{I/III}$ system, one might expect easy ring growth beyond the metallacycloheptane intermediate. However, this further ring expansion requires binding of an additional ethene molecule and hence is entropically unfavourable; we find that in terms of free energy, H transfer at the metallacycloheptane (**D** → **E**) is still preferred over ring expansion (**D** → **I** → **J**) by a margin of about 11 kcal/mol.

In any case, neither the $Cr^{I/III}$ cycle (this work) nor the $Cr^{II/IV}$ one[12] appear to involve discrete (hydride)(hexenyl) species analogous to **F**. The transition state **TS**(**F** → **E**) for the final reductive hexene elimination from **F** is simply too high in energy to compete with direct hydrogen transfer through **TS**(**D** → **E**), the difference being about 9 kcal/mol. On the other hand, this difference is not so large that one can confidently exclude this path for all possible chromium systems.

Our results suggest a possible explanation for the observation by Bercaw and co-workers[14b] of methylenecyclopentane and methylcyclopentane side products. The calculated energies of the system are such that, while reductive hydride-alkyl elimination via **TS**(**F** → **E**) is well above **TS**(**D** → **E**), the (hydride)(hexenyl) complex **G** itself is low enough in energy to be accessible. Indeed, intramolecular cyclization via **TS**(**G** → **L**) is calculated to happen *below* the level of **TS**(**F** → **E**), though still above **TS**(**D** → **E**). Thus, it seems likely that depending on the specific catalyst used, there could be systems where formation of cyclopentylmethyl complex **L**

Fig. 2. Calculated free energy profile for reactions shown in Scheme 2 occurring at chromium centre 3/4.

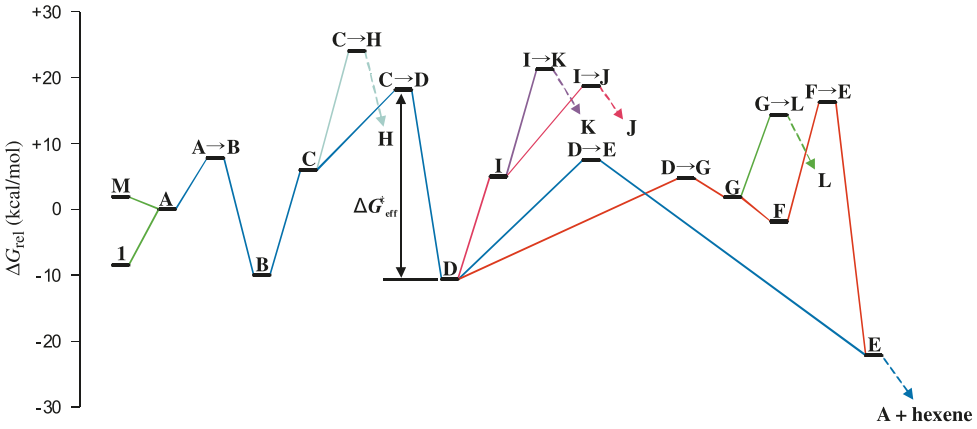

Table 1. Relative free energies (kcal/mol) for species related to trimerization with Cr fragments 3/4, 5, and 6.

	3/4		**5**		**6**	
Structure	coord, *S*	ΔG_{rel}	*S*	ΔG_{rel}	*S*	ΔG_{rel}
A	**3**, 3/2	0	3/2	0	3/2	0
TS(A → B)	**3**, 3/2	7.67	3/2	3.30	3/2	12.63
B	**3**, 3/2	–9.86	3/2	3.62	3/2	8.14
C	**4**, 3/2	5.79	3/2	6.90	3/2	7.22
TS_A(C → H)	**4**, 3/2	24.15	3/2	23.83	3/2	25.21
TS_B(C → H)	**3**, 3/2	38.90	3/2	33.86	3/2	33.18
TS(C → D)	**3**, 3/2	18.24	3/2	16.09	3/2	16.37
D	**3**, 3/2	–10.76	3/2	–3.02	3/2	–4.81
TS(D → E)	**4**, 3/2	7.60	3/2	8.91	3/2	6.82
E	**3**, 3/2	–22.31	3/2	–9.00	3/2	–9.67
(**A** + hexene)	**3**, 3/2	–18.78	3/2	–18.78	3/2	–18.78
TS(D → G)	**3**, 3/2	4.72	3/2	6.39	3/2	6.50
G	**3**, 3/2	1.94	3/2	1.61	3/2	2.27
TS(G → L)	**3**, 3/2	14.39	3/2	12.62	3/2	11.76
F	**3**, 3/2	–2.00	3/2	9.98	3/2	9.60
TS(F → E)	**4**, 3/2	16.38	3/2	16.17	3/2	15.69
I	**3**, 3/2	5.15	3/2	4.08	3/2	4.85
TS(I → J)	**3**, 3/2	18.88	3/2	14.78	3/2	15.15
TS_A(I → K)	**3**, 3/2	21.10	3/2	17.77	3/2	18.02
TS_B(I → K)	**3**, 3/2	37.47	3/2	32.37	3/2	32.32
M	**3**, 3/2	1.97	3/2	2.05	1/2	–9.97
1	(**4**), 3/2	–8.53		—		—
$(C_2H_4)_3$ complex	**3**, 3/2	22.17	1/2	30.17	1/2	33.68

Note: For structure labelling, see Scheme 2. For system **3/4**, the lowest-energy ligand coordination mode is given.

via intramolecular insertion competes with the Cβ → Cα′ hydrogen transfer reaction. Once this (irreversible) cyclization has occurred, the resulting (hydride)(cyclopentylmethyl) complex could insert an olefin in the Cr–H bond[27] and then undergo hydrogen transfer either *from* or *to* the cyclopentylmethyl group to produce the observed side products, as illustrated in Scheme 3.

Bercaw and co-workers[14c] have reported kinetic isotope effects (KIE) for trimerization of trans and cis ethylene-d_2 (4.1(1) and 3.1(1), respectively).[14c] These KIE were believed not to have a significant tunnelling component. Our calculated KIE for transfer of a single H versus D in **TS(D → E)** is 4.1, in remarkably good agreement with the experimental value.[28] However, the KIE calculated for the reductive-elimination step is not much higher (5.4), so we cannot draw any definitive conclusions from this fact alone.

Since for our cycle the β-elimination/reductive elimination steps have relatively high barriers, we checked for alternative hydrogen transfer possibilities. In olefin polymerization, chain transfer usually occurs either via β-elimination or via direct transfer of a β-hydrogen to an incoming monomer ("chain transfer to monomer"). The β-elimination path is blocked in **B** by steric constraints, but one could still envisage transfer of a β-hydrogen to an incoming ethene molecule from both **B** and **D**. We located two transition states for each of these reactions, corresponding to the "classical" bis(ole-

Scheme 3. Possible mechanism for formation of methylcyclopentane and methylenecyclopentane side products.

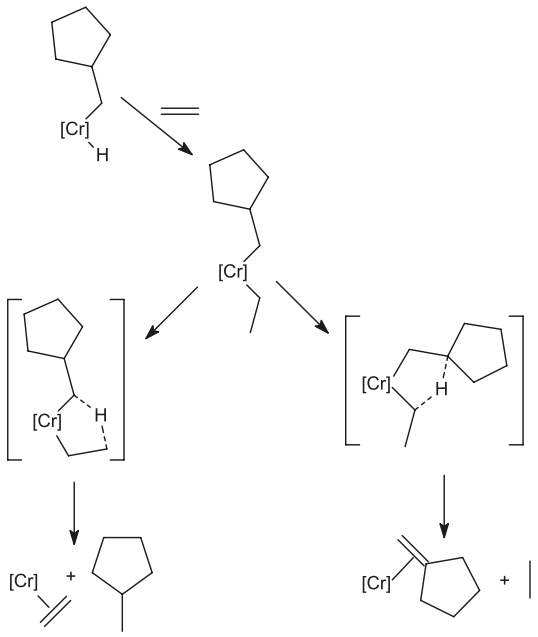

fin)hydride like $\mathbf{TS_A}$ and the "ene" like $\mathbf{TS_B}$ that have been calculated for several polymerization systems.[29] As for most relatively open polymerization catalysts, $\mathbf{TS_A}$ is preferred by a significant margin (about 16 kcal/mol) over $\mathbf{TS_B}$. However, even $\mathbf{TS_A}$ is clearly disfavoured relative to metallacycle growth (from **B**, by 6 kcal/mol) or hydrogen transfer (from **D**, by 14 kcal/mol), so that chain transfer to monomer does not seem to be a relevant side reaction in this system.

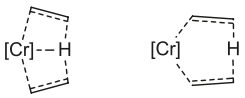

$\mathbf{TS_A}$ $\mathbf{TS_B}$

Role of the indolate ligand

For comparison, the same catalytic cycle was studied for model catalysts (*N*-methyl-pyrrole)Cr^+ (**5**) and (benzene)Cr^+ (**6**), which lack the hemilabile $AlMe_2Cl$ group but are otherwise similar to **3** and **4**.

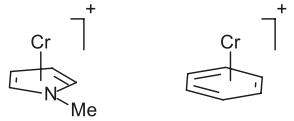

5 **6**

The calculated catalytic cycles are roughly similar, but ethene binding is consistently stronger for both of these models because the incoming ethene monomer does not have to compete with the hemilabile chloride. Nevertheless, the competition between H transfer and further metallacycle growth is very similar for all systems, **3**–**6**, since in the crucial transition states for H transfer and chain growth, chloride coordination does not occur to a significant extent.

These results would suggest that cationic (pyrrole)Cr^+ and (benzene)Cr^+ could be viable trimerization catalysts. They would be even more active than the hemilabile systems **3** and **4** since they lack the additional stabilization at the metallacycle stages **B** and **D** that cause the high effective barriers for these latter systems. We believe, however, that *some* additional form of stabilization of the chromium center is necessary to keep the catalyst alive and prevent it from undergoing unwanted side reactions. Species like **5** and **6** would be so reactive they are unlikely to survive for long.

A cationic (arene)Cr^I species would most plausibly be generated from low-spin 17-*e* (arene)$_2Cr^+$. However, arene dissociation is normally not easy: displacement of one benzene ring of $(C_6H_6)_2Cr^+$ by two molecules of ethene is calculated to be endergonic by about 10 kcal/mol, and is unlikely to happen.[30] Due to the negative charge on the ligand, the arene ring of **4** is a stronger σ-donor and poorer π-acceptor than benzene, resulting in slightly weaker binding of benzene to **4** than to **6**. Also, the chloride ligand may assist in a *stepwise* displacement of an arene from **3/4**, which should be easier than a fully dissociative mechanism. Nevertheless, the use of an arene as solvent should hinder trimerization catalysis at Cr^I, in agreement with experimental results.[14b,16]

Conclusions

Our results indicate that, in addition to the $Cr^{II/IV}$ cycle proposed by van Rensburg and Steynberg[12] a $Cr^{I/III}$ cycle is a reasonable possibility for ethene trimerization at Cr. For the activator-free system described by Gambarotta and coworkers,[16] this $Cr^{I/III}$ cycle seems the more likely one because the starting material contains Cr^I and there is no obvious oxidant present. The observed inhibition by toluene supports this interpretation, since Cr^{II} does not bind arenes strongly enough to result in inhibition of olefin binding. For the commercial Cr-pyrrolyl systems, not enough information is available to assign the oxidation state of the catalyst; both $Cr^{I/III}$ and $Cr^{II/IV}$ cycles should be considered as viable alternatives. It appears that both of these cycles involve direct Cβ → Cα′ hydrogen transfer, avoiding reductive elimination from discrete (hydride)(hexenyl) intermediates. A possible explanation for the formation of methylenecyclopentane and methylcyclopentane side products is given that does not involve a reductive hydride-alkyl elimination step. And finally, the calculated KIE for direct Cβ → Cα′ hydrogen transfer agrees well with the KIEs observed by Bercaw and co-workers[14c] for a PNP catalyst. Taken together, these results make a strong case for the occurrence of direct hydrogen transfer as a "standard" mechanistic step in chromium-catalyzed trimerization.

Supplementary data

Supplementary data for this article are available on the journal Web site (canjchem.nrc.ca) or may be purchased from the Depository of Unpublished Data, Document Delivery, CISTI, National Research Council Canada, Ottawa, ON K1A 0R6, Canada. DUD 3906. For more information on obtaining material refer to cisti-icist.nrc-cnrc.gc.ca/cms/unpub_e.shtml.

Acknowledgements

The author thanks the Canada Foundation for Innovation (CFI) and Natural Sciences and Engineering Research Council of Canada for financial support and Professor S. Gambarotta for helpful discussions.

References

(1) This article is part of a Special Issue dedicated to Professor Tom Ziegler on the occasion of his 65th birthday.

(2) (a) Briggs, J. R. *J. Chem. Soc. Chem. Commun.* **1989**, 674 doi:10.1039/c39890000674.; (b) Dixon, J. T.; Green, M. J.; Hess, F. M.; Morgan, D. H. *J. Organomet. Chem.* **2004**, *689*, 3641, and references cited there. doi:10.1016/j.jorganchem.2004.06.008.

(3) (a) Hessen, B. *J. Mol. Catal. A Chem. (Kyoto)* **2004**, *213*, 129 doi:10.1016/j.molcata.2003.10.056.; (b) Deckers, P. J. W.; Hessen, B.; Teuben, J. H. *Organometallics* **2002**, *21*, 5122 doi:10.1021/om020765a.; (c) Deckers, P. J. W.; Hessen, B.; Teuben, J. H. *Angew. Chem. Int. Ed.* **2001**, *40*, 2516. doi:10.1002/1521-3773(20010702)40:13<2516::AID-ANIE2516>3.0.CO;2-V.

(4) Andes, C.; Harkins, S. B.; Murtuza, S.; Oyler, K.; Sen, A. *J. Am. Chem. Soc.* **2001**, *123*, 7423. doi:10.1021/ja010762+. PMID:11472174.

(5) Emrich, R.; Heinemann, O.; Jolly, P. W.; Krueger, C.; Verhovnik, G. P. J. *Organometallics* **1997**, *16*, 1511. doi:10.1021/om961044c.

(6) Yu, Z. X.; Houk, K. N. *Angew. Chem. Int. Ed.* **2003**, *42*, 808. doi:10.1002/anie.200390215.

(7) Blok, A. N. J.; Budzelaar, P. H. M.; Gal, A. W. *Organometallics* **2003**, *22*, 2564. doi:10.1021/om030049o.

(8) (a) de Bruin, T. J. M.; Magna, L.; Raybaud, P.; Toulhoat, H. *Organometallics* **2003**, *22*, 3404 doi:10.1021/om030255w.; (b) de Bruin, T.; Raybaud, P.; Toulhoat, H. *Organometallics* **2008**, *27*, 4864. doi:10.1021/om800326r.

(9) (a) Tobisch, S.; Ziegler, T. *Organometallics* **2003**, *22*, 5392 doi:10.1021/om0341247.; (b) Tobisch, S.; Ziegler, T. *J. Am. Chem. Soc.* **2004**, *126*, 9059 doi:10.1021/ja048861l. PMID:15264839.; (c) Tobisch, S.; Ziegler, T. *Organometallics* **2004**, *23*, 4077 doi:10.1021/om0498100.; (d) Tobisch, S.; Ziegler, T. *Organometallics* **2005**, *24*, 256. doi:10.1021/om049362w.

(10) Morgan, M. Alpha Olefins (02/03-4), PERP Report. Nexant Chem Systems. 2004.

(11) Reagan, W. K. EP 0417477. Phillips Petroleum Company. 1991.

(12) Janse van Rensburg, W.; Steynberg, P. J. *Organometallics* **2004**, *23*, 1207. doi:10.1021/om0306269.

(13) (a) Wass, D. F. WO 02/04119. BP Chemicals Ltd. 2002.; (b) Carter, A.; Cohen, S. A.; Cooley, N. A.; Murphy, A.; Scutt, J.; Wass, D. F. *Chem. Commun. (Camb.)* **2002**, 858. doi:10.1039/b201335e. PMID:12123014.

(14) (a) Schofer, S. J.; Day, M. W.; Henling, L. M.; Labinger, J. A.; Bercaw, J. E. *Organometallics* **2006**, *25*, 2743 doi:10.1021/om0506062.; (b) Elowe, P. R.; McCann, C.; Pringle, P. G.; Spitzmesser, S. K.; Bercaw, J. E. *Organometallics* **2006**, *25*, 5255 doi:10.1021/om0601596.; (c) Agapie, T.; Labinger, J. A.; Bercaw, J. E. *J. Am. Chem. Soc.* **2007**, *129*, 14281. doi:10.1021/ja073493h. PMID:17973377.

(15) Janse van Rensburg, W.; Steynberg, P. J. *Organometallics* **2007**, *26*, 1000. doi:10.1021/om060890c.

(16) Albahily, K.; Koç, E.; Al-Baldawi, D.; Savard, D.; Gambarotta, S.; Burchell, T. J.; Duchateau, R. *Angew. Chem. Int. Ed.* **2008**, *47*, 5816. doi:10.1002/anie.200800845.

(17) (a) Ahlrichs, R.; Bär, M.; Baron, H.-P.; Bauernschmitt, R.; Böcker, S.; Ehrig, M.; Eichkorn, K.; Elliott, S.; Furche, F.; Haase, F.; Häser, M.; Hättig, C.; Horn, H.; Huber, C.; Huniar, U.; Kattannek, M.; Köhn, A.; Kölmel, C.; Kollwitz, M.; May, K.; Ochsenfeld, C.; Ohm, H.; Schäfer, A.; Schneider, U.; Treutler, O.; Tsereteli, K.; Unterreiner, B.; von Arnim, M.; Weigend, F.; Weis, P. Weiss, H. *Turbomole*, version 5; Theoretical Chemistry Group: University of Karlsruhe, Karlsruhe, Germany, 2002; (b) Treutler, O.; Ahlrichs, R. *J. Chem. Phys.* **1995**, *102*, 346. doi:10.1063/1.469408.

(18) (a) *PQS*, version 2.4. Parallel Quantum Solutions: Fayetteville, AR. 2001. The Baker optimizer is available separately from PQS upon request; (b) Baker, J. J. *Comput. Chem.* **1986**, *7*, 385 doi:10.1002/jcc.540070402.; (c) Convergence criteria used: 4×10^{-5} h on energy, 1×10^{-4} h/Bohr on max cartesian gradient.

(19) (a) Lee, C.; Yang, W.; Parr, R. G. *Phys. Rev. B* **1988**, *37*, 785 doi:10.1103/PhysRevB.37.785.; (b) Becke, A. D. *J. Chem. Phys.* **1993**, *98*, 1372 doi:10.1063/1.464304.; (c) Becke, A. D. *J. Chem. Phys.* **1993**, *98*, 5648 doi:10.1063/1.464913.; (d) All calculations were performed using the Turbomole functional "b3-lyp", which is not identical to the Gaussian "B3LYP" functional.

(20) Schäfer, A.; Horn, H.; Ahlrichs, R. *J. Chem. Phys.* **1992**, *97*, 2571. doi:10.1063/1.463096.

(21) Weigend, F.; Furche, F.; Ahlrichs, R. *J. Chem. Phys.* **2003**, *119*, 12753. doi:10.1063/1.1627293.

(22) One could imagine formation of a Al-N-Cr bridge like that in complex **2**. However, we did not examine that possibility in the present study.

(23) The low-spin state is only preferred for 17-*e* complexes such as $(C_6H_6)_2Cr^+$. For all 13-*e* and 15-*e* species, the $S = 1/2$ calculations moreover result in a high spin contamination: typical values of S^2 are 1.7–1.8, whereas the S^2 values for the $S = 3/2$ states are mostly in the range of 3.8–3.9.

(24) The scheme shows single arrows for simplicity; of course, all steps are to some degree reversible.

(25) All attempts to find a separate transition state for hydride-alkyl reductive elimination from **G** led back to the direct Cβ → Cα′ transfer **TS(D → E)**. A discrete reductive elimination TS could only be calculated when the hexenyl C=C bond was first dissociated from the Cr atom, i.e., starting from **F** to give **TS(D → E)**.

(26) Based on data given in ref. 11 for the $ClAlMe_3$ model, using the lowest-energy pyrrolate coordination mode at each stage of the reaction.

(27) Alternatively, and perhaps more likely, olefin could insert in the Cr–H bond of **G** *before* cyclization of the hexenyl group occurs. This would eventually lead to the same products.

(28) KIE calculated from standard thermodynamic free-energy calculations, not including any tunnelling estimates. Calculated secondary isotope effects are also significant, in particular for the Cα′ H having an agostic interaction with the metal (1.14).

(29) Talarico, G.; Budzelaar, P. H. M. *Organometallics* **2008**, *27*, 4098. doi:10.1021/om800313n.

(30) Displacement by *three* ethenes was found to be even less favourable, see Table 1.

Pd/X group interchange in the [Pd(Br)(PH_3)(C_6H_5)(C_6H_5X)] system — Theoretical insights from the isolobal analogy perspective[1]

Alain Dedieu and Antonio J. Mota

Abstract: DFT-B3LYP calculations have been carried out to assess the fate of the Pd/X group intermolecular exchange in the [PdBr(PH_3)(C_6H_5)(C_6H_5X)] system, where *X* is either H, an electropositive atom, or a group such as Li, Na, BH_2, AlH_2, BeH or $BeCH_3$, and an electronegative atom, or a group such as F, Cl, Br, CH_3, OH, and SH. The transfer of H is best viewed as involving the migration of a proton between the two phenyls. At variance with this result, the transfer of the more electropositive entities such as X = Li, Na, BH_2, AlH_2, BeH, or $BeCH_3$ is not complete. It stops halfway to yield a stable structure in which *X* can experience interactions with the two phenyl groups that are quite ionic. These stable structures are rationalized through isolobal analogy arguments. In the case of beryllium, the correspondence has been made also with the experimentally known cyclopentadienylberyllium borohydride system, $CpBeH_4$. The results of the DFT geometry optimization call for a re-examination of the gas-phase electron-diffraction structure determination, especially for the bond distances and angles that pertain to the two bridging hydrogens. For the halogen series X = F, Cl, or Br and for the electronegative groups CH_3, OH, or SH, the transfer between the two phenyls takes place via a two-step Pd(II)/Pd(IV) oxidative addition/reductive elimination mechanism. The associated energy barriers are nevertheless quite high, except for Br and SH for which the process might be feasible. The dimerization of the PdBr(PH_3)(C_6H_5) system is also analyzed within the isolobal analogy framework.

Key words: C–X activation, metathesis, group exchange, theoretical study, palladium.

Résumé : On a étudié, à l'aide de calculs DFT-B3LYP l'échange intramoléculaire entre les groupes PdBr(PH_3) et X, lorsque X est soit un atome d'hydrogène, un atome ou un groupe plus électropositif tel que Li, Na, BH_2, AlH_2, BeH or $BeCH_3$, soit un groupe plus électronégatif comme F, Cl, Br, CH_3, OH, SH. Le transfert de H correspond à un transfert de proton entre les deux phényles. Par contre le transfert des atomes ou des groupes plus électropositifs n'est pas complet et s'arrête à mi-chemin pour donner un complexe stable, dans lequel les interactions de X avec les deux groupes phényles ont un fort caractère ionique. On rationalise ce type de structures par des arguments basés sur le concept de l'analogie isolobale. Dans le cas du béryllium la géométrie du système $CpBeBH_4$, qui est aussi un analogue isolobal, a été optimisée. Sur la base des résultats correspondants, on suggère un réexamen de la structure expérimentale obtenue en phase gazeuse par diffraction d'électrons. Pour la série F, Cl, Br, CH_3, OH, SH, le transfert peut se faire via un mécanisme à deux étapes Pd(II)/Pd(IV) impliquant une addition oxydante suivie d'une élimination réductrice. Les barrières d'énergie associées sont cependant très élevées, sauf pour Br et SH, pour lesquels on peut imaginer un tel processus. La dimérisation du système PdBr(PH_3)(C_6H_5) est aussi étudiée sous l'angle de l'analogie isolobale.

Mots-clés : activation C–X, métathèse, échange de groupe, étude théorique, palladium.

Introduction

Synthetic organic reactions catalyzed or mediated by palladium complexes are extraordinarily numerous and different. Among them, the through-space shift of palladium between two sp^2 or an sp^3 and an sp^2 carbon atom, associated to a simultaneous C–H bond activation,[2–18] that has been observed under Heck-type or Suzuki-type conditions, has recently attracted our attention.[19–21] Its intimate mechanism is quite intriguing and still a matter of debate.[17]

Two different "intramolecular" pathways can be envisioned a priori: either an oxidative addition/reductive elimination two-step process in which a hydridopalladium(IV) intermediate is involved, see (i) in Scheme 1, or a one-step process in which the oxidation state +2 of the palladium atom is retained, see (ii) in Scheme 1. In this case, it could be considered either as a metathesis reaction of the C–H σ bond with the Pd–C bond, or as a concomitant 1,*n* shift of both the hydrogen and the palladium atoms, where the hydrogen atom is best viewed as being transferred as a proton. Our investigations also pointed out to the possibility, especially for the 1,4 shift, of an oxidative hydrogen-migration one-step mech-

Received 9 October 2008. Published on the NRC Research Press Web site at canjchem.nrc.ca on 27 March 2009.

A. Dedieu.[1] Laboratoire de Chimie Quantique, Institut de Chimie, UMR 7177 CNRS/ULP, Université de Strasbourg, 4, rue Blaise Pascal, 67000 Strasbourg, France.
A.J. Mota.[2] Departamento de Química Inorgánica, Facultad de Ciencias. Universidad de Granada, Campus de Fuentenueva, 18071 Granada, Spain.

[1]Corresponding author (e-mail: alain.dedieu@chimie.u-strasbg.fr).
[2]Corresponding author (e-mail: mota@ugr.es).

Scheme 1.

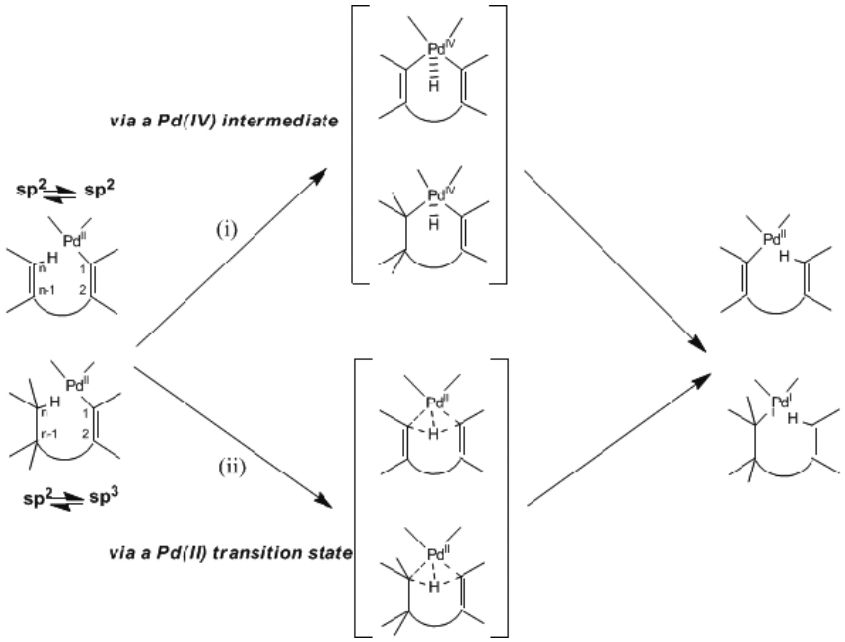

Fig. 1. Optimized structures for the one-step Pd(II) and Pd(IV) rearrangements between $PdBr(PH_3)$ and H in the $PdBr(PH_3)(C_2H_3)(C_2H_4)$ system. The enthalpy values are in kcal mol^{-1} (1 cal = 4.184 J).

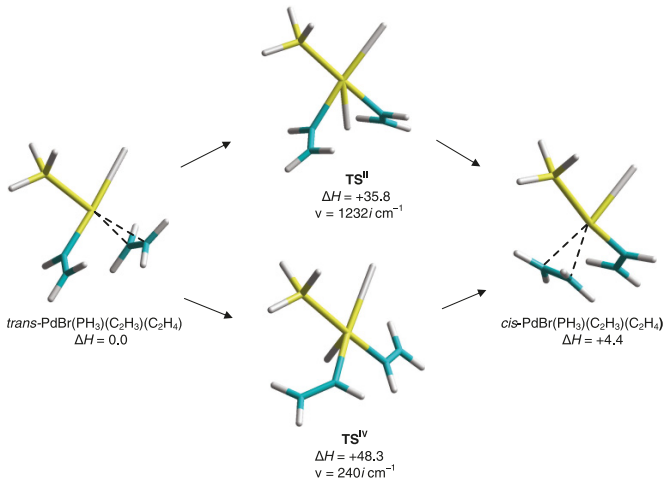

anism, in which the hydrogen is transferred as a hydride.[19–21] In fact, as stressed recently by various authors,[22–25] such clear-cut distinctions are too strict, and there is probably a monotonous evolution from one mechanism to the other, depending on the metal center and its environment. Yet in the palladium PdBr(phosphine)(biaryl) systems that we investigated, we could show that the one-step Pd(II) mechanism was favoured for $n \geq 5$ and unravelled the orbital and geometric factors that account for this feature.[20] This was done by considering the 1,∞ re-arrangement in the unconstrained $PdBr(PH_3)(C_2H_3)(C_2H_4)$ model system, both sides of the system being then allowed to adopt the more adequate position with respect to the Pd atom (see Fig. 1). As shown on Fig. 1, both "one-step" Pd(II) and Pd(IV) mechanisms were found. The one-step Pd(II) transition state is favoured by a clamping arrangement of the two organic moieties around the transferred hydrogen, in contrast to the one-step Pd(IV) transition state, for which a planar arrangement is needed (see Fig. 1) . This Pd(II) transition state $PdBr(PH_3)(C_2H_3)(C_2H_3)(H)$, with its almost linear $C_{vinyl}\cdots H\cdots C_{vinyl}$ unit, involves a proton transfer, and that was, inter alia, rationalized on the basis of the isolobal analogy[26,27] between the d^9 C_{2v} $PdBr(PH_3)$ unit and either CH_2^+ or BH_2. If one also replaces the two groups that are covalently bound to Pd by two hydrogen atoms (their isolobal analogs), one then gets for this transition state a structure that is akin to the one of the C_{2v} transition state for hydrogen scrambling in CH_5^+ or BH_5.[28–30]

Up to now, our mechanistic studies[19–21] and the related studies on sigma-bond metathesis reaction[22–25] have been limited to C–H activation. In an effort to broaden the scope of these interchange processes, we have now considered the Pd/X interchange and related processes (vide infra) in the $Pd(Br)(PH_3)(C_6H_5)(C_6H_5X)$ "model" systems, where the exchanged X group is of cationic character, viz. X = Li, Na, BH_2, AlH_2, BeH, and $BeCH_3$. Our conclusions rely on DFT calculations, but we will use the isolobal analogy as a rationalizing tool. For the sake of completion, we will also briefly report our results for anionic X groups in $Pd(Br)(PH_3)(C_6H_5)(C_6H_5X)$ systems.

Computational details

The calculations were carried out at the DFT-B3LYP level[31–33] with the Gaussian 03 program.[34] The triphenylphosphine ligand PPh_3 was modelled by PH_3. The geometries were fully optimized by the gradient technique with the following basis: For Pd, the LANL2DZ basis set is modified following the prescription of Couty and Hall.[35] In this modified basis, the innermost core electron (up to 3d) are described by the relativistic orbital-adjusted effective core potential of Hay and Wadt,[36] and the remaining outer core and valence electrons by a [341/541/31] basis set where the two outermost 5p functions of the standard LANL2DZ

Fig. 2. (*a*) Optimized structures for the one-step Pd(II) re-arrangement between $PdBr(PH_3)$ and H in the $PdBr(PH_3)(C_6H_5)(C_6H_6)$ system. The enthalpy values are in kcal mol^{-1}; (*b*) structure of the $[CH_2(C_6H_5)(C_6H_5)(H)]^+$ transition state.

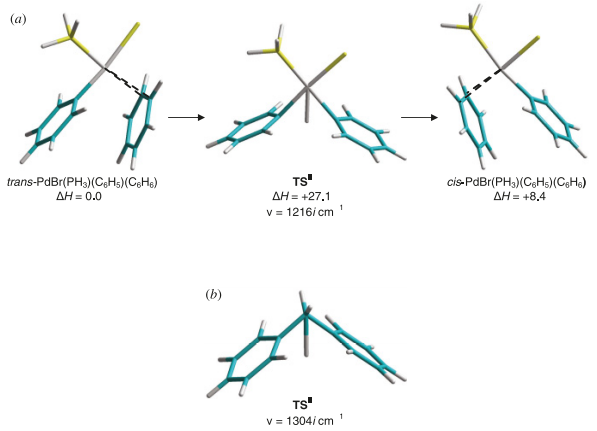

Fig. 3. (*a*) Optimized structures of the $[PdBr(PH_3)(C_6H_5)_2Li]^+$ and $[PdBr(PH_3)(C_6H_5)_2Na]^+$ systems; (*b*) Optimized structures of the $[(CH_2)(C_6H_5)(C_6H_5)(Li)]^+$ and $[(BH_2)(C_6H_5)(C_6H_5)(Li)]$ systems.

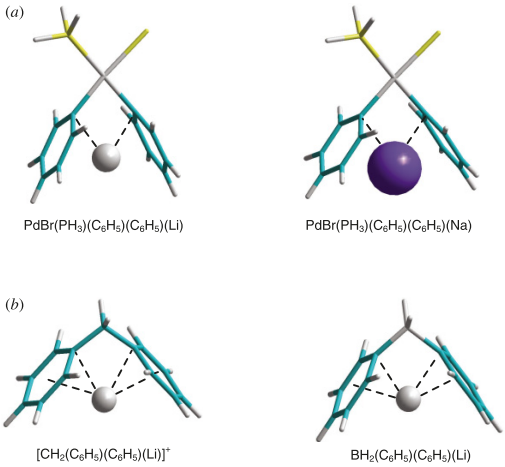

basis set have been replaced by a [41] split of the 5p function optimized by Couty and Hall.[35] For the Br atom, the quasi relativistic energy-adjusted spin-averaged effective core potential was taken from the work of the Stuttgart group, together with their [31/31] basis set,[37] to which s and p diffuse functions (with exponents of 0.0493 and 0.0363, respectively), and a d polarization function (of exponent 0.381) were added, following Radom et al.[38] The other atoms were described by the standard polarized 6–31G* basis set.[39] The cis/trans label that will be used throughout this paper refers to the relative position of the bromine atom and the carbon atom covalently bound to palladium. Note that the transfer will connect a cis structure to a trans structure and vice versa. Since both types of transfer led to similar conclusions, we will focus here on the transfer that starts from the most stable isomer, that is the trans isomer. The nature of the optimized structures, either transition states or intermediates, was assessed through a frequency calculation. Since we are dealing here with intramolecular processes, we will concentrate on enthalpy values, which were obtained by taking into account zero-point energies and the thermal motion at standard conditions (temperature of 298.15 K, pressure of 1 atm) (1 atm = 101.325 kPa). In our first study,[19] we checked that the geometrical parameters obtained with this basis set are in agreement with related experimental structures of bromo-palladium complexes and that the thermodynamic values obtained with this basis set were quite comparable to those obtained with larger basis sets.

Results and discussion

The $PdBr(PH_3)(C_6H_5)(C_6H_6)$ parent system

We will start our study by an analysis of the unsubstituted system $PdBr(PH_3)(C_6H_5)(C_6H_6)$. For this system, the results turned out to be quite similar to the ones obtained previously for $PdBr(PH_3)(C_2H_3)(C_2H_4)$[20] (see Fig. 2*a*). The one-step Pd(II) pathway is the preferred one, with a rather accessible activation barrier of 27.1 kcal mol^{-1} (enthalpy value, 1 cal = 4.184 J). In the transition state, the transferred hydrogen lies halfway between the two ipso carbon atoms and is roughly collinear with them (the C···H···C angle amounting to 166.8°). The value of the imaginary frequency (1216*i* cm^{-1}) compares well with the ones obtained previously for a one-step proton transfer.[19–21] As for $PdBr(PH_3)(C_2H_3)(C_2H_3)(H)$, one can make use of the isolobal analogy of the $PdBr(PH_3)(C_6H_5)(C_6H_5)(H)$ structure with CH_5^+ to account for the protonic character of the transferred hydrogen. The isolobal analogy between $PdBr(PH_3)$ and CH_2^+ is also best exemplified by the results of the geometry optimization that we carried out on the isolobal $[CH_2(C_6H_5)(C_6H_5)(H)]^+$ system. As shown on Fig. 2*b*, the optimized structure is quite similar to the structure of the $PdBr(PH_3)(C_6H_5)(C_6H_5)(H)$ transition state and is characterized by a single imaginary frequency of 1304*i* cm^{-1}, again typical of a through space proton transfer between two aryls.[20]

It is also noteworthy that, at variance with the $PdBr(PH_3)(C_2H_3)(C_2H_4)$ system of our previous study,[20] we could not get any one-step Pd(IV) transition state. We stressed in that study that for such a transition state to be operative, a coplanar arrangement of the two organic moieties involved in the transfer is necessary. In the $PdBr(PH_3)(C_6H_5)(C_6H_5)(H)$ system investigated here, a coplanar arrangement of the two mutually cis phenyl ligands is no longer possible due to the steric hindrance that would arise between the phenyl groups. That precludes the existence of a Pd(IV) transition state.

The $PdBr(PH_3)(C_6H_5)(C_6H_5M)$ systems (M = Li, Na)

Replacing the transferred hydrogen atom of Fig. 2*a* by either lithium or sodium led to a totally different situation, i.e., we could not in both cases find any transition state. Instead, the structure with either Li^+ or Na^+ halfway between the two carbon atoms turned out to be an "intermediate" (see Fig. 3*a*). This result is at variance with what has been found in previous computational studies of the isolobal system $[LiCH_4]^+$ [40–44] since they all conclude to the C_{3v} structure (with Li^+ bound in a trihapto fashion to three hydrogen atoms) as being the most stable one. The C_{2v} structure, in which the lithium ion is located along the C_2 axis of CH_4 is a transition structure, as in CH_5^+, although the energy

difference between the two structures, when reported[41–43] is very small (between 1 and 2 kcal mol^{-1} depending on the computational level and on whether basis set superposition error has been taken into account or not). Similar results have also been obtained for $[NaCH_4]^+$.[43] Thus, one might conclude that the isolobal analogy does not work here, since its use would lead to the wrong conclusion that the $PdBr(PH_3)(C_6H_5)(C_6H_5)(Li)$ structure should be a transition state interconnecting *cis*- and *trans*-$PdBr(PH_3)(C_6H_5)(C_6H_5Li)$. In fact this failure of the isolobal analogy is only apparent. It can be traced to the replacement of the two phenyl rings by two hydrogens "and not" to the replacement of $PdBr(PH_3)$ unit by CH_2^+. Unlike the two hydrogens, the two phenyls can experience quite strong cation–π interactions.[45] Compare for instance the affinity of Li^+ for benzene, in an η^6 fashion, with the one for CH_4: 38.3 kcal mol^{-1} instead of 12.6 kcal mol^{-1} according to Ehlers et al.,[43] who have computed both systems at the B3PW91/6–311++G(3d,2p) level. Similar values have been obtained at the B3LYP,[46] MP2 and CCSD(T) level,[47–49] and experimentally in the gas phase.[48] There have also been some reports of X-ray crystal structures of systems in which the lithium atom is η^6 bound to benzene[50] or to a phenyl ring.[51] It is therefore not surprising that the $PdBr(PH_3)(C_6H_5)(C_6H_5Li)$ system will yield a stable structure with Li^+ embedded between the two phenyl groups. Indeed the bond dissociation energy (at 0 K) of a benzene ring from the bis(benzene) $[Li(\eta^6\text{-}C_6H_6)_2]^+$ system is rather high (24.9 ± 1.6 kcal mol^{-1} experimentally, and 25.0 kcal mol^{-1} at the MP2/6–311+G(2d,2p)//MP2/6–311+G(2d,2p) level with BSSE correction).[48] At the B3LYP/6–31G*// B3LYP/6–31G* level (which is our level of calculation), we obtained a value (not BSSE corrected) of 26.2 kcal mol^{-1}.

Thus, to better reconcile our findings with the isolobal analogy concept, one should keep the two phenyl groups and replace only the $PdBr(PH_3)$ moeity by CH_2^+. One can also consider BH_2 instead of CH_2^+. This leads to$[(CH_2)(C_6H_5)(C_6H_5)(Li)]^+$ and $[(BH_2)(C_6H_5)(C_6H_5)(Li)]$ as isolobal analogs of $PdBr(PH_3)(C_6H_5)(C_6H_5)(Li)$. We indeed obtained stable structures for these two systems (see Fig. 3*b*). Note that lithium tetraphenylborate $Li(BPh_4)$ would also be an isolobal analog. $Li(BPh_4)$ is not known experimentally, since organolithium compounds usually occur as oligomers and (or) are stabilized by donor ligands.[52–60] This is in particular the case for the tetraphenylborate salts, such as $[Li(H_2O)_4][BPh_4]$,[61] $[Li(THF)_2(H_2O)_2][BPh_4]$,[62] and $[Li(CH_3OCH_2CH_2OCH_3)(H_2O)_2][BPh_4]$,[63] where the interaction with the tetraphenylborate anion takes place through hydrogen bonding between one water molecule and two phenyl groups. But in potassium and rubidium tetraphenylborate[64,65] the potassium and rubidium cations are embedded between two phenyl rings and experience M^+–π interactions, just like the Li^+ or Na^+ cations in $PdBr(PH_3)(C_6H_5)(C_6H_5)(Li)$ or $PdBr(PH_3)(C_6H_5)(C_6H_5)(Na)$. Quite interesting too is the crystal structure of lithium diferrocenyldiphenylborate·Bu_2O $[Li(OBu_2)][BFc_2Ph_2]$ **1** and of the compound $[(Li(OBu_2))_2][1,1'\text{-}Fc(BPh_3)_2]$,[66] **2,** which are again isolobal analogs of the palladium system. In these systems, Li is bound to only one dibutyl ether molecule and interacts with either two Cp rings, as sketched in **1**, or with one Cp and one phenyl ring, as sketched in **2**. Thus, these results point to the pertinence of the isolobal analogy, when used circumspectly.

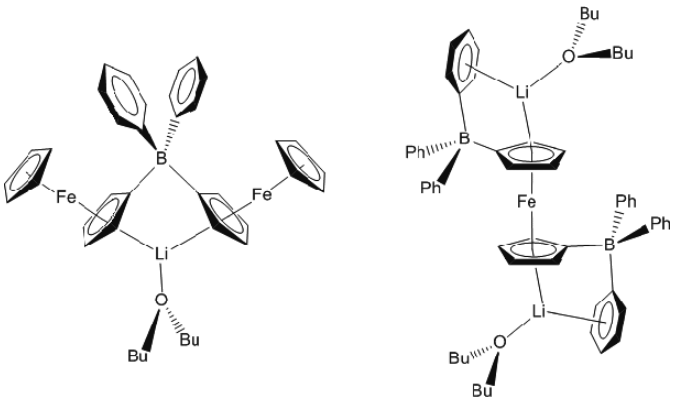

1 **2**

The details of the structure of $PdBr(PH_3)(C_6H_5)(C_6H_5)(Li)$ and the energetics of the reaction $PdBr(PH_3)(C_6H_5)$ + C_6H_5Li → $PdBr(PH_3)(C_6H_5)(C_6H_5)(Li)$ also deserve some comments. We may first note that the lithium atom does not lie exactly above the center of the phenyl rings, as in $[Li(C_6H_6)]^+$ and $[Li(C_6H_6)_2]^+$ but is displaced toward the meso carbon atoms: The Li–C_{meso} average bond distance amounts to 2.306 Å, whereas the Li–C_{ortho}, Li–C_{meta}, and Li–C_{para} average bond distances amount to 2.413, 2.611, and 2.695 Å, respectively. The Li–C_{meso} bond distance compares well with the Li–C bond distance computed for $[Li(C_6H_6)_2]^+$,[48] and is somewhat shorter than the Li–C_{meso} bond distance of 2.42 Å in **2**.[66] Note also the relatively acute C_{phenyl}-Pd-C_{phenyl} angle of 81.4°, and the fact that the two phenyl ligands are tilted slightly inward toward the Li (with the Pd-C_{meso}-C_{ortho}-C_{meta} dihedral angle amounting to 163°). This shows clearly how the complex adapts itself to maximize the interaction with lithium. The enthalpy and the Gibbs free energy for the reaction *trans*-$PdBr(PH_3)(C_6H_5)$ + C_6H_5Li → $PdBr(PH_3)(C_6H_5)(C_6H_5)(Li)$ are indeed rather large, –61.2 kcal mol^{-1} and –47.2 kcal mol^{-1}, respectively. The ΔH value is much larger than the value computed for the reaction $[(C_6H_6)Li]^+ + C_6H_6 \rightarrow [(C_6H_6)_2Li]^+$.[47] One may therefore tentatively propose the synthesis of such embedded lithium complexes through the reaction of phenyl lithium with an appropriate palladium complex. We are of course well aware that one should take into account the fact that phenyl lithium interacts with solvation molecules and that the interaction of such molecules in the first coordination sphere of lithium would reduce the magnitude of the interaction with the phenyl group, as shown theoretically by Sastry et al. for $[(C_6H_6)Li^+(H_2O)_n]$.[67] But the fact that the synthesis of **2** could be successfully achieved strengthens our present proposal.

We can finally analyze briefly the results for the Na system. Here too, the sodium atom is embedded between the two phenyl rings (see Fig. 3*a*). The Na–C_{phenyl} distances are longer than the Li–C_{phenyl} distances by 0.2–0.3 Å. A similar lengthening has been obtained in $(C_6H_6)M^+$ and $[(C_6H_6)_2]M^+$, when M is changed from Li to Na.[46–49] In line with this lengthening, one notes that the C_{phenyl}-Pd-C_{phenyl} angle is less acute (84.2°) and that the phenyl rings are also less tilted inward toward the alkali metal (the Pd-C_{meso}-C_{ortho}-C_{meta} dihedral angle value of 171° being now closer to 180°). Yet, the enthalpy and the Gibbs free en-

Fig. 4. (*a*) Optimized structure of $PdBr(PH_3)(C_6H_5)_2BH_2$; (*b*) Optimized structure of the $[BH_2(C_6H_5)_2]^-$ anion.

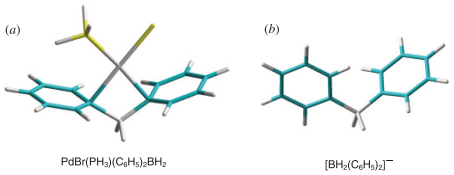

Fig. 5. (*a*) Optimized structure of $PdBr(PH_3)(C_6H_5)_2AlH_2$: front view and view along the Pd···Al line of the $PdBr(PH_3)(C_6H_5)_2AlH_2$ system; (*b*) Optimized structure of the $[PdBr(PH_3)(C_6H_5)_2]^-$ anion.

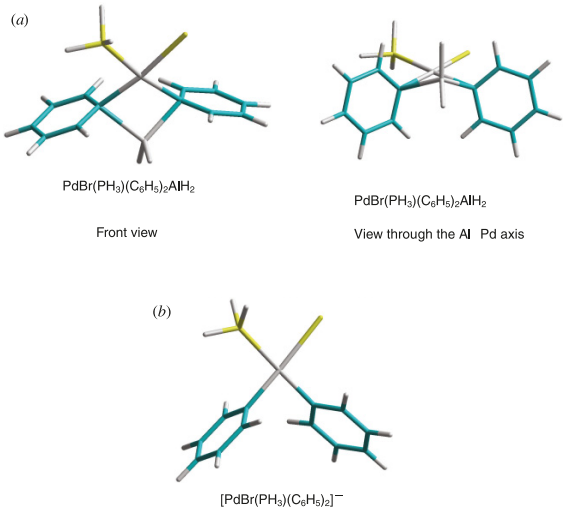

Scheme 2. Isolobal relationships between various systems incorporating the AlH_2 or $AlMe_2$ moiety.

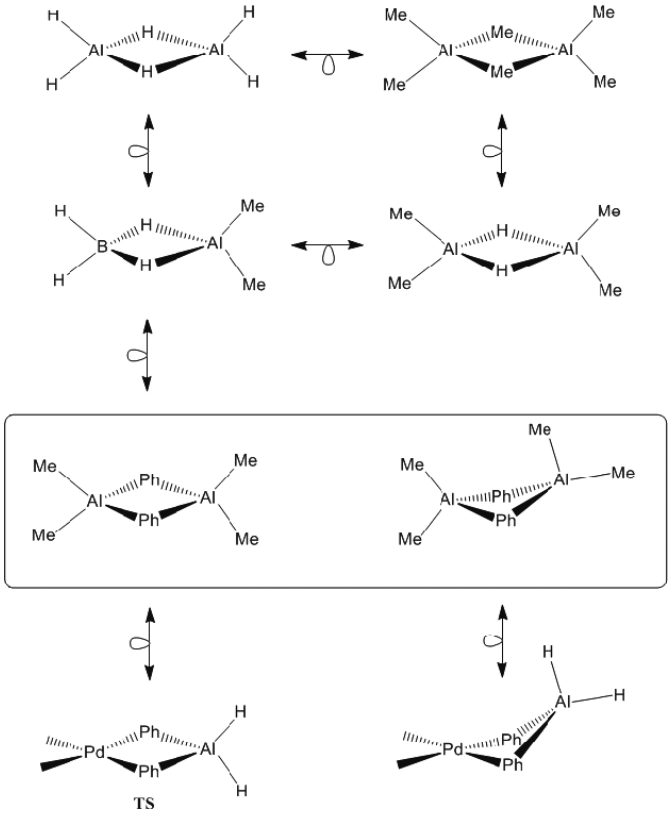

ergy of the *trans*-$PdBr(PH_3)(C_6H_5)$ + C_6H_5Na → $PdBr(PH_3)(C_6H_5)(C_6H_5)(Na)$ reaction hardly change, with values of –62.0 and –48.0 kcal mol^{-1}, respectively.

The $PdBr(PH_3)(C_6H_5)(C_6H_5AH_2)$ systems (A = B, Al)

In phenylboron dihydride, which can be considered as a model for phenylboron dihalides, the BH_2 group is of cationic character. This is also true for the AlH_2 group in $(C_6H_5)AlH_2$. We therefore investigated the fate of the reaction between $PdBr(PH_3)(C_6H_5)$ and either $(C_6H_5)BH_2$ or $(C_6H_5)AlH_2$. As in the previous paragraph, we will use the isolobal analogy to analyze the corresponding results.

The replacement of the $PdBr(PH_3)$ moiety in $PdBr(PH_3)(C_6H_5)_2BH_2$ by its isolobal analogs CH_2^+ or BH_2, and of the two phenyl groups by H, leads to the BCH_6^+ cation and to the well-known (experimentally and theoretically) diborane molecule B_2H_6. It is therefore not surprising to find as a stable structure the one shown in Fig. 4*a*, with the BH_2 group lying halfway between the two phenyl groups and the BH_2 plane perpendicular to the PdBrP plane. The BCH_6^+ cation has been theoretically studied[68–70] and found to adopt a structure somewhat analog to the one of B_2H_6, i.e., of the form $[H_2C(\mu\text{-}H)_2BH_2]^+$. Quite noticeably, the AIM analysis and the natural orbital analysis performed at the MP2/cc-pVTZ level by Zeng and Davico[70] suggest that the bonding pattern is best described as involving CH_4 in interaction with a BH_2^+ fragment. The optimized structure of Fig. 4*a* is consistent with this bonding pattern: In $PdBr(PH_3)(C_6H_5)_2BH_2$, the $[BH_2(C_6H_5)_2]$ fragment adopts a structure, which is the one of $[BH_2(C_6H_5)_2]^-$ (see Fig. 4*b*). The $PdBr(PH_3)(C_6H_5)_2BH_2$ system is therefore best described as being made of a $[BH_2(C_6H_5)_2]^-$ fragment, which is isolobal to CH_4, in interaction with $[PdBr(PH_3)]^+$, which is isolobal toBH_2^+.

If one now compares the optimized structure of $PdBr(PH_3)(C_6H_5)_2BH_2$ with the one of $PdBr(PH_3)(C_6H_5)_2AlH_2$ (see Figs. 4*a* and 5*a*), one will immediately notice that they differ primarily by the orientation of the two phenyl groups. In $PdBr(PH_3)(C_6H_5)_2BH_2$, the phenyl groups bend away from the boron atom, as in $[BH_2(C_6H_5)_2]^-$, whereas in $PdBr(PH_3)(C_6H_5)_2AlH_2$, they bend away from the palladium atom, as in $[PdBr(PH_3)(C_6H_5)_2]^-$ (see Fig. 5*b*). Thus, the $PdBr(PH_3)(C_6H_5)_2AlH_2$ system now best corresponds to the interaction of a $[PdBr(PH_3)(C_6H_5)_2]^-$ anionic fragment with the AlH_2^+ moiety. This is again consistent with the picture that one can draw from the isolobal analogy. All calculations carried out on the $H_2B(\mu\text{-}H)_2AlH_2$ system by several groups conclude to an electronic structure of the $(BH_4)^-(AlH_2)^+$ type.[71–74] Another structural feature also deserves some comments. In contrast to $PdBr(PH_3)(C_6H_5)_2BH_2$ the Pd-C-Al-C, central ring of the $PdBr(PH_3)(C_6H_5)_2AlH_2$ system is no longer planar, but folded about the Pd···Al line (by 39.3°), see the view along this line in Fig. 5*a*. Al_2H_6,[75] Al_2Me_6,[76] $[Me_2AlH]_2$,[77] and $H_2B(\mu\text{-}H)_2AlMe_2$[78] have a planar central ring, as B_2H_6 (see Scheme 2). The same holds true for $Ph_2Al(\mu\text{-}Ph)_2AlPh_2$.[79] But the X-ray crystal structure of $Me_2Al(\mu\text{-}Ph)_2AlMe_2$, which is isolobal to $PdBr(PH_3)(C_6H_5)_2AlH_2$, shows two kinds of molecules, one with a central planar ring and one with a folded central ring

Scheme 3. Structures obtained through the coupling of $Pd(Br)(C_6H_5)(PH_3)$ and $(C_6H_5)BH_2$. The enthalpies, in kcal mol^{-1}, are relative to the separated *trans*-$PdBr(PH_3)(C_6H_5)$ + $(C_6H_5)BH_2$ reactants. Relative free energy values are in italic.

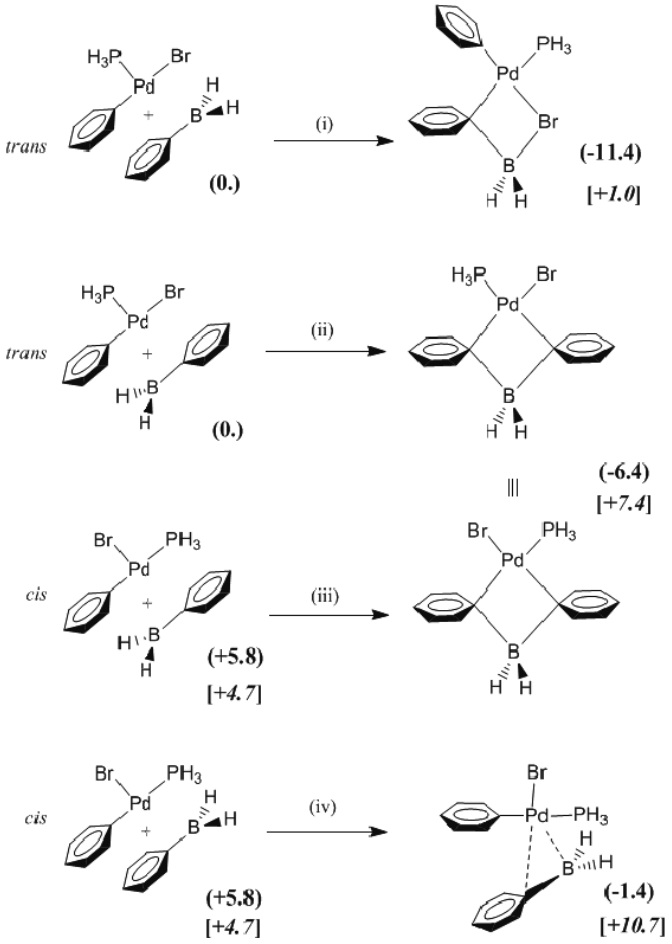

Fig. 6. Optimized structures for the reaction of $(C_6H_5)BH_2$ with *trans*-$PdBr(PH_3)(C_6H_5)$ to yield $PdBr(PH_3)(\mu\text{-}C_6H_5)_2BH_2$. The enthalpy values are in kcal mol^{-1}.

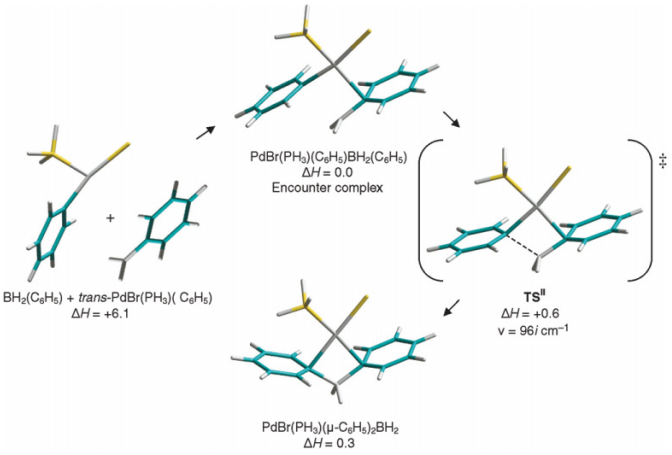

(by 13.7°).[80] In our case, the conformer with a planar central ring turned out to be the transition state for the flipping between the two folded conformers (imaginary frequency of

Fig. 7. Optimized structure of $Pd(PH_3)(C_6H_5)(\mu\text{-}Br)(\mu\text{-}C_6H_5)BH_2$.

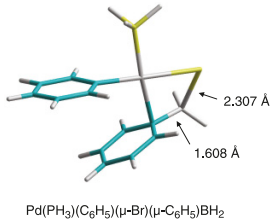

Fig. 8. (*a*) Optimized structures of the $PdBr(PH_3)(C_6H_5)_2(BeH)$ and $PdBr(PH_3)(C_6H_5)_2(BeCH_3)$ systems; (*b*) Optimized structure of $H_2B(\mu\text{-}H)_2BeCp$.

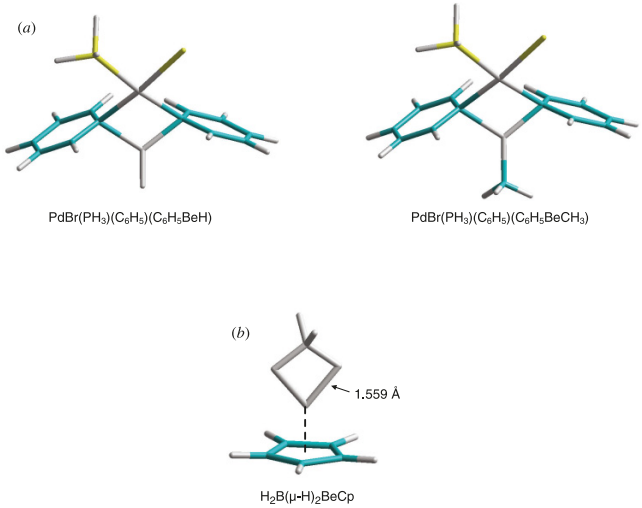

Fig. 9. Optimized structures of the different $[PdBr(PH_3)(\mu\text{-}C_6H_5)]_2$ dimers.

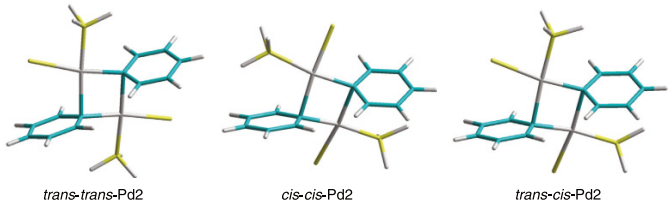

24*i* cm^{-1}). The computed energy barrier for this flipping is very low, only 1.1 kcal mol^{-1}.

The $PdBr(PH_3)(\mu\text{-}C_6H_5)_2BH_2$ and $PdBr(PH_3)(\mu\text{-}C_6H_5)_2AlH_2$ systems of Figs. 4*a* and 5*a* also differ by their stabilization with respect to the separated reactants, $PdBr(PH_3)(C_6H_5)$ and $(C_6H_5)BH_2$ on one hand for boron, and $PdBr(PH_3)(C_6H_5)$ and $(C_6H_5)AlH_2$ on the other hand for aluminium. For *trans*-$PdBr(PH_3)(C_6H_5)$, we computed a stabilization enthalpy of 6.4 kcal mol^{-1} in the former case and of 22.0 kcal mol^{-1} in the latter one (values not BSSE corrected). This is in line with the greater propensity of aluminum organyls to dimerize.[81] For *cis*-$PdBr(PH_3)(C_6H_5)$, the stabilization enthalpy is 5.8 kcal mol^{-1} larger, a value that corresponds to the destabilization of *cis*-$PdBr(PH_3)(C_6H_5)$ with respect to its isomer *trans*-$PdBr(PH_3)(C_6H_5)$.

We have investigated the reaction of $PdBr(PH_3)(C_6H_5)$ with $(C_6H_5)BH_2$ with some depth. As indicated in the Scheme 3, four modes of approach, (i) to (iv), can be de-

Table 1. Calculated and experimental structures of the $H_2B(\mu\text{-}H)_2Be(C_5H_5)$ system.

	B3LYP/6–31G*	B3LYP/6–311++G**	Experimental[a]
$(Be—C)_{av}$	1.941	1.939	1.915 (5)
Be—B	1.924	1.916	1.88 (1)
B—H_t	1.201	1.196	1.17 (3)
B—H_b	1.255	1.250	1.29 (5)
Be—H_b	1.559	1.556	1.78 (9)
Be–B–H_b	53.9	54.0	65 (4)
H_t–B–H_b	107.6	107.5	123 (9)

Note: Note: Distances are in Å; angles are in degrees.

[a]Reference Drew et al. 1972.[86]

Scheme 4*a*. Phenyl-bridged structures obtained through the homo coupling of $Pd(Br)(C_6H_5)(PH_3)$. The enthalpies, in kcal mol^{-1}, are relative to the separated *trans*-$PdBr(PH_3)(C_6H_5)$ + *trans*-$PdBr(PH_3)(C_6H_5)$ reactants. Relative free energy values are in italic.

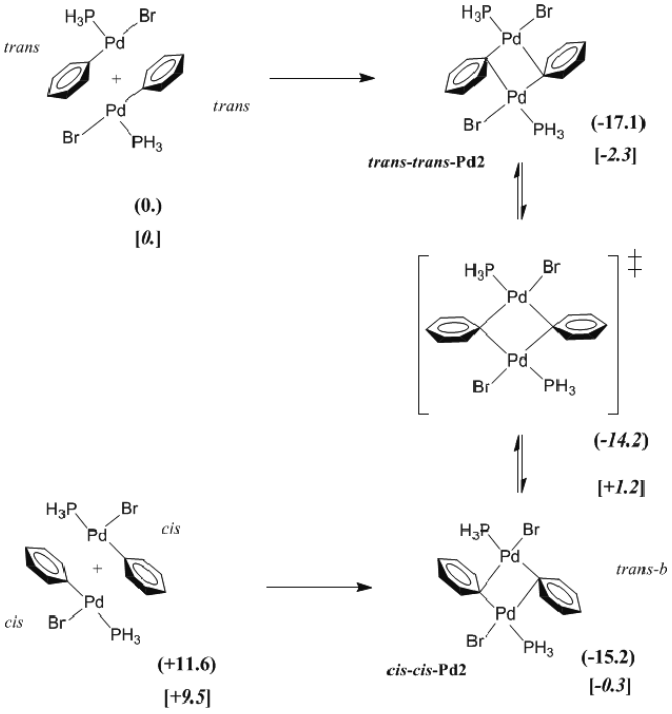

Scheme 4*b*. Phenyl-bridged structures obtained through the hetero coupling of $Pd(Br)(C_6H_5)(PH_3)$. The enthalpies, in kcal mol^{-1}, are relative to the separated *trans*-$PdBr(PH_3)(C_6H_5)$ + *trans*-$PdBr(PH_3)(C_6H_5)$ reactants. Relative free energy values are in italic.

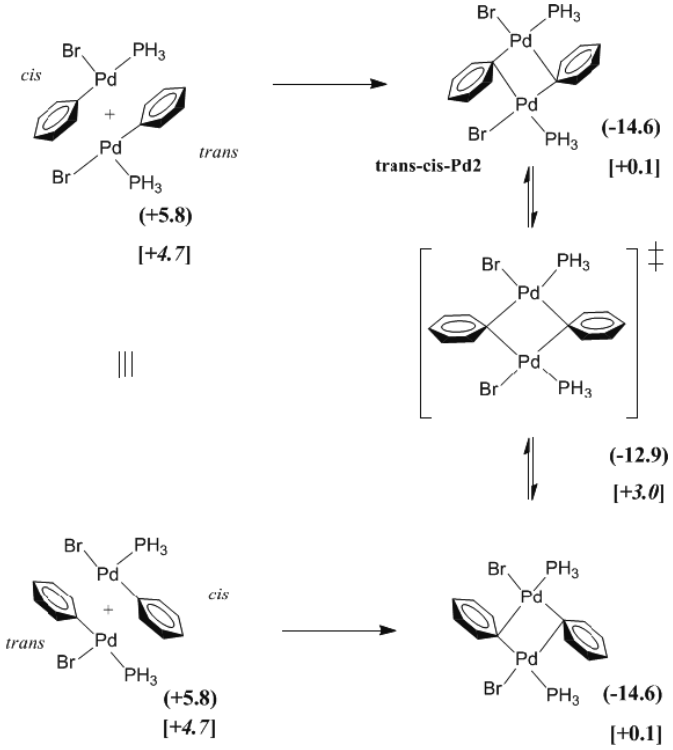

lineated, depending on whether the *cis*- or the *trans*-$PdBr(PH_3)(C_6H_5)$ complex is considered and on whether in the approach the two phenyl groups are facing each other or not. Note that (ii) and (iii) lead in fact to two identical structures. We were able to locate a transition state for the addition of $(C_6H_5)BH_2$ to *trans*-$PdBr(PH_3)(C_6H_5)$ that leads to $PdBr(PH_3)(\mu\text{-}C_6H_5)_2BH_2$ (pathway (ii), see Fig. 6). As shown in this figure, it lies 0.6 kcal mol^{-1} above an encounter complex that correspond to an η^1 coordination of the phenyl group of $(C_6H_5)BH_2$, and 0.9 kcal mol^{-1} above the product $PdBr(PH_3)(\mu\text{-}C_6H_5)_2BH_2$.

We could not find a similar reaction path for the addition of $(C_6H_5)BH_2$ to *cis*-$PdBr(PH_3)(C_6H_5)$, whatever disposition $(C_6H_5)BH_2$ may adopt. The only species that could be unambiguously characterized was a weak interaction complex schematically shown in the Scheme 3 as the outcome of pathway (iv). Finally, one should stress that $PdBr(PH_3)(\mu\text{-}C_6H_5)_2BH_2$ is not the most stable structure, the $Pd(PH_3)(C_6H_5)(\mu\text{-}Br)(\mu\text{-}C_6H_5)BH_2$ structure with one bridging phenyl and one bridging bromine, see Fig. 7, being more stable than $PdBr(PH_3)(\mu\text{-}C_6H_5)_2BH_2$ by 5 kcal mol^{-1}. We have no clear-cut explanation for this greater stability. Phenylhaloboranes Ph_nBX_{3-n} (n = 1, 2; X = F, Cl, Br, or I) are usually monomeric.[82] On the other hand, in the case of haloalanes,[81] halogens are known to be better bridging ligands than phenyls. The Br-bridged structure may be helped also by the disposition of the two phenyl rings in a π-stacking arrangement, see Fig. 7, with the closest carbon···carbon distances of about 3.5 Å.[83] As shown on Scheme 3, it may be obtained via the pathway (i). Alternatively, since the transition state and the encounter complex of pathway (*ii*) are very close in energy from *trans*-$PdBr(PH_3)(\mu\text{-}C_6H_5)_2BH_2$, it

Scheme 4*c*. Bromo-bridged structures obtained through the homo and hetero coupling of $Pd(Br)(PH_3)(C_6H_5)$. The enthalpies, in kcal mol^{-1}, are relative to the separated *trans*-$PdBr(PH_3)(C_6H_5)$ + *trans*-

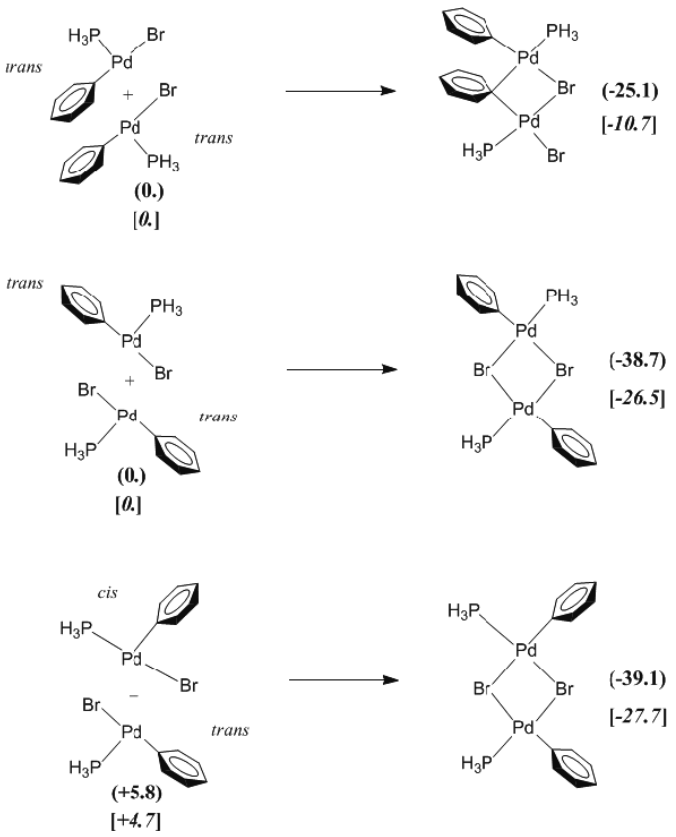

could be obtained from *trans*-$PdBr(PH_3)(\mu\text{-}C_6H_5)_2BH_2$ via a pathway that would comprise first a partial dissociation of $(C_6H_5)BH_2$, followed by a rotation of $(C_6H_5)BH_2$ around the Pd–C bond in the encounter complex, and a final recombination of the two entities to yield the μ-bromo structure.

The $PdBr(PH_3)(C_6H_5)(C_6H_5BeR)$ systems (R = H, CH_3)

The optimized structures of $PdBr(PH_3)(C_6H_5)(C_6H_5BeH)$ and $PdBr(PH_3)(C_6H_5)$ $(C_6H_5BeCH_3)$ are shown on Fig. 8*a*. As for $PdBr(PH_3)(C_6H_5)(C_6H_5AlH_2)$, we found, for each of these systems, a stable structure with a folded central ring and a transition state with a planar central ring associated to the flipping movement of this central ring. The values of the fold angle are quite similar to the one obtained in the case of AlH_2, 39.0° and 39.9° for $PdBr(PH_3)(C_6H_5)(C_6H_5BeH)$ and $PdBr(PH_3)(C_6H_5)(C_6H_5BeCH_3)$, respectively. The energy barriers are also quite low, 2.2 and 2.3 kcal mol^{-1}, respectively.

We can try to push the isolobal analogy further. Since $PdBr(PH_3)$ is isolobal to BH_2, the $PdBr(PH_3)(\mu\text{-}C_6H_5)_2BeH$ system is isolobal to $H_2B(C_6H_5)_2BeH$. If one replaces the two phenyl groups by two hydrogens, one gets the H_4BBeH system, for which the $HB(\mu\text{-}H)_3BeH$ triply bridged structure, which corresponds to the folded structure of $PdBr(PH_3)(C_6H_5)(C_6H_5BeH)$, has been found to be more stable than the $H_2B(\mu\text{-}H)_2BeH$ double-bridged structure at both the SCF and MP2 levels.[84,85] Moreover, the MP2 calculations indicated that the double-bridged structure is a transition state rather than a stable structure.[84] This is again in line with our results of the previous paragraph for $PdBr(PH_3)(C_6H_5)(C_6H_5BeH)$.

Finally, replacing H (or CH_3) by a cyclopentadienyl group leads to cyclopentadienylberyllium borohydride $CpBeBH_4$ for which the double-bridged structure $H_2B(\mu\text{-}H)_2BeCp$ has been inferred on the basis of gas-phase electron-diffraction measurements supplemented by an infrared and Raman spectra analysis.[86,87] The electron-diffraction study could not distinguish between a double- or a triple-bridged borohydride linkage. Accordingly, the bridging hydrogens were characterized by very large standard deviations (e.g., up to 0.09 Å for the $Be–H_b$ bond distance).[86] Although this system was considered in a theoretical study that dealt with the determination of ^{9}Be NMR chemical shifts,[88] its structure was not optimized. We have therefore carried out such a geometry optimization, using basis sets of increasing quality, viz. 6–31G*, 6–31G**, and 6–311++G**. All basis sets led to the double-bridged structure $H_2B(\mu\text{-}H)_2BeCp$ (Fig. 8*b*), as one could have anticipated from the isolobal analogy and in agreement with the results of the vibrational spectra.[87] Note, however, that with this example, one reaches again the limits of the concept, since the $H_2B(\mu\text{-}H)_2BeCp$ most stable structure is not folded, in contrast to the most stable structure of $PdBr(PH_3)(\mu\text{-}C_6H_5)_2(BeCH_3)$. We checked whether this might be due to the replacement of the two phenyls by two hydrogens by considering the $H_2B(C_6H_5)_2BeCp$ system. But the geometry optimization starting from a $H_2B(\mu\text{-}C_6H_5)_2BeCp$ geometry with two bridging phenyls led to the $(H)(C_6H_5)B(\mu\text{-}H)(\mu\text{-}C_6H_5)BeCp$ structure, with one bridging hydrogen and one bridging phenyl only. This structure is folded, however, with a fold angle of 21.6°. The $H_2B(\mu\text{-}C_6H_5)_2BeCp$ structure was not obtained, and that can be traced to the steric repulsion that would be experienced between the Cp ring and the two phenyl groups. In fact, the $(C_6H_5)_2B(\mu\text{-}H)_2BeCp$ structure, with two bridging hydrogens and two terminal phenyl groups turned out to be more stable by 8.3 kcal mol^{-1}, but planar. The folding of these systems seems therefore to be linked to the presence of bridging phenyls.

The values computed (at the B3LYP/6–31G* and 6–311++G** levels) for selected structural parameters of the $H_2B(\mu\text{-}H)_2BeCp$ system are reported in Table 1 together with the values deduced experimentally from the gas-phase electron-diffraction data. They generally agree, with the exception of the bridging-hydrogen values, for which large discrepancies are found: 0.22 Å for the $Be–H_b$ bond distance, 11° for the $Be\text{-}B\text{-}H_b$ angle, and 15° for the $H_t\text{-}B\text{-}H_b$ angle, whatever the basis set is. We have already mentioned the large experimental standard deviation for these parameters. Thus, we think, on the basis of our results, that the $H_2B(\mu\text{-}H)_2BeCp$ system warrants a re-investigation of its molecular structure.

The $[PdBr(PH_3)(C_6H_5)]_2$ dimer

We can use again the isolobal analogy of $PdBr(PH_3)$ with BH_2 to obtain the $[PdBr(PH_3)(\mu\text{-}C_6H_5)]_2$ dimer as the isolobal analog of the $PdBr(PH_3)(\mu\text{-}C_6H_5)_2BH_2$ system. Similarly, the dimerization reaction of $PdBr(PH_3)(C_6H_5)$ and the reaction of $PdBr(PH_3)(C_6H_5)$ with $(C_6H_5)BH_2$ should bear some resemblance. We indeed found three stable dimeric

Fig. 10. Optimized structures for the two-step Pd(IV) re-arrangement between $PdBr(PH_3)$ and Br in the $PdBr(PH_3)(C_6H_5)(C_6H_5Br)$ system. The enthalpy values are in kcal mol^{-1}. The distances are in Å.

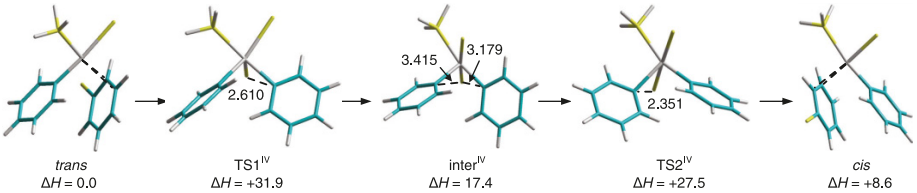

Table 2. Calculated energies for the Pd(IV) pathway in the trans–cis transformation of structures $PdBr(PH_3)(C_6H_5)(C_6H_5Y)$ (Y = F, Cl, Br, CH_3, OH, SH).

System		ΔE	ΔH	ΔG	Imaginary frequency[a]
Y = F	trans	0.0	0.0	0.0	
	$TS1^{IV}$	+54.1	+52.5	+54.0	296*i*
	$Inter^{IV}$	+37.4	+36.4	+36.7	
	$TS2^{IV}$	+55.5	+53.3	+53.7	312*i*
	cis	+9.2	+8.6	+8.1	
Y = Cl	trans	0.0	0.0	0.0	
	$TS1^{IV}$	+41.9	+40.3	+41.6	159*i*
	$Inter^{IV}$	+22.6	+21.7	+22.0	
	$TS2^{IV}$	+36.0	+34.2	+35.2	230*i*
	cis	+9.2	+8.6	+8.2	
Y = Br	trans	0.0	0.0	0.0	
	$TS1^{IV}$	+33.3	+31.9	+33.1	104*i*
	$Inter^{IV}$	+18.1	+17.4	+18.0	
	$TS2^{IV}$	+29.2	+27.5	+28.5	186*i*
	cis	+9.2	+8.6	+8.0	
Y = CH_3	trans	0.0	0.0	0.0	
	$TS1^{IV}$	+57.0	+54.7	+56.5	311*i*
	$Inter^{IV}$	+50.8	+49.0	+49.2	
	$TS2^{IV}$	+56.9	+54.7	+56.5	311*i*
	cis	+8.9	+8.3	+7.4	
Y = OH	trans	0.0	0.0	0.0	
	$TS1^{IV}$	+58.4	+56.5	+58.3	263*i*
	$Inter^{IV}$	+49.0	+47.3	+47.0	
	$TS2^{IV}$	+58.7	+56.4	+57.8	287*i*
	cis	+10.1	+9.5	+9.2	
Y = SH	trans	0.0	0.0	0.0	
	$TS1^{IV}$	+32.2	+30.9	+32.9	176*i*
	$Inter^{IV}$	+29.4	+28.5	+29.0	
	$TS2^{IV}$	+34.6	+32.9	+34.7	187*i*
	cis	+9.8	+9.2	+8.7	

Note: The values are in kcal mol^{-1}; the zero of energy for the Pd migration in $PdBr(PH_3)(C_6H_5)(C_6H_5Y)$ refers, respectively, to the corresponding trans isomers. The B3LYP total energies (in a.u.) for Y = F are E = –1046.453680, H = –1046.221620, and G = –1046.291008; for Y = Cl: E = –1406.811765, H = –1406.580727, and G = –1406.651583; for Y = Br: E = –960.001520, H = –959.770805, and G = –959.842577; for Y = CH_3: E = –986.538760, H = –986.269756, and G = –986.340732; for Y = OH: E = –1022.438885, H = –1022.194120, and G = –1022.263903; and for Y = SH: E = –1345.348696, H = –1345.111128, and G = –1345.180185.

[a]In cm^{-1}; refers to the unique imaginary frequency of the calculated transition state.

structures for $[PdBr(PH_3)(\mu\text{-}C_6H_5)]_2$ with the two phenyl rings as bridging ligands, that are denoted ***trans-trans*-Pd2**, ***cis-cis*-Pd2**, and ***trans-cis*-Pd2** in Fig. 9. ***Trans-trans*-Pd2** corresponds to the coupling of *trans*-$PdBr(PH_3)(C_6H_5)$ with another *trans*-$PdBr(PH_3)(C_6H_5)$, ***cis-cis*-Pd2** to the coupling of *cis*-$PdBr(PH_3)(C_6H_5)$ with *cis*-$PdBr(PH_3)(C_6H_5)$, and ***trans-cis*-Pd2** to the coupling of *trans*-$PdBr(PH_3)(C_6H_5)$ with *cis*-$PdBr(PH_3)(C_6H_5)$ (see Schemes 4*a* and 4*b*). Note that the ***trans-trans*-Pd2** and ***cis-cis*-Pd2** structures differ only by a flipping of the two phenyl rings (see Scheme 4*a*). They are rather close in energy, the ***trans-trans*-Pd2** structure being more stable than the ***cis-cis*-Pd2** structure by 1.9 kcal mol^{-1} (enthalpy value) only. The transition state for this synchronous flipping movement is also quite low, only 1 kcal mol^{-1} above ***cis-cis*-Pd2**. On the other hand, the ***trans-trans*-Pd2** and ***cis-cis*-Pd2** phenyl-bridged structures

are well stabilized with respect to the separated monomers, by –17.1 and –15.2 kcal mol^{-1}, respectively. Of course, entropy will work against this stabilization. When the entropy penalty is taken into account, one gets Gibbs free energy stabilization values of –2.3 kcal mol^{-1} and –0.3 kcal mol^{-1} only, the free energy barrier between the two structures amounting to 1.5 kcal mol^{-1} (from ***cis-cis*-Pd2**). We are well aware that the present entropy corrections, which assume that all molecules are an ideal gas, are probably too large.[89–93] Yet, an interesting feature may be inferred from this rather flat free energy profile, viz. that the process sketched in Scheme 4*a* provides a route for exchanging the non aromatic ligands in the three coordinated Pd(II) phenyl complex. Note that this route will be operative if there is no other dimeric structure of large thermodynamic stability. For the present "model" system, structures with one or two bridging bromines are, as expected,[94,95] much more stable than the phenyl-bridged structures (see Scheme 4*c*). But, similarly to what has been found for the existence of monomeric arylpalladium(II) halide complexes, which can be stabilized by agostic interactions,[94,96–99] there might be steric factors that favour the phenyl-bridged dimeric structure when real phosphine ligands are considered.

The $PdBr(PH_3)(C_6H_5)(C_6H_5Y)$ systems (Y = F, Cl, Br, CH_3, OH, SH)

As said in the introduction, we also considered substituents of anionic nature, namely Y = F, Cl, Br, CH_3, OH, and SH. The process that exchanges Y with $PdBr(PH_3)$ is shown in Fig. 10 for Y = Br. Not unexpectedly, it involves a classical two-step oxidative addition/reductive elimination pathway between the +2 and +4 oxidation states of Palladium. We are not aware of such a systematic theoretical study for Pd(II) systems. There have been two studies of the oxidative addition of C_6H_5I to three-coordinate Pd(II) complexes.[100,101] In contrast, for Pd(0) systems, the oxidative addition of CH_3Y to Pd and $PdCl^-$, with Y being either F, Cl, Br, or I, has been thoroughly analyzed.[102] There is also a very recent report of the oxidative addition of C_6H_5Y (with Y = Cl, Br, or I) to a PdL_2 complex, where L_2 is a pyridylpyrazol ligand.[103] Our results for the three-coordinate $PdBr(PH_3)(C_6H_5)$ substrate are reported in Table 2. As for the Pd(0) systems, the energy barrier for the oxidative addition decreases in the order F > Cl > Br. It is very high for CH_3 and OH. The lowest barriers are found for Br and SH, of the order of 30 kcal mol^{-1}. The literature values for iodine are smaller, between 10 and 15 kcal mol^{-1}.[100,101] This points to a similar reactivity order for Pd(0) and Pd(II) systems. Thus, the factors that govern the reactivity pattern (see ref. [102]) are probably similar in both oxidation states.

Conclusion

Our calculations have shown that the Pd/X group intermolecular exchange in the $[PdBr(PH_3)(C_6H_5)(C_6H_5X)]$ system is a relatively easy process when X = H, and can be viewed in this case as involving the migration of a proton between the two phenyls. At variance with this result, the transfer of entities, which are more electropositive, such as X = Li, Na, BH_2, AlH_2, BeH, or $BeCH_3$ cannot take place. Instead, one gets stable structures that correspond to an arrested transfer in which X lies halfway between the two phenyl groups and experiences interactions that are quite ionic. These stable structures can be rationalized through isolobal analogy arguments. In the case of beryllium, the correspondence has been made also with the experimentally known cyclopentadienylberyllium borohydride system, $CpBeH_4$. The results of the DFT geometry optimization call for a re-examination of the gas-phase electron-diffraction structure determination, especially for the bond distances and angles that pertain to the two bridging hydrogens. As far as the halogen series, X = F, Cl, or Br and the electronegative groups X = CH_3, OH, or SH are concerned, the transfer between the two phenyls can take place via a Pd(II)/Pd(IV) two-step oxidative addition/reductive elimination mechanism. Yet, the associated energy barriers are very high, except for Br and SH for which the process might be feasible. We have also considered the $[PdBr(PH_3)(C_6H_5)]$ dimer and analyzed its structure with μ-phenyl ligands on the basis of the isolobal analogy with the previous systems. We hope that this study will be an incentive for the synthesis of systems related to some of the models that have been analyzed here.

Acknowledgments

The calculations have been carried out at the Institut du Développement et des Ressources en Informatique Scientifique (IDRIS, Orsay). We also thank the Universidad de Granada for financial support.

References

(1) This article is part of a Special Issue dedicated to Professor T. Ziegler.
(2) Wang, L.; Pan, Y.; Jiang, X.; Hu, H. *Tetrahedron Lett.* **2000**, *41*, 725. doi:10.1016/S0040-4039(99)02154-1.
(3) Tian, Q.; Larock, R. C. *Org. Lett.* **2000**, *2*, 3329. doi:10.1021/ol000220h. PMID:11029202.
(4) Larock, R. C.; Tian, Q. *J. Org. Chem.* **2001**, *66*, 7372. doi:10.1021/jo010561o. PMID:11681950.
(5) Karig, G.; Moon, M.-T.; Thasana, N.; Gallagher, T. *Org. Lett.* **2002**, *4*, 3115. doi:10.1021/ol026426v. PMID:12201730.
(6) Campo, M. A.; Larock, R. C. *J. Am. Chem. Soc.* **2002**, *124*, 14326. doi:10.1021/ja0275481. PMID:12452705.
(7) Campo, M. A.; Huang, Q.; Yao, T.; Tian, Q.; Larock, R. C. *J. Am. Chem. Soc.* **2003**, *125*, 11506. doi:10.1021/ja035121o. PMID:13129347.
(8) Huang, Q.; Fazio, A.; Dai, G.; Tian, Q.; Larock, R. C. *J. Am. Chem. Soc.* **2004**, *126*, 7460. doi:10.1021/ja047980y. PMID:15198591.
(9) Huang, Q.; Campo, M. A.; Yao, T.; Campo, M. A.; Larock, R. C. *J. Org. Chem.* **2004**, *69*, 8251. doi:10.1021/jo048788h. PMID:15549795.
(10) Barder, T. E.; Walker, S. D.; Martinelli, J. R.; Buchwald, S. L. *J. Am. Chem. Soc.* **2005**, *127*, 4685. doi:10.1021/ja042491j. PMID:15796535.
(11) Zhao, J.; Larock, R. C. *Org. Lett.* **2005**, *7*, 701. doi:10.1021/ol0474655. PMID:15704929.
(12) Zhao, J.; Campo, M.; Larock, R. C. *Angew. Chem. Int. Ed. Engl.* **2005**, *44*, 1873. doi:10.1002/anie.200462327. PMID:15712250.
(13) Bour, C.; Suffert, J. *Org. Lett.* **2005**, *7*, 653. doi:10.1021/ol047537s. PMID:15704917.
(14) Masselot, D.; Charmant, J. P. H.; Gallagher, T. *J. Am.*

Chem. Soc. **2006**, *128*, 694. doi:10.1021/ja056964d. PMID: 16417339.
(15) Zhao, J.; Larock, R. C. *J. Org. Chem.* **2006**, *71*, 5340. doi:10.1021/jo060727r. PMID:16808524.
(16) Singh, A.; Sharp, P. R. *J. Am. Chem. Soc.* **2006**, *128*, 5998. doi:10.1021/ja060159x. PMID:16669644.
(17) Campo, M. A.; Zhang, H.; Yao, T.; Ibdah, A.; McCulla, R. D.; Huang, Q.; Zhao, J.; Jenks, W. S.; Larock, R. C. *J. Am. Chem. Soc.* **2007**, *129*, 6298. doi:10.1021/ja069238z. PMID:17451243.
(18) Ma, S.; Gu, Z. *Angew. Chem. Int. Ed. Engl.* **2005**, *44*, 7512. doi:10.1002/anie.200501298. PMID:16273558.
(19) Mota, A. J.; Dedieu, A.; Bour, C.; Suffert, J. *J. Am. Chem. Soc.* **2005**, *127*, 7171. doi:10.1021/ja050453+. PMID: 15884959.
(20) Mota, A. J.; Dedieu, A. *Organometallics,* **2006**, *25*, 3130. doi:10.1021/om060128a.
(21) Mota, A. J.; Dedieu, A. *J. Org. Chem.* **2007**, *72*, 9669. doi:10.1021/jo701701s. PMID:18001098.
(22) Lin, Z. *Coord. Chem. Rev.* **2007**, *251*, 2280. doi:10.1016/j.ccr.2006.11.006.
(23) Vastine, B. A.; Hall, M. B. *J. Am. Chem. Soc.* **2007**, *129*, 12068. doi:10.1021/ja074518f. PMID:17854189.
(24) Perutz, R. N.; Sabo-Etienne, S. *Angew. Chem. Int. Ed. Engl.* **2007**, *46*, 2578. doi:10.1002/anie.200603224. PMID: 17380532.
(25) Armélin, M.; Schlangen, M.; Schwarz, H. *Chem. Eur. J.* **2008**, *14*, 5229. doi:10.1002/chem.200800029.
(26) Hoffmann, R. *Angew. Chem. Int. Ed. Engl.* **1982**, *21*, 711. doi:10.1002/anie.198207113.
(27) Albright, T. A.; Burdett, J. K.; Whangbo, M. H. In *Orbital interactions in chemistry*; Wiley: New York, 1985; p. 402.
(28) Von Ragué Schleyer, P.; de Carneiro, J. W. M. *J. Comput. Chem.* **1992**, *13*, 997. doi:10.1002/jcc.540130810.
(29) Schreiner, P. R.; Kim, S. J.; Schaefer, H. F.; Schleyer, P. v. R. *J. Chem. Phys.* **1993**, *99*, 3716. doi:10.1063/1.466147.
(30) Scuseria, G. E. *Nature,* **1993**, *366*, 512. doi:10.1038/366512a0.
(31) Becke, A. D. *Phys. Rev. A,* **1988**, *38*, 3098. doi:10.1103/PhysRevA.38.3098. PMID:9900728.
(32) Lee, C.; Yang, W.; Parr, R. G. *Phys. Rev. B,* **1988**, *37*, 785. doi:10.1103/PhysRevB.37.785.
(33) Becke, A. D. *J. Chem. Phys.* **1993**, *98*, 5648. doi:10.1063/1.464913.
(34) Frisch, M. J.; Trucks, G. W.; Schlegel, H. B.; Scuseria, G. E.; Robb, M. A.; Cheeseman, J. R.; Montgomery, J. A., Jr.; Vreven, T.; Kudin, K. N.; Burant, J. C.; Millam, J. M.; Iyengar, S. S.; Tomasi, J.; Barone, V.; Mennucci, B.; Cossi, M.; Scalmani, G.; Rega, N.; Petersson, G. A.; Nakatsuji, H.; Hada, M.; Ehara, M.; Toyota, K.; Fukuda, R.; Hasegawa, J.; Ishida, M.; Nakajima, T.; Honda, Y.; Kitao, O.; Nakai, H.; Klene, M.; Li, X.; Knox, J. E.; Hratchian, H. P.; Cross, J. B.; Adamo, C.; Jaramillo, J.; Gomperts, R.; Stratmann, R. E.; Yazyev, O.; Austin, A. J.; Cammi, R.; Pomelli, C.; Ochterski, J. W.; Ayala, P. Y.; Morokuma, K.; Voth, G. A.; Salvador, P.; Dannenberg, J. J.; Zakrzewski, V. G.; Dapprich, S.; Daniels, A. D.; Strain, M. C.; Farkas, O.; Malick, D. K.; Rabuck, A. D.; Raghavachari, K.; Foresman, J. B.; Ortiz, J. V.; Cui, Q.; Baboul, A. G.; Clifford, S.; Cioslowski, J.; Stefanov, B.; Liu, B. G.; Liashenko, A.; Piskorz, P.; Komaromi, I.; Martin, R. L.; Fox, D. J.; Keith, T.; Al-Laham, M. A.; Peng, C. Y.; Nanayakkara, A.; Challacombe, M.; Gill, P. M. W.; Johnson, B.; Chen, W.; Wong, M. W.; Gonzalez, C.; Pople, J. A. *Gaussian 03* [computer program], Revision B.04. Gaussian Inc.: Pittsburgh, Penn. USA, 2003.
(35) Couty, M.; Hall, M. B. J. *Comput. Chem.* **1996**, *17*, 1359. doi:10.1002/(SICI)1096-987X(199608)17:11<1359::AID-JCC9>3.0.CO;2-L.
(36) Hay, P. J.; Wadt, W. R. *J. Chem. Phys.* **1985**, *82*, 299. doi:10.1063/1.448975.
(37) Bergner, A.; Dolg, M.; Küchle, W.; Stoll, H.; Preuss, H. *Mol. Phys.* **1993**, *80*, 1431. doi:10.1080/00268979300103121.
(38) Glukhovtsev, M.; Pross, A.; McGrath, M. P.; Radom, L. *J. Chem. Phys.* **1995**, *103*, 1878. doi:10.1063/1.469712 .
(39) Hehre, W. J.; Ditchfield, R.; Pople, J. A. *J.Chem. Phys.* **1972**, *56*, 2257. doi:10.1063/1.1677527 .
(40) Smith, G. D.; Jaffe, R. L.; Partridge, H. *J. Phys. Chem. A*, **1997**, *101*, 1705. doi:10.1021/jp961417n.
(41) Gadre, S.; Pingale, S. S. *J. Am. Chem. Soc.* **1998**, *120*, 7056. doi:10.1021/ja971544c.
(42) Arulmozhiraja, S.; Fuji, T.; Tokiwa, H. *Chem. Phys.* **1999**, *250*, 237. doi:10.1016/S0301-0104(99)00348-1.
(43) Ehlers, A. W.; de Koster, G. G.; Meier, R. J.; Lammertsma, K. *J. Phys. Chem. A,* **2001**, *105*, 8691. doi:10.1021/jp010627j.
(44) Fujii, T.; Iijima, S.; Iwase, K.; Arulmozhijara, S. *J. Phys. Chem. A,* **2001**, *105*, 10089. doi:10.1021/jp012113q.
(45) Ma, J. C.; Dougherty, D. A. *Chem. Rev.* **1997**, *97*, 1303. doi:10.1021/cr9603744. PMID:11851453.
(46) Cheng, J.; Zhu, W.; Tang, Y.; Zu, Y.; Li, Z.; Chen, K.; Jiang, H. *Chem. Phys. Lett.* **2006**, *422*, 455. doi:10.1016/j.cplett.2006.03.005.
(47) Feller, D.; Dixon, D. A.; Nicholas, J. B. *J. Phys. Chem. A,* **2000**, *104*, 11414. doi:10.1021/jp002631l.
(48) Amicangelo, J. C.; Armentrout, P. B. *J. Phys. Chem. A,* **2000**, *104*, 11420. doi:10.1021/jp002652f.
(49) Kim, D.; Hu, S.; Tarakeshwar, P.; Kim, K. S. J. *Phys. Chem. A,* **2003**, *107*, 1228. doi:10.1021/jp0224214.
(50) Jonas, K.; Rüsseler, W.; Angermund, K.; Krüger, C. *Angew. Chem. Int. Ed. Engl.* **1986**, *25*, 927. doi:10.1002/anie.198609271.
(51) Schiemenz, B.; Power, P. P. *Angew. Chem. Int. Ed. Engl.* **1996**, *35*, 2150. doi:10.1002/anie.199621501.
(52) Wardell, J. L. In *Comprehensive organometallic chemistry*; Wilkinson, G., Stone, F. G. A., Abel, E. W, Eds.; Pergamon Press: Oxford, UK, 1982; Vol. 1, p. 64.
(53) Wright, D. S.; Beswick, M. A. In *Comprehensive organometallic chemistry II*; Abel, E. W., Stone, F. G. A., Wilkinson, G., Eds., Pergamon Press: Oxford, USA, 1992; Vol. 1, p. 1.
(54) Schümann, U.; Kopf, J.; Weiss, E. *Angew. Chem. Int. Ed. Engl.* **1985**, *24*, 215. doi:10.1002/anie.198502151.
(55) Reich, H. J.; Green, D. P.; Medina, M. A.; Goldenberg, W. S.; Gudmundsson, B. Ö.; Dykstra, R. R.; Phillips, N. H. J. *Am. Chem. Soc.* **1998**, *120*, 7201. doi:10.1021/ja980684z.
(56) Betz, J.; Hampel, F.; Bauer, W. *J. Chem. Soc. Dalton Trans.* **2001**, 1876. doi:10.1039/b009077h.
(57) Kwon, O.; Sevin, F.; Kee, M. L. *J. Phys. Chem. A,* **2001**, *105*, 913. doi:10.1021/jp003345c.
(58) Ilkhechi, A. H.; Mercero, J. M.; Silanes, I.; Boltes, M.; Scheibitz, M.; Lerner, H.-W. *J. Am. Chem. Soc.* **2005**, *127*, 10656. doi:10.1021/ja051544+. PMID:16045353.
(59) Strohmann, C.; Dilsky, S.; Strohfeldt, K. *Organometallics,* **2006**, *25*, 41. doi:10.1021/om050794w.
(60) Sott, R.; Hakansoson, M.; Hilmersson, G. *Organometallics*, **2006**, *25*, 6047. doi:10.1021/om050872f.

(61) Bakshi, P. K.; Sereda, S. V.; Knop, O.; Falk, M. *Can. J. Chem.* **1994**, *72*, 2144. doi:10.1139/v94-272.
(62) Schodel, H.; Vaupel, T.; Bock, H. *Acta Crystallogr. C,* **1996**, *52*, 637. doi:10.1107/S0108270195012522.
(63) Butler, J. M.; Gray, G. M. *J. Chem. Cryst.* **2002**, *32*, 171. doi:10.1023/A:1020235818763.
(64) Hoffmann, K.; Weiss, E. *J. Organomet. Chem.* **1974**, *67*, 221. doi:10.1016/S0022-328X(00)82348-7.
(65) Pajzderska, A.; Maluszynska, H.; Wasicki, J. *Z. Naturforsch.* **2002**, *57a*, 847.
(66) Kaufmann, L.; Vitze, H.; Bolte, M.; Lerner, H.-W.; Wagner, M. *Organometallics,* **2007**, *26*, 1771. doi:10.1021/om061117k.
(67) Reddy, A. S.; Zipse, H.; Sastry, G. N. *J. Phys. Chem. B,* **2007**, *111*, 11546. doi:10.1021/jp075768l. PMID:17850069.
(68) Schleyer, P. v. R.; Balaban, A. T. *J. Am. Chem. Soc.* **1982**, *104*, 3771. doi:10.1021/ja00377a061.
(69) DePuy, C. H.; Gareyev, R.; Hankin, J.; Davico, D. E.; Krempp, M.; Damrauer, R. *J. Am. Chem. Soc.* **1998**, *120*, 5086. doi:10.1021/ja974005g.
(70) Zeng, X.; Davico, G. E. *J. Phys. Chem. A*, **2003**, *107*, 11565. doi:10.1021/jp036386s.
(71) Barone, V.; Minichino, C.; Lelj, F.; Nino, R. J. *Comput. Chem.* **1988**, *9*, 518. doi:10.1002/jcc.540090510.
(72) van der Woerd, M.; Lammertsma, K.; Duke, B. J.; Schaefer, H. F., III. *J. Chem. Phys.* **1991**, *95*, 1160. doi:10.1063/1.461146.
(73) Bock, C. W.; Trachtman, M.; Murphy, C.; Muschert, B.; Mains, G. J. *J. Phys. Chem.* **1991**, *95*, 2339. doi:10.1021/j100159a041.
(74) Bennett, F. R.; Connelly, J. P. *J. Phys. Chem.* **1996**, *100*, 9308. doi:10.1021/jp953315n.
(75) Wang, X.; Andrews, L.; Tam, S.; DeRose, M. E.; Fajardo, M. E. *J. Am. Chem. Soc.* **2003**, *125*, 9218. doi:10.1021/ja0353560. PMID:15369378.
(76) McGrady, G. S.; Turner, J. F. C.; Ibberson, R. M.; Praeger, M. *Organometallics* **2000**, *19*, 4398. doi:10.1021/om0004794.
(77) Downs, A. J.; Greene, T. M.; Collin, S. E.; Whitehurst, L. A.; Brain, P. T.; Morrison, C. A.; Pulham, C. R.; Stuart, B. A.; Rankin, D. W. H.; Keys, A.; Barron, A. R. *Organometallics,* **2000**, *19*, 527. doi:10.1021/om990811f.
(78) Barlow, M. T.; Downs, A. J.; Thomas, P. D. P.; Rankin, D. W. H. *J. Chem. Soc. Dalton Trans.* **1979**, 1793. doi:10.1039/dt9790001793.
(79) Malone, J. F.; McDonald, W. S. *J. Chem. Soc. Dalton Trans.* **1972**, 2646. doi:10.1039/dt9720002646.
(80) Malone, J. F.; McDonald, W. S. *J. Chem. Soc. Dalton Trans.* **1972**, 2649. doi:10.1039/dt9720002649.
(81) Elschenbroich, C.; Salzer, A. *Organometallics: A concise introduction*; VCH: Weinheim, Germany, 1992.
(82) Odom, J. D. In *Comprehensive Organometallic Chemistry*; Wilkinson, G., Pergamon Press: Oxford, UK, 1982; Vol. 1, p. 254.
(83) In addition, we are well aware that the B3LYP calculations most likely underestimates the π stacking.
(84) DeFrees, D. J.; Ragavachari, K.; Schlegel, H. B.; Pople, J. A.; Schleyer, P. v. R. *J. Phys. Chem.* **1987**, *91*, 1857. doi:10.1021/j100291a034.
(85) Bonaccorsi, R.; Charkin, O. P.; Tomasi, J. *Inorg. Chem.* **1991**, *30*, 2964. doi:10.1021/ic00015a005.
(86) Drew, D. A.; Gundersen, G.; Haaland, A. *Acta Chem. Scand.* **1972**, *26*, 2147. doi:10.3891/acta.chem.scand.26-2147.
(87) Coe, D. A.; Nibler, J. W.; Cook, T. H.; Drew, D.; Morgan, G. L. *J. Chem. Phys.* **1975**, *63*, 4842. doi:10.1063/1.431227 .
(88) Plieger, P. G.; John, K. D.; Keizer, T. S.; McCleskey, T. M.; Burrell, A. K.; Martin, R. L. *J. Am. Chem. Soc.* **2004**, *126*, 14651. doi:10.1021/ja046712x. PMID:15521785.
(89) Cooper, J.; Ziegler, T. *Inorg. Chem.* **2002**, *41*, 6614. doi:10.1021/ic020294k. PMID:12470056.
(90) Sakaki, S.; Takayama, T.; Sumimoto, M.; Sugimoto, M. *J. Am. Chem. Soc.* **2004**, *126*, 3332. doi:10.1021/ja0304345. PMID:15012164.
(91) Leung, B. O.; Reid, D. L.; Armstrong, D. A.; Rauk, A. *J. Phys. Chem. A*, **2004**, *108*, 2720. doi:10.1021/jp030265a.
(92) Braga, A. A. C.; Ujaque, G.; Maseras, F. *Organometallics* **2006**, *25*, 3647. doi:10.1021/om060380i.
(93) Deglmann, P.; Ember, E.; Hofmann, P.; Pitter, S.; Walter, O. *Chem. Eur. J.* **2007**, *13*, 2864. doi:10.1002/chem.200600396.
(94) Paul, F.; Patt, J.; Hartwig, J. F. *Organometallics*, **1995**, *14*, 3030. doi:10.1021/om00006a053.
(95) Jain, V. K.; Jain, L. *Coord. Chem. Rev.* **2005**, *249*, 3075. doi:10.1016/j.ccr.2005.06.020.
(96) Paul, F.; Patt, J.; Hartwig, J. F. *J. Am. Chem. Soc.* **1994**, *116*, 5969. doi:10.1021/ja00092a058.
(97) Louie, J.; Hartwig, J. F. *J. Am. Chem. Soc.* **1995**, *117*, 11598. doi:10.1021/ja00151a033.
(98) Stambuli, J. P.; Bühl, M.; Hartwig, J. F. *J. Am. Chem. Soc.* **2002**, *124*, 9346. doi:10.1021/ja0264394. PMID:12167009.
(99) Stambuli, J. P.; Incarvito, C. D.; Bühl, M.; Hartwig, J. F. *J. Am. Chem. Soc.* **2004**, *126*, 1184. doi:10.1021/ja037928m. PMID:14746489.
(100) Sundermann, A.; Uzan, O.; Martin, J. M. L. *Chem. Eur. J.* **2001**, *7*, 1703. doi:10.1002/1521-3765(20010417)7:8<1703::AID-CHEM17030>3.0.CO;2-K.
(101) Cardenas, D. J.; Martin-Matute, B.; Echavarren, A. M. *J. Am. Chem. Soc.* **2006**, *128*, 5033. doi:10.1021/ja056661j. PMID:16608337.
(102) de Jong, G. T.; Bickelhaupt, F. M. *J. Chem. Theory Comput.* **2007**, *3*, 514. doi:10.1021/ct600342j.
(103) Montoya, V.; Pons, J.; Branchadell, V.; Garcia-Antón, J.; Solans, X.; Font-Bardia, M.; Ros, J. *Organometallics,* **2008**, *27*, 1084. doi:10.1021/om7009182.

Glycosidic bond cleavage in deoxynucleotides — A density functional study[1]

Andrea L. Millen and Stacey D. Wetmore

Abstract: Density functional theory was used to study the glycosidic bond cleavage in deoxynucleotides with the main goal to determine the effects of the nucleobase, hydrogen bonding with the nucleobase, and the (bulk) environment on the reaction energetics. Since direct glycosidic bond cleavage is a high-energy process, two nucleophile models were considered ($HCOO^{-}\cdots H_2O$ and HO^{-}), which represent different stages of activation of a water nucleophile. The glycosidic bond cleavage barriers were found to decrease, while the reaction exothermicity increases, with an increase in the nucleobase acidity. The gas-phase barriers and reaction energies for bond cleavage in all deoxynucleotides were found to be significantly affected by hydrogen-bonding interactions with the nucleobase (by up to 30 kJ mol^{-1} depending on the nucleophile). Although the barriers increase and reaction energies become less exothermic in enzymatic and aqueous environments, the effects of the bulk environment are similar in the presence and absence of small molecules bound to the nucleobase. Therefore, the effects of hydrogen bonding with the bases are approximately the same in all environments. Our results suggest that hydrogen bonding with the nucleobase may play an important role in the glycosidic bond cleavage in both pyrimidine and purine nucleotides in a variety of environments.

Key words: hydrogen bond, density functional theory (DFT), DNA, glycosidic bond cleavage, solvation.

Résumé : On a fait appel à la théorie de la fonctionnelle de la densité pour étudier le clivage de la liaison glycosidique de désoxynucléotides dans le but principal de déterminer les effets de la nucléobase, de la liaison hydrogène avec la nucléobase et l'environnement global sur les énergies impliquées dans la réaction. Puisque le clivage direct de la liaison glycosidique est un processus impliquant une énergie élevée, on a considéré deux processus nucléophiles modèles ($HCOO^{-}\cdots H_2O$ et HO^{-}) qui représentent des stages différents de l'activation de l'eau agissant comme nucléophile. On a trouvé que, avec une augmentation de l'acidité de la nucléobase, les barrières au clivage de la liaison glycosidique diminuent avec une augmentation du caractère exothermique de la réaction. On a aussi trouvé que les barrières en phase gazeuse et les énergies réactionnelles pour le clivage de la liaison de tous les désoxynucléotides sont significativement affectées par les interactions de barrières hydrogènes avec la nucléobase (jusqu'à 30 kJ mol^{-1} suivant le nucléophile). Même si les barrières augmentent et que les énergies réactionnelles deviennent moins exothermiques dans des environnements aqueux ou enzymatiques, les effets de l'environnement global sont semblables en présence ou en l'absence de petites molécules liées à la nucléobase. Les effets des liaisons hydrogènes avec les bases sont donc approximativement les mêmes dans tous les environnements. Les résultats obtenus suggèrent que les liaisons hydrogènes avec la nucléobase peuvent jouer un ţle important sur le clivage de la liaison glycosidique dans les nucléotides tant de pyrimidines que de purines, dans une grande variété d'environnements.

Mots-clés : liaison hydrogène, théorie de la fonctionnelle de densité (TFD), clivage de liaison glycosidique, solvatation, ADN.

Introduction

The sequence of nucleobases within DNA double helices contains the genetic make-up of living organisms. To preserve this important information, the bond between the base and the deoxyribose sugar moiety is very stable.[2–8] Indeed, even some modified DNA nucleotides, which can be formed during cell damage processes or studied for applications in biotechnology or medicine, are stable. Because of the high energy associated with cleavage of the glycosidic bond, this process requires enzymes[9] such as nucleotide hydrolases[10] or phosphorylases,[11] which are involved in nucleotide salvage pathways, or DNA glycosylases,[12,13] which are involved in DNA repair pathways.

The proposed mechanisms of action of enzymes that catalyze DNA glycosidic bond cleavages generally involve attack of a nucleophile (for example, water in the case of hydrolases,[10,14–19] ricin toxin A-chain,[19,20] and some DNA glycosylases (UDG[12,13,21–24] or MutY[12,13,25]), an active site (amine) amino acid in some DNA glycosylases (hOGG1[12,13,26–28] or FPG[12,13,29–32]), and hydrogen phosphate in phosphorylases[11,33–38]). Furthermore, important roles for active site amino acids other than nucleophilic attack, including activation of the nucleophile[10,21,24] or stabilization of the departing nucleobase through proton transfer[12,13,17] or hydrogen-bonding interactions,[12,13,21,24,36] have been suggested. Unfortunately, however, the order and importance of the proposed steps vary from enzyme to enzyme, and it is

Received 14 November 2008. Accepted 18 December 2008. Published on the NRC Research Press Web site at canjchem.nrc.ca on 31 March 2009.

A.L. Millen and S.D. Wetmore.[1] Department of Chemistry and Biochemistry, University of Lethbridge, 4401 University Drive, Lethbridge, AB T1K 3M4, Canada.

[1]Corresponding author (e-mail: stacey.wetmore@uleth.ca).

not clear whether these differences are correlated with the properties of the nucleophile, the nucleobase, and (or) active site residues.

To shed light on the glycosidic bond cleavage process, previous work in our laboratory used techniques in computational chemistry to study the kinetics and thermodynamics of the glycosidic bond cleavage in 2′-deoxyuridine.[39] The goal was to understand the fundamentals of this reaction for the smallest nucleotide, independent of specific active site interactions for a particular enzyme, and thereby complement previous computational studies in the literature that have typically focused on only one feature of the glycosidic bond cleavage catalyzed by a certain enzyme (see, for example, refs. 24, 25, 28, 32, 34, and 38). Water was chosen as a nucleophile because of its importance in nature and its anticipated role in the glycosidic bond cleavage catalyzed by several enzymes.[10,12–24] The effects of hydrogen-bonding interactions between the nucleophile and (or) nucleobase and several small molecules that span a large acidity range were also considered. Our calculations revealed important information about the effects of the nucleophile, activation of the nucleophile, and interactions with the (uracil) nucleobase on this reaction.

In the present work, we extend our study to all natural nucleotides (Chart 1, R = PO_4H^-) using a truncated model (Chart 1, R = OCH_3). Understanding the effects of different factors (nucleophile activation, hydrogen bonding) on the glycosidic bond cleavage in all DNA nucleotides is important to elucidate how the nature of the nucleobase affects the reaction. Indeed, proposed mechanisms for enzymatic glycosidic bond cleavage are dependent on the nucleobase.[9–13] For example, the bond cleavage in 2′-deoxyuridine by uracil DNA glycosylase has been proposed to proceed via a base anion,[21–24] while bond cleavage in 2′-deoxyadenosine by MutY[25] or dAMP[19] has been proposed to proceed via base protonation. We also complement our previous work by considering the effects of the (bulk) environment on this important reaction for all nucleosides, including 2′-deoxyuridine.

Computational details

Previous work in our laboratory revealed that nucleotide model systems where the phosphodiester backbone at C3′ and C5′ is replaced by hydroxyl groups are inadequate for modeling the glycosidic bond cleavage within DNA because of interactions between the hydroxyl groups and the nucleophile and (or) nucleobase that cannot occur within DNA duplexes.[39] Instead, methoxyl groups were shown to be more accurate, and we use similar models in the present work (Chart 1, R = OCH_3). We note that although a smaller model (Chart 1, R = H) was found to yield similar results, previous computational studies of glycosidic bond cleavage reactions have pointed to the potentially important role of the C5′ hydroxyl group in terms of increasing base acidity, [18] and therefore we use the larger model in the present work.

Relative energies were obtained from B3LYP/6-311+G(2d,p) single-point calculations on geometries optimized at the B3LYP/6-31G(d) level, where previous work in our lab shows that 6-31G(d) geometries yield final relative energies in excellent agreement with geometries obtained using a larger (6-31+G(d,p)) basis set.[39] Scaled (0.9806) zero-point energy corrections are included in all relative energies, and basis set superposition error (BSSE) corrections are included in total energies of hydrogen-bonded complexes. Intrinsic reaction coordinate (IRC) calculations were used to confirm that transition states connect reported reactant and product complexes. Environmental effects were taken into account by performing polarizable continuum (PCM) single-point calculations on gas-phase geometries in both water (ε = 78), due to its abundance in biological systems, and ether (ε = 4), which describes an enzymatic environment between aqueous solution and an active site sequestered from water.[40] All calculations were performed with Gaussian 03.[41]

Chart 1. The natural DNA and RNA (uracil (U), thymine (T), cytosine (C), adenine (A), and guanine (G)) deoxynucleotides (R = PO_4H^-) and truncated nucleotide models (R = OCH_3) used in the present study.

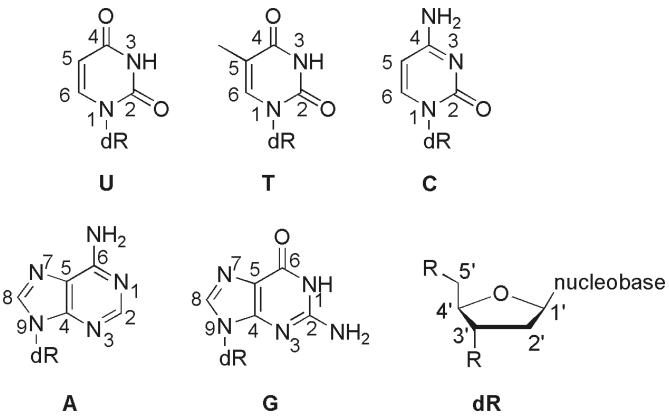

Results and discussion

As mentioned in the Introduction, the glycosidic bonds within DNA are very stable,[2–8] which means direct cleavage of the base-sugar bond is not feasible. Indeed, experimental evidence suggests that nonenzymatic bond cleavage occurs via hydrolysis.[2–8] Furthermore, previous work in our lab indicates that a sole water molecule cannot efficiently cleave the glycosidic bond in deoxyuridine,[39] which emphasizes the important catalytic role of enzymes that facilitate these bond cleavages. Since water activation through (at least partial) proton abstraction prior to nucleophilic attack has been proposed in mechanistic steps for several enzymes that cleave glycosidic bonds,[10,12–24] we previously considered the effects of different stages of water activation on the barrier to deglycosylation in 2′-deoxyuridine.[39] We found that a series of barriers is obtained by considering nucleophiles ranging from water (direct hydrolysis) to the hydroxyl anion. Since the barriers for direct hydrolysis are very large, the present work focuses on two nucleophiles, namely the hydroxyl anion (HO^-), which represents full water activation (deprotonation), and (partial) water activation by a formate ion ($HCOO^-\cdots H_2O$). Using these model nucleophiles, we consider the effects of the nature of the nucleobase, hydrogen bonding with the nucleobase, and the (bulk) environment on the kinetics and thermodynamics of the glycosidic bond cleavage in deoxynucleotides.

Fig. 1. Selected B3LYP/6-31G(*d*) bond lengths (Å) and dihedral angles (°, where χ = ∠(O1′C1′N1C2) in the pyrimidines and ∠(O1′C1′N9C4) in the purines) in reactant (RC), transition state (TS), and product (PC) complexes for glycosidic bond cleavage in deoxynucleotides involving the hydroxyl anion (HO^-) as the nucleophile.

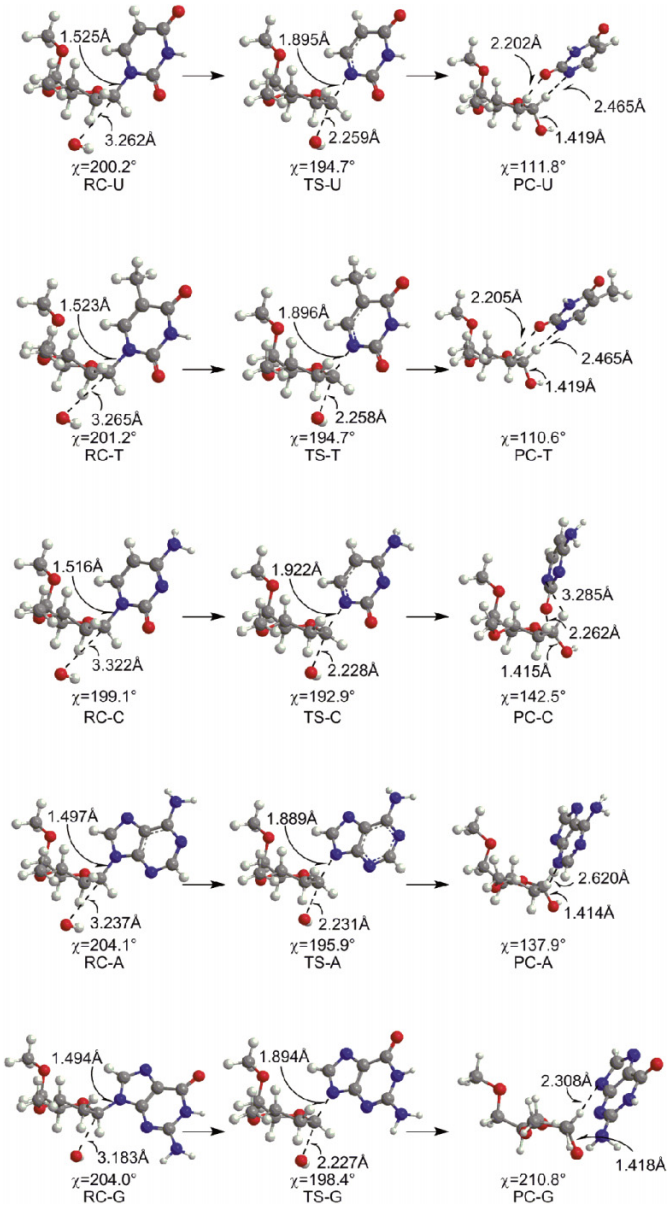

Fig. 2. Selected B3LYP/6-31G(*d*) bond lengths (Å) and dihedral angles (°, where χ = ∠(O1′C1′N1C2) in the pyrimidines and ∠(O1′C1′N9C4) in the purines) in reactant (RC), transition state (TS), and product (PC) complexes for glycosidic bond cleavage in deoxynucleotides involving formate activated water ($HCOO^-\cdots H_2O$) as the nucleophile.

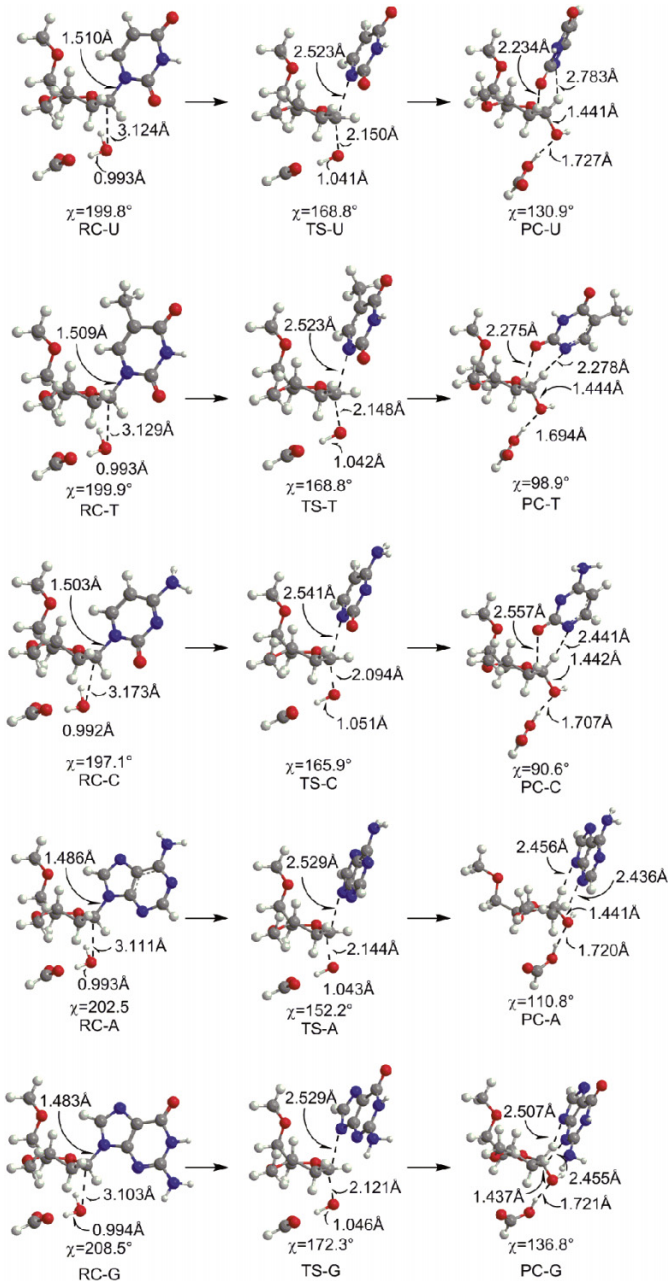

Effects of the nucleobase

The reactant, transition state, and product complexes for glycosidic bond cleavage in the natural DNA nucleotides involving the hydroxyl anion and $HCOO^-$ activated water are compared with those previously reported for uracil[39] in Figs. 1 and 2, respectively. As all transition states are formed, the nucleophile moves from a position under the sugar ring, which benefits from hydrogen-bonding interactions between the nucleophile and sugar moiety, to a position closer to C1′, while the sugar puckering changes from C3′-endo to C3′-endo-C4′-exo twist. In the transition state, the (partial) formation of a sugar cation is stabilized by charges on both the nucleophile and the departing nucleobase. In the product complex, although the final sugar puckering varies with the nucleophile and nucleobase, a bond is fully formed between the sugar and the nucleophile and the departed base is positioned above the sugar where it forms at least two (albeit weak) hydrogen bonds with sugar hydrogens. For all nucleobases, one of these hydrogen bonds involves the nucleobase ring nitrogen that previously formed the glycosidic bond (N1 for the pyrimidines and N9 for the purines, see Chart 1 for atomic numbering in the nucleobases).

Table 1. Barriers and reaction energies (kJ mol^{-1}) for the glycosidic bond cleavage in deoxynucleotides facilitated by $HCOO^{-}\cdots H_2O$ or HO^{-} nucleophiles, as well as nucleobase acidities at the glycosidic bond site (N1 in the pyrimidines and N9 in the purines).

	$HCOO^{-}\cdots H_2O$		HO^{-}		
	Barrier	Reaction energy	Barrier	Reaction energy	Acidity[b]
Uracil[a]	108.1	15.9	49.9	–163.4	1389.4
Thymine	110.3	14.0	51.6	–161.0	1396.5
Cytosine	130.4	40.9	64.9	–137.0	1442.7
Adenine	122.2	25.7	61.0	–151.3	1406.8
Guanine	127.0	35.0	60.5	–150.9	1403.6

Note: B3LYP/6-311+G(2d,p) single-point calculations were performed on B3LYP/6-31(d) geometries, and relative energies include scaled (0.9806) zero-point energy corrections.

[a]Ref. 39.

[b]Refs. 42–45, where the acidity is calculated as the enthalpy of deprotonation and therefore a decrease in the deprotonation enthalpy represents an increase in the acidity.

Chart 2. Structure and nomenclature for small molecule (XH = HF, H_2O, and NH_3) hydrogen-bonding sites in the natural nucleotides.

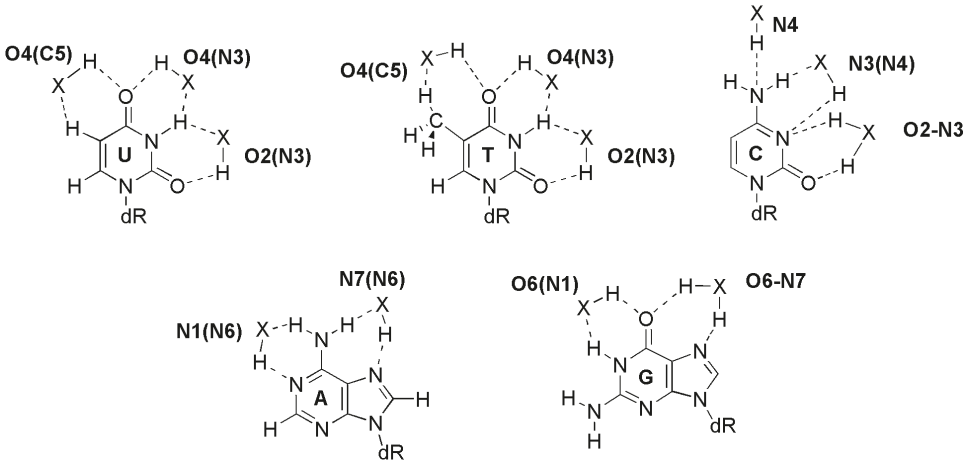

In the reaction pathway involving the $HCOO^{-}\cdots H_2O$ nucleophile (Fig. 2), water retains the proton in the transition state, although the O–H bond interacting with the formate ion is lengthened by 0.05–0.06 Å, and the proton is transferred to the formate ion upon product formation. As a result, the nucleophile cannot provide as much stabilization to the developing positive charge on the sugar moiety in this transition state compared with bond cleavage in the presence of the hydroxyl anion. Therefore, the $HCOO^{-}\cdots H_2O$ nucleophile is associated with later transition states as indicated by approximately 0.6 Å longer C1′–N distances and approximately 0.1 Å shorter distances between the nucleophile and C1′ (see Figs. 1 and 2). The end result is that the barrier for the reaction facilitated by the $HCOO^{-}\cdots H_2O$ nucleophile is larger (by a factor of approximately 2), and the reaction is less exothermic (by up to 180 kJ mol^{-1}), compared with the reaction facilitated by the hydroxyl anion for all nucleobases (Table 1).

For both nucleophile models, the magnitude of the transition barrier decreases as C > G ≈ A > T ≈ U, while the overall exothermicity of the reaction generally decreases according to U ≈ T > A ≈ G > C for $HCOO^{-}\cdots H_2O$ and as U ≈ T > A > G > C for HO^{-}. These trends follow the trend in the nucleobase acidity at the glycosidic bond site (Table 1).[42–45] Specifically, the greater the nucleobase acidity, the lower the barrier and the more exothermic the overall reaction. However, despite an approximate 50 kJ mol^{-1} difference in the acidity of the nucleobases, the barriers for glycosidic bond cleavage deviate by only 22 and 15 kJ mol^{-1} when catalyzed by $HCOO^{-}\cdots H_2O$ and HO^{-}, respectively.

The difference between the glycosidic bond cleavage barriers for the natural nucleobases as a function of the nucleophile can be understood by considering the charge on the nucleobase. Specifically, the reaction facilitated by the hydroxyl anion has the earliest transition states with the shortest C1′–N bond lengths, and therefore the nucleobases in these transition states have smaller net charges compared with the corresponding $HCOO^{-}\cdots H_2O$ reaction. As a result, the transition barrier is much less dependent on the ability of the nucleobase to stabilize the charge (or in other words, on the nucleobase acidity), and therefore the smallest range in barriers is observed for the HO^{-} nucleophile. Similarly, the amount of charge on the nucleobase in the transition states for the reaction catalyzed by activated water is less than that on the isolated uracil anion, which does not benefit from interactions with the (cationic) sugar moiety, and therefore the dependence of the barrier on the nucleobase is less than the dependence of the acidity.

In summary, although the barriers for glycosidic bond cleavage for different nucleobases follow the trend in nucleobase acidity, there is a relatively small difference between

the barriers. This suggests that factors other than the acidity likely also play an important role in promoting different mechanisms for cleavage of the glycosidic bonds in the pyrimidine compared with the purine nucleotides.

Effects of hydrogen bonding with the nucleobase

As mentioned in the Introduction, the proposed mechanisms for many enzymes that catalyze DNA glycosidic bond cleavage reactions involve proton transfer reactions or hydrogen-bonding interactions between the nucleobase substrate and active site amino acid residues. Due to the proposed formation of base anions in the mechanisms of action of some enzymes, previous work in our group considered the effects of hydrogen-bonding interactions with small molecules (HF, H_2O, and NH_3) on the (N1 or N9) acidity of the natural (and selected damaged) nucleobases.[42–45] We found that the acidity can be increased by up to 60 kJ mol^{-1}, where the magnitude of the enhancement decreases with the acidity of the small molecule bound ($HF > H_2O > NH_3$) and is more dependent on the nature of the small molecule than the nucleobase binding site (see Chart 2 for binding sites considered). Since the previous section suggests that there is a correlation between glycosidic bond cleavage barriers and nucleobase acidity, we consider the effects of various hydrogen-bonding interactions with the nucleobase on the glycosidic bond cleavage reaction in all natural deoxynucleotides.

Tables 2–6 display the effects of hydrogen bonding between the nucleobase and small molecules (XH = HF, H_2O, or NH_3) for glycosidic bond cleavage in the presence of the formate activated water and hydroxyl anion nucleophiles. Specifically, changes to the barriers ($\Delta^{\ddagger}$) and reaction energies (Δ(energy)) are reported as well as the corresponding changes in the nucleobase acidity (Δ(acidity)). Each small molecule binds to both a nucleobase proton donor and acceptor at a variety of sites, where our notation uses brackets to identify the nucleobase proton donor as defined in Chart 2.

In general, hydrogen bonding with the nucleobase decreases the barrier heights ($\Delta^{\ddagger} < 0$) and increases the reaction exothermicity (Δ(energy) < 0). The magnitude of the effect follows the same trends with respect to the small molecule bound for each nucleobase–nucleophile combination and matches the previously reported trends in the effects on the acidity. Specifically, the effect increases with the relative acidity of the small molecule bound.[42–45] Therefore, ammonia sometimes leads to a small increase in the barrier (reaction energy), while hydrogen fluoride leads to the largest decrease. The trends with respect to the binding site also follow those previously reported for the effects on the acidity,[42–45] which is dictated by the relative magnitude of the proton affinity and acidity of the nucleobase sites involved in each bidentate binding arrangement.

Although decreases in the barriers for glycosidic bond cleavage were anticipated, based on calculated increases in the nucleobase acidity due to hydrogen bonding,[42–45] we find that the results are more dependent on the nature of the small molecule interacting with the nucleobase than the identity of the nucleobase. Specifically, although there is a range in the effect of each small molecule according to the nucleobase identity and binding site, there is little overlap in the effects of different small molecules. For example, the range in the effect of hydrogen fluoride on the barrier ($\Delta^{\ddagger}$) for the reaction involving the $HCOO^{-}\cdots H_2O$ nucleophile is 13–32 kJ mol^{-1}, while the range in the effect of water is 4–15 kJ mol^{-1}. The decrease in the barrier (and increase in reaction exothermicity) found for all nucleobases suggests that hydrogen-bonding interactions can facilitate the glycosidic bond cleavage in all natural nucleotides.

We also find that the effect of hydrogen bonding with the base on the barrier height is highly dependent on the nucleophile involved in the reaction. For example, the effects of hydrogen bonding with HF on the barrier range from approximately 13 to 32 kJ mol^{-1} for the reaction involving $HCOO^{-}\cdots H_2O$ and from 8 to 15 kJ mol^{-1} for the reaction involving HO^{-}. For comparison, the effects of the same HF interactions on the nucleobase acidity range from 39 to 58 kJ mol^{-1}. Thus, in this example, the effects of hydrogen bonding on the nucleobase acidity are approximately double the effects on the barrier for the $HCOO^{-}\cdots H_2O$ nucleophile and approximately four times the effects on the barrier for the HO^{-} nucleophile. Once again, these differences can be understood in terms of the net charge on the nucleobase, where the smaller the net charge on the base (TS for hydroxyl anion < TS for activated water < isolated base anion), the smaller the effect of the hydrogen bonds on the barrier (or acidity).

In contrast, the effects of hydrogen bonding with the base on the reaction energy are generally the same for both nucleophiles (approximately 14 to 38 kJ mol^{-1}), which are approximately half the effects on the acidity. The effects on the reaction energies are independent of the nucleophile due to the similarities in the geometries of the product complexes (see Figs. 1 and 2), where the base anion receives comparable stabilization through interactions with the sugar moiety regardless of the nucleophile. Furthermore, the effects are smaller than those previously reported for the acidity since some stabilization is provided to the base by the sugar cation in the product complexes.

Although the trend in the effects of hydrogen-bonding interactions on the barriers, reaction energies, and acidities can be easily justified, the differences in the magnitudes of these effects are initially surprising. Nevertheless, the deviations can be understood by considering differences in the binding strengths of the small molecules to the neutral nucleobases compared with the reactant complexes or the anionic nucleobases compared with the transition states or product complexes. Specifically, the effect of hydrogen bonding on the acidity arises because of stronger binding to the base anion compared with the neutral base.[42–45] Similarly, the effects of hydrogen bonding on the reaction energy (barrier) can be defined as the difference between the binding strengths in the reactant and product (transition state) complexes.[39] Therefore, when binding is stronger to the reactant complex than the isolated base, the effect of hydrogen bonding on the reaction energy (barrier) is less than the effect on the acidity. Alternatively, when binding is stronger to the product (transition state) complex than the base anion, the effect of hydrogen bonding on the reaction energy (barrier) is greater than the effect on the acidity.

In summary, hydrogen bonding with the nucleobase decreases the barrier height for glycosidic bond cleavage and increases the reaction exothermicity regardless of the identity of the nucleobase or nucleophile. However, although the effect of hydrogen bonding with the base on the reaction

Table 2. Barriers and reaction energies (kJ mol^{-1}) for the glycosidic bond cleavage in deoxyuridine catalyzed by the $HCOO^{-}\cdots H_2O$ and HO^{-} nucleophiles with HF, H_2O, or NH_3 bound at various uracil sites.

			Gas[a]						Ether				Water			
O2(N3)	O4(N3)	O4(C5)	Barrier	$\Delta^{\ddagger}$ [b]	Reaction energy	Δ(energy)[c]	Acidity[d]	Δ(acidity)[d]	Barrier	$\Delta^{\ddagger}$ [b]	Reaction energy	Δ(energy)[c]	Barrier	$\Delta^{\ddagger}$ [b]	Reaction energy	Δ(energy)[c]
			$HCOO^{-}\cdots H_2O$													
			108.1		15.9		1389.4		112.1		24.4		108.6		19.6	
HF			87.3	–20.8	–11.0	–26.9	1338.0	51.4	88.7	–23.4	–6.7	–31.1	84.5	–24.1	–9.7	–29.3
	HF		89.8	–18.3	–6.6	–22.5	1346.7	42.7	94.8	–17.3	–1.9	–26.3	91.1	–17.5	–3.6	–23.2
		HF	92.3	–15.8	–8.5	–24.4	1342.5	46.9	95.6	–16.5	–3.3	–27.7	93.5	–15.1	1.4	–18.2
H_2O			100.7	–7.4	5.4	–10.5	1369.2	20.2	105.5	–6.6	15.3	–9.1	101.3	–7.3	10.2	–9.4
	H_2O		97.8	–10.3	3.2	–12.7	1373.7	15.7	104.9	–7.2	16.0	–8.4	105.6	–3.0	15.8	–3.8
		H_2O	101.8	–6.3	6.7	–9.2	1366.4	23.0	107.2	–4.9	17.2	–7.2	100.0	–8.6	8.2	–11.4
NH_3			111.1	3.0	16.4	0.5	1392.6	–3.2	116.9	4.8	28.7	4.3	112.1	3.5	25.8	6.2
	NH_3		102.6	–5.5	8.5	–7.4	1394.8	–5.4	117.5	5.4	30.3	5.9	111.9	3.3	23.4	3.8
		NH_3	110.5	2.4	17.3	1.4	1380.3	9.1	108.9	–3.2	20.1	–4.3	105.3	–3.3	15.1	–4.5
			HO^{-}													
			49.9		–163.4		1389.4		64.9		–119.0		73.0		–81.9	
HF			37.2	–12.7	–189.1	–25.7	1338.0	51.4	50.0	–14.9	–147.3	–28.3	58.5	–14.5	–107.1	–25.2
	HF		40.2	–9.7	–182.9	–19.5	1346.7	42.7	53.6	–11.3	–138.1	–19.1	60.0	–13.0	–100.4	–18.5
		HF	38.5	–11.4	–185.3	–21.9	1342.5	46.9	53.6	–11.3	–138.2	–19.2	61.0	–12.0	–100.1	–18.2
H_2O			44.4	–5.5	–174.6	–11.2	1369.2	20.2	59.5	–5.4	–128.3	–9.3	68.1	–4.9	–89.4	–7.5
	H_2O		45.9	–4.0	–172.1	–8.7	1373.7	15.7	60.9	–4.0	–124.6	–5.6	69.1	–3.9	–86.1	–4.2
		H_2O	43.1	–6.8	–176.4	–13.0	1366.4	23.0	59.4	–5.5	–128.0	–9.0	66.6	–6.4	–90.5	–8.6
NH_3			51.0	1.1	–163.1	0.3	1392.6	–3.2	67.6	1.1	–115.1	3.9	76.8	3.8	–77.8	4.1
	NH_3		51.8	1.9	–162.9	0.5	1394.8	–5.3	68.7	3.8	–114.5	4.5	76.9	3.9	–76.9	5.0
		NH_3	45.7	–4.2	–171.6	–8.2	1380.3	9.1	62.3	–2.6	–122.5	–3.5	70.2	–2.8	–85.8	–3.9

Note: B3LYP/6-311+G(2d,p) single-point calculations were performed on B3LYP/6-31G(d) geometries, where all relative energies include scaled (0.9806) zero-point energy corrections and total energies of hydrogen-bonded complexes include basis set superposition error corrections. See Chart 2 for definition of complexation sites.

[a]Ref. 39.

[b]Effect of hydrogen bonding with the nucleobase on the reaction barrier in the same environment, where negative $\Delta^{\ddagger}$ represents a decrease in the barrier height.

[c]Effect of hydrogen bonding with the nucleobase on the reaction energy in the same environment, where negative Δ(energy) represents a more exothermic reaction.

[d]Ref. 42, where a positive Δ(acidity) represents an increase in acidity.

Table 3. Barriers and reaction energies (kJ mol^{-1}) for the glycosidic bond cleavage in deoxythymidine catalyzed by the $HCOO^{-}\cdots H_2O$ and HO^{-} nucleophiles with HF, H_2O, or NH_3 bound at various thymine sites.

			Gas						Ether				Water			
O2(N3)	O4(N3)	O4(C5)	Barrier	$\Delta^{\ddagger}$ [a]	Reaction energy	Δ(energy)[b]	Acidity[c]	Δ(acidity)[c]	Barrier	$\Delta^{\ddagger}$ [a]	Reaction energy	Δ(energy)[b]	Barrier	$\Delta^{\ddagger}$ [a]	Reaction energy	Δ(energy)[b]
			$HCOO^{-}\cdots H_2O$													
			110.3		14.0		1396.5		116.4		25.7		112.6		16.8	
HF			89.1	–21.2	–8.9	–22.9	1345.3	51.2	92.2	–24.2	–2.1	–27.8	87.7	–24.9	–6.8	–23.6
	HF		94.2	–16.1	–6.0	–20.0	1354.2	42.3	99.1	–17.3	6.7	–19.0	94.4	–18.2	–0.3	–17.1
		HF	93.0	–17.3	–3.2	–17.2	1351.1	45.4	99.7	–16.7	9.8	–15.9	98.0	–14.6	7.6	–9.2
H_2O			102.4	–7.9	5.7	–8.3	1376.1	20.4	108.7	–7.7	19.0	–6.7	104.7	–7.9	17.1	0.3
	H_2O		103.6	–6.7	9.0	–5.0	1380.5	16.0	111.1	–5.3	23.1	–2.6	106.2	–6.4	16.5	–0.3
		H_2O	100.8	–9.5	6.2	–7.8	1366.6	29.9	109.3	–7.1	20.9	–4.8	107.0	–5.6	16.8	0.0
NH_3			112.4	2.1	18.6	4.6	1399.1	–2.6	120.2	3.8	33.1	7.4	114.9	2.3	28.5	11.7
	NH_3		112.2	1.9	19.5	5.5	1401.4	–4.9	120.6	4.2	34.4	8.7	115.2	2.6	26.0	9.2
		NH_3	105.1	–5.2	11.5	–2.5	1384.7	11.8	114.2	–2.2	26.6	0.9	110.9	–1.7	20.0	3.2
			HO^{-}													
			51.6		–161.0		1396.5		67.1		–114.4		73.1		–79.9	
HF			38.7	–12.9	–187.0	–26.0	1345.3	51.2	51.6	–15.5	–144.0	–29.6	59.4	–13.7	–104.9	–25.0
	HF		41.7	–9.9	–180.2	–19.2	1354.2	42.3	55.9	–11.2	–133.3	–18.9	61.5	–11.6	–96.9	–17.0
		HF	40.1	–11.5	–181.6	–20.6	1351.1	45.4	55.1	–12.0	–132.9	–18.5	63.0	–10.1	–94.2	–14.3
H_2O			46.0	–5.6	–172.2	19.9	1376.1	20.4	62.1	–5.0	–123.1	–8.7	69.9	–3.2	–85.4	–5.5
	H_2O		47.0	–4.6	–170.1	22.1	1380.5	16.0	62.3	–4.8	–120.8	–6.4	69.2	–3.9	–83.9	–4.0
		H_2O	45.3	–6.3	–172.9	18.8	1366.6	29.9	62.1	–5.0	–122.4	–8.0	67.0	–6.1	–86.0	–6.1
NH_3			52.8	1.2	–160.7	0.3	1399.1	–2.6	70.6	3.5	–110.4	4.0	78.5	5.4	–74.3	5.6
	NH_3		52.9	1.3	–160.9	0.1	1401.4	–4.9	70.3	3.2	–109.9	4.5	77.1	4.0	–74.3	5.6
		NH_3	47.6	–4.0	–168.1	–7.1	1384.7	11.8	64.4	–2.7	–118.0	–3.6	70.3	–2.8	–82.1	–2.2

Note: B3LYP/6-311+G(2d,p) single-point calculations were performed on B3LYP/6-31G(d) geometries, where all relative energies include scaled (0.9806) zero-point energy corrections and total energies of hydrogen-bonded complexes include basis set superposition error corrections. See Chart 2 for definition of complexation sites.

[a]Effect of hydrogen bonding with the nucleobase on the reaction barrier in the same environment, where negative $\Delta^{\ddagger}$ represents a decrease in the barrier height.

[b]Effect of hydrogen bonding with the nucleobase on the reaction energy in the same environment, where negative Δ(energy) represents a more exothermic reaction.

[c]Ref. 43, where a positive Δ(acidity) represents an increase in acidity.

Table 4. Barriers and reaction energies (kJ mol^{-1}) for the glycosidic bond cleavage in deoxycytidine catalyzed by the $HCOO^{-}\cdots H_2O$ and HO^{-} nucleophiles with HF, H_2O, or NH_3 bound at various cytosine sites.

			Gas						Ether				Water			
O2-N3	N3(N4)	N4	Barrier	$\Delta^{\ddagger}$ [a]	Reaction energy	Δ(energy)[b]	Acidity[c]	Δ(acidity)[c]	Barrier	$\Delta^{\ddagger}$ [a]	Reaction energy	Δ(energy)[b]	Barrier	$\Delta^{\ddagger}$ [a]	Reaction energy	Δ(energy)[b]
			$HCOO^{-}\cdots H_2O$													
			130.4		40.9		1442.7		137.8		56.7		133.6		47.1	
HF			106.6	–23.8	2.8	–38.1	1387.4	55.3	115.7	–22.1	28.7	–28.0	112.9	–20.7	29.6	–17.5
	HF		111.5	–18.9	15.1	–25.8	1394.0	48.7	119.1	–18.7	32.9	–23.8	116.3	–17.3	25.3	–21.8
		HF	111.6	–18.8	19.7	–21.2	1394.6	48.1	119.6	–18.2	41.5	–15.2	117.4	–16.2	46.1	–1.0
H_2O			115.9	–14.5	14.5	–26.4	1405.3	37.4	127.0	–10.8	40.5	–16.2	126.4	–7.2	46.0	–1.1
	H_2O		123.0	–7.4	30.1	–10.8	1422.2	20.5	133.3	–4.5	51.8	–4.9	129.1	–4.5	42.3	–4.8
		H_2O	120.7	–9.7	27.4	–13.5	1414.3	28.4	130.1	–7.7	53.7	–3.0	127.4	–6.2	58.2	11.1
NH_3			135.0	4.6	34.9	–6.0	1422.3	20.4	147.3	9.5	62.5	5.8	141.6	8.0	59.8	12.7
	NH_3		130.2	–0.2	36.1	–4.8	1441.2	1.5	141.4	3.6	60.9	4.2	136.4	2.8	51.2	4.1
			HO^{-}													
			64.9		–137.0		1442.7		81.9		–86.4		87.7		–48.7	
HF			49.9	–15.0	–163.0	–26.0	1387.4	55.3	66.4	–15.5	–108.2	–21.8	74.5	–13.2	–67.8	–19.1
	HF		53.1	–11.8	–160.6	–23.6	1394.0	48.7	70.0	–11.9	–107.5	–21.1	80.3	–7.4	–68.3	–19.6
		HF	53.5	–11.4	–158.1	–21.1	1394.6	48.1	70.6	–11.3	–105.2	–18.8	78.4	–9.3	–65.7	–17.0
H_2O			55.3	–9.6	–154.9	–17.9	1405.3	37.4	72.7	–9.2	–99.4	–13.0	82.9	–4.8	–54.0	–5.3
	H_2O		59.7	–5.2	–147.0	–10.0	1422.2	20.5	78.6	–3.3	–92.5	–6.1	87.0	–0.7	–50.2	–1.5
		H_2O	57.5	–7.4	–150.9	–13.9	1414.3	28.4	74.6	–7.3	–97.7	–11.3	81.6	–6.1	–56.2	–7.5
NH_3			69.5	4.6	–136.9	0.1	1422.3	20.4	88.7	6.8	–78.2	8.2	95.7	8.0	–38.0	10.7
	NH_3		64.7	–0.2	–139.1	–2.1	1441.2	1.5	84.2	2.3	–82.3	4.1	92.3	4.6	–41.9	6.8

Note: B3LYP/6-311+G(2d,p) single-point calculations were performed on B3LYP/6-31G(d) geometries, where all relative energies include scaled (0.9806) zero-point energy corrections and total energies of hydrogen-bonded complexes include basis set superposition error corrections. See Chart 2 for definition of complexation sites.

[a]Effect of hydrogen bonding with the nucleobase on the reaction barrier in the same environment, where negative $\Delta^{\ddagger}$ represents a decrease in the barrier height.

[b]Effect of hydrogen bonding with the nucleobase on the reaction energy in the same environment, where negative Δ(energy) represents a more exothermic reaction.

[c]Ref. 44, where a positive Δ(acidity) represents an increase in acidity.

Table 5. Barriers and reaction energies (kJ mol^{-1}) for the glycosidic bond cleavage in deoxyadenine catalyzed by the $HCOO^{-}\cdots H_2O$ and HO^{-} nucleophiles with HF, H_2O, or NH_3 bound at various adenine sites.

		Gas						Ether				Water			
N1(N6)	N7(N6)	Barrier	$\Delta^{\ddagger}$ [a]	Reaction energy	Δ(energy)[b]	Acidity[c]	Δ(acidity)[c]	Barrier	$\Delta^{\ddagger}$ [a]	Reaction energy	Δ(energy)[b]	Barrier	$\Delta^{\ddagger}$ [a]	Reaction energy	Δ(energy)[b]
		$HCOO^{-}\cdots H_2O$													
		122.2		25.7		1406.8		129.1		35.8		123.4		28.8	
HF		108.8	–13.4	7.9	–17.8	1365.2	41.6	116.3	–12.8	20.4	–15.4	112.5	–10.9	16.0	–12.8
	HF	101.7	–20.5	–2.3	–28.0	1348.7	58.1	107.5	–21.6	10.5	–25.3	103.4	–20.0	6.1	–22.7
H_2O		116.6	–5.6	17.3	–8.4	1388.5	18.3	125.4	–3.7	31.0	–4.8	120.6	–2.8	25.1	–3.7
	H_2O	113.5	–8.7	14.6	–11.1	1381.8	25.0	122.3	–6.8	28.8	–7.0	118.0	–5.4	24.3	–4.5
NH_3		122.5	0.3	25.0	–0.7	1406.9	–0.1	131.1	2.0	38.2	2.4	126.0	2.6	31.1	2.3
	NH_3	121.7	–0.5	24.3	–1.4	1403.3	3.5	131.3	2.2	38.6	2.8	124.9	1.5	32.2	3.4
		HO^{-}													
		61.0		–151.3		1406.8		79.1		–100.3		89.1		–59.0	
HF		52.0	–9.0	–168.0	–16.7	1365.2	41.6	70.4	–8.7	–115.3	–15.0	80.4	–8.7	–71.7	–12.7
	HF	47.9	–13.1	–175.9	–24.6	1348.7	58.1	65.1	–14.0	–124.2	–23.9	73.4	–15.7	–82.2	–23.2
H_2O		57.1	–3.9	–158.7	–7.4	1388.5	18.3	75.8	–3.3	–105.0	–4.7	86.2	–2.9	–62.5	–3.5
	H_2O	54.8	–6.2	–162.2	–10.9	1381.8	25.0	73.4	–5.7	–107.8	–7.5	80.8	–8.3	–67.0	–8.0
NH_3		60.9	–0.1	–152.0	–0.7	1406.9	–0.1	81.0	1.9	–97.4	2.9	90.3	1.2	–57.0	2.0
	NH_3	60.5	–0.5	–152.7	–1.4	1403.3	3.5	79.9	0.8	–98.0	2.3	87.0	–2.1	–59.0	0.0

Note: B3LYP/6-311+G(2d,p) single-point calculations were performed on B3LYP/6-31G(d) geometries, where all relative energies include scaled (0.9806) zero-point energy corrections and total energies of hydrogen-bonded complexes include basis set superposition error corrections. See Chart 2 for definition of complexation sites.

[a]Effect of hydrogen bonding with the nucleobase on the reaction barrier in the same environment, where negative $\Delta^{\ddagger}$ represents a decrease in the barrier height.

[b]Effect of hydrogen bonding with the nucleobase on the reaction energy in the same environment, where negative Δ(energy) represents a more exothermic reaction.

[c]Ref. 45, where a positive Δ(acidity) represents an increase in acidity.

Table 6. Barriers and reaction energies (kJ mol^{-1}) for the glycosidic bond cleavage in deoxyguanidine catalyzed by the $HCOO^{-}\cdots H_2O$ and HO^{-} nucleophiles with HF, H_2O, or NH_3 bound at various guanine sites.

		Gas						Ether				Water			
O6(N1)	O6-N7	Barrier	$\Delta^{\ddagger}$ [a]	Reaction energy	Δ(energy)[b]	Acidity[c]	Δ(acidity)[c]	Barrier	$\Delta^{\ddagger}$ [a]	Reaction energy	Δ(energy)[b]	Barrier	$\Delta^{\ddagger}$ [a]	Reaction energy	Δ(energy)[b]
		$HCOO^{-}\cdots H_2O$													
		127.0		35.0		1403.6		132.3		42.5		127.4		36.8	
HF		114.2	–12.8	17.9	–17.1	1368.5	35.1	119.0	–13.3	27.5	–15.0	115.1	–12.3	23.6	–13.2
	HF	95.4	–31.6	–0.8	–35.8	1353.7	49.9	106.0	–26.3	10.4	–32.1	107.3	–20.1	8.0	–28.8
H_2O		123.0	–4.0	29.3	–5.7	1393.9	9.7	129.2	–3.1	39.0	–3.5	124.2	–3.2	33.8	–3.0
	H_2O	113.5	–13.5	18.5	–16.5	1370.6	33.0	122.4	–9.9	32.1	–10.4	119.7	–7.7	31.2	–5.6
NH_3		129.5	2.5	36.7	1.7	1412.6	–9.0	135.8	3.5	46.4	3.9	129.9	2.5	39.0	2.2
	NH_3	119.5	–7.5	25.8	–9.2	1385.9	17.7	129.7	–2.6	40.7	–1.8	127.8	0.4	38.4	1.6
		HO^{-}													
		60.5		–150.9		1403.6		80.2		–103.0		90.8		–66.8	
HF		52.3	–8.2	–167.4	–16.5	1368.5	–35.1	71.9	–8.3	–118.8	–15.8	82.0	–8.8	–79.5	–12.7
	HF	47.0	–13.5	–175.1	–24.2	1353.7	–49.9	68.4	–11.8	–122.3	–19.3	78.0	–12.8	–81.8	–15.0
H_2O		57.9	–2.6	–157.0	–6.1	1393.9	–9.7	77.8	–2.4	–107.8	–4.8	90.4	–0.4	–69.4	–2.6
	H_2O	52.3	–8.2	–166.5	–15.6	1370.6	–33.0	74.0	–6.2	–113.3	–10.3	83.7	–7.1	–72.9	–6.1
NH_3		62.3	1.8	–149.6	1.3	1412.6	9.1	83.2	3.0	–99.7	3.3	93.6	2.8	–64.3	2.5
	NH_3	56.3	–4.2	–159.5	–8.6	1385.9	–17.7	78.9	–1.3	–105.1	–2.1	88.5	–2.3	–66.4	0.4

Note: B3LYP/6-311+G(2d,p) single-point calculations were performed on B3LYP/6-31G(d) geometries, where all relative energies include scaled (0.9806) zero-point energy corrections and total energies of hydrogen-bonded complexes include basis set superposition error corrections. See Chart 2 for definition of complexation sites.

[a]Effect of hydrogen bonding with the nucleobase on the reaction barrier in the same environment, where negative $\Delta^{\ddagger}$ represents a decrease in the barrier height.

[b]Effect of hydrogen bonding with the nucleobase on the reaction energy in the same environment, where negative Δ(energy) represents a more exothermic reaction.

[c]Ref. 45, where a positive Δ(acidity) represents an increase in acidity.

energies is independent of the nucleophile, the effect on the barrier is highly dependent due to differences in transition state geometries that dictate the net charge on the base. Indeed, since the magnitude of the effect can be directly correlated with the net charge on the base, the effects of hydrogen bonds on the reaction energetics are much less than those previously reported for the nucleobase acidity.[42–45] Nevertheless, the effects are still significant (up to approximately 40 kJ mol^{-1}). Furthermore, our previous study of the bond cleavage in deoxyuridine provides evidence that the glycosidic bond cleavage barrier can be further reduced by simultaneously involving more than one hydrogen-bonding interaction with the nucleobase.[39]

Environmental effects

The previous section has shown that hydrogen-bonding interactions between the nucleobase and small molecules can decrease the barrier height and increase the exothermicity of the reaction in the gas phase but to a smaller extent than the same interactions can increase the acidity of the (isolated) nucleobase. Previous work in our lab considered (bulk) environmental effects on the magnitude of the increase in acidity of natural (and damaged) nucleobases due to discrete hydrogen bonds through the implementation of continuum (PCM) solvation methods. We found that although the maximum increase in the gas-phase acidity is 60 kJ mol^{-1}, the maximum increase in enzymatic environments reduces to approximately 40 kJ mol^{-1}, and reduces further to approximately 30 kJ mol^{-1} in water. Since the present work suggests that the effects of discrete hydrogen bonds are also decreased when the reaction kinetics and thermodynamics are considered rather than the base acidity, it is of interest to evaluate the synergy between this outcome and the (bulk) environmental effects on the reaction energetics. Specifically, we must consider whether solvation further decreases the effects of hydrogen bonds on the reaction kinetics and thermodynamics reported in the present work, which may therefore make these interactions negligible to the overall reaction energetics.

Tables 2–6 compare the effects of hydrogen bonds on the kinetics and thermodynamics for glycosidic bond cleavage in the gas phase to those calculated in ether and water. As mentioned in the Computational details section, water was chosen because of its abundance in biological systems, while ether was chosen to represent enzymatic environments as a compromise between an aqueous solution and an active site sequestered from water. Furthermore, our previous work on the effects of hydrogen bonding on the nucleobase acidity shows that the results obtained in the gas phase, ether, and water span the results obtained in a wider range of solvents,[46] and therefore these dielectrics will provide representative examples of the environmental effects of interest.

The glycosidic bond cleavage barriers in the absence of small molecules interacting with the nucleobase in ether or water are only slightly larger (by less than 8 kJ mol^{-1}) than the corresponding gas phase barriers for the $HCOO^-\cdots H_2O$ nucleophile, but up to 30 kJ mol^{-1} larger for the HO^- nucleophile. The reaction energies, on the other hand, are more significantly affected due to the presence of solvent, where the $HCOO^-\cdots H_2O$ and HO^- reaction energies become less exothermic by up to approximately 15 and 90 kJ mol^{-1}, respectively.

The barriers and reaction energies for the glycosidic bond cleavage in the presence of hydrogen-bonding interactions with the nucleobase for the $HCOO^-\cdots H_2O$ nucleophile are larger and more endothermic in ether and water compared with the gas phase, where environmental effects on the barriers and reaction energies are up to approximately 26 and 32 kJ mol^{-1}, respectively. Additionally, there is no clear trend in the relative magnitude of the effects of ether or water, which suggests that there is a plateau in the (bulk) solvent effects for this nucleophile. Alternatively, the barriers systematically increase, and the reaction energies systematically become less exothermic, according to gas < ether < water for the reaction in the presence of the hydroxyl anion nucleophile, where the barriers generally increase by up to approximately 30 kJ mol^{-1} and the reaction energies generally increase by up to 100 kJ mol^{-1}.

The increases in the barriers and decreases in the reaction exothermicities in the absence and presence of hydrogen-bonding interactions with the nucleobases upon inclusion of solvation effects can be correlated with the stabilization of the nucleophile by the (bulk) solvent in the reactant complexes. Specifically, the degree of additional stabilization increases with both the charge on the nucleophile (HO^- > $HCOO^-\cdots H_2O$) and the polarity of the solvent (water > ether), and the net effect of ground state (reactant) stabilization is to increase the relative energies of the transition states and product complexes. For example, a greater degree of stabilization is provided to the hydroxyl anion nucleophile by (bulk) water than ether, which reduces the nucleophilicity in water to a greater extent and leads to larger increases in the reaction barriers. On the other hand, the formate activated water nucleophile is not affected as much as the hydroxyl anion by the bulk solvent and therefore there are smaller barrier increases for $HCOO^-\cdots H_2O$ compared with HO^-. These general conclusions for the effects of the bulk environment are supported by our previous results that considered the effects of interacting discrete molecules with the water nucleophile for the bond cleavage in deoxyuridine.[39] Specifically, the greater the stabilization provided to the hydroxyl anion (fully activated water) nucleophile though discrete hydrogen bonds, the larger the reaction barriers.

The most important finding upon consideration of environmental effects is that the changes in the gas-phase barriers and overall reaction energies upon solvation are essentially the same in the presence and absence of hydrogen-bonding interactions with the nucleobases. Therefore, the effects of hydrogen bonds with the nucleobase on the reaction barriers ($\Delta^{\ddagger}$) and energies (Δ(energy)) are approximately the same in the gas phase, ether, and water. Specifically, for both the HO^- and $HCOO^-\cdots H_2O$ nucleophiles, the deviations between the effects on the barriers in gas and ether or water are typically less than 5 kJ mol^{-1}, while the deviations in the reaction energies are generally less than 10 kJ mol^{-1}. This is a very important finding since the effects of the hydrogen bonds on the kinetics of the glycosidic bond cleavage are less than the effect on the acidity, and the effects on the acidity are further reduced upon solvation. These results emphasize the important role of discrete hydrogen-bonding interactions with the nucleobase in the glycosidic bond cleavage reaction for all deoxynucleotides.

Conclusions

The present work used computational chemistry to study the effects of the nature of the nucleobase, hydrogen bonding with the nucleobase, and the (bulk) environment on the kinetics and thermodynamics of the glycosidic bond cleavage in deoxynucleotides. Two nucleophiles were considered (HO^- and $HCOO^-\cdots H_2O$), which represent different stages of activation of a water nucleophile. In the absence of small molecules interacting with the nucleobase, the trend in the barriers and reaction energies for glycosidic bond cleavage follows the trend in the nucleobase acidities, where the greater the acidity, the smaller the barrier, and the more exothermic the reaction energy. However, the range in the reaction barriers is much less than the range in the base acidity and decreases with an increase in the charge on the nucleophile due to the promotion of earlier transition states with shorter glycosidic bond distances (and less charge on the nucleobase).

Discrete hydrogen-bonding interactions with all nucleobases decrease the barrier to glycosidic bond cleavage and increase the reaction exothermicity, but not to the same extent previous work indicates that these hydrogen bonds increase the base acidity. The magnitude of the effects depends on the small molecule bound, where the most acidic small molecules lead to the greatest effects. Although the effects on the reaction energies are the same for both nucleophiles considered in the present work, the effects on the barriers increase with a decrease in the charge on the nucleophile due to the formation of later transition states with greater charge on the nucleobase.

Environmental effects are found to increase the reaction barriers and decrease the reaction exothermicity due to stabilization of the nucleophile in reactant complexes. Since the ground state stabilization is similar regardless of whether small molecules are bound to the nucleobase, the effects of hydrogen bonding to the nucleobase are not significantly affected by the (bulk) environment and the reduction in barrier heights due to hydrogen bonding is up to approximately 30 kJ mol^{-1} in enzymatic environments depending on the nucleophile.

In summary, the most important conclusion from our work is that the effects of discrete hydrogen bonds with the nucleobase on the glycosidic bond cleavage are significant for all DNA bases in a variety of environments. Thus, although different proposed mechanisms exist for cleavage of the glycosidic bond in purine versus pyrimidine nucleotides, hydrogen bonding to the nucleobase will significantly decrease the reaction barrier regardless of the nucleotide. Future work must consider the implications of this finding for specific enzyme-catalyzed reactions since the magnitude of the effect of hydrogen bonds is dependent on the nucleophile, where different nucleophiles are often involved in cleavage of the glycosidic bond in pyrimidine versus purine nucleotides.

Acknowledgements

We thank the Natural Sciences and Engineering Research Council (NSERC), the Canada Foundation for Innovation (CFI), and the Canada Research Chair (CRC) program for financial support. ALM thanks NSERC, Alberta Ingenuity (AIF), the Alberta government, and the University of Lethbridge for graduate student scholarships. Mallory V. Mayes and Kenneth C. Hunter are acknowledged for preliminary calculations.

References

(1) This article is part of a Special Issue dedicated to Professor T. Ziegler.
(2) Voet, D.; Voet, J. G.; Pratt, C. W. *Fundamentals of biochemistry, Upgrade Edition*; Wiley Inc.: New York, USA, 2002.
(3) (a) Shapiro, R.; Danzig, M. *Biochemistry* **1972**, *11*, 23 doi:10.1021/bi00751a005. PMID:5009434.; (b) Shapiro, R.; Kang, S. *Biochemistry* **1969**, *8*, 1806. doi:10.1021/bi00833a004. PMID:5785205.
(4) (a) Piszkiewicz, D.; Bruice, T. C. *J. Am. Chem. Soc.* **1967**, *89*, 6237 doi:10.1021/ja01000a044.; (b) Piszkiewicz, D.; Bruice, T. C. *J. Am. Chem. Soc.* **1968**, *90*, 5844 doi:10.1021/ja01023a032.; (c) Piszkiewicz, D.; Bruice, T. C. *J. Am. Chem. Soc.* **1968**, *90*, 2156. doi:10.1021/ja01010a038. PMID:5644189.
(5) Cadet, J.; Teoule, R. *J. Am. Chem. Soc.* **1974**, *96*, 6517. doi:10.1021/ja00827a047. PMID:4414318.
(6) Prior, J. J.; Santi, D. V. *J. Biol. Chem.* **1984**, *259*, 2429. PMID:6546573.
(7) Zoltewicz, J. A.; Clark, D. F.; Sharpless, T. W.; Grahe, G. *J. Am. Chem. Soc.* **1970**, *92*, 1741. doi:10.1021/ja00709a055. PMID:5418456.
(8) Chernikov, A. V.; Usacheva, A. M.; Bruskov, V. I. *Biochemistry* **1996**, *61*, 35.
(9) Schramm, V. L. *Acc. Chem. Res.* **2003**, *36*, 588. doi:10.1021/ar0200495. PMID:12924955.
(10) Versees, W.; Steyaert, J. *Curr. Opin. Struct. Biol.* **2003**, *13*, 731. doi:10.1016/j.sbi.2003.10.002. PMID:14675552.
(11) Schramm, V. L. *Arch. Biochem. Biophys.* **2005**, *433*, 13. doi:10.1016/j.abb.2004.08.035. PMID:15581562.
(12) Berti, P. J.; McCann, J. A. B. *Chem. Rev.* **2006**, *106*, 506. doi:10.1021/cr040461t. PMID:16464017.
(13) Stivers, J. T.; Jiang, Y. L. *Chem. Rev.* **2003**, *103*, 2729. doi:10.1021/cr010219b. PMID:12848584.
(14) (a) Hunt, C.; Gillani, N.; Farone, A.; Rezaei, M.; Kline, P. C. *Biochim. Biophys. Acta* **2005**, *1751*, 140 PMID:16027052.; (b) Vandemeulebroucke, A.; Versees, W.; De Vos, S.; Van Holsbeke, E.; Steyaert, J. *Biochemistry* **2003**, *42*, 12902. doi:10.1021/bi0347914. PMID:14596604.
(15) (a) Versees, W.; Barlow, J.; Steyaert, J. J. *Mol. Biol.* **2006**, *359*, 331 doi:10.1016/j.jmb.2006.03.026.; (b) Bates, C.; Kendrick, Z.; McDonald, N.; Kline, P. C. *Phytochemistry* **2006**, *67*, 5 doi:10.1016/j.phytochem.2005.10.006. PMID:16300810.; (c) Horenstein, B. A.; Parkin, D. W.; Estupinan, B.; Schramm, V. L. *Biochemistry* **1991**, *30*, 10788 doi:10.1021/bi00108a026. PMID:1931998.; (d) Parkin, D. W.; Mentch, F.; Banks, G. A.; Horenstein, B. A.; Schramm, V. L. *Biochemistry* **1991**, *30*, 4586 doi:10.1021/bi00232a032. PMID:2021651.; (e) Mentch, F.; Parkin, D. W.; Schramm, V. L. *Biochemistry* **1987**, *26*, 921 doi:10.1021/bi00377a037. PMID:3552038.; (f) Parkin, D. W.; Schramm, V. L. *Biochemistry* **1987**, *26*, 913. doi:10.1021/bi00377a036. PMID:3552037.
(16) (a) Muzzolini, L.; Versees, W.; Tornaghi, P.; Van Holsbeke, E.; Steyaert, J.; Degano, M. *Biochemistry* **2006**, *45*, 773 doi:10.1021/bi0511991. PMID:16411753.; (b) Versees, W.; Loverix, S.; Vandemeulebroucke, A.; Geerlings, P.; Steyaert, J. J. *Mol. Biol.* **2004**, *338*, 1. doi:10.1016/j.jmb.2004.02.049.
(17) (a) Mazumder-Shivakumar, D.; Bruice, T. C. *Biochemistry* **2005**, *44*, 7805 doi:10.1021/bi047394h. PMID:15909995.;

(b) Mazumder, D.; Bruice, T. C. *J. Am. Chem. Soc.* **2002**, *124*, 14591. doi:10.1021/ja021088e. PMID:12465969.

(18) (a) Loverix, S.; Geerlings, P.; McNaughton, M.; Augustyns, K.; Vandemeulebroucke, A.; Steyaert, J.; Versees, W. J. *Biol. Chem.* **2005**, *280*, 14799 doi:10.1074/jbc.M413231200.; (b) Loverix, S.; Versees, W.; Steyaert, J.; Geerlings, P. *Int. J. Quantum Chem.* **2006**, *106*, 565. doi:10.1002/qua.20785.

(19) McCann, J. A. B.; Berti, P. J. *J. Am. Chem. Soc.* **2007**, *129*, 7055. doi:10.1021/ja067371l. PMID:17497857.

(20) (a) Chen, X.-Y.; Berti, P. J.; Schramm, V. L. *J. Am. Chem. Soc.* **2000**, *122*, 1609 doi:10.1021/ja992750i.; (b) Chen, X.-Y.; Berti, P. J.; Schramm, V. L. *J. Am. Chem. Soc.* **2000**, *122*, 6527 doi:10.1021/ja992751a.; (c) Roday, S.; Amukele, T.; Tyler, G. B. P. C.; Furneaux, R. H.; Schramm, V. L. *Biochemistry* **2004**, *43*, 4923. doi:10.1021/bi0498499. PMID:15109250.

(21) (a) Drohat, A. C.; Stivers, J. T. *J. Am. Chem. Soc.* **2000**, *122*, 1840 doi:10.1021/ja993254x.; (b) Drohat, A. C.; Jagadeesh, J.; Ferguson, E.; Stivers, J. T. *Biochemistry* **1999**, *38*, 11866 doi:10.1021/bi9910878. PMID:10508389.; (c) Drohat, A. C.; Xiao, G.; Tordova, M.; Jagadeesh, J.; Pankiewicz, K. W.; Watanabe, K. A.; Gilliland, G. L.; Stivers, J. T. *Biochemistry* **1999**, *38*, 11876 doi:10.1021/bi9910880. PMID:10508390.; (d) Savva, R.; McAuley-Hecht, K.; Brown, T.; Pearl, L. *Nature* **1995**, *373*, 487. doi:10.1038/373487a0. PMID:7845459.

(22) (a) Jiang, Y. L.; Ichikawa, Y.; Song, F.; Stivers, J. T. *Biochemistry* **2003**, *42*, 1922 doi:10.1021/bi027014x. PMID:12590578.; (b) Jiang, Y. L.; Drohat, A. C.; Ichikawa, Y.; Stivers, J. T. J. *Biol. Chem.* **2002**, *277*, 15385 doi:10.1074/jbc.M200634200.; (c) Jiang, Y. L.; Ichikawa, Y.; Stivers, J. T. *Biochemistry* **2002**, *41*, 7116 doi:10.1021/bi025694y. PMID:12033946.; (d) Jiang, Y. L.; Stivers, J. T. *Biochemistry* **2001**, *40*, 7710 doi:10.1021/bi010622c. PMID:11412125.; (e) Dong, J.; Drohat, A. C.; Stivers, J. T.; Pankiewicz, K. W.; Carey, P. R. *Biochemistry* **2000**, *39*, 13241 doi:10.1021/bi001437m. PMID:11052677.; (f) Drohat, A. C.; Stivers, J. T. *Biochemistry* **2000**, *39*, 11865 doi:10.1021/bi000922e. PMID:11009598.; (g) Werner, R. M.; Stivers, J. T. *Biochemistry* **2000**, *39*, 14054 doi:10.1021/bi0018178. PMID:11087352.; (h) Shroyer, M. J. N.; Bennett, S. E.; Putnam, C. D.; Tainer, J. A.; Mosbaugh, D. W. *Biochemistry* **1999**, *38*, 4834. doi:10.1021/bi982986j. PMID:10200172.

(23) (a) Bianchet, M. A.; Seiple, L. A.; Jiang, Y. L.; Ichikawa, Y.; Amzel, L. M.; Stivers, J. T. *Biochemistry* **2003**, *42*, 12455 doi:10.1021/bi035372+. PMID:14580190.; (b) Parikh, S. S.; Putnam, C. D.; Tainer, J. A. *Mutat. Res. DNA Repair* **2000**, *460*, 183 doi:10.1016/S0921-8777(00)00026-4. PMID:10946228.; (c) Werner, R. M.; Stivers, J. T. *Biochemistry* **2000**, *39*, 14054 doi:10.1021/bi0018178. PMID:11087352.; (d) Parikh, S. S.; Walcher, G.; Jones, G. D.; Slupphaug, G.; Krokan, H. E.; Blackburn, G. M.; Tainer, J. A. *Proc. Natl. Acad. Sci. U.S.A.* **2000**, *97*, 5083. doi:10.1073/pnas.97.10.5083. PMID:10805771.

(24) (a) Ma, A.; Hu, J.; Karplus, M.; Dinner, A. R. *Biochemistry* **2006**, *45*, 13687 doi:10.1021/bi061061y. PMID:17105188.; (b) Dinner, A. R.; Blackburn, G. M.; Karplus, M. *Nature* **2001**, *413*, 752 doi:10.1038/35099587. PMID:11607036.; (c) Osman, R.; Fuxreiter, M.; Luo, N. *Comput. Chem.* **2000**, *24*, 331 doi:10.1016/S0097-8485(99)00073-X. PMID:10816003.; (d) Luo, N.; Mehler, E.; Osman, R. *Biochemistry* **1999**, *38*, 9209. doi:10.1021/bi990262h. PMID:10413495.

(25) (a) McCann, J. A. B.; Berti, P. J. *J. Am. Chem. Soc.* **2008**, *130*, 5789 doi:10.1021/ja711363s. PMID:18393424.; (b) Eutsey, R.; Wang, G.; Maier, R. J. *DNA Repair (Amst.)* **2007**, *6*, 19 doi:10.1016/j.dnarep.2006.08.006. PMID:16996809.; (c) Lu, A. L.; Bai, H. B.; Shi, G. L.; Chang, D. Y. *Front. Biosci.* **2006**, *11*, 3062 doi:10.2741/2033. PMID:16720376.; (d) Livingston, A. L.; Kundu, S.; Pozzi, M. H.; Anderson, D. W.; David, S. S. *Biochemistry* **2005**, *44*, 14179 doi:10.1021/bi050976u. PMID:16245934.; (e) Pope, M. A.; David, S. S. *DNA Repair (Amst.)* **2005**, *4*, 91 doi:10.1016/j.dnarep.2004.08.004. PMID:15533841.; (f) Fromme, J. C.; Banerjee, A.; Huang, S. J.; Verdine, G. L. *Nature* **2004**, *427*, 652 doi:10.1038/nature02306. PMID:14961129.; (g) Manuel, R. C.; Hitomi, K.; Arvai, A. S.; House, P. G.; Kurtz, A. J.; Dodson, M. L.; McCullough, A. K.; Tainer, J. A.; Lloyd, R. S. J. *Biol. Chem.* **2004**, *279*, 46930 doi:10.1074/jbc.M403944200.; (h) Zharkov, D. O.; Gilboa, R.; Yagil, I.; Kycia, J. H.; Gerchman, S. E.; Shoham, C.; Grollman, A. P. *Biochemistry* **2000**, *39*, 14768. doi:10.1021/bi001538k. PMID:11101292.

(26) (a) Hamm, M. L.; Gill, T. J.; Nicolson, S. C.; Summers, M. R. *J. Am. Chem. Soc.* **2007**, *129*, 7724 doi:10.1021/ja0716453. PMID:17536801.; (b) Sidorenko, V. S.; Nevinsky, G. A.; Zharkov, D. O. *DNA Repair (Amst.)* **2007**, *6*, 317 doi:10.1016/j.dnarep.2006.10.022. PMID:17126083.; (c) Kirpota, O. O.; Zharkov, D. O.; Buneva, V. N.; Nevinsky, G. A. *Mol. Biol.* **2006**, *40*, 952 doi:10.1134/S002689330606015X.; (d) Kuznetsov, N. A.; Koval, V. V.; Zharkov, D. O.; Nevinsky, G. A.; Douglas, K. T.; Fedorova, O. S. *Nucleic Acids Res.* **2005**, *33*, 3919. doi:10.1093/nar/gki694. PMID:16024742.

(27) (a) Radom, C. T.; Banerjee, A.; Verdine, G. L. J. *Biol. Chem.* **2007**, *282*, 9182 doi:10.1074/jbc.M608989200.; (b) Banerjee, A.; Yang, W.; Karplus, M.; Verdine, G. L. *Nature* **2005**, *434*, 612 doi:10.1038/nature03458. PMID:15800616.; (c) Chung, S. J.; Verdine, G. L. *Chem. Biol.* **2004**, *11*, 1643 doi:10.1016/j.chembiol.2004.09.014. PMID:15610848.; (d) Fromme, J. C.; Bruner, S. D.; Yang, W.; Karplus, M.; Verdine, G. L. *Nat. Struct. Biol.* **2003**, *10*, 204 doi:10.1038/nsb902. PMID:12592398.; (e) Norman, D. P. G.; Chung, S. J.; Verdine, G. L. *Biochemistry* **2003**, *42*, 1564 doi:10.1021/bi026823d. PMID:12578369.; (f) Bruner, S. D.; Norman, D. P. G.; Verdine, G. L. *Nature* **2000**, *403*, 859. doi:10.1038/35002510. PMID:10706276.

(28) (a) Calvaresi, M.; Bottoni, A.; Garavelli, M. *J. Phys. Chem. B* **2007**, *111*, 6557 doi:10.1021/jp071581i. PMID:17508740.; (b) Schyman, P.; Danielsson, J.; Pinak, M.; Laaksonen, A. *J. Phys. Chem. A* **2005**, *109*, 1713 doi:10.1021/jp045686m. PMID:16833496.; (c) Osakabe, T.; Fujii, Y.; Hata, M.; Tsuda, M.; Neya, S.; Hoshino, T. *Chem-Bio Infomatics J.* **2004**, *4*, 73. doi:10.1273/cbij.4.73.

(29) (a) Amara, P.; Serre, L. *DNA Repair (Amst.)* **2006**, *5*, 947 doi:10.1016/j.dnarep.2006.05.042. PMID:16857432.; (b) Rogacheva, M. V.; Saparbaev, M. K.; Afanasov, I. M.; Kuznetsova, S. A. *Biochimie* **2005**, *87*, 1079 doi:10.1016/j.biochi.2005.05.011. PMID:15979229.; (c) Zharkov, D. O.; Shoham, G.; Grollman, A. P. *DNA Repair (Amst.)* **2003**, *2*, 839 doi:10.1016/S1568-7864(03)00084-3. PMID:12893082.; (d) Zharkov, D. O.; Shoham, G.; Grollman, A. P. *DNA Repair (Amst.)* **2003**, *2*, 839 doi:10.1016/S1568-7864(03)00084-3. PMID:12893082.; (e) Nash, H. M.; Lu, R. Z.; Lane, W. S.; Verdine, G. L. *Chem. Biol.* **1997**, *4*, 693 doi:10.1016/S1074-5521(97)90225-8. PMID:9331411.; (f) Rabow, L. E.; Kow, Y. W. *Biochemistry* **1997**, *36*, 5084. doi:10.1021/bi963005a. PMID:9125531.

(30) (a) de Jésus, K. P.; Serre, L.; Zelwer, C.; Castaing, B. *Nucleic Acids Res.* **2005**, *33*, 5936 doi:10.1093/nar/gki879.

PMID:16243784.; (b) Fromme, J. C.; Verdine, G. L. J. *Biol. Chem.* **2003**, *278*, 51543 doi:10.1074/jbc.M307768200.; (c) Fromme, J. C.; Verdine, G. L. *Nat. Struct. Biol.* **2002**, *9*, 544 PMID:12055620.; (d) Gilboa, R.; Zharkov, D. O.; Golan, G.; Fernandes, A. S.; Gerchman, S. E.; Matz, E.; Kycia, J. H.; Grollman, A. P.; Shoham, G. J. *Biol. Chem.* **2002**, *277*, 19811 doi:10.1074/jbc.M202058200.; (e) Sugahara, M.; Mikawa, T.; Kumasaka, T.; Yamamoto, M.; Kato, R.; Fukuyama, K.; Inoue, Y.; Kuramitsu, S. *EMBO J.* **2000**, *19*, 3857. doi:10.1093/emboj/19.15.3857. PMID:10921868.

(31) (a) Harbut, M. B.; Meador, M.; Dodson, M. L.; Lloyd, R. S. *Biochemistry* **2006**, *45*, 7341 doi:10.1021/bi052383p. PMID: 16752923.; (b) Zaika, E. I.; Perlow, R. A.; Matz, E.; Broyde, S.; Gilboa, R.; Grollman, A. P.; Zharkov, D. O. J. *Biol. Chem.* **2004**, *279*, 4849; (c) Koval, V. V.; Kuznetsov, N. A.; Zharkov, D. O.; Ishchenko, A. A.; Douglas, K. T.; Nevinsky, G. A.; Fedorova, O. S. *Nucleic Acids Res.* **2004**, *32*, 926 doi:10.1093/nar/gkh237. PMID:14769949.; (d) Zharkov, D. O.; Ishchenko, A. A.; Douglas, K. T.; Nevinsky, G. A. *Mutat. Res.* **2003**, *531*, 141 PMID:14637251.; (e) Ishchenko, A. A.; Vasilenko, N. L.; Sinitsina, O. I.; Yamkovoy, V. L.; Fedorova, O. S.; Douglas, K. T.; Nevinsky, G. A. *Biochemistry* **2002**, *41*, 7540. doi:10.1021/bi0121297. PMID:12056884.

(32) (a) Song, K.; Hornak, V.; Santos, C. D.; Grollman, A. P.; Simmerling, C. *Biochemistry* **2006**, *45*, 10886 doi:10.1021/bi060380m. PMID:16953574.; (b) Perlow-Poehnelt, R. A.; Zharkov, D. O.; Grollman, A. P.; Broyde, S. *Biochemistry* **2004**, *43*, 16092 doi:10.1021/bi048747f. PMID:15610004.; (c) Amara, P.; Serre, L.; Castaing, B.; Thomas, A. *Protein Sci.* **2004**, *13*, 2009. doi:10.1110/ps.04772404. PMID: 15273302.

(33) (a) Nunez, S.; Wing, C.; Antoniou, D.; Schramm, V. L.; Schwartz, S. D. *J. Phys. Chem. A.* **2006**, *110*, 463 doi:10.1021/jp051277u. PMID:16405318.; (b) Canduri, F.; dos Santos, D. M.; Silva, R. G.; Mendes, M. A.; Basso, L. A.; Palma, M. S.; de Azevedo, W. F.; Santos, D. S. *Biochem. Biophys. Res. Commun.* **2004**, *313*, 907 doi:10.1016/j.bbrc.2003.11.179. PMID:14706628.; (c) Lewandowicz, A.; Schramm, V. L. *Biochemistry* **2004**, *43*, 1458 doi:10.1021/bi0359123. PMID:14769022.; (d) Lewandowicz, A.; Shi, W. X.; Evans, G. B.; Tyler, P. C.; Furneaux, R. H.; Basso, L. A.; Santos, D. S.; Almo, S. C.; Schramm, V. L. *Biochemistry* **2003**, *42*, 6057 doi:10.1021/bi0343830. PMID:12755607.; (e) Kline, P. C.; Schramm, V. L. *Biochemistry* **1993**, *32*, 13212 doi:10.1021/bi00211a033. PMID:8241176.; (f) Kline, P. C.; Schramm, V. L. *Biochemistry* **1995**, *34*, 1153. doi:10.1021/bi00004a008. PMID:7827065.

(34) (a) Gao, X.-F.; Huang, X.-R.; Sun, C.-C. *J. Struct. Biol.* **2006**, *154*, 20 doi:10.1016/j.jsb.2005.11.014. PMID: 16469506.; (b) Deng, H.; Cahill, S. M.; Abad, J. L.; Lewandowicz, A.; Callender, R. H.; Schramm, V. L.; Jones, R. A. *Biochemistry* **2004**, *43*, 15966 doi:10.1021/bi048167i. PMID: 15595853.; (c) Nunez, S.; Antoniou, D.; Schramm, V. L.; Schwartz, S. D. *J. Am. Chem. Soc.* **2004**, *126*, 15720. doi:10.1021/ja0457563. PMID:15571394.

(35) (a) Deng, H.; Murkin, A. S.; Schramm, V. L. *J. Am. Chem. Soc.* **2006**, *128*, 7765 doi:10.1021/ja0570281. PMID: 16771490.; (b) Deng, H.; Lewandowicz, A.; Schramm, V. L.; Callender, R. *J. Am. Chem. Soc.* **2004**, *126*, 9516. doi:10.1021/ja049296p. PMID:15291536.

(36) (a) Wielgus-Kutrowska, B.; Bzowska, A. *Biochim. Biophys. Acta* **2006**, *1764*, 887 PMID:16631420.; (b) Kicska, G. A.; Tyler, P. C.; Evans, G. B.; Furneaux, R. H.; Shi, W. X.; Fedorov, A.; Lewandowicz, A.; Cahill, S. M.; Almo, S. C.; Schramm, V. L. *Biochemistry* **2002**, *41*, 14489 doi:10.1021/bi026636f. PMID:12463747.; (c) Fedorov, A.; Shi, W.; Kicska, G.; Fedorov, E.; Tyler, P. C.; Furneaux, R. H.; Hanson, J. C.; Gainsford, G. J.; Larese, J. Z.; Schramm, V. L.; Almo, S. C. *Biochemistry* **2001**, *40*, 853 doi:10.1021/bi002499f. PMID:11170405.; (d) Erion, M. D.; Stoeckler, J. D.; Guida, W. C.; Walter, R. L.; Ealick, S. E. *Biochemistry* **1997**, *36*, 11735. doi:10.1021/bi961970v. PMID:9305963.

(37) (a) Birck, M. R.; Schramm, V. L. *J. Am. Chem. Soc.* **2004**, *126*, 2447 doi:10.1021/ja039260h. PMID:14982453.; (b) Birck, M. R.; Schramm, V. L. *J. Am. Chem. Soc.* **2004**, *126*, 6882. doi:10.1021/ja0492642. PMID:15174854.

(38) Mendieta, J.; Martin-Santamaria, S.; Priego, E.-M.; Balzarini, M.-J.; Camarasa, M.-J.; Perez-Perez, M.-J.; Gago, F. *Biochemistry* **2004**, *43*, 405. doi:10.1021/bi034793o. PMID: 14717594.

(39) Millen, A. L.; Archibald, L. A. B.; Hunter, K. C.; Wetmore, S. D. *J. Phys. Chem. B* **2007**, *111*, 3800. doi:10.1021/jp063841m. PMID:17388517.

(40) (a) Blomberg, M. R. A.; Siegbahn, P. E. M.; Babcock, G. T. *J. Am. Chem. Soc.* **1998**, *120*, 8812 doi:10.1021/ja9805268.; (b) Siegbahn, P. E. M.; Blomberg, M. R. A. *Chem. Rev.* **2000**, *100*, 421 doi:10.1021/cr980390w. PMID:11749242.; (c) Blomberg, M. R. A.; Siegbahn, P. E. M. *J. Phys. Chem. B* **2001**, *105*, 9375 doi:10.1021/jp010305f.; (d) Himo, F.; Siegbahn, P. E. M. *Chem. Rev.* **2003**, *103*, 2421 doi:10.1021/cr020436s. PMID:12797836.; (e) Cho, K. B.; Gauld, J. W. *J. Am. Chem. Soc.* **2004**, *126*, 10267 doi:10.1021/ja049186i. PMID:15315438.; (f) Cho, K. B.; Gauld, J. W. *J. Phys. Chem. B* **2005**, *109*, 23706. doi:10.1021/jp054864o. PMID:16375351.

(41) Frisch, M. J.; Trucks, G. W.; Schlegel, H. B.; Scuseria, G. E.; Robb, M. A.; Cheeseman, J. R.; Montgomery, J. A., Jr.; Vreven, T.; Kudin, K. N.; Burant, J. C.; Millam, J. M.; Iyengar, S. S.; Tomasi, J.; Barone, V.; Mennucci, B.; Cossi, M.; Scalmani, G.; Rega, N.; Petersson, G. A.; Nakatsuji, H.; Hada, M.; Ehara, M.; Toyota, K.; Fukuda, R.; Hasegawa, J.; Ishida, M.; Nakajima, T.; Honda, Y.; Kitao, O.; Nakai, H.; Klene, M.; Li, X.; Knox, J. E.; Ratchian, H. P.; Cross, J. B.; Adamo, C.; Jaramillo, J.; Gomperts, R.; Stratmann, R. E.; Yazyev, O.; Austin, A. J.; Cammi, R.; Pomelli, C.; Ochterski, J. W.; Ayala, P. Y.; Morokuma, K.; Voth, G. A.; Salvador, P.; Dannenberg, J. J.; Zakrzewski, V. G.; Dapprich, S.; Daniels, A. D.; Strain, M. C.; Farkas, O.; Malick, D. K.; Rabuck, A. D.; Raghavachari, K.; Foresman, J. B.; Ortiz, J. V.; Cui, Q.; Baboul, A. G.; Clifford, S.; Cioslowski, J.; Stefanov, B. B.; Liu, G.; Liashenko, A.; Piskorz, P.; Komaromi, I.; Martin, R. L.; Fox, D. J.; Keith, T.; Al-Laham, M. A.; Peng, C. Y.; Nanayakkara, A.; Challacombe, M.; Gill, P. M. W.; Johnson, B.; Chen, W.; Wong, M. W.; Gonzalez, C.; Pople, J. A. *Gaussian 03*, Revisions D.02. Gaussian, Inc.: Wallingford, Conn., USA., 2004.

(42) Di Laudo, M.; Whittleton, S. R.; Wetmore, S. D. *J. Phys. Chem. A* **2003**, *107*, 10406. doi:10.1021/jp035496w.

(43) Whittleton, S. R.; Hunter, K. C.; Wetmore, S. D. *J. Phys. Chem. A* **2004**, *108*, 7709. doi:10.1021/jp048318r.

(44) Hunter, K. C.; Rutledge, L. R.; Wetmore, S. D. *J. Phys. Chem. A* **2005**, *109*, 9554. doi:10.1021/jp0527709. PMID: 16866407.

(45) McConnell, T. L.; Wheaton, C. A.; Hunter, K. C.; Wetmore, S. D. *J. Phys. Chem. A* **2005**, *109*, 6351. doi:10.1021/jp0509919. PMID:16833978.

(46) Hunter, K. C.; Wetmore, S. D. *J. Phys. Chem. A* **2007**, *111*, 1933. doi:10.1021/jp066641j. PMID:17302396.

An improved neural network method for solving the Schrödinger equation[1]

Sergei Manzhos and Tucker Carrington, Jr.

Abstract: We propose a neural network (NN) based algorithm for calculating vibrational energies and wave functions and apply it to problems in 2-, 4-, and 6-dimensions. By using neurons as basis functions and methods of nonlinear optimization, we are able to compute three states of a 6-D Hamiltonian using only 50 basis functions. In a standard direct product basis, thousands of basis functions would be necessary. Previous NN methods for solving the Schrödinger equation computed one level at a time and optimized all of the parameters using expensive nonlinear optimization methods. Using our approach, linear coefficients in the NN representation of wave functions are determined with methods of linear algebra and many levels are computed at the same time from one set of nonlinear NN parameters. In addition, we use radial basis function neurons to ensure the correct boundary conditions. The use of linear algebra methods makes it possible to treat systems of higher dimensionality.

Key words: neural networks, vibrational spectroscopy, numerical methods.

Résumé : On propose un algorithme basé sur un réseau neuronal (RN) pour calculer les énergies de vibration et les fonctions d'onde et on l'applique à des problèmes en 2, 4 et 6 dimensions. L'utilisation de neurones comme fonctions de base et de méthodes d'optimisation non-linéaires permettent de calculer trois états d'un hamiltonien 6-D, en n'utilisant que 50 fonctions de base. Dans une base standarde produit direct, des milliers de fonctions de base seraient nécessaires. Les méthodes antérieures de RN utilisées pour résoudre l'équation de Schrödinger calculaient un niveau à la fois et optimisaient tous les paramètres en utilisant des méthodes coûteuses d'optimisation non linéaire. Dans l'approche présentée ici, les coefficients linéaires nécessaires pour représenter des fonctions d'onde sont déterminés par une méthode de l'algèbre linéaire et il est possible de calculer plusieurs niveaux en même temps, à partir d'un seul ensemble de paramètres neuronales nonlinéaires. En plus, nous utilisons des fonctions de base radiale afin d'assurer des conditions de limite correctes. L'utilisation de méthodes de l'algèbre linéaire permet de traiter des systèmes de dimension plus élevée.

Mots-clés : réseau neuronal, spectroscopie de vibration, méthodes numériques.

I. Introduction

Using a perturbative normal mode approach, it is frequently possible to understand spectral patterns associated with low-lying energy levels of semirigid molecules, and to extract from them information about potential energy surfaces.[2,3] These methods enable one to disentangle the spectrum of a molecule to extract, for example, its equilibrium geometry and some information about its Born–Oppenheimer potential. However, to calculate high-lying levels of semirigid molecules or even low-lying levels of floppy molecules, it is necessary to calculate eigenvalues and eigenvectors of a matrix **H**, representing the nuclear Hamiltonian operator in a chosen basis.[4–7] This variational method has been successfully used to compute both high-lying vibrational states of semirigid molecules and low-lying states of weakly-bound complexes.[4–8] The principal impediment to applying it to compute spectra of small molecules, for which detailed experimental results are available, is the size of the Hamiltonian matrix. The most straightforward way to compute eigenvalues and eigenvectors is using a direct eigensolver (usually Householder transformations and the QR method).[9] The cost of such a calculation scales as N^3, where N is the size of the matrix. In many cases, the cost can be reduced by using the Lanczos algorithm.[10–14]

The basis functions used to make the calculations in refs. 4–8 and 10–14 are either products of functions of a single variable or contracted functions obtained from product basis functions. Contraction greatly reduces the size of the basis required to obtain a converged spectrum,[4–8,12,14–17] but for difficult problems, the matrices for which one must compute eigenvalues and eigenvectors are nonetheless huge. This is due to the fact that a linear variation is used: the only parameters are the coefficients of a basis set expansion. The matrix size can be reduced considerably by using flexible basis functions, which depend on parameters that are optimized. In this paper, we explore this strategy. Owing to the fact that most methods for solving the Schrödinger equation are limited by the amount of memory they require, the advantages of an approach that greatly reduces the basis size (and hence the size of the matrices or vectors one must

Received 3 December 2008. Accepted 21 January 2009. Published on the NRC Research Press Web site at canjchem.nrc.ca on 8 May 2009.

S. Manzhos.[1] Département de chimie, Université de Montréal, C.P. 6128, Succursale Centre-ville, Montreal, QC H3C 3J7, Canada.
T. Carrington, Jr..[2] Chemistry Department, Queen's University, Kingston, ON K7L 3N6, Canada.

[1]Present address: Department of Chemical System Engineering, School of Engineering, University of Tokyo, 7-3-1, Hongo, Bunkyo-ku, Tokyo 113-8656, Japan.
[2]Corresponding author (e-mail: tucker.carrington@chem.queensu.ca).

store) are compelling. Some questions to be explored: Is it possible to use functions that are flexible enough that they make a good basis for computing many energy levels? Is the cost of the parameter optimization prohibitive?

In this paper, we use neural network (NN) basis functions. Other scientists have also used NNs to solve the Schrödinger equation[18–20] but they have not used NN basis functions and have computed levels one at a time. NNs are attractive tools for solving the Schrödinger equation, because it is known that they are universal approximators,[21–24] and thought to scale favourably with dimensionality.[25–30] These advantages stem from the fact that NNs represent multidimensional functions with univariate functions but not with sums of products of functions. The difficulty of the multidimensional NN-parameter optimization problem has so far limited the application of NN-based methods to 1-, 2-, and 3-dimensional problems for which vibrational levels are obtained one at a time. We give a brief overview of NN methods for solving the Schrödinger equation in Section II.

In Section III, we present an improved NN method for solving the vibrational Schrödinger equation. Our method is better in four respects. (*i*) We simultaneously determine several energy levels and wave functions. This is done by optimizing a set of neurons for all the computed levels, i.e., the same NN hidden layer of neurons is used to make several outputs, one for each desired state. (*ii*) The linear NN parameters are determined using tools from linear algebra instead of standard minimization methods. This reduces the number of parameters one must optimize using expensive nonlinear methods. It involves finding eigenvalues and eigenvectors of "rectangular matrix pencils": recent progress[31] makes this approach feasible. (*iii*) In contrast to previous work, we use radial basis neural networks (RBFNN) and not sigmoid neural networks, in line with the argument that RBFNNs are better suited for approximating band-limited functions.[32] (*iv*) We pretrain the NN to avoid local minima.

II. Neural networks for wave functions

NNs[33–36] are flexible functions of the form

$$[1] \qquad f(y_1,\ldots,y_d)=\sum_{q=1}^{N} c_q \sigma\left(\sum_{p=1}^{d} w_{qp}y_p + b_q\right) + h$$

The one-dimensional function, σ, is called a neuron. The argument of σ is a linear combination of the coordinates; see Fig. 1, where a commonly used single hidden layer NN is shown. The final output of the NN is a linear combination of the outputs of the hidden layer. The key NN parameters are the input weights, $\boldsymbol{w}$, biases, $\boldsymbol{b}$, and output weights, $\boldsymbol{c}$. The most common choice for σ is the sigmoid function, $\sigma(x) = (1 + e^{x})^{-1}$.[24,37] It is well-known that the parameters can be adjusted to fit any function.[21–24] Mathematicians have also argued that the number of neurons required to obtain a good fit scales well with dimensionality.[25–30] Note that eq. [1] has the form of a basis expansion with neuron basis functions. The neurons should be good basis functions because they depend on many optimizable parameters. By varying the parameters, one changes the location, orientation, and extent of the basis functions.

How does one use NNs to solve the Schrödinger equation? One way to proceed[18–20] is to represent a wave function as an NN and to adjust the parameters to make the square of the norm of the residual

Fig. 1. The architecture of the commonly used single hidden layer neural network. *N* neuron inputs are formed from *d* components of the input vector. A weighted sum of the neuron outputs is the NN output. Here, neurons are labeled for the case of the most commonly used sigmoid NN: the neurons inputs are weighted *sums* of the coordinates (Σ) and the transfer function is sigmoid.

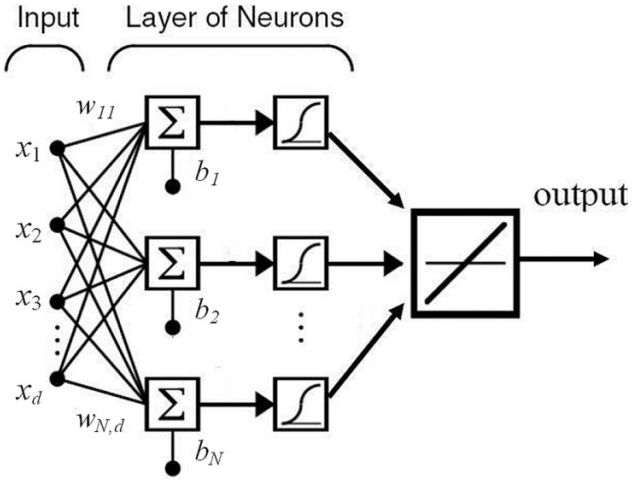

$$[2] \qquad R=\frac{\langle\psi|(\widehat{H}-E)^2|\psi\rangle}{\langle\psi|\psi\rangle} \approx \frac{\sum_{i=1}^{M}|(\widehat{H}-E)\psi({}^{i}\mathbf{y})|^2}{\sum_{i=1}^{M}|\psi({}^{i}\mathbf{y})|^2}$$

as small as possible. The ${}^{i}\mathbf{y}$ quadrature points on the right are chosen in the region where the wave function is expected to be non-negligible. If the wave function is represented as an NN, the kinetic energy operator (KEO) can be applied to the wave function analytically. In previous NN methods, NN parameters and E[19,20] or only NN parameters[18] (E being computed from the wave function) were fit to reduce R (or maximize e^{-R}) for a single state. For one-dimensional (1-D) problems, the best values of $\sqrt{R}$ were typically 2.3%–19% of the corresponding energies.[19,20] For a two-dimensional Henon–Heiles potential, the first four wave functions and levels were reported in ref. 18 with a relative error of the order of 10^{-5}. For a three-dimensional case, only the ground state for a Hamiltonian representing three coupled anharmonic oscillators was reported.[18]

III. Multilevel radial neuron matrix method

Our method is based on these ideas but improves on them in four ways; see the last paragraph of section I. Previous NN methods use general optimization techniques to determine the best values of all the NN parameters. These methods are computationally intensive because there are many parameters. Increasing the dimensionality exacerbates the problem. This is certainly one reason that previous calculations did not get beyond 3-D. All previous NN methods also use one NN per wave function. In section III.A, we outline a method that uses the same NN for a whole set of wave func-

tions and exploits a linear algebra technique to reduce the cost of the parameter optimization. In section III.B, we explain why radial basis function neurons are advantageous.

A. Combining linear and nonlinear optimization to determine several wave functions

To reduce the number of parameters that must be determined using general optimization techniques and at the same time to make it possible to compute a group of wave functions from one set of neurons, we think of the neurons as optimizable basis functions. To do so we must use a single hidden layer NN (see Eq. [1]). The simplicity of this architecture allows us to obtain a matrix equation from which we can easily determine the linear coefficients. It also greatly facilitates applying the kinetic energy operator to the NN. For example, applying the KEO of section III.E

$$[3] \qquad \widehat{T}(\boldsymbol{y}) = -\sum_{j,k=1}^{d} \gamma_{jk} \frac{\partial^2}{\partial y_j \partial y_k}$$

to the simple NN of eq. [1], one obtains

$$[4] \qquad \begin{cases} \widehat{T}\psi_k(\boldsymbol{y}) = -\sum_{i=1}^{d} c_{ik} \widetilde{\gamma}_i \sigma''(q_i) \\ \widetilde{\gamma}_i \equiv \sum_{m,n} \gamma_{mn} w_{im} w_{in} \\ q_i \equiv \sum_{j=1}^{d} w_{ij} y_j + b_i \end{cases}$$

Rather than representing each wave function with eq. [1] and optimizing a set of c_q, w_{qp}, and b_p parameters for each wave function, we optimize a single set of w_{qp} and b_p parameters to represent several wave functions and choose different c_q for each wave function, i.e.,

$$[5] \qquad \psi_k(\boldsymbol{y}) = \sum_{i=1}^{N} c_{ik} \sigma(\boldsymbol{w}_i, b_i, \boldsymbol{y}) + h_k$$

where $\psi_k(\boldsymbol{y})$ is the k^{th} wave function, and $\boldsymbol{w}_i$ is the ith row of the input weight matrix $\boldsymbol{w}$. In NN language, the network has several outputs, one for each wave function. All previous methods extract one vibrational level per neural network: to obtain many levels it is necessary to do many NN fits. As all wave functions are determined by the same potential, it is reasonable to hope that one set of NN hidden layer neurons can be used for many of them.

It is not necessary to optimize the w_{qp}, b_p, and c_q with the same method. We can use tools of linear algebra for the linear coefficients. For a given set of w_{qp} and b_p, we optimize the c_{qk} by solving a matrix equation. It is obtained by replacing the wave function in the Schrödinger equation with the NN, applying the Hamiltonian, and requiring that the Schrödinger equation be satisfied at a set of M points. One finds a generalized rectangular eigenvalue problem for the parameters c and h (see Appendix)

$$[6] \qquad (\mathbf{M} - E_k \mathbf{S})\widetilde{\boldsymbol{c}}_k = 0$$

where $\widetilde{\boldsymbol{c}}_k \equiv \begin{pmatrix} \boldsymbol{c}_k \\ h_k \end{pmatrix}$. Here $\mathbf{M}$ and $\mathbf{S}$ are rectangular matrices (of the dimension $M \times N$) depending on values of the potential and of the neurons at different points in the configuration space. This equation is somewhat analogous to the square matrix equation obtained using the collocation approach.[38] In our case, the matrices are rectangular because the number of basis functions is much smaller than the number of points used to optimize the parameters.

Fig. 2. An illustration of the band-limited character of vibrational wave functions. A vibrational wave function of a harmonic oscillator is shown along with its Fourier transform. The Fourier transform decays sharply above the frequency corresponding to the period of oscillation of the wave function (both shown by vertical lines).

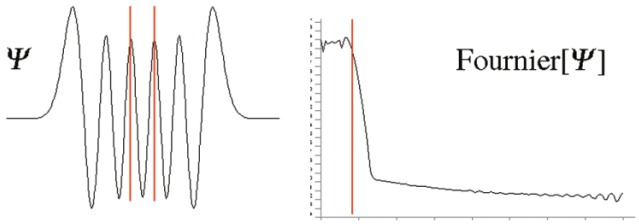

B. RBFNN wave function

When devising a NN method for computing vibrational bound state solutions of the Schrödinger equation, it is important to do something to ensure that wave functions approach zero when the molecule is pulled apart. Previous NN methods used either an amplitude-phase decomposition[19,20] or multiplied the neural network by a function that satisfies the boundary condition by construction.[18] Both these approaches, however, make the application of the KEO cumbersome for a multidimensional problem and are incompatible with the use of linear optimization for some of the NN parameters. Instead, we use so-called radial basis function (RBF) neurons as opposed to the traditional sigmoid neurons. The NN is

$$[7] \qquad \psi_k(\boldsymbol{y}) = \sum_{i=1}^{N} c_{ik} \exp\Big(- b_i^2 \sum_{j=1}^{d} (w_{ij} - y_j)^2 \Big) + h_k$$

RBFNNs have also been shown to be universal approximators.[39,40] It has recently been suggested that RBF or Gaussian neurons should be good for representing band-limited functions.[32] As vibrational wave functions are band limited, RB neurons should be a good choice for a NN Schrödinger method. Figure 2 shows, as an example, a harmonic wave function and its Fourier spectrum that decays quickly. There is also evidence that a RBF representation of a band limited function should be "free of the curse of dimensionality".[32] The RBFs we use are similar to the distributed Gaussian basis proposed in refs. 41–43. The key difference is that we optimize the parameters numerically to find the best possible basis. The parameters c_{ik} and h_k are determined with linear algebra and the other parameters with nonlinear optimization.

C. Solving the rectangular eigenvalue problem

To solve the rectangular eigenvalue problem we use an approach closely based on that of ref. 31. Note that an exact solution is not possible because the matrices are rectangular. The algorithm minimizes

Fig. 3. The architecture of the multiple output radial basis NN corresponding to eq. [7] and used in this paper.

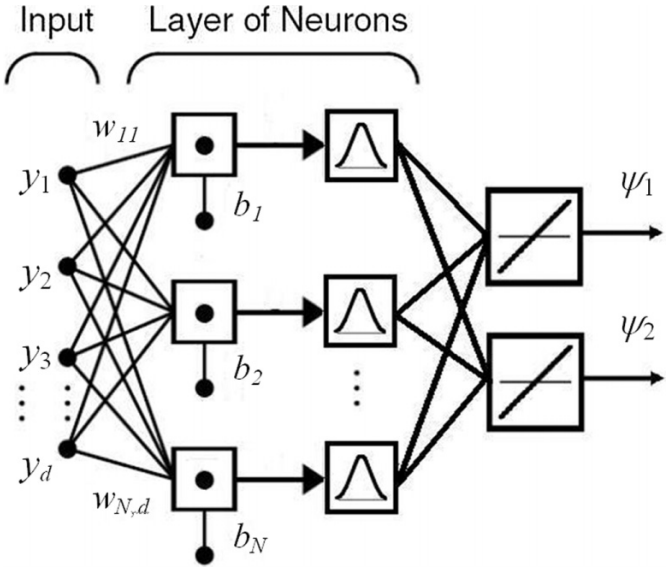

$$[8] \qquad \min \|(\mathbf{M} - E_k\mathbf{S})\tilde{c}_k\|^2/(1 + |E_k|^2)$$

It requires a guess for E_k. According to the algorithm, an approximate right eigenvector is the eigenvector corresponding to the smallest eigenvalue of $(\mathbf{M} - E_k\mathbf{S})^{\mathrm{H}}$ $(\mathbf{M} - E_k\mathbf{S})$). In ref. 31 energies are updated at each iteration by solving $\tilde{c}^H(\mathbf{S}^{\mathrm{H}} + E_k\mathbf{M}^{\mathrm{H}})(\mathbf{M} - E_k\mathbf{S})\tilde{c} = 0$ for E. We obtain somewhat better results when, instead, we update the energy by fitting the E_k together with the $\boldsymbol{w}$ and $\boldsymbol{b}$ parameters. Here superscript "H" stands for the Hermitian conjugate. See ref. 31 for more details.

We combine the Levenberg–Marquadt algorithm and solutions of the rectangular eigenvalue problem as follows. For a particular set of w_{qp}, b_p, and E_k we solve the rectangular problem to determine eigenvectors and hence approximate wave functions. From the E_k and the approximate wave functions we compute a total residual, $R_{\mathrm{T}} = \sum_k R_k^2$, where R_k is the residual of eq. [2] for the kth eigenpair. We use a nonlinear optimization method to minimize

$$[9] \qquad R_{\mathrm{T}} + \sum_k (E_k - E_k^{\mathrm{int}})^2, \text{ where } E_k^{\mathrm{int}} \equiv \frac{\int \psi_k \hat{\boldsymbol{H}} \psi_k d\boldsymbol{r}}{\int |\psi_k|^2 d\boldsymbol{r}}$$

to find the best values of w_{qp}, b_p, and E_k. Only the w_{qp}, b_p, and E_k are determined by nonlinear optimization. This reduces the cost of finding the best parameters and makes it possible to treat higher-dimensional systems. For each set of w_{qp}, b_p, and E_k values, the rectangular eigenvalue problem must be solved. Figure 3 shows schematically the architecture of the NN, the coordinates that are input, and one layer of neurons whose weighted outputs are used to construct several wave functions.

D. Avoiding local minima

When optimizing the parameters, it is critical to avoid getting stuck in a local minimum. As the dimensionality of the calculation increases, the local minimum problem becomes more severe. We propose starting with parameter values that are close to those required to represent the desired wave functions. If we know good approximate wave functions, we find these values by pretraining the NN so that it reproduces them. If we do not have good approximate wave functions, we pretrain using wave functions obtained from a separable approximation to the potential and then turn on the coupling adiabatically, drawing the parameters to the correct minimum as the coupling strength is increased. (See section III.E).

E. Test Hamiltonians and results

We tested the new NN Schrödinger solver on quadratic potentials. As the NN basis is not based on a zeroth-order approximation it is expected to work about equally well for all potentials. In the original coordinates, the potential, KEO, and energy levels are

$$[10] \qquad \begin{aligned} V(\boldsymbol{x}) &= \sum_{i=1}^{d} x_i^2 \\ \hat{T}(\boldsymbol{x}) &= -\sum_{i=1}^{d} \frac{\partial^2}{\partial x_i^2} \end{aligned}$$

$$[11] \qquad E = 2\sum_{i=1}^{d}\left(n_i + \frac{1}{2}\right)$$

The calculations are done in a new set of coordinates, $\boldsymbol{y}$, obtained from, $\boldsymbol{y} = \boldsymbol{M}\boldsymbol{x}$, where the matrix of $\boldsymbol{M}$ is used to introduce coupling. Although we compute energy levels and wave functions of a coupled Hamiltonian, the exact levels and wave function are known and can be used to assess the quality of the NN solutions. This idea has been used to test other methods for solving the Schrödinger equation.[44,45] In our tests, we used

$$[12] \qquad y = \begin{pmatrix} 1 & 0 & \cdots & 0 \\ 0.2/d & 1 & \cdots & 0 \\ \vdots & \vdots & \ddots & \vdots \\ 0.2/d & 0.2/d & \cdots & 1 \end{pmatrix} x$$

In the new coordinates

$$[13] \qquad \begin{aligned} V(\boldsymbol{y}) &= \sum_{i,j=1}^{d} a_{ij} y_i y_j \\ \hat{T}(\boldsymbol{y}) &= -\sum_{j,k=1}^{d} \gamma_{jk} \frac{\partial^2}{\partial y_j \partial y_k} \end{aligned}$$

Configuration space is randomly sampled in the region in which the potential is below twice the energy of the highest level we wish to compute. There is no need to sample on a uniform grid, it is only necessary to have points where the wave functions are nonzero. The point distribution could be used to emphasize specific regions of space. We used the following point selection scheme: a random point, ${}^n\boldsymbol{y}$, is selected within a range of y_i, large enough to include all points for which $V({}^n y) \leq V_{\max} \equiv 2E_{\max}$, where $E_{\max}$ is the energy

of the largest desirable level. The point is accepted into the dataset if

$$[14] \qquad \frac{V_{\max} - V({}^{n}\boldsymbol{y})}{V_{\max}} > rand - PdfBias$$

where *rand* is a uniformly distributed random number in the range [0, 1], and *PdfBias* is a constant also in the range [0, 1]. *PdfBias* = 1 corresponds to a uniform point distribution, while *PdfBias* = 0 results in the "inverted potential" type of distribution with more points put in low-energy regions.[46] We find that it is better to use *PdfBias* < 1 when many levels are computed, as otherwise the lower level wave functions are undersampled. Obviously, computing high-lying levels requires using both more points and more NN parameters. More points are needed because wave functions associated with higher levels span a larger region of space, and a larger NN is needed because these wave functions are more structured. We first computed seven vibrational levels in two-dimensions using one NN with 70 Gaussian neurons and with 2 500 points up to $2E_{\max}$ ($E_{\max}$ = 14.0).

The RBFNN scheme described in section III.B was programmed in Matlab.[47] The neural network architecture was programmed using the Neural Network Toolbox[48] of Matlab. The more time-consuming parts of the code are programmed in Fortran and called from the Matlab code using mex-files.[47] The parameters $\boldsymbol{w}$, $\boldsymbol{b}$, and E_k were fitted with the Levenberg–Marquardt algorithm of Matlab. The parameters $\boldsymbol{c}$ and $\boldsymbol{h}$ were determined with the method described in section III.A. Parameter values can be obtained from the authors by request. The average, over all computed levels, of the residual norm

$$[15] \qquad \langle R_k \rangle = \left\langle \frac{\sum_{i=1}^{Np} |(\hat{H} - E_k)\psi_k({}^{i}\boldsymbol{x})|^2}{\sum_{i=1}^{Np} |\psi_k({}^{i}\boldsymbol{x})|^2} \right\rangle = 0.014$$

The ratio $\sqrt{R_k}/E_k$ is small compared to what was achieved previously for a 1-D problem.[19,20] Differences between exact and computed energies, ΔE_k, are about 0.022, which is also good compared to errors of previous calculations, despite the fact that all previous calculations compute only one level at time.[18–20] The R_k and ΔE_k for different levels have similar magnitudes.

There is, to the best of our knowledge, only one published result (the ground state) for a three-dimensional coupled harmonic oscillator[18] and *no* results for a four-dimensional Schrödinger equation. Therefore, we next performed a four-dimensional calculation for the system specified by eqs. [10] – [13]. For this 4-D test, we used 5 000 randomly sampled points, 70 neuron basis functions, and achieved an average R_k of about 0.007 over the first three levels. A direct product basis would have about 10^4 functions. Figure 4 shows two-dimensional slices of the wave functions for the first three vibrational levels. A similar fit of the three lowest vibrational levels in 6-D at 5 000 points and using 50 neurons yields an average error $<R_k>$ of 0.073. For reference purposes, the E_k we determine in the 6-D fit are

Fig. 4. Two-dimensional cross-sections of wave functions for three levels of the four-dimensional Hamiltonian in transformed coordinates (y).

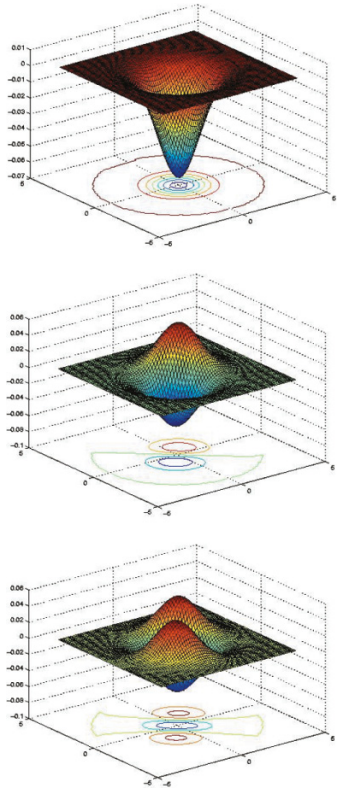

5.9638, 7.9745, and 10.1388, and the corresponding R_k are 0.0814, 0.0618, and 0.0757. The energies obtained by integrating $\int \psi_k H \psi_k dr$ are 5.9524, 7.9708, and 10.1424, and the exact energies are 6.0, 8.0, and 10.0 (see eq. [11]). This proves that with the modifications we introduced, the new scheme surpasses the previous NN Schrödinger solvers.[18–20]

Finally, we discuss how we choose initial values of the E_k and the $\boldsymbol{w}$ and $\boldsymbol{b}$ parameters. If the initial values are far from optimal, the fit is difficult. Initial values of E_k were randomly chosen in a window $E_{\text{ini}} = E_{\text{exact}} \pm 0.2$. In general, good initial values for the $\boldsymbol{w}$ and $\boldsymbol{b}$ can be determined by pretraining a RBFNN on (fitting it to) wave functions calculated on a potential reasonably close in shape to the real one. The results presented above were all obtained by pretraining to exact wave functions (which we know in the x coordinates and hence can obtain in the y coordinates). The RBFNN we use to pretrain is not fully optimized. The Gaussian widths are not varied, and Gaussians are simply added consecutively and centered at data points where the error is largest. The fit is done with the RBFNN algorithm of Matlab. R_k values obtained from the pretrained NN are typically at least two orders of magnitude larger than their post-fit counterparts. For a real problem, exact wave functions are not known. In this case, we propose starting from known wave functions for a model potential surface (e.g., an uncoupled approximation) and slowly adding the coupling or distortion to "walk" the RBFNN wave functions to the solutions for the potential of interest. To test the procedure for

Fig. 5. Wave functions for the first two vibrational levels of a 2-D version of the eq. [16] potential. They are calculated by pretraining a NN on a harmonic potential and retraining it while progressively increasing α. The circled part of the ground state wave function is very different from the Gaussian shape used in the initial stage of the pretraining.

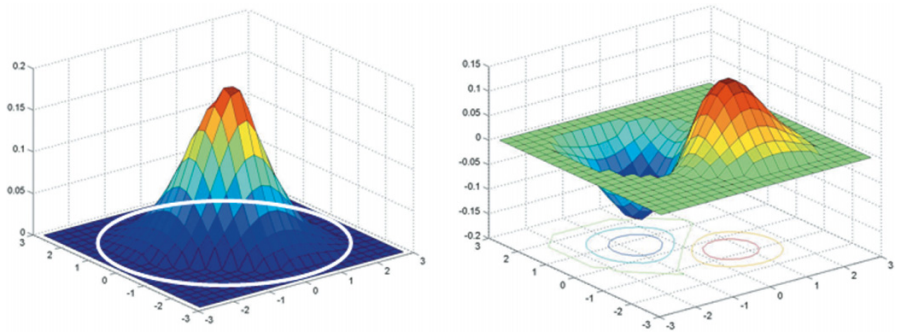

"walking" the RBFNN wave functions into a deep minimum on the parameter surface, we computed two solutions of the 2-D problem without using the exact wave functions to choose initial parameter values. A RBFNN is pretrained on the first two wave functions of an uncoupled approximation to the Hamiltonian and then the coupling strength is progressively increased by increasing α

$$[16] \qquad V(\boldsymbol{x}) = \sum_{i=1}^{d} x_i^2 + \alpha \left(\sum_{i=1}^{d} x_i \right)^2$$

where α = 0.0, 0.05, …, 1.0. At each value of α, the NN method is used to solve the Schrödinger equation and the solutions obtained are used to pretrain for the next value of α. Figure 5 shows neural network wave functions with α = 1.0: for the ground state one can clearly see that the wave function is not a Gaussian. This procedure does walk the RBF-NN wave functions into a deep minimum on the parameter surface.

IV. Conclusion

Despite recent progress, computational methods for solving the Schrödinger equation are hobbled by the basis size problem. Even if one uses contracted basis functions, the size of the basis required to compute a spectrum increases dramatically with the dimensionality of the Hamiltonian. Neuron basis functions may vitiate the basis size problem. Because they are extremely flexible, very few functions are necessary, and basis size may not increase quickly with dimension. It is encouraging that only 50 basis functions are required to solve a 6-D problem. The NN Schrödinger solver reported in this article is certainly better than previous NN solvers. It obviates the need to compute levels one by one. It uses nonlinear optimization methods only for some of the NN parameters and uses linear algebra tools for the others. Using the NN Schrödinger solver, one can obtain solutions without a potential surface: it is only necessary to know values of the potential at points.

We view a neural network representation of a wave function as an expansion in a small adaptable basis. The location, and, to some extent, shape, of the neuron basis functions are adjusted to achieve the best possible solutions for a given basis size. We have improved four aspects of previous NN Schrödinger solvers. (*i*) We compute several levels at a time from one shared layer of neurons. (*ii*) We use RBF neurons for the first time. RBF neurons automatically incorporate the correct boundary conditions. The application of the KEO to the NN is therefore clean and straightforward as no extra functions are required to impose those conditions. Other scientists have also used Gaussian basis functions,[41,42] but ours are more general and more fully optimized. (*iii*) We determine some of the NN parameters with methods of linear algebra thereby reducing the dimensionality of the parameter space in which nonlinear optimization needs to be done. (*iv*) We developed a systematic scheme for guiding the parameter optimization into the right minimum. This is done by pretraining the NN and adiabatically increasing the coupling strength.

These ideas make it possible to increase the difficulty of problems that can be solved. NN methods for solving the Schrödinger equation are at an early stage of development. The small size of the NN basis is very promising, but the optimization problem remains formidable. The method we have developed could certainly be applied to higher dimensional Hamiltonians. The largest molecules for which a spectrum has been computed using matrix methods are the protonated water dimer and CH_5^+.[49,50] To go even larger would require a huge amount of memory due to the ballooning basis size. In contrast, the NN Schrödinger solver requires only a modest basis. The NN Schrödinger solver might also be useful for computing levels in a high-lying window. The basis functions could be adapted to a particular spectral window. Other methods for computing levels in a window require storing large vectors.[51–53] NN methods for solving the Schrödinger equation are new and still being developed, but the ameliorations suggested in this paper address essential problems and advance the state of the art.

V. Acknowledgements

We thank the Natural Sciences and Engineering Research Council of Canada (NSERC) and the Canada Research Chairs programme for funding.

References

(1) This article is part of a Special Issue dedicated to Professor T. Ziegler.
(2) Papousek, D.; Aliev, M. R. *Molecular Vibrational-Rotational Spectra;* Elsevier: Amsterdam, 1982.
(3) Aliev, M. R.; Watson, J. K. G. In *Molecular Spectroscopy:*

Modern Research; Rao, K. N., Ed.; Academic Press: New York, 1985; Vol. 3, Chap. 1.
(4) Tennyson, J. *Comput. Phys. Rep.* **1986**, *4*, 1. doi:10.1016/0167-7977(86)90005-5.
(5) Bacic, Z.; Light, J. C. *Annu. Rev. Phys. Chem.* **1989**, *40*, 469. doi:10.1146/annurev.pc.40.100189.002345.
(6) Carrington, T., Jr. Vibrational Energy Level Calculations for Molecules. In *Encyclopedia of Computational Chemistry;* Schleyer, P. R., Allinger, N. L., Clark, T., Gasteiger, J., Kollman, P. A., Schaefer III, H. F., Schreiner, P. R., Eds.; John Wiley & Sons, Ltd: New York. 1998.
(7) Bowman, J. M.; Carrington, T., Jr.; Meyer, H.-D. *Mol. Phys.* **2008**, *106*, 2145. doi:10.1080/00268970802258609.
(8) Light, J. C.; Carrington, T., Jr. *Adv. Chem. Phys.* **2000**, *114*, 263. doi:10.1002/9780470141731.ch4.
(9) Press, W. H.; Teukolsky, S. A.; Vetterling, W. T.; Flannery, B. P. *Numerical Recipes in Fortran 77: The Art of Scientific Computing;* Cambridge University Press: Cambridge, 1992.
(10) McNichols, A.; Carrington, T., Jr. *Chem. Phys. Lett.* **1993**, *202*, 464. doi:10.1016/0009-2614(93)90031-U.
(11) Bramley, M. J.; Carrington, T., Jr. *J. Chem. Phys.* **1993**, *99*, 8519. doi:10.1063/1.465576.
(12) Bramley, M. J.; Carrington, T., Jr. *J. Chem. Phys.* **1994**, *101*, 8494. doi:10.1063/1.468110.
(13) Chen, R.; Guo, H. J. *Chem. Phys.* **1998**, *108*, 6068.
(14) Wang, X.-G.; Carrington, T., Jr. *J. Chem. Phys.* **2002**, *117*, 6923. doi:10.1063/1.1506911.
(15) Wang, X.-G.; Carrington, T., Jr. *J. Chem. Phys.* **2003**, *119*, 101. doi:10.1063/1.1574016.
(16) Wang, X.-G.; Carrington, T., Jr. *J. Chem. Phys.* **2004**, *121*, 2837.
(17) Wang, X.-G.; Carrington, T., Jr. *J. Chem. Phys.* **2008**, *129*, 234102. doi:10.1063/1.3027825. PMID:19102521.
(18) Lagaris, I. E.; Likas, A.; Fotiadis, D. I. *Comput. Phys. Commun.* **1997**, *104*, 1. doi:10.1016/S0010-4655(97)00054-4.
(19) Sugawara, M. *Comput. Phys. Commun.* **2001**, *140*, 366. doi:10.1016/S0010-4655(01)00286-7.
(20) Nakanishi, H.; Sugawara, M. *Chem. Phys. Lett.* **2000**, *327*, 429. doi:10.1016/S0009-2614(00)00913-1.
(21) Hornik, K.; Stinchcombe, M.; White, H. *Neural Netw.* **1990**, *3*, 551. doi:10.1016/0893-6080(90)90005-6.
(22) Hornik, K. *Neural Netw.* **1989**, *2*, 359. doi:10.1016/0893-6080(89)90020-8.
(23) Hornik, K. *Neural Netw.* **1991**, *4*, 251. doi:10.1016/0893-6080(91)90009-T.
(24) Funahashi, K. *Neural Netw.* **1989**, *2*, 183. doi:10.1016/0893-6080(89)90003-8.
(25) Kurkova, V. *Neural Netw.* **1992**, *5*, 501. doi:10.1016/0893-6080(92)90012-8.
(26) Scarselli, F.; Tsoi, A. C. *Neural Netw.* **1998**, *11*, 15. doi:10.1016/S0893-6080(97)00097-X. PMID:12662846.
(27) Barron, A. *IEEE Trans. Inf. Theory* **1993**, *39*, 930. doi:10.1109/18.256500.
(28) Chui, C.; Li, X. J. *Approximation Theory* **1992**, *70*, 131. doi:10.1016/0021-9045(92)90081-X.
(29) Mhaskar, H.; Miccheli, C. *Adv. Appl. Math.* **1992**, *13*, 350. doi:10.1016/0196-8858(92)90016-P.
(30) Mhaskar, H.; Miccheli, C. *IBM J. Res. Develop.* **1994**, *38*, 277.
(31) Boutry, G.; Elad, M.; Golub, G. H.; Milanfar, P. *SIAM J. Matrix Anal. Appl.* **2005**, *27*, 582. doi:10.1137/S0895479803428795.
(32) Mulero-Martinez, J. I. *Neurocomputing* **2007**, *70*, 1439. doi:10.1016/j.neucom.2006.05.010.
(33) Sumpter, B. G.; Getino, C.; Noid, D. W. *Annu. Rev. Phys. Chem.* **1994**, *45*, 439. doi:10.1146/annurev.pc.45.100194.002255.
(34) Zupan, J.; Gasteiger, J. *Anal. Chim. Acta* **1991**, *248*, 1. doi:10.1016/S0003-2670(00)80865-X.
(35) Widrow, B.; Lehr, M. A. *Proc. IEEE* **1990**, *78*, 1415. doi:10.1109/5.58323.
(36) Hassoun, M. H. *Fundamentals of artificial neural networks;* MIT Press: Cambridge, MA, 1995.
(37) Maiorov, V.; Pinkus, A. *Neurocomputing* **1999**, *25*, 81. doi:10.1016/S0925-2312(98)00111-8.
(38) Yang, W.; Peet, A. C. *Chem. Phys. Lett.* **1988**, *153*, 98. doi:10.1016/0009-2614(88)80139-8.
(39) Liao, Y.; Fang, S.-C.; Nuttle, H. L. W. *Neural Netw.* **2003**, *16*, 1019. doi:10.1016/S0893-6080(02)00227-7. PMID:14692636.
(40) Wu, W.; Nan, D.; Long, J.; Ma, Y. *Neural Netw.* **2008**, *21*, 1462.
(41) Poirier, B.; Light, J. C. J. *Chem. Phys.* **2000**, *113*, 211.
(42) Hamilton, I. P.; Light, J. C. J. *Chem. Phys.* **1986**, *84*, 306.
(43) Davis, M. J.; Heller, E. J. J. *Chem. Phys.* **1979**, *71*, 3383.
(44) Dawes, R.; Carrington, T., Jr. *J. Chem. Phys.* **2006**, *124*, 054102. doi:10.1063/1.2162168. PMID:16468846.
(45) Cooper, J.; Carrington, T., Jr. Unpublished results.
(46) Garashchuk, S.; Light, J. C. J. *Chem. Phys.* **2001**, *114*, 3929.
(47) *MatLab,* [7.0R14]; MathWorks, Inc.: Natick, MA, 2004.
(48) Demuth, H.; Beale, M. *Neural network toolbox user's guide*; The MathWorks, Inc.: Natick, MA, 2004.
(49) Vendrell, O.; Gatti, F.; Lauvergnat, D.; Meyer, H.-D. *J. Chem. Phys.* **2007**, *127*, 184302.
(50) Wang, X.-G.; Carrington, T., Jr. *J. Chem. Phys.* **2008**, *129*, 234102.
(51) Mandelshtam, V. A.; Taylor, H. S. J. *Chem. Phys.* **1997**, *106*, 5085.
(52) Huang, S.-W.; Carrington, T., Jr. *J. Chem. Phys.* **2000**, *112*, 8765. doi:10.1063/1.481492.
(53) Neuhauser, D. J. *Chem. Phys.* **1994**, *100*, 5076.

VII. Appendix

Herein, we derive eq. [6]. Applying the KEO of eq. [13] to the NN wave function of eq. [7] we obtain

$$[A1] \qquad T({}^n y)\psi_k({}^n y) = -4\sum_{i=1}\widehat{N}\, c_{ik} b_i^4 \widetilde{\gamma}_{in} \exp\Big(- b_i^2 \sum_{j=1}^{d} (w_{ij} - {}^n y_j)^2 \Big) + 2\gamma_0 \sum_{i=1}^{N} c_{ik} b_i^2 \exp\Big(- b_i^2 \sum_{j=1}^{d} (w_{ij} - {}^n y_j)^2 \Big)$$

with

$$[A2] \qquad \widetilde{\gamma}_{ik} \equiv \sum_{m,n} \gamma_{mn} (w_{in} - {}^k y_n)(w_{im} - {}^k y_m)$$

$$\gamma_0 \equiv \sum_n \gamma_{nn}$$

where the left superscript indexes the point at which the potential surface is evaluated. We then define a matrix $\mathbf{S}$ with elements $S_{ni} \equiv \exp\Big(- b_i^2 \sum_{j=1}^{d} (w_{ij} - {}^n y_j)^2 \Big)$, $\widetilde{\boldsymbol{S}} \equiv (\mathbf{S}|1)$, a matrix $\mathbf{S}''$ with elements $\boldsymbol{S}''_{ni} \equiv b_i^4 \widetilde{\gamma}_{in} S_{ni} - 2\gamma_0 b_i^2 S_{ni}$ and $\widetilde{\boldsymbol{S}}'' \equiv 4(\widetilde{\boldsymbol{S}}''_{ni}|0)$, where 1 and 0 are column vectors of size M with all elements equal to 1 or 0, respectively (the matrix represented by $(\mathbf{A}|\boldsymbol{v})$ is obtained by adding the column $\boldsymbol{v}$ to the matrix $\mathbf{A}$). Then, the Schrödinger equation becomes, at each point n ($V({}^n y) \equiv V_n$):

$$[A3] \qquad -\widetilde{\boldsymbol{S}}''_{ni}\widetilde{c}_{ik} + V_n \widetilde{S}_{ni}\widetilde{c}_{ik} = E_k \widetilde{S}_{ni}\widetilde{c}_{ik}$$

which has the form of eq. [6].

The application of the ONIOM hybrid method to the cycloaddition reactions of bromo-substituted 2(*H*)-pyran-2-ones[1]

Susan M. Larkin, Thom Vreven, Michael J. Bearpark, and Keiji Morokuma

Abstract: We investigate the performance of Our own N-layered Integrated molecular Orbital and molecular Mechanics (ONIOM) hybrid computational method applied to Diels–Alder reactions of bromo-2(*H*)-pyran-2-ones, combining the B3LYP/6–31G(d) method with a variety of low-level methods. We show that ONIOM is able to reproduce full B3LYP calculations, including the prediction of the stereoselectivity, which requires accurate potentials. We focus on the various ways in which the performance and potential errors of ONIOM can be analyzed, and show that the best method combination depends on the property one is interested in.

Key words: ONIOM, hybrid methods, transition structures, transition state, Diels–Alder.

Résumé : On a étudié la performance de la méthode de calcul hybride « ONIOM » appliquée aux réactions de Diels–Alder des bromo-2(*H*)-pyran-2-ones en combinant la méthode B3LYP/6-31G(d) avec une variété de méthodes de niveaux plus faibles. On a démontré que la méthode « ONIOM » permet de reproduire les calculs complets B3LYP, y compris les prédictions relatives à la stéréosélectivité qui demandent des potentiels précis. On a porté une attention particulière aux diverses façons par lesquelles on peut analyser la performance et les erreurs potentielles de la méthode « ONIOM » et on montre que la meilleure méthode de combinaison dépend de la propriété qu'on veut analyser.

Mots-clés : « ONIOM », méthodes hybrides, structures de transition, état de transition, Diels–Alder.

[Traduit par la Rédaction]

Introduction

Diels–Alder reactions of bromo-2(*H*)-pyran-2-ones are extremely useful in the synthesis of substituted ring structures, since their reactions are highly stereoselective.[2,3] These reactions are often governed by subtle features on the potential surface, which affect the relative barrier heights for competing reaction paths, and accurate methods are needed in the computational study of the stereoselectivity. The computation time needed for such methods scales unfavourably with the size of the system, and can quickly become the limiting factor in the studies, especially since one typically considers a large number of reactants and possible cycloadducts. In this paper, we investigate the applicability of Our own N-layered Integrated molecular Orbital and molecular Mechanics (ONIOM) hybrid method to such reactions. ONIOM treats different parts of the system at different levels of theory, and can reduce the computational cost dramatically compared with conventional methods.[4–10] We apply the ONIOM scheme to the cycloadditions of bromo-2(*H*)-pyran-2-ones with strongly electron-deficient and electron-rich dienophiles, methyl acrylate (MA) and methyl vinyl ether (MVE), respectively. Previously, we studied these systems with conventional (i.e., single non-hybrid) B3LYP and the 6–31G(d) basis set, which reproduced experimental results well.[11,12] This level of theory will therefore serve as "benchmark" in the assessment of the ONIOM scheme in the current work.

The focus in this work is on ways to reduce the computational cost of accurate calculations, and to give better scaling for much larger calculations. There are two traditional approaches to reduce the calculation time in computational chemistry. First, one can simply use a lower level of theory to treat the entire system. Second, when the chemical process takes place in a distinct part of the system, high-level calculations can be performed on truncated model systems. These two approximations have their obvious and severe limitations; the former may not treat the reactive center at a sufficiently high level of theory, while the latter excludes any electronic and steric effects from the part of the molecule that is not included in the truncated model.

Over the past decade, a third approach has become popular, which combines the two traditional approaches. In this hybrid approach, the full system is divided into a reactive part, which is treated at an appropriately high level of theory, while the remainder of the system is included at a less expensive level of theory. This ensures a sufficiently

Received 31 October 2008. Accepted 22 January 2009. Published on the NRC Research Press Web site at canjchem.nrc.ca on 8 May 2009.

S.M. Larkin and M.J. Bearpark.[1] Department of Chemistry, Imperial College London, South Kensington campus, London SW7 2AZ, UK.
T. Vreven. Gaussian, Inc, 340 Quinnipiac St Bldg 40, Wallingford, CT 06492 USA.
K. Morokuma.[2] Fukui Institute for Fundamental Chemistry, Kyoto University, Kyoto, 606-8103, Japan.

[1]Corresponding author (e-mail: m.bearpark@imperial.ac.uk).
[2]Present address: Cherry Emerson Center for Scientific Computation and Department of Chemistry, Emory University, Atlanta, GA 30322, USA.

high level of accuracy for the different regions of the system, while reducing the computational cost by only calculating a small part of the system with the expensive method.

A well-known class of hybrid methods is formed by the quantum mechanics / molecular mechanics (QM/MM) schemes, which combine a QM method with a MM method.[13–15] QM/MM methods have been successful in diverse areas, such as the study of enzyme mechanisms, catalysis, solvated systems, and materials.

Somewhat different from QM/MM methods is the ONIOM hybrid method. ONIOM is a generalized scheme for layered calculations. QM/MM methods can only combine a QM method with an MM method, whereas ONIOM can combine QM methods with QM methods as well as QM methods with MM methods. Transition structures can be calculated with ONIOM in general as for a conventional QM method. Furthermore, ONIOM can in principle combine any number of methods, although our current implementation is limited to three. ONIOM has been used for a wide variety of chemical problems, and has been the subject of several reviews.[16–20] In contrast to QM/MM methods, the ability of ONIOM to combine multiple QM methods allows it to include electronic interactions between the reactive and surrounding regions, which is essential for the reactions studied in the work. Besides ONIOM, there are several other methods that can combine QM methods with QM methods. The frozen and constrained DFT methods (FDFT and CDFT) embed the model in the potential from the outer-layer DFT calculation.[21–23] FDFT keeps the density fixed, whereas CDFT relaxes the density iteratively, and is somewhat similar to Yang's divide and conquer method.[24] QM/QM schemes specifically designed for semi-empirical methods in the low level, including electrostatic embedding, were presented by Cui,[25] as well as Merz.[26] Most of these schemes embed the model calculation in the potential generated by the environment, which is not explicit in our ONIOM(QM:QM) scheme. However, as will be outlined in the Computational methods, through the low-level QM calculation on the entire system, we do incorporate polarization effects, as well as electronic effects that can "cross the border". The latter, combined with the ability to use any electronic structure method, form the main strengths of ONIOM. Recently, we did present potential embedding in the ONIOM scheme, using Mulliken charges, including the calculation of gradients.[27]

Computational methods

The ONIOM energy is written as an extrapolation

$$[1] \qquad E^{\mathrm{ONIOM}} = E^{\mathrm{high}}_{\mathrm{model}} + E^{\mathrm{low}}_{\mathrm{real}} - E^{\mathrm{low}}_{\mathrm{model}}$$

"High" and "low" refer to the levels of theory. "Real" refers refer to the full system, and "model" to the part of the system that is treated at the high level of theory. The "model" system is calculated at both levels of theory, while the "real" system is calculated only at the low level of theory. All three terms involve chemically realistic systems, which allows the low level to be either QM or MM, thus forming ONIOM(QM:QM′) or ONIOM(QM:MM). This is in contrast with most other hybrid methods, which allow only QM methods to be combined with MM methods. ONIOM(QM:QM′) schemes include quantum mechanical effects between the regions, albeit at the lower of the two QM methods. This is essential for the accurate modelling of the reactions presented here, since the primary effect of the substituents is electronic.

Covalent bonding between the two regions would result in open valencies in the model system if this were just "cut out" from the full molecule. Because the model system would then no longer be representative of the real system we are investigating, we saturate these dangling bonds with hydrogen "link atoms". The gradients and higher derivatives are well-defined, and can be obtained with expressions similar to that of the energy.[8] Because of this, force constants can be calculated and transition structures characterized, which is essential for this work.

We use the level of theory of our previous study,[11,12] B3LYP with the 6–31G(d) basis set, as the benchmark or "Target", to which we compare our ONIOM results. As such, we also use B3LYP/6–31G(d) as the high-level method in our ONIOM calculations. We investigated a variety of low-level methods: the semi-empirical methods AM1 and PM3, the Hartree–Fock (HF) method with the STO-3G and 3–21G basis sets, and B3LYP with the STO-3G, 3–21G, and 6–31G basis sets. For readability, we abbreviate the STO-3G, 3–21G, and 6–31G basis sets as I, II, and III, respectively. These methods cover a wide range of computational costs and accuracies, and have all proven to be valuable in the study of organic reaction mechanisms. We do not consider ONIOM combinations with MM methods in the low level, since ONIOM(QM:MM) is not well-defined when there is bond breaking and formation within three bonds from the MM region, as cancellation of errors is incomplete.[28] Partitioning the system so that there is a three-bond separation would make the QM region too large to yield reasonable time-savings for the systems studied in this work. Instead, we used the "minimal model" of butadiene + ethene in our ONIOM calculations (Figs. 1 and 2). This implies that the effects of the substituents are entirely described by the low level of theory. All the reported energies are obtained for geometries optimized at the specific level of theory (thus using the ONIOM gradients). The calculations were carried out with a development version of the Gaussian package.[29]

Results and discussion

Each reactant pair can generate four unique products, which are denoted as 5-endo, 6-endo, 5-exo, and 6-exo. Each product is reached via a unique transition structure. In Fig. 1, we show the four transition states for 3-bromo-2(*H*)-pyran-2-ones with methyl acrylate, and in Fig. 2, we show those for 3-bromo-2(*H*)-pyran-2-ones with methyl vinyl ether. Since the rate of the reaction depends on the height of the transition-state barrier, and the energy of the separated reactants is the same for each of the four products, the stereoselectivity of the reaction depends on the "relative" energies of the four transition states. In our previous work, we saw that the differences involved are often only several kcal/mol. Therefore, the prediction of the stereoselectivity requires computational levels of theory that can accurately describe such small differences, and B3LYP/6–31G(d) is able to do so.[11,12,30] The "absolute" barrier heights are less

Fig. 1. The four possible transition structures of the cycloadditions of 3-bromo-2(*H*)-pyran-2-ones with methyl acrylate. The high-level region is rendered by ball and bond, and the remainder of the system as tube.

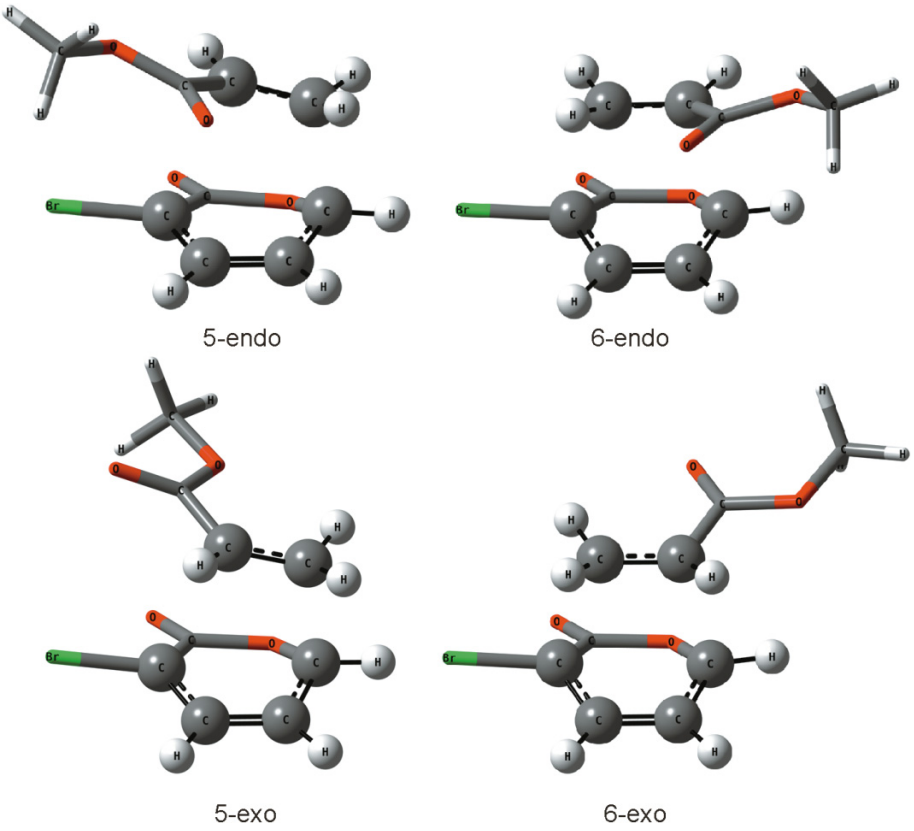

critical for the prediction of the stereoselectivity, which is in contrast with the requirements of computational methods in most other reactivity studies. Also, we are not concerned with free-energy corrections (i.e., we approximate these to be the same in each case).

We calculated the reactant energy and the barriers for all the reaction paths, at the Target and ONIOM levels of theory. As indicated in the previous paragraph, we can assess the performance of ONIOM in two ways. First, we can assess how well ONIOM is able to reproduce the absolute barriers, thus $\Delta E = E^{TS} - E^{reactant}$. This will yield the best ONIOM combination for describing reaction kinetics. Second, we can focus on the ability of ONIOM to describe the relative barriers, thus $\Delta E' = E^{TS} - E^{TS'}$. This will yield the best ONIOM combination for describing the stereoselectivity. Although it is likely that a method combination that performs well for rates also performs well for stereoselectivity, this is not necessarily the case. We will therefore test the performance in both ways, starting with the absolute barriers.

In Table 1, we show the energy barriers calculated at the ONIOM levels of theory, as well as the Target B3LYP/6–31G(d). In Table 2, we show the errors of the ONIOM barriers compared with the Target, and the root-mean-square (RMS) error values for various combinations of barriers. For a quartet of TS configurations (5-exo, 5-endo, 6-exo, and 6-endo, the RMS value is obtained from

$$[2] \qquad \mathrm{RMS}^{\mathrm{abs}} = \frac{1}{2}\sqrt{\sum_{i}^{4}[(E^{\mathrm{TS}_i}_{\mathrm{ONIOM}} - E^{\mathrm{reactant}}_{\mathrm{ONIOM}}) - (E^{\mathrm{TS}_i}_{\mathrm{Target}} - E^{\mathrm{reactant}}_{\mathrm{Target}})]^2}$$

where i refers to the four configurations, which we sum over.

First, we will look at the total MA + MVE RMS value, which is calculated from the errors of all barriers. Both the semi-empirical methods and HF/I give a value of around 3 kcal/mol, and B3LYP/II and B3LYP/III around 1 kcal/mol. HF/II is somewhat higher, about 4 kcal/mol. Looking at the MVE and MA RMS values separately, we see that they are similar, which indicates that the total RMS value is quite "stable" and not biased by a single or few large individual errors (inspection of all the individual values confirms this). The total mean error is similar to the RMS error, except for AM1 and PM3, in which case it is much lower.

Since HF/II has a total RMS error larger than HF/I, we suspect that the latter is fortuitous due to cancellation of errors, and can therefore not be considered reliable. Unlike almost all of the other methods, the AM1 and PM3 mean errors (Table 2) are much smaller than their respective RMS errors. This indicates that, on average, they perform

Fig. 2. The four possible transition structures of the cycloadditions of 3-bromo-2(*H*)-pyran-2-ones with methyl vinyl ether. The high-level region is rendered by ball and bond, and the remainder of the system as tube.

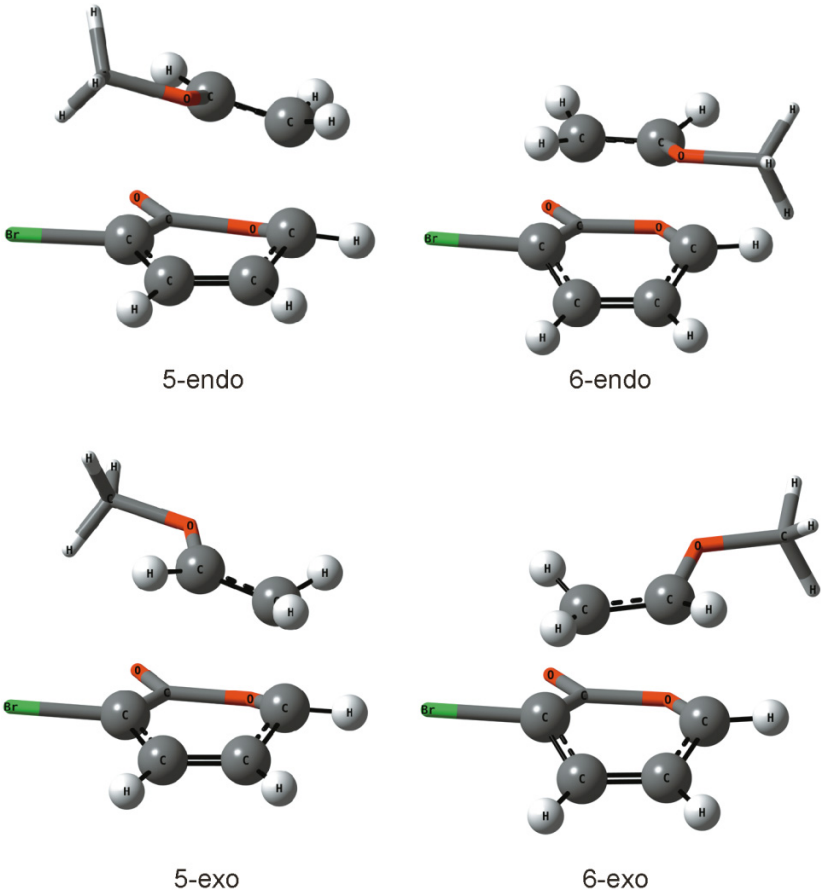

very well as low level, similar to their small mean errors as stand-alone method,[31] but the errors are less systematic. The mean error being similar to that with B3LYP methods in the low level can be explained by AM1 and PM3 being parameterized to include electron correlation. However, the form of the wave function is much simpler and not similar to that in DFT methods, which causes the error cancellation in the ONIOM extrapolation to be less systematic, and increases the total RMS error relative to the mean error.

Since B3LYP/II and B3LYP/III have very similar total RMS errors, we can consider the basis set of the former (3–21G) to be converged. On the basis of these results, we consider B3LYP/II the best choice when accurate barriers are required and AM1 or PM3 the best choice when more approximate results are sufficient.

We will now assess the ability of ONIOM to reproduce the "relative" barriers of each quartet of transition states. To do this, we need to correct for the systematic overestimation or underestimation from a low-level method for each quartet. We do this by shifting the four transition-state energies with a constant factor, *X*, so that the RMS deviation is minimized:

$$[3] \qquad \mathrm{RMS}^{\mathrm{rel}} = \frac{1}{2}\sqrt{\sum_{i}^{4}[(E^{\mathrm{TS}_i}_{\mathrm{ONIOM}} + X - E^{\mathrm{reactant}}_{\mathrm{ONIOM}}) - (E^{\mathrm{TS}_i}_{\mathrm{Target}} - E^{\mathrm{reactant}}_{\mathrm{Target}})]^2}$$

X is specific for each quartet and low-level method. Note that eq. [3] can be expressed without the reactant energies, which indicates that indeed only the transition-state energies determine the resulting RMS value, and not the barriers, thus

$$[4] \qquad \mathrm{RMS}^{\mathrm{rel}} = \frac{1}{2}\sqrt{\sum_{i}^{4}[E^{\mathrm{TS}_i}_{\mathrm{ONIOM}} - E^{\mathrm{TS}_i}_{\mathrm{Target}} + X']^2}$$

The resulting RMS value indicates how well ONIOM reproduces the Target pattern of four transition states, and is unrelated to the ability of the ONIOM combination to reproduce the absolute barriers. We show these values in Table 3, for each quartet separately, again combined for the MVE quartets and the MA quartets, and combined for all the quartets. In addition,we calculated the spread of each quartet at the Target level of theory, the minimum of

Table 1. Calculated ONIOM and Target barrier heights (kcal/mol) of the reactions of 3-bromo-, 4-bromo-, and 5-bromo-substituted 2(*H*)-pyran-2-ones with methyl acrylate (MA) and methyl vinyl ether (MVE). For low-level methods, HF denotes the Hartree–Fock method, and B3 denotes the B3LYP method. I, II, and III denote the STO-3G, 3–21G, and 6–31G basis sets, respectively.

	Low-level method								
Reactants	Configuration	AM1	PM3	HF/I	HF/II	B3/I	B3/II	B3/III	Target
MA + 3-bromo	5-endo	23.2	24.2	18.2	17.5	23.7	20.2	20.2	19.7
	5-exo	26.2	27.3	20.1	20.6	24.9	21.9	24.1	23.2
	6-endo	21.5	21.8	21.1	16.3	27.2	21.1	21.1	21.4
	6-exo	23.5	23.7	21.8	18.4	27.7	22.4	24.0	24.0
MA + 4-bromo	5-endo	21.4	24.2	18.5	17.2	25.0	21.2	21.8	21.2
	5-exo	23.9	26.4	20.1	19.2	25.9	21.8	24.8	24.2
	6-endo	19.5	22.2	18.3	16.4	23.5	20.8	22.7	21.7
	6-exo	21.4	23.5	19.0	17.8	23.9	21.6	24.8	23.6
MA + 5-bromo	5-endo	21.6	24.0	16.7	15.7	22.3	18.9	19.7	19.1
	5-exo	24.0	26.4	18.3	17.6	23.3	19.4	21.8	21.2
	6-endo	20.2	22.7	18.3	15.6	23.3	19.5	20.4	19.5
	6-exo	21.8	23.8	19.0	16.8	23.8	20.4	23.5	22.5
MVE + 3-bromo	5-endo	16.2	18.0	16.5	14.1	21.0	19.4	15.9	18.2
	5-exo	16.5	18.5	16.5	13.9	20.6	17.6	17.9	18.8
	6-endo	22.6	22.3	22.9	21.4	28.4	25.1	23.9	24.8
	6-exo	24.3	23.2	25.0	25.4	29.2	27.1	26.0	26.9
MVE + 4-bromo	5-endo	16.3	18.8	16.2	14.1	21.4	19.2	17.3	18.6
	5-exo	17.2	19.3	16.4	14.5	21.5	18.2	19.9	20.1
	6-endo	19.4	21.8	21.0	21.0	24.7	24.7	25.4	25.2
	6-exo	20.4	22.6	22.2	24.3	24.8	26.0	26.9	26.6
MVE + 5-bromo	5-endo	15.8	19.0	15.4	13.3	19.4	17.8	17.1	17.3
	5-exo	16.8	19.6	15.6	13.3	19.3	16.1	17.2	17.3
	6-endo	20.7	22.3	20.2	20.2	23.7	22.6	22.0	22.4
	6-exo	21.4	22.7	21.7	23.4	24.1	24.5	25.5	25.1

$\frac{1}{2}\sqrt{\sum_i^4 [E_{\text{Target}}^{\text{TS}_i} + X'']^2}$, which can be compared to the RMS values of the ONIOM calculation.

We first observe from Table 3 that the Target spread is different from the transition states with MA (about 1.5 kcal/mol) and the transition states with MVE (about 3.5 kcal/mol), which indicates that the four MA transition states are closer together than those for MVE. This spread serves as a measure for the required accuracy of the ONIOM potentials, i.e., if the RMS error in the ONIOM results is larger or comparable to the spread, the error is larger than the effect we are attempting to predict. This is indeed the case for AM1 and PM3 as the low level for the MA transition states, which are therefore not recommended for comparing energetics.

Related to the Target spread (Table 3), we need to comment on the basis set superposition error (BSSE) as a source of error in the ONIOM calculations. The BSSE for the high-level region is always included at the Target level of theory. But the BSSE in the low-level region will be different for the various ONIOM combinations that we consider, i.e., it depends on the basis set employed and is zero for the semi-empirical methods. If we assume that the BSSE is the same for all four structures in a quartet, the shift factor X (eq. [3] will take care of it. To test this assumption, we calculated the BSSE in the low-level region (defined as the BSSE difference between the model- and real-system calculations) for the transition states of the 3-bromo compound with MA. Of all the adducts, this quartet has the largest expected interaction in the low-level region, and will provide an upper bound for the BSSE. For the Target, however, we find that the BSSE values for the 5-endo and 5-exo structures are about 1 kcal/mol larger than the 6-endo and 6-exo structures. This clearly is related to the vicinity of the bromine to the oxygen centers in MA. Significant BSSE that affected the endo/exo ratio was observed previously.[32,33] We did not observe the same pattern using ONIOM with smaller basis sets in the low level. Since the semi-empirical methods do not include this error, we cannot expect these to provide a resolution better than 1 kcal/mol compared with the Target. However, this estimate is an upper bound, and we expect transitions states with MVE, 4-bromo, or 5-bromo compounds to have a smaller error. Indeed, we see that for all the low-level methods, MA with 3-bromo in Table 3 has the largest error of all three MA adducts.

We see that again HF/I is somewhat better than HF/II, indicating cancellation of errors. However, contrary to the results in Table 2, HF performs significantly better than the semi-empirical methods. This is most likely the result of all four transition states in a quartet having similar electron-correlation contributions to the barriers. The (systematic) errors in these contributions are then compensated for through the shift factor X in eq. [3]. The good performance of AM1 and PM3 relative to HF for the "absolute" barriers (Table 2) is mostly due to the inclusion of these correlation effects in the semi-empirical parameterization. This is not an important contribution to the "relative" barriers (Table 3), hence the swap in performance of HF and the semi-empirical methods.

Table 2. Errors of the calculated ONIOM barrier heights (kcal/mol, relative to Target) of the reactions of 3-bromo-, 4-bromo-, and 5-bromo-substituted 2(*H*)-pyran-2-ones with methyl acrylate (MA) and methyl vinyl ether (MVE), including the root-mean-square (RMS) value for each quartet of configurations, the RMS value for all the MA and all the MVE barriers and for all 24 barriers combined, and the Mean value for all barriers combined. For the low-level methods, see the caption of Table 1.

		Low-level method						
Reactants	Configuration	AM1	PM3	HF/I	HF/II	B3/I	B3/II	B3/III
MA + 3-bromo	5-endo	3.5	4.4	–1.5	–2.2	4.0	0.5	0.5
	5-exo	3.0	4.1	–3.1	–2.6	1.8	–1.3	0.9
	6-endo	0.1	0.4	–0.3	–5.1	5.7	–0.3	–0.4
	6-exo	–0.4	–0.3	–2.2	–5.6	3.7	–1.5	0.0
	RMS	2.3	3.0	2.0	4.2	4.1	1.1	0.6
MA + 4-bromo	5-endo	0.2	3.0	–2.7	–4.0	3.8	0.0	0.6
	5-exo	–0.3	2.2	–4.1	–5.0	1.7	–2.3	0.7
	6-endo	–2.2	0.5	–3.4	–5.3	1.8	–0.8	1.0
	6-exo	–2.2	–0.1	–4.6	–5.8	0.3	–1.9	1.2
	RMS	1.6	1.9	3.7	5.0	2.3	1.6	0.9
MA + 5-bromo	5-endo	2.5	4.9	–2.4	–3.4	3.2	–0.1	0.6
	5-exo	2.9	5.2	–2.8	–3.5	2.1	–1.7	0.7
	6-endo	0.7	3.2	–1.2	–3.8	3.8	0.0	1.0
	6-exo	–0.6	1.4	–3.5	–5.7	1.3	–2.1	1.0
	RMS	2.0	4.0	2.6	4.2	2.8	1.4	0.8
All MA	RMS	2.0	3.1	2.9	4.5	3.1	1.3	0.8
MVE + 3-bromo	5-endo	–2.0	–0.1	–1.6	–4.1	2.8	1.2	–2.2
	5-exo	–2.3	–0.3	–2.3	–4.9	1.8	–1.2	–0.9
	6-endo	–2.2	–2.5	–1.9	–3.4	3.6	0.3	–0.9
	6-exo	–2.5	–3.7	–1.9	–1.5	2.3	0.3	–0.8
	RMS	2.3	2.2	2.0	3.7	2.7	0.9	1.4
MVE + 4-bromo	5-endo	–2.3	0.2	–2.4	–4.5	2.8	0.6	–1.3
	5-exo	–2.8	–0.7	–3.7	–5.6	1.4	–1.9	–0.2
	6-endo	–5.8	–3.4	–4.2	–4.2	–0.5	–0.5	0.2
	6-exo	–6.2	–4.0	–4.4	–2.2	–1.7	–0.6	0.4
	RMS	4.6	2.6	3.8	4.3	1.8	1.1	0.7
MVE + 5-bromo	5-endo	–1.5	1.7	–2.0	–4.0	2.1	0.5	–0.2
	5-exo	–0.5	2.4	–1.6	–4.0	2.1	–1.2	–0.1
	6-endo	–1.7	–0.1	–2.2	–2.2	1.3	0.2	–0.4
	6-exo	–3.7	–2.4	–3.4	–1.7	–1.0	–0.6	0.4
	RMS	2.2	1.9	2.4	3.2	1.7	0.7	0.3
All MVE	RMS	3.2	2.3	2.8	3.7	2.1	0.9	0.9
MA + MVE	RMS	2.7	2.7	2.8	4.1	2.7	1.1	0.8
MA + MVE	Mean	–1.1	0.7	–2.6	–3.9	2.1	–0.6	0.1

Table 3. Minimized ONIOM root-mean-square (RMS) errors relative to the Target for each quartet of transition states (kcal/mol). These RMS values are then combined for all the MVA barriers, all the MVE barriers, and all MA and MVE barriers. The spread of the Target indicates the spread of the four transition states at the Target level of theory. For the low-level methods, see the caption of Table 1.

	Low-level method							
Reactants	AM1	PM3	HF/I	HF/II	B3/I	B3/II	B3/III	Target spread
MA + 3-bromo	1.7	2.1	1.0	1.5	1.4	0.8	0.5	1.6
MA + 4-bromo	1.1	1.3	0.7	0.6	1.2	0.9	0.2	1.2
MA + 5-bromo	1.4	1.5	0.8	0.9	1.0	0.9	0.2	1.4
All MA	1.4	1.7	0.9	1.1	1.2	0.9	0.3	1.4
MVE + 3-bromo	0.2	1.5	0.3	1.3	0.7	0.9	0.6	3.7
MVE + 4-bromo	1.7	1.7	0.8	1.2	1.7	0.9	0.7	3.3
MVE + 5-bromo	1.1	1.8	0.7	1.0	1.3	0.7	0.3	3.4
All MVE	1.2	1.7	0.6	1.2	1.3	0.8	0.5	3.5
MA + MVE	1.3	1.7	0.8	1.1	1.3	0.9	0.4	2.7

B3LYP performs again better than HF in the low level. For the MA reactant, only B3LYP/II and B3LYP/III are able to predict the splitting of the transition-state energies. However, the energy differences are very small, and for MVE, which has a larger splitting, all methods give results better than the target spread. On the basis of these results, it appears that B3LYP/III is needed for an accurate prediction of the stereoselectivity, while the semi-empirical methods are not accurate enough.

Discussion and conclusions

We showed that ONIOM is able to predict barriers as well as relative barriers for the stereoselective reactions presented in this work. In all cases, a level of theory close to the Target, such as B3LYP with the 3–21G or 6–31G basis sets, ensures reliable results. In case of the absolute barriers, the semi-empirical methods AM1 and PM3 in the low level also produce reasonable results, especially when the very low cost is taken into consideration. However, due to the small splitting of the transition states in some cases, the prediction of stereoselectivity requires very accurate potentials, and only B3LYP with the larger basis sets performs consistently well. It is clear that when benchmarking ONIOM, the low level (and partitioning) must be chosen based on the type of problem that one is interested in. However, our conclusion that B3LYP is required as low level for the stereoselectivity is directly related to the difficulty of the problem. Such small differences in TS energies are perhaps not very common or meaningful, and even the Target level of theory in this work may not be the most appropriate for predicting experimental results. When the differences are larger, as in case of MVE in the current work, HF or perhaps even the semi-empirical methods in the low level will be sufficient.

It is interesting to see that for the absolute barriers, the semi-empirical methods perform as well or better than HF, while this is reversed when the relative barriers are considered. This shows that the low level of theory in the ONIOM scheme is not only determined by the required accuracy, but also by the nature of the problem under investigation. It must be noted that the parameterization of semi-empirical methods may not be as good for bromo-containing compounds as it is for species that include only multi-valent non-hydrogen atoms. For non-bromo compounds, the performance of semi-empirical methods in ONIOM may therefore be better than what was concluded from the current work.

Since the goal of ONIOM is to reduce the overall computational cost, we will now comment on the computational times required for the various method combinations we have tested. For an energy and gradient calculation on the transition state of a bromo-substituded 2(*H*)-pyran-2-one with MA, ONIOM with AM1 or PM3 in the low level takes about one-seventh of the CPU time needed for the same calculation at the Target level of theory. This clearly makes the semi-empirical methods attractive choices for many purposes, especially since the accuracy was remarkably good for the prediction of the absolute barriers (much better than the accuracy we would expect when using the semi-empirical method on its own). Of the other promising combinations, HF/II takes about one-third of the CPU time, while B3LYP/II and B3LYP/III need just under half and just over half of the time, respectively. Although the latter reduction in computational cost may not seem very significant, it must be noted that for larger systems, the relative savings will be much larger for these combinations, particularly for carrying out frequency calculations. Savings will be further increased if a more accurate computational level of theory is used as the Target.[34]

To conclude, we have shown that ONIOM is able to reliably describe transition states in Diels–Alder cycloadditions. We envision several ways in which the proposed schemes can be useful. First, we can assume that the methods are transferable to larger systems, which cannot be benchmarked directly. In those cases, the computational savings will be more substantial than in the current work. Second, we can assume that the methods are transferable to other reactants. Having carefully benchmarked for a relatively small set will allow the quick scanning of many different reactant pairs and possible cycloadducts. Third, after benchmarking only the critical points on the potential surface, ONIOM can be used to map other parts of the surface, for example, as needed in transition-state theory (TST).

Acknowledgements

S.M.L. acknowledges an Emerson Center Visiting Fellowship to work at Emory, in addition to support from Engineering and Physical Sciences Research Council (UK) (EPSRC) grant No. GR/R75236/02.

References

(1) This article is part of a Special Issue dedicated to Professor T. Ziegler.
(2) Afarinkia, K.; Nelson, T. D.; Vinader, M. V.; Posner, G. H. *Tetrahedron* **1992**, *48*, 9111. doi:10.1016/S0040-4020(01)85607-6.
(3) Woodward, B. T.; Posner, G. H. *Adv. Cycloaddit.* **1999**, *5*, 47.
(4) Svensson, M.; Humbel, S.; Froese, R. D. J.; Matsubara, T.; Sieber, S.; Morokuma, K. *J. Phys. Chem.* **1996**, *100* (50), 19357. doi:10.1021/jp962071j.
(5) Humbel, S.; Sieber, S.; Morokuma, K. *J. Chem. Phys.* **1996**, *105* (5), 1959. doi:10.1063/1.472065.
(6) Svensson, M.; Humbel, S.; Morokuma, K. *J. Chem. Phys.* **1996**, *105*, 3654. doi:10.1063/1.472235.
(7) Maseras, F.; Morokuma, K. *J. Comput. Chem.* **1995**, *16* (9), 1170. doi:10.1002/jcc.540160911.
(8) Dapprich, S.; Komáromi, I.; Byun, K. S.; Morokuma, K.; Frisch, M. J. *J. Mol. Struct. THEOCHEM* **1999**, *461–462*, 1. doi:10.1016/S0166-1280(98)00475-8.
(9) Vreven, T.; Frisch, M. J.; Kudin, K. N.; Schlegel, H. B.; Morokuma, K. *Mol. Phys.* **2006**, *104*, 701. doi:10.1080/00268970500417846.
(10) Vreven, T.; Morokuma, K. *J. Phys. Chem. A* **2002**, *106*, 6167. doi:10.1021/jp014588n.
(11) Afarinkia, K.; Bearpark, M. J.; Ndibwami, A. *J. Org. Chem.* **2003**, *68*, 7158. doi:10.1021/jo0348827. PMID:12968865.
(12) Afarinkia, K.; Bearpark, M. J.; Ndibwami, A. *J. Org. Chem.* **2005**, *70*, 1122. doi:10.1021/jo048213k. PMID:15704944.
(13) Warshel, A.; Levitt, M. *J. Mol. Biol.* **1976**, *103*, 227. doi:10.1016/0022-2836(76)90311-9. PMID:985660.
(14) Singh, U. C.; Kollman, P. A. *J. Comput. Chem.* **1986**, *7* (6), 718. doi:10.1002/jcc.540070604.
(15) Field, M. J.; Bash, P. A.; Karplus, M. *J. Comput. Chem.* **1990**, *11* (6), 700. doi:10.1002/jcc.540110605.

(16) Vreven, T.; Morokuma, K. *J. Comput. Chem.* **2000**, *21*, 1419. doi:10.1002/1096-987X(200012)21:16<1419::AID-JCC1>3.0.CO;2-C.
(17) Vreven, T.; Morokuma, K. *Annu. Rep. Comput. Chem.* **2006**, *2*, 35. doi:10.1016/S1574-1400(06)02003-2.
(18) Morokuma, K. *Bull. Korean Chem. Soc.* **2003**, *24*, 797.
(19) Morokuma, K.; Musaev, D. G.; Vreven, T.; Basch, H.; Torrent, M.; Khoroshun, D. V. *IBM J. Res. Develop.* **2001**, *45* (3–4), 367.
(20) Bearpark, M. J.; Ogliaro, F.; Vreven, T.; Boggio-Pasqua, M.; Frisch, M. J.; Larkin, S. M.; Morrison, M.; Robb, M. A. *J. Photochem. Photobiol. A* **2007**, *190*, 207. doi:10.1016/j.jphotochem.2007.05.008.
(21) Wesolowski, T. A.; Weber, J. *Chem. Phys. Lett.* **1996**, *248*, 71. doi:10.1016/0009-2614(95)01281-8.
(22) Wesolowski, T. A.; Warshel, A. *J. Phys. Chem.* **1993**, *97*, 8050. doi:10.1021/j100132a040.
(23) Wesolowski, T. A.; Warshel, A. *J. Phys. Chem.* **1993**, *97* (30), 8050. doi:10.1021/j100132a040.
(24) Yang, W. *Phys. Rev. Lett.* **1991**, *66*, 1438. doi:10.1103/PhysRevLett.66.1438. PMID:10043209.
(25) Cui, Q.; Guo, H.; Karplus, M. *J. Chem. Phys.* **2002**, *117* (12), 5617. doi:10.1063/1.1501134.
(26) Gogonea, V.; Westerhoff, L. M.; Merz, K. M. *J. Chem. Phys.* **2000**, *113* (14), 5604. doi:10.1063/1.1290608.
(27) Hratchian, H. P.; Parandekar, P. V.; Raghavachari, K.; Frisch, M. J.; Vreven, T. *J. Chem. Phys.* **2008**, *128* (3). doi:10.1063/1.2814164. PMID:18205488.
(28) Vreven, T.; Byun, K. S.; Komáromi, I.; Dapprich, S.; Montgomery, J. A., Jr.; Morokuma, K.; Frisch, M. J. *J. Chem. Theory Comput.* **2006**, *2*, 815. doi:10.1021/ct050289g.
(29) Frisch, M. J.; Trucks, G. W.; Schlegel, H. B.; Scuseria, G. E.; Robb, M. A.; Cheeseman, J. R.; Montgomery, J. A., Jr.; Vreven, T.; Kudin, K. N.; Burant, J. C.; Millam, J. M.; Iyengar, S. S.; Tomasi, J.; Barone, V.; Mennucci, B.; Cossi, M.; Scalmani, G.; Rega, N.; Petersson, G. A.; Nakatsuji, H.; Hada, M.; Ehara, M.; Toyota, K.; Fukuda, R.; Hasegawa, J.; Ishida, M.; Nakajima, T.; Honda, Y.; Kitao, O.; Nakai, H.; Klene, M.; Li, X.; Knox, J. E.; Hratchian, H. P.; Cross, J. B.; Adamo, C.; Jaramillo, J.; Gomperts, R.; Stratmann, R. E.; Yazyev, O.; Austin, A. J.; Cammi, R.; Pomelli, C.; Ochterski, J. W.; Ayala, P. Y.; Morokuma, K.; Voth, G. A.; Salvador, P.; Dannenberg, J. J.; Zakrzewski, V. G.; Dapprich, S.; Daniels, A. D.; Strain, M. C.; Farkas, O.; Malick, D. K.; Rabuck, A. D.; Raghavachari, K.; Foresman, J. B.; Ortiz, J. V.; Cui, Q.; Baboul, A. G.; Clifford, S.; Cioslowski, J.; Stefanov, B. B.; Liu, G.; Liashenko, A.; Piskorz, P.; Komaromi, I.; Martin, R. L.; Fox, D. J.; Keith, T.; Al-Laham, M. A.; Peng, C. Y.; Nanayakkara, A.; Challacombe, M.; Gill, P. M. W.; Johnson, B.; Chen, W.; Wong, M. W.; Gonzalez, C.; Pople, J. A. Gaussian development version [computer program]. Version C.01. Gaussian, Inc., Wallingford CT. 2004.
(30) Ujaque, G.; Norton, J. E.; Houk, K. N. *J. Org. Chem.* **2002**, *67*, 7179. doi:10.1021/jo020441w. PMID:12375943.
(31) Dewar, M. J. S. *J. Phys. Chem.* **1985**, *89* (11), 2145. doi:10.1021/j100257a004.
(32) Kobko, N.; Dannenberg, J. J. *J. Phys. Chem. A* **2001**, *105* (10), 1944. doi:10.1021/jp001970b.
(33) Sodupe, M.; Rios, R.; Branchadell, V.; Nicholas, T.; Oliva, A.; Dannenberg, J. J. *J. Am. Chem. Soc.* **1997**, *119* (18), 4232. doi:10.1021/ja9628260.
(34) Bakalova, S. M.; Kaneti, J. *J. Phys. Chem. A* **2008**, *112* (50), 13006. doi:10.1021/jp803701y.

Mapping approach for quantum-classical time correlation functions[1]

Ali Nassimi and Raymond Kapral

Abstract: The calculation of quantum canonical time correlation functions is considered in this paper. Transport properties, such as diffusion and reaction rate coefficients, can be determined from time integrals of these correlation functions. Approximate quantum-classical expressions for correlation functions, which are amenable to simulation, are derived. These expressions incorporate the full quantum equilibrium structure of the system but approximate the dynamics by quantum-classical evolution where a quantum subsystem is coupled to a classical environment. The main feature of the formulation is the use of a mapping basis where the subsystem quantum states are represented by fictitious harmonic oscillator states. This leads to a full phase space representation of the dynamics that can be simulated without appeal to surface-hopping methods. The results in this paper form the basis for new simulation algorithms for the computation of quantum transport properties of large many-body systems.

Key words: mapping basis, quantum-classical dynamics, quantum correlation functions.

Résumé : Dans ce travail, on s'applique à calculer les fonctions de corrélation du temps quantique canonique. Il est possible de déterminer les propriétés de transport, tels les coefficients des vitesses de diffusion et de réaction, à partir des intégrales de temps de ces fonctions de corrélation. On a dérivé des expressions quantiques classiques approximatives pour les fonctions de corrélation qui peuvent éventuellement être utilisées en simulation. Ces expressions incorporent la structure d'équilibre quantique complète du système, mais ne donne qu'une approximation de la dynamique par le biais d'une évolution quantique classique dans lequel un sous système quantique est couplé à un environnement classique. La caractéristique principale de la formulation est l'utilisation d'une base de cartographie dans laquelle les états quantiques du sous système sont représentés par des états d'oscillateurs harmoniques fictifs. Ce traitement conduit à une représentation spatiale complète de l'espace de la dynamique qui peut être simulée sans faire appel aux méthodes de sauts de surface. Les résultats obtenus dans ce travail forment la base de nouveaux algorithmes de simulation pour le calcul des propriétés de transport de systèmes à plusieurs composantes.

Mots-clés : base de représentation, dynamique quantique classique, fonctions de corrélation quantique.

[Traduit par la Rédaction]

1. Introduction

In the investigation of condensed-phase systems, one is usually interested in the average value of some observable or in a time correlation function from which a transport coefficient can be computed. Since the basic description of matter is quantum mechanical, we are interested in the average value of a quantum-mechanical operator, which is given by $\overline{B(t)} = \mathrm{Tr}\widehat{B}(t)\widehat{\rho}(0)$, where, for a system with Hamiltonian $\widehat{H}$, the time-dependent operator satisfies the Heisenberg equation of motion,

$$[1] \qquad \frac{\mathrm{d}}{\mathrm{d}t}\widehat{B}(t) = \frac{i}{\hbar}[\widehat{H}, \widehat{B}]$$

and $\widehat{\rho}(0)$ is the initial value of the density matrix. Quantum time correlation functions of two operators $\widehat{A}$ and $\widehat{B}$ have the form,[2] $C_{\mathrm{AB}}(t) = \mathrm{Tr}(\widehat{\rho}_{\mathrm{eq}}\widehat{A}\widehat{B}(t))$, where $\widehat{\rho}_{\mathrm{eq}}$ is the quantum canonical equilibrium density matrix. Either of these quantum expressions requires a knowledge of the time evolution of a quantum operator in a many-body system that is often very large. Consequently, these general expressions are not computationally tractable, and appeal must be made to approximations if they are to be evaluated for problems of physical interest.

The approximate dynamical description we consider in this paper is quantum-classical Liouville dynamics.[4] In this formulation, the system is partitioned into two subsystems, which we call quantum subsystem and bath or environment. The partition is dictated by physical principles. For example, in electron or proton transfer problems, the electron or proton may constitute the quantum subsystem, while the environment in which the transfer takes place, a molecular group or biomolecule dissolved in a solvent, forms the bath. In quantum-classical Liouville dynamics, the bath is treated classically while retaining the full quantum character of the

Received 15 January 2009. Accepted 11 March 2009. Published on the NRC Research Press Web site at canjchem.nrc.ca on 4 May 2009.

A. Nassimi[1] and R. Kapral. Chemical Physics Theory Group, Department of Chemistry, University of Toronto, Toronton ON M5S 3H6, Canada.

[1]Corresponding author (e-mail: anassimi@chem.utoronto.ca).

quantum subsystem. In this theory, the analog of the Heisenberg equation of motion for an operator is[4,5]

$$[2] \qquad \frac{\mathrm{d}}{\mathrm{d}t}\widehat{B}_{\mathrm{W}}(X,t) = \frac{i}{\hbar}\left[\widehat{H}_{\mathrm{W}},,\widehat{B}_{\mathrm{W}}\right] - \frac{1}{2}\left(\left\{\widehat{H}_{\mathrm{W}},\widehat{B}_{\mathrm{W}}\right\} - \left\{\widehat{B}_{\mathrm{W}},\widehat{H}_{\mathrm{W}}\right\}\right)$$

where $X = (R,P)$ are the positions and momenta of the bath degrees of freedom. The subscript W indicates that operators are expressed in a partial Wigner representation, defined below. In addition to the usual quantum commutator, the equation of motion also involves a Poissson bracket denoted by { , }. While this equation is far more tractable than the full quantum equations of motion, its numerical simulation presents challenges and a number of different schemes have been constructed for this purpose.[6,7] These include Trotter-based methods that use an adiabatic basis,[8] as well as trajectory methods that use the diabatic[9] and force bases,[10] schemes based on the multiple threads algorithm,[11] and a method that utilizes the mapping basis.[12] The mapping method has proved to be especially promising for the evaluation of expectation values of operators, as shown by calculations of population relaxation in the spin-boson model, one of the standard test cases for quantum dynamics.[12] In this paper, we show how the mapping method can be extended to the computation of time correlation functions within the quantum-classical Liouville framework.

In the next section, we present the explicit expression for the quantum correlation function that forms the basis of our calculations. Section 3 outlines the mapping formulation, where subsystem quantum states are replaced by fictitious harmonic oscillator states. Section 4 reformulates the quantum correlation function in the mapping basis. This fully quantum description is exact and the dynamics is embodied in the spectral density function. A quantum-classical approximation for the spectral density dynamics is derived in Section 5. The details of this derivation are presented in the Appendix. This result is used in Section 6 to obtain the final result for the quantum-classical correlation function in the mapping basis. The conclusions of the study are presented in Section 7.

2. Correlation function

Before considering quantum-classical approximations to the dynamics, we first rewrite the exact quantum correlation function in a form that is suitable for the introduction of the mapping basis and passage to the quantum-classical limit. Suppose the quantum subsystem and bath have N_{s} and N_{b} degrees of freedom with characteristic masses m and M, respectively. To introduce a phase space description of the bath, we first introduce a coordinate representation of the bath so that the correlation function takes the form

$$\begin{aligned}
C_{AB}(t) &= \mathrm{Tr}\left(\widehat{\rho}_{eq}\widehat{A}\widehat{B}(t)\right) = \left(\mathrm{Tr}\widehat{\rho}_{eq}\widehat{A}e^{i\widehat{H}t/\hbar}\widehat{B}e^{-i\widehat{H}t/\hbar}\right) \\
&= \mathrm{Tr}'\int \mathrm{d}Q_1\mathrm{d}Q_2\mathrm{d}Q_3\mathrm{d}Q_4 \left\langle Q_1\left|\widehat{\rho}_{eq}\widehat{A}\right|Q_2\right\rangle\left\langle Q_2\left|e^{i\widehat{H}t/\hbar}\right|Q_3\right\rangle\left\langle Q_3\left|\widehat{B}\right|Q_4\right\rangle\left\langle Q_4\left|e^{-i\widehat{H}t/\hbar}\right|Q_1\right\rangle \\
&= \mathrm{Tr}'\int \mathrm{d}R_1\mathrm{d}R_2\mathrm{d}Z_1\mathrm{d}Z_2 \left\langle R_1 - \frac{Z_1}{2}\left|\widehat{\rho}_{eq}\widehat{A}\right|R_1 + \frac{Z_1}{2}\right\rangle\left\langle R_1 + \frac{Z_1}{2}\left|e^{i\widehat{H}t/\hbar}\right|R_2 - \frac{Z_2}{2}\right\rangle \\
&\qquad \times \left\langle R_2 - \frac{Z_2}{2}\left|\widehat{B}\right|R_2 + \frac{Z_2}{2}\right\rangle\left\langle R_2 + \frac{Z_2}{2}\left|e^{-i\widehat{H}t/\hbar}\right|R_1 - \frac{Z_1}{2}\right\rangle
\end{aligned} \qquad [3]$$

In these equations, Tr′ stands for a trace over the quantum subsystem degrees of freedom, and in the fourth equality above, we have made a change of variables $Q_1 = R_1 - Z_1/2$, $Q_2 = R_1 + Z_1/2$, etc.

Two further manipulations are required to cast the correlation function into a form that is suitable for the calculations using the mapping basis described below. The coordinate space matrix elements may be replaced with bath phase space functions by introducing the partial[5] Wigner transforms[13–15] of an operator and density matrix

$$[4] \qquad \left\langle R - \frac{Z}{2}\left|\widehat{B}\right|R + \frac{Z}{2}\right\rangle = \frac{1}{(2\pi\hbar)^{N_{\mathrm{b}}}}\int \mathrm{d}P\widehat{B}_W(R,P)e^{-iP\cdot Z/\hbar}, \qquad \left\langle R - \frac{Z}{2}\left|\widehat{\rho}_{\mathrm{eq}}\widehat{A}\right|R + \frac{Z}{2}\right\rangle = \int \mathrm{d}P(\widehat{\rho}_{\mathrm{eq}}\widehat{A})_{\mathrm{W}}(R,P)e^{-iP\cdot Z/\hbar}$$

Note that the partially Wigner-transformed quantities are still operators in the quantum subsystem Hilbert space. In addition, Tr′ may be written explicitly using the eigenfunctions of the Hamiltonian of the quantum subsystem. The Hamiltonian for the entire system is given by

$$[5] \qquad \widehat{H} = \frac{\widehat{P}^2}{2M} + \widehat{V}_{\mathrm{b}}(\widehat{R}) + \frac{\widehat{p}^2}{2m} + \widehat{V}_{\mathrm{s}}(\widehat{q}) + \widehat{V}_{\mathrm{c}}(\widehat{R},\widehat{q})$$

where $\widehat{P}$ and $\widehat{p}$ are momentum operators of the bath and subsystem, and $\widehat{V}_{\mathrm{b}}$, $\widehat{V}_{\mathrm{s}}$, and $\widehat{V}_{\mathrm{c}}$ are, respectively, the bath, subsystem, and coupling potentials. The coordinate operators for the subsystem and bath are $\widehat{q}$ and $\widehat{R}$, respectively. Equation [5] can be written as $\widehat{H} = \frac{\widehat{P}^2}{2M} + \widehat{V}_{\mathrm{b}} + \widehat{V}_{\mathrm{c}} + \widehat{h}_{\mathrm{s}}$, where $\widehat{h}_{\mathrm{s}} = \frac{\widehat{p}^2}{2m} + \widehat{V}_{\mathrm{s}}$ is the subsystem Hamiltonian. The eigenstates of $\widehat{h}_{\mathrm{s}}$ are defined by the eigenvalue problem $\widehat{h}_{\mathrm{s}}|\lambda\rangle = \varepsilon_\lambda|\lambda\rangle$. We suppose that there are N quantum subsystem states. Making use of subsystem

Fig. 1. Schematic representation of the mapping for a five-level system. Subsystem states are on the left and the mapping states are on the right.

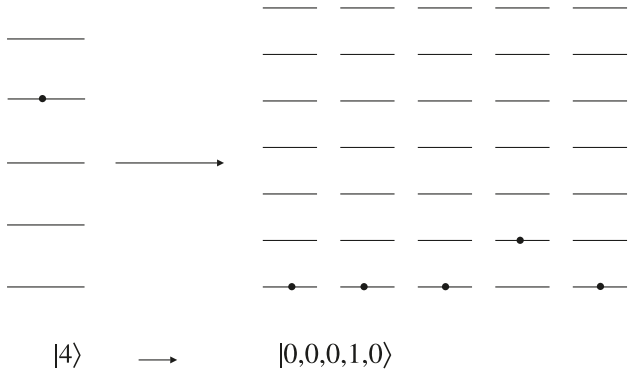

energy eigenstates as a basis and introducing the Wigner-transformed forms of $\widehat{\rho}_{eq}\widehat{A}$ and $\widehat{B}$ given in eq. [4] we have

$$[6]\qquad C_{AB}(t) = \frac{1}{(2\pi\hbar)^{N_b}} \sum_{\lambda,\lambda',\mu,\mu'=1}^{N} \int dX_1 dX_2 dZ_1 dZ_2 \left\langle \lambda \middle| (\widehat{\rho}_{eq}\widehat{A})_W(X_1) \middle| \lambda' \right\rangle \times \left\langle \lambda' \middle| \left\langle R_1 + \frac{Z_1}{2} \middle| e^{i\widehat{H}t/\hbar} \middle| R_2 - \frac{Z_2}{2} \right\rangle \middle| \mu \right\rangle \left\langle \mu \middle| \widehat{B}_W(X_2) \middle| \mu' \right\rangle \left\langle \mu' \middle| \left\langle R_2 + \frac{Z_2}{2} \middle| e^{-i\widehat{H}t/\hbar} \middle| R_1 - \frac{Z_1}{2} \right\rangle \middle| \lambda \right\rangle e^{-\frac{i}{\hbar}(P_1\cdot Z_1 + P_2\cdot Z_2)}$$

The spectral density function in the subsystem basis may be defined as

$$[7]\qquad W^{\lambda'\lambda\mu'\mu}(X_1, X_2, t) = \int dZ_1 dZ_2 \left\langle \lambda' \middle| \left\langle R_1 + \frac{Z_1}{2} \middle| e^{i\widehat{H}t/\hbar} \middle| R_2 - \frac{Z_2}{2} \right\rangle \middle| \mu \right\rangle \left\langle \mu' \middle| \left\langle R_2 + \frac{Z_2}{2} \middle| e^{-i\widehat{H}t/\hbar} \middle| R_1 - \frac{Z_1}{2} \right\rangle \middle| \lambda \right\rangle e^{-\frac{i}{\hbar}(P_1\cdot Z_1 + P_2\cdot Z_2)}$$

and contains all information needed to compute the quantum time evolution contribution to the correlation function. The spectral density defined via full Wigner transform was used by Filinov et al.[16–18] in a reformulation of the quantum correlation function. In terms of the spectral density function in the subsystem basis, the correlation function takes the form

$$[8]\qquad C_{AB}(t) = \frac{1}{(2\pi\hbar)^{N_b}} \sum_{\lambda,\lambda',\mu,\mu'}^{N} \int dX_1 dX_2 \left\langle \lambda \middle| (\widehat{\rho}_{eq}\widehat{A})_W(X_1) |\lambda'\right\rangle \langle \mu | \widehat{B}_W(X_2) | \mu' \rangle W^{\lambda'\lambda\mu'\mu}(X_1, X_2, t)$$

This expression for the quantum correlation function is exact. To compute it, the matrix elements of the forward and backward propagators must be evaluated to solve for the time dependence of the spectral density function. This is the most difficult part of the problem. A similar expression utilizing the adiabatic basis in place of the subsystem basis was derived earlier.[19] In addition to the time-dependent spectral density function, the time-independent matrix elements of the quantum operators and quantum equilibrium density matrix must also be computed to evaluate the ensemble average appearing in the definition of the correlation function. While these equilibrium quantities may be difficult to evaluate for complex systems, they are far easier to compute than the quantum time dependence, and algorithms have been developed for this purpose.[20,21]

3. Mapping basis

To construct a useful simulation algorithm for the quantum correlation function, it is convenient to use an alternative but equivalent mapping form for the quantum subsystem matrix elements of the operators that enter in its definition. A well-known mapping approach was introduced by Schwinger.[22] In his scheme, the eigenstates of the angular momentum operator are mapped onto eigenfunctions of two bosonic oscillators, and the angular momentum operators are mapped onto combinations of creation, $\hat{a}_\lambda^\dagger$, and annihilation, $\hat{a}_{\lambda'}$, operators ($\lambda,\lambda' = 1$ or 2). Such a mapping yields a simple treatment of the angular momentum problem in quantum mechanics. In this formalism, the resolution of identity is mapped to $\hat{a}_1^\dagger\hat{a}_1 + \hat{a}_2^\dagger\hat{a}_2 = 1$. This equality is used in the Holstein–Primakoff mapping scheme to eliminate one bosonic oscillator and represent angular momentum states by a single oscillator.[23] An extension of these mapping schemes was used to map discreet states of a quantum system onto fictitious harmonic oscillators, so that all degrees of freedom in the system can be treated with semiclassical approximations.[24–30] The mapping approach has also been used in other closely related contexts.[31–33]

In the mapping scheme used in this work, an N level quantum system is mapped onto N harmonic oscillators. The wave function of the system in a given quantum state is mapped onto a product of harmonic oscillator wave functions where all oscillators are in their ground state, except for one oscillator corresponding to the given quantum state, which is in its first excited state. This mapping is schematically represented in Fig. 1. Therefore, we have a physical space with a cardinality N, which is much lower than the cardinality of the Hilbert space of the N harmonic oscillators, which is infinite. More specifically, the subsystem quantum states are mapped through the relations,

$$[9] \qquad |\lambda\rangle \rightarrow |m_\lambda\rangle = |0_1, \ldots, 1_\lambda, \ldots, 0_N\rangle$$

where

$$\langle q|m_\lambda\rangle = \langle q_1, q_2, \ldots, q_N|0_1, \ldots, 1_\lambda, \ldots, 0_N\rangle = \phi_0(q_1)\ldots\phi_0(q_{\lambda-1})\phi_1(q_\lambda)\ldots\phi_0(q_N)$$

with ϕ_0 and ϕ_1, respectively, being the ground and the first excited state wave functions of an harmonic oscillator. The creation and annihilation operators on the mapping states act in the following ways[34]

$$[10] \qquad \widehat{a}_\lambda^\dagger|0\rangle = |0_1, \ldots, 1_\lambda, \ldots, 0_N\rangle = |m_\lambda\rangle \quad \text{and} \quad \widehat{a}_\lambda|m_\lambda\rangle = |0_1, \ldots, 0_N\rangle = |0\rangle$$

where

$$[11] \qquad \widehat{a}_\lambda = \sqrt{\frac{m\omega}{2\hbar}}\left(\widehat{q}_\lambda + \frac{i}{m\omega}\widehat{p}_\lambda\right), \qquad \widehat{a}_\lambda^\dagger = \sqrt{\frac{m\omega}{2\hbar}}\left(\widehat{q}_\lambda - \frac{i}{m\omega}\widehat{p}_\lambda\right), \quad \text{and} \quad [\widehat{q}_\lambda, \widehat{p}_\lambda] = i\hbar$$

We may then introduce the mapping representation of an operator $\widehat{A}$ as

$$[12] \qquad \widehat{A}_m = \sum_{\lambda\lambda'} A_{\lambda\lambda'}\widehat{a}_\lambda^\dagger\widehat{a}_{\lambda'}$$

For example, the mapping form of the Hamiltonian in eq. [5] is

$$[13] \qquad \begin{aligned}\widehat{H}_m &= \sum_{\lambda\lambda'}\left[\frac{\widehat{P}^2}{2M}\delta_{\lambda\lambda'} + \widehat{V}_{\mathrm{B}}(\widehat{R})\delta_{\lambda\lambda'} + h_{\lambda\lambda'}(\widehat{R})\right]\widehat{a}_\lambda^\dagger\widehat{a}_{\lambda'} \\ &= \frac{\widehat{P}^2}{2M} + \widehat{V}_B(\widehat{R}) + \frac{m\omega}{2\hbar}\sum_{\lambda\lambda'}h_{\lambda\lambda'}(\widehat{R})(\widehat{r}_\lambda\widehat{r}_{\lambda'} + \frac{\widehat{p}_\lambda\widehat{p}_{\lambda'}}{m^2\omega^2} - \frac{\hbar}{m\omega}\delta_{\lambda\lambda'})\end{aligned}$$

where $\widehat{h} = \frac{\widehat{p}^2}{2m} + \widehat{V}_{\mathrm{s}}(\widehat{q}) + \widehat{V}_{\mathrm{c}}(R, \widehat{q})$, and $h_{\lambda\lambda'}$ is its matrix element. We used the fact that $h_{\lambda\lambda'} = h_{\lambda'\lambda}$ in writing this expression. Note that unlike eq. [5], where $\widehat{q}$ and $\widehat{p}$ are the subsystem coordinates and momenta, in eq. [13] $\widehat{r}$ and $\widehat{p}$ are the mapping space coordinates and momenta. These quantities have dimensions equal to the number of subsystem quantum states.

From the definition in eq. [12] it is clear that the matrix elements of $\widehat{A}$ in the subsystem basis are identical to those of $\widehat{A}_m$ in the mapping basis: $\langle\lambda|\widehat{A}|\lambda'\rangle = A_{\lambda\lambda'} = \langle m_\lambda|\widehat{A}_m|m_{\lambda'}\rangle$. Consequently, any matrix element in the quantum subsystem basis can be substituted by its equivalent form in the mapping basis. We show that this substitution leads to computational advantages when simulating quantum correlation functions.

4. Correlation function in mapping basis

The matrix elements in the correlation function expression (eq. [6]) can be replaced by their mapping equivalent forms to yield

$$[14] \qquad \begin{aligned}C_{AB}(t) = \frac{1}{(2\pi\hbar)^{N_{\mathrm{b}}}}\sum_{\lambda\lambda'\mu\mu'=1}^{N}\int \mathrm{d}X_1\mathrm{d}X_2\mathrm{d}Z_1\mathrm{d}Z_2 \left\langle m_\lambda\middle|(\widehat{\rho}_{\mathrm{eq}}\widehat{A})_{Wm}(X_1)\middle|m_{\lambda'}\right\rangle \\ \times\left\langle m_{\lambda'}\middle|\left\langle R_1 + \frac{Z_1}{2}\middle|e^{i\widehat{H}_m t/\hbar}\middle|R_2 - \frac{Z_2}{2}\right\rangle\middle|m_\mu\right\rangle\left\langle m_\mu\middle|\widehat{B}_{Wm}(X_2)\middle|m_{\mu'}\right\rangle \\ \times\left\langle m_{\mu'}\middle|\left\langle R_2 + \frac{Z_2}{2}\middle|e^{-i\widehat{H}_m t/\hbar}\middle|R_1 - \frac{Z_1}{2}\right\rangle\middle|m_\lambda\right\rangle e^{-\frac{i}{\hbar}(P_1\cdot Z_1 + P_2\cdot Z_2)}\end{aligned}$$

The next step in the analysis of this correlation function is to introduce a coordinate space representation of the abstract mapping eigenfuctions. Inserting resolutions of the identity, $\int \mathrm{d}q\ |q\rangle\langle q| = 1$, and making use of the closure relation for mapping states, $\sum_\lambda \langle q'|m_\lambda\rangle\langle m_\lambda|q\rangle = \delta(q - q')$, the correlation function takes the form

$$[15] \qquad \begin{aligned}C_{AB}(t) = \frac{1}{(2\pi\hbar)^{N_{\mathrm{b}}}}\int \mathrm{d}X_1\mathrm{d}X_2\mathrm{d}Z_1\mathrm{d}Z_2\mathrm{d}q_1\mathrm{d}q_2\mathrm{d}q_4\mathrm{d}q_6 \left\langle q_1\middle|\left(\widehat{\rho}_{\mathrm{eq}}\widehat{A}\right)_{Wm}(X_1)\middle|q_2\right\rangle \\ \times\left\langle q_2\middle|\left\langle R_1 + \frac{Z_1}{2}\middle|e^{i\widehat{H}_m t/\hbar}\middle|R_2 - \frac{Z_2}{2}\right\rangle\middle|q_4\right\rangle\left\langle q_4\middle|\widehat{B}_{Wm}(X_2)\middle|q_6\right\rangle\left\langle q_6\middle|\left\langle R_2 + \frac{Z_2}{2}\middle|e^{-i\widehat{H}_m t/\hbar}\middle|R_1 - \frac{Z_1}{2}\right\rangle\middle|q_1\right\rangle e^{-\frac{i}{\hbar}(P_1\cdot Z_1 + P_2\cdot Z_2)}\end{aligned}$$

It is important to note that the dimensionality of the mapping coordinate space representation is fixed by the number of quantum states.

A phase space description of this coordinate representation can be obtained by introducing Wigner transforms of the matrix elements. Making the change of variables, $q_1 = r_1 - z_1/2$, $q_2 = r_1 + z_1/2$, etc., and using the analog of eq. [4] for the mapping coordinates, we find

$$[16] \qquad C_{AB}(t) = \frac{1}{(2\pi\hbar)^{(N_b+N)}} \int dX_1 dX_2 dx_1 dx_2 \left(\widehat{\rho}_{eq}\widehat{A}\right)_{Wm}(X_1, x_1) B_{Wm}(X_2, x_2) W(X_1, X_2, x_1, x_2, t)$$

where in analogy with the bath phase space terminology, $x = (r, p)$. The full Wigner representation of the mapping spectral density W is defined as

$$[17] \qquad W(X_1, X_2, x_1, x_2, t) = \int dZ_1 dZ_2 dz_1 dz_2 \left\langle r_1 + \frac{z_1}{2}\middle|\left\langle R_1 + \frac{Z_1}{2}\middle|e^{i\widehat{H}_m t/\hbar}\middle|R_2 - \frac{Z_2}{2}\right\rangle\middle|r_2 - \frac{z_2}{2}\right\rangle \times \left\langle r_2 + \frac{z_2}{2}\middle|\left\langle R_2 + \frac{Z_2}{2}\middle|e^{-i\widehat{H}_m t/\hbar}\middle|R_1 - \frac{Z_1}{2}\right\rangle\middle|r_1 - \frac{z_1}{2}\right\rangle e^{-\frac{i}{\hbar}(P_1\cdot Z_1 + P_2\cdot Z_2 + p_1\cdot z_1 + p_2\cdot z_2)}$$

All of these manipulations have served simply to cast the exact expression for the quantum correlation function into an equivalent exact form involving a phase-space-like representation for both the bath and the mapping version of the quantum subsystem degrees of freedom. There are advantages to defining W and deriving its dynamics rather than directly considering the dynamics of the correlation function. Not only are the algebraic manipulations simplified, but also all correlation functions for a specific system share the same spectral density. This fully quantum problem is still intractable for complex many-body systems. We now turn to the evaluation of the spectral density function in the quantum-classical limit that will provide the basis for simulation algorithms of the dynamics.

5. Quantum-classical dynamics for *W*

Given the development presented above, the dynamical problem consists in finding a tractable equation of motion for the spectral density function $W(X_1,X_2,x_1,x_2,t)$ and constructing an algorithm for its solution. The equation of motion can be derived by differentiating W with respect to time. However, to derive the quantum-classical equation for W we must introduce approximations. For this purpose we make use of an expansion in the small mass ratio $\mu = (m/M)^{1/2}$, where it is assumed that the characteristic mass M of the bath particles is much larger than m for the quantum subsystem particles. The manner in which this expansion is carried out is analogous to that discussed earlier for the quantum-classical Liouville equation (eq. [2]). More specifically, given the energy ε_0, time $t_0 = \hbar/\varepsilon_0$, and length $\lambda_m = (\hbar^2/m\varepsilon_0)^{1/2}$ units, we scale the light and heavy particle momenta, respectively, with $p_m = (m\lambda_m/t_0) = (m\varepsilon_0)^{1/2}$ and $P_M = (M\varepsilon_0)^{1/2}$. Note that the only difference between subsystem and bath particles is scaling their momenta with different factors. As the subsystem and bath are in thermal equilibrium, their average kinetic energies are equal, and therefore, on average, $p/P = \mu$, so that after scaling both subsystem and bath momenta have the same order of magnitude. After scaling variables, we obtain

$$[18] \qquad W'(R'_1, P'_1, R'_2, P'_2, r'_1, p'_1, r'_2, p'_2; t') = \int dZ'_1 dZ'_2 dz'_1 dz'_2 \left\langle r'_1 + \frac{z'_1}{2}\middle|\left\langle R'_1 + \frac{Z'_1}{2}\middle|e^{i\widehat{H}'_m t'}\middle|R'_2 - \frac{Z'_2}{2}\right\rangle\middle|r'_2 - \frac{z'_2}{2}\right\rangle \times \left\langle r'_2 + \frac{z'_2}{2}\middle|\left\langle R'_2 + \frac{Z'_2}{2}\middle|e^{-i\widehat{H}'_m t'}\middle|R'_1 - \frac{Z'_1}{2}\right\rangle\middle|r'_1 - \frac{z'_1}{2}\right\rangle e^{-i\mu^{-1}(P'_1\cdot Z'_1 + P'_2\cdot Z'_2)} e^{-i(p'_1\cdot z'_1 + p'_2\cdot z'_2)}$$

where a prime means that the variable is divided by the corresponding scaling factor. To avoid cumbersome notation, we drop the primes in the following relations. Differentiation of the scaled form of W yields the equation of motion

$$[19] \qquad \frac{\partial W(t)}{\partial t} = i\int dZ_1 dZ_2 dz_1 dz_2 dQ dq \left[\left\langle r_1 + \frac{z_1}{2}\middle|\left\langle R_1 + \frac{Z_1}{2}\middle|\widehat{H}_m\middle|Q\right\rangle\middle|q\right\rangle \times \left\langle q\middle|\left\langle Q\middle|e^{i\widehat{H}_m t}\middle|R_2 - \frac{Z_2}{2}\right\rangle\middle|r_2 - \frac{z_2}{2}\right\rangle \times \left\langle r_2 + \frac{z_2}{2}\middle|\left\langle R_2 + \frac{Z_2}{2}\middle|e^{-i\widehat{H}_m t}\middle|R_1 - \frac{Z_1}{2}\right\rangle\middle|r_1 - \frac{z_1}{2}\right\rangle - \left\langle r_1 + \frac{z_1}{2}\middle|\left\langle R_1 + \frac{Z_1}{2}\middle|e^{i\widehat{H}_m t}\middle|R_2 - \frac{Z_2}{2}\right\rangle\middle|r_2 - \frac{z_2}{2}\right\rangle \times \left\langle r_2 + \frac{z_2}{2}\middle|\left\langle R_2 + \frac{Z_2}{2}\middle|e^{-i\widehat{H}_m t}\middle|Q\right\rangle\middle|q\right\rangle\left\langle Q\middle|\left\langle q\middle|\widehat{H}_m\middle|R_1 - \frac{Z_1}{2}\right\rangle\middle|r_1 - \frac{z_1}{2}\right\rangle\right] e^{-i\mu^{-1}(P_1\cdot Z_1 + P_2\cdot Z_2)} e^{-i(p_1\cdot z_1 + p_2\cdot z_2)}$$

The mapping Hamiltonian (eq. [13] in scaled variables is $\widehat{H}_m = \frac{\widehat{P}^2}{2} + \widehat{V}_B(\widehat{R}) + \sum_{\lambda\lambda'} \frac{h_{\lambda\lambda'}(\widehat{R})}{2}(\widehat{r}_\lambda\widehat{r}_{\lambda'} + \widehat{p}_\lambda\widehat{p}_{\lambda'} - \delta_{\lambda\lambda'})$, while the scaled quantum mechanical momentum operators are $\widehat{P} = \frac{\mu}{i}\frac{\partial}{\partial Q}$ and $\widehat{p} = -i\frac{\partial}{\partial q}$. Substituting the Hamiltonian and momentum operators into eq. [19] yields

$$[20]\quad \frac{\partial W(t)}{\partial t} = i\mu^{2N_b}\int d\tilde{Z}_1 d\tilde{Z}_2 dQ dz_1 dz_2 dq e^{-i(P_1\cdot\tilde{Z}_1+P_2\cdot\tilde{Z}_2)}e^{-i(p_1\cdot z_1+p_2\cdot z_2)}$$
$$\times\left\{\left\{\left[\frac{-\mu^2}{2}\frac{\partial^2}{\partial Q^2}+V_B(Q)+\frac{1}{2}\sum_{\lambda\lambda'}h_{\lambda\lambda'}(Q)\left(q_\lambda q_{\lambda'}-\frac{\partial}{\partial q_\lambda}\frac{\partial}{\partial q_{\lambda'}}-\delta_{\lambda\lambda'}\right)\right]\right.\right.$$
$$\left.\left.\times\,\delta\left(Q-R_1-\frac{\mu\tilde{Z}_1}{2}\right)\delta\left(q-r_1-\frac{z_1}{2}\right)\right\}\left\langle q\left|\left\langle Q\left|e^{i\widehat{H}_m t}\right|R_2-\frac{\mu\tilde{Z}_2}{2}\right\rangle\right|r_2-\frac{z_2}{2}\right\rangle\right.$$
$$\times\left\langle r_2+\frac{z_2}{2}\left|\left\langle R_2+\frac{\mu\tilde{Z}_2}{2}\left|e^{-i\widehat{H}_m t}\right|R_1-\frac{\mu\tilde{Z}_1}{2}\right\rangle\right|r_1-\frac{z_1}{2}\right\rangle\right.$$
$$-\left\{\left[\frac{-\mu^2}{2}\frac{\partial^2}{\partial Q^2}+V_B(Q)+\frac{1}{2}\sum_{\lambda\lambda'}h_{\lambda\lambda'}(Q)\left(q_\lambda q_{\lambda'}-\frac{\partial}{\partial q_\lambda}\frac{\partial}{\partial q_{\lambda'}}-\delta_{\lambda\lambda'}\right)\right]\right.$$
$$\left.\times\,\delta\left(Q-R_1+\frac{\mu\tilde{Z}_1}{2}\right)\delta\left(q-r_1+\frac{z_1}{2}\right)\right\}\left\langle r_1+\frac{z_1}{2}\left|\left\langle R_1+\frac{\mu\tilde{Z}_1}{2}\left|e^{i\widehat{H}_m t}\right|R_2-\frac{\mu\tilde{Z}_2}{2}\right\rangle\right|r_2-\frac{z_2}{2}\right\rangle$$
$$\left.\times\left\langle r_2+\frac{z_2}{2}\left|\left\langle R_2+\frac{\mu\tilde{Z}_2}{2}\left|e^{-i\widehat{H}_m t}\right|Q\right\rangle\right|q\right\rangle\right\}$$

where the change of variable $\tilde{Z}_1 = Z_1/\mu$ was performed to transfer the μ dependence from the exponential to the argument of the potential energy terms, after integrations over Q and q have been performed. It is more convenient to expand a potential energy term around a small parameter rather than to deal with an oscillatory exponential.

We begin the calculation by performing the integrals over q and Q, followed by Taylor expansion of the potential energy terms around μ = 0, keeping terms up to the first order in μ. Finally, we introduce the definition of W into the resulting expression. The algebra is lengthy so it is presented in the Appendix. While the algebra leading to the result is lengthy, the final equation of motion is relatively simple. In unscaled coordinates it takes the form

$$[21]\quad \frac{\partial W(t)}{\partial t} = -\frac{1}{\hbar}\sum_{\lambda\lambda'}h_{\lambda\lambda'}(R_1)\left[r_{1\lambda}\frac{\partial}{\partial p_{1\lambda'}}-p_{1\lambda}\frac{\partial}{\partial r_{1\lambda'}}\right]W(t)+\left(\frac{P_1}{M}\cdot\frac{\partial}{\partial R_1}-\frac{\partial H_{\rm m}}{\partial R_1}\cdot\frac{\partial}{\partial P_1}\right)W(t)$$
$$+\;\frac{\hbar}{8}\sum_{\lambda\lambda'}\frac{\partial h_{\lambda\lambda'}(R_1)}{\partial R_1}\cdot\left(\frac{\partial}{\partial r_{1\lambda}}\frac{\partial}{\partial r_{1\lambda'}}+\frac{\partial}{\partial p_{1\lambda'}}\frac{\partial}{\partial p_{1\lambda}}\right)\frac{\partial}{\partial P_1}W(t)$$
$$\equiv\; i\mathscr{L}_{\rm m}(x_1,X_1)W(t)$$

Here, the Wigner transform of the Hamiltonian[15] is given by

$$[22]\quad H_{\rm m} = \frac{P^2}{2M}+V_{\rm B}(R)+\sum_{\lambda\lambda'}\frac{h_{\lambda\lambda'}(R)}{2}(r_\lambda r_{\lambda'}+p_\lambda p_{\lambda'}-\delta_{\lambda\lambda'})$$

This equation of motion is one of the principal results of this paper. It results from an expansion of the evolution operator for W to order μ and is equivalent to quantum-classical Liouville dynamics for the spectral density function.[19] The first term in eq. [21] represents the subsystem dynamics of the spectral density in the mapping phase space. The second term is the dynamics of the spectral density due to classical evolution of the bath degrees of freedom and the third term is a higher order correlation between the quantum mapping and classical degrees of freedom. The last equality defines the quantum-classical Liouville operator in the mapping basis. This equation must be solved subject to the initial condition

$$[23]\quad W(\theta) = (2\pi\hbar)^{(N_{\rm b}+N)}\delta\left(r_1-r_2\right)\delta\left(R_1-R_2\right)\delta\left(p_1-p_2\right)\delta\left(P_1-P_2\right)$$

In eq. [19], since $\widehat{H}_m$ commutes with propagator $e^{i\widehat{H}_m t}$ when differentiating with respect to time, $\widehat{H}_m$ could be placed on either side of the propagator. In this derivation, we chose to put it to the left of the propagator in the first term in eq. [19] and to the right of the propagator in the second term. If instead one places $\widehat{H}_m$ to the right of the propagator in the first term and to the left of the propagator in the second term, we can obtain an alternate form of the equation of motion[35]. The manipulations are similar to those described above and in the Appendix and are not repeated her. The resulting equation of motion is

$$[24]\quad \frac{\partial W(t)}{\partial t} = +\frac{1}{\hbar}\sum_{\lambda\lambda'}h_{\lambda\lambda'}(R_2)\left[r_{2\lambda}\frac{\partial}{\partial p_{2\lambda'}}-p_{2\lambda}\frac{\partial}{\partial r_{2\lambda'}}\right]W(t)-\left(\frac{P_2}{M}\cdot\frac{\partial}{\partial R_2}-\frac{\partial H_{\rm m}}{\partial R_2}\cdot\frac{\partial}{\partial P_2}\right)W(t)$$
$$-\frac{\hbar}{8}\sum_{\lambda\lambda'}\frac{\partial h_{\lambda\lambda'}(R_2)}{\partial R_2}\cdot\left(\frac{\partial}{\partial r_{2\lambda}}\frac{\partial}{\partial r_{2\lambda'}}+\frac{\partial}{\partial p_{2\lambda'}}\frac{\partial}{\partial p_{2\lambda}}\right)\frac{\partial}{\partial P_2}W(t)$$
$$\equiv -i\mathscr{L}_m(x_2,X_2)W(t)$$

This alternate form of the dynamics not only shows the symmetry of the dynamics of W in its variables but also allows us to move the time evolution from W to the observable B_{Wm} in the correlation function expression. The formal solution of eq. [24] is

$$[25] \qquad W(X_1, X_2, x_1, x_2, t) = e^{-i\mathscr{L}_m(x_2,X_2)t} W(X_1, X_2, x_1, x_2, 0)$$

These results will be used in the next section to derive a quantum-classical approximation to the time correlation function.

6. Quantum-classical correlation function

We can now employ the results of the last two sections to find an expression for the quantum-classical approximation to the correlation function in the mapping basis. Using eq. [25] in eq. [16], we have

$$[26] \qquad C_{AB}(t) = \frac{1}{(2\pi\hbar)^{(N_b+N)}} \int dX_1 dX_2 dx_1 dx_2 \left(\widehat{\rho}_{eq}\widehat{A}\right)_{Wm}(X_1, x_1) B_{Wm}(X_2, x_2) e^{-i\mathscr{L}_m(x_2,X_2)t} W(X_1, X_2, x_1, x_2, 0)$$

Performing an integration by parts to move the evolution operator onto the B_{Wm} and integrating over the coordinates with subscript 1, making use of the delta functions in the initial value of W, yields

$$[27] \qquad C_{AB}(t) = \int dX dx (\widehat{\rho}_{eq}\widehat{A})_{W_m}(X, x) B_{W_m}(X, x, t)$$

where $B_{Wm}(X, x, t) = e^{i\mathscr{L}_m(x,X)t} B_{Wm}(X, x)$. (We have dropped the subscripts on the phase space coordinates since this notation is no longer needed.) This expression contains the full quantum equilibrium structure of the subsystem and bath and the quantum-classical Liouville evolution of the operator $\widehat{B}$ in the mapping representation.

The evolution equation for $B_{Wm}(X,x,t)$ that one obtains in this derivation is identical to that found earlier in the calculation of the average value of an observable.[12] This evolution equation can be written in the form,

$$[28] \qquad \frac{d}{dt} B_{Wm}(x, X, t) = i\mathscr{L}_m B_{Wm}(t) = -\{H_m, B_{Wm}(t)\}_{x,X} + \frac{\hbar}{8} \sum_{\lambda\lambda'} \frac{\partial h_{\lambda\lambda'}}{\partial R} \cdot \left(\frac{\partial}{\partial r_{\lambda'}} \frac{\partial}{\partial r_\lambda} + \frac{\partial}{\partial p_{\lambda'}} \frac{\partial}{\partial p_\lambda} \right) \frac{\partial}{\partial P} B_{Wm}(t)$$

where $\{\ ,\ \}_{x,X}$ denotes a Poisson bracket in the full mapping-bath phase space of the system. The quantum-classical Liouville operator in the mapping basis can be decomposed into two terms, $i\mathscr{L}_m = i\mathscr{L}^0_m + i\mathscr{L}'_m$, where

$$[29] \qquad \begin{aligned} i\mathscr{L}^0_m &= -\{H_m, \quad\}_{x,X} \\ i\mathscr{L}'_m &= \frac{\hbar}{8} \sum_{\lambda\lambda'} \frac{\partial h_{\lambda\lambda'}}{\partial R} \cdot \left(\frac{\partial}{\partial r_{\lambda'}} \frac{\partial}{\partial r_\lambda} + \frac{\partial}{\partial p_{\lambda'}} \frac{\partial}{\partial p_\lambda} \right) \frac{\partial}{\partial P} \end{aligned}$$

The $i\mathscr{L}^0_m$ evolution operator, corresponding to the Poisson bracket in eq. [28], leads to a classical-like evolution of the coupled dynamics of the quantum mapping and classical bath phase space variables that can be simulated by Newtonian trajectories. The force field that the classical variables feel varies with time as a result of the dependence of the forces on the mapping phase space variables. If $i\mathscr{L}'_m$ is dropped in the evolution equation, $B_{Wm}(t)$ has a solution in terms of characteristics. The set of ordinary differential equations that determines its solution is

$$[30] \qquad \begin{aligned} \frac{dr_\lambda(t)}{dt} &= \frac{1}{\hbar} \sum_{\lambda'} h_{\lambda\lambda'}(R(t)) p_{\lambda'}(t) \\ \frac{dp_\lambda(t)}{dt} &= -\frac{1}{\hbar} \sum_{\lambda'} h_{\lambda\lambda'}(R(t)) r_{\lambda'}(t) \\ \frac{dR(t)}{dt} &= \frac{P(t)}{M}, \frac{dP(t)}{dt} = -\frac{\partial H_m}{\partial R(t)} \end{aligned}$$

The utility of this approximation to eq. [28] is a topic of current research. Tests of its accuracy have been carried out on the spin-boson model where eq. [28] is equivalent to full quantum dynamics and are being carried out on other model systems with nonlinear coupling between the quantum and classical degrees of freedom where eq. [28] is not exact. For the spin-boson model, eq. [30] yields results that are indistinguishable from the known exact quantum results for this system.[12] Tests being carried out on other model systems show that while the results are often in close accord with exact quantum results, sometimes discrepancies are observed that cannot be ascribed to approximations in eq. [28] for these more general interactions, and must be attributed to the use of eq. [30] for the dynamics. Consequently, further research is underway to fully characterize the contributions arising from $i\mathscr{L}'_m$ and construct algorithms that account for its action.

7. Conclusion

In the adiabatic basis, the correlation function may be evaluated in terms of an ensemble of surface-hopping trajectories.[5,7] While this simulation scheme has been used in a number of applications it is difficult to obtain accurate results for long times because of the presence of oscillating terms in the Monte Carlo sampling. In this paper, we show that it is possible to reformulate the calculation of the correlation function in the mapping basis. Simulation schemes based on this formulation do not suffer from some of the problems that arise in the implementation of surface-hopping schemes.

To evaluate the expression for the correlation function obtained in this paper, two ingredients are required. The expression involves an average over the full quantum equilibrium structure. As briefly discussed above, the computation of quantum equilibrium structure is a more tractable problem than the calculation of quantum dynamics. Nevertheless, approximations are usually required to evaluate the equilibrium structure. In the high-temperature limit it is possible to derive analytical expressions that are useful in many applications.[36–38]

The main result of this paper is the quantum-classical expression for the correlation function that involves time evolution of the quantum subsystem in the mapping basis. Provided the quantum-classical evolution is approximated by $i\mathscr{L}_m \simeq i\mathscr{L}_m^0$, the time evolution of the dynamical variable in the correlation function can be computed easily by solving a set of Newtonian-like equations. Thus, difficulties associated with the accumulation of Monte Carlo weights in the evaluation of an oscillatory function that arise in the surface-hopping solution of the quantum-classical Liouville equation in the adiabatic basis are by-passed. Of course, this simple scheme relies on the ability to neglect $i\mathscr{L}_m'$, which accounts for higher-order correlations in the dynamics. Thus, the focus of future research is on the characterization of the nature of the dynamics generated by $i\mathscr{L}_m'$ and the construction of simulation algorithms that account for its presence. The results in this paper form the basis for future applications to the calculation of transport properties, such as rate constants for nonadiabtic chemical reactions.

Acknowledgement

This work was in part supported by a grant from the Natural Science and Engineering Research Council of Canada (NSERC). AN acknowledges the support from the Lachlan Gilchrist fellowship.

References

(1) This article is part of a Special Issue dedicated to Professor T. Ziegler.
(2) Other forms of quantum correlation functions are useful in applications. These include symmetrized and Kubo transformed forms. Since relations exist among these correlation functions,[3] we restrict our considerations to this expression.
(3) Kubo, R. *Rep. Prog. Phys.* **1966**, *29*, 255. doi:10.1088/0034-4885/29/1/306.
(4) Kapral, R. *Annu. Rev. Phys. Chem.* **2006**, *57*, 129. doi:10.1146/annurev.physchem.57.032905.104702. PMID:16599807.
(5) Kapral, R.; Ciccotti, G. *J. Chem. Phys.* **1999**, *110*, 8919. doi:10.1063/1.478811.
(6) Grunwald, R.; Kelly, A.; Kapral, R. In *Energy transfer dynamics in biomaterial systems: Series in chemical physics*; Burghardt, I., Bittner, E., May, V., Micha, D. Eds.; Springer: NY. In press.
(7) Sergi, A.; Mac Kernan, D.; Ciccotti, G.; Kapral, R. *Theor. Chem. Acc.* **2003**, *110*, 49.
(8) Mac Kernan, D. M.; Ciccotti, G.; Kapral, R. *J. Phys. Chem. B* **2008**, *112*, 424. doi:10.1021/jp0761416. PMID:18154283.
(9) Donoso, A.; Martens, C. *J. Phys. Chem. A* **1998**, *102*, 4291. doi:10.1021/jp980219o.
(10) Wan, C.; Schofield, J. *J. Chem. Phys.* **2000**, *113*, 7047. doi:10.1063/1.1313525.
(11) Wan, C.; Schofield, J. *J. Chem. Phys.* **2002**, *116*, 494. doi:10.1063/1.1425835.
(12) Kim, H.; Nassimi, A.; Kapral, R. *J. Chem. Phys.* **2008**, *129* (8), 084102. doi:10.1063/1.2971041.
(13) Wigner, E. *Phys. Rev.* **1932**, *40*, 749. doi:10.1103/PhysRev.40.749.
(14) Hillery, M.; O'Connell, R.; Scully, M.; Wigner, E. *Phys. Rep.* **1984**, *106*, 121. doi:10.1016/0370-1573(84)90160-1.
(15) Imre, K.; Ozizmir, E.; Rosenbaum, M.; Zweifel, P. *J. Math. Phys.* **1967**, *8*, 1097. doi:10.1063/1.1705323.
(16) Filinov, V.; Medvedev, Y.; Kamskyi, V. *Mol. Phys.* **1995**, *85*, 711. doi:10.1080/00268979500101421.
(17) Filinov, V. *Mol. Phys.* **1996**, *88*, 1517. doi:10.1080/00268979650025605.
(18) Filinov, V. *Mol. Phys.* **1996**, *88*, 1529. doi:10.1080/00268979650025614.
(19) Sergi, A.; Kapral, R. *J. Chem. Phys.* **2004**, *121*, 7565. doi:10.1063/1.1797191.
(20) Poulsen, J.; Nyman, G.; Rossky, P. *J. Chem. Phys.* **2003**, *119*, 12179. doi:10.1063/1.1626631.
(21) Shi, Q.; Geva, E. *J. Chem. Phys.* **2003**, *118*, 8173. doi:10.1063/1.1564814.
(22) Schwinger, J. In *Quantum Theory of Angular Momentum*; Biedenharn, L.C., Van Dam, H. Eds., Academic Press: NY, 1965; p. 229.
(23) Holstein, T.; Primakoff, H. *Phys. Rev.* **1940**, *58*, 1098. doi:10.1103/PhysRev.58.1098.
(24) Stock, G.; Thoss, M. *Phys. Rev. Lett.* **1997**, *78*, 578. doi:10.1103/PhysRevLett.78.578.
(25) Muller, U.; Stock, G. *J. Chem. Phys.* **1998**, *108*, 7516. doi:10.1063/1.476184.
(26) Thoss, M.; Stock, G. *Phys. Rev. A* **1999**, *59*, 64. doi:10.1103/PhysRevA.59.64.
(27) Stock, G.; Thoss, M. In *Advances in Chemical Physics*; Wiley-IEEE: NY, 2005; Vol. 131, p. 560.
(28) Miller, W.; McCurdy, C. *J. Chem. Phys.* **1978**, *69*, 5163. doi:10.1063/1.436463.
(29) Sun, X.; Wang, H.; Miller, W. *J. Chem. Phys.* **1998**, *109*, 7064. doi:10.1063/1.477389.
(30) Miller, W. *J. Phys. Chem. A* **2001**, *105*, 2942. doi:10.1021/jp003712k.
(31) Bonella, S.; Coker, D. *J. Chem. Phys.* **2003**, *118*, 4370. doi:10.1063/1.1542883.
(32) Bonella, S.; Coker, D. *J. Chem. Phys.* **2005**, *122*, 194102. doi:10.1063/1.1896948.
(33) Dunkel, E.; Bonella, S.; Coker, D. *J. Chem. Phys.* **2008**, *129*, 114106. doi:10.1063/1.2976441.
(34) Since the harmonic oscillators are fictitious we may set $m\omega$ to 1 to simplify these expressions; however, we retain these forms both to make dimensional consistency manifest and to simplify the dynamical relations (see Section 5) by equating m to the quantum subsystem characteristic mass and ω to the inverse of the scaling time.

(35) If $\widehat{H}_m$ is placed in other locations, say, either to the right or left in both terms, the evolution operator for W is the mean of the two forms discussed in the text.
(36) Kim, H.; Hanna, G.; Kapral, R. *J. Chem. Phys.* **2006**, *125*, 084509. doi:10.1063/1.2336778.
(37) Kim, H.; Kapral, R. *J. Chem. Phys.* **2005**, *122*, 214105. doi:10.1063/1.1925268.
(38) Hanna, G.; Kapral, R. *J. Chem. Phys.* **2008**, *128*, 164520. doi:10.1063/1.2907847.

Appendix: Derivation of the dynamics

In this appendix, we give the details of the calculations needed to obtain the quantum-classical evolution equation for the spectral density function. There are ten terms in eq. [20], and because of the symmetry of the expression, it is convenient to group term i with term $i + 5$ and evaluate the contributions group by group. First, we perform the integrals over Q and q. The first and sixth terms contain $\frac{\partial^2}{\partial \tilde{Z}_1^2}$ and $\frac{\partial^2}{\partial \tilde{Z}_2^2}$, respectively, after this integration. Integration by parts with respect to $\tilde{Z}_1$ and $\tilde{Z}_2$ and summation of the results yield $\mu P_1 \cdot \frac{\partial W}{\partial R_1}$. The second and seventh terms involve bath potentials. After expansion of $V_B(R_1 \pm \frac{\mu \tilde{Z}_1}{2})$ in μ, the first and third terms in the series, which are proportional to μ^0 and μ^2, cancel, and the second terms, which are proportional to μ, yield $-\mu \frac{\partial V_B(R_1)}{\partial R_1} \cdot \frac{\partial W}{\partial P_1}$. The contribution from the fifth and tenth terms is derived similarly to yield $\frac{\mu}{2} \frac{\partial \mathrm{Tr}(h)}{\partial R_1} \cdot \frac{\partial W}{\partial P_1}$. The derivations of the third and eighth and also the fourth and fifth groups of terms are more complicated and are presented in the following two subsections.

Third and eighth terms

The sum of the third and eighth contributions to the time derivative of W is

$$[A1] \quad \left(\frac{\partial W}{\partial t}\right)_{3+8} = \frac{i\mu^{2N_b}}{2} \sum_{\lambda\lambda'} \int d\tilde{Z}_1 d\tilde{Z}_2 dz_1 dz_2 e^{-i(P_1\cdot\tilde{Z}_1 + P_2\cdot\tilde{Z}_2 + p_1\cdot z_1 + p_2\cdot z_2)}$$
$$\times \left\{ \left[h_{\lambda\lambda'}(R_1) + \frac{\partial h_{\lambda\lambda'}(R_1)}{\partial R_1} \cdot \frac{\mu\tilde{Z}_1}{2} \right] \left[r_{1\lambda} r_{1\lambda'} + r_{1\lambda} z_{1\lambda'}/2 + z_{1\lambda} r_{1\lambda'}/2 + z_{1\lambda} z_{1\lambda'}/4 \right] \right.$$
$$\left. - \left[h_{\lambda\lambda'}(R_1) - \frac{\partial h_{\lambda\lambda'}(R_1)}{\partial R_1} \cdot \frac{\mu\tilde{Z}_1}{2} \right] \left[r_{1\lambda} r_{1\lambda'} - r_{1\lambda} z_{1\lambda'}/2 - z_{1\lambda} r_{1\lambda'}/2 + z_{1\lambda} z_{1\lambda'}/4 \right] \right\}$$
$$\times \left\langle r_1 + \frac{z_1}{2} \middle| \left\langle R_1 + \frac{\mu\tilde{Z}_1}{2} \middle| e^{i\widehat{H}_m t} \middle| R_2 - \frac{\mu\tilde{Z}_2}{2} \right\rangle \middle| r_2 - \frac{z_2}{2} \right\rangle$$
$$\times \left\langle r_2 + \frac{z_2}{2} \middle| \left\langle R_2 + \frac{\mu\tilde{Z}_2}{2} \middle| e^{-i\widehat{H}_m t} \middle| R_1 - \frac{\mu\tilde{Z}_1}{2} \right\rangle \middle| r_1 - \frac{z_1}{2} \right\rangle$$

where we have performed a McLauren expansion of $h_{\lambda\lambda'}$ in the small parameter μ, and retained the first two terms. Finally, using the fact that a partial differential with respect to momentum acting on the exponential term has the same effect as multiplication by the variable z_1 or $\tilde{Z}_1$ that results from the expansion, we have

$$[A2] \quad \left(\frac{\partial W}{\partial t}\right)_{3+8} = \frac{i\mu^{2N_b}}{2} \sum_{\lambda\lambda'} \int d\tilde{Z}_1 d\tilde{Z}_2 dz_1 dz_2 \left\{ ih_{\lambda\lambda'}(R_1) \left[r_{1\lambda} \frac{\partial}{\partial p_{1\lambda'}} + r_{1\lambda'} \frac{\partial}{\partial p_{1\lambda}} \right] \right.$$
$$\left. + \frac{\mu}{2} \frac{\partial h_{\lambda\lambda'}(R_1)}{\partial R_1} \cdot \left(i \frac{\partial}{\partial P_1} \right) \left[2 r_{1\lambda} r_{1\lambda'} - \frac{1}{2} \frac{\partial}{\partial p_{1\lambda}} \frac{\partial}{\partial p_{1\lambda'}} \right] \right\} e^{-i(P_1\cdot\tilde{Z}_1 + P_2\cdot\tilde{Z}_2 + p_1\cdot z_1 + p_2\cdot z_2)}$$
$$\times \left\langle r_1 + \frac{z_1}{2} \middle| \left\langle R_1 + \frac{\mu\tilde{Z}_1}{2} \middle| e^{i\widehat{H}_m t} \middle| R_2 - \frac{\mu\tilde{Z}_2}{2} \right\rangle \middle| r_2 - \frac{z_2}{2} \right\rangle$$
$$\times \left\langle r_2 + \frac{z_2}{2} \middle| \left\langle R_2 + \frac{\mu\tilde{Z}_2}{2} \middle| e^{-i\widehat{H}_m t} \middle| R_1 - \frac{\mu\tilde{Z}_1}{2} \right\rangle \middle| r_1 - \frac{z_1}{2} \right\rangle$$
$$= -\frac{1}{2} \sum_{\lambda\lambda'} h_{\lambda\lambda'}(R_1) \left[r_{1\lambda} \frac{\partial}{\partial p_{1\lambda'}} + r_{1\lambda'} \frac{\partial}{\partial p_{1\lambda}} \right] W$$
$$- \frac{\mu}{4} \sum_{\lambda\lambda'} \frac{\partial h_{\lambda\lambda'}(R_1)}{\partial R_1} \cdot \left[2 r_{1\lambda} r_{1\lambda'} - \frac{1}{2} \frac{\partial}{\partial p_{1\lambda}} \frac{\partial}{\partial p_{1\lambda'}} \right] \frac{\partial}{\partial P_1} W$$

where in the last equality the expression for the scaled W is inserted.

Fourth and ninth terms

The sum of the fourth and ninth terms in eq. [20] is

$$
\begin{aligned}
[A3]\qquad \left(\frac{\partial W}{\partial t}\right)_{4+9} = &-\frac{i\mu^{2N_b}}{2}\int d\tilde{Z}_1 d\tilde{Z}_2 dz_1 dz_2 \sum_{\lambda\lambda'}\Bigg\{\Bigg[h_{\lambda\lambda'}\left(R_1+\frac{\mu\tilde{Z}_1}{2}\right)\frac{\partial}{\partial\left(r_1+\frac{z_1}{2}\right)_\lambda}\frac{\partial}{\partial\left(r_1+\frac{z_1}{2}\right)_{\lambda'}}\\
&\times\left\langle r_1+\frac{z_1}{2}\middle|\left\langle R_1+\frac{\mu\tilde{Z}_1}{2}\middle|e^{i\widehat{H}_m t}\middle|R_2-\frac{\mu\tilde{Z}_2}{2}\right\rangle\middle|r_2-\frac{z_2}{2}\right\rangle\Bigg]\\
&\times\left\langle r_2+\frac{z_2}{2}\middle|\left\langle R_2+\frac{\mu\tilde{Z}_2}{2}\middle|e^{-i\widehat{H}_m t}\middle|R_1-\frac{\mu\tilde{Z}_1}{2}\right\rangle\middle|r_1-\frac{z_1}{2}\right\rangle\\
&-\Bigg\{h_{\lambda\lambda'}\left(R_1-\frac{\mu\tilde{Z}_1}{2}\right)\frac{\partial}{\partial\left(r_1-\frac{z_1}{2}\right)_\lambda}\frac{\partial}{\partial\left(r_1-\frac{z_1}{2}\right)_{\lambda'}}\\
&\times\left\langle r_2+\frac{z_2}{2}\middle|\left\langle R_2+\frac{\mu\tilde{Z}_2}{2}\middle|e^{-i\widehat{H}_m t}\middle|R_1-\frac{\mu\tilde{Z}_1}{2}\right\rangle\middle|r_1-\frac{z_1}{2}\right\rangle\Bigg]\\
&\times\left\langle r_1+\frac{z_1}{2}\middle|\left\langle R_1+\frac{\mu\tilde{Z}_1}{2}\middle|e^{i\widehat{H}_m t}\middle|R_2-\frac{\mu\tilde{Z}_2}{2}\right\rangle\middle|r_2-\frac{z_2}{2}\right\rangle\Bigg\}e^{-i(P_1\cdot\tilde{Z}_1+P_2\cdot\tilde{Z}_2+p_1\cdot z_1+p_2\cdot z_2)}\\
=&-\frac{i\mu^{2N_b}}{2}\sum_{\lambda\lambda'}\int d\tilde{Z}_1 d\tilde{Z}_2 dz_1 dz_2\Bigg\{\Bigg[\left(h_{\lambda\lambda'}(R_1)+\frac{\partial h_{\lambda\lambda'}(R_1)}{\partial R_1}\frac{\mu\tilde{Z}_1}{2}\right)\\
&\times\frac{\partial}{\partial r_{1\lambda}}\frac{\partial}{\partial r_{1\lambda'}}\left\langle r_1+\frac{z_1}{2}\middle|\left\langle R_1+\frac{\mu\tilde{Z}_1}{2}\middle|e^{i\widehat{H}_m t}\middle|R_2-\frac{\mu\tilde{Z}_2}{2}\right\rangle\middle|r_2-\frac{z_2}{2}\right\rangle\Bigg]\\
&\times\left\langle r_2+\frac{z_2}{2}\middle|\left\langle R_2+\frac{\mu\tilde{Z}_2}{2}\middle|e^{-i\widehat{H}_m t}\middle|R_1-\frac{\mu\tilde{Z}_1}{2}\right\rangle\middle|r_1-\frac{z_1}{2}\right\rangle\\
&-\Bigg[\left(h_{\lambda\lambda'}(R_1)-\frac{\partial h_{\lambda\lambda'}(R_1)}{\partial R_1}\frac{\mu\tilde{Z}_1}{2}\right)\frac{\partial}{\partial r_{1\lambda}}\frac{\partial}{\partial r_{1\lambda'}}\left\langle r_2+\frac{z_2}{2}\middle|\left\langle R_2+\frac{\mu\tilde{Z}_2}{2}\middle|e^{-i\widehat{H}_m t}\middle|R_1-\frac{\mu\tilde{Z}_1}{2}\right\rangle\middle|r_1-\frac{z_1}{2}\right\rangle\Bigg]\\
&\times\left\langle r_1+\frac{z_1}{2}\middle|\left\langle R_1+\frac{\mu\tilde{Z}_1}{2}\middle|e^{i\widehat{H}_m t}\middle|R_2-\frac{\mu\tilde{Z}_2}{2}\right\rangle\middle|r_2-\frac{z_2}{2}\right\rangle\Bigg\}e^{-i(P_1\cdot\tilde{Z}_1+P_2\cdot\tilde{Z}_2+p_1\cdot z_1+p_2\cdot z_2)}
\end{aligned}
$$

Again, in the second equality we have carried out a McLauren expansion of $h_{\lambda\lambda'}$ to first order in μ. Equation [A3] itself has four terms. In the sum of the first and third subcontributions, one of the partial derivatives over r may be replaced by a partial derivative over z, and an integration by parts may be carried out. We find

$$
\begin{aligned}
[A4]\qquad &\frac{i\mu^{2N_b}}{2}\sum_{\lambda\lambda'}h_{\lambda\lambda'}(R_1)\int d\tilde{Z}_1 d\tilde{Z}_2 dz_1 dz_2 e^{-i(P_1\cdot\tilde{Z}_1+P_2\cdot\tilde{Z}_2+p_1\cdot z_1+p_2\cdot z_2)}\\
&\times\Bigg\{\Bigg[2\frac{\partial}{\partial r_{1\lambda'}}\left\langle r_1+\frac{z_1}{2}\middle|\left\langle R_1+\frac{\mu\tilde{Z}_1}{2}\middle|e^{i\widehat{H}_m t}\middle|R_2-\frac{\mu\tilde{Z}_2}{2}\right\rangle\middle|r_2-\frac{z_2}{2}\right\rangle\\
&\times\left(\frac{\partial}{\partial z_{1\lambda}}-ip_{1\lambda}\right)\left\langle r_2+\frac{z_2}{2}\middle|\left\langle R_2+\frac{\mu\tilde{Z}_2}{2}\middle|e^{-i\widehat{H}_m t}\middle|R_1-\frac{\mu\tilde{Z}_1}{2}\right\rangle\middle|r_1-\frac{z_1}{2}\right\rangle\Bigg]\\
&-\Bigg[(-2)\frac{\partial}{\partial r_{1\lambda'}}\left\langle r_2+\frac{z_2}{2}\middle|\left\langle R_2+\frac{\mu\tilde{Z}_2}{2}\middle|e^{-i\widehat{H}_m t}\middle|R_1-\frac{\mu\tilde{Z}_1}{2}\right\rangle\middle|r_1-\frac{z_1}{2}\right\rangle\\
&\times\left(\frac{\partial}{\partial z_{1\lambda}}-ip_{1\lambda}\right)\left\langle r_1+\frac{z_1}{2}\middle|\left\langle R_1+\frac{\mu\tilde{Z}_1}{2}\middle|e^{i\widehat{H}_m t}\middle|R_2-\frac{\mu\tilde{Z}_2}{2}\right\rangle\middle|r_2-\frac{z_2}{2}\right\rangle\Bigg]\Bigg\}\\
&=\sum_{\lambda\lambda'}h_{\lambda\lambda'}(R_1)p_{1\lambda}\frac{\partial}{\partial r_{1\lambda'}}W
\end{aligned}
$$

Here, we see that the two terms with a momentum multiplier are added together, while the other terms cancel each other.

The second and fourth subcontributions in eq. [A3] are treated in the following way: We replace multiplication by the variable $\tilde{Z}$ with a partial differentiation with respect to the momentum. Furthermore, the sum of these contributions is written as one half the sum of two equal contributions, the expressions appearing in eq. [A3] and the same expression but with the differentials over r replaced with those over z. Thus, the sum of the second and fourth contributions can be written as

$$
\begin{aligned}
[A5]\qquad & \frac{i\mu^{2N_b}}{2}\sum_{\lambda\lambda'}h_{\lambda\lambda'}(R_1)\int \mathrm{d}\tilde{Z}_1\mathrm{d}\tilde{Z}_2\mathrm{d}z_1\mathrm{d}z_2 e^{-i(P_1\cdot\tilde{Z}_1+P_2\cdot\tilde{Z}_2+p_1\cdot z_1+p_2\cdot z_2)} \\
& \times\left\{\left[2\frac{\partial}{\partial r_{1\lambda'}}\left\langle r_1+\frac{z_1}{2}\middle|\left\langle R_1+\frac{\mu\tilde{Z}_1}{2}\middle|e^{i\widehat{H}_m t}\middle|R_2-\frac{\mu\tilde{Z}_2}{2}\right\rangle\middle|r_2-\frac{z_2}{2}\right\rangle\right.\right. \\
& \times\left(\frac{\partial}{\partial z_{1\lambda}}-ip_{1\lambda}\right)\left\langle r_2+\frac{z_2}{2}\middle|\left\langle R_2+\frac{\mu\tilde{Z}_2}{2}\middle|e^{-i\widehat{H}_m t}\middle|R_1-\frac{\mu\tilde{Z}_1}{2}\right\rangle\middle|r_1-\frac{z_1}{2}\right\rangle\Bigg] \\
& -\left[(-2)\frac{\partial}{\partial r_{1\lambda'}}\left\langle r_2+\frac{z_2}{2}\middle|\left\langle R_2+\frac{\mu\tilde{Z}_2}{2}\middle|e^{-i\widehat{H}_m t}\middle|R_1-\frac{\mu\tilde{Z}_1}{2}\right\rangle\middle|r_1-\frac{z_1}{2}\right\rangle\right. \\
& \left.\left.\times\left(\frac{\partial}{\partial z_{1\lambda}}-ip_{1\lambda}\right)\left\langle r_1+\frac{z_1}{2}\middle|\left\langle R_1+\frac{\mu\tilde{Z}_1}{2}\middle|e^{i\widehat{H}_m t}\middle|R_2-\frac{\mu\tilde{Z}_2}{2}\right\rangle\middle|r_2-\frac{z_2}{2}\right\rangle\right]\right\} \\
& =\sum_{\lambda\lambda'}h_{\lambda\lambda'}(R_1)p_{1\lambda}\frac{\partial}{\partial r_{1\lambda'}}W
\end{aligned}
$$

If in both expressions we replace $\frac{\partial^2 A}{\partial x\partial y}B+A\frac{\partial^2 B}{\partial x\partial y}$ with $\frac{\partial^2(AB)}{\partial x\partial y}-\frac{\partial A}{\partial x}\frac{\partial B}{\partial y}-\frac{\partial A}{\partial y}\frac{\partial B}{\partial x}$, the cross terms cancel. Finally, integrating by parts over $z_{1\lambda}$ and $z_{1\lambda'}$, we obtain

$$
[A6]\qquad \frac{\mu}{8}\sum_{\lambda\lambda'}\frac{\partial h_{\lambda\lambda'}(R_1)}{\partial R_1}\cdot\left(\frac{\partial}{\partial r_{1\lambda}}\frac{\partial}{\partial r_{1\lambda'}}-4p_{1\lambda}p_{1\lambda'}\right)\frac{\partial}{\partial P_1}W
$$

Summing all the contributions from the above calculations, we find the comparatively simple result

$$
\begin{aligned}
[A7]\qquad \frac{\partial W}{\partial t} &= -\sum_{\lambda\lambda'}h_{\lambda\lambda'}(R_1)\left[r_{1\lambda}\frac{\partial}{\partial p_{1\lambda'}}-p_{1\lambda}\frac{\partial}{\partial r_{1\lambda'}}\right]W \\
&+\ \mu P_1\cdot\frac{\partial W}{\partial R_1}-\mu\frac{\partial V_B(R_1)}{\partial R_1}\cdot\frac{\partial W}{\partial P_1}-\frac{\mu}{2}\sum_{\lambda\lambda'}\frac{\partial h_{\lambda\lambda'}(R_1)}{\partial R_1}\cdot\left(r_{1\lambda}r_{1\lambda'}+p_{1\lambda}p_{1\lambda'}-\delta_{\lambda\lambda'}\right)\frac{\partial}{\partial P_1}W \\
&+\ \frac{\mu}{8}\sum_{\lambda\lambda'}\frac{\partial h_{\lambda\lambda'}(R_1)}{\partial R_1}\cdot\left(\frac{\partial}{\partial r_{1\lambda}}\frac{\partial}{\partial r_{1\lambda'}}+\frac{\partial}{\partial p_{1\lambda}}\frac{\partial}{\partial p_{1\lambda'}}\right)\frac{\partial}{\partial P_1}W
\end{aligned}
$$

Restoring unscaled coordinates, we have eq. [21] in the text.

Mechanisms for anionic butadiene polymerization with alkyl lithium species[1]

Peter Margl

Abstract: Anionic butadiene polymerization by means of [Li-polybutadienyl]$_x$ species (x = 1–6, 8) without polar agents was investigated by means of density functional theory (DFT) under conditions relevant to industrial application, namely in a low-dielectric hydrocarbon solvent and at room temperature. The calculations indicate that the dimeric and tetrameric catalyst species together account for the bulk of Li-polybutadienyl species in the polymerization mixture under typical conditions. It is likely that each type of oligomer produces its own "fingerprint" signature polymer microstructure, as there is a systematic variation in the amounts of 1,2- and 1,4-insertions as well as in the preference of *cis*- and *trans*-butadiene. According to the calculations, higher aggregated Li species tend to produce more 1,2-insertions and prefer *trans*- over *cis*-butadiene insertion, while the dimer prefers *trans*-butadiene and 1,4-insertions. The dimer closely reproduces the experimentally observed polybutadiene microstructure (5%–10% 1,2-insertion, approximately equal ratios of cis and trans units with a slight predominance of trans). The monomeric catalyst species shows a clear preference for insertion of *cis*-butadiene over *trans*-butadiene. Thus, the monomer species is predicted to be present in the polymerization mixture in very small concentrations under normal conditions and the overall polymerization is predicted to be mainly carried out by the dimeric catalyst species.

Key words: anionic polymerization, density functional theory, polymer microstructure.

Résumé : On a étudié la polymérisation anionique du butadiène à l'aide d'espèces [Li-polybutadiényle]$_x$ (x = 1–6, 8), sans agents polaires en faisant appel à la théorie de la fonctionnelle de densité, dans des conditions intéressantes pour une application industrielle, telle celle en solution dans un solvant hydrocarboné de faible coefficient diélectrique et à la température ambiante. Les calculs indiquent que les espèces dimères et tétramères du catalyseur prises ensemble correspondent à pratiquement l'ensemble des espèces Li-polybutadiényles dans le mélange de polymérisation, dans des conditions typiques. Il est probable que chaque type d'oligomère conduit à une microstructure de polymère qui lui est propre puisqu'on observe des variations systématiques dans les quantités d'insertions 1,2- et 1,4- ainsi que dans la formation préférentielle des *cis*- et *trans*-butadiènes. D'après les calculs, les espèces lithiées plus agrégées ont tendance à produire plus d'insertions 1,2 ainsi qu'une formation préférentielle *trans*-butadiènes par rapport aux *cis*- alors que les espèces dimères ont tendance à produire plus d'insertions 1,4. Le dimère permet de bien reproduire la microstructure observée expérimentalement pour le polybutadiène (5 % à 10 % d'insertion-1,2, des rapports approximativement égaux d'unités *cis*- et *trans*- avec une légère prédominance pour le trans). Les espèces du catalyseur monomère présentent une préférence marquée pour l'insertion de *cis*-butadiène par rapport au *trans*-butadiène. On peut donc prédire que l'espèce monomère n'est présente dans le mélange de polymérisation qu'à de très faibles concentrations, dans les conditions normales, et que la polymérisation globale est effectuée par les espèces du catalyseur dimère.

Mots-clés : polymérisation anionique, théorie de la fonctionnelle de la densité, microstructure d'un polymère.

[Traduit par la Rédaction]

Introduction

Living anionic polymerization is a powerful tool to produce tailor made polymers.[2] The anionic polymerization of butadiene and butadiene/styrene copolymerization is commonly initiated by alkyl lithium compounds. Such processes are commercially used to obtain polybutadiene products for high-impact plastic modification, random styrene butadiene rubber for tire tread compounds, and thermoplastic block copolymers. The area of application depends strongly on the structure of the polymer and its resulting performance characteristics. In these processes, the polymerization is generally performed in nonpolar hydrocarbon solvents. The microstructure (trans-, cis-,[3] 1,2-, and 1,4-incorporation of butadiene and sequence distribution of the styrene monomer) can be varied by the addition of polar compounds, e.g., diglyme, THF, or diethylether.

Industrial demand for ever more sophisticated polymer applications requires manufacturers of butadiene and butadiene/styrene polymers to be able to control the polymer microstructure more effectively. The research and development process for meeting this demand is generally heuristic, and modifications to alkyl-lithium-initiated polymerization towards a particular polymer microstructure are often made by using a trial-and-error method, which is expensive in terms of time and resources. Few, if any, quantitative methods exist to relate a polymer microstructure to the agents involved in the polymerization. Hence, new approaches are required to modulate and predict the micro-

Received 14 January 2009. Published on the NRC Research Press Web site at canjchem.nrc.ca on 11 May 2009.

P. Margl. Core R&D, The Dow Chemical Company, Midland, MI 48674-1776, USA. (e-mail: PMMargl@dow.com).

Fig. 1. Mechanism for butadiene (BD) polymerization. Top: initiation leading from butyl lithium to allyl lithium. Middle: 1-carbon attack leading to a linear polymer. Bottom: 3-carbon attack leading to formation of a pendant vinyl chain. Only the trans isomers are shown for simplicity.

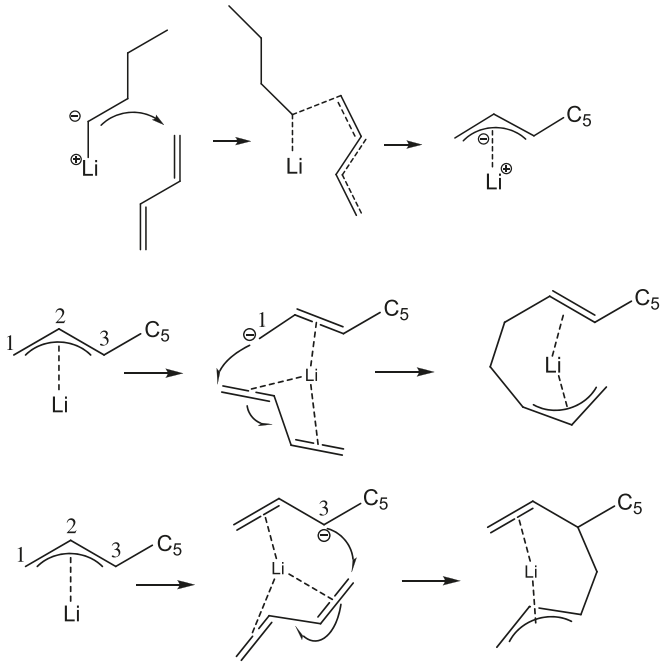

structure of the final polymer and to investigate the possibility of obtaining new products. For true microstructure engineering, a mechanism-based simulation method is desirable to assess and eventually predict the impact and effectiveness of a particular agent upon the anionic polymerization and the resulting microstructure of the polymer. A detailed understanding of the species occurring in the living polymerization mixture and their reactivities towards each other is the necessary first step towards such a predictive model.

Alkyl lithium compounds are believed to initiate butadiene polymerization by an anionic mechanism, whereby the anionic alkyl moiety acts as a nucleophile towards an olefinic monomer (Fig. 1, top). The alkyl chain attaches itself to the monomer, which then forms the new active chain end that continues the polymerization by nucleophilic attack upon the next monomer (propagation; Fig. 1, middle and bottom). The propagation step may proceed by nucleophilic attack from either the 1-carbon or the 3-carbon of the allyl chain upon the 1-carbon of the butadiene monomer. In the former case, this results in a so-called 1,4-insertion and formation of a straight chain polymer (Fig. 1, middle), whereas the latter process results in 1,2-insertion and formation of a pendant vinyl chain (Fig. 1, bottom).

The alkyl lithium chain initiators are known to exist as oligomeric or polymeric clusters in the solid state[4–8] as well as in solution.[9–13] In the postinitiation phase, all or most of the alkyl Li initiator has been converted to the allyl Li propagator species and the Li species is thought to exist in a variety of oligomeric or polymeric states.[14–17,18] The degree of aggregation, x, for polybutadienyl lithium is usually put at $x = 4$ for a wide range of concentrations.[19] Stellbrink and co-workers[14] were able to assemble a relationship between the aggregation number and the degree of butadiene polymerization in which x decays exponentially with the degree of polymerization and levels off at at a tetrameric ($x = 4$) aggregation for high monomer conversions. Throughout polymerization, giant aggregates with $x >> 1000$ were also observed, but decayed with increasing butadiene conversion.

Since the chain initiation event itself, to a first approximation, does not determine microstructure, we will review it here only insofar as it is necessary to form a basis for the understanding of the propagation reaction. However, we find it useful to establish a common baseline with prior research by applying our simulation method to the speciation of *n*-butyl lithium, which is a commonly used initiation agent. Despite its industrial importance and widespread use, anionic butadiene polymerization by alkyl lithium initiators has garnered comparatively little attention from the theoretical community. The complex, oligomeric nature of both the alkyl lithium initiator and the propagator species make molecular simulations difficult. For alkyl lithium initiator species, Verstraete et al.[20] have recently given an excellent computational description of various geometries and energetics in the gas phase. For very small aggregation numbers of the allyl lithium propagator species, Schleyer and coworkers[21] have undertaken investigations by means of Møller–Plesset theory, as have Pratt and Khan[22] by means of density functional theory (DFT). More recently, Klein and co-workers[23] have investigated the initiation and propagation steps for isoprene in the presence of monomeric ethyl lithium by first-principles molecular dynamics. Frischknecht and Milner[18] have investigated small and medium-sized aggregates of allyl lithium using the PM3 and DFT methods, with allyl lithium clusters ranging up to $x = 12$. To the best knowledge of the authors, no study to date has attempted to systematically investigate the chain propagation kinetics of relevant allyl lithium clusters for anionic butadiene polymerization by means of mechanistic, first-principles simulations. As a necessary first step towards a comprehensive, mechanistic understanding of anionic styrene/butadiene polymerization by allyl lithium, we are presenting here first-principles simulations of the chain propagation process for alkyl lithium initiated polymerization of butadiene in a nonpolar hydrocarbon solvent in the absence of any polar additives.

As our primary tool, we are using density functional theory[24] (DFT), which has consistently yielded valuable insights in a number of areas in chemistry and catalysis. The density functional calculations are performed in solution phase using the COSMO method.[25] Details of computations and their parameters can be found in the Computational section.

The present work is divided into three logical parts: In the first part, we establish a common baseline with preceding research. In the second part, we discuss various modes of chain propagation for anionic polymerization of butadiene. In the third and last part, we compare our findings with experimental data.

Results and discussion

Initiator species

To establish a common baseline with prior computational data and to gauge the effect of solvation upon the agglomer-

Table 1. Energies of $(n\text{-BuLi})_x$ clusters in solution (ε = 2) and in the gas phase (ε = 1).

	ε = 2		ε = 1		
x/(Sym)	*E**	E_B†	*E**	E_B†	Reference 20
1/(Cs)	–165.37981	0	–165.35878	0	0
2/(C2h)	–330.80032	–53	–330.78444	–88	–82.7
3/(C3h)	–496.21380	–65	–496.20350	–111	–109.6
4/(S4)	–661.64169	–80	–661.63009	–128	–127.2
5/(C5h)	–827.02648	–67	–827.00663	–112	–114.0
6/(S6)	–992.46429	–81	–992.45992	–134	–135.3
8/(S8)	–1323.27225	–77	–1323.26470	–129	—

*Total energy in hartree atomic units.
†Binding energy per Li in kJ/mol relative to separate *n*-BuLi units according to eq. [1].

Table 2. Energies of $[(allyl)Li]_x$ clusters.

x/(Sym)	*E**	$\Delta H(g)^\dagger$	$\Delta S(g)^\dagger$	$\Delta S(s)^\ddagger$	E_B§	G_B§,‡
1/(C1)	–321.46478	0.1318	343	258	0	0
2/(Ci)	–642.96232	0.2659	551	413	–43	–25
3/(C3)	–964.44661	0.4005	750	562	–46	–20
4/(S4)	–1285.94241	0.5345	891	668	–55	–23
5/(C1)	–1607.41477	0.6690	1084	813	–48	–14
6/(S6)	–1928.90854	0.8037	1255	941	–52	–17
8/(S8)	–2571.85666	1.0702	1621	1216	–45	–9

*Total energy in hartree atomic units in solution (ε = 2).
†Calculated at the 6-31G/ BP/ε = 1 level of theory with Gaussian 03. ΔH includes the zero-point energy and finite temperature effects to the energy and the enthalpy computed for 298.15 K. ΔS is given in J/mol/K.
‡Scaling factor of 0.75 applied to gas-phase entropy.
§Binding energy in kJ/mol relative to separate (allyl)Li units.

ation energies, we calculated the ground state geometries and energies of $(n\text{-BuLi})_x$ (x = 1–6, 8) clusters, where x is the degree of agglomeration. The resulting geometry types are very similar to the ones obtained by Verstraete et al.[20] The total energies obtained in the gas phase as well as in the solution phase are shown in Table 1.

The gas-phase binding energies, E_B, for clusters composed of x monomers were computed according to eq. [1], and agree very well with the binding energies presented by Verstraete et al.,[20] although these authors used a different density functional.

$$[1] \qquad E_B[x] = (E_x - x \cdot E_{monomer})/x$$

Here, E_x is the density functional total energy of oligomer of the degree of agglomeration, x. It appears that E_B reaches a minimum at x = 6, although the binding energy differences between x = 4, 6, and 8 are relatively small. On introducing a nonpolar solvent (ε = 2), a steep decrease in binding energy occurs. The binding energy is decreased by 40%–50% in going from the gas phase to solution phase. This steep drop in binding energy indicates that a large fraction of the binding energy is electrostatic. For a pure electrostatic bond, the interaction energy scales with 1/ε, and thus is expected to decrease by 50% if the dielectric contant changes from vacuum (ε = 1) to a solution with ε = 2. However, no relative structural changes are observed between the structures of the individual clusters. The most stable structure (x = 6) calculated in the gas phase is also the most stable structure in solution, and also the one detected in the X-ray analysis of the solid.[26] These results indicate that our method adequately reproduces the data given by prior calculation, but that inclusion of solvent effects, even for low dielectric solvents, is essential to the description of the system, as it substantially decreases the driving force to agglomeration.

Fig. 2. Binding energies of various $[(ally)Li]_x$ oligomers on a per monomer basis, according to eq. [1] (E_B) and eq. [2] (G_B).

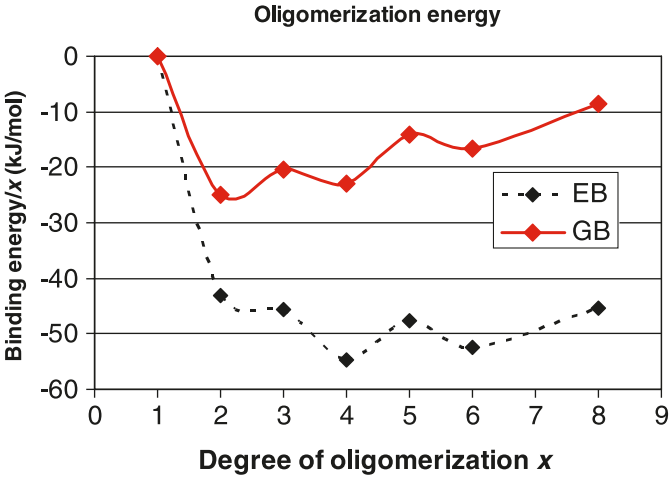

Chain propagation

Propagator species

Having found good agreement between our description of *n*-butyl lithium aggregation and data from the literature,[2,20] we performed calculations on the allyl lithium chain propa-

Fig. 3. $[(\text{Allyl})\text{Li}]_x$ structures for $x = 1$, 2, and 3.

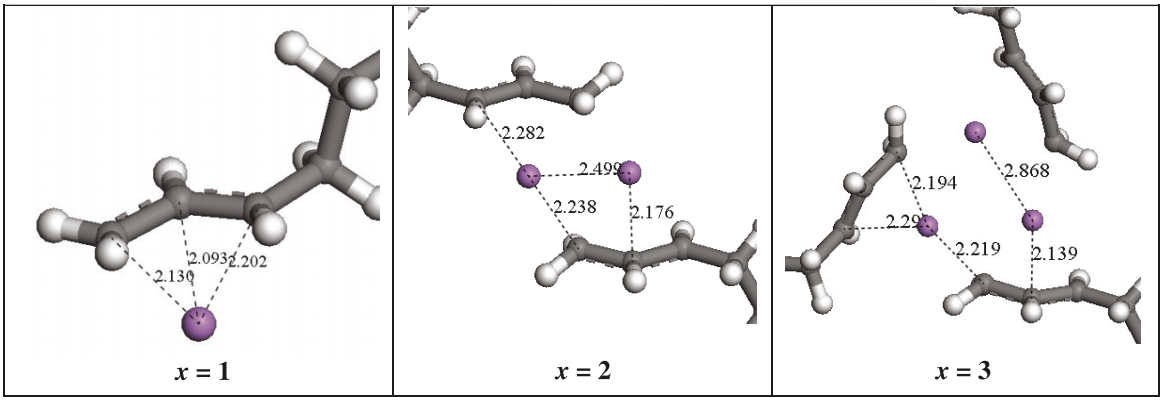

gator to obtain the nature of the active propagating species. In the same manner as above, we calculated the ground state geometries and energies of $[(n\text{-oct-2-en-1-yl})\text{Li}]_x$ (x = 1–6, 8) clusters. The *n*-oct-2-en-1-yl group was chosen since it naturally arises as the allyl species formed after the first insertion of butadiene into the Li–*n*-butyl bond. In the following, we will refer to the *n*-oct-2-en-1-yl group simply as "allyl".

From a comparison of the binding-energy columns, E_B, for solution phase ($\varepsilon = 2$) in Table 1 and Table 2 it is immediately apparent that the allyl intermediates oligomerize with substantially less driving force than the *n*-alkyl intermediates. This is due to the interaction of the allyl π system with the Li ions. The π-allyl group occupies more of the available space around each metal and thus imposes steric hindrance to further oligomerization. Further examination of Table 2 and Fig. 2 shows that the strongest per monomer binding energy occurs for $x = 4$ and 6 for the allyl system, similar to what is observed for the *n*-alkyl system (Table 1). *Free* energies of oligomerization in solution, G_B, (Table 2), which determine the amount of agglomeration in the system, may be derived from vibrational analyses of the oligomers in the gas phase according to the expression

$$[2] \quad G_B[x] = \{[E_x + \Delta H(g)_x - T\Delta S(s)_x] - x \cdot [E_{monomer} + \Delta H(g)_{monomer} - T\Delta S(s)_{monomer}]\}/x$$

In this expression, $\Delta H(g)_x$ is a thermodynamic correction applied to E_x, consisting of the zero-point energy and statistical-mechanic contributions to the enthalpy, as computed in the gase phase. $\Delta S(s)$ is the entropy of oligomer x as computed in the gas phase, corrected for the loss of entropy that accompanies transfer of a gas-phase species to solution.[27–29] This is achieved by scaling the computed gas-phase entropies $\Delta S(g)$ by a factor of 0.75 to arrive at the expression for the solution phase entropy, $\Delta S(s) = 0.75 \cdot \Delta S(g)$. This factor is approximated from data given in Abraham's paper,[29] which shows an approximate reduction of the gas-phase entropy of 20%–30% upon transfer to cyclohexane solution for polyatomic molecules.

Figure 2 shows the free energies of oligomerization G_B derived using eq. [2] at 298.15 K. It is apparent that the dimer ($x = 2$) and the tetramer ($x = 4$) are the species with the lowest free energy; the dimer being slightly favored over the tetramer. The trimer is less stable than the tetramer by a small amount (3 kJ/mol on a per Li basis). The energies of oligomerization, E_B, computed from the raw density functional energetics according to eq. [1] are also given.

Experimentally, the aggregation state of polybutadienyl lithium appears to be a complicated equilibrium of dimers, tetramers, and higher aggregation states up to giant agglomerates of $x >> 1000$.[14–19,30] Niu et al.[14] have found that the observed value of x decreases as the degree of polymerization increases, and levels off at $x \sim 4$, which agrees with our finding that the tetramer is among the most stable species. Experiment did not clarify completely whether the large aggregates consist of mixed initiator/propagator species.[14] Also, it is not entirely clear from experiment which of the oligomeric or polymeric states of polybutadienyl lithium are responsible for chain propagation.

In light of the fact that the experimental determination of the species distribution of the Li polybutadienyl system is approximate and considering that the computed free energy difference between dimer (–25 kJ/mol), trimer (–20 kJ/mol), and tetramer species (–23 kJ/mol) is close to the expected accuracy of our computations (see Computational section), we will assume throughout the remainder of this work that both the dimer, trimer, and tetramer are available for chain propagation to a similar extent.

The allyl-Li monomer (Fig. 3; left) has a well-expressed π-allyl structure, with carbons 1–3 bound tightly. It is important to note that the 1-carbon has a somewhat closer bond to Li than the 3-carbon, which will become important in the subsequent discussion of chain propagation transition states. The corresponding lowest-energy dimer (Fig. 3; middle) has C_i symmetry. In this dimer, the 1-carbon binds approximately to the midpoint of the Li–Li vector, while carbons 2 and 3 bind in π-fashion to one of the Li atoms. The Li–Li distance is shorter (2.5 Å) than in the higher oligomers. The C_3-symmetric trimer (Fig. 3; right) has the Li atoms arranged in an equilateral triangle with Li–Li distances of 2.87 Å. As in the dimer, the 1-carbon binds to the midpoint of the Li–Li vector while carbons 2 and 3 π-bond one of the Li atoms.

As shown in Fig. 4, the $[(\text{allyl})\text{Li}]_x$ structures with $x = 4$, 5, 6, and 8 have a nonplanar arrangement of Li atoms. The Li atoms in the tetramer form an irregular tetrahedron, whereas the Li atoms in the hexamer and octamer form tri-

Fig. 4. [(Allyl)Li]$_x$ structures for x = 4, 5, 6, and 8.

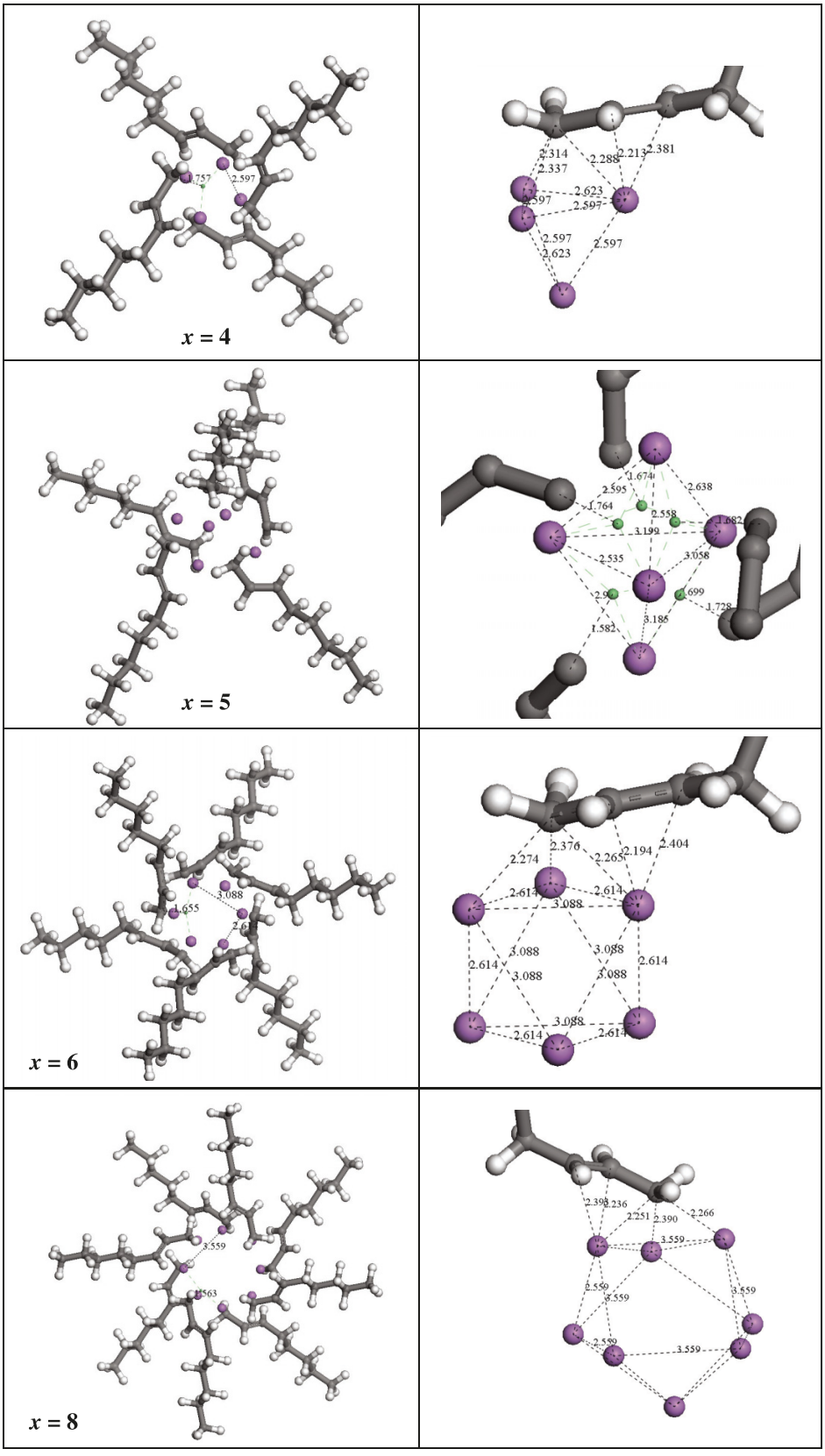

Table 3. Insertion energetics for butadiene into *cis*- and *trans*-[(allyl)Li] in solution (ε = 2).

Chain	BD isomer	Mode	E^*	$E^\dagger$	Chain	BD isomer	Mode	E^*	$E^\dagger$
Trans	Trans	1,4	–477.48717	21	Cis	Trans	1,4	–477.48442	26
Trans	Cis	1,4	–477.49216	8	Cis	Cis	1,4	–477.49154	7
Trans	Trans	1,2	–477.48915	16	Cis	Trans	1,2	–477.48816	16
Trans	Cis	1,2	–477.49170	9	Cis	Cis	1,2	–477.48804	17

*Total energy (DNP/BP/ε = 2) of the transition state in hartree atomic units.
†Activation energy in kJ/mol relative to separate allyl-Li and *trans*-butadiene.

angular and square antiprisms. The allyl chains can conveniently be considered to be connected through the 1-carbon atom to the midpoint of the isosceles triangles that form the sides of the antiprisms (x = 6, 8) or the faces of the tetrahedron (x = 4). With increasing x, the 1-carbon of the allyl chain becomes bound more closely to the midpoint of the triangle formed by the Li atoms (tetramer: 1.76 Å; hexamer: 1.66 Å; octamer: 1.56 Å). However, the π-bond distances between carbons 2 and 3 and Li stay approximately the same at 2.2–2.4 Å. The three lowest-energy $[(allyl)Li]_x$ (x = 4, 6, 8) structures have S_x symmetry. The pentamer is a somewhat special case in that the lowest energy isomer found here is of C_1 symmetry. The Li atoms in the pentamer are arranged in a distorted trigonal bipyramid, with three of the allyl chains bound to the midpoints of the triangles formed by the Li atoms of the "upper" pyramid, and the remaining two allyl chains bound to the "lower" pyramid, whereby one of the latter is bound to an edge as opposed to a surface.

Propagation from the monomer

The cis and trans isomers[31] of (allyl)Li are schematically shown in Fig. 5, together with their total and relative energies. The cis isomer is less stable by only 2 kJ/mol than the trans isomer.

Insertion may proceed by attack of either the 1-carbon or the 3-carbon of the allyl terminus of the growing chain, as shown in Fig. 1. Attack of the 1-carbon on the 1-position of butadiene (BD) leads to linear chain extension (1,4-insertion; Fig. 1, middle), whereas attack of the 3-carbon leads to formation of a pendant vinyl chain (1,2-insertion; Fig. 1, bottom). The allyl terminus of the growing chain may either have cis or trans geometry (Fig. 5). Taking into account these two factors (insertion mode and terminal isomer) as well as the fact that the inserting butadiene may either be the cis or trans isomer leads to eight (2 × 2 × 2) different insertion pathways for chain propagation from a single (allyl)Li unit.

Table 3 presents the activation energies for these eight propagation pathways, classified by the chain end isomer, the isomer of butadiene, and the insertion mode. The barriers ($E^\dagger$) are calculated relative to free *trans*- or *cis*-(allyl)Li and free *trans*-butadiene.

Examination of Table 3 shows that the barriers for insertion as measured from the isolated reactants are rather low, with the largest barrier just 26 kJ/mol above the dissociation limit of the reactants.[32] There is little difference between insertions into a trans chain end and a cis chain end. Except in one case, insertion of *cis*-butadiene into a particular chain end for a particular insertion mode is faster than insertion of *trans*-butadiene. 1,4-Insertions of *cis*-butadiene are fastest, and 1,4-insertions of *trans*-butadiene are slowest.

Fig. 5. Schematic of monomer structures used for modeling the insertion of butadiene into (*trans*-allyl)Li (left) and (*cis*-allyl)Li (right), together with their density functional total energies and relative energies (DNP/BP/ε = 2).

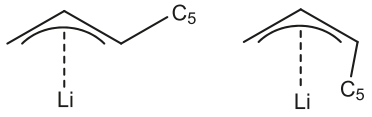

–321.4647812
0 kJ/mol

–321.4638607
2 kJ/mol

These differences between insertion paths are explained by Fig. 6, which shows the transition-state geometries for insertion into a growing chain terminated by *trans*-allyl. During insertion of *cis*-butadiene (Figs. 6*c* and 6*d*), all carbon atoms of the butadiene moiety maintain close contact to the Li atom, thus stabilizing the *cis*-BD transition state relative to the *trans*-BD one, in which the monomer cannot maintain the same degree of contact. This generally favors insertion of *cis*-BD over insertion of *trans*-BD.

1,2-Insertion of *trans*-BD ($E^\dagger$ = 16 kJ/mol) is faster than 1,4-insertion of *trans*-BD (21 kJ/mol < $E^\dagger$ < 26 kJ/mol). This is because the transition state for 1,2-insertion allows the Li atom to move towards the 1-carbon of the growing allyl chain, which is able to bind Li more strongly than the 3-carbon atom, as outlined in Fig. 3, left.

Propagation from the dimer

As shown by Table 2, the lowest energy $[(allyl)Li]_2$ species is formed from the monomer in a reaction that is 86 kJ/mol exothermic (–43 kJ/mol per monomer). Thus, a significant amount of energy would be needed to create the monomer species. However, the significantly more stable dimer species is also able to propagate the chain as outlined in Fig. 1. The dimer species that are considered for chain propagation are shown in Fig. 7, which shows the three lowest-energy $[(allyl)Li]_2$ structures with all-trans, cis/trans, and cis/cis chain ends, respectively. For simulating the insertion process into cis and trans chain ends, the all-trans and cis/trans isomers were used as they were lowest in energy.

Table 4 summarizes the insertion energetics derived with these models. A comparison with the corresponding Li monomer energetics shown in Table 3 shows that insertion of butadiene into a chain growing from an (allyl)Li dimer has a higher activation barrier (46 kJ/mol < $E^\dagger$ < 60 kJ/mol) than insertion into the corresponding (allyl)Li monomer bound chain (7 kJ/mol < $E^\dagger$ < 26 kJ/mol). The difference in the insertion barriers of *cis*- and *trans*-butadiene is less pronounced than for the (allyl)Li monomer based pathways. Cis insertion barriers are consistently higher than trans insertion barriers by 2–6 kJ/mol. 1,2-Insertions have consistently

Table 4. Insertion energetics for butadiene into the cis and trans allyl groups of all-*trans*- and *cis*/*trans*-[(allyl)Li]$_2$, respectively.

All-*trans*-[(allyl)Li]$_2$					*Cis*/*trans*-[(allyl)Li]$_2$				
Chain	BD isomer	Mode	E*	$E^{\dagger}$	Chain	BD isomer	Mode	E*	$E^{\dagger}$
Trans	Trans	1,4	–798.97521	46	Cis	Trans	1,4	–798.97206	49
Trans	Cis	1,4	–798.97422	48	Cis	Cis	1,4	–798.97093	52
Trans	Trans	1,2	–798.97219	54	Cis	Trans	1,2	–798.97028	54
Trans	Cis	1,2	–798.97018	59	Cis	Cis	1,2	–798.96785	60

*Total energy (DNP/BP/ε = 2) of transition state in hartree atomic units.
†Activation energy in kJ/mol relative to separate [(allyl)Li]$_2$ and *trans*-butadiene.

Fig. 6. Transition-state geometries for insertion of *trans*- ((*a*) and (*b*)) and *cis*-butadiene ((*c*) and (*d*)) into a growing chain with *trans*-allyl terminus. (*a*) and (*c*) show 1-carbon attack, (*b*) and (*d*) shown 3-carbon attack.

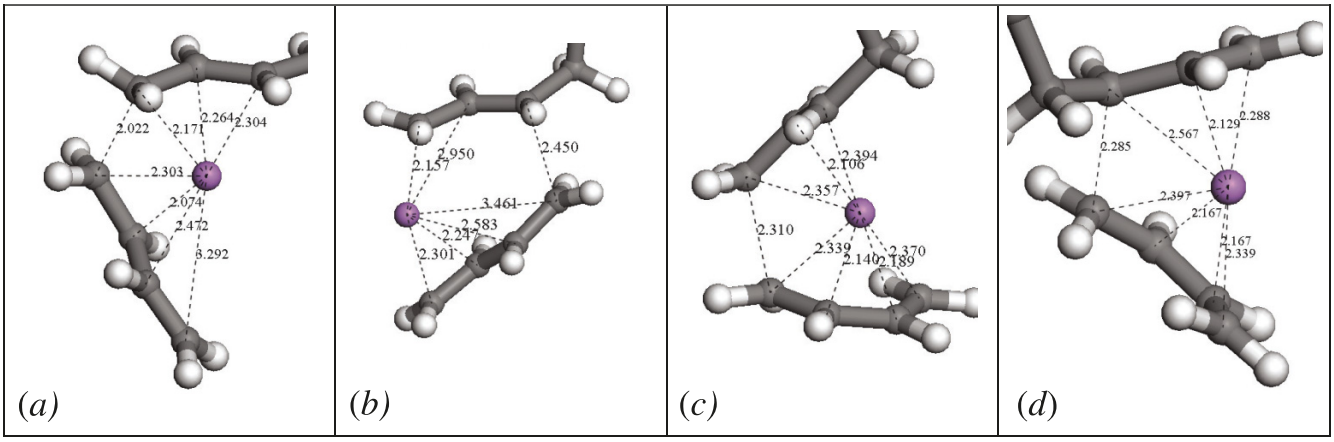

Fig. 7. Schematic of dimer structures used for modeling the insertion of butadiene into *trans*-(allyl)Li (left) and *cis*-(allyl)Li (middle). The structure to the right was not used for the study of propagation steps as it is higher in energy. Density functional total energies (DNP/BP/ε = 2) and relative energies in kJ/mol are given below each structure.

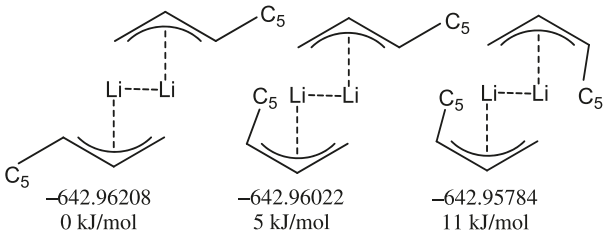

higher barriers than 1,4-insertions by approximately 5–10 kJ/mol.

The reasons for these trends can be rationalized by examining the three-dimensional structures for the (allyl)Li dimer based transition states as shown in Fig. 8 and drawn out schematically in Fig. 9.

Of the two allyl chain ends in the dimer, one partakes in the insertion process, whereas the other forms a spectator. Both lithium atoms, however, are intimately involved in stabilizing the reacting organic fragments during the transition state. The spectator ligand effectively reduces the binding surface available to the incoming butadiene and thus forces the transition state to a higher energy as compared to the monomer-based transition states in Table 3. However, due to the relatively large binding area that the Li dimer exposes towards allylic chain ends and incoming monomer, both the butadiene moiety and the chain end can maintain effective contact to Li at the transition state. This is especially apparent for 1,4-insertions (Figs. 8*a* and 8*c*).

Propagation from the trimer

The insertion energetics for two trimer species (Fig. 10), namely all-*trans*-[(*n*-oct-2-en-1-yl)Li][(*n*-pent-2-en-1-yl)Li]$_2$ and [(*cis*-*n*-oct-2-en-1-yl)Li][(*trans*-*n*-pent-2-en-1-yl)Li]$_2$, are given in Table 5. We chose to use pentenyl chains for the spectator allyl ligands as they significantly reduce computational overhead and do not significantly impact our results.

First, one notices that the barriers to 1,4-insertion into trimer-borne allyl chains are higher than for dimer- and monomer-borne allyl species. Barriers to 1,2-insertion are similar to 1,2-insertion barriers observed for dimer-borne chains. Secondly, it appears that 1,4-insertions have consistently higher barriers than 1,2-insertions, which is a reversal of the behavior observed for monomer- and dimer-based behavior. 1,2-Insertions are favored by 1–15 kJ/mol over the analogous 1,4-insertions. Also, insertion of *trans*-BD tends to have lower barriers than insertion of *cis*-BD.

Figure 11 schematically depicts the two different insertion pathways (1,4- and 1,2-insertion) occurring at a trimeric Li-allyl propagator. Both pathways are analogous to the pathways for the dimeric propagators shown in Fig. 9, in that they involve two lithium ions for stabilizing the organic fragments during the transition state. The difference between the trimer- and dimer-facilitated insertions lies in the fact that the lithium atoms in the trimer are more sterically

Fig. 8. Transition-state geometries for insertion of *trans*- ((*a*) and (*b*)) and *cis*-butadiene ((*c*) and (*d*)) into a chain growing from an all-*trans*-[(allyl)Li]$_2$. (*a*) and (*c*) show 1,4-insertions, (*b*) and (*d*) shown 1,2-insertions.

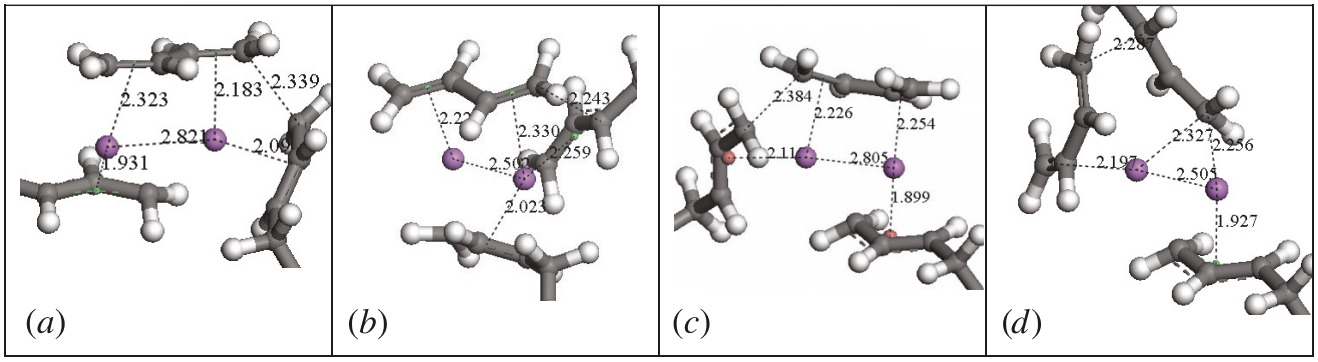

Fig. 9. Schematic drawing of butadiene insertion by 1-carbon attack (top) and 3-carbon attack (bottom) with a dimeric propagator species.

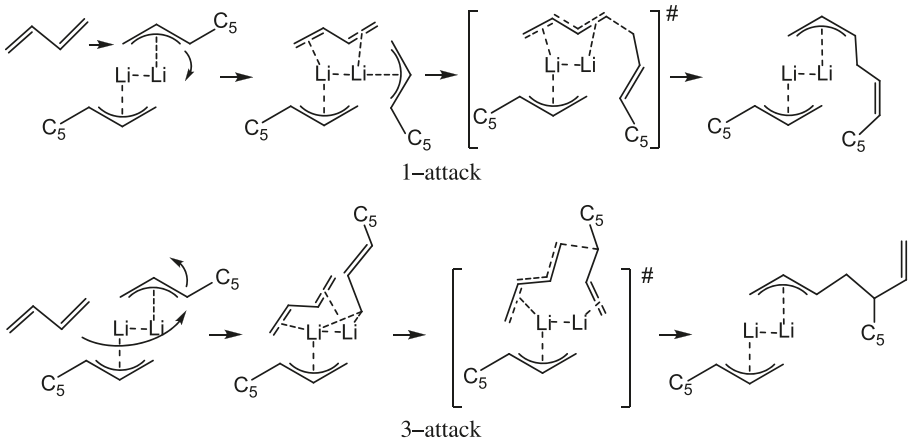

Fig. 10. Schematic of trimer structures used for modeling the insertion of butadiene into (*trans*-allyl)Li (left) and (*cis*-allyl)Li (right). Density functional total energies (DNP/BP/ε = 2) and relative energies in kJ/mol are given below each structure.

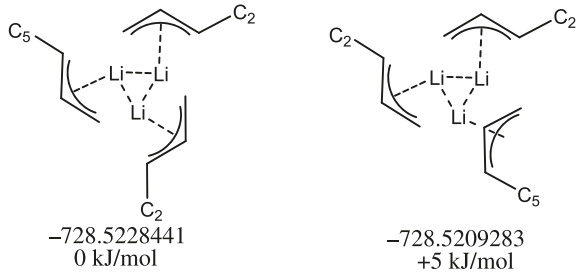

shielded, which makes it less straightforward to stabilize the transition state. This especially causes a rise in the activation barriers to 1,4-insertion, which is sterically more demanding than 1,2-insertion, because the 1-carbon that provides binding for the chain end during 1,2-insertion binds more strongly to Li than the 3-carbon atom that anchors the chain during 1,4-insertion (as seen in Fig. 6*b*). This results in a kinetic preference for 1,2-insertion.

Propagation from the tetramer

Figure 12 shows the two model systems used for simulation of butadiene insertion barriers into a butadienyl chain growing from an (allyl)Li tetramer.

As seen in Fig. 4, the lithium atoms in the tetramer are effectively shielded. This makes it harder for the incoming butadiene to stabilize itself during the transition state, and leads to comparatively high butadiene insertion barriers both during 1-carbon attack and 3-carbon attack (Table 6). Barriers range from 86 to 104 kJ/mol, which is at least 20 kJ/mol higher than what was computed for the trimer. Barriers related to 1,4-insertion are consistently higher than barriers related to 1,2-insertion by approximately 10 kJ/mol.

The reason for this becomes apparent on examination of the reaction schematics in Fig. 13. Both 1- and 3-carbon attacks can be regarded as occurring on a Li tetrahedron, three of whose faces are covered with allyl groups (oriented towards the bottom of Fig. 13). The fourth face (oriented towards the top) provides the reaction site. The incoming butadiene attacks the allyl group at the top, and partially displaces it. Throughout the transition state, both 1- and 3-carbon attack pathways derive stabilization from a close interaction of the organic moieties with the Li cluster. For the 1-carbon attack (1,4-insertion), the arrangement of spectator allyl groups around the central Li tetrahedron crowds the top face so strongly that approach of the butadiene towards the 1-carbon is only possible from the top, leading to an energetically unfavorable transition-state energy for 1,4-insertion. For 3-carbon attack (1,2-insertion), the incoming butadiene monomer is able to approach the top allyl from the side, allowing both the 1-carbon as well as the monomer to keep tight contact with the Li atoms of the cluster. Hence, 1,2-insertion is favored for the tetramer.

Table 5. Insertion energetics for butadiene into the cis and trans allyl groups of all-*trans*- and *cis*/*trans*-[(allyl)Li]$_3$, respectively.

all-*trans*-[(*n*-alk-2-enyl)Li]$_3$					*cis*$_1$/*trans*$_2$-[(*n*-alk-2-enyl)Li]$_3$				
Chain	BD isomer	Mode	*E**	*E*†	Chain	BD isomer	Mode	*E**	*E*†
Trans	Trans	1,4	–884.5307	60	Cis	Trans	1,4	–884.5309	54
Trans	Cis	1,4	–884.5277	67	Cis	Cis	1,4	–884.5276	63
Trans	Trans	1,2	–884.5350	48	Cis	Trans	1,2	–884.5313	53
Trans	Cis	1,2	–884.5334	53	Cis	Cis	1,2	–884.5302	56

*Total energy (DNP/BP/ε = 2) of transition state in hartree atomic units.
†Activation energy in kJ/mol relative to separate [(allyl)Li]$_3$ and *trans*-butadiene.

Fig. 11. Schematic drawing of butadiene insertion by 1-carbon attack (top) and 3-carbon attack (bottom) with a trimeric propagator species.

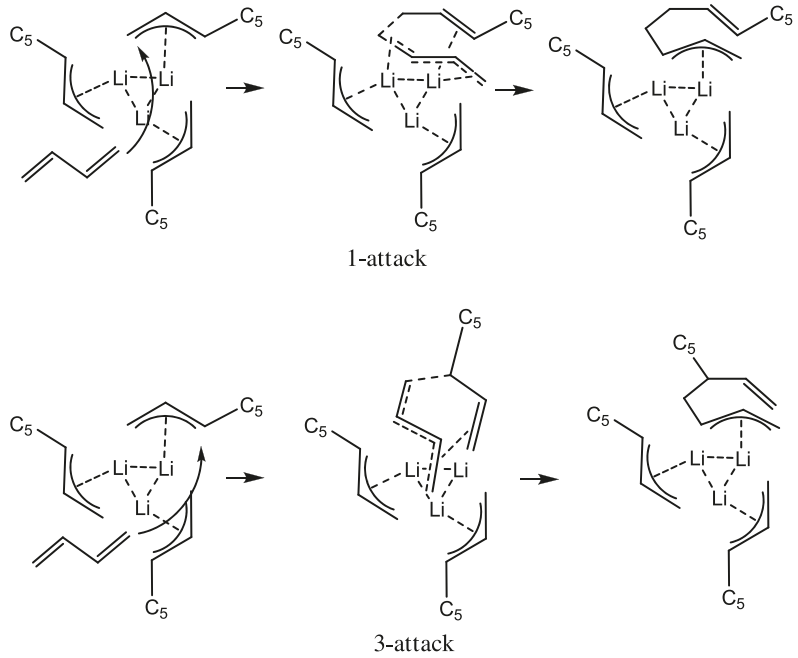

Fig. 12. Schematic of tetramer structures used for modeling the insertion of butadiene into *trans*-(allyl)Li (left) and *cis*-(allyl)Li (right).

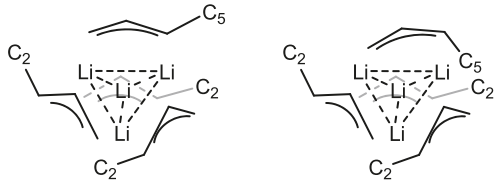

Propagation from the higher oligomers (x = 5, 6, 8)

Propagation from the higher oligomers with aggregation numbers of 5 and above was investigated only in a cursory manner. For $x = 5$, our calculations indicated that the pentamer was simply too unstable to be considered a serious candidate for polymerization, and no insertion transition-state calculations were attempted. For $x = 6$, insertion transition-state calculations with some amount of conformational sampling were done and showed that insertion of butadiene into chains growing off a hexamer would have prohibitively high barriers (>110 kJ/mol) in addition to a relatively small population of the hexamer itself. Hence, no detailed conformational sampling was done on these preliminary transition states and propagation from the hexamer is not deemed feasible. For $x = 8$, it was clear that the octamer was not present in significant amounts under the most favorable conditions imaginable in the present context, as its per monomer binding free energy is –9 kJ/mol (Table 2). The progression of insertion barriers from monomer to tetramer (Table 3–5) also did not make it likely that propagation from the octamer would be kinetically feasible. Thus, propagation from the octamer was excluded.

Comparison of polymerization kinetics

Figures 14*a*–14*d* compares butadiene insertion energetics for species with $x = 1$–4, using the thermodynamically most stable dimer species as a reference point. In this figure, the recombination energetics of relevant (allyl)Li oligomers are combined with butadiene insertion barriers to give a simple, yet meaningful impression of the accessibility of insertion transition states based on different oligomers. Figure 14 uses a relative free energy *y*-axis. For the relative thermodynamics of different oligomers, we use the free energy values as tabulated in Table 2. For free energy barriers of insertion, which we have not calculated explicitly, we use the approximation that the free energy barrier of insertion is composed according to $\Delta G^\dagger = \Delta E^\dagger - T\Delta S^\dagger$, where $\Delta E^\dagger$ is taken directly from Tables 3–6 and $T\Delta S^\dagger$ is approximated as

Table 6. Insertion energetics for butadiene into the cis and trans allyl groups of all-*trans*- and *cis*$_1$/*trans*$_3$-[(allyl)Li]$_4$, respectively.

All-*trans*-[(*n*-alk-2-enyl)Li]$_4$					*Cis*$_1$/*trans*$_3$-[(*n*-alk-2-enyl)Li]$_4$				
Chain	BD isomer	Mode	*E**	$E^{\dagger}$	Chain	BD isomer	Mode	*E**	$E^{\dagger}$
Trans	Trans	1,4	–1088.0473	104	Cis	Trans	1,4	–1088.0465	99
Trans	Cis	1,4	–1088.0492	99	Cis	Cis	1,4	–1088.0448	103
Trans	Trans	1,2	–1088.0539	86	Cis	Trans	1,2	–1088.0512	86
Trans	Cis	1,2	–1088.0501	96	Cis	Cis	1,2	–1088.0485	93

*Total energy (DNP/BP/ε = 2) of transition state in hartree atomic units.
†Activation energy in kJ/mol relative to separate [(allyl)Li]$_4$ and *trans*-butadiene.

Fig. 13. Schematic drawing of butadiene insertion by 1-carbon attack (top) and 3-carbon attack (bottom) with a tetrameric propagator species.

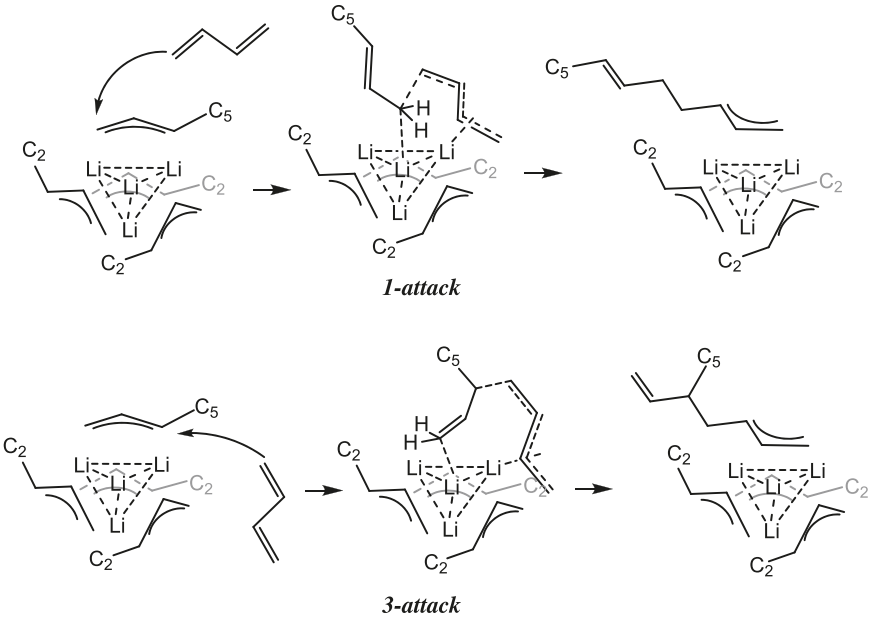

–40 kJ/mol at 298.15 K. The value of –40 kJ/mol is an approximation of the entropy loss occurring on bringing two molecules together into one and may therefore be regarded as constant over a series of similar reactions.[27,33] Although a value for $T\Delta S^{\dagger}$ of –40 kJ/mol for a bimolecular reaction appears typical from the literature, further support can be obtained by calculating the entropic correction for association between (allyl)Li and butadiene to form the corresponding insertion transition state. For this reaction, a $T\Delta S^{\dagger}_{(298.15)}$ correction of –60 kJ/mol is obtained. Applying the correction factor of 0.75 introduced above, one arrives at 45 kJ/mol for $T\Delta S^{\dagger}_{(298.15)}$ in solution, which agrees well with our standard value of –40 kJ/mol. The $T\Delta S^{\dagger}$ contributions to the insertion barrier are shown in grey, on top of the $\Delta E^{\dagger}$ values.

The monomer (Fig. 14*a*) is most efficiently created by dissociation of a dimer unit. This process is uphill in terms of free energy by 25 kJ/mol on a per monomer basis, and involves an activation barrier of 86 kJ/mol. The monomer created by this process can then insert butadiene with activation energies as low as $\Delta E^{\dagger}$ = 7 kJ/mol (Table 3). Although the propagation step from the monomer is kinetically favorable, we believe that production of the monomer itself is slow, with an effective barrier of approximately 86 kJ/mol.

The thermodynamically most efficient route to create a trimer is by recombination of three dimer units into two trimer units (Fig. 14*c*). This process is uphill by only 13 kJ/mol free energy on a per trimer basis (1.5 dimer → trimer). However, the lowest-energy butadiene insertion barrier is $\Delta E^{\dagger}$ = 48 kJ/mol above the separated trimer and butadiene reactants. This makes the total barrier relative to the (allyl)Li dimer over 100 kJ/mol in terms of free energy.

The tetramer is most efficiently created by dimerization of two dimers (Fig. 14*d*). This process is marginally endoergic (+8 kJ/mol). However, the lowest-energy butadiene insertion barrier is $\Delta E^{\dagger}$ = 86 kJ/mol high, which brings the barrier relative to the dimer up to $\Delta G^{\dagger}$ = 134 kJ/mol.

Compared to the barrier for insertion into the (resting state) dimer ($\Delta E^{\dagger}$ = 46 kJ/mol; $\Delta G^{\dagger}$ = 86 kJ/mol; Fig. 14*b*), trimer- and tetramer-based insertion transition states are not accessible from a mere thermodynamic standpoint. However, insertion into a monomer-borne allyl chain appears competitive, having an approximate barrier of 86 kJ/mol. Thus, the activation energies of monomer- and dimer-based insertions are sufficiently close that the evidence of the present calculations alone cannot rule out one in favor of the other.

We are now in a position to compare the computed butadiene polymerization behavior with the experimentally ob-

Fig. 14. From left to right: Free-energy reaction profiles for butadiene insertion into monomer, dimer, trimer, and tetramer species. Black annotations are free energies, $\Delta E^{\dagger}$ values are activation energies taken from Tables 3–6, and $T\Delta S^{\dagger}$ contributions to insertion barriers are shown in grey. All values in kJ/mol, at 298.15 K.

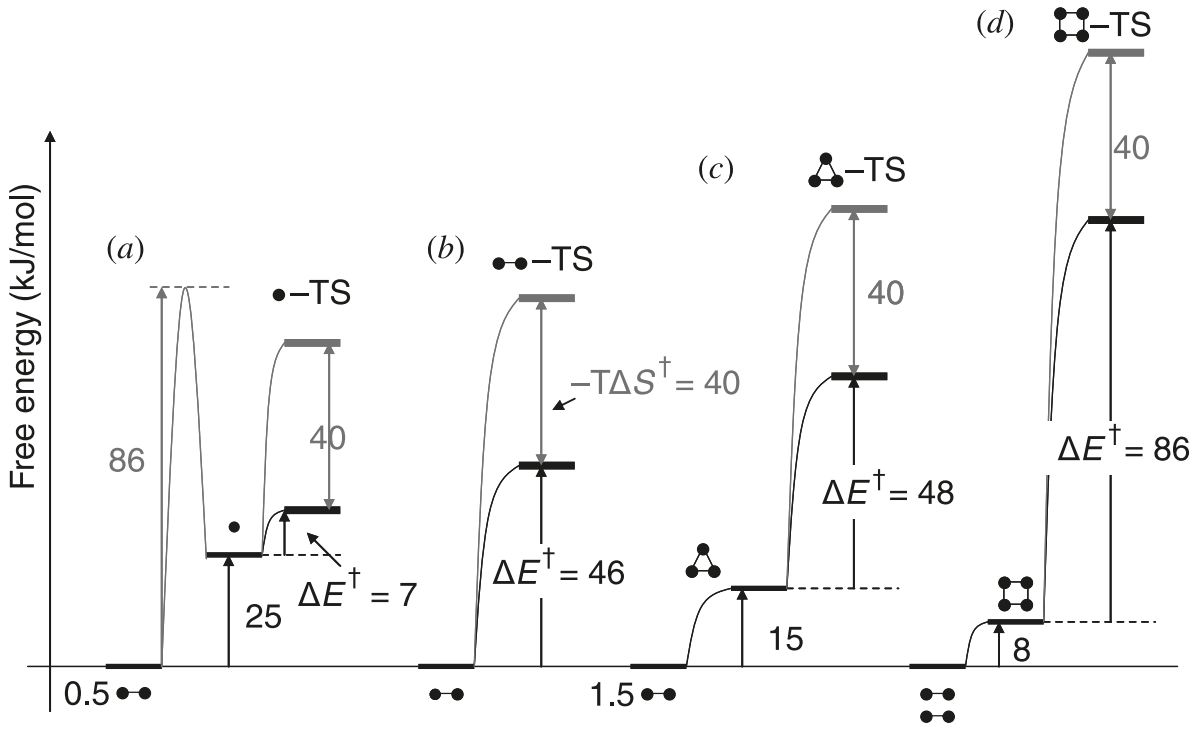

served polymerization behavior. In the absence of polar modifier agents such as THF, the alkyl lithium initiator produces predominantly straight-chain polybutadiene with only a minimal (around 5%–10%) admixture of 1,2-insertions. *Cis*- and *trans*-butadiene insertions occur with approximately equal frequency, with a slight predominance of trans insertions.

This agrees best with our results computed for the dimeric (allyl)Li species, which indicate that 3-carbon attacks (leading to 1,2-insertions) have slightly higher barriers than the corresponding 1-carbon attacks (leading to 1,4-insertions). Also, it would best agree with the computational results that $[(allyl)Li]_2$ species would produce a slight predominance of *trans*-butadiene units (see Table 4).

As stated above, butadiene insertions into a monomer-borne butadienyl chain have similar barriers. Polybutadiene produced by the monomeric (allyl)Li species would show a predominance of *cis*-BD units. This is clearly not what is observed in experiment. Realistically, we have to admit that the insertion paths for monomic and dimeric (allyl)Li species are so close in energy that even a relatively small systematic error in our simulations (e.g., 10 kJ/mol) may be responsible for skewing our results one way or the other. However, based on the mismatch between experimentally observed polymer microstructure and the microstructure computed for the (allyl)Li monomer, we conclude that the (allyl)Li monomer species is probably not the species responsible for the majority of the polymer produced.

Conclusion

Our computational results indicate that the anionic polymerization of butadiene likely proceeds from an equilibrium of propagating species and that each individual propagating species produces its own signature polymer microstructure. Within the limits of accuracy inherent in our computational approach, we have identified the dimer, trimer, and tetramer species of (allyl)Li as the most prevalent oligomers in nonpolar ($\varepsilon = 2$) solvent at room temperature. The monomeric (allyl)Li species is not present to a significant extent under the conditions investigated in this paper. The dimer is computed as being the most stable species on a per Li basis. The trimer, having uneven x, is less stable than both the dimer and tetramer. However, the relative stabilities of the species with $x = 2$, 3, and 4 are so close at the present level of calculations (G_B = 25, 20, and 23 kJ/mol, respectively) that their relative populations are difficult to predict. The clusters with even agglomeration numbers of $x > 2$ are highly symmetrical antiprisms. Higher order oligomers greater than tetramers are not present in significant amounts to affect the product distributions that are produced with this system.

The chain propagation barriers increase with increasing degree of agglomeration, x. The lowest calculated butadiene insertion barriers for each of the oligomeric species was found to be 7, 46, 48, and 86 kJ/mol for $x = 1$, 2, 3, and 4, respectively. No insertion barriers were calculated for the pentamer, which is rather unstable, as well as the hexamer and octamer, for which our calculations predict negligible populations. Computed barriers for insertion into a dimer-bound butadienyl chain would reproduce the experimentally obtained polymer microstructure closely, whereas our results for monomer-, trimer-, and tetramer-derived microstructures would not. Thus, we conclude that the dimer is the dominant propagating species at least under the commonly practiced experimental conditions.

The polybutadiene microstructures produced by different oligomers change systematically with the degree of agglomeration, *x*. For the monomer, insertion of *cis*-butadiene is significantly faster than insertion of *trans*-butadiene, which would lead to an all-*cis*-butadiene if the monomer were responsible for a significant portion of insertions. For the Li-allyl dimer, insertions of *cis*- and *trans*-butadiene occur at comparable rates, with insertion of *trans*-butadiene being slightly faster. 1-Carbon attack (leading to 1,4-insertion) is faster than 3-carbon attack (leading to 1,2-insertion) by 5–8 kJ/mol, which corresponds to a vinyl fraction of roughly 5%–10%, which is in good agreement with experiment.[2] However, given the inherent limits of accuracy of our calculations, this level of agreement may be fortuitous.

Computational

Methods

All computations in this work were performed with the DMol[3] program developed by Delley.[34] The double numeric with polarization functions (DNP) basis set and the Becke–Perdew gradient-corrected density functional[35] were used. All computations, except where noted, were performed in solution phase, using the COSMO method developed by Klamt and Schüürmann[25] as adapted by Delley for DMol,[3,36] using a dielectric constant of 2.0 to approximate a low dielectric hydrocarbon solvent that is commonly used for anionic butadiene/styrene polymerization. Geometry optimizations for locating ground state intermediates were performed until a threshold gradient of at most 10^{-3} hartree/bohr was reached. Transition-state optimizations were done by computing a Hessian from finite differences and a subsequent eigenvector following search until a threshold of at most 10^{-3} hartree/bohr was reached. Limited conformational sampling was done on both ground state intermediates and transition-state geometries. All calculations were done under C_1 symmetry except where explicitly mentioned. Free energies were calculated from vibrational frequecies using the standard thermodynamics methods.[37] Due to system size restrictions, the vibrational analyses for thermodynamic property calculations were produced on model systems with C_5 (pentenyl) chains instead of C_8 (octenyl) chains using the Gaussian 03 program,[38] the BP86 functional,[35a,39] and a 6-31G basis set.

Accuracy

From experience, we expect reaction energies or barriers for organometallic systems to carry an absolute error of approximately ±20 kJ/mol. When comparing a set of barriers for which some degree of error cancellation can be expected, such as a series of analogous reaction barriers as discussed in the present work, the error decreases sharply. We estimate the relative errors in reaction barriers to be of the order of 5 kJ/mol.

Supplementary data

Supplementary data for this article are available on the journal Web site (canjchem.nrc.ca) or may be purchased from the Depository of Unpublished Data, Document Delivery, CISTI, National Research Council Canada, Ottawa, ON K1A 0R6, Canada. DUD 3928. For more information on obtaining material, refer to cisti-icist.nrc-cnrc.gc.ca/cms/unpub_e.shtml.

Acknowledgements

The author would like to thank the Dow Chemical Company for making this research possible, and to thank Evemarie Hamann, Silvia Valenti, Sven Thiele, and David Wilson for illuminating discussions.

References

(1) This article is part of a Special Issue dedicated to Professor T. Ziegler.
(2) Hsieh, H. L.; Quirk, R. P. *Anionic Polymerization: Principles and Applications;* Marcel Dekker Inc.: New York, 1996.
(3) We use the common cis/trans nomenclature for butadiene instead of the IUPAC-recommended s-cis/s-trans nomenclature in keeping with the conventions of the polyolefins research community.
(4) Dietrich, H. *Acta Crystallogr.* **1963**, *16*, 681. doi:10.1107/S0365110X63001754.
(5) Dietrich, H. *J. Organometal. Chem. (Kyoto)* **1981**, *205*, 291. doi:10.1016/S0022-328X(00)82431-6.
(6) Weiss, E.; Lucken, E. A. C. *J. Organometal. Chem. (Kyoto)* **1964**, *2*, 197. doi:10.1016/S0022-328X(00)80512-4.
(7) Weiss, E.; Hencken, G. *J. Organometal. Chem. (Kyoto)* **1970**, *21*, 265. doi:10.1016/S0022-328X(00)83621-9.
(8) Weiss, E.; Lambertsen, T.; Schubert, B.; Cockcroft, J. K.; Wiedenmann, A. *Chem. Ber.* **1990**, *123*, 79. doi:10.1002/cber.19901230116.
(9) Lambert, C.; von Ragué Schleyer, P. *Angew. Chem. Int. Ed. Engl.* **1994**, *33*, 1129. doi:10.1002/anie.199411291.
(10) Young, R. N.; Quirk, R. P.; Fetters, L. J. *Adv. Polym. Sci.* **1984**, *56*, 1. doi:10.1007/BFb0024120.
(11) Brown, T. L. *Adv. Organomet. Chem.* **1966**, *3*, 365. doi:10.1016/S0065-3055(08)60041-6.
(12) Brown, T. L. *Pure Appl. Chem.* **1970**, *23*, 447. doi:10.1351/pac197023040447.
(13) Wakefield, B. L. *The Chemistry of Organolithium Compounds;* Pergamon Press: Oxford, 1974.
(14) Niu, A. Z.; Stellbrink, J.; Allgaier, J.; Willmer, L.; Richter, D.; Koenig, B. W.; Gondorf, M.; Willbold, S.; Fetters, L. J.; May, R. P. *Macromol. Symp.* **2004**, *215*, 1. doi:10.1002/masy.200451101.
(15) Stellbrink, J.; Allgaier, J.; Willner, L.; Richter, D.; Slawecki, T.; Fetters, L. J. *Polymer (Guildf.)* **2002**, *43*, 7101. doi:10.1016/S0032-3861(02)00450-0.
(16) Stellbrink, J.; Willner, L.; Jucknischke, O.; Richter, C.; Lindner, P.; Fetters, L. J.; Huang, J. S. *Macromolecules* **1998**, *31*, 4189. doi:10.1021/ma971890e.
(17) Niu, A. Z.; Stellbrink, J.; Allgaier, J.; Willner, L.; Radulescu, A.; Richter, D.; Koenig, B. W.; May, R. P.; Fetters, L. J. *J. Chem. Phys.* **2005**, *122*, 134906. doi:10.1063/1.1866092. PMID:15847501.
(18) Frischknecht, A. L.; Milner, S. T. *J. Chem. Phys.* **2001**, *114* (2), 1032. doi:10.1063/1.1328068.
(19) Worsfold, D. J.; Bywater, S. *Macromolecules* **1972**, *5* (4), 393. doi:10.1021/ma60028a012.
(20) Verstraete, P.; Deffieux, A.; Fritsch, A.; Rayez, J. C.; Rayez, M. T. *J. Mol. Struct. (Theochem.)* **2003**, *631*, 53. doi:10.1016/S0166-1280(03)00133-7.
(21) van Eikema Hommes, N. J. R.; von Ragué Schleyer, P.; Wu, Y. D. *J. Organomet. Chem.* **1991**, *409*, 307. doi:10.1016/0022-328X(91)80017-E.

(22) Pratt, L. M.; Khan, I. M. *J. Comput. Chem.* **1995**, *16* (9), 1067. doi:10.1002/jcc.540160903.
(23) Röthlisberger, U.; Sprik, M.; Klein, M. L. *J. Chem. Soc. Faraday Trans.* **1998**, *94* (4), 501. doi:10.1039/a707860i.
(24) (a) Hohenberg, P.; Kohn, W. *Phys. Rev.* **1964**, *136*, B864 doi:10.1103/PhysRev.136.B864.; (b) Kohn, W.; Sham, L. J. *Phys. Rev.* **1965**, *140*, A1133 doi:10.1103/PhysRev.140.A1133.; (c) Parr, R. G.; Yang, W. *Density Functional Theory of Atoms and Molecules;* Oxford University Press: New York, 1989.
(25) Klamt, A.; Schüürmann, G. *J. Chem. Soc. Perkin Trans.* **1993**, *2*, 799.
(26) Kottke, T.; Stalke, D. *Angew. Chem. Int. Ed. Engl.* **1993**, *32*, 580. doi:10.1002/anie.199305801.
(27) Leung, B.; Reid, D. L.; Armstrong, D. A.; Rauk, A. *J. Phys. Chem. A* **2004**, *108*, 2720. doi:10.1021/jp030265a.
(28) Jorgensen, W. L.; Lim, D.; Blake, J. F. *J. Am. Chem. Soc.* **1993**, *115*, 2936. doi:10.1021/ja00060a048.
(29) Abraham, M. H. *J. Am. Chem. Soc.* **1981**, *103*, 6742. doi:10.1021/ja00412a036.
(30) Watanabe, H.; Oishi, Y.; Kanaya, T.; Kaji, H.; Horii, F. *Macromolecules* **2003**, *36*, 220. doi:10.1021/ma0213697.
(31) The use of the cis/trans nomenclature for the allyl derived from butadiene is retained here although this is contrary to IUPAC standards, which recommend use of the syn/anti nomenclature. However, it allows us to discuss allyls derived from *cis*- and *trans*-butadiene without having to switch to the designators anti and syn, respectively.
(32) Butadiene π-complexes of the monomeric allyl lithium species are only marginally stable, with binding energies greater than –10 kJ/mol. Thus, they are not stable enough to form stable species at room temperature and may be ignored for the calculation of insertion barriers.
(33) Page, I. *The Chemistry of Enzyme Action;* Elsevier: Amsterdam, 1984; p 20.
(34) (a) Delley, B. *J. Chem. Phys.* **1990**, *92*, 508 doi:10.1063/1.458452.; (b) Delley, B. *J. Chem. Phys.* **2000**, *113*, 7756. doi:10.1063/1.1316015.
(35) (a) Becke, A. D. *Phys. Rev. A* **1988**, *38*, 3098 doi:10.1103/PhysRevA.38.3098. PMID:9900728.; (b) Perdew, J. P. *Physica B* **1991**, *172*, 1. doi:10.1016/0921-4526(91)90409-8.
(36) Delley, B. *Mol. Simul.* **2006**, *32*, 117. doi:10.1080/08927020600589684.
(37) McQuarrie, D. A. *Statistical Thermodynamics;* University Science Books: Mill Valley, CA, 1973.
(38) Frisch, M. J.; Trucks, G. W.; Schlegel, H. B.; Scuseria, G. E.; Robb, M. A.; Cheeseman, J. R.; Montgomery, J. A., Jr.; Vreven, T.; Kudin, K. N.; Burant, J. C.; Millam, J. M.; Iyengar, S. S.; Tomasi, J.; Barone, V.; Mennucci, B.; Cossi, M.; Scalmani, G.; Rega, N.; Petersson, G. A.; Nakatsuji, H.; Hada, M.; Ehara, M.; Toyota, K.; Fukuda, R.; Hasegawa, J.; Ishida, M.; Nakajima, T.; Honda, Y.; Kitao, O.; Nakai, H.; Klene, M.; Li, X.; Knox, J. E.; Hratchian, H. P.; Cross, J. B.; Bakken, V.; Adamo, C.; Jaramillo, J.; Gomperts, R.; Stratmann, R. E.; Yazyev, O.; Austin, A. J.; Cammi, R.; Pomelli, C.; Ochterski, J. W.; Ayala, P. Y.; Morokuma, K.; Voth, G. A.; Salvador, P.; Dannenberg, J. J.; Zakrzewski, V. G.; Dapprich, S.; Daniels, A. D.; Strain, M. C.; Farkas, O.; Malick, D. K.; Rabuck, A. D.; Raghavachari, K.; Foresman, J. B.; Ortiz, J. V.; Cui, Q.; Baboul, A. G.; Clifford, S.; Cioslowski, J.; Stefanov, B. B.; Liu, G.; Liashenko, A.; Piskorz, P.; Komaromi, I.; Martin, R. L.; Fox, D. J.; Keith, T.; Al-Laham, M. A.; Peng, C. Y.; Nanayakkara, A.; Challacombe, M.; Gill, P. M. W.; Johnson, B.; Chen, W.; Wong, M. W.; Gonzalez, C.; Pople, J. A. *Gaussian 03,* Revision D.01; Gaussian, Inc.: Wallingford CT, 2004.
(39) Perdew, J. P. *Phys. Rev. B* **1986**, *33*, 8822. doi:10.1103/PhysRevB.33.8822.

Organoplatinum(IV) complexes with functional alkyl groups and their use in supramolecular chemistry[1]

Richard H.W. Au, Lisa J. Findlay-Shirras, Neil M. Woody, Michael C. Jennings, and Richard J. Puddephatt

Abstract: The oxidative addition of alkyl bromides RCH_2Br (R = C_5H_4N, C_6H_4CN, $CH_2C_6H_4CO_2H$, or $CH_2C_6H_4CH_2CO_2H$) to dimethylplatinum(II) complexes [$PtMe_2(LL)$] (LL = diimine ligand) gives the corresponding organoplatinum(IV) complexes [$PtBrMe_2(CH_2R)(LL)$] containing functionality in the alkyl group RCH_2. The pyridyl derivatives can be protonated, while abstraction of the bromide ligand from [$PtBrMe_2(CH_2R)(LL)$] can form cationic complexes, which can react with water or form oligomers by self-assembly.

Key words: platinum, organometallic, hydrogen bond, supramolecular.

Résumé : L'addition oxydante de bromures d'alkyle, RCH_2Br [R = C_5H_4N, C_6H_4CN, $CH_2C_6H_4COOH$ ou $CH_2C_6H_4CH_2COOH$] sur des complexes de diméthylplatine(II) [$PtMe_2(LL)$] [LL = ligand diimine], conduit à la formation de complexes organoplatine(IV) [$PtBrMe_2(CH_2R)(LL)$] comportant une fonctionnalité dans le groupe alkyle RCH_2. Les dérivés pyridyles peuvent être protonés alors que l'enlèvement du ligand bromure à partir de [$PtBrMe_2(CH_2R)(LL)$] peut conduire à la formation de complexes cationiques qui peuvent réagir avec de l'eau ou former des oligomères par autoassemblage.

Mots-clés : platine, organométallique, liaison hydrogène, supramoléculaire.

[Traduit par la Rédaction]

Introduction

The oxidative addition of small molecules to platinum(II) complexes to form organoplatinum(IV) complexes can be a key step in catalysis, and so this type of reaction has been studied in great detail.[2–6] The oxidative addition can also be a key step in the synthesis of binuclear or even polymeric organoplatinum(IV) complexes, which are of interest as molecular materials.[4–8] The building up of complex structures from simple building blocks is a feature of supramolecular chemistry,[9] and organoplatinum(IV) complexes have proved to be very versatile in the development of supramolecular organometallic chemistry of the transition metals.[10–14] The stability of organoplatinum(IV) complexes towards reactions of protic reagents, oxidants, and other functional groups is an important property in allowing this chemistry to be developed.[15] This paper describes chemistry of new organoplatinum(IV) complexes in which one of the alkyl groups carries a cyanide, a pyridine, or a carboxylic acid group.

Results

Formation of organoplatinum(IV) complexes through oxidative addition reactions

The oxidative addition of 3-cyanobenzyl bromide to complexes [$PtMe_2(LL)$], **1** or **2**, where LL = 4,4′-di-*t*-butyl-2,2′-bipyridine (bu_2bipy) or di-2-pyridyl ketone (DPK), respectively, gave the products of trans oxidative addition [$PtBrMe_2(CH_2C_6H_4$-3-CN)(LL)], **3** or **4** (Scheme 1).

The complexes were readily characterized by their ^{1}H NMR spectra. For example, complex **3** gave a single methylplatinum resonance at δ = 1.51 with coupling constant ^2J(PtH) = 69 Hz, and a single Pt-CH_2 resonance at δ = 2.79 with coupling constant ^2J(PtH) = 96 Hz, indicating formation of a single symmetrical isomer. Complex **3** was also characterized by X-ray structure determination (Fig. 1). The platinum(IV) centre has octahedral stereochemistry and the cyanophenyl group lies over one of the pyridyl groups of the bu_2bipy ligand.

The reactions of complex **1** with the three isomers of bromomethylpyridine are shown in Scheme 2. The organic reagents are available only as the hydrobromide salts, because the neutral compound self-react, but the simple reaction of the bromomethylpyridinium bromides were complex. They evidently act as a source of HBr, which reacts with **1** to give methane and [$PtBrMe(bu_2bipy)$], which can itself react with bromomethylpyridine. To obtain the products of Scheme 2, the pyridinium salts were neutralized with triethylamine to generate the neutral bromomethylpyridine in situ, and this solution was then used to react with complex **1**. Each of the complexes [$PtBrMe_2(CH_2py)(bu_2bipy)$], **5**–**7**

Received 28 November 2008. Accepted 21 January 2009. Published on the NRC Research Press Web site at canjchem.nrc.ca on 20 May 2009.

R.H.W. Au, L.J. Findlay-Shirras, N.M. Woody, M.C. Jennings, and R.J. Puddephatt.[1] Department of Chemistry, University of Western Ontario, London, ON N6A 5B7, Canada.

[1]Corresponding author (e-mail: pudd@uwo.ca).

Scheme 1.

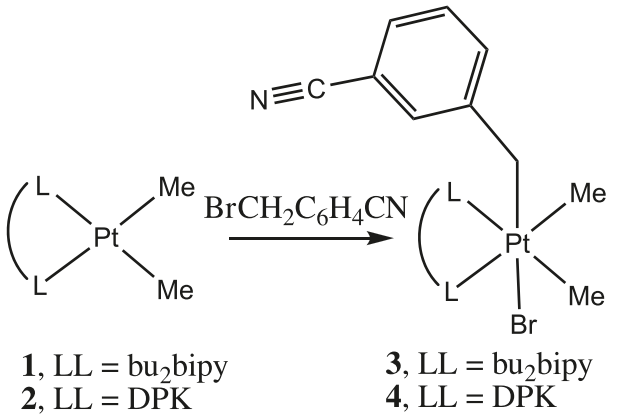

Fig. 1. Structure of [$PtBrMe_2(CH_2C_6H_4$-3-CN)(bu_2bipy)], **3**. Selected bond parameters: Pt–C(1) 2.06(1), Pt–C(2) 2.04(1), Pt–C(31) 2.10(1), Pt–N(11) 2.17(1), Pt–N(22) 2.13(1), Pt–Br 2.582(1), C(38)–N(39) 1.15(2) Å.

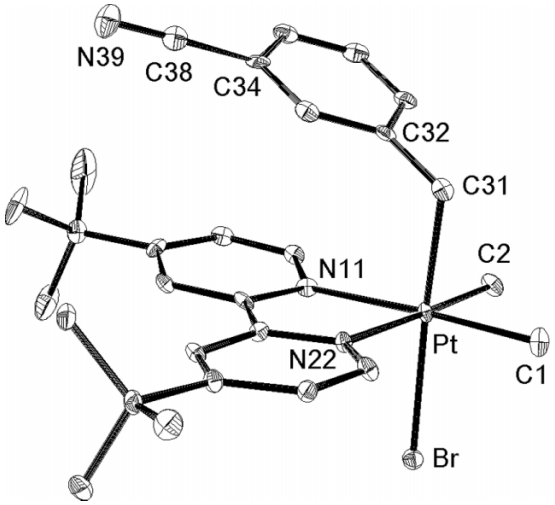

(py = 2-, 3-, or 4-C_5H_4N, respectively), gave a single methylplatinum resonance and a single $PtCH_2$ resonance in the ^{1}H NMR spectra, thus confirming that selective trans oxidative addition of the C–Br bond had occurred. The structure of complex **5** was confirmed by X-ray structure determination and is shown in Fig. 2. There are two independent molecules in the asymmetric unit, but they have similar structures and so only one is shown in Fig. 2. As in complex **3** (Fig. 1), the platinum(IV) centre has octahedral stereochemistry and the 2-pyridyl unit of the $PtCH_2$py group is π-stacked with one of the pyridyl groups of the bu_2bipy ligand.

The oxidative addition reactions of some bromomethyl derivatives of carboxylic acids are shown in Scheme 3. In all cases, *trans* oxidative addition was observed to give the products **8**–**11**. However, the DPK complexes also gave some cis isomer. Complexes **8** and **10** have been reported previously but the structures were not determined.[10]

The structure of complex **8** is shown in Fig. 3. The complex forms a hydrogen bonded dimer in the solid state with a distance of O(39)···O(40A) = O(40)···O(39A) = 2.61(1) Å. The structure of complex **10** is more complex and is illustrated in Figs. 4 and 5. The molecular structure is similar to that of complex **8** (Figs. 3 and 4), but there is disorder of the $CH_2C_6H_4CH_2CO_2H$ groups with roughly 50:50 occupation of the **A** [containing O(40) and O(41)] and **B** [containing O(60) and O(61)] forms. The supramolecular structure of **10** is more complex than for **8** (compare Figs. 3 and 5). The head-to-head dimerization of the type seen for **8** is not observed for complex **10**. Instead, the molecules of the form **A** and **B** alternate in forming hydrogen bonds O(61)=C(R)–O(60)H···O(41)=C(R)–O(40)H···Br. Molecule **A** acts as a hydrogen bond donor to the Br–Pt group of molecule **B**, and a hydrogen bond acceptor through its carbonyl oxygen atom. Molecule **B** acts as a hydrogen bond donor to the carbonyl group of molecule **A** and an acceptor through its Br–Pt group. The overall result is to form a hydrogen-bonded supramolecular polymer.

Scheme 2.

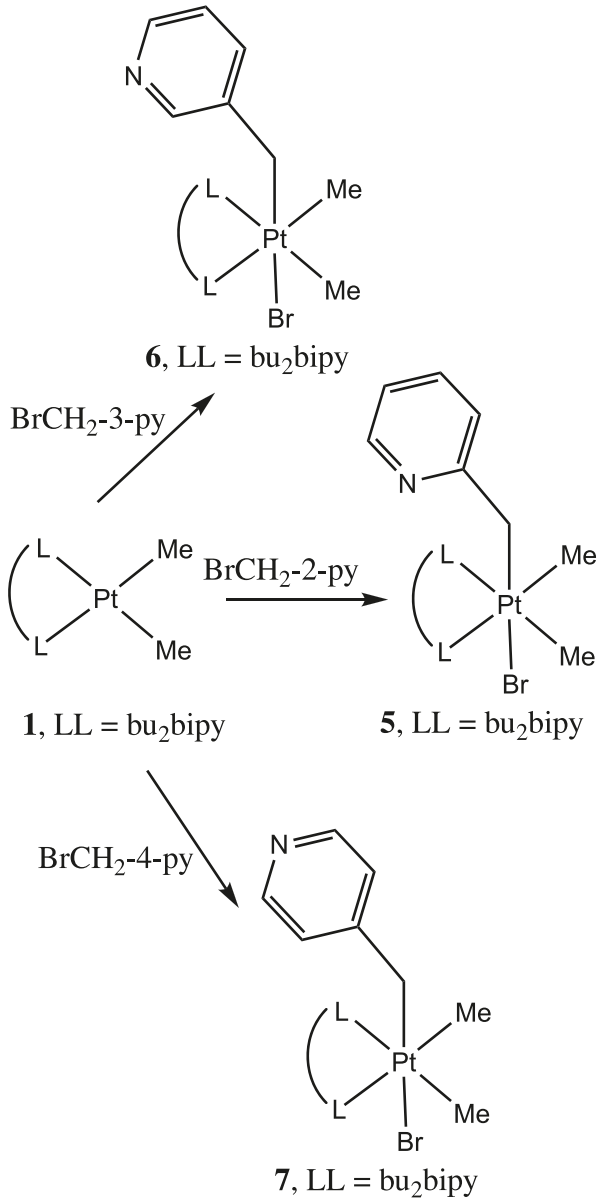

Fig. 2. The structure of [$PtBrMe_2(CH_2$-2-py)(bu_2bipy)], **5**. Selected bond distances: Pt(1)–C(1) 2.04(1), Pt(1)–C(3) 2.08(1), Pt(1)–C(31) 2.10(1), Pt(1)–N(11) 2.136(9), Pt(1)–N(22) 2.166(9), Pt(1)–Br(1) 2.5618(15) Å.

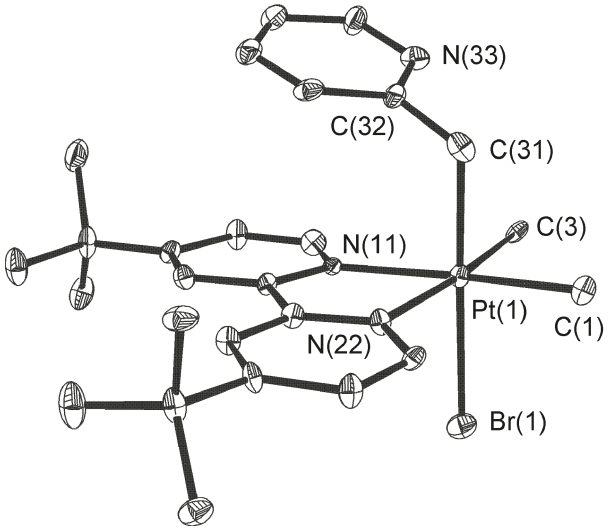

Scheme 3.

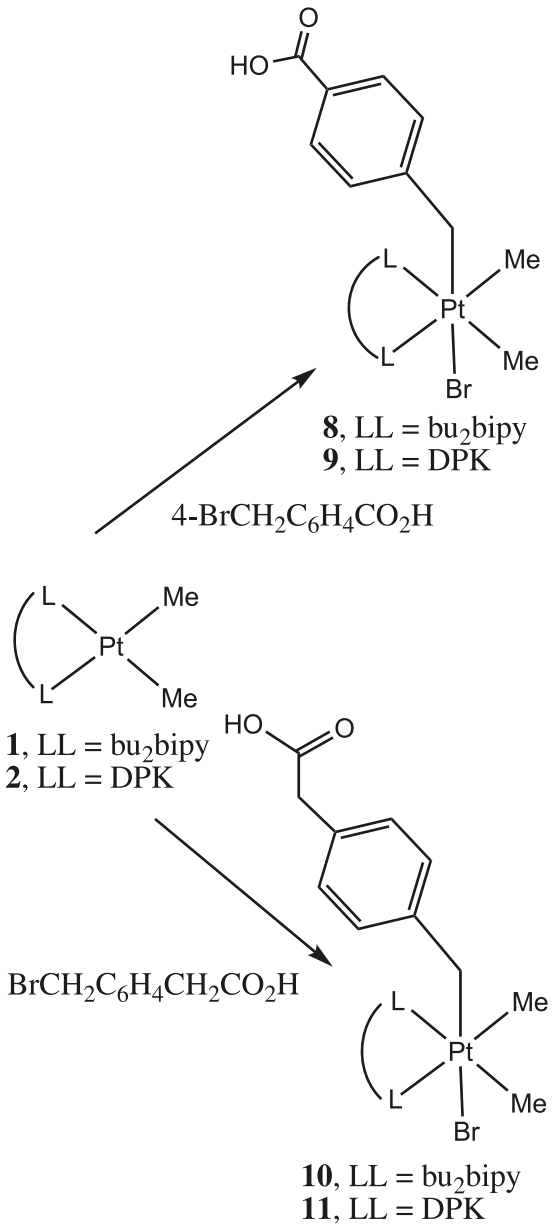

Further derivatization of the platinum(IV) complexes

The pyridyl complexes **5**–**7** could be protonated by addition of acid, as shown for the protonation of 4-pyridylmethylplatinum(IV) derivative (**7**) to give **12** in Scheme 4. The main effect on the ^{1}H NMR spectra was a shift of the $PtCH_2$ resonance on protonation. This shift defined as $\Delta(\delta) = \delta$(protonated complex) – δ(parent complex) = 1.78, 0.52, and 0.32 for the 2-, 3-, and 4-pyridylmethyl derivative, respectively. Two complications were observed in these reactions. Firstly, the reversible isomerization of **12** to the overall product of cis oxidative addition (**13**, in Scheme 4) was catalyzed by acid. It was not possible to isolate the cis isomers such as **13**, but these compounds could be identified by their NMR spectra. For example, the low symmetry of **13** leads to nonequivalent MePt resonances [δ(PtMe, axial) = 0.76, ^2J(PtH) = 72 Hz; δ(PtMe, equatorial) = 1.05, ^2J(PtH) = 68 Hz] and $PtCH^aH^b$py protons [$\delta(PtH^a) = 3.54$, ^2J(HH) = 7 Hz, ^2J(PtH) = 105 Hz; $\delta(PtH^b) = 4.41$, ^2J(HH) = 7 Hz, ^2J(PtH) = 110 Hz] in the ^{1}H NMR spectrum. The isomerization is expected to occur after bromide dissociation to give a five-coordinate intermediate [$PtMe_2(CH_2$-4-py)(bu_2bipy)]$^+$, and this reversible step is catalyzed by H^+.[16] At equilibrium, the ratio of **12**:**13** was ca. 3:1 when X = triflate. A similar isomerization occurred on protonation of the 3-pyridylmethylplatinum(IV) complex (**6**), but no cis isomer was detected on protonation of the 2-pyridylmethylplatinum(IV) complex (**5**). The second complication is that, if the group X in the acid HX can act as a ligand for platinum(IV), then partial exchange of the bromide ligand for X^- can occur. For example, crystallization of complex **7** in the presence of HCl gave complex **12** (X = Cl), but crystallographic characterization of the product showed partial displacement of the PtBr by the PtCl group to give **14** (Scheme 4, X = Cl). The structure of **12** (X = Cl) is shown in Fig. 6, showing only the Pt-Br component. The ratio of disorder components **12**:**14** (X = Cl) was refined as 0.36:0.64. The possibility of supramolecular association between the pyridyl base **7** and the acidic complexes **8** or **10** was investigated, but no such acid–base adducts could be crystallized.

The reactions of the pyridyl complexes **5**–**7** with silver salts of weakly coordinating anions were expected to occur by bromide abstraction followed by intramolecular or intermolecular coordination of the pyridine nitrogen atom to platinum(IV), as illustrated in Scheme 5.[17] The reaction of complex **5** with silver triflate occurred according to Scheme 5, and the product **15**(OTf) was isolated in analytically pure form, though single crystals could not be obtained. The ^{1}H NMR spectrum of **15** was broad at room temperature but, at –20 °C, it clearly showed two methylplatinum resonances and an [**AB**] multiplet for the $PtCH^aH^b$ protons. However, the ^{1}H NMR spectra of compounds obtained by treating the cyanobenzyl complex **3**, or the 3- or 4-pyridylmethyl complexes (**6** or **7**) with silver triflate were very complex, indicating that the self-assembly was nonse-

Fig. 3. The structure of complex **8**, showing the dimer formed by H-bonding. Selected parameters: Pt–C(31) 2.04(2), Pt–C(1) 2.08(1), Pt–C(2) 2.09(1), Pt–N(22) 2.16(1), Pt–N(11) 2.167(9), Pt–Br 2.563(2) Å. Hydrogen bond distance: O(39)···O(40A) = O(40)···O(39A) = 2.61(1) Å.

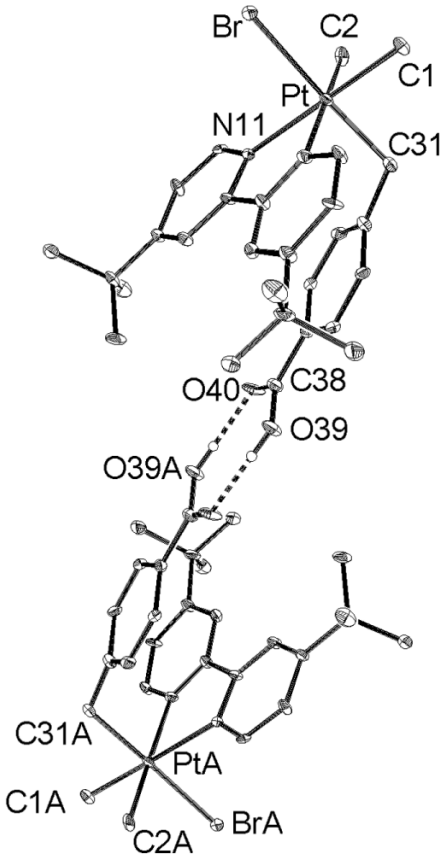

lective and gave a mixture of oligomers rather than a single product such as **16**. The unique behavior of the 2-pyridylmethyl complex (**5**) was also reflected in the ESI-MS of a solution in dichloromethane. The 2-pyridylmethyl complex (**15**), as the triflate salt, gave a molecular ion at m/z = 585, whereas the corresponding products with 3- or 4-pyridylmethyl groups gave the same envelope of peaks at m/z = 585 but also significant peaks at m/z = 1319 due to the dimer ion $[\{PtMe_2(CH_2py)(bu_2bipy)\}_2(OTf)]^+$ and, for the 4-pyridylmethyl complex only, trimer peaks.

Reaction of the toluic acid derivative (**8**) with silver tetrafluoroborate in moist solvent acetone occurred according to Scheme 6, to give the cationic aqua complex **17**, whose structure is shown in Fig. 7. The stereochemistry at the octahedral platinum(IV) centre is not changed in this reaction and so the effect is to substitute the bromide ligand by the aqua ligand. The carboxylic acid group hydrogen bonds to an acetone molecule, while one hydrogen atom of the aqua group hydrogen bonds to a second acetone molecule and the other hydrogen bonds to the tetrafluoroborate anion. It was anticipated that addition of base to complex **17** would give the carboxylate anion and that this would in turn displace the aqua ligand from a neighbouring molecule to give a dimer or, by repletion of these steps, an oligomer or polymer. However, the reaction gave only a mixture of complexes that could not be characterized.

Fig. 4. The 50:50 disordered structure of complex **10**. Selected parameters: Pt–C(1) 2.09(2), Pt–C(2) 2.07(2), Pt–C(31) 2.10(3), Pt–C(51) 2.11(3), Pt–N(11) 2.16(1), Pt–N(22) 2.18(1), Pt–Br 2.601(2) Å.

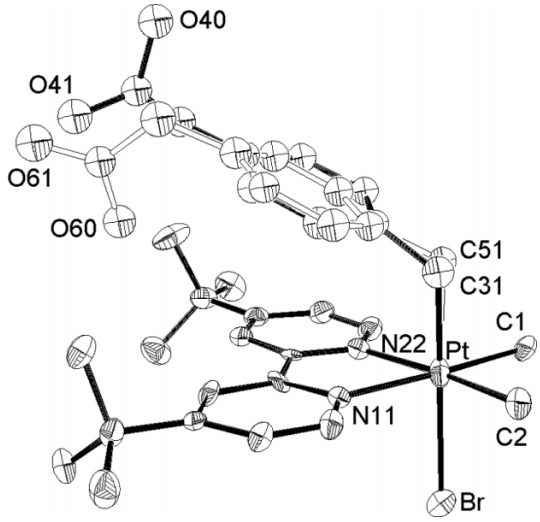

Fig. 5. The supramolecular structure of complex **10**, with alternating conformers **A** (red) and **B** (blue). Hydrogen-bonding parameters: O(40)···Br 3.26(4), O(41)···O(60) 2.67(5) Å. Other sequences, such as $(\mathbf{AABB})_n$ can be ruled out because they lead to unreasonably short contacts.

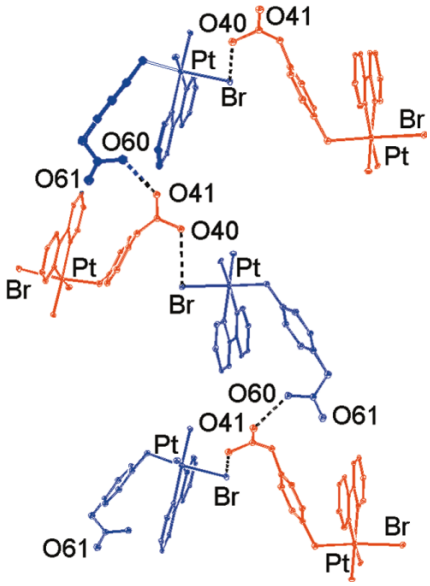

In some reactions of the platinum(IV) complexes with DPK ligands with silver salts, the carbonyl group of the DPK ligand was shown to be involved. The reaction of complex **4** with silver triflate gave the cationic complex **18**, as the triflate salt, according to Scheme 7. The two key features of complex **18** are the change in stereochemistry at platinum(IV) and the hydration of the DPK ligand to give the tridentate DPK-OH_2 ligand. None of the more symmetrical isomer, with the cyanobenzyl group trans to oxygen, was detected. In the ^{1}H NMR spectrum, complex **18** gave two methylplatinum resonances [δ = 1.18, ^2J(PtH) = 72 Hz and δ = 1.48, ^2J(PtH) = 81 Hz], and the $PtCH_2$ group gave an [AB] multiplet [δ = 3.03, ^2J(PtH) = 73 Hz; δ = 3.55,

Scheme 4.

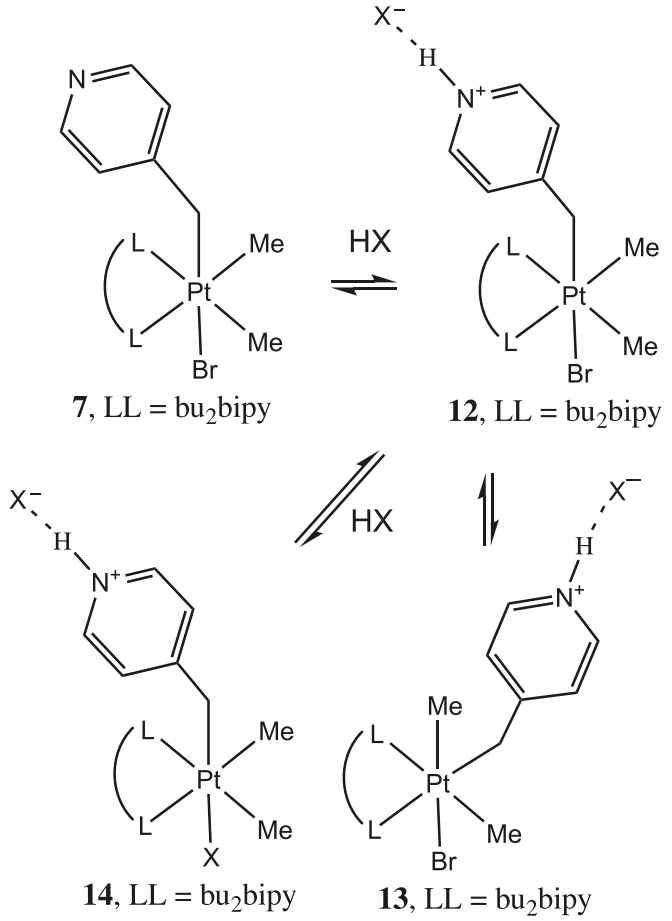

Scheme 5.

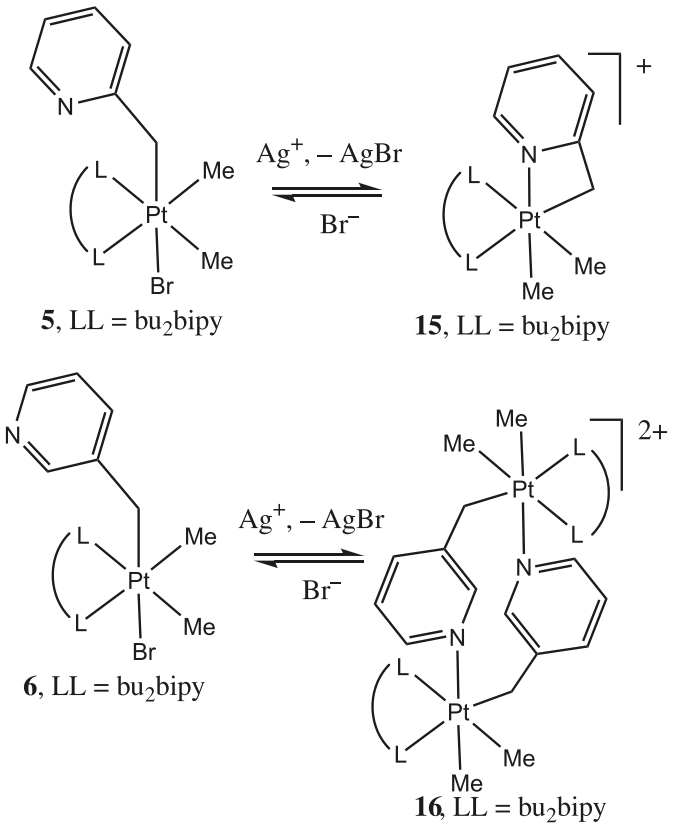

Fig. 6. The structure of disordered complex **12/14** (X = Cl), showing only component **12**. Selected bond parameters: Pt–C(1) 2.09(2), Pt–C(2) 1.99(3), Pt–C(31) 2.06(2), Pt–N(11) 2.15(2), Pt–N(22) 2.10(2), Pt–Br 2.55(2) Å. Hydrogen bond distance: N(35)···Cl(1) 3.61(3) Å.

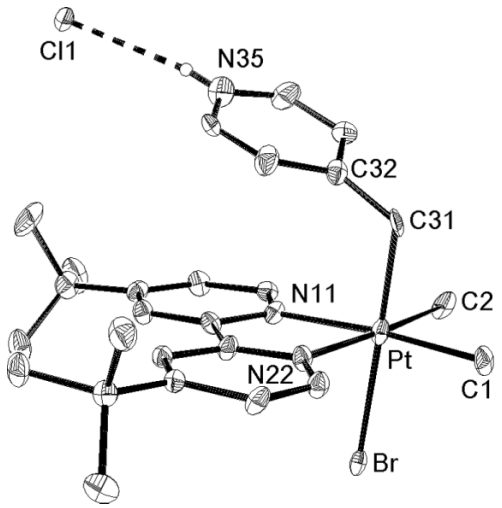

Scheme 6.

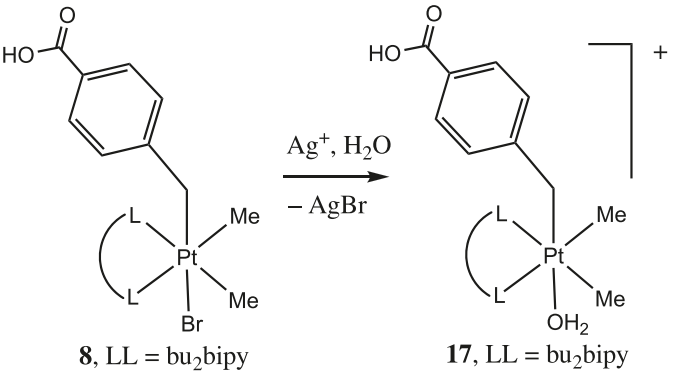

^2J(PtH) = 103 Hz; ^2J(HH) = 10 Hz], and there were two sets of pyridyl resonances. The ESI-MS gave a parent ion for **18** at *m*/*z* = 543 as well as a peak corresponding to a cation formed by loss of water at *m*/*z* = 525. In the IR spectrum, the carbonyl peak, found at 1677 cm^{-1} in **4** was absent in **18**. Hydrogen bonding between at least one of the OH groups in **18** to the cyano group was indicated by a shift in the value of ν(CN) from 2226 cm^{-1} in **4** to 2250 cm^{-1} in **18**. The peak assigned to ν(OH) was broad and centred at 3250 cm^{-1}, indicating that both OH groups are involved in hydrogen bonding. The data are most consistent with hydrogen bonding to the nitrogen atom only of the cyano group, because hydrogen bonding to the π-bond should lead to a decrease in ν(CN) whereas end-on hydrogen bonding leads to an increase,[18,19] but it is not clear if both OH groups hydrogen bond to the nitrogen atom or if one of them hydrogen bonds to the triflate anion. The stereochemical change at platinum(IV) in converting **4** to **18** (Scheme 7) is presumably in part to allow maximum hydrogen bonding. Intermolecular OH···NC hydrogen bonding could form a dimer,

Fig. 7. Structure of the aqua complex **17**[BF_4]·2acetone·hexane. Selected bond parameters: Pt–C(1) 2.049(7), Pt–C(2) 2.048(8), Pt–C(31) 2.085(8), Pt–N(11) 2.154(6), Pt–N(22) 2.171(6), Pt–O 2.224(5) Å. Hydrogen bond distances: O···F(44) 2.703(9), O···O(54) 2.43(1), O(40)···O(64) 2.729(9) Å.

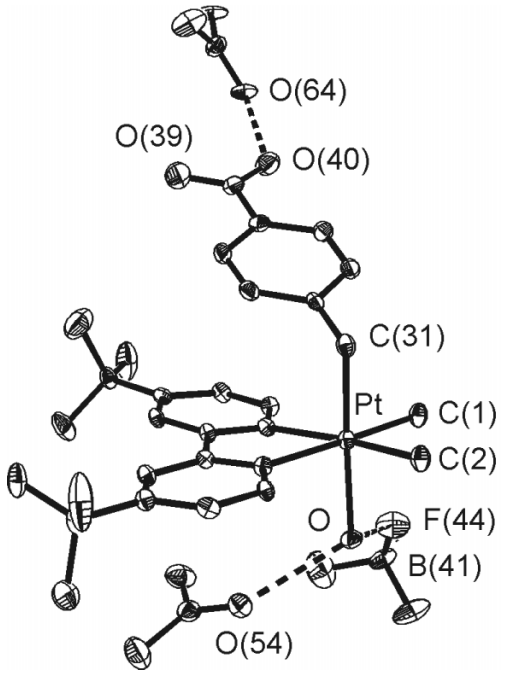

oligomer, or polymer. In the ESI-MS, an intense peak was at *m/z* = 543, corresponding to the cation **18**, and a less intense peak assigned to a dimer was observed at *m/z* = 1235 [(2 × **18**) + OTf]. No trimer or higher mass peaks were detected. There are several precedents for the hydration of the DPK ligand and for participation in hydrogen bonding of the DPK-OH_2 ligand.[20]

The reaction of complex **11** with siver trifluoroacetate occurred to give the cationic complex **19** according to Scheme 7. The reaction to give **19** occurred with a change in stereochemistry at platinum(IV) but this reaction was less selective and some trans isomer was also present. The ^{1}H NMR spectrum of the cis isomer **19** contained two methylplatinum resonances and two resonances for the $PtCH^aH^b$ protons, indicating the absence of a mirror plane of symmetry. The structure of complex **19** as the trifluoroacetate salt is shown in Fig. 8. There are two independent but similar molecules in the unit cell, and they are connected by hydrogen bonding between the carboxylic acid groups. In addition, the two OH groups of the ketone hydrate are hydrogen bonded to the trifluoroacetate anions. The hydrogen bond distances O··O are in the range of 2.59–2.65 Å. In the ESI-MS, the most intense envelope of peaks was at *m/z* = 576, corresponding to the cation **19**, with the second most intense peak at *m/z* = 558, corresponding to loss of H_2O. However, intense dimer peaks were also observed at *m/z* = 1151 [(2 × **19**) – H^+], 1133 [(2 × **19**) – H^+ – H_2O], and 1115 [(2 × **19**) – H^+ – 2H_2O]. The trifluoroacetate groups were not present in any observed fragments. These data indicate that the dimer units persist in solution, and that loss of water from the DPK-OH_2 groups occurs easily in the MS. Reactions of complex **11** with silver salts of weakly coordinating anions, such as Ag[BF_4] or Ag[PF_6], gave products that contained the cationic complex **19** but with unidentified side products. We suggest that the hydrogen bonding by the anion (Fig. 8) is significant in stabilizing **19** as the trifluoroacetate salt.

Fig. 8. Structure of the dimer of **19**·CF_3CO_2. Selected bond distances: Pt(1)–C(16) 2.05(1), Pt(1)–C(17) 2.06(1), Pt(1)–C(21) 2.08(1), Pt(1)–N(1) 2.16(1), Pt(1)–N(13) 2.17(1), Pt(1)–O(15) 2.188(9) Å. Hydrogen bond distances: O(14)···O(81) 2.62(1), O(15)···O(82) 2.59(1), O(29)···O(60) 2.61(1), O(44)···O(92) 2.65(2), O(45)···O(91) 2.56(1), O(59)···O(30) 2.61(1) Å.

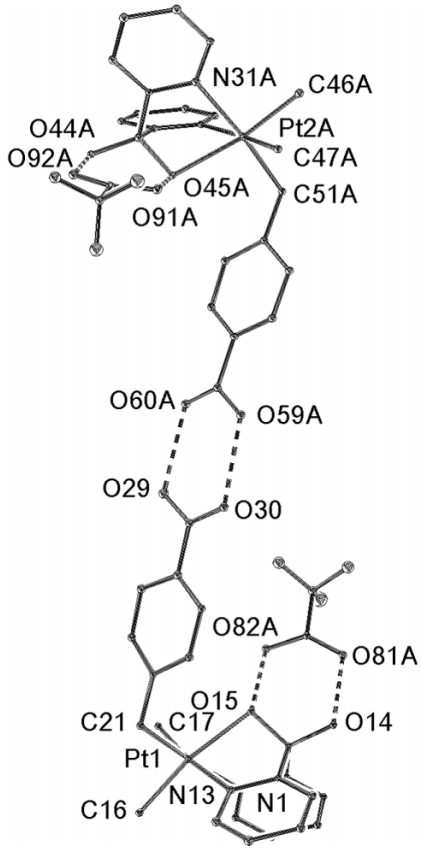

Discussion

The oxidative addition reactions to give alkyl platinum(IV) complexes tolerate a range of functional groups.[4–8,10–16] In particular, it is possible to incorporate either basic or acidic groups into the organoplatinum(IV) products.[8,10] The reactions of [$PtMe_2$(LL)] with RCH_2Br usually occur by kinetic control to give the product of trans oxidative addition, [$PtBrMe_2(CH_2R)$(LL)], by way of an ionic intermediate, [$PtMe_2(CH_2R)(LL)]^+Br^-$.[4] However, if the ionic intermediate is long-lived, or if the bromide ligand can dissociate easily, the cis isomer may also be formed.[4,16] Several cases of isomerization were observed in this work, and some insight into the reasons for this were sought by computations using density functional theory (DFT).

For the complexes [$PtBrMe_2(CH_2R)$(bipy)] or [$PtBrMe_2(CH_2R)$(DPK)], the trans isomer is calculated to be more stable than the cis isomer in all cases. The example with R = 2-pyridyl is illustrated in Figs. 9*a* and 9*b*. The trans isomer has a preferred conformation with the 2-pyridyl

Scheme 7.

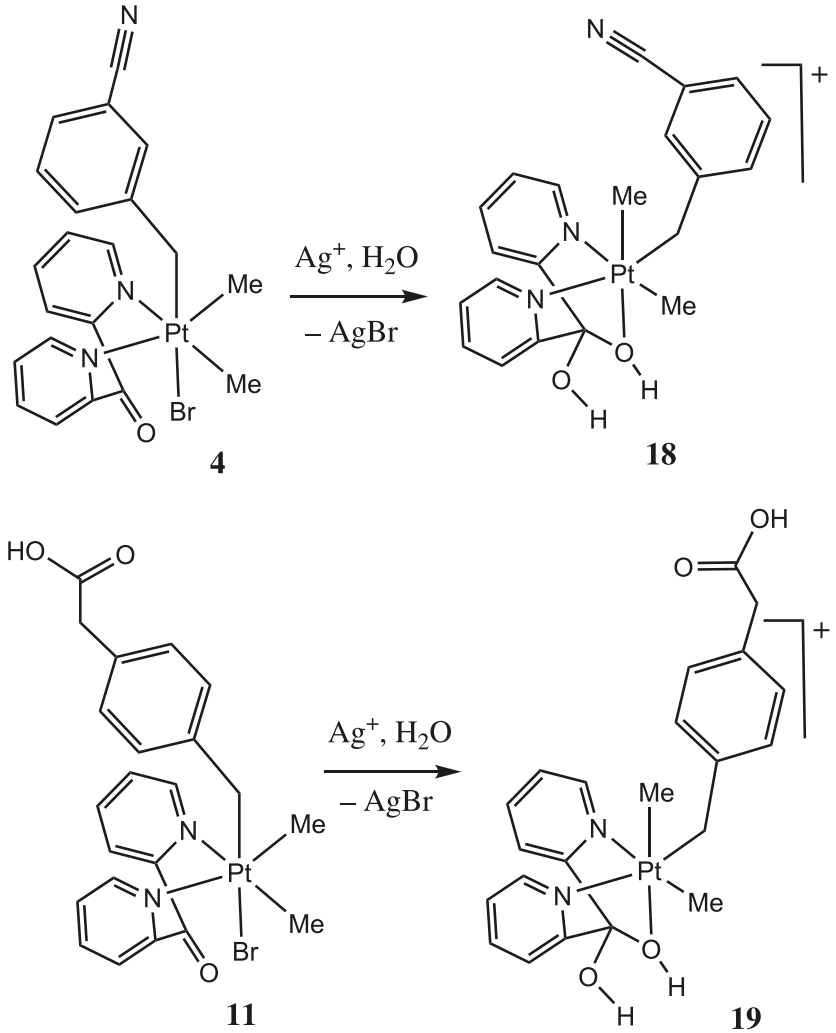

Fig. 9. Optimized structures and calculated relative energies (kJ mol^{-1}) of trans and cis isomers, respectively: (*a*), (*b*) [$PtBrMe_2(CH_2$-2-py)(bipy)]; (*c*), (*d*) [$PtMe_2(CH_2$-2-py)(OH_2)(bipy)]$^+$; (*e*), (*f*) [$PtMe_2(CH_2$-2-py)(bipy)]$^+$.

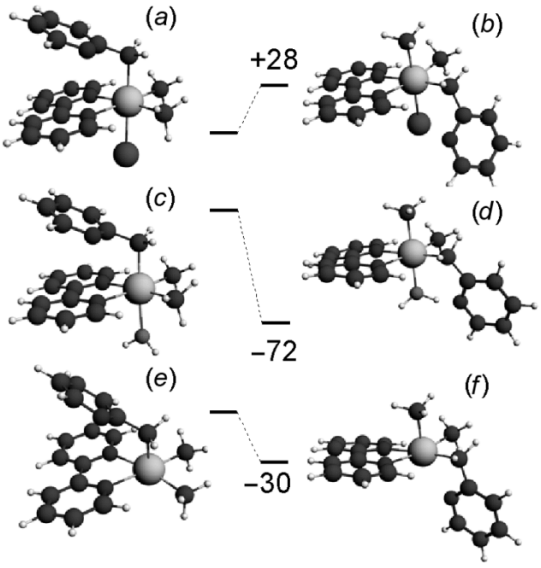

group π-stacked with the 2,2′-bipyridine ligand (Fig. 9*a*) but there is little barrier to rotation about the Pt–CH_2R bond for the cis isomer. The cis isomer can be more stable if there is a specific bonding effect in its favour. For example, the hypothetical aqua complex, [$PtMe_2(CH_2$-2-py)(OH_2)(bipy)]$^+$, is more stable as the cis isomer because an intramolecular hydrogen bond OH···N can exist between the aqua ligand and the 2-pyridyl group (Figs. 9*c*, 9*d*). Similarly, the intermediate five-coordinate complex [$PtMe_2(CH_2$-2-py)(bipy)]$^+$ is more stable as the cis isomer because the pyridylmethyl group can chelate to platinum (Figs. 9*e*, 9*f*). Ring strain in the $PtCH_2$-2-py chelate unit allows easy dissociation of the Pt–N bond. Thus, a conformation with d(Pt–N) increased from the optimized value of 2.23 Å (Fig. 9*f*) to 2.66 Å, with corresponding opening of the angle Pt–C–C(py) from 93° to 104°, was only 18 kJ mol^{-1} higher in energy. Easy reversible access to the coordinatively unsaturated square pyramidal intermediate accounts for the easy fluxionality in complex **15**.

A further complication in the chemistry of the DPK complexes arose from the ease of hydration of the ketone group. Some trimethylplatinum(IV) model complexes, used to avoid complications from cis and trans isomers in the actual complexes studied, are shown in Fig. 10. The ketone addi-

Fig. 10. Optimized structures and calculated relative energies (kJ mol^{-1}) of (*a*) [Pt(OH)Me$_3$(DPK)], (*b*) [PtMe$_3$(DPK-OH)]; (*c*) [PtMe$_3$(OH$_2$)(DPK)]$^+$, (*d*) [PtMe$_3$(DPK-OH$_2$)]$^+$; (*e*) [PtMe$_3$(OH$_2$)(DPK)][MeCO$_2$], (*f*) [PtMe$_3$(DPK-OH$_2$)][MeCO$_2$].

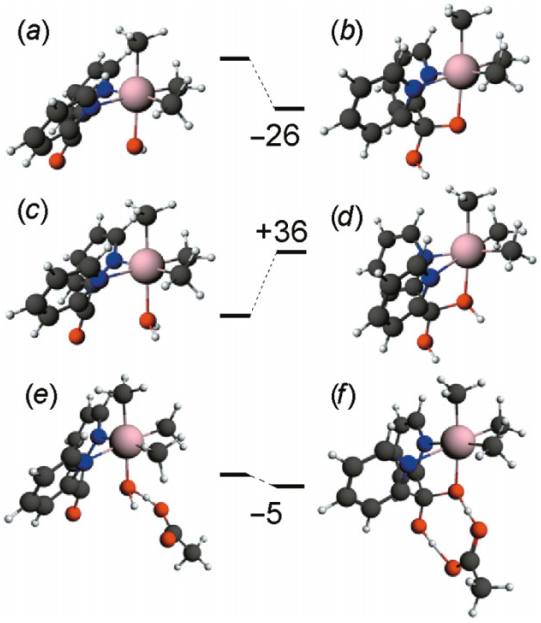

tion step is calculated to be favorable for conversion of neutral complex [Pt(OH)Me$_3$(DPK)] to [PtMe$_3$(DPK-OH)] (Figs. 10*a*, 10*b*). However, for the protonated cationic complexes [PtMe$_3$(OH$_2$)(DPK)]$^+$ and [PtMe$_3$(DPK-OH$_2$)]$^+$, the ketone addition step is unfavorable (Figs. 10*c*, 10*d*). Addition of an acetate anion, which can form a hydrogen bond with the aqua or DPK-OH$_2$ ligand, is enough to make the ketone addition step favorable, as illustrated in Figs. 10*e* and 10*f*. These calculations rationalize the observation that, in all known complexes of the DPK-OH$_2$ ligand, including complex **19**, the OH groups are involved in hydrogen bonding and that hydration is easily reversible.[20,21] The ligand DPK can form a hydrate in hydrochloric acid solution, under conditions where both pyridyl groups are protonated and there is hydrogen bonding between the C–OH groups and chloride anions, but the neutral ketone DPK is not hydrated.[22]

A feature of the complexes **18** and **19** with the DPK-OH$_2$ ligand is that the cis isomer is preferred. Calculations indicate that the trans isomer is expected to be more stable in the absence of hydrogen bonding, for both the ligand DPK and DPK-OH$_2$, as seen in Figs. 11*a*, 11*b* and Figs. 11*c*, 11*d*, respectively. For the cis isomer of the 3-cyanobenzyl derivative (**18**), intramolecular hydrogen bonding is possible and this greatly stabilizes this isomer, as illustrated in Figs. 11*e* and 11*f*. For complex **19**, intramolecular hydrogen bonding is not possible and the carboxylic acid group is involved in intermolecular hydrogen bonding (Fig. 9). In this case, the intermolecular hydrogen bonding is less favored for the trans isomer because of steric effects in the conformation with the aryl group lying over the DPK-OH$_2$ ligand and so the cis isomer is preferred.

Overall, this work has significantly expanded the range of known organoplatinum complexes containing functional alkyl groups. Some of the strengths and limitations in the use of these compounds in supramolecular chemistry are also

Fig. 11. Optimized structures and calculated relative energies (kJ mol^{-1}) of (*a*), (*b*) *trans*- and *cis*-[PtBrMe$_2$(CH$_2$-3-C$_6$H$_4$CN)(DPK)]; (*c*), (*d*) *trans*- and *cis*-[PtMe$_2$(CH$_2$-3-C$_6$H$_4$CN)(DPK-OH$_2$)]$^+$; (*e*), (*f*) *cis*-[PtMe$_2$(CH$_2$-3-C$_6$H$_4$CN)(DPK-OH$_2$)]$^+$ in conformations without and with OH···NC hydrogen bonding, respectively.

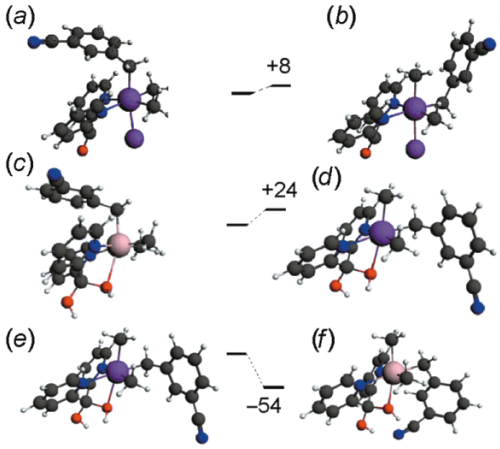

defined. The easy trans and cis isomerism and the easy hydration of the DPK ligand makes crystal engineering in these compounds challenging, and the relatively slow rate of ligand substitution at platinum(IV) limits the use of dynamic coordination chemistry for self-assembly. However, the use of hydrogen bonding for self-assembly has given interesting supramolecular dimers and a polymer, which have been structurally characterized.

Experimental

All reactions were performed under a nitrogen atmosphere using standard Schlenk techniques. The complexes [Pt$_2$Me$_4$(μ-SMe$_2$)$_2$], [PtMe$_2$(bu$_2$bipy)], [PtMe$_2$(DPK)], [PtBrMe$_2$(bu$_2$bipy)(CH$_2$-4-C$_6$H$_4$CO$_2$H)], **8**, and [PtBrMe$_2$(bu$_2$bipy)(CH$_2$-4-C$_6$H$_4$CH$_2$CO$_2$H)], **10**, were prepared using the literature methods.[10,23,21] 1-D and 2-D ^{1}H NMR spectra were recorded using a Varian Mercury 400 NMR or a Varian Inova 400 NMR spectrometer at room temperature unless specified otherwise. ESI-MS were recorded using a Micromass LCT spectrometer. DFT calculations were carried out using the Becke–Perdew exchange-correlation functional in the Amsterdam Density Functional program,[24] including first-order scalar relativistic corrections and standard parameters used in previous studies of organoplatinum compounds.[2,25]

[PtBrMe$_2$(3-CH$_2$C$_6$H$_4$CN)(bu$_2$bipy)], 3

To a solution of [PtMe$_2$(bu$_2$bipy)] (0.1096 g, 0.22 mmol) in CH$_2$Cl$_2$ (5 mL) was added a solution of α-bromo-*m*-tolunitrile (0.0463 g, 0.24 mmol) in CH$_2$Cl$_2$ (5 mL). The solution was stirred for 30 min, the volume of solvent was reduced under vacuum, and the product was precipitated by addition of pentane (10 mL) and recrystallized from CH$_2$Cl$_2$/pentane. Yield: 0.085 g (0.12 mmol). ^{1}H NMR (CD$_2$Cl$_2$) δ: 1.43 [s, 18H, *t*-Bu], 1.51 [s, 6H, ^2J(PtH) = 69 Hz, *Me*Pt], 2.79 [s, 2H, ^2J(PtH) = 96 Hz, *CH*$_2$Pt], 6.19 [t, 1H, ^4J(HH) = 2 Hz, C$_6$H$_4$-H^2], 6.76 [d, 1H, ^3J(HH) = 7 Hz, C$_6$H$_4$-H^5], 6.79 [m, 1H, ^3J(HH) = 7 Hz, ^4J(HH) = 2 Hz, C$_6$H$_4$-H^6], 6.95 [m,

1H, ^3J(HH) = 7 Hz, ^4J(HH) = 2 Hz, C_6H_4-H^4], 7.93 [dd, 2H, ^3J(HH) = 6 Hz, ^4J(HH) = 2 Hz, bipy-H^5], 7.95 [d, 2H, ^4J(HH) = 2 Hz, bipy-H^3], 8.58 [d, 2H, ^3J(HH) = 6 Hz, bipy-H^6]. ESI-MS *m*/*z*: 609 (100) [$PtMe_2$(bu$_2$bipy)(3-$CH_2C_6H_4CN$)]$^+$. Anal. calcd. for $C_{28}H_{36}BrN_3Pt$ (%): C 48.77, H 5.26, N 6.09; found: C 48.43, H 5.19, N 5.96.

[$PtBrMe_2$(3-$CH_2C_6H_4CN$)(DPK)], 4

This was prepared similarly from [$PtMe_2$(DPK)] (0.149 g, 0.36 mmol) and α-bromo-*m*-tolunitrile (0.080 g, 0.41 mmol). Yield: 0.162 g (74%). IR (cm^{-1}): ν(CN) 2226 , ν(CO) 1677. ^{1}H NMR (CD_2Cl_2) δ: 1.35 [s, 6H, ^2J(PtH) = 70 Hz, *Me*Pt], 3.14 [s, 2H, ^2J(PtH) = 96 Hz, CH_2Pt], 6.93 [d, 1H, ^3J(HH) = 7 Hz, C_6H_4-H^6], 6.97 [s, 1H, C_6H_4-H^2], 7.01 [dd, 1H, ^3J(HH) = 7 Hz, ^3J(HH) = 6 Hz, C_6H_4-H^5], 7.28 [d, 1H, ^3J(HH) = 6 Hz, C_6H_4-H^4], 7.58 [dd, 2H, ^3J(HH) = 7 Hz, ^3J(HH) = 8 Hz, ^4J(HH) = 2 Hz, bipy-H^5], 8.12 [dd, 2H, ^3J(HH) = 8 Hz, ^4J(HH) = 2 Hz, bipy-H^4], 8.22 [d, 2H, ^3J(HH) = 8 Hz, ^4J(HH) = 2 Hz, bipy-H^3], 8.52 [d, 2H, ^3J(HH) = 7 Hz, ^4J(HH) = 2 Hz, bipy-H^6]. Anal. calcd. for $C_{21}H_{20}BrN_3PtO$ (%): C 41.66, H 3.33, N 6.94; found: C 41.34, H 3.02, N 6.60.

[$PtBrMe_2$(2-$CH_2C_5H_4N$)(bu$_2$bipy)], 5

To a solution of [$PtMe_2$(bu$_2$bipy)] (0.205 g, 0.4 mmol) in CH_2Cl_2 (4 mL) was added a solution of 2-(bromomethyl)-pyridine hydrobromide (0.123 g, 0.48 mmol) and excess NEt_3 (2.5 mL) in CH_2Cl_2 (5 mL). After 10 min, water (5 mL) was added, the mixture was extracted with CH_2Cl_2 (3 × 5 mL), the extracts were dried over anhydrous $MgSO_4$, filtered, and the solvent was removed under vacuum to give the product as a white solid, which was recrystallized from CH_2Cl_2/pentane. Yield: 197 mg. ^{1}H NMR (CD_2Cl_2) δ: 1.41 [s, 18H, *t*-Bu], 1.53 [s, 6H, ^2J(PtH) = 69 Hz, *Me*Pt], 2.97 [s, 2H, ^2J(PtH) = 99 Hz, CH_2Pt], 6.56 [m, 1H, ^3J(HH) = 7 Hz, py-H^5], 6.69 [d, 1H, ^3J(HH) = 7 Hz, py-H^3], 7.06 [m, 1H, ^3J(HH) = 7 Hz, py-H^4], 7.40 [d, 2H, ^3J(HH) = 6 Hz, bipy-H^5], 7.58 [m, 1H, ^4J(HH) = 2 Hz, py-H^6], 7.94 [s, 2H, bipy-H^3], 8.51 [d, 2H, ^3J(HH) = 6 Hz, bipy-H^6]. ESI-MS *m*/*z*: 585 (100) [$PtMe_2$(bu2bipy)(2-CH_2py)]$^+$. Anal. calcd. for $C_{26}H_{36}BrN_3Pt$ (%): C 46.92, H 5.45, N 6.31; found: C 46.48, H 5.07, N 6.04.

[$PtBrMe_2$(3-$CH_2C_5H_4N$)(bu$_2$bipy)], 6

This was prepared similarly from [$PtMe_2$(bu$_2$bipy)] (0.205 g, 0.4 mmol) and 3-(bromomethyl)pyridine hydrobromide (0.123 g, 0.48 mmol). Yield: 110 mg. ^{1}H NMR (CD_2Cl_2) δ: 1.42 [s, 18H, *t*-Bu], 1.50 [s, 6H, ^2J(PtH) = 68 Hz, *Me*Pt], 2.74 [s, 2H, ^2J(PtH) = 95 Hz, CH_2Pt], 6.54 [dd, 1H, ^3J(HH) = 7.5 Hz, ^3J(HH) = 5 Hz, py-H^5], 6.77 [d, 1H, ^3J(HH) = 7.5 Hz, py-H^4], 7.41 [s, 1H, py-H^2], 7.45 [d, 2H, ^3J(HH) = 6 Hz, bipy-H^5], 7.90 [m, 1H, ^3J(HH) = 5 Hz, py-H^6], 7.93 [s, 2H, bipy-H^3], 8.56 [d, 2H, ^3J(HH) = 6 Hz, bipy-H^6]. ESI-MS *m*/*z*: 585.2 (27) [$PtMe_2$(bu$_2$bipy)(3-CH_2py)]$^+$; 1250.4 (100) [[$PtMe_2$(bu$_2$bipy)(3-CH_2py)]$^+{}_2$Br$^-$]$^+$. Anal. calcd. for $C_{26}H_{36}BrN_3Pt$ (%): C 46.92, H 5.45, N 6.31; found: C 46.71, H 5.22, N 6.08.

[$PtBrMe_2$(4-$CH_2C_5H_4N$)(bu$_2$bipy)], 7

This was prepared similarly from [$PtMe_2$(bu$_2$bipy)] (0.106 g, 0.22 mmol) and 4-(bromomethyl)pyridine hydrobromide (0.065 g, 0.26 mmol). Yield: 92 mg. ^{1}H NMR (CD_2Cl_2) δ: 1.40 [s, 18H, *t*-Bu], 1.52 [s, 6H, ^2J(PtH) = 69 Hz, *Me*Pt], 2.74 [s, 2H, ^2J(PtH) = 99 Hz, CH_2Pt], 6.17 [d, 2H, ^3J(HH) = 5 Hz, py-H^{3,5}], 7.47 [d, 2H, ^3J(HH) = 5 Hz, py-H^{2,6}], 7.74 [d, 2H, ^3J(HH) = 6 Hz, bipy-H^5], 7.94 [s, 2H, bipy-H^3], 8.54 [d, 2H, ^3J(HH) = 6 Hz, bipy-H^6]. ESI-MS *m*/*z*: 585 (7) [$PtMe_2$(bu2bipy)(4-CH_2py)]$^+$, 666 (47) [$PtBrMe_2$(bu$_2$bipy)(4-CH_2pyH)]$^+$, 1250 (100) [[$PtMe_2$(-bu$_2$bipy)(4-CH_2py)]$^+{}_2$Br$^-$]$^+$. Anal. calcd. for $C_{26}H_{36}BrN_3Pt$ (%): C 46.92, H 5.45, N 6.31; found: C 46.87, H 5.19, N 6.10.

[$PtBrMe_2$(CH_2-4-$C_6H_4CO_2H$)(DPK)], 9

To a solution of [$PtMe_2$(DPK)] (0.25 g, 0.61 mmol) in Et_2O (10 mL) was added a solution of 4-(bromomethyl)benzoic acid (0.17 g, 0.79 mmol) in Et_2O (50 mL). After 1 h, the solvent was evaporated and the product was recrystallized from CH_2Cl_2/pentane. Yield: 0.38 g (91%). ^{1}H NMR (acetone-d_6) δ: 1.36 [s, 6H, ^3J(PtH) = 71 Hz, *Me*Pt], 3.29 [s, 2H, ^3J(PtH) = 95 Hz, CH_2Pt], 6.84 [d, 2H, ^3J(HH) = 8 Hz, C_6H_4-H^2], 7.50 [d, 2H, ^3J(HH) = 8 Hz, C_6H_4-H^3], 7.73 [m, 2H, DPK-H^5], 8.25 [m, 4H, DPK-H^{3,4}], 8.61 [m, 2H, DPK-H^6]. ESI-MS *m*/*z*: 544 (100) [$PtMe_2$(CH_2-4-$C_6H_4CO_2H$)(DPK)]$^+$. Anal. calcd. for $C_{21}H_{21}BrN_2O_3Pt$ (%): C 40.40, H 3.39, N 4.49; found: C 40.10, H 3.08, N 4.12.

[$PtBrMe_2$(CH_2-4-$C_6H_4CH_2CO_2H$)(DPK)], 11

To a solution of [$PtMe_2$(DPK)] (0.061 g, 0.149 mmol) in Et_2O (4 mL) was added a solution of 4-(bromomethyl)phenylacetic acid (0.043 g, 0.188 mmol) in Et_2O (10 mL). The solvent was evaporated and the product was recrystallized from CH_2Cl_2/pentane. Yield: 0.061 g (91.1%). ^{1}H NMR (acetone-d_6) δ: 1.36 [s, 6H, ^3J(PtH) = 70 Hz, *Me*Pt], 3.19 [s, 2H, ^3J(PtH) = 92 Hz, CH_2Pt], 3.60 [s, 2H, CCH_2], 7.24 [d, 2H, ^3J(HH) = 8 Hz, C_6H_4-H^2], 7.36 [d, 2H, ^3J(HH) = 8 Hz, C_6H_4-H^3], 7.55 [m, 2H, DPK-H^5], 7.95 [m, 4H, DPK-H^{3,4}], 8.76 [m, 2H, DPK-H^6]. ESI-MS *m*/*z*: 558 (100) [$PtMe_2$(CH_2-4-$C_6H_4CH_2CO_2H$)(DPK)]$^+$. The cis isomer was identified by its ^{1}H NMR spectrum δ: 0.99 [s, 3H, ^2J(PtH) = 71 Hz, Me^a], 1.62 [s, 3H, ^2J(PtH) = 72 Hz, Me^b], 2.81 [d, lH, ^2J(H^{a}H^b) = 9 Hz, ^2J(PtH^a) = 78 Hz, PtCH^a], 3.35, 3.48 [m, 2H, ^2J(HH) = 14 Hz, CCH_2], 3.65 [d, lH, ^2J(H^{a}H^b) = 9 Hz, ^2J(PtH^b) = 98 Hz, PtCH^b]. Anal. calcd. for $C_{22}H_{23}BrN_2O_3Pt$ (%): C 41.39, H 3.63, N 4.39; found: C 41.18, H 3.53, N 4.34.

[$PtBrMe_2$(4-$CH_2C_5H_4NH$)(bu$_2$bipy)]OTf, 12/13

This was prepared in situ by addition of triflic acid (5 equiv.) to a solution of complex **7** in CD_2Cl_2. **12**: ^{1}H NMR (CD_2Cl_2) δ: 1.56 [s, 6H, ^2J(PtH) = 68 Hz, *Me*Pt], 3.07 [s, 2H, ^2J(PtH) = 106 Hz, CH_2Pt]. **13**: ^{1}H NMR (CD_2Cl_2) δ: 0.78 [s, 3H, ^2J(PtH) = 72 Hz, *Me*Pt], 1.03 [s, 3H, ^2J(PtH) = 67 Hz, *Me*Pt], 3.54 [ms, 1H, ^2J(HH) = 7 Hz, ^2J(PtH) = 78 Hz, Pt*CH*^{a}H^b], 4.40 [m, 2H, ^2J(PtH) = 110 Hz, PtCH^a*H*^{b}]. ESI-MS *m*/*z*: 666 (100) [$PtBrMe_2$(4-CH_2py-H$^+$) (bu$_2$bipy)].

Similarly prepared were the following

[$PtBrMe_2$(2-$CH_2C_5H_4NH$)(bu$_2$bipy)]OTf

^{1}H NMR (CD_2Cl_2, trans isomer) δ: 1.68 [s, 6H, ^2J(PtH) = 72 Hz, *Me*Pt], 3.75 [s, 2H, ^2J(PtH) = 115 Hz, CH_2Pt]. ESI-

MS *m*/*z*: 585 (100) [$PtMe_2$(2-CH_2py) (bu_2bipy)]$^+$, 666 (11) [$PtBrMe_2$(2-CH_2py-H^+) (bu_2bipy)].

[PtBrMe$_2$(3-CH$_2$C$_5$H$_4$NH)(bu$_2$bipy)]OTf

^{1}H NMR (CD_2Cl_2, trans isomer) δ: 1.71 [s, 6H, ^2J(PtH) = 75 Hz, *Me*Pt], 3.26 [s, 2H, ^2J(PtH) = 102 Hz, *CH*$_2$Pt]. ESI-MS *m*/*z*: 585 (100) [$PtMe_2$(3-CH_2py) (bu_2bipy)]$^+$, 666 (10) [$PtBrMe_2$(3-CH_2py-H^+) (bu_2bipy)].

[PtMe$_2$(bu$_2$bipy)(2-CH$_2$py)]OTf, 15·OTf

To a solution of [$PtBrMe_2$(2-CH_2py)(bu_2bipy)] (0.0524 g, 0.08 mmol) in CH_2Cl_2 (6 mL) was added a solution of AgOTf (0.0442 g, 0.17 mmol) in acetone (2 mL). The mixture was stirred for 20 min, decolorizing charcoal was added, the solution was filtered, and the solvent was evaporated to give the product as a pale yellow solid. Yield: 0.046 g. ^{1}H NMR (CD_2Cl_2 at –10 °C) δ: 0.56 [s, 3H, ^2J(PtH) = 69 Hz, *Me*Pt], 1.43, 1.44 [s, 18H, *t*-Bu], 1.85 [s, 3H, ^2J(PtH) = 69 Hz, *Me*Pt], 2.53, 2.62 [m, 2H, ^2J(PtH) = 99 Hz, *CH*^{a}*H*^{b}Pt], 6.95–8.95 [m, 10H, py, bipy]. ESI-MS *m*/*z*: 585 (100) [$PtMe_2$(bu_2bipy)(2-CH_2py)]$^+$. Anal. ca1cd. for $C_{27}H_{36}F_3N_3O_3PtS$ (%): C 44.14, H 4.94, N 5.72; found: C 43.76, H 5.13, N 5.41.

[{PtMe$_2$(bu$_2$bipy)(3-CH$_2$py)}$_n$]OTf$_n$, 16·OTf

This was prepared similarly from [$PtBrMe_2$(3-CH_2py)(bu_2bipy)] (0.051 g, 0.08 mmol) and AgOTf (0.047 g, 0.18 mmol). Yield: 0.041 g. ESI-MS *m*/*z*: 585 (100) [$PtMe_2$(3-CH_2py)(bu_2bipy)]$^+$, 1319 (23) [{$PtMe_2$(bu_2bipy)(3-CH_2py)}$_2$OTf]$^+$. Anal. ca1cd. for $C_{27}H_{36}F_3N_3O_3PtS$ (%): C 44.14, H 4.94, N 5.72; found: C 43.68, H 5.02, N 5.36.

[{PtMe$_2$(bu$_2$bipy)(4-CH$_2$py)}$_n$]OTf$_n$

This was prepared similarly from [$PtBrMe_2$(4-CH_2py)(bu_2bipy)] (0.0498 g, 0.075 mmol) and AgOTf (0.040 g, 0.16 mmol). Yield: 0.030 g. ESI-MS *m*/*z*: 585 (100) [$PtMe_2$(bu_2bipy)(4-CH_2py)]$^+$, 1319 (4) [$PtMe_2$(bu_2bipy)(4-CH_2py)]$^+{}_2OTf^-]^+$, 1027 (5) [$PtMe_2$(bu_2bipy)(4-CH_2py)]$^+{}_3OTf^-]^{2+}$. Anal. ca1cd. for $C_{27}H_{36}F_3N_3O_3PtS$ (%): C 44.14, H 4.94, N 5.72; found: C 43.90, H 5.13, N 5.30.

[PtMe$_2$(CH$_2$-4-C$_6$H$_4$COOH)(bu$_2$bipy)(OH$_2$)][BF$_4$], 17·BF$_4$

A solution of $AgBF_4$ (10.5 mg, 0.054 mmol) in acetone (5 mL) was added dropwise to complex **11** (38.5 mg, 0.054 mmol) in acetone (10 mL) and allowed to stir for 1 h. AgBr began to precipitate and the mixture was filtered through Celite. After 2 h of stirring at room temperature, the solvent was evaporated. The product was washed with pentane to give a white solid. Yield: 35.0 mg (88%). ^{1}H NMR (acetone-d_6) δ: 1.33 [s, br, 6H, ^2J(PtH) = 64 Hz, *Me*Pt], 1.41 [s, 18H, *t*-Bu], 2.38 [s, 2H, ^2J(PtH) = 94 Hz, *CH*$_2$Pt], 3.19 [s, br, 2H, $PtOH_2$], 6.52 [br, 2H, C_6H_4(H^2, H^6)], 7.26 [br, 2H, C_6H_4(H^3, H^5)], 7.79 [br, 2H, bipy(H^5, $H^{5'}$)], 8.55 [br, 2H, bipy(H^3, $H^{3'}$)], 8.74 [br, 2H, bipy(H^6, $H^{6'}$)]. Anal calcd. for $C_{28}H_{39}BF_4N_2O_3Pt{\cdot}Me_2CO$ (%): C 47.04, H 5.73, N 3.54; found: C 47.11, H 5.76, N 3.42.

[PtMe$_2$(3-CH$_2$C$_6$H$_4$CN)(DPK-OH$_2$)]OTf, 18·OTf

To a solution of [$PtBrMe_2$(DPK)(3-$CH_2C_6H_4CN$)] (0.056 g, 0.09 mmol) in CH_2Cl_2 (6 mL) was added a solution of AgOTf (0.026 g, 0.1 mmol) in acetone (2 mL). The mixture was stirred for 20 min, decolorizing charcoal was added, the solution was filtered, and the solvent was removed under vacuum to give a pale yellow solid, which was recrystallized from CH_2Cl_2/pentane. Yield: 0.033 g. IR (cm^{-1}): ν(OH) 3250, ν(CN) 2250, ν(C=O) absent. ^{1}H NMR (CD_2Cl_2) δ: 1.18 [s, 3H, ^2J(PtH) = 72 Hz, *Me*Pt], 1.48 [s, 3H, ^2J(PtH) = 81 Hz, *Me*Pt], 3.03 [d, 1H, ^2J(PtH) = 73 Hz, ^2J(HH) = 10 Hz, *CH*$_2$Pt], 3.55 [d, 1H, ^2J(PtH) = 103 Hz, ^2J(HH) = 10 Hz, *CH*$_2$Pt], 7.08 [t, 1H, ^3J(HH) = 8 Hz, C_6H_4-H^5], 7.24 [d, 1H, ^3J(HH) = 6 Hz, C_6H_4-H^4], 7.25 [s, 1H, C_6H_4-H^2], 7.30 [m, 1H, ^3J(HH) = 6 Hz, bipy-$H^{5'}$], 7.34 [d, 1H, ^3J(HH) = 8 Hz, C_6H_4-H^6], 7.57 [t, 1H, ^3J(HH) = 7 Hz, bipy-H^5], 7.78 [d, 1H, ^3J(HH) = 5 Hz, bipy-$H^{3'}$], 8.02 [m, 1H, ^3J(HH) = 7 Hz, bipy-H^3], 8.03 [m, 1H, ^3J(HH) = 5 Hz, bipy-$H^{4'}$], 8.05 [m, 1H, bipy-H^4], 8.08 [d, 1H, ^3J(HH) = 8 Hz bipy-$H^{6'}$], 8.44 [d, 1H, ^3J(HH) = 6 Hz bipy-H^6]. ESI-MS *m*/*z*: 495 (100) [Pt(DPK)(3-$CH_2C_6H_4CN$)]$^+$, 525 (66) [$PtMe_2$(DPK)(3-$CH_2C_6H_4CN$)]$^+$, 543 (16) [$PtMe_2$(DPK)(3-$CH_2C_6H_4CN$) + H_2O]$^+$. Anal. calcd. for $C_{22}H_{22}F_3N_3O_5PtS$ (%): C 38.15, H 3.20, N 6.07; found: C 37.90, H 3.29, N 5.77.

[PtMe$_2$(4-CH$_2$C$_6$H$_4$CH$_2$CO$_2$H)(DPK-OH$_2$)][CF$_3$CO$_2$], 19·O$_2$CCF$_3$

To a solution of [$PtBrMe_2$(4-$CH_2C_6H_4CH_2CO_2H$)(DPK)] (0.050 g, 0.0783 mmol) in Et_2O (15 mL) was added a solution of AgO_2CCF_3 (0.018 g, 0.0815 mmol) in THF (2 mL). The mixture was stirred for 30 min, decolorizing charcoal was added, the mixture was filtered, and the solvent was evaporated to give a yellow solid, which was recrystallized from ether/pentane. ^{1}H NMR (CD_2Cl_2) δ: 1.05 [s, 3H, ^2J(PtH) = 71 Hz, *Me*^{a}Pt], 1.34 [s, 3H, ^2J(PtH) = 71 Hz, *Me*^{b}Pt], 2.80 [d, lH, ^2J(H^{a}H^b) = 10 Hz, ^2J(PtH^a) = 88 Hz, *CH*^{a}Pt], 3.44, 3.47 [m, 2H, CCH_2], 3.65 [d, lH, ^2J(H^{a}H^b) = 10 Hz, ^2J(PtH^b) = 95 Hz, *CH*^{b}Pt], 6.74 [d, 2H, ^3J(HH) = 8 Hz, C_6H_4-H^3], 6.92 [d, 2H, C_6H_4-H^2], 7.20–8.33 [m, 8H, DPK]. ESI-MS (M = [$PtMe_2$(4-$CH_2C_6H_4CH_2CO_2H$)(DPK-OH_2)][CF_3CO_2]) *m*/*z*: 1151 (5) [2M-2CF_3CO_2-H_3O]$^+$, 1133 (7) [2M-2CF_3CO_2-H_3O]$^+$, 1115 (5) [2M-2CF_3CO_2-2H_2O-H)]$^+$, 576 (100) [M-CF_3CO_2]$^+$, 558 (94) [M-CF_3CO_2-H_2O]$^+$. The trans isomer was identified by its ^{1}H NMR spectrum δ: 1.13 [s, 6H, ^2J(PtH) = 71 Hz, *Me*Pt], 3.39 [s, 2H, ^2J(PtH) = 91 Hz, *CH*$_2$Pt], 3.51 [s, 2H, CCH_2]. Anal. calcd. for $C_{24}H_{25}F_3N_2O_6Pt$ (%): C 41.80, H 3.65, N 4.06; found: C 41.56, H 3.87, N 3.81.

X-ray structure determinations

A crystal was mounted on a glass fibre and data were collected using a Nonius Kappa CCD diffractometer. Details of the data collection, absorption correction, and structure refinement are given in Table 1 and in the Supplementary data. Nonhydrogen atoms were refined with anisotropic thermal parameters, except in cases of disorder. The hydrogen atom positions were calculated geometrically and were included as riding on their respective heavy atoms. Brief comments on unusual features of individual structures are given below. The accuracy of bond distances was low in some cases as a result of disorder, but the structures are all well-defined.

Table 1. Crystal data and structure refinement.

Complex	**3**	**5**	**8**	**10**	**12/14**· $CHCl_3$	**17**· $1.5Me_2CO{\cdot}0.5C_6H_{14}$	**19**·O_2CCF_3
Formula	$C_{28}H_{36}BrN_3Pt$	$C_{26}H_{36}BrN_3Pt$	$C_{28}H_{37}BrN_2O_2Pt$	$C_{29}H_{39}BrN_2O_2Pt$	$C_{27}H_{38}Br_{0.36}Cl_{4.64}N_3Pt$	$C_{35.}H_{48}BF_4N_2O_{4.5}Pt$	$C_{23}H_{23}F_3N_2O_6Pt$
Fw	689.60	665.58	708.60	722.62	792.95	856.66	675.52
T (K)	150(2)	150(2)	150(2)	298(2)	295(2)	150(2)	100(2)
λ	0.71073	0.71073	0.71073	0.71073	0.71073	0.71073	0.71073
Cryst. syst.	Orthorhombic	Monoclinic	Monoclinic	Orthorhombic	Monoclinic	Tetragonal	Triclinic
Sp. Gp.	*Pbca*	$P2_1/c$	$P2_1/n$	*Pbca*	$P2_1/c$	$P\text{-}42_1c$	*P*-1
Cell dimensions							
a (Å)	22.9401(8)	12.7645(3)	7.1812(4)	22.6325(3)	12.1138(5)	26.7467(3)	7.8246(5)
b (Å)	20.2766(6)	11.5506(3)	12.7284(7)	21.5949(3)	21.932(1)	26.7467(3)	17.515(1)
c (Å)	11.4773(4)	35.2208(9)	30.2139(17)	12.0756(2)	12.1444(6)	10.9285(2)	17.683(1)
α	90	90	90	90	90	90	87.580(4)
β	90	93.674(1)	93.785(2)	90	91.870(4)	90	85.829(4)
γ	90	90	90	90	90	90	86.391(4)
V (Å^3)	5338.6(3)	5182.2(2)	2755.7(3)	5901.9(1)	3224.8(3)	7818.1(2)	2410.5(3)
Z	8	8	4	8	4	8	4
$D_{calcd.}$ (Mg m^{-3})	1.716	1.706	1.708	1.627	1.633	1.456	1.861
μ (mm^{-1})	6.774	6.975	6.568	6.135	5.202	3.647	5.885
Reflns.	46409	50713	12865	61611	26097	76143	16428
Data/restr./param.	4719/279/306	9150/0/559	4155/288/309	5208/244/291	5675/283/337	6867/29/461	9418/596/632
Gof	1.127	1.043	1.079	1.412	1.255	1.024	1.095
R_1 ($I>2\sigma(I)$)	0.058	0.062	0.065	0.092	0.137	0.037	0.066
wR_2 (all data)	0.095	0.167	0.160	0.223	0.313	0.099	0.175

[PtBrMe$_2$(3-CH$_2$C$_6$H$_4$CN)(bu$_2$bipy)], 3

There was minor unresolved disorder of the *t*-butyl groups.

[PtBrMe$_2$(2-CH$_2$C$_5$H$_4$N)(bu$_2$bipy)], 5

There were two independent molecules in the asymmetric unit.

[PtBrMe$_2$(CH$_2$-4-C$_6$H$_4$CO$_2$H)(bu$_2$bipy)], 8

The crystal was twinned and the twinning was successfully modelled.

[PtBrMe$_2$(CH$_2$-4-C$_6$H$_4$CH$_2$CO$_2$H)(bu$_2$bipy)], 10

The CH$_2$-4-C$_6$H$_4$CH$_2$CO$_2$H groups were disordered. The disordered atoms were modeled isotropically at a 0.50/0.50 ratio.

[PtBr$_{0.36}$(Cl$_{0.64}$)Me$_2$(4-CH$_2$C$_5$H$_4$NH)(bu$_2$bipy)]Cl·CHCl$_3$, 12/14

The crystal was twinned, with evidence for a multiple twin. The twinning was not modeled successfully, and so the agreement factors are large, but the structure is clearly defined.

[PtMe$_2$(CH$_2$-4-C$_6$H$_4$CO$_2$H)(OH$_2$)(bu$_2$bipy)][BF$_4$]·1.5Me$_2$CO·0.5C$_6$H$_{14}$, 17

There was 50:50 disorder of the carboxylic acid group. In one component form, there was a hydrogen bond to an acetone molecule while, in the other component, that void contained a disordered hexane molecule, which was refined isotropically. The hexane molecule was not well-defined.

[PtMe$_2$(4-CH$_2$C$_6$H$_4$CH$_2$CO$_2$H)(DPK-OH$_2$)][CF$_3$CO$_2$], 19·O$_2$CCF$_3$

There were two independent molecules in the asymmetric unit, and they were connected through hydrogen bonds. The crystal was twinned and the twinning was successfully modeled.

Supplementary data

Supplementary data for this article are available on the journal Web site (canjchem.nrc.ca) or may be purchased from the Depository of Unpublished Data, Document Delivery, CISTI, National Research Council Canada, Ottawa, ON K1A 0R6, Canada. DUD 3933. For more information on obtaining material, refer to cisti-icist.nrc-cnrc.gc.ca/cms/unpub_e.shtml. CCDC 711234–711240 contain the X-ray data in CIF format for seven complexes for this manuscript. These data can be obtained, free of charge, via www.ccdc.cam.ac.uk/conts/retrieving.html (Or from the Cambridge Crystallographic Data Centre, 12 Union Road, Cambridge CB2 1EZ, UK; fax +44 1223 336033; or deposit@ccdc.cam.ac.uk).

Acknowledgement

We thank the Natural Sciences and Engineering Research Council of Canada (NSERC) for financial support.

References

(1) This article is part of a Special Issue dedicated to Professor T. Ziegler.
(2) Gilbert, T. M.; Hristov, I.; Ziegler, T. *Organometallics* **2001**, *20*, 1183. doi:10.1021/om0007264.
(3) Hayaki, S.; Yokogawa, D.; Sato, H.; Sakaki, S. *Chem. Phys. Lett.* **2008**, *458*, 329. doi:10.1016/j.cplett.2008.04.116.
(4) Rendina, L. M.; Puddephatt, R. J. *Chem. Rev.* **1997**, *97*, 1735. doi:10.1021/cr9704671. PMID:11848891.
(5) Jamali, S.; Nabavizadeh, S. M.; Rashidi, M. *Inorg. Chem.* **2005**, *44*, 8594. doi:10.1021/ic0511064. PMID:16271001.
(6) Jenkins, H. A.; Yap, G. P. A.; Puddephatt, R. J. *Organometallics* **1997**, *16*, 1946. doi:10.1021/om961011x.
(7) (a) Scott, J. D.; Puddephatt, R. J. *Organometallics* **5**, *1986*, 1538; (b) Monaghan, P. K.; Puddephatt, R. J. *J. Chem. Soc. Dalton* **1988**, 595. doi:10.1039/dt9880000595.
(8) Achar, S.; Puddephatt, R. J. *Organometallics* **1995**, *14*, 1681. doi:10.1021/om00004a023.
(9) (a) Braga, D.; Grepioni, F. *Acc. Chem. Res.* **2000**, *33*, 601 doi:10.1021/ar990143u. PMID:10995197.; (b) Hosseini, M. W. *Acc. Chem. Res.* **2005**, *38*, 313 doi:10.1021/ar0401799. PMID:15835878.; (c) Gerhardt, W. W.; Zacchero, A. J.; South, C. R.; Bunz, U. H. F.; Weck, M. *Chem. Eur. J.* **2007**, *13*, 4467 doi:10.1002/chem.200601601.; (d) Severin, K. *J. Chem. Soc. Chem. Comm.* **2006**, 3859.
(10) Fraser, C. S. A.; Jenkins, H. A.; Jennings, M. C.; Puddephatt, R. J. *Organometallics* **2000**, *19*, 1635. doi:10.1021/om990942g.
(11) Fraser, C. S. A.; Jennings, M. C.; Puddephatt, R. J. *J. Chem. Soc. Chem. Comm.* **2001**, 1310.
(12) Fraser, C. S. A.; Jennings, M. C.; Puddephatt, R. J. *J. Chem. Soc. Chem. Comm.* **2002**, 1224.
(13) Fraser, C. S. A.; Eisler, D. J.; Puddephatt, R. J. *Polyhedron* **2006**, *25*, 266. doi:10.1016/j.poly.2005.08.020.
(14) Zhang, F.; Jennings, M. C.; Puddephatt, R. J. *Chem. Comm.* **2007**, 1496. PMID:17406685.
(15) (a) Jain, V. K.; Rao, G. S.; Jain, L. *Adv. Organomet. Chem.* **1987**, *27*, 113 doi:10.1016/S0065-3055(08)60027-1.; (b) Canty, A. J.; Patel, J.; Rodemann, T.; Ryan, J. H.; Skelton, B. W.; White, A. H. *Organometallics* **2004**, *23*, 3466 doi:10.1021/om040023c.; (c) Mamtora, J.; Crosby, S. H.; Newman, C. P.; Clarkson, G. J.; Rourke, J. P. *Organometallics* **2008**, *27*, 5559. doi:10.1021/om800583c.
(16) Puddephatt, R. J. *Angew. Chem. Int. Ed. Engl.* **2002**, *41*, 261. doi:10.1002/1521-3773(20020118)41:2<261::AID-ANIE261>3.0.CO;2-5. PMID:12491404.
(17) The chelating 2-pyridylmethyl complexes such as hypothetical **15** are strained, and reversible ring-opening to form a dimer has precedent. Vergnaud, J.; Borissou, D. *J. Chem. Soc. Dalton* **2007**, 2370. doi:10.1039/b704993p.
(18) (a) Vinogradov, S. N.; Linnell, R. H. *Hydrogen Bonding;* Van Nostrand Reinhold: New York, 1971; (b) Jeffrey, G. A. *An Introduction to Hydrogen Bonding;* Oxford University Press: Oxford, 1997.
(19) Kryachko, E. S.; Nguyen, M. T. *J. Chem. Phys.* **2001**, *115*, 833. doi:10.1063/1.1371516.
(20) (a) Abrahams, B. F.; Hudson, T. A.; Robson, R. *Chem. Eur. J.* **2006**, *12*, 7095 doi:10.1002/chem.200600323.; (b) Papaefstathiou, G. S.; Perlepes, S. P. *Comments Inorg. Chem.* **2002**, *23*, 249 doi:10.1080/02603590213135.; (c) Padhi, S. K.; Sahu, R. *Polyhedron* **2008**, *27*, 2662 doi:10.1016/j.poly.2008.05.024.; (d) Li, C.-J.; Tong, M.-L.; Ng, S. K. *Acta Crystallogr.* **2005**, *E61*, m229.

(21) Zhang, F.; Broczkowski, M. E.; Jennings, M. C.; Puddephatt, R. J. *Can. J. Chem.* **2005**, *83*, 595. doi:10.1139/v05-028.
(22) Bock, H.; Van, T. T. H.; Schodel, H.; Dienelt, R. *Eur. J. Org. Chem.* **1998**, 585. doi:10.1002/(SICI)1099-0690(199804)1998:4<585::AID-EJOC585>3.0.CO;2-B.
(23) (a) Scott, J. D.; Puddephatt, R. J. *Organometallics* **1983**, *2*, 1643 doi:10.1021/om50005a028.; (b) Hill, G. S.; Irwin, M. J.; Levy, C. J.; Rendina, L. M.; Puddephatt, R. J. *Inorg. Synth.* **1998**, *32*, 149. doi:10.1002/9780470132630.ch25.
(24) Becke, A. D. *Phys. Rev. A* **1988**, *38*, 3098. doi:10.1103/PhysRevA.38.3098. PMID:9900728.
(25) Cooper, J.; Ziegler, T. *Inorg. Chem.* **2002**, *41*, 6614. doi:10.1021/ic020294k. PMID:12470056.

The affinity of HGGG, GHGG, GGHG, and GGGH peptides for copper(II) and the structures of their complexes — An ab initio study[1]

Stephen D. Barry, Gail A. Rickard, M. Jake Pushie, and Arvi Rauk

Abstract: The structures and relative free energies in aqueous solution of the Cu(II) complexes of the "histidine walk" peptides, $AcHGGGNH_2$, $AcGHGGNH_2$, $AcGGHGNH_2$, and $AcGGGHNH_2$, were determined as a function of pH. Numerous structures of each species were found by gaseous- and solution-phase geometry optimization at the B3LYP/6–31G(d) level, and the effect of solvation estimated by the IEFPCM continuum solvation model. Free energies of solvation of the ionic species are large and favour structures with an extended peptide chain. In all Cu(II)–peptide complexes, deprotonation of two amide groups occurs readily at or below pH 7. In each system, the most abundant species at pH 7 is a neutral 1:1 complex with N3O1 coordination pattern. Binding in the forward direction toward the C terminus is preferred. The results are compared to recent experimental spectroscopic and potentiometric studies on related systems. Alternative explanations are offered for some of the experimental observations.

Key words: copper–peptides, theoretical, DFT, prion, binding affinities, CD spectra.

Résumé : On a déterminé les structures et les énergies libres, en solutions aqueuses et en fonction du pH, des complexes de Cu(II) des peptides de la série histidine, $AcHGGGNH_2$, $ACGHGGNH_2$, $AcGGHGNH_2$ et $ACGGGHNH_2$. On a déterminé les diverses structures de chacune des espèces, en phase gazeuse et en solution, par une optimisation de la géométrie au niveau B3LYP/6-31G(d) et on a évalué l'effet de solvatation par le modèle de solvatation continue IEEPCM. Les énergies libres de solvatation des espèces ioniques sont importantes et elles favorisent les structures avec une chaîne peptidique étendue. Dans tous les complexes Cu(II)–peptide, la déprotonation de deux groupes amides se produit facilement à des pH égal ou inférieurs à 7. Dans chaque système, l'espèce la plus abondante au pH 7 est un complexe 1:1 neutre comportant un patron de coordination N3O1. La fixation est favorisée dans la direction allant vers la position C-terminale. On compare les résultats obtenus ici avec ceux rapportés récemment pour des études expérimentales spectroscopiques et potentiométriques sur des systèmes apparentés. Des explications alternatives sont proposées pour un certain nombre d'observations expérimentales.

Mots-clés : complexes cuivre–peptides, théorique, théorie de la fonctionnelle de densité (TFD), affinités de fixation, spectres de dichroïsme circulaire (DC).

[Traduit par la Rédaction]

Introduction

The pathology of many neurodegenerative diseases involves the disruption of normal trafficking of a metal ion which is ultimately related to its binding to a biologically prevalent protein or peptide. These include Alzheimer's, Parkinson's, and Huntington's diseases, as well as the prion diseases, also known as transmissible spongiform encephalopathies (TSEs), which result in the deterioration of neurons.[2,3] The misfolding of these proteins/peptides, which in some instances may involve metal binding, is believed to cause the observed neurotoxicity of these species.[2,4,5] Especially in the case of TSEs and Alzheimer's disease (AD), copper is involved in peptide–protein binding, and has been shown to be a contributor to the neurotoxicity of the beta amyloid peptide of AD.[6–9]

The prion protein, PrP, a 231 amino acid protein, is a normal component of body tissues and is found at high concentrations in the central nervous systems of humans, as well as various other species, including mammals, avians, and yeast. Prion diseases occur when the cellular form of the protein (PrP^C) is converted into its scrapie form (PrP^{Sc}), which readily aggregates. PrP selectively binds Cu(II) over other bioavailable metal ions.[10] The first Cu(II)-binding region of PrP is termed the octarepeat region, which has four or more tandem repeats of the same 8 amino acids, PHGGGWGQ, beginning at Pro60 (human numbering) and repeating at Pro68, Pro76, and Pro84 in the N-terminal domain. The link between this region and the pathology of Creutzfeldt–Jakob disease (CJD) is apparent, since individuals with extra octarepeats are more prone to developing CJD.[11,12] The association constants of Cu(II) binding to the octarepeat region are varied, but are generally accepted to be between 10^9 M^{-1} [13] and 10^6 M^{-1}.[14]

As in the case of the prion protein, and the beta amyloid peptide of AD, virtually all physiological copper is bound to

Received 11 November 2008. Accepted 21 January 2009. Published on the NRC Research Press Web site at canjchem.nrc.ca on 2 June 2009.

S.D. Barry, G.A. Rickard, M.J. Pushie, and A. Rauk.[1] Department of Chemistry, University of Calgary, Calgary, AB T2N 1N4, Canada.

[1]Corresponding author (e-mail: rauk@ucalgary.ca).

one or more His residues in tetracoordinated square-planar complexes. Experimentally, tetragonal coordination is preferred to pentacoordination.[15] Comparison of the affinity of Cu(II) for biologically available ligands, modeled theoretically with small compounds, has shown that the imidazole group of His is a better ligand than any other,[16,17] with the exception of a thiolate group (i.e., cysteine).[16] However, it is well known that Cu(II) has a considerable acidifying effect on the amide N–H bond with the consequence that one or more deprotonated amide groups may be ligands to the Cu(II) ion even at physiological pH 7.[18–21]

Detailed information about the structures of some Cu(II)–peptide complexes is available from crystallography, but information about structures in solution comes from electron paramagnetic resonance (EPR), circular dichroism (CD), and infrared (IR) and UV–vis spectroscopies, and is much less detailed. Millhauser and co-workers were able to partially clarify the binding of Cu(II) to PrP from their use of X-ray crystallography, circular dichroism, and electron paramagnetic resonance spectroscopy studies.[22–24] They determined the prominent binding modes in both solid and solvated forms at various pH values. At pH 7.4, two binding modes existed, called component 1 and component 2. The major component, component 1, has a square-planar binding environment about the Cu center consisting of three N ligands and an oxygen atom (i.e., N3O1). It was established that one of the N atoms is N_π of His and the other two are deprotonated amides of the adjacent two Gly residues. The oxygen is the carbonyl oxygen of the second Gly. In the absence of the Trp residue, i.e., HGGG or HGG, component 2 is dominant. Its binding stoichiometry was tentatively identified as N2O2. These results supported previous experimentally determined binding environments at varied pH values.[25,26] It was found that the minimum peptide sequence required to model the observed N3O1 and N2O2 environments of the full length Cu(II)-bound octarepeat region is the fragment "HGGG".[22,24]

Pushie and Rauk originally analyzed the binding of Cu to PrP at a high theoretical level,[27] using a truncated model of the "HGGG" fragment in which the N- and C-terminal groups were replaced by hydrogen atoms. Nevertheless, the analysis provided some interesting insights into the interaction between Cu and PrP, including confirming the stability of the structure and binding modes determined by Millhauser and co-workers.[22–24] This included identifying both component 1 and component 2, which were the most stable neutral and cationic structures, respectively.

Several recent theoretical[28–30] studies of models of the octarepeat region of the prion protein have appeared since this paper was in preparation. Marino et al.[28] carried out gaseous-phase calculations of the pentapeptide, Cu–HGGGW with and without an additional water molecule, on structures adapted from the crystal structure of Millhauser and coworkers (tetragonal Cu with N3O1 coordination).[23] They found that the water would not occupy a fifth site in the coordination sphere of the metal but additional stabilization ensued if the Trp residue adopted a position over the square plane. Furlan et al.[29] also adopted the crystal structure as a starting geometry and carried out 1 ps ab initio molecular dynamics simulations of Cu–HGGG and Cu–HGGGW surrounded by water. They found that a water molecule would not occupy the fifth coordination site even in the presence of the Trp residue. Riihimäki et al. carried out MD simulations with an empirical forcefield on copper bound to the full octarepeat unit, PHGGGWGQ, also adopting the crystal structure for the tetragonal copper binding environment. With an empirical forcefield, additional coordination to copper could only arise due to electrostatic attraction. A carbonyl group was able to occupy the fifth coordination site.

In the truncated HGGG model, and in the PrP octarepeats, the peptide wraps around the Cu(II) in the forward direction. This was attributed in part to the presence of the Pro residue which precludes full binding in the reverse direction. Mammalian PrP also has two additional His residues capable of Cu(II) binding within the N-terminal domain, located between the octarepeat region and the structured C-terminal domain — these are His96 and His111. The most recent reevaluation of Cu(II) coordination with this region of PrP by Jones et al. supports binding of Cu(II) at His96 and His111 in a noncooperative manner.[31] At physiological pH, the Cu(II) is bound within an N3O1 or N4 coordination environment. Binding at His96 or His111 proceeds in the reverse direction — from the anchoring His residue toward the N-terminus.

The objectives of this work are threefold: (1) determine the structures of the most stable species in which Cu(II) is bound to a peptide fragment containing an anchoring His residue, as a function of pH; (2) estimate the binding affinities of the structures; and (3) establish the propensity of the Cu(II) to coordinate in a forward or reverse direction relative to the His residue in the absence of specific interactions with side chains.

We adopt as models, the four tetrapeptides, $AcHGGGNH_2$ (**a**), $AcGHGGNH_2$ (**b**), $AcGGHGNH_2$ (**c**), and $AcGGGHNH_2$ (**d**), to which we refer simply as HGGG (**a**), GHGG (**b**), GGHG (**c**), and GGGH (**d**), respectively. These are shown in Fig. 1*a*. The overlapping nature of the models affords comparison of four distinct binding modes as illustrated in Fig. 1*b*. In each case, the Cu(II) can bind to the His residue and may coordinate an oxygen atom or an N atom from one or more of the flanking amide groups. The amide may be protonated or deprotonated. The binding may be in the forward (toward the C terminus) or reverse (toward the N terminus) direction, and may potentially bracket the His residue (middle-forward or middle-reverse). In Fig. 1 and the following figures, all structures are shown with the N-terminal acetyl group to the left.

Methods

Calculations were performed using the Gaussian 03 suite of electronic structure codes.[32] With several exceptions, all optimizations were performed in vacuo without using geometry or symmetry constraints, using the B3LYP hybrid functional method[33] and the 6–31G(d) basis set. Harmonic frequency analysis was performed at the B3LYP/6–31G(d) level, to ensure that a minimum energy stationary point was located on the potential energy surface (no imaginary frequencies). The harmonic frequency data was used to obtain enthalpies, entropies, and zero-point energies for each structure. The zero-point energies were scaled by a factor of

Fig. 1. (*a*) The most stable structures of the four peptide models in water. (*b*) An extended polyGly peptide chain with a central His residue, residues spanned by the four modes of Cu-binding, and the relationship to the four peptide models.

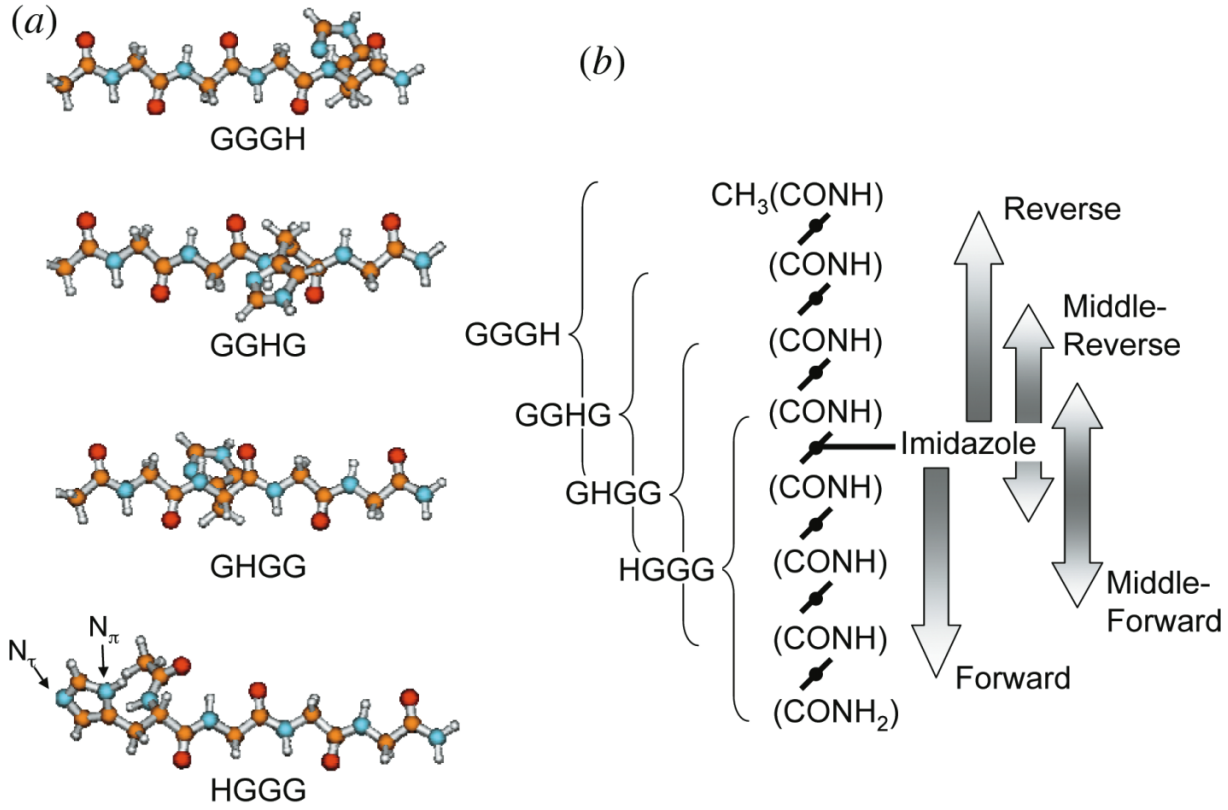

0.9806. Single point energies were calculated from optimized geometries at the B3LYP/6–311+G(2df,2p) level. These energies were used to provide more accurate relative enthalpies at 0 K.

The gaseous- and solution-phase entropies were calculated including the factor, $R\ln(n)$,[34] where R is the normal gas constant and n is an estimate of the number of conformational degrees of freedom, based on allowing 6 conformers for a free His residue, and 5 conformers for each uncoordinated Gly residue. Values of n range from $n = 1$ for some tricyclic, strongly H-bonded structures, to a maximum of $n = 1500$ for a copper-free peptide. It is important to include an estimate of n to take into account loss of conformational degrees of freedom in the formation of cyclic structures. It should be noted that an error of a factor of 2 in the estimate of n corresponds to an error of less than 2 kJ mol^{-1} in the free-energy change at 298 K, but neglect of it altogether may incur an error of as much as 18 kJ mol^{-1} (= $RT\ln(1500)$ at $T = 298$ K). We count only cyclic structures formed by coordination to the copper. Intramolecular hydrogen bonds are considered not to be stable in water. Values of n are given in the Supplementary data.

Aqueous solvation effects were modeled by using the B3LYP/6–31G(d) wave function and the self-consistent integral equation formalism of the polarizable continuum model,[35,36] as implemented in Gaussian 03 software (SCRF=IEFPCM), on the gaseous-phase-optimized geometries. The default scale factor 1.2 was used for the "united atom Hartree–Fock" (UAHF) radii of all neutral species. Selective scaling of UAHF radii was applied to charged species as follows: in cationic species, the radii of the Cu(II) ion and all atoms directly attached to it were scaled by 1.1; in anionic species, the radii of the Cu(II) ion and all formally neutral atoms directly attached to it were scaled by 1.1; the radii of atoms bearing a formal negative charge were unscaled (scale factor = 1.0). In the case of a deprotonated amide group, both the N and O atoms were unscaled. It is our experience that the selective scaling as described yields reasonably accurate absolute free energies of solvation of small charged species and the calculation of pK_a values usually to within two units.

Time-dependent (TD)[37] B3LYP with the 6–31G(d) basis, in the presence of the solvent reaction field as described above, were carried out to estimate the circular dichroism (CD)[38] spectrum for some of the species studied.

Experimental values were adopted for the free energy of solvation of the proton and water: $\Delta G_{solv}(H^+)$ = –1107 kJ mol^{-1} [39]; $\Delta G_{solv}(H_2O)$ = –16.4 kJ mol^{-1}. The value for water corresponds to the transfer of a water molecule from the gaseous phase at a concentration of 1 mol/L into aqueous medium at 55 mol/L.[40]

pK_a values reported in the text and figures were calculated from the aqueous free-energy change of the acid ionization reaction, $AH_{(aq)}{}^{m+} \rightarrow A_{(aq)}{}^{(m-1)+} + H_{(aq)}{}^{+}$. We expect that for the large systems, at the level of theoretical treatment described above, the residual errors in aqueous free-energy changes are likely to be approximately ±15 kJ mol^{-1}. This range corresponds to about ±2 pK_a units. Thus we will place emphasis only on differences that are larger than these amounts.

Fig. 2. GHGG(**b**)/Cu Structures. Ball colours: green = Cu^{2+}; orange = C; blue = N; red = O. Free-energy changes, ΔG, are in units of kJ mol^{-1} in aqueous solution.

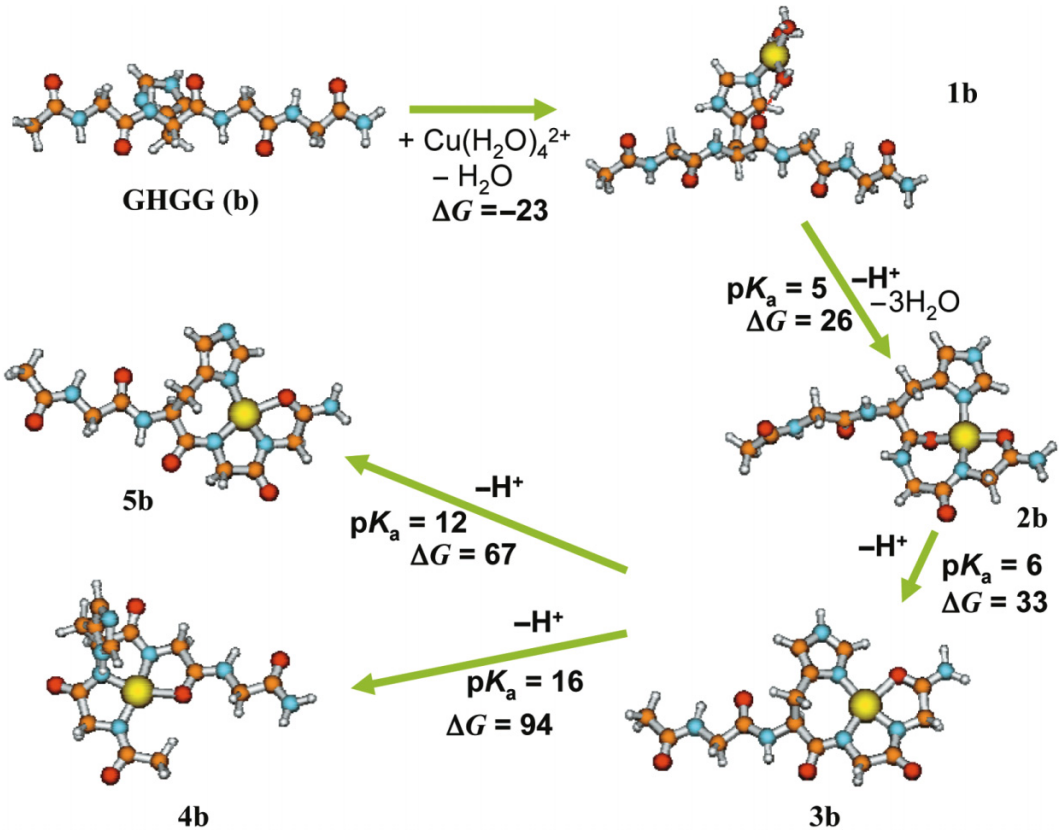

Table S1 of Supplementary data contains all primary calculated data for all species discussed below. Table S2 contains calculated CD data. The Cartesian coordinates of all species are also provided in the Supplementary data.

Results and discussion

Many conformations of each system were examined to find the most stable in solution. In most cases, the most stable conformation in the gaseous phase involved collapsed structures with a maximum number of intramolecular hydrogen bonds. However, these were often not the most stable structures in solution after addition of ΔG_{solv}; the solvent reaction field strongly favoured extended structures with a maximum exposure of the amide groups to the solvent. In the case of **1b** and **2b** (Fig. 2), there were no local minima corresponding to extended conformations in the gaseous phase, but in each case, geometry optimization with the solvent reaction field yielded a more stable conformation in solution. For these, the zero-point energy and thermal corrections were taken from the nearest gaseous-phase minimum.

The binding of Cu(II) to the peptides is strongly dependent on pH. The pK_a of a protonated His residue is approximately 7 for loss of proton from either side chain N atom. At pH < 7, both N atoms of the imidazole group are protonated, and the Cu(II) ion must compete with a proton for binding to one of the N atoms. At the present level of theory, the complexes of copper ion with water and other simple ligands are best described as tetracoordinated, having a distorted square-planar coordination sphere.[16] Since an amide carbonyl oxygen will probably not displace water from the coordination sphere, initial binding of the copper will be to one of the imidazole N atoms provided the free-energy penalty for deprotonating the N atom (= $-RT(\ln(K_a) - \ln[H^+])$ is not greater than the free energy of binding. The structures of the most stable complexes of Cu(II) with each peptide, according to the reaction,

$$[1] \quad Cu^{2+}(H_2O)_{4(aq)} + L_{(aq)} \rightarrow Cu^{2+}(H_2O)_3L_{(aq)} + H_2O_{(aq)}$$

are designated **1a**, **1b**, **1c**, and **1d**, and are shown in Figs. 3 or 4, 2, 5, and 6, respectively. In each case, the coordination is through N_τ yielding a tetracoordinated metal center. It is of interest to note that structures that are substantially more stable than **1a**, **1b**, **1c**, and **1d** *in the gaseous phase* were found by attaching the copper ion to N_π. In these cases (not shown), the copper ion is pentacoordinated. Although not part of the starting structure, the His carbonyl O atom moved into the fifth coordination site upon geometry optimization, and short H-bonds were formed between two coordinated water molecules and other carbonyl O atoms. However, the N_π-coordinated structures had significantly lower free energy of solvation, with the result that, for all systems, the most stable structures *in water*, where a *single* water is displaced, involved coordination of the aqueous copper ion through N_τ. with the peptide backbone in an extended configuration.

Since the structures are isomeric, it is possible to compare their energies. The relative $\Delta G_{(aq)}$ of **1a**, **1b**, **1c**, and **1d**, are

Fig. 3. HGGG(**a**)–Cu structures. Ball colours: green = Cu^{2+}; orange = C; blue = N; red = O. Free-energy changes, ΔG, are in units of kJ mol^{-1} in aqueous solution.

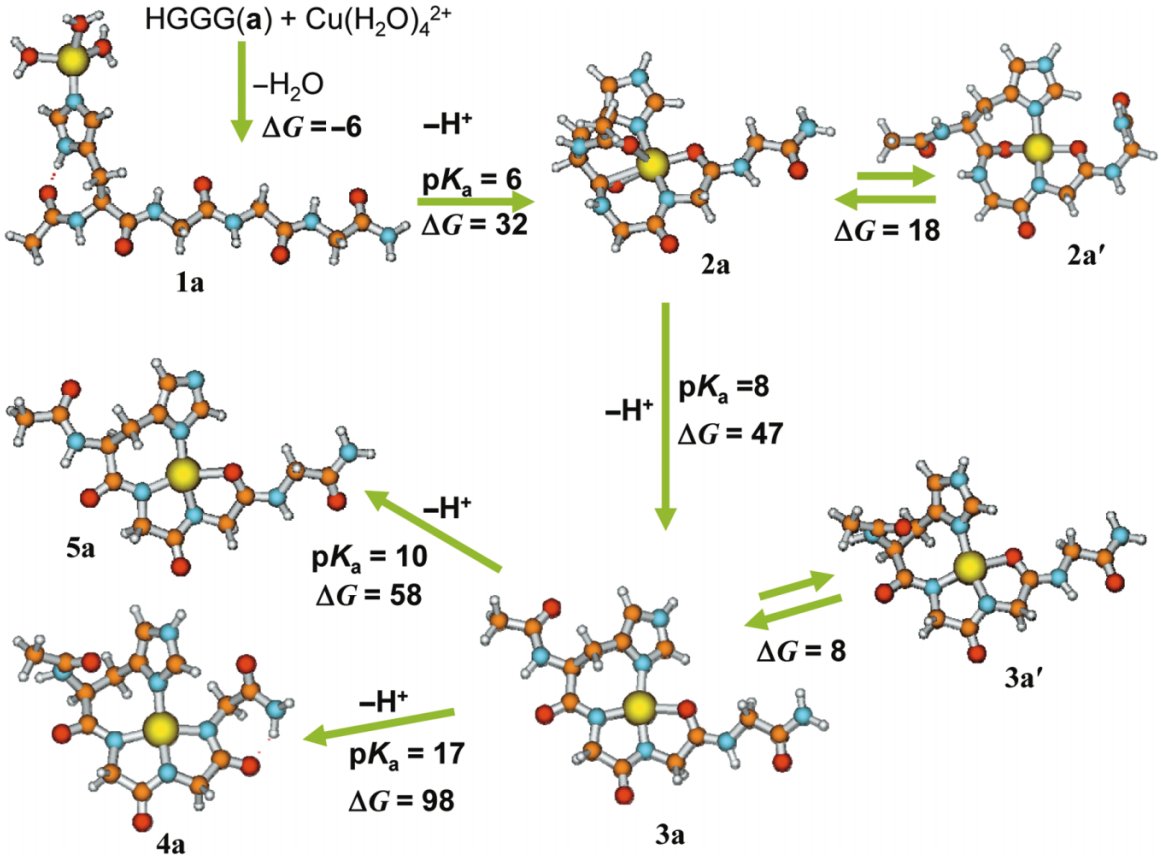

0, 5, 23, and 11 kJ mol^{-1}, respectively. We return to a discussion of the low-pH attachment of Cu(II) below when we compare the results with experiment.

The remainder of the structures discussed here are those expected to exist at higher pH. In all of these, the Cu(II) is bound to the histidine via the N_π atom of the imidazole group. The N_π atom is close enough to the peptide backbone to allow easy access to the Cu centre by amide groups that lie adjacent to the C_α of the histidine residue and in forward and reverse directions down the chain. The sequence of models permits evaluation of the energetics of chelation of the Cu in both the forward direction (toward the C terminus) and the backward direction (toward the N terminus) as illustrated in Fig. 1. We consider structures in which the Cu–peptide complex has lost a single proton (structures **2x**), two protons (structures **3x**), and three protons, either from three amide groups (**4x**), or from two amide groups and N_τ of the imidazole (**5x**). Here **x** is one of **a** (HGGG series), **b** (GHGG series), **c** (GGHG series), or **d** (GGGH series). For convenience, all of the structures in all of the figures are oriented with the N-terminus to the left and the C- terminus to the right. We briefly discuss each of the tetrapeptides separately, and then compare them.

HGGG structures

The sequence of the most stable structures of each type in the HGGG series resulting from successive proton loss, namely **1a**, **2a**, **3a**, **4a**, and **5a**, is shown in Fig. 3. Several conformations of the copper-free HGGG peptide, HGGG(**a**), were found. The most stable of these in solution, the N_π-protonated tautomer, is shown in Fig. 4. It attaches to $Cu_{(aq)}^{2+}$ with low affinity, $\Delta G_{(2)}$ = –6 ± 12 kJ /mol^{-1} to yield structure **1a** in which the Cu(II) is tetracoordinated and bound to N_τ of the imidazole.

$$[2] \quad Cu(H_2O)_4^{2+} + HGGG(\mathbf{a}) \rightarrow \mathbf{1a}/Cu(H_2O)_3^{2+} + H_2O$$

Successive loss of water leads to the other structures shown in Fig. 4. The most stable structure in which two waters of coordination remain, **1a**′, is unstable relative to the separated species (left hand side of eq. [2]) by 33 kJ mol^{-1}. Successive loss of the remaining two waters of coordination yields **1a**″ and **1a**‴, that are bound relative to the separated species by $\Delta G_{(aq)}$ = –6 kJ mol^{-1} and –17 kJ mol^{-1}, respectively. In each of **1a**′, **1a**″, and **1a**‴, the Cu(II) is pentacoordinated, with a tetragonal pyramidal geometry.

Structure **2a** (Fig. 3) is the most stable singly-deprotonated species. Of the many structures examined here, **2a** is unusual in that it has a "middle-forward" bonding configuration (see Fig. 1*b*). The pentacoordination in **2a** is probably weak. The average distance for a Cu–O bond at this level of theory is 2.00 ± 0.02 Å. The length of the fifth bond (to the O=C of His) is 2.49 Å, indicating that it is considerably weaker and may not survive in aqueous solution. Structure **2a** has nominally an N2O2 coordination pattern. It can be identified with structure II of Bonomo et al.,[21] and "component 2" of

Fig. 4. Attachment of aqueous Cu(II) to HGGG(**a**) with successive loss of water. The most stable structures of each type are shown. Ball colours: green = Cu^{2+}; orange = C; blue = N; red = O. Free-energy changes, ΔG, are in units of kJ mol^{-1} in aqueous solution.

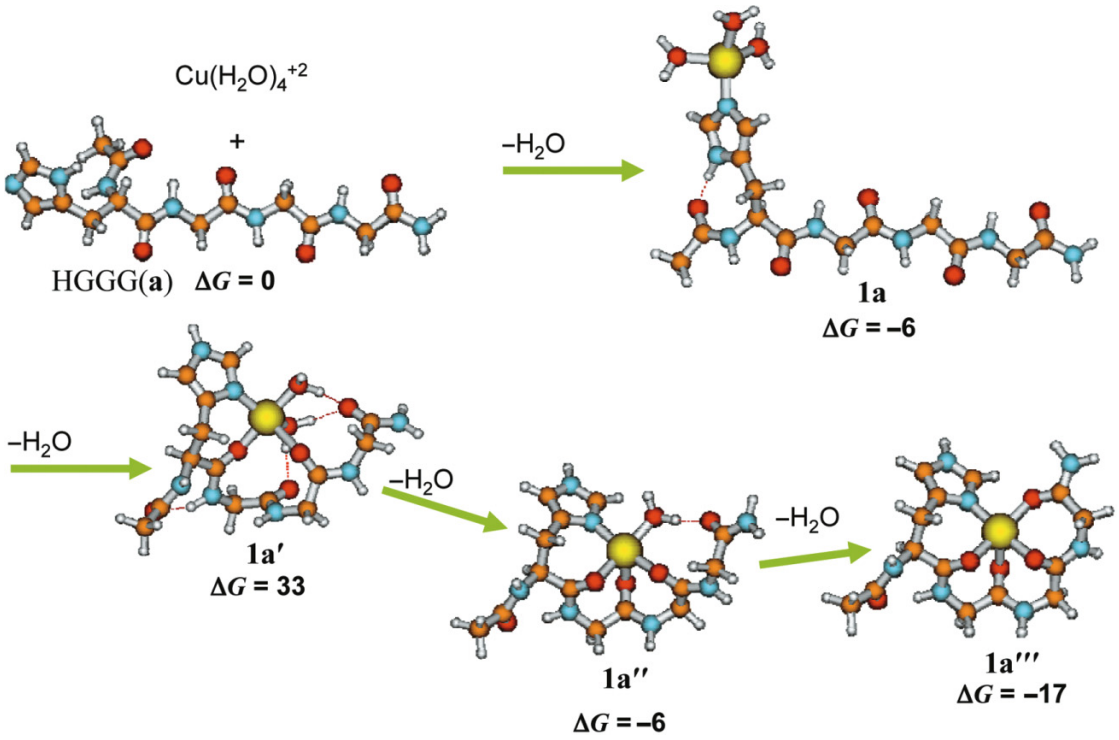

Millhauser and co-workers, and confirms their tentative N2O2 assignment.[41] The second most stable singly deprotonated structure, **2a**′ (Fig. 3), also has N2O2 coordination and is predicted to be less stable by 18 kJ mol^{-1}. As is evident from both structures **2a** and **2a**′, the first loss of a proton is predicted to occur from the N–H bond of the second Gly residue, since this permits the two strong electron pair donors, the amide group and the imidazole group, to be trans to each other in the Cu coordination shell.

Structure **2a** is predicted to have $pK_a = 8 \pm 2$, corresponding to ionization of the N–H bond of the first Gly residue, yielding **3a**. Species **3a** has N3O1 coordination in the "forward" direction, with two five-membered rings involving the two deprotonated amide groups and a coordinating carbonyl O atom, and a seven-membered ring involving the His residue. A second structure, **3a**′ (Fig. 3) with the same coordination pattern as **3a**, but with the seven-membered ring inverted, is predicted to be slightly less stable. In **3a**′, the oxygen atom of the N-acetyl group almost makes a fifth ligand to the copper ion. Either or both of **3a** and **3a**′ are candidates for structure III of Bonomo et al.,[21] and "component 1" of Millhauser and co-workers.[41]

Structure **3a** has four remaining sites for deprotonation, three from backbone N–H bonds and the N_τ–H bond of the imidazole. The latter is calculated to be the most acidic, with $pK_a = 10 \pm 2$, yielding structure **5a**. We could find no backbone N–H bond with $pK_a < 17$, i.e., corresponding to structure **4a**. Thus our results suggest that the third deprotonation is from the imidazole group rather than from the backbone. We return to this apparent disagreement with the experimental observations by Bonomo et al.[21] in the "Relationship to experimental studies" section below.

GHGG structures

In a fashion analogous to the HGGG (**a**) system, the pH-dependent origin of GHGG (**b**) structures is displayed in Fig. 2. The first attachment to the copper ion yields **1b** with binding affinity, –23 kJ mol^{-1}. Despite the availability of two amide groups preceding the His residue, the most stable coordination pattern, after loss of a single proton and three water molecules, is in the "forward" direction, yielding **2b** with N2O2 coordination. As in the case of **2a**, loss of the proton has occurred from the "i + 2" Gly residue, affording a trans orientation of the two N ligands. Loss of the proton from the "i + 1" Gly residue of **2b**, yielding **3b**, is predicted to occur more easily than in the case of **2a**, with $pK_a = 6 \pm 2$. Structure **3b** is predicted to deprotonate from N_τ–H of the imidazole with $pK_a = 12 \pm 2$, yielding **5b**. Of the structures that could be derived by further deprotonation of a backbone N–H bond, the most stable is **4b**, which has an N3O pattern of coordination and three five-membered rings. The coordination direction of **4b** is "middle-reverse" and the His residue is not involved. Structure **4b** is predicted to be 94 ± 10 kJ mol^{-1} less stable than **3b** (at pH = 7, $\Delta G_{(aq)}$(**3b** → **4b** + H^+) = 54 ± 10 kJ mol^{-1}) and 27 kJ mol^{-1} less stable than **5b**.

GGHG structures

The pH-dependent origin of GGHG(**c**) structures is displayed in Fig. 5. As was the case with **2a**, the most stable coordination pattern, after loss of a single proton and three water molecules from **1c**, is a pentacoordinated "middle" structure, **2c**. However, **2c** differs in detail from **2a**. In **2c**, the deprotonated amide N–H bond is that of the preceding (i.e., i – 1) Gly residue, again leaving the two strong N donors

Fig. 5. GGHG(**c**)–Cu structures. Ball colours: green = Cu^{2+}; orange = C; blue = N; red = O. Free-energy changes, ΔG, are in units of kJ mol^{-1} in aqueous solution.

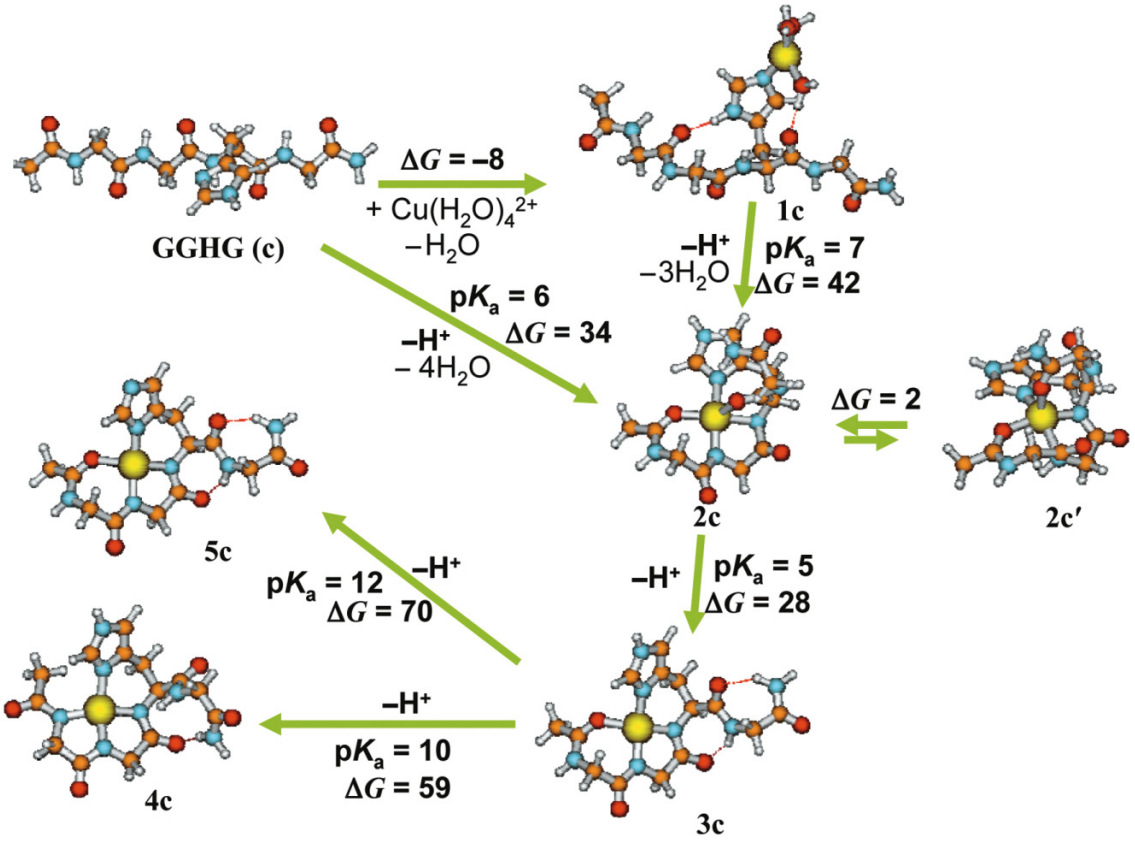

in a trans orientation in the copper coordination shell. Cis to the imidazole group is a neutral N atom of the His residue. The two remaining ligands are O atoms of the $i - 2$ Gly residue and of the His residue. The Cu–O bond lengths are 1.99 Å and 2.30 Å, respectively, indicating that the latter ligand is less strongly held and would probably be released in solution. Within 2 kJ mol^{-1} of **2c** is a second pentacoordinated structure, **2c′**, that differs in that the protonation states of the His and $i - 1$ Gly residues are reversed and the fifth coordinating O ligand is from the amidated C-terminus (formally the O atom of the $i + 2$ residue).

Loss of the proton from the N atom of the His residue of **2c** (or the $i - 1$ Gly residue of **2c′**) yields the neutral structure, **3c**, which also has the strong amide donor opposite the imidazole group and four-coordination with N3O1 ligand distribution in the reverse direction. Loss of the proton from **2c** or **2c′**, yielding **3c**, is predicted to occur very easily, with $pK_a = 5 \pm 2$. Structure **3c** is predicted to deprotonate primarily from the $i - 2$ Gly residue ($pK_a = 10 \pm 2$), yielding **4c**, and secondarily from N_τ–H of the imidazole ($pK_a = 12 \pm 2$), yielding **5c**. Structure **4c** has an N4 pattern of coordination with two five-membered rings and a six-membered ring.

GGGH structures

The pH-dependent origin of GGGH(**d**) structures is displayed in Fig. 6. The singly deprotonated structure **2d** is entirely analogous to **2c′**, except that it is four-coordinated in the reverse direction, rather than five-coordinated in the "middle-reverse" direction. In this case, the shorter C-terminus does not provide a weak fifth-coordinating ligand. Deprotonation of **2d** occurs with $pK_a = 5 \pm 2$ to yield **3d**, which has the same bonding characteristics as **3c**, namely coordination in the reverse direction with ligand pattern N3O1. Further deprotonation of **3d** is also entirely analogous to **3c**, with almost equal probability for proton loss from N_τ–H and $i - 2$ Gly residue, with the similar pK_a values, $pK_a = 12 \pm 2$, and $pK_a = 13 \pm 2$,yielding **4d** and **5d**, respectively. Like **4c**, structure **4d** has an N4 pattern of coordination with two five-membered rings and a six-membered ring.

Structural comparisons

Isomeric structures may be compared to each other. The relative aqueous free energies $\Delta G_{(aq)}$ of the most stable singly deprotonated species described above are (in kJ mol^{-1}): **2a**, 1; **2b**, 0; **2c**, 34; and **2d**, 33. The first two represent binding in the forward direction with configuration N2O2. The last two structures are bound in the reverse direction. Thus, in the case of singly deprotonated structures, binding in the forward direction is preferred.

The relative aqueous free energies $\Delta G_{(aq)}$ of the most stable doubly deprotonated species described above are (in kJ mol^{-1}): **3a**, 15; **3b**, 0; **3c**, 29; and **3d**, 27. Again, the first two represent binding in the forward direction, but with configuration N3O1. The last two structures are bound in the reverse direction, also with configuration N3O1. Thus, the neutral doubly deprotonated structures also prefer to bind in

Fig. 6. GGGH(**d**)–Cu structures. Ball colours: green = Cu^{2+}; orange = C; blue = N; red = O. Free-energy changes, ΔG, are in units of kJ mol^{-1} in aqueous solution.

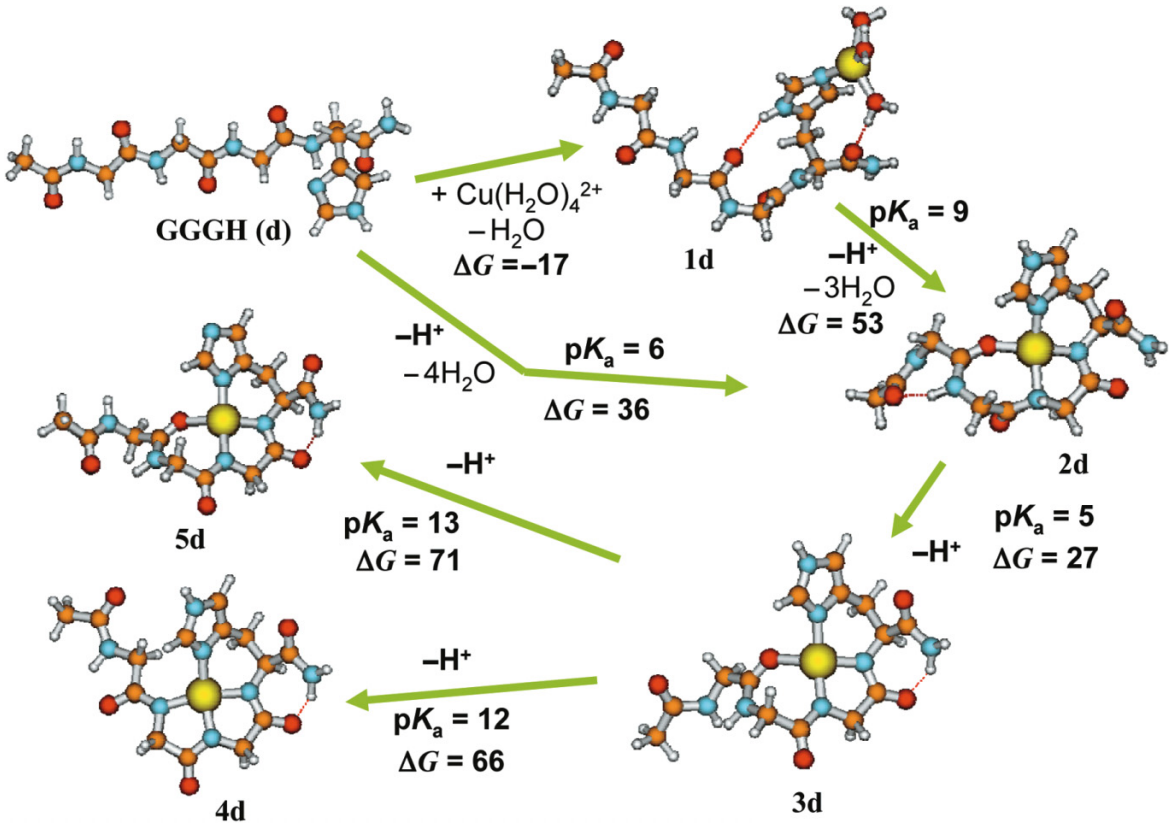

the forward direction. The difference is most pronounced in the cases of GHGG(**b**) and GGHG(**c**), which could bind in either direction. The more stable structure **3b** has a five, five, seven ring system while the less stable structure **3c** has a six, five, seven ring system. The calculated difference in the enthalpies of the two ring systems is ΔH_{298} = 14 kJ mol^{-1}. The remaining 15 kJ mol^{-1} of the difference originates primarily from the higher entropy ($-T\Delta S$ = 10 kJ mol^{-1}) and slightly more favourable solvation ($\Delta\Delta G_{solv}$ = 5 kJ mol^{-1}) of **3b**, both contributions of which are due to the longer free peptide chain in the reverse direction.

The relative aqueous free energies $\Delta G_{(aq)}$ of the most stable anionic triply backbone-deprotonated species described above are (in kJ mol^{-1}): **4a**, 25; **4b**, 5; **4c**, 0; and **4d**, 5. There is no significant difference in stability among the last three structures. Structures **4c** and **4d** exemplify reverse binding and have an N4 coordination pattern. Both structures are favoured by enthalpy over structure **4a**, ΔH_{298} = –18 kJ mol^{-1} and ΔH_{298} = –24 kJ mol^{-1}, respectively. Structure **4b** is technically a middle-reverse binding pattern that has lost the imidazole as a ligand. It is the least stable by enthalpy in the gaseous phase, but a significantly higher free energy of solvation brings it into the same range as the reverse binding structures. Thus, the calculations suggest that at high pH there is a clear preference for backbone deprotonation in the reverse direction, which yields a five, five, six ring pattern as opposed to the five, five, seven ring pattern of forward binding.[18]

Relationship to experimental studies

Protonated imidazoles of His residues have pK_a values in the range 6–7.[42] The calculated pK_as of the present systems are: HGGG(**a**)H^+, 7.5; GHGG(**b**)H^+, 12; GGHG(**c**)H^+, 6;. GGGH(**d**)H^+, 5. Thus, the values of three of the His residues lie within the error in pK_a values (±2) expected due to uncertainties in relative aqueous free energies, but the His residue of GHGG(**b**)H^+ is outside of these bounds. The reason for this is unclear.

The capping at both ends of the peptide models permits direct comparison with previous spectroscopic and potentiometric titration studies on $AcHGGGNH_2$.[21] Similar studies have also been carried out on the related systems, AcHGGG, AcGHGG, AcGGHG, and AcGGGH, in which the C-terminus was a free carboxylate group.[20] The calculated free energies of binding (eq. [1], $\Delta G_{(1)}$ are (kJ mol^{-1}): **1a**, –6; **1b**, –23; **1c**, –8; **1d**, –17. The binding free energy of the first and third is close to zero; **1b** and **1d** are predicted to be bound in water.

An experimental value, –23 kJ mol^{-1}, is available[21] for the first coordination of Cu(II) to HGGG (**a**) yielding a 1:1 complex with +2 charge. The number of waters of coordination is unknown from the experiment. In the case of the HGGG(**a**) system, we examined the successive loss of water for the Cu(II)-bound system at low pH (i.e., with net charge = +2). The results are displayed in Fig. 4. The binding affinity of the most stable structure, **1a**‴, ΔG = –17 ± 10 kJ mol^{-1}, is in satisfactory agreement with ex-

periment, but is also within the overlapping error bars of **1a**. We conclude that it is not possible to determine computationally the degree of hydration of the species arising from the first attachment of the Cu(II) ion to HGGG(**a**) with the present level of theory. Consequently, we have not pursued this course with any of the other three systems, but rather take the N_τ-bound $Cu(II)(H_2O)_3$ species **1b**, **1c**, and **1d**, as being representative. For two of these, the calculated binding affinity **1b**, ΔG = –23 kJ mol^{-1}and **1d**, ΔG = –17 kJ mol^{-1}, agree well with the experimental values based on the stability constant reported for the 1:1 complex of Cu(II) with AcGHGG and AcGGGH.[20]

In the pH range 6.5–8.5, two Cu–$AcHGGGNH_2$ complexes, corresponding to singly and doubly deprotonated species, were observed potentiometrically and spectroscopically.[21] The relative abundance of the former was always less than 15% . These may be identified with **2a** and **3a**, respectively (Fig. 3). The pK_a for loss of the second proton, 6.25, is in satisfactory agreement with that calculated for **2a** → **3a** + H^+, 8 ± 2. ESI-MS revealed a signal corresponding to protonated and sodiated forms of a neutral 1:1 Cu–$AcHGGGNH_2$ complex that notably did not contain any coordinated water molecules. A recent ESI-MS study by one of us confirmed this observation.[43] Two structures consistent with EPR and MS data were proposed for the neutral species, both of N3O1 square-planar coordination in the tetragonal plane, but differing by which terminal carbonyl oxygen atom formed the fifth coordination site.[21] The present results suggest that the neutral complex corresponds to **3a**, which has a square-planar N3O1 coordination geometry, but does not have involvement of either terminal carbonyl oxygen in the coordination sphere of the copper. In solution, this site would be transiently occupied by a water molecule.

Similar potentiometric measurements were carried out on the free terminal carboxylate system, Cu–AcHGGG, by Orfei et al.,[20] with very similar results. In that case, pK_a = 6.96 was assigned for the loss of the second proton. These authors carried out gaseous-phase modeling using the semiempirical PM3 method on the "neutral" species (actually negatively charged because of the carboxylate group) and obtained the same square-planar N3O1 coordination geometry as in **3a**, with coordinating water ligands above and below the plane.[20] In our high-level ab initio study, the fifth and sixth ligands to Cu are not stable to exchange in solution.

Both Bonomo et al.[21] and Orfei et al.[20] detected a third ionization with pK_a = 8.9, yielding a species with a negative charge (ignoring the charge of the carboxylate group). Both groups interpreted the EPR spectra as consistent with N4 coordination, in which three deprotonated amide nitrogen atoms, as well as imidazole N atom were coordinated to copper in a square-planar arrangement. ESI-MS signals collected in negative mode proved the absence of water.[21] As shown in Fig. 3, we could find no species with N4 coordination in an accessible pH range. The lowest pK_a for loss of a third amide proton from **3a** is calculated to be pK_a = 17, yielding **4a**. The lowest energy negatively charged species originates from loss of the remaining proton of the imidazole group, namely **5a**, which is formed from **3a** with pK_a = 10 ± 2. The calculated pK_a is essentially equal to the observed pK_a. Thus our data suggest that it is the imidazole that is the source of the third deprotonation, rather than a third amide group. As we show below, this conclusion is also supported by CD data. We have no explanation for the discrepancy with the EPR results.

As well as AcHGGG, Orfei et al., also examined the pH-dependent evolution of structures of Cu(II) complexes with AcGHGG, AcGGHG, and AcGGGH.[20] The stability constants for formation of a putative 1:1 Cu–peptide complex without loss of any protons were similar among all of the species, and correspond to free-energy changes in the narrow range –25 kJ mol^{-1} to –27 kJ mol^{-1}, as mentioned above. For each of these, the loss of the first proton produced a species in minor abundance compared to that derived from loss of two protons. pK_a values for both processes for all systems were in the narrow range of 6–7. We would assign structures **2b**, **2c**, and **2d** to the former and **3b**, **3c**, and **3d**, to the latter. However, we find some variability in the energetic parameters among the three systems, and the calculated data for the Cu(II)–GHGG(**b**) system, shown in Fig. 2, does not fit the observed pattern for the free terminal carboxylate systems. Experimentally, the third ionization in the case of the Cu–AcGHGG system was anomalous but the first two were not. In the case of Cu–AcGGHG and Cu–AcGGGH, as for Cu–AcHGGG, the third ionization occurred with a pK_a below 9 units, but the third ionization in the AcGHGG system had an apparent pK_a 2 units higher, and was attributed either to ionization of a bound water molecule or the imidazole.[20] An N4-coordinated pattern was not seen by EPR. In our study, the Cu–GHGG(**b**) system is unusual in several respects. Single and double deprotonation, yielding **2b** and **3b**, respectively, is predicted to occur at pH < 6. The most acidic proton of **3b** is found to be the imidazole proton, as it was in the case of **3a** but 2 pK_a units higher. The lowest energy structure that has three amide groups deprotonated is **4b**, in which the imidazole group is not coordinated to the Cu(II). This complex is 27 kJ mol^{-1} higher in energy than **5b**. By way of contrast, in both the Cu–GGHG(**c**) (Fig. 5) and Cu–GGGH(**d**) (Fig. 6) systems, the third ionization occurs with slightly higher probability from a third amide than from the imidazole group, and with very similar acidity constants.

Circular dichroism data

Orfei et al.[20] found that the high-pH CD spectra of the Cu–AcGGHG and Cu–AcGGGH systems displayed evidence of an identical chromophore. The spectra are dominated by a pair of oppositely signed bands of nearly equal intensity: Cu–AcGGHG, 600 nm (–), 500 nm (+); Cu–AcGGGH, 600 nm (–), 500 nm (+). Distinctly different chromophores were observed in the CD spectra at high pH of Cu–AcHGGG and Cu–AcGHGG. These both showed negative rotatory strength above 700 nm, a positive band near 600 nm, and a negative band near 520 nm.

To seek an explanation for the different CD spectra at high pH, we applied TD-B3LYP/6–31G(d) methodology to calculate and simulate the aqueous CD spectra of the triply deprotonated amide structures, **4a**, **4c**, and **4d**, as well as the imidazole deprotonated forms, **5a**, **5b**, **5c**, and **5d**, and the imidazole-released form, **4b**, in the spectral range studied by Orfei et al. The simulated CD spectra are displayed in Fig. 7, using Gaussian lineshapes with a half width of 0.37 eV (100 nm for a peak centred at 600 nm). Seven to

Fig. 7. Simulated CD spectra by TD-B3LYP/6–31G(*d*) in the presence of solvent reaction field: (*a*) HGGG structures **4a** and **5a**; (*b*) GHGG structures **4b** and **5b**; (*c*) GGHG structures **4c** and **5c**; (*d*) GGGH structures **4d** and **5d**.

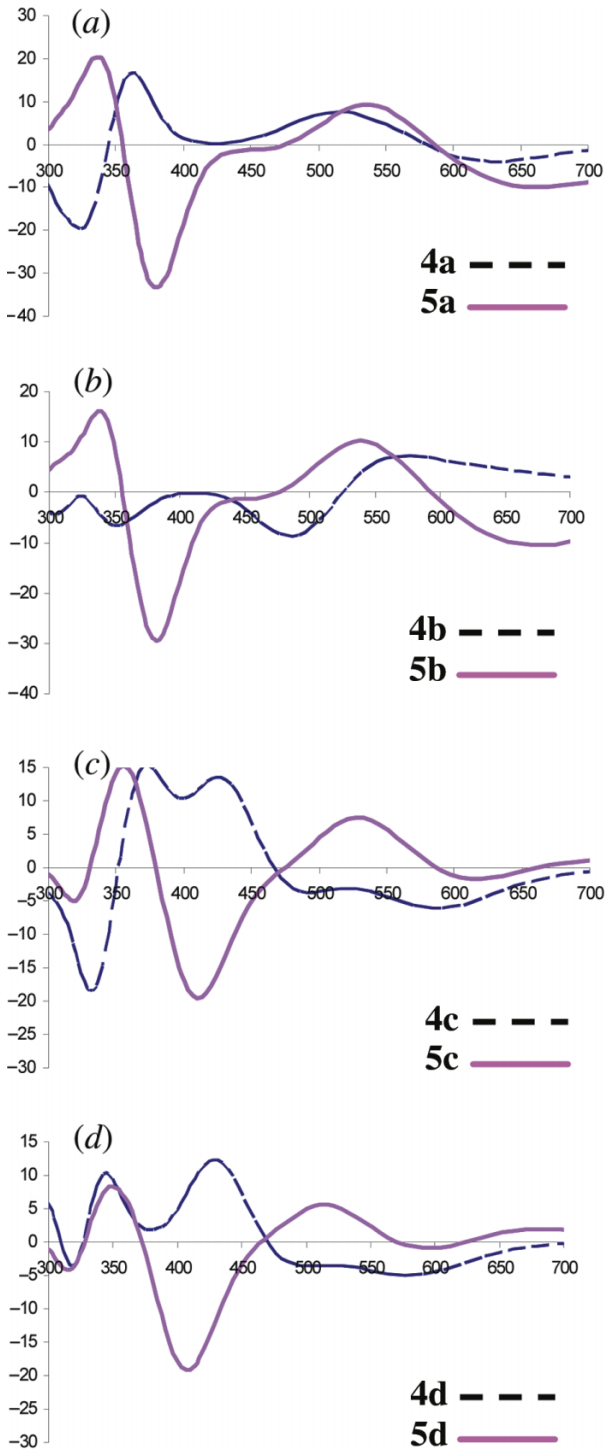

ten electronic transitions are predicted to occur on the spectral range 300–700 nm. The simulated CD spectra of the N4 species **4c** and **4d** are very similar to each other, but are qualitatively different from **4a**. The former have negative rotatory strength in the range 450–700 nm, while **4a** has a bisignate feature in the range with positive rotatory strength near 500 nm. **4b** is different again, with a negative CD band at 490 nm and positive intensity above 520 nm. The imidazole-deprotonated systems are distinct from the N4 systems. The spectra of **5c** and **5d** are almost identical to each other with CD pattern (right to left) weak (+), weak (–), medium (+), strong (–), and medium (+). The parallel systems **5a** and **5d** also have a similar pattern but have larger CD intensity in the 450–700 nm range.

Because of the limitations of the theoretical method and the fact that the systems are different, we do not expect a perfect match between our simulated spectra and the experimental spectra of Orfei et al. Nevertheless, *some* of the computed spectra reproduce the main spectral features of the experimental ones very well. For the N4 systems, **4c**, and **4d** (dashed lines in Figs. 7*c* and 7*d*), the dominant characteristic is bisignate, as are the experimental high-pH CD spectra of Cu–AcGGHG and Cu–AcGGGH, with positive rotatory strength to short wavelength and negative to longer. The calculated spectra are more complex in appearance than the experimental spectra, but reveal the multiple-transition origin of the deceptively simple spectra. The calculated spectra for the imidazole-deprotonated species **5c** and **5d** do not match the experimental spectra, thereby confirming the N4 coordination pattern for the high-pH species of the GGHG and GGGH species.

In the case of the GHGG system, the simulated CD spectrum of **5b** exactly matches the sign sequence of the experimental high-pH spectrum of Cu–AcGHGG although all the peaks are shifted to shorter wavelength. The spectrum of **4b** is very different. Thus the spectroscopic as well as energetic calculations are consistent with an imidazole-deprotonated structure for this system.

The most troublesome system is HGGG at high pH. Both Bonomo et al.[21] and Orfei et al.[20] found clear indications of N4 coordination in Cu–AcHGGGNH$_2$ and Cu–AcHGGG, respectively, by EPR. However, our calculations suggest that the most stable N4 system, **4a**, is energetically disfavoured compared to the imidazole-deprotonated species, **5a**, which has N3O1 coordination. Also the CD data of Orfei et al.[20] are quantitatively different from Cu–AcGGHG and Cu–AcGGGH which were clearly assigned as N4 above. The simulated CD spectrum of **4a** is also quantitatively different from that of **4c** and **4d**. The difference is probably due to the different direction of coordination, forward, as apposed to reverse. In our opinion, there is a better match between the experimental CD spectrum of Cu–AcHGGG obtained by Orfei et al and our simulated spectrum of **5a**. Thus, our energetic and spectroscopic calculations both point to an imidazole-deprotonated structure, **5a**, for both Cu–AcHGGG and Cu–AcHGGGNH2 at pH > 11. The discrepancy between the EPR and CD data could be resolved if the different spectroscopic techniques were sensitive to different species in solution. However, we have been unable to find an N4 species analogous to **4a** in an accessible energy range.

Summary and conclusions

The structures and relative free energies in aqueous solution of the Cu(II) complexes of the peptides, AcHGGGNH$_2$ (HGGG(**a**)), AcGHGGNH$_2$ (GHGG(**b**)), AcGGHGNH$_2$ (GGHG(**c**)), and AcGGGHNH$_2$ (GGGH(**d**)) were deter-

mined as a function of pH. Numerous structures of each species were found by gaseous phase geometry optimization and the effect of solvation estimated by the IEFPCM continuum solvation model. Free energies of solvation of the ionic species are large and favour structures with an extended peptide chain. It is rare that the most stable gaseous-phase structure is also the most stable in the aqueous phase. The solvation procedure gives satisfactory results for neutral and cationic species, but undersolvates anionic species, as judged against experimental observations at pH ≥ 8.

At low pH, the tetraaquo Cu(II) ion attaches to a single N atom of the imidazole group with the expulsion of one or more waters of coordination. In Cu–HGGG(**a**), for which all possible levels of hydration were examined, the most stable structure, **1a**‴, had no waters in the copper coordination shell, a result consistent with ESI-MS.[21,43]

In all Cu(II)–peptide complexes, deprotonation of two amide groups occurs readily at or even below physiological pH = 7. The first N–H bond to ionize is that which places the amide N atom in a trans orientation to the imidazole N atom, in the forward direction in the case of HGGG(**a**) and GHGG(**b**) (the i + 2 Gly), and in the reverse direction in the case of GGHG(**c**) and GGGH(**d**) (the i – 1 Gly). The intervening amide group in protonated form and the carbonyl of the i ± 2 Gly complete the coordination sphere of the Cu(II). The second ionization then occurs from the intervening amide group to yield a neutral 1:1 complex with N3O1 coordination pattern as the most abundant species at pH = 7.

In the case of both singly and doubly deprotonated structures, binding in the forward direction is preferred. The observation of forward binding in the crystal structure of the octarepeat region of the prion protein was tentatively attributed to the blocking effect of the proline residue immediately preceding the His. The present results suggest that forward binding would be the preferred mode in any case. It should be noted however, that it is not possible to determine the effect of side-chain interactions on the direction of binding from the present models.

The computed relative free energies of the various ionized species in the Cu–HGGG(**a**) system are in good agreement with the experimental potentiometric studies of Bonomo et al.,[21] with the exception that ionization of the third proton, which was attributed to a third amide group and observed at pH ≈ 9, is calculated to come from the imidazole at similar pH (pK_a = 10). Simulated CD spectra of the candidate high-pH species support this result.

Supplementary data

Supplementary data for this article (Table S1: Primary computed data for all species: energies, zero-point energies, thermal corrections to the enthalpy, entropies, numbers of conformations and free energies of solvation; Table S2: CD spectral data for **4a**, **5a**, **4b**, **5b**, **4c**, **5c**, **4d**, and **5d**) are available on the journal Web site (canjchem.nrc.ca) or may be purchased from the Depository of Unpublished Data, Document Delivery, CISTI, National Research Council Canada, Ottawa, ON K1A 0R6, Canada. DUD 3933. For more information on obtaining material, refer to cisti-icist.nrc-cnrc.gc.ca/cms/unpub_e.shtml. Geometries are available upon request.

References

(1) This article is part of a Special Issue dedicated to Professor T. Ziegler.

(2) Dobson, C. M. *Trends Biochem. Sci.* **1999**, *24* (9), 329–332. doi:10.1016/S0968-0004(99)01445-0. PMID:10470028.

(3) Gaggelli, E.; Kozlowski, H.; Valensin, D.; Valensin, G. *Chem. Rev.* **2006**, *106* (6), 1995–2044. doi:10.1021/cr040410w.

(4) Pan, K.-M.; Baldwin, M.; Nguyen, J.; Gasset, M.; Serban, A.; Groth, D.; Mehlhorn, I.; Huang, Z.; Fletterick, R. J.; Cohen, F. E.; Prusiner, S. B. *Proc. Natl. Acad. Sci. U.S.A.* **1993**, *90* (23), 10962–10966. doi:10.1073/pnas.90.23.10962. PMID:7902575.

(5) Kang, J.; Lemaire, H.-G.; Unterbeck, A.; Salbaum, J. M.; Masters, C. L.; Grzeschik, K.-H.; Multhaup, G.; Beyreuther, K.; Müller-Hill, B. *Nature* **1987**, *325* (6106), 733–736. doi:10.1038/325733a0. PMID:2881207.

(6) Varadarajan, S.; Yatin, S.; Aksenova, M.; Butterfield, D. A. *J. Struct. Biol.* **2000**, *130* (2-3), 184–208. doi:10.1006/jsbi.2000.4274. PMID:10940225.

(7) Huang, X.; Atwood, C. S.; Hartshorn, M. A.; Multhaup, G.; Goldstein, L. E.; Scarpa, R. C.; Cuajungco, M. P.; Gray, D. N.; Lim, J.; Moir, R. D.; Tanzi, R. E.; Bush, A. I. *Biochemistry* **1999**, *38* (24), 7609–7616. doi:10.1021/bi990438f. PMID:10386999.

(8) Huang, X.; Cuajungco, M. P.; Atwood, C. S.; Hartshorn, M. A.; Tyndall, J. D. A.; Hanson, G. R.; Stokes, K. C.; Leopold, M.; Multhaup, G.; Goldstein, L. E.; Scarpa, R. C.; Saunders, A. J.; Lim, J.; Moir, R. D.; Glabe, C.; Bowden, E. F.; Masters, C. L.; Fairlie, D. P.; Tanzi, R. E.; Bush, A. I. *J. Biol. Chem.* **1999**, *274* (52), 37111–37116. doi:10.1074/jbc.274.52.37111. PMID:10601271.

(9) Ali, F. E. A.; Barnham, K. J.; Barrow, C. J.; Separovic, F. *Aust. J. Chem.* **2004**, *57* (6), 511. doi:10.1071/CH04026.

(10) Hornshaw, M. P.; McDermott, J. R.; Candy, J. M. *Biochem. Biophys. Res. Commun.* **1995**, *207* (2), 621–629. doi:10.1006/bbrc.1995.1233. PMID:7864852.

(11) Pan, K.-M.; Baldwin, M.; Nguyen, J.; Gasset, M.; Serban, A.; Groth, D.; Mehlhorn, I.; Huang, Z.; Fletterick, R. J.; Cohen, F. E.; Prusiner, S. B. *Proc. Natl. Acad. Sci. U.S.A.* **1993**, *90* (23), 10962–10966. doi:10.1073/pnas.90.23.10962. PMID:7902575.

(12) Croes, E. A.; Theuns, J.; Houwing-Duistermaat, J. J.; Dermaut, B.; Sleegers, K.; Roks, G.; Van den Broeck, M.; van Harten, B.; van Swieten, J. C.; Cruts, M.; Van Broeckhoven, C.; van Duijn, C. M. *J. Neurol. Neurosurg. Psychiatry* **2004**, *75* (8), 1166–1170. doi:10.1136/jnnp.2003.020198. PMID:15258222.

(13) Kramer, M. L.; Kratzin, H. D.; Schmidt, B.; Römer, A.; Windl, O.; Liemann, S.; Hornemann, S.; Kretzschmar, H. *J. Biol. Chem.* **2001**, *276* (20), 16711–16719. doi:10.1074/jbc.M006554200. PMID:11278306.

(14) Garnett, A. P.; Viles, J. H. *J. Biol. Chem.* **2003**, *278* (9), 6795–6802. doi:10.1074/jbc.M209280200. PMID:12454014.

(15) Williams, R. J. P. *Eur. J. Biochem.* **1995**, *234* (2), 363–381. doi:10.1111/j.1432-1033.1995.363_b.x.

(16) Rickard, G. A.; Gomez-Balderas, R.; Brunelle, P.; Raffa, D. F.; Rauk, A. *J. Phys. Chem. A* **2005**, *109* (37), 8361–8370. doi:10.1021/jp052303r. PMID:16834228.

(17) Rulíšek, L.; Havlas, Z. *J. Am. Chem. Soc.* **2000**, *122* (42), 10428–10439. doi:10.1021/ja001265g.

(18) Raffa, D. F.; Gómez-Balderas, R.; Brunelle, P.; Rickard, G. A.; Rauk, A. *J. Biol. Inorg. Chem.* **2005**, *10* (8), 887–902. doi:10.1007/s00775-005-0038-9. PMID:16267663.

(19) Sigel, H.; Martin, R. B. *Chem. Rev.* **1982**, *82* (4), 385–426. doi:10.1021/cr00050a003.
(20) Orfei, M.; Alcaro, M. C.; Marcon, G.; Chelli, M.; Ginanneschi, M.; Kozlowski, H.; Brasuń, J.; Messori, L. *J. Inorg. Biochem.* **2003**, *97* (3), 299–307. doi:10.1016/S0162-0134(03)00283-6. PMID:14511892.
(21) Bonomo, R. P.; Cucinotta, V.; Giuffrida, A.; Impellizzeri, G.; Magrì, A.; Pappalardo, G.; Rizzarelli, E.; Santoro, A. M.; Tabbì, G.; Vagliasindi, L. I. *Dalton Trans.* **2005**, (1): 150–158. doi:10.1039/b415727c. PMID:15605159.
(22) Aronoff-Spencer, E.; Burns, C. S.; Avdievich, N. I.; Gerfen, G. J.; Peisach, J.; Antholine, W. E.; Ball, H. L.; Cohen, F. E.; Prusiner, S. B.; Millhauser, G. L. *Biochemistry* **2000**, *39* (45), 13760–13771. doi:10.1021/bi001472t. PMID:11076515.
(23) Burns, C. S.; Aronoff-Spencer, E.; Dunham, C. M.; Lario, P.; Avdievich, N. I.; Antholine, W. E.; Olmstead, M. M.; Vrielink, A.; Gerfen, G. J.; Peisach, J.; Scott, W. G.; Millhauser, G. L. *Biochemistry* **2002**, *41* (12), 3991–4001. doi:10.1021/bi011922x. PMID:11900542.
(24) Burns, C. S.; Aronoff-Spencer, E.; Legname, G.; Prusiner, S. B.; Antholine, W. E.; Gerfen, G. J.; Peisach, J.; Millhauser, G. L. *Biochemistry* **2003**, *42* (22), 6794–6803. doi:10.1021/bi027138+. PMID:12779334.
(25) Miura, T.; Hori-i, A.; Mototani, H.; Takeuchi, H. *Biochemistry* **1999**, *38* (35), 11560–11569. doi:10.1021/bi9909389. PMID:10471308.
(26) Stöckel, J.; Safar, J.; Wallace, A. C.; Cohen, F. E.; Prusiner, S. B. *Biochemistry* **1998**, *37* (20), 7185–7193. doi:10.1021/bi972827k. PMID:9585530.
(27) Pushie, M. J.; Rauk, A. *J. Biol. Inorg. Chem.* **2003**, *8* (1-2), 53–65. doi:10.1007/s00775-002-0386-7. PMID:12459899.
(28) Marino, T.; Russo, N.; Toscano, M. *J. Phys. Chem. B* **2007**, *111* (3), 635–640. doi:10.1021/jp065296v. PMID:17228921.
(29) Furlan, S.; Penna, G.; Guerrieri, F.; Morante, S.; Rossi, G. C. *J. Biol. Inorg. Chem.* **2007**, *12* (4), 571–583. doi:10.1007/s00775-007-0218-x. PMID:17333299.
(30) Riihimäki, E.-S.; Martinez, J. M.; Kloo, L. *J. Phys. Chem.* **B 2007**, *111*, 10529. doi:doi: 10.1021/jp072672i. PMID: 17696524.
(31) Jones, C. E.; Klewpatinond, M.; Abdelraheim, S. R.; Brown, D. R.; Viles, J. H. *J. Mol. Biol.* **2005**, *346* (5), 1393–1407. doi:10.1016/j.jmb.2004.12.043. PMID:15713489.
(32) Frisch, M. J.; Trucks, G. W.; Schlegel, H. B.; Scuseria, G. E.; Robb, M. A.; Cheeseman, J. R.; Montgomery, J. A., Jr.; Vreven, T.; Kudin, K. N.; Burant, J. C.; Millam, J. M.; Iyengar, S. S.; Tomasi, J.; Barone, V.; Mennucci, B.; Cossi, M.; Scalmani, G.; Rega, N.; Petersson, G. A.; Nakatsuji, H.; Hada, M.; Ehara, M.; Toyota, K.; Fukuda, R.; Hasegawa, J.; Ishida, M.; Nakajima, T.; Honda, Y.; Kitao, O.; Nakai, H.; Klene, M.; Li, X.; Knox, J. E.; Hratchian, H. P.; Cross, J. B.; Bakken, V.; Adamo, C.; Jaramillo, J.; Gomperts, R.; Stratmann, R. E.; Yazyev, O.; Austin, A. J.; Cammi, R.; Pomelli, C.; Ochterski, J. W.; Ayala, P. Y.; Morokuma, K.; Voth, G. A.; Salvador, P.; Dannenberg, J. J.; Zakrzewski, V. G.; Dapprich, S.; Daniels, A. D.; Strain, M. C.; Farkas, O.; Malick, D. K.; Rabuck, A. D.; Raghavachari, K.; Foresman, J. B.; Ortiz, J. V.; Cui, Q.; Baboul, A. G.; Clifford, S.; Cioslowski, J.; Stefanov, B. B.; Liu, G.; Liashenko, A.; Piskorz, P.; Komaromi, I.; Martin, R. L.; Fox, D. J.; Keith, T.; Al-Laham, M. A.; Peng, C. Y.; Nanayakkara, A.; Challacombe, M.; Gill, P. M. W.; Johnson, B.; Chen, W.; Wong, M. W.; Gonzalez, C.; Pople, J. A. *Gaussian 03, Revision C.02. Gaussian, Inc.*, Wallingford CT. 2004.
(33) Becke, A. D. *J. Chem. Phys.* **1993**, *98* (7), 5648. doi:10.1063/1.464913.
(34) Guthrie, J. P. *J. Phys. Chem. A* **2001**, *105* (37), 8495–8499. doi:10.1021/jp010321c.
(35) Klamt, A.; Schüürmann, G. *J. Chem. Soc., Perkin Trans. 2* **1993**, 799. doi:10.1039/p29930000799.
(36) Andzelm, J.; Kolmel, C.; Klamt, A. *J. Chem. Phys.* **1995**, *103* (21), 9312. doi:10.1063/1.469990.
(37) (a) Stratmann, R. E.; Scuseria, G. E.; Frisch, M. J. *J. Chem. Phys.* **1998**, *109* (19), 8218. doi:10.1063/1.477483.; (b) Bauernschmitt, R.; Ahlrichs, R. *Chem. Phys. Lett.* **1996**, *256* (4-5), 454–464. doi:10.1016/0009-2614(96)00440-X.; (c) Casida, M. E.; Jamorski, C.; Casida, K. C.; Salahub, D. R. *J. Chem. Phys.* **1998**, *108* (11), 4439. doi:10.1063/1.475855.
(38) (a) Helgaker, T.; Jørgensen, P. *J. Chem. Phys.* **1991**, *95*, 2595 doi:10.1063/1.460912.; (b) Bak, K. L.; Jørgensen, P.; Helgaker, T.; Ruud, K.; Jensen, H. J. A. *J. Chem. Phys.* **1993**, *98*, 8873 doi:10.1063/1.464445.; (c) Bak, K. L.; Hansen, A. E.; Ruud, K.; Helgaker, T.; Olsen, J.; Jørgensen, P. *Theor. Chim. Acta* **1995**, *90*, 441; (d) Olsen, J.; Bak, K. L.; Ruud, K.; Helgaker, T.; Jørgensen, P. *Theor. Chim. Acta* **1995**, *90*, 421; (e) Autschbach, J.; Ziegler, T.; van Gisbergen, S. J. A.; Baerends, E. J. *J. Chem. Phys.* **2002**, *116* (16), 6930. doi:10.1063/1.1436466.; (f) Hansen, A. E.; Bak, K. L. *Enantiomer* **1999**, *4*, 455.
(39) Liptak, M. D.; Shields, G. C. *J. Am. Chem. Soc.* **2001**, *123* (30), 7314–7319. doi:10.1021/ja010534f. PMID:11472159.
(40) [Calculated as the difference between $\Delta G_{(g)}(H_2O)$ and $\Delta G_{(l)}(H_2O)$, with the former corrected to the standard state of 1 M and the latter to 55 M].
(41) Chattopadhyay, M.; Walter, E. D.; Newell, D. J.; Jackson, P. J.; Aronoff-Spencer, E.; Peisach, J.; Gerfen, G. J.; Bennett, B.; Antholine, W. E.; Millhauser, G. L. *J. Am. Chem. Soc.* **2005**, *127* (36), 12647–12656. doi:10.1021/ja053254z. PMID:16144413.
(42) Moran, L. A.; Scrimgeour, K. G.; Horton, H. R.; Ochs, R. S.; Rawn, J. D. *Biochemistry*. 2nd ed. Neil Patterson Publishers, Prentice Hall, Englewood Cliffs, NJ. p. 76. 1994.
(43) Pushie, M. J.; Ross, A. R. S.; Vogel, H. *J. Anal. Chem.* **2007**, *79* (15), 5659–5667. doi:10.1021/ac070312l.

^{1}H chemical shifts in nonaxial, paramagnetic chromium(III) complexes — Application of novel pNMR shift theory[1]

Helmi Liimatainen, Teemu O. Pennanen, and Juha Vaara

Abstract: We present the first chemical application of the recent, general theory of the nuclear magnetic resonance shielding and chemical shift in paramagnetic compounds, to a set of nonaxial high-spin metallo-organic complexes. The theory is for the first time rigorous for systems of arbitrary spatial and spin symmetry, and introduces new structure to the isotropic, anisotropic but symmetric, and anisotropic and antisymmetric parts of the shielding tensor. We apply the theory using density functional calculations of the proton chemical shift in a family of nonaxial chromium(III) complexes possessing a quartet ground electronic spin state. We discuss the various contributions to the isotropic chemical shift, and compare the full theory to approximate forms appropriate to the doublet case on the one hand, and to the doublet case at the nonrelativistic limit, on the other hand. The performance of various exchange-correlation functionals in reproducing the recently measured experimental chemical shifts is evaluated.

Key words: paramagnetic NMR, chemical-shift calculation, nonaxial, high spin, density functional theory.

Résumé : La récente théorie générale du blindage et du déplacement chimique, en résonance magnétique nucléaire, des composés paramagnétiques a été appliquée pour la première fois à un ensemble de complexes organométalliques de spin élevé et non axiaux. La théorie est la pour la première fois rigoureuse pour des systèmes de symétrie spatiale et de spin arbitraire et elle introduit une nouvelle structure pour les portions isotropes, anisotropes mais symétriques et anisotropes et antisymétriques du tenseur de blindage. On a appliqué la théorie dans des calculs de fonctionnelle de la densité du déplacement chimique du proton dans une famille de complexes non axiaux du chrome(III) possédant un état de spin électronique fondamental quadruplet. On discute des diverses contributions au déplacement chimique isotrope et on les résultats obtenus avec la théorie complète avec ceux obtenus avec des versions approximatives appropriées, d'une part, au cas des doublets et, d'autre part, au cas des doublets à la limite non relativiste. On évalue la performance des diverses fonctionnelles d'échange de corrélation pour reproduire les déplacements chimiques expérimentaux mesurés récemment.

Mots-clés : RMN paramagnétique, calcul du déplacement chimique, non axial, spin élevé, théorie de la fonctionnelle de densité.

[Traduit par la Rédaction]

Introduction

Nuclear magnetic resonance (NMR) of paramagnetic substances possessing unpaired electrons (pNMR) is gaining importance in studies of magnetic matter ranging from bioinorganic chemistry[2] to materials science.[3] From the point of view of modern electronic structure theory, the field of calculation of the spectral parameters of pNMR is still in its infancy, as compared to the extensive knowledge on diamagnetic systems.[4–6]

Theory and methods of systematic quantum chemical calculation of the pNMR chemical shift, δ, have emerged during the last few years, starting from the nonrelativistic (NR) approach for doublet systems with one unpaired electron.[7] This level involves the orbital shielding, $\boldsymbol{\sigma}_{\mathrm{orb}}$, that is analogous to the closed-shell nuclear shielding, as well as the explicitly temperature-dependent, fully isotropic contact and fully anisotropic dipolar shielding contributions, $\sigma_{\mathrm{con}}\mathbf{1}$ and $\boldsymbol{\sigma}_{\mathrm{dip}}$, respectively. The latter terms arise from the hyperfine interaction of nuclei with thermally averaged electron spin density.[8] Moon and Patchkovskii[9] presented a framework for systematic extension of the theory to higher-order spin-orbit (SO) interaction-induced effects. These arise from the deviation $\Delta\mathbf{g} = \mathbf{g} - g_{\mathrm{e}}\mathbf{1}$ of the $\mathbf{g}$ tensor, used to parameterize the electronic Zeeman interaction, from the isotropic free-electron factor, g_{e}. Two more experimentally relevant terms arising from the anisotropic part of $\Delta\mathbf{g}$ were captured by the approach, namely the anisotropic contact shielding, $\boldsymbol{\sigma}_{\mathrm{c,aniso}}$, and the pseudocontact shielding, $\boldsymbol{\sigma}_{\mathrm{pc}}$, which also contributes to the isotropic shielding constant, σ.[10,11] Two of the present authors added SO corrections to the hyperfine coupling, $\mathbf{A}$, with the result that systematic light-atom shieldings in heavy-element-containing doublet systems became accessible.[12]

Extension of the pNMR shift theory to systems with more than one unpaired electron requires the incorporation of the effect of zero-field splitting (ZFS) on the spin-Zeeman sub-

Received 20 December 2008. Accepted 26 February 2009. Published on the NRC Research Press Web site at canjchem.nrc.ca on 5 June 2009.

H. Liimatainen, T.O. Pennanen, and J. Vaara.[1] Laboratory of Physical Chemistry, Department of Chemistry, P.O. Box 55 (A.I. Virtasen aukio 1), University of Helsinki, Helsinki FIN-00014, Finland.

[1]Corresponding author (e-mail: juha.t.vaara@helsinki.fi).

levels.[13] The first, approximate attempt in this direction was made by Hrobárik et al.[14] who applied a posteriori corrections to the calculated contact and dipolar shifts, formulated using the spin susceptibility tensor as an intermediate physical quantity. These authors were limited to systems possessing cylindrical spatial symmetry in their approach.

Recently, Pennanen and Vaara[15] modified the approach of Moon and Patchkovskii[9] and obtained a general expression for the pNMR shielding tensor for an arbitrary number of unpaired electrons and for an arbitrary spatial symmetry. The theory, which can be viewed as the extension of the Ramsey theory of nuclear shielding[16,17] to the open-shell situation, generalizes the symmetry of all the hyperfine shielding terms present in the doublet case.[9,12,14] In particular, several new contributions to the isotropic chemical shifts arise.[15]

In this paper we present the first chemical applications of the new theory of pNMR chemical shift, and calculate using density functional theory (DFT) the ^{1}H shifts in a family of quinolyl-functionalized Cp chromium(III) complexes, which was recently investigated experimentally by Enders and coworkers.[18] The studied complexes are illustrated in Chart 1. These $S = 3/2$ systems are of interest in studies of olefin polymerization catalysts. In ref. 18, DFT results at the B3LYP/6-311G(d) level[19–21] for the spin densities at the ^{1}H nuclei were related to the experimental hyperfine shifts. Such an approach is based on the, as such, rather realistic assumption that the contact shielding, σ_{con}, dominates the hyperfine contributions to σ.

Due to the theory presented in ref. 15, chemical shifts in such nondoublet, nonaxial open-shell molecules have now for the first time become accessible to systematic quantum chemical investigation, in which a more complete analysis in terms of the various physical contributions can be carried out. Here we present such an analysis based on a DFT implementation of the new theory,[15] and discuss the results in terms of the errors made assuming the doublet (neglecting ZFS)[12] and NR[7] theories. Furthermore, we investigate the dependence of the calculated shifts on various computational factors: selection of the basis set and exchange-correlation functional, as well as the choice between experimental X-ray[18,22] and computationally optimized molecular structures. Finally, we present linear regression fits correlating the experimental ^{1}H shifts[18] based on this more complete theoretical level than applied previously.[18]

Theory

The analysis of ref. 15 resulted in the following expression for the magnetic field independent part of the nuclear shielding tensor in open-shell, paramagnetic molecules:

$$\boldsymbol{\sigma} = \boldsymbol{\sigma}_{\mathrm{orb}} - \frac{\mu_{\mathrm{B}}}{\gamma k T}\mathbf{g}\cdot\langle\mathbf{SS}\rangle_0\cdot\mathbf{A}$$

$$\langle\mathbf{SS}\rangle_0 = \frac{\sum_n \langle n|\mathbf{SS}|n\rangle \exp\left(-E_n(0)/kT\right)}{\sum_n \exp\left(-E_n(0)/kT\right)}$$

where μ_{B}, γ, and k in the hyperfine part of the shielding (the second term on the right-hand side of the first line) are the Bohr magneton, gyromagnetic ratio of the investigated nucleus, and the Boltzmann constant, respectively. **S** is the effective spin operator used in the analysis of electron spin resonance (ESR) spectra, and the product **SS** is on the second line Boltzmann-averaged in the manifold of states, $|n\rangle$, consisting of the ground-state spin multiplet. Any excited states that are thermally accessible from the ground state would also have to be included in the averaging. In a $S = 3/2$ system, such as the present Cr(III) complexes, and neglecting electronically excited states, there are four states, $|n\rangle$, and energies, $E_n(0)$, that can be obtained by diagonalizing the ZFS part of the ESR Hamiltonian:

$$H_{\mathrm{ESR}}(0) = \mathbf{S}\cdot\mathbf{D}\cdot\mathbf{S}$$

g, **A**, and the ZFS tensor, **D**, are obtained from quantum chemical calculations, and the states, $|n\rangle$, are easily obtained in the basis of the eigenfunctions of S_z. The zero argument refers both to the absence of strong hyperfine couplings and considering the limit of vanishing magnetic field, $\mathbf{B}_0 = \mathbf{0}$. The isotropic shielding constant and chemical shift are obtained in the usual fashion as

$$\sigma = (\sigma_{xx} + \sigma_{yy} + \sigma_{zz})/3$$
$$\delta = \sigma_{\mathrm{ref}} - \sigma$$

where σ_{ref} is the shielding constant of a suitable, closed-shell reference compound.

Chart 1. Studied chromium complexes.

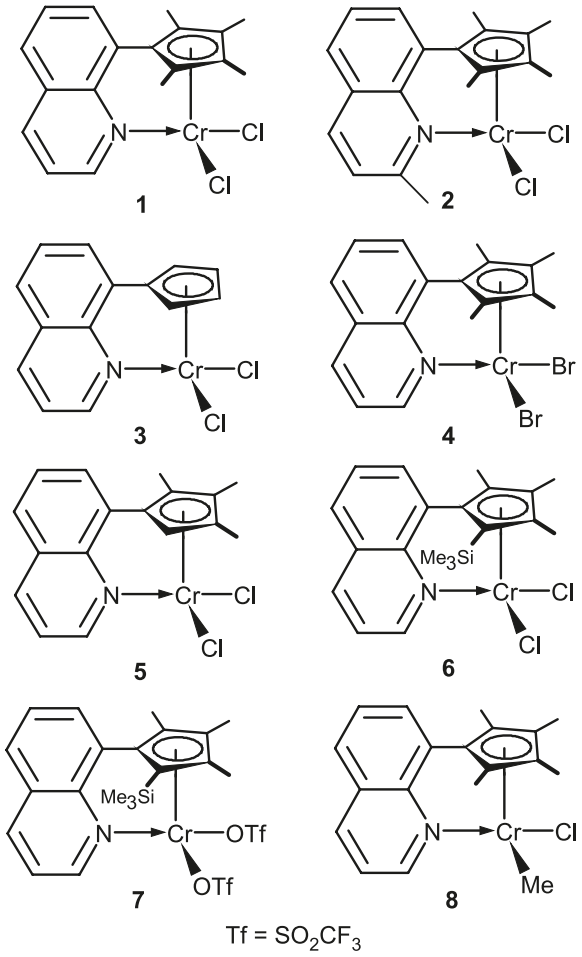

Table 1. Decomposition of the paramagnetic nuclear shielding to isotropic chemical-shift contributions.

Shift symbol	Term in $\sigma_{\varepsilon\tau}$[a]	Isotropic shift contribution		
		Full theory[b]	Doublet theory[c]	NR theory[d]
δ_{orb}	$\sigma_{\varepsilon\tau}^{orb}$	Yes	Yes	Yes
δ_{con}	$g_e\langle S_\varepsilon S_\tau\rangle_0 A_{con}$	Yes	Yes	Yes
δ_{dip}	$g_e\Sigma_b\langle S_\varepsilon S_b\rangle_0 A_{b\tau}^{dip}$	Yes	0	0
$\delta_{con,2}$	$g_e\langle S_\varepsilon S_\tau\rangle_0 A_{PC}$	Yes	Yes	—
$\delta_{dip,2}$	$g_e\Sigma_b\langle S_\varepsilon S_b\rangle_0 A_{b\tau}^{dip,2}$	Yes	0	—
δ_{ac}	$g_e\Sigma_b\langle S_\varepsilon S_b\rangle_0 A_{b\tau}^{as}$	0	0	—
$\delta_{con,3}$	$\Delta g_{iso}\langle S_\varepsilon S_\tau\rangle_0 A_{con}$	Yes	Yes	—
$\delta_{dip,3}$	$\Delta g_{iso}\Sigma_b\langle S_\varepsilon S_b\rangle A_{b\tau}^{dip}$	Yes	0	—
$\delta_{c,aniso}$	$\Sigma_a\Delta\tilde{g}_{\varepsilon a}\langle S_a S_\tau\rangle_0 A_{con}$	Yes	0	—
δ_{pc}	$\Sigma_{ab}\Delta\tilde{g}_{\varepsilon a}\langle S_a S_b\rangle A_{b\tau}^{dip}$	Yes	Yes	—

Note: The entry "yes" means that a nonvanishing contribution to δ arises from the term in question at the level considered, "0" denotes that the contribution is rigorously zero, and "–" indicates that the shielding term does not appear at all in the shielding tensor at this level.

[a]For the hyperfine terms, the contribution to the product $\mathbf{g}\cdot\langle\mathbf{SS}\rangle_0\cdot\mathbf{A}$ is indicated.

[b]General theory for arbitrary spin state,[15] neglecting hyperfine terms beyond the fourth order in the fine structure constant, $O(\alpha^4)$.

[c]Terms resulting from the doublet theory[12] where the symmetric $\langle\mathbf{SS}\rangle_0$ matrix reduces to the isotropic diagonal matrix $S(S+1)\mathbf{1}/3$.

[d]Nonrelativistic terms,[7] neglecting any terms beyond $O(\alpha^2)$.

Chart 2. Numbering of the ^{1}H nuclei in molecules **1**–**8**.

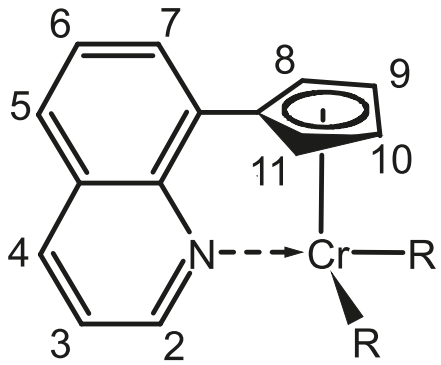

For light NMR nuclei in the presence of heavy-element or transition-metal compounds, it is convenient to analyze the hyperfine part of the shielding expression by performing a breakdown of **g** and **A** to the leading-order parts and the first-order corrections arising from the SO interaction.[9,12,14,15] For the Zeeman interaction, the **g** tensor can be decomposed as

$$\mathbf{g} = g_e\mathbf{1} + \Delta g_{iso}\mathbf{1} + \Delta\tilde{\mathbf{g}}$$

into the isotropic free-electron contribution (the first term) and the *g* shift. It is advantageous to consider the latter in separate isotropic and anisotropic parts, Δg_{iso} and $\Delta\tilde{\mathbf{g}}$, respectively. The hyperfine coupling tensor can be analogously analyzed as

$$\mathbf{A} = A_{con}\mathbf{1} + \mathbf{A}_{dip} + A_{PC}\mathbf{1} + \mathbf{A}_{dip,2} + \mathbf{A}_{as}$$

where the first two terms on the right-hand side are the nonrelativistic, isotropic contact and anisotropic dipolar couplings, respectively. The remaining terms are the isotropic (PC: "pseudocontact", not to be confused with the pseudocontact shift of pNMR), anisotropic but symmetric (dip,2), and antisymmetric (as) contributions that arise due to the relativistic SO correction.[23] Table 1 lists the contributions to the isotropic chemical shift after performing the breakdown. Besides the terms present in the full theory,[15] we also show the shift contributions resulting from an application of the doublet theory[12] as well as the result of limiting ourselves to the NR terms.[7]

Experimentally, δ_{orb} is often approximately eliminated by using a corresponding diamagnetic compound as a secondary shift reference. The true leading-order contact shift, δ_{con}, cannot be experimentally distinguished from the mathematically similar $\delta_{con,2}$ and $\delta_{con,3}$ arising from SO corrections to **A** and **g**, respectively. The pseudocontact term, δ_{pc}, arises from the interplay of anisotropic *g*-shift ($\Delta\tilde{\mathbf{g}}$) and dipolar hyperfine interaction and is useful in structure determination due to the dependence of $\mathbf{A}_{dip}$ on the molecular geometry.[2] Besides these contributions, the general shift theory[15] predicts a number of terms, the isotropic parts of which can be intermixed with δ_{pc}:δ_{dip} (the leading-order dipolar term), $\delta_{dip,2}$ and $\delta_{dip,3}$ (SO-corrections to **A** and **g**, respectively), and $\delta_{c,aniso}$ that is misleadingly termed the "anisotropic" contact term due to the property of this contribution for doublet systems. Consequently, the experimental analysis of chemical shifts based on

$$\delta = \delta_{orb} + \delta_{con} + \delta_{pc}$$

unavoidably hides interesting details that affect the quantitative, potentially also qualitative, results of, e.g., structural studies. With quantum chemical calculations it is possible to unearth the full structure of the contributions. In this con-

Table 2. Calculated chemical shifts for molecule **1** at the PBE level with different basis sets.

^{1}H signal	Exp.[18,a]	HII	HIII	HIIIt1	HIIIt2	HIIIt3	HIIIt4	HIV	HIVt1	HIVt2
2	–78.0	–181.9	–167.7	–174.3	–177.9	–180.0	–181.1	–176.8	–178.0	–184.7
3	51.8	79.0	74.3	76.6	78.0	78.8	79.2	79.1	79.7	82.4
4	–56.0	–152.3	–134.9	–141.9	–143.9	–146.3	–146.7	147.9	–148.8	–154.8
5	–15.8	–42.1	–37.1	–38.8	–39.8	–40.3	–40.6	–38.9	–39.7	–41.5
6	15.3	16.8	14.0	14.4	14.4	14.5	14.5	15.2	15.4	15.7
8 and 11	27.6	56.3	55.2	56.5	58.1	58.4	58.9	60.1	60.8	62.8
9 and 10	–41.1	–31.1	–29.3	–29.7	–30.7	–30.9	–31.2	–27.2	–27.8	–28.8

[a]Including both the orbital and hyperfine shift contributions.

text, the errors arising from analyzing either computational or experimental data for $S > 1/2$ systems in terms of the doublet theory, are also of interest.

Computational details

The starting geometries for molecules **1** and **4**–**8** were obtained from the X-ray studies reported in refs. 18 and 22. Structures for molecules **2** and **3** were generated using the molecular modeling program Maestro.[24] Geometry optimization was carried out with the BP86 exchange-correlation functional[25,26] with the def2-TZVP basis set.[27] We used the Turbomole program,[28] except for partial optimizations where only hydrogen positions were optimized. In the latter calculations, GAUSSIAN 03[29] was used. The optimized structures are available in the Supplementary data.

For calculating the pNMR chemical shift corresponding to the new theory, we used two different quantum chemical programs and combined the results and completed calculations with the independent stand-alone code by Pennanen.[15] DFT in the unrestricted Kohn–Sham formulation was applied to **g**, **A**, and **D** using the ORCA package[30] as described in refs. 31– 33, respectively. The orbital shielding was obtained using similar methods in GAUSSIAN 03.[29] The calculated shieldings were averaged between the experimentally equivalent nuclei in the methyl groups on the one hand and in the Cp ring on the other hand. The individual ^{1}H nuclei, particularly in the methyl rings, have different spin densities and, hence, different shifts at the optimized molecular structure. These minimum-energy positions can be viewed as instantaneous locations of the hydrogens in the rotational trajectory of the methyl groups, and averaging them represents an approximation to a full rotational analysis of the ^{1}H shift.

Various basis sets were tested for molecules **1** and **4** with the PBE[34] exchange-correlation functional. The Huzinaga–Kutzelnigg HII-HIV (also known as IGLO II-IV) basis sets[35] were used for the main group elements. For Br we used the primitive set by Fægri and Almlöf,[36] contracted and polarized in the same spirit as the Huzinaga–Kutzelnigg sets. For chromium we used (in the [primitive/contracted] notation) the [15s11p6d/9s7p4d] basis by Munzarová and Kaupp,[37] when the main group elements were represented with the HII or HIII basis sets. The HII sets are [5s1p/3s1p] for H, [9s5p1d/5s4p1d] for C, N, and O, [11s7p2d/7s6p2d] for Si, S, and Cl, and [16s13p10d/11s10p10d] for Br. At the HIII level the basis sets are, in the corresponding order, H: [6s2p/4s2p], C–O: [11s7p2d/7s6p2d], Si–Cl: [12s8p3d/8s7p2d], and Br: [16s13p11d/12s11p11d]. We constructed a larger [15s11p6d3f1g/11s9p6d3f1g] basis for chromium for use with the HIV basis for main group elements. This was done by uncontracting the most diffuse functions and introducing three new f-type functions and one g-type function. The new exponents were obtained from the cc-pVTZ and cc-pVQZ[38] basis sets. The HIV basis sets are H: [6s3p1d/5s3p1d], C–O: [11s7p3d1f/8s7p3d1f], and Si–Cl: [12s8p4d2f/9s8p4d2f].

Chemical shifts were calculated for molecules **1** and **4** with different exchange-correlation functionals to find out about the sensitivity of the results for this choice. HII basis was used. The tested functionals contained two generalized gradient approximation (GGA) functionals, PBE and BLYP,[26,39] and three hybrid functionals, PBE0,[34] B3LYP, and BHandHLYP.[19]

For the chemical shifts we used tetramethylsilane (TMS) as the diamagnetic reference molecule, for which orbital shieldings were calculated with GAUSSIAN 03 using the different exchange-correlation functionals and basis sets. The optimized BP86/def2-TZVP structure was employed. The calculated shielding constants at PBE/HII, PBE/HIII, and B3LYP/HII levels are 31.61, 31.36, and 31.84 ppm, respectively.

Results and discussion

The hydrogen sites are numbered in Chart 2.

Selection of basis set

The choice of the basis set must be made between accuracy and cost. Basis sets were tested for molecules **1** and **4** at the PBE level. The results are listed for molecule **1** in Table 2 (similar observations apply for molecule **4**). Mainly the valence region is improved by changing the basis between the HII, HIII, and HIV levels. The t1–t4 specification indicates the addition of 1–4 sets of tight s- and p-type primitives to the hydrogen basis to improve the description of the spin density around these centers. The tested basis sets imply that the smallest basis set, HII, gives values as accurate as the largest basis sets, due to error cancellation. The best results as compared to the experimental data[18] are obtained with the HIII basis set. For molecule **1**, and the shift at site 4, a result improved by 17.4 ppm is obtained with HIII as compared to the HII level. A reduction of the absolute value of the shift occurs between the HII and HIII sets, amounting on average to 6.7 ppm for molecule **1**.

We will mainly use the compact HII set in the following discussion, but return to the semi-empirical best choice of the HIII basis in our final results.

Fig. 1. [1]H chemical shift in molecule **1** calculated with different exchange-correlation functionals using the HII basis set.

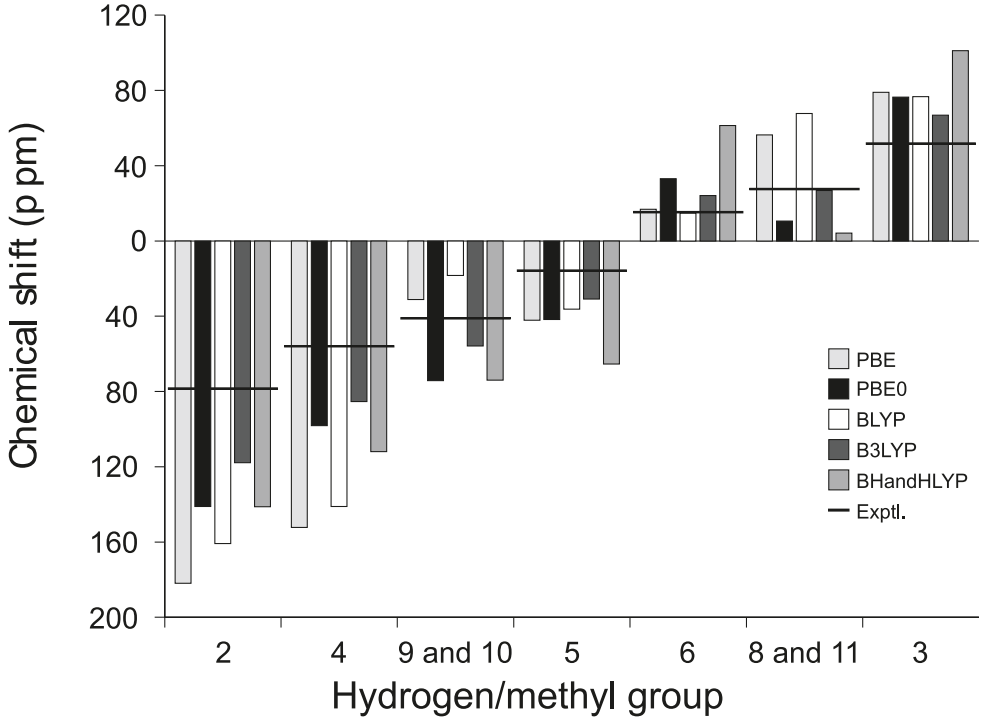

Selection of functional

Different exchange-correlation functionals have a larger impact on our results than the basis set. The comparison of shifts with different functionals is presented for molecules **1** and **4** in Figs. 1 and 2, respectively, with the HII basis. These molecules were selected because all the other molecules behave similarly to molecule **1**, whereas the Br atoms in molecule **4** affect the spin density distribution significantly. From Figs. 1 and 2 we can see that, in comparison to experiment, the best agreement is obtained with the B3LYP hybrid functional. In general, the computations exaggerate the [1]H shift range and the performance of the hybrid functionals (PBE0 and B3LYP) is better than that of the corresponding GGAs (PBE and BLYP). On the other hand, BHandHLYP is seen to fail completely for molecule **4**.

The principal values of the **g** and **D** tensors are listed for molecule 4 in Table 3. Changes between the functionals occur particularly in **D**. We see that the principal values of **D** change very much from the 20%–25% admixture of exact exchange in B3LYP and PBE0 to the 50% fraction in BHandHLYP. The last functional gives an unrealistically large anisotropy of **D**. The spin contamination was not found to change alarmingly between the functionals. The value of S^2 deviated only slightly from the formal value of 3.75.

Impact of geometry on chemical shift

Calculations were carried out for molecules 1 and 4 with three kinds of geometries. We used a fully computationally optimized structure, a structure where only the hydrogens were optimized while the other nuclei retained the X-ray positions, and the experimental X-ray structure for all nuclei. The last one was also used as the starting geometry of the optimizations. The results are listed in Table 4. For most shifts the best results are obtained with hydrogen-optimized structures, although no clear trends for a general improvement of the results can be distinguished.

Among the computational parameters that we vary in the present paper, exchange-correlation functional, basis set, and geometry, by far the greatest sensitivity of the calculated shifts is noted with respect to the choice of the functional. Besides these sources of deviation from the experimental data, solvation effects and rovibrational dynamics are expected to contribute. We do not presently model either of these effects.

Breakdown into chemical-shift terms

The different physical contributions to the chemical shifts (listed in Table 1) are broken down for molecules **1** and **4** in Tables 5 and 6, respectively. The δ_{ac} term is omitted from the tables because its contribution to the isotropic shift is zero. The largest contributions are expectedly the NR contact and orbital terms, which are numerically correctly taken into account also in the doublet theory. By far the dominating new term is δ_{dip} whose magnitude varies from 0.03 ppm to over 16 ppm. For most chemical shifts in molecules **1** and **4**, this contribution clearly exceeds the magnitude of the pseudocontact shift. It is noteworthy that in the presence of zero-field splitting, the δ_{dip} term encodes structural information of the paramagnetic molecule in a manner analogous to the δ_{pc} contribution in the more conventional analysis of pNMR spectra. Both cases share the same spin-dipole hyperfine interaction depending on the length and orientation of the vector joining the resonant NMR nucleus to the center of the electron spin density distribution. However, the role of the spin susceptibility tensor of the analysis of the pseudocontact term[2] is acquired by **D** in the novel δ_{dip} term, for $S \geq 1$ systems.

Fig. 2. [1]H chemical shift in molecule **4** calculated with different exchange-correlation functionals using the HII basis set.

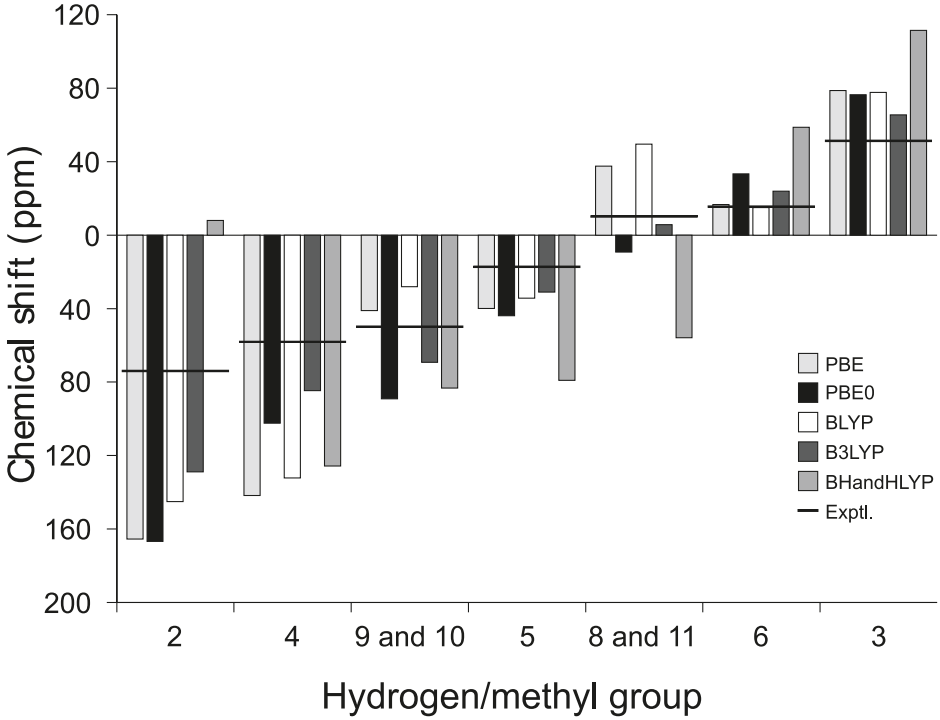

Table 3. Calculated eigenvalues of the **D** and **g** tensors of molecule **4** with different exchange-correlation functionals at the HII basis set level.

Property	Functional	Principal values		
g	PBE	2.0087	2.0105	2.0256
	PBE0	1.9994	2.0040	2.0175
	BLYP	2.0100	2.0118	2.0275
	B3LYP	2.0021	2.0063	2.0206
	BHandHLYP	1.9928	1.9990	2.0129
D	PBE	–210.76	–207.08	–203.66
	PBE0	–288.58	–272.59	–257.08
	BLYP	–210.23	–206.53	–202.83
	B3LYP	–263.74	–257.84	–244.94
	BHandHLYP	–371.42	–231.48	–218.37

Note: D tensor eigenvalues in cm^{-1}.

Table 4. Calculated [1]H chemical shifts (in ppm) for different geometries at the B3LYP/HII level for molecules **1** and **4**.

[1]H shift	Fully optimized	Optimized hydrogens	Experimental structure
Molecule 1			
2	–117.9	–105.5	–115.9
3	66.9	61.4	54.2
4	–85.3	–75.3	–77.5
5	–30.9	–25.3	–26.9
6	24.2	20.4	18.5
8 and 11	26.8	31.4	17.1
9 and 10	–55.8	–54.9	–53.9
Molecule 4			
2	–128.9	–131.0	–140.3
3	65.4	66.0	54.3
4	–84.6	–92.1	–91.8
5	–31.0	–33.3	–30.2
6	24.0	24.5	22.3
8 and 11	5.7	13.6	4.2
9 and 10	–69.3	–61.8	–63.7

The other novel dipolar terms, $\delta_{dip,2}$ and $\delta_{dip,3}$, as well as the anisotropic contact term, $\delta_{c,aniso}$, are negligible for [1]H in the present systems. In contrast, the contact terms arising from the SO corrections to the hyperfine and Zeeman interactions, $\delta_{con,2}$ and $\delta_{con,3}$, respectively, both obtain significant values, comparable to the pseudocontact contribution. The con,2 and con,3 contributions are already present in the doublet theory of ref.12.

The overall difference between molecule **4** and the other systems appear to be the enhancement of hyperfine shift terms other than the NR contact term, brought about by the Br centers of molecule **4**. This is reflected in a dramatic order of magnitude increase of the anisotropy of the ZFS tensor, e.g., from molecule **1** to molecule **4**, originating in the spin-orbit contribution to **D**. In contrast, the **g** tensor is much less influenced by the replacement of Cl by Br.

Full theory and approximations

The effect of the choice of the theoretical level was estimated by comparing the calculated chemical shifts for molecules **1** and **4** at the level of the full theory,[15] limiting the treatment to the doublet formulation (keeping, however, the correct $S(S + 1)$ factors appropriate to the quartet state), and the NR theory.[7] The results are shown in Table 7. There are cases, such as site 2 in molecule **4**, where the difference between the theories reaches up to 16 ppm due to the δ_{dip} term (vide supra). A general finding is that the difference be-

Table 5. Different physical contributions to the ^{1}H chemical shift (in ppm) for molecule **1** at the B3LYP/HII level with fully optimized structure.

^{1}H site	orb	con	dip	con,2	dip,2	con,3	dip,3	c,aniso	pc
2	8.3	–126.6	–2.61	1.30	0.013	0.48	0.010	0.002	1.01
3	7.1	59.3	0.16	0.18	0.000	–0.22	–0.001	–0.001	0.18
4	8.0	–94.7	0.82	0.00	–0.001	0.36	–0.003	0.001	0.05
5	7.7	–39.4	0.43	–0.02	–0.001	0.15	–0.002	0.001	–0.01
6	7.6	16.5	0.08	–0.04	0.000	–0.06	0.000	0.000	–0.01
7	7.7	–21.8	–0.62	–0.09	0.001	0.08	0.002	0.000	0.01
8 and 11	1.7	25.3	–0.03	–0.15	–0.002	–0.10	0.000	0.000	–0.26
9 and 10	1.9	–59.3	0.66	0.22	–0.003	0.22	–0.002	0.001	0.17

Table 6. Different physical contributions to the ^{1}H chemical shift (in ppm) for molecule **4** at the B3LYP/HII level with fully optimized structure.

^{1}H site	orb	con	dip	con,2	dip,2	con,3	dip,3	c,aniso	pc
2	8.5	–124.7	–16.14	2.11	–0.008	–0.46	–0.059	0.014	1.68
3	7.1	58.4	–1.49	0.59	–0.012	0.21	–0.005	–0.006	0.40
4	8.0	–94.3	1.31	0.22	0.010	–0.35	0.005	0.010	0.22
5	7.7	–39.7	0.74	0.09	0.009	–0.15	0.003	0.004	0.03
6	7.6	16.3	–0.14	0.00	0.005	0.06	–0.001	–0.002	–0.02
7	7.7	–21.7	–2.44	–0.18	0.003	–0.08	–0.009	0.002	–0.10
8 and 11	1.8	1.6	3.21	–0.71	–0.004	0.01	0.012	0.000	–0.50
9 and 10	2.0	–72.4	0.30	0.37	–0.011	–0.27	0.001	0.008	0.47

tween the shift obtained with the approximate theories and the full theory normally is within 0–3 ppm. The biggest changes occur for hydrogens in positions 2 and 4, and in the methyl groups bonded to the Cp ring. The deviations arise mainly from the terms that do not contribute to the isotropic shift at the approximate levels, especially the δ_{dip} term. Changes also occur in the pseudocontact term δ_{pc} when calculated at different levels of theory.

When comparing to δ_{pc}, which is often the target quantity in experimental investigations, one can see that the error is of a magnitude comparable to or larger than δ_{pc}, which ranges between 0 and 2 ppm in all molecules.

Final results

All the ^{1}H shifts of the eight molecules are reported at the B3LYP/HII level and at the extrapolated B3LYP/HIII* as well as B3LYP/HIII*//H-opt* levels in Table 8. Figure 3 visualizes the B3LYP/HII data and gives linear regression fits for that and the two extrapolated approximations. The first extrapolation, B3LYP/HIII* takes into account the effect of basis set improvement from the HII to the HIII level, evaluated using the PBE functional and added on top of the B3LYP/HII result (all at the fully BP86/def2-TZVP-optimized geometry):

$$\text{B3LYP/HIII}^* = \text{B3LYP/HII} + (\text{PBE/HIII} - \text{PBE/HII})$$

The reason for carrying out this extrapolation is that direct B3LYP/HIII calculations would be rather expensive due to the hybrid functional. Whereas it is evident that extrapolations of the present kind should be used with caution, the change of δ_{con} for the ^{1}H nuclei between the HII and HIII basis set levels is typically a decrease by 10% (PBE calculations for molecule **1**). The B3LYP and PBE functionals give, in general, different results for hyperfine properties. However, a common finding is that their basis set dependence is relatively independent of the choice of the functional. Consequently, the basis set effect represents only a quantitative modification of the shifts and the extrapolation procedure should be safe in the present case. The other extrapolation scheme additionally takes into account the

Table 7. Comparison of the general chemical-shift theory with the doublet theory of ref. 12 and the nonrelativistic theory of ref. 7 at the B3LYP/HII level (in ppm).

^{1}H site	Full theory	Error in doublet theory	Error in NR theory
Molecule 1			
2	–117.9	2.6	–0.4
3	66.9	–0.2	–0.5
4	–85.3	–0.8	–1.6
5	–30.9	–0.4	–0.8
6	24.2	0.0	–0.1
7	–14.6	0.6	0.4
8 and 11	26.8	0.1	0.5
9 and 10	–55.8	–0.7	–1.3
Molecule 4			
2	–128.9	16.2	12.9
3	65.4	1.5	0.3
4	–84.6	–1.4	–1.4
5	–31.0	–0.8	–0.7
6	24.0	0.1	0.1
7	–16.6	2.4	2.8
8 and 11	5.7	–3.2	–2.0
9 and 10	–69.3	–0.3	–0.9

Note: For the doublet or NR levels, the error with respect to the full theory is reported.

Table 8. ^{1}H chemical shifts at the B3LYP/HII level, as well as at the extrapolated B3LYP/HIII*//H-opt* and B3LYP/HIII* levels (see text).

Molecule	^{1}H site	Exp. [18,a]	B3LYP/HIII*//H-opt*[b]	B3LYP/HIII*[c]	B3LYP/HII	ΔStructure[d]	ΔBasis[e]
1	2	–78	–86.8	–103.7	–117.9	17.0	14.2
	3	51.8	57.2	62.2	66.9	–5.0	–4.7
	4	–56	–51.6	–67.9	–85.3	16.3	17.4
	5	–15.8	–19.9	–25.9	–30.9	6.0	5.0
	6	15.3	19.7	21.4	24.2	–1.7	–2.8
	7	—	–2.4	–8.6	–14.6	6.2	6.0
	8 and 11	27.6	34.4	25.7	26.8	8.7	–1.1
	9 and 10	–41.1	–49.6	–53.9	–55.8	4.3	1.9
2	2	86.7	112.7	112.7	115.2	—	–2.5
	3	51.7	45.5	45.5	48.2	—	–2.7
	4	–31.1	–39.0	–39.0	–50.1	—	11.1
	5	–4.3	–17.4	–17.4	–21.0	—	3.5
	6	19.7	15.6	15.6	18.0	—	–2.4
	7	—	–0.2	–0.2	–5.6	—	5.4
	8 and 11	25.4	16.4	16.4	17.2	—	–0.8
	9 and 10	–73.8	–95.5	–95.5	–97.1	—	1.6
3	2	–73	–100.7	–100.7	–111.7	—	11.1
	3	56	56.0	56.0	60.0	—	–4.0
	4	–46.8	–54.3	–54.3	–68.7	—	14.4
	5	–10.5	–22.9	–22.9	–26.3	—	3.5
	6	23.6	17.6	17.6	19.9	—	–2.3
	7	—	–1.5	–1.5	–7.0	—	5.5
	8 and 11	256.0	181.7	181.7	166.9	—	14.8
	9 and 10	216.0	158.3	158.3	157.5	—	0.9
4	2	–74	–121.1	–118.8	–128.9	–2.3	10.1
	3	51.3	62.4	60.5	65.4	1.9	–5.0
	4	–58.1	–73.0	–70.5	–84.6	–2.5	14.1
	5	–17.2	–25.9	–27.5	–31.0	1.6	3.5
	6	15.5	22.6	21.8	24.0	0.8	–2.2
	7	—	–9.7	–11.4	–16.6	1.7	5.2
	8 and 11	10.2	10.6	4.7	5.7	5.8	–1.0
	9 and 10	–49.9	–55.1	–66.3	–69.3	11.2	3.0
5	2	–78	–102.7	–102.7	–116.2	—	13.4
	3	50.6	60.3	60.3	65.1	—	–4.8
	4	–55.6	–65.1	–65.1	–81.7	—	16.6
	5	–16.4	–25.3	–25.3	–29.8	—	4.5
	6	15.2	20.9	20.9	23.6	—	–2.6
	7	—	–6.8	–6.8	–13.1	—	6.3
	8	19.7	21.0	21.0	22.1	—	–1.1
	9 and 10	–36.7	–47.1	–47.1	–49.0	—	1.9
	11	—	239.1	239.1	224.9	—	14.2
6	2	–75	–77.3	–103.7	–115.9	26.3	12.2
	3	51.1	57.5	61.9	64.6	–4.4	–2.7
	4	–55.9	–48.2	–68.2	–82.2	20.0	14.0
	5	–16.7	–14.8	–26.9	–30.4	12.1	3.5
	6	15.6	21.5	21.6	23.4	–0.1	–1.9
	7	—	2.9	–8.2	–13.7	11.1	5.5
	8	11.2	–73.2	31.8	32.8	–104.9	–1.1
	9	–29.3	17.7	–78.1	–80.1	95.8	2.0
	10	–38.7	–95.1	–13.0	–16.3	–82.1	3.3
	11	—	3.6	2.7	2.5	0.9	0.3
7	2	—	–73.0	–95.7	–103.7	22.7	8.0
	3	45.9	54.4	59.0	62.5	–4.6	–3.5
	4	–50.6	–60.0	–74.4	–85.6	14.5	11.1
	5	–16.3	–28.2	–31.5	–34.5	3.4	3.0
	6	14.4	20.3	23.4	25.6	–3.1	–2.2
	7	—	–7.8	–9.8	–14.6	2.0	4.8

Table 8 (*concluded*).

Molecule	^{1}H site	Exp. [18,a]	B3LYP/HIII*//H-opt*[b]	B3LYP/HIII*[c]	B3LYP/HII	ΔStructure[d]	ΔBasis[e]
	8	—	33.1	2.5	0.9	30.6	1.6
	9	–38.9	–62.0	–44.5	–48.8	–17.6	4.3
	10	–48.9	–49.1	–64.9	–69.1	15.8	4.2
	11	—	4.6	5.0	4.6	–0.3	0.4
8	2	—	–102.5	–157.6	–178.2	55.1	20.6
	3	56	74.8	93.6	100.6	–18.7	–7.1
	4	–79	–73.4	–133.1	–158.5	59.7	25.4
	5	–19.7	–29.0	–44.0	–49.9	15.0	5.9
	6	18.1	32.6	37.1	40.0	–4.5	–2.9
	7	—	–12.6	–26.4	–34.0	13.7	7.7
	8	169.0	182.7	197.8	198.7	–15.1	–0.9
	9	–52	–38.5	–92.9	–95.1	54.4	2.2
	10	41.5	–4.8	46.7	43.1	–51.4	3.5
	11	38	53.1	24.5	23.3	28.5	1.2

[a]Including both the orbital and hyperfine shift contributions.

[b]Extrapolated result as follows: B3LYP/HII + ΔBasis + ΔStructure.

[c]Extrapolated result as follows: B3LYP/HII + ΔBasis.

[d]Change induced by adopting the experimental X-ray structure for the heavy-atom framework and computationally optimized hydrogen positions: ΔStructure = PBE/HII//H-optimized – PBE/HII//fully optimized.

[e]Change induced by improving the basis set from HII to HIII: ΔBasis = PBE/HIII – PBE/HII, both at the fully optimized structure.

change of the results (for molecules other than **2**, **3**, and **5**) due to adopting the experimental X-ray structure for the heavy-atom framework, and computationally optimized hydrogen positions:

$$\text{B3LYP/HIII}^*\text{//H-opt}^* = \text{B3LYP/HIII}^* + (\text{PBE/HIII//H-opt} - \text{PBE/HII//fully opt})$$

The linear regression parameters of the three sets of data are given in Table 9. The fit parameters are noted to improve in the succession of approximations from the calculated B3LYP/HII data to the extrapolated B3LYP/HIII* and B3LYP/HIII*//H-opt* versions. That is visible in the k coefficients obtaining values closer to unity and the intercepts, b, becoming smaller. This underlines the role of the basis set as well as the experimental heavy-atom geometry for reproducing the experiment.

Despite the fact that the extrapolations improve the results on average, significant deviations from the experimental values remain. In some cases, the H-opt* step, in particular, introduces outliers that are not present in the earlier approximations. All three approximations feature the largest deviations occurring at the ends of the chemical-shift range. Signals with experimental values at around –80 ppm arise from the aromatic hydrogen atoms at site 2, which is nearest to the chromium center. The shifts experimentally at 220 and 260 ppm are due to molecule **3**, sites 8–11. These signals differ from all the other molecules because the H atoms of the Cp ring in molecule **3** are aromatic, i.e., there are no methyl groups. Other major deviations arise in the methyl groups of the Cp ring in the different molecules. It is thinkable that intramolecular dynamics, in particular the relative movement of the quinolyl and Cp ring structures with respect to each other, can affect the ^{1}H shifts of the Cp rings and the attached methyl groups.

Much of the error is expected to arise from the incompleteness of the B3LYP functional used, despite it being the best performing among the currently tried ones. The omitted solvation and rovibrational effects are likely to constitute other important error sources in our results. With the rigorous theory of pNMR shielding now at hand, it is motivating to pursue studying improved functionals and dynamic solvation effects in the context of the ^{1}H pNMR shifts in $S \geq 1$ transition metal systems.

Conclusions

A novel and general first-principles theory of pNMR nuclear shielding and chemical shift[15] was applied to molecules possessing nonaxial spatial symmetry and quartet spin state. This theory, for the first time, rigorously takes into account the effect of zero-field splitting of the ground-state electronic Zeeman manifold of $S \geq 1$ systems. The isotropic ^{1}H chemical shifts of a family of quinolyl-functionalized Cp chromium(III) complexes were calculated using DFT methods and compared to recent experimental pNMR data.[18] In particular, the selection of the exchange-correlation functional was found to be a crucial factor determining the accuracy of the predicted shifts. Overall, the B3LYP hybrid functional was found to perform best in comparison with a few GGA and other hybrid functionals. Linear regression fits of the calculated B3LYP shifts indicate improved agreement with experiment when extrapolating the data to a larger basis set and furthermore, when experimental X-ray structure is adopted for the heavy-atom framework, instead of the fully computationally optimized geometry. The remaining errors are mainly attributed to the deficiency of the B3LYP exchange-correlation functional and the fact that we did not model solvation or rovibrational effects that affect the experimental shifts.

Fig. 3. [1]H chemical shifts at the B3LYP/HII level as compared to experimental data. Linear regression lines indicate the best fits of the B3LYP/HII as well as the extrapolated B3LYP/HIII*//H-opt* and B3LYP/HIII* results (see text).

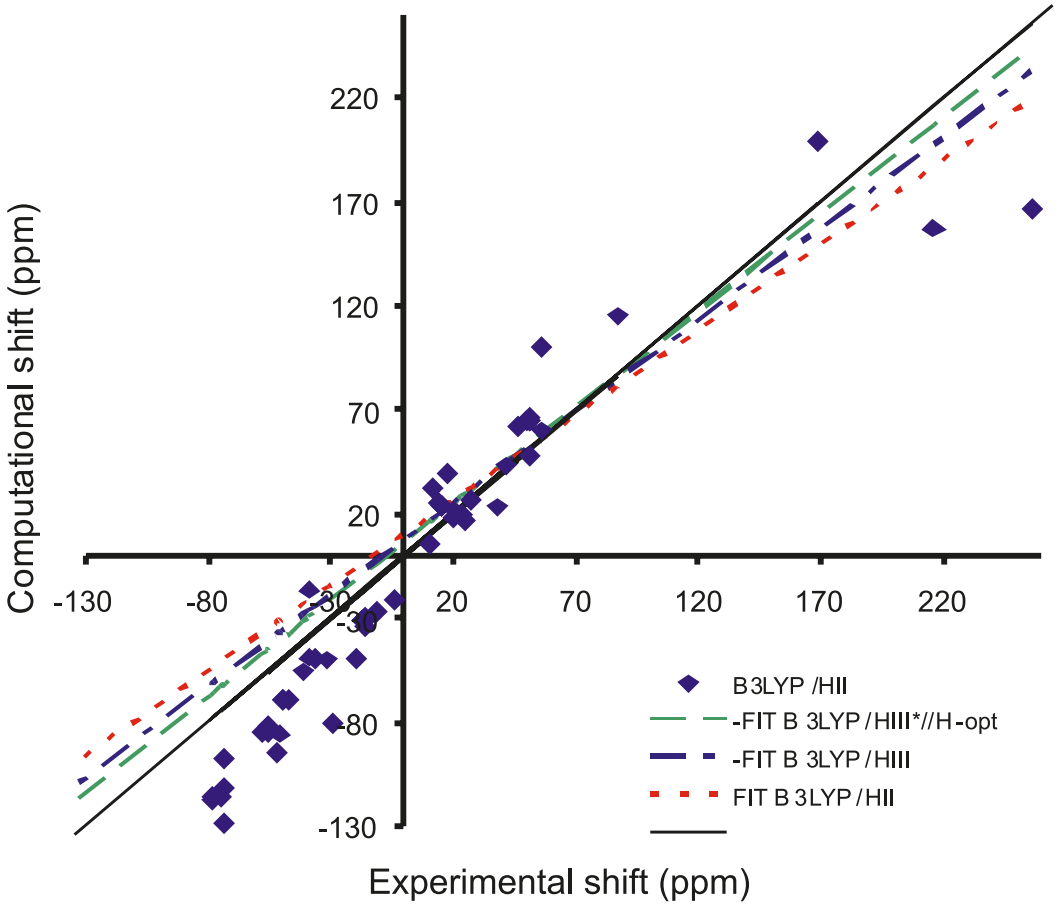

Table 9. Parameters of the linear fit of calculated [1]H chemical shifts with different approximations (see text) to the experimental data.

Approximation	*k*	*b* (ppm)
B3LYP/HII	0.82	10.4
B3LYP/HIII*	0.88	7.9
B3LYP/HIII*//H-opt*	0.93	6.6

Note: Fit to equation Exp = *k* Calc + *b*.

The calculated chemical shifts were broken down into physical contributions according to the new theory of ref. 15. The different terms arise from the expansion of the hyperfine coupling and electronic Zeeman interaction in orders α^2 of the fine structure constant, α, in the presence of the ZFS. The nonrelativistic orbital and contact shift terms, which are already correctly obtained in the approximate, earlier forms of the theory, were found to dominate the [1]H shifts. However, some of the novel isotropic shift contributions due to the ZFS effect are found to obtain significant magnitude. In particular, the nonrelativistic dipolar term, δ_{dip}, that does not enter the isotropic shift at all in the theory appropriate to doublet systems, systematically exceeds in magnitude the isotropic part of the so-called pseudocontact shift, in the present quartet molecules. The latter is traditionally used in the structure determination of paramagnetic molecules due to the spatial structure of the spin-dipole hyperfine Hamiltonian. It is argued that δ_{dip}, which features the same operator, could find similar use in $S \geq 1$ molecules.

Supplementary data

Supplementary data for this article are available on the journal Web site (canjchem.nrc.ca) or may be purchased from the Depository of Unpublished Data, Document Delivery, CISTI, National Research Council Canada, Ottawa, ON K1A 0R6, Canada. DUD 3947. For more information on obtaining material, refer to cisti-icist.nrc-cnrc.gc.ca/cms/unpub_e.shtml.

Acknowledgments

The authors are with the Finnish Center of Excellence in Computational Molecular Science. Financial support from the research funds of the University of Helsinki (HL, TOP, JV) as well as the Jenny and Antti Wihuri Fund (TOP) is gratefully acknowledged. The computational resources were partially provided by The Finnish IT Center for Science (CSC; Espoo, Finland).

References

(1) This article is part of a Special Issue dedicated to Professor T. Ziegler.
(2) Bertini, I.; Luchinat, C.; Parigi, G. *Solution NMR of Paramagnetic Molecules;* Elsevier: Amsterdam, 2001.

(3) Capsoni, D.; Bini, M.; Massarotti, V.; Mustarelli, P.; Chiodelli, G.; Azzoni, C. B.; Mozzati, M. C.; Linati, L.; Ferrari, S. *Chem. Mater.* **2008**, *20* (13), 4291–4298. doi:10.1021/cm703650c.
(4) Helgaker, T.; Jaszuński, M.; Ruud, K. *Chem. Rev.* **1999**, *99* (1), 293–352. doi:10.1021/cr960017t. PMID:11848983.
(5) *Calculation of NMR and EPR Parameters: Theory and Applications;* Kaupp, M., Bühl, M., Malkin, V. G., Eds.; Wiley-VCH: Weinheim, 2004.
(6) Autschbach, J.; Ziegler, T. *Encyclopedia of Nuclear Magnetic Resonance;* Grant, D. M., Harris, R. K., Eds.; Wiley: Chichester, 2002; Vol. 9, p 306.
(7) Rinkevicius, Z.; Vaara, J.; Telyatnyk, L.; Vahtras, O. *J. Chem. Phys.* **2003**, *118* (6), 2550–2561. doi:10.1063/1.1535904.
(8) McConnell, H. M.; Chesnut, D. B. *J. Chem. Phys.* **1958**, *28* (1), 107–117. doi:10.1063/1.1744052.
(9) Moon, S.; Patchkovskii, S. *Calculation of NMR and EPR Parameters: Theory and Applications;* Kaupp, M., Bühl, M., Malkin, V. G., Eds.; Wiley-VCH: Weinheim, 2004; p 325.
(10) McConnell, H. M.; Robertson, R. E. *J. Chem. Phys.* **1958**, *29* (6), 1361–1365. doi:10.1063/1.1744723.
(11) Kurland, R. J.; McGarvey, B. R. *J. Magn. Reson.* **1970**, *2* (3), 286–301.
(12) Pennanen, T. O.; Vaara, J. *J. Chem. Phys.* **2005**, *123* (17), 174102.
(13) Boca, R. *Theoretical foundations of molecular magnetism;* Elsevier: Amsterdam, 1999.
(14) Hrobárik, P.; Reviakine, R.; Arbuznikov, A. V.; Malkina, O. L.; Malkin, V. G.; Köhler, F. H.; Kaupp, M. *J. Chem. Phys.* **2007**, *126* (2), 024107.
(15) Pennanen, T. O.; Vaara, J. *Phys. Rev. Lett.* **2008**, *100* (13), 133002. doi:10.1103/PhysRevLett.100.133002. PMID: 18517943.
(16) Ramsey, N. F. *Phys. Rev.* **1950**, *78* (6), 699–703. doi:10.1103/PhysRev.78.699.
(17) Ramsey, N. F. *Phys. Rev.* **1953**, *91* (2), 303–307. doi:10.1103/PhysRev.91.303.
(18) Fernández, P.; Pritzkow, H.; Carbó, J. J.; Hofmann, P.; Enders, M. *Organometallics* **2007**, *26* (18), 4402–4412. doi:10.1021/om070173y.
(19) Becke, A. D. *J. Chem. Phys.* **1993**, *98* (7), 5648–5652. doi:10.1063/1.464913.
(20) Stephens, P. J.; Devlin, F. J.; Chabalowski, C. F.; Frisch, M. J. *J. Phys. Chem.* **1994**, *98* (45), 11623–11627. doi:10.1021/j100096a001.
(21) Krishnan, R.; Binkley, J. S.; Seeger, R.; Pople, J. A. *J. Chem. Phys.* **1980**, *72* (1), 650–654. doi:10.1063/1.438955.
(22) Enders, M.; Fernández, P.; Ludwig, G.; Pritzkow, H. *Organometallics* **2001**, *20* (24), 5005–5007. doi:10.1021/om010753+.
(23) Arbuznikov, A. V.; Vaara, J.; Kaupp, M. *J. Chem. Phys.* **2004**, *120* (5), 2127–2139. doi:10.1063/1.1636720. PMID: 15268351.
(24) *Maestro,* version 7.5.106; Schrödinger Inc.: Portland, OR, 2006.
(25) Perdew, J. P. *Phys. Rev. B* **1986**, *33* (12), 8822–8824. doi:10.1103/PhysRevB.33.8822.
(26) Becke, A. D. *Phys. Rev. A* **1988**, *38* (6), 3098–3100. doi:10.1103/PhysRevA.38.3098. PMID:9900728.
(27) Schäfer, A.; Huber, C.; Ahlrichs, R. *J. Chem. Phys.* **1994**, *100* (8), 5829–5835. doi:10.1063/1.467146.
(28) Ahlrichs, R.; Bär, M.; Häser, M.; Horn, H.; Kölmel, C. *Chem. Phys. Lett.* **1989**, *162* (3), 165–169. doi:10.1016/0009-2614(89)85118-8.
(29) Frisch, M. J.; Trucks, G. W.; Schlegel, H. B.; Scuseria, G. E.; Robb, M. A.; Cheeseman, J. R.; Montgomery, J. A., Jr.; Vreven, T.; Kudin, K. N.; Burant, J. C.; Millam, J. M.; Iyengar, S. S.; Tomasi, J.; Barone, V.; Mennucci, B.; Cossi, M.; Scalmani, G.; Rega, N.; Petersson, G. A.; Nakatsuji, H.; Hada, M.; Ehara, M.; Toyota, K.; Fukuda, R.; Hasegawa, J.; Ishida, M.; Nakajima, T.; Honda, Y.; Kitao, O.; Nakai, H.; Klene, M.; Li, X.; Knox, J. E.; Hratchian, H. P.; Cross, J. B.; Bakken, V.; Adamo, C.; Jaramillo, J.; Gomperts, R.; Stratmann, R. E.; Yazyev, O.; Austin, A. J.; Cammi, R.; Pomelli, C.; Ochterski, J. W.; Ayala, P. Y.; Morokuma, K.; Voth, G. A.; Salvador, P.; Dannenberg, J. J.; Zakrzewski, V. G.; Dapprich, S.; Daniels, A. D.; Strain, M. C.; Farkas, O.; Malick, D. K.; Rabuck, A. D.; Raghavachari, K.; Foresman, J. B.; Ortiz, J. V.; Cui, Q.; Baboul, A. G.; Clifford, S.; Cioslowski, J.; Stefanov, B. B.; Liu, G.; Liashenko, A.; Piskorz, P.; Komaromi, I.; Martin, R. L.; Fox, D. J.; Keith, T.; Al-Laham, M. A.; Peng, C. Y.; Nanayakkara, A.; Challacombe, M.; Gill, P. M. W.; Johnson, B.; Chen, W.; Wong, M. W.; Gonzalez, C.; Pople, J. A. *GAUSSIAN 03,* revision C.02; Gaussian, Inc.: Wallingford, CT, 2004.
(30) Neese, F. *ORCA,* version 2.6, revision 35; University of Bonn: Bonn, Germany, 2008.
(31) Neese, F. *J. Chem. Phys.* **2005**, *122* (3), 034107. doi:10.1063/1.1829047.
(32) Neese, F. *J. Chem. Phys.* **2003**, *118* (9), 3939–3948. doi:10.1063/1.1540619.
(33) Neese, F. *J. Chem. Phys.* **2007**, *127* (16), 164112. doi:10.1063/1.2772857. PMID:17979324.
(34) (a) Perdew, J. P.; Burke, K.; Ernzerhof, M. *Phys. Rev. Lett.* **1996**, *77* (18), 3865–3868. doi:10.1103/PhysRevLett.77.3865. PMID:10062328.; (b) Perdew, J. P.; Burke, K.; Ernzerhof, M. *Phys. Rev. Lett.* **1997**, *78* (7), 1396. doi:10.1103/PhysRevLett.78.1396.
(35) (a) Huzinaga, S. *Approximate Atomic Functions;* University of Alberta: Edmonton, AB, 1971; (b) Kutzelnigg, W.; Fleischer, U.; Schindler, M. *NMR Basic Principles and Progress*. Diehl, P., Flück, E., Günther, H., Kosfeld, R., Seelig, J., Eds.; Springer: Berlin, 1990.
(36) Fægri, K., Jr.; Almlöf, J. *J. Comput. Chem.* **1986**, *7* (4), 396–405. doi:10.1002/jcc.540070403.
(37) Munzarová, M.; Kaupp, M. *J. Phys. Chem. A* **1999**, *103* (48), 9966–9983. doi:10.1021/jp992303p.
(38) Balabanov, N. B.; Peterson, K. A. *J. Chem. Phys.* **2005**, *123* (6), 064107. doi:10.1063/1.1998907.
(39) Lee, C.; Yang, W.; Parr, R. G. *Phys. Rev. B* **1988**, *37*, 758.

Localized-orbital locator (LOL) profiles of transition-metal hydride and dihydrogen complexes[1,2]

Heiko Jacobsen

Abstract: A bond descriptor based on the kinetic-energy density, the localized-orbital locator (LOL), is used to characterize the nature of the chemical bond in transition-metal hydride and dihydrogen complexes. Cationic complexes of the iron triad $[MH_3(PMe_3)_4]^+$ (M = Fe, Ru, Os) serve as model compounds for transition-metal hydrogen bonding, since these complexes not only present examples for hydride as well as dihydrogen complexes, but for certain representatives, the two different types of metal–hydrogen bonds are realized within the same molecule. Both types of ligands show characteristic LOL profiles: (3,–3) Γ attractors in close vicinity to the H-atom for hydride ligands, and (3,–3) Γ attractors located between the two atoms for a dihydrogen ligand with ν_Γ-values of 0.8 and 0.9, respectively. In-between structures combine elements of the hydride and dihydrogen ligands. Relativistic effects on the relative stability of various isomers for the set of model compounds have been evaluated.

Key words: dihydrogen complexes, hydride complexes, localized-orbital locator, transition-metal complexes.

Résumé : On fait appel à un descripteur de liaison basé sur la densité de l'énergie cinétique, le localisateur d'orbitales localisées (LOL), pour caractériser la nature de la liaison chimique de l'hydrure d'un métal de transition et de ses complexes de dihydrogène. On a utilisé les complexes cationiques de la triade du fer $[MH_3(PMe_3)_4]^+$ (M = Fe, Ru, Os) comme composés modèles pour la liaison d'un hydrogène avec un métal de transition puisque ces complexes ne présentent pas uniquement des exemples pour l'hydrure et les complexes de dihydrogène, mais aussi pour certains produits représentatifs, les deux types différents de liaisons métal–hydrogène peuvent se retrouver dans la même molécule. Les deux types de ligands présentent de profils LOL caractéristiques : attracteurs (3,–3) Γ dans le proche voisinage de l'atome d'hydrogène avec les ligands hydrures et des attracteurs (3,–3) Γ situés entre les deux atomes pour un ligand dihydrogène, avec des valeurs de ν_Γ de 0,8 et 0,9 respectivement. Des structures intermédiaires combinent des éléments des ligands hydrure et dihydrogène. On a évalué les effets relativistes sur la stabilité relative de divers isomères pour l'ensemble des composés modèles de l'ensemble.

Mots-clés : complexes de dihydrogène, complexes d'hydrure, localisateur d'orbitales localisées, complexes de métaux de transition.

[Traduit par la Rédaction]

Introduction

Since Werner's work, which explored the nature of complexes between transition-metal ions and ligand entities around the beginning of the 20th century,[3] the nature of the chemical bond in transition-metal complexes continues to be an area of ongoing research activities. In particular, the coordination chemistry of saturated molecules has progressed steadily into a well-established and well-understood structural paradigm,[4] and holds the promise to be an integral player in the quest for "holy grails in chemistry", such as the solar splitting of water to hydrogen and oxygen, and carbon–hydrogen bond activation by synthetic metal complexes.[5] Since dihydrogen complexes constitute prototypes for the coordination chemistry of saturated molecules,[6] transition metal – hydrogen compounds are central to the investigation of bonding and reactivity of this class of compounds.

The discovery of transition-metal complexes with a side-on bonded H_2 ligand[7] has expanded the coordination chemistry of hydrogen from *classical* hydride ligands to *non-classical* dihydrogen complexes: they are part of an important class of compounds, in which an electron pair in a σ-bond of a ligand donates part of its electron density to the transition-metal center,[8] a bonding motif quintessential for the coordination chemistry of saturated molecules. Dihydrogen can in addition act as a σ*-acceptor through its antibonding and vacant σ* orbital. It is the fine balance between the donor and acceptor properties of the transition-metal center that determines the valence tautomerism of the H_2 ligand ranging from non-classical $M–H_2$ dihydrogen complexes to classical H–M–H bishydrides, resulting from an oxidative addition of the hydrogen molecule to the transition-metal center. In the first decade after their initial discovery, the coordination chemistry[9] as well as the reactivity[10] of dihydrogen complexes have already become subjects of extensive review articles; a fact which underlines the importance of this class of

Received 17 December 2008. Accepted 19 March 2009. Published on the NRC Research Press Web site at canjchem.nrc.ca on 5 June 2009.

H. Jacobsen.[1] KemKom, 1215 Ursulines Ave, New Orleans, LA 70116, USA. (e-mail: jacobsen@kemkom.com).

[1]Present address: Tulane University, Department of Chemistry, New Orleans, LA 70118, USA.

compounds. Dihydrogen complexes are best-viewed as a subclass of transition-metal hydrides,[11] which continue to be the focus of much research activities.[12]

With the recognition of density functional theory (DFT) as a practical tool in molecular energetics and dynamics,[13] computational chemistry began to develop into a reliable companion method to experimental investigations. DFT provides an easy and straightforward computational access to areas that were excessively difficult to tackle with conventional ab initio methodology, such as transition-metal chemistry.[14] Elementary reaction steps in organometallic chemistry have been the subject of DFT investigations early on,[15] and DFT progresses on the way of modeling chemical reactions "from balls and sticks to HOMO's and LUMO's".[16]

Chemical reactions are characterized by processes of bond breakage and bond formation, and central questions that seek for an understanding of chemical reactivity are intimately related to a detailed description of the chemical bond (its strength and its characteristics). The pool of theoretical methods of potential use for studies of inorganic reaction mechanisms is constantly expanding,[17] and so is the number of approaches that explore the nature of the chemical bond. The quantum theory of atoms in molecules (QTAIM)[18] carries the description of a chemical bond from an orbital-based approach to a definition based on the electron density of a molecular system. However, not only the charge density, but also the kinetic-energy density contains valuable information about the chemical bond. Descriptors based on the kinetic-energy density, such as the electron localization function (ELF)[19] and the localized-orbital locator (LOL),[20] provide answers to the problem of electron localization and delocalization (one of the main aspects of the nature of the chemical bond). A recent study of LOL profiles of prototypical chemical bonds demonstrates that LOL represents a conceptually simple but efficient tool in characterizing a chemical bond.[21]

In the present paper, we set out to establish LOL profiles of transition-metal hydrides and dihydrogen complexes. Molecular geometries and electron densities obtained from DFT calculations represent the basis of our analysis. We hope to establish characteristic LOL features that might be useful in characterizing the true nature of the M–H bond.

Results and discussion

We chose cationic complexes of the iron triad $[MH_3(PMe_3)_4]^+$ (M = Fe, Ru, Os) as model compounds for transition metal – hydrogen bonding. These complexes not only present examples for hydride as well as dihydrogen complexes, but for certain representatives, the two different types of metal–hydrogen bonds are realized within the same molecule, allowing for a direct comparison of different hydrogen bonding modes. Like many transition metal – hydride complexes, $[MH_3(PMe_3)_4]^+$ compounds are stereochemically nonrigid in solution, and their structures and dynamics have been investigated by X-ray diffraction studies and detailed NMR experiments.[22]

The possible coordination geometries of $[MH_3(PMe_3)_4]^+$ molecules can be classified as *P*-, *C*-, and *T*-type structures, where the nomenclature is derived from the coordination sphere of the phosphine ligands based on a square-planar, C_{2v}-butterfly, and tetrahedral arrangement, respectively. Further, one has to differentiate between classical trihydride complexes and non-classical hydride–dihydrogen systems, and we designate these types as P_c and C_c (classical), or P_n and C_n(non-classical). Chart 1 depicts the various geometries of $[MH_3(PMe_3)_4]^+$ complexes.

We note that the geometries and relative energies of various $[MH_3(PMe_3)_4]^+$ complexes have been previously studied by DFT calculations;[23,24] what we will add in the present work is a more detailed analysis of the nature of the transition metal – hydrogen bond.

Geometries of transition metal – hydride and transition metal – dihydrogen bonds

A first assessment of the nature of a HH-ligand is usually based on the distance of separation of the two hydrogen atoms, d(H–H). Most of the structural information of dihydrogen complexes is derived from their NMR properties in solution, and Morris has recently analyzed the structures and characteristic NMR properties of 17 Fe-, 98 Ru-, and 70 Os-complexes that contain a HH-ligand.[25] The question then arises of whether the HH-ligand represents a dihydrogen, bishydride, or something in between. Kubas has defined a practical, but qualitative, criterion for categorizing M–(HH) complexes. In comparison to free dihydrogen, d(H–H) = 74 pm, a complex where the H separation falls in the distance range 80 pm < d(H–H) < 100 pm represents a true dihydrogen complex, a complex with 100 pm < d(H–H) < 130 pm is a representative of an elongated dihydrogen complex, and when the HH separation falls into the range 130 pm < d(H–H) < 160 pm, we talk about a compressed bishydride, whereas the true bishydride possesses a H–H separation with d(H–H) > 160 pm.[6]

We note that there is no definite transition from one form to another in this continuum of structures, and so these definitions are somewhat arbitrary. It might be therefore helpful to develop a criterion for characterizing the nature of the M–(HH) bond that goes beyond this rather capricious criterion. Before we address this problem, we will look at the M–(HHH) geometries of our set of model compounds $[MH_3(PMe_3)_4]^+$ (M = Fe, Ru, Os).

For all model complexes, we have optimized *P*-, *C*-, and *T*-type structures without any geometric constraints that define the hydrogen atoms of the HH-ligand as classical hydride H^c or non-classical dihydrogen H^n ligands. Characteristic distances and angles of M–(HHH) coordination geometries are collected in Table 1.

The *T*-isomers contain three true classical hydride ligands H^c; the structural requirement of the pseudotetrahedral arrangement places the H^c ligands at distances between 240 pm and 270 pm from each other. As the data of Table 1 indicate, all the H^c ligands are equivalent in terms of metal to hydrogen separation. The geometries of the *T*-isomers therefore define typical Fe–H^c, Ru–H^c, and Os–H^c bond lengths. It becomes apparent from the slight deviations between the distances d(H^c–H^c) and bond angles (H^c–M–H^c) that the geometry of the *T*-isomers is best described as pseudoterahedral. However, these deviations are only minor and do not invalidate the notion of three equivalent hydride ligands.

The *P*-isomers contain two groups of hydrogen ligands, one consisting of one H and the other consists of two H

Chart 1. Structures of $[MH_3(PR)_4]^+$ compounds (M = Fe, Ru, Os; R = Me).

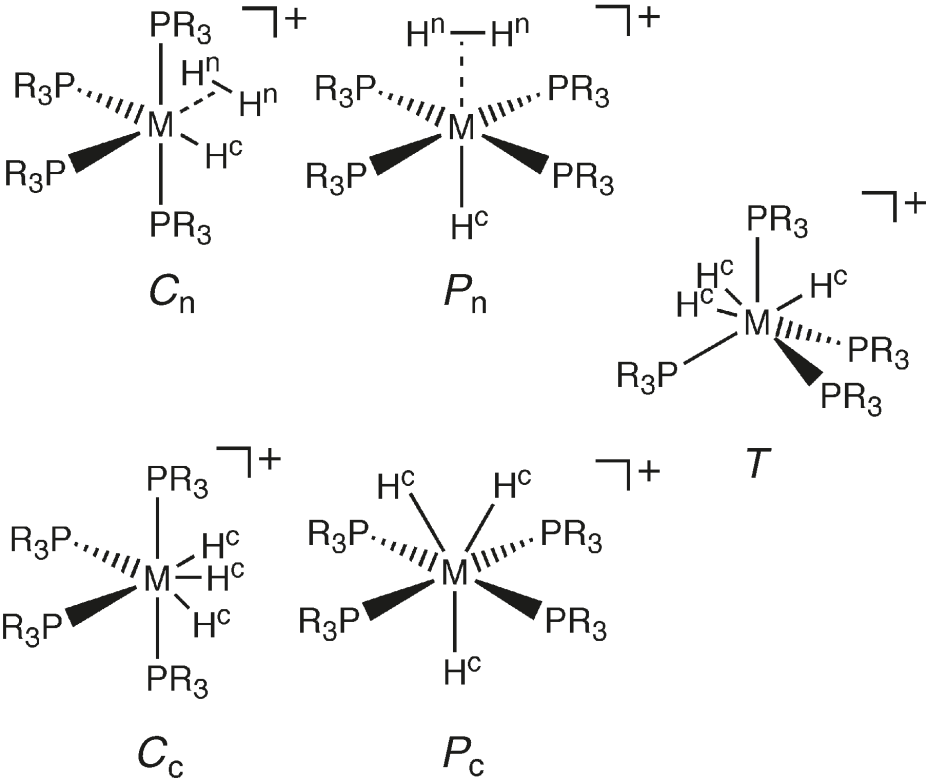

Table 1. Bond distances (in pm) and bond angles (in degree) of *T*-, *P*-, and *C*-type isomers of cationic $[MH_3(PMe_3)_4]^+$ complexes (M = Fe, Ru, Os).

	Distances (pm)				Angles (°)	
Transition metal (structure type)	d(M–H^c)	d(M–H^n)	d(H^c–H^n)	d(H^x–H^x)[a]	(H^x–M–H^x)[a]	(H^c–M–H^n)
Fe (*T*)	151	—	—	240	105	—
	151			241	106	
	151			243	107	
Ru (*T*)	163	—	—	262	107	—
	163			262	107	
	163			264	108	
Os (*T*)	166	—	—	267	107	—
	166			267	107	
	166			272	110	
Fe (P_n)	152	157	306	96	35	162
		157	306			162
Ru (P_n)	163	174	334	90	30	165
		174	334			165
Os (P_c)	168	—	—	193	71	—
	166			317	144	
	166			318	145	
Fe (C_n)	151	154	176	94	35	71
		157				
Ru (C_n)	163	166	196	98	34	73
		169				
Os (C_c)	165	—	—	168	62	—
	163			168	62	
	165					

[a]For *T* -isomers, H^x refers to H^c; for *P*- and *C*-type complexes of Fe and Ru, H^x refers to H^n; for *P*- and *C*-type complexes of Os, H^x refers to H^c.

atoms. These two groups are well-separated from each other, since they are positioned on opposite sides of the square-planar framework defined by the phosphine ligand. Whereas the single H atom naturally represents a hydride ligand, the question arises of whether the HH-entity represents a bishydride or a dihydrogen ligand. Kubas' geometric criterion characterizes the HH group in the *P*-isomers of complexes of Fe and Ru as a true H_2-complex, whereas the osmium complex contains three true hydride ligands H^c. The sum of the bond angles (H^c–M–H^c) indicates that the three H^c ligands in the Os-complex are located in the same coordination plane.

On the basis of their coordination geometries, we refer to these complexes as P_n–Fe, P_n–Ru, and P_c–Os, respectively. We were also able to locate P_c–Fe, P_c–Ru, and P_n–Os structures, which however are substantially higher in energy. We will only briefly return to these structures in the last section of our discussion, and we refer the interested reader to the Supplementary data for details. To conclude the discussion of *P*-isomers, we note that M–H^c distances for all complexes compare quite well with the standard reference values established for *T*-isomers.

The *C*-isomers possess three H-atoms in a cis arrangement, and offer various possibilities for forming hydride and dihydrogen ligands, or in between bonding situations. For the Fe- and Ru-complexes, we find two HH distances designative of the presence of a true dihydrogen ligand for one pair of neighboring H-atoms, and that indicates that there is no HH-bonding interaction for the other pair of neighboring H-atoms. The *C*-isomers of Fe and Ru compounds are to be classified as hydride–dihydrogen C_n-type complexes. The *C*-isomer of the Os complex displays H–H separations that exceed values for elongated dihydrogen and compressed dihydride complexes, and is to be classified as trishydride, a C_c-type complex. All three H^c ligands display essentially the same d(M–H^c) separation, which compares well with the value of the other trishydride, *T*-Os. The same observation holds true for the single hydride ligands in *C*-type complexes of Fe and Ru.

The geometry optimization of the cationic $[MH_3(PMe_3)_4]^+$ complexes offered no surprises; the values for M–(HHH) coordination geometries compare well with previous studies.[24] The optimized geometries however set the stage for a detailed LOL analysis, which provides insights into the nature of transition metal – hydride and transition metal – dihydrogen bonds.

LOL profiles of transition metal – hydride and transition metal – dihydrogen bonds

Before we engage in a more detailed discussion, a few remarks on LOL are in order. LOL (referred to as ν) is a measure of the relative value of the local kinetic energy τ in a mapping onto the finite range [0,1]. A value of $\nu = 1/2$ indicates that the kinetic-,energy content of the corresponding region is what would be expected from a spin-neutral electron gas of that density, and values of $\nu > 1/2$ indicate regions where electrons are localized. Ideas borrowed from the topological analysis of electron charge density[18] allow one to locate critical points and in particular (3,–3) attractors Γ in the gradient vector field of LOL.[21] Each nucleus position is associated with one attractor Γ, but LOL also features attractors between bonded atoms and in molecular regions associated with lone pairs. It is the Γ topology of LOL and its associated ν_Γ-values that serve as a guide in describing the nature of chemical bonding in molecular systems.

The chemical content of LOL is similar to that of ELF, which is also dependent on the kinetic-energy density τ. However, ELF is founded on considerations of the electron pair density, whereas LOL simply recognizes that gradients of localized orbitals are maximized when localized orbitals overlap. Moreover, LOL offers a simpler interpretation in terms of fast and slow electrons, and always falls to zero asymptotically, whereas ELF sometimes does not.[26] It appears that LOL represents a simpler function than ELF, and is more easily linked to intuitive concepts of chemical bonding.

The LOL analysis of hydrogen is a special case due to the lack of an electronic core; similar observations have been made for ELF as well.[27] The kinetic-energy density contains pertinent information in the description of Pauli repulsion,[28] and thus the region of the nucleus is not excluded for valence electrons. For element–hydrogen bonds, E–H, the hydrogen nucleus is within region of the slow moving electrons that form a covalent bond.[20] The (3,–3) attractor Γ is not found at equal distance to the E and H nuclei, but is displaced toward the hydrogen atom. For example, for the prototypical C–H covalent single bond in ethane, a Γ attractor with a ν_Γ-value of 0.92 is found, and the distance ratio between the LOL attractor and the C and H nuclei amounts to $d(\Gamma–C)/d(\Gamma–H) = 4.2$.[21] For the H–H bond in dihydrogen, no (3,–3) attractor Γ is to be found in the LOL gradient vector field because of the absence of core electrons. We will keep these two points in mind when we interpret LOL profiles of transition metal – hydride and transition metal – dihydrogen bonds.

We have analyzed the valence electron kinetic-energy density of various $[MH_3(PMe_3)]^+$ complexes, and located (3,–3) attractors Γ in the gradient vector field of LOL. Here, we restrict ourselves to the analysis of metal–ligand bonds, and the LOL profiles of ligands within the first coordination sphere around the transition-metal center for *T*-, *P*-, and *C*-type isomers are depicted in Fig. 1.

For the *T*-type trishydride complexes, we find that the classical hydride ligand is characterized by the presence of one Γ attractor located between the transition metal and the hydride with a ν_Γ-value around 0.80. This value is about 0.1 units smaller than the ν_Γ-value for the prototypical covalent C–H bond in ethane. The attractor is found in close vicinity to the H^c-ligand, with $d(\Gamma–M)/d(\Gamma–H^c)$ ratios of 8.4 for iron, 8.6 for ruthenum, and 8.8 for osmium. These ratios are about twice as large as for the covalent C–H bond in ethane. We associate the decrease in ν_Γ together with the stronger displacement of the Γ attractor toward the hydride ligand with an increased ionic character of the M–H^c bond.

For the hydride–dihydrogen P_n-isomers of Fe and Ru, the HH ligand is characterized by a Γ attractor located between the two H-atoms of the coordinated dihydrogen molecule. We recall that no Γ attractor exists in the LOL gradient vector field of free dihydrogen, and the existence of the Γ attractor indicates the presence of a σ-bond between the HH ligand and the transition-metal center. The hydride ligand again displays a Γ attractor in close vicinity to the H nu-

Fig. 1. Γ attractors and associated ν_Γ-values of *T*-, *P*-, and *C*-type isomers of cationic $[MH_3(PMe_3)]^+$ complexes (M = Fe, Ru, Os): (a) *T*–Fe, (b) *T*–Ru, (c) *T*–Os, (d) P_n–Fe, (e) P_n–Ru, (f) P_c–Os, (g) C_n–Fe, (h) C_n–Ru, and (i) C_c–Os.

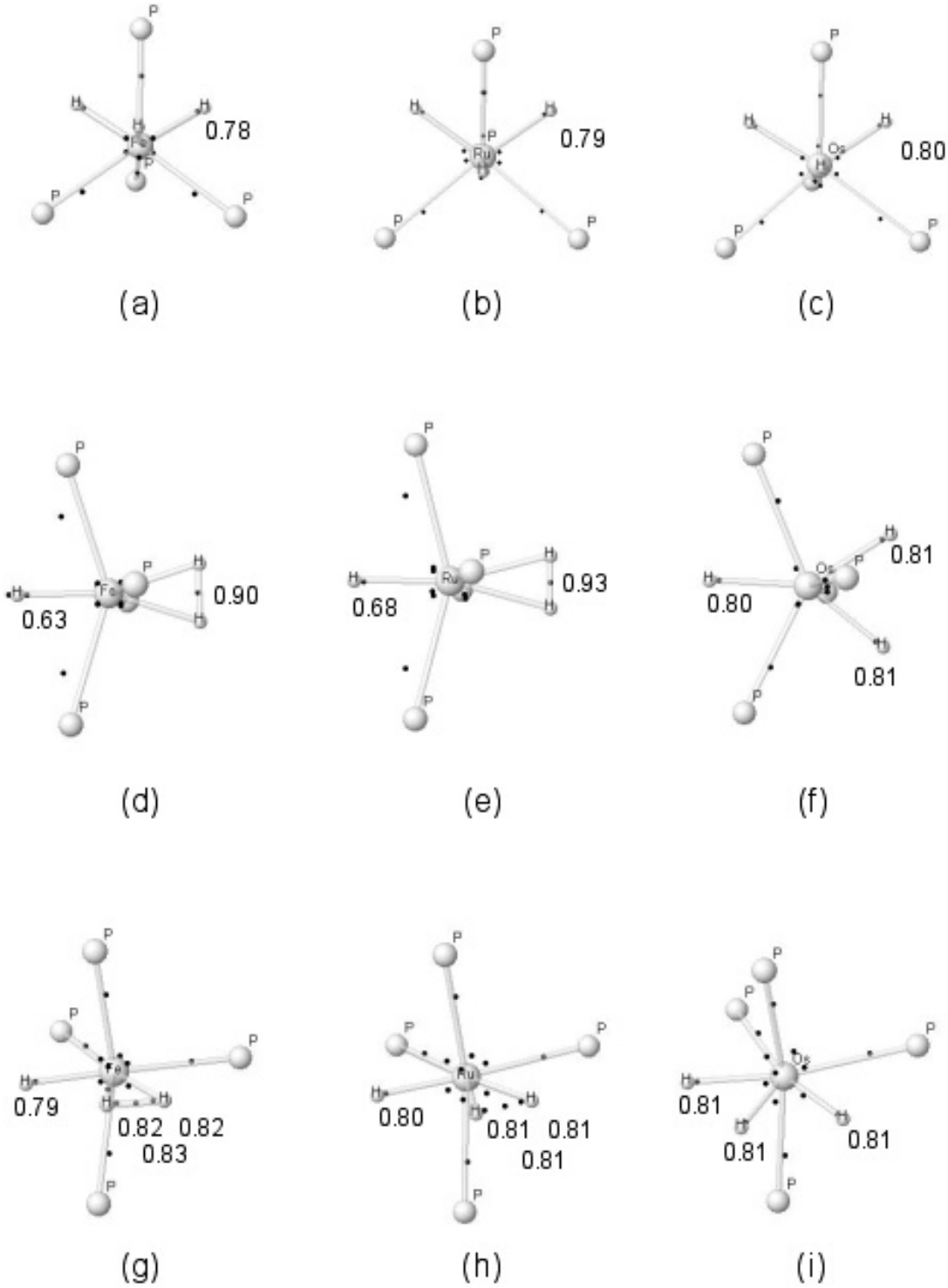

cleus; we note that the ν_Γ-value is about 0.1 to 0.15 units smaller when compared with the *T*-type trihydride compounds. Proceeding to the P_c-type isomer of Os, we find three hydride ligands characterized by Γ attractors in close vicinity to the hydrogen nuclei. The ν_Γ-values are essentially the same as found for *T*–Os, and we conclude that *T*–Os and *P*–Os constitute true structural isomers.

When we proceed to the *C*-type structures, we notice the presence of a dihydrogen ligand for the Fe- and Ru-complex, while Fig. 1 displays a Γ attractor located between the two H-atoms at close distance to each other. This feature characterizes the HH ligand as a dihydrogen ligand, bonded by σ-donation to the transition-metal center. However, whereas for the *P*-type isomers of Fe and Ru, the attractor

located between the two H-atoms was the only attractor to be found in relation to the HH ligand, whereas the HH ligand in C_n–Fe and C_n–Ru displays additional attractors in close vicinity to the H-atom, similar to those observed for hydride ligands. It appears that the HH ligand in *C*-type structures displays characteristic features of both a dihydrogen and a bishydride ligand. Although not obvious from its coordination geometry, the HH ligand in these structures represents an in-between situation between the two extremes, σ-bonded dihydrogen and ionic bishydride. The third H-ligand in C_n–Fe and C_n–Ru is clearly an independent hydride ligand, with attractor ν_Γ-values comparable to those of the related *T*-type structures. When we proceed to the *C*-type structure of osmium, no Γ attractor located between two adjacent H-atoms is to be found; the osmium isomer is a true trishydride, to be classified as C_c–Os, in accord with the assessment based on structural parameters.

LOL profiles might further be helpful in elucidating mechanistic aspects related to the afore-mentioned stereochemical non-rigidity. In particular, hydride fluxionality in transition-metal complexes has played a key role in developing mechanistic concepts, and the possible interchange of a hydrogen atom in hydride–dihydrogen complexes serves as the simplest model for σ-bond activation reactions.[29] The first ab initio studies of the model complex $[Fe(PH_3)_4H(H_2)]^+$ lead to the conclusion that the favoured mechanism for intramolecular atom exchange between the hydride and the dihydrogen moiety within the C_n-isomer is the so-called open direct transfer.[30] This exchange pathway consists of a single-step transfer of the hydrogen atom between the two ligands. In the transition state of this mechanism, the central hydrogen atom is bound to the metal center as well as to the other two hydrogen atoms, forming a trihydrogen ligand. A mechanism following an addition–elimination reaction, which would involve a true transition-metal trishydride, has been excluded on the basis of an extraordinarily high activation energy.

Since the initial investigations employ geometry constrains, the problem has been revaluated using DFT methodologies,[31] and the nature of the transition state – trishydride vs. – trihydrogen has been addressed in a QTAIM study. It turned out that qualitative differences appeared in the topological description of the chemical bonding in the transition state for the hydrogen exchange process and depends on the chosen density functional approach. From results of pure density functional calculations, the transition state had to be classified as a trishydride complex, whereas computations employing hybrid methodologies produced a transition state that, according to its bond critical points and bond paths, represents a trihydrogen situation.

It has been found that in situations where a QTAIM analysis leaves open questions and seems to be dependent of the underlying computational methodology, an LOL analysis provides a more consistent picture, independent of the theoretical method employed.[32] In the context of the present work, we analyze the transition state for hydrogen exchange within the C_n–Fe complex $[FeH_3(PMe_3)_4]^+$ as a representative example. The LOL profile for the transition state is depicted in Fig. 2.

Inspection of Fig. 2 provides an immediate answer to the question of whether the hydrogen exchange in C_n–$[FeH_3(PMe_3)]^+$ follows an open direct transfer or an addition–elimination pathway. No Γ attractors are to be found between two adjacent H-atoms, but three Γ attractors are located in close vicinity to each of the H-atoms. The ν_Γ-values are indicative of a hydride ligand (compare *T*–Fe), and according to its LOL profile, the transition state has to be classified as trishydride rather than a trihydrogen complex.

Fig. 2. Γ attractors and associated ν_Γ-values of the transition state for hydrogen exchange in C_n–$[FeH_3(PMe_3)]^+$.

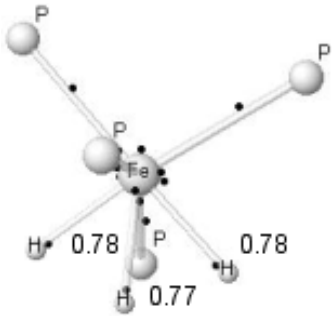

Chart 2. Relativistic influence on the d_π donor and d_σ acceptor orbitals of transition-metal fragments.

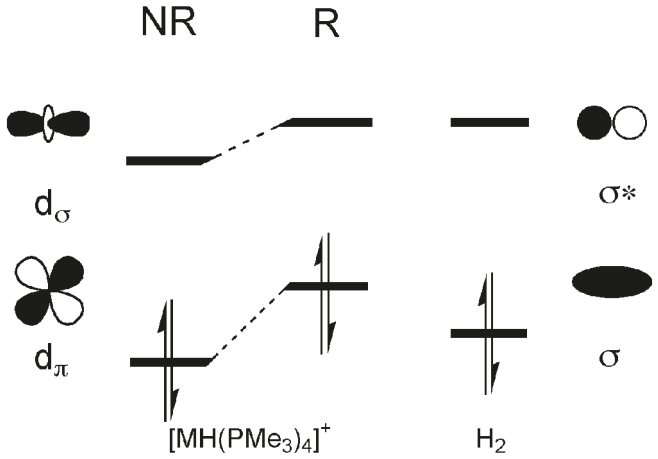

While LOL profiles obtained from the valence electron density are helpful in characterizing the nature of the M–H bond in cationic $[MH_3(PMe_3)]^+$ complexes, they do not answer questions related to different preferences for *C*-, *P*-, and *T*-isomers for classical or non-classical coordination of a HH-ligand when proceeding down group 4 from iron to osmium. There apparently exists a major influence of the core electrons on the relative stability of the various isomers. This problem has been analyzed in detail in the literature, and we conclude our discussion with a brief assessment of relative energies of some of the possible isomers.

Preference for classical or non-classical bonding of a dihydrogen ligand

A seminal paper by Ziegler analyzes the origin of the preference for bishydride complexes as opposed to dihydrogen bonding within a series of related compounds.[33] He chose transition-metal complexes of group 8 metals as representative examples, and the observed preference for a bishydride complex in the case of the heavier congener osmium was explained by a relativistic effect. Chart 2 displays this

Fig. 3. Relative energies (in kJ/mol) of *T*-, *P*-, and *C*-type isomers of cationic $[MH_3(PMe_3)]^+$ complexes (M = Fe, Ru, Os), obtained from relativistic R and non-relativistic NR calculations.

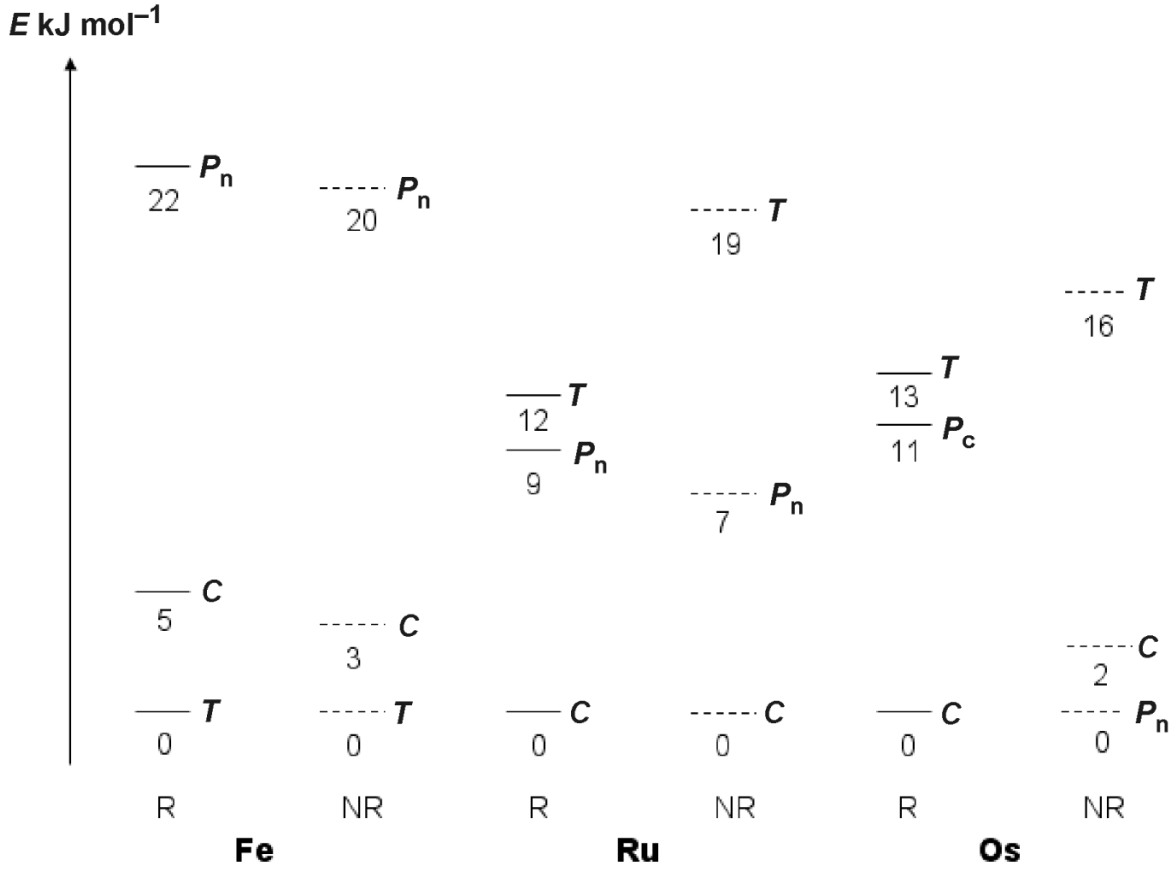

relativistic effect in terms of orbital interactions related to donation and back-donation.

Both d-based orbitals of a transition-metal fragment that are responsible for ligand bonding are raised in energy by relativity. The energy increase for d_π will enhance back-donation, since this orbital now is closer in energy to a σ* accepting orbital of a HH-ligand. On the other hand, the energy increase for d_σ will reduce donation, since the energy gap to a σ donor orbital is enlarged. The relativistic increase in the energy of the osmium d orbitals is the result of a relativistic contraction of the s and p core orbitals, which in turn reduces the effective nuclear charge experienced by electrons in the d-valence shell on osmium.[33] As a consequence of enhanced back-donation, the electron density in the σ* orbital of a HH-ligand is increased, which induces a transformation of the ligand from dihydrogen to bishydride.

This concept has been explored for other systems as well,[34] including the complexes that are the subject of the present investigation.[24] We therefore conclude with only a few remarks on the energetic preferences of different isomers, including and excluding relativistic contributions. These energy rankings are displayed in Fig. 3.

We begin with results obtained from relativistic calculations. For the iron complex, the *T*-isomer represents the most stable isomer, whereas for ruthenium and osmium complexes, this isomer is the least stable, and *C*-isomers are to be found at lowest energy values. The *T*-isomer preference for iron has been observed before,[23] and is explained by the strong donor capabilities of the trimethyl phosphine ligand together with the absence of a d-electron core. While for iron and ruthenium, the *C*- and *P*-type isomers represent non-classical structures, the osmium isomers are classical without any dihydrogen ligands. We also note that the P_n-type isomers are higher in energy than the *C*-type isomers; the reduced ν_Γ-value of the hydride ligand in Fe–P_n and Ru–P_n might be interpreted as a first indication of this fact.

When we turn to non-relativistic calculations, we observe that for iron complexes, the influence of relativistic effects is only marginal, and that the qualitative picture is not affected. For osmium on the other hand, exclusion of relativistic effects turns the classical P_c-isomer into its non-classical P_n counterpart. At the same time, we notice a decrease of the *C*–P_n energy gap when proceeding down group 8. As a consequence, without the inclusion of relativistic effects, a P_n-isomer is predicted to represent the lowest energy isomer for osmium systems.

Conclusion

We have shown how an LOL analysis might provide answers to the question at the heart of many investigations of transition-metal dihydrogen complexes: does a HH-ligand represent a dihydrogen ligand, a bishydride, or something in between? Both the hydride and the dihydrogen ligand pos-

sess their characteristic LOL profiles, and the HH-ligand of in-between structures features LOL characteristics of extremes.

The distinction between classical and non-classical bonding situation is not restricted to transition-metal hydrides, but is applied in other areas of coordinaion chemistry as well, for example, non-classical interligand interactions involving silicon-based ligands.[35] An LOL analysis might provide alternative explanations and place the discussion on firmer grounds, shifting the emphasis away from arguments that are frequently concerned with the idea of hypervalency, a concept that is often misunderstood.[36]

Computational details

Geometries have been optimized in density functional calculations carried out with the Gaussian03 system of programs,[37] which also furnished molecular valence densities used in topology analyses. The pure density functional calculations employed the PBE functional proposed by Perdew, Burke, and Ernzerhof.[38] Transition metals were modeled by a small-core,[39] as quasi-relativistic effective core potential together with a corresponding valence basis set.[40] Atoms bonded to the transition-metal center have been described by contracted Gaussian basis sets of triple zeta valence quality augmented by polarization functions (TZVP).[41] The remaining elements were described by contracted Gaussian split-valence basis sets with polarization (SVP).[42]

For optimized geometries, relative energies with and without the explicit consideration of relativistic effects have been evaluated using the ADF2006.01 program package,[43] The calculations employed the frozen-core approximation. The transition metals and atoms bonded to them have been described by a triple-ζ basis with polarization, the remaining elements were modeled by a double-ζ basis with polarization (ADF basis sets TZP and DZP, respectively). Relativistic effects have been incorporated by the zero-order regular approximation.[44]

Topological analyses of molecular electron densities employed a modified version of the program MORPHY.[45] 3D pictures were generated using the graphical package Jmol.[46]

Supplementary data

Supplementary data (Cartesian coordinates, total bond energies, zero-point energies, entropic terms, and lowest frequencies for all optimized structures and Cartesian coordinates and ν_Γ-values of (3,–3) Γ attractors) for this article are available on the journal Web site (canjchem.nrc.ca) or may be purchased from the Depository of Unpublished Data, Document Delivery, CISTI, National Research Council Canada, Ottawa, ON K1A 0R6, Canada. DUD 3950. For more information on obtaining material, refer to cisti-icist.nrc-cnrc.gc.ca/cms/unpub_e.shtml.

Acknowledgement

Computational resources were provided by the Louisiana Optical Network Initiative (LONI), and by the MoLNaC computing facilities at Dipartimento di Chimica, Università di Salerno, Italy.

References

(1) This article is part of a Special Issue dedicated to Professor T. Ziegler.
(2) Dedicated to Professor Tom Ziegler on the occasion of his 2^6th birthday (a number of substantial importance in the evolution of computer technology) and in recognition of his significant developments in the field of theoretical inorganic chemistry.
(3) Kauffman, G. B. *J. Indian Chem. Soc.* **2003**, *80*, 601.
(4) Bercaw, J. E.; Labinger, J. A. *Proc. Natl. Acad. Sci. U.S.A.* **2007**, *104* (17), 6899–6900. doi:10.1073/pnas.0700902104. PMID:17456607.
(5) Bard, A. J.; Whitesides, G. M.; Zare, R. N.; McLafferty, F. W. *Acc. Chem. Res.* **1995**, *28* (3), 91. doi:10.1021/ar00051a001.
(6) Kubas, G. J. *Proc. Natl. Acad. Sci. U.S.A.* **2007**, *104* (17), 6901–6907. doi:10.1073/pnas.0609707104. PMID:17442752.
(7) Kubas, G. J.; Ryan, R. R.; Swanson, B. I.; Vergamini, P. J.; Wasserman, H. J. *J. Am. Chem. Soc.* **1984**, *106* (2), 451–452. doi:10.1021/ja00314a049.
(8) Kubas, G. J.; *Acc. Chem. Res.* **1988**, *21* (3), 120–128. doi:10.1021/ar00147a005.
(9) Heinekey, D. M.; Oldham, W. J. *Chem. Rev.* **1993**, *93* (3), 913–926. doi:10.1021/cr00019a004.
(10) Jessop, P. G.; Morris, R. H. *Coord. Chem. Rev.* **1992**, *121* (1-2), 155–284. doi:10.1016/0010-8545(92)80067-2.
(11) Dedieu, A., Ed.; *Transition-metal hydrides*; Wiley-VCH: New York, 1992.
(12) Peruzzini, M.; Poli, R., Eds.; *Recent advances in hydride chemistry*; Elsevier: Amsterdam, 2001.
(13) Ziegler, T. *Chem. Rev.* **1991**, *91* (5), 651–667. doi:10.1021/cr00005a001.
(14) Ziegler, T. *Can. J. Chem.* **1995**, *73* (6), 743–761. doi:10.1139/v95-095.
(15) Ziegler, T. *Pure Appl. Chem.* **1991**, *63* (6), 873–878. doi:10.1351/pac199163060873.
(16) Ziegler, T. *J. Chem. Soc., Dalton Trans.* **2002**, (5): 642–652. doi:10.1039/b106126g.
(17) Ziegler, T.; Autschbach, J. *Chem. Rev.* **2005**, *105* (6), 2695–2722. doi:10.1021/cr0307188. PMID:15941226.
(18) Bader, R. F. W. *Atoms in molecules: A quantum theory*; Oxford University Press: Oxford, 1990.
(19) Becke, A. D.; Edgecombe, K. E. *J. Chem. Phys.* **1990**, *92* (9), 5397. doi:10.1063/1.458517.
(20) Schmider, H. L.; Becke, A. D. *J. Mol. Struct. THEOCHEM* **2000**, *527* (1-3), 51–61. doi:10.1016/S0166-1280(00)00477-2.
(21) Jacobsen, H. *Can. J. Chem.* **2008**, *86* (7), 695–702. doi:10.1139/V08-052.
(22) Gusev, D. G.; Hübener, R.; Burger, P.; Orama, O.; Berke, H. *J. Am. Chem. Soc.* **1997**, *119* (16), 3716–3731. doi:10.1021/ja963692t.
(23) Jacobsen, H.; Berke, H. *Chem. Eur. J.* **1997**, *3* (6), 881–886. doi:10.1002/chem.19970030608.
(24) Jacobsen, H.; Berke, H. *Chem. Ber./Rec.* **1997**, *130* (9), 1273–1277. doi:10.1002/cber.19971300916.
(25) Morris, R. H. *Coord. Chem. Rev.* **2008**, *252* (21-22), 2381–2394. doi:10.1016/j.ccr.2008.01.010.
(26) Schmider, H. L.; Becke, A. D. *J. Chem. Phys.* **2002**, *116* (8), 3184. doi:10.1063/1.1431271.
(27) Silvi, B.; Savin, A. *Nature* **1994**, *371* (6499), 683–686. doi:10.1038/371683a0.
(28) Savin, A.; Jepsen, O.; Flad, J.; Andersen, O. K.; Preuss, H.; von Schnering, H. G. *Angew. Chem., Int. Ed. Engl.* **1992**, *31* (2), 187–188. doi:10.1002/anie.199201871.

(29) (a) Crabtree, R. H. *Chem. Rev.* **1985**, *85* (4), 245–269. doi:10.1021/cr00068a002.; (b) Crabtree, R. H. *Chem. Rev.* **1995**, *95* (4), 987–1007. doi:10.1021/cr00036a005.
(30) Maseras, F.; Duran, M.; Lledós, A.; Bertrán, J. *J. Am. Chem. Soc.* **1991**, *113* (8), 2879–2884. doi:10.1021/ja00008a014.
(31) Jacobsen, H. *J. Phys. Chem. A* **2002**, *106* (25), 6189–6192. doi:10.1021/jp0257404.
(32) Jacobsen, H. *J. Comput. Chem.* **2009**, *30* (7), 1093–1102. doi:10.1002/jcc.21135. PMID:19090572.
(33) Li, J.; Dickson, R. M.; Ziegler, T. *J. Am. Chem. Soc.* **1995**, *117* (46), 11482–11487. doi:10.1021/ja00151a011.
(34) Li, J.; Ziegler, T. *Organometallics* **1996**, *15* (18), 3844–3849. doi:10.1021/om950956w.
(35) Nikonov, G. I. *J. Organomet. Chem.* **2001**, *635* (1-2), 24–36. doi:10.1016/S0022-328X(01)00843-9.
(36) Gillespie, R. J.; Silvi, B. *Coord. Chem. Rev.* **2002**, *233-234*, 53–62. doi:10.1016/S0010-8545(02)00102-9.
(37) Frisch, M. J.; Trucks, G. W.; Schlegel, H. B.; Scuseria, G. E.; Robb, M. A.; Cheeseman, J. R.; Montgomery, J. A., Jr.; Vreven, T.; Kudin, K. N.; Burant, J. C.; Millam, J. M.; Iyengar, S. S.; Tomasi, J.; Barone, V.; Mennucci, B.; Cossi, M.; Scalmani, G.; Rega, N.; Petersson, G. A.; Nakatsuji, H.; Hada, M.; Ehara, M.; Toyota, K.; Fukuda, R.; Hasegawa, J.; Ishida, M.; Nakajima, T.; Honda, Y.; Kitao, O.; Nakai, H.; Klene, M.; Li, X.; Knox, J. E.; Hratchian, H. P.; Cross, J. B.; Bakken, V.; Adamo, C.; Jaramillo, J.; Gomperts, R.; Stratmann, R. E.; Yazyev, O.; Austin, A. J.; Cammi, R.; Pomelli, C.; Ochterski, J. W.; Ayala, P. Y.; Morokuma, K.; Voth, G. A.; Salvador, P.; Dannenberg, J. J.; Zakrzewski, V. G.; Dapprich, S.; Daniels, A. D.; Strain, M. C.; Farkas, O.; Malick, D. K.; Rabuck, A. D.; Raghavachari, K.; Foresman, J. B.; Ortiz, J. V.; Cui, Q.; Baboul, A. G.; Clifford, S.; Cioslowski, J.; Stefanov, B. B.; Liu, G.; Liashenko, A.; Piskorz, P.; Komaromi, I.; Martin, R. L.; Fox, D. J.; Keith, T.; Al-Laham, M. A.; Peng, C. Y.; Nanayakkara, A.; Challacombe, M.; Gill, P. M. W.; Johnson, B.; Chen, W.; Wong, M. W.; Gonzalez, C.; Pople, J. A. *Gaussian 03*, Revision D.02; Gaussian, Inc., Wallingford: CT, 2004; Available from http://www.gaussian.com/citation_g03.htm (accessed Dec. 11, 2008).
(38) Perdew, J. P.; Burke, K.; Ernzerhof, M. *Phys. Rev. Lett.* **1996**, *77* (18), 3865–3868. doi:10.1103/PhysRevLett.77.3865. PMID:10062328.
(39) Stoll, H. *Chem. Phys. Lett.* **2006**, *429* (1-3), 289–293. doi:10.1016/j.cplett.2006.07.083.
(40) Andrae, D.; Häussermann, U.; Dolg, M.; Stoll, H.; Preuss, H. *Theor. Chim. Acta* **1990**, *77*, 123. doi:10.1007/BF01114537.
(41) Schäfer, A.; Huber, C.; Ahlrichs, R. *J. Chem. Phys.* **1994**, *100* (8), 5829. doi:10.1063/1.467146.
(42) Schäfer, A.; Horn, C. H.; Ahlrichs, R. *J. Chem. Phys.* **1992**, *97* (4), 2571. doi:10.1063/1.463096.
(43) (a) te Velde, G.; Bickelhaupt, F. M.; Baerends, E. J.; Fonseca Guerra, C.; van Gisbergen, S. J. A.; Snijders, J. G.; Ziegler, T. *J. Comput. Chem.* **2001**, *22* (9), 931–967. doi:10.1002/jcc.1056.; (b) Fonseca Guerra, C.; Snijders, J. G.; te Velde, G.; Baerends, E. *J. Theor. Chem. Acc.* **1998**, *99* (6), 391. doi:10.1007/s002140050021.; (c) *SCM*, ADF2006.01; Theoretical Chemistry, Vrije Universiteit, Amsterdam, The Netherlands, 2008; Available from http://www.scm.com (accessed Dec. 11, 2008).
(44) (a) Lenthe, E.; Baerends, E. J.; Snijders, J. G. *J. Chem. Phys.* **1993**, *99* (6), 4597. doi:10.1063/1.466059.; (b) van Lenthe, E.; Baerends, E. J.; Snijders, J. G. *J. Chem. Phys.* **1994**, *101* (11), 9783. doi:10.1063/1.467943.
(45) Popelier, P. L. A. *Comput. Phys. Commun.* **1996**, *93* (2-3), 212–240. doi:10.1016/0010-4655(95)00113-1.
(46) *JMOL: An open-source Java viewer for chemical structures in 3D*; 2008; Available from http://www.jmol.org (accessed Dec. 11, 2008).

Homolytic bond-dissociation enthalpies of tin bonds and tin–ligand bond strengths — A computational study[1]

Sarah R. Whittleton, Russell J. Boyd, and T. Bruce Grindley

Abstract: Density functional theory and second-order Møller–Plesset perturbation theory with effective core potentials have been used to calculate homolytic bond-dissociation enthalpies, *D*(Sn–X), of organotin compounds, and their performance has been assessed by comparison with available experimental bond enthalpies. The SDB-aug-cc-pVTZ basis set with its effective core potential was used to calculate the *D*(Sn–X) of a series of trimethyltin(IV) species, Me_3Sn–X, where X = H, CH_3, CH_2CH_3, NH_2, OH, Cl, and F. This is the most comprehensive report to date of homolytic Sn–X bond-dissociation enthalpies (BDEs). Effective core potentials are then used to calculate thermodynamic parameters including donor–acceptor bond enthalpies, $\overline{D}(\mathrm{Sn-X})$, for a series of tin-ligand complexes, L_2SnX_4 (X = Br or Cl, L = py, dmf, or dmtf), which are compared with previous experimental and nonrelativistic computational results. Based on computational efficiency and accuracy, it is concluded that effective core potentials are appropriate computational methods to examine bonding in organotin systems.

Key words: bond-dissociation enthalpy, trimethyltin bond-dissociation enthalpies, donor–acceptor bond enthalpy, density functional theory, effective core potential, tetrahalotin complexes.

Résumé : On a fait appel à la théorie de la fonctionnelle de la densité et à la théorie des perturbations du deuxième ordre de Møller–Plesset avec des potentiels de coeur effectifs pour calculer les enthalpies de dissociation homolytique des liaisons, *D*(Sn–X), de composés organiques de l'étain et on a évalué leurs performances par comparaison avec les enthalpies expérimentales de liaison disponibles. On a utilisé l'ensemble de base SDB-aug-cc-pVTZ avec son potentiel de coeur effectif pour calculer les valeurs des *D*(Sn–X) d'une série d'espèces organiques de l'étain, Me_3Sn–X dans lequel X = H, CH_3, CH_2CH_3, NH_2, OH, Cl et F. Il s'agit de l'étude la plus complète à date sur les enthalpies de dissociation homolytique de liaisons Sn–X (ENL). On a ensuite utilisé les potentiels de coeur effectifs pour calculer des paramètres thermodynamiques, dont les enthalpies de liaison donneur–accepteur, $\overline{D}(\mathrm{Sn-X})$, pour une série de complexes de l'étain, L_2SnX_4 (X = Br ou Cl, L = py, dmf ou dmtf), qui ont été comparées avec les résultats antérieurs obtenus d'une façon expérimentale ou par des calculs non relativistes. En se basant sur l'efficacité des calculs et leur exactitude, on peut conclure que les potentiels de coeurs sont des méthodes appropriées de calcul pour examiner les systèmes organiques de l'étain.

Mots-clés : enthalpie de dissociation de liaison, enthalpies de dissociation de liaison du triméthylétain, enthalpie de liaison donneur accepteur, théorie de la fonctionnelle de densité, potentiel de coeur efficace, complexes tétrahalogénés de l'étain.

[Traduit par la Rédaction]

Introduction

The importance of tin chemistry is attributed to the prevalence of organotin compounds in organic synthesis and materials science, as well as the industrial, agricultural, and biological applications of tin species. Our specific interests in tin chemistry focus on the use of dialkyltin(IV) intermediates (dialkylstannylene acetals) to obtain regioselective reactions of diols and polyols.[2–7] Reliable estimates of tin bond strengths in organotin compounds allow one to understand their chemistry, including bond breaking, bond making, and chemical reactivity. For organotin species, bond strengths can be reported as homolytic bond-dissociation enthalpies (BDEs) and coordinate donor–acceptor tin bond energies. Both of these bond types are involved in the chemistry of dialkylstannylene acetals and, therefore, an understanding of the nature of covalent and donor–acceptor tin bonds is essential for explaining the complex chemistry of these compounds.

The experimentally determined bond strengths of light elements are well-documented, but bond strengths involving heavier elements such as tin are harder to determine and are surprisingly sparse.[8,9] In fact, there is a lack of reliable experimental bond-dissociation enthalpy, *D*(Sn–X), values in the literature. Several studies have used thermochemical calculations to estimate the bond strengths of various Sn–X bonds[10–13] from fairly old reference values that may be unreliable.[8] In addition, some experimental studies do not yield directly determined homolytic bond-dissociation enthalpies for particular bonds, but rather report average BDEs.[14] The challenges of obtaining absolute values of experimental bond energies have

Received 13 December 2008. Accepted 20 February 2009. Published on the NRC Research Press Web site at canjchem.nrc.ca on 8 June 2009.

S.R. Whittleton, R.J. Boyd,[1] and T.B. Grindley.[2] Department of Chemistry, Dalhousie University, Halifax, NS B3H 4J3, Canada.

[1]Corresponding author (e-mail: russell.boyd@Dal.ca).
[2]Corresponding author (e-mail: bruce.grindley@Dal.ca).

led some workers to emphasize the use of relative values.[15] Computational methods have been employed to calculate tin bonds strengths,[16–26] by use of a variety of effective core potentials (ECPs). The earlier studies did not validate the results by comparison with experimental data.

The first goal of this two part study was to identify a computational method to obtain reliable estimates of the homolytic Sn–X bond-dissociation enthalpies (BDEs) for a variety of organotin species. An appropriate basis set and effective core potential used for tin was selected by comparing calculated and experimental[8,27] bond-dissociation enthalpies, D(Sn–H), for three different organotin compounds, Me_3SnH, Ph_3SnH, and Bu_3SnH (eqs. [1] and [2]). A more comprehensive study of Sn bonds (Sn–O, Sn–C, Sn–N) was precluded by the lack of reliable gas-phase bond-dissociation enthalpies for tin species.[8,9]

$$[1] \quad Y_3Sn{-}H \rightarrow Y_3Sn^{\cdot} + H^{\cdot}, \text{ where Y} = \text{Me, Bu, and Ph}$$

$$[2] \quad \text{BDE} = D(\text{Sn}{-}\text{H}) = \Delta_f H^o(Y_3Sn^{\cdot}) + \Delta_f H^o(H^{\cdot}) - \Delta_f H^o(Y_3Sn{-}H)$$

The ECP that yields the best agreement with the experimental bond-dissociation enthalpies was used subsequently to predict the D(Sn–X) of a series of trimethyltin(IV) species, Me_3Sn–X (eqs. [3] and [4]). It should be emphasized that this is not a methodological study, but instead uses the limited available experimental BDEs to verify that these ECPs are appropriate for further calculation of tin bond strengths, Me_3Sn–X. The X substituents were chosen on the basis of the prevalence of Sn–X bonds in the current experimental and computational tin literature, where typically X substituents are small, main-group elements.

$$[3] \quad Me_3Sn{-}X \rightarrow Me_3Sn^{\cdot} + X^{\cdot}, \text{ where X} = \text{H, } CH_3, \text{ } CH_2CH_3, \text{ } NH_2, \text{ OH, Cl, and F}$$

$$[4] \quad \text{BDE} = D(\text{Sn}{-}\text{X}) = \Delta_f H^o(Me_3Sn^{\cdot}) + \Delta_f H^o(X^{\cdot}) - \Delta_f H^o(Me_3Sn{-}X)$$

The second goal of this study was to examine bond strengths of donor–acceptor tin bonds, where tin(IV) acts as an acceptor to the donor ligand. These donor–acceptor, or coordinate, bonds are ubiquitous in the chemistry of tin, including catalysis,[28–30] carbohydrate chemistry,[5,7] anti-fungal agents,[31] potential antitumor drugs,[32–35] and biological systems.[36,37] In these types of coordinate systems, donor ligands bind to tin creating new Sn–L bonds, where L = N, O, S, Br, Cl, and Se. Dissociation enthalpies, reorganization energies, basis set superposition error corrections, and bond strengths were calculated using the two different effective core potentials. These thermodynamic parameters were compared to corresponding values obtained from available experimental[38–43] and nonrelativistic all-electron computational studies.[20] One of these effective core potentials will be used in further studies involving donor–acceptor tin bonds.

The complexes examined in this study (eq. [5]) are tin(IV) chlorides or bromides bound to the ligands (L) pyridine (py), *N*,*N*-dimethylformamide (dmf), or *N*,*N*-dimethylthioformamide (dmtf), with two Sn–N, Sn–O, or Sn–S bonds in each L_2SnX_4 complex. These bond strengths are defined as the mean tin(IV)-ligand coordinate bond energies, $\overline{D}$(Sn–L). The approach used to calculate $\overline{D}$(Sn–L) for the L_2SnX_4 coordinate complexes considered reorganization effects of the donor–acceptor complexes (eq. [6]).[20,44,45] Reorganization effects are caused by the increase in the tin coordination number. In L_2SnX_4 systems, the tin coordination number decreases from six to four upon dissociation, changing the geometry of the tin center from octahedral to tetrahedral. The dissociation enthalpy (ΔH^{diss}) differs from the coordinate bond energy (ΔH^{DA}) because it does not include the energies associated with the reorganization of individual donor and acceptor fragments from their geometries in the coordinate complex, ΔH^{reorg}(L) and $\Delta H^{reorg}(SnX_4)$.[20,44,45] Previous researchers have calculated reorganization energies involved in the formation of similar group-14 coordination complexes[20,44] as part of the calculation of ΔH^{DA}.

$$[5] \quad L_2SnX_4 \rightarrow SnX_4 + 2L, \text{ where X} = \text{Br or Cl; L} = \text{py, dmf, or dmtf}$$

$$[6] \quad \overline{D}(\text{Sn}{-}\text{L}) = \Delta H^{DA} = 0.5[\Delta H^{diss} + \Delta H^{reorg}(SnX_4) + 2\Delta H^{reorg}(L) + \Delta H^{BSSE}(L_2SnX_4)]$$

Computational methods

Gas-phase calculations were performed using the B3LYP density functional implemented in Gaussian 03[46] with Becke's three-parameter hybrid exchange functional (B3)[47,48] and the correlation functional of Lee, Yang, and Parr.[49] For geometry optimizations and frequency calculations, unrestricted B3LYP was used for radical species while restricted B3LYP was employed for all other compounds. MP2 single point calculations were preformed on optimized species. The D(Sn–X) and $\overline{D}$(Sn–L) values include basis set superposition error (BSSE) corrections[50] and the enthalpies include the zero point vibrational energy corrections (ZPVE). Frequency analyses were performed on the optimized geometries of the compounds and no imaginary frequencies were observed.

Previous work has shown that a variety of basis sets and effective core potentials can be used to predict the geometries of organotin compounds, $Cl_nSn(CH_3)_{4-n}$, n = 0–4, accurately.[51] However, the abilities of these ECPs to predict the thermochemistry of organotin compounds was not examined, due to a lack of thermochemical data for $Cl_nSn(CH_3)_{4-n}$. Two of these effective core potentials were shown to be appropriate for the prediction of organotin tin geometries and in this study have been evaluated for their applicability for the calculation of bond-dissociation enthalpies.[51] The first method uses the Los Alamos National Laboratory double-zeta basis set (LANL2DZdp) with diffuse and polarization functions[52] and the associated LANL2 ECP developed by Wadt and Hay.[53] The second method uses a correlation consistent, triple-zeta basis set developed by Martin and Sundermann[54] that includes diffuse and polarization functions (SDB-aug-cc-pVTZ) and was used in conjunction with the Stuttgart–Dresden–Bonn (SDB) ECP developed by Dolg and co-workers.[55] Both LANL2 and SDB are 46-electron core ECPs. It should be noted that all

Table 1. Calculated bond-dissociation enthalpies D(Sn–X) and standard deviations in bond-dissociation enthalpies (s_D) of Y_3Sn–H, Y = Me, Bu, and Ph (kJ mol^{-1}).

	Me_3Sn–H		Bu_3Sn–H		Ph_3Sn–H		
Method	D(Sn–H)	ΔD(Sn–H)	D(Sn–H)	ΔD(Sn–H)	D(Sn–H)	ΔD(Sn–H)	s_D[a]
Experiment	318.5[b]	—	326.5[c]	—	294.6[b]	—	—
LANL2DZdp	296.8	–21.7	294.0	–32.5	291.0	–3.6	27.8
SDB-aug-cc-pVTZ	301.2	–17.3	298.1	–28.4	294.6	0.0	23.5

[a]For ΔD(Sn–H) for the three compounds.
[b]Ref. 27.
[c]Ref. 8.

nontin atoms in this study (H, C, N, O, F, S, Cl, and Br) were treated at the MP2/6-311G(2d,p)//B3LYP/6-31G(d,p) level. The BSSE calculations were performed at same level as the MP2 single point calculations, using 6-311G(2d,p) for nontin atoms and LANL2DZdp or SDB-aug-cc-pVTZ for tin. The ZPVE corrections were obtained at the same level as B3LYP geometry optimizations, using 6-31G(d,p) for nontin atoms and LANL2DZdp or SDB-aug-cc-pVTZ for tin.

Results and discussion

Comparison with experimental results — D(Sn–X)

Table 1 lists the experimental bond-dissociation enthalpies, the corresponding calculated enthalpies, and the standard deviations of Y_3Sn–H, Y = Me, Bu, and Ph. The standard deviation in bond-dissociation enthalpies (s_D), defined in eq. [7], compares the calculated bond-dissociation enthalpies (D_{ci}) to the experimental values (D_e).

$$[7] \qquad s_D = \sqrt{\frac{\sum_{i=1}^{n} (D_{ci} - D_e)^2}{(n_D - 1)}}$$

The SDB-aug-cc-pVTZ basis set and ECP yields an s_D value for Y_3Sn–H of 23.3 kJ mol^{-1}, 5 kJ mol^{-1} less than that calculated using LANL2DZdp. Both methods consistently underestimate the bond-dissociation enthalpies of the three organotin molecules, by –32.5 to –3.6 kJ mol^{-1}. The experimental D(Sn–H) values increase as Y changes from Ph to Me to Bu, which is the same order found for D(Ge–H) for the respective germanium species.[9] Both ECPs predict the D(Sn–H) values for H-$SnBu_3$ to be slightly smaller than for H-$SnMe_3$, contrary to observation. Therefore, on the basis of Table 1, the effective core potential paired with the larger basis set, SDB-aug-cc-pVTZ, slightly outperforms the LANL2DZdp.

It would be ideal to compare the results from theory with experimental results for a more diverse sample of tin bonds, but this is prevented by a lack of reliable experimental data. In addition, it is unlikely that larger basis sets (QDZ) would substantially decrease the s_D values because the much larger, augmented, triple-zeta SDB basis set with polarization functions calculates Y_3Sn–H within 5 kJ mol^{-1} of LANL2DZdp. Therefore, it was decided that the SDB-aug-cc-pVTZ and its ECP would be used to calculate the Sn–X bond-dissociation enthalpies of the Me_3Sn–X compounds in the following section.

Table 2. Calculated bond-dissociation enthalpies, D(Sn–X), of Me_3Sn–X, where X = H, CH_3, CH_2CH_3, NH_2, OH, Cl, and F (kJ mol^{-1}).

X	D(Sn–X)
H	301.2
CH_3	284.8
CH_2CH_3	267.5
NH_2	324.7
OH	409.3
F	531.3
Cl	411.3

Homolytic bond-dissociation enthalpies for Me_3Sn–X

Using the SDB-aug-cc-pVTZ basis set and SDB ECP, D(Sn–X) values were calculated for a series of trimethyltin(IV) species, Me_3Sn–X, where X = H, CH_3, CH_2CH_3, NH_2, OH, Cl, and F. The results are shown in Table 2.

The calculated D(Sn–X) increase in the order of X = CH_2CH_3 < CH_3 < H < NH_2 < OH < Cl < F, as observed in other BDE studies.[25,56] This generally agrees with the trend of increasing electronegativity, confirming the strong correlation between electronegativity and bond dissociation.[18,21,57,58] Fluorine is the most electronegative substituent, resulting in a large Sn–F bond-dissociation enthalpy. One apparent discrepancy in this trend occurs for hydrogen, which has a lower electronegativity but a larger D(Sn–X) than the nitrogen and carbon species. However, this trend is seen for other series of group-14 compounds, namely for C, Si, and Ge.[59]

Experimental bond-dissociation energies of X bound to other group-14 atoms (M), reported in Table 3, can be compared to the calculated D(Sn–X) values in Table 2. The trends in D(C–X) values are in general agreement with those of the D(Sn–X) values. The experimental D(C–X) values for X = R and NH_2 are 34–103 kJ mol^{-1} larger than their respective calculated D(Sn–X) values. For X = F, OH, and Cl, the D(Sn–X) values are greater than the D(C–X) values. Fluorine, oxygen, and chlorine are electronegative atoms that draw electron density away from the polarizable tin atom, creating strong electrostatic attractions (high ionic character) that explain these larger bond-dissociation enthalpies. The largest D(Sn–X) and D(C–X) values are observed with X = F. The experimental D(Si–X) and D(Ge–X) values are also larger than their respective calculated D(Sn–X) val-

Table 3. Experimental bond-dissociation enthalpies D(M–X) of Me_3M–X, where M= C, Si, Ge and X= H, CH_3, CH_2CH_3, NH_2, OH, Cl, and F (kJ mol^{-1}).

X	D(C–X)	D(Si–X)	D(Ge–X)
H	403.9[a]	378.0[b]	343.3[c]
CH_3	366.3[a]	374.2[b]	340.0[d]
CH_2CH_3	358.3[a]	—	—
NH_2	358.7[a]	—	—
OH	401.0[a]	535.8[b]	—
F	484.7[e]	—	—
Cl	355.4[a]	473.0[b]	485.6[f]

Note: Available D(M–X) are reported and are considered only relative values in the context of this study; they are used solely to compare trends with D(Sn–X).

[a]Ref. 60.
[b]Ref. 61.
[c]Ref. 8.
[d]Ref. 62.
[e]Ref. 59.
[f]Ref. 12.

ues. Although many D(Si–X) and D(Ge–X) values are not available, the general trends agree with the other group-IV species, linking electronegativity with bond dissociation.

L_2SnX_4 complex geometries

For L_2SnX_4, the ligands can be cis or trans in the octahedral geometry (Fig. 1), and each trans isomer can exist as two possible conformers. If a ligand, such as pyridine, has a C_2 axis of symmetry, the trans conformers have D_{2h} and D_{2d} symmetry. Unsymmetric ligands, such as *N,N*-dimethylformamide (dmf) and *N,N*-dimethylthioformamide (dmtf), can exist as trans isomers with C_{2h} or C_{2v} symmetry.

The relative energies calculated for the different L_2SnX_4 complexes are significant because experimental $\overline{D}$(Sn–L) values are reported[38–43] as single values that are the summation of population-weighted contributions from all complexes formed. Trends in energy are generally consistent regardless of ECP and are discussed below.

For the $(dmf)_2SnCl_4$ complex, the relative energies are similar for three structural complexes, with the C_{2h}, C_{2v}, and cis geometries differing by less than 6.3 kJ mol^{-1}. Similarly, the energies of three unique $(dmtf)_2SnCl_4$ complexes differ by less than 3.4 kJ mol^{-1}. However, while the energies of the D_{2h} and D_{2d} $(py)_2SnCl_4$ complexes differ by less than 2 kJ mol^{-1}, the cis complexes are 13–15 kJ mol^{-1} less stable. These relative energies are consistent with those calculated previously for the $(py)_2SnX_4$ complexes.[20,63] The relative instabilities of the *cis*-$(py)_2SnCl_4$ complexes may be attributed to the greater steric repulsions between the larger py ligands than between the dmf and dmtf ligands (see Fig. 2). The steric interactions present in the *cis*-$(py)_2SnCl_4$ complex are not present in the *trans*-$(py)_2SnCl_4$ complexes where the ligands are 180° apart (Fig. 1); resulting in lower relative energies for trans species. Because the magnitudes of ligand–ligand steric interactions in *cis*-$(dmf)_2SnCl_4$ and $(dmf)_2SnCl_4$ are small, these complexes were calculated to have energies similar to those of their trans counterparts.

These relative energy trends are also found for L_2SnBr_4, where the three structural complexes yield relative energies differing by less than 8 and 6 kJ mol^{-1} for $(dmf)_2SnBr_4$ and $(dmtf)_2SnBr_4$, respectively. In these cis complexes the dmf–dmf and dmtf–dmtf interactions do not appear to be larger than the Br–Br interactions; however, the *cis*-$(py)_2SnBr_4$ complexes are calculated to be 13–15 kJ mol^{-1} less stable than the D_{2h} and D_{2d} complexes, indicating that there are significantly larger steric interactions between cis py ligands.

The calculated mean tin–ligand bond lengths (r) of L_2SnX_4, L = py, dmf, and dmtf and X = Cl and Br, using the LANL2DZdp basis set with the LANL2 ECP are reported in Table 4. The two trans complexes yield similar r(Sn–L) while cis complexes contain longer Sn–L bond lengths. The bond strengths increase in the order of r(Sn–O) < r(Sn–N) < r(Sn–S) for both L_2SnCl_4 and L_2SnBr_4, however, the r(Sn–L) bonds in bromine species are longer than the respective chlorine complexes.

Thermodynamic parameters for L_2SnX_4 complexes

The thermodynamic parameters for the L_2SnX_4 complexes shown in Table 5 include gas-phase dissociation enthalpies (ΔH^{diss}), reorganization energies ($\Delta H^{reorg}(SnX_4)$), and BSSE corrections ($\Delta H^{BSSE}(L_2SnX_4)$). These three contributions and the reorganization energies of the donor ligands ($\Delta H^{reorg}(L)$) define the tin(IV)–ligand coordinate bond energies, $\overline{D}$(Sn−L) (eq. [6]). Although the $\Delta H^{reorg}(L)$ values are included in the calculation of $\overline{D}$(Sn–L), they are not reported in Table 5 because they are almost identical regardless of the type of isomer, the identity of X, or the computational method. The ligands' reorganization energies are very small compared to those for SnX_4; $\Delta H^{reorg}(L)$ for py, dmf, and dmtf are less than 3, 10, and 1 kJ mol^{-1}, respectively.

Results in Table 5 show that the calculated values for ΔH^{diss}, $\Delta H^{reorg}(SnX_4)$, $\Delta H^{BSSE}(L_2SnX_4)$, and $\overline{D}$(Sn − L) are unique for each molecule. The BSSE correction is the smallest contribution to the total bond strength, which seems to be ruled by dissociation and reorganization energies. This is consistent with the results of the previous computational study of L_2SnX_4,[18] which are further discussed in the final section titled "comparison with previous all-electron theoretical results". However, it should be noted that to obtain the average bond strengths, $\overline{D}$(Sn−L), all enthalpies and corrections are included and the total divided by the number of bonds formed (eq. [6]). Therefore, the dissociation enthalpies and reorganization energies can be greater or less than the bond strength because of the BSSE correction and final division by two. Some interesting trends in Table 5 are discussed in the following sections.

Comparing cis and trans isomers

Trends for ΔH^{diss} mirror those seen for the relative energies of cis and trans isomers. The trans isomers for $(dmf)_2SnX_4$ and $(dmtf)_2SnX_4$ complexes have ΔH^{diss} similar in magnitude to those of the cis complexes. However, for $(py)_2SnX_4$, ΔH^{diss} for the trans isomers are approximately equal while the cis complex has a smaller dissociation enthalpy. Furthermore, for each L_2SnX_4, BSSE corrections are similar for cis and trans complexes, while calculated reorganization energies for cis complexes are much lower than for trans species. Compared to the square planar SnX_4 in

Fig. 1. Structures of the L_2SnCl_4 complexes, optimized using the LANL2DZdp basis set with the LANL2 ECP (L= py, dmf, and dmtf).

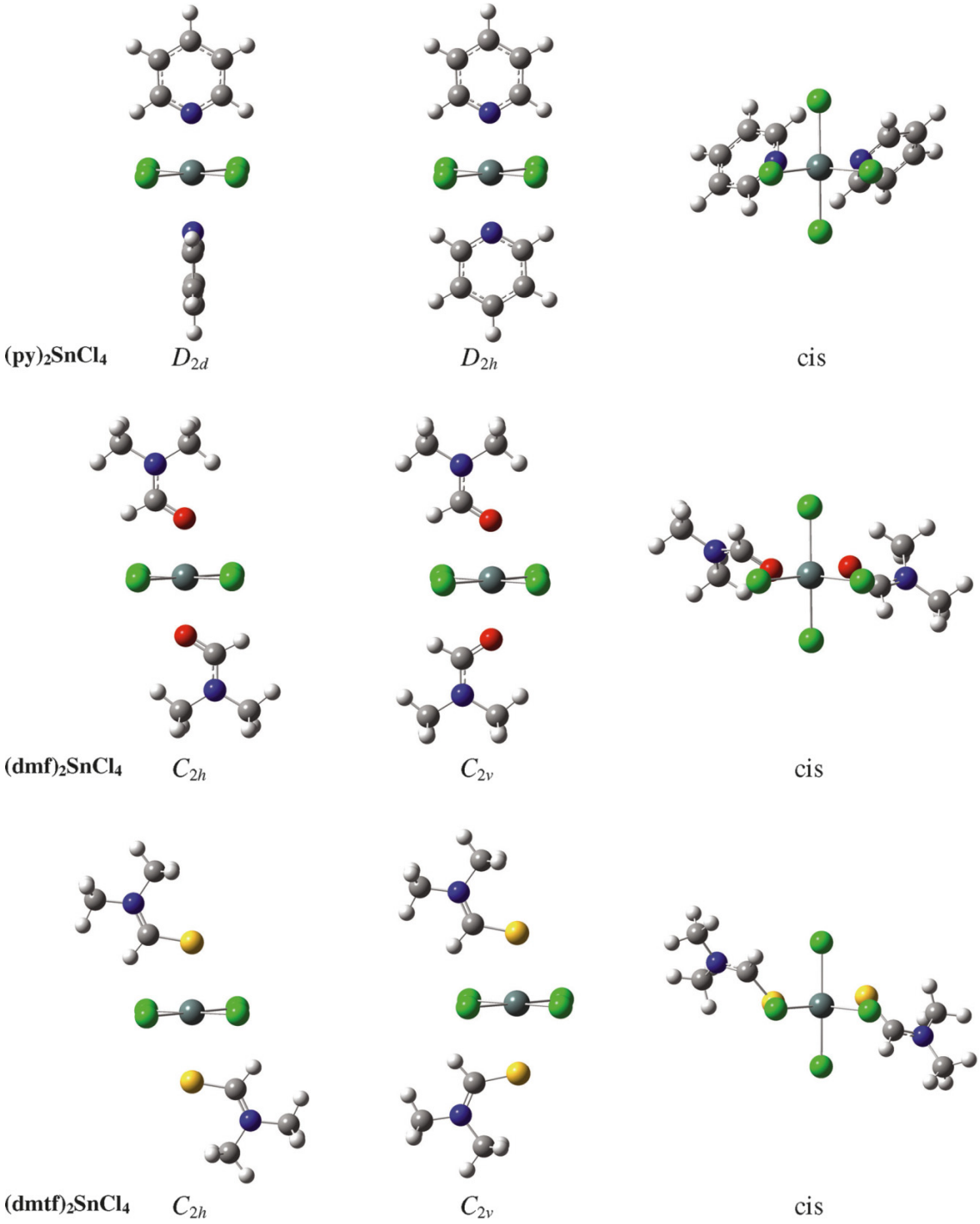

Fig. 2. Structures of the *cis*-L_2SnCl_4 complexes, optimized using the LANL2DZdp basis set with the LANL2 ECP (L = py, dmf, dmtf).

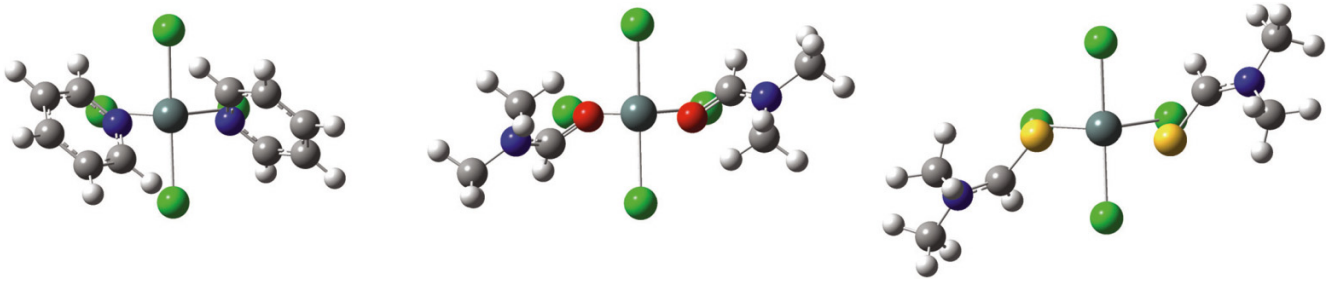

Table 4. Calculated mean tin–ligand bond lengths (r) of L_2SnX_4, optimized using the LANL2DZdp basis set with the LANL2 ECP, where L = py, dmf, and dmtf and X = Cl and Br (reported in Å).

L_2SnX_4	Structure	r(Sn–L)
$(Py)_2SnCl_4$	D_{2d}	2.280
	D_{2h}	2.279
	Cis	2.360
$(Py)_2SnBr_4$	C_{2h}	2.305
	C_{2v}	2.302
	Cis	2.387
$(Dmf)_2SnCl_4$	C_{2h}	2.161
	C_{2v}	2.160
	Cis	2.193
$(Dmf)_2SnBr_4$	D_{2d}	2.180
	D_{2h}	2.176
	Cis	2.208
$(Dmtf)_2SnCl_4$	C_{2h}	2.658
	C_{2v}	2.660
	Cis	2.740
$(Dmtf)_2SnBr_4$	C_{2h}	2.675
	C_{2v}	2.676
	Cis	2.758

Note: Bond length r(Sn–L) refers to r(Sn–N), r(Sn–O), and r(Sn–S) in py, dmf, and dmtf complexes, respectively.

the trans complex, the distorted-tetrahedral geometry of SnX_4 in cis complexes is closer in energy to the tetrahedral SnX_4 that exists upon dissociation, resulting in smaller $\Delta H^{reorg}(SnX_4)$ values. The $\Delta H^{reorg}(SnX_4)$ influences $\overline{D}$(Sn–L), as cis complexes contain weaker tin–ligand bonds than their respective trans counterparts, by as much as 26 and 27 kJ mol^{-1} in L_2SnCl_4 and L_2SnBr_4, respectively. This reflects geometric trends (Table 4), with tin–ligand bonds longer in cis complexes.

Effects of ligand choice in L_2SnX_4 complexes

The enthalpies of dissociation are affected by the choice of ligand as the magnitude of ΔH^{diss} increases from dmtf to dmf to py. BSSE energies are comparable for $(py)_2SnX_4$ and $(dmf)_2SnX_4$, and are up to 22 kJ mol^{-1} greater than $(dmtf)_2SnX_4$ complexes. The $\Delta H^{reorg}(SnX_4)$ values are consistent for every ligand because every trans geometry has the square planar tin center while cis complexes have the distorted-tetrahedral tin center. Like ΔH^{diss}, tin–ligand bonds increase in strength from $\overline{D}$(Sn–S) to $\overline{D}$(Sn–O) to $\overline{D}$(Sn–N).

Effect of X in L_2SnX_4 complex

As shown in Table 5, the choice of X affects the thermodynamic parameters of the L_2SnX_4 complexes. While BSSE corrections and the enthalpies of reorganization are comparable, the enthalpies of dissociation are generally larger in magnitude for L_2SnCl_4 than L_2SnBr_4. This affects the strength of the tin–ligand bonds, which are stronger for L_2SnCl_4 by as much as 13 kJ mol^{-1}.

Effect of computational method on L_2SnX_4 thermodynamic parameters

The foregoing discussion of the results in Table 5 focused on trends that are consistent for both effective core potentials; the choice of ECP does affect the quantitative values of dissociation, reorganization, BSSE, and bond enthalpy. Specifically, the ΔH^{diss} values from LANL2DZdp are up to 18 kJ mol^{-1} larger than those calculated using the SDB basis set. Conversely, the large SDB-aug-cc-pVTZ basis set produces BSSE and $\Delta H^{reorg}(SnX_4)$ values 9 and 13 kJ mol^{-1} larger than those with LANL2DZdp. All these values, along with reorganization energies of the ligands, contribute to the calculated bond strengths, $\overline{D}$(Sn–L), that differ by less than 9 kJ mol^{-1} between the two effective core potentials.

Computational efficiency should also be considered to determine which method is best for calculations on organotin compounds. The augmented, triple-zeta SDB-aug-cc-pVTZ basis set is larger than the double-zeta LANL2DZdp basis set. The smaller basis set requires less CPU time for geometry optimizations, and CPU times of both methods show significant time savings with LANL2DZdp (25%–90%) compared to the SDB-aug-cc-pVTZ basis set. Although these time savings are not substantial for the small organotin compounds in the present study, obtaining results with similar accuracy while using a fraction of the CPU time will be valuable in future studies of large dialkylstannylene acetal systems of interest. Therefore, based on computational accuracy and efficiency, we conclude that the LANL2DZdp basis set and ECP is an appropriate method and should be employed for further bond strength calculations of large donor-ligand tin complexes.

Comparison with previous experimental results

Table 5 includes the experimental dissociation enthalpies, calculated as the standard enthalpies for the Lewis acid/base reaction obtained for the gaseous phase using thermodynamic cycles.[38–43] For all L_2SnX_4 complexes, the $\Delta H^{diss} > 0$ indicated dissociation is not favored. However, there are noticeable discrepancies in the magnitudes of experimental and calculated dissociations. While this discrepancy may be attributed to an improper evaluation of complex energies by computational methods, other factors such possible uncertainties within the thermodynamics cycles employed in experiment may be the cause. Specifically, within these cycles the enthalpies of sublimation for the L_2SnX_4 are unknown, as the adducts decompose upon heating. Therefore, to complete the thermodynamic cycles, these enthalpies of sublimation were assumed to equal the enthalpies of vaporizations of the respective donor ligands. These assumptions may be the cause of the substantial difference between calculated and experimental dissociation enthalpies.

Comparison with previous all-electron theoretical results

The thermodynamic parameters of D_{2h} and *cis*-$(py)_2SnX_4$ complexes have been previously calculated using nonrelativistic, all-electron computational calculations employing B3LYP and basis sets of DZP quality on both tin and nontin atoms. Table 6 compares these with calculated theoretical parameters from the present study.

The effective core potentials in the present study yield dissociation energies up to 99 kJ mol^{-1} larger than the non-

Table 5. Thermodynamic parameters of L_2SnX_4 (X = Cl and Br, L = py, dmf, and dmtf) calculated with two computational methods (kJ mol^{-1}).

L_2SnX_4	Exp. ΔH^{diss}	Structure	ΔH^{diss}	$\Delta H^{reorg}(SnX_4)$	$\Delta H^{BSSE}(L_2SnX_4)$	$\overline{D}$(Sn–L)
LANL2DZdp						
$(Py)_2SnCl_4$	267.1±3.1[a]	D_{2d}	209.9	180.1	54.1	170.6
		D_{2h}	211.8	180.2	56.1	170.6
		Cis	199.2	154.0	65.4	145.8
$(Dmf)_2SnCl_4$	263.5±5.0[b]	C_{2h}	169.6	177.9	56.3	155.3
		C_{2v}	169.6	182.2	56.9	154.6
		Cis	175.9	150.3	64.5	139.4
$(Dmtf)_2SnCl_4$	263.1±2.7[b]	C_{2h}	128.3	187.6	38.2	138.0
		C_{2v}	124.9	191.1	38.2	137.9
		Cis	126.2	162.5	43.1	122.5
$(Py)_2SnBr_4$	277.2±2.7[c]	D_{2d}	190.4	177.6	51.5	160.8
		D_{2h}	191.7	177.8	52.5	161.1
		Cis	177.5	146.2	57.7	134.9
$(Dmf)_2SnBr_4$	309.0±5.6[d]	C_{2h}	148.3	175.9	53.6	144.9
		C_{2v}	148.2	180.2	54.1	146.8
		Cis	154.9	138.5	58.4	126.0
$(Dmtf)_2SnBr_4$	222.9±3.3[d]	C_{2h}	114.5	183.8	35.4	130.9
		C_{2v}	112.6	188.1	35.5	131.6
		Cis	112.0	149.8	37.0	112.0
SDB-aug-cc-pVTZ						
$(Py)_2SnCl_4$	267.1±3.1[a]	D_{2d}	198.6	191.4	58.0	168.7
		D_{2h}	198.7	191.6	58.2	168.8
		Cis	183.4	157.5	57.9	143.4
$(Dmf)_2SnCl_4$	263.5±5.0[b]	C_{2h}	152.7	187.1	61.2	148.4
		C_{2v}	151.7	191.0	61.3	149.8
		Cis	157.9	148.5	61.0	130.6
$(Dmtf)_2SnCl_4$	263.1±2.7[b]	C_{2h}	127.4	199.5	43.1	141.9
		C_{2v}	124.6	202.7	42.4	141.6
		Cis	127.1	168.2	41.2	126.8
$(Py)_2SnBr_4$	277.2±2.7[c]	D_{2d}	180.9	189.4	58.4	158.6
		D_{2h}	181.8	190.1	59.0	159.1
		Cis	166.5	151.1	57.4	132.0
$(Dmf)_2SnBr_4$	309.0±5.6[d]	C_{2h}	133.8	186.2	62.1	137.9
		C_{2v}	134.1	189.9	62.4	139.8
		Cis	142.4	140.1	62.0	118.2
$(Dmtf)_2SnBr_4$	222.9±3.3[d]	C_{2h}	116.8	196.6	43.1	134.9
		C_{2v}	111.2	199.5	42.3	133.7
		Cis	116.3	158.2	40.7	116.8

[a]Ref. 42.
[b]Ref. 40.
[c]Ref. 43.
[d]Ref. 41.

relativistic, all-electron computational results. This trend occurs for $\Delta H^{reorg}(SnX_4)$ and $\Delta H^{BSSE}(L_2SnX_4)$, where ECPs values are greater by as much as 29 kJ mol^{-1}. However, these large deviations are created because of the different basis sets and levels of theory employed in each computational study. Previous results[20] show that for Si and Ge adducts of pyridine, ΔH^{diss} values calculated using MP2 are up to 50 kJ mol^{-1} larger than those using B3LYP. Therefore, including relativistic effects using ECPs, larger basis sets, and MP2 single-point calculations leads to large discrepancies between previous computational results and those in the present study. All of these thermodynamic contributions are included in the final bond strengths listed in Table 6, where large BSSE values using MP2 leads to better agreement between computational studies. However, MP2 calculations with ECPs still lead to $\overline{D}$(Sn–N) values larger than the previous all-electron B3LYP results.

The discrepancies between our thermodynamic values and those in the literature may be, in part, due to differences in geometries. The r(Sn–N) calculated with nonrelativistic, all-electron methods are up to 0.024 Å longer than those in the present study. The previous computational study used all-electron basis sets of DZP quality and neglected relativistic effects, which results in longer bonds.[64] It should also be

Table 6. Comparison of thermodynamic parameters of $(py)_2SnX_4$ (X = Cl and Br) calculated with ECPs versus all-electron methods (kJ mol^{-1}).

L_2SnX_4	Structure	Method	ΔH^{diss}	$\Delta H^{reorg}(SnX_4)$	$\Delta H^{BSSE}(L_2SnX_4)$	$\overline{D}$(Sn–L)
$(Py)_2SnCl_4$	D_{2h}	LANL2DZdp	211.8	180.2	56.1	170.6
	D_{2h}	SDB-aug-cc-pVTZ	198.7	191.6	58.2	168.8
	D_{2h}	All-electron[a]	134.8	162.7	36[b]	141[b]
$(Py)_2SnCl_4$	Cis	LANL2DZdp	199.2	154.0	65.4	145.8
	Cis	SDB-aug-cc-pVTZ	183.4	157.5	57.9	143.4
	Cis	All-electron[a]	116.4	129.1	36[b]	114[b]
$(Py)_2SnBr_4$	D_{2h}	LANL2DZdp	191.7	177.8	52.5	161.1
	D_{2h}	SDB-aug-cc-pVTZ	181.8	190.1	59.0	159.1
	D_{2h}	All-electron[a]	96.2	164.6	36[b]	123[b]
$(Py)_2SnBr_4$	Cis	LANL2DZdp	177.5	146.2	57.7	134.9
	Cis	SDB-aug-cc-pVTZ	166.5	151.1	57.4	132.0
	Cis	All-electron[a]	78.5	129.6	32[b]	97[b]

[a]Ref. 20.

[b]Although previous studies[20,44] have included half of the BSSE correction in eq. [6], the present study includes the entire $\Delta H^{BSSE}(L_2SnX_4)$ in calculation of $\overline{D}(Sn-X)$. Therefore, we compare values calculated in the present study to BSSE corrections and bond strengths that contain the entire $\Delta H^{BSSE}(L_2SnX_4)$, which are estimated from previous work.

noted that the values obtained from the present study are closer to all-electron calculations[20] than previous studies that employed effective core potentials.[16,17]

Conclusions

Effective core potentials were used to calculate homolytic bond-dissociation enthalpies, D(Sn–X), and donor–acceptor bond enthalpies, $\overline{D}$(Sn–L), of organotin compounds. Comparing calculated to experimental values showed that ECPs are suitable computational methods to examine bond in organotin systems. The large SDB-aug-cc-pVTZ basis set and ECP was used to calculate the D(Sn–X) of a series of trimethyltin(IV) species, Me_3Sn–X. However, it was concluded, based on computational efficiency and accuracy, that the LANL2DZdp basis set and effective core potential on tin and nontin atoms described by the 6-31G(d,p) basis set is also an appropriate method for calculation of tin bond strengths. Therefore, in larger organotin systems, including the dialkylstannylene acetals of interest, the LANL2DZdp basis set and effective core potential will be employed to calculate tin bond strengths in organotin compounds.

Supplementary data

Supplementary data (archive entries for the geometry optimizations of the molecules and the radical species and the geometry optimizations for the L_2SnX_4 series of donor–acceptor complexes) for this article are available on the journal Web site (canjchem.nrc.ca) or may be purchased from the Depository of Unpublished Data, Document Delivery, CISTI, National Research Council Canada, Ottawa, ON K1A 0R6, Canada. DUD 3938. For more information on obtaining material, refer to cisti-icist.nrc-cnrc.gc.ca/cms/unpub_e.shtml.

Acknowledgements

We thank the Natural Sciences and Engineering Research Council (NSERC) for financial support. We gratefully acknowledge WestGrid for use of computer resources, and in turn the Canada Foundation for Innovation, Alberta Innovation and Science, BC Advanced Education. WestGrid equipment is provided by IBM, Hewlett Packard, and SGI. Additional computational facilities were provided in part by ACEnet, the regional high performance computing consortium for universities in Atlantic Canada. ACEnet is funded by the Canada Foundation for Innovation (CFI), the Atlantic Canada Opportunities Agency (ACOA), and the Provinces of Newfoundland & Labrador, Nova Scotia, and New Brunswick.

References

(1) This article is part of a Special Issue dedicated to Professor T. Ziegler.
(2) Grindley, T. B.; Thangarasa, R. *J. Am. Chem. Soc.* **1990**, *112* (4), 1364–1373. doi:10.1021/ja00160a012.
(3) Kong, X.; Grindley, T. B. *Can. J. Chem.* **1994**, *72* (12), 2396–2404. doi:10.1139/v94-306.
(4) Kong, X.; Grindley, T. B. *Can. J. Chem.* **1994**, *72* (12), 2405–2415. doi:10.1139/v94-307.
(5) Grindley, T. B. *Adv. Carbohydr. Chem. Biochem.* **1998**, *53*, 17–142. doi:10.1016/S0065-2318(08)60043-8. PMID: 9710969.
(6) Gonçalves, A. G.; Noseda, M. D.; Duarte, M. E. R.; Grindley, T. B. *J. Org. Chem.* **2007**, *72* (26), 9896–9904. doi:10.1021/jo701413y. PMID:18044914.
(7) Grindley, T. B. Applications of Organotin Derivatives for Carbohydrate Synthesis. In *Tin chemistry: fundamentals, frontiers, and applications;* Gielen, M., Davies, A. G.,Tiekink, E. R. T., Pannell, K.H., Eds.; John Wiley & Sons, Ltd.:Chichester, UK, 2008; p 491.
(8) Laarhoven, L. J. J.; Mulder, P.; Wayner, D. D. M. *Acc. Chem. Res.* **1999**, *32* (4), 342–349. doi:10.1021/ar9703443.
(9) Clark, K. B.; Griller, D. *Organometallics* **1991**, *10* (3), 746–750. doi:10.1021/om00049a039.
(10) Griller,D.; Kanabus-Kaminska, J. M.; Maccoll, A. *Theochem.* **1988**, *163*, 125–131.
(11) Becerra, R.; Boganov, S. E.; Egorov, M. P.; Faustov, V. I.; Krylova, I. V.; Nefedov, O. M.; Walsh, R. *J. Am. Chem. Soc.* **2002**, *124* (25), 7555–7562. doi:10.1021/ja012691k. PMID:12071766.

(12) Jackson, R. A. *J. Organomet. Chem.* **1979**, *166* (1), 17–19. doi:10.1016/S0022-328X(00)91415-3.
(13) Galli, C.; Pau, T. *Tetrahedron* **1998**, *54* (12), 2893–2904. doi:10.1016/S0040-4020(98)83025-1.
(14) Keiser, D.; Kana'an, A. S. *J. Phys. Chem.* **1969**, *73* (12), 4264–4269. doi:10.1021/j100846a038.
(15) Baldwin, J. C.; Lappert, M. F.; Pedley, J. B.; Poland, J. S. *J. Chem. Soc. Dalton Trans.* **1972**, 1943–1947. doi:10.1039/DT9720001943.
(16) Poleshchuk, O. K.; Kalinina, E. L.; Legon, A. *Russ. J. Coord. Chem.* **2003**, *29* (1), 60–65. doi:10.1023/A:1021899102470.
(17) Poleshchuk, O. K.; Shevchenko, E. L.; Branchadell, V.; Lein, M.; Frenking, G. *Int. J. Quantum Chem.* **2005**, *101* (6), 869–877. doi:10.1002/qua.20348.
(18) Shurki, A.; Hiberty, P. C.; Shaik, S. *J. Am. Chem. Soc.* **1999**, *121* (4), 822–834. doi:10.1021/ja982218f.
(19) Davydova, E. I.; Timoshkin, A. Y.; Sevastianova, T. N.; Suvorov, A. V.; Frenking, G. *Phosphorus Sulfur Silicon* **2004**, *179* (4–5), 953–954. doi:10.1080/10426500490429013.
(20) Davydova, E. I.; Timoshkin, A. Y.; Sevastianova, T. N.; Suvorov, A. V.; Frenking, G. *Theochem* **2006**, *767* (1–3), 103–111. doi:10.1016/j.theochem.2006.05.011.
(21) Bickelhaupt, F. M.; Ziegler, T.; Schleyer, P. V. *Organometallics* **1996**, *15* (5), 1477–1487. doi:10.1021/om950560k.
(22) Hao, C. T.; Kaspar, J. D.; Check, C. E.; Lobring, K. C.; Gilbert, T. M.; Sunderlin, L. S. *J. Phys. Chem. A* **2005**, *109* (9), 2026–2034. doi:10.1021/jp040743x. PMID:16833538.
(23) Whittleton, S. R.; Boyd, R. J.; Grindley, T. B. Computational methods for organotin compounds. In *Tin chemistry: fundamentals, frontiers, and applications;* Gielen, M.; Davies, A. G., Tiekink, E. R. T., Pannell, K. H.; John Wiley & Sons, Ltd.: Chichester, UK, 2008; p 267.
(24) Wakamatsu, K.; Orita, A.; Otera, J. *Organometallics* **2008**, *27* (6), 1092–1097. doi:10.1021/om701179j.
(25) Basch, H. *Inorg. Chim. Acta* **1996**, *252* (1–2), 265–279. doi:10.1016/S0020-1693(96)05326-1.
(26) Deeth, R. J.; Jenkins, H. D. B. *J. Phys. Chem. A* **1997**, *101* (26), 4793–4798. doi:10.1021/jp970374n.
(27) Drozdova, T. I.; Denisov, E. T. *Kinet. Catal.* **2002**, *43* (1), 10–18. doi:10.1023/A:1014232625544.
(28) Martynov, A. V.; Zhinkin, A. R.; Amosova, S. V. *Russ. J. Org. Chem.* **2006**, *42* (2), 190–192. doi:10.1134/S1070428002120059.
(29) Martinelli, M. J.; Vaidyanathan, R.; Pawlak, J. M.; Nayyar, N. K.; Dhokte, U. P.; Doecke, C. W.; Zollars, L. M. H.; Moher, E. D.; Khau, V. V.; Kosmrlj, B. *J. Am. Chem. Soc.* **2002**, *124* (14), 3578–3585. doi:10.1021/ja016031r. PMID:11929246.
(30) Chojnacka, A.; Piatek, A. M.; Chapuis, C.; Jurczak, J. *Tetrahedron Asymmetry* **2006**, *17* (5), 822–828. doi:10.1016/j.tetasy.2006.01.031.
(31) Ayoko, G. A.; Bonire, J. J.; Abdulkadir, S. S.; Olurinola, P. F.; Ehinmidu, J. O.; Kokot, S.; Yiasel, S. *Appl. Organomet. Chem.* **2003**, *17* (10), 749–758. doi:10.1002/aoc.520.
(32) Valla, V.; Bakola-Christianopoulou, M.; Kojic, V.; Bogdanovic, G. *Synth. React. Inorg. Met.-Org. Nano-Met. Chem.* **2007**, *37* (1), 41–51. doi:10.1080/15533170601172450.
(33) Bregadze, V. I.; Glazun, S. A.; Petrovskii, P. V.; Starikova, Z. A.; Buyanovskaya, A. G.; Takazova, R. U.; Gielen, M.; de Vos, D.; Kemmer, M.; Biesemans, M.; Willem, R. *Appl. Organomet. Chem.* **2004**, *18* (4), 191–194. doi:10.1002/aoc.599.
(34) Gielen, M.; Biesemans, M.; Willem, R. *Appl. Organomet. Chem.* **2005**, *19* (4), 440–450. doi:10.1002/aoc.771.
(35) Bonire, J. J.; Fricker, S. P. *J. Inorg. Biochem.* **2001**, *83* (2–3), 217–221. doi:10.1016/S0162-0134(00)00192-6. PMID:11237262.
(36) Pellerito, C.; Nagy, L.; Pellerito, L.; Szorcsik, A. *J. Organomet. Chem.* **2006**, *691* (8), 1733–1747. doi:10.1016/j.jorganchem.2005.12.025.
(37) Caratozzolo, R.; Bellini, E.; Melati, M. R.; Pellerito, C.; Fiore, T.; D'Agati, P.; Scopelliti, M.; Pellerito, L. *Appl. Organomet. Chem.* **2007**, *21* (2), 66–72. doi:10.1002/aoc.1175.
(38) Dunstan, P. O. *Thermochim. Acta* **2000**, *345* (2), 117–123. doi:10.1016/S0040-6031(99)00400-1.
(39) Dunstan, P. O. *Thermochim. Acta* **2001**, *369* (1–2), 9–16. doi:10.1016/S0040-6031(00)00740-1.
(40) Dunstan, P. O. *Thermochim. Acta* **2001**, *376* (1), 17–23. doi:10.1016/S0040-6031(01)00570-6.
(41) Dunstan, P. O. *Thermochim. Acta* **2002**, *389* (1–2), 25–31. doi:10.1016/S0040-6031(02)00011-4.
(42) Dunstan, P. O. *Thermochim. Acta* **2003**, *398* (1–2), 1–7. doi:10.1016/S0040-6031(02)00326–X.
(43) Dunstan, P. O. *Thermochim. Acta* **2003**, *404* (1–2), 117–123. doi:10.1016/S0040-6031(03)00102-3.
(44) Timoshkin, A. Y.; Davydova, E. I.; Sevastianova, T. N.; Suvorov, A. V.; Schaefer, H. F. *Int. J. Quantum Chem.* **2002**, *88* (4), 436–440. doi:10.1002/qua.10073.
(45) Timoshkin, A. Y.; Suvorov, A. V.; Bettinger, H. F.; Schaefer, H. F. *J. Am. Chem. Soc.* **1999**, *121* (24), 5687–5699. doi:10.1021/ja983408t.
(46) Frisch, M. J.; Trucks, G. W.; Schlegel, H. B.; Scuseria, G. E.; Robb, M. A.; Cheeseman, J. R.; Montgomery, J. A., Jr.; Vreven, T.; Kudin, K. N.; Burant, J. C.; Millam, J. M.; Iyengar, S. S.; Tomasi, J.; Barone, V.; Mennucci, B.; Cossi, M.; Scalmani, G.; Rega, N.; Petersson, G. A.; Nakatsuji, H.; Hada, M.; Ehara, M.; Toyota, K.; Fukuda, R.; Hasegawa, J.; Ishida, M.; Nakajima, T.; Honda, Y.; Kitao, O.; Nakai, H.; Klene, M.; Li, X.; Knox, J. E.; Hratchian, H. P.; Cross, J. B.; Adamo, C.; Jaramillo, J.; Gomperts, R.; Stratmann, R. E.; Yazyev, O.; Austin, A. J.; Cammi, R.; Pomelli, C.; Ochterski, J. W.; Ayala, P. Y.; Morokuma, K.; Voth, G. A.; Salvador, P.; Dannenberg, J. J.; Zakrzewski, V. G.; Dapprich, S.; Daniels, A. D.; Strain, M. C.; Farkas, O.; Malick, D. K.; Rabuck, A. D.; Raghavachari, K.; Foresman, J. B.; Ortiz, J. V.; Cui, Q.; Baboul, A. G.; Clifford, S.; Cioslowski, J.; Stefanov, B. B.; Liu, G.; Liashenko, A.; Piskorz, P.; Komaromi, I.; Martin, R. L.; Fox, D. J.; Keith, T.; Al-Laham, M. A.; Peng, C. Y.; Nanayakkara, A.; Challacombe, M.; Gill, P. M. W.; Johnson, B.; Chen, W.; Wong, M. W.; Gonzalez, C.; Pople, J. A. *Gaussian 03,* version Revision B.05; Gaussian, Inc.: Wallingford, CT, 2003.
(47) Becke, A. D. *J. Chem. Phys.* **1993**, *98* (2), 1372. doi:10.1063/1.464304.
(48) Becke, A. D. *J. Chem. Phys.* **1993**, *98* (7), 5648. doi:10.1063/1.464913.
(49) Lee, C.-H.; Yang, W.; Parr, R. G. *Phys. Rev. B* **1988**, *37* (2), 785–789. doi:10.1103/PhysRevB.37.785.
(50) Boys, S. F.; Bernardi, F. *Mol. Phys.* **1970**, *19* (4), 553–566. doi:10.1080/00268977000101561.
(51) Whittleton, S. R.; Boyd, R. J.; Grindley, T. B. *J. Phys. Chem. A* **2006**, *110* (17), 5893–5896. doi:10.1021/jp056996n. PMID:16640386.
(52) Check, C. E.; Faust, T. O.; Bailey, J. M.; Wright, B. J.; Gilbert, T. M.; Sunderlin, L. S. *J. Phys. Chem. A* **2001**, *105* (34), 8111–8116. doi:10.1021/jp011945l.

(53) Wadt, W. R.; Hay, P. J. J. *Chem. Phys.* **1985**, *82* (1), 284–298.
(54) Martin, J. M. L.; Sundermann, A. *J. Chem. Phys.* **2001**, *114* (8), 3408–3420. doi:10.1063/1.1337864.
(55) Bergner, A.; Dolg, M.; Küchle, W.; Stoll, H.; Preuß, H. *Mol. Phys.* **1993**, *80* (6), 1431–1441. doi:10.1080/00268979300103121.
(56) Boyd, S. L.; Boyd, R. J.; Bessonette, P. W.; Kerdraon, D. I.; Aucoin, N. T. *J. Am. Chem. Soc.* **1995**, *117* (34), 8816–8822. doi:10.1021/ja00139a015.
(57) Luo, Y. R.; Pacey, P. D. *Can. J. Chem.* **1993**, *71* (4), 572–577. doi:10.1139/v93-079.
(58) Luo, Y. R.; Benson, S. W. *J. Phys. Chem.* **1989**, *93* (8), 3304–3306. doi:10.1021/j100345a082.
(59) Luo, Y. R.; Benson, S. W. *J. Phys. Chem.* **1989**, *93* (21), 7333–7335. doi:10.1021/j100358a014.
(60) Blanksby, S. J.; Ellison, G. B. *Acc. Chem. Res.* **2003**, *36* (4), 255–263. doi:10.1021/ar020230d. PMID:12693923.
(61) Walsh, R. *Acc. Chem. Res.* **1981**, *14* (8), 246–252. doi:10.1021/ar00068a004.
(62) Doncaster, A. M.; Walsh, R. *J. Phys. Chem.* **1979**, *83* (5), 578–581. doi:10.1021/j100468a005.
(63) Davydova, E. I.; Sevastianova, T. N.; Timoshkin, A. Y.; Suvorov, A. V.; Frenking, G. *Int. J. Quantum Chem.* **2004**, *100* (4), 419–425. doi:10.1002/qua.20094.
(64) Pyykkö, P. *Chem. Rev.* **1988**, *88* (3), 563–594. doi:10.1021/cr00085a006.

The response of extended systems to electrostatic fields[1]

Michael Springborg and Bernard Kirtman

Abstract: The response to electrostatic fields by finite systems, which contain a large central region of chemically identical building blocks, is shown not to depend on the boundaries of the system. Consequently, we can determine this response from that of the corresponding infinite periodic system and a vector potential theoretical–computational approach is presented for doing so. Both the electronic and structural response can be obtained with our approach. In many cases, neglecting the structural response is a poor approximation. To illustrate the performance of our treatment, extensive calculations have been carried out for simple model systems. Selected results are reported.

Key words: polarization, extended systems, electrostatic fields, structural properties, electronic properties.

Résumé : On démontre que, pour des systèmes finis contenant une grande région de blocs chimiquement identiques, la réponse à des champs électrostatiques ne dépend pas des limites du système. En conséquence, on peut déterminer cette réponse à partir des systèmes infinis correspondants et on présente une approche par calculs théoriques des potentiels vectoriels qui permet d'y arriver. Avec notre approche, il est possible d'obtenir aussi bien la réponse électronique que structurelle. Dans plusieurs cas, si on néglige la réponse structurelle, on obtient une mauvaise approximation. Afin d'illustrer la performance de notre traitement, on a effectué des calculs extensifs de systèmes modèles simples. On rapporte des résultats choisis.

Mots-clés : polarisation, systèmes étendus, champs électrostatiques, propriétés structurelles, propriétés électroniques.

[Traduit par la Rédaction]

Introduction

With this contribution, we want to honor Tom Ziegler on the occasion of his 65th birthday. It happens that Tom Ziegler shares a number of life experiences with one of the present authors (MS). Both grew up and studied in Denmark, but followed a scientific career outside of Denmark. Moreover, some of their first scientific footsteps were taken under the supervision of the same person, Jens Peder Dahl.

A significant part of Tom Ziegler's research has been devoted to calculating the electronic structure properties, including experimental observables, of large systems. These properties can be interpreted as the response of the system to external perturbations. In the spirit of Tom Ziegler's work, we discuss in this contribution, the response of large systems to electrostatic fields. The systems considered contain a large inner part consisting of a repetition of the same building block. On the boundaries other groups of atoms may be found. For the sake of simplicity, we shall concentrate on quasi-one-dimensional systems, i.e., polymers or chain compounds, but our treatment can be generalized to 2D and 3D systems as well.

Received 17 December 2008. Accepted 6 March 2009. Published on the NRC Research Press Web site at canjchem.nrc.ca on 9 June 2009.

M. Springborg.[1] Physical and Theoretical Chemistry, University of Saarland, 66123 Saarbrücken, Germany.
B. Kirtman. Department of Chemistry and Biochemistry, University of California, Santa Barbara, CA 93106, USA.

[1]Corresponding author (e-mail: m.springborg@mx.uni-saarland.de).

The response of a material to spatially uniform electric fields can be described through its dipole moment, which may be expanded (in the perturbation regime) as

$$[1]\quad \mu_i(\omega) = \mu_i^{(0)}(\omega) + \sum_j \sum_{\omega_1} \alpha_{ij}(\omega;\omega_1)\cdot E_j(\omega_1) + 1/2 \sum_{jk} \sum_{\omega_1,\omega_2} \beta_{ijk}(\omega;\omega_1,\omega_2)\cdot E_j(\omega_1)E_k(\omega_2) + 1/6 \sum_{jkl} \sum_{\omega_1,\omega_2,\omega_3} \gamma_{ijkl}(\omega;\omega_1,\omega_2,\omega_3) \cdot E_j(\omega_1)E_k(\omega_2)E_l(\omega_3) + \ldots$$

Here the external field is given by

$$[2]\quad \vec{E} = \sum_j \sum_{\omega_n} E_j(\omega_n)\vec{1}_j$$

where $\vec{1}_j$ is a unit vector along the j direction (i.e., x, y, or z), and ω_n is its frequency. Furthermore, $\omega = \pm\omega_1 \pm \omega_2 \pm \ldots$ is the frequency of the molecular response[2] and $\mu_i^{(0)}(\omega)$ is the dipole moment in the absence of the field, which vanishes for $\omega \neq 0$. The quantity $\alpha_{ij}(\omega;\omega_1)$ is the linear polarizability, while $\beta_{ijk}(\omega;\omega_1,\omega_2)$, $\gamma_{ijkl}(\omega;\omega_1,\omega_2,\omega_3)$, ... are the first, second, ... hyperpolarizabilities. The fact that the non-linear responses of a material can result in frequencies different from those of the external field is very important for a number of future applications in non-linear optics (see, e.g., refs. 2–4).

In the present contribution we shall focus on the low-frequency case, where setting $\omega = \omega_1 = \omega_2 = \ldots = 0$ is a good approximation. In that case, both structural and electronic degrees of freedom will respond to the external field. From a practical point of view, the relevant property is the re-

sponse per unit volume, which in our case translates into the dipole moment, per unit,

$$[3] \qquad P = \lim_{N\to\infty} [\mu_i(N+1,\omega) - \mu_i(N,\omega)]$$

where N is the number of units in our system and P is the polarization.

A number of earlier theoretical studies, devoted to identifying the polarization of extended systems, have been based on applying eq. [3] (see, e.g., ref. 6 and references therein). As a general conclusion, it has been found that wave-function-based methods give significantly more accurate results for chain-length dependence than those that are found with density-based methods, at least as far as conventional density functionals are concerned.[7,8] There is an on-going search for more adequate functionals as discussed, for example, in refs. 9 and 10. However, that pertains to short and medium-size chains. To the knowledge of the present authors, there has been no attempt to characterize the $N \to \infty$ limit directly. Although it is not the scope of the present work, we suggest use of the methods presented here to obtain further insight into the problems of density functionals in describing responses of extended systems to electric fields.

Theoretical studies of the properties of a material exposed to an external electrostatic field face a number of challenges. Even for an isolated atom, the external field changes a bound state into a resonance. In a practical calculation, runaway solutions can be avoided by using a basis set of functions that are localized on the atom. For molecules, a second problem may occur: electrons may tunnel from one end to the other (the analogue of Zener tunneling in periodic systems). To avoid this, one may consider external fields that are not too strong. But for large systems the fields may have to be so weak that numerical accuracy will suffer.

Here we shall first demonstrate that the response of finite chains containing a long central region of repeat units is independent of how the chain is terminated. Thus, one may study infinite, periodic chains instead. It turns out to be non-trivial to formulate the polarization calculation for the periodic chain, or periodic systems in general. However, once that has been done, the resulting computational procedure can be more efficient and reliable than that of considering a large finite system.

In the past we have found it extremely useful to analyse computational performance and obtain illustrative insights through model calculations, and we shall do the same here. Our formulation for infinite periodic systems has been discussed in detail elsewhere,[11–13] but a brief review with illustrative calculations for the structural response will be provided below. Additional results for long finite chains have been presented previously.[6] For technical details, the reader is referred to those papers. Finally, we offer some concluding remarks.

Long finite chains

In this section, we shall study the responses of finite chains consisting of a long sequence of identical units plus some terminations. It will also be assumed that the chain can be split into three different parts, i.e., a central region (C) where the effects of the terminations are not felt (criteria to be specified later), and the two terminal left and right (L and R) regions. The fact that such a split can be made defines what we mean by a 'long' chain.

General considerations

When the system can be split into three segments as in Fig. 1 it can be shown that any accumulated charge, Q, is localized to the terminations. This follows from the fact that, for fixed terminations, increasing the length of the chain increases the number of units (N_C) in the central region. If there were extra charge, $\widetilde{Q}$, not localized to the terminations, then the charge per central unit (i.e., $\widetilde{Q}/N_C$) would change (unless $\widetilde{Q}$ were zero). This conflicts with being able to identify a central region with given properties.

Next we relate the dipole moment to the charge transfer between the L and R terminal regions. We assume that the chain is placed along the z axis, with $z = 0$ determined by the average of the nuclear positions in the z direction. Then, for the z component of the dipole moment, we may write

$$\begin{aligned}[4] \qquad \mu_z &= \int \rho(\vec{r}) z d\vec{r} \\ &= \int_L \rho(\vec{r}) z d\vec{r} + \int_C \rho(\vec{r}) z d\vec{r} + \int_R \rho(\vec{r}) z d\vec{r} \\ &= N_C \mu_C + \left[Z_R \int_R \rho(\vec{r}) d\vec{r} + Z_L \int_L \rho(\vec{r}) d\vec{r} \right] \\ &\quad + \left[\int_L \rho(\vec{r})(z - Z_L) d\vec{r} + \int_R \rho(\vec{r})(z - Z_R) d\vec{r} \right]\end{aligned}$$

This expression is valid whether or not an external electrostatic field is included and whether or not the structure has been relaxed accordingly. In eq. [4], $\rho(\vec{r})$ is the total density, including nuclear and electronic charges, and μ_C is the z component of the dipole moment of one of the central units. Z_R and Z_L describe the centers of the nuclear positions in the R and L regions, respectively.

To analyse eq. [4], we make a similar separation of the total charge of the system, which leads to

$$\begin{aligned}[5] \qquad Q &= \int \rho(\vec{r}) d\vec{r} \\ &= \int_L \rho(\vec{r}) d\vec{r} + \int_C \rho(\vec{r}) d\vec{r} + \int_R \rho(\vec{r}) d\vec{r} \\ &= \int_L \rho(\vec{r}) d\vec{r} + \int_R \rho(\vec{r}) d\vec{r}\end{aligned}$$

since the central units are neutral as shown above. From this equation,

$$\begin{aligned}[6] \qquad Z_R \int_R \rho(\vec{r}) d\vec{r} + Z_L \int_L \rho(\vec{r}) d\vec{r} &= (Z_R - Z_L)/2 \left[\int_R \rho(\vec{r}) d\vec{r} - \int_L \rho(\vec{r}) d\vec{r} \right] \\ &\quad + \frac{(Z_R + Z_L)}{2} Q\end{aligned}$$

Thus, we see that in eq. [4] the first term in square brackets is the dipole moment due to electron transfer from one end to the other plus a term that is non-vanishing only for a charged system. It is important to note that the last term in square brackets in eq. [4] describes local dipole moments

that arise from the charge distribution within the two terminal regions. Thus, for fixed terminations, it is the only term in this equation that does not increase with increasing chain length and, therefore, does not contribute to the dipole moment per unit as defined in eq. [3].

Instead of partitioning physical space into rigorously nonoverlapping regions, it is convenient at this point to use a different partitioning based on localized orbitals, which are confined primarily, but not exclusively, to one of the regions and are orthogonal when integrated over all space. Let us assume, then, that we have solved the electronic single-particle (Hartree–Fock or Kohn–Sham) equation,

$$[7] \qquad \hat{h}\psi_i(\vec{r}) = \epsilon_i\psi_i(\vec{r})$$

with or without the external field and with or without allowing the structure to relax in response to the field. Using an approach related to one that has been presented by Vanderbilt and King-Smith[14] (see also ref. 15), we now prove that the dipole moment per unit is independent of the terminations, except for terms that result from the transfer of an integral number of electrons from one end to the other. This result is independent of the presence of an external electrostatic field with or without structural relaxation. Therefore, the linear and nonlinear responses of the extended chain (i.e., dipole derivatives with respect to the field) are independent of the terminations.

The first step is to transform the occupied orbitals into a set of maximally localized orthogonal functions, $\{w_{np}(\vec{r})\}$ which in C will approach Wannier functions as the system becomes larger. Here, w_{np} is the pth function localized primarily to the nth cell (in the terminal regions the division into cells is arbitrary) which, however, may have tails sticking out into other cells. We can, then, write μ_z as

$$\begin{aligned}[8] \qquad \mu_z &= \sum_n \left[-\sum_p \int |w_{np}(\vec{r})|^2 z d\vec{r} + \sum_m z_{nm} Q_m \right] \\ &= \sum_{n\in C} \left[-\sum_p \int |w_{np}(\vec{r})|^2 z d\vec{r} + \sum_m z_{nm} Q_m \right] \\ &\quad + Z_L \sum_{n\in L} \left[-\sum_p \int |w_{np}(\vec{r})|^2 d\vec{r} + \sum_m Q_m \right] \\ &\quad + \sum_{n\in L} \left[-\sum_p \int |w_{np}(\vec{r})|^2 (z - Z_L) d\vec{r} \right. \\ &\qquad \left. + \sum_m Q_m (z_{nm} - Z_L) \right] \\ &\quad + Z_R \sum_{n\in R} \left[-\sum_p \int |w_{np}(\vec{r})|^2 d\vec{r} + \sum_m Q_m \right] \\ &\quad + \sum_{n\in R} \left[-\sum_p \int |w_{np}(\vec{r})|^2 (z - Z_R) d\vec{r} \right. \\ &\qquad \left. + \sum_m Q_m (z_{nm} - Z_R) \right] \end{aligned}$$

where Q_m is the charge of the mth nucleus (independent of n) and z_{nm} is the z coordinate for the position of the mth nucleus in the nth cell. In contrast to eq. [4], where the integrals are over different regions of space but the (electron) densities are completely delocalized, all integrals in eq. [8] are over the complete space, but the orbital densities are localized to different regions of space,. In eq. [8] only the 1st, 2nd, and 4th terms depend (linearly) on the size of the system and therefore only these terms will contribute to the long chain limit of the dipole moment per unit (i.e., the polarization), cf. eq [3].

Fig. 1. Schematic representation of a long finite chain separated into a central region and two terminal regions. Each dot represents a group of atoms.

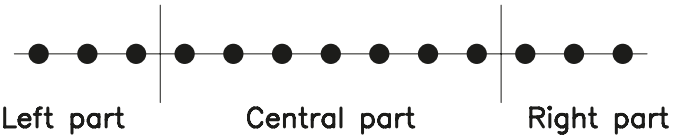

Using the w functions, the density matrix can be written in block form,

$$[9] \qquad \underline{\underline{D}} = \begin{pmatrix} \underline{\underline{D}}_L & \underline{\underline{0}} & \underline{\underline{0}} \\ \underline{\underline{0}} & \underline{\underline{D}}_C & \underline{\underline{0}} \\ \underline{\underline{0}} & \underline{\underline{0}} & \underline{\underline{D}}_R \end{pmatrix}$$

where each block $\underline{\underline{D}}_X$ is the density matrix for the region X and the submatrices $\underline{\underline{0}}$ contain elements that are exponentially vanishing as a function of the distance from the boundary between regions. As the w functions become closer to Wannier functions in C, $\underline{\underline{D}}_C$ will approach a diagonal matrix. The full density matrix is idempotent, so that each block $\underline{\underline{D}}_X$ is idempotent as well. Therefore, in the formulation of eq. [8] the w functions centered in the terminal regions are associated with an integral number of electrons.

In the formulation of eq. [4], any non-integral electron transfer between the two terminations is determined by tails of the w functions in C that extend into either R or L. To maintain neutrality there must be an exactly equal transfer of electronic charge into C from the other termination. Since the w functions of C are, by definition, independent of the termination, so is the amount of charge transfer from one end to the other, $\int_R \rho(\vec{r}) d\vec{r} - \int_L \rho(\vec{r}) d\vec{r}$. Therefore, the contribution of the first term on the rhs of eq. [6] to the dipole moment per unit is independent of the terminations. The same is true of the second term on the rhs of eq. [6] due to the fact that $Z_R + Z_L$ is unchanged by adding a unit at the center of the chain. Finally, as argued above, the last term in square brackets on the rhs of eq. [4] does not grow with chain length. Hence, its contribution to the dipole moment per unit becomes increasingly negligible as N_c increases. This completes our demonstration that the dipole moment per unit is a bulk property for sufficiently long chains.

Illustrative calculations

To illustrate the result of the preceding sub-section, calculations were carried out using a simple Hückel-like model for long finite $(AB)_{2M+1}$ chains placed along the z axis. We employed a basis set of orthonormal atomic orbitals (AOs) with one AO per atom. The system has one electron per

atom and the nuclei have charges of +1. With χ_n being the AO of the nth atom, we assume that $\langle\chi_n|\widehat{h}_0|\chi_m\rangle$ is non-vanishing only for $m = n$, $n \pm 1$, or $n \pm 2$. For $m = n$ this matrix element oscillates between $\pm\epsilon_0$ as a function of n, and in the other cases it is a linear function of the interatomic distance. The quantity $\widehat{h}_0$ is that part of the single-particle Fock (or Kohn–Sham) operator, $\widehat{h}$, that does not depend explicitly on the electrostatic field. Thus, we have

$$
\begin{aligned}
&\langle\chi_{2p+1}|\widehat{h}|\chi_{2p+1}\rangle = \epsilon_0 - E_{\mathrm{DC}}\cdot z_{2p+1}\\
&\langle\chi_{2p}|\widehat{h}|\chi_{2p}\rangle = -\epsilon_0 - E_{\mathrm{DC}}\cdot z_{2p}\\
&\langle\chi_{p}|\widehat{h}|\chi_{p+1}\rangle = -[t_1 - \alpha_1(z_{p+1} - z_p)]\\
&\langle\chi_{p}|\widehat{h}|\chi_{p+2}\rangle = -[t_2 - \alpha_2(z_{p+2} - z_p)]
\end{aligned}
\qquad [10]
$$

with z_j being the position of the jth atom and E_{DC} the external electrostatic field in the z direction. To study the dependence of the results on the the terminations, we modify the on-site energies of the terminal atoms and (or) the terminal hopping integrals:

$$
\begin{aligned}
&\langle\chi_{1}|\widehat{h}|\chi_{1}\rangle = \epsilon_0 + \epsilon_L - E_{\mathrm{DC}}\cdot z_1\\
&\langle\chi_{4M+2}|\widehat{h}|\chi_{4M+2}\rangle = -\epsilon_0 + \epsilon_R - E_{\mathrm{DC}}\cdot z_{4M+2}\\
&\langle\chi_{1}|\widehat{h}|\chi_{2}\rangle = -[t_1 - \alpha_1(z_2 - z_1)] + t_L\\
&\langle\chi_{4M+1}|\widehat{h}|\chi_{4M+2}\rangle = -[t_1 - \alpha_1(z_{4M+2} - z_{4M+1})] + t_R
\end{aligned}
\qquad [11]
$$

In eqs. [10] and [11] ϵ_0, t_1, t_2, α_1, α_2, ϵ_L, ϵ_R, t_L, and t_R are parameters whose values have been varied over a large range. Here, we shall just report typical results. The total energy is written as a sum over the energies of the occupied orbitals augmented by elastic terms and a contribution from the DC field acting on the nuclear charges, i.e.

$$
\begin{aligned}
\mathscr{E}_{\mathrm{tot}} = 2\sum_{i=1}^{\mathrm{occ}}\epsilon_i + k_1/2\sum_{p=1}^{4M+1}(z_{p+1} - z_p)^2\\
+ k_2/2\sum_{p=1}^{4M}(z_{p+2} - z_p)^2 + E_{\mathrm{DC}}\sum_{p=1}^{4M+2} z_p
\end{aligned}
\qquad [12]
$$

where the parameters k_1 and k_2 are defined so that, for the infinite periodic chain without an external field, the minimum total energy corresponds to the atomic positions

$$
z_n = [n\cdot a/2 - (4M+3)\cdot a/4] + (-1)^{n+1}u_0 \qquad [13]
$$

Here, a is the lattice constant and u_0 is a bond length alternation parameter that describes a displacement of the atoms leading to alternating shorter and longer bonds.

We set $\epsilon_0 = 0.5$, $t_1 = 2.5$, $\alpha_1 = 4.5$, $t_2 = 0.5$, and $\alpha_2 = 0.2$. Moreover, k_1 and k_2 are chosen so that the optimized structure for a vanishing field and an infinite periodic chain has $a = 2.1$ and $u_0 = 0.05$. Finally, we consider the six different terminations obtained by setting (ϵ_L, ϵ_R, t_L, t_R) equal to (0, 0, 0, 0), (0, 0.5, 0, 0), (0.5, 0, 0, 0), (0, 0, 0, 0.8), (0, 0, 0.8, 0), and (0.5, 0.5, 0.8, 0.8), respectively. Results of the calculations are shown in Fig. 2 for both the relaxed and unrelaxed geometries of a long neutral chain with $N = 2M + 1 = 81$ units. To analyse the results we define the charge transfer

$$
q = 1/2\left[\int_L \rho(\vec{r})d\vec{r} - \int_R \rho(\vec{r})d\vec{r}\right] \qquad [14]
$$

Since we employ a set of orthonormal AOs

$$
\begin{aligned}
q = 1/2\left[\sum_{n=1}^{2M}\left(1 - 2\sum_{i=1}^{2M+1}|C_{ni}|^2\right)\right.\\
\left. - \sum_{n=2M+3}^{4M+2}\left(1 - 2\sum_{i=1}^{2M+1}|C_{ni}|^2\right)\right]
\end{aligned}
\qquad [15]
$$

where C_{ni} is the coefficient of the nth AO in the ith molecular orbital. The figure shows clearly that q is independent of the termination, i.e., all six curves lie on top of each other except that for certain field strengths this quantity changes by an integer. The precise value of the field at which the jump occurs depends on the termination. Figure 2 (bottom two panels) also shows that for different terminations the dipole moment per unit, μ_z/N, follows parallel curves when plotted vs. the field. The differences between the curves are due to the charge distributions within the terminations, i.e., the last term in square brackets in eq. [4]. The fact that all curves are parallel implies that the linear and non-linear responses are independent of the termination. This is a consequence of the fact that, for these responses, the terminal regions make a negligible contribution to the total property for the entire system (cf. the discussion following eq. [6]). For the unrelaxed chains, the calculations were done using the unrelaxed geometry of the infinite, periodic chain. Although this is an approximation, we note that an optimization of the finite chain geometry would only alter the structure of the terminal regions and, accordingly, would result in rigid shifts of the curves shown in the figure. When the structure is allowed to relax correctly, the responses increase significantly as seen in the right hand panels.

Infinite periodic chains

In the preceding section we demonstrated that, for a long chain with a central region of repeating units and arbitrary terminations, the dipole moment induced by an electrostatic field is unaffected by the terminations. This means that the responses are properties of the central region. The only possible exception is associated with transfer of an integral number of electrons from one end to the other. Thus, treating an infinite periodic chain might provide a convenient alternative procedure for calculating (hyper)polarizabilities of ordinary neutral systems. In that way the terminations are removed and the various band-structure approaches that have been developed in solid state physics can be applied. However, there are theoretical problems with this alternative because the external (scalar) potential destroys the periodicity and, in addition, is unbounded. One solution is to introduce the external field through the vector potential as described below (see, e.g., refs. 16 and 17).

Calculation of the electronic energy using the vector potential approach

In this subsection we discuss our vector potential approach (VPA) for calculating the total electronic energy of a given infinite periodic structure. In the second subsection we present our procedure for optimizing the structure automatically. Within the VPA, the external electrostatic field is described by a vector potential, in contrast to the more conventional scalar potential. It has the advantage that the ex-

Fig. 2. Charge transfer, q, and dipole moment per unit, μ_z/N, as a function of applied external field, for a model chain containing 81 units. The panels on the left show the results for the field-free structure of the infinite periodic chain while the panels on the right show the results after the structure has been allowed to relax. Vertical lines indicate the field at which an integral number of electrons is transferred from one end to the other. The details of the model are described in the text and the different curves in each panel are for different terminations.

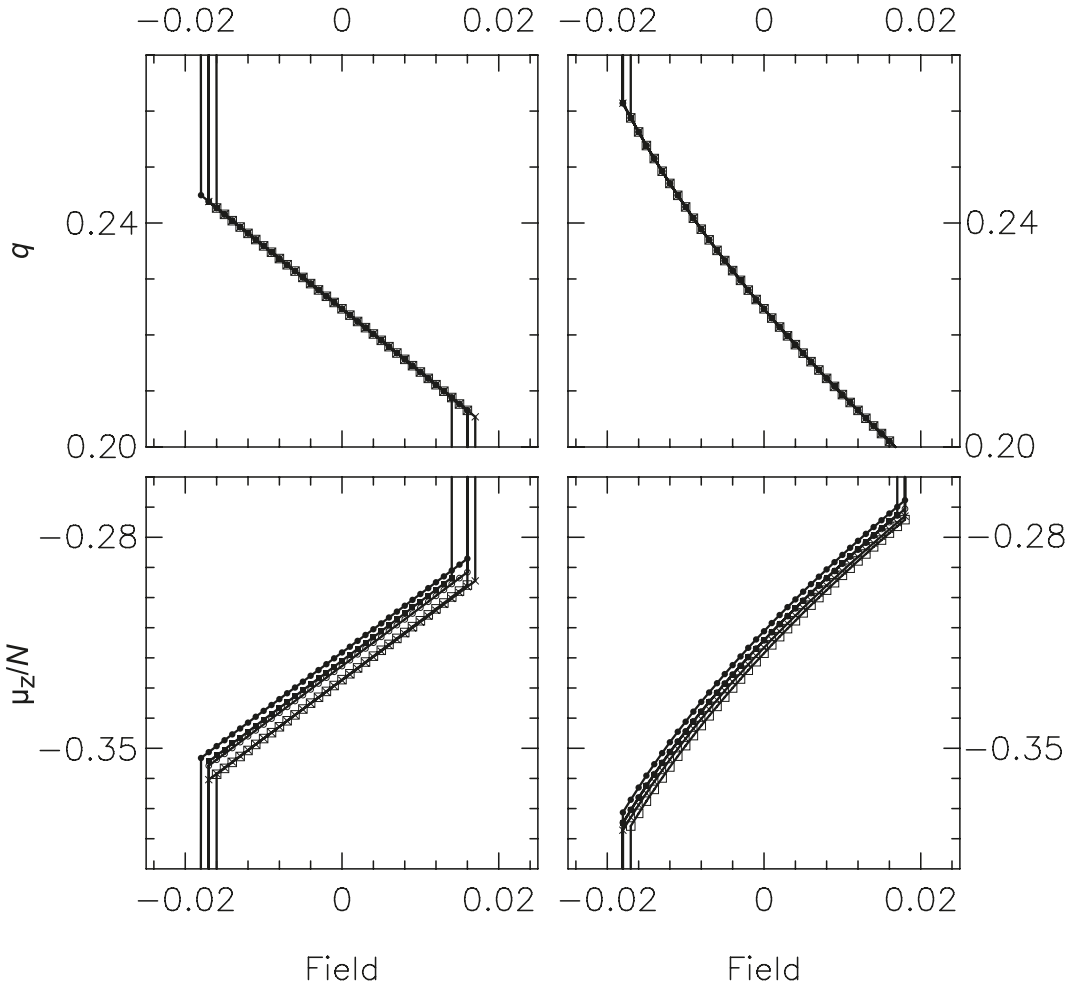

tension to time-dependent fields is trivial. Moreover, as we have shown elsewhere[13] the two approaches can be formulated identically in the static field case.

In a conventional band-structure calculation, without an electrostatic field, translational symmetry is used in writing the electronic orbitals as

$$[16] \qquad \psi_j(k, \vec{r}) = e^{ikz} u_j(k, \vec{r})$$

with j being a band index and $u_j(k, \vec{r})$ a periodic unit cell function. In a typical calculation, a finite set of K equidistant k points in the interval $[-\frac{\pi}{a}; \frac{\pi}{a}]$ is employed. Here $a = |\vec{a}|$ is the lattice constant, and the k spacing is

$$[17] \qquad \Delta k = \frac{2\pi}{Ka}$$

Thus, the Born–von Kármán (BvK) zone consists of K unit cells. For a system with B doubly filled bands, and a gap between the occupied and unoccupied orbitals, the electronic part of the polarization can, then, be expressed as[11,16,18,19]

$$[18] \qquad P_e = \frac{2i}{K} \sum_{k=1}^{K} \sum_{j=1}^{B} \langle u_j(k) | \frac{\partial}{\partial k} u_j(k) \rangle$$

in the Hartree–Fock or Kohn–Sham approach.

If we write the orbitals as a linear combination of Bloch functions formed from atom-centered basis functions, i.e.

$$[19] \qquad \psi_j(k, \vec{r}) = \sum_p C_{pj}(k) \chi_p(k, \vec{r})$$

$$\chi_p(k, \vec{r}) = \frac{1}{\sqrt{K}} \sum_m e^{ikam} \chi_{pm}(\vec{r})$$

(χ_{pm} is the pth basis function of the mth unit cell), then[16,18]

$$[20] \qquad P_e = \frac{2}{K} \sum_{j=1}^{B} \sum_{k=1}^{K} \sum_m e^{ikma} \sum_{pq} C^*_{qj}(k) \left(\underbrace{\langle \chi_{q0} | z - ma | \chi_{pm} \rangle}_{\text{charge}} + \underbrace{i \langle \chi_{q0} | \chi_{pm} \rangle \frac{d}{dk}}_{\text{current}} \right) C_{pj}(k)$$

This relation expresses the polarization as a sum of charge and current contributions. The former can be interpreted as being the expectation value of a potential that is piecewise linear and has the periodicity of the lattice. On the other hand, the latter is not the expectation value of a potential since it involves the $\frac{d}{dk}$ operator. The charge term is identical to μ_C of eq. [4], implying that the current term replaces the contributions associated with the terminations in eq. [4]. Numerical calculations for a simple model confirm this analysis.[11]

In an actual calculation of P_e the current term can easily be the source of both numerical and conceptual difficulties. The reason is that the coefficients $C_{qj}(k)$ contain a band-dependent phase factor, which is arbitrary except that it must satisfy

$$[21] \qquad C_{qj}(-\pi/a) = C_{qj}(\pi/a)$$

Because $\frac{dC_{qj}(k)}{dk}$ has to be calculated numerically in determining the response to a finite field, this arbitrariness can very easily result in severe numerical problems. We have demonstrated that a smoothing procedure which makes $C_{qj}(k)$ maximally similar to the coefficients at the neighboring k points provides an optimal solution.[12]

A more fundamental problem occurs as follows. When introducing a phase factor so that

$$[22] \qquad \widetilde{C}_{qj}(k) = C_{qj}(k)e^{i\phi_j(k)}$$

the phase angle is required to satisfy

$$[23] \qquad \phi_j(\pi/a) = \phi_j(-\pi/a) + \widetilde{n}_j \cdot 2\pi$$

However, that still leaves $\widetilde{n}_j$ as an unknown integer. Adding the contribution from all bands the polarization and the total energy will change according to

$$[24] \qquad \begin{aligned} P_e &\rightarrow P_e - a \cdot \widetilde{n} \\ \mathscr{E}_{\text{tot}} &\rightarrow \mathscr{E}_{\text{tot}} + E_{\text{DC}} \cdot a \cdot \widetilde{n} \end{aligned}$$

where $\widetilde{n} = \sum_j \widetilde{n}_j$. Thus, the total energy depends upon the product of the lattice constant a, the field E_{DC}, and an unknown integer. Despite appearing to be physically irrelevant, different values of $\widetilde{n}$ will lead to different values of a piezoelectric coefficient, defined as

$$[25] \qquad \eta = \left.\frac{da}{dE_{\text{DC}}}\right|_{E_{\text{DC}}=0}$$

which quantifies how the material changes length (or, in 3D, volume) under the influence of an external electrostatic field. Although a practical procedure is available for obtaining the value of the unknown integer, at the moment of writing we have not come up with a final prescription.

Having defined the polarization, we can write the total electronic energy for one BvK zone as

$$[26] \qquad \mathscr{E}_e(E_{\text{DC}}) = \mathscr{E}_e(0) - E_{\text{DC}} \cdot K \cdot P_e$$

where $\mathscr{E}_e(0)$ is the field-free electronic energy and P_e is defined in eq. [18]. The corresponding Hartree–Fock equation (see, e.g., refs. 12 and 13) for the crystal orbitals is

$$[27] \qquad \left\{\underline{\underline{F}}(k) - E_{\text{DC}} \cdot \left[\underline{\underline{M}}(k) + i\underline{\underline{S}}(k)\frac{\partial}{\partial k}\right]\right\} \cdot \underline{C}_j(k) = \epsilon_j(k) \cdot \underline{\underline{S}}(k) \cdot \underline{C}_j(k)$$

where $\underline{C}_j(k)$ is the (field-dependent) jth column of the matrix $\underline{\underline{C}}(k)$, and

$$[28] \qquad \begin{aligned} S_{qp}(k) &= \sum_l e^{ikal}\langle\chi_{0q}|\chi_{1p}\rangle \\ M_{qp}(k) &= \sum_l e^{ikal}\langle\chi_{0q}|z - la|\chi_{1p}\rangle \\ &= \sum_l e^{-ikal}\langle\chi_{1q}|z|\chi_{0p}\rangle \\ F_{qp}(k) &= \sum_l e^{ikal}\langle\chi_{0q}|\widehat{F}|\chi_{1p}\rangle \end{aligned}$$

are the overlap, unit cell dipole, and Fock matrix elements, respectively. Here $\widehat{F}$ is the usual Fock operator which depends on the field through the orbital coefficients (see later).

Equation [27] deserves some discussion. First, note that the quantity in square brackets replaces the dipole moment operator that would occur in a molecular treatment based on the scalar potential. This quantity preserves the translational symmetry, i.e., k remains a good quantum number even though the derivative with respect to k now appears. Second, because of this derivative, eq. [30] is not a standard matrix-eigenvalue problem. However, by using the normalization condition

$$[29] \qquad \underline{\underline{1}} = \underline{\underline{C}}^{\dagger}(k) \cdot \underline{\underline{S}}(k) \cdot \underline{\underline{C}}(k)$$

which gives

$$[30] \qquad \underline{\underline{S}}(k)\frac{\partial}{\partial k}\underline{\underline{C}}(k) = \left[\underline{\underline{S}}(k)\left(\frac{\partial}{\partial k}\underline{\underline{C}}(k)\right)\underline{\underline{C}}^{\dagger}(k)\underline{\underline{S}}(k)\right]\underline{\underline{C}}(k)$$

equation [27] can be cast into the standard form. In that event, the term in square brackets in eq. [30] (as well as the Fock matrix) has to be treated self-consistently. Third, as mentioned above, the coefficients $\underline{C}_j(k)$contain arbitrary phase factors (eq. [22]). Since $\frac{\partial}{\partial k}\overline{C}(k)$ has to be calculated numerically, in general, the occurrence of these arbitrary phase factors can cause severe numerical problems. This makes the previously described smoothing procedure of paramount importance. Due to the arbitrariness of the phase factors there is an arbitrariness in the orbital energies. Thus, upon making the substitution of eq. [22], $\epsilon_j(k)$ changes according to

$$[31] \qquad \epsilon_j(k) \rightarrow \epsilon_j(k) + E_{\text{DC}}\frac{\partial}{\partial k}\phi_j(k)$$

Although the integral of the second term over the entire band will vanish, except for possible contributions from the undetermined $\widetilde{n}_j$ in eq. [23], the field-dependent orbital energies will vary in a somewhat arbitrary fashion as one goes across the band. Thus, the usual interpretation of the orbital energies as ionization potentials or electron affinities, based on Koopmans' (Hartree–Fock) / Janak's (DFT) theorem, must be reconsidered.

Our experience has shown that it is not possible to solve eq. [27] self-consistently to arbitrary accuracy. In the itera-

tive process a convergence parameter may be defined using, for example, the magnitude of the differences between output and input coefficients $\{C_{qj}\}$. That parameter reaches a minimum and then increases. Furthermore, its value at the minimum grows as a function of the strength of the external field, $|E_{DC}|$. This numerical instability is associated with the oscillations in the band structures described by eq. [31]. In physical terms it is undoubtedly related to the onset of Zener tunneling. However a full understanding has not yet been reached.

Optimization of the structure

The total energy, at a given geometry, is the sum of the electronic and the nuclear energy,

$$[32] \qquad \mathscr{E}_{tot} = \mathscr{E}_e + \mathscr{E}_n$$

The nuclear energy contains the (classical) electrostatic interaction between the nuclei as well as the (classical) interaction between the external electrostatic field and the nuclear charges. To optimize the structure automatically, the forces, $\frac{\partial \mathscr{E}_{tot}}{\partial x}$ are normally used. Here x is a general structural coordinate such as a lattice constant or an internal parameter, whose variation does not destroy the translational symmetry. Analytical formulas for evaluation of the forces are especially helpful in this regard. For the $\frac{\partial \mathscr{E}_n}{\partial x}$ term they are easily found, whereas for $\frac{\partial \mathscr{E}_e}{\partial x}$ they are more difficult to obtain.

In our recent work,[13] we have shown how an approach of Zerner[20] for finite, molecular systems can be generalized to the present case. As usual, the field-free Hamiltonian operator is written as a sum of one- and two-electron terms,

$$[33] \qquad \widehat{H}_e = \sum_i \widehat{h}_0(\vec{r}_i) + 1/2 \sum_{i \neq j} \widehat{v}(\vec{r}_i, \vec{r}_j)$$

for which the matrix elements are

$$[34] \qquad h_{0qp}(k) = \sum_l e^{ikal} \langle \chi_{0q} | \widehat{h}_0 | \chi_{lp} \rangle$$

$$v_{q_1q_2p_1p_2}(k_1, k_2) = \frac{1}{K} \sum_{l_1, l_2, m_2} e^{ia(k_1 l_1 + k_2 l_2 - k_2 m_2)} (\langle \chi_{0q_1} \chi_{m_2 q_2} | \widehat{v} | \chi_{l_1 p_1} \chi_{l_2 p_2} \rangle - \langle \chi_{0q_1} \chi_{m_2 q_2} | \widehat{v} | \chi_{l_2 p_2} \chi_{l_1 p_1} \rangle)$$

The total electronic energy in the presence of an electrostatic field may then be written as

$$[35] \qquad \mathscr{E}_e = \sum_k \sum_{pq} D_{qp}(k) h_{0qp}(k) + \frac{1}{2} \sum_{k_1 k_2} \sum_{p_1 p_2 q_1 q_2} D_{q_1 p_1}(k_1) D_{q_2 p_2}(k_2) v_{q_1 q_2 p_1 p_2}(k_1, k_2) - E_{DC} K P_e$$

where $D_{qp}(k)$ is the (k-dependent) density matrix,

$$[36] \qquad D_{qp}(k) = \sum_j C_{qj}(k) C^*_{pj}(k)$$

constructed from the coefficients that satisfy eq. [27] with

$$[37] \qquad F_{qp}(k) = h_{0qp}(k) + \sum_{k_1} \sum_{q_1 p_1} D_{q_1 p_1}(k_1) v_{q_1 q p_1 p}(k_1, k)$$

Note that $D_{qp}(k)$ depends upon E_{DC} since the expansion coefficients C_{qj} are field-dependent. After several steps where we use the facts that (1) the polarization is real, (2) the coefficients $C_{qj}(k)$ satisfy the single-particle eq. [27], (3) the overlap matrices are Hermitian, and (4)

$$[38] \qquad \frac{\partial S_{qp}(k)}{\partial k} = -i[M_{qp}(k) - M^*_{pq}(k)]$$

we obtain

$$[39] \qquad \frac{\partial \mathscr{E}_e}{\partial x} = \sum_k \sum_{pq} D_{qp}(k) \frac{\partial h_{0qp}(k)}{\partial x} + \frac{1}{2} \sum_{k_1 k_2} \sum_{p_1 p_2 q_1 q_2} D_{q_1 p_1}(k_1) D_{q_2 p_2}(k_2) \frac{\partial v_{q_1 q_2 p_1 p_2}(k_1, k_2)}{\partial x}$$
$$- \sum_k \sum_{pq} Q_{pq}(k) \frac{\partial S_{qp}(k)}{\partial x} - \frac{\mathscr{E}_{DC}}{2} i \sum_k \sum_{pq} [R_{qp}(k) - R^*_{pq}(k)] \frac{\partial S_{qp}(k)}{\partial x}$$
$$- \frac{E_{DC}}{2} \sum_k \sum_{pq} D_{qp}(k) \left(\frac{\partial M_{qp}(k)}{\partial x} + \frac{\partial M^*_{pq}(k)}{\partial x} \right)$$

in which

Fig. 3. Comparison of the total polarization, P, for a periodic chain (open circles) with $\Delta\mu$ for a finite chain (full curve) as a function of field strength for: (*a*) field-free geometry ($N = 25$); (*b*) relaxed geometry ($N = 51$). In (*c*) the periodic chain results of (*a*) have been separated into the charge term (open circles) and the current term (full circles). All periodic chain calculations were done with $K = 60$ units in the BvK zone. For further details see the text.

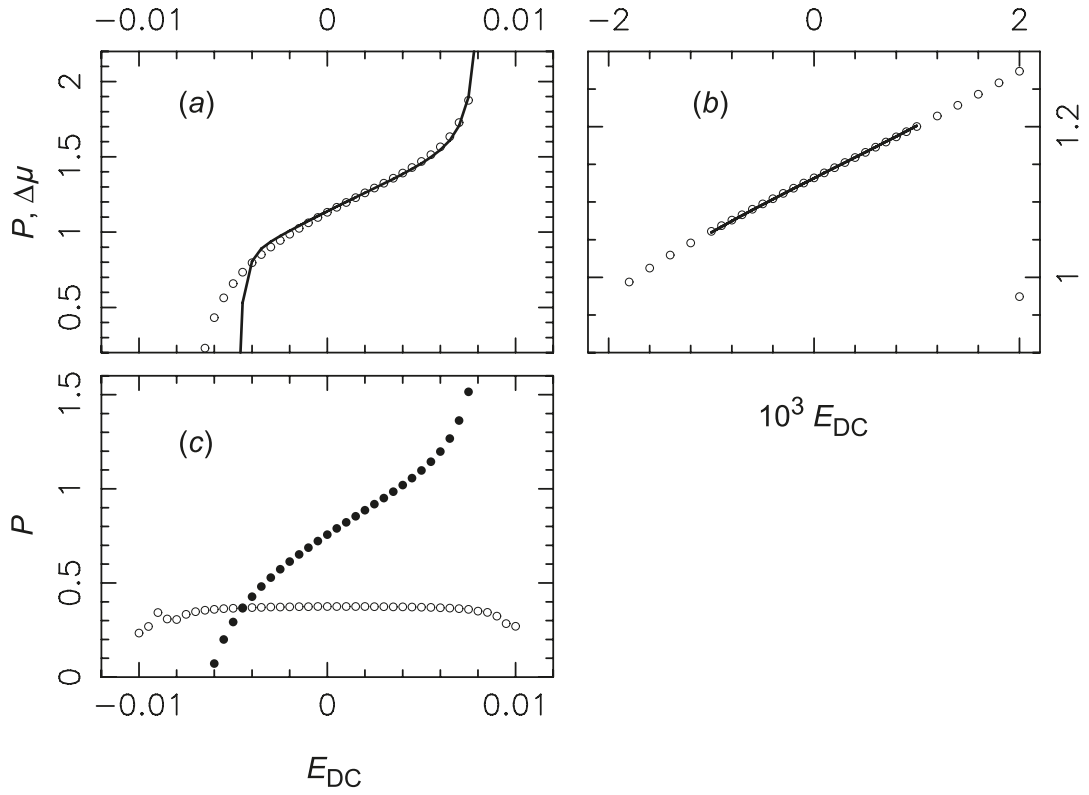

$$[40] \qquad R_{qp}(k) = \sum_j C^*_{qj}(k)\frac{\partial C_{pj}(k)}{\partial k}$$

$$Q_{qp}(k) = \sum_j \epsilon_j(k) C^*_{qj}(k) C_{pj}(k)$$

have been introduced.

Illustrative calculations

The model in the above section was extended in the following ways:[13] Instead of only one, two (orthonormal) basis functions per atom were considered and the functions of neighboring atoms were allowed to overlap. In the nearest-neighbor one-electron matrix elements $\langle \chi_{n(i)}|\hat{h}_0|\chi_{n\pm1(j)}\rangle$, with $\chi_{m(k)}$ being the kth basis function of the mth atom, (k = 1,2) were assumed to depend linearly on the distance between the atoms, whereas the next-nearest neighbor terms were set equal to zero. Moreover, $\langle \chi_{n(i)}|\hat{h}_0|\chi_{n(i)}\rangle$ was assumed to depend only on i and the (A or B) atom type. Of the (parameterized) two-electron matrix elements, only $\langle \chi_{n(i)}\chi_{n(i)}|\hat{v}|\chi_{n(i)}\chi_{n(i)}\rangle$ were assumed to be nonzero. The parameters entering into the overlap matrix and P_e were calculated from basis functions whose rectangular shape was chosen to simplify the evaluation; i.e.

$$[41] \qquad \chi_{m(1)} = \begin{cases} 1/\sqrt{w_{X1}} \text{ for } |z - z_m| \le w_{X1}/2 \\ 0 \text{ otherwise} \end{cases}$$

$$\chi_{m(2)} = \begin{cases} 1/\sqrt{w_{X2}} \text{ for } w_{X2}/4 \le |z - z_m| \le w_{X2}/2 \\ -1/\sqrt{w_{X2}} \text{ for } |z - z_m| \le w_{X2}/4 \\ 0 \text{ otherwise} \end{cases}$$

Here, X denotes whether the mth atom is of type A or B. We considered the case of four electrons per AB unit and the nuclei were each given a charge of +2 a.u.

In total, the model includes more than 20 parameters. By varying their values over a considerable range, the validity of our approach could be verified. We shall not give details of our results or values of the parameters but instead present typical calculations. More details, including values of the parameters, are available from the authors upon request.

Two different cases were studied: (1) a long finite chain of N units, for which the polarization was calculated using eq. [3], and (2) an infinite periodic chain with the electronic polarization given by eq. [20] and the nuclear polarization by the standard classical expression. Finally, we have adjusted the unknown integer $\tilde{n}$ of eq. [24] to obtain the best agreement between the finite and infinite chains.

In Fig. 3, we show typical results of our calculations. The number of k points, which is the same as the number of unit

Fig. 4. Optimized values of (top panel) the average bond length, $\frac{a}{2}$, and (bottom panel) the displacement of the atoms away from the equidistant positions, u_0 [see eq. [13], as a function of the field strength. Solid curves are for finite chains with N = 25, 26, 27, 50, 51, and 52 units, whereas the infinite chain results (dots) are for K = 60. The finite chain results for $N \simeq 25$ are those that differ most from the infinite chain results.

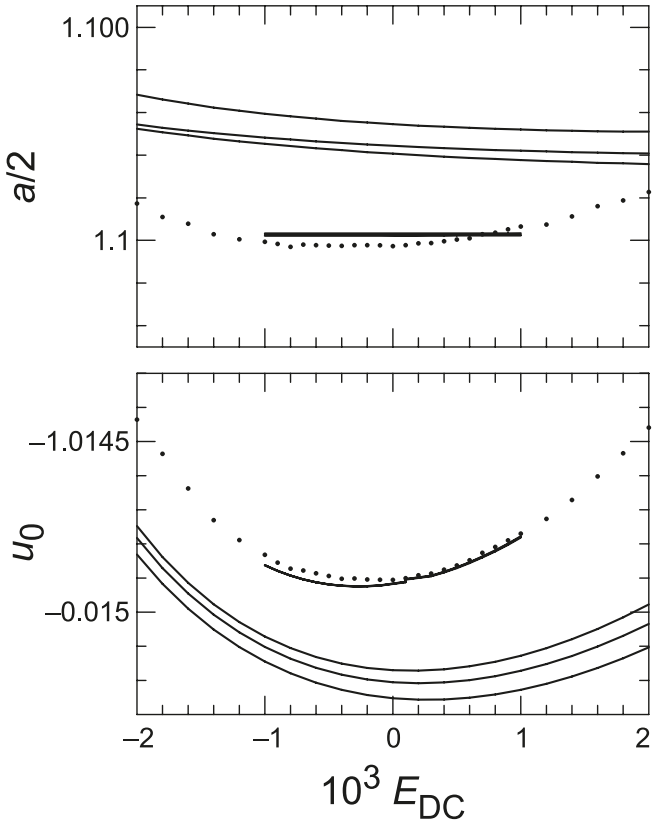

cells in the BvK zone, was set equal to K = 60 (cf. eq. [17]). According to our previous experience, this is sufficient to provide good accuracy. For the field-free structure, satisfactory agreement between the finite and infinite chains was found for N = 25, but when the structure is optimized, N = 51 was needed. Even with our simple model, the finite chain calculations for N = 51 are quite demanding, thereby providing support for the infinite periodic chain approach outlined here.

The figure clearly demonstrates that our approach for infinite periodic chains is able to reproduce the results for finite chains, when the latter are sufficiently long. When separating the polarization into the charge and current contributions [cf. Fig. 3*c*] we see that the variation in the polarization as a function of field strength is dominated by the current term, at least for this model system. Thus, the current term cannot generally be neglected.

In the present model the infinite periodic system has only two structural variables, which may be taken as the average bond length $\frac{a}{2}$ and the bond length alternation parameter u_0. Using the force expression of eq. [39] the relaxed structure was determined as a function of field strength. For comparison purposes we used the positions of the atoms in the middle of the finite chain to estimate $\frac{a}{2}$ and u_0.

The resulting parameters are shown in Fig. 4. As already observed the finite chains with 25 units are too short to allow for an accurate estimate of the infinite chain limit; at least 50 units are needed. In the latter case, the two sets of calculations yield good agreement. We believe that the small remaining differences are due to self-consistent field (SCF) convergence difficulties for the finite chains. In addition, we emphasize that the calculations for the latter are several orders of magnitude slower than those for the infinite periodic chains.

Concluding remarks

In this presentation we have demonstrated that finite chains consisting of a long sequence of identical building blocks with arbitrary terminations can be treated as if they were infinite and periodic. However, the correct procedure for determining the polarization (the dipole moment per unit) of an infinite periodic chain in an electrostatic field is not obvious. We have outlined how this problem can be solved by using the vector potential to describe the field. The resulting Hartree–Fock single particle equation has been formulated as eq. [27]. Although not presented, the analogous equation can be set up within Kohn–Sham density functional theory as well. Solving the single particle equation entails some non-trivial numerical difficulties. We have utilized a numerically stable procedure for obtaining a solution, but have also indicated some numerical and conceptual issues that remain open. Our approach allows for automatic structure optimization, with eq. [39] being the central result; again, a similar expression can be derived within the Kohn–Sham density functional theory formalism.

We have defined what is meant by a "long" chain, as used here, only in general terms, i.e., a chain for which maximally localized orbitals in the central region are unaffected by the terminations. When the property of interest is the polarization in the absence of an external field, also known as the "spontaneous" polarization, then the long chain limit will usually be reached for chains that contain on the order of 10 diatomic units. On the other hand, when higher-order responses and (or) structural relaxations are sought, we also require that contributions from the terminal regions be negligible compared to those from the central region. Then, considerably longer chains will often be required. Furthermore, when a field is turned on, our numerical results indicate that the size of the central region is reduced. This means that even larger systems are necessary before reaching the long chain limit.

Another method used to determine some of the responses to electrostatic fields is based on the application of a periodic, piecewise linear potential,

$$[42] \qquad V(z) = E_{DC} \cdot \begin{cases} z + L/4 \text{ for } -L/2 \le z \le 0 \\ -z + L/4 \text{ for } 0 \le z \le L/2 \end{cases}$$

where L is the size of the periodic repetition (which could be the size of the BvK zone). This approach has been employed, for example, by Darrigan et al.[21] Naturally, the length L must be sufficiently large to obtain accurate results. Although convergence with increasing L can be improved by taking differences, preliminary model calculations suggest that L values have to be so large that this procedure is

not useful compared to the one we have presented here. A more detailed analysis, which is beyond the scope of the present work, will be presented elsewhere.[22]

Our focus here has been on quasi-one-dimensional systems as studied by simple models. However, the treatment presented can be extended relatively easily to higher dimensions and can be implemented into parameter-free electronic structure programs. Work along these lines has already been initiated.[23] Nevertheless, by focusing on simple model systems, it has been possible to carry out extensive calculations which enabled our numerical methodology to be fully developed and tested. This would not have been possible had we solely considered accurate ab initio methods.

Acknowledgments

This work was supported by the German Research Council (DFG) through project Sp439/20. One of the authors (MS) is very grateful to the International Center for Materials Research, University of California, Santa Barbara, for generous hospitality.

References

(1) This article is part of a Special Issue dedicated to Professor T. Ziegler.
(2) Orr, B. J.; Ward, J. F. *Mol. Phys.* **1971**, *20* (3), 513–526. doi:10.1080/00268977100100481.
(3) Champagne, B.; Bishop, D. M. *Adv. Chem. Phys.* **2003**, *126*, 41–92. doi:10.1002/0471428019.ch2.
(4) Shi, S. *Contemp. Phys.* **1994**, *35* (1), 21–36. doi:10.1080/00107519408217493.
(5) Marder, S. R.; Perry, J. W. *Science* **1994**, *263* (5154), 1706–1707. doi:10.1126/science.263.5154.1706. PMID:17795376.
(6) Springborg, M.; Kirtman, B. *Chem. Phys. Lett.* **2008**, *454* (1-3), 105–113. doi:10.1016/j.cplett.2008.01.078.
(7) Champagne, B.; Perpète, E. A.; van Gisbergen, S. J. A.; Baerends, E.-J.; Snijders, J. G.; Soubra-Ghaoui, C.; Robins, K. A.; Kirtman, B. *J. Chem. Phys.* **1998**, *109* (23), 10489. doi:10.1063/1.477731.
(8) van Gisbergen, S. J. A.; Schipper, P. R. T.; Gritsenko, O. V.; Baerends, E. J.; Snijders, J. G.; Champagne, B.; Kirtman, B. *Phys. Rev. Lett.* **1999**, *83* (4), 694–697. doi:10.1103/PhysRevLett.83.694.
(9) Kirtman, B.; Bonness, S.; Ramirez-Solis, A.; Champagne, B.; Matsumoto, H.; Sekino, H. *J. Chem. Phys.* **2008**, *128* (11),o. 114108. doi:10.1063/1.2885051. PMID:18361555.
(10) Ruzsinszky, A.; Perdew, J. P.; Csonka, G. I. *Phys. Rev. A* **2008**, *78* (2),o. 022513. doi:10.1103/PhysRevA.78.022513.
(11) Springborg, M.; Kirtman, B.; Dong, Y. *Chem. Phys. Lett.* **2004**, *396* (4-6), 404–409. doi:10.1016/j.cplett.2004.08.067.
(12) Springborg, M.; Kirtman, B. *J. Chem. Phys.* **2007**, *126* (10),o. 104107. doi:10.1063/1.2711202. PMID:17362061.
(13) (a) Springborg, M.; Kirtman, B. *Phys. Rev. B* **2008**, *77* (4),o. 045102. doi:10.1103/PhysRevB.77.045102.; (b) Springborg, M.; Kirtman, B. *Phys. Rev. B* **2008**, *77* (20),o. 209901. (E). doi:10.1103/PhysRevB.77.209901.
(14) Vanderbilt, D.; King-Smith, R. D. *Phys. Rev. B* **1993**, *48* (7), 4442–4455. doi:10.1103/PhysRevB.48.4442.
(15) Kudin, K. N.; Car, R.; Resta, R. *J. Chem. Phys.* **2007**, *127* (19),o. 194902. doi:10.1063/1.2799514. PMID:18035903.
(16) Kirtman, B.; Gu, F. L.; Bishop, D. M. *J. Chem. Phys.* **2000**, *113* (3), 1294. doi:10.1063/1.481907.
(17) Bishop, D. M.; Gu, F. L.; Kirtman, B. *J. Chem. Phys.* **2001**, *114* (17), 7633. doi:10.1063/1.1356019.
(18) Blount, E. I. *Solid State Phys.* **1962**, *13*, 305.
(19) King-Smith, R. D.; Vanderbilt, D. *Phys. Rev. B* **1993**, *47* (3), 1651–1654. doi:10.1103/PhysRevB.47.1651.
(20) Zerner, M. C. In *Modern quantum chemistry: introduction to advanced electronic structure theory*. A. Szabo and N. S. Ostlund. Eds.;. Dover Publ.: Mineola, NY, 1989;; p 437 ff.
(21) Darrigan, C.; Rérat, M.; Mallia, G.; Dovesi, R. *J. Comput. Chem.* **2003**, *24* (11), 1305–1312. doi:10.1002/jcc.10274. PMID:12827671.
(22) Kirtman, B.; Ferrero, M.; Rérat, M.; Springborg, M. Unpublished.
(23) Ferrero, M.; Rérat, M.; Kirtman, B.; Dovesi, R. *J. Chem. Phys.* **2008**, *129* (24), o. 244110. doi:10.1063/1.3043366. PMID:19123498.

A time-dependent density functional theory (TDDFT) interpretation of the optical spectra of zinc phthalocyanine π-cation and π-anion radicals[1]

Angela Rosa and Giampaolo Ricciardi

Abstract: The UV–visible and near-IR spectra of the zinc phthalocyanine π-cation and π-anion radicals, $[ZnPc(-1)]^{\bullet+}$ and $[ZnPc(-3)]^{\bullet-}$, are investigated by time-dependent density functional theory (TDDFT) calculations using the pure, asymptotically correct, statistical average of (model) orbital potentials (SAOP) functional. The nature and intensity of the main spectral features are highlighted and interpreted on the basis of the ground-state electronic structure of the complexes. Similarities and differences with previous TDDFT/B3LYP results are discussed. TDDFT/SAOP results for the π-anion radical prove to be in excellent agreement with the solution spectra and generally in line with deconvolution analyses of solution absorption and magnetic circular dichroism (MCD) spectra. On the basis of these results a novel interpretation of the Q-band system is proposed. For the π-cation radical TDDFT/SAOP calculations provide a satisfactory description of the UV region of the spectrum. However, they do not reproduce accurately the energy and intensity of the Q band observed at 825 nm. The description of the Q-band region appears to be complicated by the presence of spurious non-Gouterman transitions. Furthermore, the calculations, either in the gas phase or in solution, do not account for the broad absorption near 500 nm that has been suggested to arise from a nondegenerate, *z*-polarized $^2A_{2g}$ excited state. Theory and experiment can be reconciled if the presence of an axial ligand such as CN^- is explicitly considered in the calculations. TDDFT/SAOP results for the axially ligated $[ZnPc(-1)(CN)]^{\bullet}$ species indicate that the 500 nm feature is related to the axial ligation induced symmetry lowering of the π-cation radical and this band is assigned to a *z*-polarized transition associated with the hole in the $2a_{1u}$.

Key words: metallophthalocyanine π-radicals, optical and magnetic circular dichroism (MCD) spectra, density functional theory (DFT) calculations, time-dependent density functional theory (TDDFT) calculations.

Résumé : On a étudié d'une façon théorique les spectres UV–visible et proche infrarouge des radicaux π-cationiques et π-anioniques de la phtalocyanine de zinc, $[ZnPc(-1)]^{\bullet-}$ et $[ZnPc(-3)]^{\bullet+}$, en faisant appel à la théorie de la fonctionnelle de la densité en fonction du temps (TFDFT) et une fonctionnelle pure et asymptotiquement correcte, SAOP. La nature et l'intensité des caractéristiques spectrales principales sont signalées et interprétées sur la base de la structure électronique de l'état fondamental des complexes. On discute des similarités et des différences observées avec les résultats rapportées antérieurement sur la base de calculs au niveau TFDFT/B3LYP. Les résultats obtenus pour radical π-anionique sont en excellent accord avec le spectre en solution et il est généralement en accord avec les analyses de déconvolutoin des spectres d'absorption de dichroïsme circulaire moléculaire (DCM). Sur la base de ces résultats, on propose une nouvelle interprétation pour la bande Q. Pour le radical π-cationique, les calculs au niveau TFDFT/SAOP fournissent une description satisfaisante de la région de l'UV du spectre. Toutefois, ils ne reproduisent pas d'une façon satisfaisante l'énergie et l'intensité de la bande Q observée à 825 nm. La description de la région de la bande Q semble compliquée par la présence de fausses transitions de Gouterman. De plus, les calculs, en phase gazeuse ou en solution, n'expliquent pas l'absorption large près de 500 nm pour laquelle il a été suggéré qu'elle découle d'un état excité $^2A_{2g}$ polarisé suivant l'axe *z* et qui ne serait pas dégénéré. On peut réconcilier les résultats théoriques et expérimentaux si la présence d'un ligand axial, tel un CN^-, est explicitement considérée dans les calculs. Les résultats de calculs au niveau TFDFT/SAOP pour l'espèce portant un ligand axial $[ZnPc-1)(CN)]^{\bullet}$ indiquent que l'absorption à 500 nm est reliée au fait que le ligand axial induit une réduction de la symétrie du radical π-cationique et ils attribuent cette bande à une transition polarisée selon l'axe des *z* qui serait associé avec le trou dans la $2a_{1u}$.

Mots-clés : radicaux π de métallophtalocyanines, spectres optiques et de dichroîsme circulaire moléculaire (DCM), calculs selon la théorie de la fonctionnelle de densité (TFD), calculs selon la théorie de la fonctionnelle de la densité en fonction du temps (TFDFT).

[Traduit par la Rédaction]

Received 19 November 2008. Accepted 19 March 2009. Published on the NRC Research Press Web site at canjchem.nrc.ca on 15 June 2009.

A. Rosa[1] and G. Ricciardi. Dipartimento di Chimica, Università della Basilicata, Via N. Sauro 85, 85100 Potenza, Italy.

[1]Corresponding author (e-mail: angela.rosa@unibas.it).

Introduction

The electronic and spectroscopic properties of oxidized and reduced metallophthalocyanines (MPcs) have been studied since the middle of the past century because of their involvement in photocatalysis and photoinduced redox chemistry and because of their similarity with the tetrapyrrolic species (porphyrins, chlorins, bacteriochlorins) formed as principal intermediates in a number of key biological processes, such as the primary charge-separation reactions of photosynthesis and the catalytic processes of naturally occurring hemes in catalase and peroxidase enzymes.[2–13] Oxidized and reduced MPcs have also shown potential as building blocks of photovoltaic devices. For instance, incorporating MPcs into donor–acceptor systems together with fullerenes,[14] perylenes,[15] anthraquinones,[16] carbon nanotubes,[17] or related metallomacrocycles,[18] gives rise to long-lived and highly emissive charge-separated states. MPcs may be reduced or oxidized chemically or electrochemically to give a series of negative or positive ions. For MPcs with redox nonactive metal ions, such as Mg^{2+} and Zn^{2+}, electron addition or removal is confined to the π orbitals of the Pc macrocycle. Up to four electrons can be reversibly added to the lowest unoccupied molecular orbitals (LUMOs), the twofold degenerate e_g* MOs in the D_{4h} molecular structure of MPcs, and up to two can be reversibly removed from the highest occupied molecular orbital (HOMO) of the Pc ring, the a_{1u} MO. Although spectral data concerning oxidized and reduced metallophthalocyanines have been available in the literature since the early seventies, the first band assignment was provided only in 1985 by Minor et al.[6] These authors have proposed a general assignment of the bands in the electronic absorption spectra of the cationic and anionic species for a number of MPcs based on a semiquantitative theoretical approach. Subsequently, through a combination of band deconvolution analysis of solution absorption and magnetic circular dichroism (MCD) spectra and semiempirical intermediate neglect of differential overlap (INDO) calculations, Stillman and co-workers[7–11,13,19,20] were able to provide an assignment of the optical spectra of the $[MPc(-1)]^{\bullet+}$ (M = Zn, Mg), $[MgPc(-3)]^{\bullet-}$, and $[ZnPc(-(2 + n)]^{n-}$ (n = 1–4) species as well as a general band assignment scheme for both main group and transition metal phthalocyanine anions. A band assignment for $[MgPc(-3)]^{\bullet-}$ based on INDO calculations has also been reported by Cory et al.,[12] who have also investigated the effects of Jahn–Teller (JT) distortions on the computed excitation energies. Recently, band deconvolution analyses of the absorption and MCD spectra have been used in combination with INDO calculations to interpret the optical absorption spectra of the radical anion of an electron-deficient zinc phthalocyanine.[21] Although spectral band deconvolution analyses of the absorption and MCD spectra give indications on the energy, number, and magnetic moment of the excited states contributing to each spectral region, a full characterization of the excited states requires accurate quantum mechanical calculations. Time-dependent density functional theory (TDDFT) is one of the most popular approaches for the calculation of excitation energies in quantum chemistry due to its efficiency and accuracy. It has already been used to study electron spectra for a wide range of molecules, including metallotetrapyrroles.[22] Except for special cases, such as long-range charge-transfer (CT) transitions,[23–26] TDDFT shows great promise in studies of excited states and its accuracy can be compared with the much more expensive correlated ab initio methods. In the last few years TDDFT has also been successfully applied to the calculation of the excitation energies of open-shell transition metal compounds.[27–32] Worth mentioning in this context is the recent TDDFT study by Stillman and co-workers[33] of the optical spectra of the zinc phthalocyanine π-cation and π-anion radicals, $[ZnPc(-1)]^{\bullet+}$ and $[ZnPc(-3)]^{\bullet-}$. Using the hybrid B3LYP functional, these authors came to a satisfactory description of the optical spectra of these compounds, although the assignments of several key spectral features remained problematic.

In this work, the optical spectra of $[ZnPc(-1)]^{\bullet+}$ and $[ZnPc(-3)]^{\bullet-}$ are revisited using TDDFT methods in conjunction with the sophisticated, asymptotically correct non-hybrid functional, SAOP (statistical average of orbital potentials).[34,35]This functional has been shown to provide an accurate description of the UV–visible spectra of tetrapyrrole complexes,[22,31,36,37] and in several cases, including ZnPc, proved to perform better than B3LYP[22] and other hybrid functionals.[38]

Since the compounds studied in this work are charged, we have also investigated the effect of the solvent on both the ground-state geometries and the excitation energies.

Computational details

All calculations have been performed with the program package ADF (Amsterdam Density Functional).[39–42] The geometry optimizations were carried out using the local density approximation (LDA) functional of Vosko–Wilk–Nusair (VWN),[43] plus the generalized gradient approximation (GGA), employing Becke's[44] gradient approximation for exchange and Perdew's[45] for correlation (BP86). Because this work is concerned with open-shell complexes, the spin-unrestricted density functional theory (DFT) formalism was employed. The calculated structures were verified to represent local minima by calculation of harmonic frequencies. Spin contamination, monitored by the $\langle S^2 \rangle$ expectation value, was found to be negligible in all cases. Electronic vertical excitation energies and oscillator strengths were computed using spin-unrestricted TDDFT, as implemented in ADF.[30]

Ground- and excited-state property calculations at the optimized geometries were performed using the pure, asymptotically correct, SAOP functional.[34,35] In the DFT and TDDFT calculations the all electron ADF TZ2P basis set, which is an uncontracted triple-ζ STO basis set with two polarization functions, was used.

Since the compounds studied in this work are charged, we have also carried out the calculations in solution by using the conductor-like screening model (COSMO)[46,47] as implemented in ADF.[48] The effects on the predicted geometries proved, however, to be negligible. Therefore, the excited-state properties were computed at the gas phase optimized geometries. Concerning the effect of the solvent on the excited state energies, it should be pointed out that in the ADF implementation[48] the COSMO surface charges are not explicitly considered in the TDDFT procedure other than through their influence on the ground-state density. This effectively amounts to using the ground-state surface charges

for both the ground and excited states as a first approximation to simulate the solvent effect on the excitation energies. The high-frequency component of the solvent electric susceptibility accounting for changes of the electronic structure of the solvent upon electronic excitations within the solute is not considered.

Results and discussion

Molecular structure

The interpretation of the optical and MCD spectra of MPc π-cation radicals reported so far has been based on the assumption that these species retain the D_{4h} symmetry of the parent neutral complexes.[6–9,13,19,33] Indeed, it is commonly accepted that formation of MPc π-cation radicals invariably involves removal of one electron from the $1a_{1u}$ HOMO of the Pc ring resulting in a $^2A_{1u}$ ground state. The situation is different in MPs (P = porphyrin). MPs have two nearly degenerate highest occupied MOs of a_{1u} and a_{2u} symmetry in the D_{4h} molecular framework, and removal of one electron can lead to a π-cation radical with a $^2A_{1u}$ or $^2A_{2u}$ ground state.[49–52] Neither of these pure state species, however, is stable under the D_{4h} symmetry, and both radical cation types are subject to *pseudo*-JT distortion that leads to structures with lower symmetry and states with mixed A_{1u} and A_{2u} character.[52]

Our DFT/BP86 calculations on the zinc phthalocyanine π-cation radical fully confirm the previously assumed D_{4h} structure. Geometry optimization of $[ZnPc(-1)]^{\bullet+}$ under D_{4h} symmetry constraint indeed led to a stable minimum with a $^2A_{1u}$ electronic ground state. In an attempt to capture out-of-plane distortions, unconstrained geometry optimizations of ad hoc distorted structures were also performed. However, these invariably converged to the D_{4h} structure.

Table 1 collects the most relevant bond parameters calculated for $[ZnPc(-1)]^{\bullet+}$ and $[ZnPc(-3)]^{\bullet-}$ and, for the sake of comparison, those previously reported for the neutral complex, ZnPc.[36] The orientation of the molecules and the atom labeling are shown in Fig. 1. According to the data in Table 1, removal of one electron from the $2a_{1u}$ HOMO causes a shortening of the Zn–N_p bond. A recent theoretical analysis of the structural and electronic properties of metalloporphyrin π-cation radicals also points to a contraction of the M–N_p bond length upon formation of π-cation radicals of A_{1u} type.[52] The decrease of the macrocycle core size is accompanied by changes in other geometric parameters. The largest bond lengthening is observed for the C_o–C_m bond, due to a loss of π-bonding interaction between the C_o and C_β atoms. On the other hand, significant contraction is observed for the C_m–C_m, C_β–C_o, and C_β–C_β bonds, owing to the relief of π-antibonding interaction between the involved atoms. All these changes in the bond lengths reflect the nodal pattern of the $2a_{1u}$ MO (see the plot of this orbital in Fig. 2).

Concerning the MPc π-anion radicals, the addition of one electron to the e_g* LUMOs of the neutral MPc results in the twofold degenerate ^2E_g state. Therefore, a JT distortion will take place to remove this electronic degeneracy. According to the general theory,[53,54] JT-active coordinates are of either B_{1g} or B_{2g} symmetry resulting in D_{2h} configurations of a *rhombus* or *rectangle*, respectively. Geometry optimization of $[ZnPc(-3)]^{\bullet-}$ led to a *rectangular* D_{2h} structure (the elongation is along the *y* axis) with a $^2B_{3g}$ electronic ground state. The D_{2h} *rhombic* structure, which is only 0.5 kJ/mol less stable, has an imaginary frequency (350 cm^{-1}) of B_{1g} symmetry. A JT distorted rectangular D_{2h} structure was also predicted for $[MgPc(-3)]^{\bullet-}$ by Cory et al.,[12] using both ab initio and semiempirical (INDO/1) self-consistent field approaches.

The bond parameters obtained for the equilibrium rectangular D_{2h} structure of $[ZnPc(-3)]^{\bullet-}$ indicate that the Zn–N_p bond shortens along the *y* axis and elongates along the perpendicular axis (see Table 1). The changes of the other

Table 1. Symmetry unique bond lengths (Å) and bond angles (°) for ZnPc, $[ZnPc(-1)]^{\bullet+}$, and $[ZnPc(-3)]^{\bullet-}$.

	ZnPc[a]	$[ZnPc(-1)]^{\bullet+}$	$[ZnPc(-3)]^{\bullet-}$ [b]
Bond lengths (Å)			
Zn—N_p	2.006	1.995	2.002/2.103
C_α—N_p	1.377	1.375	1.383/1.377
C_α—C_β	1.463	1.464	1.467/1.444
C_β—C_β	1.415	1.411	1.412/1.426
C_α—N_b	1.335	1.332	1.320/1.352
C_β—C_o	1.397	1.391	1.395/1.402
C_o—C_m	1.399	1.402	1.397/1.392
C_m—C_m	1.410	1.401	1.407/1.417
Bond angles (°)			
C_α–N_p–C_α	109.9	109.4	110.0/109.9
C_α–N_b–C_α	124.5	124.5	124.2
C_β–C_α–N_p	108.4	108.7	108.1/108.4
C_β–C_β–C_α	106.7	106.6	106.9/106.7
C_β–C_o–C_m	117.9	117.6	118.2/118.5
C_o–C_m–C_m	121.1	121.2	121.0/120.9

[a]Data is from ref. 36.

[b]The data in the column refer to the indole moieties bisected by the *y*/*x* axes.

Fig. 1. Atom labeling scheme for ZnPc. The elongation for the π-anion radical is along the *y* axis.

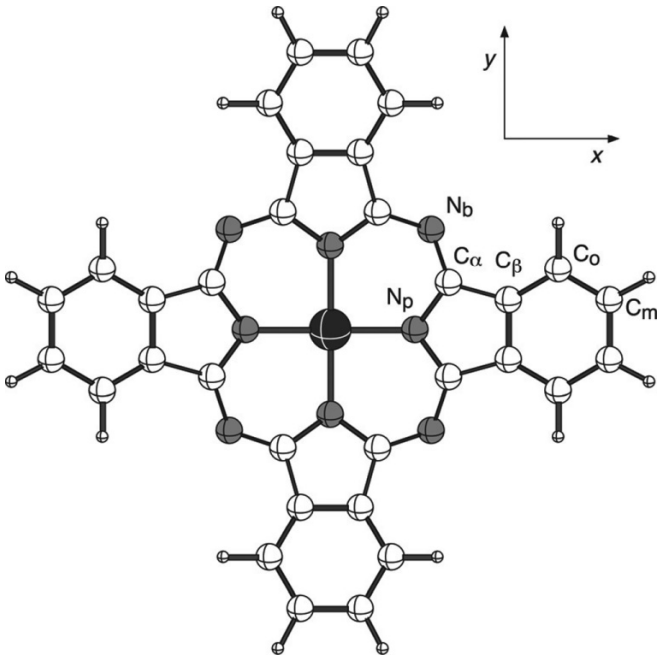

Fig. 2. DFT/SAOP ground-state molecular-orbital description of ZnPc. Double occupancy is indicated for the HOMO only. All lower lying levels are also doubly occupied. The Gouterman's four orbitals are indicated with red lines. For the sake of clarity, the N lone pairs of b_{1g}, b_{2g}, and e_u symmetry are reported in a separate column.

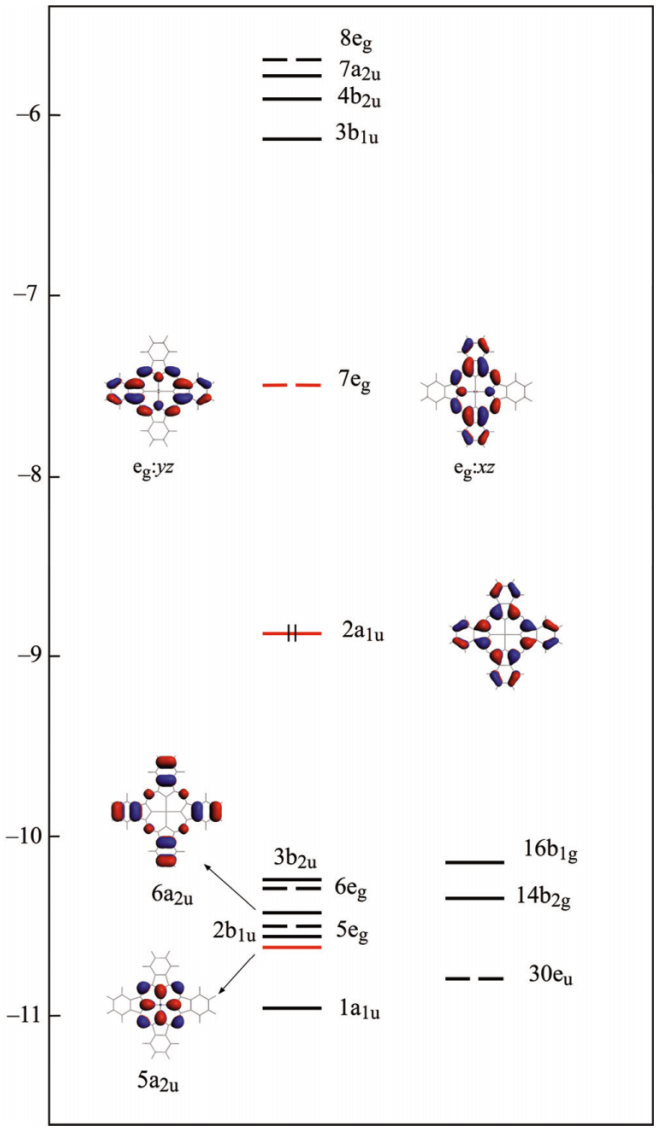

bond parameters are consistent with the nodal pattern of the *yz* component of the $7e_g$ MOs (see plots in Fig. 2), the b_{3g} SOMO (singly occupied MO) in the distorted D_{2h} structure. For instance, the C_α–N_p bond of the pyrroles bisected by the *y* axis elongates significantly on account of the increased π-antibonding interaction between the C_α and N_p atoms. In contrast, the C_α–N_p bond of the pyrroles bisected by the *x* axis remains unperturbed, which is consistent with the b_{3g} having no amplitude on the N_p atoms lying on the *x* axis.

Electronic structure

Before dealing with the excited states of $[ZnPc(-1)]^{\bullet+}$ and $[ZnPc(-3)]^{\bullet-}$, we analyze the ground-state electronic structure of these species. Our analysis is based on the Kohn–Sham (KS) MOs of DFT. The KS orbital model is very suitable for the interpretation of the electronic structure and elucidation of the character of the excitations.[55] The use of KS orbitals affords a direct connection with the linear combination of atomic orbitals (LCAO)–MO treatments based on semiempirical or Hartree–Fock (HF) orbitals that have been used so far to interpret the main spectral features of oxidized and reduced MPcs,[6,11–13,19] while having at the same time the advantage of the high accuracy of the TDDFT treatment of the excitation energies.

To discuss the ground-state electronic structure of $[ZnPc(-1)]^{\bullet+}$ and $[ZnPc(-3)]^{\bullet-}$, it is useful to take the neutral complex as the reference point. Since an extensive DFT analysis of the electronic structure of ZnPc has been previously reported,[36] only the most salient features are recalled here. The highest occupied and lowest unoccupied levels of ZnPc are shown in Fig. 2. The Gouterman MOs, i.e., the occupied $5a_{2u}$ and $2a_{1u}$ (HOMO) and the unoccupied $7e_g$ (LUMOs), are indicated with red lines. For the sake of clarity, the highest N lone pair levels are given in the right column of the level scheme of Fig. 2. Of these in-plane levels, the $16b_{1g}$ is a N_p lone pair MO, which is pushed up by antibonding with the Zn-$3d_{x^2-y^2}$ and ends up just above the set of the occupied π orbitals, but is still well below (~1.1 eV) the HOMO. The $16b_{1g}$ is actually the HOMO-1 of the molecule. The lower lying N lone pair levels shown in Fig. 2, the $14b_{2g}$ and $30e_u$, are basically N_b lone pair MOs. Of the occupied π levels, the two MOs of A_{2u} symmetry, the $6a_{2u}$ and $5a_{2u}$, have received special attention in view of their relevance to the interpretation of the absorption spectrum of ZnPc.[36] As it will be shown herein, they also play an important role in the absorption spectra of the zinc phthalocyanine π-cation and π-anion radicals. According to the level scheme of Fig. 2, quite a large energy gap separates the LUMOs from a set of closely spaced π* levels, which have large amplitude on the benzo rings. These MOs have been shown to be involved in the excitations accounting for the UV features (N, L, and C bands) of the optical spectra of ZnPc.[36]

As mentioned above, one electron oxidation of ZnPc affords a π-cation radical having a D_{4h} molecular structure and a $^2A_{1u}$ electronic ground state, with the unpaired electron residing on the $2a_{1u}\uparrow$. Consistent with the nature of the SOMO, the spin density is almost entirely localized in the p_z orbitals of the carbon atoms of the indole moieties, as inferred from Fig. 3*a* where a plot of the spin density distribution in $[ZnPc(-1)]^{\bullet+}$ is displayed. The plot of Fig. 3*a* also shows that, besides the spin density coming from the SOMO, there exists some p_z spin density on the N_p and N_b atoms. This negative spin density at the nitrogen atoms is due to a polarization effect produced by the SOMO on the double occupied π MOs having amplitude on N_p and (or) N_b atoms. When comparing the level schemes of Fig. 2 and Fig. 4 it is apparent that the outstanding difference between ZnPc and $[ZnPc(-1)]^{\bullet+}$ is the generalized, although not uniform, stabilization of occupied and virtual levels. The downward shift of the spin orbitals with N lone pair character, i.e., the $16b_{1g}$, $14b_{2g}$, and $30e_u$, is particularly large so that the ordering of the occupied orbitals is in the π-cation radical, slightly altered relative to the neutral complex. The splitting between the spin-up and spin-down levels is in general quite modest, which is in line with the delocalized character of these spin orbitals.

Fig. 3. Spin density distribution in (*a*) $[ZnPc(-1)]^{\bullet+}$ and (*b*) $[ZnPc(-3)]^{\bullet-}$.

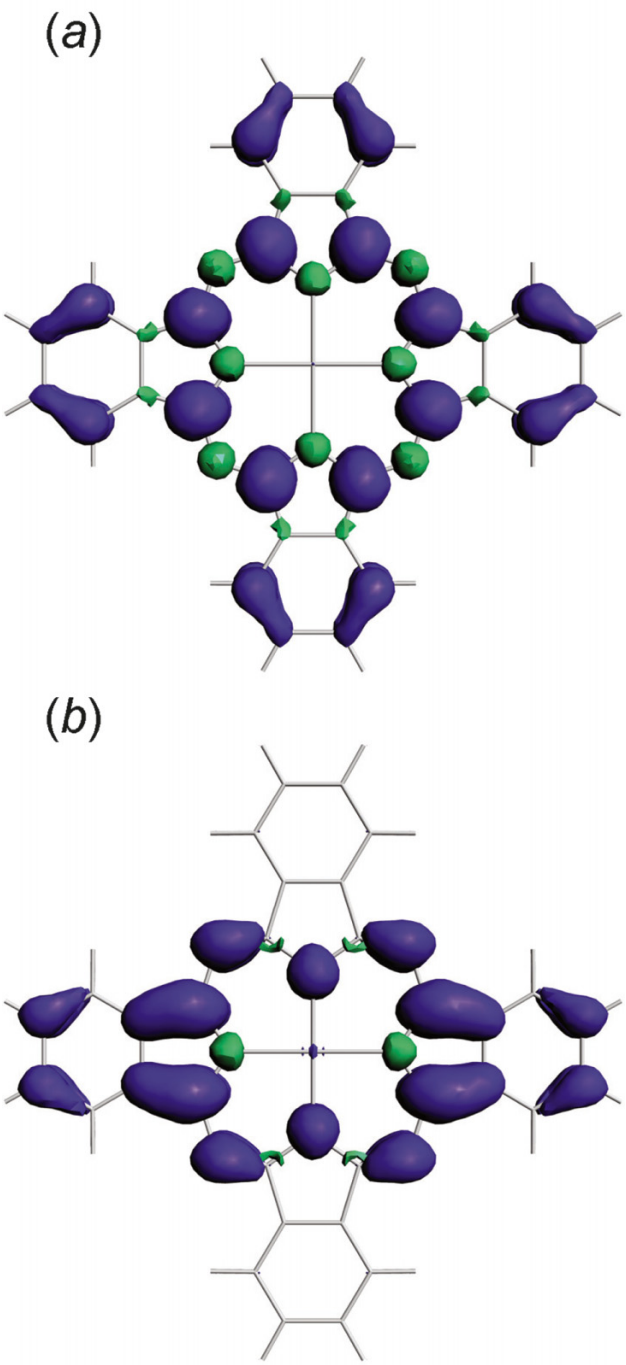

Coming now to the π-anion radical, this species has a $^2B_{3g}$ electronic ground state in the equilibrium JT distorted rectangular D_{2h} structure. The ground-state spin density distribution in $[ZnPc(-3)]^{\bullet-}$ (see Fig. 3*b*) reflects the atomic orbital composition of the SOMO, the $7b_{3g}\uparrow$, although a small amount (–0.030) of negative spin density resides on the p_z orbitals of the N_p atoms lying on the *x* axis. An energy level scheme showing the highest-occupied and lowest-unoccupied KS spin orbitals of $[ZnPc(-3)]^{\bullet-}$ is displayed in Fig. 5. When comparing the level schemes of $[ZnPc(-3)]^{\bullet-}$ and ZnPc, it is apparent that the negative charge induces a generalized destabilization of the levels. The JT splitting of the e_g and e_u levels is small, particularly in the case of the $7e_g$. The spin-down components of the JT split $7b_{3g}$ and $7b_{2g}$ MOs are actually nearly degenerate (see the level scheme of Fig. 5), with the splitting of the spin-up components being merely related to occupation of the $7b_{3g}\uparrow$.

Fig. 4. Energy-level scheme for $[ZnPc(-1)]^{\bullet+}$ obtained from spin-unrestricted DFT/SAOP calculations.

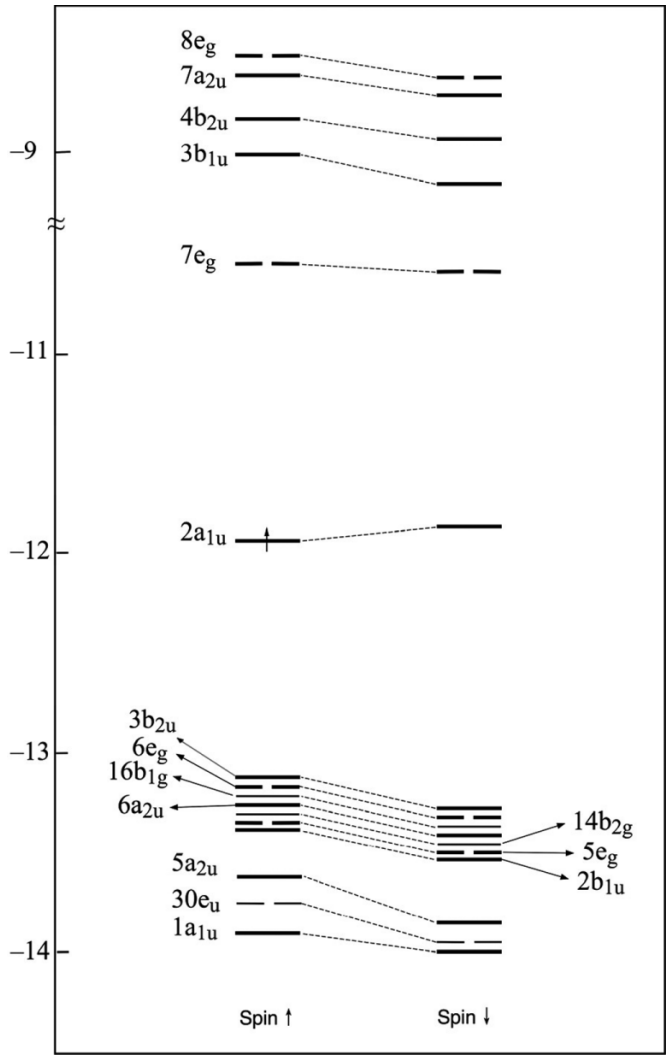

Excited states and optical spectra

[ZnPc(–1)]$^{\bullet+}$

Figure 6 displays the absorption and MCD spectra of $[ZnPc(-1)]^{\bullet+}$ recorded after controlled potential oxidation of ZnPc(Im) (Im = imidazole) dissolved in dichloromethane solution at room temperature.[8] Figure 6 also shows the absorption and MCD spectra of ZnPc(Im) before controlled coulometry oxidation. The optical spectrum of the neutral complex is characterized by an intense Q band at ~670 nm showing vibrational structure, and by a broad envelope peaking at ~330 nm followed by a weaker feature at ~270 nm, denoted as B and N bands, respectively. Band envelope deconvolution analyses of the room temperature solution absorption and MCD spectra of ZnPc(L) complexes, where L is

Fig. 5. Energy-level scheme for $[ZnPc(-3)]^{\bullet-}$ obtained from spin-unrestricted DFT/SAOP calculations.

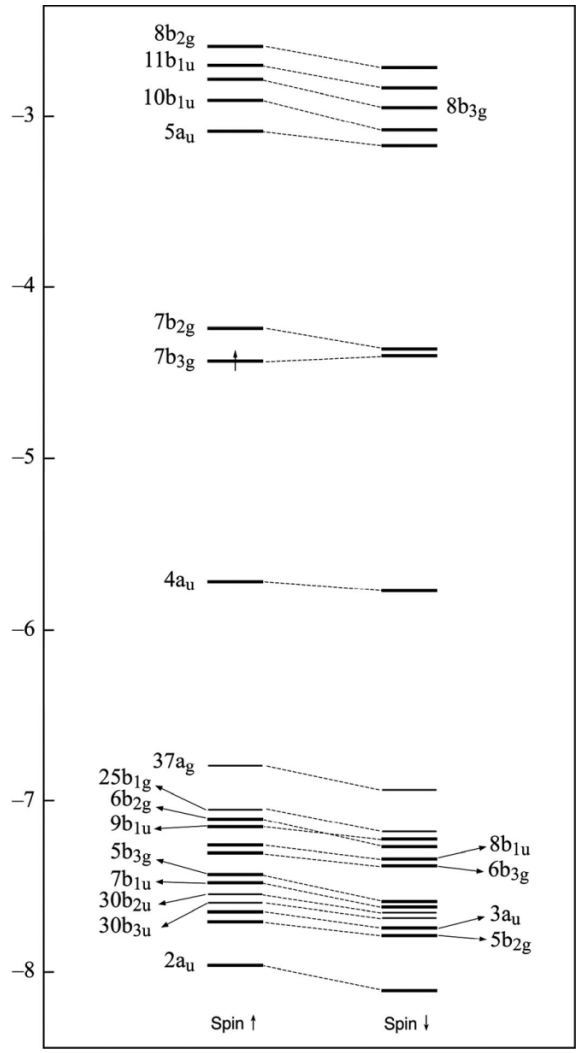

Fig. 6. Absorption and MCD spectra of ZnPc (dashed lines) and $[ZnPc(-1)]^{\bullet+}$ (solid lines) in dichloromethane. Reprinted with permission from ref. 8.

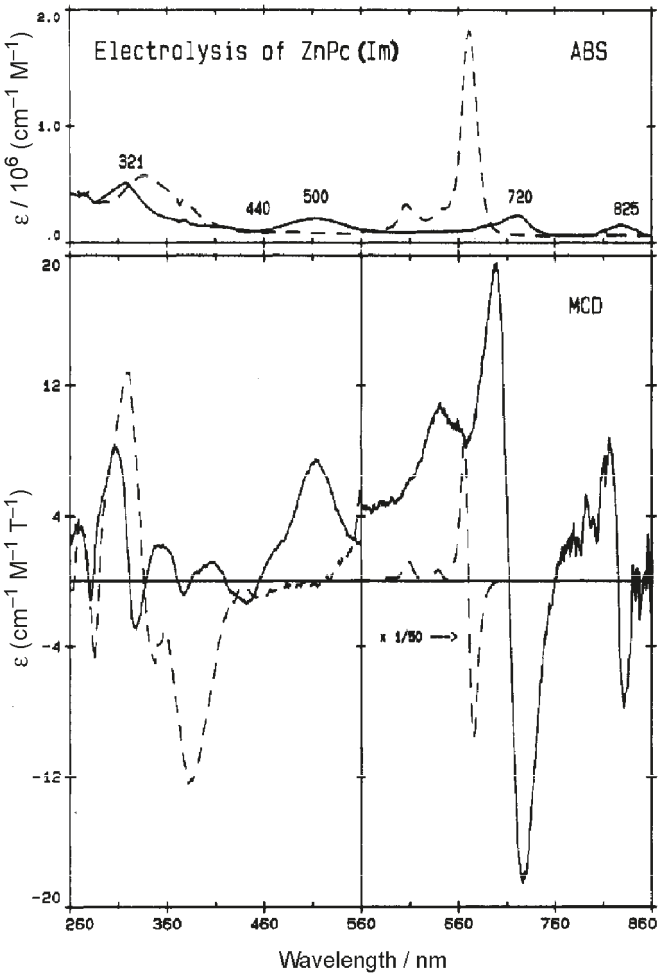

an axially coordinate cyanide, imidazole, or pyridine ligand, identified, within the B band envelope, at least two components associated to MCD *A* terms.[7] In the case of zinc phthalocyanine with cyanide, the two components of the B band, denoted as B1 and B2, were located at 386 and 331 nm, respectively. When comparing the absorption spectrum of the neutral complex with that of the π-cation radical in Fig. 6, it is apparent that upon oxidation dramatic spectral changes occur in the visible and near-IR region. The intense Q band of the neutral complex and its vibrational progression disappear, while broad and weaker bands appear at around 500, 720, and 825 nm. Less dramatic changes occur in the UV region ($\lambda < 400$ nm). These mainly consist in a blue shift and weakening of the B band envelope. Spectral deconvolution analyses of the absorption and MCD spectra of $[ZnPc(-1)]^{\bullet+}$ assigned the bands at 825 and 720 nm to transitions to ^2E_g (*x*/*y* polarized) excited states, since they are accounted for by MCD *A* terms.[7,8] More recent studies by Stillman and coworkers[33] have demonstrated that the 720 nm band arises from an electron paramagnetic resonance (EPR) silent dimeric species in equilibrium with the monomer. As for the broad band at 500 nm, it was assigned to a transition of a nondegenerate excited state since it is an intense *z*-polarized Faraday *B* term.[7] The absorption spectrum in Fig. 6 clearly indicates that the 440–250 nm region comprises several bands. Actually, a sum of 11 bands was used by Stillman and co-workers[7] to fill most of the intensity in both the absorption and MCD spectra. Of these, the bands at 424, 370, 317, and 278 nm were associated to MCD *A* terms.

The excitation energies and oscillator strengths calculated for the optically allowed ^2E_g and $^2A_{2g}$ excited states of $[ZnPc(-1)]^{\bullet+}$ up to 4.0 eV are gathered in Table 2. The TDDFT calculations were performed both in the gas phase and dichloromethane solution (the solvent used to record the absorption and MCD spectra) using the gas-phase optimized geometry of the complex. The theoretical results in the gas phase will be considered first, and then the solvent effects will be examined. As inferred from the data in Table 2, only three doubly degenerate excited states are predicted in the 860–560 nm spectral region. Of these, the 2^2E_g and 3^2E_g computed at 1.50 eV (827 nm) and 1.82 eV (681 nm), respectively, consist of the same one-electron transitions, the $2a_{1u}\uparrow \rightarrow 7e_g\uparrow$ and the $5e_g\downarrow \rightarrow 2a_{1u}\downarrow$, with approximately reversed weights. The large transition dipoles of

Table 2. Vertical excitation energies (E_{va}, eV/nm) and oscillator strengths (f) computed for the optically allowed ^2E_g and $^2A_{2g}$ excited states of $[ZnPc(-1)]^{\bullet+}$. The major one-electron transitions contributing to the SAOP solution vectors are also given.

		Gas phase		CH_2Cl_2		
State[a]	Composition[a] (%)	E	f	E	f	Exp.[b]
1^2E_g	$6e_g\downarrow \rightarrow 2a_{1u}\downarrow$ (92)	1.47/843	0.002	1.47/843	0.003	
2^2E_g	$2a_{1u}\uparrow \rightarrow 7e_g\uparrow$ (56); $5e_g\downarrow \rightarrow 2a_{1u}\downarrow$ (35)	1.50/827	0.014	1.54/807	0.030	825
3^2E_g	$5e_g\downarrow \rightarrow 2a_{1u}\downarrow$ (61); $2a_{1u}\uparrow \rightarrow 7e_g\uparrow$ (33)	1.82/681	0.583	1.87/664	0.590	
4^2E_g	$3b_{2u}\uparrow \rightarrow 7e_g\uparrow$ (82); $3b_{2u}\downarrow \rightarrow 7e_g\downarrow$ (15)	2.56/485	0.003	2.58/481	0.003	
5^2E_g	$6a_{2u}\uparrow \rightarrow 7e_g\uparrow$ (71); $6a_{2u}\downarrow \rightarrow 7e_g\downarrow$ (19)	2.70/459	0.030	2.76/449	0.032	
6^2E_g	$3b_{2u}\downarrow \rightarrow 7e_g\downarrow$ (66); $2b_{1u}\uparrow \rightarrow 7e_g\uparrow$ (18)	2.76/449	0.001	2.78/446	0.006	
7^2E_g	$2b_{1u}\uparrow \rightarrow 7e_g\uparrow$ (48); $2b_{1u}\downarrow \rightarrow 7e_g\downarrow$ (32); $3b_{2u}\downarrow \rightarrow 7e_g\downarrow$ (15)	2.77/448	0.024	2.84/437	0.015	
8^2E_g	$6a_{2u}\downarrow \rightarrow 7e_g\downarrow$ (50); $2b_{1u}\downarrow \rightarrow 7e_g\downarrow$ (23); $6a_{2u}\uparrow \rightarrow 7e_g\uparrow$ (11)	2.90/428	0.003	2.94/422	0.006	
9^2E_g	$2b_{1u}\downarrow \rightarrow 7e_g\downarrow$ (41); $6a_{2u}\downarrow \rightarrow 7e_g\downarrow$ (19); $2b_{1u}\uparrow \rightarrow 7e_g\uparrow$ (19)	2.97/417	0.475	2.97/417	0.019	424
10^2E_g	$5a_{2u}\uparrow \rightarrow 7e_g\uparrow$ (58); $5a_{2u}\downarrow \rightarrow 7e_g\downarrow$ (33)	3.05/407	0.076	3.03/409	0.404	
1^2A_{2g}	$30e_u\uparrow \rightarrow 7e_g\uparrow$ (82); $30e_u\downarrow \rightarrow 7e_g\downarrow$ (18)	3.17/391	0.001	3.24/383	0.001	
11^2E_g	$4e_g\downarrow \rightarrow 2a_{1u}\downarrow$ (48); $1a_{1u}\uparrow \rightarrow 7e_g\uparrow$ (35)	3.24/383	0.002	3.23/384	0.001	
12^2E_g	$1a_{1u}\downarrow \rightarrow 7e_g\downarrow$ (39); $4e_g\downarrow \rightarrow 2a_{1u}\downarrow$ (27); $1a_{1u}\uparrow \rightarrow 7e_g\uparrow$ (23)	3.31/375	0.001	3.35/370	0.006	
2^2A_{2g}	$30e_u\downarrow \rightarrow 7e_g\downarrow$ (82); $30e_u\uparrow \rightarrow 7e_g\uparrow$ (18)	3.38/367	0.001	3.44/360	0.002	
13^2E_g	$1a_{1u}\downarrow \rightarrow 7e_g\downarrow$ (36); $2a_{1u}\uparrow \rightarrow 8e_g\uparrow$ (19); $1a_{1u}\uparrow \rightarrow 7e_g\uparrow$ (19); $5a_{2u}\downarrow \rightarrow 7e_g\downarrow$ (16)	3.42/362	0.103	3.41/364	0.028	370
14^2E_g	$2a_{1u}\uparrow \rightarrow 8e_g\uparrow$ (74)	3.44/360	0.137	3.45/359	0.376	
15^2E_g	$5a_{2u}\downarrow \rightarrow 7e_g\downarrow$ (25); $5a_{2u}\uparrow \rightarrow 7e_g\uparrow$ (16); $4e_g\downarrow \rightarrow 2a_{1u}\downarrow$ (15); $1a_{1u}\uparrow \rightarrow 7e_g\uparrow$ (11); $1a_{1u}\downarrow \rightarrow 7e_g\downarrow$ (10)	3.83/324	1.095	3.82/324	1.106	317

Note: Only states with $f \geq 0.001$ are reported.

[a]The numbering and composition of the excited states refer to TDDFT calculations in the gas phase.

[b]Band maxima corresponding to positive MCD *A* terms obtained trough deconvolution analyses of the absorption and MCD spectra of $[ZnPc(-1)]^{\bullet+}$ in CH_2Cl_2, from refs. 7 and 33.

these transitions reinforce in the 3^2E_g and cancel in the 2^2E_g to the result that the former is by far more intense than the latter. It is evident from the data in Table 2 that neither of these excited states properly account for the energy and intensity of the band observed at 825 nm. The discrepancy between theory and experiment can be traced to the well-known failure of TDDFT to correctly calculate the energy of CT transitions.[23–26] The description of the Q-band region appears to be complicated by the presence of spurious non-Gouterman transitions out of MOs mostly localized on the benzo rings, the $5e_g$, to the highly delocalized Gouterman SOMO, the $2a_{1u}$. As these transitions have significant CT character, they are calculated at an energy that is somewhat too low and accidentally mix with the Gouterman $2a_{1u} \rightarrow 7e_g$ transitions. One way of counterbalancing this observed shortcoming of TDDFT is the admixture of a portion of "exact" HF exchange (hybrid-GGA functionals). The optimum percentage of HF exchange may vary from molecule to molecule and state to state.[56,57] However, the more exact exchange is included in the treatment, the less electron correlation is considered, again leading to wrong excitation energies. It is instructive in this respect to look at the TDDFT/B3LYP/6-31G(d) results by Stillman and co-workers[33] showing that the introduction of a 20% HF exchange is sufficient to avoid the mixing between the $2a_{1u}\uparrow \rightarrow 7e_g\uparrow$ and the $5e_g\downarrow \rightarrow 2a_{1u}\downarrow$ transitions, but at the expense of the accuracy. In the Q-band region they indeed compute only an intense ($f = 0.23$) ^2E_g excited state, which is a nearly pure (93%) $2a_{1u} \rightarrow 7e_g$ state. The calculated energy is, however, far too low compared to the experiment (950 vs 825 nm).

As for the lowest ^2E_g state, the 1^2E_g, it is a nearly pure $6e_g\downarrow \rightarrow 2a_{1u}\downarrow \pi \rightarrow \pi$ state. This state, computed at 843 nm and with a very low oscillator strength ($f = 0.002$), is likely to contribute to the broadening of the 825 nm band.

As inferred from the calculated excitation energies, a large energy gap separates the 3^2E_g from the next excited state, the 4^2E_g, which is computed at 2.56 eV (485 nm). Thus, TDDFT results confirm the vibronic origin of the weak and broad absorption to the blue of the band at 825 nm, as suggested by Stillman and co-workers.[7] They do not account, however, for the broad absorption near 500 nm. According to the absorption and MCD deconvolution analysis by Stillman and co-workers,[7,33] this band should be accounted for by a nondegenerate, z-polarized $^2A_{2g}$ excited state. However, TDDFT/SAOP calculations predict the lowest $^2A_{2g}$ state at a much higher energy, 3.17 eV (391 nm). Inclusion of the solvent effects (vide infra) does not reconcile theory and experiment.

In the region of the observed spectrum between 480 and 300 nm, TDDFT/SAOP calculations predict 12 doubly degenerate excited states, four of which, the 9^2E_g, 13^2E_g, 14^2E_g, and 15^2E_g, with sufficient intensity to be easily observed. Taking into account the near degeneracy of the 13^2E_g and 14^2E_g states, there is an excellent correspondence between the energies of the three bands of the deconvolution of Stillman and co-workers[7] and the calculated excitation energies. The bands located by the deconvolution analysis at 424, 370, and 317 nm are indeed nicely accounted for by the 9^2E_g, the two nearly degenerate 13 and 14^2E_g, and the 15^2E_g states, respectively. Comparing the present TDDFT/

Table 3. Vertical excitation energies (E_{va}, eV/nm) and oscillator strengths (f) computed for the optically allowed $^2B_{1u}$ and ^2A_u excited states of $[ZnPc(-3)]^{\bullet-}$. The major one-electron transitions contributing to the SAOP solution vectors are also given.

		Gas phase		DMF		
State[a]	Composition[a] (%)	E	f	E	f	Exp.[b]
1^2B_{1u}	$4a_u\downarrow \rightarrow 7b_{2g}\downarrow$ (58); $4a_u\uparrow \rightarrow 7b_{2g}\uparrow$ (39)	1.31/948	0.001	1.31/948	0.001	956
1^2A_u	$7b_{3g}\uparrow \rightarrow 5a_u\uparrow$ (57); $4a_u\downarrow \rightarrow 7b_{3g}\downarrow$ (43)	1.32/939	0.001	1.34/928	0.001	925
2^2B_{1u}	$7b_{3g}\uparrow \rightarrow 10b_{1u}\uparrow$ (87); $4a_u\uparrow \rightarrow 7b_{2g}\uparrow$ (12)	1.51/821	0.001	1.68/737	0.014	
3^2B_{1u}	$7b_{3g}\uparrow \rightarrow 11b_{1u}\uparrow$ (93)	1.72/723	0.010	1.88/661	0.007	
2^2A_u	$4a_u\downarrow \rightarrow 7b_{3g}\downarrow$ (53); $7b_{3g}\uparrow \rightarrow 5a_u\uparrow$ (39)	1.86/667	0.361	1.90/654	0.387	635
4^2B_{1u}	$4a_u\uparrow \rightarrow 7b_{2g}\uparrow$ (41); $4a_u\downarrow \rightarrow 7b_{2g}\downarrow$ (35)	2.06/602	0.442	2.09/594	0.425	570
4^2A_u	$4a_u\downarrow \rightarrow 8b_{3g}\downarrow$ (79); $4a_u\uparrow \rightarrow 8b_{3g}\uparrow$ (18)	2.81/441	0.001	2.87/432	0.030	
8^2A_u	$7b_{3g}\uparrow \rightarrow 6a_u\uparrow$ (39); $4a_u\uparrow \rightarrow 8b_{3g}\uparrow$ (20); $9b_{1u}\uparrow \rightarrow 7b_{2g}\uparrow$ (10); $4a_u\downarrow \rightarrow 8b_{3g}\downarrow$ (10)	3.04/408	0.116	3.12/397	0.001	
7^2B_{1u}	$8b_{1u}\downarrow \rightarrow 7b_{3g}\downarrow$ (72)	3.11/399	0.168	3.08/402	0.001	
8^2B_{1u}	$4a_u\uparrow \rightarrow 8b_{2g}\uparrow$ (59); $4a_u\downarrow \rightarrow 8b_{2g}\downarrow$ (27)	3.18/390	0.010	3.14/395	0.036	432
9^2B_{1u}	$7b_{1u}\downarrow \rightarrow 7b_{3g}\downarrow$ (87)	3.23/384	0.059	3.17/391	0.162	
10^2A_u	$7b_{1u}\uparrow \rightarrow 7b_{2g}\uparrow$ (43); $7b_{1u}\downarrow \rightarrow 7b_{2g}\downarrow$ (33)	3.29/377	0.005	3.17/391	0.027	
10^2B_{1u}	$3a_u\uparrow \rightarrow 7b_{2g}\uparrow$ (55); $3a_u\downarrow \rightarrow 7b_{2g}\downarrow$ (37)	3.24/383	0.007	3.23/384	0.070	
11^2A_u	$3a_u\downarrow \rightarrow 7b_{3g}\downarrow$ (87)	3.30/376	0.091	3.26/380	0.114	
11^2B_{1u}	$3a_u\downarrow \rightarrow 7b_{2g}\downarrow$ (42); $3a_u\uparrow \rightarrow 7b_{2g}\uparrow$ (40)	3.38/367	0.219	3.34/371	0.214	383
12^2A_u	$8b_{1u}\uparrow \rightarrow 7b_{2g}\uparrow$ (35); $8b_{1u}\downarrow \rightarrow 7b_{2g}\downarrow$ (20); $7b_{3g}\uparrow \rightarrow 7a_u\uparrow$ (16); $7b_{1u}\downarrow \rightarrow 7b_{2g}\downarrow$ (11)	3.46/358	0.564	3.51/354	0.471	364
14^2A_u	$7b_{3g}\uparrow \rightarrow 7a_u\uparrow$ (52); $2a_u\downarrow \rightarrow 7b_{3g}\downarrow$ (20)	3.88/320	0.286	3.96/313	0.267	319
15^2B_{1u}	$7b_{3g}\uparrow \rightarrow 12b_{1u}\uparrow$ (38); $4a_u\downarrow \rightarrow 9b_{2g}\downarrow$ (19); $2a_u\downarrow \rightarrow 7b_{2g}\downarrow$ (14)	3.94/315	0.232	3.99/311	0.399	

Note: Only states with $f \geq 0.001$ are reported.

[a]The numbering and composition of the excited states refer to TDDFT calculations in the gas phase.

[b]Band maxima observed in the absorption spectrum of $[ZnPc(-3)]^{\bullet-}$ in DMF at 77 K, from ref. 11.

SAOP results for $[ZnPc(-1)]^{\bullet+}$ with the previous ones for ZnPc[36] we note that the 9^2E_g has approximately the same energy, intensity, and composition as the excited state accounting for the B1 band of ZnPc, the 4^1E_u (see Table 3 in ref. 36). The same holds true for the 15^2E_g state of the π-cation radical and the excited state accounting for the B2 band in ZnPc, the 7^1E_u (see Table 3 in ref. 36). Thus, the bands located at 424 and 417 nm in the absorption and MCD spectra of $[ZnPc(-1)]^{\bullet+}$ correspond to the B1 and B2 bands of ZnPc, respectively. The B1 and B2 bands are located by TDDFT/B3LYP/6-31G(d) calculations[33] at a much higher energy, 321 and 295 nm, respectively.

The TDDFT/SAOP results in dichloromethane show that the vertical absorption energies of the excited states are scarcely (if at all) affected by solvation. As previously pointed out (see Computational details section), since the COSMO surface charges are not explicitly considered in the TDDFT procedure other than through their influence on the ground-state density, changes in vertical excitation energies upon solvation only reflect changes in the energies of the ground-state MOs. In dichloromethane, both the occupied and virtual spin orbitals are destabilized by 2.2–2.4 eV. The destabilization of the levels is not uniform, however, which causes small changes in the composition, excitation energies, and oscillator strengths of the excited states, the most relevant example being the inversion of the 13^2E_g and 14^2E_g excited states. As for the assignment of the band at 500 nm to the lowest $^2A_{2g}$ state, as suggested by Stillman and co-workers,[7] on the basis of the absorption and MCD spectra deconvolution analyses, the disagreement between theory and experiment about the location of this state still holds when solvent effects are taken into account. As a matter of fact, the lowest $^2A_{2g}$ state is calculated in dichloromethane at an even higher energy than in the gas phase (383 nm vs 391 nm), with the discrepancy between theory and experiment amounting to more than 0.7 eV (117 nm). Such a large error is unlikely, however, for TDDFT excitation energies on tetrapyrrole complexes.[22] Rather, this discrepancy might be related to the fact that the calculations have been performed for the bare $[ZnPc(-1)]^{\bullet+}$ complex, while the absorption and MCD spectra have been recorded for the axially ligated $[ZnPc(-1)L]^{\bullet+}$ (L = CN^-, Im, py) species. Although the axial ligand is not expected to significantly alter the main features of the spectra –the fitting of the absorption and MCD spectra was successfully obtained assuming a D_{4h} symmetry for the π-cation radical[7–9]– the symmetry lowering following axial ligation might allow for additional transitions, which are forbidden in the D_{4h} symmetry of the unligated π-cation radical. To verify if this is indeed the case, we have examined the ground and excited states of an axially ligated π-cation radical, $[ZnPc(-1)(CN)]^{\bullet}$. According to DFT/BP86 calculations, in $[ZnPc(-1)(CN)]^{\bullet}$ the metal center is C bound, the N bound species being 29.2 kJ/mol less stable. The complex shows a saucer-like structure of C_{4v} symmetry in the $^2A_2$ electronic ground state (see Fig. 7). As indicated by the short (1.980 Å) Zn–C(CN) distance, the interaction with the axial ligand is quite strong. Accordingly, there is a considerable displacement (0.767 Å) of the metal out of the $(N_p)_4$ plane and a significant elongation of the Zn–N_p distance relative to the unligated complex (2.125 Å vs 1.995 Å).

Fig. 7. DFT-calculated structure of [ZnPc(–1)(CN)]•. Selected bond distances (Å) are also shown.

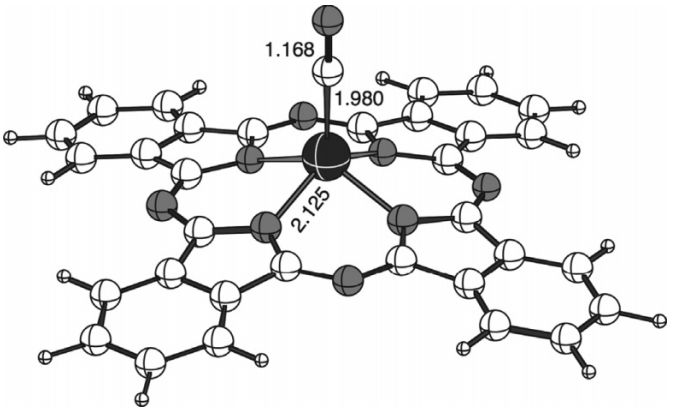

Fig. 8. Absorption and MCD spectra of [ZnPc(–3)]•– recorded in DMF, at cryogenic temperatures. Reprinted with permission from ref. 11.

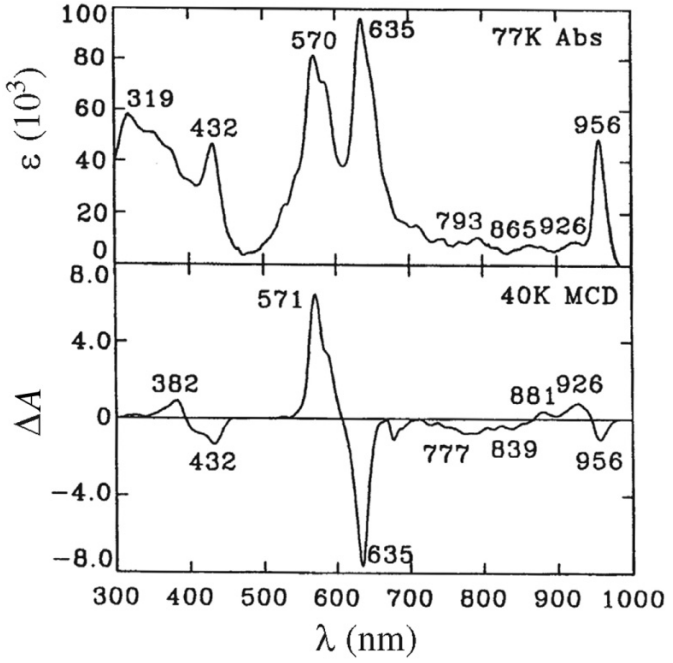

TDDFT/SAOP results in dichloromethane for the [ZnPc(–1)(CN)]• species show that axial coordination of CN^- has, as expected, very little impact on the excitation energies and oscillator strengths of the doubly degenerate ^2E excited states accounting for the salient spectral features. In the region where deconvolution analyses of the absorption and MCD spectra locate a nondegenerate transition,[7] TDDFT calculations now predict a nondegenerate excited state, the 1^2A_2, that is a plausible candidate for assignment to the broad feature at ~500 nm. This state computed at 2.25 eV (550 nm) and with oscillator strength of 0.001, is largely (96%) described by the *z*-polarized $12a_2\downarrow \rightarrow 13a_2\downarrow$ transition, which corresponds in the D_{4h} symmetry of the bare [ZnPc(–1)]•+ complex to the optically forbidden $1a_{1u}\downarrow \rightarrow 2a_{1u}\downarrow$ transition. What we find suggests that the feature appearing in the solution absorption spectra of [MPc(–1)L]•+ (M = Mg, Zn; L = CN^-, Im, py) species at ~500 originates from the axial ligation induced symmetry lowering. Notably, TDDFT calculations assign this band to a transition associated with the hole in the $2a_{1u}$, which is in line with this feature being observed in the spectra of virtually all phthalocyanine π-cation radicals,[6] but not in those of the parent neutral complexes. TDDFT/B3LYP/6-31G(d) calculations by Stillman and co-workers[33] for the chloride anion ligated π-cation radical, [ZnPc(–1)Cl]•, also locate a very weak π → π *z*-polarized excited state in the region of the 500 nm band, at 589 nm.

[ZnPc(–3)]•–

Figure 8 displays the absorption and MCD spectra of [ZnPc(–3)]•– recorded in DMF at cryogenic temperatures.[11] The absorption spectrum of the π-anion radical shows three prominent clusters of bands, centered on 960, 600, and 400 nm. Spectral deconvolution analyses of the MCD and absorption spectra of [ZnPc(–3)]•– recorded at cryogenic temperatures identified three distinct sets of coupled, oppositely signed *B* terms observed in the MCD spectrum of the complex, at 958/925, 635/569, and 434/383 nm.[11] Mack and Stillman[11] observed that the alternating – and + signs of the *B* terms (pseudo *A* terms[58,59]) that comprise the MCD envelope in the three spectral regions of the anion radical are the same as the sign alternation of the *A* terms in the parent neutral complex. These authors also pointed out that this behavior is typical of *x*- and *y*-polarized transitions to close lying, coupled excited states, and the MCD spectral features observed for [ZnPc(–3)]•–, especially the band at 958 nm, are characteristic marker bands for ring-reduced phthalocyanine radical anions.[11]

To provide an assignment of the main spectral features of [ZnPc(–3)]•–, we have computed the excitation energies and oscillator strengths of the dipole and spin allowed ^2A_u, $^2B_{1u}$, and $^2B_{3u}$ excited states of the complex, in both the gas phase and DMF solution (DMF is the solvent used to record the absorption and MCD spectra of the π-anion radical). With our choice of coordinates these states are *x*, *y*, and *z* allowed, respectively. The TDDFT results are reported in Table 3. The excited states of B_{3u} symmetry are not listed in Table 3 since they have oscillator strengths smaller than 0.001 and are therefore not relevant for the interpretation of the main spectral features. According to the TDDFT results, the lowest dipole allowed excited state is the *y*-polarized 1^2B_{1u}, computed in both the gas phase and DMF solution at 1.31 eV (948 nm) and with an oscillator strength of 0.001. The 1^2B_{1u} is a pure $4a_u \rightarrow 7b_{2g}$ π → π* state. The $4a_u \rightarrow 7b_{2g}$ transition would in the neutral species be the $2a_{1u} \rightarrow 7e_g$:*xz*, which describes the *y*-polarized component of the 1^1E_u excited state accounting for the intense Q band.[36] As inferred from the composition of the excited states given in Table 3, the higher lying, intense, 4^2B_{1u} state computed at 2.06 eV (602 nm) and 2.09 eV (594 nm) in the gas phase and DMF solution, respectively, also originates from the $4a_u \rightarrow 7b_{2g}$ transition.[60] On the basis of the calculated excitation energies and oscillator strengths, the 1^2B_{1u} and 4^2B_{1u} states can be unambiguously assigned to the bands appearing in the absorption spectrum of the π-anion radical at 956 and 570 nm, respectively. As these spectral features share with the Q band of the parent neutral complex a common electronic origin and are *y* polarized, they can be denoted as Q'_y and Q''_y. Immediately above the 1^2B_{1u} state, TDDFT calcula-

tions predict another weak dipole-allowed excited state, the *x*-polarized 1^2A_u. This state, which is computed at 1.32 eV (932 nm) in the gas phase and at slightly higher energy in DMF, is a nearly 50:50 mixture of the $7b_{3g}\uparrow \rightarrow 5a_u\uparrow$ and $4a_u\downarrow \rightarrow 7b_{3g}\downarrow$ one-electron transitions. This configuration mixing generates another excited state, the 2^2A_u, which is computed at 1.86 eV (667 nm) in the gas phase and at 1.90 (650 nm) in DMF solution. In the 1^2A_u and 2^2A_u states the mixing coefficients of the $7b_{3g}\uparrow \rightarrow 5a_u\uparrow$ and $4a_u\downarrow \rightarrow 7b_{3g}\downarrow$ transitions are such that their large transition dipole moments cancel each other in the former and add up in the latter. The energy and intensity computed for the 1^2A_u and 2^2A_u states leaves little doubt on their assignment to the features appearing in the absorption spectrum of the π-anion radical at 925 and 635 nm, respectively. As one of the transitions contributing to the 1^2A_u and 2^2A_u states, the $4a_u\downarrow \rightarrow 7b_{3g}\downarrow$, would in the neutral species be the $2a_{1u} \rightarrow 7e_g$:*yz*, which describes the *x*-polarized component of the 1^1E_u excited state accounting for the Q band,[36] the features appearing in the absorption spectrum of the π-anion radical at 925 and 635 nm can be denoted as Q'_x and Q''_x. In sum, TDDFT results indicate that the features appearing in the absorption spectrum of $[ZnPc(-3)]^{\bullet-}$ at 956, 925, 635, and 570 nm can be interpreted as deriving from the splitting of the Q(0,0) band of the neutral species into two pairs of bands, one pair (Q'_y, Q'_x) with low intensity and shifted to red, and the other pair (Q''_y, Q''_x) with high intensity and shifted to the blue. This interpretation fits in with the two pairs of bands just described being a spectral signature of virtually all phthalocyanine π-anion radicals.[6] Previous TDDFT/B3LYP results by Stillman and co-workers[33] basically provide the same description of the visible and near-IR region of the spectrum in terms of energy and composition of the excited states. These authors, however, come to a different interpretation of the four key features characterizing this spectral region.

In the spectral region comprised between the two pairs of Q bands, we compute two excited states, the 2^2B_{1u} and 3^2B_{1u}, which are dominated by the SOMO → LUMO+2 and SOMO → LUMO+4 transition, respectively. TDDFT results in the gas phase place the 2^2B_{1u} in the energy regime of the weak band appearing in the absorption spectrum of $[ZnPc(-3)]^{\bullet-}$ at ~793 nm and the 3^2B_{1u} in the red tail of the intense Q''_y band. In DMF these states shift to higher energy by some 60–80 nm (solvation stabilizes the SOMO more than the LUMO+2 and LUMO+4) to the effect that both end up in the red tail of the Q''_y band. Thus, TDDFT calculations in DMF strongly support the conclusion by Mack and Stillman[11] that the two peaks observed at 865 and 793 nm are vibrational overtones of the 956 nm and 925 nm band pair.

In the region of the observed spectrum between 450 nm and 300 nm, we compute 11^2A_u and 9^2B_{1u} excited states. The energy, composition, and intensity of some of these excited states change appreciably on going from the gas phase to the DMF solution, due to a differential stabilization in DMF of the occupied and virtual MOs involved in the pertinent one-electron transitions. In the energy regime of the band centered at 432 nm in the absorption spectrum of $[ZnPc(-3)]^{\bullet-}$ we compute, in the gas phase, two excited states with sufficient intensity to be observed, the 8^2A_u and 7^2B_{1u}. The former has a multitransitional character involving transitions from the HOMO and SOMO to MOs of the set of π* levels, which have large amplitude on the benzo rings, such as the $8b_{3g}$ and $6a_u$ (see level scheme of Fig. 5). The latter is largely described by a transition from the $8b_{1u}$ (the $6a_{2u}$ in the D_{4h} symmetry of the neutral complex) into the SOMO. The assignment of the 8^2A_u and 7^2B_{1u} states to the 432 nm band is consistent with the MCD spectra showing in correspondence of this feature a couple of oppositely signed *B* terms at 434 and 383 nm.[11] In DMF the states corresponding to the 8^2A_u and 7^2B_{1u} are the 11^2A_u and 9^2B_{1u} computed at 3.26 eV (380 nm) and 3.17 eV (391 nm), respectively. At a higher energy we compute four excited states with considerable intensity, the 11^2B_{1u}, 12^2A_u, 14^2A_u, and 15^2B_{1u}. The excitation energies and oscillator strengths computed for these states are scarcely affected by solvation. However, the composition of the lowest two, the 11^2B_{1u} and 12^2A_u, changes to some extent going from the gas phase to DMF. According to the TDDFT results in solution, the 11^2B_{1u} is a nearly 50:50 mixture of the $3a_u \rightarrow 7b_{2g}$ and $4a_u \rightarrow 8b_{2g}$ transitions and the 12^2A_u is described by the $7b_{1u}\uparrow \rightarrow 7b_{2g}\uparrow$ (30%), $2a_u\downarrow \rightarrow 7b_{3g}\downarrow$ (30%), and $8b_{1u}\downarrow \rightarrow 7b_{2g}\downarrow$ (20%) transitions. On the basis of the calculated energies and oscillator strengths, the 11^2B_{1u} and 12^2A_u are assigned to the features appearing in the UV region of the spectrum of the π-anion radical at 383 and 364 nm, respectively. As for the nearly degenerate 14^2A_u and 15^2B_{1u} excited states, they account well for the prominent peak at 319 nm. It is worth noting that these excited states are π* → π* states since they are dominated by transitions out of the SOMO into MOs of the set of π* levels, which have large amplitude on the benzo rings, viz. the $7a_u$ and $12b_{1u}$. The assignment of the intense band at 319 nm to π* → π* states is consistent with this feature being missing in the absorption spectra of the parent neutral complex.

Conclusions

An accurate description of the UV–visible and near-IR spectra of the zinc phthalocyanine π-cation and π-anion radicals, $[ZnPc(-1)]^{\bullet+}$ and $[ZnPc(-3)]^{\bullet-}$, has been provided by TDDFT calculations of the excited states of these molecules, in both the gas phase and solution. The theoretical results are in good agreement with the solution spectra and generally in line with deconvolution analyses of the solution absorption and MCD spectra. The nature and intensities of the main spectral features have been highlighted and interpreted on the basis of the ground-state electronic structure of the complexes.

For the π-cation radical, DFT calculations predict a D_{4h} molecular structure and a $^2A_{1u}$ electronic ground state, with the unpaired electron residing on the $2a_{1u}\uparrow$. TDDFT/SAOP calculations of the dipole and spin allowed ^2E_g and $^2A_{2g}$ excited states locate, in the Q-band region, two excited states, the 2^2E_g at 827/802 nm (gas phase/CH_2Cl_2) and the 3^2E_g at 681/664 nm, consisting of the same one-electron transitions, the $2a_{1u}\uparrow \rightarrow 7e_g\uparrow$ and the $5e_g\downarrow \rightarrow 2a_{1u}\downarrow$, with approximately reversed weights. The large transition dipoles of these transitions reinforce in the 3^2E_g and cancel in the 2^2E_g to the result that the former is by far more intense than the latter. Neither of these excited states properly account for the energy and

intensity of the band observed at 825 nm. The discrepancy between theory and experiment can be traced to the well-known failure of TDDFT to correctly calculate the energy of CT transitions.[23–26] The description of the Q-band region appears to be complicated by the presence of spurious non-Gouterman transitions out of MOs mostly localized on the benzo rings, such as the $5e_g$, to the highly delocalized Gouterman SOMO, the $2a_{1u}$. As these transitions have significant CT character, they are calculated at an energy that is somewhat too low and accidentally mix with the Gouterman $2a_{1u} \rightarrow 7e_g$ transitions. According to the TDDFT/B3LYP/6-31G(d) results by Stillman and co-workers,[33] the introduction of a 20% HF exchange is sufficient to avoid the mixing between the $2a_{1u}\uparrow \rightarrow 7e_g\uparrow$ and the $5e_g\downarrow \rightarrow 2a_{1u}\downarrow$ transitions, but at the expense of the accuracy. In the Q-band region they indeed compute only an intense ($f = 0.23$) ^2E_g excited state, which is a nearly pure (93%) $2a_{1u} \rightarrow 7e_g$ state. The calculated energy is, however, far too low compared to the experiment (950 vs 825 nm). In the 480–300 nm spectral region, TDDFT/SAOP calculations predict four doubly degenerate excited states with sufficient intensity to be easily observed, the 9^2E_g, 13^2E_g, 14^2E_g, and 15^2E_g. Taking into account the near degeneracy of the 13^2E_g and 14^2E_g states, there is an excellent correspondence between the calculated excitation energies and the energies of the three bands located by the deconvolution analysis of Stillman and co-workers[7] at 424, 370, and 317 nm. Analysis of the composition of the pertinent excited states reveals that the features in the absorption and MCD spectra of $[ZnPc(-1)]^{\bullet+}$ at 424 and 417 nm correspond to the B1 and B2 bands of ZnPc, respectively.

TDDFT/SAOP calculations, either in the gas phase or in solution, do not account for the broad absorption near 500 nm assigned by Stillman and co-workers[7] to a nondegenerate, *z*-polarized $^2A_{2g}$ excited state. Theory and experiment can be reconciled only if the presence of an axial ligand such as CN^- is explicitly considered in the calculations. TDDFT calculations for the axially ligated $[ZnPc(-1)(CN)]^{\bullet}$ species indicate that the 500 nm feature originates from axial ligation induced symmetry lowering and assign this band to a *z*-polarized transition associated with the hole in the $2a_{1u}$, which is in line with this feature being observed in the spectra of virtually all phthalocyanine π-cation radicals[6] but not in those of the parent neutral complexes.

Concerning the π-anion radical, this species has a $^2B_{3g}$ electronic ground state in the JT distorted rectangular D_{2h} structure. TDDFT calculations of the dipole and spin allowed ^2A_u, $^2B_{1u}$, and $^2B_{3u}$ excited states of the complex, in both the gas phase and DMF solution, indicate that the features appearing in the absorption spectrum of $[ZnPc(-3)]^{\bullet-}$ at 956, 925, 635, and 570 nm can be interpreted as derived from the splitting of the Q(0,0) band of the neutral species into two pairs of bands, one pair (Q'_y, Q'_x) with low intensity and shifted to red, and the other pair (Q''_y, Q''_x) with high intensity and shifted to the blue. This interpretation fits in with the two pairs of bands being a spectral signature of virtually all phthalocyanine π-anion radicals.[6] Previous TDDFT/B3LYP results by Stillman and co-workers[33] basically provide the same description of the visible and near-IR region of the spectrum in terms of energy and composition of the excited states. These authors, however, come to a different interpretation of the four key features characterizing this spectral region.

In the region of the observed spectrum between 450 nm and 300 nm we compute several excited states, the most intense of which nicely account for the most intense features located at 432, 383, 364, and 319 nm. In particular, the assignement of the prominent peak at 319 nm to the nearly degenerate 14^2A_u and 15^2B_{1u} $\pi^* \rightarrow \pi^*$ excited states, is consistent with this feature being missing in the absorption spectra of the parent neutral complex.

Acknowledgements

Financial support by the Università della Basilicata, Italy, is gratefully acknowledged.

References

(1) This article is part of a Special Issue dedicated to Professor T. Ziegler.
(2) Lever, A. B. P. *Adv. Inorg. Chem. Radiochem.* **1965**, *7*, 27–114. doi:10.1016/S0065-2792(08)60314-3.
(3) Clack, D. W.; Yandle, J. R. *Inorg. Chem.* **1972**, *11* (8), 1738–1742. doi:10.1021/ic50114a003.
(4) Myers, J. F.; Canham, G. W. R.; Lever, A. B. P. *Inorg. Chem.* **1975**, *14* (3), 461–468. doi:10.1021/ic50145a002.
(5) Green, J. M.; Faulkner, L. R. *J. Am. Chem. Soc.* **1983**, *105* (10), 2950–2955. doi:10.1021/ja00348a004.
(6) Minor, P. C.; Gouterman, M.; Lever, A. B. P. *Inorg. Chem.* **1985**, *24* (12), 1894–1900. doi:10.1021/ic00206a040.
(7) Nyokong, T. N.; Gasyna, Z.; Stillman, M. J. *Inorg. Chem.* **1987**, *26* (7), 1087–1095. doi:10.1021/ic00254a025.
(8) Nyokong, T.; Gasyna, Z.; Stillman, M. J. *Inorg. Chem.* **1987**, *26* (4), 548–553. doi:10.1021/ic00251a012.
(9) Ough, E. A.; Gasyna, Z.; Stillman, M. J. *Inorg. Chem.* **1991**, *30* (10), 2301–2310. doi:10.1021/ic00010a016.
(10) Mack, J.; Kirkby, S.; Ough, E. A.; Stillman, M. J. *Inorg. Chem.* **1992**, *31* (9), 1717–1719. doi:10.1021/ic00035a037.
(11) Mack, J.; Stillman, M. J. *J. Am. Chem. Soc.* **1994**, *116* (4), 1292–1304. doi:10.1021/ja00083a015.
(12) Cory, M. G.; Hirose, H.; Zerner, M. C. *Inorg. Chem.* **1995**, *34* (11), 2969–2979. doi:10.1021/ic00115a026.
(13) Mack, J.; Stillman, M. J. *Inorg. Chem.* **1997**, *36* (3), 413–425. doi:10.1021/ic960737i.
(14) Guldi, D. M.; Gouloumis, A.; Vázquez, P.; Torres, T. *Chem. Commun. (Camb.)* **2002**, 2056–2057. doi:10.1039/b205620h. PMID:12357776.
(15) Rodríguez-Morgade, M. S.; Torres, T.; Atienza-Castellanos, C.; Guldi, D. M. *J. Am. Chem. Soc.* **2006**, *128* (47), 15145–15154. doi:10.1021/ja0622195. PMID:17117866.
(16) Gouloumis, A.; González-Rodríguez, D.; Vázquez, P.; Torres, T.; Liu, S.; Echegoyen, L.; Ramey, J.; Hug, G. L.; Guldi, D. M. *J. Am. Chem. Soc.* **2006**, *128* (39), 12674–12684. doi:10.1021/ja055344+. PMID:17002361.
(17) Ballesteros, B.; de la Torre, G.; Ehli, C.; Aminur Rahman, G. M.; Agulló-Rueda, F.; Guldi, D. M.; Torres, T. *J. Am. Chem. Soc.* **2007**, *129* (16), 5061–5068. doi:10.1021/ja068240n. PMID:17397152.
(18) Claessens, C. G.; Torres, T. *Angew. Chem. Int. Ed. Engl.* **2002**, *41* (14), 2561–2565. doi:10.1002/1521-3773(20020715)41:14<2561::AID-ANIE2561>3.0.CO;2-3. PMID:12203534.
(19) Mack, J.; Stillman, M. J. *Coord. Chem. Rev.* **2001**, *219–221*, 993–1032. doi:10.1016/S0010-8545(01)00394-0.
(20) Mack, J.; Stillman, M. J. *The porphyrin handbook;* Kadish, K. M., Smith, K. M., Guilard, R., Eds.; Academic Press: Amsterdam, 2003; pp 43–116.
(21) Keizer, S. P.; Mack, J.; Bench, B. A.; Gorun, S. M.; Still-

man, M. J. *J. Am. Chem. Soc.* **2003**, *125* (23), 7067–7085. doi:10.1021/ja0299710. PMID:12783561.
(22) Rosa, A.; Ricciardi, G.; Gritsenko, O.; Baerends, E. *J. Struct. Bonding* **2004**, *112*, 49–116.
(23) Dreuw, A.; Weisman, J. L.; Head-Gordon, M. *J. Chem. Phys.* **2003**, *119* (6), 2943–2946. doi:10.1063/1.1590951.
(24) Dreuw, A.; Head-Gordon, M. *J. Am. Chem. Soc.* **2004**, *126* (12), 4007–4016. doi:10.1021/ja039556n. PMID:15038755.
(25) Dreuw, A.; Head-Gordon, M. *Chem. Rev.* **2005**, *105* (11), 4009–4037. doi:10.1021/cr0505627. PMID:16277369.
(26) Gritsenko, O.; Baerends, E. J. *J. Chem. Phys.* **2004**, *121* (2), 655–660. doi:10.1063/1.1759320.
(27) Broclawik, E.; Borowski, T. *Chem. Phys. Lett.* **2001**, *339* (5–6), 433–437. doi:10.1016/S0009-2614(01)00361-X.
(28) Dai, B.; Deng, K.; Yang, J.; Zhu, Q. *J. Chem. Phys.* **2003**, *118* (21), 9608–9613. doi:10.1063/1.1570811.
(29) Nemykin, V. N.; Basu, P. *Inorg. Chem.* **2003**, *42* (13), 4046–4056. doi:10.1021/ic0262942. PMID:12817960.
(30) Wang, F.; Ziegler, T. *Mol. Phys.* **2004**, *102* (23-24), 2585–2595. doi:10.1080/00268970420002750 80.
(31) Donzello, M. P.; Ercolani, C.; Kadish, K. M.; Ricciardi, G.; Rosa, A.; Stuzhin, P. A. *Inorg. Chem.* **2007**, *46* (10), 4145–4157. doi:10.1021/ic070038d. PMID:17444636.
(32) Soldatova, A. V.; Kim, J.; Rosa, A.; Ricciardi, G.; Kenney, M. E.; Rodgers, M. A. J. *Inorg. Chem.* **2008**, *47* (10), 4275–4289. doi:10.1021/ic7023204. PMID:18407627.
(33) Mack, J.; Kobayashi, N.; Stillman, M. J. *J. Porphyrins Phthalocyanines* **2006**, *10* (10), 1219–1237.
(34) Gritsenko, O. V.; Schipper, P. R. T.; Baerends, E. J. *Chem. Phys. Lett.* **1999**, *302* (3–4), 199–207. doi:10.1016/S0009-2614(99)00128-1.
(35) Schipper, P. R. T.; Gritsenko, O. V.; van Gisbergen, S. J. A.; Baerends, E. J. *J. Chem. Phys.* **2000**, *112* (3), 1344. doi:10.1063/1.480688.
(36) Ricciardi, G.; Rosa, A.; Baerends, E. J. *J. Phys. Chem. A* **2001**, *105* (21), 5242–5254. doi:10.1021/jp0042361.
(37) Baerends, E. J.; Ricciardi, G.; Rosa, A.; van Gisbergen, S. J. A. *Coord. Chem. Rev.* **2002**, *230* (1–2), 5–27. doi:10.1016/S0010-8545(02)00093-0.
(38) Nemykin, V. N.; Hadt, R. G.; Belosludov, R. V.; Mizuseki, H.; Kawazoe, Y. *J. Phys. Chem. A* **2007**, *111* (50), 12901–12913. doi:10.1021/jp0759731. PMID:18004829.
(39) *ADF2007.01;* SCM, Theoretical Chemistry, Vrije Universiteit: Amsterdam, The Netherlands. Available from http://www.scm.com.
(40) Baerends, E. J.; Ellis, D. E.; Ros, P. *Chem. Phys.* **1973**, *2* (1), 41–51. doi:10.1016/0301-0104(73)80059-X.
(41) Fonseca Guerra, C.; Snijders, J. G.; te Velde, G.; Baerends, E. *J. Theor. Chem. Acc.* **1998**, *99* (6), 391–403. doi:10.1007/s002140050021.
(42) te Velde, G.; Bickelhaupt, F. M.; Baerends, E. J.; Fonseca Guerra, C.; van Gisbergen, S. J. A.; Snijders, J. G.; Ziegler, T. *J. Comput. Chem.* **2001**, *22* (9), 931–967. doi:10.1002/jcc.1056.
(43) Vosko, S. H.; Wilk, L.; Nusair, M. *Can. J. Phys.* **1980**, *58* (8), 1200–1211.
(44) Becke, A. D. *Phys. Rev. A* **1988**, *38* (6), 3098–3100. doi:10.1103/PhysRevA.38.3098. PMID:9900728.
(45) Perdew, J. P. *Phys. Rev. B* **1986**, *33* (12), 8822–8824. doi:10.1103/PhysRevB.33.8822.
(46) Klamt, A.; Schürmann, G. *J. Chem. Soc., Perkin Trans. 2* **1993**, 799–805.
(47) Klamt, A.; Jonas, V. *J. Chem. Phys.* **1996**, *105* (22), 9972–9981. doi:10.1063/1.472829.
(48) Pye, C. C.; Ziegler, T. *Theor. Chem. Acc.* **1999**, *101* (6), 396–408.
(49) Prendergast, K.; Spiro, T. G. *J. Phys. Chem.* **1991**, *95* (24), 9728–9736. doi:10.1021/j100177a025.
(50) Vangberg, T.; Lie, R.; Ghosh, A. *J. Am. Chem. Soc.* **2002**, *124* (27), 8122–8130. doi:10.1021/ja011438h. PMID:12095358.
(51) Lian-Cai, X.; Zun-Yun, L.; Tian-Jing, H.; Fan-Chen, L.; Dong-Ming, C. *Chem. Phys.* **2004**, *305* (1–3), 165–174. doi:10.1016/j.chemphys.2004.06.044.
(52) Hirao, H.; Shaik, S.; Kozlowski, P. M. *J. Phys. Chem. A* **2006**, *110* (18), 6091–6099. doi:10.1021/jp0558066. PMID:16671680.
(53) Englman, R. *The Jahn–Teller effect in molecules and crystals;* Wiley: London, 1972.
(54) Bersuker, I. B. *Chem. Rev.* **2001**, *101* (4), 1067–1114. doi:10.1021/cr0004411. PMID:11709858.
(55) Rosa, A.; Ricciardi, G.; Baerends, E. J.; van Gisbergen, S. J. A. *J. Phys. Chem. A* **2001**, *105* (13), 3311–3327. doi:10.1021/jp003508x.
(56) Zhao, Y.; Truhlar, D. J. *J. Phys. Chem. A* **2006**, *110* (49), 13126–13130. doi:10.1021/jp066479k.
(57) Magyar, R. J.; Tretiak, S. *J. Chem. Theory Comput.* **2007**, *3* (3), 976–987. doi:10.1021/ct600282k.
(58) Piepho, S. B.; Schatz, P. N. *Group theory in spectroscopy with applications to magnetic circular dicroism;* Wiley: New York, 1980.
(59) Williamson, B. E.; Van Cott, T. C.; Boyle, M. E.; Misener, G. C.; Stillman, M. J.; Schatz, P. N. *J. Am. Chem. Soc.* **1992**, *114* (7), 2412–2419. doi:10.1021/ja00033a016.
(60) In molecular systems with a doublet ground-state one-electron transitions from fully occupied orbitals to virtual orbitals result in one set of quartet excited states and two sets of doublet excited states, whereas one-electron transitions from or into the singly occupied orbital result in doublet states.

Spin–orbit ab initio investigation of the UV photoinduced bond cleavage in iodotrimethylstannane[1]

N. Ben Amor and C. Daniel

Abstract: The photoinduced homolytic cleavage of the Sn–I bond in iodotrimethylstannane $(CH_3)_3SnI$, observed after UV irradiation, is investigated by means of spin–orbit ab initio calculations based on CASSCF (complete active space self-consistent field) and MS-CASPT2 (multi-state complete active space 2nd order perturbation theory) methods. The absorption electronic spectrum is characterized by ten low-lying $^{1,3}A'$ and $^{1,3}A''$ spin eigenstates corresponding to $p_y(I),p_x(I) \rightarrow \sigma^*_{SnI}$; $\sigma_{SnI} \rightarrow \sigma^*_{SnI}$ and $p_y(Sn)$, $p_x(Sn) \rightarrow \sigma^*_{SnI}$, where σ_{SnI} and σ^*_{SnI} are the bonding and anti-bonding orbitals of the Sn–I bond along the p_z axis. From the $^1A'$ electronic ground state and these ten spin eigenstates, 21 spin–orbit states are generated leading to various deactivation channels of $(CH_3)_3SnI$, corresponding to the formation of radicals $(CH_3)_3Sn^{\bullet}$ and $^{\bullet}I$ and to the ionic species $(CH_3)_3Sn^+$ and I^-. Irradiation into the upper band at 175 nm should lead to the heterolytic cleavage of the Sn–I bond to form the ionic primary products exclusively, whereas absorption into the shoulder at 250 nm induces the homolytic breaking with formation of the radical products.

Key words: ab initio, spin–orbit, UV spectroscopy, iodostannane, photodissociation.

Résumé : Faisant appel à des calculs ab initio spin-orbite basés sur des méthodes de champ autocohérent avec espace actif complet « CASSCF » et de la théorie des perturbations du second ordre, à espace actif complet et à états multiples « MS-CASPT2 », on a étudié le clivage homolytique photoinduit de la liaison Sn–I de l'iodotriméthylstannane, $(CH_3)_3SnI$, observé après une irradiation UV. Le spectre d'absorption électronique est caractérisé par dix états de spin de basses intensités, $^{1,3}A'$ et $^{1,3}A''$ qui correspondent aux transitions $p_y(I)$, $p_x(I) \rightarrow \sigma^*_{SnI}$; $\sigma_{SnI} \rightarrow \sigma^*_{SnI}$ et $p_y(Sn)$, $p_x(Sn) \rightarrow \sigma^*_{SnI}$ dans lesquelles σ_{Sn1} et σ^*_{SnI} sont les orbitales liantes et antiliantes de la liaison Sn–I le long des axes p_z. De l'état électronique fondamental $^1A'$ à ces états de spin, on peut obtenir vingt états spin–orbite qui génèrent divers canaux de désactivation du $(CH_3)_3SnI$ qui correspondent à la formation des radicaux $(CH_3)_3Sn^{\bullet}$ et $^{\bullet}I$ et aux espèces ioniques $(CH_3)_3Sn^+$ et I^-. L'irradiation dans la bande supérieure, à 175 nm, devrait conduire à un clivage hétérolytique de la liaison Sn–I avec une formation exclusive de produits primaires ioniques alors qu'une absorption dans l'épaulement à 250 nm devrait induire une scission homolytique avec formation de produits radicalaires.

Mots-clés : ab initio, spin–orbite, spectroscopie UV, iodostannane, photodissociation.

[Traduit par la Rédaction]

Introduction

In contrast to the extensive literature on the photochemistry of transition-metal complexes, and despite of the numerous potential applications of main-group metal molecules, little is known on their photoreactivity. Oxides derived from main-group compounds are characterized by large band gaps leading to high transparency in the visible–UV spectral domains. Experiments based on $(CH_3)_3SnI$, used as a precursor, confirm changes in refractive index in porous Vycor glass (PVG),[2] comparable to those obtained with Fe(CO). UV photolysis of $(CH_3)_3SnI$ adsorbed onto PVG or porous glassy matrixes enhances the refractive index relative to the bulk glass.[3–13] Subsequent heating drives the unexposed complex from the glass and, at 1200 °C, consolidates the glass, entrapping a photogenerated gradient index pattern in the glass.[12] Several experiments were undertaken to improve the optical performance of these gradient-index structures by establishing the nature of the precursor on the glass surface and identifying the photoactive excited states. Photochemistry of $(CH_3)_3SnI$ in hydrocarbon solution indicates homolytic cleavage of the Sn–I bond following 254 nm irradiation leading to $((CH_3)_3Sn)_2$ and I_2 primary products.[14] However, both products desorb from the glass during subsequent heating, thereby precluding their involvement in gradient index formation. Furthermore, UV photolysis of $(CH_3)_3SnI$ adsorbed onto PVG yields I_3^-, suggesting heterolytic cleavage of the molecule in the glass matrix. It has been pointed out that the quantum yield of the radical channel depends on the solvent medium. In nonpolar solvents, excitation leads to homolytic

Received 9 December 2008. Accepted 25 February 2009. Published on the NRC Research Press Web site at canjchem.nrc.ca on 16 June 2009.

N. Ben Amor. Université de Toulouse, UPS, LCPQ (Laboratoire de Chimie et Physique Quantiques), IRSAMC, 118 rte de Narbonne F-31062 Toulouse CEDEX, France; CNRS, UPS, LCPQ (Laboratoire de Chimie et Physique Quantiques), IRSAMC, 118 rte de Narbonne F-31062 Toulouse CEDEX, France.
C. Daniel.[1] Laboratoire de Chimie Quantique, Institut de Chimie, CNRS/Université de Strasbourg, Institut Le Bel, 4, rue Blaise Pascal, 67000 Strasbourg, France.

[1]Corresponding author (e-mail: c.daniel@chimie.u-strasbg.fr).

cleavage, while in solvent capable of acting as Lewis bases, formation of a solvent adduct switches the reactivity to heterolytic rupture of the Sn–I bond.[14] In hexane, $(CH_3)_3SnI$ exists as a four-coordinate tetrahedron, but adsorbed onto PVG, and in ethanol, the complex exists as a five-coordinate adduct with the oxygen of the surface silanol, or the alcohol, occupying the fifth coordination site. A preliminary theoretical study of the tetrahedral compound based on CASSCF/CASPT2 calculations of the low-lying singlet excited states and associated potential-energy curves (PECs) has enabled us to assign the experimental absorption spectrum and to determine two dissociative channels leading to the radical and ionic primary products $(CH_3)_3Sn^{\bullet}$ and $^{\bullet}I$ and $(CH_3)_3Sn^+ + I^-$, respectively.[15] In a more recent article, the photodissociation dynamics of this compound has been investigated in the semi-classical approximation and in the quasi-resonant approximation.[16]

The present theoretical study reports partly the quantum chemical calculations underlying this dynamical study based on wavepacket propagations on one-dim potential-energy functions obtained by nonlinear fit of the SO-MS-CASPT2 eigenvalues. This work differs from the quantum chemical study reported in ref. 15 by considering the low-lying triplet states as well as their spin–orbit interactions with the singlet excited states. Moreover, an additional state, perturbing significantly the SO-states and corresponding to the ($p_y Sn \rightarrow \sigma^*_{SnI}$) excitation, is included. To contribute to a better understanding of the complex experimental behavior described above, we aim at determining the photoactive states and the various dissociation channels accessible after UV, far-UV irradiation of tetrahedral $(CH_3)_3SnI$. In a first step, a preliminary investigation of the structural aspects related to the tin-compounds coordination lability is undertaken by means of DFT calculations. In a second step, the electronic absorption spectrum including all the singlet and triplet states between 273 nm and 176 nm is modelized in vacuum by means of spin–orbit (SO) MS-CASPT2 calculations. The PECs describing the Sn–I bond dissociation have been calculated at the same level of theory.

Methods and computational details

The geometries of $(CH_3)_3Sn^{\bullet}$, $(CH_3)_3Sn^+$, $(CH_3)_3SnI$, $(CH_3)_3SnI–OHC_2H_5$, and $(CH_3)_3SnI–OHSiH_2CH_3$ have been optimized at the DFT level of theory using the B3LYP[17] functional within the quasi-relativistic pseudopotential[18] with the associated valence basis sets for the tin centre a (4s4p) set contracted to [2s2p], for the iodine a (4s5p) set contracted to [2s3p] while all electrons split-valence basis sets[19] were used for the carbon and hydrogen atoms, respectively (9s5p) contracted to [3s2p] and (4s) contracted to [2s]. The geometry optimizations have been performed without any constraint in the C_1 symmetry group. The electronic ground state of all species is described by a singlet configuration, except for the radical, which is a doublet.

The photodissociation of $(CH_3)_3SnI$ has been modeled within a one-dimensional scheme described by the Sn–I bond elongation, without relaxation of the whole molecule with the C_s symmetry constraint. Scalar relativistic effects were included within the Douglas–Kroll Hamiltonian. The calculations are based on atomic natural orbitals-relativistic

Fig. 1. DFT-optimized geometries.

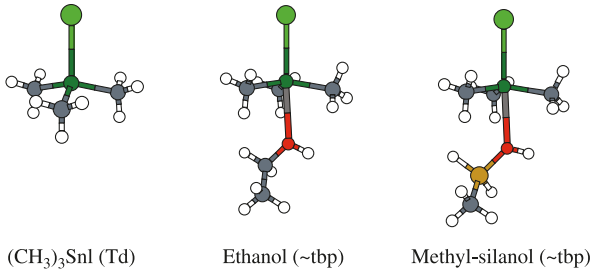

correlation consistent (ANO-RCC)[20] basis sets with the following contraction scheme: for Sn atom, a (22s19p13d5f) set contracted to [6s5p3d1f]; for I atom, a (22s19p13d5f) set contracted to [6s5p3d1f]; for C, a (14s9p4d) set contracted to [3s2p1d]; and for H, a (8s4p) set contracted to [2s1p]. To determine the potential presence of Rydberg states in the domain of energy investigated here (UV, far-UV), one more calculation has been performed, at the equilibrium geometry, with the following extended basis set: for Sn and I atoms, (22s19p13d5f3g) sets contracted to [10s9p5d3f1g]; for C, a (14s9p4d3f) set contracted to [5s4p3d1f]; and for H, a (8s4p3d) set contracted to [4s3p2d]. Since the ten first singlet or triplet states of A′ and A″ symmetries have mainly a valence character, the first contraction scheme is well-adapted to this study. The electronic ground state is described by the following electronic configuration $(\sigma_{SnC})^2\ (\sigma_{SnI})^2\ (5p_yI)^2\ (\sigma_{SnC})^2\ (5p_xI)^2$.

The electronic excited states and associated PECs have been calculated by means of complete active space self-consistent field (CASSCF) method,[21] with ten electrons correlated in ten active orbitals in coherence with our first study.[15] This active space includes the σ_{SnC} and σ_{SnI} bonding orbitals and their anti-bonding counterparts, the $5p_xI$, $5p_yI$, and virtual orbitals mainly located on methyl groups and Sn atom to keep a stable active space along the dissociation path. Ten singlet and ten triplet excited states of A′ and A″ symmetries are calculated. These rather large active space and number of states are necessary to get all the states of interest along the dissociation path. Dynamic correlation is included in subsequent multi-state complete active space 2nd order perturbation theory[22] (MS-CASPT2) calculations based on state average CASSCF reference wave functions. The multi-state approach has been preferred to the state specific approach for two reasons: (*i*) to take into account the mixing at the level of avoided crossings occurring along the Sn–I coordinate; (*ii*) to use 2nd Order energies coherent with the zero-order multi-state CASSCF wave function in SO-RASSI. To avoid intruder states, we used a level shift of 0.2. For each symmetry and spin, eight roots are coupled at second order via an effective Hamiltonian approach. The core electrons are frozen in the CASSCF as well as in the CASPT2 calculations.

The spin–orbit coupling between the different electronic states is determined by the restricted active space state interaction approach (RASSI-SO).[23] Although, the method has been conceived in the basis of RASSCF wave functions, recent works use the MS-CASPT2 results[24–26]: the diagonal elements are the correlated MS-CASPT2 energies and the off-

Table 1. DFT(B3LYP) optimized bond lengths (in Å) and bond angles (in °) of $(CH_3)_3Sn^{\bullet}$, $(CH_3)_3SnI^{+}$, $(CH_3)_3SnI$, $(CH_3)_3SnI–OHC_2H_5$, and $(CH_3)_3SnI–OHSiH_2CH_3$.

	$(CH_3)_3Sn^{\bullet}$	$(CH_3)_3Sn^{+}$	$(CH_3)_3SnI$	$(CH_3)_3SnI–OHC_2H_5$	$(CH_3)_3SnI–OHSiH_2CH_3$
Distances					
Sn—C	2.210	2.151	2.161	2.169	2.170
Sn—I	—	—	2.824	2.904	2.916
Sn—O	—	—	—	2.718	2.678
O—C/O—Si	—	—	—	1.482	1.764
C—C/Si—C	—	—	—	1.523	1.905
Angles					
C–Sn–C	108	120	113	118	118
C–Sn–I	—	—	105	99	99
Geometry	~Td (trigonal pyramidal)	Planar	~Td	~TBP	~TBP

Table 2. MS-CASPT2 transition energies (in cm^{-1}). Oscillator strengths are in parenthesis.

		ANO-RCC basis sets[a]	AIMP basis sets[b]
		MS-CASPT2	MS-CASPT2
Transition	a^1A' Total energy	–13403.802 017 hartree	–299.678 782 hartree
$a^1A' \rightarrow a^3A'$	$p_yI \rightarrow \sigma^*_{SnI}$	38 540	
$a^1A' \rightarrow a^3A''$	$p_xI \rightarrow \sigma^*_{SnI}$	38 960	
$a^1A' \rightarrow a^1A''$	$p_xI \rightarrow \sigma^*_{SnI}$	40 820 (0.03)	42 210 (0.01)
$a^1A' \rightarrow b^1A'$	$p_yI \rightarrow \sigma^*_{SnI}$	42 315 (0.02)	42 920 (0.01)
$a^1A' \rightarrow b^3A'$	$\sigma_{SnI} \rightarrow \sigma^*_{SnI}$	45 575	
$a^1A' \rightarrow c^3A'$	$p_ySn \rightarrow \sigma^*_{SnI}$	49 325	
$a^1A' \rightarrow b^3A''$	$p_xSn \rightarrow \sigma^*_{SnI}$	49 330	
$A^1A' \rightarrow b^1A''$	$p_xSn \rightarrow \sigma^*_{SnI}$	51 675 (0.09)	53 220 (0.04)
$a^1A' \rightarrow c^1A'$	$p_ySn \rightarrow \sigma^*_{SnI}$	56 240 (0.14)	
$a^1A' \rightarrow d^1A'$	$\sigma_{SnI} \rightarrow \sigma^*_{SnI}$	59 720 (0.24)	55 610 (0.81)

[a]Present work.
[b]Reference 15.

diagonal SOC elements are evaluated on the basis of first-order MS-CASPT2 wave functions (i.e., mixed CASSCF states). To take into account the interaction between the low-lying SO states involved in the absorption spectroscopy with the upper states, the SO states have been determined over spin-components of 32 MS-CASPT2 eigenstates (spin eigenstates).

The calculations have been performed either with GAUSSIAN[27] (DFT) or MOLCAS 6.2[28] (transition energies and spin–orbit coupling) quantum chemistry software.

Results and discussion

Structures

The DFT (B3LYP) equilibrium geometries of the ground state of $(CH_3)_3SnI$ and of the penta-coordinated $(CH_3)_3SnI–OHC_2H_5$ and $(CH_3)_3SnI–OHSiH_2CH_3$ are depicted in Fig. 1. Some optimized relevant distances and bond angles are reported in Table 1 for the five complexes.

As expected with the valence shell electron pair repulsion method (VSEPR),[29] the radical $(CH_3)_3Sn^{\bullet}$ and $(CH_3)_3SnI$ have very similar geometries, nearly tetrahedral (Td) and the ionic compound $(CH_3)_3Sn^{+}$ is planar.

The C–Sn–C angle in the radical $(CH_3)_3Sn^{\bullet}$ is slightly smaller than the 109.5° associated to the pure tetrahedral structure. Similarly, the C–Sn–I angle in $(CH_3)_3SnI$ is smaller than the C–Sn–C angle. In the $(CH_3)_3SnI–OHC_2H_5$ and $(CH_3)_3SnI–OHSiH_2CH_3$ complexes, the oxygen is bound to the tin, leading to nearly trigonal bipyramidal (TBP) structure of the tin, with the three methyl groups in the trigonal plan. These results confirm the experimental hypothesis,[13] namely the significant change of the structure of the trimethyltin iodine complex in a five-coordinate system when it is adsorbed on a PVG or when ethanol is added to hexane trimethyltin iodine solution.

In the present study, related to the experiment reported in hexane (poorly polar solvent), the calculations reported below have been performed for the isolated molecule in vacuum. Obviously, in a more realistic theoretical study, dedicated to environment effects on the absorption spectroscopy and photoreactivity, the calculations should be performed on the solvated structures, $(CH_3)_3SnI–OHC_2H_5$ and $(CH_3)_3SnI–OHSiH_2CH_3$ (Fig. 1), in addition to the standard solvent correction (discrete or polarized continuum models). This will be the purpose of further investigations.

Electronic absorption spectroscopy of $(CH_3)_3SnI$

The transition energies to the low-lying singlet and triplet excited states of $(CH_3)_3SnI$ have been obtained by means of CASSCF/ MS-CASPT2 calculations based on the DFT tetrahedral optimized geometry with a Sn–I equilibrium distance of 2.7 Å in the $^1A'$ electronic ground state. This value re-

Table 3. SO states and the corresponding transition energies (in cm^{-1}) of $(CH_3)_3SnI$. Oscillator strengths are in parenthesis.

		MSCASPT2 states	Spin	Orbit states	
Transition	a^1A' Total energy	–13403.802017 hartree	**aA′**	100% a^1A'	–13403.803135 hartree
$a^1A' \rightarrow a^3A'$	$p_yI \rightarrow \sigma^*_{SnI}$	38 540	aA″	58% a^3A' + 42% a^3A''	36 660 (0)
			bA′	56% a^3A' + 44% a^3A''	36 670 (0)
			bA″	75% a^3A' + 24% a^1A''	37 050 (0.003 – μ_x)
$a^1A' \rightarrow a^3A''$	$p_xI \rightarrow \sigma^*_{SnI}$	38 960	**cA′**	83% a^3A'' + 15% b^1A'	37 850 (0003 – μ_{yz})
			cA″	50% a^3A'' + 32% a^3A'+ 17% b^3A'	39 540 (0)
			eA′	54% a^3A'' + 42% a^3A'	40 820 (0.008 – μ_{yz})
$a^1A' \rightarrow a^1A''$	$p_xI \rightarrow \sigma^*_{SnI}$	40 820 (0.03)	dA″	62% a^1A'' + 22% b^3A'	40 395 (0.008 – μ_x)
$a^1A' \rightarrow b^1A'$	$p_yI \rightarrow \sigma^*_{SnI}$	42 315 (0.02)	**dA′**	63% b^1A' + 28% b^3A' + 8% a^3A''	41 695 (0.013 – μ_{yz})
$a^1A' \rightarrow b^3A'$	$\sigma_{SnI} \rightarrow \sigma^*_{SnI}$	45 575	eA″	48% b^3A' + 32% c^3A'	46 920 (0)
			gA″	73% b^3A'+ 10% b^3A'' + 9% a^3A''	47 195 (0)
			gA′	54% b^3A' + 15% b^3A'' + 15% b^1A' + 8% a^3A''	47 415 (0.003 – μ_{yz})
$a^1A' \rightarrow c^3A'$	$p_ySn \rightarrow \sigma^*_{SnI}$	49 325	fA″	56% c^3A' + 20% b^3A''	47 140 (0)
			fA′	62% c^3A' + 28% b^3A''	47 170 (0)
			hA″	72% c^3A'' + 18% b^3A'	47 675 (0.009 – μ_x)
$a^1A' \rightarrow b^3A''$	$p_xSn \rightarrow \sigma^*_{SnI}$	49 330	**hA′**	76% b^3A'' + 10% b^3A'	48 325 (0.014 – μ_{yz})
			iA′	68% b^3A'' + 30% c^3A'	48 990 (0)
			iA″	66% b^3A'' + 28% c^3A'	49 055 (0)
$a^1A' \rightarrow b^1A''$	$p_xSn \rightarrow \sigma^*_{SnI}$	51 675 (0.09)	jA″	95% b^1A''	51 770 (0.072 – μ_{yz})
$a^1A' \rightarrow c^1A'$	$p_ySn \rightarrow \sigma^*_{SnI}$	56 240 (0.14)	**jA′**	70% c^1A' + 20% c^3A''	51 645 (0.170 – μ_x)
$a^1A' \rightarrow d^1A'$	$\sigma_{SnI} \rightarrow \sigma^*_{SnI}$	59 720 (0.24)	**kA′**	71% d^1A' + 23% d^3A''	56 950 (0.016 – μ_{yz})

mained unchanged when adding SO effects. The low-lying excited states are generated by excitations from the valence-occupied orbitals of the tin and iodine to the antibonding orbital σ^*_{SnI}. The MS-CASPT2 calculated electronic Franck–Condon transitions of the complex are reported in Table 2 with the previous results obtained with Cowan–Griffin relativistic core ab initio model potential (CG-AIMP).[30]

The two studies differ by the following features: (*i*) In the present work, the scalar relativistic effects are taken into account by the Douglas–Kroll Hamiltonian, whereas they were included in the pseudopotentials in the previous study; (*ii*) the Sn–I equilibrium distance was shortened: 2.70 Å in the present study compared with 2.73 Å in the previous one. There is a good qualitative agreement between the transition energies obtained in the present work and the previous published values. The two first excited states correspond to an excitation from the iodine to the antibonding orbital σ^*_{SnI} and are followed by singlet state arising from p_xSn to σ^*_{SnI} excitation. However, an additional singlet state appeared in the Franck–Condon region, corresponding to the $p_ySn \rightarrow \sigma^*_{SnI}$ excitation. This state was found to have quite important oscillator strength. The transition energies differ by less than 1600 cm^{-1} except for the $\sigma_{SnI} \rightarrow \sigma^*_{SnI}$ state, which is calculated at 59 720 cm^{-1} vs. 55 610 cm^{-1} with the AIMP. The oscillator strengths are qualitatively equivalent, with a maximum value for the $\sigma_{SnI} \rightarrow \sigma^*_{SnI}$ ionic state in the two studies.

Spin–orbit coupling

Spin–orbit coupling (SOC) effects have been determined for all singlet and triplet states of both symmetries (32 spin eigenstates). The SO states and the corresponding transition energies of $(CH_3)_3$ SnI are presented in Table 3. The treatment of spin–orbit coupling is very sensitive to the size of

Fig. 2. Comparison between the theoretical absorption spectra of $(CH_3)_3SnI$ from MSCASPT2 and spin–orbit (SO) MSCASPT2 states.

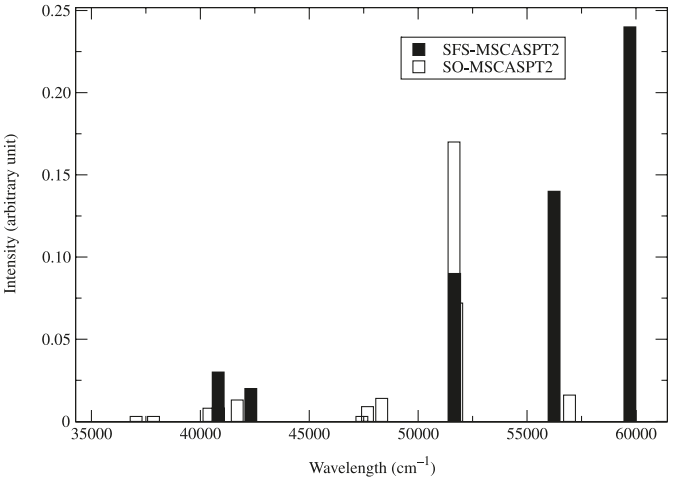

the spin eigenstates basis. In ref. 16, the SO A′ state, arising mainly from the $p_{ySn} \rightarrow \sigma^*_{SnI}$ state, has not been calculated, while it is included in the present study. Although this state has a high energy, the results are affected as a whole. For instance, the bA′ SO state with an electronic term value of 38 590 cm^{-1} in ref. 16 is now calculated at 36 670 cm^{-1} at the equilibrium distance of 2.7 Å. A greater effect is found for the ionic state, higher by more than 5000 cm^{-1}, while the $p_{ySn} \rightarrow \sigma^*_{SnI}$ state takes its place at 51645 cm^{-1}.

According to the double-group symmetry rules, the $^3A'$ states are split into two A″ and one A′ components, whereas the $^3A''$ states are split into two A′ and one A″ components. By interaction with the A′ components of the triplet spin eigenstates, the $^1A'$ electronic ground state is shifted down by

Fig. 3. SO-MSCASPT2 potential-energy curves of $(CH3)_3SnI$ as a function of the Sn–I bond distance.

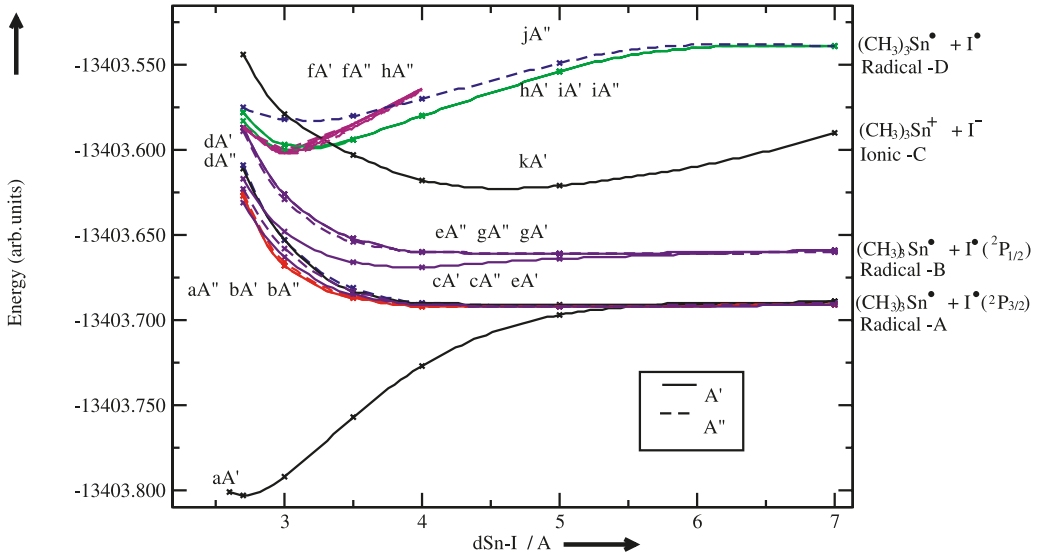

245 cm^{-1}. The $^3A'$ and $^3A''$ electronic states split into several spin–orbit states. The SO splittings of the low-lying $^3A'$ and $^3A''$ amount to 390 cm^{-1}, 500 cm^{-1}, and 530 cm^{-1} for the a^3A', b^3A', and c^3A', respectively, and are larger for the a^3A'' and b^3A'' states with values of 2970 cm^{-1} and 730 cm^{-1}, respectively.

In the Franck–Condon region, apart from the aA′ electronic ground state and the jA″ (b^1A'') state, the SO states are strongly mixed. The singlet states gain significant contributions of the triplet spin eigenstates (~20%), whereas the SO states that originate from the triplet states are nearly exclusively composed by contributions of the triplet spin eigenstates. By inclusion of the SO, transition energies increase by more than 1800 cm^{-1} for the b^3A' and a^3A'', while they decrease by 1000 cm^{-1}, 1880 cm^{-1}, 1110 cm^{-1}, and 2770 cm^{-1} for the b^3A'', a^3A', a^3A'', and d^1A', respectively.

As illustrated by Fig. 2, the theoretical absorption spectrum is broadened and less intense when SO effects are included. The decrease of the oscillator strength is a general trend also observed for $H_2M(CO)_4$.[31] This may be explained by the large contributions of the SO states arising from the triplet states in the absorbing states.

Potential-energy curves

The 1D PECs, corresponding to ten of the 11 low-lying post-SO A′-levels and ten low-lying post-SO A″-levels, are depicted in Fig. 3 as a function of the Sn–I bond distance. The post-SO-adiabatic A′-levels originate from the a^1A' electronic ground state and from the ten low-lying $^{1,3}A'$ and $^{1,3}A''$ states corresponding to p_yI, $p_xI \rightarrow \sigma^*_{SnI}$, $\sigma_{SnI} \rightarrow \sigma^*_{SnI}$ and p_ySn, $p_xSn \rightarrow \sigma^*_{SnI}$ excitations. From these 11 spin eigen states (four $^1A'$, three $^3A'$, two $^1A''$, and two $^3A''$), one may generate 11 SO A′-states and ten SO A″-states. These 21 SO states lead to various deactivation channels of $(CH_3)_3SnI$. The lowest channel radical A, which leads to $(CH_3)_3Sn^\bullet$ (J = 1/2) + $^\bullet I$ (J = 3/2), is an eightfold degenerate at infinite separation, while the next channel radical B, fourfold degenerate, gives $(CH_3)_3Sn^\bullet$ (J = 1/2) + $^\bullet I$ (J = 1/2). The third channel is nondegenerate and corresponds to the ionic channel leading to $(CH_3)_3$ $Sn^+ + I^-$ (channel ionic C). The fourth channel, radical D eightfold degenerate, leads to $(CH_3)_3Sn^\bullet + {}^\bullet I$.

The SO splitting of 6930 cm^{-1} between the radical-A and radical-B species at the asymptote corresponds roughly to the energy gap between I (J = 3/2) and I (J = 1/2) of 7600 cm^{-1} (experimental value[32]: 7595 cm^{-1}). It is worth noting that the six spin eigenstates leading to radical A and radical B by SO splitting are degenerate at the asymptote. The PECs connected to radical A (bA′, cA′, dA′, eA′, aA″, bA″, cA″, and dA″) and the upper PECs connected to radical B (eA″ and gA″) are dissociative. The gA′ SO state has bounded PECs, due to an important mixing of the b^3A' with the a^3A'' SFS in the range of 3.0–5.0 Å. The single post-SO adiabatic kA′ curve leading to the ionic species is characterized by a minimum between 4 Å and 5 Å in agreement with the PEC shown in ref.15. The upper PECs are bound along the Sn–I bond elongation. The jA′ SO state, which has the larger oscillator strength in the Franck–Condon region, becomes higher in energy, and its oscillator strength decreases (from 0.17 at d_{SnI} = 2.7 Å to 0.11 at d_{SnI} = 3.0 Å), while the ionic state kA′ has an increasing oscillator strength (0.016 to 0.61) within the same range. It was not possible to follow the jA′ state along the dissociation path. According to the shape of the PECs depicted in Fig. 3 and to the theoretical absorption spectrum represented in Fig. 2, photoinduced bond cleavage in $(CH_3)_3SnI$ may occur following three distinct mechanisms. Whereas irradiation in the upper intense band at about 52 000 cm^{-1} (195 nm) will produce radical primary products, irradiation in the shoulder at 57 000 cm^{-1} (175 nm) will lead to the formation of ionic primary products. Another shoulder, between 40 000 cm^{-1} and 42 500 cm^{-1} (250 and 235 nm), will produce radical primary products. This last mechanism explains the homolytic cleavage of the Sn–I bond observed after irradiation at 254 nm in hydrocarbon solution leading to $((CH_3)_3Sn)_2$ and I_2 primary products.[14] The branching ratio between the radical and ionic channels will depend on the solvent conditions, as suggested by the experiments reported in various media. Indeed,

the relative position and the shape of the "ionic" and "radicals" PECs should be very sensitive to the polarity of the solvents.

Conclusion

The theoretical electronic absorption spectrum of $(CH_3)_3SnI$, representative of organotin compounds, has been calculated and analyzed by means of spin–orbit accurate ab initio calculations. It has been shown that it is characterized by an intense band centered at 51 700 cm^{-1} (or 195 nm) assigned to transitions composed essentially of $p_xSn/p_ySn \rightarrow \sigma^*_{SnI}$ excitations. A shoulder starting at 40 000 cm^{-1} (or 250 nm) is attributed to A′ and A″ states corresponding to $p_xI/p_yI \rightarrow \sigma^*_{SnI}$ excitations. Irradiation in the upper band, at 175 nm, will lead to the heterolytic cleavage of the Sn–I bond, leading exclusively to the ionic primary products observed under certain experimental conditions ($(CH_3)_3SnI$ adsorbed on PVG or in polar solvents). In contrast, irradiation into the shoulder at 250 nm should induce homolytic rupture of the Sn–I bond with formation of the radicals primary products.

A preliminary study of the quantum dynamics of the photodissociation of $(CH_3)_3SnI$ suggests that population of the ionic channel in a limited range around 207 nm leads to a quantum yield of ionic products higher than 50% vs. 10% for the radical product.[16] Further work will consider other degrees of freedom, such as the umbrella angle and the environment effects, which may modify drastically the mechanism by controlling the relative position of the ionic and radical channels. Another aspect of the quantum dynamics concerns the control of the ionic/radical branching ratio. This will be the subject of new simulations based on the potentials presented here.

Acknowledgements

The calculations have been carried out at the IDRIS computer center (CNRS, Orsay) through a grant of computer time from the Conseil Scientifique.

References

(1) This article is part of a Special Issue dedicated to Professor T. Ziegler.
(2) Dong, J.; Sunil, D.; Gafney, H. D.; Schwarz, S. A. *J. Non-Cryst. Non-Cryst. Solids* **2003**, *319* (1-2), 163–173. doi:10.1016/S0022-3093(02)01916-6.
(3) Borelli, N. F.; Morse, D. L.; Schreurs, J. W. H. *J. Appl. Phys. (Berl.)* **1983**, *54* (6), 3344. doi:10.1063/1.332447.
(4) Borrelli, N. F.; Morse, D. L. *Appl. Phys. Lett.* **1983**, *43* (11), 992. doi:10.1063/1.94208.
(5) Gafney, H. D. *J. Imaging Sci.* **1989**, *33*, 37.
(6) Gafney, H. D. A photochemical approach to integrated optics. In *Chemistry in industry*; Perry, D., Ed.; American Chemical Society: Plenum Press, New York; 1997; p. 189.
(7) Gafney, H. D. *J. Macromol. Sci. Chem.* **1991**, *A27*, 1187.
(8) Mendoza, E. A.; Wolkow, E.; Sunil, D.; Wong, P.; Sokolov, J.; Rafailovich, M. H.; Den Boer, M.; Gafney, H. D. *Langmuir* **1991**, *7* (12), 3046–3051. doi:10.1021/la00060a023.
(9) Mendoza, E. A.; Wolkow, E.; Rafailovich, M. H.; Sokolov, J.; Gafney, H. D.; Hansen, A. *Mater. Res. Soc. Symp. Proc.* **1990**, *168*, 381.
(10) Sunil, D.; Rafailovich, M. H.; Sokolov, J.; Gafney, H. D.; Hansen, A. *Mater. Res. Soc. Symp. Proc.* **1990**, *168*, 387.
(11) Mendoza, E. A.; Sunil, D.; Wolkow, E.; Gafney, H. D.; Rafailovich, M. H.; Sokolov, J.; Long, G. G.; Jemian, P. R.; Schwartz, S. A.; Wilkens, B. J. *Appl. Phys. Lett.* **1990**, *57* (3), 209. doi:10.1063/1.103740.
(12) Mendoza, E. A. Ph. D. thesis, The City University of New York, 1992.
(13) Dong, J.; Devi, P. S.; Sunil, D.; Mendoza, E.; Gafney, H. D. *Inorg. Chem.* **2002**, *41* (1), 11–18. doi:10.1021/ic010051c. PMID:11782138.
(14) Mendoza, E.; Gafney, H. D. *Inorg. Chem.* **1990**, *29* (24), 4853–4854. doi:10.1021/ic00349a007.
(15) Ben Amor, N.; Daniel, C. *Coord. Chem. Rev.* **2002**, *226* (1–2), 11–15. doi:10.1016/S0010-8545(01)00451-9.
(16) Benamor, N.; Ambrosek, D.; Daniel, C.; Marquardt, R. *Chem. Phys.* **2007**, *338* (2–3), 81–89. doi:10.1016/j.chemphys.2007.05.029.
(17) (a) Lee, C.; Yang, W.; Parr, R. G. *Phys. Rev. B Condens. Matter* **1988**, *37* (2), 785–789. PMID:9944570.; (b) Becke, A. D. *Phys. Rev. A At. Mol. Opt. Phys.* **1988**, *38*, 3098; (c) Becke, A. D. *J. Chem. Phys.* **1993**, *98* (7), 5648. doi:10.1063/1.464913.
(18) Bergner, A.; Dolg, M.; Küchle, W.; Stoll, H.; Preuss, H. *Mol. Phys.* **1993**, *80* (6), 1431–1441. doi:10.1080/00268979300103121.
(19) Dunning, T. H., Jr.; Hay, P. J. In *Modern theoretical chemistry*; Schaefer, H. F., III, Ed.; Plenum: New York; 1976; Vol. 3, pp. 1–28.
(20) Roos, B. O.; Lindh, R.; Malmqvist, P.-Å.; Veryazov, V.; Widmark, P.-O. *J. Phys. Chem. A* **2004**, *108* (15), 2851–2858. doi:10.1021/jp031064+.
(21) (a) Malmqvist, P.-Å.; Rendell, A.; Roos, B. O. *J. Phys. Chem.* **1990**, *94* (14), 5477–5482. doi:10.1021/j100377a011.; (b) Roos, B. O.; Taylor, P. R.; Siegbahn, P. E. M. *Chem. Phys.* **1980**, *48* (2), 157–173. doi:10.1016/0301-0104(80)80045-0.; (c) Roos, B. O. The complete active space self-consistent field method and its applications in electronic structure calculations; In *Advances in chemical physics; ab initio methods in quantum chemistry - II*, Chap. 69; Lawley, K. P., Ed.; John Wiley & Sons Ltd.: Chichester, England; 1987; p. 399.
(22) Finley, J.; Malmqvist, P.-Å.; Roos, B. O.; Serrano-Andrés, L. *Chem. Phys. Lett.* **1998**, *288* (2–4), 299–306. doi:10.1016/S0009-2614(98)00252-8.
(23) Malmqvist, P.-Å.; Roos, B. O.; Schimmelpfennig, B. *Chem. Phys. Lett.* **2002**, *357* (3–4), 230–240. doi:10.1016/S0009-2614(02)00498-0.
(24) Roos, B. O.; Malmqvist, P.-Å. *Phys. Chem. Chem. Phys.* **2004**, *6* (11), 2919. doi:10.1039/b401472n.
(25) Ajitha, D.; Wierzbowska, M.; Lindh, R.; Malmqvist, P.-Å. *J. Chem. Phys.* **2004**, *121* (12), 5761–5766. doi:10.1063/1.1784411. PMID:15367000.
(26) Liu, Y.-J.; Ajitha, D.; Krogh, J. W.; Tarnovsky, A. N.; Lindh, R. *ChemPhysChem* **2006**, *7* (4), 955–963. doi:10.1002/cphc.200500654. PMID:16596616.
(27) Frisch, M. J.; Trucks, G. W.; Schlegel, H. B.; Scuseria, G. E.; Robb, M. A.; Cheesemann, J. R.; Zakrzewski, V. G.; Montgomery, J. A., Jr.; Stratmann, R. E.; Burant, J. C.; Dapprich, S.; Millam, J. M.; Daniels, A. D.; Kudin, K. N.; Strain, M. C.; Farkas, O.; Tomasi, J.; Barone, V.; Cossi, M.; Cammi, R.; Mennuci, B.; Pomelli, C.; Adamo, C.; Clifford, S.; Ochterski, J.; Petersson, G. A.; Ayala, P. Y.; Cui, Q.; Morokuma, K.; Malick, D. K.; Rabuck, A. D.; Raghavachari, K.; Foresman, J. B.; Cioslowski, J.; Ortiz, J. V.; Stefanov, B. B.; Liu, G.; Liashenko, A.; Piskorz, P.; Komaromi, I.; Gom-

perts, R.; Martin, R. L.; Fox, D. J.; Keith, T.; Al-Laham, M. A.; Peng, C. Y.; Nanayakkara, A.; Gonzalez, C.; Challacombe, M.; Gill, P. M. W.; Johnson, B.; Chen, W.; Wong, M. W.; Andres, J. L.; Gonzalez, C.; Head-Gordon, M.; Replogle, E. S.; Pople, J. A. *GAUSSIAN software*; Gaussian 98 Inc.: Pittsburgh PA, 1998.

(28) Karlström, G.; Lindh, R.; Malmqvist, P.-Å.; Roos, B. O.; Ryde, U.; Veryazov, V.; Widmark, P.-O.; Cossi, M.; Schimmelpfennig, B.; Neogrady, P.; Seijo, L. *Comput. Mater. Sci.* **2003**, *28* (2), 222–239. doi:10.1016/S0927-0256(03)00109-5.; (a) Andersson, K.; Barysz, M.; Bernhardsson, A.; Blomberg, M. R. A.; Carissan, Y.; Cooper, D. L.; Fülscher, M. P.; Gagliardi, L.; de Graaf, C.; Hess, B. A.; Hagberg, D.; Karlström, G.; Lindh, R.; Malmqvist, P.-Å.; Nakajima, T.; Neogrády, P.; Olsen, J.; Raab, J.; Roos, B. O.; Ryde, U.; Schimmelpfennig, B.; Schütz, M.; Seijo, L.; Serrano-Andrés, L.; Siegbahn, P. E. M.; Stålring, J.; Thorsteinsson, T.; Veryazov, V.; Widmark, P.-O. *MOLCAS software*; Lund University, 2004.

(29) (a) Gillespie, R. J.; Nyholm, R. S. *Quart. Rev.* **1957**, *11* (4), 339. doi:10.1039/qr9571100339.; (b) Gillespie, R. J. *Actual. Chim.* **1973**, *4*, 27; (c) Gillespie, R. J. *Molecular geometry*; Vna Nostrand Reihold: Londres. 1972; (d) Fontaine, G. Bulletin de l'union des physiciens, No. 591, 1977; pp. 559–568; (e) Sala-Pala, J. Bulletin de l'union des physiciens, No. 648, 1982; pp. 201–244; (f) Greenwood, N. N.; Earnshaw, E. *Chemistry of the elements*; Pergamon Press, 1984.

(30) Barandiarán, Z.; Seijo, L.; Huzinaga, S. *J. Chem. Phys.* **1990**, *93* (8), 5843. doi:10.1063/1.459580.

(31) Vallet, V.; Strich, A.; Daniel, C. *Chem. Phys.* **2005**, *311* (1-2), 13–18. doi:10.1016/j.chemphys.2004.10.036.

(32) Moore, C. E. In *National Bureau of Standards*; US government printing office, WA, 1952; Volume Circular 467.

Competition between mixing and segregation in bimetallic Ag_nRb_n clusters (n = 2–10)[1,2]

René Fournier, Shaima Zamiruddin, and Min Zhang

Abstract: We found the minimum-energy structures of Ag_nRb_n (n = 2–10) clusters by a combination of density functional theory (DFT) and taboo search global optimization. The global minimum geometry is mixed for $n \leq 4$ and segregated, with a core-shell arrangement, for $n > 4$. There is a change in the nature of the bonding, from ionic to metallic, between $n = 4$ and $n = 5$. Although metallic bonding dominates at $n > 4$, large atomic charges (in the order of ±0.5) persist. These atomic charges (negative on the interior Ag atoms, positive on the surface Rb atoms) make Ag_nRb_n clusters analogous to Zintl compounds and could prevent them from coalescing. This makes them intriguing potential building blocks for cluster-assembled materials. Ag_4Rb_4 is relatively stable compared with other Ag_nRb_n clusters; it has a nearly cubic shape, a large HOMO–LUMO gap (2 eV), and a highly ionic character with atomic charges equal to roughly ±1 au.

Key words: bimetallic clusters, nanostructured materials, global energy minima, segregation, Zintl compounds.

Résumé : Nous avons déterminé les structures d'énergie minimum d'agrégats Ag_nRb_n (n = 2–10) par une méthode qui combine la théorie de la fonctionelle de la densité avec une recherche de minima par optimisation globale (recherche tabou). Les minima globaux que nous obtenons sont des structures mixtes d'alliages pour $n \leq 4$, et des structures ségrégationnée de topologie concentrique $Ag_n@Rb_n$, pour $n > 4$. La nature des liens évolue en fonction de n, avec de fortes interactions ioniques pour $n \leq 4$ et des liens de type métallique pour $n > 4$. Cependant, des charge atomiques appréciables subsistent à $n > 4$ (charges négatives sur les atomes de Ag qui sont à l'intérieur, et charges positives sur les atomes de Rb en surface). La séparation radiale des charges rend les agrégats de Ag_nRb_n analogues aux composés Zintl, et les rend probablement stables vis-à-vis la coalescence. Cette propriété ferait des agrégats de Ag_nRb_n des unités de base intéressantes pour d'éventuels matériaux. Ag_4Rb_4 est relativement stable comparé aux autres agrégats de Ag_nRb_n et possède une structure cubique ainsi qu'une forte séparation des niveaux d'énergie des orbitales frontières (2 eV) et un fort caractère ionique avec des charges atomiques de l'ordre de ±1 au.

Mots-clés : agrégats bimétalliques, matériaux à l'échelle du nanomètre, minima globaux d'énergie, ségrégation, composés Zintl.

Introduction

The structure of small metal clusters, and particularly "bimetallic" clusters, are not well-known. The phase diagrams of bulk alloys do not give reliable predictions about possible mixing in the corresponding small bimetallic clusters.[3] For alloying, as for many other things, clusters are often very different from the bulk. Many simple questions about bimetallics A_nB_p are still open. Generally, one would like to know if A and B segregate, or if they mix to form a nanoalloy. Experimentally, the structures of bimetallic clusters A_nB_p often fall into one of these three categories: mixed, core-shell, or onion-layered.[4] There is also a fourth category, "left-right segregated", that often occurs in the bulk limit because it minimizes the A–B interfacial area. A recent computational study showed that Pd–Pt clusters described by a Gupta potential adopt different types of segregated structures depending on the value of A–B interaction parameters used in the potential.[5] One could also distinguish between various mixed structures, some of them ordered, others, random. In fact, the details of A–B ordering can be intricate even in simple theoretical models of coinage (Cu, Ag, Au) bimetallic clusters.[6]

We chose to study the series of clusters Ag_nRb_n (n = 2–10) as a model to test computational methods and tackle general questions about AB order in bimetallic clusters because (*a*) it is simple (Ag and Rb atoms have only s valence electrons), (*b*) the big difference in absolute electronegativity $\chi = (I + A)/2$ (I is the ionization energy, A is the electron affinity, χ = 4.44 eV for Ag, and χ = 2.33 eV for Rb) favors mixing but, (*c*) the big difference in cohesive energies (2.95 eV for Ag, 0.85 eV for Rb) and atomic radii (1.45 Å for Ag, 2.42 Å for Rb) favor core-shell segregation. We expect (*c*) to dominate and control the structure at large n. But small clusters, where there are few or no interior atoms, could be very different, and the size evolution of structure is non-trivial. The nature of the bonding in these small clusters is also unclear a priori. Ag and Rb both have a very low ionization energy, and many aspects of Ag_n[7] and Rb_n[8] clusters are reasonably

Received 18 December 2008. Accepted 19 March 2009. Published on the NRC Research Press Web site at canjchem.nrc.ca on 23 June 2009.

R. Fournier[1] and S. Zamiruddin. Department of Chemistry, York University, Toronto, ON M3J 1P3, Canada.
M. Zhang. Department of Physics, York University, Toronto, ON M3J 1P3, Canada.

[1]Corresponding author (e-mail: renef@yorku.ca).

well-described in the jellium model.[9] So, in a way, Ag and Rb are ideal metals. But in Ag_nRb_n, ionic interactions could be important, and maybe small clusters of Ag_nRb_n are not even metallic, after all. Clusters like Ag_nRb_n are interesting for another reason. Their presumed core-shell structure, combined to large surface charges, should prevent them from coalescing. This is important for making cluster-assembed materials. For instance, size-selected metastable $Ag_n@Rb_n$ or $Ag_n@Na_n$ clusters (the @ symbol denotes a core-shell structure with the Ag atoms inside) could be relatively stable intermediates on the way to making uniform size silver clusters embedded in ionic solids (e.g., RbCl, NaCl). In fact, one can view $Ag_n@Rb_n$ as a metal cluster analog of Zintl compounds, with a true metal (Ag) in the interior instead of a semimetal (Ge, Sn, Pb, Sb, and so forth) like in the known Zintl compounds,[10] so there is a slight possibility that it could be stable in itself.

Methods

We performed global optimization by the taboo search in descriptor space (TSDS) method.[11] All energies were calculated by density functional theory (DFT) with the Perdew–Burke–Ernzerhof (PBE)[12] generalized gradient approximation to exchange-correlation and a LANL2 double-zeta (LANL2DZ) basis set as implemented in the Gaussian 03 software package.[13] The number of possibles isomers (local minima) for elemental clusters X_n is quite large; for a 13-atom cluster, it is in the order of 1000, and the number of isomers roughly triples for every additional atom.[14] However, the number of isomers for a bimetallic cluster A_nB_n is much greater than for an elemental cluster X_{2n}. Ignoring symmetry, there are $(2n)!/(n!)^2$ ways to substitute n atoms of X by atoms of A (and the rest by atoms of B). The $(2n)!/(n!)^2$ isomers of A_nB_n that result from these different ways to occupy sites with atoms of type A or B are often called "homotops".[15] For $Ag_{10}Rb_{10}$, then, an order of magnitude estimate for the number of isomers is 10^{11}. Fortunately, the optimization problem is not as difficult as it seems because the vast majority of isomers are very high in energy, *and the low-energy isomers fall into one or a few categories that share common geometric characteristics*. The TSDS algorithm exploits these resemblences among low-energy structures to quickly identify regions of configuration space where the search is likely to succeed, and it finds GMs, or good approximations to them, with very few energy evaluations even in difficult cases.[16,17] The TSDS runs for this study consisted of $(12n^2 + 30)$ iterations, where $2n$ is the number of atoms. At every iteration, TSDS produces a structure of Ag_nRb_n with predefined nearest-neighbour (NN) distances. A few preliminary runs of local optimization on arbitrary trial geometries of small Ag_nRb_n clusters show what distances are appropriate, and they were set at 2.82 Å for Ag–Ag, 4.70 Å for Rb–Rb, and 3.65 Å for Ag–Rb. For comparison, the bulk experimental interatomic distances are 2.89 Å for Ag–Ag and 4.84 Å for Rb–Rb. Other control parameters in TSDS ensure that the majority of the $(12n^2 + 30)$ structures generated in this way are topologically distinct, but a fraction of them are "distorted copies" of previous structures. These $(12n^2 + 30)$ geometries are not local minima of the potential surface, but are near local minima. For this reason, our optimization algorithm can be viewed as having an additional approximation compared to basin hopping (BH) methods,[18] but having the advantage of being much more economical (by roughly a factor of 50) compared to BH in terms of the number of energy evaluations required. The last point is, of course, crucial for doing global optimization directly on a first-principles DFT energy surface. After the TSDS iterations are complete, the $(12n^2 + 30)$ structures are ordered according to their energy and their similarity to higher ranked structures, i.e., similar structures get pushed down the ranks. The 10 to 20 top in this order constitute the lowest energy-distinct structures: we take them as initial geometries for local optimization with Gaussian 03 PBE/LANL2DZ.

To analyze trends in the final optimized structures, we use a number of geometric descriptors. Note that these are, generally speaking, different from the descriptors used during TSDS optimization. The three basic descriptors that we use for characterizing AB order are the number of A–B NN pairs m, and two variables, c and ℓ, that quantify core-shell segregation (CSS) and left–right segregation (LRS), respectively. In the following equations, a and b are indices that label atoms of type A and B, respectively, d_{ab} is the distance between a A–B pair of atoms, R_A and R_B are the atomic radii for elements A and B, $R_{AB} = R_A \pm R_B$, $\vec{P}_a$ and $\vec{P}_b$ are position vectors of the nuclei, and $\vec{C}$ is the center of mass of the cluster calculated with fictitious masses of one for all atoms. We use a simple cut-off function of interatomic distance $f(d_{ab})$ to decide if two atoms are neighbours, and add up to get the number of AB neighbour pairs.

$$\begin{aligned} f(d_{ab}) &= 1 \text{ if } d_{ab} < 1.1R_{AB} \\ &= [1.3R_{AB} - d_{ab}]/0.2R_{AB} \text{ if } 1.1 \le d_{ab}/R_{AB} \le 1.3 \\ &= 0 \text{ if } 1.3R_{AB} < d_{ab} \\ m &= 1/2\sum_{a=1}^{n}\sum_{b=1}^{n} f(d_{ab}) \end{aligned} \quad [1]$$

The two segregation variables are simple relations between centers of mass of different types of atoms.

$$\ell = \frac{1}{n}\left|\sum_{a=1}^{n}\vec{P}_a - \sum_{b=1}^{n}\vec{P}_b\right| \quad [2]$$

$$c = \frac{1}{n}\left[\sum_{a=1}^{n}|\vec{P}_a - \vec{C}| - \sum_{b=1}^{n}|\vec{P}_b - \vec{C}|\right] \quad [3]$$

We normally do not use m, ℓ, or c directly. Instead, we calculate m, ℓ, and c for all the homotops of a given structure, or a large sample of those homotops, and estimate the average "Avg" and standard deviation "SD" of m, ℓ, and c over the sample set of homotops. We sample homotops by doing a long sequence of random A–B position interchanges, calculating m, ℓ, and c each time. We denote the values of the variables for the structure itself (parent homotop) m_0, ℓ_0, and c_0, and define relative descriptors like this:

$$M = \frac{m_0 - \text{Avg}(m)}{\text{SD}(m)} \quad [4]$$

$$L = \frac{\ell_0 - \text{Avg}(\ell)}{\text{SD}(\ell)} \quad [5]$$

Fig. 1. Isomers of Ag_3Rb_3 and their relative energies (eV).

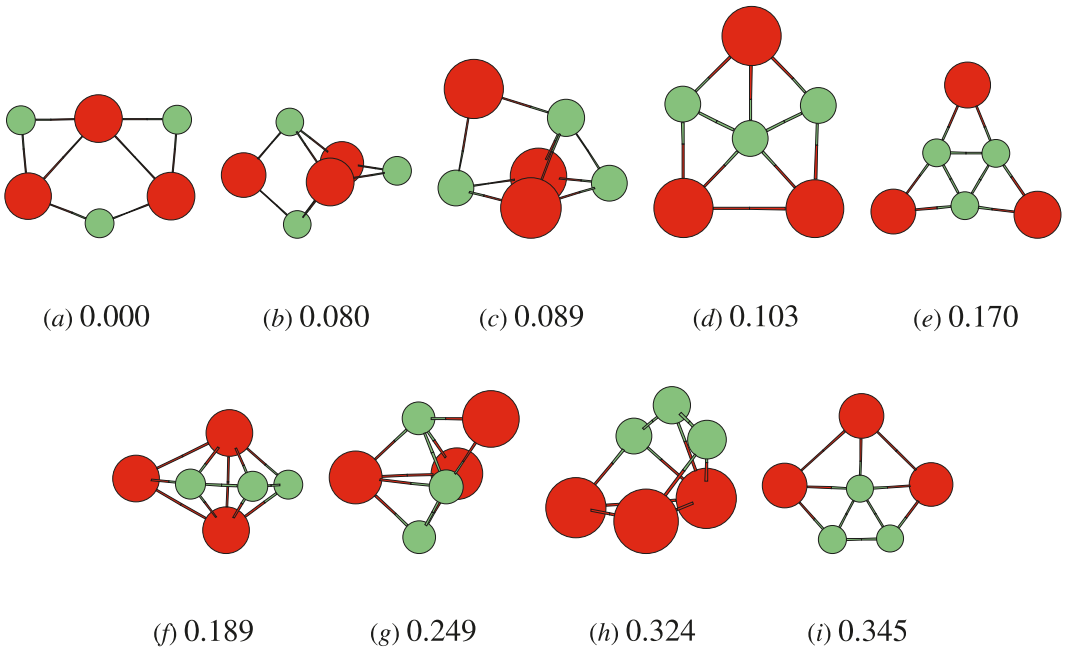

$$[6] \qquad C = \frac{c_0 - \mathrm{Avg}(c)}{\mathrm{SD}(c)}$$

So, for instance, an M value of +2.00 means that this structure has a number of A–B nearest neighbours that is larger than the average value for all of its homotops by two standard deviations; a value of zero for ℓ means that the structure has a degree of left–right segregation that is average relative to the set of all homotops to which it belongs, and so forth. Another variable that we use to quantify core-shell separation is the number of interior atoms N_i defined as follows: First, we calculate the asphericity ζ_j around each atom j by

$$[7] \qquad \zeta_j = \frac{(I_a - I_b)^2 + (I_b - I_c)^2 + (I_c - I_a)^2}{I_a^2 + I_b^2 + I_c^2}$$

where I_a, I_b, and I_c are the moments of inertia of the *neighbours* of atom j. We assign, to atom j, a number $n_j = \exp(-(\zeta_j/\zeta_0)^2)$, which tends to be close to one for interior atoms and close to zero for surface atoms, and get an effective number of interior atoms, N_i, by adding up the n_j's.

$$[8] \qquad N_i = \sum_j n_j = \sum_j \exp\left(-(\zeta_j/\zeta_0)^2\right)$$

With these definitions and $\zeta_0 = 0.0601$, we almost always get $n_j > 0.9$ for atoms that we would have classified as "interior atoms" upon visual inspection and $n_j < 10^{-5}$ for typical surface atoms. Another descriptor of geometry that we use is F_{90}, the number of 90° angles per atom. It is defined by

$$[9] \qquad F_{90} = \frac{1}{2n}\sum_j \sum_{k>\ell} \cos(\theta_{kjl} - 90°)^{100}$$

where k and ℓ index the neighbours of atom j. The exponent 100 in that formula is arbitrary, but it produces an intuitively correct count of the number of right angles.

Results and discussion

A taboo search explicitly encourages diverse solutions; therefore, it not only has a good chance of finding the global minimum (GM), but it is also likely to find many of the lowest-energy isomers. This is illustrated in Fig. 1, which shows the nine isomers found for Ag_3Rb_3 (another structure found by TSDS turned out to be a repeat of the 0.080 eV isomer). We should say a few words to put our results in perspective. We estimate that DFT-PBE gives errors of roughly 0.1 eV to 0.2 eV on relative cluster isomer energies for elements with low cohesive energy like Ag and Rb, and we believe that it is unlikely that TSDS would miss the GM but it is more likely that it would miss some (and maybe many) of the low-energy isomers. That said, there is clearly a lot of diversity among the lowest-energy structures of Ag_3Rb_3 some flat and some tridimensional, some well-mixed (e.g., 0.000 eV) and some segregated (e.g., 0.324 eV). The same is true for Ag_5Rb_5 (four very different isomers found within 0.1 eV, see Fig. 2) and Ag_6Rb_6 (three very different isomers found within 0.1 eV). The Ag_9Rb_9 and $Ag_{10}Rb_{10}$ clusters also have many isomers within 0.1 eV of the GM, but those isomers are similar, all of them have a silver core and an incomplete rubidium shell. In Fig. 3, we show the distribution of isomer energies as a function of n, and the cohesive energies of GM as a function of $N^{-1/3}$ ($N = 2n$). The number of isomers within a small energy range of the GM varies a lot. We did not find any isomer within 0.2 eV of the GM at n = 2, 4, and 8 but found five for n = 3, six for n = 5, four for n = 6, one for n = 7, four for n = 9, and six for n = 10 (some of them are indistinguishable in Fig. 3*a*).

Notwithstanding the uncertainty about the identity of the GM, it is convenient to focus on the structures and properties of the putative GM to see how they evolve with size (Figs. 3 and 4). Cohesive energies $E(N)$ of the GM (Fig. 3*b*) follow a typical trend for metal clusters; they are well-fitted by the function $E(N) = E_{bulk} + bN^{-1/3}$, with a

Fig. 2. Isomers of Ag_nRb_n ($n > 3$) within 0.10 eV of the GM and their relative energies.

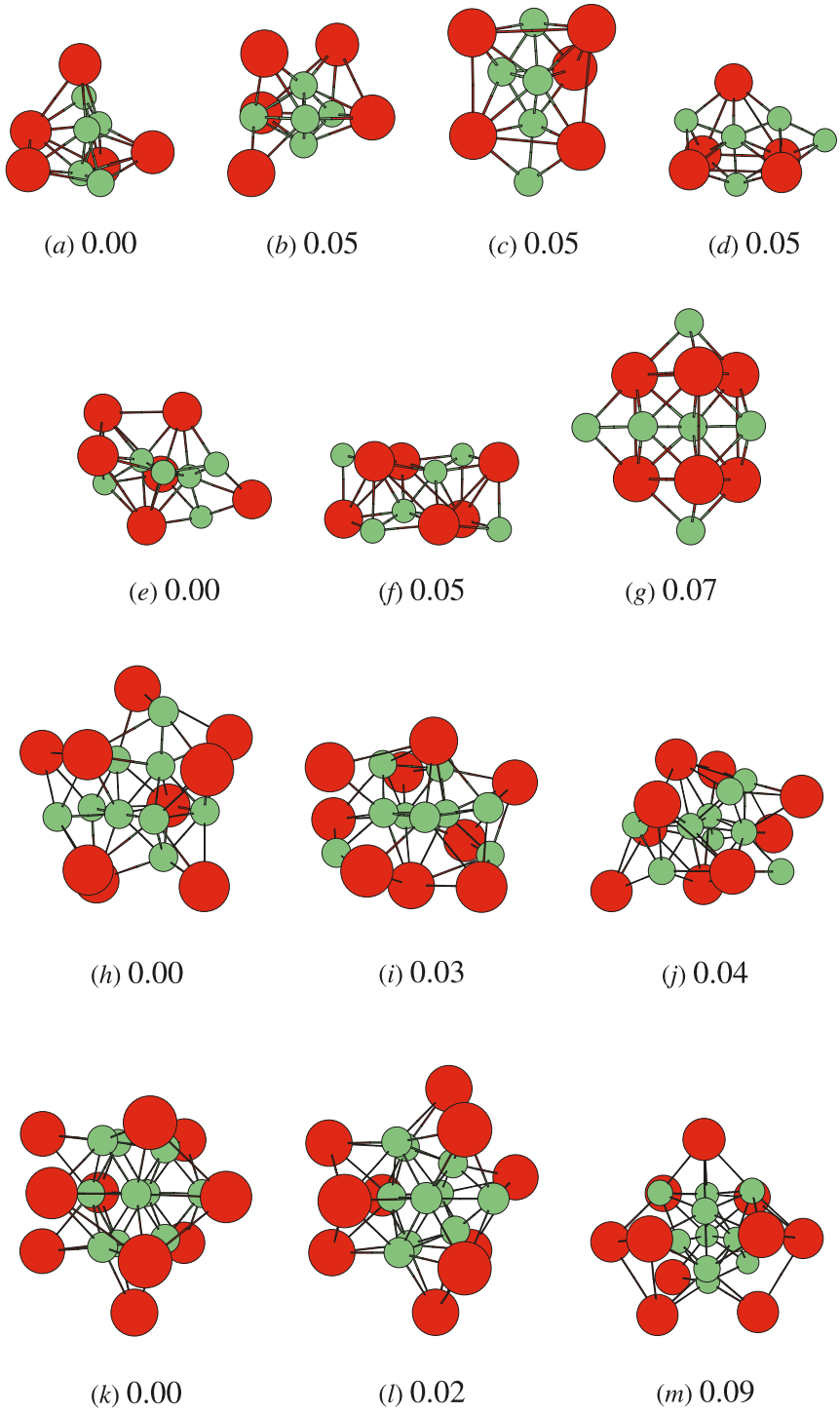

correlation coefficient of –0.9918. The intercept E_{bulk} is 1.75 eV/atom, which is 8% smaller than the average of experimental cohesive energies for Ag (2.95) and Rb (0.85). The negative of the slope (1.26) is related to surface energy: it is much smaller than the negative of the slope (3.48) that we got by fitting the Ag_n cohesive energies obtained years ago in another series of DFT calculations.[7] This is not surprising considering that the surfaces of Ag_nRb_n clusters are enriched in Rb atoms. Generally, for elemental solids and clusters, surface energy is roughly proportional to (E_c/R^2), where E_c is the cohesive energy and R is the bulk interatomic distance. So, we can get a *rough* estimate of what the slope would be for pure Rb clusters by taking $3.48 \times (0.85/2.95) \times (2.89/4.837)^2$, which is 0.36. So, the slope of 1.26 for the mixed Ag–Rb clusters must surely be very different from the pure Rb_n case also. Looking at N_i for $n = 5$ to 10, we see that it is roughly $n/4$ on average, i.e., a quarter of Ag atoms are "interior atoms" in that size interval. The weighted average $(3/4 \cdot 3.48 + 0.36)/1.75 = 1.70$ is reasonably close to 1.26, so the slope of the fit line in Fig. 3*b*

Fig. 3. Relative isomer energies, and cohesive energies of the GMs.

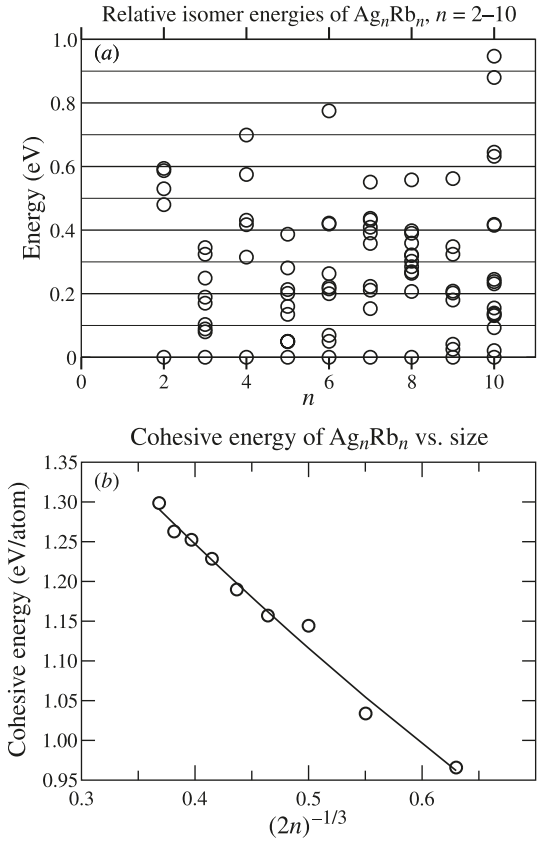

Fig. 4. Global minima.

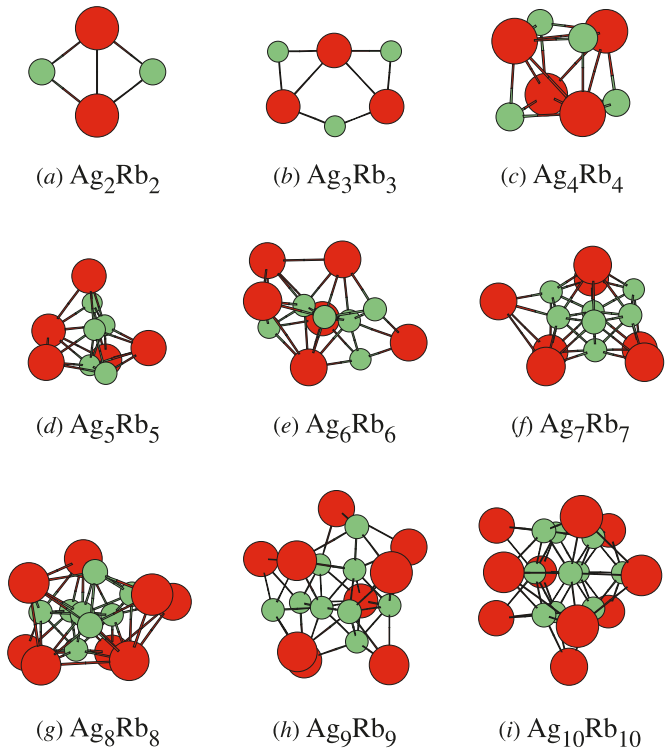

can be understood as a sort of weighted average of the surface energies of Ag and Rb. At very large n, the surface should consist entirely of Rb atoms, and the slope of a straight line fit would have to be close to –0.36, not –1.26. So, clearly, a linear function of $N^{-1/3}$ cannot fit accurately the cohesive energies of Ag_nRb_n over the entire range of n.

The n = 2–4 GM structures are very well-mixed (Figs. 4*a*–4*c*). A natural bond orbital (NBO) analysis reveals atomic charges of nearly ±0.75 in all three cases and shows that bonding is predominantly ionic. The structures in bigger clusters show a strong tendency for Ag atoms to be near the center, and by n = 8, the silver core is already fairly compact and tridimensional. The NBO analysis for $n > 4$ shows that charges are smaller (~ ± 0.50) and that a larger fraction of the valence electrons are delocalized, both of which indicate a transition from ionic to metallic bonding at around n = 5.

We also calculated atomic charges using the self-consistent charge equalization (SC QEq) method,[6,19] which is an improved version of QEq,[20] to gain more insight. In SC QEq, an electronegativity parameter χ is assigned to each element (Ag, Rb), along with parameters for the first, second, and third derivatives of χ with respect to atomic charge. These derivatives also depend on an atom's position, through its screened Coulomb interactions to other atoms, so, for instance, the Ag atoms in a given cluster do not necessarily all end up with the same charge. Atomic charges, and charge-dependent atomic electronegativities, are calculated iteratively until they satisfy the principle of electronegativity equalization.[21,22] An approximate electrostatic energy is then calculated by summing pairwise-screened Coulomb interactions. Details of the method can be found in the literature.[19] For the GM of Ag_nRb_n (n = 2, 3, and 4), the average SC QEq charges on Rb atoms are 0.76, 0.91, and 1.12, respectively. For the GM at n = 5–9, the average SC QEq charges on Rb atoms vary between 0.40 and 0.53 and have no simple relation to n, and for n = 10, it is 0.27. These SC QEq charges are not very different from the NBO charges. The SC QEq electrostatic energy per atom is strongly correlated to the average magnitude of SC QEq charges. So, the different geometric AB ordering of the GMs as a function of n, along with a simple electrostatic model that ignores quantum mechanical effects (SC QEq), are sufficient to explain some qualitative differences in bonding seen in a more rigorous (NBO) analysis. Other interesting things emerge from the SC QEq analysis. First, at $n > 4$, the average magnitudes of SC QEq charges in the GM are neither small or big compared to those in other structures found in our TSDS search. But for $n \leq 4$, the average magnitudes of SC QEq charges in the GMs are much bigger than in the other structures, which indicates ionic bonding in the GMs, and they increase as a function of size (from n = 2 to n = 4), whereas other structures show no clear trend with size. Second, the SC QEq electrostatic energies of the different isomers for a given cluster size vary over a big range: 1.1 eV (n = 2), 2.1 eV (n = 3), 3.5 eV (n = 4), 1.8 eV (n = 5), and for $n > 5$, a typical range is n/2 eV. At $n > 4$, the GMs have SC QEq electrostatic energies that are typically 2–3 eV less negative (less stable) than for the structure with most negative SC QEq electrostatic energy for that size. Third, there is a big drop in the SC QEq average Rb charge between n = 9 (0.47) and n = 10 (0.27) and, linked to that, a big drop in the mixing parameter M (Fig. 5*c*). One could say that Ag_nRb_n clusters ($n \leq 10$) are an example of a frustrated sys-

Fig. 5. Size evolution of structure and properties in the GM of Ag_nRb_n.

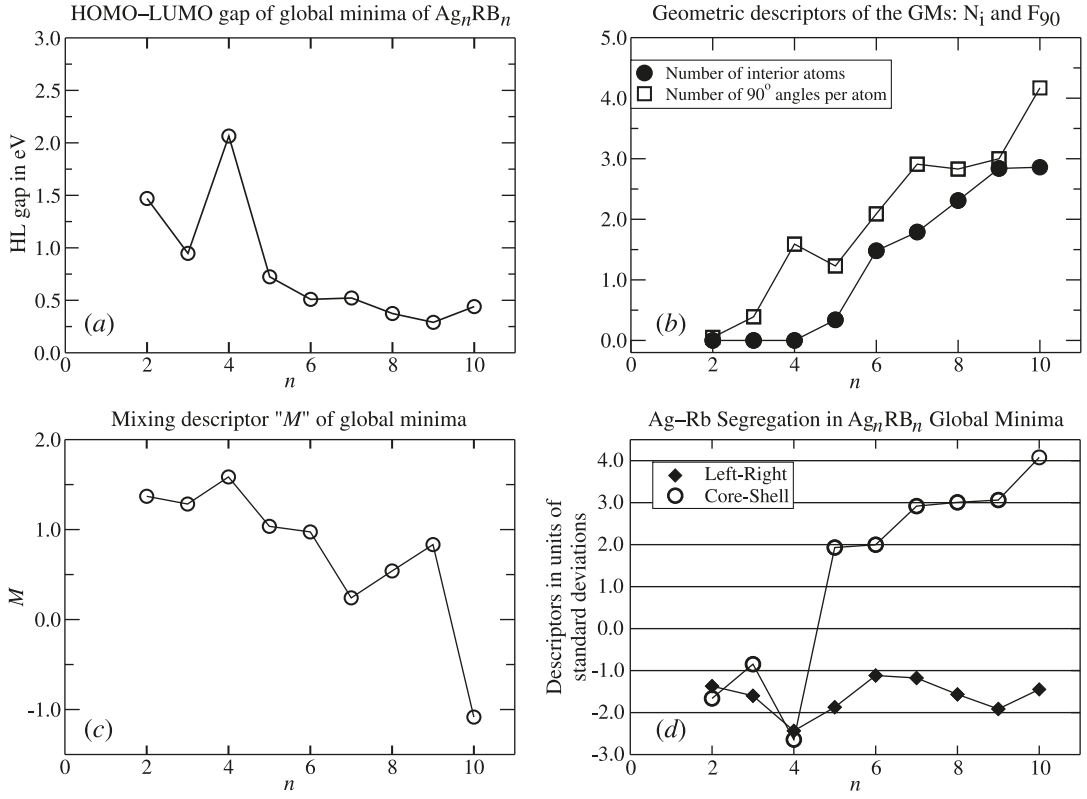

tem. Their lowest-energy structures do not necessarily minimize electrostatic energy, or surface energy (i.e., do not maximize the number of nearest neighbours). Instead, the GM structures are normally the best compromise between these two things, and evolve with size from mixed ($n \leq 4$) to "mostly core-shell segregated" ($n = 10$). We wanted to see how much difference there is between the GM of Ag_nRb_n ($n > 4$) and ideal CSS structures. To do that, we calculated the mean coordination "x" in hypothetical Ag_n clusters that consist of the n Ag atoms at their positions in the GM of Ag_nRb_n, $x(Ag;Ag_nRb_n)$; and for comparison, we calculated the mean coordinations of Ag atoms in the GM of Ag_n clusters that we had previously obtained,[7] $x(Ag;Ag_n)$. In either case, x is the mean number of Ag atom neighbours around a Ag atom. An ideal Ag_nRb_n CSS structure would have a central compact Ag_n subunit with a structure comparable to, and roughly as compact as, that of a pure Ag_n cluster. What we find, going in order from $n = 2$ to $n = 10$, is $x(Ag;Ag_nRb_n)$ = 0.0, 0.0, 0.0, 2.4, 2.3, 3.4, 3.5, 3.3, and 4.6. These values are much smaller than the corresponding $x(Ag;Ag_n)$; going again in order from $n = 2$ to $n = 10$, we have $x(Ag;Ag_n)$ = 1.0, 2.0, 2.5, 2.8, 3.0, 4.6, 4.5, 4.7, and 5.2. We see that the Ag_n subunits in Ag_nRb_n are a lot less compact than Ag_n clusters, except maybe for $n = 5$ and $n = 10$. This again shows that the GM of Ag_nRb_n ($n > 4$) represent a compromise between minimizing surface energy and maximizing ionic energy (mixing).

The size evolution of the HOMO–LUMO gap and some geometric descriptors of the GMs are shown in Fig. 5. The peak in HOMO–LUMO gap at $n = 4$ is remarkable. Two other things indicate special stability for Ag_4Rb_4: the $E(n = 4)$ point is well above the fit line of cohesive energies (Fig. 3*b*), and the second most stable isomer found for Ag_4Rb_4 is much higher (0.3 eV) than the GM (Fig. 3*a*). It is tempting to ascribe that to the eight-electron count, which is a closed shell in the jellium model. However, the difference in bulk electron densities of Ag and Rb, 0.0087 – 0.0017 = 0.0070 au, is very close to the critical value (0.0080 au) beyond which one normally sees inversion of the 2s and 1d jellium levels and magic numbers of 2, 10 (instead of 8), and 20.[3, 23] Also, the large atomic charges (NBO and SC QEq) in Ag_4Rb_4 indicate that ionic bonding is more important than delocalized metallic bonding. The SC QEq electrostatic energy, which is admittedly very approximate, amounts to 60% of the KS-DFT-PBE atomization energy of Ag_4Rb_4. Aside from the anomaly at $n = 4$, and maybe $n = 10$, HOMO–LUMO gaps decrease smoothly from $n = 2$ to $n = 10$, suggesting a gradual transition from ionic to metallic bonding.

There is a rationale for why the transition from mixed to CSS structure should occur near $n = 5$. Ionic bonding favors mixed structures at any size. On the other hand, the difference in surface energies between Ag and Rb, which is *roughly* $E_s(Ag) - E_s(Rb) \approx 0.4 \times (2.95 - 0.85) = 2.1$ eV per surface atom, favors CSS structures, i.e., it disfavors mixing, but only provided that the number of interior atoms (N_i) is not zero of course. Generally speaking, for metal clusters, one expects that N_i becomes nonzero for clusters with more than roughly 12 atoms because the 13-atom icosahedron is the smallest cluster in the polytetrahedral growth sequence with one interior atom. For structures other than polytetrahedral, N_i can become nonzero at slightly smaller or slightly bigger size. In mixed A_nB_n clusters where the el-

ement with lowest cohesive energy has a bigger atomic radius, like Ag_nRb_n, the smallest cluster size with one interior atom can occur at a smaller size, 10 atoms ($n = 5$) in our case (see Fig. 5*b*). As soon as clusters are big enough to accommodate one interior atom, the maximally mixed structure is no longer automatically favored, and the GM are generally "structures of compromise". Using a crude model (see Appendix 1), we estimate that the surface energy of a CSS structure is lower than that of a mixed (ionic) structure by an amount ΔU_s that is roughly $(2n - 8) \times 0.43$ eV in Ag_nRb_n clusters ($n > 4$). On the other hand, as we said earlier, the range in calculated SC QEq electrostatic energies among different isomers of Ag_nRb_n is roughly $0.5n$ eV. So, these two contributions to energy differences between mixed and segregated structures have comparable magnitudes, and they both scale roughly as n, which gives a rationale for why, starting with $n = 5$, the structures of GM are neither of the mixed nor the ideal (compact) core-shell type.

There remains a strong ionic character (charges of ±0.5) even in the largest clusters. This has an effect on the preferred geometries of Ag_nRb_n clusters. In particular, the number of 90° bond angles (F_{90}) per atom is large compared with other metal clusters: F_{90} varies between 1 and 4 for Ag_nRb_n ($n > 3$), and it is 2.1 for $n = 6$ (12-atom cluster) and 2.9 for $n = 7$ (14-atom cluster). The average of 2.1 and 2.9, 2.5, can be compared to the F_{90} value we found for the calculated GM of 26 different 13-atom metal clusters.[17] Of those 26 cases, only six (Tc_{13}, Ru_{13}, Rh_{13}, Re_{13}, Os_{13}, Ir_{13}) had $F_{90} > 2.5$. The large F_{90} values in those six cases were explained by the participation of d orbitals in bonding; but this explanation obviously cannot apply to Ag_nRb_n. The largest F_{90} we calculated[17] for 13-atom clusters of group 1, 2, 11, or 12 in the periodic table was 1.5 (for Zn_{13}), much smaller than 2.5. We think that the large F_{90} in Ag_nRb_n is a consequence of the large ionic contribution to bonding and the effect this has on A–B ordering, since cubic packing (as in NaCl) would minimize the electrostatic energy. The tendency to adopt structures with large F_{90} is not limited to the GM of Ag_nRb_n; several isomers (some of them not shown here) have prismatic or square arrangements of Rb atoms, e.g., Fig. 2*g* and 2*k*. It is also interesting to track the number of interior atoms, N_i, as a function of n (see Fig. 5*b*), but we are unable to predict accurately the size where $N_i = n$, i.e., the smallest cluster with n interior Ag atoms covered by a "monolayer" of n Rb atoms (this would correspond to the closure of an atomic shell in the core-shell growth sequence and could give enhanced stability). A simple geometric model leads us to predict that, within the Ag_nRb_n sequence, the Rb shell of the atoms becomes complete only at $n = 30$, *roughly*.

The mixing descriptor M and core-shell segregation parameter C (Figs. 4*j* and 4*k*) both undergo a sudden change between $n = 4$ and $n = 5$. The value of M starts off very large (at $n = 2$) and goes down but remains above zero until $n = 10$. As expected, the large electronegativity difference between Ag and Rb favors mixing. The drop of M at $n = 10$ shows that the driving force for having Ag atoms inside (difference in surface energies of Ag and Rb) is bigger than the driving force for mixing (difference in electronegativities of Ag and Rb). There is no special significance to M becoming negative at precisely $n = 10$. It happens partly because, with increasing number of atoms, there are many more ways to make highly mixed homotops, which makes the CSS structures appear poorly mixed in a relative sense (see eq. [4]). The C values get very large at $n > 4$ (+2.0 to +4.0) while L always stays negative; this shows that Ag_nRb_n has indeed a strong tendency to form core-shell structures, even for n values as small as 5.

The shape descriptor, $\eta = (2I_b - I_a - I_c)/I_a$, of the GMs of Ag_nRb_n is negative for $2n = 4$, 6, 14, 16, and 18, positive for $2n = 10$ and 12, and very nearly zero for $2n = 8$ and 20. These predictions of oblate, prolate, and spherical shapes agree with the ellipsoidal jellium model in every case except Ag_2Rb_2. The peaks in the HOMO–LUMO gap at $2n = 8$ and 20 also agree with the jellium model, but this is partly coincidental. For instance, the structure of Ag_4Rb_4 is optimal for ionic bonding (it is cubic), and also for accomodating a spherical closed-shell of eight electrons ($I_a = I_b = I_c$) as per the jellium model, but bonding in Ag_4Rb_4 is predominantly ionic. However, the agreement of DFT and EJM cluster shapes for all cases at $n \geq 5$ is probably not entirely accidental either. The EJM may be a crude model of electronic structure, but it gives a qualitatively correct relation between cluster shape and orbital symmetry and energies. These effects of shape and orbital symmetry are implicitly included in a more complete theory like DFT and may well give a small energetic preference (maybe in the order of a few tenths of eV) to structures that conform to the EJM.

In conclusion, the structures and nature of chemical bonding in Ag_nRb_n clusters evolve from mixed AB structures having ionic bonding for $n \leq 4$ to CSS structures where metallic bonding dominates but where ionic bonding is still important for $n = 5$ to 10. The Ag_4Rb_4 clusters are special for their relative stabilities and large HOMO–LUMO gaps. The geometric structures of Ag_nRb_n ($n = 5$ to 10) have a Ag core and an incomplete Rb shell, but the Ag core is not very compact. These structures are the result of a compromise between metallic and ionic contributions to bonding. Atomic charges on the Rb outer-shell atoms in $Ag_{10}Rb_{10}$ are calculated to be +0.3; this may be large enough to prevent coalescence of larger $Ag_n@Rb_n$ clusters having a complete Rb outer shell.

Acknowledgements

RF is grateful to the European Science Foundation (ESF) for supporting the *2008 Workshop on Computational Nanoalloys* where participants discussed many ideas that are relevant to the work presented here, and to the Natural Sciences and Engineering Research Council of Canada (NSERC) for research funding.

References

(1) This article is part of a Special Issue dedicated to Professor T. Ziegler.
(2) This manuscript is dedicated to Tom Ziegler on the occasion of his 65th birthday.
(3) Alonso, J. A; *Structure and properties of atomic nanoclusters*; Imperial College Press: London, 2005.
(4) Ferrando, R.; Jellinek, J.; Johnston, R. L. *Chem. Rev.* **2008**, *108* (3), 845–910. doi:10.1021/cr040090g.
(5) Paz-Borbón, L. O.; Gupta, A.; Johnston, R. L. *J. Mater. Chem.* **2008**, *18* (35), 4154. doi:10.1039/b805147j.

(6) Zhang, M.; Fournier, R. *J. Mol. Struct. THEOCHEM* **2006**, *762* (1-3), 49–56. doi:10.1016/j.theochem.2005.08.042.
(7) Fournier, R. *J. Chem. Phys.* **2001**, *115* (5), 2165. doi:10.1063/1.1383288.
(8) Bhaskar, N. D.; Frueholz, R. P.; Klimcak, C. M.; Cook, R. A. *Phys. Rev. B* **1987**, *36* (8), 4418–4421. doi:10.1103/PhysRevB.36.4418.
(9) (a) de Heer, W. A. *Rev. Mod. Phys.* **1993**, *65* (3), 611–676. doi:10.1103/RevModPhys.65.611.; (b) Brack, M. *Rev. Mod. Phys.* **1993**, *65* (3), 677–732; and refs. therein. doi:10.1103/RevModPhys.65.677.
(10) Corbett, J. D. *Angew. Chem., Int. Ed.* **2000**, *39* (4), 670–690. doi:10.1002/(SICI)1521-3773(20000218)39:4<670::AID-ANIE670>3.0.CO;2-M.
(11) Cheng, J.; Fournier, R. *Theor. Chem. Acc.* **2004**, *112*, 7.
(12) (a) Perdew, J. P.; Burke, K.; Ernzerhof, M. *Phys. Rev. Lett.* **1996**, *77* (18), 3865–3868. doi:10.1103/PhysRevLett.77.3865. PMID:10062328.; (b) Perdew, J. P.; Burke, K.; Ernzerhof, M. *Phys. Rev. Lett.* **1997**, *78* (7), 1396. doi:10.1103/PhysRevLett.78.1396.
(13) Frisch, M. J.; Trucks, G. W.; Schlegel, H. B.; Scuseria, G. E.; Robb, M. A.; Cheeseman, J. R.; Montgomery, J. A., Jr.; Vreven, T.; Kudin, K. N.; Burant, J. C.; Millam, J. M.; Iyengar, S. S.; Tomasi, J.; Barone, V.; Mennucci, B.; Cossi, M.; Scalmani, G.; Rega, N.; Petersson, G. A.; Nakatsuji, H.; Hada, M.; Ehara, M.; Toyota, K.; Fukuda, R.; Hasegawa, J.; Ishida, M.; Nakajima, T.; Honda, Y.; Kitao, O.; Nakai, H.; Klene, M.; Li, X.; Knox, J. E.; Hratchian, H. P.; Cross, J. B.; Bakken, V.; Adamo, C.; Jaramillo, J.; Gomperts, R.; Stratmann, R. E.; Yazyev, O.; Austin, A. J.; Cammi, R.; Pomelli, C.; Ochterski, J. W.; Ayala, P. Y.; Morokuma, K.; Voth, G. A.; Salvador, P.; Dannenberg, J. J.; Zakrzewski, V. G.; Dapprich, S.; Daniels, A. D.; Strain, M. C.; Farkas, O.; Malick, D. K.; Rabuck, A. D.; Raghavachari, K.; Foresman, J. B.; Ortiz, J. V.; Cui, Q.; Baboul, A. G.; Clifford, S.; Cioslowski, J.; Stefanov, B. B.; Liu, G.; Liashenko, A.; Piskorz, P.; Komaromi, I.; Martin, R. L.; Fox, D. J.; Keith, T.; Al-Laham, M. A.; Peng, C. Y.; Nanayakkara, A.; Challacombe, M.; Gill, P. M. W.; Johnson, B.; Chen, W.; Wong, M. W.; Gonzalez, C.; Pople, J. A. *Gaussian 03*, Revision C.02; Gaussian, Inc.: Wallingford, CT, 2004.
(14) (a) Chekmarev, S. F. *Phys. Rev. E Stat. Nonlin. Soft Matter Phys.* **2001**, *64* (3 Pt 2),o. 036703. PMID:11580478.; (b) Tsai, C. J.; Jordan, K. D. *J. Phys. Chem.* **1993**, *97* (43), 11227–11237. doi:10.1021/j100145a019.
(15) Jellinek, J.; Krissinel, E. B. *Chem. Phys. Lett.* **1996**, *258* (1-2), 283–292. doi:10.1016/0009-2614(96)00636-7.
(16) Fournier, R. *J. Chem. Theory Comput.* **2007**, *3* (3), 921–929. doi:10.1021/ct6003752.
(17) Sun, Y.; Zhang, M.; Fournier, R. *Phys. Rev. B* **2008**, *77* (7),o. 075435. doi:10.1103/PhysRevB.77.075435.
(18) (a) Wales, D.; Doye, J. *J. Phys. Chem. A* **1997**, *101* (28), 5111–5116. doi:10.1021/jp970984n.; (b) Doye, J.; Wales, D. *Phys. Rev. Lett.* **1998**, *80* (7), 1357–1360. doi:10.1103/PhysRevLett.80.1357.
(19) Zhang, M.; Fournier, R. *J. Phys. Chem. A* **2009**, *113* (13), 3162–3170. doi:10.1021/jp8063273. PMID:19320517.
(20) Rappe, A. K.; Goddard, W. A., III. *J. Phys. Chem.* **1991**, *95* (8), 3358–3363. doi:10.1021/j100161a070.
(21) Sanderson, R. T. *Science* **1951**, *114* (2973), 670–672. doi:10.1126/science.114.2973.670. PMID:17770191.
(22) Sanderson, R. T; *Chemical bonds and bond energy*; 2nd ed; Academic Press: New York, 1976.
(23) Baladrón, C.; Alonso, J. A. *Physica B* **1988**, *154* (1), 73–81. doi:10.1016/0921-4526(88)90019-1.
(24) Somorjai, G. A; *Introduction to surface chemistry and catalysis*; Wiley: New York, 1994.

Appendix I. Model of surface energy in mixed and core-shell A_nB_n clusters

We want to estimate the energy difference, ΔU_s, arising from the different surface area, structure, and composition at the surface of two qualitatively different types of A_nB_n cluster structures (ionic and maximally mixed (IMM), and core-shell (CS)). A model like SC QEq could be used to estimate energy differences due to electrostatics, ΔU_e. The sign of $\Delta U_s + \Delta U_e$ could then be used to make qualitative predictions of cluster structure in A_nB_n mixed clusters.

We assume that IMM clusters have a packing similar to the simple cubic crystal structure and have a cubic shape, whereas the CS clusters are spherical with atoms packed in a way similar to fcc. These assumptions clearly cannot be exact for small clusters, but they hopefully capture an essential difference in the surface-to-volume ratio for the two types. So, the volume V and surface area A of the two structure types are estimated to be

$$[A1] \qquad \begin{array}{ll} \text{IMM} & \left\{ \begin{array}{l} V = Nv\sqrt{2} \\ A = 6V^{2/3} = 7.560(Nv)^{2/3} \end{array} \right\} \\ \text{CS} & \left\{ \begin{array}{l} V = Nv \\ A = 4.836V^{2/3} = 4.836(Nv)^{2/3} \end{array} \right\} \end{array}$$

where $N = 2n$ is the number of atoms and v is the average of the bulk atomic volumes for elements A and B. The surface of an IMM cluster is assumed to have A–B composition of 50%:50%, so the surface energy for IMM can be estimated as

$$[A2] \qquad U_s = (A_{IMM}/a)E_c \times 0.4$$

where E_c is the average of the two cohesive energies ((0.85 + 2.95)/2 = 1.90 eV for Ag–Rb) and a is the square of the average of bulk A–A and B–B distances (14.9 Å^2 for Ag–Rb); a is a rough estimate of surface area per atom in a mixed ordered A–B surface. The factor 0.4 is empirical; a factor of 0.16 would be appropriate for surface atoms of macroscopic particles,[24] but the cohesive energy of very small metal clusters (those with $N_i = 0$) is often close to 60% of the bulk cohesive energy, which motivates the choice of 0.4. The composition of the surface of a CS cluster depends on the number N_i of interior atoms. If N_i is large enough, the surface of CS clusters have only atoms of type "B" (the one with lowest surface energy), and in this particular case, the surface energy of the CS cluster would be

$$[A3] \qquad U_s = (A_{CS}/R_B^2)E_{c,B} \times 0.4$$

Let us define $f_m = 7.56E_c/a$ and $f_c = 4.836E_{c,B}/R_B^2$. Then, the surface energy for IMM is $f_m \times 0.4 \times (Nv)^{2/3}$, and the surface energy of a very large CS cluster is $f_c \times 0.4 \times (Nv)^{2/3}$. For the Ag–Rb case, $0.4 \times v^{2/3} = 4.78$ Å^2. When a CS cluster is not too large, there are $N_i < n$ interior atoms, and the surface composition is not 100% B. Instead, it is closer to $(N/2 - N_i)$ atoms of A and $N/2$ atoms of B, or alter-

natively, $(N - 2N_i)$ of AB, and N_i of B. So, we calculate a factor f_x for intermediate size CS cluster like this:

[A4] $$f_x = [(N - 2N_i)f_m + N_i f_c]/(N - N_i)$$

and estimate the surface energy of the CS cluster as

[A5] $$\begin{aligned} U_s &= f_x \times 0.4 \times (Nv)^{2/3} \\ &= f_x \times 4.78 \times N^{2/3} \text{ for Ag}-\text{Rb} \end{aligned}$$

From our calculated N_i values (Fig. 5*b*), we can propose a simplified approximate relation between N_i and N, $N_i \approx (N - 4)/2$. Using this relation and the equations above, we can estimate the contribution ΔU_s to the energy difference between IMM- and CS-type structures that is specifically due to surface structure and composition. We find ΔU_s = 0, 1.8, 3.4, and 4.9 eV for N = 8, 12, 16, and 20, respectively.

Ab initio electronic structure and direct dynamics simulations of CH_3OCl[1]

Stephanie Y. Y. Wong, Pierre-Nicholas Roy, and Alex Brown

Abstract: The ground (X^1A') and two lowest lying excited singlet states ($1^1A''$ and $2^1A'$) of methyl hypochlorite have been examined using ab initio electronic structure techniques to validate computationally efficient methods, upon which direct dynamics can be based, versus high-level ones, for which direct dynamics would be intractable. Ground-state equilibrium geometries and vibrational frequencies determined using density functional theory (DFT) with the 6-31G(d) basis set are tested against coupled-cluster theory (CCSD(T)) results from the literature. Vertical excitation energies and transition dipole moments calculated at the complete active space self-consistent field CASSCF/6-31+G(d) level of theory are benchmarked against multireference configuration interaction (MRCI) results with the aug-cc-pV*X*Z (*X* = D, T, Q) family of basis sets. The excited-state gradients that will govern the classical dynamics are compared for CASSCF/6-31+G(d) versus MRCI/aug-cc-pV*X*Z (*X* = D, T). To carry out the ab initio molecular dynamics (AIMD), existing electronic structure codes have been interfaced with the molecular modelling toolkit (MMTK), an open-source program library for molecular simulation applications. We use two examples to demonstrate the use of direct dynamics in MMTK: a canonical ground-state trajectory to sample positions and momenta, and an excited-state microcanonical trajectory based on CASSCF. The work presented here forms the basis for future study of the photodissociation of CH_3OCl. As well, the implementation of AIMD within MMTK provides a useful tool for examining a variety of other research problems.

Key words: ab initio molecular dynamics, excited states, atmospheric chemistry, electronic spectroscopy.

Résumé : Faisant appel à une technique de structure électronique ab initio, on a étudié l'état fondamental (X^1A') et les deux états singulets excités de plus basse énergie ($1^1A''$ and $2^1A'$) de l'hypochlorite de méthyle afin de valider les méthodes de calcul numériques sur lesquelles des dynamiques directes pourraient être basées par opposition aux méthodes de haut niveau dont le coût serait prohibitif. Les géométries d'équilibre de l'état fondamental et les fréquences de vibration déterminées à l'aide de la théorie de la fonctionnelle de la densité (TFD) avec un ensemble de base 6-31G(d) ont été comparées avec les résultats obtenus avec la méthode CCSD(T) et rapportés dans la littérature. Les énergies d'excitation verticale et les moments dipolaires de transition calculés au niveau (CASSCF)/6-31+G(d) de la théorie avec champ autocohérent de l'espace actif complet sont utilisées comme référence et comparées aux résultats de l'interaction de configuration multiréférence (MRCI) avec des familles d'ensembles de base aug-cc-pV*X*Z (*X* = D, T, Q). Les gradients de l'état excité qui gouverneront les dynamiques classiques obtenus au niveau (CASSCF)/6-31+G(d) sont comparés avec ceux obtenus au niveau MRCI/aug-cc-pV*X*Z (*X* = D, T). Dans le but d'effectuer des calculs ab initio de dynamiques moléculaires (AIDM), on a établi une interface entre les codes existants de structure électronique et le « molecular modelling toolkit (MMTK) », une source ouverte de programmes pour des applications de simulation moléculaire. On a examiné deux exemples pour démontrer l'utilisation des dynamiques directes dans MMTK: positions et impulsions de la trajectoire d'un état fondamental canonique et une trajectoire macrocanonique d'un état excité basée sur CASSCF. Les résultats présentés ici forment la base d'une étude future sur la photodissociation du CH_3OCl. De plus, l'implantation d'AIMD dans MMTK fournit un outil utile pour étudier une variété d'autres problèmes de recherche.

Mots-clés : dynamique moléculaire ab initio, états excités, chimie de l'atmosphère, spectroscopie électronique.

I. Introduction

The stratospheric molecule CH_3OCl has been shown to be important in ozone chemistry through its role as a reservoir for Cl.[2] Therefore, it is important to understand the loss mechanisms for CH_3OCl, including its UV absorption and subsequent decomposition. Gas-phase experiments have shown there to be two CH_3OCl absorption peaks between the range of 200–400 nm. The absorption peak at 236 nm is strong and narrow while the one at 310 nm is weaker and broader.[3] Due to its structural and spectral similarities to HOCl,[4,5] it has been predicted that CH_3O and Cl would be the photolysis products.[2,5] The dominant reaction upon photolysis via either absorption peak was confirmed experimentally[6,7] as

$$[1] \qquad CH_3OCl + h\nu \rightarrow CH_3O(X^2E) + Cl(^2P)$$

where the chlorine atom could be produced in either its spin–orbit ground ($^2P_{3/2}$) or excited ($^2P_{1/2}$) state. Theoretical

Received 16 October 2008. Accepted 2 April 2009. Published on the NRC Research Press Web site at canjchem.nrc.ca on 25 June 2009.

S.Y.Y. Wong and A. Brown. Department of Chemistry, University of Alberta, Edmonton, AB T6G 2G2, Canada.
P.-N. Roy.[1] Department of Chemistry, University of Waterloo, Waterloo, ON N2L 3G1, Canada.

[1]Corresponding author (e-mail: pnroy@uwaterloo.ca).

Table 1. Equilibrium geometry of CH_3OCl at the B3LYP/6-31G(d) level of theory as compared to previous benchmark results. H_a refers to the H atom lying in the same plane as C–O–Cl, while $H_{b,c}$ are the two out-of-plane hydrogen atoms.

Parameter	This work (B3LYP/6-31G(d))	Reference 9 (CCSD(T)/6-311G(2df,2p))	Reference 11 (CCSD(T)/cc-pVTZ)
Bond lengths (Å)			
$r_{C—O}$	1.425	1.425	1.425
$r_{O—Cl}$	1.736	1.709	1.689
$r_{C—Ha}$	1.096	1.089	1.089
$r_{C—Hb,c}$	1.097	1.091	1.089
Bond/dihedral angles (°)			
$\theta_{C–O–Cl}$	110.4	109.2	109.3
$\theta_{Ha–C–O}$	103.3	104.4	—
$\theta_{Hb,c–C–O}$	111.9	111.4	—
$\tau_{Hb,c–C–O–Cl}$	62.0	61.5	—

Table 2. Vibrational frequencies and assignments (cm^{-1}) at the B3LYP/6-31G(d) level of theory compared to experimental results and previous benchmark calculations.

Assignment	This work (B3LYP/6-31G(d))	Reference 5 (Experiment)	Reference 9 (CCSD(T)/6-311G(2df,2p))	Reference 11 (CCSD(T)/cc-pVTZ)
CH_3 torsion	260	—	254	261
C–O–Cl bend	365	—	373	365
O–Cl stretch	659	680	692	661
C–O stretch	1023	1002	1046	1020
$H_{b,c}$–C–O rock	1183	1150	1180	1181
H_a–C–O rock	1206	1170	1201	1284
CH_3 umbrella	1477	1424	1467	1475
C–H asymm. bend	1487	1456	1479	1488
H_b–C–H_c scissor	1538	1471	1516	1537
CH_3 symm. stretch	3035	2820	3040	3038
H_b–C–H_c asymm. stretch	3109	2904	3117	3113
H_a–C–H_b asymm. stretch	3131	2920	3144	3133

determination of the excited states[8] demonstrated their highly repulsive nature along the Cl–O coordinate. Butler and co-workers[6] measured the velocity distributions of the photofragments resulting from photodissociation at 248 nm. All their data could be fit assuming Cl and CH_3O as the only photoproducts. They determined that the CH_3O fragments had a narrow range of internal energies (vibration and primarily rotation). Schindler et al.[7] used resonantly enhanced multiphoton ionization time-of-flight mass spectrometry to measure the Cl atom fragments produced following excitation at 308 nm and 235 or 237 nm; different wavelengths were used to detect $Cl(^2P_{3/2})$ versus $Cl(^2P_{1/2})$. The chlorine atoms were formed with nearly unity probability at both wavelengths. Interestingly, the ratio of spin-orbit excited to ground-state chlorine atoms, $Cl(^2P_{1/2})/Cl(^2P_{3/2})$, was strongly wavelength dependent with a value of 0.31 ± 0.02 at 308 nm and 1.45 ± 0.05 at 235 nm. Clearly, the photodissociation dynamics of CH_3OCl is quite rich, and thus, it is a useful model molecule for our study.

Francisco[9] completed an equilibrium structure and vibrational frequency study of CH_3OCl with density functional theory B3LYP/6-31++G(3df,3pd) and coupled-cluster theory CCSD(T)/6-311G(2df,2p) where the results show a structure similar to that of methanol. Li and Francisco[8] have determined energetics for low-lying singlet and triplet excited electronic states using complete active space self-consistent field (CASSCF) followed by internally-contracted multireference configuration interaction (MRCI) with cc-pVTZ and (or) cc-pVTZ+sp basis sets. Peyerimhoff and co-workers[10,11] have examined similar properties for CH_3OCl using CCSD(T)/cc-pVTZ (equilibrium structure and vibrational frequencies) and MRCI/cc-pVTZ+sp (vertical excitation energies). The goal of the present study is not to reproduce these results, but to demonstrate that a computationally efficient method will provide an energetically correct characterization of CH_3OCl, consistent with the previously reported findings above. The necessity for a merely "sufficient" method is to be able to conduct direct dynamics simulations. To this effect, single-point calculations along the O–Cl bond coordinate are demonstrated to semiquantitatively provide the potential-energy surface and energy gradients of the first three singlet states. In the present study, we neglect the roles that low-lying triplet states and spin-orbit coupling play in the dissociation process. In the Franck–Condon region, the singlet ground-to-triplet excited-state transitions are essentially forbidden, and, thus, the triplet states play no role in the initial excitation process. As the molecule dissociates, coupling between the singlet and triplet states becomes important as the states approach the asymptote and are energetically similar. The coupling manifests itself in the production of both $Cl(^2P_{3/2})$ and $Cl(^2P_{1/2})$ fragments. Therefore, if one wants to interpret the experimental measure-

Table 3. Vertical excitation energies (eV) and, when determined, transition dipole moments (Debye) from the ground (X^1A') to the first ($1^1A''$) and second ($2^1A'$) excited states. Present results determined at the CCSD(T)/6-311G(2df,2p) equilibrium geometry.[9]

			Transition energy (transition dipole moment)	
Reference	Basis	Method	$1^1A'' \leftarrow X^1A'$	$2^1A' \leftarrow X^1A'$
Present work	aug-cc-pVDZ	CASSCF	4.826 (0.262)	5.957 (0.430)
		MRCI	4.136 (0.052)	5.317 (0.257)
	aug-cc-pVTZ	CASSCF	4.364 (0.283)	5.804 (0.338)
		MRCI	4.132 (0.079)	5.268 (0.264)
	aug-cc-pVQZ	CASSCF	4.371 (0.324)	5.802 (0.417)
		MRCI	4.133 (0.089)	5.269 (0.270)
	6-31+G(d)	CASSCF[a]	4.313 (0.282)	5.782 (0.331)
		CASSCF[b]	4.373 (0.317)	5.867 (0.388)
Reference 8	cc-pVTZ	CASSCF	4.19	5.90
		MRCI	4.17	5.65
	cc-pVTZ+sp	CASSCF	4.53	6.00
		MRCI	4.24	5.58
Reference 10	cc-pVTZ+sp[c]	MRCI	4.13 (0.07)[d]	5.50 (0.12)[d]

[a]CASSCF (14,10).

[b]Full valence, i.e., CASSCF (20,15).

[c]Both the basis set and active space used differ from that in ref. 8.

[d]Converted from oscillator strengths, f, using $\mu = \sqrt{\frac{3f}{2E_{10}}}$.

Fig. 1. Energies at the CASSCF/6-31+G(d) level of the first three singlet states of CH_3OCl as a function of the r_{OCl} bond length. All other bond parameters fixed at those of the B3LYP/6-31G(d) ground-state equilibrium geometry. Calculations are carried out in C_1 symmetry and, therefore, the states (along with their C_s symmetries) illustrated are $1^1A = X^1A'$ (solid line + circles), $2^1A = 1^1A''$ (dashed line + squares), and $3^1A = 2^1A'$ (dotted line + diamonds).

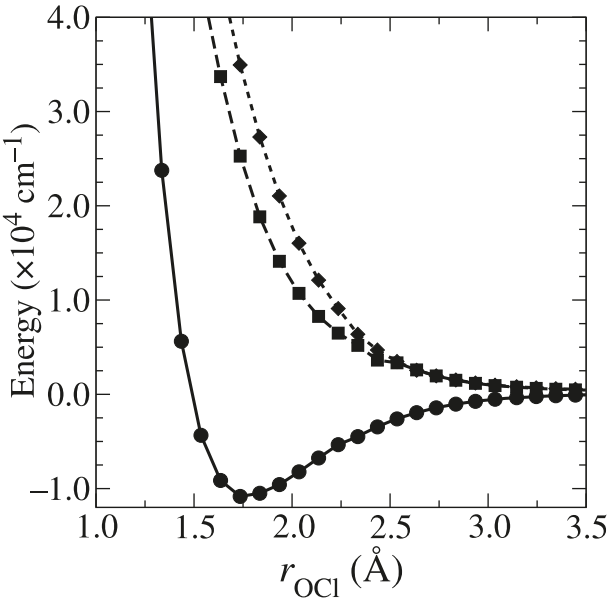

Fig. 2. Gradient projections of the first excited state ($2^1A = 1^1A''$) onto the O–Cl bond vector as a function of the r_{OCl} bond length: CASSCF/6-31+G(d) (circles), MRCI/aug-cc-pVDZ (squares), and MRCI/aug-cc-pVTZ (triangles). Other coordinates are fixed at the B3LYP/6-31G(d) optimized geometry.

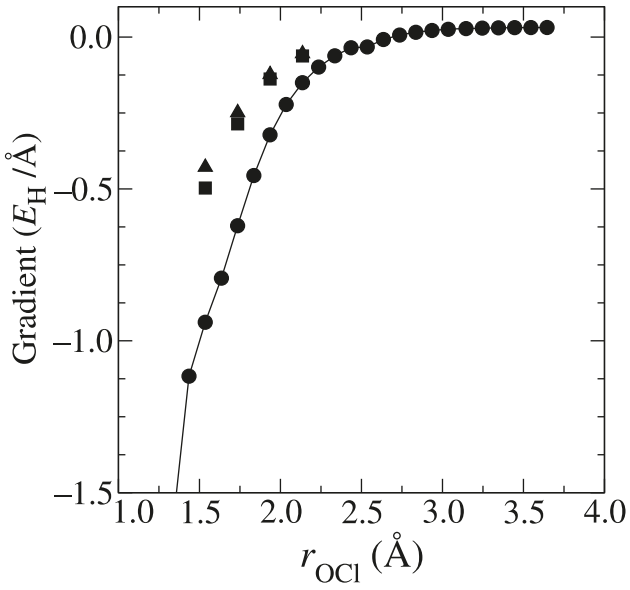

ments[7] of the branching ratio for these photoproducts, the spin-orbit coupling will have to be taken into account. This is not, however, the purpose of the present study.

In this paper, excited-state energies, gradients, and transition dipole moments for the CH_3OCl molecule determined using computational methods tractable for ab initio molecular dynamics, i.e., density functional theory (DFT) for the ground state and CASSCF for the excited states, are validated against high-level internally-contracted MRCI results. These lay the groundwork for future studies of the photodissociation of CH_3OCl. This article also reports the first implementation of ab initio molecular dynamics (AIMD) using

Fig. 3. Gradient projections of the second excited state ($3^1A = 2^1A'$) onto the O–Cl bond vector as a function of the r_{OCl} bond length: CASSCF/6-31+G(d) (circles), MRCI/aug-cc-pVDZ (squares), and MRCI/aug-cc-pVQZ (triangles). Other coordinates are fixed at the B3LYP/6-31G(d) optimized geometry.

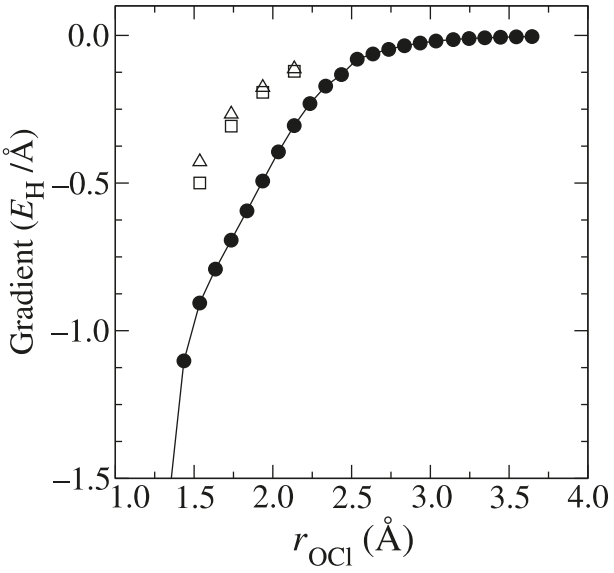

Fig. 4. The canonical distribution of C–O bond lengths (r_{CO}) for unconstrained and constrained (with C–H bond lengths fixed at their equilibrium values) dynamics. Both trajectories are at the B3LYP/6-31G(d) level of theory. Trajectory length is 9.6 ps for both unconstrained (dt = 2 fs) and constrained (dt = 4 fs) dynamics. The vertical line represents the equilibrium value.

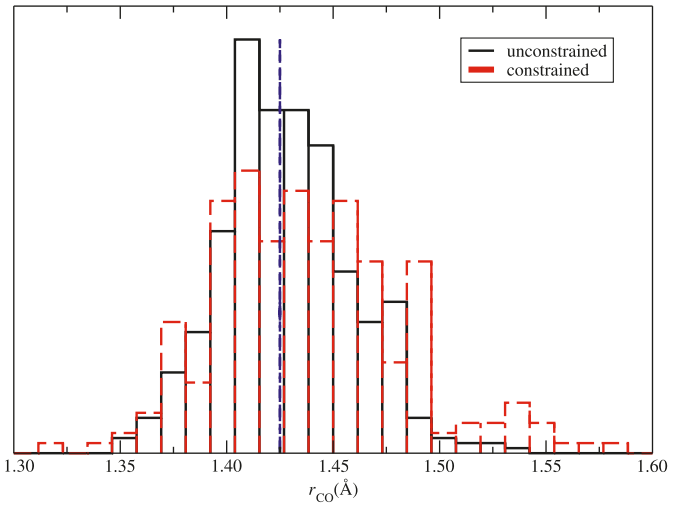

Fig. 5. The canonical distribution of O–Cl bond lengths (r_{OCl}) for unconstrained and constrained (with C–H bond lengths fixed at their equilibrium values) dynamics. Both trajectories are at the B3LYP/6-31G(d) level of theory. Trajectory length is 9.6 ps for both unconstrained (dt = 2 fs) and constrained (dt = 4 fs) dynamics. The vertical line represents the equilibrium value.

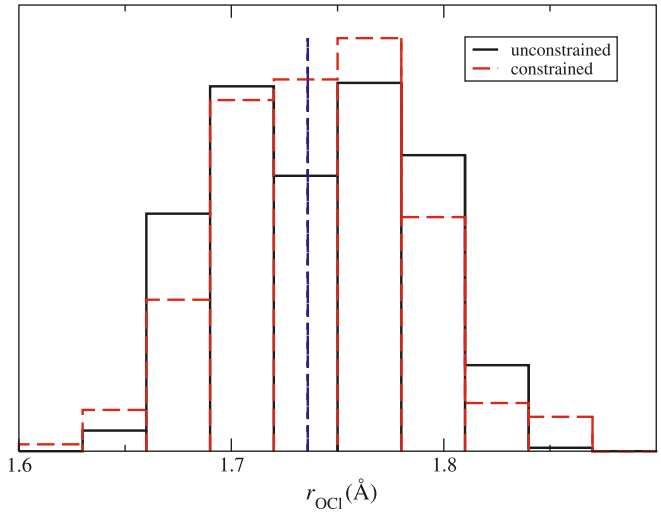

Fig. 6. The canonical distribution of the C–O–Cl bond angle (θ_{COCl}) for unconstrained and constrained (with C–H bond lengths fixed at their equilibrium values) dynamics. Both trajectories are at the B3LYP/6-31G(d) level of theory. Trajectory length is 9.6 ps for both unconstrained (dt = 2 fs) and constrained (dt = 4 fs) dynamics. The vertical line represents the equilibrium value.

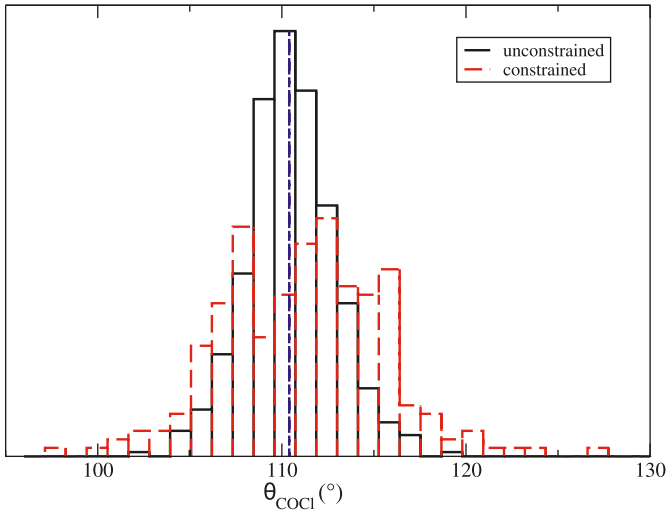

the molecular modelling toolkit (MMTK) and illustrates its use with both ground- and excited-state dynamics for CH_3OCl. Section II.A details the present and previous ab initio methods used to explore the electronic structure of CH_3OCl. The AIMD techniques are discussed in Section II.B. The static electronic structure properties are reported in Section III.A and a comparison is made between those from methods viable for AIMD and high-level benchmark results. Ground electronic state configurational sampling from AIMD for unconstrained and constrained dynamics is discussed in Section III.B. Section III.B also contains a brief discussion of AIMD for excited states of CH_3OCl. Finally, some conclusions and an outlook on future uses of AIMD with MMTK are presented in Section IV.

II. Computational methods

A. Electronic structure

There have been several previous theoretical studies of the ground-state structure and vibrational frequencies of CH_3OCl.[9,11–13] In particular, there have been two benchmark studies by Francisco[9] and by Peyerimhoff and co-workers[11]

Fig. 7. The canonical distribution of the H_a–C–O–Cl dihedral angle (τ_{H_aCOCl}) for unconstrained and constrained (with C–H bond lengths fixed at their equilibrium values) dynamics. Both trajectories are at the B3LYP/6-31G(d) level of theory. Trajectory length is 9.6 ps for both unconstrained (dt = 2 fs) and constrained (dt = 4 fs) dynamics.

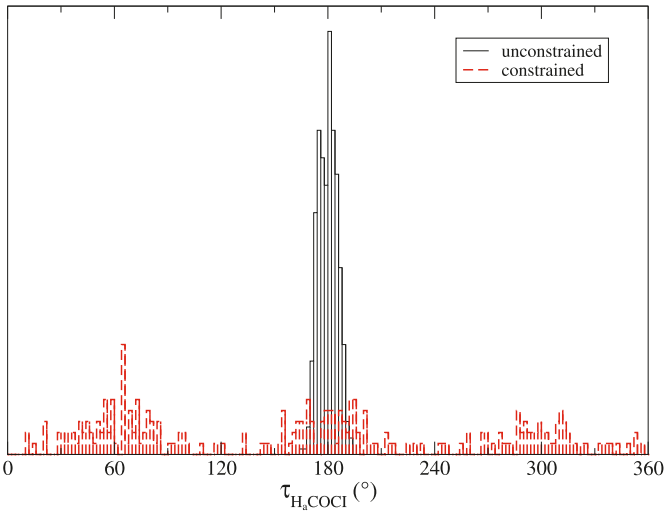

at the CCSD(T)/6-311G(2df,2p) and at the CCSD(T)/cc-pVTZ levels of theory, respectively. Unless otherwise specified, all single-point calculations reported in this article have been carried out at the equilibrium geometry determined by Francisco (see Table 1) using C_s symmetry. Since the CCSD(T) methodology is too computationally expensive for dynamics calculations, a B3LYP/6-31G(d) geometry optimization and vibrational frequency analysis were performed to assess the suitability of this level of theory for ground-state configurational sampling (see the discussion in Section II.B). The B3LYP/6-31G(d) ground-state structure (Table 1) and vibrational frequencies (Table 2) as compared to the benchmark CCSD(T) results indicate that this method and basis set provide a suitable representation for the ground-state potential-energy surface, including the equilibrium structure. For example, and as expected, the bond lengths differ by less than 0.05 Å and the angles by less than 1.3°. Importantly, the frequencies also differ by a maximum of 5% and, in most cases, are within 1% of the benchmark results.

There have only been two theoretical studies focused on surveying the lowest-lying singlet and triplet excited states for CH_3OCl.[8,10] In these studies, they have determined the energies for the lowest six singlet and triplet states (three A′ and three A″ for each spin multiplicity). From these works, the two lowest energy absorptions observed experimentally at 310 nm and 236 nm[5] are identified with excitation to the $1^1A'$ and $2^1A''$ states, respectively. These two low-lying electronic states are the focus of this work. Benchmark calculations of both vertical excitation energies and transition dipole moments have been carried out using the augmented correlation consistent family of basis sets (aug-cc-pV*X*Z, *X* = D, T, and Q).[14–16] To determine the energies and transition dipole moments, state-averaged complete active space self-consistent field (SA-CASSCF) calculations[17,18] were carried out including two A′ and one A″ states. Following the work of Li and Francisco,[8] the active space consisted of 14 electrons in 10 active orbitals (seven and three active molecular orbitals in A′ and A″ symmetry, respectively). The resulting CASSCF orbitals and wave functions were then used for internally-contracted MRCI[19,20] calculations. For the MRCI calculations, the effect of higher-order excitations on the energies was estimated using the Davidson correction.[21] All electronic structure calculations reported in this article were carried out using the MOLPRO ab initio electronic structure program.[22]

The MRCI method is suitable for single-point calculations (or even potential-energy scans) but it is far too computationally intensive to be utilized for a direct dynamics study. The benchmark calculations discussed above were used to gauge the accuracy of SA-CASSCF calculations using the same (14,10) active space as described above but with the much more modest 6-31+G(d) basis set.[23–26] The major difference was that these calculations were carried out with C_1 symmetry as they will form the basis for future excited-state dynamics studies, where the planar symmetry of the molecule will be broken. We would like to use a moderate level of theory since efficiency (speed) is of critical importance for dynamics but we would like to retain a quantitative description of the excited states. Therefore, the vertical excitation energies were determined as they provide information on the energetic accessibility of the two excited states. The transition dipoles were determined as they provide information about the relative probability of accessing either state. Finally, and perhaps most importantly, the energy gradients must be determined since they govern the classical dynamics. To assess the accuracy of the SA-CASSCF/6-31+G(d) gradients, they are compared with numerical MRCI gradients at a small number of geometries (note that analytic MRCI gradients are not available in MOLPRO). The comparison of the gradients we make involves a projection onto the O—Cl bond vector, i.e., the primary "reaction" channel, defined by

$$[2] \qquad g_{OCl} = \frac{(\vec{g}_O - \vec{g}_{Cl}) \cdot (\vec{r}_O - \vec{r}_{Cl})}{\| \vec{r}_{OCl} \|}$$

where $\vec{g}_i$ and $\vec{r}_i$ are atom Cartesian vectors of the gradient and position, respectively. The numerical MRCI gradients are computed by four-point finite difference using a displacement length of 0.01 bohr along the r_{OCl} bond coordinate.

B. Molecular dynamics

Ab initio molecular dynamics simulations on the ground electronic state were carried out using MMTK.[27] MMTK is a simulation and modelling program library written in Python and C, which has been proven to be useful for atomic systems to large biomolecules. Most of the procedures needed in conducting the dynamics is self-contained in program classes that can be called from a main code. Significantly for us, MMTK allows the ready implementation of constrained dynamics, where the bond lengths can be fixed. A proper choice of constraints can "freeze out" high-frequency vibrations, permitting the use of larger integration timesteps. To perform AIMD using MMTK, an ab initio force field class that obtains energies and gradients directly from electronic structure calculations was implemented. The electronic structure calculations were performed using the MOLPRO package.[22] The present implementation allows the use of Hartree–Fock (HF), Møller–Plesset second-order

perturbation theory (MP2), DFT, and CASSCF classical trajectories, which are methods where analytic gradients are available in MOLPRO. An ab initio force field determined using GAMESS[28] has also been developed for HF and DFT trajectories (results are not presented here). The computer code for interfacing these ab initio electronic structure packages with MMTK is available upon request from the authors.

To generate initial conditions for examining the excited-state dynamics, one requires a sampling of geometries and initial velocities from the ground electronic state. One can do this by Monte Carlo sampling or by running a canonical NVT (where N, V, and T refer to the number of particles, volume, and temperature in the system, respectively) classical trajectory on the ground-state potential-energy surface to sample both positions and momenta. In this paper, we chose the latter to demonstrate our implementation of AIMD in MMTK. A single long NVT ground-state trajectory was generated at the B3LYP/6-31G(d) level of theory and can serve as a sampling of initial conditions of the molecule prior to photoabsorption. The initial conditions of the trajectory consisted of the equilibrium geometry determined at the B3LYP/6-31G(d) level of theory (see Table 1) and velocities obtained from a Boltzmann distribution at 300 K. Dynamics were conducted using the Velocity Verlet integrator.[29] To maintain the temperature, a Nosé thermostat[30] with a time constant of 0.2 ps was used. The proper timestep was determined from NVE (where E refers to the total energy of the system) dynamics and the length of simulation determined from proper phase space coverage. These NVT trajectories were determined for both unconstrained and constrained systems. In the constrained dynamics, the r_{CH} distances were fixed at their equilibrium values. The excited-state dynamics at the CASSCF/6-31+G(d) level of theory is briefly discussed. A more detailed study of the photodissociation process is beyond the scope of this paper.

III. Results and discussion

A. Static electronic structure

The important properties for photodissociation are the vertical excitation energies from the ground state ($1^1A'$) to the low-lying excited states ($1^1A''$ and $2^1A'$) and the corresponding transition dipole moments. Our results (CASSCF and MRCI) along with previous calculations for CH_3OCl[8,10] are presented in Table 3. All the present results are determined at the CCSD(T)/6-311G(2df,2p) equilibrium geometry.[9] Examining the MRCI vertical excitation energies as a function of increasing basis set size (aug-cc-pV*X*Z, X = D, T, Q), it is clear that they are converging to the values of 4.13 eV and 5.27 eV for the $1^1A'' \leftarrow X^1A'$ and $2^1A' \leftarrow X^1A'$ excitations, respectively. The present CASSCF and MRCI excitation energies are consistent with those determined previously[8,10] and with the experimentally-determined absorption spectrum[2,5] that exhibits maxima at 4.00 eV (310 nm) and 5.25 eV (236 nm). Importantly, the CASSCF/6-31+G(d) energies, upon which we plan to base the direct dynamics, are within 0.180 eV and 0.513 eV of the MRCI/aug-cc-pVQZ results.

The square of the magnitudes of the transition dipole moments can be used to determine the probability of a transition to each excited state; presently, the transition dipole moments are treated as scalars rather than as vectors. Examining the CASSCF versus MRCI transition dipole moments for a given basis set (see Table 3), it is clear that the inclusion of dynamic correlation plays a significant role in determining their magnitudes. For example, the CASSCF/6-31+G(d) transition dipoles as compared to the MRCI/aug-cc-pVQZ results are reduced from 0.282 D ($1^1A'' \leftarrow X^1A'$) and 0.331 D ($2^1A' \leftarrow X^1A'$) to 0.089 D and 0.270 D, respectively. More importantly, the ratio of the square of the dipole moments, which is proportional to the absorption cross section, changes significantly, e.g., for the aug-cc-pVQZ basis set, $(\mu_2/\mu_1)^2 = 1.38$ for CASSCF and 9.30 for MRCI. To assess the reliability of the computed transition dipole moments, we can compare as a first-order approximation to the ratio of the experimentally determined maximum-absorption cross sections,[2,5] where $\sigma_{236}/\sigma_{310} = 9.99$. Clearly, the ratios predicted by the CASSCF calculations are incorrect while the MRCI results for the triple- and quadruple-zeta basis sets agree fairly well with experiment. For future excited-state direct dynamics work, the CASSCF results will be unable to predict correctly the relative populations of the $1^1A''$ and $2^1A'$ states. Therefore, a geometry-independent dipole will be assumed and the populations in the states will be weighted 1:9 if both states are energetically accessible.

The CASSCF/6-31+G(d) energies also need to be considered away from the ground-state equilibrium geometry as the eventual goal of the research is to examine the photodissociation dynamics, where the molecule will access geometries far from equilibrium. Figure 1 shows the potential-energy curves for the first three singlet states of CH_3OCl as determined using the CASSCF/6-31+G(d) level of theory. As expected from previous investigations,[8,10] the excited states are highly repulsive in the r_{OCl} coordinate. Since the dynamics will break the C_s symmetry of the molecule, the CASSCF calculations have been performed using C_1 symmetry, i.e., no symmetry. One difficulty with carrying out the calculations in C_1 symmetry is that root-flipping problems can occur in the asymptotic region of the potentials.

Gradients serve the purpose of providing the acceleration term in the Velocity Verlet integration scheme. Therefore, obtaining accurate forces is more important than the potential-energy curves (relative energetics), although, they are, of course, intimately related. The gradients for the first excited state ($1^1A''$ in C_s symmetry = 2^1A in C_1 symmetry) as a function of the r_{OCl} bond length (all other coordinates are fixed at the B3LYP/6-31G(d) optimized geometry) are shown in Fig. 2. The CASSCF/6-31+G(d) gradients are compared to those from MRCI/aug-cc-pVDZ and MRCI/aug-cc-pVTZ determinations at four bond lengths (r_{OCl} = 1.536, 1.736, 1.936, and 2.136 Å). The MRCI results are noticeably smaller in magnitude than the corresponding CASSCF results; the ratio of the MRCI/aug-cc-pVTZ to the CASSCF results is approximately 0.4 for all four r_{OCl} bond lengths considered. The gradients for the second excited state ([$2^1A'$ in C_s symmetry = 3^1A in C_1 symmetry], see Fig. 3) are qualitatively similar to those of Fig. 2, where now the MRCI/aug-cc-pVTZ to CASSCF ratio is approximately 0.5. Hence, we conclude that the CASSCF/6-31+G(d) gradients provide a qualitative picture for guiding the excited-state dynamics; a semiquantitative picture could be obtained through simple

scaling of the CASSCF/6-31+G(d) gradients. Importantly, the CASSCF/6-31+G(d) energy and analytic gradient calculations are reasonable in computational time (approximately 2 min per geometry) for performing AIMD while those using MRCI/aug-cc-pV*X*Z are prohibitive. Note that for $r_{OCl} > 2.5$ Å, there is a problem with root flippping as the $2^1A'$ (3^1A) state becomes lower in energy than $^1A''$ (2^1A); this is obvious due to the observation of a discontinuity in the original gradient calculations. Therefore, the potentials, Fig. 1, and gradients, Figs. 2 and 3, present results where the root flipping has been accounted for "by hand". When AIMD is determined in the excited states, the root flipping must be accounted for automatically or trajectories must be terminated before $r_{OCl} > 2.5$ Å.

B. Ground- and excited-state dynamics

Presented here are NVT ground-state trajectories at the B3LYP/6-31G(d) level of theory. In the first case, motion in all $3N - 6$ internal degrees of freedom is allowed. In the second case, to remove high frequency vibrational motions, all three C–H bonds are fixed at their equilibrium bond lengths. To determine an appropriate timestep, equivalent NVE simulations with various timesteps (dt) are run. Equilibration occurs within a few femtoseconds. By applying constraints, we are able to increase the timestep about threefold (from $\sim$2 fs in unconstrained dynamics to $\sim$5 fs with constrained dynamics) before energy conservation is violated or SCF nonconvergence occurs in the electronic structure calculation, when large timesteps lead to significant geometric and, hence, electronic, changes. The latter point is of particular importance in AIMD simulations. Therefore, the energy convergence tests are merely to show the general upper limit on dt for the unconstrained and constrained systems. As a prescription, we suggest that actual production runs should be performed at smaller timesteps.

Figures 4, 5, 6, and 7 present histograms of the r_{CO} and r_{OCl} bond lengths, the C–O–Cl bond angle, θ_{COCl}, and the torsional angle, τ_{H_aCOCl}, respectively, from 9.6 ps unconstrained and constrained NVT trajectories (dt = 2 fs and dt = 4 fs, respectively). As expected, in the ground state at this temperature, the harmonic-like C–O bond exhibits a Gaussian distribution centered about the equilibrium bond length. Similarly, the O–Cl bond, C–O–Cl bond angle and torsional angle exhibit canonical behaviour. The Cl fragment neither diverges too far from its equilibrium distance to the O nor changes exceedingly from its orientation with respect to the C–O. For the constrained simulation, note that the methyl group isomerizes and H_a occupies equivalent minima at 60°, 180°, and 300°. Taking all the above into consideration, the use of a canonical NVT trajectory to sample initial ground-state distributions is certainly feasible, although it should be implemented with care. A small enough timestep needs to be taken to prevent integrator problems, which can adversely affect ab initio calculations. Yet, the simulation must be long enough for all modes to reach the canonical limit. The use of a Monte Carlo sampling scheme may allow us to circumvent such difficulties.

Positions and momenta sampled from the constrained ground-state trajectory will serve as initial conditions for future excited-state dynamics studies. To test AIMD for excited electronic states, a short 20 fs constant energy excited-state trajectory is determined on the first excited electronic state (2^1A in C_1 symmetry) at the CASSCF/6-31+G(d) level of theory. The trajectory starts at the ground-state equilibrium geometry with no initial kinetic energy (in practice, NVT ground-state initial conditions would be used). The molecule quickly reaches the asymptotic dissociation limit ($r_{OCl} > 2.5$ Å) in about 100 timesteps (dt = 0.2 fs). Thus, a single trajectory would take only (approximately) 300 min pointing to the computational feasibility of exploring ensembles of trajectories on the excited electronic states. The entire ensemble of excited-state trajectories can then be easily parallelized.

IV. Conclusions

The three lowest-lying singlet states of methyl hypochlorite have been examined using electronic structure methods for which direct dynamics studies would be computationally feasible, i.e., B3LYP/6-31G(d) for the ground state and CASSCF/6-31+G(d) for the excited states. From this, potential-energy scans and energy gradients along the O–Cl bond were obtained with an accuracy compared to that of MRCI with the aug-cc-pV*X*Z (*X* = D, T, Q) family of basis sets. In particular, the CASSCF gradients are related to the MRCI gradients by only a factor, allowing for appropriate dynamics. Thus, this moderate method is capable of semiquantitatively representing the benchmark calculations of the CH_3OCl system at a fraction of the computational cost. We have successfully implemented direct dynamics into MMTK using the electronic structure packages MOLPRO (results presented here) and also GAMESS (results not presented here). The power of using an ab initio "on the fly" method is that any system, provided electronic structure calculations are feasible, can be studied. Implementing this method with a modular molecular dynamics package lends to portability, generalization, and great potential. Note, however, careful analysis of the single-point calculations must be done. In our case, we encountered root-flipping problems and the potential for electronic structure nonconvergence of systems far from equilibrium. We have also shown that constrained dynamics can markedly decrease simulation time.

A full dynamical study of CH_3OCl dissociation is currently underway. In theory, a large set of trajectories generated from a Boltzmann distribution of initial states can be used to produce the sampling pool of ground-state configurations from which photoexcitation (vertical excitation) can occur. However, a Monte Carlo sampling approach may be more practical. One could, for instance, sample the ground-state NVT distribution in the harmonic approximation, yielding a Monte Carlo sampling scheme where no rejection step is required. In this case, the Monte Carlo sampling would be more efficient than the molecular dynamics sampling. The dissociative nature of CH_3OCl in its excited states was demonstrated with our AIMD algorithm, and for this type of process, is highly computationally practical at this level of theory. Further investigations will involve calculating ensemble averages and other structural properties. Quantum dynamical properties are also currently being investigated based on the present tool along with semiclassical initial value representation (SC-IVR) techniques.[31–34] The present work opens the door to the development of semiclassical dy-

namics with constraints using ab initio force fields. This is an advancement over earlier work where the quantum dynamics of rigid water clusters[35,36] was studied using model potentials. Very recent work has shown the practicality of on-the-fly AIMD based semiclassical calculations[37] and the aforementioned inclusion of constraints is therefore quite timely.

V. Acknowledgment

The authors thank the Natural Sciences and Engineering Research Council of Canada (NSERC), the Canadian Foundation for Innovation and the University of Alberta for financial support. AB thanks Chen Liang for performing preliminary calculations for CH_3OCl.

References

(1) This article is part of a Special Issue dedicated to Professor T. Ziegler.
(2) Crowley, J. N.; Helleis, F.; Müller, R.; Moortgat, G. K.; Crutzen, P. J.; Orlando, J. J. *J. Geophys. Res.* **1994**, *99* (D10), 20683–20688. doi:10.1029/94JD01829.
(3) JPL-97, JPL-2002, and JPL-2006 recommended the mean values of Crowley et al.[2] and Jungkamp et al.[5]
(4) Nanbu, S.; Iwata, S. *J. Phys. Chem.* **1992**, *96* (5), 2103–2111. doi:10.1021/j100184a017.
(5) Jungkamp, T. P. W.; Kirchner, U.; Schmidt, M.; Schindler, R. N. *J. Photochem. Photobiol. A* **1995**, *91* (1), 1–6. doi:10.1016/1010-6030(95)04074-P.
(6) Krisch, M. J.; McCunn, L. R.; Takematsu, K.; Butler, L. J.; Blase, F. R.; Shu, J. *J. Phys. Chem. A* **2004**, *108* (10), 1650–1656. doi:10.1021/jp0372082.
(7) Schindler, R. N.; Liesner, M.; Schmidt, S.; Kirchner, U.; Benter, T. *J. Photochem. Photobiol. A* **1997**, *107* (1–3), 9–19. doi:10.1016/S1010-6030(96)04583-2.
(8) Li, Y.; Francisco, J. S. *J. Chem. Phys.* **1999**, *111* (18), 8384–8388. doi:10.1063/1.480180.
(9) Francisco, J. S. *Int. J. Quantum Chem.* **1999**, *73* (1), 29–35. doi:10.1002/(SICI)1097-461X(1999)73:1<29::AID-QUA3>3.0.CO;2-M.
(10) Mühlhäuser, M.; Schnell, M.; Peyerimhoff, S. D. *Mol. Phys.* **2002**, *100* (16), 2719–2725. doi:10.1080/00268970210139967.
(11) Drougas, E.; Kosmas, A. M.; Schnell, M.; Mühlhäuser, M.; Peyerimhoff, S. D. *Mol. Phys.* **2002**, *100* (16), 2653–2658. doi:10.1080/00268970210137293.
(12) He, T. J.; Chen, D. M.; Liu, F. C.; Sheng, L. S. *Chem. Phys. Lett.* **2000**, *332* (5–6), 545–552. doi:10.1016/S0009-2614(00)01307-5.
(13) Jung, D.; Chen, C. J.; Bozzelli, J. W. *J. Phys. Chem. A* **2000**, *104* (42), 9581–9590. doi:10.1021/jp001469j.
(14) Dunning, T. H., Jr. *J. Chem. Phys.* **1989**, *90* (2), 1007–1023. doi:10.1063/1.456153.
(15) Woon, D. E.; Dunning, T. H., Jr. *J. Chem. Phys.* **1993**, *98* (2), 1358–1371. doi:10.1063/1.464303.
(16) Kendall, R. A.; Dunning, T. H., Jr.; Harrison, R. J. *J. Chem. Phys.* **1992**, *96* (9), 6796–6806. doi:10.1063/1.462569.
(17) Werner, H.-J.; Knowles, P. J. *J. Chem. Phys.* **1985**, *82* (11), 5053–5063. doi:10.1063/1.448627.
(18) Knowles, P. J.; Werner, H. J. *Chem. Phys. Lett.* **1985**, *115* (3), 259–267. doi:10.1016/0009-2614(85)80025-7.
(19) Werner, H. J.; Knowles, P. J. *J. Chem. Phys.* **1988**, *89* (9), 5803–5814. doi:10.1063/1.455556.
(20) Knowles, P. J.; Werner, H. J. *Chem. Phys. Lett.* **1988**, *145* (6), 514–522. doi:10.1016/0009-2614(88)87412-8.
(21) Davidson, E. R.; Silver, D. W. *Chem. Phys. Lett.* **1977**, *52* (3), 403–406. doi:10.1016/0009-2614(77)80475-2.
(22) Werner, H.-J.; Knowles, P. J.; Lindh, R.; Schütz, M.; Celani, P.; Korona, T.; Manby, F. R.; Rauhut, G.; Amos, R. D.; Bernhardsson, A., et al. *MOLPRO: A Package of Ab Initio Programs,* version 2006.1; University College Cardiff Consultants Limited: Cardiff, UK, 2006. Available from http://www.molpro.net.
(23) Hehre, W. J.; Ditchfield, R.; Pople, J. A. J. *Chem. Phys.* **1972**, *56* (5), 2257–2261.
(24) Francl, M. M.; Pietro, W. J.; Hehre, W. J.; Binkley, J. J.; Gordon, M. S.; Defrees, D. J.; Pople, J. A. J. *Chem. Phys.* **1982**, *77* (7), 3654–3665.
(25) Hariharan, P. C.; Pople, J. A. *Theor. Chim. Acta* **1973**, *28* (3), 213–222. doi:10.1007/BF00533485.
(26) Clark, T.; Chandrasekhar, J.; Spitznagel, G. W.; Schleyer, P. V. J. *Comput. Chem.* **1983**, *4* (3), 294–301. doi:10.1002/jcc.540040303.
(27) Hinsen, K. J. *Comput. Chem.* **2000**, *21* (2), 79–85. doi:10.1002/(SICI)1096-987X(20000130)21:2<79::AID-JCC1>3.0.CO;2-B.
(28) Schmidt, M. W.; Baldridge, K. K.; Boatz, J. A.; Elbert, S. T.; Gordon, M. S.; Jensen, J. H.; Koseki, S.; Matsunaga, N.; Nguyen, K. A.; Su, S. J.; Windus, T. L.; Dupuis, M.; Montgomery, J. A. *J. Comput. Chem.* **1993**, *14* (11), 1347–1363. doi:10.1002/jcc.540141112.
(29) Swope, W. C.; Andersen, H. C.; Berens, P. H.; Wilson, K. R. J. *Chem. Phys.* **1982**, *76*, (1), 637–649.
(30) Nosé, S. *Mol. Phys.* **1984**, *52* (2), 255–268. doi:10.1080/00268978400101201.
(31) Thoss, M.; Wang, H. *Annu. Rev. Phys. Chem.* **2004**, *55* (1), 299–332. doi:10.1146/annurev.physchem.55.091602.094429. PMID:15117255.
(32) Kay, K. G. *Annu. Rev. Phys. Chem.* **2005**, *56* (1), 255–280. doi:10.1146/annurev.physchem.56.092503.141257. PMID:15929199.
(33) Miller, W. H. *Proc. Natl. Acad. Sci. U.S.A.* **2005**, *102* (19), 6660–6664. doi:10.1073/pnas.0408043102. PMID:15870209.
(34) Miller, W. H. J. *Chem. Phys.* **2006**, *125* (13), 132305.
(35) Issack, B. B.; Roy, P.-N. J. *Chem. Phys.* **2007**, *127* (5), 054105.
(36) Issack, B. B.; Roy, P.-N. J. *Chem. Phys.* **2007**, *127* (14), 144306.
(37) Tatchen, J.; Pollak, E. J. *Chem. Phys.* **2009**, *130* (4), 041103.

Computational design of ruthenium hydride olefin-hydrogenation catalysts containing hemilabile ligands[1,2]

Christopher N. Rowley and Tom K. Woo

Abstract: Three ruthenium hydridocarbonyl complexes containing bidentate hemilabile ligands have been evaluated as possible catalysts for the H_2 hydrogenation of olefins. Our previous investigations of the mainstay hydridoruthenium catalyst, $RuHCl(CO)(PR_3)_2$ (**1**), indicated that the rate-limiting olefin-insertion barrier was increased by the need for an H_2 molecule to act as a stabilizing two-electron donor. Using density functional theory (DFT) calculations, we have determined that a P,N phosphane-oxazoline would be suitable for stabilizing the metal center of the complex $RuHCl(CO)(P^iPr_3)(DZ)$, where DZ is a neutral bidentate hemilable ligand. In the reaction catalyzed by this complex, the olefin insertion occurs before the coordination of H_2, avoiding the entropic penalty of coordinating H_2. We predict that the phosphane-oxazoline containing catalyst will have higher activity than **1** and a different rate-law, zero-order in $[H_2]$. The oxazoline increases the strength of coordination of the ethylene due to stronger back-donation from destabilized Ru d-orbitals to the ethylene π^* molecular orbital.

Key words: catalyst design, catalysis, olefin, hydrogenation, DFT, hemilabile, phosphine, oxazoline.

Résumé : On a évalué la possibilité d'utiliser trois complexes hydridocarbonyle du ruthénium contenant des ligands bidentates hémilabiles comme catalyseurs pour l'hydrogénation d'oléfines. Les études antérieures effectuées avec le catalyseur traditionnel de l'hydridoruthénium, $RuHCl(CO)(PR_3)_2$, **1**, ont permis de déterminer que l'étape cinétiquement limitante à l'insertion de l'oléfine est rehaussée par la nécessité qu'une molécule d'hydrogène agisse comme donneur stabilisant de deux électrons. Se basant sur des calculs de la théorie de la fonctionnelle de la densité, on a pu déterminer qu'un ligand phosphane-oxazoline contenant un atome d'azote et un atome de phosphore devrait être approprié pour stabiliser le centre métallique du complexe $RuHCl(CO)(isoPr_3)(DZ)$ dans lequel le groupe DZ est un ligand bidentate hémilabile neutre. Dans la réaction catalysée par ce complexe, l'insertion de l'oléfine se produit avant la coordination du H_2 ce qui a pour effet d'éviter la pénalité entropique de la coordination du H_2. Sur la base des calculs, il est prédit que l'activité d'un catalyseur contenant un ligand phosphane-oxazoline sera plus élevée que celle du composé **1** et sera régit par une loi de vitesse différente, d'ordre zéro en $[H_2]$. L'oxazoline augmente la force de la coordination de l'éthylène en raison d'un pouvoir de rétrocession plus important à partir des orbitales d déstabilisée du ruthénium vers l'orbitale moléculaire π^* de l'éthylène.

Mots-clés : développement d'un catalyseur, catalyse, oléfine, hydrogénation, théorie de la fonctionnelle de la densité, hémilabile, phosphine, oxazoline.

[Traduit par la Rédaction]

Introduction

The homogeneous H_2 hydrogenation of olefins is of considerable importance in organic synthesis, fine chemical production, and polymer chemistry.[3–5] Among homogeneous catalysts, hydridoruthenium complexes of the class $RuHCl(L)(PR_3)$ are of notable use in the reduction of challenging substrates[6–12] or within a tandem ROMP-hydrogenation (ring-opening metathesis polymerization) process.[13–19]

The first example of this type of catalyst was the arylphosphine complex $RuHCl(PPh_3)_3$, reported 40 years ago by Wilkinson and co-workers.[20,21] Since then, this framework of a neutral Ru(II)–hydride with three two-electron donors has served as the basis for vast amounts of research in homogeneous hydrogenation. Variation of the two-electron donor trans to the chloride found that a strongly bonding but compact CO ligand yields exceptionally good catalytic activity.[11,12] Another branch of optimization led to the substitution of the aryl phosphines for alkyl phosphines.[22–24]

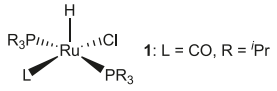

1: L = CO, R = ^{i}Pr

Computational modeling has made increasingly significant contributions in organometallic chemistry.[25,26] In particular, density functional theory (DFT) modeling of catalytic cycles has contributed greatly to catalyst design, and in some recent examples, novel catalysts have been designed computationally in advance of their synthesis.[27–30] In our own research, we have attempted to move beyond the traditional procedures for modeling organometallic reactions, which has led us to study the dynamic features of catalytic

Received 28 January 2009. Accepted 29 April 2009. Published on the NRC Research Press Web site at canjchem.nrc.ca on 25 June 2009.

C.N. Rowley and T.K. Woo.[1] Centre for Catalysis Research and Innovation, Department of Chemistry, University of Ottawa, Ottawa, ON K1N 6N5, Canada.

[1]Corresponding author (e-mail: twoo@uottawa.ca).

reaction mechanisms,[31,32] to evaluate novel catalysts prior to experiment,[33,34] and to pursue in-depth collaborations with experimentalists.[35]

One exceptionally productive collaboration sparked our interest in this class of olefin-hydrogenation catalysts. In that study, we modeled the catalytic cycle of hydridoruthenium complex **1** using DFT calculations. Kinetic studies had established that the catalytic cycle begins with the dissociation of a phosphine from the metal, although the subsequent steps were more opaque. Some published catalytic cycles proposed that the olefin undergoes insertion into the Ru–H bond to form a four-coordinate alkyl-containing intermediate.[36] Instead, we found that the putative four-coordinate ethyl intermediate formed by this insertion is not a potential-energy minimum and H_2 must be coordinated trans to the hydride prior to the insertion to stabilize this intermediate. As the coordination of H_2 is initially weak due to the trans influence of the hydride, this association is endergonic and increases the activation free energy of the rate-limiting insertion step.

This need for an external stabilizing donor led us to consider how the catalyst could be modified so that it would not be necessary for H_2 to coordinate before the insertion. In principle, another two-electron donor could be introduced to stabilize the metal in the insertion step, although a strong donor could inhibit the activity of the catalyst or induce the complex to isomerize to an inactive form. Conversely, a weak donor may not be able to coordinate trans to the hydride ligand, which has a strong trans influence.

Hemilabile ligands[37–40] could provide an elegant solution to this problem. Hemilabile ligands are polydentate ligands with at least two different coordinating groups. Notably, these coordinating groups can be chosen to have dramatically different interactions with the metal centre. Many highly active catalysts from groups 8–10 contain bidentate DZ-type hemilabile ligands with a strongly coordinating soft donor (D), such as a phosphine or carbene, and a weakly coordinating hard N or O donor (Z). The weakly coordinating donor can stabilize the metal in some steps of the catalytic cycle, but can adjust to interact weakly in other steps. A hemilabile P,N,P ligand was recently used in a related Ru(II) hydride catalyst for the dehydrogenation of alcohols[41] and the hydrogenation of esters,[42] providing precedence for this strategy. In this study, we have used DFT calculations to explore whether incorporating a DZ-type hemilabile ligand to ruthenium–hydrido catalysts similar to **1** could eliminate the need for H_2 to serve as the trans-hydride two-electron donor in the insertion step.

This paper is divided into three sections. In the first section, we present the calculated reaction profile of H_2 hydrogenation of ethylene catalyzed by the benchmark monodentate phosphine complex **1**. In the second section, we screen three potential catalysts containing DZ-type hemilabile ligands. In the last section, we model the catalytic cycle of a novel complex featuring one of these ligands.

Results and discussion

Monodentate phosphine catalyst

To provide a consistent point of comparison, we have included the reaction profile for the catalytic cycle of **1**, based on the mechanism we previously reported. The specific numerical values differ from our earlier report as we have used a different computational procedure in this report; BP86/def2-TZVP is used throughout this paper (see Computational methods for full details), while B3LYP/LACV3P+** was used in our first report. The relative energies and structures are generally consistent for both methods, although in our first report we found that a metastable nonclassical ethyl-dihydrogen intermediate formed after the insertion step. This structure is not a potential-energy minimum with the methodology used in this paper and only the $Ru(H)_2$ intermediate is present in this revised reaction profile.

Fig. 1. Catalytic cycle of ethylene hydrogenation by **1**.

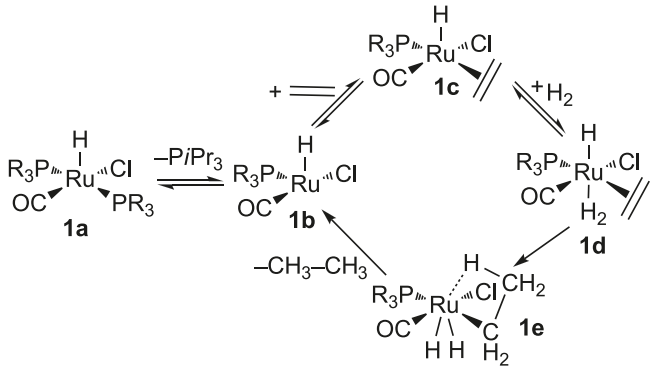

The catalytic cycle of **1** (Fig. 1) begins with the dissociation of P^iPr_3 to form a four-coordinate monophosphine complex **1b**. The olefin can then coordinate to the site vacated by the phosphine to form an η^2 metal-olefin complex (**1c**). Coordination of H_2 trans to the hydride forms **1d**, the immediate precursor to the olefin insertion. This insertion forms a metastable Ru(IV) dihydride intermediate (**1e**), which can facilely undergo reductive elimination to release the product alkane and regenerate **1b**. A path sampling study of this step demonstrated that this elimination generally occurs within 1 ps of the insertion due to localization of vibrational energy into the H–Ru–H bending mode.[33]

We have included the reaction profile of this catalytic cycle in Fig. 2. The dissociation of P^iPr_3 to form **1b** is significantly endergonic (11.8 kcal mol^{-1}). The coordination of ethylene is considerably weaker than that of the phosphine, so **1c** is only marginally more stable (10.1 kcal mol^{-1}). The reaction profile shows that **1d** is an unstable complex, at 14.6 kcal mol^{-1} with respect to the reactants. This is due to the strong trans influence of the hydride ligand and the entropic cost the complexation. As a result, subsequent olefin insertion into the ruthenium–hydride bond is the rate-limiting step on the reaction profile. Although the coordination of H_2 is weak in **1d**, our previous study[35] showed that the H_2 must be present to stabilize the metal during the insertion. The transition state of the insertion step (TS1) has a relative energy of 20.1 kcal mol^{-1}, the rate-limiting step of this profile.

The coordinated H_2 cleaves concurrently to the insertion, resulting in a Ru(IV) dihydride intermediate (**1e**), which is 1.4 kcal mol^{-1} less stable than **1d**. While Ru(IV) dihydrides had been thought to be generally less stable than the alternative non-classical $Ru(H_2)$ form,[43] a growing number of Ru(IV) dihydrides have been identified.[44–49] Given appropriate electron-donating auxiliary ligands and favourable trans

Fig. 2. Gibbs free-energy reaction profile of **1**. Free energies are given below the labels in kcal mol^{-1}.

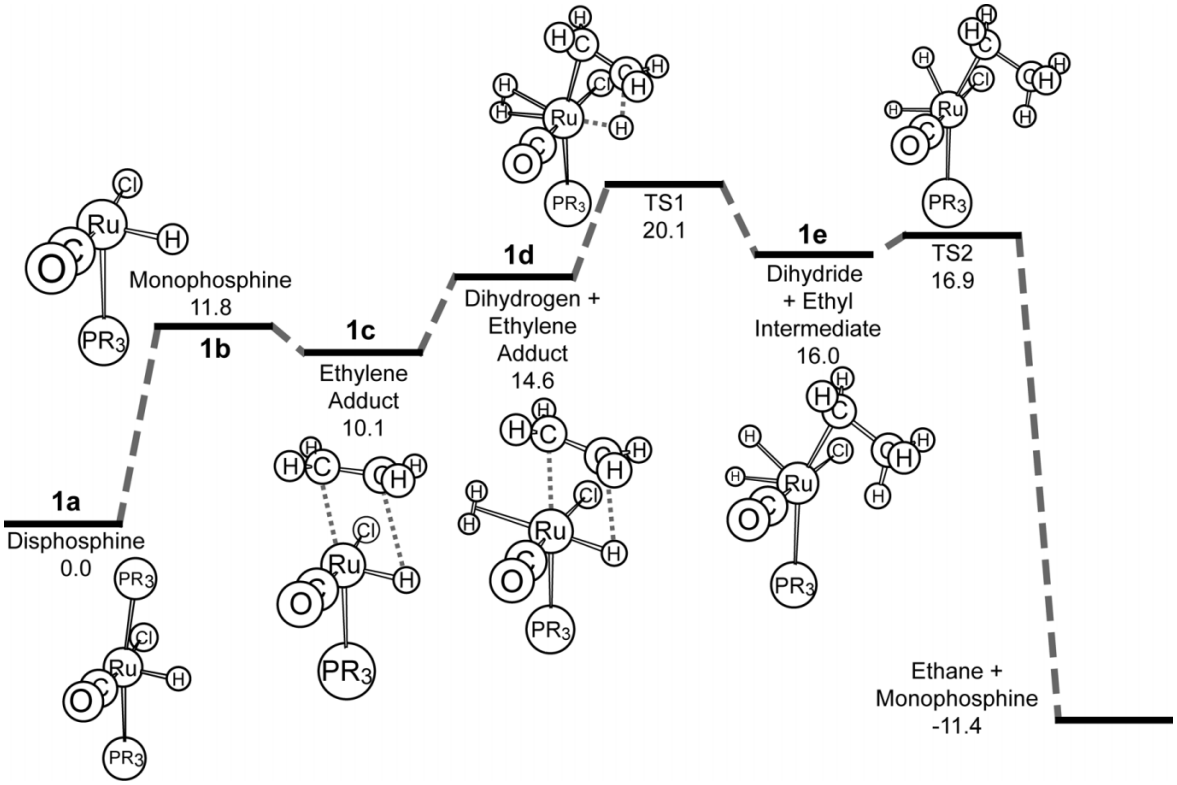

interactions, these dihydrides are viable reaction intermediates in some cases.

Potential hemilabile ligands

With the aim of identifying a ligand system that would allow the insertion to occur before the coordination of H_2, we have considered a series of complexes containing D–Z hemilabile ligands, where D is a strong donor and Z is a weak donor. In these complexes, the D donor occupies the coordinate site trans to the phosphine, while the Z donor occupies the site trans to the hydride (Fig. 3, **DZ-a**).

With the hemilabile ligand present, the catalytic cycle will be somewhat different than for **1** (Fig. 3). While the catalytic cycle still begins with the dissociation of phosphine (**DZ-b**) and the coordination of ethylene to form an olefin adduct (**DZ-c**), the donation from Z should allow the olefin insertion to occur directly from **DZ-c**. The insertion generates an alkyl-containing intermediate (**DZ-d**), which is stabilized by Z. As **DZ-d** is coordinately saturated, a ligand must dissociate to allow the coordination of H_2. Dissociation of Z would cause the complex to immediately revert to **DZ-c**, so the β-agostic interaction in **DZ-d** must be broken instead. This forms a square-pyramidal intermediate, **DZ-e**. Coordination of H_2 to this empty coordination site affords **DZ-f**, which can undergo reductive elimination to release the product and regenerate **DZ-b**.

We initially screened three catalysts containing established hemilabile ligands, **2**, **3**, and **4** with P–N, P–O, and C–N atoms acting as the DZ donors, respectively. The hemilabile ligand in **2** is diphenylphosphanodihydrooxazole, which coordinates to the metal through both the phosphine and the sp^2-hybridized N moiety. This type of ligand has been used extensively by Braunstein and co-workers in Pd-,[50] Ru-,[51,52] Cu-,[53] and Co-based[54] catalysts. **3** contains a benzamide-derived aryl phosphine, which was developed by Kwong et al. for Suzuki–Miyaura cross-coupling reactions.[55] We also evaluated **4**, where the hemilabile ligand is an N-heterocyclic carbene with a pendant pyridine group. This carbene was considered because Dharmasena et al. demonstrated that adding an N-heterocyclic carbene in the place of the alkyl phosphine in **1**, in conjunction with a more labile trans-phosphine, significantly improves hydrogenation activity.[56]

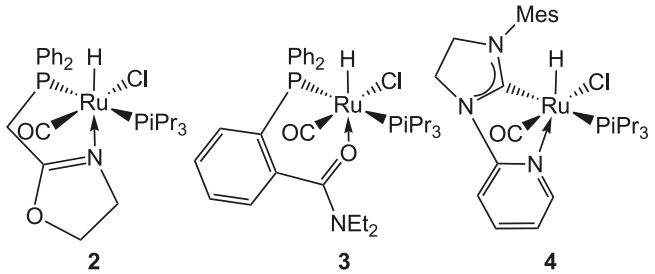

For these ligands to function effectively, they must stabilize **DZ-d** in the absence of H_2 coordinating trans to the hydride. To test this, we constructed **2d**, **3d**, and **4d**, then constrained the C–H(ag) distance to 1.1 Å to generate optimized structures corresponding to these intermediates. We then reoptimized these structures without the C–H(ag) constraint to test whether these complexes are stable. **3d** and **4d** are not potential-energy minima, as they reverted to their

Fig. 3. Catalytic cycle for H_2 hydrogenation of ethylene catalyzed by a hydridoruthenium complex with a hemilabile ligand (DZ).

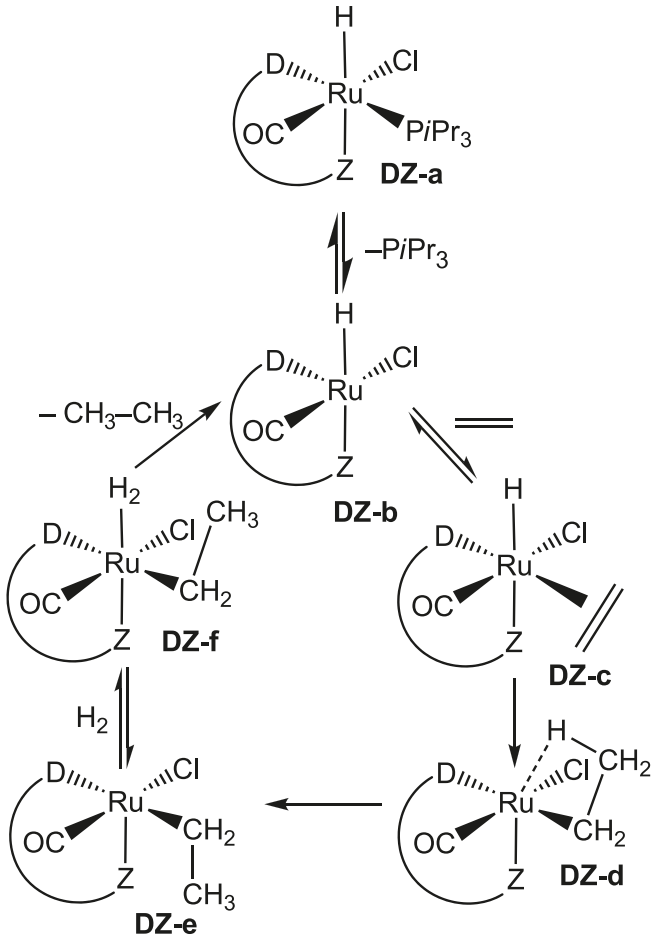

ethylene adduct structures (**3c** and **4c**, respectively), indicating that these hemilabile ligands are not sufficiently strong donors to stabilize this intermediate. The ethyl intermediate of **2** is a potential-energy minimum, indicating that the oxazoline is a strong enough donor to stabilize this intermediate. The relatively high basicity of the oxazoline, as well as the comparatively large bite angle of this ligand, appears to be critical for stabilizing the ethyl intermediate. We have focused our efforts on catalyst **2** as a result.

Evaluating the phosphaoxazoline-containing catalyst

We have calculated the full catalytic cycle for **2**, following the mechanism in Fig. 3. The reaction profile is presented in Fig. 4. The hydride is trans to the oxazoline donor in the minimum-energy isomer of the precatalyst (**2a**), although the alternative isomer where the hydride is trans to the chloride is close in energy. As in the catalytic cycle of **1**, the first step is the dissociation P^iPr_3 ligand. This forms a square-pyramidal monophosphine complex (**2b**) with a vacant coordination site trans to the remaining phosphine. This occurs more readily for this catalyst, as this step is endergonic by 6.6 kcal mol^{-1} vs. 11.8 kcal mol^{-1} for **1**. We attribute this to steric repulsion between P^iPr_3 and the oxazoline and more limited donation of the phosphine to the more electron-rich metal centre in **2**. The oxazoline–metal interaction is relatively weak in this step (the Ru–N bond order is 0.40), as the hydride has a strong trans influence (Table 1).

This step is followed by the η^2 coordination of ethylene to the vacant coordination site to form **2c**. This coordination is relatively strong, and the calculations predict a small preference to the coordination of ethylene (–0.9 kcal mol^{-1}) over the phosphine. This coordination is considerably stronger than in **1c** due to stronger back-donation interactions (vide infra).

As the oxazoline is able to stabilize the metal in this step, the insertion can proceed immediately after the coordination of ethylene (TS1). The catalytic cycle of **2** differs from **1** beginning at this step, as this insertion occurs prior to the coordination of H_2. The barrier to insertion is modest, at 6.2 kcal mol^{-1} with respect to the initial reactants, as opposed to 20.1 kcal mol^{-1} in the reaction profile of **1**. This indicates that this hemilabile ligand successfully lowers the activation free energy of the insertion step. The oxazoline begins to stabilize the metal significantly in this transition state, as the Ru–N distance decreases to 2.14 Å, and the bond order increases to 0.5.

This transition state leads to **2d**, an intermediate containing the newly formed ethyl ligand. The ethyl group interacts with the metal through an extremely strong β-agostic interaction (Ru–H(ag) = 1.75 Å; C–H(ag) = 1.27 Å). Further, this intermediate is very shallow, with a barrier of only 0.3 kcal mol^{-1} for the β-hydride elimination of the ethyl ligand. The Ru–N bond order increases even further in this step, to 0.54, indicating that the oxazoline is donating to the metal to a greater degree to stabilize this intermediate.

To coordinate H_2 to the metal, the β-agostic interaction in **2d** must be broken. As this agostic interaction is exceptionally strong and the metal is electron poor, the square-pyramidal intermediate formed in this process is 18.1 kcal mol^{-1} on the reaction profile, making this step the rate-limiting process in the catalytic cycle. With the agostic interaction broken, the oxazoline must donate strongly to the metal to stabilize this complex (**2e**); the Ru–N bond length is the shortest of any of the steps of the catalytic cycle (2.00 Å), and the Ru–N bond order is 0.73, considerably larger than in any other step. As this is the rate-limiting step, we would expect that this reaction would be zero order in $[H_2]$, unlike related Ru–monohydride catalysts, which are first order in $[H_2]$.[6,8,10,57]

This intermediate is the highest point on the reaction coordinate. The transition state preceding it would correspond to rotation of the Ru–ethyl segment to break the agostic interaction. This transition state could not be located on the potential-energy surface as this barrier is extremely flat, so we have assumed that the height of this barrier can be approximated by the energy of this intermediate.

With the β-agostic interaction broken, H_2 can coordinate to metal trans to the oxazoline, forming **2f**. This coordination is very strong, resulting in an elongation of the H–H bond to 0.92 Å. This coordination significantly stabilizes the metal and is considerably lower on the reaction profile than **2e** (7.0 kcal mol^{-1} vs. 18.1 kcal mol^{-1}).

The cleavage of dihydrogen and the elimination of the alkane occurs in a concerted fashion (TS2). This step is facile, with an energy barrier of only 11.2 kcal mol^{-1}. The metal

Fig. 4. Gibbs free-energy reaction profile of the catalytic cycle of **2**. Free energies are given below the labels in kcal mol^{-1}.

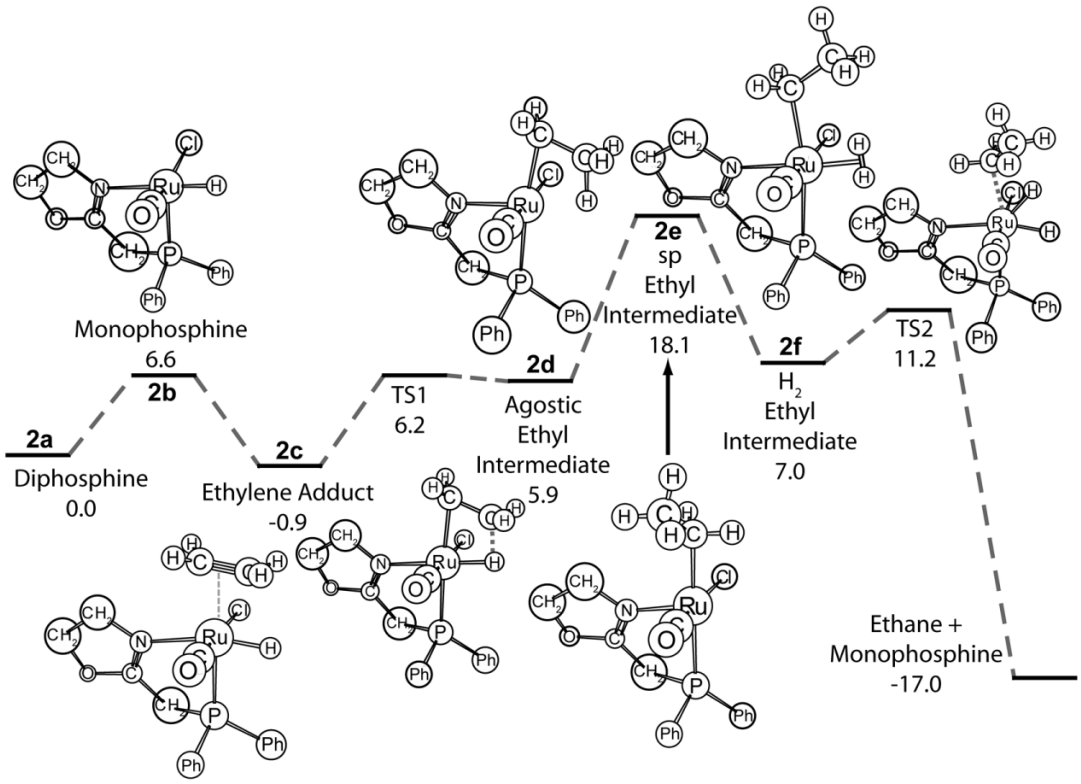

Table 1. Ru–N(oxazoline) bond lengths and Mayer bond orders for the reaction profile of **2**.

Reaction step	Ru–N bond length (Å)	Ru–N bond order
(**2a**) Diphosphine	2.35	0.37
(**2b**) Monophosphine	2.24	0.40
(**2c**) Ethylene adduct	2.24	0.41
TS1	2.14	0.50
(**2d**) β-Agostic ethyl intermediate	2.10	0.54
(**2e**) SP ethyl intermediate	2.00	0.73
(**2f**) H_2 + ethyl intermediate	2.12	0.53
TS2	2.24	0.40

Table 2. EDA of the coordination of ethylene to Ru(L) metal fragment in **1c** and **2c**.

		Energy (kcal mol^{-1})	
Component		**1**	**2**
Pauli repulsion		129.8	138.9
Electrostatic interaction		–92.1	–99.3
Orbital interactions		–66.5	–74.4
Preparation energy	Ru(L)	6.7	6.2
	Ethylene	4.4	6.1
Total		17.7	22.5

stabilizes the transition state via a partial hydridic bond with the transferred hydrogen. In contrast to **1**, no transient dihydride intermediate is formed in this elimination. Avoiding this unstable Ru(IV) dihydride intermediate is another advantage of the use of this hemilabile ligand.

Ethylene coordination

The free energy of coordination of ethylene to **1b** is exergonic by 1.7 kcal mol^{-1}, but the coordination to **2b** is exergonic by 7.7 kcal mol^{-1}. This difference is predominately due to the bond energy of the Ru–ethylene bond, which is

Table 3. Donation, back-donation, and repulsion components of CDA for Ru(L)↔ethylene interactions for the ethylene adducts of **1** and **2**.

Complex	Donation	Back-donation	Repulsion
1c	0.74	0.25	–0.41
2c	0.75	0.33	–0.45

Fig. 5. MO scheme of back-donation interaction in the complex between the monophosphine complex and ethylene for **1c** and **2c**.

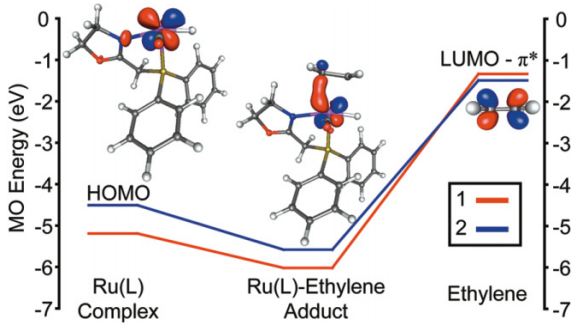

approximately 5 kcal mol^{-1} higher in **2c** than **1c** (Table 2).[58] The alternative conformation of **2c** where the oxazoline is not coordinated to the metal is 6.7 kcal mol^{-1} less stable with respect to the analogous reactants than structures where the oxazoline is coordinated, indicating that the coordination of the oxazoline causes this difference. This is surprising given that the oxazoline donor should make the metal centre more electron-rich and therefore have a lower Lewis acidity. Intrigued by this effect, we used fragment bonding analysis to investigate this further.

In the first stage of our analysis, we applied Ziegler–Morokuma energy decomposition analysis (EDA)[59–61] to complexes **1c** and **2c** (Table 2). EDA divides the bonding energy of two molecular fragments (in these cases, the ethylene ligand is one fragment, and the metal plus all the other ligands is the second fragment) into four components: the Pauli energy, the electrostatic interaction, the orbital interactions, and the preparation energies. The Pauli energy originates from the repulsion of the electron density of the two fragments, the electrostatic term includes the Coulomb interactions between the two fragments, and the orbital interactions term originates from covalent overlap between the fragment orbitals. The preparation energy results from the distortion of each fragment from their minimum-energy geometry to the geometry they adopt in the complex.

2c has a 4.8 kcal mol^{-1} stronger total bond energy than **1c** (Table 2). The Pauli repulsion term is larger for **2c**, although this repulsion is approximately cancelled by greater electrostatic interactions. Metal-fragment preparation energies are roughly equivalent, although the ethylene in **2c** has a higher preparation energy due to greater C=C bond elongation, typical of more strongly coordinated olefins. The crucial difference is that **2c** experiences 7.9 kcal mol^{-1} stronger orbital interactions. As this difference in coordination energies stems from the orbital interaction component, we next investigated the donation and back-donation interactions in complexes **1c** and **2c**.

Charge decomposition analysis (CDA) is a fragment analysis technique for investigating metal–ligand interactions[62] that is complimentary to EDA. This method calculates the relative weights of ligand-to-metal donation, metal-to-ligand back-donation, and an electron repulsion term resulting from the change in interelectron repulsion when the complex is formed. Within Dewar–Chatt–Duncanson theory,[63,64] bonding between transition-metal complexes and olefins results from two types of MO interactions: donation from the π bonding orbital of the olefin to the metal and back-donation from the metal to the π* antibonding orbital of the olefin. CDA data for the interaction between the coordinated ethylene and the metal fragment are presented in Table 3. **2c** has a distinctly higher proportion of back-donation than **1c** relative to the donation and repulsion terms. This indicates that the coordination of the oxazoline increases the interaction between the metal and the π* orbital of the ethylene.

We have identified the origin of this greater orbital interaction by examining the molecular orbitals corresponding to the metal–ethylene bonding. In each complex, the MO corresponding to back-donation is a predominantly combination of the d-character HOMO of the monophospine complex and the unoccupied ethylene π* orbital. Fragment orbital analysis shows that the Ru d-orbitals involved in this back-donation are destabilized by a repulsive interaction with the lone pair of the oxazoline (Fig. 5). This raises the energy of the back-donating Ru d-orbital, thereby reducing the energy difference between the interacting orbitals and making the interaction stronger.

As strong coordination of the olefin substrate is essential in this catalytic cycle, the increase in olefin coordination energy when the oxazoline is coordinated provides an additional benefit for the hemilabile ligand catalyst. Generally, it may be possible to increase the partitioning between ethylene and alkyl phosphines in Ru(II) complexes by introducing a hard, electron-donating ligand to destabilize filled d-orbitals. This favours bonding to olefins, which have higher back-bonding abilities than phosphines.

Conclusions

We have designed and computationally tested RuHCl(CO)(PR_3)(DZ) hydrogenation catalysts with hemilabile DZ-type ligands and compared them with an established catalyst RuHCl(CO)(P^iPr_3)$_2$ (**1**). In a previous mechanistic study of **1**, it was determined that H_2 must coordinate to the catalyst before ethylene can insert into the Ru–H bond of the catalyst. In this work, we have proposed that a hemilabile ligand could act as a two-electron donor to stabilize the metal during the insertion step such that it would not be necessary for H_2 to coordinate before ethylene coordination.

Three catalysts, **2**, **3**, and **4**, with P,N, P,O, and C,N hemilabile ligands, respectively, were computationally screened. Of the three hemilabile ligands that we considered, we determined that only a P,N coordinating phospha-oxazoline (**2**) could stabilize the metal sufficiently for the olefin inser-

tion to occur prior to coordinating H_2 to the metal. In principle, such a catalyst would be more active, as the entropic cost of weakly coordinating H_2 to the metal during the rate-limiting process is avoided.

Somewhat surprisingly, the introduction of the hemilabile ligand was found to significantly increase the olefin complexation energy relative to **1**. The reason for this was found to be a stronger Ru–ethylene back-donating interaction that was enhanced by a destabilization of the d-orbitals on the metal by the lone pair on the oxazoline ligand. This was found to lower the energy barriers associated with the ethylene coordination steps of the catalytic cycle.

On the other hand, the introduction of the hemilabile ligand has the detrimental consequence of producing a metal center that is coordinatively saturated after the insertion step. This results in an additional step where the β-agostic interaction between the newly formed alkyl ligand and the metal must be broken in to coordinate H_2. This process is rate-limiting, and we predict that the reaction should be zero-order in $[H_2]$, whereas this reaction with the traditional catalysts is known to be first-order in $[H_2]$. The formation of the intermediate with the strong β-agostic interaction therefore mitigates the rate enhancement induced by the hemilabile ligand.

The calculations presented here suggest that the overall ethylene hydrogenation barrier for the proposed hemilabile phospha-oxazoline containing catalyst, **2**, should be comparable to the more established $RuHCl(CO)PR_3)_2$, **1**, catalyst. Although simulating the reaction on the computer can never replace actually testing the catalyst in the lab, we have rationally designed a new catalyst motif based on our theoretical analysis of the parent catalyst system (**1**). This proposed catalyst motif may provide experimentalists with additional avenues to tune and optimize an important class of catalysts. For example, we believe there are opportunities to further optimize the donor properties of the hemilabile ligands as to stabilize the formation of the rate-determining ethyl intermediate (**2e**).

In addition to any rate enhancement resulting from the hemilabile ligand, the presence of the N donor may improve the catalyst lifetime. Fogg and co-workers have recently concluded that catalyst stability is critical for high activity in these systems,[11] which suggests that blocking decomposition pathways could be a fruitful approach to developing a more robust catalyst. Coordinately saturating the metal and inhibiting the dissociation of the hemilabile phosphine through the chelate effect could deter the degradation of the catalyst.

Computational methods

The calculations presented here were made with DFT,[26] as implemented in Turbomole 5.9[65] using the BP86[66,67] functional and the def2-TZVP basis set.[68] Thermal corrections were determined by reoptimizing these structures with the def2-SV(P) basis set, then running frequency analysis. We confirmed that the imaginary mode of the reported transition-state structures connects the adjacent steps in the reaction profile. Our first report used the B3LYP functional; however, the larger systems we have studied here required that we adopt a "pure" DFT functional so that the resolution-of-identity (RI)[69] approximation could be used. The BP86 calculations were benchmarked against the alternative PBE functional[70] and found to be consistent. Ziegler–Morokuma EDA analysis was performed by reoptimizing the complexes in ADF 2007.1 with the BP86 functional and the TZP basis set. Fragment orbital analysis was performed using the AOmix package.[71,72]

Acknowledgement

We thank Professor D. Fogg and Heather M. Foucault for useful discussions and getting us interested in this catalytic system. We thank the Natural Sciences and Engineering Research Council of Canada (NSERC) and the Canada Research Chairs program for funding. C.N.R. thanks NSERC for a PGS scholarship and HPCVL for research scholarships. We are also grateful to the Canadian Foundation for Innovation (CFI), the Ontario Research Fund, IBM Canada, HPCVL, and SharcNet for providing computing resources.

References

(1) This article is part of a Special Issue dedicated to Professor T. Ziegler.
(2) This paper is dedicated to Tom Ziegler to celebrate his numerous contributions to the fields of organometallic chemistry and catalysis.
(3) Blaser, H.-U.; Malan, C.; Pugin, B.; Spindler, F.; Steiner, H.; Studer, M. *Adv. Synth. Catal.* **2003**, *345* (12), 103–151. doi:10.1002/adsc.200390000.
(4) Genet, J.-P. *Acc. Chem. Res.* **2003**, *36* (12), 908–918. doi:10.1021/ar020152u. PMID:14674782.
(5) Clapham, S. E.; Hadzovic, A.; Morris, R. H. *Coord. Chem. Rev.* **2004**, *248* (21-24), 2201–2237. doi:10.1016/j.ccr.2004.04.007.
(6) McManus, N. T.; Rempel, G. L. *Rev. Macromol. Chem. Phys.* **1995**, *C35*, 239.
(7) Guo, X.-Y.; Rempel, G. L. *J. Appl. Polym. Sci.* **1997**, *65* (4), 667–675. doi:10.1002/(SICI)1097-4628(19970725)65:4<667::AID-APP5>3.0.CO;2-I.
(8) Martin, P.; McManus, N. T.; Rempel, G. L. *J. Mol. Catal. A* **1997**, *126* (2-3), 115–131. doi:10.1016/S1381-1169(97)00102-7.
(9) Pan, Q.; Rempel, G. L. *Macromol. Rapid Commun.* **2004**, *25* (8), 843–847. doi:10.1002/marc.200300275.
(10) Tangthongkul, R.; Prasassarakich, P.; Rempel, G. L. *J. Appl. Polym. Sci.* **2005**, *97* (6), 2399–2406. doi:10.1002/app.21922.
(11) Beach, N. J.; Dharmasena, U. L.; Drouin, S. D.; Fogg, D. E. *Adv. Synth. Catal.* **2008**, *350* (5), 773–777. doi:10.1002/adsc.200800056.
(12) Beach, N. J.; Blacquiere, J. M.; Drouin, S. D.; Fogg, D. E. *Organometallics* **2009**, *28* (2), 441–447. doi:10.1021/om800778h.
(13) Drouin, S. D.; Zamanian, F.; Fogg, D. E. *Organometallics* **2001**, *20* (26), 5495–5497. doi:10.1021/om010747d.
(14) Fogg, D. E. *Can. J. Chem.* **2008**, *86*, 931.
(15) Fogg, D. E.; dos Santos, E. N. *Coord. Chem. Rev.* **2004**, *248* (21-24), 2365–2379. doi:10.1016/j.ccr.2004.05.012.
(16) Louie, J.; Bielawski, C. W.; Grubbs, R. H. *J. Am. Chem. Soc.* **2001**, *123* (45), 11312–11313. doi:10.1021/ja016431e. PMID:11697983.
(17) Schmidt, B. *Pure Appl. Chem.* **2006**, *78* (2), 469–476. doi:10.1351/pac200678020469.

(18) Wasilke, J.-C.; Obrey, S. J.; Baker, R. T.; Bazan, G. C. *Chem. Rev.* **2005**, *105* (3), 1001–1020. doi:10.1021/cr020018n. PMID:15755083.
(19) Watson, M. D.; Wagener, K. B. *Macromolecules* **2000**, *33* (9), 3196–3201. doi:10.1021/ma991595p.
(20) Hallman, P. S.; Evans, D.; Osborn, J. A.; Wilkinson, G. *Chem. Commun.* **1967**, *305*, 229.
(21) Hallman, P. S.; McGarvey, B. R.; Wilkinson, G. *J. Chem. Soc. A* **1968**, *3143*.
(22) Yi, C. S.; Lee, D. W. *Organometallics* **1999**, *18* (24), 5152–5156. doi:10.1021/om990493k.
(23) Esteruelas, M. A.; Sola, E.; Oro, L. A.; Werner, H.; Meyer, U. *J. Mol. Catal.* **1988**, *45* (1), 1–5. doi:10.1016/0304-5102(88)85024-7.
(24) Esteruelas, M. A.; Sola, E.; Oro, L. A.; Werner, H.; Meyer, U. *J. Mol. Catal.* **1989**, *53* (1), 43–52. doi:10.1016/0304-5102(89)85028-X.
(25) Niu, S.; Hall, M. B. *Chem. Rev.* **2000**, *100* (2), 353–406. doi:10.1021/cr980404y. PMID:11749240.
(26) Ziegler, T.; Autschbach, J. *Chem. Rev.* **2005**, *105* (6), 2695–2722. doi:10.1021/cr0307188. PMID:15941226.
(27) Busico, V.; Cipullo, R.; Pellecchia, R.; Ronca, S.; Roviello, G.; Talarico, G. *Proc. Natl. Acad. Sci. U.S.A.* **2006**, *103* (42), 15321–15326. doi:10.1073/pnas.0602856103. PMID:17032770.
(28) Wang, Y.; Wang, J.; Su, J.; Huang, F.; Jiao, L.; Liang, Y.; Yang, D.; Zhang, S.; Wender, P. A.; Yu, Z.-X. *J. Am. Chem. Soc.* **2007**, *129* (33), 10060–10061. doi:10.1021/ja072505w. PMID:17655302.
(29) Houk, K. N.; Cheong, P. H.-Y. *Nature* **2008**, *455* (7211), 309–313. doi:10.1038/nature07368. PMID:18800129.
(30) Wondimagegn, T.; Wang, D.; Razavi, A.; Ziegler, T. *Organometallics* **2008**, *27* (24), 6434–6439. doi:10.1021/om800731y.
(31) Rowley, C. N.; Woo, T. K. *Organometallics* **2008**, *27* (24), 6405–6407. doi:10.1021/om800891w.
(32) Rowley, C. N.; Woo, T. K. *J. Am. Chem. Soc.* **2008**, *130* (23), 7218–7219. doi:10.1021/ja802219a. PMID:18481857.
(33) Rowley, C. N.; Ong, T.-G.; Priem, J.; Richeson, D. S.; Woo, T. K. *Inorg. Chem.* **2008**, *47* (24), 12024–12031. doi:10.1021/ic801739a.
(34) Rowley, C. N.; Ong, T.-G.; Priem, J.; Woo, T. K.; Richeson, D. S. *Inorg. Chem.* **2008**, *47* (20), 9660–9668. doi:10.1021/ic801028m. PMID:18811151.
(35) Rowley, C. N.; Foucault, H. M.; Woo, T. K.; Fogg, D. E. *Organometallics* **2008**, *27* (8), 1661–1663. doi:10.1021/om7012698.
(36) Crabtree, R. H. *The organometallic chemistry of the transition metals*; 4th ed; John Wiley and Sons, Inc.: Hoboken, NJ,2005.
(37) Bader, A.; Lindner, E. *Coord. Chem. Rev.* **1991**, *108* (1), 27–110. doi:10.1016/0010-8545(91)80013-4.
(38) Slone, C. S.; Weinberger, D. A.; Mirkin, C. A. *Prog. Inorg. Chem.* **1999**, *48*, 233–350. doi:10.1002/9780470166499.ch3.
(39) Weng, Z.; Teo, S.; Hor, T. S. A. *Acc. Chem. Res.* **2007**, *40* (8), 676–684. doi:10.1021/ar600003h. PMID:17461542.
(40) Kwong, F.; Chan, A. *Synlett* **2008**, 1440–1448. doi:10.1055/s-2008-1078425.
(41) Zhang, J.; Leitus, G.; Ben-David, Y.; Milstein, D. *J. Am. Chem. Soc.* **2005**, *127* (31), 10840–10841. doi:10.1021/ja052862b. PMID:16076184.
(42) Zhang, J.; Leitus, G.; Ben-David, Y.; Milstein, D. *Angew. Chem., Int. Ed.* **2006**, *45* (7), 1113–1115. doi:10.1002/anie.200503771.
(43) Morris, R. H. *Coord. Chem. Rev.* **2008**, *252* (21-22), 2381–2394. doi:10.1016/j.ccr.2008.01.010.
(44) Grünwald, C.; Gevert, O.; Wolf, J.; González-Herrero, P.; Werner, H. *Organometallics* **1996**, *15* (8), 1960–1962. doi:10.1021/om9509554.
(45) Rodriguez, V.; Donnadieu, B.; Sabo-Etienne, S.; Chaudret, B. *Organometallics* **1998**, *17* (17), 3809–3814. doi:10.1021/om980141y.
(46) Rodriguez, V.; Sabo-Etienne, S.; Chaudret, B.; Thoburn, J.; Ulrich, S.; Limbach, H.-H.; Eckert, J.; Barthelat, J.-C.; Hussein, K.; Marsden, C. J. *Inorg. Chem.* **1998**, *37* (14), 3475–3485. doi:10.1021/ic970697y. PMID:11670430.
(47) Ferrando-Miguel, G.; Wu, P.; Huffman, J. C.; Caulton, K. G. *N. J. Chem.* **2005**, *29* (1), 193. doi:10.1039/b411487f.
(48) Oliván, M.; Clot, E.; Eisenstein, O.; Caulton, K. G. *Organometallics* **1998**, *17* (14), 3091–3100. doi:10.1021/om971109r.
(49) Drouin, S. D.; Yap, G. P. A.; Fogg, D. E. *Inorg. Chem.* **2000**, *39* (23), 5412–5414. doi:10.1021/ic000102q. PMID:11154602.
(50) Braunstein, P.; Fryzuk, M. D.; Le Dall, M.; Naud, F.; Rettig, S. J.; Speiser, F. *Dalton Trans.* **2000**, 1067.
(51) Braunstein, P.; Graiff, C.; Naud, F.; Pfaltz, A.; Tiripicchio, A. *Inorg. Chem.* **2000**, *39* (20), 4468–4475. doi:10.1021/ic0000754.
(52) Braunstein, P.; Naud, F.; Rettig, S. J. *N. J. Chem.* **2001**, *25* (1), 32–39. doi:10.1039/b004786o.
(53) Braunstein, P.; Clerc, G.; Morise, X. *N. J. Chem.* **2003**, *27* (1), 68–72. doi:10.1039/b206410n.
(54) Jie, S.; Agostinho, M.; Kermagoret, A.; Cazin, C. S. J.; Braunstein, P. *Dalton Trans.* **2007**, (39): 4472–4482. doi:10.1039/b706818b. PMID:17909659.
(55) Yee Kwong, F.; Har Lam, W.; Hung Yeung, C.; Shing Chan, K.; Chan, A. S. C. *Chem. Commun. (Camb.)* **2004**, (17): 1922–1923. doi:10.1039/b407243j. PMID:15340602.
(56) Dharmasena, U. L.; Foucault, H. M.; dos Santos, E. N.; Fogg, D. E.; Nolan, S. P. *Organometallics* **2005**, *24* (6), 1056–1058. doi:10.1021/om049041k.
(57) James, B. R. In *Homogeneous hydrogenation*; John Wiley & Sons, Inc.: New York, NY, 1973; pp. 83–88.
(58) [The bond energies we report here differ slightly from those reported in Figs. 1 and 2, as we have performed this analysis in ADF using a different basis set. See Computational methods for full details.
(59) Kitaura, K.; Morokuma, K. *Int. J. Quantum Chem.* **1976**, *10* (2), 325–340. doi:10.1002/qua.560100211.
(60) Ziegler, T.; Rauk, A. *Theor. Chim. Acta* **1977**, *46*, 1.
(61) Bickelhaupt, F. M.; Baerends, E. J. Kohn–Sham density functional theory: predicting and understanding chemistry; In *Rev. Comput. Chem.* Wiley-VCH: New York, 2000; pp. 1–86.
(62) Dapprich, S.; Frenking, G. *J. Phys. Chem.* **1995**, *99* (23), 9352–9362. doi:10.1021/j100023a009.
(63) Winterton, N. Some notes on the early development of models of bonding in olefin-metal complexes; In *Modern coordination chemistry: the legacy of Joseph Chatt*; Leigh, G. J. and Winterton, N., Eds.; Royal Society of Chemistry: Cambridge, UK, 2002.
(64) Frenking, G. The Dewar–Chatt–Duncanson bonding model of transition metal-olefin complexes examined by modern quantum chemical methods;In *Modern coordination chemistry: the legacy of Joseph Chatt*; Leigh, G. J. and Winterton, N., Eds.; Royal Society of Chemistry: Cambridge, UK, 2002.
(65) Ahlrichs, R.; Bar, M.; Haser, M.; Horn, H.; Kolmel, C.

Chem. Phys. Lett. **1989**, *162* (3), 165–169. doi:10.1016/0009-2614(89)85118-8.
(66) Becke, A. D. Phys. Rev. A: At. Mol. Opt. Phys. 1988, 38.
(67) Perdew, J. P.; Yue, W. *Phys. Rev. B* **1986**, *33* (12), 8800–8802. doi:10.1103/PhysRevB.33.8800.
(68) Weigend, F.; Ahlrichs, R. *Phys. Chem. Chem. Phys.* **2005**, *7* (18), 3297–3305. doi:10.1039/b508541a. PMID:16240044.
(69) Eichkorn, K.; Treutler, O.; Ohm, H.; Haser, M.; Ahlrichs, R. *Chem. Phys. Lett.* **1995**, *240* (4), 283–289. doi:10.1016/0009-2614(95)00621-A.
(70) Perdew, J. P.; Burke, K.; Ernzerhof, M. *Phys. Rev. Lett.* **1996**, *77* (18), 3865–3868. doi:10.1103/PhysRevLett.77.3865. PMID:10062328.
(71) Gorelsky, S. I.; Lever, A. B. P. *J. Organomet. Chem.* **2001**, *635* (1-2), 187–196. doi:10.1016/S0022-328X(01)01079-8.
(72) Gorelsky, S. I. *AOMix: Program for molecular orbital analysis*; University of Ottawa, Ontario. Available from http://www.sg-chem.net. 2009.

Binding of polar monomers in the complexes with organometallic ethylene polymerization catalysts — Natural orbitals for chemical valence and energy decomposition analysis[1]

Monika Srebro, Mariusz Mitoraj, and Artur Michalak

Abstract: The binding mode of polar monomers in complexes with late-transition-metal catalysts for ethylene polymerization was studied by density functional theory (DFT) calculations. The Ziegler–Rauk energy decomposition scheme was used to characterize the geometry distortion and steric and orbital-interaction terms in the bonding energy, while Natural Orbitals for Chemical Valence (NOCV) were applied to describe the donation and back-bonding components of the bond between the monomer and the catalyst. The NOCV analysis allowed for comparison of the donor–acceptor properties of different monomers in the σ- and π-complexes. The complexes with the model, cationic Ni– or Pd–diimine catalysts, N^N–Ni(H)+ and N^N–Pd(H)+, and the neutral Ni–anilinotropone system, N^O–Ni(H), were investigated. The monomers studied included: simple olefins (Et and Pr); examples of oxygen- and nitrogen-containing polar monomers (methyl acrylate (MA), vinyl acetate (VAc), their fluorinated derivatives (FMA, FVAc), vinyl ether (VE), acrylonitrile (AN), and β-butenoic nitrile (BN); vinyl and allyl amines (VAm, PrAm); and a tertiary dimethyl vinyl amine (MVAm). The results demonstrate that the metal-based fragment has a significant influence on the relative stability of the σ- and π-complexes; the π-binding mode increases in the following order: N^N–Ni(H)+ < N^N–Pd(H)+ < N^O–Ni(H). The results of the Ziegler–Rauk bond-energy decomposition indicate that for some monomers (MA, FMA, VAc, AN, VAm, MVAm) the preference of the coordination mode has a steric (electrostatic and Pauli) origin. For other monomers (VE, FVAc, BN, PrAm) the changes in the orbital-interaction terms are important as well. The results of the NOCV analysis indicate that for both, σ- and π-coordination modes there exist components describing σ-donation and π-back-bonding. The sequences of σ-donor and π-acceptor properties of monomers in the π-complexes as well as σ-complexes are similar for the considered catalysts.

Key words: NOCV, bonding analysis, donor–acceptor properties, copolymerization of olefins with polar monomers, single-site catalysts.

Résumé : Faisant appel à des calculs basés sur la théorie de la fonctionnelle de densité (TFD), on a étudié le mode de fixation de monomères polaires dans des complexes avec des catalyseurs de métaux de transition utilisés pour la polymérisation de l'éthylène. On a fait appel au schéma de décomposition de l'énergie de Ziegler–Rauk pour caractériser la distorsion de la géométrie et des termes d'interactions orbitalaires et stériques dans l'énergie de fixation; on a aussi appliqué la théorie de la valence chimique des orbitales naturelles (VCON) pour décrire les composantes de donation et de rétrodonation de la liaison entre les divers monomères et le catalyseur. Une analyse selon la VCON a permis de faire une comparaison entre les propriétés donneur–accepteur des divers monomères dans des complexes σ- et π-. Avec ce modèle, on a étudié les catalyseurs cationiques Ni– Pd–diimine, N^N–Ni(H)+ et N^N–Pd(H)+, et le système neutre Ni–anilinotropone system, N^O–Ni(H). Les monomères examinés comprennent les oléfines simples (éthylène, Et, et propylène, Pr) ainsi que des exemples de monomères polaires contenant de l'oxygène et de l'azote, tel l'acrylate de méthyle (AM), l'acétate de vinyle (AcV) et leurs dérivés fluorés (FAM; FacV), l'éther vinylique (EV), l'acrylonitrile (AN) et le β-butènenitrile (BN), les vinylamine (Vam) et allylamiine (PrAm) et une amine tertiaire, lal diméthylvinylamine (MVAm). Les résultats démontrent que le fragment porté par le métal exerce une influence significative sur la stabilité relative des complexes σ- et π- et que le mode de fixation π augmente dans l'ordre suivant: N^N–Ni(H)+ < N^N–Pd(H)+ < N^O–Ni(H). Les résultats de la décomposition de l'énergie de liaison de Ziegler–Rauk indiquent que, pour quelques-uns des monomères (AM, FAM, AcV, AN, VAm, MVAm), la préférence du mode de coordination est d'origine stérique (électrostatique et Pauli). Pour quelques monomères (EV, FAcV, BN, PrAm), les changements dans les termes de l'interaction d'orbitale sont aussi importants. Les résultats de l'analyse selon la théorie VCON indiquent que pour les deux modes de coordination σ- et π-, il existe des composants décrivant la donation σ et la rétrocession π. Les séquences des propriétés σ-donneur et π-accepteur des monomères dans les complexes π ainsi que dans les complexes σ sont semblables pour les catalyseurs considérés.

Received 23 December 2008. Accepted 2 April 2009. Published on the NRC Research Press Web site at canjchem.nrc.ca on 26 June 2009.

M. Srebro, M. Mitoraj, and A. Michalak.[1] Department of Theoretical Chemistry, Faculty of Chemistry, Jagiellonian University, R. Ingardena 3, 30-060 Cracow, Poland.

[1]Corresponding author (e-mail: michalak@chemia.uj.edu.pl).

Mots-clés : théorie de la valence chimique des orbitales naturelles (VCON), analyse des liaisons, propriétés donneur/accepteur, copolymérisation d'oléfines avec des monomères polaires, catalyseurs à site unique.

[Traduit par la Rédaction]

Introduction

Copolymers of ethylene and higher α-olefins with monomers bearing a polar functional group have attracted the growing interest of material researchers, especially because the incorporation of even small amounts of the polar monomer into the polyolefin chain dramatically modifies polymer properties.[2] Since commercially available polar copolymers are still overwhelmingly produced in radical polymerization processes under high temperature and high pressure conditions,[3] great attention has been paid to the development of new, less expensive routes of their production.[2]

In this context, use of the organometallic single-site catalysts based on the late transition metals is especially promising,[2b,4] as they are more tolerant toward Lewis bases than early-transition-metal complexes. The development of such catalysts for random copolymerization processes would not only decrease the production costs of the copolymers, but it could additionally enable the synthesis of new materials, potentially possessing new, interesting properties.

However, only a limited number of polar vinyl monomers has so far been efficiently copolymerized with α-olefins via the coordination–insertion mechanism[5] using catalysts based on late-transition-metal complexes. A list of proposed catalysts for controlled, direct copolymerization processes includes: Brookhart Ni– and Pd–diimine catalysts,[6] which have been shown to copolymerize ethylene and higher α-olefins with acrylates and vinyl ketones;[7] salicylaldiminato Ni-complexes, developed by Grubbs et al.,[8] able to polymerize and copolymerize some polar monomers;[9] Brookhart and Gibson (imino)pyridine Fe or Co systems[10] active in the copolymerization of ethylene with vinyl chloride and vinyl acetate;[11] and the Pd(II) complexes containing anionic bidentate sulfonate ligands recently developed by Drent et al., giving rise to copolymers of ethylene with acrylates, acrylonitrile, vinyl ethers, and vinyl fluoride.[12] Consequently, in view of the great variety of available polar monomers, the design of an effective catalyst for the random copolymerization of α-olefins with monomers bearing a polar functional group still remains one of the fundamental goals of organometallic catalysis.

Simultaneously with experimental research, theoretical mechanistic studies on various aspects of homopolymerization[13,14] and copolymerization mechanisms[15,16] have been carried out to understand the factors that are important for stabilizing catalytic–active metal centers and controlling their activity and selectivity; here the contribution from the group of Prof. Tom Ziegler has been particularly significant. Basically, the copolymerization of α-olefins with polar monomers proceeds via the same reaction mechanism as that of traditional α-olefin Ziegler–Natta homopolymerization,[5] including such steps as complexation, insertion, isomerization, and termination. Nevertheless, these elementary reactions reveal some specificity compared to homopolymerization because of the presence of donor atoms provided by polar monomers.[15d] One of the most important is the formation of σ-complexes, in which the monomer is bound to the metal center by its functional group. According to the standard Cossee–Arlman mechanism for α-olefin polymerization[5] the monomer insertion into the metal–polymer chain bond may start only from the σ-complex. Thus, formation of too stable σ-complexes results in the poisoning of the catalyst. Consequently, the preferred binding mode of the nitrogen- or oxygen-containing monomers seems to be crucial for the activity of the catalyst.

The main goal of the present study is to explore the important factors that influence the binding mode of various monomers in complexes with organometallic ethylene polymerization catalysts. The list of monomers investigated in the present work includes examples of the important oxygen- and nitrogen-containing molecules containing a vinyl group, as well as simple non-polar olefins. Complexes with model, cationic Ni– or Pd–diimine catalysts,[6,7] and neutral Ni–anilinotropone systems[17] were investigated in this work. On the basis of the DFT calculations, the role of the electronic and steric factors together with the donor–acceptor properties of a series of monomers for all considered catalysts in both types of coordination modes (π- and σ-complexes) will be discussed.

To date, many theoretical methods[18–23] have been proposed to describe the bond formed between the metal center and the ligand according to the "classical" Dewar–Chatt–Duncanson model[24] of donation–back-donation in transition-metal systems. Among the most widespread there are charge decomposition analysis[19] (CDA), constrained space orbital variation[20] (CSOV), interaction-energy partitioning schemes,[21] and natural bond orbitals[22] (NBO). One of the most recently proposed approaches is based on analysis of the natural orbitals for chemical valence[23] (NOCV). A main advantage of NOCV is that it allows for the direct separation of the contributions to the deformation (differential) density, $\Delta\rho$, of the ligand → metal and metal → ligand electron charge transfer processes. The NOCV, together with the Ziegler–Rauk[21b–21c] bond-energy decomposition analysis, will be used in the present work. It was shown in our previous papers[23] that NOCV approach gives a picture in agreement with other measures of donation–back-bonding.

Computational details and the model systems

The polar monomers and the catalysts studied in the present work are shown in Fig. 1. We considered complexes of polar monomers with the model cationic diimine catalysts based on Ni and Pd[6,7] and the neutral Ni–anilinotropone catalyst.[17] As the simplest models for the active form of the respective catalysts, the hydride complexes were considered: N^N–Ni(H)+, N^N–Pd(H)+, and N^O–Ni(H), depicted in

Fig. 1. Complexes studied in the present work: models for catalysts (panel *a*), monomers (panel *b*), and optimized geometries of the acrylonitrile π- (left) and σ-complexes (right) with Ni-based diimine (top) and anilinotropone (bottom) catalysts (panel *c*).

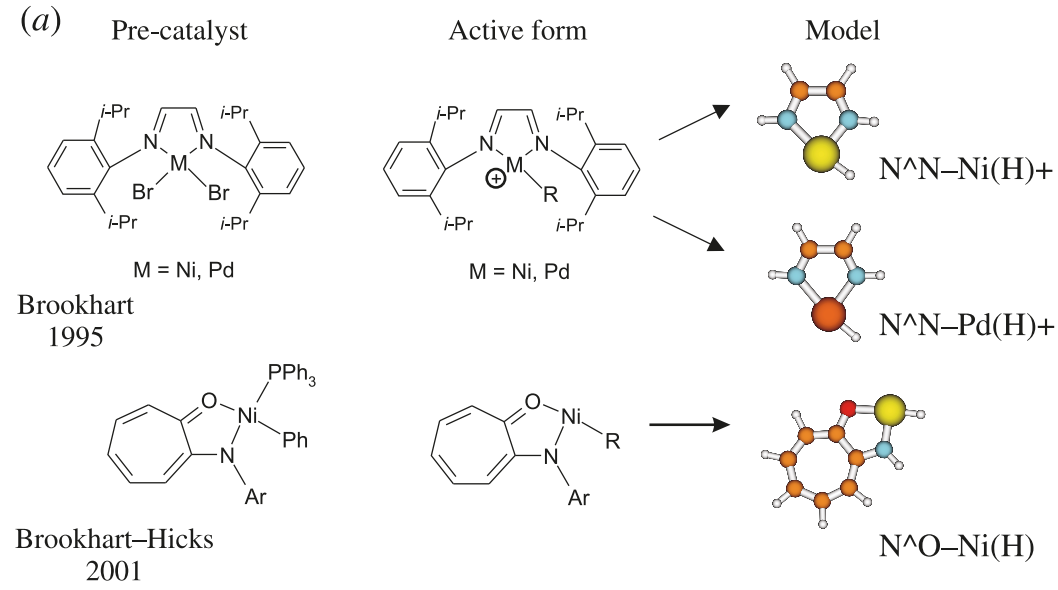

(b)

$CH_2=CH_2$ Et
$CH_2=CHCH_3$ Pr

O-monomers

$CH_2=CHCOOCH_3$	MA
$CH_2=CHCOOCF_3$	FMA
$CH_2=CHO(CO)CH_3$	VAc
$CH_2=CHO(CO)CF_3$	FVAc
$CH_2=CHOCH_3$	VE

N-monomers

$CH_2=CHCN$	AN
$CH_2=CHCH_2CN$	BN
$CH_2=CHNH_2$	VAm
$CH_2=CHCH_2NH_2$	PrAm
$CH_2=CHN(CH_3)_2$	MVAm

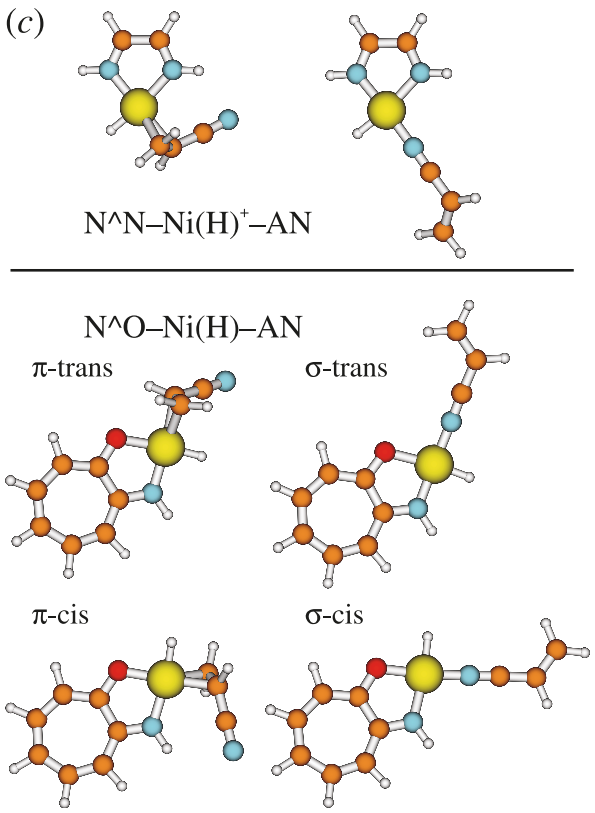

Fig. 1*a*. Since our goal was to compare two different binding modes in the complexes of various monomers, use of the hydride complexes instead of longer alkyl chains was justified here.

A list of the monomers studied is presented in Fig. 1*b*. It includes simple olefins (Et and Pr) as well as examples of oxygen- and nitrogen-containing polar monomers ("O-monomers" and "N-monomers"): methyl acrylate (MA), vinyl acetate (VAc), their fluorinated derivatives (FMA, FVAc), vinyl ether (VE), acrylonitrile (AN), and β-butenoic nitrile (BN); vinyl and allyl amines (VAm, PrAm), and an example of tertiary dimethyl vinyl amine (MVAm).

Following the mechanism of the copolymerization of α-olefins with polar monomers,[5,15d] we have considered complexes in which the polar monomer is bound to the metal center by either its double C=C bond (π-complexes), or by a donor atom (nitrogen or oxygen) of the polar group (σ-complexes). Examples of optimized structures of such

systems for acrylonitrile and the model Ni–diimine and Ni–anilinotropone catalysts are presented in Fig. 1*c*. It should be emphasized that, in the case of anilinotropone system, N^O–Ni(H), two pairs of the π- and σ-complexes are possible for each polar monomer, since it can be coordinated in the position trans or cis with respect to the nitrogen atom. However, for all monomers the trans complexes were found to be more stable (by 3.1–8.9 kcal/mol) than the corresponding cis complexes. Therefore, all the results for Ni–anilinotropone catalyst presented in this work will refer to the trans π- and σ-complexes, i.e., the most stable species.

All the results were obtained from the DFT calculations based on the Becke–Perdew exchange–correlation functional,[25] using the Amsterdam density functional[26] (ADF) program, version 2004.01. A standard triple-ζ STO basis with one set of polarization functions (TZP) was used for transition metals Ni and Pd, while a standard DZP basis set was employed for main-group elements H, C, N, and O. For fluorine, a triple-ζ STO basis with two sets of polarization functions (TZ2P) was employed. The 1s electrons of C, N, O, and F, as well as the 1s–2p electrons of Ni and 1s–3d electrons of Pd were treated as frozen core. Auxiliary s, p, d, f, and g STO functions, centered on all nuclei, were used to fit the electron density and obtain accurate Coulomb potential in each SCF cycle. Relativistic effects were considered using the first-order scalar relativistic correction.[27]

Bonding between monomers and catalysts in all systems was described using the Ziegler–Rauk bond-energy decomposition scheme[21b–21c] and the analysis of NOCV.[23]

In the Ziegler–Rauk bond-energy decomposition analysis,[21b–21c] the overall bonding energy is decomposed as

$$[1]\qquad \begin{aligned}\Delta E_{\mathrm{b}} &= \Delta E_{\mathrm{geom.}} + \Delta E_{\mathrm{tot.}} \\ &= \Delta E_{\mathrm{geom.}} + [\Delta E_{\mathrm{ster.}} + \Delta E_{\mathrm{orb.int.}}] \\ &= \Delta E_{\mathrm{geom.}} + [(\Delta E_{\mathrm{el.}} + \Delta E_{\mathrm{Pauli}}) + \Delta E_{\mathrm{orb.int.}}]\end{aligned}$$

where $\Delta E_{\mathrm{geom.}}$ is a geometry distortion term, comprising the contributions from both considered fragments (monomer and catalyst), and $\Delta E_{\mathrm{tot.}}$ is the total interaction energy of distorted reactants. The latter can be further decomposed into the orbital-interaction term, $\Delta E_{\mathrm{orb.int.}}$, and the steric contribution consisting of the electrostatic interaction and the Pauli repulsion, $\Delta E_{\mathrm{ster.}} = \Delta E_{\mathrm{el.}} + \Delta E_{\mathrm{Pauli}}$.

NOCV have been defined[23a] as the eigenvectors of the chemical valence operator of the Nalewajski–Mrozek theory of valence and bond-order indices[28]

$$[2]\qquad \hat{V}\varphi_i = v_i\varphi_i \; i = 1, \ldots, n$$

with the valence operator given in a matrix form as

$$[3]\qquad \mathbf{V} = 1/2\mathbf{\Delta P}$$

where $\mathbf{\Delta P} = \mathbf{P} - \mathbf{P^0}$ corresponds to a difference between the density matrices (*charge-and-bond-order* matrices) of a molecule **P** and promolecule $\mathbf{P^0}$. In the present work a promolecule built of two fragments (the monomer and the transition-metal-containing fragment) was considered.

One of the features of NOCV is that they can be grouped in pairs of complementary orbitals characterized by eigenvalues of opposite sign and the same absolute value[23a,23f]

$$[4]\qquad \hat{V}\varphi_{-k} = -v_k\varphi_{-k},\ \hat{V}\varphi_k = v_k\varphi_k,\ k = 1, \ldots, n/2$$

Using eq. [4], the deformation density, $\Delta\rho = \rho(\text{complex}) - \rho(\text{fragments})$, can be written in terms of the NOCV-pairs as

$$[5]\qquad \Delta\rho(r) = \sum_{k=1}^{n/2} v_k[-\varphi^2_{-k}(r) + \varphi^2_k(r)] \equiv \sum_{k=1}^{n/2} \Delta\rho_k(r)$$

In eq. [5] an eigenvalue v_k corresponds to the fraction of electron density that is transferred from the φ_{-k} orbital to the φ_k orbital, when the molecule is formed from the fragments. Thus, a complementary pair of NOCV defines a channel for electron charge transfer between the molecular fragments.[23a] The total charge transferred in this channel is:

$$[6]\qquad \Delta q_k = v_k$$

It should be also pointed out that only a few pairs of orbitals contribute to bonding, and a large majority of eigenvalues v_k are practically equal to zero. Thus, there exist only a few non-vanishing $\Delta\rho_{\mathrm{k}}$ components.

It has been found for many transition-metal complexes,[23a–23e] that among the $\Delta\rho_{\mathrm{k}}$ contributions, it is often possible to recognize components with negative sign on one fragment (i.e., an outflow of charge density from it) and the positive on the other fragment (i.e., an accumulation of charge density). Thus, in such a case, NOCV led to a separation of the charge transfer channels corresponding to donation–back-donation and the respective eigenvalue, v_k provides a quantitative measure of a donor–acceptor ability of the two fragments in the complex.

However, a separation of the donation and back-donation channels is not always naturally achieved. In some systems the two channels are inherently mixed. It will be demonstrated later that this is the case of the π-complexes of polar monomers. Thus, to characterize donor–acceptor properties of the monomers in the π-complexes one has to apply additional constraints or different approaches. In the present study, we have applied the CSOV-like[20] technique combined with the NOCV analysis. This will be discussed in a more detailed way in further parts of this work.

Results and discussion

In the following we will first discuss the energetic preference of the σ- and π-binding mode for different monomers in the complexes with the model catalysts. Further, the results of the Ziegler–Rauk bond-energy decomposition analysis will be presented to rationalize the observed changes in the preference of the binding mode in terms of the orbital-interaction, steric, and geometry distortion components to the bond-energy. Finally, the NOCV picture of bonding will be presented and used to compare the donor–acceptor properties of a series of monomers in the σ- and π-complexes.

The energetic preference of the binding mode: σ-complexes vs. π-complexes

The differences in the energies of the π-complex and σ-complex ($\Delta E(\pi\text{–}\sigma) = E(\pi) - E(\sigma)$) for all studied polar monomers bound to the transition-metal-based fragments are collected in Fig. 2 and Table 1. Since the positive or negative value of $\Delta E(\pi\text{–}\sigma)$ corresponds to the preference for σ-

Fig. 2. The preference of the co-monomer binding mode for all the studied systems, measured by the energy difference between the π- and σ-complexes, $\Delta E(\pi-\sigma)$.

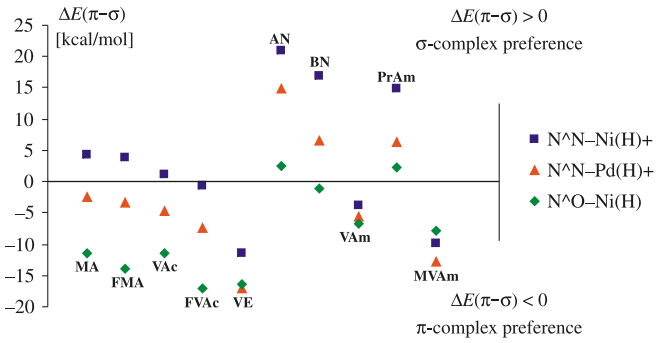

Table 1. The differences in the energies of the π- and σ-complexes, ($\Delta E(\pi-\sigma) = E(\pi) - E(\sigma)$).

	$\Delta E(\pi$-$\sigma)$ [kcal/mol]		
	N^N–Ni(H)+	N^N–Pd(H)+	N^O–Ni(H)
MA	4.20	–2.55	–11.43
FMA	3.81	–3.31	–14.01
VAc	1.14	–4.67	–11.37
FVAc	–0.73	–7.29	–17.07
VE	–11.50	–17.04	–16.46
AN	21.03	14.79	2.40
BN	17.00	6.66	–1.19
VAm	–3.87	–5.62	–6.82
PrAm	14.82	6.22	2.19
MVAm	–9.84	–12.74	–7.81

complex or π-complex preference, respectively, a lower (more negative) $\Delta E(\pi-\sigma)$ value describes a higher preference of the π-binding mode. Thus, Fig. 2 illustrates which binding mode is preferred for each monomer in the complexes with different model catalysts, and allows us to discuss how this preference varies with the change of the transition-metal-based fragment.

It is clearly seen from Fig. 2 that the polar monomers can be divided into three groups: (1) the monomers with a noticeable preference for σ-complex for all model catalysts (AN and PrAm), (2) the monomers for which the π-complex is preferred (FVAc, VE, VAm, and MVAm), and (3) the monomers with variable preference of the binding mode, depending on transition-metal fragment (MA, FMA, VAc, BN).

Furthermore, comparing the metal-containing fragments, the highest $\Delta E(\pi-\sigma)$ values were generally obtained for the cationic Ni–diimine systems, followed by the cationic Pd–diimine complexes and the neutral Ni–anilinotropone systems. There are, however, two exceptions, VE and MVAm, for which the $\Delta E(\pi-\sigma)$ values change in the order N^N–Ni(H)+ > N^O–Ni(H) > N^N–Pd(H)+ and N^O–Ni(H) > N^N–Ni(H)+ > N^N–Pd(H)+, respectively.

The increase in the π-binding mode preference when Pd replaces Ni in the cationic diimine model catalyst is in agreement with the previous DFT calculations for related systems; the qualitatively similar trend was observed by Ziegler and Michalak for O-monomers and by Ziegler and Deubel for N-monomers.[15e,16a] The differences between $\Delta E(\pi-\sigma)$ values obtained here and in refs. 15e and 16a result from differences in the structure of model complexes. Specifically, in the present work hydride complexes were studied, whereas in refs. 15e and 16a the results for propyl and ethyl complexes were presented.

A decrease in the $\Delta E(\pi-\sigma)$ values in the order N^N–Ni(H)+ > N^N–Pd(H)+ > N^O–Ni(H) reflects a decrease in the positive charge on the metal in these complexes. It has been shown previously[15e] that for MA complexes with Ni– and Pd–diimine systems the electrostatic component is the major factor determining the preference of the binding mode. However, the results of Fig. 2 and Table 1 indicate that for different monomers the shift in the $\Delta E(\pi-\sigma)$ values is not constant when going from Ni–diimine to Pd–diimine, and in particular to Ni–anilinotropone complexes. This suggests that for some polar monomers a difference in the orbital-interaction components for σ- and π-complexes may also change with a change of the catalyst.

Monomers ranked according to their $\Delta E(\pi-\sigma)$ value are in the order: AN > BN > PrAm > MA > FMA > VAc > FVAc > VAm > MVAm > VE in the cationic Ni–diimine complex; this order is preserved for the Pd–diimine complex, with one minor exception (VAm > FVAc). In the neutral complexes the sequence is slightly different: AN > PrAm > BN > VAm > MVAm > VAc > MA > FMA > VE > FVAc, with all the N-monomers exhibiting higher $\Delta E(\pi-\sigma)$ values than the O-monomers.

Ziegler–Rauk bond-energy decomposition analysis for the σ- and π-complexes

Let us now examine the origin of the difference between these transition-metal-based fragments in terms of the Ziegler–Rauk bond-energy decomposition analysis.

To facilitate the discussion, in Fig. 3 we schematically present the differences in the contributions to the bond-energies between Pd– and Ni-based complexes and the two binding modes (π- and σ-) for AN and VE monomers used as examples. The left-hand side of the figure (panels *a*–*c*) shows the results for both diimine systems (N^N–Pd(H)+ and N^N–Ni(H)+), while the middle part (panels *d*–*f*) refers to the comparison between the Pd–diimine and Ni–anilinotropone catalysts (N^N–Pd(H)+ and N^O–Ni(H)). For completeness, the results for N^N–Ni(H)+ and N^O–Ni(H) are compared in the right-hand side of the figure. The same kind of diagram was used in ref. 15e to analyze the differences between the σ- and π-complexes of MA and VAc with the Ni– and Pd-diimine catalyst. In these diagrams, the differences between the two binding modes (for the same catalyst) are shown horizontally, whereas the differences between the two catalysts (for the same binding mode) are shown vertically.The arrows point to the preferred complex of the respective pair and the numbers correspond to the differences in the orbital-interaction (panels *a*, *d*, and *g*), steric (panels *b*, *e*, and *h*), and geometry distortion contributions (panels *c*, *f*, and *i*), $\Delta[\Delta E_{\text{orb.int.}}]$, $\Delta[\Delta E_{\text{ster.}}]$ and $\Delta[\Delta E_{\text{geom.}}]$, respectively.

We will start the discussion from the comparison between the two binding modes for AN and VE in the Ni- and Pd-based diimine model catalysts. It was demonstrated previously by Ziegler and Michalak for MA and VAc[15e] that the difference between these two catalysts has a mainly steric (electrostatic and Pauli repulsion) origin.

Fig. 3. Schematic representation of the differences ($\Delta[\Delta E]$ in kcal/mol) in the contributions to the bonding energies between the σ- and π-complexes of AN and VE monomers with the Ni- and Pd-based Brookhart catalysts (left), the Ni-based anilinotropone and Pd-based Brookhart catalysts (middle), and the Ni-based anilinotropone and Ni-based Brookhart catalysts (right). Respective panels display the differences in the orbital-interaction, $\Delta[\Delta E_{orb.int.}]$, (*a*, *d*, and *g*), steric, $\Delta[\Delta E_{ster.}]$, (*b*, *e*, and *h*), and geometry distortion contributions, $\Delta[\Delta E_{geom.}]$, (*c*, *f*, and *i*). The arrows point to the preferred complex of the considered pair.

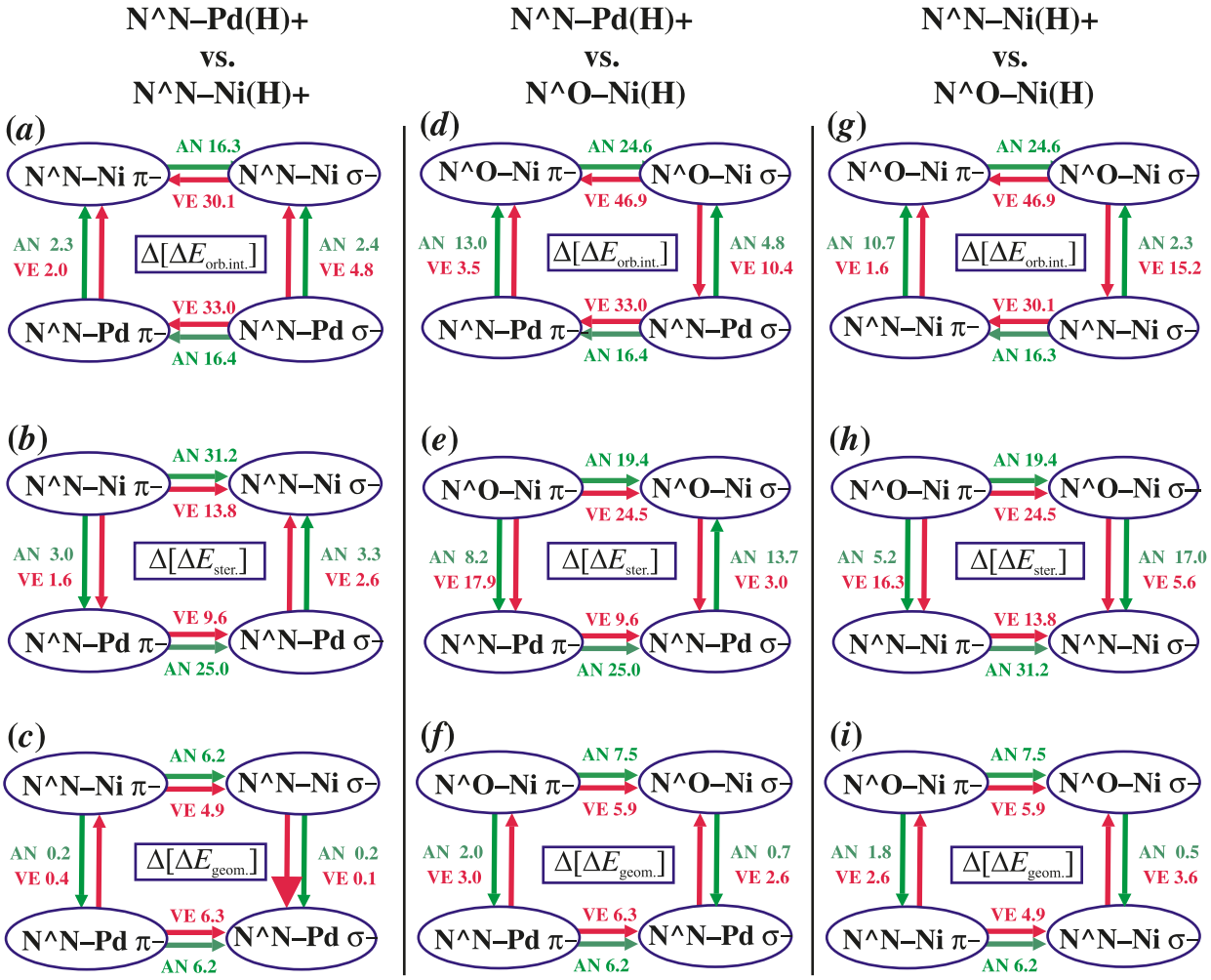

Our results for AN lead to a similar conclusion. As far as the comparison between the two coordination modes is concerned (a "horizontal" comparison), there is practically no difference in the orbital-interaction contribution to the bonding energy (16.3 vs. 16.4 kcal/mol), nor in the geometry distortion term (6.2 kcal/mol for both catalysts). The steric term, on the other hand, shows a substantial difference (31.2 vs. 25.0 kcal/mol). A "vertical" comparison (Ni– and Pd– π-complexes vs. σ-complexes) leads to a similar conclusion: there is practically no difference in the orbital-interaction (2.3 vs. 2.4 kcal/mol) and the geometry distortion components (0.2 kcal/mol for both systems), whereas the steric terms are qualitatively different: the steric destabilization of the π-complex is lower for Pd by 3.0 kcal/mol, wherease for the σ-complex it is higher by 3.3 kcal/mol.

However, for VE the difference in the orbital-interaction term becomes noticeable in both the "horizontal" (30.1 vs. 33.0 kcal/mol) and "vertical" (2.0 vs. 4.8 kcal/mol) cases. The corresponding differences for the steric component are of comparable magnitude. Thus, it may be concluded that in the case of VE, the difference between the Ni– and Pd–diimine catalysts is not completely determined by the steric term; the orbital-interaction component is as well important.

Similar analysis performed for all the monomers shows that for MA, FMA, VAc, AN, VAm, and MVAm the differences in the orbital-interaction terms are insignificant compared to those in steric terms, as far as the comparison between Ni– and Pd-catalysts is concerned. For VE, FVAc, BN, and PrAm, however, the difference in the Ni- and Pd-complexes has both a steric and electronic (orbital-interaction) origin.

Comparing the cationic Pd–diimine catalyst with the neutral Ni–anilinotropone catalyst (Figs. 3*d*–3*f*), the "horizontal" differences in the orbital-interaction term are non-negligible for both monomers (24.6 vs. 16.4 kcal/mol for AN, and 46.9 vs. 33.0 kcal/mol for VE), and qualitatively comparable with the differences in the corresponding steric components (19.4 vs. 25.0 kcal/mol for AN, and 24.5 vs. 9.6 kcal/mol for VE). A "vertical" comparison of the bond-energy components leads to the same conclusions. A similar picture can be drawn for the other monomers.

Fig. 4. Contours of the NOCV (panel *a*) and corresponding contributions to the deformation density, $\Delta\rho$, (panel *b*) characterizing the bond formed between the Ni–diimine complex, N^N–Ni(H)+, and MA in the σ-complex. The contour values are 0.1 au for orbitals and 0.01 au for the $\Delta\rho$ contributions.

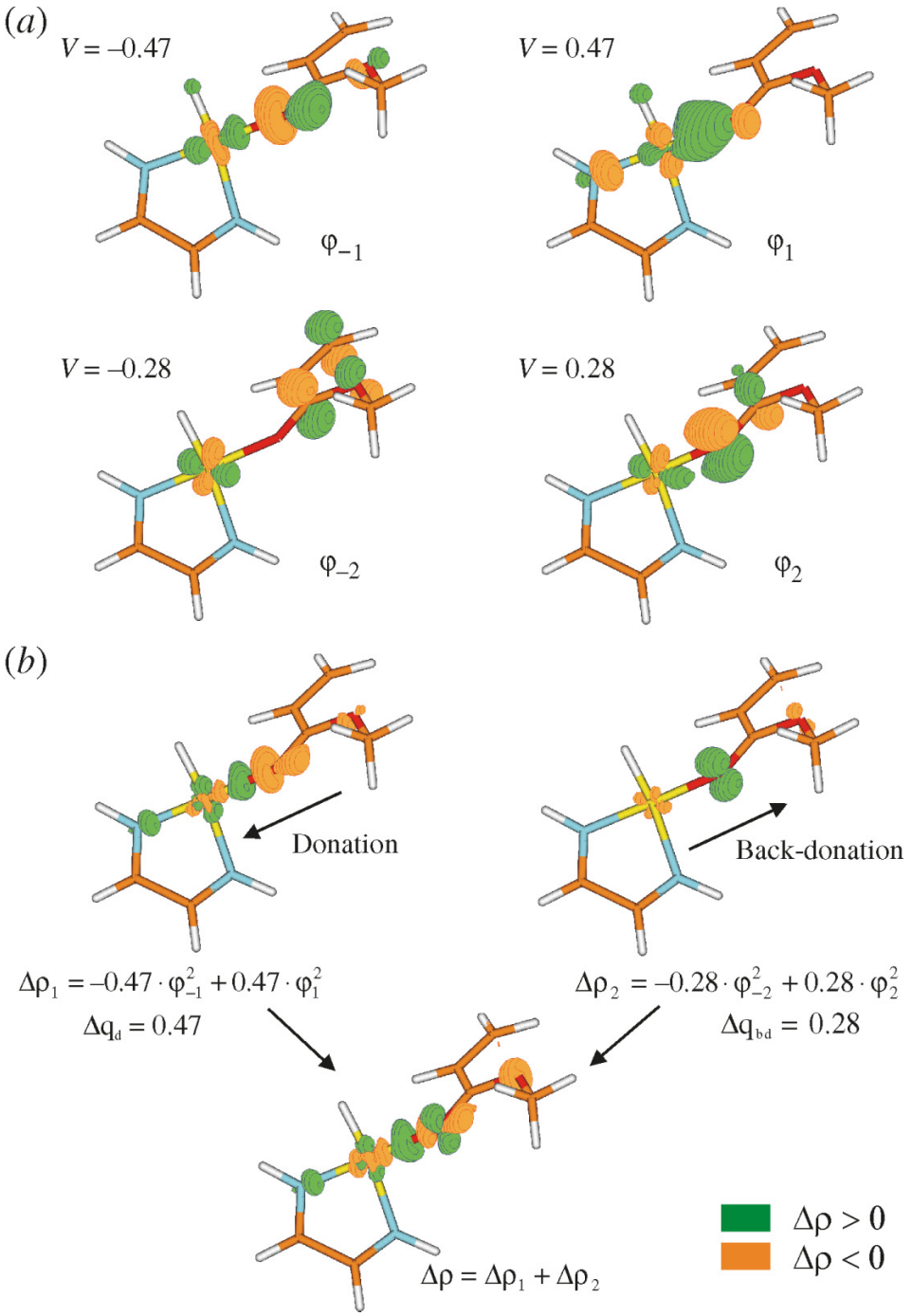

NOCV description of bonding in the σ-complexes and π-complexes

As an example of the NOCV-representation of bonding in the σ-complexes, in Fig. 4 the NOCV are presented that describe the bond between methyl acrylate and the Ni–diimine catalyst, N^N–Ni(H)+.

There are two pairs of NOCV localized in the bond region. The first pair, corresponding to $|v_1|$=0.47, represent a bonding and anti-bonding orbital of σ-character. The second pair, corresponding to $|v_2|$=0.28, represent a bonding and anti-bonding orbital of π-character.

In Fig. 4*b*, the corresponding contributions to the deformation density $\Delta\rho$ are shown. The first pair of NOCV describes a channel for the ligand → metal electron transfer (donation). The second pair represents the metal → ligand π-back-bonding. Thus, NOCV allow one to separate the donation and back-donation channels and the corresponding NOCV-eigenvalues that provide measures of the donation–

Fig. 5. Contours of the NOCV (panel *a*) and corresponding contributions to the deformation density, $\Delta\rho$, (panel *b*) characterizing the bond formed between the Ni–diimine complex, N^N–Ni(H)+, and MA in the π-complex. The contour values are 0.1 au for orbitals and 0.01 au for the $\Delta\rho$ contributions.

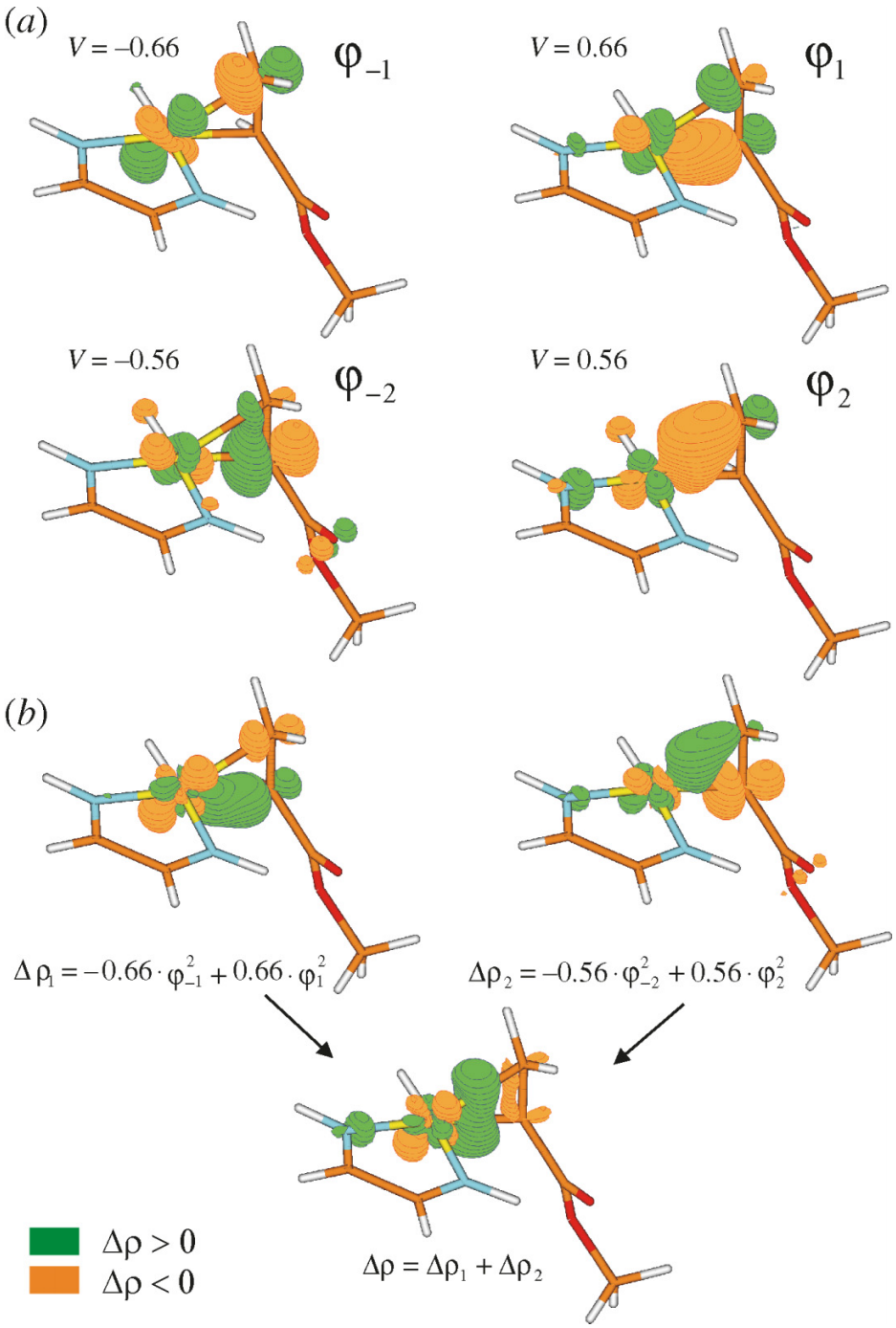

back-bonding charge flows ($\Delta q_d = \nu_1 = 0.47$ and $\Delta q_d = \nu_2 = 0.28$) can be used to characterize the donor–acceptor properties of different monomers.

It is worth mentioning that for the σ-complex, the charge transfer due to π-back-bonding is undoubtedly non-negligible. The NOCV analysis performed for the complexes with different monomers shows similar features. A detailed comparison of the donor–acceptor properties of considered polar monomers will be presented in the next section.

Let us now characterize the bond between the monomer and the metal fragment in the π-complexes in terms of NOCV. As an example, the Ni–diimine complex with methyl acrylate is shown in Fig. 5. The NOCV for this system together with the corresponding contribution to the deformation density are presented in Figs. 5*a* and 5*b*, respectively.

As we mentioned earlier, in this case there is no clear separation between the donation–back-bonding channels. Each of the two pairs describes a localized covalent bond

Fig. 6. Contributions to the deformation density, $\Delta\rho$, for the bond formed between the Ni–diimine complex, N^N–Ni(H)+, and MA in the π-complex obtained using CSOV-like technique combined with the NOCV analysis by the elimination of the virtual orbitals on the monomer (panel *a*) and the virtual orbitals on the metal fragment (panel *b*) from the basis. The contour value is 0.01 au.

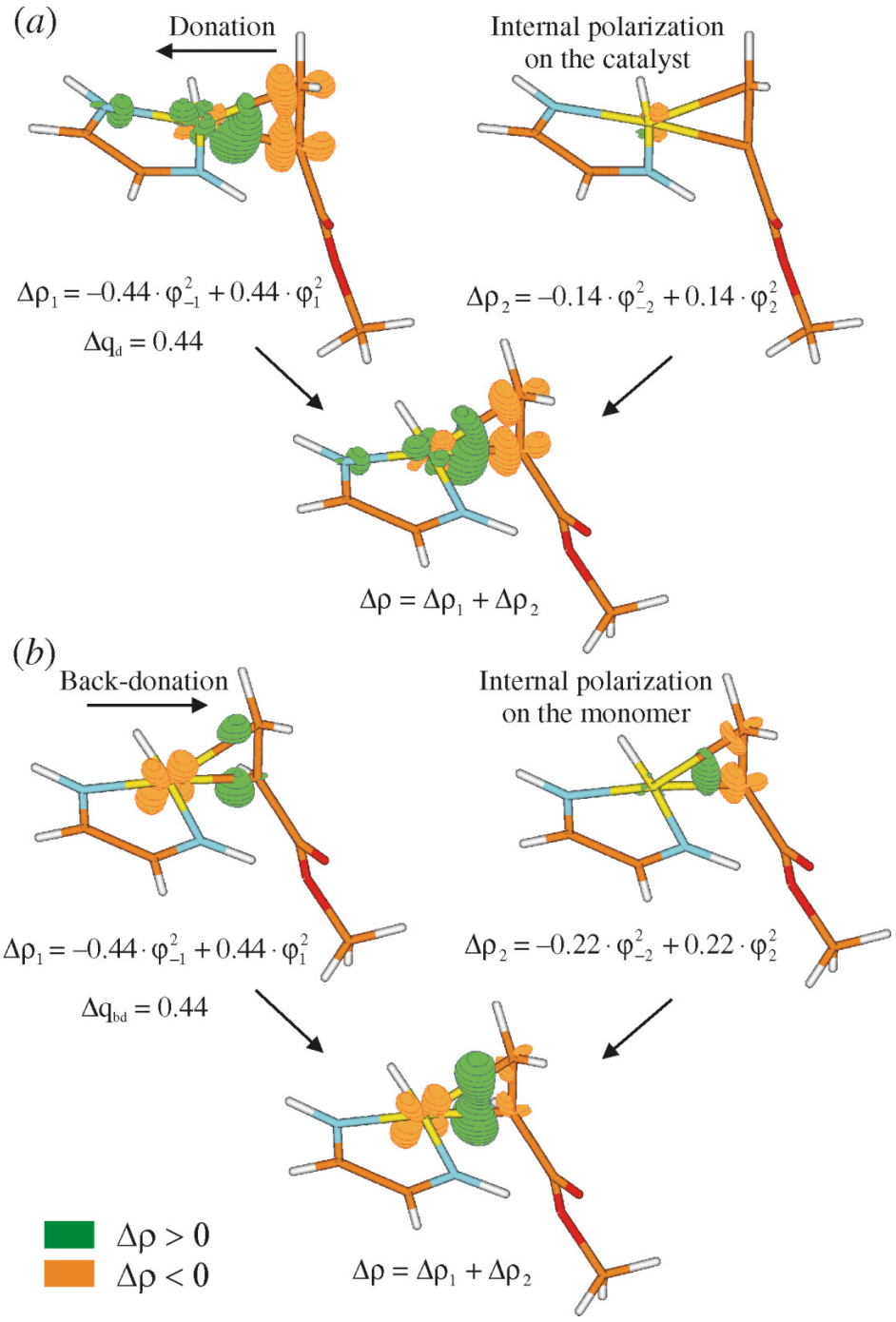

between one carbon atom of MA and the metal (positive $\Delta\rho$), with a negative $\Delta\rho$ contribution in the vicinity of the other carbon atom. Thus, NOCV-eigenvalues cannot be directly used as measures of the donation–back-bonding charge flows.

Thus, to characterize the donor–acceptor properties of different monomers in the π-complexes, one has to use an additional constraint or approximation. In the present study, we have applied the CSOV-like[20] technique combined with the NOCV approach. Specifically, the NOCV analysis was repeated, based on the results of the DFT calculations in which (1) the virtual orbitals on the monomer were removed from the basis, to characterize the ligand → metal donation, and (2) the virtual orbitals on the metal fragment were removed from the basis, to describe independently the metal → ligand back-bonding.

The NOCV-contributions to the bond between the monomer and the metal fragment obtained for N^N–Ni(H)$^+$–MA

Fig. 7. σ-Donor (panel *a*) and π-acceptor (panel *b*) properties of polar monomers in the σ-complexes with N^O–Ni(H), N^N–Ni(H)+, and N^N–Pd(H)+ measured by the NOCV eigenvalues, Δq_d and Δq_{bd}, respectively.

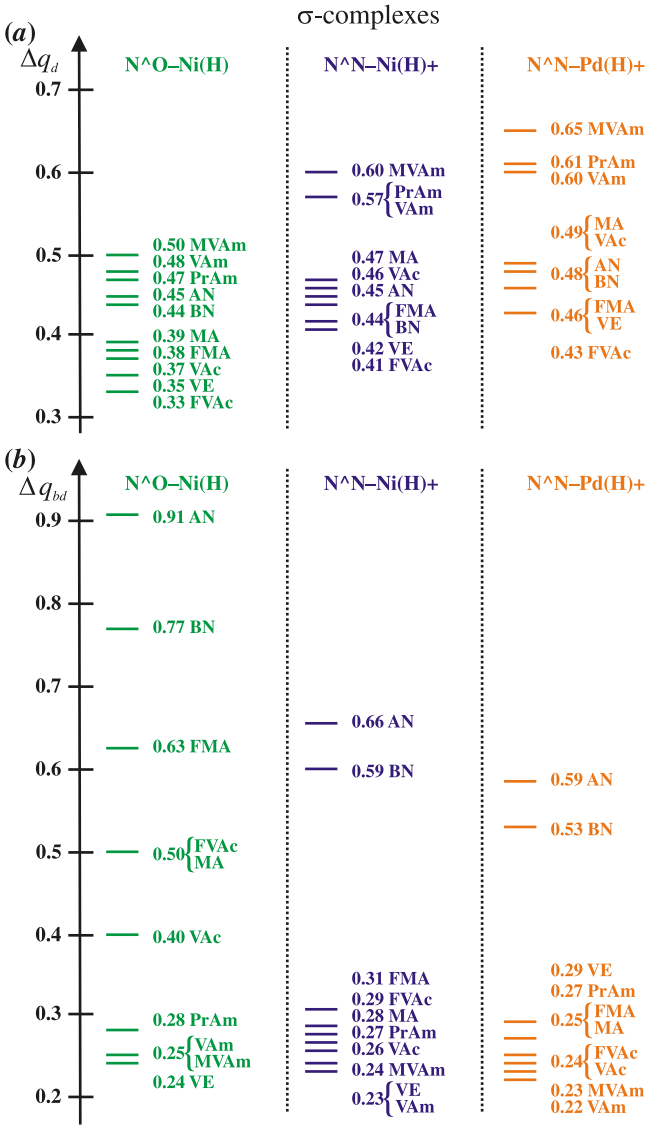

π-complex are presented in Fig. 6*a* and 6*b*, respectively. It is clearly seen that the donation (Fig. 6*a*) and the back-bonding (Fig. 6*b*) are characterized by similar Δq_d and Δq_{bd} values (0.44).

In addition to pure donation–back-bonding channels, the NOCV pairs describing internal polarization of the catalyst and the monomer are present, when the CSOV-like technique is applied. The eigenvalues corresponding to these polarization channels are relatively large. However, they are comparable for all the monomers. Thus, a comparison of the donor–acceptor properties of different monomers based on the NOCV donation and back-donation channels obtained within a CSOV-like approach is justified. In the next section a comparison of the donor–acceptor properties of monomers in the π-complexes based on the similar NOCV analysis will be presented.

Fig. 8. σ-Donor (panel *a*) and π-acceptor (panel *b*) properties of polar monomers in N^O–Ni(H), N^N–Ni(H)+, and N^N–Pd(H)+ based π-complexes, measured by the NOCV eigenvalues, Δq_d and Δq_{bd}, respectively.

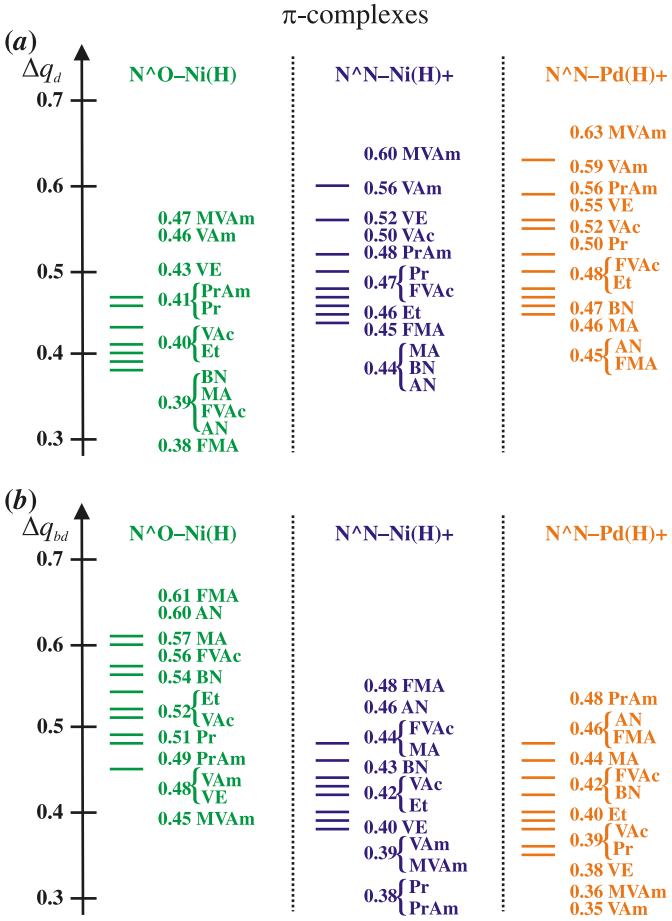

Comparison of the donor–acceptor properties of monomers in the σ-complexes

Figure 7 collects Δq_d and Δq_{bd} values calculated for all the σ-complexes studied in the present work, i.e., for all polar monomers and all transition-metal-based fragments. We will start the discussion with the σ-donor properties of the monomers, measured by the Δq_d value, i.e., the eigenvalue for NOCV describing the donation process (Fig. 7*a*). Let us first look at the Δq_d values calculated for N^N–Ni(H)+ based complexes (the middle part of the figure). The highest values of Δq_d were obtained for amine monomers: MVAm (0.60), and PrAm and VAm (0.57). Other N-monomers, as well as all O-monomers are characterized by relatively close values of Δq_d, lower in comparison with amines, ranging from 0.47 to 0.41, with the highest values obtained for MA, VAc, and AN (0.47, 0.46, and 0.45), intermediate for FMA and BN (0.44), and the lowest for VE and FVAc (0.42 and 0.41). Thus, MA and VAc monomers reveal slightly better σ-donor properties (higher Δq_d values by 0.03 and 0.05, respectively) compared to their fluorinated analogues, FMA and FVAc.

The right-hand side of Fig. 7*a* shows the Δq_d values calculated for σ-complexes with the Pd–diimine system,

Table 2. Comparison of the results calculated for the model and real catalysts (see Fig. 9).

Monomer (property)	N^N–Pd(H)+	N^N–Pd(Pr)+[a]	(N^N)[real]–Pd(Pr)+[a]
Donation from NOCV			
Et (Δq_d)	0.48	0.49	0.52
MA (Δq_d)	0.46	0.47	0.48
Back-bonding from NOCV			
Et (Δq_{bd})	0.40	0.42	0.44
MA (Δq_{bd})	0.44	0.45	0.45
Distances (Å)			
Et ($R_{Pd–C1}$, $R_{Pd–C2}$)	2.184, 2.205	2.219, 2.240	2.227, 2.235
MA ($R_{Pd–C1}$, $R_{Pd–C2}$)	2.173, 2.189	2.207, 2.254	2.230, 2.269
π- and σ-Complexes energy difference (kcal/mol)			
MA/ΔE(π-σ)	–2.55	–3.40	–3.01

[a]optimized geometries from ref. 15e.

Fig. 9. The model and real systems compared in Table 2.

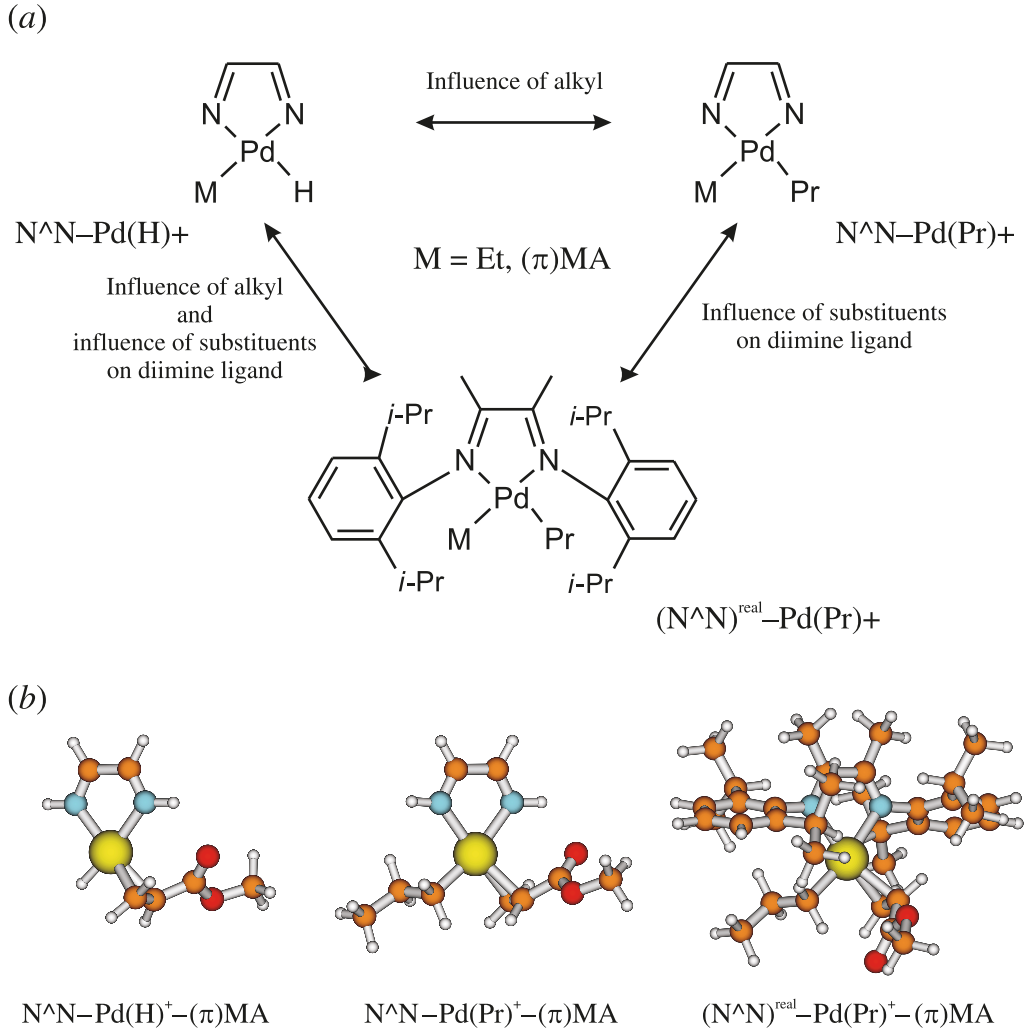

N^N–Pd(H)+. As can be seen from the figure, changing the metal in the Brookhart catalysts introduces only small changes in the Δq_d values: they are all slightly increased (by 0.02–0.05) in the N^N–Pd(H)+ based system compared to the Ni–diimine catalyst. Furthermore, the monomer sequence does not change compared to the Ni-catalyst; only the positions of monomers characterized by close σ-donation eigenvalues are exchanged.

Let us now discuss the σ-donor properties of the monomers bound in N^O–Ni(H) based σ-complexes (the left-hand side of Fig. 7*a*). In this case the eigenvalues are visibly decreased compared to N^N–Ni(H)+ complexes (by 0.06–

Fig. 10. Two-dimensional maps of donor–acceptor properties for monomers binding in transition-metal-based σ-complexes (panel *a*) and π-complexes (panel *b*).

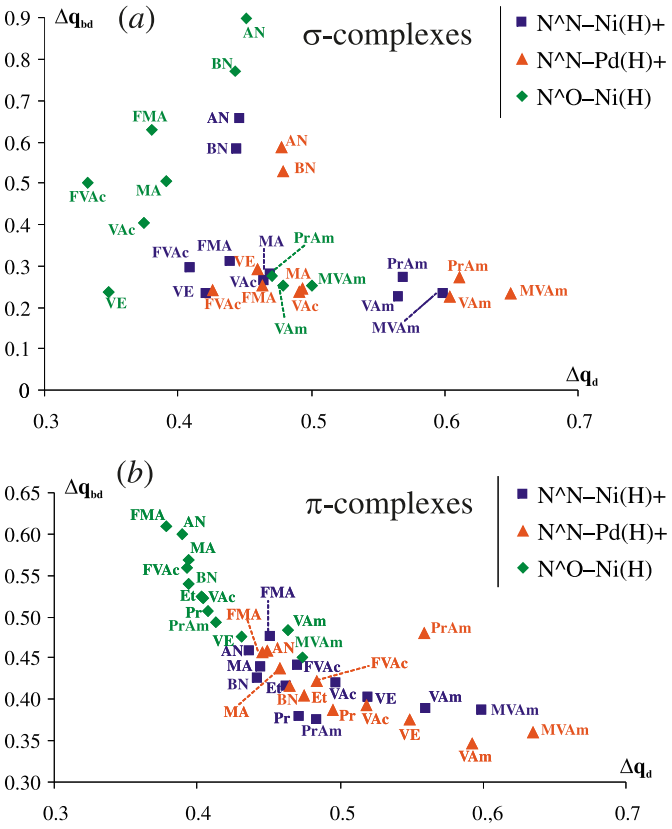

0.10); the only exceptions are AN and BN, for which the Δq_d values remain unchanged. Furthermore, in this case there is a clear distinction between the N-monomers and O-monomers, with the former revealing higher values of Δq_d (0.50–0.44) than the latter (0.39–0.33).

In conclusion, the sequence of monomers ordered according to their σ-donor properties is hardly dependent on the transition-metal-based fragment, starting with the amine monomers as the strongest σ-donors, and ending with VE and FVAc as the weakest σ-donors. Only monomers characterized by close the Δq_d values can exchange their position. Furthermore, MA and VAc reveal slightly higher values of Δq_d in comparison with the corresponding fluorinated systems, FMA and FVAc. It is also clearly seen that the Δq_d values are shifted upwards in the sequence: N^O–Ni(H) < N^N–Ni(H)+ < N^N–Pd(H)+ with more significant increase in the first step, i.e., from the neutral Ni–anilinotropone to the cationic Ni–diimine system.

We will now focus on the π-acceptor properties of the polar monomers bound in the same group of σ-complexes. Figure 7*b* presents the Δq_{bd} values corresponding to the NOCV eigenvalues describing the back-donation electron transfer.

Again, we will start the discussion with the N^N–Ni(H)+ case, for which the results are shown in the middle part of Fig. 7*b*. Clearly, the best π-acceptor properties (the highest values of Δq_{bd}) are demonstrated by both nitrile monomers, i.e., AN and BN (0.66 and 0.59). All other polar monomers studied in the present work are characterized by relatively close Δq_{bd} eigenvalues, ranging from 0.31 to 0.23, significantly lower than AN and BN: FMA (0.31) > FVAc (0.29) > MA (0.28) > PrAm (0.27) > VAc (0.26) > MVAm (0.24) > VE ≈ VAm (0.23). Further, it is seen that the MA and VAc monomers show slightly lower π-acceptor eigenvalues than their fluorinated analogues, FMA and FVAc. It is also worth emphasizing that amine monomers, which are characterized by the highest Δq_d values, reveal the lowest Δq_{bd} values.

For the Pd–diimine system the results are very similar to its Ni-analogue, with a small decrease in all the values for the Pd complexes. In the case of the neutral Ni–anilinotropone catalyst, the Δq_{bd} values are higher than for the cationic systems. Nevertheless, the order of monomers remains unchanged; as noted previously, only the monomers characterized by very close values exchange their positions.

To conclude, the results of the NOCV analysis indicate that the nitrile monomers in the σ-binding mode can be classified as the strongest, whereas the amine systems together with VE are the weakest π-acceptors. Further, the absolute values of Δq_{bd} are shifted down in the sequence: N^O–Ni(H) > N^N–Ni(H)+ > N^N–Pd(H)+.

Comparing the monomer donor–acceptor ranking, one can notice that amine monomers are characterized by the highest Δq_d values, and simultaneously the lowest Δq_{bd} values (the strongest σ-donors and the weakest π-acceptors). However, stronger σ-donor ability is not always accompanied by weaker π-acceptor properties. VE can be used here as an example, since it is weakest in both the σ-donor and π-acceptor ability.

Comparison of the donor–acceptor properties of monomers in the π-complexes

The Δq_d and Δq_{bd} values, determined for all the π-complexes, are collected in Fig. 8. Let us first discuss the σ-donor properties of monomers in the π-coordination mode (Fig. 8*a*), starting with Ni–diimine system. The Δq_d values calculated for N^N–Ni(H)+ based π-complexes are shown in the middle part of Fig. 8*a*. Similarly to the corresponding σ-complexes, the best σ-donor abilities are demonstrated by the vinyl amine monomers, MVAm and VAm (Δq_d = 0.60 and 0.56, respectively). Other monomers reveal relatively close values of Δq_d, varying from 0.52 to 0.44. Among them, the highest Δq_d values were obtained for VE, VAc, and PrAm (0.52, 0.50, and 0.48), intermediate for Pr, FVAc (0.47), and Et (0.46), and the lowest for FMA and MA (0.45 and 0.44) and both nitrile monomers, BN and AN (0.44). Furthermore, comparing the σ-donor abilities of simple olefins and the polar monomers, it can be noticed that Et and Pr are located in the middle of the range, revealing the intermediate values of Δq_d.

Let us now consider the σ-donor properties of monomers bound to the metal center in the Pd–diimine system. The results presented in the right-hand side of Fig. 8*a* show close similarity to those characterizing the Ni-based system. Finally, for monomers binding in N^O–Ni(H) based π-complexes presented in the left-hand side of Fig. 8*a*, the Δq_d values are noticeably decreased in comparison with N^N–Ni(H)+ (by 0.05–0.13). However, as noted previously, the monomer sequence remains almost unchanged. Again, only

the positions of monomers characterized by close σ-donation eigenvalues are exchanged.

We will now analyze the π-acceptor properties of monomers binding in the π-complexes. The quantitative measures of metal → monomer π-back-donation processes, Δq_{bd} values are collected in Fig. 8*b*. We will start the discussion with the results obtained for N^N–Ni(H)+ systems (the middle part of the figure). In this case, all monomers are characterized by close values of Δq_{bd}, ranging from 0.48 to 0.38. The highest Δq_{bd} values were obtained for FMA and AN (0.48 and 0.46), intermediate for FVAc and MA (0.44) and BN (0.43) together with VAc and Et (0.42), and the lowest for VE (0.40), both vinyl amine monomers, VAm and MVAm (0.39), and Pr and PrAm (0.38). It should be also pointed out that the results obtained for these systems correspond very well with a common intuitive way of thinking of the ligand properties (the stronger σ-donor, the weaker π-acceptor).

Comparing the π-acceptor properties of monomers binding in the Ni- and Pd-based Brookhart catalysts (the middle and the right-hand side of Fig. 8*b*), it is clearly seen that the replacement of Ni with Pd does not introduce any significant differences in the values of Δq_{bd}, nor in the sequence of monomers. Specifically, all monomers in the π-complexes with the Pd–diimine catalyst are characterized by relatively close values of Δq_{bd}, varying from 0.48 to 0.38. As far as the π-acceptor eigenvalues determined for the complexes with the neutral anilinotropone catalyst are concerned (the left-hand side of Fig. 8*b*), a visible shift upwards in the absolute values of Δq_{bd} is observed. Again, the sequence of monomers remains almost the same.

Thus, AN, MA, and both fluorinated monomers, FMA and FVAc, can be classified as the strongest, and the amine monomers as the weakest π-acceptors. The analysis of both Δq_d and Δq_{bd} values indicates that in the case of the π-complexes, the σ-donor and π-acceptor abilities of the monomers are strongly coupled, i.e., the monomers which are characterized by the highest Δq_d values, reveal the lowest Δq_{bd} values, and vice versa.

In the present study, we analyzed the complexes of different monomers with *model* catalysts in which the bulky substituents were replaced by hydrogen atoms. Further, the olefin–hydride complexes were used, while in the catalytic cycle, the alkyl complexes are present. Use of the model systems is justified by the fact that we focus on the donor–acceptor properties, determined mainly by the orbital–interaction terms. Thus, it can be expected that they are independent from the steric terms, mostly affected by the bulky substituents. However, some *indirect* steric influence on the orbital-interaction exists, since the steric bulk alters the coordination geometry, especially the monomer–metal distance.

Therefore, it is important to compare the results obtained for the model systems and for the real catalysts. Such a comparison is presented in Table 2 for the ethylene and methyl acrylate complexes with Pd-based catalysts shown in Fig. 9. Here, we compared the model olefin–hydride and olefin–propyl complexes, N^N–Pd(H)+ and N^N–Pd(Pr)+, as well as the olefin–propyl complexes with the real catalyst, $(N^N)^{real}$–Pd(Pr)+.

The results presented in Table 2 confirm that use of the model systems is indeed justified as far as the donor–acceptor properties are concerned. Even for the monomers such as Et and MA, which are characterized by relatively close donation and back-bonding NOCV descriptors, their order is preserved. The absolute NOCV eigenvalues change by 0.01–0.04 in the model and real systems. However, the difference in the σ- and π-bonding energies is visibly affected (by ~ ±0.5 kcal/mol relative to the real catalyst), as shown in the previous studies.[15,16]

To conclude the results of the NOCV analysis performed for all monomers in both σ- and π-coordination mode, the values of Δq_d and Δq_{bd} are presented in the form of a two-dimensional map, separately for σ-complexes (Fig. 10*a*) and π-complexes (Fig. 10*b*). In both cases the absolute Δq_d value (the σ-donor property) increases and the Δq_{bd} value (π-acceptor property) decreases, in the sequence of the transition-metal-based fragments: N^O–Ni(H) → N^N–Ni(H)+ → N^N–Pd(H)+. These differences are more pronounced in the neutral and the cationic systems than the Ni– and Pd–diimine complexes.

Concluding remarks

In this article, we analyzed the binding mode of a series of polar monomers in complexes with late-transition-metal catalysts for ethylene polymerization. The σ- and π-complexes with the model, cationic Ni– and Pd–diimine catalysts, N^N–Ni(H)+ and N^N–Pd(H)+, and the neutral Ni–anilinotropone system, N^O–Ni(H), were investigated. The Ziegler–Rauk energy decomposition scheme was used to characterize the geometry distortion, and steric and orbital-interaction terms in the bonding energy, while NOCV were applied to quantitatively describe donation and back-bonding components of the bond between the monomer and the catalyst. Further, NOCV analysis allowed for comparison of the donor–acceptor properties of different monomers in the σ- and π-complexes.

In agreement with earlier theoretical studies,[15,16] the results demonstrate that the metal-based fragment has a significant influence on the relative stability of the σ- and π-complexes. Generally, the preference of the π-binding mode increases in the following order: N^N–Ni(H)+ < N^N–Pd(H)+ < N^O–Ni(H). Thus, for the neutral catalyst, the preference of the π-coordination is enhanced. The results of the Ziegler–Rauk bond-energy decomposition indicate that for some monomers (MA, FMA, VAc, AN, VAm, and MVAm) the preference of the coordination mode has a steric (electrostatic and Pauli) origin, as found previously for methyl acrylate.[15e] However, for other monomers (VE, FVAc, BN, and PrAm) the changes in the orbital-interaction terms are important as well.

The results of the NOCV analysis indicate that for both σ- and π-coordination modes there exist components describing σ-donation and π-back-bonding. Furthermore, the sequences of σ-donor and π-acceptor properties of monomers in the π-complexes as well as σ-complexes are nearly the same for all model catalysts studied. The absolute values of Δq_d are shifted upwards and the absolute values of Δq_{bd} are shifted downwards in the sequence of metal-based fragments: N^O–Ni(H) < N^N–Ni(H)+ < N^N–Pd(H)+ with a more pronounced effect observed for N^O–Ni(H). However, the

change of the metal center in the diimine systems has a relatively small effect on the donor–acceptor ability of the coordinated monomer.

In the case of the π-complexes, the strong "coupling" between σ-donor and π-acceptor properties of monomers can be observed. In a series of the monomers studied, the better the monomer's σ-donor ability is (the higher Δq_d), the worse its σ-acceptor character becomes (the lower Δq_{bd}). However, for the σ-coordination mode, such a relationship between donor and acceptor properties is not a rule. This is in agreement with our previous NOCV analysis for other transition metal complexes.[23b]

Supplementary data

Supplementary data for this article are available on the journal Web site (canjchem.nrc.ca) or may be purchased from the Depository of Unpublished Data, Document Delivery, CISTI, National Research Council Canada, Ottawa, ON K1A 0R6, Canada. DUD 3956. For more information on obtaining material, refer to cisti-icist.nrc-cnrc.gc.ca/cms/unpub_e.shtml.

Acknowledgement

This article is dedicated to prof. Tom Ziegler on the occasion of his 65th birthday. This work was supported by a research grant No. N204 227534 (2275-B-H03–2008–34) from the Ministry of Science and Higher Education in Poland.

References

(1) This article is part of a Special Issue dedicated to Professor T. Ziegler.

(2) (a) *Functional polymers: Modern synthetic methods and novel structures*; Patil, A. O.; Schulz, D. N.; Novak, B. M., Eds.; ACS Symposium Series 704. American Chemical Society: WA, 1998; (b) Boffa, L. S.; Novak, B. M. *Chem. Rev.* **2000**, *100* (4), 1479–1494; and refs. cited therein. doi:10.1021/cr990251u. PMID:11749273.

(3) Doak, K. W. In *Encyclopedia of polymer science and engineering*; H. F. Mark, Ed.; John Wiley and Sons: New York, 1986; Vol. 6., p. 386.

(4) (a) Britovsek, G. J. P.; Gibson, V. C.; Wass, D. F. *Angew. Chem. Int. Ed.* **1999**, *38* (4), 428–447. doi:10.1002/(SICI)1521-3773(19990215)38:4<428::AID-ANIE428>3.0.CO;2-3.; (b) Ittel, S. D.; Johnson, L. K.; Brookhart, M. *Chem. Rev.* **2000**, *100* (4), 1169–1204. doi:10.1021/cr9804644. PMID:11749263.; (c) Gibson, V. C.; Spitzmesser, S. K. *Chem. Rev.* **2003**, *103* (1), 283–316. doi:10.1021/cr980461r. PMID:12517186.

(5) (a) Cossee, P. *Tetrahedron Lett.* **1960**, *1* (38), 12–16. doi:10.1016/S0040-4039(01)99340-2.; (b) Cossee, P. *J. Catal.* **1964**, *3* (1), 80–88. doi:10.1016/0021-9517(64)90095-8.; (c) Arlman, E. J. *J. Catal.* **1964**, *3* (1), 89–98. doi:10.1016/0021-9517(64)90096-X.; (d) Arlman, E. J.; Cossee, P. *J. Catal.* **1964**, *3* (1), 99–104. doi:10.1016/0021-9517(64)90097-1.; (e) Arlman, E. J. *J. Catal.* **1966**, *5* (1), 178–189. doi:10.1016/S0021-9517(66)80137-9.

(6) (a) Johnson, L. K.; Killian, C. M.; Brookhart, M. *J. Am. Chem. Soc.* **1995**, *117* (23), 6414–6415. doi:10.1021/ja00128a054.; (b) Killian, C. M.; Tempel, D. J.; Johnson, L. K.; Brookhart, M. *J. Am. Chem. Soc.* **1996**, *118* (46), 11664–11665. doi:10.1021/ja962516h.; (c) Svejda, S. A.; Johnson, L. K.; Brookhart, M. *J. Am. Chem. Soc.* **1999**, *121* (45), 10634–10635. doi:10.1021/ja991931h.; (d) Tempel, D. J.; Johnson, L. K.; Huff, R. L.; White, P. S.; Brookhart, M. *J. Am. Chem. Soc.* **2000**, *122* (28), 6686–6700. doi:10.1021/ja000893v.

(7) (a) Johnson, L. K.; Mecking, S.; Brookhart, M. *J. Am. Chem. Soc.* **1996**, *118* (1), 267–268. doi:10.1021/ja953247i.; (b) Mecking, S.; Johnson, L. K.; Wang, L.; Brookhart, M. *J. Am. Chem. Soc.* **1998**, *120* (5), 888–899. doi:10.1021/ja964144i.

(8) Wang, C.; Friedrich, S.; Younkin, T. R.; Li, R. T.; Grubbs, R. H.; Bansleben, D. A.; Day, M. W. *Organometallics* **1998**, *17* (15), 3149–3151. doi:10.1021/om980176y.

(9) Younkin, T. R.; Connor, E. F.; Henderson, J. I.; Friedrich, S. K.; Grubbs, R. H.; Bansleben, D. A. *Science* **2000**, *287* (5452), 460–462. doi:10.1126/science.287.5452.460. PMID:10642541.

(10) (a) Small, B. L.; Brookhart, M.; Bennett, A. M. *J. Am. Chem. Soc.* **1998**, *120* (16), 4049–4050. doi:10.1021/ja9802100.; (b) Britovsek, G. J. P.; Gibson, V. C.; McTavish, S. J.; Solan, G. A.; White, A. J. P.; Williams, D. J.; Britovsek, G. J. P.; Kimberley, B. S.; Maddox, P. J. *Chem. Commun. (Camb.)* **1998**, (7): 849–850. doi:10.1039/a801933i.

(11) Boone, H. W.; Athey, P. S.; Mullins, M. J.; Philipp, D.; Muller, R.; Goddard, W. A. *J. Am. Chem. Soc.* **2002**, *124* (30), 8790–8791. doi:10.1021/ja0260061. PMID:12137520.

(12) (a) Drent, E.; van Dijk, R.; van Ginkel, R.; van Oort, B.; Pugh, R. I. *Chem. Commun. (Camb.)* **2002**, *7* (7), 744–745. doi:10.1039/b111252j. PMID:12119702.; (b) Luo, S.; Vela, J.; Lief, G. R.; Jordan, R. F. *J. Am. Chem. Soc.* **2007**, *129* (29), 8946–8947. doi:10.1021/ja072562p. PMID:17595087.; (c) Kochi, T.; Noda, S.; Yoshimura, K.; Nozaki, K. *J. Am. Chem. Soc.* **2007**, *129* (29), 8948–8949. doi:10.1021/ja0725504. PMID:17595086.; (d) Weng, W.; Shen, Z.; Jordan, R. F. *J. Am. Chem. Soc.* **2007**, *129* (50), 15450–15451. doi:10.1021/ja0774717. PMID:18027953.; (e) Vera, J.; Lief, G. R.; Shen, Z.; Jordan, R. F. *Organometallics* **2007**, *26* (26), 6624–6635. doi:10.1021/om700869c.

(13) (a) Angermund, K.; Fink, G.; Jensen, V. R.; Kleinschmidt, R. *Chem. Rev.* **2000**, *100* (4), 1457–1470. doi:10.1021/cr990373m. PMID:11749271.; (b) Rappé, A. K.; Skiff, W. M.; Casewit, C. J. *Chem. Rev.* **2000**, *100* (4), 1435–1456. doi:10.1021/cr9902493. PMID:11749270.; (c) Woo, T. K.; Fan, L.; Ziegler, T. *Organometallics* **1994**, *13* (6), 2252–2261. doi:10.1021/om00018a019.; (d) Lohrenz, J. C. W.; Woo, T. K.; Ziegler, T. *J. Am. Chem. Soc.* **1995**, *117* (51), 12793–12800. doi:10.1021/ja00156a017.; (e) Lohrenz, J. C. W.; Woo, T. K.; Fan, L.; Ziegler, T. *J. Organomet. Chem.* **1995**, *497* (1-2), 91–104. doi:10.1016/0022-328X(95)00110-C.; (f) Woo, T. K.; Margl, P. M.; Lohrenz, J. C. W.; Blöch, P. E.; Ziegler, T. *J. Am. Chem. Soc.* **1996**, *118* (51), 13021–13030. doi:10.1021/ja962525q.; (g) Musaev, D. G.; Froese, R. D. J.; Svensson, M.; Morokuma, K. *J. Am. Chem. Soc.* **1997**, *119* (2), 367–374. doi:10.1021/ja9628314.; (h) Deng, L.; Margl, P.; Ziegler, T. *J. Am. Chem. Soc.* **1997**, *119* (5), 1094–1100. doi:10.1021/ja962860e.; (i) Deng, L.; Woo, T. K.; Cavallo, L.; Margl, P. M.; Ziegler, T. *J. Am. Chem. Soc.* **1997**, *119* (26), 6177–6186. doi:10.1021/ja970226a.; (j) Musaev, D. G.; Svensson, M.; Morokuma, K.; Strömberg, S.; Zetterberg, K.; Siegbahn, P. E. M. *Organometallics* **1997**, *16* (9), 1933–1945. doi:10.1021/om961033j.; (k) Woo, T. K.; Margl, P. M.; Ziegler, T.; Blöchl, P. E. *Organometallics* **1997**, *16* (15), 3454–3468. doi:10.1021/om970126d.; (l) Fro-

ese, R. D. J.; Musaev, D. G.; Morokuma, K. *J. Am. Chem. Soc.* **1998**, *120* (7), 1581–1587. doi:10.1021/ja9728334.;

(14) (a) Margl, P.; Deng, L.; Ziegler, T. *J. Am. Chem. Soc.* **1998**, *120* (22), 5517–5525. doi:10.1021/ja9742139.; (b) Margl, P.; Deng, L.; Ziegler, T. *Organometallics* **1998**, *17* (5), 933–946. doi:10.1021/om9707578.; (c) Musaev, D. G.; Froese, R. D. J.; Morokuma, K. *Organometallics* **1998**, *17* (9), 1850–1860. doi:10.1021/om9711032.; (d) Deng, L.; Ziegler, T.; Woo, T. K.; Margl, P.; Fan, L. *Organometallics* **1998**, *17* (15), 3240–3253. doi:10.1021/om9803164.; (e) Margl, P.; Deng, L.; Ziegler, T. *J. Am. Chem. Soc.* **1999**, *121* (1), 154–162. doi:10.1021/ja981995c.; (f) Deng, L.; Margl, P.; Ziegler, T. *J. Am. Chem. Soc.* **1999**, *121* (27), 6479–6487. doi:10.1021/ja984385l.; (g) Woo, T. K.; Ziegler, T. *J. Organomet. Chem.* **1999**, *591* (1-2), 204–213. doi:10.1016/S0022-328X(99)00449-0.; (h) Margl, P.; Deng, L.; Ziegler, T. *Organometallics* **1999**, *18* (26), 5701–5708. doi:10.1021/om990392m.; Musaev, D. G.; Morokuma, K. *Top. Catal.* **1999**, *7* (1/4), 107–123. doi:10.1023/A:1019147313488.; Chan, M. S. W.; Deng, L.; Ziegler, T. *Organometallics* **2000**, *19* (14), 2741–2750. doi:10.1021/om000055+.; Khoroshun, D. V.; Musaev, D. G.; Vreven, T.; Morokuma, K. *Organometallics* **2001**, *20* (10), 2007–2026. doi:10.1021/om010126k.; (i) Liu, Y.; Zhang, M.; Drew, M. G. B.; Yang, Z.-D.; Liu, Y. *J. Mol. Struct. THEOCHEM* **2005**, *726* (1-3), 277–283. doi:10.1016/j.theochem.2005.04.027.; Collins, S.; Ziegler, T. *Organometallics* **2007**, *26* (26), 6612–6623. doi:10.1021/om700833b.

(15) (a) Koga, M.; Morokuma, K. *J. Am. Chem. Soc.* **1986**, *108* (20), 6136–6144. doi:10.1021/ja00280a005.; (b) Margl, P.; Ziegler, T. *J. Am. Chem. Soc.* **1996**, *118* (31), 7337–7344. doi:10.1021/ja960697h.; (c) Margl, P.; Ziegler, T. *Organometallics* **1996**, *15* (26), 5519–5523. doi:10.1021/om960521o.; (d) Michalak, A.; Ziegler, T. *J. Am. Chem. Soc.* **2001**, *123* (49), 12266–12278. doi:10.1021/ja010876l. PMID:11734027.; (e) Michalak, A.; Ziegler, T. *Organometallics* **2001**, *20* (8), 1521–1532. doi:10.1021/om0009886.; (f) von Schenck, H.; Strömberg, S.; Zetterberg, K.; Ludwig, M.; Åkermark, B.; Svensson, M. *Organometallics* **2001**, *20* (13), 2813–2819. doi:10.1021/om000926f.; (g) Philipp, D. M.; Muller, R. P.; Goddard, W. A., 3rd; Storer, J.; McAdon, M.; Mullins, M. *J. Am. Chem. Soc.* **2002**, *124* (34), 10198–10210. doi:10.1021/ja0157705. PMID:12188685.;

(16) (a) Deubel, D. V.; Ziegler, T. *Organometallics* **2002**, *21* (8), 1603–1611. doi:10.1021/om010662c.; (b) Deubel, D. V.; Ziegler, T. *Organometallics* **2002**, *21* (21), 4432–4441. doi:10.1021/om0202975.; (c) Michalak, A.; Ziegler, T. *Organometallics* **2003**, *22* (10), 2069–2079. doi:10.1021/om030072+.; (d) Michalak, A.; Ziegler, T. *Organometallics* **2003**, *22* (13), 2660–2669. doi:10.1021/om021044e.; (e) Szabo, M. J.; Jordan, R. F.; Michalak, A.; Piers, W. E.; Weiss, T.; Yang, S.-Y.; Ziegler, T. *Organometallics* **2004**, *23* (23), 5565–5572. doi:10.1021/om049485g.; (f) Szabo, M. J.; Galea, N. M.; Michalak, A.; Yang, S.-Y.; Groux, L. F.; Piers, W. E.; Ziegler, T.; *J. Am. Chem. Soc.* **2005**, *127* (42), 14692–14703. doi:10.1021/ja052350x. PMID:16231923.; (g) Yang, S.-Y.; Szabo, M. J.; Michalak, A.; Weiss, T.; Piers, W. E.; Jordan, R. F.; Ziegler, T. *Organometallics* **2005**, *24* (6), 1242–1251. doi:10.1021/om049015m.; (h) Szabo, M. J.; Galea, N. M.; Michalak, A.; Yang, S.-Y.; Groux, L. F.; Piers, W. E.; Ziegler, T.; Theoretical Study Based on Acrylonitrile and the Brookhart Diimine Catalyst. *Organometallics* **2005**, *24* (9), 2147–2156. doi:10.1021/om049018z.; (i) Haras, A.; Anderson, G. D. W.; Michalak, A.; Rieger, B.; Ziegler, T. *Organometallics* **2006**, *25* (19), 4491–4497. doi:10.1021/om060250+.

(17) (a) Hicks, F. A.; Brookhart, M. *Organometallics* **2001**, *20* (15), 3217–3219. doi:10.1021/om010211s.; (b) Hicks, F. A.; Jenkins, J. C.; Brookhart, M. *Organometallics* **2003**, *22* (17), 3533–3545. doi:10.1021/om030142c.

(18) (a) Ziegler, T.; Autschbach, J. *Chem. Rev.* **2005**, *105* (6), 2695–2722; and refs. cited therein. doi:10.1021/cr0307188. PMID:15941226.; (b) Suresh, C. H.; Koga, N. *Inorg. Chem.* **2002**, *41* (6), 1573–1578. doi:10.1021/ic0109400. PMID:11896726.; (c) Fantucci, P.; Polezzo, S.; Sironi, M.; Bencini, A. *J. Chem. Soc., Dalton Trans.* **1995**, *24* (24), 4121. doi:10.1039/dt9950004121.; (d) González-Blanco, Ò.; Branchadell, V. *Organometallics* **1997**, *16* (25), 5556–5562. doi:10.1021/om9705214.; (e) Ruiz-Morales, Y.; Ziegler, T. *J. Phys. Chem. A* **1998**, *102* (22), 3970–3976. doi:10.1021/jp973308u.

(19) (a) Frenking, G.; Fröhlich, N. *Chem. Rev.* **2000**, *100* (2), 717–774; and refs. therein. doi:10.1021/cr9804011. PMID:11749249.; (b) Dapprich, S.; Frenking, G. *J. Phys. Chem.* **1995**, *99* (23), 9352–9362. doi:10.1021/j100023a009.; (c) Ehlers, A. W.; Dapprich, S.; Vyboishchikov, S. F.; Frenking, G. *Organometallics* **1996**, *15* (1), 105–117. doi:10.1021/om950697a.; (d) Frenking, G.; Wichmann, K.; Fröchlich, N.; Grobe, J.; Golla, W.; Van, D. L.; Krebs, B.; Läge, M. *Organometallics* **2002**, *21* (14), 2921–2930. doi:10.1021/om020311d.

(20) (a) Pacchioni, G.; Bagus, P. S. *Inorg. Chem.* **1992**, *31* (21), 4391–4398. doi:10.1021/ic00047a029.; (b) Bagus, P. S.; Hermann, K.; Bauschlicher, C. W. *J. Chem. Phys.* **1984**, *80* (9), 4378. doi:10.1063/1.447215.

(21) (a) Morokuma, K. *J. Chem. Phys.* **1971**, *55* (3), 1236. doi:10.1063/1.1676210.; (b) Ziegler, T.; Rauk, A. *Inorg. Chem.* **1979**, *18* (7), 1755–1759. doi:10.1021/ic50197a006.; (c) Ziegler, T.; Rauk, A. *Inorg. Chem.* **1979**, *18* (6), 1558–1565. doi:10.1021/ic50196a034.

(22) Reed, A. E.; Curtiss, L. A.; Weinhold, F. *Chem. Rev.* **1988**, *88* (6), 899–926; and refs. therein.. doi:10.1021/cr00088a005.

(23) (a) Mitoraj, M.; Michalak, A. *J. Mol. Model.* **2007**, *13* (2), 347–355. doi:10.1007/s00894-006-0149-4. PMID:17024408.; (b) Mitoraj, M.; Michalak, A. *Organometallics* **2007**, *26* (26), 6576–6580. doi:10.1021/om700754n.; (c) Mitoraj, M.; Michalak, A. *J. Mol. Model.* **2008**, *14* (8), 681–687. doi:10.1007/s00894-008-0276-1. PMID:18278526.; (d) Michalak, A.; Mitoraj, M.; Ziegler, T. *J. Phys. Chem. A* **2008**, *112* (9), 1933–1939. doi:10.1021/jp075460u. PMID:18266342.; (e) Mitoraj, M.; Zhu, H.; Michalak, A.; Ziegler, T. *Int. J. Quantum Chem.* **2009**, in press; (f) Radoń, M. *Theor. Chem. Acc.* **2008**, *120* (4-6), 337–339. doi:10.1007/s00214-008-0428-5.

(24) (a) Dewar, M. J. S. *Bull. Soc. Chim.* **1951**, *18*, C71; (b) Chatt, J.; Duncanson, J. A. *J. Chem. Soc.* **1953**, *3*, 2939. doi:10.1039/jr9530002939.

(25) (a) Becke, A. D. *Phys. Rev. A* **1988**, *38* (6), 3098–3100. doi:10.1103/PhysRevA.38.3098. PMID:9900728.; (b) Perdew, J. P. *Phys. Rev. B* **1986**, *34* (10), 7406. doi:10.1103/PhysRevB.34.7406.; (c) Perdew, J. P. *Phys. Rev. B* **1986**, *33* (12), 8822–8824. doi:10.1103/PhysRevB.33.8822.

(26) (a) te Velde, G.; Bickelhaupt, F. M.; Baerends, E. J.; Fonseca Guerra, C.; Van Gisbergen, S. J. A.; Snijders, J. G.; Ziegler, T. *J. Comput. Chem.* **2001**, *22* (9), 931–967; and refs. therein. doi:10.1002/jcc.1056.; (b) Baerends, E. J.; Ellis, D. E.; Ros, P. *Chem. Phys.* **1973**, *2* (1), 41–51. doi:10.1016/0301-0104(73)80059-X.; (c) Baerends, E. J.; Ros, P.

Chem. Phys. **1973**, *2* (1), 52–59. doi:10.1016/0301-0104(73)80060-6.; (d) Tevelde, G.; Baerends, E. J. *J. Comput. Phys.* **1992**, *99* (1), 84–98. doi:10.1016/0021-9991(92)90277-6.; (e) Fonseca, C. G.; Visser, O.; Snijders, J. G.; TeVelde, G.; Baerends, E. J. In *Methods and Techniques in Computational Chemistry*. METECC-95. E. Clementi, G. Corongiu, Eds.;. STEF: Cagliari, Italy, 1995; p. 305.

(27) (a) Ziegler, T.; Baerends, E. J.; Snijders, J. G.; Ravenek, W.; Tschinke, V. *J. Phys. Chem.* **1989**, *93* (8), 3050–3056. doi:10.1021/j100345a036.; (b) Snijders, J. G.; Baerends, E. J. *Mol. Phys.* **1978**, *36* (6), 1789–1804. doi:10.1080/00268977800102771.; (c) Snijders, J. G.; Baerends, E. J.; Ros, P. *Mol. Phys.* **1979**, *38* (6), 1909–1929. doi:10.1080/00268977900102941.

(28) (a) Nalewajski, R. F.; Köster, A. M.; Jug, K. *Theor. Chim. Acta* **1993**, *85*, 463 doi:10.1007/BF01112985.; (b) Nalewajski, R. F.; Mrozek, J. *Int. J. Quantum Chem.* **1994**, *51* (4), 187–200. doi:10.1002/qua.560510403.; (c) Nalewajski, R. F.; Formosinho, S. J.; Varandas, A. J. C.; Mrozek, J. *Int. J. Quantum Chem.* **1994**, *52* (5), 1153–1176. doi:10.1002/qua.560520504.; (d) Nalewajski, R. F.; Mrozek, J. *Int. J. Quantum Chem.* **1996**, *57* (3), 377–389. doi:10.1002/(SICI)1097-461X(1996)57:3<377::AID-QUA11>3.0.CO;2-1.; (e) Nalewajski, R. F.; Mrozek, J.; Mazur, G. *Can. J. Chem.* **1996**, *74* (6), 1121–1130. doi:10.1139/v96-126.; (f) Nalewajski, R. F.; Mrozek, J.; Michalak, A. *Int. J. Quantum Chem.* **1997**, *61* (3), 589–601. doi:10.1002/(SICI)1097-461X(1997)61:3<589::AID-QUA28>3.0.CO;2-2.; (g) Nalewajski, R. F.; Mrozek, J.; Michalak, A. *Pol. J. Chem.* **1998**, *72*, 1779; (h) Michalak, A.; DeKock, R. L.; Ziegler, T. *J. Phys. Chem. A* **2008**, *112* (31), 7256–7263. doi:10.1021/jp800139g. PMID:18627137.

An investigation of $(C_5H_5)Fe(C_5H_4–C(OBF_3)–CH_3)$[1,2]

Francis O. Ogini, Philip J. W. Elder, James F. Britten, and Ignacio Vargas-Baca

Abstract: Acetylferrocene readily forms an adduct with BF_3. The product is a neutral model for protonated acetylferrocene, a species that is a crucial intermediate in the formation of 1,3,5-trisferrocenyl-benzene and other conjugated heterometallic derivatives by cyclocondensation. The title compound's structure was determined in the solid state by X-ray diffraction and its spectroscopic properties were examined in detail, particularly the electronic excitation spectrum, which confirms the previous identification of the in situ generated protonated ketone.

Key words: organometallic ketones, BF_3 adducts, ferrocenyl cations, density functional theory (DFT) calculations.

Résumé : L'acétylferrocène forme facilement un adduit avec le BF_3. Le produit est un modèle neutre pour un acétylferrocène, une espèce qui est un intermédiaire crucial dans la formation du 1,3,5-trisferrocényl-benzène et d'autres dérivés hétérométalliques par cyclocondensation. La structure du composé mentionné dans le titre a été déterminée à l'état solide par diffraction des rayons X et on a examiné ses propriétés spectroscopiques en détail, en particulier son spectre d'excitation électronique qui confirme l'identification antérieure de la cétone protonée générée in situ.

Mots-clés : cétones organométalliques, adduits avec le BF_3, cations ferrocényles, calculs d'après la théorie de la fonctionnelle de la densité (TFD).

[Traduit par la Rédaction]

Introduction

Aldehydes and ketones are weak bases, with the typical pK_a values of their conjugated acids being below –6, e.g., –6.99 in the case of benzaldehyde and –6.04 for acetophenone.[3] A wide variety of organometallic functional groups can increase the basicity of a carbonyl group. This is attributed to a stabilizing effect on the positive charge of the protonated form. Examples of such groups include ferrocenyl (Fc = $(C_5H_5)Fe(C_5H_4)$), cymantrenyl (Cym = $(CO)_3Mn(C_5H_4)$),[4] (cyclobutadienyl)$Fe(CO)_3$,[5] (cyclobutadienyl)$Co(C_5H_5)$,[6] and (cyclobutadienyl)$Cr(CO)_2NO$.[7] Indeeed, the pK_a values of $[(CO)_3Mn(C_5H_4–C(OH)–CH_3)]^+$ and $[(C_5H_5)Fe(C_5H_4–C(OH)–CH_3)]^+$ (**1**) are –4.0 and –2.6, respectively.[8] Such protonated species are considered key intermediates in the acid-catalyzed oligomerization of the ketones,[9] which yields 3,1 disubstituted (*E*)-2-buten-1-ones (**2**) and 1,3,5-trisubstituted benzenes (**3**). The relative yields of the heterometallic condensation products from mixtures of acetylferrocene (**4**) and acetylcymantrene has been rationalized by considering the relative stabilities of those cations. Such a condensation process begins with a striking colour change, which was attributed to the formation of the cationic intermediates. That interpretation was supported by calculations of the electronic spectra of simplified models of the cations and the reactants. The shape of the calculated spectra and the relative position of the first excitation bands were in reasonable agreement with the experimental data. However, conclusive identification of the chromophores was precluded by the inherent reactivity of the transient intermediates.

In lieu of protons, Lewis acids can be used to induce the condensation reaction of ketones and aldehydes. Such activation is usually explained with two different effects: (*i*) enhancement of the acidity of the α-hydrogens of a ketone or an aldehyde, which promotes enolization[10] and (*ii*) enhancement of the electrophilicity of the carbonylic carbon.[11–13] The practical uses of this type of Lewis acid activation in organic chemistry have been reviewed.[13]

Lewis acid catalysts that are useful in this context include the trihalides of group-13 elements.[3,14–16] Thermochemical and theoretical studies of BF_3–Carbonyl adducts have shown that coordination of BF_3 transforms simple carbonyl compounds into gas-phase superacids and superelectrophiles with enhancements in acidity of up to 50 kcal/mol and hydride affinity of up to 66 kcal/mol.[10] On the other hand, α-deprotonation results in strengthening of the B–O bond, increasing the bond energy from 11 kcal/mol in the carbonyl adduct to 60 kcal/mol in the BF_3-enolate[10] Correspondingly, addition of H^- to the carbonyl carbon also increases the B–O bond energy to 78 kcal/mol.[10] Both the enolate and the alkoxide forms enable stabilization of negative charge by the fluorine atoms.

Here, we report the isolation of a stable adduct of **4** with BF_3, compound **5**, which is in effect a neutral analogue to the cation $[(C_5H_5)Fe(C_5H_4–C(OH)–CH_3)]^+$. The product was isolated in pure form, structurally characterized by single crystal X-ray crystallography and studied by electronic, vibrational, and NMR spectroscopy. These experimental observations were analyzed and interpreted in comparison to the results of computational modeling.

Received 8 January 2009. Accepted 19 March 2009. Published on the NRC Research Press Web site at canjchem.nrc.ca on 29 June 2009.

F.O. Ogini, P.J.W. Elder, J.F. Britten, and I. Vargas-Baca.[1] Department of Chemistry, McMaster University, 1280 Main Street West, Hamilton, ON L8S 4M1, Canada.

[1]Corresponding author (e-mail: vargas@chemistry.mcmaster.ca).

Experimental

Materials and methods

All manipulations of air- and moisture-sensitive materials were performed under an atmosphere of dry nitrogen in a glovebox or using standard Schlenk techniques. Pentane and methylene chloride were carefully dried over CaH_2. Acetylferrocene and $BF_3{\cdot}OEt_2$ were purchased from Sigma-Aldrich and used as received. $^1H/^{13}C$ and $^{11}B/^{19}F$ NMR spectra were acquired on Bruker AC 500 and AC 600 spectrometers, respectively. Chemical shifts for ^1H and ^{13}C are reported in ppm with respect to $Si(CH_3)_4$ and were determined using the resonances of the residual proton and the natural-abundance ^{13}C in $CDCl_3$ as internal standards. Chemical shifts for ^{11}B and ^{19}F spectra are reported with respect to $BF_3{\cdot}OEt_2$ and $CFCl_3$ (respectively) and were measured using an internal standard of $BF_3{\cdot}OEt_2$. Infrared spectra were recorded in pellets of anhydrous AgCl using a Bio-Rad FTS-40 spectrometer with a 4 cm^{-1} resolution. Ultraviolet–visible spectra were recorded on a Cary 300 ultraviolet/visible spectrophotometer. Raman spectra were recorded on a Bruker RFS 100/s at –78 °C. Melting points (uncorrected) of samples in sealed capillaries were measured on a Thomas Hoover melting-point apparatus.

Preparation of $[(C_5H_5)Fe(C_5H_4–C(O–BF_3)–CH_3)]$ (5)

Mixing of a diethyl ether solution of acetylferrocene (2 mmol in 2 mL) and $BF_3{\cdot}OEt_2$ (2 mmol) resulted in the immediate appearance of a purple coloration. The adduct was quantitatively recovered in pure form (by ^1H NMR) after evaporation of the solvent. Moisture-sensitive dark purple crystals of the adduct were grown by vapor diffusion of pentane into a chloroform solution at –30 °C over 2 d, mp 124–126 °C. UV–vis (10.8 mmol L^{-1} in CH_2Cl_2) λ_{max} (nm), [Abs]: 290 [1.76], 350 [0.38], 505 [0.25]. ^1H NMR (500 MHz, $CDCl_3$, T = –50 °C, ppm) δ: 5.33 (H8, ddd, $^3J_{H9–H8}$ = 2.8 Hz, $^3J_{H8-H7}$ = 2.7 Hz, $^4J_{H8–H6}$ = 1.2 Hz), 5.24 (H7, ddd, $^3J_{H7-H6}$ = 2.8 Hz, $^4J_{H7-H9}$ = 1.4 Hz), 5.18 (H9, ddd, $^4J_{H9–H6}$ = 1.3 Hz), 4.90 (H6, ddd). ^{13}C NMR (125 MHz, $CDCl_3$, T = 50 °C) δ: 209.89 (C11), 80.91 (C7, C8), 75.15 (C10), 74.20 (C9), 73.31 (C_5H_5), 70.78 (C6), 23.57 (CH_3). ^{19}F NMR (470 MHz, $CDCl_3$, T = –50 °C) δ: –148.8 (s). ^{11}B NMR (160 MHz, $CDCl_3$, T = 50 °C) δ: –0.11 (s). IR (AgCl, cm^{-1}): 1534 (νCO), 1312 and 1339 ($C_{ring}–C_\alpha$). Raman (cm^{-1}): 1534 (νCO), 1312 and 1339 ($C_{ring}–C_\alpha$).

X-ray crystallography (see the Supplementary data section for the supplementary crystallographic data for this paper)

A single crystal of $[(C_5H_5)Fe(C_5H_4–C(O–BF_3)–CH_3)]$ was mounted on a nylon loop at –78 °C using a high-density perfluoropolyether oil. Data were collected on a P4 Bruker diffractometer upgraded with a Bruker SMART 1000 CCD detector and a rotating anode utilizing Mo Kα radiation (λ = 0.7103 Å, graphite monochromator) equipped with an Oxford cryosystems cryostat. A full sphere of reciprocal lattice was scanned by 0.36° steps in ω with a crystal-to-detector distance of 4.9 cm. Preliminary orientation matrices were obtained from the first frames using SMART.[17] The collected frames were integrated using the preliminary orientation matrices, which were updated every 100 frames. Final cell parameters were obtained by refinement on the positions of reflections with $I > 10\sigma(I)$ after integration of all the frames using SAINT.[17] The structure was solved by Patterson methods and refined by full-matrix least squares on all F2 data using SHELXTL.[18] The non-H atoms were refined anisotropically, while H atoms were constrained to idealized positions using appropriate riding models. Molecular graphics were produced using ORTEP-3.[19]

Fig. 1. Ultraviolet–visible absorption spectra of **4**, 10.8 mmol/L, in CH_2Cl_2 (—), 70% (*v*/*v*) H_2SO_4/ethanol (- - -), both from ref. 8, and CH_2Cl_2 with one molar equivalent of BF_3 (·····).

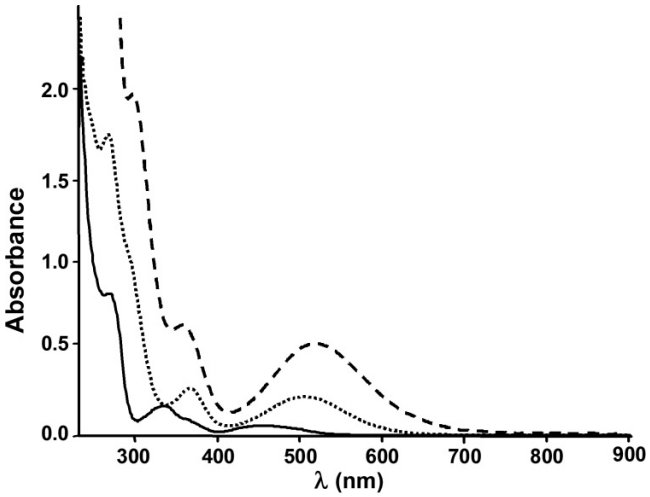

Table 1. Summary of crystallographic data for **5**.

	5
Formula	$C_{12}H_{12}BF_3FeO$
Formula weight	295.88
Radiation (wavelength, Å)	0.71073
Temperature (K)	173(2)
Crystal system	Triclinic
Space group	*P*-1
a (Å)	10.124(6)
b (Å)	10.268(6)
c (Å)	12.790(8)
α (°)	67.040(9)
β (°)	88.165(10)
γ (°)	76.282(10)
Volume ($Å^3$)	1186.5(13)
Z	4
$\delta_{calcd.}$ (g/cm^3)	1.656
μ (mm^{-1})	1.291
$R_1{}^a$	0.0642
$wR_2{}^b$	0.1582

$^aR_1 = \Sigma||F_o| - |F_c||/\Sigma|F_o|$.
$^bwR_2 = (\Sigma w||F_o| - |F_c||^2/\Sigma w|F_o|^2)^{1/2}$.

Computational methods

All calculations were performed using the ADF density functional theory (DFT) package (versions 2006.01 to 2008.01).[20–22] The adiabatic local density approximation (ALDA) was used for the exchange-correlation kernel[23,24] and the differentiated static LDA expression was used with the Vosko–Wilk–Nusair parametrization.[25] The optimization

Fig. 2. ORTEP of the asymmetric unit in the crystal of **5** (50% thermal ellipsoids); hydrogen atoms are omitted for clarity. The C_5H_5 rings are disordered; the major component of each is shown.

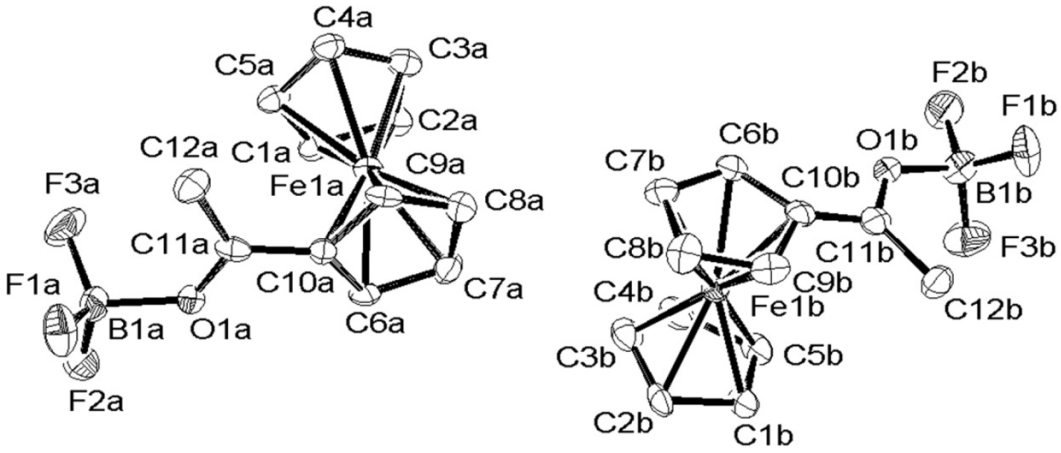

Table 2. Experimental (X-ray diffraction) and calculated (DFT) magnitudes of selected bond lengths and angles of **5**.

	Enantiomer		
	a	b	Calculated
Bond lengths (Å)			
Fe(1)—C(6)	2.038(5)	2.037(5)	2.030
Fe(1)—C(7)	2.068(5)	2.067(5)	2.060
Fe(1)—C(8)	2.063(6)	2.075(6)	2.061
Fe(1)—C(9)	2.015(5)	2.013(6)	2.036
Fe(1)—C(10)	2.006(5)	2.018(6)	2.025
Fe(1)—C(11)	2.908(6)	2.883(6)	2.942
O(1)—B(1)	1.536(8)	1.539(8)	1.618
O(1)—C(11)	1.265(6)	1.270(6)	1.268
F(1)—B(1)	1.372(8)	1.363(8)	1.367
F(2)—B(1)	1.373(8)	1.369(8)	1.381
F(3)—B(1)	1.370(7)	1.380(8)	1.392
Bond angles (°)			
F(2)–B(1)–F(1)	111.5(5)	112.5(6)	114.4
F(2)–B(1)–F(3)	112.1(5)	111.4(6)	112.7
F(1)–B(1)–F(3)	111.9(6)	111.2(5)	113.5
F(1)–B(1)–O(1)	108.0(5)	107.9(5)	103.3
F(2)–B(1)–O(1)	104.6(5)	104.9(5)	106.9
F(3)–B(1)–O(1)	108.8(5)	108.6(5)	104.9
C(11)–O(1)–B(1)	126.2(5)	125.6(4)	125.0
O(1)–C(11)–C(10)	117.4(5)	116.1(5)	117.1
O(1)–C(11)–C(12)	123.0(5)	122.2(5)	121.3

Table 3. Calculated 14 lowest electronic transitions of **4** and **5**.

	4			**5**		
	E (eV)	λ (nm)	*f*	*E* (eV)	λ (nm)	*f*
1a	2.90	428	0.00043	2.31	537	0.00061
2a	3.07	404	0.01150	2.55	486	0.00557
3a	3.21	386	0.00065	2.75	451	0.00985
4a	3.68	337	0.00007	3.52	353	0.00081
5a	3.73	332	0.00248	3.69	336	0.00003
6a	3.88	320	0.00004	3.71	334	0.00068
7a	3.95	314	0.00060	3.85	322	0.04180
8a	4.08	304	0.00096	3.88	320	0.00020
9a	4.20	295	0.00105	4.08	304	0.00694
10a	4.26	291	0.00006	4.12	301	0.00158
11a	4.37	284	0.00631	4.37	284	0.01023
12a	4.49	276	0.06709	4.42	280	0.00069
13a	4.52	274	0.00012	4.67	266	0.11951
14a	4.76	261	0.00086	4.84	256	0.00797

of model geometries was gradient-corrected with the exchange and correlated functionals of the gradient correction proposed in 1988 by Becke,[26] Perdew,[27] and Lee, Yang and Parr.[28] Preliminary geometry optimizations were conducted using a double-ζ basis set with frozen cores corresponding to the configuration of the preceding noble gas and one set of polarization functions; the resulting structures were refined using a triple-ζ all electron basis set with two polarization functions. The geometry optimizations were followed by a vibrational calculation[29,30] to verify that all the computed frequencies were real. Electronic excitations were calculated using time-dependent density functional theory (TDDFT) as implemented within the ADF package; the statistical average of different model potentials for occupied Kohn–Sham (KS) orbitals (SAOP)[31,32] was used for the exchange-correlation potentials in the zeroth-order KS equations.

Results and discussion

Preliminary experiments and synthesis

The early stages of the acid-catalyzed cyclocondensation of acetylferrocene are characterized by a strong colour change from orange to purple, due to the appearance of a strong absorption band with λ_{max} at 490 nm in the UV–visible absorption spectrum (Fig. 1). Very similar colour and spectral changes are observed when a small amount of H_2SO_4 is added to a solution of **4** in ethanol. Although it is reasonable to attribute the new absorption band to the cation **1**, other intermediates, such as the enol $(C_5H_5)Fe(C_5H_4–C(OH)=CH_2)$, could not be ruled out a priori. It was therefore necessary to isolate and characterize the coloured species. Initial attempts in this respect were based on multiple combinations of protic acids (trichloroacetic, trifluoroacetic, acetic, sulfuric, and hydrochloric acid) and organic solvents (acetonitrile, methylene chloride, hexanes, pentane, ethanol, chloroform, tetrahydrofuran, and ether; pure and mixtures) at different temperatures

Fig. 3. Transition densities for the most intense transitions in the electronic spectra of **4** and **5**. Clear and dark lobes represent positive and negative lobes, respectively.

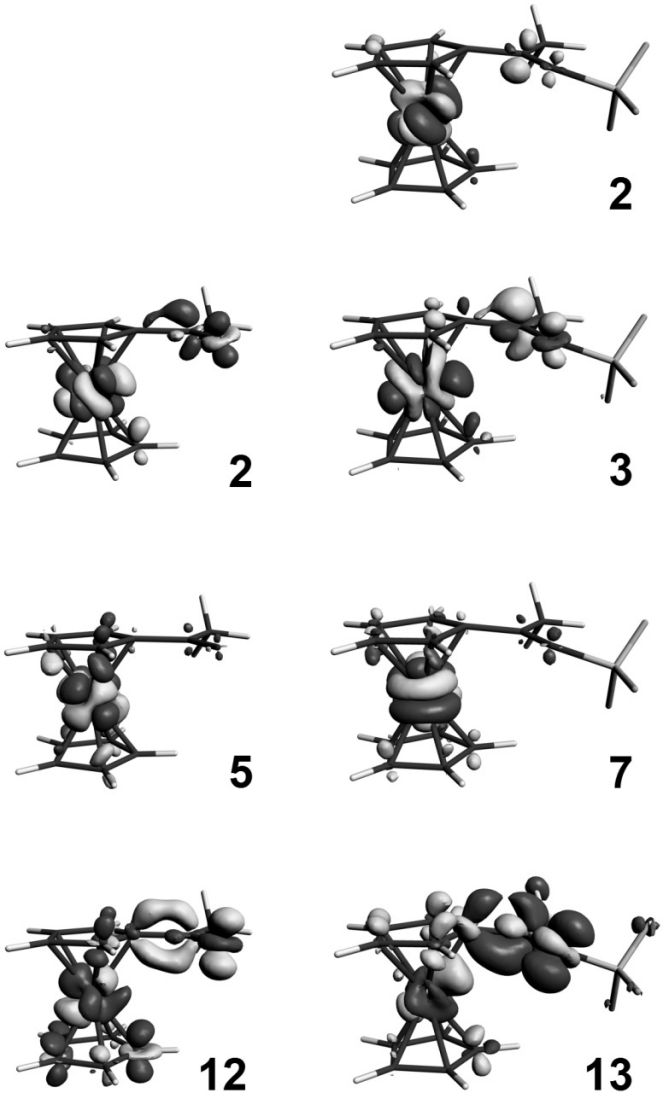

(25 °C, 0 °C, –30 °C). Each attempt invariably led to the separation of an oily phase, which could not be purified and characterized further.

Because all attempts to crystallize the coloured intermediate were unsuccessful, the preparation of Lewis acid–base adducts of **4** with group-13 trihalides ($InCl_3$, $AlCl_3$, and BF_3) was attempted. In each case, the expected colour and spectral changes were observed in solution, with the spectrum of the **4**-BF_3·OEt_2 mixtures resembling very closely that of **4** in acidic medium (Fig. 1). The mixtures with $InCl_3$ and $AlCl_3$ separated as oils and were impossible to purify. In contrast, the equimolar combination of **4** and BF_3·OEt_2 yielded almost quantitatively a dark purple microcrystalline solid, which was easily recrystallized.

Molecular structure

The crystal structure of **5** was determined by X-ray diffraction, and final results are summarized in Table 1. The molecule of the Lewis acid–base adduct is chiral and the unit cell contains the two enantiomers within the asymmetric unit (Fig. 2). The Cp rings are nearly 50% disordered. Selected internal dimensions of both molecules are summarized in Table 2, where the magnitudes of individual pairs are equal within statistical error. The adduct displays a boron centre with tetrahedral geometry, with B–F bond distances in the range of 1.363(8)–1.380(8) Å. The B–O bond lengths of 1.536(8) and 1.539(8) Å are comparable to the average 1.561(22) Å observed in other adducts of BF_3 with ketones.[33,34,35] The F–B–F bond angles, which vary between 111.2°(5) and 112.5°(6), are comparable to those observed in the X-ray structure of $C_6H_6CHO{\cdot}BF_3$ (110.2°(6)–111.3°(5)).[36] The C=O bond shows significant lengthening in both enantiomers, with respect to the distance observed in acetylferrocene,[37] r(C=O) = 1.211(7) Å.

The increase of the C=O bond is complemented by a substantial contraction of the C_{Cp}–Cα bond. The values for this bond distance, 1.423(7) and 1.420(8) Å for each enantiomer, are well below the 1.470(8) Å measured in the parent ketone; it is very close to the 1.416(9) Å observed in the X-ray structure of $[(C_5H_5)Fe(C_5H_4{=}C(C_6H_5)_2)]^+$ $(BF_4)^-$,[38] but slightly longer than the 1.357(5) Å of the neutral iron fulvene complex, $(CO)_3Fe(C_5H_4{=}C(C_6H_5)_2)$.[39] The pattern of change in bond lengths is typical of donor–acceptor interactions[40] and, in this case, can be interpreted as the result of the adoption of a fulvene Lewis structure.

Table 4. Calculated atomic charges (au) of selected atoms or fragments in the molecules of **4** and **5**.

	Voronoi		Hirshfeld		NPA	
	4	**5**	**4**	**5**	**4**	**5**
Fe(1)	–0.03	–0.02	0.09	0.10	0.30	0.31
C_6H_5	0.07	0.14	0.01	0.08	–0.10	–0.02
C_6H_4	0.01	0.07	–0.02	0.05	–0.20	–0.14
C(11)	0.16	0.20	0.16	0.21	0.55	0.62
O	–0.27	–0.12	–0.26	–0.12	–0.54	–0.53
CH_3	0.07	0.13	0.03	0.07	–0.01	0.05
BF_3		–0.41		–0.38		–0.31

Fig. 4. Vibrational spectra (top: infrared, bottom: Raman) of acetylferrocene (·····) and its BF_3 adduct (—). Selected assignments: (a) ν(C=O), (b) $\nu(C_{ring}{-}C_\alpha)$.

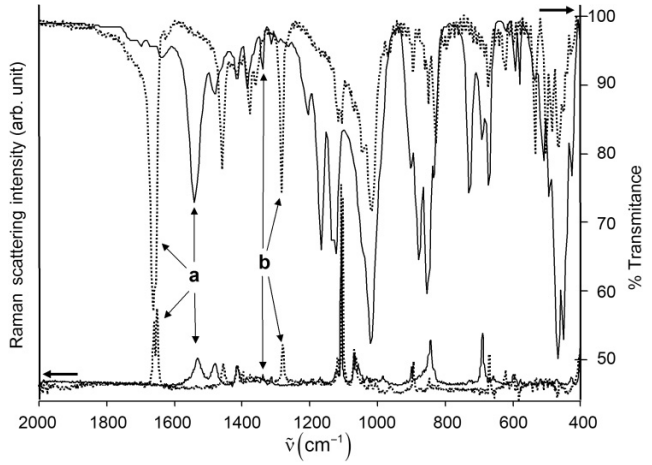

Fig. 5. Selected normal vibrational modes. **4**: (**a**) ν(C=O), (**b**) ν(C_{ring}–C_α); **5**: (**c**) ν(C–O), (**d**) and (**e**) ν(C_{ring}=C_α).

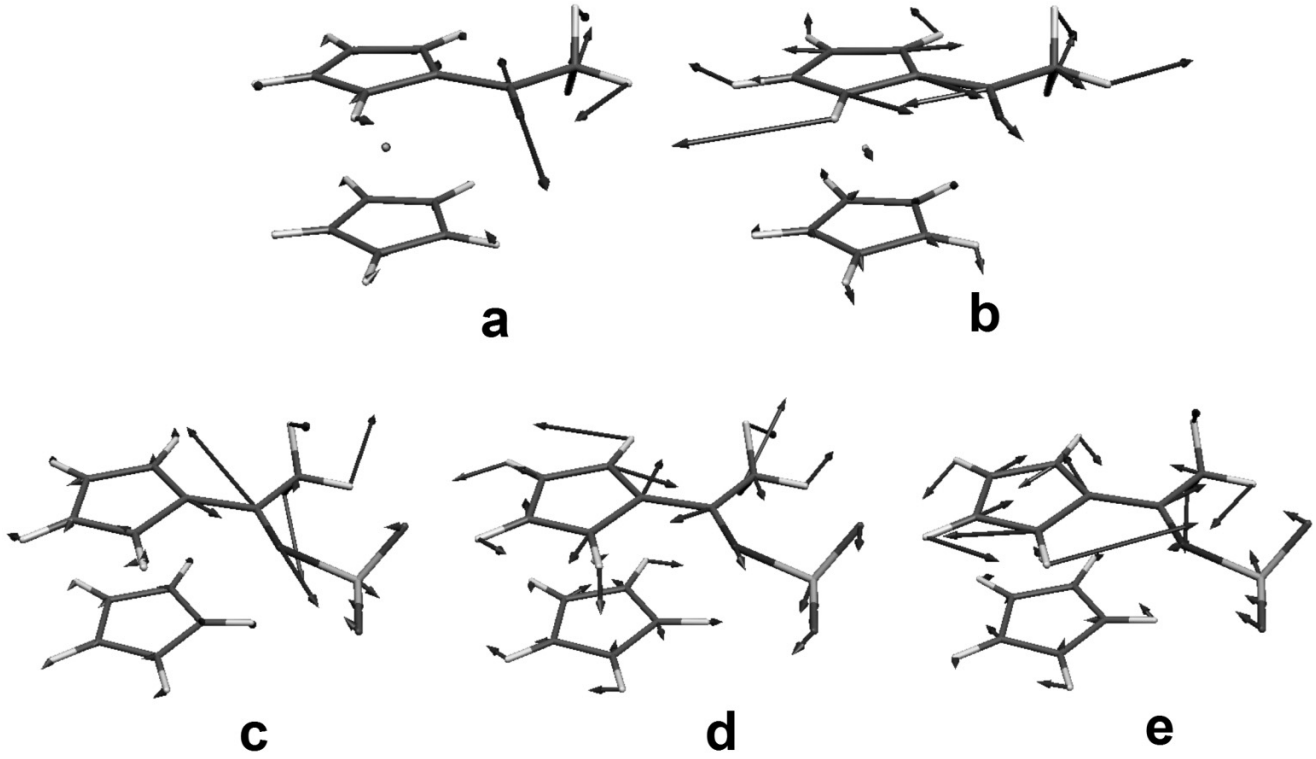

Both enantiomers also exhibit a displacement of the O–C_α–C_{Me} exocyclic moiety below the plane of the Cp ring, to enable coordination of the metal by C_g. The corresponding Fe(1)–C(11) bond distances are 2.908(6) Å and 2.883(6) Å, the angles described by the C(10)–C(11) bond and the plane of the five-membered ring are 10.4° and 12.7°. Such geometrical features are characteristic of cyclopentadienyl organometallic cations[38,41–43] in which the bent geometry is interpreted as a consequence of the electron deficiency at the α–Carbon; overlap of the vacant p with a filled d orbital of the metal is thought to stabilize the molecule.[41,42] The dip angle of **5** is less pronounced than that observed in α-ferrocenylcarbocations such as $[(C_5H_5)Fe(C_5H_4C(C_6H_5)_2)]^+BF_4^-$ (20.7°; r(Fe···C_α): 2.715(6) Å).[38] Fulvene complexes of electron richer iron atoms usually display a different structure, for example, in the X-ray structure of $(CO)_3Fe(C_5H_4C(C_6H_5)_2)$ the C_α atom bends away from the metal to a distance of 3.679 Å and has an exo fold angle of 18.5°.[39]

The above geometric features are well reproduced by DFT calculations. The optimized molecular dimensions are compared to the experimental values in Table 2. Most calculated bond distances fall within 3σ of the measured values, larger deviations are observed for bond angles. The most significant differences are in those dimensions that involve the metal atom and the B–O bond.

Electronic absorption spectra

The UV–vis absorption spectra of **4** and **5** are similar to each other: both display three absorption bands above 240 nm. The most important differences between them are the red shift and increased intensity of the first band of the BF_3 adduct. When TDDFT calculations were used to interpret the spectrum of **1** using the models $[(C_5H_5)Fe(C_5H_4C(O)H)]$ and $[(C_5H_5)Fe(C_5H_4C(OH)H)]^+$, the first band was attributed to a M–L charge transfer involving the $\pi^*_{C=O}$ empty orbital.[8] In this work, we calculated the first 40 transitions of **4** and **5**, used these to model the total absorption spectra, and identified the main contributions to the lowest three bands of each compound. There was good agreement in the shape and relative intensity of the bands, although their λ_{max} was underestimated by up to 45 nm. This analysis revealed that, remarkably, each band in the spectrum of **4** has essentially the same nature as the corresponding band of **5**. The first absorption originates in charge transfer transitions (**4**: 2a; **5**: 2a, 3a) from the metal–Centred HOMO-1 (and HOMO-2 in the case of **5**) to the $\pi^*_{C=O}$ LUMO. The second band arises from the excitation of d electrons to M–C_{cp} antibonding orbitals. The third band is the result of a transition from M–C bonding orbitals to the LUMO. The lowest 14 transitions of these compounds are listed in Table 3 and Fig. 3 presents the transition densities for the most prominent excitations of both molecules, calculated as

$$[1] \qquad \rho_{ge}(r) = \psi^*_g(r)\psi_e(r)$$

The red shift corresponds to the decrease of the HOMO–LUMO gap as the ligand acquires a fulvene character, the C=C bond shortens and the C–O bond elongates. The relative magnitudes of calculated oscillator strengths were consistent with the observed increase of intensity of the bands upon adduct formation. An explanation for the observed change of absorption intensity can be proposed from simple arguments based on the Lewis structures; the BF_3 adduct molecule is more polar, hence, the transition moments are larger. The calculated dipole moments (3.5 and 9.8 D for **4** and **5**, respectively) support this interpretation.

Fig. 6. Variable temperature NMR spectra of **5**; (*a*) ^{13}C, (*b*) ^{1}H.

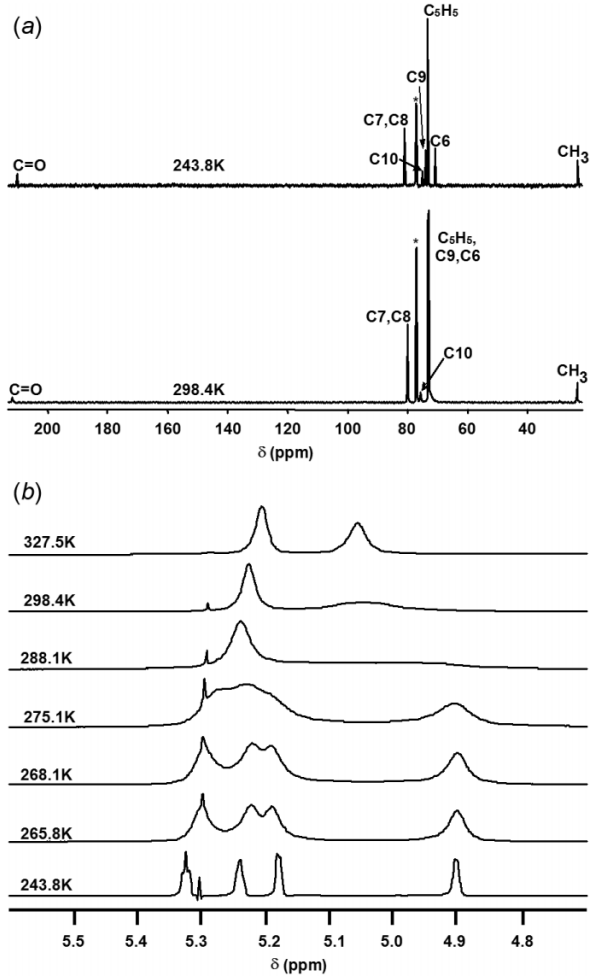

Fig. 7. Calculated potential-energy profile for the rotation of the C_{ring}–C_{α} bond of **5**.

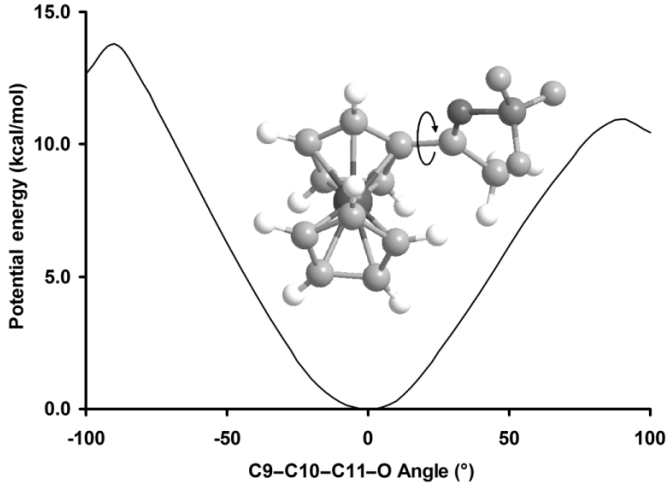

To examine the origin of the change in dipole moment upon binding to the Lewis acid, the atomic charges of **4** and **5** were calculated using methods based on electron density (Voronoi deformation density[44] and Hirshfeld[45]), as well as the natural population analysis (NPA).[46,47] The results are summarized in Table 4. The three schemes do attribute a significantly negative character to the BF_3 group. However, the the organometallic fragment bears only a small amount of charge, which doesn't significantly change upon coordination of BF_3, instead it is the carbon atom of the carbonyl group which bears the largest increase of charge.

Vibrational spectroscopy

The normal modes of **4** and its donor–acceptor complexes are already discussed in detail elsewhere.[48,49] For the purposes of this study, the most relevant sections of the vibrational spectrum correspond to the stretch vibrations of the C–O and C_{ring}–C_{α} bonds. Both the infrared and Raman spectra of solid **5** are compared to those of **4** in Fig. 4.

The ν(C–O) band is readily perturbed by bonding to BF_3. In the case of **4,** it is observed at 1683 cm^{-1} in the infrared spectrum; in Raman, the centrosymmetric character of the crystal splits the band and two maxima appear at 1681 cm^{-1} and 1671 cm^{-1}. These peaks are absent in the spectra of **5**; instead, broad and intense bands appear at 1534 cm^{-1} in both techniques. The shift of this vibration to lower wavenumbers is consistent with the decrease of bond order upon formation of the donor–acceptor adduct and parallels the observations made for other adducts of Lewis acids with carbonyl compounds.[50–52] DFT calculations showed that in both molecules the ν(C–O) vibrations have little mixing with other interatomic motions (Fig. 5) and, without scaling, the calculated shift is from 1670 to 1542 cm^{-1}.

Similarly, the increase of bond order makes the ν(C_{ring}–C_{α}) sensitive to Lewis acids, in principle.[53] However, DFT calculations show that this stretch is coupled to changes in other bonds (Fig. 5). The mode that best corresponds to this vibration in **4** is calculated at 1261 cm^{-1} and is assigned to the absorption band at 1280 cm^{-1}, in agreement with Pavlík et al.[49] According to the calculations, the stretch of the C_{ring}–C_{α} is strongly coupled in **5** and contributes to two modes at 1324 and 1302 cm^{-1}. Experimentally, in the spectra of **5** there is no significant band at 1280 cm^{-1} and new vibrations appear at 1312 cm^{-1} and 1339 cm^{-1}.

NMR spectroscopy

The dynamic structure of **5** in $CHCl_3$ solution was examined using variable temperature (VT) NMR spectroscopy from 203.0–328.0 K under N_2 in a sealed glass tube. ^{1}H and ^{13}C NMR spectral assignments for **5** were accomplished using two-dimensional methods (including HSQC and HMBC), the magnitudes of the coupling constants, and the relative chemical shifts of the observed peaks. The final assignments were consistent with published studies of a variety of ferrocenyl carbenium ions.[54] In comparison to **4**, the room temperature ^{1}H and ^{13}C NMR spectra of **5** display high frequency shifts for most resonances, except those of C(10) and C(11), which is consistent with the fulvenoid structure acquired by the acetylcyclopentadienyl ligand upon protonation. The double bond character restricts the rotation of the C_{ring}–C_{α} bond, as it has been observed in ferrocenyl carbenium ions.[55–63] Consistently, the five ^{13}C peaks observed at room temperature, split at 243.8 K (Fig. 6*a*). However, only seven bands are discernible because the resonances of C(7) and C(8) remain coincident at 80.91 ppm. In the room temperature ^{1}H spectrum, the peaks of H(6), H(7), H(8), and H(9) appear as two broad singlets at 5.05 and

5.23 ppm, which split upon cooling into four signals at 243.8 K (Fig. 6*b*), while all other peaks remained unchanged. At 238.0 K, all the coupling constants in the ^{1}H NMR spectrum become discernible; they all fall within the range of values observed for monosubstituted cyclopentadienyl rings.[64] Lineshape simulations and an Eyring analysis[65] provided a rotational barrier of 13.7 kcal/mol. The magnitude is comparable to the 10.9 kcal/mol that correspond to the smaller barrier evaluated with DFT calculations of the potential energy as a function of the rotation of the C(10)–C(11) bond (Fig. 7). This barrier is smaller than the 16.6–21.2 kcal/mol measured for cations prepared from 1-hydroxyalkylferrocenes in acidic medium.[62] Similarly, the DFT calculated barrier for restricted rotation after protonation of 3-ferrocenyl-2,4,5-triphenylcyclopentadienone[66] was over 19 kcal/mol but it could not be experimentally determined.

Conclusions

The Lewis acid–base adduct, $[(C_5H_5)Fe(C_5H_4–C(OBF_3)–CH_3)]$, features an alkoxyfulvene moiety, which results from electron reorganization of the acetylcyclopentadienyl ligand upon attachment of the borane to the oxygen atom. This is the same type of structural change that has been attributed to the protonation of the ligand. The electronic excitation spectrum of the compound does reproduce the observations made by UV–vis spectroscopy at the beginning of the cyclocondensation reaction of acetylferrocene, providing confirmation of the identity of the coloured intermediate. On the other hand, DFT calculations do model accurately the structure and some spectroscopic properties of this compound.

Supplementary data

Supplementary data for this article are available on the journal Web site (canjchem.nrc.ca) or may be purchased from the Depository of Unpublished Data, Document Delivery, CISTI, National Research Council Canada, Ottawa, ON K1A 0R6, Canada. DUD 3968. CCDC 714002 contains the supplementary crystallographic data for this manuscript. These data can be obtained, free of charge, via www.ccdc.cam.ac.uk/conts/retrieving.html (Or from the Cambridge Crystallographic Data Centre, 12 Union Road, Cambridge CB2 1EZ, UK; fax +44 1223 336033; or deposit@ccdc.cam.ac.uk).

Acknowledgment

This project was supported by grants from the Natural Sciences and Engineering Research Council of Canada (NSERC), the Canada Foundation for Innovation (CFI), and the Ontario Innovation Trust (OIT). This work was made possible by the facilities of the Shared Hierarchical Academic Research Computing Network (SHARCNET:www.sharcnet.ca).

References

(1) This article is part of a Special Issue dedicated to Professor T. Ziegler.
(2) This paper is dedicated to Professor Tom Ziegler, hoping that it illustrates the extent to which his work has enabled a deep understanding of organometallic and inorganic systems.
(3) Culbertson, G.; Pettit, R. *J. Am. Chem. Soc.* **1963**, *85* (6), 741–743. doi:10.1021/ja00889a020.
(4) Gupta, H. K.; Reginato, N.; Ogini, F. O.; Brydges, S.; McGlinchey, M. J. *Can. J. Chem.* **2002**, *80* (11), 1546–1554. doi:10.1139/v02-152.
(5) Davis, R. E.; Simpson, H. D.; Grice, N.; Pettit, R. *J. Am. Chem. Soc.* **1971**, *93* (24), 6688–6690. doi:10.1021/ja00753a068.
(6) Seyferth, D.; Merola, J. S. *J. Organomet. Chem.* **1978**, *160* (1), 275–290. doi:10.1016/S0022-328X(00)91220-8.
(7) Rausch, M. D.; Mintz, E. A.; Macomber, D. W. *J. Org. Chem.* **1980**, *45* (4), 689–695. doi:10.1021/jo01292a028.
(8) Ogini, F. O.; Ortin, Y.; Mahmoudkhani, A. H.; Cozzolino, A. F.; McGlinchey, M. J.; Vargas-Baca, I. *J. Organomet. Chem.* **2008**, *693* (11), 1957–1967. doi:10.1016/j.jorganchem.2008.02.013.
(9) Teplyakov, M. M. *Usp. Khim.* **1979**, *48* (2), 344–361.
(10) Ren, J.; Cramer, C. J.; Squires, R. R. *J. Am. Chem. Soc.* **1999**, *121* (11), 2633–2634. doi:10.1021/ja9840899.
(11) Nelson, S. G. *Tetrahedron Asymmetry* **1998**, *9* (3), 357–389. doi:10.1016/S0957-4166(97)00634-4.
(12) Evans, D. A.; Nelson, J. V.; Vogel, E.; Taber, T. R. *J. Am. Chem. Soc.* **1981**, *103* (11), 3099–3111. doi:10.1021/ja00401a031.
(13) Paterson, I. *Pure Appl. Chem.* **1992**, *64* (12), 1821–1830. doi:10.1351/pac199264121821.
(14) Schinzer, D. *Selectivities in Lewis acid promoted reactions*; Kluwer: Dordrecht, 1988.
(15) Taylor, M. J.; Brothers, P. J. *The chemistry of aluminum, gallium, indium, tallium*; Downs, A. J., Ed.; Blackie: London, 1993; Vol. 111.
(16) Brown, M. A.; Tuck, D. G. *Can. J. Chem.* **2000**, *78* (5), 536–541. doi:10.1139/cjc-78-5-536.
(17) *SMART* and *SAINT*: *Area detector control and integration software*; Siemens AXS, Inc.: Madison, WI, 1995.
(18) *SHEXTL 5*, 10th ed.; Bruker AXS, Inc.: Madison, WI, 1997.
(19) Farrugia, L. J. *J. Appl. Cryst.* **1997**, *30* (5), 565. doi:10.1107/S0021889897003117.
(20) te Velde, G.; Bickelhaupt, F. M.; Baerends, E. J.; Fonseca Guerra, C.; van Gisbergen, S. J. A.; Snijders, J. G.; Ziegler, T. *J. Comput. Chem.* **2001**, *22* (9), 931–967. doi:10.1002/jcc.1056.
(21) Fonseca Guerra, C.; Snijders, J. G.; Te Velde, G.; Baerends, E. J. *Theor. Chem. Acc.* **1998**, *99* (6), 391–403. doi:10.1007/s002140050021.
(22) *ADF,* versions 2002.03–2008.01; SCM, *Theoretical chemistry*; Vrije Universiteit: Amsterdam, The Netherlands. Available from http://www.scm.com.
(23) van Gisbergen, S. J. A.; Snijders, J. G.; Baerends, E. J. *J. Phys. Rev. Lett.* **1997**, *78* (16), 3097–3100. doi:10.1103/PhysRevLett.78.3097.
(24) Van Gisbergen, S. J. A.; Snijders, J. G.; Baerends, E. J. *J. Chem. Phys.* **1998**, *109*, 10644–10656. doi:10.1063/1.477762.
(25) Vosko, S. H.; Wilk, L.; Nusair, M. *Can. J. Phys.* **1980**, *58* (8), 1200–1211.
(26) Becke, A. D. *Phys. Rev. A* **1988**, *38* (6), 3098–3100. doi:10.1103/PhysRevA.38.3098. PMID:9900728.
(27) Perdew, J. P. *Phys. Rev. B* **1986**, *33* (12), 8822–8824. doi:10.1103/PhysRevB.33.8822.
(28) Lee, C.; Yang, W.; Parr, R. G. *Phys. Rev. B* **1988**, *37* (2), 785–789. doi:10.1103/PhysRevB.37.785.

(29) Fan, L. Y.; Ziegler, T. *J. Chem. Phys.* **1992**, *96* (12), 9005–9012. doi:10.1063/1.462258.
(30) Fan, L. Y.; Ziegler, T. *J. Phys. Chem.* **1992**, *96* (17), 6937–6941. doi:10.1021/j100196a016.
(31) Gritsenko, O. V.; Schipper, P. R. T.; Baerends, E. J. *Chem. Phys. Lett.* **1999**, *302* (3–4), 199–207. doi:10.1016/S0009-2614(99)00128-1.
(32) Schipper, P. R. T.; Gritsenko, O. V.; van Gisbergen, S. J. A.; Baerends, E. J. *J. Chem. Phys.* **2000**, *112* (3), 1344–1352. doi:10.1063/1.480688.
(33) Ryu, D. H.; Lee, T. W.; Corey, E. J. *J. Am. Chem. Soc.* **2002**, *124* (34), 9992–9993. doi:10.1021/ja027468h. PMID: 12188655.
(34) Corey, E. J.; Rohde, J. J.; Fischer, A.; Azimioara, M. D. *Tetrahedron Lett.* **1997**, *38* (1), 33–36. doi:10.1016/S0040-4039(96)02248-4.
(35) Corey, E. J.; Loh, T.-P.; Sarshar, S.; Azimiora, M. *Tetrahedron Lett.* **1992**, *33* (46), 6945–6948. doi:10.1016/S0040-4039(00)60902-4.
(36) Reetz, M. T.; Huellmann, M.; Massa, W.; Berger, S.; Rademacher, P.; Heymanns, P. *J. Am. Chem. Soc.* **1986**, *108* (9), 2405–2408. doi:10.1021/ja00269a044.
(37) Sato, K.; Katada, M.; Sano, H.; Konno, M. *Bull. Chem. Soc. Jpn.* **1984**, *57* (9), 2361–2365. doi:10.1246/bcsj.57.2361.
(38) Behrens, U. J. *Organomet. Chem.* **1979**, *182* (1), 89–98. doi:10.1016/S0022-328X(00)85878-7.
(39) Edelmann, F.; Lubke, B.; Behrens, U. *Chem. Ber.* **1982**, *115* (4), 1325–1331. doi:10.1002/cber.19821150408.
(40) Gutmann, V. *The donor–acceptor approach to molecular interactions*; Plenum Press: New York, 1978.
(41) McGlinchey, M. J.; Girard, L.; Ruffolo, R. *Coord. Chem. Rev.* **1995**, *143*, 331–381. doi:10.1016/0010-8545(95)01131-8.
(42) Barlow, S.; Cowley, A.; Green, J. C.; Brunker, T. J.; Hascall, T. *Organometallics* **2001**, *20* (25), 5351–5359. doi:10.1021/om010667+.
(43) Buisson, D. H.; Sigel, H.; Cais, M.; Herbstein, F. H. *Angew. Chem. Int. Ed. Engl.* **1972**, *11* (11), 1025. doi:10.1002/anie.197210251. PMID:4630316.
(44) Fonseca Guerra, C.; Handgraaf, J.-W.; Baerends, E. J.; Bickelhaupt, F. M. *J. Comput. Chem.* **2004**, *25* (2), 189–210. doi:10.1002/jcc.10351.
(45) Hirshfeld, F. L. *Theor. Chim. Acta* **1977**, *44* (2), 129–138. doi:10.1007/BF00549096.
(46) Reed, A. E.; Weinstock, R. B.; Weinhold, F. A. *J. Chem. Phys.* **1985**, *83* (2), 735–746. doi:10.1063/1.449486.
(47) Reed, A. E.; Curtiss, L. A.; Weinhold, F. *Chem. Rev.* **1988**, *88* (6), 899–926. doi:10.1021/cr00088a005.
(48) Lippincott, E. R.; Nelson, R. D. *Spectrochim. Acta* **1958**, *10* (3), 307–329.
(49) Pavlík, I.; Handlíř, K.; Dvořák, V. *Collect. Czech. Chem. Commun.* **1965**, *30*, 3052.
(50) Susz, B. P.; Chalandon, P. *Helv. Chim. Acta* **1958**, *41* (5), 1332–1341. doi:10.1002/hlca.19580410519.
(51) Lappert, M. F. *J. Chem. Soc.* **1962**, 542. doi:10.1039/jr9620000542.
(52) Cotton, F. A.; Leto, J. R. *J. Chem. Phys.* **1959**, *30* (4), 993–998. doi:10.1063/1.1730142.
(53) Pavlík, I.; Handlíř, K. *Collect. Czech. Chem. Commun.* **1966**, *31*, 1958.
(54) Cais, M. *Tet. Lett.* **1966**, *7* (15), 1695–1701. doi:10.1016/S0040-4039(01)99779-5.
(55) Lukasser, J.; Angleitner, H.; Schottenberger, H.; Kopacka, H.; Schweiger, M.; Bildstein, B.; Ongania, K. H.; Wurst, K. *Organometallics* **1995**, *14* (12), 5566–5578. doi:10.1021/om00012a025.
(56) Watts, W. E. *J. Organomet. Chem.* **1981**, *220* (2), 165–172. doi:10.1016/S0022-328X(00)90104-9.
(57) Kenny, T. P. E.; Knipe, A. C.; Watts, W. E. *J. Organomet. Chem.* **1981**, *413* (1–3), 257–261. doi:10.1016/0022-328X(91)80054-N.
(58) Habib, M. J. A.; Park, J.; Watts, W. E. *J. Chem. Soc. C* **1970**, 2556–2563. doi:10.1039/j39700002556.
(59) Abram, T. S.; Watts, W. E. *J. Chem. Soc., Perkin Trans. 1* **1977**, 1522–1526. doi:10.1039/p19770001522.
(60) Koch, E. *Tett. Lett.* **1985**, *26* (12), 1493–1496. doi:10.1016/S0040-4039(00)98533-2.
(61) Dannenberg, J.; Levenberg, M.; Richards, J. *Tetrahedron* **1973**, *29* (11), 1575–1584. doi:10.1016/S0040-4020(01)83399-8.
(62) Turbitt, T. D.; Watts, W. E. *J. Chem. Soc., Perkin Trans. 2* **1974**, 177–184. doi:10.1039/p29740000177.
(63) Cerichelli, G.; Floris, B.; Ortaggi, G. *J. Organomet. Chem.* **1974**, *78* (2), 241–252. doi:10.1016/S0022-328X(00)89846-0.
(64) Johnston, P.; Loonat, M. S.; Ingham, W. L.; Carlton, L.; Coville, N. J. *Organometallics* **1987**, *6* (10), 2121–2127. doi:10.1021/om00153a016.
(65) Bain, A. D. *Prog. Nucl. Magn. Reson. Spectrosc.* **2003**, *43* (3–4), 63–103. doi:10.1016/j.pnmrs.2003.08.001.
(66) Harrington, L. E.; Vargas-Baca, I.; Reginato, N.; McGlinchey, M. J. *Organometallics* **2003**, *22* (4), 663–669. doi:10.1021/om020820f.

Chemical bonding and aromaticity in metalloporphyrins[1,2]

Ferran Feixas, Miquel Solà, and Marcel Swart

Abstract: We report here the chemical bonding and aromaticity patterns in metalloporphyrins, which were obtained with density functional theory (DFT) calculations at the OPBE/TZP level. This level of theory was previously shown to be very accurate for determining spin-state splittings [*J. Chem. Theory Comput.* **2008**, *4*, 2057] of transition-metal complexes. We considered metalloporphyrins along the first-row transition metals (Sc–Zn) extended with alkaline-earth metals (Mg, Ca) and several second-row transition metals (Ru, Pd, Ag, Cd). An energy decomposition analysis was performed to study the metal–ligand interactions, which showed that almost all complexes are significantly stabilized through (covalent) orbital interactions. The only exception is with calcium as the central metal, which interacts with the porphyrin mainly through electrostatic interactions. Furthermore, we studied aromaticity patterns for these complexes by looking at a number of (structural and electronic) aromaticity descriptors, for both the inner-ring and outer-ring of the porphyrin and of the pyrroles. The inner-ring (N16) aromaticity is shown to be unaffected by metal complexation, while the outer-ring (N20) and the pyrrole (N5) aromaticities are found to increase significantly in the metal coordinated porphyrins.

Key words: porphyrins, transition-metal complexes, aromaticity, density functional theory.

Résumé : On a déterminé les patrons de liaison chimique et d'aromaticité de métalloporphyrines à l'aide de calculs selon la théorie de la fonctionnelle de densité, au niveau OPBE/TZP. Il a été démontré antérieurement que ce niveau de la théorie est très précis dans la détermination des couplages de métaux de spin [*J. Chem. Theory Comput.* **2008**, *4*, 2057] dans des complexes d'états de transition. On a considéré les métalloporphyrines des métaux de transition de la première période (Sc–Zn) avec leurs métaux alcalino-terreux (Mg, Ca) et plusieurs métaux de transition de la deuxième période (Ru, Pd, Ag, Cd). On a effectué une analyse de l'énergie de décomposition dans le but d'étudier les interactions métal–ligand; elle a démontré que pratiquement tous les complexes sont fortement stabilisés par des interactions orbitalaires covalentes. La seule exception est le calcium qui comme métal central, interagit avec la porphyrine principalement par le biais d'interactions électrostatiques. De plus, on a étudié les patrons d'aromaticité de ces complexes en examinant un certain nombre descripteurs d'aromaticité (structural et électronique) tant des cycles internes que des cycles externes de la porphyrine et des pyrroles. On a démontré que l'aromaticité du cycle interne (N16) n'est pas affectée par une complexation métallique alors que les aromaticités du cycle externe (N20) et du pyrrole (N5) augmentent d'une façon significative dans les porphyrines en coordination avec un métal.

Mots-clés : porphyrines, complexes de métaux de transition, aromaticité, théorie de la fonctionnelle de la densité.

[Traduit par la Rédaction]

Introduction

Metalloporphyrins play an important role in biology and catalysis, in which they are observed with a multitude of central metals and peripheral substituents (see Fig. 1).[3–6] The most common of them is formed by the heme group where the central particle is usually an iron(II) or iron(III) ion.[7] This heme group serves a wide range of functions, ranging from electron transfer or oxygen carrier to hydroxylation oxidant.[8,9] To be able to perform this wide range of functions, both the axial ligands to iron and the nature of the immediate protein environment around the heme seem to play an important role. In many cases, however, the active species of a heme-containing enzyme is too reactive to be isolated and characterized, which is for instance the case for the catalytic cycle of P450 enzymes.[10] For that reason, there is an overwhelming amount of experimental studies that use more simple and smaller metal complexes.[11] Many of these are based on, e.g., tetraphenylporphyrin (TPP), octaethylporphyrin (OEP), or phtalocyanines (PC). The relationship between the porphyrin orbitals and the UV–vis spectra of several porphyrin systems was reported some years ago by Baerends and co-workers,[12] which was recently shown to hold also for magnetic circular dichroism (MCD) spectra by Ziegler and co-workers.[13] Furthermore, the synergy between substituents, core-saddling, and meso-phenyl twisting was reported by Rosa and co-workers.[14]

Here, we are interested in the "naked" (metallo)porphyrins, i.e., the porphyrin without peripheral substituents

Received 20 January 2009. Accepted 23 February 2009. Published on the NRC Research Press Web site at canjchem.nrc.ca on 29 June 2009.

F. Feixas and M. Solà.[1] Institut de Química Computacional and Departament de Química, Universitat de Girona, Campus Montilivi, 17071 Girona, Spain.
M. Swart.[2] Institut de Química Computacional and Departament de Química, Universitat de Girona, Campus Montilivi, 17071 Girona, Spain; Institució Catalana de Recerca i Estudis Avançats (ICREA), 08010 Barcelona, Spain.

[1]Corresponding author (e-mail: miquel.sola@udg.edu).
[2]Corresponding author (e-mail: marcel.swart@icrea.es).

Fig. 1. Typical metalloporphyrin systems.

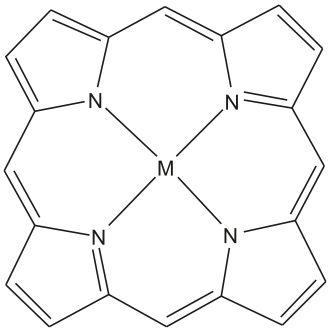

"naked" metalloporphyrin

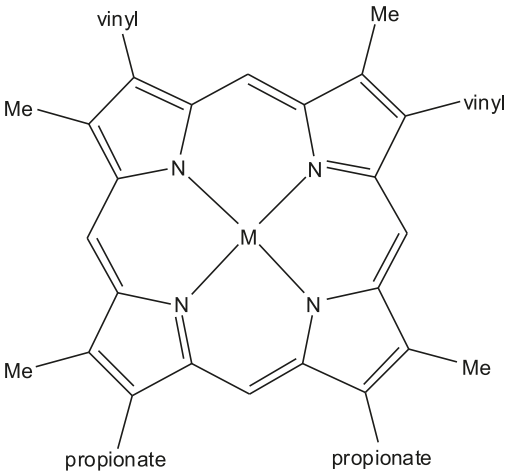

heme group

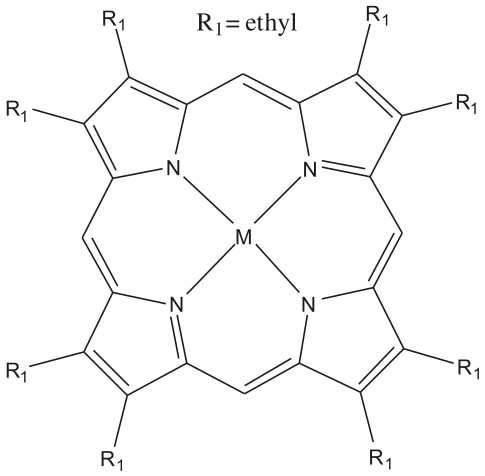

octaethyl-metalloporphyrin

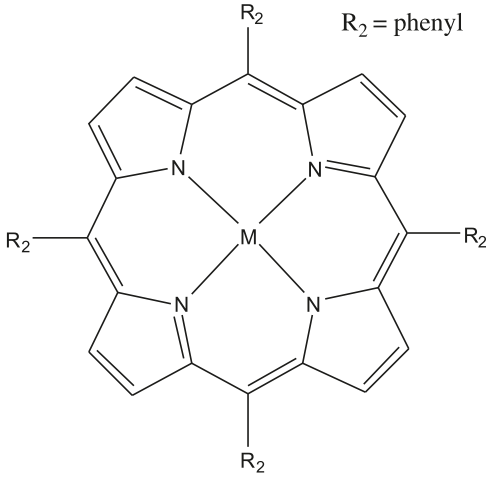

tetraphenyl-metalloporphyrin

and axial ligands. In particular, we are interested in the metal–ligand bonding interactions and aromaticity, and how these are influenced by the nature of the central metal and (or) spin-state. Recently, validation studies of density functional theory (DFT)[15] functionals by some of us[16,17] have shown the excellent performance of the OPBE[18–20] functional for spin-state splittings of transition-metal complexes, which is corroborated by good results in other studies.[21–34] Moreover, also for NMR chemical shifts and reaction barriers, OPBE seems to perform significantly better than other DFT functionals.[22,24,26,35] In a very recent systematic investigation of the influence of the basis set on the spin-state energies and geometries of iron compounds with the OPBE functional,[36] we have obtained reliable and consistent results when using Slater-type orbital (STO) and large Gaussian-type orbital (GTO) basis sets. Therefore, we have used the OPBE functional together with an STO basis set of triple-ζ quality to study metalloporphyrins along the first-row transition metals (Sc–Zn), extended with alkaline-earth metals (Mg, Ca) and several second-row transition metals (Ru, Pd, Ag, Cd). For those metal ions with multiple spin-states in close proximity, we have studied all spin-states separately.

Computational details

The calculations using the unrestricted formalism have been performed with the Amsterdam density functional (ADF) suite of program.[37] MOs were expanded in an uncontracted set of STOs of triple-ζ quality containing diffuse functions and one set of polarization functions (TZP). Energies and gradients were calculated using the local density approximation (LDA; Slater exchange and VWN correlation) with gradient-corrections (GGA) for exchange (OPTX)[19] and correlation (PBE)[20] included self-consistently, i.e., the OPBE functional.[18] Geometries were optimized with a locally modified version of the QUILD program[38] using adapted delocalized coordinates[39] until the maximum gradient component was less than 1.0×10^{-5} au. The frequen-

cies of all complexes were calculated to ensure that they correspond to minima.

For some spin-states of the transition-metal complexes, an energy decomposition analysis (EDA)[40] has been performed to study the chemical bonding in these compounds. In this EDA analysis, the total energy ΔE_{total} for the heterolytic association[26] reaction between the metal, M(II), cation and the porphyrin ligand, Por, with charge –2 ($M^{2+} + Por^{2-} \rightarrow MPor$) results directly from the Kohn–Sham molecular orbital (KS-MO) model[40] and is made up of two major components: preparation and interaction. The preparation energy contains the energy needed to bring the cation and ligands together from their isolated equilibrium geometry to the positions they attain in the complex, and consists of the deformation energy ΔE_{deform} and the energy needed to excite, e.g., the iron(II) cation from its quintuplet ground state to the spin state (with corresponding orbital occupations) it attains in the complex (ΔE_{valexc}). Note that the latter do not concur to the ones of the isolated cation, and can thus not be compared to experimental ionization energies for the metal(II) cation. Moreover, for the ground state of the isolated metal(II) cation, we use the "average of configuration" (AOC) approach,[41] which is a one-determinant approximation to the true atomic state, and serves here mainly as reference energy. The interaction energy gives the subsequent interaction between the cation on one side, and the porphyrin ligand on the other, and consists of Pauli repulsion ΔE_{Pauli}, electrostatic interactions ΔE_{elstat}, and the (covalent) orbital interactions ΔE_{orbint} (see Supplementary data for full details).

Descriptors of aromaticity

As a structure-based measure, we have employed the harmonic oscillator model of aromaticity (HOMA) index, defined by Kruszewski and Krygowski[42] as

$$[1] \qquad \mathrm{HOMA} = 1 - \alpha/n\sum_{i=1}^{n}(R_{opt} - R_i)^2$$

where n is the number of bonds considered, and α is an empirical constant (for C–C and C–N bonds, α = 257.7 and 93.5, respectively) fixed to give HOMA = 0 for a model nonaromatic system, and HOMA = 1 for a system with all bonds equal to an optimal value R_{opt} (1.388 and 1.334 Å for C–C and C–N bonds, respectively), assumed to be achieved for fully aromatic systems. R_i stands for a running bond length. This index has been found to be one of the most effective structural indicators of aromaticity.[43]

In addition, two aromaticity criteria (FLU and MCI) based on electron delocalization measures have been employed. These indices measure the cyclic electron delocalization of mobile electrons in aromatic rings. The electron delocalization is measured by means of the so-called delocalization indices (DIs), or, in a more general nomenclature, the electron sharing indices (ESI). The ESI value between atoms A and B, δ(A,B), is obtained by double integration of the exchange-correlation density ($\gamma_{XC}(\vec{\mathbf{r}}_1, \vec{\mathbf{r}}_2)$) over the molecular space regions corresponding to atoms A and B

$$[2] \qquad \delta(\mathrm{A,B}) = -2\int_{\mathrm{A}}\int_{\mathrm{B}}\gamma_{XC}(\vec{\mathbf{r}}_1, \vec{\mathbf{r}}_2)\mathrm{d}\vec{\mathbf{r}}_1\mathrm{d}\vec{\mathbf{r}}_2$$

For single-determinant closed or open-shell wave functions, one obtains

$$[3] \qquad \delta(\mathrm{A,B}) = 2\sum_{i,j} S_{ij}(\mathrm{A})S_{ij}(\mathrm{B})$$

The summations in eq. [3] run over all occupied molecular spin orbitals (MSOs). S_{ij}(A) is the overlap between MSOs i and j within the molecular space assigned to atom A, the elements of the so-called atomic overlap matrices (AOM). δ(A,B) provides a quantitative idea of the number of electrons delocalized or shared between atoms A and B. Although several atomic partitions may be used in the ESI definition, the most popular one is that where the partition is carried out in the framework of the quantum theory of atoms-in-molecules (QTAIM) of Bader,[44] by which atoms are defined from the condition of zero-flux gradient in the one-electron density, $\rho(\mathbf{r})$. The aromatic fluctuation index (FLU)[45] is based on the fact that aromaticity is related to the *cyclic* delocalized circulation of π-electrons, and is constructed not only considering the amount of electron sharing between contiguous atoms, which should be substantial in aromatic molecules, but also taking into account the similarity in terms of electron sharing between adjacent atoms. Let us consider a ring structure of N atoms represented by the following string $\mathcal{A} = (A_1, A_2, \ldots, A_N)$, whose elements are ordered according to the connectivity of the atoms in the ring. For such ring, the FLU index is defined as

$$[4] \qquad \mathrm{FLU}(\mathcal{A}) = \frac{1}{N}\sum_{i=1}^{N}\left[\left(\frac{V(A_i)}{V(A_{i-1})}\right)^{\alpha} \times \left(\frac{\delta(A_i, A_{i-1}) - \delta_{ref}(A_i, A_{i-1})}{\delta_{ref}(A_i, A_{i-1})}\right)\right]^2$$

where $A_0 \equiv A_N$ and half the values of V(A) is recognized by some authors as the atomic valence defined as

$$[5] \qquad V(A_i) = \sum_{A_j \neq A_i}\delta(A_i,A_j)$$

and α is a simple function to make sure that the first term in eq. [4] is always greater than or equal to 1, thus taking the values

$$[6] \qquad \alpha = \begin{cases} 1 & V(A_i) > V(A_{i-1}) \\ -1 & V(A_i) \leq V(A_{i-1}) \end{cases}$$

The $\delta_{ref}(A_i, A_{i-1})$ reference values are δ_{ref}(C,C) = 1.389 e and δ_{ref}(C,N) = 1.204 e (the δ_{ref}(C,C) and δ_{ref}(C,N) values in benzene and pyridine, respectively, at the OPBE/TZVP level). FLU is close to 0 in aromatic species, and differs from it in non-aromatic ones. Second, we have employed the multicenter index (MCI),[46] whose formula reads

$$[7] \qquad \mathrm{MCI}(\mathcal{A}) = \frac{1}{2N}\sum_{P(\mathcal{A})} I_{ring}(\mathcal{A})$$

where $P(\mathcal{A})$ stands for a permutation operator which interchanges the atomic labels $A_1, A_2, \ldots, A_N$ to generate up to the $N!$ permutations of the elements in the string A. In turn, I_{ring} is defined as[47,48]

$$[8] \qquad I_{\text{ring}}(\mathcal{A}) = \sum_{i_1,i_2,\ldots,i_N} n_{i_1} \ldots n_{i_N} S_{i_1 i_2}(A_1) S_{i_2 i_3}(A_2) \ldots S_{i_N i_1}(A_N)$$

where n_i is the occupancy of orbital i. For the series of indices used, the lower the FLU index, and the higher the HOMA and MCI values, the more aromatic the rings.

Calculation of AOM and computation of FLU and MCI have been performed with the AIMPAC[49] and ESI-3D[50] collection of programs. These two programs work with GTO basis sets. In consequence, single-point calculations at the OPBE/TZP(STO)-optimized geometries have been performed with the Gaussian 03[51] program at the OPBE level of theory with a TZVP basis set[52] to generate the wave function and obtain the necessary AOM.

Calculation of these ESIs with DFT cannot be performed exactly because the electron-pair density is not available at this level of theory.[53] As an approximation, we have used the Kohn–Sham orbitals obtained from a DFT calculation to compute Hartree–Fock-like DIs through eq. [3] that does not account for electron correlation effects. In practice, the values of the ESIs obtained using this approximation are generally closer to the Hartree–Fock (HF) values than correlated ESIs obtained with a configuration interaction method.[53,54]

The numerical accuracy of the QTAIM calculations has been assessed using two criteria: (*i*) the integration of the Laplacian of the electron density ($\nabla^2\rho(r)$) within an atomic basin must be close to zero, and (*ii*) the number of electrons in a molecule must be equal to the sum of all the electron populations of the molecule, and also equal to the sum of all the localization indices and half of the DIs in the molecule. For all atomic calculations, integrated absolute values of $\nabla^2\rho(r)$ were always less than 0.001 au. For all molecules, errors in the calculated number of electrons were always below 0.01 au.

Finally, we have not used NICS[55] values in our discussion because, for complexed porphyrins, the results obtained are largely influenced by the nature of the metal center.[56]

Results and discussion

We have studied the chemical bonding and aromaticity of metalloporphyrins, where we considered both first-row (Sc–Zn) and second-row (Ru, Pd, Ag, Cd) transition metals and alkaline-earth metals (Mg, Ca). This series of metals comprises the metalloporphyrins that are observed experimentally[4–6,57] (although the latter are in many cases with substituents present on the porphyrin ring). For those metal ions with several spin states in close proximity (Fe, Ru, Mn, and so forth), we studied each spin state separately but will limit our discussion here to the ground state; data for the other spin states can be found in the Supplementary data. Previous theoretical studies focused either on only a small subset of these metalloporphyrins (e.g., Fe, Co, Ni, Cu, Zn in refs. 58 and 59), on the time-dependent (TD) DFT properties of a number of (metallo)porphyrins,[12,60] on the effect of the axial ligand,[3] or on comparing porphyrins with porphyrin analogues.[12,61,62] However, a complete study on the full set of metalloporphyrins, consistently studied with the same DFT functional and basis set, has to the best of our knowledge never been done before.

For most systems, there was no problem with spin contamination, as indicated by the expectation values of the S^2 operator, which gave values very close to the pure spin-state values (0.0 for singlet, 0.75 for doublet, 2.0 for triplet, 3.75 for quartet, 6.0 for quintet, and 8.75 for sextet). For four singlet systems (^{1}Cr, ^{1}Fe, ^{1}Ru, and ^{1}Ti) and one doublet system (^{2}V), the spin contamination was however substantial and had to be corrected. For the singlet systems, the S^2 value was 1.0, indicating that the contaminated system contained 50% of a triplet state, while for the doublet system, the S^2 value was 1.75, indicating an admixture of 33% of a quartet state. This spin-contamination correction[63] is easily handled by the QUILD program for both the geometry optimization and energy calculation.

The spin density was in almost all cases located mainly on the metal, with two exceptions. The quintet state of ruthenium–porphyrin is in fact obtained from the coupling of a Ru(III) quartet with a porphyrin^{3-} doublet. Furthermore, the triplet state of palladium–porphyrin is in fact obtained through the coupling of a Pd(II) singlet with a porphyrin^{2-} triplet.

Geometry and ground state of the metalloporphyrins

The geometry of all metalloporphyrins was optimized for each spin state separately within a number of symmetry representations (C_{2v}, C_{4v}, D_{4h}, and S_4) for the geometry. In all these cases, the orbitals and densities were described by C_{2v} symmetry, in which the metal d orbitals are more conveniently treated. This separation of the geometric vs. orbital point-group symmetry is one of the advantages of using the QUILD program in our studies. For most of the systems we studied, the actual symmetry imposed was irrelevant because the optimizations ended up in D_{4h} symmetry. For a small number of systems however (see Table 1), the most stable configuration was found with the metal ion displaced from the porphyrin plane (i.e., within C_{4v} symmetry). For two of them (chromium–porphyrin and nickel–porphyrin), this out-of-plane distortion has no effect, since it occurs in the triplet state, which is significantly less stable than the corresponding ground states, by 40 and 21 kcal mol^{-1}, respectively. It is another matter for the scandium– and calcium–porphyrins, for which it is observed in the ground state. For the calcium—porphyrin, this out-of-plane distortion is significant (0.86 Å) in similar fashion to that observed for a larger porphyrin system (where it is 1.21 Å out of the N_4 plane).[57]

The calculated spin ground states (see Table 1) of the metalloporphyrins correspond to those observed experimentally,[7] i.e., we find a quintet for chromium, a sextet for manganese, a triplet for iron, and a doublet for cobalt. For many of these systems, the experimental situation is such that no clear determination of the ground state of the "naked" metalloporphyrin can be made. For instance, for the early transition metals (Ti, V), the porphyrin system is most frequently obtained with an oxygen bound to the metal (the oxo-compound). Also, other axial ligands are usually present, which are known to have a determining influence on the spin ground state. For instance, in the catalytic cycle of cytochrome P450s, a spin flip occurs from a doublet to a sextet state after substrate binding in the active site of the enzyme. For cytochrome P450cam, the substrate is found to be anchored to a tyrosine residue present in the active site in close proximity of the heme, and not directly ligated to iron. However, in the process of substrate binding, six water mol-

Table 1. Metal–nitrogen and out-of-plane distances (Å) and relative spin-state energies (kcal mol^{-1}) for the metalloporphyrins studied.

	Metal–nitrogen distance			Out-of-plane distance[a]			Spin-state energy		
Metal	Low	Intermediate	High	Low	Intermediate	High	Low	Intermediate	High
^{2}Ag	2.115	—	—	—	—	—	—	—	—
^{1}Ca	2.274	—	—	0.857	—	—	—	—	—
^{1}Cd	2.154	—	—	—	—	—	—	—	—
^{2,4}Co	1.972	2.043	—	—	—	—	0	19.5	—
^{1,3,5}Cr	2.001[b]	2.044	2.038	—	0.119	—	83.5[b]	40.3	0
^{2}Cu	2.021	—	—	—	—	—	—	—	—
^{1,3,5}Fe	1.975[b]	1.983	2.055	—	—	—	30.2[b]	0	6.4
^{1}Mg	2.065	—	—	—	—	—	—	—	—
^{2,4,6}Mn	1.997	2.006	2.087	—	—	—	47.9	0.6	0
^{1,3}Ni	1.963	2.029	—	—	0.043	—	0	20.6	—
^{1,3}Pd	2.041	2.056	—	—	—	—	0	45.0	—
^{1,3,5}Ru	2.034[b]	2.043	2.042	—	—	—	19.5[b]	0	33.5
^{2}Sc	2.107	—	—	0.270	—	—	—	—	—
^{1,3}Ti	2.051[b]	2.064	—	—	—	—	12.4[b]	0	—
^{2,4}V	2.031[b]	2.050	—	—	—	—	33.2[b]	0	—
^{1}Zn	2.055	—	—	—	—	—	—	—	—

[a]Out-of-plane distances are only given for those systems with C_{4v} symmetry; within D_{4h}, this distance is zero because of symmetry.
[b]Corrected for spin contamination.

ecules are expelled from the active site, one of which was previously present as axial ligand to iron. Therefore, the spin flip merely reflects the change from six-coordinate iron to five-coordinate iron. Nevertheless, based on trends in experimental data, it was (correctly) predicted that the "naked" unligated iron(II)–porphyrin should be a pure intermediate-spin complex. This is corroborated by our OPBE data,[64] for which there now exists the consensus that it gives the correct spin ground state of transition-metal complexes in general, and for iron complexes in particular.[16,17]

Chemical bonding in the metalloporphyrins

The optical spectrum of porphyrins and analogues is well-understood in terms of the Gouterman model,[12] but a similarly simple model for understanding the metal–ligand interactions themselves is not yet available. Recently however, a generalization of these interactions in terms of their spin-state preferences has been put forward.[17,26] It successfully explains the spin ground state of transition-metal complexes in terms of a compromise between Hund's rule of maximum multiplicity and metal–ligand covalent interactions. Initially, it was proposed for metal–ligand interactions in metallocenes, but later was shown to hold also for challenging iron complexes that contain the mono- and di-pyridylmethylamine ligands. Key ingredient in these studies was the application of an energy decomposition analysis (EDA),[40] which describes the metal–ligand interactions in terms of the preparation and interaction components (see Computational details). Here, we have likewise applied the EDA analysis to study the metal–ligand interactions in terms of the heterolytic association reaction between the cationic metal M^{2+} and the anionic porphyrin ligand (Por^{2-}), see Table 2 (and Table S1 for the data of the different spin states). As anticipated, the interaction between the metal and porphyrin is, for a large part, electrostatic in nature. This shows up clearly in the EDA analysis where the electrostatic interactions contribute between –528 and –658 kcal mol^{-1} to the total metal–ligand interactions. This range of ~130 kcal mol^{-1} between the different metalloporphyrins is accompanied by Pauli repulsion interactions that are (with the exception of Mg–Por, see below) found within a range of ~180 kcal mol^{-1}, e.g., between +134 and +311 kcal mol^{-1}. More discriminating however are the (covalent) orbital interactions, which are found in the range from –223 to –467 kcal mol^{-1}. In most cases, the orbital interactions are sufficiently large to overcome the Pauli repulsion, and therefore positively contribute to the metal–ligand interactions. Moreover, for the stable metalloporphyrins, such as nickel–porphyrin or iron–porphyrin, the orbital interactions are significantly large compared with Pauli repulsion such that a substantially enhanced total energy (> –700 kcal mol^{-1}) is obtained. The only exceptions to this rule are the alkaline earth metals Mg and Ca, for which the (covalent) orbital interactions are much reduced (–223 to –229 kcal mol^{-1}). For calcium–porphyrin, the metal–ligand interaction is therefore purely electrostatic, as the Pauli repulsion of 250 kcal mol^{-1} more or less cancels the (covalent) orbital interactions. Surprisingly enough, this is not the case for magnesium–porphyrin, where the small (covalent) orbital interactions (of –223 kcal mol^{-1}) are still substantially larger than the Pauli repulsion (of +81 kcal mol^{-1}). Therefore, for all metalloporphyrins (except the calcium–porphyrin), the covalent interactions are one of the most important factors that determine their stabilities. Moreover, the fact that the metal–ligand interac-

Table 2. Energy decomposition analysis (kcal mol^{-1}) for metalloporphyrins.

	^{1}Mg	^{1}Ca	^{2}Sc	^{3}Ti	^{4}V	^{5}Cr	^{6}Mn	^{3}Fe	^{2}Co	^{1}Ni	^{2}Cu	^{1}Zn	^{3}Ru	^{1}Pd	^{2}Ag	^{1}Cd
Preparation	3.7	2.9	9.3	8.5	6.9	10.0	5.3	85.0	81.1	101.1	10.1	4.5	58.4	71.8	6.8	6.2
ΔE_{deform}	*3.7*	*2.9*	*9.1*	*8.2*	*6.4*	*6.5*	*3.7*	*12.9*	*14.1*	*15.8*	*7.3*	*4.5*	*7. 5*	*6.9*	*4.8*	*6.2*
ΔE_{valexc}	*0.0*	*0.0*	*0.2*	*0.3*	*0.5*	*3.5*	*1.6*	*72.1*	*67.0*	*85.3*	*2.8*	*0.0*	*50.9*	*64.9*	*2.0*	*0.0*
Interaction	–669.3	–539.5	–648.7	–677.8	–695.4	–725.3	–667.8	–788.1	–823.2	–864.3	–778.9	–719.4	–776.4	–844.2	–734.1	–628.0
ΔE_{Pauli}	*81.4*	*249.9*	*232.7*	*220.4*	*201.6*	*205.1*	*175.5*	*194.4*	*189.2*	*208.9*	*146.5*	*134.1*	*310.6*	*265.4*	*244.2*	*205.5*
ΔE_{elstat}	*–527.7*	*–560.0*	*–574.6*	*–582.0*	*–584.4*	*–592.2*	*–580.0*	*–602.7*	*–603.3*	*–606.4*	*–585.0*	*–576.7*	*–657.9*	*–650.2*	*–612.7*	*–595.0*
ΔE_{orbint}	*–223.0*	*–229.4*	*–306.8*	*–316.1*	*–312.6*	*–338.1*	*–263.3*	*–379.8*	*–409.1*	*–466.9*	*–340.5*	*–276.8*	*–429.2*	*–459.4*	*–365.6*	*–238.4*
Total	–665.6	–536.6	–639.4	–669.3	–688.5	–715.3	–662.5	–703.1	–742.1	–763.2	–768.8	–714.9	–718.0	–772.4	–727.3	–621.8

Note: Obtained at OPBE/TZP for the heterolytic association reaction: $M^{2+} + Por^{2-}$.

Fig. 2. Correlation between vibrational frequency and metal – porphyrin-core distance.

tions in calcium–porphyrin are only electrostatic in nature, and not covalent, might explain why this is the only metalloporphyrin where the metal is found far away from the porphyrin plane and at the longest M–N bond distances. Both the out-of-plane distorsion and the large Ca–N bond distance lead to smaller orbital overlaps and, consequently, low orbital-interaction energies.

Correlation between frequency and metal-core distance

In the 1970s, there were a number of papers that describe the relationship between resonance Raman frequencies and structural properties of metalloporphyrins. Initially, it was suggested that one particular frequency (at ~1590 cm^{-1}) could be used as probe for the metal being out-of-plane or in-plane. This was later on[5] corrected to show a correlation between this frequency and the metal – porphyrin-core distance. Since we have computed here both the metal–core distances and the vibrational frequencies, we thought it might be interesting to establish if there exists a relationship between the vibrational frequencies at ~1590 cm^{-1} region, and either the out-of-plane distance of the metal or the metal – porphyrin-core distance. Shown in Fig. 2 is, for each of the systems, the largest vibrational frequency in the 1500–1700 cm^{-1} region as function of the metal – porphyrin-core distance. This figure shows a clear correlation between the two, i.e., the larger the metal – porphyrin-core distance, the smaller the frequency, which corroborates the notions by Spaulding and co-workers.[5]

Aromaticity of the metalloporphyrins

We have investigated the aromaticity of the metalloporphyrins using several descriptors (see Computational details). We noticed several interesting trends. For the HOMA and FLU analysis, we looked at a number of different patterns, i.e., either the inner ring (N16) or the outer ring (N20), or the pyrrole rings (N5) (see Fig. 3 for the description of these different patterns). For the MCI measures, we only analyzed the N5 rings because of the computational cost of generating up to 16! and 20! permutations of the members of the N16 and N20 rings. The inner-ring and pyrrole-ring patterns had previously been used by Krygowski, Schleyer, and co-workers in combination with the HOMA and NICS analyses to investigate aromaticity in (metallo)-

Fig. 3. Inner ring, outer ring, and pyrrole patterns.

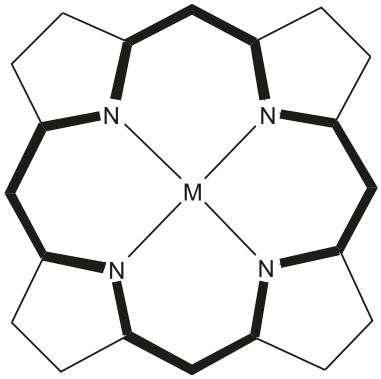

Inner ring

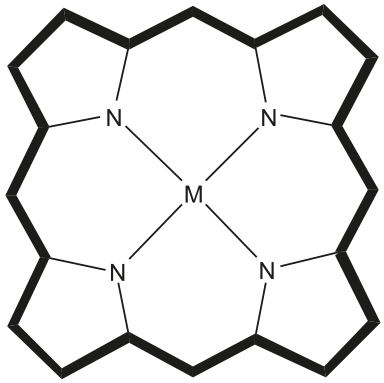

Outer ring

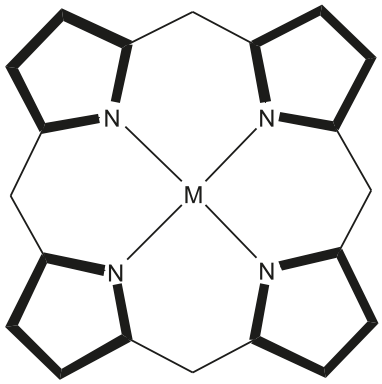

Pyrroles

porphyrins.[65] However, they looked mainly at experimentally obtained structures (of non-"naked" porphyrins) and only investigated one metalloporphyrin (Mg(II)–porphyrin) together with isolated porphyrin and porphyrin dianion by quantum chemistry.

To understand the behavior of aromaticity in metalloporphyrins, the analysis of free base porphyrin ($PorH_2$) has been performed, and the HOMA, FLU, and MCI values are given in Table 3. In the free base porphyrin, two out of the four pyrrole rings are protonated. In previous work, it has been demonstrated by means of HOMA and NICS calculations that the aromaticity of two pyrrole rings with an NH group is higher than the other two deprotonated rings.[65,66] This is attributed to the fact that five-membered rings (5-MRs) with an NH group have six π-electrons and behave like true pyrrole rings in contrast to deprotonated rings that formally possess only five π-electrons. Both the aromatic ring current shielding (ARCS) analysis[67] and the calculation of the induced ring current[68,69] show a strong diamagnetic current in the 5-MRs in porphyrin with an inner H atom of the similar magnitude as the pyrrole molecule, whereas the pyrrole rings without the H atom present much lower local ring currents. In the latter 5-MRs, the C_2H_2 group was considered by Krygowski, Schleyer, and co-workers as simple exocyclic bridges.[65] The same trends were found in an imidazole-containing analogue of porphycene,[70] in porphyrazine and tautomers of triazoleporphyrazine,[71] and in N-confused porphyrins.[72] Our calculated HOMA, FLU, and MCI values follow the expected trends, and the rings with an NH group are closer to the free-pyrrole values than the 5-MRs with the N group (see Table 3). Deprotonation of $PorH_2$ leads to its dianion (Por^{2-}). The charge is distributed over the whole molecule, and the symmetry of the molecule becomes D_{4h}. The aromaticity of inner N16 is more or less the same as in $PorH_2$ but the four N5 pyrrole rings are less aromatic according to HOMA and FLU values. This trend also showed up in the study by Krygowski and Schleyer[65] for a large number of experimental crystal structures. Finally, MCI results indicate that the aromaticity of the 5-MRs with an NH group remains unaltered, while that of the 5-MRs with the N group is slightly increased.

In $PorH_2$ and Por^{2-}, the number of contributing π electrons is 18 in N16 and 22 in N20, consistent with the $(4n + 2)$ rule for aromatic monocycles. In agreement with previous studies,[65,68,69] the aromaticity of the inner N16 ring is higher than that of the N20 ring that contains the C_2H_2 group of the 5-MRs acting as simple exocyclic bridge. To obtain the neutral deprotonated porphyrin (Por), the removal of two electrons causes the localization of π electrons, and the symmetry of the system becomes D_{2h}. It is worth mentioning here that the localization/delocalization patterns are not simply the result of the π-bonding, as it was shown that π-bonding in itself is distortive while it is actually the σ-bonding that tends to favor delocalized structures.[73–81] Therefore, Por has 16 and 20 π electrons in N16 and N20 consistent with the $(4n)$ rule of antiaromaticity. So, the aromaticity of N16, N20, and N5 clearly decreases in Por. The diatropic (aromatic) ring current in Por^{2-} and paratropic (antiaromatic) in Por were reported by Steiner and co-workers.[69] Therefore, HOMA, FLU, and MCI reproduce the expected trends for free-base porphyrins ($PorH_2$, Por^{2-}, and Por).

The metalloporphyrins studied in this work contain the metal M(II) cation and the dianion porphyrin ligand ($M^{2+} + Por^{2-} \rightarrow MPor$). We have studied the behavior of aromaticity in the N16, N20, and N5 rings upon complexation of the metal dication (see Table 4). First, we have analyzed the aromaticity of inner N16 and outer N20 in Por^{2-} and MPor. As far as N16 is concerned, one can see that the aromaticity keeps almost unchanged after metal complexation, which

Table 3. HOMA, FLU, and MCI measures for Pyrrole, Porphyrin ($PorH_2$), Por, and Por^{2-}.

	HOMA(N16)	HOMA(N20)	HOMA(N5)	FLU(N16)	FLU(N20)	FLU(N5)	MCI(N5)
Pyrrole			0.860			0.006	0.046
$PorH_2$	0.923	—	0.723(H)	0.006	—	0.017(H)	0.029(H)
			0.421			0.023	0.020
Por	0.701	0.118	0.255	0.018	0.035	0.034	0.018
Por^{2-}	0.897	0.330	0.399	0.005	0.027	0.024	0.029

Table 4. HOMA, FLU, and MCI (in electrons) measures for Por^{2-} and MPor.

Metal	HOMA(N16)	HOMA(N20)	HOMA(N5)	FLU(N16)	FLU(N20)	FLU(N5)	MCI(N5)
Por^{2-}	0.897	0.330	0.399	0.005	0.027	0.024	0.029
^{2}Ag	0.938	0.598	0.605	0.004	0.020	0.020	0.025
^{1}Ca	0.906	0.574	0.591	0.003	0.020	0.018	0.026
^{1}Cd	0.879	0.525	0.579	0.004	0.020	0.019	0.026
^{2}Co	0.918	0.726	0.672	0.004	0.018	0.018	0.024
^{4}Co	0.944	0.683	0.644	0.004	0.018	0.016	0.025
^{1}Cr	0.892	0.798	0.711	0.005	0.016	0.017	0.023
^{3}Cr	0.906	0.803	0.750	0.006	0.021	0.027	0.024
^{5}Cr	0.934	0.710	0.663	0.004	0.018	0.018	0.025
^{2}Cu	0.951	0.695	0.656	0.004	0.019	0.018	0.026
^{1}Fe	0.909	0.745	0.680	0.004	0.017	0.018	0.024
^{3}Fe	0.912	0.752	0.687	0.005	0.016	0.015	0.025
^{5}Fe	0.933	0.696	0.656	0.004	0.018	0.019	0.024
^{1}Mg	0.934	0.658	0.637	0.003	0.019	0.017	0.026
^{2}Mn	0.911	0.734	0.666	0.005	0.016	0.020	0.022
^{4}Mn	0.904	0.782	0.706	0.006	0.016	0.020	0.022
^{6}Mn	0.926	0.641	0.630	0.004	0.019	0.018	0.026
^{1}Ni	0.917	0.724	0.677	0.005	0.018	0.019	0.024
^{3}Ni	0.948	0.689	0.650	0.004	0.019	0.018	0.026
^{1}Pd	0.954	0.692	0.656	0.005	0.019	0.019	0.025
^{3}Pd	0.930	0.794	0.770	0.007	0.016	0.019	0.025
^{1}Ru	0.911	0.754	0.684	0.004	0.017	0.018	0.024
^{3}Ru	0.923	0.734	0.676	0.004	0.017	0.015	0.024
^{5}Ru	0.871	0.883	0.783	0.009	0.010	0.009	0.027
^{2}Sc	0.867	0.775	0.717	0.006	0.013	0.011	0.027
^{1}Ti	0.869	0.797	0.699	0.007	0.014	0.022	0.018
^{3}Ti	0.890	0.749	0.677	0.005	0.015	0.017	0.023
^{2}V	0.869	0.797	0.699	0.007	0.014	0.022	0.018
^{4}V	0.890	0.749	0.677	0.005	0.015	0.017	0.023
^{1}Zn	0.944	0.671	0.642	0.004	0.019	0.018	0.026

was also observed by Krygoswki and Schleyer in their study of a large number of experimental crystal structures.[65] So, the inner ring keeps the aromatic character of Por^{2-} with HOMA values close to 1 and the FLU index close to 0. Usually the spin state with high N16 aromaticity corresponds to the ground state but there are some exceptions, like in Ni and Fe. As we have commented before, the outer N20 ring of Por^{2-} is significantly less aromatic because the electrons of the pyrrole ring are highly localized in C–C bonds. However, after complexation, the aromaticity of N20 MPor increases significantly, the alternation between C–C decreases, and the electrons are delocalized both in the N16 and N20 rings. The aromaticity of N5 in metalloporphyrins increases and becomes quite close to that of NH rings in $PorH_2$. This increase in the aromatic character of the outer N20 and N5 rings is attributed to two main factors: polarization of the π-cloud and charge transfer. The polarization of the π-cloud is caused by the divalent positive charge of the metal that moves the more polarizable π-electrons near to the N atoms. As a result, the N5 rings become more aro-

matic (and the N20 pathway too) as they approach the formally six π-electron count from the initial five π-electrons. This is what is observed for ^{1}Mg, ^{1}Ca, ^{6}Mn, and ^{1}Zn that have, in general, small orbital interactions (see Table 2). In these cases, these orbital interactions are mainly due to polarization and not to two-electron – two-orbital interactions. This effect was already reported by Steiner and co-workers[69] who calculated the total π current density maps of model systems obtained by replacement of the Mg^{2+} cation in MgPor by charges Z_e, $ZPor^{2-}$(Z = 0, Z = 2, and Z = 4). For Z = 2, the current density is almost the same as in MgPor. So, the ring current is bifurcated, and N16 and N20 are both aromatic. The replacement of Mg^{2+} by Z = 0 ring current presents a reduction of bifurcation in favor of the inner N16, and Z = 4 favors outer N20. So, the increase of central charge leads to a decrease of aromaticity in N16 and an increase in N20. For the rest of the MPor, apart from polarization, there are significant two-electron – two-orbital interactions as can be seen from the orbital interaction terms in the EDA. These orbital interactions are basically σ-donation from the N lone pair to empty d orbitals of the metal and π-retrodonation from filled d orbitals to the π-system of Por^{2-}. As a consequence of retrodonation, there is an increase in the π-population of the 5-MRs that makes them more aromatic. This is especially clear in the case of ^{5}Ru. As we showed before, the quintet state of ruthenium porphyrin is obtained from the coupling of Ru(III) quartet with a porphyrin(3–) doublet. In this case, the aromaticity of N20 is the highest and the aromaticity of N16 is the lowest among the metalloporphyrins analyzed. As we mentioned, the increase of the central charge leads to a strong delocalization of the outer N20 and decrease of the inner N16.

Finally, it is worth noting that the MCI descriptor shows only a small reduction upon metal complexation, and hardly makes any difference between the different metal ions or spin states present. This index did already not differentiate between aromaticities of the 5-MRs in $PorH_2$ and Por^{2-} (Table 3).

Conclusions

We have studied chemical bonding and aromaticity patterns in metalloporphyrins using DFT at the OPBE/TZP level. A number of the complexes showed spin contamination, which was corrected for using standard techniques within the QUILD program that can be used for both the energy and the geometry optimization. The geometry optimization was performed with QUILD using a number of geometric symmetries (C_{2v}, C_{4v}, D_{4h}, and S_4), together with C_{2v} symmetry for the orbitals within the ADF program. Nevertheless, for most complexes, the final geometry turned out to be D_{4h}. Four complexes were found to be more stable within C_{4v} symmetry, in which the metal was found slightly displaced from the porphyrin plane. Only for calcium was this out-of-plane distortion significantly large (0.86 Å), which concurs with a recent crystal structure of a related calcium–porphyrin complex.

The chemical bonding in these complexes was studied with an energy decomposition analysis, which showed, as anticipated, strong electrostatic interactions between the metal(II) cation and the porphyrin dianion. For most complexes, this was accompanied by significant (covalent) orbital interactions, apart from calcium–porphyrin that showed mainly electrostatic interactions.

Finally, we have studied aromaticity patterns in these transition-metal complexes using a number of (structural and electronic) aromaticity descriptors. The inner-ring (N16) aromaticity is hardly affected by the complexation of the metal cation, i.e., it keeps the aromatic character of the porphyrin dianion. On the other hand, the aromaticity of the 5-MR (N5) and the outer-ring (N20) aromaticity are significantly enhanced by the presence of the metal. This increase in the aromatic character of the outer N20 and N5 rings is attributed to two main factors: polarization of the π-cloud and charge transfer.

Supplementary data

Supplementary data (detailed description of the components of the energy decomposition analysis, EDA analysis for all spin-states, and Cartesian coordinates of the transition-metal complexes) for this article are available on the journal Web site (canjchem.nrc.ca) or may be purchased from the Depository of Unpublished Data, Document Delivery, CISTI, National Research Council Canada, Ottawa, ON K1A 0R6, Canada. DUD 3965. For more information on obtaining material, refer to cisti-icist.nrc-cnrc.gc.ca/cms/unpub_e.shtml.

Acknowledgments

This study was financially supported by Spanish research projects (CTQ2008–03077/BQU and CTQ2008–06532/BQU) and a DURSI project (No. 2005SGR-00238). F.F. thanks Spanish MICINN for the doctoral fellowship No. AP2005–2997.

References

(1) This article is part of a Special Issue dedicated to Professor T. Ziegler.
(2) Dedicated to Prof. Tom Ziegler as a proof of our admiration for his brilliant contributions to chemistry.
(3) Jones, D. H.; Hinman, A. S.; Ziegler, T. *Inorg. Chem.* **1993**, *32* (10), 2092–2095. doi:10.1021/ic00062a035.
(4) Irikura, K. K.; Beauchamp, J. L. *J. Am. Chem. Soc.* **1991**, *113* (7), 2767–2768. doi:10.1021/ja00007a069.
(5) Spaulding, L. D.; Chang, C. C.; Yu, N.-T.; Felton, R. H. *J. Am. Chem. Soc.* **1975**, *97* (9), 2517–2525. doi:10.1021/ja00842a032.
(6) Furhop, J. H.; Kadish, K. M.; Davis, D. G. *J. Am. Chem. Soc.* **1973**, *95* (16), 5140–5147. doi:10.1021/ja00797a008. PMID:4354829.
(7) Scheidt, W. R.; Reed, C. A. *Chem. Rev.* **1981**, *81* (6), 543–555. doi:10.1021/cr00046a002.
(8) Bren, K. L.; Kellogg, J. A.; Kaur, R.; Wen, X. *Inorg. Chem.* **2004**, *43* (25), 7934–7944. doi:10.1021/ic048925t. PMID:15578827.
(9) Loew, G. H.; Harris, D. L. *Chem. Rev.* **2000**, *100* (2), 407–420. doi:10.1021/cr980389x. PMID:11749241.
(10) Limberg, C. *Angew. Chem. Int. Ed.* **2003**, *42* (48), 5932–5954. doi:10.1002/anie.200300578.
(11) Lombardi, A.; Nastri, F.; Pavone, V. *Chem. Rev.* **2001**, *101* (10), 3165–3190. doi:10.1021/cr000055j. PMID:11710067.
(12) Baerends, E. J.; Ricciardi, G.; Rosa, A.; van Gisbergen, S. J.

A. *Coord. Chem. Rev.* **2002**, *230* (1-2), 5–27. doi:10.1016/S0010-8545(02)00093-0.
(13) Peralta, G. A.; Seth, M.; Ziegler, T. *Inorg. Chem.* **2007**, *46* (22), 9111–9125. doi:10.1021/ic7008545. PMID:17914806.
(14) Rosa, A.; Ricciardi, G.; Baerends, E. J. *J. Phys. Chem. A* **2006**, *110* (15), 5180–5190. doi:10.1021/jp060931i. PMID:16610842.
(15) Koch, W.; Holthausen, M. C. *A chemist's guide to density functional theory*; Wiley-VCH: Weinheim, 2000.
(16) Swart, M.; Groenhof, A. R.; Ehlers, A. W.; Lammertsma, K. *J. Phys. Chem. A* **2004**, *108* (25), 5479–5483. doi:10.1021/jp049043i.
(17) Swart, M. *J. Chem. Theory Comput.* **2008**, *4* (12), 2057–2066. doi:10.1021/ct800277a.
(18) Swart, M.; Ehlers, A. W.; Lammertsma, K. *Mol. Phys.* **2004**, *102* (23-24), 2467–2474. doi:10.1080/00268970420002750l7.
(19) Handy, N. C.; Cohen, A. J. *J. Mol. Phys.* **2001**, *99*, 403. doi:10.1080/00268970010018431.
(20) Perdew, J. P.; Burke, K.; Ernzerhof, M. *Phys. Rev. Lett.* **1996**, *77* (18), 3865–3868. doi:10.1103/PhysRevLett.77.3865. PMID:10062328.
(21) Conradie, J.; Ghosh, A. *J. Phys. Chem. B* **2007**, *111* (44), 12621–12624. doi:10.1021/jp074480t. PMID:17935317.
(22) Zhang, Y.; Wu, A.; Xu, X.; Yan, Y. *Chem. Phys. Lett.* **2006**, *421* (4-6), 383–388. doi:10.1016/j.cplett.2006.01.095.
(23) Zhang, Y.-Q.; Luo, C.-L. *J. Phys. Chem. A* **2006**, *110* (15), 5096–5101. doi:10.1021/jp056446p. PMID:16610830.
(24) Wu, A.; Zhang, Y.; Xu, X.; Yan, Y. *J. Comput. Chem.* **2007**, *28* (15), 2431–2442. doi:10.1002/jcc.20641. PMID:17722026.
(25) Wasbotten, I.; Ghosh, A. *Inorg. Chem.* **2006**, *45* (13), 4910–4913. doi:10.1021/ic0602493. PMID:16780311.
(26) Swart, M. *Inorg. Chim. Acta* **2007**, *360* (1), 179–189. doi:10.1016/j.ica.2006.07.073.
(27) Groenhof, A. R.; Ehlers, A. W.; Lammertsma, K. *J. Am. Chem. Soc.* **2007**, *129* (19), 6204–6209. doi:10.1021/ja0685654. PMID:17441718.
(28) Derat, E.; Kumar, D.; Neumann, R.; Shaik, S. *Inorg. Chem.* **2006**, *45* (21), 8655–8663. doi:10.1021/ic0610435. PMID:17029376.
(29) Romo, S.; Fernández, J. A.; Maestre, J. M.; Keita, B.; Nadjo, L.; de Graaf, C.; Poblet, J. M. *Inorg. Chem.* **2007**, *46* (10), 4022–4027. doi:10.1021/ic062030u. PMID:17447755.
(30) Rong, C.; Lian, S.; Yin, D.; Shen, B.; Zhong, A.; Bartolotti, L.; Liu, S. *J. Chem. Phys.* **2006**, *125* (17),o. 174102. doi:10.1063/1.2378830. PMID:17100424.
(31) Liao, M.-S.; Watts, J. D.; Huang, M.-J. *J. Comput. Chem.* **2006**, *27* (13), 1577–1592. doi:10.1002/jcc.20458. PMID:16868988.
(32) Liao, M.-S.; Watts, J. D.; Huang, M.-J. *J. Phys. Chem. A* **2007**, *111* (26), 5927–5935. doi:10.1021/jp070734z. PMID:17559200.
(33) Zein, S.; Borshch, S. A.; Fleurat-Lessard, P.; Casida, M. E.; Chermette, H. *J. Chem. Phys.* **2007**, *126* (1), 014105. doi:10.1063/1.2406067. PMID:17212488.
(34) Conradie, J.; Ghosh, A. *J. Chem. Theory Comput.* **2007**, *3* (3), 689–702. doi:10.1021/ct600337j.
(35) Acosta-Silva, C.; Branchadell, V. Unpublished results shown at DFT2007 congress. 2007.
(36) Güell, M.; Luis, J. M.; Solà, M.; Swart, M. *J. Phys. Chem. A* **2008**, *112* (28), 6384–6391. doi:10.1021/jp803441m. PMID:18572904.
(37) Baerends, E. J.; Autschbach, J.; Bérces, A.; Berger, J. A.; Bickelhaupt, F. M.; Bo, C.; de Boeij, P. L.; Boerrigter, P. M.; Cavallo, L.; Chong, D. P.; Deng, L.; Dickson, R. M.; Ellis, D. E.; van Faassen, M.; Fan, L.; Fischer, T. H.; Fonseca Guerra, C.; van Gisbergen, S. J. A.; Groeneveld, J. A.; Gritsenko, O. V.; Grüning, M.; Harris, F. E.; van den Hoek, P.; Jacob, C. R.; Jacobsen, H.; Jensen, L.; Kadantsev, E. S.; van Kessel, G.; Klooster, R.; Kootstra, F.; van Lenthe, E.; McCormack, D. A.; Michalak, A.; Neugebauer, J.; Nicu, V. P.; Osinga, V. P.; Patchkovskii, S.; Philipsen, P. H. T.; Post, D.; Pye, C. C.; Ravenek, W.; Romaniello, P.; Ros, P.; Schipper, P. R. T.; Schreckenbach, G.; Snijders, J. G.; Solà, M.; Swart, M.; Swerhone, D.; te Velde, G.; Vernooijs, P.; Versluis, L.; Visscher, L.; Visser, O.; Wang, F.; Wesolowski, T. A.; van Wezenbeek, E. M.; Wiesenekker, G.; Wolff, S. K.; Woo, T. K.; Yakovlev, A. L.; Ziegler, T. *ADF 2007.01*; SCM: Amsterdam, The Netherlands, 2007.
(38) Swart, M.; Bickelhaupt, F. M. *J. Comput. Chem.* **2008**, *29* (5), 724–734. doi:10.1002/jcc.20834. PMID:17902157.
(39) Swart, M.; Bickelhaupt, F. M. *Int. J. Quantum Chem.* **2006**, *106* (12), 2536–2544. doi:10.1002/qua.21049.
(40) Bickelhaupt, F. M.; Baerends, E. J. *Kohn–Sham density functional theory: Predicting and understanding chemistry*; In *Reviews in computational chemistry*, Vol. 15; Wiley-VCH: New York, 2000; pp. 1.
(41) Baerends, E. J.; Branchadell, V.; Sodupe, M. *Chem. Phys. Lett.* **1997**, *265* (3-5), 481–489. doi:10.1016/S0009-2614(96)01449-2.
(42) Kruszewski, J.; Krygowski, T. M. *Tetrahedron Lett.* **1972**, *13* (36), 3839–3842. doi:10.1016/S0040-4039(01)94175-9.
(43) Krygowski, T. M.; Cyrański, M. K. *Chem. Rev.* **2001**, *101* (5), 1385–1420. doi:10.1021/cr990326u. PMID:11710226.
(44) Bader, R. F. W. Atoms in molecules: A quantum theory. Clarendon, Oxford. 1990.
(45) Matito, E.; Duran, M.; Solà, M. *J. Chem. Phys.* **2005**, *122* (1), 014109. doi:10.1063/1.1824895.
(46) Bultinck, P.; Rafat, M.; Ponec, R.; Van Gheluwe, B.; Carbó-Dorca, R.; Popelier, P. *J. Phys. Chem. A* **2006**, *110* (24), 7642–7648. doi:10.1021/jp0609176. PMID:16774209.
(47) Giambiagi, M.; Giambiagi, M. S.; dos Santos, C. D.; de Figueiredo, A. P. *Phys. Chem. Chem. Phys.* **2000**, *2* (15), 3381–3392. doi:10.1039/b002009p.
(48) Lain, L.; Torre, A.; Bochicchio, R. C.; Ponec, R. *Chem. Phys. Lett.* **2001**, *346* (3-4), 283–287. doi:10.1016/S0009-2614(01)00974-5.
(49) Biegler-König, F. W.; Bader, R. F. W.; Tang, T.-H. *J. Comput. Chem.* **1982**, *3*, 317. doi:10.1002/jcc.540030306.
(50) Matito, E. *ESI-3D: Electron sharing indexes program for 3D molecular space partitioning*; Available from http://iqc.udg.es/~eduard/ESI. Institute of Computational Chemistry: Girona, 2006.
(51) Frisch, M. J.; Trucks, G. W.; Schlegel, H. B.; Scuseria, G. E.; Robb, M. A.; Cheeseman, J. R.; Montgomery, J. A., Jr.; Vreven, T.; Kudin, K. N.; Burant, J. C.; Millam, J. M.; Iyengar, S. S.; Tomasi, J.; Barone, V.; Mennucci, B.; Cossi, M.; Scalmani, G.; Rega, N.; Petersson, G. A.; Nakatsuji, H.; Hada, M.; Ehara, M.; Toyota, K.; Fukuda, R.; Hasegawa, J.; Ishida, M.; Nakajima, T.; Honda, Y.; Kitao, O.; Nakai, H.; Klene, M.; Li, X.; Knox, J. E.; Hratchian, H. P.; Cross, J. B.; Bakken, V.; Adamo, C.; Jaramillo, J.; Gomperts, R.; Stratmann, R. E.; Yazyev, O.; Austin, A. J.; Cammi, R.; Pomelli, C.; Ochterski, J. W.; Ayala, P. Y.; Morokuma, K.; Voth, G. A.; Salvador, P.; Dannenberg, J. J.; Zakrzewski, V. G.; Dapprich, S.; Daniels, A. D.; Strain, M. C.; Farkas, O.; Malick, D. K.; Rabuck, A. D.; Raghavachari, K.; Foresman, J. B.; Ortiz, J. V.; Cui, Q.; Baboul, A. G.; Clifford, S.; Cio-

slowski, J.; Stefanov, B. B.; Liu, G.; Liashenko, A.; Piskorz, P.; Komaromi, I.; Martin, R. L.; Fox, D. J.; Keith, T.; Al-Laham, M. A.; Peng, C. Y.; Nanayakkara, A.; Challacombe, M.; Gill, P. M. W.; Johnson, B.; Chen, W.; Wong, M. W.; Gonzalez, C.; Pople, J. A. *Gaussian 03*, revision C.04; Gaussian, Inc.: Pittsburgh, PA, 2003.

(52) Schäfer, A.; Huber, C.; Ahlrichs, R. *J. Chem. Phys.* **1993**, *100*, 5829.

(53) Poater, J.; Solà, M.; Duran, M.; Fradera, X. *Theor. Chem. Acc.* **2002**, *107*, 362.

(54) Matito, E.; Solà, M.; Salvador, P.; Duran, M. *Faraday Discuss.* **2007**, *135*, 325. doi:10.1039/b605086g. PMID:17328437.

(55) Schleyer, P. R.; Maerker, C.; Dransfeld, A.; Jiao, H.; Hommes, N. J. R. E. *J. Am. Chem. Soc.* **1996**, *118* (26), 6317–6318. doi:10.1021/ja960582d.

(56) Feixas, F.; Jiménez-Halla, J. O. C.; Matito, E.; Poater, J.; Solà, M. *Pol. J. Chem.* **2007**, *81*, 783.

(57) Bonomo, L.; Lehaire, M.-L.; Solari, E.; Scopelliti, R.; Floriani, C. *Angew. Chem. Int. Ed.* **2001**, *40* (4), 771–774. doi:10.1002/1521-3773(20010216)40:4<771::AID-ANIE7710>3.0.CO;2-X.

(58) Liao, M.-S.; Scheiner, S. *J. Chem. Phys.* **2002**, *117*, 205–219. doi:10.1063/1.480872.

(59) Kozlowski, P. M.; Bingham, J. R.; Jarzecki, A. A. *J. Phys. Chem. A* **2008**, *112* (50), 12781–12788. doi:10.1021/jp801696c.

(60) Patchkovskii, S.; Ziegler, T. *J. Am. Chem. Soc.* **2000**, *122* (14), 3506–3516. doi:10.1021/ja994041a.

(61) Liao, M.-S.; Scheiner, S. J. *Comput. Chem.* **2002**, *23* (15), 1391–1403. doi:10.1002/jcc.10142.

(62) Rosa, A.; Baerends, E. J. *Inorg. Chem.* **1994**, *33* (3), 584–595. doi:10.1021/ic00081a029.

(63) Wittbrodt, J. M.; Schlegel, H. B. *J. Chem. Phys.* **1996**, *105*, 6574.

(64) Groenhof, A. R.; Swart, M.; Ehlers, A. W.; Lammertsma, K. *J. Phys. Chem. A* **2005**, *109* (15), 3411–3417. doi:10.1021/jp0441442. PMID:16833677.

(65) Cyrański, M. K.; Krygowski, T. M.; Wisiorowski, M.; Van Eikema Hommes, N. J. R.; Schleyer, P. v. R. *Angew. Chem., Int. Ed.* **1998**, *37* (1-2), 177–180. doi:10.1002/(SICI)1521-3773(19980202)37:1/2<177::AID-ANIE177>3.0.CO;2-H.

(66) Campomanes, P.; Menéndez, M. I.; Cárdenas-Jirón, G. I.; Sordo, T. L. *Phys. Chem. Chem. Phys.* **2007**, *9* (42), 5644. doi:10.1039/b709198b. PMID:17960251.

(67) Jusélius, J.; Sundholm, D. *Phys. Chem. Chem. Phys.* **2000**, *2* (10), 2145–2151. doi:10.1039/b000260g.

(68) Steiner, E.; Fowler, P. W. *ChemPhysChem* **2002**, *3* (1), 114–116. doi:10.1002/1439-7641(20020118)3:1<114::AID-CPHC114>3.0.CO;2-A. PMID:12465482.

(69) Steiner, E.; Soncini, A.; Fowler, P. W. *Org. Biomol. Chem.* **2005**, *3* (22), 4053. doi:10.1039/b511913h. PMID:16267582.

(70) Sargent, A. L.; Hawkins, I. C.; Allen, W. E.; Liu, H.; Sessler, J. L.; Fowler, C. J. *Chem. Eur. J.* **2003**, *9* (13), 3065–3072. doi:10.1002/chem.200204694.

(71) Islyaikin, M. K.; Ferro, V. R.; García de la Vega, J. M. *J. Chem. Soc., Perkin Trans. 2* **2002**, *2*, 2104–2109. doi:10.1039/b207034k.

(72) Furuta, H.; Maeda, H.; Osuka, A. *J. Org. Chem.* **2001**, *66* (25), 8563–8572. doi:10.1021/jo016051b. PMID:11735539.

(73) Shaik, S.; Hiberty, P. C. *J. Am. Chem. Soc.* **1985**, *107* (11), 3089–3095. doi:10.1021/ja00297a013.

(74) Ou, M. C.; Chu, S. Y. *J. Phys. Chem.* **1994**, *98* (4), 1087–1089. doi:10.1021/j100055a008.

(75) Solà, M.; Mestres, J.; Duran, M. *J. Phys. Chem.* **1995**, *99* (27), 10752–10758. doi:10.1021/j100027a013.

(76) Shaik, S.; Shurki, A.; Danovich, D.; Hiberty, P. C. *Chem. Rev.* **2001**, *101* (5), 1501–1540. doi:10.1021/cr990363l. PMID:11710231.

(77) Kovačević, B.; Barić, D.; Maksić, Z. B.; Müller, T. *ChemPhysChem* **2004**, *5* (9), 1352–1364. doi:10.1002/cphc.200400061. PMID:15503393.

(78) Hiberty, P. C.; Shaik, S. *Phys. Chem. Chem. Phys.* **2004**, *6* (2), 224. doi:10.1039/b310496f.

(79) Pierrefixe, S. C. A. H.; Bickelhaupt, F. M. *Chem. Eur. J.* **2007**, *13* (22), 6321–6328. doi:10.1002/chem.200700206.

(80) Pierrefixe, S. C. A. H.; Bickelhaupt, F. M. *J. Phys. Chem. A* **2008**, *112* (50), 12816–12822. doi:10.1021/jp800514n.

(81) Pierrefixe, S. C. A. H.; Bickelhaupt, F. M. *Aust. J. Chem.* **2008**, *61* (3), 209. doi:10.1071/CH08043.

Hetero-Diels–Alder reactions involving $Fe(CO)_3$-coordinated dienal and formyltrimethylenemethane catalyzed by Lewis acids — A theoretical study[1]

Carles Acosta-Silva, Òscar González-Blanco, and Vicenç Branchadell

Abstract: The hetero-Diels–Alder reactions of butadiene with $Fe(CO)_3$-coordinated formylbutadiene and formyltrimethylenemethane catalyzed by Lewis acids have been theoretically studied through density functional calculations. The results obtained show that, for the reaction with (formylbutadiene)$Fe(CO)_3$, the kinetically most favourable product is the one corresponding to the attack of butadiene on the *s-cis* conformer of the formylbutadiene fragment when the reaction is catalyzed by BF_3, and the one corresponding to the attack on the *s-trans* conformer when the catalyst is $TiCl_4$. On the other hand, for the reaction with (formyltrimethylenemethane)$Fe(CO)_3$ catalyzed by BF_3, the product corresponding to the attack on the *s-trans* conformer is predicted to be favoured. These results have been interpreted through an energy decomposition analysis of the potential-energy barriers.

Key words: $Fe(CO)_3$ complexes, hetero-Diels–Alder reactions, density functional theory, Lewis acid catalysis.

Résumé : Faisant appel à la méthode de calcul de la fonctionnelle de la densité, on a étudié d'une façon théorique les réactions d'hétéro-Diels–Alder catalysées par des acides de Lewis du butadiène avec du formylbutadiène et du formyltriméthylèneméthane coordinés au $Fe(CO)_3$. Les résultats obtenus montrent que, pour la réaction avec le (formylbutadiène)$Fe(CO)_3$ catalysée par le BF_3, le produit le plus favorable d'un point de vue cinétique correspond à celui obtenu par une attaque du butadiène sur le conformère *s-cis* du fragment formylbutadiène alors que pour la réaction catalysée par le $TiCl_4$ le produit le plus favorable correspond à une attaque sur le conformère *s-trans*. Par ailleurs, pour la réaction avec le (formyltriméthylèneméthane)$Fe(CO)_3$, catalysée par le BF_3, les calculs prédisent que le produit favorisé serait celui correspondant à une attaque sur le conformère *s-trans*. On interprète ces résultats par le biais d'une analyse par décomposition de l'énergie des barrières à l'énergie potentielle.

Mots-clés : complexes $Fe(CO)_3$, réactions hétéro-Diels-Alder, théorie de la fonctionnelle de la densité, catalyse par un acide de Lewis.

[Traduit par la Rédaction]

Introduction

Diene tricarbonyl iron complexes are very valuable tools in organic synthesis.[2–12] The iron tricarbonyl unit is a very efficient protecting group for 1,3-diene and facilitates an excellent chirality transfer to the stereogenic centers created close to it. Moreover, the iron tricarbonyl unit directs the *anti* attack to the vicinal groups.

Experimental results suggest that the stereochemistry of the reactions taking place in unsaturated systems in positions vicinal to the organometallic unit is determined by the conformational bias of the reactant.[7–9] In this way, the addition of a nucleophile to a carbonyl group vicinal to a diene iron tricarbonyl moiety may lead to two different products, depending on the *s-cis* or *s-trans* conformation of the carbonyl group (see Scheme 1).

The *s-cis–s-trans* conformational equilibrium in this kind of compound has been theoretically studied,[13] and the results obtained were in good agreement with the diastereoselectivities experimentally observed in addition reactions.

A carbonyl group vicinal to diene iron tricarbonyl may also participate in cycloaddition reactions such as the hetero-Diels–Alder reaction reported by Donaldson et al.[14] In this case, a different ratio between diastereomers was obtained depending on the Lewis acid used as catalyst. In the presence of BF_3, the major product was the one corresponding to the attack of the *s-cis* conformer, whereas in the presence of $TiCl_4$, the product coming from the *s-trans* conformer was predominant . The same kind of dependence on the Lewis acid has been observed by Harvey and Selchau for the addition of several nucleophiles to the carbonyl group of (dienal)$Fe(CO)_3$ complexes.[11]

A similar hetero-Diels–Alder reaction has also been reported for a (formyltrimethylenemethane)$Fe(CO)_3$ complex.[15] In this case, the reaction catalyzed by BF_3 leads to the diastereomer corresponding to the attack of the *s-trans* conformer as the only product.

Received 19 January 2009. Accepted 11 March 2009. Published on the NRC Research Press Web site at canjchem.nrc.ca on 30 June 2009.

C. Acosta-Silva, Ò. González-Blanco, and V. Branchadell.[1] Departament de Química, Universitat Autònoma de Barcelona, 08193 Bellaterra (Barcelona), Spain.

[1]Corresponding author (e-mail: vicenc.branchadell@uab.cat).

Scheme 1.

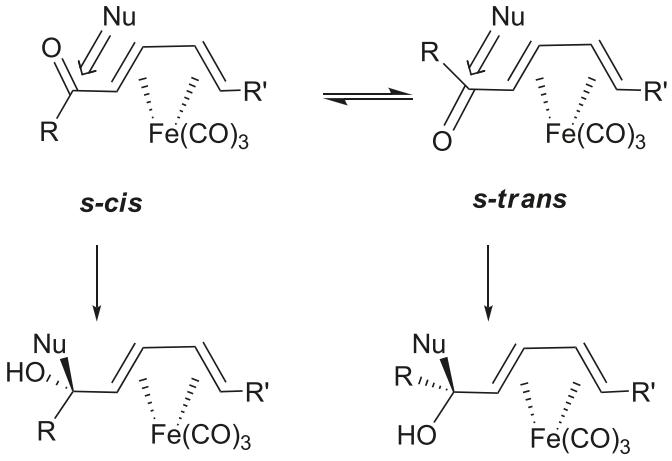

In this paper, we report a theoretical study of the hetero-Diels–Alder reactions of butadiene with formylbutadiene and formyltrimethylenemethane $Fe(CO)_3$ complexes catalyzed by Lewis acids. Our goals are to establish the role played by the conformational preferences of these complexes in the outcome of the reactions and to understand the different effect of the Lewis acids in the stereochemistry of the reactions.

Computational details

The geometries of all stationary points were optimized using the BPW91[16,17] density functional method with a LANL2DZ basis set[18] supplemented with d polarization functions for B, C, O, F, and Cl (LANL2DZ(d)). This basis set includes effective core potentials for the inner shells of Fe, Ti (up to 2p), and Cl, with a double-ζ expansion for the valence shells. For H, B, C, O, and F, the D95 basis set[19] was used. Harmonic vibrational frequencies were calculated for all structures to characterize them as energy minima (all frequencies are real) or transition states (one and only one imaginary frequency). All these calculations were carried out using the Gaussian-03 program.[20] To correct for possible deficiencies of the basis set, the energies of all structures were recalculated with the same functional and a larger basis set. These calculations were done with the ADF program[21] using a TZP basis set. This basis set is a triple-ζ basis set of uncontracted Slater orbitals supplemented by polarization functions (f for Fe and Ti; d for B, C, O, F, and Cl; and p for H). The inner shells of all atoms were treated with the frozen core approximation.[22]

Solvent effects were included using the CPCM method[23] implemented in the Gaussian-03 program. We used diethyl ether as solvent (ε = 4.335). Calculations in solution were done for geometries optimized in the gas phase. The hetero-Diels–Alder reaction between butadiene and acrolein was used as a model to check how the results change when geometries are optimized including the solvent effect. The obtained structures are shown as Supplementary data. The length of the forming C–O and C–C bonds vary by 0.085 and 0.067 Å, respectively, while the potential-energy barrier changes by only 0.1 kcal mol^{-1}.

Scheme 2.

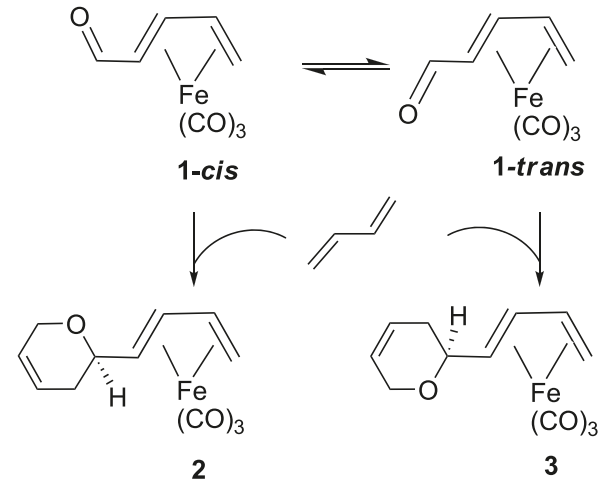

Scheme 3.

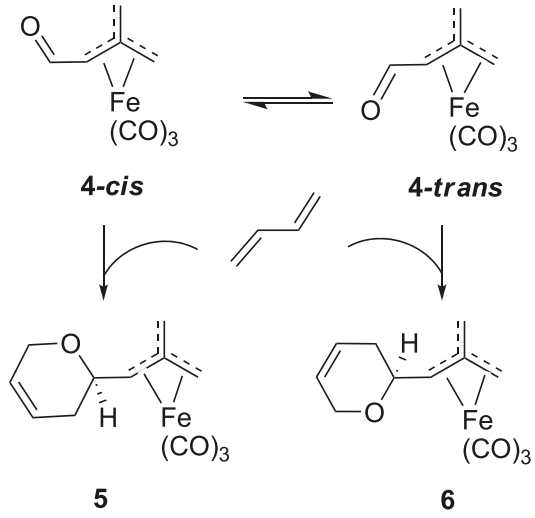

The reported reaction energies and potential-energy barriers correspond to those calculated with the TZP basis set for the gas phase results and they have been corrected with the solvation energies computed with the LANL2DZ(d) basis set. Regarding the Gibbs energies, the reported values were computed from energies calculated with the TZP basis set and zero-point correction, and thermal energies and entropy were computed with the LANL2DZ(d) basis set. For bimolecular processes in solution, the correction associated to the change of reference state between gas phase (1 atm) and solution (1 mol L^{-1}) was included.

Results and discussion

We studied the reactions of butadiene with (formylbutadiene)$Fe(CO)_3$ **1** (see Scheme 2) and with (formyltrimethylenemethane) $Fe(CO)_3$ **4** (Scheme 3).

In both cases, the presence of the bulky $Fe(CO)_3$ group directs the attack *anti* with respect to this group. There are two different conformations arising from the rotation around the C–C(carbonyl) bond: *s-cis* and *s-trans*. The attack of butadiene to each one of these two conformers would lead to

Fig. 1. Structures of conformers of **1** and of their complexes with Lewis acids. Selected interatomic distances in Å.

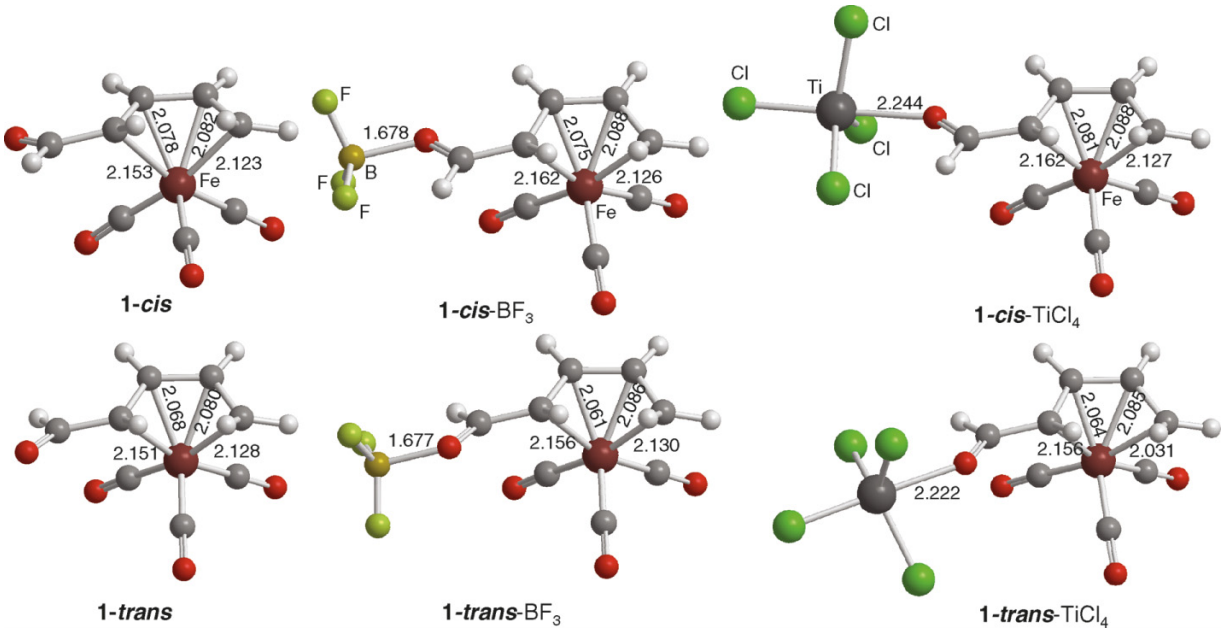

Fig. 2. Structures of conformers of **4** and of their complexes with BF_3. Selected interatomic distances in Å.

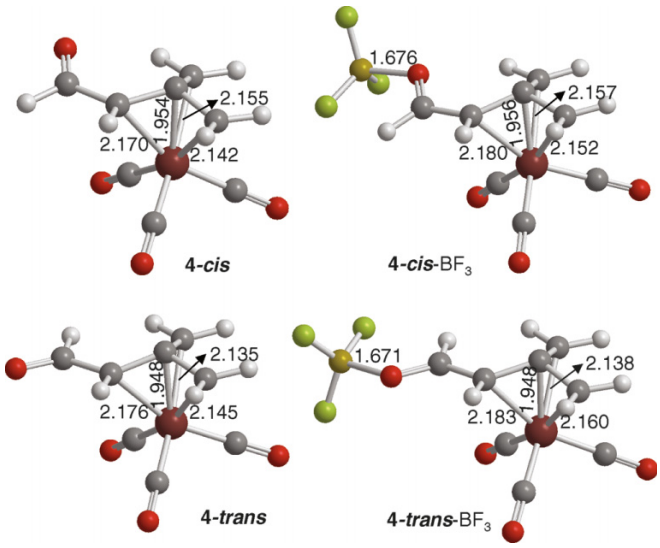

the formation of two diasteromers, **2** and **3**, for the reaction of **1,** and **5** and **6** for the reaction of **4**.

Figures 1 and 2 show the structures of *s-cis* and *s-trans* conformers of **1** and **4** and of their respective complexes with Lewis acids. Table 1 presents the relative energies of both conformers as well as their interconversion energy barriers.

The coordination of the Lewis acid always takes place in the plane of the carbonyl group with the Lewis acid *syn* with respect to the aldehydic hydrogen atom.[24]

Complexes with *trans* coordination were also studied, but they are higher in energy than those shown in Fig. 1. For **1**-*cis*, the coordination of BF_3 to one of the CO ligands was also considered, but the calculation led to a B–O distance of 2.98 Å.

For $TiCl_4$, the coordination of the carbonyl group led to a trigonal bipyramidal environment, with the oxygen occupying one of the axial positions.[25]

Other coordination modes were also explored for **1**-*cis*-$TiCl_4$, such as the out-of-plane coordination to the carbonyl group and the formation of a chelate complex involving the carbonyl group of the aldehyde and one of the CO ligands, but the system evolved to the structure shown in Fig. 1.

Table 1 shows that in all cases the *s-trans* conformer is the most stable one, the largest Gibbs energy difference between both conformers being 1.8 kcal mol^{-1} for **4**-BF_3 in solution. The Gibbs activation energies associated to the *s-trans–s-cis* conformational rearrangements are lower than 9 kcal mol^{-1} for the uncomplexed systems, and increase to values larger than 11 kcal mol^{-1} when the carbonyl group is complexed by a Lewis acid. For **1**-BF_3, there is a significant increase due to solvation.

We studied the reactions of **1**, **4**, and their complexes with Lewis acids with butadiene. For the uncatalyzed reactions, we considered both *endo* and *exo* transition states, the *endo* ones being the most favourable ones in all cases.

The structures of the transition states corresponding to all reactions are shown in Figs. 3 and 4, whereas those of the reaction products can be found in the Supplementary data.

Table 2 presents the values of the potential-energy barriers and Gibbs activation energies of all reactions. As we can observe, in all cases the potential-energy barriers for the cycloaddition reactions are notably larger than the *s-cis–s-trans* rearrangement barriers (see Table 1), so that an equilibrium between both conformers may be assumed.

For the catalyzed reactions, the inclusion of the solvent effect leads to a larger decrease in the Gibbs activation energies than for the uncatalyzed processes.

Regarding the geometries of the transition states, we can observe that, for the uncatalyzed reactions, the C–C and C–O bonds being formed are of similar lengths. By contrast, coordination of a Lewis acid produces a notable asymmetry in the transition states. A similar effect has already been

Table 1. Reaction and activation energies[a] and Gibbs energies[a,b] for the *s-trans–s-cis* conformational rearrangements of **1**, **4**, and their complexes with Lewis acids.

	Lewis acid	ΔE		$\Delta E^{\ddagger}$		ΔG		$\Delta G^{\ddagger}$	
1	—	0.0	(0.9)	7.7	(8.4)	0.2	(1.1)	7.6	(8.3)
	BF_3	0.2	(0.5)	11.6	(17.5)	0.1	(0.4)	11.1	(17.0)
	$TiCl_4$	0.6	(1.1)	10.3	(12.2)	0.0	(0.5)	10.0	(11.8)
4	—	0.6	(1.3)	7.7	(8.5)	0.7	(1.4)	7.6	(8.5)
	BF_3	1.4	(1.5)	12.4	(14.8)	1.6	(1.8)	11.9	(14.3)

[a]In kcal mol^{-1}. Referred to the *s-trans* conformer of each complex. In parentheses, values computed in diethyl ether solution.
[b]At 298.15 K and 1 atm.

Fig. 3. Structures of the transition states corresponding to the reactions of butadiene with **1** and its complexes with BF_3 and $TiCl_4$. Selected interatomic distances in Å. Hydrogen atoms have been omitted for clarity.

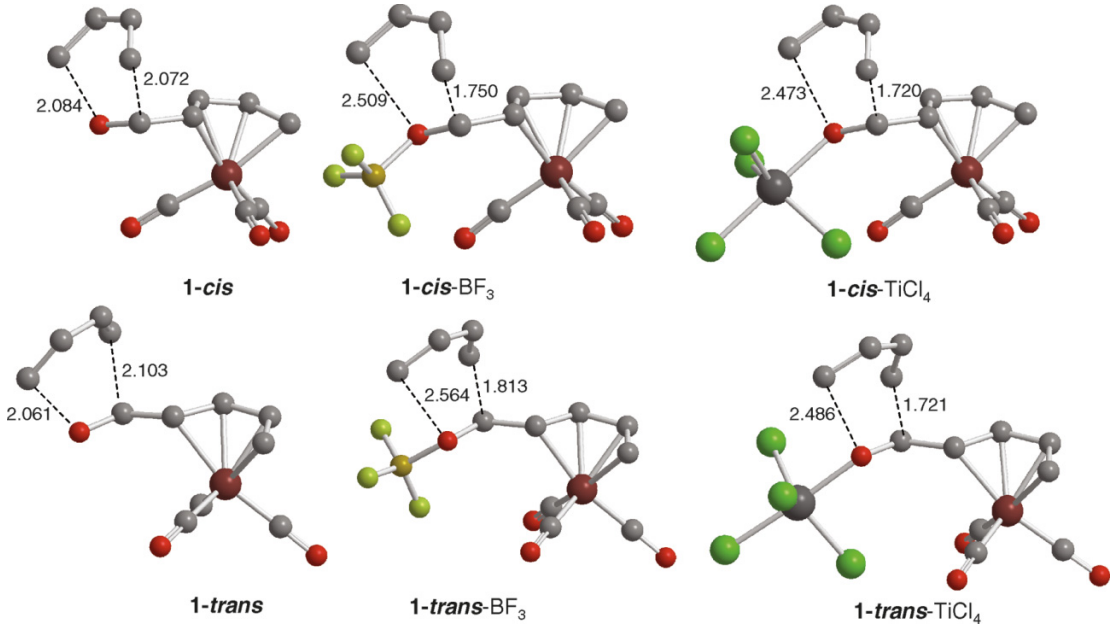

observed for hetero-Diels–Alder reactions of formaldehyde with butadiene catalyzed by BH_3[26] and of methyl vinyl ketone with furan catalyzed by BF_3.[27]

As we can observe in Table 2, for the reaction between **1** and butadiene catalyzed by BF_3, the attack to the *s-cis* conformer is the kinetically most favourable. The difference in energy barriers in solution leads to a predicted **3**:**2** ratio of 76.5:23.5 at 298.15 K, in excellent agreement with the experimental 75:25 ratio.[14] On the other hand, for the reaction catalyzed by $TiCl_4$ the attack to the *s-trans* conformer becomes the most favourable one with a predicted **3**:**2** ratio at 298.15 K of 34:66. In this case, the experimentally observed ratio is 21:79, so that the agreement is only qualitative.[14] For the reaction in the absence of a Lewis acid, the results predict that the attack to the *s-trans* conformer would also be the most favourable one.

Regarding the reactions between **4** and butadiene, the results presented in Table 2 show that in the absence of a Lewis acid the attack to the *s-trans* conformer is the most favourable one, while catalysis by BF_3 increases this preference. In this case, the difference between Gibbs activation energy barriers is not large enough to be consistent with the experimental results, since only a product like **6** was exper-

Fig. 4. Structures of the transition states corresponding to the reactions of butadiene with **4** and its complexes with BF_3. Selected interatomic distances in Å. Hydrogen atoms have been omitted for clarity.

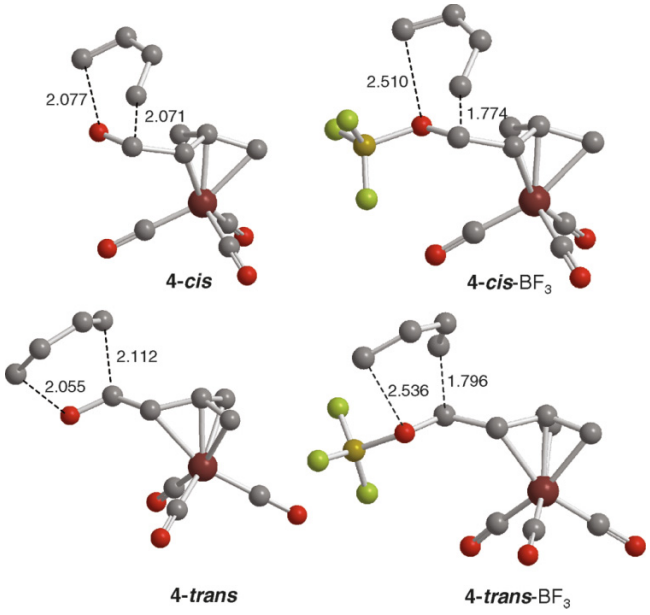

Table 2. Potential-energy barriers[a] and Gibbs activation energies[a,b] for the reactions of **1** and **4** with butadiene.

	Lewis acid	Conformer	Product	$\Delta E^{\ddagger}$		$\Delta G^{\ddagger}$	
1	—	*cis*	**2**	26.9	(28.1)	41.4	(38.8)
		trans	**3**	27.8	(28.0)	41.6	(37.9)
	BF_3	*cis*	**2**	20.5	(18.6)	36.6	(30.9)
		trans	**3**	20.8	(19.7)	36.5	(31.6)
	$TiCl_4$	*cis*	**2**	29.2	(25.2)	45.5	(37.7)
		trans	**3**	28.9	(24.6)	45.4	(37.3)
4	—	*cis*	**5**	27.5	(27.3)	41.8	(37.8)
		trans	**6**	27.5	(27.4)	41.1	(37.3)
	BF_3	*cis*	**5**	22.1	(19.7)	38.5	(32.3)
		trans	**6**	21.4	(19.3)	37.3	(31.4)

[a]In kcal mol^{-1}. Referred to the *s-trans* conformer of each complex. In parentheses, values computed in diethyl ether solution.
[b]At 298.15 K and 1 atm (gas phase) or 1 mol L^{-1} (solution).

Table 3. Energy decomposition analysis of the potential-energy barriers[a] of the reactions of **1** and **4** with butadiene.

	Lewis acid	Conformer	E_{prep}	E_{Pauli}	E_{elstat}	E_{orb}	$\Delta E^{\ddagger}$
1	—	*cis*	35.5	113.6	–48.7	–73.5	26.9
		trans	35.7	110.5	–47.0	–71.4	27.8
	BF_3	*cis*	50.9	169.4	–73.4	–126.4	20.5
		trans	47.0	150.3	–64.7	–111.8	20.8
	$TiCl_4$	*cis*	63.0	198.0	–85.0	–146.8	29.2
		trans	62.6	196.2	–83.9	–146.0	28.9
4	—	*cis*	36.6	115.0	–49.3	–74.8	27.5
		trans	35.3	110.2	–46.8	–71.2	27.5
	BF_3	*cis*	52.7	170.2	–73.6	–127.2	22.1
		trans	48.9	159.3	–68.4	–118.4	21.4

[a]In kcal mol^{-1}. See text for definitions.

imentally observed,[15] whereas the predicted **5**:**6** ratio at 298.15 K is actually only 18:82. In general, there is a good qualitative agreement between our results, obtained for reactions with butadiene, and the experimental observations made for reactions with substituted derivatives of butadiene. In most cases, the kinetically preferred products arise from the attack of the diene to the most stable conformer of the iron tricarbonyl complex. The only exception is the reaction of **1** catalyzed by BF_3.

For the catalyzed reactions, the selectivity of the reactions may also be predicted from gas phase potential-energy barriers instead of Gibbs activation energies in solution. For this reason, we carried out an energy partition analysis[28] to determine the origin of the selectivity.

The potential-energy barrier ($\Delta E^{\ddagger}$) for a cycloaddition reaction between a carbonyl group and butadiene can be partitioned into several terms[29]:

$$\Delta E^{\ddagger} = E_{prep} + E_{Pauli} + E_{elstat} + E_{orb}$$

The preparation energy, E_{prep}, is the energy necessary to distort the reactant molecules from their equilibrium geometries to the geometries they have at the transition state. E_{Pauli} is the Pauli repulsion term associated with closed-shell repulsions between both fragments at the transition state. E_{elstat} is the electrostatic interaction energy arising from the interaction between both fragments, each one having the electron density that it would have in the absence of the other fragment. The orbital interaction term, E_{orb}, arises when the electron densities of both fragments are allowed to relax and accounts for charge transfer and polarization. The results obtained from this analysis are shown in Table 3.

Table 4. LUMO energies of **1**, **4**, and their complexes with Lewis acids and charge transfer at the transition states of their reactions with butadiene.

	Lewis acid	Conformer	ε_{LUMO}[a]		Q[b]
1	—	*cis*	–3.171	(–3.609)	0.164
		trans	–3.112	(–3.542)	0.156
	BF_3	*cis*	–4.302	(–5.347)	0.359
		trans	–4.229	(–5.279)	0.349
	$TiCl_4$	*cis*	–4.210	(–5.334)	0.362
		trans	–4.148	(–5.333)	0.362
4	—	*cis*	–3.296	(–3.735)	0.173
		trans	–3.232	(–3.637)	0.163
	BF_3	*cis*	–4.389	(–5.429)	0.369
		trans	–4.321	(–5.334)	0.359

[a]Computed at the BPW91/TZP level of calculation, in eV. Values in parentheses correspond to the fragments with the distorted geometries corresponding to the transition states of the reactions with butadiene.
[b]Net charge in the butadiene fragment at the transition state determined from Hirshfeld[30] population analysis in au.

In all cases, the Pauli repulsion term favours the attack to the *s-trans* conformers, whereas the electrostatic and orbital interaction terms favour the attack to the *s-cis* conformers. Since the *s-trans* conformers are more stable than the *s-cis* ones, the preparation energy is lower for the attack to the *s-trans* conformers, with the exception of the reaction of **1** in the absence of a Lewis acid. For this reaction, formation of the product arising from the attack to the *s-cis* conformer is the most favourable one kinetically. As we can observe in the *cis* transition state, the sum of the electrostatic and orbital interaction terms overcompensates for the larger Pauli repulsion.

In the reaction catalyzed by BF_3, the same trends are observed. However, when the reaction is catalyzed by $TiCl_4$, the contribution of the preparation energy and Pauli repulsion to the differences between energy barriers becomes dominant and the formation of the product arising from the attack to the *s-trans* conformer is predicted to be the most favourable one.

Regarding the uncatalyzed reaction between **4** and butadiene, the computed energy barrier has the same value for the attacks to both conformers of **4**. In the presence of BF_3, the sum of the contribution of preparation and Pauli repulsion terms dominates over the contribution of the electrostatic and orbital interaction terms, so that the formation of the product arising from the attack to the *s-trans* conformer becomes kinetically favoured.

In all reactions, butadiene acts as an electron donor, so that the most important interaction between fragment molecular orbitals involves the HOMO of butadiene and the LUMO of the organometallic fragment. Table 4 shows the energies of the LUMO of **1**, **4**, and their complexes with Lewis acids at their equilibrium geometries and at the geometries corresponding to the transition states of the reactions with butadiene and the charge transfer between butadiene and the organometallic fragments at these transition states.

Complexation of **1** or **4** by a Lewis acid stabilizes the LUMO and so increases the electrophilicity of the carbonyl group. As a consequence, the absolute value of the orbital interaction term (see Table 3) and the charge transfer from butadiene to the organometallic fragment at the transition state (see Table 4) increase. This fact is associated with a notable decrease of the distance between butadiene and the carbonylic carbon atom at the transition state, which also leads to an increase in the Pauli repulsion energy and in the absolute value of the electrostatic term.

The coordination by a Lewis acid always tends to favour the transition states corresponding to the *s-trans* conformers. In the uncatalyzed reaction between **1** and butadiene, the attack on the *s-cis* conformer of **1** is kinetically favoured. The difference between energy barriers decreases when the reaction is catalyzed by BF_3, but the formation of **2** is still kinetically favourable. Complexation by $TiCl_4$ makes the transition state corresponding to the attack to the *s-trans* conformer the lowest in energy, so that the formation of **3** becomes kinetically favoured over the formation of **2**.

Regarding the reaction between **4** and butadiene, for the uncatalyzed process there is no preference for either of the two possible transition states. In this case, the effect of BF_3 complexation makes the formation of **6** the kinetic most favourable process.

Concluding remarks

We have studied the hetero-Diels–Alder reactions of butadiene with (formylbutadiene)$Fe(CO)_3$ (**1**) and (formyltrimethylenemethane)$Fe(CO)_3$ (**4**) catalyzed by Lewis acids. The potential-energy barriers of these reactions are always larger than the barriers associated with the *s-cis*–*s-trans* conformational rearrangement of the formyl group, so that an equilibrium between both conformers may be assumed. In all cases the *s-trans* conformer is the most favourable one. However, the reactions with butadiene leading to the formation of the most favourable diastereomers do not always involve the most stable conformer of the corresponding reactant. In the reaction between **1** and butadiene catalyzed by BF_3, the most favourable product corresponds to the attack of butadieneon the *s-cis* conformer of **1**. On the other hand when the reaction is catalyzed by $TiCl_4$, the most favourable attack takes place on the *s-trans* conformer. In the reaction between **4** and butadiene catalyzed by BF_3, the kinetically most favourable diasteromer corresponds to the attack of butadiene on the *s-trans* conformer of **4**. All these results may be interpreted through an energy partition analysis of the potential-energy barriers. According to this analysis, complexation by a Lewis acid tends to favour the reaction with *s-trans* conformers, since steric repulsion dominates over electrostatic and orbital interaction terms which favour the attack to *s-cis* conformers. In the reaction between **1** and butadiene, catalysis by BF_3 decreases the selectivity with respect to the uncatalyzed reaction, while with $TiCl_4$ the selectivity is reversed. Finally, for the reaction between **4** and butadiene, the catalyst increases the preference for the attack to the *s-trans* conformer of **4**.

Supplementary data

Supplementary data for this article (structures of the transition state of the reaction between butadiene and acrolein in the gas phase and in diethyl ether solution, structures of the reaction products and reaction energies of the reactions of **1** and **4** with butadiene) are available on the journal Web site (canjchem.nrc.ca) or may be purchased from the Depository of Unpublished Data, Document Delivery, CISTI, National Research Council Canada, Ottawa, ON K1A 0R6, Canada. DUD 3967. For more information on obtaining material, refer to cisti-icist.nrc-cnrc.gc.ca/cms/unpub_e.shtml.

Acknowledgment

Financial support from Ministerio de Ciencia e Innovación (CTQ2007–61704/BQU) and Generalitat de Catalunya (2005SGR-103) is gratefully acknowledged.

References

(1) This article is part of a Special Issue dedicated to Professor T. Ziegler.
(2) Koerner von Gustorf, E. A.; Fischer, I. *The organic chemistry of iron*; Academic Press: New York, 1978, Vol. 1.
(3) Koerner von Gustorf, E. A.; Fischer, I. *The organic chemistry of iron*; Academic Press: New York, 1981, Vol. 2.
(4) Davies, S. G. *Organotransition metal chemistry: Applications to organic synthesis*; Pergamon: Oxford, 1981.
(5) Pearson, A. J. *Metallo-organic chemistry*; Wiley: New York, 1985.

(6) Grée, R. *Synthesis* **1989**, *1989* (05), 341–355. doi:10.1055/s-1989-27250.
(7) Cox, R. L.; Ley, V. S. *Chem. Soc. Rev.* **1998**, *27*, 301. doi:10.1039/a827301z.
(8) Takemoto, Y.; Yoshikawa, N.; Baba, Y.; Iwata, C.; Tanaka, T.; Ibuka, T.; Ohishi, H. *J. Am. Chem. Soc.* **1999**, *121* (39), 9143–9154. doi:10.1021/ja991889q.
(9) Knölker, H. J. *Chem. Rev.* **2000**, *100* (8), 2941–2962. doi:10.1021/cr990267k. PMID:11749311.
(10) Prahlad, V.; El-Ahl, A. A. S.; Donaldson, W. A. *Tetrahedron Asymmetry* **2000**, *11* (15), 3091–3102. doi:10.1016/S0957-4166(00)00280-9.
(11) Harvey, D. F.; Selchau, V. B. *J. Org. Chem.* **2000**, *65* (8), 2282–2286. doi:10.1021/jo991193f. PMID:10789436.
(12) Williams, I.; Kariuki, B. M.; Reeves, K.; Cox, L. R. *Org. Lett.* **2006**, *8*, 4398. doi:10.1021/o10611321.
(13) González-Blanco, O.; Branchadell, V.; Grée, R. *Chem. Eur. J.* **1999**, *5* (6), 1722–1727. doi:10.1002/(SICI)1521-3765(19990604)5:6<1722::AID-CHEM1722>3.0.CO;2-U.
(14) Donaldson, W. A.; Tao, C.; Bennett, D. W.; Grubisha, D. S. *J. Org. Chem.* **1991**, *56* (14), 4563–4566. doi:10.1021/jo00014a049.
(15) Kleindl, P. J.; Donaldson, W. A. *J. Org. Chem.* **1997**, *62* (12), 4176–4179. doi:10.1021/jo970234+.
(16) Becke, A. D. *Phys. Rev. A* **1988**, *38* (6), 3098–3100. doi:10.1103/PhysRevA.38.3098. PMID:9900728.
(17) (a) Wang, Y.; Perdew, J. P. *Phys. Rev. B* **1991**, *44* (24), 13298–13307. doi:10.1103/PhysRevB.44.13298.; (b) Perdew, J. P.; Jackson, K. A.; Pederson, M. R.; Singh, D. J.; Fiolhais, D. C. *Phys. Rev. B* **1992**, *46* (11), 6671–6687. doi:10.1103/PhysRevB.46.6671.
(18) Hay, P. J.; Wadt, W. R. *J. Chem. Phys.* **1985**, *82* (1), 299. doi:10.1063/1.448975.
(19) Dunning, T. H.; Hay, P. J. In *Modern theoretical chemistry*; Schaeffer, H. F., III., Ed. Plenum: New York, 1976; Vol. 3, p. 1.
(20) Frisch, M. J.; Trucks, G. W.; Schlegel, H. B.; Scuseria, G. E.; Robb, M. A.; Cheeseman, J. R.; Montgomery, J. A., Jr.; Vreven, T.; Kudin, K. N.; Burant, J. C.; Millam, J. M.; Iyengar, S. S.; Tomasi, J.; Barone, V.; Mennucci, B.; Cossi, M.; Scalmani, G.; Rega, N.; Petersson, G. A.; Nakatsuji, H.; Hada, M.; Ehara, M.; Toyota, K.; Fukuda, R.; Hasegawa, J.; Ishida, M.; Nakajima, T.; Honda, Y.; Kitao, O.; Nakai, H.; Klene, M.; Li, X.; Knox, J. E.; Hratchian, H. P.; Cross, J. B.; Bakken, V.; Adamo, C.; Jaramillo, J.; Gomperts, R.; Stratmann, R. E.; Yazyev, O.; Austin, A. J.; Cammi, R.; Pomelli, C.; Ochterski, J. W.; Ayala, P. Y.; Morokuma, K.; Voth, G. A.; Salvador, P.; Dannenberg, J. J.; Zakrzewski, V. G.; Dapprich, S.; Daniels, A. D.; Strain, M. C.; Farkas, O.; Malick, D. K.; Rabuck, A. D.; Raghavachari, K.; Foresman, J. B.; Ortiz, J. V.; Cui, Q.; Baboul, A. G.; Clifford, S.; Cioslowski, J.; Stefanov, B. B.; Liu, G.; Liashenko, A.; Piskorz, P.; Komaromi, I.; Martin, R. L.; Fox, D. J.; Keith, T.; Al-Laham, M. A.; Peng, C. Y.; Nanayakkara, A.; Challacombe, M.; Gill, P. M. W.; Johnson, B.; Chen, W.; Wong, M. W.; Gonzalez, C.; Pople, J. A. *Gaussian 03*, revision C.02; Gaussian, Inc.: Wallingford, CT, 2004.
(21) (a) te Velde, G.; Bickelhaupt, F. M.; Baerends, E. J.; Fonseca Guerra, C.; van Gisbergen, S. J. A.; Snijders, J.; Ziegler, T. *J. Comput. Chem.* **2001**, *22* (9), 931–967. doi:10.1002/jcc.1056.; (b) Theoretical Chemistry, S. C. M. *ADF: Amsterdam density functional software*, 2007.01; Vrije Universiteit: Amsterdam, The Netherlands. Available from http://www.scm.com.
(22) Baerends, E. J.; Ellis, D. E.; Ros, P. *Chem. Phys.* **1973**, *2* (1), 41–51. doi:10.1016/0301-0104(73)80059-X.
(23) (a) Klamt, A.; Schüürmann, G. *J. Chem. Soc., Perkin Trans. 2* **1993**, 799; doi:10.1039/p29930000799.;(b) Barone, V.; Cossi, M. *J. Phys. Chem. A* **1998**, *102* (11), 1995–2001. doi:10.1021/jp9716997.; (c) Cossi, M.; Rega, N.; Scalmani, G.; Barone, V. *J. Comput. Chem.* **2003**, *24* (6), 669–681. doi:10.1002/jcc.10189. PMID:12666158.
(24) Branchadell, V.; Oliva, A. *J. Am. Chem. Soc.* **1991**, *113* (11), 4132–4136. doi:10.1021/ja00011a011.
(25) Branchadell, V.; Oliva, A. *J. Am. Chem. Soc.* **1992**, *114* (11), 4357–4364. doi:10.1021/ja00037a049.
(26) McCarrick, M. A.; Wu, Y. D.; Houk, K. N. *J. Org. Chem.* **1993**, *58* (12), 3330–3343. doi:10.1021/jo00064a020.
(27) Avalos, M.; Babiano, R.; Bravo, J. L.; Cintas, P.; Jiménez, J. L.; Palacios, J. C.; Silva, M. A. *J. Org. Chem.* **2000**, *65* (20), 6613–6619. doi:10.1021/jo000752b. PMID:11052109.
(28) (a) Ziegler, T.; Rauk, A. *Theor. Chim. Acta* **1978**, *46*, 1; doi:10.1007/BF00551648.(b) Ziegler, T.; Rauk, A. *Inorg. Chem.* **1979**, *18* (6), 1558–1565. doi:10.1021/ic50196a034.
(29) For an application of this kind of analysis to potential-energy barriers, see: Lecea, B.; Ayerbe, M.; Arrieta, A.; Cossío, F. P.; Branchadell, V.; Ortuño, R. M.; Baceiredo, A. *J. Org. Chem.* **2007**, *72* (2), 357–366. doi:10.1021/jo061662v. PMID:17221950.
(30) Hirshfeld, F. L. *Theor. Chim. Acta* **1977**, *44* (2), 129–138. doi:10.1007/BF00549096.

Nonlinear time-dependent density functional theory studies of the ionization of CO_2 by ultrashort intense laser pulses[1]

Emmanuel Penka Fowe and André Dieter Bandrauk

Abstract: Time-dependent density functional theory (TDDFT) studies of the ionization of CO_2 by intense laser pulses (3.50×10^{14}, 1.40×10^{15}, 2.99×10^{15}, and 1.25×10^{16} W/cm^2) at 800 nm ($\omega = 0.0584$ au) are presented in the nonlinear nonpertubative regime. Special emphasis is placed on elucidating molecular orbital orientation and various peak-intensities effects on the ionization processes. The results reveal that molecular orbital ionizations are strongly sensitive to their symmetry and the laser intensities. Most notably, we found that with a proper choice of the laser intensity (3.5×10^{14} W/cm^2), the sensitivity is strong enough such that the nature and symmetry of the highest occupied molecular orbital (HOMO) can be directly probed and visualized from the angular dependence of laser-induced ionization. At higher intensities, ionization is found to occur also from inner orbitals, thus complicating the imaging of simple orbitals. A time-dependent electron-localization function (TDELF) is used to get a visual insight on the time evolution process of the electron density.

Key words: TDDFT, orbital ionization, molecular ionization, molecular symmetry, TDELF.

Résumé : Opérant dans un régime non perturbant et non linéaire, on a effectué des études selon la théorie de la fonctionnelle de la densité en fonction du temps (TFDFT) de l'ionisation du CO_2 par des pulsations laser intenses ($3{,}50 \times 10^{14}$; $1{,}40 \times 10^{15}$; $2{,}99 \times 10^{15}$ et $1{,}25 \times 10^{16}$ W/cm^2) à 800 nm ($\omega = 0{,}0584$ au). On a placé une emphase spéciale sur l'élucidation de l'orientation de l'orbitale moléculaire et sur les effets des intensités des divers pics sur les processus d'ionisation. Les résultats révèlent que l'ionisation des orbitales moléculaires est très sensible à leur symétrie et aux intensités laser. La caractéristique la plus notable observée a trait au fait qu'avec un choix approprié d'intensité laser ($3{,}50 \times 10^{14}$ W/cm^2), la sensibilité est suffisamment forte que la nature et la symétrie de l'orbitale moléculaire haute occupée peuvent être directement examinées et visualisées à partir de la dépendance angulaire de l'ionisation induite par le laser. À des intensités plus élevées, on a trouvé que l'ionisation se produit aussi à partir des orbitales internes et que cette situation complique la visualisation des orbitales simples. On a fait appel à une fonction de localisation électronique en fonction du temps (FLEFT) pour obtenir une meilleure compréhension du processus d'évolution de la densité électronique en fonction du temps.

Mots-clés : théorie de la fonctionnelle de la densité en fonction du temps (TFDFT), ionisation d'orbitale, ionisation moléculaire, symétrie moléculaire, fonction de localisation électronique en fonction du temps (FLEFT).

[Traduit par la Rédaction]

Introduction

In the last two decades, the interaction of atoms and molecules with intense laser pulses has attracted widespread research. One of the reasons is that laser fields induce interesting nonlinear electron dynamics, such as multiphoton ionization[2] (MPI), above-threshold ionization[3] (ATI), and tunnelling ionization[4] (IT). Numerous experiments on the molecular ionization have been performed[5–7] thanks to the refinement technique[8] of the molecular orientation and alignment. More recently, tomography[9] imaging has emerged as a powerful tool to obtain the shape of the active molecular orbital. While experimental efforts for better understanding of the ionization processes are growing, theoretical investigations are still limited, even though computational power is increasing rapidly. Our group (Kamta and Bandrauk[10]) has developed recently, for one-electron systems[11] (H_2^+, HeH^{++}, and H_3^{++}), an approach of solving exactly the time-dependent Schrödinger equation (TDSE) to investigate the sensitivity of the orientation dependence of molecular ionization to the symmetry and the electron distribution in active molecular orbitals, based on Born–Oppenheimer (fixed nuclei) and dipole approximations ($r << \lambda$, where r is the dimension of charges and λ is the wavelength of the electric field). For the theoretical study of multielectrons system, the so-called ADK[12] (Ammosov–Delone–Krainov) model.

In the ADK, one commonly assumes that each electron moves independently in the ionization single-electron approximation where only the weakest bound valence electron interacts with the laser. The ionization process is also treated

Received 18 December 2008. Accepted 6 March 2009. Published on the NRC Research Press Web site at canjchem.nrc.ca on 30 June 2009.

E.P. Fowe and A.D. Bandrauk.[1] Laboratoire de Chimie Théorique, Faculté des Sciences, Université de Sherbrooke, Sherbrooke, QC J1K 2R1, Canada.

[1]Corresponding author (e-mail: Andre.Dieter.Bandrauk@USherbrooke.ca).

by tunnelling in the laser field of one-center expansions of a field-free multicenter function. The MO-ADK theory does not account for the many-electron effect, including the change of screening such as those discussed in the density functional approach. The theory also does not extend to regions where tunneling ionization is not the dominant ionization mechanism.

The major difficulties in the theoretical study of molecular systems in a laser field reside on the multicenter nature of the molecule, including the treatment of the electron–electron interactions.[10,11]

In this paper, we study the ionization process of CO_2 in an intense few laser field. CO_2 is an important molecule present in the earth's atmosphere, volcanic gases, oceans, ice cores in Antarctica, and so forth. It plays a primordial role in the photosynthesis process of plants, in human physiology, and in atmospheric processes. Its electronic structure determination via ionization has been the subject of several studies.[6,7,13] Villeneuve et al.[7] have obtained the angular dependence of ionization of linear molecules N_2, O_2, and CO_2 by recording the ion yield as a function of the angle between the polarization axis of the ionizing field and the main axis of the alignment distribution. Their fitted-results from the deconvolution of the ionization yield with the alignment distribution yield a butterfly-like distribution from the π symmetry of the HOMO of O_2 and CO_2; additionally, the angular dependence of the ionization of carbon dioxide is narrowness and peaks at 46° to the laser field, whereas the MO-ADK model predicts 25°. We remarked that in Fig. 6 in a previous work,[14] where single-electron π-orbital probabilities bend to smaller angles with increasing atoms separation, since there is no electron repulsion. So, the difference may be regarded as the manifestation of multielectron interactions effects, which are not properly take into account in the MO-ADK models.

To analyze the electron dynamics of the ionization process in CO_2, we have considered various laser pulse intensities and durations to probe the behaviour (symmetry and orientation) of the different molecular orbitals in the presence of a few cycles intense laser pulse. We have used the time-dependent density functional theory[15] approach, TDDFT, in the nonlinear nonperturbative regime (beyond conventional linear response theory,[16] which is extensively used nowadays for different spectroscopy properties[17]). This method is found to give a good compromise between accuracy and computer time, and is currently used.[18] Because details of our theoretical approach are given elsewhere,[19] we briefly review the formulation necessary for the present study in strong laser fields.

For a visual understanding of the electron motion on CO_2 during the time propagation under strong laser pulses, we used the time-dependent approach of the electron-localization function (ELF).[20–22] Conceptually, the physical idea is based on the fact that a highly localized electron repels other electrons stronger. Then, the ELF makes use of the probability to find a second like-spin electron in the vicinity of the first one as a measure for electronic localization. When applied to molecules, ELF's usefulness stem from the manner it allows to show a clear separation between the core and valence electron, and also shows covalent bonds and lone pairs, in the spirit of valence-shell electron-pair repulsion theory (VSEPR).

Nonpertubative TDDFT

Kohn–Sham formalism

The TDDFT method provides the most detailed and feasible ab initio approach for tackling many-body problems. Density functional theory (DFT) as first introduced by Hohenberg and Kohn,[23] and extended by Kohn and Sham (KS[24]) is based on the existence of an exact mapping between one-particle density and external potentials. This leads to the density of the interacting system being obtained from the density of an auxiliary system of non-interacting particles moving in an effective local single-particle potential. A time-dependent generalization of DFT was provided by Runge and Gross,[15] showing that there is a one-to-one correspondence between the external (time-dependent) potential, $\upsilon_{ext}(r,t)$, and the time-dependent one-electron density, $n(r,t)$, for many-body systems evolving from a fixed initial state. The time-dependent electronic density is written as[25]

$$[1] \qquad n(r,t) = \sum_{\sigma=\uparrow,\downarrow} n_\sigma(r,t) = \sum_{\sigma=\uparrow,\downarrow} \sum_{i}^{N_\sigma} |\psi_{i\sigma}(r,t)|^2$$

where, N_σ is the number of the electrons in the spin state σ and $\psi_{i\sigma}$ (r,t) is the orbital obtained through the time-dependent KS equations (in au):

$$[2] \qquad i\frac{\partial}{\partial t}\psi_{i\sigma}(r,t) = \left[-\frac{1}{2}\nabla^2 + \upsilon_{\text{eff}}(r,t)\right]\psi_{i\sigma}(r,t)$$

where

$$[3] \qquad \upsilon_{\text{eff}}(r,t) = \upsilon_{\text{ext}}(r,t) + \upsilon_{\text{h}}(r,t) + \upsilon_{\text{xc},\sigma}(r,t)$$

The first term is the external potential, due to the interaction of the electron with an external laser field and the nuclei, while the second term accounts for the classical hartree electrostatic interaction between electrons, and the third, the exchange correlation (xc) potential includes all non-trivial many body effects, and has an extremely complex (and essentially unknown) functional[19,24] dependence on the density. This dependence is non-local both in space and in time; thus, the quality of numerical solutions of eq. [2] will depend on the quality of the approximation to the xc potential used. KS proposed a simple approximation to xc, the local density approximation (LDA[26]). This functional uses the knowledge of the xc energy of the homogeneous electron gas[27] and has turned out to be quite adequate for a number of applications in time-independent problems.

Time-dependent electron-localization function (TDELF)

The ELF is a method for the mapping of electron-pair probability in multielectron systems. It was first introduced by Becke and Edgecombe[22] as a descriptor of electronic localization, using arguments based on the conditional same-spin pair probability function, generally for the Hartree–Fock approach. Thereafter, the function was readapted for DFT by Savin et al.[28] They interpreted the ELF in terms of the excess of local kinetic energy density due to the Pauli repulsion, and the Thomas–Fermi kinetic energy density for a homogeneous electron gas used as reference. Here, we briefly recall the definitions of the extension of the ELF for the time-dependent processes,[20,21] the time-dependent ELF, or TDELF, $\eta(r,t)$, is given as

Fig. 1. DFT/LDA images of the molecular orbitals of CO_2. Only the five highest occupied molecular orbitals are plotted.

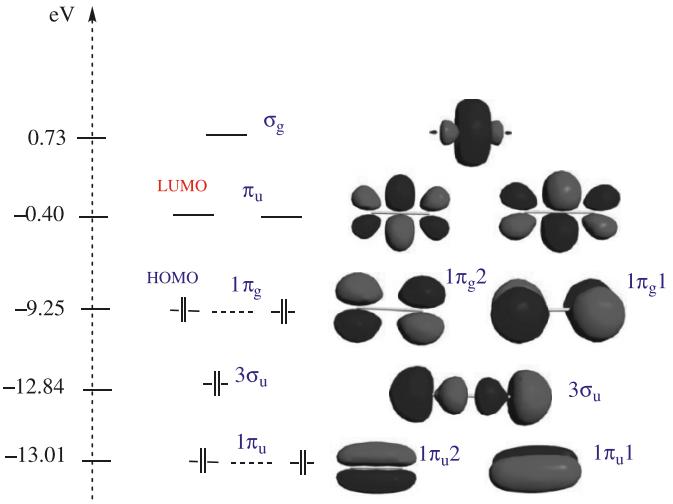

$$[4a] \qquad \eta(r,t) = \frac{1}{1 + [C(r,t)/C_h(r,t)]^2}$$

where

$$[4b] \qquad C(r,t) = \sum_{\sigma} \left\{ \sum_{i=1}^{N_\sigma} |\nabla \psi_{i\sigma}(r,t)|^2 - \frac{1}{4}\frac{[\nabla n_\sigma(r,t)]^2}{n_\sigma(r,t)} - \frac{j_\sigma^2(r,t)}{n_\sigma(r,t)} \right\}$$

$$[4c] \qquad C_h(r,t) = \frac{3}{5}(6\pi^2)^{2/3} n_\sigma(r,t)^{5/3}$$

j_σ^2 is the squared modulus of the current density. $C(r,t)$ measures the probability of finding one electron in the near vicinity of a reference like-spin electron at position r and time t. Thus, the Pauli repulsion between two like-spin electrons, described by the smallness of $C(r,t)$, is taken as a measure of the electron localization. $C_h(r,t)$ is the corresponding factor found for uniform electron gas, i.e., a homogeneous electron gas whose density is the same as that of the real system. Equation [4*b*] is valid only for one-determinantal wave functions, and therefore lends itself to be used within the context of HF or DFT. This expression has a convenient scaling factor to obtain values between 0 and 1. High values, $\eta(r,t) \rightarrow 1$, are associated to a high probability to find an electron pair, whereas the value $\eta(r,t) = 0.5$ indicates that the effect of the Pauli repulsion is the same as in the uniform electron gas of the same density. When applied to molecules, an analysis of the ELF shows a clear separation between the core and valence electron pairs (bonds and lone pairs) in the spirit of the Lewis theory. So, the ELF performs a partition of real molecular space into chemically meaningful regions and has been proven useful for describing the nature of the chemical bond in a wide variety of situations in comparison with electron densities.[21,29] In the present work, the TDELF will be used for the time-resolved observation of the molecular ionization, and can thus provide a visual understanding of the particle dynamic (most notably lone-pair and bond electrons) under strong laser pulses.

Fig. 2. Normalized total population, $\beta(t)$, as a function of laser intensities I (W/cm^2).

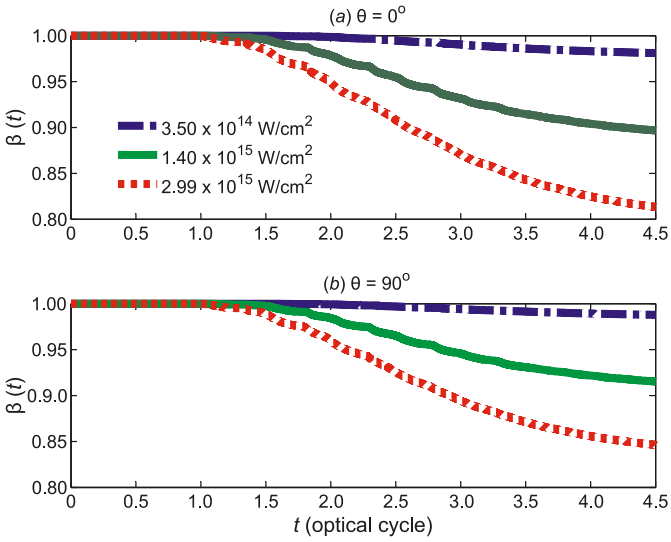

Computational details

The TDDFT KS equation, eq. [2], was discretized in space using grid technique combined with the Troullier–Martin pseudopotential,[30] and the resulting computer code was parallelized to run on a massively parallel processor. We have placed a CO_2 molecule in a large three-dimensional (3D) cubic grid cell (atomic units au, are used) of dimension a = 64 au The uniform finite-difference grid spacing, Δa = 0.26 au, was used for numerical integration, and the convergence of the calculations was checked against results with slightly smaller grid spacing. The external potential caused by an intense laser field is assumed to arise from an oscillating electric field with a cosinoidal envelope of the form:

$$[5] \qquad \upsilon_{ext}(r,t) = r \cdot E(t);\ E(t) = A_o \cos^2\left(\frac{\pi(t - 2\tau - t_o)}{2\tau}\right)\sin(\omega t)$$

A_o is the maximum field strength, τ is half of the total pulse duration, ω = 0.0584 au, and t_o is chosen such that $|t\text{-}t_o| < \tau$. The laser field linear polarization is set parallel to the molecular axis (z), and we have defined θ as the molecular orientation angle. The total area, $\int_{-\infty}^{+\infty} E(t)dt = 0$ ensures no spurious static effects.[4] The time-dependent equations are solved using the approximated enforced time-reversal symmetry method[31] to propagate the electronic wave functions with the time step Δt = 0.003 au. This method was found stable and provided a correct energy,[32] norm conservation, and was less computer-time-consuming than a Crank–Nicolson scheme.[33] We have used the local density approximation (LDA) of Perdew and Zunger[34] to represent the exchange-correlation potential υ_{xc}. To absorb the electrons reflecting spuriously at the boundary of the box, we included an imaginary poten-

Fig. 3. KS orbital population, $N(t)$, as a function of the laser intensities I (W/cm^2); only the relevant KS orbitals, which possess an important response to the laser fields, are shown with their label. Upper (*a*): the laser is parallel to the CO_2 axis, and bottom (*b*): the laser is perpendicular to the CO_2 axis.

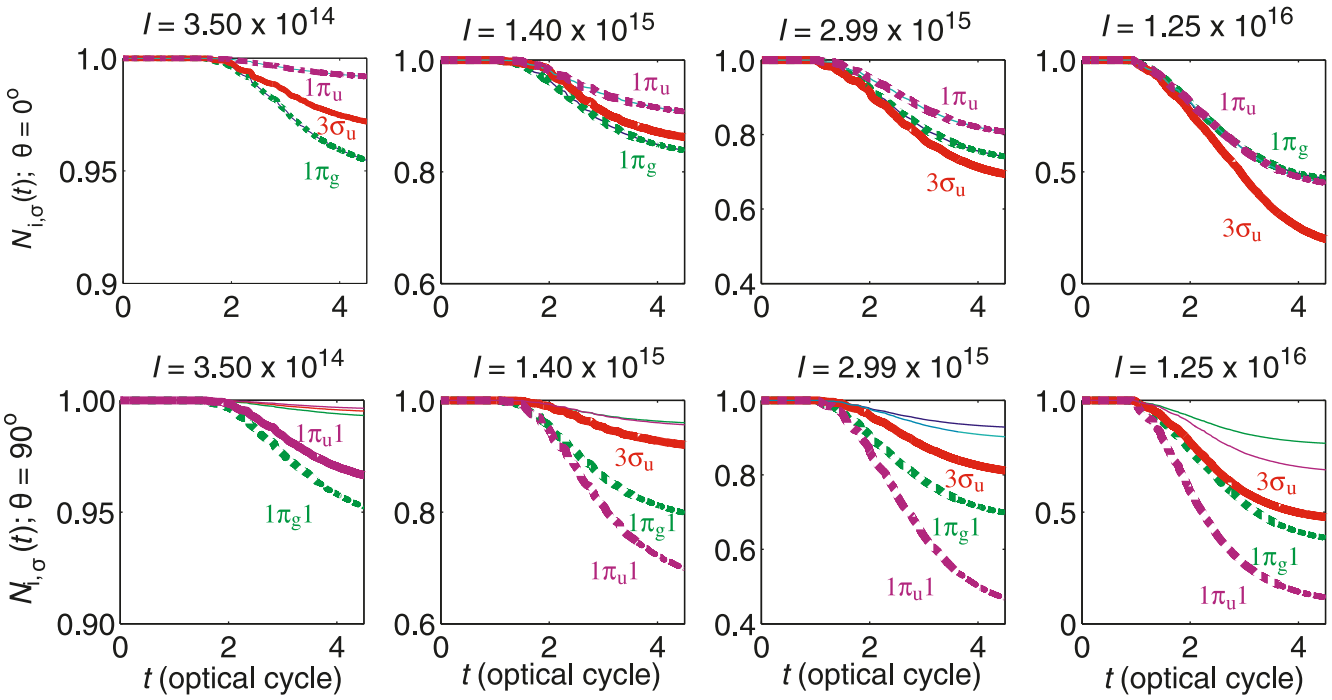

tial[35] in the Hamiltonian of the system. Thus, once the time-dependent wave functions and the time-dependent electron density were obtained, we have easily calculated the time-dependent ionization probability, $P_{i,\sigma}$, of an individual spin-orbital according to

$$[6] \qquad P_{i,\sigma} = 1 - N_{i,\sigma}(t)$$

where

$$[7] \qquad N_{i,\sigma}(t) = \langle \psi_{i,\sigma}(t) | \psi_{i,\sigma}(t) \rangle$$

is the time-dependent population (suvival probability) of the i,σ-th spin-population. In the grid, the number of the electrons inside the box is given as

$$[8] \qquad N_{\text{bound}}(t) = \int_{\text{inside the box}} d^3r \; n(r,t)$$

and the normalized remaining electron population is

$$[9] \qquad \beta(t) = \frac{\int_{\text{inside the box}} d^3r \; n(r,t)}{\int_{\text{inside the box}} d^3r \; n(r,0)} = e^{-\Gamma t}$$

Γ is the ionization rate, and

$$n\,(r,0) = \sum_{\sigma=\uparrow,\downarrow} n_\sigma(r,0) = \sum_{\sigma=\uparrow,\downarrow} \sum_{i}^{N_\sigma} |\psi_{i\sigma}(r,0)|^2$$

is the total number of electrons in the initial state (without external field). The ionization yield probability, $\gamma(t_f)$, computed at the final time, t_f, of the propagation is then deduced as the following difference:

$$[10] \qquad \gamma(t_f) = 1 - \beta(t_f)$$

and the KS orbital ionization, $\delta(t_f)$, is deduced as

$$[11] \qquad \delta(t_f) = 1 - N_{i,\sigma}(t_f)$$

Results and discussion

Electronic analysis and ionization potential in DFT/LDA

The relevant information of the ground-state geometry of CO_2 is that the molecule is linear and the computed CO bond length is 1.161 Å, which is in good agreement with the experimental[36] value (CO = 1.162 Å).

The analysis of the electronic structure from the DFT-KS equation is depicted in Fig. 1. The five highest occupied KS molecular orbitals with their phases are presented. The nodal properties, which correctly reflect the g and u character of the orbitals, are visible. One finds that the highest occupied molecular orbital (HOMO), $1\pi_g$, is antibonding. It is formed of π lobes lying perpendicular to the internuclear axis and located on the oxygen atoms. We note from our DFT/LDA calculation that the energies of the $1\pi_u$ and $3\sigma_u$ are close (we have found a difference of the magnitude of 0.2 eV). Recently, it has been established that Kohn–Sham orbitals are physically[37] sound and are expected to be more suitable for use in qualitative molecular-orbital theory than either Hartree–Fock or semiempirical orbitals. In fact, the exact exchange–correlation potential, υ_{xc}, should give the exact ionization potential (IP) corresponding to the negative of the KS HOMO energy ($-\varepsilon_{HOMO}$). In the present work, due to the LDA approximation, we have carried out the calculation of IP by the computation of the vertical ionization potential. This is done by a proper subtraction of the total

Fig. 4. Computed and measured ionization yield, $\gamma(t_f)$, as a function of the angle, θ, between the CO_2 molecule and the laser beam: (*a*) experimental angular[6] distributions for correlated (CO^+, O^+) ion pairs produced by the dissociation of CO_2^+ by (8 fs, 800 nm central wavelength and 1×10^{14} W/cm^2) laser pulses; (*b*) data from Villeneuve et al.[7] (1.1×10^{14} W/cm^2); (*c*) simulated angular distributions of the first ionization[6] from ADK theory; (*d*) results from the TDDFT of this work.

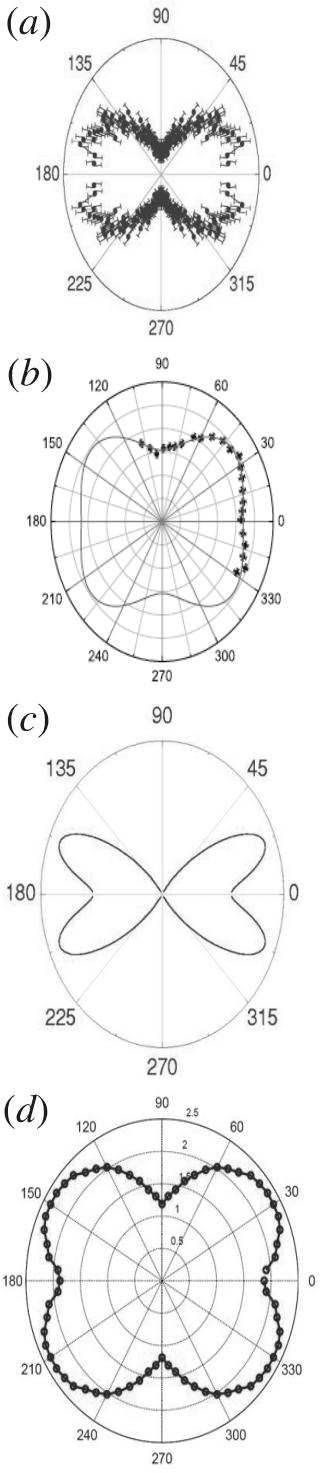

Fig. 5. TDDFT/LDA polar coordinate representation of the ionization probability of CO_2 for (*a*) the Homo, $1\pi_u$, and (*b*) the Homo-1, $3\sigma_u$, MOs vs. the orientation angle θ. Laser parameters are $I = 3.5 \times 10^{14}$ W/cm^2, $\omega = 0.0584$ au, and the total pulse duration is 4 optical cycles (10.8 fs).

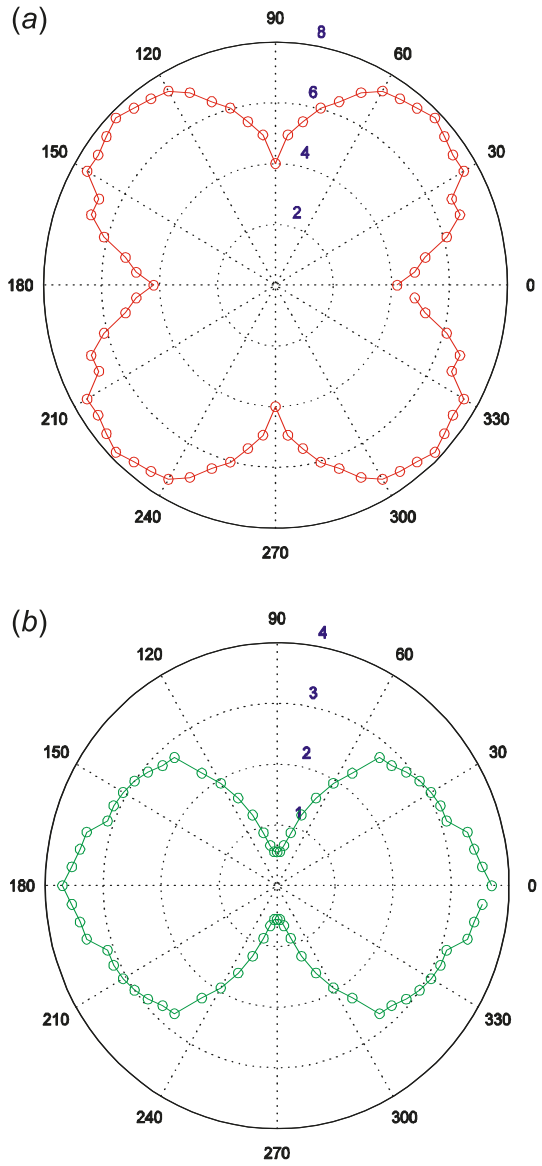

energies for the neutral and the cation obtained at the equilibrium geometry of the neutral. One has to emphasize that "vertical" here means the underlying assumption that no geometrical structural changes occur during the ionization process. The computed value of the vertical IP is 14.26 eV, which is near to the available experimental[38] data 13.77 eV.

CO_2 ionization

Our time-dependent calculation allows a detailed analysis of the ionization process as it evolves with time. From the initial ground state, we have propagated in time the KS orbitals, and computed the ionization factor according to eq. [9]. We display in Fig. 2 the dependence of the total normalized remaining population, $\beta(t)$, with different laser peaks intensities (3.50×10^{14}, 1.40×10^{15}, and 2.99×10^{15} W/cm^2) at

Fig. 6. DFT/LDA representation of the ELF for the ground state of CO_2: isosurfaces (bottom) of the ELF with a value of 0.85 reveal the lone pairs (a) as lobes on the oxygen atoms and contour maps (top) of the ELF for throughout the plane containing all atoms. The most localized electron regions, which correspond to the lone pair (a) and the CO bond (b), are clearly visible.

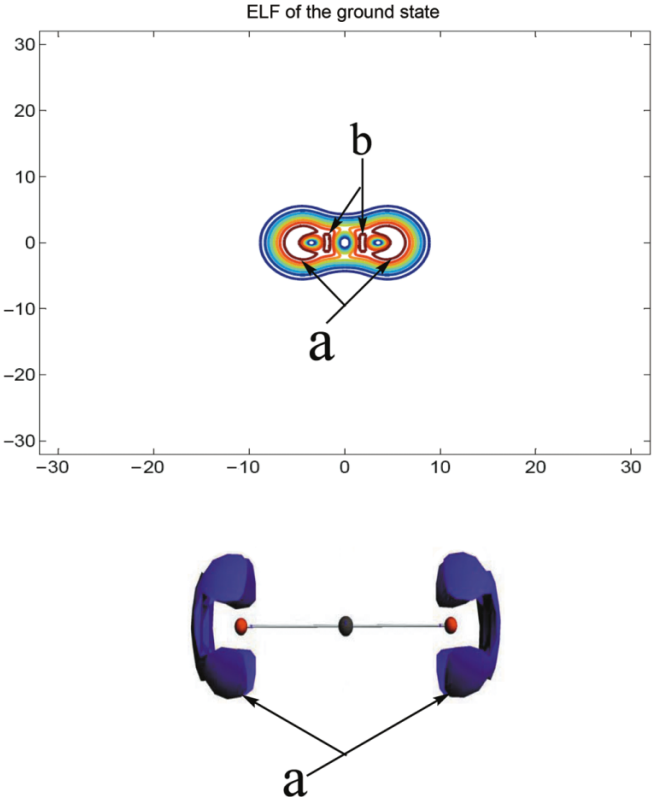

800 nm wavelength. Calculations have been done for four optical cycle pulse duration.

Two molecular orientations have been considered, $\theta = 0^\circ$ and $\theta = 90^\circ$. One observes a strong dependence of the remaining electron population, $\beta(t)$, on the laser intensities. So, the higher the laser intensity, the lower the remaining electron population. A close look reveals that the ionization is sensitive to the orientation, θ, of the molecule with respect to the laser field; ionization at $\theta = 0^\circ$ is higher than that at $\theta = 90^\circ$. Similar results have been observed in H_2^+ from exact TDSE calculations.[10]

Orbital influence on the ionization

To gain a better understanding of the ionization dynamics as a function of the orbital symmetries, we investigate, in Fig. 3, the time-dependent evolution of some relevant KS molecular orbitals by the aid of eq. [7].

The ionization rate of each KS, $\Gamma_i = -(\ln(N_{i,\sigma}(t))/t$ for the molecular orbital, $\psi_i(r,t)$ can be obtained as the slope of the decay of the population in time (see Supplementary data, Table S) of its orbital norm (see eqs. [9]–[10]). The laser (electric) field is assumed to be either parallel ($\theta = 0^\circ$) or perpendicular ($\theta = 90^\circ$) to the CO_2 molecular axis, and the internuclear distance for the molecule is fixed at its equilibrium distance. Results for four laser intensities, 3.50×10^{14}, 1.40×10^{15}, 2.99×10^{15}, and 1.25×10^{16} W/cm^2, are shown. According to the molecular orientation, we have subdivided Fig. 3 in two parts, named respectively, Fig. 3*a* where $\theta = 0^\circ$ and Fig. 3*b* with $\theta = 90^\circ$. In Fig. 3*a*, one sees that for symmetry reason, the two components of each π orbital have the same behaviour. One finds also that the KS molecular orbitals are sensitive to the applied laser field intensities, so at lower intensities, 3.50×10^{14} and 1.40×10^{15} W/cm^2, it emerges that the $1\pi_g$ molecular orbital shows the dominant response to the field and is followed by the inner $3\sigma_u$ orbital whose ionization is growing with the laser intensities. For the last two intensities, 2.99×10^{15} and 1.25×10^{16} W/cm^2, the inner $3\sigma_u$ molecular orbital presents the dominant response to the field, whereas the effect of the valence $1\pi_g$ orbital on the ionization process is decreasing and is getting closer to that of the $1\pi_u$ orbital, probably resulting from the enhancement of the coupling between these orbitals, which results in charge–resonance enhanced ionization (CREI), enhanced ionization in H_2^+ at large internuclear distance.[11] Our results show that the orientation effect of the orbital plays a key role in the ionization process. In regard to our data, we can say that the anisotropy of the ionization of CO_2 is more significant at smaller laser intensities where the expected higher valence orbital is more active, whereas at higher intensity, the inner, $3\sigma_u$ electrons whose orbital orientation is parallel to the polarization direction of the laser field ionizes faster.

Figure 3*b* treats the cases of the laser oriented perpendicularly to the CO_2 molecular axis, the symmetry contribution of the different components of the π orbital (e.g, π_g components are renamed π_g1 and π_g2) is broken, as a consequence of their orientation, i.e., each component of the KS π orbital is feeling the presence of the laser field in a different way. At lower intensity, 3.50×10^{14} W/cm^2, as in the previous analysis, the $1\pi_g$ molecular orbital shows the dominant response to the field and is followed by the inner $1\pi_u$ orbital. As the intensity is increasing, the response effect of the $1\pi_u$ orbital becomes more and more pronounced than that of $1\pi_g$. This behaviour illustrates a rather complicated correlated response of the orientation of the different orbitals to the intense laser field. Meanwhile, one of the main results is that at 3.50×10^{14} W/cm^2, the $1\pi_g$ orbital remains the most influenced by the laser. Thus, it appears that at 3.50×10^{14} W/cm^2, single ionization of CO_2 occurs predominantly by ionization of the valence electron of the HOMO. To see the effect of the laser pulse duration, τ, on the ionization process, we have calculated, for 3.50×10^{14} W/cm^2, the orbital ionization during 10 laser pulse cycles, and we have found that it is increasing with the pulse duration, and more importantly, the electron is always ionized from HOMO, the highest occupied molecular orbital $1\pi_g$.

To analyze the details of the angular-dependent ionization rate of CO_2, the corresponding ionization probability, $\gamma(t_f)$, eq. [10] vs. the orientation angle, θ, is plotted in polar coordinates in Fig. 4. Some experimental data are also showed for comparison. The calculations were performed with, θ, varying from 0° to 90° (5° angle step) and were reflected to the rest of the trigonometric circle to give a complete picture. It appears from our result that the ionization rate peaks somewhere between 30° and 40°, and shows minima at 0° and 90°. This, because the HOMO has a nodal plane containing (or perpendicular to) the molecular axis, is giving

Fig. 7. Snapshot of the TDELF for 3.5×10^{14} W/cm^2 (left and noted (*a*) in the text) and for 1.25×10^{16} W/cm^2 (right and noted (*b*) in the text).

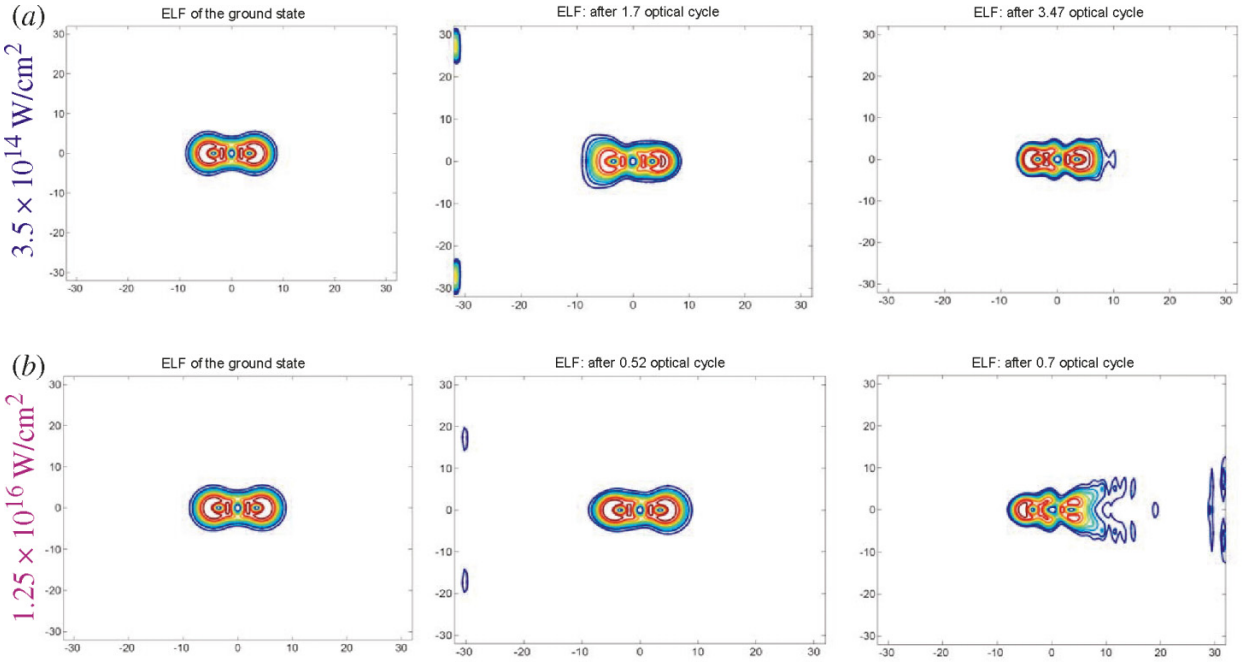

rise to a low probability for ionization when aligned parallel (or perpendicular) to the laser electric field, and this is corroborated by exact TDSE calculations in H_2^+.[10]

Furthermore, the ionization at $\theta = 0^\circ$ is higher compared with that at $\theta = 90^\circ$, in good correlation with our orbital ionization results in Fig. 3. More generally, our plot (Fig. 4*d*) exhibits a butterfly pattern, which is characteristic of the $1\pi_g$ orbital and clearly shows a good agreement with the experimental result (Fig. 4*b*).[7] The nonzero and negligible ionization at $\theta = 0^\circ$ and $\theta = 90^\circ$ reflects contributions from the $3\sigma_u$ orbital at $\theta = 0^\circ$ and the $1\pi_u$ at $\theta = 90^\circ$. We repeated the previous operation to image the $3\sigma_u$ and $1\pi_u$ molecular orbitals by the calculation of the molecular-orbital ionization from the eq. [11]. The results are shown in Fig. 5. We find once again that for the selected molecular orbitals, our model reproduces the shape of the corresponding ground-state molecular orbital. However, one observes an absence of nodal planes on the $1\pi_u$ molecular orbital, and a lengthening of the form of the $3\sigma_u$ molecular orbital. This may be regarded as the result of a coupling of the selected MO with some virtual orbitals.[10]

TDELF analysis

The two-dimensional representation of the ELF isosurfaces for the ground state of CO_2 is presented in Fig. 6. The figure depicts a slab of the ELF passing through the plane containing the molecule. The most localized domains are clearly visible, and they correspond to the lone pairs on the oxygen atoms and the C–O bond electrons.

The comparison of ELFs in the ground state and during the time propagation (TDELF) is showed in Fig. 7*a* for 3.5×10^{14} W/cm^2 and in Fig. 7*b* for 1.25×10^{16} W/cm^2. We point out that the induced dipoles from $1\pi_u$ (HOMO) and $3\sigma_u$ (HOMO-1) are polarized in opposite direction. In Fig. 7*a*, one sees that after 1.7 optical cycles, the first electronic perturbation occurs as expected on the lone pairs of the oxygen atom and while the two domains (lone pair and C–O bond) are subsequently affected by the laser field during the propagation, we note that the perturbation is much higher on lone pairs. In Fig. 7*b*, our results show that at the very beginning of the interaction of CO_2 with the laser field (after 0.52 optical cycle), as previously, one observes that the electronic perturbation appears on the lone pairs of the oxygen, but thereafter and suddenly, it is greatly exceeded by that emerging from the C–O bond domain. It will remain so throughout the simulation. These observations are consistent with our findings in Fig. 3. We add a table of the ionization rate, which shows the increasing importance of inner orbitals with the laser intensities.

Conclusion

In this work, orbital populations, $N_{i,\sigma}(r, t)$, and ionization yields, $\gamma(t_f)$, have been computed for CO_2 molecule with different laser intensities from a nonlinear nonpertubative TDDFT approach.[19,25] In view of all results, we conclude that both the symmetry of the KS orbitals and the laser intensities play an important role in the ionization process. We showed that for 3.5×10^{14} W/cm^2, the orientation dependence of the ionization probability maps the electron distribution in the active orbital, thereby allowing to image the contour of electron density distributions in molecules. We have introduced time-dependent electronic localization function, TDELF, to visualize the ionization dynamics. Further refinements are required, since it is a well-known property of the static DFT/LDA that the single-particle ionization threshold is underestimated,[19] due to the wrong asymptotic behaviour of the KS potential or the self interaction error (SI).[25,37] The SI effect arises from the interaction of an electron with itself, and it is related to Coulomb energy of the KS Hamiltonian, which is not, in contrast to the Hartree–

Fock (HF) and post-HF approach, totally cancelled by the exchange contribution. Work to improve the cancellation of the SI by either the mixing in of half-and-half exchange, combining a (local) GGA exchange functional with the (nonlocal) HF (so-called hybrid functionals[39]) or by using the exact exchange based on the optimized effective potential[40] (OEP) as developed by Krieger, Li, and Iafrate (KLI[41]), is in progress for orbital functionals to include memory effects and derivative discontinuities.[7,42]

Supplementary data

Supplementary data for this article are available on the journal Web site (canjchem.nrc.ca) or may be purchased from the Depository of Unpublished Data, Document Delivery, CISTI, National Research Council Canada, Ottawa, ON K1A 0R6, Canada. DUD 3959. For more information on obtaining material, refer to cisti-icist.nrc-cnrc.gc.ca/cms/unpub_e.shtml.

Acknowledgement

The authors would like to express their thanks to the Natural Sciences and Engineering Research Council of Canada (NSERC) and the Canadian Institute for Photonic Innovations (CIPI) for funding this research on the theory of the intense laser – molecule interaction and Réseau Québécois de Calcul de Haute Performance (RQCHP), for parallel computer time. The authors are also thankful to Dr. L. Kamta, Dr. S. Chelkowski, Dr. N. Nguyen, and Dr. H. Lu for their helpful discussions.

References

(1) This article is part of a Special Issue dedicated to Professor T. Ziegler.

(2) (a) Lin, S. H.; Fujimura, Y.; Neusser, H. J.; Schlag, E. W. *Multiphoton spectroscopy of molecules*; Academic Press: London, 1984; (b) Bandrauk, A. *Molecules in laser fields*; M. Dekker: New York, 1994.

(3) (a) Gavrila, M. *Atoms in intense fields*; Academic Press: New York, 1992; (b) Lewenstein, M.; Kulander, K. C.; Schafer, K. J.; Bucksbaum, P. H. *Phys. Rev. A* **1995**, *51* (2), 1495–1507. doi:10.1103/PhysRevA.51.1495. PMID:9911736.

(4) Brabec, T.; Krausz, F. *Rev. Mod. Phys.* **2000**, *72* (2), 545–591. doi:10.1103/RevModPhys.72.545.

(5) (a) l'Huillier, A.; Lompre, L. A.; Mainfray, G.; Manus, C. *Phys. Rev. A* **1983**, *27* (5), 2503–2512. doi:10.1103/PhysRevA.27.2503.; (b) Perry, M. D.; Landen, O. L.; Szöke, A.; Campbell, E. M. *Phys. Rev. A* **1988**, *37* (3), 747–760. doi:10.1103/PhysRevA.37.747. PMID:9899717.; (c) Chin, S. L.; Rolland, C.; Corkum, P. B.; Kelly, P. *Phys. Rev. Lett.* **1988**, *61* (2), 153–156. doi:10.1103/PhysRevLett.61.153. PMID:10039046.; (d) Mainfray, G.; Manus, C. *Rep. Prog. Phys.* **1991**, *54* (10), 1333–1372. doi:10.1088/0034-4885/54/10/002.; (e) Larochelle, S.; Talebpour, A.; Chin, S. L. *J. Phys. At. Mol. Opt. Phys.* **1988**, *31* (6), 1201–1214. doi:10.1088/0953-4075/31/6/008.; (f) Litvinyuk, I. V.; Lee, K. F.; Dooley, P. W.; Rayner, D. M.; Villeneuve, D. M.; Corkum, P. B. *Phys. Rev. Lett.* **2003**, *90* (23),o. 233003. doi:10.1103/PhysRevLett.90.233003. PMID:12857255.

(6) Alnaser, A. S.; Maharjan, C. M.; Tong, X. M.; Ulrich, B.; Ranitovic, P.; Shan, B.; Chang, Z.; Lin, C. D.; Cocke, C. L.; Litvinyuk, I. V. *Phys. Rev. A* **2005**, *71* (3),o. 031403. doi:10.1103/PhysRevA.71.031403.

(7) Pavičić, D.; Lee, K. F.; Rayner, D. M.; Corkum, P. B.; Villeneuve, D. M. *Phys. Rev. Lett.* **2007**, *98* (24),o. 243001. doi:10.1103/PhysRevLett.98.243001. PMID:17677961.

(8) Stapelfeldt, H.; Seideman, T. *Rev. Mod. Phys.* **2003**, *75* (2), 543–557. doi:10.1103/RevModPhys.75.543.

(9) Itatani, J.; Levesque, J.; Zeidler, D.; Niikura, H.; Pépin, H.; Kieffer, J. C.; Corkum, P. B.; Villeneuve, D. M. *Nature* **2004**, *432* (7019), 867–871. doi:10.1038/nature03183. PMID:15602553.

(10) (a) Kamta, G. L.; Bandrauk, A. D. *Phys. Rev. A* **2004**, *70* (1),o. 011404. doi:10.1103/PhysRevA.70.011404.; (b) Kamta, G. L.; Bandrauk, A. D. *Phys. Rev. A* **2005**, *71* (5),o. 053407. doi:10.1103/PhysRevA.71.053407.; (c) Kamta, G. L.; Bandrauk, A. D. *Laser Phys.* **2005**, *15*, 502.

(11) (a) Bandrauk, A. D.; Barmaki, S.; Chelkowski, S.; Kamta, G. L. In *Progress in ultrafast intense laser science*; Vol. III; Yamanouchi, K., Chin, S. L., Agostini, P., and Ferrante, G., Eds.; Springer: New York, 2007; (b) Bandrauk, A. D.; Barmaki, S.; Kamta, G. L. *Phys. Rev. Lett.* **2007**, *98* (1),o. 013001. doi:10.1103/PhysRevLett.98.013001. PMID:17358471.

(12) (a) Ammosov, M. V.; Delone, N. B.; Krainov, V. P. *Sov. Phys. JETP* **1986**, *64*, 1191; (b) Ammosov, M. V.; Delone, N. B.; Krainov, V. P. *Zh. Eksp. Teor. Fiz* **1986**, *91*, 2008.

(13) (a) Chen, Y.; Li, Y.; Yang, S.; Liu, J. *Phys. Rev. A* **2008**, *77* (3),o. 031402. doi:10.1103/PhysRevA.77.031402.; (b) Lin, C. D.; Tong, X. M. *J. Photochem. Photobiol. Chem.* **2006**, *182* (3), 213–219. doi:10.1016/j.jphotochem.2006.04.027.; (c) Kono, H.; Koseki, S.; Shiota, M.; Fujimura, Y. *J. Phys. Chem. A* **2001**, *105* (23), 5627–5636. doi:10.1021/jp003848i.; (d) Gühr, M.; McFarland, B. K.; Farrell, J. P.; Bucksbaum, P. H. *J. Phys. At. Mol. Opt. Phys.* **2007**, *40* (18), 3745–3755. doi:10.1088/0953-4075/40/18/013.; (e) Yudin, G. L.; Ivanov, M. Y. *Phys. Rev. A* **2001**, *64* (1),o. 013409. doi:10.1103/PhysRevA.64.013409.; (f) Nalda, R.; Heesel, E.; Lein, M.; Hay, N.; Velotta, R.; Springate, E.; Castillejo, M.; Marangos, J. P. *Phys. Rev. A* **2004**, *69* (3),o. 031804. doi:10.1103/PhysRevA.69.031804.

(14) Lagmago Kamta, G.; Bandrauk, A. D. *Phys. Rev. A* **2006**, *74* (3),o. 033415. doi:10.1103/PhysRevA.74.033415.

(15) Runge, E.; Gross, E. K. U. *Phys. Rev. Lett.* **1984**, *52* (12), 997–1000. doi:10.1103/PhysRevLett.52.997.

(16) Marques, M. A. L.; Ullrich, C. A.; Nogueira, F.; Rubio, A.; Burke, K.; Gross, E. K. U. *Time-dependent density functional theory*; Springer: Berlin, 2006.

(17) (a) Casarin, M.; Finetti, P.; Vittadini, A.; Wang, F.; Ziegler, T. *J. Phys. Chem. A* **2007**, *111* (24), 5270–5279. doi:10.1021/jp071561g. PMID:17523609.; (b) Seth, M.; Autschbach, J.; Ziegler, T. *J. Chem. Theory Comput.* **2007**, *3* (2), 434–447. doi:10.1021/ct600283t.; (c) Seth, M.; Ziegler, T.; Banerjee, A.; Autschbach, J.; van Gisbergen, S. J. A.; Baerends, E. J. J. *Chem. Phys.* **2004**, *120*, 10942.

(18) (a) Chu, X.; Chu, S. *Phys. Rev. A* **2004**, *70* (6),o. 061402. doi:10.1103/PhysRevA.70.061402.; (b) Dundas, D.; Rost, J. M. *Phys. Rev. A* **2005**, *71* (1),o. 013421. doi:10.1103/PhysRevA.71.013421.; (c) Nobusada, K.; Yabana, K. *Phys. Rev. A* **2004**, *70* (4),o. 043411. doi:10.1103/PhysRevA.70.043411.; Marques, M. A. L.; Gross, E. K. U. *Annu. Rev. Phys. Chem.* **2004**, *55* (1), 427–455. doi:10.1146/annurev.physchem.55.091602.094449. PMID:15117259.

(19) Ullrich, C. A.; Bandrauk, A. D. In *Time-dependent density functional theory*; Burke, K and Marques, M., Eds.; Springer: New York, 2006; p. 357.

(20) Erdmann, M.; Gross, E. K. U.; Engel, V. *J. Chem. Phys.*

2004, *121* (19), 9666–9670. doi:10.1063/1.1806812. PMID: 15538889.
(21) Burnus, T.; Marques, M. A. L.; Gross, E. K. U. *Phys. Rev. A* **2005**, *71* (1),o. 010501. doi:10.1103/PhysRevA.71.010501.
(22) Becke, A. D.; Edgecombe, K. E. *J. Chem. Phys.* **1990**, *92* (9), 5397. doi:10.1063/1.458517.
(23) Hohenberg, P.; Kohn, W. *Phys. Rev.* **1964**, *136* (3B)(3B), B864–B871. doi:10.1103/PhysRev.136.B864.
(24) Kohn, W.; Sham, L. J. *Phys. Rev.* **1965**, *140* (4A)(4A), A1133–A1138. doi:10.1103/PhysRev.140.A1133.
(25) Nguyen, H. S.; Bandrauk, A. D.; Ullrich, C. A. *Phys. Rev. A* **2004**, *69* (6), o. 063415. doi:10.1103/PhysRevA.69.063415.
(26) Kohn, W.; Sham, L. *Phys. Rev.* **1965**, *140* (4A)(4A), A1133–A1138. doi:10.1103/PhysRev.140.A1133.
(27) Ceperley, D. M.; Alder, B. J. *Phys. Rev. Lett.* **1980**, *45* (7), 566–569. doi:10.1103/PhysRevLett.45.566.
(28) Savin, A.; Flad, H.-J.; Flad, J.; Preuß, H.; von Schnering, H. G. *Angew. Chem.* **1992**, *104* (2), 185–186. doi:10.1002/ange.19921040211.
(29) (a) Pilme, J.; Silvi, B.; Alkhani, M. *J. Phys. Chem.* **2003**, *107A*, 4506; (b) Kohout, M.; Wagner, F.; Grin, Y. *Theor. Chem. Acc.* **2002**, *108*, 150; (c) Fowe, E. P.; Therrien, B.; Süss-Fink, G.; Daul, C. *Inorg. Chem.* **2008**, *47* (1), 42–48. doi:10.1021/ic7007914. PMID:18052334.; (d) Fuentealba, P.; Savin, A. *J. Phys. Chem. A* **2001**, *105* (51), 11531–11533. doi:10.1021/jp012004b.; (e) Räsänen, E.; Castro, A.; Gross, E. K. U. *Phys. Rev. B* **2008**, *77* (11),o. 115108. doi:10.1103/PhysRevB.77.115108.
(30) (a) Troullier, N.; Martins, J. L. *Solid State Commun.* **1990**, *74* (7), 613–616. doi:10.1016/0038-1098(90)90686-6.; (b) Troullier, N.; Martins, J. L. *Phys. Rev. B* **1991**, *43* (3), 1993–2006. doi:10.1103/PhysRevB.43.1993.; (c) Castro, A.; Appel, H.; Oliveira, M.; Rozzi, C. A.; Andrade, X.; Lorenzen, F.; Marques, M. A. L.; Gross, E. K. U.; Rubio, A. *Phys. Status Solidi, B Basic Res.* **2006**, *243* (11), 2465–2488. doi:10.1002/pssb.200642067.
(31) Castro, A.; Marques, M. A. L.; Rubio, A. *J. Chem. Phys. Rev A* **2004**, *121*, 3425.
(32) (a) Yabana, K.; Bertsch, G. F. *Phys. Rev. B* **1996**, *54* (7), 4484–4487. doi:10.1103/PhysRevB.54.4484.; (b) Yan-Ping, Z.; Feng-Shou, Z.; Ke-Lai, M.; Guo-Qing, X. *Commun. Theor. Phys.* **2007**, *47* (5), 901–904. doi:10.1088/0253-6102/47/5/027.
(33) Crank, J.; Nicolson, P.; Hartree, D. R. *Proc. Camb. Philos. Soc.* **1947**, *43* (01), 50. doi:10.1017/S0305004100023197.
(34) Perdew, J. P.; Zunger, A. *Phys. Rev. B* **1981**, *23* (10), 5048–5079. doi:10.1103/PhysRevB.23.5048.
(35) (a) Fevens, T.; Jiang, H. *SIAM J. Sci. Comput.* **1999**, *21* (1), 255. doi:10.1137/S1064827594277053.; (b) Bandrauk, A. D.; Lu, H. Z. *Phys. Rev. A* **2005**, *72* (2),o. 023408. doi:10.1103/PhysRevA.72.023408.
(36) Jiang, H.; Novak, I. *J. Mol. Struct.* **2003**, *645* (2–3), 177.
(37) (a) Baerends, E. J.; Gritsenko, O. V. *J. Chem. Phys.* **1997**, *101*, 5383; (b) Chong, D. P.; Gritsenko, O. V.; Baerends, E. J. *J. Chem. Phys.* **2002**, *116* (5), 1760. doi:10.1063/1.1430255.; (c) Wolfe, S.; Shi, Z.; Brion, C. E.; Rolke, J.; Zheng, Y.; Cooper, G.; Chong, D. P.; Hu, C. Y. *Can. J. Chem.* **2002**, *80* (3), 222–227. doi:10.1139/v01-201.; (d) García, J. I.; Martinez-Merino, V.; Mayoral, J. A. *J. Org. Chem.* **1998**, *63* (7), 2321–2324. doi:10.1021/jo972174d.; (e) Parr, R. G.; Yang, W. *Density functional theory of atoms and molecules*; Oxford University Press: Oxford, 1989; (f) Zheng, Y.; Rolke, J.; Cooper, G.; Brion, C. E. *J. Electron Spectrosc. Relat. Phenom.* **2002**, *123* (2-3), 377–388. doi:10.1016/S0368-2048(02)00034-8.
(38) (a) Kikoin, I. K. *Tables of physical quantities*; Atomizdat: Moscow, 1976 [in Russian]; (b) Anishchenko, Y. V. *J. Appl. Spectrosc.* **1997**, *64* (6), 866–868. doi:10.1007/BF02678875.
(39) Ciofini, I.; Adamo, C.; Chermette, H. *Chem. Phys.* **2005**, *309* (1), 67–76. doi:10.1016/j.chemphys.2004.05.034.
(40) (a) Talman, J. D.; Shadwick, W. F. *Phys. Rev. A* **1976**, *14* (1), 36–40. doi:10.1103/PhysRevA.14.36.; (b) Sharp, R. T.; Horton, G. K. *Phys. Rev.* **1953**, *90* (2), 317. doi:10.1103/PhysRev.90.317.
(41) Krieger, J. B.; Li, Y.; Iafrate, G. J. *Phys. Rev. A* **1992**, *45* (1), 101–126. doi:10.1103/PhysRevA.45.101. PMID: 9906704.
(42) (a) Maitra, N. T.; Burke, K.; Woodward, C. *Phys. Rev. Lett.* **2002**, *89* (2),o. 023002. doi:10.1103/PhysRevLett.89.023002. PMID:12096991.; (b) Mundt, M.; Kümmel, S. *Phys. Rev. A* **2006**, *74* (2),o. 022511. doi:10.1103/PhysRevA.74.022511.

A solid-state ^{31}P NMR study of 1:1 silver–triphenylphosphine complexes — Interpretation of $^{1}J(^{107,109}Ag,^{31}P)$ values[1,2]

Fu Chen, Se-Woung Oh, and Roderick E. Wasylishen

Abstract: High-resolution solid-state ^{31}P NMR spectroscopy was used to investigate a series of 1:1 silver–triphenylphosphine complexes, $[Ph_3PAgX]_n$, where X is a monovalent anion and n = 1, 2, 3, 4, or ∞. The ^{31}P CP MAS NMR spectra reveal the number of distinct phosphorus sites in these complexes as well as the $|^{1}J(^{109}Ag,^{31}P)|$ values, which range from 401 ± 10 Hz ($X = N_3^-$) to 869 ± 10 Hz ($X = SO_3CF_3^-$). The data obtained here and in earlier investigations indicate that $|^{1}J(^{109}Ag,^{31}P)|$ values for silver–tertiary phosphine complexes decrease as Ag–P bond lengths increase. This experimental conclusion is supported by DFT calculations, which also indicate that the Fermi-contact mechanism is the only important spin–spin coupling mechanism for $^{1}J(^{109}Ag,^{31}P)$ in these complexes. In addition, the crystal structure of a silver–triphenylphosphine trifluoroacetate tetramer was determined using X-ray crystallography, and the structure of a silver–triphenylphosphine chloride tetramer was reinvestigated.

Key words: silver(I)–triphenylphosphine complexes, solid-state ^{31}P NMR, $^{1}J(^{107,109}Ag,^{31}P)$ values, DFT calculations.

Résumé : On a fait appel à la RMN du ^{31}P en phase solide et à haute résolution pour étudier une série de complexes 1:1 argent:triphénylphosphine, $[Ph_3PAgX]_n$ dans lesquels X est un anion monovalent et n = 1, 2, 3, 4, ou ∞. Les spectres RMN du ^{31}P par la technique de polarisation croisée avec rotation à l'angle magique (PC RAM) révèlent le nombre de sites distincts de phosphore dans ces complexes ainsi que les valeurs de $|^{1}J(^{109}Ag,^{31}P)|$ qui s'échelonnent de 401 ± 10 Hz ($X = N_3^-$) jusqu'à 869 ± 10 Hz ($X = SO_3CF_3^-$). Les données obtenues dans ce travail et dans d'autres effectués antérieurement indiquent que les valeurs de $|^{1}J(^{109}Ag,^{31}P)|$ pour les complexes d'argent avec des phosphines tertiaires diminuent avec une augmentation de la longueur des liaisons Ag–P. Cette conclusion expérimentale est en accord avec les résultats de calculs effectués d'après la théorie de la fonctionnelle de la densité (TFD), ce qui indique aussi que le mécanisme de contact de Fermi est le seul mécanisme important de couplage spin–spin affectant la valeur de $^{1}J(^{109}Ag,^{31}P)$ dans ces complexes. De plus, faisant appel à la diffraction des rayons X, on a déterminé la structure cristalline d'un tétramère d'argent et de trifluoroacétate de triphénylphosphine et on a réétudié la structure du tétramère d'argent et du chlorure de triphénylphosphine.

Mots-clés : complexes d'argent(I) et de triphénylphosphine, RMN du ^{31}P en phase solide, valeur de $^{1}J(^{109}Ag,^{31}P)$, calculs selon la théorie de la fonctionnelle de la densité (TFD).

[Traduit par la Rédaction]

Introduction

Coinage-metal tertiary phosphine complexes $[L_mMX]_n$, where L is a tertiary phosphine ligand, m = 1–4, M is Cu(I), Ag(I), or Au(I), X is a monovalent anion, and n = 1, 2, 3, 4, or ∞, have attracted much interest because they display a wide variety of structure types involving a range of metal coordination numbers.[3–14] Most of these studies have involved ligands such as triphenylphosphine (Ph_3P), tricyclohexylphosphine (Cy_3P), 1-phenyldibenzylphosphole (DBP), 1-phenyl-3,4-dimethylphosphole (DMPP), butyldiphenylphosphine (Ph_2BuP), or other closely related phosphines. For most group-11 metal phosphine complexes, the metal oxidation state is +1 and the valence electron configuration is nd^{10}. This electron configuration generally leads to complexes with low coordination numbers, typically two, three, or four. Vibrational and NMR spectroscopy as well as X-ray diffraction are critical tools for characterizing group-11 transition-metal phosphine complexes. In particular, solid-state ^{31}P NMR spectroscopy has been demonstrated to be significantly important in providing insights about molecular structure and bonding in the complexes; for example, see refs. 9–27.

The most common structure for the 1:1 coinage-metal tertiary phosphine complexes of the type $[LMX]_n$ are the cubane and chair structures (Scheme 1).[10,28–31] However, several other structures are also known, depending on the steric requirements of both the ligand L and the anion X.[32–38] The number of distinct phosphorus sites or metal–phosphorus bonds in these complexes can be identified by the number of distinct ^{31}P chemical shifts from NMR spectroscopy. Here, we illustrate the value of solid-state ^{31}P NMR spectroscopy in characterizing a series of 1:1 silver–

Received 14 March 2009. Accepted 21 April 2009. Published on the NRC Research Press Web site at canjchem.nrc.ca on 2 July 2009.

F. Chen, S. Oh,[1] and R.E. Wasylishen.[2] Department of Chemistry, Gunning/Lemieux Chemistry Centre, University of Alberta, Edmonton, AB T6G 2G2, Canada.

[1]Present address: Department of Chemistry, Mokpo National University, Muan, Chonnam 534-729, Republic of Korea.
[2]Corresponding author (e-mail: Roderick.Wasylishen@ualberta.ca).

Scheme 1.

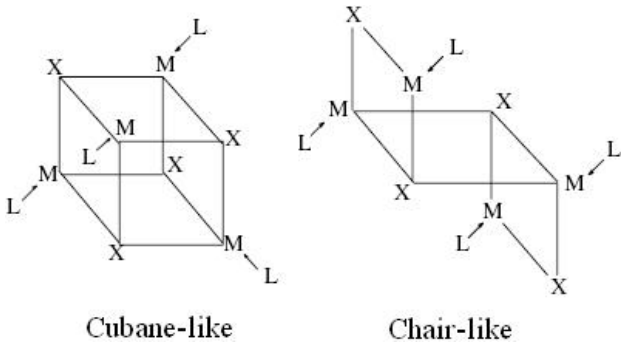

triphenylphosphine complexes of the type $[Ph_3PAgX]_n$. In general, for these complexes, each distinct phosphorus site consists of four peaks in the ^{31}P NMR spectrum, two due to ^{109}Ag–^{31}P indirect spin–spin coupling (^{109}Ag, I = 1/2, N.A. = 48.2%, $\gamma = -1.2518 \times 10^7$ rad s^{-1} T^{-1}) and two due to ^{107}Ag–^{31}P indirect spin–spin coupling (^{107}Ag, I = 1/2, N.A. = 51.8%, $\gamma = -1.0889 \times 10^7$ rad s^{-1} T^{-1})[39]; the $^1J(^{109}Ag,^{31}P)$ values are approximately 1.15 times those for $^1J(^{107}Ag,^{31}P)$ because ^{109}Ag has a slightly larger (in magnitude) magnetogyric ratio than ^{107}Ag. It should be mentioned that, on the basis of first-principles calculations (vide infra), the $^1J(^{109}Ag,^{31}P)$ and $^1J(^{107}Ag,^{31}P)$ values reported here are negative.

Earlier, Nelson and co-workers found a linear relationship between $^1J(^{63,65}Cu,^{31}P)$ and the inverse cube of the Cu–P bond length, $1/r^3_{CuP}$ for a series of copper(I)–tertiary phosphine complexes.[9–11] They also found a linear relationship between ^1J(Ag,P) and $1/r^3_{AgP}$ for $[(Ph_3P)_nAgNO_3]$ (n = 1–4),[10,11] although at that time the number of silver–tertiary phosphine complexes for which both solid-state ^{31}P NMR and X-ray crystal structure data had been reported was limited. The authors suggested that these results indicate that the Fermi-contact mechanism is the dominant mechanism for $^1J(^{63,65}Cu,^{31}P)$ and $^1J(^{107,109}Ag,^{31}P)$. However, based on these observations alone, such a conclusion is difficult to prove. For example, in the "simple" hydrogen molecule where the Fermi-contact mechanism completely dominates, ^1J(H,H) increases as the bond length increases.[40–42] In this study, we have examined several silver–tertiary phosphine complexes to determine if indeed there is a correlation between experimental ^1J(Ag,P) values and the Ag–P bond length as reported by Nelson.[10,11] We have also carried out density functional theory (DFT) calculations of ^1J(Ag,P) to determine whether the experimental trends are reproduced and to determine the dominant mechanism contributing to ^1J(Ag,P) values.

Background and theory

Ramsey[43] first described the theory of indirect nuclear spin–spin coupling in 1953, using second-order perturbation theory, in terms of three mechanisms, which together account for the interaction of the coupled nuclei with the electronic network of the molecule. These mechanisms, generally denoted as the spin-orbital (SO), spin-dipolar (SD), and Fermi-contact (FC) mechanisms, have been described in numerous review articles and textbooks (see ref. 44 for an example). In 1964, Pople and Santry[45] presented an approximate molecular orbital description of spin–spin coupling, which was later extended by Buckingham and Love.[46] Following Ramsey,[43] the isotropic indirect spin–spin coupling, ^nJ(A,B), can be written as a sum of three contributions,

$$[1] \qquad {}^nJ(A,B) = {}^nJ(A,B)_{SO} + {}^nJ(A,B)_{SD} + {}^nJ(A,B)_{FC}$$

The SO mechanism describes the interaction between the nuclear magnetic moment and the orbital magnetic moment arising from the motion of the electrons and can be further divided into diamagnetic SO (DSO) and paramagnetic SO (PSO) contributions; the former depends on the ground electronic state while the latter involves allowed excitations between the ground and singlet excited states. The PSO mechanism contributes significantly to both the isotropic J and the anisotropy of the **J** tensor in the presence of formal multiple bonds.[47] The second mechanism, SD, is the interaction between the nuclear magnetic moment and the magnetic field arising from the spin of the electrons not located at the nucleus. The FC mechanism accounts for the interaction between a nuclear spin and an electron spin which has a finite probability of being at the nucleus (i.e., s electrons); this term is purely isotropic and hence does not contribute to anisotropy of the **J** tensor. In addition to the three mechanisms discussed above, there is also a purely anisotropic SD × FC cross term, which only contributes to the anisotropic **J** tensor and does not contribute to J.[46] In 1977, Pyykkö[48] extended Ramsey's nonrelativistic theory to include relativistic effects; other relativistic theories have since been presented.[49,50] For any given spin–spin coupling tensor, all these mechanisms may be important;[51] however, in the early literature, it was common to assume that the FC mechanism was the most important contribution to the isotropic J.

In this study, ^1J(Ag,P) values were calculated for model complexes, $[(CH_3)_3PAgX]$, with different monovalent anions using DFT. This method was selected because of its applicability to relatively large systems as opposed to ab initio methods, which are currently limited to small molecules containing relatively light atoms.

Experimental

Sample preparation

Because silver compounds are generally light sensitive, all synthetic work was undertaken in a dark room and where appropriate, the reactions were carried out in dry solvents under an N_2 atmosphere. All silver salts and triphenylphosphine, Ph_3P, were purchased from Sigma-Aldrich Chemicals, Inc. Most 1:1 silver–triphenylphosphine complexes, silver triphenylphosphine halides, $[Ph_3PAgX]_4$ (X = Cl, Br, I),[28–31] silver triphenylphosphine trifluoromethane sulfonate, $[Ph_3PAgSO_3CF_3]_3$,[32,33] silver triphenylphosphine acetate, $[Ph_3PAgOC(O)CH_3]_4$,[34] silver triphenylphosphine bromate, $[Ph_3PAgBrO_3]_4$,[35] silver triphenylphosphine nitrate, $[Ph_3PAgNO_3]_\infty$,[20,36] silver triphenylphosphine azide, $[Ph_3PAgN_3]_n$,[36] silver triphenylphosphine nitrite, $[Ph_3PAgNO_2]_\infty$,[37] and silver triphenylphosphine quinine,[38] were prepared as reported in the literature. Silver triphenylphosphine trifluoroacetate, $[Ph_3PAgOC(O)CF_3]_4$, and silver triphenylphosphine hexafluorophosphate, $[Ph_3PAgPF_6]_n$,

Table 1. Selected single-crystal X-ray diffraction parameters for some 1:1 silver–triphenylphosphine complexes.

Compound	Space group	Phosphorus sites in the asymmetric unit	r_{AgP} (avg.) (Å)	Reference
$[Ph_3PAgCl]_4$	*Pbcn* (60)	2	2.386(1)	This work
			2.371(1)	
$[Ph_3PAgBr]_4$	*R*3*c* (161)	2	2.418(1)	30
			2.431(4)	
$[Ph_3PAgI]_4$ (cubane)	$P2_1/c$ (14)	4	2.455(1)	31
			2.459(1)	
			2.456(2)	
			2.462(2)	
$[Ph_3PAgI]_4$ (chair)	*P*-1 (2)	2	2.455(1)	31
			2.431(1)	
$[Ph_3PAgCO_2CH_3]_4$	$P2_1/c$ (14)	2	2.374(3)	34
			2.355(2)	
$[Ph_3PAgCO_2CF_3]_4$	$P2_1/c$ (14)	2	2.354(1)	This work
			2.355(1)	
$[(Ph_3P)_2AgBrO_3]$	*P*-1 (2)	2	2.418(1)	35
			2.434(1)	
$[Ph_3PAgSO_3CF_3]_3$	$P2_1/c$ (14)	3	2.341(5)	35
			2.327(5)	
			2.362(6)	
$[Ph_3PAgNO_2]_\infty$	$P2_1/c$ (14)	1	2.392(1)	37
$[Ph_3PAgNO_3]_\infty$	$P2_1/c$ (14)	Phase I	2.376(2)	20
		Phase II	2.357(2)	

were synthesized using the same method as for $[Ph_3PAgOC(O)CH_3]_4$.[34] Silver triphenylphosphine thiocyanate, $[Ph_3PAgSCN]_n$, and silver triphenylphosphine cyanate, $[Ph_3PAgCNO]_n$, were synthesized following the method used for the preparation of $[Ph_3PAgN_3]_n$.[36]

Single-crystal X-ray diffraction

Single-crystal X-ray diffraction data were acquired for two complexes, $[Ph_3PAgCl]_4$ and $[Ph_3PAgOC(O)CF_3]_4$, using a Bruker PLATFORM/SMART 1000 CCD diffractometer (Mo Kα, λ = 0.71073 Å graphite monochromator). Structures for $[Ph_3PAgCl]_4$ and $[Ph_3PAgOC(O)CF_3]_4$ were solved by direct methods using DIRDIF-99[52] and refined with SHELXL-93.[53] A single crystal of $[Ph_3PAgCl]_4$ was slowly recrystallized from a mixture of $CHCl_3$ and ether; 35517 reflections were collected in the range $4.54^\circ < 2\theta < 52.62^\circ$, of which 6863 were independent. A single crystal of $[Ph_3PAgOC(O)CF_3]_4$ was slowly recrystallized from toluene; 25974 reflections were collected in the range $5.24^\circ < 2\theta < 53.24^\circ$, of which 8459 were independent.

Solid-state ^{31}P NMR spectroscopy

Phosphorus-31 NMR spectra were acquired using a Chemagnetics CMX Infinity 200 (B_0 = 4.70 T) spectrometer as well as Bruker Avance 300 (B_0 = 7.05 T) and 500 (B_0 = 11.75 T) NMR spectrometers with the combination of standard cross-polarization (CP), magic angle spinning (MAS), and proton decoupling. Samples were packed in 4 mm o.d. rotors. Proton 90° pulse widths of 2.5 or 4.0 μs, contact times of 3 or 5 ms, and pulse delays of 10 to 120 s were used to acquire most ^{31}P NMR spectra. Phosphorus-31 chemical shifts were referenced with respect to 85% aqueous phosphoric acid by setting the isotropic peak of an external solid ammonium dihydrogen phosphate sample to 0.81 ppm.[54] All spectra were acquired at ambient temperature with a sample spinning frequency of 3.0 or 5.0 kHz.

Theoretical calculations of ^1J(Ag,P)

To reduce computational times, the phenyl groups for the 1:1 silver–triphenylphosphine complexes were replaced with methyl groups. The effect of different monovalent anions, $[(CH_3)_3PAgX]$ (X = Cl, Br, I, CN, NC, OCH_3, OC(O)H and $OC(O)CH_3$) on ^1J(Ag,P), was investigated. The molecular structures used to generate the nuclear coordinates for the ^1J(Ag,P) calculations were obtained from geometries optimized using Gaussian 03.[55] The optimizations were performed using the B3LYP functional with the DZVP basis set for Ag, the LANL2DZ basis set for I, and the 6–31G* basis set for the remaining atoms. The same functional and basis sets were also employed to calculate ^1J(Ag,P) with the same program.

DFT calculations of ^1J(Ag,P) were also performed using the CPL module[56–59] of the ADF program (ADF 2005.01).[60–64] The Vosko–Wilk–Nusair (VWN) local density approximation,[65] with the Becke–Perdew generalized gradient approximation (GGA),[66–68] was used for the exchange-correlation functional. Relativistic calculations including spin-orbital and scalar corrections were carried out using the zeroth-order regular approximation (ZORA) formalism.[69–72] The FC, SD, PSO, and DSO mechanisms were included in all *J* calculations; a description of these mechanisms, as implemented in the ZORA formalism, has been presented.[73] The basis sets available with the ADF program consist of Slater-type functions. The TZ2P basis set is of triple-ζ quality with two sets of polarization functions while the DZP basis set is of double-ζ quality with one set of polarization func-

Table 2. Solid-state ^{31}P NMR chemical shifts and $|^1J(^{107,109}Ag,^{31}P)|$ values for $[Ph_3PAgX]_n$.

$[Ph_3PAgX]_n$						
X	*n*	Site	$\delta_{iso}(^{31}P)$ (ppm)	$\|^1J(^{107}Ag,^{31}P)\|$ (Hz)	$\|^1J(^{109}Ag,^{31}P)\|$ (Hz)	$\|^1J(Ag,P)\|$ (Hz)
Cl	4	1	9.2±0.2	586±10	663±10	—
		2	3.1±0.2	593±10	681±10	—
Br	4	1	5.1±0.2	—	—	593±15[a]
		2	0.1±0.2	—	—	564±15[a]
I (cubane)	4	1	–4.3±0.2	476±10	542±10	—
		2	–6.4±0.2	446±10	513±10	—
		3	–8.0±0.2	483±10	564±10	—
		4	–9.1±0.2	425±10	476±10	—
I[a] (chair)	4	1	2.5±0.2	—	—	508±15[a]
		2	–1.5±0.2	—	—	479±15[a]
CO_2CH_3	4	1	14.0±0.2	693±10	806±10	—
		2	12.9±0.2	681±10	776±10	—
CO_2CF_3	4	1	15.4±0.2	673±10	771±10	—
		2	13.8±0.2	674±10	771±10	—
BrO_3[b]	1	2	4.9±0.5	—	—	490±15[a]
SO_3CF_3	3	1	17.1±0.2	742±10	850±10	—
		2	15.7±0.2	752±10	869±10	—
		3	11.2±0.2	732±10	840±10	—
PF_6	2/4	1	19.8±0.2	772±10	869±10	—
		2	12.7±0.2	742±10	840±10	—
NO_3[c]		Phase I	13.2±0.2	707±14	815±14	—
	∞	Phase II	12.0±0.2	719±14	830±14	—
NO_2	∞	1	5.2±0.2	625±10	723±10	—
N_3	4	1	10.6±0.2	361±10	401±10	—
		2	9.1±0.2	360±10	404±10	—
		3	3.2±0.2	399±10	446±10	—
		4	1.6±0.2	399±10	447±10	—
SCN	2/4	1	9.4±0.2	558±10	618±10	—
		2	2.4±0.2	516±10	598±10	—
CNO	3	1	17.0±0.2	605±10	698±10	—
		2	15.0±0.2	640±10	728±10	—
		3	11.4±0.2	620±10	718±10	—
quinine	1	1	11.8±0.2	527±10	596±10	—

[a]Average $^1J(^{107}Ag,^{31}P)$ and $^1J(^{109}Ag,^{31}P)$.
[b]The molecular formula is $[(Ph_3P)_2AgBrO_3]$.
[c]Reference 20.

tions. For relativistic calculations, the TZ2P basis set, optimized for ZORA calculations, was used for the silver, phosphorus, oxygen, carbon, nitrogen, chlorine, bromine, and iodine nuclei, while the DZP basis set was used for the hydrogen atoms.

Results and discussion

Solid-state ^{31}P NMR spectroscopy

Selected single-crystal X-ray diffraction data for several of the 1:1 silver–triphenylphosphine complexes considered here are summarized in Table 1. Phosphorus-31 chemical shifts and ^1J(Ag,P) values measured for these complexes in the solid state are summarized in Table 2.

X = Cl⁻, Br⁻, and I⁻

The single-crystal X-ray diffraction data (see Supplementary data) for $[Ph_3PAgCl]_4$ indicate that this compound possesses a distorted cubane-like structure with C_2 symmetry along the *b*-axis. There are two distinct phosphorus sites with two crystallographically equivalent phosphorus atoms in each. These results are in agreement with previous X-ray results.[29] A ^{31}P NMR spectrum of an MAS sample of $[Ph_3PAgCl]_4$ is shown in Fig. 1*a*. As mentioned earlier, each distinct phosphorus site generally consists of four peaks in the ^{31}P NMR spectrum due to the indirect spin–spin coupling of ^{109}Ag–^{31}P and of ^{107}Ag–^{31}P. Thus, the eight peaks in the isotropic region indicate that there are two distinct phosphorus sites, in agreement with the single-crystal X-ray diffraction data. The isotropic chemical shifts are 9.2 ± 0.2 and 3.1 ± 0.2 ppm. The $|^1J(^{109}Ag,^{31}P)|$ values corresponding to the two phosphorus sites are 663 ± 10 and 681 ± 10 Hz, whereas the $|^1J(^{107}Ag,^{31}P)|$ values are 586 ± 10 and 593 ± 10 Hz, respectively.

A ^{31}P NMR spectrum of an MAS sample of $[Ph_3PAgBr]_4$ recrystallized from a mixture of $CHCl_3$ and ether is shown in Fig. 1*b*. The four peaks in the isotropic region indicate that there are also two distinct phosphorus sites with isotropic chemical shifts of 5.1 ± 0.2 and 0.1 ± 0.2 ppm; in this case, $^1J(^{107}Ag,^{31}P)$ cannot be resolved from $^1J(^{109}Ag,^{31}P)$. The line

Fig. 1. Solid-state ^{31}P NMR spectra of MAS samples (ν_{rot} = 5 kHz) of (*a*) $[Ph_3PAgCl]_4$, (*b*) $[Ph_3PAgBr]_4$, (*c*) $[Ph_3PAgI]_4$, (cubane-like), and (*d*) $[Ph_3PAgI]_4$ (chair-like) acquired at room temperature. The labels, A, B, C, and D correspond to distinct phosphorus sites for each complex.

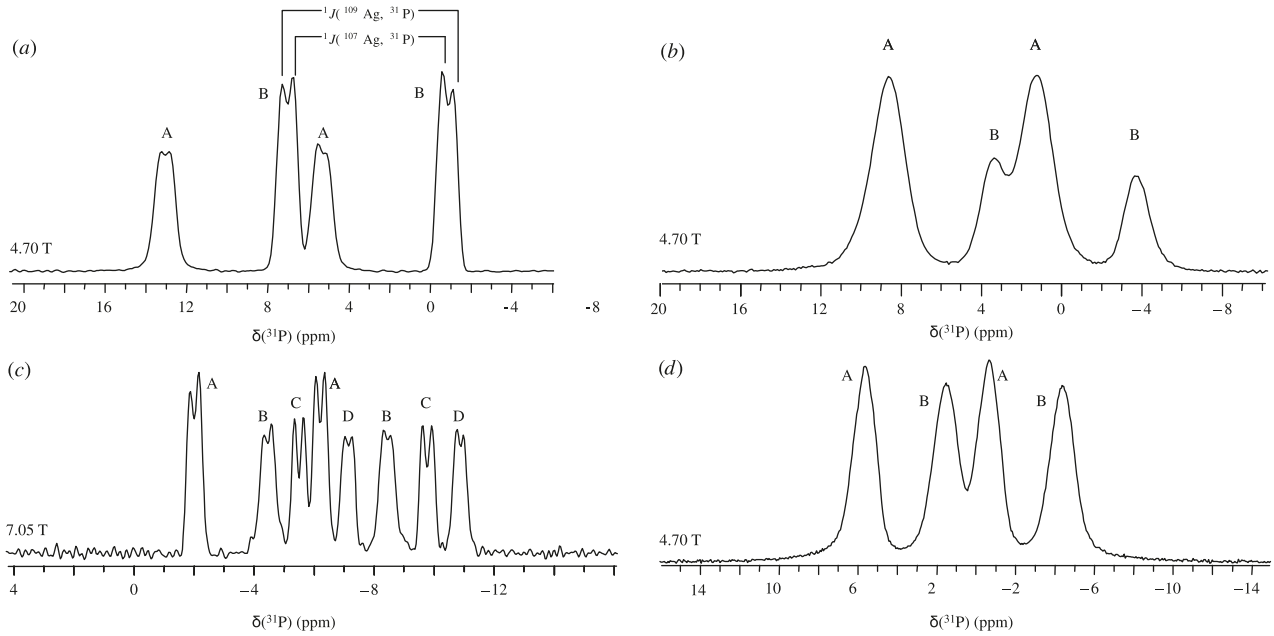

broadening in the experimental spectra are attributed to ^{79,81}Br–^{31}P residual dipolar interactions. The average $|^1J(^{107,\ 109}Ag,^{31}P)|$ values corresponding to the two phosphorus sites are 593 ± 15 and 564 ± 15 Hz, respectively. From the reported single-crystal X-ray data, the distorted cubane-like structure of $[Ph_3PAgBr]_4$ has C_3 symmetry, with three phosphorus atoms that are crystallographically equivalent and one distinct site,[30] consistent with the ~3:1 ratio of integrated intensities for the two ^{31}P sites.

$[Ph_3PAgI]_4$ is known to crystallize in a cubane-like or chair-like structure, depending on how it is recrystallized.[31] According to the literature,[31] $[Ph_3PAgI]_4$ recrystallized from a mixture of $CHCl_3$ and ether has the cubane-like structure; the ^{31}P NMR spectrum of an MAS sample of this polymorph is shown in Fig. 1*c*. The sixteen peaks in the isotropic region indicate that there are four distinct phosphorus sites in the unit cell; the ^{31}P chemical shifts and $^1J(^{107,109}Ag,^{31}P)$ values are listed in Table 2. The ^{31}P NMR results are in agreement with the reported distorted cubane-like structure with C_1 symmetry,[31] in which all four phosphorus atoms are crystallographically distinct. Chair-like $[Ph_3PAgI]_4$ was obtained by recrystallizing the complex in a mixture of CH_2Cl_2 and ether; the ^{31}P NMR spectrum of an MAS sample of this polymorph, shown in Fig. 1*d*, indicates that there are two distinct phosphorus sites in this complex, in agreement with the centrosymmetric C_i chair-like geometry.[31] However, unlike for the cubane-like structure, the pair of doublets for each phosphorus site, arising from indirect spin–spin coupling to both ^{107}Ag and ^{109}Ag, is not resolved; the reason for this is unclear. Possibly, ^{127}I–^{31}P residual dipolar coupling contributes to the ^{31}P NMR linewidth in the chair-like complex. Cubane-like and chair-like $[Ph_3PAgI]_4$ have different $|^1J(Ag,P)|$ values and ^{31}P chemical shifts for each phosphorus site, although the average $|^1J(Ag,P)|$ values for the two polymorphs are similar, approximately 490 Hz. The spectra shown in Figs. 1*c* and 1*d* provide an excellent example of the sensitivity of ^{31}P NMR spectra to polymorphism.

X = $CO_2CF_3^-$, $CO_2CH_3^-$, BrO_3^-, $SO_3CF_3^-$, and PF_6^-

The structure of $[Ph_3PAgOC(O)CF_3]_4$ determined by single-crystal X-ray diffraction (see Supplementary data), shown in Fig. 2*a*, as well as those for $[Ph_3PAgOC(O)CH_3]_4$,[34] and $[Ph_3PAgBrO_3]_4$,[35] indicate that these complexes have an Ag_2O_2 core and possess a centrosymmetric C_i pseudo-chair-like geometry with two distinct phosphorus sites. Phosphorus-31 NMR spectra of MAS samples of $[Ph_3PAgOC(O)CF_3]_4$ are shown in Fig. 3*a*; those for $[Ph_3PAgOC(O)CH_3]_4$ are similar. The eight well-resolved peaks in the isotropic regions of the spectra for these compounds indicate that there are indeed two distinct phosphorus sites.[34]

Unfortunately, we were unable to prepare $[Ph_3PAgBrO_3]_4$ following the literature method.[35] However, the ^{31}P NMR spectrum (not shown) of an MAS sample of the compound is similar to that for $[(Ph_3P)_2AgBrO_3]$ published previously.[35] The ^{31}P NMR spectrum indicates that there are two similar phosphorus sites with similar $|^1J(Ag,P)|$ values, 490 ± 15 Hz (Table 2), in agreement with the literature values for $[(Ph_3P)_2AgBrO_3]$.[35] Thus, the compound prepared here is $[(Ph_3P)_2AgBrO_3]$, not $[Ph_3PAgBrO_3]_4$.

The molecular structure of $[Ph_3PAgSO_3CF_3]_3$ (Fig. 2*b*) consists of one unique silver atom (Ag1) in a trigonal-planar arrangement bonded to a phosphorus atom (P1) of one phosphine and to two oxygen atoms from different triflate units. There are two other silver atoms in the structures (Ag2 and Ag3), each in distorted tetrahedral configurations bonded to the phosphorus atom (P2 or P3) of one phosphine and three oxygen atoms from different triflate units.[32,33] This indicates that the bonding environments about P2 and P3 are similar

Fig. 2. Molecular structures of (*a*) $[Ph_3PAgOC(O)CF_3]_4$ (see Supplementary data for further details) and (*b*) $[Ph_3PAgSO_3CF_3]_3$.[32,33] For clarity, the fluorine atoms of the CF_3 groups are not shown.

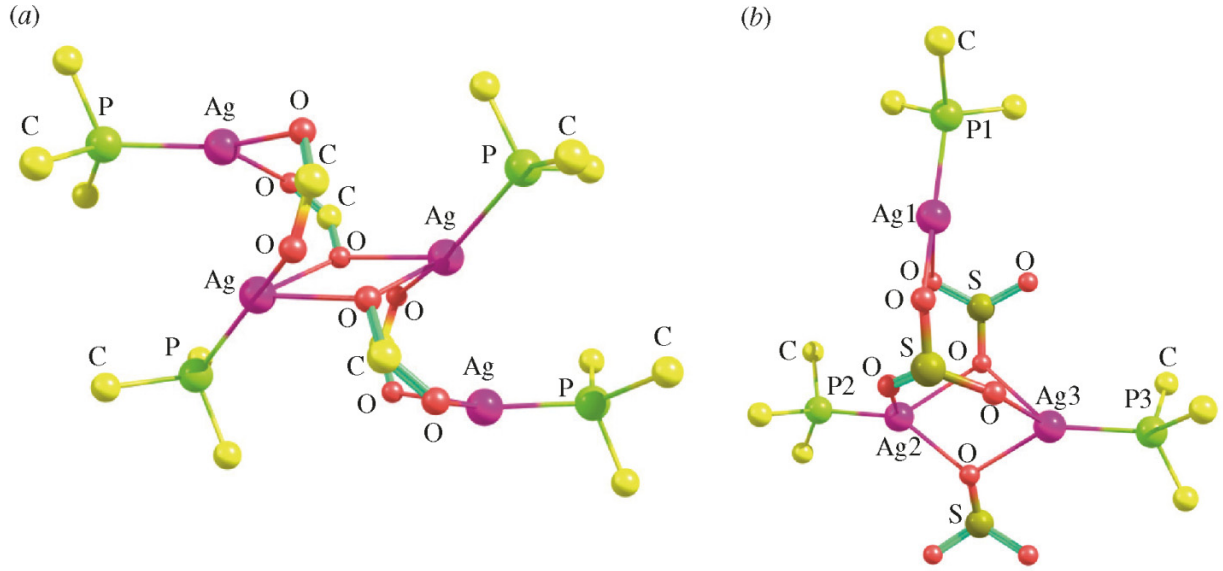

Fig. 3. Solid-state ^{31}P NMR spectra of MAS samples (ν_{rot} = 5 kHz) of (*a*) $[Ph_3PAgOC(O)CF_3]_4$, (*b*) $[Ph_3PAgSO_3CF_3]_3$, (*c*) $[Ph_3PAgNO_2]_\infty$, and (*d*) $[Ph_3PAgN_3]_4$ acquired at room temperature and at the indicated magnetic field strengths. The labels, A, B, C, and D correspond to distinct phosphorus sites for each complex.

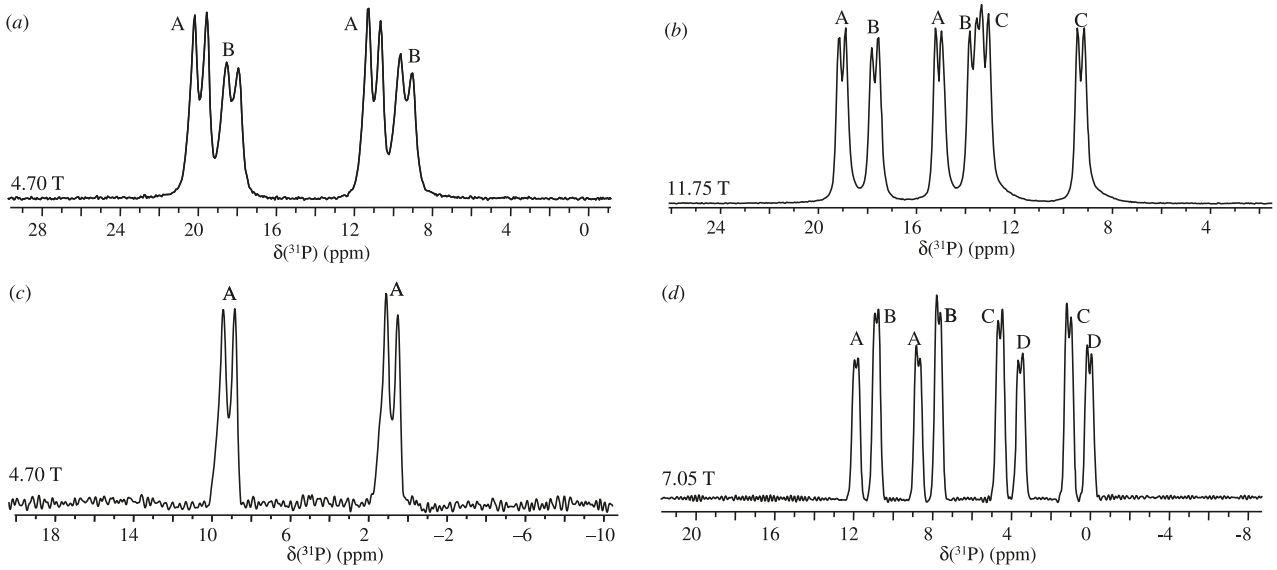

and that of P1 is different, consistent with the ^{31}P NMR spectrum of an MAS sample shown in Fig. 3*b*: there are three distinct phosphorus sites, two of which have similar chemical shifts and $^1J(^{107\,109}Ag,^{31}P)$ values (Table 2).

Single-crystal structural data for silver–triphenylphosphine hexafluorophosphate, $[Ph_3PAgPF_6]_n$, are unavailable. Phosphorus-31 NMR spectra of MAS samples of $[Ph_3PAgPF_6]_n$, which are similar to that shown in Fig. 3*a*, indicate that there are two distinct phosphorus sites of equal population for the PPh_3 group in this complex, suggesting the molecular formula is either $[Ph_3PAgPF_6]_2$ or $[Ph_3PAgPF_6]_4$.

X = NO_3^- and NO_2^-

The structure of $[Ph_3PAgNO_3]_\infty$ determined by X-ray diffraction measurements at 193 and 295 K, and the ^{31}P chemical shifts as well as $^1J(^{107,109}Ag,^{31}P)$ values (Table 2) have been reported previously.[20] Because $[Ph_3PAgNO_3]_\infty$ undergoes a phase transition at 299 K, different NMR parameters are obtained above and below this temperature.[20]

Single-crystal X-ray diffraction data indicate that the structure of $[Ph_3PAgNO_2]_\infty$[37] at 295 K is similar to that of $[Ph_3PAgNO_3]_\infty$.[20] Both are monoclinic with the same space group, $P2_1/c$ (No. 14), and similar unit cell parameters: a = 10.2430(14) Å, b = 18.521(3) Å, c = 9.1373(12) Å, β = 90.596(3)° for $[Ph_3PAgNO_3]_\infty$[20]; a = 10.191(1) Å, b = 8.906(2) Å, c = 18.086(2) Å, β = 88.281(3)° for $[Ph_3PAgNO_2]_\infty$.[37] For $[Ph_3PAgNO_3]_\infty$, shown in Fig. 4*a*, the silver atom is coordinated with two oxygen atoms from one $-NO_3^-$ group, one oxygen atom from another $-NO_3^-$ group and the phosphorus atom of the $-PPh_3$ group.[20] For

Fig. 4. Molecular structures of (*a*) $[Ph_3PAgNO_3]_\infty$[20] and (*b*) $[Ph_3PAgNO_2]_\infty$.[37]

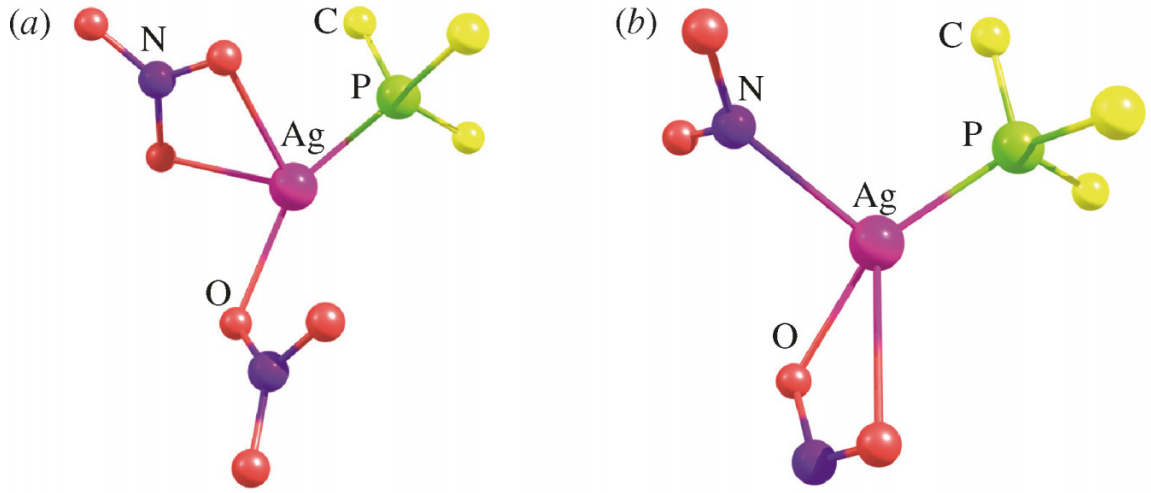

$[Ph_3PAgNO_2]_\infty$, shown in Fig. 4*b*, the silver atom is coordinated with the two oxygen atoms of one $-NO_2^-$ group, the nitrogen atom of another $-NO_2^-$ group and the phosphorus atom of the $-PPh_3$ group.[37]

The ^{31}P NMR spectrum of an MAS sample of $[Ph_3PAgNO_2]_\infty$ shows that there is one phosphorus site (Fig. 3*c*). The ^{31}P chemical shift is different from the value $\delta(^{31}P)$ = 16.1 ppm obtained in solution, probably arising from a different silver coordination environment for $[Ph_3PAgNO_2]_\infty$ dissolved in solvent; however, the $|^1J(^{109}Ag,^{31}P)|$ value obtained for the solid sample is in agreement with that obtained for a sample in solution, 769 Hz.[37]

X = N_3^-, SCN$^-$, and CNO$^-$

For the three silver–triphenylphosphine pseudo-halide complexes, $[Ph_3PAgN_3]_n$, $[Ph_3PAgSCN]_n$, and $[Ph_3PAgCNO]_n$, single-crystal data are unavailable, and all attempts to grow suitable single-crystals for X-ray diffraction failed. The ^{31}P NMR spectrum (Fig. 3*d*) for the X = N_3^- complex indicates four distinct phosphorus sites, suggesting that the molecular formula is $[Ph_3PAgN_3]_4$. The ^{31}P NMR spectra for the X = SCN^- complex, which are similar to those shown for the X = Cl^- complex in Fig. 1*a*, indicate two distinct phosphorus sites, so the formula is likely either $[Ph_3PAgSCN]_2$ or $[Ph_3PAgSCN]_4$. The ^{31}P NMR spectra for the X = CNO^- complex, which are similar to that shown in Fig. 3*b*, indicate three distinct phosphorus sites; thus, the molecular formula is probably $[Ph_3PAgCNO]_3$.

X = quinine

The silver atom of silver-triphenylphosphine quinine nitrate is coordinated to the phosphine and the tertiary nitrogen atom (Scheme 2).[38] A ^{31}P NMR spectrum of an MAS sample of this compound is similar to that shown for the X = NO_2^- complex in Fig. 3*c*. The spectrum indicates that there is a single phosphorus site, in agreement with the structure of this complex.[38] The ^{31}P chemical shift is in agreement with that obtained for a sample in solution, 12.4 ppm.[38]

Summary of solid-state ^{31}P NMR results

For those $[Ph_3PAgX]_n$ complexes with X-ray diffraction data, solid-state ^{31}P NMR spectra contain the number of distinct phosphorus sites predicted from this data. We have shown that solid-state ^{31}P NMR spectroscopy can provide information concerning the number of distinct phosphorus sites from the distinct ^{31}P NMR chemical shifts. In addition, the ^1J(Ag,P) values were also determined for these complexes from solid-state ^{31}P NMR spectroscopy. The ^{31}P NMR parameters including chemical shifts and ^1J(Ag,P) values for many silver–phosphine complexes are unavailable from solution NMR measurements because these complexes are often insoluble in non-coordinating solvents.

Scheme 2.

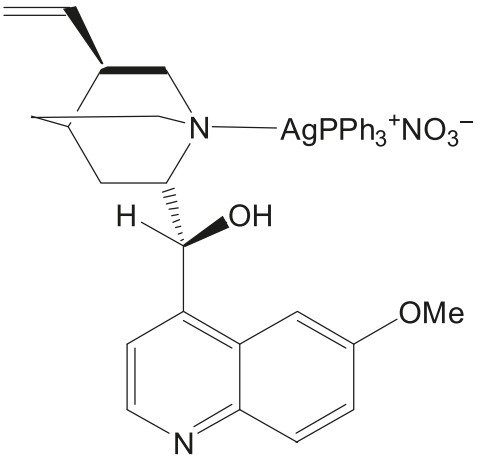

Relationship between $|^1J(^{107,\,109}Ag,^{31}P)|$ and Ag–P bond-length

Experimental results

Table 3 summarizes the average $|^1J$(Ag,P)| values and the average Ag–P bond lengths for the silver–tertiary phosphine complexes which have been investigated by both solid-state ^{31}P NMR spectroscopy and single-crystal X-ray diffraction. Average $|^1J$(Ag,P)| values and bond lengths are taken for complexes with multiple $|^1J$(Ag,P)| values and P sites since we are unable to assign these to a specific Ag–P bond. As discussed earlier, Nelson and co-workers[9–11] found a linear relationship between $^1J(^{63,65}Cu,^{31}P)$ and $1/r^3_{CuP}$ for a series of

Table 3. Reported $|^1J(^{107,109}Ag,^{31}P)|$ values obtained from solid-state ^{31}P NMR and Ag–P bond-lengths obtained from single-crystal X-ray diffraction for a variety of silver–tertiary phosphine complexes.

Compound	$\|^1J$(Ag,P)$\|$ (avg.) (Hz)	r_{AgP} (avg.) (Å)	Reference	Compound	$\|^1J$(Ag,P)$\|$ (avg.) (Hz)	r_{AgP} (avg.) (Å)	Reference
$[(DBP)_2AgCl]_2$	316	2.515	11	$[Ph_3PAgCO_2CF_3]_4$	723	2.354	This work
$[(Ph_2Bu)AgCl]_4$	633	2.364	14	$[(Ph_3P)_2AgBrO_3]$	466[a]	2.426	35
$[(Ph_2Bu)AgBr]_4$	610	2.407	14	$[Ph_3PAgSO_3CF_3]_3$	798[a]	2.343	32
$[(Ph_2Bu)AgI]_4$	510	2.432	14	$[Ph_3PAgNO_2]_\infty$	674[a]	2.392	37
$[Cy_3PAgCl]_2$	648	2.354	78	$[Ph_3PAgNO_3]_\infty$	768	2.367	20
$[Cy_3PAgBr]_2$	612	2.374	78	$[(Ph_3P)_2AgNO_3]$	470	2.442	22
$[Cy_3PAgI]_4$	500	2.454	78	$[(Ph_3P)_3AgNO_3]$	310	2.567	22
$[Cy_3PAgI]_2$·0.5py	552	2.415	78	$[(Ph_3P)_4AgNO_3]$	190	2.657	22
$[(Cy_3P)_2AgCN]$	322	2.480	79	$[(Ph_3P)_2AgBr]$	394	2.458	12
$[(Cy_3P)_2AgCl]$	400	2.471	79	$[(Ph_3P)_4Ag_2Cl_2]$·$2CHCl_3$	400	2.482	12
$[(Cy_3P)_2AgBr]$	396	2.473	79	$[(Ph_3P)_4Ag_2Br_2]$·$2CHCl_3$	385	2.496	12
$[(Cy_3P)_2AgI]$	386	2.479	79	$[(Ph_3P)_2AgO_2CH]$	432	2.426	80
$[(Cy_3P)_2AgSCN]$	404	2.487	79	$[(Ph_3P)_2AgO_2CH]$·$2HCO_2H$	517	2.426	80
$[(Cy_3P)_2AgCNO]$	413	2.456	79	$[(Ph_3P)_3AgO_2CH]$	237	2.513	81
$[(Cy_3P)_2AgNO_3]$	473	2.446	79	$[(Ph_3P)_3AgO_2CH]$·HCO_2H	323	2.523	81
$[Ph_3PAgCl]_4$	631	2.378	[a]	$[(Ph_3P)_4Ag_2(SO_4)]$·$2H_2O$	473	2.455	82
$[Ph_3PAgBr]_4$	579[a]	2.425	30	$[(Ph_3P)_4Ag_2(SeO_4)]$·$2H_2O$	445	2.449	82
$[Ph_3PAgI]_4$ (cubane)	491[a]	2.458	31	$[(Ph_3P)_2Ag(HSO_4)]$·$2H_2O$	484	2.432	82
$[Ph_3PAgI]_4$ (chair)	494[a]	2.443	31	$[(Ph_3P)_2Ag(HSeO_4)]$·$2H_2O$	463	2.433	82
$[Ph_3PAgCO_2CH_3]_4$	740[a]	2.365	34	$[(Ph_3P)_2Ag(H_2PO_4)]$·$2H_2PO_4$	449	2.473	82
$[Ph_3PAgCO_2CF_3]_4$	723	2.354	[a]				

[a]This work.

Fig. 5. Plot of experimental $|^1J(Ag,P)|$ versus (*a*) $1/r^3_{AgP}$ ($R = 0.935$), (*b*) $1/r^2_{AgP}$ ($R = 0.932$), (*c*) $1/r_{Ag,P}$ ($R = 0.927$), and (*d*) $r_{Ag,P}$ (see Table 3) for a variety of silver–tertiary phosphine complexes. The lines in (*a*), (*b*), and (*c*) were obtained by using the linear regression method.

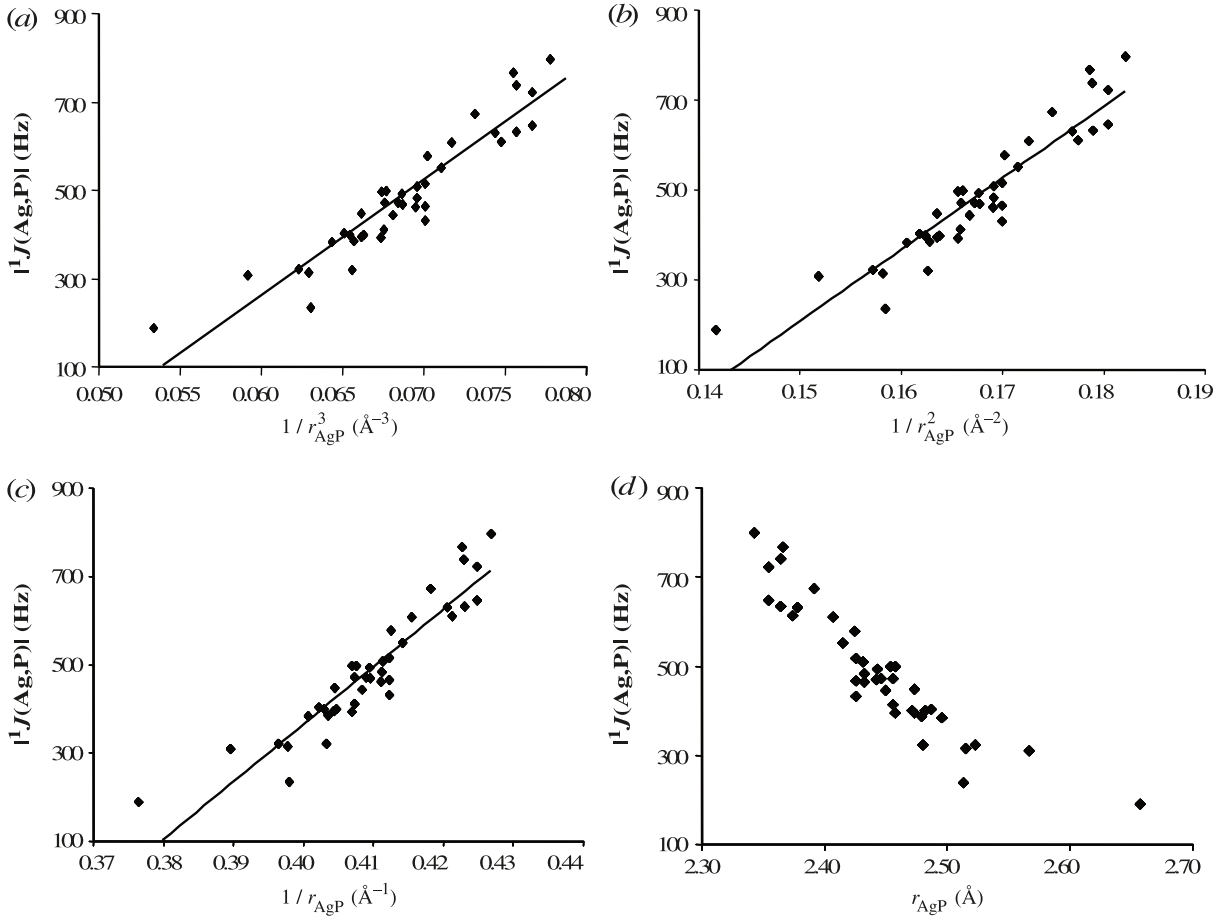

copper(I)–tertiary phosphine complexes as well between $|^1J(Ag,P)|$ and $1/r^3_{AgP}$ for $[(Ph_3P)_nAgNO_3]$ ($n = 1 - 4$). Similarly, a plot of $|^1J(Ag,P)|$ vs. $1/r^3_{AgP}$ for the series of silver–tertiary phosphine complexes, shown in Fig. 5*a*, suggests a linear relationship between these parameters. However, there is no obvious theoretical reason for expecting a linear relationship between $|^1J(Ag,P)|$ and $1/r^3_{AgP}$.[43–47] Furthermore, plots between $|^1J(Ag,P)|$ and $1/r^2_{AgP}$ or $1/r_{AgP}$, shown in Figs. 5*b* and 5*c*, respectively, are reasonably linear; thus, there is no reason for plotting $|^1J(Ag,P)|$ as a linear function of $1/r^3_{AgP}$. Clearly, plots of $J(Ag,P)$ vs. $1/(r_{AgP})^n$ are not very sensitive to n. To demonstrate that $|^1J(Ag,P)|$ values are related to bond length, we have simply plotted $|^1J(Ag,P)|$ versus r_{AgP}, see Fig. 5*d*. It is obvious that the magnitudes of $^1J(Ag,P)$ are very sensitive to the variation of r_{AgP}; $|^1J(Ag,P)|$ values decrease with increasing r_{AgP} for silver–tertiary phosphine complexes. The $|^1J(Ag,P)|$ values have a wide range, *i.e.*, 798–190 Hz, and r_{AgP} values range from 2.343 to 2.657 Å. Similar empirical trends also exist for other metal complexes, such as $^1J(^{63,65}Cu,^{31}P)$ vs. r_{CuP},[9–11] $^1J(^{195}Pt,^{31}P)$ vs. r_{PtP}[74–76] and $^1J(^{113}Cd,^{14}N)$ vs. r_{CdN}.[77]

Theoretical calculations

To shed light on the origins of the correlation between $|^1J(Ag,P)|$ values and r_{AgP}, we have carried out quantum chemistry calculations as outlined below. The geometries of model complexes $[(CH_3)_3PAgX]$ for $[Ph_3PAgX]$, $X^- = Cl^-$, Br^-, I^-, CN^-, NC^-, OCH_3^-, $OC(O)H^-$, and $OC(O)CH_3^-$, were optimized using the B3LYP functional. Calculated $^1J(^{109}Ag,^{31}P)$ values for these model complexes were obtained at the DFT level using both the Gaussian 03 and ADF packages. The optimized r_{AgP} and calculated $^1J(^{109}Ag,^{31}P)$ values are summarized in Table 4. The $^1J(^{109}Ag,^{31}P)$ values obtained for the same model complex from both calculations differ, depending on the basis sets (see Experimental section) employed. However, both calculation methods suggest that the magnitudes of the calculated $^1J(Ag,P)$ values for these model complexes are also very sensitive to the variation of r_{AgP}; the trends between the calculated $|^1J(^{109}Ag,^{31}P)|$ values and r_{AgP} are in agreement with experimental results. A plot of calculated $|^1J(^{109}Ag,^{31}P)|$ values, obtained with the ADF package, vs. r_{AgP} for these model complexes is shown in Fig. 6*a*. The $^1J(Ag,P)$ values were also calculated for model complexes $[(CH_3)_3PAgX]$, where $X = Cl^-$, Br^-, and I^-, by varying r_{AgP} and keeping all other structural parameters constant. The plot of calculated $|^1J(^{109}Ag,^{31}P)|$ values vs. r_{AgP} for these complexes (Fig. 6*b*) shows that the $|^1J(^{109}Ag,^{31}P)|$ values are very sensitive to r_{AgP} and have a negative slope, in agreement with the experimental results. The calculations performed with both ADF and Gaussian 03 packages indicate that the FC term com-

Table 4. Calculated $^1J(^{109}Ag,^{31}P)$ values for $[Me_3PAgX]$ (see text for details).

$[Me_3PAgX]$:	ADF (2005.01)		Gaussian 03		
X	^1J(Ag,P) (Hz)	FC (total %)	^1J(Ag,P) (Hz)	FC (total %)	r_{AgP} (Å)
Cl	–441	99.7	–386	98.9	2.475
Br	–418	99.5	–359	98.8	2.488
I	–370	99.2	—	—	2.504
CN	–460	99.8	–391	99.0	2.464
NC	–373	99.6	–309	98.7	2.491
OCH_3	–603	99.7	–477	99.4	2.417
OC(O)H	–507	99.7	–434	99.1	2.454
$OC(O)CH_3$	–522	99.8	–440	99.1	2.454

Fig. 6. Plot of $|^1J(Ag,P)|$ values calculated with ADF versus $r_{Ag,P}$ for (*a*) $[Me_3PAgX]$, where X is a monovalent anion (see Table 4) and (*b*) $[Me_3PAgX]$, where X = Cl^- (squares), Br^- (triangles), and I^- (prisms).

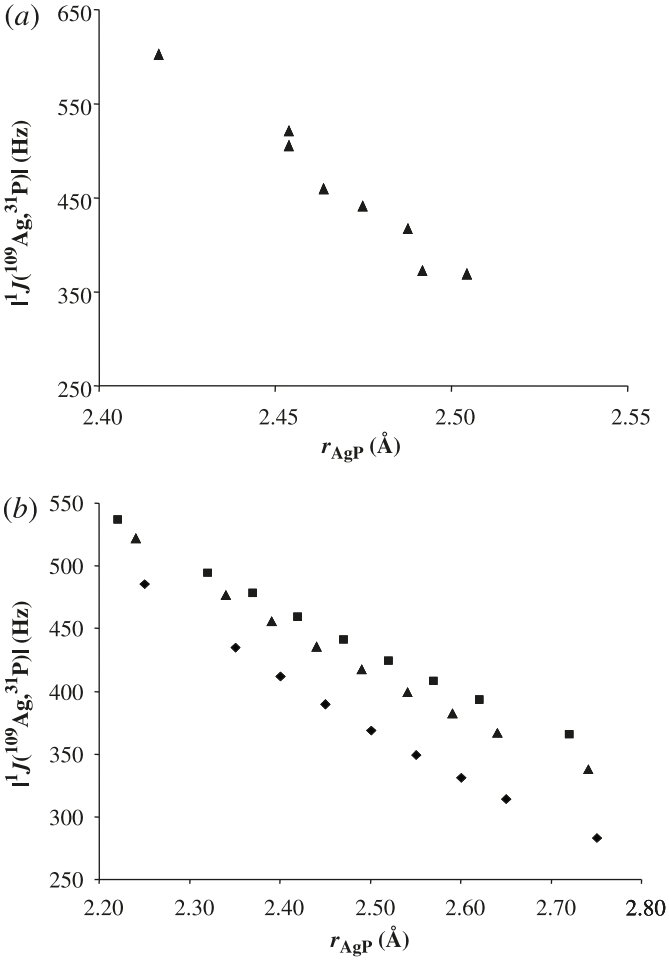

pletely dominates the $^1J(^{109}Ag,^{31}P)$ (Table 4), in agreement with the suggestions by Nelson and co-workers.[9–11]

Conclusions

Solid-state ^{31}P NMR spectroscopy has been used to investigate a series of silver–triphenylphosphine complexes of the type $[Ph_3PAgX]_n$. The number of distinct P sites revealed in the high-resolution solid-state ^{31}P NMR spectra of $[Ph_3PAgX]_n$ are consistent with the available crystal structures. The ability to identify the number of distinct phosphorus sites by solid-state ^{31}P CP/MAS NMR spectroscopy is particularly useful when X-ray diffraction data are unavailable. The $|^1J(^{109}Ag,^{31}P)|$ values for those complexes investigated here range from 401 ± 10 Hz (X = N_3^-) to 869 ± 10 Hz (X = $SO_3CF_3^-$). The data obtained here and in earlier literature indicate that $|^1J(Ag,P)|$ values decrease with increasing r_{AgP} for silver–tertiary phosphine complexes. This conclusion is supported by DFT calculations which also indicate that the Fermi-contact mechanism is the only important spin–spin coupling mechanism contributing to $^1J(Ag,P)$.

Supplementary data

Supplementary data for this article are available on the journal Web site (canjchem.nrc.ca) or may be purchased from the Depository of Unpublished Data, Document Delivery, CISTI, National Research Council Canada, Ottawa, ON K1A 0R6, Canada. DUD 3963. For more information on obtaining material, refer to cisti-icist.nrc-cnrc.gc.ca/cms/unpub_e.shtml. CCDC 724007 and 724008 contain the X-ray data in CIF format for for $[Ph_3PAgCl]_4$ and $[Ph_3PAgOC(O)CF_3]_4$ for this manuscript. These data can be obtained, free of charge, via www.ccdc.cam.ac.uk/conts/retrieving.html (or from the Cambridge Crystallographic Data Centre, 12 Union Road, Cambridge CB2 1EZ, UK; fax +44 1223 336033; or deposit@ccdc.cam.ac.uk).

Acknowledgements

We thank Guy Bernard for many helpful comments and discussions, and Scott Kroeker for obtaining preliminary experimental ^{31}P NMR data for some of the silver halide triphenylphosphine complexes many years ago. We are also grateful to Robert McDonald and Michael Ferguson in the X-ray Crystallography laboratory for acquiring the X-ray data. We acknowledge WestGrid for allowing the use of their clusters for Gaussian 03 calculations. REW is a Canada Research Chair in Physical Chemistry and would like to acknowledge the Natural Sciences and Engineering Research Council of Canada (NSERC) for funding. SWO is grateful to Mokpo National University, Republic of Korea for an award under the Professors' training program. Finally, we thank a referee for pointing out that a plot of $\log_{10}|^1J(Ag,P)|$ versus r_{AgP} has a slope of –2.0 (R = 0.944); however, the theoretical significance of this relationship is unknown and we prefer to state that it is simply an empirical observation.

References

(1) This article is part of a Special Issue dedicated to Professor T. Ziegler.

(2) This article is dedicated to Professor Tom Ziegler in recognition of his contributions to science in Canada.

(3) Hathaway, B. J. In *Comprehensive Coordination Chemistry*;. G. Wilkinson, Ed.; Pergamon: Oxford, 1987; Vol. 5, p. 533.

(4) Lancashire, R. J In *Comprehensive coordination chemistry*;. G. Wilkinson, Ed.; Pergamon: Oxford, 1987; Vol. 5, p. 775.

(5) Puddephatt, R. J. In *Comprehensive coordination chemistry*;. G. Wilkinson, Ed.; Pergamon: Oxford, 1987; Vol. 5, p. 861.

(6) Bowmaker, G. A.; Hart, R. D.; Jones, B. E.; Skelton, B. W.; White, A. H. *J. Chem. Soc., Dalton Trans.* **1995**, (18): 3063. doi:10.1039/dt9950003063.

(7) Bowmaker, G. A.; Healy, C.; Kildea, J. D.; White, A. H. *Spectrochim. Acta A Mol. Biomol. Spectrosc.* **1988**, *44,* 1219. doi:10.1016/0584-8539(88)80096-5.

(8) Bowmaker, G. A.; Hanna, J. V.; Hart, R. D.; Healy, P. C.; White, A. H. *Aust. J. Chem.* **1994**, *47*, 25. doi:10.1071/CH9940025.

(9) Attar, S.; Bowmaker, G. A.; Alcock, N. W.; Frye, J. S.; Bearden, W. H.; Nelson, J. H. *Inorg. Chem.* **1991**, *30* (25), 4743–4753. doi:10.1021/ic00025a013.

(10) Nelson, J. H. *Concepts Magn. Reson.* **2002**, *14* (1), 19–78. doi:10.1002/cmr.10001.

(11) Attar, S.; Alcock, N. W.; Bowmaker, G. A.; Frye, J. S.; Bearden, W. H.; Nelson, J. H. *Inorg. Chem.* **1991**, *30* (22), 4166–4176. doi:10.1021/ic00022a016.

(12) Bowmaker, G. A.; Effendy, H.; Hanna, J. V.; Healy, P. C.; Skelton, B. W.; White, A. H. *J. Chem. Soc., Dalton Trans.* **1993**, (9): 1387. doi:10.1039/dt9930001387.

(13) Bowmaker, G. A.; de Silva, E. N.; Healy, P. C.; Skelton, B. W.; White, A. H. *J. Chem. Soc., Dalton Trans.* **1999**, (6): 901–908. doi:10.1039/a808778d.

(14) Bowen, R. J.; Camp, D.; Effend, y; Healy, P. C.; Skelton, B. W.; White, A. H. *Aust. J. Chem.* **1994**, *47*, 693. doi:10.1071/CH9940693.

(15) Bowmaker, G. A.; Dyason, J. C.; Healy, P. C.; Engelhardt, L. M.; Pakawatchai, C.; White, A. H. *J. Chem. Soc., Dalton Trans.* **1987**, (5): 1089. doi:10.1039/dt9870001089.

(16) Bowmaker, G. A.; Engelhardt, L. M.; Healy, P. C.; Kildea, J. D.; Papasergio, R. I.; White, A. H. *Inorg. Chem.* **1987**, *26* (21), 3533–3538. doi:10.1021/ic00268a023.

(17) Bowmaker, G. A.; Cotton, J. D.; Healy, P. C.; Kildea, J. D.; Silong, S. B.; Skelton, B. W.; White, A. H. *Inorg. Chem.* **1989**, *28* (8), 1462–1466. doi:10.1021/ic00307a009.

(18) Baker, L. J.; Bowmaker, G. A.; Camp, D.; Effendy.; Healy, P. C.; Schmidbaur, H.; Steigelmann, O.; White, A. H. *Inorg. Chem.* **1992**, *31* (17), 3656–3662. doi:10.1021/ic00043a029.

(19) Baker, L. J.; Bowmaker, G. A.; Hart, R. D.; Harvey, P.; Healy, P. C.; White, A. H. *Inorg. Chem.* **1994**, *33* (18), 3925–3931. doi:10.1021/ic00096a016.

(20) Oh, S.-W.; Bernard, G. M.; Wasylishen, R. E.; McDonald, R.; Ferguson, M. J. *Can. J. Chem.* **2005**, *83* (10), 1721–1730. doi:10.1139/v05-174.

(21) Brown, S. S. D.; Salter, I. D.; Smith, D. J.; Clayden, N. J.; Dobson, C. M. *J. Organomet. Chem.* **1991**, *408* (3), 439–450. doi:10.1016/0022-328X(91)83213-N.

(22) Alyea, E. C.; Malito, J.; Attar, S.; Nelson, J. H. *Polyhedron* **1992**, *11* (18), 2409–2413. doi:10.1016/S0277-5387(00)83532-9.

(23) Barron, P. F.; Dyason, J. C.; Healy, P. C.; Engelhardt, L. M.; Skelton, B. W.; White, A. H. *J. Chem. Soc., Dalton Trans.* **1986**, (9): 1965. doi:10.1039/dt9860001965.

(24) Wu, G.; Wasylishen, R. E.; Pan, H.; Liu, C. W.; Fackler, J. P., Jr.; Shang, M. *Magn. Reson. Chem.* **1995**, *33* (9), 734–738. doi:10.1002/mrc.1260330908.

(25) Liu, C. W.; Pan, H.; Fackler, J. P., Jr.; Wu, G.; Wasylishen, R. E.; Shang, M. *J. Chem. Soc., Dalton Trans.* **1995**, (22): 3691. doi:10.1039/dt9950003691.

(26) Davila, R. M.; Staples, R. J.; Elduque, A.; Harlass, M. M.; Kyle, L.; Fackler, J. P., Jr. . *Inorg. Chem.* **1994**, *33* (25), 5940–5945. doi:10.1021/ic00103a049.

(27) Khan, M. N. I.; Staples, R. J.; King, C.; Fackler, J. P.; Winpenny, R. E. P. *Inorg. Chem.* **1993**, *32* (25), 5800–5807. doi:10.1021/ic00077a025.

(28) Teo, B. K.; Calabrese, J. C. *J. Am. Chem. Soc.* **1975**, *97* (5), 1256–1257. doi:10.1021/ja00838a057.

(29) Teo, B. K.; Calabrese, J. C. *Inorg. Chem.* **1976**, *15* (10), 2467–2474. doi:10.1021/ic50164a031.

(30) Teo, B. K.; Calabrese, J. C. *J. Chem. Soc. Chem. Commun.* **1976**, (6): 185. doi:10.1039/c39760000185.

(31) Teo, B. K.; Calabrese, J. C. *Inorg. Chem.* **1976**, *15* (10), 2474–2486. doi:10.1021/ic50164a032.

(32) Terroba, R.; Hursthouse, M. B.; Laguna, M.; Mendia, A. *Polyhedron* **1999**, *18* (6), 807–810. doi:10.1016/S0277-5387(98)00361-1.

(33) Bardají, M.; Crespo, O.; Laguna, A.; Fischer, A. K. *Inorg. Chim. Acta* **2000**, *304* (1), 7–16. doi:10.1016/S0020-1693(00)00052-9.

(34) Blues, E. T.; Drew, M. G. B.; Femi-Onadeko, B. *Acta Crystallogr.* **1977**, *B33*, 3965. doi:10.1107/S056774087701262X.

(35) Cingolani, A.; Effendy, E.; Hanna, J. V.; Pellei, M.; Pettinari, C.; Santini, C.; Skelton, B. W.; White, A. H. *Inorg. Chem.* **2003**, *42* (16), 4938–4948. doi:10.1021/ic034243e. PMID:12895118.

(36) Stein, R. A.; Knobler, C. *Inorg. Chem.* **1977**, *16* (2), 242–245. doi:10.1021/ic50168a005.

(37) Cingolani, A.; Effendy.; Pellei, M.; Pettinari, C.; Santini, C.; Skelton, B. W.; White, A. H. *Inorg. Chem.* **2002**, *41* (25), 6633–6645. doi:10.1021/ic020375g. PMID:12470058.

(38) Hubel, R.; Polborn, K.; Beck, W. *Eur. J. Inorg. Chem.* **1999**, *1999* (3), 471–482. doi:10.1002/(SICI)1099-0682(199903)1999:3<471::AID-EJIC471>3.0.CO;2-H.

(39) Harris, R. K.; Becker, E. D.; Cabral de Menezes, S. M.; Goodfellow, R.; Granger, P. *Solid State Nucl. Magn. Reson.* **2002**, *22* (4), 458–483. doi:10.1006/snmr.2002.0063. PMID:12637147.

(40) Bacskay, G. B. *Chem. Phys. Lett.* **1995**, *242* (4-5), 507–513. doi:10.1016/0009-2614(95)00765-V.

(41) Hush, N. S. *J. Am. Chem. Soc.* **1997**, *119* (7), 1717–1719. doi:10.1021/ja963150b.

(42) Vizioli, C. V.; Ruiz de Azua, M. C. *Mol. Phys.* **2000**, *98*, 891. doi:10.1080/00268970050025501.

(43) Ramsey, N. F. *Phys. Rev.* **1953**, *91* (2), 303–307. doi:10.1103/PhysRev.91.303.

(44) Vaara, J.; Jokisaari, J.; Wasylishen, R. E.; Bryce, D. L. *Prog. Nucl. Magn. Reson. Spectrosc.* **2002**, *41* (3-4), 233–304. doi:10.1016/S0079-6565(02)00050-X.

(45) Pople, J. A.; Santry, D. P. *Mol. Phys.* **1964**, *8* (1), 1–18. doi:10.1080/00268976400100011.

(46) Buckingham, A. D.; Love, I. *J. Magn. Reson.* **1970**, *2*, 338.

(47) Jameson, C. J. *In* Multinuclear NMR. *Edited by* J. Mason. Plenum Press, New York. pp. 89–131. 1987.

(48) Pyykkö, P. *Chem. Phys.* **1977**, *22* (2), 289–296. doi:10.1016/0301-0104(77)87013-4.

(49) Aucar, G. A.; Contreras, R. H. *J. Magn. Reson.* **1991**, *93*, 413.

(50) Aucar, G. A.; Oddershede, J. *Int. J. Quantum Chem.* **1993**, *47* (6), 425–435. doi:10.1002/qua.560470603.
(51) Blizzard, A. C.; Santry, D. P. J. *Chem. Phys.* **1971**, *55*, 950.
(52) Beurskens, P. T.; Beurskens, G.; de Gelder, R.; Garcia-Granda, S.; Israel, R.; Gould, R. O.; Smits, J. M. M. The DIRDIF-99 program system [computer program]. Crystallography Laboratory, University of Nijmegen, Nijmegen, The Netherlands. 1999.
(53) Sheldrick, G. M. *SHELXL-93* [computer program]; University of Göttingen: Göttingen, Germany, 1993.
(54) Bryce, D. L.; Bernard, G. M.; Gee, M.; Lumsden, M.; Eichele, K.; Wasylishen, R. E. *Can. J. Anal. Sci. Spectrosc.* **2001**, *46*, 46.
(55) Frisch, M. J.; Trucks, G. W.; Schlegel, H. B.; Scuseria, G. E.; Robb, M. A.; Cheeseman, J. R.; Montgomery, J. A., Jr.; Vreven, T.; Kudin, K. N.; Burant, J. C.; Millam, J. M.; Iyengar, S. S.; Tomasi, J.; Barone, V.; Mennucci, B.; Cossi, M.; Scalmani, G.; Rega, N.; Petersson, G. A.; Nakatsuji, H.; Hada, M.; Ehara, M.; Toyota, K.; Fukuda, R.; Hasegawa, J.; Ishida, M.; Nakajima, T.; Honda, Y.; Kitao, O.; Nakai, H.; Klene, M.; Li, X.; Knox, J. E.; Hratchian, H. P.; Cross, J. B.; Bakken, V.; Adamo, C.; Jaramillo, J.; Gomperts, R.; Stratmann, R. E.; Yazyev, O.; Austin, A. J.; Cammi, R.; Pomelli, C.; Ochterski, J. W.; Ayala, P. Y.; Morokuma, K.; Voth, G. A.; Salvador, P.; Dannenberg, J. J.; Zakrzewski, V. G.; Dapprich, S.; Daniels, A. D.; Strain, M. C.; Farkas, O.; Malick, D. K.; Rabuck, A. D.; Raghavachari, K.; Foresman, J. B.; Ortiz, J. V.; Cui, Q.; Baboul, A. G.; Clifford, S.; Cioslowski, J.; Stefanov, B. B.; Liu, G.; Liashenko, A.; Piskorz, P.; Komaromi, I.; Martin, R. L.; Fox, D. J.; Keith, T.; Al-Laham, M. A.; Peng, C. Y.; Nanayakkara, A.; Challacombe, M.; Gill, P. M. W.; Johnson, B.; Chen, W.; Wong, M. W.; Gonzalez, C.; Pople, J. A. *Gaussian 03*, revision C.04; Gaussian, Inc.: Wallingford, CT, 2004.
(56) Dickson, R. M.; Ziegler, T. *J. Phys. Chem.* **1996**, *100* (13), 5286–5290. doi:10.1021/jp951930l.
(57) Autschbach, J.; Ziegler, T. *J. Chem. Phys.* **2000**, *113* (3), 936. doi:10.1063/1.481874.
(58) Autschbach, J.; Ziegler, T. *J. Chem. Phys.* **2000**, *113* (21), 9410. doi:10.1063/1.1321310.
(59) Khandogin, J.; Ziegler, T. *Spectrochim. Acta [A]* **1999**, *55* (3), 607–624. doi:10.1016/S1386-1425(98)00265-0.
(60) Baerends, E. J.;te Velde, B.; Rauk, A.; Ziegler, T. and collaborators. *ADF 2005.01* Scientific computing and modelling, theoretical chemistry, Vrije Universiteit: Amsterdam. Available from http://www.scm.com.
(61) Baerends, E. J.; Ellis, D. E.; Ros, P. *Chem. Phys.* **1973**, *2* (1), 41–51. doi:10.1016/0301-0104(73)80059-X.
(62) Versluis, L.; Ziegler, T. *J. Chem. Phys.* **1988**, *88* (1), 322. doi:10.1063/1.454603.
(63) Tevelde, G.; Baerends, E. J. *J. Comput. Phys.* **1992**, *99* (1), 84–98. doi:10.1016/0021-9991(92)90277-6.
(64) Fonseca Guerra, C.; Snijders, J. G.; te Velde, G.; Baerends, E. *J. Theor. Chem. Acc.* **1998**, *99* (6), 391. doi:10.1007/s002140050021.
(65) Vosko, S. H.; Wilk, L.; Nusair, M. *Can. J. Phys.* **1980**, *58*, 1200.
(66) Becke, A. D. *Phys. Rev. A* **1988**, *38* (6), 3098–3100. doi:10.1103/PhysRevA.38.3098. PMID:9900728.
(67) Perdew, J. P. *Phys. Rev. B* **1986**, *33* (12), 8822–8824. doi:10.1103/PhysRevB.33.8822.
(68) Perdew, J. P. *Phys. Rev. B* **1986**, *34* (10), 7406. doi:10.1103/PhysRevB.34.7406.
(69) Chang, C.; Pelissier, M.; Durand, P. *Phys. Scr.* **1986**, *34* (5), 394–404. doi:10.1088/0031-8949/34/5/007.
(70) van Lenthe, E.; Baerends, E. J.; Snijders, J. G. *J. Chem. Phys.* **1993**, *99*, 4597. doi:10.1063/1.466059.
(71) van Lenthe, E.; Baerends, E. J.; Snijders, J. G. *J. Chem. Phys.* **1994**, *101* (11), 9783. doi:10.1063/1.467943.
(72) van Lenthe, E.; van Leeuwen, R.; Baerends, E. J.; Snijders, J. G. *Int. J. Quantum Chem.* **1996**, *57* (3), 281–293. doi:10.1002/(SICI)1097-461X(1996)57:3<281::AID-QUA2>3.0.CO;2-U.
(73) Forgeron, M. A. M.; Gee, M.; Wasylishen, R. E. *J. Phys. Chem. A* **2004**, *108* (22), 4895–4908. [and references therein]. doi:10.1021/jp040034j.
(74) Hitchcock, P. B.; Jacobson, B.; Pidcock, A. *J. Chem. Soc., Dalton Trans.* **1977**, (20): 2038. doi:10.1039/dt9770002038.
(75) Mason, R.; Meek, D. W. *Angew. Chem. Int. Ed. Engl.* **1978**, *17* (3), 183–194. doi:10.1002/anie.197801831.
(76) Mather, G. G.; Pidcock, A.; Rapsey, G. J. N. *J. Chem. Soc., Dalton Trans.* **1973**, (20): 2095. doi:10.1039/dt9730002095.
(77) Eichele, K.; Wasylishen, R. E. *Inorg. Chem.* **1994**, *33* (13), 2766–2773. doi:10.1021/ic00091a017.
(78) Bowmaker, G. A.; Effendy.; Harvey, P. J.; Healy, P. C.; Skelton, B. W.; White, A. H. *J. Chem. Soc., Dalton Trans.* **1996**, (12): 2459. doi:10.1039/dt9960002459.
(79) Bowmaker, G. A.; Effendy.; Harvey, P. J.; Healy, P. C.; Skelton, B. W.; White, A. H. *J. Chem. Soc., Dalton Trans.* **1996**, (12): 2449. doi:10.1039/dt9960002449.
(80) Bowmaker, G. A.; Effendy.; Hanna, J. V.; Healy, P. C.; Millar, G. J.; Skelton, B. W.; White, A. H. *J. Phys. Chem.* **1995**, *99* (12)(Skelton), 3909–3917. doi:10.1021/j100012a008.
(81) Bowmaker, G. A.; Hanna, J. V.; Rickard, C. E. F.; Lipton, A. S. *J. Chem. Soc., Dalton Trans.* **2001**, (1): 20–28. doi:10.1039/b007796h.
(82) Bowmaker, G. A.; Hanna, J. V.; Healy, P. C.; Reid, J. C.; Rickard, C. E. F.; White, A. H. *J. Chem. Soc., Dalton Trans.* **2000**, (5): 753–762. doi:10.1039/a908427d.

TRIBUTE

A tribute to Tom Ziegler

Biographical sketch — From Copenhagen to Calgary

Tom Ziegler was born in Copenhagen in 1945. He received his M.Sc. degree from the University of Copenhagen in 1972 in the field of Theoretical Chemistry, and his Ph.D. from the University of Calgary, in 1978 in the area of Inorganic/Theoretical Chemistry. After postdoctoral studies at the Free University in Amsterdam and McMaster University, he returned to Calgary in 1981, first as an NSERC University Research Fellow, and then Assistant Professor in 1986. He moved quickly through the ranks to Full Professor in 1993. Between 1996 and 1999, he held a Canada Council Killam Professorship, and two years later, in 2001, became a Tier 1 Canada Research Chair in Theoretical Inorganic Chemistry in recognition of his world-class achievements.

Tom is one of the earliest proponents of density functional theory (DFT), an electronic structure scheme that today is widely accepted as the method of choice in the description of large molecules. He began his life-long development work on a DFT-based computer code during his graduate years (1972–1978) as a Ph.D. student in Calgary under my supervision. This project has since been carried out in collaboration with the group of E. J. Baerends at the Free University in Amsterdam. It has resulted in the powerful Amsterdam density functional (ADF) program package that is widely used and still under development. The applications of this program have in particular been in the area of transition-metal chemistry, a field Tom became acquainted with as an M.Sc. student in Copenhagen under the supervision of J. P. Dahl and C. J. Ballhausen.

During the period 1978–1992, Tom's group (together with a few other sites, including that of D. Salahub in Montréal) demonstrated that DFT in the formulation by their Canadian compatriot A. Becke from Queens University was able to predict molecular energetics and structures with higher accuracy than the traditional electronic structure methods, and at a much lower computational cost. The work on structure and energetics culminated in an influential review paper (*Chem. Rev.* 1991), as well as the general acceptance of DFT in the Becke formulation, as the electronic structure theory of choice for large molecules.

Since 1992, Tom has demonstrated the power of DFT in applications to homogeneous catalysis in a number of highly cited papers mainly concentrating on olefin polymerization. Several petrochemical companies in Europe, Japan, and North America have supported this work. His polymerization research has considerably enhanced our understanding of the different role played by early and late transition metals as polymerization catalysts. More recently, Tom has turned towards heterogeneous catalysis in connection with research on solid oxide fuel cells (SOFC) and Fischer–Tropsch synthesis, again with substantial support from industry and government.

The Ziegler group has at the same time extended the number of molecular properties that can be modelled by DFT. In the period 1992–2000, the group introduced one of the first DFT codes for calculations of NMR chemical shifts and spin–spin coupling parameters as well as the ESR g- and A-tensors. These codes were based on methods that included relativistic effects and could as a result treat catalytic transition-metal systems with heavy metals. The NMR and ESR work is currently being extended to metal surfaces. Another ongoing development of use in homogenous and bioinorganic catalysis has been methods that can calculate electronic (ECD) and magnetic (MCD) circular dichroism. The group is currently applying their ECD and MCD codes to a number of metallo-enzymes. Other developments worth mentioning are their bonding analysis scheme with more than 1000 citations as well as their molecular dynamics method that makes it possible to optimize transition-state structures on the free energy surface.

Most recently, Tom has embarked on a critical assessment of the way in which we describe excited states. He has shown that the currently used method based on time-dependent DFT can be reformulated into a more simple static and time-independent method based on variation theory. The new formulation promises to extend the capability of DFT in studies of excited states.

Tom has been a Visiting Professor at a number of famous universities, the Institute of Molecular Sciences in Okazaki, Japan, the Free University in Amsterdam, and the University of Fribourg in Switzerland. Most recently, in 2008, he was the Lise–Meitner Lecturer at the Lise–Meitner–Minerva Center for Computational Quantum Chemistry in Israel.

Over the course of his career, he has won numerous awards, including a CNC-IUPAC Award (1988), the CSC's Alcan Award (1994), the Award in Pure and Applied Inorganic Chemistry (2000), and Steacie Award (2005). He was elected Fellow of the Royal Society of Canada in 1997, Fellow of the Royal Danish Academy of Sciences and Letters in 2000, and Fellow of the International Academy of Quantum Molecular Science in 2007. In 2004, Tom was awarded the prestigious Schrödinger Medal, the highest award of the World Association for Theoretically Oriented Chemists (WATOC).

Tom has also made significant contributions to the chemical community, serving on the Advisory Boards of *Organometallics* (1998–2001), and *Journal of Computational Chemistry* (2005–2009), and as a member of the NSERC Grant Selection Committee for Analytical and Physical Chemistry (1998–2001), the Fellowship Selection Committee for the Royal Society of Canada (2001–2004), and as Secretary, Academy of Science, Royal Society of Canada (2000–2004). Many of his students and co-workers have gone on to hold academic positions at various Canadian and International Universities, or have accepted industrial positions.

Tom is one of the two most cited chemists in Canada with over 7000 citations, and ranks in the top 100 most cited in the World with an H-index of 70. The number and quality of the papers submitted to this dedicated issue of the *Canadian Journal of Chemistry* attests to the breadth and reach of his influence in the chemical, theoretical, and computational community.

Arvi Rauk
Calgary, Alberta, Canada

Can. J. Chem. Downloaded from www.nrcresearchpress.com by Sichuan Normal University on 09/14/12
For personal use only.

HOMMAGE

Hommage à Tom Ziegler

Tom Ziegler est né à Copenhague en 1945. Il a obtenu une maîtrise ès sciences en chimie théorique de l'Université de Copenhague (1972), puis un doctorat dans le domaine de la chimie inorganique théorique de l'Université de Calgary (1978). Après ses études postdoctorales à l'Université libre d'Amsterdam et à l'Université McMaster, il est de retour à Calgary en 1981, tout d'abord à titre de chercheur universitaire du CRSNG, et ensuite à titre de professeur adjoint en 1986. Il a rapidement gravi les échelons pour atteindre le poste de professeur titulaire en 1993. Entre 1996 et 1999, il a obtenu une bourse de recherche Killam du Conseil des arts du Canada. Deux ans plus tard, en 2001, il est devenu titulaire de la chaire de recherche du Canada (niveau 1) en chimie inorganique théorique pour ses réalisations incomparables.

Tom est l'un des partisans de la première heure de la théorie de la fonctionnelle de la densité (TFD), un schéma de structure électronique généralement accepté de nos jours comme la méthode préconisée pour décrire les grosses molécules. Il a commencé ses travaux de recherche, qui le suivront tout au long de sa carrière, sur un code informatique basé sur la TFD au cours de son doctorat (1972–1978) à Calgary, sous ma direction. Depuis, ce projet est réalisé en collaboration avec l'équipe d'E. J. Baerends de l'Université libre d'Amsterdam. Ces travaux ont donné lieu au puissant logiciel ADF (Amsterdam Density Functional), couramment utilisé et encore en développement. Les applications de ce logiciel se situent particulièrement dans le domaine de la chimie des métaux de transition, discipline dont Tom a pris connaissance au cours de ses études à la maîtrise sous la direction de J. P. Dahl et de C. J. Ballhausen, à Copenhague.

Entre 1978 et 1992, l'équipe de Tom (ainsi que quelques autres laboratoires, dont celui de D. Salahub, à Montréal) a démontré que la TFD, dans la formulation issue de leur compatriote canadien A. Becke de l'Université Queen's, pouvait prédire la structure et l'énergie des molécules avec une plus grande précision qu'en utilisant les méthodes de structure électronique traditionnelles, et ce, à un coût bien moindre en temps de calcul. Les travaux sur la structure et l'énergétique ont été couronnés aussi bien par la parution d'un article de synthèse influent (*Chemical Reviews,* 1991) que par l'acceptation générale de la TFD selon la formulation de Becke comme étant la théorie de la structure électronique à préconiser pour les grosses molécules.

Depuis 1992, Tom démontre la puissance de la TFD dans des applications à la catalyse homogène dans de nombreux articles fréquemment cités qui portent principalement sur la polymérisation de l'oléfine. Plusieurs sociétés pétrochimiques en Europe, au Japon et en Amérique du Nord ont financé ces travaux. Ses recherches sur la polymérisation ont grandement contribué à l'amélioration de notre connaissance du rôle différent que jouent les métaux de transition précoce et tardive comme catalyseurs de la polymérisation. Plus récemment, Tom s'est tourné vers la catalyse hétérogène relative aux travaux effectués sur les piles à combustible à oxyde solide (piles SOFC) et sur la synthèse de Fischer–Tropsch grâce, encore une fois, à l'aide importante de l'industrie et du gouvernement.

Au même moment, l'équipe de Ziegler a accru le nombre de propriétés moléculaires qui pouvaient être modélisées par la TFD. Entre 1992 et 2000, cette équipe a mis en place l'un des premiers codes de la TFD pour calculer aussi bien les déplacements chimiques en RMN et les paramètres de couplage spin–spin que les tenseurs g et A en RPE. Ces codes reposaient sur des méthodes qui comprenaient les effets relativistes; l'équipe a donc pu traiter des systèmes catalytiques de métaux de transition à base de métaux lourds. On étend actuellement les travaux en RMN et en RPE aux surfaces métalliques. Le développement actuel d'une autre utilisation en catalyse homogène et bioorganique consiste à mettre au point des méthodes qui permettent de calculer le dichroïsme circulaire électronique (DCE) et magnétique (DCM). L'équipe applique actuellement ses codes de DCE et de DCM à de nombreux métalloenzymes. On ne peut passer sous silence d'autres innovations apportées par cette équipe comme le schéma d'analyse des liaisons, cité à plus de 1000 occasions, et la méthode de dynamique moléculaire qui permet d'optimiser les structures des états de transition sur la surface d'énergie libre.

Tout récemment, Tom a entrepris une évaluation critique de la façon dont on décrit les états d'excitation. Il a montré que la méthode utilisée actuellement, fondée sur la TFD en fonction du temps, peut être reformulée en une méthode plus simple, statique et indépendante du temps, et fondée sur la théorie de la variation. Cette nouvelle formulation annonce un potentiel accru de la TFD dans des études portant sur les états d'excitation.

Tom a été professeur invité dans plusieurs universités prestigieuses, soit l'Institut des sciences moléculaires d'Okazaki (Japon), l'Université libre d'Amsterdam et l'Université de Fribourg (Suisse). Tout récemment, en 2008, il a été nommé maître de conférence Lise–Meitner au Lise–Meitner–Minerva Center for Computational Quantum Chemistry (Israël).

Tout au long de sa carrière, Tom a gagné de nombreux prix, dont celui du CNC-UICPA (1988), le prix Alcan de la SCC (1994), le prix de chimie inorganique pure ou appliquée (2000) et le prix Steacie (2005). Il a été élu membre de la Société royale du Canada (1997), membre de l'Académie royale danoise des sciences et des lettres (2000), et membre de l'Académie internationale des sciences moléculaires quantiques (2007). En 2004, Tom a reçu la prestigieuse médaille Schrödinger, la plus haute distinction remise par la World Association for Theoretically Oriented Chemists (WATOC).

Tom a contribué de façon importante au milieu de la chimie en siégeant au comité consultatif des revues *Organometallics* (1998–2001) et *Journal of Computational Chemistry* (2005–2009), et à titre de membre du Comité de sélection des subventions du CRSNG pour la chimie analytique et physique (1998–2001), de membre du Comité de sélection des bourses pour la Société royale du Canada (2001–2004), et de secrétaire pour l'Académie des sciences de la Société royale du Canada (2000–2004). Beaucoup de ses étudiants et collègues occupent maintenant des postes dans diverses universités canadiennes ou étrangères, ou dans l'industrie.

Fort de plus de 7000 citations à son actif, Tom est l'un des deux chimistes les plus cités au Canada, et il se situe parmi les cent premiers chimistes les plus cités dans le monde avec un indice h de 70. Le nombre et la qualité des articles soumis à ce numéro spécial de la *Revue canadienne de chimie* attestent l'ampleur et la portée de son influence dans le milieu de la chimie, de la théorie et de l'informatique.

Arvi Rauk
Calgary (Alberta), Canada

Can. J. Chem. Downloaded from www.nrcresearchpress.com by Tianjin University of Technology on 09/16/12
For personal use only.

TRIBUTE

DFT — Das Future Tool

"Das Future Tool" was the title of the group T-shirt[1] that we had made for Tom Ziegler as graduate students in the early nineties. In those days, DFT was only beginning to gain popularity in theoretical chemistry community. Tom had just published his influential review article "Approximate Density Functional Theory as a Practical Tool in Molecular Energetics and Dynamics" in *Chem. Rev.* and had organized one of the first, if not the first, ACS symposium dedicated solely to DFT titled "Chemical Applications of Density Functional Theory" at the spring national meeting in Anaheim. Even the Gaussian suite of programs had finally incorporated DFT into their G92 package (However, not with the original G92 release but as a later interim release they dubbed G92/DFT).

Nonetheless, even at that time, there were a large number of detractors in the theoretical chemistry community who were skeptical of DFT and considered it just another semi-empirical method.[2] Tom, however, realized that DFT was "Das Future Tool" long before then and in fact had started to develop DFT as a practical tool in chemistry some ten years before beginning in the late 1970s. In those "early days", there was an even more skeptical attitude towards DFT in the theoretical chemistry community. For example, Tom's first NSERC operating grant, intended to run his whole research program, was a mere $5000 per year. Even adjusting 1982 dollars for inflation which brings this grant amount to $10 585 in today's dollars, that is a very skeptical level of funding. Things have dramatically changed since the 1980s. Not only is Tom's research funding level much higher, but DFT is now the quantum chemical method of choice for most researchers.

One impressive aspect of Tom's body of work is that he is able to communicate both to "hard core" theoretical chemists interested in fundamental theory, as well as non-theoretical chemists who were interested in gaining a deeper understanding of their chemistry from a theoretical point of view. Tom's work has always focused on two equally important aspects of computational chemistry, namely the development of new methodology and its application to problems of chemical relevance. Owing to this duality, Tom's work has inspired theoretically as well as experimentally inclined researchers alike. This is evidenced by that fact that Tom is one of Canada's most highly cited chemists with a towering H-index of 70.

Tom's kaleidoscopic research interests present many different facets. If five out of Tom's former graduate students were asked to name their favorites out of all his contributions to science, five different answers would probably be generated – be it his work on molecular structure and properties, or on the nature of the chemical bond, or on relativistic effects which led to the Dutch Revolution in the theory of relativity, be it his work on NMR calculations or his contributions to catalysis or DFT based molecular dynamics. With all the different hats that Tom wears, DFT is the common denominator that amalgamates his many interests, from the early days up to the present time. Based on his work done in fulfillment of a Ph.D. degree, Tom published a seminal work in which he became aware of and circumvented the problem of calculating reliable bond energies by DFT. The transition state method was at the heart of many research topics that Tom worked on in the beginning of his career. Now, some thirty years later, Tom tackles excited states as well as solid states in search for answers to many relevant chemical problems.

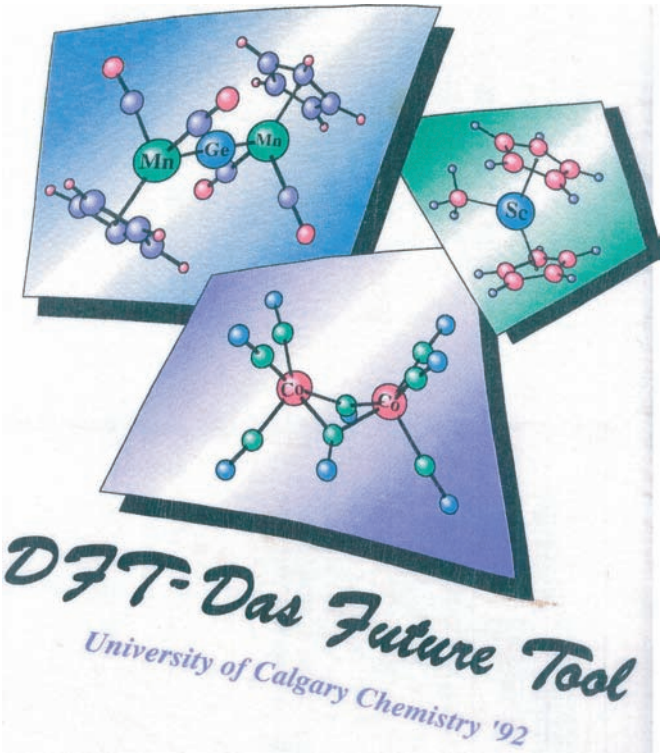

Tom and his Calgary group were certainly pivotal in the meteoric rise of DFT as a powerful tool in chemical research. Tom was not only an early pioneer some 25 years ago, but he has continued to make significant contributions to fundamental DFT theory and its applications to chemical systems since then. In these two special issues of *Can. J. Chem.*, we wish to celebrate Tom Ziegler's vision and many contributions to chemistry. It was a privilege to be a group member in the early nineties and to witness our then whimsical interpretation of DFT (Das Future Tool) become a reality alongside one of its most influential contributors.[2]

Heiko Jacobsen
New Orleans, Louisiana, USA

Tom Woo
Ottawa, Ontario, Canada

[1]The T-shirt featured images of "large" organometallic complexes, that were chosen not only for their aesthetic beauty and symmetry, but also to symbolize the fact that DFT could treat these systems accurately and with a practical amount of computing effort, when, at the time, no other quantum chemical methods could do so. There was also an ongoing discussion as to whether we should use "Der" or "Das". From a German language point of view "Der" may be better but we opted for "Das".

[2]We recall a number of heated debates at the ACS meeting in Anaheim involving some of the "unconverted".

Can. J. Chem. Downloaded from www.nrcresearchpress.com by Sichuan Normal University on 09/14/12
For personal use only.

HOMMAGE

DFT — Das Future Tool (TFD: l'outil de l'avenir)

« Das Future Tool » (l'outil de l'avenir) était le titre inscrit sur le t-shirt[1] que nous, l'équipe d'étudiants diplômés, avions fait confectionner pour Tom Ziegler au début des années 1990. À cette époque, la TFD commençait à gagner en popularité dans le milieu de la chimie théorique. Tom venait tout juste de publier son article de synthèse influent intitulé « Approximate Density Functional Theory as a Practical Tool in Molecular Energetics and Dynamics » (la théorie approximative de la fonctionnelle de la densité comme outil pratique en énergétique et en dynamique moléculaires) dans la revue *Chemical Reviews*. Par ailleurs, il avait organisé l'un des premiers, sinon le premier symposium de l'ACS consacré uniquement à la TFD et intitulé « Chemical Applications of Density Functional Theory » (applications chimiques de la théorie de la fonctionnelle de la densité) lors de la réunion printanière nationale qui avait eu lieu à Anaheim. Même la suite logicielle de la société Gaussian avait fini par incorporer la TFD dans son progiciel G92 (pas lors de la sortie de la première version de ce progiciel, mais plutôt dans une version provisoire ultérieure appelée G92/DFT).

Néanmoins, même à cette époque, il y avait un grand nombre de détracteurs dans le milieu de la chimie théorique qui demeuraient sceptiques par rapport à la TFD et qui la considéraient uniquement comme une autre méthode semi-empirique[2]. Cependant, Tom s'est rendu compte que la TFD était « l'outil de l'avenir » bien avant et qu'en fait, il avait commencé à concevoir la TFD comme outil pratique en chimie quelque dix ans auparavant, soit à la fin des années 1970. À cette époque, le scepticisme à l'égard de la TFD était encore plus grand dans le milieu de la chimie théorique. À titre d'exemple, la première subvention pour dépenses courantes de recherche qu'a reçue Tom du CRSNG, et qui visait à assurer le fonctionnement de son programme de recherche en entier, n'atteignait que 5000 $ par année. Même en tenant compte de l'inflation depuis 1982, ce qui porte le montant de cette subvention à 10 585 $ en dollars actuels, il s'agit d'un niveau de financement qui témoigne de ce scepticisme. Toutefois, les choses ont considérablement changé depuis les années 1980. Non seulement le niveau de financement en recherche de Tom est beaucoup plus important, mais la TFD est maintenant la méthode préconisée par la plupart des chercheurs en chimie quantique.

Un aspect impressionnant des travaux de Tom réside dans le fait qu'il réussit à joindre aussi bien le « noyau dur » de chimistes théoriciens qui s'intéressent à la théorie fondamentale que les chimistes non théoriciens qui désirent obtenir une meilleure compréhension de leur discipline d'un point de vue théorique. Les travaux de Tom ont toujours porté essentiellement sur deux aspects de la chimie informatique tout aussi importants l'un que l'autre, à savoir la conception d'une nouvelle méthodologie et son application aux problèmes ayant une pertinence chimique. Grâce à cette dualité, les travaux de Tom inspirent autant les chercheurs théoriciens qu'expérimentaux,

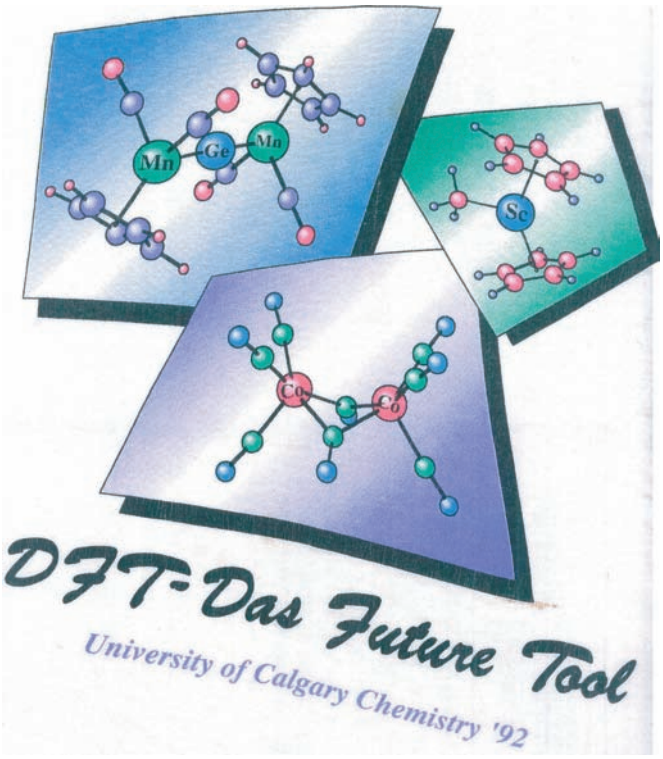

comme le prouve le fait que Tom est l'un des chimistes les plus cités au Canada avec un indice h de 70.

En constante évolution, les travaux de recherche de Tom présentent de multiples facettes. Si on demandait à cinq des anciens étudiants diplômés de Tom de nommer la contribution à la science qu'ils préfèrent parmi toutes celles qu'il a apportées, on obtiendrait probablement cinq réponses différentes. Mentionnons, à titre d'exemples, ses travaux sur la structure et les propriétés moléculaires, sur la nature de la liaison chimique ou sur les effets relativistes qui ont mené à la révolution néerlandaise de la théorie de la relativité, ou encore ses travaux sur des calculs en RMN ou ses contributions à la catalyse ou à la dynamique moléculaire fondée sur la TFD. Peu importe les fonctions occupées par Tom, la TFD constitue le dominateur commun qui amalgame ses nombreux sujets de prédilection, depuis ses débuts jusqu'à aujourd'hui. À partir de ses travaux effectués au cours de son doctorat, Tom a publié un ouvrage novateur dans lequel il s'est rendu compte du problème de fiabilité des calculs des énergies de liaison par la TFD et l'a contourné. La méthode de l'état de transition était au cœur de nombreux sujets de recherche sur lesquels Tom a travaillé au début de sa carrière. Maintenant, quelque trente ans plus tard, Tom s'attaque aussi bien aux états excités qu'aux états solides, à la recherche de réponses à de nombreux problèmes chimiques importants.

1. Ce t-shirt comportait des images de « gros » complexes organométalliques choisis non seulement pour leur esthétisme et leur symétrie, mais également pour symboliser le fait que la TFD pouvait traiter ces systèmes de façon précise et avec un volume acceptable de calculs informatisés quand, à cette époque, aucune autre méthode de chimie quantique ne permettait de le faire. Il y avait également des discussions constantes autour de l'utilisation de « Der » ou de « Das ». Du point de vue de la linguistique allemande, « Der » serait plus juste, mais nous avons opté pour « Das ».

Can. J. Chem. Downloaded from www.nrcresearchpress.com by Tianjin University of Technology on 09/16/12
For personal use only.

Tom et son équipe de Calgary ont certainement joué un rôle crucial dans l'ascension fulgurante de la TFD comme outil puissant de recherche en chimie. Tom n'a pas seulement été un précurseur il y a quelque 25 ans, il continue, depuis ce temps, à contribuer grandement à la théorie fondamentale de la TFD et à ses applications dans les systèmes chimiques. Dans ces deux numéros spéciaux de la *Revue canadienne de chimie*, nous voulons célébrer la vision de Tom Ziegler et ses nombreuses contributions apportées à la chimie. Ce fut un privilège de faire partie de cette équipe, au début des années 1990, et d'être témoins du fait que notre interprétation fantaisiste à l'époque de la TFD (l'outil de l'avenir) soit devenue réalité, et ce, en œuvrant aux côtés d'un de ses contributeurs les plus influents.[2]

Heiko Jacobsen
La Nouvelle-Orléans (Louisiane), É.-U.

Tom Woo
Ottawa (Ontario), Canada

Can. J. Chem. Downloaded from www.nrcresearchpress.com by Tianjin University of Technology on 09/16/12
For personal use only.

2. On se souviendra de plusieurs débats houleux avec certains des « non-convertis » lors de la réunion de l'ACS, à Anaheim.

Quasi-classical trajectory calculation of the Ba + HBr chemical reaction

Wen Wen Xia, Ning Lu, Haiyang Zhong, and Li Yao

Abstract: The results of the reaction between Ba atom and HBr are studied by using the quasi-classical trajectory (QCT) calculation on extended London–Eyring–Polanyi–Sato (LEPS) potential-energy surface (PES). The vibrational distribution, reaction cross section, and rotational alignment of the product BaBr have been calculated. The calculations predict that the reaction cross section decreases, while the translation energy and rotational energy increase with the increasing of collision energy. It has been found that low collision energy favors the abstraction reaction, whereas high collision energy leads to an insertion reaction. The calculated results agree with the experimental data and some relative theoretical results as well.

Key words: QCT, LEPS PES, vibrational distribution, reaction cross section, rotational alignment.

Résumé : On a réalisé une étude théorie de la réaction entre un atome de baryum et du HBr en faisant appel à des calculs de trajectoire quasi-classique (TQC) sur une surface d'énergie potentielle (SEP) étendue de London–Eyring–Polanyi–Santo (LEPS). On a calculé la distribution vibrationnelle, la section droite de la réaction et l'alignement rotation du produit BaBr. Les calculs ont permis de prédire que, une augmentation de l'énergie de collision s'accompagne d'une diminution de la section droite de la réaction alors que l'énergie de translation et l'énergie de rotation augmentent. On a trouvé qu'une faible énergie de collision favorise une réaction d'abstraction alors qu'une énergie de collision élevée conduit à une insertion. Les résultats calculés sont en bon accord avec les données expérimentales ainsi qu'avec certains résultats théoriques.

Mots-clés : trajectoire quasi-classique (TQC), LEPS SEP, distribution vibrationnelle, section droite de réaction, alignement réactionnel.

[Traduit par la Rédaction]

Introduction

Along with the interaction of experiments and theories in the field, the study of molecular reaction dynamics has obtained great development and extraordinary achievements in recent decades. The first quasi-classical trajectory (QCT) method that investigated the reaction collisions were carried out during the 1930s.[1] Since the 1960s, QCT method has developed rapidly.[2] From the experimental part, by means of electric field, supersonic molecular beam, and laser,[3–5] the translational energy, electric state, and vibration state of the reagent molecules can be well-prepared. The alignment of the rotation state under the same experimental conditions could also be obtained. By using the technologies of chemiluminescence (CL), laser-induced fluorescence (LIF), and cross molecular beam,[6,7] the nascent internal energy states of the molecular product can be detected. Similarly, the velocity and space-angle distributions of the product can also be measured.

In practice, LIF, which uses tunable dye lasers, has been employed to measure the reaction product's internal-state distribution, and actually most of these LIF studies were conducted under thermal collision-energy environment. In 1980, Siegel and Schultz[8] performed a lot of experimental work on the Ba + HBr reaction using the LIF method. They measured the vibrational distribution, mean product energies, and the total reaction cross section of the product BaBr. From the experiment, they concluded that only the change of the collision energy can slightly influence the vibrational distribution. They also determined that the mean rotational energy increases with the increasing collision energy and the total reaction cross section decreases as the collision energy is raised. Kasuya and co-workers[9] studied the crossed beam reaction (Ba + CH_3Br) by means of the LIF method when the collision energy was controlled in the range from 2.9 to 4.9 kcal/mol. Through the systematic simulation of the observed LIF spectra, they found that an increase of the collision energy brought about a drastic decrease of the vibrational excitation. Recently, in 2002, Zhang et al.[10] calculated the exothermic reaction Ba + HF based on the extended LEPS PES using the QCT method. They carried out the vibrational distribution, the internal-energy distribution, and product rotational alignment of the Ba + HF reaction. In their article, they described the reaction mechanism as two pathways, abstraction and insertion. There also exist some other studies on the reaction between an alkaline earth metal atom and a hydrogen halide molecule, such as Ba + HF,[11–17] Ba + HCl,[8,12,18] and Ba + HI.[12,19–23]

On all accounts, by means of the QCT method and some dynamics calculation, the experiment is able to be simulated, and the reaction principle can be further proved and discussed. So, in this paper, we calculate the vibrational distribution, product rotational alignment, reaction cross section, and some other results of the reaction Ba + HBr → BaBr + H and analyze the differences between the experimental re-

Received 9 February 2009. Accepted 14 April 2009. Published on the NRC Research Press Web site at canjchem.nrc.ca on 17 June 2009.

W.W. Xia, N. Lu, H.-Y. Zhong, and L. Yao.[1] Department of Physics, Dalian Maritime University, Dalian 116026, China.

[1]Corresponding author (e-mail: yaoli@newmail.dlmu.edu.cn).

sults and the theoretical ones. In the conclusions, we provide a reasonable explanation of the experimental results.

Theory

Potential-energy surface (PES)

The PES is the basis of the analysis and calculation of the reaction rate and reaction mechanism in the study of the molecular reaction dynamics. The London–Eyring–Polanyi–Sato (LEPS) PES is the one that has been widely used. In fact, we must use accurate PES to study the kinetic property of the Ba + HBr reaction; however, obtaining an intact PES is not an easy work. This is the reason why a lot of people use this primary PES in their calculations. In our calculation, we used the LEPS PES, which is just suitable for systems such as three or pseudo-three-body systems. Compared with other methods, such as QM and ab initio, QCT was a good fit for our request.

As for the system of ABC, semi-empirical generalized LEPS PES can be interpreted as follows[24]:

$$[1]\qquad U(R_1,R_2,R_3) = Q_1 + Q_2 + Q_3 - \{1/2[(J_1 - J_2)^2 + (J_2 - J_3)^2 + (J_3 - J_1)^2]\}^{1/2}$$

R_i, Q_i, and J_i represent the nuclear separation of diatomic molecule, the Coulomb integral, and exchange integral of electron, respectively.

$$[2]\qquad Q_i = \frac{D_e}{4 \times (1 + S_i)}[X_i^2(3 + S_i) - 2X_i(1 + 3S_i)]$$

$$[3]\qquad J_i = \frac{D_e}{4 \times (1 + S_i)}[X_i^2(1 + 3S_i) - 2X_i(3 + S_i)]$$

where

$$[4]\qquad X_i = \exp[-\beta_i(R_i - R_i^0)]$$

S_i is an adjustable parameter (so-called Sato parameter), and D_e, β_i, and R_i^0 are the Morse parameters of the diatom. D_e is defined as the classical dissociation energy, β_i stands for the spectrum constant, and R_i^0 is the equilibrium nuclear separation. Subscript i = 1, 2, 3 indicates Ba–Br, H–Br, and Ba–H, respectively. All the parameters are presented in Table 1. In our calculation, we used the adjustable parameters, which are called Sato parameter, given in Table 1 to obtain more reasonable PES. Although the Sato parameters do not have any physical meaning, we can use them to achieve the main feature about the PES and dynamical properties of the Ba + HBr reaction in our work. When we adjusted the Sato parameters, we had to compare our calculation results with the experimental results. If they correspond with each other, the Sato parameters are appropriate. If they do not, then we have to re-adjust the Sato parameters. When we found the right Sato parameters for one experimental result, we used the same Sato parameters to calculate the other experimental results.

Quasi-classical trajectory calculation

In the present study, the conventional quasi-classical algorithm, which is sixth order symplectic routine with energy conservation checked[17] is employed for the numerical solution of the classical Hamilton's equations in three dimensions. The calculations of the product vibrational distribution, reaction cross section, and rotational alignment for the Ba + HBr reaction had been performed on LEPS PES by means of QCT method. To compare with the experimental measurements of the product state distribution for the Ba + HBr reaction,[8] the collision energy was chosen to be 0.51 eV in this work. In our calculations, a batch of 100 000 trajectories was run for the case and also the integration step size was chosen to be 0.1 fs. Trajectories were initiated at a Ba–HBr inter-nuclear separation of 15 Å and HBr molecule at the v = 0 and j = 0 levels. The parameters should be suitable to guarantee the conservation of total energy and angular momentum. The calculated results deviate slightly from the experimental ones because of the number limitation of trajectories.

Table 1. Parameters are calculated at the mp2/lanl2dz level using Gaussion03 program of the LEPS PES for the Ba + HBr reaction.

Species	D_e (eV)	β_i (Å^{-1})	R_0 (Å)	S_i
BaBr	2.6667	1.202	3.2323	0.370
HBr	3.7838	1.998	1.4608	0.220
BaH	0.7771	1.553	2.54	0.578

Product rotational alignment

It is a simple method to describe the degree of polarization of $\vec{J}'$, which is through the center of mass-frame orientation and alignment parameters. During reactive encounter, the total angular momentum is conserved $\vec{J} + \vec{L} = \vec{J}' + \vec{L}'$, where $\vec{L}$ and $\vec{L}'$ are the reagent and product orbital momenta, respectively. When the reagent angular momentum $\vec{J}$ is small (as is common), the product rotation can only result from $\vec{L}$. The distribution of the rotational angular momentum $\vec{J}'$ of the product molecule, which is mainly determined by $\vec{L}$, can be described by a function $f(\theta)$, where θ is the angle between $\vec{J}'$ and the relative velocity vector $\vec{K}$. $f(\theta)$ can be expanded in a set of Legendre polynomials[25]

$$[5]\qquad f(\theta) = \sum a_l P_l(\cos\theta)$$

l = 2 indicates the product rotational alignment

$$[6]\qquad a_2 = 5\langle P_2(\cos\theta)\rangle = 5\langle P_2(\vec{J}' \cdot \vec{K})\rangle$$

$$[7]\qquad \langle P_2(\vec{J}' \cdot \vec{K})\rangle = 1/2\langle 3\cos^2\theta - 1\rangle$$

where P_2 is the second Legendre momentum, and the brackets indicate an average over the distribution of $\vec{J}'$ about $\vec{K}$.[26]

Apparently, the heavy–heavy–light (HHL) mass combination leads to the product rotation being strongly aligned about the reagents' relative velocity, and $\langle P_2(\vec{J}' \cdot \vec{K})\rangle$ should be equal to –0.5. However, the HHL mass combination is not strictly proper for the Ba + HBr reaction any more. The calculated $\langle P_2(\vec{J}' \cdot \vec{K})\rangle$ values, which are less than –0.5, first decrease then increase slightly and then decrease with increasing the collision energy.

Results and discussion

The internal-energy state was described by two quantum numbers (v, j), and the internal-energy state of reagent is

Table 2. Selected values of b_{max} at different collision energies in the Ba + HBr reaction.

E_{col} (eV)	b_{max} (Å^2)
0.1	4.0
0.12	3.87
0.2	3.55
0.3	3.40
0.4	3.33
0.51	3.25

Fig. 1. The contour plot of LEPS PES for the Ba + HBr reaction. The unit of the R is Å and of the energy is erg × 10^{16}.

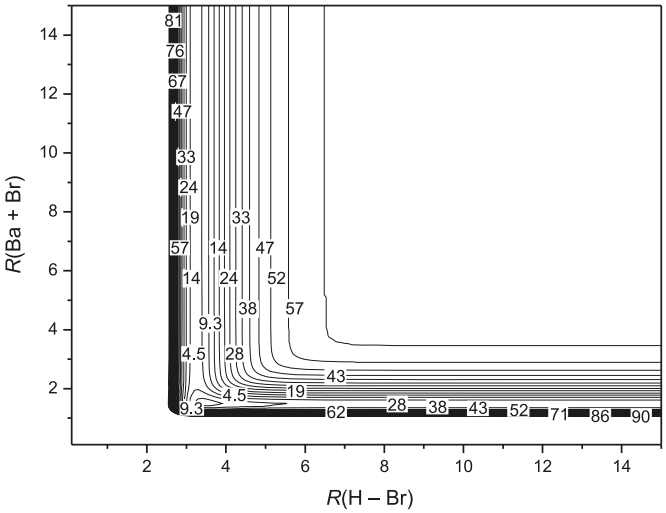

the lowest ($v = 0, j = 0$) because the reagent was "frozen" in the crossed molecular beam experiment.[24] So, the point of Ba + HBr (0, 0) can be the start point in every trajectory. Prior to the calculation, the biggest impact parameter b_{max} must be confirmed, and for different collision energies, the values of b_{max} are shown in Table 2.

In terms of the results of the LIF and the molecular beam,[8] there are several special laws in the Ba + HBr reaction: (*i*) the vibrational excitation of the product BaBr is very high, and the reaction cross section is big too; (*ii*) the collision energy of the reagent plays an important role in the internal-energy distribution and vibrational distribution.

LEPS potential-energy surface (PES)

The features of the PES are the most basic conditions to obtain the information of a chemical reaction. When we know as much information as possible about the PES, then we can study problems like the energy distribution and the product rotational alignment. The extended LEPS PES for the Ba + HBr → BaBr + H reaction is constructed using parameters listed in Table 1. Figure 1 shows the contour plot of this LEPS PES of the collinear configuration of Ba–Br–H. The values of the potential barrier and the potential well are the important data of the reaction potential-energy surface in the QCT calculation. From Fig. 1, one can see that in this reaction, there is a shallow barrier located in the entrance path whose value is 4.5 kcal/mol, and the potential energy decreases gradually from the entrance

Fig. 2. Vibrational distribution of the BaBr product in collision energy 11.761 kcal/mol. The experimental results are from ref. 16.

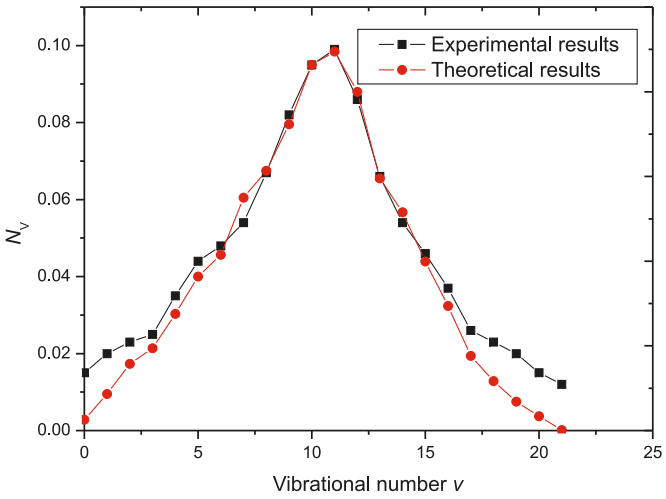

($R_{Sr,CH_3Br} = \infty$, corresponding to reactants) to the exit ($R_{CH_3,SrBr} = \infty$, corresponding to products). Because the shallow barrier, the reaction cross section decreases first from 0.1 eV to 0.16 eV, then it increases slightly and reaches the maximum value at 0.165 eV, after that it decreases with the increase of the collision energy.

Vibrational distribution

The vibrational distribution of the product BaBr versus collision energy using QCT is shown in Fig. 2. Obviously, Fig. 2 shows that the experimental and calculated results tend to be similar when the vibrational energy is changed.

It can be seen from Fig. 2 that as v is increased, when the value of E_{col} is 11.761 kcal/mol, N_v first increases then decreases. When the value of v is 11, the value of N_v reaches its maximum, which is 0.098. The computational results are different from the experimental ones at the high vibrational quantum numbers. Clearly, the QCT result in the present work is in good agreement with the experimental data.

Reaction cross section

The absolute cross section of the state reaction in the trajectory calculation can be obtained, and its formula and estimate of error are

$$[8] \qquad \sigma_r(E_{col}, v, j) \approx \pi b_{max}^2 \frac{N_r(E_{col}, v, j)}{N(E_{col}, v, j)}$$

$$[9] \qquad \Delta\sigma_r \approx \pi b_{max}^2 \frac{N_r}{N}\left(\frac{N - N_r}{N_r N}\right)^{1/2} = \sigma_r\left(\frac{N - N_r}{N_r N}\right)^{1/2}$$

where N_r is the number of reaction trajectories, and N is the total number of trajectories, while b_{max} is the maximum-impact parameter and $\Delta\sigma_r$ is the estimate of error of σ_r. The relative cross section can be obtained through the experiment, while the absolute cross section can be obtained through the calculation.

The product channel BaBr results of the present and elder's are integrated to get the reaction cross section for the Ba + HBr reaction to compare our result with the experimental results.[8]

Fig. 3. The reaction cross section versus the collision energy for the Ba + HBr reaction. The experimental results are from ref. 16.

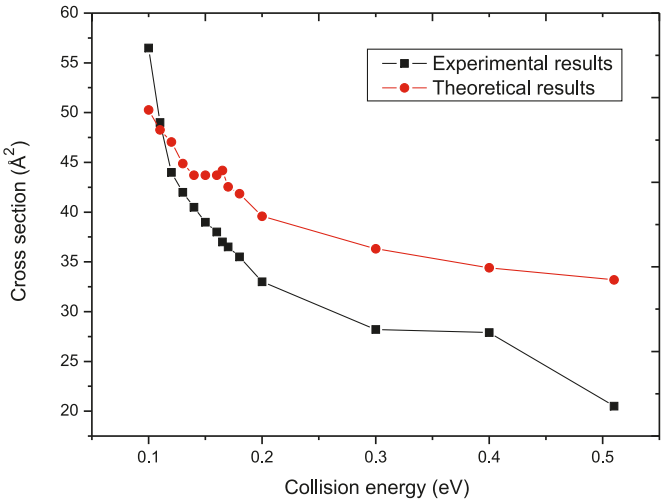

Fig. 4. Maximum-impact parameter b^2_{max} as a function of collision energy. The experimental results are from ref. 16.

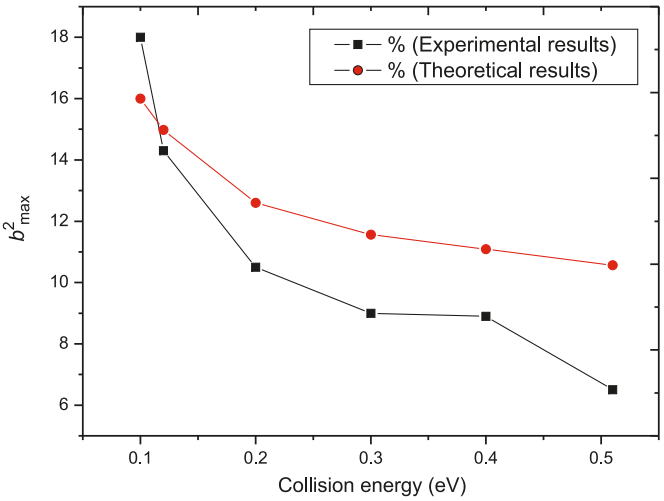

Fig. 5. The product rotational alignment of the Ba + HBr reaction versus the collision energy on LEPS PES.

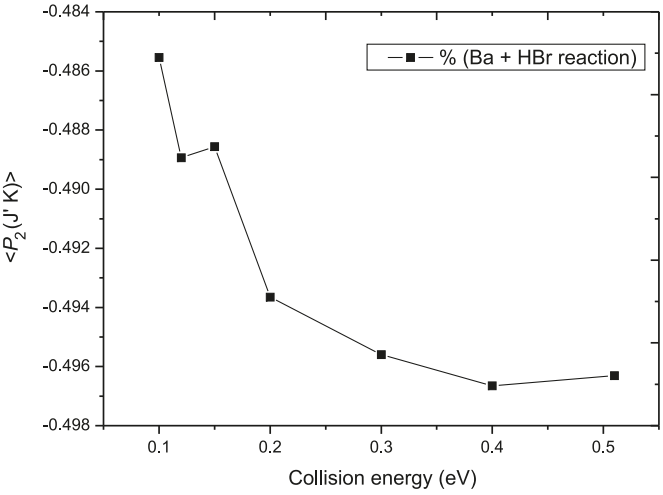

Fig. 6. Mean product energies for BaBr. The experimental results are from ref. 16.

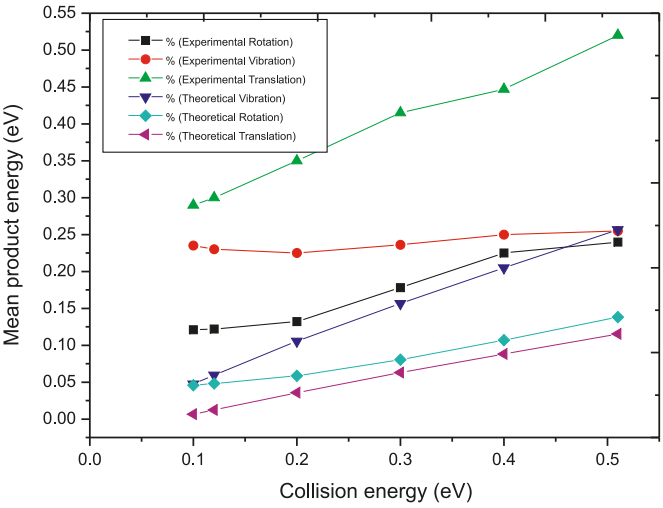

Equation [8] has been used to determine the reaction cross sections, which are given in Fig. 3 for the Ba + HBr → BaBr + H reaction.

The reaction cross section decreases from 50 Å^2 to 33 Å^2 as the calculated increase in the collision energy from 0.1 eV to 0.51 eV takes place. It is very interesting to find the high reaction cross sections at low energies, while low reaction cross sections are found at high energies.

From Fig. 3, it can be seen that the QCT calculation on the PES posts a strong impact on producing BaBr for the Ba + HBr reaction. The decrease of σ_r with E_{col} agrees with the general behavior of exothermic chemical reactions with little or no activation energy, and it can be rationalized as a decrease of b_{max}. We can see from Fig. 3 that as the collision energy increases, the reaction cross sections decrease first and then increase lightly to the maximum value when the collision energy is 0.165 eV then decrease again. These results are consistent with the results of LEPS PES whose potential barrier value is 4.5 kcal/mol. Figure 4 shows the distribution of b^2_{max} when the collision energy increases. Therefore, the values of our reaction cross sections are in the same range (from 50 Å^2 to 33 Å^2) as the experimental results. Clearly, the QCT-computed results of reaction cross section are in good agreement with the experimental data.

Product rotational alignment

The product rotational alignment of the HHL mass-combination reaction, a function of the collision energy, was independent of the characters of the PES. It just increases as the collision energy increases. Whether it is the attractive or the repulsive PES, it can be seen that the product rotational alignment depends on the collision energy slightly.

The Ba + HBr reaction, which is the reaction of interest in this paper, belongs to the HHL-type of reactions. The product rotational alignment tendency of BaBr versus collision energy is shown in Fig. 5.

The variation of $\langle P_2(\vec{J}' \cdot \vec{K}) \rangle$ with the change in the R group in R–Br molecules is probably due to the difference

of the mass factor.[27] The expected values for $\langle P_2(\vec{J}' \cdot \vec{K})\rangle$ are between 0.0 (randomly aligned) and –0.5 (completely aligned).[27] Usually, when $|L| \gg |J|$ and $|L'| \ll |J'|$ are satisfied, the maximum product rotational alignment occurs.[27] The first condition is satisfied for reactions with large cross section, while the typical HHL mass-configuration reaction system leads to the second condition.[27] The product rotational alignment decreases as the collision energy increases, which is achieved by the significant disposal of angular momentum into product orbital motion, and this happens in the condition of high energy.

The excessive translation energy will turn into rotational and translational excitation, as we have already known, and the collision energy is allocated in the rotation momentum in a great measure, which also can be detected from the distinct increment of the alignment. The reaction between an alkaline earth atom (M) and a hydrogen halide (HX) to produce MX + H constitutes a series of related results. In the reaction, two pathways are under discussion, which are abstraction and insertion.

When Ba is attacking HBr on the area that is closer to the Br, there is an attractive area, while Ba on the area closer to the H, is on a repulsive area. The initial velocity was modulated by the action field, which shows that the reaction was affected by the collision energy of the reagent in the following manner: when Ba is close to HBr on the repulsive area and the collision energy is so little that it cannot conquer the repel, Ba prefers the attractive area, and the insertion reaction will occur. At this moment, the vibrational excitation of the product BaBr is strong. When the collision energy of the Ba and HBr is big enough to conquer the repel action, Ba and HBr become close to each other to some degree, and now the bond of H–Br fracture suddenly, and this is the abstraction reaction, which shows that the vibrational excitation is weak, while the translation energy of the product is high. The abstraction reaction is favored by low collision energy, while the insertion reaction is more likely to occur at high collision energy based on the dynamical calculation of this reaction. The progress of reaction is prolonged because of the transfer, which will make the life of the complex long.

For the Ba + HBr reaction, QCT calculations on PES show a great preference for producing BaBr. The reason is probably that the center of mass of the HBr molecule is closer to the Br atom; for the attack of Ba to this end of the molecule, it implies a greater cone of acceptance and thus reproducing the preference for the BaBr product well. The reaction cross section and the product rotational alignment as the function of the collision energy are given in this paper. It is interesting that the reaction cross section and product rotational alignment were all affected by the collision energy.

Other result

Figure 6 shows the mean product energies for BaBr. It can be seen from Fig. 6 that the nearly constant mean vibrational energy reflects the insensitivity of N_v against variations of the E_{col}. It presents the energy dependence of the mean rotational energy. Figure 6 also contains the mean translational energy E_{trans} of the product. It was obtained by subtracting the mean energies E_{vib} and E_{rot} from the totally available energy E_{col}. A constant equivalent to the error in the dissociation energy of BaBr may offset the curves for E_{trans}.

Conclusions

Research on the dependence of the product vibrational distribution, reaction cross section, the product rotational alignment, and other distributions on the collision energy for the Ba + HBr reaction has been carried out. Through the QCT method, the studies of those rules have been performed on LEPS PES at different collision energies. In summary, it is shown that the QCT calculations are in good agreement with the experimental data for the exothermic reaction of Ba + HBr. Comparing the dynamic calculated results on constructed semi-empirical extended LEPS PES with the experimental results, we can know that the extended LEPS PES under the "quasi-three-body" approximation condition can describe the main dynamic rules of multiatomic reaction system well. The calculation shows that when the reagent is in the vibrational ground state, the vibrational distribution of the product BaBr increases and then decreases. The relationship between the product rotational alignment and the collision energy depends greatly on mass combination. The calculated results show that the product rotational alignment decreases when the collision energy of reagent increases. With the increasing of collision energy, the reaction cross section also decreases, while mean product energies increase. The reaction mechanism was discussed using the obtained conclusion that the rule of reaction dynamics, which depends on the reactant collision energy can be explained by the bi-model (abstraction reaction and insertion reaction). Moreover, abstraction is much more probable at low collision energy, and insertion becomes more probable to occur at high collision energy. As mentioned above, the calculated results for the Ba + HBr rection are consistent with the experimental ones.

Acknowledgements

This work was supported by the National Natural Science Foundation of China (Grant No. 10704012) and the Natural Science Foundation of Liaoning Province (Grant No. 2006Z064).

References

(1) Eyring, H.; Polanyi, M. Z. *Phys. Chem. (Leipzig) Abt. B* **1931**, *12,* 279.
(2) Aoiz, F. J.; Banares, L.; Herrero, V. J. *J. Chem. Soc., Faraday Trans.* **1998**, *94* (17), 2483–2500. doi:10.1039/a803469i.
(3) Irvin, J. A.; Dagdigian, P. J. *J. Chem. Phys.* **1980**, *73* (1), 176. doi:10.1063/1.439911.
(4) Karny, Z.; Zare, R. N. *J. Chem. Phys.* **1978**, *68* (8), 3360. doi:10.1063/1.436242.
(5) Brooks, P. R. *Science* **1976**, *193* (4247), 11–16. doi:10.1126/science.193.4247.11. PMID:17793988.
(6) Prisant, M. G.; Rettner, C. T.; Zare, R. N. *J. Chem. Phys.* **1981**, *75* (5), 2222. doi:10.1063/1.442335.
(7) Lin, K. C.; Urena, A. G. *Int. Rev. Phys. Chem.* **2007**, *26* (2), 289–352. doi:10.1080/01442350701211180.
(8) Siegel, A.; Schultz, A. J. *Chem. Phys.* **1980**, *72*, 6227.
(9) Munakata, T.; Matsumi, Y.; Kasuya, T. *J. Chem. Phys.* **1983**, *79* (4), 1698. doi:10.1063/1.446014.

(10) Zhang, X.; Xie, T. X.; Zhao, M. Y.; Han, K. L. *Chin. J. Chem. Phys.* **2002**, *15*, 169.
(11) Torres-Filho, A.; Pruett, J. G. *J. Chem. Phys.* **1982**, *77* (2), 740. doi:10.1063/1.443890.
(12) Cruse, H. W.; Dagdigian, P. J.; Zare, R. N. *Faraday Discuss. Chem. Soc.* **1973**, *55*, 277. doi:10.1039/dc9735500277.
(13) Pruett, J. G.; Zare, R. N. *J. Chem. Phys.* **1976**, *64* (4), 1774. doi:10.1063/1.432355.
(14) Gupta, A.; Perry, D. S.; Zare, R. N. *J. Chem. Phys.* **1980**, *72* (11), 6237. doi:10.1063/1.439082.
(15) Torres-Filho, A.; Pruett, J. G. *J. Chem. Phys.* **1982**, *77* (2), 740. doi:10.1063/1.443890.
(16) Zare, R. N. *Faraday Discuss. Chem. Soc.* **1979**, *67*, 7. doi:10.1039/dc9796700007.
(17) Zhang, X.; Han, K. L. *Int. Quant. Chem.* **2006**, *106* (8), 1815–1819. doi:10.1002/qua.20929.
(18) Feldman, D.; Lengel, R. K.; Zare, R. N. *Chem. Phys. Lett.* **1977**, *52* (3), 413–417. doi:10.1016/0009-2614(77)80477-6.
(19) Mims, C. A.; Lin, S. M.; Hem, R. R. *J. Chem. Phys.* **1972**, *57* (8), 3099. doi:10.1063/1.1678726.
(20) Noda, C.; Mckillop, J. S.; Johnson, M. A.; Waldeck, J. R.; Zare, R. N. *J. Chem. Phys.* **1986**, *85* (2), 856. doi:10.1063/1.451293.
(21) Alberti, M.; Gimenez, X.; Aguilar, A.; Urena, A. G. *Mol. Phys.* **1995**, *85* (5), 949–963. doi:10.1080/00268979500101581.
(22) Tsekouras, A. A.; Leach, C. A.; Kalogerakis, K. S.; Zare, R. N. *J. Chem. Phys.* **1992**, *97* (10), 7220. doi:10.1063/1.463547.
(23) Zhao, D.; Zare, R. N. *J. Chem. Phys.* **1992**, *97* (9), 6208. doi:10.1063/1.463983.
(24) Han, K. L.; Zheng, X. G.; Sun, B. F.; He, G. Z.; Zhang, R. Q. *Chem. Phys. Lett.* **1991**, *181* (5), 474–478. doi:10.1016/0009-2614(91)90383-K.
(25) Han, K. L.; He, G. Z.; Lou, N. Q. *J. Chem. Phys.* **1996**, *105* (19), 8699. doi:10.1063/1.472651.
(26) Chen, M. D.; Han, K. L.; Lou, N. Q. *Chem. Phys. Lett.* **2002**, *357* (5-6), 483–490. doi:10.1016/S0009-2614(02)00585-7.
(27) Han, K. L.; Zhang, L.; Xu, D. L.; He, G. Z.; Lou, N. Q. *J. Phys. Chem. A* **2001**, *105* (13), 2956–2960. doi:10.1021/jp002181x.

Photoelectrochemical studies on poly[1-(2-aminophenyl)pyrrole] — Creation of a photoactive inorganic–organic semiconductor interface (IOI)

Kasem K. Kasem, Sara Menges, and Stephenie Jones

Abstract: The compound 2-APPy [1-(2-aminophenyl)pyrrole] as an organic phase in an inorganic–organic semiconductor interface (IOI) assembly was the subject of photoelectrochemical studies in aqueous solutions. Results show that thin films of poly(2-APPy) can be prepared using oxidative electropolymerization. Furthermore, absorption spectroscopic studies indicate that the protonated 2-APPy polymer's ionization potential (IP) is 4.7 eV, the electron affinity (EA) is 1.90 eV, and a gap of 2.80 eV separates the higher occupied molecular orbital's (HOMO) and lower unoccupied molecular orbital's (LUMO) energy levels of this polymer. Impedance measurements under illumination show an increase in the film charge capacitance compared with those measured under darkened conditions. The behavior of the poly(2-APPy) film as a host for redox-active dopants was also explored. The results show that the film did not alter the redox potentials of a large dopant such as $PMo_{12}O_{40}^{3-}$. The photoactivities of the IOI assemblies consisting of 2-APPy and nanoparticles of ZnO, and of Fe_2O_3 were investigated using fluorescence emissions. Results show that the fluorescence emissions generated by 2-APPy were quenched by 5% and 55% on ZnO and on Fe_2O_3, respectively. The charge injection rate constants, k_{ct}, at the inorganic metal oxide–2-APPy interface, were calculated.

Key words: poly[1-(2-aminophenyl)pyrrole], photoelectrochemistry, semiconductors, material, charge transfer.

Résumé : Opérant en solutions aqueuses, on a effectué des études photoélectrochimiques sur un assemblage du 1-(2-aminophényl)pyrrole (2-APPy)dans une interface inorganique/organique semiconductrice (IIO). Les résultats obtenus montrent qu'il est possible de préparer le poly(2-APPy) par électropolymérisation oxydante. De plus les études spectroscopiques d'absorption indiquent que le potentiel d'ionisation (PI) du polymère 2-APPy protoné est égal à 4,7 eV; l'affinité électronique (AE) est de 1,90 eV et que 2,80 eV séparent les niveaux d'énergie de l'orbitale moléculaire haute occupée (HO) et de l'orbitale moléculaire basse vacante (BV) de ce polymère. Des mesures d'impédance sous illumination mettent en évidence une augmentation dans la capacitance de la charge du film par comparaison avec celles mesurées en l'absence d'illumination. On a aussi examiné le comportement du film de poly-2-APPy comme hôte pour des dopants redox actifs. Les résultats montrent que le film n'altère pas les potentiels redox d'un dopant volumineux, tel le $PMo_{12}O_{40}^{3-}$. Les photoactivités des assemblages d'interfaces inorganique/organique semi-conductrices formées de 2APPy et de nanoparticules de ZnO et de Fe_2O_3 ont aussi été examinées à l'aide d'émission de fluorescence. Les résultats montrent que les émissions de fluorescence générées par le 2-APPy sont piégées respectivement par 5% et 55% de ZnO et de Fe_2O_3. On a calculé les constantes d'injection de charge, k_{ct}, à l'interface oxyde métallique inorganique/2-APPy.

Mots-clés : poly[1-(2-aminophényl)pyrrole], photoélectrochimie, semiconducteurs, matériau, transfert de charge.

[Traduit par la Rédaction]

Introduction

The interest in developing sensitizers that improve interfacial charge transfer and suppress charge recombination substantiates the need for a wider investigation of organic semiconductors. Organic compounds with semiconducting character have been developed during the last two decades. These types of semiconductors have the potential to minimize the hole–electron recombination rates by polaron production. They also have a proven resistance to photocorrosion and mitigate some of the other disadvantages of inorganic semiconductors as well. Integrating these organic semiconductors at the interface between inorganic semiconductors and electrolytes[1–5] could enhance the process of charge separation and further charge transfer.

Understanding the photoinduced electron-transfer process in organic semiconductors requires correlating their molecular structure and band structure to their observed photoelectrochemical responses.[6–8] Some extrinsic semiconducting properties such as the capacity to transport charge generated by light, which is injected by electrodes or provided by chemical dopants, has been exhibited by many conjugated organic compounds.[1–8] 2-APPy, a conjugated organic molecule, containing both aniline and pyrrole units has the

Received 3 July 2008. Accepted 30 April 2009. Published on the NRC Research Press Web site at canjchem.nrc.ca on 17 July 2009.

K.K. Kasem,[1] S. Menges, and S. Jones. Department of Nat. Info. Math. Sciences, Indiana University Kokomo, Kokomo, IN 46904, USA.

[1]Corresponding author (e-mail: kkasem@iuk.edu).

potential to exhibit these extrinsic properties. Many studies have been carried out on pyrrole-[9–18] and on aniline-related polymers.[19–22] These studies showed noticeable differences in the polymerization mechanisms and in the chemical, electrochemical, and photoelectrochemical behavior of the polymeric films. These studies also showed that both aniline- and pyrrole-related polymers possess the capability for charge injection and (or) transfer. Due to the limitations imposed by the stability requirements and the scope of applications of these polymers, the structure of 2-APPy substantiates interest to explore its potential as an organic semiconductor using photoelectrochemical studies.

The present work focuses on the investigation of the electropolymerization of 2-APPy and a study of the behavior of this polymer towards charge injection from the electrode and from the dopant in aqueous electrolytes. This study was also extended to investigate UV–vis absorption and fluorescence emission spectra to explore the light induced charge transfer process in this compound. Photoelectrochemical and spectroscopic data obtained for 2-APPy were integrated to investigate its semiconductor properties and information related to its band structure including its ionization potential (IP), electron affinity (EA), and band gap (BG or E_g). Adsorption of this compound in monomer or polymer form on metal oxides (inorganic semiconductors) creates assemblies that consist of inorganic–organic interfaces (IOI). Gaining intrinsic information about charge transfer behavior across this IOI was another goal of this study.

Experimental

Reagents

1-(2-Aminophenyl)pyrrole (Sigma-Aldrich) and all other reagents were of an analytical grade. All solutions, unless otherwise stated, were prepared using deionized water.

Instrumentation

All electrochemical experiments were carried out using a conventional three electrode cell consisting of a Pt wire as a counter electrode, Ag/AgCl as the reference electrode, and GCE (glassy-carbon electrode) as the working electrode. A BAS 100W electrochemical analyzer (Bioanalytical Co.) was used to perform the electrochemical and impedance studies. X-ray photoelectron spectroscopy (XPS) was performed using PerkinElmer 5500 ESCA. An Amery 1000A was used to produce scanning electron micrographs of the polymer films. A UV–vis spectrophotometer was used to generate absorption spectra of the thin solid films on ITO electrodes. FTIR (Thermo Nicolet 4100s) was used to confirm the existence of the amino group (NH_2) within the polymer phase.

Fluorescence lifetime measurements

Fluorescence lifetime measurements were performed using a Chronos (ISS, Champaign, IL) with a laser diode as the excitation source.

Impedance measurement

Impedance measurements were carried out within a frequency range between 0.1 mHz and 1 KHz.

Fig. 1. (A) Oxidative electropolymerization cyclic voltamograms of 1-(2-aminophenyl)pyrrole in a 50% acetonitrile/water mixture containing 0.5 mol/L H_2SO_4 on a GCE. Scan rate: 100 mV/s. (B) XPS for poly(2-APPy) on a GCE . The inset is the scanning electron micrograph of the polymer film.

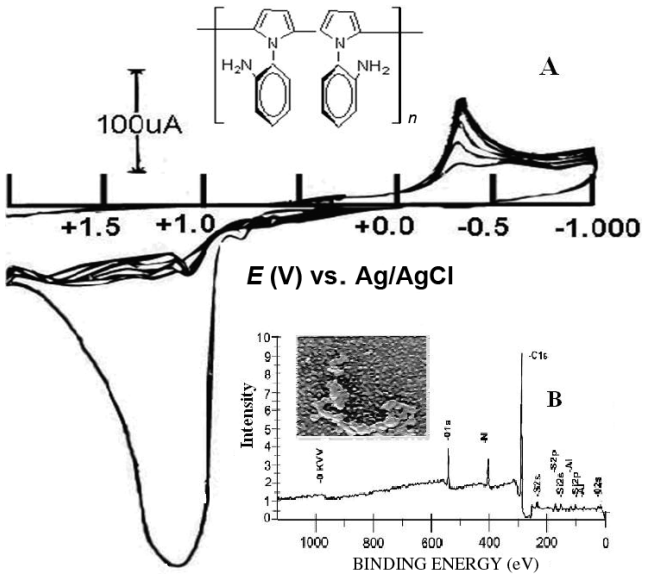

Fig. 2. Electropolymerization in a 50% acetonitrile/water mixture containing 0.5 mol/L H_2SO_4 of (A) aniline and (B) a mixture of aniline and pyrrole on a GCE. Scan rate: 100 mV/s. (Note the scans' numbers.)

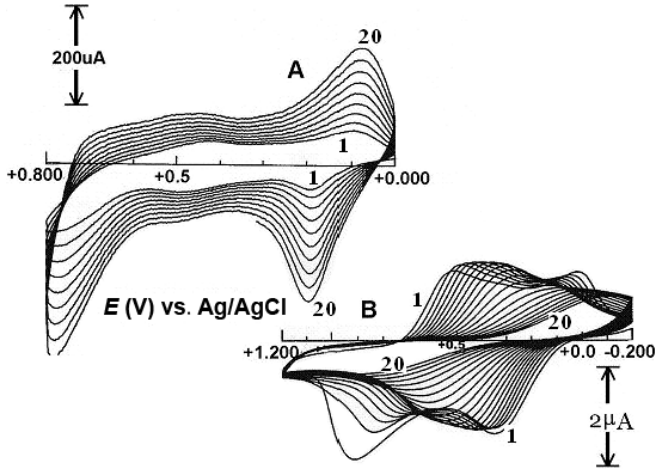

Results and discussion

Electropolymerization of 2-APPy

Because of the stability limitations of the dopant used ($PMo_{12}O_{40}^{3-}$) in this study, a mixture of 50% acetonitrile/water was used as a solvent throughout the study. Within the potential window of –1.0 to 2.0 V, 2-APPy polymerized and lost its monomer identity. No reduction or oxidation peaks were evident for 2-APPy when the potential was scanned between –1.0 and 0.9 V during cyclic voltammetric (CV) experiments. Therefore, the only electrochemical behavior observed was that of poly(2-APPy). Oxidative electropolymerization of 2-APPy was used to generate thin films of poly(2-APPy). Figure 1A is a display of the repeti-

Fig. 3. (A) CV in 0.5 mol/L $HClO_4$ of a GCE modified with poly(2-APPy) (dashed line) and a mixture of polyaniline and pyrrole (solid line). (B) CV of a GCE modified with poly(2-APPy) in 0.5 mol/L $HClO_4$ (solid line) and in 0.5 mol/L $KClO_4$ (dashed line).

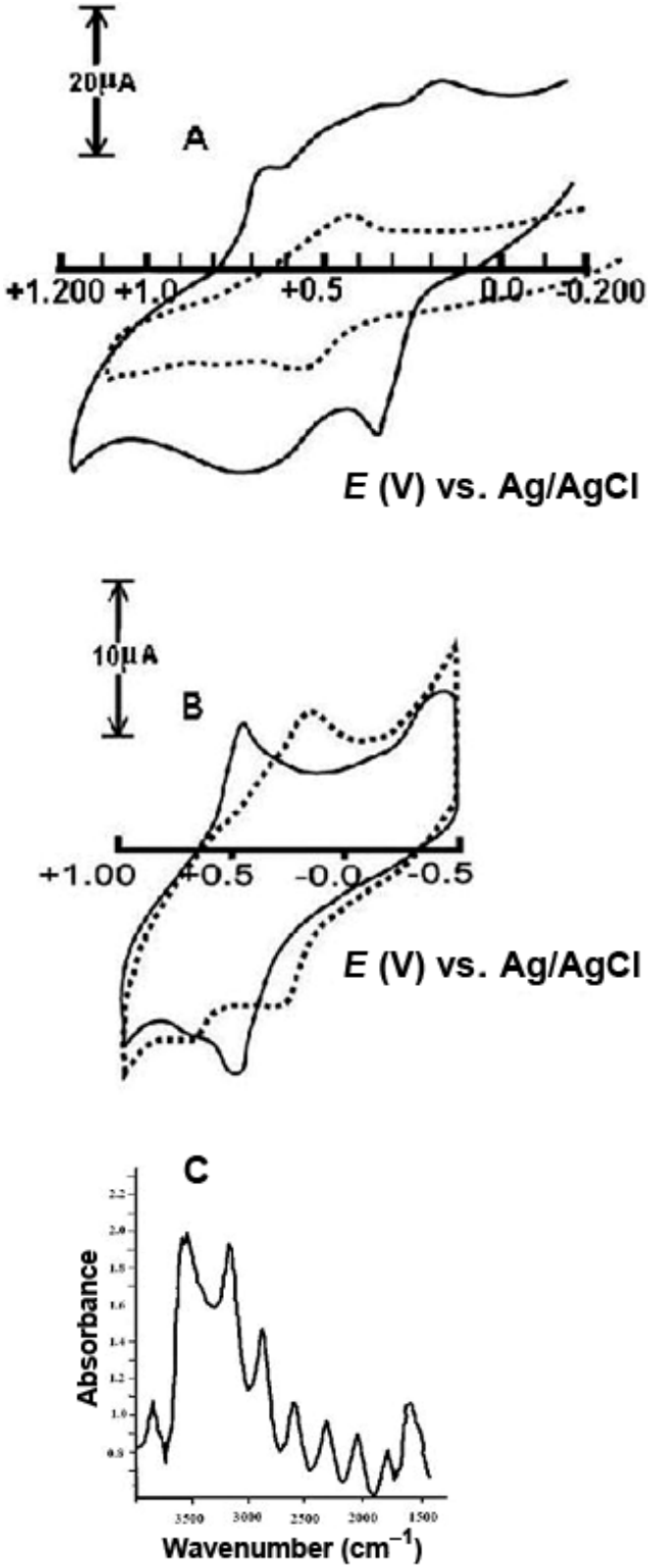

Fig. 4. CV of immobilized $PMo_{12}O_{40}^{3-}$ anions in poly(2-APPy) in a 50% dioxane/water mixture containing 0.5 mol/L H_2SO_4

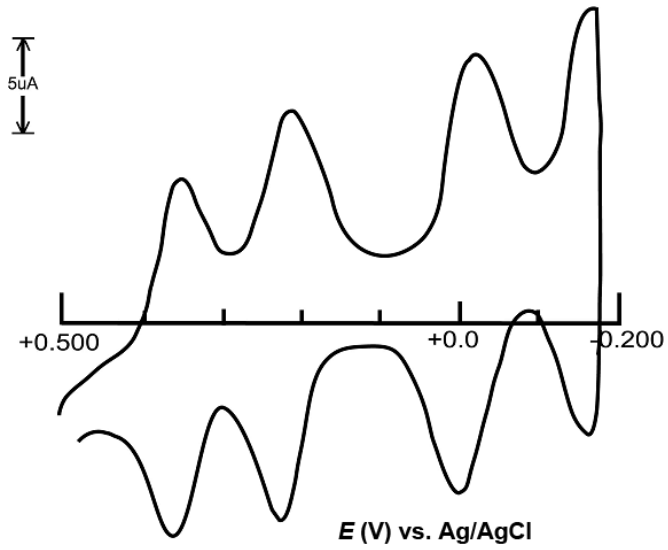

Fig. 5. Steady-state absorption spectra of thin film of 2-APPy on ITO.

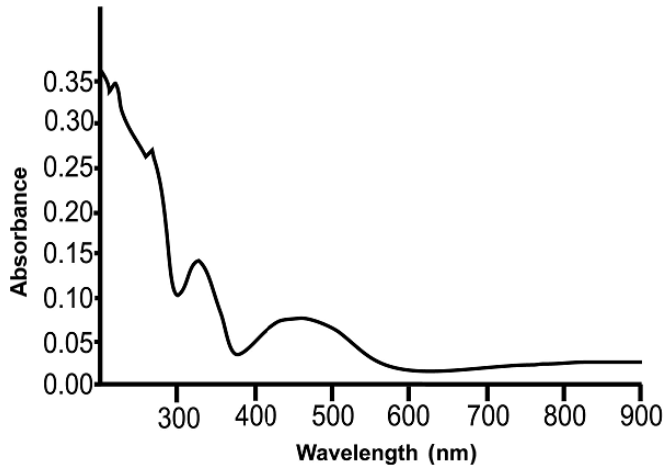

Diagram 1. Energy-level diagram for poly(2-APPy) film based on the determined values for E_g, IP, and EA.

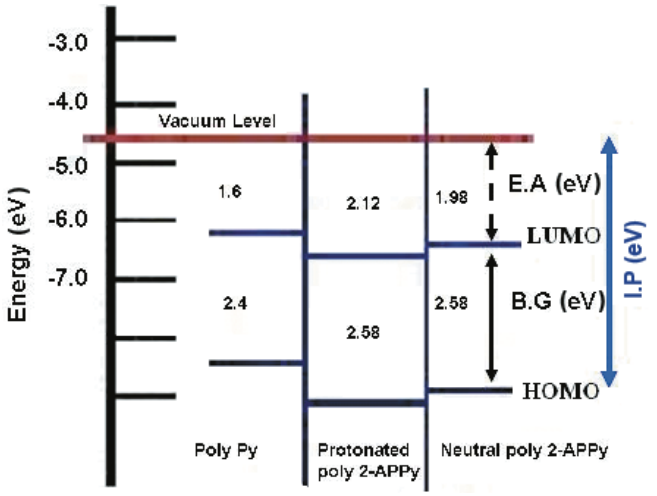

Fig. 6. Admittance plot of poly(2-APPy) at 0.0 V (trace 1 and 2) and at –0.79 V (trace 3 and 4). Traces 2 and 4 are under illumination. (The inset is the equivalent circuit.)

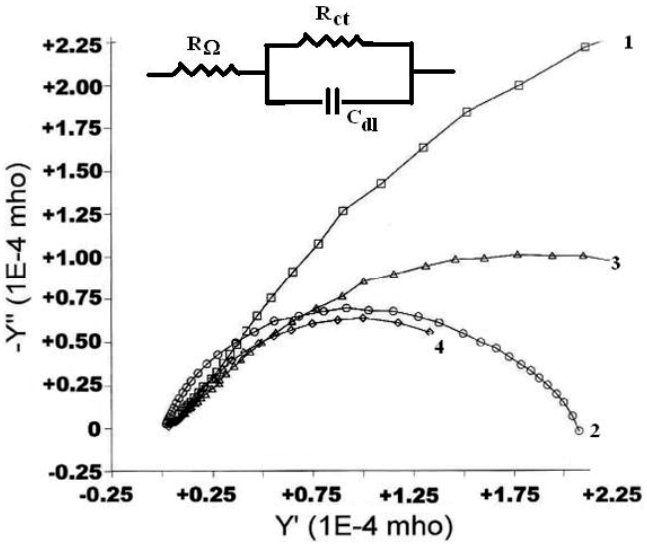

Table 1. Electrochemical impedance data for poly(2-APPy).

	Measured film capacitance	
Applied potential vs Ag/AgCl	0.00 V	–0.800 V
Dark	190 nF	400 nF
Light	187 nF	1.32 μF

tive cycling of the potential of the GCE between –1.0 V and 2.0 V versus the Ag/AgCl in 50% acetonitrile/water mixture containing 0.5 mol/L H_2SO_4 and 5 mmol/L monomer. As the positive potential scanning started at 0.0 V, a shoulder anodic peak appeared at 0.75 V, followed by the large broad irreversible oxidation wave, which were recorded in the first cycle. The anodic peak current of this irreversible anodic wave started to decay as the cycling continued. The 2-APPy monomer has three active sites that can initiate the polymerization process. The drop of the anodic peak current in the second and subsequent cycles can be attributed to the semiconducting nature of the polymer film and to the high degree of cross-linking that hinders the contact of monomer species with the electrode surface.

To get an understanding of the polymerization process of 2-APPy consider the fact that 2-APPy is a combination of pyrrole and aniline units. The CV of the electropolymerization of aniline (Fig. 2A) gives a CV wave where the anodic and cathodic peak currents grow with the successive scan (note the scan number). The CV of the electropolymerization of pyrrole under similar conditions gives an irreversible anodic wave during the first scan followed by a significant drop of anodic current, which reflects a passive film nature. On the other hand, the CV of electropolymerization of an equiconcentration aniline/pyrrole mixture shows a decay of both anodic and cathodic current (note the scan number) with succession potential scans (Fig. 2B). This indicates that pyrrole is the dominating component in the mixture under the experimental conditions. Although Fig. 2B does not resemble Fig. 1, the commonality between these two figures is the decay of the current after the first scan, which reflects the passive nature of the generated films.

Fig. 7. Fluorescence emission spectra of (a) 2-APPy on SiO_2 colloidal solution, (b) 2-APPy on SiO_2 colloidal solution with 5% Fe_2O_3 particles, and (c) 2-APPy on SiO_2 colloidal solution with 5% ZnO particles.

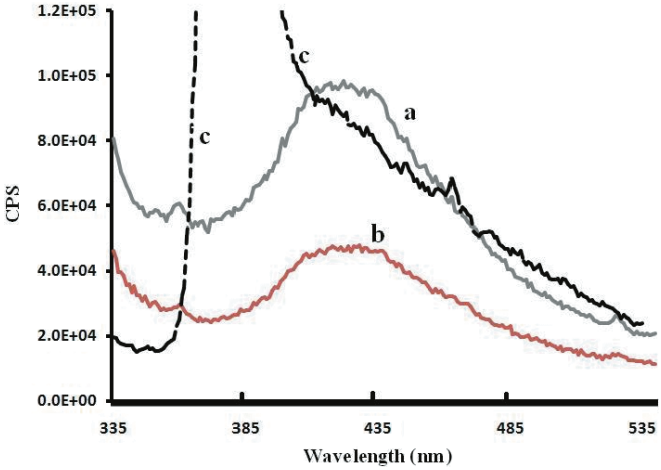

Diagram 2. Relative energy levels at poly(2-APPy) and Fe_2O_3.

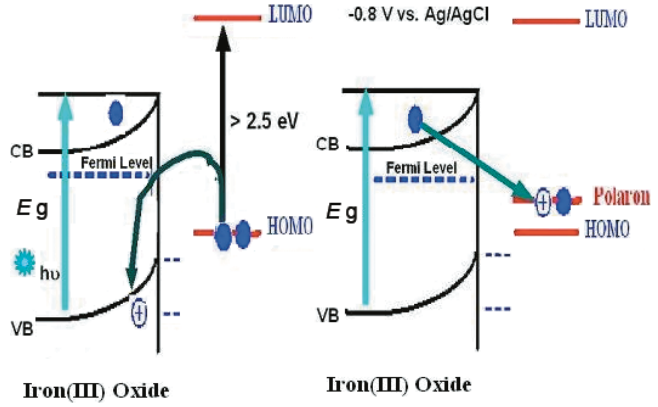

Polymeric film characterizations

Figure 3A illustrates the CV for the electrode modified with a thin film of poly(2-APPy) (dashed line) overlaid with the CV for an electrode modified with a thin film of the polymer generated from an aniline/pyrrole monomer mixture (solid line) in 0.5 mol/L $HClO_4$. Under the experimental conditions, the noticeable difference between these two polymer films is that polypyrrole did not show any redox peaks within the experimental potential window (CV are not shown); therefore, polypyrrole is redox inactive. This leads us to conclude that the polymerization of 2-APPy is controlled by the pyrrole portion of 1-(2-aminophenyl)pyrrole, while the redox behavior of poly(2-APPy) is quite different from what might be expected from the aniline part in the polymer. Recalling that in an acidic solution, the pyrrole ring in the monomer is more stable than that of the aniline, and it is easier to quaternize (protonate) the N-terminal NH_2 group on the phenyl ring versus the N within the pyrrole ring. Under the experimental conditions, the quaternized amino group will hinder participation of the aniline side of the monomer in the polymerization process. Furthermore, IR

studies indicate the presence of amino groups within the neutral polymer film (peaks at 1633 and 3385 cm^{-1} represent scissoring and aromatic stretching of NH_2 vibrations, respectively). These facts support our assumption that electropolymerization through the pyrrole ring within 2-APPy is kinetically favored. The fact that 2-APPy polymerization is achieved using oxidative electropolymerization suggests that a cation radical has played an important role in initiation of the propagation steps of the polymerization process. The mechanism and the kinetics of the electropolymerization will be the subject of future investigation.

Electrochemical behavior of poly(2-APPy)

The redox behavior of poly(2-APPy) in 0.5 mol/L $HClO_4$ is displayed in Fig. 3B (solid line). The CV shows a reversible wave at $E^{0'} = 0.45$ V and an ill-overlapping anodic wave at $\approx$0.7 V. Also present is a broad cathodic wave between –0.4 and –0.06 V. In 0.5 mol/L $KClO_4$ (a neutral electrolyte), although the reversible wave shows up at $E^{0'} = 0.175$ V, an irreversible anodic peak appears at $\approx$0.7 V and a broad cathodic peak appears between –0.4 and –0.06 V (Fig. 3B dashed line). Considering the fact that polypyrrole is electrochemically inactive within the experimental potential window, the cyclic voltammetric behavior described above as displayed in Fig. 3B, can be explained as follows: The reversible CV wave can be attributed to aniline activity within the polymer film. Aniline (in one of the polymer segments) acts as a functional group for the charge injection that takes place through the amino group in L (Leucoemeraldine). Furthermore, these side reactions can lead to the formation of cation radicals ($L^{\bullet+}$), and their protonated forms (LH_2^{2+})[23] during the potential cycling. The CV wave at 0.175 V in the neutral electrolyte is due to the unprotonated form of the polymer. The protonated forms require a more positive potential to be oxidized. This explains the positive shift of the formal potential ($E^{0'}$) from 0.175 V in a neutral electrolyte to 0.450 V in an acidic electrolyte. The ill-developed anodic peak shown at $\approx$ 0.7 V is pH independent, and is attributed to further oxidations of the L form to $L^{\bullet+}$ to form PH_2^{2+} (protonated pernigraline). The lack of a cathodic peak makes perfect reversible behavior impossible. However, it is noticeable that the reduction peaks in the CV wave in acidic and in neutral media are greater than the anodic peaks. This may be due to the reduction of the PH_2^{2+} (formed at 0.7 V) that causes these waves to overlap. This also may indicate that the reduction of PH_2^{2+} is quasi-reversible.

Performing a CV in both the absence and the presence of oxygen indicates that peaks appear in the potential range between –0.4 and –0.06 V due to the reduction of trapped O_2. Figure 3B also indicates that the protonated film of poly(2-APPy) possesses less capacitive current than the unprotonated film.

Poly(2-APPy) film was subjected to XPS and IR studies. IR results show peaks at 1633 and 3385 cm^{-1}, which indicates aromatic NH_2 group scissoring and stretching vibrations, respectively. The XPS results are displayed in Fig. 1B. It can be noticed that the N peak is $\approx$20% of that of the C peak. This reflects the N to C ratio in the monomer. The inset in Fig. 1B is the scanning electron micrograph of the polymer films, which describes some discontinuity in the film matrices as indicated by small and large particles.

Ion-exchange properties of poly(2-APPy)

Poly(2-APPy) acts as an anion dopant exchange polymer. The quaternized N centers within an acidic solution produces ion pairing with electrolyte anions such as SO_4^{2-} or ClO_4^-. Doping this film with large redox anions becomes possible because of these centers. Phosphomolybdate anions ($PMo_{12}O_{40}^{3-}$) were incorporated in the poly(2-APPy). The CV for poly(2-APPy) doped with $PMo_{12}O_{40}^{3-}$ is displayed in Fig. 4. The well-developed consecutive redox waves of $PMo_{12}O_{40}^{3-}$ indicate that the doped redox oxoanion underwent multiple electron transfers (2 e^- each) without interference from the host film. This behavior is similar to that previously reported for the $PMo_{12}O_{40}^{3-}$'s CV in a liquid electrolyte only.[24] It is worth noticing the lack of the host film's CV wave appearing in the displayed CV. This indicates that the rates of charge transfer among Mo(VI) centers in $PMo_{12}O_{40}^{3-}$ are greater than that in the film network structure, and that the charge transfer process is not hindered by the conjugate Π electrons of the polymer. Furthermore, poly(2-APPy) doped with $PMo_{12}O_{40}^{3-}$ exhibits less capacitive current than that undoped one. The incorporated oxoanions have electrochromic properties that can be used to manipulate the photonic properties of poly(2-APPy) that are doped with $PMo_{12}O_{40}^{3-}$ assemblies.

Optical activities of poly(2-APPy)

Absorption spectra of poly(2-APPy) thin films deposited over ITO (indium–tin oxide glass) are displayed in Fig. 5. In this figure, we can identify a broad absorption peak in the wavelength range of 430–490 nm. This broad absorption peak corresponds to an E_g range from 2.8 to 2.5 eV. This is also an indication of energy intervals with high density states that represent HOMO (higher occupied molecular orbitals) and LUMO (lower unoccupied molecular orbitals). The absorbed photons are consumed in generating charge carriers, probably by an extrinsic mechanism.

Energy map of poly(2-APPy)

To draw the energy map of the studied organic semiconductor film of poly(2-APPy), along with the band gap (E_g), parameters such as IP and EA are required. Furthermore, these parameters are needed to explain the electrical and optical properties of the film. Relating electrochemical data, such as the onset oxidation potential (E'_{ox}), the onset reduction potential (E'_{Red}), and the band gap, leads to an understanding of the integrated energy diagram of the film. Onset potentials can be estimated from the intersection of the two tangents drawn at the rising oxidation current and the background current in the CV using the following formula:[25]

$$[1] \qquad E_{ox} = E'_{ox} + E_{\text{reference electrode}} \approx E_{vac} + 4.6\,\text{eV}$$

As Ag/AgCl was used as a reference electrode (E^0 = 0.197 V vs normal hydrogen electrode (NHE)), and $E_{vac} \approx 0$, the above equation can be written as follows:

$$[2] \qquad \text{IP} \approx E'_{ox} + 4.4\,\text{eV}$$

Considering the energy gap between HOMO (valence band) and LUMO (conduction band) to be the band gap (E_g), and the energy gap between the LUMO and vacuum

level to be the electron affinity (EA), we can write the following equation:

$$[3] \quad IP = EA + E_g$$

The determined E'_{ox} obtained for the protonated polymer ($\approx$0.3 V) generates a 4.70 eV for IP, and a 2.12 eV for EA. In neutral media (unprotonated film), quantities for IP and EA are 4.56 eV and 1.98 eV, respectively. The reported low solid state EAs of poly(2-APPy) reflect an electron donor nature (p-type) and can be compared to those reported for PBZT {poly[*p*-(2-hydroxy)phenylenebenzbisthiazole]}.[26,27] To draw the energy diagram of poly(2-APPy) we recognize that IP and EA values can be influenced by polarization effects and structural relaxation. This would explain why conjugated polymers do not present an energy band similar to that of inorganic crystalline semiconductors, but rather they show energy intervals with a high density of states representing HOMO or LUMO of the polymer chain segments. Diagram 1 displays an energy-level diagram for poly(2-APPy) film that is based on the determined values for E_g, IP, and EA assuming molecular symmetry conditions.

Electrochemical impedance studies

Impedance studies were carried out at two potentials, with and without illumination. These conditions were used to demonstrate the effect of charge transfer and injection induced by electrochemical or photonic methods. The admittance plots at 0.0 V and $\approx$–0.8 V, taken both in the dark and under illumination, are displayed in Fig. 6. The simplified equivalent circuit that describes the data is displayed in Fig. 6, where R_{ct}, C_{dl}, and R_{Ω} are the charge transfer resistance, double layer capacitance, and ohmic solution resistance, respectively. Impedance studies at 0.0 V (below the onset oxidation potential) would give some information about the film in the absence of charge removal. Studies under illumination (Fig. 6, trace 2) at this potential will indicate the photonic effects only (if any photonic effects are present). Previous studies[15] reported that E_{fb} (the flat band potential) of polypyrrole derivatives is $\approx$–0.8 V versus the Ag/AgCl electrode. Impedance studies were performed at $\approx$–0.8 V to determine the effect of illumination (Fig. 6, trace 4) on electrical properties such as charge injection and capacitance of the film. The lack of band bending at E_{fb}, and the lack of band features for organic semiconductors suggests that a higher density of states, and consequently greater capacitance, was created at –0.8 V rather than at 0.0 V. Impedance measurements and calculations of the film capacities were performed as described in ref. 28 and summarized in Table 1. The data displayed in Table 1 show that:

At 0.00 V illumination there was no tangible change in the charge capacitance in the film. This is consistent with the fact that the applied potential is less than the onset oxidation of the film assembly. Therefore, no charges can be removed and no anions from the electrolyte will be incorporated.

Capacitance measured under an applied potential closer to the E_{fb}, while in the dark, almost doubles at 0.00 V. This can be attributed to the reduction of molecular oxygen that is entrapped within the film forming superoxides (O^{2-}), and these cause further changes at the film–electrolyte interface at the flat band potential.

Upon illumination at –0.800 V, the capacitance is 3.3 times that measured in the dark. This is an evidence of charge injection and the formation of a new dielectric system. Further, it suggests that this capacitance increase indicates restructuring of the double layer at the film–electrolyte interface. This is because double layer illumination causes an increase in the temperature at the electrode–electrolyte interface, which causes a drop in double layer capacitance ($C\alpha\ T^{-1}$) . The charge injection as a direct interaction of the polymer network structure with the electrolyte anions takes place concurrently with the double layer restructuring process. This may include photoinduced film polarity as a major factor in the film capacitance. Furthermore, illumination does not change the equivalent circuit of the film but rather changes the capacitor charge.

Potential integration with inorganic semiconductor assembly

Charge injection from one system to the other depends on, first, the potential maps (conduction and valence band) in the inorganic semiconductor and the higher unoccupied and lower occupied molecular orbitals (HUMO–LOMO) of the organic semiconductor; second, it depends on the lifetime of the excited state of each semiconductor; and third, it depends on the amount of overlapping between the band gaps of these two systems. Fluorometric emission studies indicate that the 2-APPy monomer and its polymer generated an emission when excited with a 320 nm source. The lifetime of the excited state of the monomer was measured to be 299 ps (rate constant of charge injection (k_{ct}) = $3.3 \times 10^9\ s^{-1}$), while that of the polymer was 437 ps (with k_{ct} = $2.3 \times 10^{9}\ s^{-1}$). Such elongation of the lifetime in the polymer is attributed to the increasing of the LUMO in the polymer compared with that in the monomer. The polymer maintained the conjugated structure, which allows coordination of LUMOs of the polymer units. These LUMOs can accommodate the excited electrons for some time before these electrons return to the ground state. The studies show that 2-APPy in colloidal SiO_2 gives a strong emission at λ = 360 nm (Fig. 7a). While the greater band gap of SiO_2 explains the lack of absorption of emitted photons from 2-APPy, it also indicates that the LUMO of 2-APPy is far below the conduction band in SiO_2.

IOI involving Fe_2O_3

A colloidal system of SiO_2 containing 5% iron oxide and the 2-APPy shows a great quenching of emission (drop of 55%) as displayed in Fig. 7b. This observation indicates that the junction at iron oxide colloidal particles–2-APPy interface has a band-energy structure that favors this emission absorption. The fact that the flat band potential of poly(2-APPy) is more negative than that of the conduction band (CB) of Fe_2O_3 (CB = –0.58 vs Ag/AgCl) would explain the observed quenching of emission in the presence of Fe_2O_3. Schematic Diagram 2 illustrates the relative band structure of poly(2-APPy) and Fe_2O_3. The fluorescence lifetime of 2-APPy is 0.437 ns. The shorter lifetime of the organic semiconductor excited state compared to that reported for Fe_2O_3 suggests that organic semiconductors will inject

charges into the iron colloidal particles because the hole in the valence band (VB) has a longer life than the hole generated from 2-APPy. These electrons can be injected to neutralize the holes in the VB of Fe_2O_3. This will certainly reduce the electron–hole recombination process. The lifetime of the polaron created in the organic semiconductor will determine whether these polarons will be partially or totally used in an oxidation of the chemical agent in conjunction with this illuminated IOI. It is worth noting that the Fe_2O_3 – 2-APPy assembly acts as a potential capturer of UV solar radiation and makes it available for absorption at a longer wavelength for a dopant with a correspondent band gap.

IOI involving ZnO

Aqueous colloidal solution of nanoparticles of ZnO containing 2-APPy was subject to fluorescence emission studies. The results are displayed in Fig. 7c. Unlike d^5 Fe_2O_3, a d^{10} ZnO–2-APPy assembly shows a sharp emission peak at 370 nm with emission tails at longer wavelengths ($\approx$430 nm). Although such behavior was reported for ZnO quantum dots (QDs)[29] and for other oxides,[30,31] we expect that the emission at 430 nm is due to 2-APPy only. This is due to the lack of excess OH^- that causes the emission at this wavelength. Figure 7c indicates that very small emissions were absorbed by the ZnO–2-APPy assembly. This can be attributed to the high barrier potential[32] at this interface (calculated to be 3.4 eV), and the low EA of ZnO (2.09 eV), which categorizes it as a p-type semiconductor. A p–p junction interface does not promote charge injection. Establishing a database about this organic semiconductor–metal oxide interface would find greater application relevant to organic light emitting diodes.[33] Further studies will be performed on inorganic–organic interface (IOI) systems to investigate the effect in lowering the electron–hole recombination rate and suppressing the photo-corrosion of an inorganic semiconductor.

Conclusions

The results obtained in this study represent an attempt to establish a database regarding the photoelectrochemical behavior of 2-APPy. The photoelectrochemical studies on 2-APPy indicate that this compound possesses the characteristics of a p-type organic semiconductor. Studies also show that the course of the polymerization process of this compound was different from those of the parent compounds. Although this work answers some questions, it, however, raises more questions that need to be answered in future detailed studies.

References

(1) Güllü, O.; Biber, M.; Turut, A. *J. Mater Sci. Mater.Electron.* **2008**, *19* (10), 986–991. doi:10.1007/s10854-007-9431-1.

(2) Ruden, P. P.; Albrecht, J. D.; Smith, D. L. In *Organic thin-film electronics*, Materials Research Society Symposium Proceedings; Warrendale, PA, 2005; Arias, A. C., Tessler, N., Burgi, L., Emerson, J. A., Eds.; 2005; p 871E.

(3) Tada, H. *Oyo Butsuri* **2007**, *76* (11), 284.

(4) Abe, T.; Nagai, K.; Matsukawa, T.; Tajiri, A.; Norimatsu, T. *J. Solid State Electrochem.* **2006**, *11* (2), 303–309. doi:10.1007/s10008-006-0108-0.

(5) Chikamatsu, M.; Itakura, A.; Yoshida, Y.; Azumi, R.; Kikuchi, K.; Yase, K. *J. Photochem. Photobiol. A* **2006**, *182* (3), 245–249. doi:10.1016/j.jphotochem.2006.06.09.

(6) Tachikawa, T.; Choi, J. R.; Fujitsuka, M.; Majima, T. *J. Phys. Chem. C* **2008**, *112* (36), 14090–14101. doi:10.1021/jp803620v.

(7) de Boer, R. W. I.; Gershenson, M. E.; Morpurgo, A. F.; Podzorov, V. *Condensed matter*; Los Alamos National Laboratory, Preprint Archive: Los Alamos, New Mexico, 2004; Vol. 11.

(8) Gundlach, L.; Ernstorfer, R.; Willig, F. *Appl. Phys., A Mater. Sci. Process.* **2007**, *88* (3), 481–495. doi:10.1007/s00339-007-4054-1.

(9) Kossmehl, G.; Chatzitheodorou, G. In *IUPAC 28th Macromolecular Symposium*, Proceedings of IUPAC Macro 82, Amherst, Mass., July 12–16, 1982; 1982; p 419.

(10) Yang, H.; Kwak, J. *J. Phys. Chem. B* **1997**, *101* (5), 774–781. doi:10.1021/jp962903d.

(11) Singh, R.; Narula, A. K. *Appl. Phys. Lett.* **1997**, *71* (19), 2845–2847. doi:10.1063/1.120151.

(12) Tan, T. T.; Gardner, J. W.; Farrington, J.; Bartlett, P. N. *Int. J. Electron.* **1994**, *77* (2), 173–184. doi:10.1080/00207219408926045.

(13) Hamer, W. J.; Koene, L.; de Wit, J. H. W. *Mater. Corros.* **2004**, *55* (9), 653–658. doi:10.1002/maco.200303778.

(14) Ren, X.; Pickup, P. G. *J. Phys. Chem.* **1993**, *97* (20), 5356–5362. doi:10.1021/j100122a029.

(15) Ogawa, K.; Rasmussen, S. C. *Macromolecules* **2006**, *39* (5), 1771–1778. doi:10.1021/ma052490r.

(16) Audebert, P.; Sadki, S.; Miomandre, F.; Hapiot, P.; Chane-Ching, K. *N. J. Chem.* **2003**, *27* (5), 798–804. doi:10.1039/b210906a.

(17) Sarac, A.; Sonmez, G. *Polym. Int.* **2002**, *51* (7), 594–600. doi:10.1002/pi.914.

(18) Rapta, P.; Neudeck, A.; Petr, A.; Dunsch, L. *J. Chem. Soc., Faraday Trans.* **1998**, *94* (24), 3625–3630. doi:10.1039/a806423g.

(19) Bazito, F. F. C.; Córdoba de Torresi, S. I. *Polymer (Guildf.)* **2006**, *47* (4), 1259–1266. doi:10.1016/j.polymer.2005.11.076.

(20) Oyama, N.; Kazuyuki, C.; Yukio, O.; Takeo, O.; Kaishi, N. K. *Bull. Chem. Japan* **1985**, *6*, 1172.

(21) Pekmez, N. *J. Electroanal. Chem.* **1994**, *370* (1–2), 223–229. doi:10.1016/0022-0728(93)03156-J.

(22) Pron, A.; Rannou, P.; Zagorska, M. *Electronic and optical properties of conjugated molecular systems in condensed phases*; Research Signpost: Kerala, India, **2003;** Vol. *10*, p 529.

(23) Tatarets, A. L.; Fedyunyayeva, I. A.; Dyubko, T. S.; Povrozin, Y. A.; Doroshenko, A. O.; Terpetschnig, E. A.; Patsenker, L. D.; Patsenker, L. D. *Anal. Chim. Acta* **2006**, *570* (2), 214–223. doi:10.1016/j.aca.2006.04.019. PMID:17723402.

(24) Kasem, K.; Schultz, F. A. *Can. J. Chem.* **1995**, *73* (6), 858–864. doi:10.1139/v95-107.

(25) Micaroni, L.; Nart, F. C.; Hummelgen, L. A. *J. Solid State Electrochem.* **2002**, *7* (1), 55–59. doi:10.1007/s10008-002-0289-0.

(26) Osaheni, J. A.; Jenekhe, S. A. *Chem. Mater.* **1995**, *7* (4), 672–682. doi:10.1021/cm00052a011.

(27) Osaheni, J. A.; Jenekhe, S. A. *Chem. Mater.* **1992**, *4* (6), 1282–1290. doi:10.1021/cm00024a031.

(28) Hunter, T. B.; Tyler, P. S.; Smyrl, W. H.; White, H. S. *J. Electrochem. Soc.* **1987**, *134* (9), 2198–2204. doi:10.1149/1.2100851.

(29) Monticone, S.; Tufeu, R.; Kanaev, A. V. *J. Phys. Chem. B* **1998**, *102* (16), 2854–2862. doi:10.1021/jp973425p.

(30) Fessenden, R. W.; Kamat, P. V. *J. Phys. Chem.* **1995**, *99* (34), 12902–12906. doi:10.1021/j100034a032.
(31) Liu, D.; Hug, G. L.; Kamat, P. V. *J. Phys. Chem.* **1995**, *99* (45), 16768–16775. doi:10.1021/j100045a043.
(32) Davis, C.; Kasem, K. K. *Bull. Mater. Sci.* **2008**, *31* (7), 925–929.
(33) Tadayyon, S. *Org. Electron.* **2004**, *5* (4), 199–205. doi:10.1016/j.orgel.2003.12.002.

Synthesis of both isomers of aziridine derived from the mixture of *cis*- and *trans*-limonene oxide

Hossein Mehrabi

Abstract: A short and efficient route is described for both isomers of aziridine derived from the commercially available 1:1 mixture of limonene oxides. The process is amenable to scale-up and allows easy access to multigram quantities of these useful chiral building blocks.

Key words: cis- and *trans*-limonene oxide, β-amino alcohol, *o*-tosylation, limonene aziridine.

Résumé : On a décrit une méthode courte et efficace d'obtention des deux isomères de l'aziridine qui peut être obtenue à partir d'un mélange 1 :1 commercialement disponible d'oxydes de limonène. Le processus pourrait être amener à produire de grandes quantités et il permet d'accéder facilement à des quantités multigrammes de ces importants intermédiaires chiraux.

Mots-clés : oxydes des *cis*- et *trans*-limonène, β-amino alcool, *o*-tosylation, aziridine du limonène.

[Traduit par la Rédaction]

Terpenes, particularly limonenes, are an important class of naturally occurring chiral compounds widely used in organic synthesis either as starting materials in the synthesis of optically pure molecules[1] or as the chiral core of the numerous chiral auxiliaries or asymmetric ligands employed in enantioselecive transformations.[2] In the majority of cases, the ligands derived from terpenes are amino alcohols as opposed to diamines, and the use of diamines as ligands in asymmetric synthesis is well-established.[3] The simplest way to access diamines in an enantiomerically pure form is from stereoselective ring opening of chiral aziridines.[4]

While methods for the synthesis of chiral epoxides, and thus chiral amino alcohols, have been an area of active research interest for some time, the area of asymmetric aziridination has only recently become implemented.[4] An alternative to this approach would be to utilize molecules from the chiral pool and develop chemistry to transform them into optically active aziridines. The most obvious starting materials to carry out such transformations would be amino acids, and indeed numerous methods have been developed for the transformation of amino acids into the corresponding optically pure aziridines[4,5] via the corresponding amino alcohols. Although, this would offer simple, rapid access to a number of diamines, the flexible nature of the amino acids side chain would not be suitable for developing chiral ligands.[6] Thus, the attention of our group was turned to the naturally occurring terpenes, the substituents of which are in geometrically defined environments as a result of the rigidity of the ring systems. In conjunction with our program to develop ligands for such asymmetric transformations, as well as our general interest in the chemistry of these naturally occurring chiral building blocks,[7] our group aimed to obtain the aziridines derived from limonene in diastereomericaly pure form. While several methods for the preparation of terpene aziridines have been reported, they vary in their degree of regio- and diastereo-selectivity.[8]

Herein, a method is reported for the selective synthesis of either diastereomer of aziridine from the commercially available 1:1 mixture of limonene oxides.

The separation of limonene oxide diastereomers by distillation is difficult,[9] though partial separation has been achieved by this method.[10] However, to separate the epoxides, there are chemical methods of isomer resolution based on the difference in rates of the *cis*-limonene oxide and *trans*-limonene oxide opening either by amines[10,11] or via hydrolysis.[12,13] Trans-diaxial ring opening of the *trans*-limonene oxide is more facile; hence, this isomer reacts faster than the other one, and this difference can be exploited in the separation of the corresponding products.

The reaction of a 1:1 mixture of *trans*-limonene oxide (**1a**) and *cis*-limonene oxide (**1b**) with ethanolamine gave a mixture of the β-amino alcohol (**2a**) and the unreacted *cis*-limonene oxide (**1b**).[12a] The *cis*-limonene oxide was recovered from the reaction mixture in 85% yield after a simple distillation in greater than 98% purity. The crude β-amino alcohol was purified by isolation of the oxalate salt, followed by treatment with potassium hydroxide to give the free base,[10b] which was subsequently recrystallizad (Scheme 1).

The selectivity observed in these reactions can be explained by the inherent conformational difference between *cis*- and *trans*-limonene oxides (Scheme 2). Because of its large *A* value, the isopropenyl group prefers the equatorial orientation in both the *cis*- and *trans*-isomers. For the *trans*-isomer, **1a**, an S_N2-type reaction with ethanolamine can be envisioned to occur at the less hindered C-2 carbon through a thermodynamically stable chair-like transition state (Scheme 2A). In contrast, for S_N2-type attack at the C-2 carbon atom to occur, the *cis*-isomer would have to attain the unfavorable, energetically demanding "boat-like" transition state. Consequently, the *cis*-isomer is left largely unreacted (Scheme 2B).

Received 21 January 2009. Accepted 24 April 2009. Published on the NRC Research Press Web site at canjchem.nrc.ca on 17 July 2009.

H. Mehrabi. Department of Chemistry, Rafsanjan Vali-e-Asr University, Rafsanjan 77176, Iran. (e-mail: mehraby_h@yahoo.com).

Scheme 1.

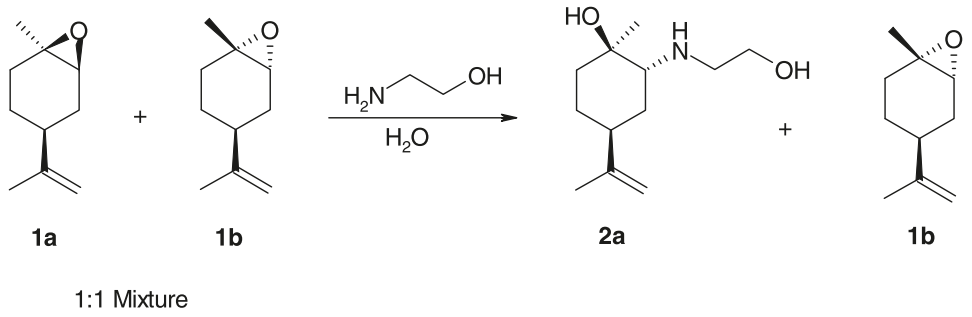

Scheme 2.

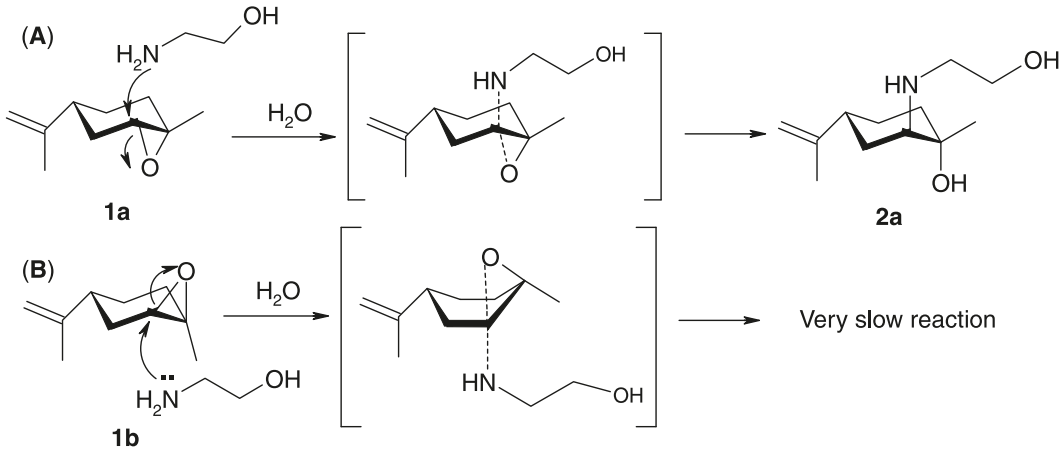

Scheme 3.

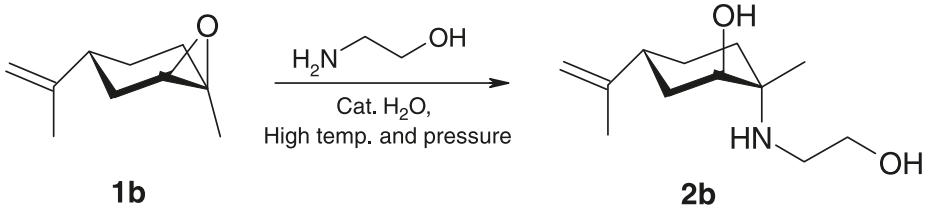

Scheme 4.

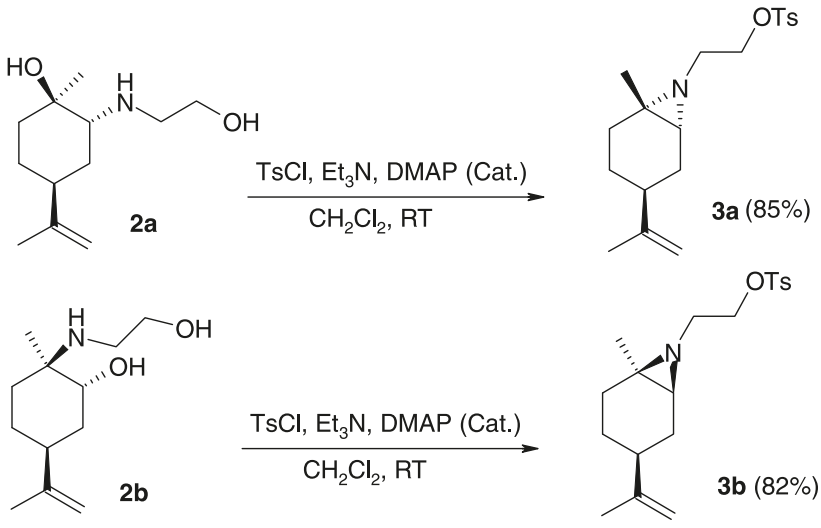

The amino alcohol **2b** can be prepared from the recovered pure *cis*-limonene oxide and ethanolamine under high temperature and pressure (sealed tube) in the presence of a catalytic amount of water.[14] Epoxide ring opening of the cis-diastereomer provides amino alcohol where the amine is attached to the more C-1 carbon atom (Scheme 3).

The products **2a** and **2b** were fully characterized by elemental analyses, IR, ^{1}H NMR, ^{13}C NMR, and mass spectrometry (see Appendix I).

It was thought that the *o*-tosylation and cyclization could be performed in a single operation starting from the β-amino alcohols **2a** and **2b** (Scheme 4). Therefore, the reaction involved 1.0 equiv. of β-amino alcohol with 2.5 equiv. of tosyl chloride and excess (3.0 equiv.) triethylamine in CH_2Cl_2 and in the presence of a catalytic amount of DMAP (see Appendix II), observing that the expected chiral aziridines **3a** and **3b** were formed cleanly after 24 h with high yields. When these conditions were applied at a larger scale (10 g), the reaction showed to be equally effective, giving comparable yields of the final compound (**3a,** 8.5 g and **3b,** 8.2 g).

The structure of compounds **3a** and **3b** were confirmed by their analytical and spectroscopic data (^{1}H NMR, ^{13}C NMR, IR, and MS) (see Appendix II). The coupling constants of the aziridinyl proton of **3b** (2.62, dd, $^3J_{HH}$= 16.8 Hz, $^3J_{HH}$= 2.4 Hz, N–C**H**) showed a clear difference from the aziridinyl proton of **3a** (2.62, dd, $^3J_{HH}$= 10.4 Hz, $^3J_{HH}$= 5.6 Hz, N–C**H**).

In conclusion, this paper reports an efficient and convenient procedure for the highly selective synthesis of either diastereomer of aziridine derived from limonene starting from the commercially available 1:1 mixture of limonene oxides. It is important to point out that the reaction was performed on a 10 g scale, which allowed the preparation of high quantities of the target aziridines in a single step and using a simple protocol.

Acknowledgements

The author is thankful to the Office of Graduate Studies of the Rafsanjan Vali-e-Asr University for financial support.

References

(1) (a) For examples of synthesis, utilizing limonene as the chiral template, see: Van Tamelen, E. E.; Anderson, R. J. *J. Am. Chem. Soc.* **1972**, *94* (23), 8225–8228. doi:10.1021/ja00778a047. PMID:5079966.; (b) Pawson, B. A.; Cheung, H.-C.; Gurbaxani, S.; Saucy, G. *J. Am. Chem. Soc.* **1970**, *92* (2), 336–343. doi:10.1021/ja00705a641.; (c) Baudouy, R.; Prince, P. *Tetrahedron* **1989**, *45* (7), 2067–2074. doi:10.1016/S0040-4020(01)80068-5.; (d) Paquette, L. A.; Kang, H.-J. *J. Am. Chem. Soc.* **1991**, *113* (7), 2610–2621. doi:10.1021/ja00007a039.; (e) Mori, K.; Kato, M. *Tetrahedron Lett.* **1986**, *27* (8), 981–982. doi:10.1016/S0040-4039(00)84154-4.; (f) Marron, B. E.; Nicolaou, K. C. *Synthesis* **1989**, *1989* (07), 537–539. doi:10.1055/s-1989-27309.; (g) Tius, M. A.; Kerr, M. A. *Synth. Commun.* **1988**, *18* (16), 1905–1911. doi:10.1080/00397918808068256.; (h) Dauphin, G. *Synthesis* **1979**, *1979* (10), 799–801. doi:10.1055/s-1979-28835.; (i) Kaneda, M.; Takahashi, R.; Litaka, Y.; Shibata, S. *Tetrahedron Lett.* **1972**, *13* (45), 4609–4611. doi:10.1016/S0040-4039(01)94378-3.; (j) Wender, P. A.; Singh, S. K. *Tetrahedron Lett.* **1990**, *31* (18), 2517–2520. doi:10.1016/0040-4039(90)80114-2.; (k) ApSimon. J., Ed.; In *The total synthesis of natural products*; Vol. 4, 1981; p. 610; (l) Hudlicky, T.; Luna, H.; Barbieri, G.; Kwart, L. D. *J. Am. Chem. Soc.* **1988**, *110* (14), 4735–4741. doi:10.1021/ja00222a035.; (m) Hudlicky, T.; Radesca-Kwart, L.; Li, L.; Bryant, T. *Tetrahedron Lett.* **1988**, *29* (27), 3283–3286. doi:10.1016/0040-4039(88)85141-4.; (n) Pinto, L.; Dupont, J.; Souza, R. F.; Gusmao, K. B. *Catal. Commun.* **2008**, *9* (1), 135–139. doi:10.1016/j.catcom.2007.05.025.

(2) (a) For examples, see: Goralski, C. T.; Chrisman, W.; Hasha, D. L.; Nicholson, L. W.; Rudolf, P. R.; Zakett, D.; Singaram, B. *Tetrahedron Asymmetry* **1997**, *8* (23), 3863–3871. doi:10.1016/S0957-4166(97)00566-1.; (b) Masui, M.; Shioiri, T. *Tetrahedron* **1995**, *51* (30), 8363–8370. doi:10.1016/0040-4020(95)00447-G.; (c) Masui, M.; Shiori, T. *Synlett* **1995**, 49; (d) Kauffman, G. S.; Harris, G. D.; Dorow, R. L.; Stone, B. R. P.; Parsons, R. L. J., Jr.; Pesti, J. A.; Magnus, N. A.; Fortunak, J. M.; Confalone, P. N.; Nugent, W. A. *Org. Lett.* **2000**, *2* (20), 3119–3121. doi:10.1021/ol006321x. PMID:11009360.; (e) Noyori, R.; Kitamura, M.; Suga, S.; Kawai, K. *J. Am. Chem. Soc.* **1986**, *108* (22), 7117. doi:10.1021/ja00282a054.; (f) Szakonyi, Z.; Hetenyi, A.; Fulop, F. *Tetrahedron* **2008**, *64* (6), 1034–1039. doi:10.1016/j.tet.2007.07.065.

(3) Togni, A.; Venanzi, L. M. *Angew. Chem., Int. Ed. Engl.* **1994**, *33* (5), 497–526. doi:10.1002/anie.199404971.

(4) (a) For recent reviews on aziridines, including their synthesis in optically active form and their ring-opening reactions, see: Sweeney, J. B. *Chem. Soc. Rev.* **2002**, *31* (5), 247–258. doi:10.1039/b006015l. PMID:12357722.; (b) McCoull, W.; Davis, F. A. *Synthesis* **2000**, *2000* (10), 1347–1365. doi:10.1055/s-2000-7097.; (c) Atkinson, R. S. *Tetrahedron* **1999**, *55* (6), 1519–1559. doi:10.1016/S0040-4020(98)01199-5.; (d) Jacobsen, E. N.; Pfaltz, A.; Yamamoto, H., Eds.; In *Comprehensive asymmetric catalysis*; Vol. 2; Springer-Verlag: Berlin, Heidelberg: New York, 1999; p. 607; (e) Osborn, H. M. I.; Sweeney, J. B. *Tetrahedron Asymmetry* **1997**, *8*(11), 1693–1715. doi:10.1016/S0957-4166(97)00177-8.; (f) Tanner, D. *Angew. Chem., Int. Ed. Engl.* **1994**, *33* (6), 599–619. doi:10.1002/anie.199405991.; (g) Tanner, D. *Pure Appl. Chem.* **1993**, *65* (6), 1319–1328. doi:10.1351/pac199365061319.

(5) (a) For examples of ring closure of amino alcohols and their derivatives, see: Kelly, J. W.; Eskew, N. L.; Evans, S. A. *J. Org. Chem.* **1986**, *51* (1), 95–97. doi:10.1021/jo00351a020.; (b) Kuyl-Yeheskiely, E.; Lodder, G. A.; van der Marel, G. A.; Van Boom, J. H. *Tetrahedron Lett.* **1992**, *33* (21), 3013. doi:10.1016/S0040-4039(00)79586-4.; (c) Pfister, J. R. *Synthesis* **1994**, 969; (d) Song, L.; Servajean, V.; Thierry, J. *Tetrahedron* **2006**, *62* (15), 3509–3516. doi:10.1016/j.tet.2006.02.003.

(6) (a) An exception to this would be to utilize proline as the amino acid, and derivatives of this important synthon have been widely used as chiral auxilaries. For example, see: Soai, K.; Okawa, A.; Tatsuya, K.; Ogawa, K. *J. Am. Chem. Soc.* **1987**, *109* (23), 7111–7115. doi:10.1021/ja00257a034.; (b) Krzemiński, M. P.; Wojtczak, A. *Tetrahedron Lett.* **2005**, *46* (48), 8299–8302. doi:10.1016/j.tetlet.2005.09.172.; (c) Watts, C. C.; Thoniyot, P.; Cappuccio, F.; Verhagen, J.; Gallagher, B.; Singaram, B. *Tetrahedron Asymmetry* **2006**, *17* (8), 1301–1307. doi:10.1016/j.tetasy.2006.04.025.

(7) (a) For a review on ClickChem, see: Kolb, H. C.; Finn, M. G.; Sharpless, K. B. *Angew. Chem., Int. Ed.* **2001**, *40* (11), 2004–2021. doi:10.1002/1521-3773(20010601)40:11<2004::AID-ANIE2004>3.0.CO;2-5.; (b) Bulut, A.; Aslan, A.; Izgü, E. Ç.; Dogan, Ö. *Tetrahedron Asymmetry* **2007**, *18* (8), 1013–1016. doi:10.1016/j.tetasy.2007.04.013.

(8) (a) For examples, see: Davis, C. E.; Bailey, J. L.; Lockner, J. W.; Coates, R. M. *J. Org. Chem.* **2003**, *68* (1), 75–82. doi:10.1021/jo026506c. PMID:12515464.; (b) Bochvic, B.; Kapuscinski, J.; Olejniczak, B. *Roczniki Chem.* **1971**, *45*, 869; (c) Subbaraj, A.; Rao, O. S.; Lwowski, W. *J. Org. Chem.* **1989**, *54* (16), 3945–3952. doi:10.1021/jo00277a037.; (d) Bergmeier, S. C.; Seth, P. P. *Tetrahedron Lett.* **1999**, *40* (34), 6181–6184. doi:10.1016/S0040-4039(99)01210-1.; (e) Parrish, E.; Nes, W. D. *Synth. Commun.* **1988**, *18* (2), 221–226. doi:10.1080/00397918808077348.; (f) Tiecco, M.; Testaferri, L.; Santi, C.; Tomassini, C.; Santoro, S.; Marini, F.; Bagnoli, L.; Temperini, A. *Tetrahedron* **2007**, *63* (50), 12373–12378. doi:10.1016/j.tet.2007.09.047.

(9) Fractional distillation is possible but extremely inefficient: Royals, E. E.; Leffingwell, J. C. *J. Org. Chem.* **1966**, *31* (6), 1937–1944. doi:10.1021/jo01344a062.

(10) (a) Steiner, D.; Sethofer, S. G.; Goralski, C. T.; Singaram, B. *Tetrahedron Asymmetry* **2002**, *13* (14), 1477–1483. doi:10.1016/S0957-4166(02)00342-7.; (b) Chrisman, W.; Camara, J.; Marcellini, K.; Singaram, B.; Goralski, C.; Hasha, D.; Rudolf, P.; Nicholson, L.; Borodychuk, K. *Tetrahedron Lett.* **2001**, *42* (34), 5805–5807. doi:10.1016/S0040-4039(01)01135-2.; (c) Voronkov, M. V.; Kanamarlapudi, R. C.; Richardson, P. *Tetrahedron Lett.* **2005**, *46* (40), 6907–6910. doi:10.1016/j.tetlet.2005.08.009.

(11) (a) Under harsh conditions, both epoxides can be opened with dimethylamine, and the corresponding amino alcohols can be separated by salt formation and crystallization. For examples of this and the susbsequent conversion of the amino alcohols back to the diastereomerically pure epoxides, see: Baker, R.; Borges, M.; Cooke, N. G.; Herbert, R. H. *J. Chem. Soc., Chem. Commun.* **1987**, (6): 414. doi:10.1039/c39870000414.; (b) Newhall, W. F. *J. Org. Chem.* **1964**, *29* (1), 185–187. doi:10.1021/jo01024a042.

(12) (a) For examples, see: Steiner, D.; Ivison, L.; Goralski, C. T.; Appell, R. B.; Gojkovic, J. R.; Singaram, B. *Tetrahedron Asymmetry* **2002**, *13* (21), 2359–2363. doi:10.1016/S0957-4166(02)00646-8.; (b) Jones, J.; dos Santos, A. G.; de Lima Castro, F. *Synth. Commun.* **1996**, *26* (14), 2651–2656. doi:10.1080/00397919608004581.; (c) Cole-Hamilton, D. J.; Salles, L.; Nixon, A. F.; Russell, N. C.; Clarke, R.; Pogorzelec, P. *Tetrahedron Asymmetry* **1999**, *10* (8), 1471–1476. doi:10.1016/S0957-4166(99)00136-6.; (d) van der Werf, M. J.; Jongejan, H.; Franssen, M. C. R. *Tetrahedron Lett.* **2001**, *42* (32), 5521–5524. doi:10.1016/S0040-4039(01)01037-1.

(13) (a) Enzyme-mediated hydrolysis has been reported, see: Weijers, C. A. G. M. *Tetrahedron Asymmetry* **1997**, *8* (4), 639–647. doi:10.1016/S0957-4166(97)00012-8.; (b) van der Werf, M. J.; Orru, R. V. A.; Overkamp, K. M.; Swarts, H. J.; Osprian, A.; de Bont, J. A. M.; Faber, K. *Appl. Microbiol. Biotechnol.* **1999**, *52* (3), 380. doi:10.1007/s002530051535.

(14) Watts, C. C.; Thoniyot, P.; Hirayama, L. C.; Romano, T.; Singaram, B. *Tetrahedron Asymmetry* **2005**, *16* (10), 1829–1835. doi:10.1016/j.tetasy.2005.03.036.

Appendix I

The data for 2a

Pale yellow oil, yield: 9.0 g (85%). $[\alpha]_D^{25}$ –29.8 (*c*1.0, $CHCl_3$). IR ν(cm^{-1}, KBr): 3332 (broad), 1441, 1044, 887. ^1H NMR (400 MHz, $CDCl_3$) δ: 1.27 (3H, s, CH_3), 1.46–1.90 (6H, m, $3CH_2$), 1.72 (3H, s, CH_3), 2.27 (1H, m, CH), 2.73 (2H, td, $^3J_{HH}$= 6.4 Hz, $^2J_{HH}$= 2.8 Hz, N–CH_2), 3.64 (2H, td, $^3J_{HH}$= 6.4 Hz, $^2J_{HH}$= 2.8 Hz, O–CH_2), 3.81 (1H, t, $^3J_{HH}$= 7.2 Hz, N–CH), 4.68 (2H, s, =CH_2) ppm. ^{13}C NMR (100 MHz, $CDCl_3$) δ: 26.3 (CH_3), 26.6 (CH_3), 29.5 (CH_2), 33.8 (CH_2), 37.1 (CH_2), 43.2 (CH), 48.9 (N–CH_2), 63.6 (C), 65.4 (O–CH_2), 78.7 (N–CH), 115.3 (C=**C**H_2), 150.6 (**C**=CH_2) ppm. MS (EI, 70 eV) *m*/*z* (%): 213 (M^+, 27), 156 (55), 143 (39), 114 (100), 83 (52). Anal. calcd. for $C_{12}H_{23}NO_2$ (213.3): C, 67.57; H, 10.87; N, 6.57. Found: C, 67.68; H, 10.91; N, 6.54.

The data for 2b

Pale orange oil, yield: 8.3 g (78%). $[\alpha]_D^{25}$ –46.3 (*c*1.0, $CHCl_3$). IR ν(cm^{-1}, KBr): 3334 (broad), 1440, 1044, 884. ^1H NMR (400 MHz, $CDCl_3$) δ: 1.11 (3H, s, CH_3), 1.49–1.99 (6H, m, $3CH_2$), 1.73 (3H, s, CH_3), 2.30 (1H, m, CH), 2.69 (2H, td, $^3J_{HH}$= 5.2 Hz, $^2J_{HH}$= 2.4 Hz, N–CH_2), 3.61 (2H, td, $^3J_{HH}$= 5.2 Hz, $^2J_{HH}$= 2.4 Hz, O–CH_2), 3.64 (1H, t, $^3J_{HH}$= 6.8 Hz, O–CH), 4.74 (2H, s, =CH_2) ppm. ^{13}C NMR (100 MHz, $CDCl_3$) δ: 26.0 (CH_3), 26.5 (CH_3), 30.1 (CH_2), 35.5 (CH_2), 37.9 (CH_2), 42.3 (CH), 47.3 (N–CH_2), 59.4 (C), 66.5 (O–CH_2), 81.7 (O–CH), 113.7 (C=**C**H_2), 153.5 (**C**=CH_2) ppm. MS (EI, 70 eV) *m*/*z* (%): 213 (M^+, 14), 156 (87), 143 (22), 114 (100), 83 (38). Anal. calcd. for $C_{12}H_{23}NO_2$ (213.3): C, 67.57; H, 10.87; N, 6.57. Found: C, 67.73; H, 10.77; N, 6.52.

Appendix II

General procedure for the preparation of compounds 3a and 3b

Et_3N (0.10 mol) was added to a cooled (0 °C) solution of the starting β-amino alcohols **2a** and **2b** (0.03 mol), TsCl (0.07 mol), and DMAP (30 mg) in dry CH_2Cl_2 (200 mL). The mixture was allowed to reach RT and stirred at this temperature for 24 h after which a saturated NH_4Cl solution (100 mL) was added. The mixture was extracted with CH_2Cl_2 (3 × 50 mL), and the organic fractions were collected, dried over Na_2SO_4, filtered, and the solvent removed in vacuo, affording the desired aziridines (**3a** and **3b**) after flash column chromatography purification (hexane/AcOEt 8:2).

The data for 3a

White powder, yield: 8.91 g (85%), mp 111–113 °C. $[\alpha]_D^{25}$ +24.7 (*c*1.0, $CHCl_3$). IR ν(cm^{-1}, KBr): 1643, 1596, 1374, 1330, 1124, 1088. ^1H NMR (400 MHz, $CDCl_3$) δ: 1.37 (3H, s, CH_3), 1.67 (3H, s, CH_3), 1.35–1.70 and 2.21 (6H, m, $3CH_2$), 1.86 (1H, m, CH), 2.41 (3H, s, CH_3), 2.62 (1H, dd, $^3J_{HH}$= 10.4 Hz, $^3J_{HH}$= 5.6 Hz, N–CH), 2.83 and 3.90 (2H, m, N–CH_2), 3.67 and 4.08 (2H, m, O–CH_2), 4.63 and 4.68 (2H, 2s, =CH_2), 7.30 (2H, d, $^3J_{HH}$= 8.0 Hz, 2CH), 7.61 (2H, d, $^3J_{HH}$= 8.0 Hz, 2CH) ppm. ^{13}C NMR (100 MHz, $CDCl_3$) δ: 16.4 (CH_3), 22.9 (CH_3), 23.5 (CH_3), 29.4 (CH_2), 34.0 (CH_2), 38.3 (CH_2), 46.7 (CH), 52.4 (N–CH_2), 62.3 (O–CH_2), 69.3 (N–CH), 78.8 (N–C), 112.3 (C=**C**H_2), 129.5 (CH), 130.3 (CH), 137.2 (C), 146.7 (C), 150.9 (**C**=CH_2) ppm. MS (EI, 70 eV) *m*/*z* (%): 349 (M^+, 13), 194 (100), 155 (38), 91 (42), 65 (21). Anal. calcd. for $C_{19}H_{27}NO_3S$ (349.5): C, 65.30; H, 7.79; N, 4.01. Found: C, 65.31; H, 7.73; N, 4.00.

The data for 3b

White powder, yield: 8.59 g (82%), mp 110–111 °C. $[\alpha]_D^{25}$ –56.1 (*c*1.0, $CHCl_3$). IR ν(cm^{-1}, KBr): 1645, 1597,

1374, 1333, 1123, 1087. ^{1}H NMR (400 MHz, $CDCl_3$) δ: 1.35 (3H, s, CH_3), 1.68 (3H, s, CH_3), 1.38–1.73 and 2.22 (6H, m, $3CH_2$), 1.86 (1H, m, CH), 2.43 (3H, s, CH_3), 2.62 (1H, dd, $^{3}J_{HH}$= 16.8 Hz, $^{3}J_{HH}$= 2.4 Hz, N–CH), 2.85 and 3.92 (2H, m, N–CH_2), 3.67 and 4.09 (2H, m, O–CH_2), 4.66 and 4.70 (2H, 2s, =CH_2), 7.31 (2H, d, $^{3}J_{HH}$= 8.0 Hz, 2CH), 7.63 (2H, d, $^{3}J_{HH}$= 8.0 Hz, 2CH) ppm. ^{13}C NMR (100 MHz, $CDCl_3$): δ = 17.8 (CH_3), 23.1 (CH_3), 23.6 (CH_3), 29.5 (CH_2), 34.2 (CH_2), 39.5 (CH_2), 46.6 (CH), 52.2 (N–CH_2), 62.7 (O–CH_2), 69.2 (N–CH), 78.9 (N–C), 111.6 (C=**C**H_2), 129.3 (CH), 131.9 (CH), 138.5 (C), 145.5 (C), 150.3 (**C**=CH_2) ppm. MS (EI, 70 eV) *m*/*z* (%): 349 (M^+, 9), 194 (100), 155 (16), 91 (37), 65 (14). Anal. calcd. for $C_{19}H_{27}NO_3S$ (349.5): C, 65.30; H, 7.79; N, 4.01. Found: C, 65.32; H, 7.70; N, 4.02.

Commercial ZrO_2 as a new, efficient, and reusable catalyst for the one-step synthesis of quinolines in solvent-free conditions

Mona Hosseini-Sarvari

Abstract: Commercially available zirconia (ZrO_2) is reported as an extremely efficient catalyst for the synthesis of quinolines. A one-step reaction of 2-aminoarylketones and a carbonyl compound (Friedlander reaction) took place under solvent-free conditions to afford the corresponding quinolines in good-to-high yields in the presence of ZrO_2. Furthermore, the catalyst is reused several times without any significant loss of its catalytic activity.

Key words: ZrO_2, Quinoline, Friedlander reaction, solvent-free, 2-aminoarylketones.

Résumé : On a observé que la zircone commercialement disponible est un catalyseur extrêmement efficace pour la synthèse des quinoléines. En présence de ZrO_2, la réaction de Friedlander, une réaction en une étape entre une 2-aminoarylcétones et un composé carbonylé, se produit dans des conditions sans solvant pour conduire aux quinoléines correspondantes avec des rendements allant de bons à excellents. De plus, on peut réutiliser le catalyseur à plusieurs reprises sans perte significative de son activité catalytique.

Mots-clés : ZrO_2, réaction de Friedlander, sans solvant, 2-aminoarylcétones.

[Traduit par la Rédaction]

Introduction

Quinolines are well-known for a wide range of medicinal properties and for being used as antimalarial, antiasthmatic, antihypertensive, antibacterial, and tyrosine-kinase-inhibiting agents.[1] They also undergo hierarchical self-assembly into a variety of nano- and meso-structures with enhanced electronic and photonic functions.[2] Thus, a great deal of effort has been drawn to develop new and efficient synthetic routes to quinoline derivatives. Among several routes to quinoline synthesis, an acid- or base-catalyzed condensation followed by a cyclodehydration between a 2-aminoarylketone and a carbonyl compound containing a reactive α-methylene group, namely the Friedlander reaction, is one of the simplest and straightforward methods.[3] This classical method is still not fully satisfactory with regard to the relatively low yield, harsh reaction conditions, side reactions, and also under base-catalyzed conditions. In addition, *o*-aminobenzophenone fails to react with simple ketones such as cyclohexanone and β-ketoesters.[4] Recently, modified methods employing $ZnCl_2$, $SnCl_2$, $Bi(OTf)_3$, $AuCl_3$, $CeCl_3$, and so forth[5,6] have been reported for the synthesis of quinolines. In these methods, the catalyst is destroyed during the work-up and cannot be recovered. However, development of a new catalyst, which can be reused, commercially available, new, and simplest for the synthesis of this important class of heterocyclic compounds is of demand.

Received 12 January 2009. Accepted 18 March 2009. Published on the NRC Research Press Web site at canjchem.nrc.ca on 28 July 2009.

M. Hosseini-Sarvari. Department of Chemistry, Shiraz University, Shiraz 71454, I.R. Iran. (e-mail: hossaini@susc.ac.ir).

Today, active surfaces, such as metal oxides, play an ever growing role in organic synthesis and are widely employed not only for preparative organic reactions but also in the industry. Such reactions normally proceed under mild conditions, with high chemo-, regio-, and stereo-selectivities, securing simpler isolation procedures compared with similar reactions in solution.[7,8]

Results and discussion

Herein, I have studied the reaction of ethylacetoacetate with 2-aminoacetophenone in the presence of metal oxides as a model reaction in solvent-free conditions (Table 1). The progress of the reaction was monitored by TLC and ^1H NMR spectra from the reaction mixture.

For the first time, it is shown (Table 1) that certain metal oxides are active catalysts for the interaction studied, particularly ZrO_2, TiO_2, and both acidic and basic types of Al_2O_3. So, by considering the reaction time and yield, ZrO_2 was found to be the most effective in comparison with other metal oxides that were chosen. Subsequently, a series of substituted quinolines were synthesized following the same method using this catalyst (Scheme 1, Table 2). Interestingly, cyclic ketones, such as cyclohexanone and cyclopentanone, reacted with 2-arylketones to afford the respective tricyclic quinolines. The reaction is fairly general, clean, and efficient. The experimental procedure is very simple. The good-to-high yield transformation did not form any significant amounts of undesirable side products.

The condensation of 2-aminoarylketones (**2**) (R^3 = Me, Ph; R^4 = H, Cl) with unsymmetrical 1,3-diones (**1**) gave exclusively the regioisomer **3** if the two carbonyl groups present in **1** had dissimilar reactivity with regard to enamine

Scheme 1.

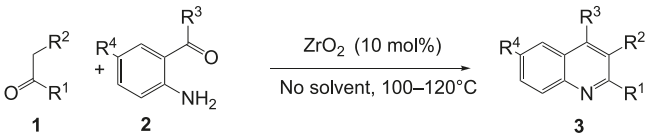

formation. However, the condensation of 2-aminoarylketones (**2**) with ethyl-4,4,4-trifluoro-3-oxobutanoate led to regioisomeric mixtures of quinolines **3** and **4**, respectively (Table 2, entries 3 and 12). This can be discussed by the similar activity of the two carbonyl groups present in ethyl-4,4,4-trifluoro-3-oxobutanoate, where the actual mechanism seems to be that the enamine formation may proceed in the condensation step; however, in this case, it is rather an iminoether (**4c**, **4l**).

From an environmental point of view, it is desirable to minimize the amount of waste for organic transformation. In this context, the catalyst was recycled for subsequent runs. The recyclability of the catalyst was investigated using a model reaction of the synthesis of quinoline **3a** in the presence of 10 mol% of the catalyst in solvent-free conditions. After the completion of the reaction (monitored by TLC), EtOAc was added to the reaction mixture and then filtered to separate the catalyst. The recycled catalyst was used for further runs, and it was found that its activity does not show any significant decrease even after six runs. It should be noted that although no solvents are used in the reaction itself, but to separate the catalyst and for the isolation and purification of the products, quantitative amounts of solvent are used.

In summary, the present protocol is the first example of ZrO_2-catalyzed synthesis of quinolines in benign conditions. The advantages of this method are the use of a cheap and commercially available catalyst. No toxic reagents, solvents, or byproducts were involved, and no laborious purifications were necessary. These conditions are also environment-friendly, cost-effective, and possess high generality to make our methodology industrialized as a valid contribution to the existing methodologies in the field of quinoline synthesis.

Experimental

Chemicals were purchased from Fluka, Merck, BDH, and Aldrich Chemical Companies. Progress of the reactions was followed by TLC using silica gel polygrams SIL G/UV 254 plates. NMR spectra were recorded on a Bruker DPX 250 MHz instrument. Microanalyses were performed on a PerkinElmer 240-B microanalyzer.

General procedure

To a mixture of 2-aminoaryl ketone (1 mmol) and a methylene carbonyl compound (1.5 mmol) ZrO_2 (0.12 g, 10 mol%) was added. The mixture was heated in an oil bath at 100–120 °C, and the reaction was monitored by TLC. After the reaction was complete, EtOAc was added to the reaction mixture, which was filtered to separate the catalyst. The organic solvent was removed under reduced pressure. After purification by chromatography on silica gel (*n*-hexane/ethyl acetate, 70:30), the product was obtained. The structures of the products were confirmed by ^{1}H NMR, IR, and comparison with authentic samples obtained commercially or prepared by reported methods. All products are known and were characterized by ^{1}H NMR, IR, and mass spectral data, which were found to be identical to those described in the literature, and for the new compounds, complete spectroscopic data are described below.

Table 1. ^{1}H NMR spectroscopic monitoring of the reaction of ethylacetoacetate (**1a**, 1.5 mmol) with 2-aminoacetophenone (**2a**, 1 mmol) at 100 °C under solvent-free condition.

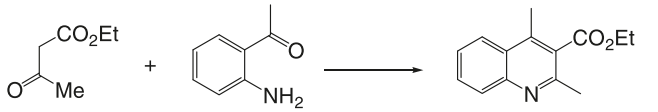

Entry	Active surface[a]	Time (h)	Yield (%)
1	MgO	24	40
2	TiO_2	8	90
3	CaO	24	73
4	ZnO	11	90
5	Al_2O_3 (acidic type)	6	82
6	Al_2O_3 (basic type)	9	80
7	ZrO_2	4	98

[a]10 mol% of the metal oxide was used as catalyst.

Compound (3c)

Light yellow solid. ^{1}H NMR (250 MHz, $CDCl_3$) δ_H: 7.23–7.33 (4H, m, Ar*H*), 3.95–4.03 (2H, m, –OC*H*$_2$CH$_3$), 2.33 (3H, s, ArC*H*$_3$), 1.13 (3H, t, *J* =7.05 Hz, –OCH$_2$C*H*$_3$). ^{13}C NMR (62.9 MHz, $CDCl_3$) δ_C: 15.3, 17.2, 64.7, 108.1, 115.2, 122.3, 128.9 (–*C*F$_3$), 119.2, 124.5, 124.8, 128.8, 131.3, 134.6, 145.3, 147.6, 148.9, 171.3. MS (ESI) *m*/*z*: 283 (M^+ + H). HR-MS calcd. for $C_{14}H_{12}F_3NO_2$ (M^+ + H): 283.2490, found: 283.2489. Anal. calcd. for $C_{14}H_{12}F_3NO_2$: C, 59.37; H, 4.27%. Found: C, 59.12; H, 4.00.

Compound (4c)

Light yellow solid. ^{1}H NMR (250 MHz, $CDCl_3$) δ_H: 7.50–7.93 (4H, m, Ar*H*), 4.39 (2H, m, –OC*H*$_2$CH$_3$), 2.60 (3H, s, ArC*H*$_3$), 1.31 (3H, t, *J* = 7.05 Hz, –OCH$_2$C*H*$_3$). ^{13}C NMR (62.9 MHz, $CDCl_3$) δ_C: 15.4, 17.5, 65.1, 107.5, 115.1, 122.5, 129.2 (–*C*F$_3$), 100.2, 162.5, 124.8, 128.9, 130.4, 130.9, 132.7, 141.7, 151.4, 185.0. MS (ESI) *m*/*z*: 283 (M^+ + H). HR-MS calcd. for $C_{14}H_{12}F_3NO_2$ (M^+ + H): 283.2490, found: 283.2489. Anal. calcd. for $C_{14}H_{12}F_3NO_2$: C, 59.37; H, 4.27%. Found: C, 59.20; H, 4.03.

Compound (3l)

Light yellow solid. ^{1}H NMR (250 MHz, $CDCl_3$) δ_H: 7.40–8.50 (9H, m, Ar*H*), 5.25 (2H, m, –OC*H*$_2$CH$_3$), 1.96 (3H, t, *J* =7.06 Hz, –OCH$_2$C*H*$_3$). ^{13}C NMR (62.9 MHz, $CDCl_3$) δ_C: 31.2, 65.8, 107.1, 119.2, 122.3, 128.8 (–*C*F3), 116.0, 122.5, 126.4, 126.9, 127.7, 127.8, 128.1, 128.2, 128.5, 128.7, 130.9, 137.5, 148.0, 161.2. MS (ESI) *m*/*z*: 345 (M^+ + H). HR-MS calcd. for $C_{19}H_{14}F_3NO_2$ (M^+ + H): 345.3190, found: 345.3189. Anal. calcd. for $C_{19}H_{14}F_3NO_2$: C, 66.09; H, 4.09%. Found: C, 66.02; H, 4.00.

Compound (4l)

Light yellow solid. ^{1}H NMR (250 MHz, $CDCl_3$) δ_H: 7.13–7.28 (9H, m, Ar*H*), 4.00 (2H, m, –OC*H*$_2$CH$_3$), 1.08 (3H, t, *J* = 7.06 Hz, –OCH$_2$C*H*$_3$). ^{13}C NMR (62.9 MHz, $CDCl_3$)

Table 2. Quinolines synthesis using ZrO_2 (10 mol%) as catalyst under solvent-free conditions.

Entry	R^1	R^2	R^3	R^4	Product	Time (h)	Yields[a] (%)	Mp (°C)
1	Me	CO_2Et	Me	H	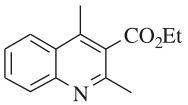 **3a**	4	98	Oil (oil)[5h]
2	Me	CO_2CH_2Ph	Me	H	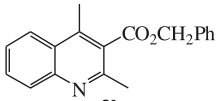 **3b**	2.5	93	54–57
3	CF_3	CO_2Et	Me	H	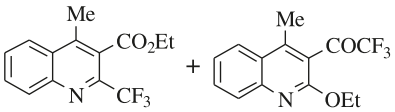 **3c** + **4c**	2	95 (70:30)[b]	**3c:** 86–88 **4c:** (97–100)
4	Me	CO_2Me	Me	H	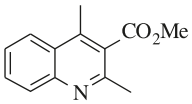 **3d**	3	98	Oil
5	$-COCH_2CMe_2CH_2-$		Me	H	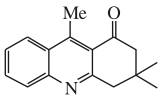 **3e**	4	90	103–105 (105–106)[5m]
6	$-CO(CH_2)_3-$		Me	H	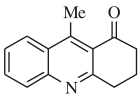 **3f**	4	86	78–79 (78)[5h]
7	Me	COMe	Me	H	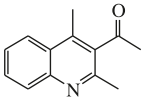 **3g**	6	65	Oil (oil)[5m]
8	$-(CH_2)_2-$		Me	H	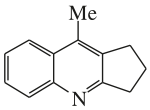 **3h**	6	60	54–56 (58–56)[5m]
9	$-(CH_2)_3-$		Me	H	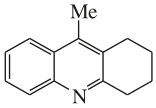 **3i**	6	65	75–78 (75–77)[5m]
10	Me	CO_2Et	Ph	H	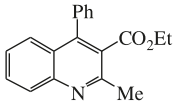 **3j**	3	95	95–97 (96)[5h]

Table 2. *Concluded.*

Entry	R^1	R^2	R^3	R^4	Product	Time (h)	Yields[a] (%)	Mp (°C)
11	Me	CO_2CH_2Ph	Ph	H	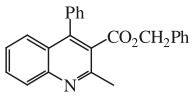 **3k**	2.5	90	89–91 (90–93)[6c]
12	CF_3	CO_2Et	Ph		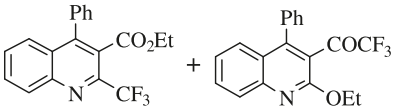 **3l** **4l**	2.5	95 (70:30)[b]	**3l:** 165–167 **4l:**192–194
13	Me	CO_2Me	Ph	H	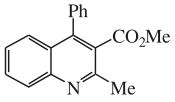 **3m**	3	95	131–133 (132–134)[6d]
14	$-COCH_2CMe_2CH_2-$		Ph	H	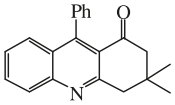 **3n**	3.5	92	189–191 (191)[5h]
15	$-CO(CH_2)_3-$		Ph	H	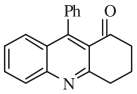 **3o**	4	90	156–158 (158)[5h]
16	Me	COMe	Ph	H	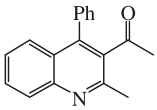 **3p**	5.5	70	110–112 (113)[5h]
17	$-(CH_2)_2-$		Ph	H	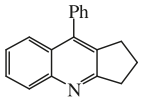 **3q**	5	72	131–133 (132)[5h]
18	$-(CH_2)_3-$		Ph	H	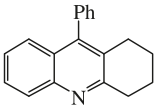 **3r**	5	68	137–139 (139)[5h]
19	Me	CO_2Et	Ph	Cl	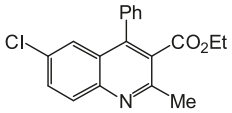 **3s**	2.5	95	105–107 (108)[4]
20	$-CO(CH_2)_3-$		Ph	Cl	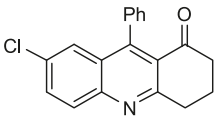 **3t**	3	90	160–162 (163)[4]

[a] Isolated yields.
[b] The ratios of regioisomers **3** and **4** were determined by ^1H NMR.

δ_C: 49.5, 66.9, 108.2, 121.1, 123.5, 129.0 (–*CF3*), 119.3, 126.0, 126.6, 127.1, 127.8, 127.9, 128.2, 128.4, 128.8, 129.1, 133.3, 137.8, 149.3, 201.5. MS (ESI) *m/z*: 345 (M^+ + H). HR-MS calcd. for $C_{19}H_{14}F_3NO_2$ (M^+ + H): 345.3190, found: 345.3189. Anal. calcd. for $C_{19}H_{14}F_3NO_2$: C, 66.09; H, 4.09%. Found: C, 66.00; H, 4.05.

Acknowledgement

The support of this work by the Shiraz University Research Council is gratefully acknowledged.

References

(1) (a) Sinden, R. E.; Morris, H. R.; Billker, O.; Lindo, V.; Panico, M.; Etienne, A. E.; Paxton, T.; Dell, A.; Rogers, M. *Nature* **1998**, *392* (6673), 289–292. doi:10.1038/32667. PMID: 9521324.; (b) Roma, G.; Di Braccio, M.; Grossi, G.; Mattioli, F.; Ghia, M. *Eur. J. Med. Chem.* **2000**, *35* (11), 1021–1035. doi:10.1016/S0223-5234(00)01175-2. PMID:11137230.; (c) Chen, Y.-L.; Fang, K.-C.; Sheu, J.-Y.; Hsu, S.-L.; Tzeng, C.-C. J. *Med. Chem.* **2001**, *44* (14), 2374–2377. doi:10.1021/jm0100335.

(2) (a) Agrawal, A. K.; Jenekhe, S. A. *Macromolecules* **1991**, *24* (25), 6806–6808. doi:10.1021/ma00025a044.; (b) Zhang, X.; Shetty, A. S.; Jenekhe, S. A. *Macromolecules* **1999**, *32* (22), 7422–7429. doi:10.1021/ma990960+.; (c) Jenekhe, S. A.; Lu, L.; Alam, M. M. *Macromolecules* **2001**, *34* (21), 7315–7324. doi:10.1021/ma0100448.

(3) (a) Friedlander, P. *Chem. Ber.* **1882**, *15*, 2572; (b) Cheng, C. C.; Yan, S. *J. Org. React.* **1982**, *28*, 37.

(4) Fehnel, E. A. *J. Heterocycl. Chem.* **1967**, *4* (4), 565–570. doi:10.1002/jhet.5570040417.

(5) (a) Strekowski, L.; Czamy, A. *J. Fluor. Chem.* **2000**, *104* (2), 281–284. doi:10.1016/S0022-1139(00)00252-9.; (b) Hu, Y. Z.; Zhang, G.; Thummel, R. P. *Org. Lett.* **2003**, *5* (13), 2251–2253. doi:10.1021/ol034559q. PMID:12816421.; (c) Arcadi, A.; Chiarini, M.; Di Giuseppe, S.; Marinelli, F. *Synlett* **2003**, (2): 0203–0206. doi:10.1055/s-2003-36798.; (d) McNaughton, B. R.; Miller, B. L. *Org. Lett.* **2003**, *5* (23), 4257–4259. doi:10.1021/ol035333q. PMID:14601974.; (e) Yadav, J. S.; Reddy, B. V.; Premalatha, K. *Synlett* **2004**, (6): 963–966. doi:10.1055/s-2004-822898.; (f) Yadav, J. S.; Reddy, B. V.; Sreedhar, P.; Rao, R. S.; Nagaiah, K. *Synthesis* **2004**, *2004* (14), 2381–2385. doi:10.1055/s-2004-831185.; (g) Mogilaiah, K.; Reddy, C. S. *Synth. Commun.* **2003**, *33* (18), 3131–3134. doi:10.1081/SCC-120023427.; (h) Desai, U. V.; Mitragotri, S. D.; Thopate, T. S.; Pore, D. M.; Wadganokar, P. P. *ARKIVOK* **2006**, *xv*, 198; (i) Atechian, S.; Nock, N.; Norcross, R. D.; Ratni, H.; Thomas, A. W.; Verron, J.; Masciadri, R. *Tetrahedron* **2007**, *63* (13), 2811–2823. doi:10.1016/j.tet.2007.01.050.; (j) Das, B.; Damodar, K.; Chowdhury, N.; Kumar, R. A. *J. Mol. Catal. A* **2007**, *274* (1-2), 148–152. doi:10.1016/j.molcata.2007.04.034.; (k) Jia, C.-S.; Zhang, Z.; Tu, S.-J.; Wang, G.-W. *Org. Biomol. Chem.* **2006**, *4* (1), 104–110. doi:10.1039/b513721g. PMID:16358003.; (l) Bose, D. S.; Kumar, R. K. *Tetrahedron Lett.* **2006**, *47* (5), 813–816. doi:10.1016/j.tetlet.2005.11.075.; (m) Wang, G.-W.; Jia, C.-S.; Dong, Y.-W. *Tetrahedron Lett.* **2006**, *47* (7), 1059–1063. doi:10.1016/j.tetlet.2005.12.053.;

(6) (a) Yadav, J. S.; Purushothama Rao, P.; Sreenu, D.; Rao, R. S.; Naveen Kumar, V.; Nagaiah, K.; Prasad, A. R. *Tetrahedron Lett.* **2005**, *46* (42), 7249–7253. doi:10.1016/j.tetlet.2005.08.042.; (b) Yadav, J. S.; Subba Reddy, B. V.; Sunitha, V.; Srinivasa Reddy, K.; Ramakrishna, K. V. S. *Tetrahedron Lett.* **2004**, *45* (42), 7947–7950. doi:10.1016/j.tetlet.2004.08.128.; (c) Ghassamipour, S.; Sardarian, A. R. *Tetrahedron Lett.* **2009**, *50* (5), 514–519. doi:10.1016/j.tetlet.2008.09.097.; (d) Muscia, G. C.; Bollini, M.; Carnevale, J. P.; Bruno, A. M.; Asis, S. E. *Tetrahedron Lett.* **2006**, *47* (50), 8811–8815. doi:10.1016/j.tetlet.2006.10.073.

(7) (a) Banerjee, A. K.; Laya, M. S.; Vera, W. J. *Russ. Chem. Rev.* **2001**, *70* (11), 971–990. doi:10.1070/RC2001v070n11ABEH000642.; (b) Sharghi, H.; Hosseini-Sarvari, M. *J. Chem. Res.* **2000**, 24.; (c) Sharghi, H.; Hosseini, M. *Synthesis* **2002**, *2002* (08), 1057–1060. doi:10.1055/s-2002-31964.; (d) Sharghi, H.; Hosseini-Sarvari, M. *Tetrahedron* **2002**, *58* (52), 10323–10328. doi:10.1016/S0040-4020(02)01417-5.; (e) Sharghi, H.; Hosseini-Sarvari, M. *J. Chem. Res. (s)* **2003**, *3*, 176; (f) Sarvari, M. H.; Sharghi, H. *J. Org. Chem.* **2004**, *69* (20), 6953–6956. doi:10.1021/jo0494477. PMID: 15387635.; (g) Hosseini-Sarvari, M. *Synthesis* **2005**, *2005* (05), 787–790. doi:10.1055/s-2005-861826.; (h) Hosseini-Sarvari, M.; Sharghi, H. *Tetrahedron* **2005**, *61* (46), 10903–10907. doi:10.1016/j.tet.2005.09.002.; (i) Hosseini-Sarvari, M.; Sharghi, H. *J. Org. Chem.* **2006**, *71* (17), 6652–6654. doi:10.1021/jo060847z. PMID:16901164.; (j) Hosseini-Sarvari, M.; Sharghi, H.; Etemad, S. *Chin. J. Chem.* **2007**, *25* (10), 1563–1567. doi:10.1002/cjoc.200790288.; (k) Hosseini-Sarvari, M. *Acta Chim. Slov.* **2007**, *54*, 345; (l) Hosseini-Sarvari, M.; Sharghi, H. *Phos. Silicon. Sulf.* **2007**, *182* (9), 2125–2130. doi:10.1080/10426500701372355.; (m) Hosseini-Sarvari, M. *Synth. Commun.* **2008**, *38* (6), 832–840. doi:10.1080/00397910701845274.;

(8) (a) Hosseini-Sarvari, M. *Can. J. Chem.* **2008**, *86* (1), 65–71. doi:10.1139/V07-135.; (b) Hosseini-Sarvari, M. *Tetrahedron* **2008**, *64* (23), 5459–5466. doi:10.1016/j.tet.2008.04.016.; (c) Hosseini-Sarvari, M.; Etemad, S. *Tetrahedron* **2008**, *64* (23), 5519–5523. doi:10.1016/j.tet.2008.03.095.; (d) Hosseini-Sarvari, M. *Act. Chim. Slov.* **2008**, 440; (e) Hosseini-Sarvari, M.; Sharghi, H.; Etemad, S. *Helv. Chim. Acta* **2008**, *91* (4), 715–724. doi:10.1002/hlca.200890072.

Rearrangement mechanisms for azoxypyridines and azoxypyridine *N*-oxides in the 100% H_2SO_4 region — The Wallach rearrangement story comes full circle[1]

Erwin Buncel, Sam-Rok Keum, Srinivasan Rajagopal, and Robin A. Cox

Abstract: Kinetic studies of the Wallach rearrangements of four azoxypyridines, four azoxypyridine *N*-oxides, and one azoxypyridine *N*-methiodide have been carried out in the 100% H_2SO_4 acidity region. For all of the β-isomers in the study the reactions proceeded at a spectrally measurable rate, and the log observed rate constants were found to be linear functions of the log $H_3SO_4^+$ concentration, as previously found for azoxybenzene itself, suggesting that the reaction mechanism for these substrates is the same as that previously deduced for axozybenzene, i.e., a general-acid-catalysis A-S_E2 process. For the α-azoxypyridines no reaction could be observed at all. The two α-azoxypyridine *N*-oxides in the study did react, albeit very slowly, but for these two compounds the log observed rate constants were not linear functions of the log $H_3SO_4^+$ concentration, but were instead found to be linear in the H_0 acidity function, which is known for the 100% H_2SO_4 acidity region. It follows that the reaction mechanism for these α-isomers is a different one, presumably an A1 process. This mechanism was proposed back in 1963 for azoxybenzene, but has never actually been observed for any substrate before the work reported in this study. Thus, the Wallach rearrangement story can be said to have come full circle.

Key words: azoxypyridines, azoxypyridine *N*-oxides, Wallach rearrangement, reactivities, mechanisms.

Résumé : Opérant dans la région d'acidité du H_2SO_4 à 100 %, on a effectué des études cinétiques sur les réarrangements de Wallach de quatre azoxypyridines, de quatre *N*-oxydes d'azoxypyridines et d'un *N*-méthiodure d'azoxypyridine. Pour tous les isomères β de l'étude, les réactions procèdent à des vitesses spectroscopiquement mesurables et on a trouvé que le log des constantes de vitesse observées sont linéaires avec le log de la concentration en $H_3SO_4^+$, tel qu'on l'avait observé antérieurement avec l'azoxybenzène lui-même, ce qui suggère que le mécanisme de la réaction pour ces substrats est le même que celui déduit antérieurement pour l'azoxybenzène, c'est-à-dire un processus de catalyse acide générale, A-S_E2. Pour les α-azoxypyridines, on n'a observé aucune réaction. Les deux *N*-oxydes de la α-azoxypyridne réagissent, mais la réaction est toutefois très lente et les log des constantes de vitesses de ces deux produits ne donnent pas de relation linéaire avec le log de la concentration en $H_3SO_4^+$; elles sont toutefois linéaires avec une fonction d'acidité H_0 qui est connue pour la réaction d'acidité du H_2SO_4 à 100 %. On peut donc en conclure que le mécanisme de la réaction pour les isomères α est différent, probablement un processus A1. Ce mécanisme avait déjà été proposé en 1963 pour l'azoxybenzène, mais il n'avait jamais été observé avec un substrat avant celui rapporté dans ce travail. On peut donc dire que l'histoire du réarrangement de Wallach a retrouvé son point de départ.

Mots-clés : azoxypyridines, *N*-oxydes d'azoxypyridines, réarrangement de Wallach, réactivités, mécanismes.

[Traduit par la Rédaction]

Introduction

Many of the kinetic and other studies of the Wallach rearrangement, discovered in 1880[2] and shown below for azoxybenzene **1**, have been extensively reviewed, along with other aromatic rearrangements.[3] Over the years, this reaction has proven to occupy a pivotal position in physical organic chemistry, providing unique insights into reaction mechanisms. For instance, it was the first reaction for which a general-acid-catalysis mechanism in strong aqueous acid media was proved to take place,[4,5] the possibility having been suggested previously.[6] Catalysis by the species H_2SO_4 and $H_3SO_4^+$ occurred in concentrated H_2SO_4, but not by $(H^+)_{aq}$ (or H_3O^+), which was found to be not a strong enough

Received 17 March 2009. Accepted 22 April 2009. Published on the NRC Research Press Web site at canjchem.nrc.ca on 20 July 2009.

Dedicated to the memory of Yvonne Chiang (Mrs. Jerry Kresge), wife, mother, fine chemist.

E. Buncel,[1] S.-R. Keum,[2,3] and S. Rajagopal. Department of Chemistry, Queen's University, Kingston, ON K7L 3N6, Canada.
R.A. Cox.[4] 16 Guild Hall Drive, Scarborough, ON M1R 3Z8, Canada.

[1]Corresponding author (e-mail: buncele@chem.queensu.ca).
[2]Corresponding author (e-mail: keum@korea.ac.kr).
[3]Present address: Korea University, Department of New Materials Chemistry, Jochiwon 339700, South Korea.
[4]Corresponding author (e-mail: robin.a.cox@sympatico.ca).

acid species to catalyze the reaction.[4] This was again shown to be the case, quite strikingly, when the reaction was found not to take place at all in $HClO_4$, a stronger acid than H_2SO_4 in H_0 terms, but containing no acidic species other than H_3O^+ and other $(H^+)_{aq}$.[7] Since that time, other general-acid-catalysis mechanisms have been found, for instance, in benzamide hydrolysis,[8] and others proposed[8] in concentrated aqueous acids.

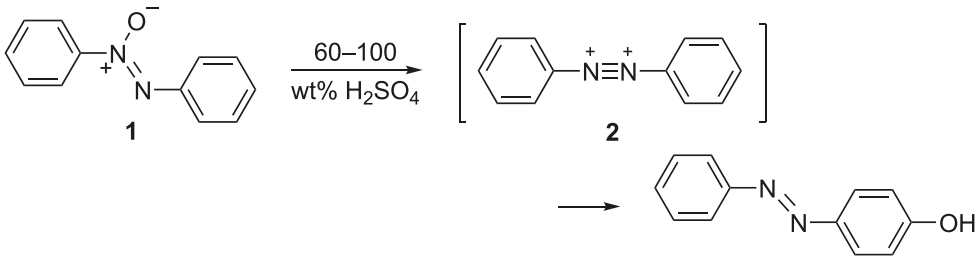

The first kinetic study of the reaction of azoxybenzene,[9,10] which we reported as early as 1963,[9] quantified the relationship between substrate protonation ($pK_{BH}^+ = -5.18$[11]) and rearrangement, and demonstrated the requirement for a second proton transfer;[10] the proposed mechanism involved the formation of a dicationic intermediate, which at the time we wrote as having the structure **2**.[9,10] However, recent accurate theoretical calculations on several dicationic intermediates shown to be present in various Wallach rearrangements[12] indicate that the structure is more accurately rendered as **3**, with the positive charges being almost entirely situated on the two rings, not on the nitrogens, which retain their lone pairs.[12] Dicationic intermediates can actually be observed as stable species in suitable superacid media.[13]

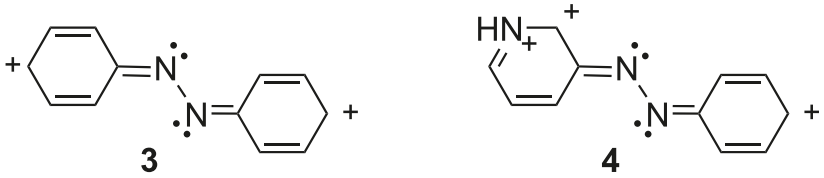

This prompted the question as to whether a tricationic species, for instance **4**, could be generated on going to heteroaromatic structures. (For clarity only one resonance form is given for **3** and for **4**.) We have found, using modern theoretical calculations, that the charge distributions in di- (or tri-) cationic intermediates like this can have dramatic effects on their reactivities,[11] and we developed a novel method of showing this by using the differences in charge distribution over the two halves of the species concerned.[11] The latter study used a series of azoxypyridines and azoxypyridine *N*-oxides. One of the observations that the calculation results helped to explain was the large reactivity difference found between α- and β-isomers of these molecules,[11,14] and this paper deals in detail with their kinetic behaviour; it happens that as well as the reaction rates being quite different, the reaction mechanisms are different as well. The compounds used in this study, **5**–**13**, are shown below, in the protonated forms, which are the true reactants,[11] the parent species being entirely monoprotonated under the reaction conditions used. (Except for **13**, the counteranions would be sulfate or bisulfate.) The α and β nomenclature is used here in preference to the formal NNO and ONN nomenclature, simply because of the convenience. The pK_{BH}^+ values for diprotonation of those molecules for which these could be measured have been given before.[11]

Experimental

We have reported the syntheses of **5**–**12** previously.[11,15] The methiodide **13** has also been reported;[15] in brief, it was obtained from **6** by methylation, refluxing **6** with a slight excess of methyl iodide for 5 h and recrystallizing the resulting red-brown crystals from ethanol. The acid solutions, in the 100% H_2SO_4 range, were prepared from 96% H_2SO_4 and fuming 30% oleum, and their concentrations determined accurately by conductivity measurements according to Gillespie and Wasif.[16] Reaction rates were determined spectrophotometrically by the "direct method".[10,11]

The 90%–100% H_2SO_4 acidity region is interesting and not particularly complex, the only species present being H_3O^+ (there is no free water), HSO_4^-, $H_3SO_4^+$, and undissociated H_2SO_4 molecules.[4] Accurate H_2SO_4 activities are available,[17] and with these and the value of $(7.8 \pm 1.7) \times 10^{-4}$ mol^2 l^{-2} given by Liler[18] for the best value for the autoprotolysis constant of H_2SO_4 at 25 °C (combined from several sources) it is possible to calculate the concentrations (although not the activities) of the species $H_3SO_4^+$ and HSO_4^- between 90% and 100% H_2SO_4 (at 25 °C). This was done. Above 100% H_2SO_4 the medium becomes much more complex, as $H_2S_2O_7$ and higher sulfur acids are formed, together with the ions resulting from their dissociation, and species concentrations cannot be calculated. However, acidity functions for these media are available;[19] the one used in this work is the one generally called H_0, measured at "room temperature" by Gillespie, Peel, and Robinson.[20] This scale was determined using the protonation equilibria of aromatic nitro compounds, which protonate on an oxygen of the nitro group, and was adjudged suitable to use in this work because of the similarity of the nitro compounds to the azoxy compounds used here. (The other acidity scale in these media, measured by Frederick and Poulter[21] and called H_A, uses protonated uracils and related compounds as indicators and was adjudged to be less suitable.)

All of the observed pseudo-first-order rate constants, k_ψ, at different sulfuric acid concentrations, some at 50 °C and some at 65 °C, obtained for **6** and for **8**–**13** are given as Supplementary data in Tables S1–S7, together with the H_0 values used and the values calculated for the $H_3SO_4^+$ concentrations. Rate constants at 25 °C were already available for **1**,[10,22] and no reaction could be observed for **5** or for **7**.

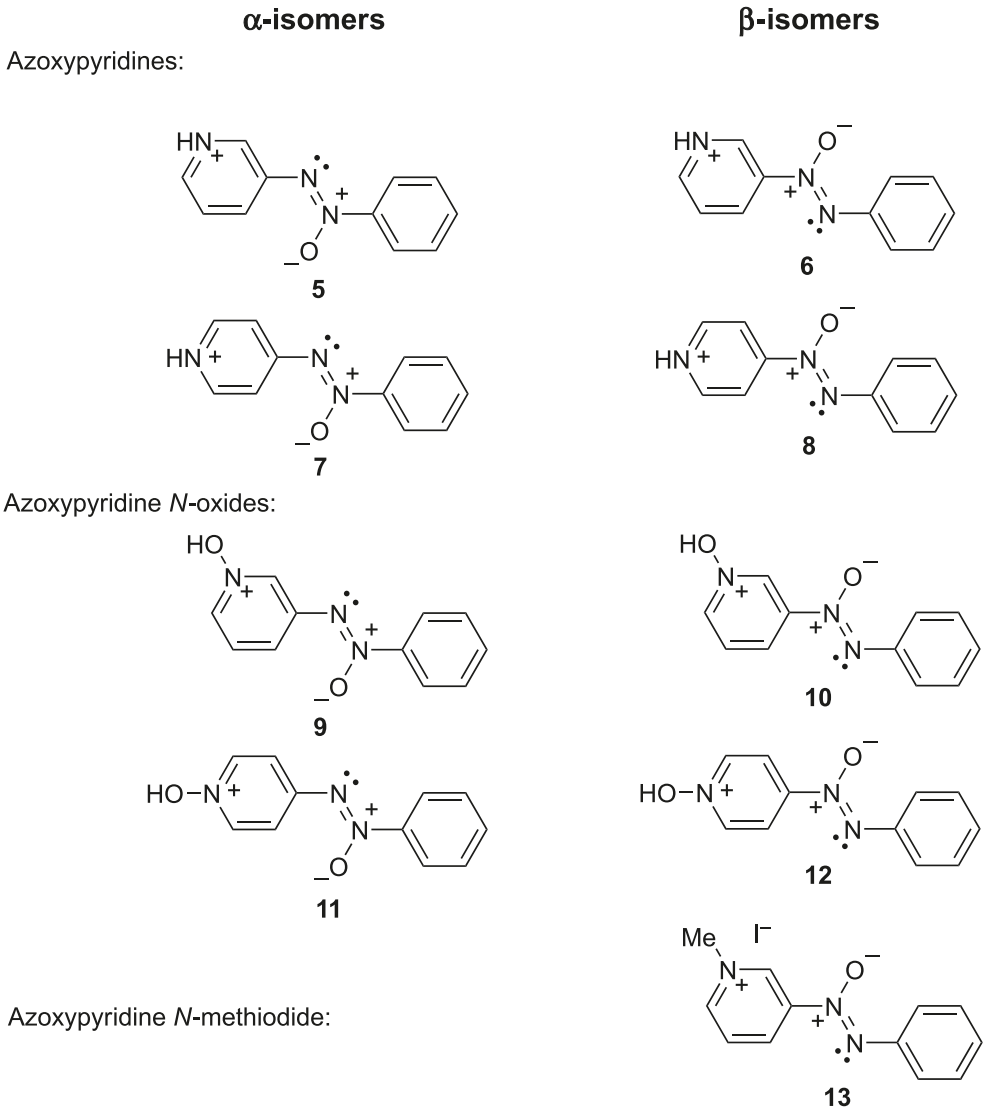

Results

Previously, we found that the log observed rate constants for **1** were a linear function of the log $H_3SO_4^+$ concentration at sulfuric acid concentrations between 90% and 100%,[4] and the same was also found to be true, at least under some circumstances, for hexamethylazoxybenzene[5] and some azoxynaphthalenes.[23] Shown in Fig. 1 are the log rate constants for azoxybenzene **1**[10,21] plotted against the log $H_3SO_4^+$ concentrations as recalculated for this work; as it can be seen, the linearity is excellent. For these data log rate constant plots against $-H_0$ are known to exhibit multiple curvature.[4]

It therefore seemed reasonable to plot the log rate constant results obtained in this work against the log $H_3SO_4^+$ concentrations in the same way. Dealing with the β-isomers first: Fig. 2 demonstrates the excellent linearity obtained for the azoxypyridines **6** and **8**, and Fig. 3 that obtained for the azoxypyridine *N*-oxide **12** at two temperatures; the results for **10** were very similar. For **10** and **12**, results at two temperatures were available; although both temperatures gave linear plots, the slopes were not the same, but we attach little significance to this as the rate data were obtained by two different workers at different times. There could be other reasons. The results for the *N*-methiodide **13** are shown in Fig. 4, which, as might be expected, exhibits very similar behaviour to that of **10**. It is shown in Fig. 5 that the observed log rate constants for **10** and **12** are in fact not linear in $-H_0$. The observed slopes, intercepts, etc. for the various correlations in this paper, many of which are shown in Figs. 1–4, are collected together in Table 1.

The α-isomers behaved differently, however; in fact, no reaction at all was observed for the azoxypyridines **5** and **7**. The azoxypyridine *N*-oxides **9** and **11** did react, but much more slowly than did the β-isomers under the same conditions. The log rate constants were not linear in the log

Fig. 1. Plot of log observed rate constants for **1** at 25 °C against the log $H_3SO_4^+$ concentration.

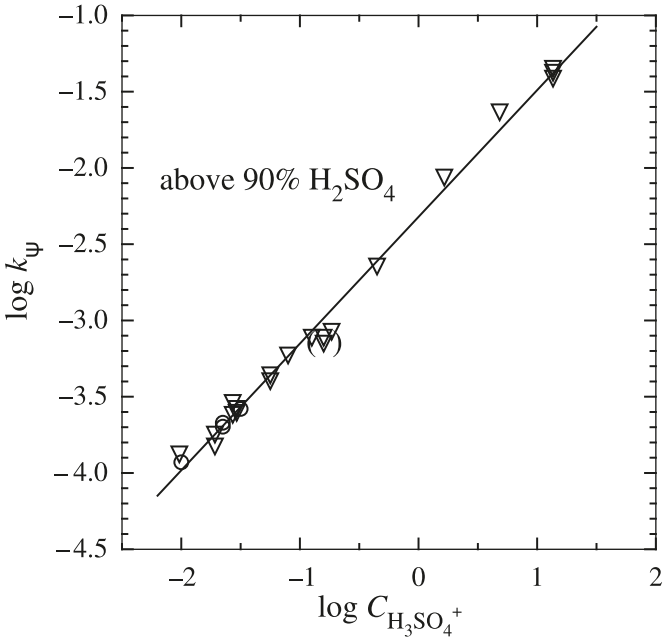

Fig. 2. Plot of the log observed rate constants for **6** and **8** at 50 °C against the log $H_3SO_4^+$ concentration.

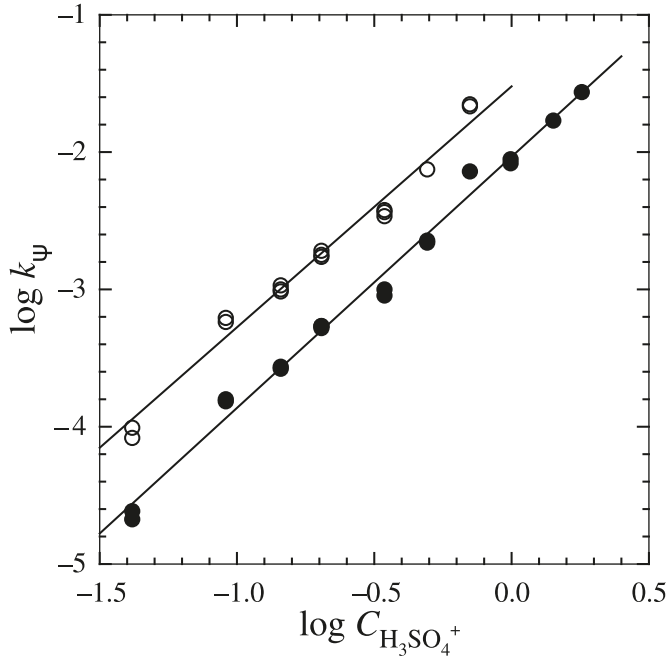

Fig. 3. Plot of the log observed rate constants for **12** at 50 °C (lower) and 65 °C (upper) against the log $H_3SO_4^+$ concentration.

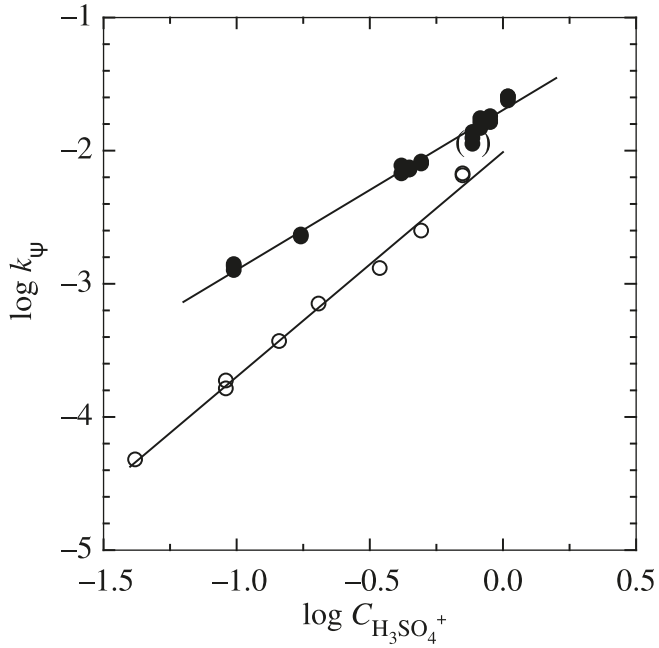

Fig. 4. Plot of the log observed rate constants for **13** at 50 °C against the log $H_3SO_4^+$ concentration.

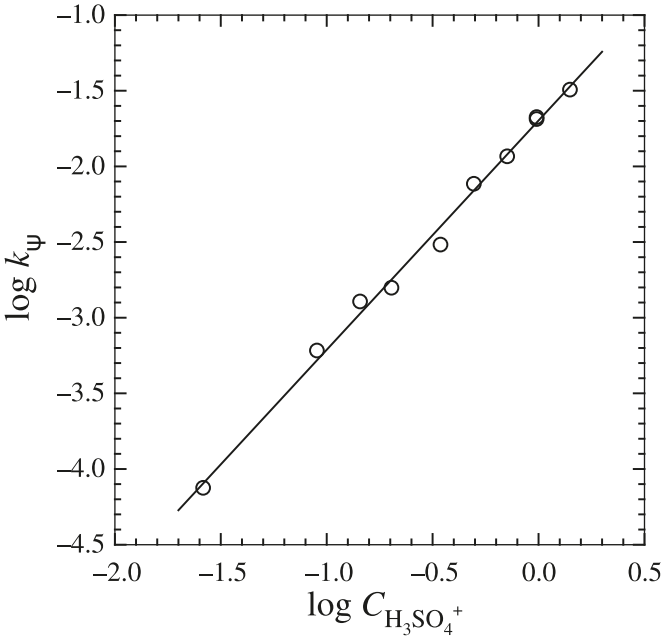

$H_3SO_4^+$ concentration, as is illustrated in Fig. 6, however, when the log rate constants for **9** and **11** were instead plotted against the $-H_0$ acidity function for this medium,[20] excellent linearity resulted, as can be seen from Fig. 7. The slopes, etc. of these plots are also given in Table 1.

Discussion

The excess acidity (*X*-function) method, developed for the study of the mechanisms of reactions in acid media,[17] has proved itself to be an excellent tool for this task.[17] However, it does not work well in the 90%–100% H_2SO_4 acidity range, primarily because an extrapolation to pure water is required, which is unrealistic here. It does not work at all above 99.5% H_2SO_4, as the *X*-function cannot be defined in this region,[17] and clearly extrapolating to pure water from oleum solutions, which contain no water at all, is not reasonable. Similarly, the Bunnett–Olsen[24] and Bunnett[25] methods, both of which require the water activity, cannot be used in media, which contain no free water either.

Therefore, in this acidity region it is more reasonable to ascertain whether the log rate constants can achieve linearity

Fig. 5. Plot of the log observed rate constants for **10** and **12** at 50 °C against $-H_0$, illustrating the lack of linearity in these plots for the β-isomers.

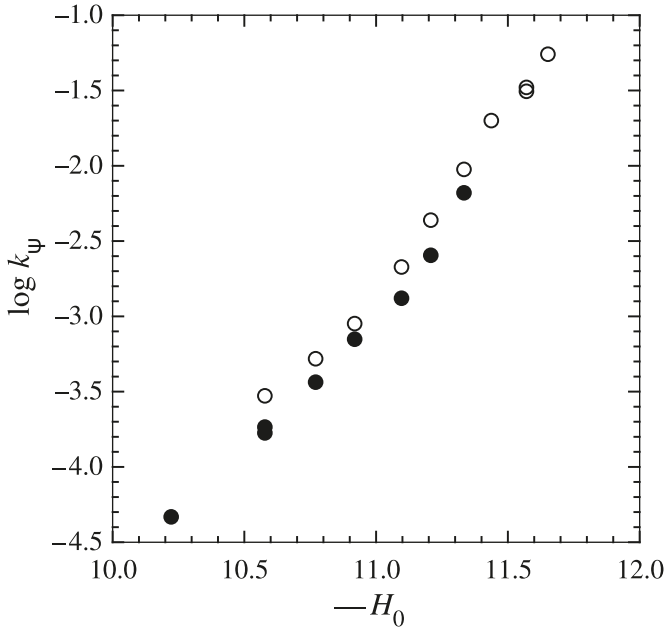

when plotted against known species activities or concentrations, or against a reliable acidity function.[26] The fact of linearity is what is actually important. The slopes and intercepts of these lines may not mean much, as there is little data with which to compare them, but at least some meaning can be attached to the relative values. As mentioned above, 90%–100% aqueous sulfuric acid is not a particularly complex medium, only four species being present, H_3O^+, HSO_4^-, $H_3SO_4^+$, and H_2SO_4, and the concentrations of all of them can be calculated.

Much previous work[3–5] has led to the conclusion that azoxybenzene itself reacts with undissociated H_2SO_4 molecules in sulfuric acid, which is more dilute than 90%, and with $H_3SO_4^+$ at higher concentrations. The reaction scheme has been given recently[11] and need not be repeated here. The linearity against log $C_{H_2SO_4^+}$ also found for all of the β-isomers in this study strongly suggests the same mechanism applies to them. The azoxybenzene mechanism, modified so as to apply to **6**, is given here as Scheme 1; the same Scheme 1 (with suitable atom arrangements) also applies to **8**, **10**, **12**, and **13**.

The α-isomers, however, behave differently; no reaction could be observed at all for **5** and **7**, while for **9** and **11** the log rate constants are not linear functions of log $C_{H_2SO_4^+}$, but are instead linear in $-H_0$ (see Figs. 6 and 7). Linearity in different acidity functions has long been attributed to the A1 and A-S_E2 reaction mechanisms;[17,18,26] this is part of the original Zucker–Hammett hypothesis.[27] We have just ruled out an A-S_E2 process for this reaction, leaving an A1 reaction as the only possibility. A likely reaction scheme for this process is given for **9** in Scheme 2. (In Schemes 1 and 2 the proton in dilute acid media is written as having the form $H^+(H_2O)_n$, as this is the most likely situation applying there.[8])

The reaction mechanism shown in Scheme 2 is in fact analogous to one proposed for azoxybenzene **1** itself as far back as 1963,[9,10] but never actually observed in practice for any substrate until now. A second protonation of the monoprotonated substrate **9**, $pK_{SH^+} = -10.49$,[11] occurs first. Following this, the (third) proton transfer to the azoxy OH group, giving **14**, is a pre-equilibrium process, rather than being concerted with water loss and di- (actually tri-) cationic intermediate formation as in Scheme 1, and the actual rate-determining step is loss of water to give the intermediate as shown in Scheme 2. (In Scheme 2, no attempt is made to show the full electron flow from **14** to the intermediate, as this would look confusing.) The actual concentration of the triprotonated precursor must be vanishingly small, even at these acidities, and the formation of the intermediate from it is an uphill process, as we found when we calculated the charge distributions in these species,[11] and so the reaction is very slow. Once the intermediate is formed it will react with almost anything nucleophilic very quickly, probably a bisulfate ion at these acidities, as shown. The difference from the β-isomers is that, for these, intermediate formation is downhill in energy,[11] and so it can be concerted with the third proton transfer.

The information in Table 1 is useful for internal comparisons of the reactions of **1** and **5**–**13**, but very few other correlations of this type are available for other reactions, and so other comparisons are difficult; for instance, the similar reaction found in the hydrolysis of benzamides at high acidity involves $(H^+)_{aq}$ as the catalyzing acid, not $H_3SO_4^+$.[8] We can make no reliable use of the information obtained at different temperatures for two reasons: (*i*) because the log rate constant data, obtained at 50 °C or at 65 °C, is plotted as functions of $H_3SO_4^+$ concentrations calculated at 25 °C (or an acidity function measured at room temperature); and (*ii*) there is no reliable "acidity" at which to calculate them, since any value will also have variations due to different species concentrations built into it (for instance, we cannot extrapolate to "pure water", as we can when using the excess acidity method[17]).

Having said that, there are some conclusions to draw from the information in Table 1. The intercept values for **10** and the corresponding methiodide **13** are about the same, as would be expected. The β-3-isomers react consistently faster than do the β-4-isomers, by about 0.3 of a log unit. The β-4-isomers **8** and **12** react at the same rate, whereas the azoxypyridine **6** reacts slightly faster than does the azoxypyridine *N*-oxide **10**. Little difference seems apparent between the axoxypyridines and the azoxypyridine *N*-oxides. Most of the differences can be explained by considering the charge separation in the various reaction intermediates, and we have already done this.[11] Little difference is apparent between the intercepts for the α-isomers **9** and **11**. Some comments can be made about the slopes listed in Table 1: it seems that the reaction temperature may have a large effect on them, looking at the differences between the 50 °C and 65 °C results for **10** and **12**, but unfortunately, they are in opposite directions for these two; however, the slope for **1** at 25 °C is much smaller than all of the other slopes. The behaviour of the α-isomers **9** and **11** seem much the same as one another.

Table 1. Slopes, intercepts, etc. for the observed log rate correlations for **1**, **6**, and **8**–**13**.

Substrate	T (°C)	Slope	Intercept	r^a	N^b	$\pm\sigma^c$
Against log $C_{H_3SO_4^+}$						
1 (see Fig. 1)	25	0.831±0.013	–2.321±0.018	0.997	25(1)	0.066
5			No reaction			
6 (see Fig. 2)	50	1.755±0.063	–1.521±0.051	0.990	18	0.099
7			No reaction			
8 (see Fig. 2)	50	1.829±0.041	–2.034±0.028	0.995	21	0.091
10	50	1.806±0.035	–1.754±0.019	0.998	13(1)	0.054
10	65	2.44±0.19	–1.413±0.043	0.954	18	0.095
12 (see Fig. 3)	50	1.687±0.057	–2.011±0.044	0.995	10	0.072
12 (see Fig. 3)	65	1.201±0.024	–1.695±0.012	0.995	27(1)	0.041
13 (see Fig. 4)	50	1.515±0.039	–1.697±0.028	0.997	10	0.065
Against $-H_0$						
9 (see Fig. 6)	65	2.587±0.070	–35.72±0.83	0.994	18	0.11
11 (See Fig. 6)	65	2.34±0.12	–32.3±1.4	0.986	12	0.12

Note: Errors given are standard deviations.

[a]Correlation coefficient.

[b]Number of points. Any rejected by the program used as being off the line, to 95% confidence, are in parentheses here and in the figures.[17]

[c]Root-mean-square deviation between experimental and fitted points.

Fig. 6. Plot of the log observed rate constants for **9** and **11** at 65 °C against the log $H_3SO_4^+$ concentration, illustrating the lack of linearity in these plots for the α-isomers.

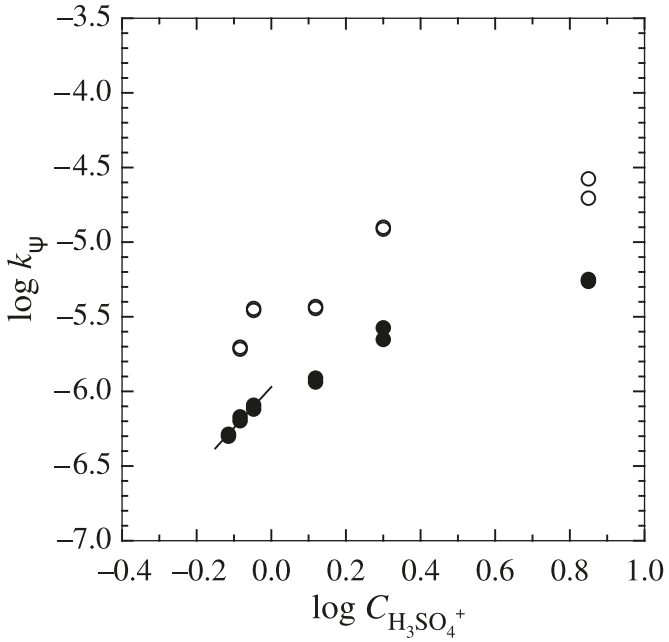

Fig. 7. Plot of the log observed rate constants for **9** and **11** at 65 °C against $-H_0$.

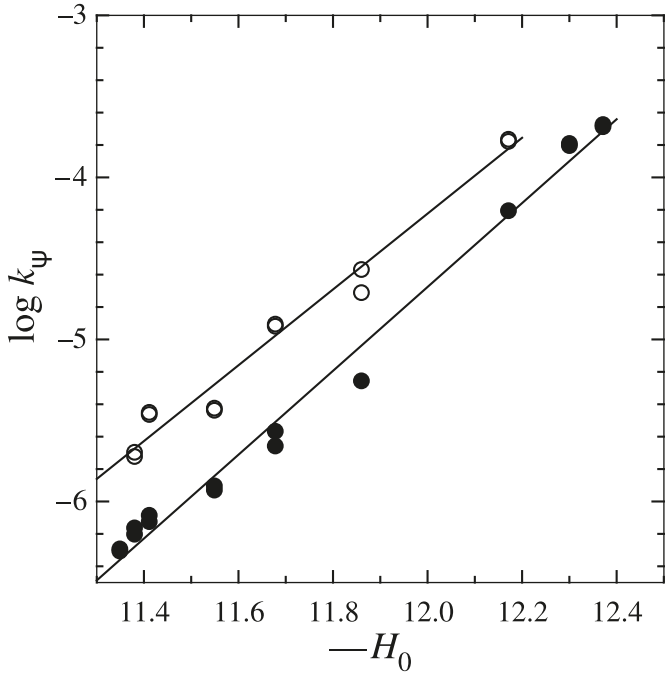

General conclusions

Having delineated the various possible Wallach rearrangement mechanisms in the 100% H_2SO_4 region, it is of interest that in more dilute acid media another reaction mechanism is possible, proceeding via the monoprotonated species,[5,23] but only for those azoxy compounds in which the intermediate species can be stabilized in some way. For instance, by the retention of full aromaticity in one of the aromatic rings of several azoxynaphthalenes.[23] If formation of one of these is not possible, the general-acid-catalysis mechanism of **1** is followed,[23] thus completing the spectrum of Wallach rearrangement mechanisms resulting from structural changes, as one traverses the H_2SO_4 acidity region from dilute to moderately concentrated to highly concentrated and oleum media. Moreover, analogies between the Wallach and benzidine rearrangements are apparent,[28] such as two possible mechanisms also being possible in this case, involving mono- and di-cationic reaction pathways.[29]

This whole class of azo and azoxy compounds and the reactions they undergo have contributed much to our understanding of physical organic chemistry. For instance, we have found that there are two different pathways for the

Scheme 1.

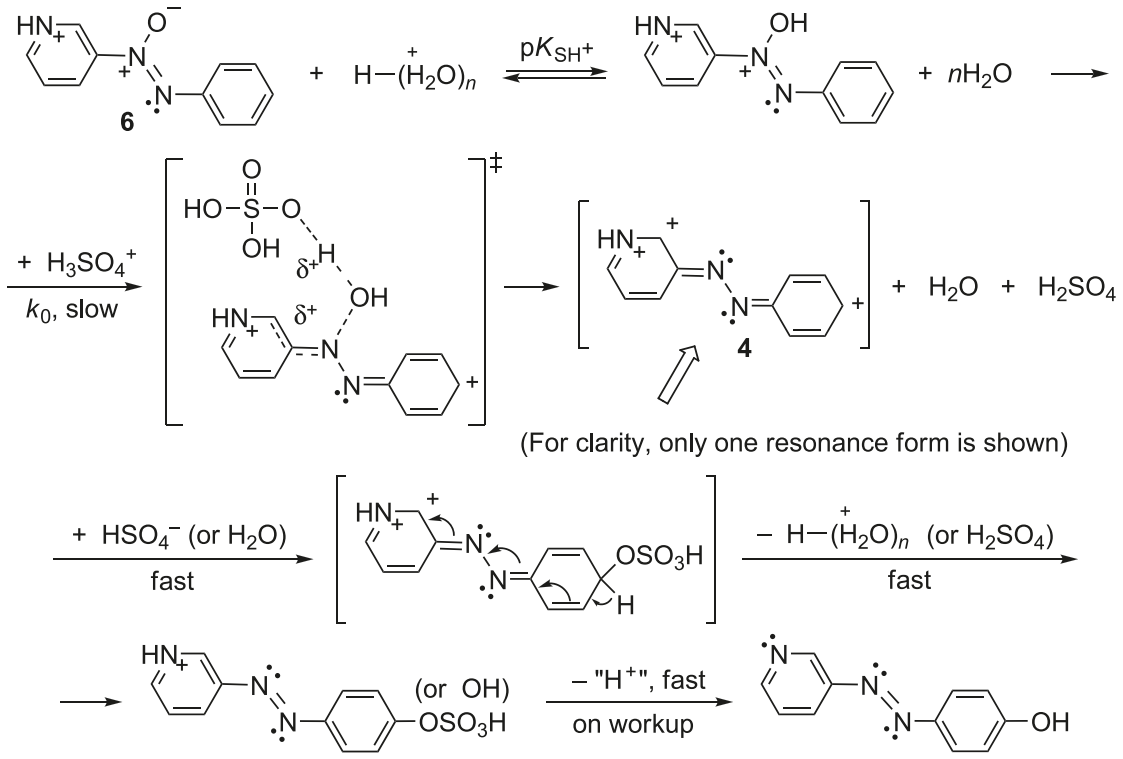

Scheme 2.

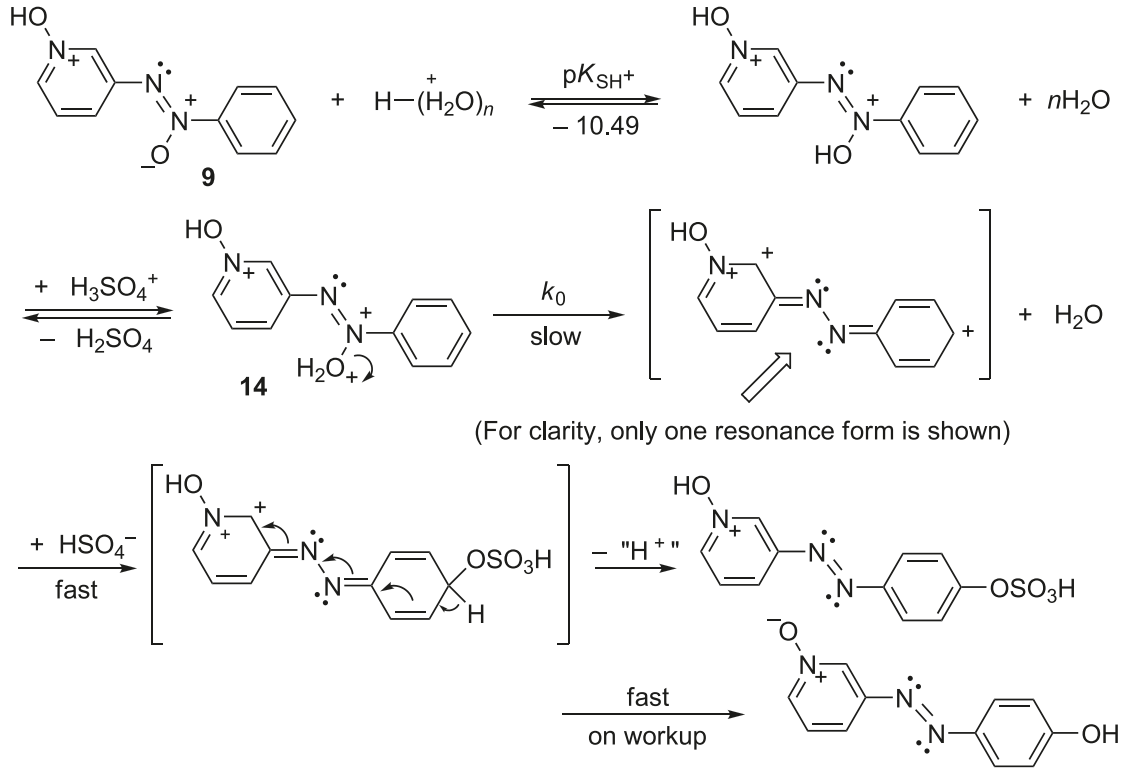

acid hydrolysis of the two methoxy groups in 4-[(3,4-dimethoxyphenyl)azo]pyridine,[30] and an excess acidity analysis of the acid-catalyzed aryl hydroxylation of phenylazopyridines showed that the reaction was an A2 process with nucleophilic attack of HSO_4^- or H_2O on the diprotonated substrate in the slow step.[31]

More generally, studies of the heteroaromatic azoxyarene series led to the examination of the solvatochromic behaviour of hydroxyazo products and their analogs, and the establishment of the π^*_{azo} solvent polarity scale.[32] More recently, we have been studying azo moieties as optical transducers, through light absorption, energy transfer, and

cis/trans isomerism, for molecular photo switching.[33] This continues to be a very fruitful area of research.

Supplementary data

Supplementary data for this article are available on the journal Web site (canjchem.nrc.ca) or may be purchased from the Depository of Unpublished Data, Document Delivery, CISTI, National Research Council Canada, Ottawa, ON K1A 0R6, Canada. DUD 3970. For more information on obtaining material, refer to cisti-icist.nrc-cnrc.gc.ca/cms/unpub_e.shtml.

Acknowledgments

Financial support of this research through a grant by the Natural Sciences and Engineering Research Council of Canada to EB, and from Queen's University via teaching assistantships (to S-RK and SR) is gratefully acknowledged.

References

(1) Part 28 of the series "Studies of azo and azoxy dyestuffs" of which Part 27 is ref. 11.
(2) Wallach, O.; Belli, E. *Chem. Ber.* **1880**, *13* (1), 525–527.
(3) (a) Shine, H. J. *Aromatic rearrangements*; Elsevier: New York, 1967; (b) Buncel, E. *Mechanisms of molecular migrations*; Thyagarajan, B. S., Ed. Wiley: New York, 1968; Vol. 1, pp 61–119; (c) Buncel, E. *Acc. Chem. Res.* **1975**, *8* (4), 132–139. doi:10.1021/ar50088a004.; (d) Cox, R. A.; Buncel, E. *The chemistry of the hydrazo, azo, and azoxy groups*; Patai, S., Ed. Wiley: London, 1975; Vol. 1, pp 775–859; (e) Cox, R. A.; Buncel, E. *The chemistry of the hydrazo, azo, and azoxy groups*; Patai, S., Ed. Wiley: London, 1997; Vol. 2, pp 569–602.
(4) Cox, R. A. *J. Am. Chem. Soc.* **1974**, *96* (4), 1059–1063. doi:10.1021/ja00811a018.
(5) Cox, R. A.; Buncel, E. *J. Am. Chem. Soc.* **1975**, *97* (7), 1871–1875. doi:10.1021/ja00840a045.
(6) (a) Kresge, A. J.; Hakka, L. E.; Mylonakis, S. G.; Sato, Y. *Discuss. Faraday Soc.* **1965**, *39*, 75–83. doi:10.1039/df9653900075.; (b) Kresge, A. J.; Chiang, Y.; Fitzgerald, P. H.; McDonald, R. S.; Schmid, G. H. *J. Am. Chem. Soc.* **1971**, *93* (19), 4907–4908. doi:10.1021/ja00748a043.
(7) Bolduc, R.; Buncel, E.; Cox, R. A.; Kitzul, R. B. Unpublished results quoted in ref. 2d.
(8) Cox, R. A. *Can. J. Chem.* **2008**, *86* (4), 290–297. doi:10.1139/V08-015.
(9) Buncel, E.; Lawton, B. T. *Chem. Ind. (London)* **1963**, 1835.
(10) Buncel, E.; Lawton, B. T. *Can. J. Chem.* **1965**, *43* (4), 862–875. doi:10.1139/v65-113.
(11) Buncel, E.; Keum, S.-R.; Rajagopal, S.; Kiepek, E.; Cox, R. A. *Can. J. Chem.* **2008**, *86* (4), 298–304. doi:10.1139/V08-016.
(12) Cox, R. A.; Fung, D. Y. K.; Csizmadia, I. G.; Buncel, E. *Can. J. Chem.* **2003**, *81* (6), 535–541. doi:10.1139/v03-049.
(13) Olah, G. A.; Dunne, K.; Kelly, D. P.; Mo, Y. K. *J. Am. Chem. Soc.* **1972**, *94* (21), 7438–7447. doi:10.1021/ja00776a029.
(14) Buncel, E.; Keum, S.-R. *J. Chem. Soc. Chem. Commun.* **1983**, 578–579. doi:10.1039/c39830000578.
(15) Buncel, E.; Keum, S.-R.; Cygler, M.; Varughese, K. I.; Birnbaum, G. I. *Can. J. Chem.* **1984**, *62* (8), 1628–1639. doi:10.1139/v84-280.
(16) Gillespie, R. J.; Wasif, S. *J. Chem. Soc.* **1953**, 215–221.
(17) Cox, R. A. *Adv. Phys. Org. Chem.* **2000**, *35*, 1–66. doi:10.1016/S0065-3160(00)35011-0.
(18) Liler, M. *Reaction mechanisms in sulfuric acid*; Academic Press: New York, 1971; p 79.
(19) Cox, R. A.; Yates, K. *Can. J. Chem.* **1983**, *61* (10), 2225–2243. doi:10.1139/v83-388.
(20) Gillespie, R. J.; Peel, T. E.; Robinson, E. A. *J. Am. Chem. Soc.* **1971**, *93* (20), 5083–5087. doi:10.1021/ja00749a021.
(21) Frederick, G. D.; Poulter, C. D. *J. Am. Chem. Soc.* **1975**, *97* (7), 1797–1801. doi:10.1021/ja00840a031.
(22) Buncel, E.; Strachan, W. M. J. *Can. J. Chem.* **1970**, *48* (2), 377–382. doi:10.1139/v70-055.
(23) Cox, R. A.; Dolenko, A. J.; Buncel, E. *J. Chem. Soc. Perkin Trans. 2* **1975**, 471.
(24) Bunnett, J. F.; Olsen, F. P. *Can. J. Chem.* **1966**, *44* (16), 1917–1931.
(25) Bunnett, J. F. *J. Am. Chem. Soc.* **1961**, *83* (24), 4973–4977. doi:10.1021/ja01485a021.
(26) Rochester, C. H. *Acidity functions*; Academic Press: New York, 1970.
(27) Zucker, L.; Hammett, L. P. *J. Am. Chem. Soc.* **1939**, *61* (10), 2791–2798. doi:10.1021/ja01265a067.
(28) Buncel, E. *Can. J. Chem.* **2000**, *78* (10), 1251–1271. doi:10.1139/cjc-78-10-1251.
(29) Banthorpe, D. V.; Hughes, E. D.; Ingold, C. K. *J. Chem. Soc.* **1964**, 2864–2901. doi:10.1039/jr9640002864.
(30) Cox, R. A.; Onyido, I.; Buncel, E. *J. Am. Chem. Soc.* **1992**, *114* (4), 1358–1363. doi:10.1021/ja00030a034.
(31) Cheon, K.-S.; Cox, R. A.; Keum, S.-R.; Buncel, E. *J. Chem. Soc. Perkin Trans. 2* **1998**, 1231.
(32) Buncel, E.; Rajagopal, S. *J. Org. Chem.* **1989**, *54* (4), 798–809. doi:10.1021/jo00265a017.
(33) (a) Abdallah, D.; Ghani, M. A. A.; Cunningham, M. F.; Kazmaier, P. M.; Keoshkerian, B.; Buncel, E. *Can. J. Chem.* **2004**, *82* (9), 1393–1402. doi:10.1139/v04-107.; (b) Ghani, M. A. A.; Abdallah, D.; Kazmaier, P. M.; Keoshkerian, B.; Buncel, E. *Can. J. Chem.* **2004**, *82* (9), 1403–1412. doi:10.1139/v04-106.

Studies on chemo- and diastereo-selectivity of the Diels–Alder reactions of sulfinyltoluquinones with cyclopentadiene

Andrea L. F. de Sousa, José E. P. Cardoso Filho, Blanka Wladislaw, Liliana Marzorati, and Claudio Di Vitta

Abstract: Sulfinyltoluquinones (**2a**–**2c**) were submitted to thermal or catalyzed [4+2] cycloaddition reactions with cyclopentadiene. For *p*-tolylsulfinyltoluquinones (**2b**) and (**2c**), almost complete C2–C3-chemo- and *unlike*-diastereoselectivity was achieved by catalysis with $ZnBr_2$, yielding adducts **6**. Under thermal conditions, Diels–Alder reaction took place at the C5–C6 double bonds of quinones **2a**–**2c**, generating mixtures of diastereoisomeric *like*- and *unlike*-adducts **4**.

Key words: Diels–Alder reaction, sulfinyltoluquinones, sulfinyl group, stereochemical control, π-facial selectivity.

Résumé : On a soumis les sulfinyltoluquinones (**2a**–**2c**) à des réactions de cycloaddition thermiques ou catalysées avec le cyclopentadiène. Avec le $ZnBr_2$ comme catalyseur, les *p*-tolylsulfinyltoluquinones (**2b**) et (**2c**) conduisent à la formation des adduits **6** et la diastéréosélectivité chimique et dissemblable au niveau de la liaison C2–C3 est pratiquement complète. Dans des conditions thermiques, la réaction de Diels–Alder se produit au niveau des doubles liaisons C5–C6 des quinones **2a**–**2c** qui conduit à la formation d'adduits **4** sous la forme de mélanges diastéréomères semblables et dissemblables.

Mots-clés : réaction de Diels–Alder, sulfinyltoluquinones, groupe sulfinyle, contrôle stéréochimique, sélectivité de la face π.

[Traduit par la Rédaction]

Introduction

The Diels–Alder (DA) reaction remains as one of the most powerful methods for the construction of cyclic systems with potential for stereochemical control of up to four stereogenic centers in only one step.[1,2] Many natural products like steroids,[3] alkaloids,[4] and terpenoids,[5] among others,[6] were synthesized by using quinones as dienophiles. However, due to the lack of π-facial selectivity, during the cycloaddition step, many of the above-mentioned syntheses proceeded in a racemic way. Only by the intervention of chiral enantiopure dienes[7] or quinones,[8] or by employing chiral Lewis acids or catalysts,[9,10] it was possible to conduct asymmetric DA reactions leading to enantiopure or enantioenriched adducts. Although resolution steps after the DA reaction may also be applied, the loss of material, intrinsically associated to the resolution process, limits its synthetic usefulness.

Recently, we became interested in an alternative synthesis of the enantiomerically pure adducts **1** (Fig. 1). It should be mentioned that (+)-**1a** was prepared by Corey et al.[10] to be used as precursors of natural products like (+)-hirsutene, (–)-corioline, pleurotellol, and pleurotellic acid via the photothermal olefinic metathesis methodology (PTOM).[5b,5d,5h]

Received 12 November 2008. Accepted 15 April 2009. Published on the NRC Research Press Web site at canjchem.nrc.ca on 27 July 2009.

A.L.F. de Sousa, J.E.P. Cardoso Filho, B. Wladislaw, L. Marzorati, and C. Di Vitta.[1] Instituto de Química da Universidade de São Paulo, Av. Prof. Lineu Prestes 748, Cidade Universitária, São Paulo SP 05508 900, Brazil.

[1]Corresponding author (e-mail: cldvitta@iq.usp.br).

Considering the ability of the sulfinyl group to control the chemo- and π-facial diastereoselectivity in DA reactions,[11] especially in the case of benzoquinones acting as dienophiles, the synthesis of adducts (+)- or (–)-**1** by π-facial discrimination of enantiopure sulfinyltoluquinones (**2a**–**2c**) (Fig. 2) seemed quite feasible to us.

Only two reports were found in the literature for the DA reactions of sulfinylbenzoquinones (**3**), bearing a group different from hydrogen at C3.[12,13] Carreño and Ruano[12] reported a complete chemoselectivity but a moderate π-facial diastereoselectivity (40%–60% de under catalytic conditions vs. 0% de under thermal conditions) for the DA reaction of cyclopentadiene with benzoquinones (+)-(*SS*)-**3** (X = Cl) and (+)-(*SS*)-**3** (X = Et) with exclusive formation of cycloadducts by reaction at the C5–C6 double bond. Better results were obtained when 2,3-dimethyl-1,3-butadiene was employed (40%–72% de under catalytic conditions vs. 20%–34% de under thermal conditions). Similar π-facial diastereoselectivity but complete reversal of chemoselectivity was observed for the thermal DA reaction of (+)-(*SS*)-**3** (X = CN)[13] (at C2–C3; 0% de for cyclopentadiene and 58%–84% de for 1-methoxy-1,3-butadiene).

Results and discussion

To evaluate the chemo- and diastereo-selectivity of toluquinones, (±)-**2b** and (±)-**2c** (R = *p*Tol, *i*Pr, and *i*Bu) were prepared by addition of the corresponding thiols to the 2,6- and 2,5-dimethylbenzoquinones,[14] respectively, followed by subsequent oxidation at sulfur with H_2O_2/SeO_2,[15] and of the aromatic ring with CAN.[12] As for the synthesis of quinone **2a**, although the analogous compound (+)-**3** (X = Et) could be obtained by the reaction[12] of (+)-**3** (X = H) with $Zn(Et)_2$,

Fig. 1. Diels–Alder adducts between toluquinones and cyclic dienes.

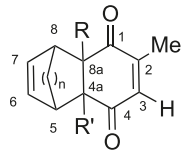

1

(**a**) R = H, R' = Me, for *n* = 1
(**b**) R = Me, R' = H, for *n* = 1
(**c**) R = R' = H, for *n* = 2

Fig. 2. Sulfinyltoluquinones prepared by our group (**2**) and by Carreño and Ruano[12,13] (**3**; X = Cl, Et, and CN).

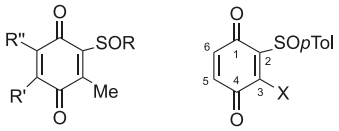

2 **3**

(**a**) R = *p*Tol, R' = R'' = H
(**b**) R = *p*Tol, R' = Me; R'' = H
(**c**) R = *p*Tol, *i*Pr or *i*Bu, R' = H; R'' = Me

Scheme 1. Synthesis of toluquinone (+)-(*SS*)-**2a**.

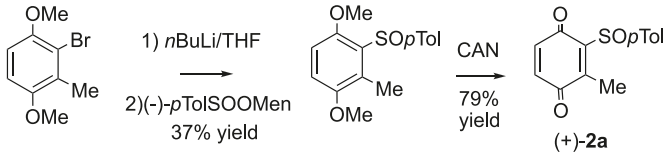

Scheme 2. Diels–Alder adducts formed by attack of cyclopentadiene to both sides of C5–C6 double bond of (+)-(*SS*)-**2a**.

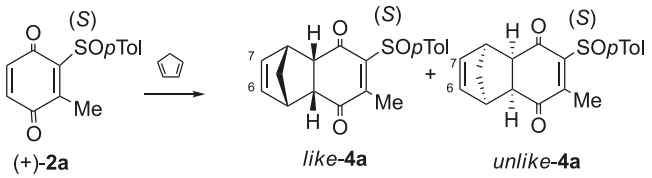

(+)-**2a** *like*-**4a** *unlike*-**4a**

Fig. 3. Representation of the *s-cis* conformation between the S–O and C2–C3 bonds for adducts (+)-**5**.

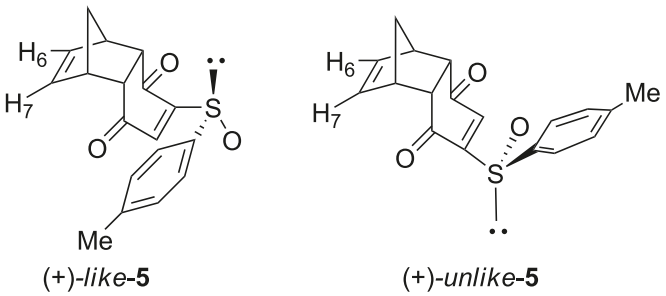

(+)-*like*-**5** (+)-*unlike*-**5**

Scheme 3. Diels–Alder adducts formed by attack of cyclopentadiene to both sides of C5–C6 double bonds of racemic toluquinones **2b** and **2c**, considering only the (*SS*) isomers.

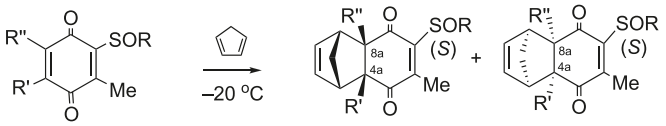

(±)-**2b** (R = pTol; R' = Me; R'' = H) (±)-*like*-**4b** (1) : (±)-*unlike*-**4b** (1)
(±)-**2c** (R = pTol; R' = H; R'' = Me) (±)-*like*-**4c** (4) : (±)-*unlike*-**4c** (1)

the same precursor proved to be unreactive toward $Zn(Me)_2$. In a search for an alternative methodology, we tried the reaction of 2-bromo-1,4-dimethoxy-3-methylbenzene[16] with *n*BuLi, followed by the quenching of the lithiated aromatic compound with methyl *p*-toluenesulfinate. However, better yields (37%) of sulfinylated product were obtained by using (*SS*)-menthyl *p*-toluenesulfinate as sulfinylating agent. After subsequent oxidation of the obtained aromatic compound with CAN, quinone (+)-**2a** was isolated in 79% yield (Scheme 1).

Due to the deactivating effect of the methyl group on the C2–C3 double bond of (+)-**2a**, its chemoselective DA reaction with cyclopentadiene yielded an inseparable mixture of adducts *like*-**4a**[17] and *unlike*-**4a**, resulting from the approach of the diene to each side of the C5–C6 double bond (Scheme 2).

Evidence for the formation of such isomeric adducts was provided by the inspection of the ^{1}H NMR spectrum of the reaction crude mixture, which revealed, for the absorptions of the norbornenyl hydrogens, only two clusters: one, at 6.07, and the other, centered at 5.71 ppm (composed by two separated multiplets at 5.89 and 5.53 ppm), suggesting the absence of adducts arising from the cycloaddition at the C2–C3 double bond of the quinone. A 1.3:1 integral ratio was obtained for the olefinic clusters in favor of signals at 6.07 ppm.

It should be mentioned that a different result was reported by Carreño et al.[18] for the analogous DA reaction performed using (+)-(*SS*)-**3** (X = H). In that case, the H6/H7 lower field signals (6.13 vs 5.85/4.82 ppm) corresponded to the less abundant isomer. According to the authors, for the major isomer ((+)-*like*-**5**; Fig. 3) the S–O and the C2–C3 bonds would lie in an *s-cis*-favored conformation, in which the *p*-tolyl ring would shield the H6/H7 protons. Such effect would be absent in the other isomer ((+)-*unlike*-**5**[18]), which would be formed by cycloaddition to the C5–C6 top (*re*) face of the (+)-(*SS*)-**3** (X = H).

When (±)-**2b** was treated with cyclopentadiene, under the same conditions (Scheme 3), a mixture of two adducts was obtained, as evidenced by the ^{1}H NMR spectra of the crude mixture, which presented only two pairs of signals in the olefinic region. Additionally, two doublets, at 2.77 and 2.92 ppm (J = 3.9 Hz), attributed to H8a of the (±)-*like*-**4b** and (±)-*unlike*-**4b** adducts (Scheme 3), respectively, were also observed, indicating that *endo*-cycloadditions took place chemoselectively at both sides of the C5–C6 double bond. For this mixture, a 1:1 ratio for the isomeric (±)-**4b** adducts could be determined by integration of the absorptions, at 6.06/6.02 and at 5.96/5.56 ppm. However, for toluquinone (±)-**2c** (R = *p*Tol) (Scheme 3), a 4:1 mixture of adducts was obtained. Accordingly, in this case, signals at lower field (6.14/6.01 ppm) were attributed to H6/H7 of the most abundant (±)-*like*-**4c** (R = *p*Tol), and those at 5.82/5.67 ppm were attributed to the (±)-*unlike*-**4c** (R = *p*Tol) isomer.

Fig. 4. Representation of the *s-trans* conformation between the S–O and C2–C3 bonds for adducts *unlike*-**4**.

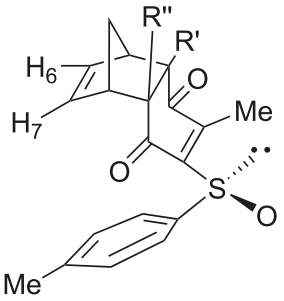

unlike-**4**

Thermal DA reactions of cyclopentadiene with sulfinyltoluquinones **2c** (R = *i*Pr) and **2c** (R = *i*Bu) yielded mixtures of adducts for which the most abundant isomers (ratios: 2.3 to 1, for R = *i*Pr; 4 to 1, for R = *i*Bu) presented H6/H7 absorptions at 6.04/6.21 ppm for R = *i*Pr and at 6.04/6.23 ppm for R = *i*Bu. For the minor isomers, the corresponding H6/H7 signals were observed at 6.04/6.13 ppm (R = *i*Pr) and at 6.04/6.15 ppm (R = *i*Bu).

Considering that, in the case of adducts arising from benzoquinone (+)-(*SS*)-**3**, the major isomer presents H6/H7 ^{1}H NMR absorptions at higher field in comparison with the minor isomer, and that the opposite was observed starting from toluquinones (+)-**2a** and (±)-**2c** (for R = *p*Tol), and assuming the same π-facial diastereoselectivity for the DA reaction of all three quinones, the observed lower-field absorptions for H6/H7 of the *unlike*-**4** adducts can only be explained if, in these compounds, an *s-trans* conformation (instead of an *s–cis* conformation) between the S–O and C2–C3 bonds is assumed (Fig. 4). Accordingly, for the *like*-**4c** and *unlike*-**4c** (R = *i*Pr and *i*Bu) adducts, for which no *p*-tolyl shielding effects are expected, similar chemical shifts values were observed for H6/H7.

However, a reversed π-facial diastereoselectivity for the DA reactions of quinones (+)-**2a** and (±)-**2c**, as compared with that for (+)-(*SS*)-**3** (X = H), with preferential *unlike* approach of the diene to the top (*re*) face of (+)-**2a** and (±)-**2c**, considering the *SS* configuration, giving rise to the *unlike*-**4a** and (±)-*unlike*-**4c** (R = *p*Tol) adducts, could not be discarded. Thus, aiming to elucidate the stereochemistry of adducts **4**, and to obtain diastereoisomerically pure compounds, required for the synthesis of enantiomerically pure **1**, we decided to essay some catalytic conditions for the DA reactions with toluquinones **2**.

When quinone (+)-**2a** was submitted to the $ZnBr_2$-catalyzed DA reaction with cyclopentadiene, the same chemo- and diastereo-selectivities were observed as compared with the thermal process. However, a completely reversed π-facial diastereoselection was observed for (±)-**2c** (R = *p*Tol) under $BF_3{\cdot}Et_2O$ catalysis (see Table 1), as the most abundant adduct is the one with the H6/H7 signals at higher field. Furthermore, when (±)-**2b** and (±)-**2c** (R = *p*Tol) were treated with $ZnBr_2$, only one product was formed in each case. The ^{1}H NMR spectra of these last adducts showed no doublets for the ring-junction hydrogens, but the presence of a broad singlet at 5.88 ppm (in the case of (±)-**2b**) and of a quartet at 6.13 ppm (J is ~1.5 Hz) in the case of (±)-**2c** (R = *p*Tol) indicated that the DA reactions took place at the C2–C3 double bond for both quinones. Thus, assuming the sterically favoured *unlike-endo* approach of the diene to the bottom face of the chelates formed between $ZnBr_2$ and toluquinones (±)-**2b** or (±)-**2c** (R = *p*Tol), products (±)-*unlike*-**6b** and (±)-*unlike*-**6c** could be advanced (Scheme 4).

The catalytic DA reactions of cyclopentadiene with toluquinones **2c** (R = *i*Pr or *i*Bu; see Table 1) showed similar results and, in some cases, it became possible to separate and isolate pure adducts by flash chromatography.

Having in hands the diastereomerically pure adducts **4c**, and due to the unambiguous structure assignment for compounds *unlike*-**6c** (R = *p*Tol or *i*Bu), we envisaged that the stereochemical outcome of the DA reactions of (+)-**2b** and (±)-**2c** could be determined by comparison of the $[\alpha]_D$ values of the enantiomerically pure desulfurized compounds arising from *like*- or *unlike*-**4c** and *unlike*-**6**. Therefore, if the initially proposed structures for compounds (±)-*like*-**4c** and (±)-*unlike*-**4c** were correct, the same enantiomer would result from desulfurization of the (*SS*)-*like*-**4c** and the (*SS*)-*unlike*-**6c** compounds. On the other hand, enantiomeric products would result from desulfurization of adducts (*SS*)-*unlike*-**4c** and the (*SS*)-*unlike*-**6c**. Furthermore, these desulfurized compounds would correspond to the desired enantiomerically pure forms of adduct **1a**.

To establish the best experimental conditions for the removal of the sulfinyl group, racemic *unlike*-**6c** and *like*-**4c** and *unlike*-**4c** were submitted to the reactions with three different desulfurizing agents. Thus, reaction of (±)-*unlike*-**6c** (R = *p*Tol) with aluminum amalgam[19] yielded, after 3 h at 0 °C, an equimolar mixture of adduct (±)-**1a** and its corresponding (±)-C2–C3-dihydro derivative **7**[20] (Scheme 5). This last compound was also obtained when aluminum amalgam was used for reduction of (±)-*like*- or *unlike*-**4c** (R = *i*Bu). The use of Ni_2B[21] resulted in the formation of the (±)-C6–C7-dihydro derivative (±)-**8**, starting from (±)-*unlike*-**6c** (R = *p*Tol) but converted (±)-*unlike*-**4c** (R = *i*Pr) into (±)-**1a** in low yield (12%) (Scheme 5). On the other hand, employing Raney–Ni[22] for desulfurizing (±)-*unlike*-**6c** (R = *p*Tol), an equimolar mixture of (±)-**7** and (±)-**8** was obtained. However, by using deactivated Raney–Ni,[23] we were able to obtain pure (±)-**1a**, although in a moderate yield (50%) (Scheme 5).

Having established the conditions for the successful synthesis of adduct (±)-**1a** by desulfurization of (±)-*unlike*-**6c** (R = *p*Tol) and *unlike*-**4c** (R = *i*Pr), we prepared the optically active quinones (*SS*)-**2c** (R = *p*Tol) and (*SR*)-**2c** (R = *i*Pr) to compare the $[\alpha]_D$ values of their desulfurized cyclopentadiene DA adducts. Thus, by treating 3-bromo-1,4-dimethoxy-2,5-dimethylbenzene[24] with *n*BuLi, followed by quenching with the adequate sulfinylating agent, toluquinones (+)-(*SS*)-**2c** (R = *p*Tol) and the (–)-(*SR*)-**2c** (R = *i*Pr) were isolated[25] after oxidation with CAN. Next, cyclopentadiene was used for the reactions with (+)-**2c** (R = *p*Tol) chelated with $ZnBr_2$, and with (–)-**2c** (R = *i*Pr) complexed with $BF_3{\cdot}Et_2O$. After desulfurization of the corresponding obtained adducts (Scheme 6), the observed $[\alpha]_D$ value for the resulting adducts **1a**,[10a] was +7.6 in both cases, thus confirming the initially proposed relative configurations for adducts **4**.

Table 1. Diels–Alder catalytic reactions of cyclopentadiene with (±)-**2c**.

Entry	R	Condition	Time (days)[a]	*like*-**4c**[b]	*unlike*-**4c**[b]	*unlike*-6**c**[b]
1	*p*Tol[c]	$BF_3{\cdot}Et_2O$	14	1	2.3	—
2	*p*Tol[c]	$ZnBr_2$	3	—	—	1
3	*i*Bu	$BF_3{\cdot}Et_2O$	8	1	2	—
4	*i*Bu	$ZnBr_2$	5	—	1	2.5
5	*i*Pr[d]	$BF_3{\cdot}Et_2O$	4	—	1	—

[a]At –20 °C.

[b]In this Table, *like*-**4c** and *unlike*-**4c** adducts were named according to the chemical shifts of H6 and H7: *like* for highest and *unlike* for lowest chemical shifts, respectively.

[c]Also prepared in an enantiomericaly pure *SS* form.

[d]Prepared in racemic and in enantiomerically pure *SR* form.

Scheme 4. Modes of approaching of cyclopentadiene to both faces of C2–C3 double bonds of racemic chelates formed between $ZnBr_2$ and toluquinones **2b** and **2c**, considering only the (*SS*) isomers.

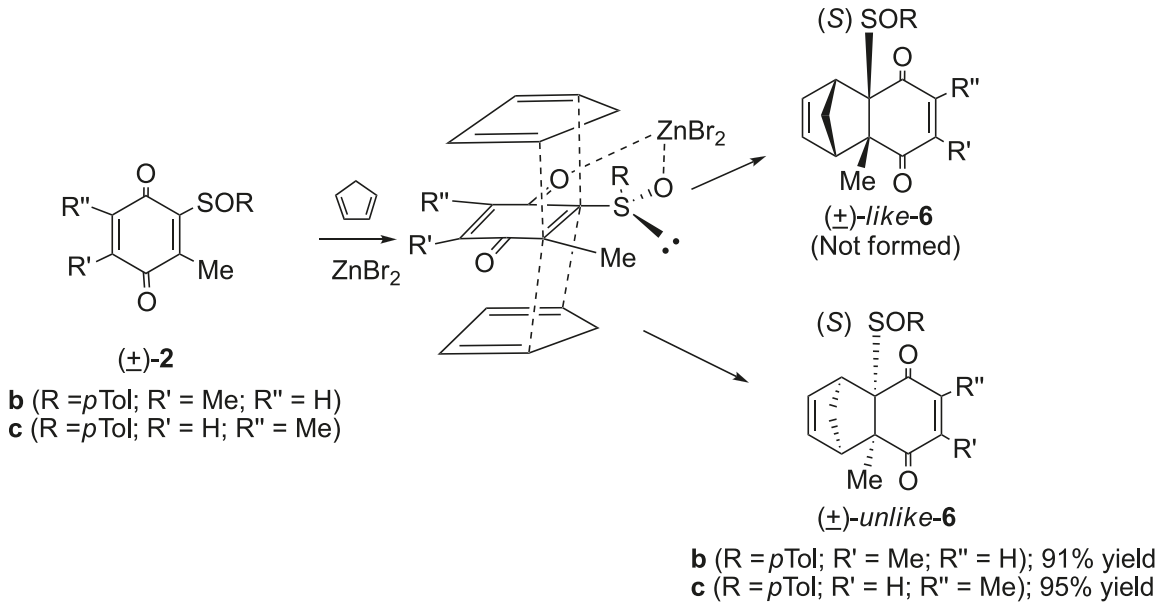

Conclusion

The above results indicate that the same stereochemical outcome is observed for the DA reactions of cyclopentadiene with sulfinylbenzo- and sulfinyl-toluquinones, despite the presence of an extra methyl group attached to the C5–C6 double bond of such toluquinones. However, in the case of adducts **4**, the C2 methyl group sterically interacts with the sulfinyl group, thus imposing an *s-trans* conformation between the S–O and the C2–C3 bonds, causing, in the case of *p*Tol derivatives, a shielding effect on the olefinic hydrogens (H6/H7) only for the *unlike* adducts.

It should be also mentioned that we could establish the adequate conditions for the synthesis of (+)-**1a**, a valuable precursor for synthesis of (+)-hirsutene, (–)-corioline, pleurotellol, and pleurotellic acid.

Experimental

General

Melting points were determined on a Koffler micro hot stage and are uncorrected. ^{1}H NMR spectra were recorded with a Bruker AC 200 or a Varian INOVA 300 spectrometer using TMS as an internal standard. ^{13}C NMR spectra were recorded on the same instruments at 50 or 75 MHz, and are referenced against the central line of the solvent signal ($CDCl_3$ triplet at 77.0 ppm). The coupling constants (*J*) are given in Hz. IR spectra were obtained with a BOMEN instrument (KBr pellets for all compounds). TLC was carried out on Merck silica-gel TLC-cards. All reagents and solvents were used as received from commercial suppliers.

Sulfinyl 1,4-benzoquinones (±)-2b and (±)-2c (R = *p*Tol, *i*Bu, and *i*Pr)

(±)-**2b** and (±)-**2c** (R = *p*Tol, *i*Bu, and *i*Pr) were prepared by the following three-step procedure.

Step 1: addition of thiol to quinone[14]

To a solution of quinone (2.2 mmol) in ethanol (10 mL) was added dropwise a solution of the thiol (2.2 mmol) in ethanol (10 mL), under stirring and at room temperature. After 2 h, the solvent was removed under vacuum, and the residue was submitted to flash chromatography.

3-(Isobutylthio)-2,5-dimethylbenzene-1,4-diol was obtained as a colorless oil, in 96% yield, using hexane/ethyl acetate (6:1) as eluting solvent. δ_H (300 MHz, $CDCl_3$): 1.02 (d, 6H, *J* = 6.6), 1.76 (m, 1H), 2.21 (s, 3H), 2.41 (s, 3H),

Scheme 5. Products arising from reactions of adducts (±)-*unlike*-**6c** and (±)-*unlike* **4c** with desulfurizing agents.

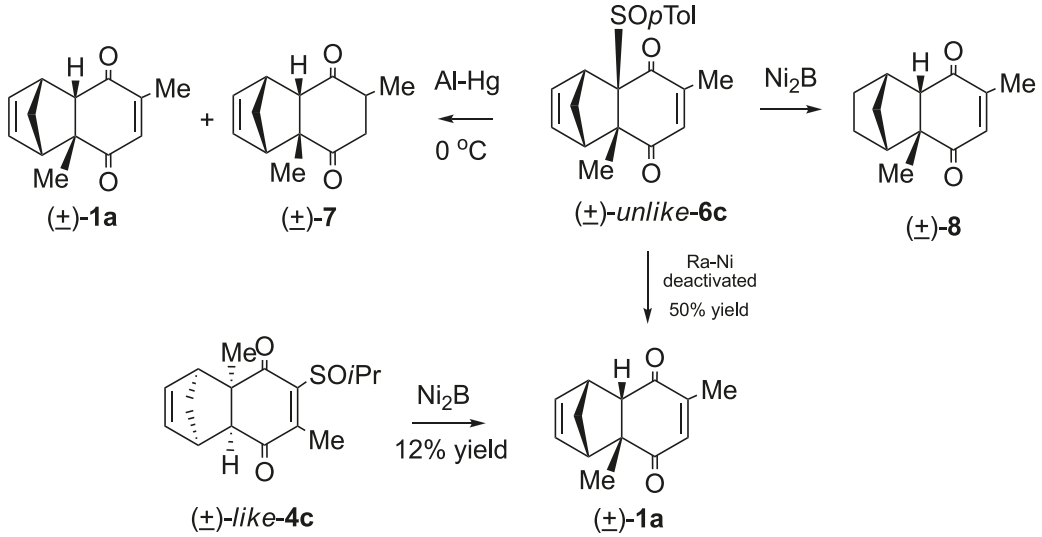

Scheme 6. Product resulting from desulfurization of the Diels–Alder adducts between cyclopentadiene and toluquinones (+)-(*SS*)-**2c** and (–)-(*SR*)-**2c**.

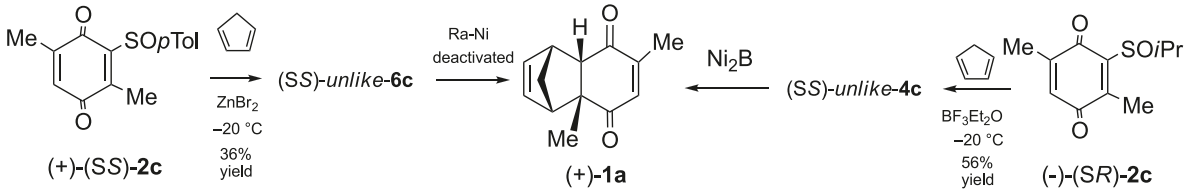

2.48 (d, 2H, J = 6.9), 4.30 (s, 1H), 6.62 (s, 1H), 6.83 (s, 1H). δ_C (75 MHz, $CDCl_3$): 14.5, 16.7, 22.4, 29.2, 45.5, 119.2, 120.2, 121.9, 125.6, 146.9, 149.9. Elemental analysis (%) ($C_{12}H_{18}O_2S$): C 63.7, H 8.0 (calcd.); C 63.2, H 7.8 (found).

3-(Isopropylthio)-2,5-dimethylbenzene-1,4-diol was obtained as a white solid, in 82% yield, using hexane/ethyl acetate (6:1) as eluting solvent. Mp 71–74 °C. δ_H (300 MHz, $CDCl_3$): 1.23 (d, 6H, J = 6.6), 2.22 (s, 3H), 2.40 (s, 3H), 3.05 (m, 1H, J = 6.4), 4.32 (s, 1H), 6.64 (s, 1H), 6.84 (s, 1H). Elemental analysis (%) ($C_{11}H_{16}O_2S$): C 62.2, H 7.6 (calcd.); C 61.8, H 7.8 (found).

Step 2: oxidation at the sulfur atom[15]

To a water cooled solution of the sulfanylbenzene-1,4-diol (1.1 mmol) in methanol (3 mL) was slowly added a solution of H_2O_2 30% (0.11 mL; 1.1 mmol) and SeO_2 (0.12 g; 1.1 mmol) in water (1 mL). After 1 h, water (5 mL) was added, and the mixture was extracted with $CHCl_3$. After drying (Na_2SO_4) and concentration, the solid sulfinyl derivative was isolated.

(±)-2,5-Dimethyl-3-(*p*-tolylsulfinyl)benzene-1,4-diol was obtained, in 74% yield, starting from 2,5-dimethyl-3-(*p*-tolylthio)benzene-1,4-diol,[14] and was used without purification. Mp 171–174 °C. δ_H (300 MHz, $CDCl_3$): 2.13 (s, 3H), 2.22 (s, 3H), 2.38 (s, 3H), 4.80 (bs, 1H), 6.70 (s, 1H), 7.28 (d, 2H, J = 7.5), 7.56 (d, 2H, J = 7.5), 10.61 (bs, 1H). δ_C (75 MHz, $CDCl_3$): 11.6, 15.2, 21.4, 119.2, 121.3, 125.8, 126.7, 130.3, 139.8, 142.3, 145.7, 152.4.

(±)-3,5-Dimethyl-2-(*p*-tolylsulfinyl)benzene-1,4-diol was obtained, in 90% yield, starting from 3,5-dimethyl-2-(*p*-tolylthio)benzene-1,4-diol.[14] Mp 163–165 °C. IR (KBr, cm^{-1}): 1428, 1471, 2915, 3133, 3314. δ_H (300 MHz, $CDCl_3$): 2.20 (s, 3H), 2.22 (s, 3H), 2.38 (s, 3H), 4.63 (bs, 1H), 6.57 (s, 1H), 7.27 (d, 2H, J = 7.8), 7.56 (d, 2H, J = 8.1), 10.49 (s, 1H). δ_C (75 MHz, $CDCl_3$): 12.6, 16.9, 21.8, 119.2, 119.6, 122.1, 126.2, 130.1, 130.7, 140.5, 142.7, 145.4, 154.3. Elemental analysis (%) ($C_{15}H_{16}SO_3$): C 65.2, H 5.8 (calcd.); C 64.9, H 5.8 (found).

(±)-3-(Isobutylsulfinyl)-2,5-dimethylbenzene-1,4-diol was obtained, as a colorless oil, in 87% yield, starting from 3-(isobutylthio)-2,5-dimethylbenzene-1,4-diol. δ_H (300 MHz, $CDCl_3$): 1.12 (d, 3H, J = 6.6), 1.16 (d, 3H, J = 6.6), 2.14 (s, 3H), 2.16 (s, 3H), 2.25 (m, 1H), 2.63 (dd, 1H, *vic* J = 9.3 and *gem* J = 13.2), 3.36 (dd, 1H, *vic* J = 4.8 and *gem* J = 12.9), 4.62 (bs, 1H), 6.70 (s, 1H), 10.51 (s, 1H). δ_C (75 MHz, $CDCl_3$): 11.4, 15.3, 21.6, 22.9, 24.4, 62.6, 118.6, 121.0, 121.3, 126.8, 146.0, 152.9.

(±)-3-(Isopropylsulfinyl)-2,5-dimethylbenzene-1,4-diol was obtained, in 79% yield, starting from 3-(isopropylthio)-2,5-dimethylbenzene-1,4-diol. Mp 129–132 °C. δ_H (300 MHz, $CDCl_3$): 1.24 (d, 3H, J = 6.8), 1.45 (d, 3H, J = 6.8), 2.14 (s, 3H), 2.16 (s, 3H), 3.39 (h, 1H, J = 6.5), 6.73 (s, 1H). δ_C (75 MHz, $CDCl_3$): 12.4, 15.6, 16.0, 17.1, 54.0, 119.3, 120.4, 121.8, 126.7, 146.3, 153.2.

Step 3: oxidation with CAN

To a solution of the sulfinyl derivative (1.0 mmol) in MeCN (10 mL) was added 5 mL of an aqueous solution of CAN (3.0 mmol), and the resulting mixture was stirred for 1 h at room temperature. After removal of half volume of the solvent, the quinone was extracted with CH_2Cl_2. The ex-

tract was dried (Na_2SO_4) and concentrated under vacuum, resulting in a red solid.

(±)-2,5-Dimethyl-3-(*p*-tolylsulfinyl)cyclohexa-2,5-diene-1,4-dione, (±)-2c (R = *p*Tol), was obtained from (±)-2,5-dimethyl-3-(*p*-tolylsulfinyl)benzene-1,4-diol in 82% yield. Mp 138–139 °C. δ_H (300 MHz, $CDCl_3$): 2.02 (s, 3H), 2.40 (s, 3H), 2.49 (s, 3H), 6.64 (s, 1H), 7.31 (m, 2H), 7.64 (m, 2H). δ_C (75 MHz, $CDCl_3$): 9.9, 16.0, 22.0, 125.3, 130.5, 134.1, 140.0, 142.0, 146.1, 146.5, 147.5, 185.2, 186.2. Elemental analysis (%) ($C_{15}H_{14}SO_3$): C 65.7, H 5.1 (calcd.); C 65.3, H 5.5 (found).

(±)-3,5-Dimethyl-2-(*p*-tolylsulfinyl)cyclohexa-2,5-diene-1,4-dione, (±)-2b, was obtained from (±)-3,5-dimethyl-2-(*p*-tolylsulfinyl)benzene-1,4-diol in 90% yield. Mp 100–102 °C. IR (KBr, cm^{-1}): 1630, 1647, 1665, 3044. δ_H (300 MHz, $CDCl_3$): 2.04 (d, 3H, J = 1.8), 2.39 (s, 3H), 2.49 (s, 3H), 6.54 (q, 1H, J = 1.5), 7.30 (d, 2H, J = 7.8), 7.63 (d, 2H, J = 8.1). δ_C (75 MHz, $CDCl_3$): 9.6, 16.5, 21.7, 125.2, 130.4, 133.2, 140.0, 141.9, 146.1, 147.0, 147.2, 184.8, 187.1. Elemental analysis (%) ($C_{15}H_{14}SO_3$): C 65.7, H 5.1 (calcd.); C 65.2, H 5.0 (found).

(±)-2,5-Dimethyl-3-(isobutylsulfinyl)cyclohexa-2,5-diene-1,4-dione, (±)-2c (R = *i*Bu), was obtained from (±)-3-(isobutylsulfinyl)-2,5-dimethylbenzene-1,4-diol in 87% yield. Mp 75–78 °C. IR (KBr, cm^{-1}): 1650, 1603, 1466, 1438, 1042. δ_H (300 MHz, $CDCl_3$): 1.12 (d, 3H, J = 6.6), 1.19 (d, 3H, J = 6.9), 2.05 (d, 3H, J = 1.5), 2.25 (m, 1H), 2.45 (s, 3H), 3.22 (dd, 1H, J = 4.8 and 12.9), 3.26 (dd, 1H, *vic* J = 4.5 and 12.3), 6.69 (q, 1H, J = 1.8). δ_C (75 MHz, $CDCl_3$): 9.4, 15.7, 21.6, 23.2, 24.9, 63.4, 134.3, 145.9, 146.3, 148.4, 185.5, 185.8. Elemental analysis (%) ($C_{12}H_{16}SO_3$): C 60.0, H 6.7 (calcd.); C 59.2, H 6.5 (found).

(±)-2,5-Dimethyl-3-(isopropylsulfinyl)cyclohexa-2,5-diene-1,4-dione, (±)-2c (R = *i*Pr), was obtained from (±)-3-(isopropylsulfinyl)-2,5-dimethylbenzene-1,4-diol in 78% yield. Mp 83–84 °C. IR (KBr, cm^{-1}): 1665, 1650, 1595, 1465, 1432, 1059. δ_H (300 MHz, $CDCl_3$): 1.35 (d, 3H, J = 6.9), 1.40 (d, 3H, J = 7.2), 2.05 (d, 3H, J = 1.8), 2.44 (s, 3H), 3.43 (h, 1H, J = 7.9), 6.70 (q, 1H, J = 1.8). δ_C (75 MHz, $CDCl_3$): 9.7, 15.2, 15.8, 17.7, 53.4, 134.4, 144.2, 146.3, 149.9, 185.7, 185.8. Elemental analysis (%) ($C_{11}H_{14}SO_3$): C 58.4, H 6.2 (calcd.); C 58.7, H 6.0 (found).

Sulfinyltoluquinones (+)-2a, (+)-2c (R = *p*Tol), and (–)-2c (R = *i*Pr)

(+)-**2a**, (+)-**2c** (R = *p*Tol) and (–)-**2c** (R = *i*Pr) were prepared by a two-step procedure, as described below, by employing the adequate combination of bromo-1,4-dimethoxyarene and the sulfinylating agent.

Step 1

To a cooled solution (–20 °C) of *n*BuLi (3.0 mmol) in ethyl ether (5 mL) was added a solution of the bromo-1,4-dimethoxy-arene (2.7 mmol) in ethyl ether (5 mL). After 1 h at –20 °C, a solution of the sulfinylating agent (3.3 mmol) in ethyl ether (5.0 mL) was slowly added. The mixture was stirred for 2 h at –20 °C and for 1 h at RT. Cold aqueous saturated ammonium chloride (50 mL) was added to the mixture, and the organic layer was separated. The aqueous phase was extracted with ethyl ether (25 mL), and the extracts were dried ($MgSO_4$) and concentrated. The resulting sulfoxide was isolated by column chromatography.

(–)-(*S*,*S*)-1,4-Dimethoxy-2-methyl-3-(*p*-tolylsulfinyl)benzene was obtained, in 37% yield, from 2-bromo-1,4-dimethoxy-3-methylbenzene[16] and (*S*,*S*)-menthyl *p*-toluenesulfinate. $[\alpha]_D$ –115 (*c* 1.8, CH_2Cl_2). δ_H (300 MHz, $CDCl_3$): 2.36 (s, 3H), 2.41 (s, 3H), 3.71 (s, 3H), 3.77 (s, 3H), 6.74 (d, 2H, J = 9.0), 6.90 (d, 1H, J = 9.0), 7.21 (d, 2H, J = 8.4), 7.43 (d, 2H, J = 8.4). δ_C (75 MHz, $CDCl_3$): 11.3, 21.2, 56.3, 56.6, 110.1, 114.5, 124.3, 129.2, 130.2, 132.1, 139.5, 141.5, 152.4, 152.7. Elemental analysis (%) ($C_{16}H_{18}SO_3 \cdot 1/2H_2O$): C 64.2, H 6.4 (calcd.); C 64.2, H 6.0 (found).

(–)-(*S*,*S*)-1,4-Dimethoxy-2,5-dimethyl-3-(*p*-tolylsulfinyl)-benzene was obtained, in 37% yield, from 3-bromo-1,4-dimethoxy-2,5-dimethylbenzene[24] and (*S*,*S*)-menthyl *p*-toluenesulfinate. Mp 132–135 °C. $[\alpha]_D$ –123.7 (*c* 1, $CHCl_3$). δ_H (300 MHz, $CDCl_3$): 2.28 (s, 3H), 2.29 (s, 3H), 2.36 (s, 3H), 3.70 (s, 3H), 3.81 (s, 3H), 6.77 (s, 1H), 7.23 (m, 2H), 7.44 (m, 2H). δ_C (75 MHz, $CDCl_3$): 10.4, 16.0, 21.2, 56.0, 62.1, 116.6, 124.3, 124.8, 127.0, 129.4, 129.9, 136.8, 139.7, 141.6, 151.0, 154.4. Elemental analysis (%) ($C_{17}H_{20}SO_3$): C 67.1, H 6.6 (calcd.); C 66.8, H 6.7 (found).

(+)-(*S*,*R*)-3-(Isopropylsulfinyl)-1,4-dimethoxy-2,5-dimethylbenzene was obtained, in 45% yield as a colorless oil, from 3-bromo-1,4-dimethoxy-2,5-dimethylbenzene[24] and 1,2:5,6-di-*O*-isopropylidene-α-D-glucofuranosyl (+)-(*R*)-2-propanesulfinate.[25] $[\alpha]_D$ + 91 (*c* 0.45, $CHCl_3$). δ_H (300 MHz, $CDCl_3$): 1.05 (d, 3H, J = 6.9), 1.44 (d, 3H, J = 6.9), 2.28 (s, 3H), 2.45 (s, 3H), 3.64 (m, 1H), 3.80 (s, 3H), 3.81 (s, 3H), 6.75 (s, 1H). δ_C (75 MHz, $CDCl_3$): 10.9, 15.8, 16.6, 16.7, 52.0, 55.9, 61.7, 115.8, 127.1, 129.4, 133.9, 150.7, 154.1

Step 2

To a solution of the sulfoxide (1.0 mmol) in MeCN (5 mL) was added 5 mL of an aqueous solution of CAN (2.5 mmol), and the resulting mixture was stirred 1 h at room temperature. After removal of half volume of the solvent, the quinone was extracted with CH_2Cl_2 (two portions of 20 mL). The extract was dried (Na_2SO_4) and concentrated under vacuum, yielding a solid.

(+)-(*S*,*S*)-2-Methyl-3-(*p*-tolylsulfinyl)cyclohexa-2,5-diene-1,4-dione, (+)-2a, was obtained, in 79% yield, from 1,4-dimethoxy-2-methyl-3-(*p*-tolylsulfinyl)benzene. Mp 107–109 °C. $[\alpha]_D$ +898 (*c* 0.50, CH_2Cl_2). δ_H (300 MHz, $CDCl_3$): 2.40 (s, 3H), 2.50 (s, 3H), 6.70 (d, 1H, J = 9.9), 6.80 (d, 1H, J = 9.9), 7.31 (d, 2H, J = 8.7), 7.63 (d, 2H, J = 8.7). δ_C (75 MHz, $CDCl_3$): 9.2, 21.3, 124.8, 130.1, 136.0, 136.8, 139.2, 141.7, 146.0, 146.8, 184.3, 185.9. Elemental analysis (%) ($C_{14}H_{12}SO_3 \cdot 1/2H_2O$): C 62.4, H 4.9 (calcd.); C 62.9, H 4.7 (found).

(+)-(*S*,*S*)-2,5-Dimethyl-3-(*p*-tolylsulfinyl)cyclohexa-2,5-diene-1,4-dione, (+)-2c (R = *p*Tol), was obtained as a red solid, in 71% yield, from (–)-(*S*,*S*)-1,4-dimethoxy-2,5-dimethyl-3-(*p*-tolylsulfinyl)benzene. Mp 136–139 °C. $[\alpha]_D$ +440 (*c* 0.40, $CHCl_3$). Spectroscopic data are identical to those described for (±)-**2c** (R = *p*Tol).

(–)-(*S*,*R*)-3-(Isopropylsulfinyl)-2,5-dimethylcyclohexa-2,5-diene-1,4-dione, (–)-2c (R = *i*Pr), was obtained as a red solid, in 79% yield, from (+)-(*S*,*R*)-3-(isopropylsulfinyl)-1,4-

dimethoxy-2,5-dimethylbenzene. Mp 82–84 °C. $[\alpha]_D$ –806 (*c* 0.2, $CHCl_3$). Spectroscopic data are identical to those reported for (±)-**2c** (R = *i*Pr).

Diels–Alder reactions

Thermal conditions

A solution of sulfinyl-1,4-benzoquinone (1.0 mmol) and cyclopentadiene (3.0 mmol) in CH_2Cl_2 (2 mL) was stirred at –20 °C. After complete consumption of the quinone, the solvent was removed under vacuum, and the DA adduct was isolated by column chromatography.

Catalytic conditions

A solution of sulfinylquinone (1.0 mmol) and the Lewis acid (see Table 1) in CH_2Cl_2 (2 mL) was stirred at –20 °C for 1 h, and at room temperature for 1 h. The mixture was cooled to –20 °C, and cyclopentadiene (3.0 mmol) was added. The mixture was stirred at –20 °C, and after complete consumption of the quinone, the solvent was removed under vacuum, and the adduct was isolated by column chromatography.

(±)-*Like*-4b was isolated as a yellow solid, in 40% yield, using hexane/ethyl acetate (4.5:1) as eluting solvent. Mp 97–99 °C. IR (KBr, cm^{-1}): 1329, 1659, 1673, 2977. δ_H (300 MHz, $CDCl_3$): 1.47 (s, 3H), 1.48 (m, 1H), 1.65 (m, 1H), 2.32 (s, 3H), 2.39 (s, 3H), 2,92 (d, 1H, *J* = 3.9), 3.04 (s, 1H), 3.35 (s, 1H), 5.56 (m, 1H), 5.96 (m, 1H), 7.29 (m, 2H), 7.55 (m, 2H). δ_C (75 MHz, $CDCl_3$): 9.9, 21.8, 26.8, 46.8, 49.3, 53.5, 54.2, 58.1, 125.2, 130.4, 135.0, 141.8, 138.6, 139.5, 151.9, 152.8, 196.9, 201.7. Elemental analysis (%) ($C_{20}H_{20}SO_3$): C 70.6, H 5.9 (calcd.); C 69.9, H 6.2 (found).

(±)-*Unlike*-4b was isolated as a yellow oil, in 30% yield, using hexane/ethyl acetate (4.5:1) as eluting solvent. δ_H (300 MHz, $CDCl_3$): 1.41 (s, 3H), 1.54 (m, 1H), 1.64 (m, 1H), 2.37 (s, 3H), 2.39 (s, 3H), 2.77 (d, 1H, *J* = 3.9), 3.06 (s, 1H), 3.39 (s, 1H), 6.02 (m, 1H), 6.06 (m, 1H), 7.29 (m, 2H), 7.60 (m, 2H). δ_C (75 MHz, $CDCl_3$): 10.8, 21.8, 27.0, 47.0, 49.5, 53.6, 54.4, 58.2, 125.4, 130.4, 135.6, 138.4, 140.0, 141.9, 151.7, 153.0, 196.2, 201.5.

(±)-*Like*-4c (R = *p*Tol) was isolated as a yellow oil in admixture with (±)-*unlike*-**4c** (R = *p*Tol), using hexane/ethyl acetate (3.5:1) as eluting solvent. δ_H (300 MHz, $CDCl_3$): 1.25 (s, 3H), 1.55 (m, 2H), 2.39 (s, 3H), 2.40 (s, 3H), 2.80 (d, 1H, *J* = 3.9), 3.04 (m, 1H), 3.42 (m, 1H), 6.01 (m, 1H), 6.14 (m, 1H), 7.29 (m, 2H), 7.58 (m, 2H).

(±)-*Unlike*-4c (R = *p*Tol) was isolated as a yellow oil in admixture with (±)-*like*-**4c** (R = *p*Tol) using hexane/ethyl acetate (3.5:1) as eluting solvent. δ_H (300 MHz, $CDCl_3$): 1.49 (s, 3H), 1.55 (m, 2H), 2.35 (s, 3H), 2.40 (s, 3H), 2.86 (d, 1H, *J* = 3.9), 3.04 (m, 1H), 3.40 (m, 1H), 5.67 (dd, 1H, *J* = 3.0 and 2.4), 5.82 (dd, 1H, *J* = 3.0 and 2.4), 7.58 (m, 2H), 7.49 (m, 2H).

(±)-*Like*-4c (R = *i*Bu) was isolated as a yellow oil, in 22% yield, using hexane/ethyl acetate (2:1) as eluting solvent. δ_H (300 MHz, $CDCl_3$): 1.10 (d, 3H, *J* = 6.6), 1.16 (d, 3H, *J* = 6.6), 1.49 (s, 3H), 1.65 (m, 2H), 2.30 (m, 1H), 2.31 (s, 3H), 2.70 (dd, 1H, *J* = 4.2 and 12.6), 2.92 (d, 1H, *J* = 4.2), 3.08 (bs, 1H), 3.20 (dd, 1H, *J* = 4.5 and 12.6), 3.44 (bs, 1H), 6.04 (m, 1H), 6.23 (m, 1H).

(±)-*Unlike*-4c (R = *i*Bu) was isolated as a yellow oil, in 20% yield, using hexane/ethyl acetate (2:1) as eluting solvent. δ_H (300 MHz, $CDCl_3$): 1.10 (d, 3H, *J* = 6.6), 1.16 (d, 3H, *J* = 6.6), 1.49 (s, 3H), 1.65 (m, 2H), 2.30 (m, 1H), 2.40 (s, 3H), 2.70 (dd, 1H, *J* = 4.2 and 12.6), 2.92 (d, 1H, *J* = 4.2), 3.15 (m, 2H), 3.44 (m, 1H), 6.04 (m, 1H), 6.15 (m, 1H).

(±)-*Like*-4c (R = *i*Pr) was isolated as a yellow oil, in 25% yield, using hexane/ethyl acetate (3:1). δ_H (300 MHz, $CDCl_3$): 1.29 (d, 3H, *J* = 6.6), 1.35 (d, 3H, *J* = 6.6), 1.49 (s, 3H), 1.59 (m, 2H), 2.31 (s, 3H), 2.91 (d, 1H, *J* = 3.9), 3.09 (bs, 1H), 3.45 (m, 1H), 3.48 (m, 1H), 6.04 (m, 1H), 6.21 (m, 1H).

(±)-*Unlike*-4c (R = *i*Pr) was isolated as a yellow oil, in 60% yield, using hexane/ethyl acetate (3:1) as eluting solvent. δ_H (300 MHz, $CDCl_3$): 1.29 (d, 3H, *J* = 6.0), 1.37 (d, 3H, *J* = 6.0), 1.52 (s, 3H), 1.60 (m, 2H), 2.38 (s, 3H), 2.90 (d, 1H, *J* = 3.3), 3.09 (bs, 1H), 3.37 (m, 1H), 3.50 (bs, 1H), 6.04 (m, 1H), 6.13 (m, 1H). δ_C (75 MHz, $CDCl_3$): 9.6, 15.3, 18.0, 26.9, 46.8, 49.6, 53.8, 53.9, 57.3, 135.5, 138.7, 149.8, 155.7, 197.8, 200.8.

(±)-*Unlike*-6b (R = *p*Tol) was isolated, in 91% yield, as a yellow solid by employing hexane/ethyl acetate (3.5:1) as eluting solvent. δ_H (200 MHz, $CDCl_3$): 1.66 (m, 1H), 1.75 (d, 3H, *J* = 1.5), 1.81 (s, 3H), 2.29 (m, 1H), 2.41 (s, 3H), 3.24 (bs, 1H), 4.02 (bs, 1H), 5.88 (q, 1H, *J* = 1.2), 6.05 (m, 1H), 6.22 (m, 1H), 7.27 (m, 2H), 7.49 (m, 2H). δ_C (50 MHz, $CDCl_3$): 16.3, 21.5, 25.0, 43.3, 49.6, 54.3, 57.5, 81.4, 126.2, 129.2, 136.8, 137.4, 139.4, 140.3, 142.6, 149.6, 191.2, 201.4.

(±)-*Unlike*-6c (R = *p*Tol) was isolated, in 95% yield, as a yellow solid, using hexane/ethyl acetate (3.5:1) as eluting solvent. Mp 111–114 °C. δ_H (300 MHz, $CDCl_3$): 1.24 (d, 3H, *J* = 1.5), 1.68 (m, 1H), 1.85 (s, 3H), 2.23 (m, 1H), 2.40 (s, 3H), 3.25 (bs, 1H), 4.09 (bs, 1H), 6.05 (m, 1H), 6.13 (q, 1H, *J* = 1.5), 6.23 (m, 1H), 7.28 (m, 2H), 7.48 (m, 2H). δ_C (75 MHz, $CDCl_3$): 15.3, 21.3, 25.6, 43.3, 50.2, 54.4, 58.0, 81.3, 126.1, 129.7, 136.4, 136.6, 137.7, 140.4, 142.3, 153.2, 192.0, 200.4. Elemental analysis (%) ($C_{20}H_{20}SO_3$): C 70.6, H 5.9 (calcd.); C 70.7, H 6.0 (found).

(–)-*Unlike*-6c (R = *p*Tol) was isolated as a yellow oil, in 36% yield, employing hexane/ethyl acetate (3.5:1) as eluting solvent. $[\alpha]_D$ –134 (*c* 0.5, $CHCl_3$). Spectroscopic data are identical to those described for (±)-*unlike*-**6c** (R = *p*Tol).

(±)-*Unlike*-6c (R = *i*Bu) was isolated as a yellow oil, in 34% yield, using hexane/ethyl acetate (2:1) as eluting solvent. δ_H (300 MHz, $CDCl_3$): 1.08 (d, 3H, *J* = 6.9), 1.10 (d, 3H, *J* = 6.9), 1.50 (s, 3H), 1.61 (m, 1H), 2.02 (d, 3H, *J* = 1.5), 2.20 (m, 1H), 2.30 (m, 1H), 2.35 (m, 1H), 2.45 (m, 1H), 2.50 (dd, 1H, *J* = 3.9 and 4.2), 3.20 (bs, 1H), 3.95 (bs, 1H), 6.10 (dd, 1H, *J* = 2.7 and 3.0), 6.24 (dd, 1H, *J* = 2.7 and 3.0), 6.50 (q, 1H, *J* = 1.5). δ_C (75 MHz, $CDCl_3$): 15.9, 21.7, 22.8, 23.4, 25.4, 43.2, 50.3, 55.2, 57.6, 60.5, 136.5, 138.4, 140.5, 153.1, 193.1, 200.6.

(–)-*Unlike*-4c (R = *i*Pr) was isolated as a yellow oil, in 56% yield, using hexane/ethyl acetate (6:1). $[\alpha]_D$ –132 (*c* 0.5, $CHCl_3$). Spectroscopic data are identical to those described for (±)-*unlike*-**4c** (R = *i*Pr).

Desulfurization reactions

Using Al–Hg

To a solution of the DA adduct (0.42 mmol) in THF/water (9:1; 12 mL), pieces of aluminum foil[19] (1.0 g; recently immersed into a $HgCl_2$ aqueous solution and washed

with ethanol and ethyl ether) were added, and the mixture was stirred at room temperature for 3.5 h. The solids were filtered off, and the solvent was removed under vacuum. The residue was submitted to flash chromatography separation.

Using Raney–Ni

A suspension of Raney–Ni (W2[22] or deactivated;[23] ~1 mL of the decanted solid metal) in ethanol (5 mL) was added to a solution of the DA adduct (0.45 mmol) in ethanol (10 mL) under stirring at room temperature. The desulfurization process was monitored by the consumption of the DA adduct (by TLC). The residual metal was removed by filtration, and the solvent was evaporated under vacuum. The residue was purified by flash chromatography.

Using Ni_2B[21]

To a well-stirred mixture of the DA adduct (0.21 mmol) and $NiCl_2{\cdot}6H_2O$ (0.10 g; 0.42 mmol) in methanol/THF (3:1; 12 mL) at 0 °C, $NaBH_4$ (0.050 g; 1.3 mmol) was added, resulting in a black solid. After 15 min, the mixture was filtered over Celite, and the solvent was removed under vacuum. The residue was dissolved in CH_2Cl_2 (20 mL) and washed with water (20 mL). After drying (Na_2SO_4) and concentration under vacuum, the residue was purified by flash chromatography.

(±)-4a,7-Dimethyl-1,2,3,4,4a,8a-hexahydro-1,4-methano-naphthalene-5,8-dione, 8, was isolated as a colorless oil, in 40% yield, using hexane/ethyl acetate (3:1) as eluting solvent. δ_H (300 MHz, $CDCl_3$): 1.25 (s, 3H), 1.35 (m, 1H), 1.45 (m, 2H), 1.69 (m, 1H), 1.97 (bs, 2H), 2.02 (d, 3H, J = 1.5), 2.48 (bs, 1H), 2.56 (dd, 1H, J = 1.5 and 1.8), 2.86 (bs, 1H), 6.56 (q, 1H, J = 1.5).

Supplementary data

Supplementary data for this article are available on the journal Web site (canjchem.nrc.ca) or may be purchased from the Depository of Unpublished Data, Document Delivery, CISTI, National Research Council Canada, Ottawa, ON K1A 0R6, Canada. DUD 3978. For more information on obtaining material, refer to cisti-icist.nrc–Cnrc.gc.ca/cms/unpub_e.shtml.

Acknowledgement

We acknowledge Fundação de Amparo à Pesquisa do Estado de São Paulo (FAPESP), Conselho Nacional de Desenvolvimento Científico e Tecnológico (CNPq), and Coordenação de Aperfeiçoamento de Pessoal de Nível Superior (CAPES) for financial support.

References

(1) Nicolaou, K. C.; Snyder, S. A.; Montagnon, T.; Vassilikogiannakis, G. *Angew. Chem., Int. Ed. Engl.* **2002**, *41* (10), 1668–1698. doi:10.1002/1521-3773(20020517)41:10<1668::AID-ANIE1668>3.0.CO;2-Z.

(2) Desimoni, G.; Tacconi, G.; Barco, A.; Pollini, G. P. *Natural products synthesis through pericyclic reactions*; ACS Monograph 180; American Chemical Society: WA. 1983.

(3) (a) Woodward, R. B.; Sondheimer, F.; Taub, D.; Heusler, K.; McLamore, W. M. *J. Am. Chem. Soc.* **1952**, *74* (17), 4223–4251. doi:10.1021/ja01137a001.; (b) Dickinson, R. A.; Kubela, R.; MacAlpine, G. A.; Stojanac, Z.; Valenta, Z. *Can. J. Chem.* **1972**, *50* (14), 2377–2380. doi:10.1139/v72-379.

(4) (a) Gates, M.; Tschudi, G. *J. Am. Chem. Soc.* **1956**, *78* (7), 1380–1393. doi:10.1021/ja01588a033.; (b) Woodward, R. B.; Bader, F. E.; Bickel, H.; Frey, A. J.; Kierstead, R. W. *Tetrahedron* **1958**, *2* (1-2), 1–57. doi:10.1016/0040-4020(58)88022-9.

(5) (a) Yamakawa, K.; Satoh, T. *Chem. Pharm. Bull. (Tokyo)* **1977**, *25*, 2535; (b) Mehta, G.; Reddy, A. V. *J. Chem. Soc., Chem. Commun.* **1981**, (15): 756. doi:10.1039/c39810000756.; (c) Mehta, G.; Reddy, D. S.; Murty, A. N. *J. Chem. Soc., Chem. Commun.* **1983**, (15): 824. doi:10.1039/c39830000824.; (d) Mehta, G.; Murthy, A. N.; Reddy, D. S.; Reddy, A. V. *J. Am. Chem. Soc.* **1986**, *108* (12), 3443–3452. doi:10.1021/ja00272a046.; (e) Mehta, G.; Murthy, A. N.; Reddy, D. S. K. *Tetrahedron Lett.* **1987**, *28* (13), 1467–1468. doi:10.1016/S0040-4039(00)95955-0.; (f) Mehta, G.; Umarye, J. D. *Tetrahedron Lett.* **2001**, *42* (10), 1991–1993. doi:10.1016/S0040-4039(01)00051-X.; (g) Nicolaou, K. C.; Vassilikogiannakis, G.; Mägerlein, W.; Kranich, R. *Angew. Chem., Int. Ed. Engl.* **2001**, *40* (13), 2482–2486. doi:10.1002/1521-3773(20010702)40:13<2482::AID-ANIE2482>3.0.CO;2-A. PMID:11443672.; (h) Mehta, G.; Murthy, A. S. K. *Tetrahedron Lett.* **2003**, *44* (28), 5243–5246. doi:10.1016/S0040-4039(03)01215-2.

(6) (a) Inouye, Y.; Kakisawa, H. *Bull. Chem. Soc. Jpn.* **1969**, *42* (11), 3318–3323. doi:10.1246/bcsj.42.3318.; (b) Ichihara, A.; Oda, K.; Kobayashi, M.; Sakamura, S. *Tetrahedron Lett.* **1974**, *15* (48), 4235–4238. doi:10.1016/S0040-4039(01)92130-6.; (c) Ichihara, A.; Kimura, R.; Oda, K.; Sakamura, S. *Tetrahedron Lett.* **1976**, *17* (51), 4741–4744. doi:10.1016/S0040-4039(00)93014-4.; (d) Kraus, G. A.; Taschner, M. J. *J. Org. Chem.* **1980**, *45* (6), 1175–1176. doi:10.1021/jo01294a058.; (e) Larsen, D. S.; O'Shea, M. D.; *J. Chem. Soc., Perkin Trans.* 1 **1995**, 1019; (f) Mehta, G.; Islam, K. *Tetrahedron Lett.* **2003**, *44* (17), 3569–3572. doi:10.1016/S0040-4039(03)00621-X.; (g) Mehta, G.; Islam, K. *Tetrahedron Lett.* **2003**, *44* (35), 6733–6736. doi:10.1016/S0040-4039(03)01643-5.; (h) Mehta, G.; Pan, S. C. *Tetrahedron Lett.* **2005**, *46* (17), 3045–3048. doi:10.1016/j.tetlet.2005.03.019.; (i) Tapia, R. A.; Villalobos, L.; Salas, C. *Synthesis* **2007**, *2007* (24), 3773–3775. doi:10.1055/s-2007-990895.

(7) (a) Edwards, W. D.; Gupta, R. C.; Raynor, C. M.; Stoodley, R. J. *J. Chem. Soc., Perkin Trans. 1* **1991**, (8): 1913. doi:10.1039/p19910001913.; (b) Kim, K.; Sulikowski, G. A. *Angew. Chem., Int. Ed. Engl.* **1995**, *34* (21), 2396–2398. doi:10.1002/anie.199523961.; (c) Carreño, M. C.; Ribagorda, M.; Somoza, A.; Urbano, A. *Angew. Chem., Int. Ed. Engl.* **2002**, *41* (15), 2755–2757. doi:10.1002/1521-3773(20020802)41:15<2755::AID-ANIE2755>3.0.CO;2-A. PMID:12203475.; (d) Boezio, A. A.; Jarvo, E. R.; Lawrence, B. M.; Jacobsen, E. N. *Angew. Chem., Int. Ed. Engl.* **2005**, *44* (37), 6046–6050. doi:10.1002/anie.200502178. PMID:16108082.; (e) Carreño, M. C.; Somoza, A.; Ribagorda, M.; Urbano, A. *Chem. Eur. J.* **2007**, *13* (3), 879–890. doi:10.1002/chem.200600809.

(8) (a) Beagley, B.; Curtis, A. D. M.; Pritchard, R. G.; Stoodley, R. J. *J. Chem. Soc., Perkin Trans. 1* **1992**, (15): 1981. doi:10.1039/p19920001981.; (b) Kraus, G. A.; Li, J.; Gordon, M. S.; Jensen, J. H. *J. Org. Chem.* **1995**, *60* (5), 1154–1159. doi:10.1021/jo00110a017.; (c) Gill, M.; Harte, M. F.; Ten, A. *Aust. J. Chem.* **2000**, *53* (4), 245. doi:10.1071/CH99091.; (d) Carreño, M. C.; García Ruano, J. L.; Toledo, M. A. *Chem. Eur. J.* **2000**, *6* (2), 288–291. doi:10.1002/

(SICI)1521-3765(20000117)6:2<288::AID–CHEM288>3.0.CO;2-2.; (e) Caygill, G. B.; Larsen, D. S.; Brooker, S. *J. Org. Chem.* **2001**, *66* (22), 7427–7431. doi:10.1021/jo015839r. PMID:11681957.; (f) Chaplin, J. H.; Edwards, A. J.; Flynn, B. L. *Org. Biomol. Chem.* **2003**, *1* (11), 1842–1844. doi:10.1039/b302522e. PMID:12945762.

(9) (a) Larsen, D. S.; O'Shea, M. D.; Brooker, S. *Chem. Commun. (Camb.)* **1996**, (2): 203. doi:10.1039/cc9960000203.; (b) White, J. D.; Choi, Y. *Org. Lett.* **2000**, *2* (15), 2373–2376. doi:10.1021/ol0001463. PMID:10930287.; (c) Nicolaou, K. C.; Vassilikogiannakis, G.; Magerlein, W.; Kranich, R. *Chem. Eur. J.* **2001**, *7* (24), 5359–5371. doi:10.1002/1521-3765(20011217)7:24<5359::AID-CHEM5359>3.0.CO;2-Z.; (d) Jarvo, E. R.; Lawrence, B. M.; Jacobsen, E. N. *Angew. Chem., Int. Ed. Engl.* **2005**, *44* (37), 6043–6046. doi:10.1002/anie.200502176. PMID:16134190.

(10) (a) Ryu, D. H.; Corey, E. J. *J. Am. Chem. Soc.* **2003**, *125* (21), 6388–6390. doi:10.1021/ja035393r. PMID:12785777.; (b) Sprott, K. T.; Corey, E. J. *Org. Lett.* **2003**, *5* (14), 2465–2467. doi:10.1021/ol034706k. PMID:12841756.; (c) Hu, Q.-Y.; Zhou, G.; Corey, E. J. *J. Am. Chem. Soc.* **2004**, *126* (42), 13708–13713. doi:10.1021/ja046154m. PMID:15493929.; (d) Liu, D.; Canales, E.; Corey, E. J. *J. Am. Chem. Soc.* **2007**, *129* (6), 1498–1499. doi:10.1021/ja068637r. PMID:17283985.

(11) (a) Ruano, J. L. G.; Plata, B. C. *Top. Curr. Chem.* **1999**, *204*, 1–126. doi:10.1007/3-540-48956-8_1.; (b) Nenajdenko, V. G.; Krasovskiy, A. L.; Balenkova, E. S. *Tetrahedron* **2007**, *63* (51), 12481–12539. doi:10.1016/j.tet.2007.10.018.

(12) Carreño, M. C.; Ruano, J. L. G.; Toledo, M.; Urbano, A. *Tetrahedron Lett.* **1994**, *35* (52), 9759–9762. doi:10.1016/0040-4039(94)88379-3.

(13) García Ruano, J. L.; Alemparte, C. *J. Org. Chem.* **2004**, *69* (4), 1405–1408. doi:10.1021/jo035629+. PMID:14961705.

(14) Brown, E. R.; Finley, K. T.; Reeves, R. L. *J. Org. Chem.* **1971**, *36* (19), 2849–2853. doi:10.1021/jo00818a026.

(15) Drabowicz, J.; Mikolajczyk, M. *Synthesis* **1978**, *1978* (10), 758–759. doi:10.1055/s-1978-24881.

(16) Selander, H.; Nilsson, J. L. G.; Liaaen-Jensen, S.; Watson, K. J.; Svensson, S. *Acta Chem. Scand.* **1972**, *26*, 2433–2440. doi:10.3891/acta.chem.scand.26-2433.

(17) *Like* and *unlike* adducts result from the approach of diene at the *si* and *re* face of the double bond (considering the end of the double bond that is next to the sulfur atom) of an (*SS*)-substituted quinone molecule, respectively, cf. Seebach, D.; Prelog, V. *Angew. Chem., Int. Ed. Engl.* **1982**, *21*, 654.

(18) Carreño, M. C.; García Ruano, J. L.; Toledo, M. A.; Urbano, A.; Remor, C. Z.; Stefani, V.; Fischer, J. *J. Org. Chem.* **1996**, *61* (2), 503–509. doi:10.1021/jo951438y. PMID:11666967.

(19) Corey, E. J.; Chaykovsky, M. *J. Am. Chem. Soc.* **1964**, *86* (8), 1639–1640. doi:10.1021/ja01062a039.

(20) Chapman, D. D.; Musliner, W. J.; Gates, J. W., Jr. *J. Chem. Soc. C* **1969**, (1): 124. doi:10.1039/j39690000124.

(21) Truce, W. E.; Perry, F. M. *J. Org. Chem.* **1965**, *30* (4), 1316–1317. doi:10.1021/jo01015a550.

(22) Mozingo, R.; Wolf, D. E.; Harris, S. A.; Folkers, K. *J. Am. Chem. Soc.* **1943**, *65* (6), 1013–1016. doi:10.1021/ja01246a005.

(23) Teich, S.; Curtin, D. Y. *J. Am. Chem. Soc.* **1950**, *72* (6), 2481–2483. doi:10.1021/ja01162a035.

(24) Smith, L. I.; Nichols, J. *J. Am. Chem. Soc.* **1943**, *65* (9), 1739–1747. doi:10.1021/ja01249a025.

(25) The *SR* configuration was chosen because of the availability of the sulfinylating agent 1,2:5,6-di-*O*-isopropylidene-α-D-glucofuranosyl (+)-(*R*)-2-propanesulfinate in our laboratory; prepared according to Fernandez, I.; Khiar, N.; Llera, J. M.; Alcudia, F. *J. Org. Chem.* **1992**, *57*, 6789.

Aluminum nitrate and silica sulfuric acid as efficient nitrating media for the mononitration of phenols under mild and heterogeneous conditions

Arash Ghorbani-Choghamarani, Hamid Goudarziafshar, Mohsen Nikoorazm, and Somaieh Yousefi

Abstract: A variety of phenol derivatives were successfully nitrated via combination of $Al(NO_3)_3{\cdot}9H_2O$ and silica sulfuric acid in the presence of wet SiO_2 (50% *w*/*w*) in dichloromethane at room temperature with moderate-to-good yields.

Key words: nitration, phenol, heterogeneous conditions, aluminum nitrate [$Al(NO_3)_3{\cdot}9H_2O$], silica sulfuric acid (SiO_2–OSO_3H).

Résumé : Opérant à la température ambiante, dans le dichlorométhane et faisant appel à une combinaison de $Al(NO_3)_2{\cdot}9H_2O$ et d'acide sulfurique lié à de la silice, en présence de SiO_2 humide (50 % *w*/*w*), on a réalisé avec succès la nitration des dérivés du phénol, avec des rendements allant de modérés à bons.

Mots-clés : nitration, phénol, conditions hétérogènes, nitrate d'aluminium [$Al(NO_3)_2{\cdot}9H_2O$], acide sulfurique lié à de la silice (SiO_2–OSO_3H).

[Traduit par la Rédaction]

Introduction

Nitrophenols have been identified in the atmospheric gas phase and in cloud and rainwater.[1] Nitration of organic substrates is a widely studied reaction of great industrial significance, as many nitro-compounds are extensively utilized and act as intermediates for the manufacture of plastics, dyes, perfumes, drugs, and pharmaceuticals.[2] However, nitration in a manufacturing process requires the use of potent mixtures of concentrated or fuming nitric acid with sulfuric acid, leading to excessive acid-waste streams and added expense.[3] Nitrophenols are very important organic intermediates, and hence, it is still interesting to develop regiospecific pollution-free nitrating procedures for phenolic compounds under mild conditions.[4] Even though various nitrating reagents for the nitration of phenols have been emerged in the recent years,[5–10] many of these methods still suffer from some drawbacks, including low selectivity, low yields of products, tedious work-up, toxicity, and expensive reagents.

Recent research has demonstrated that the heterogeneous reagent systems have many advantages, such as simple experimental procedures, mild reaction conditions, and minimization of chemical waste as compared with the liquid-phase counterparts.[11–16]

Received 27 February 2009. Accepted 28 May 2009. Published on the NRC Research Press Web site at canjchem.nrc.ca on 27 July 2009.

A. Ghorbani-Choghamarani,[1] H. Goudarziafshar, M. Nikoorazm, and S. Yousefi. Department of Chemistry, Faculty of Science, Ilam University, P.O. Box 69315516 Ilam, Iran.

[1]Corresponding author (e-mail: arashghch58@yahoo.com).

Therefore, we decided to design new heterogeneous media for the selective mononitration of phenolic compounds.

Result and discussion

In this article, we report a new, simple, cheap, and convenient protocol for the mononitration of phenols using SiO_2–OSO_3H and $Al(NO_3)_3{\cdot}9H_2O$ in the presence of wet SiO_2 (50% *w*/*w*) under mild and heterogeneous conditions. Silica sulfuric acid can be readily prepared via the reported procedure by Zolfigol (Scheme 1).[17]

A wide variety of substituted phenols were nitrated by silica sulfuric acid (SiO_2–OSO_3H) (**I**) and aluminum nitrate [$Al(NO_3)_3{\cdot}9H_2O$] (**II**) in the presence of wet SiO_2 (50%, *w*/*w*) in dichloromethane (Scheme 2).

The nitration reactions were performed at room temperature with moderate-to-good yields, and the results are summarized in Table 1.

The mixing of the nitrating agents and phenols in dichloromethane and stirring the resulting heterogeneous mixture at room temperature can selectively produce mononitrated phenols. Highly pure mononitrophenols can be obtained by flash column chromatography. A combination of aluminum nitrate nine hydrate and silica sulfuric acid can act as a solid nitrating agent, which can be readily weighed, handled, and used in the presence of moist SiO_2. Water molecules or wet SiO_2 are necessary for the nitration of phenols. Therefore, we think that wet SiO_2 acts as a heterogeneous effective surface area for in situ generation of HNO_3.

In summary, herein, we report an efficient method for the selective nitration of phenols under mild and heterogeneous conditions with acceptable yields. Furthermore, this method exhibits substrate versatility, mild reaction conditions, easy and clean work-up of products.

Table 1. Mononitration of phenols to their corresponding nitro derivatives using silica sulfuric acid (**I**), $Al(NO_3)_3{\cdot}9H_2O$ (**II**), and wet SiO_2 (50% *w*/*w*) in dichloromethane at room temperature.

Entry	Substrate	Product	Reagent/substrate (mmol)[a] I	II	Time (min)	Yields[b] %	Mp or bp (°C) found	Mp or bp (°C) reported
1	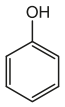	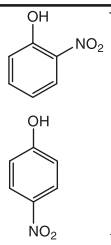	0.225	1	25	36 43	42–44 110–111	44–46[18] 111–113[18]
2	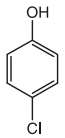	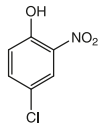	0.225	1.5	5 (h)	56	83–85	89[18]
3	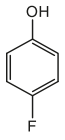	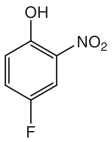	0.225	1.5	6.5 (h)	59	72–74	73[18]
4	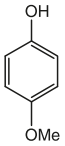	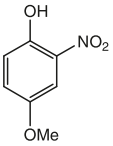	0.225	0.5	165	56	78–79	54–56[18]
5	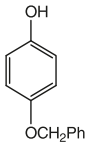	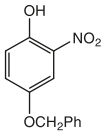	0.225	0.7	195	75	67–69	61–66[18]
6	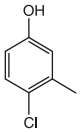	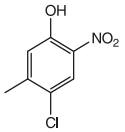	0.225	0.5	110	60	130–132	—
7	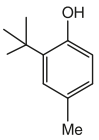	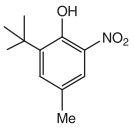	0.225	0.7	5 (h)	88	89–90	—
8	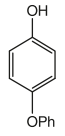	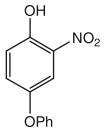	0.225	1	20	72	Oil	—

Scheme 1. Preparation of silica sulfuric acid (SiO_2–OSO_3H).

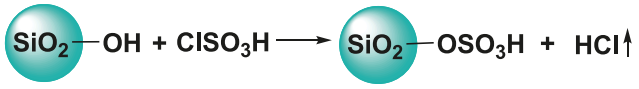

Scheme 2. Mononitration of phenol derivatives.

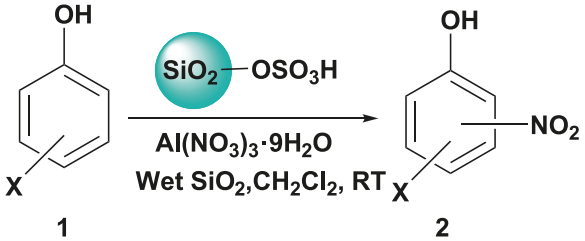

Table 1. *Concluded.*

Entry	Substrate	Product	Reagent/substrate (mmol)[a] I	II	Time (min)	Yields[b] %	Mp or bp (°C) found	Mp or bp (°C) reported
9	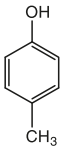	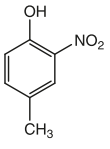	0.225	0.5	225	61	30–32	29–31[18]
10	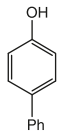	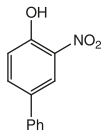	0.225	1	20	52	68–69	61–63[18]
11	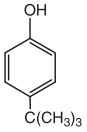	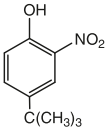	0.225	0.7	35	54	Oil	—
12	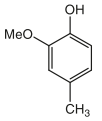	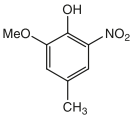	0.225	1	15	59	75–77	—
13	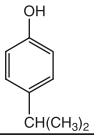	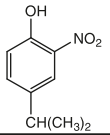	0.225	0.7	25	63	Oil	—

[a] Wet SiO_2 : substrate = 0.2 g : 1 mmol.
[b] Yields after purification by column chromatography.

Experimental section

The chemicals and solvents were purchased from Fluka, Merck, and Aldrich chemical companies and were used without further purifications.

Mononitration of 4-chloro-3-methylphenol with silica sulfuric acid, $Al(NO_3)_3{\cdot}9H_2O$, and wet SiO_2 (a typical procedure)

A suspension of 4-chloro-3-methylphenol (0.142 g, 1 mmol), silica sulfuric acid (0.225 g), wet SiO_2 (50% *w*/*w*, 0.2 g), and $Al(NO_3)_3{\cdot}9H_2O$ (0.143 g, 0.5 mmol) in CH_2Cl_2 (5 mL) was stirred at room temperature for 110 min (the progress of the reaction was monitored by TLC) and then filtered. Anhydrous Na_2SO_4 (1.5 g) was added to the filtrate. After 15 min, the resulting mixture was also filtered; CH_2Cl_2 was removed by distillation in a water bath. Crude product was purified by flash silica-gel column chromatography using CH_2Cl_2 as eluent and pure product obtained in 60% yield (0.112 g). Crystalline pale yellow solid, mp 130–132 °C. ^{1}H NMR (400 MHz, $CDCl_3$) δ: 10.46 (s, 1H), 8.10 (s, 1H), 7.27 (s, 1H), 7.07 (s, 1H), 2.43 (s, 3H) ppm. ^{13}C NMR (100 MHz, $CDCl_3$) δ: 153.4, 147.6, 131.8, 125.8, 124.5, 121.4, 20.8 ppm.

4-tert-*Buthyl-2-nitrophenol*

Yellow oil. ^{1}H NMR (400 MHz, $CDCl_3$) δ: 10.49 (s, 1H), 8.07 (s, 1H), 7.63–7.66 (d, 1H, *J* = 8.8 Hz), 7.09–7.12 (d, 1H, *J* = 8.8 Hz), 1.33 (s, 9H) ppm. ^{13}C NMR (100 MHz, $CDCl_3$) δ: 153.0, 143.6, 135.4, 132.9, 120.8, 119.5, 34.3, 31.0 ppm.

*2-Nitro-4-*iso*-propylphenol*

Yellow oil. ^{1}H NMR (400 MHz, $CDCl_3$) δ: 10.48 (s, 1H), 7.94 (s, 1H), 7.47–7.49 (d, 1H, *J* = 7.6 Hz), 7.09–7.11 (d, 1H, *J* = 8.8 Hz), 2.89–2.96 (septet, 1H, *J* = 8 Hz), 1.25–1.27 (d, 6H, *J* = 8 Hz) ppm. ^{13}C NMR (100 MHz, $CDCl_3$) δ: 153.3, 141.2, 136.4, 133.3, 121.9, 119.7, 33.1, 23.7 ppm.

2-Nitro-4-phenoxyphenol

Yellow oil. ^{1}H NMR (400 MHz, $CDCl_3$) δ: 10.41 (s, 1H), 7.7–7.71 (m, 1H), 7.34–7.4 (m, 3H), 7.16–7.18 (m, 2H), 6.99–7.0 (m, 2H) ppm. ^{13}C NMR (100 MHz, $CDCl_3$) δ: 156.6, 151.2, 149.8, 133.3, 130.1, 129.6, 124.1, 121.1, 118.6, 113.6 ppm.

2-tert-*Buthyl-4-methyl-2-nitrophenol*

Crystalline pale yellow solid, mp 89–90 °C. ^{1}H NMR (400 MHz, $CDCl_3$) δ: 11.43 (s, 1H), 7.79 (s, 1H), 7.38 (s, 1H), 2.32 (s, 3H), 1.43 (s, 9H) ppm. ^{13}C NMR (100 MHz, $CDCl_3$) δ: 153.1, 140.2, 136.1, 133.8, 128.6, 122.2, 35.4, 29.3, 20.7 ppm.

2-Methoxy-4-methyl-2-nitrophenol

Crystalline pale yellow solid, mp 75–77 °C. ^{1}H NMR (400 MHz, $CDCl_3$) δ: 10.64 (s, 1H), 7.49 (s, 1H), 6.96 (s, 1H), 3.94 (s, 3H), 2.34 (s, 3H) ppm. ^{13}C NMR (100 MHz, $CDCl_3$) δ: 149.6, 144.3, 133.4, 128.9, 122.0, 119.2, 115.2, 56.6, 20.9 ppm.

Acknowledgment

This work was supported by the research facilities of Ilam University, Ilam, Iran.

References

(1) Heal, M. R.; Harrison, M. A. J.; Cape, J. N. *Atmos. Environ.* **2007**, *41* (17), 3515–3520. doi:10.1016/j.atmosenv.2007.02.003.

(2) Mallick, S.; Parida, K. M. *Catal. Commun.* **2007**, *8* (10), 1487–1492. doi:10.1016/j.catcom.2006.12.023.

(3) Yi, W.-B.; Cai, C. *Synth. Commun.* **2006**, *36* (20), 2957–2961. doi:10.1080/00397910600773700.

(4) Selvam, J. J. P.; Suresh, V.; Rajesh, K.; Reddy, S. R.; Venkateswarlu, Y. *Tetrahedron Lett.* **2006**, *47* (15), 2507–2509. doi:10.1016/j.tetlet.2006.02.057.

(5) Nandurkar, N. S.; Bhanushali, M. J.; Jagtap, S. R.; Bhanage, B. M. *Ultrason. Sonochem.* **2007**, *14* (1), 41–45. doi:10.1016/j.ultsonch.2006.01.005. PMID:16563845.

(6) Anuradha, V.; Srinivas, P. V.; Aparna, P.; Rao, J. M. *Tetrahedron Lett.* **2006**, *47* (28), 4933–4935. doi:10.1016/j.tetlet.2006.05.017.

(7) Heravi, M. M.; Benmorad, T.; Bakhtiari, K.; Bamoharram, F. F.; Oskooie, H. H. *J. Mol. Catal. Chem.* **2007**, *264* (1-2), 318–321. doi:10.1016/j.molcata.2006.09.014.

(8) Rajagopal, R.; Srinivasan, K. V. *Synth. Commun.* **2003**, *33* (6), 961–966. doi:10.1081/SCC-120016360.

(9) Budde, C. L.; Beyer, A.; Munir, I. Z.; Dordick, J. S.; Khmelnitsky, Y. L. *J. Mol. Catal., B Enzym.* **2001**, *15* (1-3), 55–64. doi:10.1016/S1381-1177(01)00004-2.

(10) Barletta, B.; Bolzacchini, E.; Meinardi, S.; Orlandi, M.; Rindone, B. *Environ. Sci. Technol.* **2000**, *34* (11), 2224–2230. doi:10.1021/es990844m.

(11) Zolfigol, M. A.; Salehi, P.; Ghorbani-Choghamarani, A.; Shahamirian, M. *Synth. Commun.* **2007**, *37* (11), 1817–1823. doi:10.1080/00397910701316276.

(12) Mohammadpoor-Baltork, I.; Tangestaninejad, S.; Hojati, S. F. *J. Iran. Chem. Soc.* **2008**, *5*, S65.

(13) Zolfigo, M.; Amani, K.; Ghorbani-Choghamarani, A.; Hajjami, M.; Ayazinasrabadi, R.; Jafari, S. *Catal. Commun.* **2008**, *9* (8), 1739–1744. doi:10.1016/j.catcom.2008.01.029.

(14) Zolfigol, M.; Shirini, F.; Ghorbani-Choghamarani, A. *Synthesis* **2006**, 2043–2046. doi:10.1055/s-2006-942396.

(15) Mohammadpoor-Baltork, I.; Ghorbani-Choghamarani, A.; Baghbanzadeh, M. *J. Iran. Chem. Soc.* **2006**, *3*, 73.

(16) Zolfigol, M. A.; Amani, K.; Hajjami, M.; Ghorbani-Choghamarani, A. *Monatsh. Chem.* **2008**, *139* (8), 895–899. doi:10.1007/s00706-008-0868-6.

(17) Zolfigol, M. A. *Tetrahedron* **2001**, *57* (46), 9509–9511. doi:10.1016/S0040-4020(01)00960-7.

(18) Zolfigol, M.; Shirini, F.; Ghorbani-Choghamarani, A. *Phosphorus Sulfur Silicon* **2003**, *178* (9), 2019–2025. doi:10.1080/10426500390228701.

Theoretical study of the electronic spectra of *s*-triazine vapour

Delano P. Chong

Abstract: The ionization and excitation spectra of valence and core electrons of *s*-triazine in the gas phase are studied with ab initio, density functional, and semi-empirical methods. The results are compared with available experimental data and previous calculations. New estimates are proposed for the ionization energies of both valence and core electrons. The calculated excitation energies are consistent with experiment.

Key words: ionizations, photoelectron spectra, excitations, UV absorption, electron spectra, *s*-triazine, core-electron binding energies, ESCA, DFT.

Résumé : Faisant appel à des méthodes de calculs semi-empiriques, ab initio et selon la théorie de la fonctionnelle de la densité, on a étudié les spectres d'excitation et d'ionisation des électrons de coeur et de valence de la *s*-triazine en phase gazeuse. On compare les résultats de ces calculs avec les données expérimentales disponibles et les résultats de calculs antérieurs. On propose de nouvelles évaluations pour les énergies d'ionisation des électrons de valence et de coeur. Les énergies d'excitation calculées sont cohérentes avec les résultats expérimentaux.

Mots-clés : ionisations, spectres photoélectroniques, excitations, absorption UV, spectres électroniques, *s*-triazine, énergies de liaison des électrons de coeur, spectroscopie électronique pour l'analyse chimique (SEAC), théorie de la fonctionnelle de densité (TFD).

[Traduit par la Rédaction]

Introduction

The photoelectron spectra of 1,3,5-(*sym*)-triazine ($C_3N_3H_3$) vapour were reported by several workers in 1972.[1–4] The assignments of some of the bands were somewhat tentative, since the interpretation of the photoelectron spectra was based on the use of Rydberg transitions,[1] extended Hückel treatments,[2] or the perfluoro effect,[3,4] and vertical ionization energies (VIEs) within 0.3 eV of each other can easily be misinterpreted. In my opinion, none of the assignments is completely correct, and the best estimates of the VIEs of gas-phase *s*-triazine are presented in Table 1.

On the other hand, although the excitation spectrum[1,5,6] was better understood, the Rydberg-like assignments, such as *n*s and *n*p (leaving the centre of the Rydberg orbitals unspecified), are not entirely satisfactory. Experimental studies of the excitation of the core electrons of *s*-triazine were more recent,[7–9] but the core-electron binding energies (CEBEs) have only been estimated from similar molecules,[7] and those values are quite different from ab initio[8] and density functional theory (DFT) calculations.[9]

As is well-known, *s*-triazine is planar with D_{3h} symmetry. The purpose of this work is to calculate the ionization and excitation spectra of both valence and core electrons of *s*-triazine in the gas phase with various theoretical methods and to compare the results with the available experimental data. The calculations are performed with standard program packages. The motivation for this work is partly to stimulate experimentalists to try similar computations for the interpretation of their observed electron spectra after they see the encouraging results of this work.

Received 24 March 2009. Accepted 22 May 2009. Published on the NRC Research Press Web site at canjchem.nrc.ca on 28 July 2009.

D.P. Chong. Department of Chemistry, 2036 Main Mall, The University of British Columbia, Vancouver, BC V6T 1Z1, Canada. (e-mail: chong@chem.ubc.ca).

Computational details

Electron spectra are generally not very sensitive to small variations in geometry. Since the experimental geometry of gas-phase *s*-triazine (D_{3h} symmetry) has been determined by electron diffraction,[10] it is used instead of optimizing the geometry theoretically. However, the angles around each carbon do not add up to 360° exactly, with the H–C–N angle having the largest uncertainty. I therefore decided to use a value of 116.95° for the H–C–N angle instead of the reported value of 116.9° ± 0.1°.[10] For runs with Gaussian03 program package,[11] Dunning's cc-pVTZ basis set[12] is used, while the aug-TZP basis set of Slater-type orbitals[13,14] is chosen for runs with the Amsterdam density functional (ADF) program.[15]

Results and discussions

Valence ionizations

In the absence of significant shake-up satellite bands, the most reliable method for the computation of VIEs is outer-valence Green's function (OVGF). This is true for our molecule *s*-triazine as well, as shown in Table 2, with an average absolute deviation (AAD) of 0.34 eV from experiment. The $1a_2''$ and the doubly degenerate $1e''$ orbitals are similar to the familiar π-MOs of benzene. In the OVGF output, there is no calculated VIE between $1e''$ cation at 11.69 eV and the $1e''$ cation at 13.23 eV, confirming the suggestion

Table 1. Observed vertical ionization energies (in eV) of gas-phase *s*-triazine.

Fridh et al.[1]		Gleiter et al.[2]		Robin et al.,[3] Brundle et al.[4]		Best estimate from all three	
VIE	Species	VIE	Species	VIE	Species	VIE	Species
10.4	6e′	10.37	e′	10.41	e′	10.39	6e′
12.0	1e″	11.67	e″	11.71[a]	π_2 and π	11.69	1e″
13.3	$1a_2''$	13.21	a_1'	13.25	a_1'	13.23	$5a_1'$
14.7	5e′	14.67	a_2''	14.65	π_1	14.66	5e′ [b]
15.0[c]	$6a_1'$	14.88	e′	14.85		14.87	$1a_2''$ [b]
17.6	$1a_2'$			17.94		17.8	$1a_2'$
18.2	$5a_1'$			18.2[d]		18.2	$4a_1'$ [b]
22.0	4e′			22.3		22.2	4e′

[a]Omitting 12.2 eV due to Jahn–Teller splitting.
[b]Based on various calculations; see Table 2.
[c]In light of refs. 2–4, 15.0 eV is a more likely value than 15.8 eV for the VIE from their Fig. 1.
[d]From their Fig. 4.

Table 2. Vertical ionization energies (in eV) of gas-phase s-triazine.

Observed[a]	Species[a]	This work						1973	1990
		OVGF[b]	0.55GF2[b]	mKT(SAOP)[c]	ΔE(PBE0)[c,d]	ΔE(mPW1PW)[c,d]	HAM/3	INDO/2[e]	MRINDO/S[f]
10.39	6e′	10.51	10.62	11.07	10.84	10.90	10.39	10.4	10.38
11.69	1e″	11.77	11.69	12.86	12.43	12.45	11.89	11.1	11.19
13.23	$5a_1'$	13.75	13.92	13.73	13.38	13.43	13.18	13.5	13.88
14.66	5e′	15.08	15.39	14.97	15.14	15.21	14.82	14.8	14.10
14.87	$1a_2''$	15.27	15.57	15.80	15.42	15.44	14.59	15.8	14.90
17.8	$1a_2'$	18.23	18.50	18.08	18.22	18.26	16.88	21.6	17.01
18.2	$4a_1'$	18.64	19.08	17.98	18.07	18.12	17.32	23.6	20.93
AAD (*N*)[g]		0.34 (7)	0.56 (7)	0.58 (7)	0.42 (7)	0.45 (7)	0.36 (7)	0.42 (5)	0.45 (5)

[a]See Table 1.
[b]With cc-pVTZ basis set.
[c]With aug-TZP basis set.
[d]With electron density from V_{xc} = SAOP.
[e]Ridley and Zerner.[22]
[f]Prasad and Rai.[23]
[g]Average absolute deviation for *N* entries.

of Robin et al.[4] that the observed peak at 12.2 eV is due to Jahn–Teller effects. Because of the D_{3h} symmetry, most of the occupied σ-MOs exist in combinations of a_1' and e′. For example, the N1s cores become $1a_1'$ and 1e′ MOs; and those of C1s, $2a_1'$, and 2e′.

The shortcut approximations, parametrized second-order Green's function (pGF2),[16] and meta-Koopmans' theorem (mKT),[17] fare less well, with AAD = 0.56 and 0.58 eV, respectively. The latest DFT methods[18] are ΔE(PBE0) and ΔE(mPW1PW) for the density obtained with the exchange–correlation potential V_{xc} known as statistical averaging of orbital potential (SAOP),[19,20] perform reasonably well, with AAD = 0.42 and 0.45 eV, respectively. Of the semi-empirical MO methods, the heavily parametrized HAM/3,[21] outperforms the others,[22,23] not only in giving a lower AAD, but also in providing VIE estimates for more MOs, as shown in Table 2.

The calculation of adiabatic ionization energies (except the lowest one) is more difficult because one needs to optimize the geometry of each cationic state of interest. In this work, the geometry of the ground-state cation of *s*-triazine was first optimized with the exchange–correlation functional E_{xc} known as PW91 using the polarized triple-zeta TZP basis set in the ADF program package. Then, the energy difference between parent and cation was computed with the method of coupled-cluster with single and double excitations and perturbative correction due to triple excitations CCSD(T) using the polarized valence triple-zeta basis set 6–311G(d,p) in the Gaussian03 program. The adiabatic ionization energy thus obtained is 10.05 eV, in excellent agreement with the observed value of 10.01 eV.[1]

In short, the combination of past experimental and present theoretical studies provides a better interpretation of the photoelectron spectra of *s*-triazine vapour.

Valence excitations

One of the nice features of the exchange–correlation potential V_{xc} = SAOP is its correct asymptotic behavior, leading to reliable excitation energies from time-dependent DFT (TDDFT) calculations, as indicated by previous studies,[13,19,20,24,25] provided one uses adequate basis sets such as aug-TZP. As an example, the excitation energies of the N_2 molecule as calculated by various methods are compared in Table 3. It can be seen that, in favorable situa-

Table 3. Vertical excitation energies (in eV) of N_2.

	Obs[a]	TDDFT(SAOP)[c]	MRCC[d]	FCI[e]	IH-FS-CCSD[f]	TDDFT(CAM-B3LYP)[g]	IH-FS-CCSDT[h]
$^3\Sigma_u^+$	7.75	7.88	7.56		7.73		7.91
$^3\Pi_g$	8.04	7.83	8.05		8.07		8.15
$^3\Delta_u$	8.88	8.82	8.93		8.93		9.21
$^1\Pi_g$	9.31	9.35	9.27	9.58	9.29	9.38	9.61
$^3\Sigma_u^-$	9.67	9.65	9.86		9.91		10.02
$^1\Sigma_u^-$	9.92	9.65	10.09	10.33	9.99	9.21	10.33
$^1\Delta_u$	10.27	10.22	10.54	10.72	10.48	9.68	10.73
$^3\Pi_u$	11.19	10.89	11.19		11.20		11.42
$^3\Sigma_g^+$	12.00	11.93	11.75		11.98		
$^1\Sigma_g^+$	12.20	12.37	12.20		13.06	11.80	
$^1\Pi_u$	12.90[b]	13.14	12.84	13.61		12.27	13.77
$^1\Sigma_u^+$	12.98[b]	12.86	12.82			12.32	

[a]Oddershede et al.,[26] except as noted.
[b]Stahel et al.[27]
[c]Time-dependent DFT with SAOP potential.[13]
[d]Multireference coupled-cluster method.[28]
[e]Full CI.[29]
[f]Intermediate Hamiltonian Fock-space coupled-cluster method with singles and doubles.[30]
[g]Time-dependent DFT with CAM-B3LYP functional.[31]
[h]Intermediate Hamiltonian Fock-space coupled-cluster method with singles, doubles, and triples.[32,33]

Table 4. Valence singlet excitations in eV (*f*-values in parentheses) of *s*-triazine.

UV	Assignment	EELS[a]	Assignment[c]	TDDFT(SAOP)		INDO/2[b]	MRINDO/S[c]
				ΔE (*f*-value) state	excitation	ΔE (*f*-value) state	ΔE (*f*-value) state
4.59[d]	$^1A_2''$	4.5 strong	$^1A_2''$	4.30 (0.01) $^1A_2''$	$6e' \rightarrow 2e''$	4.56 (0.04) $^1A_2''$	3.22 (0.02) $^1A_2''$
7.12[e]	$^1E'$	7.77 very strong	$^1E'$	7.20 (1.52) $^1E'$	$1e'' \rightarrow 2e''$	7.59 (0.84) $^1E'$	5.34 (0.05) $^1E'$
		8.6		8.00 (0.05) $^1E'$	$6e' \rightarrow 7e'$		6.82 (0.11) $^1E'$
			$6e' \rightarrow 4p$	8.24 (0.04) $^1E'$	$6e' \rightarrow 7a_1'$		6.85 (0.12) $^1E'$
				8.94 (0.04) $^1E'$	$6e' \rightarrow 8e'$		7.08 (0.02) $^1E'$
							7.11 (0.03) $^1E'$
							7.87 (0.36) $^1E'$
							7.89 (0.36) $^1E'$
		9.37		9.20 (0.06) $^1E'$	$1a_2'' \rightarrow 2e''$		
			$1e'' \rightarrow 3p$	9.60 (0.01) $^1A_2''$	$6e' \rightarrow 3e''$		
				9.80 (0.04) $^1A_2''$	$1e'' \rightarrow 7e'$		
		10.6	$1e'' \rightarrow 4p$	10.23 (0.03) $^1E'$	$1e'' \rightarrow 2a_2''$ and $3a_2''$		
				10.30 (0.19) $^1E'$	$6e' \rightarrow 2a_2'$		
				10.37 (0.09) $^1E'$	$6e' \rightarrow 8a_1'$		

Note: Excluding excitations with calculated *f*-values < 0.0.01 and metatable states above 10.4 eV.
[a]Fridh et al.[1]
[b]Ridley and Zerner.[22]
[c]Prasad and Rai.[23]
[d]Brinen and Goodman.[5]
[e]Brinen et al.[6]

tions, our procedure of TDDFT(SAOP)/aug-TZP can be as reliable as the other methods. In this work, TDDFT is used with V_{xc} = SAOP to compute the excitation of valence electrons of *s*-triazine vapour. The results are compared with experiment and other studies in Table 4.

Excitations of valence electrons for *s*-triazine in different solutions and in solid state, studied by various workers, are beyond the scope of the present work. For gas-phase *s*-triazine, there have been very few studies.[1,5,6,34] The most reliable data seem to be from the electron-impact energy-loss spectrum reported by Fridh et al.[1] The intensity in electron energy-loss spectra (EELS), of course, does not correspond to *f*-values.

The lowest triplet states from our calculation are $^3A_2''$ at 3.85 eV and $^3E''$ at 3.92 eV, which probably correspond to the triplet at 3.59 eV for *s*-triazine crystal.[34] The first singlet peak with nonzero *f*-value from our calculation is $^1A_2''$ at 4.30 eV, compared with $^1A_2''$ at 4.5 eV observed in EELS,[1]

Table 5. CEBEs (in eV) of gas-phase *s*-triazine.

	Core hole	Method	C1s	N1s
Apen et al. (1993)[7]			290.6	404.9
Duflot et al. (2005)[8]	Localized	SCF	294.15	405.70
		MP2	293.28	406.14
Vall-Ilosera et al. (2008)[9]		B88P86	292.95	405.5
This work	Localized core hole	PW86PW91	293.30	405.83
	Symmetry MO	PW86PW91	282.49	393.35
Best estimate			293.3	405.8

Table 6. Inner-shell excitation spectra (in eV) of gas-phase *s*-triazine.

This work				Apen et al.[7]		Duflot et al.[8]					Vall-Ilosera et al.[9]			
	ΔE	TV	Relative intensity	IS-EELS	TV	IS-EELS	TV	CIS + MP2	TV	Relative intensity	Near-edge XAS	TV	ΔKS	TV
C1s														
e″	275.85	6.64	1	286.2 e″	7.1	286.16	7.14 π*	286.32	6.96	1	285.9	7.4	285.49	7.46 e″
e′	279.08	3.41	0.39	287.5	5.8									
a_1'	279.16	3.33	0.75	290.1 a_2''	3.2	290.09	3.21 σ*	289.83	3.45	0.064				
a_2''	279.50	2.99	0.24	290.8	2.5	290.84	2.46 π*	290.73	2.55	0.128	288.8	4.5	289.36	3.59 a_2''
a_1'	279.66	2.83	3.16											
e′	279.69	2.80	0.22								290.5	2.8	290.40	2.55 e′
a_2''	279.98	2.51	0.33											
IP	282.49	(0)		293.3	(0)	293.3	(0)	293.28	(0)		293.3	(0)	292.95	(0)
N1s														
e″	386.84	6.51	1	398.8 e″	7.0	398.84	6.96	399.05	7.09	1 π*	398.9	6.9	398.36	7.14 e″
a_1'	390.07	3.28	0.24								399.9	5.9		
a_2''	390.19	3.16	0.69	402.9 a_2''	2.9	402.92	2.88	404.03	2.11	0.116 π*	402.9	2.9	402.34	3.16 a_2''
e′	390.67	2.68	0.99			404.12	1.68	404.10	2.04	0.152 π*				
IP	393.35	(0)		405.8	(0)	405.8	(0)	406.14	(0)		405.8	(0)	405.5	(0)

and the maximum absorption at 4.59 eV in low-resolution UV spectra.[5] The very intense excitation to the ^{1}E′ state at 7.77 eV from EELS and the estimated maximum UV at 7.12 eV in the high-resolution UV spectrum are confirmed by our 7.20 eV with *f*-value > 1.5 for ^{1}E′ state from the 1e″ to 2e″ excitation. However, the $^1A_1'$ state for the same 1e″ to 2e″ excitation is calculated with no intensity, even though the calculated energy of 6.88 eV agrees well with the observed ~6.7 eV. The reason for the disagreement in intensity is probably the neglect of vibronic interactions in this work. The interpretation of the higher energy peaks is tentative.

Core-electron ionizations

There does not appear to be any reported measurement(s) of the CEBEs of *s*-triazine vapour. Apen et al[7] estimated the C1s and N1s values from similar molecules while Duflot et al.[8] made ab initio calculations and Vall-Ilosera et al.[9] did DFT computations for them. In this work, DFT calculations are also performed but with an exchange–correlation functional E_{xc} known as PW86x-PW91c, which has been shown to lead to reliable CEBEs for C, N, O, and F.[35] Moreover, it is well-known that the calculated values for symmetric core holes for equivalent nuclei are much less reliable than those for localized core holes.[36] Table 5 presents best estimates, obtained by this work, of the CEBEs of C1s and N1s in *s*-triazine based on the results of MP2,[8] B88P86,[9] and the present PW86PW91 calculations. I believe that 293.3 and 405.8 eV are better estimates of the CEBEs of C1s and N1s than the previous estimates of Apen et al.[7]

Core-electron excitations

Excitations from core electrons in degenerate symmetry MOs are difficult to treat in this work's approach because core holes are better approximated by localized holes, but localizing a core hole would reduce the full symmetry of the symmetric molecule. Moreover, this work's simplification of limiting the TDDFT treatment to excitations from the core levels gives only estimates of the oscillator strengths. To overcome the localized versus delocalized difficulty, term values (TVs) are compared in Table 6.

Although this work's calculated value of 6.51 eV for the TV of N1s going to 2e″ MO deviates from the observed value around 7 eV, the assignment of the two main bands in the N1s excitations to 2e″ and $2a_2'$ are definitely confirmed. However, the assignment of the observed N1s excitation at 399.9 eV by Vall-Ilosera et al.[9] and that at 404.12 eV by Duflot et al.[8] remain uncertain.

Except for the first excitation from C1s to the 2e″ LUMO, the excitations from C1s are not well-understood. The second main band at 290.1 eV was assigned to $2a_2'$ by Apen et al.[7] The value corresponds well to 290.09 eV observed but Duflot et al.,[8] who however assigned it to π* MO. The TV

value of this work and estimated intensity seem to favour the assignment to $6a_1'$, supporting Duflot et al.

Conclusions

In this work, previous photoelectron spectra of *s*-triazine vapour are reviewed and the best estimates of the vertical ionization energies are presented in Table 1, and the results of ab initio, DFT, and semi-empirical MO methods are compared in Table 2. As expected, the best method is OVGF, and the best semi-empirical method is HAM/3. On the other hand, the approach of TDDFT(SAOP)/aug-TZP provides a good interpretation of the experimental excitation spectra of valence electrons.

Spectra of core-electron are usually more difficult. Based on previous and present calculations, more reliable values for the core-electron binding energies than the previous estimates from similar molecules are proposed. Although the core excitations from C1s and N1s to the π^* MOs of e'' and a_2' are definitely confirmed, the identity of other levels are less certain.

Acknowledgment

The author is grateful to the Natural Sciences and Engineering Research Council of Canada (NSERC) for financial support.

References

(1) Fridh, C.; Åsbrink, L.; Jonsson, Ö.; Lindholm, E. *Int. J. Mass Spectrom. Ion Phys.* **1972**, *8* (2), 85–99. doi:10.1016/0020-7381(72)80001-9.

(2) Gleiter, R.; Heilbronner, E.; Hornung, V. *Helv. Chim. Acta* **1972**, *55*, 28.

(3) Robin, M. B.; Kueble, N. A.; Brundle, C. R. In Electron spectroscopy; Shirley, D.A., Ed.; North-Holland Publishing Co.: Amsterdam, 1972; p. 351.

(4) Brundle, C. R.; Robin, M. B.; Kuebler, N. A. *J. Am. Chem. Soc.* **1972**, *94* (5), 1466–1475. doi:10.1021/ja00760a008.

(5) Brinen, J. S.; Goodman, L. *J. Chem. Phys.* **1961**, *35* (4), 1219. doi:10.1063/1.1732026.

(6) Brinen, J. S.; Hirt, R. C.; Schmitt, R. G. *Spectrochim. Acta [A]* **1962**, *18*, 863.

(7) Apen, E.; Hitchcock, A. P.; Gland, J. L. *J. Phys. Chem.* **1993**, *97* (26), 6859–6866. doi:10.1021/j100128a019.

(8) Duflot, D.; Sidhoum, K.; Flament, J.-P.; Giuliani, A.; Heinesch, J.; Hubin-Franskin, M.-J. *Eur. Phys. J. D* **2005**, *35* (2), 239–248. doi:10.1140/epjd/e2005-00193-6.

(9) Vall-llosera, G.; Gao, B.; Kivimäki, A.; Coreno, M.; Álvarez Ruiz, J.; de Simone, M.; Ågren, H.; Rachlew, E. *J. Chem. Phys.* **2008**, *128* (4),o. 044316. doi:10.1063/1.2822985. PMID:18247958.

(10) Pyckhout, W.; Callaerts, I.; van Alsenoy, C.; Geise, H. J.; Almenningen, A.; Seip, R. *J. Mol. Struct.* **1986**, *147* (3-4), 321–329. doi:10.1016/0022-2860(86)80386-6.

(11) Frisch, M. J.; Trucks, G. W.; Schlegel, H. B.; Scuseria, G. E.; Robb, M. A.; Cheeseman, J. R.; Montgomery, J. A., Jr.; Vreven, T.; Kudin, K. N.; Burant, J. C.; Millam, J. M.; Iyengar, S. S.; Tomasi, J.; Barone, V.; Mennucci, B.; Cossi, M.; Scalmani, G.; Rega, N.; Petersson, G. A.; Nakatsuji, H.; Hada, M.; Ehara, M.; Toyota, K.; Fukuda, R.; Hasegawa, J.; Ishida, M.; Nakajima, T.; Honda, Y.; Kitao, O.; Nakai, H.; Klene, M.; Li, X.; Knox, J. E.; Hratchian, H. P.; Cross, J. B.; Adamo, C.; Jaramillo, J.; Gomperts, R.; Stratmann, R. E.; Yazyev, O.; Austin, A. J.; Cammi, R.; Pomelli, C.; Ochterski, J. W.; Ayala, P. Y.; Morokuma, K.; Voth, G. A.; Salvador, P.; Dannenberg, J. J.; Zakrzewski, V. G.; Dapprich, S.; Daniels, A. D.; Strain, M. C.; Farkas, O.; Malick, D. K.; Rabuck, A. D.; Raghavachari, K.; Foresman, J. B.; Ortiz, J. V.; Cui, Q.; Baboul, A. G.; Clifford, S.; Cioslowski, J.; Stefanov, B. B.; Liu, G.; Liashenko, A.; Piskorz, P.; Komaromi, I.; Martin, R. L.; Fox, D. J.; Keith, T.; Al-Laham, M. A.; Peng, C. Y.; Nanayakkara, A.; Challacombe, M.; Gill, P. M. W.; Johnson, B.; Chen, W.; Wong, M. W.; Gonzalez, C.; Pople, J. A. *Gaussian 03*, revision B.05; Gaussian, Inc.: Pittsburgh, PA, 2003.

(12) Dunning, T. H. *J. Chem. Phys.* **1989**, *90* (2), 1007. doi:10.1063/1.456153.

(13) Chong, D. P. *Mol. Phys.* **2005**, *103* (6), 749–761; note: the volume and page numbers of ref. 20 should read 34 and 31, respectively. doi:10.1080/00268970412331333618.

(14) Chong, D. P. *Chem. Phys. Lett.* **2007**, *441* (4-6), 209–212. doi:10.1016/j.cplett.2007.05.034.

(15) *ADF program system*, release 2007.01; Scientific Computing & Modeling: NV, Amsterdam, 2006. For a comprehensive description of ADF, see: te Velde, G.; Bickelhaupt, F. M.; Baerends, E. J.; Fonseca Guerra, C.; van Gisbergen, S. J. A.; Snijders, J. G.; Ziegler, T. J. *Comput. Chem.* **2001**, *22* (9), 931–967. doi:10.1002/jcc.1056.

(16) Hu, C.-H.; Chong, D. P.; Casida, M. E. *J. Electron Spectrosc. Relat. Phenom.* **1997**, *85* (1-2), 39–46. doi:10.1016/S0368-2048(97)00037-6.

(17) Chong, D. P.; Gritsenko, O. V.; Baerends, E. J. *J. Chem. Phys.* **2002**, *116* (5), 1760. doi:10.1063/1.1430255.

(18) Segala, M.; Chong, D. P. *J. Electron. Spectrosc. Rel. Phenom.* **2009**, *171*, 18–23.

(19) Schipper, P. R. T.; Gritsenko, O. V.; van Gisbergen, S. J. A.; Baerends, E. J. *J. Chem. Phys.* **2000**, *112* (3), 1344. doi:10.1063/1.480688.

(20) Grüning, M.; Gritsenko, O. V.; van Gisbergen, S. J. A.; Baerends, E. J. *J. Chem. Phys.* **2001**, *114* (2), 652. doi:10.1063/1.1327260.

(21) Lindholm, E.; Åsbrink, L. In *Molecular orbitals and their energies, studied by the semiempirical HAM method*; Springer-Verlag: Berlin, 1985.

(22) Ridley, J.; Zerner, M. *Theor. Chim. Acta* **1973**, *32* (2), 111–134. doi:10.1007/BF00528484.

(23) Prasad, R. S.; Rai, B. N. *Theor. Chim. Acta* **1990**, *77* (5), 343–357. doi:10.1007/BF01120134.

(24) Falzon, C. T.; Chong, D. P.; Wang, F. *J. Comput. Chem.* **2006**, *27* (2), 163–173; note: the detail of ref. 41 should read "...1978, private communication to C.W. Bauschlicher". doi:10.1002/jcc.20330. PMID:16312016.

(25) Chong, D. P.; Takahata, Y. *Chem. Phys. Lett.* **2006**, *418* (1-3), 286–291. doi:10.1016/j.cplett.2005.10.091.

(26) Oddershede, J.; Gruner, N. E.; Diercksen, G. H. F. *Chem. Phys.* **1985**, *97* (2-3), 303–310. doi:10.1016/0301-0104(85)87039-7.

(27) Stahel, D.; Leoni, M.; Dressler, K. *J. Chem. Phys.* **1983**, *79* (6), 2541. doi:10.1063/1.446166.

(28) Ben-Shlomo, S. B.; Kaldor, U. *J. Chem. Phys.* **1990**, *92* (6), 3680. doi:10.1063/1.457824.

(29) Christiansen, O.; Koch, H.; Jorgensen, P.; Olsen, J. *Chem. Phys. Lett.* **1996**, *256* (1-2), 185–194. doi:10.1016/0009-2614(96)00394-6.

(30) Musiał, M.; Meissner, L.; Kucharski, S. A.; Bartlett, R. J. *J. Chem. Phys.* **2005**, *122* (22),o. 224110. doi:10.1063/1.1926278. PMID:15974654.

(31) Peach, M. J. G.; Benfield, P.; Helgaker, T.; Tozer, D. J. *J. Chem. Phys.* **2008**, *128* (4),o. 044118. doi:10.1063/1.2831900. PMID:18247941.
(32) Musial, M.; Bartlett, R. *J. Chem. Phys. Lett.* **2008**, *457* (1-3), 267–270. doi:10.1016/j.cplett.2008.04.004.
(33) Musial, M.; Bartlett, R. J. *J. Chem. Phys.* **2008**, *129* (24),o. 244111. doi:10.1063/1.3046453. PMID:19123499.
(34) Berstein, E. R.; Smalley, R. E. *J. Chem. Phys.* **1973**, *58* (6), 2197. doi:10.1063/1.1679493.
(35) Takahata, Y.; Chong, D. P. *J. Electron Spectrosc. Relat. Phenom.* **2003**, *133* (1-3), 69–76; and references therein. doi:10.1016/j.elspec.2003.08.001.
(36) Chong, D. P. *J. Electron Spectrsoc. Rel. Phenom.* **2007**, *159* (1-3), 94–96. doi:10.1016/j.elspec.2007.01.005.

A test of various computational solvation models on a set of "difficult" organic compounds

J. Peter Guthrie and Igor Povar

Abstract: Various dielectric continuum models in Gaussian 03, based on the SCRF approach, PCM, CPCM, DPCM, IEFPCM, IPCM, and SCIPCM, have been tested on a set of 54 highly polar, generally polyfunctional compounds for which experimental solvation energies are available. These compounds span a range of 13 kcal/mol in ΔG_t. The root-mean-square (RMS) errors for the full set of compounds range from 2.48 for DPCM to 1.77 for IPCM. For each method, classes of compounds which were not handled well could be identified. If these classes of compounds were omitted, the performance improved, and ranged from 1.58 (PCM, 39 compounds) to 1.02 (IPCM, 42 compounds). Models in the PCM family (PCM, CPCM, DPCM, and IEFPCM) with the recommended UAHF or UAKS sets of radii rely on a highly parameterized definition of the solvent cavity. Where this parameterization was inadequate, the calculated solvation energies were less reliable. This has been demonstrated by devising a new parameterization for PCM and halogen compounds, which markedly improves performance for polyhalogen compounds. The effective radius for the portion of the cavity centered on a halogen atom was assumed to be linear in the electron-withdrawing or -donating properties of the rest of the molecule as measured by Hammett σ (for halogens on aromatic rings) or Taft σ* (for halogens on aliphatic carbons). This new parameterization for PCM was tested on a set of 45 aliphatic and 22 aromatic polyhalogen compounds and shown to do well. IPCM, which was already the best of the methods in Gaussian, can be considerably improved by a parameterization to allow for cavitation, dispersion, and hydrogen bonding. A large set of compounds was used for the parameterization to have multiple examples for each parameter and as far as possible to have molecules with multiple instances of each structural feature. In the end, 15 parameters were found to be defined by the data for 241 compounds. With this parameter set, the RMS error for the set used for fitting was 0.81 kcal/mol, and the RMS error for the original set of 54 compounds was 0.85. With this new parameterization, IPCM is clearly the best of the methods available in Gaussian 03.

Key words: solvation energy, polyfunctional molecules, computational chemistry, parameterization, IPCM.

Résumé : Utilisant un ensemble de 54 composés hautement polaires et généralement polyfonctionnels pour lesquels des données expérimentales sur les énergies de solvatation sont disponibles, on a évalué divers modèles diélectriques continus dans la gaussienne 03, basée sur l'approche du champ réactionnel autocohérent (CRAC), dans des modèles du continuum polarisable divers, tel le modèle apparenté à un conducteur « CPCM », le modèle diélectrique « DPCM », le modèle dans un formalisme d'équation intégrale « IEFPCM », le modèle avec surface d'isodensité « IPCM » ou son équivalente en champ autocohérent « SPICM ». Les valeurs du ΔG_t pour ces composés s'étalent sur une plage de 13 kcal/mol. La valeur quadratique moyenne (VQM) des erreurs pour l'ensemble des composés varie de 2,48 pour la méthode « DPCM » à 1,77 pour l' « IPCM ». Pour chacune des méthodes, il a été possible de bien identifier des classes de produits qui ne pouvaient pas être examinés. Si on omet ces classes de produits, la performance s'améliore et elle varie de 1,58 (« PCM », 39 composés) à 1,02 (« IPCM », 42 composés). Les modèles de la famille « PCM » « PCM, CPCM, DPCM, IEFPCM » utilisés avec les ensembles recommandés de rayons atomiques d'atome unis de Hartree–Fock « UAHF » ou de "UAKS" reposent sur une définition hautement paramétrisée de la cavité du solvant. Lorsque cette paramétrisation n'était pas adéquate, les énergies de solvatation étaient moins fiables. On a démontré ce point en mettant au point une nouvelle paramétrisation pour la méthode "PCM" et les composés halogénés qui a permis d'améliorer grandement la performance pour les dérivés polyhalogénés. On fait l'hypothèse que le rayon effectif de la portion de la cavité centrée sur un atome d'halogène est linéaire dans le caractère électroaffinitaire ou électrodonneur du reste de la molécule, tel que mesuré par les valeurs σ de Hammett (pour les atomes d'hydrogène sur les noyaux aromatiques) et σ* de Taf (pour les atomes d'halogène sur les carbones aliphatiques). On a testé cette nouvelle paramétrisation dans le modèle « PCM » sur un ensemble de 45 composés polyhalogénés aliphatiques et 22 aromatiques et on a montré qu'elle donne de bons résultats. La méthode « IPCM » qui était déjà la meilleure des méthodes gaussiennes peut être considérablement améliorée par une paramétrisation qui tient compte de la cavitation de la dispersion et des liaisons hydrogènes. Afin de couvrir plusieurs exemples de chacun des paramètres et pour avoir des molécules comportant de multiples instances de chacune des caractéristiques structurales, on a utilisé un large ensemble de composés pour effectuer la paramétrisation. On a trouvé que les paramètres sont définis par les données relatives à 241 composés. Avec cet ensemble de paramètres, l'erreur quadratique moyenne pour l'ensemble utilisé est de 0,81 kcal/mol alors qu'elle était de 0,85 pour l'ensemble original de 54 composés. Avec cette nouvelle paramétrisation, la méthode "IPCM" est nettement la meilleure disponible dans la gaussienne 03.

Received 19 January 2009. Accepted 9 April 2009. Published on the NRC Research Press Web site at canjchem.nrc.ca on 28 July 2009.

J.P. Guthrie[1] and I. Povar. Department of Chemistry, The University of Western Ontario, London, ON N6A 5B7, Canada.

[1]Corresponding author (e-mail: peter.guthrie@uwo.ca).

Mots-clés : énergie de solvatation, molécules polyfonctionnelles, chimie théorique, paramétrisation, modèle du continum polarisable avec surface d'isodensité « IPCM ».

[Traduit par la Rédaction]

Introduction

Reading the literature might leave one with the impression that the problem of calculating solvation energies with precision similar to experiment, i.e., errors less than 1 kcal/mol, had been solved. Barone et al. have stated that "mean error ... below 0.20 kcal/mol for ... 43 neutral solutes";[1] Takano and Houk tested several methods and reported that with CPCM, the mean absolute deviation was 1.10 kcal/mol for 30 neutrals.[2] Based on our previous work on solvation energies,[3] we were skeptical of these implicit claims that general solutions to the problem of calculating solvation energies for any organic molecules had been achieved because these approaches were based on calculations for simple molecules. Hine and Mookerjee[4] found that additivity schemes allowed the calculation of solvation energies for monofunctional compounds but that polyfunctional compounds were much harder because of distant polar interactions. We have reported a parameterization for distant polar interactions, which allowed the calculation of the solvation energies for polyfunctional molecules,[3] and have had occasion to determine solvation energies for a number of polar polyfunctional molecules in the course of work concerned with reactive species in solution.[5–11]

In the present work, we have carried out a critical examination of various solvation models in current use, focused on compounds expected to be difficult. These compounds are highly polar and mostly polyfunctional, belonging to a variety of chemical classes. It was our expectation that many of the currently available solvation models, which are often parameterized to fit a range of relatively simple compounds, were likely to have difficulty with polyfunctional compounds.

As will be seen in this report, this is what we have found: all of the methods tested had problems with some of the test compounds and showed systematic errors. We will demonstrate that for halogens, the popular UAHF model is seriously under-parameterized and will show how it can be improved. We will also report that a small number of parameters permit the IPCM method to be significantly improved so that it becomes the best of the currently available continuum models.

Our long term goal is to establish a reliable general approach for the calculation of equilibrium constants for reactions in solution and especially for the formation of reactive intermediates (for which models of known solvation energy are frequently unavailable). Such equilibrium constants are often unknown and difficult to measure; computation would be an attractive alternative. The equilibrium constant in solution for the rate-determining step is a key input datum for calculation of the rate of a reaction by no-barrier theory.[12–16] Calculation of equilibrium constants in the gas phase is close to being a solved problem, at least for small molecules.[17–21] The difficulty is to have a general method for calculating solvation energies with chemical accuracy.

During the past few years, there has been increasing interest in calculating solvation free energies via self-consistent reaction field (SCRF) methodologies, involving the inclusion of a dielectric continuum model of the solvent in an electronic structure calculation. For a dielectric continuum model, the solute, treated as having a low dielectric constant, is in a cavity outside of which the solvent has its continuum dielectric constant. Definition of the cavity surface is crucial and commonly based on either scaled atomic radii or parameterized atomic radii adjusted to give good results.

The IPCM, isodensity polarizable continuum model,[22] simplifies the cavity definition by a modification of the original formalism. In this model, the solute cavity is determined by a specific value of the electronic isodensity contour (typically in the range 0.0004 – 0.001). This quantity defines the cavity boundary in terms of a surface of constant electron density for the solute. In this method, for a given solvent at a given theoretical level, there is only one parameter. The IPCM process, however, is not fully self-consistent. SCIPCM overcomes this problem as it contains a suitable term, which couples the isodensity and solute Hamiltonian. Consequently, the isodensity surface can either be based on a gas-phase calculation (IPCM) or can be determined self-consistently in the SCF procedure, i.e., taking account of the effect of solvation on the isodensity contours (SCIPCM).[22–27] Unfortunately, SCIPCM is prone to convergence failures. Neither IPCM nor SCIPCM as implemented in Gaussian03 makes any attempt to calculate a non-electrostatic contribution to ΔG_s. Published results[22,26,28] have shown that a value of 0.0004 for the isodensity parameter is a good choice and closely reproduces molar volumes of the liquid phase.

In general, the interactions of the solute with the solvent depend on the geometry of the solute, and in principle, the computation of solvation energies should use an average over solute geometries. In practice, this procedure is usually replaced by a single calculation using either the optimized gas-phase geometry or the optimized solution-phase geometry. On the other hand, geometry reoptimization in the presence of the solvent has a limited effect on the computed solvation energy.[1]

Solvation energies can be calculated with different standard states for gas and solution; two of the commonest are ΔG_s (1 mol/L to 1 mol/L) and ΔG_t (1 atm to 1 mol/L). Both are legitimate: ΔG_t is the most convenient for calculating free energies in solution (normal standard state 1 mol/L) from free energies in the gas phase (normal standard state 1 atm); ΔG_s is more convenient when thinking about the solvation process because it has no arbitrary entropic contribution from a change in concentration scales. In this paper, we will mainly use ΔG_t but will sometimes find it convenient to use ΔG_s.

Computational methodology

Initial three-dimensional geometries of the chemical structures were generated and optimized using the PCModel molecular modeling program.[29] Equilibrium geometries were

obtained for most compounds by the optimization at Hartree–Fock (RHF) or density functional (B3LYP)[30,31] levels of electronic structure theory using the 6–31+G(d,p) basis set in the gas phase. For molecules which have more than one possible conformation, the conformation with the lowest electronic energy was chosen. Each final optimized geometry was confirmed by RHF/6–31+G** or B3LYP/6–31+G** frequency calculations to be a real minimum on the potential-energy surface with no imaginary frequencies. The optimized geometries were used in subsequent single-point calculations of solvation energies with the same basis set. The solvent was always water at 25 °C.

For most compounds, calculations (geometry optimizations and solvation calculations) were carried out at two levels: (*a*) RHF/6–31+G** and (*b*) B3LYP/6–31+G**. For a few compounds, we carried out the geometry optimization and single-point calculations using correlated ab initio levels of theory, MP2 and MP4, with the 6–31+G(d,p) and 6–311+G(2df,2p) basis sets for MP2 and 6–31+G(d,p) for MP4. In the case of the isodensity methods IPCM and SCIPCM, the size of the solvent cavity was calculated with an isodensity value of 0.0004 and a dielectric constant of 78.39 for aqueous solution. For the PCM calculations carried out with the Gaussian03 suite of programs, we typically used the default settings, with radii from the United Atom Topological Model optimized at the HF/6–31G(d) level of theory (specified with RADII=UAHF), and the default scaling factor. All calculations were carried out with Gaussian03 or Gaussian98[32] series of programs.

We used the ideal gas at 1 atm as the reference state for the gas phase and 1 mol/L ideal solution with an infinitely dilute reference state for aqueous solution in all solvation energy calculations. Thus, we were calculating the free energy of transfer of a compound from the gas at 1 atm to 1 mol/L aqueous solution, ΔG_t. Solvation energies calculated by Gaussian are for transfer from the gas at 1 mol/L to aqueous solution at 1 mol/L, ΔG_s. The relationship for the solvation energy between the 1 atm standard state (e.g., energy of transfer, ΔG_t) and 1 mol/L standard state (ΔG_s) is

$$[1] \qquad \Delta G_t = \Delta G_s + RT\ln(\tilde{R}T)$$

where $\tilde{R} = 0.082053\ \mathrm{K}^{-1}$. At 298 K, $RT\ln(\tilde{R}T)$ equals 1.896 kcal/mol. All experimental data were converted to these reference states

Results

We began with a somewhat arbitrary set of polar molecules to use as a test set, strongly biased by the availability of experimental solvation free energies. This test set is given in Table 1; we recommend that this set of data or one similarly biased towards polar polyfunctional molecules be used for any test of solvation models. Figure 1 shows the performance of all methods which we examined on the test set of compounds. These results for various methods at two levels of theory for this test set of 54 compounds can be found in the Supplementary data (Tables S1 to S5). The SCIPCM method failed to converge for all compounds, so the number of points for this model is only 42; see Supplementary data (Table S6) for details. Table 2 gives a summary of the performance of the various models. The immediate conclusion is that none of the currently available methods is very good when challenged with difficult compounds. This is very unfortunate because it is for such difficult polar polyfunctional compounds that general computational methods are most needed. For simple monofunctional compounds, additivity methods are quite successful, and computationally very cheap. On reviewing the data and looking for classes of compounds which posed problems for each method, we could recognize the following problem classes: for IPCM and SCIPCM, amides, hydrogen bonding bases, and polyfluorinated compounds; for PCM and its relatives (CPCM, DPCM, IEFPCM), orthoesters, amides, SO compounds, and PO compounds. In some cases, there were members of the problem classes that were handled correctly, but each class of compounds was either all included or all excluded. These reduced sets of compounds are, not surprisingly, handled much better as also shown in Fig. 1. The numbers of compounds left in the data sets are IPCM, 42; PCM and its variants, 39; and SCIPCM, 31. In both cases, IPCM is the best method with a root-mean-square error (RMSE) of 1.79 for 54 compounds (full set), and 1.02 for 42 compounds (restricted set).

IPCM and SCIPCM do badly on any compounds where the experimental ΔG_s is positive (or where ΔG_t is more positive than +1.90 kcal/mol), such as hydrocarbons and polyfluoro compounds. Although adding the non-electrostatic contribution for such compounds, from a PCM calculation, improved these values, adding this contribution to all 54 compounds in the full set led to a poorer RMSE: this is documented for IPCM in the Supplementary data (Table S7). We prefer to work with ΔG_t, but Gaussian03 reports values leading naturally to ΔG_s, and the problem is that ΔG_s calculated by IPCM is never positive.

Since IPCM failed for fluorocarbons and hydrocarbons, we had to consider the possibility that part of the problem was the omission of any term for the cost of cavity formation. To see how general the problem was, we examined a number of hydrocarbons and found that IPCM does not lead to correct ΔG_s values for hydrocarbons. We carried out calculations on simple hydrocarbons of various sizes and also on cyclohexanone, chosen as a molecule with considerable hydrocarbon character, five CH_2s, and one polar group. The results, Supplementary data (Table S8), showed that calculated solvation free energies for hydrocarbons were in error by about 2 kcal/mol, but that ΔG_s for cyclohexanone was correctly calculated.

Since there seemed to be a problem for both IPCM and PCM with fluorocarbon compounds, we did a more extensive examination of halocarbons both by IPCM and PCM. The results, in Table S9, show that for brominated compounds, IPCM is somewhat better, RMSE = 1.19 vs. 2.62 for PCM; for chlorinated compounds, IPCM is good, RMSE = 0.54 and PCM is poor, RMSE = 3.65; and for fluorinated compounds, PCM is slightly better, RMSE = 2.89, than IPCM, RMSE = 3.36, though neither is very good. We examined plots of ΔG_{calc} vs. ΔG_{obs}, Fig. 2, and found that for both methods, solvation energies for fluorinated compounds are invariably more negative than they should be. For chlorinated compounds, the correlation was very bad for PCM, while IPCM gives a fairly good correlation. For brominated compounds and IPCM, the points were scattered about the line of perfect correlation, while with PCM, there is a strong tendency for ΔG_{calc} to be

Table 1. Experimental free energies of transfer for the initial test set.

Compound	ΔG_t	Compound	ΔG_t
Methanesulfonyl chloride	–2.97[a]	Ethylene glycol diacetate	–4.44[n]
Nitromethane	–2.30[b]	1,1-Diacetoxyethane	–3.07[n]
2,2,2-Trifluoroethanol	–2.41[c]	3,3,3-Trimethoxypropionitrile	–4.50[k]
Dimethyl sulfoxide	–6.81[d]	1,1-Diethoxyethane	–1.38[n]
Methyl methanesulfonate	–2.97[a]	1,2-Diethoxyethane	–1.64[n]
Dimethyl sulfate	–3.20[e]	Trimethyl orthomethoxyacetate	–3.83[k]
Dimethyl sulfide	0.36[f]	*N*,*N*′-Dimethyl piperazine	–5.68[n]
Methyl trifluoroacetate	0.80[g]	Cyanobenzene	–2.32[h]
Imidazole	–7.91[i]	Phenyl formate	–1.9[j]
Methyl formate	–0.88[l]	Benzyl bromide	–0.48[n]
Methyl chloroacetate	–2.10[k]	Benzyl chloride	–0.03[n]
Methyl acetate	–1.45[l]	Methyl phenyl sulfide	–0.84[m]
Dimethoxymethane	–1.03[n]	Diethyl malonate	–4.10[n]
Trimethyl orthophosphate	–6.56[o]	*m*-Bis-trifluoromethylbenzene	2.97[n]
Methyl cyanoacetate	–4.82[k]	Phenyl trifluoroethyl ether	0.61[p]
Bis-2-chloroethyl ether	–2.33[n]	Methyl *p*-nitrobenzoate	–4.98[q]
1,4-Dioxane	–3.15[r]	Methyl benzoate	–1.88[l]
Sulfolane	–6.78[s,t]	Diethyl succinate	–3.81[n]
1,2-Dimethoxyethane	–2.94[n]	*N*,*N*-Dimethyl *p*-nitrobenzamide	–10.05[q]
Trimethyl orthoformate	–2.52[v]	Methyl *p*-methoxybenzoate	–3.43[q]
Diethyl sulfide	0.47[f]	*N*-Methyl-*N*-(2,2,2-trifluoroethyl)-aniline	–0.02[u]
Trimethyl orthotrifluoroacetate	1.10[g]	*N*,*N*-Dimethylbenzamide	–7.39[q]
N-Methylmorpholine	–4.44[n]	Glycerol triacetate	–6.94[n]
Trimethyl orthochloroacetate	–2.69[k]	*N*,*N*-dimethyl-*p*-methylbenzamide	–7.86[q]
Methyl *t*-butyl ether	–0.31[n]	*N*,*N*-Dimethyl-*p*-methoxybenzamide	–9.11[q]
Trimethyl orthoacetate	–2.52[v]	Trimethyl orthobenzoate	–2.14[k]
Nitrobenzene	–2.22[w]	Phenyl diethyl orthoformate	–3.33[x]

[a]Reference 11.

[b]Reference 35.

[c]Reference 36.

[d]Reference 37. Estimated from Henry's law constant, k_H = 97350, obtained at 25 °C by interpolation using the temperature-dependence equation.

[e]Reference 38.

[f]Reference 39.

[g]Reference 5.

[h]Reference 40.

[i]Reference 8.

[j]Reference 41.

[k]Reference 7.

[l]Reference 42.

[m]Reference 4.

[n]Reference 3.

[o]Reference 43.

[p]Lu, J. Ph.D. thesis; The University of Western Ontario, 1994.

[q]Reference 9.

[r]Reference 44.

[s]Calculated from activity coefficient data at 30, 40, and 50 °C (reference 45) and vapor pressure calculated from the Antoine parameters in Reference 46: see Supplementary data, Appendix 10.

[t]Reference 45.

[u]Reference 10.

[v]Reference 6.

[w]Reference 47.

[x]Calculated from solubility and estimated vapor pressure as described in Supplementary data, Appendix 11.

too negative. It is noteworthy that PCM and IPCM show similar errors for fluorinated hydrocarbons; whatever the problem is for IPCM and these molecules, it is not just the absence of non-electrostatic contributions in IPCM, since PCM does poorly despite having such contributions.

Since it became clear that there were serious problems when PCM was used for polyhalogenated molecules, we investigated whether the problem might be inadequate parameterization in the standard UAHF model for the radii used to define the cavity. The UAHF parameterization for F, Cl, and

Fig. 1. Plots of ΔG_t^{calc} vs. ΔG_t^{exptl} for the various solvent models. First, with the full data set (except for SCIPCM for which some calculations failed to converge) and then with selected data sets, omitting compound classes which caused problems for particular methods. Full data set of 54 compounds: (a) IPCM; (b) SCIPCM (only 42 compounds); (c) PCM; (d) CPCM; (e) DPCM. Selected data sets: (f) IPCM, 42 compounds; (g) SCIPCM, 31 compounds; (h) PCM, 39 compounds; (i) CPCM, 39 compounds; (j) DPCM, 39 compounds. The lines are the lines of perfect correlation and lines displaced by one or two times the RMSE.

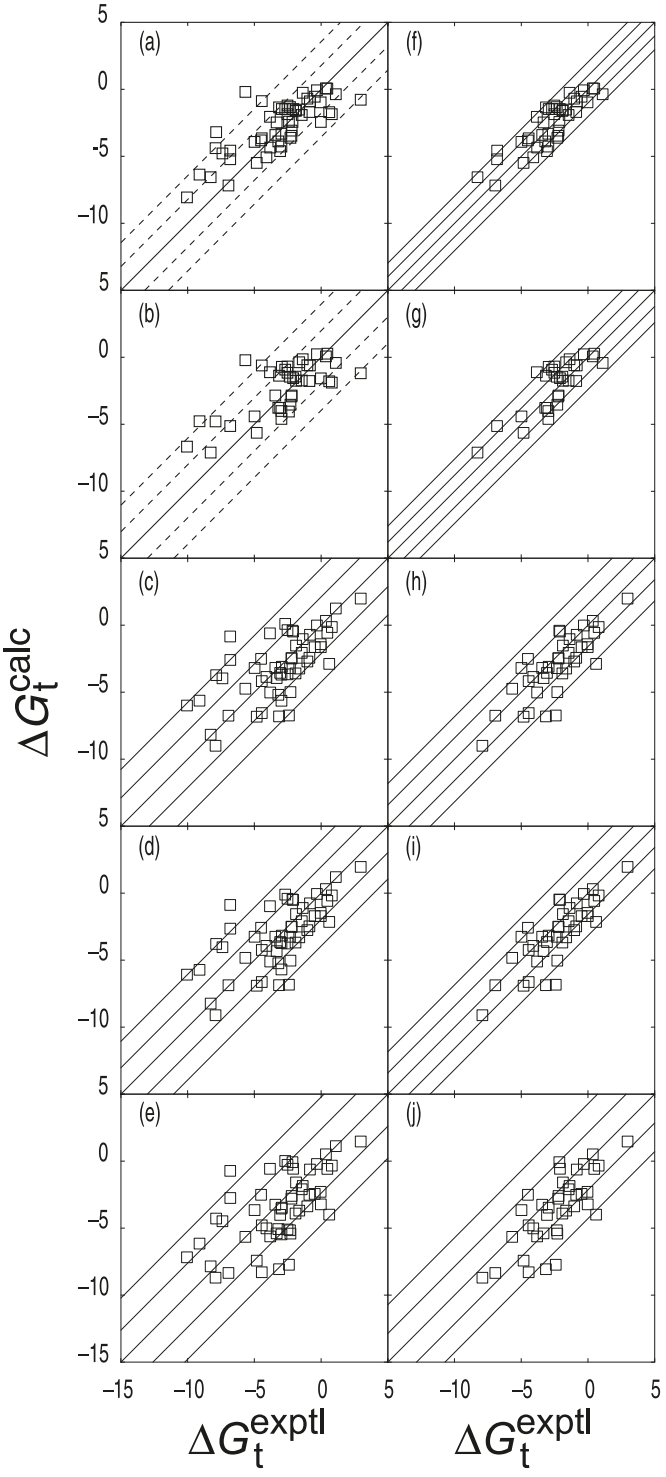

Table 2. Comparison of the RMSE for free energies of transfer calculated with different solvation models.

Method	Number of compounds	RMSE (kcal/mol) RHF/6–31+G**	RMSE (kcal/mol) B3LYP/6–31+G**
IPCM	54[a]	2.11	1.79, 0.85[b]
PCM (IEFPCM)	54[a]	2.13	2.31
CPCM	54[a]	2.09	2.02
DPCM	54[a]	2.40	2.48
SCIPCM	42[c]	2.18	2.14
IPCM	42[d]	1.47	1.02
PCM	39[d]	1.59	1.50
CPCM	39[d]	1.58	1.56
DPCM	39[d]	2.14	1.97
SCIPCM	31[d]	1.52	1.19

[a]The list of compounds is presented in Tables S1–S4.

[b]Using free energies of transfer corrected using the set of 14 parameters based on 194 compounds, as described in the text.

[c]The list of compounds is presented in Table S5.

[d]Leaving out those classes of compounds for which the method fails.

Br was based on CH_3F, C_6H_5Cl, CH_3Cl, and CH_3Br.[1] Specifically, we treated the radius for a halogen atom as a linear function of the electron-withdrawing properties of groups in the rest of the molecule. The idea behind this was that electron-withdrawing substituents would cause the halogen atom to bear less partial negative charge and thus to contract. To make determining the parameters relatively simple, we used only compounds with only one halogen environment per molecule. For aromatic compounds, the Hammett σ values[33] for the substituents affecting a halogen were used. For aliphatic compounds, the Taft σ* values[33] for substituents on the carbon bearing the halogen were used. First, we adjusted the radius for the compounds with all halogens in the same environment to give a good fit to experimental values. Then, we did a linear fit of these radii to the sum of appropriate sigma values:

$$[2] \qquad \begin{cases} \mathbf{r} = \mathbf{r_0} + \mathbf{a}\sum\sigma \\ \mathbf{r} = \mathbf{r_0} + \mathbf{a}^*\sum\sigma^* \end{cases}$$

In this way, we determined the parameters in Table 3. Tables S10 and S11 and Fig. 3 show that with our refinement in the cavity definition, solvation energies for polyhalogenated compounds are calculated with much better accuracy than with the default radii. The procedure for a calculation with new radii is illustrated in the Supplementary data, Appendix 6.

It seems very likely that similar improvements could be achieved for other functional groups if one wished to take the time. The more important lesson is that methods such as PCM are totally dependent on the quality and appropriateness of the parameterization and will fail very badly for any compounds which do not match the parameterization in place.

Early in this work, we examined whether the use of a higher level of theory (larger basis set or MP2 in place of RHF or B3LYP) would lead to better results for some of the more difficult compounds: the results (Table S12) showed that this led at best to slight improvement and often to poorer results. A similar test on a few small molecules using MP4 in place of RHF or B3LYP led to similar conclusions; see Supplementary data in Table S13.

Fig. 2. Plots of ΔG_t^{calc} vs. ΔG_t^{exptl} for halogenated compounds, using IPCM and PCM. (a) Fluoro compounds by IPCM; (b) chloro compounds by IPCM; (c) bromo compounds by IPCM; (d) fluoro compounds by PCM; (e) chloro compounds by PCM; (f) bromo compounds by PCM. The lines are the lines of perfect correlation and lines displaced by one or two times the RMSE.

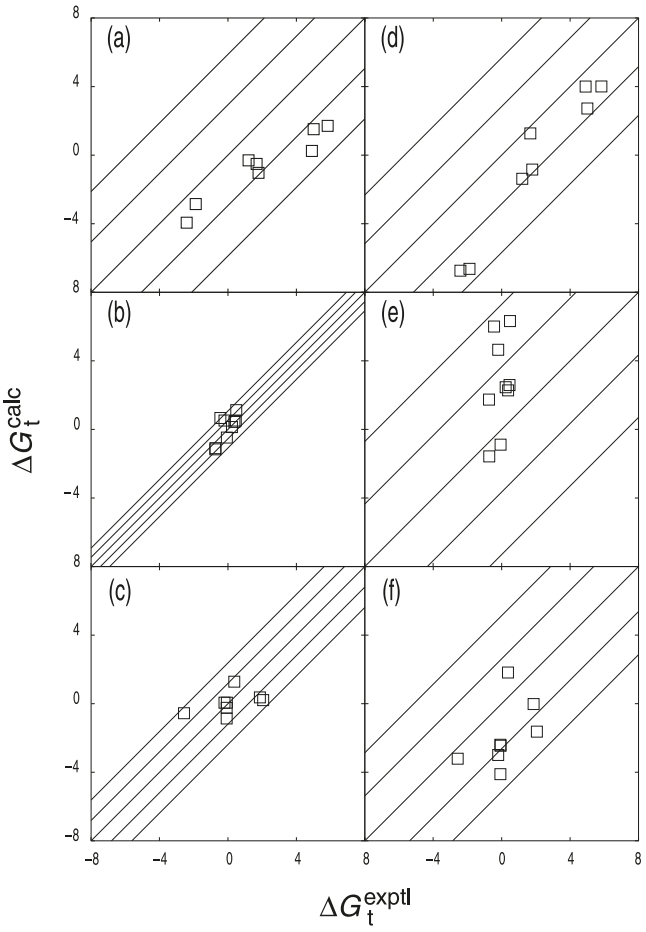

Having found that improved parameterization to incorporate a physically reasonable model dramatically improved the performance of PCM for halocarbons, we were led to ask if a modest parameterization would improve the performance of IPCM, which was already the best of the methods in Gaussian03, for the test set of compounds. The deficiencies, which we hoped to address, were the lack of any accounting for the cost of forming a cavity, the lack of any accounting for dispersion interactions, and the lack of any explicit accounting for hydrogen bonds (and particularly the covalent component of hydrogen bonds). To address these issues, we put in a constant term, a term in the molecular volume of the solute (taken as the final value reported during an IPCM calculation), and a term for the presence of a ring (these first three terms should allow for the cost of cavitation), terms for each kind of atom with a lone pair and each π-bonded feature (hoping that these terms would account for dispersion and hydrogen bonding with solvent as hydrogen donor), and a term for the presence of an acidic hydrogen (thus far limited to species containing OH). We had expected to need terms in the basicity or acidity of each hydrogen bonding group, but found that the pK_a of the relevant feature was only significant

Table 3. The parameters of the linear regression equations.

Halogen	$\mathbf{r_0}$	**a** or **a***	Correlation coefficient
For aliphatic polyhalogen compounds: $\mathbf{r} = \mathbf{r}_0 + \mathbf{a}^*\Sigma\,\sigma^*$			
F[a]	1.792±0.01	–0.011±0.00	–0.980
Cl[b]	2.119±0.05	–0.050±0.01	–0.923
Cl[b,c]	2.161±0.07	–0.051±0.01	–0.913
Br[d]	**2.176±0.01**	**–0.034±0.00**	**–0.996**
For aromatic polyhalogen compounds: $\mathbf{r} = \mathbf{r}_0 + \mathbf{a}\Sigma\,\sigma$			
Cl[e]	1.991±0.02	–0.145±0.02	–0.967
Br[f]	2.082±0.02	–0.068±0.07	–0.695

[a]Compounds used in the linear least-squares data-fitting: CF_4; CHF_3; and CH_3CHF_2.

[b]Compounds used in the linear least-squares fitting: 1,2-$C_2H_4Cl_2$; 1,1-$C_2H_4Cl_2$; 1,1,2,2-$C_2H_2Cl_4$; 1,1,1-$C_2H_3Cl_3$; C_2Cl_6.

[c]Taking into account the presence of conformational isomerism.

[d]Compounds used in the linear least-squares fitting: 1,3-dibromopropane; 1,4-dibromobutane; 1,1,2,2-tetrabromoethane; CH_2BrCH_2Br; and CH_2Br_2.

[e]Compounds used in the linear least-squares fitting: 1,3-$C_6H_4Cl_2$; 1,3,5-$C_6H_3Cl_3$; 1,2,4,5-$C_6H_2Cl_4$; C_6HCl_5; C_6Cl_6.

[f]Compounds used in the linear least-squares fitting: *m*-$C_6H_4Br_2$; *p*-$C_6H_4Br_2$, and *p*-$C_6H_4BrCH_3$.

for amines; for hydroxyl compounds, the corresponding parameter was not defined by the data. This can be rationalized as a consequence of the dual nature of the hydroxyl group, functioning as both a hydrogen bond donor and acceptor. A change which increases acidity strengthens hydrogen-donor properties but weakens hydrogen-acceptor properties; these effects would be expected to cancel. For amines, only the hydrogen-bond-acceptor property matters, since NH is too weakly acidic to hydrogen bond significantly to water. In this simpler situation, electronic effects of substituents do matter. Some functional groups did not require terms (i.e., if such a term were included, the coefficient was not meaningfully determined by least squares); these were NO_2, CN, SO_2, and alkene. All are so weakly basic that they are unlikely to engage in hydrogen bonding to water. There was a meaningful contribution for the presence of a ring. Carboxylic acids could be treated as CO plus OH, and the OH parameter served for alcohols, phenols, and carboxylic acids. Carboxylate ester is not CO plus O; it could be treated as CO alone. This can be rationalized as a consequence of resonance delocalization making the ether oxygen of an ester much less polarizable or hydrogen-bondable, while similar resonance for a carboxylic acid increases the hydrogen-bonding ability of the OH in a way that compensates for the loss of basic properties of the hydroxyl oxygen. Amides with strong resonance delocalization show no sign of nitrogen basicity but have enhanced carbonyl oxygen basicity. Trimethyl phosphate was left in the set because it was found to be well-behaved if one treated the P(+)–O(–) as a carbonyl, and the phosphate ester oxygens as ethers (no p–π resonance). Dimethyl sulfoxide was the only sulfoxide for which we had data and would require special treatment (treat S(+)–O(–) as a carbonyl and the S as a thioether sulfur), so it was not included.

The parameters were evaluated by least-squares fitting to an augmented set of 241 compounds with numerous simple compounds added so that each parameter was based on at least 7 instances. After most of this work was completed,

Fig. 3. Plots of ΔG_t^{calc} vs. ΔG_t^{exptl} (kcal/mol) for halogenated compounds, using both the original and revised radii for halogen atoms and the PCM method. (□) original radii; (△) revised radii. (a) and (c) Aromatic compounds; (b) and (d) aliphatic compounds. The lines are the lines of perfect correlation and lines displaced by one or two times the RMSE.

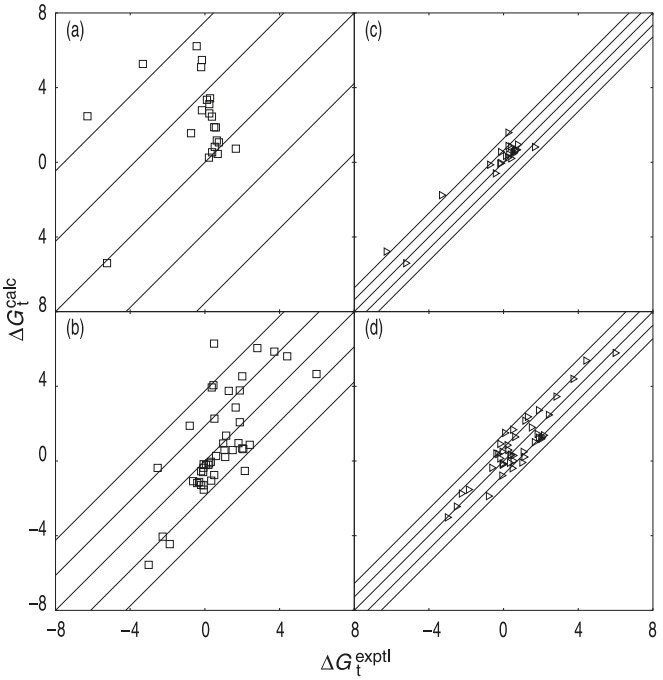

we derived another set of solvation energies for polar compounds for use in a Blind Challenge. [34] The best defined values from this set were added to the data set as part of the 241 compounds. The data were fit to

$$[3] \qquad \Delta G_t^{obs} = \Delta G_t^{calc} + A_0 + \sum n_i A_i$$

where A_0 is a constant term, n_i is the number of times the ith structural feature appears, and A_i is the corresponding parameter. Least-squares fitting provided the parameters in Table 4. The n_i values for all 241 compounds are given in Table S14.

A few compounds posed problems and were deleted from an initial, larger, set. Although phenols and anilines required no special treatment in most cases, *p*-nitroaniline deviated severely. This was attributed to the increased polarizability of this highly delocalized molecule; this compound was deleted from the data set. A number of molecules did not converge with the isodensity parameter set at 0.0004; such compounds, often highly polarizable as for example 4-amino-4′-nitroazobenzene, were not used in fitting. At the moment, we do not know how to extend the IPCM solvation method to this class of highly polarizable compounds. 2,4-Dinitrophenol was the only example with an intramolecular hydrogen bond; it was described by [O] and not [OH] and was fitted satisfactorily with this description. With this parameterization, ultimately using 15 parameters (after trial parameters, which were not defined by the data had been deleted), the overall RMSE for 241 compounds was 0.81. The parameters are surprisingly close to being orthogonal; the only terms in the covariance matrix greater than 0.7 were

Table 4. Parameters for additive corrections to IPCM solvation energies.

Number	Parameter	Value for 241 compounds	Uncertainty
1	Constant	–1.094	0.208
2	Volume	–0.00042	0.00022
3	[F]	–0.454	0.042
4	[Br]	0.638	0.110
5	[O]	1.023	0.095
6	[ring]	0.545	0.132
7	[Cl]	0.446	0.052
8	[ROH]	2.653	0.173
9	[benzene ring]	0.308	0.155
10	[S]	0.921	0.236
11	[CONR2]	5.316	0.306
12	[N]	1.996	0.274
13	pK_a^N	0.0183	0.0053
14	[P=S]	–0.926	0.491
15	[C=O]	0.828	0.145

Fig. 4. Free energies of transfer calculated using IPCM solvation energies and energies corrected using the new parameters; results are shown for the large data set (241 compounds; (a) raw IPCM values, (b) parameters from the large data set); and the original test set (54 compounds; (c) raw IPCM values, (d) parameters from the large data set). The lines are the lines of perfect correlation and lines displaced by one or two times the RMSE.

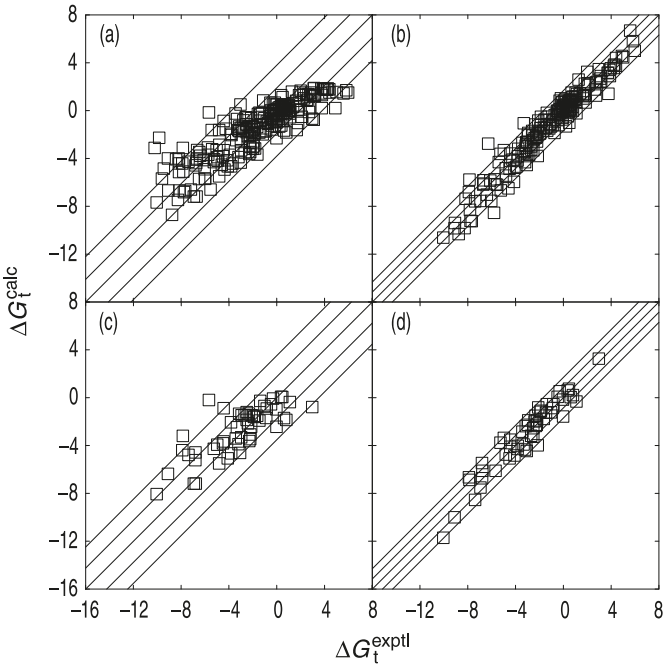

for parameters 1 and 2 (constant and volume) and parameters 12 and 13 (N and pK_a of N). See Supplementary data, Table S14, for this set of compounds. The parameters are close to the ideal of being at the atomic rather than the group level, which leads to an inherently small number of possible parameters. The major exception is the amide parameter, which is specific to one functional group. Given a larger data set including more functional groups, it might be possible to derive a better and less specific description. That

one parameter does for all hydroxyl containing compounds (alcohols, phenols, and carboxylic acids) and two for all basic nitrogen compounds shows the general simplicity of the parameterization.

We also tested the various methods on the original test set of 54 compounds (using the parameter for [C=O ↔ C^+–O^-] for [P^+–O^-] and [S^+–O^-] in sulfinyl but not sulfonyl compounds (sulfonyl compounds are distinctly less basic and would not hydrogen bond)), and treating sulfinyl sulfur as a thioether. When this was done, we obtained the results shown in Fig. 4, and documented in Table S15; the RMSE value was 0.85. Figure 4 demonstrates that, with this parameterization, the results are distinctly better than the raw IPCM solvation energies. The role of the parameterization seems to be to correct small deficiencies in the IPCM model while the computational method does most of the work of calculating solvation free energy. With this new parameterization, IPCM is clearly the best of the methods currently available.

Summary and conclusions

Tests of solvation models must use a wide range of compounds to indicate how well they perform. IPCM is the best of the solvation methods in Gaussian03 as it stands, and with parameterization to compensate for its deficiencies, it becomes even better.

PCM and CPCM give rather similar results for the test set (RMSE = 2.13 and 2.09) and both are very good for classes of compounds falling within their parameterization. They are much poorer for compounds which do not. We illustrate this by showing that results for polyhalogenated compounds are dramatically improved by further parameterization of atomic radii for the halogens. The RMSE improved from 2.64 to 0.67 for 67 halogenated compounds with our new parameterization. Presumably, similar improvements could be obtained by additional parameterization for other groups.

A serious problem for users of continuum solvation methods is that PCM or CPCM give no warning when a compound contains structural features not covered by the parameterization, and then give unreliable results for such compounds. Users of these versions of the polarized continuum models in Gaussian must realize that they are all semiempirical and consequently their performance for a particular compound depends on whether all the structure features of that compound are well-described by the parameters of the method.

There is a great need for more experimental data to test computational methods for solvation energies and where necessary to allow parameterization. The problem is that where the need for data is greatest (polar functional groups, polyfunctional molecules containing such groups), the experiments are difficult.

While this paper was in press, we learned of an excellent computational solvation method based on IEF-PCM developed by Chuanjie Wu and Jay Ponder (personal communication from Prof. Ponder).

Supplementary data

Supplementary data for this article are available on the journal Web site (canjchem.nrc.ca) or may be purchased from the Depository of Unpublished Data, Document Delivery, CISTI, National Research Council Canada, Ottawa, ON K1A 0R6, Canada. DUD 3976. For more information on obtaining material, refer to cisti-icist.nrc-cnrc.gc.ca/cms/unpub_e.shtml.

References

(1) Barone, V.; Cossi, M.; Tomasi, J. *J. Chem. Phys.* **1997**, *107* (8), 3210. doi:10.1063/1.474671.

(2) Takano, Y.; Houk, K. *J. Chem. Theory Comput.* **2005**, *1* (1), 70–77. doi:10.1021/ct049977a.

(3) Guthrie, J. P. *Can. J. Chem.* **1991**, *69* (12), 1893–1903. doi:10.1139/v91-274.

(4) Hine, J.; Mookerjee, P. K. *J. Org. Chem.* **1975**, *40* (3), 292–298. doi:10.1021/jo00891a006.

(5) Guthrie, J. P. *Can. J. Chem.* **1976**, *54* (2), 202–209. doi:10.1139/v76-032.

(6) Guthrie, J. P. *J. Am. Chem. Soc.* **1973**, *95* (21), 6999–7003. doi:10.1021/ja00802a021.

(7) Guthrie, J. P.; Cullimore, P. A. *Can. J. Chem.* **1980**, *58* (13), 1281–1294. doi:10.1139/v80-201.

(8) Guthrie, J. P.; Pike, D. C. *Can. J. Chem.* **1987**, *65* (8), 1951–1969. doi:10.1139/v87-326.

(9) Guthrie, J. P.; Pike, D. C.; Lee, Y. C. *Can. J. Chem.* **1992**, *70* (6), 1671–1683. doi:10.1139/v92-210.

(10) Guthrie, J. P.; Barker, J.; Cullimore, P. A.; Lu, J.; Pike, D. C. *Can. J. Chem.* **1993**, *71* (12), 2109–2122. doi:10.1139/v93-262.

(11) Guthrie, J. P.; Gallant, R. T. *Can. J. Chem.* **2000**, *78* (10), 1295–1298. doi:10.1139/cjc-78-10-1295.

(12) Guthrie, J. P.; Pitchko, V. *J. Am. Chem. Soc.* **2000**, *122* (23), 5520–5528. doi:10.1021/ja992991q.

(13) Guthrie, J. P. *Bioorg. Chem.* **2002**, *30* (1), 32–52. doi:10.1006/bioo.2001.1231. PMID:11955001.

(14) Guthrie, J. P. *ChemPhysChem* **2003**, *4* (8), 809–816. doi:10.1002/cphc.200200327. PMID:12961977.

(15) Guthrie, J. P.; Pitchko, V. *J. Phys. Org. Chem.* **2004**, *17* (6-7), 548–559. doi:10.1002/poc.763.

(16) Guthrie, J. P. *Can. J. Chem.* **2005**, *83* (1), 1–8. doi:10.1139/v04-172.

(17) Fabian, W. M. F. *Monatsh. Chem.* **2008**, *139* (4), 309–318. doi:10.1007/s00706-007-0798-8.

(18) Schwabe, T.; Grimme, S. *Acc. Chem. Res.* **2008**, *41* (4), 569–579. doi:10.1021/ar700208h. PMID:18324790.

(19) Baboul, A.; Curtiss, L.; Redfern, P.; Raghavachari, K. *J. Chem. Phys.* **1999**, *110* (16), 7650. doi:10.1063/1.478676.

(20) Guthrie, J. *J. Phys. Chem. A* **2001**, *105* (40), 9196–9202. doi:10.1021/jp010355k.

(21) Guthrie, J. P. *J. Phys. Chem. A* **2001**, *105* (37), 8495–8499. doi:10.1021/jp010321c.

(22) Foresman, J. B.; Keith, T. A.; Wiberg, K. B.; Snoonian, J.; Frisch, M. J. *J. Phys. Chem.* **1996**, *100* (40), 16098–16104. doi:10.1021/jp960488j.

(23) Lee, I.; Kim, C.; Lee, I.; Kim, C. *J. Phys. Chem. A* **2000**, *104* (26), 6332–6337. doi:10.1021/jp9938361.

(24) Cramer, C.; Truhlar, D. Continuum solvation models. In *Solvent effects and chemical reactivity*; Tapia, O. and Bertran, J., Eds.; Kluwer: Dordrecht, 1996.

(25) Cramer, C. J.; Truhlar, D. G. *Chem. Rev.* **1999**, *99* (8), 2161–2200. doi:10.1021/cr960149m. PMID:11849023.

(26) Wiberg, K.; Rablen, P.; Rush, D.; Keith, T. *J. Am. Chem. Soc.* **1995**, *117* (15), 4261–4270. doi:10.1021/ja00120a006.

(27) Cossi, M.; Barone, V.; Cammi, R.; Tomasi, J. *Chem. Phys.*

Lett. **1996**, *255* (4-6), 327–335. doi:10.1016/0009-2614(96)00349-1.
(28) Wiberg, K.; Keith, T.; Frisch, M.; Murcko, M. *J. Phys. Chem.* **1995**, *99* (22), 9072–9079. doi:10.1021/j100022a019.
(29) *PCMODEL*; Serena Software: Box 3076, Bloomington, IN. 1993.
(30) Becke, A. D. J. *Chem. Phys.* **1993**, *98*, 5648.
(31) Lee, C.; Yang, W.; Parr, R. G. *Phys. Rev. B* **1988**, *37* (2), 785–789. doi:10.1103/PhysRevB.37.785.
(32) Gaussian_for_NSERC. *Gaussian 98*, Revision A9; Gaussian Inc., 1998.
(33) Perrin, D. D.; Dempsey, B.; Serjeant, E. P. In *pK_a prediction for organic acids and bases*; Chapman and Hall: London. 1981.
(34) Guthrie, J. P. *J. Phys. Chem. B* **2009**, *113* (14), 4501–4507. doi:10.1021/jp806724u.
(35) Rohrschneider, L. *Anal. Chem.* **1973**, *45* (7), 1241–1247. doi:10.1021/ac60329a023.
(36) Rochester, C. H.; Symonds, J. R. *J. Chem. Soc., Faraday Trans. I* **1973**, *69*, 1577. doi:10.1039/f19736901577.
(37) Watts, S.; Brimblecombe, P. *Environ. Technol. Lett.* **1987**, *8* (1), 483–486. doi:10.1080/09593338709384509.
(38) Guthrie, J. P. *Can. J. Chem.* **1978**, *56* (17), 2342–2354. doi:10.1139/v78-385.
(39) Przyjazny, A.; Janicki, W.; Chrzanowsi, W.; Staszewski, R. *J. Chromatogr. A* **1983**, *280* (1), 249–260. doi:10.1016/S0021-9673(00)91567-X.
(40) Andonianhaftvan, J.; Taft, R. S. *J. Chem. Soc., Perkin Trans. 2* **1994**, *2*, 1777.
(41) Nicholls, A.; Mobley, D. L.; Guthrie, J. P.; Chodera, J. D.; Bayly, C. I.; Cooper, M. D.; Pande, V. S. *J. Med. Chem.* **2008**, *51* (4), 769–779. doi:10.1021/jm070549+. PMID: 18215013.
(42) Guthrie, J. P. *Can. J. Chem.* **1992**, *70* (4), 1042–1054. doi:10.1139/v92-139.
(43) Wolfenden, R.; Williams, R. J. *Am. Chem. Soc.* **1983**, *105* (4), 1028–1031. doi:10.1021/ja00342a063.
(44) Cabani, S.; Conti, G.; Lepori, L. *Trans. Faraday Soc.* **1971**, *67*, 1943. doi:10.1039/tf9716701943.
(45) Benoit, R. L.; Choux, G. *Can. J. Chem.* **1968**, *46* (20), 3215–3219. doi:10.1139/v68-533.
(46) Stephenson, R. M.; Malanowski, S. In *Handbook of thermodynamics of organic compounds*; Elsevier: Amsterdam, 1987.
(47) Abraham, M. H.; Whiting, G. S.; Fuchs, R.; Chambers, E. J. *J. Chem. Soc., Perkin Trans. 2* **1990**, 291.

Hafnium–phosphinimide complexes

Osamah Alhomaidan, Gregory C. Welch, Guangcai Bai, and Douglas W. Stephan

Abstract: A series of phosphinimide complexes of Hf are prepared and characterized. Reaction of the phosphinimine *t*-Bu_3PNH with $Hf(NEt_2)_4$ gave (*t*-$Bu_3PN)Hf(NEt_2)_3$ (**1**) but this species was not readily converted to the corresponding $HfCl_3$-derivative. The reaction of 2 equiv. of *t*-Bu_3PNH with $Hf(NEt_2)_4$, however, gave (*t*-$Bu_3PN)_2Hf(NEt_2)_2$ (**2**), which was readily converted to (*t*-$Bu_3PN)_2HfCl_2$ (**3**) and (*t*-$Bu_3PN)_2HfMe_2$ (**4**). Employing *t*-Bu_3PNLi and $HfCl_4$ afforded (*t*-$Bu_3PN)_3HfCl$ (**5**) while reaction with $CpHfCl_3$ gave rise to ligand redistribution reactions affording (*t*-$Bu_3PN)_2HfCl_2$ and Cp_2HfCl_2. However, Cp(*t*-$Bu_3PN)_2HfCl$ (**7**) was prepared by treating (*t*-$Bu_3PN)_2HfCl_2$ with CpNa. The related species of Cp_2(*t*-$Bu_3PN)HfCl$ (**8**) was synthesized by the reaction of Cp_2HfCl_2 and *t*-Bu_3PNLi. Ligand redistribution was avoided in the reaction of Cp^*HfCl_3 as Cp^*(*t*-$Bu_3PN)HfCl_2$ (**9**) and Cp^*(*i*-$Pr_3PN)HfCl_2$ (**10**) were readily obtained and derivatized as Cp^*(*t*-$Bu_3PN)Hf(NMe_2)_2$ (**11**) and Cp^*(*t*-$Bu_3PN)HfMe_2$ (**12**), respectively. Similarly, $((Me_3Si)_2C_5H_3)$(*t*-$Bu_3PN)HfCl_2$ (**13**) was converted to $((Me_3Si)_2C_5H_3)$(*t*-$Bu_3PN)HfMe_2$ (**14**). Reactions with Lewis acid activators were used to prepare Cp^*(*t*-$Bu_3PN)HfMe(THF)MeB(C_6F_5)_3$ (**15**), (Cp^*(*t*-$Bu_3PN)HfMe)(B$(C_6F_5)_4$) (**16**), and (*t*-$Bu_3PN)_2Hf(H_2B(C_6F_5)_2)_2$ (**17**). Preliminary testing of **3**, **9**, and **13** in ethylene polymerization is reported. Compounds **3**, **4**, **7**, **9**, and **17** are characterized crystallographically.

Key words: hafnium, phosphinimide, ligand redistribution, cyclopentadienyl ligands, ethylene polymerization.

Résumé : On a préparé et caractérisé une série de complexes de Hf avec le phosphinimide. La réaction de la phosphinimine *t*-Bu_3PNH avec le $Hf(NEt_2)_4$ conduit à la formation du composé (*t*-$Bu_3PN)Hf(NEt_2)_3$ (**1**); toutefois, cette espèce ne se transforme pas facilement en dérivé $HfCl_3$ corrrespondant. Toutefois, la réaction de 2 equiv. de *t*-Bu_3PNH avec du $Hf(NEt_2)_4$ conduit à la formation de (*t*-$BuPN)_2Hf(NEt_2)_2$ (**2**) qu'on peut facilement transformer en (*t*-$Bu_3PN)_2HfCl_2$ (**3**) et en (*t*-$Bu_3PN)_2HfNe_2$ (**4**). L'utilisation de (*t*-BuPNLi) et de $HfCl_4$ conduit à la formation de (*t*-$Bu_3PN)_2HfCl$ (**5**) alors que la réaction avec du $CpHfCl_3$ conduit à une réaction de redistribution de ligand conduisant au (*t*-$Bu_3PN)_2HfCl_2$ et au Cp_2HfCl_2. Toutefois, on a pu préparer le Cp(*t*-$Bu_3PN)_2HfCl$ (**7**) par traitement du (*t*-$Bu_3PN)_2HfCl_2$ avec du CpNa. On a effectué la synthèse de l'espèce apparentée Cp_2(*t*-$Bu_3PN)HfCl$ (**8**) par réaction du Cp_2HfCl_2 avec le *t*-Bu_3PNLi. La réaction de redistribution des ligands a été évitée dans la réaction du Cp^*HfCl_3 et il a été possible d'obtenir facilement de Cp^*(*t*-$Bu_3PN)HfCl_2$ (**9**) et Cp^*(*t*-$BuPN)HfCl_2$ (**10**) et de les transformer en dérivés Cp^*(*t*-$Bu_3PN)Hf(NMe_2)_2$ (**11**) et Cp^*(*t*-$BuPN)Hf(NMe_2)_2$ (**12**) respectivement. De la même manière, on a pu transformer le produit $[(Me_3Si)_2C_5H_3]$(*t*-$Bu_3PN)HfCl_2$ (**13**) en $[(Me_3Si)_2C_5H_3]$(*t*-$Bu_3PN)HfCl_2Me_2$ (**14**). On a fait appel à des réactions avec des activateurs d'acide de Lewis pour préparer les produits Cp^*(*t*-BuPH)HgMe(THF)MeB$(C_6F_5)_3$ (**15**), (Cp^*(*t*-$Bu_3PN)HfMe)(B(C_6F_5)_4$) (**16**) et (*t*-$Bu_3PN)Hf(H_2B(C_6F_5)_2)_2$ (**17**). On rapporte les résultats préliminaires de l'évaluation des composés **3**, **9** et **13** dans des polymérisations de l'éthylène. Les structures des composés **3**, **4**, **7**, **9** et **17** ont été caractérisées par cristallographie.

Mots-clés : hafnium, phosphonimide, redistribution de ligand, ligands cyclopentadiényles, polymérisation de l'éthylène.

[Traduit par la Rédaction]

Introduction

The drive to discover new homogeneous catalysts for olefin polymerization has stimulated much research over the last 25 years. Several reviews have described such studies.[1–9] While synthetic routes to a large number of potential catalysts have been developed, only very few have been shown to operate effectively under commercial conditions.[10] One system that has indeed been commercialized is based on the early metal derivatives of a cyclopentadienyl-amide ligand,[11] affording the so-called "constrained geometry catalysts".[12–15] Another system that has drawn considerable recent attention is that based on the "FI" catalysts developed by researchers at the Mitsui Chemical Co.[7,16–20] During the last decade, we have studied olefin polymerization catalysts based on Ti-phosphinimide complexes and examined in detail the structure–activity relationship,[21–33] as well as the mechanisms of deactivation.[34–39] These systems yield highly active olefin polymerization catalysts[10,40] and indeed, some of these systems are also operative under commercially relevant conditions.[10,31,40]

While the majority of early metal catalysts have been derived from Ti or Zr complexes,[1–9] we have also probed the reactivity of V[41] and Cr[42] phosphinimide complexes. Derivatives of the third-row element Hf have drawn much less attention, presumably due to the high stability of Hf–C bonds.[43] Nonetheless, recent publications have described nonmetallocene Hf complexes, which are highly active for olefin polymerization. These systems incorporated bis(phenoxy-imine) ligands (Fig. 1*a*),[44–47] first introduced by Mitsui

Received 19 March 2009. Accepted 14 May 2009. Published on the NRC Research Press Web site at canjchem.nrc.ca on 28 July 2009.

O. Alhomaidan, G.C. Welch, G. Bai, and D.W. Stephan.[1,2] Department of Chemistry & Biochemistry, University of Windsor, Windsor, ON N9B 3P4, Canada.

[1]Corresponding author (e-mail: dstephan@chem.utoronto.ca).
[2]Present address: Department of Chemistry, University of Toronto, 80 St. George St. Toronto, ON M5S 3H6, Canada.

researchers for the FI catalysts. In addition, researchers at Dow have described Hf systems based on the pyridyl-amido ligand depicted in Fig. 1*b*.[48–50] In this paper, we describe synthetic routes to a series of Hf–phosphinimide derivatives. The reactivity of these species with Lewis acid activators is considered and a preliminary evaluation of the polymerization activity is presented.

Experimental section

General considerations

All preparations were performed under an atmosphere of dry O_2-free N_2 employing either Schlenk-line techniques or a Vacuum Atmospheres inert atmosphere glovebox. Solvents were purified employing Grubbs-type column systems manufactured by Innovative Technologies or were distilled from the appropriate drying agents under N_2. ^1H and ^{13}C NMR spectra were recorded on Bruker Avance 300 and 500 spectrometers. Deuterated benzene, toluene, and methylene chloride were purchased from Cambridge Isotopes Laboratories, vacuum distilled from the appropriate drying agents, and freeze-pump-thaw degassed (three times). Trace amounts of protonated solvents were used as references, and ^1H and $^{13}C\{^1H\}$ NMR chemical shifts are reported relative to $SiMe_4$. $^{31}P\{^1H\}$, $^{11}B\{^1H\}$, and ^{19}F NMR spectra were referenced to external 85% H_3PO_4, $BF_3{\cdot}Et_2O$, and $CFCl_3$, respectively. Combustion analyses were performed at the University of Windsor Chemical Laboratories employing a PerkinElmer CHN Analyzer. High temperature gel permeation chromatography (GPC) data were provided by the technical staff at NOVA Chemicals Corporation. *t*-Bu_3PNLi[51] and $(Me_3SiC_5H_4)HfCl_3$[52] were prepared as previously reported.

Synthesis of (*t*-Bu_3PN)$Hf(NEt_2)_3$ (1)

t-Bu_3PNH (0.46 g, 2.119 mmol) was dissolved in 5 mL of toluene and then added dropwise to a toluene solution (10 mL) containing $Hf(NEt_2)_4$ (1.0 g, 2.119 mmol) at room temperature. The light yellow solution was heated overnight at 70 °C. Toluene was removed under vacuum to give a crystalline white solid (1.27 g, 2.077 mmol, 96%). ^1H NMR (C_6D_6): 3.60 (q, ^3J = 7.3 Hz, 12H, NCH_2CH_3), 1.29 (t, ^3J = 7.3 Hz, 18H, NCH_2CH_3), 1.28 (d, $^3J_{PH}$ = 13.0 Hz, 27H, P-*t*-Bu). $^{13}C\{^1H\}$ NMR (C_6D_6): 44.3 (NCH_2CH_3), 40.4 (d, $^1J_{PC}$ = 48 Hz, P-*t*-*Bu*), 30.0 (P-*t*-Bu), 16.9 (NCH_2CH_3). ^{31}P NMR (C_6D_6): 38.5. Anal. calcd. for $C_{24}H_{57}N_4PHf$: C 47.16, H 9.40, N 9.17; found: C 46.88, H 9.24, N 9.59.

Synthesis of (*t*-$Bu_3PN)_2Hf(NEt_2)_2$ (2)

t-Bu_3PNH (0.93 g, 4.279 mmol) was dissolved in 5 mL of toluene and then added dropwise to toluene solution (10 mL) containing $Hf(NEt_2)_4$ (1.0 g, 2.119 mmol) at room temperature. The solution was refluxed for 12 h. Toluene was removed under vacuum to give an orange oil. It was dissolved in pentane (5 mL) and stirred for 10 min. Removing pentane under vacuum gave a colorless crystalline solid (1.55 g, 2.052 mmol, 96%). ^1H NMR (C_6D_6): 3.79 (q, ^3J = 7.3 Hz, 8H, NCH_2CH_3), 1.38 (d, $^3J_{PH}$ = 12.5 Hz, 54H, *t*-Bu), 1.36 (t, ^3J = 7.3 Hz, 12 H, NCH_2CH_3). $^{13}C\{^1H\}$ NMR (C_6D_6): 44.8 (NCH_2CH_3), 40.7 (d, $^1J_{PC}$ = 45 Hz, P-*t*-*Bu*), 30.4 (P-*t*-Bu), 16.9 (NCH_2CH_3). ^{31}P NMR (C_6D_6): 35.8.

Fig. 1. Recent examples of Hf olefin-polymerization catalysts.

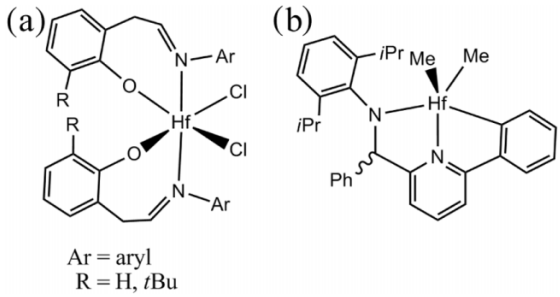

Anal. calcd. for $C_{32}H_{74}N_4P_2Hf$: C 50.88, H 9.87, N 7.42; found: C 50.73, H 10.13, N 6.99.

Synthesis of (*t*-$Bu_3PN)_2HfCl_2$ (3)

Compound **2** (1.00 g, 1.323 mmol) was dissolved in 10 mL of toluene. Me_3SiCl (1.40 mL, 10.590 mmol) was added dropwise to the clear solution at room temperature. A white solid started forming in a few minutes. It was stirred for 8 h and the volatiles removed under vacuum. The white solid was washed with hexanes (5 mL) and then dried under vacuum (0.85 g, 1.257 mmol, 95%). ^1H NMR (C_6D_6): 1.28 (d, $^3J_{PH}$ = 10.0 Hz, 54H, P-*t*-Bu). $^{13}C\{^1H\}$ NMR (C_6D_6): 41.0 (d, $^1J_{PC}$ = 48 Hz, P-*t*-*Bu*), 30.0 (P-*t*-Bu). ^{31}P NMR (C_6D_6): 41.3. Anal. calcd. for $C_{24}H_{54}N_2P_2HfCl_2$: C 42.26, H 7.98, N 4.11; found: C 42.68, H 8.11, N 4.28.

Synthesis of (*t*-$Bu_3PN)_2HfMe_2$ (4)

Compound **3** (0.10 g, 0.147 mmol) was dissolved in 10 mL of diethyl ether. MeMgBr (3 mol/L, 0.19 mL; 0.588 mmol) was added dropwise at room temperature. The solution was stirred overnight and then pumped to dryness. The product was extracted with hot hexanes (10 mL) and then filtered through celite. Removing hexanes under vacuum gave a white solid (0.09 g, 0.145 mmol, 93%). ^1H NMR (C_6D_6): 1.33 (d, $^3J_{PH}$ = 10.5 Hz, 54H, P-*t*-Bu), 0.42 (s, 6H, $HfMe_2$). $^{13}C\{^1H\}$ NMR (C_6D_6): 41.6 ($HfMe_2$), 40.7 (d, $^1J_{PC}$ = 45 Hz, P-*t*-Bu), 30.1 (P-*t*-Bu). ^{31}P NMR (C_6D_6): 37.2. Anal. calcd. for $C_{26}H_{60}N_2P_2Hf$: C 48.70, H 9.43, N 4.37; found: C 48.54, H 9.79, N 4.28.

Synthesis of (*t*-$Bu_3PN)_3HfCl$ (5)

$HfCl_4$ (0.50 g, 1.561 mmol) was suspended in 5 mL of THF. *t*-Bu_3PNLi (1.05 g, 4.685 mmol) in 5 mL of THF was added quickly at room temperature. The suspension became clear within 30 min. It was stirred for another 8 h and the volatiles removed under vacuum. The product was dissolved in 15 mL of toluene and then filtered through celite. The solution was concentrated to ca. 3 mL and then stored in a freezer at −35 °C for 48 h. A white solid precipitated, which was isolated and dried under vacuum (0.83 g, 0.961 mmol, 62%). ^1H NMR (C_6D_6): 1.44 (d, $^3J_{PH}$ = 12.0 Hz, 81H, P-*t*-Bu). $^{13}C\{^1H\}$ NMR (C_6D_6): 41.1 (d, $^1J_{PC}$ = 45 Hz, P-*t*-Bu), 30.7 (P-*t*-Bu). ^{31}P NMR (C_6D_6): 36.0. Anal. calcd. for $C_{36}H_{81}N_3P_3HfCl$: C 50.11, H 9.46, N 4.87; found: C 50.13, H 9.71, N 4.95.

Synthesis of (*t*-$Bu_3PN)_3HfMe$ (6)

Compound **5** (0.20 g, 0.231 mmol) was dissolved in 5 mL of diethyl ether. MeMgBr (3 mol/L, 0.23 mL, 0.693 mmol)

was added dropwise at room temperature. The solution was stirred for 4 h and the volatiles removed under vacuum. The product was extracted with hexanes (2 × 5 mL) and then filtered through celite. Removing hexanes under vacuum gave a white solid (0.17 g, 0.201 mmol, 87%). ^{1}H NMR (C_6D_6): 1.44 (d, $^3J_{PH}$ = 12.0 Hz, 81H, P-*t*-Bu), 0.36 (s, 3H, HfMe). ^{13}C{^{1}H} NMR (C_6D_6): 41.0 (d, $^1J_{PC}$ = 45 Hz, P-*t-Bu*), 30.7 (P-*t*-Bu), 29.1 (HfMe). ^{31}P NMR (C_6D_6): 34.1. Anal. calcd. for $C_{37}H_{84}N_3P_3HfCl$: C 52.75, H 10.05, N 4.99; found: C 52.63, H 9.99, N 4.95.

Synthesis of Cp(*t*-Bu$_3$PN)$_2$HfCl (7)

Compound **3** (0.13 g, 0.191 mmol) was dissolved in 5 mL of THF. Solid CpNa (16.78 mg, 0.191 mmol) was added to the above at −35 °C. The solution was stirred at room temperature for 8 h and the volatiles removed under vacuum. The product was dissolved in 7 mL of toluene and then filtered through celite. Toluene was removed under vacuum to give a white solid (0.13 g, 0.183 mmol, 95%). ^{1}H NMR (C_6D_6): 6.57 (s, 5H, Cp), 1.31 (d, $^3J_{PH}$ = 12.5 Hz, 54H, P-*t*-Bu). ^{13}C{^{1}H} NMR (C_6D_6): 110.7 (Cp), 41.1 (d, $^1J_{PC}$ = 48 Hz, P-*t*-Bu), 30.4 (P-*t*-Bu). ^{31}P NMR (C_6D_6): 37.4. Anal. calcd. for $C_{29}H_{59}N_2P_2HfCl$: C 48.94, H 8.36, N 3.94; found: C 48.86, H 8.61, N 3.71.

Synthesis of Cp$_2$(*t*-Bu$_3$PN)HfCl (8)

Cp_2HfCl_2 (0.85 g, 2.24 mmol) was dissolved in 10 mL of THF. Solid *t*-Bu$_3$PNLi (0.50 g, 2.24 mmol) was added in portions at room temperature. The cloudy solution was stirred for 24 h and then pumped to dryness. The product was dissolved in 10 mL of toluene and then filtered through celite. The solution was concentrated to ~5 mL and then stored in a freezer at −35 °C for 48 h. A pale yellow solid precipitated, which was isolated and dried under vacuum (0.97 g, 1.73 mmol, 77%). ^{1}H NMR (C_6D_6): 6.15 (s, 10H, Cp), 1.18 (d, $^3J_{PH}$ = 12.5 Hz, 27H, P-*t*-Bu). ^{13}C{^{1}H} NMR (C_6D_6): 111.9 (s, Cp), 41.3 (d, $^1J_{PC}$ = 45 Hz, P-*t*-Bu), 30.3 (s, P-*t*-Bu). ^{31}P{^{1}H} NMR (C_6D_6): 40.8. Anal. calcd. for $C_{22}H_{37}NPHfCl$: C 47.15, H 6.65, N 2.50; found: C 46.90, H 6.30, N 2.23.

Synthesis of Cp*(*t*-Bu$_3$PN)HfCl$_2$ (9)

Cp*$HfCl_3$ (1.09 g, 2.595 mmol) was suspended in 10 mL of toluene. Solid *t*-Bu$_3$PNLi (0.58 g, 2.597 mmol) was added in portions at room temperature. The cloudy solution was stirred for 24 h and then filtered through celite. The solution was concentrated to ~5 mL and then stored in a freezer at −35 °C for 48 h. A white solid precipitated, which was isolated, washed with pentane, and then dried under vacuum (1.30 g, 2.163 mmol, 83%). ^{1}H NMR (C_6D_6): 2.19 (s, 15H, Cp*), 1.21 (d, $^3J_{PH}$ = 12.5 Hz, 27H, P-*t*-Bu). ^{13}C{^{1}H} NMR (C_6D_6): 121.0 (*Cp**), 41.3 (d, $^1J_{PC}$ = 45 Hz, P-*t-Bu*), 30.0 (P-*t*-Bu), 12.3 (Cp*). ^{31}P NMR (C_6D_6): 46.3. Anal. calcd. for $C_{22}H_{42}NPHfCl_2$: C 43.97, H 7.04, N 2.33; found: C 44.08, H 7.07, N 2.34.

Synthesis of Cp*(*i*-Pr$_3$PN)HfCl$_2$ (10)

Cp*$HfCl_3$ (0.11, 0.262 mmol) was suspended in 3 mL of toluene. Solid *i*-Pr$_3$PNLi (0.05 g, 0.276 mmol) was added in portions at room temperature. The cloudy solution was stirred overnight and then filtered through celite. Toluene was removed under vacuum to give a white solid (94 mg, 0.168 mmol, 64%). ^{1}H NMR (C_6D_6): 2.19 (s, 15H, Cp*), 1.64 (m, 3H, PC*H*), 0.95 (dd, $^3J_{PH}$ = 14.0 Hz, ^3J = 7.0 Hz, 18H, *i*-Pr). ^{13}C{^{1}H} NMR (C_6D_6): 120.9 (Cp*), 26.9 (d, $^1J_{PC}$ = 58 Hz, P*C*H), 17.3 (P-*i*-Pr), 12.3 (Cp*). ^{31}P NMR (C_6D_6): 35.3. Anal. calcd. for $C_{19}H_{36}NPHfCl_2$: C 40.83, H 6.49, N 2.51; found: C 41.22, H 6.64, N 2.48.

Synthesis of Cp*(*t*-Bu$_3$PN)Hf(NMe$_2$)$_2$ (11)

Compound **9** (100 mg, 0.166 mmol) was dissolved in 3 mL of THF. Me_2NLi (50 mg, 0.980 mmol) was dissolved in 3 mL of THF and then added dropwise to the above solution at room temperature. The solution was stirred for 36 h and the volatiles removed under vacuum. The product was extracted with hexanes (10 mL) and then filtered through celite. Hexanes were removed under vacuum to give a crystalline solid (91 mg, 0.147 mmol, 88%). ^{1}H NMR (C_6D_6): 3.10 (s, 12H, NMe_2), 2.19 (s, 15H, Cp*), 1.28 (d, $^3J_{PH}$ = 12.0 Hz, 27H, P-*t*-Bu). ^{13}C{^{1}H} NMR (C_6D_6): 116.9 (*Cp**), 46.4 (NMe_2), 40.3 (d, $^1J_{PC}$ = 45 Hz, P-*t-Bu*), 30.1 (P-*t*-Bu), 12.1 (Cp*). ^{31}P NMR (C_6D_6): 38.1. Anal. calcd. for $C_{26}H_{54}N_3PHf$: C 50.51, H 8.80, N 6.80; found: C 50.28, H 8.54, N 6.64.

Synthesis of Cp*(*t*-Bu$_3$PN)HfMe$_2$ (12)

Compound **9** (0.71 g, 1.181 mmol) was suspended in 8 mL of diethylether. MeMgBr (3 mol/L, 1.97 mL, 5.905 mmol) was added dropwise at room temperature. The cloudy solution was stirred for 12 h and the volatiles removed under vacuum. The product was extracted with hot hexanes (2 × 8 mL) and then filtered through celite. Removing hexanes under vacuum gave a white solid (0.62 g, 1.107 mmol, 95%). ^{1}H NMR (C_6D_6): 2.11 (s, 15H, Cp*), 1.24 (d, $^3J_{PH}$ = 11.0 Hz, 27H, P-*t*-Bu), −0.03 (s, 6H, $HfMe_2$). ^{13}C{^{1}H} NMR (C_6D_6): 116.5 (*Cp**), 41.7 ($HfMe_2$), 41.0 (d, $^1J_{PC}$ = 45 Hz, P-*t-Bu*), 30.1 (P-*t*-Bu), 11.9 (Cp*). ^{31}P NMR (C_6D_6): 40.3. Anal. calcd. for $C_{24}H_{48}HfNP$: C 51.46, H 8.64, N 2.50; found: C 51.07, H 8.59, N 2.43.

Synthesis of (Me$_3$Si)$_2$Cp(*t*-Bu$_3$PN)HfCl$_2$ (13)

$(Me_3Si)_2CpHfCl_3$ (0.10 g, 0.202 mmol) was dissolved in 5 mL of toluene. Solid *t*-Bu$_3$PNLi (0.45 g, 0.202 mmol) was added to the above at room temperature. The clear solution was stirred at room temperature for a week upon which it became cloudy and the volatiles removed under vacuum. The product was extracted with hot hexanes (5 mL) and then filtered through celite. Hexanes were removed to give a colorless oil, which solidified on standing for a few hours as a white material (0.08 g, 0.118 mmol, 59%). ^{1}H NMR (C_6D_6): 7.01 (t, ^4J = 2.1 Hz, 1H, H2 of Cp″), 6.81 (d, ^4J = 2.1 Hz, 2H, H3 and H4 of Cp″), 1.17 (d, $^3J_{PH}$ = 13.0 Hz, 27H, P-*t*-Bu), 0.46 (s, 18H, $SiMe_3$). ^{13}C{^{1}H} NMR (C_6D_6): C1, C2, and C3 of Cp″ not seen, 120.9 (C4 and C5 of Cp″), 41.4 (d, $^1J_{PC}$ = 45 Hz, P-*t-Bu*), 30.0 (P-*t*-Bu), 0.73 ($SiMe_3$). ^{31}P NMR (C_6D_6): 45.0. Anal. calcd. for $C_{23}H_{48}NPSi_2HfCl_2$: C 40.91, H 7.17, N 2.07; found: C 40.59, H 7.06, N 1.94.

Synthesis of (Me$_3$Si)$_2$Cp(*t*-Bu$_3$PN)HfMe$_2$ (14)

Compound **13** (0.15 g, 0.222 mmol) was dissolved in 3 mL of diethylether. MeMgBr (3 mol/L, 0.37 mL,

Table 1. Crystallographic data.

Crystal	**3**	**4**	**7**	**9**	**17** $0.5(C_6H_5Me)$
Formula	$C_{24}H_{54}Cl_2HfN_2P_2$	$C_{26}H_{60}HfN_2P_2$	$C_{36}H_{81}ClHfN_3P_3$	$C_{22}H_{42}Cl_2HfNP$	$C_{51.5}H_{62}B_2F_{20}HfN_2P_2$
Formula weight	682.02	641.19	862.89	600.93	1351.08
Crystal system	Triclinic	Monoclinic	Monoclinic	Monoclinic	Monoclinic
Space group	*P*-1	$P2_1/n$	$P2_1/c$	$P2_1/n$	$P2_1/n$
a (Å)	13.185(4)	13.2389(11)	21.720(6)	11.855(7)	15.423(10)
b (Å)	15.486(5)	16.5993(13)	12.784(4)	16.683(10)	15.819(5)
c (Å)	16.407(5)	15.5844(13)	17.046(5)	13.521(8)	24.116(10)
α (deg)	89.845(4)				
β (deg)	89.878(4)	106.5240(10)	108.883(3)	97.072(6)	102.001(19)
γ (deg)	73.037(4)				
V (Å^3)	3204.4(17)	3283.3(5)	4479(2)	2654(3)	5755(5)
Z	4	4	4	4	4
D(calcd.) (g cm^{-1})	1.414	1.297	1.280	1.504	1.545
Absorption coeff.,μ (cm^{-1})	3.536	3.289	2.521	4.200	2.013
Data collected	36389	31134	42099	22502	54604
Data $F_o^2 > 3\sigma(F_o^2)$	14392	5785	7884	4623	10154
Variables	559	280	397	244	712
R	0.0335	0.0240	0.0280	0.0630	0.0326
Rw	0.0792	0.0597	0.0825	0.1744	0.0816
GOF	1.043	1.037	0.762	1.297	1.029

Note: Data collected at 20 °C with Mo Kα radiation (λ = 0.71069 Å). $R = \Sigma(F_o - F_c)/\Sigma F_o$. $R_w = \{\sum[w(F_o^2 - F_c^2)^2]/\sum[w(F_o)^2]\}^{1/2}$

1.110 mmol) was added dropwise at room temperature. The solution was stirred for 8 h and the volatiles removed under vacuum. The product was extracted with hexanes (5 mL) and then filtered through celite. Hexanes were removed to give a crystalline white solid (0.12 g, 0.189 mmol, 86%). ^{1}H NMR (C_6D_6): 6.75 (t, ^4J = 1.6 Hz, 1H, H2 of Cp″), 6.54 (d, ^4J = 1.6 Hz, 2H, H3 and H4 of Cp″), 1.22 (d, $^3J_{PH}$ = 12.5 Hz, 27H, P-*t*-Bu), 0.38 (s, 18H, $SiMe_3$), 16 (s, 6H, $HfMe_2$). $^{13}C\{^1H\}$ NMR (C_6D_6): 125.2 (C1 and C3 of Cp″), 123.4 (C2 of Cp″), 41.1 (d, $^1J_{PC}$ = 47 Hz, P-*t-Bu*), 39.9 ($HfMe_2$), 30.1 (P-*t*-Bu), 1.0 ($SiMe_3$). ^{31}P NMR (C_6D_6): 39.8 Anal. calcd. for $C_{25}H_{54}NPSi_2Hf$: C 42.58, H 7.72, N 1.99; found: C 42.50, H 7.60, N 1.93.

Synthesis of Cp*(*t*-Bu$_3$PN)HfMe(THF)MeB(C$_6$F$_5$)$_3$ (15)

Compound **12** (50 mg, 0.089 mmol) was dissolved in 2 mL of CH_2Cl_2 containing 72 µL of THF (10 equiv.). $B(C_6F_5)_3$ (45 mg, 0.088 mmol) was dissolved in 2 mL of CH_2Cl_2 and then added dropwise to the above solution at room temperature. The colorless solution was stirred for 30 min and then pumped to dryness to give a white solid, washed with pentane (3 mL), and then dried under vacuum (91 mg, 0.079 mmol, 89%). ^{1}H NMR (CD_2Cl_2): 4.13 (br, 4H, OCH_2CH_2), 2.11 (s, 15H, Cp*), 2.03 (br, 4H, OCH_2CH_2), 1.39 (d, $^3J_{PH}$ = 13.5 Hz, 27H, P-*t*-Bu), 0.47 (br s, 3H, $MeB(C_6F_5)_3$), 0.27 (s, 3H, HfMe). $^{13}C\{^1H\}$ NMR (CD_2Cl_2): 149.0 (dm, $^1J_{CF}$ = 225 Hz, *o*-C_6F_5), 138.1 (dm, $^1J_{CF}$ = 240 Hz, *p*-C_6F_5), 137.1 (dm, $^1J_{CF}$ = 240 Hz, *m*-C_6F_5), 121.9 (*Cp**), 121.9 (*Cp**), 75.9 (OCH_2CH_2), 41.1 (d, $^1J_{PC}$ = 46 Hz, P-*t-Bu*), 29.8 (P-*t*-Bu), 29.1 (HfMe), 26.0 (OCH_2CH_2), 11.7 (Cp*), 11.0 (br, $CH_3B(C_6F_5)_3$). ^{19}F NMR (CD_2Cl_2, 282 MHz): −133.59 (d, $^3J_{FF}$ = 22 Hz, 6F, *o*-F), −165.71 (t, $^3J_{FF}$ = 20 Hz, 3F, *p*-F), −168.25 (m, 6F, *m*-F). ^{31}P NMR (CD_2Cl_2): 51.3. ^{11}B NMR (CD_2Cl_2, 96 MHz): −14.9. The extreme air sensitivity of this species precluded satisfactory elemental analysis.

Synthesis of (Cp*(*t*-Bu$_3$PN)HfMe)(B(C$_6$F$_5$)$_4$) (16)

Compound **12** (50 mg, 0.09 mmol) and $(Ph_3C)(B(C_6F_5)_4)$ (82 mg, 0.09 mmol) were dissolved in 2 mL of CH_2Cl_2 in two separate vials. The borate solution was added dropwise to the other at −35 °C. The clear yellow solution was stirred for 15 min and the volatiles removed under vacuum to give an orange foam. It was washed with benzene (3 × 3 mL) and then dried under vacuum for 12 h. ^{1}H NMR (CD_2Cl_2): 2.07 (s, 15H, Cp*), 1.40 (d, $^3J_{PH}$ = 13.0 Hz, 27H, *t*-Bu), 0.03 (s, HfMe). $^{13}C\{^1H\}$ NMR (CD_2Cl_2): 148.7 (d, $^1J_{CF}$ = 240 Hz, *o*-C_6F_5), 138.8 (dm, $^1J_{CF}$ = 240 Hz, *p*-C_6F_5), 136.9 (d, $^1J_{CF}$ = 247 Hz, *m*-C_6F_5), 120.1 (s, *Cp**), 41.8 (s, HfMe), 41.5 (d, $^1J_{PC}$ = 45 Hz, *t*-Bu), 30.0 (s, *t*-Bu), 11.7 (s, $C_5(CH_3)_5$). ^{19}F NMR (CD_2Cl_2): −133.5 (s, 8F, *o*-F), −164.1 (t, $^3J_{FF}$ = 20 Hz, 4F, *p*-F), −168.0 (m, 8F, *m*-F). ^{31}P NMR (CD_2Cl_2): 48.2. ^{11}B NMR (CD_2Cl_2, 96 MHz): −16.9. The extreme air sensitivity of this species precluded satisfactory elemental analysis.

Synthesis of (*t*-Bu$_3$PN)$_2$Hf(H$_2$B(C$_6$F$_5$)$_2$)$_2$ (17)

Compound **4** (15 mg, 0.023 mmol) and $HB(C_6F_5)_2$ (33 mg, 0.093 mmol) were combined in a small vial containing 1 mL of benzene. The vial was capped and sonicated for 10 min at room temperature. The cloudy solution was heated at 50 °C for 30 min until it became clear. The product precipitated as colorless crystals on cooling to room temperature. The solvent was removed under vacuum to give a white solid. The solid was washed thoroughly with hexanes (5 × 2 mL) to remove $MeB(C_6F_5)_2$ and side products and then dried under vacuum (25 mg, 0.019 mmol, 83%). ^{1}H NMR (C_6D_6): 4.67 (br q, µ-H, J_{HB} = 65 Hz, 4H), 0.92 (d, $^3J_{PH}$ = 10 Hz, 54H, *t*-Bu). $^{13}C\{^1H\}$ NMR (C_6D_6): 148.3 (d, $^1J_{CF}$ = 241 Hz, *o*-C_6F_5), 139.5 (dm, $^1J_{CF}$ = 250 Hz, *p*-C_6F_5), 138.1 (d, $^1J_{CF}$ = 245 Hz, *m*-C_6F_5), 40.2 (d, $^1J_{PC}$ = 45 Hz, *t*-Bu), 29.2 (s, *t*-Bu). ^{19}F NMR (C_6D_6): −130.7 (s, 8F, *o*-F), −157.8 (t, $^3J_{FF}$ = 28 Hz, 4F, *p*-

F), −163.9 (m, 8F, *m*-F). ^{31}P NMR (C_6D_6): 47.2. ^{11}B NMR (C_6D_6): −15.0 (t, J_{BH} = 65 Hz). Anal. calcd. for $C_{48}H_{58}B_2F_{20}N_2P_2Hf$: C 44.18, H 4.48, N 2.15; found: C 44.09, H 4.33, N 2.03.

X-ray data collection and reduction

Crystals were manipulated and mounted in capillaries in a glovebox, thus maintaining a dry, O_2-free environment for each crystal. Diffraction experiments were performed on a Siemens SMART System CCD diffractometer. The data ($4.5^\circ < 2\theta < 45^\circ - 50.0^\circ$) were collected in a hemisphere of data in 1329 frames with 10 s exposure times. The observed extinctions were consistent with the space groups in each case. A measure of decay was obtained by recollecting the first 50 frames of each data set. The intensities of reflections within these frames showed no statistically significant change over the duration of the data collections. The data were processed using the SAINT and SHELXTL processing packages. An empirical absorption correction based on redundant data was applied to each data set. Subsequent solution and refinement was performed using the SHELXTL solution package.

Structure solution and refinement

Non-hydrogen atomic scattering factors were taken from the literature tabulations.[53] The heavy atom positions were determined using direct methods employing the SHELXTL direct methods routine. The remaining non-hydrogen atoms were located from successive difference Fourier map calculations. The refinements were carried out by using full-matrix least-squares techniques on F, minimizing the function $\omega(F_o - F_c)^2$ where the weight, ω, is defined as $4F_o^2/2\sigma(F_o^2)$ and F_o and F_c are the observed and calculated structure factor amplitudes, respectively. In the final cycles of each refinement, all non-hydrogen atoms were assigned anisotropic temperature factors in the absence of disorder or insufficient data. In the latter cases, atoms were treated isotropically. C−H atom positions were calculated and allowed to ride on the carbon to which they are bonded assuming a C−H bond length of 0.95 Å. H-atom temperature factors were fixed at 1.10 times the isotropic temperature factor of the C-atom to which they are bonded. The H-atom contributions were calculated, but not refined. The locations of the largest peaks in the final difference Fourier map calculation as well as the magnitude of the residual electron densities in each case were of no chemical significance. Additional details are provided in the Supplementary data.

Polymerization protocol

For comparable results, routine standards were run regularly to ensure reproducibility. The polymerizations were performed in a 1 L Buchi reactor system. Following assembly, the reactor vessel and solvent storage unit were refilled with nitrogen via four refill and evacuation cycles over at least 90 min. Approximately 600 mL of toluene was transferred to the solvent storage container from the purification column. The solvent was purged with dry nitrogen for 20 min and then transferred to the reactor vessel by differential pressure. The solvent was stirred at 1500 ± 5 rpm and the temperature was kept constant at 30 ± 2 °C. The system was then exposed to ethylene via five vent and refill cycles. The precatalyst, cocatalyst, and scrubber stock solutions were freshly prepared and loaded into syringes in a glovebox, then transferred to the reactor immediately before injection to limit the possibility of catalyst decomposition. A prepared solution of TiBAl (3.0 mL) was injected into the reaction vessel through the catalyst injection inlet and allowed to stir for 5 min. The prepared precatalyst solution (1.0 mL) was injected, followed immediately with the injection of the $B(C_6F_5)_3$ solution (1.5 mL) into the reactor vessel. The mixture was stirred at 1500 ± 5 rpm at 30 °C under 2 atm (1 atm = 101.325 kPa) of dynamic ethylene flow for 10 min. The temperature and ethylene flow rate were recorded manually at regular intervals. After 5−10 min, the polymerization was stopped by closing the ethylene inlet valve and venting the reactor, the stirring was stopped, and the reactor was disassembled. The contents of the reactor were emptied into a 4 L beaker containing approximately 100 mL of 10% HCl (*v*/*v*) in MeOH. The precipitated polymer was collected by filtration, washed with toluene and acetone, and dried overnight. The resulting polymer was weighed and polymerization activity calculated.

Scheme 1. Synthetic routes to **1**−**4**.

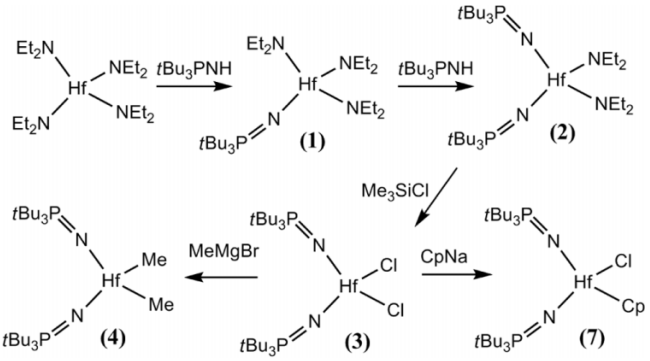

Results and discussion

The dehalosilylation reaction of silyl-phosphinimides and a titanium halide proved to be a simple and successful method for the preparation of titanium-phosphinimide complexes. However, this method does not work well for zirconium.[54] Previously, several phosphinimide complexes of Zr and Hf have been prepared at high temperature using an equimolar amount of KF to remove a N-silyl substituent as the by-product Me_3SiF.[54,55] However, the most convenient route to Zr compounds involves either salt metathesis (LiCl) or alkane or amine elimination. Thus, using these latter methods we targeted Hf−phosphinimide complexes.

The parent phosphinimine, *t*-Bu_3PNH, was reacted stoichiometrically with $Hf(NEt_2)_4$ to afford (*t*-Bu_3PN)$Hf(NEt_2)_3$ (**1**) in 96% yield (Scheme 1). Subsequent treatment of **1** with excess Me_3SiCl in an effort to affect amide cleavage and prepare (*t*-Bu_3PN)$HfCl_3$ proved to be problematic. Based on spectroscopic data it appeared Me_3SiCl effects nonselective Hf−N bond cleavage.

Similarly, reaction of *t*-Bu_3PNH with $Hf(NEt_2)_4$ in a 2:1 ratio afforded the species (*t*-$Bu_3PN)_2Hf(NEt_2)_2$ (**2**) in 96% yield. In contrast to the above species, **2** reacts cleanly at room temperature with excess Me_3SiCl to give (*t*-$Bu_3PN)_2HfCl_2$ (**3**). This compound showed a singlet at 41.3 ppm and a doublet at 1.28 ppm in the ^{31}P NMR and ^{1}H

Fig. 2. ORTEP drawings of (a) **3** and (b) **4**; 20% thermal ellipsoids are shown. Hydrogen atoms are omitted for clarity. Selected bond distances (Å) and angles (°): **3**: Hf(1)—N(2) 1.922(3), Hf(1)—N(1) 1.927(3), Hf(1)—Cl(1) 2.3855(13), Hf(1)—Cl(2) 2.3856(14), P(1)—N(1) 1.569(3), P(2)—N(2) 1.570(4); N(2)−Hf(1)−N(1) 111.22(15), N(2)−Hf(1)−Cl(1) 109.81(12), N(1)−Hf(1)−Cl(1) 108.87(12), N(2)−Hf(1)−Cl(2) 109.70(12), N(1)−Hf(1)−Cl(2) 109.89(12). Cl(1)−Hf(1)−Cl(2) 107.27(6), P(1)−N(1)−Hf(1) 175.0(3), P(2)−N(2)−Hf(1) 168.3(2); **4**: Hf(1)—N(2) 1.946(3), Hf(1)—N(1) 1.948(3), Hf(1)—C(26) 2.237(4), Hf(1)—C(25) 2.251(5), N(1)—P(1) 1.554(3), N(2)—P(2) 1.555(3); N(2)−Hf(1)−N(1) 114.92(13), N(2)−Hf(1)−C(26) 108.74(15), N(1)−Hf(1)−C(26) 110.11(15), N(2)−Hf(1)−C(25) 109.69(17), N(1)−Hf(1)−C(25) 109.06(18), C(26)−Hf(1)−C(25) 103.73(17), P(1)−N(1)−Hf(1) 170.8(2), P(2)−N(2)−Hf(1) 175.7(2).

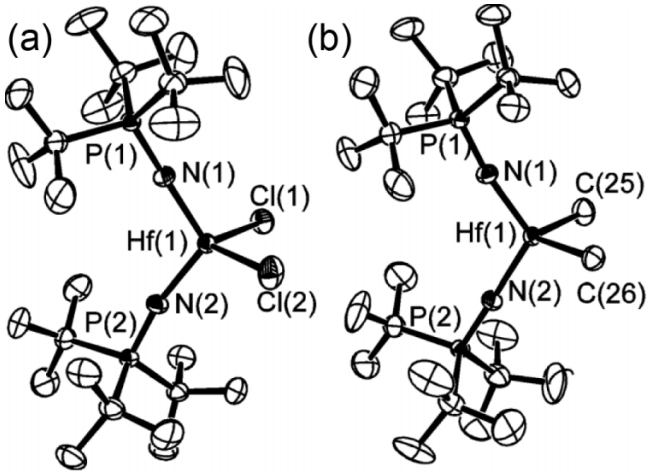

NMR spectra, respectively. The pseudotetrahedral arrangement around Hf was confirmed by X-ray crystallography (Fig. 2*a*). The Hf−N distances were found to be 1.922(3) Å and 1.927(3) Å and the Hf−Cl distances were 2.3855(13) Å and 2.3856(14) Å. The P−N−Hf angles (175.0(3)° and 168.3(2) °) are approximately linear and typical of early metal phosphinimide complexes.[54,56] This geometry suggests the presence of some degree of multiple bonding character in the Hf−N bond.

Compound **3** was subsequently alkylated with MeMgBr to give (t-$Bu_3PN)_2HfMe_2$ (**4**) as a white solid in 93% yield. An upfield shift in ^{31}P NMR at 37.2 ppm is consistent with the presence of electron donating methyl substituents. The structure of **4**, determined by X-ray crystallography (Fig. 2*b*), was similar to **3**, although the Hf−N bonds were longer at 1.946(3) and 1.948(3) Å. In addition, the P−N bonds (1.554(3) and 1.555(3) Å) were shorter, a consequence of the more electron-rich Hf.

It has been previously shown that efforts to prepare Zr analogs of **3** and **4** employing (t-Bu_3PNLi) and $ZrCl_4$ were unsuccessful as the tris ligand complexes, (t-$Bu_3PN)_3ZrCl$, were preferentially formed.[36] In a similar fashion, reactions of the lithium phosphinimide with $HfCl_4$ in a 1:1 ratio did not give (t-$Bu_3PN)HfCl_3$. Instead, a product mixture was evidenced by ^{31}P NMR spectroscopy. However, by employing a 3:1 ratio of reagents the phosphinimide compound (t-$Bu_3PN)_3HfCl$ (**5**) was prepared and isolated in 62% yield. The structure of this white product (**5**) was also confirmed crystallographically (Fig. 3). The Hf−N bonds in

Scheme 2. Synthetic routes to **5** and **6**.

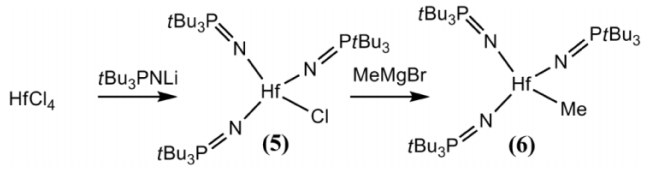

Fig. 3. ORTEP drawing of **5**; 20% thermal ellipsoids are shown. Hydrogen atoms are omitted for clarity. Selected bond distances (Å) and angles (°): Hf(1)—N(3) 1.969(3), Hf(1)—N(2) 1.971(3), Hf(1)—N(1) 1.983(3), Hf(1)—Cl(1) 2.4272(13), P(1)—N(1) 1.551(4), P(2)—N(2) 1.557(3), P(3)—N(3) 1.561(3); N(3)−Hf(1)−N(2) 111.16(16), N(3)−Hf(1)−N(1) 112.93(16), N(2)−Hf(1)−N(1) 110.95(15), Hf(1)−Cl(1) 107.64(11), N(2)−Hf(1)−Cl(1) 106.50(11), N(1)−Hf(1)−Cl(1) 107.31(11), P(1)−N(1)−Hf(1) 164.8(2), P(2)−N(2)−Hf(1) 165.0(2), P(3)−N(3)−Hf(1) 168.1(2).

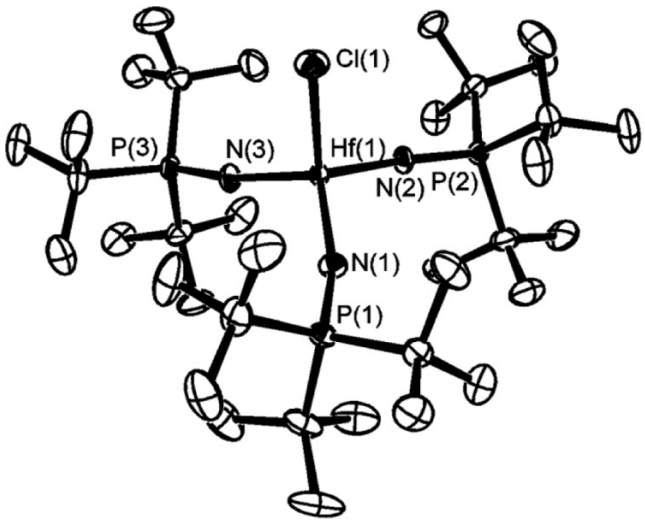

5 (1.969(3), 1.971(3), and 1.983(3) Å) were longer than those seen in **3**, presumably a result of reduced Lewis acidity and greater steric congestion at Hf. The methylated analog (t-$Bu_3PN)_3HfMe$ (**6**) was obtained from the treatment of **5** with MeMgBr. This species exhibited a sharp ^{31}P NMR signal at 34.1 ppm and two ^1H NMR signals, a doublet at 1.44 ppm for *tert*-butyl groups and a singlet at 0.36 ppm for methyl protons, consistent with the formulation.

Complexes of the form Cp(t-$Bu_3PN)MCl_2$ (M = Ti, Zr) have been shown to be active olefin polymerization catalysts.[30,56,57] Thus, the Hf analog was targeted. Reaction of 1equiv. of t-Bu_3PNLi with $CpHfCl_3$ was performed. The product showed a single ^{31}P NMR resonance at 41.3 ppm and two ^1H NMR signals, a singlet at 5.82 ppm for the cyclopentadienyl group and a doublet at 1.28 ppm for *tert*-butyl protons. The ^{31}P and ^1H NMR spectra for the phosphinimide ligand correspond to those observed for **3** while the ^1H NMR resonance attributed to the cyclopentadienyl group corresponds to that seen for Cp_2HfCl_2. Indeed, **3** was isolated as a crystalline product from this reaction mixture and its identity confirmed crystallographically. It is noteworthy that the reaction of $IndHfCl_3$ with t-Bu_3PNLi proceeding in a similar fashion yielded **3** and Ind_2HfCl_2. Attempts to probe the mechanism of this ligand redistribution reaction were

Scheme 3. Proposed ligand redistribution process to **3**.

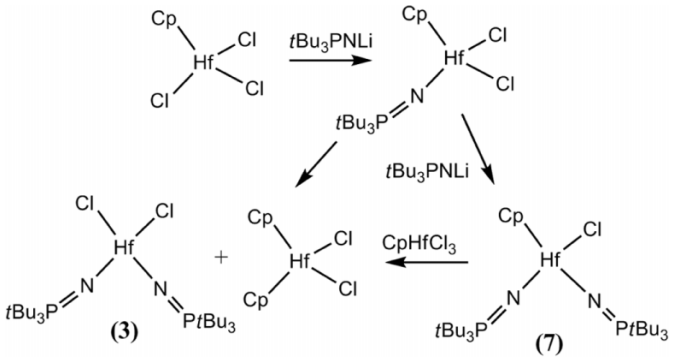

performed by a variable temperature ^{31}P NMR spectroscopy. Although solubility was problematic, on mixing at 15 °C, a broad resonance at 56.6 ppm was observed, which slowly transformed to a sharp signal at 41.3 ppm corresponding to **3**. One possible mechanism could involve metathesis generating Cp(*t*-Bu_3PN)$HfCl_2$,which then undergoes ligand redistribution to give (*t*-$Bu_3PN)_2HfCl_2$ and Cp_2HfCl_2. Alternatively, the improved solubility of Cp(*t*-Bu_3PN)$HfCl_2$ could result in a second metathesis to give Cp(*t*-$Bu_3PN)_2HfCl$, which could then react with $CpHfCl_3$ to give the two redistribution products (Scheme 3). This would suggest that the initial species giving rise to the resonance at 56.6 ppm could be Cp(*t*-Bu_3PN)$HfCl_2$, although the mechanistic details of this disproportionation were not confirmed.

The proposed intermediate in the latter mechanism, Cp(*t*-$Bu_3PN)_2HfCl$ (**7**), was prepared independently in 95% yield by treating (*t*-$Bu_3PN)_2HfCl_2$ with an equimolar amount of CpNa. Compound **7** gave rise to ^{31}P resonance at 37.4 ppm and a ^1H NMR signal at 6.57 ppm arising from the cyclopentadienyl protons. This species is stable on its own at elevated temperature. However, upon addition of a stoichiometric amount of $CpHfCl_3$, **7** reacts to give **3** and Cp_2HfCl_2, thus supporting the role of **7** in the ligand redistribution process described above. In a related and analogous synthesis, the species Cp_2(*t*-Bu_3PN)HfCl (**8**) was readily synthesized in 77% isolated yield by reacting Cp_2HfCl_2 with *t*-Bu_3PNLi.

While the species Cp(*t*-Bu_3PN)$HfCl_2$ was not accessible, use of substituted cyclopentadienyl groups afforded the target species that were stable with respect to ligand redistribution. For example, Cp*$HfCl_3$ reacts with *t*-Bu_3PNLi smoothly to give Cp*(*t*-Bu_3PN)$HfCl_2$ (**9**) as evidenced by NMR data. The pseudotetrahedral arrangement about Hf was unambiguously confirmed by X-ray crystallography (Fig. 4). The Hf−N distance was found to be 1.925(7) Å while the Hf−Cl distances were 2.398(3) Å and 2.402(3) Å, which are quite similar to those in **3**. Additionally, the approximately linear P−N−Hf vector (163.2(4)°) in **9** is significantly larger than that observed in $(Hf_3Cl_6(NPMe_3)_5)^+(Hf_2Cl_7(NPMe_3)_2)^-$ (133.1(8)°, 125.9(6)°, and 132.6(8)°),[55] where the phosphinimide ligand bridges two Hf atoms.

In addition, reaction of Cp*$HfCl_3$ with *i*-Pr_3PNLi afforded Cp*(*i*-Pr_3PN)$HfCl_2$ (**10**). The ^1H NMR signal attributable to the Cp* group was observed at 2.19 ppm, downfield from that seen for $Cp^*_2HfCl_2$ (1.88 ppm). The halide atoms in **9** could be readily replaced with amides or methyl groups via reaction with $LiNMe_2$ or MeMgBr, affording Cp*(*t*-$Bu_3PN)Hf(NMe_2)_2$ (**11**) and Cp*(*t*-Bu_3PN)$HfMe_2$ (**12**) in yields of 88% and 95%, respectively (Scheme 4).

Fig. 4. ORTEP drawing of **9**; 20% thermal ellipsoids are shown. Hydrogen atoms are omitted for clarity. Selected bond distances (Å) and angles (°): Hf(1)—N(1) 1.925(7), Hf(1)—Cl(2) 2.398(3), Hf(1)—Cl(1) 2.402(3), N(1)—P(1) 1.574(8); N(1)−Hf(1)−Cl(2) 104.3(2), N(1)−Hf(1)−Cl(1) 103.3(2), Cl(2)−Hf(1)−Cl(1) 103.46(12), P(1)−N(1)−Hf(1) 163.2(4).

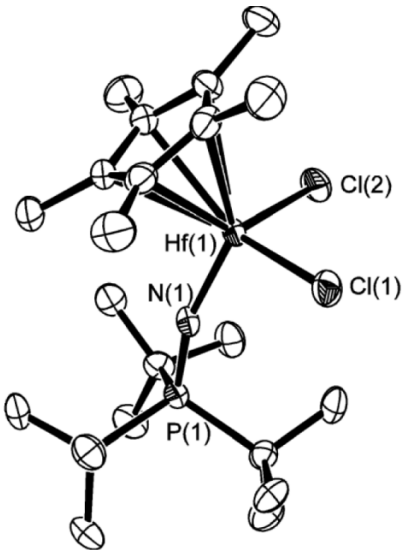

Scheme 4. Synthetic routes to **9**−**14**.

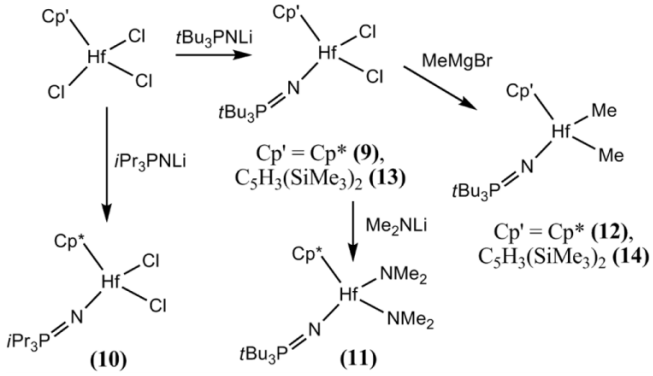

In a procedure similar to that employed for the synthesis of **8**, other cyclopentadienyl derivatives could be employed. For example, $((Me_3Si)_2C_5H_3)HfCl_3$ reacted stoichiometrically with *t*-Bu_3PNLi to form $((Me_3Si)_2C_5H_3)$(*t*-Bu_3PN)$HfCl_2$ (**13**). This reaction proceeded slowly, presumably as a result of the sterically demanding substituents on the Cp-ring. Nonetheless, this afforded **13** in 59% isolated yield. Compound **13** exhibits a sharp ^{31}P NMR signal at 45.0 ppm and four ^1H NMR resonances at 7.01, 6.81, 1.17, and 0.46 ppm attributable to the Cp, *tert*-butyl, and trimethylsilyl groups, respectively. This species was readily alkylated with MeMgBr to give $((Me_3Si)_2C_5H_3)$(*t*-Bu_3PN)$HfMe_2$ (**14**) as a crystalline white solid in a high yield of 86% (Scheme 4).

The reactions of Lewis acid activators are commonly used to generate cationic species, which serve as single-site catalysts in olefin polymerization.[58] Reaction of **12** with $B(C_6F_5)_3$ in CH_2Cl_2 under various conditions, showed no clear indica-

Scheme 5. Reactions of Hf−dialkyls with boranes.

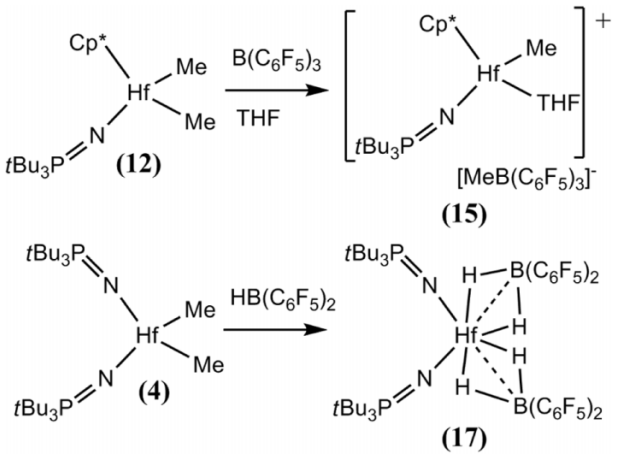

tion of the formation of a cationic species by NMR spectroscopy. However, reaction in the presence of THF afforded [Cp*(*t*-Bu_3PN)HfMe(THF)][$MeB(C_6F_5)_3$] (**15**) in 89% yield (Scheme 5). The ^{1}H NMR spectrum showed a broad singlet at 0.47 ppm attributable to the Me-B and a sharp singlet at 0.27 ppm attributable to the Hf−Me. The sharp ^{11}B NMR signal at −14.9 ppm confirmed a tetracoordinate boron environment.[59] In a similar fashion, methyl-abstraction by [Ph_3C][$B(C_6F_5)_4$] from **12** affords the cationic species [Cp*(*t*-Bu_3PN)HfMe][$B(C_6F_5)_4$] (**16**). In this species, the Hf−Me gave rise to a broad singlet at 0.03 ppm in the ^{1}H NMR spectrum, while a sharp ^{11}B NMR signal was observed at −16.9 ppm. This reactivity towards Lewis acids resembles that of the analogous Zr species, Cp(*t*-Bu_3PN)$ZrMe_2$.[60]

The corresponding reactions of **4** with $B(C_6F_5)_3$ or [Ph_3C][$B(C_6F_5)_4$] gave complex mixtures of unidentified products. However, **4** was found to react cleanly with $(C_6F_5)_2BH$ at room temperature. The resulting product was isolated as a white solid (**17**) in 89% yield. The ^{1}H NMR spectrum exhibited a resonance centered at 4.67 ppm consisting of four broad peaks separated by 65 Hz. The ^{11}B NMR showed a triplet at −15.00 ppm. This complex (**17**) was further confirmed by X-ray crystallography and confirmed to be (*t*-Bu_3PN)$_2$Hf($H_2B(C_6F_5)_2$)$_2$ (Scheme 5, Fig. 5). The Hf−N distances in **17** were found to be 1.909(3) Å and 1.921(3) Å, while the P−N−Hf angles were nearly linear at 177.4(2)° and 173.3(2)°. The Hf−B distances of 2.588(5) Å and 2.655(4) Å were consistent with the close proximity of one *ortho*-F of a C_6F_5 group (Hf···F 2.678(3) Å). This interaction was not seen in the related zirconocene complex, $Cp_2Zr(H_2B(C_6F_5)_2)_2$.[61]

Preliminary testing of the ability of compounds **3**, **9**, and **13** to effect ethylene polymerization was probed. The polymerizations were performed for 5 min at 30 °C, under 2 atm of ethylene, and using Al(*i*-Bu)$_3$ as a scavenger. Employing 500 equiv. of methylaluminoxane (MAO) as the alkylatingand activating reagent, negligible amounts of polyethylene were obtained. Similarly, using **12** and **14** while employing 2 equiv. of $B(C_6F_5)_3$ as the activator, no polymer formation occurred. However, activation of **12** and **14** with [Ph_3C][$B(C_6F_5)_4$] gave rise to activities of 5900 and 5800 g/mol/h/atm, respectively. This compares to 6400 and 8000 g/mol/h/atm, obtained for Cp_2HfMe_2 and Cp(*t*-Bu_3PN)$TiMe_2$, respectively, under the same condition. The insolubility of the resulting polyethylene, which precluded GPC data infers high molecular weight. Similar observations have been made for other phosphinimide-based olefin polymerization catalysts.[54]

Fig. 5. ORTEP drawing of **17**; 20% thermal ellipsoids are shown. Hydrogen atoms are omitted for clarity. Selected bond distances (Å) and angles (°): Hf(1)—N(1) 1.909(3), Hf(1)—N(2) 1.921(3), Hf(1)—B(1) 2.588(5), Hf(1)—B(2) 2.655(4), Hf(1)—F(16) 2.678(3), P(1)—N(1) 1.594(3), P(2)—N(2) 1.587(3); N(1)−Hf(1)−N(2) 112.85(14), N(1)−Hf(1)−B(1) 104.05(14), N(2)−Hf(1)−B(1) 111.07(15), N(1)−Hf(1)−B(2) 101.36(14), N(2)−Hf(1)−B(2) 113.45(14), B(1)−Hf(1)−B(2) 113.32(15), P(1)−N(1)−Hf(1) 177.4(2), P(2)−N(2)−Hf(1) 173.3(2).

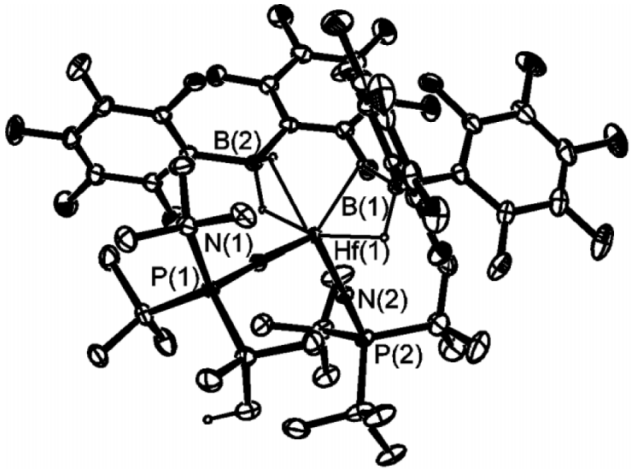

Conclusions

Phosphinimide complexes of hafnium can be synthesized either by salt metathesis or amine elimination. Cyclopentadienyl redistribution precludes the synthesis of Cp(*t*-Bu_3PN)$HfCl_2$, although use of bulkier substituted cyclopentadienyl ligands readily affords the analogous derivatives. Activation of several Hf−phosphinimide-dihalide species proved to be inactive in olefin polymerization upon activation by MAO. In contrast, activation of dimethyl analogs by [Ph_3C][$B(C_6F_5)_4$] generate catalysts of moderate activity.

Supplementary data

Supplementary data for this article are available on the journal Web site (canjchem.nrc.ca) or may be purchased from the Depository of Unpublished Data, Document Delivery, CISTI, National Research Council Canada, Ottawa, ON K1A 0R6, Canada. DUD 3979. For more information on obtaining material, refer to cisti-icist.nrc-cnrc.gc.ca/cms/unpub_e.shtml. CCDC 732437−732441 contain the X-ray data in CIF format for this manuscript. These data can be obtained, free of charge, via www.ccdc.cam.ac.uk/conts/retrieving.html (Or from the Cambridge Crystallographic Data Centre, 12 Union Road, Cambridge CB2 1EZ, UK; fax +44 1223 336033; or deposit@ccdc.cam.ac.uk).

Acknowledgements

Financial support from the Natural Sciences and Engineering Research Council of Canada (NSERC) and NOVA

Chemicals Corporation is gratefully acknowledged. OA is grateful for the financial support from the Saudi Basic Industries Corporation (SABIC). DWS is grateful for the award of a Canada Research Chair.

References

(1) Britovsek, G. J. P.; Gibson, V. C.; Wass, D. F. *Angew. Chem., Int. Ed. Engl.* **1999**, *38* (4), 428−447. doi:10.1002/(SICI)1521-3773(19990215)38:4<428::AID-ANIE428>3.0.CO;2-3.

(2) Coates, G. W. *J. Chem. Soc. Dalton Trans.* **2002**, 467−475. doi:10.1039/b111226k.

(3) Ewart, S. W.; Baird, M. C.Olefin Polymerization by Monocyclopentadienyl compounds of Titanium, Zirconium and Hafnium. *In Metallocene-Based Polyolefins*; John Wiley & Sons: New York, **2000**; *Vol. 1*, p 119.

(4) Gibson, V. C.; Spitzmesser, S. K. *Chem. Rev.* **2003**, *103* (1), 283−316. doi:10.1021/cr980461r. PMID:12517186.

(5) Margl, P.; Deng, L.; Ziegler, T. *Top. Catal.* **1999**, *7* (1/4), 187−208. doi:10.1023/A:1019176119849.

(6) Marks, T. J. Chen, Y.-X. *In* U.S. Cont.-in-part of U.S. 16,087,460. Northwestern University, USA. pp. 15 pp. 2001.

(7) Matsui, S.; Mitani, M.; Fujita, T. *Petrotech (Tokyo)* **2001**, *24*, 11−14.

(8) McKnight, A. L.; Waymouth, R. M. *Chem. Rev.* **1998**, *98* (7), 2587−2598. doi:10.1021/cr940442r. PMID:11848972.

(9) Resconi, L.; Cavallo, L.; Fait, A.; Piemontesi, F. *Chem. Rev.* **2000**, *100* (4), 1253−1346. doi:10.1021/cr9804691. PMID:11749266.

(10) Stephan, D. W.; Guerin, F.; Spence, R. E. H.; Koch, L.; Gao, X.; Brown, S. J.; Swabey, J. W.; Wang, Q.; Xu, W.; Zoricak, P.; Harrison, D. G. *Organometallics* **1999**, *18* (11), 2046−2048. doi:10.1021/om981026q.

(11) Shapiro, P. J.; Bunel, E.; Schaefer, W. P.; Bercaw, J. E. *Organometallics* **1990**, *9* (3), 867−869. doi:10.1021/om00117a055.

(12) Chen, Y.-X.; Marks, T. J. *Organometallics* **1997**, *16* (16), 3649−3657. doi:10.1021/om970288+.

(13) Stevens, J. C. *Stud. Surf. Sci. Catal.* **1994**, *89*, 277−284. doi:10.1016/S0167-2991(08)63042-6.

(14) Stevens, J. C. *Stud. Surf. Sci. Catal.* **1996**, *101*, 11−20. doi:10.1016/S0167-2991(96)80211-4.

(15) Stevens, J. C.; Timmers, F. J.; Wilson, D. R.; Schmidt, G. F.; Nickias, P. N.; Rosen, R. K.; Knight, G. W.; Lai, S. Y. (Dow Chemical Co., USA). Eur. Pat. Appl. EP 416815-A2, Mar 13, 1991.

(16) Matsui, S.; Fujita, T. *Catal. Today* **2001**, *66* (1), 63−73. doi:10.1016/S0920-5861(00)00605-2.

(17) Matsui, S.; Mitani, M.; Saito, J.; Matsukawa, N.; Tanaka, H.; Nakano, T.; Fujita, T. *Chem. Lett.* **2000**, 554−555. doi:10.1246/cl.2000.554.

(18) Matsui, S.; Mitani, M.; Saito, J.; Tohi, Y.; Makio, H.; Matsukawa, N.; Takagi, Y.; Tsuru, K.; Nitabaru, M.; Nakano, T.; Tanaka, H.; Kashiwa, N.; Fujita, T. *J. Am. Chem. Soc.* **2001**, *123* (28), 6847−6856. doi:10.1021/ja0032780.

(19) Matsukawa, N.; Matsui, S.; Mitani, M.; Saito, J.; Tsuru, K.; Kashiwa, N.; Fujita, T. *J. Mol. Catal. Chem.* **2001**, *169* (1−2), 99−104. doi:10.1016/S1381-1169(01)00050-4.

(20) Saito, J.; Mitani, M.; Mohri, J.; Yoshida, Y.; Matsui, S.; Ishii, S.; Kojoh S.; Kashiwa, N.; Fujita, T. *Angew. Chem., Int. Ed. Engl.* **2001**, *40* (15), 2918−2920. doi:10.1002/1521-3773(20010803)40:15<2918::AID-ANIE2918>3.0.CO;2-S. PMID:11500909.

(21) Beddie, C.; Hollink, E.; Wei, P.; Gauld, J.; Stephan, D. W. *Organometallics* **2004**, *23* (22), 5240−5251. doi:10.1021/om049545i.

(22) Brown, S. J.; Gao, X.; Harrison, D. G.; McKay, I.; Koch, L.; Wang, Q.; Xu, W.; Spence, R. E.; Stephan, D. W. *Chem. Abstr.* **2000**, *132*, 123057a.

(23) Brown, S. J.; Gao, X.; Kowalchuk, M. G.; Spence, R. E. H.; Stephan, D. W.; Swabey, J. *Can. J. Chem.* **2002**, *80* (11), 1618−1624. doi:10.1139/v02-170.

(24) Cabrera, L.; Hollink, E.; Stewart, J. C.; Wei, P.; Stephan, D. W. *Organometallics* **2005**, *24* (6), 1091−1098. doi:10.1021/om0492202.

(25) Carraz, C.-A.; Stephan, D. W. *Organometallics* **2000**, *19* (19), 3791−3796. doi:10.1021/om0003178.

(26) Graham, T. W.; Kickham, J.; Courtenay, S.; Wei, P.; Stephan, D. W. *Organometallics* **2004**, *23* (13), 3309−3318. doi:10.1021/om049826q.

(27) Guérin, F.; Beddie, C. L.; Stephan, D. W.; Spence, R. E. H.; Wurz, R. *Organometallics* **2001**, *20* (16), 3466−3471. doi:10.1021/om010298h.

(28) Spence, R. E. V. H.; Brown, S. J.; Wurz, R. P.; Jeremic, D.; Stephan, D. W. (Nova Chemicals (International) S.A. Switzerland) PCT Int. Appl. WO. 2000-CA978 20000824, CA 99-2282070D, 2001.

(29) Stephan, D. W. *Can. J. Chem.* **2002**, *80* (2), 125−132. doi:10.1139/v01-203.

(30) Stephan, D. W.; Stewart, J. C.; Guerin, F.; Courtenay, S.; Kickham, J.; Hollink, E.; Beddie, C.; Hoskin, A.; Graham, T.; Wei, P.; Spence, R. E. H.; Xu, W.; Koch, L.; Gao, X.; Harrison, D. G. *Organometallics* **2003**, *22* (9), 1937−1947. doi:10.1021/om020954t.

(31) Stephan, D. W.; Stewart, J. C.; Harrison, D. G. Nova Chemicals (International) S.A., Switzerland. Eur. Pat. Appl. Ep. 1999, 21 pp.

(32) Sung, R. C. W.; Courtenay, S.; McGarvey, B. R.; Stephan, D. W. *Inorg. Chem.* **2000**, *39* (12), 2542−2546. doi:10.1021/ic9913051. PMID:11197008.

(33) Yue, N. L. S.; Stephan, D. W. *Organometallics* **2001**, *20* (11), 2303−2308. doi:10.1021/om0101184.

(34) Guérin, F.; Stephan, D. W. *Angew. Chem., Int. Ed.* **1999**, *38* (24), 3698−3701. doi:10.1002/(SICI)1521-3773(19991216)38:24<3698::AID-ANIE3698>3.0.CO;2-X.

(35) Guérin, F.; Stephan, D. W. *Angew. Chem., Int. Ed.* **2000**, *39* (7), 1298−1300. doi:10.1002/(SICI)1521-3773(20000403)39:7<1298::AID-ANIE1298>3.0.CO;2-W.

(36) Guérin, F.; Stewart, J. C.; Beddie, C.; Stephan, D. W. *Organometallics* **2000**, *19* (16), 2994−3000. doi:10.1021/om0002069.

(37) Kickham, J. E.; Guérin, F.; Stephan, D. W. *J. Am. Chem. Soc.* **2002**, *124* (38), 11486−11494. doi:10.1021/ja0260972. PMID:12236763.

(38) Kickham, J. E.; Guerin, F.; Stewart, J. C.; Stephan, D. W. *Angew. Chem., Int. Ed.* **2000**, *39* (18), 3263−3266. doi:10.1002/1521-3773(20000915)39:18<3263::AID-ANIE3263>3.0.CO;2-H.

(39) Kickham, J. E.; Guérin, F.; Stewart, J. C.; Urbanska, E.; Ong, C. M.; Stephan, D. W. *Organometallics* **2001**, *20* (6), 1175−1182. doi:10.1021/om001047w.

(40) Stephan, D. W.; Stewart, J. C.; Guerin, F.; Spence, R. E. H.; Xu, W.; Harrison, D. G. *Organometallics* **1999**, *18* (7), 1116−1118. doi:10.1021/om980955e.

(41) Hawkeswood, S. B.; Stephan, D. W. *Inorg. Chem.* **2003**, *42* (17), 5429−5433. doi:10.1021/ic030151d. PMID:12924917.

(42) Wei, P. R.; Stephan, D. W. *Organometallics* **2003**, *22* (10), 1992−1994. doi:10.1021/om030169w.
(43) Cotton, F. A.; Wilkinson, G.; Murillo, C. A.; Bochmann, M. *Advanced Inorganic Chemistry;* Wiley: New York, 1999; pp 877−895.
(44) Makio, H.; Fujita, T. *Bull. Chem. Soc. Jpn.* **2005**, *78* (1), 52−66. doi:10.1246/bcsj.78.52.
(45) Makio, H.; Tohi, Y.; Saito, J.; Onda, M.; Fujita, T. *Macromol. Rapid Commun.* **2003**, *24* (15), 894−899. doi:10.1002/marc.200300020.
(46) Ishii, S.; Furuyama, R.; Matsukawa, N.; Saito, J.; Mitani, M.; Tanaka, H.; Fujita, T. *Macromol. Rapid Commun.* **2003**, *24* (7), 452−456. doi:10.1002/marc.200390072.
(47) Axenov, K. V.; Klinga, M.; Lehtonen, O.; Koskela, H. T.; Leskela, M.; Repo, T. *Organometallics* **2007**, *26* (6), 1444−1460. doi:10.1021/om060753f.
(48) Domski, G. J.; Lobkovsky, E. B.; Coates, G. W. *Macromolecules* **2007**, *40* (9), 3510−3513. doi:10.1021/ma062824s.
(49) Boussie, T. R.; Diamond, G. M.; Goh, C.; Hall, K. A.; LaPointe, A. M.; Leclerc, M. K.; Murphy, V.; Shoemaker, J. A. W.; Turner, H.; Rosen, R. K.; Stevens, J. C.; Alfano, F.; Busico, V.; Cipullo, R.; Talarico, G. *Angew. Chem. Int. Ed.* **2006**, *45* (20), 3278−3283. doi:10.1002/anie.200600240.
(50) Zuccaccia, C.; Macchioni, A.; Busico, V.; Cipullo, R.; Talarico, G.; Alfano, F.; Boone, H. W.; Frazier, K. A.; Hustad, P. D.; Stevens, J. C.; Vosejpka, P. C.; Abboud, K. A. *J. Am. Chem. Soc.* **2008**, *130* (31), 10354−10368. doi:10.1021/ja802072n. PMID:18613668.
(51) Courtenay, S.; Wei, P.; Stephan, D. W. *Can. J. Chem.* **2003**, *81* (12), 1471−1476. doi:10.1139/v03-162.
(52) Winter, C. H.; Zhou, X. X.; Dobbs, D. A.; Heeg, M. J. *Organometallics* **1991**, *10* (1), 210−214. doi:10.1021/om00047a051.
(53) Cromer, D. T.; Waber, J. T. *International Tables for X-Ray Crystallography;* Ibers, J. A., Hamilton, W. C. Eds; Kynoch: Birmingham, **1974**; Vol. *4*, p 71.
(54) Dehnicke, K.; Krieger, M.; Massa, W. *Coord. Chem. Rev.* **1999**, *182* (1), 19−65. doi:10.1016/S0010-8545(98)00191-X.
(55) Grun, M.; Weller, F.; Dehnicke, K. *Z. Anorg. Allg. Chem.* **1997**, *623* (1−6), 224−230. doi:10.1002/zaac.19976230137.
(56) Stephan, D. W. *Organometallics* **2005**, *24* (11), 2548−2560. doi:10.1021/om050096b.
(57) Hollink, E.; Stewart, J. C.; Wei, P.; Stephan, D. W. *J. Chem. Soc. Dalton Trans.* **2003**, 3968. doi:10.1039/b308114a.
(58) Chen, E. Y. X.; Marks, T. J. *Chem. Rev.* **2000**, *100* (4), 1391−1434. doi:10.1021/cr980462j. PMID:11749269.
(59) Blackwell, J. M.; Sonmor, E. R.; Scoccitti, T.; Piers, W. E. *Org. Lett.* **2000**, *2* (24), 3921−3923. doi:10.1021/ol006695q. PMID:11101454.
(60) Yue, N.; Hollink, E.; Guerin, F.; Stephan, D. W. *Organometallics* **2001**, *20* (21), 4424−4433. doi:10.1021/om010433q.
(61) Hollink, E.; Wei, P.; Stephan, D. W. *Organometallics* **2004**, *23* (7), 1562−1569. doi:10.1021/om030631c.

Triterpenes of *Commiphora holtziana* oleo-gum resin

Lawrence Onyango Arot Manguro, Sylvia Awino Opiyo, Eberhardt Herdtweck, and Peter Lemmen

Abstract: Chemical analysis of the acetone extract of *Commiphora holtziana* gum resin has led to the isolation of triterpenes characterized as methyl 3-oxo-1α,19α,28-trihydroxyurs-12-en-24-oate (**1**), methyl 3β-acetyl-2α,11α,19α,28-tetrahydroxyurs-12-en-24-oate (**2**), methyl 3β,11α-diacetyl-1α,2α,28-trihydroxyurs-12-ene-24-oate (**3**), and 3β,28-diacetyl-1α,2α,25-trihydroxydammar-23-ene (**4**). The known compounds isolated from the same extract included cabraleadiol monoacetate (**5**), mansumbinol (**6**), 3β-acetylamyrin (**7**), 3α-acetylboswellic acid (**8**), 2-methoxy-8,12-epoxygermacra-1(10),7,11-trien-6-one (**9**), 2-methoxy-5-acetylfuranogermacra-1(10),7,11-trien-6-one (**10**), furadienone (**11**), 2-methoxy-5-acetyl-4-furanogermacra-1(10)*Z*-en-6-one (**12**), α-amyrin (**13**), sistosterol (**14**) and stigmasterol 3-*O*-acetate (**15**). Structural elucidation was carried out using spectroscopic and physical methods as well as by comparison with the literature data.

Key words: Commiphora holtziana, Burseraceae, triterpenes, gum-oleo-resin exudate.

Résumé : L'analyse chimique des produits extraits à l'acétone à partir de la gomme résine *Commiphora hostziana* a permis d'extraire des triterpènes caractérisés comme le 3-oxo-1α,19α,28-trihydroxyurs-12-én-24-oate de méthyle (**1**), le 3β-acétyl-2α,11α,19α,28-tétrahydroxyurs-12-én-24-oate de méthyle (**2**), le 3β,11α-diacétyl-1α,2α,28-trihydroxyurs-12-én-24-oate de méthyle (**3**) et le 3β,28-diacétyl-1α,2α,25-trihydroxydamma-23-ène (**4**). On a aussi isolé les produits connus suivants: monoacétate de cabraléadiol (**5**), mansumbinol (**6**), 3β-amyrine (**7**), acide 3-α-acétylboswellique (**8**), 2-méthoxy-8,12-époxy-germacra-1(10),7,11-trién-6-one (**9**), 2-méthoxy-5-acétylfuranogermacra-1(10),7,11-trién-6-one (**10**), furadiénone (**11**), 2-méthoxy-5-acétyl-4-furanogermacra-1(10)*Z*-én-6-one (**12**), α-amyrine (**13**), sistostérol (**14**) et 3-*O*-acétate du stigmastérol (**15**). L'élucidation des structures a été réalisée à l'aide de méthodes physiques et spectroscopiques ainsi que par comparaison avec des données tirées de la littérature.

Mots-clés : Commiphora holtziana, Burseraceae, triterpènes, exsudate de gomme-oléo-résine.

[Traduit par la Rédaction]

Introduction

The genus *Commiphora* (*Burseraceae*) is widely distributed in the tropics and subtropics, particularly in Africa, Asia, and Australia.[1] Over 46 *Commiphora* species are acclimatized in the northeastern province of Kenya, and a good number of them are characterized by oleo-resin exudates used in medicine, food, and perfumery industries.[2] *Commiphora holtziana* (syn. *Commiphora erythraea*) is one such species growing in the wild and produces resin, an article of commerce.[3] The plant is used in the indigenous system of medicine as a remedy for microbial infections, anti-inflammatory, and as an acaricide.[4,5] Previous chemical analyses of the plant resin exudate yielded 2-methoxy-8,12-epoxygermacra-1(10),7,11-trien-6-one, 2-methoxy-5-acetylfuranogermacra-1(10),7,11-trien-6-one, and furadienone.[5,6] In the present study, steam-distilled residue of *C. holtziana* resin exudate was examined chemically leading to the isolation and identification of triterpenes of ursane and dammarane types.

Received 9 December 2008. Accepted 19 February 2009. Published on the NRC Research Press Web site at canjchem.nrc.ca on 28 July 2009.

L.O.A. Manguro[1] and S.A. Opiyo. Maseno University, Chemistry Department, P. O. Box 333, Maseno, Kenya.
E. Herdtweck. Technical University Munich, Institute of Inorganic Chemistry, Lichtenbergstrasse 4, 85747 Garching, Germany.
P. Lemmen. Technical University Munich, Institute of Organic Chemistry and Biochemistry, Lichtenbergstrasse 4, 85747 Garching, Germany.

[1]Corresponding author (e-mail: kamanguro@yahoo.com).

Experimental part

General experimental procedure

IR data were recorded on a PerkinsElmer FTIR 600 series. NMR data were measured in $CDCl_3$ and $CDCl_3$ + DMSO-d_6 on a Bruker DRX-400 NMR spectrometer operating at 400 and 100 MHz, respectively. MS data were obtained on a MAT 8200A instrument of Varian (Bremen). Preparative HPLC was performed on an instrument of JASCO labor und daten technik GmBH (RP-18, 250 × 20 mm, 7.4 μm JASCO Kromasil 100).

Oleo-gum resin material

Oleo-gum resins were collected from *C. holtziana* trees in Samburu district of Kenya by Mr. Norman Gachathi in March 2002 and were kept in a deep freezer in sealed polyethylene bags. Voucher specimens were confirmed after comparison with authentic herbarium samples at the Kenya Forestry Research Institute, Muguga, Kenya.

Chart 1.

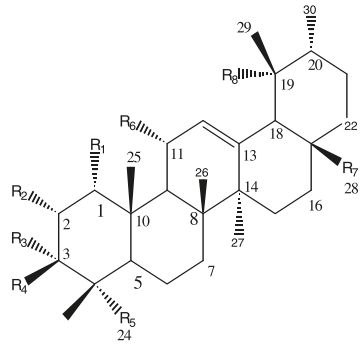

1: $R_1 = R_8 = OH$, $R_2 = R_6 = H$, $R_3 = R_4 = O$, $R_5 = CO_2Me$, $R_7 = CH_2OH$

2: $R_1 = R_3 = H$, $R_2 = R_6 = R_8 = OH$, $R_4 = OAc$, $R_5 = CO_2Me$, $R_7 = CH_2OH$

3: $R_1 = R_2 = OH$, $R_3 = R_8 = H$, $R_4 = R_6 = OAc$, $R_5 = CO_2Me$, $R_7 = CH_2OH$

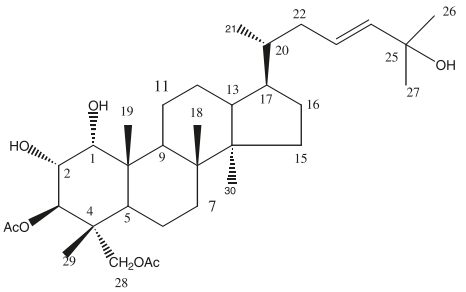

4

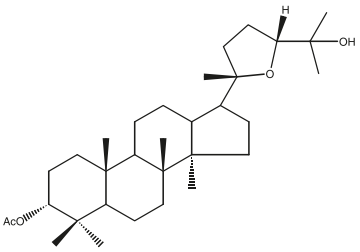

5

Extraction and isolation

Steam-distilled residues of the resin (~1 kg) were extracted at room temperature with acetone (2.5 L) for 5 days. The extract was filtered and concentrated to give a brownish gummy material (350 g). Approximately 245 g was dissolved in a small amount of acetone and then adsorbed onto silica gel. Removal of acetone under reduced pressure yielded a free-flowing mass that was chromatographed over silica gel (medium pressure, pressure ~ 1 bar); eluted with *n*-hexane/EtOAc mixtures with increasing concentration of the more polar solvent, EtOAc, followed by EtOAc/MeOH mixtures (9:1, 4:1, 7:3, and 2:1), and elution concluded with MeOH, affording 250 fractions (100 mL each) whose compositions were monitored by TLC (eluent: *n*-hexane/EtOAc (9:1, 4:1, 2:1) and EtOAc/MeOH (9:1, 4:1). Those showing similar TLC profiles were combined, resulting into four pools (I–IV). Pool I (fractions 1–105, 35 g), an oily resinous material was further purified by medium-pressure chromatography to afford 2-methoxy-8,12-epoxygermacra-1(10), 7,11-trien-6-one (**9,** 78 mg), furadienone (**11,** 105 mg), 2-methoxy-5-acetylfuranogermacra-1(10),7,11-trien-6-one (**10,** 62 mg), and 2-methoxy-5-acetyl-4-furanogermacra-1(10)*Z*-en-6-one (**12,** 85 mg).[6–8] Fractions 111–170 constituted pool II (25 g) and was found to contain four major spots, which were resolved into α-amyrin (**13**, 200 mg), sistosterol (**14**, 104 mg), stigmasterol 3-*O*-acetate (**15**, 84 mg), and mansumbinol (**6,** 65 mg), using *n*-hexane/ethyl acetate (4:1, 3:2).[9–11] Pool III (fractions 171–205, 10 g) upon repeated fractionation using *n*-hexane/ethyl acetate (3:2, 1:2), collecting 20 mL each, allowed the isolation of 3β-acetylamyrin (**7,** 150 mg), 3α-acetylboswellic acid (**8,** 97 mg),[12,13] methyl-3β,11α-diacetyl-1α,2α,28trihydroxyurs-12-ene-24-oate (**3**, 35 mg), and cabraleadiol monoacetate (**5**, 95 mg).[14] Pool IV (21 g) was a gummy material, and its constituents were resolved into individual compounds using preparative HPLC (eluent: acetonitrile/H_2O, 35:65), mobile flow rate 10 mL min^{-1}, injecting 10 μL each time. The process afforded methyl 3-oxo-1α,19α, 28-trihydroxyurs-12-en-24-oate (**1**, 65 mg), methyl-3β-acetyl-2α,11α,19α,28-tetrahydroxyurs-12-en-24-oate (**2**, 87 mg), and 3β, 24-diacetyl-1α,2α,25-trihydroxydammar-23-ene (**4**, 75 mg).

Compound 1

Colorless amorphous powder, mp > 250 °C. $[\alpha]_D^{25}$ +13 (MeOH, *c* 0.05). UV (CH_3CN) λ_{max} (nm): 202 (log ε 3.4). IR ν_{max} (KBr) (cm^{-1}): 3430–3300 (OH), 2950, 2863, 1719 (CO_2Me), 1706 (C=O), 1646 (C=C), 1450, 1380, 1260, 1190, 1020, 960. ^1H NMR ($CDCl_3$ + DMSO-d_6, 400 MHz): see Table 1. ^{13}C NMR ($CDCl_3$ + DMSO-d_6, 100 MHz): data are in Table 2. EIMS *m/z* (%): 516 $[M]^+$ (1), 498 $[M - H_2O]^+$ (3), 480 $[M - 2H_2O]^+$ (7), 448 (2), 440 (3), 266 $[C_{15}H_{22}O_4]^+$ (10), 250 $[C_{16}H_{26}O_2]^+$ (3), 248 (15), 238 (100), 232 (1), 231 (45), 219 (17), 207 (2), 203 (11), 201 (21), 189 (75), 173 (27), 119 (55), 95 (34), 56 (48). HR-EIMS *m/z*: 516.3589 $[M]^+$, (calcd. for $C_{31}H_{48}O_6$: 516.3473).

Compound 2

Colorless amorphous powder, mp > 250 °C. $[\alpha]_D^{25}$ +73 (MeOH, *c* 0.2). UV λ_{max} (nm): 206 (log ε 4.0). IR ν_{max} (KBr) (cm^{-1}): 3420 (OH), 2950, 2856, 1732 (ester), 1721 (CO_2Me), 1640 (C=C), 1450, 1376, 1245, 1221, 1130, 980. ^1H NMR ($CDCl_3$ + DMSO-d_6, 400 MHz): see Table 1. ^{13}C NMR ($CDCl_3$ + DMSO-d_6, 100 MHz): see Table 2. EIMS *m/z* (%): 540 $[M - 2H_2O]^+$ (6), 522 (2), 481 (3), 310 $[C_{17}H_{26}O_5]^+$ (1), 292 (4), 266 $[C_{16}H_{26}O_3]^+$ (5), 250 (7), 249 $[C_{15}H_{21}O_4]^+$ (21), 248 $[C_{16}H_{24}O_2]^+$ (4), 235 $[C_{15}H_{23}O_2]^+$ (12), 231 $[C_{16}H_{23}O]^+$ (100), 213 (8), 218 $[C_{15}H_{22}O]^+$ (10), 203 (2), 189 (21). HR-ESIMS *m/z*: 576.3834 $[M + Na]^+$, (calcd. for $C_{33}H_{52}O_8Na$: 576.3827).

Compound 3

Colorless amorphous powder, mp > 250 °C. $[\alpha]_D^{25}$ +7.9 ($CHCl_3$, *c* 0.5). UV λ_{max} (nm): 198 (log ε 4.1). IR ν_{max} (KBr) (cm^{-1}): 3540 (OH), 2945, 2870, 1736 (ester), 1725 (CO_2CH_3), 1635 (C=C), 1460, 1382, 1250, 1120, 1040, 950. ^1H NMR ($CDCl_3$, 400 MHz): see Table 1. ^{13}C NMR ($CDCl_3$, 100 MHz): see Table 2. EIMS *m/z* (%): 618 $[M]^+$ (3), 600 $[M - H_2O]^+$ (1), 587 (4), 582 (2), 569 (6), 558 $[M - CH_3COOH]^+$ (11), 551 (7), 527 (9), 498 $[M - 2CH_3COOH]^+$ (6), 491 (11), 467 (2), 441 (1), 431 (5), 410 (1), 408 (3), 326

Table 1. ^{1}H NMR spectra of compounds **1**–**5**.

C	**1**	**2**	**3**	**4**	**5**
1	3.60 t (10.0, 4.5)	1.96 dd (12.0, 4.6), 0.94 dd (12.0, 9.0)	3.75 d (3.6)	3.60 d (4.5)	1.94 m, 1.12 m
2	1.84 m, 1.54 m	3.65 ddd (12.4 10.0, 3.2)	3.50 dd (10.2, 3.4)	3.77 dd (11.0, 3.3)	1.66 m, 1.59 m
3	—	4.50 d (11.6)	4.40 d (12.0)	4.65 d (12.4)	4.56 d (4.6)
4	—	—	—	—	—
5	1.02 m	1.00 m	0.98 m	0.92 m	0.84 m
6	1.68 m, 1.43 m	1.63 m, 1.40 m	1.62 m, 1.38 m	1.65 m, 1.35 m	1.54 m, 1.43 m
7	1.44 m, 1.24 m	1.56 m, 1.27 m	1.54 m, 1.28 m	1.46 m, 1.20 m	1.52 m, 1.25 m
8	—	—	—	—	—
9	1.66 dd (12.7, 6.6)	1.98 dd (10.3, 4.0)	1.95 d (9.3)	1.36 m	1.33 m
10	—	—	—	—	—
11	2.00 m, 1.92 m	3.70 dd (10.2, 3.6)	4.23 dd (8.8, 3.4)	1.47 m, 1.28 m	1.48 m, 1.16 m
12	5.26 br s	5.21 br s	5.25 br s	1.74 m, 1.16 m	1.63 m, 1.22 m
13	—	—	—	1.60 m	1.62 m
14	—	—	—	—	—
15	1.74 m, 1.16 m	1.60 m, 1.13 m	1.86 m, 1.01 m	1.46 m, 1.10 m	1.45 m, 0.96 m
16	1.92 m, 1.58 m	2.01 m, 1.62 m	1.96 m, 0.96 m	1.56 m, 1.42 m	1.69 m, 1.30 m
17	—	—	—	1.75 m	1.86 m
18	2.36 s	2.38 s	1.75 d (12.5)	0.94 s	0.95 s
19	—	—	1.53 m	0.86 s	0.88 s
20	1.20 m	1.17 m	1.46 m	1.30 m	—
21	1.58 m, 1.18 m	1.35 m, 1.17 m	1.51 m, 1.29 m	0.95 d (6.5)	1.02 s
22	1.86 m, 1.61 m	1.70 m, 1.51 m	1.59 m, 1.23 m	1.44 m, 1.06 m	1.90 m, 1.66 m
23	1.16 s	1.15 s	1.13	5.64 m	1.84 m, 1.76 m
24	—	—	—	5.58 m	3.45 dd (10.6, 5.3)
25	0.98 s	0.99 s	0.94 s	—	—
26	1.10 s	1.18 s	1.15 s	1.36 s	1.32 s
27	1.22 s	1.20 s	1.17 s	1.36 s	1.32 s
28	4.00 d (10.6), 3.80 d (10.6)	4.20 (11.0), 3.90 d (11.0)	4.10 d (11.1), 3.86 d (11.1)	0.95 s	0.88 s
29	1.30 s	1.33 s	0.88 d (6.8)	1.04 s	0.82 s
30	0.89 d (6.6)	0.95 d (6.7)	0.87 d (6.6)	0.84 s	0.89 s
CO_2*Me*	3.54 s	3.46 s	3.50 s	—	—
OCO*Me*	—	1.98 s	2.00 s, 2.03 s	1.99 s, 2.02 s	2.01 s

Table 2. ^{13}C NMR of compounds **1**–**5**.

C	1	2	3	4	5
1	73.4	46.2	71.5	74.3	38.8
2	44.1	67.6	74.0	72.0	24.7
3	216.0	78.2	80.1	80.0	81.0
4	54.2	55.0	54.0	42.2	37.6
5	48.4	48.8	48.3	43.5	54.7
6	20.8	18.1	20.6	20.3	18.3
7	33.2	32.4	33.1	36.2	34.8
8	39.4	39.8	40.4	40.8	41.4
9	38.4	48.2	46.7	46.8	51.1
10	38.9	38.6	40.6	37.4	37.4
11	23.8	71.4	79.5	25.7	22.0
12	127.3	126.0	125.4	33.0	27.0
13	140.0	141.6	139.0	42.6	43.2
14	42.4	43.6	42.3	52.4	50.0
15	27.2	28.8	28.1	36.2	32.4
16	23.7	26.0	23.4	27.9	25.8
17	46.1	47.4	45.9	54.2	49.7
18	52.6	54.0	37.8	15.8	16.0
19	72.8	72.4	39.9	16.3	16.6
20	43.0	42.6	37.8	35.7	86.6
21	26.9	27.2	31.8	18.8	24.4
22	36.9	38.4	38.5	36.2	35.5
23	14.1	16.1	14.4	126.3	26.8
24	181.4	179.7	180.8	141.4	86.2
25	16.0	15.0	14.2	79.9	73.0
26	16.8	16.9	17.0	25.3	26.6
27	26.3	25.0	26.5	25.1	27.0
28	66.6	65.7	67.5	26.4	16.6
29	28.7	26.7	26.3	19.7	28.0
30	16.9	17.0	16.8	16.1	17.3
CO_2*Me*	53.0	54.5	54.0		
O*C*OMe		171.0	170.1, 169.5	170.3, 169.8	171.1
OCO*Me*		23.0	23.8, 24.1	24.1, 23.5	22.8

$[C_{17}H_{26}O_6]^+$ (5), 298 (1), 292 $[C_{18}H_{28}O_3]^+$ (11), 266 $[C_{15}H_{22}O_4]^+$ (15), 261 $[C_{17}H_{25}O_2]^+$ (10), 249 $[C_{15}H_{21}O_3]^+$ (20), 234 (3), 232 $[C_{16}H_{24}O]^+$ (12), 231 (1), 201 $[C_{15}H_{21}]^+$ (100), 198 (41), 174 (23), 95 (51), 69 (70). HR-EIMS *m/z*: 618.2354 $[M]^+$, (calcd. for $C_{35}H_{54}O_9$: 618.2337).

Compound 4

Colorless amorphous powder, mp 248–250 °C. $[\alpha]_D^{25}$ 116 ($CHCl_3$, *c* 0.02). UV λ_{max} (nm): 228 (log ε 4.1). IR ν_{max} (KBr) (cm^{-1}): 3500 (OH), 1736 (ester), 1644 (C=C). ^1H NMR ($CDCl_3$, 400 MHz): see Table 1. ^{13}C NMR ($CDCl_3$, 100 MHz): see Table 2. EIMS *m/z* (%): 558 $[M - H_2O]^+$ (4), 540 $[M - 2H_2O]^+$ (13), 516 $[M - HOAc]^+$ (4), 435 (22), 420 (3), 373 (31), 250 (42), 189 (100), 109 (75). HR-ESIMS *m/z:* 599.2495 $[M + Na]^+$, (calcd. for $C_{34}H_{56}O_7{}^+Na$: 599.2431).

Compound 5

Colorless crystals, mp151–153 °C. $[\alpha]_D^{25}$ + 61° ($CHCl_3$, *c* 0.1). IR ν_{max} (KBr) (cm^{-1}): 3440 (OH), 2952, 2860, 1734 (ester), 1450, 1380, 1255, 1145, 1040, 1020, 970. ^1H NMR ($CDCl_3$, 400MHz): see Table 1. ^{13}C NMR ($CDCl_3$, 100 MHz): see Table 2. CIMS *m/z* (%): 502 $[M]^+$ (9), 442 $[M - HOAc]^+$ (12), 424 $[M - H_2O - HOAc]^+$ (9), 292 (11), 249 (15), 248 (20), 213 (10), 218 (36), 201 (100).

Fig. 1. Key NOESY correlations for compounds **3** and **4**.

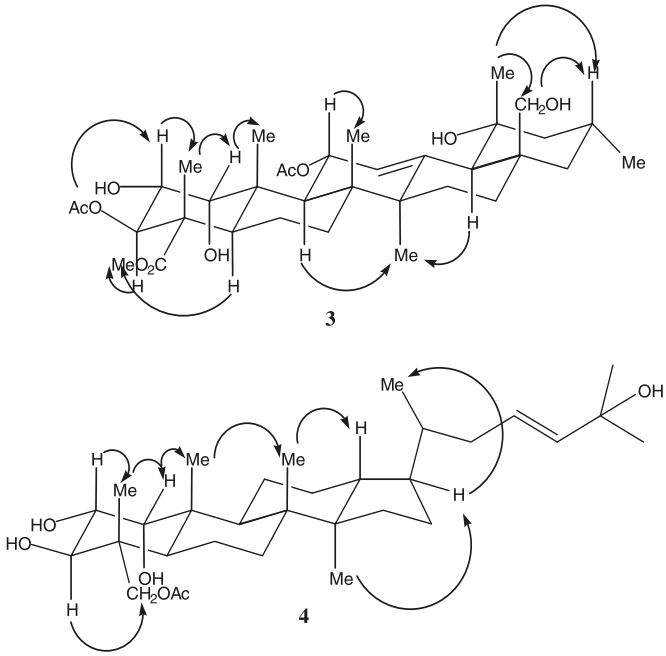

Results and discussion

Fractionation of the acetone extract of *C. holtziana* yielded compounds (**1**–**4**) together with eleven known ones (**5–15**) identified on the basis of spectroscopic and physical methods.

Compound **1**, isolated as colorless amorphous powder afforded positive Liebermann–Burchard test, suggesting the presence of a triterpene or sterol skeleton. Its molecular-ion peak at *m/z* 516.3589 (calcd. *m/z* 516.3473) by accurate mass measurement corresponds to the formula $C_{31}H_{48}O_6$, confirmed by ^{13}C NMR and DEPT spectra, which exhibited 31 carbon atoms resolved into 9 methylenes, 7 methyls, 6 methines, and 9 quaternary. The ^1H NMR spectrum (Table 1) indicated five tertiary methyls (δ 1.30, 1.22, 1.10, 1.06, 0.98), a methoxy carbonyl (δ 3.54), a secondary methyl group (δ 1.16, d, *J* = 6.6 Hz, CH_3-30), an oxymethine (δ 3.60, t, *J* = 10.0, 4.5 Hz, H-1), a terminal hydroxymethylene (δ 4.00, d, *J* = 10.6 Hz, H-28b; δ 3.80, d, *J* = 10.6 Hz, H-28a), and a trisubstituted double bond (δ 5.26, d, *J* = 4.0 Hz, H-12). In combination with the characteristic EIMS fragmentation ions at *m/z* 266 $[C_{15}H_{22}O_4]^+$ and 250 $[C_{16}H_{26}O_2]^+$ attributed to retro-Diels–Alder cleavage between C-9 and C-11, and between C-8 and C-14 bonds, it suggested that compound **1** is either an ursane- or oleanane-type triterpene containing a keto, two hydroxyls, a methyl carbonyl, and a terminal hydroxymethylene functional group. On the basis of the cleavage, it was suggested that the oxo, one hydroxyl, and the methoxy carbonyl were present in the rings A/B, whereas the terminal hydroxymethylene and another hydroxyl group were positioned in the rings C/D part of the molecule.[15–19] The ^1H NMR singlet peak at δ 2.36 is a characteristic signal for the H-18 of an ursane-type with 19-O-substitution.

Fig. 2. ORTEP-style plot of compound **5** showing the atom-numbering scheme and the solid-state conformation. Thermal ellipsoids are drawn at the 50% probability level.

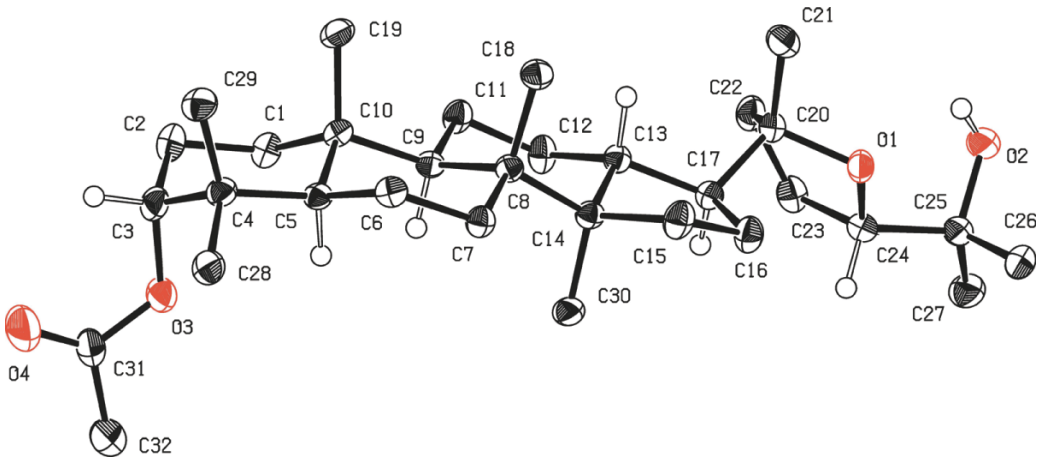

Together with the ^{13}C NMR olefinic carbon signals at δ 127.3 (C-12) and δ 140.0 (C-13) and an oxygen bearing quaternary carbon at δ 72.8 (C-19), it confirmed the 19α-hydroxyurs-12-ene skeleton for the compound.[17,20] The positions of the substituents and their stereochemistry were established by 2D experiments, whereby the key proton resonances were assigned by gHSQC correlations. The long-range correlation (gHMBC) showed significant cross peaks between H-1 (δ 3.60) and C-3 (δ 216.0), between H-18 (δ 2.36) and C-19 (δ 72.8) and C-28 (δ 66.6), between H-5 (δ 1.02) and C-24 (δ 181.4), and between H-18 and C-20 (δ 43.0). The position of a hydroxyl-bearing methine proton at δ 3.60 (H-1) was confirmed to be at C-1, as its carbon resonance (δ 73.4) showed a gHMBC correlation with Me-25, a fact further corroborated by the ^{13}C NMR shielded resonances for C-5 (δ 48.4) and C-9 (δ 38.4), respectively.[21] The stereochemistry of the hydroxyl group at C-1 was determined as α and axial on the basis of NOESY cross peaks between H-1 and Me-23 and also between H-1 and Me-25. This was further supported by the coupling $J_{H\text{-}1/H\text{-}2}$ (cis) = 4.5 Hz consistent with the 1α-hydroxy-substituted ring A, which is in agreement with literature report for rings A/B part of 1α-hydroxy-3-oxoolean-12-en-oic acid.[21] Thus, based on the results, compound **1** was concluded to be methyl-3-oxo-1α,19α,28-trihydroxyurs-12-en-24-oate.

Compound **2** was isolated as colorless powder from CH_2Cl_2/MeOH (9:1). According to EIMS, ^{13}C NMR, and DEPT, its composition is $C_{33}H_{52}O_8$, consistent with nine degrees of unsaturation. Data from ^1H and ^{13}C NMR (Tables 1 and 2) indicated a secondary metabolite with a structure similar to that of compound **1**. The major structural difference is the additional acetyl group (δ 1.98) and two oxygenated methines (δ 4.50, d, J = 11.6 Hz, H-3; δ 3.70, dd, J = 10.2, 3.6 Hz, H-11). Both the ^1H and ^{13}C NMR depicted data typical of a triterpene of ursane skeleton containing a double bond between C-12 and C-13.[17,22,23] Support for this conclusion was further provided by the mass spectrum. Retro-Diels–Alder cleavage, characteristic of Δ^{12}-pentacyclic triterpenes, leads to m/z 310 $[C_{17}H_{26}O_5]^+$ and 250 $[C_{16}H_{26}O_2]^+$. The fragments at m/z 249 $[C_{15}H_{21}O_4]^+$, resulting from m/z 310, and those at m/z 232 $[C_{16}H_{24}O]^+$ and 201 $[C_{16}H_{21}]^+$, resulting from m/z 250, indicated the presence of hydroxyl, acetyl, and a methoxy carbonyl group in rings A/B, whereas another hydroxyl, an oxymethylene and an oxygenated tertiary methyl group were in rings D/E part of the molecule.[24] This was further corroborated by the singlet proton signal at δ 2.38 (H-18), typical of 19α-hydroxyurs-12-ene skeleton, which correlated with C-28 (δ 65.7), C-12 (δ 126.0), and C-20 (δ 42.6) in the HMBC spectrum. On the other hand, in the ^1H–^1H homonuclear chemical correlation spectrum, the comparatively low field oxymethine proton at δ 4.50 correlated with one proton and hence was assigned to C-3, further evidenced by gHSQC correlation between H-3 (δ 4.50) and C-3 (δ 78.2). The large coupling constant (J = 11.6 Hz) allowed the assignment of β and equatorial orientation of the acetyl group. Similarly, the positions of two hydroxyl-bearing methine protons at δ 3.65 (ddd, J = 12.4, 10.0, 3.2 Hz, H-2) and δ 3.70 (d, J = 10.2, 3.6 Hz, H-11) and their disposition as both α was suggested by the coupling constants, which agreed well with 2α, 11α-dihydroxy substitution on rings A/C,[25,26] respectively, and were confirmed by gHMBC cross peaks between H-2 (δ 3.65) and C-4 (δ 55.0), and between H-11 (δ 3.70) and C-13 (δ 141.6). Spin-decoupled and NOESY experiments allowed the complete assignment of the stereochemistry of compound **2**. Thus, on the basis of accrued data, **2** was concluded to be methyl 3β-acetyl-2α,11α,19α,28- tetrahydroxyurs-12-en-24-oate.

Compound **3** was isolated as colorless powder from CH_2Cl_2–MeOH (9:1). It afforded an IR spectrum indicating the presence of hydroxyl, ester, methoxylated carbonyl group, and a double bond (3540, 1734, 1725, 1635 cm^{-1}). Its ^1H NMR spectrum showed a vinyl proton (δ 5.25, br s, H-12), an oxymethine proton (δ 4.40, d, J = 12.0 Hz, H-3), an allylic methine proton attached to an oxygen functionality (δ 4.23, d, J = 8.8, 3.4 Hz, H-11), a terminal hydroxymethylene (δ 4.10, d, J = 11.1 Hz) and δ 3.86 (d, J = 11.1 Hz, CH_2-28), two hydroxy methine protons (δ 3.50, dd, J = 10.2, 3.4 Hz, H-2; δ 3.75, d, J = 3.6 Hz, H-1), two acetyl groups (δ 2.03, 2.00, both singlets), four tertiary methyls (δ 1.17, δ 1.15, δ 1.13, δ 0.94), and two secondary methyl groups (δ 0.88, d, J = 6.8 Hz, Me-29; δ 0.87, d, J = 6.6 Hz, Me-30). The compound exhibited an HR-EIMS molecular ion peak at m/z 618.2354, compatible with the formula $C_{35}H_{54}O_9$. Other significant peaks at m/z 326 $[C_{17}H_{26}O_6]^+$

and 234 $[C_{16}H_{26}O]^+$ were in accord with the retro-Diels–Alder cleavage, typical of C-12 unsaturated pentacyclic triterpenes.[27] From the fragmentation pattern, it was evident that rings A/B contained two hydroxyls, an acetyl, and a methoxy carbonyl group, a fact that was evidenced by the daughter ions at *m/z* 266 $[C_{15}H_{22}O_4]^+$ and 249 $[C_{15}H_{21}O_3]^+$ from the ions *m/z* 326 $[C_{17}H_{26}O_6]^+$. Similarly, fragments at *m/z* 261 $[C_{17}H_{25}O_2]^+$, 232 $[C_{16}H_{24}O]^+$, and 201 $[C_{15}H_{21}]^+$ signified the presence of another acetoxy and an hydroxymethylene group in the rings D/E. The foregoing conclusions were confirmed by gHSQC and gHMBC experiments; in particular, the gHMBC correlations observed between H-18 (δ 1.75) and C-28 (δ 67.5), between H-11 (δ 4.23) and C-13 (δ 139.0), and between H-5 (δ 0.98) and C-24 (δ 180.8) and C-3 (δ 80.1). The relative stereochemistry of substituents was assigned by NOESY experiments (Fig. 1). Therefore, on the basis of spectroscopic data, as well as comparison with known compounds, **3** was structurally concluded to be methyl 3β,11α-diacetyl-1α,2α,28-trihydroxyurs-12-en-24-oate.

Compound **4** was obtained as colorless powder, mp 248–250 °C after crystallization from a CH_2Cl_2/MeOH. Its molecular formula, $C_{34}H_{56}O_7$, was deduced from the HR-ESIMS molecular ions at *m/z* 599.2495 $[M + Na]^+$ (calcd. 599.2431) and by quantification of methyls, methylenes, methines, and quaternary carbon atoms revealed in the ^{13}C NMR and DEPT spectra. The IR spectrum displayed significant bands at 3500, 1736, and 1644 cm^{-1}, signifying the presence of OH, ester, and a carbon–carbon double bond, respectively. The EIMS fragment peaks at *m/z* 558 $[M - H_2O]^+$, 540 $[M - 2H_2O]^+$, and 516 $[M - HOAc]^+$ are characteristic features of the dammarane skeleton with two acetoxy and two hydroxyl groups in the rings A/B.[20,28] The ^1H NMR spectrum corroborated the findings by showing nine signals for methyl groups, two of them acetoxy, a fact further supported by two ester carbonyl peaks at δ 170.3 and δ 169.8 with corresponding methyls at δ 24.1 and δ 23.5, respectively. A singlet at δ 1.36, typical of a hydroxyl isopropyl moiety, and signals of an isolated double bond at δ 5.64 and δ 5.58 evidenced the presence of a $–CH(CH_3)–CH_2–CH=C(CH_3)_2–OH$ system in the C-17 side chain.[12] This was confirmed by ^1H-detected gradient heteronuclear single quantum coherence (gHSQC) experiments where the two peaks at δ 126.3 (C-23) and δ 141.4 (C-24) represented the isolated double bond while the other peak at δ 79.9 corresponded to hydroxy isopropyl moiety. Further insight into the structure of **4** was provided by close examination of both the mass spectrum and the ^1H NMR data, whereby the EIMS fragments in combination with ^1H NMR peaks at δ 4.65 (d, J = 12.4 Hz, H-3), δ 3.77 (dd, J = 11.0, 3.3 Hz, H-2), and δ 3.60 (d, J= 4.5 Hz, H-1) confirmed the presence of an acetoxy and three oxymethines linked in a $CH_{eq}(O-H_{ax})–CH_{eq}(OH_{ax})–CH_{ax}(OAc_{eq})–CCH_3(CH_2OAc)$ system requiring the two oxymethine protons to be at C-1 and C-2 both as α, while the acetoxy to be at C-3 as β[20,28] and was consistent with gHSQC, gHMBC, and NOESY correlations (Fig. 1). On this basis, the structure of compound **4** was concluded as 3β,28-diacetyl-1α,2α,25-trihydroxydammar-23-ene.

Compound **5** was isolated as colorless crystals from *n*-hexane/EtOAc (2:1). Its HR-EIMS showed a peak at *m/z* 502.4074 $[M]^+$, corresponding to the formula $C_{32}H_{54}O_4$. The ^1H and ^{13}C NMR spectral data revealed a close relationship, if not identity, with cabraleadiol monoacetate.[14] However, HMQC and HMBC experiments lead to minor but possibly significant differences from the reported ^1H NMR spectrum data, as concluded from HETCOR experiments. Thus, the structure of **5** was validated by an X-ray crystallographic study (Fig. 2) to be cabraleadiol monoacetate.[29]

Supplementary data

Supplementary data for this article are available on the journal Web site (canjchem.nrc.ca) or may be purchased from the Depository of Unpublished Data, Document Delivery, CISTI, National Research Council Canada, Ottawa, ON K1A 0R6, Canada. DUD 3974. For more information on obtaining material, refer to cisti-icist.nrc-cnrc.gc.ca/cms/unpub_e.shtml. CCDC 727028 contains the X-ray data in CIF format for this manuscript. These data can be obtained, free of charge, via www.ccdc.cam.ac.uk/conts/retrieving.html (or from the Cambridge Crystallographic Data Centre, 12 Union Road, Cambridge CB2 1EZ, UK; fax +44 1223 336033; or deposit@ccdc.cam.ac.uk).

Acknowlegements

The authors are grateful to the African Academy of Science (AAS) for providing funds that initiated the research. Alexander von Humboldt foundation is sincerely thanked for the fellowship awarded to L. Manguro that made part of analysis done at Technische Universitaet Munich, Germany. Prof. Thomas Bach, Director of the Institute of Organic Chemistry and Biochemistry, Technical University of Munich, is highly appreciated for accepting to host L. Manguro. Mr. Norman Gachathi of Kenya Forestry Research Institute is acknowledged for identification and collection of the plant products. Mr. Liu of Quangzhou Institute of Chemistry, Chinese Academy of Sciences, is acknowledged for NMR data analysis of some compounds.

References

(1) Dale, I.; Greenway, P. G. In *Kenya trees and shrubs*; Buchanan's Kenya Ltd: Nairobi, 1961; pp 86–95.
(2) Trease, G. E.; Evans, W. C. In *Pharmacognosy*; 11th ed.; Balliere Tindall: London, 1988; pp. 463–475.
(3) Provan, G. J.; Waterman, P. G. *Phytochemistry* **1988**, *27*, 3841.
(4) Kokwaro, J. O. *Medicinal plants of East Africa*; East African Literature Bureau: Nairobi, 1976; pp. 76–83.
(5) Maradufu, A. *Phytochemistry* **1982**, *21* (3), 677–680. doi:10.1016/0031-9422(82)83164-6.
(6) Dekebo, A.; Dagne, E.; Hansen, L. K.; Gautum, O. R.; Aasen, A. J. *Tetrahedron Lett.* **2000**, *41* (50), 9875–9878. doi:10.1016/S0040-4039(00)01752-4.
(7) Brieskorn, C. H.; Noble, P. *Tetrahedron Lett.* **1980**, *21* (16), 1511–1514. doi:10.1016/S0040-4039(00)92760-6.
(8) Heinz Brieskorn, C.; Noble, P. *Phytochemistry* **1983**, *22* (5), 1207–1211. doi:10.1016/0031-9422(83)80223-4.
(9) Dekebo, A.; Dagne, E.; Hansen, L. K.; Gautum, O. R.; Aasen, A. J. *Phytochemistry* **2002**, *59*, 399.
(10) Manguro, L. O. A.; Gitiomi, J. K.; Mukonyi, K. W. *Planta Med.* **1996**, *32*, 85.

(11) Cambie, R. C.; Raharjo, A. F. X.; Rutledge, P. S.; Woodgate, P. D. *N. Z. J. Bot.* **1993**, *31*, 425.
(12) Manguro, L. O. A.; Ugi, I.; Lemmen, P. *Japan. Chem. Pharm. Bull. (Tokyo)* **2003**, *51* (5), 483–486. doi:10.1248/cpb.51.483.
(13) Mathias, L.; Ivo, J. C.; Vieira, R. B.; Edson, R. F. *J. Braz. Soc.* **2000**, *11*, 195.
(14) Hisham, A.; Ajitha Bai, M. D.; Fujimoto, Y.; Hara, N.; Shimada, H. *Magn. Reson. Chem.* **1996**, *34* (2), 146–150. doi:10.1002/(SICI)1097-458X(199602)34:2<146::AID-OMR850>3.0.CO;2-U.
(15) Manguro, L.; Onyango Okwiri, S.; Lemmen, P. *Phytochemistry* **2006**, *67* (24), 2641–2650. doi:10.1016/j.phytochem.2006.07.025. PMID:16973190.
(16) Machocho, A. K.; Kiprono, P. C.; Grinberg, S.; Bittner, S. *Phytochemistry* **2003**, *62* (4), 573–577. doi:10.1016/S0031-9422(02)00619-2. PMID:12560028.
(17) Takahashi, H.; Hirata, S.; Minami, H.; Fukuyama, Y. *Phytochemistry* **2001**, *56* (8), 875–879. doi:10.1016/S0031-9422(00)00493-3. PMID:11324921.
(18) Ohtani, K.; Mavi, S.; Hostettman, K. *Phytochemistry* **1993**, *33* (1), 83–86. doi:10.1016/0031-9422(93)85400-L.
(19) Napoli, L.; Picialli, G.; Picialli, V.; Santacrose, C.; Carolla, R. *Phytochemistry* **1992**, *31* (11), 3965–3968. doi:10.1016/S0031-9422(00)97564-2.
(20) Wandji, J.; Tillequin, F.; Mulholland, D. A.; Shirri, J. C.; Tsabang, N.; Seguin, E.; Verite, P.; Libot, F.; Fomum, Z. T. *Phytochemistry* **2003**, *64* (4), 845–849. doi:10.1016/S0031-9422(03)00495-3. PMID:14559279.
(21) Nick, A.; Wright, A. D.; Sticher, O.; Rali, T. *Phytochemistry* **1995**, *40* (6), 1691–1695. doi:10.1016/0031-9422(95)00491-O.
(22) Sukumar, E.; Balakrishma, K.; Bhima-Rao, R.; Kundu, A. B. *Phytochemistry* **1995**, *38* (1), 275–276. doi:10.1016/0031-9422(94)00581-D.
(23) Mahato, B. S.; Kundu, P. A. *Phytochemistry* **1994**, *37* (6), 1517–1575. doi:10.1016/S0031-9422(00)89569-2.
(24) Lontsi, D.; Sondangam, B. L.; Martin, M. T.; Bodo, B. *Phytochemistry* **1998**, *48* (1), 171–174. doi:10.1016/S0031-9422(97)00789-9.
(25) Cáceres-Castillo, D.; Mena-Rejón, G. J.; Cedillo-Rivera, R.; Quijano, L. *Phytochemistry* **2008**, *69* (4), 1057–1064. doi:10.1016/j.phytochem.2007.10.016. PMID:18061220.
(26) Chen, I. H.; Chang, F. R.; Wu, C. C.; Chen, S. L.; Hsieh, P. W.; Yen, H. F.; Du, Y. C.; Wu, Y. C. *J. Nat. Prod.* **2006**, *69* (11), 1543–1546. doi:10.1021/np060369n. PMID:17125218.
(27) Shen, T.; Wan, W.; Yuan, H.; Kong, F.; Guo, H.; Fan, P.; Lou, H. *Phytochemistry* **2007**, *68* (9), 1331–1337. doi:10.1016/j.phytochem.2007.01.013. PMID:17343886.
(28) Siddiqui, B. S.; Sultana, I.; Sabira, B. F. *Phytochemistry* **2000**, *54* (8), 861–865. doi:10.1016/S0031-9422(00)00058-3.
(29) Qiu, S. X.; Nguyen, V. H.; Le, T. X.; Gu, J. Q.; Lobkovsky, E.; Tran, C. K.; Soejarto, D. D.; Clardy, J.; Pezzuto, J. M.; Dong, Y.; Mai, V. T.; Le, M. H.; Fong, H. H. S. *Phytochemistry* **2001**, *56* (7), 775–780. doi:10.1016/S0031-9422(00)00463-5. PMID:11314967.

Design, chemical synthesis, and in vitro biological evaluation of simplified estradiol–adenosine hybrids as inhibitors of 17β-hydroxysteroid dehydrogenase type 1

Marie Bérubé and Donald Poirier

Abstract: A series of estradiol (E_2) derivatives were designed to interact with both the substrate- and the cofactor-binding sites of 17β-hydroxysteroid dehydrogenase type 1 (17β-HSD1). These analogues of potent E_2–adenosine hybrid inhibitor EM-1745, where the adenosine moiety was replaced by a more stable benzene derivative, were synthesized from estrone using alkene cross-metathesis and Sonogashira coupling reactions as key steps. In vitro biological evaluation of these steroid derivatives revealed that a spacer of 13 methylenes, between the 16β-position of E_2 and the adenosine mimic bearing a carboxylic acid group, gave the best inhibition of 17β-HSD1.

Key words: 17β-hydroxysteroid dehydrogenase, enzyme, inhibitor, steroid, metathesis, Sonogashira coupling.

Résumé : Plusieurs dérivés de l'estradiol (E_2) ont été préparés pour interagir avec le site de liaison du substrat et le site de liaison du cofacteur de la 17β-hydroxystéroïde déshydrogénase type 1 (17β-HSD1). Ces analogues du puissant inhibiteur EM-1745, un hybride E_2–adénosine dont la partie adénosine a été remplacée par un dérivé benzylique plus stable, ont été obtenus à partir de l'estrone en utilisant la métathèse de Grubbs et le couplage de Sonogashira comme étapes clé. L'évaluation biologique in vitro de ces dérivés stéroïdiens a montré qu'une chaîne ayant 13 groupes méthylènes, entre la position 16β du stéroïde E_2 et le noyau benzylique porteur d'un acide carboxylique, provoquait la meilleure inhibition de l'enzyme 17β-HSD1.

Mots-clés : 17β-hydroxystéroïde déshydrogénase, enzyme, inhibiteur, stéroïde, métathèse, couplage de Sonogashira.

Introduction

17β-Hydroxysteroid dehydrogenase type 1 (17β-HSD1) or human estradiol dehydrogenase [E.C.1.1.1.62] was partially purified from human placenta by Langer and Engel in 1958.[1] It is a 327-amino-acids protein that exists as a homodimer. This enzyme preferentially catalyzes the transformation of estrone (E_1) into estradiol (E_2), the most potent estrogen, using NAD(P)H as cofactor (Fig. 1),[2–7] but also catalyzes the reduction of dehydroepiandrosterone (DHEA) into 5-androstene-3β,17βdiol (Δ^5-diol).[4] 17β-HSD1 activities have been found in many human tissues such as placenta, ovary, endometrium, liver, and breast.[8] In peripheral tissues such as the breast, enzyme substrates come from circulating DHEA-sulfate (DHEAS) or E_1-sulfate (E_1S), which are converted into DHEA and E_1 by steroid sulfatase.[9–11]

E_2 and Δ^5-diol have, respectively, high and weak affinity for the estrogen receptor (ER). The resulting receptor–estrogen complex produces estrogenic effects. Thus, in estrogen-dependent breast cancer, activation of ER by E_2 is crucial for the stimulation of growth of tumour cells. In fact, E_2 concentration has been found to be significantly higher in breast tumours than in normal breast tissue.[12,13] Furthermore, the intratumoral E_2 levels are high in postmenopausal patients with very low serum E_2 levels; a study aimed at explaining this revealed that the expression of 17β-HSD1 and the E_2/E_1 ratio are higher in breast cancer tissues of postmenopausal patients than in those of premenopausal ones.[14] Such results suggest that the accumulation of E_2 in breast cancer tissue is mainly caused by the intracrine activity of 17β-HSD1. In fact, because E_2 increases breast-cancer-cell proliferation, inhibition of 17β-HSD1 activity constitutes a good way to reduce tumour estrogen levels, thus promoting tumour regression. Consequently, the steroidogenic enzyme 17β-HSD1 is an interesting therapeutic target for the treatment of estrogen-sensitive diseases such as breast cancer.

The design of potent 17β-HSD1 inhibitors has been attempted during the past decades, but progress was not significant enough to justify their use in the treatment of estrogen-sensitive diseases.[15–17] However, interesting clini-

Received 6 March 2009. Accepted 5 May 2009. Published on the NRC Research Press Web site at canjchem.nrc.ca on 30 July 2009.

This article is dedicated to Dr. Robert H. Burnell, a retired professor from the Department of Chemistry at Laval University (Québec City, Canada) who passed away in November of 2008, for his creative contribution to the field of natural product synthesis and his inspiring mentorship.

M. Bérubé and D. Poirier.[1] Laboratory of Medicinal Chemistry, CHUQ (CHUL)-Research Center and Laval University, Québec City, QC G1V 4G2, Canada.

[1]Corresponding author (e-mail: donald.poirier@crchul.ulaval.ca).

Fig. 1. Roles of 17β-HSD1 in the formation of estrogens E_2 and Δ^5-diol from precursor steroids E_1 and DHEA.

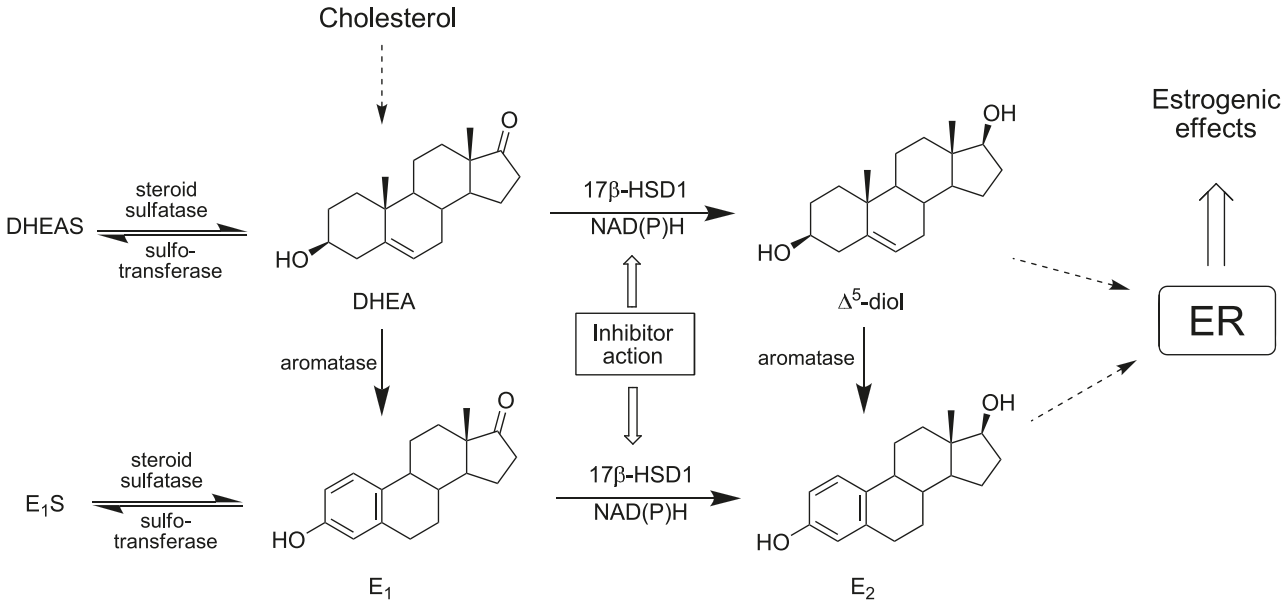

Fig. 2. Main interactions (hydrogen bonds only) of the potent inhibitor EM-1745 (**1**) with amino acids of 17β-HSD1. E_2 and adenosine moieties interact with the substrate- and the cofactor-binding sites of the enzyme, respectively.

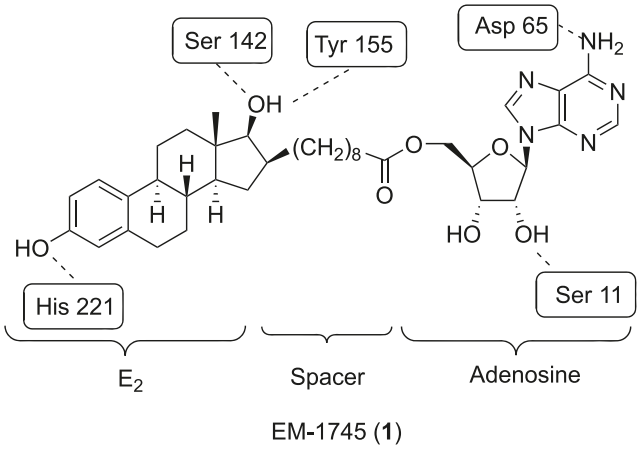

Fig. 3. Proposed simplified hybrid inhibitors of 17β-HSD1 (compounds **2**–**18**) and targeted main interactions with the enzyme.

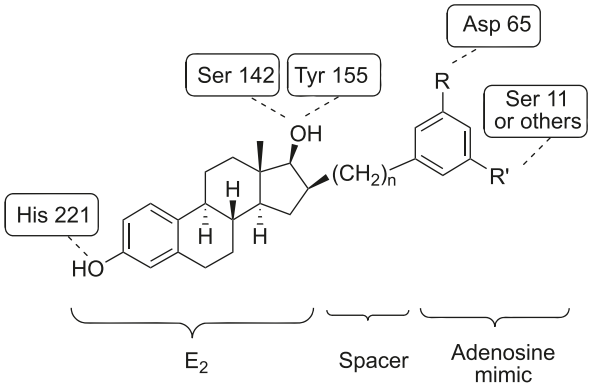

2–4 (R = NH_2, R' = CH_2COOMe, *n* = 13, 14, and 15)
5–8 (R = NH_2, R' = CH_2COOH, *n* = 13, 14, 15, and 17)
9–11 (R = NH_2, R' = CH_2CH_2OH, *n* = 13, 14, and 15)
12 (R = NH_2, R' = CH_2CH_2Br, *n* = 13)
13 (R = NH_2, R' = $CH_2CH_2OPO_3Me_2$, *n* = 13)
14–16 (R = NH_2, R' = $(CH_2)_mCOOH$, *n* = 13, *m* = 0, 2, and 3)
17 (R = H, R' = CH_2COOH, *n* = 13)
18 (R = NH_2, R' = H, *n* = 13)

cal success has been achieved in reducing mammary tumours with inhibitors of aromatase, another enzyme involved in the biosynthesis of E_2.[18–20] Based on three-dimensional structures of 17β-HSD1 and on structure–activity relationship (SAR) studies, inhibitors that could interact with both the substrate- and the cofactor-binding sites were designed.[21–23] EM-1745 (**1**) (Fig. 2), one of these E_2–adenosine hybrid compounds, inhibited the transformation of E_1 into E_2 by 17β-HSD1 with an IC_{50} value of 52 nmol/L.[22] Furthermore, EM-1745 (**1**) was crystallized inside the enzyme, and X-ray analysis confirmed that it interacts with both the substrate- and the cofactor-binding sites.[23]

EM-1745 (**1**) is however a complex molecule. To become a potential drug, it needs to be simplified to improve its in vivo stability and enzyme inhibitory activity. Special care needs to be taken for the ester link and the adenosine moiety.[24] With that in mind, simplified hybrid inhibitors were then designed using the main interaction between EM-1745 (**1**) and the enzyme (compounds **2**–**18**, Fig. 3). The E_2 core was kept for interacting with His221, Ser142, and Tyr155, as well as with the hydrophobic residues that recognize the steroid substrate. Adenosine mimics were designed keeping in mind that the primary amino group of the adenosine template forms a strong interaction with Asp65. Other functionalities, such as an ester, a carboxylic acid, an alcohol, a bromide, and a phosphotriester, were added on the aniline core to potentially interact with Ser11 or other amino acids in this area of the enzyme. The carboxylic acid and the phosphotriester were chosen because they should interact in a way similar to that of a phosphate group. In fact, the cofactor NADPH has a better affinity than NADH for this en-

Scheme 1. First chemical approach: synthesis of **27**. Reagents, conditions, and yields: (a) MsCl, Et_3N, DCM, 0 °C, 15 min (97%); (b) 2nd generation Grubbs' catalyst, DCM, reflux, 16 h (67%); (c) 10% Pd/C, H_2, EtOAc, RT, 16 h; (d) NaI, acetone, reflux, 16 h; (e) DHP, *p*-TSA, DCM, RT, 3 h (57% for three steps); (f) (i) CuI, vinylMgBr, THF, −40 °C, 15 min; (ii) HMPA, $P(OEt)_3$, −40 °C to RT, 3 h (89%); (g) tributyl(vinyl)tin, $Pd(PPh_3)_2Cl_2$, toluene, 75 °C, 4 h (88%); (h) 2nd generation Grubbs' catalyst, DCM, reflux, 16 h (34%). Mes: mesityl or 2,4,6-trimethylphenyl; Cy: cyclohexyl.

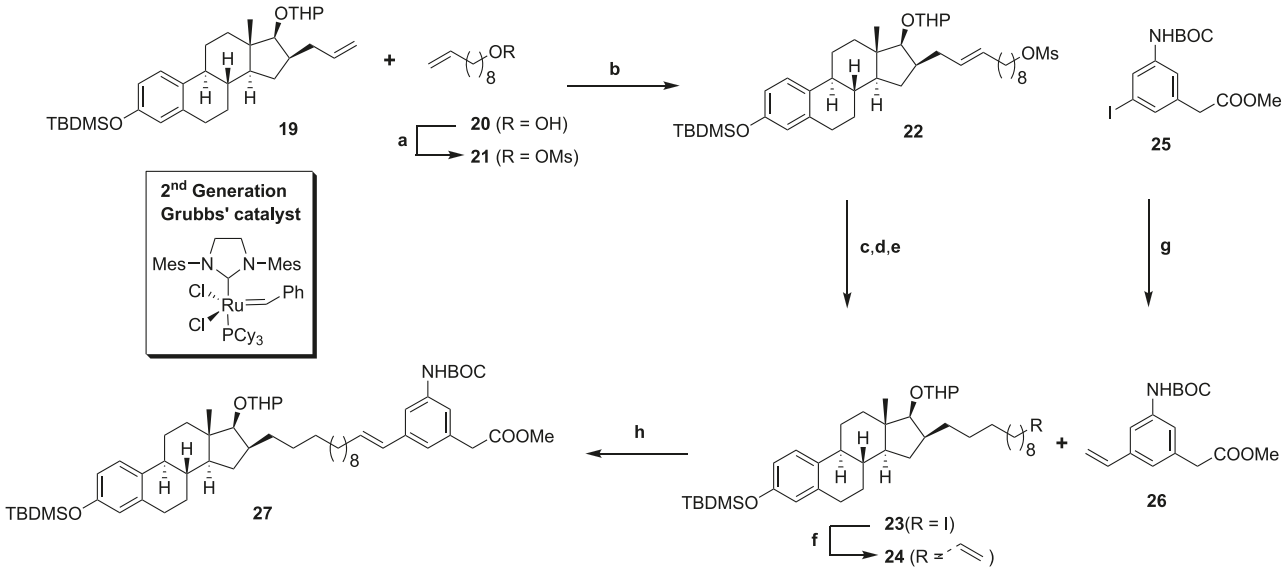

zyme, and the main structural difference between these two cofactors is a phosphate group on the C2′ of the adenosine moiety.[25] Furthermore, the ester function in EM-1745 (**1**) was removed and the E_2 nucleus was joined to the adenosine mimic by an alkyl chain, the length of which needs to be optimized (n = 13−17). We report herein two chemical approaches developed to synthesize compounds **2**−**18**. The in vitro biological evaluation of compounds **2**−**18** as inhibitors of 17β-HSD1 is also reported and discussed.

Results and discussion

Chemistry

The first approach to synthesize simplified hybrid inhibitors of 17β-HSD1 is presented in Scheme 1. The bisubstrate compound **27** was obtained by two cross-metathesis reactions[26] used as key steps to join E_2 and the adenosine mimic represented by an aniline derivative. Briefly, 9-decenol (**20**) was activated as the mesylate **21** using standard conditions and then linked to diprotected 16β-allyl-E_2 (**19**)[27] using the 2nd generation Grubbs' catalyst in refluxing dichloromethane (DCM) to afford **22** in 67% yield. Formation of a side product resulting from the metathesis of two molecules of steroid **19** was also observed. Hydrogenation of olefin **22** followed by substitution of the mesylate by an iodide afforded **23**. Partial deprotection of the C17β-OTHP group however necessitated a subsequent protective step.

For the next step, our first idea was to obtain a terminal olefin similar to **24** by dehydrohalogenation. However, no terminal olefin was observed when **23** was treated with various bases (DBU, KOH, and *t*-BuOK) under different conditions. In fact, there are few dehydrohalogenation methodologies to prepare unconjugated terminal olefins in good yields and mild conditions. Although we later resolved this synthetic problem by developing a new methodology for obtaining terminal olefins,[28] we applied another strategy for the synthesis of **24**. This terminal olefin was easily obtained by addition of a vinyl cuprate on iodide **23** using hexamethylphosphoramide (HMPA) and triethyl phosphite as additives.[29]

Synthesis of aniline derivative **25** was described in our earlier report.[30] Addition of a vinyl group on **25** using Stille coupling procedure (tributyl(vinyl)tin, $Pd(PPh_3)_2Cl_2$, toluene, 75 °C)[31] afforded **26** in an excellent 88% yield. The next step was to join by cross-metathesis the side chain of **24** to the adenosine mimic **26** using the 2nd generation Grubbs' catalyst. However, the bisubstrate compound **27** was obtained in only 34% yield. Furthermore, the main product recovered after the reaction came from the metathesis of two steroids **24** that was obtained in 47% yield. Because product **27** was only obtained in low yield and synthesis of starting materials for this reaction necessitated numerous steps (nine steps for the synthesis of **24** from commercially available estrone and six steps for the synthesis of **26** from 2,6-diiodo-4-nitroaniline), a new synthetic strategy was developed.

This second synthetic approach for the preparation of simplified hybrid inhibitors was reported by us earlier as a short communication.[30] Briefly, an olefinic aldehyde (Scheme 2), used to elaborate the alkyl side-chain spacer, was joined to steroid **19** through cross-metathesis (Scheme 3). The aldehyde was transformed into an alkyne, and a Sonogashira coupling was used to link the steroid/spacer to the adenosine mimic **25** in excellent yields.

The first step in this approach was to synthesize spacers of various lengths as outlined in Scheme 2. Depending on the spacer length, the synthesis of aldehydes **37**−**39** started from the commercially available olefin **33** or the commercially available bromides **31** and **32**. However, for the synthesis of the aldehyde **40**, no olefin or bromide with the appropriate length were available from commercial sources. Bromide **30** was then synthesized in a good 80% yield from

Scheme 2. Second chemical approach: synthesis of spacers **37**−**40**. Reagents, conditions, and yields: (a) 2nd generation Grubbs' catalyst, DCM, reflux, 72 h (80%); (b) NaI, acetone, reflux, 16 h; (c) (i) CuI, vinylMgBr, THF, −40 °C, 15 min; (ii) HMPA, $P(OEt)_3$, −40 °C to RT, 3 h (60%−71% for two steps); (d) TPAP, NMO, molecular sieves, DCM, RT, 1 h (65%−94%).

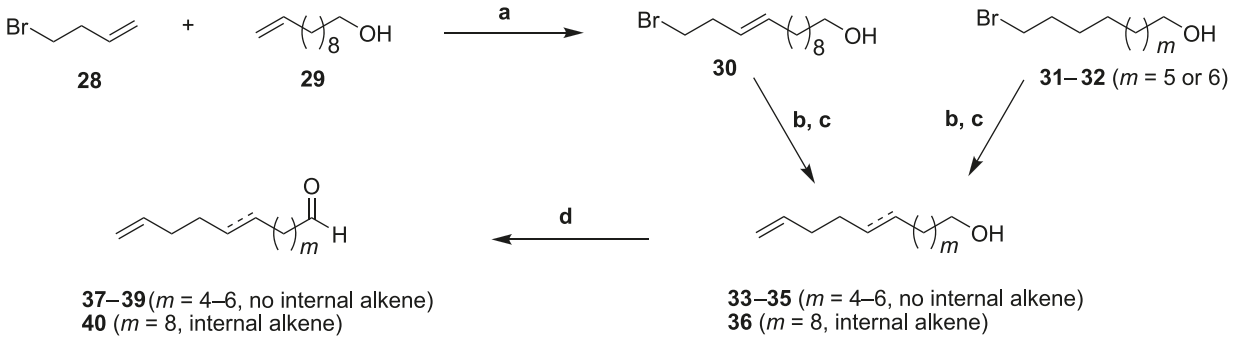

the cross-metathesis of 4-bromobutene (**28**) and 10-undecenol (**29**) with the 2nd generation Grubbs' catalyst. Iodination of bromides **30**−**32** using Finkelstein conditions followed by addition of a vinyl cuprate as described above afforded olefins **34**−**36** in 60%−71% yields for two steps. Alcohols **33**−**36** were next subjected to a tetrapropylammonium perruthenate (TPAP) oxidation to gain aldehydes **37**−**40**.

The next steps, as illustrated in Scheme 3, were to join the three components: the steroid **19**, a spacer originating from aldehydes **37**−**40**, and the adenosine mimic **25**. A cross-metathesis of steroid **19**[27] and freshly prepared aldehydes **37**−**40** using the 2nd generation Grubbs' catalyst provided compounds **41**−**44**. Hydrogenation of internal olefin(s) catalyzed by palladium followed by treatment with lithium diisopropylamide (LDA), (trimethylsilyl)diazomethane, and heat afforded alkynes **45**−**48** in 15%−33% yields for three steps.[32] Finally, applying optimized Sonogashira coupling procedure ($Pd(PPh_3)_4$, CuI, Et_3N),[33] alkynes **45**−**48** were added to aryl iodide **25**,[30] giving **49**−**52** in excellent yields (91%−95%).

Molecular diversity was next added on the adenosine mimic moiety as described in Scheme 4. Depending on the type of functional group introduced, two synthetic procedures were applied. The first procedure was used to synthesize ester, carboxylic acid, and alcohol derivatives. Hydrolysis of the three protective groups (TBDMS, THP, and BOC) under acid conditions, followed by hydrogenation of the alkyne, provided ester derivatives **2**−**4** and **53** in 41%−66% yield for two steps. To obtain the salt-free product, the crude product−NH_2·HCl, resulting from the hydrolysis step, was treated with a solution of Cs_2CO_3 in MeOH. Carboxylic acid derivatives **5**−**8** and alcohol derivatives **9**−**11** were, respectively, obtained from esters **2**−**4** and **53** by acid hydrolysis or by hydride reduction. The second procedure was used to prepare bromide and phosphotriester derivatives **12** and **13**, respectively. To avoid formation of side products, the bromide and the phosphotriester needed to be introduced before removal of protective groups. Thus, reduction of ester **49** with $LiAlH_4$ afforded alcohol **54** in good yield of 80%. From **54**, the bromide **55** was obtained by reaction with CBr_4 and PPh_3 in DCM. Phosphotriester **56** was obtained by treatment of alcohol **54** with CBr_4 and $P(OMe)_3$ in pyridine.[34] Bromide **12** and phosphotriester **13** were finally obtained by hydrolysis of the three protective groups and hydrogenation of alkyne as described above.

Scheme 3. Second chemical approach: synthesis of **49**−**52**. Reagents, conditions, and yields: (a) **37**−**40**, 2nd generation Grubbs' catalyst, DCM, reflux, 16 h; (b) 10% Pd/C, H_2, EtOAc, RT, 16 h; (c) (i) LDA, $TMSCHN_2$ (2.0 mol/L in hexanes), THF, −78 °C, 1 h; (ii) reflux, 3 h (15%−33% for three steps); (d) **25**, CuI, Et_3N, $Pd(PPh_3)_4$, benzene, 40 °C, 3 h (91%−95%).

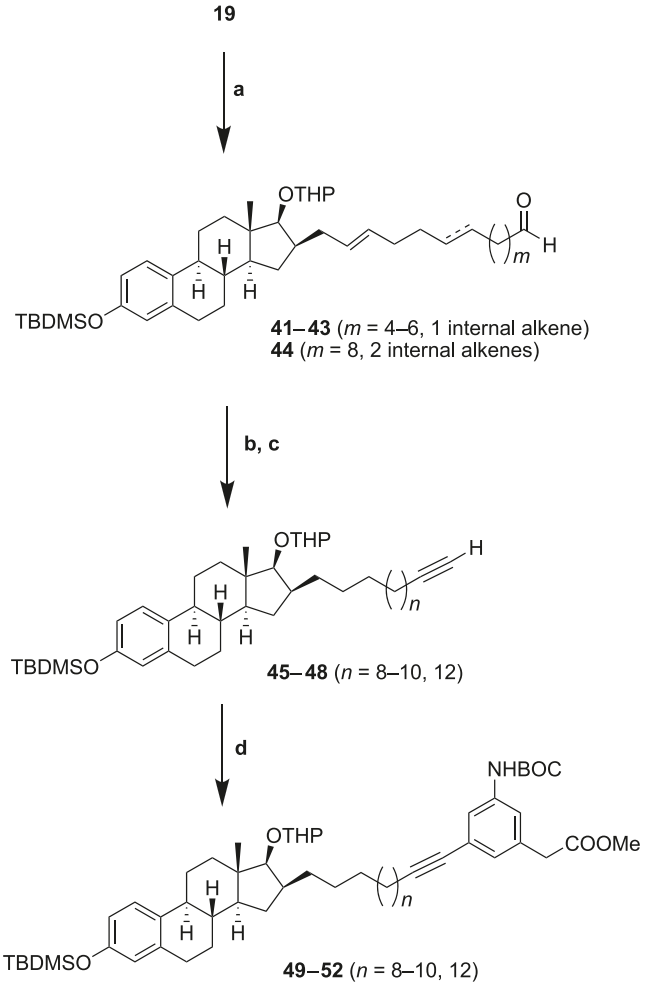

As described in the Biological activity section, the best inhibitor of 17β-HSD1 obtained amongst compounds **2**−**13** is the carboxylic acid derivative **5** with an alkyl-side-chain spacer of 13 methylenes. To improve its inhibitory potency, new inhibitors **14**−**16** were designed by changing the dis-

Scheme 4. Introduction of molecular diversity: synthesis of **2**−**13**. Reagents, conditions, and yields: (a) (i) HCl (4 mol/L in dioxane), DCM, MeOH, RT, 16 h; (ii) Cs_2CO_3, MeOH, 15 min; (b) 10% Pd/C, H_2, EtOAc, RT, 16 h (41%−66% for two steps); (c) HCl (1 N in H_2O), THF, reflux, 2 to 5 h (58%−91%); (d) $LiAlH_4$, THF, 0 °C, 4 to 16 h (45%−87%); (e) $LiAlH_4$, THF, 0 °C to RT, 2 to 16 h (80%); (f) CBr_4, PPh_3, DCM, 0 °C, 15 min to 4 h (70%); (g) CBr_4, $P(OMe)_3$, pyridine, RT, 3 h (82%); (h) HCl (4 mol/L in dioxane), DCM, MeOH, RT, 16 h; (i) 10% Pd/C, H_2, EtOAc, RT, 16 h (Bromide derivative: 25% for two steps); (j) 10% Pd/C, H_2, MeOH, RT, 16 h (Phosphotriester derivative: 35% for two steps).

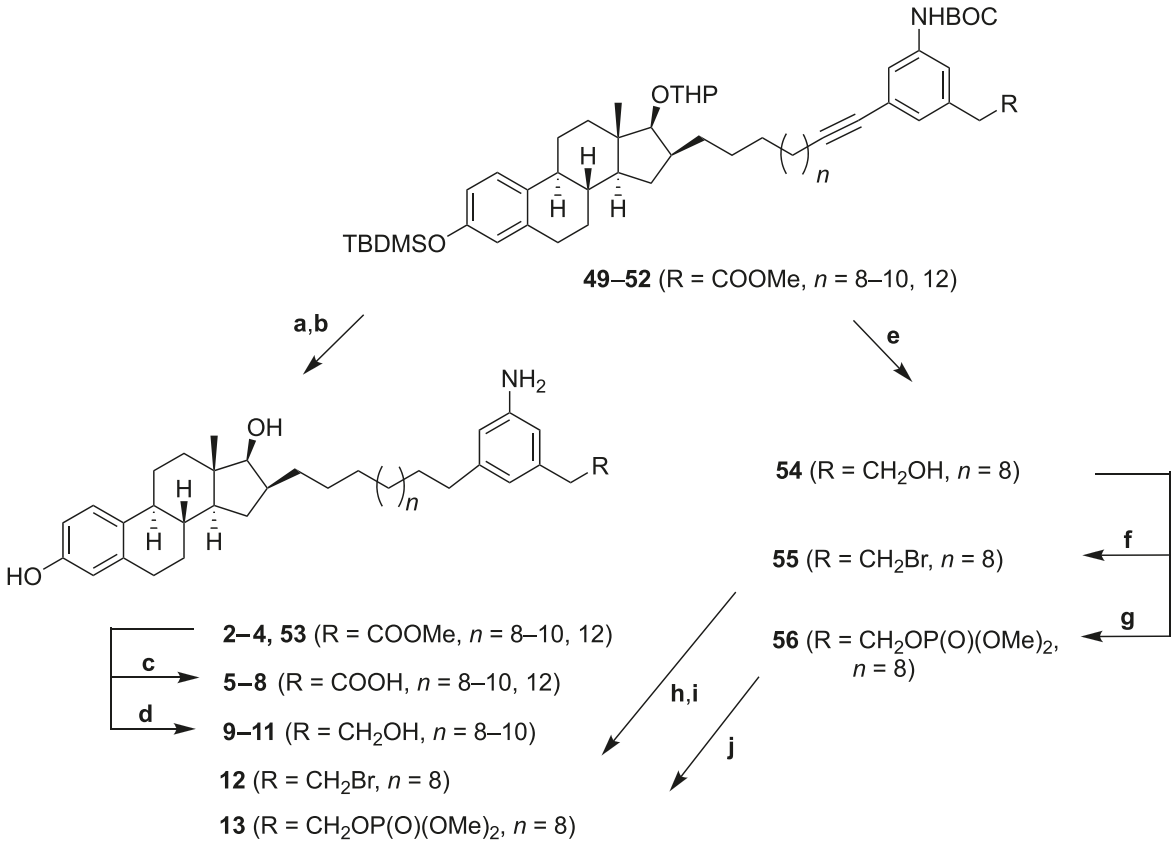

tance between the carboxylic acid and the aryl group (m = 0−3). Two compounds, **17** and **18**, bearing only a carboxylic acid or an amino group were also prepared to complement our SAR study.

First of all, the new adenosine mimic template had to be synthesized (Scheme 5). Starting from **57**,[30] an intermediate in the synthesis of adenosine mimic **25**, ester **59** was synthesized in three steps. Oxidative hydroboration of olefin **57** afforded alcohol **58** in 74% yield. Oxidation with Jones' reagent, followed by esterification with (trimethylsilyl)diazomethane in MeOH, provided ester **59** in 76% yield for the two steps. Synthesis of ester **61** began with a cross-metathesis between olefin **57** and methyl acrylate used in large excess to obtain **60** in an excellent 87% yield. However, when hydrogenation catalyzed by Pd/C was used in EtOAc or MeOH, reduction of the olefin was not observed. Thus, hydrogenation catalyzed by PtO_2 in anhydrous THF was necessary to reduce the olefin and provide **61** in 93% yield. Esters **64** (m = 0) and **65** (m = 1, no amino group) were obtained by esterification of their corresponding carboxylic acids **62**[35,36] and **63**.

The synthesis of carboxylic acid derivatives **14**−**17** and aniline derivative **18** was achieved using a methodology similar to that used for the synthesis of **5**−**8** as summarized in Scheme 6. Briefly, a Sonogashira coupling of alkyne **45** with adenosine mimics **59**, **61**, and **64**−**66** afforded **67**−**71** in 66%−74% yields. Hydrolysis of protective groups (TBDMS, THP, and BOC) in acid conditions, followed by hydrogenation of the alkyne, afforded final compound **18** and esters **72**−**75**, which after hydrolysis with LiOH in refluxed acetone provided derivatives **14**−**17**. Control compound **79** that should only interact with the cofactor-binding site was also prepared as outlined in Scheme 7. This compound was synthesized easily using the same Sonogashira coupling strategy described above for the preparation of **5**−**8** and **14**−**18**. Final compounds **2**−**18** and **79**, which were needed for our SAR study, were carefully purified by flash column chromatography and fully characterized by IR, ^{1}H NMR, ^{13}C NMR, and HR-MS to validate their structure.

Biological activity

The inhibition of the transformation of [^{14}C]-E_1 (0.1 μmol/L) into [^{14}C]-E_2 by compounds **2**−**18** and **79** was evaluated with homogenated HEK-293 cells transfected with a vector encoding for 17β-HSD1.[37] NADH (0.1 mmol/L) was added as cofactor, and the enzymatic assay was performed at pH and temperature close to physiological conditions (pH = 7.4 and T = 37 °C). The first series of simplified hybrid inhibitors, compounds **2**−**13**, were tested at two concentrations: 0.1 and 1 μmol/L, and the results are presented

Scheme 5. Synthesis of new adenosine mimics **59**, **61**, **64**, and **65**. Reagents, conditions, and yields: (a) (i) BH_3·THF, THF, 0 °C, 3 h; (ii) NaOH (3 N in H_2O), H_2O_2 (30% *w*/*v*), 2 h, RT (74%); (b) Jones' reagent, acetone, 0 °C, 90 min; (c) $TMSCHN_2$ (2.0 mol/L in hexanes), MeOH, 0 °C, 10 min (**59**: 76% for two steps, **64**: 93%, **65**: 99%); (d) methyl acrylate, 2nd generation Grubbs' catalyst, DCM, reflux, 16 h (87%); (e) H_2, PtO_2, THF, RT, 16 h (93%).

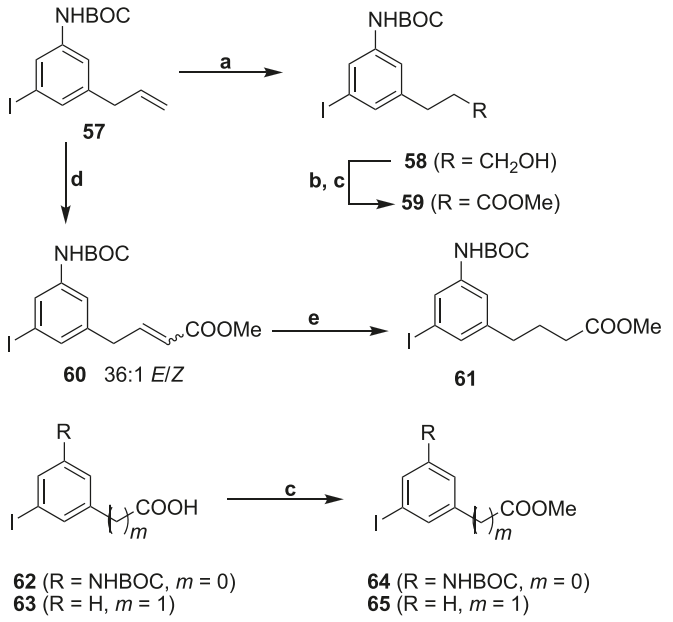

in Table 1 as percentage of 17β-HSD1 inhibition or IC_{50} values (the concentration that inhibited 50% of enzyme activity).

Two points must be highlighted in these results. First, carboxylic acid derivatives **5**–**7** are by far the best inhibitors of that series with percentages of inhibition varying from 88% to 90% at 1 μmol/L. On the opposite, esters **2**–**4**, alcohols **9**–**11**, bromide **12**, and phosphotriester **13** presented almost no inhibition of 17β-HSD1. Second, varying the length of the alkyl-side-chain spacer had almost no effect on the inhibition of 17βHSD1. In fact, the inhibition of the enzyme by carboxylic derivatives **5**–**7** (from 13 to 15 methylenes) varied only from 88% to 90% at 1 μmol/L. To determine the optimal spacer length, a compound with a longer side-chain spacer (**8**, n = 17 methylenes) was prepared. As presented in Table 1, compound **5**, with an alkyl spacer of 13 methylenes, is the best inhibitor with an IC_{50} of 56 nmol/L. Compounds **6**–**8**, with spacers of 14, 15, or 17 methylenes, inhibit the enzyme slightly less effectively compared with compound **5** with IC_{50} of 83, 99, and 108 nmol/L, respectively. In fact, compound **5** is a better inhibitor than compounds **6**–**8** by less than twofold. These biological results confirm that the alkyl-side-chain spacer is very flexible and that its length may vary to a certain extent. However, shortening it too much would result in a huge drop of inhibition as was observed in the SAR study carried out to develop hybrid inhibitor EM-1745 (**1**).[22] In addition to its better inhibitory potency, a spacer of 13 methylenes was chosen to continue the SAR study because the synthesis of the aldehyde spacer **37** required only one synthetic step, as compared with three steps for the 14- and 15-methylene spacers (**38** and **39**, respectively) and four steps for the 17-methylene one (**40**).

Scheme 6. Synthesis of **14**–**18**. Reagents, conditions, and yields: (a) CuI, Et_3N, $Pd(PPh_3)_4$, benzene, 40 °C, 3 h (66%–74%); (b) HCl (4 mol/L in dioxane), DCM, MeOH, RT, 2 h (for **70**) or 16 h (for **67**–**69**); (c) HCl (5% *v*/*v* in MeOH), DCM, RT, 1 h (for **71**, 81%); (d) 10% Pd/C, H_2, EtOAc, RT, 16 h (**72**–**75**: 54%–75% for two steps, **18**: 67%); (e) LiOH (1 mol/L in H_2O), acetone, reflux, 1 h (66%–78%).

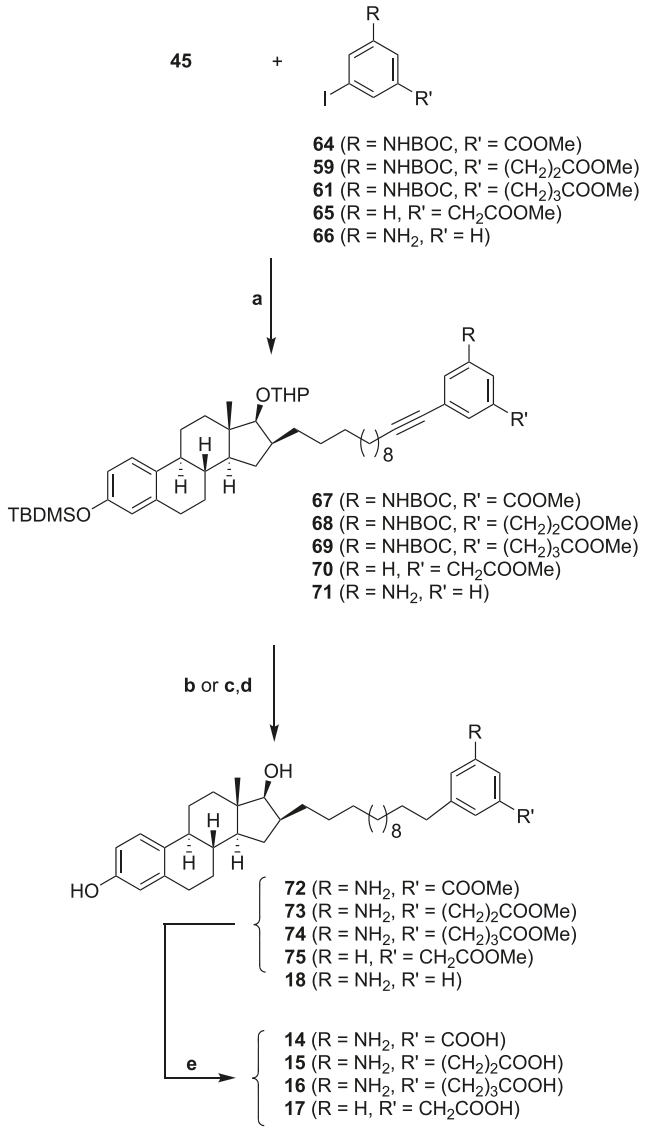

As presented above, carboxylic acid derivatives **5**–**8** give better inhibition than the other derivatives synthesized. To explain this result, speculation on the main interactions between inhibitor **5** and 17β-HSD1 was attempted. Starting from X-ray analysis of the crystallized EM-1745 (**1**)/17β-HSD1 complex,[23] we assumed that the E_2 moiety of **5** would form the same interactions with His221, Ser142, and Tyr155 as the E_2 moiety of EM-1745 (**1**) (see Figs. 2 and 3). Moreover, the amino and the carboxylic acid groups of compound **5** should, respectively, interact with Asp65 and Ser11 found in the cofactor-binding site, as observed for the adenosine moiety of EM-1745 (**1**). Furthermore, 17β-HSD1 prefers cofactor NADPH over NADH,[25] and the structural difference between these two entities is the presence of a phosphate

Scheme 7. Synthesis of monosubstrate compound **79**. Reagents, conditions, and yields (a) CuI, Et_3N, $Pd(PPh_3)_4$, benzene, 40 °C, 1 h (88%); (b) HCl (1 N in H_2O), THF, reflux, 4 h (94%); (c) 10% Pd/C, H_2, MeOH, RT, 16 h (75%).

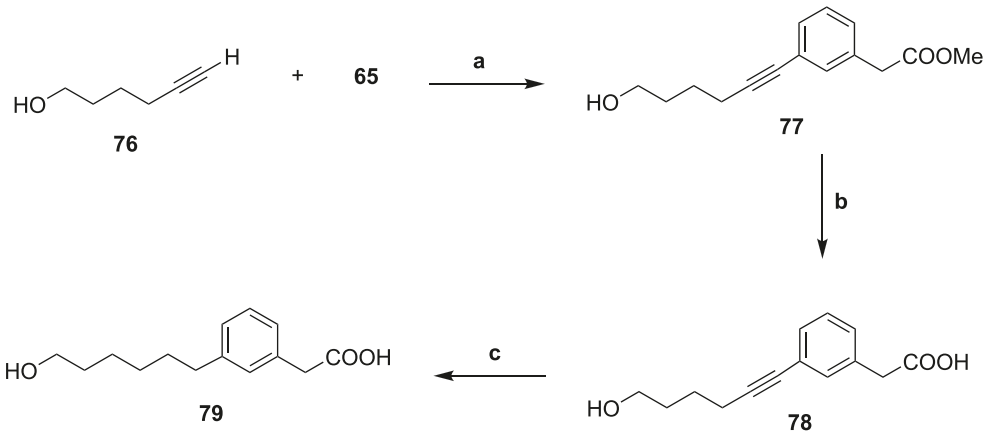

Table 1. Inhibition of 17β-HSD1 by simplified hybrid inhibitors **2**–**13** and known inhibitors.

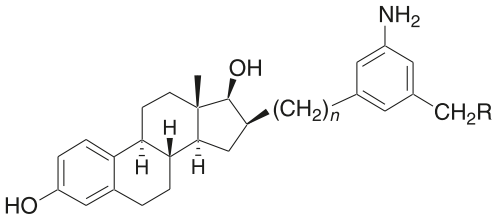

			Inhibition (%)		
Compound	R	*n*	At 0.1 μmol/L	At 1 μmol/L	IC_{50} (nmol/L)
2	COOMe	13	0	14	Nd
3	COOMe	14	0	26	Nd
4	COOMe	15	12	45	Nd
5	COOH	13	22	88	56±3
6	COOH	14	40	90	83±8
7	COOH	15	42	90	99±31
8	COOH	17	Nd	Nd	108±5
9	CH_2OH	13	6	6	Nd
10	CH_2OH	14	2	4	Nd
11	CH_2OH	15	22	16	Nd
12	CH_2Br	13	11	33	Nd
13	$CH_2OPO_3Me_2$	13	0	12	Nd
1	—	—	95	98	7.8±0.2
E_1	—	—	Nd	Nd	847±78
EM-251	—	—	19	57	239±122

Note: Nd: not determined. For the transformation of [^{14}C]-E_1 (0.1 μmol/L) into [^{14}C]-E_2. The error for screening assay was ± 10%. See Experimental section for more details.

group on the adenosine C2′. Accordingly, NADPH was also crystallized with the enzyme, and X-ray analysis revealed that the phosphate group forms its main interactions with three amino acids: Ser11, Arg37, and Lys195.[38] The disappointing inhibitory activity obtained with the phosphate derivative **13** suggests no interaction between this dimethylated phosphate group and one of the three amino acids identified by X-ray analysis (Ser11, Arg37, and Lys195). Considering the best inhibition results provided by compounds **5**–**8**, the carboxylic acid probably interacts with at least one of these amino acids. This hypothesis remains however to be confirmed by docking studies, or better, by crystallization of compound **5** with 17β-HSD1.

To improve the interactions between the adenosine mimic part of **5** and the enzyme, we next undertook the optimization of the distance between the carboxylic acid (COOH) and the aniline moiety. Compounds **14**–**16** were then synthesized as described above (Schemes 5 and 6) with a spacer of 0 to 3 methylenes between the COOH group and the aryl moiety. Compounds **17** and **18**, bearing only one of the components, respectively, the carboxylic acid and the amino group, were also prepared. Compounds **5** and **14**–**18** were next tested to determine their potential to inhibit the 17β-HSD1 activity at 0.1 and 1 μmol/L, and the results are presented in Table 2. Compounds **5** and **14**–**16** gave almost the same percentages of inhibition with 22% to 29% and 89% to

Table 2. Inhibition of 17β-HSD1 by simplified hybrid inhibitors **5** and **14**–**18** and known inhibitors.

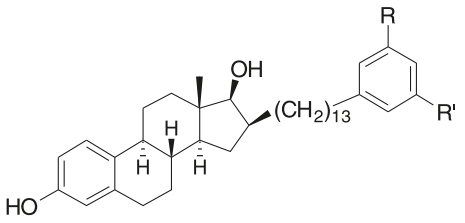

			Inhibition (%)	
Compound	R	R′	At 0.1 μmol/L	At 1 μmol/L
5	NH_2	CH_2COOH	27	91
14	NH_2	COOH	22	90
15	NH_2	$(CH_2)_2COOH$	29	92
16	NH_2	$(CH_2)_3COOH$	22	89
17	H	CH_2COOH[a]	49	92
18	NH_2	H	5	66
79	—	—	—	30
1	—	—	90	96
E_1	—	—	20	60

Note: For the transformation of [^{14}C]-E_1 (0.1 μmol/L) into [^{14}C]-E_2. The screening assay error was ± 10%. See experimental section for more details.

[a]Inhibition of compound **17** is statistically different ($P < 0.01$) from inhibition of compounds **5** and **14**–**16**.

92% at 0.1 and 1 μmol/L, respectively. Thus, the distance between the aryl group and the carboxylic acid did not affect the inhibition of 17β-HSD1. Compound **18**, which bears no carboxylic acid, gave, as expected, lower inhibition with, respectively, 5% and 66% at 0.1 and 1 μmol/L. However, with only a carboxylic acid on the aryl (no amino group), compound **17** gave a surprisingly higher inhibition with 49% and 92% at 0.1 and 1 μmol/L, respectively. This last result reveals that the positions of the carboxylic acid and the amino group are not optimal and, consequently, opens the door to additional optimization studies.

However, when simplified hybrid inhibitors are compared to the activity of EM-1745 (**1**), the inhibitory potency of carboxylic acid derivatives **5** and **14**–**17** was weaker at 0.1 μmol/L (22%–49% compared with 90% for **1**). To verify that our best simplified hybrid inhibitors, compounds **5** and **14**–**17**, kept their bisubstrate characteristics, compound **79**, which should interact only with the cofactor-binding site of the enzyme, was synthesized (Scheme 7) and tested as inhibitor of 17β-HSD1. The monosubstrate compound showed, as expected, almost no inhibition (30% at 1 μmol/L). When tested in the same conditions, the monosubstrate 16β-nonyl-E_2 gave the same results (no enzyme inhibition).[22] Furthermore, unlabeled E_1, which interacts only with the substrate-binding site, gave lower inhibition (60% at 1 μmol/L) than compounds **5** and **14**–**17** (89%–92% at 1 μmol/L). According to IC_{50} values (Table 1), inhibitor **5** (56 nmol/L) is only seven times less potent than EM-1745 (7.8 nmol/L), but four times more potent than EM-251 (239 nmol/L),[39] a known inhibitor of 17β-HSD1, and 15 times more potent than unlabeled E_1. Thus, **5** and **14**–**17** cause more interactions with the enzyme than E_1, and they should interact with both the substrate- and the cofactor-binding site of 17β-HSD1 as EM-1745 (**1**).

Conclusion

Two chemical approaches were investigated in the preparation of simplified hybrid inhibitors of 17β-HSD1 represented by compounds **2**–**18**. The first approach uses two olefin cross-metathesis reactions as key steps to join the steroid, the spacer, and the adenosine mimic, but failed to give satisfactory results because of the very low cross-metathesis yield for the coupling of the spacer and the adenosine mimic. However, the second approach, using an olefin cross-metathesis and a Sonogashira coupling as key steps, was more effective, giving a better coupling yield of the spacer to the adenosine mimic. Using this new approach, a series of steroid derivatives (compounds **2**–**18**) were synthesized as simplified hybrid inhibitors of 17β-HSD1. These compounds featured ester, carboxylic acid, alcohol, bromide, phosphotriester, and (or) amine as functional groups to interact with the cofactor-binding site, and an E_2 nucleus to bind in the substrate-binding site. Inhibitory potency of these compounds was tested on homogenated HEK-293 cells overexpressing 17β-HSD1 activity. Carboxylic acid derivatives **5**–**8** and **14**–**17** were found to be the best bisubstrate inhibitors of that group. A small effect on the inhibition was observed when varying the length of the alkyl-side-chain spacer between the steroid and the adenosine mimic (n = 13, 14, 15, and 17), but no effect was observed according to the length of the alkyl chain between the aryl and the carboxylic acid group (m = 0–3). The inhibition potency of carboxylic acid derivatives **5**–**8** and **14**–**17** was weaker than the potency of bisubstrate inhibitor EM-1745 (**1**), but higher than that of known inhibitors that interact only with one binding site like unlabeled E_1, EM-251, and **79**. In addition, even if compounds **5**–**8** and **14**–**17** are less potent than EM-1745, they should be more stable, since they have no ester group and no

ribose moiety. Furthermore, a better inhibition of 17β-HSD1 was surprisingly observed with compound **17** that contains only a carboxylic acid group (no amine) on the adenosine mimic. This result suggests that better hybrid inhibitors than **17** could be obtained with the optimization of the position of the carboxylic acid and the amino groups on the adenosine mimic. Docking studies using 3D structure of crystallized EM-1745/17β-HSD1 complex will be undertaken to achieve this task.

Experimental

General methods

Reagents were obtained from Sigma-Aldrich Canada Co. (Oakville, ON, Canada) except for 3-iodophenylacetic acid purchased from Matrix Scientific (Colombia, SC, USA). The tricyclohexylphosphine [1,3-bis(2,4,6-trimethylphenyl)-4,5-dihydroimidazol-2-ylidene] [benzylidine] ruthenium(IV)dichloride (2nd generation Grubbs' catalyst) was purchased from Strem Chemicals (Newburyport, MA, USA) and Sigma-Aldrich Canada Co. (Oakville, ON, Canada). Usual solvents were obtained from Fisher Scientific and VWR (Ville Mont-Royal, QC, Canada) and were used as received. Anhydrous solvents were purchased from Aldrich and VWR in SureSeal bottles, which were kept under positive argon pressure. Tetrahydrofuran (THF) was distilled from sodium/benzophenone under argon. All anhydrous reactions were performed under positive argon pressure in oven-dried glassware. Thin-layer chromatography (TLC) was performed on 0.25 mm silica gel 60 F_{254} plates (Whatman, Maidstone, UK), and compounds were visualized by exposure to UV light (254 nm) and (or) with a solution of ammonium molybdate/sulphuric acid/water (with heating). Flash chromatography was performed on Silicycle 60 (Quebec, QC, Canada) 230−400 mesh silica gel. IR spectra were obtained neat, from KBr pellets or from a thin film of the solubilized compound on NaCl pellets (usually in CH_2Cl_2). They were recorded on a PerkinElmer series 1600 FTIR spectrophotometer (Norwalk, CT, USA); only significant bands are reported (in cm^{-1}). ^1H and ^{13}C NMR spectra were recorded with a Bruker AC/F 300 spectrometer (Billerica, MA, USA) at 300 and 75 MHz, respectively, and a Bruker AVANCE 400 spectrometer at 400 (^1H) and 100 (^{13}C) MHz. The chemical shifts (δ) are expressed in ppm and referenced to chloroform (7.26 and 77.0 ppm), acetone (2.07 and 206.0 ppm), or methyl sulfoxide (2.51 and 39.5 ppm) for ^1H and ^{13}C, respectively. Duplication of ^1H NMR signals was observed for all THP derivatives (presence of two stereoisomers). Low-resolution mass spectra (LR-MS) were recorded with an LCQ Finnigan apparatus (San Jose, CA, USA) equipped with an atmospheric pressure chemical ionization (APCI) source on positive or negative mode. High-resolution mass spectra (HR-MS) were provided by the Regional Laboratory for Instrumental Analysis (Université de Montréal, Montréal, QC, Canada).

Synthesis of compound 27 using the first chemical approach

Synthesis of 9-decenyl methanesulfonate (21)

To a solution of 9-decen-1-ol (1.0 mL, 5.6 mmol) in anhydrous DCM (30 mL) under an argon atmosphere at 0 °C were added Et_3N (1.2 mL, 8.4 mmol) and methanesulfonyl chloride (0.48 mL, 6.2 mmol). The mixture was stirred for 15 min at 0 °C and extracted with DCM. The organic phase was washed with an aqueous solution of HCl (1 N) and brine, dried over $MgSO_4$, filtered, and evaporated to dryness. Purification by flash chromatography (hexanes/EtOAc, 8:2) afforded **21** (1.27 g, 97% yield) as a colourless oil. IR (neat) ν: 3075 (C−H, alkene), 1640 (C=C, alkene), 1355 and 1176 (O=S=O). ^1H NMR (400 MHz, $CDCl_3$) δ: 1.34 (m, 5 × CH_2), 1.73 (m, CH_2CH$_2$OS), 2.02 (m, CH_2CH=CH$_2$), 2.99 (s, CH_3), 4.20 (t, J = 6.6 Hz, CH_2OS), 4.95 (m, CH=CH_2), 5.79 (m, CH=CH$_2$). ^{13}C NMR (100 MHz, $CDCl_3$) δ: 25.3, 28.7, 28.8 (2×), 29.0, 29.1, 33.6, 37.2, 70.1, 114.1, 139.0.

*Synthesis of 9-undecen-11-[3′-(***tert***-butyldimethylsilyloxy)-17′β-(tetrahydro-2***H***-pyran-2-yl-oxy)-estra-1′,3′,5′(10′)-trien-16′β-yl)-methanesulfonate (22)*

A mixture of 16β-allyl-estradiol (**19**)[27] (3.00 g, 5.87 mmol), 9-decenyl methanesulfonate (**21**) (2.75 g, 11.7 mmol), and 2nd generation Grubbs' catalyst (500 mg, 0.587 mmol) in dry DCM (100 mL) was refluxed for 16 h under an argon atmosphere. The crude mixture was preadsorbed on silica gel, and a flash chromatography was performed (hexanes/EtOAc, 9:1 to 8:2) to afford **22** (2.83 g, 67%) as a viscous yellowish oil. IR (film) ν: 1352 and 1174 (O=S=O). ^1H NMR (400 MHz, $CDCl_3$) δ: 0.18 (s, Si$(CH_3)_2$), 0.79 and 0.84 (2s, 18′-CH_3), 0.80 to 2.35 (CH and CH_2 of steroid skeleton and alkyl chain), 0.97 (s, SiC$(CH_3)_3$), 2.79 (m, 6′-CH_2), 3.01 (s, CH_3SO), 3.51 and 3.95 (2m, OCH_2 of THP), 3.72 and 3.79 (2d, J = 10.0 Hz, 17′α-CH), 4.23 (t, J = 6.6 Hz, CH_2SO), 4.64 and 4.74 (2m, CH of THP), 5.38 (m, CH=CH), 6.55 (s, 4′-CH), 6.61 (d, J = 8.2 Hz, 2′-CH), 7.11 (m, 1′-CH). LR-MS calculated for $C_{41}H_{69}O_6SSi$ $[M + H]^+$ 717.5, found 717.2 *m*/*z*.

*Synthesis of 13-[3′-(***tert***-butyldimethylsilyloxy)-17′β-(tetrahydro-2***H***-pyran-2-yl-oxy)-estra-1′,3′,5′(10′)-trien-16′β-yl)-tridecene (24)*

Hydrogenation

A suspension of steroid **22** (2.76 g, 3.85 mmol) and 10% Pd/C (414 mg) in EtOAc (150 mL) was stirred at room temperature under hydrogen atmosphere. After 16 h, the resulting suspension was filtered through a pad of Celite, and EtOAc was evaporated to dryness. ^1H NMR analysis of the crude mixture revealed the disappearance of alkene protons that were at 5.38 ppm.

Iodination

The crude product (2.72 g, 3.78 mmol) was dissolved in acetone (50 mL), and NaI (1.98 g, 13.2 mmol) was added. The reaction mixture was refluxed for 16 h. The product was then extracted with EtOAc, and the organic phase was washed with a saturated aqueous solution of $Na_2S_2O_3$ and washed with brine, dried over $MgSO_4$, filtered, and evaporated to dryness. Flash chromatography (hexanes/EtOAc, 95:5) afforded a mixture of **23** and 17β-OH form of **23** that was protected again as a THP derivative (dihydropyran, *p*-TSA, DCM, RT, 3 h) using a previously described procedure.[27] Then, **23** (2.12 g, 57% yield for three steps) was obtained as a white solid.

Vinylation

CuI (484 mg, 2.54 mmol) was suspended in anhydrous THF (5 mL) under an argon atmosphere. The mixture was cooled to −40 °C and vinylmagnesium bromide (1 mol/L in THF) (7.63 mL, 7.63 mmol) was added. The reaction was stirred for 15 min at −40 °C. Then, HMPA (0.880 mL, 5.08 mmol) and triethyl phosphite (0.880 mL, 5.08 mmol) were added, and the mixture was stirred for 5 min at −40 °C. **23** (1.91 g, 2.54 mmol) was added, and the reaction mixture was stirred for 1 h at −40 °C and for 2 h at room temperature. The reaction was quenched by the addition of a saturated solution of NH_4Cl. The crude product was extracted with EtOAc, washed with brine, dried over $MgSO_4$, filtered, and evaporated under reduced pressure.

Purification by flash chromatography (hexanes/EtOAc, 95:5) yielded **24** (1.48 g, 89% yield) as a colourless viscous oil. IR (film) ν: 1640 (C=C, alkene). ^{1}H NMR (300 MHz, $CDCl_3$) δ: 0.18 (s, $Si(CH_3)_2$), 0.79 and 0.83 (2s, 18′-CH_3), 0.80 to 2.35 (CH and CH_2 of steroid skeleton and alkyl chain), 0.97 (s, $SiC(CH_3)_3$), 2.79 (m, 6′-CH_2), 3.52 and 3.95 (2m, OCH_2 of THP), 3.72 and 3.79 (2d, J = 9.6 Hz, 17′α-CH), 4.62 and 4.75 (2m, CH of THP), 4.97 (m, CH_2=CH), 5.81 (m, CH=CH_2), 6.55 (d, J = 2.2 Hz, 4′-CH), 6.60 (d, J = 8.3 Hz, 2′-CH), 7.11 (m, 1′-CH). LR-MS calculated for $C_{42}H_{71}O_3Si$ $[M + H]^+$ 651.5, found 651.3 *m*/*z*.

Synthesis of methyl 2-(3′-*tert*-butoxycarbonylamino-5′-vinylphenyl)-acetate (26)

To a solution of **25**[30] (800 mg, 2.04 mmol) in anhydrous toluene (68 mL) under an argon atmosphere were added tributyl(vinyl)tin (1.8 mL, 6.1 mmol) and $Pd(PPh_3)_2Cl_2$ (143 mg, 0.204 mmol). The reaction was stirred for 4 h at 75 °C and quenched by addition of H_2O. The product was extracted with EtOAc, and the organic phase was washed with brine, dried over $MgSO_4$, filtered, and evaporated to dryness. The crude product was purified by flash chromatography (hexanes/EtOAc, 9:1) to gain **26** (520 mg, 88% yield) as a yellowish oil. IR (film) ν: 3344 (NH, carbamate), 1728 (C=O, ester and carbamate). ^{1}H NMR (300 MHz, acetone-d_6) δ: 1.50 (s, $(CH_3)_3$C of *N*-BOC), 3.62 (s, CH_2COOCH_3), 3.65 (s, $COOCH_3$), 5.24 (d, J = 11.1 Hz, 1H of CH=CH_2), 5.78 (dd, J_1 = 17.6 Hz, J_2 = 1.1 Hz, 1H of CH=CH_2), 6.72 (dd, J_1 = 17.6 Hz, J_2 = 10.9 Hz, CH=CH_2), 7.05 (s, 6′-CH), 7.45 (s, 2′-CH), 7.59 (s, 4′-CH), 8.44 (s, NH). ^{13}C NMR (75 MHz, acetone-d_6) δ: 28.3 (3×), 41.2, 51.8, 79.8, 114.2, 115.1, 119.3, 122.0, 136.1, 137.5, 138.8, 140.8, 153.5, 171.9. LR-MS calculated for $C_{16}H_{20}NO_4^-$ $[M - H]^-$ 290.1, found 290.2 *m*/*z*.

Synthesis of methyl 2-{3′-(tert-butoxycarbonylamino)-5′-[13″-(3‴-(tert-butyldimethylsilyloxy)-17‴β-(tetrahydro-2H-pyran-2-yl-oxy)-estra-1‴,3‴,5‴(10‴)-trien-16‴β-yl)-tridecenyl]-phenyl}-acetate (27)

A mixture of steroid **24** (860 mg, 1.32 mmol), adenosine mimic **26** (500 mg, 1.71 mmol), and 2nd generation Grubbs' catalyst (112 mg, 0.132 mmol) in dry DCM (20 mL) was refluxed for 16 h under an argon atmosphere. The solvent was evaporated, and the crude product was purified by flash chromatography (hexanes/EtOAc, 97:3 to 93:7) to afford **27** (413 mg, 34% yield) as a white foam. IR (film) ν: 3364 (NH, carbamate), 1732 (C=O, ester and carbamate). ^{1}H NMR (300 MHz, $CDCl_3$) δ: 0.18 (s, $Si(CH_3)_2$), 0.79 and 0.83 (2s, 18‴-CH_3), 0.80 to 2.30 (CH and CH_2 of steroid skeleton and alkyl chain), 0.97 (s, $SiC(CH_3)_3$), 1.51 (s, $(CH_3)_3$C of *N*-BOC), 2.78 (m, 6‴-CH_2), 3.52 and 3.96 (2m, OCH_2 of THP), 3.57 (s, CH_2COOCH_3), 3.68 (s, $COOCH_3$), 3.71 and 3.79 (2d, J = 10.2 Hz, 17‴α-CH), 4.62 and 4.75 (2m, CH of THP), 6.26 (m, CH=CH), 6.48 (s, NH), 6.55 (s, 4‴-CH), 6.60 (d, J = 8.3 Hz, 2‴-CH), 6.93 (s, 6′-CH), 7.12 (m, 1‴-CH, 2′-CH), 7.29 (s, 4′-CH). LR-MS calculated for $C_{56}H_{86}NO_4Si^-$ $[M - H]^-$ 912.6, found 912.5 *m*/*z*.

Synthesis of spacers 37–40

Synthesis of 13-bromo-10-tridecenol (30)

A mixture of 4-bromobutene (**28**) (3.0 mL, 29.6 mmol), 10-undecenol (**29**) (23.7 mL, 118 mmol), and the 2nd generation Grubbs' catalyst (1.25 g, 1.48 mmol) in dry DCM (200 mL) was refluxed for 3 days under an argon atmosphere. The crude mixture was purified by flash chromatography (hexanes/EtOAc, 8:2) to afford **30** (6.46 g, 80% yield) as a colourless oil. IR (neat) ν: 3365 (OH). ^{1}H NMR (400 MHz, $CDCl_3$) δ: 1.25 (m, 6 × CH_2), 1.53 (m, CH_2CH_2OH), 1.97 (m, CH_2CH_2CH=CH), 2.02 (s, OH), 2.51 (q, J = 7.0 Hz, CH_2CH_2Br), 3.34 (m, CH_2Br), 3.59 (m, CH_2OH), 5.35 and 5.50 (2m, CH=CH). ^{13}C NMR (75 MHz, $CDCl_3$) δ: 25.6, 28.8, 29.0, 29.2, 29.3, 29.5, 32.4, 32.6, 32.9, 35.9, 62.8, 126.3, 133.9. LR-MS calculated for $C_{13}H_{26}BrO$ $[M + H]^+$ 277.1 and 279.1, found 276.9 and 278.9 *m*/*z*.

General procedure to synthesize 34–36

The iodination and vinylation procedures described above for the synthesis of **24** were used without modification except that 5 and 4 equiv. of vinylmagnesium bromide were used for the synthesis of **35** and **36**, respectively, instead of 3 equiv. It is noteworthy that alcohol **33** is commercially available.

11-Dodecenol (34)

We reported earlier the synthesis and characterization of **34**.[40]

12-Tridecenol (35)

Colourless oil (4.24 g, 71% yield for two steps). IR (neat) ν: 3355 (OH), 1641 (C=C, alkene). ^{1}H NMR (400 MHz, $CDCl_3$) δ: 1.26 (m, 8 × CH_2), 1.55 (m, CH_2CH_2OH), 2.02 (m, CH_2CH=CH_2), 3.62 (t, J = 6.6 Hz, CH_2OH), 4.95 (m, CH=CH_2), 5.80 (m, CH=CH_2). ^{13}C NMR (75 MHz, $CDCl_3$) δ: 25.7, 28.9, 29.1, 29.4, 29.5 (4×), 32.7, 33.8, 63.0, 114.0, 139.2.

Pentadeca-10,14-dien-1-ol (36)

Colourless oil (3.65 g, 70% yield for two steps). IR (neat) ν: 3332 (OH), 1641 (C=C, alkene). ^{1}H NMR (400 MHz, $CDCl_3$) δ: 1.26 (m, 6 × CH_2), 1.54 (m, CH_2CH_2OH), 1.90 to 2.10 (m, 3 × CH_2CH=CH_2 and OH), 3.60 (t, J = 7.4 Hz, CH_2OH), 4.97 (m, CH=CH_2), 5.39 (m, CH=CH), 5.80 (m, CH=CH_2). ^{13}C NMR (75 MHz, $CDCl_3$) δ: 25.7, 29.1, 29.4 (2×), 29.5 (2×), 31.9, 32.5, 32.7, 33.8, 62.8, 114.4, 129.3, 130.8, 138.4. LR-MS calculated for $C_{15}H_{29}O$ $[M + H]^+$ 225.2, found 225.1 *m*/*z*.

General procedure to synthesize 37–40

The TPAP oxidation procedure that we described previously for the synthesis of 10-undecenal (**37**)[30] was used without modification.

11-Dodecenal (38)

We reported earlier the synthesis and characterization of **38**.[40]

12-Tridecenal (39)

Colourless oil (2.66 g, 67% yield). IR (neat) ν: 2713 (C–H, aldehyde), 1728 (C=O, aldehyde), 1641 (C=C, alkene). ^{1}H NMR (300 MHz, $CDCl_3$) δ: 1.25 (m, 7 × CH_2), 1.60 (m, CH_2CH$_2$CHO), 2.02 (m, CH_2CH=CH$_2$), 2.41 (dt, J_1 = 7.4 Hz, J_2 = 1.6 Hz, CH_2CHO), 4.95 (m, CH=CH_2), 5.78 (m, CH=CH$_2$), 9.74 (t, J = 1.6 Hz, CHO). ^{13}C NMR (75 MHz, $CDCl_3$) δ: 22.0, 28.9, 29.1 (2×), 29.3, 29.4 (2×), 29.5, 33.8, 43.9, 114.1, 139.2, 203.0.

Pentadeca-10,14-dien-1-al (40)

Colourless oil (2.61 g, 74% yield). IR (neat) ν: 2715 (C–H, aldehyde), 1728 (C=O, aldehyde), 1640 (C=C, alkene). ^{1}H NMR (400 MHz, $CDCl_3$) δ: 1.28 (m, 6 × CH_2), 1.61 (m, CH_2CH$_2$CHO), 1.90 to 2.10 (m, 3 × CH_2CH=), 2.41 (dt, J_1 = 7.4 Hz, J_2 = 1.6 Hz, CH_2CHO), 4.97 (m, CH=CH_2), 5.40 (m, CH=CH), 5.80 (m, CH=CH$_2$), 9.75 (t, J = 1.6 Hz, CHO). ^{13}C NMR (75 MHz, $CDCl_3$) δ: 22.0, 29.0, 29.1, 29.2, 29.3, 29.5, 32.0, 32.5, 33.8, 43.9, 114.4, 129.4, 130.8, 138.5, 202.9.

Synthesis of 49–52 using the second chemical approach

General procedure to synthesize 45–48

The procedure that we described previously for the synthesis of **45** from **37**[30] was used without modification to prepare alkynes **46**, **47**, and **48**, from aldehydes **38**, **39**, and **40**, respectively.

14-[3′-(*tert*-butyldimethylsilyloxy)-17′β-(tetrahydro-2*H*-pyran-2-yl-oxy)-estra-1′,3′,5′(10′)-trien-16′β-yl]-tetradecyne (46)

Colourless viscous oil (801 mg, 15% yield for three steps). IR (film) ν: 3313 (C–H, alkyne). ^{1}H NMR (300 MHz, acetone-d_6) δ: 0.20 (s, Si(CH$_3$)$_2$), 0.82 and 0.86 (2s, 18′-CH$_3$), 0.99 (s, SiC(CH$_3$)$_3$), 0.80 to 2.35 (CH and CH_2 of steroid skeleton and alkyl chain), 2.18 (dt, J_1 = 6.8 Hz, J_2 = 2.5 Hz, CH$_2$C≡C), 2.33 (t, J = 2.7 Hz, C≡C–H), 2.83 (m, 6′-CH$_2$), 3.47 and 3.95 (2m, OCH$_2$ of THP), 3.74 and 3.79 (2d, J = 10.0 Hz, 17′α-CH), 4.63 and 4.73 (2m, CH of THP), 6.58 (s, 4′-CH), 6.63 (d, J = 8.8 Hz, 2′-CH), 7.15 and 7.17 (2d, J = 8.4 Hz, 1′-CH). LR-MS calculated for $C_{43}H_{71}O_3Si$ [M + H]$^+$ 663.5, found 663.3 *m*/*z*.

15-[3′-(*tert*-butyldimethylsilyloxy)-17′β-(tetrahydro-2*H*-pyran-2-yl-oxy)-estra-1′,3′,5′(10′)-trien-16′β-yl]-pentadecyne (47)

Colourless viscous oil (1.36 g, 33% yield for three steps). IR (film) ν: 3312 (C–H, alkyne). ^{1}H NMR (400 MHz, acetone-d_6) δ: 0.20 (s, Si(CH$_3$)$_2$), 0.82 and 0.87 (2s, 18′-CH$_3$), 1.00 (s, SiC(CH$_3$)$_3$), 0.90 to 2.35 (CH and CH_2 of steroid skeleton and alkyl chain), 2.18 (dt, J_1 = 6.8 Hz, J_2 = 2.6 Hz, CH$_2$C≡C), 2.33 (t, J = 2.6 Hz, C≡C-H), 2.81 (m, 6′-CH$_2$), 3.48 and 3.92 (2m, OCH$_2$ of THP), 3.74 and 3.80 (2d, J = 10.0 Hz, 17′α-CH), 4.63 and 4.73 (2m, CH of THP), 6.58 (d, J = 2.4 Hz, 4′-CH), 6.64 (d, J = 8.5 Hz, 2′-CH), 7.15 and 7.17 (2d, J = 5.7 Hz, 1′-CH). LR-MS calculated for $C_{44}H_{73}O_3Si$ [M + H]$^+$ 677.5, found 677.4 *m*/*z*.

17-[3′-(*tert*-butyldimethylsilyloxy)-17′β-(tetrahydro-2*H*-pyran-2-yl-oxy)-estra-1′,3′,5′(10′)-trien-16′β-yl]-heptadecyne (48)

Colourless viscous oil (636 mg, 24% yield for three steps). IR (film) ν: 3313 (C–H, alkyne). ^{1}H NMR (400 MHz, acetone-d_6) δ: 0.20 (s, Si(CH$_3$)$_2$), 0.82 and 0.87 (2s, 18′-CH$_3$), 1.00 (s, SiC(CH$_3$)$_3$), 0.90 to 2.35 (CH and CH_2 of steroid skeleton and alkyl chain), 2.18 (m, CH$_2$C≡C), 2.33 (t, J = 2.6 Hz, C≡C–H), 2.81 (m, 6′-CH$_2$), 3.48 and 3.92 (2m, OCH$_2$ of THP), 3.75 and 3.80 (2d, J = 10.0 Hz, 17′α-CH), 4.64 and 4.73 (2m, CH of THP), 6.58 (d, J = 2.3 Hz, 4′-CH), 6.64 (d, J = 8.4 Hz, 2′-CH), 7.15 and 7.17 (2d, J = 5.6 Hz, 1′-CH). LR-MS calculated for $C_{46}H_{77}O_3Si$ [M + H]$^+$ 705.6, found 705.5 *m*/*z*.

General procedure to synthesize 49–52

The procedure that we described previously for the synthesis of **49**[30] was used without modification for the synthesis of **50**–**52**. The chemical synthesis of **25** was also described in this earlier report.

Methyl 2-{3′-(*tert*-butoxycarbonylamino)-5′-[14″-(3‴-(*tert*-butyldimethylsilyloxy)-17‴β-(tetrahydro-2*H*-pyran-2-yl-oxy)-estra-1‴,3‴,5‴(10‴)-trien-16‴β-yl)-tetradecynyl]-phenyl}-acetate (50)

Viscous yellowish oil (540 mg, 61% yield (non-optimized)). IR (film) ν: 3354 (NH, carbamate), 1732 (C=O, ester and carbamate). ^{1}H NMR (400 MHz, acetone-d_6) δ: 0.20 (s, Si(CH$_3$)$_2$), 0.82 and 0.86 (2s, 18‴-CH$_3$), 1.00 (s, SiC(CH$_3$)$_3$), 1.50 (s, (CH$_3$)$_3$C of *N*-BOC), 1.00 to 2.35 (CH and CH_2 of steroid skeleton and alkyl chain), 2.42 (t, J = 6.9 Hz, CH$_2$–C≡C), 2.81 (m, 6‴-CH$_2$), 3.47 and 3.92 (2m, OCH$_2$ of THP), 3.60 (s, CH_2COOMe), 3.66 (s, COOCH$_3$), 3.74 and 3.79 (2d, J = 10.0 Hz, 17‴α-CH), 4.63 and 4.73 (2m, CH of THP), 6.58 (d, J = 2.0 Hz, 4‴-CH), 6.64 (d, J = 8.4 Hz, 2‴-CH), 6.97 (s, 6′-CH), 7.16 (m, 1‴-CH), 7.45 (s, 2′-CH), 7.58 (s, 4′-CH), 8.46 (s, NH). LR-MS calculated for $C_{57}H_{86}NO_7Si$ [M – H]$^-$ 924.6, found 924.5 *m*/*z*.

Methyl 2-{3′-(*tert*-butoxycarbonylamino)-5′-[15″-(3‴-(*tert*-butyldimethylsilyloxy)-17‴β-(tetrahydro-2*H*-pyran-2-yl-oxy)-estra-1‴,3‴,5‴(10‴)-trien-16‴β-yl)-pentadecynyl]-phenyl}-acetate (51)

White foam (1.41 g, 95% yield). IR (film) ν: 3353 (NH, carbamate), 1732 (C=O, ester and carbamate). ^{1}H NMR (400 MHz, acetone-d_6) δ: 0.20 (s, Si(CH$_3$)$_2$), 0.82 and 0.86 (2s, 18‴-CH$_3$), 1.00 (s, SiC(CH$_3$)$_3$), 1.50 (s, (CH$_3$)$_3$C of *N*-BOC), 1.00 to 2.35 (CH and CH_2 of steroid skeleton and alkyl chain), 2.42 (t, J = 7.0 Hz, CH$_2$–C≡C), 2.81 (m, 6‴-CH$_2$), 3.48 and 3.92 (2m, OCH$_2$ of THP), 3.60 (s, CH_2COOMe), 3.66 (s, COOCH$_3$), 3.73 and 3.79 (2d, J = 10.0 Hz, 17‴α-CH), 4.63 and 4.73 (2m, CH of THP), 6.58 (d, J = 2.2 Hz, 4‴-CH), 6.64 (d, J = 8.4 Hz, 2‴-CH), 6.97 (s, 6′-CH), 7.16 (m, 1‴-CH), 7.45 (s, 2′-CH), 7.58 (s, 4′-CH), 8.48 (s, NH). LR-MS calculated for $C_{58}H_{88}NO_7Si$ [M – H]$^-$ 938.6, found 938.5 *m*/*z*.

Methyl 2-{3′-(tert-butoxycarbonylamino)-5′-[17″-(3‴-(tert-butyldimethylsilyloxy)-17‴β-(tetrahydro-2H-pyran-2-yloxy)-estra-1‴,3‴,5‴(10‴)-trien-16‴β-yl)-heptadecynyl]-phenyl}-acetate (52)

Yellowish foam (219 mg, 91% yield). IR (film) ν: 3356 (NH, carbamate), 1736 (C=O, ester and carbamate). ^{1}H NMR (400 MHz, acetone-d_6) δ: 0.20 (s, Si(CH$_3$)$_2$), 0.82 and 0.86 (2s, 18‴-CH$_3$), 1.00 (s, SiC(CH$_3$)$_3$), 1.49 (s, (CH$_3$)$_3$C of *N*-BOC), 1.00 to 2.35 (CH and CH$_2$ of steroid skeleton and alkyl chain), 2.43 (t, J = 6.9 Hz, CH$_2$−C≡C), 2.81 (m, 6‴-CH$_2$), 3.48 and 3.91 (2m, OCH$_2$ of THP), 3.61 (s, C*H*$_2$COOMe), 3.66 (s, COOCH$_3$), 3.74 and 3.79 (2d, J = 10.0 Hz, 17‴α-CH), 4.63 and 4.73 (2m, CH of THP), 6.58 (d, J = 2.3 Hz, 4‴-CH), 6.64 (d, J = 8.5 Hz, 2‴-CH), 6.97 (s, 6′-CH), 7.16 (m, 1‴-CH), 7.45 (s, 2′-CH), 7.58 (s, 4′-CH), 8.49 (s, NH). LR-MS calculated for $C_{60}H_{92}NO_7Si$ [M − H]$^-$ 966.7, found 966.5 *m*/*z*.

Introduction of molecular diversities: synthesis of 2−13

General procedure to synthesize ester derivatives 2−4 and 53

Esters **2**−**4** and **53** were synthesized in two steps from **49**−**52**. The first step is an acid treatment to remove the three protective groups, and the second is the hydrogenation of alkyne catalyzed by palladium. The procedure that we described previously for the synthesis of **2**[30] was used without modification except that 8 equiv. of HCl (4 mol/L) in dioxanes were used for the synthesis of **3**, **4**, and **53** instead of 4 equiv.

Methyl 2-{3′-amino-5′-[14″-(3‴,17‴β-dihydroxy-estra-1‴,3‴,5‴(10‴)-trien-16‴β-yl)-tetradecyl]-phenyl}-acetate (3)

Colourless viscous oil (83 mg, 62% yield for two steps). IR (film) ν: 3372 (OH and NH$_2$), 1732 (C=O, ester). ^{1}H NMR (400 MHz, acetone-d_6) δ: 0.80 (s, 18‴-CH$_3$), 0.95 to 2.35 (CH and CH$_2$ of steroid skeleton and alkyl chain), 2.45 (t, J = 7.4 Hz, 1″-CH$_2$), 2.78 (m, 6‴-CH$_2$), 3.44 (s, C*H*$_2$COOMe), 3.62 (m, COOCH$_3$, 17‴β-OH), 3.74 (dd, J_1 = 9.7 Hz, J_2 = 5.7 Hz, 17‴α-CH), 4.53 (s, NH$_2$), 6.37 (s, 6′-CH), 6.42 (s, 2′-CH and 4′-CH), 6.54 (d, J = 2.5 Hz, 4‴-CH), 6.60 (dd, J_1 = 8.4 Hz, J_2 = 2.6 Hz, 2‴-CH), 7.10 (d, J = 8.4 Hz, 1‴-CH), 8.06 (s, 3‴-OH). ^{13}C NMR (75 MHz, acetone-d_6) δ: 12.7, 26.8, 28.0, 28.7 to 30.2 (11C under solvent peaks), 30.4, 31.8, 32.3, 33.0, 36.2, 38.3, 39.1, 40.9, 41.2, 44.5 (2×), 49.2, 51.5, 81.9, 113.1 (2×), 113.6, 115.5, 118.4, 126.6, 131.7, 135.3, 138.0, 144.0, 148.8, 155.5, 172.1. HR-MS calculated for $C_{41}H_{62}NO_4$ [M + H]$^+$ 632.46734, found 632.46636 *m*/*z*.

Methyl 2-{3′-amino-5′-[15″-(3‴,17‴β-dihydroxy-estra-1‴,3‴,5‴(10‴)-trien-16‴β-yl)-pentadecyl]-phenyl}-acetate (4)

Colourless viscous oil (115 mg, 53% yield for two steps). IR (film) ν: 3376 (OH and NH$_2$), 1734 (C=O, ester). ^{1}H NMR (400 MHz, acetone-d_6) δ: 0.80 (s, 18‴-CH$_3$), 0.95 to 2.35 (CH and CH$_2$ of steroid skeleton and alkyl chain), 2.46 (t, J = 7.5 Hz, 1″-CH$_2$), 2.78 (m, 6‴-CH$_2$), 3.44 (s, C*H*$_2$COOMe), 3.56 (d, J = 5.4 Hz, 17‴β-OH), 3.62 (s, COOCH$_3$), 3.74 (dd, J_1 = 9.8 Hz, J_2 = 5.4 Hz, 17‴α-CH), 4.53 (s, NH$_2$), 6.37 (s, 6′-CH), 6.42 (s, 2′-CH and 4′-CH), 6.54 (d, J = 2.6 Hz, 4‴-CH), 6.60 (dd, J_1 = 8.4 Hz, J_2 = 2.6 Hz, 2‴-CH), 7.11 (d, J = 8.4 Hz, 1‴-CH), 7.97 (s, 3‴-OH). ^{13}C NMR (100 MHz, acetone-d_6) δ: 13.0, 27.1, 28.2, 29.1 to 30.3 (12C under solvent peaks), 30.6, 32.0, 32.5, 33.2, 36.4, 38.6, 39.4, 41.2, 41.5, 44.79, 44.82, 49.5, 51.7, 82.2, 113.4, 113.8, 115.8, 118.7, 124.5, 126.8, 132.0, 135.6, 138.2, 144.3, 149.1, 155.7, 172.2. HR-MS calculated for $C_{42}H_{64}NO_4$ [M + H]$^+$ 646.48299, found 646.48402 *m*/*z*.

Methyl 2-{3′-amino-5′-[17″-(3‴,17‴β-dihydroxy-estra-1‴,3‴,5‴(10‴)-trien-16‴β-yl)-heptadecyl]-phenyl}-acetate (53)

Yellowish viscous oil (61 mg, 41% yield for two steps). IR (film) ν: 3376 (OH and NH$_2$), 1732 (C=O, ester). ^{1}H NMR (400 MHz, acetone-d_6) δ: 0.80 (s, 18‴-CH$_3$), 0.95 to 2.35 (CH and CH$_2$ of steroid skeleton and alkyl chain), 2.46 (t, J = 7.5 Hz, 1″-CH$_2$), 2.78 (m, 6‴-CH$_2$), 3.45 (s, C*H*$_2$COOMe), 3.54 (d, J = 5.4 Hz, 17‴β-OH), 3.62 (s, COOCH$_3$), 3.72 (dd, J_1 = 9.8 Hz, J_2 = 5.5 Hz, 17‴α-CH), 4.54 (s, NH$_2$), 6.37 (s, 6′-CH), 6.41 and 6.42 (2s, 2′-CH and 4′-CH), 6.54 (d, J = 2.5 Hz, 4‴-CH), 6.60 (dd, J_1 = 8.4 Hz, J_2 = 2.6 Hz, 2‴-CH), 7.11 (d, J = 8.4 Hz, 1‴-CH), 7.96 (s, 3‴-OH). ^{13}C NMR (100 MHz, acetone-d_6) δ: 12.9, 27.1, 28.2, 29.1 to 30.3 (14C under solvent peaks), 30.6, 32.1, 32.5, 33.2, 36.4, 38.6, 39.4, 41.2, 41.4, 44.77, 44.81, 49.4, 51.7, 82.1, 113.3, 113.4, 113.8, 115.8, 118.6, 126.9, 132.0, 135.6, 138.3, 144.3, 149.2, 155.7, 172.2. LR-MS calculated for $C_{44}H_{68}NO_4$ [M + H]$^+$ 674.5, found 674.3 *m*/*z*.

General procedure to synthesize carboxylic acid derivatives 5−8

The procedure that we described previously for the synthesis of **5**[30] was used without modification for the synthesis of **5**−**8**. Completion of the reaction was monitored by TLC (2 to 5 h).

2-{3′-Amino-5′-[14″-(3‴,17‴β-dihydroxy-estra-1‴,3‴,5‴(10‴)-trien-16‴β-yl)-tetradecyl]-phenyl}-acetic acid (6)

White foam (31 mg, 91% yield). IR (KBr) ν: 3600−2400 (OH, carboxylic acid), 3374 (OH and NH$_2$), 1718 (C=O, carboxylic acid). ^{1}H NMR (400 MHz, CDCl$_3$ and few drops of DMSO-d_6) δ: 0.62 (s, 18‴-CH$_3$), 0.65 to 2.25 (CH and CH$_2$ of steroid skeleton and alkyl chain), 2.41 (t, J = 7.7 Hz, 1″-CH$_2$), 2.66 (m, 6‴-CH$_2$), 3.40 (s, C*H*$_2$COOH), 3.58 (d, J = 9.9 Hz, 17‴α-CH), 6.45 (d, J = 2.4 Hz, 4‴-CH), 6.51 (dd, J_1 = 8.4 Hz, J_2 = 2.5 Hz, 2‴-CH), 6.71 (m, 2′-CH and 4′-CH, 6′-CH), 6.98 (d, J = 8.4 Hz, 1‴-CH). ^{13}C NMR (75 MHz, CDCl$_3$ and few drops of DMSO-d_6) δ: 12.2, 26.0, 27.2, 28.3, 29.1, 29.3 (9×), 29.6, 31.0, 31.3, 32.1, 35.4, 37.4, 38.1, 38.9 to 40.6 (1C under DMSO peaks), 40.8, 43.66, 43.75, 48.2, 81.8, 112.5, 115.0, 117.6, 117.9, 123.0, 125.9, 131.0, 135.5, 137.5, 139.3, 144.4, 154.5, 173.0. HR-MS calculated for $C_{40}H_{60}NO_4$ [M + H]$^+$ 618.45169, found 618.45187 *m*/*z*.

2-{3′-Amino-5′-[15″-(3‴,17‴β-dihydroxy-estra-1‴,3‴,5‴(10‴)-trien-16‴β-yl)-pentadecyl]-phenyl}-acetic acid (7)

White foam (43 mg, 75% yield). IR (KBr) ν: 3600−2300 (OH, carboxylic acid), 3370 (OH and NH$_2$), 1711 (C=O,

carboxylic acid). ^{1}H NMR (400 MHz, $CDCl_3$ and few drops of DMSO-d_6) δ: 0.67 (s, 18‴-CH_3), 0.75 to 2.30 (CH and CH_2 of steroid skeleton and alkyl chain), 2.40 (t, J = 7.6 Hz, 1″-CH_2), 2.70 (m, 6‴-CH_2), 3.39 (s, CH_2COOH), 3.62 (d, J = 10.0 Hz, 17‴α-CH), 6.44 (s, 4‴-CH), 6.49 (s_{br}, 2′-CH, 4′-CH, and 6′-CH), 6.55 (dd, J_1 = 8.4 Hz, J_2 = 2.4 Hz, 2‴-CH), 7.02 (d, J = 8.4 Hz, 1‴-CH). ^{13}C NMR (100 MHz, $CDCl_3$ and few drops of DMSO-d_6) δ: 12.2, 26.1, 27.3, 28.4, 29.17, 29.24, 29.3, 29.4 (8×), 29.6, 31.0, 31.3, 32.2, 35.6, 37.6, 38.2, 39.9, 41.1, 43.8, 43.9, 48.4, 82.0, 112.7, 114.4, 114.8, 115.0, 121.0, 125.9, 131.2, 135.3, 137.6, 139.4, 144.2, 154.5, 173.5. HR-MS calculated for $C_{41}H_{62}NO_4$ $[M + H]^+$ 632.46734, found 632.46688 *m*/*z*.

2-{3′-Amino-5′-[17″-(3‴,17‴β-dihydroxy-estra-1‴,3‴,5‴(10‴)-trien-16‴β-yl)-heptadecyl]-phenyl}-acetic acid (8)

Yellowish foam (42 mg, 72% yield). IR (KBr) ν: 3700−2300 (OH, carboxylic acid), 3369 (OH and NH_2), 1713 (C=O, carboxylic acid). ^{1}H NMR (400 MHz, $CDCl_3$ and few drops of DMSO-d_6) δ: 0.62 (s, 18‴-CH_3), 0.80 to 2.25 (CH and CH_2 of steroid skeleton and alkyl chain), 2.40 (t, J = 7.6 Hz, 1″-CH_2), 2.66 (m, 6‴-CH_2), 3.40 (s, CH_2COOH), 3.57 (d, J = 10.0 Hz, 17‴α-CH), 6.43 (d, J = 2.2 Hz, 4‴-CH), 6.50 (dd, J_1 = 8.4 Hz, J_2 = 2.4 Hz, 2‴-CH), 6.78 (m, 2′-CH, 4′-CH, and 6′-CH), 6.96 (d, J = 8.5 Hz, 1‴-CH). ^{13}C NMR (75 MHz, $CDCl_3$ and few drops of DMSO-d_6) δ: 12.2, 26.0, 27.1, 28.3, 29.0, 29.1, 29.3 (11×), 29.5, 31.0, 31.3, 32.0, 35.4, 37.4, 38.0, 38.9 to 40.5 (1C under DMSO peaks), 40.9, 43.6, 43.7, 48.2, 81.7, 112.5, 115.0, 115.3, 115.7, 122.0, 125.8, 131.0, 135.2, 137.4, 142.1, 144.1, 154.5, 173.3. HR-MS calculated for $C_{43}H_{66}NO_4$ $[M + H]^+$ 660.49863, found 660.49790 *m*/*z*.

General procedure to synthesize alcohol derivatives 9−11

The procedure that we described previously for the synthesis of **9**[30] was used without modification for the synthesis of **9**−**11** except that 1.1 to 3 equiv. of $LiAlH_4$ were used. Completion of the reaction was monitored by TLC (4 to 16 h).

2-{3′-Amino-5′-[14″-(3‴,17‴β-dihydroxy-estra-1‴,3‴,5‴(10‴)-trien-16‴β-yl)-tetradecyl]-phenyl}-ethyl alcohol (10)

Yellowish foam (15 mg, 45% yield). IR (film) ν: 3400 (OH and NH_2). ^{1}H NMR (400 MHz, acetone-d_6) δ: 0.79 (s, 18‴-CH_3), 0.75 to 2.35 (CH and CH_2 of steroid skeleton and alkyl chain), 2.44 (t, J = 7.7 Hz, 1″-CH_2), 2.65 (t, J = 7.3 Hz, CH_2CH$_2$OH), 2.79 (m, 6‴-CH_2), 3.58 (m, 17‴β-OH and CH$_2$OH), 3.70 (m, CH_2OH and 17‴α-CH), 4.44 (s_{br}, NH_2), 6.32 (s, 6′-CH), 6.36 (s, 2′-CH and 4′-CH), 6.54 (d, J = 2.5 Hz, 4‴-CH), 6.60 (dd, J_1 = 8.4 Hz, J_2 = 2.6 Hz, 2‴-CH), 7.11 (d, J = 8.4 Hz, 1‴-CH), 8.01 (s, 3‴-OH). ^{13}C NMR (75 MHz, acetone-d_6) δ: 12.9, 27.1, 28.2, 28.9 to 30.4 (11C under solvent peaks), 32.1, 32.5, 33.2, 36.3, 36.5, 38.5, 39.3, 40.2, 41.2, 44.8 (2×), 49.4, 63.8, 82.1, 113.4, 115.7, 117.7, 118.0, 124.2, 126.8, 132.0, 138.2, 140.7, 143.9, 152.6, 155.7. HR-MS calculated for $C_{40}H_{62}NO_3$ $[M + H]^+$ 604.47242, found 604.47243 *m*/*z*.

2-{3′-Amino-5′-[15″-(3‴,17‴β-dihydroxy-estra-1‴,3‴,5‴(10‴)-trien-16‴β-yl)-pentadecyl]-phenyl}-ethyl alcohol (11)

Colourless viscous oil (25 mg, 61% yield). IR (film) ν: 3354 (OH and NH_2). ^{1}H NMR (400 MHz, acetone-d_6) δ: 0.80 (s, 18‴-CH_3), 0.85 to 2.35 (CH and CH_2 of steroid skeleton and alkyl chain), 2.44 (t, J = 7.7 Hz, 1″-CH_2), 2.65 (t, J = 7.3 Hz, CH_2CH$_2$OH), 2.78 (m, 6‴-CH_2), 3.57 (m, 17‴β-OH and CH$_2$OH), 3.71 (m, CH_2OH and 17‴α-CH), 4.43 (s_{br}, NH_2), 6.33 (s, 6′-CH), 6.36 (s, 2′-CH and 4′-CH), 6.54 (d, J = 2.5 Hz, 4‴-CH), 6.60 (dd, J_1 = 8.4 Hz, J_2 = 2.6 Hz, 2‴-CH), 7.11 (d, J = 8.5 Hz, 1‴-CH), 7.97 (s, 3‴-OH). ^{13}C NMR (100 MHz, acetone-d_6) δ: 13.0, 27.2, 28.3, 29.1 to 30.3 (11C under solvent peaks), 30.4, 30.7, 32.4, 32.6, 33.3, 36.6, 38.7, 39.5, 40.5, 41.3, 44.88, 44.92, 49.6, 64.1, 82.3, 113.2, 113.4, 113.5, 115.9, 118.7, 126.9, 132.1, 138.3, 140.6, 144.1, 149.0, 155.8. HR-MS calculated for $C_{41}H_{64}NO_3$ $[M + H]^+$ 618.48807, found 618.48783 *m*/*z*.

*Synthesis of 2-{3′-(***tert***-butoxycarbonylamino)-5′-[13″-(3‴-(***tert***-butyldimethylsilyloxy)-17‴β-(tetrahydro-2***H***-pyran-2-yl-oxy)-estra-1‴,3‴,5‴(10‴)-trien-16‴β-yl)-tridecynyl]-phenyl}-ethyl alcohol (54)*

The procedure that we described previously for the synthesis of **9**[30] was used without modification except that 1.2 equiv. of $LiAlH_4$ were used instead of 1 equiv. Purification by flash chromatography using hexanes/EtOAc (8:2) as eluent afforded **54** as white foam (491 mg, 80% yield). IR (film) ν: 3340 (OH and NH carbamate), 1718 (C=O, carbamate). ^{1}H NMR (400 MHz, acetone-d_6) δ: 0.21 (s, Si(CH$_3$)$_2$), 0.82 and 0.86 (2s, 18‴-CH_3), 1.00 (s, SiC(CH$_3$)$_3$), 0.95 to 2.35 (CH and CH_2 of steroid skeleton and alkyl chain), 1.49 (s, (CH$_3$)$_3$C of *N*-BOC), 2.42 (t, J = 7.0 Hz, CH$_2$−C≡C), 2.75 (t, J = 6.7 Hz, CH_2CH$_2$OH), 2.81 (m, 6‴-CH_2), 3.48 and 3.91 (2m, OCH$_2$ of THP), 3.74 (m, 17‴α-CH and CH_2OH), 4.63 and 4.73 (2m, CH of THP), 6.58 (d, J = 2.3 Hz, 4‴-CH), 6.64 (d, J = 8.4 Hz, 2‴-CH), 6.92 (s, 6′-CH), 7.16 (2d, J = 5.8 Hz, 1‴-CH), 7.37 (s, 2′-CH), 7.53 (s, 4′-CH), 8.39 (s_{br}, NH). LR-MS calculated for $C_{55}H_{84}NO_6Si$ $[M - H]^-$ 882.6, found 882.6 *m*/*z*.

*Synthesize of 2-{3′-(***tert***-butoxycarbonylamino)-5′-[13″-(3‴-(***tert***-butyldimethylsilyloxy)-17‴β-(tetrahydro-2***H***-pyran-2-yl-oxy)-estra-1‴,3‴,5‴(10‴)-trien-16‴β-yl)-tridecynyl]-phenyl}-ethyl bromide (55)*

To a solution of alcohol **54** (150 mg, 0.172 mmol) in anhydrous DCM under an argon atmosphere at 0 °C were added PPh_3 (90 mg, 0.344 mmol) and CBr_4 (114 mg, 0.344 mmol). The reaction mixture was stirred for 3.5 h at 0 °C. Then, a saturated aqueous solution of $NaHCO_3$ was added to quench the reaction, and the product was extracted with DCM. The organic phases were washed with brine, dried over $MgSO_4$, filtered, and evaporated to dryness. The crude product was purified by flash chromatography (hexanes/EtOAc, 8:2) to afford a mixture of the desired, deprotected form of **55** (113 mg, 70% yield). Desired product **55** was collected with its deprotected form (without THP) as a minor compound produced during this bromination reaction, since the next step was to hydrolyze protective groups under acid conditions. Only the characterization of the major compound **55** is described. Colourless viscous oil (113 mg, 70%

yield). ^{1}H NMR (400 MHz, acetone-d_6) δ: 0.21 (s, $Si(CH_3)_2$), 0.82 and 0.86 (2s, 18‴-CH_3), 0.85 to 2.35 (CH and CH_2 of steroid skeleton and alkyl chain), 1.00 (s, $SiC(CH_3)_3$), 1.50 (s, $(CH_3)_3C$ of *N*-BOC), 2.43 (t, *J* = 7.0 Hz, $CH_2-C\equiv C$), 2.81 (m, 6‴-CH_2), 3.12 (t, *J* = 7.3 Hz, CH_2CH_2Br), 3.47 and 3.92 (2m, OCH_2 of THP), 3.68 (t, *J* = 7.4 Hz, CH_2Br), 3.73 and 3.79 (2d, *J* = 9.9 Hz, 17‴α-CH), 4.63 and 4.73 (2m, CH of THP), 6.58 (d, *J* = 2.4 Hz, 4‴-CH), 6.64 (d, *J* = 8.5 Hz, 2‴-CH), 6.97 (s, 6′-CH), 7.15 (m, 1‴-CH), 7.42 (s, 2′-CH), 7.57 (s, 4′-CH), 8.46 (s_{br}, NH).

*Synthesize of dimethyl 2-{3′-(***tert***-butoxycarbonylamino)-5′-[13″-(3‴-(***tert***-butyldimethylsilyloxy)-17‴β-(tetrahydro-2***H***-pyran-2-yl-oxy)-estra-1‴,3‴,5‴(10‴)-trien-16‴β-yl)-tridecynyl]-phenyl}-ethyl phosphate (56)*

In a round-bottom flask, alcohol **54** (300 mg, 0.345 mmol) and CBr_4 (171 mg, 0.517 mmol) were purged under an argon atmosphere for 10 min. Then, pyridine (2.3 mL) and $P(OMe)_3$ (163 μL, 1.38 mmol) were added. The reaction mixture was stirred for 3 h at room temperature. Then, the product was extracted with EtOAc. The organic phase was washed with an aqueous solution of $CuSO_4$ 1 mol/L and re-extracted with EtOAc. The combined organic phases were washed with H_2O and brine, dried over $MgSO_4$, filtered, and evaporated to dryness. Purification by flash chromatography (hexanes/EtOAc, 6:4) provided **56** (275 mg, 82% yield) as a yellowish solid. IR (film) ν: 3284 (NH carbamate), 1727 (C=O, carbamate). ^{1}H NMR (400 MHz, acetone-d_6) δ: 0.20 (s, $Si(CH_3)_2$), 0.82 and 0.86 (2s, 18‴-CH_3), 1.00 (s, $SiC(CH_3)_3$), 0.95 to 2.35 (CH and CH_2 of steroid skeleton and alkyl chain), 1.49 (s, $(CH_3)_3C$ of *N*-BOC), 2.42 (t, *J* = 6.9 Hz, $CH_2-C\equiv C$), 2.81 (m, 6‴-CH_2), 2.95 (t, *J* = 6.7 Hz, $CH_2CH_2OP(O)(OMe)_2$), 3.48 and 3.91 (2m, OCH_2 of THP), 3.67 (d, $^3J_{PH}$ = 11.1 Hz, 2 × OMe), 3.74 and 3.79 (2d, *J* = 9.8 Hz, 17‴α-CH), 4.23 (q, *J* = 7.0 Hz, $CH_2CH_2O-P(O)(OMe)_2$), 4.63 and 4.73 (2m, CH of THP), 6.58 (d, *J* = 2.1 Hz, 4‴-CH), 6.64 (d, *J* = 8.4 Hz, 2‴-CH), 6.98 (s, 6′-CH), 7.16 (m, 1‴-CH), 7.44 (s, 2′-CH), 7.56 (s, 4′-CH), 8.48 (s, NH). LR-MS calculated for $C_{57}H_{90}NO_9PSiNa$ $[M + Na]^+$ 1014.6, found 1014.5 *m*/*z*.

Synthesize of 2-{3′-amino-5′-[13″-(3‴,17‴β-dihydroxy-estra-1‴,3‴,5‴(10‴)-trien-16‴β-yl)-tridecyl]-phenyl}-ethyl bromide (12)

Deprotection

A solution of **55** (80 mg, 0.086 mmol) in dry DCM (0.5 mL) and dry MeOH (0.5 mL) under an argon atmosphere was treated with HCl (4 mol/L in dioxane) (160−255 μL, 0.858 mmol). The resulting mixture was stirred at room temperature for 16 h. The reaction was quenched by addition of a saturated aqueous $NaHCO_3$ solution, and extraction was performed with DCM. The organic phase was washed with brine, dried over $MgSO_4$, filtered, and evaporated to dryness under reduced pressure. Purification of the crude product by flash chromatography (hexanes/EtOAc, 8:2) afforded a mixture of the desired products (NH_2) and its salt (NH_2·HCl).

Hydrogenation

To a solution of the deprotected form of alkyne **55** (35 mg, 0.054 mmol) in EtOAc (2 mL) was added 10% Pd/C (7 mg). This mixture was stirred for 16 h under a hydrogen atmosphere at room temperature. The resulting suspension was filtered through Celite, washed with EtOAc, and the filtrate was evaporated to dryness. The crude compound was purified by flash chromatography (hexanes/EtOAc, 8:2 to 7:3) to provide a mixture of bromide derivative **12** and its salt (NH_2·HCl). White foam (12 mg, 25% yield for two steps). IR (film) ν: 3356 (OH and NH_2). ^{1}H NMR (400 MHz, acetone-d_6) δ: 0.80 (s, 18‴-CH_3), 1.00 to 2.35 (CH and CH_2 of steroid skeleton and alkyl chain), 2.46 and 2.58 (2t, *J* = 7.7 Hz, 1″-CH_2), 2.77 (m, 6‴-CH_2), 2.99 and 3.11 (2t, *J* = 7.6 Hz, CH_2CH_2Br), 3.56 (s_{br}, 17‴β-OH), 3.60 and 3.68 (2t, *J* = 7.6 Hz, CH_2Br), 3.73 (d, *J* = 9.2 Hz, 17‴α-CH), 6.40 (m, 2′-CH, 4′-CH and 6′-CH), 6.54 (s, 4‴-CH), 6.60 (d, *J* = 8.4 Hz, 2‴-CH), 6.83 (s, NH_2), 7.11 (d, *J* = 8.5 Hz, 1‴-CH), 7.98 (s, 3‴-OH). ^{13}C NMR (75 MHz, acetone-d_6) δ: 12.9, 27.1, 28.2, 28.9 to 30.4 (10C under solvent peaks), 30.5, 32.0, 32.5, 33.2, 34.1, 36.2, 38.5, 39.3, 39.7, 41.2, 44.76, 44.81, 49.4, 82.1, 113.3, 115.7, 117.9, 118.7, 124.2, 126.9, 132.0, 138.3, 140.4, 144.4, 146.4, 155.7. HR-MS calculated for $C_{39}H_{59}BrNO_2$ $[M + H]^+$ 652.37237, found 652.37128 *m*/*z*.

Synthesize of dimethyl 2-{3′-amino-5′-[13″-(3‴, 17‴β-dihydroxy-estra-1‴,3‴,5‴(10‴)-trien-16‴β-yl)-tridecyl]-phenyl}-ethyl phosphate (13)

The procedure described above for the synthesis of **12** was used without modification except that MeOH was used as solvent in the hydrogenation step instead of EtOAc. Deprotected form of **56** and phosphotriester derivatives were purified by flash chromatography using hexanes/EtOAc (2:8) followed by DCM/MeOH (97:3) as eluent. Compound **13** was obtained as a mixture with its salt (NH_2·HCl). Yellowish foam (22 mg, 35% yield for two steps). IR (film) ν: 3364 (OH and NH_2). ^{1}H NMR (400 MHz, acetone-d_6) δ: 0.80 (s, 18‴-CH_3), 0.85 to 2.35 (CH and CH_2 of steroid skeleton and alkyl chain), 2.46 and 2.57 (2t, *J* = 7.7 Hz, 1″-CH_2), 2.78 (m, 6‴-CH_2), 2.83 and 2.94 (2t, *J* = 6.8 Hz, $CH_2CH_2OP(O)(OMe)_2$), 3.65 (d, $^3J_{PH}$ = 11.1 Hz, 2 × OMe), 3.72 (d, *J* = 9.8 Hz, 17‴α-CH), 4.18 and 4.21 (2q, *J* = 7.1 Hz, $CH_2OP(O)(OMe)_2$), 6.40 (m, 2′-CH, 4′-CH and 6′-CH), 6.54 (s, 4‴-CH), 6.60 (d, *J* = 8.4 Hz, 2‴-CH), 6.81 (s, NH_2), 7.11 (d, *J* = 8.4 Hz, 1‴-CH). ^{13}C NMR (100 MHz, acetone-d_6) δ: 13.0, 27.2, 28.3, 29.1 to 30.3 (10C under solvent peaks), 30.6, 32.1, 32.6, 33.3, 36.3, 37.2, 38.7, 39.5, 41.3, 44.86, 44.92, 49.6, 54.15, 54.22, 68.5 (68.6), 82.1, 113.4, 115.8, 118.2, 118.4, 124.4, 126.9, 132.1, 138.3, 138.9, 144.4, 151.8, 155.8. HR-MS calculated for $C_{41}H_{65}NO_6P$ $[M + H]^+$ 698.45440, found 698.45359 *m*/*z*.

Synthesis of new adenosine mimics 59, 61, 64, and 65

*Synthesis of 3-(3′-***tert***-butoxycarbonylamino-5′-iodophenyl)-propanol (58)*

To a solution of alkene **57**[30] (100 mg, 0.278 mmol) in anhydrous THF (3 mL) under an argon atmosphere at 0 °C was added BH_3·THF (1.0 mol/L in THF, 0.64 mL, 0.64 mmol). The mixture was stirred 3 h at 0 °C. Then, 3 N aqueous NaOH (0.23 mL, 0.695 mmol) and 30% (*w*/*v*) hydrogen peroxide (0.17 mL, 1.53 mmol) were added. After 2 h at room temperature, the reaction was quenched with water, and extraction was performed with EtOAc. The organic phase was

washed with brine, dried over $MgSO_4$, filtered, and evaporated to dryness. The crude product was purified by flash chromatography (hexanes/EtOAc, 6:4) to give 77 mg (74% yield) of the desired alcohol **58** as a white foam. IR (film) ν: 3316 (OH and NH carbamate), 1700 (C=O carbamate). ^{1}H NMR (400 MHz, acetone-d_6) δ: 1.49 (s, $(CH_3)_3C$ of *N*-BOC), 1.80 (m, CH_2CH_2OH), 2.64 (t, J = 7.5 Hz, $CH_2CH_2CH_2OH$), 3.58 (m, CH_2OH), 3.67 (t, J = 5.4 Hz, OH), 7.25 (s, 6′-CH), 7.40 (s, 2′-CH), 7.90 (s, 4′-CH), 8.49 (s, NH). ^{13}C NMR (75 MHz, acetone-d_6) δ: 28.2 (3×), 32.2, 34.9, 61.3, 80.1, 94.4, 118.2, 124.7, 131.8, 141.6, 146.1, 153.2. LR-MS calculated for $C_{14}H_{19}INO_3$ $[M - H]^-$ 376.0, found 375.9 *m/z*.

*Synthesis of methyl 3-(3′-***tert***-butoxycarbonylamino-5′-iodophenyl)-propanoate (59)*

Oxidation

To a solution of alcohol **58** (329 mg, 0.872 mmol) in acetone (44 mL) was added dropwise Jones' reagent (0.48 mL of a $CrO_3 \cdot H_2SO_4$, 2.7 mol/L solution) at 0 °C, and the reaction mixture was stirred for 90 min. Then, 2-propanol (few drops) and brine were added. Acetone was partially evaporated under reduced pressure, the mixture was extracted with EtOAc. The organic phase was dried over $MgSO_4$, filtered, and evaporated to dryness.

Esterification

The crude acid was dissolved in anhydrous MeOH (9 mL) under an argon atmosphere at 0 °C. $TMSCHN_2$ (2.0 mol/L in hexanes, 2.6 mL, 5.2 mmol) was added slowly, and the mixture was stirred for 10 min at 0 °C. Then, MeOH was removed under reduced pressure. The crude product was purified by flash chromatography (hexanes/EtOAc, 9:1) to afford ester **59** (269 mg, 76% yield for two steps) as a white foam. IR (film) ν: 3339 (NH, carbamate), 1725 (C=O, ester and carbamate). ^{1}H NMR (400 MHz, acetone-d_6) δ: 1.49 (s, $(CH_3)_3C$ of *N*-BOC), 2.63 (t, J = 7.6 Hz, CH_2COOMe), 2.86 (t, J = 7.6 Hz, CH_2CH_2COOMe), 3.63 (s, $COOCH_3$), 7.29 (s, 6′-CH), 7.40 (s, 2′-CH), 7.93 (s, 4′-CH), 8.49 (s, NH). ^{13}C NMR (75 MHz, acetone-d_6) δ: 28.3 (3×), 30.9, 35.5, 51.5, 80.3, 94.5, 118.2, 125.3, 131.8, 141.8, 144.5, 153.3, 173.0. LR-MS calculated for $C_{15}H_{19}INO_4$ $[M - H]^-$ 404.0, found 403.9 *m/z*.

*Synthesis of methyl 4-(3′-***tert***-butoxycarbonylamino-5′-iodophenyl)-2-butenoate (60)*

Alkene **57**[30] (500 mg, 1.39 mmol) was dissolved in anhydrous DCM (23 mL) under an argon atmosphere. Methyl acrylate (2.5 mL, 27.8 mmol) and the 2nd generation Grubbs' catalyst (118 mg, 0.139 mmol) were added. The reaction mixture was refluxed for 16 h. Then, DCM was removed under reduced pressure, and the crude product was purified by flash chromatography (hexanes/EtOAc, 9:1) to yield **60** (505 mg, 87% yield, 36:1 *E*/*Z* as determined by integration of peaks at 5.91 and 6.02 ppm in the ^{1}H NMR spectrum) as a white amorphous solid. IR (film) ν: 3335 (NH, carbamate), 1700 (C=O, conjugated ester and carbamate), 1654 (C=C, conjugated alkene). ^{1}H NMR (400 MHz, acetone-d_6) δ: 1.49 (s, $(CH_3)_3C$ of *N*-BOC), 3.53 (dd, J_1 = 7.0 Hz, J_2 = 1.1 Hz, CH_2CH=), 3.68 (s, $COOCH_3$), 5.91 (dt, J_1 = 15.6 Hz, J_2 = 1.6 Hz, CH=C*H*−COOMe), 7.03 (dt, J_1 = 15.5 Hz, J_2 = 7.0 Hz, CH_2CH=CH), 7.28 (s, 6′-CH), 7.42 (s, 2′-CH), 7.97 (s, 4′-CH), 8.56 (s, NH). ^{13}C NMR (75 MHz, acetone-d_6) δ: 28.2 (3×), 38.0, 51.4, 80.3, 94.6, 118.5, 122.7, 125.5, 132.0, 141.8, 142.0, 147.4, 153.2, 166.6. LR-MS calculated for $C_{16}H_{19}INO_4$ $[M - H]^-$ 416.0, found 415.9 *m/z*.

*Synthesis of methyl 4-(3′-***tert***-butoxycarbonylamino-5′-iodophenyl)-butanoate (61)*

To a solution of alkene **60** (240 mg, 0.57 mmol) in anhydrous THF (6 mL) was added PtO_2 (60 mg). This mixture was stirred for 16 h under a hydrogen atmosphere at room temperature. The resulting suspension was filtered through Celite, and THF was evaporated under reduced pressure. Purification by flash chromatography (hexanes/EtOAc, 85:15) afforded **61** (222 mg, 93% yield) as a white solid. IR (film) ν: 3342 (NH, carbamate), 1720 (C=O, ester and carbamate). ^{1}H NMR (400 MHz, acetone-d_6) δ: 1.49 (s, $(CH_3)_3C$ of *N*-BOC), 1.89 (dt, J_1 = 15.2 Hz, J_2 = 7.5 Hz, CH_2CH_2COOMe), 2.35 (t, J = 7.4 Hz, CH_2COOMe), 2.60 (t, J = 7.5 Hz, $CH_2CH_2CH_2COOMe$), 3.63 (s, $COOCH_3$), 7.26 (s, 6′-CH), 7.39 (s, 2′-CH), 7.93 (s, 4′-CH), 8.49 (s, NH). ^{13}C NMR (75 MHz, acetone-d_6) δ: 27.0, 28.3 (3×), 33.4, 35.0, 51.4, 80.2, 94.5, 118.3, 125.1, 131.8, 141.8, 145.4, 153.3, 173.6. LR-MS calculated for $C_{16}H_{21}INO_4$ $[M - H]^-$ 418.0, found 417.9 *m/z*.

*Synthesis of methyl 3-***tert***-butoxycarbonylamino-5-iodophenyl)-benzoate (64)*

The starting material **62** was obtained according to an already described procedure.[35,36] The esterification procedure described above for the synthesis of **59** was used without modification. Purification by flash chromatography (hexanes/EtOAc, 9:1) yielded ester **64** (962 mg, 93% yield) as a white solid. IR (film) ν: 3343 (NH, carbamate), 1710 (C=O, ester and carbamate). ^{1}H NMR (400 MHz, $CDCl_3$) δ: 1.52 (s, $(CH_3)_3C$ of N-BOC), 3.90 (s, $COOCH_3$), 6.70 (s, NH), 7.86 (dd, J_1 = 2.0 Hz, J_2 = 1.5 Hz, 6-CH), 8.02 (t, J = 1.5 Hz, 4-CH), 8.16 (s, 2-CH). ^{13}C NMR (75 MHz, $CDCl_3$) δ: 28.2 (3×), 52.5, 81.3, 94.0, 118.6, 131.0, 132.1, 132.7, 139.6, 152.2, 165.4. LR-MS calculated for $C_{13}H_{15}INO_4$ $[M - H]^-$ 376.0, found 376.0 *m/z*.

Synthesis of methyl 2-(3′-iodophenyl)-acetate (65)

The procedure described above for the synthesis of **59** was used without modification. Purification by flash chromatography (hexanes/EtOAc, 95:5) afforded ester **65** (263 mg, 99% yield) as a colourless oil. IR (film) ν: 1738 (C=O, ester). ^{1}H NMR (400 MHz, $CDCl_3$) δ: 3.57 (s, CH_2), 3.70 (s, $COOCH_3$), 7.06 (t, J = 7.8 Hz, 5′-CH), 7.25 (d, J = 7.4 Hz, 6′-CH), 7.61 (d, J = 7.9 Hz, 4′-CH), 7.64 (s, 2′-CH). ^{13}C NMR (75 MHz, $CDCl_3$) δ: 40.5, 52.2, 94.4, 128.6, 130.2, 136.1, 136.2, 138.2, 171.4. LR-MS calculated for $C_9H_{10}IO_2$ $[M + H]^+$ 277.0, found 276.8 *m/z*.

Synthesis of 14−18 using the second chemical approach

General procedure to synthesize 67−71

The Sonogashira coupling procedure described previously[30] for the synthesis of **49** was used without modification except for the synthesis of **71** where 2 equiv. of 3-iodoaniline were used instead of 1 equiv.

Methyl 3-*tert*-butoxycarbonylamino-5-[13′-(3″-(*tert*-butyldimethylsilyloxy)-17″β-(tetrahydro-2*H*-pyran-2-yl-oxy)-estra-1″,3″,5″(10″)-trien-16″β-yl)-tridecynyl]-benzoate (67)

Yellowish foam (249 mg, 72% yield). IR (film) ν: 3355 (NH, carbamate), 1732 (C=O, ester), 1712 (C=O, carbamate). ^{1}H NMR (400 MHz, acetone-d_6) δ: 0.20 (s, $Si(CH_3)_2$), 0.81 and 0.85 (2s, 18″-CH_3), 1.00 (s, $SiC(CH_3)_3$), 1.00 to 2.40 (CH and CH_2 of steroid skeleton and alkyl chain), 1.51 (s, $(CH_3)_3C$ of *N*-BOC), 2.45 (t, J = 6.9 Hz, CH_2–C≡C), 2.80 (m, 6″-CH_2), 3.48 and 3.94 (2m, OCH_2 of THP), 3.72 and 3.78 (2d, J = 10.0 Hz, 17″α-CH), 3.89 (s, $COOCH_3$), 4.62 and 4.72 (2m, CH of THP), 6.57 (d, J = 1.8 Hz, 4″-CH), 6.63 (d, J = 8.4 Hz, 2″-CH), 7.15 (m, 1″-CH), 7.63 (d, J = 1.4 Hz, 6-CH), 7.89 (s, 4-CH), 8.20 (d, J = 1.5 Hz, 2-CH), 8.71 (s, NH). LR-MS calculated for $C_{55}H_{87}N_2O_7Si$ [M + NH_4]$^+$ 915.6, found 915.8 *m*/*z*.

Methyl 3-{3′-*tert*-butoxycarbonylamino-5′-[13″-(3‴-(*tert*-butyldimethylsilyloxy)-17‴β-(tetrahydro-2H-pyran-2-yl-oxy)-estra-1‴,3‴,5‴(10‴)-trien-16‴β-yl)-tridecynyl]-phenyl}-propanoate (68)

Yellowish foam (263 mg, 74% yield). IR (film) ν: 3354 (NH, carbamate), 1732 (C=O, ester and carbamate). ^{1}H NMR (400 MHz, acetone-d_6) δ: 0.20 (s, $Si(CH_3)_2$), 0.82 and 0.86 (2s, 18‴-CH_3), 1.00 (s, $SiC(CH_3)_3$), 1.00 to 2.35 (CH and CH_2 of steroid skeleton and alkyl chain), 1.49 (s, $(CH_3)_3C$ of *N*-BOC), 2.42 (t, J = 6.9 Hz, CH_2–C≡C), 2.62 (t, J = 7.6 Hz, CH_2COOMe), 2.81 (m, 6‴-CH_2), 2.86 (t, J = 7.7 Hz, CH_2CH$_2$COOMe), 3.47 and 3.92 (2m, OCH_2 of THP), 3.63 (s, $COOCH_3$), 3.73 and 3.78 (2d, J = 10.0 Hz, 17‴α-CH), 4.63 and 4.72 (2m, CH of THP), 6.58 (s, 4‴-CH), 6.63 (d, J = 8.4 Hz, 2‴-CH), 6.92 (s, 6′-CH), 7.16 (m, 1‴-CH), 7.37 (s, 2′-CH), 7.54 (s, 4′-CH), 8.43 (s, NH). LR-MS calculated for $C_{57}H_{91}N_2O_7Si$ [M + NH_4]$^+$ 943.7, found 943.8 *m*/*z*.

Methyl 4-{3′-*tert*-butoxycarbonylamino-5′-[13″-(3‴-(*tert*-butyldimethylsilyloxy)-17‴β-(tetrahydro-2*H*-pyran-2-yl-oxy)-estra-1‴,3‴,5‴(10‴)-trien-16‴β-yl)-tridecynyl]-phenyl}-butanoate (69)

Yellowish viscous oil (238 mg, 66% yield). IR (film) ν: 3342 (NH, carbamate), 1734 (C=O, ester and carbamate). ^{1}H NMR (400 MHz, acetone-d_6) δ: 0.20 (s, $Si(CH_3)_2$), 0.82 and 0.86 (2s, 18‴-CH_3), 1.00 (s, $SiC(CH_3)_3$), 1.00 to 2.30 (CH and CH_2 of steroid skeleton, alkyl chain and CH_2CH$_2$COOMe), 1.49 (s, $(CH_3)_3C$ of *N*-BOC), 2.34 (t, J = 7.4 Hz, CH_2COOMe), 2.42 (t, J = 7.0 Hz, CH_2–C≡C), 2.60 (t, J = 7.6 Hz, CH_2CH$_2$CH$_2$COOMe), 2.81 (m, 6‴-CH_2), 3.46 and 3.91 (2m, OCH_2 of THP), 3.63 (s, $COOCH_3$), 3.73 and 3.79 (2d, J = 10.0 Hz, 17‴α-CH), 4.63 and 4.72 (2m, CH of THP), 6.58 (d, J = 2.2 Hz, 4‴-CH), 6.64 (dd, J_1 = 6.7 Hz, J_2 = 2.2 Hz, 2‴-CH), 6.89 (s, 6′-CH), 7.16 (m, 1‴-CH), 7.37 (s, 2′-CH), 7.53 (s, 4′-CH), 8.42 (s, NH). LR-MS calculated for $C_{58}H_{90}NO_7Si$ [M + H]$^+$ 940.6, found 940.4 *m*/*z*.

Methyl 2-{3′-[13″-(3‴-(*tert*-butyldimethylsilyloxy)-17‴β-(tetrahydro-2*H*-pyran-2-yl-oxy)-estra-1‴,3‴,5‴(10‴)-trien-16‴β-yl)-tridecynyl]-phenyl}-acetate (70)

Yellowish viscous oil (220 mg, 72% yield). IR (film) ν: 1742 (C=O, ester). ^{1}H NMR (400 MHz, acetone-d_6) δ: 0.21 (s, $Si(CH_3)_2$), 0.82 and 0.86 (2s, 18‴-CH_3), 1.00 (s, $SiC(CH_3)_3$), 1.00 to 2.35 (CH and CH_2 of steroid skeleton and alkyl chain), 2.43 (t, J = 6.9 Hz, CH_2–C≡C), 2.81 (m, 6‴-CH_2), 3.47 and 3.92 (2m, OCH_2 of THP), 3.66 (s, CH_2COOCH_3), 3.74 and 3.79 (2d, J = 10.0 Hz, 17‴α-CH), 4.63 and 4.73 (2m, CH of THP), 6.58 (s, 4‴-CH), 6.64 (d, J = 8.4 Hz, 2‴-CH), 7.15 (m, 1‴-CH), 7.30 (m, 2′-CH, 4′-CH, 5′-CH and 6′-CH). LR-MS calculated for $C_{51}H_{80}N_2O_5Si$ [M + NH_4]$^+$ 814.6, found 814.8 *m*/*z*.

3-[13′-(3″-(*tert*-butyldimethylsilyloxy)-17″β-(tetrahydro-2H-pyran-2-yl-oxy)-estra-1″,3″,5″(10″)-trien-16″β-yl)-tridecynyl]-aniline (71)

Yellowish viscous oil (151 mg, 71% yield). IR (film) ν: 3460 and 3354 (NH_2). ^{1}H NMR (400 MHz, acetone-d_6) δ: 0.21 (s, $Si(CH_3)_2$), 0.82 and 0.86 (2s, 18″-CH_3), 1.00 (s, $SiC(CH_3)_3$), 1.00 to 2.35 (CH and CH_2 of steroid skeleton and alkyl chain), 2.39 (t, J = 6.9 Hz, CH_2–C≡C), 2.81 (m, 6″-CH_2), 3.49 and 3.92 (2m, OCH_2 of THP), 3.74 and 3.79 (2d, J = 9.7 Hz, 17″α-CH), 4.69 (m, CH of THP and NH_2), 6.58 (d, J = 2.1 Hz, 4″-CH), 6.62 (m, 2″-CH, 4-CH and 6-CH), 6.71 (d, J = 1.7 Hz, 2-CH), 7.00 (t, J = 7.8 Hz, 5-CH) 7.16 (m, 1″-CH). LR-MS calculated for $C_{48}H_{74}NO_3Si$ [M + H]$^+$ 740.5, found 740.6 *m*/*z*.

General procedure to synthesize 72–75

The same procedure described above for the preparation of **12** was used without modification except that 15% *w*/*w* of 10% Pd/C was used instead of 20% *w*/*w* in the hydrogenation step. The salt product (NH_2·HCl) was not observed for compounds **72**–**75**.

Methyl 3-amino-5-[13′-(3″, 17″β- dihydroxy-estra-1″,3″,5″(10″)-trien-16″β-yl)-tridecyl]-benzoate (72)

White solid (98 mg, 63% yield for two steps). IR (film) ν: 3368 (OH and NH_2), 1704 (C=O, ester). ^{1}H NMR (400 MHz, acetone-d_6) δ: 0.79 (s, 18″-CH_3), 0.95 to 2.35 (CH and CH_2 of steroid skeleton and alkyl chain), 2.54 (t, J = 7.5 Hz, 1′-CH_2), 2.78 (m, 6″-CH_2), 3.56 (d, J = 5.4 Hz, 17″βOH), 3.74 (dd, J_1 = 9.8 Hz, J_2 = 5.5 Hz, 17″α-CH), 3.82 (s, $COOCH_3$), 4.84 (s, NH_2), 6.54 (d, J = 2.5 Hz, 4″-CH), 6.60 (dd, J_1 = 8.4 Hz, J_2 = 2.6 Hz, 2″-CH), 6.77 (s, 4-CH), 7.13 (m, 1″-CH, 2-CH and 6-CH), 7.97 (s, 3″-OH). ^{13}C NMR (100 MHz, acetone-d_6) δ: 12.9, 27.1, 28.2, 29.1 to 30.2 (9C under solvent peaks), 30.3, 30.6, 32.0, 32.6, 33.2, 36.3, 38.5, 39.3, 41.2, 44.7, 44.8, 49.4, 51.8, 82.1, 113.2, 113.4, 115.8, 118.5, 119.4, 126.9, 131.6, 132.0, 138.3, 144.5, 149.3, 155.7, 167.6. LR-MS calculated for $C_{39}H_{58}NO_4$ [M + H]$^+$ 604.4, found 604.6 *m*/*z*.

Methyl 3-{3′-amino-5′-[13″-(3‴, 17‴β- dihydroxy-estra-1‴,3‴,5‴(10‴)-trien-16‴β-yl)-tridecyl]-phenyl}-propanoate (73)

Yellowish viscous oil (97 mg, 63% yield for two steps). IR (film) ν: 3366 (OH and NH_2), 1734 (C=O, ester). ^{1}H NMR (400 MHz, acetone-d_6) δ: 0.80 (s, 18‴-CH_3), 0.95 to 2.35 (CH and CH_2 of steroid skeleton and alkyl chain), 2.44 (t, J = 7.5 Hz, 1″-CH_2), 2.55 (t, J = 7.8 Hz, CH_2COOMe), 2.76 (m, 6‴-CH_2, CH_2CH$_2$COOMe), 3.54 (d, J = 5.4 Hz, 17‴β-OH), 3.62 (s, $COOCH_3$), 3.73 (dd, J_1 = 9.8 Hz, J_2 = 5.6 Hz, 17‴α-CH), 4.46 (s, NH_2), 6.32 (s, 6′-CH), 6.35 (s, 2′-CH and 4′-CH), 6.54 (d, J = 2.4 Hz, 4‴-CH), 6.60 (dd, J_1 = 8.4 Hz, J_2 = 2.6 Hz, 2‴-CH), 7.11 (d, J = 8.4 Hz, 1‴-

CH), 7.96 (s, 3‴-OH). ^{13}C NMR (100 MHz, acetone-d_6) δ: 12.9, 27.1, 28.2, 29.1 to 30.2 (8C under solvent peaks), 30.3, 30.5, 30.6, 31.5, 32.1, 32.5, 33.2, 36.1, 36.5, 38.6, 39.4, 41.2, 44.7, 44.8, 49.4, 51.4, 82.1, 112.5, 113.2, 113.4, 115.8, 117.7, 126.8, 132.0, 138.3, 142.0, 144.2, 149.1, 155.7, 173.8. LR-MS calculated for $C_{41}H_{62}NO_4$ [M + H]$^+$ 632.5, found 632.6 *m*/*z*.

Methyl 4-{3′-amino-5′-[13″-(3‴, 17‴β- dihydroxy-estra-1‴,3‴,5‴(10‴)-trien-16‴β-yl)-tridecyl]-phenyl}-butanoate (74)

Yellowish viscous oil (81 mg, 64% yield for two steps). IR (film) ν: 3377 (OH and NH_2), 1732 (C=O, ester). ^{1}H NMR (400 MHz, acetone-d_6) δ: 0.80 (s, 18‴-CH_3), 0.95 to 2.35 (CH and CH_2 of steroid skeleton, alkyl chain and CH_2CH$_2$COOMe), 2.32 (m, CH_2COOMe), 2.46 (m, 1″-CH_2), 2.58 (m, *J* = 7.8 Hz, CH_2CH$_2$CH$_2$COOMe), 2.78 (m, 6‴-CH_2), 3.56 (m, 17‴β-OH), 3.62 (s, $COOCH_3$), 3.73 (dd, J_1 = 9.8 Hz, J_2 = 5.9 Hz, 17‴α-CH), 4.45 (s, NH_2), 6.33 (m, 2′-CH, 4′-CH and 6′-CH), 6.54 (d, *J* = 2.2 Hz, 4‴-CH), 6.59 (d, *J* = 8.4 Hz, 2‴-CH), 7.11 (d, *J* = 8.5 Hz, 1‴-CH), 7.97 (s, 3‴-OH). ^{13}C NMR (75 MHz, acetone-d_6) δ: 12.9, 27.0, 27.2, 28.2, 28.9, 29.1 to 30.2 (7C under solvent peaks), 30.3, 30.4, 30.6, 32.1, 32.5, 33.2, 33.5, 35.6, 36.5, 38.5, 39.3, 41.1, 44.8 (2×), 49.4, 51.3, 82.1, 112.7, 113.0, 113.3, 115.7, 118.0, 126.8, 131.9, 138.2, 142.8, 144.0, 149.0, 155.7, 173.8. LR-MS calculated for $C_{42}H_{64}NO_4$ [M + H]$^+$ 646.5, found 646.3 *m*/*z*.

Methyl 2-{3′-[13″-(3‴, 17‴β- dihydroxy-estra-1‴,3‴,5‴(10‴)-trien-16‴β-yl)-tridecyl]-phenyl}-acetate (75)

The deprotection step was carried out in 2 h instead of 16 h. Purification by flash chromatography (hexanes/EtOAc, 8:2) afforded **75** (105 mg, 75% yield for two steps) as a white foam. IR (film) ν: 3400 (OH), 1732 (C=O, ester). ^{1}H NMR (400 MHz, acetone-d_6) δ: 0.80 (s, 18‴-CH_3), 0.95 to 2.35 (CH and CH_2 of steroid skeleton and alkyl chain), 2.61 (t, *J* = 7.6 Hz, 1″-CH_2), 2.78 (m, 6‴-CH_2), 3.55 (d, *J* = 5.4 Hz, 17‴β-OH), 3.62 (s, CH_2COOCH$_3$), 3.65 (s, $COOCH_3$) 3.73 (dd, J_1 = 9.7 Hz, J_2 = 5.6 Hz 17‴α-CH), 6.54 (d, *J* = 2.4 Hz, 4‴-CH), 6.60 (dd, J_1 = 8.4 Hz, J_2 = 2.6 Hz, 2‴-CH), 7.12 (m, 1‴-CH, 2′-CH, 4′-CH and 6′-CH), 7.23 (t, *J* = 7.4 Hz, 5′-CH), 7.97 (s, 3‴-OH). ^{13}C NMR (75 MHz, acetone-d_6) δ: 12.9, 27.0, 28.2, 28.9, 29.1 to 30.1 (8C under solvent peaks), 30.4, 30.6, 32.1, 32.5, 33.2, 36.2, 38.5, 39.3, 41.1, 41.2, 44.8 (2×), 49.4, 51.7, 82.1, 113.3, 115.7, 126.8, 127.2, 127.5, 128.9, 130.0, 131.9, 135.1, 138.2, 143.6, 155.7, 172.1. LR-MS calculated for $C_{40}H_{62}NO_4$ [M+NH$_4$]$^+$ 620.5, found 620.6 *m*/*z*.

General procedure to synthesize 14–17

To a solution of esters **72**–**75** (40–68 mg, 0.066–0.113 mmol) in acetone (2.0–3.5 mL) was added LiOH (1 mol/L in H_2O, 2.0–3.5 mL). The mixture was refluxed for 1 h and quenched by addition of an aqueous solution of HCl (1 N) until it reached pH 7. Then, a saturated $NaHCO_3$ aqueous solution was added, and extraction was performed with EtOAc. The organic phase was washed with brine, dried over $MgSO_4$, filtered, and evaporated to dryness. The crude product was purified by flash chromatography (DCM/MeOH, 97:3 to 90:10) to provide carboxylic acids **14**–**17** (26–44 mg, 66%–78% yield).

3-amino-5-[13′-(3″,17″β-dihydroxy-estra-1″,3″,5″(10″)-trien-16″β-yl)-tridecyl]-benzoic acid (14)

Yellowish foam (26 mg, 66% yield). IR (KBr) ν: 3600–2300 (OH, carboxylic acid), 3415 (OH and NH_2), 1694 (C=O, carboxylic acid). ^{1}H NMR (400 MHz, DMSO-d_6) δ: 0.65 (s, 18″-CH_3), 0.80 to 2.25 (CH and CH_2 of steroid skeleton and alkyl chain), 2.45 (t, *J* = 7.4 Hz, 1′-CH_2), 2.69 (m, 6″-CH_2), 3.55 (d, J_1 = 9.4 Hz, 17″α-CH), 4.39 (s_{br}, 17″β-OH), 5.21 (s_{br}, NH_2), 6.43 (d, *J* = 2.2 Hz, 4″-CH), 6.50 (dd, J_1 = 8.3 Hz, J_2 = 2.4 Hz, 2″-CH), 6.58 (s, 4-CH), 6.92 (s, 2-CH), 6.98 (d, *J* = 1.7 Hz, 6-CH), 7.03 (d, *J* = 8.5 Hz, 1″-CH), 9.03 (s_{br}, COOH). ^{13}C NMR (75 MHz, DMSO-d_6) δ: 12.7, 26.1, 27.2, 28.4, 28.7, 28.9, 29.1 (7×), 29.5, 30.9, 31.7, 32.3, 35.2, 37.5, 38.2, 38.7 to 40.3 (1C under solvent peaks), 43.6, 43.7, 48.2, 80.5, 112.3, 112.7, 114.9, 116.9, 117.9, 126.0, 130.5, 131.6, 137.2, 142.9, 148.7, 154.9, 168.1. HR-MS calculated for $C_{38}H_{56}NO_4$ [M + H]$^+$ 590.42039, found 590.42017 *m*/*z*.

3-{3′-amino-5′-[13″-(3‴,17‴β-dihydroxy-estra-1‴,3‴,5‴(10‴)-trien-16‴β-yl)-tridecyl]-phenyl}-propanoic acid (15)

Yellowish foam (42 mg, 78% yield). IR (KBr) ν: 3600–2400 (OH, carboxylic acid), 3378 (OH and NH_2), 1708 (C=O, carboxylic acid). ^{1}H NMR (400 MHz, DMSO-d_6) δ: 0.65 (s, 18‴-CH_3), 0.80 to 2.30 (CH and CH_2 of steroid skeleton and alkyl chain), 2.35 (t, *J* = 7.5 Hz, 1″-CH_2), 2.42 (t, *J* = 7.9 Hz, CH_2COOH), 2.61 (t, *J* = 7.5 Hz, CH_2CH$_2$COOH), 2.70 (m, 6‴-CH_2), 3.55 (d, J_1 = 9.5 Hz, 17‴α-CH), 4.85 (s_{br}, NH_2), 6.18 (s, 6-CH), 6.20 (s, 2′-CH and 4′-CH), 6.43 (d, *J* = 2.2 Hz, 4‴-CH), 6.49 (dd, J_1 = 8.4 Hz, J_2 = 2.4 Hz, 2‴-CH), 7.03 (d, *J* = 8.5 Hz, 1‴-CH). ^{13}C NMR (75 MHz, DMSO-d_6) δ: 12.7, 26.1, 27.2, 28.3, 28.8, 29.0, 29.1 (7×), 29.5, 30.6, 31.0, 31.7, 32.3, 35.4, 35.6, 37.5, 38.2, 38.7 to 40.3 (1C under solvent peaks), 43.6 (2×), 48.2, 80.5, 111.3, 111.8, 112.7, 114.9, 116.0, 126.0, 130.5, 137.1, 141.2, 142.8, 148.4, 154.9, 174.0. HR-MS calculated for $C_{40}H_{60}NO_4$ [M + H]$^+$ 618.45169, found 618.45148 *m*/*z*.

4-{3′-amino-5′-[13″-(3‴,17‴β-dihydroxy-estra-1‴,3‴,5‴(10‴)-trien-16‴β-yl)-tridecyl]-phenyl}-butanoic acid (16)

Yellowish foam (43 mg, 66% yield). IR (KBr) ν: 3600–2300 (OH, carboxylic acid), 3384 (OH and NH_2), 1707 (C=O, carboxylic acid). ^{1}H NMR (400 MHz, DMSO-d_6) δ: 0.65 (s, 18‴-CH_3), 0.80 to 2.10 (CH and CH_2 of steroid skeleton, alkyl chain and CH_2CH$_2$COOH), 2.18 (t, *J* = 7.3 Hz, CH_2COOH), 2.36 (m, 1″-CH_2, CH_2CH$_2$CH$_2$COOH), 2.69 (m, 6‴-CH_2), 3.55 (d, J_1 = 9.5 Hz, 17‴α-CH), 4.41 (s_{br}, 17″β-OH), 4.87 (s_{br}, NH_2), 6.14 (s, 6′-CH), 6.19 (s, 2′-CH and 4′-CH), 6.43 (d, *J* = 2.2 Hz, 4‴-CH), 6.50 (dd, J_1 = 8.3 Hz, J_2 = 2.3 Hz, 2‴-CH), 7.03 (d, *J* = 8.5 Hz, 1‴-CH). ^{13}C NMR (100 MHz, DMSO-d_6) δ: 12.7, 26.1, 26.3, 27.2, 28.4, 28.8, 29.0, 29.1 (5×), 29.2, 29.3, 29.5, 31.0, 31.8, 32.3, 33.2, 34.7, 35.4, 37.6, 38.2, 38.9 to 40.2 (1C under solvent peaks), 43.6, 43.7, 48.2, 80.5, 111.5, 111.7, 112.7, 115.0, 116.4, 126.1, 130.6, 137.2, 141.9, 142.7, 148.5,

154.9, 174.5. HR-MS calculated for $C_{41}H_{62}NO_4$ [M + H]$^+$ 632.46734, found 632.46672 *m/z*.

2-{3′-[13″-(3‴,17‴β-dihydroxy-estra-1‴,3‴,5‴(10‴)-trien-16‴β-yl)-tridecyl]-phenyl}-acetic acid (17)

White gummy solid (44 mg, 66% yield). IR (KBr) ν: 3600−2400 (OH, carboxylic acid), 3400 (OH), 1708 (C=O, carboxylic acid). ^{1}H NMR (400 MHz, DMSO-d_6) δ: 0.65 (s, 18‴-CH_3), 0.80 to 2.30 (CH and CH_2 of steroid skeleton and alkyl chain), 2.51 (m, 1″-CH_2 under solvent peaks), 2.70 (m, 6‴-CH_2), 3.50 (s, CH_2COOH), 3.55 (d, J_1 = 9.5 Hz, 17‴α-CH), 6.43 (d, J = 2.3 Hz, 4‴-CH), 6.50 (dd, J_1 = 8.4 Hz, J_2 = 2.4 Hz, 2‴-CH), 7.06 (m, 1‴-CH, 2′-CH, 4′-CH and 6′-CH), 7.19 (t, J = 8.0 Hz, 5′-CH). ^{13}C NMR (75 MHz, DMSO-d_6) δ: 12.7, 26.1, 27.2, 28.3, 28.7, 28.9, 29.0 (4×), 29.1, 29.2, 29.5, 29.6, 31.1, 31.7, 32.3, 35.1, 37.5, 38.2, 38.7 to 40.3 (1C under solvent peaks), 41.0, 43.59, 43.63, 48.2, 80.5, 112.7, 114.9, 126.0, 126.4, 126.7, 128.1, 129.3, 130.5, 135.1, 137.1, 142.2, 154.9, 172.8. HR-MS calculated for $C_{39}H_{57}O_4$ [M + H]$^+$ 589.4179, found 589.4202 *m/z*.

Synthesis of 3-[13′-(3″, 17″β- dihydroxy-estra-1″,3″,5″(10″)-trien-16″β-yl)-tridecyl]-aniline (18)

Compound **71** (133 mg, 0.180 mmol) was dissolved in a minimum amount of DCM (~0.5 mL). Then, a solution of concentrated HCl in MeOH (5% *v*/*v*, 3.6 mL) was added. The mixture was stirred for 1 h at room temperature. The reaction was quenched by addition of H_2O, followed by evaporation of MeOH. Then, a saturated solution of $NaHCO_3$ was added, and extraction was performed with EtOAc. The organic phase was washed with brine, dried over $MgSO_4$, filtered, and evaporated to dryness. Purification by flash chromatography (hexanes/EtOAc, 8:2 to 7:3) afforded the deprotected product (79 mg, 81%) as a white foam. This compound was then hydrogenated, using the hydrogenation procedure described previously for the synthesis of **12**, except that 15% *w*/*w* of 10% Pd/C were used instead of 20% *w*/*w*, to afford **18** (49 mg, 67% yield) as a white foam. IR (film) ν: 3366 (OH and NH_2). ^{1}H NMR (400 MHz, acetone-d_6) δ: 0.80 (s, 18″-CH_3), 0.95 to 2.35 (CH and CH_2 of steroid skeleton and alkyl chain), 2.47 (t, J = 7.5 Hz, 1′-CH_2), 2.78 (m, 6″-CH_2), 3.58 (d, J = 5.4 Hz, 17″β-OH), 3.73 (dd, J_1 = 9.7 Hz, J_2 = 5.4 Hz, 17″α-CH), 4.50 (s, NH_2), 6.43 (d, J = 7.4 Hz, 6-CH), 6.47 (dd, J_1 = 7.9 Hz, J_2 = 1.4 Hz, 4-CH), 6.52 (s, 2-CH), 6.54 (d, J = 2.5 Hz, 4″-CH), 6.60 (dd, J_1 = 8.4 Hz, J_2 = 2.6 Hz, 2″-CH), 6.95 (t, J = 7.7 Hz, 5-CH), 7.11 (d, J = 8.4 Hz, 1″-CH), 8.00 (s, 3″-OH). ^{13}C NMR (75 MHz, acetone-d_6) δ: 12.9, 27.0, 28.1, 28.9, 29.1 to 30.2 (8C under solvent peaks), 30.4, 30.6, 32.1, 32.5, 33.1, 36.4, 38.5, 39.3, 41.1, 44.7 (2×), 49.3, 82.1, 112.4, 113.3, 115.1, 115.7, 117.5, 126.8, 129.4, 131.9, 138.2, 144.0, 148.9, 155.7. HR-MS calculated for $C_{37}H_{56}NO_2$ [M + H]$^+$ 546.43056, found 546.43092 *m/z*.

Synthesis of monosubstrate 79

Synthesis of methyl 2-[3′-(6″-hydroxyhex-1″-ynyl)-phenyl]-acetate (77)

The Sonogashira coupling procedure described previously[30] for the synthesis of **49** was used without modification except that 2 equiv. of **76** were used instead of 1.2 equiv., and the reaction mixture was stirred for 1 h at 40 °C instead of 3 h. Purification by flash chromatography (hexanes/EtOAc, 7:3) gained **77** (156 mg, 88% yield) as colourless oil. IR (film) ν: 3390 (OH), 1732 (C=O, ester). ^{1}H NMR (400 MHz, acetone-d_6) δ: 1.69 (m, 2 × CH_2), 2.46 (m, CH_2−C≡C), 3.54 (m, OH), 3.61 (m, CH_2OH), 3.66 (s, CH_2COOCH_3), 7.29 (m, 2′-CH, 4′-CH, 5′-CH, and 6′-CH). ^{13}C NMR (100 MHz, acetone-d_6) δ: 19.5, 26.0, 32.8, 40.8, 52.0, 61.9, 81.1, 91.0, 125.0, 129.2, 129.5, 130.6, 133.1, 135.7, 171.5. LR-MS calculated for $C_{15}H_{19}O_3$ [M + H]$^+$ 247.1, found 247.1 *m/z*.

Synthesis of 2-[3′-(6″-hydroxyhex-1″-ynyl)-phenyl]-acetic acid (78)

The procedure that we described previously[30] for the synthesis of **5** was used without modification except that the reaction mixture was stirred at reflux for 4 h instead of 5 h. Purification by flash chromatography (DCM/MeOH, 97:3 to 70:30) afforded **78** (128 mg, 94% yield) as a white viscous oil. IR (film) ν: 3700−2200 (OH, carboxylic acid), 3322 (OH), 3420 (OH), 1711 (C=O, carboxylic acid). ^{1}H NMR (400 MHz, $CDCl_3$ and few drops of MeOH-d_4) δ: 1.67 (m, 2 × CH_2), 2.41 (t, J = 6.7 Hz, CH_2−C≡C), 3.54 (s, CH_2COOH), 3.64 (t, J = 6.1 Hz, CH_2OH), 7.22 (m, 2′-CH, 4′-CH, 5′-CH, and 6′-CH). ^{13}C NMR (100 MHz, acetone-d_6) δ: 19.1, 24.9, 31.7, 40.9, 62.1, 80.7, 90.1, 124.1, 128.4, 128.6, 130.1, 132.4, 134.2, 174.2. LR-MS calculated for $C_{14}H_{15}O_3$ [M − H]$^-$ 231.1, found 231.0 *m/z*.

Synthesis of 2-[3′-(6″-hydroxyhexyl)-phenyl]-acetic acid (79)

The general hydrogenation procedure described for the synthesis of **13** was used without modification. Purification by flash chromatography (DCM/MeOH, 95:5 to 70:30) provided **79** (72 mg, 75% yield) as a white solid. IR (film) ν: 3700−2400 (OH, carboxylic acid), 3398 (OH), 1711 (C=O, carboxylic acid). ^{1}H NMR (400 MHz, $CDCl_3$ and few drops of MeOH-d_4) δ: 1.32 (m, 2 × CH_2), 1.52 (t, J = 6.9 Hz. CH_2CH$_2$OH), 1.60 (t, J = 7.1 Hz, 5″-CH_2), 2.58 (t, J = 7.6 Hz, 6″-CH_2), 3.57 (t, J = 6.6 Hz, CH_2OH), 3.58 (s, CH_2COOH), 7.11 (m, 2′-CH, 4′-CH, and 6′-CH), 7.22 (t, J = 7.4 Hz, 5′-CH). ^{13}C NMR (100 MHz, acetone-d_6) δ: 25.4, 28.8, 31.1, 32.4, 35.6, 41.1, 62.7, 126.4, 127.2, 128.4, 129.4, 133.8, 143.0, 175.2. HR-MS calculated for $C_{14}H_{21}O_3$ [M + H]$^+$ 237.14852, found 237.14839 *m/z*.

Enzymatic assay: inhibition of 17β-HSD1 in homogenated cells

This enzymatic assay was performed as previously described.[37] Briefly, HEK-293 cells transfected with a 17β-HSD1 cDNA fragment were sonicated in 50 mmol/L sodium phosphate buffer (pH 7.4), containing 20% glycerol and 1 mmol/L EDTA to obtain cellular fragmentation. The cytosol fraction containing the enzyme was isolated as the supernatant after centrifugation (100 000*g*, 5 min, 4 °C). The enzymatic reaction was performed at 37 °C for 2 h in 1 mL of a solution, which included 870 μL of 50 mmol/L sodium phosphate buffer (pH 7.4, 20% glycerol and 1 mmol/L EDTA), 100 μL of 1 mmol/L NADH in phosphate buffer, 10 μL of 10 μmol/L [^{14}C]-estrone in ethanol (54 mCi/mmol, American Radiolabeled Chemicals Inc., St-Louis, MO, USA),

10 μL of the indicated inhibitor dissolved in ethanol, and 10 μL of diluted enzymatic source in phosphate buffer. Each inhibitor was assessed in duplicate (Table 1) or in triplicate (Table 2). To obtain the IC_{50} values, each inhibitor was assessed in duplicate at 0.001, 0.01, 0.03, 0.06, 0.1, 0.3, 0.6, 1, 10, and 30 μmol/L. Afterward, radiolabeled steroids were extracted twice from the reaction mixture by 1 mL of diethyl ether. The organic phases were pooled and evaporated to dryness with nitrogen. Residues were dissolved in 50 μL of DCM, applied on silica gel 60 F_{254} thin-layer chromatography plates (EMD Chemicals Inc., Gibbstown, NJ, USA), and eluted with a mixture of toluene/acetone (4:1). Substrate ([^{14}C]-E_1) and metabolite ([^{14}C]-E_2) were identified by comparison with reference steroids and quantified using the Storm 860 system (Molecular Dynamics, Sunnyvale, CA, USA). The percentage of transformation of [^{14}C]-E_1 into [^{14}C]-E_2 was calculated as follows: % transformation = $100 \times [[^{14}C]\text{-}E_2 / ([^{14}C]\text{-}E_2 + [^{14}C]\text{-}E_1)]$, and subsequently, % inhibition = $100 \times$ [(% transformation without inhibitor − % transformation with inhibitor) / % transformation without inhibitor]. The IC_{50} values were calculated using an unweighted iterative least-squares method for four-parameters logistic curve fitting (DE_{50} program, CHUL Research Center, Québec, QC, Canada).

Supplementary data

Supplementary data (^{1}H NMR spectra and ^{13}C NMR spectra of compounds tested as inhibitors of 17β-HSD1) for this article are available on the journal Web site (canjchem.nrc.ca) or may be purchased from the Depository of Unpublished Data, Document Delivery, CISTI, National Research Council Canada, Ottawa, ON K1A 0R6, Canada. DUD 3985. For more information on obtaining material, refer to cisti-icist.nrc-cnrc.gc.ca/cms/unpub_e.shtml.

Acknowledgements

This work was supported by the Canadian Institutes of Health Research (CIHR) (D.P. for an operating grant, and M.B. for a scholarship). We thank Dr. Van Luu-The for providing HEK-293 cells overexpressing 17β-HSD1. We are grateful to Fatima Kamal for chemical synthesis of intermediate compound **19** and to Julie Lefebvre for performing some of the enzymatic assays. We also thank Ms. Sylvie Méthot for careful reading of the manuscript.

References

(1) Langer, L. J.; Engel, L. L. *J. Biol. Chem.* **1958**, *233* (3), 583−588. PMID:13575417.

(2) Penning, T. M. *Endocr. Rev.* **1997**, *18* (3), 281−305. doi:10.1210/er.18.3.281. PMID:9183566.

(3) Labrie, F.; Luu-The, V.; Lin, S. X.; Labrie, C.; Simard, J.; Breton, R.; Bélanger, A. *Steroids* **1997**, *62* (1), 148−158. doi:10.1016/S0039-128X(96)00174-2. PMID:9029730.

(4) Luu-The, V. *J. Steroid Biochem. Mol. Biol.* **2001**, *76* (1-5), 143−151. doi:10.1016/S0960-0760(00)00155-2. PMID:11384872.

(5) Vihko, P.; Härkönen, P.; Soronen, P.; Törn, S.; Herrala, A.; Kurkela, R.; Pulkka, A.; Oduwole, O.; Isomaa, V. *Mol. Cell. Endocrinol.* **2004**, *215* (1-2), 83−88. doi:10.1016/j.mce.2003.11.021. PMID:15026178.

(6) Moeller, G.; Adamski, J. *Mol. Cell. Endocrinol.* **2006**, *248* (1-2), 47−55. doi:10.1016/j.mce.2005.11.031. PMID:16413960.

(7) Poirier, D. *Drug Dev. Res.* **2008**, *69* (6), 304−318. doi:10.1002/ddr.20263.

(8) Martel, C.; Rhéaume, E.; Takahashi, M.; Trudel, C.; Couët, J.; Luu-The, V.; Simard, J.; Labrie, F. *J. Steroid Biochem. Mol. Biol.* **1992**, *41* (3-8), 597−603. doi:10.1016/0960-0760(92)90390-5. PMID:1314080.

(9) Poirier, D.; Ciobanu, L. C.; Maltais, R. *Exp. Opin. Ther. Patents* **1999**, *9* (8), 1083−1099. doi:10.1517/13543776.9.8.1083.

(10) Hanson, S. R.; Best, M. D.; Wong, C. H. *Angew. Chem. Int. Ed.* **2004**, *43* (43), 5736−5763. doi:10.1002/anie.200300632.

(11) Reed, M. J.; Purohit, A.; Woo, L. W. L.; Newman, S. P.; Potter, B. V. L. *Endocr. Rev.* **2004**, *26* (2), 171−202. doi:10.1210/er.2004-0003. PMID:15561802.

(12) Vermeulen, A.; Deslypere, J. P.; Paridaens, R.; Leclercq, G.; Roy, F.; Heuson, J. C. *Eur. J. Cancer Clin. Oncol.* **1986**, *22* (4), 515−525. doi:10.1016/0277-5379(86)90121-5. PMID:3015631.

(13) Geisler, J.; Berntsen, H.; Lonning, P. E. *J. Steroid Biochem. Mol. Biol.* **2000**, *72* (5), 259−264. doi:10.1016/S0960-0760(00)00036-4. PMID:10822015.

(14) Miyoshi, Y.; Ando, A.; Shiba, E.; Taguchi, T.; Tamaki, Y.; Noguchi, S. *Int. J. Cancer* **2001**, *94* (5), 685−689. doi:10.1002/ijc.1525. PMID:11745463.

(15) Poirier, D. *Curr. Med. Chem.* **2003**, *10* (6), 453−477. PMID:12570693.

(16) Gobec, S.; Brozic, P.; Rizner, T. L. *Curr. Med. Chem.* **2008**, *15* (2), 137−150. doi:10.2174/092986708783330629. PMID:18220769.

(17) Day, J. M.; Tutill, H. J.; Purohit, A.; Reed, M. J. *Endocr. Relat. Cancer* **2008**, *15* (3), 665−692. doi:10.1677/ERC-08-0042. PMID:18541621.

(18) Santen, R. J. *Steroids* **2003**, *68* (7-8), 559−567. doi:10.1016/S0039-128X(03)00096-5. PMID:12957661.

(19) Briest, S.; Davidson, N. E. *Rev. Endocr. Metab. Disord.* **2007**, *8* (3), 215−228. doi:10.1007/s11154-007-9039-z. PMID:17486453.

(20) Li, J. J. *Aromatase inhibitors for breast cancer: exemestane (Aromasin), anastrazole (Arimidex) and letrozole (Femara)*; In *The art of drug synthesis*; Johnson, D.S. and Li, J.J., Eds.; Wiley: Hoboken, NJ, 2007; pp.31−38.

(21) Poirier, D.; Boivin, R. P.; Bérubé, M.; Lin, S.-X. *Synth. Commun.* **2003**, *33*, 3183−3191. doi:10.1081/SCC-120023440.

(22) Poirier, D.; Boivin, R. P.; Tremblay, M. R.; Bérubé, M.; Qiu, W.; Lin, S. X. *J. Med. Chem.* **2005**, *48* (26), 8134−8147. doi:10.1021/jm058235e. PMID:16366595.

(23) Qiu, W.; Campbell, R. L.; Gangloff, A.; Dupuis, P.; Boivin, R. P.; Tremblay, M. R.; Poirier, D.; Lin, S. X. *FASEB J.* **2002**, *16* (13), 1829−1831. PMID:12223444.

(24) Fournier, D.; Poirier, D.; Mazumdar, M.; Lin, S. X. *Eur. J. Med. Chem.* **2008**, *43* (11), 2298−2306. doi:10.1016/j.ejmech.2008.01.044. PMID:18372081.

(25) Lin, S. X.; Shi, R.; Qiu, W.; Azzi, A.; Zhu, D. W.; Dabbagh, H. A.; Zhou, M. *Mol. Cell. Endocrinol.* **2006**, *248* (1-2), 38−46. doi:10.1016/j.mce.2005.11.035. PMID:16480815.

(26) Connon, S. J.; Blechert, S. *Angew. Chem. Int. Ed.* **2003**, *42* (17), 1900−1923. doi:10.1002/anie.200200556.

(27) Tremblay, M. R.; Poirier, D. *J. Comb. Chem.* **2000**, *2*, 48−65.

(28) Bérubé, M.; Kamal, F.; Poirier, D. *Synthesis* **2006**, 3085−3091.

(29) Wang, Y.; Romo, D. *Org. Lett.* **2002**, *4* (19), 3231−3234. doi:10.1021/ol026438g. PMID:12227756.
(30) Bérubé, M.; Poirier, D. *Org. Lett.* **2004**, *6* (18), 3127−3130. doi:10.1021/ol048820u. PMID:15330604.
(31) Cornejo, A.; Fraile, J. M.; García, J. I.; García-Verdugo, E.; Gil, M. J.; Legarreta, G.; Luis, S. V.; Martínez-Merino, V.; Mayoral, J. A. *Org. Lett.* **2002**, *4* (22), 3927−3930. doi:10.1021/ol026787a. PMID:12599494.
(32) Miwa, K.; Aoyama, T.; Shioiri, T. *Synlett* **1994**, *1994* (02), 107−108. doi:10.1055/s-1994-22755.
(33) Nicolaou, K. C.; Dai, W. M.; Hong, Y. P.; Baldridge, K. K.; Siegel, J. S.; Tsay, S. C. *J. Am. Chem. Soc.* **1993**, *115* (18), 7944−7953. doi:10.1021/ja00071a003.
(34) Oza, V. B.; Corcoran, R. C. *J. Org. Chem.* **1995**, *60* (12), 3680−3684. doi:10.1021/jo00117a018.
(35) Auman, B. C.; Myers, T. L.; Higley, D. P. *J. Polym. Sci. Part Polym. Chem.* **1997**, *35* (12), 2441−2451. doi:10.1002/(SICI)1099-0518(19970915)35:12<2441::AID-POLA14>3.0.CO;2-7.
(36) Choi, K.; Hamilton, A. D. *J. Am. Chem. Soc.* **2001**, *123* (10), 2456−2457. doi:10.1021/ja005772+. PMID:11456908.
(37) Tremblay, M. R.; Lin, S. X.; Poirier, D. *Steroids* **2001**, *66* (11), 821−831. doi:10.1016/S0039-128X(01)00116-7. PMID:11576622.
(38) Mazza, C.; Breton, R.; Housset, D.; Fontecilla-Camps, J. C. *J. Biol. Chem.* **1998**, *273* (14), 8145−8152. doi:10.1074/jbc.273.14.8145. PMID:9525918.
(39) Sam, K. M.; Boivin, R. P.; Auger, S.; Poirier, D. *Bioorg. Med. Chem. Lett.* **1994**, *4* (17), 2129−2132. doi:10.1016/S0960-894X(01)80115-3.
(40) Bérubé, M.; Laplante, Y.; Poirier, D. *Med. Chem.* **2006**, *2* (4), 329−347. doi:10.2174/157340606777724086. PMID:16848745.

AWARD LECTURE / CONFÉRENCE D'HONNEUR

2008 Macromolecular Science and Engineering Division Award Lecture — Conjugated polymers: From micro-electronics to genomics

Mario Leclerc, Ahmed Najari, and Serge Beaupré

Abstract: Conjugated polymers have received a lot of attention, since they combine the best features of metals or semiconductors with those of synthetic polymers. For instance, solar cells based on poly(2,7-carbazole) derivatives have revealed power-conversion efficiencies up to 6%. This class of materials could lead to printable and flexible photovoltaic devices. Moreover, water-soluble luminescent polythiophenes have allowed the specific, rapid, and ultra-sensitive detection of unlabelled DNA, RNA, or proteins. This new optical detection mechanism is based on electrostatic interactions between a cationic polythiophene derivative and negatively charged oligonucleotides. This method makes now possible the rapid assessment of the identity of single nucleotide polymorphisms (SNPs), genes, and pathogens without the need for nucleic acid amplification.

Key words: conjugated polymers, plastic electronics, biosensors, polyfluorenes, polythiophenes, polycarbazoles.

Résumé : Les polymères conjugués suscitent beaucoup d'intérêt puisqu'ils combinent les propriétés des métaux ou des semiconducteurs à celles des polymères synthétiques. Par exemple, des piles solaires fabriquées à l'aide de dérivés du poly(2,7-carbazole) ont montré des efficacités de conversion énergétique de l'ordre de 6 %. Cette classe de matériaux pourrait donc conduire à la mise en place de dispositifs photovoltaïques flexibles et imprimables. Par ailleurs, des polythiophènes luminescents et solubles dans l'eau ont permis une détection rapide, spécifique, ultra-sensible et directe d'ADN, d'ARN ou de protéines. Ce nouveau mécanisme de détection optique utilise les interactions électrostatiques entre un dérivé cationique du polythiophène et les charges négatives de sondes à base d'oligonucléotides. Cette méthode rend maintenant possible l'identification rapide de mutations génétiques, de gènes spécifiques ou de pathogènes sans le recours d'amplification du matériel génomique.

Mots-clés : polymères conjugués, électronique plastique, biocapteurs, polyfluorènes, polythiophènes, polycarbazoles.

Introduction

In the field of micro-electronics and medicine, polymeric materials were traditionally used in applications such as packaging and electrical insulators. However, new opportunities emerged with the discovery of conducting polymers in 1977.[1] After more than 30 years of progress, these unusual polymeric materials can now be utilized as transparent antistatic coatings, modified electrodes, electrochromic windows, biosensors, transistors, light-emitting diodes, conducting photoresists, photovoltaic cells, and so forth.[2,3] The significance of this class of polymers has been outlined by the awarding of the 2000 Nobel Prize in Chemistry to the three scientists (H. Shirakawa, A.G. MacDiarmid, and A.J. Heeger) who pioneered this novel research field. This attribution of the Nobel Prize recognizes also indirectly a fruitful collaboration between two chemists and one physicist.

As often happens in science, the discovery of conducting polymers was accidental. A student of the Shirakawa's laboratory was working on Ziegler–Natta (1963 Nobel Prize in Chemistry) polymerization of acetylene. By accident, this student prepared a thousand times more concentrated catalyst than required and obtained a polyacetylene thin film, which looked like an aluminum foil instead of the usual dark, powdery material.[4] During a visit to the University of Tokyo, Prof. MacDiarmid (University of Pennsylvania) met Prof. Shirakawa and invited him to come to Philadelphia to investigate in more detail this new form of polyacetylene.[5] In collaboration with Prof. A.J. Heeger, this trio discovered that upon partial oxidation or reduction (so-called doping reaction), the conductivity of polyacetylene increases more than a billionfold (up to 100 S/cm).[6] Electrical conductivities up to 10^5 S/cm are obtained with some forms of polyacetylene. The delocalized electronic structure (alternation of single and double bonds) of polyacetylene (see Scheme 1A) is responsible for such good intrachain and interchain mobility

Received 9 April 2009. Accepted 21 May 2009. Published on the NRC Research Press Web site at canjchem.nrc.ca on 1 August 2009.

M. Leclerc,[1] A. Najari, and S. Beaupré. Canada Research Chair on Electroactive and Photoactive Polymers, Département de Chimie, Université Laval, Québec, QC G1V 0A6, Canada.

[1]Corresponding author (e-mail: Mario.Leclerc@chm.ulaval.ca).

Scheme 1. The chemical structure of polyacetylene (A), polypyrrole (B), polythiophene (C), polyaniline (D), poly(3-alkylthiophene)s (E), regioregular poly(3-alkythiophene)s (F), poly(3-alkoxy-4-methylthiophene)s (G), and poly(3,4-ethylenedioxythiophene) (H).

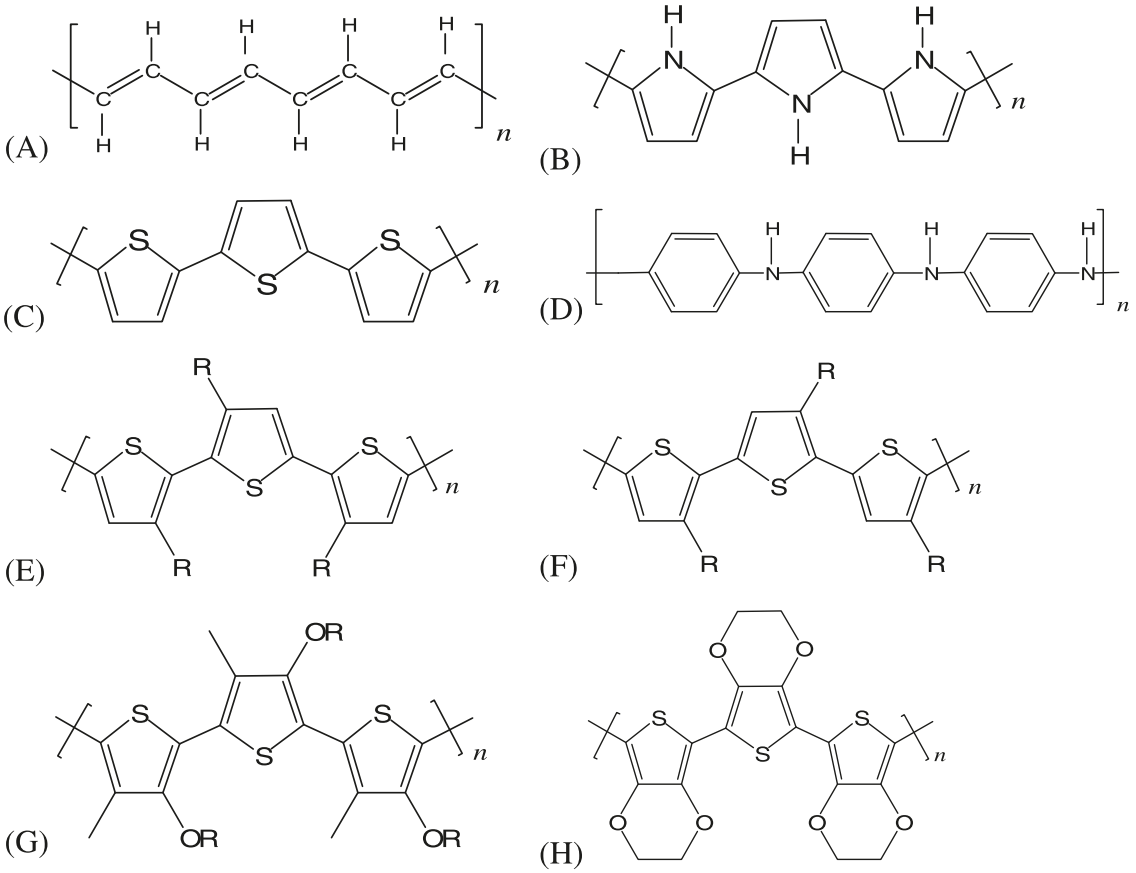

of the charge carriers (radical cations and dications) created upon doping. This delocalized (conjugated) structure is also responsible for strong absorption in the UV–visible range. Unfortunately, this first conducting polymer is difficult to process and unstable in presence of oxygen or water. Rapidly, chemists investigated the more stable, aromatic conjugated polymers. This paper will review advances in this research field together with some significant contributions from our laboratory.

Aromatic conducting polymers

In the beginning of the 1980s, a lot of studies were devoted to electropolymerized polypyrrole[7] (Scheme 1B), polythiophene[8] (Scheme 1C), and polyaniline[9] (Scheme 1D). This method has the advantage of being able to prepare thin films of these infusible and insoluble conjugated polymers in one step. However, the ultimate goal was and still is the development of polymeric materials that "combine" the electrical and optical properties of metals and semiconductors with the processing advantages and mechanical properties of commodity polymers. For this purpose, substituted conjugated polymers were prepared, since the unsubstituted parent polymers are not melt- or solution-processable owing to strong interchain interactions and chain stiffness. Experiments carried out on substituted polyacetylenes[10] and polyanilines[11] revealed that the presence of bulky substituents forces a twisting of the backbone that led to processable but poorly conjugated materials with reduced electrical properties. A breakthrough occurred with the synthesis of highly conjugated, conducting, and processable poly(3-alkylthiophene)s [12] (Scheme 1E).

Following these first studies on the synthesis and characterization of processable poly(3-alkylthiophene)s, it became quite clear that the synthesis of well-defined head-to-tail coupled (which should give the lowest steric hindrance from the side chains and, possibly, a more efficient three-dimensional packing) conjugated polymers should lead to a significant improvement in the performance of these polymeric materials.[13] Therefore, in attempts to bring more reliable synthetic procedures to the field of electronic materials, a variety of synthetic tools were utilized and allowed significant advances in this research field. These investigations have led to the discovery of new and interesting conjugated structures, such as well-defined regioregular poly(3-alkylthiophene)s [14] (Scheme 1F), poly(3-alkoxy-4-methylthiophenes)s [15] (Scheme 1G), and poly(3,4-ethylenedioxythiophene) (also called PEDOT)[16] (Scheme 1H). Up to now, regioregular poly(3-alkylthiophene)s exhibit the highest conductivities (up to 1000 S/cm) for processable conjugated polymers but alkoxy-substituted polythiophenes show the best compromise between processability, conductivity, and air-stability.[14,16,17]

Polymeric light-emitting diodes

In the 1990s, the focus shifted from the synthesis of metallic-like conductors to the design of stable semi-conducting poly-

Scheme 2. Schematic description of a polymer light-emitting diode (PLED).

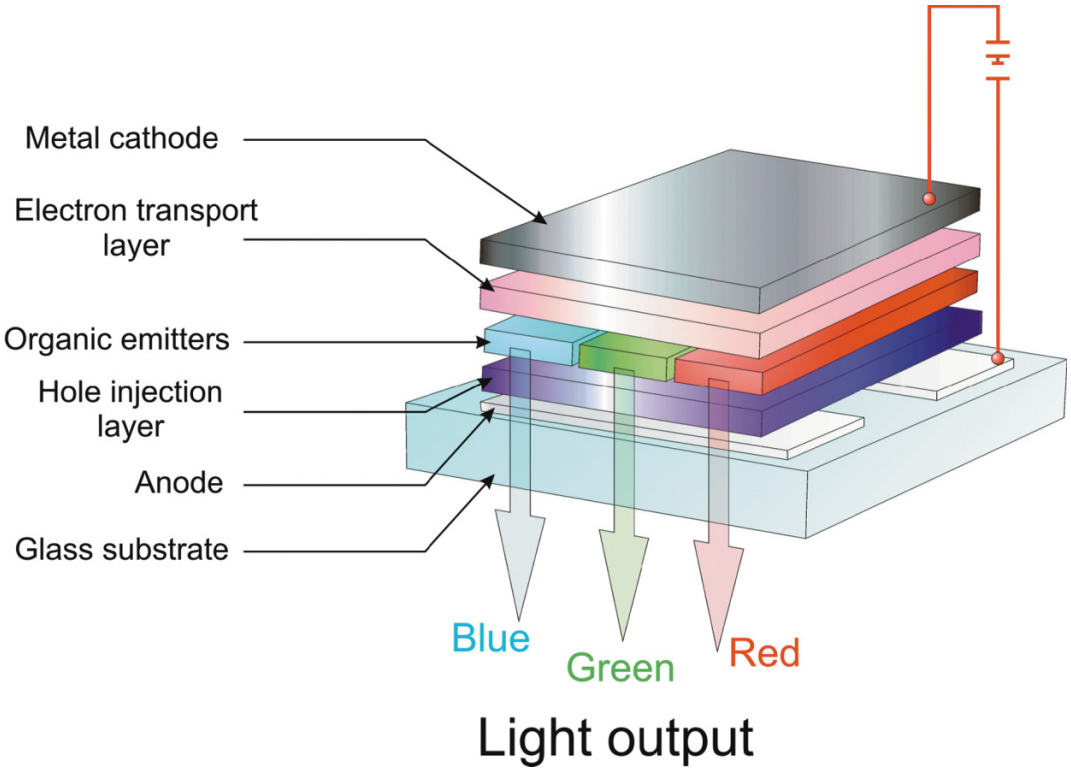

mers. This new driving force is based on the aim to set up the so-called plastic electronics where micro-electronic devices could be printed on flexible substrates. For instance, the last 15–20 years have witnessed the emergence of conjugated (undoped, semi-conducting) polymers in light-emitting diodes (PLEDs).[18] The basic structure of a polymeric light-emitting diode consists of a positive hole-injecting electrode (usually transparent) with a high work function such as ITO or a conducting polymer, a negative electron-injecting electrode with a low work function such as Al, In, Mg, or Ca, and the light-emitting polymer film sandwiched between these two electrodes. In this layered structure, the injected holes and electrons migrate across the polymer layer, combine to form excitons, which then decay with photon emission (see Scheme 2). Depending upon the chemical structure of the emissive polymer, different colors can be obtained.

Among all reported conjugated polymers, our synthetic procedures (based on Suzuki cross-coupling reactions, see Scheme 3) for the preparation of well-defined poly(2,7-fluorene) derivatives[19] rapidly received a lot of attention, since this class of polymeric materials can emit light ranging from blue to red.[20] However, blue-light-emitting poly(2,7-fluorene)s show some problems of stability, probably owing to an oxidative electro- and photo-degradation.[21] To try to solve this problem, we reported the first syntheses of poly(2,7-carbazole) derivatives.[22] Indeed, carbazole-based conjugated polymers exhibit many advantages: the nitrogen atom can be easily functionalized with a large variety of substituents to modulate the physical properties without increasing the steric hindrance near the backbone, and its fully aromatic configuration provides good chemical and environmental stabilities. Following our first reports, optimized

Scheme 3. Suzuki cross-coupling reaction for the synthesis of poly(2,7-fluorene) derivatives.

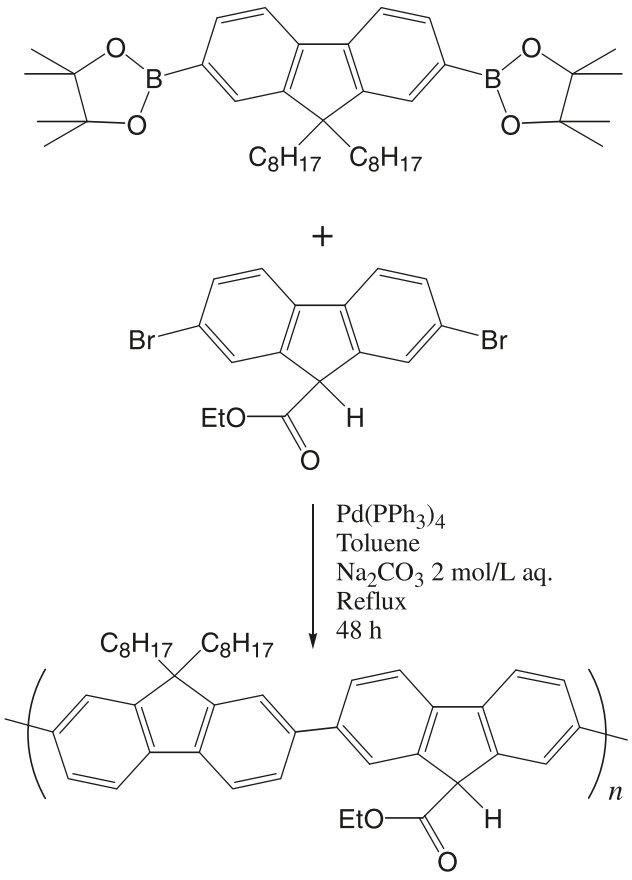

Scheme 4. Synthesis of a processable poly(2,7-carbazole) derivative.

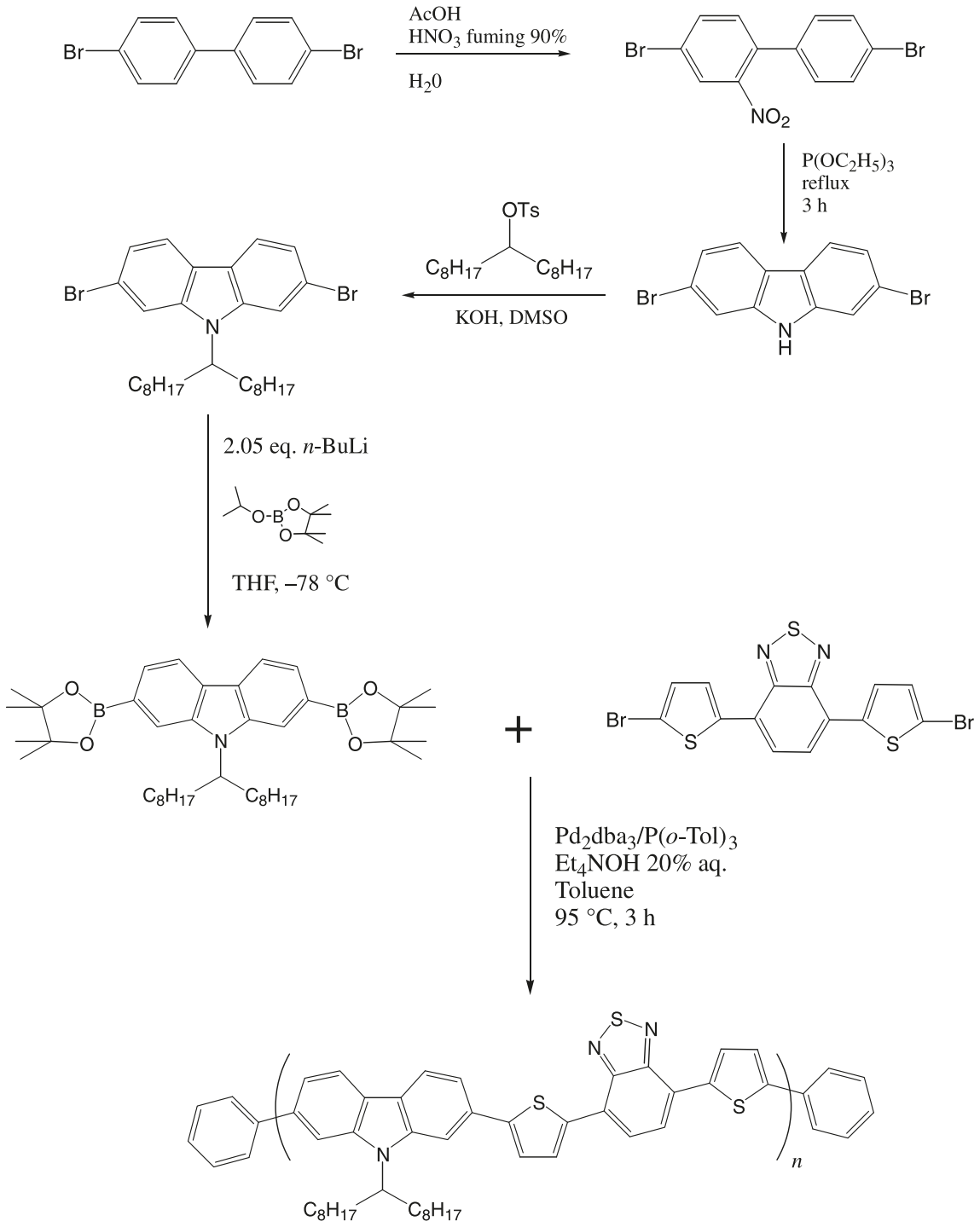

synthetic strategies have been reported to improve the simplicity and the efficiency of the preparation of such poly(2,7-carbazole) derivatives[23] (see Scheme 4). Unfortunately, PLEDs made of poly(2,7-carbazole)s generally suffered from improper balance of charge injection and charge transport. In other words, the hole mobility is favoured, and that limits the efficiencies of the resulting light-emitting diodes.[24] Therefore, despite some stability issues, poly(2,7-fluorene) derivatives remain the most widely-studied polymers for light-emitting applications.[25]

Polymeric photovoltaic cells

If one reverses the energy input, instead of a light-emitting diode, one obtains a photovoltaic device (Scheme 5). Interestingly, solar cells are becoming more and more attractive because they represent a green and renewable energy alternative to fossil energy and nuclear power. Along these lines, polymer bulk heterojunction (BHJ) solar cells based on composites of electron-donating and hole-transporting conjugated polymers and electron-accepting and electron-

Scheme 5. Schematic description of a bulk-heterojunction photovoltaic device.

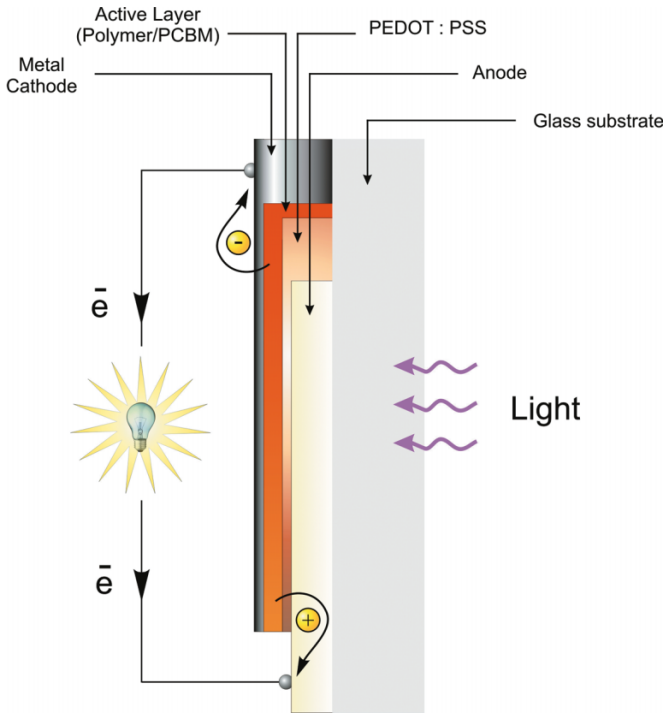

transporting fullerenes offer promise for the realization of a low-cost, printable, portable, and flexible renewable source of energy.[26] The fundamental BHJ concept involves self-assembly of nano-scale heterojunction by spontaneous phase separation of the polymeric donor and the fullerene acceptor (usually PCBM). During the past decade, research has mainly focused on regioregular poly(3-alkylthiophene)s, as the donor and power-conversion efficiencies about 5% were recently reported.[27] However, the performances of these polymers are somehow limited by their relatively large band gap and the limited possibilities to modulate their physical properties. Therefore, besides those recent advances, there is still a need for new polymeric materials to go beyond the 5% efficiency.

As mentioned above, poly(2,7-carbazole) derivatives exhibit good hole mobilities and should therefore be considered as promising candidates for photovoltaic applications. Among them, poly[*N*-9″-heptadecanyl-2,7-carbazole-*alt*-5,5-(4′,7′-di-2-thienyl-2′,1′,3′-benzothiadiazole)] (PCDTBT, see Scheme 4) has allowed to obtain a power-conversion efficiency up to 6%.[28] These remarkable results are partly explained by the optimized morphology of the active layer by which electron transfer and charge transport can be facilitated. Moreover, the synthetic flexibility of carbazole-containing conjugated copolymers should lead to an easy modulation of their electronic structures to better harvest the solar radiation. For instance, new low-band-gap poly(2,7-carbazole) derivatives have just been reported, and high power-conversion efficiencies are anticipated from these new polymeric materials.[29] Clearly, more efficient polymeric solar cells are foreseen in a near future. In addition, efficient polymeric solar cells mean high mobilities, and this research program should therefore also lead to highly efficient transistors.[30]

Scheme 6. Schematic description of conformational transition in polythiophenes.

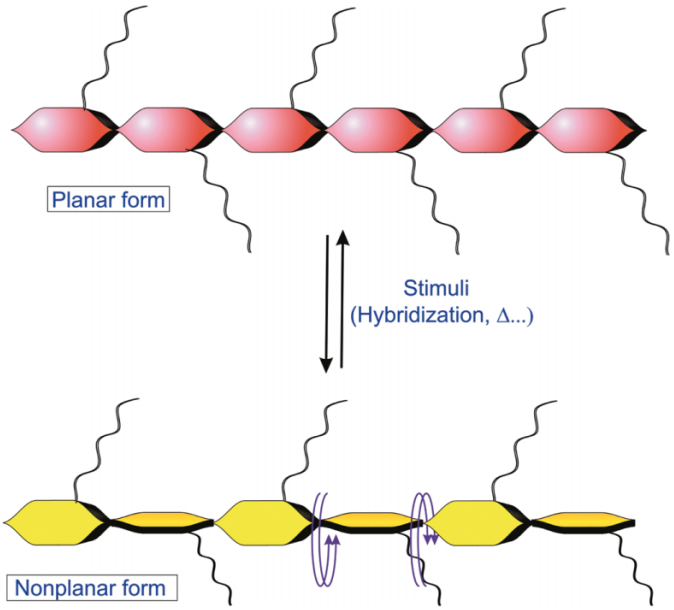

Optical biosensors

Optical and electrical sensors have become another important research topic for conjugated and electroactive polymers.[31] For instance, some neutral conjugated polymers (mainly polythiophenes) can undergo striking color changes upon exposure to various external stimuli. In most cases, these optical changes seem to be related to a conformational transition of the polymer backbone, from a planar to nonplanar form (Scheme 6), triggered by adequately functionalized and field-responsive side chains.[32] In addition to optical transitions induced by heating (thermochromism) or solvent quality changes (solvatochromism),[31,33] we have generated new phenomena with different regioregular poly(3-alkoxy-4-methylthiophene) derivatives, including the detection of ions (ionochromism),[34] UV radiation (dual photochromism),[35] and molecular recognition of chemical or biological moieties (affinitychromism).[36] In addition to the use of colorimetric detection, a modification of the conformation of a conjugated polymer can also modify its luminescence. Conjugated polymers are very sensitive to minor perturbations due to amplification by a collective system response and offer then a key advantage over small-molecule-based sensors.[37]

Along these lines, our recent studies have been mainly devoted to the detection of DNA and proteins.[38] More precisely, we have developed a new concept that utilizes a water-soluble, cationic polythiophene derivative as a polymeric stain that can specifically transduce the binding of an appropriate single-stranded DNA probe to its target into a clear optical signal. This simple, rapid, and selective methodology is based on conformationally flexible polyelectrolytes and complementary electrostatic interactions. For example, the starting neutral polythiophene–oligonucleotide complex is red in solution (aggregated and planar form) and presents a weak fluorescence. After hybridization with a perfect-match target, the solution becomes yellow and more fluorescent because of the formation of a so-called triplex structure. The fluorescence signal, measured at 570 nm,

Scheme 7. Schematic description of the proposed signal amplification detection mechanism based on the conformation change of a cationic polythiophene and energy transfers for ultrasensitive, selective, and rapid DNA detection.

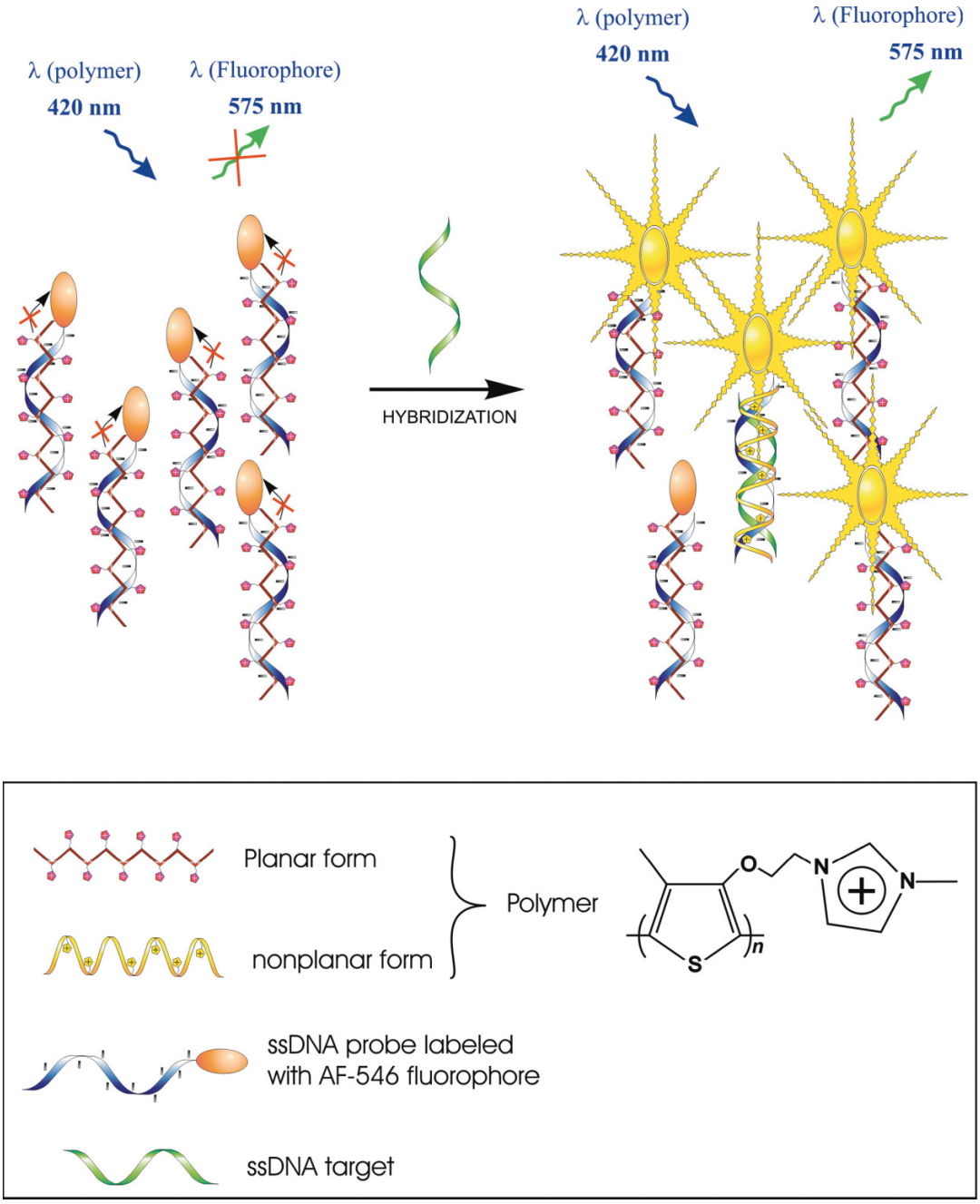

shows a clear contrast between perfect complementary targets and those having two or even one mismatch. A slightly different approach has even allowed the detection of a few copies of a human-gene target (Scheme 7). In this last case, oligonucleotide capture probes are labelled with a fluorophore whose excitation spectrum gets a good overlap with the emission spectrum of the polymer. It seems that through Förster resonance energy transfer (FRET), one polythiophene donor can rapidly transfer its energy to a large number of neighbouring acceptors. This new and exciting but still unclear amplification phenomenon is called fluorescence chain reaction (FCR). Interestingly, recent studies have shown the possibility to transfer these methodologies to micro-arrays.[39] On the basis of these recent advances, we are currently targeting the development of PCR-free methods for genotyping, diagnostics, and so forth.

Conclusion and perspectives

From all these examples, it is quite evident that conjugated polymers promise a bright future. Research is not only conducted into academic institutions but many small and large companies are now involved in R & D projects devoted to conducting and semi-conducting polymers. On the basis of this tremendous momentum, it is firmly believed that the next few years should show how the design and the

better understanding of the structure–property relationships in conjugated polymers have contributed to address important society problems such as the production of renewable energy with minimum detrimental effects on the environment or the development of simple and inexpensive tests for the rapid detection and identification of genes, infections, and so forth. As Benjamin Braddock is told in The Graduate, the future is in plastics…

Acknowledgements

We would like to thank all students and collaborators who have participated to our research activities described here and whose names are cited in the references. Behind these scientific results, there were and still are students and scientists totally devoted to the development of conjugated polymers and to their future utilization in our day-to-day life. We would like also to acknowledge the Natural Sciences and Engineering Research Council (NSERC) of Canada and the Fonds Québécois de Recherche sur la Nature et les Technologies (FQRNT) for their continuous financial support over the years. We sincerely hope that our governments will continue to see their support to basic sciences as a very important investment in our next generation of scientists and as a source of socio-economical development. Finally, we would like to thank colleagues at Université Laval for their support and collaboration to our research program.

References

(1) Shirakawa, H.; Louis, E. J.; MacDiarmid, A. G.; Chiang, C. K.; Heeger, A. J. *J. Chem. Soc., Chem. Commun.* **1977**, (16): 578. doi:10.1039/c39770000578.

(2) Skotheim, T. A.; Reynolds, J. R., Eds.; In *Handbook of conducting polymers*, 3rd ed.; Marcel Dekker: New York, 2007.

(3) Hadziioannou, G.; Malliaris, G. G., Eds.; In *Semiconducting polymers*, 2nd ed., Wiley-VCH: Weinheim, 2007.

(4) Shirakawa, H. *Angew. Chem., Int. Ed.* **2001**, *40* (14), 2574. doi:10.1002/1521-3773(20010716)40:14<2574::AID-ANIE2574>3.0.CO;2-N.

(5) MacDiarmid, A. *Angew. Chem., Int. Ed.* **2001**, *40* (14), 2581–2590. doi:10.1002/1521-3773(20010716)40:14<2581::AID-ANIE2581>3.0.CO;2-2.

(6) Heeger, A. J. *Angew. Chem., Int. Ed.* **2001**, *40* (14), 2591–2611. doi:10.1002/1521-3773(20010716)40:14<2591::AID-ANIE2591>3.0.CO;2-0.

(7) Diaz, A. F.; Kanazawa, K. K.; Gardini, G. P. *J. Chem. Soc., Chem. Commun.* **1979**, (14): 635. doi:10.1039/c39790000635.

(8) Tourillon, G.; Garnier, F. *J. Electroanal. Chem.* **1982**, *135* (1), 173–178. doi:10.1016/0022-0728(82)90015-8.

(9) Diaz, A. F.; Logan, J. A. *J. Electroanal. Chem.* **1980**, *111* (1), 111–114. doi:10.1016/S0022-0728(80)80081-7.

(10) (a) Petit, M. A.; Soum, A. H.; Leclerc, M.; Prud'homme, R. E. *J. Polym. Sci. Polym. Phys. Ed.* **1987**, *25* (2), 423–433. doi:10.1002/polb.1987.090250213.; (b) Leclerc, M.; Prud'homme, R. E. *Macromolecules* **1987**, *20* (9), 2153–2159. doi:10.1021/ma00175a018.

(11) (a) Leclerc, M.; Guay, J.; Dao, L. H. *Macromolecules* **1989**, *22* (2), 649–653. doi:10.1021/ma00192a024.; (b) D'Aprano, G.; Leclerc, M.; Zotti, G. *Macromolecules* **1992**, *25* (8), 2145–2150. doi:10.1021/ma00034a013.; (c) D'Aprano, G.; Leclerc, M.; Zotti, G.; Schiavon, G. *Chem. Mater.* **1995**, *7* (1), 33–42. doi:10.1021/cm00049a008.

(12) (a) Sato, M. A.; Tanaka, S.; Kaeriyama, K. *J. Chem. Soc., Chem. Commun.* **1986**, (11): 873. doi:10.1039/c39860000873.; (b) Jen, K. Y.; Miller, G. G.; Elsenbaumer, R. L. *J. Chem. Soc., Chem. Commun.* **1986**, (17): 1346. doi:10.1039/c39860001346.; (c) Sugimoto, R.; Takeda, S.; Gu, H. B.; Yoshino, Y. *Chem. Express* **1986**, *1*, 635; (d) Hotta, S.; Rughooputh, S. D. D. V.; Heeger, A. J.; Wudl, F. *Macromolecules* **1987**, *20* (1), 212–215. doi:10.1021/ma00167a038.; (e) Roncali, J.; Garreau, R.; Yassar, A.; Marque, P.; Garnier, F.; Lemaire, M. *J. Phys. Chem.* **1987**, *91* (27), 6706–6714. doi:10.1021/j100311a030.

(13) Leclerc, M.; Diaz, F. M.; Wegner, G. *Makromol. Chem.* **1989**, *190* (12), 3105–3116. doi:10.1002/macp.1989.021901208.

(14) (a) McCullough, R. D.; Lowe, R. D. *J. Chem. Soc., Chem. Commun.* **1982**, 70; (b) Chen, T. A.; Rieke, R. D. *J. Am. Chem. Soc.* **1992**, *114* (25), 10087–10088. doi:10.1021/ja00051a066.; (c) McCullough, R. D. *Adv. Mater.* **1998**, *10* (2), 93–116. doi:10.1002/(SICI)1521-4095(199801)10:2<93::AID-ADMA93>3.0.CO;2-F.

(15) (a) Leclerc, M.; Daoust, G. *J. Chem. Soc., Chem. Commun.* **1990**, (3): 273. doi:10.1039/c39900000273.; (b) Daoust, G.; Leclerc, M. *Macromolecules* **1991**, *24* (2), 455–459. doi:10.1021/ma00002a018.

(16) (a) Heywang, G.; Jonas, F. *Adv. Mater.* **1992**, *4* (2), 116–118. doi:10.1002/adma.19920040213.; (b) Kirchmeyer, S.; Reuter, K. J. *Mater. Chem.* **2005**, *15* (21), 2077. doi:10.1039/b417803n.

(17) (a) Faïd, K.; Cloutier, R.; Leclerc, M. *Macromolecules* **1993**, *26* (10), 2501–2507. doi:10.1021/ma00062a017.; (b) Chayer, M.; Faïd, K.; Leclerc, M. *Chem. Mater.* **1997**, *9* (12), 2902–2905. doi:10.1021/cm970238v.; (c) Leclerc, M.; Faïd, K. *Adv. Mater.* **1997**, *9* (14), 1087–1094. doi:10.1002/adma.19970091404.; (d) Sheina, E. E.; Khersonsky, S. M.; Jones, E. G.; McCullough, R. D. *Chem. Mater.* **2005**, *17* (13), 3317–3319. doi:10.1021/cm050083o.

(18) (a) Burroughes, J. H.; Bradley, D. D. C.; Brown, A. R.; Marks, R. N.; Mackay, K.; Friend, R. H.; Burns, P. L.; Holmes, A. B. *Nature* **1990**, *347* (6293), 539–541. doi:10.1038/347539a0.; (b) Kraft, A.; Grimsdale, A. C.; Holmes, A. B. *Angew. Chem., Int. Ed.* **1998**, *37* (4), 402. doi:10.1002/(SICI)1521-3773(19980302)37:4<402::AID-ANIE402>3.0.CO;2-9.

(19) (a) Ranger, M.; Rondeau, D.; Leclerc, M. *Macromolecules* **1997**, *30* (25), 7686–7691. doi:10.1021/ma970920a.; (b) Ranger, M.; Leclerc, M. *Can. J. Chem.* **1998**, *76* (11), 1571–1577. doi:10.1139/cjc-76-11-1571.; (c) Ranger, M.; Leclerc, M. *Macromolecules* **1999**, *32* (10), 3306–3313. doi:10.1021/ma981443e.

(20) (a) Donat-Bouillud, A.; Lévesque, I.; Tao, Y.; D'Iorio, M.; Beaupré, S.; Blondin, P.; Ranger, M.; Bouchard, J.; Leclerc, M. *Chem. Mater.* **2000**, *12* (7), 1931–1936. doi:10.1021/cm0001298.; (b) Leclerc, M. J. *Polym. Sci. Polym. Chem. Ed.* **2001**, *39* (17), 2867–2873. doi:10.1002/pola.1266.; (c) Beaupré, S.; Leclerc, M. *Adv. Funct. Mater.* **2002**, *12* (3), 192. doi:10.1002/1616-3028(200203)12:3<192::AID-ADFM192>3.0.CO;2-U.; (d) Chen, S. A.; Lu, H. H.; Huang, C. W. *Adv. Polym. Sci.* **2008**, *212*, 49.

(21) Scherf, U.; List, E. J. W. *Adv. Mater.* **2002**, *14* (7), 477–487. doi:10.1002/1521-4095(20020404)14:7<477::AID-ADMA477>3.0.CO;2-9.

(22) (a) Morin, J.-F.; Leclerc, M. *Macromolecules* **2001**, *34* (14), 4680–4682. doi:10.1021/ma010152u.; (b) Zotti, G.; Schiavon, G.; Zecchin, S.; Morin, J.-F.; Leclerc, M. *Macromolecules*

2002, *35* (6), 2122–2128. doi:10.1021/ma011311c.; (c) Morin, J.-F.; Leclerc, M. *Macromolecules* **2002**, *35* (22), 8413–8417. doi:10.1021/ma020880x.; (d) Morin, J.-F.; Drolet, N.; Tao, Y.; Leclerc, M. *Chem. Mater.* **2004**, *16* (23), 4619–4626. doi:10.1021/cm0499390.

(23) (a) Dierschke, F.; Grimsdale, A. C.; Müllen, K. *Synthesis* **2003**, 2470; (b) Morin, J.-F.; Leclerc, M.; Adès, D.; Siove, A. *Macromol. Rapid Commun.* **2005**, *26* (10), 761–778. doi:10.1002/marc.200500096.; (c) Boudreault, P.-L. T.; Blouin, N.; Leclerc, M. *Adv. Polym. Sci.* **2008**, *212*, 99; (d) Blouin, N.; Leclerc, M. *Acc. Chem. Res.* **2008**, *41* (9), 1110–1119. doi:10.1021/ar800057k. PMID:18656967.

(24) (a) Morin, J.-F.; Beaupré, S.; Leclerc, M.; Lévesque, I.; D'Iorio, M. *Appl. Phys. Lett.* **2002**, *80* (3), 341. doi:10.1063/1.1433917.; (b) Kobayashi, N.; Kijima, M. *Appl. Phys. Lett.* **2007**, *91* (8), 081113. doi:10.1063/1.2773740.

(25) Grimsdale, A. C.; Müllen, K. *Adv. Polym. Sci.* **2008**, *212*, 1.

(26) (a) Yu, G.; Gao, J.; Hummelen, J. C.; Wudl, F.; Heeger, A. J. *Science* **1995**, *270* (5243), 1789–1791. doi:10.1126/science.270.5243.1789.; (b) Scharber, M. C.; Mühlbacher, D.; Koppe, M.; Denk, P.; Waldauf, C.; Heeger, A. J.; Brabec, C. J. *Adv. Mater.* **2006**, *18* (6), 789–794. doi:10.1002/adma.200501717.; (c) Thompson, B. C.; Fréchet, J. M. J. *Angew. Chem., Int. Ed.* **2008**, *47* (1), 58–77. doi:10.1002/anie.200702506.

(27) (a) Li, G.; Shrotriya, V.; Huang, J.; Yao, Y.; Moriarty, T.; Emery, K.; Yang, Y. *Nat. Mater.* **2005**, *4* (11), 864–868. doi:10.1038/nmat1500.; (b) Ma, W.; Yang, C.; Ging, X.; Lee, K.; Heeger, A. J. *Adv. Funct. Mater.* **2005**, *15* (10), 1617–1622. doi:10.1002/adfm.200500211.

(28) (a) Blouin, N.; Michaud, A.; Leclerc, M. *Adv. Mater.* **2007**, *19* (17), 2295–2300. doi:10.1002/adma.200602496.; (b) Blouin, N.; Michaud, A.; Gendron, D.; Wakim, S.; Blair, E.; Neagu-Plesu, R.; Belletête, M.; Durocher, G.; Tao, Y.; Leclerc, M. *J. Am. Chem. Soc.* **2008**, *130* (2), 732–742. doi:10.1021/ja0771989. PMID:18095689.; (c) Park, S. H.; Roy, A.; Beaupré, S.; Cho, S.; Coates, N.; Moon, J. S.; Moses, D.; Leclerc, M.; Lee, K.; Heeger, A. J. *Nat. Photonics* **2009**, *3* (5), 297–302. doi:10.1038/nphoton.2009.69.

(29) Zou, Y.; Gendron, D.; Badrou-Aïch, R.; Najari, A.; Tao, Y.; Leclerc, M. *Macromolecules* **2009**, *42* (8), 2891–2894. doi:10.1021/ma900364c.

(30) Klauk, H., Eds; In *Organic electronics*; Wiley-VCH: Weinheim, 2006.

(31) (a) Leclerc, M. *Adv. Mater.* **1999**, *11* (18), 1491–1498. doi:10.1002/(SICI)1521-4095(199912)11:18<1491::AID-ADMA1491>3.0.CO;2-O.; (b) Liu, B.; Bazan, G. C. *Chem. Mater.* **2004**, *16* (23), 4467–4476. doi:10.1021/cm049587x.; (c) Herland, A.; Inganäs, O. *Macromol. Rapid Commun.* **2007**, *28* (17), 1703–1713. doi:10.1002/marc.200700281.; (d) Ho, H. A.; Najari, A.; Leclerc, M. *Acc. Chem. Res.* **2008**, *41* (2), 168–178. doi:10.1021/ar700115t. PMID:18198841.

(32) (a) DiCésare, N.; Belletête, M.; Marrano, C.; Leclerc, M.; Durocher, G. *J. Phys. Chem. A* **1999**, *103* (7), 795–802. doi:10.1021/jp983186l.; (b) DiCésare, N.; Belletête, M.; Leclerc, M.; Durocher, G. *J. Phys. Chem. A* **1999**, *103* (7), 803–811. doi:10.1021/jp983187d.; (c) DiCésare, N.; Belletête, M.; Rivera Garcia, E.; Leclerc, M.; Durocher, G. *J. Phys. Chem. A* **1999**, *103* (20), 3864–3875. doi:10.1021/jp9901085.; (d) DiCésare, N.; Belletête, M.; Durocher, G.; Leclerc, M. *Chem. Phys. Lett.* **1997**, *275* (5-6), 533–539. doi:10.1016/S0009-2614(97)00777-X.; (e) Garreau, S.; Leclerc, M.; Errien, N.; Louarn, G. *Macromolecules* **2003**, *36* (3), 692–697. doi:10.1021/ma021358d.; (f) Le Bouch, N.; Auger, M.; Leclerc, M. *Macromol. Chem. Phys.* **2008**, *209* (24), 2455–2462. doi:10.1002/macp.200800365.

(33) (a) Rughooputh, S. D. D. V.; Hotta, S.; Heeger, A. J.; Wudl, F. J. *Polym. Sci. Polym. Phys. Ed.* **1987**, *25*, 1071; (b) Roux, C.; Leclerc, M. *Macromolecules* **1992**, *25* (8), 2141–2144. doi:10.1021/ma00034a012.; (c) Roux, C.; Bergeron, J. Y.; Leclerc, M. *Makromol. Chem.* **1993**, *194* (3), 869–877. doi:10.1002/macp.1993.021940311.; (d) Robitaille, L.; Leclerc, M. *Macromolecules* **1994**, *27* (7), 1847–1851. doi:10.1021/ma00085a028.; (e) Roux, C.; Leclerc, M. *Chem. Mater.* **1994**, *6* (5), 620–624. doi:10.1021/cm00041a011.; (f) Faïd, K.; Fréchette, M.; Ranger, M.; Mazerolle, L.; Lévesque, I.; Leclerc, M.; Chen, T.-A.; Rieke, R. D. *Chem. Mater.* **1995**, *7* (7), 1390–1396. doi:10.1021/cm00055a018.; (g) Yang, C.; Orfino, F. P.; Holdcroft, S. *Macromolecules* **1996**, *29* (20), 6510–6517. doi:10.1021/ma9604799.

(34) (a) Lévesque, I.; Leclerc, M. *Chem. Mater.* **1996**, *8* (12), 2843–2849. doi:10.1021/cm960373s.; (b) Ho, H. A.; Leclerc, M. *J. Am. Chem. Soc.* **2003**, *125* (15), 4412–4413. doi:10.1021/ja028765p. PMID:12683798.

(35) Lévesque, I.; Leclerc, M. *Macromolecules* **1997**, *30* (15), 4347–4352. doi:10.1021/ma961892j.

(36) (a) Faïd, K.; Leclerc, M. *J. Chem. Soc., Chem. Commun.* **1996**, 2761; (b) Faïd, K.; Leclerc, M. *J. Am. Chem. Soc.* **1998**, *120* (21), 5274–5278. doi:10.1021/ja9802753.; (c) Bernier, S.; Garreau, S.; Béra-Abérem, M.; Gravel, C.; Leclerc, M. *J. Am. Chem. Soc.* **2002**, *124* (42), 12463–12468. doi:10.1021/ja027387l. PMID:12381187.

(37) Thomas, S. W., 3rd; Joly, G. D.; Swager, T. M. *Chem. Rev.* **2007**, *107* (4), 1339–1386. doi:10.1021/cr0501339. PMID:17385926.

(38) (a) Ho, H. A.; Boissinot, M.; Bergeron, M. G.; Corbeil, G.; Doré, K.; Boudreau, D.; Leclerc, M. *Angew. Chem., Int. Ed.* **2002**, *41* (9), 1548–1551. doi:10.1002/1521-3773(20020503)41:9<1548::AID-ANIE1548>3.0.CO;2-I.; (b) Ho, H. A.; Leclerc, M. *J. Am. Chem. Soc.* **2004**, *126* (5), 1384–1387. doi:10.1021/ja037289f. PMID:14759196.; (c) Doré, K.; Dubus, S.; Ho, H. A.; Lévesque, I.; Brunette, M.; Corbeil, G.; Boissinot, M.; Boivin, G.; Bergeron, M. G.; Boudreau, D.; Leclerc, M. *J. Am. Chem. Soc.* **2004**, *126* (13), 4240–4244. doi:10.1021/ja038900d. PMID:15053613.; (e) Ho, H. A.; Doré, K.; Boissinot, M.; Bergeron, M. G.; Tanguay, R. M.; Boudreau, D.; Leclerc, M. *J. Am. Chem. Soc.* **2005**, *127* (36), 12673–12676. doi:10.1021/ja053417j. PMID:16144416.; (f) Sigurdson, C. J.; Nilsson, K. P. R.; Hornemann, S.; Manco, G.; Polymenidou, M.; Schwarz, P.; Leclerc, M.; Hammarström, P.; Wüthrich, K.; Aguzzi, A. *Nat. Methods* **2007**, *4* (12), 1023–1030. doi:10.1038/nmeth1131. PMID:18026110.

(39) (a) Nilsson, K. P. R.; Inganäs, O. *Nat. Mater.* **2003**, *2* (6), 419–424. doi:10.1038/nmat899. PMID:12754497.; (b) Najari, A.; Ho, H. A.; Gravel, J.-F.; Nobert, P.; Boudreau, D.; Leclerc, M. *Anal. Chem.* **2006**, *78* (22), 7896–7899. doi:10.1021/ac061650+. PMID:17105186.; (c) Béra-Abérem, M.; Najari, A.; Ho, H. A.; Gravel, J.-F.; Nobert, P.; Boudreau, D.; Leclerc, M. *Adv. Mater.* **2006**, *18* (20), 2703–2707. doi:10.1002/adma.200601651.; (d) Zheng, W.; He, L. *J. Am. Chem. Soc.* **2009**, *131* (10), 3432–3433. doi:10.1021/ja809175q. PMID:19243094.; (e) Yang, X.; Zhao, X.; Zuo, X.; Wang, K.; Wen, J.; Zhang, H. *Talanta* **2009**, *77* (3), 1027–1031. doi:10.1016/j.talanta.2008.08.001. PMID:19064086.

Iodine-catalyzed efficient synthesis of chalcones by grinding under solvent-free conditions

Hongshe Wang and June Zeng

Abstract: Chalcones are useful intermediates in organic synthesis and exhibit a large number of different biological activities. Chalcones have been synthesized in high yields by Claisen–Schmidt condensation of substituted acetophenones with various aromatic aldehydes in the presence of 10 mol% of iodine at room temperature by grinding under solvent-free conditions.

Key words: iodine, chalcones, Claisen–Schmidt condensation, grinding, solvent-free.

Résumé : Les chalcones sont des intermédiaires importants en synthèse organique et elles présentent un grand nombre d'activités biologiques diverses. On a réalisé la synthèse de chalcones avec des rendements élevés, par le biais d'une condensation de Claisen–Schmidt d'acétophénones substituées avec divers aldéhydes aromatiques, en présence de 10 moles % d'iode, à la température ambiante, par simple broyage dans des conditions sans solvant.

Mots-clés : iode, chalcones, condensation de Claisen–Schmidt, broyage, sans solvant.

[Traduit par la Rédaction]

Introduction

Chalcones and their derivatives are useful intermediates in organic synthesis.[1] Many chalcone derivatives display interesting pharmacological and biological activities.[2] Therefore, much attention has been paid to the synthesis of chalcones. Traditionally, chalcones are obtained via Claisen–Schmidt condensation carried out using alkaline hydroxides as catalysts.[3] However, the poor selectivity, generation of wastes, and laborious separation techniques make these catalysts practically inconvenient. Thus, more efficient methods have been developed for the synthesis of chalcones, which include the use of NaOH,[4] $FeCl_3 \cdot 6H_2O$,[5] $SOCl_2$/EtOH,[6] $BF_3 \cdot Et_2O$,[7] sulfonic-acid-functionalized organosilica materials,[8] $ZrCl_4$,[9] bamboo char sulfonic acid,[10] and ionic liquid[11] microwave[12] and ultrasonic irradiation.[13] However, some of the previously reported procedures have various disadvantages, such as long reaction times, special efforts needed to prepare the catalysts, high temperatures, and the use of expensive reagents and hazardous solvents. Thus, there is scope for further improvement involving more environment-friendly and milder reaction conditions.

With the increasing public concern over environmental pollution, it is of great importance for chemists to come up with new approaches that are less hazardous to human health and environment. The use of environmentally benign solvents, like water, and solvent-free reactions represent very powerful green chemical technology procedures from both the economical and synthetic points of view.[14] Grinding under solvent-free conditions is an environment-friendly method for the organic synthesis reactions.

In recent years, molecular iodine has been considered as an inexpensive and readily available catalyst for a variety of organic transformations.[15] In continuation to our work on studying iodine-catalyzed reactions,[16] we report herein an efficient and convenient procedure for the synthesis of chalcones from substituted acetophenones and various aromatic aldehydes via Claisen–Schmidt condensation in the presence of a catalytic amount of iodine at room temperature by grinding under solvent-free conditions (Scheme 1).

Results and discussion

To determine the efficiency of this procedure, we carried out the reaction of acetophenone with benzaldehyde using various other Lewis acids, such as $InCl_3$, $FeCl_3$, $ZnCl_2$, $(NH_4)_2Fe(SO_4)_2$, $Bi(NO_3)_3$, $Al_2(SO_4)_3$, and $Mg(ClO_4)_2$ at room temperature by grinding under solvent-free conditions (Table 1). Among these catalysts, I_2 was found to be the most effective catalyst for this conversion. As for the amount of the catalyst used, we found that 10 mol% of I_2 is sufficient to promote reaction efficiently (Table 2). No reaction was observed when acetophenone was reacted with benzaldehyde under similar conditions in the absence of I_2 even after grinding for 180 min. Any excess of I_2 beyond this loading did not show any further increase in conversion and yield. Use of less than the required catalyst loading resulted in low yields.

Received 14 March 2009. Accepted 8 June 2009. Published on the NRC Research Press Web site at canjchem.nrc.ca on 4 August 2009.

H. Wang[1] and J. Zeng. Shaanxi Key Laboratory for Phytochemistry, Department of Chemistry and Chemical Engineering, Baoji University of Arts and Sciences, Baoji 721013, P. R. China.

[1]Corresponding author (e-mail: hongshewang@126.com).

Scheme 1.

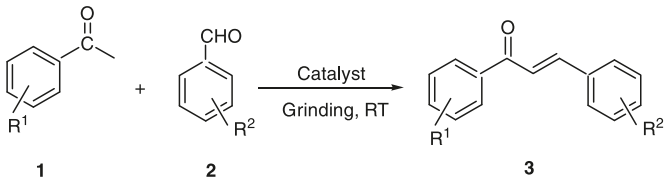

Table 1. Claisen–Schmidt condensation of acetophenone with benzaldehyde catalyzed by different catalysts.

Entry	Catalyst (mol%)	Time (min)	Yield[a] (%)
1	$InCl_3$ (50)	20	30
2	$FeCl_3$ (50)	20	30
3	$ZnCl_2$ (50)	20	20
4	$(NH_4)_2Fe(SO_4)_2$ (50)	20	20
5	$Bi(NO_3)_3$ (50)	20	40
6	$Al_2(SO_4)_3$ (50)	20	55
7	$Mg(ClO_4)_2$ (30)	10	72
8	I_2 (10)	5	91

Note: The reaction was performed with 1 mmol of benzaldehyde and 1 mmol of acetophenone by grinding at room temperature.

[a]Isolated yield.

To explore the generality of this method, a series of chalcones were prepared under the optimized reaction conditions. By this method, the reactions were carried out simply by mixing a variety of substituted acetophenones and substituted benzaldehydes in the presence of a catalytic amount (10 mol%) of iodine at room temperature by grinding under solvent-free conditions, and the results are summarized in Table 3. The components of the mixture were ground together in a mortar with a pestle for several minutes. In all the cases, the reactions proceeded smoothly to afford the corresponding products in good-to-excellent yields using ethanol recrystallization. Their physical properties were determined, and the structures were confirmed by ^{1}H and ^{13}C NMR, IR, and MS. All acetophenones and benaldehydes with either electron-withdrawing or electron-donating substitutes, such as nitro, and methoxy groups on aromatic rings produced a satisfactory yield ranging from 83% to 95%. It was found from ^{1}H NMR spectral data that all chalcones were with trans configuration.

In conclusion, we have developed a new methodology to prepare a variety of chalcones in the presence of a catalytic amount of iodine at room temperature by grinding under solvent-free conditions. The advantages, such as the easy procedure, shorter reaction times, green and clean to the environment, mild reaction conditions, and high yields, make our method an attractive alternative to the preparation of chalcones.

Experimental

Melting points were determined on an XT4A electrothermal apparatus equipped with a microscope. ^{1}H NMR and ^{13}C NMR spectra were recorded on a Bruker Avance 400 spectrometer (^{1}H: 400 MHz, ^{13}C: 100 MHz) in $CDCl_3$ with TMS as an internal standard. Mass spectra were measured by HP5973 spectrometer. IR spectra were measured on a Nicolet FTIR-750 spectrometer. The benzaldehyde was distilled prior to use. All other reagents were commercially available products and were used without further purification.

Table 2. Effect of different amounts of iodine on the reaction of benzaldehyde with acetophenone.

Entry	I_2 (mol%)	Time (min)	Yield[a](%)
1	0	180	0
2	1	20	46
3	5	10	73
4	10	5	91
5	15	5	92
6	20	5	91

Note: The reaction was carried out at room temperature by grinding under solvent-free conditions.

[a]Isolated yield.

General procedure for the synthesis of chalcones

A mixture of acetophenone (1 mmol), benzaldehyde (1 mmol), and iodine (0.1 mmol) was ground in a mortar with a pestle (the mortar and pestle are thoroughly cleaned between runs) at room temperature until the reaction was completed (monitored by TLC). The reaction mixture was treated with 5% aqueous sodium thiosulfate. The precipitated products were then separated, washed with water, and recrystallized from ethanol to afford the pure products.

Except for compounds **3d**, **3e**, **3h**, and **3l**, all the products are known compounds. The spectroscopic and physical data for all known compounds corresponded to those given in the literatures.

*3-(4-*N,N*-Dimethylaminophenyl)-1-phenyl-2-propen-1-one (3d)*

IR (KBr) ν: 2922, 1649, 1565, 1529 cm^{-1}. ^{1}H NMR (400 MHz, $CDCl_3$) δ: 3.05 (s, 6H), 6.73 (d, J = 8.0 Hz, 2H), 7.35 (d, J = 16.0 Hz, 1H), 7.46 (d, J = 8.0 Hz, 2H), 7.55 (m, 3H), 7.80 (d, J = 16.0 Hz, 1H), 8.00 (d, J = 5.6 Hz, 2H). ^{13}C NMR ($CDCl_3$, 100 MHz) δ: 42.31, 110.13, 111.06, 119.11, 123.24, 128.23, 129.06, 133.10, 139.07, 145.19, 162.16, 190.08. MS (EI) m/z (%): 251 (M^+, 100), 250 (34), 236 (2), 222 (11), 207 (11), 174 (43), 105 (16). Anal. calcd. for $C_{17}H_{17}NO$: C, 81.27; H, 6.77; N, 5.59. Found: C, 81.16; H, 6.86; N, 5.67.

3-(2-Hydroxyphenyl)-1-phenyl-2-propen-1-one (3e)

IR (KBr) ν: 3386, 1662, 1591, 1562, 1498, 1392, 800, 762 cm^{-1}. ^{1}H NMR (400 MHz, $CDCl_3$) δ: 6.60 (m, 3H), 7.23 (d, J = 16.0 Hz, 1H), 7.41 (d, J = 8.0 Hz, 1H), 7.54 (m, 3H), 7.71 (d, J = 16.0 Hz, 1H), 8.01 (d, J = 8.0 Hz, 2H), 9.68 (s, 1H). ^{13}C NMR ($CDCl_3$, 100 MHz) δ: 110.96, 111.63, 119.79, 123.91, 128.62, 129.32, 129.86, 131.05, 133.53, 138.61, 145.11, 162.84, 166.17, 190.87. MS (EI) m/z (%): 224 (M^+, 66), 207 (100), 206 (2), 222 (16), 147 (71), 119 (31), 105 (65). Anal. calcd. for $C_{15}H_{12}O_2$: C, 80.36; H, 5.36. Found: C, 80.23; H, 5.45.

Table 3. Synthesis of chalcones catalyzed by iodine.

Entry	Product	R^1	R^2	Time (min)	Yield[a] (%)	Mp (lit.) (°C)
1	**3a**	H	H	5	91	57–58 (56–57)[7]
2	**3b**	H	4-CH_3	5	90	94–95 (93–94)[5]
3	**3c**	H	3-NO_2	5	92	143–144 (144–145)[5]
4	**3d**	H	4-$N(CH_3)_2$	8	88	102–103
5	**3e**	H	2-OH	5	89	142–143
6	**3f**	4-CH_3	H	5	90	54–55 (53–54)[17]
7	**3g**	4-NO_2	H	5	95	118–119 (117–119)[13]
8	**3h**	2,4-$(OCH_3)_2$	3-NO_2	10	87	168–170
9	**3i**	4-Br	4-OH	8	92	179–181 (180–182)[13]
10	**3j**	3-OCH_3	2-NO_2	10	91	88–90 (99–90)[13]
11	**3k**	2,4-$(OH)_2$	4-$N(CH_3)_2$	10	85	181–183 (180–182)[13]
12	**3l**	2,4-$(OCH_3)_2$	4-OCH_3	10	83	33–35

Note: All the reactions were performed with 10 mol% of iodine at room temperature by grinding under solvent-free conditions.

[a]Isolated yields.

1-(2,4-Dimethoxyphenyl)-3-(3-nitrophenyl)-2-propen-1-one (3h)

IR (KBr) ν: 3055, 2965, 2843, 1658, 1605, 1573, 1403, 813, 646 cm^{-1}. ^1H NMR (400 MHz, $CDCl_3$) δ: 3.90 (s, 3H), 3.98 (s, 3H), 6.50 (m, 2H), 7.48 (m, 4H), 7.61 (d, J = 16.0 Hz, 1H), 7.82 (d, J = 16.0 Hz, 1H), 8.01 (d, J = 8.0 Hz, 1H). ^{13}C NMR ($CDCl_3$, 100 MHz) δ: 55.96, 114.98, 120.66, 121.73, 125.06, 126.98, 129.09, 130.05, 134.64, 139.13, 142.60, 145.43, 164.44, 191.87. MS (EI) m/z (%): 313 (M^+, 58), 296 (30), 285 (83), 165 (100), 151 (33). Anal. calcd. for $C_{17}H_{15}NO_5$: C, 65.18; H, 4.79; N, 4.40. Found: C, 65.11; H, 4.71; N, 4.55.

1-(2,4-Dimethoxyphenyl)-3-(4-methoxyphenyl)-2-propen-1-one (3l)

IR (KBr) ν: 3050, 1651, 1600, 1573, 1510, 1441, 1330, 1015, 980, 821, 772, 680 cm^{-1}. ^1H NMR (400 MHz, $CDCl_3$) δ: 3.86 (s, 6H), 3.97 (s, 3H), 6.36 (m, 2H), 6.95 (d, J = 8.0 Hz, 2H), 7.40 (d, J = 16.0 Hz, 1H), 7.51 (d, J = 8.0 Hz, 2H), 7.80 (d, J = 16.0 Hz, 1H), 8.00 (d, J = 8.0 Hz, 1H). ^{13}C NMR ($CDCl_3$, 100 MHz) δ: 55.73, 114.01, 114.69, 119.43, 121.21, 128.75, 129.87, 130.11, 133.89, 140.03, 144.30, 161.64, 163.54, 190.77. MS (EI) m/z (%): 298 (M^+, 100), 283 (82), 255 (10). Anal. calcd. for $C_{18}H_{18}O_4$: C, 72.48; H, 6.04. Found: C, 72.33; H, 6.03.

Acknowledgments

This work was financially supported by the Educational Committee of Shaanxi Province (Nos. 08JZ09 and 09JK332) and Baoji University of Arts and Sciences (No. Zk064).

References

(1) (a) Ranu, B. C.; Hajra, A.; Jana, U. *Synlett* **2000**, 75; (b) Katritzky, A. R.; Abdel-Fattah, A. A.; Tymoshenko, D. O.; Essawy, S. A. *Synthesis* **1999**, *1999* (12), 2114–2118. doi:10.1055/s-1999-3637.

(2) (a) Liu, M.; Wilairat, P.; Go, M. L. J. *Med. Chem.* **2001**, *44* (25), 4443–4452. doi:10.1021/jm0101747.; (b) Kumar, S. K.; Hager, E.; Pettit, C.; Gurulingappa, H.; Davidson, N. E.; Khan, S. R. J. *Med. Chem.* **2003**, *46* (14), 2813–2815. doi:10.1021/jm030213+.

(3) (a) Edwards, M. L.; Stemerick, D. M.; Sunkara, P. S. J. *Med. Chem.* **1990**, *33* (7), 1948–1954. doi:10.1021/jm00169a021.; (b) Alcantara, A. R.; Marinas, J. K.; Sinisterra, J. V. *Tetrahedron Lett.* **1987**, *28* (14), 1515–1518. doi:10.1016/S0040-4039(01)81030-3.

(4) Toda, F.; Tanaka, K.; Hamai, K. *J. Chem. Soc., Perkin Trans. 1* **1990**, (11): 3207. doi:10.1039/p19900003207.

(5) Zhang, X.; Niu, H.; Wang, J. *J. Chem. Res. Synop.* **2003**, 33.

(6) Petrov, O.; Ivanova, Y.; Gerova, M. *Catal. Commun.* **2008**, *9* (2), 315–316. doi:10.1016/j.catcom.2007.06.013.

(7) Narender, T.; Reddy, K. P. *Tetrahedron Lett.* **2007**, *48* (18), 3177–3180. doi:10.1016/j.tetlet.2007.03.054.

(8) Shylesh, S.; Samuel, P. P.; Srilakshmi, C.; Parischa, R.; Singh, A. P. *J. Mol. Catal. Chem.* **2007**, *274* (1-2), 153–158. doi:10.1016/j.molcata.2007.04.040.

(9) Kumar, A.; Akanksha. *J. Mol. Catal. Chem.* **2007**, *274* (1-2), 212–216. doi:10.1016/j.molcata.2007.05.016.

(10) Xu, Q.; Yang, Z.; Yin, D.; Zhang, F. *Catal. Commun.* **2008**, *9* (7), 1579–1582. doi:10.1016/j.catcom.2008.01.007.

(11) Fan, D.; Cheng, J.; Fei, Z.; Gong, K.; Liu, Z. *Catal. Commun.* **2008**, *9* (6), 1394. doi:10.1016/j.catcom.2007.11.039.

(12) Zhou, J. F.; Zhou, J. F. *Synth. Commun.* **2002**, *32* (21), 3289–3294. doi:10.1081/SCC-120014034.

(13) Huang, D.; Jiang, G. Q. *Chin. J. Org. Chem.* **2002**, *22*, 1057.

(14) (a) Rothenberg, G.; Downie, A. P.; Raston, C. L.; Scott, J. L. *J. Am. Chem. Soc.* **2001**, *123* (36), 8701–8708. doi:10.1021/ja0034388. PMID:11535074.; (b) Jeon, S. J.; Li, H.; Walsh, P. J. *J. Am. Chem. Soc.* **2005**, *127* (47), 16416–16425. doi:10.1021/ja052200m. PMID:16305227.

(15) (a) Sun, G.; Wang, Z. *Tetrahedron Lett.* **2008**, *49* (33), 4929–4932. doi:10.1016/j.tetlet.2008.05.146.; (b) Liu, B.; Ji, S. J. *Synth. Commun.* **2008**, *38* (8), 1201–1211. doi:10.1080/00397910701866254.; (c) Deb, M. L.; Bhuyan, P. J. *Synlett* **2008**, 325; (d) Zhang, X.; Rao, W.; Chan, P. W. H. *Synlett* **2008**, 2204; (e) Lucas, R.; Vergnaud, J.; Teste, K.; Zerrouki, R.; Sol, V.; Krausz, P. *Tetrahedron Lett.* **2008**, *49* (38), 5537–5539. doi:10.1016/j.tetlet.2008.07.058.; (f) Yadav, J. S.; Reddy, B. V. S.; Narasimhulu, G.; Satheesh, G. *Tetrahedron Lett.* **2008**, *49* (39), 5683–5686. doi:10.1016/j.tetlet.2008.07.085.; (g) Wang, J.; Xu, F. X.; Lin, X. F.; Wang, Y. G. *Tetrahedron Lett.* **2008**, *49* (35), 5208–5210. doi:10.1016/j.tetlet.2008.06.024.; (h) Yadav, J. S.; Reddy, B. V. S.; Gopal, A. V. H.; Kumar, G. G. K. S. N.; Madavi, C.; Kunwar,

A. C. *Tetrahedron Lett.* **2008**, *49* (28), 4420–4423. doi:10.1016/j.tetlet.2008.05.014.

(16) (a) Wang, H. S.; Zeng, J. E. *Chin. J. Chem.* **2008**, *26* (1), 175–178. doi:10.1002/cjoc.200890017.; (b) Wang, H. S.; Zhao, L. F.; Du, Z. M. *Chin. J. Chem.* **2006**, *24* (1), 135–137. doi:10.1002/cjoc.200690009.; (c) Wang, H. S.; Zeng, J. E. *Chin. Chem. Lett.* **2007**, *18* (12), 1447–1450. doi:10.1016/j.cclet.2007.10.024.

(17) Huang, D.; Wang, J.; Hu, Y.; Zhang, Y.; Tang, J. *Synth. Commun.* **2002**, *32* (7), 971–979. doi:10.1081/SCC-120003144.

Ruthenium-catalyzed efficient routes to oxindole derivatives

Khalil Tabatabaeian, Manouchehr Mamaghani, Nosratollah Mahmoodi, and Alireza Khorshidi

Abstract: Ruthenium-catalyzed preparation of oxindoles from one-pot trimerization of indoles under oxidative conditions and from electrophilic substitution reaction of indoles with isatins or isatin-derived imines under very mild reaction conditions is reported.

Key words: ruthenium, oxindoles, isatins, indoles, oxidative conditions.

Résumé : On a réalisé la préparation d'oxindoles par la réaction de trimérisation monotope d'indoles dans des conditions oxydantes et catalysée par le ruthénium ainsi que par la réaction de substitution électrophile d'indoles avec des isatines ou des imines dérivées de l'isatine, dans des conditions réactionnelles très douces.

Mots-clés : ruthénium, oxindoles, isatines, indoles, conditions oxydantes.

[Traduit par la Rédaction]

Introduction

Various indole derivatives occur in many pharmacologically and biologically active compounds,[1] and the chemistry of indoles has been and continues to be one of the most active areas of heterocyclic chemistry.[2,3] Isatins are also familiar for their biological activity. Oxindoles are well-known amongst different isatin derivatives and are useful as antibacterials, antiinflammatories, and laxatives.[4,5] Although these heterocyclic compounds were recently isolated from plants, for example, the marine alkaloid Convolutamydine A from the marine bryozoan *Amathia convoluta*,[6] oxindole derivatives have been prepared by different methods, such as the reaction of indoles and isatin in acid conditions,[7] silica sulfuric acid catalysis,[8] $KAl(SO_4)_2$ catalysis under microwave conditions,[9] bismuth triflate catalysis,[10] and few others. All of these methods have their own drawbacks, such as long reaction times, non-environment-friendly solvents, low yields of products, and so forth. Recently, we have been involved in the study of the catalytic activity of ruthenium towards organic reactions.[11–14] As a matter of fact, many organic transformations, which involve ruthenium species as catalyst, are known and well-documented.[15–17] We found that ruthenium chloride hydrate smoothly acts as homogeneous catalyst in one-pot trimerization of indoles under oxidative conditions and also in condensation of indoles with isatins or isatin-derived imines, providing the desired oxindoles in high yields under mild reaction conditions and using a relatively easy work-up.

Received 2 March 2009. Accepted 28 May 2009. Published on the NRC Research Press Web site at canjchem.nrc.ca on 7 August 2009.

K. Tabatabaeian,[1] M. Mamaghani, N. Mahmoodi, and A. Khorshidi. Department of Chemistry, Faculty of Sciences, The University of Guilan, P. O. Box: 41335-1914, Iran.

[1]Corresponding author (e-mail: Taba@guilan.ac.ir).

Results and discussion

A recent report on the trimerization of indole through laccase catalysis,[18] along with previous reports, such as iodine-catalyzed trimerization,[19] prompted us to evaluate the trimerization of indoles under ruthenium catalysis. We have recently reported the efficient condensation of indoles with aldehydes or ketones using $RuCl_3{\cdot}nH_2O$ as homogeneous catalyst.[11] To obtain oxindoles directly from indoles, as it is shown in Scheme 1, the scheme of reaction involves in situ oxidation to isatins and then condensation of the latter with excess indoles.

In an optimized procedure, treatment of indole (3 mmol) with hydrogen peroxide (3 mmol) in the presence of $RuCl_3{\cdot}nH_2O$ (5 mol%) in methanol (5 mL) at 50 °C for 120 min gave the corresponding 3,3-di(1*H*-indole-3-yl)indolin-2-one as a white solid precipitate, which was easily purified (see Experimental section). NMR data were consistent with those previously reported for 3,3-di(1*H*-indole-3-yl)indolin-2-one (**1a**),[20] while laccase catalysis was shown to produce 2,2-di(1*H*-indol-3-yl)indolin-3-one.[18] From a mechanistic point of view, initial oxidation of indole to isatin followed by the coordination of C3-located carbonyl group of isatin with ruthenium and then aldol condensation may be responsible for the formation of products, while laccase catalysis proceeds via a different pathway.[18] A mechanistic pathway for oxidation under ruthenium catalysis could be found in our previous report.[14] As shown in Table 1, indoles bearing substitution on 2- or 3-position failed to produce the desired products (Table 1, entries 5 and 6) probably because of oxidation to products other than isatin.

To further explore the formation of oxindoles, the condensation reaction of indoles and isatins was examined. In the condensation of indole (2 mmol) with isatin (1 mmol) in the presence of $RuCl_3{\cdot}nH_2O$ catalyst (5 mol%) in methanol (3 mL) at 50 °C, the reaction furnished an excellent yield of the product **1a** in a rather short time (95%, 5 min). This may be due to the fact that the product is insoluble in the

Scheme 1. Trimerization of indole under oxidative conditions.

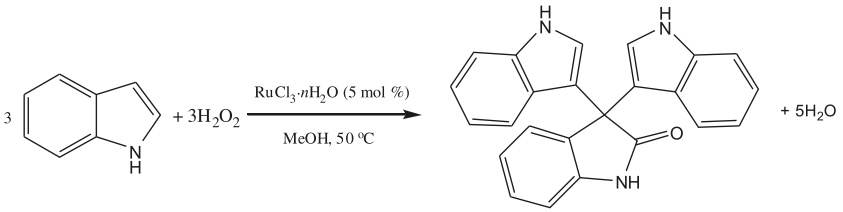

reaction solvent. As shown in Table 2, this method worked with a variety of substrates. In most cases, the products are insoluble in the reaction solvent, and a simple filtration and rinsing (with methanol) work-up provides spectroscopically pure products. One interesting example is the reaction of 3-methylindole with isatin (Table 2, entry 4), which provided the alcohol product **4b**, while other reported methods failed for this reaction. $RuCl_3 \cdot nH_2O$ was found to be an efficient catalyst in the view of handling, temperature, yields, and reaction times as indicated in comparison with the reported methods.[7–10]

Although bis-indolylalkanes were usually prepared by nucleophilic addition of indoles to aldehydes, the addition of indoles to Schiff bases is also studied. However, the reactivity of Schiff bases is lower in comparison with aldehydes. Some reports in this context involve the reaction of indoles with aromatic aldimines in low-to-moderate yields in the presence of BF_3 etherate or Me_3SiCl,[21] $InCl_3$-catalyzed addition to aromatic aldimines in an extremely difficult procedure,[22] and the addition of indoles to *N-tert*-butanesulfinylaldimines, which requires long reaction times.[23] We found that isatin-derived imines bearing an electron-withdrawing group on the amine moiety, also, react with indoles in a smooth fashion to provide the desired oxindoles as an alternative route (Scheme 2). Typical results in this context are listed in Table 3. To ensure that the products were not formed from isatin due to hydrolysis of aldimine in the presence of Ru^{III}, a control reaction was set up without indole, and no isatin was detected (checked by TLC). To the best of our knowledge, this is the first report on efficient addition of indoles to aldimines. Here again, the unique feature of the protocol is the insolubility of the products in the reaction solvent, offering an easy work-up.

Conclusion

In conclusion, we have developed convenient routes to oxindole derivatives.

Experimental

General

IR spectra were recorded on a Shimadzu FTIR-8400S spectrometer. ^1H NMR spectra were obtained on a Bruker DRX-500 Avance spectrometer and ^{13}C NMR spectra were obtained on a Bruker DRX-125 Avance spectrometer. Chemical shifts of ^1H and ^{13}C NMR spectra were expressed in ppm downfield from tetramethylsilane. Melting points were measured on a Büchi Melting Point B-540 instrument and are uncorrected. Elemental analyses were performed by a Carlo-Erba EA1110 CNNO-S analyzer and agreed with the calculated values. Microwave irradiation was performed in a LBP125 microwave oven.

Scheme 2. Ru^{III}-catalyzed condensation of indoles with an isatin-derived aldimine.

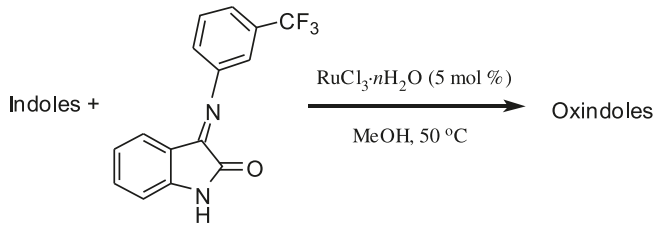

Materials

All materials were purchased from Merck and used without further purification.

General procedure for trimerization of indoles under oxidative condensations

To a solution of indole (3 mmol) and $RuCl_3 \cdot nH_2O$ (10.7 mg, 0.05 mmol) in methanol, H_2O_2 (340 mg of a 30% solution) was added, and the reaction mixture was heated in an oil bath at 50 °C under reflux conditions for the time specified in Table 1. After completion of the reaction, the white solid precipitate was filtered and washed with cold methanol until removal of all traces of impurities (checked by TLC), providing the product **1a** (273 mg, 75%). The same procedure was used for the other products, except for products **3a** (Table 1, entry 3), **4b**, and **5b** (Table 2, entries 4 and 5, respectively), which were purified by preparative TLC (*n*-hexane/ethyl acetate 10:5).

Characterization data for the products

3,3-Di(1H-indol-3-yl)indolin-2-one, 1a

White solid, mp 310–312 °C. IR (KBr) ν (cm^{-1}): 758, 1012, 1103, 1336, 1473, 1614, 1706, 3056, 3280, 3323, 3427. ^1H NMR (500 MHz, $CDCl_3$, 25 °C) δ: 6.51 (2H, t, J = 7.5 Hz), 6.59 (1H, t, J = 7.5 Hz), 6.62 (2H, s), 6.69 (1H, d, J = 7.7 Hz), 6.72 (2H, t, J = 7.5 Hz), 6.88 (1H, t, J = 7.6 Hz), 6.97 (1H, d, J = 7.4 Hz), 7.02 (4H, t, J = 7.65 Hz), 9.78 (1H, s), 9.89 (2H, s) ppm. ^{13}C NMR (125 MHz, $CDCl_3$, 25 °C) δ: 53.41, 110.48, 112.47, 115.14, 119.01, 119.13, 121.62, 122.26, 125.05, 125.21, 126.55, 128.70, 135.45, 137.77, 142.17, 179.60 ppm. Anal. calcd. for $C_{24}H_{17}N_3O$: C, 79.32; H, 4.72; N, 11.56. Found: C, 79.35; H, 4.75; N, 11.55.

1-Methyl-3,3-bis(1-methyl-1H-indol-3-yl)indolin-2-one, 2a

White solid, mp 232–234 °C. IR (KBr) ν (cm^{-1}): 742, 1014, 1083, 1128, 1157, 1251, 1334, 1371, 1467, 1608, 1714, 2925, 3051. ^1H NMR (500 MHz, $CDCl_3$, 25 °C) δ: 3.40 (3H, s), 3.74 (6H, s), 6.92 (2H, s), 6.99 (2H, t, J = 7.4 Hz), 7. 04 (1H, d, J = 7.8 Hz), 7.08 (1H, t, J = 7.5 Hz), 7.21 (2H, t, J = 7.5 Hz), 7.32 (2H, d, J = 8.3 Hz), 7.35 (2H,

Table 1. Ru-catalyzed trimerization of indoles under oxidative conditions.

Entry[a]	Indole	Product	Time (min)	Yield[b](%)
1	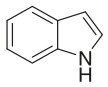	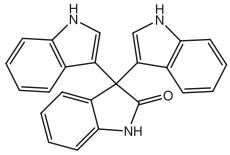 **1a**	120	75[c]
2	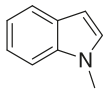	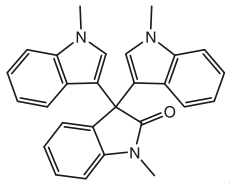 **2a**	80	80[c]
3	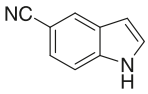	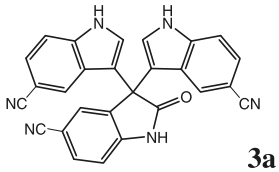 **3a**	150	65
4	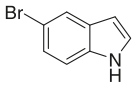	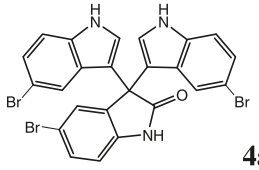 **4a**	150	68
5	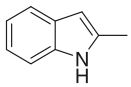	—	—	—
6	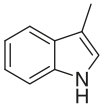	—	—	—

[a] All products were characterized by ^{1}H NMR, ^{13}C NMR, and IR data.
[b] Isolated yields.
[c] Identified by comparison with authentic samples.[20]

d, *J* = 8.1 Hz), 7.38 (1H, t, *J* = 7.4 Hz), 7.51 (1H, d, *J* = 7.3 Hz) ppm. ^{13}C NMR (125 MHz, $CDCl_3$, 25 °C) δ: 27.08, 33.20, 53.19, 108.62, 109.72, 114.17, 119.43, 121.84, 121.96, 123.13, 125.72, 126.89, 128.46, 129.19, 134.74, 138.20, 143.38, 178.30 ppm. Anal. calcd. for $C_{27}H_{23}N_3O$: C, 79.97; H, 5.72; N, 10.36. Found: C, 79.95; H, 5.74; N, 10.35.

3,3-Di(5-cyano-1H-indole-3-yl)-5-cyanoindolin-2-one, 3a

White solid, mp 289–291 °C. IR (KBr) ν (cm^{-1}): 754, 812, 1470, 1618, 1704, 2224, 3259, 3340. ^{1}H NMR (500 MHz, $CDCl_3$, 25 °C) δ: 6.94 (2H, d, *J* = 2.5 Hz), 7.01 (1H, d, *J* = 8.3 Hz), 7.18 (2H, dd, *J* = 8.3, 1.3 Hz), 7.29 (1H, d, *J* = 8.5 Hz), 7.33 (2H, d, *J* = 8.3 Hz), 7.53 (1H, s), 7.69 (2H, s), 10.45 (1H, s), 10.78 (2H, s) ppm. ^{13}C NMR (125 MHz, $CDCl_3$, 25 °C) δ: 53.10, 102.13, 110.87, 113.19, 115.98, 121.44, 122.60, 124.68, 125.39, 125.99, 126.98, 128.84, 133.86, 139.47, 141.49, 179.70 ppm. Anal. calcd. for $C_{27}H_{14}N_6O$: C, 73.96; H, 3.22; N, 19.17. Found: C, 74.01; H, 3.24; N, 19.17.

3,3-Di(5-bromo-1H-indole-3-yl)-5-bromoindolin-2-one, 4a

White solid, mp 286–288 °C. IR (KBr) ν (cm^{-1}): 653, 677, 751, 799, 888, 1103, 1464, 1618, 1714, 3281, 3323, 3429. ^{1}H NMR (500 MHz, $CDCl_3$, 25 °C) δ: 6.85 (2H, s), 6.96 (1H, d, *J* = 8.5 Hz), 7.02 (2H, dd, *J* = 8.7, 1.7 Hz), 7.10 (1H, d, *J* = 8.5 Hz), 7.16 (2H, d, *J* = 8.5 Hz), 7.27 (1H, s), 7.40 (2H, s), 9.99 (1H, s), 10.33 (2H, s) ppm. ^{13}C NMR (125 MHz, $CDCl_3$, 25 °C) δ: 53.75, 110.54, 112.87, 113.65, 114.66, 122.65, 123.99, 124.65, 125.68, 126.49, 127.99, 128.49, 134.35, 136.40, 141.89, 179.86 ppm. Anal. calcd. for $C_{24}H_{14}Br_3N_3O$: C, 48.03; H, 2.35; N, 7.00. Found: C, 48.07; H, 2.33; N, 7.03.

3,3-Di(2-methyl-1H-indole-3-yl)indolin-2-one, 3b

White solid, mp 297–299 °C. IR (KBr) ν (cm^{-1}): 611, 686, 740, 760, 1018, 1176, 1298, 1421, 1458, 1616, 1712, 2927, 3055, 3330, 3417. ^{1}H NMR (500 MHz, $CDCl_3$, 25 °C) δ: 2.11 (3H, s), 2.30 (3H, s), 6.41 (1H, d, *J* = 7.6 Hz), 6.80–6.85 (3H, m), 6.98–7.09 (4H, m), 7.37 (2H,

Table 2. Ru^{III}-catalyzed condensation of indoles with isatin.

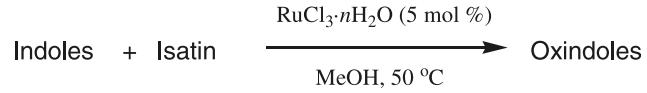

Entry[a]	Indole	Product	Time (min)	Yield[b] (%)
1	Indole	**1a**	5	95[c]
2	1-Methylindole	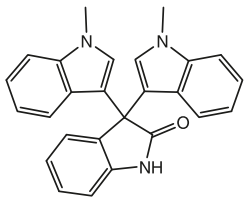 **2b**	5	90[c]
3	2-Methylindole	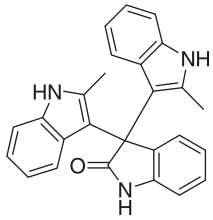 **3b**	5	98
4	3-Methylindole	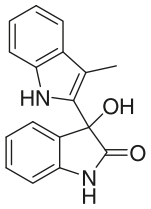 **4b**	60	75
5	5-Cyanoindole	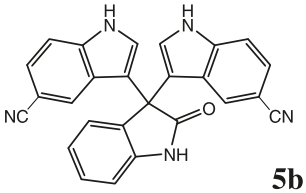 **5b**	30	78
6	5-Bromoindole	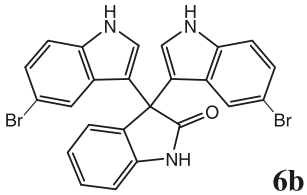 **6b**	10	92

[a]All products were characterized by ^{1}H NMR, ^{13}C NMR, and IR data.
[b]Isolated yields.
[c]Identified by comparison with authentic sample.[20]

d, J = 7.5 Hz), 7.82 (1H, d, J = 7.6 Hz), 7.92 (1H, d, J = 8.2 Hz), 10.39 (1H, s), 10.51 (1H, s), 10.92 (1H, s) ppm. ^{13}C NMR (125 MHz, $CDCl_3$, 25 °C) δ: 13.87, 14.05, 53.28, 110.21, 110.29, 111.21, 111.27, 118.78, 118.84, 120.15, 120.21, 120.46, 120.63, 122.13, 126.32, 127.90, 128.54, 128.68, 132.84, 134.81, 135.76, 135.83, 136.44, 142.06, 180.21 ppm. Anal. calcd. for $C_{26}H_{21}N_3O$: C, 79.77; H, 5.41; N, 10.73. Found: C, 79.78; H, 5.40; N, 10.72.

3-Hydroxy-3-(3-methyl-1*H*-indol-2-yl)indolin-2-one, 4b

White solid. IR (KBr) ν (cm^{-1}): 748, 1001, 1064, 1093, 1124, 1209, 1242, 1328, 1467, 1622, 1685, 1716, 2833, 2941,

Table 3. Ru^{III}-catalyzed condensation of indoles with aldimine.

Entry[a]	Indole	Product	Time (min)	Yield[b] (%)
1	Indole	**1a**	1	85[c]
2	1-Methylindole	**2b**	15	88[c]
3	2-Methylindole	**3b**	20	75
4	5-Cyanoindole	**5b**	60	67
5	5-Bromoindole	**6b**	60	70

[a]All products were characterized by ^{1}H NMR, ^{13}C NMR, and IR data.
[b]Isolated yields.
[c]Identified by comparison with authentic samples.[20]

3222, 3357. ^{1}H NMR (500 MHz, $CDCl_3$, 25 °C) δ: 2.01 (1H, br), 2.08 (3H, s), 6.90 (1H, d, J = 7.8 Hz), 7.16 (1H, t, J = 7.1 Hz), 7.21 (1H, t, J = 7.0 Hz), 7.29–7.34 (3H, m), 7.44 (1H, d, J = 7.4 Hz), 7.58 (1H, d, J = 7.8 Hz), 8.30 (1H, s), 8.75 (1H, s) ppm. ^{13}C NMR (125 MHz, $CDCl_3$, 25 °C) δ: 9.59, 97.47, 110.74, 111.17, 111.38, 119.12, 119.93, 122.81, 123.69, 126.55, 129.62, 129.77, 130.24, 131.28, 135.37, 140.91, 178.08 ppm. Anal. calcd. for $C_{17}H_{14}N_2O_2$: C, 73.37; H, 5.07; N, 10.07. Found: C, 73.43; H, 5.10; N, 10.09.

3,3-Di(5-cyano-1*H*-indole-3-yl)indolin-2-one, 5b

White solid, mp 273–275 °C. IR (KBr) ν (cm^{-1}): 752, 810, 1101, 1228, 1346, 1469, 1618, 1670, 1706, 2223, 3259, 3338. ^{1}H NMR (500 MHz, $CDCl_3$, 25 °C) δ: 6.87 (1H, t, J = 7.0 Hz), 6.91–6.95 (3H, m), 7.10–7.18 (4H, m), 7.31 (2H, d, J = 8.3 Hz), 7.62 (2H, s), 9.98 (1H, s), 10.64 (2H, s) ppm. ^{13}C NMR (125 MHz, $CDCl_3$, 25 °C) δ: 52.93, 102.03, 110.85, 113.14, 115.98, 121.45, 122.59, 124.62, 125.32, 125.99, 126.98, 128.81, 133.79, 139.47, 141.39, 179.39 ppm. Anal. calcd. for $C_{26}H_{15}N_5O$: C, 75.53; H, 3.66; N, 16.94. Found: C, 75.55; H, 3.65; N, 16.94.

3,3-Di(5-bromo-1*H*-indole-3-yl)indolin-2-one, 6b

White solid, mp 264–266 °C. IR (KBr) ν (cm^{-1}): 651, 675, 750, 798, 885, 1101, 1463, 1562, 1616, 1712, 3280, 3323, 3427. ^{1}H NMR (500 MHz, $CDCl_3$, 25 °C) δ: 6.75 (2H, d, J = 2.4 Hz), 6.79 (1H, t, J = 7.4 Hz), 6.86 (1H, d, J = 7.7 Hz), 6.97 (2H, dd, J = 8.6, 1.7 Hz), 7.02–7.08 (4H, m), 7.32 (2H, d, J = 1.3 Hz), 9.87 (1H, s), 10.12 (2H, s) ppm. ^{13}C NMR (125 MHz, $CDCl_3$, 25 °C) δ: 53.65, 110.43, 112.32, 113.51, 114.64, 122.27, 123.65, 124.47, 125.42, 126.29, 127.89, 128.40, 134.26, 136.29, 141.50, 179.64 ppm. Anal. calcd. for $C_{24}H_{15}Br_2N_3O$: C, 55.31; H, 2.90; N, 8.06. Found: C, 55.35; H, 2.92; N, 8.05.

Acknowledgements

The authors are grateful to the Research Council of Guilan University for the partial support of this study.

References

(1) Zhang, H.-C.; Ye, H.; Moretto, A. F.; Brumfield, K. K.; Maryanoff, B. E. *Org. Lett.* **2000**, *2* (1), 89–92. doi:10.1021/ol991255o. PMID:10814253.

(2) Gilchrist, T. L. In *Heterocyclic chemistry*; Academic Press: London, 1997; p. 231.

(3) Humphrey, G. R.; Kuethe, J. T. *Chem. Rev.* **2006**, *106* (7), 2875–2911. doi:10.1021/cr0505270. PMID:16836303.

(4) Popp, F. D. *J. Heterocycl. Chem.* **1984**, *21* (5), 1367–1368. doi:10.1002/jhet.5570210523.

(5) Garrido, F.; Ibanez, J.; Gonalons, E.; Giraldez, A. *Eur. J. Med. Chem.* **1975**, *10*, 143.

(6) Kamano, Y.; Zhang, H. P.; Ichihara, Y.; Kizu, H.; Komiyama, K.; Itokawa, H.; Pettit, G. R. *Tetrahedron Lett.* **1995**, *36* (16), 2783–2784. doi:10.1016/0040-4039(95)00395-S.

(7) Bergman, J.; Eklund, N. *Tetrahedron* **1980**, *36* (10), 1445–1450. doi:10.1016/0040-4020(80)85060-5.

(8) Mohammadizadeh, M. R.; Karimi, A. R. *Catal. Commun.* **2006**, *7* (10), 752–755. doi:10.1016/j.catcom.2006.01.026.

(9) Azizian, J.; Mohammadi, A. A.; Karimi, N.; Mohammadizadeh, M. R. *J. Chem. Res. Synop.* **2004**, *6*, 424.

(10) Yadav, S. S.; Subbareddy, B. V.; Kamakolanu, U. G. *Synthesis* **2006**, *2006* (24), 4121–4123. doi:10.1055/s-2006-950373.

(11) Tabatabaeian, K.; Mamaghani, M.; Mahmoodi, N. O.; Khorshidi, A. *Can. J. Chem.* **2006**, *84* (11), 1541–1545. doi:10.1139/V06-159.

(12) Tabatabaeian, K.; Mamaghani, M.; Mahmoodi, N. O.; Khorshidi, A. *J. Mol. Catal. A* **2007**, *270* (1-2), 112–116. doi:10.1016/j.molcata.2007.01.038.

(13) Tabatabaeian, K.; Mamaghani, M.; Mahmoodi, N. O.; Khorshidi, A. *Tetrahedron Lett.* **2008**, *49* (9), 1450–1454. doi:10.1016/j.tetlet.2008.01.001.

(14) Tabatabaeian, K.; Mamaghani, M.; Mahmoodi, N. O.; Khorshidi, A. *Catal. Commun.* **2008**, *9* (3), 416–420. doi:10.1016/j.catcom.2007.07.024.

(15) Murahashi, S.-I. In *Ruthenium in organic synthesis*; Wiley-VCH: New York, 2004.

(16) Bruneau, C.; Dixneuf, P. H. In *Ruthenium catalysts and fine chemistry*; Springer, 2004.

(17) Murai, S. In *Activation of unreactive bonds and organic synthesis*; Springer, 1999.

(18) Ganachaud, C.; Garfagnoli, V.; Tron, T.; Iacazio, G. *Tetrahedron Lett.* **2008**, *49* (15), 2476–2478. doi:10.1016/j.tetlet.2008.02.021.

(19) Janosik, T.; Bergman, J. *Heterocycles* **2002**, *57* (7), 1273. doi:10.3987/COM-02-9477.

(20) Wang, S.-Y.; Ji, S.-J. *Tetrahedron* **2006**, *62* (7), 1527–1535. doi:10.1016/j.tet.2005.11.011.

(21) Banerji, J.; Kumar, M.; Sarkar, S. *Indian J. Chem.* **1983**, *22*, 27.

(22) Wynne, J. H.; Stalick, W. M. *J. Org. Chem.* **2002**, *67* (16), 5850–5853. doi:10.1021/jo020049i. PMID:12153292.

(23) Bowen, K.; Qin, Y.; He, Q.; Huang, Z.; Wang, F. *Tetrahedron Lett.* **2005**, *46* (10), 1751–1753. doi:10.1016/j.tetlet.2004.12.140.

Phenolic constituents of *Phellodendron chinense* bark

Xue-Hu Li, Wen-Juan Zhang, Huan-Yang Qi, and Yan-Ping Shi

Abstract: The bark of *Phellodendron chinense* is a very important herbal medicine in traditional Chinese medicine. In a detailed phytochemical investigation, a new phenolic lactone, 2β,3β-dihydroxy-3α-vanilloylmethyl-γ-lactone (named as phellolactone) (**1**), and nine known phenolic compounds (**2–10**) were isolated from the bark of *P. chinense* Schneid. Their structures were characterized by spectroscopic methods, including IR, UV, HR-ESI-MS, NMR, and chemical transformation analysis.

Key words: Phellodendron chinense, Rutaceae, Phenolic constituents, Phellolactone.

Résumé : L'écorce du *Phellodendron chinense* est un produit très important dans la médication chinoise traditionnelle. Dans une étude phytochimique détaillée de l'écorce du *P. chinense* Schneid, on a isolé une nouvelle lactone phénolique, la 2β,3β-dihydroxy-3α-vanilloylméthyl-γ-lactone (dénommée phellolactone) (**1**) et neuf nouveaux composés phénoliques (**2–10**). Les structures ont été caractérisées par des méthodes spectroscopies, dont l'IR, l'UV, la spectrométrie de masse à haute résolution avec ionisation par électronébulisation, la RMN et l'analyse des transformations chimiques.

Mots-clés : Phellodendron chinense, rutaceae, constituants phénoliques, phellolactone.

[Traduit par la Rédaction]

Introduction

Phellodendron chinense Schneid (Rutaceae) is a deciduous tree found widely in Southwest China. The bark extracts of the tree have been used for the treatment of meningitis, bacillary dysentery, pneumonia, tuberculosis, and liver cirrhosis in traditional Chinese medicine.[1] However *Phellodendron amurense* is listed as invasive species in both the United States and Canada.[2] Previous phytochemical investigations of this plant revealed the presence of some alkaloids, flavonoids, and coumarins.[3–5] In the continuous search for new and bioactive components from traditional Chinese medicine, we selected the bark of *P. chinense*. This paper details the isolation and identification of eleven phenolic components obtained from *P. chinense*, two of the eleven components are new compounds.

Results and discussion

The 95% ethanol extract of the *P. chinense* was subjected to column chromatography to give a new phenolic lactone (**1**) (Fig. 1), together with nine other known phenolic compounds (**2–10**) (Fig. 1). The structures of the known compounds were elucidated using 1D and 2D NMR spectroscopic data and compared with those reported in the literature.

Phellolactone (**1**) was obtained as colorless oil. Its molecular formula, $C_{13}H_{14}O_8$, was deduced from HR-ESI-MS data at *m/z* 321.0582 $[M + Na]^+$ (calcd.: 321.0581 for $C_{13}H_{14}O_8Na$). The IR spectrum showed absorption bands for hydroxyl (3410 cm^{-1}), ester carbonyl (1706 and 1786 cm^{-1}), and phenyl (1599, 1516, and 1462 cm^{-1}) groups. The UV spectrum displayed maximal absorptions at 210, 258, and 292 nm. The CD spectrum showed negative Cotton effect at 212 and 225 nm.

In the ^1H and ^{13}C NMR spectra (Table 1), the aromatic signals at δ_H 7.61 (d, J = 8.0 Hz, H-6′), 7.57 (s, H-2′), and 6.88 (d, J = 8.0 Hz, H-5′) were assigned to a 1,3,4-trisubstituted benzene ring. An oxymethine signal at δ_H 4.64 (m, H-2) and two oxymethylene signals at δ_H 4.42 (m, H-5), δ_H 4.26 (d, J = 10.0 Hz, H-4a), and δ_H 4.44 (m, H-4b), as well as the five carbon resonances at δ_C 64.3 (C-5), 69.6 (C-2), 71.4 (C-4), 75.1 (C-3), and 174.5 (C-1) implied the presence of a five-carbon substructure. The HMBC correlations of H-2 and H-4 with C-1 (Fig. 2), combined with the IR absorption band at 1786 cm^{-1}, indicated that the five-carbon substructure should include a γ-lactone moiety with two hydroxyl groups. The functional groups could be attached by key correlations in the HMBC experiment (Fig. 2). The correlations of H-2′ and H-6′ with C-7′ indicated that the carbonyl carbon (C-7′) at δ_C 165.1 was connected to the C-1′ of the benzene ring. The correlation of the methoxyl protons at δ_H 3.87 (s, 3H) with C-3′ indicated that it was connected to C-3′. Therefore, compound **1** should include a vanilloyl moiety, and both substructures could also be put together by observable correlation between H-5 and C-7′ in the HMBC.

The NOE correlation of H-2 with H-5b was an important evidence for the cis-orientation of H-2 and H-5b, but two

Received 21 March 2009. Accepted 22 June 2009. Published on the NRC Research Press Web site at canjchem.nrc.ca on 18 August 2009.

X.-H. Li and W.-J. Zhang. Key Laboratory for Natural Medicine of Gansu Province, Lanzhou Institute of Chemical Physics, Chinese Academy of Sciences, Lanzhou 730000, P. R. China; The Graduate University of Chinese Academy of Sciences, Chinese Academy of Sciences, Beijing 100039, P. R. China.
H.-Y. Qi and Y.-P. Shi.[1] Key Laboratory for Natural Medicine of Gansu Province, Lanzhou Institute of Chemical Physics, Chinese Academy of Sciences, Lanzhou 730000, P. R. China.

[1]Corresponding author (e-mail: shiyp@lzb.ac.cn).

Fig. 1. Structures of compounds **1**–**10**.

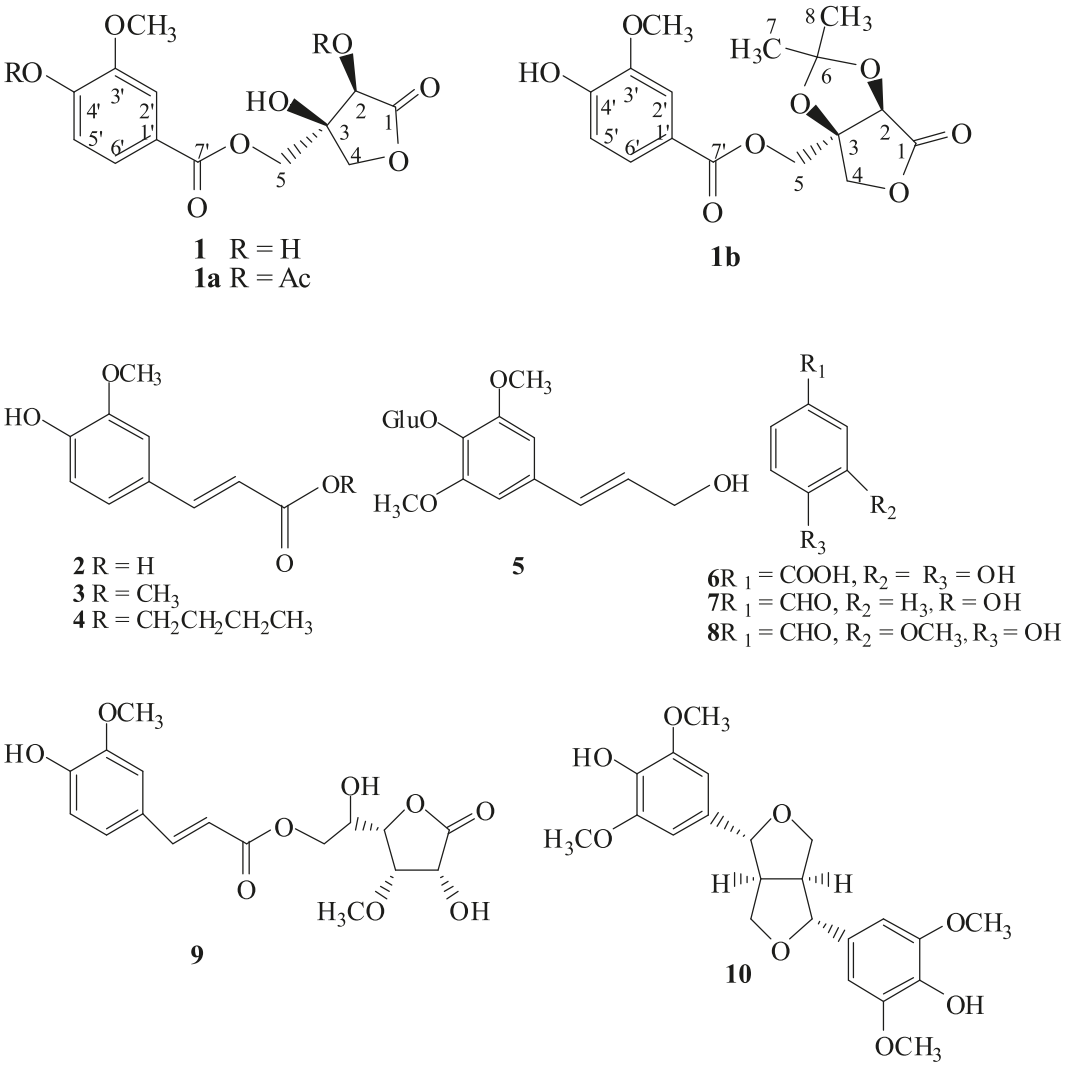

key proton signals of the H-4b and H-5 could not be exactly distinguished (Table 1). To further confirm the relative configuration of compound **1** by NMR techniques, this material was transformed into the acetate **1a**. HR-ESI-MS of the acetylated product **1a** (Fig. 1) gave a molecular ion peak at *m*/*z* 400.1233 $[M + NH_4]^+$ ($C_{17}H_{18}O_{10}N$). The assignments of all proton signals and carbon signals were established from the results of the 1D and 2D NMR as shown in Table 1. Additionally, a clear correlation was observed in NOESY experiment of **1a** between H-5 and H-2; it is another important evidence for the cis-orientation of H-2 and C-5, and the correlation of the methoxyl protons at δ_H 3.87 (s, 3H) with C-2′ confirmed that the methoxy was connected to C-3′. So, the structure of phellolactone **1** was elucidated as 2β,3β-dihydroxy-3α-vanilloylmethyl-γ-lactone and named as phellolactone after the plant (Fig. 1).

Phellolactone-2,3-acetonide (**1b**) was obtained as colorless oil. The molecular formula of **1b** was established as $C_{16}H_{18}O_8$ on the basis of HR-ESI-MS analysis (*m*/*z* 356.1330 $[M + NH_4]^+$, calcd.: 356.1340) with eight degrees of unsaturation. The IR spectrum showed absorption bands for the ester carbonyl (1712 cm^{-1}) and phenyl (1598, 1516, and 1425 cm^{-1}) groups. The presence of acetonide was indicated by a strong absorption of a geminal dimethyl (1362 cm^{-1}) and a dioxolane ring (1095 and 1223 cm^{-1}). The structure of **1b** was determined also from the ^1H and ^{13}C NMR spectra (Table 1) and compared with the corresponding data of phellolactone (**1**). The additional resonance corresponding to two methyl singlets at δ_H 1.44 and 1.49, a downfield shift of H-2 (0.13 ppm) in the ^1H NMR spectrum (Table 1), and the carbon signals at δ_C 115.1, 27.9, and 27.4, together with downfield shifts of C-2 (7.3 ppm) and C-3 (9.1 ppm), against **1b** in the ^{13}C NMR spectrum (Table 1), implyed that **1b** could be an acetonide of **1** originating from the addition of an acetone unit with the OH groups attached to C-2 and C-3. HMBC correlations of H-2 and of H-7/8 with C-6 were observed, and therefore, the gross structure of **1b** was depicted.

Additionally, a clear correlation between H-5 and H-2 could be observed in NOESY experiment of **1b**, and it confirmed the cis-orientation of H-2 and C-5. So, compound **1b** could be confirmed as phellolactone-2,3-acetonide (Fig. 1). Since acetone has been used as a solvent in the isolation and purification of these compounds, compound **1b** should be an artifact resulting from the isolation process. When we repeated the isolation procedure without acetone, compound

Table 1. ^{1}H NMR (400 MHz) and ^{13}C NMR (100 MHz) spectral data of Compounds **1**, **1a**, and **1b**.

	1[a]		**1a**[b]		**1b**[b]	
Position	δ_H (*J* in Hz)	δ_C	δ_H (*J* in Hz)	δ_C	δ_H (*J* in Hz)	δ_C
1		174.5 s		170.5 s		173.6 s
2	4.64 s	69.6 d	5.67 s	69.9 d	4.77 s	76.9 d
3		75.1 s		72.5 s		84.7 s
4a	4.26 d (10.0)	71.4 t	4.35 s	75.9 t	4.43 d (10.4)	72.9 t
4b	4.44 m[c]				4.50 d (10.4)	
5a	4.42 m[c]	64.3 t	4.31 d (12.0)	65.1 t	4.45 s	63.8 t
5b			4.48 d (12.0)			
6						115.1 s
7					1.44 s	27.4 q
8					1.49 s	27.9 q
1′		120.3 s		127.4 s		120.8 s
2′	7.57 s	112.2 d	7.59[c]	113.5 d	7.48 d (2.0)	111.7 d
3′		146.8 s		151.3 s		146.4 s
4′		151.2 s		144.1 s		150.7 s
5′	6.88 d (8.0)	114.2 d	7.08 d (8.8)	123.0 d	6.92 d (8.4)	114.3 d
6′	7.61 d (8.0)	123.6 d	7.58[c]	122.6 d	7.57 dd (8.4, 2.0)	124.3 d
7′		165.1 s		165.3 s		165.5 s
3′-OCH_3	3.87 s	55.0 q	3.86 s	56.1 q	3.92 s	56.1 q
Ac				169.2, 20.3 168.6, 20.5		

[a]In acetone-d_6.
[b]In $CDCl_3$.
[c]Overlapped signals.

Fig. 2. The key HMBC correlations (H→C) of **1**.

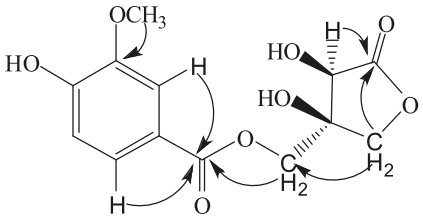

1b was not observed by TLC, which confirmed the conclusion above.

The remaining compounds were characterized as ferulic acid (**2**),[6] methyl ferulate (**3**),[7] *n*-butyl ferulate (**4**),[8] syringin (**5**),[9] protocatechuic acid (**6**),[10] *p*-hydroxybenzaldehyde (**7**),[11] vanillin (**8**),[12] amurenlactone A (**9**),[13] and (–)(–) syringaresinol (**10**)[14] (Fig. 1) by comparison with their reported physical and spectroscopic data. Compounds **3**, **4**, **6**, **9**, and **10** were isolated and identified from this plant species for the first time.

Experimental

General experimental procedures

Optical rotations were recorded in $CHCl_3$ using a PerkinElmer 241 polarimeter. UV spectra were measured on a Spect 50-UV–vis instrument (Analytic Jena AG). IR spectra were measured on an FTS 165-IR spectrometer (Bio-Rad, USA). CD spectra were recorded on an Olis DSM 10000 spectrophotometer. ^{1}H NMR (400 MHz), ^{13}C NMR (100 MHz), and 2D NMR were recorded on a Varian INOVA-400 FTNMR spectrometer (USA) in $CDCl_3$ with TMS as internal standard. HR-ESI-MS (high resolution electrospray ionization mass spectrometry) was determined on a Bruker APEX II. EI-MS was determined on a HP 5988A MS (70 eV). Separation and purification were performed by column chromatography (CC) over silica gel. Silica gel (200–300 mesh), used for CC, and silica gel (GF_{254}) for TLC were supplied by the Qingdao Marine Chemical Factory, Qindao, P. R. China. Spots were detected on the TLC under UV light or by heating over 110 °C after spraying with 98% H_2SO_4/EtOH (*v*/*v*, 5:95).

Plant material

The commercial bark of *P. chinense*, which was collected from Sichuan province and was authenticated by Dr. Huan-Yang Qi in Lanzhou Institute of Chemical Physics, Chinese Academy of Sciences, Lanzhou, was obtained from Lanzhou Ltd. Co. of Fuxinhou herbal medicines. A voucher specimen (No. ZY2007P001) is deposited at the Key Laboratory for Natural Medicine of Gansu Province.

Extraction and isolation

The air-dried and powdered bark of *P. chinense* (9.8 kg) was extracted three times with 95% ethanol under reflux. The extract was obtained by vacuum concentration, suspended in water, and successively extracted with petroleum ether, ethyl acetate, and *n*-butanol. The ethyl acetate fraction was subjected to silica-gel CC, eluted with $CHCl_3$/MeOH (*v*/*v*, 20:1–1:1) to afford eight fractions (fractions 1–8). Fraction 2 was separated on CC over silica gel (200–300 mesh) with $CHCl_3$/acetone (15:1) to give crude **2**, which was further isolated and purified on a silica-gel column (200–300 mesh) with petroleum ether/acetone (2:1) to give the pure compound **2** (15.0 mg). Fraction 3 was subjected to a silica-gel

eluting with petroleum ether/acetone (4:1) to yield **7** (12.0 mg) and **8** (10.0 mg). Fraction 4 was purified by repeated CC over silica gel, eluted by petroleum ether and acetone (2:1) to provide **1b** (8.0 mg) and **1** (30 mg). Fraction 5 was chromatographed on silica gel and eluted with $CHCl_3$/acetone (4:1) to produce **6** (11.0 mg). Fraction 6 was separated by silica-gel chromatography using $CHCl_3$/acetone (3:1) to yield **9** (20.0 mg) and **10** (9.0 mg). From the *n*-butanol fraction, compounds **3** (13.0 mg), **4** (15.0 mg), and **5** (20.0 mg) were isolated after repeated column chromatography and recrystallization. In addition, fraction 4 was checked by TLC (run by $CHCl_3$/MeOH, 15:1) to find compound **1**, not **1b**.

Phellolactone (2β,3β-dihydroxy-3α-vanilloylmethyl-γ-lactone)

Colorless oil. $[\alpha]_D^{20}$ + 12.0 (*c* 0.1, $CHCl_3$). UV (MeOH) λ_{max} (log ε):210, 258, 292 nm. IR (film) ν_{max}: 3410 (OH), 2922, 2851, 1786, 1706 (ester carbonyl function), 1598, 1705, 1598, 1516, 1462, 1429, 1371, 1287, 1220, 1122, 1015, 879, 763 cm^{-1}. ^1H and ^{13}C NMR: see Table 1. HR-ESI-MS *m*/*z* calcd. for $C_{13}H_{14}O_8Na$: 321.0581 $[M + H]^+$; found: 321.0582.

Phellolactone-2,3-acetonide

Colorless oil. IR (film) ν_{max}: 3003, 1794, 1712 (ester carbonyl function), 1425, 1362, 1284, 1223, 1095, 1029, 531 cm^{-1}. ^1H and ^{13}C NMR: see Table 1. HR-ESI-MS *m*/*z* calcd. for $C_{16}H_{22}O_8N$: 356.1340 $[M + NH_4]^+$; found: 356.1330.

Acknowledgment

The work was supported by the National 863 Program of China (No. 2007AA09Z403), the National Key Technology Research and Development Program of China (No. 2007BAI37B05), and the Natural Science Foundation of Gansu Province (No. 0710RJZA120).

References

(1) Shiao, P. G. *Photocatalogue of Traditional Chinese Medicine;* Taiwan Business Publication Company: Taipei, 1989; Vol. 3, p. 86.
(2) USDS FS FHTET. *Invasive Plants of Asian Origin Established in the US and Their Natural Enemies* [Online]; 2005; p. 131–132. www.invasive.org/weeds/asian/phellodendron.pdf (accessed April 1, 2005).
(3) el Izzi, A.; Benie, T.; Thieulant, M. L.; Le Men-Olivier, L.; Duval, J. *Planta Med.* **1992**, *58* (03), 229–233. doi:10.1055/s-2006-961441. PMID:1409976.
(4) Guo, S. H.; Zhou, M. H.; Li, S. M.; Li, Y. Q. *Journal of Jinan University (Natural Science)* **1998**, *19*, 68.
(5) Zobel, A. M.; Brown, S. A. *Can. J. Bot.* **1991**, *69* (3), 485–488. doi:10.1139/b91-065.
(6) Yang, X. D.; Xu, L. Z.; Yang, S. L. *China Journal of Chinese Materia Medica* **1988**, *36*, 5004.
(7) Bohlmann, F.; Zdero, C. *Chem. Ber.* **1977**, *110* (2), 487–490. doi:10.1002/cber.19771100211.
(8) Vafiadi, C.; Topakas, E.; Wong, K. Y.; Suckling, L. D.; Christakopoulos, P. *Tetrahedron* **2005**, *16* (2), 373–379. doi:10.1016/j.tetasy.2004.11.037.
(9) Wu, L. J.; Shen, Y.; Zheng, J.; Wu, B. *Chinese J. Magn. Reson.* **1999**, *16*, 465.
(10) Yin, T.; Liu, H.; Wang, F.; Zhao, Y. Y. *Acta Pharmacol. Sin.* **2008**, *43*, 67.
(11) Li, P.; Zuo, T. T.; Wang, X. Q.; Wu, S. H.; Zhang, G. G. *Chinese J. Med. Chem.* **2008**, *18*, 374.
(12) Numata, A.; Kawai, K.; Takahashi, C. *Phytochemistry* **1992**, *31*, 3373.
(13) Zhou, H. Y.; Wang, D.; Cui, Z. *J. Asian Nat. Prod. Res.* **2008**, *10* (5), 409–413. doi:10.1080/10286020801966534. PMID:18464078.
(14) Buske, A.; Schmidt, J.; Porzel, A.; Adam, G. *Phytochemistry* **1997**, *46* (8), 1385–1388. doi:10.1016/S0031-9422(97)00488-3.

Synthesis and properties of ladder-type 1,4-dihydro-1,4-phosphasilins

Yi Ren, Thomas Linder, and Thomas Baumgartner

Abstract: The synthesis and advanced characterization of a series of extended dithieno[2,3-*b*:3′,2′-*e*][1,4-dihydro-1,4]phosphasilins is reported, and their suitability as new building blocks for organic electronics is evaluated. Synthesis of basic, as well as benzo-extended dithienophosphasilins, can be achieved using appropriate 2,3-dibromothiophene precursors in a two-step protocol introducing the silicon and phosphorus centers subsequently. Both ladder-type materials show the typical reactivity of trivalent phosphorus species and can quantitatively be converted into the corresponding oxides or gold complexes, the latter exemplified with the basic dithienophosphasilin. Their optoelectronic properties were found to be inferior to those of related dithieno[3,2-*b*:2′,3′-*d*]phospholes, indicating a disruption of the π-conjugation in the molecular scaffold. X-ray crystallographic studies revealed that the molecular scaffold is planar in the oxidized benzo-extended material, whereas the basic dithieno materials show some small deviation from planarity. Density functional theory calculations suggest all materials to be planar, with the exception of the benzo-extended trivalent phosphasilin. This structure–property study illustrates that the disruption of the π-conjugation in the molecular scaffold of the extended phosphasilins is exclusively due to the presence of the silicon center and its electronic effects, rather than structural features.

Key words: phosphorus heterocycles, silicon heterocycles, organic electronics, thiophene, π-conjugation.

Résumé : On a effectué la synthèse et la caractérisation avancée d'une série étendue de dithiéno[2,3-*b*:3′,2′-*e*][1,4-dihydro-1,4-]phosphasilines et on a évalué la possibilité de les utiliser dans la synthèse de composés organiques électroniques. On peut réaliser la synthèse du produit de base ainsi que de diverses benzodithiénophosphasilines en utilisant comme précurseurs des 2,3-dibromothiophènes appropriés dans un protocole en deux étapes au cours desquelles on introduit les centres siliciés et phosphorés ultérieurement. Les deux types de matériaux en échelle présentent la réactivité type des espèces contenant du phosphore trivalent et ils peuvent être transformés quantitativement en oxydes correspondants ou en complexes d'or, un exemple de ce dernier ayant été préparé avec la dithiénophosphasiline basique. On a trouvé que leurs propriétés optoélectroniques sont inférieures à celles des dithiéno[2,3-*b*:3′,2′-*d*]phospholes, ce qui indique qu'il se produit une interruption dans la conjugaison π dans l'échafaudage moléculaire. Les études cristallographiques par diffusion des rayons X révèlent que l'échafaudage moléculaire est plan dans les dérivés benzo-condensés oxydés alors que les matériaux dithiéno de base présentent de faibles déviations par rapport à la planéité. Des calculs à base de la théorie de la fonctionnelle de la densité suggèrent que tous les matériaux doivent être plans, à l'exception de la benzophosphasiline trivalente. L'étude structure propriété illustre le fait que la disruption de la conjugaison π dans l'échafaudage moléculaire de phosphasilines étendues est exclusivement due à la présence du centre silicium et de ses effets électroniques et n'a rien à voir avec ses caractéristiques structurales.

Mots-clés : hétérocycles du phosphore, hétérocycles du silicium, électroniques organiques, thiophène, conjugaison π.

[Traduit par la Rédaction]

Introduction

Organic π-conjugated materials have received significant attention in recent years owing to their beneficial photophysical and electronic properties that provide intriguing opportunities for the field of organic electronics. Their semiconducting properties, in particular, show great potential for application in electronic devices such as molecular or polymer-based light-emitting diodes, photovoltaic cells, field-effect transistors, and sensory materials.[1–5]

Surprisingly, organophosphorus π-conjugated materials have received relatively little attention up until recently, despite the fact that the incorporation of σ^3,λ^3-phosphorus centers allows for a number of facile, nearly quantitative chemical modifications to be performed that significantly impact the materials' electronic structure.[6] The versatile reactivity of trivalent phosphorus centers allows for the preparation of entire families of materials from a single precursor, through oxidation or complexation of the phosphorus center.[7] Well-defined molecular systems thus allow for the investigation of important structure–property relationships through the systematic variation of the model's chemical structure that may then be used subsequently to tailor the materials' properties towards certain applications.[6a]

Received 19 May 2009. Accepted 16 June 2009. Published on the NRC Research Press Web site at canjchem.nrc.ca on 18 August 2009.

Y. Ren, T. Linder, and T. Baumgartner.[1] Department of Chemistry, University of Calgary, 2500 University Drive NW, Calgary, AB T2N 1N4, Canada.

[1]Corresponding author (e-mail: thomas.baumgartner@ucalgary.ca).

Chart 1. Relevant, ring-annelated dithieno- and dibenzo-heterocycles reported in the literature.

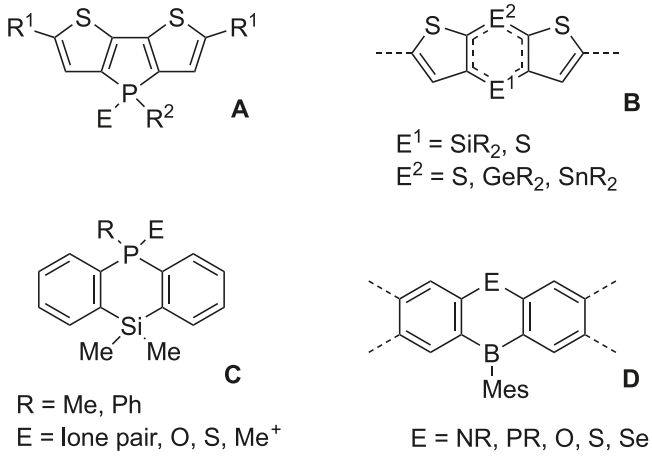

A few years ago, we introduced the dithieno[3,2-*b*:2′,3′-*d*]phosphole system (Chart 1A) as a new building block for π-conjugated materials.[8] This system conjoins two thiophene subunits with a central phosphole moiety via annelation. Fused bithiophene materials are generally promising candidates for an application in organic electronics, as they provide a high degree of π-conjugation due to their rigidified, planar structure that intrinsically affords smaller HOMO–LUMO (highest occupied molecular obrital – lowest unoccupied molecular orbital) gaps.[9] Our extensive, systematic investigations to date have revealed that this is also true for the dithienophosphole system and we were able to confirm a doping function for the phosphorus center, rather than it being an integral part of the π-conjugated system.[8]

The materials obtained in the context of our studies display intriguing photophysical properties with respect to emission wavelengths, intensity, and tunability that are far superior over those of related dibenzophospholes;[10,11] the parent dithienophosphole scaffold is strongly blue-light emitting with photoluminescence efficiencies of up to 90%. Notably, its photophysical properties can efficiently be tuned by simple modifications at either the phosphorus center (E = lone pair) via oxidation (E = O, S), complexation with main group centers (E = BH_3, CH_3^+) or transition metals (E = [M]), or by variation of the substitution pattern (R^1 on the thieno units or R^2 on the central phosphorus atom; see Chart 1).[6f,8,11]

Expanding our work on dithienophospholes, in this paper we now report our initial structure–property investigations on a new class of ladder-type, π-conjugated materials with a central 6-membered, 1,4-dihydro-1,4-phosphasilin ring (Chart 1B; E^1 = PPh, E^2 = $SiMe_2$). We were interested in how the addition of an additional silylene group within the molecular scaffold of dithienophospholes would impact the structure and properties of the resulting class of materials. It should be mentioned in this context that the number of reported six-membered, heterocyclic fused bithiophene materials to date is limited to a few thia-silins,[12,13] -germins, and -stannins (Chart 1B),[12] as well as dithieno-1,2-disilins[14]; most of the dithieno materials reported to date showcase five-membered central heterocycles.[9a] Although dibenzophosphasilins (Chart 1C) have been reported by Skvortsov, Toldov, and co-workers[15] in the early 1990s, and

Scheme 1. Synthesis and reactivity of the dithienophosphasilin (**3**).

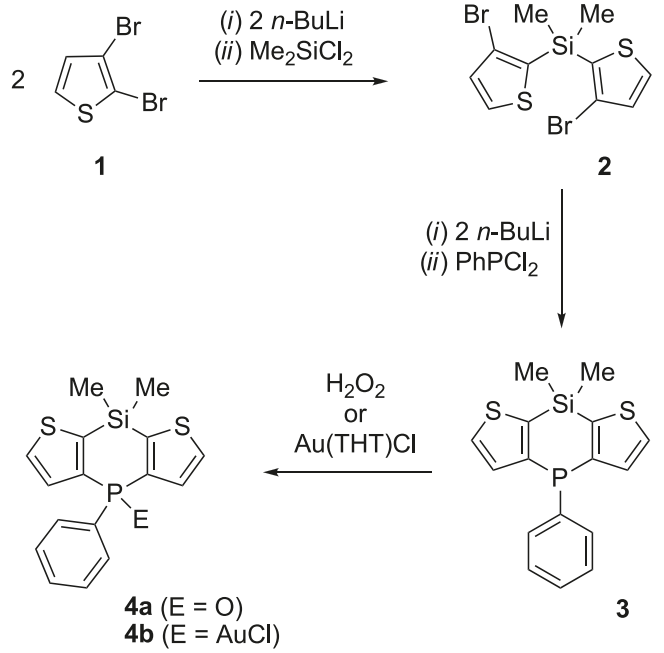

Nakayama and co-workers[16] have reported somewhat related phospha-sila-thienotrypticenes in 1993, neither manuscript focuses on organic electronics. It is noteworthy, however, that Kawashima and co-workers[17] have recently reported a series of dibenzoborin-based materials (Chart 1D) that show very promising optoelectronic features for a potential application in organic electronics.

This present investigation now explores the synthetic accessibility and properties of dithieno[2,3-*b*:3′,2′-*e*][1,4-dihydro-1,4]phosphasilins, and the chemical versatility of the phosphorus center for additional fine-tuning. The study is further supported by theoretical investigations to gain a deeper understanding of the properties of this new ladder-type system.

Results and discussion

Synthesis and characterization

The synthesis of the targeted dithienophosphasilin (**3**) (Scheme 1) is straightforward using 2,3-dibromothiophene as starting material. Due to the ortho-directing effect of the sulfur atom, the 2-position of the thiophene is favored towards selective lithiation with *n*-butyllithium at –78 °C. Subsequent treatment with 0.5 equiv. of Me_2SiCl_2 affords the formation of the dithienyldimethylsilane (**2**) in good yield (80%). The further addition of 2 equiv. of *n*-butyllithium at –78 °C allows for the remaining bromo-substituents of **2** to be lithiated, and the central six-membered ring is closed by addition of $PhPCl_2$, providing **3** in a similarly high yield (80%). The dithienophosphasilin (**3**) shows a ^{31}P NMR resonance at δ = –20.7 ppm that is related to those of dithienophospholes (cf.: δ = –20 ± 3 ppm).[8,10] A ^{29}Si NMR shift of δ = –17.7 ppm further supports the successful formation of **3**;[18] the same is true for the ^1H and ^{13}C NMR data. As mentioned in the introduction, the trivalent phosphorus center in **3** is an excellent site for further modification, allowing for the generation of a whole family of new materi-

als. To verify this important tool of organophosphorus π-conjugated materials[6a] for this new ladder-type system, we have performed two representative chemical modifications converting **3** into the corresponding oxide **4a** by treatment with hydrogen peroxide, and the gold complex **4b** by treatment with Au(THT)Cl at room temperature, respectively (Scheme 1). The distinct lowfield shifted ^{31}P NMR resonances observed for the modified compounds **4a** (δ = 11.5 ppm) and **4b** (δ = 5.4 ppm) clearly support the successful transformation, as they again relate fairly well to the values of the corresponding dithienophosphole oxides and gold complexes;[8,11] the same is true for the ^{1}H and ^{13}C NMR data. The ^{29}Si NMR resonances, on the other hand, are less of a clear indicator, as they remain essentially unchanged at δ = –17.8 ppm (**4a**) and δ = –17.6 ppm (**4b**).

To our surprise, however, none of the three phosphasilin materials, **3**, **4a**, or **4b**, showed any notable fluorescence, which is in stark contrast to strongly emitting dithienophospholes.[8,11] This indicates that the incorporation of the silicon center appears to disrupt the π-conjugation across the system by essentially separating the chromophore into two independent thiophene units. The observation is also supported by the UV–vis spectroscopic data of the three compounds that only show narrow absorptions in the deep UV region of the optical spectrum at λ_{max} = 236 nm for **3**, 237 nm for **4a**, and 250 nm for **4b** (cf. thiophene: λ_{max} = 230 nm).[19]

The investigations on the related dibenzophosphasilins have illustrated that their scaffold is nonplanar at the P–Si sites, and the central ring generally shows a pronounced boat conformation. Furthermore, the resulting dihedral angle between the two halves of the molecule was found to depend on the chemical nature of the P center.[15] To verify whether the scaffold in the dithienophosphasilin system is also bent (or planar), we have investigated the solid-state structures of the two modified species, **4a** and **4b**. We were able to obtain single crystals suitable for X-ray diffraction studies of both compounds at room temperature from acetone solutions. The structure of **4a** shows two independent molecules in the unit cell, both of which show a somewhat bent molecular scaffold with dihedral angles amounting to approximately 20° and 17.5° (Fig. 1). In contrast to the dibenzo system, the central phosphasilin ring in both molecules is fairly planar, with the silicon center showing a slightly more pronounced deviation from planarity (Si: 0.31/0.32 Å; P: 0.20/0.13 Å). The bond lengths of the molecular scaffold suggest two isolated thiophene units without significant conjugation across the central phosphasiline ring, which is in line with the features observed for the dibenzophosphasilins.[15]

The gold complex **4b**, on the other hand, exhibits an essentially planar central phosphasiline ring (deviation: 0.17 Å for Si and 0.15 Å for P), and the rest of the molecular scaffold shows a significantly smaller deviation from planarity (~11°; Fig. 2). Remarkably, the dithienophosphasilin scaffold of **4b** is bent towards the exocyclic phenyl ring, whereas in **4a** the opposite direction is observed (away from phenyl group). The bond lengths and angles of the molecular scaffold of **4b** support a comparably more delocalized electronic structure within the central 1,4-phosphasilin ring. Whereas endocyclic C–C bonds are significantly elongated (C3–C4: 1.382(7) Å, C5–C6: 1.371(8) Å), when compared

Fig. 1. Two views of the molecular structure of **4a** in the solid state (50% probability level; H atoms are omitted for clarity). Selected bond lengths (Å) and angles (°): P1—O1 1.496(4), C1—C2 1.368(9), C2—C3 1.437(8), C3—C4 1.383(8), C5—C6 1.377(8), C6—C7 1.433(8), C7—C8 1.358(9), P1—C3 1.789(6), P1—C6 1.800(6), P1—C11 1.807(5), Si1—C4 1.863(6), Si1—C5 1.870(6), Si1—C21 1.855(7), Si1—C22 1.860(6); dihedral angle at P–Si axis: 20.09/17.46.

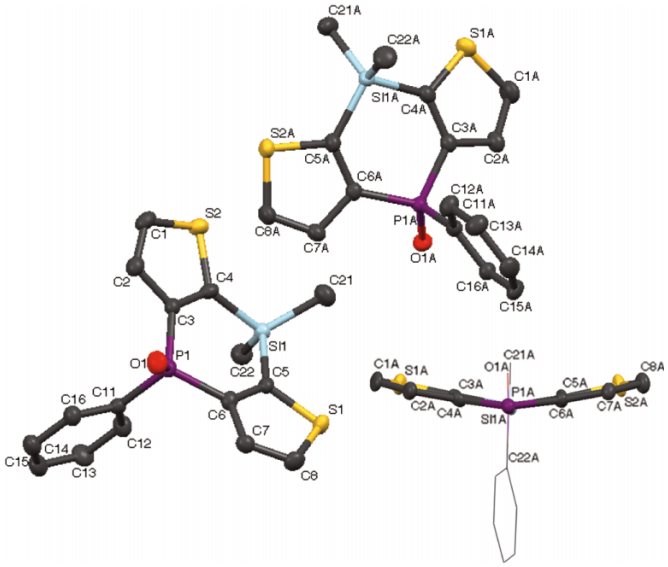

Fig. 2. Two views of the molecular structure of **4b** in the solid state (50% probability level; H atoms are omitted for clarity). Selected bond lengths (Å) and angles (°): Au1—Cl1 2.2861(13), Au1—P1 2.2297(13), C1—C2 1.358(8), C2—C3 1.423(7), C3—C4 1.382(7), C5—C6 1.371(8), C6—C7 1.433(7), C7—C8 1.355(9), P1—C3 1.802(5), P1—C6 1.810(6), P1—C11 1.813(6), Si1—C4 1.853(6), Si1—C5 1.865(6), Si1—C21 1.856(6), Si1—C22 1.858(6); P1–Au1–Cl1 178.24(5); dihedral angle at P–Si axis: 10.94.

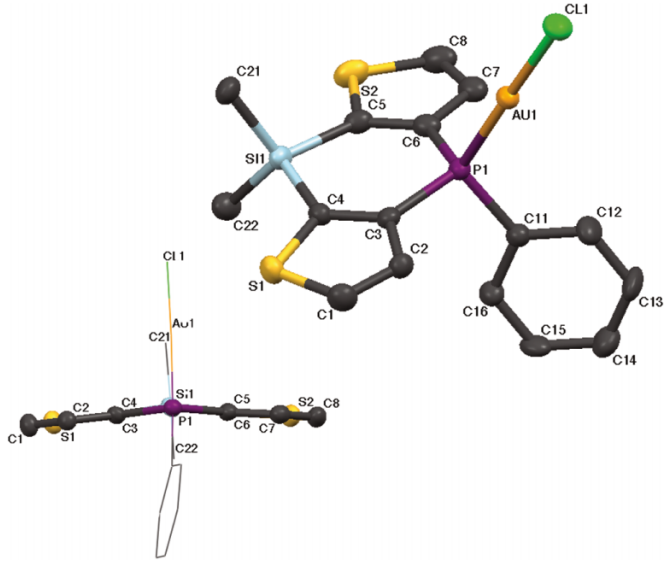

with the peripheral C1–C2 and C7–C8 bonds at 1.358(8) and 1.355(9) Å, respectively, the endocyclic Si–C (1.865(6) and 1.856(6) Å) and P–C bonds (1.802(5) and 1.810(6) Å)

Scheme 2. Synthesis and chemical modification of the benzoannelated dithienophosphasilin (**7**).

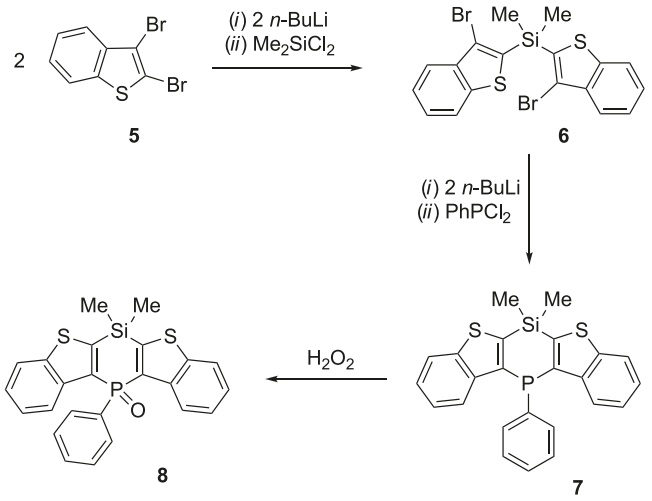

are similar in length to the respective exocyclic Si–C/P–C bonds within the margin of error (Fig. 2).

The bond lengths between the gold center and P1 (2.2297(13) Å) or Cl1 (2.2861(13) Å) relate well to those observed for the dithienophosphole system.[11b,11e] Remarkably, **4b** exists as a monomer in the solid state and shows no intermolecular contacts through aurophilic interactions. Although we have observed this feature with the dithienophosphole system once before,[11b] related complexes usually show dimerization through aurophilic interactions in the solid state.[11e,20] The monomeric structure of **4b** can, however, be explained through sterics, as the somewhat bulky dimethylsilylene group does not easily allow for π-stacking interactions between two neighboring dithienophosphasilines brought together in a potential dimer, as observed in the dimeric dithienophosphole gold complexes.

To potentially reduce the band gap of the dithienophosphasiline scaffold and to increase the degree of delocalization for improved optoelectronic properties of the materials, we have targeted corresponding benzo-extended dithienophosphasilins next. We could recently confirm this feature with the benzo-extended dithienophosphole system that does indeed show a smaller band gap than the parent system.[21] Synthesis of the corresponding benzoannelated dithienophosphasilin is possible in a protocol similar to that for the parent dithienophosphasilins (vide supra), using 2,3-dibromobenzo[*b*]thiophene as starting material. Selective lithiation with *n*-butyllithium and treatment with Me_2SiCl_2 affords the silane (**6**), which can then be converted into the extended phosphasilin (**7**) with another 2 equiv. of *n*-BuLi and 1 equiv. of $PhPCl_2$ (Scheme 2).

Compared to the non-benzoannelated phosphasilin (**3**), compound **7** shows a highfield shifted ^{31}P NMR resonance at δ = –36.5 ppm and a somewhat lowfield shifted ^{29}Si NMR resonance at δ = –16.9 ppm that suggest a significantly different structure for **7**, likely involving a more strongly bent central phosphasilin ring (vide infra). Oxidation with hydrogen peroxide affords the oxidized species **8** with a ^{31}P NMR shift at δ = 11.3 ppm that, on the other hand, is very similar to that of the non-extended oxide **4a**. The ^{29}Si NMR resonance at δ = –17.1 ppm is again only slightly shifted

Fig. 3. Two views of the molecular structure of **8** in the solid state (50% probability level; H atoms are omitted for clarity). Selected bond lengths (Å) and angles (°): P1—O1 1.4878(18), C5—C6 1.410(4), C6—C7 1.452(3), C7—C8 1.378(4), C9—C10 1.379(4), C10—C11 1.450(4), C11—C12 1.415(4), P1—C7 1.801(3), P1—C10 1.803(3), P1—C21 1.810(3), Si1—C8 1.862(3), Si1—C9 1.860(3), Si1—C31 1.860(3), Si1—C32 1.854(3); dihedral angle at P–Si axis: 4.81/5.83; helical torsion angle: 10.5/12.

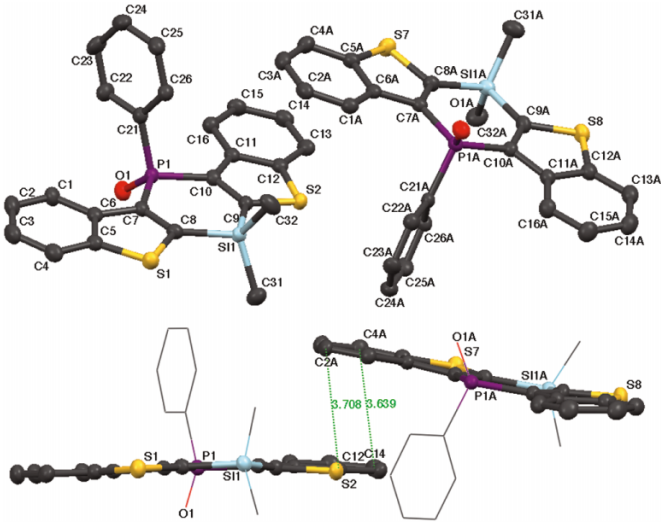

from that of **6**. However, neither of the extended compounds shows any noteworthy fluorescence emission indicating that the extension of the π-conjugated system in **7** and **8** is not sufficient enough to significantly enhance the photophysical properties of the materials. Again, UV–vis spectroscopic data suggest that the central phosphasiline ring breaks the system down into two independent benzothiophene chromophores without delocalization across the entire scaffold (λ_{max} = 232 nm for **7**, 237 nm for **8**). To confirm the planarity of the system and to support the electronic 'decoupling effect' of the central phosphasilin ring, we have also studied the structure of **8** in the solid state. Suitable single crystals for an X-ray diffraction study were obtained from a concentrated acetone solution at room temperature.

The structure of **8** in the solid state shows two independent molecules in the unit cell that each overlap with parts of one of their terminal benzene rings (Fig. 3). This overlap gives rise to some π-stacking type interactions in the typical range of 3.6–3.7 Å. The bond lengths of **8** are similar to those of a related benzoannelated dithienophosphole oxide[21] and reflect a somewhat delocalized electronic system similar to **4b**. The exocyclic Si–C (1.860(7) Å by average) and P–C bonds (1.805(10) Å by average) of the central rings relate well to the other two phosphasiline systems reported herein. In terms of the molecular geometries, the scaffold of **8** is indeed significantly more planar than those of compounds **4a** and **4b**; the central phosphasilin ring is perfectly planar. Surprisingly, however, both independent molecules of **8** show the onset of a helical structure, although the terminal benzene subunits are too far away from each other for claiming steric issues to be responsible. There are also no distinct intermolecular interactions that could cause the twisting from planarity; electronic factors appear to be intrinsically responsible for the unusual helicity that generates a dihedral torsion

angle of 11°–12° between the C1(C1A) and C16(C16A) atoms in each of the two molecules.

Computational investigations

To better understand the observed properties of the new dithienophosphasilin materials, we have optimized the structures of **3**, **4a**, **7**, and **8** on the B3LYP-6/31G* level of theory.[22] The density functional theory (DFT) calculations suggest that three of the materials, **3**, **4a**, and **8**, are planar, whereas **7** is significantly bent at the P–Si axis with a dihedral angle of ca. 30° between the two benzothiophene halves. These observations relate well to the observed ^{31}P NMR resonances for the four compounds and the observed molecular structures of **4a** (and **4b**) and **8** in the solid state. The planar structures clearly suggest that geometry is not a factor in the inferior photophysical properties. In fact, the frontier orbitals for all four compounds extend well over the whole π-conjugated framework, irrespective of the molecular geometry. However, the energy of the frontier orbitals can be used to explain the observed properties. The generally lower energy levels of the HOMOs as well as the higher energy levels of the LUMOs lead to significantly increased band gaps for the phosphasiline-based materials ranging from E_{bg} = 5.06 eV for **3** to E_{bg} = 4.57 eV for **7** that are basically more than 1 eV larger than those for related dithienophospholes.[8b,21] Notably, the band gap of the phosphasilin even increases when the phosphorus center is oxidized (**4a**: E_{bg} = 5.36 eV, **8**: E_{bg} = 4.60 eV), which is contrary to the phosphole system, where the LUMO can generally be stabilized significantly leading to smaller band gaps in the dithienophosphole oxides.[8b,11f,21] These observations support an inherently different electronic structure for the phosphasilin-based materials, although they should theoretically be able to allow for delocalization of the π-system via hyperconjugative σ*–π* interactions through the Si centers.[23]

Conclusions

In conclusion, we have synthesized a series of dithieno[2,3-*b*:3′,2′-*e*][1,4-dihydro-1,4]phosphasilins that extend our studies on the dithieno[3,2-*b*:2′,3′-*d*]phosphole system. Our studies have shown that the phosphasilin framework can efficiently be constructed in two steps and subsequent modification of the central phosphorus atom allows for the formation of a family of derivatives. Investigations of their properties, however, have revealed that the incorporation of an additional silylene center within the scaffold of dithienophospholes significantly impacts the photophysical properties of the materials, not necessarily due to nonplanar geometries, but significantly increased band gaps (>4.5 eV). As a result, no strong fluorescence emission is observed for the phosphasiline system, which is in stark contrast to the dithienophosphole system.

Experimental section

General procedures

Reactions were carried out in dry glassware and under inert atmosphere of purified nitrogen using Schlenk techniques. Solvents were dried using an MBRAUN solvent purification system. *n*-BuLi (2.5 mol/L in hexane), 2,3-dibromothiophene, and hydrogen peroxide (30% in water) were used as received. Dichlorodimethylsilane and phenyldichlorophosphane were distilled prior to use. 2,3-Dibromo-benzo[*b*]thiophene[24] and Au(THT)Cl[25] were prepared by literature methods. ^{1}H NMR, ^{13}C{^{1}H} NMR, ^{31}P{^{1}H} NMR, and ^{29}Si{^{1}H} NMR spectra were recorded on a Bruker AC200, Bruker DMX-300, or Bruker DRX-400 spectrometer. Chemical shifts were referenced to external 85% H_3PO_4 (^{31}P) or tetramethylsilane (TMS) (^{13}C, ^{1}H, ^{29}Si). Elemental analyses were performed at the Department of Chemistry at the University of Calgary. Mass spectrometry (chemical ionization) was performed using a Finigan SSQ700 and Waters GCTOF Premier instrument. Optical spectroscopy was performed with dichloromethane solutions using a Jasco FP-6600 spectrofluorometer and UV-Vis-NIR Cary 5000 spectrophotometer.

X-ray crystallography

Crystallographic data for **4a**, **4b**, and **8** are summarized in Table 1 (also see the Supplementary data). Diffraction data were collected on a Nonius Kappa CCD diffractometer using monochromated Mo Kα radiation (λ = 0.71073 Å) at –80 °C (**4b**) and –100 °C (**4a**, **8**). The data sets were corrected for Lorentz and polarization effects, and empirical absorption correction was applied to the net intensities. The structures were solved by direct methods and refined using SHELX.[26] After full-matrix least-squares refinement of the nonhydrogen atoms with anisotropic thermal parameters, the hydrogen atoms were placed in calculated positions using a riding model. Refinement of the structure model for **4a** resulted in unsatisfactory agreement factors (wR_2 = 0.44, R_1 = 0.13) and high residual electron density (2 e Å^{-3}). Comparison of observed and calculated intensities showed that the most disagreeable reflections were consistently associated with much higher observed intensities than expected. This feature was interpreted as the effect of intensity addition due to nonmerohedral twinning with the help of PLATON;[27] the same twin law was confirmed for a second crystal. Refinement of an intensity data set taking into account the overlap of ca. 80% of the reflections resulted in a batch scale factor of 0.15 for the smaller individual. Due to incomplete overlap of reflections, the final agreement factors are still higher than in the case of the untwinned structures; the residual electron density dropped to 0.9 e Å^{-3}.

Bis(3-bromothiophen-2-yl)dimethylsilane (2)

To the solution of 2,3-dibromothiophene (**1**) (0.918 g, 3.79 mmol) in Et_2O (20 mL), *n*-BuLi (1.52 mL, 3.79 mmol) was added dropwise at –78 °C. After stirring for 40 min, Me_2SiCl_2 (0.245 g, 1.897 mmol) was added dropwise at this temperature. After another 15 min at –78 °C, the reaction was allowed to warm up, and stirred overnight at room temperature. Subsequently, the mixture was filtered through neutral alumina and the solvent was removed under vacuum, affording a light yellow oil (yield: 0.580 g, 80%). ^{1}H NMR (400 MHz, $CDCl_3$, ppm) δ: 7.52 (d, $^{2}J_{HH}$ = 4.8 Hz, 2H, thiophene), 7.13 (d, $^{2}J_{HH}$ = 4.8 Hz, 2H, thiophene), 0.81 (s, 6H, Si(CH_3)$_2$). MS (CI) *m*/*z*: 383.4 [*M* + H]$^{+}$.

Compound 3

To the solution of bis(3-bromothiophen-2-yl)dimethylsilane (0.986 g, 2.58 mmol) in Et_2O (200 mL), *n*-BuLi (2.06 mL, 5.16 mmol) was added dropwise at –78 °C. After

Table 1. X-ray crystallographic data of compounds **4a**, **4b**, and **8**.

Crystal	**4a**	**4b**	**8**
Empirical formula	$C_{16}H_{15}OPS_2Si$	$C_{16}H_{15}AuClPS_2Si$	$C_{24}H_{19}OPS_2Si$
Formula weight	346.5	562.9	446.6
Crystal system	Triclinic	Monoclinic	Triclinic
Space group	*P*-1	$P2_1/c$	*P*-1
Color	Colourless	Colourless	Colourless
a (Å)	8.7170(4)	12.2520(3)	11.6690(4)
b (Å)	9.3890(5)	11.8560(3)	14.3750(4)
c (Å)	20.0570(9)	13.0200(3)	14.4700(3)
α (°)	87.147(3)	90	100.554(2)
β (°)	85.979(3)	102.8980(10)	108.293(2)
γ (°)	89.964(3)	90	104.8340(10)
V (Å^3)	1635.47(14)	1843.56(8)	2133.96(10)
Z	4	4	4
T (K)	173(2)	193(2)	173(2)
μ (Mo Kα) (mm^{-1})	0.492	8.496	0.394
F(000)	720	1072	928
Crystal size (mm^{-1})	0.21 × 0.18 × 0.15	0.23 × 0.20 × 0.18	0.21 × 0.20 × 0.20
$\rho_{calcd.}$ (g cm^{-3})	1.407	2.028	1.390
θ range (°)	2.04–27.64	1.71–27.47	1.55–27.45
No. of reflections	12730	8063	17652
No. of unique data	7040	4200	9549
R_{int}	0.0381	0.0253	0.0283
Reflections/parameters ratio	7040/0/380	4200/0/199	9549/0/603
R_1, [$I > 2\sigma(I)$]	0.0780	0.0255	0.0464
wR_2 (all data)	0.2360	0.0935	0.1468
GoF on F^2	1.106	1.254	1.152
Completeness (%)	94.3	99.6	98.5
Largest diff. peak and hole (e Å^{-3})	0.912 and –0.576	0.941 and –1.243	0.742 and –0.782

stirring at this temperature for 40 min, $PhPCl_2$ (0.462 g, 2.58 mmol) was added dropwise. The reaction was then allowed to warm up quickly and was left stirring overnight at room temperature. The mixture was subsequently filtered through neutral alumina and evaporated to dryness. The pure product **3** was obtained as white solid after recrystallization from pentane at room temperature (yield: 0.682 g, 80%). ^{1}H NMR (400 MHz, $CDCl_3$, ppm) δ: 7.66 (dd, $^3J_{HH}$ = 4.8 Hz, $^4J_{HP}$ = 2.0 Hz, 2H, thiophene), 7.36–7.32 (m br, 2H, Ph), 7.28–7.25 (m br, 3H, Ph), 7.14 (dd, $^3J_{HH}$ = 4.8 Hz, $^3J_{HP}$ = 4.0 Hz, 2H, thiophene), 0.56 (d, $^4J_{HP}$ = 6.4 Hz, 6H, Si(CH_3)$_2$). ^{13}C{^{1}H} NMR (100 MHz, $CDCl_3$, ppm) δ: 145.0 (d, $^1J_{CP}$ = 10.3 Hz, ipso-Ar), 138.9 (d, $^1J_{CP}$ = 15.9 Hz, ipso-Ph), 135.3 (d, $^2J_{CP}$ = 1.9 Hz, thiophene), 133.3 (d, $^3J_{CP}$ = 21.1 Hz, thiophene), 132.4 (d, $^2J_{CP}$ = 34.1 Hz, thiophene), 131.2 (d, $^2J_{CP}$ = 10.2 Hz, *o*-Ph), 128.9 (s, *p*-Ph), 128.4 (d, $^3J_{CP}$ = 7.6 Hz, *m*-Ph), 1.6 (s, Si(CH_3)$_2$), 1.4 (d, J_{CP} = 2.3 Hz, Si(CH_3)$_2$). ^{31}P{^{1}H} NMR (162 MHz, $CDCl_3$, ppm) δ: –20.7. ^{29}Si{^{1}H} NMR (80 MHz, $CDCl_3$, ppm) δ: –17.7 (s). HR-MS *m*/*z* calcd. for [*M* + H]$^+$: 330.0122; found: 330.0113.

Compound 4a

To the solution of dithienophosphasilin (**3**) (0.800 g, 2.42 mmol) in $CHCl_3$ (20 mL), H_2O_2 (3 mL, 30% aqueous solution) was added at room temperature. After stirring overnight, all volatiles were removed under vacuum. Pure product **4a** was obtained as a white solid after recrystallization from Et_2O at room temperature (yield: 0.713 g, 85%). ^{1}H NMR (400 MHz, $CDCl_3$, ppm) δ: 7.76 (dd, $^3J_{HP}$ = 4.8 Hz, $^4J_{HH}$ = 1.6 Hz, 2H, thiophene), 7.61–7.56 (m, 4H, thiophene and Ph), 7.46–7.35 (m, 3H, Ph). ^{13}C{^{1}H} NMR (100 MHz, $CDCl_3$, ppm) δ: 143.3 (d, $^3J_{CP}$ = 19.2 Hz, thiophene), 142.0 (d, $^2J_{CP}$ = 109.4 Hz, ipso-thiophene), 135.4 (d, $^2J_{CP}$ = 108.1 Hz, ipso-Ph), 133.0 (d, $^2J_{CP}$ = 15.5 Hz, thiophene), 131.4 (d, $^4J_{CP}$ = 2.8 Hz, *p*-Ph), 131.1 (d, $^3J_{CP}$ = 15.8 Hz, thiophene), 130.3 (d, $^2J_{CP}$ = 10.6 Hz, *o*-Ph), 128.5 (d, $^3J_{CP}$ = 7.6 Hz, *m*-Ph), 1.7 (s, Si(CH_3)$_2$), 1.1 (s, Si(CH_3)$_2$). ^{31}P{^{1}H} NMR (162 MHz, $CDCl_3$, ppm) δ: 11.5 (s). ^{29}Si{^{1}H} NMR (80 MHz, $CDCl_3$, ppm) δ: –17.8 (d, $^3J_{SiP}$ = 9.04 Hz). Elemental anal. calcd. (%) for $C_{16}H_{15}OPS_2Si$ (346.48): C 55.46, H 4.36; found: C 55.19, H 4.44.

Compound 4b

To the solution of dithienophosphasilin (**3**) (0.984 g, 2.98 mmol) in CH_2Cl_2 (20 mL), Au(THT)Cl (0.827 g, 2.98 mmol) was added at room temperature. After stirring overnight, all volatiles were removed under vacuum. The crude product was washed with acetone and pentane affording the pure product **4b** as a white solid (yield: 1.005 g, 60%). ^{1}H NMR (400 MHz, $CDCl_3$, ppm) δ: 7.81 (dd, $^3J_{HH}$ = 4.8 Hz, $^4J_{HH}$ = 2.0 Hz, 2H, thiophene), 7.53–7.47 (m, 2H, *o*-Ph), 7.44 (dd, *J* = 5.6 Hz, *J* = 4.8 Hz, 2H, thiophene), 7.43–7.35 (m, 3H, Ph), 0.62 (d, J_{HP} = 35.6 Hz, 6H, Si(CH_3)$_2$). ^{13}C{^{1}H} NMR (100 MHz, $CDCl_3$, ppm) δ: 141.6 (d, $^2J_{CP}$ = 10.9 Hz, thiophene), 135.4 (d, $^1J_{CP}$ = 66.8 Hz, ipso-thiophene), 131.9 (d, $^1J_{CP}$ = 62.1 Hz, ipso-Ph), 133.2 (d, $^2J_{CP}$ = 14.7 Hz, thiophene), 133.0 (d, $^3J_{CP}$ = 8.4 Hz, thiophene), 132.7 (s, *p*-Ph), 131.7 (d, $^2J_{CP}$ = 2.6, Hz, *o*-Ph),

129.2 (d, $^3J_{CP}$ = 12.2 Hz, *m*-Ph), 1.6 (s, Si(CH_3)$_2$), 1.0 (s, Si(CH_3)$_2$). $^{31}P\{^1H\}$ NMR (162 MHz, $CDCl_3$, ppm) δ: 5.4 (s). $^{29}Si\{^1H\}$ NMR (80 MHz, $CDCl_3$, ppm) δ: –17.6 (d, $^3J_{SiP}$ = 7.74 Hz). Elemental anal. calcd. (%) for $C_{16}H_{15}AuClOPS_2Si$ (562.90): C 34.14, H 2.69; found: C 34.19, H 2.99.

Bis(3-bromobenzo[*b*]thiophen-2-yl)dimethylsilane (6)

To the solution of 2,3-dibromobenzo[*b*]thiophene (**5**) (1.038 g, 3.56 mmol) in Et_2O (30 mL), *n*-BuLi (1.420 mL, 3.56 mmol) was added dropwise at –78 °C. After stirring at this temperature for 40 min, Me_2SiCl_2 (0.2294 g, 3.555 mmol) was added dropwise. After stirring for another 15 min at –78 °C, the reaction was allowed to warm up and was left stirring overnight at room temperature. The mixture was subsequently filtered through neutral alumina. Pure product **6** was obtained as a white solid by recrystallization from Et_2O (yield: 0.520 g, 60%). ^1H NMR (400 MHz, $CDCl_3$, ppm) δ: 7.85 (m, 4H, benzo), 7.43 (m, 4H, benzo), 0.88 (s, 6H, Si(CH_3)$_2$).

Compound 7

To the solution of bis(3-bromobenzo[*b*]thiophen-2-yl)-dimethylsilane (**6**) (0.558 g, 1.16 mmol) in Et_2O (200 mL), *n*-BuLi (0.930 mL, 2.31 mmol) was added dropwise at –78 °C. After stirring for 50 min, $PhPCl_2$ (0.207 g, 1.157 mmol) was added dropwise at –78 °C. The reaction was allowed to warm up quickly to room temperature and then left stirring overnight. The mixture was subsequently filtered through neutral alumina and evaporated to dryness. The pure product **7** was obtained as a white solid by recrystallization from acetone at 0 °C (0.300 g, 60%). ^1H NMR (400 MHz, $CDCl_3$, ppm) δ: 8.17–8.14 (m, 2H), 7.97–7.94 (m, 2H), 7.53–7.49 (m, 2H), 7.39–7.35 (m, 4H), 7.19–7.15 (m, 3H), 0.70 (J_{HP} = 18.4 Hz, 6H, Si(CH_3)$_2$). $^{13}C\{^1H\}$ NMR (100 MHz, $CDCl_3$, ppm) δ: 143.7 (d, $^2J_{CP}$ = 6.5 Hz, thiophene), 142.8 (d, $^1J_{CP}$ = 30.1 Hz, ipso-thiophene), 139.3 (d, $^3J_{CP}$ = 3.8 Hz, thiophene), 138.4 (d, $^2J_{CP}$ = 11.5 Hz, thiophene), 137.0 (d, $^1J_{CP}$ = 8.4 Hz, ipso-Ph), 133.3 (d, $^2J_{CP}$ = 20.6 Hz, *o*-Ph), 129.0 (s, *p*-Ph), 128.6 (d, $^3J_{CP}$ = 7.7 Hz, *m*-Ph), 125.0 (s, benzo), 124.3 (s, benzo), 123.6 (d, $^3J_{CP}$ = 12.8 Hz, benzo), 1.5 (s, Si(CH_3)$_2$), 1.0 (d, $^4J_{CP}$ = 4.2 Hz, Si(CH_3)$_2$). $^{31}P\{^1H\}$ NMR (162 MHz, $CDCl_3$, ppm) δ: –36.5 (s). $^{29}Si\{^1H\}$ NMR (80 MHz, $CDCl_3$, ppm) δ: –16.9 (s). HR-MS *m/z* calcd for $[M + H]^+$: 430.0435; found: 430.0435.

Compound 8

To the solution of the benzanellated dithienophosphasilin (**7**) (0.500 g, 1.16 mmol) in $CHCl_3$ (20 mL), H_2O_2 (3 mL, 30% aqueous solution) was added at room temperature. After stirring overnight, all volatiles were removed under vacuum. The pure product **8** was obtained as a white solid after recrystallization from Et_2O at room temperature (yield: 0.415 g, 80%). ^1H NMR (400 MHz, $CDCl_3$, ppm) δ: 8.52–8.48 (m, 2H), 7.94–7.92 (m, 2H), 7.84–7.78 (m, 2H), 7.39–7.33 (m, 7H), 0.75 (J_{HP} = 14.8 Hz, 6H, Si(CH_3)$_2$). $^{13}C\{^1H\}$ NMR (100 MHz, $CDCl_3$, ppm) δ: 145.5 (d, $^2J_{CP}$ = 18.1 Hz, thiophene), 143.5 (d, $^3J_{CP}$ = 12.8 Hz, thiophene), 140.9 (d, $^2J_{CP}$ = 15.1 Hz, thiophene), 136.2 (d, $^1J_{CP}$ = 109.4 Hz, ipso-thiophene), 134.2 (d, $^1J_{CP}$ = 106.4 Hz, ipso-Ph), 131.4 (d, $^4J_{CP}$ = 2.7 Hz, *p*-Ph), 130.8 (d, $^3J_{CP}$ = 10.7 Hz, *m*-Ar), 128.6 (d, $^2J_{CP}$ = 12.6 Hz, *o*-Ph), 125.5 (s, benzo), 125.2 (s, benzo), 125.1 (s, benzo), 122.1 (s, benzo), 1.3 (s, Si(CH_3)$_2$), 0.5 (s, Si(CH_3)$_2$). $^{31}P\{^1H\}$ NMR (162 MHz, $CDCl_3$, ppm) δ: 11.3 (s). $^{29}Si\{^1H\}$ NMR (80 MHz, $CDCl_3$, ppm): –17.1 (d, $^3J_{SiP}$ = 11.0 Hz). Elemental anal. calcd. (%) for $C_{24}H_{19}OPS_2Si$ (446.60): C 64.55, H 4.29; found: C 63.78, H 4.29.

Supplementary data

Supplementary data for this article are available on the journal Web site (canjchem.nrc.ca) or may be purchased from the Depository of Unpublished Data, Document Delivery, CISTI, National Research Council Canada, Ottawa, ON K1A 0R6, Canada. DUD 3992. For more information on obtaining material, refer to cisti-icist.nrc-cnrc.gc.ca/cms/unpub_e.shtml. CCDC 732433–732435 contain the X-ray data in CIF format for seven complexes for this manuscript. These data can be obtained, free of charge, via www.ccdc.cam.ac.uk/conts/retrieving.html (Or from the Cambridge Crystallographic Data Centre, 12 Union Road, Cambridge CB2 1EZ, UK; fax +44 1223 336033; or deposit@ccdc.cam.ac.uk).

Acknowledgements

Financial support by the Natural Sciences and Engineering Research Council of Canada (NSERC) and the Canada Foundation for Innovation (CFI) is gratefully acknowledged. We thank Alberta Ingenuity for a graduate scholarship (Y.R.) and a New Faculty Award (T.B.). We would also like to thank Ulli Englert (RWTH Aachen University) for his help with the X-ray diffraction data of **4a**.

References

(1) Skotheim, T. A.; Reynolds, J. R., Eds. *Handbook of Conducting Polymers*, 3rd ed.; CRC-Press: Boca Raton, 2007.

(2) (a) Murphy, A. R.; Fréchet, J. M. J. *Chem. Rev.* **2007**, *107* (4), 1066–1096. doi:10.1021/cr0501386. PMID:17428023.; (b) Allard, S.; Forster, M.; Souharce, B.; Thiem, H.; Scherf, U. *Angew. Chem. Int. Ed.* **2008**, *47* (22), 4070–4098. doi:10.1002/anie.200701920.; (c) Ong, B. S.; Wu, Y.; Li, Y.; Liu, P.; Pan, H. *Chem. Eur. J.* **2008**, *14* (16), 4766–4778. doi:10.1002/chem.200701717.; (d) Anthony, J. E. *Angew. Chem. Int. Ed.* **2008**, *47* (3), 452–483. doi:10.1002/anie.200604045.

(3) Müllen, K.; Scherf, U., Eds. *Organic Light Emitting Devices;* Wiley-VCH: Weinheim, 2006.

(4) (a) Thompson, B. C.; Fréchet, J. M. J. *Angew. Chem. Int. Ed.* **2008**, *47* (1), 58–77. doi:10.1002/anie.200702506.; (b) Günes, S.; Neugebauer, H.; Sariciftci, N. S. *Chem. Rev.* **2007**, *107* (4), 1324–1338. doi:10.1021/cr050149z. PMID:17428026.

(5) (a) Thomas, S. W., III; Joly, G. D.; Swager, T. M. *Chem. Rev.* **2007**, *107* (4), 1339–1386. doi:10.1021/cr0501339. PMID:17385926.; (b) McQuade, D. T.; Pullen, A. E.; Swager, T. M. *Chem. Rev.* **2000**, *100* (7), 2537–2574. doi:10.1021/cr9801014. PMID:11749295.

(6) (a) Baumgartner, T.; Réau, R. *Chem. Rev.* **2006**, *106* (11), 4681–4727. doi:10.1021/cr040179m.; (b) Mathey, F. *Angew. Chem. Int. Ed.* **2003**, *42* (14), 1578–1604. doi:10.1002/anie.200200557.; (c) Gates, D. P. *Top. Curr. Chem.* **2005**, *250*, 107–126. doi:10.1007/b100983.;(d) Hissler, M.; Dyer, P. W.; Réau, R. *Top. Curr. Chem.* **2005**, *250*, 127–163. doi:10.1007/b100984.; (e) Jin, Z.; Lucht, B. L. *J. Organomet. Chem.* **2002**, *653* (1–2), 167–176. doi:10.1016/S0022-328X(02)01171-3.; (f) Hobbs, M. G.; Baumgartner, T. *Eur.*

J. Inorg. Chem. **2007**, *2007* (23), 3611–3628. doi:10.1002/ejic.200700236.

(7) (a) Dillon, K.; Mathey, F.; Nixon, J. F. *Phosphorus: The Carbon Copy;* John Wiley and Sons Ltd.: Chichester, 1998; (b) Regitz, M., Ed. *Houben Weyl, Methods of Organic Chemistry, Vol. E1 & E2: Organic Phosphorus Compounds I & II;* Thieme: Stuttgart, 1982; (c) Mathey, F.; Sevin, A. *Molecular Chemistry of the Transition Metals;* Wiley: Chichester. 1996.

(8) (a) Baumgartner, T.; Neumann, T.; Wirges, B. *Angew. Chem. Int. Ed.* **2004**, *43* (45), 6197–6201. doi:10.1002/anie.200461301.; (b) Baumgartner, T.; Bergmans, W.; Kárpáti, T.; Neumann, T.; Nieger, M.; Nyulászi, L. *Chem. Eur. J.* **2005**, *11* (16), 4687–4699. doi:10.1002/chem.200500152.

(9) (a) Baumgartner, T. *J. Inorg. Organomet. Poly. Mater.* **2005**, *15* (4), 389–409. doi:10.1007/s10904-006-9013-3.; (b) Zhang, X.; Matzger, A. J. *J. Org. Chem.* **2003**, *68* (25), 9813–9815. doi:10.1021/jo035241e. PMID:14656112.; (c) Hong, S. Y.; Song, J. M. *J. Chem. Phys.* **1997**, *107* (24), 10607. doi:10.1063/1.474175.

(10) Su, H.-C.; Fadhel, O.; Yang, C.-J.; Cho, T.-Y.; Fave, C.; Hissler, M.; Wu, C.-C.; Réau, R. *J. Am. Chem. Soc.* **2006**, *128* (3), 983–995. doi:10.1021/ja0567182. PMID:16417390.

(11) (a) Baumgartner, T.; Wilk, W. *Org. Lett.* **2006**, *8* (3), 503–506. doi:10.1021/ol0529288. PMID:16435870.; (b) Dienes, Y.; Eggenstein, M.; Neumann, T.; Englert, U.; Baumgartner, T. *J. Chem. Soc., Dalton Trans.* **2006**, 1424–1433. doi:10.1039/b509277a. PMID:16518512.; (c) Neumann, T.; Dienes, Y.; Baumgartner, T. *Org. Lett.* **2006**, *8* (3), 495–497. doi:10.1021/ol052911p. PMID:16435868.; (d) Durben, S.; Dienes, Y.; Baumgartner, T. *Org. Lett.* **2006**, *8* (25), 5893–5896. doi:10.1021/ol062580w. PMID:17134299.; (e) Dienes, Y.; Durben, S.; Kárpáti, T.; Neumann, T.; Englert, U.; Nyulászi, L.; Baumgartner, T. *Chem. Eur. J.* **2007**, *13* (26), 7487–7500. doi:10.1002/chem.200700399.; (f) Ren, Y.; Dienes, Y.; Hettel, S.; Parvez, M.; Hoge, B.; Baumgartner, T. *Organometallics* **2009**, *28* (3), 734–740. doi:10.1021/om800874d.

(12) Lee, K.-H.; Ohshita, J.; Kunai, A. *Organometallics* **2004**, *23* (22), 5365–5371. doi:10.1021/om0496479.

(13) Fauré, S.; Valentin, B.; Rouzaud, J.; Gornitzka, H.; Castel, A.; Rivière, P. *Inorg. Chim. Acta* **2000**, *305* (1), 46–52. doi:10.1016/S0020-1693(00)00111-0.

(14) Ohshita, J.; Nodono, M.; Kai, H.; Watanabe, T.; Kunai, A.; Komaguchi, K.; Shiotani, M.; Adachi, A.; Okita, K.; Harima, Y.; Yamashita, K.; Ishikawa, M. *Organometallics* **1999**, *18* (8), 1453–1459. doi:10.1021/om980918n.

(15) (a) Skvortsov, N. K.; Bel'skii, V. K.; Kostenko, N. L. *Metalloorg. Khim.* **1990**, *3*, 1057; (b) Skvortsov, N. K.; Toldov, S. V. *Zh. Obshch. Khim.* **1994**, *64*, 1784.

(16) Ishii, A.; Takaki, I.; Nakayama, J.; Hoshino, M. *Tetrahedron Lett.* **1993**, *34* (51), 8255–8258. doi:10.1016/S0040-4039(00)61404-1.

(17) (a) Agou, T.; Kobayashi, J.; Kawashima, T. *Org. Lett.* **2005**, *7* (20), 4373–4376. doi:10.1021/ol051537q. PMID:16178536.; (b) Agou, T.; Kobayashi, J.; Kawashima, T. *Inorg. Chem.* **2006**, *45* (22), 9137–9144. doi:10.1021/ic061055q. PMID:17054375.; (c) Agou, T.; Kobayashi, J.; Kawashima, T. *Org. Lett.* **2006**, *8* (11), 2241–2244. doi:10.1021/ol060539n. PMID:16706496.; (d) Agou, T.; Kobayashi, J.; Kawashima, T. *Chem. Commun. (Camb.)* **2007**, 3204–3206. doi:10.1039/b706418g. PMID:17653389.; (e) Agou, T.; Kobayashi, J.; Kawashima, T. *Chem. Eur. J.* **2007**, *13* (28), 8051–8060. doi:10.1002/chem.200700622.; (f) Kobayashi, J.; Kato, K.; Agou, T.; Kawashima, T. *Chem. Asian J.* **2009**, *4* (1), 42–49. doi:10.1002/asia.200800302. PMID:19021190.; (g) Agou, T.; Sekine, M.; Kobayashi, J.; Kawashima, T. *Chem. Eur. J.* **2009**, *15* (20), 5056–5062. doi:10.1002/chem.200802159.; (h) Agou, T.; Sekine, M.; Kobayashi, J.; Kawashima, T. *Chem. Commun. (Camb.)* **2009**, 1894–1896. doi:10.1039/b818505k.

(18) Moreau, C.; Serein-Spirau, F.; Bordeau, M.; Biran, C.; Dunoguès, J. *J. Organomet. Chem.* **1996**, *522* (2), 213–221. doi:10.1016/0022-328X(96)06333-4.

(19) Fichou, D., Ed. *Handbook of Oligo- and Polythiophenes;* Wiley-VCH: Weinheim, 1998.

(20) Dienes, Y.; Englert, U.; Baumgartner, T. *Z. Anorg. Allg. Chem.* **2009**, *635* (2), 238–244. doi:10.1002/zaac.200800425.

(21) Dienes, Y.; Eggenstein, M.; Kárpáti, T.; Sutherland, T. C.; Nyulászi, L.; Baumgartner, T. *Chem. Eur. J.* **2008**, *14* (32), 9878–9889. doi:10.1002/chem.200801549.

(22) Frisch, M. J.; Trucks, G. W.; Schlegel, H. B.; Scuseria, G. E.; Robb, M. A.; Cheeseman, J. R.; Montgomery, J. A., Jr.; Vreven, T.; Kudin, K. N.; Burant, J. C.; Millam, J. M.; Iyengar, S. S.; Tomasi, J.; Barone, V.; Mennucci, B.; Cossi, M.; Scalmani, G.; Rega, N.; Petersson, G. A.; Nakatsuji, H.; Hada, M.; Ehara, M.; Toyota, K.; Fukuda, R.; Hasegawa, J.; Ishida, M.; Nakajima, T.; Honda, Y.; Kitao, O.; Nakai, H.; Klene, M.; Li, X.; Knox, J. E.; Hratchian, H. P.; Cross, J. B.; Bakken, V.; Adamo, C.; Jaramillo, J.; Gomperts, R.; Stratmann, R. E.; Yazyev, O.; Austin, A. J.; Cammi, R.; Pomelli, C.; Ochterski, J. W.; Ayala, P. Y.; Morokuma, K.; Voth, G. A.; Salvador, P.; Dannenberg, J. J.; Zakrzewski, V. G.; Dapprich, S.; Daniels, A. D.; Strain, M. C.; Farkas, O.; Malick, D. K.; Rabuck, A. D.; Raghavachari, K.; Foresman, J. B.; Ortiz, J. V.; Cui, Q.; Baboul, A. G.; Clifford, S.; Cioslowski, J.; Stefanov, B. B.; Liu, G.; Liashenko, A.; Piskorz, P.; Komaromi, I.; Martin, R. L.; Fox, D. J.; Keith, T.; Al-Laham, M. A.; Peng, C. Y.; Nanayakkara, A.; Challacombe, M.; Gill, P. M. W.; Johnson, B.; Chen, W.; Wong, M. W.; Gonzalez, C.; Pople, J. A. *Gaussian 03*, revision E.01; Gaussian Inc.: Wallingford, CT, 2007.

(23) (a) Herrema, J. K.; van Hutten, P. F.; Gill, R. E.; Wildeman, J.; Wieringa, R. H.; Hadziioannou, G. *Macromolecules* **1995**, *28* (24), 8102–8116. doi:10.1021/ma00128a020.; (b) Tamao, K.; Yamaguchi, S.; Shiro, M. *J. Am. Chem. Soc.* **1994**, *116* (26), 11715–11722. doi:10.1021/ja00105a012.; (c) Yamaguchi, S.; Tamao, K. *J. Chem. Soc., Dalton Trans.* **1998**, 3693–3702. doi:10.1039/a804491k.; (d) Hissler, M.; Dyer, P. W.; Réau, R. *Coord. Chem. Rev.* **2003**, *244* (1–2), 1–44. doi:10.1016/S0010-8545(03)00098-5.

(24) Barbarella, G.; Favaretto, L.; Zanelli, A.; Gigli, G.; Mazzeo, M.; Anni, M.; Bongini, A. *Adv. Funct. Mater.* **2005**, *15* (4), 664–670. doi:10.1002/adfm.200400172.

(25) Usón, R.; Laguna, A.; Laguna, M.; Briggs, D. A.; Murray, H. H.; Fackler, J. P., Jr. *Inorg. Synth.* **1989**, *26*, 85–91. doi:10.1002/9780470132579.ch17.

(26) Sheldrick, G. M. *Acta Crystallogr.* **2008**, *A64*, 112–122. doi:10.1107/S0108767307043930.

(27) Spek, A. L. *J. Appl. Cryst.* **2003**, *36* (1), 7–13. doi:10.1107/S0021889802022112.

Dammarane triterpenoid saponins from *Bacopa monnieri*

Pamita Bhandari, Neeraj Kumar, Bikram Singh, and Inderjeet Kaur

Abstract: *Bacopa monnieri* is a well-known Ayurvedic Indian medicinal plant traditionally used as a memory enhancer. Its memory-enhancing effect is mainly attributed to dammarane triterpenoid saponins. In the present study, two new dammarane-type triterpenoid saponins, bacopaside-XI (**1**) and bacopaside-XII (**2**), together with known compounds, bacopaside IV, bacopaside V, and apigenin, were isolated from the aerial parts of the *B. monnieri*. The structures of the new saponins were elucidated as 3-*O*-[α-L-arabinofuranosyl(1→3)]-6-*O*-sulfonyl-β-D-glucopyranosyl pseudojujubogenin (**1**) and 3-*O*-{β-D-glucopyranosyl(1→3)[α-L-arabinofuranosyl(1→2)]-β-D-glucopyranosyl}-20-*O*-α-L-arabinopyranosyl pseudojujubogenin (**2**) on the basis of extensive investigations of 1D and 2D NMR (HMQC and HMBC), ESI-QTOF-MS/MS spectroscopic methods, and chemical evidences.

Key words: scrophulariaceae, *Bacopa monnieri*, triterpenoid saponins, bacopaside-XI, bacopaside-XII.

Résumé : Le *Bacopa monnieri* est un plante médicinale bien connue chez les indiens ayurvediques où elle est utilisée pour améliorée la mémoire. Cet effet est généralement attribué aux saponines triterpénoïdes dammarane. Dans la présente étude sur les parties aériennes du *B. monnieri*, on a isolé deux nouvelles saponines triterpénoïdes du type dammarane, le bacopaside-XI (**1**) et le bacopaside-XII (**2**) aux côtés de composés connus, dont le bacopaside-IV, le bacopaside-V et l'apigénie. Faisant appel à des études extensives de données chimiques, de RMN mono- et bidimensionnelles (« HMQC » et « HMBC ») et de spectrométrie de masse (« ESI-QTOF-MS/MS »), on a élucidé les structures des nouvelles saponines, la 3-*O*-[α-L-arabinopyranosyl-(1→3)-6-*O*-sulfonyl-β-D-glucopyranosylpseudojujubogénine (**1**) et la 3-*O*-{β-D-glucopyranosyl(1→3)[α-L-arabinofuranosyl(1→2)]-β-D-glucopyranosyl}-20-*O*-L-arabinopyranosylpseudojujubogénine (**2**).

Mots-clés : scrofulariacée, *Bacopa monnieri*, sapogénines triterpénoïdes, bacopaside-XI, bacopaside-XII.

[Traduit par la Rédaction]

Introduction

Bacopa monnieri (L) WETTST. (Scrophulariaceae) (commonly known as "Brahmi") is a reputed medicinal herb, found throughout the Indian subcontinent in wet and marshy places.[1] It is used in the Ayurvedic system of medicine as a brain tonic and memory enhancer, for the improvement of intellect, and as a revitalizer of sensory organs.[2] It is claimed to be useful in the treatment of cardiac, respiratory,[3] and neuropharmacological[4] disorders like insomnia, insanity, depression, psychosis, epilepsy, and stress. In addition, *B. monnieri* is reported to show anti-inflamatory, antiulcerogenic, anti-*Helicobactor pylori*, anthemintic, adaptogenic, anticancer, cardiotonic, bronchodilatatory, and mast-cell-stabilizing activities.[3,5,6]

The major chemical constituents isolated and characterized from *B. monnieri* are dammarane-type triterpenoid saponins with jujubogenin or psuedojujubogenin as aglycone. These saponins include bacosides A_1–A_3, bacopasaponins A–G, bacopasides I–VIII.[7,8] The pharmacological effects of *B. monnieri* are mainly attributed to these saponins, especially bacoside A and bacoside B, which are therefore, considered as bioactive marker compounds for this species.[9] The composition of bacoside A, and bacoside B, has been established very recently as a mixture of four triglycosidic and four diglycosidic saponins, respectively (bacoside A as a mixture of bacoside A_3, bacopaside II, 3-*O*-{α-L-arabinofuranosyl-(1→2)-[β-D-glucopyranosyl-(1→3)]-α-L-arabinopyranosyl} jujubogenin, and bacopasaponin C; and bacoside B as a mixture of bacopaside N1, bacopaside N2, bacopaside-IV, and bacopaside-V).[10,11] Besides saponins, cucurbitacins,[12] phenylethanoid glycosides, flavonoids, and alkaloids, such as brahmine and herpestine,[13] were also reported. In continuation to our work on the isolation of novel bioactive molecules from the western Himalayan bioresources, here, we report two new dammarane-type triterpenoid saponins from *B. monnieri*.[12,14–18]

Results and discussion

Defatted powdered aerial parts of *B. monnieri* were extracted with methanol/water (50:50), concentrated, and kept overnight. The extract was filtered and fractionated with EtOAc and *n*-BuOH, successively. The EtOAc extract was chromatographed over Diaion HP-20 resin, which resulted in the isolation of two new triterpenoid saponins (Fig. 1).

Received 3 April 2009. Accepted 22 June 2009. Published on the NRC Research Press Web site at canjchem.nrc.ca on 19 August 2009.

P. Bhandari, N. Kumar, and B. Singh.[1] Natural Plant Products Division, Institute of Himalayan Bioresource Technology (CSIR), Palampur (Himachal Pradesh) 176 061, India.
I. Kaur. Himachal Pradesh University, Shimla (Himachal Pradesh) 170 005, India.

[1]Corresponding author (e-mail: bikram_npp@rediffmail.com).

Fig. 1. Structures of bacopaside-XI (**1**) and bacopaside-XII (**2**).

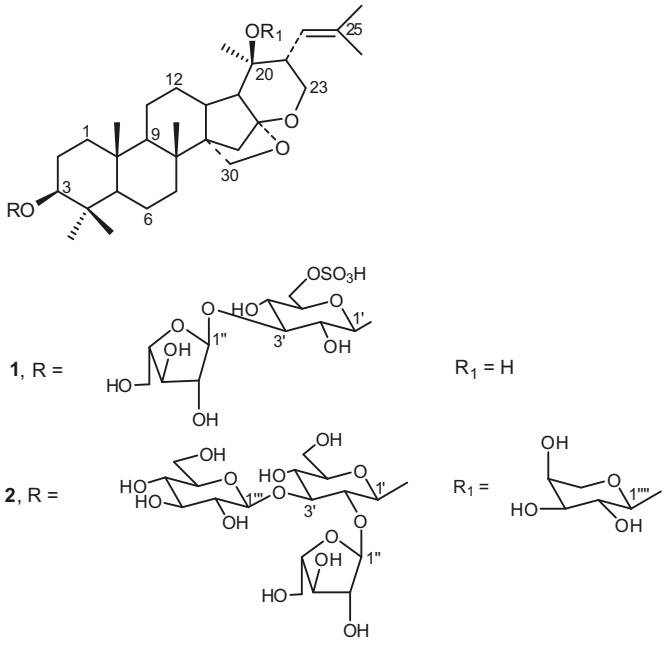

Compound **1** was obtained as a white amorphous powder, which showed a positive Liebermann–Burchard test for triterpenoids. The HR-ESI-QTOF-MS displayed a pseudomolecular ion peak at *m/z* 847.0171 $[M + H]^+$ (calcd. 847.0191) corresponded to the formula $C_{41}H_{66}O_{16}S$. Its IR spectrum showed a strong and broad band at 3430 cm^{-1} due to multiple hydroxyl groups in the compound. The IR absorptions at 1220 and 809 cm^{-1} were observed due to the presence of sulfate group. The ^1H NMR spectrum (Table 1) of **1** exhibited seven methyl singlets at δ 0.59 (3H-19), 0.93 (3H-18), 0.95 (3H-29), 1.16 (3H-28), 1.27 (3H-26), 1.49 (3H-27), and 1.57 (3H-21). In ^{13}C NMR spectrum (Table 2), these methyls were observed at δ 16.1 (C-19), 18.6 (C-18), 16.2 (C-29), 27.5 (C-28), 26.9 (C-26), 18.2 (C-27), and 25.8 (C-21). Two olefinic signals were observed at δ 123.0 and 132.7 for C-24 and C-25 positions of the isobutenyl group. The presence of a ketal group (C-16) and an oxygen-bearing methylene (C-30) in aglycone moiety was evidenced from its ^{13}C NMR signals at δ 110.1 and δ 65.9, respectively. On the basis of NMR spectral data and the saponins previously isolated from this species, the aglycone was identified as pseudojujubogenin.[2,19–21] In ^1H NMR, the upfield signals of H-23 at δ 3.78 (1H, d, J = 10.2) and 3.70 (overlapped) and further upfield of C-23, C-24, and C-25 (δ 65.6, 123.0, and 132.7, respectively) in ^{13}C NMR confirmed the aglycone as pseudojujubogenin. Two anomeric proton and carbon signals were observed for the presence of two sugar moieties at δ 5.06 (1H, d, J = 7.8 Hz), 6.18 (1H, brs), and δ 104.9 and 109.8, respectively. The anomeric signals, their coupling constants, together with ^{13}C NMR values clearly indicated the identity of the sugars as α-L-arabinofuranosyl and β-D-glucopyranosyl. These sugars were further confirmed by TLC analysis of the acid-hydrolyzed product with authentic sugars. The attachment of a sugar moiety to the C-3 of aglycone and interglycosidic linkage (C-3′–C-1″) was confirmed by downfield shifting of C-3 (δ 88.4) and C-3′ (δ 84.7) NMR signals (α-effect) and upfield shifting of neighbouring carbon signals (β-effect). The linkages were further confirmed by HMQC and HMBC spectral studies (Fig. 2).

ESI-QTOF-MS/MS of **1** (*m/z* 847) displayed the fragment ion peak at *m/z* 767 $[M + H - 80]^+$, indicating the loss of a sulfate group. In ^{13}C NMR, a downfield shift of ~3.00 ppm in C-6′ signal and an upfield shift (γ effect) of ~2.00 ppm in C-5′ signal suggested the attachment of a sulfate group at C-6′. Further, two fragments at *m/z* 635 $[M + H - 80 - 132]^+$ and 473 $[M + H - 80 - 132 - 162]^+$ were observed due to the sequential release of a pentose and a desulfated hexose sugars, respectively. Thus, on the basis of the above-mentioned spectroscopic evidences, the structure of compound **1** was unambiguously assigned as 3-*O*-[α-L-arabinofuranosyl (1→3)]-6-*O*-sulfonyl-β-D-glucopyranosyl pseudojujubogenin and named as bacopaside-XI (Fig. 1).

Compound **2** was obtained as a white amorphous powder. Its positive ESI-QTOF-MS showed a pseudomolecular ion peak at *m/z* 1061.5453 $[M + H]^+$ (calcd. 1061.5454), which corresponded to the molecular formula $C_{52}H_{84}O_{22}$. Detailed ^1H and ^{13}C NMR spectrum study indicated that compound **2** shared the same aglycone as compound **1**. ^1H and ^{13}C NMR spectrum exhibited four anomeric proton and carbon signals for the presence of four sugar moieties at δ 4.63 (1H, d, J = 8.0 Hz), 6.01(1H, brs), 4.95 (overlapped with water signal), and 4.63 (1H, d, J = 7.1 Hz), and at δ 105.5, 110.1, 104.6, and 98.7, respectively. The anomeric signals, their coupling constants, together with ^{13}C NMR values clearly indicated the identity of sugars as β-D-glucopyranosyl, α-L-arabinofuranosyl and α-L-arabinopyranosyl. The sugars were further confirmed by TLC analysis of the acid-hydrolyzed product of compound **2** by comparison with authentic sugar samples.The attachment of sugar units to C-3 and C-20 of aglycone as well as intersugar linkages (C-2′–C-1″ and C-3′–C-1‴) were determined by downfield shifting of C-3 (δ 88.4), C-20 (δ 75.1), C-2′ (δ 78.2), and C-3′ (δ 88.4) NMR signals and upfield shifting of the neighbouring carbon signals. The linkages were further confirmed by HMQC and HMBC spectral studies (Fig. 3).

ESI-QTOF-MS/MS of **2** (*m/z* 1061) displayed the fragment ion peak at *m/z* 929 $[M + H - 132]^+$, representing the loss of a pentose sugar unit. Further, the fragment ion was observed at *m/z* 473 $[M + H - 132 - 162 - 132 - 162]^+$, indicating the loss of four sugar moieties. Thus, on the basis of the above-mentioned spectroscopic evidences, the structure of compound **2** was unambiguously assigned as 3-*O*-{β-D-glucopyranosyl(1→3)[α-L-arabinofuranosyl(1→2)]-β-D-glucopyranosyl}-20-*O*-α-L-arabinopyranosyl pseudojujubogenin and named as bacopaside-XII (Fig. 1).

Experimental

General methods

Melting points were determined on a Barnstead Electrothermal 9100. Optical rotation was determined on Horiba Sepa-300 Polarimeter, and IR spectra were recorded on a PerkinElmer 1760 FTIR spectrometer with KBr discs. Mass spectra were recorded on QTOF-Micro of Waters Micromass. NMR experiments were performed on a Bruker Avance-300 spectrometer. Diaion HP-20 for column chromatography, TLC silica gel 60 F_{254} plates, and all other chemicals used were purchased from Merck India Ltd.

Table 1. ^{1}H NMR (300.13 MHz) spectral data of **1** and **2** in pyridine-d_5.

	1 m (*J*, Hz)	**2** m (*J*, Hz)
Proton		
H-18	0.93 (3H, s)	0.95 (3H, s)
H-19	0.59 (3H, s)	0.57 (3H, s)
H-21	1.57 (3H, s)	1.57 (3H, s)
H-26	1.27 (3H, s)	1.27 (3H, s)
H-27	1.49 (3H, s)	1.49 (3H, s)
H-28	1.16 (3H, s)	1.16 (3H, s)
H-29	0.95 (3H, s)	0.95 (3H, s)
H-3	3.16 ((1H, dd, *J* = 11.4, 4.4)	3.14 ((1H, dd, *J* = 11.0, 4.2)
H-13	2.72 (1H, m)	2.78 (1H, m)
H-23	3.78 (d, *J* = 10.2), 3.70[b])	3.78 (d, *J* = 10.2), 3.74[b])
H-24	5.76 (1H, d, *J* = 10.2)	5.76 (1H, d, *J* = 9.6)
Glu		
H-1′	5.06 (1H, d, *J* = 7.8)	4.63 (1H, d, *J* = 8.0)
H-2′	3.99[a]	4.10
H-3′	4.37	4.22
H-4′	4.41	3.78
H-5′	3.91	4.38
H-6′	4.78, 5.03	4.49, 4.22
Ara (*f*)		
H-1″	6.18 (1H, brs)	6.01 (1H, brs)
H-2″	5.06	4.95[a]
H-3″	3.88	3.90
H-4″	4.78	4.69
H-5″	4.37	4.22
Glu		
H-1‴		4.95[a]
H-2‴		4.10
H-3‴		4.95[a]
H-4‴		4.11
H-5‴		4.22
H-6‴		4.38, 4.22
20-*O*-Ara (*p*)		
H-1⁗		4.63 ((1H, d, *J* = 7.1 Hz)
H-2⁗		4.38
H-3⁗		4.10
H-4⁗		4.30[b]
H-5⁗		4.22[b]

[a]Overlapped with water signal.
[b]Overlapped signals.

Plant material

The plant material was collected in May 2006 from the Institute of Himalayan Bioresource Technology (IHBT) farm, Palampur, Himachal Pradesh, India.

Extraction and isolation

Air-dried powdered aerial parts of *B. monnieri* (2.2 kg) were defatted with petroleum ether (bp 60–80 °C) in a soxhlet. The defatted material was extracted with MeOH/H_2O (1:1, 3 × 2 L) in a percolator at room temperature. The combined MeOH percolations were concentrated followed by dilution with MeOH (250 mL) and kept overnight at room temperature. A deep green residue was precipitated, which was filtered. The filtrate was concentrated, dissolved in water, and partitioned with EtOAc and *n*-BuOH, successively. The EtOAc and *n*-BuOH fractions were dried under vacuum to yield 43.3 g and 57.9 g extracts, respectively. The EtOAc fraction (10.0 g) was subjected to column chromatography on Diaion HP-20 (500 g) and eluted with pure water followed by increasing polarity of methanol as 10%, 20%, 30%, 50%, 70%, 90%, and 100%. A total of 196 fractions (100 mL each) were collected sequentially and combined on the basis of the TLC pattern. Fractions 177–182, eluted with methanol/water (90:10), afforded compound **1** (25 mg) as a white amorphous powder after crystallization in methanol. Fractions 191–196, eluted with pure methanol, yielded compound **2** (20 mg) as a white amorphous powder.

Table 2. ^{13}C NMR (75.46 MHz) spectral data of **1** and **2** in pyridine-d_5.

Carbon	1	2	Carbon	1	2
1	38.5	38.5	1′ Glu	104.5	105.5
2	26.5	26.5	2′	71.6	78.2
3	88.4	88.4	3′	84.7	88.4
4	39.6	39.6	4′	68.5	70.0
5	55.9	55.9	5′	75.0	75.0
6	18.0	18.0	6′	65.6	61.8
7	35.8	35.8	1″ Ara (*f*)	109.8	110.1
8	36.8	36.8	2″	83.3	83.6
9	52.8	52.8	3″	77.7	77.7
10	36.7	36.7	4″	83.6	84.7
11	21.5	21.5	5″	61.8	61.8
12	27.5	27.5	1‴ Glu		104.6
13	35.8	35.8	2‴		75.4
14	51.2	51.2	3‴		77.7
15	35.2	35.2	4‴		71.6
16	110.1	110.1	5‴		78.2
17	51.0	51.0	6‴		61.8
18	18.6	18.2	20-*O*-1‴Ara (*p*)		98.7
19	16.1	16.1	2‴		73.0
20	70.1	75.1	3‴		75.0
21	25.8	25.8	4‴		70.0
22	46.0	46.0	5‴		66.0
23	65.6	65.6			
24	123.0	123.6			
25	132.7	133.0			
26	26.9	26.9			
27	18.2	18.2			
28	27.5	27.5			
29	16.2	16.3			
30	65.9	65.9			

Fig. 2. HMBC (→) correlations of bacopaside-XI (**1**).

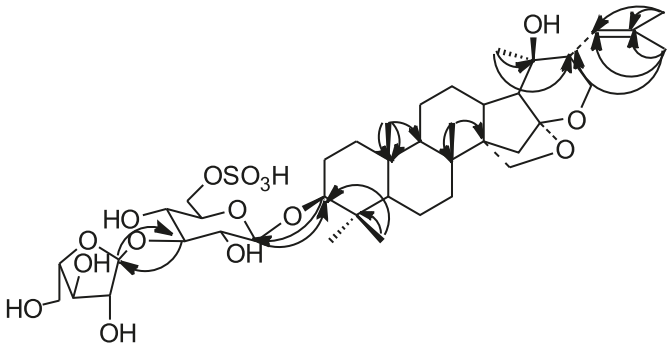

Bacopaside-XI (1)

White amorphous powder; mp 268–270 °C. $[\alpha]_D^{29}$ – 27.2 (*c* = 0.5, MeOH). IR (KBr) ν_{max} cm^{-1}: 3430, 2932, 2860, 1639, 1460, 1380, 1282, 1220, 1074, and 809. ^{1}H NMR (300.13 MHz, Py-d_5): see Table 1. ^{13}C NMR (75.46 MHz, Py-d_5): see Table 2. HR-ESI-QTOF-MS (positive) *m/z*: 847.0171 $[M + H]^+$ (calcd. for $C_{41}H_{66}O_{16}S$: 847.0191). MS^2 *m/z*: 767 $[M + H - 80]^+$, 635 $[M + H - 80 - 132]^+$, 473 $[M + H - 80 - 132 - 162]^+$, 455 $[M + H - 80 - 132 - 162 - H_2O]^+$, 437 $[M + H - 80 - 132 - 162 - 2 \times H_2O]^+$, 419$[M + H - 80 - 132 - 162 - 3 \times H_2O]^+$, 295 [glu + arabinofuranose + H]$^+$.

Fig. 3. HMBC (→) correlations of bacopaside-XII (**2**).

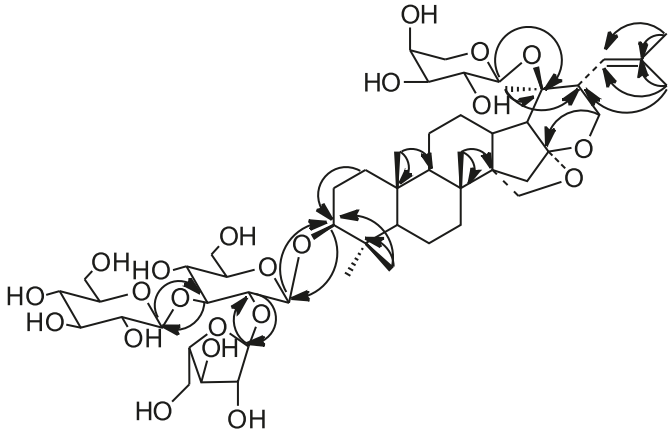

Bacopaside-XI (2)

White amorphous powder; mp 262–265 °C. $[\alpha]_D^{29}$ – 35.2 (*c* 0.5, MeOH). IR (KBr) ν_{max} cm^{-1}: 3425, 2932, 2860, 1641, 1465, 1380, 1280, and 1078. ^{1}H NMR (300.13 MHz, Py-d_5): see Table 1. ^{13}C NMR (75.46 MHz, Py-d_5): see Table 2. HR-ESI-QTOF-MS (positive) *m/z*: 1061.5453 $[M + H]^+$ (calcd. for $C_{52}H_{84}O_{22}$: 1061.5454). MS^2 *m/z*: 929 $[M + H - 132]^+$, 767 $[M + H - 132 - 162]^+$, 635 $[M + H - 132 - 162 - 132]^+$, 473 $[M + H - 132 - 162 - 132 - 162]^+$, 455

$[M + H - 132 - 162 - 132 - 162 - H_2O]^+$, 437 $[M + H - 132 - 162 - 132 - 162 - 2 \times H_2O]^+$, 419 $[M + H - 132 - 162 - 132 - 162 - 3 \times H_2O]^+$.

Acid hydrolysis of saponins

Saponins **1** and **2** (15 mg each) were refluxed with 2 mol/L HCl in aq. MeOH (10 mL) at 90 °C for 4 h. The reaction mixture was cooled, diluted with water (10 mL), and extracted with $CHCl_3$. The aquous part was neutralized with Ag_2CO_3 and filtered. The filtrate was concentrated under reduced pressure and examined for sugars by TLC using authentic sugars. Arabinose and glucose sugars were identified in both the saponins. Two spots were observed corresponding to arabinose (R_f = 0.45) and glucose (R_f = 0.25) in both the compounds.

Supplementary data

Supplementary data for this article are available on the journal Web site (canjchem.nrc.ca) or may be purchased from the Depository of Unpublished Data, Document Delivery, CISTI, National Research Council Canada, Ottawa, ON K1A 0R6, Canada. DUD 3997. For more information on obtaining material, refer to cisti-icist.nrc-cnrc.gc.ca/cms/unpub_e.shtml.

Acknowledgements

Authors are grateful to the Director of the Institute of Himalayan Bioresource Technology (IHBT), Palampur, for providing necessary facilities. Authors also thank the Council of Scientific and Industrial Research – Extra Mural Research (CSIR–EMR) for awarding the Senior Research Fellowship to Ms. P.B. Technical assistance from Mr. Ramesh Kumar are gratefully acknowledged.

References

(1) Kapoor, L. D. In *Handbook of Ayurvedic Medicinal Plants*; CRC Press: Boca Raton, 1990.
(2) Garai, S.; Mahato, S. B.; Ohtani, K.; Yamasaki, K. *Phytochemistry* **1996**, *43* (2), 447–449. doi:10.1016/0031-9422(96)00250-6. PMID:8862037.
(3) Nadkarni, K. M. In *The Indian Materia Medica;* South Asia Books: Columbia, MO, 1988.
(4) Vohora, S. B.; Khanna, T.; Athar, M. *Fitoterapia* **1997**, *68*, 361.
(5) Jain, P.; Khanna, N. K.; Trehan, N.; Pendse, V. K.; Godhwani, J. L. *Indian J. Exp. Biol.* **1994**, *32* (9), 633–636. PMID:7814042.
(6) Russo, A.; Borrelli, F. *Phytomedicine* **2005**, *12* (4), 305–317. doi:10.1016/j.phymed.2003.12.008. PMID:15898709.
(7) Chakravarty, A. K.; Sarkar, T.; Nakane, T.; Kawahara, N.; Masuda, K. *Chem. Pharm. Bull. (Tokyo)* **2002**, *50* (12), 1616–1618. doi:10.1248/cpb.50.1616. PMID:12499603.
(8) Zhou, Y.; Shen, Y. H.; Zhang, C.; Su, J.; Liu, R. H.; Zhang, W. D. *J. Nat. Prod.* **2007**, *70* (4), 652–655. doi:10.1021/np060470s. PMID:17343408.
(9) Deepak, M.; Amit, A. *Phytomedicine* **2004**, *11* (2-3), 264–268. doi:10.1078/0944-7113-00351. PMID:15070183.
(10) Deepak, M.; Sangli, G. K.; Arun, P. C.; Amit, A. *Phytochem. Anal.* **2005**, *16* (1), 24–29. doi:10.1002/pca.805. PMID:15688952.
(11) Sivaramakrishna, C.; Rao, C. V.; Trimurtulu, G.; Vanisree, M.; Subbaraju, G. V. *Phytochemistry* **2005**, *66* (23), 2719–2728. doi:10.1016/j.phytochem.2005.09.016. PMID:16293276.
(12) Bhandari, P.; Kumar, N.; Singh, B.; Kaul, V. K. *Phytochemistry* **2007**, *68* (9), 1248–1254. doi:10.1016/j.phytochem.2007.03.013. PMID:17442350.
(13) Kumar, N.; Singh, B.; Bhandari, P.; Gupta, A. P.; Uniyal, S. K.; Kaul, V. K. *Phytochemistry* **2005**, *66* (23), 2740–2744. doi:10.1016/j.phytochem.2005.10.002. PMID:16293275.
(14) Kumar, N.; Singh, B.; Gupta, A. P.; Kaul, V. K. *Tetrahedron* **2006**, *62* (18), 4317–4322. doi:10.1016/j.tet.2006.02.070.
(15) Kumar, N.; Singh, B.; Kaul, V. K. *Nat. Prod. Commun.* **2006**, *1*, 623–626.
(16) Kumar, N.; Singh, B.; Bhandari, P.; Gupta, A. P.; Kaul, V. K. *Chem. Pharm. Bull. (Tokyo)* **2007**, *55* (6), 912–914. doi:10.1248/cpb.55.912. PMID:17541193.
(17) Kumar, N.; Singh, B.; Bhandari, P.; Gupta, A. P.; Kaul, V. K. *Nat. Prod. Commun.* **2007**, *2*, 633–636.
(18) Bhandari, P.; Kumar, N.; Singh, B.; Kaul, V. K. *Chem. Pharm. Bull. (Tokyo)* **2006**, *54* (2), 240–241. doi:10.1248/cpb.54.240. PMID:16462073.
(19) Rastogi, S.; Pal, R.; KulshreshthaDK. *Phytochemistry* **1994**, *36* (1), 133–137. doi:10.1016/S0031-9422(00)97026-2. PMID:7764837.
(20) Garai, S.; Mahato, S. B.; Ohtani, K.; Yamasaki, K. *Phytochemistry* **1996**, *42* (3), 815–820. doi:10.1016/0031-9422(95)00936-1. PMID:8768327.
(21) Mahato, S. B.; Garai, S.; Chakravarty, A. K. *Phytochemistry* **2000**, *53* (6), 711–714. doi:10.1016/S0031-9422(99)00384-2. PMID:10746885.

In situ high-pressure study of ammonia borane by Raman and IR spectroscopy

Shuntai Xie, Yang Song, and Zhenxian Liu

Abstract: Pressure-induced structural transformations of the ammonia borane complex ($NH_3{\cdot}BH_3$) were investigated in diamond anvil cells by Raman spectroscopy and synchrotron IR spectroscopy up to 14 GPa at room temperature. Starting with a disordered tetragonal structure, $NH_3{\cdot}BH_3$ is found to undergo several transformations upon compression as monitored by in situ Raman measurements. These transformations are indicated by the sequential changes of characteristic Raman modes as well as by the pressure dependence of these modes. Synchrotron IR absorption spectroscopy provided supplementary and consistent information about the structural evolution of $NH_3{\cdot}BH_3$ under compression. Decompression measurements on $NH_3{\cdot}BH_3$ suggest the pressure-induced transformations are reversible in the entire pressure region. The combined Raman and IR data allowed analysis of possible high-pressure structures of $NH_3{\cdot}BH_3$. Our study significantly complements previous high-pressure Raman studies by providing new information on the structures and stabilities of $NH_3{\cdot}BH_3$.

Key words: ammonia borane, hydrogen storage, high pressure, Raman spectroscopy, IR spectroscopy, diamond anvil cell.

Résumé : Opérant à la température et à des pressions allant jusqu'à 14 GPa et faisant appel à la spectroscopie Raman et à la spectroscopie infrarouge (IR) synchrotron avec une cellule avec contre-partie de diamant, on a étudié les transformations induites par la pression du complexe ammoniac-borane ($NH_3{\cdot}BH_3$). Tel qu'on a pu l'observer par des mesures Raman in situ, on a trouvé que, par compression, le $NH_3{\cdot}BH_3$ subit plusieurs transformations à partir de sa structure tétragonale désordonnée initiale. Ces transformations sont caractérisées par des changements séquentiels des modes Raman caractéristiques ainsi que par l'influence de la pression sur ces modes. La spectroscopie d'absorption IR synchrotron fournit des informations supplémentaires et consistantes au sujet de l'évolution structurale du $NH_3{\cdot}BH_3$ soumis à une compression. Des mesures de décompression sur le $NH_3{\cdot}BH_3$ suggèrent que les transformations induites par la pression sont réversibles sur l'ensemble de la région de pression. Les données combinées des spectroscopies Raman et IR permettent de faire une analyse des structures du $NH_3{\cdot}BH_3$ à haute pression. Ce travail apporte des compléments aux études antérieures par spectroscopie Raman en fournissant de nouvelles informations sur les structures et les stabilités du $NH_3{\cdot}BH_3$.

Mots-clés : ammoniac-borane, emmagasinage de l'hydrogène, haute pression, spectroscopie Raman, spectroscopie infrarouge, cellule avec contre-partie de diamant.

[Traduit par la Rédaction]

Introduction

The ammonia borane complex ($NH_3{\cdot}BH_3$) has received intensive investigation in recent years because of its promising potential as a hydrogen storage material.[1,2] Ammonia borane is a chemical hydride with high gravimetric (19.6 wt% H) and volumetric (145 gH L^{-1}) hydrogen density and low molecular mass (30.7 g mol^{-1}). At room temperature and ambient pressure, $NH_3{\cdot}BH_3$ is a stable solid, neither flammable nor explosive. Heating $NH_3{\cdot}BH_3$ releases hydrogen at temperatures from 350 to 410 K to yield polyaminoborane $(BH_2NH_2)_x$.[3–5] The reaction is moderately exothermic (ΔH = –21 kJ mol^{-1}).[6] Continued heating releases a second equivalent hydrogen at temperatures from 380 to 470 K, yielding polyiminoborene $(BHNH)_x$ and trace quantities of borazine $(B_3N_3H_6)$.[6–9]

In addition to the hydrogen storage development, the molecular and electronic structures of ammonia borane are of fundamental interest. Although the ammonia borane complex is isoelectronic with gaseous ethane at ambient conditions, it contains a highly polarized dative N→B bond (μ = 5.1 D) formed by the electron donor–acceptor pair. The N→B bond has a dissociation energy of ~130 kJ mol^{-1},[10] which is much stronger than a typical van der Waals interaction. In addition, this dative bond is much shorter (1.58 Å)[11] in the molecular solid than in the gas phase (1.67 Å).[12] As a result, ammonia borane forms a stable molecular solid under ambient conditions that is characterized by strong dipole–dipole interactions in the crystalline network. More significantly, this complex is known to contain "dihydrogen" bonding. A dihydrogen bond is an unconventional hydrogen bond with, for example, N–H···H–B intermolecular interactions in $NH_3{\cdot}BH_3$ crystals, with 2.02 Å being the shortest H–H distance.[11] Typically, dihydrogen bonding is characterized by a short H–H contact distance (<2.2 Å) and a strongly bent angle (i.e., the angle between N–H and H–B). The effects of dihydrogen bonding on the

Received 19 March 2009. Accepted 23 June 2009. Published on the NRC Research Press Web site at canjchem.nrc.ca on 20 August 2009.

S. Xie and Y. Song.[1] Department of Chemistry, The University of Western Ontario, London, ON N6A 5B7, Canada.
Z. Liu. Geophysical Laboratory, Carnegie Institution of Washington, DC 20015, USA.

[1]Corresponding author (e-mail: yang.song@uwo.ca).

vibrational dynamics of the molecular crystal were recently demonstrated using incoherent inelastic neutron scattering.[13] These structural characteristics, including bond strength, bond length, and the directionality of dihydrogen bonding, critically determine the molecular and crystal symmetries and, therefore, the stabilities of $NH_3{\cdot}BH_3$.

$NH_3{\cdot}BH_3$ crystal structures have been examined using X-ray diffraction techniques.[14–16] At room temperature, $NH_3{\cdot}BH_3$ adopts a tetragonal structure with the space group $I4mm$ (C_{4v}^9) and cell parameters $a = b = 5.240$ Å and $c = 5.028$ Å.[15–18] Each unit cell contains two molecules occupying 2a Wyckoff sites with a C_{3v} molecular axis that coincides with the C_{4v} site symmetry (Fig. 1*a*).[16–18] This molecular crystal undergoes a phase transition from an orientationally disordered tetragonal phase to an orthorhombic structure (Fig. 1*b*) when cooled to 225 K, resulting in a significant change in the lattice dynamics. However, the molecular structure of the $NH_3{\cdot}BH_3$ molecule is preserved.[19] This orthorhombic structure was shown to have the space group $Pmn2_1$ with two molecules per unit cell and the parameters $a = 5.517$ Å, $b = 4.742$ Å, and $c = 5.020$ Å. At this temperature the NH_3 and BH_3 groups are "frozen" such that an ordered structure with a staggered conformation is formed with coinciding N–B and c axes. The crystal structure reveals that the complex has C_s symmetry only, although a recent low-temperature ^{2}H NMR study suggests that the symmetry of the molecule is very close to C_{3v}, and, therefore, it largely retains its symmetric gas-phase structure.[20]

Furthermore, $NH_3{\cdot}BH_3$ has been studied extensively using vibrational spectroscopy under varying conditions. Early IR and Raman studies on ammonia borane and its isotopologues focused on the nature and behaviour of the B–N bond.[21–23] Subsequent studies investigated the vibrational frequencies of ammonia borane (and its isotopologues) using an argon matrix[21] and by performing computational work on free molecules.[24,25] More recently, Hess et al.[19] have used Raman spectroscopy to study single-crystal ammonia borane complexes at temperatures as low as 88 K. In addition, ammonia borane has been studied under pressures as high as 4 GPa using Raman spectroscopy[22,26] to investigate the pressure effects of dihydrogen bonds on the crystalline network. It is well known that the vibrational frequencies of molecular solids under pressure exhibit a blue shift because the corresponding chemical bonds stiffen as a result of the compression. In contrast, it has been well documented that, during compression, the stretching mode of A–H shifts to lower frequencies when A–H acts as the proton donor and forms an A–H···A hydrogen bond, which subsequently weakens the A–H bond. By analogy, an N–H···H–B dihydrogen bond is expected to form in the ammonia borane complex because of the short distance between the two hydrogens, where N–H acts as the proton donor and H–B acts as the proton acceptor. This dihydrogen bond model is confirmed by the observation of a red shift in the N–H stretch frequency and a blue shift in the B–H stretch frequency with increasing pressures.[22,26] In addition, pressure-induced phase transitions were reported in both studies, but with different transition pressures and detailed spectroscopic features.[22,26]

Although ammonia borane has been studied extensively, more questions remain about the structures and properties of ammonia borane at higher pressure regions. For example, will ammonia borane form any other structures in addition to the observed tetragonal and orthorhombic phases? Will the continuous weakening of the N–H bond when compressed result in dissociation or other chemical transformations in which hydrogen is discharged? Addressing these questions, especially the possibility of hydrogen discharge and reverse processes with pressure variations, is of fundamental interest for developing this potential hydrogen storage material. Therefore, it is critical to investigate the stability, inter- and intra-molecular interactions, transformations, and reversibility of ammonia borane subjected to greater compression. Here we report the in situ high-pressure study of $NH_3{\cdot}BH_3$ by Raman and IR spectroscopy using synchrotron light sources up to 14 GPa using the diamond anvil cell (DAC) technique.[27] We note that this complex was recently studied under pressures as high as 20 GPa using Raman spectroscopy by Lin et al.[28] In this study, two new possible phase transitions were identified at 5 and 12 GPa. Although we observed some similar ammonia borane transitions, we also observed new pressure-induced structural transformations. To our knowledge, this is the first time that IR measurements, which provide sensitive and quantitative structural information, have been performed on this complex at high pressures in situ. In addition, we obtained the first high-quality spectroscopic data in the lattice region, especially in the far-IR spectral measurements. The combined spectroscopic techniques used allowed us to perform an in-depth analysis on the high-pressure structures and stabilities of the complex. Compared with previous Raman studies, this study provides the most comprehensive understanding of the pressure behaviours and structures of $NH_3{\cdot}BH_3$.

Fig. 1. Ambient-pressure crystal structures and temperature-induced transitions of $NH_3{\cdot}BH_3$. The coordinate systems showing the orientations of the unit cell are indicated. The color codes for atoms are: boron (pink), nitrogen (blue), and hydrogen (white). (*a*) The tetragonal structure of $NH_3{\cdot}BH_3$ with space group $I4mm$ ($Z = 1$) at room temperature is shown. Because of the orientational disorder associated with the free rotation of the NH_3 and BH_3 groups, the hydrogen atoms are not shown. (*b*) The ordered orthorhombic structure of $NH_3{\cdot}BH_3$ formed at 225 K with space group $Pmn2_1$ ($Z = 2$) is shown.

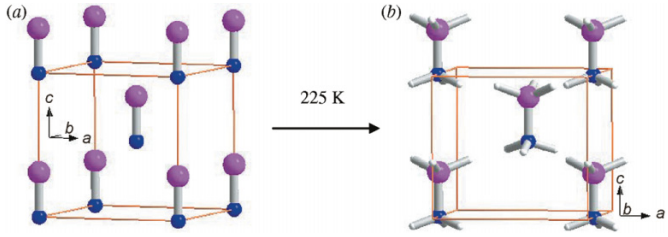

Experimental

Ammonia borane as a fine crystalline white powder with ~97% purity was purchased from Sigma-Aldrich and used without further purification. The purity was checked by ambient-pressure Raman spectroscopy and all observed Raman modes were found to be associated with the complex without any unassignable modes that originated from impurities. A symmetrical DAC with two type-I diamonds each with a 400 μm culet was used for the high-pressure Raman meas-

urements, while a pair of type II diamonds with a culet size of 300 μm was used for the IR measurements. A stainless steel gasket sample chamber was preindented to 70 μm thickness, and a 150 μm wide hole was drilled in the center. $NH_3{\cdot}BH_3$ was loaded in a MBraun LABmaster 130 glovebox equipped with a 20× microscope on the front panel. A dry inert atmosphere of <20 ppm O_2 and H_2O was maintained to accommodate the hygroscopicity of the material. The samples were loaded at room temperature with slightly elevated ambient pressures and then carefully pressurized incrementally. After each pressure change, the samples were allowed to equilibrate for a few minutes before subsequent spectroscopic measurements were taken. A few ruby (Cr^{3+} doped α-Al_2O_3) chips were used as a pressure calibrant and carefully placed inside the gasket chamber before the sample was loaded. The pressure was determined by using the R_1 ruby fluorescence line pressure shift with an accuracy of ±0.05 GPa under quasi-hydrostatic conditions.[29] For the entire pressure region, ruby fluorescence spectra obtained on different ruby chips across the sample chamber indicated no significant pressure gradient. The ruby spectral profiles suggested no obvious non-hydrostatic effects, particularly at the lower pressure regions (e.g., <10 GPa). Therefore, no pressure transmission media were used.

Raman experiments were carried out with a customized Raman microspectroscopy system constructed in our lab. A 488 nm line from an Innova Ar^+ laser (Coherent Inc.) was used as the excitation source. The laser was focused to <5 μm on the sample by an Olympus 20× objective and a 15× eyepiece and a digital camera allowed precise alignment of the focused laser beam. The Raman scattering signal was collected by the same objective lens with backscattering geometry. The Rayleigh scattering was removed by a pair of notch filters that enabled a spectral range >100 cm^{-1} to be measured before the total scattered photons were focused on the entrance slit of a spectrometer. The scattered light was then dispersed using an imaging spectrograph that housed a 0.5 m focal distance monochromator equipped with multiple gratings. A 1800 lines/mm grating with 0.1 cm^{-1} resolution was used. The Raman signal was recorded using an ultrasensitive, liquid nitrogen cooled, back-illuminated, charge-coupled device (CCD) detector from Acton. The system was calibrated using neon lines with an uncertainty of ±1 cm^{-1}. As a result of the strong diamond T_{2g} Raman mode at 1334 cm^{-1}, the spectra were collected in ranges of 50 to 1300 cm^{-1} and 1400 to 3500 cm^{-1} in several dispersive collection windows. These frequency ranges allowed all active ammonia borane Raman modes to be observed. The Raman signal was collected for 20 s for each window, and the average laser power on the sample was maintained at ~30 mW. Pressure effects on ammonia borane were examined both in the compression and decompression directions. All experiments were conducted at room temperature at pressures of up to 13.5 GPa and reproduced several times.

Infrared experiments were performed at the U2A beamline at the National Synchrotron Light Source (NSLS) at Brookhaven National Laboratory (BNL). The IR beam from the storage ring was extracted through a wedged diamond window from a source in a 40 × 40 mrad solid angle and was collimated to a 3.8 cm diameter beam before entering a Bruker IFS 66V vacuum FTIR spectrometer in conjunction with three microscope systems. The spectrometer was equipped with a number of beam splitters and detectors including a silicon bolometer and MCT. For mid-IR measurements, the IR beam was focused onto the sample by a Bruker IR microscope and then the spectrum was collected in transmission mode by the MCT detector in the 600–4000 cm^{-1} spectral range. The far-IR spectra of $NH_3{\cdot}BH_3$ were collected using a customized IR microscope with high collection efficiency and recorded by the bolometer in the 100–600 cm^{-1} spectral region. A resolution of 4 cm^{-1} was used in all IR measurements. For IR measurements, a sample thickness of 35 μm was used to allow sufficient IR transmission measurements. For all measurements, mid-IR spectra were collected through a 30 × 30 μm^2 aperture, whereas the effective IR transmission area covered the entire sample (i.e., a circle of ~90 μm in diameter) for the far-IR measurements. The reference spectrum, i.e., the diamond anvil absorption at ambient pressure, was later divided as background from each sample spectrum to obtain the absorbance. IR spectra in the decompression sequence (in ~2 GPa decrements) were also collected to investigate the reversibility of the pressure effect.

Results and discussion

Raman spectra of $NH_3{\cdot}BH_3$ during compression

Raman spectra of ammonia borane were collected from ambient pressures up to 13.5 GPa. Selected spectra are shown in Fig. 2 in four regions based on the molecular nature of the complex: the lattice region (50–600 cm^{-1}), the B–N stretching, the BH_3/NH_3 deformations and NBH rocking region (600–1650 cm^{-1}), the B–H stretching region (2100–2700 cm^{-1}), and the N–H stretching region (2750–3400 cm^{-1}).

At ambient pressure and room temperature, $NH_3{\cdot}BH_3$ crystallizes into a tetragonal phase with space group *I*4*mm* with two $NH_3{\cdot}BH_3$ molecules per unit cell.[16–18] Using factor group analysis[19], 12 distinct modes, including 11 internal modes plus one lattice librational mode, are predicted to be both Raman and IR active for the tetragonal phase of $NH_3{\cdot}BH_3$. Initially, a Raman spectrum measured at room temperature and ambient pressure is depicted at the bottom of Figs. 2*a*–2*d*. As shown, all Raman active modes except one (i.e., B–N torsion mode ν_6) are observed as predicted, in good agreement with previously reported Raman data.[19] Mode assignments are labeled in Fig. 2 and listed in Table 1. Compared with those observed in Ar-matrix isolated molecules, the N–H stretching modes (ν_7 and ν_1) in our powder sample are significantly red-shifted by 67 and 84 cm^{-1}, respectively, as a result of the dihydrogen bond in the solid phase. The analogous B–H modes (ν_8 and ν_2) are blue-shifted by 39 and 60 cm^{-1}, respectively. The assignment of the B–N stretching mode, which was originally assigned to be 787 cm^{-1} in ether solution by Taylor and Cluff[21], has long been disputed. Taylor and Cluff's assignment was confirmed by Sawodny and Goubeau[23] with a similar value of 776/790 cm^{-1} ($^{11}B/^{10}B$); however, it was reassigned by Smith et al.[30] to be 968/987 cm^{-1} ($^{11}B/^{10}B$) in argon matrices and by Jagielska et al.[31] to be 1005 cm^{-1} using an ab initio calculation.[31] In our research, we observed the B–N stretching mode (ν_5/ν_5') at 783/798 cm^{-1} ($^{11}B/^{10}B$), consistent with the original assignment and some recent observations,[22,26,28] indicating that the

Fig. 2. Selected Raman spectra of $NH_3{\cdot}BH_3$ collected at room temperature on compression in the spectral region of (*a*) 50–600 cm^{-1}, (*b*) 600–1650 cm^{-1}, (*c*) 2100–2700 cm^{-1}, and (*d*) 27503400 cm^{-1}. The relative intensities are normalized and thus are directly comparable. Because of the intense T_{2g} Raman mode of the diamond anvil at 1332 cm^{-1}, the region of 1270–1440 cm^{-1} is truncated in (*b*).The pressures in GPa are labeled for each spectrum. The assignments of Raman modes are labeled for several spectra. Unassigned peaks are labeled with asterisks (see text). The spectra are offset vertically for clarity.

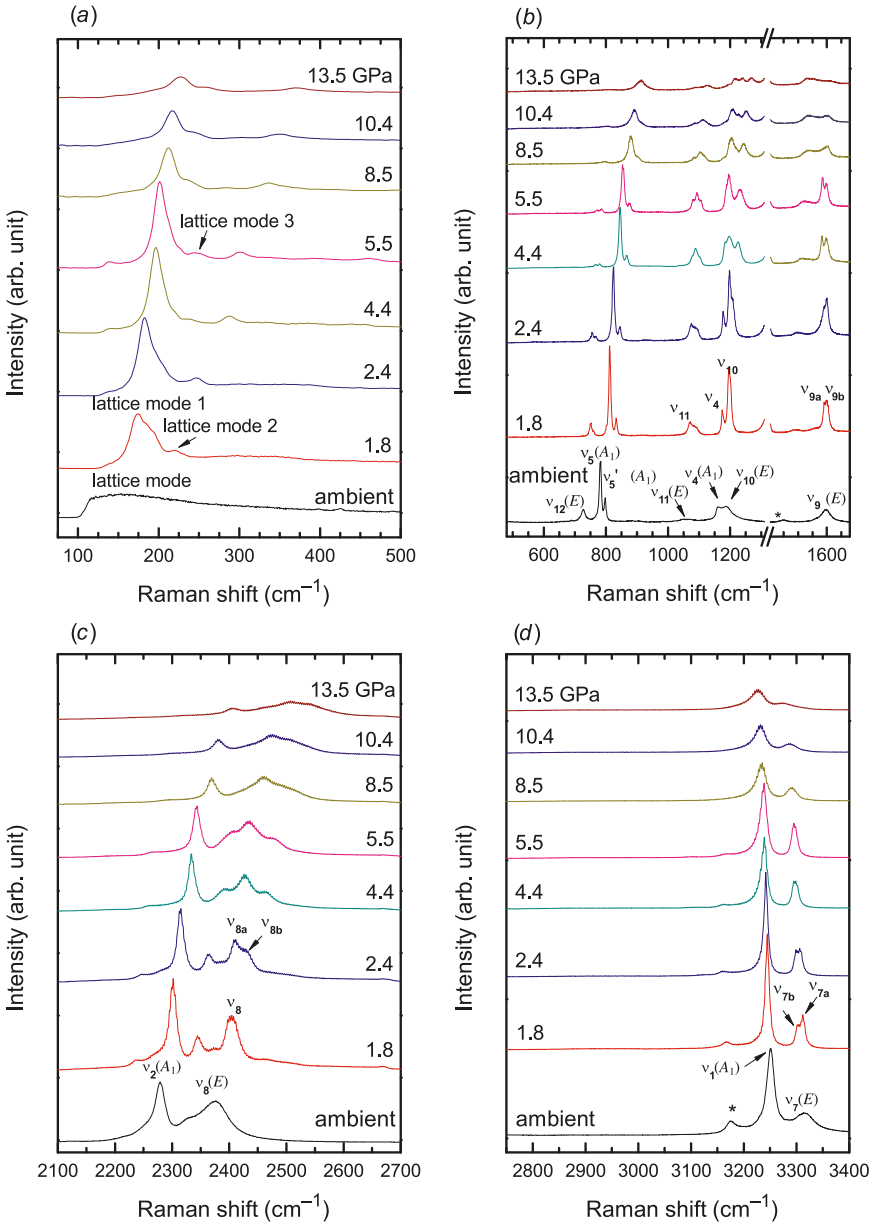

structure and behaviour of $NH_3{\cdot}BH_3$ in argon matrices is closer to the gas phase than the solid phase. For peaks at 1067 and 728 cm^{-1}, the NBH rocking modes (ν_{11} and ν_{12}) assignment of Hess et al.[19] was adopted, which are described as rocking motions involving planes of hydrogen atoms from both the NH_3 and BH_3 groups. Several previously observed but unassigned peaks, such as those at 3175 and 1447 cm^{-1}, for example, are also seen.[19,22,26] On the basis of limited polarized measurements,[19] the peak at 3175 cm^{-1} is assigned as polarized, whereas the peak at 1447 cm^{-1} is a depolarized mode.

Upon compression from ambient pressure to 1.8 GPa, a phase transition can be identified by the splitting of the modes with *E* symmetry, as well as the by the significant narrowing of the lattice mode (Fig. 2). For instance, the doubly degenerate modes ν_7 (asymmetrical N–H stretching) at 3319 cm^{-1} and ν_9 (NH_3 deformation) at 1595 cm^{-1} each split into two modes, i.e., ν_{7a}/ν_{7b} (3303 cm^{-1}/3312 cm^{-1}) and ν_{9a}/ν_{9b} (1593 cm^{-1}/1602 cm^{-1}). The phase transition is also apparent by the development of the lattice mode near 141 cm^{-1} at ambient pressure, which becomes more pronounced and finally evolves into two lattice modes at 174 and 220 cm^{-1} at 1.8 GPa. The sharp lattice modes strongly suggest a phase transition from the disordered tetragonal structure at ambient pressure to an ordered structure at 1.8 GPa. It is also noted that modes ν_4 and ν_{10}, which are

Table 1. Raman modes of ammonia borane observed under different conditions.

This work (cm^{-1})[a]	Ether solution (cm^{-1})[b]	Crystal (cm^{-1})[c]	Crystal (cm^{-1})[d]	Powder (cm^{-1})[e]	Assignment	Mode
3319	3309	3316	3316	3312	ν_7 (E)	Asym. N–H stretch
3253	3183	3250	3255	3245	ν_1 (A_1)	Sym. N–H stretch
2376	2316	2328	n.o.	2316	ν_8 (E)	Asym. B–H stretch
2280	2285	2279	2280	2277	ν_2 (A_1)	Sym. B–H stretch
1595	1600	1600	1596	1597	ν_9 (E)	NH_3 deformation
1377	n.o.	1357	1375	1374	ν_3 (A_1)	NH_3 deformation
1188	1175	1189	1185	1165	ν_{10} (E)	BH_3 deformation
1161	n.o.	1155	1158	n.o.	ν_4 (A_1)	BH_3 deformation
1067	1060	1065	1066	1058	ν_{11} (E)	NBH rock
798	n.o.	800	798	790	ν_5'(A_1)	^{10}B–N stretch
783	787	784	782	776	ν_5 (A_1)	^{11}B–N stretch
728	n.r.	727	726	715	ν_{12} (E)	NBH rock
141	n.r.	n.r.	175[f]	n.r.	Lattice mode	

Note: n.o., not observed; n.r., not reported.

[a]Measured at room temperature and ambient pressure.
[b]From ref. 21.
[c]From ref. 19.
[d]From ref. 22.
[e]From ref. 23, at low temperature.
[f]Raman shift at 1.9 GPa (see text).

very close to each other at ambient pressure, become sharply resolved at 1.8 GPa, whereas the very weak NBH rocking mode ν_{11} (1067 cm^{-1}) is greatly enhanced. In addition, a new peak appears at 2344 cm^{-1}, which was also observed but unassigned in some earlier studies.[19,22,26,28] This unassigned mode is likely a depolarized band.[19]

Upon further compression to 13.5 GPa, rich Raman features were observed to reveal the pressure-induced structural revolutions. As seen in Fig. 2*a*, the most prominent peak in the lattice in the whole pressure region is lattice mode 1, which appears at 174 cm^{-1} at 1.8 GPa. This mode becomes sharper and more intense as pressures increase to 5.5 GPa, at which point it noticeably broadens with decreasing intensity when compressed to 13.5 GPa. Lattice mode 2, although very weak at 1.8 GPa, is a characteristic mode of the new phase that is different than the disordered tetragonal structure and remains distinct as pressures increase to 13.5 GPa. The most prominent change in the lattice region is the observation of a third lattice mode at 245 cm^{-1} at 5.5 GPa, indicating a possible transformation of the crystal structure of $NH_3{\cdot}BH_3$. In addition, a clearly developed mode at 140 cm^{-1} was also observed at this pressure. These new modes, together with lattice mode 2, become weaker with increasing pressure such that only lattice mode 1 remains the dominant mode at 13.5 GPa. We note that in previous Raman studies only two lattice modes were observed in all pressure regions,[28] which is in strong contrast to our results. It is likely that the missing mode at 140 cm^{-1} is associated with the detection limit achieved.

The internal modes in the spectral region 600–1650 cm^{-1} (Fig. 2*b*), including the ν_{12}, ν_{11}, ν_{10}, and ν_9 modes when compressed to 2.4 GPa, are characterized by further splitting of the doubly degenerate modes with E symmetry during compression. Upon further compression to 5.5 GPa, these modes exhibit the maximum splitting with the exception of ν_7, which merged into a singlet. Continuous compression from 5.5 to 8.5 GPa results in merging with a markedly reduced intensity for most of the modes. All modes are significantly broadened when compressed above 13.5 GPa. These observations are in general agreement with those of Lin et al.,[28] except for the detailed profile of a few bands. For instance, the NH_3 deformation mode (ν_9) at ~1600 cm^{-1} that exhibits clear splitting up to 5.5 GPa shows a drastically different profile: no splitting was observed in the entire pressure region.[28]

The splitting at ν_5 mode is due to an isotopic effect rather than the removal of degeneracy. The ^{11}B and ^{10}B contributions to the B–N symmetric stretch (ν_5 and ν_5') are readily apparent up to 8.5 GPa. Both ^{11}B–N (ν_5) and ^{10}B–N (ν_5') stretching modes are sharp in the pressure region under 5.5 GPa, whereas ν_5' is much weaker than ν_5 because of the lower abundance of ^{10}B (19.9%). The frequency difference at 8.5 GPa is ~19–21 cm^{-1}, which is larger than that observed under ambient conditions (i.e., 15 cm^{-1}). However, this value is still in agreement with the frequency difference of 18 cm^{-1} reported by Custelcean and Dreger[22] and of 20 cm^{-1} observed by Lin et al.[28]

The symmetric B–H stretching mode ν_2 (A_1), one of the most intense Raman bands at ambient pressure, exhibits a pressure-induced blue shift and weakening (Fig. 2*c*); it becomes significantly broadened above 8.5 GPa. The doubly degenerate asymmetric B–H stretching mode ν_8 readily splits when compressed to 2.4 GPa, exhibiting a strongly asymmetric doublet labeled as ν_{8a} and ν_{8b}. As pressures continue to increase, mode ν_{8a} becomes most pronounced at 4.4 GPa and subsequently becomes much broader at higher pressures (e.g, 8.5 GPa) because of coalescence with ν_{8b} and a nearby depolarized peak.[19] In contrast to the BH stretching modes, both the symmetric and asymmetric N–H stretching modes shift to red with increasing pressures (Fig. 2*d*). The symmetric N–H stretching mode ν_1 with A_1 symmetry, the most intense $NH_3{\cdot}BH_3$ Raman band in the en-

Fig. 3. Pressure dependences of the Raman shift of $NH_3{\cdot}BH_3$ on compression for (*a*) the lattice modes, (*b*) the BH_3 deformation (ν_{10a}, ν_{10b}, and ν_4) and NH_3 deformation (ν_{9a} and ν_{9b}) modes, (*c*) the $^{11}B–N/^{10}B–N$ stretch (ν_5/ν_5') modes, (*d*) the NBH rock (ν_{12a}, ν_{12b}, ν_{11a}, ν_{11b}, and ν_{11c}) modes, and (*e*) the N–H stretch (ν_{7a}, ν_{7b}, and ν_1) and B–H stretch (ν_{8a}, ν_{8b}, and ν_2) modes. Different symbols denote Raman modes with different origins. The solid lines crossing the solid symbols are based on linear fit. The vertical dashed lines indicate the proposed phase boundaries.

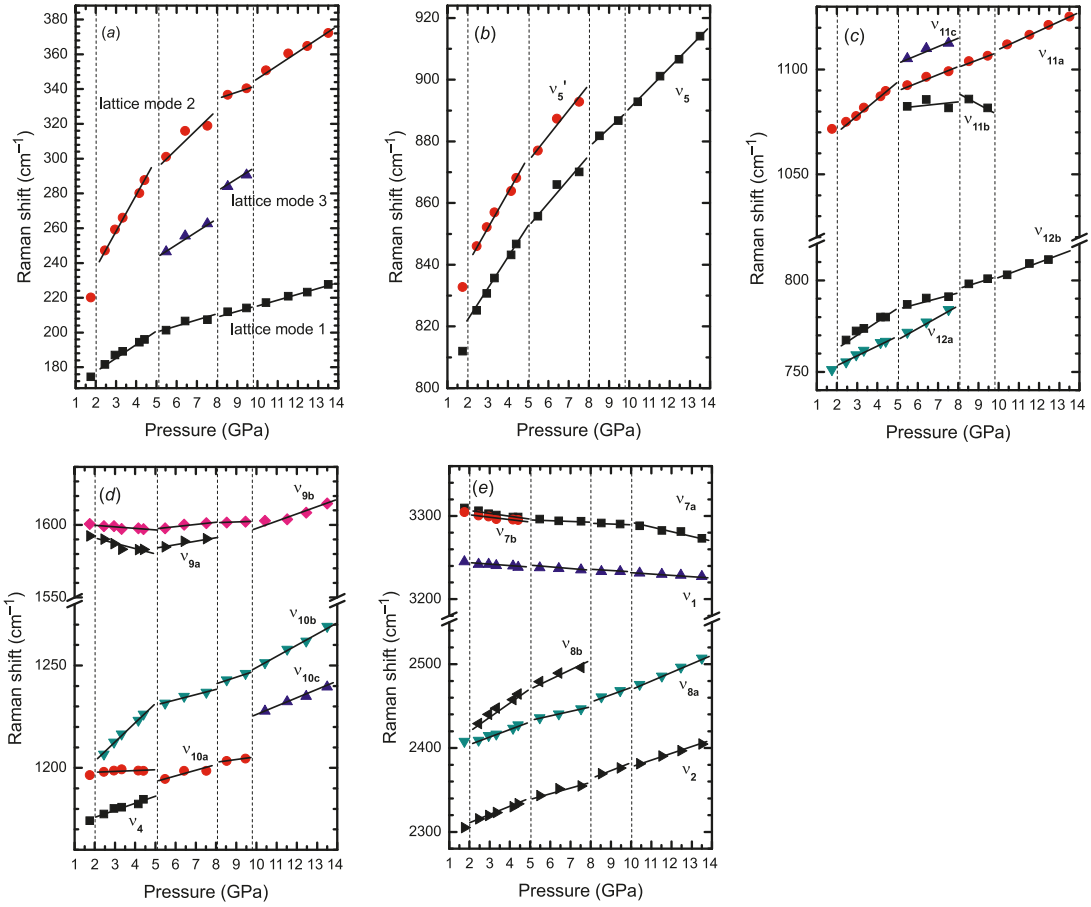

tire pressure region, becomes much broader and weaker when compressed to 8.5 GPa. The asymmetric N–H stretching mode ν_7 (*E*) that displays a doublet (ν_{7a} and ν_{7b}) at 1.8 GPa becomes a convoluted mode on compression. Similar to the ν_1 mode, this mode also broadens markedly beyond 8.5 GPa. Above 13.5 GPa, this mode is barely visible. These observations are consistent with those of Lin et al.[28]

Pressure effects on Raman modes of $NH_3{\cdot}BH_3$

To confirm the possible phase transformations on compression, the pressure dependence (i.e., Raman shift versus pressure) of selected Raman modes are depicted in Fig. 3. Calculated pressure coefficients ($d\nu/dP$ (cm^{-1} GPa^{-1})) for the monitored peaks obtained by linear regression of the experimental data are listed in Table 2. Phase transitions are further indicated when sharp differences in pressure coefficients are observed. Compared with previous analysis,[28] more phase boundaries were identified in this study.

In general, most Raman modes exhibit pressure-induced blue shifts, consistent with the finding that the bonds stiffen upon compression. However, both the symmetric and asymmetric N–H stretching modes (ν_7 and ν_1) undergo red shifts with increasing pressures in all pressure regions (i.e., $d\nu/dP < 0$), indicating the weakening of the N–H bond. This is believed to be a result of the lengthening of the N–H bond owing to the formation and strengthening of the dihydrogen bonding (N–H···H–B) as pressures increase. In strong contrast, the stretching modes (ν_8 and ν_2) involving the B–H proton acceptor group in the dihydrogen bond exhibit large blue shifts with pressure. For example, $d\nu_8/dP$ has the largest pressure coefficients (16.1 and 10.3 cm^{-1} GPa^{-1} in the 2.4–5.5 and >10.4 GPa pressure regions, respectively) indicating the significant strengthening of B–H bonding with decreasing bond length. Because the N–H and B–H bond strengths become strongly disproportionate when compressed, and the B–N bond is strengthened ($d\nu_5/dP > 0$), it is reasonable to speculate that at certain high pressures, the N–H bond may break and new materials may form.

As shown in Fig. 3 and Table 2, the pressure dependences of the major Raman modes collectively indicate several distinct pressure regions at which $NH_3{\cdot}BH_3$ could exist as different phases. These pressure regions are 2.4–5.5, 5.5–8.5, 8.5–10.4, and >10.4 GPa, which we label as phases III, IV, V, and VI, respectively (phases I and II are the known room-temperature tetragonal phase and low-temperature orthorhombic phase, respectively). In general, the pressure coefficients of the stretching modes are noticeably larger for phase III than for phase IV, which are larger than those for

Table 2. Pressure dependence of the Raman modes of $NH_3{\cdot}BH_3$ on compression.

			$d\nu/dP$ (cm^{-1} GPa^{-1})			
Mode	Assignment	Raman shift (cm^{-1})[a]	Phase III (2.4–5.5 GPa)	Phase IV (5.5–8.5 GPa)	Phase V (8.5–10.4 GPa)	Phase VI (>10.4 GPa)
Lattice mode 1		141	6.3	2.9	2.4	3.3
Lattice mode 2			17.8	8.6	4.0	6.7
Lattice mode 3				7.8	7.1	8.2
Asym. N–H stretch	ν_{7a}	3319	–3.1/–2.7[b]	–1.2	–1.6	–4.6
Sym. N–H stretch	ν_1	3253	–1.5	–0.9	–1.1	–1.3
Asym. B–H stretch	ν_8	2376	8.7/16.1[c]	5.3/8.3[c]	7.8	10.3
Sym. B–H stretch	ν_2	2280	9.2	5.6	7.4	7.6
^{11}B–N stretch	ν_5	783	5.2	3.7	5.3	6.8
^{10}B–N stretch	ν_5'	798	6.2	5.0		
NBH rock	ν_{11a}	1067	6.1	3.3	2.8	4.4
	ν_{11b}			0.6/3.6[d]	0.2	
	ν_{12}	728	5.2/6.2[e]	6.1/2.0[e]	3.0	4.1
NH_3 deformation	ν_9	1595	–2.3/–0.6[f]	2.7/1.7[f]	0.5	3.9
	ν_3	1377	–0.3	–0.8		
BH_3 deformation	ν_{10a}	1067	0.3	1.9	1.2	
	ν_{10b}		8.3	2.6	1.3	5.6/3.7[g]
	ν_4	1161	3.1			

[a]Measured at ambient pressure and room temperature.
[b]ν_{7a}/ν_{7b}.
[c]ν_{8a}/ν_{8b}.
[d]ν_{11b}/ν_{11c}.
[e]ν_{12a}/ν_{12b}.
[f]ν_{9a}/ν_{9b}.
[g]ν_{10b}/ν_{10c}.

phase V. The pressure coefficients of the rocking and deformation modes, however, do not exhibit consistent trends along phase transformations. Interestingly, the pressure coefficients of these modes seem to become larger again when compressed beyond 10.4 GPa. In summary, although the phase boundaries of 2.4 and 5.5 GPa observed in this study can be roughly aligned with those at 2 and 5 GPa noted previously,[28] new phase boundaries along with more high-pressure phases are observed in the present study.

Raman spectra of $NH_3{\cdot}BH_3$ during decompression

The reversibility of pressure effects on molecular structures provides important information on transformation mechanisms. Therefore, upon compression of $NH_3{\cdot}BH_3$ to the highest pressure of 13.7 GPa, we conducted Raman measurements on decompression all the way down to a near ambient pressure. Selected spectra are depicted in Fig. 4. In general, the change in the Raman profile is very gradual on decompression. At 13.7 GPa, one lattice mode and ν_5, ν_4, ν_{10}, ν_9, ν_8, ν_1, and ν_7 modes resolve. Starting at 6.2 GPa, the ν_2 mode at 2362 cm^{-1} recovers from decompression. Simultaneously, the ν_1 and ν_7 modes are completely deconvoluted. Further decompression to 4.0 GPa results in the development of ν_5', ν_{511}, and $\nu_{9a,b}$ modes. The onset pressure for the observation of ν_{12} and ν_4 along decompression is 2.3 GPa. When the pressure is reduced to 0.8 GPa, the Raman profile is almost identical to that at 1.8 GPa on compression. These observations suggest that, although there is some hysteresis upon decompression characterized by "delayed" back-transformations, the pressure-induced phase transitions are reversible in the entire pressure range in this study.

Mid-IR spectra of $NH_3{\cdot}BH_3$

Figure 5*a* shows the mid-IR absorption spectrum of $NH_3{\cdot}BH_3$ measured at room temperature and at 1.5 GPa (the first pressure point on compression). According to a factor group analysis,[19] all spectral active modes of $NH_3{\cdot}BH_3$ are both IR and Raman active. Therefore, the fundamental IR modes can be assigned by comparing our IR spectrum with previous IR and Raman measurements as reported in Table 3. In addition, vibrational frequencies observed from low-temperature inelastic neutron scattering (INS) measurements, which have no selection rules, are also listed to confirm the assignments in the spectra region below 1400 cm^{-1}.[25] In contrast to the Raman spectra, many more IR bands are observed as a result of overtones and (or) combinations of fundamental modes, which are labeled with asterisks in Fig. 5*a*. For instance, a new band is observed at 3479 cm^{-1}, which is very close to the combination of ν_{11} and ν_3 as $2\nu_{11} + \nu_3$, where ν_{11} = 1055 cm^{-1} and ν_3 = 1362 cm^{-1}. Similarly, the bands at 2674, 2123, and 1483 cm^{-1} are likely to be overtones of ν_3 (1362 cm^{-1}), ν_{11} (1055 cm^{-1}), and ν_{12} (751 cm^{-1}) as $2\nu_3$, $2\nu_{11}$, and $2\nu_{12}$, respectively. The band at 1767 cm^{-1} is not coincident with any combination of internal modes, but it is likely a combination of lattice modes and internal modes. Although some modes could not be distinguished because of the saturated absorptions in regions 1050–1250 cm^{-1} and 3150–3400 cm^{-1}, all

Fig. 4. Selected Raman spectra of $NH_3{\cdot}BH_3$ on decompression from 13.7 GPa all the way down to ambient pressure. The relative intensities are normalized and thus are directly comparable. The pressures in GPa are labeled for each spectrum. The spectra are offset vertically for clarity.

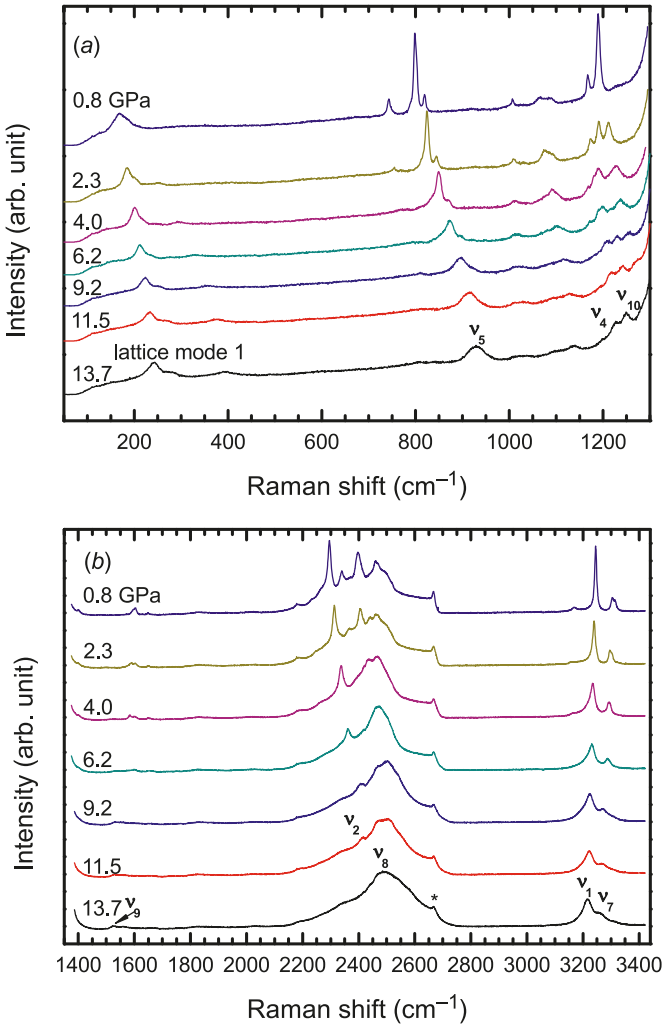

fundamental internal modes except a BH_3 deformation mode and an N–H stretching mode were observed, which is in agreement with previous Raman and IR data.[21–23]

Figure 6*a* shows the IR absorption spectra of $NH_3{\cdot}BH_3$ when compressed to 13.7 GPa at room temperature. Compared with Raman measurements on compression, the pressure evolution of the $NH_3{\cdot}BH_3$ bands is very gradual and lacks distinctive profile changes, which is mainly associated with the extremely strong or even saturated absorptions in most of the spectral regions. In addition, the absorption is markedly enhanced as pressures increase such that the multiple bands in the spectral region of 1000–1600 cm^{-1} convolute to two broad bands at 13.7 GPa. As a result, it is difficult to visualize phase transitions from the IR spectra. The only discernable profile change occurs at 7.8 GPa as indicated by the broadening of the ν_{12} mode and by the enhanced intensity of the ν_8 mode. However, the pressure dependences of the IR bands shown in Fig. 7 and Table 4 show roughly consistent pressure-induced phase transitions

Fig. 5. Synchrotron mid-IR absorption spectrum of $NH_3{\cdot}BH_3$ collected at room temperature and (*a*) 1.5 GPa upon compression in comparison with (*b*) 0.3 GPa upon decompression in the spectral region 600–3800 cm^{-1}. The assignments of the fundamental modes are shown above the corresponding IR bands. The IR bands labeled with asterisks are overtones or combinations of lattice modes and (or) internal modes (see text).

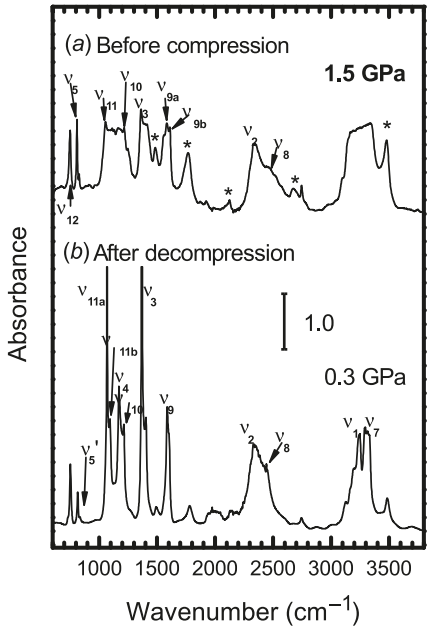

as established by our Raman measurements. Generally, most of the IR modes exhibit blue shifts with increasing pressure, consistent with the pressure-induced bond stiffening. For example, a pressure coefficient as large as 26.8 cm^{-1} GPa^{-1} is observed for the B–H stretching mode ν_8 in the pressure region of 7.8–10.8 GPa. Although the N–H stretching modes cannot be monitored owing to strong absorption, the NH_3 deformation modes (ν_{9a}, ν_{9b}, and ν_3) exhibit unambiguous red shifts, yielding consistent information obtained by Raman measurements interpreted as the weakening of N–H bonds with the formation of dihydrogen bonds.

After compressing $NH_3{\cdot}BH_3$ to pressures as high as 13.7 GPa, we conducted IR measurements on decompression to near ambient pressures (e.g., 0.3 GPa). Selected spectra are depicted in Fig. 6*b* and compared with the compression data in Fig. 6*a*. Apparently, the decompression data provide more information because the absorption is markedly reduced as the sample thins out after the compression–decompression cycle. For instance, when the pressure is reduced to 8.9 GPa, the previously saturated ν_4 and ν_{11} bands are resolved. Furthermore, IR bands ν_1 and ν_7 are clearly visible when decompressed to 2.9 GPa. Finally, as seen in Fig. 5*b*, all modes observed before compression at 1.5 GPa are recovered after decompression at 0.3 GPa. These observations indicate that the structural transformations upon compression are completely reversible in the entire pressure region, consistent with our Raman measurements.

Far-IR spectra of $NH_3{\cdot}BH_3$

Using the unique synchrotron far-IR setup dedicated to in situ high-pressure measurements, we obtained the first far-IR

Table 3. Assignment of IR fundamental frequencies for $NH_3{\cdot}BH_3$ in comparison with Raman data.

IR (cm^{-1})		INS (cm^{-1})	Raman (cm^{-1})		Assignment	IR bands
This work[a]	Reference 30[b]	Reference 25[c]	This work[d]	Reference 19[e]		
	3386		3303/3312[f]	3316	ν_7 (E)	Asym. N–H stretch
	3337		3244	3250	ν_1 (A_1)	Sym. N–H stretch
2453	2415		2404	2328	ν_8 (E)	Asym. B–H stretch
2337	2340		2302	2279	ν_2 (A_1)	Sym. B–H stretch
1584/1610[g]	1608		1593/1602[g]	1600	ν_9 (E)	NH_3 deformation
1362	1343	1368	1371	1357	ν_3 (A_1)	NH_3 deformation
1216	1186	1189	1198	1189	ν_{10} (E)	BH_3 deformation
	1175	1177	1174	1155	ν_4 (A_1)	BH_3 deformation
1055	1052	1080	1070	1065	ν_{11} (E)	NBH rock
828	987		832	800	ν_5 (A_1)	^{10}B–N stretch
810	968	798	812	784	ν_5'	^{11}B–N stretch
751	603	737	751	727	ν_{12} (E)	NBH rock

Note: INS, inelastic neutron scattering.

[a]Measured at room temperature and 1.5 GPa.

[b]At low temperature.

[c]Using inelastic neutron scattering at 30 K.

[d]Measured at room temperature and 1.8 GPa.

[e]At room temperature.

[f]Frequencies for ν_{7a}/ν_{7b}.

[g]Frequencies for ν_{9a}/ν_{9b}.

$NH_3{\cdot}BH_3$ absorption spectra at 13.5 GPa. Similar to the mid-IR region, the lattice modes in the far-IR region at 100–600 cm^{-1} are overwhelmed by extremely strong absorptions that do not allow individual modes to be identified. Therefore, we performed a compression to 13.5 GPa stepwise (the IR spectra are not shown on compression) and then measured the IR absorption on decompression with selected spectra, shown in Fig. 8*a*. At the highest pressure, two lattice modes at 294 cm^{-1} (band 1) and 415 cm^{-1} (band 2) are clearly observed. Compared with the Raman lattice region (Figs. 2*a* and 3*a*), band 1 is close to the Raman lattice mode 3 by extrapolation, whereas band 2 is a new lattice mode (IR active only). On decompression, both modes shift to lower frequencies. When decompressed to 3.5 GPa, band 1 displays enhanced absorption but subsequently diminishes into a shoulder peak when decompressed to 1.2 GPa. At this pressure, only one major band with a frequency of 210 cm^{-1} is observed, which is comparable with the Raman lattice mode 2 (219 cm^{-1}) at 1.8 GPa, but with strongly contrasting intensities.

We plotted the frequencies of the IR active modes observed in the lattice region as a function of pressure on both compression and decompression (Fig. 8*b*). Again, owing to strong absorption, $NH_3{\cdot}BH_3$ produces a broad, saturated band below 3.3 GPa upon compression. At this pressure, a clearly defined band evolved at 420 cm^{-1} (as band 3 in Fig. 8*b*) and rapidly shifted to higher frequencies ($d\nu/dP$ = 18.8 cm^{-1} GPa^{-1}) as pressures increased to 9.5 GPa when the intensity diminished almost completely. Interestingly, this band is not observed in this pressure region upon decompression, but only displays barely visible intensities below 3.5 GPa. As seen in Fig. 8, bands 1 and 2 could not be distinguished from the saturated bands until the sample was compressed to 8.5 GPa, at which point they remain resolved up to the highest pressure. Upon decompression, however, these two modes exhibit different pressure dependences (i.e., smaller pressure coefficients) than when compressed, indicating that back transformation is more sluggish owing to hysteresis. The pressure dependences of both these modes show a distinct change around 5.5 GPa, coinciding with one of the transition pressures established by our Raman measurements.

Discussion

In previous Raman studies of $NH_3{\cdot}BH_3$ in the low pressure range (i.e., <4 GPa),[22,26] two solid-to-solid transitions at 0.5 and 1.4 GPa were found by Trudel and Gilson,[26] which is different from Custelcean and Dreger's study[22] in which only one phase transition was found (at 0.8 GPa). This discrepancy may result from the differences in the hydrostatic conditions used in the two studies. Both of our Raman and IR measurements are in general agreement with these two studies in terms of phase regions, i.e., the spectroscopic features observed below and above 2 GPa roughly align with those before and after the phase transitions observed below 1.5 GPa in both studies, except that we extend the previously observed second high-pressure phase from 4 to ~5.8 GPa (we label this as phase III), which is in qualitative agreement with Lin et al.'s study.[28] Above this pressure, our Raman and IR measurements show two more phase transitions at 8.5 and 10.4 GPa, whereas the only transition observed in Lin et al.'s study was near 12 GPa.[28] In addition to the different boundaries, differences in Raman profiles, such as those in the lattice region, were also observed. One possible explanation is that our materials had a different purity and crystallinity: we used a reagent grade with a purity of 97% (purchased directly from Sigma-Aldrich), whereas Lin et al.[28] used synthetic laboratory and heat-treated samples with an unknown purity. In addition, as discussed in the following, the phase transitions are characterized by

Fig. 6. Synchrotron mid-IR spectra of $NH_3{\cdot}BH_3$ in the spectral range of 600–3800 cm^{-1} measured at room temperature for selected pressures (indicated in GPa above each spectrum) on (*a*) compression and (*b*) decompression. The absorbance has been normalized with respect to the beam current of the synchrotron light source. The spectra are offset vertically for clarity.

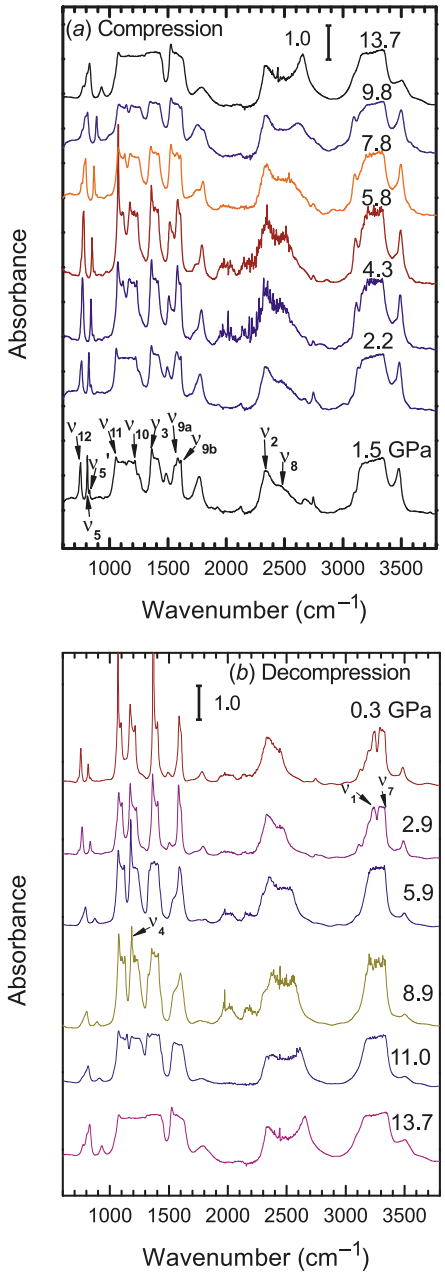

Fig. 7. Pressure dependences of IR frequencies of $NH_3{\cdot}BH_3$ for internal modes on compression. Different symbols denote different IR origins with assignments labeled on the right-hand side. The vertical dashed lines indicate one of the proposed phase boundaries.

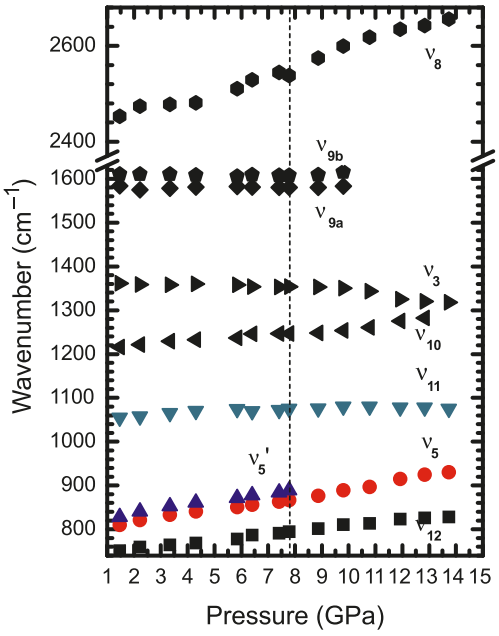

subtle changes in the unit cell without major, irreversible modifications. Such transitions are generally sensitive to compression conditions and therefore may be affected by additional factors such as kinetics. Nevertheless, our parallel measurements yielded reproducible and consistent results.

Then the remaining question is what are the possible structures of high-pressure phases of ammonia borane induced by compression and decompression. To our knowledge, no in situ high-pressure X-ray diffraction study of this complex has been reported. Therefore, these combined Raman and IR spectroscopic measurements, especially in the lattice region, provide important insight for understanding the high-pressure structures of the ammonia borane complex. Unfortunately, Hess et al.'s[19] recent low-temperature Raman study does not include lattice data, and lattice features were not analyzed in depth in any of the previous high-pressure Raman studies because of measurement limitations.[22,26]

For the phase below 2.4 GPa, the Raman measurement at 1.8 GPa (Fig. 2*a*) and IR measurement at 1.2 GPa (Fig. 8*a*) in the present study clearly indicate that there are at least two lattice modes associated with this phase. It is known that high pressures and low temperatures often induce similar phase transitions for many materials that have normal *P–T* phase diagrams. Therefore, to assume that the low-pressure phase has the same or similar crystal structure as the low-temperature orthorhombic phase is reasonable and can be examined for consistency by the observed spectroscopic features. Using factor group analysis, the orthorhombic structure ($Pmn2_1$) with two molecular units per unit cell has the following lattice modes[19]:

$$[1]\quad \Gamma^{NH_3{\cdot}BH_3}_{\text{lattice vib.}} = A_1 + A_2 + B_2$$
$$\Gamma^{NH_3{\cdot}BH_3}_{\text{lattice lib.}} = A_1 + 2A_2 + 2B_1 + B_2$$

where Γ_{vib} and Γ_{lib} are the irreducible representations for lattice vibration (translation) and lattice liberation (rotation), respectively. Species A_2 is Raman active and A_1, B_1, and B_2 are both IR and Raman active. Thus, nine lattice modes are predicted with all Raman active modes and six are IR active. Apparently, the two lattice modes observed are only a subset of the predicted modes if the assumed crystal structure is correct. Because the notch filters used in our Raman system and far-IR setup at the synchrotron beamline do not

Table 4. Pressure coefficients of the observed IR bands of $NH_3{\cdot}BH_3$ on compression.

		$d\nu/dP$ (cm^{-1} GPa^{-1})			
IR bands	Assignment	Phase III (2.8–5.8 GPa)	Phase IV (5.8–7. 8 GPa)	Phase V (7. 8–10.8 GPa)	Phase VI (>10.8 GPa)
Asym. B–H stretch	ν_8	12.6	14.6	26.8	12.4
^{11}B–N stretch	ν_5	7.6	8.1	10.6	8.5
^{10}B–N stretch	ν_5'	8.3			
NBH rock	ν_{11}	4.0	0.9	2.0	–1.6
	ν_{12}	5.1	5.5	6.5	2.6
NH_3 deformation	ν_{9a}/ν_{9b}	0.8/–2.2	–0.8/–1.4	1.4/3.8	
	ν_3	–0.1	0.0	–5.0	–3.8
BH_3 deformation	ν_{10}	2.9	0.6	6.6	8.0

allow unambiguous measurements below 100 cm^{-1}, it is possible that some additional lower frequency lattice modes were not detected. Nevertheless, the additional splitting features observed in the internal mode region, such as those for the ν_{11}, ν_9, and ν_7 modes, strongly suggest the structure is orthorhombic rather than tetragonal.

The next high-pressure phase (phase III, 2.4–5.5 GPa) may have a structure very similar to the low-pressure orthorhombic phase. This is indicated by the similarity of the lattice profile both in the Raman and IR measurements as well as in the more prominent splittings observed for the ν_{12}, ν_{11}, ν_8, and ν_9 modes. These observations strongly suggest enhanced intermolecular interactions as a result of compression as manifested by the largest pressure coefficient (Table 2) observed among all pressure regions. In addition, the bending deformation modes for BH_3 and NH_3 (i.e., ν_{10} and ν_9, respectively) at 2.4 GPa have a broad profile, indicating some degree of rotational disorder for NH_3–BH_3 along its molecular axis at this pressure. Upon compression, both modes split into narrower doublet peaks that suggests that the free rotation of the BH_3 and NH_3 groups is likely hindered by pressure and thus the complex may undergo a rotational disorder–order process in this pressure region. We note that our observation is in contrast to that of Lin et al.[28] where the splitting of these modes is lacking in this pressure region.

From 5.5 to 8.5 GPa, the complex undergoes a more prominent structural modification. In this region, up to four Raman lattice modes and three IR lattice modes were observed. The Raman frequencies are 139, 201, 246, and 301 cm^{-1} at 5.5 GPa, whereas the IR frequencies observed at the same pressure are 241, 344, and 467 cm^{-1}. However, the IR bands at 241 and 344 cm^{-1} measured during decompression are known to exhibit higher frequencies than those measured on compression owing to hysteresis. Therefore, we linearly extrapolated the high-pressure frequencies of IR bands 1 and 2 (Fig. 8*b*) to 5.5 GPa to obtain the corrected "compression" data (215 and 311cm^{-1}). As a result, these two major IR bands are roughly aligned with the two major Raman bands at 201 and 301 cm^{-1} as observed in other pressure regions, suggesting the new modes are 139 and 246 cm^{-1} for Raman measurements and 467 cm^{-1} for IR measurements. Again, because the observed Raman and IR modes are generally a subset of the predicted ones, it is difficult to perform a full factor group analysis without crystal structures. However, these observations can temporarily rule out a significant change to the factor group of the $NH_3{\cdot}BH_3$ crystal lattice, especially changes to centrosymmetric groups such as D_{2h} for orthorhombic or C_{2h} for monoclinic systems. The observation of new lattice modes can be interpreted as enhanced correlation field interactions within the C_{2v} factor group or even lower symmetry groups, such as those for monoclinic systems. X-ray diffraction measurements are required to understand the detailed structures of this $NH_3{\cdot}BH_3$ phase.

Above 8.5 GPa, both the Raman and IR spectra are characterized by significant profile broadening in almost all spectral regions. Split Raman modes are merged into broad bands with significantly reduced intensity (e.g., ν_{11}, ν_9, and ν_8), whereas the lattice modes measured both by Raman and IR spectroscopy become much weaker and broad. Above 10.4 GPa, the number of lattice modes in both Raman and IR measurements is reduced, whereas the remaining modes undergo continuing weakening and broadening. These observations suggest that the $NH_3{\cdot}BH_3$ complex is transforming from an ordered crystalline structure to a possibly disordered or ultimately amorphous structure when compressed to high enough pressures. The phase between 8.5 and 10.4 GPa can be considered as an intermediate phase for the disordering process, whereas the phase above 10.4 GPa is characterized by significant disordering. Although pressure gradients at high pressure may contribute to the profile broadening, our ruby fluorescence measurements across the sample suggest that the non-hydrostatic effect contributes only very insignificantly to this broadening.

In Lin et al.'s[28] analysis of the possible high-pressure structures based on the features of a few characteristic internal modes and the observation of two lattice modes, it is proposed that the crystal structure is unaltered in the entire pressure region. However, the additional lattice modes observed by our Raman and IR measurements clearly indicate that there is a possible pressure-induced formation of new crystal structures. They further speculate that the dimerization of ammonia borane complex may be associated with one of the high pressure phases. Again, if dimerization occurs, more internal modes with different vibrational frequencies are expected. In addition, dimerization implies that the number of the molecular unit Z halves per unit cell, which is contradictory to the observation that there was an increase in the number of lattice mode. In situ X-ray diffraction measurements are required to resolve the discrepancy between the structural interpretation of the two spectroscopic studies.

Fig. 8. (*a*) Synchrotron far-IR spectra of $NH_3{\cdot}BH_3$ in the spectral range of 100 to 700 cm^{-1} measured at room temperature for selective pressures (indicated in GPa above each spectrum) on decompression. The absorbance has been normalized with respect to the beam current of the synchrotron light source. The spectra are offset vertically for clarity. (*b*) Pressure dependences of IR frequencies of $NH_3{\cdot}BH_3$ for lattice modes. The solid symbols denote frequencies observed on compression and open symbols denote frequencies for decompression. The vertical dashed lines indicate one of the proposed phase boundaries.

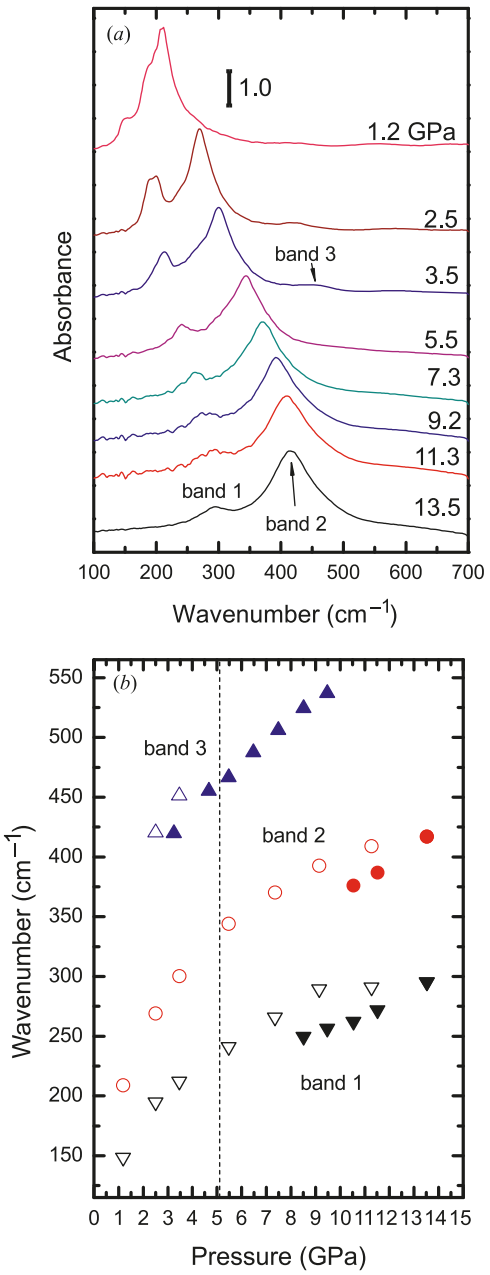

Finally, it is clear that both the Raman and IR measurements show that the pressure-induced transformations of the $NH_3{\cdot}BH_3$ complex are reversible upon decompression. The almost identical spectroscopic details in both Raman and IR internal mode regions before and after compression indicate that the chemical structure of the complex is completely unaltered by pressure and thus $NH_3{\cdot}BH_3$ is stable (i.e., no hydrogen release) up to the highest pressure yielded in this study. However, the different profiles of the lattice modes from both Raman and IR measurements suggest that crystalline structures may have been modified by pressure, even if very slightly. In addition, hysteresis has been observed in most of the pressure regions upon decompression. Our observations agree with those of Custelcean and Dreger,[22] who also found all pressure-induced transformations were reversible at <4 GPa, but that there was some hysteresis. Hysteresis is typically considered to be a result of kinetics-mediated transformations characterized by some barriers. To overcome the kinetic barrier, it would be interesting to investigate the pressure-induced transformations at elevated temperatures.

Conclusions

Using Raman and synchrotron IR spectroscopy, we investigated the pressure behaviour of the ammonia borane complex as a promising hydrogen storage material. In the low pressure region (<2 GPa), we discovered that the complex undergoes a structural transformation from a disordered tetragonal to an ordered, possibly orthorhombic, structure, consistent with previous Raman studies. Upon further compression, our Raman and IR measurements identified several solid-to-solid transformations with phase boundaries that roughly occurred at 2.4, 5.5, 8.5, and 10.4 GPa. These transformations are characterized by distinctive profiles and the pressure dependences of characteristic modes. Spectroscopic measurements on decompression suggest that these pressure-induced transformations are reversible within the intact chemical structure of the $NH_3{\cdot}BH_3$ complex, with possible modifications to the crystal structures. Analysis of combined Raman and IR measurements, especially the lattice features, suggests that $NH_3{\cdot}BH_3$ structures below 5.5 GPa resemble a low-pressure orthorhombic structure, whereas in the higher pressure regions, $NH_3{\cdot}BH_3$ complexes may undergo transformations to disordered or amorphous structures. Detailed high-pressure structural information needs to be confirmed by in situ X-ray diffraction measurements.

Acknowledgements

Y.S. acknowledges support from a Discovery Grant and a Research Tools and Instruments Grant from the Natural Sciences and Engineering Research Council of Canada (NSERC), the Leaders Opportunity Fund from the Canadian Foundation for Innovation (CFI), and the Early Researcher Award from the Ontario Ministry of Research and Innovation. IR measurements were performed at the U2A beamline at the NSLS at BNL. The U2A beamline is supported by COMPRES, the Consortium for Materials Properties Research in Earth Sciences under NSF Cooperative Agreement EAR06-49658, US Department of Energy (DOE), (CDAC), and NSF (DMR).

References

(1) Xiong, Z. T.; Yong, C. K.; Wu, G. T.; Chen, P.; Shaw, W.; Karkamkar, A.; Autrey, T.; Jones, M. O.; Johnson, S. R.; Edwards, P. P.; David, W. I. F. *Nat. Mater.* **2007**, *7* (2), 138–141. doi:10.1038/nmat2081. PMID:18157135.

(2) Dixon, D. A.; Gutowski, M. *J. Phys. Chem. A* **2005**, *109* (23), 5129–5135. doi:10.1021/jp0445627. PMID:16833867.
(3) Stowe, A. C.; Shaw, W. J.; Linehan, J. C.; Schmid, B.; Autrey, T. *Phys. Chem. Chem. Phys.* **2007**, *9* (15), 1831–1836. doi:10.1039/b617781f. PMID:17415495.
(4) Hu, M. G.; Geanangel, R. A.; Wendlandt, W. W. *Thermochim. Acta* **1978**, *23* (2), 249–255. doi:10.1016/0040-6031(78)85066-7.
(5) Sit, V.; Geanangel, R. A.; Wendlandt, W. W. *Thermochim. Acta* **1987**, *113* (1), 379–382. doi:10.1016/0040-6031(87)88340-5.
(6) Wolf, G.; Baumann, J.; Baitalow, F.; Hoffmann, F. P. *Thermochim. Acta* **2000**, *343* (1-2), 19–25. doi:10.1016/S0040-6031(99)00365-2.
(7) Jaenicke-Rossler, K.; Leitner, G. *Thermochim. Acta* **2002**, *391* (1-2), 159–168. doi:10.1016/S0040-6031(02)00173-9.
(8) Baumann, J.; Baitalow, E.; Wolf, G. *Thermochim. Acta* **2005**, *430* (1-2), 9–14. doi:10.1016/j.tca.2004.12.002.
(9) Stephens, F. H.; Pons, V.; Tom Baker, R. *Dalton Trans.* **2007**, (25): 2613–2626. doi:10.1039/b703053c. PMID: 17576485.
(10) Haaland, A. *Angew. Chem. Int. Ed. Engl.* **1989**, *28* (8), 992–1007. doi:10.1002/anie.198909921.
(11) Klooster, W. T.; Koetzle, T. F.; Siegbahn, P. E. M.; Richardson, T. B.; Crabtree, R. H. *J. Am. Chem. Soc.* **1999**, *121* (27), 6337–6343. doi:10.1021/ja9825332.
(12) Thorne, L. R.; Suenram, R. D.; Lovas, F. J. *J. Chem. Phys.* **1983**, *78* (1), 167. doi:10.1063/1.444528.
(13) Kathmann, S. M.; Parvanov, V.; Schenter, G. K.; Stowe, A. C.; Daemen, L. L.; Hartl, M.; Linehan, J.; Hess, N. J.; Karkamkar, A.; Autrey, T. *J. Chem. Phys.* **2009**, *130* (2),o. 024507. doi:10.1063/1.3042270. PMID:19154038.
(14) Hughes, E. W. *J. Am. Chem. Soc.* **1956**, *78* (2), 502–503. doi:10.1021/ja01583a074.
(15) Shore, S. G.; Parry, R. W. *J. Am. Chem. Soc.* **1955**, *77* (22), 6084–6085. doi:10.1021/ja01627a103.
(16) Hoon, C. F.; Reynhardt, E. C. *J. Phys. Chem.* **1983**, *16* (32), 6129–6136. doi:10.1088/0022-3719/16/32/007.
(17) Demaison, J.; Liévin, J.; Császár, A. G.; Gutle, C. *J. Phys. Chem. A* **2008**, *112* (19), 4477–4482. doi:10.1021/jp710630j. PMID:18422295.
(18) Bowden, M. E.; Gainsford, G. J.; Robinson, W. T. *Aust. J. Chem.* **2007**, *60* (3), 149. doi:10.1071/CH06442.
(19) Hess, N. J.; Bowden, M. E.; Parvanov, V. M.; Mundy, C.; Kathmann, S. M.; Schenter, G. K.; Autrey, T. *J. Chem. Phys.* **2008**, *128* (3),o. 034508. doi:10.1063/1.2820768. PMID:18205511.
(20) Cho, H.; Shaw, W. J.; Parvanov, V.; Schenter, G. K.; Karkamkar, A.; Hess, N. J.; Mundy, C.; Kathmann, S.; Sears, J.; Lipton, A. S.; Ellis, P. D.; Autrey, S. T. *J. Phys. Chem. A* **2008**, *112* (18), 4277–4283. doi:10.1021/jp7117696. PMID:18407708.
(21) Taylor, R. C.; Cluff, C. L. *Nature* **1958**, *182* (4632), 390–391. doi:10.1038/182390a0.
(22) Custelcean, R.; Dreger, Z. A. *J. Phys. Chem. B* **2003**, *107* (35), 9231–9235. doi:10.1021/jp035267+.
(23) Sawodny, W.; Goubeau, J. *Z. Phys. Chem. (Frankfurt)* **1965**, *44*, 227.
(24) Dillen, J.; Verhoeven, P. *J. Phys. Chem. A* **2003**, *107* (14), 2570–2577. doi:10.1021/jp027240g.
(25) Allis, D. G.; Kosmowski, M. E.; Hudson, B. S. *J. Am. Chem. Soc.* **2004**, *126* (25), 7756–7757. doi:10.1021/ja048215m. PMID:15212505.
(26) Trudel, S.; Gilson, D. F. R. *Inorg. Chem.* **2003**, *42* (8), 2814–2816. doi:10.1021/ic026275s. PMID:12691593.
(27) Hemley, R. J.; Mao, H. K. *In High-Pressure Phenomena*, Proceedings of the International School of Physics Enrico Fermi, Vol. 147; Hemley, R. J., Chiarotti, G.L., Bernasconi, M., Ulivi, L., Eds.; IOS Press: Amsterdam, 2002; p. 3.
(28) Lin, Y.; Mao, W. L.; Drozd, V.; Chen, J. H.; Daemen, L. L. *J. Chem. Phys.* **2008**, *129* (23),o. 234509. doi:10.1063/1.3040276. PMID:19102540.
(29) Mao, H. K.; Xu, J.; Bell, P. M. *J. Geophys. Res.* **1986**, *91* (B5), 4673–4676. doi:10.1029/JB091iB05p04673.
(30) Smith, J.; Seshadri, K. S.; White, D. *J. Mol. Spectrosc.* **1973**, *45* (3), 327–337. doi:10.1016/0022-2852(73)90205-1.
(31) Jagielska, A.; Moszynski, R.; Piela, L. *J. Chem. Phys.* **1999**, *110* (2), 947. doi:10.1063/1.478139.

Rhodium(I)–(*N*-heterocyclic carbene)–diphosphine complexes

Hongsui Sun, Xiao-Yan Yu, Paolo Marcazzan, Brian O. Patrick, and Brian R. James

Abstract: Reactions of $[RhCl(COE)(IPr)]_2$ (**1**) and $[RhCl(COE)(IMes)]_2$ (**2**) (COE = cyclooctene; IPr = *N*,*N*′-bis(2,6-diisopropylphenyl)imidazolin-2-ylidene; IMes = *N*,*N*′-bis(2,4,6-trimethylphenyl)imidazolin-2-ylidene) with the diphosphines $Ph_2P(CH_2)_nPPh_2$ and 1,2-bis(diphenylphosphino)benzene (dppbz) give the *N*-heterocyclic carbene (NHC)–diphosphine–rhodium(I) complexes: $RhCl(NHC)[Ph_2P(CH_2)_nPPh_2]$ [NHC = IPr, *n* = 1 (**3**); NHC = IMes, *n* = 1 (**4**); NHC = IPr, *n* = 2 (**5**); NHC = IMes, *n* = 2 (**6**); NHC = IPr, *n* = 4 (**7**); NHC = IMes, *n* = 4 (**8**)] and RhCl(NHC)(dppbz) [NHC = IPr (**9**); NHC = IMes (**10**)]. All the complexes are characterized by ^1H, $^{31}P\{^1H\}$, and $^{13}C\{^1H\}$ NMR spectroscopy, elemental analysis, and mass spectrometry. Complexes **3**, **7**, and **9** are also characterized crystallographically. In benzene solution, the complexes decompose in the presence of O_2 with formation of the diphosphine dioxide, whereas reaction with CO leads to replacement of the NHC ligand to give known carbonyl–diphosphine complexes.

Key words: rhodium, *N*-heterocyclic carbenes, bis(diphenylphosphino) ligands, crystallography.

Résumé : Les réactions du $[RhCl(COE)(IPr)]_2$ (**1**) et du $[RhCl(COE)(IMes)]_2$ (2) [COE = cyclooctène; IPr = *N*,*N*′-bis(2,6-diisopropylphényl)imidazoline-2-ylidène; IMes = *N*,*N*′-bis(2,4,6-triméthylphényl)imidazoline-2-ylidène] avec les diphosphines $Ph_2P(CH_2)_nPPh_2$ et 1,2-bis(diphénylphosphino)benzène (dppbz) conduisent à la formation de complexes carbène *N*-hétérocyclique (NHC)–diphosphine–rhodium(I): $RhCl(NHC)[Ph_2P(CH_2)_nPPh_2]$ [NHC = IPr, *n* = 1 (**3**); NHC = IMes, *n* = 1 (**4**); NHC = IPr, *n* = 2 (**5**); NHC = IMes, *n* = 2 (**6**); NHC = IPr, *n* = 4 (**7**); NHC = IMes, *n* = 4 (**8**)] et RhCl(NHC)(dppbz) [NHC = IPr (**9**); NHC = IMes (**10**)]. Tous les complexes ont été caractérisés par des analyses élémentaires, par spectroscopie RMN du ^1H, du $^{31}P\{^1H\}$ et du $^{13}C\{^1H\}$ et par spectrométrie de masse. Les complexes **3**, **7** et **9** ont aussi été caractérisés par diffraction des rayons X. En solution dans le benzène, les complexes se décomposent en présence de O_2 avec formation d'oxyde de diphosphine, alors qu'une réaction avec le CO conduit au remplacement du ligand NHC pour conduire aux complexes carbonyl–diphosphines connus.

Mots-clés : rhodium, carbènes *N*-hétérocycliques, ligands bis(diphénylphosphino), cristallographie.

[Traduit par la Rédaction]

Introduction

A just-published special issue of *European Journal of Inorganic Chemistry* demonstrates the growing interest in transition-metal *N*-heterocyclic carbene (NHC) complexes.[1] Seven of the papers in the issue are concerned with Rh–NHC chemistry, including one from our group, which describes reactions of $[RhCl(COE)(NHC)]_2$ complexes with H_2 and with CO, where COE is cyclooctene and NHC is either *N*,*N*′-bis(2,6-diisopropylphenyl)imidazolin-2-ylidene (IPr) or *N*,*N*′-bis(2,4,6-trimethylphenyl)imidazolin-2-ylidene (IMes).[2] More generally, studies on Rh–NHC systems often pertain to comparisons with the chemistry and catalytic activity of Rh–tertiary phosphine systems, i.e., with replacement of PR_3 ligand(s) by NHC ligand(s) or use of mixed NHC–tertiary phosphine species.[2–5] Of prime interest to our group is the interaction of O_2 with Rh(I) complexes containing coordinated NHC ligands with or without ancillary phosphine ligands. We have shown that RhCl(NHC)(P–N) and *cis*-$RhCl(NHC)(PPh_3)_2$ complexes oxidatively add O_2 to generate "standard" six-coordinate Rh(III)–peroxide species (see Scheme 1), where P–N = *P*,*N*-chelated *o*-(diphenylphosphino)-*N*,*N*-dimethylaniline and NHC = IPr or IMes;[5] in an as yet unpublished work, our X-ray data for a five-coordinate $RhCl(IPr)_2(O_2)$ are also consistent with a peroxide.[6] However, recent communications by Crudden and coworkers[3,4a] report that $RhCl(NHC)_2(O_2)$ (NHC = IPr or IMes) and $RhCl(IMes)(PPh_3)(O_2)$ are best described as being Rh(I) singlet oxygen species. In efforts to understand the nature of this important discrepancy, we decided to synthesize Rh(I)–diphosphine–NHC complexes in the hope that their reactivity toward O_2 might prove helpful — a hope that was not fulfilled!

Received 5 May 2009. Accepted 7 July 2009. Published on the NRC Research Press Web site at canjchem.nrc.ca on 21 August 2009.

This tardy article is dedicated to Professor R.J. Puddephatt on the occasion of his 66th birthday (should have been submitted last year for his 65th!), and in recognition of his contributions to the development of Canadian organometallic chemistry. This article is a belated contribution to a Special Issue dedicated to Professor R.J. Puddephatt (Canadian Journal of Chemistry, January 2009).

H. Sun, X.-Y. Yu, P. Marcazzan, B.O. Patrick, and B.R. James.[1] Department of Chemistry, The University of British Columbia, Vancouver, BC V6T 1Z1, Canada.

[1]Corresponding author (e-mail: brj@chem.ubc.ca).

Experimental section

General procedures

All manipulations were performed under an atmosphere of dry Ar using standard Schlenk techniques or in a glove box. Solvents (Fisher Scientific) were dried using standard procedures and, before use, were purged with a stream of Ar. C_6D_6 (Cambridge Isotope Laboratory) was distilled from Na and stored under Ar. The diphosphines were used as received from Strem Chemicals. Complexes $[RhCl(COE)(IPr)]_2$ (**1**) and $[RhCl(COE)(IMes)]_2$ (**2**) were prepared by our literature procedure.[5] NMR spectra were recorded in C_6D_6 at room temperature (~20 °C) either on a Bruker AV 400 or AV 300 spectrometer, data being reported in ppm relative to TMS with the solvent signals as internal references (^{1}H, δ 7.16; ^{13}C, δ 128.38); ^{31}P{H} NMR shifts are relative to external 85% H_3PO_4. *J* values are given in Hz (s = singlet, d = doublet, *t* = triplet, spt = septet, m = multiplet, br = broad, ps = pseudo); assignments were sometimes aided by the use of ^{13}C{^{1}H}-APT and ^{1}H–^{13}C{^{1}H}–HSQC experiments. Mass spectra were obtained on a Kratos MS-50 spectrometer operating in the EI mode or on a Bruker Biflex IV spectrometer operating with a MALDI ion source. Elemental analyses were done on a Carlo Erba EA 1108 elemental analyzer.

RhCl(IPr)($Ph_2PCH_2PPh_2$) (3)

63.8 mg (0.05 mmol) of **1** and 38.5 mg (0.10 mmol) of dppm were dissolved in C_6H_6 (6 mL). The resulting yellow solution became orange on being stirred at room temperature for 5 h and was then concentrated to ~2 mL; hexane (~2 mL) was then added to precipitate the product, which was filtered off and dried in vacuo. Yield: 85 mg (93%). ^{1}H NMR δ: 0.53 (6H, d, J = 6.7, Me), 1.00 (6H, d, J = 6.7, Me), 1.16 (6H, d, J = 6.7, Me), 1.89 (d, 6H, J = 6.7, Me), 3.35 (br t, 2H, J_{HP_A} = 9.0, J_{HP_B} = 8.7, PCH_2P), 3.62 (spt, 2H, J = 6.7, CHMe$_2$), 3.74 (spt, 2H, J = 6.7, CHMe$_2$), 6.79 (s, 2H, NCH), 6.88 (ps t, 6H, *m*-Ph (4H) + *m*-IPr (2H)?), 6.96–6.99 (m, 8H, *o*-Ph (4H) + *p*-Ph (4H)?), 7.23 (t, 2H, $^3J_{HH}$ = 7.6, *p*-IPr), 7.30–7.37 (ps t, 6H, *m*-Ph (4H) + *m*-IPr (2H)?), 7.88–7.95 (m, 4H, *o*-Ph). ^{13}C{H} NMR δ: 22.87, 24.36, 26.87, 27.03, 29.09, 29.69, 48.29 (dd, J_{CP} = 19, J_{CP} = 30, PCH$_2$P), 123.78, 124.52, 124.91, 128.05, 128.21, 128.31, 128.88, 129.48, 129.77, 133.01 (d, J_{CP} = 22, C_{Ph}P), 133.96 (d, J_{CP} = 12, C_{Ph}P), 136.35, 136.65, 136.73, 137.02, 138.13, 144.89, 149.16, 195.45 (ddd, J_{CP_A} = 10, J_{CP_B} = 48, J_{CRh} = 128, Rh–*C*). ^{31}P{H} NMR: AB portion of the P_A, P_B, Rh (ABX) spin system simulated by the parameters: δ_A = –35.68, δ_B = –20.92, J_{AB} = 101.0, J_{AX} = 104.0, J_{BX} = 178.0 (see text). MS (EI) (*m*/*z*): 910 [M]$^+$, 387 [IPr – 1]$^+$. Anal calcd. for $C_{52}H_{58}N_2ClP_2Rh$: C 68.55, H 6.42, N 3.08; found: C 68.8, H 6.4, N 2.9. X-ray quality crystals of **3** containing 0.5 mol C_6H_6 solvate were grown by layering a C_6H_6 solution of the compound with hexane.

RhCl(IMes)($Ph_2PCH_2PPh_2$) (4)

The synthetic procedure for complexes **4**–**10** follows that given for **3**; here, 55.0 mg (0.05 mmol) of **2**, 38.6 mg (0.10 mmol) of dppm, and C_6H_6 (5 mL) were used. Yield: 74 mg (89%). ^{1}H NMR δ: 1.73 (s, 6H, *o*-Me), 2.22 (s, 6H, *o*-Me), 2.77 (s, 6H, *p*-Me), 3.40 (br t, 2H, J_{HP_A} = 9.1, J_{HP_B} = 8.8, PCH_2P), 6.25 (s, 2H, NCH), 6.60 (s, 2H, *m*-IMes), 6.88 (s, 2H, *m*-IMes), 6.95–7.09 (m, 12H, *o*-Ph (4H) + *m*-Ph (4H) + *p*-Ph (4H)?), 7.43–7.49 (m, 4H, *m*-Ph), 7.80–7.87 (m, 4H, *o*-Ph). ^{13}C{H} NMR δ: 19.45 (Me), 21.02 (Me), 21.61 (Me), 51.11 (dd, J_{CP} = 18, J_{CP} = 23, PCH$_2$P), 122.93 (NCH), 122.97 (NCH), 128.99, 129.40, 130.31, 131.70, 131.92, 133.84 (d, J_{CP} = 20, C_{Ph}P), 133.96 (d, J_{CP} = 16, C_{Ph}P), 135.35, 136.69, 136.98, 137.79, 138.07, 138.33, 138.54, 193.15 (ddd, J_{CP_A} = 10, J_{CP_B} = 47, J_{CRh} = 129, Rh–*C*). ^{31}P{H} NMR: AB portion of the P_A, P_B, Rh (ABX) spin system simulated by the parameters δ_A = –33.57, δ_B = –19.93, J_{AB} = 107.0, J_{AX} = 102.0, J_{BX} = 179.0 (see text). MS (EI) (*m*/*z*): 826 [M]$^+$, 790 [M – HCl]$^+$, 303 [IMes – 1]$^+$. Anal. calcd. for $C_{46}H_{46}N_2ClP_2Rh$: C 66.81, H 5.61, N 3.39; found: C 66.8, H 5.6, N 3.3.

RhCl(IPr)($Ph_2PCH_2CH_2PPh_2$) (5)

Complex **5** was prepared using 50.0 mg (0.04 mmol) of **1**, 31.0 mg (0.08 mmol) of dppe, and 10 mL C_6H_6. Yield: 66 mg (91%). ^{1}H NMR δ: 0.40 (d, 6H, J = 6.8, Me), 0.90 (d, 6H, J = 6.8, Me), 1.11 (d, 6H, J = 6.8, Me), 1.42–1.64 (m, 4H, CH_2-dppe), 1.68 (d, 6H, J = 6.8, Me), 3.38 (m, 2H, CHMe$_2$), 3.81 (m, 2H, CHMe$_2$), 6.81 (s, 2H, NCH), 6.87 (d, 2H, J = 7.4, *m*-IPr), 6.93 (t, 4H, J = 7.0, *m*-Ph), 7.02 (t, 2H, J = 7.0, *p*-Ph), 7.07–7.14 (m, 6H, *o*-Ph (4H) + *p*-Ph (2H)?), 7.26 (t, 2H, J = 7.7, *p*-IPr), 7.35 (d, 2H, J = 7.6, *m*-IPr), 7.45 (t, 4H, J = 8.5, *m-Ph*), 7.73–7.78 (m, 4H, *o*-Ph). ^{13}C{H} NMR δ: 22.90, 24.34, 27.04, 27.17, 28.90, 29.71, 32.84 (d, J_{CP} = 25, CH$_2$), 33.17 (d, J_{CP} = 23, CH$_2$), 123.90, 124.86, 124.94, 127.83, 127.92, 127.98, 128.93, 129.16, 129.75, 133.64 (d, J_{CP} = 12, C_{Ph}P), 135.16 (d, J_{CP} = 12, C_{Ph}P), 136.20, 136.60, 137.94, 138.25, 144.91, 149.61, 196.72 (dd, J_{CP} ~ 48, J_{CRh} = 121). ^{31}P{H} NMR δ: 62.10 (dd, $^2J_{PP}$ = 38, $^1J_{RhP}$ = 123), 65.84 ($^2J_{PP}$ = 38, $^1J_{RhP}$ = 208). MS (EI) (*m*/*z*): 924 [M]$^+$, 536 [M – IPr]$^+$, 387 [IPr – 1]$^+$. Anal. calcd. for $C_{53}H_{60}N_2ClP_2Rh$: C 68.81, H 6.54, N 3.03; found: C 68.5, H 6.4, N 3.0.

RhCl(IMes)($Ph_2PCH_2CH_2PPh_2$) (6)

Complex **6** was prepared using 75.0 mg (0.07 mmol) of **2**, 54.0 mg (0.14 mmol) of dppe, and 10 mL C_6H_6. Yield: 98 mg (86%). ^{1}H NMR δ: 1.23–1.24 (m, 4H, CH_2-dppe), 1.61 (s, 6H, *o*-Me), 2.23 (s, 6H, *o*-Me), 2.79 (s, 6H, *p*-Me), 6.23 (s, 2H, NCH), 6.60 (s, 2H, *m*-IMes), 6.85 (s, 2H, *m*-IMes), 6.97–7.11 and 7.04–7.08 (m, 12H, *o*-Ph (4H) + *m*-Ph(4H) + *p*-Ph (4H)?), 7.51 (t, 4H, J = 8, *m*-Ph), 7.80 (m, 4H, *o*-Ph). ^{13}C{H} NMR δ: 19.72 (Me), 21.56 (Me), 21.59 (Me), 32.05 (d, J_{CP} = 25, CH$_2$), 32.40 (d, J_{CP} = 25, CH$_2$), 123.16 (NCH), 127.77, 127.86, 127.93, 128.87, 128.93, 129.01, 129.14, 130.39, 134.52 (d, J_{CP} = 11, C_{Ph}P), 135.04 (d, J_{CP} = 10, C_{Ph}P), 135.58, 137.57, 138.49, 138.53, 139.04, 139.36. AB portion of the P_A, P_B, Rh (ABX) spin system simulated by the parameters δ_A = –64.26, δ_B = –64.96, J_{AB} = 36.6, J_{AX} = 125.7, J_{BX} = 205.7 (see text). MS (EI) (*m*/*z*): 840 [M]$^+$, 804 [M – HCl]$^+$, 536 [M – IMes]$^+$, 303 [IMes – 1]$^+$. Anal. calcd. for $C_{47}H_{48}N_2ClP_2Rh$: C 67.13, H 5.76, N 3.33; found: C 67.0, H 5.8, N 3.23.

RhCl(IPr)[$Ph_2P(CH_2)_4PPh_2$] (7)

Complex **7** was prepared by using 63.8 mg (0.05 mmol) of **1**, 42.7 mg (0.10 mmol) of dppb, and 10 mL C_6H_6. Yield: 76 mg (80%). ^{1}H NMR δ: 0.59 (br s, 6H, Me), 1.05 (m,

12H, Me), 1.29 (br s, 6H, Me), 1.72 (br s, 4H, CH_2), 1.85 (br s, 4H, CH_2), 3.56 (br s, 4H, CHMe$_2$), 6.89 (s, 2H, NCH), 6.98–7.08 (m, 16H, *Ar*), 7.30–7.41 (m, 10H, *Ar*). ^{13}C{H} NMR δ: 21.86 (Me), 23.89 (*C*H$_2$), 23.97, 25.14, 25.58 (d, J_{CP} = 20, P*C*H$_2$), 27.34 (Me), 29.64 (Me), 29.73 (Me), 30.24 (*C*H$_2$), 36.17 (d, J_{CP} = 25, P*C*H$_2$), 123.61, 124.05, 125.20, 127.15 (d, J_{CP} = 9, C_{Ph}P), 128.30, 128.69, 128.93, 129.03, 129.61, 131.42, 131.51, 131.58, 133.36 (d, J_{CP} = 11, C_{Ph}P), 145.10, 150.55. ^{31}P{H} NMR δ: 13.85 ($^2J_{PP}$ = 48, $^1J_{RhP}$ = 114), 48.94 (dd, $^2J_{PP}$ = 48, $^1J_{RhP}$ = 208). MS (MALDI) (*m*/*z*): 952 [M]$^+$. Anal. calcd. for $C_{55}H_{64}ClN_2P_2Rh$: C 69.30, H 6.77, N 2.94; found: C 69.5, H 6.7, N 3.1. X-ray quality crystals of **7** were grown by layering a C_6H_6 solution of the compound with hexane.

RhCl(IMes)[Ph$_2$P(CH$_2$)$_4$PPh$_2$] (8)

The yellow complex **8** was obtained using 75.0 mg (0.07 mmol) of **2**, 58.0 mg (0.14 mmol) of dppb, and 10 mL of benzene. Yield: 91 mg (77%). ^{1}H NMR δ: 1.91 (s, 6H, *o*-Me), 2.09 (m, 4H, CH_2), 2.26 (s, 6H, *o*-Me), 2.46 (br s, 4H, CH_2), 2.83 (s, 6H, *p*-Me), 6.29 (s, 2H, NCH), 6.75 (s, 2H, *m*-IMes), 6.90–7.11 (m, 14H, *o*-Ph (4H) + *m*-Ph (4H) + *p*-Ph (4H) + *m*-IMes (2H)?), 7.32 (t, 4H, *J* = 8, *m*-Ph), 7.62 (m, 4H, *o*-Ph). ^{13}C{H} NMR δ: 19.90 (Me), 21.89 (Me), 22.48 (Me) 24.08 (*C*H$_2$), 32.74 (d, *J* = 18, P–*C*H$_2$), 32.99 (*C*H$_2$), 122.03, 122.05, 123.11, 126.84 (d, J_{CP} = 10, C_{Ph}P), 127.64, 127.82, 129.13, 129.54 (d, J_{CP} = 8, C_{Ph}P), 133.44, 134.39, 134.65, 134.92, 135.43, 135.68, 137.38, 137.41, 138.20, 138.60, 138.90, 144.34. ^{31}P{H} NMR δ: 12.38 (dd, $^2J_{PP}$ = 48, $^1J_{RhP}$ = 118), 54.04 ($^2J_{PP}$ = 48, $^1J_{RhP}$ = 207). MS (MALDI) (*m*/*z*): 868 [M]$^+$. Anal. calcd. for $C_{49}H_{52}ClN_2P_2Rh$: C 67.70, H 6.04, N 3.23; found: C 67.9, H 6.0, N 3.3.

RhCl(IPr)(Ph$_2$PC$_6$H$_4$PPh$_2$) (9)

The orange complex **9** was obtained using 55.0 mg (0.04 mmol) of **1** and 44.0 mg (0.10 mmol) of dppbz in 5 mL of C_6H_6. Crystalline material contained 0.5 mol solvate C_6H_6. Yield: 82 mg, 96%. Dried material was of the formulation $C_{57}H_{60}ClN_2P_2Rh$. ^{1}H NMR δ: 0.70 (d, 6H, *J* = 6.7, Me), 0.90 (d, 6H, *J* = 6.7, Me), 1.10 (d, 6H, *J* = 6.7, Me), 1.65 (d, 6H, *J* = 6.5, Me), 3.37 (m, 2H, CHMe$_2$), 3.91 (m, 2H, CHMe$_2$), 6.72 (br s, 2H, NCH), 6.80–6.82 (m, 4H, *m*-Ph), 6.89–6.95 (br t, 6H, *J* ~ 6.5), 7.09–7.15 (m, 8H), 7.25 (d, 2H, *J* = 7.6), 7.43 (ps t, 6H), 7.81 (m, 4H). ^{13}C{H} NMR δ: 22.73, 24.27, 26.99, 27.14, 29.21, 29.62, 123.63, 124.99, 127.87, 127.97, 128.32, 128.51, 128.69, 128.92, 129.10, 129.81, 133.10, 133.22, 135.13 (d, J_{CP} = 11, $C_{C_6H_4}$P?), 137.10 (d, J_{CP} = 45, C_{Ph}P?), 138.55, 139.57 (d, J_{CP} = 36, C_{Ph}P?), 144.47, 149.05, 194.96 (ddd, J_{CP_A} = 11, J_{CP_B} = 48, J_{CRh} = 122, Rh–*C*). ^{31}P{H} NMR δ: 65.96 (dd, $^2J_{PP}$ = 39, $^1J_{RhP}$ = 205), 71.36 ($^2J_{PP}$ = 39, $^1J_{RhP}$ = 124). MS (EI) (*m*/*z*): 972 [M]$^+$, 387 [IPr – 1]$^+$. Anal. calcd: C 70.35, H 6.22, N 2.88; found: C 70.6, H 6.3, N 2.7. The layering method given for complex **3** yielded X-ray quality crystals of **9** again containing 0.5 mol C_6H_6 solvate.

RhCl(IMes)(Ph$_2$PC$_6$H$_4$PPh$_2$) (10)

The orange complex **10** was obtained using 55.0 mg (0.05 mmol) of **2** and 44.0 mg (0.10 mmol) of dppbz in 5 mL of C_6H_6. Yield: 71 mg (80%). ^{1}H NMR δ: 1.62 (s, 6H, *o*-Me), 2.16 (s, 6H, *o*-Me), 2.74 (s, 6H, *p*-Me), 6.21 (s, 2H, NCH), 6.53 (s, 2H, *m*-IMes), 6.66–6.71 (m, 2H, *o*-C_6H_4), 6.74 (s, 2H, *m*-IMes), 6.95–7.04 (m, 12H, *o*-Ph (4H) + *m*-Ph (4H) + *p*-Ph (4H)), 7.25 (ps t, 2H, *m*-C_6H_4), 7.67 (t, 4H, *J* = 8.6, *m*-Ph), 7.79 (m, 4H, *o*-Ph). ^{13}C{H} NMR δ: 18.58, 20.79, 122.48, 127.09, 127.18, 127.25, 127.34, 127.81, 127.96, 128.16, 128.37, 128.88 (d, J_{CP} = 3, C_{Ph}P?), 129.21 (d, J_{CP} = 4, C_{Ph}P?), 129.65, 130.57, 130.70, 131.68, 131.83, 133.99, 134.11, 134.22, 134.32, 134.68, 136.38, 136.80, 137.53, 137.64, 138.02, 138.36, 192.32 (dd, J_{CP} ~ 9, J_{CRh} = 118, Rh–*C*). ^{31}P{H} NMR: AB portion of the P_A, P_B, Rh (ABX) spin system simulated by the parameters δ_A = –66.77, δ_B = –67.33, J_{AB} = 39.60, J_{AX} = 206.8, J_{BX} = 125.6 (see text). MS (EI) (*m*/*z*): 888 [M]$^+$, 303 [IMes – 1]$^+$. Anal. calcd. for $C_{51}H_{48}ClN_2P_2Rh$: C 68.90, H 5.45, N 3.15; found: C 69.0, H 5.3, N 3.3.

X-ray crystallographic analysis of complexes 3, 7, and 9

Measurements were made at 173.0(1) K on a Bruker X8 APEX diffractometer with graphite-monochromated Mo-Kα radiation (0.71 069 Å). Data were collected and integrated using the Bruker SAINT software package[7] and were corrected for absorption effects using the multi-scan SADABS technique.[8] All structures were solved by direct methods,[9] and refinements were performed using the SHELXTL program.[10] All non-hydrogen atoms were refined anisotropically and all H atoms were included in calculated positions but not refined.

Crystal data for 3

$C_{52}H_{58}N_2ClP_2Rh{\cdot}0.5C_6H_6$, fw = 949.31, orange tablet, size 0.15 mm × 0.20 mm × 0.50 mm, monoclinic, space group *P* 2$_1$/*n* (No. 14), *a* = 11.0616(2) Å, *b* = 21.9905(4) Å, *c* = 20.1095(4) Å, β = 90.774(1)°, *V* = 4891.2(2) Å^3, *Z* = 4, D_{calcd} = 1.291 g cm^{-3}, μ = 0.507 mm^{-1}. *F*(000) = 1988.00, 62 508 total reflections (11 674 independent of symmetry, 8726 for $I > 2\sigma(I)$), 558 variables, residuals (refined on F^2, all data): *R*1 = 0.038, *wR*2 = 0.088.

Crystal data for 7

$C_{55}H_{64}N_2ClP_2Rh$, fw = 952.33, orange plate, size 0.20 mm × 0.25 mm × 0.50 mm, monoclinic, space group *P* 2$_1$/*n* (No. 14), *a* = 11.1595(6) Å, *b* = 20.971(1) Å, *c* = 20.938(1) Å, β = 95.693(2)°, *V* = 4875.8(5) Å^3, *Z* = 4, D_{calcd} = 1.299 g cm^{-3}, μ = 0.509 mm^{-1}. *F*(000) = 2000.00, 69 860 total reflections (11 679 independent of symmetry, 9737 for $I > 2\sigma(I)$), 558 variables; residuals (refined on F^2, all data): *R*1 = 0.037, *wR*2 = 0.067.

Crystal data for 9

$C_{57}H_{60}N_2ClP_2Rh{\cdot}0.5C_6H_6$, fw = 1011.32, orange plate, size 0.04 mm × 0.15 mm × 0.25 mm, triclinic, space group *P*-1 (No. 2), *a* = 12.6856(8) Å, *b* = 17.438(1) Å, *c* = 24.693(2) Å, α = 80.911(3)°, β = 81.812(2)°, γ = 86.156(3)°, *V* = 5333.1(6) Å^3, *Z* = 4, D_{calcd} = 1.256 g cm^{-3}, μ = 0.476 cm^{-1}. *F*(000) = 2116.00, 69 026 total reflections (18 891 independent of symmetry, 14 480 for $I > 2\sigma(I)$), 1200 variables, residuals (refined on F^2, all data): *R*1 = 0.061, *wR*2 = 0.103. The material crystallized with two molecules of the Rh-complex, one C_6H_6 molecule and one additional solvent molecule, in the asymmetric unit; the solvent

resembled hexane, but could not be modeled satisfactorily and was thus removed from the model, with the SQUEEZE program[11] used to correct data for any residual electron density found in the space formerly occupied by the solvent.

Scheme 1. Reactions of O_2 with some Rh–*N*-heterocyclic carbene (NHC)–phosphine complexes.

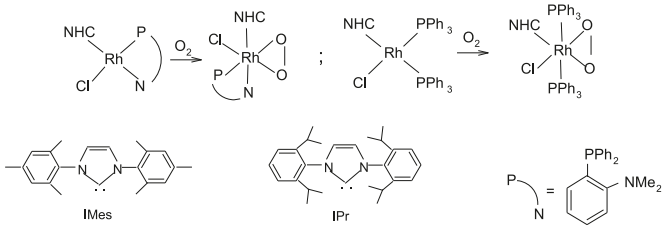

Reactivity of the complexes

The complexes (~0.05 mmol) were dissolved in C_6D_6 (1 mL), and a sample (~0.7 mL) of the solution was placed in a J-Young NMR tube and subjected to an atmosphere of O_2, CO, or H_2 at room temperature; $^{31}P\{^1H\}$ NMR spectral changes were then monitored.

Results and discussion

Synthesis and spectroscopic characterization of complexes

The diphosphines $Ph_2P(CH_2)_nPPh_2$ (n = 1, dppm; n =2, dppe; n = 4, dppb) and 1,2-bis(diphenylphosphino)benzene (dppbz) react at room temperature with $[RhCl(COE)(NHC)]_2$ complexes in benzene to give yellow RhCl(NHC)(P–P) species in 77%–96% isolated yields (NHC = IPr or IMes, and P–P is the chelating diphosphine). All eight complexes (**3**–**10**) have been synthesized (see Scheme 2) and well characterized by elemental analysis, ^1H, $^{31}P\{^1H\}$, and $^{13}C\{^1H\}$ NMR spectroscopy, mass spectrometry and, for **3**, **7**, and **9**, by X-ray crystallography.

The solution NMR data for the complexes are generally straightforward, and most of the shifts are readily assigned based on previously reported data, for example, for *cis*-$RhCl(NHC)(PPh_3)_2$ and RhCl(NHC)(P–N) species (see Scheme 1).[5] All the complexes show a ^1H singlet for NC*H* between δ_H 6.79–6.89 and 6.21–6.29 for the IPr- and IMes-containing species, respectively. The IPr species **3**, **5**, and **9** show four sets of doublets for inequivalent IPr–Me groups, with coupling of ~6.7 Hz to a IPr–methine proton; the doublets indicate restricted rotation about the Rh–C bond or, less likely, the N_{imid}–C_{arene} bond.[12] Complex **7** shows broad signals for these methyls, presumably because of the relative greater flexibility of the dppb chelate ring, which might allow for more rotational motion.[13] The Me signals are sometimes shifted downfield (e.g., to δ_H 1.89 for **3**), which could result from a deshielding effect from a phenyl ring of the diphosphine (see the following section for the structure of **3**). The IPr–methine protons appear as two septets (for **3**), two multiplets (for **5**), or one broad singlet (for **7**). For each of the IMes species **4**, **6**, **8**, and **10**, the Me protons are seen as three singlets at δ_H ~2.8, ~2.2, and between 1.9 and 1.6, implying that the two *o*-Me groups on one aromatic ring are inequivalent, consistent again with some restricted rotation.

Scheme 2. Synthesis of complexes and their numbering.

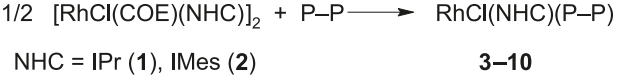

NHC	dppm	dppe	dppb	dppbz
IPr	**3**	**5**	**7**	**9**
IMes	**4**	**6**	**8**	**10**

Fig. 1. The experimental (upper) and simulated (lower) $^{31}P\{^1H\}$ NMR spectra of RhCl(IPr)(dppm) (**3**). δ_{P_A} = –35.68, δ_{P_B} = –20.92, J_{AB} = 101.0 Hz, J_{RhP_A} = 104.0 Hz, J_{RhP_B} = 178.0 Hz.

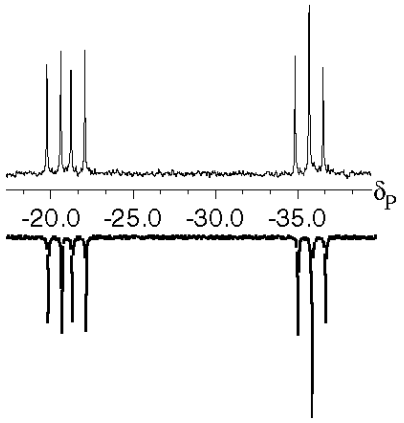

The two singlets seen for the *m*-protons of the IMes ligand similarly imply inequivalence of these protons within one ring; the same description has been noted for the analogous *cis*-$RhCl(IMes)(PPh_3)_2$ complex.[4j] Where possible, we have assigned the *m*- and *p*-protons of the IPr ligand, the *m*-protons of the IMes ligand, and the phenyl protons of the PPh_2 groups, based on (*i*) expected splitting patterns (e.g., the *m*-H of IPr and of IMes are doublets and singlets, respectively, and the *p*-H of IPr is a triplet),[2,5,14] (*ii*) data for free IPr and IMes,[15], and (*iii*) data for the free diphosphines.[16] The more tentative assignments of these aromatic protons are indicated by a query (?) in the Experimental section. The CH_2 protons of the carbon backbone of the diphosphine ligand in **5**–**8** appear as a multiplet or broad singlets. Those of dppm in **3** and **4** are seen as a broadened triplet, which is in fact a set of overlapping doublets that result from two equivalent protons coupling to the two inequivalent P atoms; the ^{31}P-decoupled spectra showed a slightly broadened singlet.

The $^{31}P\{^1H\}$ NMR spectra reveal the expected inequivalent P atoms. For **5** and **7**–**9**, first-order spectra show doublets of doublets with J_{PP} values of 48–38 Hz and J_{RhP} values of 123–114 and 208–205 Hz (for the P atom cis and trans to Cl, respectively[4d,4e,5]). For the other complexes, the spectra are more complex ABX systems but are readily simulated. Figure 1 shows the data for **3** and those of **4** (the other dppm derivative) are very similar: the J_{PP} values are now ~100 Hz, with J_{RhP} values of ~100 and 180 Hz, respectively, for the P atoms cis and trans to Cl. The ABX spectra of **6** (Fig. 2) and **10** are similar to each other, with J_{PP} and

Fig. 2. The experimental (upper) and simulated (lower) $^{31}P\{^1H\}$ NMR spectra of RhCl(IMes)(dppe) (**6**) δ_{P_A} = –64.26, δ_{P_B} = –64.96, J_{AB} = 36.6 Hz, J_{RhP_A} = 125.7 Hz, J_{RhP_B} = 205.7 Hz.

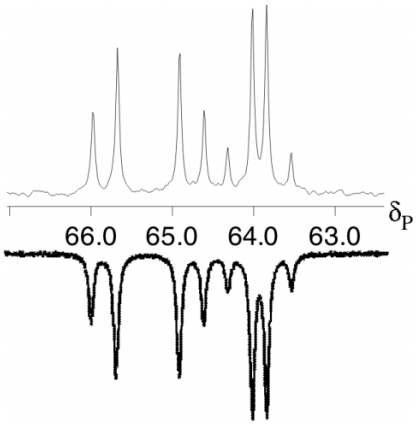

J_{RhP} values close to those seen in the first-order spectra of **5** and **7**–**9**. Spectra akin to those of Fig. 2 have been noted previously for analogous *cis*-RhCl(IMes)$[P(OPh)_3]_2$ species.[4e]

The expected ddd pattern (coupling to Rh and inequivalent P atoms) in the $^{13}C\{^1H\}$ spectra for the Rh–*C* signals is seen at δ ~195 for **3**, **4**, and **9**, with J_{RhC} being ~125 Hz and the J_{PC} values being ~10 and ~50 Hz. For **5** and **10**, only somewhat broader dd patterns are seen, whereas for **6**–**8** these signals are not seen and are presumably broadened into the baseline by some exchange processes, reflecting a relatively labile Rh–carbene bond (see the last section on the reactivity toward CO); the flexibility of the dppb ring might account in part for the lack of the Rh–*C* signal in **7** and **8**. The non-appearance of carbene-carbon resonances in Rh–NHC species is not unusual.[2,4e,5] There is no question about the identity of the complexes, which are all essentially square-planar Rh(I) species, with some distortion induced by the chelating phosphines, as seen particularly in the structure of **3**, the dppm derivative (see the following section). For **3** and **4**, the $^{13}C\{^1H\}$ signal for the P*C*H_2P carbon is seen as a doublet of doublets at δ ~50 with J_{CP} values for the inequivalent P atoms in the 18–30 Hz range. For complexes **5**–**10**, $^{13}C\{^1H\}$ signals for the C atoms attached to P atoms are seen as doublets in the expected regions δ_C 25–36 and 125–139, respectively, for alkyl and aryl carbons; uncertain assignments are again indicated by ?.

Mass spectral data reveal the parent peak for all the complexes using either the EI mode (for **3**–**6**, **9**, and **10**) or the MALDI-TOF ion source (for **7** and **8**).

Structural characterization of 3, 7, and 9

The crystal structures of **3**, **7**, and **9** (all containing IPr) were established by X-ray analysis; the molecular structures and selected bond lengths and angles are shown in Figs. 3, 4, and 5, respectively. Complex **3** crystallized with one-half of a benzene molecule, whereas **9** crystallized as two independent molecules with one benzene molecule and one additional solvent molecule (likely hexane) in the asymmetric unit; **7** was nonsolvated. The essentially square-planar structures show some distortion, particularly in the dppm of **3** where the P1–Rh–P2 bond angle is 72.81° and the adjacent

Fig. 3. ORTEP diagram of RhCl(IPr)(dppm) (**3**) with 50% probability thermal ellipsoids; H atoms are omitted for clarity. Selected bond lengths (Å) and angles (°): Rh1—C1, 2.067(2); Rh1—Cl1, 2.3793(6); Rh1—P1, 2.2005(6); Rh1—P2, 2.2516(6); P1—C28, 1.854(2); P2—C28, 1.845(2); C1–Rh1–Cl1, 90.30(6); Cl1–Rh1–P2, 93.94(2); P2–Rh1–P1, 72.81(2); P1–Rh1–C1, 103.07(6); C1–Rh1–P2, 175.28(6); Cl1–Rh1–P1, 166.32(2).

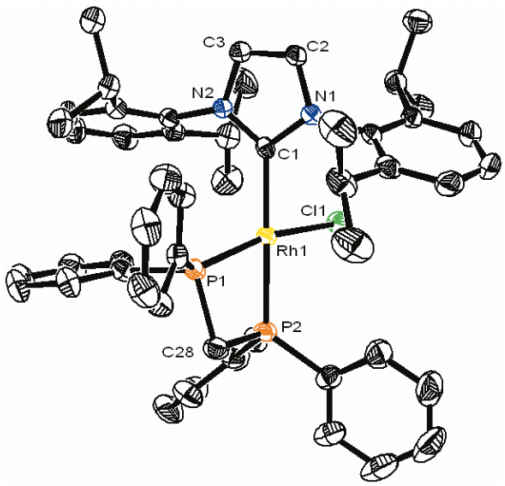

Fig. 4. ORTEP diagram of RhCl(IPr)(dppb) (**7**) with 50% probability thermal ellipsoids; H atoms are omitted for clarity. Selected bond lengths (Å) and angles (°): Rh1—C1, 2.0484(15); Rh1—Cl1, 2.3846(4); Rh1—P1, 2.2888(4); Rh1—P2, 2.2043(4); P1—C28, 1.8427(18); P2—C31, 1.8681(16); C1–Rh1–Cl1, 86.01(4); Cl1–Rh1–P1, 82.569(15); P1–Rh1–P2, 91.046(15); P2–Rh1–C1, 100.39(4); C1–Rh1–P1, 168.34(4); Cl1–Rh1–P2, 173.587(15).

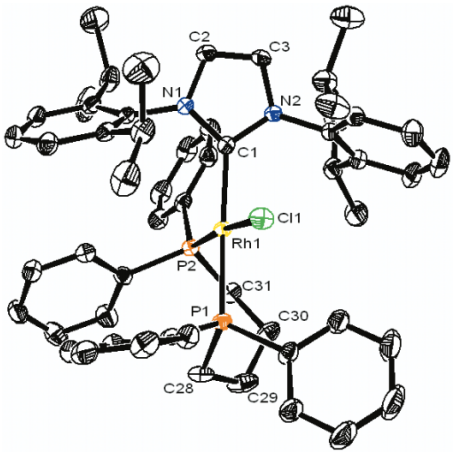

Cl1–Rh1–P2 and P1–Rh1–C1 bond angles are 93.94 and 103.07(6)°, respectively. In **7**, the more flexible dppb allows for a P1–Rh–P2 bond angle of 91.05°. Steric interactions between the IPr and a PPh_2–phenyl ring are evident in all three structures, this accounting for cis C–Rh–P angles of ~100°. The Rh–C and Rh–Cl bond lengths are in the established range for such chloro(carbene)–Rh(I or III) complexes.[2,5,4d,17–21] In all three complexes, the Rh–P bond trans to the carbene is 0.04–0.08 Å longer than the one cis to the carbene, a finding compatible with data for *cis*-RhCl(IMes)$(PPh_3)_2$, where the difference is about 0.09 Å.[4d] Our data also agree with a finding from Crudden's group that

Fig. 5. ORTEP diagram of RhCl(IPr)(dppbz) (**9**) with 50% probability thermal ellipsoids; the other independent molecule in the asymmetric unit, and H atoms, are omitted for clarity. Selected bond lengths (Å) and angles (°): Rh1—C1, 2.101(3); Rh1—Cl1, 2.3929(8); Rh1—P2, 2.2239(8); Rh1—P1, 2.1796(9); P1—C28, 1.852(3); P2—C33, 1.832(3); C1–Rh1–Cl1, 91.58(8); Cl1–Rh1–P2, 83.92(3); P2–Rh1–P1, 85.30(3); P1–Rh1–C1, 99.66(8); C1–Rh1–P2, 173.14(9); Cl1–Rh1–P1, 173.73(3).

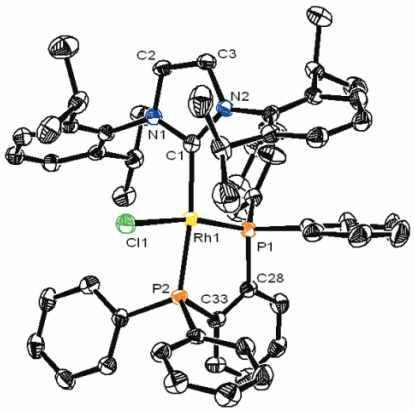

Rh–P bonds in *cis*-RhCl(NHC)$(PPh_3)_2$ complexes are marginally shorter (by up to 0.03 Å) than corresponding bonds in $RhCl(PPh_3)_3$ and *trans*-RhCl(CO)$(PPh_3)_2$;[4d] in the case of RhCl(IPr)(dppbz) (**9**), the difference is up to 0.08 Å. Data from Herrmann's group on other chloro(carbene)phosphine–phosphite–Rh(I) complexes[18] also support this finding, which is likely general within analogous Rh–carbene and Rh–phosphine species.

Reactivity of the complexes

Complexes **3**–**10** are all highly soluble in benzene, toluene, CH_2Cl_2, $CHCl_3$, and polar aprotic solvents, but are insoluble in solvents such as hexane. In the solid state, these complexes are air-stable, but in solution (e.g., in C_6H_6/C_6D_6), they are sensitive to air or oxygen and rapidly decompose at room temperature with formation of free diphosphine dioxide, as demonstrated by in situ $^{31}P\{^1H\}$ NMR data; singlets were seen at δ_P = 24.4, 12.2, 31.7, and 32.0, respectively, for the dioxides of dppm, dppe, dppb, and dppbz, in agreement with literature data,[22,23] and were identical to values measured by in situ oxidation of the free diphosphine in C_6D_6 with H_2O_2. The reactivity toward O_2 of these diphosphine complexes is markedly different to that of the analogous *cis*-RhCl(NHC)$(PPh_3)_2$ complex, which under the same conditions undergoes irreversible oxidative addition to form a Rh(III)–peroxide that contains, however, *trans*-PPh_3 ligands (see Scheme 1)[5]; this peroxide is stable in both the solid state, and even in solution shows no sign of decomposition to $OPPh_3$ over 24 h in air.[5] The necessarily cis-chelating diphosphines clearly do not allow for formation at ambient conditions of a stable peroxide, although the chelated P–N ligand mentioned in the Introduction (Scheme 1) does so.[5] Whether oxidation of the diphosphines occurs via an intermediate with coordinated O_2 requires detailed low-temperature studies. Loss of a chelating diphosphine as the dioxide during oxygenation of a Rh(I)–tris(pyrazolyl)borate–dppe complex in solution in attempts to study formation of peroxide species has been demonstrated previously,[22] although the chelating diphosphine ligands are retained when $Rh(dppm)_2^+$ and $Rh(dppe)_2^+$ react in solution with O_2 at ambient conditions to form the respective *cis*-Rh(P–P)$_2(O_2)^+$ peroxide species, where (P–P) is the chelating diphosphine.[13b] Our findings at this stage on the reactivity of O_2 toward the RhCl(NHC)(P–P) complexes unfortunately cannot contribute to the question of the nature of the coordinated O_2 in Rh–NHC complexes with and without an ancillary phosphine ligand, in which singlet oxygen has been suggested (see Introduction).[3,4a] Studies on such systems are ongoing.

Reaction of a benzene solution of RhCl(NHC)(dppe) [NHC = IPr (**5**), IMes (**6**)] with CO at ambient conditions rapidly precipitated a yellow solid, which was recrystallized by layering of a CH_2Cl_2 solution of the compound with hexane. The material, however, was shown by elemental analysis and $^{31}P\{^1H\}$ NMR and IR spectroscopies to be the known compound RhCl(CO)(dppe).[24,25] Reactions of CO with the dppm and dppb analogues (complexes **3**, **4**, **7**, and **8**) also resulted in displacement of the NHC ligand by CO as shown by in situ ^1H NMR, when resonances of the free carbenes were generated.[26]

The Rh products were not investigated, but are presumed to be the well-known dimeric, bridged-diphosphine complexes *trans*-$[RhCl(CO)]_2(\mu$-P–P$)_2$ that are formed with dppm and dppb.[25] The substitution of an NHC ligand by CO, to the best of our knowledge, has not been reported, and implies a relatively labile NHC ligand; indeed, substitution of IMes by PPh_3 has been reported (see the following).[3,4f] Within Rh–NHC–carbonyl systems, $RhCl(CO)(NHC)_2$[2,14,27] and $RhCl(CO)_2(NHC)$[2,19,28] complexes have been synthesized by reacting CO with Rh–NHC precursors, whereas RhCl(CO)(PPh_3)(NHC) has been made from $RhCl(PPh_3)_2$(NHC) and CO.[3,4d,4f,4j]

The RhCl(NHC)(P–P) complexes in benzene solution do not react with H_2 at ambient conditions. Known hydrido complexes of the type $Rh(H)_2Cl(NHC)_2$ and $[Rh(H)_2Cl(NHC)]_2$ have been made by reaction of H_2 with Rh(I)–NHC precursors,[2,3,14,27] whereas Rh–hydrido–NHC species have also been generated via intramolecular C–H activation of the Me group of IMes.[14,29] Hydrido derivatives of Rh–NHC–phosphine species have not yet been reported.

Supplementary data

Supplementary data for this article are available on the journal Web site (http://canjchem.nrc.ca) or may be purchased from the Depository of Unpublished Data, Document Delivery, CISTI, National Research Council Canada, Building M-55, 1200 Montreal Road, Ottawa, ON K1A 0R6, Canada. DUD 3999. For more information on obtaining material refer to http://cisti-icist.nrc-cnrc.gc.ca/eng/ibp/cisti/collection/unpublished-data.html. CCDC numbers 739246–739248 contain the crystallographic data for complexes **3**, **7**, and **9**, respectively. These data can be obtained, free of charge, via www.ccdc.cam.ac.uk/conts/retrieving.html (or from the Cambridge Crystallographic Data Centre, 12 Union Road, Cambridge CB2 1EZ, UK; fax +44 1223 336033; or deposit@ccdc.cam.ac/uk).

Acknowledgment

We thank the Natural Sciences and Engineering Research Council of Canada (NSERC) for financial support.

References

(1) Special Issue: *N*-Heterocyclic carbene complexes. *Eur. J. Inorg. Chem.* **2009** No. 13, 1663–2007.

(2) Yu, X.-Y.; Sun, H.; Patrick, B. O.; James, B. R. *Eur. J. Inorg. Chem.* **2009**, No. 13, 1752–1758. doi:10.1002/ejic.200801169.

(3) Praetorius, J. M.; Crudden, C. M. *J. Chem. Soc., Dalton Trans.* **2008**, (31), 4079–4094. doi:10.1039/b802114g.

(4) (a) Praetorius, J. M.; Allen, D. P.; Wang, R.; Webb, J. D.; Grein, F.; Kennepohl, P.; Crudden, C. M. *J. Am. Chem. Soc.* **2008**, *130* (12), 3724–3725. doi:10.1021/ja7108213. PMID: 18321109.; (b) Yang, L.; Kruger, A.; Neels, A.; Albrecht, M. *Organometallics* **2008**, *27* (13), 3161–3171. doi:10.1021/om800110c.; (c) Herrmann, W. A.; Frey, G. D.; Herdtweck, E.; Steinbeck, M. *Adv. Synth. Catal.* **2007**, *349* (10), 1677–1691. doi:10.1002/adsc.200700079.; (d) Chen, A. C.; Allen, D. P.; Crudden, C. M.; Wang, R.; Decken, A. *Can. J. Chem.* **2005**, *83* (6–7), 943–957. doi:10.1139/v05-106.; (e) Allen, D. P.; Crudden, C. M.; Calhoun, L. A.; Wang, R.; Decken, A. *J. Organomet. Chem.* **2005**, *690* (24-25), 5736–5746. doi:10.1016/j.jorganchem.2005.07.037.; (f) Allen, D. P.; Crudden, C. M.; Calhoun, L. A.; Wang, R. *J. Organomet. Chem.* **2004**, *689* (20), 3203–3209. doi:10.1016/j.jorganchem.2004.07.021.; (g) Neveling, A.; Julius, G. R.; Cronje, S.; Esterhuysen, C.; Raubenheimer, H. G. *J. Chem. Soc., Dalton Trans.* **2005**, (1), 181–192. doi:10.1039/b414040k.; (h) Poyatos, M. M.; Uriz, P.; Mata, J. A.; Claver, C.; Fernandez, E.; Peris, E. *Organometallics* **2003**, *22* (3), 440–444. doi:10.1021/om0205748.; (i) Grasa, G. A.; Moore, Z.; Martin, K. L.; Stevens, E. D.; Nolan, S. P.; Paquet, V.; Lebel, H. *J. Organomet. Chem.* **2002**, *658* (1-2), 126–131. doi:10.1016/S0022-328X(02)01638-8.; (j) Chen, A. C.; Ren, L.; Decken, A.; Crudden, C. M. *Organometallics* **2000**, *19* (18), 3459–3461. doi:10.1021/om0003739.; (k) Cetinkaya, B.; Ozdemir, I.; Dixneuf, P. H. *J. Organomet. Chem.* **1997**, *534* (1-2), 153–158. doi:10.1016/S0022-328X(96)06927-6.

(5) Yu, X.-Y.; Patrick, B. O.; James, B. R. *Organometallics* **2006**, *25* (20), 4870–4877. doi:10.1021/om060576i.

(6) Yu, X.-Y.; Sun, H.; Patrick, B. O.; James, B. R The University of British Columbia, Vancouver, BC. Unpublished data, 2009.

(7) Bruker AXS. *SAINT*, version 7.03A. Bruker AXS Inc.: Madison, WI, 1997–2003.

(8) Bruker AXS. *SADABS*, version 2.10; Bruker Nonius area detector scaling and absorption correction. Bruker AXS Inc.: Madison, WI, 2003.

(9) Altomare, A.; Burla, M. C.; Cammalli, G.; Cascarano, M.; Giacovazzo, C.; Guagliardi, A.; Moliterni, A. G. G.; Poidori, G.; Spagna, A. *J. Appl. Cryst.* **1999**, *32* (1), 115–119. doi:10.1107/S0021889898007717.

(10) Bruker AXS. *SHELXTL*, version 5.1. Bruker AXS Inc.: Madision, WI, 1997.

(11) van der Sluis, P.; Spek, A. L. *Acta Crystallogr.* **1990**, *A46*, 194–201. doi:10.1107/S0108767389011189.

(12) Park, K. H.; Kim, S. Y.; Chan, S. U.; Chung, Y. K. *Eur. J. Org. Chem.* **2003**, *2003* (22), 4341–4345. [and references therein]. doi:10.1002/ejoc.200300487.

(13) (a) Zhou, Z.; Facey, G.; James, B. R.; Alper, H. *Organometallics* **1996**, *15* (10), 2496–2503. doi:10.1021/om960112s.; (b) James, B. R.; Mahajan, D. *Can. J. Chem.* **1980**, *58* (10), 996–1004. doi:10.1139/v80-157.

(14) Huang, J.; Stevens, E. D.; Nolan, S. P. *Organometallics* **2000**, *19*, (6), 1194–1197. doi:10.1021/om990922e.

(15) (a) Jafarpour, L.; Stevens, E. D.; Nolan, S. P. *J. Organomet. Chem.* **2000**, *606* (1), 49–54. doi:10.1016/S0022-328X(00)00260-6.; (b) Arduengo, J. A., III; Dias, H. V. R.; Harlow, R. L.; Kline, M. *J. Am. Chem. Soc.* **1992**, *114* (14), 5530–5534. doi:10.1021/ja00040a007.

(16) James, B. R.; Mahajan, D. *Can. J. Chem.* **1979**, *57* (2), 180–187. doi:10.1139/v79-030.

(17) Yu, X. Y.; Patrick, B. O.; James, B. R. *Organometallics* **2006**, *25* (9), 2359–2363. doi:10.1021/om060030w.

(18) Herrmann, W. A.; Frey, G. D.; Herdtweck, E.; Steinbeck, M. *Adv. Synth. Catal.* **2007**, *349* (10), 1677–1691. doi:10.1002/adsc.200700079.

(19) Herrmann, W. A.; Baskakov, D.; Herdtweck, E.; Hoffmann, S. D.; Bunlaksananusorn, T.; Rampf, F.; Rodefield, L. *Organometallics* **2006**, *25* (10), 2449–2456. doi:10.1021/om060098b.

(20) Song, G.; Zhang, Y.; Li, X. *Organometallics* **2008**, *27* (8), 1936–1943. doi:10.1021/om800109a.

(21) Jiménez, M. V.; Pérez-Torrente, J. J.; Bartolomé, M. I.; Gierz, V.; Fernando, F. J.; Oro, L. A. *Organometallics* **2008**, *27* (2), 224–234. doi:10.1021/om700728a.

(22) Takahashi, Y.; Hashimoto, M.; Hikichi, S.; Moro-oka, Y.; Akita, M. *Inorg. Chim. Acta* **2004**, *357* (6), 1711–1724. doi:10.1016/j.ica.2003.12.022.

(23) (a) Cyr, P. W. Ph.D. Dissertation, The University of British Columbia, Vancouver, BC, 2001. p. 24; (b) MacFarlane, K. S.; Rettig, S. J.; Liu, Z.; James, B. R. *J. Organomet. Chem.* **1998**, *557* (2), 213–219. doi:10.1016/S0022-328X(97)00758-4.; (c) Bressan, M.; Morvillo, A. *Inorg. Chem.* **1989**, *28* (5), 950–953. doi:10.1021/ic00304a028.; (d) Berners-Price, S. J.; Norman, R. E.; Sadler, P. J. *J. Inorg. Biochem.* **1987**, *31* (3), 197–209. doi:10.1016/0162-0134(87)80005-3. PMID:2828542.

(24) (a) Hieber, W.; Kummer, R. *Chem. Ber.* **1967**, *100* (1), 148–159. doi:10.1002/cber.19671000119.; (b) Mague, J. T.; Mitchener, J. P. *Inorg. Chem.* **1969**, *8* (1), 119–125. doi:10.1021/ic50071a028.

(25) Sanger, A. R. *J. Chem. Soc., Dalton Trans.* **1977**, (2), 120–129. doi:10.1039/dt9770000120.

(26) (a) Arduengo, A. J.; Dias, H. V. R.; Harlow, R. L.; Kline, M. *J. Am. Chem. Soc.* **1992**, *114* (14), 5530–5534. doi:10.1021/ja00040a007.; (b) Arduengo, A. J.; Krafczyk, R.; Schmutzler, R.; Craig, H. A.; Georlich, J. R.; Marshall, W. J.; Unverzagt, M. *Tetrahedron* **1999**, *55* (51), 14523–14534. doi:10.1016/S0040-4020(99)00927-8.

(27) Praetorius, J. M.; Wang, R.; Crudden, C. M. *Eur. J. Inorg. Chem.* **2009**, No. 13, 1746–1751. doi:10.1002/ejic.200801191.

(28) (a) Bittermann, A.; Härter, P.; Herdtweck, E.; Hoffmann, S. D.; Herrmann, W. A. *J. Organomet. Chem.* **2008**, *693* (12), 2079–2090. doi:10.1016/j.jorganchem.2008.01.039.; (b) Fürstner, A.; Alcarazo, M.; Krause, H.; Lehmann, C. W. *J. Am. Chem. Soc.* **2007**, *129* (42), 12676–12677. doi:10.1021/ja076028t. PMID:17910460.

(29) Scott, N. M.; Dorta, R.; Stevens, E. D.; Correa, A.; Cavallo, L.; Nolan, S. P. *J. Am. Chem. Soc.* **2005**, *127* (10), 3516–3526. doi:10.1021/ja043249f. PMID:15755173.

Morphology-dependent luminescence from ZnO nanostructures — An X-ray excited optical luminescence study at the Zn K-edge

Olga Lobacheva, Michael W. Murphy, Jun Young Peter Ko, and Tsun-Kong Sham

Abstract: ZnO nanostructures have been synthesized by thermal evaporation on Si substrates. It is found that the morphologies of the nanostructures are governed by growth conditions such as temperature, carrier-gas flow rate, and the nature of the substrate (with and without a catalyst). We report X-ray excited optical luminescence from ZnO nanostructures of distinctly different morphologies in the energy and time domain using excitation photon energies across the Zn K-edge. X-ray excited optical luminescence (XEOL) and X-ray absorption near edge structure (XANES) study has clearly shown the morphology dependence of the ZnO optical properties. A correlation of luminescence with morphology, size, and crystallinity emerges.

Key words: ZnO nanostructures, XEOL, TRXEOL, XANES, vapour deposition.

Résumé : On a synthétisé des nanostructures de ZnO par évaporation thermique de substrats contenant de l'étain. On a trouvé que les morphologies des nanostructures sont gouvernées par les conditions de croissance, la vitesse d'écoulement du gaz porteur et la nature du substrat, avec ou sans catalyseur. Utilisant des énergies photoniques d'excitation sur l'arête K du zinc, on a pu observer de la luminescence optique excitée par les rayons X à partir de nanostructures de ZnO de morphologies comportant des différences importantes dans le domaine du temps et de l'énergie. Des études de luminescence optique excitée par les rayons X « XEOL » et par la spectroscopie de la structure fine d'absorption des rayons X près du seuil « XANES » ont clairement démontré l'importance de la morphologie sur les propriétés optiques du ZnO. Il en émerge une corrélation entre la luminescence et la morphologie, la taille et la cristallinité.

Mots-clés : nanostructures de ZnO, luminescence optique excitée par les rayons X « XEOL », spectroscopie de la structure fine d?absorption des rayons X près du seuil « XANES », dépôt de vapeur.

[Traduit par la Rédaction]

Introduction

Zinc oxide, a wide-band-gap semiconductor (E_g = 3.37 eV at room temperature), ranks high among oxide semiconductors for its unique properties. With suitable doping, the band gap of ZnO can be tuned from 3.0 eV to 4.28 eV.[1,2] Relatively large exciton binding energy (60 meV) makes zinc oxide a desirable technological material for electronic and photonic applications, such as UV lasers and light emitters.[3] It can also be used in the fabrication of gas sensors, varistors, and piezoelectronic devices.[4–6]

The properties of zinc oxide have been under investigation for decades.[7] The shift from bulk to nanosized materials has introduced new electronic and optical properties due to surface effects, defect formations, and quantum confinement. Using different synthesis methods, the growth of ZnO nanostructures on a number of substrates with and without catalyst has been successfully controlled. A variety of ZnO nanostructures have been produced, including nanowires, nanorods, nanoneedles, nanobelts, nanotubes, nanoparticles, nanosprings, and nanorings.[8–17]

Here, we report (*i*) the synthesis of ZnO nanowires and nanorods on a long slab of a silicon (100) wafer substrate with and without Au catalyst using a thermal evaporation technique, and (*ii*) the optical properties of ZnO nanostructures using X-ray excited optical luminescence (XEOL) and X-ray absorption near edge structure (XANES) across the Zn K-edge.[18,19]

In XEOL, X-ray photon excites the core electron into previously unoccupied levels or into the continuum. The core hole produced by the X-ray photon gets immediately filled with electrons from shallower levels. The process is accompanied by the emission of photo and Auger electrons as well as fluorescence photons, which can produce even more secondary electrons and holes on their track during the thermalization process. Thus, the absorption of a single X-ray photon can lead to more than one electron-hole pair. The thermalization process of electrons and holes is very fast and ends up with holes in the top of the valence band and electrons in the bottom of the conduction band. Radiative recombination of the holes and the electrons via excitonic deexcitation produces optical luminescence with energy close to that of the band gap, and energy transfer to defect levels lying within the band gap produces much broader emission bands in longer wavelengths.

Received 7 April 2009. Accepted 17 June 2009. Published on the NRC Research Press Web site at canjchem.nrc.ca on 21 August 2009.

O. Lobacheva, M.W. Murphy, J.Y.P. Ko, and T.-K. Sham.[1] Department of Chemistry, The University of Western Ontario, London, ON N6A 5B7, Canada.

[1]Corresponding author (e-mail: tsham@uwo.ca).

By tuning the X-ray energy across an absorption edge in an excitation process, it is often possible to investigate the site-specific optical response of light-emitting material upon X-ray absorption. In addition, the time structure of the synchrotron enables time-resolved X-ray excited optical luminescence (TRXEOL) measurements, providing information about lifetime and dynamics of the radiative de-excitation.[18,19] Combining XEOL and XANES has been proven to be a very powerful method for the studies of the origin of luminescence of materials, especially nanostructures.[20,21] XANES refers to the study of the absorption coefficient in the vicinity of an absorption edge up to ~50 eV above the threshold, and it probes the unoccupied densities of states (LUMO and so forth in molecules) above the Fermi level via bound-to-bound and bound-to-quasi-bound dipole transitions. XEOL excited across absorption edges and the corresponding XANES can be element-, site-, and excitation-channel-specific, since X-ray edges are unique to the element and chemically sensitive when the probing photon is sufficiently monochromatic (as is often the case at synchrotron light sources).[18,19]

Experimental procedures

ZnO nanostructures of interest were deposited on a slab of Si (100) wafer, which was pre-washed in ethanol and distilled water as described previously.[10] Briefly, an alumina boat containing Zn powder (99.99%, Alfa Aesar) was placed in the centre of a quartz tube, which was then mounted inside a horizontal tube furnace (Fig. 1). A carrier gas (argon) was introduced into the system at one end of the tube with a flow rate (typically of 75–80 sccm). The other end of the quartz tube was open to air. The substrate, a slab of Si wafer ~0.5 inch wide, was placed downstream of the alumina boat. We fabricated nanostructures on both clean and colloidal Au (colloid solution of thiol-capped gold nanoparticles) covered substrates. To track the influence of the catalyst on the morphology of the grown nanostructures, colloid Au was deposited on half of the Si slab along its length.

Inside the furnace, the gold particles on the substrate act as a catalyst during the growth by the vapour–liquid–solid (VLS) mechanism. ZnO (or Zn) vapour dissolves in the catalyst droplet forming Au/Zn alloy. When the concentration reaches supersaturation at a given temperature, ZnO nanorods begin to grow on the droplet–substrate interface. As shown in previous work,[9–11,22] the nanostructures thus prepared consist of zinc oxide without detectable Au impurities along the length. A catalyst particle locates on the tip of the nanorod as expected for a VLS mechanism. ZnO nanostructures can also be fabricated without any catalyst. In this case, the ZnO growth occurs by vapour–solid (VS) process, which initiates with the formation of Zn nucleus on the substrate surface. However, in a number of cases, the presence of catalyst provides an aligned nanostructure growth with a smaller size and a more uniform distribution.[23]

The temperature in the growth region was determined by the position of the substrate relative to the center of the furnace. It was calibrated by a thermocouple. Typically, the temperature in the growth region of interest was 15–20 °C less than that in the center of the furnace.

ZnO samples thus obtained appear as a grey-white coating on the surface of the Si wafer with a slowly varying morphology along the thermal gradient of the slab. When excited by an ultraviolet lamp, these samples produced green emission. Differences in synthesis conditions (the thermal gradient of the substrate, deposition time, carrier-gas flow rate, and the nature of the substrate) result in a variety of morphologies.[24,25] This combinatorial approach provides some very desirable specimens for the studies of the morphology dependence of the optical properties of ZnO nanostructure. Selected areas of uniform morphology (nanowires and nanorods) will be reported here.

Fig. 1. Schematic diagram of the ZnO nanostructure fabrication process.

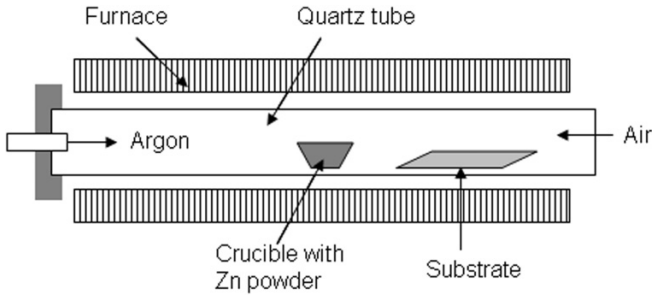

Images of the fabricated nanostructures were obtained at the Nanofabrication Facility of the University of Western Ontario using a LEO 1530 field-emission scanning electron microscope (FE SEM) fitted with a laser interferometer-controlled stage. SEM images were taken at EHT = 2 kV and a working distance of 5 mm.

XEOL and TRXEOL experiments were carried out on the PNC/XOR beamline (20-BM) at the Advanced Photon Source (APS) at Argonne National Laboratory with APS running at the top-up mode (100 mA, 24 bunches, ~100 ps pulse, and 153 ns repetition rate). We used the optical signal as the start and the synchrotron pulse as the stop in a pump-probe arrangement. Light was collected using a JY H-10 optical monochromator equipped with a Hamamatsu 943–02 PMT and suitable delays. Briefly, fast and slow time windows are selected from the decay curve of the zero-order light emitted by the specimen for time-gated measurements. Thus, TRXEOL only collects light emitted within this time window subsequent to excitation ($t = 0$). We also recorded the Zn K-edge XANES using the yield of ungated and time-gated optical emission. More details have been described previously.[18,20]

Results and discussions

SEM images

We show some representative morphologies in Fig. 2, which presents SEM images of several ZnO nanostructures. ZnO nanowires (Figs. 2a and 2b) were grown on the same region of the Si wafer without and with Au catalyst, respectively, according to the following conditions: the temperature in the center of the furnace was 570 °C, and the argon flow rate was 75 sccm. The samples were collected at a distance of 12 cm from the furnace center. Temperature in the growth region was ~550 °C. Figure 2a shows the nanowires grown on the clean Si substrate with an average diameter of ~70 nm, and Fig. 2b depicts nanowires grown on the Si substrate with Au catalyst with an average diameter of ~50 nm.

Fig. 2. SEM images of ZnO samples: (a) ZnO nanowires (NW) grown on clean Si and (b) on Si substrate with Au catalyst; and (c) ZnO nanorods (NR) grown on clean Si and (d) on Si substrate with Au catalyst .

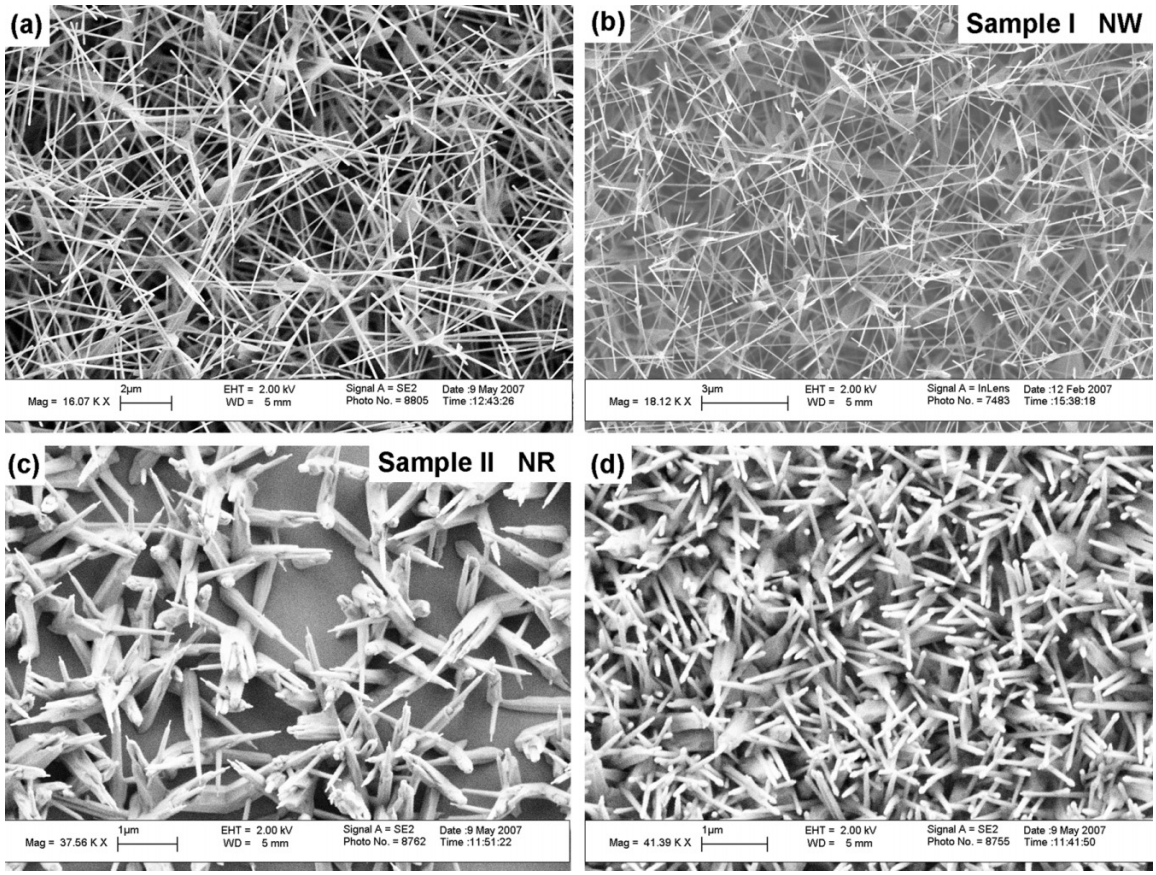

In both cases, some ribbon structures can be seen beneath the nanowires. At other locations along the slab, we also found nanoparticles and nanowires grown on clean Si and Si with Au catalyst, respectively.

ZnO nanorods shown in Figs. 2c and 2d were produced without and with Au catalyst under conditions different from to those shown in Figs. 2a and 2b: the furnace temperature was 550 °C, and Ar gas flow rate was 80 sccm. They were grown at a distance of 9 cm from the furnace center (the temperature was ~530 °C). Nanorods fabricated on clean Si substrate are ~300 nm in diameter with taper tips of ~90 nm (Fig. 2c). Nanorods grown with catalyst are ~350 nm in diameter with taper tips of ~70 nm (Fig. 2d). Nanostructures produced at other locations have similar morphology (nanorods with pointed tips) though different diameters. In general, the use of catalyst has led to a dense nanostructure growth (e.g., Fig. 2d), whereas nanorods produced without catalyst tend to expose part of the substrate (e.g., Fig. 2c).

The nanowires and nanorods obtained in this experiment are randomly oriented on the substrate without any preferential direction even when grown with catalyst. Apparently, using colloidal gold on a flat substrate could not align the growth because it is difficult to obtain the uniform coverage of the substrate with gold.

XEOL and time-resolved XEOL (TRXEOL)

For further characterization on the morphology-dependent optical properties, we chose one sample from each pair with distinctly different morphology: the 50 nm nanowires (NW) (marked as sample I) grown with Au catalyst (Fig. 2b), and 300 nm nanorods (NR) (marked as sample II) grown on clean Si (Fig. 2c).

In ZnO, light emission typically consists of a sharp peak with energy close to the band-gap energy (excitonic peak) and a broad-band emission due to defect levels formed within the band gap. More often than not, except in the case of a near-perfect nanocrystal,[12,26] green emission due to oxygen vacancies is observed on undoped ZnO nanostructures.[7,25] XEOL spectra from NW (sample I) and NR (sample II) are shown in Fig. 3. These XEOL spectra were excited at Zn K-edge (at 9660 eV).

From Fig. 3, we see that both samples show a weak near-band-gap emission at 392 nm (3.16 eV), and broad green bands at 492 nm (2.52 eV) and 530 nm (2.34 eV) (defect emission). NW exhibits a much stronger green emission than the NR (partly due to a denser packing of the materials). The inset in Fig. 3 presents a more revealing comparison (the same spectra normalized to the green emission). It can be seen that, for NW, the defect emission prevails, while for NR, the near-band-gap emission peak is relatively intense and comparable to the defect emission. The dominant broad-band green emission relative to near-band-gap emission for the NW can be explained by the presence of more oxygen-based surface defects in comparison with the relatively large NR. During vapour deposition in the quartz tube with argon as a carrier gas, the synthesis occurs in an oxygen-deficient

Fig. 3. XEOL from ZnO nanowire (sample I) and nanorod (sample II) excited with photon energy at the Zn K-edge of ZnO; the inset plot is normalized to the maximum intensity of the green emission.

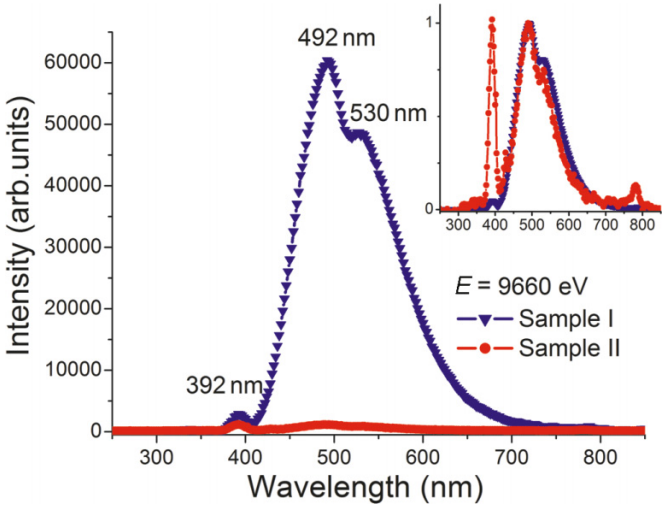

atmosphere, which leads to the formation of oxygen vacancies in the grown ZnO nanostructures. On the nanoscale, defects tend to collect in the surface area so to decrease the strain energy. It is reasonable to assume that NRs have a lower concentration of oxygen-vacancy defects than NWs, which have higher surface-to-volume ratio in comparison with NRs. The larger branching ratio (intensity of the individual peak over the overall intensity) of the near-band-gap emission for the NR compared with that of the NW suggests that the NR sample is superior in crystallinity. It was shown previously that near-perfect nanocrystals exhibit luminescence predominantly in the near-band-gap region.[12,26]

Figure 4 shows the ungated XEOL and the fast-window (0–10 ns), intermediate-window (0–50 ns), and slow-window (50–150 ns) time-gated TRXEOL from ZnO NW (sample I). These time windows are set such that only optical photons coming through the preset time interval are counted.[27] The fast-window gated XEOL shows that the branching ratio of the near-band-gap emission is the largest compared with that of the ungated XEOL and the slower time windows. With the time window opened up to 50 ns, both peaks are still present but the branching ratio of the defect emission increases markedly. With the slow window (50–150 ns), the near-band-gap peak at 392 nm completely disappears. This observation confirms that the near-band-gap emission is fast and the defect emission, which results from energy transfer through secondary processes, is relatively slow.[27]

The ungated XEOL and TRXEOL from ZnO NR are displayed in Fig. 5. The fast-time-gated (0–10 ns) XEOL contains only the 392 nm peak, which suggests a significant drop in defects compared with the ZnO NW. The defect emission becomes apparent with the 0–50 ns window. A small peak at about 427 nm is observed, and it conceivably originates from the exposed surface oxide of the Si substrate.[28] In the slow-window-gated XEOL (50–150 ns), defect emission predominates. Although no specific measurements of the decay lifetime have been made for the two samples, these TRXEOL results are consistent with other ZnO nanostructure studies, i.e., the near-band-gap emission is fast and its intensity is strongly correlated to the crystallinity of the nanostructure.[26] It is also interesting to note that bulk single crystal yields a defect-rich luminescence.[27] It is most likely that near-perfect crystal can only be obtained in the nano regime, and these materials will exhibit an XEOL with dominant near-band-gap luminescence.

Fig. 4. Time-resolved XEOL from ZnO NW (sample I) excited at the Zn K-edge: ungated and with selected time window at 0–10 ns, 0–50 ns, and 50–150 ns (time window available for timing is 153 ns).

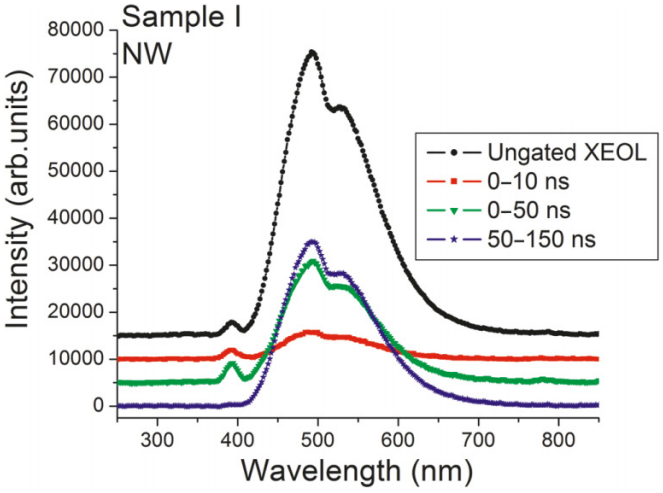

Fig. 5. Time-resolved XEOL from ZnO NR (sample II) excited at the Zn K-edge: ungated and with selected time window at 0–10 ns, 0–50 ns, and 50–150 ns. The spike with some periodicity is the electronic noise pick up from the hutch. They are not apparent in Fig. 3 where the signal is 20 times stronger.

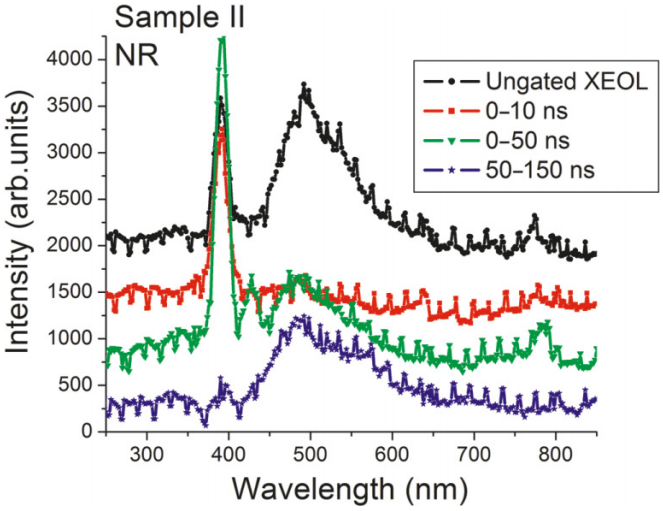

Zn K-edge XANES

Normalized Zn K-edge XANES, shown in Fig. 6a, were recorded with photoluminescence yield (PLY) using zero-order light (the entire optical emission was collected by tuning the optical monochromator to zero-order). PLY is proportional to the absorption coefficient if the X-ray energy absorbed by the system is converted to visible light with the same efficiency across the absorption edge and the sample is sufficiently thin. On the whole, absorption spectra from the two samples have the same features as that of ZnO single crystal. Interestingly, while the PLY XANES for the NR

Fig. 6. (a) Zn K-edge XANES for ZnO NW (sample I) and ZnO NR (sample II) recorded with PLY (zero order); (b) the PLY (time-gated) XANES for a 1 mm thick ZnO (0001) single crystal. Note that PLY for the single crystal has been inverted (thickness effect, see ref. 27).

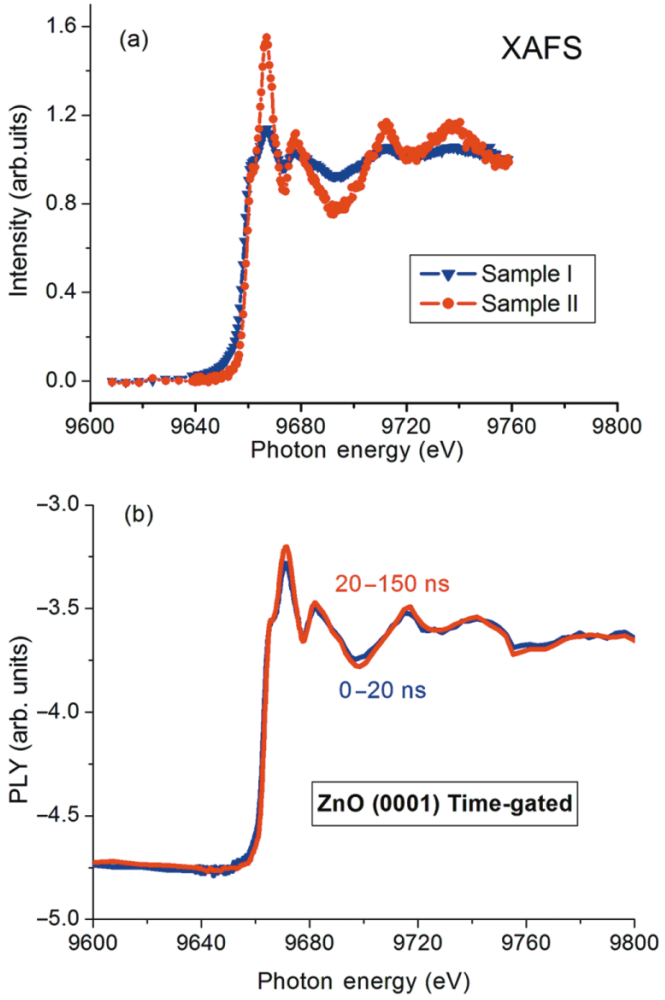

(highly crystalline) is exactly the same as XANES recorded in total electron yield or transmission, the PLY XANES for the thin nanowires exhibits considerable broadening and reduced modulation amplitude. At first glance, the latter observation is analogous to XANES recorded in X-ray fluorescence yield observed in a concentrated sample and is attributed to saturation effect. However, if we examine this problem closely, it becomes clear that both samples are too thin to exhibit the thickness effect in the PLY XANES, since the one-absorption length for ZnO below and above the Zn K-edge is about 60 and 10 micron (1 micron = 1 μm), respectively, whereas our sample thickness is in the order of microns at best. Thus, the dramatic difference in the PLY XANES between NW (~50 nm) and NR (~300 nm) indicates that conversion from X-ray energy to optical photons is less efficient per photon absorbed for the NW than for NR.

Since PLY collects the zero-order light dominated by defect emission resulting largely from secondary processes (e.g., energy loss from fluorescence X-rays and Auger electrons), there will be little contribution to the optical channel if fluorescence X-rays and Auger electrons leave the system without losing its energy. This is more likely to happen for a 50 nm than a 300 nm 1D system, since the former has a larger fraction of its atoms on the surface and a more confined region for the secondary process to take place. Thus, the broadening observed in the PLY for the NW specimen is attributed to the confinement or truncation for the secondary process. In a nanostructure, the thermalization track that creates secondary electrons and holes is truncated by the limited dimension, reducing the quantum efficiency of the secondary process, which plays an important part in the optical de-excitation process via energy transfer to the defect sites. For comparison, time-gated XANES from a ZnO (0001) single crystal with two different time windows are also shown in Fig. 6b.[27] Note that the negative scale means that the PLY for the single crystal (1 mm thick) actually recorded was inverted due to thickness effect.[19]

Summary and conclusion

In summary, we have shown that ZnO nanostructures with varying morphologies can be prepared with a combinatorial approach using the thermal gradient of the substrate and other relevant preparation conditions and that optical emission from ZnO nanostructures is morphology- and crystallinity-dependent. Thin ZnO nanowires, prepared with catalyst, produce strong green-defect emission. ZnO nanorods, prepared without catalyst, exhibit a relatively intense near-band-gap emission. TRXEOL spectra from these samples show that the green-emission lifetime is much longer than the near-band-gap-emission lifetime. This observation confirms previously observed morphology-crystallinity correlation with luminescence in that the larger the branching ratio for the near-band-gap emission, the closer to the perfection of the nanocrystal.[12,20] We also observed that the zero-order PLY XANES at the Zn K-edge is a good representative of the normal XANES for ZnO nanomaterial with good crystallinity and a desired thickness (less than one absorption length). Thus, a combined XEOL and XANES study provides additional insight for the luminescent properties of nanomaterials in terms of crystallinity, defect, morphology, and size.

Acknowledgements

Research at UWO is supported by the Natural Sciences and Engineering Research Council (NSERC) of Canada, Canada Foundation for Innovation (CFI), Ontario Innovation Trust (OIT), and Canada Research Chair (CRC). PNC/XOR is supported by the US Department of Energy – Basic Energy Sciences, a Major Facilities Access grant from NSERC, the University of Washington, Simon Fraser University, and the Advanced Photon Source. Technical assistance from Dr Robert Gordon is gratefully acknowledged.

References

(1) Makino, T.; Segawa, Y.; Kawasaki, M.; Ohtomo, A.; Shiroki, R.; Tamura, K.; Yasuda, T.; Koinuma, H. *Appl. Phys. Lett.* **2001**, *78* (9), 1237. doi:10.1063/1.1350632.

(2) Yang, W.; Hullavarad, S. S.; Nagaraj, B.; Takeuchi, I.; Sharma, R. P.; Venkatesan, T.; Vispute, R. D.; Shen, H. *Appl. Phys. Lett.* **2003**, *82* (20), 3424. doi:10.1063/1.1576309.

(3) Zhang, C. F.; Dong, Z. W.; You, G. J.; Qian, S. X.; Deng, H. *Opt. Lett.* **2006**, *31* (22), 3345–3347. doi:10.1364/OL.31.003345. PMID:17072418.
(4) Feng, P.; Wan, Q.; Wang, T. H. *Appl. Phys. Lett.* **2005**, *87* (21), 213111. doi:10.1063/1.2135391.
(5) Pillai, S. C.; Kelly, J. M.; McCormack, D. E.; Ramesh, R. *Mater. Sci. Technol.* **2004**, *20* (8), 964–968. doi:10.1179/026708304225019821.
(6) Williams, T. M.; Hunter, D.; Pradhan, A. K.; Kityk, I. V. *Appl. Phys. Lett.* **2006**, *89* (4), 043116. doi:10.1063/1.2236211.
(7) Özgür, Ü.; Alivov, Ya. I.; Liu, C.; Teke, A.; Reshchikov, M. A.; Dogan, S.; Avrutin, V.; Cho, S.-J.; Morkoç, H. *J. Appl. Phys.* **2005**, *98* (4), 041301. doi:10.1063/1.1992666.
(8) Lorenz, M.; Lenzner, J.; Kaidashev, E. M.; Hochmuth, H.; Grundmann, M. *Ann. Phys.(Leipzig)* **2004**, *13* (12), 39–42. doi:10.1002/andp.200310040.
(9) Fu, H.; Li, H.; Jie, W.; Zhang, C. *Ceram. Int.* **2007**, *33* (6), 1119–1123. doi:10.1016/j.ceramint.2006.03.024.
(10) Magalhaes-Paniago, R.; Lacerda, R. G. *Adv. Mater.* **2008**, *20* (8), 1499–1504. doi:10.1002/adma.200701612.
(11) Hejazi, S. R.; Hosseini, H. R. M.; Ghamsari, M. S. *J. Alloy. Comp.* **2008**, *455* (1-2), 353–357. doi:10.1016/j.jallcom.2007.01.100.
(12) Sun, X. H.; Lam, S.; Sham, T. K.; Heigl, F.; Jürgensen, A.; Wong, N. B. *J. Phys. Chem. B* **2005**, *109* (8), 3120–3125. doi:10.1021/jp044926v. PMID:16851331.
(13) Chen, B. J.; Sun, X. W.; Xu, C. X. *Ceram. Int.* **2004**, *30* (7), 1725–1729. doi:10.1016/j.ceramint.2003.12.140.
(14) Li, Q.; Kumar, V.; Li, Y.; Zhang, H.; Marks, T. J.; Chang, R. P. H. *Chem. Mater.* **2005**, *17* (5), 1001–1006. doi:10.1021/cm048144q.
(15) Bardhan, R.; Wang, H.; Tam, F.; Halas, N. J. *Langmuir* **2007**, *23* (11), 5843–5847. doi:10.1021/la070146c.
(16) Wang, Z. L. *J. Phys. Condens. Matter* **2004**, *16* (25), R829–R858. doi:10.1088/0953-8984/16/25/R01.
(17) Ding, Y.; Kong, X. Y.; Wang, Z. L. *Phys. Rev. B* **2004**, *70* (23), 235408. doi:10.1103/PhysRevB.70.235408.
(18) Sham, T. K.; Rosenberg, R. A. *ChemPhysChem* **2007**, *8* (18), 2557–2567. doi:10.1002/cphc.200700226. PMID:17994661.
(19) Sham, T. K. *Int. J. Nanotechnol.* **2008**, *5* (9/10/11/12), 1194. doi:10.1504/IJNT.2008.019837.
(20) Heigl, F.; Lam, S.; Regier, T.; Coulthard, I.; Sham, T. K. *J. Am. Chem. Soc.* **2006**, *128* (12), 3906–3907. doi:10.1021/ja060243c. PMID:16551087.
(21) Zhou, X. T.; Heigl, F.; Murphy, M. W.; Sham, T. K.; Regier, T.; Coulthard, I.; Blyth, R. I. R. *Appl. Phys. Lett.* **2006**, *89* (21), 213109. doi:10.1063/1.2387476.
(22) Agarwal, D. C.; Chauhan, R. S.; Avasthi, D. K.; Sulania, I.; Kabiraj, D.; Thakur, P.; Chae, K. H.; Chawla, A.; Chandra, R.; Ogale, S. B.; Pellegrini, G.; Mazzoldi, P. *J. Phys. D Appl. Phys.* **2009**, *42* (3), 035310. doi:10.1088/0022-3727/42/3/035310.
(23) Ito, D.; Jespersen, M. L.; Hutchison, J. E. *ACS Nano* **2008**, *2* (10), 2001–2006. doi:10.1021/nn800438m. PMID:19206444.
(24) Kim, T. Y.; Kim, J. Y.; Kumar, M. S.; Suh, E.-K.; Nahm, K. S. *J. Cryst. Growth* **2004**, *270* (3-4), 491–497. doi:10.1016/j.jcrysgro.2004.07.009.
(25) Schmidt-Mende, L.; MacManus-Driscoll, J. L. *Mater. Today* **2007**, *10* (5), 40–48. doi:10.1016/S1369-7021(07)70078-0.
(26) Rosenberg, R. A.; Shenoy, G. K.; Tien, L.-C.; Norton, D.; Pearton, S.; Sun, X. H.; Sham, T. K. *Appl. Phys. Lett.* **2006**, *89* (9), 093118. doi:10.1063/1.2245440.
(27) Heigl, F.; Sun, X. H.; Lam, S.; Sham, T. K.; Gordon, R. A.; Brewe, D.; Rosenberg, R. A.; Shenoy, G. K.; Yablonskikh, M.; MacNaughton, J.; Moewes, A. X-ray Absorption Fine Structure. Proceedings of XAFS13: 13th International Conference, Stanford, California, USA, July 9–14, 2006. Hedman, B., Pianetta, P., Eds.; AIP Conference Proceedings: New York, 2007; 734–737.
(28) Sham, T. K.; Naftel, S. J.; Kim, P.-S. G.; Sammynaiken, R.; Tang, Y. H.; Coulthard, I.; Moewes, A.; Freeland, J. W.; Hu, Y.-F.; Lee, S. T. *Phys. Rev. B* **2004**, *70* (4), 045313. doi:10.1103/PhysRevB.70.045313.

Structural analysis of phosphatidyl choline lipids and glycerol precursors

Annick Goursot, Tzonka Mineva, Sailaja Krishnamurty, and Dennis R. Salahub

Abstract: The structures and stabilities of the glycerol (G) and glycerol 3-phosphate (G3P) isomers have been calculated in the gas phase, using an ab initio density functional theory (DFT) method. The different conformational structures are shown to be at the origin of the various phospholipid conformers, except, obviously, for the alkyl chain torsions. The G3P conformations have been examined taking into account the experimental structures of the complexation sites in the glycerol kinase (GK) and glycerol 3-phosphate acyl transferase (G3PAT) enzymes, which correspond to the first and second steps of the "de novo" phospholipid biogenesis, respectively. The conformational analysis of the glycerophosphate skeleton is shown to determine most of the structural characteristics of the phosphatidyl choline lipids, which differ by the length of their diacyl chains, i.e., dilauroyl (DL), dimyristoyl (DM), and dipalmitoyl (DP) phosphatidylcholines (PC). Higher energy conformers with kinks in the acyl chains have been found, in preparation for molecular dynamics studies of the chain melting phase transformation.

Key words: glycerol, glycerol 3-phosphate, phosphatidylcholines, DLPC, DMPC, DPPC, conformational analysis, density functional theory, DFT-D.

Résumé : Les structures et stabilités relatives du glycérol (G) et du glycérol 3-phosphate (G3P) ont été calculées en phase gaseuze avec une méthode ab initio, basée sur la théorie de la fonctionnelle de la densité (TFD). A l'exception des formes gauches des chaînes alkyles, les différentes conformations de ces molécules sont effectivement à l'origine des conformères possibles des phospholipides. Les conformations de G3P ont été analysées en considérant les structures expérimentales des sites de complexation des enzymes glycérol kinase (GK) et glycérol 3-phosphate acyl transférase (G3PAT) qui correspondent, respectivement, aux deux premières étapes de la biosynthèse « de novo » des phospholipides. L'analyse conformationnelle du squelette glycérophosphate montre qu'il détermine la plupart des caractéristiques structurales des lipides phosphatidylcholines qui diffèrent par la longueur de leurs chaînes alkyles, c.-à-d. dilauroyl (DL), dimyristoyl (DM) et dipalmitoyl (DP) phosphatidylcholines (PC). Des conformères d'énergie plus élevée, présentant des formes gauches dans les chaînes alkyles, ont été étudiés en relation avec les simulations par dynamique moléculaire des transformations structurales des chaînes, au cours de la transition principale de phase.

Mots-clés : glycérol, glycérol 3-phosphate, phosphatidylcholine, DLPC, DMPC, DPPC, analyse conformationnelle, théorie de la fonctionnelle de la densité, TFD-D.

Introduction

Phospholipids and proteins are the main components of biological membranes, separating the cell and its various constituents from their environment. Cell membranes also have different functional roles, including protein synthesis, ion pumps and channels, receptor molecules, energy production and storage, and so forth. This versatility is due to the large range of phospholipid and protein structures, which can be involved in the membrane bilayers. The necessary fluid plasticity of these bilayers is obtained by the regulation of the lipid composition in the membrane. This regulation is accomplished by the "de novo" synthesis of the lipids in the various compartments of the cells of all living organisms.[1]

The synthesis protocol, in particular for the glycerophospholipids studied in this work, is a long and complex pathway, which starts with the enzymatic phosphorylation of the glycerol molecule and proceeds by three further successive enzymatic reactions.[2,3] The phospholipid molecule is thus built step by step through different enzyme-catalyzed reactions. The location in the enzymes of the different substrate-binding sites and their selectivity have not been identified unambiguously.[4–8] The structures of the phospholipid molecules synthesized and transferred to the membranes have thus not been determined, and there is no information concerning the existence of possible different conformers.

The presence of such conformers within phospholipid bilayers in their liquid-crystalline state has, however, been

Received 30 December 2008. Accepted 22 February 2009. Published on the NRC Research Press Web site at canjchem.nrc.ca on 29 July 2009.

This article is part of a Special Issue dedicated to Professor T. Ziegler.

A. Goursot and T. Mineva. UMR 5253 CNRS/ENSCM/UM2/UM1, Institut Charles Gerhardt Montpellier, 8 rue de l'École Normale, 34296 Montpellier cedex 5, France.
S. Krishnamurty. Functional Materials Division, Central Electrochemical Research Institute, Karaikudi 630 006, Tamilnadu, India.
D.R. Salahub.[1] Department of Chemistry and Institute for Biocomplexity and Informatics, University of Calgary, 2500 University Drive NW, Calgary, AB T2N 1N4, Canada.

[1]Corresponding author (e-mail: dennis.salahub@ucalgary.ca).

Fig. 1. Nomenclature of the atoms and torsion angles: (a) the glycerol molecule; (b) the DMPC molecule; (c) the DMPC molecule with parallel (T1) and perpendicular (T2) alkyl chains.

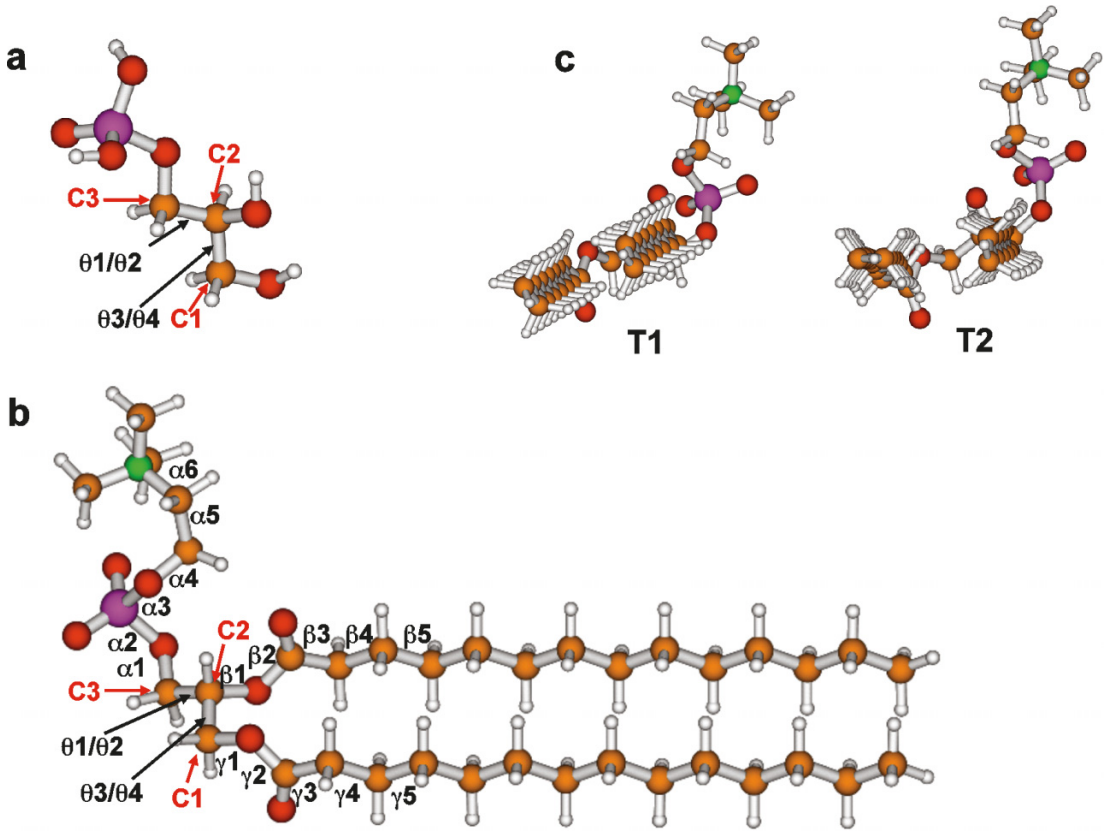

suggested from NMR experiments, that have also provided some structural information on the overall structure of the lipids.[9,10] X-ray diffraction data demonstrate the possible presence of two structurally different molecules in the solid-crystalline state of a few phospholipids.[11,12] In a previous theoretical work on the dimyristoyl phosphatidylcholine (DMPC) molecule, we have shown that several conformational structures can exist (minima on the potential-energy surface), a number of them having comparable energies.[13] The dynamics of the individual DMPC has been studied for a series of temperatures, and the nature of lipid melting has been elucidated.[14] The existence in the membranes of different lipid conformers, even iso-energetic ones, depends, of course, on the barriers for their in situ interconversion. One may also infer that the synthesis pathway itself selects the lipid conformations within the specific enzymatic catalytic sites at one or at several steps of the synthesis.

In this work, we present the structures and stabilities of the glycerol (G) and glycerol 3-phosphate (G3P) isomers, calculated in the gas phase, using an ab initio density functional theory (DFT) method. We show that their different conformational structures are at the origin of the various phospholipid conformers, except, obviously, for the alkyl chain torsions. The G3P conformations are then examined taking into account the experimental structures found for the complexation sites in the glycerol kinase (GK) and glycerol 3-phosphate acyl transferase (G3PAT) enzymes, which correspond to the first and second steps of the "de novo" phospholipid biogenesis, respectively. Finally, the conformational analysis of the glycerophosphate skeleton is shown to determine most of the structural characteristics of the phosphatidyl choline lipids, which differ by the length of their diacyl chains, i.e., DMPC, dilauroyl (DL), and dipalmitoyl (DP) phosphatidylcholines (PC).

Computational methods

Models

The carbon numbering (C1, C2, and C3), illustrated in Figs. 1 and 2, refers to the standard biochemical nomenclature defined for the glycerol molecule: if the hydroxyl group on C2 is oriented to the left, C1 is the carbon below and C3 the carbon above. When the hydroxyl on C3 is phosphorylated, the glycerol 3-phosphate molecule formed is chiral. Its in vivo synthesis produces, following the stereospecific numbering (sn) system, the sn-glycerol 3-phosphate. The diacyl phosphatydilcholine lipids have been generally characterized as a head group or α chain that is connected through one CH_2 group (C3 carbon) to two glycerolipid β and γ chains, as shown in Fig. 1b. The nomenclature defining the characteristic lipid torsion angles is illustrated in Fig. 1.

In addition, for a better understanding of the torsion angles, we have chosen to partition the molecule into four building blocks, labelled as head (H), neck (N), body (B), and tails. The head is built from the $N(CH_3)_3$–CH_2–CH_2–PO_4 atoms and is described by the α1 to α6 torsion angles. The neck includes the glycerol C3–C2–C1 fragment, characterized by the θ1 and θ2 angles, and defines the orientation of the head with respect to the carbonyl groups and the tails. The body is formed by the next two O–CO–CH_2–CH_2

Fig. 2. The glycerol conformers with the standard nomenclature: C2, secondary carbon; C3, carbon where phosphorylation will occur.

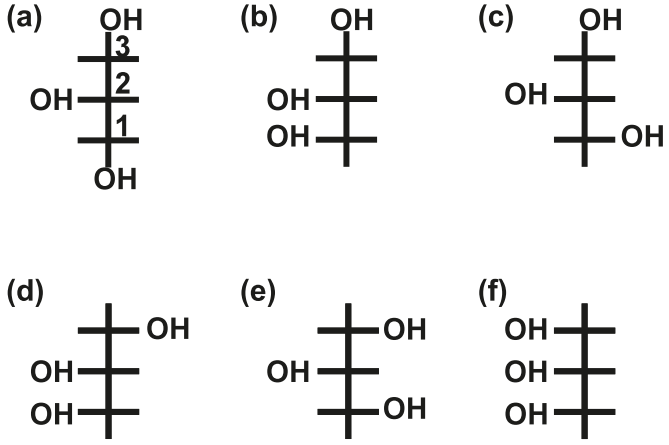

groups of the β and γ chains and is characterized by the θ3, θ4, β1 to β4, and γ1 to γ4 torsion angles. The tails consist of the two β and γ alkane chains and are defined by the β_n and γ_n torsions with $n \geq 5$. Following the calculations for the DMPC molecule,[13] for the search of the ground-state conformers, only trans β and γ angles ($n \geq 5$) have been considered for the starting geometries.

The DLPC and DPPC lipid molecules differ from DMPC only in their hydrocarbon chain lengths, namely, 12, 14, and 16 carbons for DLPC, DMPC, and DPPC, respectively.

Methods

The calculations were performed in the framework of density functional theory (DFT), using a linear combination of Gaussian orbitals, as implemented in the deMon2k program.[15] All calculations were performed using the revised PBE exchange functional (revPBE)[16] and the LYP[17] correlation functional, augmented by a damped empirical correction for dispersion-like interactions,[18] referred to as DFT-D. This DFT-D approach is necessary to account for the stabilizing interaction between the alkyl chains.[19]

DFT-optimized double-zeta plus valence polarization (DZVP) basis sets[20] were employed for all atoms, associated with automatically generated functions up to l = 2 for fitting the density.[15] The exchange-correlation potential was numerically integrated on an adaptive grid.[21] The grid accuracy was set to 10^{-5} in all calculations. The Coulomb energy was calculated by the variational fitting procedure proposed by Dunlap, Connolly, and Sabin.[22,23] A quasi-Newton method in internal redundant coordinates with analytical energy gradients was used for the structure optimization.[24] The convergence was based on the Cartesian gradient and displacement vectors with a threshold of 10^{-4} and 10^{-3} au, respectively.

Results and discussion

Conformational analysis of the glycerol and glycerol 3-phosphate molecules

The in vivo phosphatidyl choline lipid synthesis involves first the phosphorylation of glycerol in the GK enzyme, at the expense of ATP (adenosine triphosphate). The product formed is exclusively the G3P molecule (phosphate group at C3), which is further esterified at the free primary alcohol with one fatty acid molecule by an acyl transferase enzyme using an acyl carrier protein (ACP) or an acyl coenzyme A (CoA) as substrate. A second esterification at the secondary carbon leads further to a phosphatidate or phosphatidic acid including two fatty acid chains. The phosphatidate phosphatase enzyme, which regulates the glycerolipid synthesis, catalyzes its hydrolysis into diacylglycerol (or diglyceride). The reaction of this molecule with the cytidine diphosphate (CDP)-choline (via a transferase enzyme) leads finally to a phosphatidyl choline lipid.[25]

Table 1. Relative energies (ΔE in kcal/mol), dipole moment (D), and characteristic torsion angles (θ in degrees) of the different glycerol isomers (without internal hydrogen bonds).

Name	ΔE	Dipole moment (D)	θ1/θ2[a]	θ3/θ4[a]
a	0.6	3.4	178/59	180/–60
b	0.0	3.9	68/–55	182/–54
c	2.5	2.0	184/59	60/180
d	1.7	1.5	74/–50	61/185
e	2.7	1.9	–68/170	58/182
f	0.0	3.3	76/–50	–50/76

[a]The θ angles are defined in Fig. 1.

The G3P molecule provides, in some sense, the precursor of the neck–body skeleton (Fig. 1) that is common to all glycerophospholipids. The catalytic reaction forming G3P occurs at a site of the GK enzyme, which forms a complex with Mg-ATP and the G molecule. Structural information on this site has been provided by several X-ray studies[4,26,27] and molecular dynamics simulations.[28,29]

Chemically, the G molecule is achiral, since the two –CH_2OH groups are equivalent. The total number of combinations of the three OH relative positions reduces to six, taking into account mirror-image structures. Figure 2 illustrates these isomers.

The GK active site for glycerol phosphorylation is a deep cleft where ATP and glycerol are stabilized. The X-ray structures of GK show that the glycerol molecule forms hydrogen bonds with several residues.[4,27] Therefore, it is reasonable to assume that, during the glycerophosphate synthesis, external hydrogen bonds rather than internal ones are favoured. The calculated relative stabilities of the G isomers without internal hydrogen bonds are displayed in Table 1, along with the dipole-moment values and characteristic torsion angles, as defined in Fig. 1. These torsion angles are also characteristic of the final phospholipid, once the phosphocholine head and acyl chains have been bound. It is interesting to note that three glycerol structures are competitive at the lowest energy, i.e., the a, b, and f isomers (Fig. 2), which correspond very clearly to the largest dipole moments. The calculated ΔE values are only indicative of the possible conformers in the GK channel, since they do not take into account the interaction of glycerol with the surrounding residues. It is interesting to note that two types of "necks" (180/60 and 60/–60) and "bodies" (180/–60 and –60/60) are represented among the a, b, and f isomers.

The crystallization of GK leads to tetrameric structures, which are inactive forms of the enzyme.[26] Among the mono-

mers, a "closed" and an "open" form were distinguished.[27] The glycerol conduction to the GK enzyme-binding site could be facilitated by its hydrogen bonding with the surrounding GK residues more than with water molecules, due to the deepness of the GK cleft that argues for poor accessibility to the solvent.[27] The processing of glycerol from the cleft opening to the catalytic site could be helped by fluctuations of its large dipole moment interacting with the electric field along the cleft. MD simulations have shown that the protein attracts a substrate with a strong dipole moment, requiring its change of orientation at some positions in the cleft.[28] Binding the glycerol at the catalytic site is performed through tight hydrogen bonds to the closest residues (Asp245, Arg83, and Tyr135). All of these features would be in favour of promoting the a, b, and f isomers in the GK site.

X-ray structures of GK (pdb access 1glf[26] and 1glj[27]) also contain glycerol molecules. The structures of the glycerol molecule inside the tetramers are different in the "closed" and the "open" forms, with neck and body torsion angles very comparable to the conformer a for pdb.1glf ("closed" GK structure) and to a deformed f conformer (torsions of about 100°–120° instead of 60°–70°) for pdb.1glj ("open" GK structure).

The phosphorylation of one $-CH_2OH$ group of glycerol leads to a chiral C2 carbon in the sn-glycerol-3 phosphate. Starting from each of the six glycerol isomers allows one to generate the possible glycerol phosphate isomers. There are, in fact, nine topologically different structures, due to the lowering of the molecular symmetry. The presence of the phosphate group generates also additional rotational isomers, taking into account the rotation of the $-PO_3H_2$ group around the C3–O bond. Variations of the C2–C3–O–P torsion angle, α1, when sterically possible, leads to more rotational isomers. It must be noted that most of these rotations generate a steric strain due to the P=O or P–OH groups being confined too close to the atoms of the free primary CH_2OH group. In the same spirit as for the glycerol molecule, intramolecular hydrogen bonds have been avoided. After geometry optimization, 12 isomers were obtained with relative total energies within a range of 0 to about 4.0 kcal/mol. The five most stable structures (between 0 and 1.5 kcal/mol) are reported in Table 2. They are labelled by priming the letter of the original glycerol conformers. The isomers a′ and f′ are the counterparts of the a and f glycerol isomers mentioned above. They could thus both exist as products of the GK phosphorylation. These two isomers have different θ1/θ2 and θ3/θ4 values. It is thus not clear why the other isomers of equivalent energies, differing by either θ1/θ2 or θ3/θ4, could be much less stabilized through their interaction with the GK residues. It seems possible that the glycerol 3-phosphate, already before binding the acyl chains and the phosphatidyl choline head, has some structures with comparable energies.

The site and the mechanism of acylation of the G3P primary alcohol have not yet been completely elucidated. However, the X-ray structure of the squash G3PAT enzyme has been reported, and a presumptive G3P binding site is identified.[6,7] A fatty acid binding site is also proposed, in which the reactive thio ester group of the acyl-coA is located in the vicinity of the C1 alcohol of G3P. Thus, at present, there are no experimental data, which specifically contradict the possibility of finding several different conformers for the precursors of phospholipids.

Table 2. Relative energies and characteristic torsion angles of the glycero-3-phosphate most stable isomers. The primed labels correspond to the non-primed labels used for glycerol (Fig. 1).

Isomers	ΔE (kcal/mol)	θ1/θ2	θ3/θ4	α1
a′	0.7	180/60	180/–60	180
b′	0.8	70/-60	180/–60	180
e_1'	0.8	60/185	70/–60	90
e_2'	0.8	50/180	–70/180	70
f′	0.0	60/–70	–70/60	–100

Fig. 3. Damped empirical dispersion energies for the DLPC (triangles), DMPC (circles), and DPPC (squares) ground-state conformers. The conformers are ordered from left to the right as follows: $H1N1B_{A1}$, $H1N3B_{A1}$, $H2N3B_{A1}$, $H1N1B_{A2}$, $H1N2B_{A2}$, $H2N2B_{A2}$, and $H2N2B_{B1}$. The filled symbols are for T1 isomers and the open symbols are for T2 isomers.

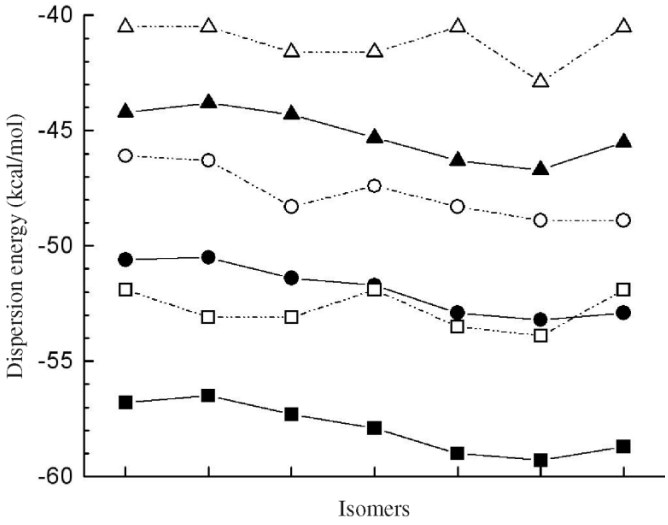

Structural analysis of the DLPC, DMPC, and DPPC molecules

Ground-state conformers with all trans chains

As in the case of the DMPC molecule, the DFT-D energy optimization for the DLPC and DPPC isomers led to 14 conformers in the range between 0 and 2 kcal/mol. The 14 lowest isoenergetic conformers are subsequently grouped into two sets of structures, differing by the mutual orientations of the carbon skeletons of the β and γ alkyl chains: in the first group of seven lowest energy structures, these two carbon skeletons are in two parallel planes (T1), and in the second half of the minimum-energy conformers, the two carbon skeletons are in two perpendicular planes (T2) (Fig. 1*c*). For a given T1 or T2 orientation of the hydrocarbon chains, the ground-state conformers arise from the following combinations between two heads (H1, H2), three necks (N1, N2, and N3) and three bodies (B_{A1}, B_{A2}, and B_{B1}): $H1N1B_{A1}$, $H1N3B_{A1}$, $H2N3B_{A1}$, $H1N1B_{A2}$, $H1N2B_{A2}$, $H2N2B_{A2}$, and $H1N1B_{B1}$.

These conformational structures are described in detail for the DMPC molecules in ref. 13. Their averaged α, β, and γ

Table 3. Relative energies in kcal/mol with respect to all-trans conformers of the DPPC, DMPC, and DLPC gauche isomers ($H1N1B_{A2}T2$) at various positions of the chain.

Kinks position *n*	DPPC (16C)	DMPC (14C)	DLPC (12C)	Tetradecane $C_{14}H_{30}$
***n* = 16**				
60	0.72			
300	0.80	—	—	
Average	0.76			
***n* = 14**				
60	0.85	0.75		0.65
300	1.10	0.66	—	
Average	0.98	0.70		
***n* = 12**				
60	1.09	0.84	0.88	0.46
300	1.29	1.10	0.61	
Average	1.19	0.97	0.74	
***n* = 10**				
60	1.21	1.00	0.75	0.45
300	1.22	1.18	0.63	
Average	1.21	1.09	0.69	
***n* = 8**				
60	1.40	1.11	0.87	0.45
300	0.89	0.92	0.58	
Average	1.15	1.01	0.72	
***n* = 6**				
60	1.02	0.87	0.73	0.46
300	0.24	0.20	0.30	
Average	0.63	0.53	0.51	

angles and their mutual combinations leading to those ground-state isomers are not affected by the chain length, e.g., the same arrangement of α, β, and γ chains is obtained for the DLPC, DMPC, and DPPC molecules. As a consequence, the characteristic geometries of the head, body, and neck conformations display very similar structural parameters. The displacement of the polar head with respect to the β or γ alkyl chains in the various isomers is characterized by the distances of the closest C=O oxygen to the choline N atom (N···C=O) and to the non-ester phosphate O atom (P=O···O=C). These distances do not vary with the chain length.

The 14 isomers have the same relative energy stability for the DLPC, DMPC, and DPPC molecules. The computed damped empirical dispersion energies, E_{disp}, plotted in Fig. 3, indicates an increase of approximately 3.1 kcal/mol per CH_2 unit for the lipids with 12, 14, and 16 carbons in the alkyl chains in their T1 and T2 arrangements. This value is somewhat smaller than the E_{disp} increase of 3.8 kcal/mol per CH_2 in the case of *n*-alkane dimers (from butane to dodecane) in their most stable arrangement.[19] The averaged DFT-D empirical dispersion in the T1 isomers is higher than the average value for the T2 isomers. This difference increases slightly with the chain length, e.g., E_{disp} of T1 isomers is higher by 3.8, 4.0, and 5.2 kcal/mol for the DLPC, DMPC, and DPPC molecules, respectively. The E_{disp} difference for both tail arrangements correlates with the difference between the β and γ hydrocarbon chain separation in T1 and T2. The relative dispersion energy in the case of isomers with parallel tails (T1) follows a very similar trend for the three lipid molecules as seen from Fig. 3. This regular behaviour is not so well-respected for the T2 isomers for a particular diacyl PC lipid. It indicates, thus, some influence of the chain length when T2 chains are coupled with a specific head and body conformation. However, this "discrepancy" is less than 3%–4% of the dispersion energy values.

Higher energy structures with gauche conformers in the alkyl chains

Gauche chain conformers are predominantly formed in phospholipid aggregates in their liquid phase. The relative energies of the possible gauche conformers with one kink per alkyl chain, optimized at $T = 0$ K, with respect to the all trans structures are presented in Table 3 for the DLPC, DMPC, and DPPC $H1N1B_{A2}T2$ isomers. For comparison, relative energies between gauche and trans isomers of tetradecane are reported in the same table. The torsions in Table 3 follow the nomenclature indicated in Fig. 1 for the β and γ chains. In contrast to tetradecane, the gauche conformers in DLPC, DMPC, and DPPC are not degenerate with, however, insignificant relative energy variations for three of the four possible gauche conformers in the DLPC molecule. Interestingly, comparable stability is obtained for the structures with a kink at the free end of the C12, C14, and C16 chains. The DPPC gauche conformers follow the behaviour of DMPC: the least stable structures are those with kinks in the middle of the hydrocarbon chains (at β_n, γ_n = 8, 10, 12 for DPPC and β_n, γ_n = 8, 10 for DMPC); the most stable conformation is the one with a torsion of 300° at β_n, γ_n = 6. The latter is obtained also for the DLPC molecules.

Comparison of the G3P and phospholipid conformers

The precursor G3P values of θ1/θ2 and θ3/θ4, characterizing the "neck" and "body", respectively, correspond to those found for the complete phospholipid structures. Indeed, if one considers all the isomers of Table 2, the three phospholipid necks are found with the combinations 180/60 (N1), 60/–60 (N2), and 60/180 (N3). Since G3P has no acyl chains, only three types of body exist: two of them correspond to those found for the phospholipids: B_A and B_B, with the θ3/θ4 values of 180/60 and 60/–60, respectively. The value of –70/180, (e'_2 in Table 2), related to two opposite OH groups at the C1 and C2 carbons, i.e., acyl chains in opposite directions, would not lead to the formation of phospholipid bilayers. Actually, this configuration (opposite acyl chains) was reported in NMR studies for PC lipids at low concentration in water, i.e., isolated molecules or very small aggregates.[9] In the same work, the B_A and B_B conformers were proposed as the only two present in the PC lipid bilayers, related with specific ^{1}H NMR signals (rotamers A and B, respectively, in ref. 9).

We thus see that G3P already provides the basis of the conformations found for the final phospholipids, moreover corresponding to similar energies. The bonding of the β and then γ acyl chains and finally that of the head α chain will allow the possibility of two relative orientations for the carbonyl groups (splitting B_A into B_{A1} and B_{A2}) and for the alkyl chains (T1 and T2).

If the G3P isoenergetic structures are not specifically selected in the G3PAT enzyme at the binding site with the fatty acyl chain, more than one or a few different neck and body conformers could exist in the final phospholipids. Indeed, at the two next steps, i.e., dephosphorylation and addition of the phosphocholine, one could assume that the glycerol backbone and the acyl chains will keep their conformations. The existence of more than one phospholipid conformer in the "de novo" synthesis is thus not unreasonable.

Conclusion

The different conformational structures of the glycerol (G) and glycerol 3-phosphate (G3P) molecules have been shown to be at the origin of the various phospholipid conformers, except, obviously, for the alkyl chain torsions. Conformations lacking internal hydrogen bonds are imposed by the enzymes involved in the synthesis, and these persist through the various subsequent steps of the synthesis, adding the tails and the head. The conformational analysis of the glycerophosphate skeleton determines most of the structural characteristics of the phosphatidyl choline lipids, which differ by the length of their diacyl chains, i.e., DLPC, DMPC, and DPPC.

Higher energy conformers with kinks in the acyl chains have been found, in preparation for molecular dynamics studies of the chain melting phase transformation, which will be published elsewhere.[30] The comparison of their relative energies with respect to the acyl chain length shows that DLPC, the shortest lipid to form bilayers, may have a different thermodynamical behaviour at the melting transition from the other two lipids, displaying more similar gauche energies along the alkyl chains.

Acknowledgements

The French computer center (CCRT) is acknowledged for a grant of computer time. D.R.S. thanks the Natural Sciences and Engineering Research Council of Canada (NSERC) for on going Discovery Grant support and WestGrid for access to computing resources.

References

(1) Fagone, P.; Jackowski, S. *J. Lipid Res.* **2008**, *50* (Suppl.), S311–S316. doi:10.1194/jlr.R800049-JLR200. PMID:18952570.
(2) Kennedy, E. P. *J. Biol. Chem.* **1953**, *201*, 399.
(3) Thorner, J. W.; Paulus, H. *J. Biol. Chem.* **1973**, *248*, 3922.
(4) Mao, C.; Ozer, Z.; Zhou, M.; Uckun, F. M. *Biochem. Biophys. Res. Commun.* **1999**, *259* (3), 640–644. doi:10.1006/bbrc.1999.0816. PMID:10364471.
(5) Slabas, A. R.; Simon, W. R.; Schierer, T. P.; Kroon, J.; Fawcett, T.; Hayman, M.; Gilroy, J.; Nishida, I.; Murata, N.; Rafferty, J.; Turnbull, A.; Rice, D. *Biochem. Soc. Trans.* **2000**, *28* (6), 677–679. doi:10.1042/BST0280677. PMID:11171167.
(6) Slabas, A. R.; Kroon, J. T. M.; Scheirer, T. P.; Gilroy, J. S.; Hayman, M.; Rice, D. W.; Turnbull, A. P.; Rafferty, J. B.; Fawcett, T.; Simon, W. J. *J. Biol. Chem.* **2002**, *277* (46), 43918–43923. doi:10.1074/jbc.M206429200.
(7) Turnbull, A. P.; Rafferty, J. B.; Sedelnikova, S. E.; Slabas, A. R.; Schierer, T. P.; Kroon, J. T. M.; Simon, J. W.; Fawcett, T.; Nishida, I.; Murata, N.; Rice, D. W. *Structure* **2001**, *9* (5), 347–353. doi:10.1016/S0969-2126(01)00595-0. PMID:11377195.
(8) Agarwal, A. K.; Sukumaran, S.; Bartz, R.; Barnes, R. I.; Garg, A. J. *Endocrinology* **2007**, *193* (3), 445–457. doi:10.1677/JOE-07-0027.
(9) Hauser, H.; Pascher, I.; Sundell, S. *Biochemistry* **1988**, *27* (26), 9166–9174. doi:10.1021/bi00426a014. PMID:3242620.
(10) Hong, M.; Schmidt-Rohr, K.; Zimmermann, H. *Biochemistry* **1996**, *35* (25), 8335–8341. doi:10.1021/bi953083i.
(11) Pearson, R. H.; Pascher, I. *Nature* **1979**, *281* (5731), 499–501. doi:10.1038/281499a0. PMID:492310.
(12) Pascher, I.; Sundell, S.; Harlos, K.; Eibl, H. *Biochim. Biophys. Acta* **1987**, *896* (1), 77–88. doi:10.1016/0005-2736(87)90358-0. PMID:3790589.
(13) Krishnamurty, S.; Stefanov, M.; Mineva, T.; Bégu, S.; Devoisselle, J. M.; Goursot, A.; Zhu, R.; Salahub, D. R. *J. Phys. Chem. B* **2008**, *112* (42), 13433–13442. doi:10.1021/jp804934d. PMID:18817435.
(14) Krishnamurty, S.; Stefanov, M.; Mineva, T.; Bégu, S.; Devoisselle, J. M.; Goursot, A.; Zhu, R.; Salahub, D. R. *ChemPhysChem* **2008**, *9* (16), 2321–2324. doi:10.1002/cphc.200800511. PMID:18924197.
(15) Köster, A. M.; Calaminici, P.; Casida, M. E.; Flores-Moreno, R.; Geudtner, G.; Goursot, A.; Heine, T.; Ipatov, A.; Janetzko, F.; Martin del Campo, J.; Patchkovskii, S.; Reveles, J. U.; Salahub, D. R.; Vela, A. *The deMon developers*; Cinvestav, Mexico. 2006.
(16) Zhang, Y.; Yang, W. *Phys. Rev. Lett.* **1998**, *80* (4), 890. doi:10.1103/PhysRevLett.80.890.
(17) Lee, C.; Yang, W.; Parr, R. G. *Phys. Rev. B Condens. Matter Mater. Phys.* **1988**, *37*, 785.
(18) Zhang, Y.; Yang, W. *Phys. Rev. Lett.* **1998**, *80* (4), 890. doi:10.1103/PhysRevLett.80.890.
(19) Goursot, A.; Mineva, T.; Kevorkyants, R.; Talbi, D. *J. Chem. Theory Comput.* **2007**, *3* (3), 755–763. doi:10.1021/ct600373f.

(20) Godbout, N.; Salahub, D. R.; Andzelm, J.; Wimmer, E. *Can. J. Chem.* **1992**, *70* (2), 560–571. doi:10.1139/v92-079.
(21) Köster, A. M.; Flores-Moreno, R.; Reveles, J. U. *J. Chem. Phys.* **2004**, *121* (2), 681. doi:10.1063/1.1759323.
(22) Dunlap, B. I.; Connolly, J. W. D.; Sabin, J. R. *J. Chem. Phys.* **1979**, *71* (12), 4993. doi:10.1063/1.438313.
(23) Mintmire, W.; Dunlap, B. I. *Phys. Rev. A* **1982**, *25* (1), 88–95. doi:10.1103/PhysRevA.25.88.
(24) Reveles, J. U.; Köster, A. M. *CJ. Comput. Chem.* **2004**, *25*, 1109. doi:10.1002/jcc.20034.
(25) Alberts, B.; Johnson, A.; Lewis, J.; Raff, M.; Roberts, K.; Walter, P. In *Molecular biology of the cell*, 5th ed.; Garland Science, Taylor & Francis Group: New York, 2008.
(26) Feese, M. D.; Faber, H. R.; Bystrom, C. E.; Pettigrew, D. W.; Remington, S. J. *Structure* **1998**, *6* (11), 1407–1418. doi:10.1016/S0969-2126(98)00140-3. PMID:9817843.
(27) Bystrom, C. E.; Pettigrew, D. W.; Branchaud, B. P.; O'Brien, P.; Remington, S. J. *Biochemistry* **1999**, *38* (12), 3508–3518. doi:10.1021/bi982460z. PMID:10090737.
(28) Grayson, P.; Tajkhorshid, E.; Schulten, K. *Biophys. J.* **2003**, *85* (1), 36–48. doi:10.1016/S0006-3495(03)74452-X. PMID: 12829462.
(29) Schlick, T. *Biophys. J.* **2003**, *85* (1), 1–4. doi:10.1016/S0006-3495(03)74448-8. PMID:12829458.
(30) Mineva, T.; Krishnamurty, S.; Goursot, A.; Salahub, D. R. Unpublished results.

Exact exchange-correlation potentials in spin-density functional theory and their discontinuities at unit electron number

John P. Perdew and Espen Sagvolden

Abstract: The exact exchange-correlation potential of Kohn–Sham density functional theory is known to jump discontinuously by a spatial constant as the average electron number, N, crosses an integer in an open system of fluctuating electron number, with important physical consequences for charge transfers and band gaps. We have recently constructed an essentially exact exchange-correlation potential v_{xc} for N electrons ($0 \le N \le 2$) in the presence of a $-1/r$ external potential, i.e., for a ground ensemble of H^+ ion, H atom, and H^- ion densities. That construction illustrates the discontinuity at $N = 1$, where it equals $I_H - A_H$, the positive difference between the ionization energy and the electron affinity of the hydrogen atom. Here we construct the corresponding essentially exact spin-up and spin-down exchange-correlation potentials $v_{xc,\uparrow}$ and $v_{xc,\downarrow}$ of the Kohn–Sham spin-density functional theory, more commonly used for electronic structure calculations, for the ground ensemble with most-negative z-component of spin (or equivalently in the presence of a uniform magnetic field of infinitesimal strength). The potentials v_{xc}, $v_{xc,\uparrow}$, and $v_{xc,\downarrow}$, which vanish as $r \to \infty$ (except when N approaches an integer from above), are identical for $0 \le N \le 1$ and for $N = 2$ but not for $1 < N < 2$. We find that the majority or spin-down potential has a spatially constant discontinuity at $N = 1$ equal to $I_H - A_H$. The minority or spin-up potential has a discontinuity which is this constant in one order of limits, but is a spatially varying function in a different order of limits. This order-of-limits problem is a consequence of a special circumstance: the vanishing of the spin-up density at $N = 1$.

Key words: density functional theory, spin-density functional theory, exchange-correlation potential, derivative discontinuity, integer discontinuity.

Résumé : Il est bien connu que le potentiel exact d'échange-corrélation de la théorie de la fonctionnelle de densité de Kohn–Sham augmente considérablement par le biais d'une constante spatiale quand le nombre moyen d'électron, N, change de nombre entier dans un système ouvert comportant un nombre variable d'électron et que cette variation comporte des conséquences physiques importantes pour les transferts de charge et les énergies entre les bandes interdites. On a récemment développé un potentiel essentiellement exact d'échange-corrélation, v_{xc}, pour N électrons ($0 \le N \le 2$), en présence d'un potentiel externe a $-1/r$, à savoir pour un ensemble fondamental des densités ioniques de l'ion H^+, de l'atome H et de l'anion H^-. Cette construction illustre la discontinuité au niveau $N = 1$, où elle est égale à $I_H - A_H$, la différence positive entre l'énergie d'ionisation et l'affinité électronique de l'atome d'hydrogène. Dans ce travail, on construit les potentiels essentiellement exacts correspondants d'échange-corrélation des spins positifs et négatifs, $v_{xc,\uparrow}$ et $v_{xc,\downarrow}$, de la théorie de la fonctionnelle de densité de spin de Kohn–Sham qui est généralement utilisée pour les calculs de structure électronique, pour l'ensemble fondamental avec des composantes de spin z plus négatives (ou, d'une façon équivalente, en présence d'un champ magnétique uniforme de force infinitésimale). Les potentiels v_{xc}, $v_{xc,\uparrow}$, et $v_{xc,\downarrow}$, qui disparaissent quand $r \to \infty$ (excepté quand la valeur de N s'approche d'un nombre entier en venant du haut), sont identiques pour $0 \le N \le 1$ et pour $N = 2$, mais pas pour $1 < N < 2$. On a trouvé que la majorité ou le potentiel à spin descendant comporte une discontinuité de constante spatiale pour $N = 1$ qui est égale à $I_H - A_H$. La minorité ou le potentiel à spin croissant comporte une discontinuité qui est constante dans un ordre de limite, mais qui est une fonction variant dans l'espace dans un ordre différent de limites. Le problème de l'ordre des limites est une conséquence d'une circonstance spéciale, à savoir la disparition de la densité du spin croissant à $N = 1$.

Mots-clés : théorie de la fonctionnelle de densité, théorie de la fonctionnelle de densité de spin, potentiel d'échange-corrélation, discontinuité de nombre entier.

[Traduit par la Rédaction]

Received 20 January 2009. Accepted 19 March 2009. Published on the NRC Research Press Web site at canjchem.nrc.ca on 11 August 2009.

This article is part of a Special Issue dedicated to Professor T. Ziegler. This work is dedicated to Tom Ziegler, whose fundamental and applied work in Kohn–Sham spin-density functional theory is of enduring value.

J.P. Perdew.[1] Department of Physics and Quantum Theory Group, Tulane University, New Orleans, LA 70118. USA.
E. Sagvolden. University of California, Irvine, Department of Chemistry, 1102 Natural Sciences II, Irvine, CA 92697-2025, USA.

[1]Corresponding author (e-mail: perdew@tulane.edu).

Kohn–Sham theory[1–4] is used throughout quantum chemistry and condensed-matter physics to find the nonrelativistic ground-state energy E and electron spin densities $n_\uparrow(\mathbf{r})$ and $n_\downarrow(\mathbf{r})$ of a collection of mutually interacting electrons in a scalar external potential $v(\mathbf{r})$. The theory is exact in principle, although in practice the exchange-correlation energy $E_{xc}[n_\uparrow,n_\downarrow]$ as a functional of the spin densities must be approximated. Computational efficiency is achieved because the equations to be solved are those for an auxiliary system of noninteracting electrons moving in an effective potential, which is the sum of the external potential, a Hartree electrostatic potential

$$[1] \qquad u([n];\mathbf{r}) = \int d^3r' \quad n(\mathbf{r}')/|\mathbf{r}' - \mathbf{r}|$$

(where $n = n_\uparrow + n_\downarrow$ is the total density), and a spin-dependent exchange-correlation potential which is the functional derivative

$$[2] \qquad v_{xc,\sigma}([n_\uparrow, n_\downarrow];\mathbf{r}) = \delta E_{xc}/\delta n_\sigma(\mathbf{r})$$

The functional derivative is defined so that

$$[3] \qquad \delta E_{xc} = \sum\nolimits_\sigma \int d^3r [\delta E_{xc}/\delta n_\sigma(\mathbf{r})]\delta n_\sigma(\mathbf{r})$$

If the number N_σ of electrons of spin σ is not allowed to vary ($\delta N_\sigma = \int d^3r\, \delta n_\sigma(\mathbf{r}) = 0$), then the potential $v_{xc,\sigma}$ contains an arbitrary additive constant.

A conceptually simpler version[1] of exact Kohn–Sham theory predicts the ground-state energy E and total electron density $n(\mathbf{r})$ from a functional $E_{xc}[n]$ of the total density and its functional derivative $v_{xc}([n];\mathbf{r})$. This theory was extended to open systems of fluctuating electron number by Perdew, Parr, Levy, and Balduz.[5] Such an open system can be described by an ensemble of wave functions with different electron numbers. Alternatively, the closed system comprising the open system and its electron reservoir can be described by a single wave function.[6] Since the average electron number N in the open system can then vary continuously, there is no arbitrary constant in the corresponding v_{xc}. The energy E was found to vary linearly between adjacent integers, with derivative discontinuities at the integers. The potential v_{xc} was found to jump discontinuously by a constant at integer N, and otherwise to tend to zero as $r \to \infty$ [6–8].

The discontinuity of the potential explains (*i*) why the band structure of the exact Kohn–Sham potential underestimates the fundamental band gap of a solid,[9–12] and (*ii*) why neutral molecules really dissociate to neutral atoms of integer electron number,[5,6] although semilocal approximations to E_{xc} often predict dissociation to atoms of fractional charge,[13] and more generally why semilocal approximations overly favor charge transfer.[14–16] In a closed system composed of isolated open subsystems, the exact Kohn–Sham potential can develop a different constant region[6] around each open system to prevent spurious charge transfer. Only fully nonlocal approximations, such as those of refs. 16–18, can properly describe such effects. Semilocal approximations, which display no discontinuity of v_{xc}, can work well only when all occupation numbers in a compact isolated open subsystem are integers.[3,19]

Recently, the discontinuity of v_{xc} at integer N has been questioned by Zahariev and Wang.[20] In response,[21] we have rigorously established the existence of a nonzero, spatially constant discontinuity at $N = 1$, and illustrated it by construction of an essentially exact v_{xc} for N electrons ($0 \le N \le 2$) in the presence of a $-1/r$ external potential. A similar construction, using accurate numerical densities instead of analytic ones, was given earlier by Savin, Colonna, and Pollet.[22] We have also made the spatially constant discontinuity more plausible at integer N greater than 1, and have pointed out[23] the error in the argument of ref. 20. However, our work has been done within total-density functional theory,[1] and not within the spin-density functional theory[2] that is almost always employed in practical applications (because its approximations are more accurate for open-shell spin-polarized systems, even in the absence of an external magnetic field). Thus, here we will extend our results to spin-density functional theory. While a general discussion of the discontinuity in this theory has been presented by Chan,[24] we will present a particularly clear and simple argument for the special case $0 \le N \le 2$, which establishes the nonzero discontinuity beyond all doubt. Ayers and Yang[25] have recently discussed some other formal issues of spin-density functional theory.

An ensemble is a collection of wave functions and their probabilities, with density and energy given by probability-weighted averages. As shown in Ref. 5 (and in more detail in ref. 26), the ground ensembles for N between adjacent integers $J - 1$ and J are composed of the ground states for the $J - 1$ and J electron systems, provided that (as expected) the ionization energy is greater than the electron affinity for all bound states of integer electron number. The ground states for integer electron number can be degenerate or nondegenerate.

Although the ground state of H^- is a spin singlet, the ground state of H is a spin doublet. We employ a ground ensemble in which the spin densities are probability-weighted averages of the spin densities of the contributing ground-state wave functions. By the arguments of ref. 5, the ground ensemble for $0 \le N \le 1$ must be composed of the H^+ ion (no electrons), the spin-up H atom, and the spin-down H atom, i.e.,

$$[4] \qquad \begin{array}{ll} n_\uparrow = \varepsilon n_H & (N_\uparrow = \varepsilon) \\ n_\downarrow = (N-\varepsilon) n_H & (N_\downarrow = N - \varepsilon) \\ n = N n_H & (N = N) \end{array}$$

for $0 \le \varepsilon \le N$). Similarly, the ground ensemble for $1 < N \le 2$ must be composed of the spin-up H atom, the spin-down H atom, and the H^- ion, i.e.,

$$[5] \qquad \begin{array}{ll} n_\uparrow = (N-1) n_{H^-}/2 + \varepsilon n_H & (N_\uparrow = N - 1 + \varepsilon) \\ n_\downarrow = (N-1) n_{H^-}/2 + (2 - N - \varepsilon) n_H & (N_\downarrow = 1 - \varepsilon) \\ n = (N-1) n_{H^-} + (2-N) n_H & (N = N) \end{array}$$

for $0 \le \varepsilon \le 2 - N$. The spin-disorder parameter ε measures the deviation of each N-electron ground ensemble from the one of most negative z-component of spin. Note that, for a given $N = N_\uparrow + N_\downarrow$ and in the absence of an external magnetic field, there is a continuous ground-level degeneracy labeled by ε or by $N_\downarrow - N_\uparrow$. The parameters we can control are N and ε, or equivalently $N_\uparrow$ and $N_\downarrow$ (the latter both in the

range from 0 to 1, inclusive). Within total-density functional theory, we choose ε so that $n_\uparrow = n_\downarrow = n/2$, i.e., $\varepsilon = N/2$ for $0 \le N \le 1$ and $\varepsilon = 1 - N/2$ for $1 < N \le 2$. Within spin-density functional theory, the ensemble with as much down spin as possible is attained in the limit $\varepsilon \to 0^+$ (and all potentials are evaluated before this limit is taken). This limit yields the nondegenerate ground ensemble in the presence of a uniform magnetic field of infinitesimal strength along the *z*-axis. For the exact energy in the $(N_\uparrow,N_\downarrow)$ plane, see Fig. 1 of ref. 27.

Note that the spin densities (but not their derivatives) are continuous functions of *N* in the interval $0 \le N \le 2$. At $N = 0$, $n_\uparrow = n_\downarrow = 0$. At $N = 2$, $n_\uparrow = n_\downarrow = (n_{H^-})/2$. At $N = 1$ in density functional theory $n_\uparrow = n_\downarrow = n_H/2$, but in spin density functional theory $n_\uparrow = 0$ and $n_\downarrow = n_H$.

For $0 \le N \le 2$, there are at most two occupied or partly occupied orbitals, with occupation numbers $N_\uparrow$ and $N_\downarrow$ and shapes proportional to $n_\uparrow^{1/2}$ and $n_\downarrow^{1/2}$. The Kohn–Sham eq.[1,2] is

$$[6] \qquad [(-1/2)\nabla^2 - 1/r + u([n];r) + v_{xc,\sigma}]n_\sigma^{1/2} = e_\sigma n_\sigma^{1/2}$$

Let $E(N_\uparrow,N_\downarrow)$ be the ground-ensemble energy for average spin electron numbers $N_\uparrow$ and $N_\downarrow$. By Janak's theorem,[28] $e_\sigma = \partial E/\partial N_\sigma$, where the derivative is taken at constant $N_{-\sigma}$. Since the external magnetic field vanishes, the energy *E* depends only upon $N = N_\uparrow + N_\downarrow$, and not at all upon $N_\downarrow - N_\uparrow$, making $\partial E/\partial N_\sigma = dE/dN = \mu$, where μ is also the chemical potential of the reservoir:

$$[7] \qquad \mu = \begin{matrix} -I_H & (0 \le N \le 1) \\ -A_H & (1 < N \le 2) \end{matrix}$$

where $I_H = 0 - E_H = 0.50000$ hartree is the ionization energy of the H atom and $A_H = E_H - E_{H^-} = 0.02775$ hartree is the electron affinity of the H atom. Janak's theorem applies here for all occupation numbers in the closed interval from 0 to 1, including the end points. At the end points, the derivative is one-sided. Thus

$$[8] \qquad v_{xc,\sigma} = \mu + 1/r - u([n];r) + (1/2)\nabla^2 n_\sigma^{1/2}/n_\sigma^{1/2}$$

Equation [8] (along with eqs. [1], [4], [5], and [7]) determines the exact exchange-correlation potentials we seek. Note that the choice $\varepsilon = 0$ in eq. [4] would leave $v_{xc,\uparrow}$ of eq. [8] undefined for $N \le 1$. The hydrogen atom density $n_H(r)$ is a simple and familiar analytic function. In ref. 21, we have constructed an accurate analytic model for the H^- ion density $n_{H^-}(r)$.

Although we have invoked Kohn–Sham orbitals and Janak's theorem to derive eq. [8], this equation can also be found from the Euler equations for the spin densities, since the non-interacting kinetic energy functional for $N_\uparrow \le 1$ and $N_\downarrow \le 1$ is the sum of von Weizsaecker functionals for $n_\uparrow$ and $n_\downarrow$[21].

The result for $0 \le N \le 1$ is especially simple, because it involves only the density of the H atom. We easily find

$$[9] \qquad v_{xc,\sigma} = -Nu([n_H];r)$$

independent of σ and ε. In this range, exchange and correlation simply provide a self-interaction correction to the Hartree potential.

Fig. 1. The exact exchange-correlation potential v_{xc} of total-density functional theory, for average electron number *N* around 1 in the $-1/r$ external potential. To the eye, the lower curves $N = 0.999$ and $N = 0.9999$ coincide. Note the jump by a positive constant as *N* increases through 1, and the asymptotic ($r \to \infty$) vanishing of all plotted curves.

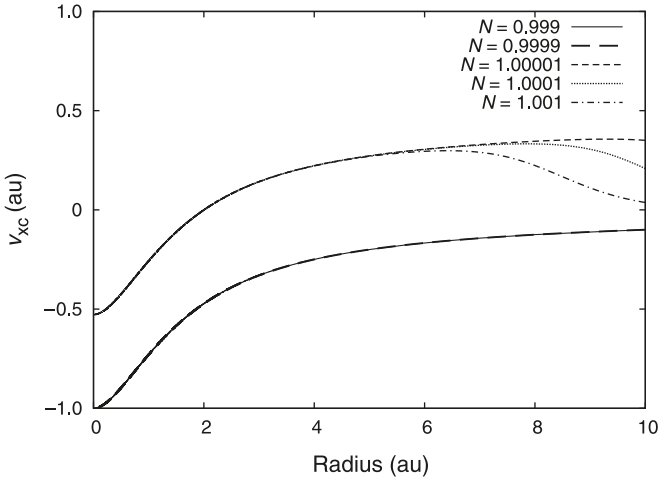

Figures 1, 2, and 3 illustrate our results for v_{xc}, $v_{xc,\downarrow}$, and $v_{xc,\uparrow}$, respectively, for values of *N* just below and just above 1. Figure 1 repeats Fig. 1 of ref. 21, for ease of comparison with total-density functional theory, while Figs. 2 and 3 for spin-density functional theory are new to this work.

The first thing to notice is that all the plotted potentials tend to 0 as $r \to \infty$. This is a simple consequence of eq. [8]: $1/r$ and $u([n];r)$ vanish in this limit, while the known asymptotic exponential decays of n_H and n_{H^-} [7] make the last term of eq. [8] tend to $-\mu$.

The second thing to notice is that the plotted potentials display a discontinuity as *N* crosses the integer 1. The discontinuity is the spatial constant $I_H - A_H$, except in Fig. 3, where the discontinuity of $v_{xc,\uparrow}$ at $N = 1$ is a function of *r*. This is also a simple consequence of eq. [8]: $1/r$, $u([n];r)$ and n_σ are all continuous in *N*, while μ jumps up by $I_H - A_H$ when *N* crosses 1. The last term of eq. [8] is also continuous, so long as n_σ is nonzero at $N = 1$. This is the case for all $\varepsilon > 0$ in eqs. [4] and [5], so the $\varepsilon \to 0^+$ limit of the discontinuity is $I_H - A_H$. But for $v_{xc,\uparrow}$ this result is only for the order of limits in which $N \to 1^+$ before $\varepsilon \to 0^+$. In the opposite order of limits, as illustrated in Fig. 3, the discontinuity of $v_{xc,\uparrow}$ is spatially varying. The latter ($\varepsilon \to 0^+$ first) is the one relevant to the nondegenerate ground ensemble in the presence of an infinitesimal magnetic field. The order-of-limits problem is manifest in the expression $\{\nabla^2[(N-1)n_{H^-} + \varepsilon n_H]^{1/2}\}/[(N-1)n_{H^-} + \varepsilon n_H]^{1/2}$.

For $0 \le N \le 1$, there is no difference between v_{xc}, $v_{xc,\uparrow}$, and $v_{xc,\downarrow}$. For *N* just above 1, there is a strong similarity between the majority-spin $v_{xc,\downarrow}$ (for most-negative z-component of spin) and v_{xc}. There is, however, a discernable difference in the approach to zero as $r \to \infty$, which is slower in $v_{xc,\downarrow}$ because $n_\downarrow$ has more of n_H when the *z* component of spin is most negative.

In summary, we have constructed exact exchange-correlation potentials for *N* electrons ($0 \le N \le 2$) in the presence of a $-1/r$ external potential, within both density

Fig. 2. The exact down- or majority-spin exchange-correlation potential $v_{xc,\downarrow}$ of spin-density functional theory, for average electron number N around 1 in the $-1/r$ external potential, and for the ground ensemble with the most-negative possible z component of spin. To the eye, the lower curves $N = 0.999$ and $N = 0.9999$ coincide. Note the jump by a positive constant as N increases through 1, and the asymptotic vanishing of all plotted curves.

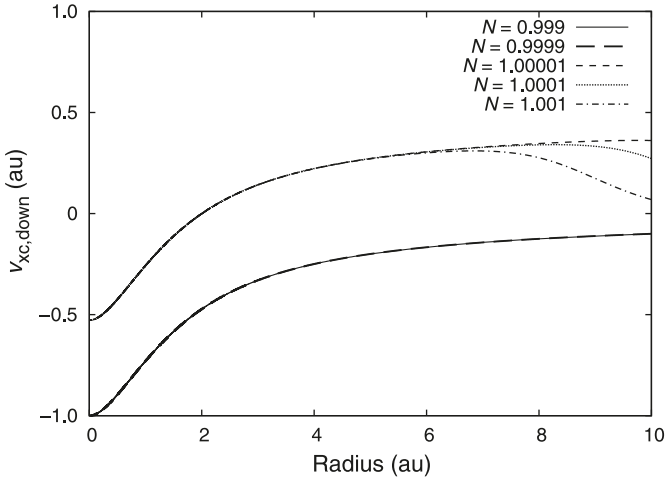

Fig. 3. The exact up- or minority-spin exchange-correlation potential $v_{xc,\uparrow}$ of spin-density functional theory, for average electron number N around 1 in the $-1/r$ external potential, and for the ground ensemble with the most-negative possible z component of spin. To the eye, the lower curves $N = 0.999$ and $N = 0.9999$ coincide, and the upper curves $N = 1.00001$, $N = 1.0001$, and $N = 1.001$ also coincide. Note the jump by a positive spatially-varying function as N increases through 1, and the asymptotic vanishing of all plotted curves.

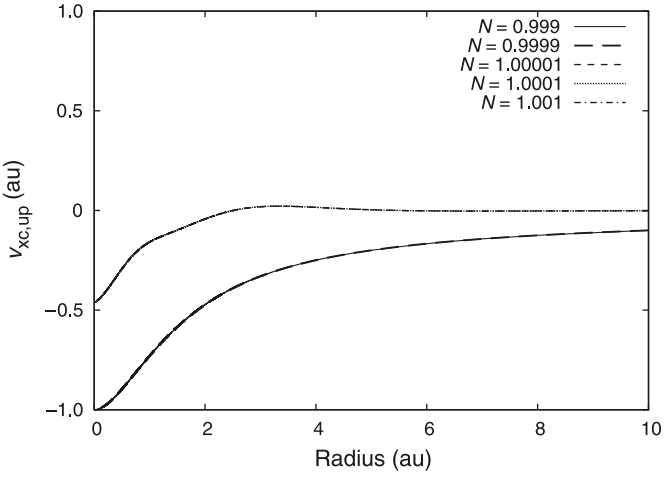

functional and spin-density functional theories. All these potentials vanish as $r \to \infty$ for all noninteger N, and all display a discontinuity at $N = 1$. The discontinuity is the spatial constant $I_H - A_H$ for the density functional potentials, and for the majority-spin but not in an important order of limits for the minority-spin potential in the spin-density functional for the case of most-negative z-component of spin. The spatial dependence of the discontinuity in the minority-spin or $\uparrow$ potential, displayed in Fig. 3, is a consequence of the special situation $n_\uparrow = 0$ at $N = 1$.

The results we have found here have a simple and direct generalization to N electrons ($0 \le N \le 2$) in the presence of *any* spin-independent external potential that vanishes as $r \to \infty$, since the degeneracy of spin $\uparrow$ and spin $\downarrow$ one-electron ground states persists, permitting the use of $N_\uparrow - N_\downarrow$ as an independent variable describing a continuum of degenerate ground-level ensembles for fixed $N_\uparrow - N_\downarrow$. For any one-electron system in the absence of a magnetic field, we earlier proved[23] that $I - A$ is positive. A weaker generalization to many-electron systems (up to the maximum number that can be bound) has also been established.[29] Moreover, the high-density limit of $I - A$ under uniform density scaling for any one-electron system has been shown to be twice the Hartree electrostatic energy[30,31] of the scaled density.

Physically, we can introduce a uniform magnetic field B along the z axis, and a temperature T. Our approach, which sets $B = T = 0$ at the start, provides unambiguous answers for the spin-dependent exchange-correlation potentials. If instead we had set $T = 0$ from the start, but had then taken the limit $B \to 0$, then $v_{xc,\uparrow}$ would have been undefined for $0 \le N \le 1$, where $n_\uparrow = 0$. Our Fig. 1 is found in the order of limits $B \to 0$ first, then $T \to 0$, while our Figs. 2 and 3 are found in the opposite order of limits.

Acknowledgments

The work of J.P.P. was supported in part by the US National Science Foundation under grant DMR-0501588.

References

(1) Kohn, W.; Sham, L. J. *Phys. Rev.* **1964**, *136* (3B), B864–B871. doi:10.1103/PhysRev.136.B864.
(2) von Barth, U.; Hedin, L. *J. Phys. Chem.* **1972**, *5* (13), 1629–1642. doi:10.1088/0022-3719/5/13/012.
(3) Ziegler, T.; Rauk, A.; Baerends, E. J. *Theoret. Chim. Acta,* **1977**, *46*, 1. doi:10.1007/BF00551648.
(4) Fiolhais, C.; Nogueira, F.; Marques, M., Eds. *A primer in density functional theory;* Springer: Berlin, 2003.
(5) Perdew, J. P.; Levy, M.; Balduz, J. *Phys. Rev. Lett.* **1982**, *49* (23), 1691–1694. doi:10.1103/PhysRevLett.49.1691.
(6) Perdew, J. P. In *Density functional methods in physics;* Dreizler, R. M. and da Providencia, J., Eds.; Plenum: New York, 1985.
(7) Levy, M.; Perdew, J. P.; Sahni, V. *Phys. Rev. A* **1984**, *30* (5), 2745–2748. doi:10.1103/PhysRevA.30.2745.
(8) Almbladh, C.-O.; von Barth, U. *Phys. Rev. B* **1985**, *31* (6), 3231–3244. doi:10.1103/PhysRevB.31.3231.
(9) Perdew, J. P.; Levy, M. *Phys. Rev. Lett.* **1983**, *51* (20), 1884–1887. doi:10.1103/PhysRevLett.51.1884.
(10) Sham, L. J.; Schlueter, M. *Phys. Rev. Lett.* **1983**, *51* (20), 1888–1891. doi:10.1103/PhysRevLett.51.1888.
(11) Grüning, M.; Marini, A.; Rubio, A. *Phys. Rev. B* **2006**, *74* (16),o. 161103. (R). doi:10.1103/PhysRevB.74.161103.
(12) Mori-Sánchez, P.; Cohen, A. J.; Yang, W. *Phys. Rev. Lett.* **2008**, *100* (14),o. 146401. doi:10.1103/PhysRevLett.100.146401. PMID:18518055.
(13) Ruzsinszky, A.; Perdew, J. P.; Csonka, G. I.; Vydrov, O. A.; Scuseria, G. E. *J. Chem. Phys.* **2006**, *125* (19),o. 194112. doi:10.1063/1.2387954. PMID:17129094.
(14) Tozer, D. J. *J. Chem. Phys.* **2003**, *119* (24), 12697. doi:10.1063/1.1633756.
(15) Ruzsinszky, A.; Perdew, J. P.; Csonka, G. I. *Phys. Rev. A* **2008**, *78* (2), 022513. doi:10.1103/PhysRevA.78.022513.

(16) Patchkovskii, S.; Ziegler, T. *J. Chem. Phys.* **2002**, *116* (18), 7806. doi:10.1063/1.1468640.
(17) Perdew, J. P.; Zunger, A. *Phys. Rev. B* **1981**, *23* (10), 5048–5079. doi:10.1103/PhysRevB.23.5048.
(18) Vydrov, O. A.; Scuseria, G. E.; Perdew, J. P. *J. Chem. Phys.* **2007**, *126* (15),o. 154109. doi:10.1063/1.2723119. PMID: 17461616.
(19) Perdew, J. P.; Ruzsinszky, A.; Csonka, G. I.; Vydrov, O. A.; Scuseria, G. E.; Staroverov, V. N.; Tao, J. *Phys. Rev. A* **2007**, *76* (4),o. 040501. doi:10.1103/PhysRevA.76.040501.
(20) Zahariev, F. E.; Wang, Y. A. *Phys. Rev. A* **2004**, *70* (4),o. 042503. doi:10.1103/PhysRevA.70.042503.
(21) Sagvolden, E.; Perdew, J. P. *Phys. Rev. A* **2008**, *77* (1),o. 012517. doi:10.1103/PhysRevA.77.012517.
(22) Savin, A.; Colonna, F.; Pollet, R. *Int. J. Quantum Chem.* **2003**, *93* (3), 166–190. doi:10.1002/qua.10551.
(23) Sagvolden, E.; Perdew, J. P.; Levy, M. *Phys. Rev. A* **2009**, *79* (2),o. 026501. doi:10.1103/PhysRevA.79.026501.
(24) Chan, G. K.-L. *J. Chem. Phys.* **1999**, *110* (10), 4710. doi:10.1063/1.478357.
(25) Ayers, P. W.; Yang, W. *J. Chem. Phys.* **2006**, *124* (22),o. 224108. doi:10.1063/1.2200884. PMID:16784264.
(26) Sagvolden, E. *Phys. Rev. A* **2006**, *74* (2),o. 022506. doi:10.1103/PhysRevA.74.022506.
(27) Mori-Sánchez, P.; Cohen, A. J.; Yang, W. *Phys. Rev. Lett.* **2009**, *102* (6),o. 066403. doi:10.1103/PhysRevLett.102.066403. PMID:19257614.
(28) Janak, J. F. *Phys. Rev. B* **1978**, *18* (12), 7165–7168. doi:10.1103/PhysRevB.18.7165.
(29) Levy, M.; Sagvolden, E.; Perdew, J. P. Unpublished results.
(30) Gori-Giorgi, P.; Savin, A. *Int. J. Quantum Chem.* **2009**, *109*, 2410 doi:10.1002/qua.22021 .
(31) Gori-Giorgi, P.; Perdew, J. P. Unpublished results.

A DFT/MM analysis of the effect of ligand substituents on asymmetric hydrogenation catalyzed by rhodium complexes with phosphine–phosphinite ligands

Steven M. A. Donald, Anton Vidal-Ferran, and Feliu Maseras

Abstract: DFT and DFT/MM calculations are carried out on the rate-determining step of the addition of dihydrogen to methyl-(*N*)-acetylaminoacrylate catalyzed by a rhodium catalyst containing a bidentate phosphine–phosphinite ligand. DFT calculations reproduce the experimental results, while DFT/MM calculations do not. The failure of DFT/MM methods for this particular problem is analyzed through a series of calculations with different partitions between the DFT and MM regions, which show that electronic effects of all ligand substituents considered are critical. The analysis of these electronic effects provides key information on the role of each of the substituents in the outcome of the overall catalytic process.

Key words: asymmetric hydrogenation, density functional theory, quantum mechanics/molecular mechanics methods, enantioselectivity.

Résumé : Opérant sur la base de la TDF et de la TDF/MM, on a effectué des calculs sur l'étape cinétiquement limitante de l'addition du dihydrogène sur le *N*-acétylaminoacrylate de méthyle, catalysée par un catalyseur de rhodium contenant un ligand phosphine–phosphinite bidentate. Les calculs sur la base de la TDF permettent de reproduire les résultats expérimentaux alors que ceux effectués sur la base de la TDF/MM ne le permettent pas. On a analysé les causes de l'échec des méthodes TDF/MM dans ce problème particulier en effectuant une série de calculs avec différentes partitions entre les régions TDF et MM qui montrent que les effets électroniques de tous les ligands substituants considérés jouent un rôle critique. L'analyse de ces effets électroniques fournit de l'information pertinente sur le rôle de chacun de substituants dans le résultat du processus catalytique global.

Mots-clés : hydrogénation asymétrique, théorie de la fonctionnelle de la densité, méthodes de la mécanique quantique/mécanique moléculaire, énantiosélectivité.

[Traduit par la Rédaction]

Introduction

Over the past three decades, the field of asymmetric catalysis, in general, and asymmetric hydrogenation, in particular, has received considerable interest in academia with the notable contributions of Knowles, Noyori, and Sharpless "for their work on chirally catalyzed hydrogenation and oxidation reactions" leading to their Nobel Prize awards in 2001.[1] Furthermore, the broad applicability of chiral compounds as drugs,[2] polymers,[3] biological probes,[4] and new materials[5] means that an entire industry focused on chirality has taken form. The never-ending search for new chiral compounds is now one of the most prominent areas of modern chemistry.

The abundance of experimental data for catalytic asymmetric hydrogenation lends itself very well to kinetic and computational investigations into the mechanism of this important reaction.[6] However, the only clear conclusion from this research is that the precise mechanism is highly dependent on the exact combination of ligand, substrate, and solvent.[7] Significant progress has been made for specific systems, although we have not yet reached the stage where we can make confident predictions on the behaviour of any ligand that experimental chemists can come to design.

Whilst computer power has risen steadily over the years, it is still the case that high accuracy calculations on large, electronically complex systems such as biological or large organometallic compounds are not practicable. Even though density functional theory offers a good compromise between accuracy and efficiency,[8] there are systems for which a full

Received 5 January 2009. Accepted 6 March 2009. Published on the NRC Research Press Web site at canjchem.nrc.ca on 11 August 2009.

This article is part of a Special Issue dedicated to Professor T. Ziegler. This article is dedicated to Professor Tom Ziegler to celebrate his numerous contributions to the field of computational chemistry.

S.M.A. Donald. Institute of Chemical Research of Catalonia (ICIQ), Av. Països Catalans 16, 43007 Tarragona, Catalonia, Spain.
A. Vidal-Ferran. Institute of Chemical Research of Catalonia (ICIQ), Av. Països Catalans 16, 43007 Tarragona, Catalonia, Spain; Catalan Institution for Research and Advanced Studies (ICREA), Passeig Lluís Companys 23, 08018 Barcelona, Catalonia, Spain.
F. Maseras.[1] Institute of Chemical Research of Catalonia (ICIQ), Av. Països Catalans 16, 43007 Tarragona, Catalonia, Spain; Departament de Química, Universitat Autònoma de Barcelona, 08193 Bellaterra, Catalonia, Spain.

[1]Corresponding author (e-mail: fmaseras@iciq.es).

Scheme 1. Asymmetric hydrogenation by catalyst **1**.

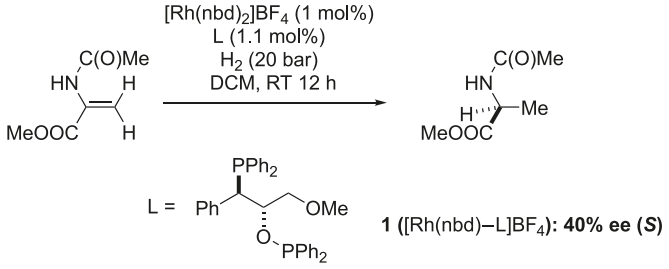

description at this level of theory is seen as too costly. Whilst the common approach of reducing the size of the system by using a "model" where bulky substituents on the ligands are replaced by a hydrogen atom (e.g., removal of phenyl substituents from PPh_3 to give a simple PH_3 ligand) describe the metal–ligand interactions relatively well, they will neglect ligand–ligand interactions. In systems where the steric interactions in the full ligand system play a vitally important role in determining enantioselectivity, the full ligand must be computed. Hybrid quantum mechanics/molecular mechanics (QM/MM) approaches, which offer a description of the full system in a reasonable time, have proven to be an extremely useful tool to the computational chemist. In particular, the IMOMM[9] (integrated molecular orbital and molecular mechanics) and ONIOM[10] (our own N-layered integrated molecular orbital and molecular mechanics) approaches have been quite successful for organometallic systems and homogeneous catalysis.[11] By partitioning the molecule, only the most important section, the metal and its close surroundings, is modelled at the more costly QM level whilst the rest of the molecule is modelled within the MM section. Many examples are available on the successful application of QM/MM methods in catalytic systems including hydrogenation,[12] hydroformylation,[13] sulfoxidation,[14] and olefin polymerization.[15]

We describe here results of the application of the ONIOM method to the study of the asymmetric hydrogenation of methyl-(*N*)-acetylaminoacrylate by the bidentate phosphine–phosphinite (Rh^I) catalyst **1**, recently published by some of us and shown in Scheme 1.[16]

Results and discussion

Computational details

We computed the complete mechanistic scheme according to Landis et al.,[8b] comprising the following stages:

(A) Addition of dihydrogen to the catalyst–substrate adduct to form a five-coordinate dihydrogen intermediate (**MolH_2**).

(B) Oxidative addition of dihydrogen to give the dihydride intermediate (**DIHY**).

(C) Migratory insertion of the β-carbon of the olefin into a Rh–H bond to form an alkyl hydride complex with a C–H···Rh agostic bond (**ALHYag**).

(D) Breaking of the agostic bond to give a five-coordinate alkyl hydride (**ALHY**).

(E) C–H reductive elimination to form the product, bound to the metal by the two carbonyl oxygens (**Prod**).

Fig. 1. Four possible catalyst–substrate adducts.

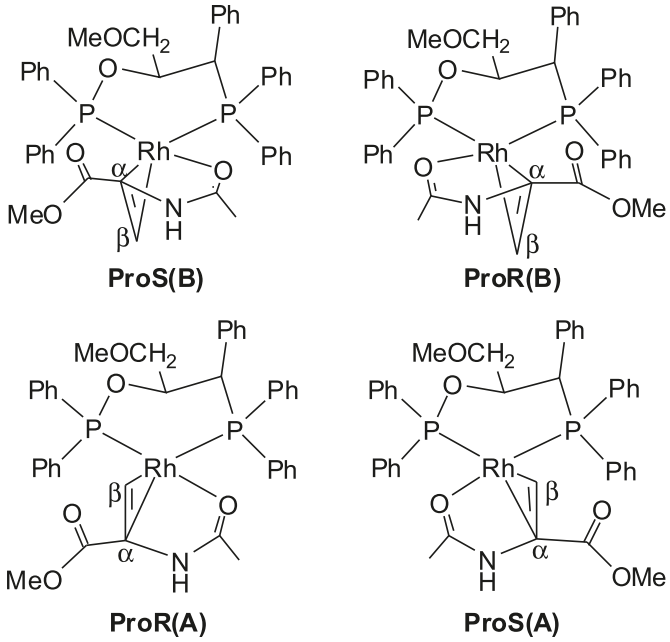

The choice of partition in such systems is of crucial importance and can lead to significant error if the partition is cut too close to the metal centre, as highlighted in a previous study on cobalamins by this group.[17] The study on the DuPHOS system by Landis et al. utilized a three-layer ONIOM approach, describing the core atoms at the DFT level, the phospholane rings at the Hartree–Fock ab inito level, and the phospholane-ring methyl groups with the universal force field (UFF).[18]

In the catalytic system under study, the ligand is non-C_2-symmetric, giving two sets of catalyst–substrate diastereomers (sets A and B, shown in Fig. 1), each diastereomer representing a possible hydrogenation manifold. Also, the catalyst contains considerably more degrees of freedom than the DuPHOS system due to a flexible six-membered backbone and freely rotating phenyl substituents on the phosphorous atoms (P-phenyls). Given the conformational flexibility, a conformation search for the catalyst–substrate adducts and the key transition states was deemed essential. This was carried out using the Monte Carlo rigid conformational scan within the Macromodel program.[19] The lowest energy conformations from each search were then optimized using the two-layer ONIOM method implemented in Gaussian 03,[20] partitioned by placing all four P-phenyls and both backbone substituents in UFF as illustrated in Fig. 2. The model system was described with the B3LYP[21] hybrid density functional, using the Stuttgart RECP and associated basis sets[22] on rhodium and phosphorous with added f (ζ^{Rh} = 1.35) and d (ζ^{P} = 0.387) polarization functions, respectively.[23] The backbone ring, substrate, and dihydrogen molecule were described with the 6–31G(d) basis.[24] The rest of the system (including the P-phenyl groups and the methoxymethyl and phenyl backbone substituents) was described using UFF.

DFT/MM vs. full DFT

Both sets of diastereomers and their possible hydrogenation manifolds were computed, and it was found that hydro-

Fig. 2. Structural comparison of the **RMolH$_2$-TS** and **SMolH$_2$-TS** structures at ONIOM and DFT levels. Ball and stick notation represents DFT atoms, whereas stick notation represents MM atoms.

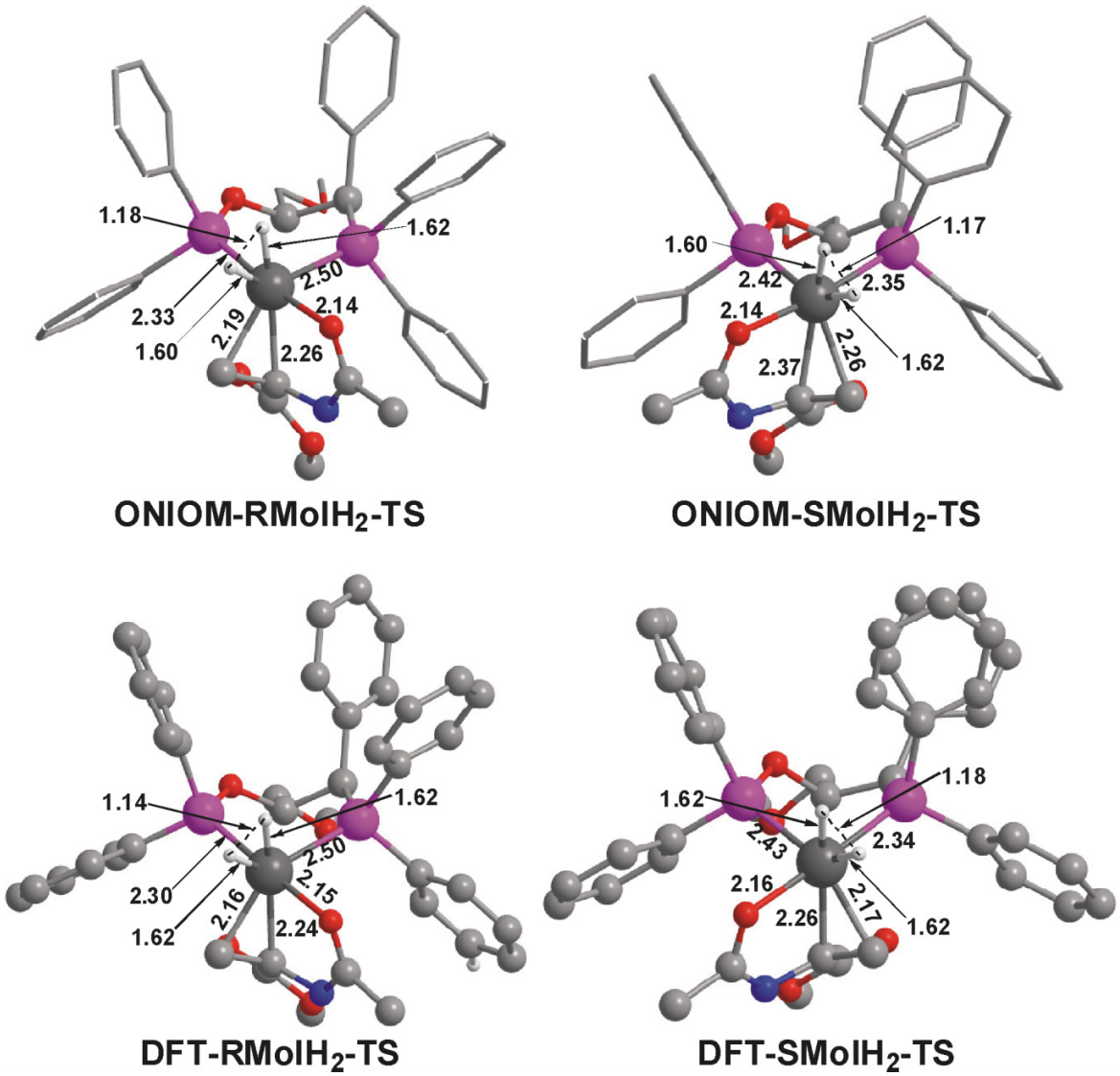

genation from the two B diastereomers, where the bulky α-substituents of the substrate are present in the same face as the backbone phenyl group, was much higher in energy than hydrogenation of the A diastereomers due to increased steric crowding. The B diastereomers are thus highly unlikely to contribute to product formation. In both A-manifolds, the oxidative addition of dihydrogen (**MolH$_2$-TS**) is clearly the rate-determining step; however, the potential energy of the R transition state is 1.88 kcal/mol lower than that of the S transition state, in sharp contrast with the experimentally reported enantiomeric excess of 40% (S), which represents a difference of 0.7 kcal/mol in favour of forming the S product. Inclusion of free-energy correction to the potential energy improves this situation slightly, but still with a 0.83 kcal/mol favourability for R. However, a full-DFT singlepoint calculation on the **MolH$_2$-TS** structures (describing the previously UFF atoms at the 6–31G basis level) reveals an even greater preference for the R pathway (4.15 kcal/mol). This suggests an underlying problem with the ONIOM model itself. Optimization of the two transition-state structures at the full-DFT level results in significant relaxation of the S-isomer, which becomes more stable than the R-isomer by 1.20 kcal/mol and just 0.80 kcal/mol after zero-point and PCM solvation corrections. This translates to an enantiomeric excess of 60% ee (vs. 40% ee experimentally).

Figure 2 shows the structures of the R and S oxidative-addition transition states at the ONIOM and full-DFT levels. At the DFT level, the catalyst backbone increases the space available to the substrate via rotation throughout the six-membered backbone ring. Also in **SMolH$_2$-TS**, the M–C$_\alpha$ and M–C$_\beta$ distances are much longer in the ONIOM model than in the DFT model (M–C$_\alpha$ = 2.37 Å vs. 2.26 Å and M–C$_\beta$ = 2.26 Å vs. 2.17 Å, respectively).

To investigate the effect of the force field, we performed IMOMM[9] test calculations on the oxidative-addition transition states, using the MM3 force field to describe the MM region. IMOMM is a very similar scheme to ONIOM, the application here owing only to the availability of the MM3 force field. IMOMM single-point calculations on the ONIOM-optimized geometries reveal a greater preference

Fig. 3. The four principal UFF regions.

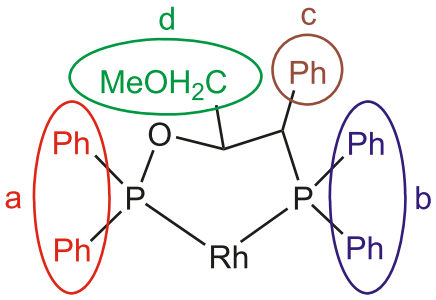

for the R-product (by 2.54 kcal/mol) and optimization at the IMOMM method still favours the R-product, but by 1.29 kcal/mol, representing a slight (0.59 kcal/mol) improvement over the ONIOM results. Whilst MM3 performs a better job than UFF in this system, the electronic effects of the ligands are still not sufficiently well-described. It is thus clear that, for this particular system, the reproduction of the critical experimental parameter, the enantiomeric excess, can only be accomplished by full DFT calculations, including geometry optimization,. It is nevertheless still possible to apply the DFT/MM approach to analyze the electronic effect of each of the regions of the system.[25]

Partitioning effects on the enantioselectivity

Given the problems, described above, with the DFT/MM partition originally applied, it was decided to carry out a detailed and systematic probe of the effect of changing the partitioning of the molecule on the relative energies of the R and S oxidative-addition transition states. The ONIOM method (and the UFF force field) was used for this study due to the easier program use than that of IMOMM, even though the MM3 force field is more accurate. The four principal UFF regions (phosphinite-phenyls (a), phosphine phenyls (b), backbone phenyl (c), and backbone methoxymethyl (d), see Fig. 3) in the initial partition system were systematically placed within the model system of the ONIOM calculation at the DFT level of theory. Single-point calculations were used to keep a consistent geometry, enabling an accurate assessment of the difference in both DFT and UFF brought about by changing the partitioning system.

Table 1 shows the changes in relative ONIOM extrapolated energies, DFT model energies, and UFF model energies for every possible partitioning of the molecule. It reveals that there is significant variation in the final ONIOM energy depending on the partitioning system used. Looking at the two components of the ONIOM energies, the DFT on the model section varies slightly, and the difference is mostly on the UFF component. The chemical relevance of this result is however dubious because of the different partitions used.

The most striking result from Table 1 is the large variation of the energetics. The simplest behaviour would have been a smooth variation between the –1.88 kcal/mol corresponding to the ONIOM calculation with the smallest QM region and the –4.15 kcal/mol corresponding to the full QM calculation. Instead, the energy differences between transition states leading to the R and S products oscillate widely within a range between –9.48 and +4.10 kcal/mol. To shed some light within this unexpected disarray, we decided to analyze the individual effect of each of the substituent blocks by assuming their contributions are additive.

We first computed the effect of the MM to QM replacement of each substituent from the original ONIOM calculation. To do this, we calculated the change in the R–S difference when introducing a given block in the QM region. For instance, the effect of the a substituents was estimated by the subtraction ΔEp(R–S)(a) – ΔEp(R–S)(original). The difference between –8.93 and –1.88 yielded a very large effect of –7.05 kcal/mol for the a block, the two phenyl substituents in the phosphinite centre. The corresponding values for the b, c, and d blocks, computed in a similar way, were +5.98, +1.17, and –1.89 kcal/mol, respectively.

We repeated then the same procedure starting from the full DFT calculation, labelled as abcd in Table 1. This means that we evaluated the effect of the a substituents by the subtraction ΔE_p(R–S)(abcd) – ΔE_p(R–S)(bcd). The resulting values for the a, b, c, and d blocks were in this case –5.56, +3.23, +0.18, and –0.51 kcal/mol, respectively.

The two procedures do not produce exactly the same values, because the effects of the blocks are not exactly additive, but the trends seem to be well-reproduced. It is clear that blocks a and b, the substituents on the phosphorous, have a large effect, above 3 kcal/mol each, and in opposite directions. The substituents on the backbone have a smaller effect, below 2 kcal/mol, but still significant for enantioselectivity calculations.

The analysis could be further refined by introduction of cross-terms, where the effect of having together two blocks in the QM region could be considered. These cross-terms could be easily computed from the results in Table 1, but a simple check shows that the cross-terms are always a minor correction, and their introduction would complicate the analysis of the chemical implications of the results.

Effect of phenyl substituents on phosphorous

The use of an MM or a QM representation of the phenyl substituents on the phosphorous atoms has a large effect on the computed enantiomeric excess. This effect is masked to a certain extent when the four phenyl substituents are considered as a block (ab calculation differs *only* by 1.83 kcal/mol from the original partition) because the a and b blocks have opposite effects, but it is very clear when one block is in the QM region and the other one in the MM region (a, b, ac, ad, bc, bd, acd, and bcd calculations).

The introduction of the a block in the QM region greatly favours (by –7.05 or –5.56 kcal/mol, depending on the estimation method) the transition state going to the R product. Inspection of the geometries in Fig. 2 shows no obvious steric differences associated to these particular phenyl substituents, so the difference is likely of an electronic nature. Bond distances around rhodium provide key information on the nature of these electronic effects. The Rh–P distances corresponding to the phosphinite side are 2.33 and 2.42 Å in **ONIOM-RMolH$_2$-TS** and **ONIOM-SMolH$_2$-TS**, respectively. The distance is 0.09 Å shorter for the structure leading to the R product because of the different trans influence of the substrate regions across the rhodium centre. In the R isomer, the position trans to phosphinite is occupied by the weakly coordinating carbonyl group, while it is occupied by the more strongly binding olefin group in the S isomer. The

Table 1. Effect of the partitioning system on the relative R and S oxidative-addition transition-state energies. Systems are labelled according to which UFF regions (see Fig. 3) are added to DFT.

Partitioning system	ΔEp(R–S) (ONIOM)	ΔEp(R–S) (DFT only)	ΔEp(R–S) (UFF only)
Original	–1.88	–6.45	+4.58
a	–8.93	–4.80	–4.13
b	+4.10	–5.11	+9.21
c	–0.69	–5.13	+4.44
d	–3.77	–7.93	+4.16
ab	–3.71	–3.57	–0.14
ac	–6.94	–2.96	–3.98
ad	–9.48	–4.78	–4.69
bc	+3.38	–5.62	+9.00
bd	+2.09	–6.94	+9.03
cd	–2.57	–6.98	+4.41
abc	–3.64	–3.58	–0.06
abd	–4.33	–3.88	–0.46
acd	–7.38	–3.23	–4.16
bcd	+1.41	–7.79	+9.21
abcd	–4.15	–4.15	—

introduction of the phenyl substituents in the QM region has an important effect on phosphorous basicity, because they are represented by hydrogen atoms in the QM part of the ONIOM calculation. This increase of basicity is much more stabilizing when a weaker ligand is in the trans position, which is the case for the transition state going to the R product. This is further confirmed by geometrical changes observed in the full DFT optimizations, also shown in Fig. 2. The corresponding Rh–P distances are reduced by 0.03 Å (from 2.33 to 2.30) when going from **ONIOM-RMolH$_2$-TS** to **DFT-RMolH$_2$-TS**, but are lengthened by 0.01 Å (from 2.42 to 2.43) when going from **ONIOM-SMolH$_2$-TS** to **DFT-SMolH$_2$-TS**. Therefore, use of the DFT description for the a region stabilizes the transition state leading to the R product, heavily favouring the formation of this product.

In view of the results for the a block, it is not surprising that introduction of the b block, the phenyl substituents on the phosphine side, to the QM region has an opposite effect, increasing the stability of the transition state going to the S product. The weakly coordinating carbonyl ligand is in a position trans to the phosphine in **SMolH$_2$-TS**, whereas the olefin is trans to the phosphine in **RMolH$_2$-TS**. Comparing the ONIOM- and DFT-optimized geometries, the Rh–P distances are unchanged (2.50 Å) going from **ONIOM-RMolH$_2$-TS** to **DFT-RMolH$_2$-TS**, but decrease by 0.01 Å (from 2.35 to 2.34) when going from **ONIOM-SMolH$_2$-TS** to **DFT-SMolH$_2$-TS**. Additionally in the S-transition states, the Rh–O distance increases by 0.02 Å (from 2.14 to 2.16) when comparing the respective ONIOM and DFT geometries. Thus, a DFT description of the phosphine stabilizes the S transition state and results in an increase of the amount of predicted S product.

A chemically relevant conclusion of this analysis is that the enantiomeric excess can be affected by modification of the electronic properties of the phosphorous donor groups, for instance by placing electron-releasing or electron-withdrawing substituents on the phenyl rings. Substituent electronic effects in asymmetric catalysis have recently been reviewed by Flanagan and Guiry.[26] Moreover, our results suggest that the electronic effects of the phosphorous donors on the enantiomeric excess should be opposite, depending on whether the modification is performed on the phosphinite phenyls or on the phosphine phenyls.

Effect of substituents on the backbone

The use of an MM or a QM representation of the backbone substituents (phenyl and methoxymethyl) has a smaller effect than that of the phosphorous phenyl substituents, but it is still large enough to have an important effect on the computed enantiomeric excess. In fact the difference can be as large as 1.89 kcal/mol between the original and the d partition schemes, which differ only in the QM or MM representation of the methoxymethyl group.

Again, inspection of the structures in Fig. 2 shows no obvious steric difference. The presence of direct electronic effects is in this case also hard to justify, because of the relative distance in terms of single bonds from the rhodium centre. The c group, a phenyl, is bound to an sp^3 carbon, which is bound to a phosphorous, which is only afterwards bound to rhodium. Also, the methoxymethyl group d is one single bond farther away from the metal. The key in this case seems to be in the conformational flexibility of the six-membered ring defined by the metal and the phosphine–phosphinite chelating ligand.

The ring has a clear boat conformation in **ONIOM-RMolH$_2$-TS**, but it is distorted towards a chair arrangement in **ONIOM-SMolH$_2$-TS**. The reasons for this behaviour are probably related to non-trivial steric interactions between the phosphorous phenyls and the substrate, but the relevant outcome for this discussion is that the backbone substituents occupy different positions. Phenyl c has a more axial-like arrangement in the structure going to the S product. The methoxymethyl group d is always equatorial, but points upwards (in Fig. 2 orientation) in **ONIOM-RMolH$_2$-TS,** and downwards in **ONIOM-RMolH$_2$-TS**. The electronic preference of the phenyl and methoxymethyl substituents for this different placements in the six-membered ring seems to be different from that of the hydrogen atoms used in the DFT/

MM calculation, and because of this, it is necessary to consider a full DFT description for a proper reproduction of the experimental results.

The analysis of the role of the backbone substituents is less conclusive than that of the phosphorous substituents because the interactions at play seem more subtle. However, there is also a chemically relevant message in the sense that, because of the conformational flexibility of the ligand, it is possible to affect the enantiomeric excess through modifications in the electronic effects of substituents that are relatively far away from the metal reaction centre.

Concluding remarks

The computational study of the addition of dihydrogen to methyl-(*N*)-acetylaminoacrylate catalyzed by a bidentate phosphine–phosphinite rhodium catalyst shows that the experimentally reported enantiomeric excess cannot be properly reproduced by hybrid QM/MM calculations. The degree of conformational flexibility in the system and the differing electronic nature of the two phosphorous donor groups are not well-described by MM methods, resulting in poor description of the experimental enantiomeric excess. A full DFT description must instead be applied in this case. Another option would be to use a method such as Q2MM, developed by Wiest, Norrby, and co-workers,[27] to generate a custom molecular mechanics force-field with all the MM parameters required to accurately describe this system. However, generation of accurate MM parameters via this method requires the creation of a representative training data set based on DFT optimizations of the rate-determining transition states in similar flexible systems with non-identical phosphorous donors, which is also not a trivial task. Moreover, we suspect that one of the reasons why force fields work better in other systems is because of their superior symmetry. With C_2, or C_s, chelating phosphines, the electronic effects on both phosphorus centers are compensated, which is not the case for intrinsically C_1 systems as the one discussed here.

Whilst the results of the DFT/MM methods are disappointing, the critical analysis of these results is highly informative on the chemical role of the different regions of the catalyst. The performance of a series of single-point calculations with different DFT/MM partitions leads to an explanation as to why each of the regions considered requires a QM description, and to a better understanding of its role on the overall chemistry of the system. In particular, we have characterized the following effects: (*a*) the presence of substituents increasing the basicity of the phosphinite centre favours the formation of the R product, (*b*) substituents increasing the basicity of the phosphine centre favour the formation of the S product, although by a lesser extent, and (*c*) substituents in the backbone have a smaller yet relevant role on selectivity, although their effect is not easy to predict a priori. These qualitative observations will guide us in the design of modifications of the catalytic system that will be studied in the near future by full DFT and experimental methods.

Acknowledgement

Ministerio de Ciencia e Innovación (MICINN) (Grants CTQ2005–02193/BQU, CTQ2008–00950/BQU, CTQ2008–06866-CO2–02/BQU), Departament d'Universitats, Recerca i Societat de la Informació (DURSI) (Grants 2005SGR225, 2005SGR715), Consolider Ingenio 2010 (CSD2006–0003), and the Institute of Chemical Research of Catalonia (ICIQ) Foundation are acknowledged for financial support.

References

(1) (a) Knowles, W. S. *Angew. Chem., Int. Ed.* **2002**, *41* (12), 1998. doi:10.1002/1521-3773(20020617)41:12<1998::AID-ANIE1998>3.0.CO;2-8.; (b) Noyori, R. *Angew. Chem., Int. Ed.* **2002**, *41* (12), 2008. doi:10.1002/1521-3773(20020617)41:12<2008::AID-ANIE2008>3.0.CO;2-4.; (c) Sharpless, K. B. *Angew. Chem., Int. Ed.* **2002**, *41* (12), 2024. doi:10.1002/1521-3773(20020617)41:12<2024::AID-ANIE2024>3.0.CO;2-O.

(2) (a) Christopherson, R. I.; Lyons, S. D.; Wilson, P. K. *Acc. Chem. Res.* **2002**, *35* (11), 961–971. doi:10.1021/ar0000509. PMID:12437321.; (b) Gallou, I.; Senanayake, C. H. *Chem. Rev.* **2006**, *106* (7), 2843–2874. doi:10.1021/cr050970a. PMID:16836302.

(3) (a) Xiong, R. G.; Zuo, J. L.; You, X. Z.; Abrahams, B. F.; Bai, Z. P.; Che, C. M.; Fun, H. K. *J. Chem. Soc. Chem. Commun.* **2000**, 2061.; (b) Green, M. M.; Cheon, K.-S.; Yang, S.-Y.; Park, J.-W.; Swansburg, S.; Liu, W. *Acc. Chem. Res.* **2001**, *34* (8), 672–680. doi:10.1021/ar010009l. PMID:11513575.; (c) Zech, G.; Kunz, H. *Chem. Eur. J.* **2004**, *10* (17), 4136–4149. doi:10.1002/chem.200400253.

(4) (a) Peri, R.; Padmanabhan, S.; Rutledge, A.; Singh, S.; Triggle, D. J. J. *Med. Chem.* **2000**, *43* (15), 2906–2914. doi:10.1021/jm000028l.; (b) Kumar, C. V.; Buranaprapuk, A.; Sze, H. C. *J. Chem. Soc. Chem. Commun.* **2001**, 297; (c) Nakagawa, H.; Kobori, Y.; Yoshida, M.; Yamada, K. *J. Chem. Soc. Chem. Commun.* **2001**, 2692.

(5) (a) Mallia, V. A.; Tamaoki, N. *Chem. Soc. Rev.* **2004**, *33* (2), 76. doi:10.1039/b106617j.; (b) Cornelissen, J. J. L. M.; Rowan, A. E.; Nolte, R. J. M.; Sommerdijk, N. A. J. M. *Chem. Rev.* **2001**, *101* (12), 4039–4070. doi:10.1021/cr990126i. PMID:11740926.; (c) Harmata, M. *Acc. Chem. Res.* **2004**, *37* (11), 862–873. doi:10.1021/ar030164v. PMID:15612676.

(6) (a) Landis, C. R.; Halpern, J. *J. Am. Chem. Soc.* **1987**, *109* (6), 1746–1754. doi:10.1021/ja00240a025.; (b) Brown, J. M. *Chem. Soc. Rev.* **1993**, *22* (1), 25. doi:10.1039/cs9932200025.; (c) Noyori, R. In *Asymmetric catalysis in organic synthesis*; John Wiley and Sons, Inc.: New York, 1994; p. 16; (d) Brown, J. M. In *Comprehensive asymmetric catalysis*; Vol. 1; Jacobsen, E. N., Pfalz, A., Yamamoto, H., Eds.; Springer: Berlin, 1999; p. 119.

(7) (a) Gridnev, I. D.; Imamoto, T. *Acc. Chem. Res.* **2004**, *37* (9), 633–644. doi:10.1021/ar030156e. PMID:15379579.; (b) Gridnev, I. D.; Imamoto, T.; Hoge, G.; Kouchi, M.; Takahashi, H. *J. Am. Chem. Soc.* **2008**, *130* (8), 2560–2572. doi:10.1021/ja076542z. PMID:18237166.; (c) Donoghue, P. J.; Helquist, P.; Wiest, O. *J. Org. Chem.* **2007**, *72* (3), 839–847. doi:10.1021/jo0619276. PMID:17253803.; (d) Heinrich, H.; Giernoth, R.; Bargon, J.; Brown, J. M. *J. Chem. Soc. Chem. Commun.* **2001**, 1296.

(8) (a) Ziegler, T. *Can. J. Chem.* **1995**, *73* (6), 743–761. doi:10.1139/v95-095.; (b) Ziegler, T. *J. Chem. Soc., Dalton Trans.* **2002**, (5): 642–652. doi:10.1039/b106126g.

(9) (a) Maseras, F.; Morokuma, K. *J. Comput. Chem.* **1995**, *16* (9), 1170–1179. doi:10.1002/jcc.540160911.; (b) Woo, T. K.; Cavallo, L.; Ziegler, T. *Theor. Chem. Acc.* **1998**, *100*, 307.

(10) (a) Svensson, M.; Humbel, S.; Froese, R. D. J.; Matsubara, T.; Sieber, S.; Morokuma, K. *J. Phys. Chem.* **1996**, *100*

(50), 19357–19363. doi:10.1021/jp962071j.; (b) Vreven, T.; Byun, K. S.; Komaromi, I.; Dapprich, S.; Montgomery, J. A.; Morokuma, K.; Frisch, M. J. *J. Chem. Theory Comput.* **2006**, *2* (3), 815–826. doi:10.1021/ct050289g.

(11) (a) Ujaque, G.; Maseras, F. *Struct. Bond.* **2004**, *112*, 117; (b) Balcells, D.; Maseras, F. *N. J. Chem.* **2007**, *31* (3), 333. doi:10.1039/b615528f.; (c) Bo, C.; Maseras, F. *Dalton Trans.* **2008**, (22): 2911–2919. doi:10.1039/b718076d. PMID:18493624.

(12) (a) Landis, C. R.; Hilfenhaus, P.; Feldgus, S. *J. Am. Chem. Soc.* **1999**, *121* (38), 8741–8754. doi:10.1021/ja991606u.; (b) Feldgus, S.; Landis, C. R. *J. Am. Chem. Soc.* **2000**, *122* (51), 12714–12727. doi:10.1021/ja0019373.; (c) Feldgus, S.; Landis, C. R. *Organometallics* **2001**, *20* (11), 2374–2386. doi:10.1021/om010060t.

(13) (a) Matsubara, T.; Koga, N.; Ding, Y.; Musaev, D. G.; Morokuma, K. *Organometallics* **1997**, *16* (5), 1065–1078. doi:10.1021/om960785a.; (b) Carbó, J. J.; Maseras, F.; Bo, C.; van Leeuwen, P. W. N. M. *J. Am. Chem. Soc.* **2001**, *123* (31), 7630–7637. doi:10.1021/ja0101678. PMID:11480985.

(14) (a) Balcells, D.; Maseras, F.; Lledós, A. *J. Org. Chem.* **2003**, *68* (11), 4265–4274. doi:10.1021/jo034052t. PMID: 12762725.; (b) Balcells, D.; Maseras, F.; Ujaque, G. *J. Am. Chem. Soc.* **2005**, *127* (10), 3624–3634. doi:10.1021/ja0435384. PMID:15755184.

(15) (a) Woo, T. K.; Fan, L.; Ziegler, T. *Organometallics* **1994**, *13* (6), 2252–2261. doi:10.1021/om00018a019.; (b) Guerra, G.; Cavallo, L.; Moscardi, G.; Vacatello, M.; Corradini, P. *J. Am. Chem. Soc.* **1994**, *116* (7), 2988–2995. doi:10.1021/ja00086a031.; (c) Musaev, D. G.; Froese, R. D. I.; Morokuma, K. *Organometallics* **1998**, *17* (9), 1850–1860. doi:10.1021/om9711032.; (d) Resconi, L.; Cavallo, L.; Fait, A.; Piemontesi, F. *Chem. Rev.* **2000**m, *100* (4), 1253–1346. doi:10.1021/cr9804691. PMID:11749266.

(16) Fernández-Pérez, H.; Pericàs, M. A.; Vidal-Ferran, A. *Adv. Synth. Catal.* **2008**, *350* (13), 1984–1990. doi:10.1002/adsc.200800311.

(17) Balcells, D.; Drudis-Solé, G.; Besora, M.; Dölker, N.; Ujaque, G.; Maseras, F.; Lledós, A. *Faraday Discuss.* **2003**, *124*, 429–441, discussion 443–455. doi:10.1039/b211473a. PMID:14527230.

(18) Rappe, A. K.; Casewit, C. J.; Colwell, K. S.; Goddard, W. A., III; Skiff, W. M. *J. Am. Chem. Soc.* **1992**, *114* (25), 10024–10035. doi:10.1021/ja00051a040.

(19) Mohamadi, F.; Richards, N. G. J.; Guida, W. C.; Liskamp, R.; Lipton, M.; Caufield, C.; Chang, G.; Hendrickson, T.; Still, W. C. *J. Comput. Chem.* **1990**, *11* (4), 440–467. doi:10.1002/jcc.540110405.

(20) Frisch, M. J.; Trucks, G. W.; Schlegel, H. B.; Scuseria, G. E.; Robb, M. A.; Cheeseman, J. R.; Montgomery, J. A., Jr.; Vreven, T.; Kudin, K. N.; Burant, J. C.; Millam, J. M.; Iyengar, S. S.; Tomasi, J.; Barone, V.; Mennucci, B.; Cossi, M.; Scalmani, G.; Rega, N.; Petersson, G. A.; Nakatsuji, H.; Hada, M.; Ehara, M.; Toyota, K.; Fukuda, R.; Hasegawa, J.; Ishida, M.; Nakajima, T.; Honda, Y.; Kitao, O.; Nakai, H.; Klene, M.; Li, X.; Knox, J. E.; Hratchian, H. P.; Cross, J. B.; Bakken, V.; Adamo, C.; Jaramillo, J.; Gomperts, R.; Stratmann, R. E.; Yazyev, O.; Austin, A. J.; Cammi, R.; Pomelli, C.; Ochterski, J. W.; Ayala, P. Y.; Morokuma, K.; Voth, G. A.; Salvador, P.; Dannenberg, J. J.; Zakrzewski, V. G.; Dapprich, S.; Daniels, A. D.; Strain, M. C.; Farkas, O.; Malick, D. K.; Rabuck, A. D.; Raghavachari, K.; Foresman, J. B.; Ortiz, J. V.; Cui, Q.; Baboul, A. G.; Clifford, S.; Cioslowski, J.; Stefanov, B. B.; Liu, G.; Liashenko, A.; Piskorz, P.; Komaromi, I.; Martin, R. L.; Fox, D. J.; Keith, T.; Al-Laham, M. A.; Peng, C. Y.; Nanayakkara, A.; Challacombe, M.; Gill, P. M. W.; Johnson, B.; Chen, W.; Wong, M. W.; Gonzalez, C.; Pople, J. A. *Gaussian 03*, Revision C.02; Gaussian Inc.: Wallingford CT, 2004.

(21) (a) Becke, A. D. *Phys. Rev. A* **1988**, *38* (6), 3098–3100. doi:10.1103/PhysRevA.38.3098. PMID:9900728.; (b) Lee, C.; Yang, W.; Parr, R. G. *Phys. Rev. B* **1988**, *37* (2), 785–789. doi:10.1103/PhysRevB.37.785.

(22) Andrae, D.; Häusserman, U.; Dolg, M.; Stoll, H.; Preuss, H. *Theor. Chim. Acta* **1990**, *77*, 123. doi:10.1007/BF01114537.

(23) (a) Ehlers, A. W.; Böhme, M.; Dapprich, S.; Gobbi, A.; Höllwarth, A.; Jonas, V.; Köhler, K. F.; Stegmann, R.; Veldkamp, A.; Frenking, G. *Chem. Phys. Lett.* **1993**, *208* (1-2), 111–114. doi:10.1016/0009-2614(93)80086-5.; (b) Höllwarth, A.; Böhme, M.; Dapprich, S.; Ehlers, A. W.; Gobbi, A.; Jonas, V.; Köhler, K. F.; Stegmann, R.; Veldkamp, A.; Frenking, G. *Chem. Phys. Lett.* **1993**, *208* (3-4), 237–240. doi:10.1016/0009-2614(93)89068-S.

(24) Hehre, W. J.; Ditchfield, R.; Pople, J. A. J. *Chem. Phys.* **1972**, *56*, 2257.

(25) (a) Barea, G.; Maseras, F.; Jean, Y.; Lledós, A. *Inorg. Chem.* **1996**, *35* (22), 6401–6405. doi:10.1021/ic960440k. PMID: 11666786.; (b) Maresca, O.; Maseras, F.; Lledós, A. *N. J. Chem.* **2004**, *28*, 625. doi:10.1039/b311926b.

(26) Flanagan, S. P.; Guiry, P. J. *J. Organomet. Chem.* **2006**, *691* (10), 2125–2154. doi:10.1016/j.jorganchem.2006.01.063.

(27) (a) Donoghue, P. J.; Helquist, P.; Norrby, P. O.; Wiest, O. *J. Chem. Theory Comput.* **2008**, *4* (8), 1313–1323. doi:10.1021/ct800132a.; (b) Donoghue, P. J.; Helquist, P.; Norrby, P. O.; Wiest, O. *J. Am. Chem. Soc.* **2009**, *131* (2), 410–411. doi:10.1021/ja806246h. PMID:19140780.

Aromaticity in pericondensed cyclopenta-fused polycyclic aromatic hydrocarbons determined by density functional theory nucleus-independent chemical shifts and the Y-rule — Implications in oil asphaltene stability

Yosadara Ruiz-Morales

Abstract: The characterization of the stability of the fused aromatic region (FAR) in oil asphaltenes in terms of kinetic and thermodynamic stability is primary. Such an understanding is important if we are to get the optimal use from the heavy fraction of any crude oil. The FAR region is composed of pericondensed cyclopenta-fused polycyclic aromatic hydrocarbon compounds (CPPAHs) with N, S, and O heteroatoms. The Clar model, which states that the most important representation of a PAH is one having the maximum number of disjoint π-sextets, depicted by inscribed circles, and a minimum number of fixed double bonds, captures the essence of the kinetic and thermodynamic stability arguments. This model is readily employed for complex aromatics of the sort to be considered for asphaltenes. In the present research we prove that the aromaticity of CPPAHs can be assessed by using the qualitative easy-to-apply Y-rule. In the literature, it is proven that the Y-rule is applicable to elucidate the aromaticity of benzenoid PAHs and it has been validated for pericondensed benzenoid PAHs but not for pericondensed CPPAHs. Here, we verify that it is applicable for CPPAHs. The applicability of the Y-rule has been theoretically proven by comparing the π-electronic distribution obtained with it with the one obtained from nucleus-independent chemical shift (NICS) calculations at the density functional theory (DFT) level. The importance of doing this is that due to the polydispersity in the composition of the oil asphaltenes, and to understand their aromatic core structure, it is necessary to be able to asses the aromaticity of many cyclopenta-fused PAHs (possibly more than 500), of different sizes (up to 15 rings between hexagons and pentagons), and different spatial rearrangements in a quick but realistic and effective way. To try to do this with NICS will be very time consuming and computationally expensive, especially in the case of big systems.

Key words: aromaticity, nucleus-independent chemical shifts (NICS), Y-rule, cyclopenta-fused PAHs, asphaltenes.

Résumé : En termes de stabilité cinétique et thermodynamique, la caractérisation de la stabilité de la région aromatique condensée (RAC) des asphaltènes d'huile est primaire. Une telle compréhension est important si on veut pouvoir faire un usage optimal de la fraction lourde des huiles brutes. La région aromatique condensée est formée d'hydrocarbures aromatiques polycycliques cyclopentaniques péri-condensés (HAP-CP) dans lesquels on retrouve des atomes d'azote, de soufre ou d'oxygène comme hétéroatomes. Le modèle de Clar qui spécifie que la représentation la plus importante d'un HAP est de posséder un nombre maximal de sextets π décrits par des cercles insérés et un nombre minimal de doubles liaisons fixes décrit l'essence des arguments de stabilité cinétique et thermodynamique. Ce modèle est facilement utilisable pour les produits aromatiques complexes de la sorte retrouvée dans les asphaltènes. Dans le présent travail, on montre que l'aromaticité des HAP-CP peut être évaluée en utilisant la règle-Y qui est facile à appliquer d'un point de vue qualitatif. Dans la littérature, il est prouvé que la règle-Y peut être utilisée pour élucider l'aromaticité de HAP benzénoïdes et elle a aussi été validée pour les HAP benzénoïdes péricondensés, mais pas pour les HAP-CP péricondensés. On vérifie donc ici qu'elle est aussi applicable à ces dérivés. L'applicabilité de la règle-Y a été démontrée d'une façon théorique en comparant la distribution électronique obtenue grâce à elle avec celle obtenue à partir de calculs de déplacements chimiques indépendants des noyaux (DCIN) au niveau de la théorie de la fonctionnelle de la densité. L'importance de cette démarche est que, en raison de la polydispersité dans la composition des asphaltènes de l'huile et afin de mieux comprendre leur structure aromatique fondamentale, il est nécessaire d'être capable d'évaluer l'aromaticité de plusieurs HAP-CP (possible plus de cinq cents), de tailles différentes (allant jusqu'à 15 noyaux hexagonaux ou pentagonaux) et d'arrangement spatial différent d'une façon rapide, mais réaliste et efficace. Il serait très long et d'un point de vue de temps de calcul très coûteux d'essayer de faire ces évaluations à l'aide de calculs DCIN.

Received 22 December 2008. Accepted 6 March 2009. Published on the NRC Research Press Web site at canjchem.nrc.ca on 24 August 2009.

This article is part of a Special Issue dedicated to Professor T. Ziegler.

Y. Ruiz-Morales. Programa de Ingeniería Molecular, Instituto Mexicano del Petróleo, Eje Lázaro Cárdenas Norte 152, México D.F. 07730, México. (e-mail: yruiz@imp.mx).

Mots-clés : aromaticité, calculs de déplacements chimiques indépendants des noyaux (DCIN), règle-Y, HAP condensés à des cyclopentanes, asphaltènes.

[Traduit par la Rédaction]

Introduction

Polycyclic aromatic hydrocarbons (PAHs) containing, by periannulation, at least one unsaturated five-membered ring, cyclopenta (CP) moiety, and fused to six-membered ring perimeters (CPPAHs) are important in several contexts.[1,2] CPPAHs are of considerable chemical importance and biological relevance. This stems from their identity as substructures of fullerenes and carbon nanotubes[3,4] and their potential to show unusual (photo)physical properties, e.g., facile (consecutive) one-electron reduction processes,[5] anomalous fluorescence,[6] and deviant aromatic character,[7] and, their presence, in charged form, in the interstellar medium.[8] UV–vis spectra are strongly modulated by the distribution and number of pentagons,[9,10] high electron affinities,[11,12] and characteristic up-field shifted ^{1}H NMR chemical shifts.[9,10,13] Theoretical interest follows from the role of CPPAHs as probes for the magnetic criteria of aromaticity, and they have been extensively investigated from this point of view.[14–18] In addition, CPPAHs were found to possess bioactivity.[19] This is of interest since CPPAHs have been identified as prevalent environmental pollutants that are invariably generated during incomplete combustion processes.[20]

Due to their biological activity, there is a need to assess the importance of CPPAHs as products of the incomplete combustion of hydrocarbon fuels.[21] CPPAHs have been observed as pyrolysis products of anthracene[22,23] and pyrene[24] and as combustion products of benzene,[25] ethylene flames,[26] and ethylenenaphthalene mixtures.[27] Wornat et al.[28] reported the identification of CPPAHs as products of the rapid pyrolysis of an Australian brown coal.

CPPAHs are also present in the fused aromatic ring region (FAR region) of oil asphaltenes. The asphaltenes[29] are a very important class of petroleum, impacting virtually all aspects of resource use. Optimization of production and processing of crude oils behooves proper chemical understanding of the asphaltenes. The vision of petroleomics, including establishment of structure–function relationships of crude oils and asphaltenes, mandates determination of asphaltene molecular structure. Nevertheless, many basic features of the molecular architecture of asphaltenes have been the subject of long debate.[29] The presence of asphaltenes have a negative impact on both the physical and chemical properties of heavy oils and increase the difficulties of crude oil utilization by impacting the processability of these heavy hydrocarbons. In catalytic processes, asphaltenes cause severe catalyst deactivaton.[30–35] Asphaltenes are defined in terms of a solubility classification, not by chemical structure, due to the difficulty of defining their structure experimentally. A widely used definition of petroleum asphaltenes is that they are the petroleum component that is insoluble in *n*-heptane and soluble in toluene.[30–35]

Asphaltenes are polycyclic aromatic compounds similar to the polycyclic aromatic hydrocarbons (PAHs) but containing heteroatoms (N, O, S), some in cyclopentafused rings, and alkyl side chains in their structure.[36] To understand the chemistry and aggregation of asphaltenes, it is essential to know the size and structure of their fused aromatic ring (FAR) region. The characterization of the stability of the FAR region in asphaltenes in terms of kinetic and thermodynamic stability is primary. The defining terms of pericondensed and catacondensed are subordinate to the stability considerations. Regarding geometry, the terms pericondensed versus catacondensed are generally used where pericondesation refers to single bridgehead carbons attached to three rings, while catacondensation refers to aromatic carbons shared by at most two rings. PAHs can be investigated by their characteristic electronic absorption and fluorescence emission spectra. The relation of these PAHs to crude oils and asphaltenes can be established. In particular, systematic rules governing the optical absorption spectra of PAHs in terms of the number of fused rings, their geometry, and their heteroatom content have been developed[37–40] but not in terms of the number of cyclopenta-fused rings.

To understand the optical properties of asphaltene PAHs, it is essential to determine their molecular geometry by measurement. This has been accomplished in part by carbon X-ray Raman spectroscopy.[41–43] It has been established that aromatic sextet carbon dominates asphaltene PAHs; this is most likely due to the significantly enhanced stability of sextet carbon over that of isolated double bond carbon (within the Clar representation).[37–40] The Clar model,[44,45] which states that the most important representation of a PAH is one having the maximum number of disjoint π-sextets (depicted by inscribed circles) and a minimum number of fixed double bonds, captures the essence of the kinetic and thermodynamic stability arguments enabling a simple heuristic for assessing stability. FARs with more sextet carbon are more aromatic and more kinetically and thermodynamically stable; that is, they gain in stability due to delocalization of π-electrons within the resonant sextets. FARs with increased isolated double bond carbon are much more reactive and unstable; that is, they are kinetically and thermodynamically less stable.

With asphaltene PAH geometry completely understood, it will be possible to decipher the known optical properties[46] of crude oils and asphaltenes. It has been shown that the major characteristics of the optical absorption and fluorescence emission spectra of asphaltenes are understandable in terms of PAHs with, most probably, seven fused rings and a distribution with four to ten rings.[46,47] Recently, the results of molecular orbital (MO) calculations on 523 selected benzenoid PAHs have been used to create an ensemble of possible asphaltene molecular structures.[48] These PAHs are selected in terms of having acceptable ratios of isolated double bond carbon to sextet carbon. However, it is still necessary to conclude on the distribution and size of the CPPAHs present in the FAR region of asphaltenes. For this, it is essential to be able to know the aromaticity of the CPPAH systems. For the

case of the benzenoid PAHs, the Clar representation or model is readily employed for complex aromatics of the sort to be considered for asphaltenes. We extended these concepts using a methodology with the simple sobriquet "the Y-rule".[37–39] The Y-rule establishes the most important and most kinetically and thermodynamically stable representation, in terms of π-sextets and double bonds, for any pericondensed *benzenoid* PAH. Regarding reactivity, it is well-known that a PAH is attacked at the position of the double bonds because it requires less energy to break these bonds than to break a π-sextet. Thus, the Clar structures found with the Y-rule also give information about where it is most likely that chemical reactivity would take place. These simple methods are tied to stability arguments and shown to yield asphaltene structures found experimentally.[46–48]

Previously, we verified theoretically the performance of a proposed modification of the basic postulates of the Clar aromatic sextet theory, called the Y-rule,[37–39] which determines the relative aromaticity of each hexagonal ring in pericondensed benzenoid polycyclic aromatic hydrocarbons (peri-PAHs). The Y-rule for constructing Clar-type aromatic sextet formulas for benzenoid peri-PAHs was also examined, and the limits of its applicability were established.[40] The π-electronic distribution obtained by the Clar sextet principle (or model) as determined by the Y-rule was compared with the π-electronic distribution obtained from nucleus-independent chemical shift (NICS) calculations for various series of benzenoid peri-PAHs.[39] The NICS values were used to assess the relative aromaticities of the individual rings in the peri-PAH compounds. It was found that the simple heuristic Y-rule predicts for all the calculated systems the same relative aromaticities given by the NICS calculations, and for the case of peri-systems with very high symmetry (like the compact peri-PAHs) it reinforces the picture derived from the NICS calculations. In these cases, the NICS results can be complex due to symmetry. The advantages of the qualitative Y-rule are that it is of particular importance for the case of large peri-PAHs, as it takes few minutes to be applied following a very easy methodology, and it provides a quick answer about the aromaticity and location of the resonant sextets in peri-PAH compounds without having to carry out theoretical chemistry calculations that take time and that can be costly depending on the size of the system.

The aromaticity of benzenoid PAHs has been highly studied. The widely used notion of the aromatic sextet is usually attributed to Armit and Robinson,[49] but was originally introduced in 1922 by Crocker.[50] Clar[44,45] employed the notion of the aromatic sextet to account for the aromaticity of PAHs by studying their reactivity, NMR properties, and UV spectra and combining the experimental facts with his intuition. The quantitative criteria commonly used to assess the aromaticity of molecules are based on energetic, geometric, and magnetic properties.[51–61] Energetic criteria are based on homodesmotic,[62] isodesmic,[63] or isomerization reactions.[64] Greater bond-length alternation is assumed to be associated with a decrease in aromatic character. Geometric treatments such as HOMA[54–56] (harmonic oscillator model of aromaticity) are typically used to deduce the degree of aromaticity from bond distances. Magnetic criteria also are quite effective in discerning aromaticity, as the ability to sustain a diatropic ring current is the defining characteristic of aromatic species.[57–59] The use of NICS, "nucleus-independent chemical shift," as a measure of aromaticity is straightforward and well-established.[50,51,65] It has already been demonstrated in the literature[39,66–72] that the NICS values represent strong theoretical support for Clar's picture of aromatic π-sextets.

If one considers that asphaltenes are essentially stable for geologic time, then unstable aromatic structures are ruled out. The optical absorption spectra of asphaltenes exhibit an exponential decrease in the neighborhood of 650 nm, showing that large graphitic structures with very low energy electronic absorption do not constitute a significant component of the asphaltene fraction. Likewise, asphaltene fluorescence emission spectra, which exhibit significant intensity in the range of 400–650 nm, reflect the nature and type of FAR structures present in asphaltenes. However, this optical absorption and emission data when considered alone has limited use in particular for the determination of aromatic structures. The utility of this data is greatly expanded when comparing it with the aromaticity for the many possible candidates, pericondensed CPPAHs, for asphaltenes. Understanding the implications of different ring geometries and sizes on stability also provides essential information about governing heuristics for the asphaltene aromatics.[37,38]

To understand the number of rings (in terms of the ratio of five-member rings and six-member rings), size, and geometry of the cyclopenta-PAHs present in the aromatic region of the asphaltenes it is necessary to understand their stability, which is directly related to their aromaticity and in turn to the observed optical properties of asphaltenes. In previous studies,[37,38,46–48] we found that the stability and reactivity of asphaltene molecules is closely associated to the stability and reactivity of their benzenoid polycyclic aromatic hydrocarbon core. We systematically analyzed the relationship between the structure of PAH isomers and the number of resonant sextets present. The number of resonant sextets in the structure is closely related to the HOMO–LUMO gap magnitude and thus to the observed optical properties of asphaltenes. Due to the polydispersity in the composition of the oil asphaltenes it is important to be able to assess the aromaticity of many cyclopenta-PAHs, of different sizes and spatial rearrangements, in a quick but realistic and effective way.

The goal of the present work is to verify the applicability of the Y-rule to pericondensed cyclopenta-fused polycyclic aromatic hydrocarbons by comparing the π-electronic distribution obtained with it with the one obtained from nucleus-independent chemical shift (NICS) calculations for various neutral CPPAHs. The advantages of the qualitative Y-rule are that it is of particular importance for the case of large peri-PAHs, it takes few minutes to be applied following a very easy methodology, and it provides a quick answer about the aromaticity and location of the resonant sextets in peri-PAH compounds without having to carry out theoretical chemistry calculations that take time and that can be costly depending on the size of the system. Therefore, if the Y-rule is applicable to CPPAHs then it will be used in a following investigation to asses the aromaticity of more than 500 CPPAHs from four to fifteen rings and to withdraw conclu-

sions of the size and stability of the CPPAHs in asphaltenes by comparing with the optical properties of asphaltenes.

In the section named "Results and discussion" a detail discussion on the Y-rule and its application and on the definition of NICS will be provided.

Computational details

We studied 25 neutral pericondensed cyclopenta-fused polycyclic aromatic hydrocarbons (peri-CPPAHs). The structure optimization of the CPPAH systems was done by performing quantum density functional theory (DFT) calculations. The self-consistent generalized gradient GGA with the exchange-correlation potential of Perdew–Wang 91[73] was used along with the DNP basis set (triple ζ numerical basis set)[74] with a radial cut off of 3.7 Å; as implemented in the DMol3 code.[74–76] The DNP basis uses double-numeric quality basis set; approximately two atomic orbitals for each one occupied in free atom, with polarization functions, i.e., functions with an angular momentum of one higher than that of the highest occupied orbital in the free atom. The size of the DNP basis sets are comparable to 6-31G** sets.[77] However, the numerical basis set is much more accurate than a Gaussian basis set of the same size.

The nucleus-independent chemical shift (NICS) calculations were carried out using the GIAO-DFT[78,79] method as implemented in the Gaussian 98[77] package using the optimized structures. A dummy atom was located on the molecular plane at the geometrical center of each hexagon in the CPPAH structures to calculate the NICS(0). The Becke's 1988 functional,[80] which includes the Slater exchange along with corrections involving the gradient of the density was used together with the correlation functional of Lee, Yang, and Parr,[81] which includes both local and nonlocal terms, i.e., B3LYP functional was used. It is well-known that the shielding tensor and NICS are very sensitive to the quality and size of the basis set used.[82,83] Schleyer and co-workers[60,61,68,71] recommend the use of the 6-31G(d) basis. However, a sufficiently large basis is needed for an accurate description of the chemical shift. Therefore, we used a basis set that is augmented with two sets of polarization functions, i.e., the 6-31G(d, p) or 6-31G** basis set.[77]

In some figures we use a combination of an Arabic number with a Roman number. The Arabic number corresponds to the number of the structure and the Arabic number corresponds to the several Clar-type structures of that CPPAH.

Results and discussion

Nucleus-independent chemical shift (NICS)

The nucleus-independent chemical shift (NICS) was introduced by Schleyer et al.[60] in 1996 as a new aromatic index, which is defined as the negative value of the absolute isotropic magnetic shielding at some selected point in space, e.g., at the center of a ring that is being probed, NICS(0), or one angstrom above the geometrical center of the ring that is being probed, NICS(1). The NICS data are reported with the reverse signs to conform to the NMR chemical shift signs conventions (negative upfield and positive downfield). Significant negative (i.e., magnetically shielded) NICS values in interior positions of rings or cages indicated the presence of induced diatropic ring currents or "aromaticity" whereas positive values (i.e., deshielded) at each position denote paratropic ring currents and "antiaromaticity".[60] The NICS criterion is now widely applied[65,69] in many ab initio and density functional studies, which have demonstrated that NICS is a useful indicator of aromaticity and generally correlates well with the energetic, geometric, and magnetic criteria for aromaticity.[65,70]

The diamagnetic contribution, which is negative in the NICS convention, stems from the circulation of ground state density (diatropic or diamagnetic current) originated from the coupling of occupied CC(π) and CH molecular orbitals by the applied magnetic field. On the other hand, the paramagnetic contribution, which is positive in the NICS convention, stems from the circulation of current density (paratropic or paramagnetic current) originated from the coupling of occupied and virtual CC(σ) molecular orbitals by the applied magnetic field.[39]

Fig. 1. Studied bowl-shaped or curved pericondensed cyclopenta-fused polycyclic aromatic hydrocarbons (bowl-shaped CPPAHs).

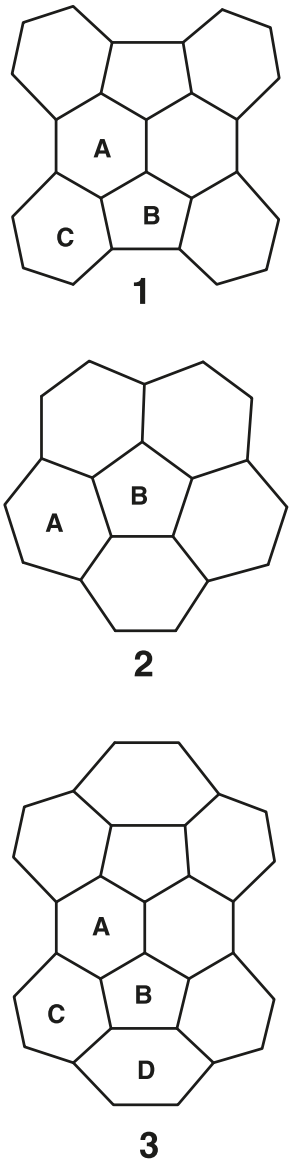

Fig. 2. Studied planar pericondensed cyclopenta-fused polycyclic aromatic hydrocarbons (planar CPPAHs).

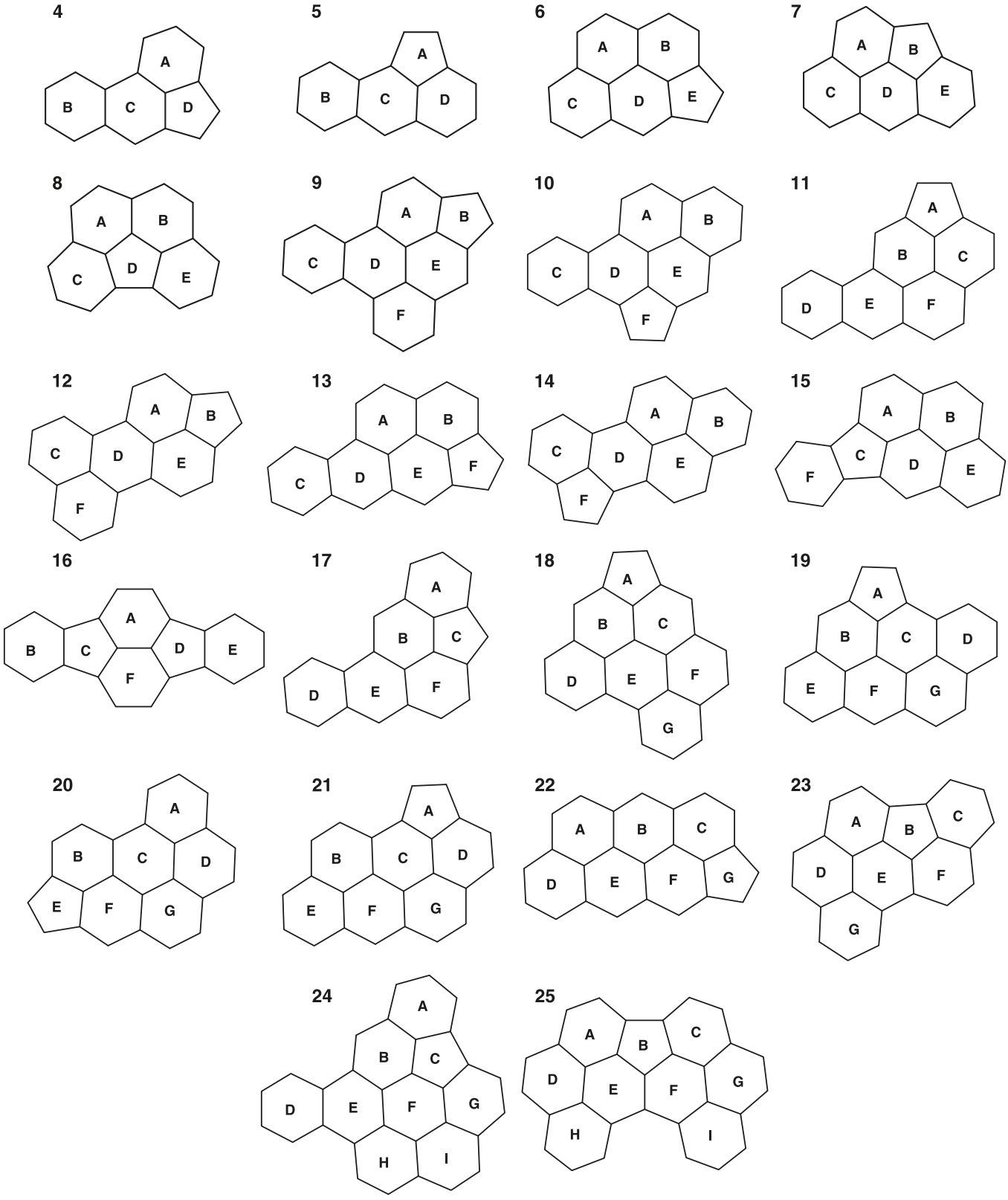

The Y-rule in identifying Clar-type structures

Recently, a modified version of the Clar theory has been proposed.[37–39] The new approach was applied to numerous benzenoid PAHs and its surprisingly good agreement with other, more sophisticated, theoretical assessments of local aromaticity (in particular, the Schleyer's NICS values, cf. refs. 60, 65, 68, and 84) was extensively discussed. On the other hand, some general features of the new method, in-

Table 1. Calculated NICS(0) for the bowl-shaped or curved CPPAHs presented in Fig. 1.

CPPAH number	*n*FAR[a]	Formula	Name	NICS(0) in each ring			
				A	**B**	**C**	**D**
1	8FAR	$C_{26}H_{12}$		–5.6[b]	+3.9b[b]	–10.0[b]	
2	6FAR	$C_{20}H_{10}$	Dibenzo[*ghi,mno*]fluoranthene or corannulene	–7.3 (–8.6)[b]	+9.6 (+7.6)[b]		
3	10FAR	$C_{30}H_{12}$		–6.5[b]	+6.8[b]	–9.4[b]	–8.1[b]

[a]Number of total fused aromatic rings (*n*FAR).

[b]Reference 86.

cluding the limits of its applicability, have been established.[40] The new version of the Clar theory is named "the Y-rule". The Y-rule applies to benzenoid PAHs possessing carbon atoms that simultaneously belong to three hexagons. Such carbon atoms are usually referred to as "internal" or also "Y-carbons". Benzenoid PAHs containing internal carbon atoms are classified as perifusenes or pericondensed (in contrast to catafusenes or catacondensed that, by definition, do not possess internal carbon atoms).

In both the original formulation of the Clar theory and its several later variants, sextets of π-electrons are located in particular hexagons of the benzenoid molecule, indicating domains of increased π-electron contents and (or) local aromaticity. The Y-rule offers a new, original, and easy-to-apply criterion for locating aromatic sextets in pericondensed benzenoids.

The Y-rule is formulated as follows:

> (*a*) The aromatic sextets are to be located so as to cover all internal carbon atoms. If not all Y-carbon atoms can be covered by aromatic sextets, then the highest possible Y-carbons must be covered.
>
> (*b*) Provided condition (*a*) is obeyed, the number of aromatic sextets must be as large as possible.
>
> (*c*) If several Clar-type structures satisfy conditions (*a*) and (*b*), then the one with the highest symmetry, provided such exists, is chosen, i.e., considered as most important.
>
> (*d*) If the Clar-type structure obtained by means of requirements (*a*), (*b*), and (*c*) is unique, then it is expected to represent the basic features of the π-electron distribution, and local aromaticity.
>
> (*e*) If there are several Clar-type structures obeying the requirements (*a*), (*b*), and (*c*), then the conclusions about π-electron distribution, and local aromaticity are drawn from their superposition.

The details and many examples on the application of the Y-rule are exemplified in ref. 39 and will not be discussed here in great detail.

The π-electronic distribution for CPPAHs obtained by the Clar sextet principle as determined by the Y-rule and NICS(0) calculations

In Fig. 1 and Fig. 2 the studied pericondensed cyclopentafused polycyclic aromatic hydrocarbons (CPPAHs) are presented. The letters in the structures in these figures are for identifying each ring and refer to the information given in Table 1 and Table 2. Table 1 lists the values of the calculated NICS(0) for bowl-shaped or curved CPPAHs, presented in Fig. 1, while Table 2 lists the values of the calculated NICS(0) for planar CPPAHs, presented in Fig. 2. A total of 25 CPPAHs are studied.

As mentioned in the "Computational details" section, the geometry optimization structure of the CPPAH systems was done by performing quantum density functional theory (DFT) calculations. In Fig. 3 the comparison between the calculated and the experimental X-ray structure for compound **2** is displayed. As it can be seen in Fig. 3, there is a good agreement between the calculated bond distances and the experimental data. The differences in bond lengths are not greater than 0.022 Å.

The π-electronic distribution for bowl-shaped or curved CPPAHs obtained by the Clar sextet principle as determined by the Y-rule and NICS(0) calculations

Table 1 lists the values of the calculated NICS(0) for bowl-shaped or curved CPPAHs, presented in Fig. 1. We calculated the NICS(0) for corannulene, **2**, but the data for compounds **1** and **3** were obtained from the literature.[86] Also, for compound **2** we obtained NICS(0) data from the literature,[86] and compared it with our calculated data. Two different NICS(0) values are obtained for corannulene, **2**, that correspond to the rings labeled A and the rings labeled B. The calculated NICS(0) compares well with the reported data for **2**, see Table 1, and the differences stem from the fact that the optimization of the structures in ref. 86 for compounds **1**, **2**, and **3** were calculated with the semiempirical AM1 method and the basis set used for the NICS calculation was less accurate, 6-31G*.[86] However, the general tendency and conclusion on the aromaticity for compound **2** is the same.

From the total NICS values presented in Table 1, and as proposed by Schleyer et al.,[60] see the section titled "Nucleus-independent chemical shift (NICS)" and in ref. 39, we consider that the highest negative NICS(0) in each structure corresponds to the presence of a sextet in that given ring. Therefore, for compound **1,** which contains 26 π-electrons and a total of eight fused rings (8FAR), the sextets are located in the rings labeled as C, NICS(0)= –10.0, giving a total of four resonant sextets that comprise 24 π-electrons, see Fig. 1 and Fig. 4. Thus, the remaining two π-electrons are located in the rings A and no density is presented in rings B, which have a positive NICS(0) value, +3.9, see Table 1. When distributing the double bonds, taking care of not exceeding the valence of any of the carbon atoms, it is only possible to locate one double bond in the A-hexagons. Therefore, the π-density in the A-hexagons involves a double bond that is right at the junction of the A-rings, see Fig. 4.

Table 2. Calculated NICS(0) for the planar CPPAHs presented in Fig. 2.

CPPAH number	*n*FAR[a]	Formula	Name	NICS(0) in each ring								
				A	**B**	**C**	**D**	**E**	**F**	**G**	**H**	**I**
4	4FAR	$C_{16}H_{10}$	Acephenanthrene or cyclopenta[*jk*]phenanthrene	–8.20	–9.64	–5.50	+3.15					
5	4FAR	$C_{16}H_{10}$	Aceanthrylene or cyclopenta[*de*]anthracene	+4.41	–8.18	–10.27	–7.11					
6	5FAR	$C_{18}H_{10}$	Cyclopenta[*cd*]pyrene	–4.60	–10.72	–10.97	–4.17	+4.13				
7	5FAR	$C_{18}H_{10}$	Benzo[*mno*]aceanthrylene	+4.91	+7.92	–3.67	–8.00	–5.43				
8	5FAR	$C_{18}H_{10}$	Benzo[*ghi*]fluoranthene	–7.39	–7.39	–7.93	+7.26	–7.93				
9	6FAR	$C_{22}H_{12}$	Benzo[*l*]cyclopenta[*cd*]pyrene	–9.43	+4.03	–8.74	–0.92	–4.43	–10.27			
10	6FAR	$C_{22}H_{12}$	Indeno[5,6,7,1-*defg*]chrysene	–6.00	–10.75	–10.08	–9.68	–2.58	+4.10			
11	6FAR	$C_{22}H_{12}$	Benzo[*def*]cyclopenta[*qr*]chrysene	+4.40	–5.26	–9.81	–10.14	–9.84	–2.44			
12	6FAR	$C_{22}H_{12}$	Cyclopenta[*cd*]perylene	–5.83	+1.86	–7.50	+4.89	–5.83	–7.50			
13	6FAR	$C_{22}H_{12}$	Indeno[1,7,6,5-*cdef*]chrysene	–5.94	–10.46	–10.10	–9.80	–2.29	+3.87			
14	6FAR	$C_{22}H_{12}$	Indeno[1,7-*ab*]pyrene	–6.62	–11.64	–8.04	–8.62	–2.42	+4.88			
15	6FAR	$C_{22}H_{12}$	Indeno[1,2,3-*cd*]pyrene	–10.93	–4.68	+4.94	–4.41	–11.51	–6.75			
16	6FAR	$C_{22}H_{12}$	Indeno[1,2,3-*cd*]fluoranthene	–4.47	–4.92	+9.42	+9.42	–4.92	–4.47			
17	6FAR	$C_{22}H_{12}$	Phenanthro[10,1,2,3-*cdef*]fluorene	–6.38	–7.97	+6.18	–8.26	–1.46	+3.72			
18	7FAR	$C_{24}H_{12}$	Indeno[5,6,7,1-*pqra*]perylene	+4.28	–4.54	–10.13	–9.85	+1.59	–6.02	–10.88		
19	7FAR	$C_{24}H_{12}$	Benz[*mno*]indeno[5,6,7,1-*defg*]chrysene	+4.43	+1.75	–8.69	–12.19	–11.51	–9.32	–2.23		
20	7FAR	$C_{24}H_{12}$	Benzo[*ghi*]cyclopenta[*cd*]perylene	–10.69	–9.12	+0.95	–5.74	+3.25	–4.60	–10.71		
21	7FAR	$C_{24}H_{12}$	Dibenzo[*def,mno*]cyclopenta[*hi*]chrysene	+5.75	–2.10	–7.86	–9.69	–11.35	–8.72	–1.78		
22	7FAR	$C_{24}H_{12}$	Benz[*mno*]indeno[1,7,6,5-*cdef*]chrysene	–2.14	–9.23	–11.16	–11.48	–8.63	–1.75	+4.24		
23	7FAR	$C_{24}H_{12}$	Acenaphtho[1,2,3-*cde*]pyrene	–10.03	+7.34	–7.62	–4.56	–2.32	–6.98	–11.14		
24	9FAR	$C_{30}H_{14}$	Dibenz[*e,ghi*]indeno[1,2,3,4-*pqra*]perylene	–7.38	–8.49	+8.96	–8.04	+1.20	–0.68	–9.27	–10.58	–3.92
25	9FAR	$C_{30}H_{14}$	Dibenzo[*mn,qr*]fluoreno [2,1,9,8,7-*defghi*]naphthacene	–9.56	+8.59	–9.56	–4.05	–2.17	–2.17	–4.05	–11.10	–11.10

[a]Number of total fused aromatic rings (*n*FAR).

Fig. 3. Comparison between the calculated and the experimental X-ray structure (values in parenthesis are from ref. 85) for corannulene, compound **2**.

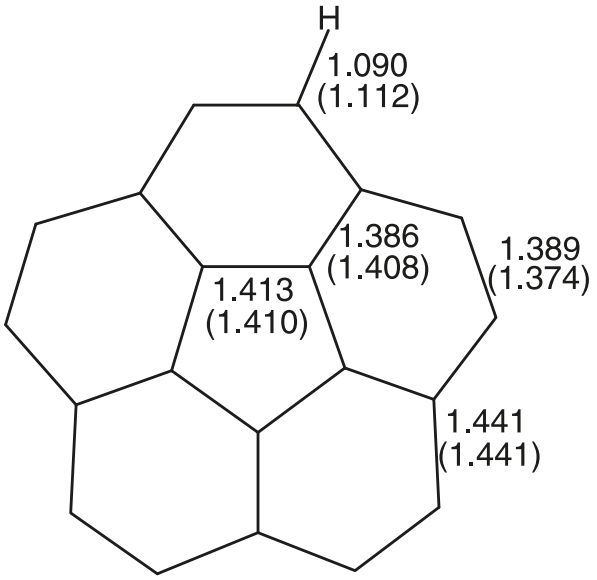

The application of the Y-rule to compound **1** is presented in Fig. 5. The CPPAH **1** presents a total of six Y-carbons or internal carbons, which are highlighted in bold in Fig. 5. There are two possibilities to accommodate as many as possible π-electrons in sextets covering all the Y-carbons and without overcoming the carbon atoms valence. These two possibilities are shown in Fig. 5 and are labeled as **1**-**I** and **1**-**II**. The solid circles and the open circles represent aromatic resonant sextets in both cases. Following the Y-rule enunciate (e), see above, the pictorial superposition of both distributions, **1**-**I** and **1**-**II**, shown as **1**-**III** is equivalent to the distribution **1**-**IV**. Because it cannot be possible to have simultaneous adjacent sextets without overcoming carbon atoms valences, then there is a double bond right at the junction of the A-hexagons, as shown in structure **1**-**IV**. The π-electronic distribution given by the NICS(0), Fig. 4, for compound **1** agrees with the distribution obtained with the Y-rule and presented as **1**-**IV** in Fig. 5.

Compound **2** has a total of 20 π-electrons and a total of six fused aromatic rings (6FAR), and according to the NICS(0) results, see Table 1 and Fig. 1, the sextets are located in all the external hexagonal rings, as shown in **2**-**I** in Fig. 4. However, there cannot be simultaneously adjacent sextets without overcoming the carbon atoms valence. Therefore, the structure **2**-**II**, in Fig. 4, where there is a double bond right at the junction of the external hexagons, is more appropriate and explains the obtained NICS(0).

Four different Clar-type structures are found for compound **2** by applying the Y-rule, which are presented in Fig. 6, named **2**-**I**, **2**-**II**, **2**-**III**, and **2**-**IV**. Compound **2** has a total of five Y-carbons or internal carbons that are highlighted in bold in Fig. 6. For CPPAH **2** it is not possible to cover all the Y-carbons with resonant sextets without exceeding the carbon atoms valence. In each of the four Clar-type structures there is one Y-carbon atom that is not covered by sextet. The pictorial superposition of the four Clar-type structures provides structure **2**-**V,** which is equivalent to the structure **2**-**VI**, see Fig. 6. The π-electronic distribution given by the NICS(0), Fig. 4, for compound **2** agrees with the distribution obtained with the Y-rule and presented as **2**-**VI** in Fig. 6.

Fig. 4. π-Electronic distribution obtained with NICS(0) for bowl-shaped CPPAHs.

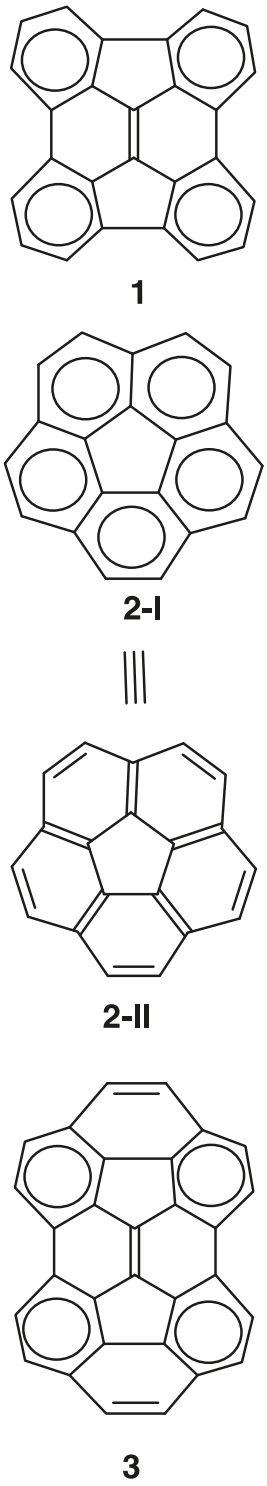

The CPPAH **3** has a total of thirty π-electrons and a total of ten fused aromatic rings (10FAR). According to the

Fig. 5. π-Electronic distribution obtained with the Y-rule for the bowl-shaped CPPAH compound **1**.

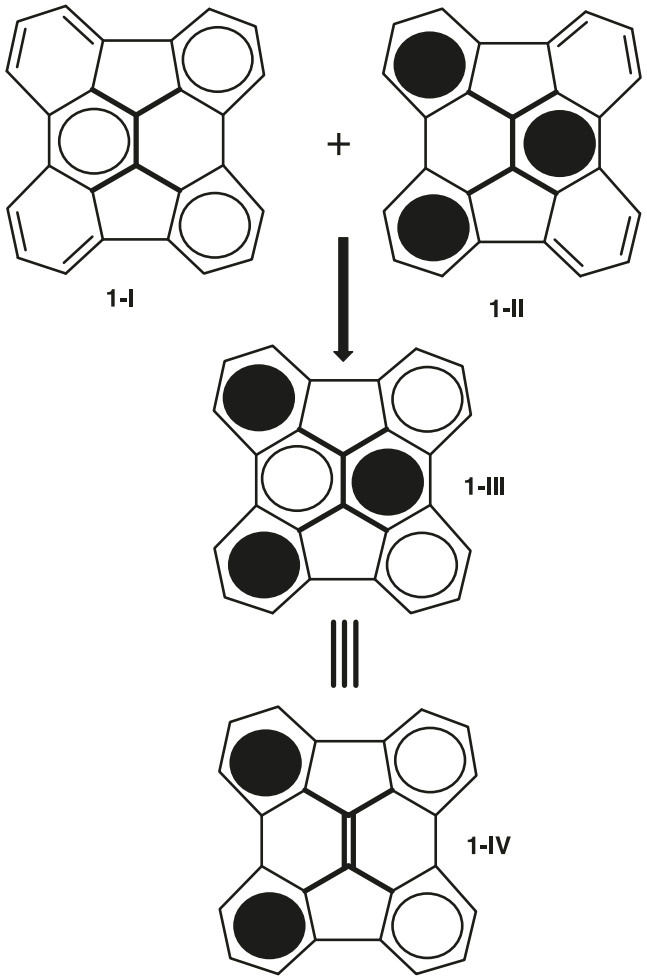

NICS(0) results, see Table 1 and Fig. 1, the sextets are located in the C-hexagons, which have the highest NICS(0) value, –9.4, giving a total of four resonant sextets. The remaining six π-electrons are located in rings A and D, see Fig. 1 and Fig. 4. The B-rings have a positive NICS(0) value, +6.8; thus, they have no electron density.

The π-electronic distribution obtained by the Y-rule for CPPAH **3** is presented in Fig. 7. Compound **3** has a total of ten Y-carbons highlighted in bold in Fig. 7. For this compound it is not possible to cover all the Y-carbons with resonant sextets without overcoming carbon atoms valence. Two Y-carbons are not covered by sextets. In Fig. 7 several Clar-type structures with three resonant sextets each are presented as **3-1** to **3-VIII**, however, the only one structure that covers all the Y-carbons, except two, and presents the highest possible number of resonant sextets is the Clar-type structure **3-IX**, thus, this is the π-electronic distribution obtained with the Y-rule. Again, the π-electronic distribution obtained with the Y-rule agrees with the one obtained with the NICS calculation, see Fig. 4 and Fig. 7.

For the case of all the studied bowl-shaped CPPAHs, the π-electronic distribution obtained with the Y-rule agrees with the π-electronic distribution obtained with the NICS(0) calculation.

Fig. 6. π-Electronic distribution obtained with the Y-rule for the bowl-shaped CPPAH compound **2**, corannulene.

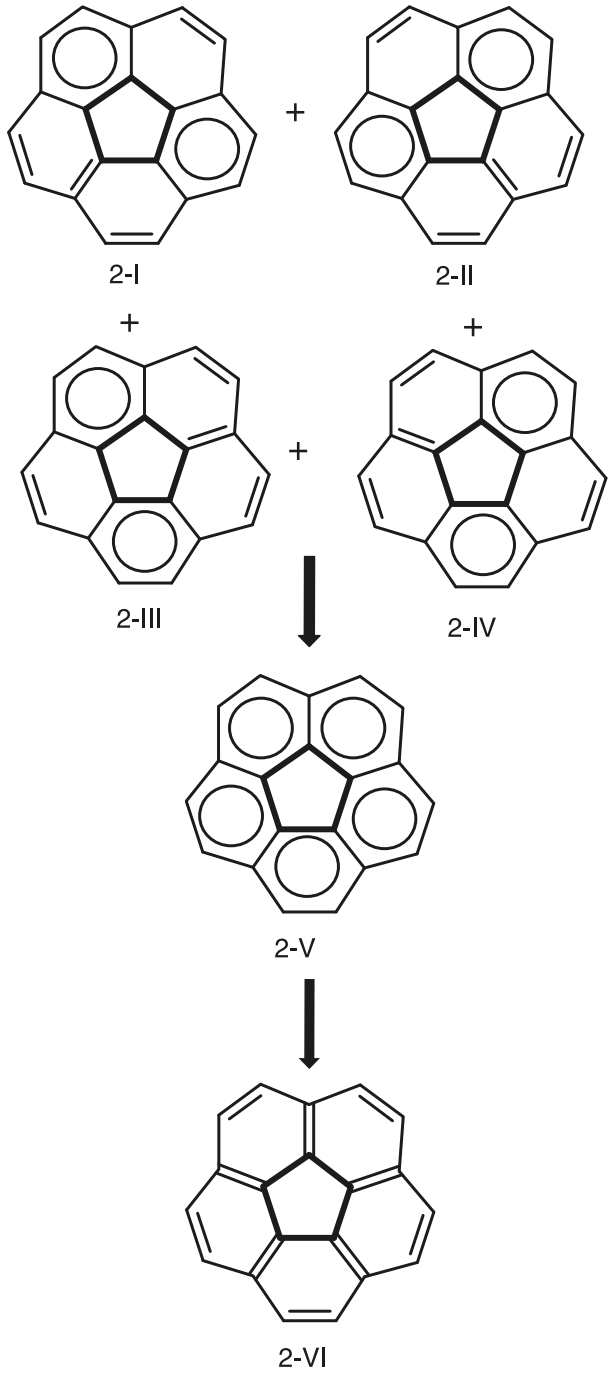

The π-electronic distribution for planar CPPAHs obtained by the Clar sextet principle as determined by the Y-rule and NICS(0) calculations

In this section, the π-electronic distribution in planar CPPAHs with a total of fused rings from 4FAR to 9FAR, and with 16–30 π-electrons, is presented. This section follows the same principles as those explained in the former sections, therefore, in this section we will discuss only some particular cases in detail but not all cases.

In Table 2, the calculated NICS(0) values for the planar CPPAHs shown in Fig. 2 are presented. In general, it is ob-

Fig. 7. π-Electronic distribution obtained with the Y-rule for the bowl-shaped CPPAH compound **3**.

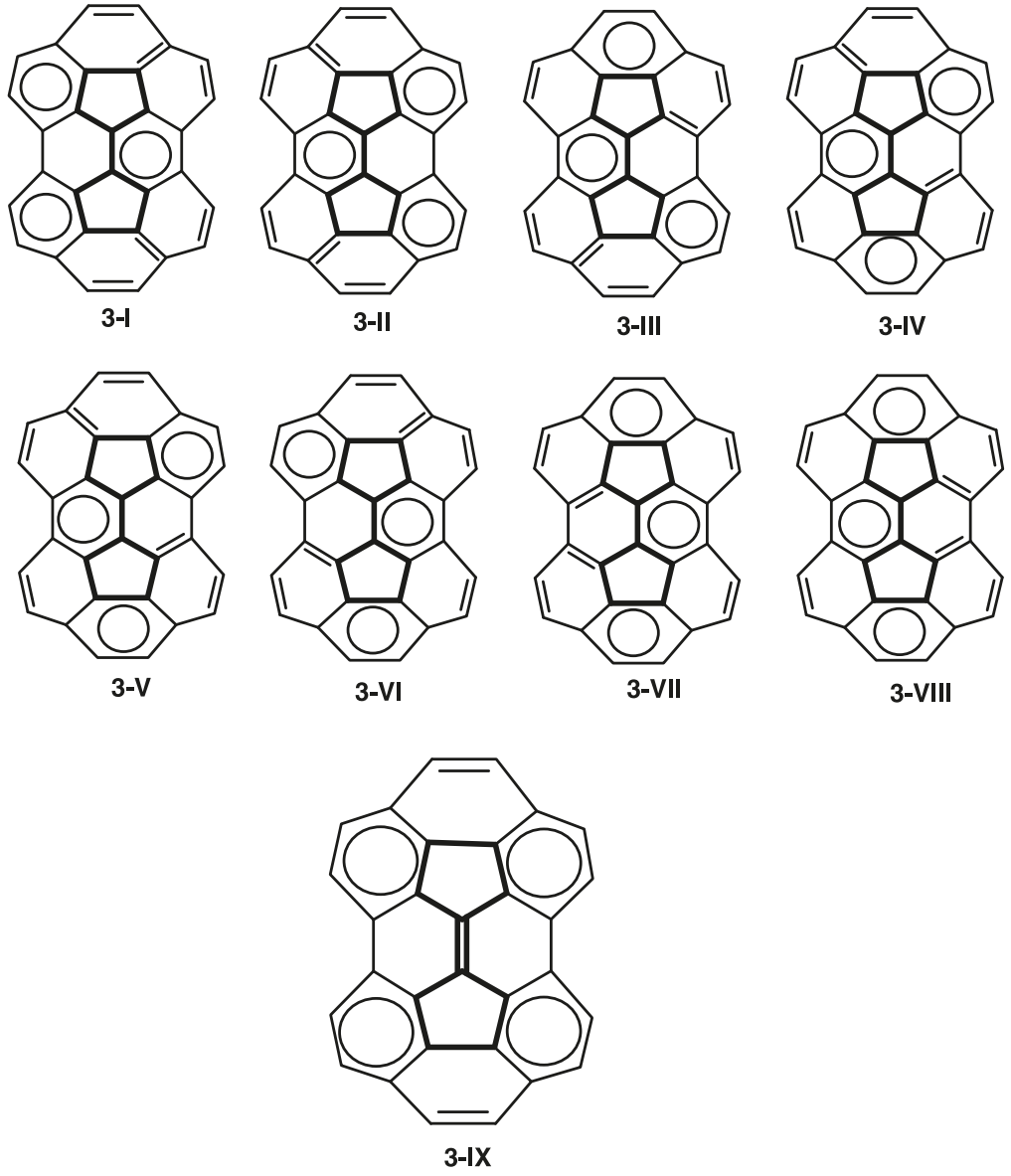

served that six-membered rings vicinal to a five-member ring are less aromatic than those not directly connected to a five-member ring, which is in agreement with data reported in the literature,[7,86] see, for example, data for compounds **12** and **15**. An analysis of the NICS values given in Table 2, as done in the former section, provides the Clar-type structures shown in Fig. 8 (for labels, see Fig. 2).

The arrow shown in Fig. 8, see structures **10**–**13**, means that there is sextet migration[39,45] between the signaled hexagons because their NICS(0) values are too close or are too close to the highest NICS(0) in the molecule to discern where the sextet is located. In the case of structures **8**, **12**, **16**, **19**, **21**–**23**, and **25**, see Fig. 8, the double bonds right at the junction of hexagons stem from the fact that the NICS(0) are too close but far from the highest value in the molecule.

In Fig. 9 the π-electronic distribution obtained with the Y-rule for the planar CPPAHs is presented. In all the cases the Y-carbon are highlighted in bold. The 4FAR systems (**4** and **5**) have one Y-carbon, see Fig. 9. The 5FAR systems (**6**, **7**, and **8**) have three Y-carbons. The 6FAR systems (**9**–**17**) have three Y-carbons, except for the system **16** that has two Y-carbons. The 7FAR systems (**18**–**23**) have five Y-carbons. Finally, the 9FAR systems (**24** and **25**) have seven Y-carbons. As it can be seen, the number of Y-carbons in CPPAHs is given by odd numbers while it is given by even numbers in benzenoid PAHs.[39]

As it can be seen by comparing Fig. 8 and Fig. 9, there is a good agreement between the π-electronic distribution obtained with the Y-rule and the NICS(0) values. The application of the Y-rule for some of the planar CPPAHs is given in Fig. 10. The application of the Y-rule for these examples is carried out as explained in the former section.

Implications in oil asphaltenes stability

Under high-temperature pyrolysis conditions, CPPAH appear to be more stable than their benzenoid counterparts,[87]

Fig. 8. π-Electronic distribution obtained with the NICS(0) calculations for the planar CPPAHs.

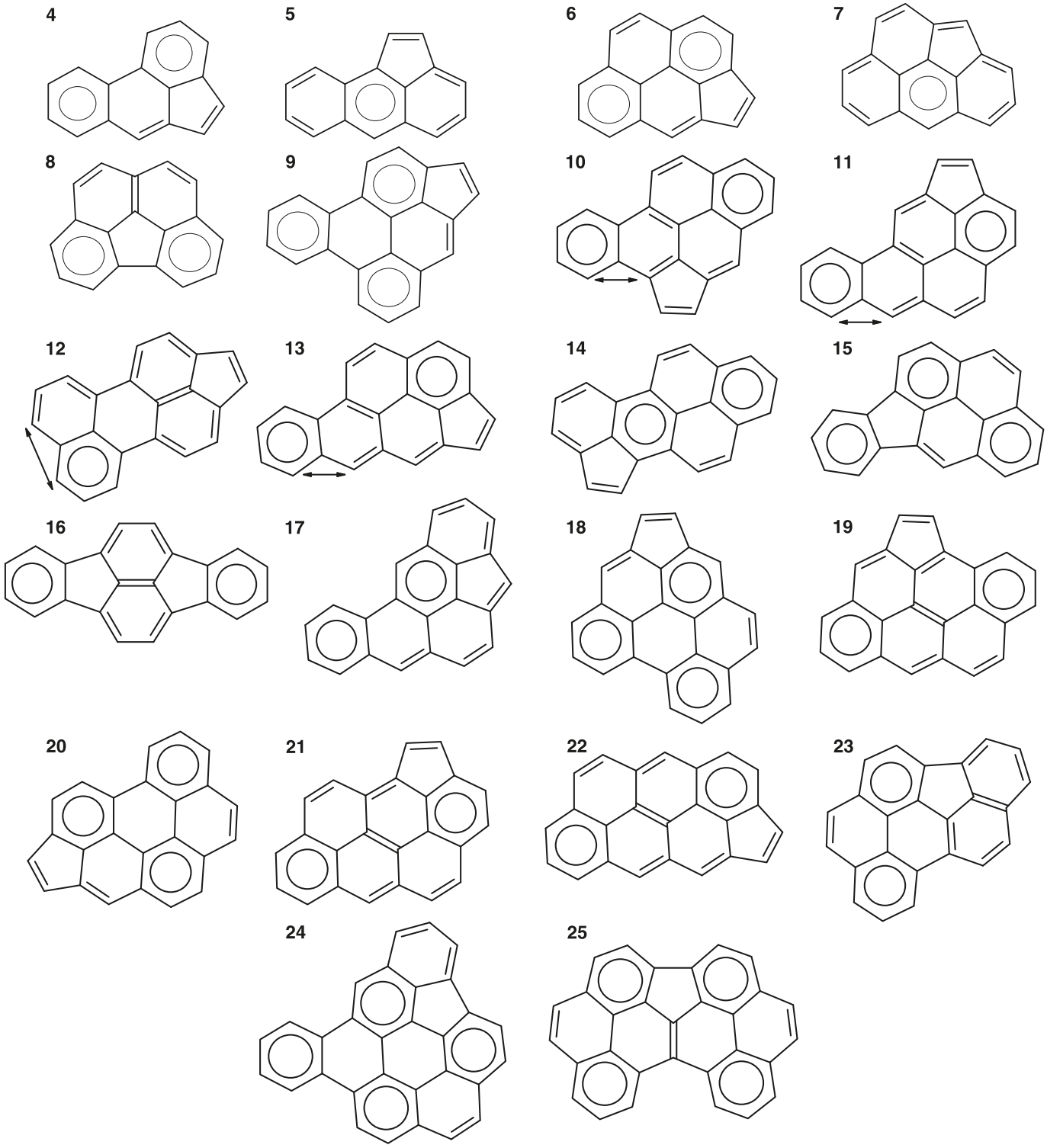

which suggests that CPPAH may survive in combustion regimes where more common PAH are known to break down. This stability is associated with the aromaticity of the CPPAHs, as proven for the case of PAHs.[37,38] The addition of pentagonal ring(s) to the benzenoid PAHs might form new Y-carbons that will lead to more possibilities for carbon sextet. However, due to the fact that asphaltenes present a very specific stability, it is important to find out how many sextets in CPPAHs are present in asphaltenes. As proven here this is going to be possible by using the Y-rule to elucidate the aromaticity of many CPPAHs candidates with the same optical properties as asphaltenes.

Andreatta et al.[88] have used high-Q high-resolution ultrasonic spectroscopy to detect the onset of aggregation in asphaltene solutions and micelle formation with standard surfactants. These authors have shown that the molecular

Fig. 9. π-Electronic distribution obtained with the Y-rule for the planar CPPAHs.

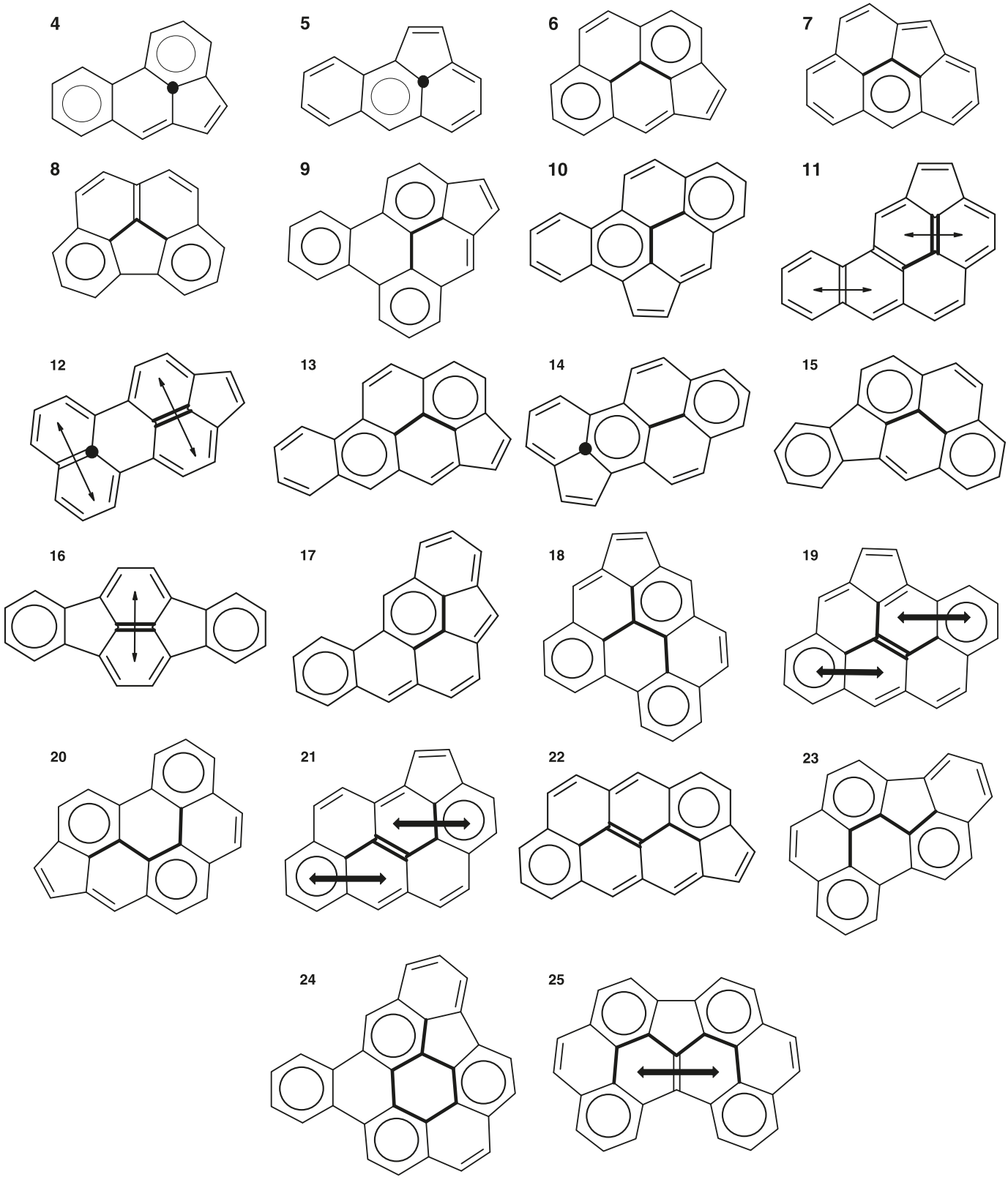

size and molecular architecture of asphaltenes can be used to understand primary aggregate formation of asphaltenes. Therefore, to establish structure–function relationships for the case of aspaltenes, in particular to relate molecular structure with solubility, it is necessary to understand the asphaltenes molecular architecture, stability, as well as their polydispersity. Thus, the importance of the present work in establishing the asphaltene molecular architecture.

Fig. 10. π-Electronic distribution obtained with the Y-rule for the planar CPPAHs compounds **8**, **11**, **16**, and **25**.

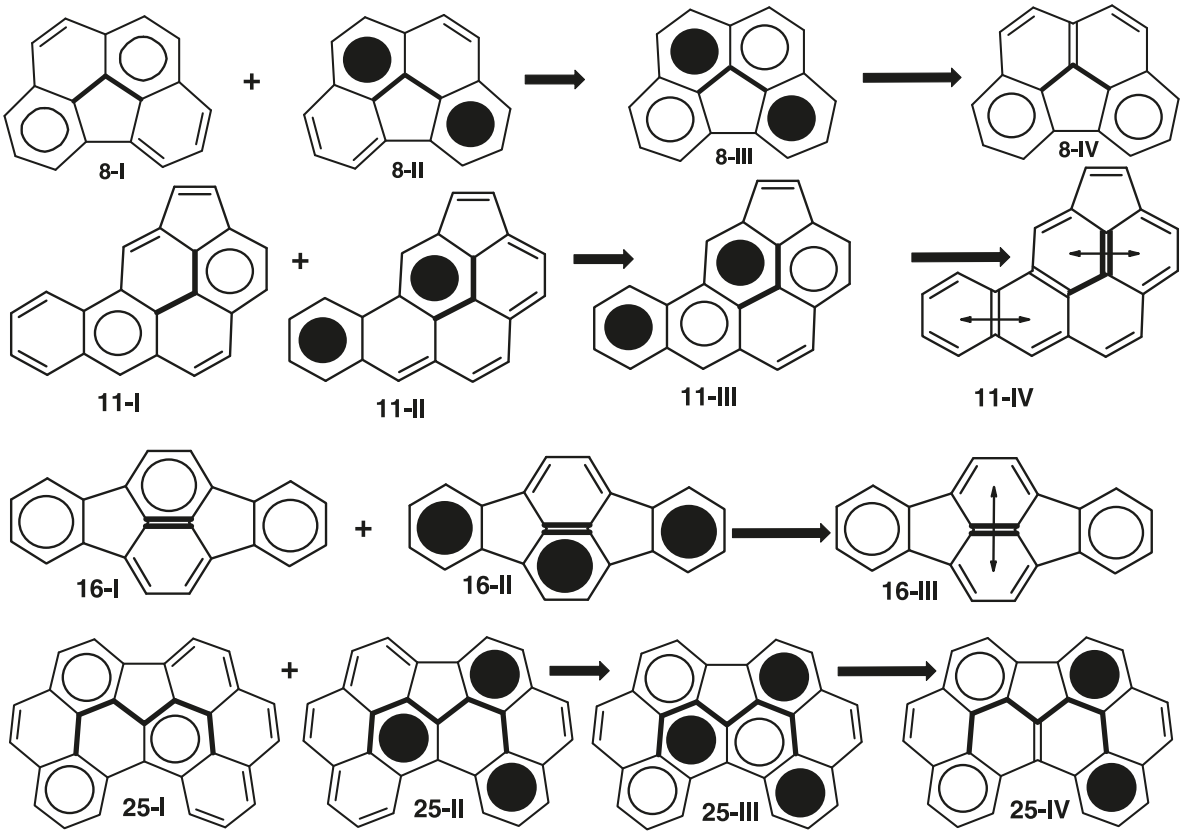

There are potentially different stages of aggregation in asphaltenes, for instance, as proposed in the Yen model, which consists of a hierarchy of aggregation for asphaltene solutions.[88,89] Different hierarchies of aggregation correspond to different energies of interaction. Andreatta et al.[88] have shown that the growth and its termination of nanoaggregates can be understood directly from molecular structural considerations.[88] The polydispersity in a standard asphaltene sample ensures nanoaggregate initiation from the least soluble molecular fraction and nanoaggregate termination from the most soluble fraction, thereby creating a stable (nano)colloidal suspension. The resulting nanoaggregates resembles a "hairy tennis ball" with alkanes surrounding the outside. The governing chemical principles of asphaltenes that determine solubility and thus define asphaltenes have shown to be van der Waals (and polar) attraction of their aromatic ring systems versus steric repulsion of their alkane chains. Asphaltene molecules are relatively small having mean molecular weights of 750 g/mol. This restriction on molecular structure enables identification of key dynamics of asphaltene behavior, thereby extending the Yen model. This "modified Yen model" or equivalently the "Yen–Mullins model" includes: (1) the restriction of small molecular size of asphaltene molecules and (2) showing the effect of asphaltene intermolecular interactions on the dynamics of aggregate formation. Therefore, the determination or elucidation of the aromatic penta-fused PAH aromatic core in asphaltenes and their polydispersity is necessary to understand asphaltene nanoaggregation. As proven in the present work the Y-rule is a necessary tool to determine the stability of the CPPAHs structural candidates that show similar optical properties as the asphaltene chromophores.

Conclusions

One of the main interests in the oil industry is to understand the aggregation process of oil asphaltenes to be able to come up with methods, either chemical or physicochemical, as inhibitors, for example, to avoid the economical losses, during the extraction, transportation, and refining of petroleum, and to get the optimal use from the heavy fraction of any crude oil. To do this it is necessary to know the structure of asphaltenes. Asphaltenes are defined operationally, due to the many difficulties to elucidate their structure from experimental results. Asphaltenes present polydispersity because they are actually mixtures of cyclopenta-fused polycyclic aromatic compounds (CPPAHs) with N, S, and O atoms in their structure and aliphatic chains. The structure of the oil asphaltenes is ruled by stability. They present a very particular stability, which has been measured experimentally by their optical properties. This stability is closely related to their aromaticity. Therefore, to elucidate the complete structure of asphaltenes their aromaticity has to be known. Because asphaltenes are mixtures there may be thousand of possibilities of CPPAHs, of different size (in terms of number of fused rings) and structure, that compose their aromatic core. Thus, the necessity to be able to asses the aromaticity of CPPAHs in a quick and easy way arises. CPPAHs with an aromaticity close to the one presented by asphaltenes will be good structural candidates but hundreds of CPPAHs will have to be analyzed to be able to get to conclusions on the

asphaltenes structure that is close to reality. The need of finding a proper method that allows us to predict the aromaticity, in an easy way, of CPPAHs is required.

In this work, we have studied the local aromaticity of cyclopenta-fused polycyclic aromatic compounds (CPPAHs) by means of the qualitative Y-rule method and the well-accepted quantitative theoretical method NICS (nucleus-independent chemical shift). The quick and easy to apply Y-rule has been proven in the literature[37,39] to compare well with NICS results for the case of benzenoid PAHs but its capabilities for CPPAHs had not been proven. This last point is addressed in the present work.

A comparison of the π-electronic distribution obtained by the Clar sextet principle, or model, as determined by the Y-rule and the π-electronic distribution obtained from nucleus-independent chemical shift (NICS) calculations show that both methodologies agree. Therefore, the aromaticitity in CPPAHs may be calculated with both methodologies. The advantages of the qualitative Y-rule are that it is of particular importance for the case of large CPPAHs, it takes few minutes to be applied following a very easy methodology, and it provides a quick answer about the aromaticity and location of the resonant sextets without having to carry out theoretical calculations that take time and that can be costly depending on the size of the system. We have found that the five-member ring in the CPPAHs presents a low electron density, it is not aromatic, and presents a NICS value that is positive. This conclusion is also reached with the Y-rule.

We suggest that the use of drawing circles in each hexagon of the σ-frame in CPPAHs, to represent the distribution of the π-density, must be discouraged. This practice has been done due to the fact that it was not possible to know, in an easy way, where the resonant sextets and the double bonds are located.

We can now continue our investigations on the structure of oil asphaltenes and we will be able to apply the Y-rule to asses the stability of hundreds of CPPAHs and choose those, as possible asphaltene candidates, with the carbon ratio (ratio between carbon atoms in sextets and carbon atoms in double bonds) close to the measured asphaltene ratio.[38,41–43,46–48] Also, the effect on the stability by the introduction of heteroatoms in the CPPAH core will be studied. However, it is known experimentally that the replacement of carbon in PAH compounds with heteroatoms typically results in red-shift (higher wavelength) of the fluorescence maximum if there is any spectral effect.[90]

The Yen–Mullins model, which enables identification of key dynamics of asphaltene behavior requires the elucidation of the molecular architecture of the aromatic penta-fused PAH aromatic core in asphaltenes and their polydispersity to understand asphaltene nanoaggregation. As proven in the present work the Y-rule is a helpful tool in determining the stability of the CPPAHs structural candidates that show similar optical properties as the asphaltene chromophores.

Acknowledgements

This research has been supported under projects D.00406 and D.00265 of the Instituto Mexicano del Petróleo. The assistance of Dr. Fernando Alvarez-Ramirez with geometry optimizations, with the DMol3 method, is gratefully acknowledged.

References

(1) Harvey, R. G. *Polycyclic Aromatic Hydrocarbons*; Wiley-VCH: New York, 1997.

(2) Todorov, P. D.; Koper, C.; van Lenthe, J. H.; Jenneskens, L. W. *Chem. Phys. Lett.* **2008**, *454* (1–3), 30–35. doi:10.1016/j.cplett.2008.01.065.

(3) Jenneskens, L. W.; Sarobe, M.; Zwikker, J. W. *Pure Appl. Chem.* **1996**, *68* (2), 219–224. doi:10.1351/pac199668020219.

(4) Scott, L. T. *Pure Appl. Chem.* **1996**, *68* (2), 291–300. doi:10.1351/pac199668020291.

(5) Koper, C.; Sarobe, M.; Jenneskens, L. W. *Phys. Chem. Chem. Phys.* **2004**, *6* (2), 319–327. doi:10.1039/b312234d.

(6) Gooijer, C.; Kozin, I.; Velthorst, N. H.; Sarobe, M.; Jenneskens, L. W. *Spectrochim. Acta A Mol. Biomol. Spectrosc.* **1998**, *54* (10), 1443–1449; see also references therein. doi:10.1016/S1386-1425(98)00045-6.

(7) Havenith, R. W. A.; Jiao, H.; Jenneskens, L. W.; van Lenthe, J. H.; Sarobe, M.; Schleyer, P. R.; Kataoka, M.; Necula, A.; Scott, L. T. *J. Am. Chem. Soc.* **2002**, *124* (10), 2363–2370. doi:10.1021/ja011538n. PMID:11878993.

(8) Malloci, G.; Mulas, G.; Cappellini, G.; Fiorentini, V.; Porceddu, I. *Astron. Astrophys.* **2005**, *432* (2), 585–594; see also references therein. doi:10.1051/0004-6361:20042246.

(9) Sarobe, M.; Snoeijer, J. D.; Jenneskens, L. W.; Slagt, M. Q.; Zwikker, J. W. *Tetrahedron Lett.* **1995**, *36* (46), 8489–8492. doi:10.1016/0040-4039(95)01747-6.

(10) Sarobe, M.; Flink, S.; Jenneskens, L. W.; van Poecke, B. L. A.; Zwikker, J. W. *J. Chem. Soc. Chem. Commun.* **1995**, 2415–2416. doi:10.1039/C39950002415.

(11) Haddon, R. C. The fullerenes: Powerful Carbon-based Electron Acceptors; In *The Fullerenes: New Horizons for the Chemistry, Physics and Astrophysics of Carbon;* Kroto, H. W., Walton, D. R. M., Eds.; Cambridge University Press: Cambridge, UK, 1993; p 53.

(12) Sarobe, M. Polycyclic Aromatic Hydrocarbons Under High Temperature Conditions: Consequences For Carbon Build-up During Combustion and Fullerene Formation Processes. Ph.D. Thesis, Utrecht University, Utrecht, The Netherlands, 1998; Chapter 9.

(13) Scott, L. T.; Necula, A. *J. Org. Chem.* **1996**, *61* (1), 386–388. doi:10.1021/jo9516087.

(14) Coulson, C. A.; Mallion, R. B. *J. Am. Chem. Soc.* **1976**, *98* (2), 592–598. doi:10.1021/ja00418a045.

(15) Fowler, P. W.; Zanasi, R.; Cadioli, B.; Steiner, E. *Chem. Phys. Lett.* **1996**, *251* (3–4), 132–140. doi:10.1016/0009-2614(96)00120-0.

(16) Subramanian, G.; Schleyer, P. R.; Jiao, H. *Organometallics* **1997**, *16* (11), 2362–2369; see also references therein. doi:10.1021/om970008q.

(17) Orendt, A. M.; Facelli, J. C.; Bai, S.; Rai, A.; Gossett, M.; Scott, L. T.; Boerio-Goates, J.; Pugmire, R. J.; Grant, D. M. *J. Phys. Chem. A* **2000**, *104* (1), 149–155; see also references therein. doi:10.1021/jp993057k.

(18) Steiner, E.; Fowler, P. W.; Jenneskens, L. W. *Angew. Chem.* **2001,** *113* (2), 375–379. doi:10.1002/1521-3757(20010119)113:2<375::AID-ANGE375>3.0.CO;2-7.

(19) Otero-Lobato, M. J.; Kaats-Richters, V. E.; Koper, C.; Vlietstra, E. J.; Havenith, R. W.; Jenneskens, L. W.; Seinen, W. *Mutat. Res.* **2005**, *581* (1–2), 115–132; see also references therein. PMID:15725611.

(20) Betowski, L. D.; Enlow, M.; Riddick, L.; Aue, D. H. *J. Phys. Chem. A* **2006**, *110* (47), 12927–12946; see also references therein. doi:10.1021/jp065785v. PMID:17125310.
(21) Ledesma, E. B.; Kalish, M. A.; Wornat, M. J.; Nelson, P. F.; Mackie, J. C. *Energy Fuels* **1999**, *13* (6), 1167–1172. doi:10.1021/ef990036g.
(22) Wornat, M. J.; Sarofim, A. F.; Lafleur, A. L. *Symp. (Int.) Combust.* **1992**, *24* (1), 955–963.
(23) Wornat, M. J.; Vriesendorp, F.; Lafleur, A. L.; Plummer, E. F.; Necula, A.; Scott, L. *Polycyclic Aromat. Compd.* **1999**, *13* (2), 221–240. doi:10.1080/10406639908020548.
(24) Mukherjee, J.; Sarofim, A. F.; Longwell, J. P. *Combust. Flame* **1994**, *96* (3), 191–200. doi:10.1016/0010-2180(94)90008-6.
(25) Marsh, N. D.; Wornat, M. J.; Scott, L. T.; Necula, A.; Lafleur, A. L.; Plummer, E. F. *Polycyclic Aromat. Compd.* 2000, *13* (4), 379–402. doi:10.1080/10406630008233852.
(26) Lafleur, A. L.; Howard, J. B.; Taghizadeh, K.; Plummer, E. F.; Scott, L. T.; Necula, A.; Swallow, K. C. *J. Phys. Chem.* **1996**, *100* (43), 17421–17428. doi:10.1021/jp9605313.
(27) Lafleur, A. L.; Taghizadeh, K.; Howard, J. B.; Anacleto, J. F.; Quilliam, M. A. *J. Am. Soc. Mass Spectrom.* **1996**, *7* (3), 276–286. doi:10.1016/1044-0305(95)00651-6.
(28) Wornat, M. J.; Vernaglia, B. A.; Lafleur, A. L.; Plummer, E. F.; Taghizadeh, K.; Nelson, B. F.; Li, C.-Z.; Necula, A.; Scott, L. *Symp. (Int.) Combust.* **1998**, *27* (2), 1677–1686.
(29) Mullins, O. C., Sheu, E. Y., Hammami, A., Marshall, G., Eds.; *Asphaltene, Heavy Oils and Petroleomics*; Springer: New York, 2007.
(30) Chilingarian, G. V.; Yen, T. F. *Bitumens, Asphalts, and Tar Sands*; Elsevier: New York, 1978.
(31) Speight, J. G. *The Chemistry and Technology of Petroleum*; Marcel Dekker: New York, 1980; pp 189–252.
(32) Tissot, P. B.; Welte, D. H. *Petroleum Formation and Occurrence*, 2nd ed.; Springer-Verlag: Berlin, 1984.
(33) Bunger, J. W.; Li, N. C., Eds.; *Chemistry of Asphaltenes*; American Chemical Society: Washington, 1984.
(34) Sheu, E. Y.; Mullins, O. C., Eds.; *Asphaltenes: Fundamentals and Applications*; Plenum Press: New York, 1995.
(35) Mullins, O. C.; Sheu, E. Y., Eds.; *Structures and Dynamics of Asphaltenes*; Plenum Press: New York, 1998.
(36) Chilingarian, G. V.; Yen, T. F., Eds.; *Bitumens, Asphalts, and Tar Sands*; Elsevier: New York, 1978.
(37) Ruiz-Morales, Y. Molecular Orbital Calculations and Optical Transitions of PAHs and Asphaltenes; In *Asphaltene, Heavy Oils and Petroleomics*; Mullins, O. C., Sheu, E. Y., Hammami, A., Marshall, A. G., Eds.; Springer: New York, 2007; Chapter 4.
(38) Ruiz-Morales, Y. *J. Phys. Chem. A* **2002**, *106* (46), 11283–11308. doi:10.1021/jp021152e.
(39) Ruiz-Morales, Y. *J. Phys. Chem. A* **2004**, *108* (49), 10873–10896. doi:10.1021/jp040179q.
(40) Gutman, I.; Ruiz-Morales, Y. *Polycyclic Aromat. Compd.* **2007**, *27* (1), 41–49. doi:10.1080/10406630601134268.
(41) Bergmann, U.; Mullins, O. C. Carbon X-ray Raman Spectroscopy of PAHs and Asphaltenes. In *Asphaltene, Heavy Oils and Petroleomics*; Mullins, O. C., Sheu, E. Y., Hammami, A., Marshall, A. G., Eds.; Springer: New York, 2007; Chapter 5.
(42) Bergmann, U.; Mullins, O. C.; Cramer, S. P. *Anal. Chem.* **2000**, *72* (11), 2609–2612. doi:10.1021/ac990730t. PMID:10857643.
(43) Bergmann, U.; Groenzin, H.; Mullins, O. C.; Glatzel, P.; Fetzer, J.; Cramer, S. P. *Chem. Phys. Lett.* **2003**, *369* (1–2), 184–191. doi:10.1016/S0009-2614(02)02003-1.
(44) Clar, E. *Polycyclic Hydrocarbons*; Springer-Verlag: Berlin, 1964.
(45) Clar, E. *The Aromatic Sextet*; John Wiley & Sons: London, 1972.
(46) Ruiz-Morales, Y.; Wu, X.; Mullins, O. C. *Energy Fuels* **2007**, *21* (2), 944–952. doi:10.1021/ef0605605.
(47) Ruiz-Morales, Y.; Mullins, O. C. *Energy Fuels* **2007**, *21* (1), 256–265. doi:10.1021/ef060250m.
(48) Ruiz-Morales, Y.; Mullins, O. C. *Energy Fuels* **2009**, *23* (3), 1169–1177. doi:10.1021/ef800663w.
(49) Armitt, J. W.; Robinson, R. *J. Chem. Soc., Trans.* **1925**, *127*,1604–1617. doi:10.1039/CT9252701604.
(50) Crocker, E. C. *J. Am. Chem. Soc.* **1922**, *44* (8), 1618–1630. doi:10.1021/ja01429a002.
(51) Jiao, H.; Schleyer, P. v. R.; Mo, Y.; McAllister, M. A.; Tidwell, T. T. *J. Am. Chem. Soc.* **1997**, *119* (30), 7075–7083. doi:10.1021/ja970380x.
(52) Krygowski, T. M.; Cyranski, M. K.; Czarnocki, Z.; Hafelinger, G.; Katritzky, A. R. *Tetrahedron* **2000**, *56* (13), 1783–1796. doi:10.1016/S0040-4020(99)00979-5.
(53) Schleyer, P. v. R.; Jiao, H. *Pure Appl. Chem.* **1996**, *68* (2), 209–218. doi:10.1351/pac199668020209.
(54) Kruszewski, J.; Krygowski, T. M. *Tetrahedron Lett.* **1972**, *13* (36), 3839–3842. doi:10.1016/S0040-4039(01)94175-9.
(55) Krygowski, T. M. *J. Chem. Inf. Comput. Sci.* **1993**, *33* (1), 70–78. doi:10.1021/ci00011a011.
(56) Krygowski, T. M.; Cyranski, M. K. *Tetrahedron* **1996**, *52* (5), 1713–1722. doi:10.1016/0040-4020(95)01007-6.
(57) Pople, J. A.; Untch, K. G. *J. Am. Chem. Soc.* **1966**, *88* (21), 4811–4815. doi:10.1021/ja00973a009.
(58) Minkin, V. L.; Glukhovtsev, M. N.; Simkin, B. Y. *Aromaticity and Antiaromaticity*; Wiley: New York, 1986.
(59) Garrat, P. J. *Aromaticity*; Wiley: New York, 1986.
(60) Schleyer, P. v. R.; Maerker, C.; Dransfeld, A.; Jiao, H.; van Eikema Hommes, N. J. R. *J. Am. Chem. Soc.* **1996**, *118* (26), 6317–6318. doi:10.1021/ja960582d.
(61) Schleyer, P. v. R.; Manoharan, M.; Wang, Z. X.; Kiran, B.; Jiao, H.; Puchta, R.; van Eikema Hommes, N. J. *Org. Lett.* **2001**, *3* (16), 2465–2468. doi:10.1021/ol016217v. PMID:11483036.
(62) George, P.; Trachtman, M.; Brett, A. M.; Bock, C. W. *J. Chem. Soc. Perkin Trans.* **1972**, *2*, 1036.
(63) Hehre, W. J.; Ditchfield, R.; Radom, L.; Pople, J. A. *J. Am. Chem. Soc.* **1970**, *92* (16), 4796–4801. doi:10.1021/ja00719a006.
(64) Schleyer, P. v. R.; Pühlhofer, F. *Org. Lett.* **2002**, *4* (17), 2873–2876. doi:10.1021/ol0261332. PMID:12182577.
(65) Chen, Z.; Wannere, C. S.; Corminboeuf, C.; Puchta, R.; Schleyer, P. v. R. *Chem. Rev.* **2005**, *105* (10), 3842–3888. doi:10.1021/cr030088+.
(66) Schleyer, P. v. R.; Manoharan, M.; Jiao, H.; Stahl, F. *Org. Lett.* **2001**, *3* (23), 3643–3646. doi:10.1021/ol016553b. PMID:11700102.
(67) Randić, M. *Chem. Rev.* **2003**, *103* (9), 3449–3606. doi:10.1021/cr9903656. PMID:12964878.
(68) Moran, D.; Stahl, F.; Bettinger, H. F.; Schaefer, H. F., III; Schleyer, P. v. R. *J. Am. Chem. Soc.* **2003**, *125* (22), 6746–6752. doi:10.1021/ja034497z. PMID:12769585.
(69) Schleyer, P. v. R. *Chem. Rev.* **2001**, *101* (5), 1115–1118. doi:10.1021/cr0103221.
(70) Patchkovskii, S.; Thiel, W. *J. Mol. Model.* **2000**, *6* (2), 67–75; see also references therein. doi:10.1007/PL00010736.

(71) Schleyer, P. v. R.; Jiao, H.; van Eikema Hommes, N. J. R.; Malkin, V. G.; Malkina, O. *J. Am. Chem. Soc.* **1997**, *119* (51), 12669–12670. doi:10.1021/ja9719135.
(72) Schleyer, P. v. R.; Manoharan, M.; Wang, Z.-X.; Kiran, B.; Jiao, H.; Puchta, R. N.; van Eikema Hommes, N. J. *Org. Lett.* **2001**, *3* (16), 2465–2468. doi:10.1021/ol016217v. PMID:11483036.
(73) Perdew, J. P.; Wang, Y. *Phys. Rev. B* **1992**, *45* (23), 13244–13249. doi:10.1103/PhysRevB.45.13244.
(74) Delley, B. J. *Chem. Phys.* **1990**, *92* (1), 508–517. doi:10.1063/1.458452.
(75) Delley, B. J. *Chem. Phys.* **2000**, *113* (18), 7756–7764. doi:10.1063/1.1316015.
(76) *DMol3,* release 4.0; User Guide; Accelrys, Inc.: San Diego, CA, 2001.
(77) Frisch, M. J.; Trucks, G. W.; Schlegel, H. B.; Scuseria, G. E.; Robb, M. A.; Cheeseman, J. R.; Zakrzewski, V. G.; Montgomery, J. A., Jr.; Stratmann, R. E.; Burant, J. C.; Dapprich, S.; Millam, J. M.; Daniels, A. D.; Kudin, K. N.; Strain, M. C.; Farkas, O.; Tomasi, J.; Barone, V.; Cossi, M.; Cammi, R.; Mennucci, B.; Pomelli, C.; Adamo, C.; Clifford, S.; Ochterski, J.; Petersson, G. A.; Ayala, P. Y.; Cui, Q.; Morokuma, K.; Malick, D. K.; Rabuck, A. D.; Raghavachari, K.; Foresman, J. B.; Cioslowski, J.; Ortiz, J. V.; Stefanov, B. B.; Liu, G.; Liashenko, A.; Piskorz, P.; Komaromi, I.; Gomperts, R.; Martin, R. L.; Fox, D. J.; Keith, T.; Al-Laham, M. A.; Peng, C. Y.; Nanayakkara, A.; Gonzalez, C.; Challacombe, M.; Gill, P. M. W.; Johnson, B. G.; Chen, W.; Wong, M. W.; Andres, J. L.; Head-Gordon, M.; Replogle, E. S.; Pople, J. A. *Gaussian 98*, revision A.7; Gaussian, Inc.: Pittsburgh, PA, 1998.
(78) Ditchfield, R. *Mol. Phys.* **1974**, *27* (4), 789–807. doi:10.1080/00268977400100711.
(79) Wolinski, K.; Hinton, J. F.; Pulay, P. *J. Am. Chem. Soc.* **1990**, *112* (23), 8251–8260. doi:10.1021/ja00179a005.
(80) Becke, A. D. *Phys. Rev. A* **1988**, *38* (6), 3098–3100. doi:10.1103/PhysRevA.38.3098. PMID:9900728.
(81) Lee, C.; Yang, W.; Parr, R. G. *Phys. Rev. B* **1988**, *37* (2), 785–789. doi:10.1103/PhysRevB.37.785.
(82) Chesnut, D. B. *Annual reports on NMR spectroscopy;* Webb, G. A., Ed. Academic Press: New York, 1994; Vol. 29.
(83) Kutzelnigg, W.; Fleischer, U.; Schindler, M. *NMR - Basic Principles and Progress*; Springer-Verlag: Berlin, 1990; Vol. 23, p 165.
(84) Hajgató, B.; Ohno, K. *Chem. Phys. Lett.* **2004**, *385* (5–6), 512–518. doi:10.1016/j.cplett.2004.01.029.
(85) Hedberg, L.; Hedberg, K.; Cheng, P.; Scott, L. T. *J. Phys. Chem. A* **2000**, *104* (32), 7689–7694. doi:10.1021/jp0015527.
(86) Poater, J.; Fradera, X.; Duran, M.; Sola, M. *Chem. Eur. J.* **2003**, *9* (5), 1113–1122. doi:10.1002/chem.200390128.
(87) Marsh, N. D.; Wornat, M. J.; Scott, L. T.; Necula, A.; Lafleur, A. L.; Plummer, E. F. *Polycyclic Aromat. Compd.* **2000**, *13* (4), 379–402. doi:10.1080/10406630008233852.
(88) Andreatta, G.; Bostrom, N.; Mullins, O. C. Ultrasonic Spectroscopy of Asphaltene Aggregation. In *Asphaltene, Heavy Oils and Petroleomics*; Mullins, O. C., Sheu, E. Y., Hammami, A., Marshall, A. G., Eds.; Springer: New York, 2007; Chapter 9; also see references therein.
(89) Yen, T. F. *Am. Chem. Soc. Dic. Petroleum Chem. Prep.* **1990**, *35*, 312.
(90) Mullins, O. C. In *Asphaltenes: Fundamentals and Applications*; Sheu, E. Y.; Mullins, O. C., Eds.; Plenum Press: New York, 1995; Chapter 2.

Towards a computational treatment of polyoxometalates in solution using QM methods and explicit solvent molecules

Pere Miró, Josep M. Poblet, Josep Bonet Ávalos, and Carles Bo

Abstract: This study is aimed at developing an explicit solvent model for highly charged species such as polyoxometalates. The model includes solvent molecules in the first solvation shell explicitly, and long-range bulk effects and counterions as a set of single point charges. The model strongly stabilizes the electronic structure of the Keggin anion. The energies of the Kohn–Sham orbitals obtained using our model lie very close to those computed using the COSMO continuum solvent model; moreover, the total solvation energy evaluated with our model compares well to the value calculated by COSMO.

Key words: polyoxometalates, solvation, DFT, MD, discrete models.

Résumé : Cette étude a été réalisée dans le but de développer un modèle de solvant explicite pour les espèces fortement chargées, tels les polyoxométalates. Le modèle comprend explicitement des molécules de solvant dans la première couche de solvatation et les effets globaux à longue distance ainsi que les contre-ions sous la forme de charges ponctuelles. Le modèle stabilise fortement la structure électronique de l'anion Keggin. Les énergies des orbitales Kohn–Sham obtenues à l'aide de notre modèle sont très proches de celles calculées à l'aide du modèle de solvant continu COSMO; de plus, l'énergie totale de solvatation évaluée à l'aide de notre modèle se compare bien avec celle calculé à l'aide du modèle COSMO.

Mots-clés : polyoxométalates, solvatation, théorie de la fonctionnelle de la densité, modèles discrets, MD.

[Traduit par la Rédaction]

Introduction

The introduction of solvent effects in quantum chemical studies is nowadays an almost standard procedure thanks to the development of several continuum solvent models, which efficiently introduce the effect of solvent molecules by treating the solvent as a structureless continuum.[1–20] Although these solvation methods for uncharged molecules experienced notable advances in the last years, for charged species the models implicitly assume that no ion-pairing occurs and neglect the direct effects of counter ions and of other species in the liquid media. However, in the field of polyoxometalates (POMs), experiments demonstrate the dramatic influence of the environment on the electronic properties of POMs in solution. For instance, Weinstock et al.[21] reported that the redox potentials of Keggin anions strongly depend on the counter-ion and on the ionic force of the solution. Our group has been pioneering the theoretical study of the electronic structure of POMs during the last two decades[22–24] (by using mainly ADF), and realized that computational assessment of the redox properties of these species has to somehow include solvent effects. However, continuum solvent models are not able to introduce in their formulations the explicit nature of the counter-ion (such as Li^+, Na^+, or K^+), nor the ionic force of the solution. Therefore, there is a need to go one step further, and introduce those effects for reproducing such experimental results.

The conductor-like Screening Model (COSMO) developed by Klamt[2–4] as implemented in the ADF program package by Pye and Ziegler[1] is of common use in the polyoxometalate field. The present study makes use of COSMO as reference. Note that for a neutral species, continuum solvent models include the electrostatic effect of a polarized dielectric (with total charge equal to zero) onto the electron density of the solute. This mimics the interactions of solvent molecules with the solute. However, for a charged species,

Received 15 January 2009. Accepted 6 March 2009. Published on the NRC Research Press Web site at canjchem.nrc.ca on 5 September 2009.

This article is part of a Special Issue dedicated to Professor T. Ziegler. This article is dedicated to Prof. Tom Ziegler on the occasion of his 65th birthday.

P. Miró. Institute of Chemical Research of Catalonia (ICIQ), Av. Països Catalans 16, 43007 Tarragona, Spain.
J.M. Poblet. Departament de Química Física i Química Inorgànica, Universitat Rovira i Virgili, Av. Marcel·lí Domingo s/n, 43007 Tarragona, Spain.
J.B. Ávalos. Departament d'Enginyeria Química, ETSEQ, Universitat Rovira i Virgili, Avinguda dels Països Catalans 26, 43007 Tarragona, Spain.
C. Bo.[1] Institute of Chemical Research of Catalonia (ICIQ), Av. Països Catalans 16, 43007 Tarragona, Spain; Departament de Química Física i Química Inorgànica, Universitat Rovira i Virgili, Av. Marcel·lí Domingo s/n, 43007 Tarragona, Spain.

[1]Corresponding author (e-mail: cbo@iciq.es).

since the total charge of the dielectric is not zero but equal to the charge of the species with opposite sign, in addition to the solvent effects, the continuum model must include the effects of the counter-ions too.

In recent papers, we described how classical molecular dynamics simulations applied to Keggin anions (see Fig. 1, $[XW_{12}O_{40}]^{n-}$, X = P, Si, Al; n = 3, 4, 5) in liquid water enabled the study of the structure of solvent water molecules around the polyoxometalates, and the effect of cations in the dynamic properties of POMs.[25] Also, the likely formation of ion pairs was discussed. Moreover, the same techniques have been applied to investigate the structure of water encapsulated in the giant Mo_{132} nanocapsule.[26] Other groups also demonstrated the usefulness of classical MD in the study of ion aggregation in concentrated solutions of Keggin anions in aqueous and methanol solvents.[27] Given that we had at hand snapshots of instant configurations of the solvent water molecules and the counter-ions around the Keggin anion, we decided to use this data to develop an explicit solvation model and investigate the effects of solvent water molecules, long-range solvent effects, and counter-ion effects on the electronic structure of POMs. In this paper, we report the results of such a study, and discuss how this microscopic model of the solvent compares to the COSMO continuum solvent model. The final goal is to develop a cheap and standard protocol that would include the effect of additional species in solution and simulate as closely as possible the nature of the liquid media that is used in the real-life laboratory.

Computational details

Classical molecular dynamics simulations were carried out using the GROMACS 3.2 program.[28] Two water models were considered, the SPC/E[29] and the TIP3P.[30,31] Lennard-Jones parameters and atomic charges for the polyoxometalate were developed previously in our group[32] and used here also. The polyoxometalate was kept rigid during the simulation. For Na^+ cations, the parameters developed by Lee et al.[33] were used. Quantum mechanical calculations were carried out using DFT-based methods implemented in the ADF2004 program[34–37] The local spin density approximation characterized by the electron gas exchange was used with Vosko–Wilk–Nusair[38] (VWN) parameterization for correlation and Becke and Perdew[39–42] nonlocal corrections were added to the exchange and correlation energy, respectively. The basis set was composed of triple ξ+ polarization (TZP) Slater basis sets extracted from the ADF library. The quasirelativistic scalar ZORA formalism with corrected core potentials was used.[43–47]

First solvation shell

Modeling the first solvation shell properly was our first goal, since in many cases (metal ions, highly charged species, proteins, etc.) specific interactions operate between the solute and the solvent molecules. These interactions originate with hydrogen bonds and van der Waals forces, which are poorly described with continuum models. Solvent molecules may be highly structured around the solute; thus the treatment of solvent in such species often uses an explicit model.

The Keggin anion has a high negative charge and polarizes the surrounding water molecules, which form multiple hydrogen bonds with the external oxygens of the polyoxometalate. To describe these interactions as accurately as possible, we decided to include the first solvation shell explicitly in the DFT calculation.

Fig. 1. A Keggin anion $[PW_{12}O_{40}]^{3-}$ surrounded by some water molecules.

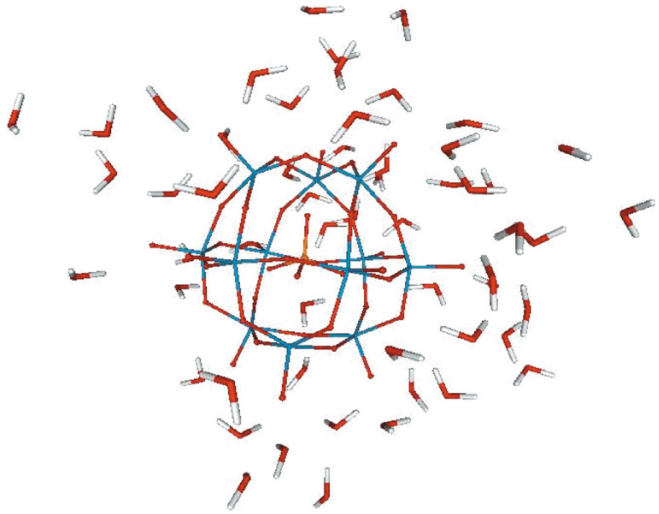

Several configurations of the solvent around the polyoxometalate were chosen from molecular dynamics simulations with two different water models, the SPC/E and the TIP3P. A preliminary study was carried out with a system that included the polyoxometalate and the first 24 neighboring water molecules. For both types of water the variations in binding energy, energies of the frontier orbitals HOMO and LUMO, and their gap, are rather similar, but in TIP3P the variations in HOMO and LUMO energies are slighly lower than in SPC/E model (see Supplementary data). Also the convergence of the SCF process was better in TIP3P than in SPC/E, probably because the H–O–H angle in SPC/E (109.47°) is larger than in a real water molecule. The H–O–H angle in TIP3P water molecules is 105.52°. As a result of this previous study all the configurations were taken from simulations that used TIP3P model.

The next question to answer was how many water molecules the first solvation shell has to contain. To answer this question, a set of calculations was carried out increasing the size of the first solvation shell (24, 49, 74, 99), and the interactions between water molecules and the POM. and water molecules with themselves were analyzed. Following Goddard's protocol,[48] we estimated the energy of the hydrogen bond between water molecules by using the same set of water clusters $(H_2O)_n$ (n = 1 to 16) (see Supplementary data). Using the DFT method described above, we obtained a value of 5.13 kcal mol^{-1}, which is only 0.55 kcal mol^{-1} smaller than the value obtained using the X3LYP functional.[48] Then, we assessed the number of hydrogen bonds between water molecules in the solvation shell and the number of hydrogen bonds between the polyoxometalate and the solvent by performing a series of single point fragment calculations. This assumption was made because our interest was to see whether the number of hydrogen bonds between the solvent and the polyoxometalate converges or not when the number of solvent molecules in the solvation shell increases.

Fig. 2. Number of hydrogen bonds between water molecules and between water and polyoxometalate in different systems.

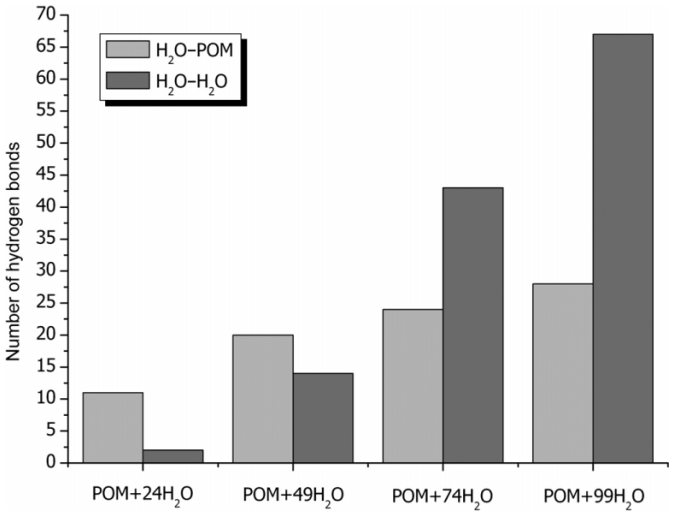

Figure 2 shows the number of hydrogen bonds between water molecules and between water and the polyoxometalate, in systems with different numbers of water molecules in the first solvation shell. The number of hydrogen bonds between water molecules increased with the size of the solvation shell; the number of hydrogen bonds with the polyoxometalate increased significantly from a shell of 24 water molecules to a shell of 49, but above 49, the increase remains nearly constant. Above 49 water molecules in the first solvation shell, the increase in the number of hydrogen bonds can be explained as an increase in interaction between water bulk and the polyoxometalate, and not to a true increase in the number of hydrogen bonds since the POM surface is already fully covered by solvent molecules. Since the computational cost strongly depends on the number of water molecules, we considered that 49 molecules in the solvation shell was a suitable number.

By introducing explicit water molecules in the DFT calculation, the Kohn–Sham molecular orbitals suffered a strong stabilization, as shown in Fig. 3. The effect is stronger when 24 and 49 water molecules are included, and seems to converge afterward. This stabilization is directly related to the addition of extra water molecules, but it is worth noting that it affects all the orbitals equally. In Fig. 3, HOMO and LUMO energies and the HOMO–LUMO gaps are shown, and it is clearly seen that the addition of water molecules in the first solvation shell shift both the HOMO and the LUMO down, while the HOMO–LUMO gap remains nearly constant (standard deviation 0.07 eV) in all cases. The addition of 99 water molecules is not enough to reach the effect of COSMO, since the levels still appear about 4 eV above.

Long-range electrostatic solvent effects

The second effect that one has to take into account is the long-range electrostatic interactions with the bulk of the solvent. This effect is also present in solids and well known as the Madelung field. Following the same approach as above, we prepared a set of calculations for a unique solvent configuration, with an increasing number of solvent molecules represented as point charges (using the TIP3P parameters,

Fig. 3. Energies of the HOMO and the LUMO (lines and left scale), and energy gap (dots and right scale).

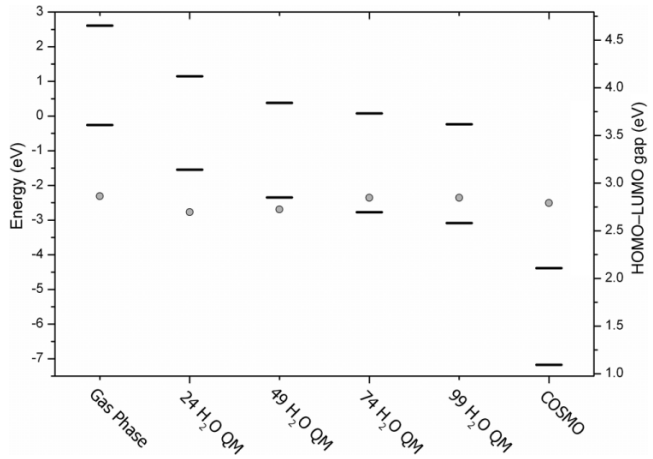

Fig. 4. Energies of HOMO (black line) and LUMO (red line) as function of the number of water molecules included as point charges.

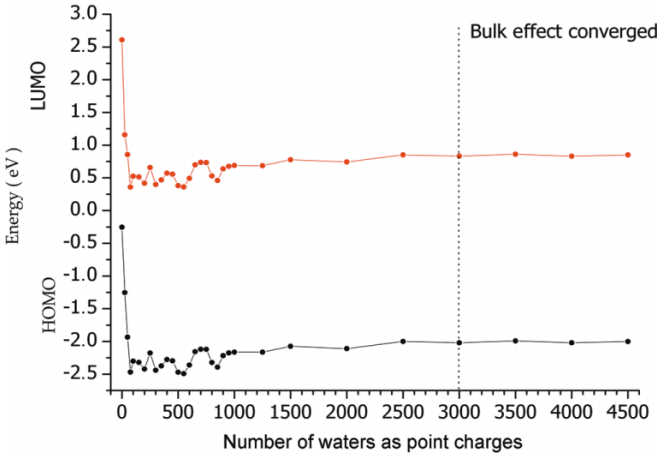

i.e., 3 point charges per molecule) in spherical shells, and performed a single point calculation to explore how many solvent shells should be included until reaching convergence. As before, we recorded the energies of the HOMO and the LUMO levels. Figure 4 plots the HOMO and LUMO energies as a function of the number of water molecules. Note that when few water molecules were included, the orbitals were strongly stabilized by more than 2 eV, and that after the first 150 water molecules a fluctuation in the energies was observed. After including 3000 water molecules, the HOMO and LUMO energies remained constant; therefore we considered that the electrostatic field converged at this point. Note also that the HOMO–LUMO gap remained constant, since the electrostatic field created by the set of point charges is isotropic.

Counter-ion effects

In addition to the specific interactions between the first solvation shell and the POM, and the long-range electrostatic field created by the bulk solvent, the remaining term is the effect associated with the counter-ions. In this case, since the POM is $[PW_{12}O_{40}]^{3-}$, three Na^+ cations must be included.

Fig. 5. Energies for the eight highest occupied and lowest empty levels for the different models. (Black: levels belonging to the POM; red: levels of water molecules; dark grey: occupied levels; light grey: empty levels).

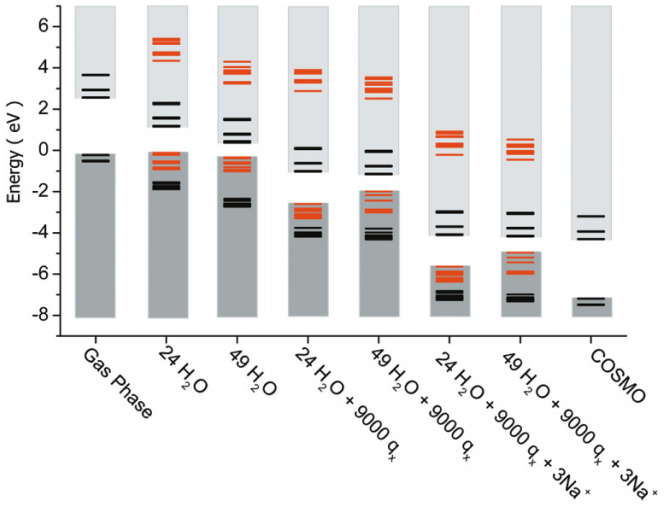

At this point we identified two approaches for including the counter-ions in our model, either as three single point charges at locations extracted from a snapshot, or as a spherical distribution at a given radius. Since we had access to the radial distribution function, g(r), of the sodium cations computed from the simulation, we used that information to determine a reasonable value for the radius of a spherical charge distribution. A plot of g(r) of Na^+ is included in the Supplementary data. By using the intensity (I_n) of g(r) at each distance form the center of the anion (r_n), we defined a weighted-averaged radius <r> of the distribution as:

$$[1] \qquad \langle r \rangle = \frac{\sum_n I_n r_n}{n}$$

Thus, we computed <r> = 14.28 Å, and created a spherical distribution of 1446 point charges, with a total charge equal to the charge of the polyoxometalate with opposite sign, i.e., –3. By including this additional set of point charges, we obtained energies for the HOMO (–6.988 eV) and for the LUMO (–4.172 eV) that were quite close to the values produced by a continuum solvent model such as COSMO (–7.183 and –4.308 eV, respectively).

In Fig. 5, the reader can observe the progressive stabilization of the electronic structure of the POM in the different models. The first system in the left hand side corresponds to a gas phase calculation without any solvent effect. Moving to the right, the effect of the first solvation shell with 24 or 49 water molecules, the effect of the bulk as a set of 9000 point charges, and finally the effect of the three sodium cations are included step by step. As a reference, the energies for HOMOs and LUMOs obtained in a COSMO calculation are shown on the right hand side. Note the nice agreement between the largest model and COSMO.

Discussion

The model, including the first solvent shell explicitly, the solvent bulk, and the counter-ions as point charges, is able to achieve the same stabilization of the electronic structure of a Keggin $[PW_{12}O_{40}]^{3-}$ anion as the COSMO continuum solvent model. As we mentioned in the introduction, COSMO includes two effects of different types, one arising from the solvent and the other one due to the neutralization of the charge by the counter-ions. Our model includes both these effects, and enables us to quantify and analyze them separately. By increasing the complexity of the solvation model step by step, it allow us to evaluate different terms, namely, the stabilization energies due to the counter-ions (E^c), due to the first solvation shell (E^{ss}), and due to the bulk (E^{bulk}). This task is easily carried out by selecting a suitable fragment and by evaluating its energy. To accomplish this, we selected different models as shown in Table 1, and defined E^c, E^{ss}, and E^{bulk} as follows: The stabilization energy due to the counter-ions is $E^c = (E_1 - E_2)$, that due to the first solvation shell is $E^{ss} = (E_3 - E_4 - E_5)$, and that due to the bulk as $E^{bulk} = ((E_2 - E_3) - (E_6 - E_5))$.

Table 1. Models and the corresponding labels and binding energies.

Label	System	Energy (ev)
E_1	POM + 49 H_2O + 9000q_x + counter-ions	–1168.25
E_2	POM + 49 H_2O + 9000q_x	–1164.66
E_3	POM + 49 H_2O	–1136.8
E_4	POM	–442.97
E_5	49 H_2O	–689.90
E_6	49 H_2O + 9000q_x	–713.50

Table 2. Solvation Energy terms (values in eV).

	COSMO	Our model
E^{solv}	–10.88	–11.78
E^{ss}	—	–3.51
E^{bulk}	—	–4.68
E^c	—	–3.59

Therefore, we can also evaluate the total solvation energy as the sum of the three terms, E^c, E^{ss}, and E^{bulk} . This total solvation energy, computed by using our microscopic solvent model, can be directly compared with solvation energy computed using the COSMO continuum model. The comparison in Table 2 shows the almost perfect agreement between the two models. The three distinct terms are quite similar in value, indicating that hey contribute to stabilizing the solute in a similar way.

Conclusions

We presented a study aimed at developing an explicit solvation model and applied it to highly charged species, a Keggin polyoxometalate. The model makes use of DFT-based methods as implemented in the ADF program, and of instant configurations of the solvent molecules extracted from classical molecular dynamics simulations. The model includes, step by step, the specific effects of the first solvation shell, since solvent molecules in this shell are explicitly introduced in the DFT calculation. The long-range electrostatic effects created by the bulk of the solvent and by the

counter-ions are introduced in the model through the use of point charges.

The model strongly stabilizes the molecular orbitals of the Keggin anion, and reaches a degree of stabilization fully comparable to COSMO, which was used as a reference. This stabilization is progressive, and increases with the complexity of the model. In addition, the model enables quantifying the effects of the solvent and the counter-ions by splitting the total solvation energy into three terms. The sum of these terms directly compares and nicely agrees with the solvation energy computed by COSMO.

The main limitation of the results presented here is the lack of sampling. All the results were obtained using just one solvent configuration. We think that by increasing the number of configurations a better model could be developed. On the other hand, the model presented here is a first step towards the computational modeling of complex polyoxometalate systems, which should explicitly include additional electrolytes used in the experiments to fix the ionic force. We think that this challenge could be achieved in the near future.

Supplementary data

Supplementary data for this article are available on the journal Web site (canjchem.nrc.ca) or may be purchased from the Depository of Unpublished Data, Document Delivery, CISTI, National Research Council Canada, Ottawa, ON K1A 0R6, Canada. DUD 3989. For more information on obtaining material, refer to cisti-icist.nrc-cnrc.gc.ca/cms/unpub_e.shtml.

Acknowledgments

P.M. is indebted to the Autonomous Government of Catalonia for a grant (2007FIC00043) and is supported by the University and Research Commission of Innovation, the University and Enterprise Department of Catalan Government, and the European Social Fund. We are indebted to the Ministerio de Ciencia e Innovación (MICINN) of the Government of Spain (Grants CTQ2008–06549-C02–01/BQU, CTQ2008–06549-C02–02/BQU, CTQ2008- 06469/PPQ, and Consolider Ingenio 2010 CSD2006–0003), to the CIRIT of the Catalan Government (Grants 2005SGR00715 and 2005SGR00104), and to the Institute of Chemical Research of Catalonia (ICIQ) Foundation for financial support.

References

(1) Pye, C. C.; Ziegler, T. *Theor. Chem. Acc.* **1999**, *101*, 396–408. doi:10.1007/s002140050457.

(2) Klamt, A.; Schuurmann, G. *J. Chem. Soc., Perkin Trans. 2* **1993**, 799–805. doi:10.1039/p29930000799.

(3) Klamt, A.; Jonas, V. *J. Chem. Phys.* **1996**, *105* (22), 9972–9981. doi:10.1063/1.472829.

(4) Klamt, A. *J. Phys. Chem.* **1995**, *99* (7), 2224–2235. doi:10.1021/j100007a062.

(5) Wong, M.; Frisch, M.; Wiberg, K. *J. Am. Chem. Soc.* **1991**, *113* (13), 4776–4782. doi:10.1021/ja00013a010.

(6) Wong, M.; Wiberg, K.; Frisch, M. *J. Chem. Phys.* **1991**, *95* (12), 8991–8998. doi:10.1063/1.461230.

(7) Wong, M.; Wiberg, K.; Frisch, M. *J. Am. Chem. Soc.* **1992**, *114* (2), 523–529. doi:10.1021/ja00028a019.

(8) Wong, M.; Wiberg, K.; Frisch, M. *J. Am. Chem. Soc.* **1992**, *114* (5), 1645–1652. doi:10.1021/ja00031a017.

(9) Barone, V.; Cossi, M. *J. Phys. Chem. A* **1998**, *102* (11), 1995–2001. doi:10.1021/jp9716997.

(10) Barone, V.; Cossi, M.; Tomasi, J. *J. Chem. Phys.* **1997**, *107* (8), 3210–3221. doi:10.1063/1.474671.

(11) Barone, V.; Cossi, M.; Tomasi, J. *J. Comput. Chem.* **1998**, *19* (4), 404–417. doi:10.1002/(SICI)1096-987X(199803)19:4<404::AID-JCC3>3.0.CO;2-W.

(12) Cancès, E.; Mennucci, B.; Tomasi, J. *J. Chem. Phys.* **1997**, *107* (8), 3032–3041. doi:10.1063/1.474659.

(13) Cossi, M.; Barone, V.; Cammi, R.; Tomasi, J. *Chem. Phys. Lett.* **1996**, *255* (4-6), 327–335. doi:10.1016/0009-2614(96)00349-1.

(14) Cossi, M.; Barone, V.; Mennucci, B.; Tomasi, J. *Chem. Phys. Lett.* **1998**, *286* (3-4), 253–260. doi:10.1016/S0009-2614(98)00106-7.

(15) Mennucci, B.; Tomasi, J. *J. Chem. Phys.* **1997**, *106* (12), 5151–5158. doi:10.1063/1.473558.

(16) Mierts, S.; Scrocco, E.; Tomasi, J. *Chem. Phys.* **1981**, *55* (1), 117–129. doi:10.1016/0301-0104(81)85090-2.

(17) Miertus, S.; Tomasi, J. *Chem. Phys.* **1982**, *65* (2), 239–245. doi:10.1016/0301-0104(82)85072-6.

(18) Tomasi, J.; Mennucci, B.; Cances, E. *J. Mol. Struct. THEOCHEM* **1999**, *464* (1-3), 211–226. doi:10.1016/S0166-1280(98)00553-3.

(19) Forti, F.; Barril, X.; Luque, F. J.; Orozco, M. *J. Comput. Chem.* **2008**, *29* (4), 578–587. doi:10.1002/jcc.20814.

(20) Cramer, C. J.; Truhlar, D. G. *Acc. Chem. Res.* **2008**, *41* (6), 760–768. doi:10.1021/ar800019z.

(21) Grigoriev, V.; Hill, C.; Weinstock, I. *J. Am. Chem. Soc.* **2000**, *122* (14), 3544–3545. doi:10.1021/ja993862c.

(22) Poblet, J. M.; López, X.; Bo, C. *Chem. Soc. Rev.* **2003**, *32* (5), 297–308. doi:10.1039/b109928k. PMID:14518183.

(23) López, X.; de Graaf, C.; Maestre, J.; Bénard, M.; Rohmer, M.-M; Bo, C.; Poblet, J. M. *J. Chem. Theory Comput.* **2005**, *1* (5), 856–861. doi:10.1021/ct050040z.

(24) López, X.; Fernandez, J.; Poblet, J. M. *Dalton Trans.* **2006**, 1162–1167. doi:doi: 10.1039/b507599h.

(25) Leroy, F.; Miró, P.; Poblet, J. M.; Bo, C.; Bonet Avalos, J. *J. Phys. Chem. B* **2008**, *112* (29), 8591–8599. doi:10.1021/jp077098p. PMID:18590304.

(26) Mitra, T.; Miró, P.; Tomsa, A.-R.; Merca, A.; Bögge, H.; Ávalos, J. B.; Poblet, J. M.; Bo, C.; Müller, A. *Chem. Eur. J.* **2009**, *15* (8), 1844–1852. doi:10.1002/chem.200801602.

(27) Chaumont, A.; Wipff, G. *Phys. Chem. Chem. Phys.* **2008**, *10*, 6940. doi:10.1039/b810440a.

(28) Lindahl, E.; Hess, B.; van der Spoel, D. *J. Mol. Model.* **2001**, *7*, 306–317. doi:10.1007/s008940100045.

(29) Berendsen, H.; Grigera, J.; Straatsma, T. *J. Phys. Chem.* **1987**, *91* (24), 6269–6271. doi:10.1021/j100308a038.

(30) Jorgensen, W.; Chandrasekhar, J.; Madura, J.; Impey, R.; Klein, M. *J. Chem. Phys.* **1983**, *79* (2), 926–935. doi:10.1063/1.445869.

(31) Jorgensen, W.; Madura, J. *Mol. Phys.* **1985**, *56* (6), 1381–1392. doi:10.1080/00268978500103111.

(32) López, X.; Nieto-Draghi, C.; Bo, C.; Avalos, J. B.; Poblet, J. M. *J. Phys. Chem. A* **2005**, *109* (6), 1216–1222. doi:10.1021/jp046862u. PMID:16833432.

(33) Lee, S. H.; Rasaiah, J. C. *J. Phys. Chem.* **1996**, *100* (4), 1420–1425. doi:10.1021/jp953050c.

(34) te Velde, G.; Bickelhaupt, F. M.; Baerends, E. J.; Guerra, C.; van Gisbergen, S. J. A.; Snijders, J. G.; Ziegler, T. *J. Comput. Chem.* **2001**, *22* (9), 931–967. doi:10.1002/jcc.1056.

(35) te Velde, G.; Baerends, E. J. *J. Comput. Phys.* **1992**, *99* (1), 84–98. doi:10.1016/0021-9991(92)90277-6.
(36) Fonseca Guerra, C.; Snijders, J. G.; te Velde, G.; Baerends, E. J. *Theor. Chem. Acc.* **1998**, *99* (6), 391–403. doi:10.1007/s002140050021.
(37) Baerends, E. J.; Ros, P. *Chem. Phys.* **1973**, *2* (1), 41–51. doi:10.1016/0301-0104(73)80059-X.
(38) Vosko, S. H.; Wilk, L.; Nusair, M. *Can. J. Phys.* **1980**, *58*, 1200–1211. doi:10.1139/p80-159.
(39) Becke, A. D. *Phys. Rev. A* **1988**, *38*, 3098. doi:10.1103/PhysRevA.38.3098.
(40) Becke, A. D. *J. Chem. Phys.* **1986**, *84* (8), 4524. doi:10.1063/1.450025.
(41) Perdew, J. P. *Phys. Rev. B* **1986**, *33*, 8822–8824. doi:10.1103/PhysRevB.33.8822 .
(42) Perdew, J. P. *Phys. Rev. B* **1986**, *34*, 7406. doi:10.1103/PhysRevB.34.7406.
(43) van Lenthe, E.; Ehlers, A.; Baerends, E. *J. Chem. Phys.* **1999**, *110* (18), 8943–8953. doi:10.1063/1.478813.
(44) van Lenthe, E.; Baerends, E. J.; Snijders, J. G. *J. Chem. Phys.* **1993**, *99* (6), 4597–4610. doi:10.1063/1.466059.
(45) van Lenthe, E.; Baerends, E.; Snijders, J. *J. Chem. Phys.* **1994**, *101* (11), 9783–9792. doi:10.1063/1.467943.
(46) van Lenthe, E.; Snijders, J.; Baerends, E. *J. Chem. Phys.* **1996**, *105* (15), 6505–6516. doi:10.1063/1.472460.
(47) van Lenthe, E.; van Leeuwen, R.; Baerends, E.; Snijders, J. *Int. J. Quantum Chem.* **1996**, *57* (3), 281–293. doi:10.1002/(SICI)1097-461X(1996)57:3<281::AID-QUA2>3.0.CO;2-U.
(48) Su, J.; Xu, X.; Goddard, W. *J. Phys. Chem. A* **2004**, *108* (47), 10518–10526. doi:10.1021/jp047502+.

Kohn–Sham DFT and ligand-field theory — Is there a synergy?

Claus E. Schäffer and Jesper Bendix

Abstract: In forming electronic states of the partially filled shell of transition-metal atomic and molecular systems, real, symmetry-based, fixed, Kohn–Sham eigenorbitals can be used to bridge KS-states with strong-field, ligand-field states. Thereby, DFT computations, restrained by the use of these frozen orbitals of the so-called average-of-configuration type, allow a central-field modeling of the partially filled shell whose Hamiltonian matrix consists of mutually orthogonal diagonal and non-diagonal parts, of which only the former can be computed. Mutually orthogonal operators of ligand-field theory are particularly suited to parameterize the energy "data" obtained from the bridges between molecular Kohn–Sham DFT states and ligand-field states. With the d^2 configuration as the simplest example encompassing both ligand-field and interelectronic repulsion, each one-electron parameter, though defined by energy differences of perturbed d orbitals, is associated with a 45×45, diagonal, theoretical, strong-field-type coefficient matrix of the ligand field repulsion model (LFR), which is mapped in a one-to-one fashion onto a likewise diagonal KS-DFT computational energy matrix. For sets of mutually orthogonal operators, the mapping determines the value of any such ligand-field parameter as a scalar product between the DFT matrix and the coefficient matrix of the associated ligand-field operator. Each and every two-electron parameter of LFR is in the same strong-field function basis associated with a 45×45 coefficient matrix that includes a non-diagonal part. This matrix, nevertheless, by the formation of a scalar product with the appropriate diagonal, computational DFT matrix, provides the value of the two-electron parameter. In spite of the lacking non-diagonal DFT information, its non-diagonal elements of the two-electron interelectronic repulsion matrices are indirectly accessible through the parameterization based upon the computed diagonal DFT matrices combined with the mapping of the DFT energy results onto the parametric LFR. In this way, LFR delivers back to DFT a quantification of the deviation of the systems' eigenbasis from the DFT-computed states, which are defined by having unit occupation numbers. This work focuses firstly on using the LFR model for forming a full DFT energy matrix and dissecting it into mutually orthogonal one- and two-electron parts and secondly on the use of the two-electron parts to obtain a complete ligand-field image of a nephelauxetic, molecular atom, intrinsic of the chemical system.

Key words: Kohn–Sham DFT, average-of-configuration, ligand-field theory, interelectronic repulsion, mutually orthogonal operators.

Résumé : Dans la formation des états électroniques de la couche partiellement remplie des systèmes atomiques et moléculaires d'un métal de transition, on peut utiliser les orbitales propres de Kohn-Sham DFT, réelles, fixes et basées sur la symétrie pour faire le pont avec des états de champ de ligand dans la formulation de champ fort. Il est donc possible que des calculs selon la théorie de la fonctionnelle de la densité (TFD) restreints par l'utilisation de ces orbitales fixes du type connu sous le nom de configuration moyenne puisse permettre d'utiliser un modèle à champ central d'une couche partiellement remplie dont la matrice de l'hamiltonien serait formée de parties mutuellement orthogonales diagonales et non diagonales desquelles on ne calculerait que les premières. Les opérateurs mutuellement orthogonaux de la théorie du champ de ligand sont particulièrement appropriés pour déterminer les paramètres des données d'énergie obtenues à partir des ponts entre des états moléculaires de la TFD selon Kohn–Sham et les états du champ de ligand. Avec la configuration d^2 comme exemple le plus simple recouvrant le champ de ligand ainsi que la répulsion interélectronique, chaque paramètre pour un électron, même s'il a été défini par des différences d'énergie d'orbitales d perturbées, est associé à une matrice 45×45, diagonale, théorique avec un coefficient du type champ fort du modèle de la répulsion du champ de ligand (RCL) qui peut être décrit d'une façon un à un sur une diagonale apparentée d'une matrice d'énergie calculée de la théorie de la fonctionnelle de la densité selon Kohn–Sham (TFD-KS). Pour les ensembles d'opérateurs mutuellement orthogonaux, la représentation permet

Received 20 December 2008. Accepted 19 March 2009. Published on the NRC Research Press Web site at canjchem.nrc.ca on 5 September 2009.

This article is part of a Special Issue dedicated to Professor T. Ziegler.

Abbreviations: KS-DFT, Kohn–Sham DFT or molecular orbital DFT; ADF, Amsterdam density functional; AOC, average-of-configuration (when all the spin orbitals of the partially filled shell are equally oocupied); WFT, wave-function theory; HF, Hartree–Fock; LFT, ligand-field theory; LFR, ligand-field repulsion model; LF, ligand field (a one-electron model operator); R, repulsion (a two-electron model operator); SCS, the Slater–Condon–Shortley model of interelectronic repulsion; PMT, the parametric multiplet term model of effective interelectronic repulsion; SCF, self-consistent field.

C.E. Schäffer[1] and J. Bendix. Department of Chemistry, University of Copenhagen, Universitetsparken 5, DK-2100, Denmark.

[1]Corresponding author (e-mail: ces@kiku.dk).

d'attribuer une valeur pour chacun des paramètres de champ de ligand sous la forme du produit scalaire entre la matrice de la TFD et le coefficient de la matrice du l'opérateur du champ de ligand qui lui est associé. Tous et chacun des paramètres à deux électrons du coefficient du type champ fort du modèle de la RCL fait partie de la même fonction de base du champ fort associé avec le coefficient d'une matrice 45×45 qui inclut une partie non diagonale. En raison de sa formation par un produit scalaire impliquant une matrice TFD diagonale calculée appropriée, cette matrice fournit le paramètre à deux électrons, malgré tout. Même s'il manque l'information TFD non diagonale, ses éléments non diagonaux des matrices de répulsion interélectroniques à deux électrons sont indirectement accessibles par le biais de la paramétrisation basée sur les matrices diagonales TFD calculées combinées avec la représentation de l'énergie TFD conduit à l'obtention de la RCL paramétrisée. De cette façon, la RCL fournit à la TFD une quantification de la déviation des bases propres du système à partir d'états calculés par la TFD qui sont définies par des nombres d'occupation d'unités. Ce travail est principalement orienté vers l'usage du modèle de la RCL pour créer une matrice complète d'énergie TFD et sur sa dissection en parties à un et à deux électrons mutuellement orthogonales et ensuite vers l'utilisation des parties à deux électrons pour obtenir une image à champ de ligand complète d'un atome moléculaire néphélauxétique, intrinsèque du système chimique.

Mots-clés : théorie de la fonctionnelle de densité de Kohn–Sham (TFD-KS), moyenne de configuration, théorie du champ de ligand, répulsion interélectronique, opérateurs mutuellement orthogonaux.

[Traduit par la Rédaction]

Introduction

A paper by Ziegler at al.[1] implied that Kohn–Sham DFT was capable of providing an energy that corresponds to an expectation value of a Hamiltonian of a wave-function description of a molecule. This capability has been used in recent years to illuminate and revive ligand-field theory. Tom told us in Danish, after having been elected a member of the Danish Royal Society of Humanities and Sciences, that he, 40 years ago, had attended a course on ligand-field theory, given by one of us at our university. He added with a smile that he had not appreciated it. Then, last August in Vålådalen, Sweden, at the 50th anniversary of the Löwdin summer schools on quantum chemistry, he expressed that he had come to appreciate it. We therefore thought it would be appropriate for this Special Issue of the *Canadian Journal of Chemistry* to illustrate some of the possible synergies between KS-DFT and ligand-field theory as we see them.[2–6]

At first, we emphasize that the novelty here is a more thorough discussion of the consequences of using KS-DFT as a tool replacing spectroscopic results. Our eyes are those of experimentalists and ligand-field theoreticians. We summarize that the ligand-field repulsion model (LFR), whose Hamiltonian does not contain the spin, is the sum of a ligand-field part and an interelectronic repulsion part, both acting on a d^q configuration. For half a century, it has been known that two apparently rather different formulations of this "quantitative LFR", the weak-field and the strong-field formulation, are mathematically equivalent. The weak field is diagonal in the interelectronic repulsion (R), the strong field in the ligand-field (LF) parameters. The number of LF parameters is determined by the symmetry of the ligand field and the particular choice of parameters may also be made on the basis of symmetry. The most famous LF parameter is the so-called spectrochemical parameter or cubic-field splitting parameter Δ, which for a metal complex of T_d symmetry is defined as the one-electron energy difference between the $e(T_d)$ and the $t_2(T_d)$ set of "d" orbitals, where the quotation marks refer to the fact that the orbitals of the molecular situation have a d orbital parentage. Once the one-electron parameters have been defined, the concept of the strong-field function basis is defined physically. In conventional LFR, all d^q functions are naturally chosen to be eigenfunctions of $\hat{S}^2$, as the Hamiltonian of LFR commutes with this operator.

Recent developments based upon a KS-DFT model have focused on the requirements of this model. The fact that the energies, which in our context are obtainable by the use of KS-DFT as a computational model, correspond to d^q functions that are single Slater determinants[2] means that the computed energies in wave-function theory are expectation values, rather than eigenvalues, of the Hamiltonian, and the associated KS state functions must be conceived as eigenfunctions of $\hat{S}_z$ rather than $\hat{S}^2$. Nevertheless, the energies directly obtained from KS-DFT belong to a strong-field situation of LFR, but the energies are different from those of the conventional situation. In LFR, the energy matrix based upon single Slater determinants is much further away from being diagonal than is the case in the conventional strong-field description. Thus, a major part of the effect of the exchange integrals is contained in the non-diagonal elements of this single-determinant basis, which we shall call for short the DFT-basis. This partial loss of the exchange-information from the DFT computations would seem to be a fatal problem and is of course a problem in a general sense. However, LFR operates by its determination of energy parameters that allow the eigenfunctions to be determined through the model, and from the eigenfunctions, all the other properties, which are consequences of the model. Here, the KS-DFT mimicking of LFR has up until now[2–6] been extremely useful because its computational results have agreed well with the empirical data on which ligand-field theory built its well-known successes in inorganic chemistry as well as its pedagogical successes.[7] Therefore, KS-DFT already has the status of being a valuable supplement or, even to a certain extent, a replacement of spectroscopic experiments.

This story also seems like a little miracle in view of the fact that ligand-field theory is so horribly simple that no one would ever have thought that it could be supported computationally in such a fundamental way. Moreover, in our previous work, our main focus was the interelectronic

repulsion (R) of ligand-field theory rather than the ligand field, LF, itself. However, our analyses cast light upon the combined model, LFR, and left the result that the model Hamiltonian matrix of LFR, after having been associated with computed KS-DFT energies, contained more information[6] regarding the partially filled shell than was extractable from KS-DFT without LFR.

Here, we focus upon the extraction of this additional information from the bridging between DFT and LFR in the hope that LFR can deliver some credit back to DFT, which has the deficiency of partially hiding the two-electron interaction energies.

The KS-DFT description

An unusual property of Kohn–Sham DFT: fractional occupation numbers

The one-electron density is introduced into KS-DFT by means of KS-orbitals. This feature of KS-DFT allows non-integer occupation numbers to be associated with well-defined computed energies. Thus, when the issue is a mimicking of LFR, the ten d spin-orbitals may be all occupied evenly so as to define the eigenorbitals of a totally symmetrical atomic or molecular system. This particular choice of occupation numbers, named the average-of-configuration, AOC,[2,3,8,9,10] has been suggested as the first step of these kinds of computations. The fact that the energy associated with the AOC is not the average energy of the configuration was at the same time pointed out.[8] If KS-DFT is constrained by the use of "average-of-configuration" frozen orbitals, an additional one-to-one relationship between unit occupation number pairs of KS spin orbitals and d^2 Slater determinants based upon real d orbitals can be established.[2,3] This means that KS-DFT molecular "d^2" energies can be equated with d^2-parameterized energies of the ligand-field theory. These energies may comprise effective two-electron operator contributions.

Many years ago, Ziegler et al. argued[1] that unit (combined with zero) occupation numbers were the key to bridging from the Hartree–Fock–Slater model to wave function theory in the form of Slater determinants. Unit occupation numbers of the AOC spin-orbitals make the basis for the mimicking of LFR, the AOC being the basis for the KS-DFT definition of the fixed (frozen) orbitals.

The ligand-field repulsion description

Quantitative ligand-field theory and the orthogonal operators formalism

LFR is a sum of operators: a sum of one-electron operators representing LF and of two-electron operators representing R. Both kinds of operators act on the configuration d^q (or p^q or f^q) and when the chemical system is molecular and the l value of the orbitals becomes subclassifiable (for example, for d orbitals in tetrahedral symmetry as $t_2(T_d)$ and $e(T_d)$), the R part of LFR causes this model to include a subconfiguration interaction, for example, the interaction[3] between the $^3T_1$ states of the subconfigurations et_2 and t_2^2 is a part of LFR. By the inclusion of this type of correlation, LFR reaches in this special respect beyond Hartree–Fock.

LFR is often formulated on a symmetry basis. Then, an inherent heterogeneity is revealed by the fact that the LF operators, which are defined upon a d^1 function space, have the symmetry assumed for the molecular system, while the R part, which is defined on a d^2 function space, is parameterized by the Slater–Condon–Shortley (SCS) parameters or equivalent sets, or even sets richer in parameters, such as the parametric multiplet term (PMT) sets. These parameterizations imply spherical symmetry. The consequence of these essentially different definitions is that the LF and R operators are mutually orthogonal on d^2 (vide infra) and remain so for the other d^q configurations (see ref. 22 and refs. cited therein). Another consequence is that quantitative LFR encompasses a central-field view on ligand-field theory (LFT) by parameterizing the R part as if the chemical system were spherical and by using basis orbitals that are eigenfunctions of the angular momentum operator $\hat{l}^2$. Moreover, by letting the LF part be defined solely by the symmetry of the chemical system, the theoretical part of LFR lies to 100% in the angular factors.

In the last two decades, we have used the SCS model in terms of the parameters D and E,[11] whose associated coefficient operators are mutually orthogonal alternatives to the conventionally used non-orthogonal operators of the Racah B and C parameters. D is Jørgensen's 50 year old spin-pairing energy parameter,[12] which we have analyzed to have a spin as well as a seniority origin, and E is the supplementary parameter of the SCS model, which, in addition, is connected with D by its associated coefficient operator being orthonormal to that of D. The orthogonality means that the parameter value can be obtained as a scalar product between the LFR Hamiltonian operator and the coefficient operators of the parameters; the normality means that the values of D and E are directly comparable in the following sense: for an atomic system, the sum of the squares of the barycentered eigenvalues, $<\hat{H}_R|\hat{H}_R>$, is a sum of the following two contributions from the parameters

$$[1] \qquad <\hat{H}_R|\hat{H}_R> = D^2 <\hat{Q}[D]|\hat{Q}[D]> + E^2 <\hat{Q}[E]|\hat{Q}[E]>$$

The important point here being that no cross terms occur, contrary to the case with the conventional parameterizations of the SCS model.

About 30 years ago, it became the custom among atomic spectroscopists to embody their observations in a quantum mechanical modeling, which gradually became more and more refined and provided with more and more well-defined parameters that were able to accurately reproduce their data sets. We used one of these models, which had a Lie-group history among theoretical physicists[13] and which encompassed all d^q configurations under one symmetry roof, and another one developed by the atomic spectroscopists,[14] which we slightly modified for our purposes, namely the determinations of spin-orbit parameters as accurately as possible from the spectroscopic J-level data.[15] We named our model the parametrical multiplet term model (PMT) because it used the energies of the multiplet terms as its major parameters. These multiplet term parameters are not directly determinable from spectroscopy, whereas their spin-orbital components, their levels are. Thus, by optimizing the energies of the multiplet terms, the standard deviations on the spin-orbit coupling constants based upon the full spectro-

scopic information, that is, the complete set of experimental energy data for all the levels of the d^q configuration, became minimized.

In our DFT work on atomic systems,[2,4] the PMT model was used in the first place to obtain a maximally flexible repulsion description intended to mimick the experimental data tightly.[4] However, when comparing the results of the computed PMT energies with those of the SCS model by confronting these two sets of "data" with experimental energy data, it turned out that the SCS model gave the better agreement.

For d^2 systems, the extension of the SCS model to the PMT model is particularly simple and instructive. Thus, the PMT model has a Hamiltonian acting on the full d^2 function space just as the SCS model does. Moreover, the four parameters, which the PMT model requires for obtaining a 100% fitting of the energy differences between the five multiplet terms of d^2, can be chosen in such a way that a contraction[4,6] by discarding two of the parameters results in the SCS model.

The superstructure of the ligand-field repulsion model: weak-field and strong-field limits

The weak-field and strong-field representations of LFR are equivalent representations connected by a unitary transformation. The former one is diagonal in R, the latter one in LF. If real functions are used as the orbital basis and the two-electron functions are chosen to be eigenfunctions of $\widehat{S}^2$, the transformation matrix is equal to a permutationally symmetrized Racah-lemma matrix,[16] which means that it is purely symmetry-determined. The concepts of the weak-field and strong-field limits refer to the energy expressions of the diagonal elements of the corresponding matrices. We shall refer to the special strong-field diagonal whose functions are single Slater determinants, and therefore eigenfunctions of $\widehat{S}_z$, but not necessarily also eigenfunctions of $\widehat{S}^2$, as DFT-based (vide infra).

By attaching unit occupation numbers to the frozen "d" spin orbitals that are molecular orbital eigenorbitals of KS-DFT, chemical situations arise, which translate to Slater determinants of WFT and LFR. These Slater determinants are diagonal in LF, and therefore belong to the class normally associated with the limiting strong-ligand field. It should be emphasized that this never means that R is not present. Therefore, although the concepts of the weak- and the strong-ligand-field limits are mathematically symmetrical concepts, this symmetry does not hold chemically because in the weak-field limit, the LF is actually not present and its radial parameters therefore cannot avoid being vanishing.

The fact that the conventional LFR model is semi-empirical in the sense that the angular factors make up all its theory while the radial factors are purely empirical is responsible for the success of the model. That is not to say that this fact ever provided an understanding of why it furnished the model with such a width within the chemistries of systems with partially filled shells of atomic parentage. However, the new fact that the empirical parameters of LFR have now become so satisfactorily computationally available came as a complete surprise because of the extreme simplicity of the model. We chose to emphasize this by using the term "data" for the set of energy expectation values obtained by the computational DFT model.

The AOC computation is unique in a chemical sense and from the point of view of WFT; chemically, because it is used to define the complete orbital basis so that it is adapted to the symmetry of the chemical system, and from a WFT point of view, because it is defined by fractional occupation numbers. Last but not least, the AOC computation is also unique within our approach by being the only restricted computation for any given chemical system that involves an SCF computation.

The fact that this SCF computation consists of a series of consecutive steps furnishes a quantification of the conventional qualitative superstructure of ligand-field theory: For a molecular system, the starting point of the iterative SCF procedure is the completely ionic situation as far as orbital occupation numbers are concerned. Then, the atomic orbitals, while keeping their occupation numbers unchanged, are gradually modified so as to end up being Kohn–Sham molecular orbitals, which are quantitatively specified. In this way, the qualitative superstructure of semi-empirical LFT has become quantitatively illustrated by the AOC computation.

Sets of mutually orthogonal conglomerate operators for describing LFR

The Hamiltonian of LFR acting on a d^q configuration can, for a cubic system using the SCS model, be written in the simple form

$$[2]\qquad \widehat{H}_{LFR} = E_{av}\widehat{1} + \Delta\widehat{Q}[\Delta] + R\widehat{Q}[R] = E_{av}\widehat{1} + \Delta\widehat{Q}[\Delta] + D\widehat{Q}[D] + E\widehat{Q}[E]$$

where E_{av} is the average energy of d^q, D is Jørgensen's spin-pairing energy parameter, and E is the spatial energy parameter. In the first term, $\widehat{1}$ is the scalar operator whose matrix in all function bases is a unit matrix, $\Delta\widehat{Q}[\Delta]$ is the ligand-field operator, and $\widehat{Q}[D]$ and $\widehat{Q}[E]$ are mutually orthogonal coefficient operators, which are diagonal when the ligand field is vanishing so that the symmetry is spherical. Moreover, all the coefficient operators are orthogonal to $\widehat{1}$ by being barycentered.

Mutual orthogonality of two operators $\widehat{A}$ and $\widehat{B}$ is, when the function bases are real, defined by the scalar product relationship

$$[3]\qquad \langle \widehat{A} \mid \widehat{B} \rangle = \sum_{i,j} \mathbf{A}_{ij}\mathbf{B}_{ij} = 0$$

and this operator overlap[16] is accordingly independent of the function basis. A useful corollary to eq. [3] is that it also defines the scalar product of the matrices.

The value of an energy parameter can be found by forming the overlap (or scalar product) between the Hamiltonian operator and the coefficient operator associated with the parameter. We have, for example, using eq. [2]

$$[4]\qquad < \widehat{H}_{LFR}|\widehat{Q}[D] >= D < \widehat{Q}[D]|\widehat{Q}[D] >$$

as a consequence of the orthogonality between, on one hand, the LF and R operators, and on the other hand, between $\widehat{Q}[D]$ and $\widehat{Q}[E]$.

If H_{LFR} is replaced by H_{obs}, where H_{obs} is hypothetically

assumed to be an exact observation of the complete H_{LFR} matrix referring to a known function basis, then the value obtained for D is identical to the value obtained by a least-squares procedure, and the fitting will be 100%. An analogous description applies to a non-exact observation except that there will now be a residual diagonal matrix, which by the very procedure is orthogonal to the matrix of $\widehat{Q}[D]$. When all the three barycentered parameters of eq. [2] have been determined, the self overlap or norm square of the residual matrix is the total variance of the fitting. The norm squares of the operators depend on the function space (but not on the function basis). However, the concept of the diagonal norm square is useful provided the basis is defined and interesting. Then, the ratio between the diagonal norm square and the full norm square is the degree of diagonality, which is always of interest if the elements of the diagonal are the observations. For d^2, the norm square of $\widehat{1}$ equals 45, and the same is true for the diagonal norm square. The norm squares of the SCS coefficient operators, $\widehat{Q}[D]$ and $\widehat{Q}[E]$,[4,11] are by their definition equal to 400/7 with the consequence that the Landé-like formula applies

$$[5] \qquad E_{av}[S{=}0] - E_{av}[S{=}1] = 2D$$

For the norm square, area, of $\widehat{H}_R$ the equation

$$[6] \qquad < \widehat{H}_R|\widehat{H}_R >= 45(E_{av})^2 + (400/7)D^2 + (400/7)E^2$$

tells that the area of the model Hamiltonian is equal to the sum of the squares of the normalized parameters, which is an expression of extended Pythagorean form that we use when the associated coefficient operators are normalized to unity over the full function space, here d^2. For the sum of the squares of the observed Hamiltonian matrix minus the total variance, the expression in eq. [6] applies as well.

The norm square has a further use based upon the following statement: Because two operators $\widehat{Q}[D]$ and $\widehat{Q}[E]$ say, have the same norm squares, then if $D > E$, the contributions of D to the area of LFR is also larger than that of E. This statement has, of course, a quantitative corollary.

The experimental information is, in practice, never complete. The most common situation for the semi-empirical LFR is that a limited number of eigenvalue differences are the observed quantities and the problem is to use the model to find the eigenbasis corresponding to the parameter values that diagonalize the parametric energy matrix. By using KS-DFT, we obtain the special LFR situation that the number of "observations" is mathematically maximal but the kind of observation is far from being perfect because the "experimental" method, that is, computation of the DFT energies dictates the DFT-basis in which the R operators are not diagonal and for some operators far from diagonal. The orthogonal operator's formalism is especially effective for analyzing this situation when it is applied to the complete function basis in which case the scalar product procedure is available for determining the individual parameters. However, since we have no "observations" relating to the non-diagonal elements of LFR in the DFT-basis, only the diagonal part of this matrix contributes to the scalar products.

For the chemical system being a molecular d^q system of lower symmetry than cubic, the ligand-field terms of the same form and in the same basis as that contained in eq. [2] must be chosen hierarchically and added. These terms are then mutually orthogonal one-electron terms, which automatically are orthogonal also to the two-electron terms, and they are favored by being diagonal in the DFT-basis,[13,17] which means that the one- and two-electron operators are also diagonally orthogonal in this basis. Looking back at the atomic chemical system, one has to remember that here the curious feature applies that the DFT computation model nevertheless requires the DFT strong-field basis even though the radial parameters of LF are zero.

Fig. 1. Illustration of three mutually orthogonal components of LFR in the DFT-basis. With the basis fixed, mutual operator orthogonality and mutual matrix orthogonality become synonymous (cf. eq. [3]). Only the two horizontal parts can be DFT-computed. Once the R parameters have been computed, the non-diagonal component of LFR is also known.

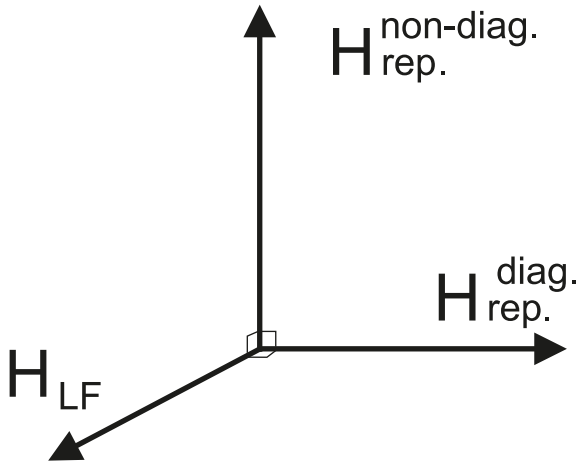

In any given function basis, a simple operator or a composite operator such as $\widehat{Q}[R]$ of eq. [2] can be divided into diagonal and non-diagonal parts, which by their very structure (eq. [3]) are mutually orthogonal. This situation is illustrated in Fig. 1.

Classification of the Slater determinantal functions of the DFT basis

In our study of atomic d^q ions,[2] we considered the use of orbitals that were characterized by m_l values and thus were complex linear combinations of real d orbitals. With just one example, this choice was demonstrated to be an impossible one. Thus, the Slater determinant |(2)(1)| with M_S = 1 is clearly a pure ^{3}F function. On the other hand, the determinant |(3)(–1)|, likewise with M_S = 1, corresponds to the same one-electron density and thus the same DFT energy, but consists of 60% ^{3}F and 40% ^{3}P, as can be read from the Wigner coefficients for coupling the two d functions to obtain F and P symmetries. This kind of problem is avoided if real orbitals are used. Thus, our problem is to find parametric expressions for the LFR energies of Slater determinants built upon real orbitals. These are linear spherical harmonics for which a lot of symmetry information has accumulated[18] during the LFT era. The LF energy contribution of our strong-field determinants is just the sum of the one-electron energies. So, we are left with the R terms, expressed in a

real Slater-determinant basis, using for instance some parameterization of the SCS model.

The symmetry analysis turned out to be simple, but extraordinary (Table 1). The obvious properties of the Slater determinants are their being eigenfunctions of the spin component operator $\widehat{S}_z$ and their two-electron energy expectation values accordingly expressible in terms of Coulomb integrals (J) and exchange integrals (K). When d^2 Slater determinants are eigenfunctions of $\widehat{S}_z$ with M_S values of 1 or –1, this implies that they are also eigenfunctions of $\widehat{S}^2$ with energies of the form J–K. However, when such single Slater determinants have $M_S = 0$, they cannot simultaneously be eigenfunctions of $\widehat{S}^2$ unless the orbitals are doubly occupied, in which case they belong to class 0 of Table 1 with energy J_0. For these reasons, the 45 Slater determinants of d^2 can immediately be separated into three classes whose expectation values of the coefficient operator $\widehat{Q}[D]$ are tabulated in Table 1.

Class 0 encompasses the doubly occupied class consisting of five determinants, all with the Coulomb energy J_0. Class 1 has the singly occupied orbitals with $M_S = 0$ with an energy equal to a specific Coulomb energy, for example $J(xy,zx)$ referring to the two Slater determinants $|(xy)(zx)|$ with the columns $m_s = 1/2$ and $m_s = -1/2$ and vice versa. There are 20 members in this class. Finally, class 2 also has singly occupied orbitals, but in this case, the Slater determinants have $|M_S| = 1$. Again, there are 20 members whose energy expressions are J–K, where K refers to the exchange integral, for example $K(xy,zx)$. Altogether, there are 45 Slater determinants as required by the Pauli principle for two equivalent d electrons. The three classes are separated in energy in the SCS model solely by Jørgensen's spin-pairing energy parameter D.

Table 1. Symmetry analysis.

	Strong-field labeled repulsion integral	Degeneracy	$\widehat{Q}[D]$	$\widehat{Q}[E]$
Class 0	J_0	5	40/21	0
Class 1	$J_{\delta\delta}$	2	4/21	20/21
	$J_{\sigma\pi}$	4	4/21	12/21
	$J_{\pi\pi}$ and $J_{\pi\delta}$	10	4/21	–4/21
	$J_{\sigma\delta}$	4	4/21	–12/21
Class 2	$J_{\delta\delta}$–$K_{\delta\delta}$	2	–14/21	30/21
	$J_{\sigma\pi}$–$K_{\sigma\pi}$	4	–14/21	18/21
	$J_{\pi\pi}$–$K_{\pi\pi}$ and $J_{\pi\delta}$–$K_{\pi\delta}$	10	–14/21	–6/21
	$J_{\sigma\delta}$–$K_{\sigma\delta}$	4	–14/21	–18/21

The five Slater determinants of class 0 can be illustrated by just one of the d orbitals; for example, $|(xy)(xy)|$, of course with $M_S = 0$. The functions of this class are degenerate for atomic systems. The class 1 and class 2 Slater determinants are both divided into energy subclasses, which in the SCS model are separated by another energy parameter,[9] denoted by E. This parameter is proportional to the historically extremely important energy difference between ^3P and ^3F (and in particular between ^4P and ^4F of the configuration d^3, which has provided a dominant part of all the information we have about nephelauxetism) and thereby also to the Racah parameter B when this is combined with the other Racah parameter C.[4] A symmetry property of the spatial part of the real d orbitals[4] is responsible for the pair-interaction subclasses of the SCS model as well as the PMT model.

The coefficients to the parameter E of the SCS model are given in Table 1 in terms of matrix elements of the associated coefficient operator $\widehat{Q}[E]$. In order of decreasing repulsion energy, the spatial part of the subclasses may be labeled by

[7]

			Number of determinants
Subclass 1	δ−δ	$e2t_23(T_d)$	1
Subclass 2	σ−π	$e1t_22$, $e1t_21$	2
Subclass 3	π−π	t_21t_23, t_22t_23, t_21t_22, $e2t_21$, $e2t_22$	5
Subclass 4	σ−δ	e1e2	2

where the individual subclasses are defined by the lambda values of the real linear spherical harmonics[18b–18d] combined with the components of the symmetry species of T_d. It should be noted that the π–π subclass of Slater determinants (for reasons of spatial symmetry)[4] includes the π–δ subclass, as for example $|(zx)(yz)|$, which clearly has the same repulsion energy as $|(zx)(xy)|$.

Common to class 1 and class 2 are the relative expectation energy differences between the subclasses,[4] cf. Table 1. Thus, while the energy difference between subclass 1 and subclass 2 equals that between subclasses 3 and 4, the energy difference between subclass 2 and subclass 3 is twice that. Explicit details have been tabulated in ref. 4 (Chapter 4) and are illustrated in Fig. 2.

It should be noted that an approximate adherence to these parametric expressions for the KS-DFT energies could be observed immediately on inspection of the computed AOC-KS-DFT Slater-determinant energies; at first for our atomic computations[2] and then for the molecular ones.[3,4] From an intuitive point of view, this agreement, even if approximate, is surprising, since the KS-DFT fundamentally is one-electron density-based and yet here provides remarkable results concerning two-electron interaction energies, even for the Slater determinants built up from molecular orbitals.

Partial quenching of the total spin operator in the strong-field, single-determinant bases — The spin symmetry problem of the class 1 Slater determinants, its analysis, and solution

The class 1 Slater determinants (Table 1) consist of pairs that are related to each other by a permutation of their columns. With the first functions associated with $m_s = 1/2$ and the second one with $m_s = -1/2$, $|(xy)(zx)|$ and $|(zx)(xy)|$ make

Fig. 2. The relative, symmetry-determined interlectronic repulsion interactions within the d-shell, cf. eq. [7] and the surrounding text. The figure illustrates particularly the symmetry obtained by linear adapatation of the basis functions, where detailed specification of the components is unnecessary.

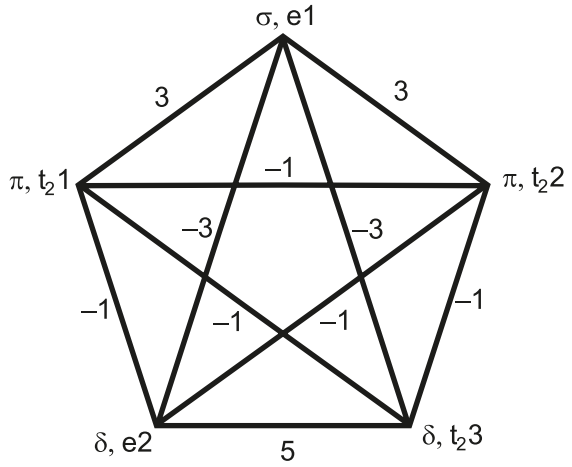

up an example of such a pair. In WFT, these two determinants, which are eigenfunctions of $\widehat{S}_z$ with eigenvalue zero, both have the diagonal elements J_3 and are connected by a non-diagonal element equal to the exchange integral K_3, where the subindices refer to the subclass 3 of eq. [7] (see also Table 1 and Fig. 2). Diagonalization of the corresponding two-by-two matrix

$$[8] \qquad \begin{bmatrix} J_3 & K_3 \\ K_3 & J_3 \end{bmatrix}$$

provides us with the eigenfunctions of $\widehat{S}^2$, and this use of WFT for all the orbital pairs was implemented in two previous papers[4,6] to adapt the directly obtained KS-DFT energies so as to obtain the singlet eigenenergies J_3+K_3 and triplet eigenenergies J_3-K_3. The function basis implied in this energy adaptation was called the spin basis (sb, eigenfunctions of $\widehat{S}^2$) as opposed to the DFT-basis, which was called the Slater-determinant basis (db, eigenfunctions of $\widehat{S}_z$).

An alternative way of bridging between LFR and KS-DFT is to adapt the conventional basis of LFR (the sb) to the DFT-basis (db). This can be accomplished by transforming the appropriate pairs of $\widehat{S}^2$ eigenstates with $M_S = 0$, which are those occurring in a standard strong-field LFR calculation, into the corresponding eigenstates of $\widehat{S}_z$.

Illustration of the PMT model by use of the definition of its spin and seniority operators' diagonal parts in the KS-DFT basis

Certain fundamental observations are necessary before the spin and seniority separators can be defined in strong-field bases in general and in the DFT-basis in particular:

(*i*) The ^{1}S term is the only state among the 45 states of d^2, which has the pure seniority equal to *zero*. The meaning of this concept is that if ^{1}S of d^2 is viewed mathematically as a member of the d^q group of configurations incorporating all q, then another ^{1}S term has already occurred at $q = 0$. This q value of the first ^{1}S term is the seniority number v of the second one.

(*ii*) The ^{1}S state of d^2 is an equally weighted linear combination of the five states of class 0 of Table 1, each of which consists of doubly occupied d orbitals. This means that these five states are distinguished from the remaining 40 states of d^2 by seniority. This fact combined with the operator barycentration suffices to define the operator $\widehat{Q}[D_v^{DFT}]$ (up to a constant of proportionality).

(*iii*) Denoting the class expectation values of $\widehat{S}^2$ by $<\widehat{S}^2>$, these remaining 40 states fall by virtue of $\widehat{S}^2$ into two classes, each containing 20 functions. These classes are characterized by $<\widehat{S}^2> = 1$ when $M_S = 0$ and by $<\widehat{S}^2> = S(S+1) = 2$ when $M_S = |1|$. Thereby, the operator $\widehat{Q}[D_v^{DFT}]$ has been defined (up to a constant of proportionality).

For the operators $\widehat{Q}[D_v^{DFT}]$ and $\widehat{Q}[D_s^{DFT}]$, which separate by seniority and spin, respectively, a comparison with Table 1 is illustrative. The top right suffix marks the function basis that has been chosen for the definition of the mutually orthogonal operators.

The spatial separators are subspace separators, one applying to the $<\widehat{S}^2> = 1$ subspace and the other one to the $<\widehat{S}^2> = 2$ subspace of functions. Thereby, the diagonal matrix elements of the spatial operators, $\widehat{Q}[E_1^{DFT}]$ and $\widehat{Q}[E_2^{DFT}]$, respectively, are obtained from the pentagon numbers of Fig. 2 (again up to a constant of proportionality). The diagonal elements of the matrices of all the four operators in the DFT-basis appear in Table 2.

The use of KS-DFT in mimicking LFR: the treatment of "data"

We take the sum of the squares of the barycentered computed energies in the DFT-basis as a measure of the magnitude, "area", of the "data" information available for fitting KS-DFT energies to the diagonal elements of LFR in the DFT-basis. These energies are elements of a diagonal matrix $H_{?obs"}$ to be treated as a genuine H_{obs} and correspond to H_{LFR} when this is also expressed in the DFT-basis. Then, the diagonal part of the overlaps, which is analogous to eq. [4], provides us with all the radial parameters, LF as well as R parts, and when all the parametrical terms are subtracted from $H_{?obs"}$, we are left with a diagonal matrix whose norm square is equal to the total variance of a linear least-squares fitting.

There is, however, something rotten in the state of Denmark: KS-DFT is unable to provide the non-diagonal elements of this modeling, which are symmetry required by the 1:1 relationship in the DFT-basis between the states of LFR and the corresponding ones of KS-DFT.[4,6] Thus, we are lacking the non-diagonal DFT matrix elements to proceed directly to the diagonalization of a hypothetical full DFT energy matrix.

However, by virtue of the parametrical nature of LFR, we are able to use the diagonal of the LFR only, obtain the R parameter values, and then proceed indirectly by means of these parameter values to obtain the non-diagonal elements.

Table 2. DFT-computed energies for Cr^{4+} and CrF_4 (outer columns, in μm^{-1}) for all strong-field DFT-based functions of the d^2 configuration. The single Slater-determinant functions are specified by the symmetries of their rows, named by components of symmetry species of T_d (cf. eq. [7]. Column headings are named after the associated parameters. The middle columns of single-digit numbers are the matrix elements of the PMT coefficient operators, which were defined by their diagonal elements in the DFT-basis . The remaining columns are the terms that add up to scalar products (involving either of the outer columns). For example, the second column to the left refers to the overlap $\hat{H}^{DFT}[Cr^{4+}]|\hat{Q}[D_v^{DFT}]$.

Cr^{4+}	$D_v(Cr^{4+})$	$D_S(Cr^{4+})$	$E[S^2=1]$ (Cr^{4+})	$E[S^2=2]$ (Cr^{4+})	D_v	D_S	$E[S^2=1]$	$E[S^2=2]$	Δ		Function	$D_v(CrF_4)$	$D_S(CrF_4)$	$E[S^2=1]$ (CrF_4)	$E[S^2=2]$ (CrF_4)	CrF_4
1.30281	10.42248	0	0	0	8	0	0	0	1.2	1	αe1βe1	–3.7372	0	0	0	–0.46715
1.26333	10.10664	0	0	0	8	0	0	0	–0.8	2	$\alpha t_2 2\beta t_2 2$	11.87792	0	0	0	1.48474
1.26333	10.10664	0	0	0	8	0	0	0	–0.8	3	$\alpha t_2 1\beta t_2 1$	11.87792	0	0	0	1.48474
1.26298	10.10384	0	0	0	8	0	0	0	–0.8	4	$\alpha t_2 3\beta t_2 3$	11.87792	0	0	0	1.48474
1.26298	10.10384	0	0	0	8	0	0	0	1.2	5	αe2βe2	–3.83600	0	0	0	–0.47950
–0.55429	0.55429	–0.55429	1.66287	0	–1	1	–3	0	0.2	6	$\alpha e 1\beta t_2 3$	0.43896	–0.43896	1.31688	0	–0.43896
–0.55429	0.55429	–0.55429	1.66287	0	–1	1	–3	0	0.2	7	$\beta e 1\alpha t_2 3$	0.43896	–0.43896	1.31688	0	–0.43896
–0.55429	0.55429	–0.55429	1.66287	0	–1	1	–3	0	1.2	8	αe1βe2	1.50227	–1.50227	4.50681	0	–1.50227
–0.55429	0.55429	–0.55429	1.66287	0	–1	1	–3	0	1.2	9	βe1αe2	1.50227	–1.50227	4.50681	0	–1.50227
–0.31722	0.31722	–0.31722	0.31722	0	–1	1	–1	0	–0.8	10	$\alpha t_2 2\beta t_2 3$	–0.74304	0.74304	–0.74304	0	0.74304
–0.31722	0.31722	–0.31722	0.31722	0	–1	1	–1	0	–0.8	11	$\beta t_2 2\alpha t_2 3$	–0.74304	0.74304	–0.74304	0	0.74304
–0.31722	0.31722	–0.31722	0.31722	0	–1	1	–1	0	–0.8	12	$\alpha t_2 1\beta t_2 3$	–0.74304	0.74304	–0.74304	0	0.74304
–0.31722	0.31722	–0.31722	0.31722	0	–1	1	–1	0	–0.8	13	$\beta t_2 1\alpha t_2 3$	–0.74304	0.74304	–0.74304	0	0.74304
–0.31716	0.31716	–0.31716	0.31716	0	–1	1	–1	0	–0.8	14	$\alpha t_2 2\beta t_2 1$	–0.74304	0.74304	–0.74304	0	0.74304
–0.31716	0.31716	–0.31716	0.31716	0	–1	1	–1	0	–0.8	15	$\beta t_2 2\alpha t_2 1$	–0.74304	0.74304	–0.74304	0	0.74304
–0.31534	0.31534	–0.31534	0.31534	0	–1	1	–1	0	0.2	16	$\alpha t_2 2\beta e 2$	0.32199	–0.32199	0.32199	0	–0.32199
–0.31534	0.31534	–0.31534	0.31534	0	–1	1	–1	0	0.2	17	$\beta t_2 2\alpha e 2$	0.32199	–0.32199	0.32199	0	–0.32199
–0.31534	0.31534	–0.31534	0.31534	0	–1	1	–1	0	0.2	18	$\alpha t_2 1\beta e 2$	0.32199	–0.32199	0.32199	0	–0.32199
–0.31534	0.31534	–0.31534	0.31534	0	–1	1	–1	0	0.2	19	$\beta t_2 1\alpha e 2$	0.32199	–0.32199	0.32199	0	–0.32199
0.20898	–0.20898	0.20898	0.62694	0	–1	1	3	0	0.2	20	$\alpha e 1\beta t_2 2$	0.07334	–0.07334	–0.22002	0	–0.07334
0.20898	–0.20898	0.20898	0.62694	0	–1	1	3	0	0.2	21	$\beta e 1\alpha t_2 2$	0.07334	–0.07334	–0.22002	0	–0.07334
0.20898	–0.20898	0.20898	0.62694	0	–1	1	3	0	0.2	22	$\alpha e 1\beta t_2 1$	0.07334	–0.07334	–0.22002	0	–0.07334
0.20898	–0.20898	0.20898	0.62694	0	–1	1	3	0	0.2	23	$\beta e 1\alpha t_2 1$	0.07334	–0.07334	–0.22002	0	–0.07334
0.44515	–0.44515	0.44515	2.22575	0	–1	1	5	0	0.2	24	$\alpha t_2 3\beta e 2$	–0.04295	0.04295	0.21475	0	0.04295
0.44515	–0.44515	0.44515	2.22575	0	–1	1	5	0	0.2	25	$\beta t_2 3\alpha e 2$	–0.04295	0.04295	0.21475	0	0.04295
–1.19464	1.19464	1.19464	0	3.58392	–1	–1	0	–3	0.2	26	$\alpha e 1\alpha t_2 3$	0.75978	0.75978	0	2.27934	–0.75978
–1.19464	1.19464	1.19464	0	3.58392	–1	–1	0	–3	1.2	27	αe1αe2	1.83274	1.83274	0	5.49823	–1.83274
–0.96376	0.96376	0.96376	0	0.96376	–1	–1	0	–1	–0.8	28	$\alpha t_2 2\alpha t_2 3$	–0.42058	–0.42058	0	–0.42058	0.42058
–0.96304	0.96304	0.96304	0	0.96304	–1	–1	0	–1	–0.8	29	$\alpha t_2 1\alpha t_2 3$	–0.42058	–0.42058	0	–0.42058	0.42058
–0.96304	0.96304	0.96304	0	0.96304	–1	–1	0	–1	–0.8	30	$\alpha t_2 2\alpha t_2 1$	–0.42058	–0.42058	0	–0.42058	0.42058
–0.94421	0.94421	0.94421	0	0.94421	–1	–1	0	–1	0.2	31	$\alpha t_2 2\alpha e 2$	0.63716	0.63716	0	0.63716	–0.63716
–0.94421	0.94421	0.94421	0	0.94421	–1	–1	0	–1	0.2	32	$\alpha t_2 1\alpha e 2$	0.63716	0.63716	0	0.63716	–0.63716
–0.42578	0.42578	0.42578	0	–1.27734	–1	–1	0	3	0.2	33	$\alpha e 1\alpha t_2 2$	0.38486	0.38486	0	–1.15458	–0.38486
–0.42578	0.42578	0.42578	0	–1.27734	–1	–1	0	3	0.2	34	$\alpha e 1\alpha t_2 1$	0.38486	0.38486	0	–1.15458	–0.38486
–0.20012	0.20012	0.20012	0	–1.00060	–1	–1	0	5	0.2	35	$\alpha t_2 3\alpha e 2$	0.26994	0.26994	0	–1.34970	–0.26994
–1.19464	1.19464	1.19464	0	3.58392	–1	–1	0	–3	0.2	36	$\beta e 1\beta t_2 3$	0.75978	0.75978	0	2.27934	–0.75978
–1.19464	1.19464	1.19464	0	3.58392	–1	–1	0	–3	1.2	37	βe1βe2	1.83274	1.83274	0	5.49823	–1.83274
–0.96376	0.96376	0.96376	0	0.96376	–1	–1	0	–1	–0.8	38	$\beta t_2 2\beta t_2 3$	–0.42058	–0.42058	0	–0.42058	0.42058
–0.96304	0.96304	0.96304	0	0.96304	–1	–1	0	–1	–0.8	39	$\beta t_2 1\beta t_2 3$	–0.42058	–0.42058	0	–0.42058	0.42058
–0.96304	0.96304	0.96304	0	0.96304	–1	–1	0	–1	–0.8	40	$\beta t_2 2\beta t_2 1$	–0.42058	–0.42058	0	–0.42058	0.42058

Table 2 (*concluded*).

Cr^{4+}	$D_v(Cr^{4+})$	$D_s(Cr^{4+})$	$E[S^2=1]$ (Cr^{4+})	$E[S^2=2]$ (Cr^{4+})	D_v	D_S	$E[S^2=1]$	$E[S^2=2]$	Δ		Function	$D_v(CrF_4)$	$D_s(CrF_4)$	$E[S^2=1]$ (CrF_4)	$E[S^2=2]$ (CrF_4)	CrF_4
−0.94421	0.94421	0.94421	0	0.94421	−1	−1	0	−1	0.2	41	$\beta t_2 2\beta e2$	0.63716	0.63716	0	0.63716	−0.63716
−0.94421	0.94421	0.94421	0	0.94421	−1	−1	0	−1	0.2	42	$\beta t_2 1\beta e2$	0.63716	0.63716	0	0.63716	−0.63716
−0.42578	0.42578	0.42578	0	−1.27734	−1	−1	0	3	0.2	43	$\beta e1\beta t_2 2$	0.38486	0.38486	0	−1.15458	−0.38486
−0.42578	0.42578	0.42578	0	−1.27734	−1	−1	0	3	0.2	44	$\beta e1\beta t_2 1$	0.38486	0.38486	0	−1.15458	−0.38486
−0.20012	0.20012	0.20012	0	−1.00060	−1	−1	0	5	0.2	45	$\beta t_2 3\beta e2$	0.26994	0.26994	0	−1.34970	−0.26994

This situation is a little bit curious and it therefore triggers the imagination enough to ask the question: Can a method be found to squeeze this additional "area" of information out of KS-DFT computations?

Comparison of a set of atomic and a set of molecular DFT "data"

Tables 2 and 3 illustrate how the DFT computations of the atomic ligand-field system, Cr^{4+}, and the molecular one, CrF_4, can be compared by taking advantage of the present formalism of mutual orthogonalities among all the model operators. In particular, the effective two-electron operators, which in LFR are described as interelectronic repulsion operators, are used to define and characterize the atomic part of CrF_4.

Intrinsic molecular atoms and nephelauxetism

Tables 2 and 3 illustrated the well-defined concept of a weak-field complex by the naked Cr^{4+} system, which is atomic and which, in LFR, is characterized by having a vanishing ligand field. A strong-field complex can, strictly speaking, not be exemplified because this would, for symmetry reasons, require the R parameters by analogy to be vanishing, a situation which for physical reasons cannot be realized. However, the tables illustrate by their quantitative contents that CrF_4 is not too far from being a so-called strong-field complex because its degree of diagonality in the DFT-basis is not too far from unity, in fact it is equal to $20.82/26.49 \approx 0.79$, that is, the ratio between the magnitudes of the information contribution of LF relative to that of LFR (Table 3).

Another aspect of Tables 2 and 3 is that if the ligand-field contribution to the analysis of CrF_4 is discarded, we are, for each R parameter, left with two LFR-parametric pictures that are identical, one for Cr^{4+} and one for CrF_4. And, since one of these pictures an atom, both do. We shall emphasize this property of LFR by considering the atomic R image associated with CrF_4, that of a molecular atom. There is one such 45×45 matrix picture for each R coefficient operator, and it is the same for all molecules of the same symmetry. Interestingly, for this purpose, the symmetry of Cr^{4+} has T_d symmetry, which is undeniable. The individuality appears when these matrices are weighted by their associated parameters, and the ratio between these weight factors for CrF_4 relative to that for Cr^{4+} exemplifies a so-called nephelauxetic ratio,[19–23] β, of which there are four in Table 3, one for each PMT parameter. A cumulative nephelauxetic ratio can be obtained from the square root of the ratio between the two values for $< \hat{H}_R | \hat{H}_R >$

$$[9] \qquad \beta^{\text{global}} = \sqrt{\frac{\langle \hat{H}_R(CrF_4) | \hat{H}_R(CrF_4) \rangle}{\langle \hat{H}_R(Cr^{4+}) | \hat{H}_R(Cr^{4+}) \rangle}} = 0.525$$

Thereby, we have obtained a global, multiparameter-based expression of nephelauxetism. This word refers to an expansion of the electronic cloud of the partially filled shell. It originated in the discovery, empirical or semi-empirical, of a phenomenon that manifests itself in reduced values for

Table 3. Parameter values resulting from the analysis of barycentered DFT calculated (ADF 2003, LDA)[24] data (Table 2) by use of orthogonal set of (LF)R operators. The first five lines give the parameter values extracted by the scalar product method. The following five lines list the contributions to the total area of the (LF)R Hamiltonian from each of the contributing conglomerate operator terms. In the following two lines, the sums corresponding to the cumulated contribution from, respectively, the R and the LFR are given. When the small residuals (variances) in the penultimate line are added to the LFR area, the total area of the DFT data is (re)covered.

	Cr^{4+}	CrF_4	β
Δ	0	–1.0413	
D_v	0.19705	0.10074	0.511
D_S	0.31957	0.15924	0.498
$E[<S^2>=1]$	0.12709	0.06080	0.478
$E[S^2=2]$	0.12713	0.06259	0.492
$(\Delta)^2 < \hat{Q}[\Delta] \mid \hat{Q}[\Delta] >$	0	20.8186	
$(D_v)^2 < \hat{Q}[D_v] \mid \hat{Q}[D_v] >$	13.9781	3.6541	
$(D_s)^2 < \hat{Q}[D_s] \mid \hat{Q}[D_s] >$	4.0851	1.0144	
$(E[<S^2>=1])^2 < \hat{Q}[E[<S^2>=1]] \mid \hat{Q}[E[<S^2>=1]] >$	2.1319	0.4881	
$(E[S^2=2])^2 < \hat{Q}[E[S^2=2]] \mid \hat{Q}[E[S^2=2]] >$	2.1335	0.5172	
$< \hat{H}_R \mid \hat{H}_R >$	22.3286	5.6738	
$< \hat{H}_{LFR} \mid \hat{H}_{LFR} >$	22.3286	26.4924	
$< \hat{H}_{RES} \mid \hat{H}_{RES} >$	0.0055	0.0253	
$< \hat{H}_{DFT} \mid \hat{H}_{DFT} >$	22.3341	26.5177	

all the R parameters for all molecular systems with a partially filled shell.

A final remark brings us back to the extent of the coverage of the KS-DFT computations at this time. The DFT energies contribute only to the diagonal of all these R matrices, whereas the non-diagonal elements are derivations due to the complete LFR formalism.

Conclusion

Kohn–Sham DFT is a useful tool for supplementing our data bank on the spectroscopy of transition-metal atoms and molecules with a partially filled shell. The approach to obtaining the one-electron and two-electron parameters of ligand-field theory is, in principle, objective. The only remaining degrees of freedom, which are unimportant in the present context, and for which standards exist, are the choice of functionals, the KS-DFT function basis, and the implementation.

The energy information extractable from KS-DFT is not, however, very straightforward, even after the DFT sets of functionals have been chosen. Two extraordinary features of the mimicking of the ligand-field repulsion model, LFR, by KS-DFT computation of its radial parameters have been illuminated.

First, only the values of the diagonal elements of a certain so-called strong-field energy matrix can be DFT-computed. The consequence of this fact is that the one-electron parameters of the ligand field itself often dominate in the extraction of information from the computed energies. Even for the computation on atoms, where only the interelectronic repulsion operators are in play, the low degree of diagonality of these operators in the DFT-basis reduces the accuracy by which the associated parameters can be obtained. However, once values of these parameters have been obtained, the non-diagonal elements that are necessary to obtain eigenvalues must be delivered by the simple ligand-field formalism. The question is: Can something be done about this status of KS-DFT? The present situation seems rather unfortunate from a more general point of view. Another way of asking the same question is: Can eigenenergies be obtained by DFT without taking advantage of ligand-field theory?

Second, unit occupation numbers of the KS-DFT spin eigenorbitals define system states that are eigenfunctions of $\hat{S}_z$, rather than $\hat{S}^2$, and whose computed energies can be interpreted and parameterized. Translated into a wave-function formulation, these states are single Slater determinants. From the point of view of ligand-field theory, they are strong-field functions, some of which are different from conventional strong-field functions by not being eigenfunctions of $\hat{S}^2$. This happens in d^2 for 20 out of the 45 state functions with the consequence that the exchange is moved out of the diagonal relative to the situation of the usual ligand-field, strong-field functions, which are eigenfunctions of $\hat{S}^2$. This curious situation may have more general stratifications.

This paper's main contribution has been to unravel the intertwining of the contributions from the one-electron and two-electron effective operators of the LFR by the method of mutually orthogonal operators. Moreover, this method allows the separation of the spin and seniority parts of the repulsion from the spatial parts. These results have been illustrated by the LFR concept of the molecular atom as the central atom inside the complex. This molecular atom was illustrated quantitatively by a common matrix expression for a given two-electron coefficient operator for all chemical members of a general class of complexes with the symmetry and number of electrons in the partially filled shell in common and an individual matrix for the conglomerate operators for each specific complex. These statements include the ma-

trices of the central ion because its symmetry covers that of any complex.

Finally, the conventional LFR Hamiltonian matrix has been modified to the DFT-adapted function basis, which is an eigenbasis of $\widehat{S}_z$, rather than $\widehat{S}^2$.

References

(1) Ziegler, T.; Rauk, A.; Baerends, E. J. *Theor. Chim. Acta* **1977**, *43* (3), 261–271. doi:10.1007/BF00551551.

(2) Anthon, C.; Schäffer, C. E. *Coord. Chem. Rev.* **2002**, *226* (1-2), 17–38. doi:10.1016/S0010-8545(01)00449-0.

(3) Anthon, C.; Bendix, J.; Schäffer, C. E. *Inorg. Chem.* **2003**, *42* (13), 4088–4097. doi:10.1021/ic0262233. PMID:12817966.

(4) Anthon, C.; Bendix, J.; Schäffer, C. E. *Struct. Bond.* **2004**, *107*, 207–301.

(5) Anthon, C.; Bendix, J.; Schäffer, C. E. *Inorg. Chem.* **2004**, *43* (24), 7882–7886. doi:10.1021/ic049507r. PMID:15554654.

(6) Bendix, J.; Anthon, C.; Schäffer, C. E. *Coord. Chem. Rev.* **2009**, *253* (5-6), 575–593. doi:10.1016/j.ccr.2008.09.010.

(7) Schäffer, C. E. In *Wave Mechanics ? The First 50 Years;* Price, W. C., Chissick, S. S., and Ravensdale. T., Eds.; Butterworths: London, 1973; Chap. 12, pp 174–192.

(8) Baerends, E. J.; Branchadell, V.; Sodupe, M. *Chem. Phys. Lett.* **1997**, *265* (3-5), 481–489. doi:10.1016/S0009-2614(96)01449-2.

(9) Atanasov, M.; Daul, C. A.; Rauzy, C. *Chem. Phys. Lett.* **2003**, *367* (5-6), 737–746. doi:10.1016/S0009-2614(02)01762-1.

(10) Atanasov, M.; Daul, C. A.; Rauzy, C. *Struct. Bond.* **2004**, *106*, 97–125.

(11) Brorson, M.; Schäffer, C. E. *Inorg. Chem.* **1988**, *27* (14), 2522–2530. doi:10.1021/ic00287a030.

(12) Jørgensen, C. K. *Modern Aspects of Ligand-Field Theory;* North-Holland,: Amsterdam, 1971.

(13) Cerkaski, M.; Judd, B. R.; Leavitt, R. C.; Lister, G. M. S. *J. Phys. B* **1990**, *23* (14), 2197–2204. doi:10.1088/0953-4075/23/14/008.

(14) Uylings, P. H. M. *J. Phys. B Atomic Mol. Phys.* **1984**, *17* (12), 2375–2392. doi:10.1088/0022-3700/17/12/009.

(15) Bendix, J.; Brorson, M.; Schäffer, C. E. *Inorg. Chem.* **1993**, *32* (13), 2838–2849. doi:10.1021/ic00065a010.

(16) (a) Schäffer, C. E. *Physica A* **1982**, *114* (1-3), 28–49. doi:10.1016/0378-4371(82)90257-6.; (b) Bendix, J.; Schäffer, C. E.; Brorson, M. *Coord. Chem. Rev.* **1989**, *94* (1), 181–241. doi:10.1016/0010-8545(89)80048-7.

(17) Brorson, M.; Damhus, T.; Schäffer, C. E. *Comments Inorg. Chem.* **1983**, *3* (1), 1–34. doi:10.1080/02603598308078126.

(18) (a) Schäffer, C. E. *Struct. Bond.* **1968**, *5*, 68–95. doi:10.1007/BFb0118847.; (b) Schäffer, C. E. *Pure Appl. Chem.* **1970**, *24* (2), 361–392. doi:10.1351/pac197024020361.; (c) Harnung, S. E.; Schäffer, C. E. *Struct. Bond.* **1972**, *12*, 201–255. doi:10.1007/BFb0117544.; (d) Harnung, S. E.; Schäffer, C. E. *Struct. Bond.* **1972**, *12*, 257–295. doi:10.1007/BFb0117545.; (e) Schäffer, C. E. *Struct. Bond.* **1973**, *14*, 69–110. doi:10.1007/BFb0016872.; (f) Schäffer, C. E. *Theor. Chim. Acta* **1974**, *34* (4), 237–243. doi:10.1007/BF02399011.

(19) Schäffer, C. E.; Jørgensen, C. K. *J. Inorg. Nucl. Chem.* **1958**, *8*, 143–148. doi:10.1016/0022-1902(58)80176-1.

(20) Schäffer, C. E. *J. Inorg. Nucl. Chem.* **1958**, *8*, 149–154. doi:10.1016/0022-1902(58)80177-3.

(21) Jørgensen, C. K. *Prog. Inorg. Chem.* **1962**, *4*, 73–124. doi:10.1002/9780470166055.ch2.

(22) Bendix, J.; Brorson, M.; Schäffer, C. E. ACS Symposium Series 565; American Chemical Society: Washington, DC, 1994; Chap. 18. pp 213–225.

(23) Schäffer, C. E. *Inorg. Chim. Acta* **2000**, *300–302* (1), 1035–1076. doi:10.1016/S0020-1693(99)00599-X.

(24) All DFT computations were performed using the ADF program package: Velde, G.; Baerends, E. J. *Comput. Phys.* **1992**, *99* (1), 84–98. doi:10.1016/0021-9991(92)90277-6.

Comprehensive study of some well-known molecular numerical integration methods

Aisha El-Sherbiny and Raymond A. Poirier

Abstract: In a previous study, we compared, both in terms of accuracy and efficiency, the performance of some of the well-known grids, which use the Becke partitioning scheme for molecular numerical integration. We concluded, based on the number of electrons only, that the MultiExp grid performed well compared with the grids proposed by Becke, Gill et al., and Treutler and Ahlrichs. In this work, we re-examine the performance of the same set of grids in addition to the SG-0 grid and a benchmark grid. These grids are evaluated by integrating the Hartree–Fock electron density to calculate the number of electrons, dipole moment, potential energy, and Coulomb repulsion energy. Our results show that, except for the large benchmark grid, none of these grids were completely satisfactory.

Key words: numerical integration, radial quadrature, ab initio, electron density.

Résumé : Dans une étude antérieure, on a comparé en termes d'exactitude et d'efficacité, la performance de quelques grilles bien connues qui font appel au schéma de partition de Becke pour l'intégration numérique. On a conclu, sur la base uniquement du nombre d'électrons, que la grille MultiExp donne de bonnes performances par comparaison avec les grilles proposées par Becke, Gill et al. et Treutler et Ahlrichs. Dans ce travail, on réexamine la performance du même ensemble de grilles, plus la grilles SG-0 et une autre grille reconnue. On a évalué ces grilles en intégrant la densité électronique de Hartree–Fock pour calculer le nombre d'électrons, le moment dipolaire, l'énergie potentielle et l'énergie de répulsion coulombienne. Les résultats obtenus montrent que, à l'exception de la grosse grille bien connue, aucune des autres grilles ne donne des résultats complètement satisfaisants.

Mots-clés : intégration numérique, quadrature radiale, ab initio, densité électronique.

[Traduit par la Rédaction]

Introduction

The use of numerical integration in quantum chemistry has become routine, especially in density functional theory (DFT). Grid-based numerical solutions of the Hartree–Fock (HF) equations of polyatomic molecules have also been considered.[1] In general, the accuracies of numerical quadrature methods are evaluated by integrating the electron density for the total number of electrons, for the total DFT energy, or specifically, for the exchange-correlation energy, which are compared to a larger grid as in refs. 2, 3, and 4–6. In this paper, we use an approach similar to Pérez-Jordá et al.,[7] where we use numerical quadrature methods to integrate properties for which the exact analytical results are known, namely, the Hartree–Fock wave function. In addition to calculating the total number of electrons N_{el}, we also calculate the electron–nuclear potential energy V_{ne}, dipole moment, μ, and Coulomb potential energy V_{ee} using the Hartree–Fock wave function and calculate these properties numerically using the HF density. Therefore, the values of V_{ne}, μ, and V_{ee} calculated using the HF wave function serve as exact values to compare with those calculated by numerical integration. We also compare our results to a benchmark grid, a large version of the SG-1 grid[2] with 100 radial points and 1202 angular points for a total of 12 200 angular points. In this work, we examine our implementation of six standard grids: the MultiExp grid by Gill and Chien,[8] the Becke grid,[9] the Treutler and Ahlrichs (TA) grid,[3] our modified version of TA,[10] TAnew, the SG-1 grid by Gill et al.,[2] and the more recent SG-0 MultiExp grid by Chien and Gill.[11] The radial quadrature formulas for these grids are given in Table 1. The accuracy of the quadrature depends on a number of factors: the function being integrated, the choice of the radial grid, the angular grid used, the radial scale factor R (See Table 1), on which it is quite dependent, the radial mapping, and ultimately on the total number of grid points used. Although other efficient types of grids exist,[6,12,13] all the grids investigated in this work use the Becke partitioning scheme.[9] In addition, we investigate how the accuracy of these grids vary with the size of the system. To our knowledge, the "size consistency" of these grids has not been investigated. It is important that grids perform equally well for different systems. For that reason, the grids are tested using a total of 89 different molecules (Table 2), including ground states, ions, complexes, and transition states. The molecules are divided into seven sets. The first three sets represent molecules containing first-, second-, and third-row atoms. The other four sets represent transition states, ions, complexes, and peptides. The peptides consist of one to five glycine amino acids (1G to 5G).

Received 19 December 2008. Accepted 7 April 2009. Published on the NRC Research Press Web site at canjchem.nrc.ca on 5 September 2009.

This article is part of a Special Issue dedicated to Professor T. Ziegler.

A. El-Sherbiny and R.A. Poirier.[1] Memorial University, Department of Chemistry, St. John's, NL A1B 3X7, Canada.

[1]Corresponding author (e-mail: rpoirier@mun.ca).

Table 1. The mappings, roots, and weights for the radial quadrature grids investigated.

Grid	Mapping	Roots	Weights
Becke	$r_i = R\frac{1+x_i}{1-x_i}$	$x_i = \cos\left(\frac{i\pi}{n+1}\right)$	$w_i = \frac{2\pi}{n+1}\frac{(1+x_i)^{5/2}}{(1-x_i)^{7/2}}R^3$
SG-1	$r_i = R\frac{x_i^2}{(1-x_i)^2}$	$x_i = \left(\frac{i}{n+1}\right)$	$w_i = \frac{2}{n+1}\frac{x_i^5}{(1-x_i)^7}R^3$
TA	$r_i = \frac{R}{\ln 2}(1+x_i)^{\alpha}\ln(\frac{2}{1-x_i})$	$x_i = \cos\left(\frac{i\pi}{n+1}\right)$	$w_i = \left(\frac{R}{\ln 2}\right)^3(1+x_i)^{3\alpha}\left(\ln\frac{2}{1-x_i}\right)^3\left(\sqrt{\frac{1+x_i}{1-x_i}}\right)\ln\frac{1-x_i}{2}+\alpha\left(\sqrt{\frac{1-x_i}{1+x_i}}\right)\left(\left(\frac{\pi}{n+1}\right)\right)$
MultiExp	$R_i = -R\ln x_i$	x_i	$w_i = \left(\frac{a}{x}\right)R^3$

Table 2. Sets of molecules used for evaluating the numerical integration calculations.

First row			Second row		Complexes	Third row	Peptides	Ions
BF_3	H_2	CH_3O^-	Cl_2	CS	H_2O–H_2O	AsH_3	1G	H_3O^+
BH_3	Li_2	Benzaldehyde	PH_3	ClF	H_2O–CO_2	CH_3Br	2G	$HCOO^-$
BeH_2	F_2	Cytosine	CH_3Cl	HOCl	FH–NH_3	H_2Se	2G	$ArNH_3^+$
C_2H_2	LiH	Ethyltosylate	CH_2Cl_2	Mg	FH–H_2O	GeH_4	4G	$NH_3^+CH_2COO^-$
C_2H_4	LiF	Naphthalene	CCl_4	NaCl	FH–FH	Ge_2H_6	5G	
CF_4	NH_3	Uracil	CH_3SiH_3	P_2	FH–N_2	Ge_3H_8		TS[a]
$CH_2CHCOOH$	CO	Formamidine	CH_3PH_2	PH	FH–NCH	Ge_4H_{10}		F^-/ CH_3F
CH_2F_2	CO_2	CH_3CONH_2	CH_3SH	PF_5	FH–CO	Ge_5H_{12}		Cl^-/CH_3Cl
$CH_2(CH_3)_2$	CH_4	H_2CO	$CH_2(SiH_3)_2$	SF_6	CH_2O_2–CH_2O_2			F^-/ CH_3Cl
CH_3F	H_2O		$CH_2(PH_2)_2$	SO				H_2O/CH_3F
CH_3NH_2	H_2O_2		$CH_2(SH)_2$	SO_2				CN^-/CH_3CH_2–OSO_2
CH_3OH	HCOOH		pNO_2BzCl[b]	SiO				CN^-/–BzCl

[a]Transition states.

[b]*p*-Nitrobenzylchloride.

Method

All calculations were performed with program MUNgauss.[14] The different grids along with the total number of grid points associated with each grid are given in Table 3. For the MultiExp grids, the atomic space is divided into three regions (core, middle, and outer). For the 20, 25, and 30 radial grids, the space is divided into (6,6,8), (6,8,11), and, (6,10,14), respectively. For each radial region, a spherical grid of six angular points was used for the core and 86 for the middle region. For the outer region, three different spherical grids of 110, 194, and 302 angular points were used. The largest grid gives 5124 [(6 × 6) + (10 × 86) + (14 × 302)] grid points. The notations 20(110), 20(194), 20(302), 25(110), 25(194), 25(302), 30(110), 30(194), and 30(302) denote the MultiExp grids with 20, 25, or 30 radial points with 6–86–110, 6–86–194, or 6–86–302 angular grids. All calculations were performed using the 6–31G(d) basis set and HF/6–31G(d) optimized structures. For each set of molecules listed in Table 2, the mean absolute error, MAE, is calculated as

$$[1] \qquad \mathrm{MAE} = \sum_i |P^i_{\mathrm{NI}} - P^i_{\mathrm{HF}}|/N$$

where P^i_{NI} is the value of the molecular property, N_{el}, V_{ne}, V_{ee}, or μ calculated using numerical integration for a molecule *i*, and P^i_{HF} is the corresponding molecular property calculated using HF. *N* is the number of molecules in each set. The radial scale factor *R* (see Table 1) was optimized[9] for Ge, As, Se, and Br in the molecules CH_3GeH_3, CH_3AsH_2, CH_3SeH, and CH_2Br_2, respectively. For SG-0 and SG-1, values of *R* are only available for elements up to argon, whereas for TA and TAnew, *R* values are available for up to krypton.

Results and discussion

Number of electrons

The total number of electrons is calculated by integrating the HF electron density using the equation:

$$[2] \qquad N_{\mathrm{el}} = \int \rho(\boldsymbol{r})\mathrm{d}\boldsymbol{r}$$

Table 4 gives the MAE of the integration of the electron density for the seven sets of molecules described above with the 15 grids mentioned previously. The MAEs range from 1.2×10^{-2} (TA) to 2.5×10^{-8} (benchmark). For molecules containing first-row atoms, the accuracy of the integration of the electron density using the MultiExp grid with 20 radial points improves slightly as the angular grid for the outermost region increases from 110 angular points to 194, but it does not improve by further increasing the number of angular points to 302. The accuracy improves slightly by increasing the size of the outermost grid using the MultiExp grid with 25 radial points. The 30(302) grid is the most accurate,

Table 3. Number of points of the atomic grids.

	Atom			
Grid	H, He	Li–Ne	Na–Ar	K–Kr
20(110)	1432	1432	1432	1432
20(194)	2104	2104	2104	2104
20(302)	2968	2968	2968	2968
25(110)	1934	1934	1934	1934
25(194)	2858	2858	2858	2858
25(302)	4046	4046	4046	4046
30(110)	2436	2436	2436	2436
30(194)	3612	3612	3612	3612
30(302)	5124	5124	5124	5124
Becke	2200	6790	7760	8730
TA[a]	3300	5890	6572	7506
TAnew	2484	4990	5960	6930
SG-1[b]	3752	3816	3760	NA
SG-0[c]	1438	1162–1494	1344–1536	NA
Benchmark	A larger version of SG-1 with 100 radial points and a single grid of 1202 angular points			

[a]These values are taken from ref. 3.

[b]These values are taken from ref. 2.

[c]The number of points varies from one atom to another. The SG-0 grid used here is slightly larger than the one in ref. 11. Due to an error in the 18 angular point grid, we used 26 angular points.

Table 4. Mean absolute errors (MAEs) for the number of electrons, eq. [2].

Grid	First	Second	Third	TS[a]	Complexes	Ions	Peptides
20(110)	4.3e–04	9.2e–04	8.2e–03	6.0e–04	4.5e–04	6.7e–04	1.3e–03
20(194)	2.5e–04	6.3e–04	8.4e–03	2.8e–04	4.2e–04	4.3e–04	6.8e–04
20(302)	2.4e–04	6.5e–04	8.5e–03	1.9e–04	4.2e–04	3.0e–04	6.2e–04
25(110)	5.1e–04	6.2e–04	6.1e–03	6.8e–04	4.1e–04	7.8e–04	7.1e–04
25(194)	1.2e–04	3.6e–04	6.2e–03	1.2e–04	2.1e–04	1.5e–04	2.4e–04
25(302)	7.9e–05	3.2e–04	6.2e–03	1.7e–04	2.0e–04	4.6e–05	2.7e–04
30(110)	4.7e–04	5.7e–04	5.9e–03	6.5e–04	2.6e–04	7.6e–04	8.8e–04
30(194)	6.9e–05	2.2e–04	6.0e–03	8.5e–05	5.2e–05	1.4e–04	1.1e–04
30(302)	2.9e–05	1.8e–04	6.0e–03	1.1e–04	4.7e–05	3.1e–05	1.2e–05
Becke	5.6e–04	8.4e–04	4.5e–03	2.5e–03	3.5e–04	3.8e–04	2.8e–03
TA	2.2e–03	2.7e–03	1.2e–02	2.9e–03	1.7e–03	1.9e–03	4.8e–03
TAnew	1.8e–04	8.3e–05	2.5e–04	1.2e–04	4.6e–05	1.3e–04	2.8e–04
SG-1	1.3e–04	2.9e–04	NA	2.2e–04	4.1e–05	2.2e–04	2.1e–04
SG-0	3.7e–04	5.0e–04	NA	7.0e–04	2.1e–04	4.4e–04	5.2e–04
Benchmark	3.4e–08	1.2e–07	NA	1.5e–07	2.5e–08	8.4e–08	6.0e–08[b]

Note: See Table 2 for list of molecules.

[a]Transition states.

[b]Only 1G and 2G peptides are calculated.

while 25(302) and 30(194) are almost of the same accuracy. The SG-0 and Becke grids are of comparable accuracies to our implementation of the MultiExp grid with 20 radial points. The least accurate grid is TA. Our new implementation of the TA grid, TAnew,[10] is almost an order of magnitude more accurate than the original TA grid. The SG-1 and TAnew grids give almost the same accuracy. For molecules containing first- and second-row atoms, third column of Table 4, a similar trend is found for the MultiExp grids. The worst accuracy is given by the TA grid. The TAnew grid is the most accurate grid and is more accurate than TA by more than an order of magnitude. For molecules containing third-row atoms, TA is again the least accurate and the best accuracy is given by TAnew, while Becke and the nine MultiExp grids give nearly the same accuracy. For the transition states, 30(194) is the most accurate and TA is the least accurate. The performance of the MultiExp grids improves slightly by increasing the number of angular points in the outermost region. For complexes, 30(194), 30(302), TAnew, and SG-1 grids give better accuracies than the rest of the grids. The TA grid is the least accurate, almost two orders of magnitude less accurate than TAnew. For ions, 25(302) and 30(302) are the most accurate and TA is the least accurate. TAnew and SG-1 grids are of comparable accuracies. Performance of the smaller SG-0 grid is similar to our implementation of the MultiExp grid. For peptides, the

Table 5. Mean absolute errors of the dipole moment, μ (au), eq. [3].

Grid	First	Second	Third	TS[a]	Complexes	Ions	Peptides
20(110)	9.0e–04	1.7e–03	2.0e–02	1.4e–03	1.2e–03	1.7e–03	9.5e–03
20(194)	6.1e–04	3.7e–04	2.2e–02	5.6e–04	8.4e–04	7.0e–04	5.6e–03
20(302)	5.3e–04	5.0e–04	2.2e–02	5.0e–04	8.8e–04	4.9e–04	4.4e–03
25(110)	8.7e–04	1.4e–03	1.5e–02	9.9e–04	9.3e–04	1.9e–03	6.7e–03
25(194)	3.5e–04	4.4e–04	1.7e–02	2.6e–04	2.9e–04	1.6e–04	1.0e–03
25(302)	2.9e–04	2.6e–04	1.7e–02	2.9e–04	2.6e–04	2.3e–05	1.9e–03
30(110)	7.3e–04	1.4e–03	1.5e–02	1.1e–03	9.9e–04	1.9e–03	7.5e–03
30(194)	2.4e–04	2.7e–04	1.6e–02	1.9e–04	2.3e–04	2.5e–04	9.0e–04
30(302)	1.5e–04	1.5e–04	1.6e–02	1.8e–04	1.7e–04	9.1e–05	1.8e–04
Becke	8.6e–04	1.9e–03	1.3e–02	3.4e–03	1.7e–03	6.0e–04	2.0e–02
TA	4.6e–03	4.9e–03	3.7e–02	7.7e–03	6.5e–03	6.2e–03	4.6e–02
TAnew	3.9e–04	2.1e–04	3.5e–04	3.2e–04	2.0e–04	4.8e–04	2.1e–03
SG-1	2.8e–04	3.3e–04	NA	4.7e–04	1.7e–04	3.9e–04	2.1e–03
SG-0	7.1e–04	1.3e–03	NA	1.3e–03	1.1e–03	8.0e–04	2.4e–03
Benchmark	4.2e–08	2.0e–07	NA	1.9e–07	1.3e–07	1.1e–07	1.9e–07[b]

Note: See Table 2 for list of molecules.

[a]Transition states.

[b]Only 1G and 2G peptides are calculated.

30(302) grid is the most accurate, while TA is the least accurate. The small 20(110) grid and the large Becke grid are of similar accuracy and generally of lower accuracy than the other grids. The 25(194), 25(302), 30(194), TAnew, and SG-1 grids have similar MAEs of around 2.0×10^{-4}, an order of magnitude less than that of the most accurate 30(302) grid. The MAEs for the benchmark grid are in the range of 1.2×10^{-7} to 2.5×10^{-8}, which is extremely accurate. For all of the seven sets, the best accuracies are for the 30(194), 30(302), TAnew, and SG-1 grids, while the performance of the 25(194) is reasonable.

Dipole moment

The electronic component of the dipole moment is calculated numerically using

$$[3] \qquad \mu = \int \rho(\boldsymbol{r})\boldsymbol{r}\mathrm{d}\boldsymbol{r}$$

The dipole moment (scalar) is calculated for all the molecules in Table 2, including those possessing a zero dipole by symmetry. Table 5 gives MAEs for the different test sets with the15 grids. The MAEs range from 4.6×10^{-2} au (TA) to 4.2×10^{-8} au (benchmark). For molecules containing first-row atoms, except for the TA grid, which gave an MAE of 4.6×10^{-3} au, the MAEs for the rest of the 13 grids are in the range of 9.0×10^{-4} au [20(110)] to 1.5×10^{-4} au [30(302)]. However, an improvement can be noticed as the number of angular points is increased in the outermost region from 110 to 194, and almost no improvement is observed by increasing to 302 angular points for 20, 25, or 30 radial points. The same observation can be made for molecules containing second-row atoms. Table 5 shows that, for molecules containing atoms from the second and third rows, the TA grid was the least accurate. TAnew is more accurate than TA and of the same accuracy as SG-1. It also shows that the SG-0 grid performed as well as the 20(110) MultiExp grid. For molecules containing third-row atoms, the MAE is almost the same and in the range of 3.7×10^{-2} au to 1.3×10^{-2} au for the nine MultiExp grids, Becke, and TA grids, while the MAE of TAnew is 3.5×10^{-4} au, two orders of magnitude less than all of the other grids. For transition states, the error in calculating the dipole moment using 20(194) MultiExp grid is less than using 20(110). However, the error does not decrease by using the larger 20(302) grid. The same pattern is also observed with the MultiExp grids of 25 radial points. The accuracy does not improve by increasing the grid size from 25(194) to 25(302), but the error decreases by increasing the grid from 25(110) to 25(194). The same trend can be also observed in the dipole moment calculated using the MultiExp grids of 30 radial points. For complexes, the accuracies of 20(110), Becke, TA, and SG-0 are of the same order of magnitude (10^{-3} au), and these grids are less accurate than the rest of the grids. It also shows that TAnew and SG-1 are almost of the same accuracy. For ions, 20(110), 25(110), and 30(110) grids give almost the same accuracy, which is less than the rest of the grids. The grid 25(302) gave the best accuracy, even better than 30(302). TAnew is as accurate as SG-1, while SG-0 is almost as accurate as 20(194). For peptides, the Becke and TA grids were the least accurate grids, while 30(302) was the most accurate. Again, TAnew and SG-1 have the same accuracy. The general trend amongst the MultiExp grids is also clear. An angular grid of 194 angular points gives better accuracy than 110, while 302 does not offer an improvement over the 194 grid. The benchmark grid is again excellent for all sets with an MAE of around 1.0×10^{-7} au. As in the case of number of electrons, the best performance for all sets was obtained by using 30(194), 30(302), TAnew, and SG-1. Of those, the 30(194) grid is the most economical.

Potential energy

The electron–nuclear potential energy is calculated numerically using

$$[4] \qquad V_{\mathrm{ne}} = \sum_{\mathrm{A}} Z_{\mathrm{A}} \int \frac{\rho(\boldsymbol{r})}{|\boldsymbol{r} - \boldsymbol{R}_{\mathrm{A}}|}\mathrm{d}\boldsymbol{r}$$

where $\boldsymbol{R}_{\mathrm{A}}$ is the position of the atom A of atomic charge Z_{A}. Table 6 gives the MAEs for the potential energy. For V_{ne},

Table 6. Mean absolute errors of the potential energy, V_{ne} (μH), eq. [4].

Grid	First	Second	Third	TS[a]	Complexes	Ions	Peptides
20(110)	7.9e+05	1.5e+07	1.5e+08	9.8e+06	5.9e+05	6.1e+05	2.0e+06
20(194)	7.9e+05	1.5e+07	1.5e+08	9.9e+06	5.9e+05	6.1e+05	2.0e+06
20(302)	7.9e+05	1.5e+07	1.5e+08	9.9e+06	5.9e+05	6.1e+05	2.0e+06
25(110)	3.8e+05	7.4e+06	1.2e+08	4.8e+06	2.8e+05	3.1e+05	1.0e+06
25(194)	3.8e+05	7.4e+06	1.2e+08	4.8e+06	2.8e+05	3.0e+05	1.0e+06
25(302)	3.8e+05	7.4e+06	1.2e+08	4.8e+06	2.8e+05	3.0e+05	1.0e+06
30(110)	1.9e+05	3.7e+06	1.3e+08	2.4e+06	1.4e+05	1.5e+05	4.8e+05
30(194)	1.9e+05	3.7e+06	1.3e+08	2.4e+06	1.4e+05	1.5e+05	4.7e+05
30(302)	1.9e+05	3.7e+06	1.3e+08	2.4e+06	1.4e+05	1.4e+05	4.8e+05
Becke	6.0e+03	2.9e+04	6.8e+05	4.8e+04	4.8e+03	3.1e+03	6.4e+04
TA	1.6e+04	3.9e+04	1.8e+05	3.0e+04	1.8e+04	3.1e+04	6.7e+04
TAnew	2.2e+03	5.8e+03	3.0e+05	5.7e+03	1.8e+03	1.0e+03	6.2e+03
SG-1	1.5e+03	6.5e+03	NA	4.4e+03	8.0e+02	3.1e+03	3.8e+03
Benchmark	15.8	337.0	NA	195.5	10.9	10.4	21.6[b]

Note: See Table 2 for list of molecules.

[a]Transition states.

[b]Only 1G and 2G peptides are calculated.

Table 7. Mean absolute errors of the Coulomb energy,V_{ee} (μH), eq. [6].

Grid	First	Second	Third	TS[a]	Complexes	Ions	Peptides
20(110)	2.7e+03	8.3e+03	3.8e+05	5.2e+03	2.7e+03	3.3e+03	1.5e+04
20(194)	3.2e+03	5.7e+03	3.8e+05	3.5e+03	3.2e+03	5.0e+03	1.3e+04
20(302)	3.1e+03	6.1e+03	3.8e+05	3.0e+03	3.2e+03	3.9e+03	1.2e+04
25(110)	9.0e+03	1.1e+04	4.4e+05	4.0e+03	1.9e+03	4.0e+03	7.3e+03
25(194)	2.2e+03	9.5e+03	4.4e+05	3.1e+03	9.8e+02	1.1e+03	3.6e+03
25(302)	1.8e+03	9.4e+03	4.5e+05	3.0e+03	9.3e+02	6.5e+02	4.2e+03
30(110)	2.3e+03	5.7e+03	4.4e+05	5.1e+03	1.1e+03	3.7e+03	9.4e+03
30(194)	4.8e+02	3.4e+03	4.4e+05	7.9e+02	1.9e+02	1.2e+03	1.2e+03
30(302)	2.4e+02	3.1e+03	4.4e+05	1.2e+03	2.3e+02	2.8e+02	2.9e+02
Becke	2.9e+03	5.1e+03	6.8e+04	1.5e+04	1.8e+03	1.2e+03	2.9e+04
TA	7.9e+03	2.1e+04	1.4e+05	1.5e+04	8.3e+03	1.4e+04	3.4e+04
TAnew	9.9e+02	6.8e+02	2.2e+03	8.4e+02	1.5e+02	4.4e+02	2.9e+03
SG-1	7.3e+02	2.4e+03	NA	1.2e+03	2.7e+02	1.5e+03	1.9e+03
SG-0	2.5e+03	9.5e+03	NA	5.0e+03	2.2e+03	2.8e+03	5.5e+03
Benchmark	3.8e–01	1.8	NA	1.6	2.2e–01	2.3e–01	2.1[b]

Note: See Table 2 for list of molecules.

[a]Transition states.

[b]Only 1G and 2G peptides are calculated.

the errors are significantly larger than the other two properties and can be as high as 10^8 μH. For molecules containing first-row atoms, the highest MAE is given by the MultiExp grid of 20 radial points (7.9×10^5 μH), while the lowest is given by SG-1 (1.5×10^3 μH). The nine MultiExp grids from 20(110) to 30(302) give MAEs around 10^5 μH. For TAnew, the MAE is very close to that of SG-1 (10^3 μH). For molecules containing second-row atoms, the 20(110), 20(194), and 20(302) grids gave MAEs of about 10^7 μH, while the MAEs for the rest of the MultiExp grids are around 10^6 μH. The most accurate grid is TAnew, followed by SG-1. For molecules containing third-row atoms, the nine MultiExp grids gave similar accuracies, while TA is slightly more accurate than TAnew. For transition states, the MultiExp grid of 20 radial points is the least accurate. Increasing the size of the outermost grid for the MultiExp grid of 20 radial points did not change the accuracy significantly, which is the same for MultiExp grids of 25 and 30 radial points. The most accurate grid for transition states is SG-1, followed by TAnew. For complexes, the MultiExp grid of 20 radial points was the least accurate grid, while SG-1 is the most accurate. For complexes and ions, performance of the nine MultiExp grids is similar to the transition states. The most accurate grid for complexes is SG-1, while TAnew is the most accurate grid for ions. For peptides, SG-1 is the most accurate grid, followed by TAnew. The error in calculating the potential energy drops significantly when the benchmark grid is used, but is still relatively high. This huge error in potential energy suggests that the grids currently used for numerical integration are not suitable for the calculation of potential energy ($1/r$ type functions) and that numerical integration is very dependent on the form of the function to be integrated. Although the errors in calculating the potential energy using all of the 14 grids are large, the TAnew and SG-1 grids performed relatively better than the rest of the grids. Although the potential energy need not be

Table 8. The error in the Coulomb energy, V_{ee} (μH), for peptides using Becke, TA, TAnew, SG-1, SG-0, and Benchmark.

Peptide	Becke	TA	TAnew	SG-1	SG-0	Benchmark
1G	–3570	–7580	–382	–263	–215	0.6
2G	21100	–49000	–1260	–1390	–6460	3.6
3G	6070	–20100	–2960	783	–4350	6.8
4G	14200	–86200	–3960	–1440	–8710	13.4
5G	98900	–5260	5890	5700	–7990	24.9
MAE	28768	33628	2890	1915	5545	9.8

Table 9. The new radial scale factors (R) for atoms from the first and second rows and the corresponding accuracies for the 20(110) grid.

Atom	Molecule	R	Accuracy[a]
H	H_2	0.852	6.5
Li	LiH	1.700	4.3
C	CH_4	1.233	8.3
N	NH_3	1.042	7.1
O	H_2O	0.756	7.5
F	HF	0.694	7.6
Na	Na_2	2.008	7.6
Mg	Mg_2	1.851	7.6
Si	SiH_4	1.573	6.3
P	PH_3	1.445	6.3
S	H_2S	1.356	6.1
Cl	HCl	1.268	6.0

Note: Optimized to give the best accuracy in V_{ee}.

[a]As defined by eq. [7].

Table 10. The error in Coulomb energy (μH) for molecules containing second-row atoms using two sets of radial scale factors (R).

	Error in V_{ee}	
Molecule	R_1[a]	R_2[b]
Cl_2	–9.2e+03	–3.4e+03
ClF	–1.3e+03	5.9e+03
HOCl	–3.7e+03	2.7e+03
$p$$NO_2$BzCl[c]	4.9e+04	5.2e+04
NaCl	–1.8e+04	1.8e+03
CH_3Cl	–2.9e+03	3.2e+02
CCl_4	–7.8e+02	1.2e+04
CH_2Cl_2	–2.8e+03	4.2e+03
Mg	5.4e+04	1.3e+03
P_2	–4.5e+03	–2.9e+02
PF_5	–1.7e+03	1.6e+04
PH	–2.2e+03	1.0e+03
$CH_2(PH_2)_2$	–1.1e+04	–3.3e+03
CH_3PH_2	–4.2e+03	–1.8e+03
CS	–1.1e+03	8.6e+02
SF_6	5.4e+03	2.6e+04
SO	–2.1e+03	3.8e+03
SO_2	4.7e+03	3.3e+03
$CH_2(SH)_2$	–8.5e+03	–2.6e+03
CH_3SH	–1.9e+03	1.2e+03
SiO	–2.2e+02	5.7e+03
CH_3SiH_3	–2.0e+03	2.6e+03
$CH_2(SiH_3)_2$	–4.1e+03	3.7e+03
MAE	8 280	7 231

[a]Optimized to give the best accuracy in number of electrons.

[b]Optimized to give the best accuracy in V_{ee}.

[c]p-Nitrobenzylchloride.

calculated using numerical integration, our results do clearly show that all grids except perhaps the benchmark grid are not sufficiently large to accurately integrate such a function.

Coulomb repulsion energy V_{ee}

Although we investigated the double numerical integration to calculate the Coulomb energy,

$$[5] \qquad V_{ee} = \int\int \frac{\rho(\boldsymbol{r}_1)\rho(\boldsymbol{r}_2)}{|\boldsymbol{r}_{12}|} d\boldsymbol{r}_1 d\boldsymbol{r}_2$$

like V_{ne}, the errors are quite large and in the order of 10^5 to10^7 μH. Even with the benchmark grid, the error is still extremely high and in the range of 9.1×10^4 to 3.1×10^5 μH. In Table 7, we report the MAEs in the Coulomb energy using a more realistic approach.

$$[6] \qquad V_{ee} = \int \rho(\boldsymbol{r}_2) \left[\sum_{\mu\nu} P_{\mu\nu} \int \frac{\Phi_\mu(\boldsymbol{r}_1)\Phi_\nu(\boldsymbol{r}_1) d\boldsymbol{r}_1}{|\boldsymbol{r}_{12}|} \right] d\boldsymbol{r}_2$$

$P_{\mu\nu}$is a density matrix element, ρ is the charge density, and Φ_μ and Φ_ν are basis functions. The first integral, in the brackets, was performed analytically, while the second integral was performed numerically. Table 7 shows that in some cases, the larger MultExp grids give larger errors than the smaller grids. A likely explanation for this apparently odd behaviour may be due to the values used for radial scale factors. Since R is optimized to give the best accuracy in the integration of the electron density, by re-optimizing R to give the most accurate Coulomb energy, these grids may perform in a more reliable fashion. From Table 7, for molecules containing first-row atoms, the most accurate grid is 30(302) and the second most accurate is 30(194), and both of them are slightly more accurate than TAnew and SG-1. Compared with the rest of the grids, SG-0 is of an average accuracy. The least accurate grid is the 25(110) MultiExp grid. While the error for the 14 grids was in the range of 239 to 8960 μH, the error for the benchmark grid was incredibly small (0.38 μH). For molecules containing second-row atoms, TAnew is by far the most accurate and its MAE is almost 30 times less than that of TA. SG-1 follows TAnew in accuracy. Of the nine MultiExp grids, the least accurate grid is the 25(110) grid, which is less accurate than the

Table 11. Simultaneous optimization of the radial scale factors in SO and SO_2 for the 20(110), 30(194), and 30 (86110,302) MultExp grids.

		Error in V_{ee} (μH)	
R (O, S)	Source of R values	SO	SO_2
20(110) grid			
R(0.8791, 1.3600)	From reference 2[2]	–2.1e+3	+4.7e+3
R(0.756, 1.356)	Values in Table 9	+3.8e+3	+3.3e+3
R(0.84951, 1.35912)	Optimized for SO	+1.9e–2	–5.6e+3
R(0.70553, 1.36832)	Optimized for SO	–3.0e–2	–1.1e+4
R(0.77242, 1.36338)	Optimized for SO_2	+3.6e+2	+4.2e–2
R(0.82052, 1.35320)	Optimized for SO_2	+4.7e+3	–1.7e–2
30(194) grid			
R(0.8791, 1.3600)	From reference 2[2]	+2.5e+3	+2.6e+3
R(0.756, 1.356)	Values in Table 9	+4.3e+3	+3.4e+3
R(0.97327, 1.40363)	Optimized for SO	–3.0e–3	+3.1e+2
R(0.61331, 1.43874)	Optimized for SO_2	+2.9e+3	+8.5e–1
30(302) grid			
R(0.97267, 1.40289)	Optimized for SO	–1.2e–1	+3.6e+2
R(0.93148, 1.40419)	Optimized for SO_2	–1.7e+2	+8.1e–2
30 radial grid with an angular grid of 86110,302			
R(1.01561, 1.40533)	Optimized for SO	–3.6e–1	+2.0e+1
R(1.02062, 1.40502)	Optimized for SO_2	+2.2e+1	–4.9

smaller grids 20(110) and SG-0. The error varied from 675 μH (TAnew) to 11133 μH [25(110)]. The 20(194), 20(302), 30(110), and Becke grids are of similar accuracy, although they differ in size. The benchmark grid is extremely accurate with an MAE of only1.81 μH. For molecules containing atoms from the third-row, TAnew is the most accurate grid. The largest error is for the MultiExp grid 25(302), which is a relatively large grid. Again, the large errors for molecules containing third-row atoms, 445 333 μH for 25(302), points to a serious problem either with the optimization of the radial scale factor *R* or the MultiExp grid size. However, since the radial scale factor for the third-row atoms was optimized using the same technique used for the first- and second-row atoms (see ref. 10) we expect that the 20, 25, or 30 radial-points grids are not large enough to calculate the Coulomb repulsion energy. Both Becke and TA grids are more accurate than the nine MultiExp grids. For transition states, the MultiExp grids performance is reasonable. For the 20, 25, and 30 radial MultiExp grids, the MAE decreases slightly as the outermost angular grid increases from 110 to 194 angular points. However, the accuracy does not increase much as the size increases from 194 to 302 angular points. The 30(194) grid is the most accurate, followed by TAnew. SG-0 has an MAE almost equivalent to that of the 20(110), 25(110), and 30(110) grids. The MAE for the benchmark grid is only 1.63 μH. For complexes, TAnew continued to be the most accurate, followed by the 30(194) grid, while TA is the least accurate. For ions, 30(302) is the most accurate, followed by TAnew. Again, TA is by far the least accurate grid. For peptides, 30(302) is the most accurate, while 30(194) is the second most accurate. In general, the accuracy of SG-0 was consistent with that of 20(110). The overall performance of the TAnew and SG-1 grids for the seven sets was the best. In general, the 30(194) and 30(302) gave relatively small MAEs; however, their poor performance for molecules containing third-row atoms makes them unreliable.

Some interesting observations

Table 8 gives the error in the Coulomb repulsion energy using the Becke, TA, TAnew, SG-1, SG-0, and benchmark grids for a series of five peptides ranging in size from one to five glycine amino acids (1G to 5G). It is obvious from the table that the Coulomb repulsion energy is in some cases underestimated, while in other cases it is overestimated and that the error changes randomly as the size of the peptide increases. This is true even with some of the larger and more accurate grids, TAnew and SG-1. For example, SG-1 predicts the error for the 3G peptide to be smaller than the error for the 2G peptide and the error with TAnew jumps from –3 960 μH for the 4G peptide to +5 890 μH for the 5G peptide. The error in V_{ee} increases consistently with the size of the peptide only when the benchmark grid is used. Using the benchmark grid, the error increased from 0.6 μH for 1G peptide to 24.9 μH for 5G peptide, which is a relatively large error, given the size of the benchmark grid. Since the benchmark grid is very time-consuming, one can only wonder how big the error would be for much larger peptides and just how reliable the numerical integration would be using smaller grids. These results suggest that comparing systems of different sizes could lead to serious errors due to the inconsistency in the results even for the larger grids.

The effect of the radial scale factor (*R*) on the integration

In our previous paper,[10] the radial scale factors for the MultiExp grid were optimized to give the best accuracy in the number of electrons. Here, we investigate the possibility of optimizing the *R* values to give the best accuracy in V_{ee} for molecules containing first- and second-row atoms. Table 9

Table 12. Error in all five properties studied in order of increasing grid size for CH_3CONH_2.

Grid	Number of grid points	Number of electrons	V_{ne} (μH)	Dipole (au)	V_{ee} (μH)
SG-0	12618	7.80e–05	4.56e+05	1.52e–03	–2.00e+02
20(110)	18504	–1.97e–04	6.11e+05	7.08e–04	1.43e+03
25(110)	23454	–4.52e–04	3.03e+05	2.56e–04	–2.03e+03
20(194)	24552	1.62e–04	6.09e+05	4.22e–04	2.52e+03
30(110)	28404	–3.49e–04	1.57e+05	2.02e–04	–9.20e+02
25(194)	31770	–7.43e–05	3.01e+05	–1.27e–05	–8.76e+02
20(302)	32328	1.78e–04	6.09e+05	4.91e–04	2.62e+03
NTA	32380	5.27e–04	–2.78e+03	–8.34e–04	1.77e+03
SG-1	33864	1.68e–05	–4.20e+02	1.17e–04	1.93e+02
Becke	38160	–2.20e–04	–2.74e+03	–2.50e–05	1.84e+02
30(194)	38988	1.78e–05	1.56e+05	–6.28e–05	1.60e+02
TA	40060	–1.74e–03	2.13e+04	6.75e–03	–1.02e+04
25(302)	42462	–7.08e–05	3.01e+05	8.22e–05	–8.14e+02
30(302)	52596	2.16e–05	1.55e+05	2.82e–05	2.18e+02
Benchmark	1081800	–1.80e–08	–1.16e+01	–9.33e–09	–4.11e–01

Table 13. Error in all five properties studied in order of increasing grid size for CH_3SiH_3.

Grid	Number of grid points	Number of electrons	V_{ne} (μH)	Dipole (au)	V_{ee} (μH)
20(110)	11456	–1.29e–04	8.00e+06	1.79e–04	–1.98e+03
SG-0	11570	–7.54e–05	2.21e+06	–2.16e–04	–4.18e+03
25(110)	15472	–2.08e–04	3.85e+06	–2.10e–04	2.91e+03
20(194)	16832	6.39e–05	8.00e+06	5.06e–04	–1.23e+03
30(110)	19488	–1.79e–04	1.94e+06	–2.26e–04	–9.97e+02
25(194)	22864	–6.16e–07	3.85e+06	1.02e–04	3.72e+03
20(302)	23744	6.95e–05	8.00e+06	4.93e–04	–1.17e+03
NTA	25854	–1.32e–04	3.45e+03	–1.62e–04	–3.67e+02
Becke	27750	–4.05e–03	2.42e+04	–8.99e–03	–1.64e+04
30(194)	28896	2.70e–05	1.94e+06	8.83e–05	–1.49e+02
SG-1	29896	–2.26e–05	–2.40e+03	–1.07e–04	–4.24e+02
TA	32262	–2.16e–03	2.25e+04	–7.99e–04	–1.05e+04
25(302)	32368	1.16e–07	3.85e+06	8.28e–05	3.74e+03
30(302)	40992	2.53e–05	1.94e+06	5.68e–05	–1.63e+02
Benchmark	961600	–2.43e–08	–2.19e+02	–8.06e–08	–4.82e–01

gives the new R values for the MultiExp 20(110) grid along with the accuracy defined as

$$[7] \qquad \text{accuracy} = -\log_{10}\left|\frac{\text{approx}}{\text{exact}} - 1\right|$$

where approx is the value of the Coulomb energy calculated using numerical integration, and exact is the HF value. Table 10 shows the error in the Coulomb potential V_{ee} calculated using the previous set of R values, R_1, and the new set of R values, R_2. The overall MAE decreased only slightly from 8 280 μH to 7 231 μH. However, from Table 10, we notice that the error for the set of molecules containing chlorine did not change systematically. The error did not change for $p$$NO_2$BzCl, but changed in sign for HOCl and CH_2Cl_2, and decreased slightly for Cl_2, and dramatically changed in both sign and magnitude for NaCl, CH_3Cl, CCl_4, and ClF. The same pattern can be observed for the set of molecules containing phosphorous, P_2, PF_5, PH, CH_3PH_2, and CH_2 PH_2 PH_2 as well as the set containing sulfur SO, SO_2, CH_3SH, and CH_2SHSH. Of special interest is the comparison of the molecules SO and SO_2. The error changed sign for SO, while it changed sign and increased more than an order of magnitude for SO_2. This analysis shows that the accuracy of the numerical integration using MultiExp grid is highly sensitive to the change in the radial scale factor. This dependence on R could explain the odd behaviour of MultiExp grid where a larger grid, 25(110), gave an overall MAE larger than that of the smaller grid 20(110) (see the third column of Table 7). To test whether further improvements are possible, we have performed simultaneous optimization of both the radial scale factors for oxygen and sulfur in SO and SO_2 using an optimization algorithm described in ref. 15, in which the gradients are calculated numerically. The radial scale factors are chosen to minimize the error, $|V_{ee}(\text{NI}) - V_{ee}(\text{HF})|$, and since the optimized values depend on the initial R values used, several optimized values are reported. In Table 11, we report the error in the Coulomb repulsion energy using different radial scale factors. It is

obvious from these results that the error in Coulomb repulsion energy is quite sensitive to the radial scale factors. Although it is possible to substantially reduce the error in V_{ee} by optimizing R values for SO or SO_2, no values of R can reduce errors in V_{ee} equally for both SO and SO_2.

Numerical integration efficiency

Number of points of the atomic grid

Table 3 gives the number of points for the atomic grids. The number of grid points for SG-0 from hydrogen to chlorine is in the range of 1328 to 1496, which makes it one of the smallest grids and comparable in size to the 20(110) grid. Table 3 shows that, except for H and He, the largest grid is the Becke grid followed by the TA grid. Also Table 3 shows that, except for H and He, the TAnew grid is larger than the SG-1 grid, the 30(194) grid is comparable in size to the SG-1 grid, and the 25(194) grid is medium in size between the SG-0 and SG-1 grids. To better measure grid convergence, errors for the five properties studied are reported in Tables 12 and 13 for CH_3CONH_2 and CH_3SiH_3, respectively. In both Table 12 and Table 13, the grids are arranged in increasing grid size. From the smallest (SG-0) to the largest [30(302)], the MultiExp grids generally perform equally. It can be seen that the larger grids are not necessarily the most accurate grids and that the mapping and the radial quadrature play a crucial rule in determining the accuracy of the numerical integration.

Conclusions

The performance for a number of well-known grids, including the most recently developed SG-0 grid, and a large benchmark grid, was examined. We used numerical integration to calculate the number of electrons, dipole moment, potential energy, and Coulomb repulsion energy. In general, the most accurate grids are our new implementation of the Trutler and Alhrichs grid, TAnew, and the standard grid, SG-1. Increasing the size of the outermost grid of the MultiExp grid from 110 to 194 angular points improved the accuracy, but increasing it further to 302 angular points did not. All the grids were very inaccurate in calculating the potential energy. The Coulomb energy calculations showed the inconsistency of the performance of the MultiExp grid. Also, the inconsistent behaviour of the numerical integration, specifically with calculating Coulomb energy, was noticed with some of the larger grids such as SG-1 and TAnew. For compounds containing third-row elements, it is interesting to note that when using the MultiExp grids, the errors are very insensitive to the angular grid used in the outer region. This would suggest that the error is mainly arising from the core or middle regions.

References

(1) (a) Shiozaki, T.; Hirata, S. *Phys. Rev. A* **2007**, *76* (4), 040503. doi:10.1103/PhysRevA.76.040503.; (b) Becke, A. D.; Dickson, R. M. *J. Chem. Phys.* **1990**, *92* (6), 3610. doi:10.1063/1.457869.

(2) Gill, P. M. W.; Johnson, B. G.; Pople, J. A. *Chem. Phys. Lett.* **1993**, *209* (5-6), 506–512. doi:10.1016/0009-2614(93)80125-9.

(3) Treutler, O.; Ahlrichs, R. J. *Chem. Phys.* **1995**, *102* (1), 346.

(4) Mura, M. E.; Knowles, P. J. *J. Chem. Phys.* **1996**, *104* (24), 9848. doi:10.1063/1.471749.

(5) Köster, A. M.; Flores-Moreno, R.; Reveles, J. U. *J. Phys. Chem.* **2004**, *121* (2), 681. doi:10.1063/1.1759323.

(6) Rodríguez, J. I.; Thompson, D. C.; Ayers, P. W.; Köster, A. M. *J. Chem. Phys.* **2008**, *128* (22),o. 224103. doi:10.1063/1.2931563. PMID:18554002.

(7) Pérez-Jordá, J. M.; Becke, A. D.; San-Fabian, E. *J. Chem. Phys.* **1994**, *100* (9), 6520. doi:10.1063/1.467061.

(8) Gill, P. M. W.; Chien, S.-H. *J. Comput. Chem.* **2003**, *24* (6), 732–740. doi:10.1002/jcc.10211. PMID:12666165.

(9) Becke, A. D. *J. Chem. Phys.* **1988**, *88* (4), 2547. doi:10.1063/1.454033.

(10) El-Sherbiny, A.; Poirier, R. A. *J. Comput. Chem.* **2004**, *25* (11), 1378–1384. doi:10.1002/jcc.20063. PMID:15185332.

(11) Chien, S. H.; Gill, P. M. W. *J. Comput. Chem.* **2006**, *27* (6), 730–739. doi:10.1002/jcc.20383. PMID:16518882.

(12) te Velde, G.; Baerends, E. J. *J. Comput. Phys.* **1992**, *99* (1), 84–98. doi:10.1016/0021-9991(92)90277-6.

(13) Pederson, M. R.; Jackson, K. A. *Phys. Rev.* **1990**, *B41*, 7453.

(14) Poirier, R. A. *MUNgauss,* Fortran 90 version. Chemistry Department, Memorial University of Newfoundland, St. John's, NL. With contributions from S.D. Bungay, A. El-Sherbiny, T. Gosse, J. Hollett, D. Keefe, A. Kelly, C.C. Pye, D. Reid, M. Shaw, Y. Wang, and J. Xidos. 2001.

(15) Davidon, W. C. *Math. Program.* **1975**, *9* (1), 1–30. doi:10.1007/BF01681328.

Finite-temperature effects in enzymatic reactions — Insights from QM/MM free-energy simulations

Hans Martin Senn, Johannes Kästner, Jürgen Breidung, and Walter Thiel

Abstract: We report potential-energy and free-energy data for three enzymatic reactions: carbon–halogen bond formation in fluorinase, hydrogen abstraction from camphor in cytochrome P450cam, and chorismate-to-prephenate Claisen rearrangement in chorismate mutase. The results were obtained by combined quantum mechanics/molecular mechanics (QM/MM) optimizations and two types of QM/MM free-energy simulations (free-energy perturbation and umbrella sampling) using semi-empirical or density-functional QM methods. Based on these results and our previously published free-energy data on electrophilic substitution in *para*-hydroxybenzoate hydroxylase, we discuss the importance of finite-temperature effects in the chemical step of enzyme reactions. We find that the entropic contribution to the activation barrier is generally rather small, usually of the order of 5 kJ mol^{-1} or less, consistent with the notion that enzymes bind and pre-organize the reactants in the active site. A somewhat larger entropic contribution is encountered in the case of chorismate mutase where the pericyclic transition state is intrinsically more rigid than the chorismate reactant (also in the enzyme). The present results suggest that barriers from QM/MM geometry optimization may often be close to free-energy barriers for the chemical step in enzymatic reactions.

Key words: QM/MM, combined quantum mechanics/molecular mechanics, free-energy methods, free-energy perturbation, enzyme reactions.

Résumé : On rapporte les données d'énergie potentielle et d'énergie libre pour trois réactions enzymatiques, soit la formation d'une liaison carbone-halogène avec la fluorinase, l'enlèvement d'un hydrogène à partir du camphre avec le cytochrome P450cam et un réarrangement de Claisen chorismate à préphénate avec une chorismate mutase. Les résultats ont été obtenus par des optimisations MQ/MM semi-empiriques ou de la théorie de la fonctionnelle de la densité (TFD) et deux types de simulations d'énergie libre MQ/MM (perturbation de l'énergie libre et échantillonnage parapluie). Sur la base de ces résultats et des résultats d'énergie libre publiés antérieurement pour la substitution électrophile avec l'hydroxylase de *p*-hydroxybenzoate, on discute de l'importance d'effets de température finie sur l'étape chimique des réactions enzymatiques. Il a été observé que la contribution entropique à la barrière d'activation est relativement faible, généralement inférieure à 5 kJ mol^{-1}, en accord avec la notion que les enzymes se lient et organisent les réactifs dans le site actif. On rencontre une contribution entropique un peu plus importante dans le cas de la chorismate mutase pour laquelle l'état de transition péricyclique est intrinsèquement plus rigide que le réactif chorismate, aussi dans l'enzyme. Les résultats présentés ici suggèrent que les barrières obtenues à partir de l'optimisation MQ/MM de la géométrie se rapprochent souvent des barrières d'énergie libre pour l'étape chimique des réactions enzymatiques.

Mots-clés : MQ/MM, combinaison de mécanique quantique et de mécanique moléculaire, méthodes de l'énergie libre, perturbation de l'énergie libre, réactions enzymatiques.

[Traduit par la Rédaction]

Introduction

Combined quantum mechanics/molecular mechanics (QM/MM) approaches are the method of choice for treating chemical reactions in enzymes,[1–4] providing an efficient and accurate description of complex biomolecular systems. They allow detailed insights into the mechanisms of enzyme reactions; see, e.g., refs. 3–5 for recent overviews. The QM/MM method is essentially a potential-energy method. However, the key quantity to characterize chemical systems and proc-

Received 22 January 2009. Accepted 12 May 2009. Published on the NRC Research Press Web site at canjchem.nrc.ca on 16 September 2009.

This article is part of a Special Issue dedicated to Professor T. Ziegler.

H.M. Senn,[1,2] J. Kästner,[3,4] J. Breidung, and W. Thiel.[5] Max-Planck-Institut für Kohlenforschung, D-45470 Mülheim an der Ruhr, Germany.

[1]Corresponding author (e-mail: senn@chem.gla.ac.uk).
[2]Present address: WestCHEM and Department of Chemistry, University of Glasgow, Glasgow G12 8QQ, UK.
[3]Corresponding author (e-mail: kaestner@theochem.uni-stuttgart.de).
[4]Present address: University of Stuttgart, D-70569 Stuttgart, Germany.
[5]Corresponding author (e-mail: thiel@mpi-muelheim.mpg.de).

esses is the free energy. The free-energy difference between two states is directly related to the probability of finding the system in one state or the other. For an *NVT* system with constant number of particles, *N*, constant volume, *V*, and constant temperature, *T*, the relevant free energy is the Helmholtz free energy, *A*,

$$[1] \qquad A = U - TS$$

The free energy is composed of the internal energy, *U* (which is the potential energy plus the zero-point vibrational energy plus finite-temperature corrections, which are usually small), and the entropic contribution, –*TS*. At temperatures $T > 0$ K, knowledge of the energy alone is therefore not sufficient to determine the free energy. A higher-energy state with high entropy may be more favourable (that is, have a lower free energy) than a low-energy state with low entropy (see Fig. 1). The entropy can be related, loosely speaking, to the size of the configuration space available to the system at a given temperature.

In quantum chemistry, the conventional approach to computing the free energy of a molecule is based on the rigid-rotor/harmonic-oscillator (RRHO) approximation,[7] where the partition function is formulated under the assumptions that the molecule as a whole rotates as a rigid body and that all intramolecular motions can be treated as harmonic vibrations. However, when applied to large biomacromolecular systems, the RRHO treatment is problematic for several reasons: (*i*) A full vibrational analysis is computationally very costly or even prohibitive for systems typically encountered when modeling enzymatic reactions (several 1000 to 10 000 atoms). (*ii*) There are many "soft", anharmonic degrees of freedom in a (solvated) biomolecule for which the harmonic-oscillator approximation is inadequate. (*iii*) Even if the above points could be resolved, there remains a major issue: The RRHO approach is applied at a stationary point (minimum or transition state) obtained from a potential-energy minimization procedure. However, for large systems, this configuration will be just one of very many of similar energy, and one cannot assume it to be *the* representative structure.[8]

A more appropriate approach for biomolecular systems is therefore to calculate free energies from some type of sampling procedure at finite temperature that is able to explore, at least locally, the configuration space available to the system. The sampling can be done either with Monte Carlo or molecular-dynamics (MD) simulation techniques; we will restrict ourselves here to MD-based methods. The general idea is to express the free-energy difference between two states as a statistical-thermodynamical average that can be evaluated by sampling the appropriate ensemble (e.g., the canonical, or *NVT*, ensemble or the isothermal–isobaric, or *NPT*, ensemble).

Over the last few years, numerous studies have been reported that combine QM/MM methods with a variety of sampling techniques to calculate reaction and activation free energies of enzymatic processes; see refs. 3, 4, and 9 for recent reviews. In the present contribution, we have used QM/MM free-energy perturbation (FEP) as well as umbrella sampling (US) to investigate several enzyme reactions, namely, the halogenation step in fluorinase, the hydrogen-abstraction step in cytochrome P450cam, and the Claisen rearrangement in chorismate mutase. We will incorporate into the discussion previously reported free-energy results on other systems and obtained by other methods. From the combined body of data, we will attempt to draw more general conclusions on the effect of finite temperature on the chemical step of these, and perhaps other, enzymatic reactions.

Fig. 1. The high-energy state x_2 has a lower (more favourable) free energy than x_1 because of its higher entropy, indicated by the larger width of the potential well (adapted from ref. 6).

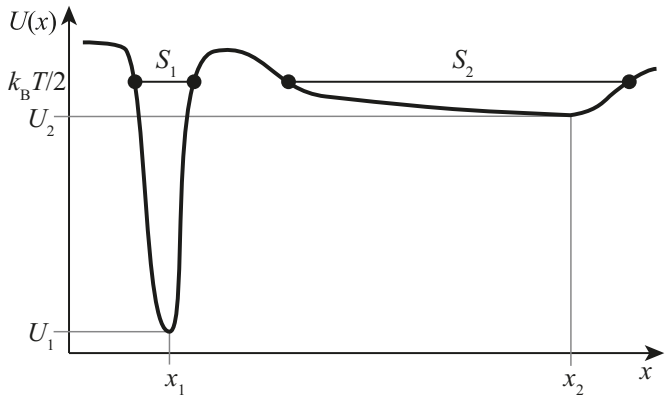

We will begin by briefly outlining our QM/MM method and discuss the QM/MM free-energy perturbation method, with which the majority of results herein were obtained. We will then introduce the three enzymatic reactions studied and provide computational details. The Results section will present potential-energy and free-energy data for the reactions, which will subsequently be discussed with a view on the importance of finite-temperature effects in the chemical step of enzyme reactions. We will finish with some conclusions.

Theoretical background

The QM/MM energy

Here, we outline our QM/MM scheme to facilitate the following discussion and introduce some notation. In brief, we use an additive scheme with hydrogen link atoms and electrostatic embedding with charge shifting.[3,10–13] The total (potential) energy of the entire system is written as

$$[2] \qquad E_{\mathrm{QM/MM}}(\mathbf{R}_{\mathrm{QM}},\mathbf{R}_{\mathrm{MM}}) = E_{\mathrm{QM}}(\mathbf{R}_{\mathrm{QM}};\mathbf{R}_{\mathrm{MM}}) + E_{\mathrm{MM}}(\mathbf{R}_{\mathrm{MM}}) + E_{\mathrm{QM-MM}}(\mathbf{R}_{\mathrm{QM}},\mathbf{R}_{\mathrm{MM}})$$

where $\mathbf{R}_{\mathrm{QM}}$ and $\mathbf{R}_{\mathrm{MM}}$ are the coordinates of the QM and the MM atoms, respectively; link atoms are included in $\mathbf{R}_{\mathrm{QM}}$ to simplify the notation. $E_{\mathrm{QM}}(\mathbf{R}_{\mathrm{QM}};\mathbf{R}_{\mathrm{MM}})$ is the electronic energy of the QM system in the presence of the MM point charges, but *without* accounting for the electrostatic interaction with the surrounding MM atoms (see below). $E_{\mathrm{MM}}(\mathbf{R}_{\mathrm{MM}})$ is the energy of the MM atoms as calculated by the classical force field. All QM–MM interactions are collected in $E_{\mathrm{QM-MM}}(\mathbf{R}_{\mathrm{QM}},\mathbf{R}_{\mathrm{MM}})$:

$$[3] \qquad E_{\mathrm{QM-MM}} = E^{\mathrm{b}}_{\mathrm{QM-MM}} + E^{\mathrm{vdW}}_{\mathrm{QM-MM}} + E^{\mathrm{el}}_{\mathrm{QM-MM}}$$

$E^{\mathrm{b}}_{\mathrm{QM-MM}}$ and $E^{\mathrm{vdW}}_{\mathrm{QM-MM}}$ contain the bonded (typically bond stretching, angle bending, torsion) and van der Waals interactions between the QM and the MM atoms, respectively. These terms are calculated at the force-field level. The elec-

trostatic QM–MM interaction, E^{el}_{QM-MM}, is treated within the electrostatic embedding scheme, that is, the QM electron density is polarized by the MM charges. This is achieved by including the point charges into the QM Hamiltonian, which amounts to solving the SCF equations in the presence of the point-charge field. The corresponding electronic Hamiltonian thus reads (in atomic units)

$$\begin{aligned}\widehat{H}_{SCF} &= \widehat{H}_0 + \widehat{H}^{el}_{QM-MM} \\ &= \widehat{H}_0 - \sum_i^{\text{electrons}} \sum_k^{\text{point charges}} \frac{q_k}{|\,\mathbf{r}_i - \mathbf{R}_k\,|} \\ &\quad + \sum_\alpha^{\text{QM nuclei}} \sum_k^{\text{point charges}} \frac{Z_\alpha q_k}{|\,\mathbf{R}_\alpha - \mathbf{R}_k\,|}\end{aligned} \quad [4]$$

where $\widehat{H}_0$ designates the gas-phase Hamiltonian of the QM system. The converged SCF energy obtained by the QM program therefore includes *both* the energy of the QM system alone *and* its interaction with the point charges, that is

$$\begin{aligned}E_{SCF} &= \langle \Psi_{QM/MM} | \widehat{H}_0 + \widehat{H}^{el}_{QM-MM} | \Psi_{QM/MM} \rangle \\ &= E_{QM} + E^{el}_{QM-MM}\end{aligned} \quad [5]$$

With the corresponding polarized wave function $\Psi_{QM/MM}$, we can write the energy of the QM system in its environment (but *without* the interaction with the environment) as

$$E_{QM}(\mathbf{R}_{QM};\mathbf{R}_{MM}) = \langle \Psi_{QM/MM} | \widehat{H}_0 | \Psi_{QM/MM} \rangle \quad [6]$$

To evaluate E_{QM} with a standard QM program, we can perform one single SCF cycle using $\widehat{H}_0$ and the polarized wave function.

Free energies from QM/MM molecular-dynamics simulations

Various free-energy methods (such as thermodynamic integration, slow growth, fast growth, free-energy perturbation, or umbrella sampling) have long been developed and used within the framework of classical MD simulations.[14–19] In principle, all these approaches can be applied with a QM/MM, rather than an MM, potential-energy function. An excellent overview of ab initio QM/MM free-energy calculations has recently been given by Hu and Yang.[9] Most commonly, QM/MM free-energy calculations are used to compute the potential of mean force (PMF) along a distinguished coordinate. Usually, the system is driven along this one-dimensional reaction coordinate (RC) from the initial to the final state using constraints (thermodynamic integration, slow growth, fast growth) or restraints (umbrella sampling). The free-energy difference is then obtained by integrating the mean force of constraint or by reconstructing the probability distribution along the reaction coordinate, respectively.

Although feasible in principle, the extended sampling required to produce converged free energies makes these approaches rather expensive when implemented with a QM/MM potential. With a semi-empirical QM method, full QM/MM sampling is well-affordable, as shown here for the chorismate mutase case or in other work from our laboratory.[20–23] However, when a first-principles (ab initio or density functional theory) QM method is required to accurately treat the reactive process, full QM/MM MD simulations become highly computationally demanding, if not prohibitive, even by modern standards (but see, e.g., ref. 24 for an ab initio QM/MM MD study). To alleviate the computational cost of such simulations, methods have been devised that avoid the sampling of the QM region; among them, QM/MM FEP has been widely used. Recent free-energy techniques even allow the computation of the minimum free-energy path and the optimization of stationary points on the free-energy surface.[25–28] QM/MM has also been combined with metadynamics[29–31] as a sampling technique.[32]

QM/MM free-energy perturbation

Here, we first summarize our implementation of the QM/MM FEP method[23] and discuss related schemes thereafter. QM/MM FEP is based on Zwanzig's perturbation formula[33] that expresses the free-energy difference between two states a and b as the exponential average of the potential-energy change between a and b, the (canonical ensemble) average being taken over configurations representative of state a

$$\Delta A^{a\to b} = -k_B T \ln\langle \exp\{-\Delta E^{a\to b}/(k_B T)\}\rangle^a \quad [7]$$

where k_B is Boltzmann's constant and T the temperature. Note that this is not a perturbation treatment in the usual sense; in the limit of complete sampling, eq. [7] is exact. By exchanging the labels of the states, one obtains a "backward" perturbation $\Delta A^{b\to a} = -\Delta A^{a\to b}$.

The basic idea in QM/MM FEP is to use a sequence of QM/MM-optimized structures, typically along a reaction coordinate, as the states and to keep the QM part fixed in each state. The free-energy difference between two states (a, b) along the reaction coordinate is then evaluated by sampling, at the MM level, the energy difference between the QM part being in configuration a to being in configuration b

$$\Delta A^{a\to b}_{env} = -k_B T \ln\langle \exp\{-\Delta E^{a\to b}_{pert}/(k_B T)\}\rangle^a_{MM} \quad [8]$$

with

$$\begin{aligned}\Delta E^{a\to b}_{pert} &= E_{QM-MM}\left(\mathbf{R}^b_{QM}, \mathbf{R}_{MM}(t)\right) \\ &\quad - E_{QM-MM}\left(\mathbf{R}^a_{QM}, \mathbf{R}_{MM}(t)\right)\end{aligned} \quad [9]$$

E_{QM-MM} is the QM–MM interaction energy as defined in eq. [3]; $\mathbf{R}_{MM}(t)$ is the instantaneous configuration of the MM atoms; $\mathbf{R}^a_{QM}$ and $\mathbf{R}^b_{QM}$ are the configurations of the QM atoms fixed in state a and b, respectively.

The subscript "env" in eq. [8] is a reminder that the free-energy difference thus obtained only accounts for the environment and the QM–MM coupling. The free-energy change due to the fixed QM part can simply be approximated in a first step by the corresponding potential-energy difference

$$\Delta A_{QM} \approx \Delta E_{QM} \quad [10]$$

where the QM energy is as defined in eq. [6]. If the two states are stationary points, one can apply the harmonic-oscillator approximation to the QM part to calculate the zero-point vibrational energy, ΔE^{ZPE}_{QM}; the thermal contributions to the internal energy, ΔU^{th}_{QM}; and the entropy contribution, $-T\Delta S_{QM}$:

$$[11] \qquad \Delta A_{QM} = \Delta E_{QM} + \Delta E_{QM}^{ZPE} + \Delta U_{QM}^{th} - T\Delta S_{QM}$$

The final free-energy difference between two stationary points thus becomes

$$[12] \qquad \Delta A = \Delta A_{env} + \Delta A_{QM}$$

Keeping the QM part fixed during the sampling is the first crucial approximation that makes QM/MM FEP computationally viable. The second key approximation is made when calculating the electrostatic QM–MM term. Within the electrostatic embedding scheme, where the QM–MM electrostatic interaction is calculated at the QM level, each change in the configuration of the MM atoms in principle triggers a QM calculation (i.e., a full SCF) to adapt the QM electron density to the new MM positions. We can eliminate the need for these QM calculations in two steps: Firstly, we introduce the approximation that the density will not change when the MM atoms move (frozen-density approximation). The QM–MM electrostatic interaction is then still calculated at the QM level but requires only one SCF cycle. Secondly, we approximate the (frozen) QM density by a point-charge model. Specifically, at each point along the reaction coordinate, we fit a set of point charges, placed on the QM atoms, to reproduce the electrostatic potential of the true density in the vicinity of the QM region (ESP charges). The QM–MM electrostatic interaction, E_{QM-MM}^{el}, during the sampling is thus approximated by the interaction of the ESP charges with the surrounding MM charges, $E_{QM-MM}^{el,ESP}$.

Note that we apply the ESP charge model not only in the calculation of $\Delta E_{pert}^{a\to b}$ but also to evaluate E_{QM} as

$$[13] \qquad E_{QM} = E_{SCF} - E_{QM-MM}^{el,ESP}$$

(cf. eqs. [5] and [6]). This not only eliminates the need for additional SCF cycles altogether but also leads to a consistent description of the QM–MM electrostatic interaction throughout the procedure.

Using the ESP charges, all terms in $\Delta E_{pert}^{a\to b}$ can therefore be evaluated at the classical level, which makes the sampling highly computationally efficient. The computational bottleneck of the procedure is shifted from the sampling to the QM/MM optimizations required to determine the points along the reaction coordinate. In our present implementation, we calculate $\Delta E_{pert}^{a\to b}$ in each MD step (i.e., typically every 1 fs). However, because MD data are correlated, it would actually be sufficient to evaluate $\Delta E_{pert}^{a\to b}$ less frequently as it is done in the related QTCP approach, e.g., every 100 to 1000 MD steps (0.1 to 1 ps).

We validated the different approximations involved in QM/MM FEP using the activation energy of the OH transfer in the enzyme *p*-hydroxybenzoate hydroxylase (PHBH) at the AM1/GROMOS level.[23] As shown in Table 1, the two methods using full QM/MM MD sampling, thermodynamic integration, and umbrella sampling, agree with each other very well and can therefore be considered as a reference. FEP with a full SCF in each sampling step to evaluate E_{QM-MM}^{el} provides a free-energy barrier that is 4–5 kJ mol^{-1} higher. This difference is statistically significant and reflects the approximations introduced by keeping the QM atoms fixed:[1] The dynamics of the environment is decoupled from the dynamics of the QM region.[2] The QM region is not treated dynamically but within the harmonic approximation. The further approximations of the QM/MM FEP approach that make the evaluation of E_{QM-MM}^{el} viable (the frozen-density approximation and the representation of the density by ESP charges) have almost no effect on the result, which differs from FEP with full SCF by 2 kJ mol^{-1}, which is barely statistically significant. We can therefore conclude that the approximations of the QM/MM FEP method lead to deviations in the computed free energies from the fully sampled reference in the order of a few kJ mol^{-1}, which is very acceptable given the massive reduction in computational effort. The major contribution to the deviation stems from keeping the QM region frozen; representing the density by point-charges does not significantly affect the result.

Table 1. Activation free energy of the OH transfer in the enzyme PHBH calculated at the AM1/GROMOS level using different free-energy methods.

Method	$\Delta^{\ddagger}A$ (kJ mol^{-1})[b]	Reference
Thermodynamic integration	101	20
Umbrella sampling	102	23
FEP (full SCF)[a]	106	23
FEP (frozen density)[a]	108	23
FEP (ESP charges)[a]	108	23

[a]The $\Delta^{\ddagger}A$ values from FEP include the QM thermal and entropic terms ($\Delta U_{QM}^{th} - T\Delta S_{QM}$) obtained within the harmonic approximation for the QM part, but are *exclusive* of the zero-point vibrational energy (ΔE_{QM}^{ZPE}) to make them comparable to the thermodynamic-integration and umbrella-sampling results.

[b]The statistical uncertainty of $\Delta^{\ddagger}A$ is 1–2 kJ mol^{-1}.

We also implemented and tested different schemes for handling the link atoms in the FEP approach and found that their effect on the results is small.[23] Moreover, we verified the validity of the ESP fit for densities described by extended basis sets.

Related FEP methods

The QM/MM FEP method described in the previous section is essentially an implementation of the QM/MM-FE method introduced by Zhang et al.,[34] with which it shares all its key features. Rod and Ryde[35,36] presented a closely related approach called QTCP (quantum thermodynamic-cycle perturbation). However, they derived it from slightly different assumptions. They start from a subtractive QM/MM scheme with mechanical embedding, where the QM atoms bear some type of point charges to begin with and the QM–MM electrostatic interaction is described at the classical level. To improve upon this, they introduce two additional FEP calculations (the vertical legs of their thermodynamic cycle) at the initial and final states that recover the free-energy difference due to changing the charge model of the QM region from point charges to a polarizable density. That is, they additionally sample perturbations, in our notation, of the type

$$[14] \qquad \begin{aligned} \Delta E_{pert}^{MM\to QM/MM} &= E_{SCF}\left(\mathbf{R}_{QM}^{a}, \mathbf{R}_{MM}(t)\right) \\ &\quad - E_{QM-MM}^{el,classical}\left(\mathbf{R}_{QM}^{a}, \mathbf{R}_{MM}(t)\right) \end{aligned}$$

(see eq. [16] in ref. 36). $E_{QM-MM}^{el,classical}$ is the QM–MM electro-

static interaction calculated using any kind of point-charge model, not necessarily ESP charges, for the QM region.

This full QTCP scheme is obviously rather costly because of the QM sampling required to evaluate the vertical legs of the cycle. Rod and Ryde therefore introduce approximations akin to the ones used in the QM/MM FEP approach, which eliminate the sampling for the vertical legs: The QM density is kept frozen during the sampling, and the density is represented by ESP charges derived from a QM/MM calculation of the initial state. With these approximations, QTCP essentially becomes equivalent to QM/MM FEP or QM/MM-FE, respectively.

The idea of the QTCP approach to use the FEP formalism to calculate the free-energy due to a change in computational level at the same configuration, rather than between two configurations, was previously exploited by Warshel and co-workers[37] and has been applied also by others.[38–40]

System setups and computational details

Fluorinase

System overview

The enzyme 5′-fluoro-5′-deoxyadenosine synthase (FDAS or fluorinase for short) from the soil bacterium *Streptomyces cattleya* is the only native enzyme known to date to catalyze the formation of C–F bonds.[41] It uses fluoride and *S*-adenosine-L-methionine (SAM) as substrates to produce 5′-fluoro-5′-deoxyadenosine (FDA); see Scheme 1. The enzyme is a hexamer in solution, consisting of a dimer of tightly bound C_3-symmetric homotrimers; each monomer is a chain of 299 amino-acid residues. The trimer unit features three equivalent active sites at the monomer interfaces.

We have previously investigated the C–F bond formation in fluorinase in detail using QM/MM optimization methods at the DFT/CHARMM level.[42] The active site with bound SAM and fluoride is shown in Fig. 2. The position of the fluoride, which is not present in the experimental structure, was determined from classical MD simulations and QM/MM optimizations. In agreement with experimental evidence,[43] we found that the attack of the fluoride at the C5′ position of SAM follows an S_N2-type mechanism. Our study revealed interesting details about the involvement of active-site residues in fluoride binding and produced reaction and activation energies.

Herein, we will report reaction and activation energies for the reaction with the other halides (Cl^-, Br^-, I^-) and free reaction and activation energies for the complete halide series.

System setup

The preparation and setup of fluorinase system was described in detail in ref. 42. In summary, we used a complete trimer unit and hydrated one of the three equivalent active sites with a sphere of water of 25 Å radius centered on the sulfur atom of SAM, which amounts to a total of 17 596 atoms. Inside the hydrated sphere, we defined an active region in which the atoms were free to move while the remaining atoms were kept frozen. To be consistent with previous work,[42] the active region for the optimization of reactant, transition, and product states for the other halides was a shell of 8 Å around SAM and the halide (1394 atoms). For the reaction-profile optimizations and the FEP simulations, the active region was a sphere of 17 Å radius containing 2947 atoms.

Scheme 1. C–F bond formation catalyzed by fluorinase.

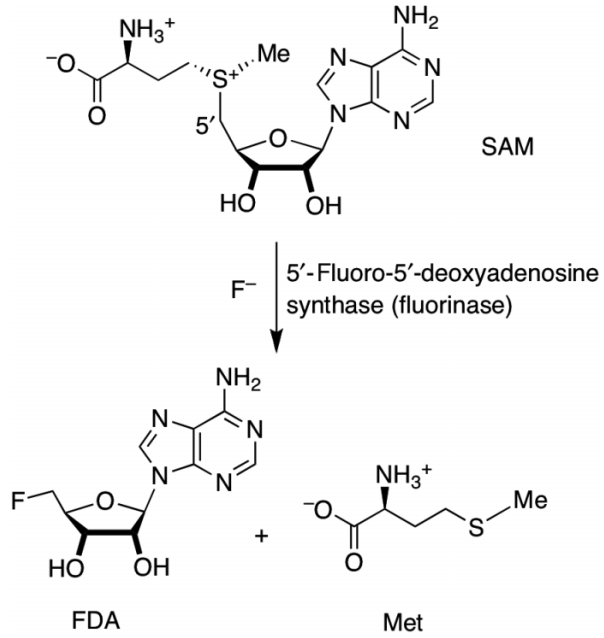

Fig. 2. QM/MM optimized structure of the active site of fluorinase. SAM is shown in ball-and-stick representation; fluoride as a green ball; selected active site residues as sticks; and hydrogen bonds are indicated in orange. The protein chains of the two monomers that form the active site are sketched in grey and yellow, respectively.

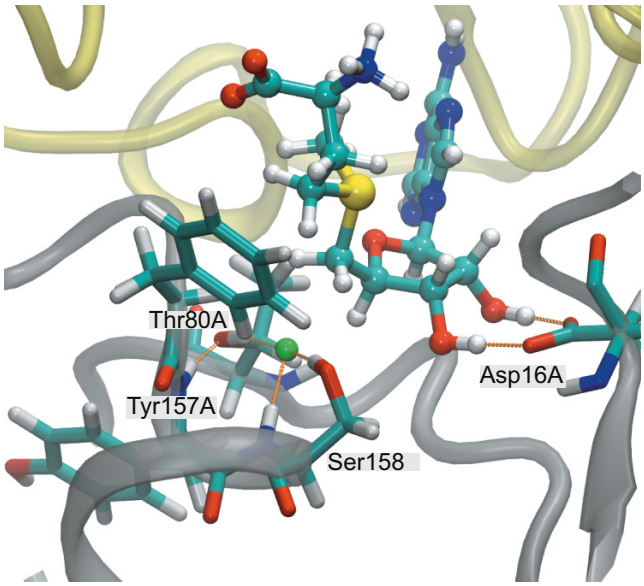

The QM/MM calculations were carried out at the DFT(BP86)/CHARMM level with the modular program package ChemShell.[13,44] QM energy and gradient were provided by TURBOMOLE,[45–49] interfaced to ChemShell. The resolution of the identity (RI) approximation[50–53] was employed with the BP86 functional.[54–57] The def2-TZVP[58,59] basis set was used, augmented with one diffuse function on all atoms (TZVP+; see Supplementary data);[41] the core

electrons of iodine were described by an effective core potential (def2-ecp)[60]. MM energy and gradient were evaluated by ChemShell's internal force-field driver using the CHARMM22[61] all-atom topology and parameter data; the MM electrostatic interactions were fully calculated. The QM electron density was electrostatically embedded into the field of the rigid MM point charges by including them into the QM Hamiltonian. The charge-shift scheme was applied at the QM/MM boundary,[13] and no electrostatic QM/MM cutoff was employed. The QM part contained SAM without the 2-ammoniopropanoate moiety, that is, 5′-(*S*,*S*-dimethylsulfonio)-5′-deoxyadenosine, the covalent bond across the QM/MM boundary being saturated with a H link atom (39 QM atoms).

QM/MM geometry optimizations were performed with a linearly scaling algorithm in hybrid delocalized coordinates (HDLCOpt)[62] as implemented in ChemShell. The residues for the optimization algorithm were the standard amino-acid residues. In microiterative transition-state searches, the core region, for which the Hessean is calculated, included the halide, C(5′)H_2, and S; full details can be found in the Supporting Information to ref. 42.

Structure optimizations with other halides

Starting from the reactant, transition, and product states obtained for the native fluoride,[42] we optimized the respective states for chloride, bromide, and iodide by replacing the halide and re-optimizing the active region. This procedure allowed the local environment to adjust to the different sizes and charge distributions of the halides, but it does not account for longer-range effects.

QM/MM reaction profile and harmonic frequencies

The reaction coordinate was defined as the difference between the bond being broken and the bond being formed, $\xi = d(\text{S–C5}) - d(\text{C5′–X})$, where X = F, Cl, Br, I. The reaction profiles were calculated by QM/MM optimizations from $\xi = -1.0$ to 2.2 Å (full profile, for F) or $\xi = -1.4$ to 0.4 Å (profiles from reactant to transition state only, for Cl, Br, I) initially in steps of 0.2 Å. If the FEP forward and backward simulations at a given RC step showed convergence problems, the step size was reduced by inserting additional optimization points. This was only necessary in certain parts of the profile between the transition and the product state. In this region of the RC, the fluoride anion gradually becomes a fluoro substituent bearing a much smaller charge, which leads to a rearrangement of the hydrogen bonding around the fluorine.

To calculate the QM contribution to the free energy at the stationary points from the harmonic approximation, numerical second derivatives were calculated at these points for the QM region (partial Hessean including the QM atoms and the MM boundary atom, consistent with link-atom method 4)[23] using ChemShell. Two displacements of 0.01 au were done per degree of freedom; the SCF convergence was tightened for the Hessean calculations (scfconv 10, grid m4).

Free-energy perturbations

For each QM/MM-optimized structure along the RC, a set of ESP charges for the QM atoms was derived by fitting to the electrostatic potential at the positions of the 200 MM atoms nearest to the QM region. With the QM region (plus the MM boundary atom) held fixed, the active region of the system was then equilibrated by QM/MM MD at 300 K under *NVT* conditions. The QM–MM electrostatic interaction in all simulations was evaluated at the classical level using the ESP charges. The MD time step was 1 fs. The Berendsen thermostat[63] ($\tau_T = 0.1$ ps) was used during the first 10 ps of the equilibration phase; the Nosé–Hoover chain thermostat[64–67] (with a chain length of 4; $\tau_{NHC} = 0.02$ ps, corresponding to $\tilde{\nu}_{NHC} = 375$ cm^{-1}) thereafter. The total equilibration time was 50 ps at each RC point.

The FEP simulations were then carried out; both forward and backward perturbations were done. The sampling time per step was 20 ps, of which the first ps was always discarded. The data of the remaining 19 ps were subjected to coarse-graining and statistical tests as described in ref. 20. Additional data were discarded as necessary to obtain a series with trend-free mean and variance. Note that the sampling length effectively used to calculate the average therefore varies between steps. The maximum deviation between forward and backward perturbation at a given RC step was about 3 kJ mol^{-1}; typical deviations were <1 kJ mol^{-1} (Fig. 3).

The discontinuities in the sampled free-energy increments in Fig. 3 are caused by non-continuous changes between the optimized structures along the reaction path that are not explicitly included in the RC. For example, the dip at $\xi = 0.7$ Å is related to the breaking of a hydrogen bond and the formation of a new one in the vicinity of the fluoride ion in the MM part. This hydrogen-bond rearrangement causes the decrease in A_{env} (plotted in Fig. 3), which is, however, counterbalanced by an increase in E_{QM}. Therefore, the sum $A(\xi) = E_{QM} + A_{env}$ is smooth (see Fig. 7). Such discontinuous changes in the environment free energy that arise from shifts between the QM energy and the environment energy due to structural rearrangements in the MM region do not disappear with longer sampling or smaller steps in ξ; note that the associated error bars are not larger than those for other points along the reaction coordinate.

On the other hand, there are features like the one at $\xi = 1.3$ Å (with a larger sampling error and a larger difference between forward and backward perturbation relative to other points) that are related to structural rearrangements in the QM part. Their error bars would be reduced by adding more steps in ξ. In the present case, this was not done at $\xi = 1.3$ Å because the error bar was still deemed acceptable and because the point does not contribute to the barrier, which is of primary interest here.

P450cam

System overview

The cytochrome P450 enzymes constitute a superfamily of haem monooxygenases that perform a variety of essential functions, such as detoxification and biosynthesis, in nearly all living species. They catalyze a variety of oxidation processes, including aliphatic and aromatic hydroxylation, epoxidation, and heteroatom oxidation. The extensive theoretical work on these enzymes has been reviewed.[68] QM/MM studies in our laboratory[69–84] (see ref. 4 for a summary) have focused on P450cam from the bacterium *Pseudomonas putida*, which catalyzes the selective hydroxylation of camphor at

Fig. 3. FEP-sampled environment free-energy increments, $\delta A_{env}(\xi_i \rightarrow \xi_{i+1})$ and $\delta A_{env}(\xi_{i+1} \rightarrow \xi_i)$ for the forward and backward perturbations, respectively, along the reaction coordinate for the fluorination reaction in fluorinase. The increments are plotted at ξ_{i+1} for both sampling directions; hence, there is no value at $\xi_1 = -1.0$ Å. The error bars show the statistical uncertainty (standard deviation of sampled mean). Black line: Forward perturbations; red dashed line: backward perturbations.

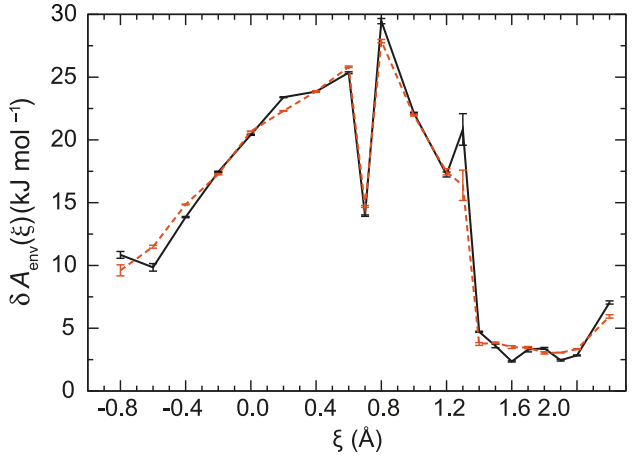

C5 to the exo alcohol (Scheme 2). The crucial reactive intermediate is an iron(IV)-oxo species (Compound I) with three unpaired electrons that give rise to almost degenerate doublet and quartet states. Compound I is able to abstract an aliphatic hydrogen from the substrate. Subsequently, the substrate radical thus generated recombines with the iron(III) hydroxo ligand to form the hydroxylated product.

We have previously studied the hydrogen-abstraction step in P450cam at the DFT(B3LYP)/CHARMM level by QM/MM optimizations.[71,77,78,80] Herein, we report on FEP simulations of this step.

System setup

We started from an optimized hydrogen-abstraction transition state obtained previously. The details of preparing and setting up the system have been published previously.[71,77,78,80] The procedures used were conceptually and technically very similar to the ones described above for fluorinase. We only highlight system-specific differences from here on. The enzyme was fully hydrated by enclosing it into a water shell of 15 Å, the outer 10 Å of which were kept fixed; the total system size is about 24 000 atoms. The active region contained 444 atoms in optimizations and 7439 atoms for the FEP simulations. The QM region included 51 atoms (region R1):[71,77,78,80] the oxy-haem without the side chains; the thiolate S of the distal cysteine; and the $C(4)HC(5)H_2C(6)H_2$ fragment of camphor. Twelve hydrogen link atoms were used to saturate the bonds across the QM–MM boundary; the QM region therefore was [FeO(porphine)(SH)] + propane. The electronic structure was described by the B3LYP functional[54,55,85–88] as implemented in TURBOMOLE. The basis set of double-ζ quality denoted B1[71,77,78,80] was used. All calculations were done in the quartet state ($S = 3/2$). The MM region was described by the CHARMM22[61] force field. All QM/MM calculations were done with ChemShell.

Scheme 2. Hydrogen abstraction from camphor by Compound I of P450cam.

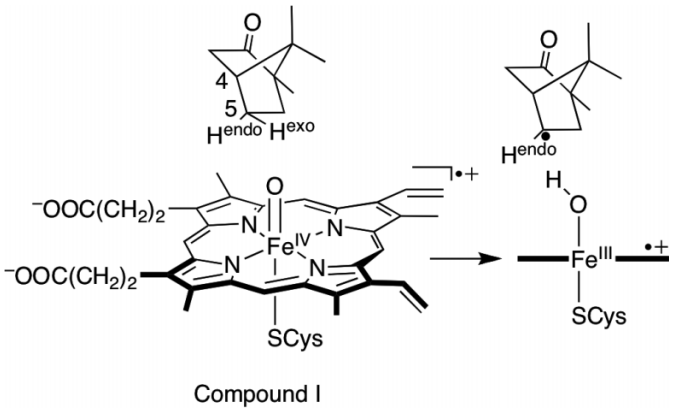

QM/MM reaction profile and FEP simulations

The reaction coordinate was defined as the difference between the bond being broken and the bond being formed, $\xi = d(C5–H^{exo}) - d(H^{exo}–O)$. Starting from the optimized transition state, the reaction profile was produced initially from $\xi = -1.2$ to 1.4 Å in steps of 0.2 Å and subsequently refined to a step size of 0.1 Å. Frequency calculations at the stationary points were not performed for this case.

At the transition state, the system was equilibrated for 30 ps at 300 K (time step of 1 fs) with the QM part and MM boundary atoms being frozen in addition to the outer water layer (7388 active atoms). For the other points along the RC, the QM region of the equilibrated TS was replaced by the QM/MM-optimized QM region of the respective point and then re-equilibrated for 20 ps. A cutoff of 15.9 Å was used for the non-bonded MM–MM interactions with a pair-list updated every 25 steps. No QM/MM cut-off was applied.

For the FEP simulations, both forward and backward perturbations were performed. The sampling time at each RC point was 20 ps. Only the trend-free[20] part (no less than 8 ps) of the data was used to calculate the average. The P450cam system is particular in that it has rather many link atoms.[12] The impact of different link-atom treatments is therefore more pronounced. With steps of 0.2 Å and link-atom method 4,[23] where both QM and MM boundary atoms and the link atoms are perturbed, the sampled free-energy differences deviated between the forward and backward perturbation by 19 kJ mol^{-1} on average, which was considered unacceptable. Applying link-atom method 2,[23] where the MM boundary atoms remain unperturbed, the average deviation between the forward and backward perturbation was still 15 kJ mol^{-1}. Only by reducing the step size to 0.1 Å and using link-atom method 4, we obtained an acceptable agreement (maximum deviation of 7 kJ mol^{-1}) between forward and backward perturbations. Only these results will be discussed below.

Chorismate mutase

System overview

The enzyme chorismate mutase catalyzes the Claisen rearrangement of chorismate to prephenate, without covalent-

bond formation between the substrate and the enzyme (Scheme 3). The reaction, a rare example of a pericyclic reaction in biochemistry, is a key step of the shikimate pathway for the synthesis of aromatic amino acids in plants, fungi, and bacteria. It has been the subject of numerous theoretical studies devoted to the structure of the enzyme–substrate complex, reaction pathways, and the role of specific residues in transition-state stabilization. It has also served as an important case for testing and developing theories on the origin of enzymatic catalysis. A summary of recent theoretical work is provided in ref. 4. Here, we have investigated the Claisen rearrangement in the *Bacillus subtilis* chorismate mutase (BsCM) by means of umbrella-sampling free-energy simulations at the semi-empirical QM/MM level.

Preparation and setup

Full details about system preparation and setup, methods, and programs can be found in the Supplementary data. All simulations were performed with the program CHARMM[89,90] using the self-consistent-charge density-functional tight-binding (SCC-DFTB) method[91,92] for the QM region (substrate, 24 atoms) and the CHARMM22[61] all-atom force field for the MM region (protein and solvent atoms, 13 397 atoms). No electrostatic QM/MM cut-off was employed; MM electrostatic interactions were treated with the extended electrostatics method.[90,93]

The initial coordinates of BsCM bound to a transition-state analogue (TSA) were obtained from the Protein Data Bank (PDB code 2CHT). The crystal structure[94] consists of four trimers in the asymmetric unit; only the first one was retained. The TSA in the active site at the interface between chains A and B was converted to chorismate; the other two TSA molecules were removed. The BsCM–chorismate complex was hydrated with a 30 Å sphere of water. Protein and substrate atoms within 17 Å from the origin of the sphere and all (crystallographic and added) water molecules within 30 Å were free to move (active region). The system was then subjected to QM/MM MD simulations under *NVT* conditions (time step 1 fs). After 200 ps of equilibration, 10 snapshots were taken every 10 ps as initial configurations for the subsequent QM/MM simulations. Depending on the snapshot, the active region included about 9850 atoms.

Umbrella-sampling simulations

The free energy of activation and the free energy of reaction of chorismate to prephenate in the active site of BsCM were obtained from umbrella-sampling[95] simulations along a reaction coordinate defined as the difference between the lengths of the breaking C–O and the forming C–C bond. The biased MD simulations consisted of two parts: First, the snapshots were equilibrated in the reactant state (ξ = –2.5 Å) at 300 K for 20 ps. Then, the RC was sequentially changed from –2.5 Å to 2.5 Å in steps of 0.1 Å (51 windows). In each window, the system was sampled for 10 ps, and RC data were collected in every time step. Only the data of the last 9 ps were used for the analysis. The sampling was then repeated in the backward direction starting from ξ = 2.5 Å.

We used umbrella integration (UI)[21,22] as well as the weighted histogram analysis method (WHAM)[96] to combine the windows of the US simulations. The number of bins was always chosen to be 500. Using 1000 bins left the free-energy results virtually unchanged for either UI or WHAM. UI and WHAM yielded essentially identical results, differing by no more than 0.8 kJ mol^{-1}. The root-mean-square deviation (RMSD) between UI and WHAM results was 0.4 kJ mol^{-1} for the activation free energies and 0.2 kJ mol^{-1} for the reaction free energies. The values reported below were obtained using UI.

Scheme 3. Claisen (allyl vinyl ether to 4,5-unsaturated ketone) rearrangement of chorismate to prephenate in chorismate mutase.

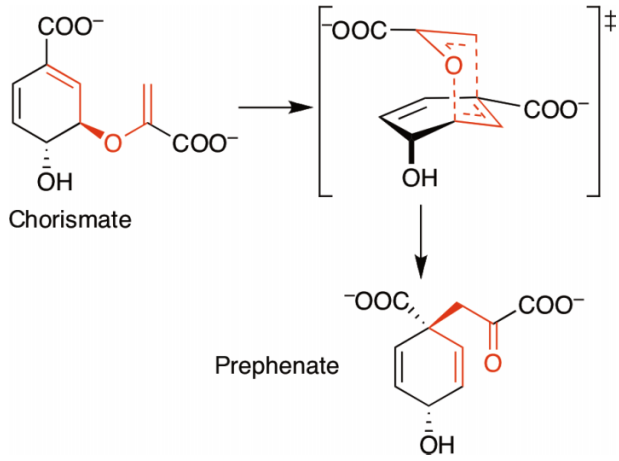

Potential-energy profiles

Complementary to the free-energy reaction profiles obtained from US, we also calculated potential-energy profiles for all the snapshots. The structures were energy-minimized and then subjected to reaction-path calculations using the same RC definition as for the US simulations. The reaction pathways were calculated in both the forward and backward direction. To precisely locate minima and maxima in the reaction profiles, the energy curves were fitted by cubic splines.

Results

Fluorinase

Optimizations with halides other than fluoride

The QM/MM-optimized reactant states with bound SAM and halide for all four halides are shown in Fig. 4. It can be seen that the structures are largely superimposable and only minor adjustments have taken place (here and below, structure were superimposed by aligning all fixed atoms). The structures with Cl^- and Br^- in particular are nearly identical. While the chosen optimization procedure does not allow for larger rearrangements, the stable binding position of SAM is explained by the highly specific recognition in the binding site through multiple hydrogen bonds with the adenine part and salt bridges and hydrogen bonds to the zwitterionic amino acid of the methionyl part. Additionally, the ribose part is held in position by the double hydrogen bond to Asp 16A. The halide binding site is in all cases formed by hydrogen bonds from the side-chain OH and the backbone NH of Ser 158A and the side-chain OH of Thr 80A. Selected structural parameters of the reactant states are collected in Table 2. The trends seen along the halide series follow the expected pattern. With increasing size of the halide, and

Fig. 4. Superimposed optimized reactant states for the complete halide series in the fluorinase: F (red), Cl (white), Br (salmon), and I (blue); for clarity, the halides are all represented by a sphere of the same size.

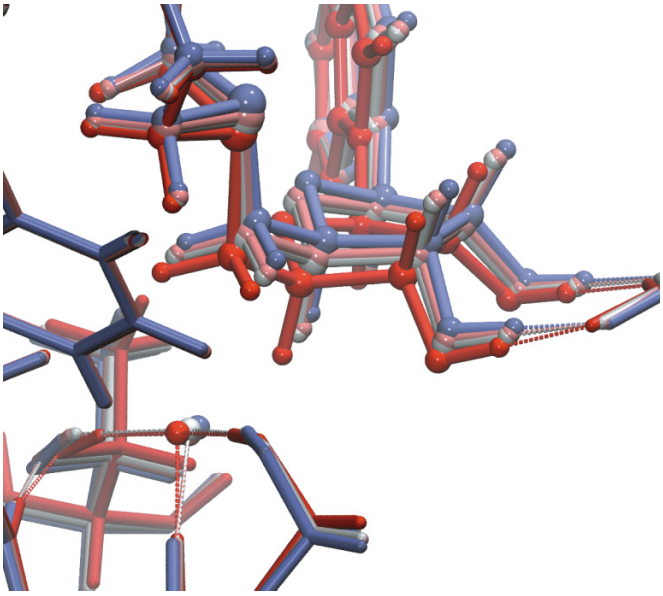

thus decreasing charge density, the hydrogen-bonding distances to the halide become monotonically longer. The biggest changes are seen from F to Cl and then from Br to I, while the Cl and Br systems are very similar. The distance between the halide and the attacked C5′ also increases along the series. However, only the change from F to Cl is larger than the other two. The slightly lengthened C5′–S bond for F compared with the other halides suggests an increased degree of activation towards nucleophilic attack.

The optimized transition states are presented in Table 3 and Fig. 5. The pertinent changes between reactant and transition state have already been discussed for fluoride[42] and apply also to the other halides, i.e., the C5′–S bond is essentially broken, the X–C5′ bond is partially formed, and the coordination around C5′ is trigonal-planar; in brief, it is a nearly ideal S_N2 transition state. As the reaction progresses, the attacking halide's negative charge is increasingly delocalized over the substrate as the interaction between halide and substrate increases. This is reflected in weakened hydrogen bonds to the halide, especially the Thr 80A OH···X bond is starting to break at the transition state. The hydrogen bonds from Ser 158A, however, are only slightly lengthened at this stage, somewhat more for F than for the other halides. In the product states (Table 4 and Fig. 6), the X–C5′ bond is fully formed and the methionine leaving group is well-separated from the halogenated deoxynucleoside. Only the hydrogen bond from the Ser 158 amide NH to the halogen is retained. Remarkably, the halogen position does not differ very much along the series, despite the differences in C5′–X bond lengths (the C–I bond is 0.7 Å longer than the C–F bond). The RMSD from F is between 0.1 Å (Br) and 0.4 Å (I); the ribose unit as a whole is displaced relative to the F system by 0.3 Å (Cl, Br) to 0.5 Å (I). To accommodate the longer C5′–X bonds for the heavier halogens, while keeping the halogen itself almost at the same position, the exocyclic torsion about C4′–C5′ needs to adjust. There are

Table 2. Selected bond lengths, hydrogen-bonding distances, and RC values (in Å) in the optimized reactant states (RS) in the fluorinase for all the halides.

	F	Cl	Br	I
d(C5′, S)	1.85	1.84	1.83	1.83
d(X, C5′)	2.76	2.99	3.12	3.24
ξ_{RS} (opt)	–0.91	–1.15	–1.29	–1.41
d(Ser158A OH···X)	1.79	2.26	2.32	2.58
d(Ser158A NH···X)	1.82	2.14	2.16	2.40
d(Thr80 OH···X)	1.82	2.25	2.29	2.54

Table 3. Selected bond lengths, hydrogen-bonding distances, and RC values (in Å) in the optimized transition states (TS) in the fluorinase for all the halides.

	F	Cl	Br	I
d(C5′, S)	2.47	2.53	2.57	2.51
d(X, C5′)	1.93	2.23	2.34	2.50
ξ_{TS} (opt)	0.54	0.30	0.23	0.01
d(Ser158A OH···X)	1.85	2.30	2.34	2.59
d(Ser158A NH···X)	1.92	2.17	2.19	2.42
d(Thr80 OH···X)	2.06	2.45	2.54	2.72

Fig. 5. Superimposed optimized transition states for the complete halide series in fluorinase: F (red), Cl (white), Br (salmon), and I (blue); for clarity, the halides are all represented by a sphere of the same size.

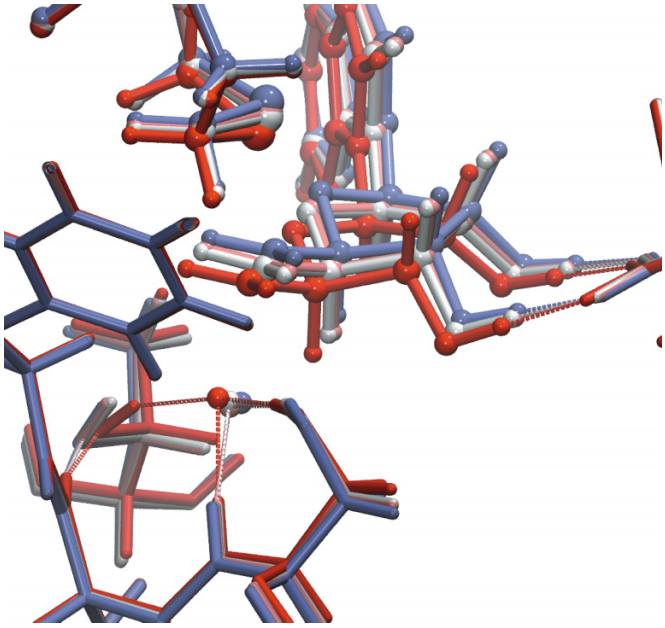

experimental structures available of the fluoro-[41] and the chloro-product.[97] Essentially, they agree perfectly with the QM/MM-optimized structures, which validates our approach.

The energetic data from the optimizations of the stationary points are summarized in Table 5. They reveal three main results: (*i*) The reaction is exothermic only with fluoride, while it is endothermic with the other halides; (*ii*) the forward barrier is lowest for fluoride; (*iii*) therefore, the backward barriers for the other halides are significantly

Table 4. Selected bond lengths, hydrogen-bonding distances, RC values (in Å), and torsion angles η about C4′–C5′ in the optimized product states (PS) in fluorinase for all the halides.

	F	Cl	Br	I
d(C5′, S)	3.44	3.45	3.44	3.47
d(X, C5′)	1.43	1.80	1.95	2.13
ξ_{PS} (opt)	2.01	1.65	1.49	1.34
d(Ser158A NH···X)	2.00	2.27	2.28	2.50
η(O4′, C4′, C5′, X)	100.2°	93.7°	93.5°	87.6°

Fig. 6. Superimposed optimized product states for the complete halide series in fluorinase: F (red), Cl (white), Br (salmon), and I (blue); for clarity, the halogens are all represented by a sphere of the same size.

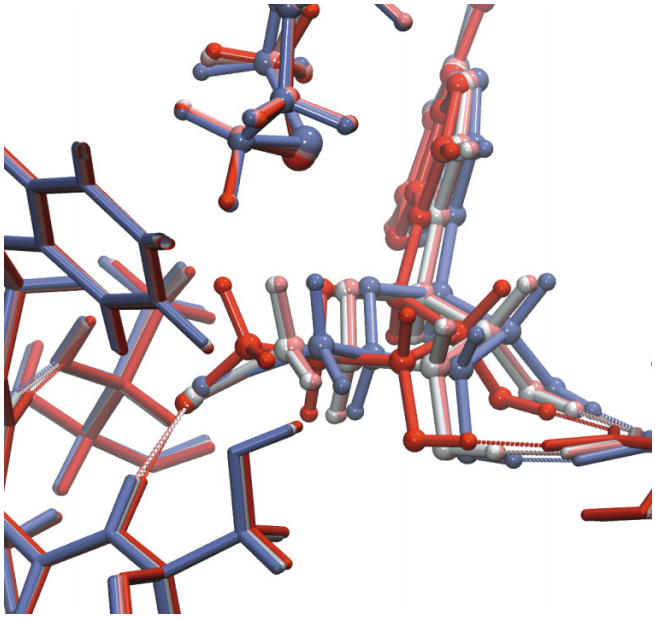

lower than the backward barrier for fluoride. Fluorinase thus has a clear preference in the C–X bond-forming step for fluorination over other halogenations. This is also reflected in the extent to which the C–X bond has formed in the transition state (Table 5), which, in agreement with the Hammond postulate, shows an earlier transition state for fluoride than for the other halides.

The calculated preference for fluoride over chloride is in agreement with the experimental data:[97] Fluorinase was found to act also as a chlorinase, however, with the equilibrium of the reaction being shifted to the reactant side and with much lower activity, as expected from the calculated reaction and activation energies. The measured ratio of effective rate constants of the forward reactions with fluoride and chloride corresponds to a difference in activation energy ($\Delta\Delta^{\ddagger}G$ at 298 K) of 12 kJ mol^{-1}. The excellent agreement with the calculated difference of 10 kJ mol^{-1} is certainly fortuitous; however, it again provides support for the validity of our approach in the present case.

Experimentally, no activity has been observed with bromide or iodide. Our results would not suggest such a discrimination between, e.g., chloride and bromide, although the reaction with bromide is more endothermic and has a somewhat higher barrier. However, it should be kept in mind that we have investigated only the C–X bond-forming step, while the halide selectivity may well be determined earlier in the mechanism. For instance, the halide-binding step, which will involve the (partial) replacement of the halide's hydration water by interactions with the protein, may well be decisive for the halide selectivity.[98,99] It is interesting to note that the recently reported SAM chlorinase SalL,[100] which is structurally, and thus presumably also mechanistically, similar to fluorinase, accepts chloride, bromide, and iodide, but not fluoride, as halide substrate.

Table 5. Reaction and activation energies (in kJ mol^{-1}) as well as relative lengths of the forming and breaking bonds in the TS for C–X bond formation in fluorinase. Data from QM/MM optimizations of stationary points (at BP86/def2-TZVP+/CHARMM level).

	F	Cl	Br	I
ΔE	–22	16	35	22
$\Delta^{\ddagger}E$(fw)	59	69	74	65
$\Delta^{\ddagger}E$(bw)	81	53	39	43
d(X–C5′)$_{TS}$/d(X–C5′)$_{PS}$	1.35	1.24	1.20	1.17
d(C5′–S)$_{TS}$/d(C5′–S)$_{RS}$	1.34	1.38	1.40	1.37

Free energies

The forward activation free energies obtained from the FEP simulations for C–X bond formation in fluorinase with X = F, Cl, Br, and I are collected in Table 6. We also provide the contributions of the individual components that sum up to the total free-energy difference according to eqs. [11] and [12]. With fluoride only, we determined the complete free-energy profile from reactants to products (Fig. 7), which allowed us to calculate also the reaction free energy: $\Delta_r A$ = –19.5 ± 0.6 kJ mol^{-1} (composed of $\Delta_r A_{env}$ = 261.9 ± 0.6 kJ mol^{-1}, $\Delta_r E_{QM}$ = –275.1 kJ mol^{-1}, $\Delta_r E_{QM}^{ZPE}$ = 0.0 kJ mol^{-1}, and $\Delta_r U_{QM}^{th} - T\Delta_r S_{QM}$ = –6.3 kJ mol^{-1}).

Comparing the free energies (excluding ΔE_{QM}^{ZPE}) with the corresponding potential energies from Table 5, the main conclusion is that the effect of finite temperature on the reaction and activation energies investigated is small (<3 kJ mol^{-1}) in this case. Without the ZPE and finite-temperature contributions to the free energy from to the QM part, the potential-energy and free-energy profiles are essentially identical from the reactant up to the transition state (shown for fluoride in Fig. 7). Also the values of the reaction coordinate at the stationary points of the free-energy curve differ only insignificantly from their potential-energy counterparts.

An explanation for this small difference between potential and free energies in the reactive step can be found in the high degree of pre-organization and pre-orientation provided by the active site. The reactants are ideally set up and held in place for the S_N2 process by their various interactions with the protein throughout the reaction. Moreover, only minimal adjustments to the active-site structure are necessary to accommodate either the reactants or the products. There is therefore not much room for thermal and entropic contributions to the free energy.

Cytochrome P450cam

The results for the hydrogen abstraction from camphor by Compound I of cytochrome P450cam are summarized in Table 7. Like for fluorinase, the differences between poten-

Table 6. Activation free energy (for the forward reaction, $\Delta^{\ddagger}A$(fw), in kJ mol^{-1}) and its components according to eqs. [11] and [12] from QM/MM FEP for C–X bond formation in fluorinase. Also given are the values of the reaction coordinate (in Å) at the stationary points of the free-energy profile.

	F	Cl	Br	I
$\Delta^{\ddagger}A$(fw)	53.5±0.6	64.5±1.7	71.2±0.3	61.5±1.0
$\Delta^{\ddagger}A_{env}$	123.2±0.6	110.4±1.7	118.2±0.3	103.4±1.0
$\Delta^{\ddagger}E_{QM}$	–64.5	–40.1	–40.5	–36.1
$\Delta^{\ddagger}E_{QM}^{ZPE}$	–4.6	–4.8	–5.3	–5.1
$\Delta^{\ddagger}U_{QM}^{th} - T\Delta^{\ddagger}S_{QM}$	–0.6	–1.0	–1.2	–0.7
ξ_{RS} (FEP)	–0.84	–1.15	–1.25	–1.41
ξ_{TS} (FEP)	0.51	0.28	0.23	0.02

Fig. 7. Reaction profile of the C–F bond formation in fluorinase. Dashed line: Potential-energy profile; solid line: free-energy profile. Note that the free-energy curve only includes $\Delta A_{env} + \Delta E_{QM}$ because the harmonic approximation for the calculation of the QM ZPE and finite-temperature terms is valid only at stationary points.

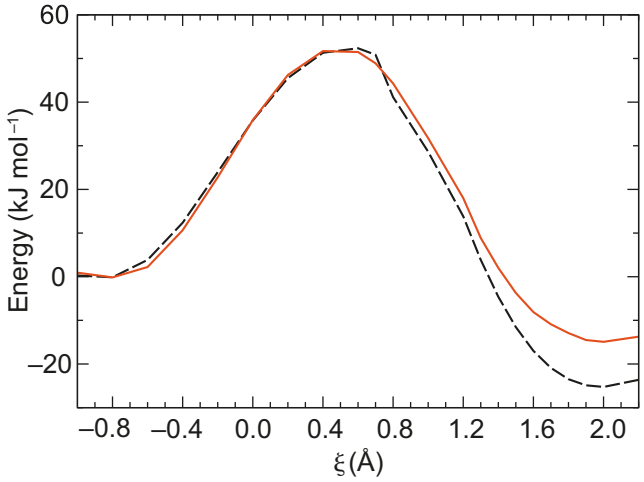

tial and free energies are small (see Fig. 8), although we note that the free-energy values here were calculated as $\Delta A_{env} + \Delta E_{QM}$ only (i.e., not including the ZPE and finite-temperature contributions from the QM part). Previous gas-phase model calculations at the B3LYP level[66] gave ZPE and enthalpic finite-temperature corrections to the QM barrier of –18 and +2 kJ mol^{-1}, respectively. Thus, the overall finite-temperature contribution remains small (nominally 4 kJ mol^{-1}, ignoring $\Delta^{\ddagger}S_{QM}$), while the ZPE correction to the barrier is significant for hydrogen transfer and should be applied to both ΔE and ΔA. The values of the reaction coordinate at the stationary points differ only slightly between the potential-energy and free-energy profiles, respectively: ξ_{RS} = –0.99/–1.03 Å (opt/FEP); ξ_{TS} = 0.17/0.18 Å; ξ_{PS} = 1.10/1.07 Å. Again, the small effect of finite temperature on structure and energetics of the hydrogen-abstraction reaction can be attributed to the pre-orientation of the bound reactants. Figure 9 shows the optimized TS; camphor is seen to be hydrogen-bonded to an active-site Tyr residue.

Chorismate mutase

Table 8 reports the activation and reaction energies obtained by optimizations for the conversion of chorismate to

Table 7. Activation and reaction energies (in kJ mol^{-1}) for the hydrogen abstraction in P450cam. Both potential energies and free energies are given.

	Forward barrier	Reaction energy
ΔE(opt)	71	42
ΔA(FEP)	73±2	48±2
ΔA_{env}	–15±2	–19±2
ΔE_{QM}	88	67

Note: Free energies do not include the QM ZPE and finite-temperature terms.

Fig. 8. Reaction profile of the H-abstraction in P450cam. Dashed line: Potential-energy profile; solid line: free-energy profile. Note that the free-energy curve only includes $\Delta A_{env} + \Delta E_{QM}$.

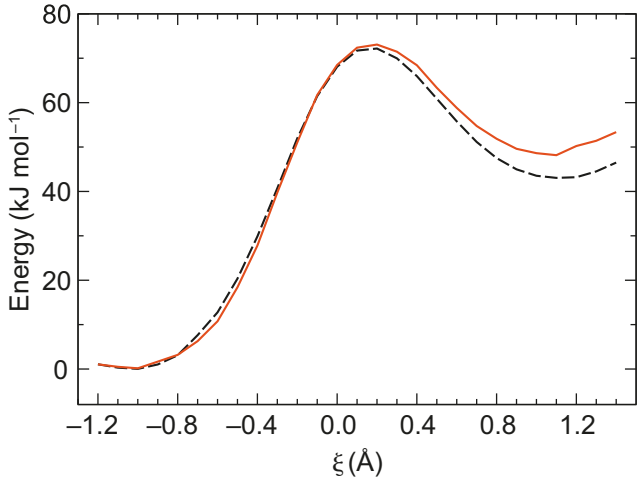

prephenate in *B. subtilis* chorismate mutase. The values for the barrier range from 21.8 to 38.7 kJ mol^{-1} across the forward and backward scans of the 10 snapshots, with a mean of $\Delta^{\ddagger}E$ = 27.5 ± 1.2 kJ mol^{-1} (the error bar indicated is the single standard deviation of the mean over the 20 values, corresponding to a confidence level of 68%). The reaction energies cover the interval from –68.5 to –98.4 kJ mol^{-1}; the mean is $\Delta_r E$ = –83.5 ± 1.9 kJ mol^{-1}. The standard deviations of the individual energy values are 5.3 kJ mol^{-1} and 8.3 kJ mol^{-1}, respectively. The difference between forward and backward scan for a given snapshot is at most 1.0 and 0.5 kJ mol^{-1} for $\Delta^{\ddagger}E$ and $\Delta_r E$, respectively. The associated RMSD (forward vs. backward) is 0.3 kJ mol^{-1} for the barriers and 0.2 kJ mol^{-1} for the reaction energies.

Multiple potential-energy profiles for the reaction of interest were previously calculated with hybrid DFT QM/MM methods (B3LYP/6–31G(d)/CHARMM27).[101] From 16 different reaction pathways, an average reaction barrier of 50.2 kJ mol^{-1} was obtained, with a standard deviation of 7.1 kJ mol^{-1}. Like in the present work, a large spread of the calculated barriers from 37.7 to 62.8 kJ mol^{-1} was reported. The differences in barrier height between the 16 QM/MM reaction profiles were explained by differences in the microstructure of the active site. Another research group[102] performed reaction-path calculations for the rearrangement of chorismate to prephenate in BsCM at various QM/MM levels of theory. At the B3LYP/6–31+G(d)/CHARMM22 level, they calculated $\Delta^{\ddagger}E$ = 37.4 kJ mol^{-1} and $\Delta_r E$ = –81.6 kJ

Fig. 9. Transition-state structure for the hydrogen abstraction from camphor in cytochrome P450cam. Camphor and haem are represented as all-atom ball-and-stick models. The residues of the binding pocket are shown as sticks; only hydrogen atoms involved in hydrophobic interactions or H-bonds (Tyr) with camphor are shown. Colour code: C cyan, H white, N blue, O red, S yellow, Fe orange.

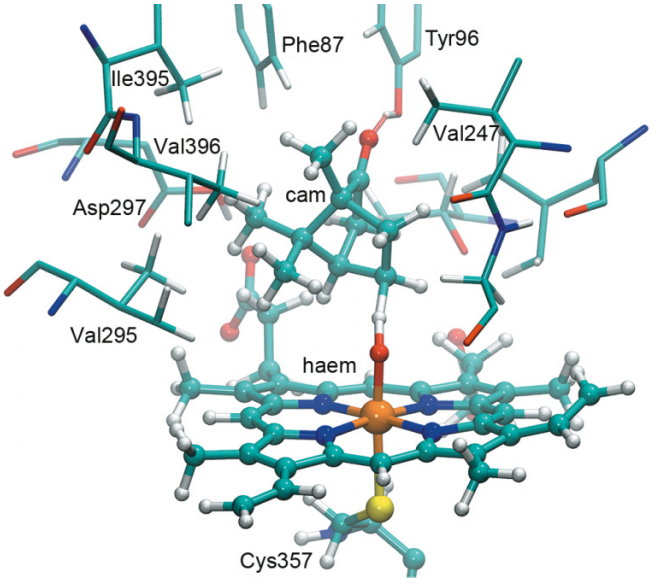

mol^{-1}, while their best estimates (34.3 and –96.7 kJ mol^{-1}, respectively) were obtained using MP2 instead of B3LYP. We also refer to ref. 102 for an overview of previous theoretical results. The experimental value[103] for the activation enthalpy is $\Delta^{\ddagger}H$ = 53.1 ± 1.7 kJ mol^{-1} (at 298 K). Comparing the calculated value for $\Delta^{\ddagger}E$ to the experimental result for $\Delta^{\ddagger}H$, as is usually done in the literature,[101] the experimental barrier is clearly underestimated by the present value of $\Delta^{\ddagger}E$ = 27.5 ± 1.2 kJ mol^{-1}; the relative error is –48%.

The Helmholtz free energies of activation and reaction for the Claisen rearrangement of chorismate to prephenate in BsCM calculated with US for the 10 snapshots are shown in Table 9. It should be noted that free energies from US (and other techniques where the full system is sampled by classical mechanics) do not include any ZPE contributions. The $\Delta^{\ddagger}A$ values from forward and backward runs range from 30.8 to 46.1 kJ mol^{-1}, with a mean of 36.5 ± 0.8 kJ mol^{-1}, which is thus our best estimate for the activation free energy. The $\Delta_r A$ values lie within a range of –67.6 to –88.6 kJ mol^{-1}; the mean is –75.2 ± 1.3 kJ mol^{-1}. The standard deviation of the individual values amounts to 3.5 and 5.7 kJ mol^{-1} for the $\Delta^{\ddagger}A$ and $\Delta_r A$ data, respectively. We note that propagating the statistical sampling errors reported in Table 9 would produce smaller error bars for the mean (0.3 and 0.5 kJ mol^{-1}, respectively). However, these would not properly represent the distribution of the individual values.

The free-energy barriers obtained from the forward and backward runs on a given snapshot agree within 5 kJ mol^{-1}; the RMSD is 4.4 kJ mol^{-1}. The 30 ps and 40 ps snapshots are exceptions where the deviation is larger (6.7 and 9.4 kJ mol^{-1} in absolute value, respectively). For the reaction free energies, four snapshots (10 ps, 40 ps, 80 ps, and 90 ps) have a forward-versus-backward difference of >5 kJ mol^{-1} in absolute value (9.5, 7.7, 13.5, and 11.6 kJ mol^{-1}, respectively). The RMSD is 7.0 kJ mol^{-1}. The variability of values between sampling directions for the same snapshot as well as between different snapshots may be explained as a consequence of yet incomplete sampling. The distribution could be narrowed by equilibrating more extensively in each window and (or) additional sampling.[20]

Table 8. Potential energies of activation and of reaction (in kJ mol^{-1}) for the conversion of chorismate to prephenate in chorismate mutase.

	Forward scan		Backward scan	
Snapshot (ps)	$\Delta^{\ddagger}E$	$\Delta_r E$	$\Delta^{\ddagger}E$	$\Delta_r E$
10	26.0	–80.4	26.0	–80.5
20	22.6	–98.4	22.6	–98.3
30	23.4	–92.0	22.4	–92.5
40	38.7	–76.3	38.5	–76.6
50	30.7	–85.7	30.7	–85.7
60	21.8	–87.3	21.8	–87.3
70	31.7	–76.0	31.8	–75.9
80	22.6	–83.4	22.5	–83.6
90	28.4	–68.5	28.4	–68.6
100	29.8	–85.9	29.8	–86.1

Table 9. Free energies of activation and of reaction (in kJ mol^{-1}) obtained with US for the conversion of chorismate to prephenate in chorismate mutase.

	Forward sampling		Backward sampling	
Snapshot (ps)	$\Delta^{\ddagger}A$	$\Delta_r A$	$\Delta^{\ddagger}A$	$\Delta_r A$
10	36.8±1.2	–75.1±2.3	33.9±1.3	–84.6±2.2
20	38.3±1.2	–73.3±2.1	34.6±1.2	–75.7±2.1
30	40.8±1.3	–69.1±2.1	34.1±1.1	–73.2±2.0
40	36.7±1.4	–75.3±2.3	46.1±1.3	–67.6±2.2
50	32.8±1.2	–73.1±2.2	34.6±1.1	–74.5±2.1
60	38.5±1.3	–74.3±2.3	40.5±1.3	–74.8±2.3
70	35.2±1.3	–73.0±2.4	34.2±1.4	–74.6±2.3
80	34.5±1.3	–74.0±2.2	30.8±1.3	–87.5±2.2
90	36.8±1.2	–77.0±2.3	33.3±1.3	–88.6±2.3
100	37.6±1.4	–68.4±2.3	39.0±1.3	–69.3±2.2

Note: US free energies do not include ZPE contributions.

The present result for the free energy of activation of 36.5 ± 0.8 kJ mol^{-1} agrees well with the value of 33.5 kJ mol^{-1} obtained from multiple-steering MD simulations employing a DFT QM/MM Hamiltonian.[104] In the same study, the reaction free energy was calculated to be about –88 kJ mol^{-1}, which lies at the lower end of the present range of $\Delta_r A$ values. Recently,[105] the free-energy profile was calculated by ab initio QM/MM combined with constrained MD-FEP simulations, yielding 41.4 kJ mol^{-1} for the free-energy barrier and about –84 kJ mol^{-1} for the reaction free energy. The experimental value[103] for the Gibbs free energy of activation is 64.4 kJ mol^{-1} (298 K). All the calculations above thus clearly underestimate the barrier. The relative error for the present free-energy barrier (–43%) is similar to the one of the activation enthalpy (–48%).

The overall finite-temperature effect on the barrier, calculated from our best estimates for $\Delta^{\ddagger}A$ and $\Delta^{\ddagger}E$ (see above), is $T\Delta^{\ddagger}S - \Delta^{\ddagger}U_{th}$ = –9.0 ± 1.4 kJ mol^{-1} at T = 300 K. It is dominated by the entropic contribution, since the change of the thermal contribution to the internal energy, $\Delta^{\ddagger}U_{th}$, is

generally very small. Alternatively, we can calculate individual values for the finite-temperature effect on the barrier for all the snapshots (forward and backward direction) reported in Tables 8 and 9. The corresponding 20 values range from –18.7 to +2.0 kJ mol^{-1}, with a mean of –8.9 ± 1.2 kJ mol^{-1} and a standard deviation of 5.6 kJ mol^{-1}. Obviously, both estimates for the finite-temperature effect on the barrier are close to each other (–9.0 ± 1.4 vs. –8.9 ± 1.2 kJ mol^{-1}) and in good agreement with the experimental[103] value of $T\Delta^{\ddagger}S$ = –11.4 ± 1.5 kJ mol^{-1} at T = 298 K. The difference between free and potential energy is thus larger in this case than for the two systems discussed above.

The finite-temperature effect on the reaction energy can be computed analogously either from our best estimates for $\Delta_r A$ and $\Delta_r E$ (see above) or from the corresponding individual snapshot values, which yields –8.3 ± 2.3 and –8.3 ± 2.6 kJ mol^{-1}, respectively. The 20 snapshot values range from –25.1 to +20.0 kJ mol^{-1}, with a standard deviation of 11.6 kJ mol^{-1} (indicating a larger scatter than in the case of the barriers).

Discussion

In this paper, we have presented potential-energy and free-energy data from QM/MM optimizations and MD-based simulations for the carbon–halide bond formation in fluorinase, the hydrogen abstraction from camphor by Compound I in cytochrome P450cam, and the chorismate-to-prephenate rearrangement in *B. subtilis* chorismate mutase. For the purpose of discussion, we complement these results with similar data obtained for the OH transfer in *para*-hydroxybenzoate hydroxylase (PHBH). The free energy of activation in PHBH at the AM1/GROMOS level is 101 kJ mol^{-1} (average from thermodynamic-integration runs on 10 snapshots; individual values range from 95 to 106 kJ mol^{-1}).[20] The potential-energy barriers obtained from geometry optimizations of the corresponding snapshots at the same level vary between 90 and 109 kJ mol^{-1} (avg. 100 kJ mol^{-1}). The finite-temperature contribution to the barrier is thus small for PHBH; nominally (judging from the average values) of the order of 1 kJ mol^{-1}, which is well within the statistical uncertainty of the thermodynamic-integration simulations and the RMS deviation of the results for the different snapshots.

For chorismate mutase, the availability of data from ten different snapshots (with a forward and a backward value each; Tables 8 and 9) enables us to assess the uncertainty of "single-snapshot" results. Statistically, a measurement falls within an interval of ±2σ around the mean with 95% probability, where σ is the sample standard deviation. Treating the 20 data points as statistically independent, one obtains 2σ error bars of 10.6 and 7.0 kJ mol^{-1} for $\Delta^{\ddagger}E$ and $\Delta^{\ddagger}A$, respectively, and of 16.6 and 11.4 kJ mol^{-1} for $\Delta_r E$ and $\Delta_r A$, respectively. Alternatively, one may consider the maximum deviations from the mean, which are 11.2 ($\Delta^{\ddagger}E$), 9.6 ($\Delta^{\ddagger}A$), 15.0 ($\Delta_r E$), and 13.4 ($\Delta_r A$) kJ mol^{-1}. Combining these values with the PHBH snapshot data,[20] we can assign a rather approximate, but practically useful, error bar of about 10 kJ mol^{-1} for (free) energy differences obtained on a single snapshot of a biomolecular system. The errors tend to be smaller for free energies than for potential energies because the former involve sampling. Also, they appear to be somewhat smaller for barriers than for reaction energies.

If one wants to improve on the accuracy of a "single-snapshot" value, be it a free-energy difference obtained from some kind of sampling technique or, even more so, a potential-energy difference obtained by optimizations, it is necessary to perform calculations for several independent snapshots extracted from extended MD simulations. Such a protocol is arguably the most practical way to include effects due to the variability of the wider environment into QM/MM results.

Leaving reaction energies aside, we now focus on activation barriers, in particular on the entropic contributions to barriers. Strictly speaking, the results obtained from umbrella sampling or thermodynamic integration represent $T\Delta S - \Delta U_{th}$, but since ΔU_{th} is generally small (of the order of 1 kJ mol^{-1}), we shall use the term "entropic contribution" for these quantities (as well as for $T\Delta^{\ddagger}S$ itself). We find the calculated entropic contribution (at 300 K unless noted otherwise) to be small for fluorinase, P450cam, and PHBH (between 1 and 4 kJ mol^{-1} in absolute value); only for BsCM, it is somewhat higher (9 kJ mol^{-1}). To put these values into perspective, we have compared to gas-phase data. The Claisen rearrangement in BsCM lends itself particularly well to such a comparison because the reaction is intramolecular, which makes the choice of gas-phase model obvious, and is experimentally known to have a sizeable entropic contribution to the barrier also in the enzyme.

We have calculated the activation free-energy for the rearrangement of chorismate to prephenate in the gas phase at SCC-DFTB level and obtained (at 300 K) $T\Delta^{\ddagger}S$ = –13.6 kJ mol^{-1} ($\Delta^{\ddagger}G$ = 94.0 kJ mol^{-1}; the chorismate reactant was taken to be in the reactive conformation). Compared with our value in the enzyme of –9.0 kJ mol^{-1}, the activation entropy is therefore 50% higher in the gas phase. This substantial reduction of the entropic contribution in the enzyme is attributed to the pre-organization of the reactant in the active site that is found to be significant even for an intramolecular process like the Claisen rearrangement. The reduced, but still fairly large, negative activation entropy in the enzyme is rationalized by considering the tight, rather rigid pericyclic TS. In the chorismate reactant, even when enzyme-bound, the interaction between the two reacting carbon atoms is only weakly preformed and leaves sufficient motional freedom to the fragments, which are only connected by the C–O bond. In the TS, however, both the forming C–C and the breaking C–O interactions are partial covalent bonds, with correspondingly low flexibility with respect to distance and orientation. So, in a case like this, where the reaction has a high (negative) activation entropy related to the intrinsic structure of the TS, the pre-organization of the reactant by the enzyme can only partially compensate for it.

The situation is rather different for the other enzymatic reactions studied herein. They are bimolecular processes and as such inherently entropically disfavoured in the gas phase because of the loss of translational degrees of freedom. For the H-abstraction from camphor by Compound I, $T\Delta^{\ddagger}S$ = –43 kJ mol^{-1} in the gas phase at the B3LYP level.[68] This high entropy contribution is essentially annihilated in the chemical step in the enzyme (to –2 kJ mol^{-1}) owing to the binding and pre-organization of the reactants in the ac-

tive site. The dominating influence of the pre-orientation of the reactants in intermolecular reactions is also illustrated in PHBH. Gas-phase calculations of the barrier with respect to a pre-reactant complex, where the translational degrees of freedom have already been lost, yield $T\Delta^{\ddagger}S$ = –5 kJ mol^{-1} at the AM1 level. In the enzyme, the entropic contribution is further reduced to –1 kJ mol^{-1}, which can again be explained by motionally restricting interactions of the reactants with the protein; in this case, the hydrogen bond of the transferring OH to a proline residue in the TS plays a special role.[20]

For fluorinase, finally, we do not have suitable gas-phase reference data. However, for an intermolecular S_N2 substitution, $T\Delta^{\ddagger}S$ in the gas phase is expected to be strongly negative relative to separated reactants. In the enzyme, most of the entropic contribution should be quenched, which we find indeed to be the case (–0.9 to 2.5 kJ mol^{-1}).

Conclusions

In this contribution, we have reported potential-energy and free-energy data for three enzymatic reactions: carbon–halogen bond formation in fluorinase, hydrogen abstraction from camphor in cytochrome P450cam, and chorismate-to-prephenate Claisen rearrangement in chorismate mutase. The results were obtained by semi-empirical or DFT QM/MM optimizations and two types of QM/MM free-energy simulations (free-energy perturbation and umbrella sampling). On the basis of these results and our previously published free-energy data for PHBH, we have discussed the importance of finite-temperature effects in the chemical step of enzyme reactions. Consistent with the notion that enzymes bind and pre-organize the reactants in the active site, we find that the entropic contribution to the activation barrier tends to be small, particularly when compared with an intermolecular process in the gas phase. In the latter case, the enzyme will "quench" the part of the entropic contribution that is related to the association of the reactants. If a reaction has a transition state that is intrinsically tight (compared with the reactant) due to the specific type of bond-making and -breaking, there may still be a sizeable entropic contribution to the barrier of the reaction in the enzyme, as seen in the chorismate mutase case. Furthermore, it should be emphasized that there will undoubtedly be considerable finite-temperature effects associated with the binding of the reactants preceding the chemical step that are well worth investigating by free-energy techniques. On the other hand, when focusing on localized chemical events in the catalytic cycle of an enzyme, the present evidence suggests that QM/MM optimization studies may often provide barriers that are close to the corresponding free-energy barriers. Our results also highlight the importance of performing biomolecular QM/MM optimizations or free-energy simulations on several snapshots taken from MD simulations if one wants to improve the accuracy of energy differences beyond about 10 kJ mol^{-1}.

Supplementary data

Supplementary data for this article are available on the journal Web site (canjchem.nrc.ca) or may be purchased from the Depository of Unpublished Data, Document Delivery, CISTI, National Research Council Canada, Ottawa, ON K1A 0R6, Canada. DUD 5257. For more information on obtaining material, refer to cisti-icist.nrc-cnrc.gc.ca/cms/unpub_e.shtml.

Acknowledgements

We thank A. Altun for providing P450cam input data, N. Otte for help with the CHARMM setup and many valuable discussions, and A. Koslowski for his program to perform spline fits of potential-energy curves.

References

(1) Warshel, A.; Levitt, M. *J. Mol. Biol.* **1976**, *103* (2), 227–249. doi:10.1016/0022-2836(76)90311-9. PMID:985660.

(2) Lin, H.; Truhlar, D. G. *Theor. Chem. Acc.* **2007**, *117* (2), 185–199. doi:10.1007/s00214-006-0143-z.

(3) Senn, H. M.; Thiel, W. In *Atomistic Approaches in Modern Biology;* Reiher, M., Ed.; Topics in Current Chemistry, Vol. 268; Springer: Berlin, 2007; pp 173–290.

(4) Senn, H. M.; Thiel, W. *Angew. Chem. Int. Ed.* **2009**, *48*, 1198–1229.

(5) Senn, H. M.; Thiel, W. *Curr. Opin. Chem. Biol.* **2007**, *11* (2), 182–187. doi:10.1016/j.cbpa.2007.01.684. PMID:17307018.

(6) van Gunsteren, W. F.; Bakowies, D.; Baron, R.; Chandrasekhar, I.; Christen, M.; Daura, X.; Gee, P.; Geerke, D. P.; Glättli, A.; Hünenberger, P. H.; Kastenholz, M. A.; Oostenbrink, C.; Schenk, M.; Trzesniak, D.; van der Vegt, N. F. A.; Yu, H. B. *Angew. Chem. Int. Ed.* **2006**, *45* (25), 4064–4092. doi:10.1002/anie.200502655.

(7) McQuarrie, D. A. *Statistical Mechanics;* University Science Books: Sausalito, CA, 2000.

(8) Klähn, M.; Braun-Sand, S.; Rosta, E.; Warshel, A. *J. Phys. Chem. B* **2005**, *109* (32), 15645–15650. doi:10.1021/jp0521757. PMID:16852982.

(9) Hu, H.; Yang, W. *Annu. Rev. Phys. Chem.* **2008**, *59* (1), 573–601. doi:10.1146/annurev.physchem.59.032607.093618. PMID:18393679.

(10) Sherwood, P.; de Vries, A. H.; Collins, S. J.; Greatbanks, S. P.; Burton, N. A.; Vincent, M. A.; Hillier, I. H. *Faraday Discuss.* **1997**, *106*, 79–92. doi:10.1039/a701790a.

(11) de Vries, A. H.; Sherwood, P.; Collins, S. J.; Rigby, A. M.; Rigutto, M.; Kramer, G. J. *J. Phys. Chem. B* **1999**, *103* (29), 6133–6141. doi:10.1021/jp9913012.

(12) Sherwood, P. In *Modern Methods and Algorithms of Quantum Chemistry;* Grotendorst, J., Ed.; NIC Series, Vol. 1; John von Neumann Institute of Computing: Jülich, 2000; pp 257–277.

(13) Sherwood, P.; de Vries, A. H.; Guest, M. F.; Schreckenbach, G.; Catlow, C. R. A.; French, S. A.; Sokol, A. A.; Bromley, S. T.; Thiel, W.; Turner, A. J.; Billeter, S. R.; Terstegen, F.; Thiel, S.; Kendrick, J.; Rogers, S. C.; Casci, J.; Watson, M.; King, F.; Karlsen, E.; Sjøvoll, M.; Fahmi, A.; Schäfer, A.; Lennartz, C. *J. Mol. Struct. (Theochem)* **2003**, *632*, 1–28.

(14) Beveridge, D. L.; DiCapua, F. M. *Annu. Rev. Biophys. Biophys. Chem.* **1989**, *18* (1), 431–492. doi:10.1146/annurev.bb.18.060189.002243. PMID:2660832.

(15) Straatsma, T. P.; McCammon, J. A. *Annu. Rev. Phys. Chem.* **1992**, *43* (1), 407–435. doi:10.1146/annurev.pc.43.100192.002203.

(16) van Gunsteren, W. F.; Daura, X.; Mark, A. E. *Helv. Chim. Acta* **2002**, *85* (10), 3113–3129. doi:10.1002/1522-2675(200210)85:10<3113::AID-HLCA3113>3.0.CO;2-0.

(17) Trzesniak, D.; Kunz, A.-P. E.; van Gunsteren, W. F. *ChemPhysChem* **2007**, *8* (1), 162–169. doi:10.1002/cphc.200600527. PMID:17131434.
(18) Chipot, C.; Pohorille, A., Eds. *Free Energy Calculations: Theory and Applications in Chemistry and Biology;* Springer Ser. Chem. Phys., Vol. 86; Springer: Berlin, 2007.
(19) Christen, M.; van Gunsteren, W. F. *J. Comput. Chem.* **2008**, *29* (2), 157–166. doi:10.1002/jcc.20725. PMID:17570138.
(20) Senn, H. M.; Thiel, S.; Thiel, W. *J. Chem. Theory Comput.* **2005**, *1* (3), 494–505. doi:10.1021/ct049844p.
(21) Kästner, J.; Thiel, W. *J. Chem. Phys.* **2005**, *123* (14),o. 144104. doi:10.1063/1.2052648. PMID:16238371.
(22) Kästner, J.; Thiel, W. *J. Chem. Phys.* **2006**, *124* (23),o. 234106. doi:10.1063/1.2206775. PMID:16821906.
(23) Kästner, J.; Senn, H. M.; Thiel, S.; Otte, N.; Thiel, W. *J. Chem. Theory Comput.* **2006**, *2* (2), 452–461. doi:10.1021/ct050252w.
(24) Wang, S.; Hu, P.; Zhang, Y. *J. Phys. Chem. B* **2007**, *111* (14), 3758–3764. doi:10.1021/jp067147i. PMID:17388541.
(25) Fleurat-Lessard, P.; Ziegler, T. *J. Chem. Phys.* **2005**, *123* (8),o. 084101. doi:10.1063/1.1948367. PMID:16164276.
(26) Yang, S.-Y.; Hristov, I.; Fleurat-Lessard, P.; Ziegler, T. *J. Phys. Chem. A* **2005**, *109* (1), 197–204. doi:10.1021/jp045943n. PMID:16839106.
(27) Hu, H.; Lu, Z.; Yang, W. *J. Chem. Theory Comput.* **2007**, *3* (2), 390–406. doi:10.1021/ct600240y. PMID:19079734.
(28) Hu, H.; Lu, Z.; Parks, J. M.; Burger, S. K.; Yang, W. *J. Chem. Phys.* **2008**, *128* (3),o. 034105. doi:10.1063/1.2816557. PMID:18205486.
(29) Iannuzzi, M.; Laio, A.; Parrinello, M. *Phys. Rev. Lett.* **2003**, *90* (23),o. 238302. doi:10.1103/PhysRevLett.90.238302. PMID:12857293.
(30) Ensing, B.; De Vivo, M.; Liu, Z. W.; Moore, P.; Klein, M. L. *Acc. Chem. Res.* **2006**, *39* (2), 73–81. doi:10.1021/ar040198i. PMID:16489726.
(31) Laio, A.; Gervasio, F. L. *Rep. Prog. Phys.* **2008**, *71* (12),o. 126601. doi:10.1088/0034-4885/71/12/126601.
(32) Stanton, C. L.; Kuo, I.-F. W.; Mundy, C. J.; Laino, T.; Houk, K. N. *J. Phys. Chem. B* **2007**, *111* (43), 12573–12581. doi:10.1021/jp074858n. PMID:17927240.
(33) Zwanzig, R. W. *J. Chem. Phys.* **1954**, *22* (8), 1420–1426. doi:10.1063/1.1740409.
(34) Zhang, Y.; Liu, H.; Yang, W. *J. Chem. Phys.* **2000**, *112* (8), 3483–3492. doi:10.1063/1.480503.
(35) Rod, T. H.; Ryde, U. *Phys. Rev. Lett.* **2005**, *94* (13),o. 138302. doi:10.1103/PhysRevLett.94.138302. PMID:15904045.
(36) Rod, T. H.; Ryde, U. *J. Chem. Theory Comput.* **2005**, *1* (6), 1240–1251. doi:10.1021/ct0501102.
(37) Bentzien, J.; Muller, R. P.; Florián, J.; Warshel, A. *J. Phys. Chem. B* **1998**, *102* (12), 2293–2301. doi:10.1021/jp973480y.
(38) Valiev, M.; Garrett, B. C.; Tsai, M.-K.; Kowalski, K.; Kathmann, S. M.; Schenter, G. K.; Dupuis, M. *J. Chem. Phys.* **2007**, *127* (5),o. 051102. doi:10.1063/1.2768343. PMID:17688327.
(39) Valiev, M.; Bylaska, E. J.; Dupuis, M.; Tratnyek, P. G. *J. Phys. Chem. A* **2008**, *112* (12), 2713–2720. doi:10.1021/jp7104709. PMID:18298106.
(40) Woods, C. J.; Manby, F. R.; Mulholland, A. J. *J. Chem. Phys.* **2008**, *128* (1),o. 014109. doi:10.1063/1.2805379. PMID:18190187.
(41) Dong, C.; Huang, F.; Deng, H.; Schaffrath, C.; Spencer, J. B.; O'Hagan, D.; Naismith, J. H. *Nature* **2004**, *427* (6974), 561–565. doi:10.1038/nature02280. PMID:14765200.
(42) Senn, H. M.; O'Hagan, D.; Thiel, W. *J. Am. Chem. Soc.* **2005**, *127* (39), 13643–13655. doi:10.1021/ja053875s. PMID:16190730.
(43) Cadicamo, C. D.; Courtieu, J.; Deng, H.; Meddour, A.; O'Hagan, D. *ChemBioChem* **2004**, *5* (5), 685–690. doi:10.1002/cbic.200300839. PMID:15122641.
(44) *ChemShell, a computational chemistry shell*. Available from http://www.chemshell.org.
(45) *TURBOMOLE*, 5.7.1. Available from http://www.turbomole.com. 2004.
(46) Ahlrichs, R.; Bär, M.; Häser, M.; Horn, H.; Kölmel, C. *Chem. Phys. Lett.* **1989**, *162* (3), 165–169. doi:10.1016/0009-2614(89)85118-8.
(47) Häser, M.; Ahlrichs, R. *J. Comput. Chem.* **1989**, *10*, 104–111. doi:10.1002/jcc.540100111.
(48) Horn, H.; Weiss, H.; Häser, M.; Ehrig, M.; Ahlrichs, R. *J. Comput. Chem.* **1991**, *12*, 1058–1064. doi:10.1002/jcc.540120903.
(49) Treutler, O.; Ahlrichs, R. *J. Chem. Phys.* **1995**, *102* (1), 346–354. doi:10.1063/1.469408.
(50) Eichkorn, K.; Treutler, O.; Öhm, H.; Häser, M.; Ahlrichs, R. *Chem. Phys. Lett.* **1995**, *240* (4), 283–289. doi:10.1016/0009-2614(95)00621-A.
(51) Eichkorn, K.; Treutler, O.; Öhm, H.; Häser, M.; Ahlrichs, R. *Chem. Phys. Lett.* **1995**, *242* (6), 652–660. doi:10.1016/0009-2614(95)00838-U.
(52) Eichkorn, K.; Weigend, F.; Treutler, O.; Ahlrichs, R. *Theor. Chem. Acc.* **1997**, *97*, 119–124.
(53) von Arnim, M.; Ahlrichs, R. *J. Comput. Chem.* **1998**, *19* (15), 1746–1757. doi:10.1002/(SICI)1096-987X(19981130)19:15<1746::AID-JCC7>3.0.CO;2-N.
(54) Becke, A. D. *Phys. Rev. A* **1988**, *38* (6), 3098–3100. doi:10.1103/PhysRevA.38.3098. PMID:9900728.
(55) Vosko, S. H.; Wilk, L.; Nusair, M. *Can. J. Phys.* **1980**, *58*, 1200–1211.
(56) Perdew, J. P. *Phys. Rev. B* **1986**, *33* (12), 8822–8824. doi:10.1103/PhysRevB.33.8822.
(57) Perdew, J. P. *Phys. Rev. B* **1986**, *34* (10), 7406. doi:10.1103/PhysRevB.34.7406.
(58) Weigend, F.; Ahlrichs, R. *Phys. Chem. Chem. Phys.* **2005**, *7* (18), 3297–3305. doi:10.1039/b508541a. PMID:16240044.
(59) Weigend, F. *Phys. Chem. Chem. Phys.* **2006**, *8* (9), 1057–1065. doi:10.1039/b515623h. PMID:16633586.
(60) Peterson, K. A.; Figgen, D.; Goll, E.; Stoll, H.; Dolg, M. *J. Chem. Phys.* **2003**, *119* (21), 11113–11123. doi:10.1063/1.1622924.
(61) Wiorkiewicz-Kuczera, J.; Karplus, M. *J. Phys. Chem. B* **1998**, *102* (18), 3586–3616. doi:10.1021/jp973084f.
(62) Billeter, S. R.; Turner, A. J.; Thiel, W. *Phys. Chem. Chem. Phys.* **2000**, *2* (10), 2177–2186. doi:10.1039/a909486e.
(63) Berendsen, H. J. C.; Postma, J. P. M.; van Gunsteren, W. F.; DiNola, A.; Haak, J. R. *J. Chem. Phys.* **1984**, *81* (8), 3684–3690. doi:10.1063/1.448118.
(64) Nosé, S. *J. Chem. Phys.* **1984**, *81* (1), 511–519. doi:10.1063/1.447334.
(65) Nosé, S. *Mol. Phys.* **1984**, *52* (2), 255–268. doi:10.1080/00268978400101201.
(66) Hoover, W. G. *Phys. Rev. A* **1985**, *31* (3), 1695–1697. doi:10.1103/PhysRevA.31.1695. PMID:9895674.
(67) Martyna, G. J.; Klein, M. L.; Tuckerman, M. *J. Chem. Phys.* **1992**, *97* (4), 2635–2643. doi:10.1063/1.463940.
(68) Shaik, S.; Kumar, D.; de Visser, S. P.; Altun, A.; Thiel, W. *Chem. Rev.* **2005**, *105* (6), 2279–2328. doi:10.1021/cr030722j. PMID:15941215.

(69) Schöneboom, J. C.; Lin, H.; Reuter, N.; Thiel, W.; Cohen, S.; Ogliaro, F.; Shaik, S. *J. Am. Chem. Soc.* **2002**, *124* (27), 8142–8151. doi:10.1021/ja026279w. PMID:12095360.
(70) Lin, H.; Schöneboom, J. C.; Cohen, S.; Shaik, S.; Thiel, W. *J. Phys. Chem. B* **2004**, *108* (28), 10083–10088. doi:10.1021/jp0493632.
(71) Schöneboom, J. C.; Cohen, S.; Lin, H.; Shaik, S.; Thiel, W. *J. Am. Chem. Soc.* **2004**, *126* (12), 4017–4034. doi:10.1021/ja039847w. PMID:15038756.
(72) Schöneboom, J. C.; Thiel, W. *J. Phys. Chem. B* **2004**, *108* (22), 7468–7478. doi:10.1021/jp049596t.
(73) Schöneboom, J. C.; Neese, F.; Thiel, W. *J. Am. Chem. Soc.* **2005**, *127* (16), 5840–5853. doi:10.1021/ja0424732. PMID:15839682.
(74) Altun, A.; Thiel, W. *J. Phys. Chem. B* **2005**, *109* (3), 1268–1280. doi:10.1021/jp0459108. PMID:16851091.
(75) Hirao, H.; Kumar, D.; Thiel, W.; Shaik, S. *J. Am. Chem. Soc.* **2005**, *127* (37), 13007–13018. doi:10.1021/ja053847+. PMID:16159296.
(76) Kumar, D.; Hirao, H.; de Visser, S. P.; Zheng, J.; Wang, D.; Thiel, W.; Shaik, S. *J. Phys. Chem. B* **2005**, *109* (42), 19946–19951. doi:10.1021/jp054754h. PMID:16853579.
(77) Altun, A.; Guallar, V.; Friesner, R. A.; Shaik, S.; Thiel, W. *J. Am. Chem. Soc.* **2006**, *128* (12), 3924–3925. doi:10.1021/ja058196w. PMID:16551096.
(78) Altun, A.; Shaik, S.; Thiel, W. *J. Comput. Chem.* **2006**, *27* (12), 1324–1337. doi:10.1002/jcc.20398. PMID:16788908.
(79) Zheng, J.; Wang, D.; Thiel, W.; Shaik, S. *J. Am. Chem. Soc.* **2006**, *128* (40), 13204–13215. doi:10.1021/ja063439l. PMID:17017800.
(80) Zheng, J.; Altun, A.; Thiel, W. *J. Comput. Chem.* **2007**, *28* (13), 2147–2158. doi:10.1002/jcc.20701. PMID:17450550.
(81) Altun, A.; Shaik, S.; Thiel, W. *J. Am. Chem. Soc.* **2007**, *129* (29), 8978–8987. doi:10.1021/ja066847y. PMID:17595079.
(82) Altun, A.; Kumar, D.; Neese, F.; Thiel, W. *J. Phys. Chem. A* **2008**, *112* (50), 12904–12910. doi:10.1021/jp802092w.
(83) Wang, D.; Zheng, J.; Shaik, S.; Thiel, W. *J. Phys. Chem. B* **2008**, *112* (16), 5126–5138. doi:10.1021/jp074958t. PMID:18386859.
(84) Wang, D.; Thiel, W. *J. Mol. Struct. (Theochem)* **2009**, *898*, 90–96.
(85) Lee, C.; Yang, W.; Parr, R. G. *Phys. Rev. B* **1988**, *37* (2), 785–789. doi:10.1103/PhysRevB.37.785.
(86) Becke, A. D. *J. Chem. Phys.* **1993**, *98* (7), 5648–5652. doi:10.1063/1.464913.
(87) Stephens, P. J.; Devlin, J. F.; Chabalowski, C. F.; Frisch, M. J. *J. Phys. Chem.* **1994**, *98* (45), 11623–11627. doi:10.1021/j100096a001.
(88) Hertwig, R. H.; Koch, W. *Chem. Phys. Lett.* **1997**, *268* (5-6), 345–351. doi:10.1016/S0009-2614(97)00207-8.
(89) *CHARMM*, c33b1. Available from http://www.charmm.org. 2006.
(90) Brooks, B. R.; Bruccoleri, R. E.; Olafson, B. D.; States, D. J.; Swaminathan, S.; Karplus, M. *J. Comput. Chem.* **1983**, *4* (2), 187–217. doi:10.1002/jcc.540040211.
(91) Elstner, M.; Porezag, D.; Jungnickel, G.; Elsner, J.; Haugk, M.; Frauenheim, T.; Suhai, S.; Seifert, G. *Phys. Rev. B* **1998**, *58* (11), 7260–7268. doi:10.1103/PhysRevB.58.7260.
(92) Cui, Q.; Elstner, M.; Kaxiras, E.; Frauenheim, T.; Karplus, M. *J. Phys. Chem. B* **2001**, *105* (2), 569–585. doi:10.1021/jp0029109.
(93) Stote, R. H.; States, D. J.; Karplus, M. *J. Chim. Phys.* **1991**, *88*, 2419–2433.
(94) Chook, Y. M.; Ke, H.; Lipscomb, W. N. *Proc. Natl. Acad. Sci. U.S.A.* **1993**, *90* (18), 8600–8603. doi:10.1073/pnas.90.18.8600. PMID:8378335.
(95) Torrie, G. M.; Valleau, J. P. *Chem. Phys. Lett.* **1974**, *28* (4), 578–581. doi:10.1016/0009-2614(74)80109-0.
(96) Kumar, S.; Bouzida, D.; Swendsen, R. H.; Kollman, P. A.; Rosenberg, J. M. *J. Comput. Chem.* **1992**, *13* (8), 1011–1021. doi:10.1002/jcc.540130812.
(97) Deng, H.; Cobb, S. L.; McEwan, A. R.; McGlinchey, R. P.; Naismith, J. H.; O'Hagan, D.; Robinson, D. A.; Spencer, J. B. *Angew. Chem. Int. Ed.* **2006**, *45* (5), 759–762. doi:10.1002/anie.200503582.
(98) Zhu, X.; Robinson, D. A.; McEwan, A. R.; O'Hagan, D.; Naismith, J. H. *J. Am. Chem. Soc.* **2007**, *129* (47), 14597–14604. doi:10.1021/ja0731569. PMID:17985882.
(99) Blasiak, L. C.; Drennan, C. L. *Acc. Chem. Res.* **2009**, *42* (1), 147–155. doi:10.1021/ar800088r. PMID:18774824.
(100) Eustáquio, A. S.; Pojer, F.; Noel, J. P.; Moore, B. S. *Nat. Chem. Biol.* **2008**, *4* (1), 69–74. doi:10.1038/nchembio.2007.56. PMID:18059261.
(101) Claeyssens, F.; Ranaghan, K. E.; Manby, F. R.; Harvey, J. N.; Mulholland, A. J. *Chem. Commun. (Camb.)* **2005**, (40): 5068–5070. doi:10.1039/b508181e. PMID:16220173.
(102) Woodcock, H. L., III; Hodošček, M.; Gilbert, A. T. B.; Gill, P. M. W.; Schaefer, H. F., III; Brooks, B. R. *J. Comput. Chem.* **2007**, *28* (9), 1485–1502. doi:10.1002/jcc.20587. PMID:17334987.
(103) Kast, P.; Asif-Ullah, M.; Hilvert, D. *Tetrahedron Lett.* **1996**, *37* (16), 2691–2694. doi:10.1016/0040-4039(96)00338-3.
(104) Crespo, A.; Martí, M. A.; Estrin, D. A.; Roitberg, A. E. *J. Am. Chem. Soc.* **2005**, *127* (19), 6940–6941. doi:10.1021/ja0452830. PMID:15884923.
(105) Ishida, T. *J. Chem. Phys.* **2008**, *129*,o. 125105.

NMR line shapes from AB spin systems in solids — The role of antisymmetric spin–spin coupling

Kristopher J. Harris, David L. Bryce, and Roderick E. Wasylishen

Abstract: NMR parameters such as indirect nuclear spin–spin coupling (**J**), nuclear magnetic shielding ($\boldsymbol{\sigma}$), direct dipolar coupling (**D**), and electric field gradient (**V**) are properly described by second-rank tensors. Each may be decomposed into isotropic, symmetric, and antisymmetric components; the number of these three components which may be nonzero is a distinguishing attribute of each interaction tensor. The rank-1 antisymmetric portion of **J** ($\mathbf{J}^{anti}$) holds the distinction of remaining the only nonzero part of these fundamental NMR interaction tensors which has never been observed experimentally. Accordingly, effects from $\mathbf{J}^{anti}$ are usually ignored, but it is important to consider when this is valid. An experimental strategy for observing $\mathbf{J}^{anti}$ in powdered samples of tightly coupled homonuclear spin pairs, based on ideas originally presented by Andrew and Farnell (*Mol. Phys.* 1968, **15**, 157), is described. The theory of Andrew and Farnell is extended to powder samples, and methods for analyzing NMR spectra from powdered samples are presented. It is found that, in certain rare cases, $\mathbf{J}^{anti}$ has the potential to affect the NMR line shapes from AB spin systems, but that even in these systems, the most intense features of the spectra are not affected and may be analyzed independently of $\mathbf{J}^{anti}$. Furthermore, $\mathbf{J}^{anti}$ will only have an observable effect on the NMR spectra when its magnitude is comparable with that of J_{iso} and with the difference in chemical shifts (in Hz) between the two sites. Finally, the first experimental attempts to measure $\mathbf{J}^{anti}$ are reported, and experimental proof that no elements of $\mathbf{J}^{anti}(^{119}Sn,^{119}Sn)$ in hexa(*p*-tolyl)ditin are larger than 2900 Hz is given. The benefits of modern double-quantum filtering NMR pulse sequences in isolating effects from $\mathbf{J}^{anti}$ are also illustrated.

Key words: J coupling, solid-state NMR spectroscopy, indirect nuclear spin–spin coupling, ^{119}Sn NMR, symmetry, NMR relaxation, antisymmetric tensor.

Résumé : Les interactions de RMN, tel le couplage spin-spin nucléaire indirect (**J**), le blindage magnétique nucléaire ($\boldsymbol{\sigma}$), le couplage dipolaire direct (**D**) et le gradient du champ électrique (**V**) peuvent être décrits correctement par des tenseurs de deuxième rang. Chacune peut être décomposée en composants isotropes, symétriques et antisymétriques; le nombre de ces trois composants qui peut être différente de zéro est un attribut caractéristique de chaque tenseur d'interaction. La portion antisymétrique de rang 1 de **J** ($\mathbf{J}^{anti}$) se distingue par le fait qu'il s'agit de la seule partie de ces tenseurs fondamentaux d'interaction RMN dont la valeur est différente de zéro qui n'a pas encore été observée expérimentalement. Il en découle qu'on ignore généralement les effets attribuables à $\mathbf{J}^{anti}$, mais il est important de considérer quand cela est valide. On décrit une stratégie expérimentale basée sur les idées proposées originalement par Andrew et Farnell (*Mol. Phys.* 1968, **15**, 157) pour observer $\mathbf{J}^{anti}$ dans des échantillons en poudre de paires de spin homonucléaires fortement couplés. La théorie de Andrew et Farnell a été étendue aux échantillons en poudre et on présente des méthodes qui permettent d'analyser les spectres RMN des échantillons en poudre. On a trouvé que dans certains rares cas, le couplage $\mathbf{J}^{anti}$ a le pouvoir d'affecter les formes des raies RMN des systèmes de spin AB, mais que même avec ces systèmes, les caractéristiques les plus intenses des spectres ne sont pas affectées et elles peuvent être analysées indépendamment de $\mathbf{J}^{anti}$. De plus, $\mathbf{J}^{anti}$ n'aura un effet observable sur les spectres RMN que lorsque son amplitude sera comparable à celle de J_{iso} et à la différence dans les déplacements chimiques (en Hz) entre les deux sites. Finalement, on rapporte les premiers efforts experimentaux à mesurer $\mathbf{J}^{anti}$, et on démontre experimentallement qu'il n'y a pas d'éléments de $\mathbf{J}^{anti}(^{119}Sn, ^{119}Sn)$ plus grand que 2900 Hz dans l'hexa(*p*-tolyl)di-étain. On illustre aussi les bénéfices des séquences modernes d'impulsions RMN avec filtrage à double quantum pour isoler les effets de $\mathbf{J}^{anti}$.

Mots-clés : couplage *J*, spectroscopie RMN à l'état solide, couplage spin-spin nucléaire indirect, RMN du ^{119}Sn, relaxation RMN, tenseur antisymmétrique.

[Traduit par la Rédaction]

Received 14 March 2009. Accepted 5 May 2009. Published on the NRC Research Press Web site at canjchem.nrc.ca on 16 September 2009.

This article is part of a Special Issue dedicated to Professor T. Ziegler. This article is dedicated to Professor Tom Ziegler in recognition of his many important contributions to science and in particular his central role in the development of methods to calculate NMR parameters.

K.J. Harris, D.L. Bryce,[1] and R.E. Wasylishen.[2] Department of Chemistry, University of Alberta, Edmonton, AB T6G 2G2, Canada.

[1]Present address: Department of Chemistry, University of Ottawa, Ottawa, ON K1N 6N5, Canada.
[2]Corresponding author (e-mail: Roderick.Wasylishen@ualberta.ca).

Introduction

One of the most useful aspects of NMR spectroscopy for relating spectroscopic observables to molecular structure and dynamics is the inherent orientation dependence of the fundamental NMR interactions.[1] This orientation dependence is routinely taken advantage of in solid-state NMR spectroscopy to determine, for example, internuclear coupling tensors, magnetic shielding tensors, and electric field gradient tensors. Over the last decade, this orientation dependence has also been exploited in solution NMR spectroscopy by employing dilute liquid crystalline solvents which introduce a small degree of molecular alignment, thereby preventing complete isotropic averaging of direct dipolar coupling tensors and magnetic shielding tensors.[2–7] Clearly, an improved understanding of the tensor nature of NMR interactions is desirable.

The most important fundamental NMR parameters in diamagnetic molecules include the electric field gradient (**V**) and nuclear magnetic shielding ($\boldsymbol{\sigma}$), as well as the direct dipolar (**D**), and indirect nuclear spin–spin (**J**) coupling, and are properly represented by second-rank tensors.[8] The **J** tensor may be written in Cartesian form as follows, with up to nine elements[9]

$$[1] \qquad \mathbf{J} = \begin{bmatrix} J_{xx} & J_{xy} & J_{xz} \\ J_{yx} & J_{yy} & J_{yz} \\ J_{zx} & J_{zy} & J_{zz} \end{bmatrix}$$

In general, any second-rank tensor may be decomposed into three contributions. The rank-0 contribution is independent of orientation, and is given by (for **J**)

$$[2] \qquad J_{iso} = \frac{1}{3}\mathrm{Tr}(\mathbf{J}) = \frac{1}{3}(J_{xx} + J_{yy} + J_{zz})$$

This term is also commonly known as the "scalar" coupling constant in the NMR spectroscopy literature of both solids and solutions. The isotropic portions of the **V** and **D** tensors are zero, while the isotropic part of $\boldsymbol{\sigma}$ is simply the nuclear magnetic shielding constant, σ_{iso}. The shielding tensor and the isotropic shielding constant are directly related to the experimentally observable chemical shift tensor ($\boldsymbol{\delta}$) and isotropic chemical shift (δ_{iso}). Thus, the nonzero isotropic portions of NMR interaction tensors (J_{iso}, δ_{iso}) are routinely measured.

The rank-2 symmetric part of **J** is given by

$$[3] \qquad \mathbf{J}^{sym} = \frac{1}{2}(\mathbf{J} + \mathbf{J}^{t}) - J_{iso}\mathbf{1} \xrightarrow{\text{to PAS}} \mathbf{J}^{sym,PAS} = \begin{bmatrix} J_{11} - J_{iso} & 0 & 0 \\ 0 & J_{22} - J_{iso} & 0 \\ 0 & 0 & J_{33} - J_{iso} \end{bmatrix}$$

where $\mathbf{J}^{t}$ is the transpose of **J,** and "symmetric" refers to the fact that $J_{ij}^{sym} = J_{ji}^{sym}$ in any axis system. As shown in eq. [3], when $\mathbf{J}^{sym}$ is represented in its principal axis system (PAS) there are no off-diagonal elements and the diagonal elements are referred to as the principal components. Note that, although there are three principal components, their sum is zero and $\mathbf{J}^{sym,PAS}$ therefore contains only two independent elements. However, it should be noted that $\mathbf{J}^{sym}$ is only fully described if its eigenvectors, i.e., the vectors that form its PAS, are known in addition to the two independent elements of $\mathbf{J}^{sym,PAS}$. Because the PAS can be specified via three Euler angles that relate it to some reference frame in the molecule, $\mathbf{J}^{sym}$ is generally described as containing five independent parameters. By definition, the principal components are ordered $|J_{33} - J_{iso}| \geq |J_{11} - J_{iso}| \geq |J_{22} - J_{iso}|$.[10,11] The **V**, **D**, and $\boldsymbol{\sigma}$ tensors can all have nonzero rank-2 symmetric contributions, but of course this depends on symmetry for **V** and $\boldsymbol{\sigma}$. For example, the nuclear quadrupolar coupling constant (C_Q) and asymmetry parameter (η_Q) are characteristic of $\mathbf{V}^{sym}$; the direct dipolar coupling constant used to extract internuclear distances from NMR measurements is characteristic of $\mathbf{D}^{sym}$; anisotropy and asymmetry parameters describing nuclear magnetic shielding and chemical shift tensors are representations of $\boldsymbol{\sigma}^{sym}$. Thus, experimental measurements of the symmetric parts of **V**, **D**, and $\boldsymbol{\sigma}$ (or $\boldsymbol{\delta}$), are routinely made. Measurements of the principal components of $\mathbf{J}^{sym}$ are not nearly as straightforward;[11,12] nevertheless, much effort has been directed at making such measurements in the gas phase, in liquid crystal solutions, and in the solid state so that a body of reliable data now exists.[13,14] Quantum chemical calculation of **J** tensors is an important tool in the interpretation of experimental results,[15–25] and advances in this area are reviewed regularly.[13,26–28]

The rank-1 antisymmetric contribution to the NMR interaction tensors is zero for **V** and **D**, but not for $\boldsymbol{\sigma}$ or **J**. For the **J** tensor, this contribution is given by[10,11]

$$[4] \qquad \mathbf{J}^{anti} = \frac{1}{2}(\mathbf{J} - \mathbf{J}^{t}) = \frac{1}{2}\begin{bmatrix} 0 & J_{xy} - J_{yx} & J_{xz} - J_{zx} \\ J_{yx} - J_{xy} & 0 & J_{yz} - J_{zy} \\ J_{zx} - J_{xz} & J_{zy} - J_{yz} & 0 \end{bmatrix} \equiv \begin{bmatrix} 0 & J_{yx}^{anti} & J_{zx}^{anti} \\ -J_{yx}^{anti} & 0 & J_{zy}^{anti} \\ -J_{zx}^{anti} & -J_{zy}^{anti} & 0 \end{bmatrix}$$

This component of **J** is designated antisymmetric because of the obvious form of the matrix in eq. [4]. While $\mathbf{J}^{sym}$ can be diagonalized through a change of basis, $\mathbf{J}^{anti}$ remains in the form shown in eq. [4] under any choice of coordinate system. Because there is no obvious reference frame for $\mathbf{J}^{anti}$, the simplest method is to report $\mathbf{J}^{anti}$ in the PAS of $\mathbf{J}^{sym}$; however, it should be noted that symmetry may require one or more elements of $\mathbf{J}^{anti}$ to be zero in a particular coordinate system, in which case the tensor will still appear to have 6 entries (three unique) in other coordinate systems (compare with $\mathbf{J}^{sym}$ versus $\mathbf{J}^{sym,PAS}$). In summary, the rank-0 portion of **J** contains one independent parameter, the rank-2 symmetric portion contains five, and the rank-1 antisymmetric portion contains three. Any **J** tensor can therefore be represented in an arbitrary coordinate system using the six independent elements of J_{iso} + $\mathbf{J}^{sym}$ + $\mathbf{J}^{anti}$, and three Euler angles relating the coordinate system to the PAS of $\mathbf{J}^{sym}$.

It has been shown that the antisymmetric components of $\boldsymbol{\sigma}$ affect the spectrum in second order only, causing small peak shifts and (or) subtle pattern changes.[10,29,30] While direct effects on the spectra would generally be very small and thus difficult to detect, the components of $\boldsymbol{\sigma}^{anti}$ can contribute to nuclear spin relaxation, but only two reports of their influ-

ence on relaxation have been published.[31,32] Wi and Frydman have shown that cross-correlations with the quadrupolar Hamiltonian can make direct detection of $\boldsymbol{\sigma}^{anti}$ more tenable, and have reported the antisymmetric components of the ^{59}Co chemical shift tensor in cobalt(III) tris(acetylacetonate), referenced to 1M $K_3[Co(CN)_6]_{(aq)}$, as $\delta_{zx}^{anti} = 1000 \pm 500$ ppm, $\delta_{zy}^{anti} = -1000 \pm 500$ ppm, $\delta_{xy}^{anti} = 1000 \pm 1000$ ppm.[33] Nuclear spin relaxation measurements, similar to those used for $\boldsymbol{\sigma}^{anti}$, could provide a method to detect the antisymmetric part of $\mathbf{J}$,[34,35] while another experimental strategy may arise from the symmetry-based pulse-sequence design methodology developed by Levitt and co-workers.[36]

The rank-1 antisymmetric part of the $\mathbf{J}$ tensor remains as the only contribution to the four fundamental NMR interactions which has yet to be measured experimentally. In 1968, Andrew and Farnell tackled this problem by considering a pair of spin-1/2 nuclei in a single crystal, taking into account the full second-rank tensor nature of the chemical shift, the direct dipolar coupling tensor, and the indirect nuclear spin–spin coupling tensor.[37] Under rapid MAS, the chemical shift tensors are averaged to their isotropic values for each of the two nuclei involved; the direct dipolar coupling tensor is averaged to its isotropic value (zero); the isotropic *J*-coupling constant manifests itself in a fashion analogous to the situation observed in solution, and the anisotropic rank-2 part of the $\mathbf{J}$ tensor is averaged to zero. The most interesting aspect of their analysis, however, is with regards to the antisymmetric rank-1 part of $\mathbf{J}$, which is averaged to zero in solution, but *not under MAS conditions*.[37,38] The theory laid out by Andrew and Farnell alone does not provide much insight into what types of chemical systems may actually lead to an experimental observation of $\mathbf{J}^{anti}$, and a discussion of such considerations is presented here. Additionally, the theory is extended to include averaging over the orientations of a micro-crystalline powdered sample, and methods for analyzing the resultant line shapes are presented. In the present paper, the discussion describes one strategy for the measurement of $\mathbf{J}^{anti}$ and details some initial experimental attempts at its characterization.

Theory

The theory for describing NMR spectra from a pair of non-equivalent spin-1/2 nuclei in solution or in the solid state without effects from $\mathbf{J}^{anti}$ is well established.[39–41] The full Hamiltonian operator for a homonuclear pair of spin-1/2 nuclei in a stationary sample is

$$[5] \quad h^{-1}\widehat{H} = -(2\pi)^{-1}\gamma\widehat{\mathbf{I}}(1-\boldsymbol{\sigma}_I)\mathbf{B}_0 - (2\pi)^{-1}\gamma\widehat{\mathbf{S}}(1-\boldsymbol{\sigma}_s)\mathbf{B}_0 + \widehat{\mathbf{I}}\cdot\mathbf{J}\cdot\widehat{\mathbf{S}} + \widehat{\mathbf{I}}\cdot\mathbf{D}\cdot\widehat{\mathbf{S}}$$

After breaking the interaction tensors into their isotropic, symmetric, and antisymmetric components, and dropping nonsecular[42] terms, the effects of MAS in averaging orientation dependencies can be included. It is well known that all terms in the secular Hamiltonian containing $\mathbf{J}^{sym}$ and $\mathbf{D}$ average to zero, and also that the secular part of $\hat{\mathbf{I}}\cdot\boldsymbol{\sigma}_I\cdot\mathbf{B}_0$ is averaged to $\sigma_I\hat{I}_Z$ when $\mathbf{B}_0$ is along the laboratory *Z* axis;[37] this last result uses σ_I as notation for the isotropic shielding (i.e., 1/3 the trace of $\boldsymbol{\sigma}_I$). Therefore, the secular Hamiltonian under MAS can be defined as

$$[6] \quad h^{-1}\widehat{H}_0^{MAS} = -\nu_L[(1-\sigma_I)\widehat{I}_Z + (1-\sigma_S)\widehat{S}_Z] + J_{iso}\widehat{I}_Z\widehat{S}_Z + \frac{1}{2}J_{iso}(\widehat{I}_+\widehat{S}_- + \widehat{I}_-\widehat{S}_+) + \widehat{\mathbf{I}}\cdot\mathbf{J}^{anti,MAS}\cdot\widehat{\mathbf{S}}$$

where $\nu_L = (2\pi)^{-1}\gamma B_0$, and $\mathbf{J}^{anti,MAS}$ is the MAS average of $\mathbf{J}^{anti}$, and an infinitely fast MAS rate is assumed. Line-shape simulations for solid samples generally neglect the term containing $\mathbf{J}^{anti,MAS}$; however, Andrew and Farnell have presented a theory including effects from the antisymmetric portion of $\mathbf{J}$ on solid-state NMR spectra from a pair of spin-1/2 nuclei in a single crystal undergoing MAS.[37] We first review Andrew and Farnell's results for NMR spectra from a single crystal, and then extend the theory to include the orientational distribution of a powder sample. Methods for analyzing the resultant powder pattern in terms of the components of $\mathbf{J}^{anti}$ are then discussed.

The Antisymmetric J-coupling Hamiltonian

Returning to a stationary single crystal in the lab frame, the only secular terms in the antisymmetric *J*-coupling Hamiltonian between spins *I* and *S* are the two involving $J_{YX}^{anti,L}$:

$$[7] \quad \begin{aligned} h^{-1}\widehat{H}^{anti} &= \widehat{\mathbf{I}}\cdot\mathbf{J}^{anti,L}\cdot\widehat{\mathbf{S}} \\ h^{-1}\widehat{H}_0^{anti} &= J_{YX}^{anti,L}(\widehat{I}_X\widehat{S}_Y - \widehat{I}_Y\widehat{S}_X) \\ &= i\frac{1}{2}J_{YX}^{anti,L}(\widehat{I}_+\widehat{S}_- - \widehat{I}_-\widehat{S}_+) \end{aligned}$$

Because $\widehat{H}_0^{anti}$ contains only the flip-flop operator involving spins *I* and *S*, it has a negligible effect on the energy levels unless the spins *I* and *S* have nearly equal chemically shifted Zeeman interactions; accordingly, $\mathbf{J}^{anti}$ only affects NMR spectra from AB spin systems. The only step remaining before we can predict spectra using the Hamiltonian in eq. [6] is determination of the MAS average of $J_{YX}^{anti,L}$.

Under MAS, the orientation of each crystallite will become time-dependent, so it is convenient to consider the tensor in the lab frame, $\mathbf{J}^{anti,L}$, as being derived from its representation in the crystallite axis system depicted in Fig. 1*a*, $\mathbf{J}^{anti,C}$, using direction cosines:[43]

$$[8] \quad J_{YX}^{anti,L} = \begin{bmatrix} (a_{Yx}a_{Xy} - a_{Yy}a_{Xx})J_{yx}^{anti,C} \\ +(a_{Yx}a_{Xz} - a_{Yz}a_{Xx})J_{zx}^{anti,C} \\ +(a_{Yy}a_{Xz} - a_{Yz}a_{Xy})J_{zy}^{anti,C} \end{bmatrix}$$

In eq. [8], each a_{Uv} is the cosine of the angle between lab-frame axis U and crystallite axis v. If some external motion causes the molecular orientation to change, each direction cosine will be time-dependent. After including expressions for the time dependence of each a_{Uv}, the average value of $J_{YX}^{anti,L}$ under external motion can be derived (see ref. 44 for an instructive example where U is the laboratory Z axis and the external motion is MAS). Under isotropic tumbling, the time average of $J_{YX}^{anti,L}$ is zero, but not for a solid undergoing MAS.[37] It is convenient to use the notation $A(\Theta)$ for the average value of $J_{YX}^{anti,L}$ under MAS, because it acts as an effective antisymmetric coupling constant which differs for each orientation, Θ, of the crystallite.[37] The effect of $\mathbf{J}^{anti}$ is therefore to add the following term to the secular Hamiltonian for an AB spin system under MAS:

Fig. 1. (*a*) Coordinate system and conventions used in the expressions for the $A(\Theta)$ distribution. The lab frame is defined by the axes X, Y, Z; the axis of sample rotation is r_{rot}, which is at the "magic angle" of $\cos^{-1}(1/\sqrt{3})$ relative to the Z axis; and the crystallite axis system in which **J** is represented is described with the vectors x, y, z. Angles given as ξ_a are those between axis *a* of the crystallite frame and r_{rot}. (*b*) Normalized projections of the crystallite axes x, y, z on the plane perpendicular to r_{rot} shown in (*a*) are labelled p_x, p_y, p_z. Rotation of these projected vectors by –90° about r_{rot} are annotated as the corresponding primed vectors p'_x, p'_y, p'_z, and angles given as $\varepsilon_{ab'}$ are those between p_a and p'_b ($\varepsilon_{yx'}$ is shown as an example).

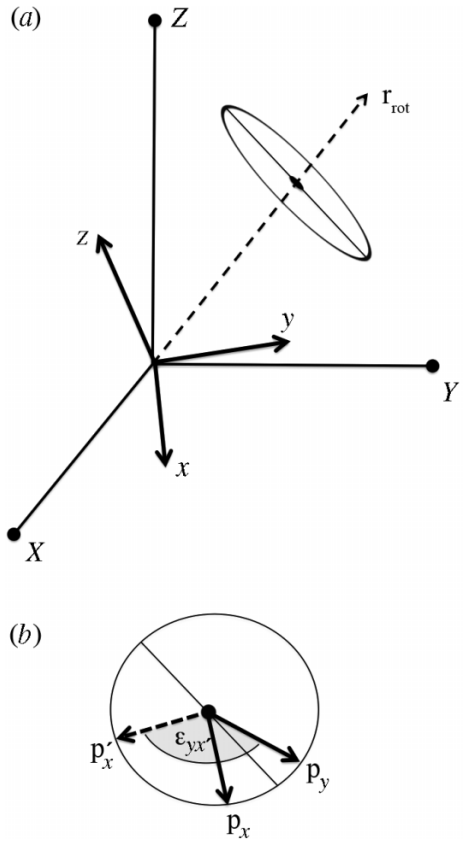

$$[9] \qquad h^{-1}\widehat{H}_0^{\text{anti,MAS}} = i\frac{1}{2}A(\Theta)(\widehat{I}_+\widehat{S}_- - \widehat{I}_-\widehat{S}_+)$$

Andrew and Farnell have provided an expression for the effective antisymmetric coupling constant for a crystallite undergoing MAS, see eq. [39] of reference 37. Application of a few algebraic manipulations produces an analogous, but slightly simpler, form for $A(\Theta)$:

$$[10] \qquad A(\Theta) = 1/\sqrt{3}\begin{bmatrix} (\sin\xi_y \sin\xi_x \cos\varepsilon_{yx'})J_{yx}^{\text{anti,C}} \\ +(\sin\xi_z \sin\xi_x \cos\varepsilon_{zx'})J_{zx}^{\text{anti,C}} \\ +(\sin\xi_z \sin\xi_y \cos\varepsilon_{zy'})J_{zy}^{\text{anti,C}} \end{bmatrix}$$

Equation [10] makes use of the coordinate system and definitions shown in Fig. 1. As described in the previous section, the components of $\mathbf{J}^{\text{anti,C}}$ are those in the crystallite reference frame shown in Fig. 1, which could be, for example, the PAS of $\mathbf{J}^{\text{sym}}$. While the depiction in Fig. 1 is for the crystallite axis system at time zero, all angles in eq. [10] are constant during the motion of the rotor, reflecting the fact that the value of $A(\Theta)$ for each crystallite is independent of time. Furthermore, the rotational independence of the expression requires that any crystallites whose initial orientations are related to each other by rotation around the sample's spinning axis are characterized by the same value of $A(\Theta)$. However, any crystallites whose orientations do not become superimposed by the motion of the rotor will exhibit a different value of $A(\Theta)$, and a powder will therefore be characterized by a distribution of these effective coupling constants.

It is interesting to contrast the effects of MAS on $\mathbf{J}^{\text{anti}}$ with its effect on the other anisotropic terms in the secular Hamiltonian. By defining $\boldsymbol{\sigma}^{\text{sym}}$ analogously to the definition of $\mathbf{J}^{\text{sym}}$ in eq. [3], the only orientation dependence, discounting $J_{YX}^{\text{anti,L}}$, is contained in terms involving $\boldsymbol{\sigma}^{\text{sym}}$, $\mathbf{J}^{\text{sym}}$, and **D**. For these more familiar terms, the secular Hamiltonian's dependence on crystallite orientation is encoded in direction cosines between the applied magnetic field and the principal component axes of the involved tensor, i.e., terms of the form a_{Zv}.[37] Because the average squared value under MAS (or in solution) for this form of direction cosine, $\langle a_{Zv}^2 \rangle$, is 1/3 for any crystallite orientation, the average of each secular Hamiltonian term involving $\boldsymbol{\sigma}^{\text{sym}}$, $\mathbf{J}^{\text{sym}}$, and **D** is zero.[37,44] This averaging explains why these three terms need not be included in the Hamiltonian, and do not affect spectra of samples undergoing MAS (at a sufficiently rapid rate). All of the orientation-dependent terms in the secular Hamiltonian other than $\widehat{H}_0^{\text{anti}}$ depend on the angles between each crystallite axis and the lab-frame Z axis, while $\widehat{H}_0^{\text{anti}}$ instead depends on the angles between each crystallite axis system and the lab-frame X and Y axes. Because the direction cosines describing the value of $J_{YX}^{\text{anti,L}}$ are of a different form, the effect of MAS on $\mathbf{J}^{\text{anti}}$ differs from its effect on $\boldsymbol{\sigma}^{\text{sym}}$, $\mathbf{J}^{\text{sym}}$, and **D**; accordingly, the average value of $J_{YX}^{\text{anti,L}}$ under MAS is not zero, but a constant, $A(\Theta)$, that differs for each nondegenerate crystallite orientation.

The $A(\Theta)$ distribution

To predict NMR spectra using the above Hamiltonian operator it is necessary to determine the shape of the $A(\Theta)$ distribution, and this was investigated here using numerical powder averaging. To investigate the behaviour of $A(\Theta)$ independent of the magnitude of the $\mathbf{J}^{\text{anti,C}}$ components, it is convenient to scale eq. [10] by the largest component of $\mathbf{J}^{\text{anti,C}}$. Considering first the case when J_{zy}^{anti} is the largest element,

$$[11] \qquad A(\Theta) = J_{zy}^{\text{anti,C}}(1/\sqrt{3})\begin{bmatrix} (\sin\xi_y \sin\xi_x \cos\varepsilon_{yx'})c_{yx} \\ +(\sin\xi_z \sin\xi_x \cos\varepsilon_{zx'})c_{zx} \\ +(\sin\xi_z \sin\xi_y \cos\varepsilon_{zy'}) \end{bmatrix}$$
$$= J_{zy}^{\text{anti,C}} \times f_{zy}(\Theta; c_{yx}, c_{zx})$$

where $f_{zy}(\Theta; c_{yx}, c_{zx})$ is a function of the crystallite orientation, which is again denoted by Θ. The function $f_{zy}(\Theta; c_{yx}, c_{zx})$ involves only the ratio of elements in $\mathbf{J}^{\text{anti,C}}$ through the parameters $c_{ij} = J_{ij}^{\text{anti,C}}/J_{zy}^{\text{anti,C}}$; note that while the theoretical range for these parameters is $-1 \le c_{ij} \le 1$, all results were found to be independent of the sign of the c_{ij} constants. See the Experimental section for specific details on the numeri-

Fig. 2. (*a*) Numerically generated plots of $f_{zy}(\Theta; c_{yx}, c_{zx})$ versus fraction of crystallites displaying that value; (*i*) The smallest range of the f_{zy} distribution, $\pm 1/\sqrt{3}$, is found with the parameters $c_{yx} = c_{zx} = 0$; (*ii*) The largest range of the f_{zy} distribution, ±1, occurs when $c_{yx} = c_{zx} = 1$; (*iii*) Example of the range found for the f_{zy} distribution with intermediate values of the c_{ij} constants, in this plot, $c_{yx} = 0$ and $c_{zx} = 0.8$. (*b*) Plot of $f_{zy}^2(\Theta; c_{yx}, c_{zx})$, with parameters $c_{yx} = c_{zx} = 1$, the same as in (*a*) (*ii*).

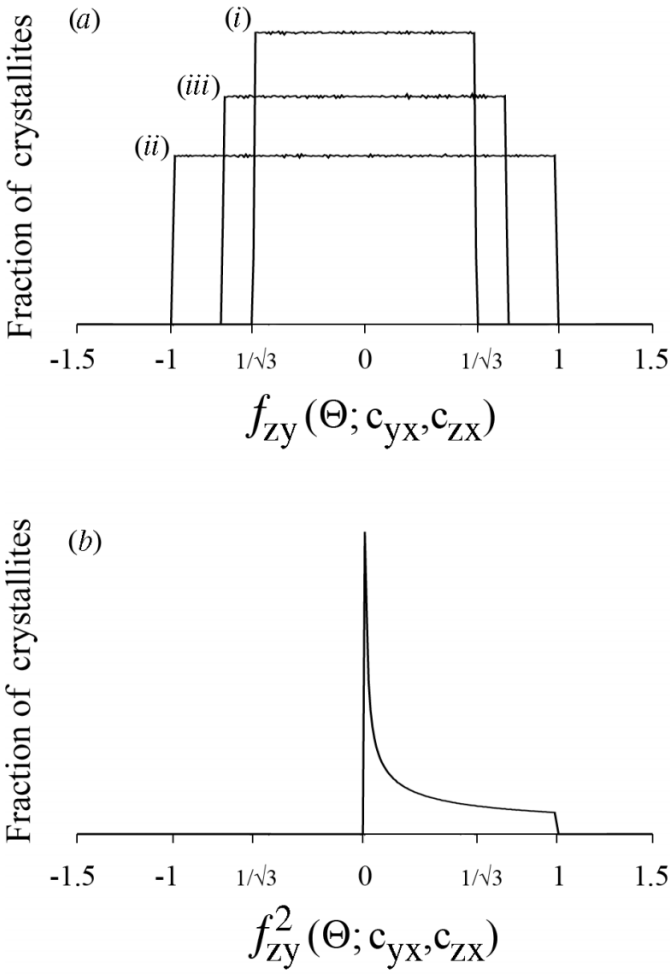

cal calculations. As shown in Fig. 2*a*, all values of f_{zy} between $\pm 1/\sqrt{3}$ are equally probable when $J_{zy}^{anti,C}$ is the only component of $\mathbf{J}^{anti,C}$, while all values in the range ±1 are populated equally when $J_{yx}^{anti,C} = J_{zx}^{anti,C} = J_{zy}^{anti,C}$. For all other values of the c_{ij} constants, the upper and lower limits of f_{zy} were found to be intermediate between the extremes of $\pm 1/\sqrt{3}$ and ±1 mentioned above, and all values of the distribution were also found equally probable. There appears to be no obvious connection between the specific limits of f_{zy} and the c_{ij} constants, except in the two cases of $c_{yx} = c_{zx} = 0$ or 1. Results obtained under the assumption that either $J_{yx}^{anti,C}$ or $J_{zx}^{anti,C}$ are the largest component of $\mathbf{J}^{anti,C}$ are entirely analogous. In summary, a powdered sample is populated equally by crystallites displaying all values of $A(\Theta)$ between $-A_{max}$ and $+A_{max}$, where A_{max} is between 1 and $1/\sqrt{3}$ of the largest component of $\mathbf{J}^{anti,C}$.

As will be shown below, values for the transition frequencies depend on $A^2(\Theta)$ rather than on $A(\Theta)$. The $f_{zy}^2(\Theta; c_{yx}, c_{zx})$ distribution is displayed in Fig. 2*b*, where the increasing probability towards zero is apparent. Interestingly, there is a striking similarity between $f_{zy}^2(\Theta; c_{yx}, c_{zx})$ and the powder pattern for an isolated spin-1/2 nucleus with an axially symmetric magnetic shielding tensor. From the shape of the distribution in Fig. 2*b*, and the range of A_{max} noted above, it may be seen that the most probable value of A^2 is zero, and the observed values of $A^2(\Theta)$ will cover the range between 0 and A_{max}^2, where A_{max}^2 is between 1 (when $J_{yx}^{anti,C} = J_{zx}^{anti,C} = J_{zy}^{anti,C}$) and 1/3 (when two components of $\mathbf{J}^{anti}$ are zero) of the largest squared component of $\mathbf{J}^{anti,C}$.

NMR spectra from a single crystal

From the above considerations, the secular Hamiltonian for one crystallite containing an "isolated" AB spin pair under fast MAS averaging must incorporate the usual terms involving isotropic nuclear magnetic shieldings for both nuclei and the isotropic *J*-coupling, and, additionally, must include the antisymmetric *J*-coupling term defined above

$$[12]\quad h^{-1}\widehat{H}_0^{MAS} = -\nu_L[(1-\sigma_I)\widehat{I}_Z + (1-\sigma_S)\widehat{S}_Z] + J_{iso}\widehat{I}_Z\widehat{S}_Z + \frac{1}{2}J_{iso}(\widehat{I}_+\widehat{S}_- + \widehat{I}_-\widehat{S}_+) + i\frac{1}{2}A(\Theta)(\widehat{I}_+\widehat{S}_- - \widehat{I}_-\widehat{S}_+)$$

To predict the NMR spectrum resulting from this Hamiltonian, one must first find the energy levels. For spin-1/2 nuclei, taking the Zeeman states as basis functions, the nonzero elements of the Hamiltonian matrix are the diagonal ones,

$$[13]\quad \begin{aligned} \langle\alpha\alpha|h^{-1}\widehat{H}_0^{MAS}|\alpha\alpha\rangle &= -\nu_L\left[1-\frac{1}{2}(\sigma_I+\sigma_S)\right]+\frac{1}{4}J_{iso} \\ \langle\alpha\beta|h^{-1}\widehat{H}_0^{MAS}|\alpha\beta\rangle &= +\nu_L\left[\frac{1}{2}(\sigma_I-\sigma_S)\right]-\frac{1}{4}J_{iso} \\ \langle\beta\alpha|h^{-1}\widehat{H}_0^{MAS}|\beta\alpha\rangle &= -\nu_L\left[\frac{1}{2}(\sigma_I-\sigma_S)\right]-\frac{1}{4}J_{iso} \\ \langle\beta\beta|h^{-1}\widehat{H}_0^{MAS}|\beta\beta\rangle &= +\nu_L\left[1-\frac{1}{2}(\sigma_I+\sigma_S)\right]+\frac{1}{4}J_{iso} \end{aligned}$$

and two off-diagonal entries which contain contributions from J_{iso} and $A(\Theta)$:

$$[14]\quad \begin{aligned} \langle\beta\alpha|h^{-1}\widehat{H}_0^{MAS}|\alpha\beta\rangle &= \frac{1}{2}[J_{iso} - iA(\Theta)] \\ \langle\alpha\beta|h^{-1}\widehat{H}_0^{MAS}|\beta\alpha\rangle &= \frac{1}{2}[J_{iso} + iA(\Theta)] \end{aligned}$$

Both $|\alpha\alpha\rangle$ and $|\beta\beta\rangle$ are eigenfunctions of $\widehat{H}_0^{MAS}$, and their eigenvalues are simply given by the first and last expressions of eq. [13]. The two remaining eigenfunctions can be obtained in the usual way by diagonalizing the 2×2 submatrix containing the four remaining nonzero matrix elements.[41] Resulting from this diagonalization is the set of energy levels and wave functions given in Table 1, where

Table 1. Energy levels and wave functions for an AB spin system under MAS, including the effects of $\mathbf{J}^{anti}$.

Wave function[a]	Energy level[a]	m_T[a]
$\psi_1 = \|\alpha\alpha\rangle$	$E_1 = -\nu_L\left[1 - \frac{1}{2}(\sigma_I + \sigma_S)\right] + \frac{1}{4}J_{iso}$	+1
$\psi_2 = Q^{-1}\{[J_{iso} + iA(\Theta)]\|\alpha\beta\rangle + [C - \Delta_S]\|\beta\alpha\rangle\}$	$E_2 = -\frac{1}{4}J_{iso} + \frac{1}{2}C$	0
$\psi_3 = Q^{-1}\{[C - \Delta_S]\|\alpha\beta\rangle - [J_{iso} - iA(\Theta)]\|\beta\alpha\rangle\}$	$E_3 = -\frac{1}{4}J_{iso} - \frac{1}{2}C$	0
$\psi_4 = \|\beta\beta\rangle$	$E_4 = +\nu_L\left[1 - \frac{1}{2}(\sigma_I + \sigma_S)\right] + \frac{1}{4}J_{iso}$	–1

Note: See ref. 37 for analogous expressions.

[a]See text for definitions of constants.

Table 2. Transition frequencies and intensities for an AB spectrum, incorporating isotropic chemical shifts and the full **J** tensor.

Transition	Frequency	Relative intensity[a]
$\nu_{3,4}$	$\nu_L\left[1 - \frac{1}{2}(\sigma_I + \sigma_S)\right] + \frac{1}{2}C + \frac{1}{2}J_{iso}$	$1 - \frac{J_{iso}}{C}$
$\nu_{1,2}$	$\nu_L\left[1 - \frac{1}{2}(\sigma_I + \sigma_S)\right] + \frac{1}{2}C - \frac{1}{2}J_{iso}$	$1 + \frac{J_{iso}}{C}$
$\nu_{2,4}$	$\nu_L\left[1 - \frac{1}{2}(\sigma_I + \sigma_S)\right] - \frac{1}{2}C + \frac{1}{2}J_{iso}$	$1 + \frac{J_{iso}}{C}$
$\nu_{1,3}$	$\nu_L\left[1 - \frac{1}{2}(\sigma_I + \sigma_S)\right] - \frac{1}{2}C - \frac{1}{2}J_{iso}$	$1 - \frac{J_{iso}}{C}$

[a]See text for definitions of constants.

the following definitions have been used to simplify the expressions:

$$[15] \qquad \Delta_S = \nu_L(\sigma_I - \sigma_S)$$

$$[16] \qquad C = \sqrt{J_{iso}^2 + A^2(\Theta) + \Delta_s^2}$$

$$[17] \qquad Q = \sqrt{2C(C - \Delta_S)}$$

Here, Δ_S is the difference between the magnetic shieldings of the two sites, measured in Hz. All results reduce to match those of the classic expressions for an AB spin system in the limit of $A^2(\Theta) = 0$.

The allowed transitions are those where m_T, the eigenvalue of the operator for the z-component of total spin angular momentum $(\hat{I}_Z + \hat{S}_Z)$ changes by ±1,[41] and values of m_T for each wave function are reported in Table 1. Frequencies for each allowed transition are given in Table 2. Relative intensities for each transition may be determined from the absolute squares of the matrix elements of $\hat{F}_- = \hat{I}_- + \hat{S}_-$ between the involved wave functions,[41] and are also reported in Table 2. The spectrum expected from a single crystal undergoing MAS is presented in Fig. 3*a*, and is analogous to the textbook example of an AB spectrum in solution (where $\mathbf{J}^{anti}$ has no effect); however, for a solid sample under MAS, the splitting between the two central lines is increased when $A(\Theta)$ is nonzero. It is interesting to note that when $A(\Theta)$ is of substantial magnitude compared with J_{iso}, the relative intensities of the outer two transitions increase relative to the case when $A(\Theta)$ is negligible (for the same ratio of J_{iso} to the chemical shift difference between the two sites).

NMR spectra from powdered samples

Because each crystallite of a powder has a different value of $A(\Theta)$, each will produce a different four-line NMR spectrum. The separation between the two inner peaks is $C - |J_{iso}|$, and because C is a function of A^2, the inner peaks will form powder patterns. The outer two peaks will also have a line shape because, in every crystallite, each is separated by J_{iso} from the respective inner peak. The smallest separation between the inner two peaks occurs for crystallites with $A^2(\Theta) = 0$, designated as $C = C_0$ in Fig. 3*b*, and this will also be the most intense portion of the line shape as it is the most probable value of $A^2(\Theta)$. Crystallites with increasing values of $A^2(\Theta)$ will produce NMR spectra with an increasing separation between the inner peaks, but with decreasing intensity because of the smaller probability of $A^2(\Theta)$; see Fig. 3*b*. The two outer peaks of the spectrum of each crystallite will mimic that of the inner two, producing the total NMR spectrum given in Fig. 3*b*.

The form of the spectrum in Fig. 3*b* illustrates the information that can be derived from it. The spacings between the most intense parts of the four line shapes are independent of the antisymmetric components of **J**, so these can be analyzed according to the methods used for AB NMR spectra of solution samples.[41,45,46] Because the intensity of the outer two peaks is generally too small to measure, it is usually necessary to obtain NMR spectra at two applied magnetic field strengths (or from two isotopomers) to separate the value of J_{iso} from that of Δ_S. The largest splitting observed between the inner two transitions of Fig. 3*b* occurs for crystallites where $C = C_{max}$, from which eq. [16] can be solved for A_{max}. And, as noted above, the absolute value of the largest of the three components of $\mathbf{J}^{anti,C}$ is between $1A_{max}$ and $\sqrt{3}A_{max}$. Interestingly, it is not necessary to fit the entire line shape, because all of the information comes from the breadth of the peak. Analysis of the NMR line shape from an AB spin system under MAS therefore provides the values of J_{iso} and Δ_S, and a measure of the largest component of $\mathbf{J}^{anti,C}$.

It is worth noting that symmetry requirements on the number of components in $\mathbf{J}^{anti,C}$, see below, may make it possible to fix the values of the c_{ij} constants and thereby reduce the noted range of $1A_{max}$ to $\sqrt{3}A_{max}$ that experiments can place on the largest component of $\mathbf{J}^{anti,C}$. We also note

Fig. 3. (*a*) General four-line NMR spectrum for a homonuclear AB spin pair in a single crystal undergoing fast MAS, taking into account isotropic chemical shifts, isotropic *J* coupling, and antisymmetric *J* coupling. Adapted from reference 37. Note that for a tightly coupled spin pair, the two outer lines will be much less intense than the two central lines. (*b*) NMR spectrum corresponding to part (*a*), but for a powdered sample; C_0 is the value of C when $A^2 = 0$, and C_{max} is the value of C when $A^2 = A^2_{max}$. Specific data used for this example are $\Delta_S = J_{iso} = 50$ Hz, $J^{anti}_{zy} = 100$ Hz, and $J^{anti}_{yx} = J^{anti}_{zx} = 0$. The zero frequency in both spectra is $\nu_L[1–1/2(\sigma_I + \sigma_S)]$.

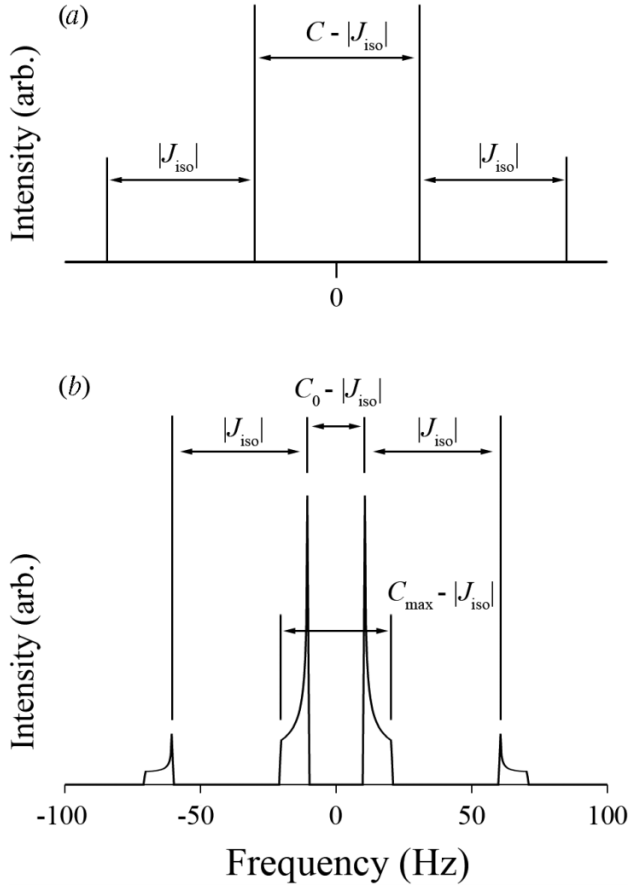

that the above results are independent of the choice used for the crystallite axis system. The PAS of $\mathbf{J}^{sym}$ can be used, but any crystallite axis system related by a set of three Euler angles could be chosen; accordingly, the experiment would provide an upper limit on the largest component of $\mathbf{J}^{anti}$ transformed to the new coordinate system. As the conclusions must remain valid under a change of the crystallite coordinate system, the final result is an upper limit of $\sqrt{3}A_{max}$ on the largest component of $\mathbf{J}^{anti}$ as represented in any coordinate system. No orientation information regarding $\mathbf{J}^{anti}$ is produced by the experiment.

Geometric interpretation of the antisymmetric component

The above discussion is focussed on deriving the effect of $\mathbf{J}^{anti}$ on the NMR spectrum. It is possible to gain some insight into the character of the antisymmetric component by using some simple geometric arguments. Consider a system

Fig. 4. Depiction of the geometry used in the classical mechanics example. In the coordinate system shown, the example angular momentum vectors are shifted to the same origin; (*a*) $\vec{S}$ along the *x* axis, and $\vec{I}$ along the *y* axis; (*b*) the vectors are interchanged, with $\vec{I}$ now along the *x* axis and $\vec{S}$ along the *y* axis.

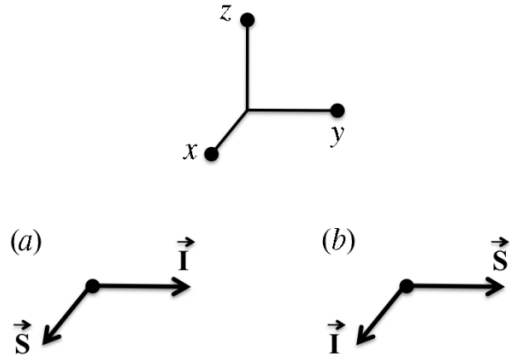

in classical mechanics whose energy is governed by the analogous equation $E^{classical} = \vec{\mathbf{I}} \cdot \mathbf{J}^{trial} \cdot \vec{\mathbf{S}}$, where

$$[18] \qquad \mathbf{J}^{trial} = \begin{bmatrix} 0 & J_{xy} & 0 \\ J_{yx} & 0 & 0 \\ 0 & 0 & 0 \end{bmatrix}$$

In this example, only the J_{xy} and J_{yx} elements (the only terms that affect the quantum energy levels) are nonzero. In the example orientations shown in Fig. 4, the classical energy, $E^{classical} = J_{xy}I_xS_y + J_{yx}I_yS_x$, is unaltered when the orientations of the two vectors are interchanged if $\mathbf{J}^{trial}$ is symmetric, but is reversed if $\mathbf{J}^{trial}$ is antisymmetric. In general, an indirect coupling tensor will have both symmetric and antisymmetric components; the symmetric portion encodes the contribution to the energy that is the same when the two angular momentum vectors are interchanged, and the antisymmetric component represents a contribution to the energy that is equal and opposite. Linear combination of the two components allows the equation to represent any difference in the energetics when the orientation of the two angular momentum vectors is interchanged. A similar geometric description of $\mathbf{J}^{anti}$ has been given by Robert and Weisenfeld.[38]

This geometric picture provides an interesting way to interpret $\mathbf{J}^{anti}$; however, it is important to consider which part of the picture is quantum mechanically relevant. For there to be an antisymmetric component in $\mathbf{J}$, there does have to be a difference in energy when the directions of the nuclear spins are interchanged in the fashion shown in Fig. 4. However, one does not measure $\mathbf{J}^{anti}$ by placing the spins in the two orientations shown in the Figure; instead, the difference in the total energy (Hamiltonian operator) terms describing these orientations causes an extra flip-flop type operator to be active. Because it is represented by such an operator, $\mathbf{J}^{anti}$ affects the energy levels of a tightly coupled AB spin system by mixing the $|\alpha\beta\rangle$ and $|\beta\alpha\rangle$ levels.

Selection of appropriate spin systems and compounds

In this section, we seek to establish some practical requirements for the observation of spectral features induced by $\mathbf{J}^{anti}$. There are several requirements which must be satis-

fied to ensure the feasibility of measuring $\mathbf{J}^{anti}$. Even if all the requirements are satisfied, there is no guarantee that $\mathbf{J}^{anti}$ will be of significant magnitude to be measured unambiguously. The requirements may be divided into those which concern the nuclear spin interactions of the nucleus to be observed, and those that describe the structural and symmetry properties of the molecule to be studied. The following discussion aims to demonstrate that after consideration of all requirements, only a small fraction of molecules are likely to provide an observation of $\mathbf{J}^{anti}$. The discussion is focussed on powdered samples; however, measurement of $\mathbf{J}^{anti}$ from a single crystal has many of the same general requirements.

The first requirement is that a chemical system must be found for which the two nuclei are strongly J coupled and for which their isotropic chemical shift difference is as small as possible. This requirement may be understood by considering the Hamiltonian, eq. [12], where it may be seen that the only occurrence of A is as the coefficient of a flip-flop type operator. And, in the usual fashion, a flip-flop operator only affects the energy levels when the two involved spins have Larmor frequencies which don't differ by much more than the magnitude of its coefficient. This behaviour is also encoded in the energy-level expressions through the value of C, eq. [16], where it may be seen that the influence of A on the spectrum increases as the magnitude of A increases relative to the chemical shift difference. Because of the necessity of a small difference in chemical shifts, a homonuclear spin pair will be required. A pair of magnetically equivalent nuclei, which constitute an A_2 spin pair and give rise to identical chemical shifts, is not a suitable spin pair since J coupling between these nuclei will not manifest itself in the NMR spectrum. Hence, what is required is an isolated pair of bonded nuclei which are nearly (but not exactly) crystallographically equivalent, so they will have very similar isotropic chemical shifts, but are likely to have a large indirect nuclear spin–spin coupling interaction. Since the chemical shift difference is smaller in Hz at lower applied magnetic field strengths, in some cases the observation of $\mathbf{J}^{anti}$ will only be possible at low applied magnetic field strengths. Measurement of $\mathbf{J}^{anti}$ is therefore one of the unusual cases where it is advisable to use the lowest possible external magnetic field strength.

The second requirement within the present strategy is that one must have a chemical system for which there is an effectively isolated pair of spin-1/2 nuclei. Quadrupolar nuclei are not feasible candidates due to the typically dominant quadrupolar interaction; however, it is possible that another method for measuring antisymmetric J coupling may involve quadrupolar nuclei as the quadrupolar interaction was used by Wi and Frydman to estimate the antisymmetric part of the chemical shift tensor.[33] Isotopes such as ^{1}H, ^{19}F, and possibly $^{203/205}$Tl will likely not be suitable due to strong homonuclear dipolar couplings preventing them from forming isolated spin pairs. Lastly, because of the fact that spin *pairs* must be observed, the spectral intensity will scale with natural abundance squared, and as such, natural abundance will play an important role in selecting a nucleus (unless isotopic labelling is available).

Although Abragam states that the components of $\mathbf{J}^{anti}$ are expected to be negligible relative to the symmetric part of $\mathbf{J}$,[47,48] multiconfigurational self-consistent field calculations on ClF_3 and OF_2 have indicated that the magnitudes of the components of the $\mathbf{J}^{anti}$ tensor are comparable to those of the principal components of the $\mathbf{J}^{sym}$ tensor in these compounds.[49] Thus, a spin pair with a large value of J_{iso} favours the likelihood of there being an antisymmetric component of substantial magnitude. This requirement rules out certain spin pairs including ^{13}C and ^{15}N because in a magnetic field of 4.7 T, e.g., the value of $^{1}J_{iso}(^{13}C,^{13}C)$ would have to be well in excess of 50 Hz for a spin pair with a chemical shift difference of 1 ppm. Such a situation is not likely given that one-bond carbon–carbon coupling constants are typically on the order of 50 Hz.[50] Because J_{iso} values generally become larger moving down any group in the periodic table, the heavier elements present the best chance of possessing observable $\mathbf{J}^{anti}$ components.

Table 3. Number of independent components of $\mathbf{J}^{anti}$ for each point group, assuming the two nuclei are not exchanged by a symmetry operation.[38,53]

Point group symmetry about the two coupled nuclei	Number of unique antisymmetric components
C_1	3
C_s, C_n ($n > 2$)	1
All others	0

Practically, one must be concerned with the chemical shift anisotropy of the nuclei in the AB pair. Heavier nuclei such as ^{199}Hg and ^{207}Pb tend to have substantial CS tensor spans.[51,52] When carrying out a MAS NMR experiment on a powdered sample, this fact introduces the additional complication that the spectral intensity is distributed over a large spectral width in the form of spinning sidebands. Thus, not only would a large span reduce the effective signal-to-noise ratio of the NMR spectrum, but it would also complicate the appearance and interpretation of the spectrum. Hence it is preferable to find a system for which the nuclei have relatively small CS tensor spans. This requirement is not critical, especially if a single-crystal NMR experiment is to be performed. However, this discussion is focussed on measurements made using powdered samples.

The molecule under study must be of sufficiently low symmetry about the bond axis of the coupled nuclei to ensure that the antisymmetric component of $\mathbf{J}$ is not forced to be zero by symmetry. The number of symmetry-allowed components in $\mathbf{J}^{anti}$ under various point groups is presented in Table 3 (see also references 38 and 53).

While the anisotropy of the symmetric part of the $\boldsymbol{\sigma}$ tensor may pose a challenge in the acquisition of high-quality NMR spectra of the AB spin pair, we do not expect the antisymmetric component of $\boldsymbol{\sigma}$ to hamper or influence the measurement of $\mathbf{J}^{anti}$ by this method. The effect of $\boldsymbol{\sigma}^{anti}$ on NMR line shapes is generally expected to be very small.[10,29,30] However, in some cases it is possible for the inclusion of extra terms in the Hamiltonian to magnify effects from the typically nonsecular terms involving $\boldsymbol{\sigma}^{anti}$, e.g., a strong quadrupolar interaction is known to have such an effect.[33] Inspection of the wave functions in Table 1 shows that this is not the case with $\widehat{H}^{anti,MAS}$, as terms in the Hamiltonian containing $\boldsymbol{\sigma}^{anti}$ remain nonsecular. Accordingly, we do not expect the predicted effects of $\mathbf{J}^{anti}$ to be obscured by the presence of $\boldsymbol{\sigma}^{anti}$ terms.

In the present work, the nuclei deemed most suitable for a definitive measurement of $\mathbf{J}^{anti}$ are ^{29}Si, ^{31}P, ^{77}Se, $^{111/113}$Cd, $^{115/117/119}$Sn, $^{123/125}$Te, and ^{129}Xe. There is also a possibility that some heavier nuclei could provide valuable results, particularly if single crystal spectra are investigated using MAS.

Data collection and analysis

Now that the most promising candidates for the observation of homonuclear antisymmetric *J* coupling have been narrowed down, suitable compounds must be identified. Tin seems to be the most promising element due to the high receptivities of the ^{119}Sn and ^{117}Sn isotopes, in addition to moderate chemical shift anisotropies and well-developed synthetic chemistry. Tellurium is another promising element, and some tellurium systems are also discussed.

Tellurium-125 solid-state NMR spectroscopy of diaryl ditellurium compounds

Tellurium-125 CP MAS NMR spectra were acquired from *p*,*p*′-dimethoxydiphenyl ditelluride, **I**; *p*,*p*′-ditolyl ditelluride, **II**; 1-naphthyl ditelluride, **III**; and diphenyl ditelluride, **IV**. One-bond ^{125}Te–^{125}Te coupling constants are generally of significant magnitude, e.g., $^1J_{iso}(^{125}Te, ^{125}Te)$ in $(Me_4N)_2Te_2$ is ±3568 Hz in the solid state,[54] making these promising samples for investigations of $\mathbf{J}^{anti}$. However, measurement of antisymmetric *J* coupling in the present case is hampered in several ways. First, there is a large tellurium chemical shift anisotropy[55] which distributes the powder pattern across ~1200 ppm. Second, the chemical shift difference between the tellurium sites, e.g., 74.4 ppm or 4698 Hz at 4.7 T for **II**, is of the same order of magnitude as the expected value of J_{iso}, thereby reducing the "AB" character of the spin system. The situation is even less promising in the case of **I**, for which there are two molecules in the asymmetric unit.[56] This distributes the desired ^{125}Te NMR signal over twice as many sites, thereby reducing the signal-to-noise ratio. In summary, ^{125}Te NMR spectra of these compounds were of such poor quality that the resonances from the AB spin pairs could not be resolved at 4.7 T (spectra not shown), and there was therefore no opportunity for detecting whether the components of the AB spectrum possessed a line shape.

Tin-119 solid-state NMR spectroscopy of hexa(*p*-tolyl)ditin

Many ditin compounds of the type $R_3Sn–SnR_3$ possess magnetically equivalent tin atoms which are related by an inversion centre. Others have C_{3v} symmetry, which by symmetry requires all elements of $\mathbf{J}^{anti}$ to be zero.[38,53] One candidate that satisfies the stringent requirements is hexa(*p*-tolyl)ditin (**V**), which has two crystallographically nonequivalent tin atoms[57] (Fig. 5). Solution ^{119}Sn NMR in $CDCl_3$ has provided a value of δ_{iso} = –141.9 ppm for the then chemically equivalent tin atoms, and a value of $^1J_{iso}(^{119}Sn,^{119}Sn)$ of 4570 Hz.[57]

The ^{119}Sn CP MAS NMR spectrum of solid powdered **V** acquired at 7.05 T is presented in Fig. 6*a*; ^{119}Sn and ^{117}Sn CP MAS spectra were also obtained at 4.70 T (not shown). The form of the spectrum, which appears more complicated than the four-line ideal spectrum presented in Fig. 3, is due to the fact that the ^{119}Sn isotope is not 100% abundant. We also note that nearly all of the spectral intensity is concentrated in the centrebands, as ^{119}Sn CP NMR spectra of a stationary sample of **V** indicate a CS tensor span for tin of less than 200 ppm. Values for the NMR parameters derived from these spectra are presented in Table 4. The isotropic chemical shifts of the two Sn sites in **V** are easily determined as –142.5 and –154.2 ppm from the peaks of the uncoupled ^{119}Sn nuclei, providing a value for Δ_S of 1310 ± 20 Hz. In Fig. 6*a*, the splittings (i) and (ii) between the outer two pairs of lines reflect the couplings of sites 1 and 2 to ^{117}Sn nuclei. These two couplings are found to be the same (as expected), and the spectra yield a final value of 4175 ± 20 Hz for $^1J_{iso}(^{119}Sn,^{117}Sn)$ in **V**. Because isotope effects are expected to be insubstantial here,[58] a value for $^1J_{iso}(^{119}Sn,^{119}Sn)$ of

Fig. 5. Structure of hexa(*p*-tolyl)ditin. (*a*) View along the tin–tin bond; (*b*) side view. Hydrogen atoms are omitted for clarity.

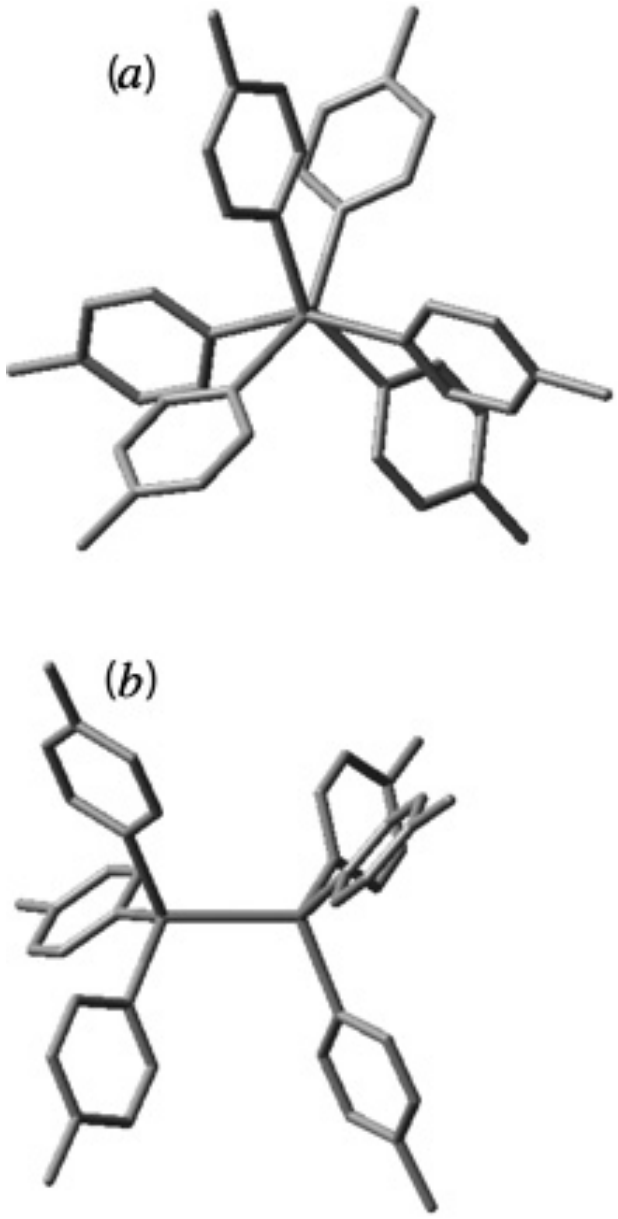

Fig. 6. (*a*) Tin-119 VACP MAS spectrum of hexa(*p*-tolyl)ditin obtained at 7.05 T. The two dominant peaks result from the uncoupled nuclei, and are therefore far more intense than peaks from the coupled isotopomers. The splitting (*i*) is equal to $^1J_{iso}(^{119}Sn, ^{117}Sn)$ for site 1 and the splitting (ii) is $^1J_{iso}(^{119}Sn, ^{117}Sn)$ for site 2. The splitting corresponding to $C_0 - |J_{iso}(^{119}Sn, ^{119}Sn)|$ is also marked in the figure. (*b*) Tin-119 POST-C7 spectrum of hexa(*p*-tolyl)ditin also obtained at 7.05 T, where the double-quantum pulse sequence filters out all but homonuclear spin pairs, leaving only the central part of the AB pattern. The edges of the line shape provide a maximum value for $C_{max} - |J_{iso}(^{119}Sn, ^{119}Sn)|$, and therefore of the largest component of $\mathbf{J}^{anti}$.

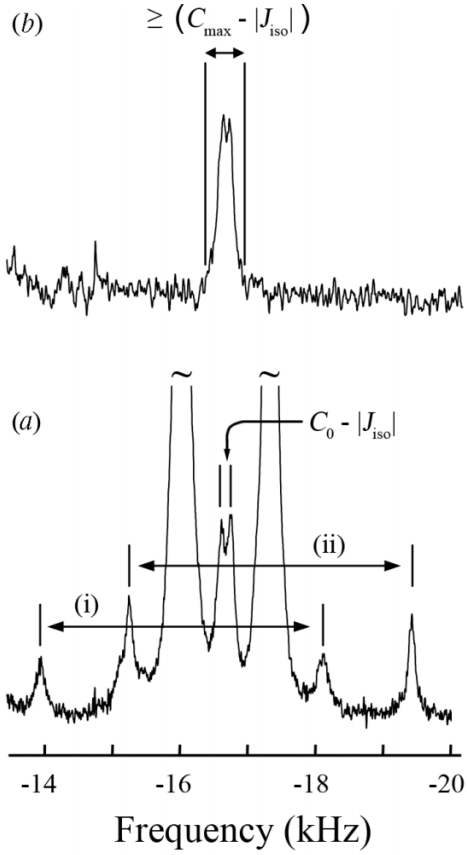

4368 Hz may be obtained through multiplication by the ratio of the magnetogyric ratios, $\gamma(^{119}Sn)/\gamma(^{117}Sn)$.[9] The splitting $C_0 - |J_{iso}|$, see Fig. 6*a*, is 140 ± 50 Hz, which agrees within error with the splitting of 192 ± 7 Hz expected from the above values of J_{iso} and Δ_S. Note that for molecules containing two ^{119}Sn nuclei, the two outer transitions are not observed in the ^{119}Sn NMR spectrum shown in Fig. 6*a*. Because the integrated intensity of each of the transitions is approximately 2.2% of each of the inner transitions, it would be extremely difficult to observe them. It would be possible to observe effects of $\mathbf{J}^{anti}$ solely from the inner transitions; however, spectral crowding by peaks from the other isotopomers prevents observation of the entire line shape and could be responsible for obscuring the effects of $\mathbf{J}^{anti}$.

In an effort to determine some line shape for the inner two peaks, a two-dimensional *J*-resolved ^{119}Sn NMR spectrum was obtained at 4.70 T.[59,60] In the *J*-resolved experiment, heteronuclear dipolar interactions as well as anisotropic chemical shifts are refocused at the top of the echo, thereby providing better resolution in the indirect (F_1) dimension.[59] Furthermore, because the peaks from the AB pattern are separated along the F_1 dimension, this experiment presents the opportunity to observe some anisotropic line shape that could be obscured in the one-dimensional spectrum. Shown in Fig. 7 is a 2D *J*-resolved ^{119}Sn CP MAS NMR spectrum of hexa(*p*-tolyl)ditin. The projection of this spectrum onto the isotropic dimension corresponds to the one-dimensional CP MAS spectrum. In the indirect *J*-resolved dimension, the splitting $C_0 - |J_{iso}(^{119}Sn,^{119}Sn)|$ is much better resolved than it is in the isotropic dimension, and therefore provides a more accurate measurement. The precision of the measurement in the indirect dimension is limited by the number of points which define the spectrum. In the spectrum shown in Fig. 7, 16 points define the 200 Hz spectral window in the indirect dimension, thereby providing one data point every 12.5 Hz. The splitting $C_0 - |J_{iso}(^{119}Sn,^{119}Sn)|$ is 85.0 ±

Table 4. Tin-119 NMR parameters determined for hexa(*p*-tolyl)ditin.

Parameter	Value
δ_{iso}(site 1)	–142.5±0.2 ppm
δ_{iso}(site 2)	–154.2±0.2 ppm
$J_{iso}(^{119}Sn,^{119}Sn)$	4368±20 Hz
$\mathbf{J}^{anti}(^{119}Sn,^{119}Sn)$ elements	<2900 Hz

Fig. 7. 2D *J*-resolved ^{119}Sn CP MAS NMR spectrum of hexa(*p*-tolyl)ditin obtained at 4.70 T. The isotropic chemical shifts of the uncoupled nuclei in sites 1 and 2 are indicated. The splitting $C_0 - |J_{iso}(^{119}Sn,^{119}Sn)|$ is easily resolved in the second dimension.

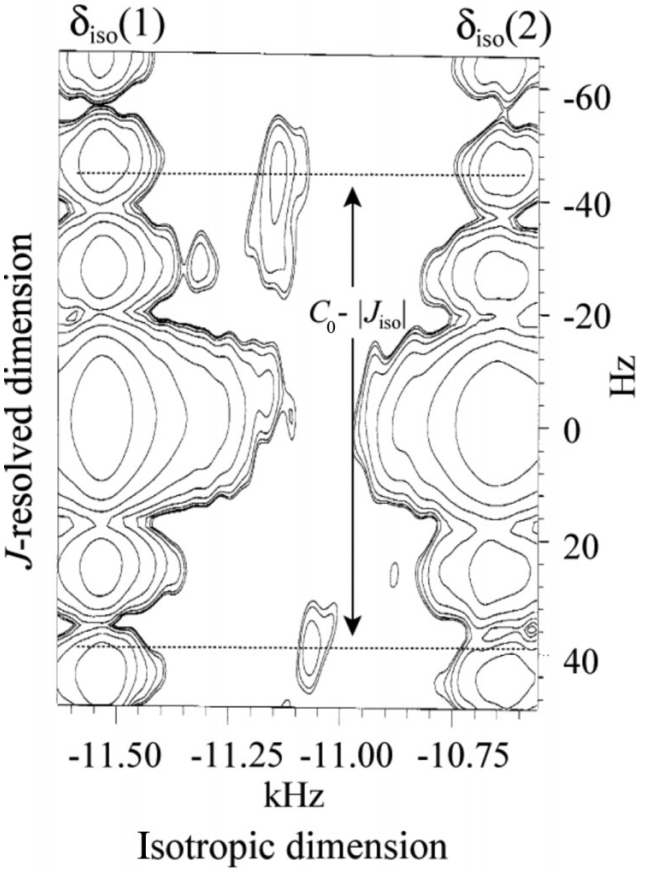

12.5 Hz, which compares favourably with the splitting of 87 ± 5 Hz expected from J_{iso} and the Δ_S = 875 ± 20 Hz measured from the 1D spectrum. Unfortunately, when the signal is spread out into two dimensions, the signal-to-noise ratio of the inner two peaks of the AB spectrum is reduced such that any line shape present was not detected.

Another method of decongesting the spectral overlap seen in Fig. 6*a* is to use a double-quantum filter, DQF, to remove any peaks that do not arise from a homonuclear spin pair. The spectrum shown in Fig. 6*b* is an example of this method where we have used the POST-C7 experiment which leaves only peaks from ^{119}Sn nuclei that are relatively strongly dipolar coupled to one another.[61,62] The spectrum in Fig. 6*b* therefore corresponds to that of Fig. 6*a*, except that only the inner two peaks from the AB spin system remain. Before providing a concrete evaluation, we note that A_{max} only produces a significant effect on the spectrum when its magnitude is comparable to both J_{iso} and Δ_S. For example, the breadth of the each of the inner peaks of Fig. 3*b*, $C_{max} - C_0$, would only be 11 Hz if A_{max} were 450 Hz (10% of J_{iso}). Comparing the DQF spectrum to the theoretical form of Fig. 3*b* shows that the edges of the peaks in the DQF spectrum provide an upper limit to C_{max}, and therefore an upper limit on the largest element of $\mathbf{J}^{anti}$. The breadth of the AB doublet is 500 Hz, which translates into a value of 1700 Hz for A_{max}, and A_{max} is from 1 to $1/\sqrt{3}$ of the largest element of $\mathbf{J}^{anti}$. The DQF spectrum therefore provides an upper limit of 2900 Hz for the largest element of $\mathbf{J}^{anti}$ in compound **V**.

In cases where a peak shoulder is directly observed, an exact value of A_{max} can be extracted; however, only the peak width can be determined from the presented spectrum of hexa(*p*-tolyl)ditin, and therefore only an upper limit on A_{max} can be reported. It should also be noted that line broadening from other sources acts to increase the upper limit provided by this analysis. For example, the sample calculation presented in the preceding paragraph shows that even if A_{max} were zero in this compound, line broadening causing an apparent increase in $C_{max} - C_0$ of only 11 Hz would lead to an upper limit of 450 Hz for A_{max}. Because of interference from line-broadening effects, the actual value of $\mathbf{J}^{anti}$ elements may be anywhere between 0 and the upper limit of 2900 Hz. Despite the limitations of analyzing a spectrum for which the theoretically expected shoulder is not observed, it is interesting that we can place a definite upper limit on $\mathbf{J}^{anti}$ elements.

Experimental and theoretical implications

Given that quantum chemical calculations have shown that the magnitudes of $\mathbf{J}^{anti}$ elements have the potential to be comparable to those of $\mathbf{J}^{sym}$,[49] it is important to consider their effect on NMR spectra. Effects from $\mathbf{J}^{anti}$ have generally been ignored in spectral analysis, despite the fact that Andrew and Farnell have predicted measureable effects on AB spectra from single crystals spinning at the magic angle.[37] Aside from interest in $\mathbf{J}^{anti}$ itself, it is important to consider whether the presence of large elements in $\mathbf{J}^{anti}$ could lead to errors when analyzing AB spectra of powders undergoing MAS. While an observable difference in peak position is predicted for each crystallite, it is found here that the most probable frequency, i.e., the highest part of each peak, is independent of $\mathbf{J}^{anti}$. Therefore, one need not worry about $\mathbf{J}^{anti}$ introducing errors in determinations of the other NMR observables.

While the above theory shows that it is possible to analyze spectra independently of $\mathbf{J}^{anti}$, the discussion also presents a strategy for its measurement. The fundamental reason for measuring the antisymmetric parts of NMR interaction tensors, and indeed for measuring the anisotropic symmetric parts, is to make use of the fact that up to nine independent elements are available for a given interaction tensor (see eq. [1]). Routine use is made of the isotropic portions of the chemical shift and *J*-coupling tensors; the availability of up to eight more parameters to describe a given interaction signifies the opportunity to provide much more complete descriptions of the nuclear environment.

The potential existence of sizable antisymmetric contributions to **J** also has other important implications. For example, the different mechanisms which contribute to *J* coupling are listed in Table 5, where it may be seen that each mechanism possesses different symmetry properties.[63] Because $\mathbf{J}^{anti}$ contains no contribution from the Fermi-contact (FC) coupling mechanism, measurement of a nonzero antisymmetric coupling constant would represent some of the most convincing experimental evidence for non-FC contributions to **J**. Furthermore, it is noted that in principle the antisymmetric part of **J** contributes to nuclear spin relaxation although its effect has never been observed experimentally.[34,35] While the experimental strategy described herein is applicable to tightly coupled homonuclear spin pairs, antisymmetric *J* coupling is a general phenomenon which will in principle affect nuclear spin relaxation even in situations where it cannot be measured directly. That heteronuclear *J* couplings may contain important antisymmetric contributions has been demonstrated by high-level quantum chemical calculations on selected systems.[49]

Table 5. Relationships between the mechanisms which contribute to **J** and the symmetry properties of **J**.[63]

Mechanism	Isotropic	Symmetric	Antisymmetric
DSO	✓	✓	✓
PSO	✓	✓	✓
FC	✓	×	×
SD	✓	✓	✓
FC×SD	×	✓	×

Conclusions

The present work has described an experimental strategy for measuring the antisymmetric part of indirect nuclear spin–spin coupling tensors for tightly coupled (AB) homonuclear spin pairs in solid samples undergoing MAS. Considerations for identifying appropriate spin systems and chemical compounds have been developed, and we also note that modern quantum-chemical calculations would likely be helpful in selecting suitable candidate molecules. Analysis of spectra from samples undergoing MAS, which averages all interactions other than $\mathbf{J}^{anti}$ to their isotropic values, appears to be an ideal strategy. $\mathbf{J}^{anti}$ would affect

spectra from stationary samples, but it would be difficult to separate $\mathbf{J}^{anti}$ from the orientationally dependent $\mathbf{J}^{sym}$ and **D** interactions (even with single crystal data). The effect of $\mathbf{J}^{anti}$ components on NMR line shapes from powdered samples undergoing MAS is derived, and the method of spectral analysis discussed. The main finding is that NMR peak shapes from AB spin systems will be affected, but that the most intense portion of the spectra may be analyzed independent of $\mathbf{J}^{anti}$. It is also found that $\mathbf{J}^{anti}$ must be comparable in magnitude to J_{iso} and the difference in chemical shifts between the two sites to affect the NMR spectra. In particular, the method of analysis allows one to determine a measure of the largest element of $\mathbf{J}^{anti}$. Using this approach, the ^{119}Sn NMR spectrum of hexa(*p*-tolyl)ditin was analyzed to show that all elements of $\mathbf{J}^{anti}$ in this compound must be smaller than 2900 Hz.

Experimental details

p,*p*′-Dimethoxydiphenyl ditelluride, **I**, (dark red powder), *p*,*p*′-ditolyl ditelluride, **II**, (orange powder), 1-naphthyl ditelluride, **III**, (light orange powder), and diphenyl ditelluride, **IV**, (orange powder) were obtained from Sigma-Aldrich. Tellurium-125 one-dimensional VACP MAS NMR spectra of compounds **I**-**IV** were acquired on a Chemagnetics CMX Infinity 200 spectrometer operating at a frequency of 63.16 MHz. MAS rates of at least 10 kHz were found to be essential to resolve spinning sidebands satisfactorily; a double-resonance 4 mm MAS probe was used for all experiments. Telluric acid, $Te(OH)_6$, was used as a cross-polarization setup sample.[64] Typical experimental parameters were: 10–20 s recycle delay, 2.50 μs π/2 pulse, 10.0 ms contact time, 76.8 ms acquisition time, 4k–8k scans recorded. High-power proton decoupling was used for all experiments. For compounds **I**, **II**, and **IV**, the temperature around the sample was kept below room temperature, typically ≈ 10 °C, to prevent melting of the samples.

Hexa-(*p*-tolyl)ditin, **V**, (white powder) was synthesized following a procedure adapted from references 65 and 66. The compound was recrystallized from benzene, which apparently affords the type-B polymorph.[57] Tin-119 VACP MAS NMR spectra of powdered samples of hexa(*p*-tolyl)ditin were acquired at a frequency of 74.63 MHz using a Chemagnetics CMX Infinity 200 spectrometer, or at 112.01 MHz with a Bruker Avance 300 spectrometer. Tin-117 VACP MAS NMR spectra were acquired at 71.31 MHz using a Chemagnetics CMX Infinity 200 spectrometer. A 4 mm DR MAS probe was used for all experiments. Tetracyclohexyltin was used as a setup sample and secondary chemical shift reference, δ_{iso} = –97.35 ppm, with respect to a solution of $SnMe_4$ at 0 ppm.[67,68] All ^{119}Sn and ^{117}Sn CP/MAS experiments used a 40 s recycle delay, 5–6 ms contact times, and either 2.40 μs (at 4.70 T) or 4.00 μs π/2 pulses. High-power proton decoupling ($\gamma B_1/2\pi$ > 60 kHz) was used for all experiments. The POST-C7 pulse sequence[61,62] was used to provide a double-quantum filtered ^{119}Sn spectrum; an MAS rate of 8.929 kHz and an experimentally optimized ^{119}Sn B_1 field near the theoretical maximum of 62.5 kHz was applied. The DQ conversion efficiency of the POST-C7 sequence was found to be approximately half the theoretical value of 47% for the 895.96 μs DQ excitation block used.[69] Heteronuclear decoupling was applied only during the acquisition period of the POST-C7 experiment.[70] Two-dimensional *J*-resolved ^{119}Sn MAS NMR spectra[59,60] were acquired using similar parameters, with 16 points acquired in the indirect dimension, a spectral window of 200 Hz in the indirect dimension, and 128 scans per increment.

Numerical calculations of the $A(\Theta)$ distribution and its effect on NMR spectra were performed with purpose-built C code. The powder distribution was generated by calculating the value of $f_{zy}(\Theta;c_{yx},c_{zx})$, see eq. [11], for a large set of crystallite orientations;[71] orientations were generated in the rotor frame, to take advantage of the above-noted rotational symmetry of $f_{zy}(\Theta;c_{yx},c_{zx})$ about the axis of sample rotation. Specifically, crystallites were initially aligned with z along r_{rot}, then rotated about r_{rot} through the angle α ($0 < \alpha < 2\pi$), and then about the initial *y* axis through the angle β ($0 < \beta < \pi$). A total of 832039 crystallite orientations were used, where the α and β Euler angles were sampled according to the Zaremba–Conroy–Wolfsberg, ZCW, distribution.[72–74] Each ξ_a and ε_{ab} angle in eq. [11] was then calculated using standard linear algebra, and used to create plots of $f_{zy}(\Theta;c_{yx},c_{zx})$, $f_{zy}^2(\Theta;c_{yx},c_{zx})$, or the NMR spectral frequencies.

Acknowledgments

We thank all members of the solid-state NMR group at the University of Alberta for helpful comments. We are grateful to Professor Cynthia Jameson for advice. K.J.H. thanks the province of Alberta and the University of Alberta for funding. We thank the Natural Sciences and Engineering Research Council (NSERC) of Canada for research grants. R.E.W. thanks the University of Alberta for financial support and also thanks the Canada Research Chairs Program for funding a Canada Research Chair in Physical Chemistry held by R.E.W. at the University of Alberta.

References

(1) Frydman, L. *Annu. Rev. Phys. Chem.* **2001**, *52* (1), 463–498. doi:10.1146/annurev.physchem.52.1.463. PMID:11326072.
(2) Tjandra, N.; Bax, A. *Science* **1997**, *278* (5340), 1111–1114. doi:10.1126/science.278.5340.1111. PMID:9353189.
(3) Tolman, J. R.; Flanagan, J. M.; Kennedy, M. A.; Prestegard, J. H. *Proc. Natl. Acad. Sci. U.S.A.* **1995**, *92* (20), 9279–9283. doi:10.1073/pnas.92.20.9279. PMID:7568117.
(4) Prestegard, J. H.; al-Hashimi, H. M.; Tolman, J. R. *Q. Rev. Biophys.* **2000**, *33* (4), 371–424. doi:10.1017/S0033583500003656. PMID:11233409.
(5) Simon, B.; Sattler, M. *Angew. Chem. Int. Ed.* **2002**, *41* (3), 437–440. doi:10.1002/1521-3773(20020201)41:3<437::AID-ANIE437>3.0.CO;2-3.
(6) de Alba, E.; Tjandra, N. *Prog. Nucl. Magn. Reson. Spectrosc.* **2002**, *40* (2), 175–197. doi:10.1016/S0079-6565(01)00042-5.
(7) Bryce, D. L.; Grishaev, A.; Bax, A. *J. Am. Chem. Soc.* **2005**, *127* (20), 7387–7396. doi:10.1021/ja051039c. PMID:15898787.
(8) Duer, M. J. *Introduction to Solid-State NMR Spectroscopy*. Blackwell Publishing Limited: Oxford, UK, 2004.
(9) Jameson, C. J. Spin–Spin Coupling. In *Multinuclear NMR*. Mason, J., Ed; Plenum Press: New York, 1987; pp. 89.
(10) Haeberlen, U. High Resolution NMR in Solids: Selective

Averaging. In *Advances in Magnetic Resonance*. Supplement 1. Waugh, J. S., Ed.; Academic Press: New York, 1976.
(11) Wasylishen, R. E. Indirect Nuclear Spin–Spin Coupling Tensors. In *Encyclopedia of Nuclear Magnetic Resonance*; Grant, D. M. and Harris, R. K., Eds.; Wiley: Chichester, UK., 2002; Vol. 9, pp 274–282.
(12) Wasylishen, R. E. Dipolar and Indirect Coupling Tensors in Solids. In *Encyclopedia of Nuclear Magnetic Resonance*; Grant, D. M. and Harris. R. K., Eds.; Wiley: Chichester, UK, 1996; Vol. 3, pp 1685–1694.
(13) Vaara, J.; Jokisaari, J.; Wasylishen, R. E.; Bryce, D. L. *Prog. Nucl. Magn. Reson. Spectrosc.* **2002**, *41* (3-4), 233–304. doi:10.1016/S0079-6565(02)00050-X.
(14) Bryce, D. L.; Wasylishen, R. E. *Acc. Chem. Res.* **2003**, *36* (5), 327–334. doi:10.1021/ar020271+. PMID:12755642.
(15) Autschbach, J.; Ziegler, T. *J. Chem. Phys.* **2000**, *113* (3), 936. doi:10.1063/1.481874.
(16) Autschbach, J.; Ziegler, T. *J. Chem. Phys.* **2000**, *113* (21), 9410. doi:10.1063/1.1321310.
(17) Dickson, R. M.; Ziegler, T. *J. Phys. Chem.* **1996**, *100* (13), 5286–5290. doi:10.1021/jp951930l.
(18) Khandogin, J.; Ziegler, T. *Spectrochim. Acta [A]* **1999**, *55* (3), 607–624. doi:10.1016/S1386-1425(98)00265-0.
(19) Bryce, D. L.; Wasylishen, R. E. *Inorg. Chem.* **2002**, *41* (12), 3091–3101. doi:10.1021/ic020025u. PMID:12054987.
(20) Bryce, D. L.; Wasylishen, R. E. *J. Am. Chem. Soc.* **2000**, *122* (13), 3197–3205. doi:10.1021/ja9942134.
(21) Bryce, D. L.; Wasylishen, R. E.; Autschbach, J.; Ziegler, T. *J. Am. Chem. Soc.* **2002**, *124* (17), 4894–4900. doi:10.1021/ja012596b. PMID:11971740.
(22) Autschbach, J.; Ziegler, T. Relativistic Computation of NMR Shieldings and Spin–Spin Coupling Constants. In *Encyclopedia of Nuclear Magnetic Resonance*; Grant, D. M. and Harris, R. K., Eds.; Wiley: Chichester, UK, 2002; Vol. 9, pp 306–321.
(23) Autschbach, J.; Le Guennic, B. *J. Chem. Educ.* **2007**, *84*, 156.
(24) Autschbach, J. *Coord. Chem. Rev.* **2007**, *251* (13-14), 1796–1821. doi:10.1016/j.ccr.2007.02.012.
(25) Autschbach, J. The Calculation of NMR Parameters in Transition Metal Complexes. In *Structure and Bonding: Principles and Applications of Density Functional Theory in Inorganic Chemistry I;* Kaltsoyanis, N. and McGrady, J. E. , Eds; Springer-Verlag: Berlin, DE. 2004, Vol. 112, pp 1–48.
(26) Helgaker, T.; Jaszuński, M.; Pecul, M. *Prog. Nucl. Magn. Reson. Spectrosc.* **2008**, *53* (4), 249–268. doi:10.1016/j.pnmrs.2008.02.002.
(27) Krivdin, L. B.; Contreras, R. H. *Annu. Rep. Nucl. Magn. Reson. Spectrosc.* **2007**, *61*, 133.
(28) Helgaker, T.; Jaszuński, M.; Ruud, K. *Chem. Rev.* **1999**, *99* (1), 293–352. doi:10.1021/cr960017t. PMID:11848983.
(29) Schneider, R. F. *J. Chem. Phys.* **1968**, *48* (11), 4905. doi:10.1063/1.1668154.
(30) Ding, S.; Ye, C. *Chem. Phys. Lett.* **1990**, *170* (2-3), 277–282. doi:10.1016/0009-2614(90)87128-E.
(31) Anet, F. A. L.; O' Leary, D. J.; Wade, C. G.; Johnson, R. D. *Chem. Phys. Lett.* **1990**, *171* (5-6), 401–405. doi:10.1016/0009-2614(90)85237-7.
(32) Chenon, M. T.; Coupry, C.; Werbelow, L. G. *J. Phys. Chem.* **1992**, *96* (2), 561–566. doi:10.1021/j100181a013.
(33) Wi, S.; Frydman, L. *J. Chem. Phys.* **2002**, *116* (4), 1551. doi:10.1063/1.1406533.
(34) Blicharski, J. S. *Z. Naturforsch. A: Astrophys. Phys. Phys. Chem.* **1972**, *27*, 1355.
(35) Spiess, H. W. Rotation of Molecules and Nuclear Spin Relaxation. In *NMR Basic Principles and Progress;*. Diehl, P., Fluck, E., and Kosfeld, R, Eds.; Springer-Verlag: Berlin, DE, 1978; Vol. 15, pp 55–214.
(36) Levitt, M. H. Symmetry-Based Pulse Sequences in Magic-Angle Spinning Solid-State NMR. In *Encyclopedia of Nuclear Magnetic Resonance*; Grant, D. M. and Harris, R. K., Eds.; Wiley: Chichester, UK; 2002; Vol. 9, pp 165–194.
(37) Andrew, E. R.; Farnell, L. F. *Mol. Phys.* **1968**, *15* (2), 157–165. doi:10.1080/00268976800100931.
(38) Robert, J. B.; Wiesenfeld, L. *Phys. Rep.* **1982**, *86* (7), 363–401. doi:10.1016/0370-1573(82)90164-8.
(39) VanderHart, D. L.; Gutowsky, H. S. *J. Chem. Phys.* **1968**, *49* (1), 261. doi:10.1063/1.1669820.
(40) Zilm, K. W.; Grant, D. M. *J. Am. Chem. Soc.* **1981**, *103* (11), 2913–2922. doi:10.1021/ja00401a001.
(41) Corio, P. L. *Structure of High-Resolution NMR Spectra;* Academic Press: New York, 1966.
(42) Levitt, M. H. *Spin Dynamics: Basics of Nuclear Magnetic Resonance*. John Wiley and Sons: Chichester, UK; 2001; Appendix 17.5.
(43) Nye, J. F. *Physical Properties of Crystals: Their Representation by Tensors and Matrices*; Oxford University Press: Oxford, UK; 1985.
(44) Harris, R. K. *Nuclear Magnetic Resonance Spectroscopy: A Physicochemical View*; Pearson Education Limited: Essex, UK; 1987; Appendix 5.
(45) Hahn, E. L.; Maxwell, D. E. *Phys. Rev.* **1952**, *88* (5), 1070–1084. doi:10.1103/PhysRev.88.1070.
(46) Anderson, W. A. *Phys. Rev.* **1956**, *102* (1), 151–167. doi:10.1103/PhysRev.102.151.
(47) Abragam, A. *Principles of Nuclear Magnetism;* Adair, R. K., Elliott, R. J., Marshall, W. C., Wilkinson, D. H., Eds.; International Series of Monographs on Physics; Clarendon Press: Oxford; 1961.
(48) Abragam, A.; Goldman, M. In *Nuclear Magnetism: Order and Disorder*; Krumhansl, J. A., Marshall, W., Wilkinson, D. H., Eds.; International Series of Monographs on Physics; Clarendon Press: Oxford, UK, 1982; Chapter 2, Section A(*c*).
(49) Bryce, D. L.; Wasylishen, R. E. *J. Am. Chem. Soc.* **2000**, *122* (45), 11236–11237. doi:10.1021/ja002043l.
(50) Wasylishen, R. E. In *Annual Reports on NMR Spectroscopy*; Webb, G. A., Ed.; Academic Press: London, UK, 1977; Vol. 7, pp 245–291.
(51) Ambrosius, F.; Klaus, E.; Schaller, T.; Sebald, A. *Z. Naturforsch A: Phys. Sci.* **1995**, *50*, 423.
(52) van Bramer, S. E.; Glatfelter, A.; Bai, S.; Dybowski, C.; Neue, G. *Concepts Magn. Reson.* **2002**, *14* (6), 365–387. doi:10.1002/cmr.10042.
(53) Buckingham, A. D.; Pyykkö, P.; Robert, J. B.; Wiesenfeld, L. *Mol. Phys.* **1982**, *46* (1), 177–182. doi:10.1080/00268978200101171.
(54) Batchelor, R. J.; Einstein, F. W. B.; Gay, I. D.; Jones, C. H. W.; Sharma, R. D. *Inorg. Chem.* **1993**, *32* (20), 4378–4383. doi:10.1021/ic00072a036.
(55) Bryce, D. L.; Wasylishen, R. E. Unpublished results.
(56) Ludlow, S.; McCarthy, A. E. *J. Organomet. Chem.* **1981**, *219* (2), 169–176. doi:10.1016/S0022-328X(00)83009-0.
(57) Schneider, C.; Dräger, M. *J. Organomet. Chem.* **1991**, *415* (3), 349–362. doi:10.1016/0022-328X(91)80135-7.
(58) Jameson, C. J. The Dynamic and Electronic Factors in Isotope Effects on NMR Parameters. In *Isotopes in the Physical and Biomedical Sciences*. Buncel, E., Jones. J. R., Eds.; Elsevier: Amsterdam, NL, 1991; Vol. 2, pp 1–55.

(59) Wu, G.; Wasylishen, R. E. *Inorg. Chem.* **1992**, *31* (1), 145–148. doi:10.1021/ic00027a030.
(60) Wu, G.; Wasylishen, R. E. *Organometallics* **1992**, *11* (10), 3242–3248. doi:10.1021/om00046a021.
(61) Lee, Y. K.; Kurur, N. D.; Helmle, M.; Johannessen, O. G.; Nielsen, N. C.; Levitt, M. H. *Chem. Phys. Lett.* **1995**, *242* (3), 304–309. doi:10.1016/0009-2614(95)00741-L.
(62) Hohwy, M.; Jakobsen, H. J.; Edén, M.; Levitt, M. H.; Nielsen, N. C. *J. Chem. Phys.* **1998**, *108* (7), 2686. doi:10.1063/1.475661.
(63) Buckingham, A. D.; Love, I. *J. Magn. Reson.* **1970**, *2*, 338. doi:10.1016/0022-2364(70)90104-6.
(64) Collins, M. J.; Ripmeester, J. A.; Sawyer, J. F. *J. Am. Chem. Soc.* **1987**, *109* (13), 4113–4115. doi:10.1021/ja00247a047.
(65) Krause, E. *Ber.* **1918**, *51*, 912.
(66) Krause, E.; Becker, R. *Ber.* **1920**, *53B*, 173.
(67) Lippmaa, E. T.; Alla, M. A.; Pehk, T. J.; Engelhardt, G. *J. Am. Chem. Soc.* **1978**, *100* (6), 1929–1931. doi:10.1021/ja00474a051.
(68) Harris, R. K.; Sebald, A. *Magn. Reson. Chem.* **1987**, *25* (12), 1058–1062. doi:10.1002/mrc.1260251208.
(69) Graf, R.; Demco, D. E.; Hafner, S.; Spiess, H. W. *Solid State Nucl. Magn. Reson.* **1998**, *12* (2-3), 139–152. doi:10.1016/S0926-2040(98)00058-7. PMID:9809786.
(70) Marin-Montesinos, I.; Brouwer, D. H.; Antonioli, G.; Lai, W. C.; Brinkmann, A.; Levitt, M. H. *J. Magn. Reson.* **2005**, *177* (2), 307–317. doi:10.1016/j.jmr.2005.07.020. PMID:16169757.
(71) Laboratory for Biomolecular NMR Spectroscopy. Angular distribution set. University of Aarhus, Aarhus DK. Available from http://bionmr.chem.au.dk/download/simpson/crystal_files (accessed 12 August 2009)
(72) Zaremba, S. K. *Ann. Mat. Pura. Appl.* **1966**, *73* (1), 293–317. doi:10.1007/BF02415091.
(73) Conroy, H. *J. Chem. Phys.* **1967**, *47* (12), 5307. doi:10.1063/1.1701795.
(74) Cheng, V. B.; Suzukawa, H. H., Jr.; Wolfsberg, M. *J. Chem. Phys.* **1973**, *59* (8), 3992. doi:10.1063/1.1680590.

Jones and magnetoelectric birefringence of pure substances — A computational study

Antonio Rizzo, Dmitry Shcherbin, and Kenneth Ruud

Abstract: We present the first investigation of condensed-phase effects on the Jones (and magnetoelectric) birefringence of a set of nondipolar (CCl_4 and CS_2) and dipolar (nitro- and chloro-benzene) molecules using a recent implementation of the polarizable continuum model for cubic response functions at the time-dependent density-functional level of theory. The condensed-phase calculations have been performed on the neat liquids of the sample molecules using a nonequilibrium solvation scheme to properly account for the solute–solvent interactions in the presence of a frequency-dependent electromagnetic field. It is demonstrated that the condensed-phase effects as modelled by the polarizable continuum model can be substantial, increasing the observable birefringence by more than sixty percent in the case of CCl_4, and by a factor of more than three for CS_2. Solvent effects are also substantial for the dipolar molecules, leading to an enhancement by a factor of roughly five for nitrobenzene and by a bit less than 30% for chlorobenzene. Comparison is made with the results of experiment. Our calculated anisotropies confirm that the effect is below current experimental detection limits for CCl_4 and CS_2. We compute Jones constants of the same order of magnitude as the upper limits given in experiment for nitro- and chlorobenzene.

Key words: birefringences, non linear optical properties, computational chemistry, density functional theory, polarizable continuum method.

Résumé : Faisant appel à une récente implantation du modèle du continuum polarisable des fonctions cubiques de réponse au niveau dépendant du temps de la théorie de la fonctionnelle de densité, on a réalisé la première étude des effets d'une phase condensée sur la biréfringence de Jones (et magnétoélectrique) d'un ensemble de molécules dipolaires (nitro- et chlorobenzène) et d'autres qui ne le sont pas (CCl_4 et CS_2). Les calculs de phase condensée ont été effectués sur des liquides purs des molécules échantillonnées en utilisant un schéma de solvatation qui n'est pas en équilibre pour bien tenir compte des interactions soluté–solvant en présence d'un champ électromagnétique dépendant de la fréquence. On a démontré que les effets de phase condensée, tels que représentés par le modèle du continuum polarisable, peuvent être substantiels et augmenter la biréfringence observable par plus de soixante pour-cent dans le cas du tétrachlorure de carbone et par un facteur supérieur à trois pour le disulfure de carbone. Les effets de solvant sont aussi substantiels pour les molécules dipolaires; ils conduisent à des augmentations qui correspondent à un facteur pratiquement égal à cinq dans le cas du nitrobenzène et d'un peu moins de 30 % pour le chlorobenzène. Une comparaison est faite avec les résultats expérimentaux. Les anisotropies calculées confirment que, pour le CCl_4 et le CS_2 l'effet est inférieur aux limites actuelles de détection expérimentale. On a aussi calculé les constantes de Jones du même ordre de grandeur que les limites supérieures expérimentales pour le nitro- et le chlorobenzène.

Mots-clés : biréfringence, propriétés optiques non linéaires, chimie théorique, théorie de la fonctionnelle de densité, méthode du continuum polarisable.

[Traduit par la Rédaction]

Introduction

Jones linear birefringence (JB) is the anisotropy of the refractive index observed when linearly polarized monochromatic light interacts with matter in the presence of external uniform electric and magnetic induction fields applied parallel to each other and perpendicular to the direction of propagation of the light beam.

The theory of the effect, predicted by Jones as early as 1948,[1] was laid down by Graham and Raab;[2] see also ref. 3. The birefringence is bilinear in the electric and magnetic induction field strengths, relating the observable to relevant

Received 6 January 2009. Accepted 24 March 2009. Published on the NRC Research Press Web site at canjchem.nrc.ca on 16 September 2009.

This article is part of a Special Issue dedicated to Professor T. Ziegler. It is a great pleasure for us to dedicate this work to one of the masters in understanding the origins of electric and magnetic responses of molecules, Prof. Tom Ziegler, on the occasion of his 65th birthday.

A. Rizzo.[1] Istituto per i Processi Chimico-Fisici del Consiglio Nazionale delle Ricerche (IPCF-CNR), Area della Ricerca, via G. Moruzzi 1, I-56124 Pisa, Italy.
D. Shcherbin and K. Ruud. Centre for Theoretical and Computational Chemistry, Department of Chemistry, University of Tromsø, N-9037 Tromsø, Norway.

[1]Corresponding author (e-mail: rizzo@ipcf.cnr.it).

molecular optical property tensors. It is characterized by a pair of axes bisecting those of the two traditional birefringences, the Kerr[4,5] and Cotton–Mouton[6,7] birefringences. Rikken and co-workers have been able to detect and measure JB in liquids.[8–10] These studies have been extended also to the analysis of the so-called "Magneto-electric birefringence" (MEB),[11,12] a different (from the experimental point of view) type of birefringence also bilinear in the strength of the electric and magnetic induction field strengths and which appears when the three directions (propagation, electric field, and magnetic induction field) are mutually orthogonal.[13] The optical axes of MEB are the same as for Kerr and Cotton–Mouton. The molecular expression for the corresponding anisotropy in fluids turns out to be identical to that for the JB,[14] and from now on we will only refer to the latter, with the understanding that the results presented below will apply to both experiments, JB and MEB.

Linear birefringences such as Jones and magnetoelectric birefringence are in principle powerful tools for polarization–optical studies which can have applications in the field of crystals, of biology, and of polymer science. Experimental interest stems also from the challenges that the measurement of tiny ellipticities poses, and which in recent years have led to the development of ever more sophisticated optics and detection hardware. These measurements are moreover often performed to calibrate optical apparatus designed for the detection of such elusive and fundamental properties as vacuum polarization. Indeed quantum electrodynamics predicts that vacuum should exhibit yet undetected Cotton–Mouton, Kerr, Jones, and magnetoelectric birefringences.[15,16] Magnetoelectric Jones dichroism has also been discussed.[17–19]

Rizzo and Coriani have identified the relevant response functions entering the expression for the birefringence.[20] The authors determined ab initio estimates of the observable, the anisotropy of the refractive index for the light polarized at +45 and –45 degrees with respect to the direction of polarization of the light in JB, in some atomic systems (He, Ne, Ar, Kr) and in a few linear molecules (H_2, N_2, C_2H_2, and CO). These estimates were obtained using the techniques provided by modern response theory, in particular the coupled cluster singles and doubles (CCSD) model.[21–23] The study involved the determination of mixed electric dipole – magnetic dipole – electric quadrupole linear, quadratic, and cubic response functions,[24–32] and it was later extended to benzene[33] and hexafluorobenzene,[34] where the relevant quantities were obtained using Density Functional Theory (DFT) approaches.[35,36] For a discussion of the subject, see also refs. 37 and 38, whereas issues arising when studying birefringences in condensed phase are analyzed in ref. 39.

In this paper we extend the study of Jones birefringence to include the effects of the condensed phase to estimate the optical anisotropy induced by mixed static electric and magnetic fields in some of the pure liquids which were the subject of the experimental study of Roth and Rikken in ref. 9. In particular, we focus on two non-dipolar (CCl_4 and CS_2) and two dipolar (nitro- and chlorobenzene) molecules. The effect of the environment is included via a polarizable continuum model (PCM)[40,41] in its integral equation formulation (IEF–PCM),[41–44] taking advantage of recent developments of linear,[45] quadratic[46], and cubic[47,48] frequency-dependent PCM response theory at the time-dependent DFT level of theory. A nonequilibrium solvation scheme is adopted, as this allows us to properly take into account the solute–solvent interactions in the presence of a frequency-dependent electromagnetic field.

Experiments were performed on a series of eleven samples, including molecular liquids and solutions of varying structural complexity, and it involved the measurements of Jones birefringence together with the Cotton–Mouton and Kerr effects.[9] Of the eleven molecules analyzed experimentally, it was only possible to measure the absolute values of Jones birefringence for three of the samples, and these three species were all metal complexes containing manganese, iron, or titanium, which have low-lying strong charge-transfer transitions of approximately octupolar symmetry and which also possess a permanent electric dipole moment. Although it is clearly of interest to explore the Jones birefringence of these metal complexes, the challenges faced in providing accurate DFT results for charge-transfer states of transition metal complexes would make it difficult to assess the quality of the calculated results. For this reason we here focus instead on somewhat simpler molecular liquids, for which experiment could only establish upper limits for the birefringence.[9,10]

In the following, we will briefly define the important quantities determining the JB, connecting these molecular quantities to the experimental observables, and outline the computational approach utilized in this work. A section will be devoted to the details on the calculations performed here. The results obtained for pure liquid CCl_4, CS_2, and chloro- and nitrobenzene are then presented and discussed. We end the paper by a brief summary of our most important findings.

Theory

Graham and Raab[2] obtained the following general expression for the anisotropy of the refractive index, indicated as $n_{-45^\circ} - n_{+45^\circ}$, in Jones birefringence

$$[1]\qquad n_{-45^\circ} - n_{+45^\circ} = \frac{NE_xB_x}{30\varepsilon_0 c_0} \times\left\{ \mathcal{G}^{(3)}_{para} + \mathcal{G}^{(3)}_{dia} + \mathcal{A}'^{,(3)} + \frac{1}{kT}[\mathcal{G}^{(2)}_{para} + \mathcal{G}^{(2)}_{dia} + \mathcal{A}'^{,(2)}]\right\}$$

where, using the Einstein summation convention for repeated Greek indices,

$$[2]\qquad \mathcal{G}^{(3)}_{para} = 3G^{para}_{\alpha\beta\alpha\beta} + 3G^{para}_{\alpha\beta\beta\alpha} - 2G^{para}_{\alpha\alpha\beta\beta}$$

$$[3]\qquad \mathcal{G}^{(3)}_{dia} = 3G^{dia}_{\alpha\beta\alpha\beta} + 3G^{dia}_{\alpha\beta\beta\alpha} - 2G^{dia}_{\alpha\alpha\beta\beta}$$

$$[4]\qquad \mathcal{A}'^{,(3)} = -\frac{\omega}{2}\varepsilon_{\alpha\beta\gamma}(a'_{\alpha\beta\delta\delta\gamma} + a'_{\alpha\beta\delta\gamma\delta})$$

$$[5]\qquad \mathcal{G}^{(2)}_{para} = \mu_\alpha(3G^{para}_{\alpha\beta\beta} + 3G^{para}_{\beta\alpha\beta} - 2G^{para}_{\beta\beta\alpha})$$

$$[6]\qquad \mathcal{G}^{(2)}_{dia} = \mu_\alpha(3G^{dia}_{\alpha\beta\beta} + 3G^{dia}_{\beta\alpha\beta} - 2G^{dia}_{\beta\beta\alpha})$$

$$[7]\qquad \mathcal{A}'^{,(2)} = -\frac{\omega}{2}\varepsilon_{\alpha\beta\gamma}(\mu_\gamma a'_{\alpha\beta\delta\delta} + \mu_\delta a'_{\alpha\beta\delta\gamma})$$

In the equations above, N is the number density, ε_0 is the electric constant, c_0 is the speed of light in vacuo, k is Boltz-

mann's constant, T is the temperature, and ω is the circular frequency of the radiation. E_x and B_x represent the x components of the electric E and magnetic B fields, respectively, and μ_α is the α component of the permanent electric dipole moment. We have thus assumed that the radiation propagates along the z axis, whereas the fields are applied along the x axis. In eqs. [4] and [7], $\varepsilon_{\alpha\beta\gamma}$ represents the Levi-Civita alternating tensor.

The remaining tensors in eqs. [2]–[7] were identified in terms of frequency-dependent response functions in ref. 20 as

$$[8]\quad a'_{\alpha\beta\gamma\delta}(-\omega;\omega,0) = a'_{\alpha\gamma\beta\delta}(-\omega;\omega,0) = -\Im\langle\langle\mu_\alpha;q_{\beta\gamma},m_\delta\rangle\rangle_{\omega,0} = i\langle\langle\mu_\alpha;q_{\beta\gamma},m_\delta\rangle\rangle_{\omega,0}$$

$$[9]\quad a'_{\alpha\beta\gamma\delta\varepsilon}(-\omega;\omega,0,0) = a'_{\alpha\gamma\beta\delta\varepsilon}(-\omega;\omega,0,0) = \Im\langle\langle\mu_\alpha;q_{\beta\gamma},m_\delta,\mu_\varepsilon\rangle\rangle_{\omega,0,0} = -i\langle\langle\mu_\alpha;q_{\beta\gamma},m_\delta,\mu_\varepsilon\rangle\rangle_{\omega,0,0}$$

$$[10]\quad G^{para}_{\alpha\beta\gamma}(-\omega;\omega,0) = \Re\langle\langle\mu_\alpha;m_\beta,m_\gamma\rangle\rangle_{\omega,0} = \langle\langle\mu_\alpha;m_\beta,m_\gamma\rangle\rangle_{\omega,0}$$

$$[11]\quad G^{para}_{\alpha\beta\gamma\delta}(-\omega;\omega,0,0) = -\Re\langle\langle\mu_\alpha;m_\beta,m_\gamma,\mu_\delta\rangle\rangle_{\omega,0,0} = -\langle\langle\mu_\alpha;m_\beta,m_\gamma,\mu_\delta\rangle\rangle_{\omega,0,0}$$

$$[12]\quad G^{dia}_{\alpha\beta\gamma}(-\omega;\omega) = -\Re\langle\langle\mu_\alpha;\xi^{dia}_{\beta\gamma}\rangle\rangle_\omega = -\langle\langle\mu_\alpha;\xi^{dia}_{\beta\gamma}\rangle\rangle_\omega$$

$$[13]\quad G^{dia}_{\alpha\beta\gamma\delta}(-\omega;\omega,0) = \Re\langle\langle\mu_\alpha;\xi^{dia}_{\beta\gamma},\mu_\delta\rangle\rangle_{\omega,0} = \langle\langle\mu_\alpha;\xi^{dia}_{\beta\gamma},\mu_\delta\rangle\rangle_{\omega,0}$$

The last equalities hold for real electronic wave functions. The operators involved in the definitions of the response functions are the electric dipole (μ), magnetic dipole (m), traced electric quadrupole (q), and diamagnetic susceptibility (ξ^{dia}) operators

$$[14]\quad \mu_\alpha = -\sum_i r_{ia}$$

$$[15]\quad m_\alpha = -\frac{1}{2}\sum_i (r_i \times p_i)_\alpha = -\frac{1}{2}\sum_i \varepsilon_{\alpha\beta\gamma} r_{i\beta} p_{i\gamma} = -\frac{1}{2}\sum_i l_{i\alpha}$$

$$[16]\quad q_{\alpha\beta} = -\sum_i r_{i\alpha} r_{i\beta}$$

$$[17]\quad \xi^{dia}_{\beta\gamma} = \frac{1}{4}\sum_i (r_{i\beta} r_{i\gamma} - r_{i\delta} r_{i\delta}\delta_{\beta\gamma})$$

where the sum runs only over the electrons and the standard notation for cartesian components of the position ($r_{i\alpha}$), angular momentum ($l_{i\alpha}$), and linear momentum ($p_{i\alpha}$) operators of electron i is used. The traced form of the electric quadrupole moment operator was adopted, following the derivation of Graham and Raab.[2] Gauge invariance of the observable anisotropy of the refractive index, eq. [1], was proven in ref. 20.

We will report the birefringence per unit density (ρ), unit electric and unit magnetic fields, $[\Delta n]$, given as

$$[18]\quad [\Delta n] = \frac{n_{-45^\circ} - n_{+45^\circ}}{\rho E_x B_x} = \frac{N_a}{30\varepsilon_0 c_0 M}\times\left\{J_0 + \frac{J_T}{T}\right\} = [\Delta n^{(0)}] + \frac{[\Delta n^{(T)}]}{T}$$

where N_a is Avogadro's number and M is the molar mass. If the latter is given in g mol^{-1}, and the quantity in graph parentheses is computed in atomic units, $[\Delta n]$ is obtained in units of cm^4 g^{-1} V^{-1} T^{-1}, using the following expression

$$[19]\quad [\Delta n] \approx 2.25681\times 10^{-19}\times\frac{1}{M[\mathrm{g\ mol^{-1}}]}\times\left\{J_0 + \frac{J_T}{T}\right\}[\mathrm{au}]$$

The quantities J_0 and J_T are easily identified as, see above,

$$[20]\quad J_0 = \mathcal{G}^{(3)}_{para} + \mathcal{G}^{(3)}_{dia} + \mathcal{A}'^{,(3)}$$

$$[21]\quad J_T = \frac{1}{k}[\mathcal{G}^{(2)}_{para} + \mathcal{G}^{(2)}_{dia} + \mathcal{A}'^{,(2)}]$$

Note that in the case of a gas with molar volume V_m, eq. [18] can be employed upon substitution of ρ with $\frac{M}{V_m}$. In the case of a perfect gas at pressure P, $\rho = \frac{MP}{N_a kT}$. Below we will refer to $[\Delta n]$ as the "specific" birefringence.

In experiment, the measurements are analyzed using a definition of the Jones birefringence that involves a Jones constant K_J,[9] defined through the relationship

$$[22]\quad \Delta n = n_{-45^\circ} - n_{+45^\circ} = k_J \lambda \boldsymbol{E}\cdot\boldsymbol{B}$$

and involving explicitly the wavelength of the radiation, λ. It is easy to show that

$$[23]\quad k_J = \frac{N_a\rho}{30\varepsilon_0 c_0 M\lambda}\times\left\{J_0 + \frac{J_T}{T}\right\} \approx 2.25681\times 10^{-12}\times\frac{\rho[\mathrm{g\ cm^{-3}}]}{\lambda[\mathrm{nm}]\times M[\mathrm{g\ mol^{-1}}]}\times\left\{J_0 + \frac{J_T}{T}\right\}[\mathrm{au}]$$

with the resulting value of the Jones constant being given in units of V^{-1} T^{-1} when the density, molar mass, and wavelength are given in the SI units specified above in square parentheses, whereas again the quantity in graph parentheses is computed in atomic units.

In the polarizable continuum model, pioneered by Tomasi and co-workers,[40,41] and exploited here in the particular formulation given by the integral-equation formalism (IEF),[43,49,50] the solvent is described as a homogeneous, polarizable dielectric medium characterized by a set of di-

Fig. 1. A sketch of the geometry arrangement for the four molecule studied here.

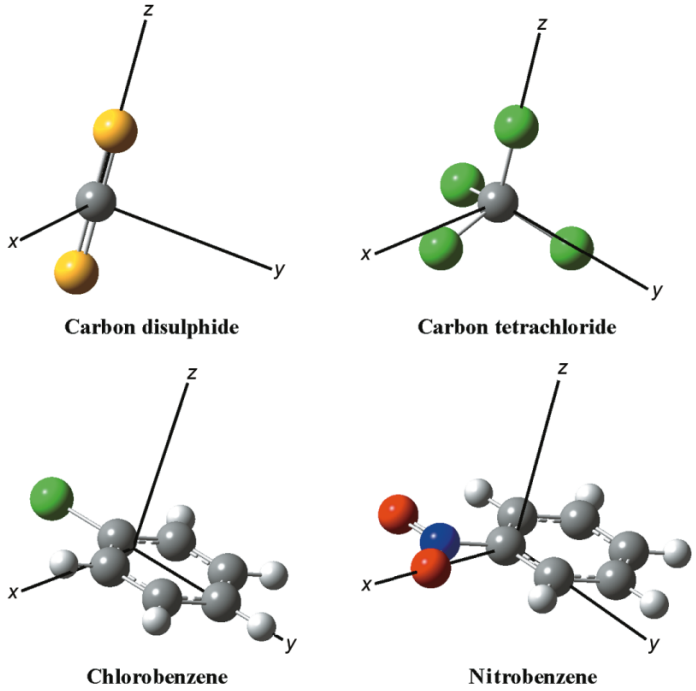

electric constants, normally restricted to a static and an optical dielectric constant, whereas the solvated molecule is placed in a cavity within the dielectric medium. The cavity can be given any arbitrary shape, and it is built from a set of interlocking spheres. As also done in this work, it is customary to center the spheres on the heavy atoms of the solvated molecules, with radii determined by the functional nature of the heavy atom and optimized against experimental solvation energies. A nonequilibrium solvation scheme is adopted, to properly account for the solute–solvent interactions in the presence of a frequency-dependent electromagnetic field.

We have developed a second-quantization formalism for the PCM[44] at the Hartree–Fock and multiconfigurational level of theory, later extended to DFT.[51] In the present work we will utilize the DFT formulation of the PCM model in combination with linear, quadratic, and cubic response functions. Indeed, building on the original implementation of linear,[24,52] quadratic,[25,35] and cubic[26,36] response theory at the Hartree–Fock, multiconfigurational Hartree–Fock and DFT levels of theory, in recent years we have been extending the PCM to the linear,[45] quadratic,[46,53,54] and recently also cubic[48] response theory levels. In the latter case, work is in progress to extend the formalism from the Hartree–Fock / density functional level of theory also to multiconfigurational self-consistent field wave functions.[55] Indeed, the present study is only the second analytic study of fourth-order, frequency-dependent molecular properties using PCM, though we note that PCM studies of fourth-order molecular properties have been carried out using mixed analytic and numerical methods.[56,57] Since the present work is an application of the method development mentioned above, we do not give further details on the implementation of the response function within the PCM framework, referring the interested reader instead to the original references.

Computational details

Calculations have been carried out for CCl_4, CS_2, chlorobenzene (C_5H_5Cl) and nitrobenzene ($C_5H_5NO_2$), four of the systems analyzed experimentally by Roth and Rikken.[9] A sketch of the geometry arrangement for the four systems in our calculations is given in Fig. 1. For each of these systems we have performed three sets of calculations of the property:

(1) in the one labelled below as "gas", the molecules are treated as being in the gas phase, and no solvent model is included;
(2) in the one labelled as "pcm", both the geometry optimization and the calculation of the properties are made with the introduction of the IEF polarizable continuum model;
(3) in the one labelled "pcm/gas", the geometry optimization is carried out on the isolated molecule, and the PCM is employed only for the calculation of the properties.

This sequence of calculations allows us to assess the extent to which the condensed phase affects the observable both through the change of geometry and through the change in the electromagnetic response.

All geometries were optimized at the DFT level of theory, using the 3-parameter exchange functional of Becke[58] in combination with the Lee–Yang–Parr correlation functional,[59] commonly referred to as the B3LYP functional.[60] For the geometry optimizations, both in gas phase and in the liquids, we have used Dunning's correlation-consistent basis set of triple-zeta quality (cc-pVTZ).[61] The cavities surrounding the solvated molecules have been created by adding spheres around all the heavy atoms in the molecules. These radii have been determined according to the United Atom Topological Model.[62] The parameters employed in the PCM calculations are given in Table 1.

Table 1. The parameters of the PCM calculations, cavity radii (R_{cav}, Å) and permittivities (ε and ε_∞).

Molecule	ε	ε_∞	Atom	R_{cav}
CCl_4	2.129	2.228	C	1.7
			Cl	1.81
CS_2	2.632	2.663	C	1.7
			S	1.85
$C_6H_5NO_2$	35.6	2.418	C	1.9
			N	1.6
			O	1.5
C_6H_5Cl	5.59	2.418	C (H)[a]	1.9
			C (Cl)[a]	1.7
			Cl	1.8

[a]In parenthesis the atom to which carbon is bound.

For a higher-order molecular property such as Jones birefringence, the choice of basis set is important to obtain reliable results. In many of our earlier studies of nonlinear birefringences, the strength of the augmented correlation-consistent basis sets[63] have been demonstrated. A detailed investigation of the basis set convergence of the different contributions to the Jones birefringence is beyond the scope of the present work, and will be presented in a forthcoming publication in which we will also consider the effects of using London orbitals on the basis set convergence of the property.[64] However, the dependence of the different cubic response function contributions to the temperature-independent contribution of the Jones birefringence is illustrated for CCl_4 in the gas phase in Table 2. From the data in Table 2, the importance of diffuse functions can be easily appreciated. The data also indicates that the daug-cc-pVTZ basis set[63] represents a good compromise between accuracy and computational feasibility, and this basis set has thus been used for all the subsequent data presented in this paper. The wavelength λ = 632.8 nm, as used in experiment, was selected. The calculations were carried out using a parallel version[48,65,66] of the Dalton 2.0 program.[67]

Results and discussion

In Table 3 we have collected the results obtained for the isolated molecules and for the neat liquids of the four molecules investigated here. In addition to presenting the results for the isolated molecules at their optimized geometries in the gas phase, and the corresponding values obtained for the liquid phase optimized geometries using PCM, we also report the results obtained when the gas-phase optimized structures were used in PCM property calculations. Comparison of the change in the calculated properties when going from the gas to the liquid phase, keeping the geometry fixed, gives us an indication of the importance of the direct solvation effects as described by the PCM, whereas the changes induced going from the properties calculated in the liquid phase at the gas-phase optimized structure to the liquid-phase optimized structure, gives us a feeling for the indirect condensed phase effects due to the relaxation of the molecular geometry occurring in the presence of the surrounding molecules. When presenting data for the specific birefringence $[\Delta n]$ or for the Jones constant k_J, a temperature of 294.15 K, the room temperature at which the experiment was performed, is assumed.

Table 2. The molecular hyperpolarizabily contributions to the observable Jones birefringence in CCl_4 in the gas phase (in 10^{-4} atomic units). λ = 632.8 nm.

Basis set	$\mathcal{G}^{(3)}$	$\mathcal{A}'^{,(3)}$	J_0
aug-cc-pVDZ	–0.05396	–0.02129	–0.07525
aug-cc-pVTZ	0.49060	–0.02718	0.46342
aug-cc-pVQZ	0.97413	–0.03452	0.93961
daug-cc-pVDZ	0.61868	–0.03613	0.58255
daug-cc-pVTZ	1.16912	–0.04742	1.12170
daug-cc-pVQZ	1.22630	–0.05036	1.17594

Note:
$$\mathcal{G}^{(3)}_{para} = 3G^{para}_{\alpha\beta\alpha\beta} + 3G^{para}_{\alpha\beta\beta\alpha} - 2G^{para}_{\alpha\alpha\beta\beta}$$
$$\mathcal{G}^{(3)}_{dia} = 3G^{dia}_{\alpha\beta\alpha\beta} + 3G^{dia}_{\alpha\beta\beta\alpha} - 2G^{dia}_{\alpha\alpha\beta\beta}$$
$$\mathcal{G}^{(3)} = G^{(3)}_{para} + G^{(3)}_{dia}$$
$$\mathcal{A}'^{,(3)} = -\frac{\omega}{2}\varepsilon_{\alpha\beta\gamma}(a'_{\alpha\beta\delta\delta\gamma} + a'_{\alpha\beta\delta\gamma\delta})$$

The change from the gas phase to the pure liquid, as modelled by PCM, is remarkable, leading to a general increase in the magnitude of the birefringence, with a change ranging at room temperature from around 25% for chlorobenzene to a notable factor of about five, for nitrobenzene. The anisotropy increases by ≈60% for CCl_4, and by ≈250% for CS_2. We also note that the effect of the condensed phase is larger for the temperature-independent contribution, see J_0 or $[\Delta n^{(0)}]$ in Table 3, than for the temperature-dependent one, see J_T or $[\Delta n^{(T)}]$, for chlorobenzene, whereas the reverse happens for nitrobenzene. Note that $[\Delta n^{(0)}]$ and $[\Delta n^{(T)}]$ are referred to as temperature-independent and temperature-dependent contributions, respectively, due to the explicit dependence on the temperature of the right-hand side term in eq. [18]. This separation into a temperature-independent and a temperature-dependent contribution is rigorous only for ideal gases at constant pressure. In the case of solutions, the dependence on T is implicit in both $[\Delta n^{(0)}]$ and $[\Delta n^{(T)}]$ through the temperature dependence of the density ρ.

Almost all of the notable influence of the condensed phase on the property is due to the effect on the linear and nonlinear response properties, in particular for the two non-dipolar molecular liquids. For the latter, the modifications induced on the geometry of the molecule yield negligible changes in the property: the difference between the "pcm/gas" and "pcm" results is less than 0.1% for CCl_4 and CS_2. For chlorobenzene, the same difference is about 3.2%. In nitrobenzene, the pcm/gas results for the specific birefringence are approximately 7.5% larger than those obtained in the pcm approximation. In the case of polar molecules, the solvent-induced geometry changes are therefore of some relevance, although still somewhat limited, when compared to the changes induced directly by the solvent on the molecular properties. The influence of the introduction of a condensed phase model in the geometry optimization is in general larger on the temperature-dependent than on the temperature-independent contribution, with J_0 in chlorobenzene being remarkably insensitive to the change of geometry. Due to the general predominance of the T-dependent contribution (J_T) over the T-independent one (J_0) on the observable $[\Delta n]$, the dependence of the latter on both direct (through changes in the molecular properties) and indirect

Table 3. Jones birefringence of pure liquids. Definitions in the text. λ = 632.8 nm. For the last three columns the temperature is T = 294.15 K.

Molecule	M (g mol^{-1})	ρ (g cm^{-3})[a]	Calculation	$J_0 \times 10^{-3}$ ($e^4 a_0^8 m_e \hbar^{-4}$)	$J_T \times 10^{-6}$ ($e^4 a_0^8 m_e \hbar^{-4} K$)	$[\Delta n^{(0)}] \times 10^{18}$ (cm^4 g^{-1} V^{-1} T^{-1})	$[\Delta n^{(T)}] \times 10^{13}$ (cm^4 K g^{-1} V^{-1} T^{-1})	$[\Delta n] \times 10^{18}$ (cm^4 g^{-1} V^{-1} T^{-1})	$k_J \times 10^{12}$ (V^{-1} T^{-1})	k_J(exp) $\times 10^{12}$ (V^{-1} T^{-1})[b]
CCl_4	153.82	1.594	gas	11.2170		16.46		16.46		<3
			pcm	18.4443		27.06		27.06	0.38	
			pcm/gas	18.4332		27.04		27.04	0.68	
CS_2	76.14	1.266	gas	2.4218		7.18		7.18		<2
			pcm	8.5910		25.46		25.46	0.51	
			pcm/gas	8.5918		25.47		25.47	0.51	
$C_6H_5NO_2$	123.11	1.196	gas	10.3059	12.7904	18.89	0.23	98.60		
			pcm	49.7811	71.5742	91.26	1.31	537.31	10.16	<3
			pcm/gas	48.2210	78.4964	88.40	1.44	577.59	10.92	
C_6H_5Cl	112.56	1.106	gas	9.0841	–24.4360	18.21	–0.49	–148.35		<2
			pcm	24.7276	–34.3668	49.58	–0.69	–184.67	–3.23	
			pcm/gas	24.7548	–33.5169	49.63	–0.67	–178.83	–3.13	

[a]Source: http://www.sigmaaldrich.com/sigma-aldrich/home.html.
[b]Reference 9.

(through changes in the molecular geometry) condensed-phase effects reflects roughly that observed for J_T.

It is interesting to go into a somewhat more detailed analysis of the effect of the PCM in the study of JB. In particular, the extent to which changes induced on the different response functions provide some insight into the mechanisms that govern the remarkable effect of the solvent, as modeled by the dielectric continuum model. In Table 4, the $\mathcal{G}^{(3)}_{para}$, $\mathcal{G}^{(3)}_{dia}$, $\mathcal{A}'^{,(3)}$, $\mathcal{G}^{(2)}_{para}$, $\mathcal{G}^{(2)}_{dia}$, and $\mathcal{A}'^{,(2)}$ contributions, defined in eqs. [2]–[7], are given for the different calculations carried out in the present study.

The condensed-phase effect on the temperature-independent contributions is larger for the mixed electric field – magnetic field hyperpolarizabilities, $\mathcal{G}^{(3)} = \mathcal{G}^{(3)}_{para} + \mathcal{G}^{(3)}_{dia}$, than for the one originating from the interaction of electric dipole, electric quadrupole , and magnetic dipole, $\mathcal{A}'^{,(3)}$. For all contributions to J_0 (or $[\Delta n^{(0)}]$), the dielectric medium leads to a positive increase in the value of the individual mixed hyperpolarizabilities. The condensed-phase effects are substantial on both $\mathcal{G}^{(3)}$ and $\mathcal{A}'^{,(3)}$, the solvent shift being often larger than the gas phase value itself. However, since $\mathcal{A}'^{,(3)}$ is at most $\approx$17% (in the "gas" calculation on CS_2) and in general less than about 8% of the whole $\mathcal{G}^{(3)} + \mathcal{A}'^{,(3)}$ T-independent term, J_0 is dominated by $\mathcal{G}^{(3)}$ and the condensed-phase shift on J_0 is thus mainly determined by the shift of the $\mathcal{G}^{(3)}$ contribution. $\mathcal{G}^{(3)}_{para}$ and $\mathcal{G}^{(3)}_{dia}$ have opposite sign, and the percentage change between "pcm" and "gas" results is a factor of 2–3 larger for the former than for the latter. This percentage is magnified to some extent by the partial cancellation occurring when the two contribution are summed up.

For the two dipolar substituted benzenes, switching from gas to liquid phase induces an increase in J_0 by roughly a factor of two and four for Cl^- and NO_2^- benzene, respectively. This increase results from a combination of the changes in all quadratic and cubic response functions, being possibly slightly larger for $\mathcal{A}'^{,(3)}$ than for $\mathcal{G}^{(3)}_{para}$ or $\mathcal{G}^{(3)}_{dia}$, when the latter two contributions are considered separately. Once again, the partial cancellation occurring between $\mathcal{G}^{(3)}_{para}$ and $\mathcal{G}^{(3)}_{dia}$ when they are combined magnifies the effect for the overall $\mathcal{G}^{(3)}$ combination.

For chlorobenzene, the effect of the change of phase from gas to liquid on the temperature-dependent J_T term, is larger for the contribution involving the quadrupolar interaction, $\mathcal{A}'^{,(2)}$, than for the electric dipole – magnetic dipole contribution, $\mathcal{G}^{(2)}$, in contrast to the behavior noted above for J_0. The former increases roughly by 105%, the latter by about 45%, in absolute value, going from the gas to the liquid. The cancellation between "para" and "dia" contributions to $\mathcal{G}^{(2)}$ has therefore, relatively speaking, a contained effect. Since the electric dipole – magnetic dipole linear and quadratic response functions give the dominant (more than 90%) contribution to J_T through $\mathcal{G}^{(2)}$, the effect of moving from gas to liquid phase is essentially determined by the change in this contribution.

For nitrobenzene, we first note that a quite efficient cancellation between $\mathcal{G}^{(2)}_{para}$ and $\mathcal{G}^{(2)}_{dia}$ in the "gas" calculation yields a relatively small value of $\mathcal{G}^{(2)}$, a bit more than half

Table 4. Jones birefringence of pure liquids. The molecular polarizability and hyperpolarizabily contributions to the observable (au). λ = 632.8 nm.

		$\mathcal{G}^{(3)}_{para}$	$\mathcal{G}^{(3)}_{dia}$	$\mathcal{G}^{(3)}$	$A'^{,(3)}$	$\mathcal{G}^{(2)}_{para}$	$\mathcal{G}^{(2)}_{dia}$	$\mathcal{G}^{(2)}$	$A'^{,(2)}$
Molecule	Calcd.	$\times 10^{-4}$				$\times 10^{-2}$			
	gas	2.47657	–1.30745	1.16912	–0.04742				
CCl_4	pcm	3.47917	–1.56917	1.91000	–0.06557				
	pcm/gas	3.47773	–1.56889	1.90884	–0.06552				
	gas	1.60209	–1.31987	0.28222	–0.04005				
CS_2	pcm	2.68682	–1.75960	0.92722	–0.06811				
	pcm/gas	2.68648	–1.75925	0.92723	–0.06805				
	gas	2.68383	–1.59852	1.08531	–0.05472	–5.41908	5.57302	0.15394	0.25111
$C_6H_5NO_2$	pcm	7.72942	–2.59088	5.13854	–0.16043	–8.50952	10.20587	1.69635	0.57027
	pcm/gas	7.55874	–2.57664	4.98211	–0.16001	–8.01908	9.94891	1.92983	0.55601
	gas	2.74256	–1.75998	0.98258	–0.07417	–2.28224	1.44590	–0.83634	0.06250
C_6H_5Cl	pcm	5.11015	–2.48218	2.62797	–0.15521	–3.63348	2.41700	–1.21648	0.12815
	pcm/gas	5.10812	–2.47827	2.62985	–0.15437	–3.56908	2.38146	–1.18761	0.12619

Note:
$$\mathcal{G}^{(3)}_{para} = 3\mathcal{G}^{para}_{\alpha\beta\alpha\beta} + 3\mathcal{G}^{para}_{\alpha\beta\beta\alpha} - 2\mathcal{G}^{para}_{\alpha\alpha\beta\beta}$$
$$\mathcal{G}^{(3)}_{dia} = 3\mathcal{G}^{dia}_{\alpha\beta\alpha\beta} + 3\mathcal{G}^{dia}_{\alpha\beta\beta\alpha} - 2\mathcal{G}^{dia}_{\alpha\alpha\beta\beta}$$
$$\mathcal{G}^{(3)} = \mathcal{G}^{(3)}_{para} + \mathcal{G}^{(3)}_{dia}$$
$$\mathcal{A}'^{,(3)} = -\frac{\omega}{2}\varepsilon_{\alpha\beta\gamma}(a'_{\alpha\beta\delta\delta\gamma} + a'_{\alpha\beta\delta\gamma\delta})$$
$$\mathcal{G}^{(2)}_{para} = \mu_\alpha(3\mathcal{G}^{para}_{\alpha\beta\beta} + 3\mathcal{G}^{para}_{\beta\alpha\beta} - 2\mathcal{G}^{para}_{\beta\beta\alpha})$$
$$\mathcal{G}^{(2)}_{dia} = \mu_\alpha(3\mathcal{G}^{dia}_{\alpha\beta\beta} + 3\mathcal{G}^{dia}_{\beta\alpha\beta} - 2\mathcal{G}^{dia}_{\beta\beta\alpha})$$
$$\mathcal{G}^{(2)} = \mathcal{G}^{(2)}_{para} + \mathcal{G}^{(2)}_{dia}$$
$$\mathcal{A}'^{,(2)} = -\frac{\omega}{2}\varepsilon_{\alpha\beta\gamma}(\mu_\gamma a'_{\alpha\beta\delta\delta} + \mu_\delta a'_{\alpha\beta\delta\gamma})$$

the size of the corresponding $\mathcal{A}'^{,(2)}$ contribution, see Table 4. Nitrobenzene in the gas phase is therefore the only occurrence in this work of Jones birefringence where a major part is played by one of the two quadrupolar contributions, specifically by $\mathcal{A}'^{,(2)}$. Moving to the "pcm" calculation, we note that although the "para" and "dia" contributions to $\mathcal{G}^{(2)}$ increase (in absolute value) *only* by 60 to roughly 80%, their combination increases by as much as about 1000%. This more than compensates for a corresponding increase of $\approx$130% in $\mathcal{A}'^{,(2)}$, and therefore the whole T-dependent contribution J_T, and consequently the whole observable, show a remarkable increase in the specific anisotropy by more than one order of magnitude.

For the nonpolar molecules, CCl_4 and CS_2, only the temperature-independent contribution survives in eq. [18]. Our calculations for the Jones constant yield k_J values of 0.68×10^{-12} and 0.51×10^{-12} V^{-1} T^{-1}, for CCl_4 and CS_2, respectively. These ab initio estimates are well below the upper limits given by Roth and Rikken,[9] of 3×10^{-12} and 2×10^{-12} V^{-1} T^{-1}, respectively. The relative magnitude of the effect is predicted correctly, with the birefringence, still too weak to be seen by the apparatus used in ref. 9, being apparently slightly stronger for CCl_4 than for CS_2.

In the case of the two dipolar monosubstituted benzenes, we first note that the temperature-dependent contribution has the same sign with respect to its temperature-independent counterpart for nitrobenzene, the former being from four times (gas phase) to about six times (liquid phase) larger than the latter at room temperature. For chlorobenzene under the same conditions, J_T, which carries a negative sign, ranges from ten times (gas phase) to about five times (liquid phase) larger than J_0 (which is instead positive). At room temperature, $[\Delta n^{(0)}]$ therefore yields a substantial contribution to the Jones birefringence of the two substituted benzenes studied here, more for the nitro- than for the chloro-substituted benzene. This evidence for Jones (and magnetoelectric) birefringence is roughly in line with the behavior of more "traditional" linear birefringences such as the Kerr, Cotton–Mouton, or Buckingham[68–70] birefringences. On the other hand, for these birefringences, very often the dominating importance of the temperature-dependent contribution at room temperature, invariably associated with lower-order, often linear, response functions and being due to the reorientation of the molecular multipoles in the presence of the external perturbations, is indeed very notable.[37–39]

At 294.15 K, the predicted Jones constant is $k_J = 10.2 \times 10^{-12}$ and $k_J = -3.23 \times 10^{-12}$ V^{-1} T^{-1}, for nitro- and chlorobenzene, respectively. The ab initio estimates are therefore of the same order of magnitude as the upper limits given by Roth and Rikken,[9] again 3×10^{-12} and 2×10^{-12} V^{-1} T^{-1}, for the two systems, respectively. The relative order of magnitude is again reproduced. We also note that the sign of the birefringence of chlorobenzene is opposite to that predicted for the other three systems studied here. Our results allow us to predict that minor improvements in the efficiency of the detection system should permit the observation of an ellipticity induced by crossed electric and magnetic induction fields, in the classical experimental setup of Jones and magnetoelectric birefringences, for liquid chloro-, and even better, for liquid nitrobenzene.

Summary

We have presented the result of an ab initio Time Dependent Density Functional Theory (TD–DFT) study of Jones birefringence in the liquid phase for four systems (CCl_4, CS_2, and nitro- and chlorobenzene) which were part of the set of eleven substances analyzed in an experimental study by Roth and Rikken.[9] The calculations, performed using the B3LYP functional with correlation-consistent basis sets of d-aug-cc-pVTZ quality, exploit the recently developed linear, quadratic, and cubic formulations of analytical response theory within a nonequilibrium, IEF polarizable continuum model. The effects of the interactions appearing in the liquid phase on both the frequency-dependent mixed electric and magnetic linear and nonlinear responses and on the geometry have been analyzed.

The effect of the condensed phase on the birefringence is remarkable. The response changes dramatically for all four systems studied here, in all cases increasing, albeit to a different extent. At room temperature, the specific anisotropy [Δn] almost doubles for CCl_4, and it is more than three times larger for CS_2 because of the interactions occurring in the liquid, as mimicked by the polarizable continuum model. Nitrobenzene, where the change in phase yields an increase of the JB by a factor of about five, is the liquid exhibiting the strongest response, whereas in chlorobenzene the changes induced by the introduction of the PCM are limited to an increase of the birefringence by 25% at room temperature.

Almost the whole enhancement arises from the effect of the dielectric medium on the response functions, more so for the higher-order (quadratic and especially cubic) response functions, contributing to the so-called temperature-independent contribution to [Δn], than for the linear and quadratic response functions entering the temperature-dependent contribution. Nitrobenzene is an exception to this general trend, where a near cancellation between the "para" and "dia" contributions arising due to the electric dipole – magnetic dipole interactions in the T-dependent term is responsible for the remarkable enhancement of the birefringence observed in the liquid-phase calculations. The changes in the geometry induced by the solvent is essentially negligible for CCl_4 and CS_2, and it has a minor effect in the case of nitrobenzene and (to a lesser extent) chlorobenzene.

The temperature-dependent contribution to the observable is, where present and as usually observed in other classical linear birefringence, stronger than the temperature-independent contribution. We predict birefringences of decreasing intensities in the order nitrobenzene > chlorobenzene > CCl_4 > CS_2, with the Jones constants k_J ranging (in absolute value) from a maximum of 10.2×10^{-12} to a minimum of 0.51×10^{-12} V^{-1} T^{-1} in this sequence. The sign of the anisotropy is opposite (negative) in chlorobenzene with respect to the other three molecules. With a resolution limited to $\Delta n_J \approx 2 \times 10^{-12}$, in an applied magnetic field of 17 T and an applied electric field of 2.5×10^5 V m^{-1}, and with a path length of 25 mm, the upper limits coming from experiment are 3×10^{-12} for nitrobenzene and CCl_4 and 2×10^{-12} for chlorobenzene and CS_2.[9] In the case of CCl_4 and CS_2, our study confirms that the birefringence cannot be measured with the apparatus used by Roth and Rikken.[9] Theory, at our level of approximation, predicts that the JB of chloro- and (even more) nitrobenzene are at the edge of the current detection limits at room temperature, and they might be measured with minor improvements in the detection limits of the apparatus employed by the authors of ref. 9.

A discussion on the level of confidence of our results, taking all approximations into account, has been done in several other instances in the past. This study is carried out at roughly the same computational level as some recent studies on other linear birefringences, as for example the studies in the gas phase of benzene and hexafluorobenzene,[33,34] or, even more to the point, the study[71] of condensed phase effects on magnetochiral birefringence.[72–76] The reader should refer to those papers, or to refs. 37, 38, and 39, for an in-depth analysis.

Acknowledgment

This work has received support from the Norwegian Research Council through a Centre of Excellence Grant (Grant No. 179568/V30), a YFF grant to KR (Grant No. 162746/V00), and a grant of computer time from the Norwegian Supercomputing Program.

References

(1) Jones, R. C. *J. Opt. Soc. Am.* **1948**, *38* (8), 671. doi:10.1364/JOSA.38.000671.
(2) Graham, E. B.; Raab, R. E. *Proc. R. Soc. Lond. A Math. Phys. Sci.* **1983**, *390* (1798), 73–90. doi:10.1098/rspa.1983.0123.
(3) Ross, H. J.; Sherborne, B. S.; Stedman, G. E. *J. Phys. At. Mol. Opt. Phys.* **1989**, *22* (3), 459–473. doi:10.1088/0953-4075/22/3/011.
(4) Kerr, J. *Philos. Mag.* **1875**, *4* (50), 337.
(5) Kerr, J. *Philos. Mag.* **1875**, *4* (50), 416.
(6) Cotton, A.; Mouton, M. *C. R. Acad. Sci.* **1905**, *141*, 317.
(7) Cotton, A.; Mouton, M. *C. R. Acad. Sci.* **1905**, *141*, 349.
(8) Rikken, G. L. J. A.; Raupach, E.; Roth, T. *Physica B* **2001**, *294–295*, 1.
(9) Roth, T.; Rikken, G. L. J. A. *Phys. Rev. Lett.* **2000**, *85* (21), 4478–4481. doi:10.1103/PhysRevLett.85.4478. PMID:11082575.
(10) Roth, T. Experimental verification of the Jones birefringence induced in liquids. Diplomarbeit, Darmstadt University of Technology and Grenoble High Magnetic Field Laboratory, 2000.
(11) Pockels, F. *Radium* **1913**, *10* (5), 152–159. doi:10.1051/radium:01913001005015201.
(12) Baranova, N. B.; Bogdanov, Y. V.; Zel'dovich, B. Y. *Sov. Phys. Usp.* **1977**, *20* (10), 870–877. doi:10.1070/PU1977v020n10ABEH005470.
(13) Roth, T.; Rikken, G. L. J. A. *Phys. Rev. Lett.* **2002**, *88* (6),o. 063001. doi:10.1103/PhysRevLett.88.063001. PMID: 11863802.
(14) Graham, E. B.; Raab, R. E. *Mol. Phys.* **1984**, *52* (5), 1241–1249. doi:10.1080/00268978400101911.
(15) Rikken, G. L. J. A.; Rizzo, C. *Phys. Rev. A* **2001**, *63* (1),o. 012107. doi:10.1103/PhysRevA.63.012107.
(16) Rikken, G. L. J. A.; Rizzo, C. *Phys. Rev. A* **2003**, *67* (1),o. 015801. doi:10.1103/PhysRevA.67.015801.
(17) Andrews, D. L.; Daniels, G. J.; Stedman, G. E. *J. Phys. At. Mol. Opt. Phys.* **2003**, *36* (20), L357–L364. doi:10.1088/0953-4075/36/20/L02.

(18) Budker, D.; Stalnaker, J. E. *Phys. Rev. Lett.* **2003**, *91* (26), 263901. doi:10.1103/PhysRevLett.91.263901. PMID:14754051.
(19) Mironova, P. V.; Ovsiannikov, V. D.; Chernushkin, V. V. *J. Phys. At. Mol. Opt. Phys.* **2006**, *39* (23), 4999–5011. doi:10.1088/0953-4075/39/23/016.
(20) Rizzo, A.; Coriani, S. *J. Chem. Phys.* **2003**, *119* (21), 11064. doi:10.1063/1.1622927.
(21) Purvis, G. D.; Bartlett, R. J. *J. Chem. Phys.* **1982**, *76* (4), 1910. doi:10.1063/1.443164.
(22) Hättig, C.; Christiansen, O.; Koch, H.; Jørgensen, P. *Chem. Phys. Lett.* **1997**, *269* (5-6), 428–434. doi:10.1016/S0009-2614(97)00311-4.
(23) Hättig, C.; Christiansen, O.; Jørgensen, P. *Chem. Phys. Lett.* **1998**, *282* (2), 139–146. doi:10.1016/S0009-2614(97)01227-X.
(24) Olsen, J.; Jørgensen, P. *J. Chem. Phys.* **1985**, *82*, 3235. doi:10.1063/1.448223.
(25) Hettema, H.; Jensen, H. J. A.; Jørgensen, P.; Olsen, J. *J. Chem. Phys.* **1992**, *97*, 1174. doi:10.1063/1.463245.
(26) Jonsson, D.; Norman, P.; Ågren, H. *J. Chem. Phys.* **1996**, *105* (15), 6401. doi:10.1063/1.472493.
(27) Olsen, J.; Jørgensen, P. In *Modern Electronic Structure Theory;* Yarkony, D. R., Ed.;. World Scientific: Singapore, 1995; Vol. 2, pp. 857–990.
(28) Koch, H.; Jørgensen, P. *J. Chem. Phys.* **1990**, *93*, 3333. doi:10.1063/1.458814.
(29) Halkier, A.; Koch, H.; Christiansen, O.; Jørgensen, P.; Helgaker, T. *J. Chem. Phys.* **1997**, *107*, 849. doi:10.1063/1.474384.
(30) Christiansen, O.; Hättig, C.; Jørgensen, P. *Int. J. Quantum Chem.* **1998**, *68*, 1. doi:10.1002/(SICI)1097-461X(1998)68:1<1::AID-QUA1>3.0.CO;2-Z.
(31) Christiansen, O.; Koch, H.; Jørgensen, P. *Chem. Phys. Lett.* **1995**, *243* (5-6), 409–418. doi:10.1016/0009-2614(95)00841-Q.
(32) Christiansen, O.; Koch, H.; Jørgensen, P. *J. Chem. Phys.* **1995**, *103*, 7429. doi:10.1063/1.470315.
(33) (a) Rizzo, A.; Cappelli, C.; Jansík, B.; Jonsson, D.; Sałek, P.; Coriani, S.; Ågren, H. *J. Chem. Phys.* **2004**, *121* (18), 8814–8830. doi:10.1063/1.1802771. PMID:15527345.; (b) Rizzo, A.; Cappelli, C.; Jansík, B.; Jonsson, D.; Salek, P.; Coriani, S.; Ågren, H.; Wilson, D. J. D.; Helgaker, T.; Junquera–Hernández, J. M.; Sánchez de Merás, A. M. J.; Sánchez-Marín, J. *J. Chem. Phys.* **2008**, *129* (3),o. 039901. doi:10.1063/1.2946699.
(34) (a) Rizzo, A.; Cappelli, C.; Jansík, B.; Jonsson, D.; Sałek, P.; Coriani, S.; Wilson, D. J. D.; Helgaker, T. U.; Ågren, H. *J. Chem. Phys.* **2005**, *122* (23),o. 234314. doi:10.1063/1.1935513. PMID:16008448.; (b) Rizzo, A.; Cappelli, C.; Jansík, B.; Jonsson, D.; Salek, P.; Coriani, S.; Wilson, D. J. D.; Helgaker, T. U.; Ågren, H. *J. Chem. Phys.* **2008**, *129* (3),o. 039901. doi:10.1063/1.2946699.
(35) Salek, P.; Jonsson, D.; Vahtras, O.; Ågren, H. *J. Chem. Phys.* **2002**, *117*, 9630. doi:10.1063/1.1516805.
(36) Jansík, B.; Salek, P.; Jonsson, D.; Vahtras, O.; Ågren, H. *J. Chem. Phys.* **2005**, *122* (5),o. 054107. doi:10.1063/1.1811605.
(37) Rizzo, A.; Coriani, S. *Adv. Quantum Chem.* **2005**, *50*, 143–184. doi:10.1016/S0065-3276(05)50008-X.
(38) Christiansen, O.; Coriani, S.; Gauss, J.; Hättig, C.; Jørgensen, P.; Pawlowski, F.; Rizzo, A. In *Non-Linear Optical Properties of Matter: From Molecules to Condensed Phases*; Papadopoulos, M. G., Sadlej, A. J., and Leszczynski, J., Eds.;. Challenges and Advances in Computational Chemistry and Physics; Springer: Dordecht, The Netherlands, 2006; Vol. 1, . pp 51–99..
(39) Rizzo, A. In *Continuum solvation methods in Chemical Physics: Theory and Application*. Mennucci, B. and Cammi, R., Eds.;. Wiley: Chichester, England, 2007; pp 252–264.
(40) Miertus, S.; Scrocco, E.; Tomasi, J. *Chem. Phys.* **1981**, *55* (1), 117–129. doi:10.1016/0301-0104(81)85090-2.
(41) Tomasi, J.; Mennucci, B.; Cammi, R. *Chem. Rev.* **2005**, *105* (8), 2999–3094. doi:10.1021/cr9904009. PMID:16092826.
(42) Cammi, R.; Tomasi, J. *J. Comput. Chem.* **1995**, *16* (12), 1449–1458. doi:10.1002/jcc.540161202.
(43) Cancès, E.; Mennucci, B. *J. Math. Chem.* **1998**, *23* (3/4), 309–326. doi:10.1023/A:1019133611148.
(44) Cammi, R.; Frediani, L.; Mennucci, B.; Tomasi, J.; Ruud, K.; Mikkelsen, K. V. *J. Chem. Phys.* **2002**, *117* (1), 13. doi:10.1063/1.1480871.
(45) Cammi, R.; Frediani, L.; Mennucci, B.; Ruud, K. *J. Chem. Phys.* **2003**, *119* (12), 5818. doi:10.1063/1.1603728.
(46) Frediani, L.; Ågren, H.; Ferrighi, L.; Ruud, K. *J. Chem. Phys.* **2005**, *123* (14),o. 144117. doi:10.1063/1.2055180. PMID:16238384.
(47) Ferrighi, L.; Frediani, L.; Fossgaard, E.; Ruud, K. *J. Chem. Phys.* **2006**, *125* (15),o. 154112. doi:10.1063/1.2357925. PMID:17059244.
(48) Ferrighi, L.; Frediani, L.; Ruud, K. *J. Phys. Chem. B* **2007**, *111* (30), 8965–8973. doi:10.1021/jp0721191. PMID:17628096.
(49) Cancès, E.; Mennucci, B.; Tomasi, J. *J. Chem. Phys.* **1997**, *107* (8), 3032. doi:10.1063/1.474659.
(50) Mennucci, B.; Cancès, E.; Tomasi, J. *J. Phys. Chem. B* **1997**, *101* (49), 10506–10517. doi:10.1021/jp971959k.
(51) Ruud, K.; Frediani, L.; Cammi, R.; Mennucci, B. *Int. J. Mol. Sci.* **2003**, *4* (3), 119–134. doi:10.3390/i4030119.
(52) Helgaker, T.; Wilson, P. J.; Amos, R. D.; Handy, N. C. *J. Chem. Phys.* **2000**, *113* (8), 2983. doi:10.1063/1.1287056.
(53) Ferrighi, L.; Frediani, L.; Cappelli, C.; Salek, P.; Ågren, H.; Helgaker, T.; Ruud, K. *Chem. Phys. Lett.* **2006**, *425* (4-6), 267–272. doi:10.1016/j.cplett.2006.04.112.
(54) Solheim, H.; Frediani, L.; Ruud, K.; Coriani, S. *Theor. Chem. Acc.* **2008**, *119* (1-3), 231–244. doi:10.1007/s00214-006-0235-9.
(55) Ferrighi, L.; Frediani, L.; Ruud, K. *J. Chem. Phys.* In press.
(56) Cappelli, C.; Mennucci, B.; Tomasi, J.; Cammi, R.; Rizzo, A.; Rikken, G.; Mathevet, R.; Rizzo, C. *J. Chem. Phys.* **2003**, *118* (23), 10712. doi:10.1063/1.1571813.
(57) Cappelli, C.; Mennucci, B.; Cammi, R.; Rizzo, A. *J. Phys. Chem. B* **2005**, *109* (39), 18706–18714. doi:10.1021/jp053097q. PMID:16853406.
(58) Becke, A. D. *Phys. Rev. A* **1988**, *38* (6), 3098–3100. doi:10.1103/PhysRevA.38.3098. PMID:9900728.
(59) Lee, C.; Yang, W.; Parr, R. G. *Phys. Rev. B* **1988**, *37* (2), 785–789. doi:10.1103/PhysRevB.37.785.
(60) Becke, A. D. *J. Chem. Phys.* **1993**, *98* (7), 5648. doi:10.1063/1.464913.
(61) Dunning, T. H. *J. Chem. Phys.* **1989**, *90* (2), 1007. doi:10.1063/1.456153.
(62) Barone, V.; Cossi, M.; Tomasi, J. *J. Chem. Phys.* **1997**, *107* (8), 3210. doi:10.1063/1.474671.
(63) Woon, D. E.; Dunning, T. H., Jr. *J. Chem. Phys.* **1994**, *100* (4), 2975. doi:10.1063/1.466439.
(64) Thorvaldsen, A. J.; Shcherbin, D.; Jonsson, D.; Ruud, K.; Rizzo, A. Unpublished results.
(65) Norman, P.; Jonsson, D.; Ågren, H.; Dahle, P.; Ruud, K.;

Helgaker, T.; Koch, H. *Chem. Phys. Lett.* **1996**, *253* (1-2), 1–7. doi:10.1016/0009-2614(96)00246-1.
(66) Fossgård, E.; Ruud, K. *J. Comput. Chem.* **2006**, *27* (3), 326–333. doi:10.1002/jcc.20343.
(67) KJEMI. Dalton, an ab initio electronic structure program, Release 2.0. Available from http://www.kjemi.uio.no/software/dalton/dalton.html. 2005.(accessed 20 August 2009)
(68) Buckingham, A. D. *J. Chem. Phys.* **1959**, *30* (6), 1580. doi:10.1063/1.1730242.
(69) Buckingham, A. D.; Disch, R. L.; Dunmur, D. A. *J. Am. Chem. Soc.* **1968**, *90* (12), 3104–3107. doi:10.1021/ja01014a023.
(70) Buckingham, A. D.; Disch, R. L. *Proc. Roy. Soc. A* **1963**, *273* (1353), 275–289. doi:10.1098/rspa.1963.0088.
(71) Jansík, B.; Rizzo, A.; Frediani, L.; Ruud, K.; Coriani, S. *J. Chem. Phys.* **2006**, *125* (23),o. 234105. doi:10.1063/1.2404661. PMID:17190545.
(72) Groenewege, M. P. *Mol. Phys.* **1962**, *5* (6), 541–563. doi:10.1080/00268976200100641.
(73) Baranova, N. B.; Bogdanov, Y. V.; Zel'dovich, B. Y. *Opt. Commun.* **1977**, *22* (2), 243–247. doi:10.1016/0030-4018(77)90028-1.
(74) Baranova, N. B.; Zel'dovich, B. Y. *Mol. Phys.* **1979**, *38* (4), 1085–1098. doi:10.1080/00268977900102261.
(75) Barron, L. D.; Vrbancich, J. *Mol. Phys.* **1984**, *51* (3), 715–730. doi:10.1080/00268978400100481.
(76) Barron, L. D. *Molecular Light Scattering and Optical Activity*; Cambridge University Press: Cambridge, UK, 2004; 2nd revised and expanded ed.

Mechanism of dihydride formation and hydrogen/deuterium exchange in a cationic iridium(III) complex

Luigi Cavallo, Steven P. Nolan, and Heiko Jacobsen

Abstract: In this manuscript, we provide a theoretical rationalization of the mechanisms that control double H_2 addition to an unsaturated 14 e cationic Ir(III) complex to yield a dihydride Ir(III) complex. Further, we also present two mechanisms that can explain the experimentally observed incorporation of deuterium into the *tert*-Butyl (^{t}Bu) groups of the *N*-heterocyclic I^{t}Bu ligands.

Key words: homogeneous catalysis, hydrogenation, deuteration, *N*-heterocyclic carbene, density functional calculations.

Résumé : Dans ce travail, on rapporte une rationalisation théorique des mécanismes qui contrôlent la double addition de H_2 sur le complexe cationique insaturé de Ir(III) conduisant à la formation d'un dihydrure complexe de Ir(III). De plus, on présente deux mécanismes qui pourraient expliquer l'incorporation observée expérimentalement de deutérium dans les groupes *tert*-butyles des ligands I^{t}Bu de l'hétérocycle azoté.

Mots-clés : catalyse homogène, hydrogénation, deutération, carbène *N*-hétérocyclique, calculs de la fonctionnelle de la densité.

[Traduit par la Rédaction]

Introduction

Coordinatively unsaturated transition-metal complexes containing hydride ligands are of remarkable interest because of their potential role in catalysis.[1–6] Due to their unsaturated nature, the structural characterization and a detailed understanding of the chemical mechanics of these complexes are often difficult. A few years ago, we reported a detailed characterization of an unsaturated 14 e cationic iridium(III) complex, $[Ir(I^tBu')_2]^+$, **1** in Chart 1, presenting a double cyclometalated structure.[7]

We suggested that **1** is remarkably stabilized by the two *N*-heterocyclic carbene (NHC) ligands that act as π-electron donors into empty d orbitals of the metals. The highly unsaturated nature of **1** prompted us to examine its reactivity with dihydrogen.[8] Exposure of **1** to H_2 gas resulted in the formation of the dihydride cationic complex **2**, whose X-ray structure evidenced strong agostic interaction with CH_3 groups of the I^{t}Bu NHC ligands. Interestingly, extended exposure of **1** to D_2 resulted in expected D atoms in the hydride position, but also in the unexpected complete deuteration of *tert*-Butyl (^{t}Bu) groups. Finally, undeuterated **2** can be regenerated by extended exposure to H_2, while the cyclometalated complex can be regenerated by exposure of **2** to CO, to yield **3**, which indicates that all the reactivity described above is reversible.

While the overall chemical scenario is already provided by the experiments, the details of the mechanisms behind this interesting chemical behavior are unknown. To shed light on this point, we decided to carry out density functional calculations (DFT) on the interaction of the bare, cationic iridium complex **1** $[Ir(I^tBu')_2]^+$ with molecular hydrogen. The goal of the present investigation is twofold: (*i*) to clarify the mechanism of formation of the iridium dihydride complex **2** $[Ir(H)_2(I^tBu)_2]^+$, assumed to occur as depicted in Scheme 1, and (*ii*) to elucidate possible pathways for hydrogen exchange and intramolecular C–H activation.

Computational details

For the sake of computational efficiency, the I^{t}Bu ligand has been replaced by an IEt ligand; this simplification only restricts the proper description of the steric properties of the carbene ligand, whereas it can be expected that electronic and bonding properties are rather well-reproduced. We further note that the IEt ligand is a suitable model ligand when agostic interactions are to be considered.

Our nomenclature is such that Et refers to a free ethyl group of an NHC ligand, whereas Et′ describes an ethyl group involved in cyclometalation.

The DFT calculations were carried out with the Gaussian03 program suite[9] and utilized the pure BP86 functional.[10–12] The basis set employed for the main-group elements is the split-valence plus one polarization function basis set of Ahlrichs and co-workers (SVP keyword in G03),[13] while for iridium, we used the Stuttgard–Dresden

Received 5 April 2009. Accepted 14 May 2009. Published on the NRC Research Press Web site at canjchem.nrc.ca on 17 September 2009.

This article is part of a Special Issue dedicated to Professor T. Ziegler.

L. Cavallo.[1] Dipartimento di Chimica, Università di Salerno, Italy.
S.P. Nolan. School of Chemistry, University of St. Andrews, St-Andrews, KY16 9ST UK.
H. Jacobsen. KemKom, 1215 Ursulines Ave, New Orleans, LA 70116, USA.

[1]Corresponding author (e-mail: lcavallo@unisa.it).

Chart 1.

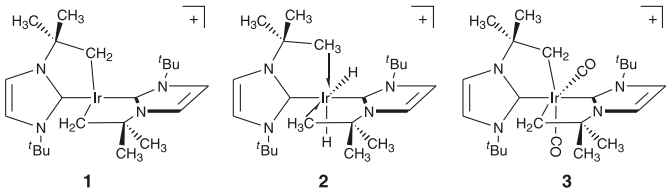

Scheme 1. Proposed mechanism for Ir–hydride formation.

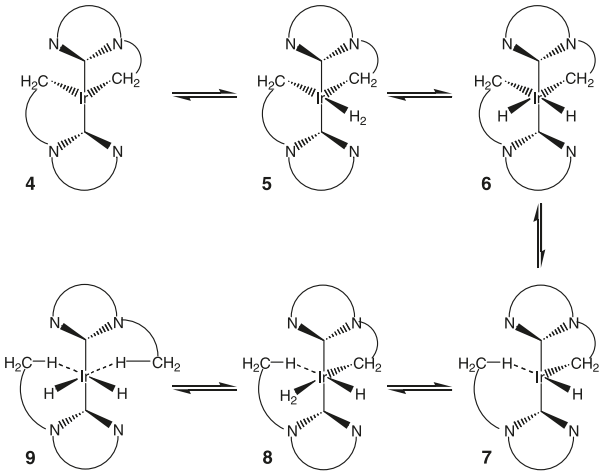

basis set, and a pseudopotential representation of the sixty innermost core electrons has been selected (SDD keyword in G03).[14] H atoms in special bonding situations, such as hydride ligands, have been described by the enlarged triple-ζ plus one polarization function basis set of Ahlrichs (TZVP keyword in G03).[15] All calculations refer to the gaseous phase and are not corrected for solvation. All stationary points have been characterized by frequency analysis, and transition states were checked to have one imaginary frequency for which the vibrational displacement vector corresponds to a molecular motion along the assumed reaction coordinate. The free energies discussed in the text are derived by standard analysis at 298 and 200 K.

Results and discussion

Hydrogenation of $[Ir(IEt')_2]^+$

The molecular geometry of the optimized complex $[Ir(IEt')_2]^+$ **4** is displayed in Fig. 1. The structure of the C_2-symmetric complex $[Ir(I^tBu')_2]^+$ **1** has been determined by X-ray crystallography, and was described as highly distorted, divacant octahedral. The bond angles around the transition-metal center amount to 79°, 98°, 111°, and 175°. The optimized geometry of the model system **4** compares well with that of the real system **1**, both in terms of symmetry and distorted coordination geometry. In particular, neither the crystal structure nor the DFT geometry indicates the presence of any agostic interactions that stabilize the electron-deficient transition-metal center.

Complex **4** reacts with two molecules of hydrogen to form the iridium dihydride complex $[Ir(H)_2(IEt)_2]^+$ **9**. The optimized geometry of complex **9** is also displayed in Fig. 1. Complex **9** is of C_2 symmetry; the Ir–H bond length is 156 pm, which is in the expected range for a transition-metal hydride bond. Characteristic for **9** are the agostic interactions in trans position to the hydride ligands; the presence of the agostic bonds together with the coordination geometry around the transition-metal center suggest that complex **9** is indeed best-described as an octahedral complex.

Fig. 1. Optimized geometry of complexes **4** and **9**. Selected bond lengths (in pm) in **4**: Ir—C_{Im}: 205; Ir—C_{Et} = 203; selected bond angles in **4**: C_{Im}–Ir–C_{Et}: 80°, 99°; C_{Im}–Ir–C_{Im}: 176°; C_{Et}–Ir–C_{Et}: 119°. Selected bond lengths (in pm) in **9**: Ir—C_{Im}: 206; Ir—H = 156; Ir···H = 203; selected bond angles in **9**: C_{Im}–Ir–C_{Im}: 179°; H–Ir–H: 84°.

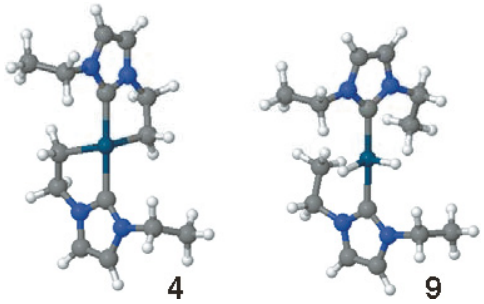

While structure **9** is stabilized by a double agostic interaction, structure **4** is not. The reason is in the constraint imposed by the five-membered metallacyle structure that pulls the Et groups of the IEt′ ligands away from the metal center (the Ir–C_{Im}–N(Et′) and Ir–C_{Im}–N(Et) angles are equal to 115° and 140°, respectively).

We have estimated the strength of the agostic interaction by optimizing a geometry **9′** in which one of the ethyl groups was rotated away from the iridium center; and the value of $\Delta E_{agostic}$ = 13 kJ/mol suggests that cleavage of the agostic bond does not account for a sizeable energetic barrier for formation of a dihydrogen complex of compound **9**. This fact will be of importance at a later point of our discussion.

The addition of the first molecule of hydrogen to complex **4** that eventually yields the monohydride complex $[Ir(H)(IEt')(IEt)]]^+$ **7** is a three-step process (see Scheme 1). First, complex **4** loosely binds a hydrogen molecule, and forms the dihydrogen complex $[Ir(H_2)(IEt')_2]^+$ **5**. We have calculated the energetics for formation of complex **5**, eq. [1].

$$[1] \qquad [Ir(IEt')_2]^+ + H_2 \rightarrow [Ir(H_2)(IEt')_2]^+$$

For the process shown in eq. [1], the value of ΔG (298 K) amounts to +18 kJ/mol, and decreases with decreasing temperature, ΔG (200 K) = 6 kJ/mol. Thus, the first step of hydrogen addition is a slightly endoergonic step.

Once dihydrogen is coordinated to the iridium center, the addition of hydrogen proceeds via a dihydride intermediate **6** to the monohydride **7**. The formation of complexes **6** and **7** occur through the respective transition states [**5**–**6**] and [**6**–**7**]. The energy profile for the addition of the first H_2 molecule corresponds to the first part of the conversion pathway **4** → **9**, as displayed in Fig. 2.

The first transition state [**5**–**6**] is reached with an activation energy of 88 kJ/mol and corresponds to the step of cleavage of the H–H bond of the coordinated hydrogen molecule. The intermediate **6** is 79 kJ/mol higher in energy than the H_2 adduct **5**. The second transition state [**6**–**7**] requires an activation energy of only 4 kJ/mol and corresponds to the

Fig. 2. Energy profile for the conversion reaction **4** → **9**.

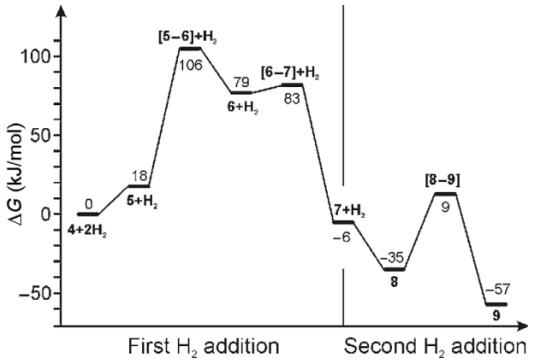

Fig. 3. Optimized geometries of the complexes relevant for the first H_2 addition.

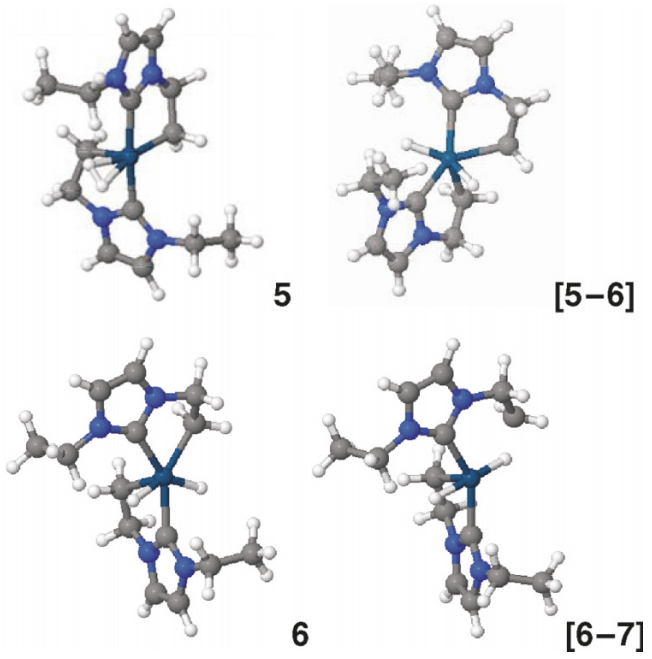

formation of the H–C bond. Transition state [**6**–**7**] collapses into intermediate **7** that is 24 kJ/mol more stable than the H_2 adduct **5**. Formation of the monohydride complex **7** represents an exoergonic process with ΔG (298 K) = –6 kJ/mol and ΔG (200 K) = –16 kJ/mol, respectively.

Optimized geometries of species relevant for the first H_2 addition are displayed in Fig. 3, and we will briefly discuss relevant geometric parameters for the complexes involved in the first hydrogen-addition process. Compared with the bare cation **4**, the dihydrogen adduct **5** shows elongated Ir–C bonds of d(Ir–C_{Im}) = 206 pm and 207 pm, and d(Ir–C_{Et}) = 209 pm and 210 pm, respectively. The bond angle ∠(C_{Et}–Ir–C_{Et}) decreases to 95°. This indicates that H_2 coordination has an influence on the coordination geometry around the Ir center, which changes from highly distorted divacant octahedral to monovacant octahedral. The Ir–H bond lengths amount to d(Ir–H) = 178 pm. The H–H bond with d(H–H) = 87 pm is slightly elongated, compared with the free ligand, d(H–H) = 74 pm, indicating that H–H bond cleavage is initiated by simple coordination to the metal center.

Fig. 4. Optimized geometry of complexes relevant for the second H_2 addition.

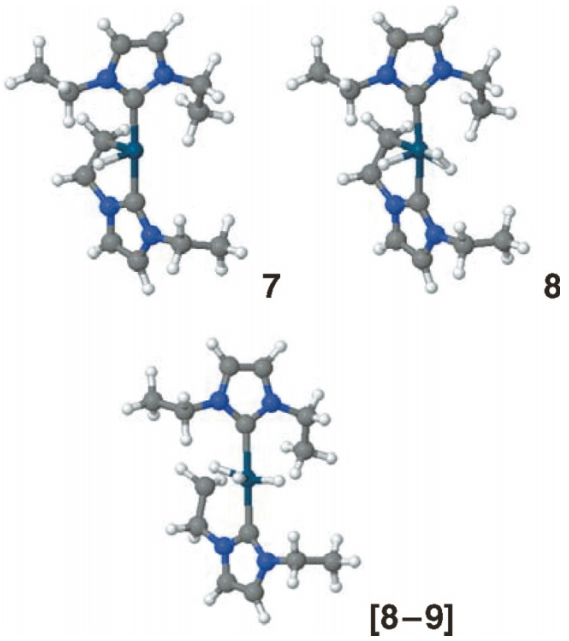

The first transition state [**5**–**6**] shows short Ir–H contacts of 157 pm and 165 pm, respectively, and a long H–H separation of 290 pm. These geometric parameters suggest that the first transition state has to be classified as late transition state, with the H–H bond being broken and the Ir–H bonds being almost completely formed.

Intermediate **6** displays pentagonal-pyramidal coordination around the transition-metal center. The two H atoms, the two C_{Im} atoms, and one of the C_{Et} atoms span the pentagonal coordination plane around Ir. The respective X_1–Ir–X_2 angles (X_1, X_2 = H, C_{Im}, C_{Et}) amount to 75°, 69°, 69°, 72°, and 74°, summing up to 359°. The two Ir–H distances remain at 157 pm and 165 pm. The hydride ligand with the shorter Ir–H separation is positioned cis to the C_{Et} atom with a H–C_{Et} separation of 229 pm, and will eventually be transferred to the adjacent ethyl group.

In the second transition state [**6**–**7**], the respective Ir–C_{Et} is already broken, d(Ir–C_{Et}) = 265 pm, and the relevant distances for the H atom that is transferred from the transition metal to the ethyl group are d(H–Ir) = 166 pm and d(H–C_{Et}) = 158 pm, respectively. With respect to the migrating H-atom, transition state [**6**–**7**] is best classified as early transition state, consistent with the fact that only a small energetic barrier separates transition state [**6**–**7**] from intermediate **7**.

The optimized geometry of complex **7** is displayed in Fig. 4 together with structures relevant for H_2 addition. Important bond distances, and especially the Ir–H separation compare well with those calculated for the dihydride **9**. One short Ir–H contact with one of the hydrogen atoms of an ethyl group suggests the presence of an agostic interaction in trans position to the hydride ligand, and complex **7** is again best-described as monovacant octahedral.

Complex **7** binds dihydrogen stronger than complex **4**, and forms the dihydrogen complex $[Ir(H)(H_2)(IEt')(IEt)]^+$ **8**. We have calculated the energetics for the formation of complex **8**, eq. [2].

Scheme 2. Proposed mechanism for deuterium incorporation into the I^{t}Bu C–H bonds.

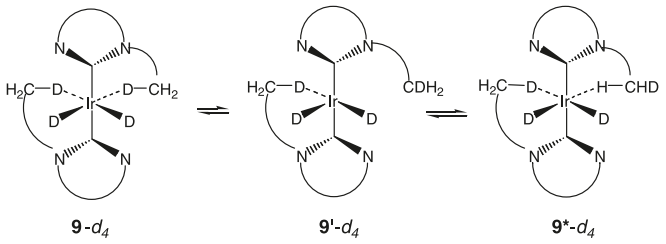

$$[2] \qquad [\mathrm{Ir(H)(IEt')(IEt)}]^+ + \mathrm{H_2} \rightarrow [\mathrm{Ir(H)(H_2)(IEt')(IEt)}]^+$$

For the process shown in eq. [2], the values of ΔG (298 K) = –29 kJ/mol and ΔG (200 K) = –51 kJ/mol were calculated, demonstrating that the monohydride **7** binds dihydrogen about 30 kJ/mol stronger than complex **4**. Thus, the first step of addition of a second hydrogen molecule is now an exoergonic step.

Optimized geometries of species relevant for the second H_2 addition are displayed in Fig. 4. The dihydrogen ligand in complex **8** binds to the transition-metal center with Ir–H distances of 177 pm, and shows an elongated H–H bond of 88 pm. The H_2 coordination geometry in complex **8** is similar to that found for complex **5**. Since the H_2 coordinates in trans position to the IEt′ group, it is the hydride ligand of complex **7** that will be transferred to the ethyl group. The incoming H_2 ligand is cleaved under coordination to the transition-metal center and will transform into the two hydride ligands of complex **9**. Geometric parameters calculated for transition state [**8**–**9**] corroborate this mechanistic proposal. In [**8**–**9**], the H_2 is almost completely transformed into two hydride ligands, which is indicated by the Ir–H bond lengths of 164 pm and a H–H separation of 158 pm. The Ir–C_{Et} bond is broken in transition state [**8**–**9**], indicated by the long Ir–C_{Et} separation of 253 pm. The hydride ligand of the transition-state complex now shows a short Ir–H bond distance of 139 pm, but is also in close contact to the C atom of the separating IEt′ group, with a H–C separation of 186 pm

The dihydride complex **9** is reached by addition of H_2 via transition state [**8**–**9**], which requires an activation energy $\Delta G^{\ddagger}$ (298 K) of 44 kJ/mol. Compared with the H_2 adduct **8**, the dihydride complex **9** is favored by 22 kJ/mol in terms of total energy. The energy profile for the second H_2 addition is also displayed in Fig. 2.

Deuterium incorporation into the I^{t}Bu C–H bonds

In this section, we discuss a possible mechanism that leads to deuterium incorporation into the ^{t}Bu groups. Complex **4** is an important intermediate in the process of incorporating external hydrogen or deuterium into hydride positions and possibly into I^{t}Bu or IEt positions. During the reaction of **1** with D_2, rapid incorporation of D into other I^{t}Bu positions is also observed, leading to complete deuteration on both the hydride and I^{t}Bu positions upon extended exposure to D_2 gas. One reaction that is of relevance for multiple D incorporation into ^{t}Bu positions is illustrated for the model complex **9**-d_4 in Scheme 2.

We briefly commented on the energetics of the agostic interaction, and we now will consider the reaction shown in Scheme 2 in terms of free-energy values. The release of the agostic interaction, which leads from complex **9**-d_4 to **9**′-d_4, proceeds with ΔG (298 K) = –2 kJ/mol and ΔG (200 K) = 2 kJ/mol. In terms of free energy, the agostic interaction is a weak interaction, and as to be expected is upset by the effect of higher temperature. Thus, the release and reformation of the agostic interaction is a facile process in solution. Under the assumption that the rotation of the deutero-methyl group in **9**′-d_4 is essentially free, the agostic interaction might be re-established to give complex **9***-d_4. This complex serves as a precursor from which incorporation of additional deuterium atoms into the I^{t}But or IEt groups might occur. We further note that the effect of deuteration affects the energetics of the agostic bond by about 0.5 kJ/mol.

Scheme 3. Proposed mechanism for H/D exchange.

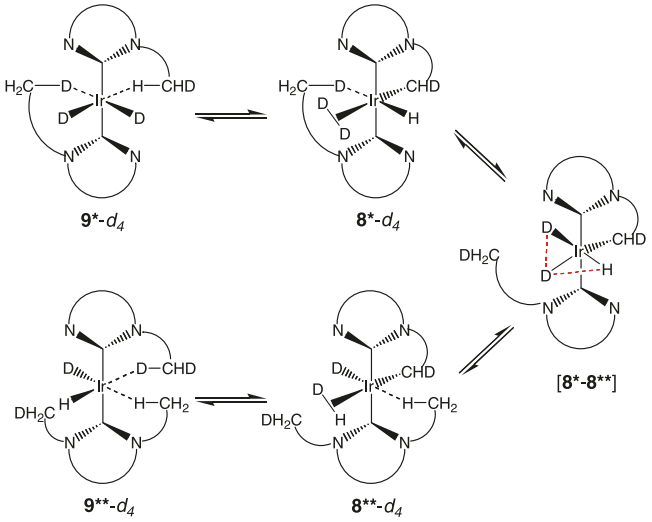

Fig. 5. Optimized geometry of the transition state [**8***–**8****] for intramolecular deuterium/hydrogen scrambling.

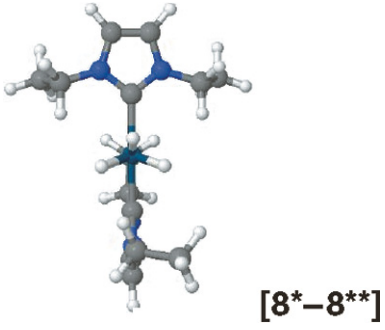

A possible mechanism for incorporation of additional deuterium atoms into the IEt position of complex **9***-d_4 is outlined in Scheme 3.

Complex **9***-d_4 undergoes a step of oxidative addition of the agostic C–H bond that leads to formation of the dideuterium hydride complex **8***-d_4. Intramolecular deuterium/hydrogen scrambling leads to the formation of complex **8****-d_4 possessing a deuteride ligand and a coordinated HD molecule. Addition of the HD ligand then furnishes complex **9****-d_4 in which one of the IEt groups is now doubly deuterated. Repeatedly running through this reaction sequence will eventually furnish the deuterated compound.

Scheme 4. Proposed mechanism to explain full deuteration of the I^{t}Bu C–H bonds.

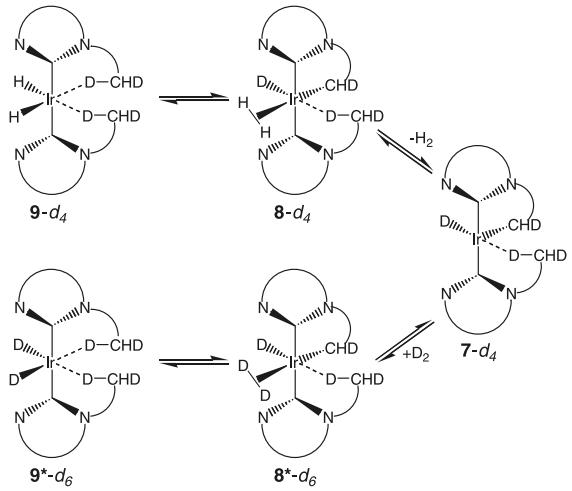

Scheme 5. Reaction profile for intramolecular deuterium/hydrogen scrambling through intermediate **10**.

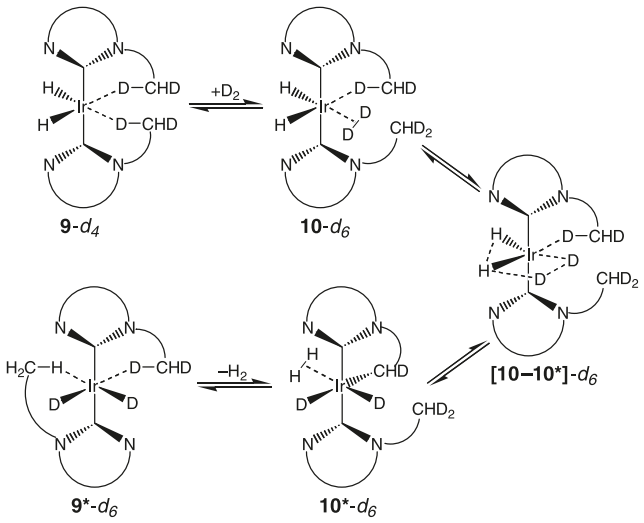

Fig. 6. Reaction profiles for intramolecular deuterium/hydrogen scrambling.

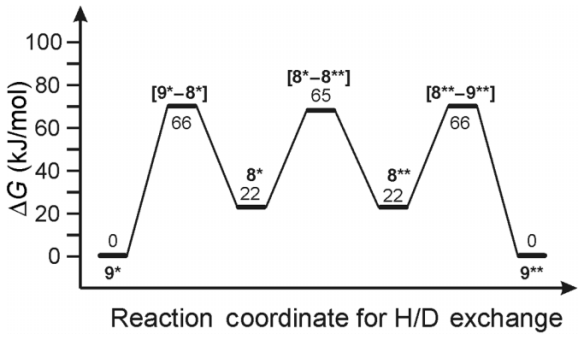

Fig. 7. Optimized geometries of dihydride–dihydrogen complexes **10** and **10a** and of the transition state [**10**–**10a**] for their interconversion.

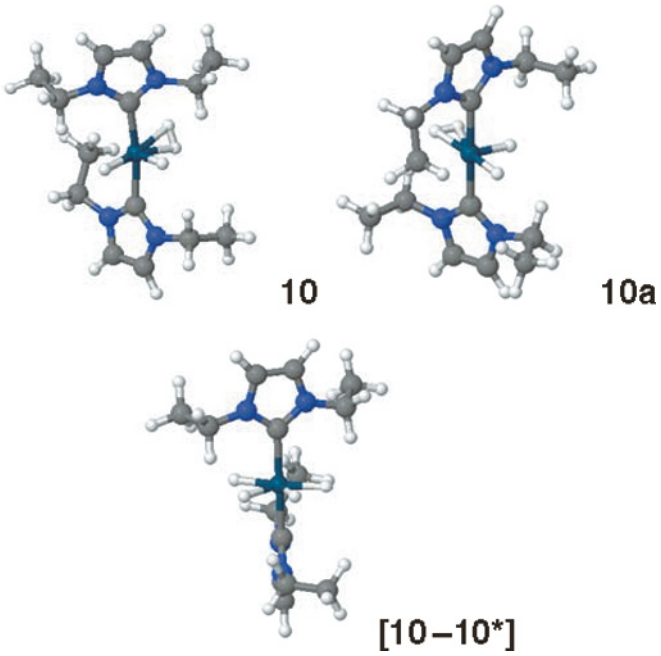

The optimized geometry of the hydrogen analogue of the transition state [**8***–**8****] is presented in Fig. 5.

The Ir–H bond lengths amount to 157, 164, and 157 pm, respectively, and are slightly elongated compared with the Ir–H distances optimized for local minimum geometries (vide supra). The longest Ir–H(D) separation is associated with a H(D)–ligand in central position, one H(D) atom of the former hydrogen(deuterium) molecule being transferred to the hydride ligand to form a new H_2(DH) molecule. Compared with complex **8**, the transition state [**8***–**8****] is reached with an activation energy of 43 kJ/mol. The complete energy profile from **9*** to **9**** is sketched in Fig. 6. The activation energy is comparable to the activation energy for addition of H_2 via transition state [**8**–**9**], which transforms the hydride–dihydrogen complex **8** into the dihydride **9**. This suggests that during the process of hydrogenation, a complex such as **8****-d_4 is accessible in terms of energetic requirements.

After complex **9**-d_4 has exchanged two H atoms on the I^{t}Bu arms with the two deuteride ligands of Ir to form a **9**-d_4 complex with the four D atoms incorporated into the ^{t}Bu groups as C–D bonds, the most intuitive mechanism to explain complete deuteration of the I^{t}Bu C–H bonds is a reductive elimination of H_2 from the two Ir–H bonds (i.e., the reverse of step **8** → **9** in Fig. 2), followed by substitution of the coordinated H_2 molecule by a D_2 molecule (i.e., the reverse of step **7** → **8** in Fig. 2 through a dissociative or associative pathway), as shown in Scheme 4.

Nevertheless, considering that **9** possesses a vacant coordination site, we explored its reactivity toward H_2 or D_2. This mechanism is based on a scenario in which the dihydride $[Ir(H)_2(IEt)_2]^+$ **9** itself forms a complex with molecular hydrogen, $[Ir(H)_2(H_2)(IEt)_2]^+$, from which further deuterium incorporation into the Et groups can proceed as shown in Scheme 5.

For the molecular hydrogen adduct to **9**, we have calculated two possible structures, referred to as **10** and **10a**, respectively. Optimized geometries are displayed in Fig. 7. In complex **10**, the dihydrogen ligand is oriented perpendicular to the $H_{Hydride}$–Ir–$H_{Hydride}$ plane, whereas in complex **10a**, all

Fig. 8. Energy profiles to account for full deuteration of the Et groups, see Schemes 4 and 5.

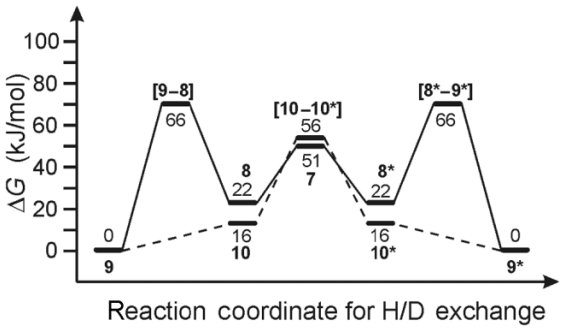

four hydrogen atoms connected to Ir are to be found within the same plane. Complex **10a** is 4 kJ/mol higher in energy than complex **10**, which indicates that the dihydrogen ligand can freely rotate without a substantial barrier. The bond distances of the dihydrogen ligand to the transition-metal center, d(Ir–H) = 181 pm and 182 pm, are slightly longer than those of the dihydrogen complexes **5** and **8** (vide supra).

To estimate the likelihood that a dihydrogen–dihydride complex might be a possible intermediate in a hydride exchange/incorporation, we have calculated the energetics for formation of complex **10**, eq. [3].

$$[3] \qquad [Ir(H)_2(IET)_2]^+ + H_2 \rightarrow [Ir(H)_2(H_2)(IEt)_2]^+$$

For the process shown in eq. [3], values of ΔG (298 K) = +16 kJ/mol and ΔG (200 K) = 6 kJ/mol were calculated, similar to the values found for H_2 binding to complex **4**. Although the formation of complex **10** represents an endoergonic reaction, it requires less of an energetic barrier than the reductive elimination **9** → **8**, see also Fig. 6. At this point, hydride/hydrogen exchange process can proceed through transition state [**10–10***], displayed in Fig. 7. Transition state [**10–10***], which is 40 kJ/mol higher in energy than complex **10** at 298 K, represents a tetrahydride coordination, with Ir–H distances between 158 pm and 167 pm and the terminal H atoms forming the longer bonds. We note that, in [**10–10***], all four hydride ligands are located in a coordination plane around Ir.

It is interesting to note that, in transition state [**10–10***], all hydride ligands are separated from each other at least by 160 pm. Structures **10**, **10a**, and transition state [**10–10***] readily explain the hydrogen/deuterium exchange in complex **9**. When complex $[Ir(H)_2(IEt)_2]^+$ **9***-d_4 is exposed to an atmosphere of deuterium, a deuterium dihydride $[Ir(H)_2(D_2)(IEt)_2]^+$ **10**-d_6 can be formed, from which the Icorresponding transition state **[10–10*]** can be reached. Transition state **[10–10*]** leads to the formation of the hydrogen dideuteride $[Ir(D)_2(H_2)(IEt)_2]^+$ **10***-d_6, which can dissociate H_2 to form the dideuteride complex $[Ir(D)_2(IEt)_2]^+$ **9-**d_6. According to the mechanism discussed in Scheme 4, complex **9**-d_6 then allows for incorporation of deuterium into the I^{t}Bu or IEt positions to form the dihydride complex $[Ir(H)_2(IEt)_2]^+$ **9***-d_6.

As for a comparison between the two possible mechanisms for complete deuteration of the NHC ligands from **9***-d_4, our calculations suggest that the **9** → **10** pathway is lower in energy that the **9** → **8** → **7** pathway, see Fig. 8.

Conclusions

In this manuscript, we provided a detailed characterization of the mechanisms that control the reactivity of an unsaturated 14 e cationic Ir(III) complex toward molecular hydrogen. Specifically, our calculations indicate the following:

(*i*) Double H_2 addition to the starting unsaturated complex **4** to give the dihydride complex **9** is a relatively easy process, with the second H_2 addition proceeding easier than the first H_2 addition.

(*ii*) Incorporation of deuterium into the ^{t}Bu groups can be rationalized by a reductive elimination of H_2 from two Ir–H bonds from **9**, followed by substitution of the coordinated H_2 molecule by a D_2 molecule. However, an alternative mechanism that starts with H_2 binding to **9**, with successive formation of an intermediate that resembles a tetrahydride intermediate, is also possible.

Supplementary data

Supplementary data for this article are available on the journal Web site (canjchem.nrc.ca) or may be purchased from the Depository of Unpublished Data, Document Delivery, CISTI, National Research Council Canada, Ottawa, ON K1A 0R6, Canada. DUD 5262. For more information on obtaining material, refer to cisti-icist.nrc-cnrc.gc.ca/cms/unpub_e.shtml.

Acknowledgement

This work was supported by Istituto di Scienza e Tecnologia dei Materiali (INSTM) (Cineca Grant Key-project 2008). SPN acknowledges support from the European Research Council (ERC) for an Advanced Researcher Grant (FUNCAT).

References

(1) Collman, J. P.; Hegedus, L. S.; Norton, J. R.; Finke, R. G. In *Principles and Applications of Organotransition-metal Chemistry;* University Science: Mill Valley, CA, 1987.

(2) Herrmann, W. A.; Cornils, B. *Angew. Chem. Int. Ed. Engl.* **1997**, *36* (10), 1048–1067. doi:10.1002/anie.199710481.

(3) Crabtree, R. H. *Acc. Chem. Res.* **1990**, *23* (4), 95–101. doi:10.1021/ar00172a001.

(4) Zassinovich, G.; Mestroni, G.; Gladiali, S. *Chem. Rev.* **1992**, *92* (5), 1051–1069. doi:10.1021/cr00013a015.

(5) Arndtsen, B. A.; Bergman, R. G.; Mobley, T. A.; Peterson, T. H. *Acc. Chem. Res.* **1995**, *28* (3), 154–162. doi:10.1021/ar00051a009.

(6) Arndtsen, B. A.; Bergman, R. G. *Science* **1995**, *270* (5244), 1970–1973. doi:10.1126/science.270.5244.1970.

(7) Scott, N. M.; Dorta, R.; Stevens, E. D.; Correa, A.; Cavallo, L.; Nolan, S. P. *J. Am. Chem. Soc.* **2005**, *127* (10), 3516–3526. doi:10.1021/ja043249f. PMID:15755173.

(8) Scott, N. M.; Pons, V.; Stevens, E. D.; Heinekey, D. M.; Nolan, S. P. *Angew. Chem. Int. Ed.* **2005**, *44* (17), 2512–2515. doi:10.1002/anie.200463000.

(9) Frisch, M. J.; Trucks, G. W.; Schlegel, H. B.; Scuseria, G. E.; Robb, M. A.; Cheeseman, J. R.; Zakrzewski, V. G.; Montgomery, J. A. J.; Stratmann, R. E.; Burant, J. C.; Dapprich, S.; Millam, J. M.; Daniels, A. D.; Kudin, K. N.; Strain, M. C.; Farkas, O.; Tomasi, J.; Barone, V.; Cossi, M.; Cammi, R.; Mennucci, B.; Pomelli, C.; Adamo, C.; Clifford, S.;

Ochterski, J.; Petersson, G. A.; Ayala, P. Y.; Cui, Q.; Morokuma, K.; Malick, D. K.; Rabuck, A. D.; Raghavachari, K.; Foresman, J. B.; Cioslowski, J.; Ortiz, J. V.; Stefanov, B. B.; Liu, G.; Liashenko, A.; Piskorz, P.; Komaromi, I.; Gomperts, R.; Martin, R. L.; Fox, D. J.; Keith, T.; Al-Laham, M. A.; Peng, C. Y.; Nanayakkara, A.; Gonzalez, C.; Challacombe, M.; Gill, P. M. W.; Johnson, B.; Chen, W.; Wong, M. W.; Andres, J. L.; Gonzalez, C.; Head-Gordon, M.; Replogle, E. S.; Pople, J. A. *Gaussian03;* Gaussian, Inc.: Pittsburgh, PA, 2003.

(10) Becke, A. D. *Phys. Rev. A* **1988**, *38* (6), 3098–3100. doi:10.1103/PhysRevA.38.3098. PMID:9900728.

(11) Perdew, J. P. *Phys. Rev. B* **1986**, *33* (12), 8822–8824. doi:10.1103/PhysRevB.33.8822.

(12) Perdew, J. P. *Phys. Rev. B* **1986**, *34* (10), 7406. doi:10.1103/PhysRevB.34.7406.

(13) Schäfer, A.; Horn, H.; Ahlrichs, R. *J. Chem. Phys.* **1992**, *97* (4), 2571. doi:10.1063/1.463096.

(14) Leininger, T.; Nicklass, A.; Stoll, H.; Dolg, M.; Schwerdtfeger, P. *J. Chem. Phys.* **1996**, *105* (3), 1052. doi:10.1063/1.471950.

(15) Schäfer, A.; Huber, C.; Ahlrichs, R. *J. Chem. Phys.* **1994**, *100* (8), 5829. doi:10.1063/1.467146.

Tests of an exact-exchange-based density-functional theory on transition-metal complexes

Erin R. Johnson and Axel D. Becke

Abstract: We have compiled a benchmark set of mean ligand-removal enthalpies for 32 transition-metal complexes of relevance in organometallic and catalysis chemistry. Our recent exact-exchange-based density-functional model, DF07 (*J. Chem. Phys.* **2007**, *127* (12), 124108), is assessed on this benchmark set along with other representative GGA, meta-GGA, and hybrid functionals. DF07 performs remarkably well, despite its exact-exchange foundation, indicating that it properly describes nondynamical correlation in transition-metal–ligand bonds.

Key words: density-functional theory, electronic structure methods, computational chemistry.

Résumé : On a compilé un ensemble de référence des enthalpies moyennes d'enlèvement d'un ligand à partir de trente-deux complexes pertinents à la catalyse et la chimie organométallique. On a évalué le modèle de fonctionnelle de densité à base d'échange exact proposé récemment, DF07 (*J. Chem. Phys.* **2007**, *127* (12), 124108), sur cet ensemble de référence ainsi que sur l'autre GCA, la méta-GCA, ainsi que d'autres fonctionnelles hybrides. La performance du modèle DF07 est remarquablement bonne malgré sa fondation d'échange exact, ce qui indique qu'elle décrit correctement la corrélation non dynamique des liaisons entre un ligand et un métal de transition.

Mots-clés : théorie de la fonctionnelle de densité, méthodes de la structure électronique, chimie des calculs théoriques.

[Traduit par la Rédaction]

Introduction

Density-functional theory (DFT) has achieved widespread popularity in computational chemistry thanks to its balance between computational cost and accuracy. DFT results now approach chemical accuracy for heats of formation and bond-dissociation enthalpies in main-group chemistry. However, recent benchmarking studies have revealed that approximate density functionals are susceptible to much larger errors in transition-metal chemistry,[1–3] in the order of 10 kcal/mol per bond. This is far from the level of accuracy needed for chemical applications. These recent results are at odds with the good agreement between DFT and experiment seen in earlier organometallic and catalysis applications by, e.g., Ziegler, Woo, and co-workers.[4]

We have recently introduced an exact-exchange-based density functional,[5] DF07, which explicitly models all three distinct correlation types in chemistry: dynamical, nondynamical, and dispersion. DF07 performs very well on a variety of main-group benchmark sets, giving excellent thermochemical properties and barrier heights.[6] However, this does not necessarily translate into good performance in transitional-metal chemistry. Indeed, DF07 might be expected to suffer even larger errors in transitional-metal chemistry than conventional DFTs, since it is based on exact (Hartree–Fock) exchange.

Transition-metal chemistry is notoriously problematic for Hartree–Fock-based theories due to the importance of both dynamical and nondynamical correlation. Veillard[7] states that the HF orbitals tend to be too localized on the metal atom or the ligands due to the small spatial extent of the d orbitals. Consequently, HF predicts the metal–ligand bonds to be too ionic. Inclusion of nondynamical correlation remedies this problem by increasing the covalent character of the metal–ligand bonds. MP2 theory, the simplest ab initio approach to incorporate electronic correlation, does not fully capture the effects of correlation in transition-metal–ligand bonds. In transition-metal carbonyls,[8] MP2 overestimates the bond energies with errors in the order of 20 kcal/mol per bond. Even basis-set-extrapolated CCSD(T) theory may yield large errors in some transition-metal systems (e.g., in TiF_2, the error is 16.6 kcal/mol per bond[9]). For the atomization energies of a set of 10 transition-metal halides and oxides, CCSD(T) gives overall results much closer to experiment than HF or MP2, with a mean absolute error (MAE) of 3.4 kcal/mol per bond.[9]

In this work, the performance of DF07[5] is assessed on a benchmark set consisting of mean ligand-removal standard enthalpies of 32 3d-transition-metal complexes. Our benchmark set differs from those of recent studies[1–3] in that we focus on closed-shell complexes of relevance in organometallic and catalysis chemistry. The exact-exchange character of DF07 is tested by comparing with several pure and hybrid density functionals.

Received 8 January 2009. Accepted 19 March 2009. Published on the NRC Research Press Web site at canjchem.nrc.ca on 17 September 2009.

This article is part of a Special Issue dedicated to Professor T. Ziegler.

E.R. Johnson. Department of Chemistry, Duke University, Durham, NC 27708, USA.
A.D. Becke.[1] Department of Chemistry, Dalhousie University, Halifax, NS B3H 4J3, Canada.

[1]Corresponding author (e-mail: axel.becke@dal.ca).

The benchmark set

Recent DFT benchmarking studies on dissociation enthalpies of transition-metal compounds have focused primarily on diatomics and triatomics[1–3] due to the availability of accurate reference data. These are frequently open-shell systems, with very high multiplicity in some cases. Our aim in this work is to assess the performance of density functionals on a benchmark set that better represents systems of interest to transition-metal chemists. Our set consists of mean ligand-removal standard enthalpies for 32 closed-shell molecules. The set is restricted to 3d transition metals to minimize relativistic effects inherent in the experimental data.[10] Reference data with large error bars are excluded as well. Mean ligand-removal enthalpies were obtained using experimental heats of formation to determine total fragmentation enthalpies of the transition-metal complex into free transition-metal atom(s) and neutral ligands, and dividing by the total number of metal–ligand bonds (and metal–metal bonds where applicable). The experimental heats of formation are from NIST[11] for all species except the cyclopentadienyl radical.[12]

Note that one molecule in the benchmark set, $Fe(CO)_4$, has a triplet ground state, which lies approximately 2 kcal/mol lower in energy than the singlet.[13] The dissociation enthalpy of $Fe(CO)_4$ is computed for the singlet state because the triplet energy is highly sensitive to the level of theory.[13] Since the energy difference between the triplet and singlet states is small, this has minimal effect on the resultant error statistics.

Computational methods

All geometry optimizations and frequency calculations were performed with B3LYP/6–31G(2df,p)[14,15] as in the G3X procedure,[16] using the Gaussian 03 program.[17] The quality of B3LYP/6–31G(2df,p) geometries in transition-metal complexes such as these is assessed in the Appendix. Single-point energy calculations were then performed with the 6–311++G(3df,3pd) basis set and a selection of eight popular functionals: BLYP,[15,18] B3LYP,[14,15] BP86,[18,19] B3P86,[14,19] PBE,[20] PBE0,[21] TPSS,[22] and TPSSh.[23] Single-point post-LSDA[24] calculations were also carried out on all species with the basis-set-free NUMOL program[25] to obtain DF07 electronic energies.

The various exchange and correlation terms in the DF07 functional are thoroughly reviewed in ref. 5. The DF07 functional has the form:[5]

$$[1]\qquad E_{XC}^{DF07} = E_X^{exact} + a_{NDC}^{opp}U_{NDC}^{opp} + a_{NDC}^{par}U_{NDC}^{par} + a_{DC}^{opp}E_{DC}^{opp} + a_{DC}^{par}E_{DC}^{par} + E_{disp}^{BR}(a_1,a_2) + a_{RC}(E_X^{B86} - E_X^{B88})$$

where E_X^{exact} is the exact exchange energy, U_{NDC} is the potential energy of nondynamical correlation,[26] and E_{DC} is the dynamical correlation energy,[27] with the superscripts indicating opposite or parallel electron spins. E_{disp}^{BR} is the BR variant of our dispersion energy (see ref. 5) dependent on two universal cutoff parameters a_1 and a_2, and $(E_X^{B86} - E_X^{B88})$ is a Pauli repulsion correction. The seven parameters were fit simultaneously to 222 main-group atomization energies and to binding energies of 45 van der Waals complexes.[5] Each parameter in DF07 is related to a well-defined physical effect, and the value of each parameter concurs with physical intuition.

To illustrate the importance of the nondynamical correlation terms in DF07, we also performed calculations with Hartree–Fock exchange corrected for dynamical correlation only. This functional, which we call HFBR, has the form:

$$[2]\qquad E_{XC}^{HFBR} = E_X^{exact} + E_{DC}^{opp} + E_{DC}^{par}$$

where E_{DC}[27] is the same dynamical correlation energy as in DF07. There are no empirical fit parameters in HFBR.

Since we are computing ligand-removal enthalpies, calculations must also be performed on free transition-metal atoms. This has been the source of great vexation in previous density-functional benchmark studies.[2,3] The treatment of degenerate states in atomic systems is a long-standing fundamental problem in DFT.[28] Density-functional calculations on transition-metal atoms are particularly problematic due to the numerous possible ways, having inequivalent densities, of occupying the d orbitals. The problem is compounded by the issue of real orbitals versus complex orbitals. We have recently demonstrated[29] that all possible single-determinantal angular-momentum eigenstates in the ground-state terms of the open-shell 3d and 4d transition-metal atoms are nearly degenerate, as they should be, in the current-density-corrected DFT of Becke and Roussel.[30,31] None of the five possible density-distinct occupation schemes of the *real* atomic orbitals in d^2-type configurations is an angular-momentum eigenstate. However, we found[29] that the current-density-corrected ground-state energies are well-reproduced in d^2-type configurations if the two electrons/holes occupy the d_{z^2} and the d_{xy} or the $d_{x^2-y^2}$ real orbitals (the e orbitals in tetrahedral or octahedral symmetry groups). In d^1-type configurations, occupancy of the d_{z^2} orbital is the preferred choice, giving a proper angular-momentum eigenstate. Since not all density functionals can be easily corrected for current-density dependence, these simple rules provide a convenient real-orbital occupation formula for calculations on free transition-metal atoms. In the present work, experimental ground-state electronic configurations were used for the free transition-metal atoms, and the above real-orbital occupancies were used throughout.

Results and discussion

The calculated and experimental mean ligand-removal enthalpies are shown in Table 1. DF07 gives an MAE of 2.3 kcal/mol, a mean error (ME) of 0.2 kcal/mol, and a maximum error (MaxE) of 7.1 kcal/mol for TiF_2O. These errors are only slightly worse than for the set of 76 main-group bond-dissociation enthalpies in ref. 32 (MAE of 1.7 kcal/mol, ME of –0.4 kcal/mol, and MaxE of 6.8 kcal/mol for the C–C bond in cyanomethane[6]). On the present transition-metal set, HFBR gives an MAE of 30.2 kcal/mol, an ME of –28.5 kcal/mol, and a MaxE of –91.5 kcal/mol for TiO_2. This demonstrates that the post-HF correlation terms in DF07 recover essentially all of the nondynamical correlation energy in these transition-metal complexes.

The other density functionals considered also perform reasonably well on our transition-metal set. The pure DFTs

Table 1. Mean ligand-removal enthalpies of benchmark transition-metal complexes, in kcal/mol.

Complex	BLYP	B3LYP	BP86	B3P86	PBE	PBE0	TPSS	TPSSh	HFBR	DF07	Experimental
$TiBr_4$	92.5	87.1	97.4	92.6	98.5	90.4	96.9	93.6	54.6	93.7	87.9
$Ti(C_5H_5)_2Cl_2$	85.8	83.3	94.3	91.3	96.7	90.4	95.1	92.5	43.1	91.3	91.0
$TiCl_4$	105.2	100.6	110.8	106.1	111.9	103.8	109.8	106.5	63.4	105.3	102.8
$TiCl_2O$	129.3	121.5	135.2	127.5	136.2	123.5	131.6	126.7	68.0	126.1	120.3
TiF_4	147.7	140.2	151.2	144.1	152.0	139.6	148.0	143.2	75.7	145.3	139.9
TiF_2O	155.9	145.9	160.5	151.1	161.3	145.4	155.4	149.4	71.4	150.9	143.8
TiO_2	166.0	149.1	173.2	157.0	173.8	148.5	163.9	154.4	61.1	153.7	152.6
$Cr(CO)_5$	29.7	22.8	34.1	26.9	35.0	24.3	33.9	29.6	24.5	25.0	23.4
$Cr(pyridine)(CO)_5$	28.5	22.8	32.8	26.9	33.9	24.8	32.9	29.3	24.4	25.4	24.5
$Cr(piperidine)(CO)_5$	28.3	22.7	32.7	26.8	33.9	24.7	32.8	29.2	24.5	25.5	25.3
$Cr(pyrazole)(CO)_5$	28.6	22.9	32.9	27.0	34.0	24.9	33.0	29.3	24.0	25.5	25.4
$Cr(CO)_6$	30.6	24.8	35.2	29.2	36.3	27.1	35.2	31.5	24.5	26.9	25.6
$Cr(C_6H_6)(CO)_3$	31.0	23.4	37.4	29.4	38.8	26.8	37.8	33.0	32.0	27.9	29.8
CrO_3	128.2	105.7	131.2	109.0	130.5	98.8	122.2	110.2	138.1	110.3	114.6
$Mn_2(CO)_{10}$	28.6	20.3	34.9	26.4	36.4	23.6	34.8	29.6	6.3	22.9	22.7
$Mn(COCH_3)(CO)_5$	29.9	22.3	36.1	28.2	37.4	25.5	35.7	30.9	7.5	25.0	24.5
$Mn(C_6H_5)(CO)_5$	31.6	24.3	37.8	30.2	39.1	27.6	37.4	32.8	10.3	27.2	26.2
$MnH(CO)_5$	34.7	27.4	40.7	33.0	41.2	29.7	40.3	35.7	12.7	29.0	27.4
$MnCl(CO)_5$	31.0	23.9	36.9	29.5	38.0	26.8	36.9	32.3	8.8	25.8	30.7
$Fe(CO)_4$	33.7	23.4	39.4	29.8	40.8	26.9	37.4	31.7	1.1	25.8	24.7
$Fe(C_2H_4)(CO)_4$	30.9	23.3	37.6	30.3	39.4	28.5	36.8	32.3	3.3	26.1	27.1
$Fe(CO)_5$	34.0	25.9	40.4	32.6	42.0	30.5	39.2	34.4	3.8	28.4	28.0
$FeH_2\ (CO)_4$	41.3	35.4	46.8	41.1	46.9	38.3	45.8	42.3	17.3	36.8	38.1
$Fe(C_5H_5)_2$	75.9	65.8	90.1	80.7	93.6	78.8	91.9	85.3	24.5	79.1	85.5
$Co_2(CO)_8$	40.4	26.4	39.0	32.2	50.5	30.0	45.0	34.7	2.1	31.2	30.6
$CoH(CO)_4$	46.8	34.6	45.6	39.8	55.1	36.9	50.7	41.6	10.8	38.1	36.9
$Ni(CO)_4$	36.2	29.4	41.7	34.5	43.2	32.5	41.3	37.1	0.0	34.5	35.3
$Ni(CO)_3$	41.0	32.6	46.5	37.6	47.9	35.0	45.6	40.5	–6.8	39.1	38.8
CuCl	78.9	78.8	84.7	84.4	86.0	83.4	85.9	84.9	43.5	85.9	87.9
CuF	94.8	89.8	97.3	93.0	98.2	89.3	96.6	93.1	48.6	96.5	102.6
$Zn(C_2H_5)_2$	29.4	30.7	34.5	35.6	36.2	35.7	34.7	34.6	6.9	35.0	37.3
$Zn(CH_3)_2$	37.4	38.5	42.6	43.5	44.3	43.4	42.1	41.9	14.2	41.9	44.1
MAE	6.3	4.3	9.4	3.5	10.9	2.7	8.6	4.5	30.2	2.3	—
ME	3.4	–4.1	8.6	1.6	10.4	–1.3	7.9	3.1	–28.5	0.2	—
MaxE	13.6	–19.6	20.6	–9.6	21.2	–15.8	14.4	–9.5	–91.5	7.1	—

Note: Experimental data are from NIST (ref. 11) except for the heat of formation of the cyclopentadienyl radical (from ref. 12). MAE: mean absolute error. ME: mean error. MaxE: maximum error.

give MAEs of 6.3–10.9 kcal/mol and tend to over-bind, as we would expect. The hybrid DFTs give MAEs of 2.7–4.5 kcal/mol. In general, the performance of the various functionals on this transition-metal benchmark set mirrors their performance for main-group atomization energies.[5,33] We conclude that there is little qualitative difference in the ability of density functionals to predict accurate thermochemistry for main-group or transition-metal complexes. This explains the transferability of DFTs to organometallic and catalysis applications despite their relatively poor performance for small transition-metal molecules.[1–3]

We note that all of the DFTs considered will have problems with the dissociation energies of metal–metal multiple bonds, as observed by Furche and Perdew.[2] These problems arise because approximate functionals cannot describe near-degeneracies, as occur in the stretching of chemical bonds.[34,35] Transition-metal dimers, with their weakly interacting 3d atomic orbitals, have near-degeneracies even at equilibrium geometries. In these cases, DF07 will give even larger errors than pure DFTs and hybrid functionals, since it is based on Hartree–Fock exchange.

Conclusions

In this work, we have compiled a new thermochemical benchmark set consisting of mean ligand-removal enthalpies of transition-metal complexes. This set is more representative of inorganic chemistry than other recent data sets consisting primarily of small transition-metal molecules.[1–3] We have assessed the performance of our recently published exact-exchange-based density functional, DF07,[5] and several popular pure and hybrid DFTs. DF07 gives the best agreement with experiment of the functionals considered, with results approaching chemical accuracy. DF07 nicely recovers the nondynamical correlation effects that are important in metal–ligand bonds. We also observe that, for the present set of closed-shell transition-metal complexes, the errors of the selected density functionals are similar to the errors typically seen in main-group thermochemistry.

Supplementary data

Supplementary data for this article are available on the journal Web site (canjchem.nrc.ca) or may be purchased from the Depository of Unpublished Data, Document Delivery, CISTI, National Research Council Canada, Ottawa, ON K1A 0R6, Canada. DUD 5266 . For more information on obtaining material, refer to cisti-icist.nrc-cnrc.gc.ca/cms/unpub_e.shtml.

Acknowledgments

This work is supported by the Natural Sciences and Engineering Research Council of Canada (NSERC), the Canada Council for the Arts through a Killam Research Fellowship to ADB, the Killam Trust of Dalhousie University, and ACEnet (the Atlantic Computing Excellence network).

References

(1) Riley, K. E.; Merz, K. M., Jr. *J. Phys. Chem. A* **2007**, *111* (27), 6044–6053. doi:10.1021/jp0705931. PMID:17571862.

(2) Furche, F.; Perdew, J. P. *J. Chem. Phys.* **2006**, *124* (4),o. 044103. doi:10.1063/1.2162161. PMID:16460145.

(3) Zhao, Y.; Truhlar, D. G. *J. Chem. Phys.* **2006**, *124*, 224105 doi:10.1063/1.2202732.

(4) (a) See for example: Woo, T. K.; Margl, P. M.; Blochl, P. E.; Ziegler, T. *J. Phys. Chem. B* **1997**, *101* (40), 7877–7880. doi:10.1021/jp9717296.; (b) Deng, L. Q.; Woo, T. K.; Cavallo, L.; Margl, P. M.; Ziegler, T. *J. Am. Chem. Soc.* **1997**, *119* (26), 6177–6186. doi:10.1021/ja970226a.; (c) Ziegler, T. *Can. J. Chem.* **1995**, *73* (6), 743–761. doi:10.1139/v95-095.

(5) Becke, A. D.; Johnson, E. R. *J. Chem. Phys.* **2007**, *127* (12),o. 124108. doi:10.1063/1.2768530. PMID:17902894.

(6) Johnson, E. R.; Becke, A. D. *J. Chem. Phys.* **2008**, *128* (12),o. 124105. doi:10.1063/1.2894878. PMID:18376906.

(7) Veillard, A. *Chem. Rev.* **1991**, *91* (5), 743–766. doi:10.1021/cr00005a006.

(8) Hyla-Kryspin, I.; Grimme, S. *Organometallics* **2004**, *23* (23), 5581–5592. doi:10.1021/om049521b.

(9) DeYonker, N. J.; Peterson, K. A.; Steyl, G.; Wilson, A. K.; Cundari, T. R. *J. Phys. Chem. A* **2007**, *111* (44), 11269–11277. doi:10.1021/jp0715023. PMID:17500547.

(10) Balabanov, N. B.; Peterson, K. A. *J. Chem. Phys.* **2005**, *123* (6),o. 064107. doi:10.1063/1.1998907.

(11) Afeefy, H. Y.; Liebman, J. F.; Stein, S. E. Neutral Thermochemical Data. Available from http://webbook.nist.gov/chemistry. National Institute of Standards and Technology, 2008.

(12) Nunes, P. M.; Agapito, F.; Costa Cabral, B. J.; Borges dos Santos, R. M.; Martinho Simões, J. A. *J. Phys. Chem. A* **2006**, *110* (15), 5130–5134. doi:10.1021/jp060325n. PMID:16610835.

(13) Carreón-Macedo, J. L.; Harvey, J. N. *Phys. Chem. Chem. Phys.* **2006**, *8* (1), 93–100. doi:10.1039/b513325d. PMID:16482248.

(14) Becke, A. D. *J. Chem. Phys.* **1993**, *98* (7), 5648. doi:10.1063/1.464913.

(15) Lee, C.; Yang, W.; Parr, R. G. *Phys. Rev. B* **1988**, *37* (2), 785–789. doi:10.1103/PhysRevB.37.785.

(16) Curtiss, L. A.; Redfern, P. C.; Raghavachari, K.; Pople, J. A. *J. Chem. Phys.* **2001**, *114* (1), 108. doi:10.1063/1.1321305.

(17) Frisch, M. J.; Trucks, G. W.; Schlegel, H. B.; Scuseria, G. E.; Robb, M. A.; Cheeseman, J. R.; Montgomery, J. A., Jr.; Vreven, T.; Kudin, K. N.; Burant, J. C.; Millam, J. M.; Iyengar, S. S.; Tomasi, J.; Barone, V.; Mennucci, B.; Cossi, M.; Scalmani, G.; Rega, N.; Petersson, G. A.; Nakatsuji, H.; Hada, M.; Ehara, M.; Toyota, K.; Fukuda, R.; Hasegawa, J.; Ishida, M.; Nakajima, T.; Honda, Y.; Kitao, O.; Nakai, H.; Klene, M.; Li, X.; Knox, J. E.; Hratchian, H. P.; Cross, J. B.; Bakken, V.; Adamo, C.; Jaramillo, J.; Gomperts, R.; Stratmann, R. E.; Yazyev, O.; Austin, A. J.; Cammi, R.; Pomelli, C.; Ochterski, J. W.; Ayala, P. Y.; Morokuma, K.; Voth, G. A.; Salvador, P.; Dannenberg, J. J.; Zakrzewski, V. G.; Dapprich, S.; Daniels, A. D.; Strain, M. C.; Farkas, O.; Malick, D. K.; Rabuck, A. D.; Raghavachari, K.; Foresman, J. B.; Ortiz, J. V.; Cui, Q.; Baboul, A. G.; Clifford, S.; Cioslowski, J.; Stefanov, B. B.; Liu, G.; Liashenko, A.; Piskorz, P.; Komaromi, I.; Martin, R. L.; Fox, D. J.; Keith, T.; Al-Laham, M. A.; Peng, C. Y.; Nanayakkara, A.; Challacombe, M.; Gill, P. M. W.; Johnson, B.; Chen, W.; Wong, M. W.; Gonzalez, C.; Pople, J. A. *Gaussian 03,* Revision C.02; Gaussian Inc.: Wallingford, CT, 2004.

(18) Becke, A. D. *Phys. Rev. A* **1988**, *38* (6), 3098–3100. doi:10.1103/PhysRevA.38.3098. PMID:9900728.

(19) Perdew, J. P. *Phys. Rev. B* **1986**, *33* (12), 8822–8824. doi:10.1103/PhysRevB.33.8822.

(20) Perdew, J. P.; Burke, K.; Ernzerhof, M. *Phys. Rev. Lett.* **1996**, *77* (18), 3865–3868. doi:10.1103/PhysRevLett.77.3865. PMID:10062328.

(21) Adamo, C.; Barone, V. J. *J. Chem. Phys.* **1999**, *110* (13), 6158. doi:10.1063/1.478522.
(22) Tao, J.; Perdew, J. P.; Staroverov, V. N.; Scuseria, G. E. *Phys. Rev. Lett.* **2003**, *91* (14),o. 146401. doi:10.1103/PhysRevLett.91.146401. PMID:14611541.
(23) Staroverov, V. N.; Scuseria, G. E.; Tao, J.; Perdew, J. P. *J. Chem. Phys.* **2003**, *119* (23), 12129. doi:10.1063/1.1626543.
(24) Perdew, J. P.; Wang, Y. *Phys. Rev. B* **1992**, *45* (23), 13244–13249. doi:10.1103/PhysRevB.45.13244.
(25) (a) Becke, A. D. *Int. J. Quantum Chem. Symp.* **1989**, *23*, 599; (b) Becke, A. D.; Dickson, R. M. *J. Chem. Phys.* **1990**, *92* (6), 3610. doi:10.1063/1.457869.
(26) Becke, A. D. *J. Chem. Phys.* **2005**, *122* (6),o. 064101. doi:10.1063/1.1844493. PMID:15740361.
(27) Becke, A. D. *Int. J. Quantum Chem. Symp.* **1994**, *52* (S28), 625–632. doi:10.1002/qua.560520855.
(28) Becke, A. D. *Int. J. Quantum Chem.* **1985**, *27* (5), 585–594. doi:10.1002/qua.560270507.
(29) Johnson, E. R.; Dickson, R. M.; Becke, A. D. *J. Chem. Phys.* **2007**, *126* (18),o. 184104. doi:10.1063/1.2723118. PMID:17508789.
(30) Becke, A. D. *J. Chem. Phys.* **2002**, *117* (15), 6935. doi:10.1063/1.1503772.
(31) Becke, A. D. *Can. J. Chem.* **1996**, *74* (6), 995–997. doi:10.1139/v96-110.
(32) Johnson, E. R.; Clarkin, O. J.; DiLabio, G. A. *J. Phys. Chem. A* **2003**, *107* (46), 9953–9963. doi:10.1021/jp035315q.
(33) Curtiss, L. A.; Raghavachari, K.; Redfern, P. C.; Pople, J. A. *J. Chem. Phys.* **1997**, *106* (3), 1063. doi:10.1063/1.473182.
(34) Cohen, A. J.; Mori-Sánchez, P.; Yang, W. *Science* **2008**, *321* (5890), 792–794. doi:10.1126/science.1158722. PMID:18687952.
(35) Cohen, A. J.; Mori-Sánchez, P.; Yang, W. *J. Chem. Phys.* **2008**, *129* (12),o. 121104. doi:10.1063/1.2987202. PMID:19044996.
(36) Bühl, M.; Kabrede, H. *J. Chem. Theory Comput.* **2006**, *2* (5), 1282–1290. doi:10.1021/ct6001187.
(37) Mitin, A. V.; Baker, J.; Pulay, P. *J. Chem. Phys.* **2003**, *118* (17), 7775. doi:10.1063/1.1563619.

Appendix: Assessment of geometries

In this work, B3LYP/6–31G(2df,p) was used for geometry optimizations and zero-point energy calculations. This is the theory/basis-set combination recommended in the G3X thermochemical procedure[16] for geometry and frequency calculations. Since B3LYP/6–31G(2df,p) is not commonly used in transition-metal chemistry, we assess its performance in computing bond lengths in organometallic complexes in this Appendix (note that the basis-set polarization designation 2df actually means 2fg on a transition-metal atom).

In Table A1, we compare 18 optimized B3LYP/6–31G(2df,p) bond lengths for complexes in our benchmark set with available experimental data from refs. 2 and 36. The mean absolute error in these 18 bond lengths is 0.02 Å. The largest errors, 0.08 and 0.09 Å, occur in the late transition-metal systems $Co_2(CO)_8$ and CuF, respectively, in agreement with the findings of others.[37] This level of accuracy in geometries is quite adequate for thermochemical benchmarking purposes.

Table A1. Calculated B3LYP/6–31G(2df,p) bond lengths for benchmark transition-metal complexes in Å.

Compound	Bond	B3LYP	Experimental
TiF_4	Ti—F	1.74	1.75[a]
$TiCl_4$	Ti—Cl	2.17	2.17[b]
$Cr(CO)_6$	Cr—C	1.91	1.92[a]
$Cr(C_6H_6)(CO)_3$	Cr—C (C_6H_6)	2.23	2.21[b]
$Cr(C_6H_6)(CO)_3$	Cr—C (CO)	1.85	1.86[b]
$Mn_2(CO)_{10}$	Mn—Mn	2.96	2.98[a]
$Mn_2(CO)_{10}$	Mn—C_{ax}	1.80	1.80[a]
$Mn_2(CO)_{10}$	Mn—C_{eq}	1.85	1.87[a]
$Fe(CO)_5$	Fe—C_{ax}	1.81	1.81[a]
$Fe(CO)_5$	Fe—C_{eq}	1.80	1.83[a]
$Fe(C_5H_5)_2$	Fe—C	2.06	2.06[a]
$Fe(C_2H_4)(CO)_4$	Fe—C (C_2H_4)	2.11	2.12[b]
$Fe(C_2H_4)(CO)_4$	Fe—C_{ax}	1.81	1.82[b]
$Fe(C_2H_4)(CO)_4$	Fe—C_{eq}	1.79	1.81[b]
$CoH(CO)_4$	Co—C_{eq}	1.79	1.82[b]
$Co_2(CO)_8$	Co—Co	2.61	2.53[a]
$Ni(CO)_4$	Ni—C	1.81	1.84[a]
CuF	Cu—F	1.66	1.75[a]
Mean absolute error		0.02	—

[a]Experimental data are from ref. 2.
[b]Experimental data are from ref. 36. ax: axial. eq: equatorial.

A comparative study on the LDA + *U* and hybrid functional methods on the description of the electronic structure of $YTiO_3$ under high pressure

Z. Song, J.J. Yang, and J.S. Tse

Abstract: The electronic structures of $YTiO_3$ under pressure have been studied with LDA + *U* (local density approximation + Hubbard parameter) and hybrid functional methods. From matching the experimental band gaps, the Hubbard *U* and hybrid functional mixing parameters were determined. It is found that both parameters vary with the pressure. Analysis of the electronic structures indicates that the description of the chemical bonding is also dependent on the method of choice.

Key words: density functional theory, Hubbard Model, hybrid function, electronic structure, high pressure.

Résumé : On a étudié les structures électroniques du $YTiO_3$ sous pression en faisant appel aux méthodes LDA + *U* et de la fonction hybride. En utilisant les séparations de bandes, on a déterminé les paramètres de mélange Hubbard *U* et de la fonction hybride. On a trouvé que les deux paramètres varient avec la pression. L'analyse des structures électroniques indique que la description de la liaison chimique dépend aussi du choix de la méthode.

Mots-clés : théorie de la fonctionnelle de la densité, modèle de Hubbard, fonction hybride, structure électronique, pression élevée.

[Traduit par la Rédaction]

Introduction

The field of electronic structure calculation is at a momentous stage, with rapid advances in basic theory, new algorithms, computational methods, and new computer architectures. There are basically two numerical approaches based on the Hartree–Fock (HF) and the density functional theory (DFT),[1] respectively. Within the independent particle approximation, both methods have several known shortcomings for a correct description of the electronic structure of highly correlated systems. The HF method, which neglects electron correlation effects, often overestimates the energy gap between the occupied and conduction band of solids. Although the DFT is formally exact, but with many approximations, for example, the local spin density approximation (LSDA), it tends to symmetrically underestimate the band gap. Well-known examples are the transition-metal oxides, FeO, MnO, and NiO.[2,3] This shortcoming has led to the erroneous prediction of a metallic ground state for FeO and very small band gaps in MnO and NiO.[4–6] The deficiency of these methods in the prediction of excited-state properties can be amended by advanced treatments of the electron correlation effect. For example, through configuration interaction (CI) methods in the HF-based theory and the extension of the LSDA to include nonlocal interactions through perturbative theory, such as the *GW* method.[7] However, the extension of these methods are rather computationally demanding and expensive to apply in the study of the electronic structure of highly correlated solids.

Recent studies have shown that the HF-based methods[2,8] can be improved substantially with the so-called hybrid functional approach. In essence, the HF Hamiltonian is augmented by introducing an exchange-correlation function computed from the DFT method. On the other hand, DFT tends to emphasize delocalization of the valence electrons and yields a smaller gap between occupied and unoccupied states. To amend this problem, an ad hoc scheme with a semi-empirical correction to the DFT energy functional is introduced to include a model Hamiltonian depending on *U*, which is the "on-site" electron–electron (Coulomb) repulsion. This method is known as the LDA + *U* (local density approximation + Hubbard parameter) method.[9,10]

The goal of this investigation is to compare the results on the electronic properties obtained from the LDA + *U* and hybrid functional methods and to obtain the description of chemical bonding in $YTiO_3$ at ambient and high pressure. $YTiO_3$ was chosen as a prototype of transition-metal oxides due to the considerable experimental and theoretical work already reported. Most importantly, the band gap of $YTiO_3$ as a function of external pressure has been determined recently from synchrotron infrared experiments.[11] This experi-

Received 16 February 2009. Accepted 17 July 2009. Published on the NRC Research Press Web site at canjchem.nrc.ca on 19 September 2009.

This article is part of a Special Issue dedicated to Professor T. Ziegler.

Z. Song, J. Yang, and J. Tse.[1] Department of Physics and Engineering Physics, University of Saskatchewan, Saskatoon, SK S7N 5E2, Canada.

[1]Corresponding author (e-mail: john.tse@usask.ca).

mental data is very useful as it offers an opportunity to evaluate the pressure dependence of the electron correlation effects and band gap energies over a wide pressure range.

The ground-state electronic structure of $YTiO_3$ under ambient pressure has previously been studied by a variety of theoretical calculations. A calculation using the full-potential linear augmented plane wave method within the LSDA reproduced the experimentally observed ferromagnetism, but erroneously predicted a metallic ground state.[6] The insulating behaviour was attributed to unfounded lattice distortions.[12] Later, the electronic structure of $YTiO_3$ was studied using the generalized gradient approximation (GGA), but the calculation failed to reproduce its insulating nature.[13] The band gap only appeared with the introduction of the LDA + U model. A calculation on the orbital ordering in $YTiO_3$ at ambient pressure using LSDA had been reported.[14] The orbital ordering was found to be in good agreement with the experiment and the HF results. The relationship between lattice distortion and the magnetic behaviour has also been reported recently.[15] Lately, dynamical mean-field theory (DMFT) calculations[16,17] demonstrated the importance of the interplay between correlation effects and cation covalency in suppressing the orbital fluctuations leading to an insulating state.[18] The DMFT[16,17] maps a model Hamiltonian involving highly correlated d electrons (e.g., the Hubbard model) onto a self-consistent quantum impurity model and then solved exactly (e.g., numerically by the Monte Carlo method), is the current method of choice for the treatment of highly correlated systems. However, the computational expenditure is significantly more demanding than that of the standard LDA + U[9,10] and hybrid functional methods.[19–21] In the LDA + U method, the atom-centered Hubbard parameter, U, can be estimated theoretically from atomic[22–24] or cluster models[25] and recently, self-consistently from band calculations using the linear response method.[26] However, the application of the LDA + U method becomes more complicated for high pressure solids where atoms are compressed against each other since it is not certain whether a unique choice of U is possible over a large pressure range. In previous studies of electronic structure of transition-metal oxides at high pressure employing LDA + U, a constant U parameter was always assumed. The validity of this assumption has yet to be tested.

The purpose of this study is to understand the pressure dependence of the on-site Coulomb parameter, U, in the LDA + U theory and the amount of mixing (mixing parameter A) used in the hybrid density functional theory. This can be achieved by treating U and A as empirical parameters and optimize their values by matching the calculated with the experimental band gap at select pressures. The questions to be addressed are (*i*) if there were any discernible trends in these parameters with pressure and (*ii*) did the calculated electronic structure depend on the theoretical model? The present study is a prelude for future work on the nonempirical determination of the U parameters[26] at high pressure.

This paper is organized as follows. First, a brief description of the methods and essential computational details will be given. This is followed by the presentation of the results obtained from LDA + U and hybrid functional methods. Finally, the electronic structures of $YTiO_3$ obtained from both methods will be compared and discussed.

Theoretical and computational details

The LDA + U theory

The LDA + U method is designed to account for strong electron correlation in LDA theory by an additional Hubbard-like Hamiltonian including on-site interactions,[9,10] E_U, which depends on the electron occupancy (n). To first order, the total Hamiltonian becomes[9,10]

$$[1] \qquad E_{\mathrm{DFT}+U} = E_{\mathrm{DFT}}[\rho^\sigma] + E_U[\{n^\sigma_{jj'}\}]$$

where ρ^σ is the charge density for spin-σ electrons and $n^\sigma_{jj'}$ is the density matrix for correlated electrons (σ is the spin index, j and j' are the orbital indices). A simple rotationally invariant LDA + U Hamiltonian of the form,[27]

$$[2] \qquad E_{\mathrm{DFT}+U} = E[\rho^\sigma] + \frac{(U-J)}{2}\sum_\sigma \left[\left(\sum_j n^\sigma_{jj}\right) - \left(\sum_{jl} n^\sigma_{jl} n^\sigma_{lj}\right)\right]$$

is employed in the present calculations. J is the intra-atomic exchange interaction. The corresponding potential V^σ_{ij} is given by

$$[3] \qquad V^\sigma_{ij} = \frac{\delta E[\rho^\sigma]}{\delta n^\sigma_{ij}} + (U-J)\left[\frac{1}{2}\delta_{jl} - \delta^\sigma_{jl}\right]$$

In this study, the U parameter is treated as an empirical parameter and evaluated from a comparison of the calculated and experimental band gaps. A fixed value of J = 0.64 eV was used throughout.

Computational details

The program VASP (Vienna ab initio simulation package)[29] was employed in this study. VASP is a software package for performing ab initio electronic calculations using pseudopotentials method with a plane wave basis set.[1] The approach implemented in VASP is based on the local density approximation (LDA) with an extension to the LDA + U approximation. The interaction between ions and electrons is described by pseudopotentials and allows a considerable reduction of the number of plane waves for transition metals and first row elements like C and O. Projector-augmented wave (PAW) potentials[30,31] for Ti, Y, and O were taken from the pseudopotential library distributed with the VASP code. The Perdew–Burke–Ernzonhof (PBE) exchange-correlation functional[32] was used. A Monkhorst–Pack[33] 8 × 6 × 8 k-mesh was used for the energy sampling of the first Brillouin zone (BZ). $YTiO_3$ is an open-shell system, all calculations were performed in the spin-unrestricted (spin-polarized) formalism.[34] Since only the Ti 3d orbitals are occupied at the top of the valence band (vide infra), the on-site Coulomb correction, U, is applied to the Ti atom only. Full geometry optimization was performed at selected pressure points.

Hybrid functional method

Since the HF theory neglects the correlation effects, an empirical extension to improve the accuracy is to include some form of correlation energy. The hybrid functional theory is based on the adiabatic connection between the HF and DFT. Applying the adiabatic connection, the exchange-correlation (XC) energy is given as

$$[4] \qquad E_{XC} = \int_0^1 U_{XC}^{\lambda} \, d\lambda$$

where λ "connects" the noninteracting Kohn–Sham reference system (λ = 0) to the fully-interacting systems (λ = 1) through a continuum of partially interacting systems ($0 \leq \lambda \leq 1$), all of which have the same density $n(r)$.[20] The advantage of the hybrid method is that for a given system, if an optimal coupling parameter, λ, can be found, it will balance the deficiency inherent in both the HF and DFT methods. The mixing of the DFT functional helps to introduce correlation effects into the Hamiltonian.

A practical "hybrid" scheme was introduced by Becke.[21] In this method, the exchange-correlation energy is expressed as the arithmetic average of the exact Kohn–Sham exchange of the local spin density approximation (LSDA) exchange-correlation potential,

$$[5] \qquad E_{XC} = 0.5E_X + 0.5U_{XC}^{LSDA}$$

Test calculations on atomic systems gave promising results on atomic exchange-correlation energies, atomization energies, and ionization potentials. This method was later extended to the hybrid functional formalism employing a three-parameter exchange-correlation (B3LYP) expression with the parameters obtained in a semi-empirical manner.[21] Using this hybrid functional, excellent results on the atomization energies of molecules in good accordance with experimental values were obtained. For isolated molecules, the accuracy of this method rivals that of the more sophisticated HF-based correlation methods but at a fraction of the computational expense.

In this study, a simplified form of the hybrid functional is employed with the exchange-correlation energy given by Ref. 8,

$$[6] \qquad E_{XC} = (1 - A)E_X^{LSA} + AE_X^{HF} + E_C^{VWM}$$

The E_{XC} potential is then a simple sum of the individual energy components, the local density approximation (LDA) exchange (E_X^{LDA}), the Hartree–Fock (E_X^{HF}), and the correlation energy functional of Vosko–Wilk–Nusair (VWM, E_C^{VWM}). By tuning the mixing parameter A between 0 and 1, the progression from pure LDA to pure HF exchange can be followed. This approximate hybrid functional has been applied to calculate the band gap on a number of solid semiconductors with good results.

Computational details

The localized basis set program CRYSTAL for periodic systems[35] was used for the hybrid functional calculations. Atomic double zeta valence basis sets augmented with diffuse functions for Y, Ti, and O atoms were taken from the tabulation found at http://www.tcm.phy.cam.ac.uk/~mdt26/crystal.html. In view of the large amount of computational resources required, the electronic structures at four selected pressures were computed using the optimized structures determined from the LDA + U calculations. This protocol was verified on $YTiO_3$ at ambient pressure via the calculation of the forces acting on the atoms in the crystal using the hybrid functional method. Even without full geometry optimization, the residual forces were found to be acceptably small.

Fig. 1. A perspective view of the crystal structure of $YTiO_3$.

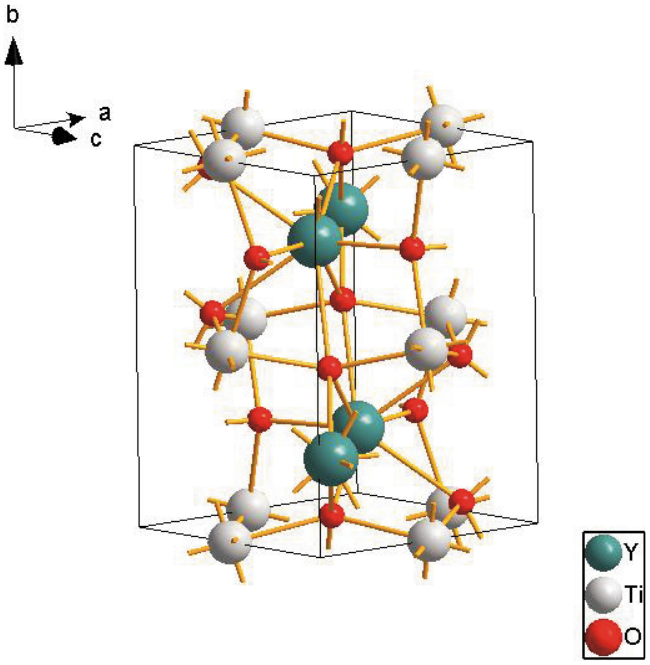

Results

$YTiO_3$ crystallized in the tetragonal space group *Pnma*[11,36] and the structure is depicted in Fig. 1. The Y atom has three valence electrons ($4d^15s^2$) and the Ti atom has four valence electrons ($3d^25s^2$). Formally, each oxygen atom can accommodate two more electrons forming an O^{2-} anion. If the charge transfer was completed, all of the electrons in the Y atom will be removed and only one electron will be left in the Ti 3d orbitals. According to the crystal field theory, in an ideal octahedral environment, this single electron will occupy the t_{2g} orbital. Moreover, it is expected that the valence bands consist mostly of Y–O and Ti–O bonding levels with the singly occupied electron in the Ti 3d orbitals at the top of the valence bands. In reality, although each Ti atom in the crystal structure is surrounded by six O atoms, there are three distinct Ti–O bonds of 2.0161, 2.0232, and 2.0769 Å.[11,36] The O–Ti–O angles range from 87°–90°. Therefore, the local environment of the Ti atom is distorted from the ideal octahedral environment, thus lifting the degeneracy of the t_{2g} orbitals. The single Ti 3d electron then occupies the lowest band and the spin multiplicity of the ground state wave function is a doublet. In the ensuing discussion, we simply refer to the singly filled band as "lower t_{2g}" and the lowest empty band as "higher t_{2g}". The empty e_g band is located at a higher energy.

LDA + *U* method

Before embarking on a detailed analysis of the electronic structure, the reliability of the LDA + U method and the choice of computational parameters used in the present calculations are examined from the comparison of calculated and experimental unit cell parameters. The theoretical predicted lattice constants at zero pressure of a = 5.7705 Å, b = 7.6719 Å, and c = 5.3675 Å, using an optimal U parameter of 2.7 eV (see below) are in exceedingly good agreement with the experimental[11] values of a = 5.6790 Å, b =

Fig. 2. Comparison of experimental and calculated lattice constants for $YTiO_3$.

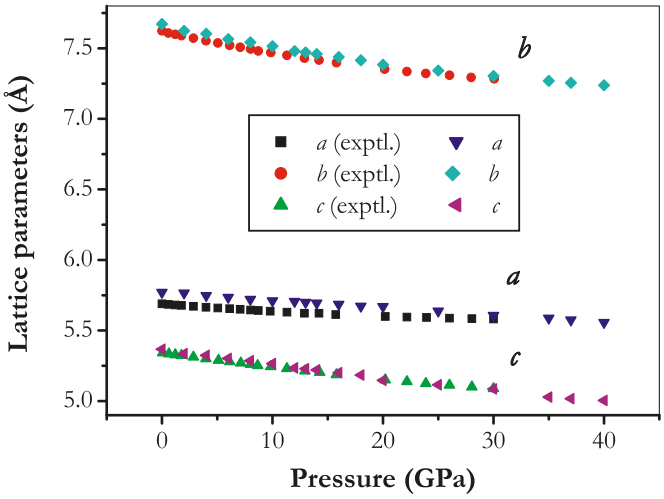

7.6110 Å, and c = 5.3160 Å. The atomic coordinates (theoretical values in parentheses): Y (0.07294(0.0749), 1/2, 0.97925(0.9764)), O1(0.4580 (0.4544), 1/2, 0.1213(0.1260)), and O2 (0.3095(0.3101), 0.0579(0.0585), 0.6909(0.6904)) are also in good accord with observed values. Over the pressure range from 0 to 25 GPa where experimental data is available, the agreement between the calculated and observed lattice parameters is consistently good (Fig. 2).

Since the observed maximum band gap energy of $YTiO_3$ is ~0.652 eV or ~5300 cm^{-1},[11] it can be measured conveniently with midinfrared optical absorption under pressure at ambient temperature. Quasi-hydrostatic conditions were ensured by the use of two different pressure transmission media: solid N_2 and KCl. The experimental results show that the band gap decreases almost linearly with increasing pressure. From 1.6 to 16 GPa,[11] the band gap energy reduces by ~2000 cm^{-1} (or 0.25 eV). No closure of the band gap is observed in the experiment up to 16 GPa. The band gap energies, ΔE, for pressures > 16 GPa were obtained from the extrapolation of a linear fit to experimental data,

$$[7] \qquad \Delta E(P)\,(\mathrm{cm}^{-1}) = 5300 - 145 \times P\,(\mathrm{GPa})$$

The derived optimal U parameters are summarized in Fig. 3. The U parameter obtained at zero pressure of 2.70 eV with a fixed J of 0.64 eV is consistent with the theoretically calculated U and J parameters of 2.75 eV and 0.81 eV, respectively[15] (converted from the Kanamori definition, see ref. 15). A general trend emerges on the pressure dependence of the optimal U parameters. At low pressure, from 0 to 4 GPa, the U parameter is not sensitive to the change in pressure and remains constant at 2.70 eV. This observation helps to understand the apparent success on the assumption of a constant U parameter in previous applications to mineral oxide systems at low pressure. It is likely that the change in electron correlation effects at low pressure is quite small and does not affect the electronic structure to a significant extent. This assumption, however, is certainly not valid over a broader range of pressures. The U parameter shows a slow steady decrease from 4 to 12 GPa and drops more rapidly for pressures above 12 GPa.

Fig. 3. Variation of calculated U parameter with pressure. The curve is a polynomial fit of the calculated data using eq. [7] (see text).

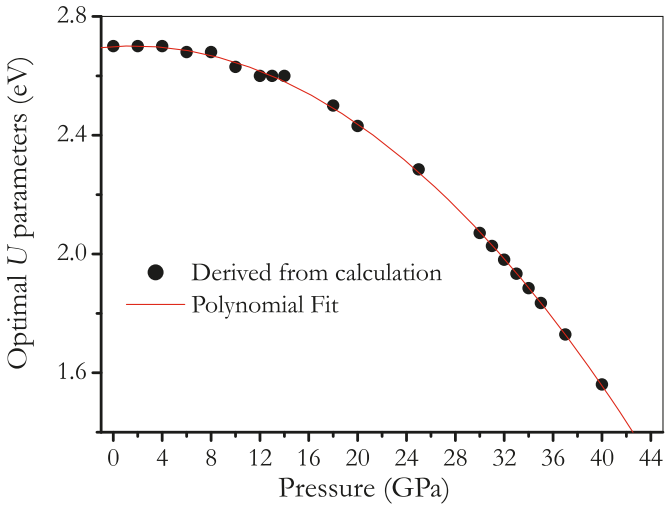

Fig. 4. Comparison of hybrid functional calculated and experimental band gaps for $YTiO_3$. Note that the band closure is predicted at 32 GPa from the extrapolation of the polynomial fit to the experimental data (see text).

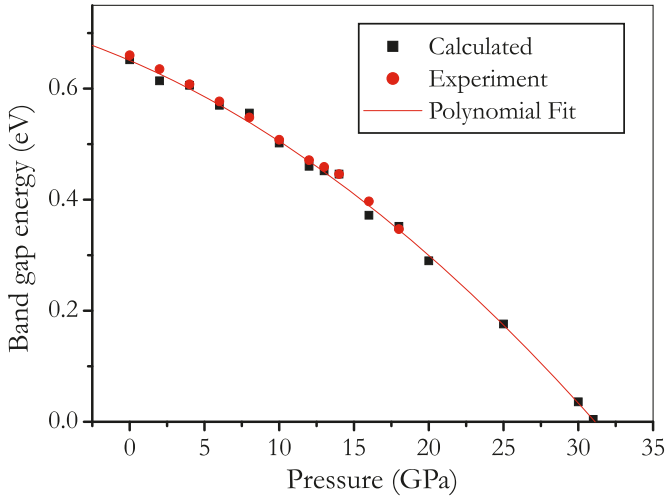

The experimental and calculated band gaps for $YTiO_3$ from 0 to 40 GPa are shown in Fig. 4. From LDA + U calculations, it is shown that $YTiO_3$ will become metallic at 32 GPa. This value is consistent with the estimation from the extrapolation of the experimental band gap energies.[11] The result, however, disagrees with a recent theoretical calculation where the electronic gap closure was suggested to occur at ~100 GPa,[37] which is almost three times that of the present estimated pressure. It should be noted that in this earlier calculation, a constant U parameter was employed throughout the entire pressure range.[37] As shown here, this assumption is invalid and therefore the pressure of the closure of the band gap would be seriously overestimated. It is noteworthy that at 32 GPa, the pressure at which $YTiO_3$ was predicted to become metallic, the derived U parameter is 1.98 eV, which is 33% smaller than the ambient value of 2.70 eV. Using a polynomial fit to the calculated results (Fig. 3), the extrapolated pressure where U = 0 is

Fig. 5. Total and projected density of state (DOS) of Ti in $YTiO_3$ calculated using LDA + U and hybrid functional methods at (a) 0 GPa (U = 2.70 eV), (b) 16 GPa (U = 2.50 eV), (c) 0 GPa (A = 0.145), and (d) 16 GPa (A = 0.13). U is the Hubbard parameter and A is the mixing parameter (see text).

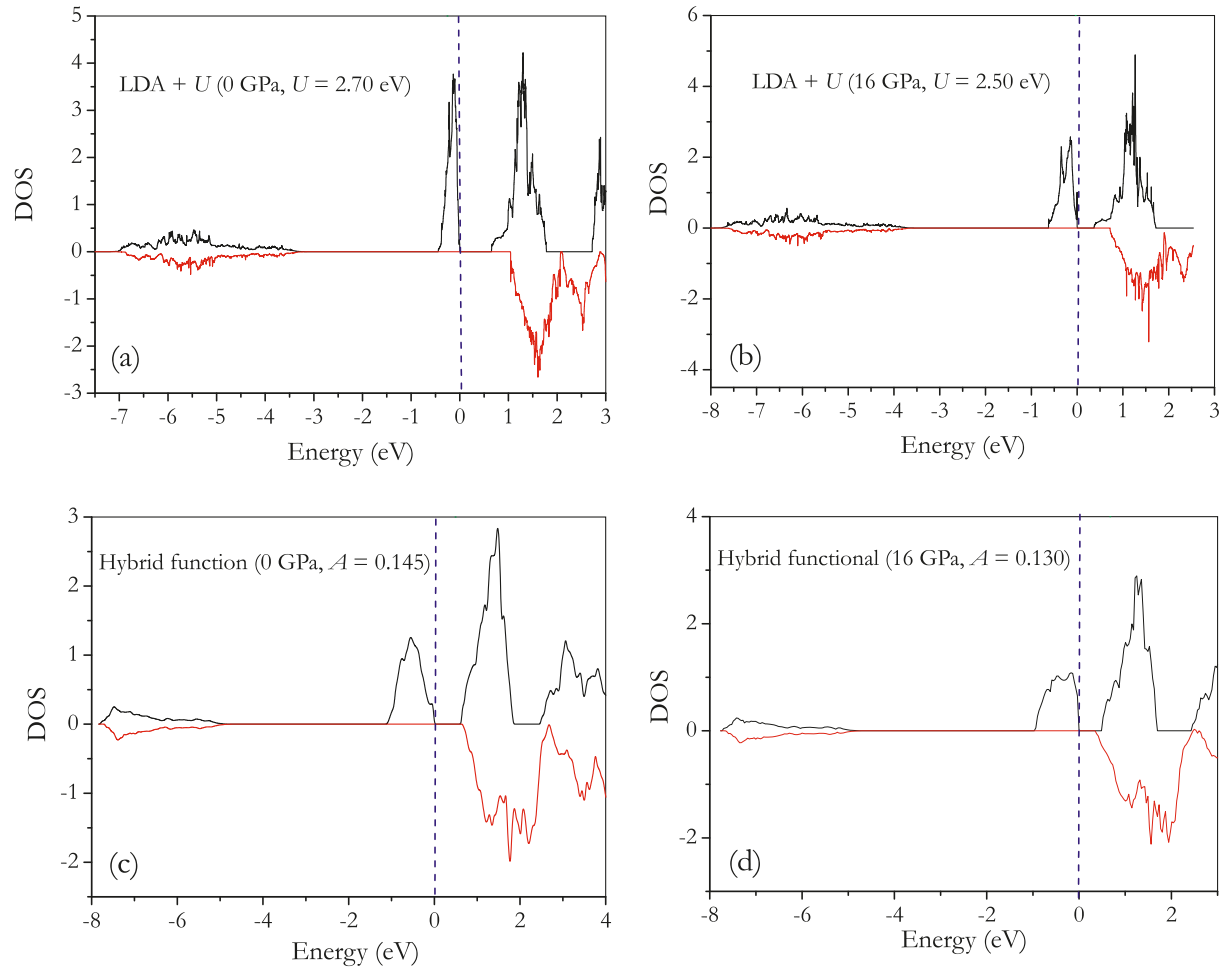

60 GPa. This value is significantly higher than the metallization pressure. This result suggests that even in the metallic state, the effect of on-site repulsion of the Ti 3d electron is not negligible (i.e., $U \neq 0$). This raises the question as to whether the standard LDA method should be used in highly correlated metallic systems.

The calculated trend of the dependence of the U parameter with pressure provides an insight into the behaviour of the electron repulsive interactions in $YTiO_3$. Since the U parameter is added to the Ti atoms to alleviate the problem of overestimated delocalization of valence electrons, a smaller U at high pressure indicates that the effect of delocalization becomes more dominant. It is consistent with the expectation that the overlap between Ti and the surrounding oxygen atoms will become more significant with decreasing Ti–O distances at high pressure. Consequently, the valence electrons should be more delocalized. As a result, the importance of the on-site Coulomb repulsion becomes less significant.

To understand the electronic structure of the occupied Ti 3d band, situated at the top of the valence band, the density of electronic state (DOS) and the projection (PDOS) into the individual components, i.e., d_{xy}, d_{yz}, d_{z^2}, d_{xz}, and $d_{x^2-y^2}$, will be used to assist the characterization and interpretation of the electron orbitals. The coordinate frame for the orbital projection is the orthorhombic crystal frame. It should be noted that although the local Cartesian coordinate frame of the TiO_6 unit does not coincide precisely with the crystal system, the principal (z) axis of the TiO_6 unit is tilted only about 14° from the crystallographic c axis. Thus, the projected d orbital DOS are convenient and useful guides to elucidate the electronic structure, in particular, for later comparison with the hybrid functional calculations. The total DOS of the dominant valence bands of Ti at 0 and 16 GPa are shown in Figs. 5a and 5b, respectively. For convenience, the energy scale is set to zero (E = 0) at the top of the valence band.

As discussed above, the degeneracy of the t_{2g} band is lifted by the local symmetry and the t_{2g} band is further decomposed into a singly filled band and an empty band. As shown in the DOS, the band width of lower t_{2g} band is very narrow ($\sim$0.5 eV). There is a "pseudo" band gap of 2–3 eV between the lower t_{2g} band and the broad band ranging from –3 to –8 eV. This broad band is mostly oxygen, which is in character with the contribution from both Ti–O and Y–O bonding. The large band width indicates strong dispersion, i.e., strong bonding interactions. Since this study is fo-

cussed on the Ti atom, in ensuing discussions, this low energy band is simply referred as the "Ti–O" band. At all pressures, the DOS of spin-up and spin-down Ti–O bands are nearly identical and, therefore, electrons in this band are perfectly paired. Close to the top of the valence, there is a predominantly Ti 3d t_{2g} spin-up band occupied by a single electron, which resulted in the doublet ground state of $YTiO_3$. In Fig. 5, it is observed that, except for d_{z^2} and d_{xz} orbitals, the highest energy electronic band at the top of the valence level shows a clear dip. This can be attributed to the splitting of the Ti t_{2g} orbitals due to deviation of the local symmetry from the ideal octahedron environment.

The population of the Ti 3d t_{2g} orbitals can be calculated from integrating the DOS in an energy window comprising only the uppermost Ti 3d valence band. The results are summarized in Table 1. At zero pressure, the population of the t_{2g} orbitals is 0.723 e. As describe above, crystal field theory analysis of the formal charges in $YTiO_3$ expected only one electron to reside in the Ti 3d orbitals. The theoretical results confirm this analysis. It is also clear that the orbitals d_{xy}, d_{yz}, and $d_{x^2-y^2}$ are main contributors to the electron occupancies of Ti 3d states. Also, the electron occupancies of the orbitals d_{xy} and $d_{x^2-y^2}$ decrease with increasing pressure. Conversely, the electron occupancy of orbital d_{yz} increases with increasing pressure. In passing, it should be mentioned that the total DOS at zero pressure obtained here compares very well with that from a previous LDA + U calculation, which employed a slightly different U parameter of 3 eV.[23] It is reassuring that, although not totally unexpected, the calculated total DOS are almost identical.

Hybrid functional method

The procedure in finding the "optimal" mixing parameter, A, in eq. [6] at a given pressure is similar to the LDA + U calculations. For example, to reproduce the experimental band gap energy at zero pressure, trial calculations are performed with mixing parameters in the range 0.13–0.80. It was found that when $A = 0.145$, the hybrid functional calculation reproduced the observed band gap energy of 0.66 eV. Similar calculations were repeated at 8, 16, and 25 GPa and the optimal A values are summarized in Table 2. It is shown that the optimal mixing parameter decreases with increasing pressure. Therefore, the Hartree exchange term becomes less important with increasing pressure. This observation is not unexpected. Similar to the case of the LDA + U method, the on-site Coulomb parameter, U, becomes smaller as the pressure is increased. Again, the reason is due to the increase in orbital overlap and the system becomes more metallic at high pressure. Incidentally, extrapolation of the mixing parameter to $A = 0$ gives a pressure of 31 GPa, which is in agreement with the predicted metallization pressure from experiment and from LDA + U calculations (vide supra). There appears to be no single mixing parameter that is appropriate to reproduce the electronic structure for the entire pressure range.

Analyses of the total and projected density of states on the results obtained from hybrid functional calculations were performed. Figures 5c and 5d show the total density of states of the Ti 3d orbitals at 0 and 16 GPa, respectively. Two electronic bands are found below the Fermi level (0 eV). The Ti–O band is located between –8 and –5 eV.

Table 1. Electron occupancy of Ti 3d t_{2g} below the top of valence band calculated with the LDFA + U method at different pressures.

	0 GPa	8 GPa	12 GPa	16 GPa	25 GPa	32 GPa
d_{xy}	0.197	0.159	0.139	0.132	0.119	0.112
d_{yz}	0.208	0.220	0.230	0.234	0.245	0.255
d_{z^2}	0.073	0.085	0.090	0.093	0.099	0.106
d_{xz}	0.020	0.027	0.033	0.036	0.042	0.048
$d_{x^2-y^2}$	0.227	0.227	0.223	0.219	0.209	0.191
Sum	0.723	0.718	0.714	0.714	0.714	0.712

Table 2. Optimal mixing parameters (A) using hybrid functional method for $YTiO_3$ at selected pressures.

Pressure (GPa)	Optimal mixing parameter (A)
0	0.145
8	0.140
16	0.130
25	0.085

Table 3. Electron occupancy of Ti 3d states in $YTiO_3$ predicted from hybrid functional calculations at selected pressures.

	0 GPa	8 GPa	16 GPa	25 GPa
d_{xy}	0.263	0.218	0.209	0.153
d_{yz}	0.160	0.177	0.187	0.214
d_{z^2}	0.104	0.107	0.112	0.125
d_{xz}	0.043	0.029	0.046	0.060
$d_{x^2-y^2}$	0.208	0.221	0.212	0.195
Sum	0.778	0.752	0.766	0.747

The lower Ti 3d t_{2g} band extends from –1.3 eV to the top of the valence band (0 eV). In the Ti–O bonding band, the occupancies of the spin-up and spin-down bands are also identical. The isolated spin-up bands are entirely due to spin-polarized lower Ti 3d t_{2g} states.

The total and projected density of state (PDOS) profiles of the Ti atom obtained by the hybrid functional method are similar to the LDA + U method. There are, however, subtle differences, which will be discussed in the next section when the results obtained by both methods are compared. It is suffice to say that the Ti 3d valence band is relatively narrow (band width is $\sim$1 eV) and is well separated from the Ti–O band by 3 eV. The band width of the Ti–O and Y–O bonding band extends from –5 to –8 eV. This is about 1 eV smaller than the LDA + U prediction. Integrating the PDOS of the isolated lower Ti 3d t_{2g} spin-up band in the energy window from –2 to 0 eV gives the electron occupancies of the individual d orbitals. The results at different pressures are reported in Table 3. From Table 3, it is again shown that d_{xy}, d_{yz}, d_{z^2}, and $d_{x^2-y^2}$ orbitals are main contributors to the electron occupancies of Ti d bands. The electron occupancy of the d_{xy} orbital decreases with increasing pressure, whereas, the electron occupancies of d_{yz} and d_{z^2} orbitals increase with increasing pressure. The trends obtained here are in broad agreement with the LDA + U results (see Table 1), although the details are somewhat different.

Table 4. Band widths of Ti–O, occupied Ti 3d t_{2g}, and pseudo-gap below the top of the valence band.

	0 GPa		8 GPa		16 GPa		25 GPa	
Width (eV)	LDA + *U*	Hybrid	LDA + *U*	Hybrid	LDA + *U*	Hybrid	LDA + *U*	Hybrid
Ti–O	3.8	3	3.6	3	4.1	3	4.2	3
Ti 3d t_{2g}	0.5	1	0.5	1	0.6	1	0.7	1
Pseudo-gap	2.7	3.6	3	3.7	3	3.7	3	3.6

Discussions

The results reported above show that both the LDA + *U* and hybrid functional methods can reproduce the observed band gap energies of $YTiO_3$ at different pressures by adjusting the relevant *U* and *A* parameters. The electronic structures from the analysis of the density of states were presented. In the ensuing discussion, details on the electronic structures predicted by the two methods are compared.

First, the occupied valence band at zero pressure computed with both approaches is discussed. For convenience, the energy at the top of the valence band is set arbitrarily to 0 eV. As shown in the DOS (Fig. 5), there are two distinct bands within the energy window from 0 to –8 eV corresponding to Ti 3d t_{2g} orbitals and "Ti–O" bonding orbitals (vide supra). However, widths of the valence bands calculated from the two methods are obviously very different. In the LDA + *U* scheme, the width of the Ti–O band is 3.8 eV. In comparison, the Ti–O width calculated using the hybrid functional method is 3 eV which is 0.8 eV smaller. A broader band width indicates that the "covalency" of Ti–O bonding predicted by the LDA + *U* method is more dominant than from the hybrid functional method. In contrast, the calculated Ti 3d t_{2g} band width of 0.5 eV by LDA + *U* is much smaller than the 1 eV width obtained by the hybrid functional method. The larger calculated band width by the latter method may be due to the inclusion of nonlocal exchange.[39] The widening of the valence band width has also been reported in a recent application of the hybrid functional method to the adsorption of CO on metal surfaces.[40]

It is also noted that the "pseudo-gap" energies, the energy difference from the top of the Ti–O band to the bottom of the Ti 3d band, are also different between the two approaches. The calculated pseudo-gap by LDA + *U* is about 2.7 eV, which is 0.9 eV smaller than that obtained from the hybrid functional method of 3.6 eV. A larger band width indicates that stronger Ti–O interactions were predicted by the hybrid functional method. Taken in all, there are quantitative differences in the description of chemical bonding between the LDA + *U* and hybrid functional methods. The results indicate that the hybrid functional method tends to prefer more ionic Ti–O interactions. This interpretation is consistent with the smaller Ti–O band width and larger Ti 3d to Ti–O pseudo-gap energy as compared to the LDA + *U*. At the same time, the Ti 3d t_{2g} band obtained from the hybrid functional method seems to experience a larger crystal field since that band width is almost double that predicted by the LDA + *U* method.

We now proceed to analyze the occupied Ti 3d t_{2g} band at high pressure in more detail. As indicated in the calculation of the DOS, the Ti 3d t_{2g} band is nearly 100% spin-polarized by both methods. The DOS calculated with the LDA + *U* method (Fig. 5) also showed that the occupied Ti 3d t_{2g} are split into two subbands. The splitting, however, is not as clear in the hybrid functional results. The lifting of the Ti 3d t_{2g} degeneracy is due to the local oxygen environment around the Ti atom not being perfectly octahedral. The magnitude of the splitting is related to interactions with the oxygen atoms. A comparison of the calculated band widths at different pressures is given in Table 4. At 8, 16, and 25 GPa, widths of Ti 3d t_{2g} bands are calculated to be almost constant at 1 eV by hybrid functional method. In comparison, widths of the corresponding bands obtained from LDA + *U* of 0.5, 0.6, and 0.7 eV at 8, 16, and 25 GPa, respectively, are slightly dependent on the pressure. A similar trend is also observed in the Ti–O band width. While the band widths were predicted to be constant at 3 eV by hybrid functional calculations, the LDA + *U* calculated widths at 8, 16, and 25 GPa of 3.6, 4.1, and 4.2 eV, respectively, show an increase of the band width with pressure. Both methods, however, predicted that the "pseudo band gap" between the Ti–O and Ti 3d t_{2g} bands is relatively insensitive to the pressure. The pseudo-gaps at 8, 16, and 25 GPa predicted by LDA + *U* are 3 eV compared with the 3.7 eV by the hybrid functional. Thus, the hybrid functional method gave a smaller Ti–O band and a larger pseudo-gap. This observation is consistent with the suggestion that the latter method tends to predict a more ionic Ti–O interaction.

Tables 1 and 3 summarize the Ti 3d occupancies in $YTiO_3$. The general trend is very similar between LDA + *U* and hybrid functional methods with a total Ti 3d occupancy close to 0.7 e. The difference in the absolute values calculated from LDA + *U* and hybrid functional methods is small and may be attributed to different *k*-point sets and integration schemes used. In LDA + *U* calculations, the tetrahedron integration method[41] was used for Brilluoin zone integration whilst the Fourier–Legendre interpolation scheme was employed in the hybrid functional calculations.[35]

The theoretical results reported here show that the details of the electronic structure predicted by LDA + *U* and hybrid functional methods are quite different. Consequently, the nature of the chemical bonding on $YTiO_3$ reflected by the two methods is also different. Results from this investigation inevitably lead to the following question: since the description of the chemical bonding is dependent on the method of calculation, which method is more reliable? So far we have only limited experimental results, with the measured band gap energies as a reference. There is no sufficient experimental evidence in the literature on $YTiO_3$ and, as a matter of fact, on other systems to make a judicial choice of either method.

It is noteworthy that the LDA + *U* calculations very well reproduced the experimental cell parameters over the entire pressure range (Fig. 2). The agreement in the calculated and

observed atomic positions is equally excellent up to 13 GPa. Based on Rietveld analysis of the powder diffraction patterns, a sudden change in the shortening trend of the Ti–O bond lengths was reported at 13 GPa.[11] The change has led to the conclusion that the orbital ordering, the occupancy of the singly occupied orbital, has changed to Ti $3d_{xy}$. The experimental observation was not reproduced by the calculations in which no discontinuity in the Ti–O bond lengths was revealed. It is tempting to attribute this discrepancy to possible artefacts in the structural refinement of high pressure powder patterns. However, failure of the LDA + *U* calculations at this pressure cannot be ruled out. Further experimental study (e.g., measurement of magnetic properties) at high pressure is needed to confirm the change in the orbital ordering.

Conclusions

In this study, using $YTiO_3$ as an example, it is found that the experimental band gap can be reproduced by varying the appropriate *U* and *A* parameters in LDA + *U* and hybrid functional methods, respectively. However, analysis of the electronic structure shows that the details of the electronic structure are quite different between the two methods indicating there are significant differences in the description of the nature of the chemical bonding. A conclusive evaluation on the reliability of the LDA + *U* and hybrid functional methods cannot be reached in this investigation, mainly due to a lack of experimental information for direct comparison. This investigation, however, invites future experimental studies on the electronic properties of $YTiO_3$ and other related systems. For example, the recent advance in charge-compensation detection of photoelectrons from insulating systems enable accurate measurements of the valence band from X-ray photoelectron spectra.[42] These spectra are invaluable for the direct comparison with the calculated electronic density of states of the occupied bands. For the characterization of empty states, X-ray photoemission experiments will be most useful. On the theoretical aspect, a future direction is to explore new methods for the ab initio prediction of the *U* parameter. Higher level approximations such as the DMFT[16,17] may be a good model to treat correlation effects. This method is under active development and there are issues still needed to be understood before the method can be employed for general computation.

References

(1) Martin, R. M. *Electronic Structure: Basic Theory and Practical Methods;* Cambridge University Press: Cambridge, England, 2004.

(2) de P. R. Moreira, I.; Illas, F.; Martin, R.L. *Phys. Rev. B* **2002**, *65* (15), 155102. doi:10.1103/PhysRevB.65.155102.

(3) Engel, E. In *A Primer in Density Functional Theory;* Fiolhais, C., Nogueira, F., Marques, M., Eds.; Sprinter-Verlag: Berlin, 2003.

(4) Terakura, K.; Oguchi, T.; Williams, A. R.; Kübler, J. *Phys. Rev. B* **1984**, *30* (8), 4734–4747. doi:10.1103/PhysRevB.30.4734.

(5) Leung, T. C.; Chan, C. T.; Harmon, B. N. *Phys. Rev. B* **1991**, *44* (7), 2923–2927. doi:10.1103/PhysRevB.44.2923.

(6) Dufek, P.; Blaha, P.; Schwarz, K. *Phys. Rev. B* **1994**, *50* (11), 7279–7283. doi:10.1103/PhysRevB.50.7279.

(7) For a recent review see: Carter, E. A. *Science* **2008**, *321* (5890), 800–803. doi:10.1126/science.1158009. PMID: 18687955.

(8) Muscat, J.; Wander, A.; Harrison, N. M. *Chem. Phys. Lett.* **2001**, *342* (3–4), 397–401. doi:10.1016/S0009-2614(01)00616-9.

(9) Anisimov, V. I.; Zaanen, J.; Andersen, O. K. *Phys. Rev. B* **1991**, *44* (3), 943–954. doi:10.1103/PhysRevB.44.943.

(10) Liechtenstein, A. I.; Anisimov, V. I.; Zaanen, J. *Phys. Rev. B* **1995**, *52* (8), R5467–R5470. doi:10.1103/PhysRevB.52.R5467.

(11) Loa, I.; Wang, X.; Syassen, K.; Roth, H.; Lorenz, T.; Hanfland, M.; Mathis, Y. L. *J. Phys. Condens. Matter* **2007**, *19* (40), 406223. doi:10.1088/0953-8984/19/40/406223.

(12) Fujitani, H.; Asano, S. *Phys. Rev. B* **1995**, *51* (4), 2098–2102. doi:10.1103/PhysRevB.51.2098.

(13) Sawada, H.; Terakura, K. *Phys. Rev. B* **1998**, *58* (11), 6831–6836. doi:10.1103/PhysRevB.58.6831.

(14) Sawada, H.; Hamada, N.; Terakura, K. *Physica B* **1997**, *237–238*, 46–47. doi:10.1016/S0921-4526(97)00043-4.

(15) Solovyev, I. V. *Phys. Rev. B* **2006**, *74* (5), 054412. doi:10.1103/PhysRevB.74.054412.

(16) Georges, A.; Kotliar, G.; Krauth, W.; Rozenberg, M. J. *Rev. Mod. Phys.* **1996**, *68* (1), 13–125. doi:10.1103/RevModPhys.68.13.

(17) Kotliar, G.; Volhardt, D. *Physics Today* **2004**, *57* (1), 53–54.

(18) Pavarini, E.; Biermann, S.; Poteryaev, A.; Lichtenstein, A. I.; Georges, A.; Andersen, O. K. *Phys. Rev. Lett.* **2004**, *92* (17), 176403. doi:10.1103/PhysRevLett.92.176403. PMID:15169176.

(19) Becke, A. D. *J. Chem. Phys.* **1993**, *98* (2), 1372–1377. doi:10.1063/1.464304.

(20) Becke, A. D. *J. Chem. Phys.* **1988**, *88* (2), 1053–1062. doi:10.1063/1.454274.

(21) Becke, A. D. *J. Chem. Phys.* **1993**, *98* (7), 5648–5652. doi:10.1063/1.464913.

(22) Hybertsen, M. S.; Schlüter, M. *Phys. Rev. B* **1989**, *39* (13), 9028–9041. doi:10.1103/PhysRevB.39.9028.

(23) Solovyev, I. V.; Dederichs, P. H.; Anisimov, V. I. *Phys. Rev. B* **1994**, *50* (23), 16861–16871. doi:10.1103/PhysRevB.50.16861.

(24) Madsen, G. K. H.; Novak, P. *Europhys. Lett.* **2005**, *69* (5), 777–783. doi:10.1209/epl/i2004-10416-x.

(25) Mosey, N. J.; Carter, E. A. *Phys. Rev. B* **2007**, *76* (15), 155123. doi:10.1103/PhysRevB.76.155123.

(26) Cococcioni, M.; de Gironcoli, S. *Phys. Rev. B* **2005**, *71* (3), 035105. doi:10.1103/PhysRevB.71.035105.

(27) Dudarev, S. L.; Savrasov, S. Y.; Humphreys, C. J.; Sutton, A. P. *Phys. Rev. B* **1998**, *57* (3), 1505–1509. doi:10.1103/PhysRevB.57.1505.

(28) (a) Solovyev, I. V. *Phys. Rev. B* **2006**, *73* (15), 155117. doi:10.1103/PhysRevB.73.155117.; (b) Becke, A. D. *J. Chem. Phys.* **1993**, *98* (2), 1372–1377. doi:10.1063/1.464304.

(29) (a) Kresse, G.; Furthmuller, J. *Comput. Mater. Sci.* **1996**, *6* (1), 15–50. doi:10.1016/0927-0256(96)00008-0.; (b) Kresse, G.; Furthmuller, J. *Phys. Rev. B* **1996**, *54* (16), 11169–11186. doi:10.1103/PhysRevB.54.11169.

(30) Blöchl, P. E. *Phys. Rev. B* **1994**, *50* (24), 17953–17979. doi:10.1103/PhysRevB.50.17953.

(31) Kresse, G.; Joubert, D. *Phys. Rev. B* **1999**, *59* (3), 1758–1775. doi:10.1103/PhysRevB.59.1758.

(32) Perdew, J. P.; Burke, K.; Ernzerhof, M. *Phys. Rev. Lett.* **1996**, *77* (18), 3865–3868. doi:10.1103/PhysRevLett.77.3865. PMID:10062328.

(33) Monkhorst, J.; Pack, J. D. *Phys. Rev. B* **1976**, *13* (12), 5188–5192. doi:10.1103/PhysRevB.13.5188.
(34) Pople, J. A.; Nesbet, R. K. *J. Chem. Phys.* **1954**, *22* (3), 571. doi:10.1063/1.1740120.
(35) (a) Pisani, C.; Dovesi, R.; Roetti, C. *Hartree–Fock Ab Initio Treatment of Crystalline Systems;* Springer-Verlag: Berlin, 1988; (b) Saunders, V. R.; Dovesi, R.; Roetti, C.; Orlando, R.; Zicovich-Wilson, C. M.; Harrison, N. M.; Doll, K.; Civalleri, B.; Bush, I. D'Arco, Ph.; Llunell, M. *CRYSTAL 2003 User's Manual;* University of Torino: Torino, Italy, 2003.
(36) MacLean, D. A.; Ng, H.; Greedan, J. E. *J. Solid State Chem.* **1979**, *30* (1), 35–44. doi:10.1016/0022-4596(79)90127-0.
(37) Pavarini, E.; Yamasaki, A.; Nuss, J.; Andersen, O. K. *New J. Phys.* **2005**, *7* (188), 1–89. doi:10.1088/1367-2630/7/1/188.
(38) Okatov, S.; Poteryaev, A.; Lichtenstein, A. *Europhys. Lett.* **2005**, *70* (4), 499–505. doi:10.1209/epl/i2004-10513-x.
(39) Solovyev, I. V. *Phys. Rev. B* **1999**, *60* (12), 8550–8558. doi:10.1103/PhysRevB.60.8550.
(40) Stroppa, A.; Termentzidis, K.; Paier, J.; Kresse, G.; Hafner, J. *Phys. Rev. B* **2007**, *76* (19), 195440. doi:10.1103/PhysRevB.76.195440.
(41) Blöchl, P.; Jepsen, O.; Andersen, O. K. *Phys. Rev. B* **1994**, *49* (23), 16223–16233. doi:10.1103/PhysRevB.49.16223.
(42) Zakaznova-Herzog, V. P.; Skinner, W. *Phys. Rev. B* **2005**, *72* (20), 205113. doi:10.1103/PhysRevB.72.205113.

The analog of Koopmans' theorem for virtual Kohn–Sham orbital energies

Oleg Gritsenko and Evert Jan Baerends

Abstract: An analog of Koopmans' theorem is formulated for the energies, ε_a, of virtual Kohn–Sham (KS) molecular orbitals (MOs) from the requirement that the KS theory provides, in principle, not only the exact electron density, but also its exact response. The starting point is the Kohn–Sham analog of Koopmans' theorem, relating the vertical ionization energies, I_i, to the energies, ε_i, of the occupied MOs (Chong, D.P.; Gritsenko, O.V.; Baerends, E.J. *J. Chem. Phys.* **2002,** *116,* 1760). Combining this with the coupled-perturbed equations of time-dependent density functional theory (TDDFT), exact relations between the energies, ε_a, of virtual KS MOs and the excitation energies, ω_{ia}, and vertical ionization energies (VIPs), I_i, are obtained. In the small matrix approximation for the coupling matrix **K** of TDDFT, two limiting cases of these relations are considered. In the limit of a negligible matrix element, $K_{ia,ia}$, the energy, ε_a, can be interpreted as (minus) the energy of ionization from the $\phi_i \rightarrow \phi_a$ excited state, $\varepsilon_a \approx -I_a$, where $-I_a$ is defined from the relation $I_i = \omega_{ia} + I_a$. This relation breaks down in special cases, such as charge-transfer transitions and the HOMO–LUMO (highest occupied molecular orbital – lowest unoccupied molecular orbital) transition of a dissociating electron-pair bond (also of charge-transfer character). The present results highlight the important difference between virtual orbital energies in the Kohn–Sham model ($\varepsilon_a \approx -I_a$) and in the Hartree–Fock model ($\varepsilon_a \approx -A_a$). Kohn–Sham differences $\varepsilon_a - \varepsilon_i$ approximate the excitation energy, ω_{ia}, while Hartree–Fock differences $\varepsilon_a^{\mathrm{HF}} - \varepsilon_i^{\mathrm{HF}}$ do not approximate excitation energies but approximate the difference of an ionization energy and an electron affinity, $I_i - A_a$.

Key words: Koopmans' theorem, density functional theory, Kohn–Sham, orbital energies.

Résumé : On formule un théorème analogue à celui de Koopmans pour les énergies ε_a des orbitales moléculaires (OM) de Kohn–Sham (KS) à partir de la condition selon laquelle la théorie de KS fournit, en principe, non seulement la densité électronique exacte, mais aussi sa réponse exacte. Le point de départ l'analogue de Kohn–Sham du théorème de Koopmans qui relie les énergies d'ionisation verticale, I_i, aux énergies ε_i des OM occupées (Chong, D.P.; Gritsenko, O.V.; Baerends, E.J. *J. Chem. Phys.* **2002,** *116,* 1760). En combinant ceci avec les équations couplées-perturbées de la théorie de la fonctionnelle de densité dépendante du temps (TFDDT), on a pu obtenir les relations exactes entre les énergies ε_a des OM virtuelles de KS et les énergies d'excitation, ω_{ia}, et les énergies d'ionisation verticale (EIV), I_i. Dans l'approximation de la petite matrice pour la matrice couplante de TFDDT, on considère deux cas limites de ces relations. Dans la limite d'un élément de matrice négligeable, $K_{ia,ia}$, on peut interpréter l'énergie ε_a comme étant la valeur négative de l'énergie d'ionisation à partir de l'état excité $\phi_i \rightarrow \phi_a$, $\varepsilon_a \approx -I_a$, dans laquelle $-I_a$ est défini par la relation $I_i = \omega_{ia} + I_a$. Cette relation ne tient pas dans certains cas, tel celui des transitions de transfert de charge et celui de la transition des OM HO à BV d'une paire d'électrons d'une liaison qui se dissocie (qui comporte aussi un caractère de transfert de charge). Les résultats obtenus dans ce travail mettent en évidence l'importante différence entre les énergies des orbitales virtuelles dans le modèle de Kohn–Sham ($\varepsilon_a \approx -I_a$) et dans le modèle de Hartree–Fock ($\varepsilon_a \approx -A_a$). Les différences $\varepsilon_a - \varepsilon_i$ de Kohn–Sham correspondent à une approximation de l'énergie d'excitation ω_{ia} alors que les différences de Hartree–Fock, $\varepsilon_a^{\mathrm{HF}} - \varepsilon_i^{\mathrm{HF}}$ ne correspondent pas à une approximation des énergies d'excitation, mais à une approximation de la différence d'une énergie d'ionisation et d'une affinité électronique, $I_i - A_a$.

Mots-clés : théorème de Koopmans, théorie de la fonctionnelle de la densité, Kohn–Sham, énergie des orbitales.

[Traduit par la Rédaction]

Received 28 December 2008. Accepted 19 March 2009. Published on the NRC Research Press Web site at canjchem.nrc.ca on 18 September 2009.

This article is part of a Special Issue dedicated to Professor T. Ziegler.

O. Gritsenko. Afdeling Theoretische Chemie, Vrije Universiteit, De Boelelaan 1083, 1081 HV Amsterdam, The Netherlands.
E.J. Baerends.[1] Afdeling Theoretische Chemie, Vrije Universiteit, De Boelelaan 1083, 1081 HV Amsterdam, The Netherlands; Center for Superfunctional Materials, Dep. of Chemistry, Pohang University of Science and Technology, Pohang, South-Korea.

[1]Corresponding author (e-mail: baerends@few.vu.nl).

1. Introduction

The requirement that the occupied Kohn–Sham (KS) molecular orbitals (MOs), ϕ_i, of density functional theory (DFT)[1,2] yield the exact (fully correlated) electron density, ρ,

$$[1.1] \qquad \rho_{\mathrm{s}}(\mathbf{r}_1) = \sum_i^H |\phi_{\mathrm{i}}(\mathbf{r}_1)|^2 = \rho^{\mathrm{exact}}(\mathbf{r}_1)$$

can be shown to lend physical meaning to the energies ε_i.[3–6] The latter appear in the one-electron KS equations

$$[1.2] \qquad \left\{-\frac{1}{2}\nabla^2 + v_s(\mathbf{r})\right\}\phi_\mu(\mathbf{r}) = \varepsilon_\mu\phi_\mu(\mathbf{r})$$

in which the local potential, v_s, is unique (fully determined by the requirement that ρ_s is exact). Equation [1.2] has the doubly occupied orbitals ($\mu \leq H = N/2$), for which we use indices $i, j, \ldots$, as the lowest solutions, but also leads to virtual ($\mu = a, b, \ldots$) MOs (throughout the paper atomic units are used and closed-shell systems are considered).

The analog of Koopmans' theorem for Kohn–Sham DFT formulated in refs. 3–6 provides the interpretation of ε_i as approximate vertical ionization potentials (VIPs):

$$[1.3] \qquad \varepsilon_i \approx -I_i$$

The quality of this approximation depends on the strength of satellite ionizations accompanying the considered primary ionization[5] in the photoemission spectrum; the KS one-electron energy is a weighted average over the primary ionization potential and its satellites, so the relation $\varepsilon_i \approx -I_i$ is more closely obeyed for MOs with ionizations that have little satellite structure, i.e., in particular for outer valence MOs.[3] Earlier, the exact identity, $\varepsilon_H \approx -I_H$, was established for the highest occupied MO (HOMO), ϕ_H, from the analysis of the long-range asymptotics of the KS equations (eq. [1.2]).[7–12] Indeed, there are no satellites to the first ionization potential. For the upper valence orbitals with generally weak satelites, the exact Kohn–Sham ε_i differ from the I_i by only ~0.1 eV, while the deviation of Hartree–Fock (HF) orbital energies from the I_i typically exceeds 1 eV. Formulated initially for closed-shell systems,[3] the identification of the Kohn–Sham orbital energies as approximate ionization energies was extended later to open-shell systems.[4,6] We continue to call this identification the analog of Koopmans' theorem in DFT, although it should be kept in mind that Koopmans' theorem in Hartree–Fock invokes, apart from the Hartree–Fock approximation, the frozen orbital approximation for the ion, while in Kohn–Sham DFT the identification is with vertical ionization to electronically relaxed and correlated ions, the approximation stemming from the averaging in the Kohn–Sham case over the primary ionization and its satellites (with weights according to the intensities). The deviations are much smaller than in the Hartree–Fock case.

While the orbital energies of both the occupied KS MOs and the occupied Hartree–Fock MOs can both be related to vertical ionization energies, the interpretation of the energies, ε_a, of virtual MOs in these theories must be different. Indeed, according to the canonical Koopmans' theorem,[13] the energies of virtual HF MOs are interpreted as approximate electron affinities (in the frozen orbital Hartree–Fock approximation). This agrees with the nature of the nonlocal one-electron HF potential which, for virtual HF MOs, describes an electron interacting with all N electrons of the system (an added electron). Unlike this, in the KS theory both occupied and virtual MOs are solutions in the same potential v_s describing interaction with $(N-1)$ electrons. Because of this, ε_a represents an "excited" electron interacting with $(N-1)$ electrons, rather than an "extra" electron interacting with N electrons. In particular, as was concluded in ref. 14 from the analysis of the long-range asymptotics of the KS equations, the energy differences between exact (not local density approximation (LDA) or generalized gradient approximation (GGA)) Rydberg type KS MO energies and HOMO energy should be good approximations to the energies of the corresponding Rydberg type excitations because the diffuseness of the Rydberg orbitals leads to a vanishing contribution from the coupling matrix (see below). In ref. 15 excited-state ensemble DFT was employed to express the difference of a virtual orbital energy and the HOMO energy, $\varepsilon_k - \varepsilon_H$, as the difference of the expectation values of the $\phi_H \rightarrow \phi_k$ excited KS determinant, Φ^k_{ES}, and ground state Kohn–Sham determinants for the full (interacting) Hamiltonian, $\langle\Phi^k_{ES}|\hat{H}|\Phi^k_{ES}\rangle - \langle\Phi_s|\hat{H}|\Phi_s\rangle$, plus the ϕ_k matrix element of the, unfortunately unknown, difference between the KS potentials for the excited state ensemble and the ground state.

More general energy differences $(\varepsilon_a - \varepsilon_i)$ between virtual and occupied orbitals obtained with standard DFT local density generalized gradient approximations (GGA) appear to be fair zero-order estimates of the valence excitation energies, ω_α ($\alpha = i \rightarrow a$), as obtained in time-dependent density functional theory (TDDFT),[16–27] at least for excitations in compact molecules or for intrafragment excitations in larger systems. To extend this agreement between ω_α and approximate $(\varepsilon_a - \varepsilon_i)$ to the abovementioned case of Rydberg excitations, model potentials that are improved with respect to those of the LDA or GGA models so that they have the qualitatively correct shape, have been proposed.[28–33] The Kohn–Sham orbital energy differences appear naturally as zero-order estimates of the excitation energies in Görling's[34] perturbation treatment of excited state DFT, which takes the Kohn–Sham system as zero order, but it is not clear in that approach if these zero-order estimates would be any more accurate than Hartree–Fock orbital energy differences.

In this paper, an analog of Koopmans' theorem is formulated for the energies, ε_a, of virtual KS MOs. In section 2 the exact KS potential, v_s, is considered under two requirements; first, that it produces the exact density ρ via eqs. [1.1], [1.2], and second, that it exhibits the proper change $\delta v_s(\omega)$ to yield the exact density response, $\delta\rho(\omega)$, to a frequency-dependent change, $\delta v_{ext}(\omega)$, of the external potential. With these requirements in section 3, the analog of Koopmans' theorem for the energies of the occupied MOs is combined with the coupled-perturbed equations of TDDFT to obtain exact relations between the energies, ε_a, of virtual KS MOs and the VIPs, I_i, as well as the excitation energies, ω_α. We analyze these relations in the small matrix approximation for the coupling matrix $\mathbf{K}$ of TDDFT, which neglects coupling of the $i \rightarrow a$ excitation with $j \rightarrow b$ excitations. Two limiting cases are considered. In the limit of a negligible matrix element, $K_{ia,ia}$, the energy, ε_a, can be interpreted as (minus) the energy of ionization of the corresponding excited state, $\varepsilon_a \approx -I_a$. Of course there may be several excited states corresponding to $i \rightarrow a$ when i and (or) a belong to a degenerate level, and for a given a there are many choices for the occupied orbital, i. The condition of negligible $K_{ia,ia}$ leads to a unique I_a that is the same for all excited states $i \rightarrow a$ to which this condition applies. We will consider the consequences of small but nonnegligible $K_{ia,ia}$ for the definition of I_a in section 3. The opposite limit of a large $K_{ia,ia}$, which is known to occur when the occupied bonding and empty antibonding orbitals of a chemical bond become nearly degenerate upon bond dissociation, leads to $\varepsilon_a \approx -I_i$.

In this particular case, the orbital energy difference, $\varepsilon_a - \varepsilon_i$ (≈ 0 in the homonuclear case), is not a good approximation of the excitation energy, ω_{ia}, which can still be quite large, at least for the singlet excited state (many eVs). So, no longer does $\varepsilon_a \approx -I_i + \omega_{ia}$, and in general when $K_{ia,ia}$ is not negligible, the association $\varepsilon_a \approx -I_a$ is not valid; $-I_i + \omega_{ia}$ for an $i \rightarrow a$ excitation with large $K_{ia,ia}$ will be rather different from the $-I_j + \omega_{ja} \approx -I_a$ values of excitations $j \rightarrow a$ for which the condition that $K_{ja,ja}$ is small does hold. In section 4 the implications of the present "Koopmans' theorem" for the virtual orbital energies, ε_a, for DFT and TDDFT are drawn, and the difference with Hartree–Fock is stressed.

2. Conditions on the KS potential

By definition, the KS potential, v_s, is that unique local potential that yields the exact density, ρ, with eqs. [1.1] and [1.2] and the correct change, $\delta v_s(\omega)$, produces the exact density response, $\delta\rho(\omega)$, to a change of the external potential, $\delta v_{ext}(\omega)$. From an analysis of the "response" part of $v_s(\mathbf{r}) = v_{xc}^{hole}(\mathbf{r}) + v_{c,kin}(\mathbf{r}) + v^{resp}(\mathbf{r})$,[35] one can establish the analog of Koopmans' theorem for the energies, ε_i, of the $H = N/2$ occupied KS MOs, starting from the exact relations between ε_i and VIPs, I_j, which have been derived in ref. 3.

$$[2.1] \qquad \varepsilon_i = T_i[\{I_j\}]$$

where

$$[2.2] \qquad T_i = \sum_k^H M_{ik}^{-1} \left(\sum_j^\infty P_{kj} I_j + \varepsilon_k^{resp} \right)$$

In eq. [2.2], $\mathbf{M}^{-1}$ is the inverse matrix of the $H \times H$ matrix of $1/\rho$ weighted overlap integrals, M_{ik}, between the occupied KS MO densities, $|\phi_i|^2$ and $|\phi_k|^2$,

$$[2.3] \qquad M_{ik} = 2 \int \frac{|\phi_i(\mathbf{r}_1)|^2 |\phi_k(\mathbf{r}_1)|^2}{\rho(\mathbf{r}_1)} d\mathbf{r}_1$$

and P_{kj} is the $H \times \infty$ matrix of $1/\rho$ weighted overlap integrals between the MO densities, $|\phi_k|^2$, and the densities, $|d_j|^2$, of the Dyson orbitals, d_j, associated with the vertical ionizations from ground state, $\Psi_0^N(x_1, x_2, \ldots, x_N)$, to ion states, $\Psi_j^{N-1}(x_2, x_3, \ldots, x_N)$,

$$[2.4] \qquad \begin{aligned} d_j(x_1) &= \sqrt{N} \int \Psi_j^{N-1}(x_2, x_3, \ldots, x_N) * \Psi_0^N(x_1, x_2, \ldots, x_N) dx_2, \ \ldots, dx_N \\ P_{kj} &= 2 \int \frac{|\phi_k(\mathbf{r}_1)|^2 |d_j(\mathbf{r}_1)|^2}{\rho(\mathbf{r}_1)} d\mathbf{r}_1 \end{aligned}$$

ε_k^{resp} is the orbital expectation value of the response part, v_{resp},[35] of v_s

$$[2.5] \qquad \varepsilon_k^{resp} = \int |\phi_k(\mathbf{r}_1)|^2 v_{resp}(\mathbf{r}_1) \, d\mathbf{r}_1$$

Furthermore, with its change, $\delta v_s(\omega)$, in response to the external change, $\delta v_{ext}(\omega)$, the potential, v_s, yields the correct density response, $\delta\rho(\omega)$,[36]

$$[2.6] \qquad \delta\rho(\mathbf{r}_1, \omega) = \int \chi_s(\mathbf{r}_1, \mathbf{r}_2, \omega) \delta v_s(\mathbf{r}_2, \omega) d\mathbf{r}_2$$

where χ_s is the non-interacting KS density response function (here and in the rest of the paper we consider real MOs):

$$[2.7] \qquad \chi_s(\mathbf{r}_1, \mathbf{r}_2, \omega) = \sum_i^H \sum_{a>H} \frac{4(\varepsilon_a - \varepsilon_i)}{\omega^2 - (\varepsilon_a - \varepsilon_i)^2} \phi_i(\mathbf{r}_1) \phi_a(\mathbf{r}_1) \phi_a(\mathbf{r}_2) \phi_i(\mathbf{r}_2)$$

Subdividing $\delta v_s(\omega)$ into the external perturbing potential, $\delta v_{ext}(\omega)$ and the "coupling" part representing the response of the electronic part (Hartree-exchange-correlation, Hxc) of the potential due to the induced density change, $\delta v_{Hxc}(\omega)$, one can re-write eq. [2.6] as follows:

$$[2.8] \qquad \delta\rho(\mathbf{r}_1, \omega) = \int \chi_s(\mathbf{r}_1, \mathbf{r}_2, \omega) [\delta v_{ext}(\mathbf{r}_2, \omega) + \delta v_{Hxc}(\mathbf{r}_2, \omega)] \, d\mathbf{r}_2$$

where $\delta v_{Hxc}(\omega)$ is obtained with the Hartree-xc kernel, $f_{Hxc}(\omega)$,

$$[2.9] \qquad \delta v_{Hxc}(\mathbf{r}_2, \omega) = \int f_{Hxc}(\mathbf{r}_2, \mathbf{r}_3, \omega) \delta\rho(\mathbf{r}_3, \omega) \, d\mathbf{r}_3$$

From eqs. [2.8], [2.9], and the alternative representation of $\delta\rho(\omega)$

$$[2.10] \qquad \delta\rho(\mathbf{r}_1, \omega) = \int \chi(\mathbf{r}_1, \mathbf{r}_2, \omega)\delta v_{\text{ext}}(\mathbf{r}_2)\, \mathrm{d}\mathbf{r}_2$$

follows the expression for $f_{\text{Hxc}}(\omega)$

$$[2.11] \qquad f_{\text{Hxc}}(\mathbf{r}_1, \mathbf{r}_2, \omega) = \chi_s^{-1}(\mathbf{r}_1, \mathbf{r}_2, \omega) - \chi^{-1}(\mathbf{r}_1, \mathbf{r}_2, \omega)$$

In eq. [2.11], $\chi^{-1}(\omega)$ is the inverse of the interacting density–density response function, χ, in eq. [2.10]

$$[2.12] \qquad \chi(\mathbf{r}_1, \mathbf{r}_2, \omega) = \sum_\alpha \frac{2\omega_\alpha}{\omega^2 - \omega_\alpha^2} \langle\Psi_0|\widehat{\rho}(\mathbf{r}_1)|\Psi_\alpha\rangle\langle\Psi_\alpha|\widehat{\rho}(\mathbf{r}_2)|\Psi_0\rangle$$

where $\widehat{\rho}$ is the density operator, Ψ_0 and Ψ_α are the ground and the excited state wave functions, and $\omega_\alpha = E_\alpha - E_0$ are the corresponding excitation energies. Using the orbital expansion of $\delta\rho(\omega)$ in eqs. [2.8] and [2.9], one arrives at the following eigenvalue equations of TDDFT:[16]

$$[2.13] \qquad (\varepsilon_a - \varepsilon_i)^2 F_{ia}^\alpha + 2\sum_{jb} \sqrt{\varepsilon_a - \varepsilon_i} K_{ia,jb}(\omega_\alpha) \sqrt{\varepsilon_b - \varepsilon_j} F_{jb}^\alpha = \omega_\alpha^2 F_{ia}^\alpha$$

In eq. [2.13] the (super)vector, F_{ia}^α, yields the oscillator strength, q_α, of the corresponding excitation with the energy, ω_α, while the coupling (super)matrix, $\mathbf{K}(\omega)$, contains the integrals of the Hxc kernel, $f_{\text{Hxc}}(\omega)$,

$$[2.14] \qquad K_{ia,jb}(\omega) = 2\int \mathrm{d}\mathbf{r}_1 \mathrm{d}\mathbf{r}_2 \phi_i(\mathbf{r}_1)\phi_a(\mathbf{r}_1)\phi_j(\mathbf{r}_2)\phi_b(\mathbf{r}_2) f_{\text{Hxc}}(\mathbf{r}_1, \mathbf{r}_2, \omega)$$

Equations [2.1], [2.2], and [2.13] represent a set of relations obeyed by the eigenvalues of the exact KS potential. From this set, exact relations between ε_a, ω_α, and I_i will be derived in the next section.

3. Relations between ε_a, ω_α, and I_i

We combine the analog of Koopmans' theorem (eqs. [2.1] and [2.2] for the energies of the occupied MOs) with the coupled-perturbed equations of TDDFT by inserting eq. [2.1] in eq. [2.13] to obtain

$$[3.1] \qquad \Big(\varepsilon_a - T_i(\mathbf{I})\Big)^2 F_{ia}^\alpha + 2\sum_{jb} \sqrt{\Big(\varepsilon_a - T_i(\mathbf{I})\Big)\Big(\varepsilon_b - T_j(\mathbf{I})\Big)} K_{ia,jb}(\boldsymbol{\varepsilon}, \mathbf{I}; \omega_\alpha) F_{jb}^\alpha = \omega_\alpha^2 F_{ia}^\alpha$$

where we have collected the set of ionization energies in the vector $\mathbf{I}$, and the set of orbital energies in the vector $\boldsymbol{\varepsilon}$. The coupling matrix $\mathbf{K}$ is denoted as a function of $\boldsymbol{\varepsilon}$ and $\mathbf{I}$ as follows from eqs. [2.7], [2.11], [2.12], and [2.14]. Summing eq. [3.1] over the indices i and α, and separating the terms, which contain ε_a explicitly, we obtain, for all a, the following coupled equations:

$$[3.2] \qquad A_a\varepsilon_a^2 + B_a\varepsilon_a + \sum_{i,j\neq i}^{H} \sqrt{\Big(\varepsilon_a - T_i(\mathbf{I})\Big)\Big(\varepsilon_a - T_j(\mathbf{I})\Big)} C_{iaja} + \sum_{ij}^{H} \sum_{b\neq a} \sqrt{\Big(\varepsilon_a - T_i(\mathbf{I})\Big)\Big(\varepsilon_b - T_j(\mathbf{I})\Big)} D_{iajb} + G_a = 0$$

where

$$[3.3] \qquad A_a = \sum_i^H \sum_\alpha F_{ia}^\alpha$$

$$[3.4] \qquad B_a = 2\sum_i^H \sum_\alpha \{-T_i(\mathbf{I}) + K_{ia,ia}(\boldsymbol{\varepsilon}, \mathbf{I}; \omega_\alpha)\} F_{ia}^\alpha$$

$$[3.5] \qquad C_{iaja} = 2\sum_\alpha K_{ia,ja}(\boldsymbol{\varepsilon}, \mathbf{I}; \omega_\alpha) F_{ja}^\alpha$$

$$[3.6] \qquad D_{iajb} = 2\sum_\alpha K_{ia,jb}(\boldsymbol{\varepsilon}, \mathbf{I}; \omega_\alpha) F_{jb}^\alpha$$

$$[3.7] \qquad G_a = \sum_i^H \sum_\alpha \{T_i^2(\mathbf{I}) - 2T_i(\mathbf{I}) K_{ia,ia}(\boldsymbol{\varepsilon}, \mathbf{I}; \omega_\alpha) - \omega_\alpha^2\} F_{ia}^\alpha$$

These equations represent exact relations between ε_a on the one hand, and I_i and ω_α on the other hand. The energies of the virtual KS MOs, ε_a, and the excitation energies, ω_α, appear in eqs. [3.2]–[3.7] explicitly, and implicitly in the coupling matrix

K. In turn, VIPs, I_i, appear in the functional dependence eqs. [2.1] and [2.2] of the energies, ε_i, of occupied KS MOs on the $\{I_j\}$. Taken together, eqs. [2.1], [2.2], [3.2], and [3.3] constitute a set of exact relations connecting both occupied (eqs. [2.1] and [2.2]) and virtual (eqs. [3.1] and [3.2]) KS MOs with the VIPs.

The equations for the virtual KS orbital energies simplify very much in case that the approximation $T_i(\mathbf{I}) \approx -I_i$ is valid. As discussed in ref. 5, this is a reasonable approximation when $\varepsilon_i^{\text{resp}}$ is negligible and when the $H \times \infty$ matrix $\mathbf{M}^{-1}\mathbf{P}$ consists of a leading $H \times H$ unit matrix and contains negligible matrix elements in its remaining columns. These conditions are met when ϕ_i is an upper valence orbital, in which case the satellite structure to the main peak representing the "orbital ionization", $(\phi_i)^{-1}$, in the photoelectron spectrum, is weak (it is absent for the HOMO); the absence of satellite structure is equivalent with negligible columns $j > H$ of $\mathbf{M}^{-1}\mathbf{P}$. Applying in addition the small matrix approximation, which means that effectively the off-diagonal elements, $K_{ia,jb}$, connecting the $i \rightarrow a$ excitation with $j \rightarrow b$ excitations are neglected, one obtains a simple "pseudoquadratic" equation for $(\varepsilon_a + I_i)$:

$$[3.8] \qquad (\varepsilon_a + I_i)^2 + 2(\varepsilon_a + I_i)K_{ia,ia}(\boldsymbol{\varepsilon}, \mathbf{I}; \omega_\alpha) - \omega_\alpha^2 = 0$$

where α denotes the excited state corresponding to the $i \rightarrow a$ orbital excitation. We have here assumed that both i and a are nondegenerate; degeneracy will be considered below. From eq. [3.8], it follows that the relation between ε_a, I_i and ω_α depends essentially on the magnitude of the coupling matrix element, $K_{ia,ia}$. We consider two limiting cases.

In the first place, when $K_{ia,ia}$ is small, and using as definition of the ionization energy, I_a, of the excited state the difference between the ground state ionization energy from orbital, ϕ_i, minus the excitation energy, ω_α,

$$[3.9] \qquad I_a = I_i - \omega_\alpha$$

we obtain approximately (writing $K = K_{ia,ia}$),

$$[3.10] \qquad \varepsilon_a \approx -I_i + \omega_\alpha - K + \frac{1}{2}\frac{K^2}{\omega} = -I_a - K + \frac{1}{2}\frac{K^2}{\omega}$$

With negligible $K_{ia,ia}$, eq. [3.10] leads immediately to the interpretation of the energy, ε_a, of the virtual orbital, ϕ_a, as (minus) the energy of ionization, I_a, of the corresponding excited state, which by definition is the difference between the ground state ionization energy from orbital ϕ_i, minus the excitation energy ω_α, $I_a = I_i - \omega_\alpha$. The condition of negligible $K_{ia,ia}$ is rather strong. For instance, it implies that the difference between the $K_{ia,ia}$ matrix element for the singlet and the triplet excited states corresponding to the $i \rightarrow a$ orbital excitation is also negligible, i.e., $\omega_{ia}^S = \omega_{ia}^T$, and $I_a = I_i - \omega_{ia}^{S,T}$ is defined. In general, we should expect $-\varepsilon_a$ to be in-between the ionization energies from the excited triplet and singlet states, and the average ionization energy could be defined as I_a, i.e., $-\varepsilon_a \approx I_i - (\omega_{ia}^S + \omega_{ia}^T)/2 \equiv I_a$.

Of course ϕ_i and (or) ϕ_a may belong to a symmetry–degenerate set of levels. The ionization energy, I_i, will still be unique: if ϕ_i belongs to the nth set of levels $(n\gamma)$ of irrep symmetry, Γ, of the point group, ionization from any of the degenerate $\phi_j \in n\Gamma$ leads to one of the degenerate states of the manifold of doublet states, $^2\Gamma$, of the ionized system. If ϕ_a belongs to irrep Δ, orbital excitations from the manifold of orbitals, $\{\phi_i\}$, belonging to the nth level of Γ symmetry, $\{\phi_i\} \in n\Gamma$, to the manifold of orbitals, $\{\phi_a\} \in m\Delta$, will lead to excited states belonging to the irreps contained in $\Gamma \times \Delta$. In the small matrix approximation one retains the coupling amongst the *ia* pairs, but neglects all coupling of the *ia* pairs to *jb* pairs with $\{\phi_j\} \notin n\Gamma$ and (or) $\{\phi_b\} \notin m\Delta$. Diagonalization of the small matrix results in a diagonal matrix, where the ω_α^2 will be on the diagonal. Of course, each ω_α appears as many times as the order of the irrep to which the α excited state belongs. The diagonalization is essentially a diagonalization of the **K** matrix, because ε_a and I_i are the same in the whole small matrix. We label the eigenvectors with $\alpha,\beta,\ldots$ Suppose α is an eigenvector belonging to irrep $\Lambda \in \Gamma \times \Delta$, then we obtain again equations of the form of eq. [3.8] (as many identical equations as the order of Λ),

$$[3.11] \qquad (\varepsilon_a + I_i)^2 + 2(\varepsilon_a + I_i)K_{\alpha\alpha}(\boldsymbol{\varepsilon}, \mathbf{I}; \omega_\alpha) - \omega_\alpha^2 = 0$$

where it should be understood that the **K** matrix in the $\{\alpha\}$ basis is diagonal. We would now obtain equations like eq. [3.10] for the relation of ε_a with each of the ω_α, α being one of the excited states of the $\Gamma \times \Delta$ manifold. It is natural to define I_a as the average ionization energy from these excited states,

$$[3.12] \qquad I_a = -I_i + \frac{1}{d}\sum_{\alpha \in \Gamma \times \Delta} \omega_\alpha$$

and average eq. [3.10] like the equations for ε_a that can be obtained from eq. [3.11] to obtain

$$[3.13] \qquad \varepsilon_a \approx -I_i + \frac{1}{d}\sum_{\alpha \in \Gamma \times \Delta} \omega_\alpha - \frac{1}{d}\sum_{\alpha \in \Gamma \times \Delta} K_\alpha + O(K^2) = I_a - \frac{1}{d}\sum_{\alpha \in \Gamma \times \Delta} K_\alpha + O(K^2)$$

Here, d is the total number of excited states resulting from $n\Gamma \rightarrow m\Delta$ excitations. Equation [3.13] yields the interpretation of the virtual orbital energy, ε_a, as the average ionization energy from the excited state manifold of the $n\Gamma \rightarrow m\Delta$ excitations. The "error" is of first order in the diagonal elements, $K_{\alpha\alpha}$, which in practice are usually small, see the examples below. A typical case where this approximation breaks down (the charge-transfer excitation) will be discussed below.

Finally, we have to realize that the orbital, i, or the manifold, $n\Gamma$, that we have chosen to consider in the definition of I_a, is not unique. A further averaging would involve all the occupied orbital levels from which excitations to ϕ_a can be carried out:

$$[3.14] \qquad I_a = \sum_i^H \left[-I_i + \frac{1}{d} \sum_{\alpha \in \Gamma_i \times \Delta} \omega_\alpha \right]$$

Altogether, we obtain the approximate identification

$$[3.15] \qquad \varepsilon_a \approx -I_a$$

where I_a is either the ionization energy from a specific excited state (eq. [3.9]), or from an average over excited states belonging to a particular manifold defined by a degenerate occupied level and (or) degenerate virtual level (eq. [3.13]), or finally an average over the excitations from all occupied orbitals to the virtual orbital, ϕ_a. The important point is that ε_a is such an ionization energy, not an electron affinity, see below.

Equations [3.10], [3.13], and [3.14] can be considered as an analog of Koopmans' theorem for the energies of virtual KS MOs. Conversely, of course, they tell us that the excitation energy, ω_α, is approximately equal to a virtual-occupied orbital energy difference when we apply the KS Koopmans theorem, $\varepsilon_i \approx -I_i$,

$$[3.16] \qquad \varepsilon_a - \varepsilon_i \approx I_i - I_a \approx \omega_\alpha$$

We emphasize that this is a radically different approximate interpretation of the Kohn–Sham than of the Hartree–Fock virtual orbital energy. It is easily seen that the Koopmans frozen orbital assumption for the negative ion with an added electron in the virtual orbital, ϕ_a, results in $\varepsilon_a^{\mathrm{HF}}$ being approximately minus the electron affinity, A_a, for addition of an electron to orbital ϕ_a, which creates an excited negative ion state (and the negative ion ground state if ϕ_a is the lowest unoccupied molecular orbital, LUMO),

$$\varepsilon_a^{\mathrm{HF}} = E_{\mathrm{froz}}^{\mathrm{HF}}[M^-(\phi_a)^1] - E^{\mathrm{HF}}[M] \approx -A_a$$

Using the frozen orbital and Hartree–Fock approximations for the ionization energy out of an occupied orbital, the standard Koopmans' theorem is obtained

$$-\varepsilon_i^{\mathrm{HF}} = E_{\mathrm{froz}}^{\mathrm{HF}}[M^+(\phi_i)^{-1}] - E^{\mathrm{HF}}[M] \approx I_i$$

It is observed that the virtual-occupied orbital energy difference in the Hartree–Fock case is approximately

$$\varepsilon_a^{\mathrm{HF}} - \varepsilon_i^{\mathrm{HF}} = I_i - A_a$$

In the Hartree–Fock model, the virtual-occupied orbital energy difference is totally different from an excitation energy, it is the difference of an ionization energy and an electron affinity. This very important difference between KS and HF models of course reflects the fact that the virtual orbital energy in the Kohn–Sham model represents an excited electron in the *same* potential as the electrons in the occupied orbitals, whereas in the Hartree–Fock model the virtual orbital energy represents an *added* electron that sees a more repulsive potential (repulsion with N electrons) than the electrons in the occupied orbitals (repulsion with $N-1$ electrons).

Let us now consider the opposite limit of large $K_{ia,ia}$, still in the small matrix approximation. It is well known that in charge-transfer transitions, where in the long distance limit the transition density, $\phi_i(\mathbf{r})\phi_a(\mathbf{r})$, goes to zero, the exchange-correlation kernel, f_{xc}, has to diverge,[37] so that the total contribution of the coupling matrix term, $\sqrt{\varepsilon_a - \varepsilon_i}K_{ia,ia}\sqrt{\varepsilon_a - \varepsilon_i}F_{ia}^{\alpha}$, in eq. [2.13] remains finite and the excitation energy, ω_{ia}, differs from the simple orbital energy difference, $\varepsilon_a - \varepsilon_i$. In that case, it is clear that eq. [3.8] will no longer afford the approximation $\varepsilon_a \approx -I_i + \omega_{ia}$. In other words, for excitations to a virtual orbital, ϕ_a, from an orbital, ϕ_i, which is in a different spatial region (no differential overlap with ϕ_a), the excitation energy, ω_{ia}, no longer leads to a quantity, $-I_i + \omega_{ia}$, which is approximately equal to the quantities, $-I_j + \omega_{ja} = -I_a$, we obtained for the small $K_{ja,ja}$ cases ("normal" excitations where ϕ_j is in the same spatial region as ϕ_a). In the extreme case that $K_{ia,ia}$ would diverge, $K_{ia,ia} \to \infty$, a finite excitation energy, ω_{ia}, would only be obtained in eq. [3.8] if the energy, ε_a, would tend to $-I_i$,

$$[3.17] \qquad \varepsilon_a \approx -I_i$$

There is a case where it is known that $K_{ia,ia}$ diverges. This happens for the HOMO (bonding orbital) → LUMO (antibonding orbital) transition in the case of a dissociating electron pair bond.[38] In that particular case the orbital energies of the HOMO and LUMO become degenerate, so the difference, $\varepsilon_a - \varepsilon_i$, tends to zero. Nevertheless, it is known that the excitation energy does not go to zero, and will in the homonuclear case even go to rather high energy as the excited state is a mixture of the ionic states A^+-A^- and A^--A^+. The excitation energy, ω_{ia}, is not zero and therefore is not approximately equal to $\varepsilon_a - \varepsilon_i \approx 0$, which according to eq. [2.13] implies that the contribution of the coupling matrix term is significant. The term with the coupling matrix is not negligible because the divergence of $K_{ia,ia}$ leads to a significant contribution in spite of the small $(\varepsilon_a - \varepsilon_i)$ factor. We conclude that in the case of large or even diverging $K_{ia,ia}$, the relation $\varepsilon_a \approx -I_i + \omega_{ia}$ does not hold, and the quantity I_a we have defined should only relate to the difference $-I_i + \omega_{ia}$ for ionization/excitation from an orbital, ϕ_i, for which $\phi_i \to \phi_a$ is not a charge transfer transition.

4. Energies of virtual orbitals and excitations — An illustration with the N_2 molecule

To illustrate numerically the interpretation of the KS virtual orbital energies, ε_a, given in the previous section and their relation to the excitation energies, ω_{ia}, we consider in this section the example of the prototype N_2 molecule.[33] Figure 1 presents the energy levels of the frontier KS MOs of N_2. They are calculated with the approximate exchange-correlation (xc) potential obtained with the statistical average of (different) orbital potentials (SAOP),[31,39] which reproduces closely the features of the KS xc potential for small prototype systems, see Fig. 1 in ref. 33.

According to the SAOP calculation, the highest occupied MO (HOMO) is the $3\sigma_g$ MO of the σ bond N–N, while the $1\pi_u$ level of the π bonds lies somewhat lower (see Fig. 1). This corresponds to the experimental assignment of the lowest ionization of N_2. Unlike this, the HF theory incorrectly

Fig. 1. Orbital energy diagram for the occupied and virtual orbitals of N_2 according to a Kohn–Sham calculation (SAOP potential). Orbital energies in eV.

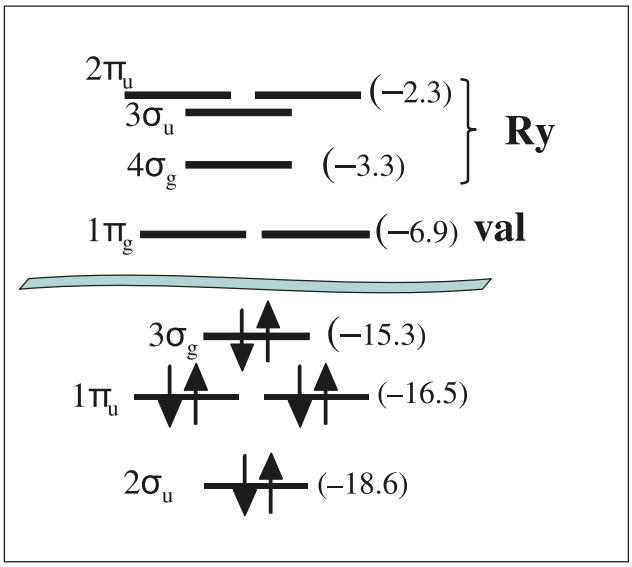

predicts $1\pi_u$ as the HOMO. Another characteristic feature of the KS spectrum are the negative energies of the virtual MOs (see Fig. 1). They reflect the binding nature of the KS potential, which, as was mentioned above, is a shared potential for both occupied and virtual KS MOs. The lowest unoccupied MOs (LUMO) are the valence antibonding $1\pi_g$ MOs of the π bonds, the next is the Rydberg-type $4\sigma_g$ MO, while the antibonding $3\sigma_u$ MO (which also has significant Rydberg character) and the Rydberg type $2\pi_u$ MOs lie at higher energies (see Fig. 1).

Table 1 compares the experimental and TDDFT energies, ω_{ia}, of the $3\sigma_g \rightarrow 3\sigma_u$ and $3\sigma_g \rightarrow 2\pi_u$ excitations as well as the corresponding oscillator strengths, f. According to the percentages of single excitation character given in Table 1, there is indeed rather little admixture of other single excitations. The theoretical quantities are calculated within the adiabatic local density approximation (ALDA) for the Hxc kernel, $f_{Hxc}(\omega)$, with the SAOP and LDA potentials as well as with the Becke–Perdew generalized gradient approximation (GGA) for the potential. We note that the calculated $3\sigma_g \rightarrow 2\pi_u$ excitation should, according to the analysis of ref. 40, be associated with the experimental $c^1\Pi_u$ band, and not with $o^1\Pi_u$ as surmised in ref. 33. One can see from Table 1 that the SAOP ω_{ia} value for $3\sigma_g \rightarrow 3\sigma_u$ is very close to experiment, while for the $3\sigma_g \rightarrow 2\pi_u$ excitation it makes a small error of ~0.2 eV. In contrast, the LDA/GGA excitation energies are much too low (several eV) compared to the experimental ones. The trend observed reflects the incorrect shape of the LDA/GGA xc potentials, which are not attractive enough in the bulk molecular region, see Fig. 1 of ref. 33. This produces orbital energies for these potentials that are typically too high by ~5 eV, at least for the valence orbitals (such as $3\sigma_g$), which have large amplitude in the molecular region. Since the orbital energies of the diffuse Rydberg orbitals do not only, or not primarily, probe the molecular region but rather the outer and large distance regions, where all potentials are close to zero anyway, the orbital energies of the Rydberg states are not so different between the approximate LDA/GGA potentials and the SAOP (or highly accurate Kohn–Sham) potentials. This holds for the diffuse $3\sigma_u$ and $2\pi_u$ orbitals. For LDA/GGA therefore, the orbital energy gap, $\varepsilon_a - \varepsilon_i$, is much too small, which leads to much too small calculated excitation energies. The deficiency of the LDA/GGA potentials masks the simple relations we are discussing in this paper of the true Kohn–Sham system between orbital energies and ionization energies (from both the occupied and the virtual orbitals) as well as excitation energies.

Table 1. The excitation energies, ω (in eV), oscillator strengths, f, and the assigned orbital transitions for two excitations of N_2. The percentages refer to the percentage character that the specific single excitation has in the eigenvector of the TDDFT calculation. The $1\pi_u \rightarrow 1\pi_g$ excitation leads to the states $^{1,3}\Sigma_u^+$, $^{1,3}\Sigma_u^-$, $^{1,3}\Delta_u$. The $\Delta\varepsilon = \varepsilon_{1\pi g} - \varepsilon_{1\pi u}$ is compared in this case to the average calculated and experimental excitation energies for these states.

	$\Delta\varepsilon$	SAOP	BP	LDA	Experimental
$3\sigma_g \rightarrow 3\sigma_u$		98%	100%	100%	$c'^1\Sigma_u^+$
ω	13.0	12.9	10.4	10.5	12.9
f		0.219	0.003	0.003	0.279
$3\sigma_g \rightarrow 2\pi_u$		99%	100%	100%	$c^1\Pi_u$
ω	13.0	12.95	10.36	10.51	13.2
f		0.122	0.004	0.006	0.145
$1\pi_u \rightarrow 1\pi_g$					
ω^{av}	9.6	9.9	10.0	10.0	10.0

The deficient LDA/GGA potentials may not affect the diffuse (Rydberg) orbital energies so much, but they do distort the shapes of these orbitals. We note that the calculated oscillator strengths in the SAOP model potential correspond well with the experimental f values (the oscillator strengths are notoriously difficult quantities, and order of magnitude agreement is already quite good). However, as the LDA/GGA potentials lack the correct Coulombic $-1/r$ behavior, but decay to zero much more rapidly (exponentially), they do not support the extended Rydberg-type MOs. The latter are too much contracted in LDA/GGA, which leads to much too low oscillator strengths, f. By its construction, the SAOP xc potential is free from the abovementioned drawbacks, which results in the observed excellent agreement between the SAOP and experimental quantities (see Table 1).

A remarkable feature of the present results is that the experimental/SAOP ω_{ia} of Table 1 nearly coincide with the corresponding orbital energy differences of Fig. 1. Indeed, the energy difference of 13.0 eV between the $3\sigma_g$ and $3\sigma_u$ MOs (see Fig. 1) is only 0.1 eV higher than the experimental/SAOP ω_{ia} of 12.9 eV (see Table 1). Furthermore, the energy difference of 13.0 eV between the $3\sigma_u$ and $2\pi_u$ MOs differs from the SAOP ω_{ia} by only 0.2 eV (see Table 1). This indicates, in the considered cases, a negligible contribution of the coupling matrix **K** to the calculated TDDFT excitation energies, ω_{ia}, with the latter being reproduced rather accurately with the virtual-occupied orbital energy differences. Then, the analog of Koopmans' theorem for the energies of virtual KS MOs of the previous section can be applied, so that the energies, ε_a, of the virtual orbitals $3\sigma_u$ and $2\pi_u$ can be interpreted as (minus) the energies of ionization, I_a, of the corresponding excited states.

Table 1 also includes the experimental and TDDFT data on the valence $1\pi_u \rightarrow 1\pi_g$ excitations in the N_2 molecule. In this case, the degenerate $1\pi_u \rightarrow 1\pi_g$ KS orbital transitions (bonding π to antibonding π^*) correspond to a manifold of excited states ($^{1,3}\Sigma_u^+$, $^{1,3}\Sigma_u^-$,$^{1,3}\Delta_u$) ranging from 7.75 to 14.2 eV. In contrast to the other excitations it is also a genuine valence transition, without Rydberg character. According to eq. [3.12] and [3.13], ε_a ($a = 1\pi_g$) is interpreted as the averaged ionization energy from these excited states, so that the orbital energy difference, $\Delta\varepsilon = \varepsilon_a$ ($a = 1\pi_g$) $- \varepsilon_i$ ($i = 1\pi_u$), is to be compared with the average energy of the $1\pi_u \rightarrow 1\pi_g$ excitations. Table 1 presents the experimental as well as the SAOP, BP, and LDA energies, ω^{av}, averaged over the six excited states. It has been observed that for valence excitations, in contrast to Rydberg excitations, SAOP, BP, and LDA all have good performance, since all valence orbitals, both the occupied and unoccupied ones, have their main amplitude in the molecular region and are all shifted in the same way by the deficient LDA and GGA potentials. In this case, all models perfectly reproduce the experimental average excitation energy of 10.0 eV. It is to be noted that the $\Delta\varepsilon$ value of 9.6 eV is also fairly close to this average (see Table 1). This provides further numerical support to our interpretation (3.15) of $-\varepsilon_a$ as the (average) ionization energy of the relevant excited state(s). It has to be cautioned that the excited states in this case correspond to a valence excitation and so are not of purely single excitation type, there is considerable mixing with other single excitations. This mixing is different for different states. Such mixing is neglected in the approximate Koopmans' theorem for the virtual orbital energies. Moreover, the diagonal $K_{\alpha\alpha}$ matrix elements are not negligible here, since they account for the spread of the energies of the excited states resulting from the $1\pi_u \rightarrow 1\pi_g$ excitation. The average of the $K_{\alpha\alpha}$ is apparently still fairly small. But it is clear, of course, that the relation of orbital energy differences to (average) excitation energies remains a qualitative correspondence rather than a quantitative equality.

5. Conclusions

In this paper, from the requirement that the KS system delivers not only the exact density, but also its response, the exact relations between the orbital energies of virtual KS orbitals, vertical ionization potentials, and excitation energies are obtained. To establish these ε_a, I_a and ($\varepsilon_a - \varepsilon_i$), ω_{ia} relations, the eigenvalue equations of time-dependent density functional theory are combined with the relations between the energies of the occupied KS MOs and VIPs, which have been derived earlier.[3–5]

We consider approximations to these exact relations in order to establish the DFT analog of Koopmans' theorem. Within the small matrix approximation of TDDFT and in the limit of small coupling matrix **K**, the energy, ε_a, of a virtual orbital is interpreted as (minus) the energy of ionization, I_a, of the corresponding excited state. This holds for the predominantly single electronic excitations in compact molecules or for intrafragmental excitations in larger systems. The opposite limit of large **K** is much more special. It occurs for charge-transfer transitions, and an example of very large (diverging) $K_{ia,ia}$ is the case of near-degenerate HOMO, ϕ_i, and LUMO, ϕ_a, occurring in the dissociating electron pair bond (with the excitation $\phi_i \rightarrow \phi_a$ also leading to a charge-transfer excited-state). In these cases, one does not have the relation $\varepsilon_a \approx -I_a$, but in the latter case the relation $\varepsilon_a \approx -I_i$ holds.

The present results are related to the previous ones of ref. 14 in a similar way as the analog of the Koopmans' theorem for the occupied KS MOs[3] is related to the previous work.[11] Indeed, in ref. 11 the long-range asymptotics of the KS equations were analyzed to provide the physical meaning of the HOMO, while in ref. 3 the exact relations between the energy, ε_i, of an arbitrary occupied MO and the manifold of VIPs, $\{I_k\}$, were obtained, from which the physical meaning of ε_i was derived. Analogously, the long-range asymptotics of the KS equations were analyzed in ref. 14 to consider the energy differences between Rydberg type KS MOs and HOMO as good approximations to the energies of the corresponding Rydberg type excitations. And in the present paper, the exact relations between the energy, ε_a, of an arbitrary virtual orbital and the manifold of VIPs, $\{I_k\}$, and excitation energies, $\{\omega_\alpha\}$, are obtained, with which a physical meaning is attributed to ε_a for small coupling matrix **K**.

The present results show the important qualitative difference between virtual MOs of the KS and HF theories; in the latter theory, according to the canonical Koopmans' theorem, the energies of virtual orbitals are interpreted as the affinities, $-A_a$, to an extra electron. This implies that the orbital energy difference, $\varepsilon_a^{HF} - \varepsilon_i^{HF}$, is not close to an excitation energy, but to the difference of an ionization energy and an electron affinity, $I_i - A_a$. In contrast, in the KS theory the energy of a virtual orbital, ε_a, can be interpreted, under certain conditions, as the ionization energy, $-I_a$, from the corresponding excited state. Moreover, the virtual-occupied orbital energy differences were shown to approximate the excitation energies, $\varepsilon_a - \varepsilon_i \approx \omega_{ia}$. Since the Kohn–Sham occupied orbital energies have already received the interpretation of approximate ionization energies, $\varepsilon_i \approx -I_i$, one obtains $\varepsilon_a \approx -I_i + \omega_{ia}$, which is by definition $-I_a$, consistent with the interpretation of ε_a noted above.

6. Acknowledgement

This research was supported by the WCU (World Class University) program (EJB) through the Korea Science and Engineering Foundation funded by the Ministry of Education, Science and Technology (Project No. R32-2008-000-10180-0). OVG was supported by the Netherlands Foundation for Scientific Research (NWO), project 700.52.302.

References

(1) Hohenberg, P.; Kohn, W. *Phys. Rev.* **1964**, *136* (3B), 864–871. doi:10.1103/PhysRev.136.B864.
(2) Kohn, W.; Sham, L. J. *Phys. Rev.* **1965**, *140* (4A), 1133–1138. doi:10.1103/PhysRev.140.A1133.
(3) Chong, D. P.; Gritsenko, O. V.; Baerends, E. J. *J. Chem. Phys.* **2002**, *116* (5), 1760–1772. doi:10.1063/1.1430255.
(4) Gritsenko, O. V.; Baerends, E. J. *J. Chem. Phys.* **2002**, *117* (20), 9154–9159. doi:10.1063/1.1516800.
(5) Gritsenko, O. V.; Braida, B.; Baerends, E. J. *J. Chem. Phys.* **2003**, *119* (4), 1937–1950. doi:10.1063/1.1582839.
(6) Gritsenko, O. V.; Baerends, E. J. *J. Chem. Phys.* **2004**, *120* (18), 8364–8372. doi:10.1063/1.1698561. PMID:15267759.

(7) Perdew, J. P.; Parr, R. G.; Levy, M.; Balduz, J. L. *Phys. Rev. Lett.* **1982**, *49* (23), 1691–1694. doi:10.1103/PhysRevLett.49.1691.
(8) Perdew, J. P.; Levy, M. *Phys. Rev. Lett.* **1983**, *51* (20), 1884–1887. doi:10.1103/PhysRevLett.51.1884.
(9) Levy, M.; Perdew, J. P.; Sahni, V. *Phys. Rev. A* **1984**, *30* (5), 2745–2748. doi:10.1103/PhysRevA.30.2745.
(10) Almbladh, C. O.; Pedroza, A. C. *Phys. Rev. A* **1984**, *29* (5), 2322–2330. doi:10.1103/PhysRevA.29.2322.
(11) Almbladh, C. O.; von Barth, U. *Phys. Rev. B* **1985**, *31* (6), 3231–3244. doi:10.1103/PhysRevB.31.3231.
(12) Perdew, J. P.; Levy, M. *Phys. Rev. B* **1997**, *56* (24), 16021–16028. doi:10.1103/PhysRevB.56.16021.
(13) Koopmans, T. *Physica* **1934**, *1* (1–6), 104–113. doi:10.1016/S0031-8914(34)90011-2.
(14) Savin, A.; Umrigar, C. J.; Gonze, X. *Chem. Phys. Lett.* **1998**, *288* (2–4), 391–395. doi:10.1016/S0009-2614(98)00316-9.
(15) Levy, M.; Nagy, A. *Phys. Rev. A* **1999**, *59* (2), 1687–1689. doi:10.1103/PhysRevA.59.1687.
(16) Casida, M. In *Recent Advances in Density Functional Methods;* Chong, D. P., Ed.; World Scientific: Singapore. 1995; Vol. 1.
(17) van Gisbergen, S. J. A.; Snijders, J. G.; Baerends, E. J. *J. Chem. Phys.* **1995**, *103* (21), 9347–9354. doi:10.1063/1.469994.
(18) Gross, E. U. K.; Dobson, J. F.; Petersilka, M. *Top. Curr. Chem.* **1996**, *181*, 81–172. doi:10.1007/BFb0016643.
(19) Bauernschmitt, R.; Ahlrichs, R. *Chem. Phys. Lett.* **1996**, *256* (4–5), 454–464. doi:10.1016/0009-2614(96)00440-X.
(20) van Gisbergen, S. J. A.; Koostra, F.; Schipper, P. R. T.; Gritsenko, O. V.; Snijders, J. G.; Baerends, E. *J. Phys. Rev. A* **1998**, *57* (4), 2556–2571. doi:10.1103/PhysRevA.57.2556.
(21) Stratmann, R. E.; Scuseria, G. E.; Frisch, M. J. *J. Chem. Phys.* **1998**, *109* (19), 8218–8224. doi:10.1063/1.477483.
(22) van Gisbergen, S. J. A.; Snijders, J. G.; Baerends, E. J. *Comput. Phys. Commun.* **1999**, *118* (2–3), 119–138. doi:10.1016/S0010-4655(99)00187-3.
(23) Görling, A.; Heinze, H. H.; Ruzankin, S. P.; Staufer, M.; Rösch, N. *J. Chem. Phys.* **1999**, *110* (6), 2785–2799. doi:10.1063/1.477922.
(24) Hirata, S.; Head-Gordon, M. *Chem. Phys. Lett.* **1999**, *302* (5–6), 375–382. doi:10.1016/S0009-2614(99)00137-2.
(25) Rosa, A.; Ricciardi, G.; Gritsenko, O.; Baerends, E. J. *Struct. Bond* **. 2004**, *112*, 49116. doi:10.1007/b12224.
(26) Burke, K.; Werschnik, J.; Gross, E. K. U. *J. Chem. Phys.* **2005**, *123* (6), 062206. doi:10.1063/1.1904586.
(27) Dreuw, A.; Head-Gordon, M. *Chem. Rev.* **2005**, *105* (11), 4009–4037. doi:10.1021/cr0505627. PMID:16277369.
(28) Baerends, E. J.; van Leeuwen, R.; *Phys. Rev. A* **1994**, *49* (4), 2421–2431. doi:10.1103/PhysRevA.49.2421. PMID:9910514.
(29) Casida, M. E.; Jamorski, C.; Casida, K. C.; Salahub, D. R. *J. Chem. Phys.* **1998**, *108* (11), 4439–4449. doi:10.1063/1.475855.
(30) Tozer, D. J.; Handy, N. C. *J. Chem. Phys.* **1998**, *109* (23), 10180–10189. doi:10.1063/1.477711.
(31) Schipper, P. R. T.; Gritsenko, O. V.; van Gisbergen, S. J. A.; Baerends, E. J. *J. Chem. Phys.* **2000**, *112* (3), 1344–1352. doi:10.1063/1.480688.
(32) Grüning, M.; Gritsenko, O. V.; van Gisbergen, S. J. A.; Baerends, E. J. *J. Chem. Phys.* **2001**, *114* (2), 652–660. doi:10.1063/1.1327260.
(33) Grüning, M.; Gritsenko, O. V.; van Gisbergen, S. J. A.; Baerends, E. J. *J. Chem. Phys.* **2002**, *116* (22), 9591–9601. doi:10.1063/1.1476007.
(34) Görling, A. *Phys. Rev. A* **1996**, *54* (5), 3912–3915. doi:10.1103/PhysRevA.54.3912. PMID:9913938.
(35) Baerends, E. J.; Gritsenko, O. V. *J. Phys. Chem. A* **1997**, *101* (30), 5383–5403. doi:10.1021/jp9703768.
(36) Gross, E. K. U.; Kohn, W. *Adv. Quantum Chem.* **1990**, *21*, 255–291. doi:10.1016/S0065-3276(08)60600-0.
(37) Gritsenko, O. V.; Baerends, E. J. *J. Chem. Phys.* **2004**, *121* (2), 655–660. doi:10.1063/1.1759320. PMID:15260591.
(38) Gritsenko, O. V.; van Gisbergen, S. J. A.; Görling, A.; Baerends, E. J. *J. Chem. Phys.* **2000**, *113* (19), 8478–8484. doi:10.1063/1.1318750.
(39) Gritsenko, O. V.; Schipper, P. R. T.; Baerends, E. *J. Chem. Phys. Lett.* **1999**, *302* (3–4), 199–207. doi:10.1016/S0009-2614(99)00128-1.
(40) Neugebauer, J.; Baerends, E. J.; Nooijen, M. *J. Chem. Phys.* **2004**, *121* (13), 6155–6166. doi:10.1063/1.1785775. PMID:15446909.

Mechanistic insight into the selective trans-1,4-polymerization of butadiene by terpyridine–iron(II) complexes — A computational study

Sven Tobisch

Abstract: The density functional theory (DFT) method has been employed to unravel mechanistic intricacies of the 1,4-polymerization of 1,3-butadiene mediated by the $[(\eta^3\text{-}RC_3H_4)Fe^{II}(C_{15}H_{11}N_3)(\eta^2\text{-}C_4H_6)]^+$ terpyridine–iron(II) active catalyst species. The π-allyl-insertion mechanism is operative for chain growth, whilst the alternative σ-allyl-insertion mechanism has been explicitly demonstrated as being inoperable. This study elucidates the mechanism of cis–trans regulation and unveils the factors that govern the observed high trans-1,4 stereoselectivity, in particular, the discriminative role of allylic isomerization. An atactic *trans*-1,4-polydiene is expected from polymerization of a terminally monosubstituted butadiene, the experimental results of which have not been reported thus far.

Key words: 1,3-diene polymerization, reaction mechanisms, structure–reactivity relationships, iron complexes, density functional calculations.

Résumé : La méthode DFT a été employée afin d'éclaircir les subtilités de la 1,4-polymérisation du 1,3-butadiène assistée par les espèces terpyridine–fer(II) ($[(\eta^3\text{-}RC_3H_4)Fe^{II}(C_{15}H_{11}N_3)(\eta^2\text{-}C_4H_6)]^+$) catalytiquement actives. Le mécanisme selon l'insertion π-allylique se déroule pour la croissance de chaine tandis que le mécanisme alternatif selon l'insertion σ-allylique a été explicitement démontré comme inopérable. Cette étude élucide le mécanisme de la régulation cis–trans et dévoile les facteurs gouvernant la haute stéréoselectivité trans-1,4 observée, en particulier le rôle discriminatoire de l'isomérisation allylique. Un *trans*-1,4-polydiène atactique est attendu à partir de la polymérisation d'un butadiène monosubstitué en position terminale. Ces résultats expérimentaux n'ont pas été reportés jusque-là.

Mots-clés : polymérisation du 1,3-diène, mécanismes réactionnels, relations structure–réactivité, complexes de fer, calculs de la fonctionnelle de la densité.

[Traduit par la Rédaction]

Introduction

The metal-catalyzed polymerization of 1,3-dienes is a key process in the chemical industry and as such has triggered considerable research efforts in both academia and industry.[1–5] Structurally defined allyl-transition-metal complexes and Ziegler–Natta systems have been established as being competent in catalysing the stereoselective polymerization of 1,3-dienes.[6] These catalyst systems are superior to other initiators due to their ability to effect the C–C bond formation in a highly chemo-, regio- and stereo-selective fashion.[7] 1,3-Diene polymerization mediated by various catalyst systems has furthermore been the subject of computational mechanistic examination.[8–10]

Recently, the group of Yasuda[11] has reported a set of iron compounds based on the motif of the 2,2′:6′,2″-terpyridine (terpy) tridentate N_3 ligand, which upon activation with modified methylaluminoxane (MMAO) are capable of effecting homo- and co-polymerization of 1,3-butadiene and isoprene. The substituents on the terpy's phenyl rings have been found to regulate catalytic performance and stereoselectivity.[11] Aryl groups in 6,6′ positions bearing sterically demanding substituents inhibit the catalysis completely, presumably because these ligands block the iron centre against diene attack, which prevents any insertion event. Conversely, Fe(terpy) compounds in which the 6,6′ positions are unsubstituted, thereby ensuring sufficient openness around the metal centre, display good polymerization performance.[11]

The $FeCl_3$(terpy) **0**/MMAO system with an unsubstituted terpy ligand is unique among all the reported systems. It leads to a highly active catalyst that affords a polybutadiene of predominant trans-1,4 structure (96% trans-1,4, 0% cis-1,4, and 4% 1,2-enchainment, Chart 1).[11] This observation prompted a mechanistic exploration of the title process by employing the density functional theory (DFT) method as an established and predictive means to aid in mechanistic

Received 22 December 2008. Accepted 6 March 2009. Published on the NRC Research Press Web site at canjchem.nrc.ca on 25 September 2009.

This article is part of a Special Issue dedicated to Professor T. Ziegler. This article is dedicated to Professor T. Ziegler on the occasion of his 65th birthday.

S. Tobisch. University of St Andrews, School of Chemistry, Purdie Building, North Haugh, St Andrews KY16 9ST, United Kingdom. (e-mail: st40@st-andrews.ac.uk).

Chart 1.

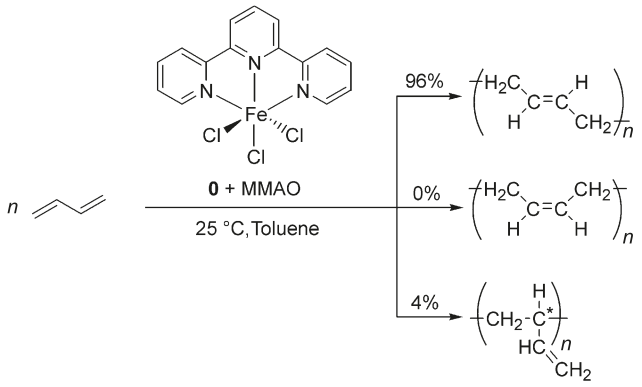

Scheme 1. Precursor activation and chain initiation. Stars indicate vacant sites, which could be occupied by the butadiene monomer or solvent molecules.

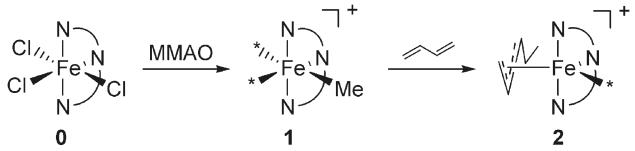

Scheme 2. Proposed mechanisms for chain growth in 1,3-diene polymerization: σ-allyl-insertion mechanism vs π-allyl-insertion mechanism.

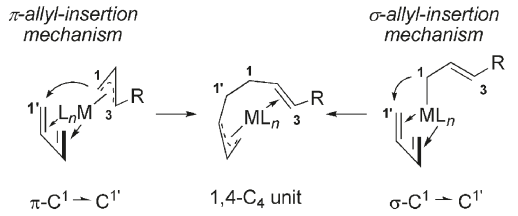

understanding. The objective of the present study is twofold, first, to elucidate the mechanism behind the catalytic performance of this catalyst system and secondly, to unveil the factors that govern the high trans-1,4 stereoselectivity. Moreover, the present mechanistic investigation enables one to predict what type of 1,4-polydiene to expect for terminally monosubstituted butadienes, the result of which has not been reported thus far by experiment.

General aspects of the polymerization cycle

The catalyst precursor **0** requires activation by MMAO,[11] which likely effects halide abstraction, methylation, and methyl anion abstraction at the iron centre together with its reduction due to the presence of the strong organylating and reducing MMAO agent. These steps have precedence in organo-iron chemistry. As an example, Yamamoto and co-workers[12] reported that $Fe^{III}(acac)_3$ transforms into $Fe^{II}Me_2(PPh_3)_3$ upon treatment with triphenylphosphine in the presence of trimethylaluminium. It is thus reasonable to assume that upon activation with MMAO the cationic $[(Me)Fe^{II}(terpy)]^+$ species, **1**, with two vacant coordination sites, is formed (Scheme 1). Butadiene insertion into the Fe–Me linkage of **1** then initiates polymer chain growth to give rise to the cationic $[(C_5H_9)Fe^{II}(terpy)]^+$ species, **2**, bearing one empty coordination site (Scheme 1).

Scheme 3. Anti–cis and syn–trans correlation of the transition-metal-mediated 1,4-polymerization of 1,3-butadiene exemplified for η^4-butadiene insertion into the η^3-butenyl–metal linkage (R denotes the polybutadienyl chain).

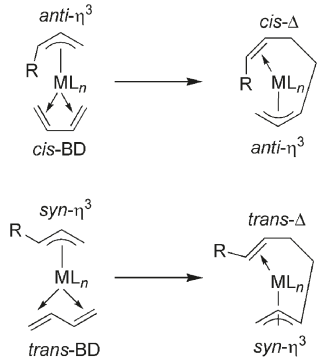

Scheme 4. Interconversion of syn and anti forms of the η^3-butenyl–metal linkage through an $\eta^1(C^3)$-σ intermediate (R denotes the polybutadienyl chain).

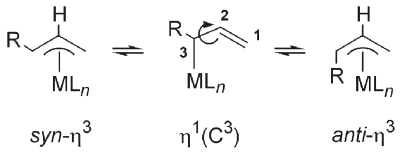

Polymer chain growth does proceed through repeated monomer insertion into the pentenyl–iron linkage of **2**. Hence, $[(RC_3H_4)Fe^{II}(terpy)(C_4H_6)]^+$ represents the catalytically active species in the productive enchainment cycle. Two mechanisms have been proposed for the chain growth step (Scheme 2). Firstly, Cossee and Arlmann[13] assumed, in their so-called σ-allyl-insertion mechanism, the η^1-σ-allyl-metal form in reactive intermediates. Taube and co-workers,[2,14] on the other hand, suggested that butadiene inserts into the η^3-π-allyl-metal bond, which is the so-called π-allyl-insertion mechanism. Detailed computational examination has identified the π-allyl-insertion mechanism as being operative for a variety of early and late transition metal-based catalysts.[8]

In contrast to olefin polymerization, enchainment of 1,3-butadiene is characterized by a greater diversity as the reactive butadiene and allylic units can adopt various forms. Butadiene can coordinate at the metal centre in monodentate (η^2) or bidentate (η^4) mode, from either the s-trans or s-cis configuration. The terminal reactive butyl group of the growing polybutadienyl chain, on the other hand, can be bound to the metal centre in η^3-π or η^1-σ mode and can adopt syn and anti configurations, which are interconvertible. According to the generally accepted anti–cis and syn–trans correlation,[6e] the configuration of the butenyl–metal linkage in the kinetic insertion product is determined by the configuration of the inserting monomer (Scheme 3). An *anti*- or *syn*-butenyl group is generated if butadiene inserts from its s-cis (anti insertion) or s-trans (syn insertion) configuration, respectively. Moreover, the polymer chain is extended by a C_4-unit with a cis or trans double bound, for butadiene to insert into the *anti*- or *syn*-butenyl group, respectively.

As mentioned before, interconversion of the syn and anti forms of the butenyl–metal linkage is another important elementary step, which can play a decisive role in cis–trans

Scheme 5. Catalytic reaction cycle for 1,4-polymerization of 1,3-butadiene with $[(\eta^3\text{-}RC_3H_4)Fe^{II}(C_{15}H_{11}N_3)(\eta^2\text{-}C_4H_6)]^+$ (**3π**) as the active catalyst species. Rival pathways for insertion of *cis*- and *trans*-butadiene into the *anti*-butenyl–Fe^{II} linkage (via k_c(cis) and k_c(trans)) affording a cis-1,4 polymer unit and into the *syn*-butenyl–Fe^{II} linkage (via k_t(cis) and k_t(trans)) affording a trans-1,4 polymer unit, together with the isomerization of the η^3-butenyl–Fe^{II} terminal group of the polymer chain (via $k_{a/s}$, $k_{s/a}$) are shown. The conformations of the key species (for notation, see the text) participating at the various pathways are schematically depicted. The *anti*- and *syn*-butenyl forms for **3** and **4** are labelled by **a** and **s**, respectively, whilst an additional **c** and **t** is used to distinguish between species that are involved in the routes for *cis*-butadiene and *trans*-butadiene insertion, respectively.

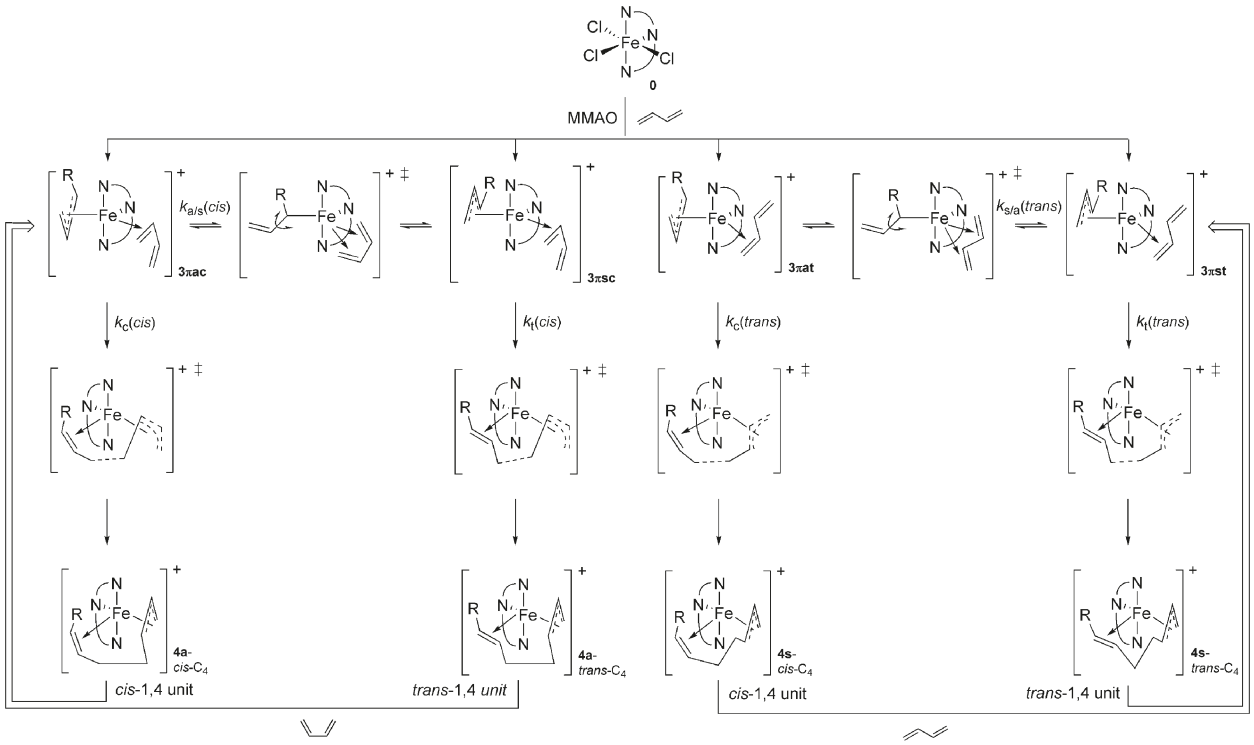

stereoregulation of the polymerization process (see below). Scheme 4 displays schematically the process for complexes with ligand architectures that allow η^3-π-butenyl–metal ligation. The isomerization of *syn*- and *anti*-η^3-butenyl forms preferably proceed by means of a η^3-π ⇄ $\eta^1(C^3)$-σ transformation of the butenyl group, followed by internal rotation of the vinyl group around the formal C^2–C^3 single bond. This has been supported by evidence provided by both experimental[15,16] and computational[17] studies.

Results and discussion

The computational exploration of butadiene polymerization is divided into two parts. The first part investigates elementary events of the tentative catalytic cycle for chain growth (Scheme 5) and also the initiation of the polymer growth commencing from **1**. The various conceivable stereochemical pathways for C–C bond formation have been thoroughly examined for both of the proposed mechanisms (Scheme 2). Special attention has been attributed to determining the spin state preferably adopted by the Fe^{II}(terpy) species when traversing the most accessible pathways. Hence, the whole account of possible singlet, triplet, and quintet states has been comprehensively examined. The free-energy profile of the productive enchainment cycle is presented in the second part. Further sections elucidate the mechanism of cis–trans stereoregulation and discuss the implications for the tacticity control of the 1,4-polymerization process.

Table 1. Gibbs free-energy profile (singlet PES) for insertion of butadiene (BD) into the Fe^{II}–Me bond of $[(Me)Fe^{II}(C_{15}H_{11}N_3)]^+$ (**1**).

Insertion path	**1**-**BD**	TS[**1**-**BD**–**2**]	**2**
trans-Butadiene	–17.3 (**1**-*t*BD)	1.5	–30.3 (**2s**)
cis-Butadiene	–16.1 (**1**-*c*BD)	3.1	–26.6 (**2a**)

Note: The free energies of activation ($\Delta G^{\ddagger}$) and reaction (ΔG) are given relative to {**1** + *trans*-C_4H_6} (singlet PES), in kilocalories per mole.

DFT calculations employed the Tao–Perdew–Staroverov–Scuseria (TPSS) functional[18] in conjunction with flexible basis sets of triple-ζ quality (TZVP[19]) for optimization of key stationary points. The good to excellent performance of the TPSS functional for a wide range of applications, with transition metal complexes in particular, has been demonstrated previously.[20] The final energies were obtained from single-point calculations at the TPSSh level[18,20a,21] using the same basis sets. This DFT method has recently been reported to accurately describe spin-states energetics for first row transition metal complexes.[22] The influence of the solvent (toluene)[11] was taken into explicit consideration by making use of a continuum model. All the key stationary points were fully located with inclusion of solvation by using the conductor-like screening model (COSMO) method.[23] The effect of the counteranion was neglected. Although its influence cannot be excluded a priori, the cationic catalyst model employed herein is likely to provide a realistic description of the studied proc-

Table 2. Gibbs free-energy profile (singlet PES) for the butadiene insertion step of the 1,4-polymerization of 1,3-butadiene with $[(\eta^3\text{-}C_4H_7)Fe^{II}(C_{15}H_{11}N_3)(\eta^2\text{-}C_4H_6)]^+$ (**3π**) as the active catalyst species.

Isomer	**3π**	TS[**3π**-**4**]	**4**
Route for *trans*-butadiene insertion			
syn-*re*/*re*	0.0 (**3πst**)	17.4	–7.5 (**4s**-*trans*-C_4)
syn-*re*/*si*	0.1 (**3πst**)	17.5	–7.4 (**4s**-*trans*-C_4)
anti-*re*/*re*	3.9 (**3πat**)	23.1	–4.2 (**4s**-*cis*-C_4)
anti-*re*/*si*	3.6 (**3πat**)	23.4	–4.7 (**4s**-*cis*-C_4)
Route for *cis*-butadiene insertion			
syn-*re*/*re*	3.8 (**3πsc**)	21.2	–3.4 (**4a**-*trans*-C_4)
syn-*re*/*si*	3.8 (**3πsc**)	21.3	–3.3 (**4a**-*trans*-C_4)
anti-*re*/*re*	7.5 (**3πac**)	27.2	–0.3 (**4a**-*cis*-C_4)
anti-*re*/*si*	7.6 (**3πac**)	27.3	–0.5 (**4a**-*cis*-C_4)

Note: The various stereoisomers are denoted according to the enantiofaces of the two reactive butenyl and butadiene units that are involved in the various stereochemical pathways: syn and anti refers to the butenyl group's configuration, followed by a description of the enantioface of the butenyl group (first) and of butadiene (second); see Scheme 6. Due to the symmetry of the Fe(terpy) backbone, *re*/*re* and *si*/*si* and also *re*/*si* and *si*/*re* stereoisomers are identical. The free energies of activation ($\Delta G^{\ddagger}$) and reaction (ΔG) are given relative to the most stable isomer of **3π**, viz. $[(syn\text{-}\eta^3\text{-}C_4H_7)Fe^{II}(terpy)(trans\text{-}\eta^2\text{-}C_4H_6)]^+$ (syn-*re*/*re* **3πst**) (singlet PES), in kilocalories per mole.

Table 3. Gibbs free-energy profile (singlet PES) for the butadiene insertion step of the 1,4-polymerization of 1,3-butadiene with $[(\eta^1(C^1)\text{-}C_4H_7)Fe^{II}(C_{15}H_{11}N_3)(\eta^4\text{-}C_4H_6)]^+$ (**3σ**) as the active catalyst species.

Isomer	**3σ**	TS[**3σ**-**4**]	**4**
Route for *trans*-butadiene insertion			
syn-*re*/*re*	17.0 (**3σst**)	34.9	–7.2 (**4s**-*trans*-C_4)
syn-*re*/*si*	17.1 (**3σst**)	35.0	–7.4 (**4s**-*trans*-C_4)
anti-*re*/*re*	18.2 (**3σat**)	36.2	–4.2 (**4s**-*cis*-C_4)
anti-*re*/*si*	18.3 (**3σat**)	36.0	–4.7 (**4s**-*cis*-C_4)
Route for *cis*-butadiene insertion			
syn-*re*/*re*	18.2 (**3σsc**)	36.1	–3.4 (**4a**-*trans*-C_4)
syn-*re*/*si*	18.4 (**3σsc**)	36.2	–3.3 (**4a**-*trans*-C_4)
anti-*re*/*re*	20.3 (**3σac**)	38.5	–0.3 (**4a**-*cis*-C_4)
anti-*re*/*si*	20.4 (**3σac**)	38.7	–0.5 (**4a**-*cis*-C_4)

Note: The various stereoisomers are denoted according to the enantiofaces of the two reactive butenyl and butadiene units that are involved in the various stereochemical pathways: syn and anti refers to the butenyl group's configuration, followed by a description of the enantioface of the butenyl group (first) and of butadiene (second); see Scheme 6. Due to the symmetry of the Fe(terpy) backbone, *re*/*re* and *si*/*si* and also *re*/*si* and *si*/*re* stereoisomers are identical. The free energies of activation ($\Delta G^{\ddagger}$) and reaction (ΔG) are given relative to the most stable isomer of **3π**, viz. $[(syn\text{-}\eta^3\text{-}C_4H_7)Fe^{II}(terpy)(trans\text{-}\eta^2\text{-}C_4H_6)]^+$ (syn-*re*/*re* **3πst**) (singlet PES), in kilocalories per mole.

Table 4. Gibbs free-energy profile (singlet PES) for isomerization of the terminal butenyl group of the growing polymer chain in **3π**.

	syn-η^3-Butenyl	TS_{ISO}[a]	*anti*-η^3-Butenyl
trans-BD ($k_{s/a}$(trans))	0.0 (**3πst**)	36.3/32.5	3.6 (**3πat**)
cis-BD ($k_{a/s}$(cis))	3.8 (**3πac**)	35.1/32.9	7.6 (**3πsc**)

Note: The free energies of activation ($\Delta G^{\ddagger}$) and reaction (ΔG) are given relative to the most stable isomer of **3π**, viz. $[(syn\text{-}\eta^3\text{-}C_4H_7)Fe^{II}(terpy)(trans\text{-}\eta^2\text{-}C_4H_6)]^+$ (syn-*re*/*re* **3πst**) (singlet PES), in kilocalories per mole.

[a]Rotational isomerization via inward/outward trajectories has been examined; see Scheme 7.

ess: the Fe^{II} centre always adopts a six coordinate geometry in all the formally cationic key stationary structures.

The mechanistic conclusions drawn in this study were based on the computed free-energy profiles for relevant elementary steps of the chain growth process (see Scheme 5). Table 1 summarizes the energy profile for chain initiation, while the energetics of chain growth events are collated in Tables 2–4 for the favourable singlet potential energy sur-

Fig. 1. Selected structural parameters (Å) of the optimized structures of key stationary points (singlet PES) for insertion of *trans*-butadiene (top) and *cis*-butadiene (bottom) into the Fe^{II}–Me bond of $[(Me)Fe^{II}(terpy)]^+$ (**1**).

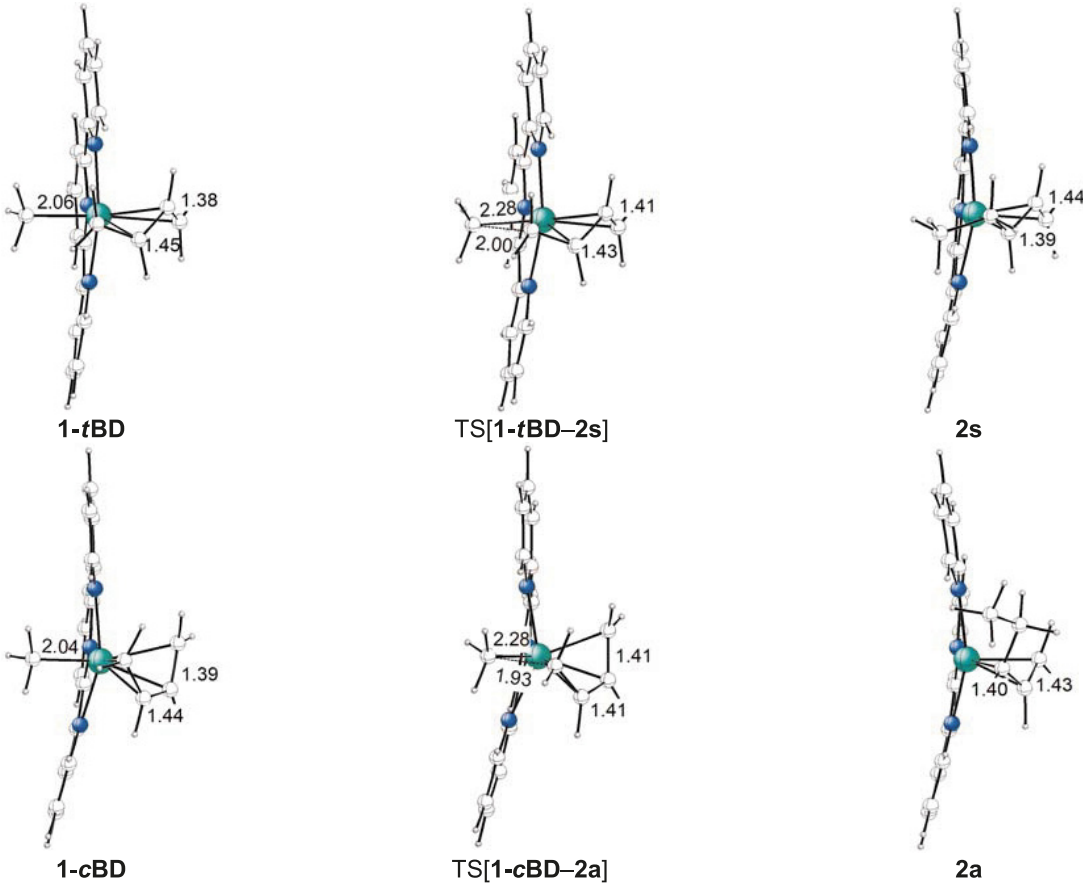

face (PES). The full account of investigated singlet, triplet, and quintet spin states for all the steps is included in the Supplementary data.

Initiation of polymer chain growth

Chain propagation is initiated by capture of a butadiene unit by the methyl precursor (**1**) to form the π-complex (**1**-BD). It comes as no surprise that butadiene binds preferably in a bidentate mode (Fig. 1), hence, occupying the two empty sites available in **1** in a process that is strongly exergonic and proceeding in an essentially barrierless fashion (Table 1).[24] Remarkably, *trans*-butadiene binds somewhat stronger (ΔG = –17.3 kcal mol^{-1}, Table 1) than *cis*-butadiene in the π-complex. The favourable of the two initiation routes commences from **1**-*t*BD and features the insertion of *trans*-η^4-butadiene into the Fe–Me bond to furnish $[(syn\text{-}\eta^3\text{-}C_5H_9)Fe^{II}(terpy)]^+$ (**2s**). This step has a free energy of activation that amounts to 18.8 kcal mol^{-1} and is driven by a thermodynamic force of 13.0 kcal mol^{-1} (Table 1). The generation of the *anti*-η^3-pentenyl species (**2a**) via the rival *cis*-η^4-butadiene insertion route is found to be also viable, but somewhat disfavoured on both kinetic and thermodynamic grounds. Overall, chain initiation is predicted to be a relatively rapid, irreversible transformation with an activation energy that is of similar magnitude as the turnover-limiting barrier for the dominant trans-1,4 enchainment (see below). This leads to the conclusion that chain initialisation is unlikely to cause an induction period.

Elementary events of the chain growth process

General reaction course

Based on the general features of 1,3-diene polymerization discussed before, Scheme 5 shows a plausible catalytic cycle for 1,4-polymerization of butadiene with the cationic $[(\eta^3\text{-}RC_3H_4)Fe^{II}(C_{15}H_{11}N_3)(\eta^2\text{-}C_4H_6)]^+$ (**3π**) as the active catalyst compound. It comprises various possible enchainment paths. After **0** → **1** activation of the catalyst precursor and subsequent **1** → **2** chain initiation, butadiene uptake onto **2** affords **3π** representing the active species of the productive enchainment cycle. Generation of a new C_4-unit can proceed via alternative routes for *cis*-butadiene or *trans*-butadiene insertion. Each of the two routes has two rival pathways for butadiene to insert into the *anti*- or *syn*-butenyl–Fe^{II} bond, thereby giving rise to a cis-1,4 (k_c) or trans-1,4 (k_t) polymer unit, respectively. Traversing the *cis*-butadiene insertion route (via k_c(cis) or k_t(cis), left side in Scheme 5), an *anti*-butenyl group is regenerated as the reactive chain end in the η^3,η^2-polybutadienyl–Fe^{II} insertion produces **4a**. *Cis*-butadiene capture by **4a** to initially afford **3πac** starts a new loop through the chain-growth cycle. Intermediate **4s** with a *syn*-η^3-butenyl-terminated polybutadienyl chain is generated along the route for *trans*-butadiene insertion (via k_c(trans) or k_t(trans), right hand side in Scheme 5), giving rise to **3πst** after *trans*-butadiene uptake to continue chain growth. For each of the insertion routes, the anti and syn forms of **3π** and **4** are interconvertible and presumably in equilibrium.

Scheme 6. Enantiomeric forms of the η^3-butenyl–metal (syn and anti configurations) and the η^2-butadiene–metal (s-cis and s-trans configurations) coordination (R denotes the polybutadienyl chain).

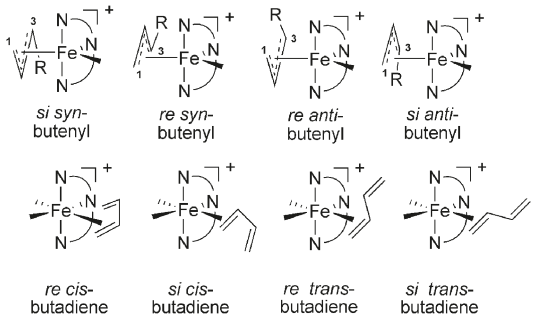

This is indicated in Scheme 5 for butenyl isomerization in **3π** through $k_{a/s}$(cis) and $k_{s/a}$(trans). It becomes evident from Scheme 5 that isomerization is indispensable for the generation of trans-1,4 polymer units along the *cis*-butadiene insertion route (via k_t(cis)) and likewise for the production of a cis-1,4 polybutadiene (via k_c(trans)) for the case that *trans*-butadiene insertion is favourable.

Butadiene π-complex

An octahedral configuration is expected for a six-coordinated d^6-metal centre such as Fe^{II} from orbital interaction considerations.[25] Hence, $[(\eta^3\text{-butenyl})Fe^{II}(terpy)(\eta^2\text{-butadiene})]^+$ (**3π**) and $[(\eta^1\text{-butenyl})Fe^{II}(terpy)(\eta^4\text{-butadiene})]^+$ (**3σ**) are conceivable forms of the π-complex. The configurations of the reactive butadiene (s-cis and s-trans) and butenyl (anti and syn) units and also their enantioface involved in chain propagation are of importance for the stereocontrol of the polymerization process. Scheme 6 depicts the stereoisomers (in *re*/*si* terminology)[26] of η^2-butadiene–Fe^{II} and η^3-butenyl–Fe^{II} ligations.[27] All the possible isomers of key stationary points, which participate in the various stereochemical pathways for chain propagation, have been carefully explored (Tables 2, 3). The $[(RC_3H_4)Fe^{II}(C_{15}H_{11}N_3)(C_4H_6)]^+$ complex, with R = CH_3 as an adequate representation of the growing polybutadienyl chain,[8b,8d,8e,8g] was used as a catalyst model.

For all the various forms of the butadiene π-complex, the singlet spin state represents the ground state. Alternative triplet and quintet spin states are well-separated from the singlet state and are found at higher energies (cf. Table S2a–S3b in the Supplementary data). The most stable form is characterized by a η^3-butenyl–Fe^{II} ligation with butadiene bound in a monodentate mode (Table 2, Fig. 2). The σ-butenyl form (**3σ**), on the other hand, is seen to be distinctly less favourable by about 17 kcal mol^{-1} (Table 3, Fig. 3). Hence, $[(\eta^3\text{-butenyl})Fe^{II}(terpy)(\eta^2\text{-butadiene})]^+$ (**3π**) is the dominant form of the active catalyst complex. For the coordinatively, relatively open terpyridine–iron architecture, which provides sufficient space around the iron centre for η^3-butenyl–Fe^{II} ligation and to capture a butadiene unit, sterics are found to play a minor role in determining the stability of **3π**. Instead, electronic factors prevail. Owing to the mainly covalent character of the butenyl–Fe^{II} interaction, the syn-η^3 form is more stable than the anti-η^3 form by about 3.5 kcal mol^{-1} (Table 2). This is similar to the findings for the several Ni^{II}-based polymerization catalysts,[8a–8f] but contrasts sharply with the situation for highly ionic crotyl-Li complexes,[28] where the anti form is predominant. Interestingly, the syn–anti gap ($\Delta G \sim 1.3$ kcal mol^{-1}, Table 3) is significantly reduced by more than half in **3σ**, but the syn-η^1 form is nevertheless more stable. With regard to butadiene coordination, the η^2-trans form is generally found to be more stable than its η^2-*cis* analogues. Because the electronic stabilization is of comparable magnitude for the two forms, the diversity in stability can simply be traced back to the higher stability of s-trans butadiene relative to its s-cis form (ΔG = 3.6 kcal mol^{-1}),[29] an amount that agrees roughly with the assessed gap between *trans*-η^2- and *cis*-η^2-butadiene forms of **3π**. As anticipated for the open terpy-Fe architecture, the enantioface of the reacting units (i.e., *re*/*re* vs *re*/*si* stereoisomers, see Table 2 and Scheme 6) influences the stability of **3π** to a marginal extent only, thereby reflecting that sterics is of minor importance.

Overall, $[(\eta^3\text{-butenyl})Fe^{II}(terpy)(\eta^2\text{-butadiene})]^+$ (**3π**) is the dominant form of the active catalyst species. Its various isomers, with the *syn*-η^3-butenyl/*trans*-η^2-butadiene isomer (**3πst**) being the most stable, are separated by a few kcal mol^{-1} only. Hence, all the isomers are present in certain concentrations that are determined by their relative stability, provided that isomerization is facile. In contrast, the σ-form (**3σ**) is predicted to be highly unfavourable energetically. Although stabilized by a chelating η^4- butadiene, **3σ** is separated by $\sim$17 kcal mol^{-1} from **3π**.

Butadiene insertion into the Fe^{II}–butenyl linkage

Similar to what has been found for precursor **3**, the transition state for C–C bond formation and also the polybutadienyl–Fe^{II} insertion product **4**, preferably adopts the singlet spin state whilst traversing the most accessible pathways. Hence, chain propagation proceeds at the singlet PES and does not involve any spin-state crossing. For all key stationary points the triplet and quintet states are found at higher energies, well-separated from the low-spin singlet ground state (see the Supplementary data). This also holds true for the two alternative insertion mechanisms (see Scheme 2)

Chain propagation proceeding via butadiene insertion into the η^3-butenyl–Fe^{II} and $\eta^1(C^1)$-butenyl–Fe^{II} linkages has been probed explicitly. The key stationary points participating in these processes are characterized structurally in Figs. 2 and 3, whereas the energy profiles are collated in Tables 2 and 3, respectively. Inspection of key stationary points for the π-butenyl insertion (Fig. 2) reveals that chain growth commences from **3π** and takes place via TS[**3π-4**] that constitutes the insertion of (*cis* or *trans*)-η^2-butadiene into a somewhat distorted (*syn* or *anti*)-η^3-butenyl–Fe^{II} linkage. The TS[**3π-4**] appears at a distance of $\sim$1.75–1.85 Å of the emerging C–C σ-bond and is characterized by a quasi-planar four-membered cis arrangement of the butadiene's double bond that is inserted, the terminal butenyl-C^1 and the iron centre. Decay of the transition state leads to the η^3, η^2-polybutadienyl–Fe^{II} compound (**4**) where the growing polybutadienyl chain is ligated to iron by its terminal η^3-butenyl group and its first double bond. Along the alternative process that starts from **3σ**, the C–C bond formation takes place at $\sim$2.0–2.1 Å in the quasi-planar four-membered TS[**3σ–4**] featuring the (*trans* or *cis*)- η^4-butadiene insertion into an elongated (*syn* or *anti*)-η^1-butenyl–Fe^{II} bond (Fig. 3). Fol-

Fig. 2. Selected structural parameters (Å) of the optimized structures of key stationary points (singlet PES) for insertion of *trans*-butadiene (top) and *cis*-butadiene (bottom) into the *syn*-η^3-butenyl–Fe^{II} bond in $[(\eta^3\text{-}C_4H_7)Fe^{II}(terpy)(\eta^2\text{-}C_4H_6)]^+$ (**3π**) along the most accessible stereochemical pathway.

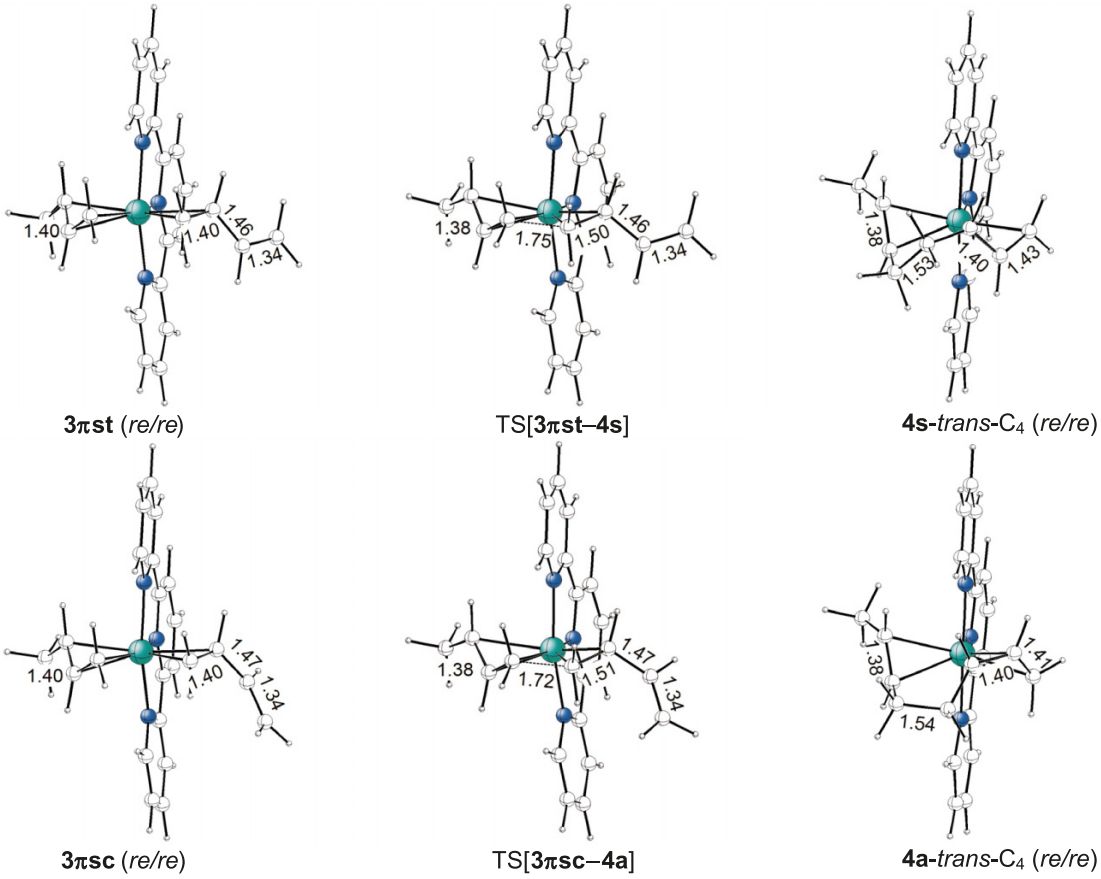

lowing the reaction path further, the η^3-butenyl terminal group is readily regenerated from the former η^4-butadiene unit together with a recoordinating polybutadienyl chain, hence the insertion product (**4**) that is formed along the alternative insertion processes are identical. The next loop through the cycle would first require an $\eta^3 \rightarrow \eta^1(C^1)$ conversion of the terminal butenyl group prior to η^4-butadiene insertion via TS[**3σ-4**]. The comparison of the energy profile for the most feasible pathways of the alternative insertion mechanisms (i.e., *trans*-butadiene insertion into the *syn*-butenyl–Fe^{II} bond, Tables 2, 3) reveals that insertion into the η^3-butenyl–Fe^{II} bond is distinctly preferred kinetically ($\Delta G^{\ddagger}$ = 17.4 kcal mol^{-1}) against the σ-butenyl insertion ($\Delta G^{\ddagger}$ = 33.9 kcal mol^{-1}). The substantial kinetic gap of 16.5 kcal mol^{-1} ($\Delta\Delta G^{\ddagger}$) between the two mechanisms indicates that insertion into the barely reactive σ-butenyl form is almost entirely precluded kinetically. This leads to the following conclusions: (*i*) The thermodynamically favourable η^3-butenyl form is also preferably involved in C–C bond formation; (*ii*) conversely, $\eta^1(C^1)$-butenyl species are predicted to be at high energy, well-separated from η^3-butenyl congeners and hence do not participate along the most accessible pathway for chain growth; (*iii*) the π-allyl insertion mechanism is operative, whilst the σ-allyl mechanism is clearly rendered inoperable.

Focusing now exclusively on the π-allyl insertion mechanism (Table 2, Fig. 2), careful analysis of the located TS[**3π-4**] structures reveals that the unsubstituted terpy ligand provokes a rather modest congestion around the iron centre. As a result, unfavourable interactions of the reactive units with the ligand backbone are of minor importance, such that the propensity of the various stereoisomers of **3π** to undergo C–C bond formation is predominantly dictated by electronic factors. The higher stability of η^2-*trans*-butadiene isomers (**3π(s/a)t**) relative to η^2-*cis*-butadiene isomers (**3π(s/a)c**) is paralleled in the TS structures. Leaving the possible discriminating role of allylic isomerization in the enchainment cycle out of consideration, by assuming facile isomerization events, DFT predicts that η^2-*trans*-butadiene insertion into the *syn*-η^3- (k_t(trans) with $\Delta G^{\ddagger}$ = 17.4 kcal mol^{-1}) and *anti*-η^3-butenyl–Fe^{II} linkage (k_c(trans) with $\Delta G^{\ddagger}$ = 23.1 kcal mol^{-1}) are the more accessible pathways to furnish a new 1,4-trans and 1,4-cis polymer unit, respectively. Of particular note, the trans–cis gap of 3.7–4.0 kcal mol^{-1} for **3πs** and **3πa** remains almost unchanged in the TS structures, thereby indicating that traversing the alternative k_t(cis) and k_c(cis) pathways is less probable. The assessed trans–cis gap coincides nicely with the disparity in stability between s-trans and s-cis butadiene (ΔG = 3.6 kcal mol^{-1}).[29] This is quite understandable for butadiene to insert in η^2-mode, i.e., formally as a vinylethylene, because of the lack of extra stabilization by a chelating η^4-butadiene, which may lead to differentiation between trans and cis isomers. The higher reactivity of the *syn*-η^3-butenyl form together

Fig. 3. Selected structural parameters (Å) of the optimized structures of key stationary points (singlet PES) for insertion of *trans*-butadiene (top) and *cis*-butadiene (bottom) into the *syn*-$\eta^1(C^1)$-butenyl–Fe^{II} bond in $[(\eta^1\text{-}C_4H_7)Fe^{II}(terpy)(\eta^4\text{-}C_4H_6)]^+$ (**3σ**) along the most accessible stereochemical pathway.

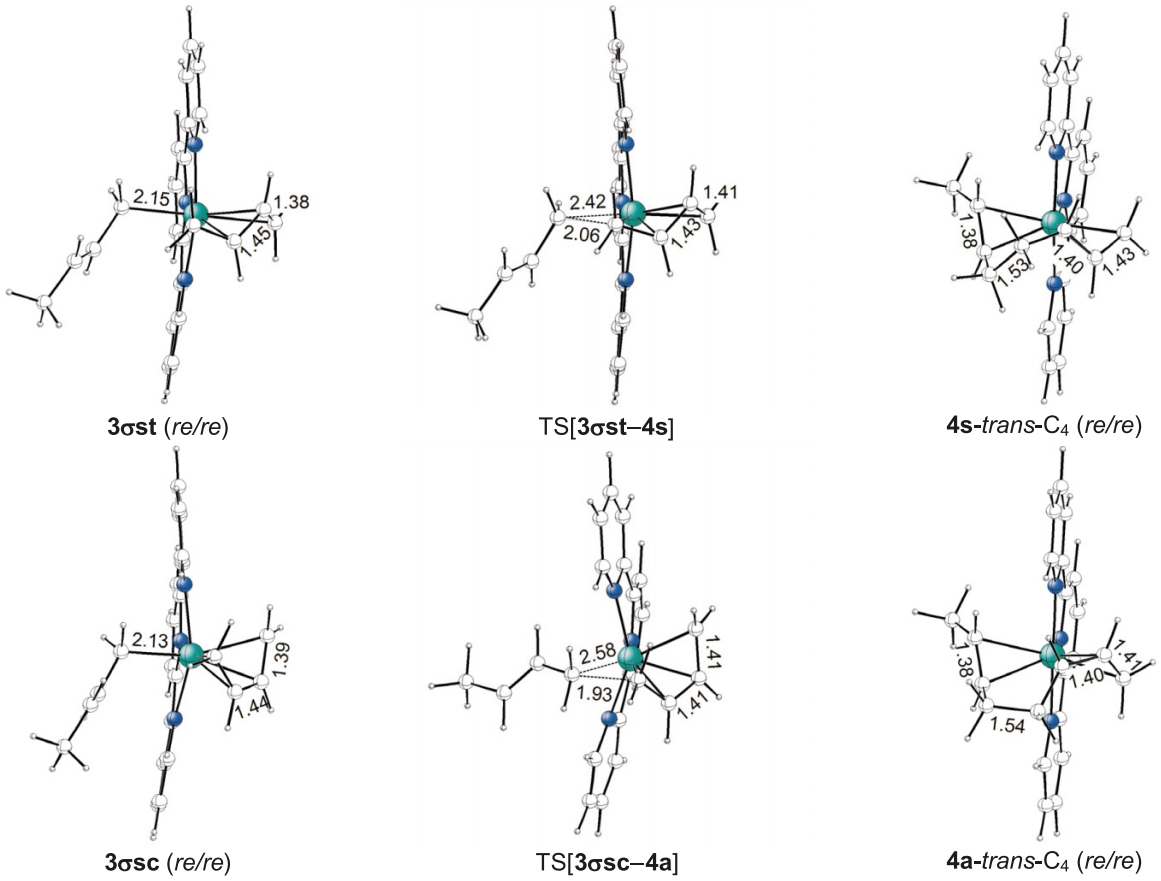

3σst (*re/re*) TS[**3σst–4s**] **4s-***trans*-C_4 (*re/re*)

3σsc (*re/re*) TS[**3σsc–4a**] **4a-***trans*-C_4 (*re/re*)

Scheme 7.

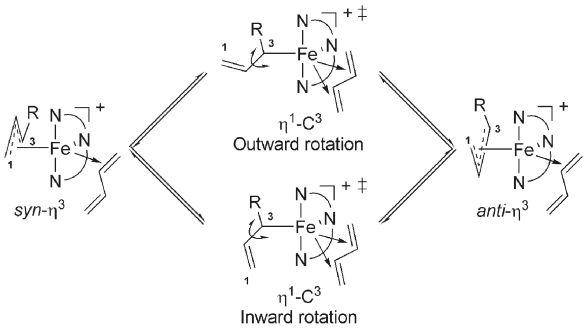

with the higher stability of s-trans butadiene are seen to dictate the propensity of the various stereoisomers of **3π** for C–C bond formation. Although it is of no mechanistic relevance for the studied catalyst system, it is worth mentioning that the gap in reactivity for *anti*- and *syn*-$\eta^1(C^1)$-butenyl isomers is significantly reduced to ~2.0–2.5 kcal mol^{-1} ($\Delta\Delta G^{\ddagger}$, Table 3) when compared to ~5.7–6.0 kcal mol^{-1} for η^3-butenyl–Fe^{II} forms

Allylic isomerization

The interconversion of the syn and anti forms of the terminal reactive η^3-polybutadienyl group is investigated next. Two trajectories are conceivable (Scheme 7)[17,30] for allylic isomerization to proceed by inward and outward rotation of the vinyl group around the formal C^2–C^3 single bond. This is exemplified in Scheme 7 for the butadiene-assisted process. Rotational isomerization taking place in **3π** or **4** has been examined. The most accessible pathway does evolve through a $\eta^1(C^3)$-butenyl-TS structure that benefits from a stabilizing η^4-butadiene complexation. The alternatively imaginable coordination of the polybutadienyl chain by its double bonds of the ultimate and (or) penultimate polymer units, however, is found to be less effective in stabilizing the TS structure. Hence, allylic isomerization preferably takes place in the butadiene π-complex (**3π**). Figure 4 shows rotational TS structures for isomerization via the *cis*-butadiene insertion route ($k_{a/s}$(cis), see Scheme 5) proceeding through inward and outward trajectories, whilst the energetics for both $k_{a/s}$(cis) and $k_{s/a}$(trans) events is collected in Table 4. *Cis*-butadiene insertion leads exclusively to anti-η^3 **4a**, from which **3πac** is readily regenerated by capture of a new butadiene unit. The most accessible isomerization pathway encounters first the anti-η^3 → anti-$\eta^1(C^3)$ butenyl conversion to be followed by rotational isomerization through the $\eta^1(C^3)$-butenyl TS_{ISO}, giving rise initially to a syn-$\eta^1(C^3)$ transient species, which transforms readily thereafter into the energetically preferred syn-η^3 species (**3πsc**). Careful inspection of the reaction path indicated that $\eta^3 \rightleftarrows \eta^1(C^3)$ butenyl transformation is a smooth process proceeding in an almost barrierless fashion,[31] which is essentially driven by the thermodynamic gap between the two

Fig. 4. Selected structural parameters (Å) of the optimized TS structures (singlet PES) for rotational isomerization of the terminal η^3-butenyl–Fe^{II} linkage via $k_{a/s}$(cis) proceeding through inward and outward trajectories.

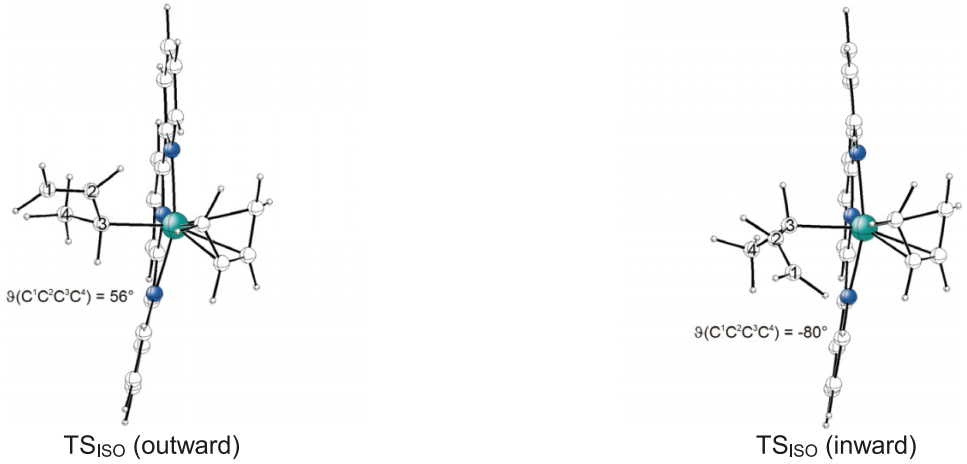

Scheme 8. Free-energy profile (singlet PES) for 1,4-polymerization of 1,3-butadiene with $[(\eta^3\text{-}RC_3H_4)Fe^{II}(C_{15}H_{11}N_3)(\eta^2\text{-}C_4H_6)]^+$ (**3π**) as the active catalyst species proceeding through competing routes for insertion of *cis*-butadiene (left) and *trans*-butadiene (right).Viable pathways are drawn in blue colour, whilst pathways that are inaccessible are indicated in red colour. The assessed reaction heat for *trans*-1,4 enchainment (ΔG = 9.2 kcal mol^{-1}) has been subtracted from polybutadienyl–Fe^{II} compounds (**4s** and **4a**). R = CH_3.

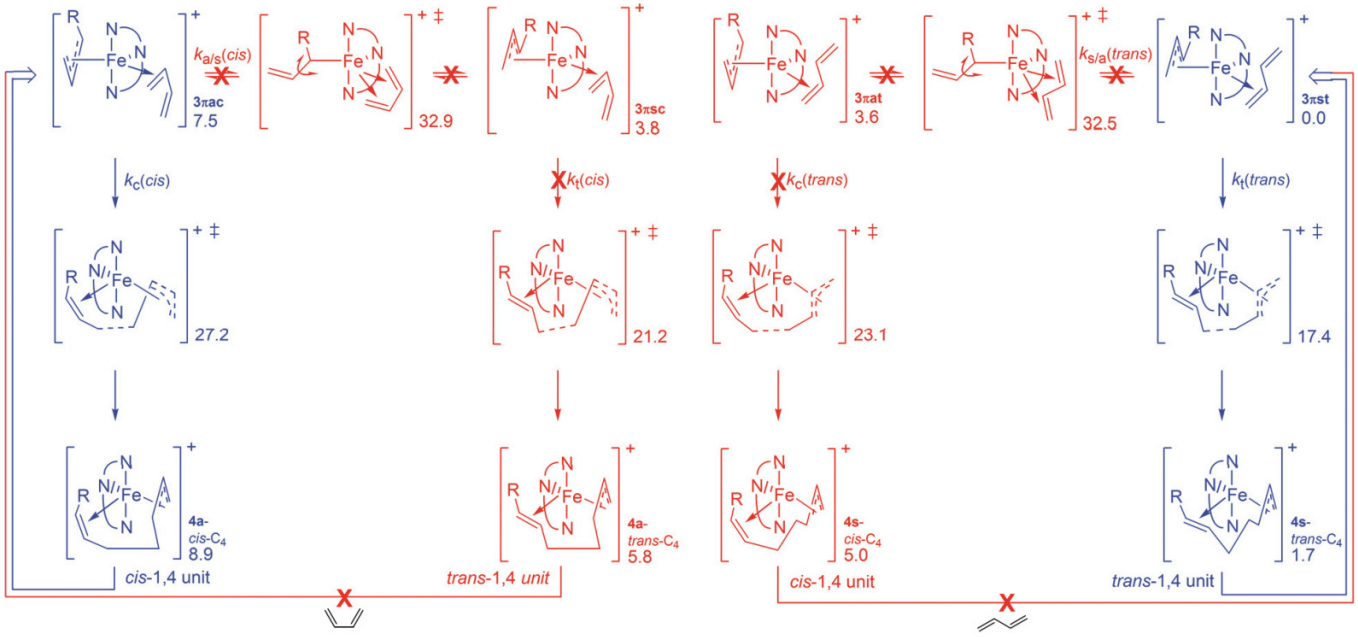

forms. Hence, TS_{ISO} is the highest point to be traversed along the most accessible pathways.

Although TS_{ISO} features a chelating η^4-butadiene (Fig. 4), a substantial activation energy is associated with rotational isomerization. The total barrier[32] for $k_{s/a}$(trans) occurring along the *trans*-butadiene insertion route and for $k_{a/s}$(cis) encountered along the *cis*-butadiene insertion route is predicted to be almost identical and amounts to 32.5–32.9 kcal mol^{-1} (Table 4). The outward rotation of the vinyl group is the more accessible pathway. Conversely, unfavourable interactions between the vinyl group and the terpy-Fe backbone are seen to disfavour the transition state of the inward trajectory. Overall, butenyl group isomerization (Table 4) is predicted to be considerably more demanding kinetically when compared with butadiene insertion (Table 2), thereby indicating that isomerization is slower than C–C bond formation ($k_{ins} >> k_{iso}$).

Productive chain growth cycle

Free-energy profile

The condensed Gibbs free-energy profile for relevant steps of the tentative catalytic cycle (Scheme 5) is displayed in Scheme 8. It is comprised of various pathways for each of these steps to follow the operative mechanistic route; viz. the η^2-butadiene insertion into the η^3-butenyl–Fe^{II} linkage proceeding through rival pathways for trans-1,4 enchainment (k_t(trans), k_t(cis)) and cis-1,4 enchainment (k_c(cis), k_c(trans)), the butadiene-assisted isomerization of the η^3-butenyl–Fe^{II}

Scheme 9. Reaction energy profile (singlet PES) for trans-1,4 enchainment of butadiene by the $[Fe^{II}(C_{15}H_{11}N_3)(RC_3H_4)(C_4H_6)]^+$ catalyst species via alternative routes for *trans*-butadiene insertion (left) and *cis*-butadiene insertion (right). The assessed reaction heat for trans-1,4 enchainment (ΔG = 9.2 kcal mol^{-1}) has been subtracted from polybutadienyl–Fe^{II} products (**4s** and **4a**), respectively. R = CH_3, R′ = $C_4H_6CH_3$.

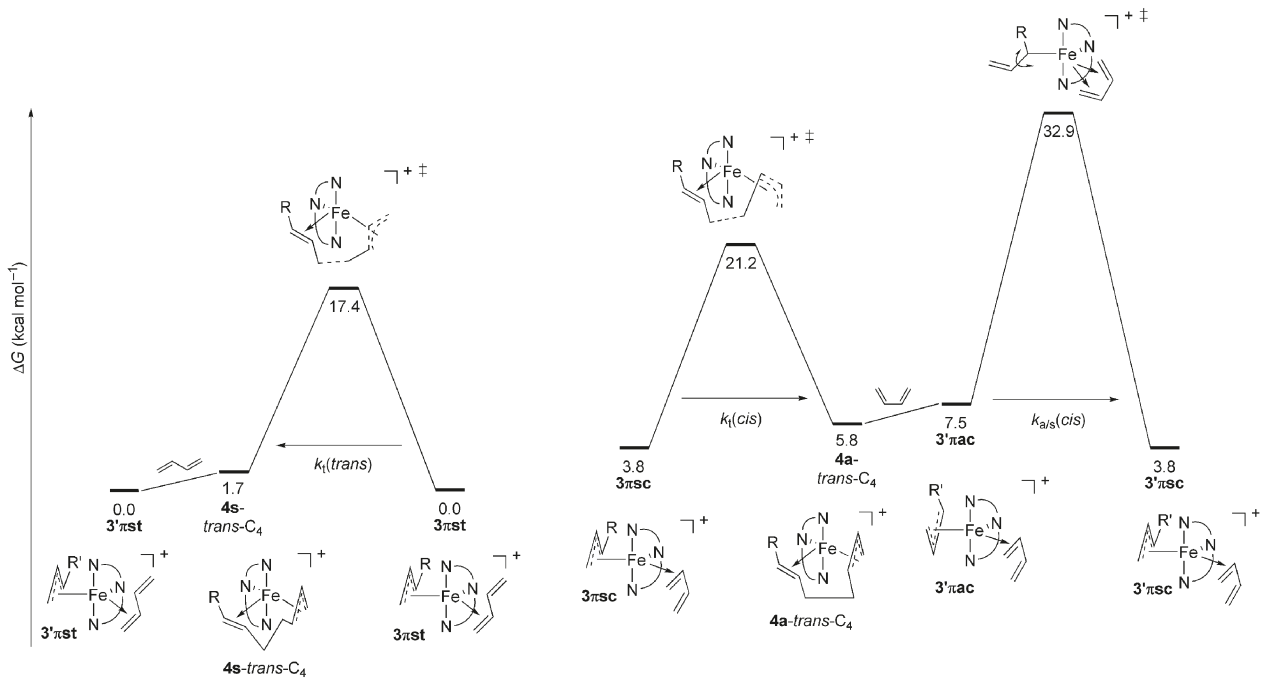

functionality of the growing polybutadienyl chain, and the facile butadiene capture of the polybutadienyl–Fe^{II} compound (**4**) to readily regenerate the active catalyst species (**3π**). The reaction heat for regular trans-1,4 enchainment has been excluded from Scheme 8. Viable pathways for trans-1,4 and cis-1,4 enchainment are drawn in blue, whilst inaccessible pathways are indicated in red. The likelihood of the various pathways to be traversed in the productive enchainment cycle is discussed in the next section. Of all the various steps, allylic isomerization is connected with the overall highest activation barrier, whilst butadiene insertion is considerably more favourable kinetically. DFT predicts that $[(syn\text{-}\eta^3\text{-}RC_3H_4)Fe^{II}(C_{15}H_{11}N_3)(trans\text{-}\eta^2\text{-}C_4H_6)]^+$ (**3πst**) is the most stable species in the productive cycle for trans-1,4 enchainment and is therefore likely to represent the catalyst resting state.

Mechanism of cis–trans regulation

As shown before, insertion of *trans*-η^2-butadiene into the *syn*-η^3- and *anti*-η^3-butenyl–Fe^{II} bond are the more accessible of the rival pathways for generation of a trans-1,4 and cis-1,4 polymer unit, respectively (see the Butadiene π-complex section). Accordingly, trans-1,4 and cis-1,4 enchainment should proceed through k_t(trans) and k_c(trans), respectively. For k_c(trans) to become accessible, however, a sufficiently facile syn–anti isomerization (k_{sa}(trans)) is required. DFT predicts that allylic isomerization is significantly more kinetically demanding than butadiene insertion, and the gap amounts to 5.7–15.1 kcal mol^{-1} ($\Delta\Delta G^{\ddagger}$).[33] This leads to the conclusion that isomerization is kinetically disabled relative to C–C bond formation and, as such, *syn*- and *anti*-butenyl forms of **3π** and **4** are not in rapid equilibrium. As a consequence, the configuration of the terminal butenyl group and also the mode of enchainment is entirely dictated by the configuration of the inserting butadiene. Hence, trans-1,4 enchainment exclusively proceeds via k_t(trans) through repeated *trans*-η^2-butadiene insertion into the *syn*-η^3-butenyl–Fe^{II} linkage and a regular cis-1,4 polymer is produced via k_c(cis) by repeated insertion of *cis*-η^2-butadiene into the *anti*-η^3-butenyl–Fe^{II} bond (cf. Scheme 8). The alternative k_t(cis) and k_c(trans) pathways for trans-1,4 and cis-1,4 enchainment, which necessitates a sufficiently fast $k_{a/s}$(cis) anti–syn and $k_{s/a}$(trans) syn–anti isomerization, respectively, cannot be traversed because of the slow isomerization (i.e., k_c(cis) >> $k_{a/s}$(cis) and k_t(trans) >> $k_{s/a}$(trans)). This is illustrated in Scheme 9 for rival trans-1,4 enchainment paths.

The trans-1,4 enchainment via k_t(trans) has a total activation barrier[32] of 17.4 kcal mol^{-1}, whilst the transition state encountered along k_c(cis) to generate a regular *cis*-1,4 polybutadiene is 9.8 kcal mol^{-1} ($\Delta\Delta G^{\ddagger}$) higher in free energy. Considering the magnitude of the assessed kinetic gap,[34] cis-1,4 enchainment appears to be kinetically prevented. Hence, DFT predicts that k_t(trans) is almost exclusively traversed in the productive enchainment cycle, thereby giving rise to a polybutadiene of predominantly trans-1,4 structure, which is in accordance with observed selectivity (Chart 1).[11] Moreover, the predicted turnover-limiting barrier of 17.4 kcal mol^{-1} compares favourably with reported performance data.[11] Although no data are available for polymerization of butadiene,[11] an effective barrier of 18.3 kcal mol^{-1} can be estimated from the reported activity for isoprene polymerization.[35] The good agreement of effective kinetics obtained by theory and experiment, although appearing somewhat fortuitous, can serve as an example for demonstrating the substantial predictive values that computational mechanistic studies can nowadays accomplish.

Generation of tactic trans-*1,4-polydienes*

The polymerization of a chiral butadiene with an asymmetrically substituted methylene group leads to the generation of a tactic 1,4-polydiene. An isotactic, syndiotactic, or atactic polymer is formed, dependent on whether the chiral centres possess an identical, alternating, or random configuration in subsequent chain growth events. It is generally agreed that the chirality of the two carbon centres that generate the C–C bond determines the tacticity of 1,4-polydienes.[6e] Hence, the enantiofaces of the reactive butenyl and butadiene units in the TS for chain propagation is of crucial importance. As an example, multiple insertion events to involve identical enantiofaces would give rise to an isotactic 1,4-polydiene.

The structure of a polymer obtained from polymerising a terminally monosubstituted butadiene by $FeCl_3$(terpy) **0**/MMAO has not been reported thus far by experiment.[11] However, the precise insight into the enchainment process detailed by the present study, brings us to a position to predict its structure. As analysed in the Butadiene π-complex section, steric interactions between the butenyl and butadiene units and the Fe(terpy) backbone are small in the TS structure and also in **3π** and **4**. As a result, the assessed energy profiles for *re*/*re* and *re*/*si* stereochemical pathways (cf. Scheme 6 and Table 2 for further details) of an individual insertion path (viz. k_t(trans), k_c(trans), k_t(cis), and k_c(cis)) are virtually congruent (Table 2). The TS structures of syn-*re*/*re* ($\Delta G^{\ddagger}$ = 17.4 kcal mol^{-1}) and syn-*re*/*si* ($\Delta G^{\ddagger}$ = 17.5 kcal mol^{-1}) pathways for trans-1,4 enchainment via k_t(trans) are almost energetically degenerate. Hence, DFT predicts an equal likelihood for the two pathways to be traversed in trans-1,4 enchainment. As a consequence, an atactic *trans*-1,4-polydiene, which lacks any stereoregularity within the methylene groups, is generated in polymerization of a terminally monosubstituted butadiene by the sterically relatively open **0**/MMAO catalyst system.

Concluding remarks

Presented herein is a computational study of the 1,4-polymerization of 1,3-butadiene mediated by a recently developed, highly active, trans-1,4 regulating terpyridine–iron catalyst. The [$Fe^{III}Cl_3$(terpy)] catalyst precursor is likely to be converted into [(Me)Fe^{II}(terpy)]$^+$ in the presence of MMAO. Subsequent butadiene insertion into the Fe–Me linkage then initiates polymer chain growth, where [$Fe^{II}(C_{15}H_{11}N_3)(\eta^3\text{-}RC_3H_4)(\eta^2\text{-}C_4H_6)]^+$ (**3π**) represents the catalytically active species in the productive enchainment cycle. Alternative mechanistic routes and pathways of all crucial elementary steps have been carefully explored for the various conceivable spin states by means of a reliable DFT method. All the studied chain initiation, chain propagation, and allylic isomerization events are found to preferably proceed at the singlet PES. Chain growth employs the π-allyl-insertion mechanism and takes place preferably by η^2-butadiene insertion into the η^3-butenyl terminal group. Conversely, the alternative suggested mechanism via $\eta^1(C^1)$-butenyl–Fe^{II} species (**3σ**) is seen to be inoperable. The likelihood of traversing rival insertion pathways is predominantly determined on electronic grounds, whilst steric factors have a small influence only for the sterically relatively open catalyst studied. The *syn*-η^3-butenyl–Fe^{II} form of **3π** is more stable than its anti counterpart and displays a higher propensity to undergo C–C bond formation, whilst η^2-butadiene preferably inserts from prevalent s-trans configuration. Isomerization of the η^3-butenyl–Fe^{II} group, to preferably proceed via a rotational $\eta^1(C^3)$-butenyl–Fe^{II} TS structure that is stabilized by a chelating η^4-butadiene, is found to exert a profound influence on cis–trans regulation. DFT predicts that isomerization is disabled kinetically relative to butadiene insertion, thereby indicating that syn and anti forms of **3π** and **4** are not in rapid equilibrium. Hence, all enchainment pathways that involve an isomerization event, are rendered inaccessible due to slow isomerization. Trans-1,4 enchainment does proceed through repeated *trans*-η^2-butadiene insertion into the *syn*-η^3-butenyl–Fe^{II} linkage with an effective barrier of 17.4 kcal mol^{-1}. This pathway is almost exclusively traversed, thereby giving rise to a polybutadiene of a predominantly 1,4-trans structure, since the competing cis-1,4-generating pathway is kinetically disabled. All these aspects match with experimental observations and rationalise them. For polymerization of a terminally monosubstituted butadiene, an atactic *trans*-1,4-polydiene is predicted, the structure of the generated polymer structure has, however, not been reported thus far by experiment.

Computational details

All DFT calculations were performed with the program package TURBOMOLE.[36] The nonempirical meta-GGA functional developed by Tao, Perdew, Staroverov, and Scuseria,[18] which is usually termed TPSS in the literature, was utilized together with the RI-*J* approximation[37] for the optimization of key stationary points. All elements were represented by Ahlrich's valence triple-ζ TZVP basis set[19a] with polarization functions on all atoms. For Fe, the TZVP set[19a] supplemented by two diffuse p functions[19b] contracted to (842111/63111/411) was used. The good to excellent performance of the TPSS functional for a wide range of applications including transition metal complexes has been demonstrated previously.[20] All the Fe^{II}(terpy) key stationary points were located for the singlet, triplet, and quintet spin states. Unrestricted calculations were performed in all cases to avoid singlet instabilities. It is well-known that pure functionals favour low-spin configurations, whilst conversely, the exact exchange contribution in hybrid functionals leads to a bias towards high-spin states. With regard to relative spin-state energetics, a version of B3LYP with 15% exact exchange has been reported to perform better for $Fe^{II}(phen)_2(NCS)_2$ complexes,[38a] and a version of BP86 with 10% exchange was found to provide the best results for some {FeNO} and {FeO2} compounds.[38b] Hence, refined energies were obtained from single-point calculations at the hybrid TPSS level, i.e., TPSSh with 10% exchange,[21] for TPSS(COSMO)-optimized geometries by using the same basis set. This DFT method has recently been reported to provide accurate spin-state energetics for first row transition metal complexes.[22] The reaction paths were explored by the growing string method,[39] in which two string fragments (commencing from reactant and product side, respectively) are grown until the two fragments join. As this was performed in mass-weighted coordinates, an approximate to the minimum energy path (MEP) was obtained. This identified the reactant and product states to be linked to the associated

transition state. The approximate saddle point connected with the MEP was subjected to an exact localization of the TS structure. All stationary points were located by utilizing analytical/numerical gradients/Hessians according to standard algorithms and were identified exactly by the curvature of the potential-energy surface at these points corresponding to the eigenvalues of the Hessian. All reported transition-state structures possess exactly one negative Hessian eigenvalue, whilst all other stationary points exhibit exclusively positive eigenvalues. The reaction and activation enthalpies and free energies (ΔH, $\Delta H^{\ddagger}$ and ΔG, $\Delta G^{\ddagger}$ at 298 K and 1 atm) were evaluated according to standard textbook procedures[40] using computed harmonic frequencies. The frequency analysis was conducted for stationary points that were located with an alternative basis set, consisting of the aforementioned basis set for Fe and Ahlrich's split-valence SV(P) basis set[41] with polarisation functions on main group atoms, but not on hydrogen. This level of basis-set quality has been reported as a reliable tool for the assessment of structural parameters and vibrational frequencies;[42] hence, this protocol allows an affordable and accurate determination of thermodynamic state functions. Enthalpies were reported as ΔE + zero point energy corrections at 0 K + thermal motion corrections at 298 K and Gibbs free energies were obtained as $\Delta G = \Delta H - T\Delta S$ at 298 K. The influence of the solvent was taken into explicit consideration by making use of a continuum model. The experimentally used toluene solvent[11] was described as a homogeneous, isotropic dielectric medium (characterized by its relative static dielectric permittivity, ε = 2.379 at 298 K)[43] within the conductor-like screening model (COSMO) due to Klamt and Schüürmann[23] as implemented in TURBOMOLE.[44] Nonelectrostatic contributions to solvation were not included. The solvation effects were included self-consistently, and all the key species were fully located including solvation. The fitted atomic COSMO radii (r_H = 1.3 Å, r_C = 2.0 Å, r_N = 1.83 Å)[45a] have been used in combination with a radius of 2.22 Å[45b] for Fe. The mechanistic conclusions drawn in this study were based on the computed Gibbs free-energy profile of the overall reaction for experimental condensed phase conditions. All the drawings were prepared by employing the StrukEd program.[46]

Supplementary data

Supplementary data (Tables S2a–S4ab giving the energetics for triplet and quintet spin states for all the investigated species) for this article are available on the journal Web site (canjchem.nrc.ca) or may be purchased from the Depository of Unpublished Data, Document Delivery, CISTI, National Research Council Canada, Ottawa, ON K1A 0R6, Canada. DUD 5265. For more information on obtaining material, refer to cisti-icist.nrc-cnrc.gc.ca/cms/unpub_e.shtml.

References

(1) La Flair, R. T.; Wolf, U.U. In *Ullmann's Encyclopedia of Industrial Chemistry,* 5th ed.; Verlag Chemie: Weinheim, Germany, 1993; Vol. A23, pp 273–282.

(2) Taube, R.; Sylvester, G. In *Applied Homogeneous Catalysis with Organometallic Complexes;* Cornils, B., Herrmann, W. A.., Eds.; VCH: Weinheim, Germany, 1996; pp 280–318.

(3) Durand, J. P.; Dawans, F.; Teyssie, P. *J. Polym. Sci.* **1970**, *8* (4), 979–990. doi:10.1002/pol.1970.150080414.

(4) Porri, L.; Giarrusso, A.; Ricci, G. *Prog. Polym. Sci.* **1991**, *16* (2–3), 405–441. doi:10.1016/0079-6700(91)90024-F.

(5) Thiele, S. K.-H.; Wilson, D. R. *J. Macromol. Sci. Part C Polym. Rev.* **2003**, *C43* (4), 581–628. doi:10.1081/MC-120025979.

(6) (a) Porri, L.; Natta, G.; Gallazzi, M. C. *Chim. Ind.* **1964**, *46*, 428–429; (b) Dolgoplosk, B. A.; Babitskii, B. D.; Kormer, V. A.; Lobach, M. I.; Tinyakova, E. T. *Dokl. Akad. Nauk SSSR* **1965**, *164*, 1300; (c) Wilke, G.; Bogdanovic, B.; Hardt, P.; Heimbach, P.; Keim, W.; Kröner, M.; Oberkirch, W.; Tanaka, K.; Steinrucke, E.; Walter, D.; Zimmermann, H. *Angew. Chem. Int. Ed. Engl.* **1966**, *5* (2), 151–164. doi:10.1002/anie.196601511.; (d) Durand, J. P.; Dawans, F.; Teyssie, Ph. *J. Polym. Sci.* Part B Polym. Lett. **1968**, *B6* (10), 757–761. doi:10.1002/pol.1968.110061015.; (e) Porri, L.; Giarrusso, A. In *Comprehensive Polymer Science;* Eastmond, G. C., Ledwith, A., Russo, S., Sigwalt, B., Eds.; Pergamon: Oxford, UK, 1989; Vol. 4, Part II, pp 53–108; (f) Taube, R.; Windisch, H.; Maiwald, St. *Macromol. Symp.* **1995**, *89*, 395–409; (g) Hou, Z.; Kaita, S.; Wakatsuki, Y. *Pure Appl. Chem.* **2001**, *73* (2), 291–294. doi:10.1351/pac200173020291.; (h) Campora, J.; del Mar Conejo, M.; Reyes, M. L.; Mereiter, K.; Passaglia, E.; *Chem. Comm* **2003**, 78–79. doi:10.1039/b209838e.;(i) Thuilliez, J.; Monteil, V.; Spitz, R.; Boisson, C. *Angew. Chem. Int. Ed.* **2005**, *44* (17), 2593–2596. doi:10.1002/anie.200462019.; (j) O'Connor, A. R.; White, P. S.; Brookhart, M. *J. Am. Chem. Soc.* **2007**, *129* (14), 4142–4143. doi:10.1021/ja070364s. PMID:17371029.

(7) (a) Teyssie, Ph.; Julemont, M.; Thomassin, J. M.; Walkiers, E.; Warin, R. In *Coordination Polymerization;* Chien, J.C.W., Ed.; Academic Press: New York, 1975; pp 327–347; (b) Boor, J., Jr. *Ziegler–Natta Catalysts and Polymerizations;* Academic Press: New York, 1979; (c) Porri, L. In *Structural Order in Polymers;* Ciardelli, F., Giusti, P., Ed.; Pergamon Press: Oxford, UK, 1981; pp 51–62.

(8) (a) Tobisch, S.; Bögel, H.; Taube, R. *Organometallics* **1996**, *15* (16), 3563–3571. doi:10.1021/om960038d.; (b) Tobisch, S.; Bögel, H.; Taube, R. *Organometallics* **1998**, *17* (6), 1177–1196. doi:10.1021/om9705923.; (c) Tobisch, S.; Taube, R. *Organometallics* **1999**, *18* (25), 5204–5218. doi:10.1021/om990356n.; (d) Tobisch, S.; Taube, R. *Chem. Eur. J.* **2001**, *7* (17), 3681–3695. doi:10.1002/1521-3765(20010903)7:17<3681::AID-CHEM3681>3.0.CO;2-J.; (e) Tobisch, S. *Chem. Eur. J.* **2002**, *8* (20), 4756–4766. doi:10.1002/1521-3765(20021018)8:20<4756::AID-CHEM4756>3.0.CO;2-W.; (f) Tobisch, S. *Acc. Chem. Res.* **2002**, *35* (2), 96–104. doi:10.1021/ar010001b. PMID: 11851387.; (g) Tobisch, S. *Macromolecules* **2003**, *36* (16), 6235–6244. doi:10.1021/ma034369v.; Tobisch, S. *Organometallics* **2003**, *22* (13), 2729–2740. doi:10.1021/om030059p.; (i) Tobisch, S. J. *Mol. Struct. (Theochem)* **2006**, *771* (1–3), 171–179. doi:10.1016/j.theochem.2006.03.036.; (i) Tobisch, S.; Taube, R. *Organometallics* **2008**, *27* (10), 2159–2162. doi:10.1021/om701214u.

(9) Kaita, S.; Koga, N.; Hou, Z.; Doi, Y.; Wakatsuki, Y. *Organometallics* **2003**, *22* (15), 3077–3082. doi:10.1021/om030162e.

(10) (a) Guerra, G.; Cavallo, L.; Corradini, P.; Fusco, R. *Macromolecules* **1997**, *30* (4), 677–684. doi:10.1021/ma960136a.; (b) Peluso, A.; Improta, R.; Zambelli, A. *Macromolecules* **1997**, *30* (8), 2219–2227. doi:10.1021/ma960957f.; (c) Pe-

luso, A.; Improta, R.; Zambelli, A. *Organometallics* **2000**, *19* (4), 411–419. doi:10.1021/om980940g.; (d) Costabile, C.; Milano, G.; Cavallo, L.; Guerra, G. *Macromolecules* **2001**, *34* (23), 7952–7960. doi:10.1021/ma010673h.; (e) Costabile, C.; Guerra, G.; Longo, P.; Pragliola, S. *Macromolecules* **2004**, *37* (6), 2016–2020. doi:10.1021/ma035892c.; (f) Costabile, C.; Milano, G.; Cavallo, L.; Longo, P.; Guerra, G.; Zambelli, A. *Polymer (Guildf.)* **2004**, *45* (2), 467–485. doi:10.1016/j.polymer.2003.10.084.; (g) Costabile, C.; Guerra, G.; Longo, P.; Pragliola, S. *Macromolecules* **2005**, *38* (15), 6327–6335. doi:10.1021/ma0504926.; (h) Costabile, C.; Pragliola, S.; Pelosi, L.; Longo, P. *Polymer (Guildf.)* **2007**, *48* (11), 3059–3065. doi:10.1016/j.polymer.2007.03.058.

(11) Nakayama, Y.; Baba, Y.; Yasuda, H.; Kawakita, K.; Ueyama, N. *Macromolecules* **2003**, *36* (21), 7953–7958. doi:10.1021/ma0300802.

(12) (a) Kubo, Y.; Yamamoto, A.; Ikeda, S. *J. Organomet. Chem.* **1972**, *46* (2), C50–C52. doi:10.1016/S0022-328X(00)88306-0.; (b) Kubo, Y.; Pu, L. S.; Yamamoto, A.; Ikeda, A. *J. Organomet. Chem.* **1975**, *84* (3), 369–378. doi:10.1016/S0022-328X(00)91402-5.

(13) (a) Cossee, P. In *Stereochemistry of Macromolecules;* Ketley, A. D., Ed.; Marcel Dekker: New York, 1967; Vol. 1, pp 145–175; (b) Arlman, E. J. *J. Catal.* **1966**, *5* (1), 178–189. doi:10.1016/S0021-9517(66)80137-9.

(14) (a) Taube, R.; Gehrke, J.-P.; Böhme, P. *Wiss. Zeitschr. Techn. Hochschule Leuna-Merseburg* **1987**, *39*, 310; (b) Taube, R. In *Metalorganic Catalysts for Synthesis and Polymerization;* Kaminsky, W., Ed.; Springer-Verlag: Berlin, 1999; p 531.

(15) (a) Faller, J. W.; Thomsen, M. E.; Mattina, M. J. *J. Am. Chem. Soc.* **1971**, *93* (11), 2642–2653. doi:10.1021/ja00740a011.; (b) Lukas, J.; van Leeuwen, P. W. N. M.; Volger, H. C.; Kouwenhoven, A. P. *J. Organomet. Chem.* **1973**, *47* (1), 153–163. doi:10.1016/S0022-328X(00)92851-1.

(16) Vrieze, K. In *Dynamic Nuclear Magnetic Resonance Spectroscopy;* Jackman, L. M., Cotton, F. A., Ed.; Academic Press; New York, 1975; pp 441–487.

(17) Tobisch, S.; Taube, R. *Organometallics* **1999**, *18* (16), 3045–3060. doi:10.1021/om9810302.

(18) (a) Dirac, P. A. M. *Proc. R. Soc. Lond.* **1929**, *A123* (792), 714–733. doi:10.1098/rspa.1929.0094.; (b) Slater, J. C. *Phys. Rev.* **1951**, *81* (3), 385–390. doi:10.1103/PhysRev.81.385.; (c) Perdew, J. P.; Wang, Y. *Phys. Rev.* **1992**, *B45* (23), 13244–13249. doi:10.1103/PhysRevB.45.13244.; (d) Tao, J.; Perdew, J. P.; Staroverov, V. N.; Scuseria, G. E. *Phys. Rev. Lett.* **2003**, *91* (14), 0146401. doi:10.1103/PhysRevLett.91.146401. PMID:14611541.; (e) Perdew, J. P.; Tao, J.; Staroverov, V. N.; Scuseria, G. E. *J. Chem. Phys.* **2004**, *120* (15), 6898–6911. doi:10.1063/1.1665298. PMID:15267588.

(19) (a) Schäfer, A.; Huber, C.; Ahlrichs, R. *J. Chem. Phys.* **1994**, *100* (8), 5829. doi:10.1063/1.467146.; (b) Wachters, A. J. H. *J. Chem. Phys.* **1970**, *52* (3), 1033. doi:10.1063/1.1673095.

(20) (a) Staroverov, V. N.; Scuseria, G. E.; Tao, J.; Perdew, J. P. *J. Chem. Phys.* **2003**, *119* (23), 12129. doi:10.1063/1.1626543.; (b) Zhao, Y.; Truhlar, D. G. *J. Chem. Theory Comput.* **2005**, *1* (3), 415–432. doi:10.1021/ct049851d.; (c) Furche, F.; Perdew, J. P. *J. Chem. Phys.* **2006**, *124* (4), 044103. doi:10.1063/1.2162161. PMID:16460145.

(21) Staroverov, V. N.; Scuseria, G. E.; Tao, J.; Perdew, J. P. *J. Chem. Phys.* **2004**, *121* (22), 011507. doi:10.1063/1.1795692.

(22) Jensen, K. P. *Inorg. Chem.* **2008**, *47* (22), 10357–10365. doi:10.1021/ic800841t. PMID:18855376.

(23) (a) Klamt, A.; Schüürmann, G. *J. Chem. Soc. Perkin Trans. 2* **1993**, 799–806. doi:10.1039/P29930000799.; (b) Klamt, A. In *Encyclopedia of Computational Chemistry;* von R. Schleyer, P., Ed.; Wiley: Chichester, 1998; Vol. I, pp 604–615.

(24) Examination by a linear-transit approach gave no indication that a significant barrier is associated with this event.

(25) Albright, T. A.; Burdett, J. K.; Whangbo, M.-H. *Orbital Interactions in Chemistry;* John Wiley & Sons: New York, 1985.

(26) Hanson, K. R. *J. Am. Chem. Soc.* **1966**, *88* (12), 2731–2742. doi:10.1021/ja00964a022.

(27) The *re*/*si* terminology is applied with regard to the chirality of the butenyl-C^3 centre for the η^3-butenyl–metal ligation.

(28) Schleyer, P. R.; Kaneti, J.; Wo, Y.-D.; Chandrasekhar, J. *J. Organomet. Chem.* **1992**, *426* (2), 143–157. doi:10.1016/0022-328X(92)83041-F.

(29) (a) The calculated stability difference of ΔG (298 K) = 3.6 kcal mol^{-1} (TPSSh) agrees reasonably well with the best experimental value of ΔH (0 K) = 2.84 kcal mol^{-1}. For experimental references see: Lipnick, R.; Garbisch, E. W. *J. Am. Chem. Soc.* **1973**, *95* (19), 6370–6375. doi:10.1021/ja00800a034.; (b) Carreira, L. A. *J. Chem. Phys.* **1975**, *62* (10), 3851. doi:10.1063/1.431009.; (c) Durig, J. R.; Bucy, W. E.; Cole, A. R. H. *Can. J. Phys.* **1975**, *53* (19), 1832–1837. doi:10.1139/p75-234.; (d) Squillacote, M. E.; Sheridan, R. S.; Chapman, O. L.; Anet, F. A. L. *J. Am. Chem. Soc.* **1979**, *101* (13), 3657–3659. doi:10.1021/ja00507a042.; (e) Furukawa, Y.; Takeuchi, H.; Hasrada, I.; Tasumi, M. *Bull. Chem. Soc. Jpn.* **1983**, *56* (2), 392–399. doi:10.1246/bcsj.56.392.; (f) Fisher, J. J.; Michl, J. *J. Am. Chem. Soc.* **1987**, *109* (4), 1056–1059. doi:10.1021/ja00238a012.; (g) Arnold, B. R.; Balaji, V.; Michl, J. *J. Am. Chem. Soc.* **1990**, *112* (5), 1808–1812. doi:10.1021/ja00161a025.

(30) Gobbi, A.; Frenking, G. *J. Am. Chem. Soc.* **1994**, *116* (20), 9275–9286. doi:10.1021/ja00099a052.

(31) All attempts to precisely localise the TS for $\eta^3 \rightleftarrows \eta^1(C^3)$ butenyl conversion were unsuccessful because the PES is rather flat in this region.

(32) Total activation barriers are given relative to the most abundant isomer of **3π**, viz. [(*syn*-η^3-C_4H_7)Fe^{II}(terpy)(*trans*-η^2-C_4H_6)]$^+$ (**3πst**).

(33) The disparity in free energy between k_c(cis) and $k_{a/s}$(cis) of 5.7 kcal mol^{-1} and between k_t(trans) and $k_{s/a}$(trans) of 15.1 kcal mol^{-1} represent the lower and upper limits of the kinetic gap for insertion and isomerisation events (cf. Tables 2 and 4).

(34) The assessed kinetic gap of 9.8 kcal mol^{-1} ($\Delta\Delta G^{\ddagger}$) between k_c(trans) and k_t(trans) pathways transforms into a relative likelihood of $\sim 6.5 \times 10^{-7}$: 100 (298.15 K) for cis-1,4 and trans-1,4 enchainment events on application of Stefan–Boltzmann statistics.

(35) The effective free energy of activation for the polymerization of 1,3-butadiene with the studied terpyridine–iron(II) catalyst has been estimated from available experimental data (ref. 11) by the following somewhat crude approximation: with an activity of 6 kg of isoprene (mol of Fe)$^{-1}$ h^{-1} at 298 K, one obtains an effective rate constant of $k_{eff} \sim 0.0245$ s^{-1}. Low temperature (253 K) measurements indicate that polymerization of butadiene is about 10 times faster then isoprene polymerization. The so adapted $k_{eff} \sim 0.245$ s^{-1} corresponds to $\Delta G^{\ddagger} \sim 18.3$ kcal mol^{-1} upon application of the Eyring equation with $k = (2.08 \times 10^{10}) \times T \times \exp(-\Delta G^{\ddagger}/RT)$].

(36) (a) Ahlrichs, R.; Bär, M.; Häser, M.; Horn, H.; Kölmel, C. *Chem. Phys. Lett.* **1989**, *162* (3), 165–169. doi:10.1016/0009-2614(89)85118-8.; (b) Treutler, O.; Ahlrichs, R. *J. Chem. Phys.* **1995**, *102* (1), 346–354. doi:10.1063/1.469408.
(37) (a) Vahtras, O.; Almlöf, J.; Feyereisen, M. W. *Chem. Phys. Lett.* **1993**, *213* (5-6), 514–518. doi:10.1016/0009-2614(93)89151-7.; (b) Eichkorn, K.; Treutler, O.; Öhm, H.; Häser, M.; Ahlrichs, R. *Chem. Phys. Lett.* **1995**, *242* (6), 652–660. doi:10.1016/0009-2614(95)00838-U.
(38) (a) Reiher, M. *Inorg. Chem.* **2002**, *41* (25), 6928–6935. doi:10.1021/ic0258911. PMID:12470092.; (b) Schenk, G.; Pau, M. Y. M.; Solomon, E. I. *J. Am. Chem. Soc.* **2004**, *126* (2), 505–515. doi:10.1021/ja036715u. PMID:14719948.
(39) (a) Peters, B.; Heyden, A.; Bell, A. T.; Chakraborty, A. *J. Chem. Phys.* **2004**, *120* (17), 7877–7886. doi:10.1063/1.1691018. PMID:15267702.; (b) Heyden, A. personal communication.
(40) McQuarrie, D. A. *Statistical Thermodynamics;* Harper & Row: New York, 1973.
(41) Schäfer, A.; Huber, C.; Ahlrichs, R. *J. Chem. Phys.* **1992**, *97* (4), 2571–2577. doi:10.1063/1.463096.
(42) Koch, W.; Holthausen, M. C. *A Chemist's Guide to Density Functional Theory,* 2nd ed.; Wiley-VCH; Weinheim, Germany, 2001.
(43) Lide, D. R., Ed. *CRC Handbook of Chemistry and Physics,* 84th ed; CRC Press: New York, 2003–2004.
(44) Schäfer, A.; Klamt, A.; Sattel, D.; Lohrenz, J. C. W.; Eckert, F. *Phys. Chem. Chem. Phys.* **2000**, *2* (10), 2187–2193. doi:10.1039/b000184h.
(45) (a) Klamt, A.; Jonas, V.; Bürger, Th.; Lohrenz, J. C. W. *J. Phys. Chem. A* **1998**, *102* (26), 5074–5085. doi:10.1021/jp980017s.; (b) Bondi, A. *J. Phys. Chem.* **1964**, *68* (3), 441–451. doi:10.1021/j100785a001.
(46) Dettmann, J. *StrukEd.* QCsoft: Merseburg, Germany, 1992–1999. Available at http://www.struked.de.

Bis(cyclopentadienyl)dihydrido Mo and W complexes as Lewis bases — A computational study about their adducts with BX_3 (X = F, Cl) and $Al(CH_3)_3$

Mario Amati and Francesco Lelj

Abstract: A computational investigation about the Lewis acid–base adducts between bases Cp_2MH_2 (M = Mo, W) and acids BX_3 (X = F, Cl) and $Al(CH_3)_3$ is presented. Density functional methods based on pure and hybrid correlation-exchange functionals and relativistic corrections based on the zero order relativistic approximation (ZORA) have been applied. A comparison with experimental data has been addressed to give insights about the nature of the acid–base interaction with the aim to evaluate the role of the transition metal in charge donation toward the acid centre. In this respect, the likelihood of proposed criteria for recognizing the presence of transition-metal direct charge donation has been discussed.

Key words: metallocenes, Lewis basicity, density functional theory (DFT), atoms in molecules (AIM), zero order relativistic approximation (ZORA).

Résumé : On a effectué une étude théorique des adduits acide–base de Lewis entre les bases Cp_2MH_2 (M = Mo, W) et les acides BX_3 (X = F, Cl) et $Al(CH_3)_3$. On a utilisé les méthodes de la fonctionnelle de la densité en faisant appel à des fonctionnelles de corrélation-échange pures ainsi qu'hybrides et on a appliqué des corrections relativistes basées sur l'approximation relativiste d'ordre zéro (AROZ). Une comparaison avec les données expérimentales a été réalisée afin d'obtenir des informations sur la nature de l'interaction acide–base qui permettraient d'évaluer le rôle du métal de transition dans le transfert de charge vers le centre acide. Dans cette optique, on discute du potentiel d'utilité des critères proposés pour reconnaître la présence d'un transfert de charge direct de la part du métal de transition.

Mots-clés : métallocènes, basicité de Lewis, théorie de la fonctionnelle de la densité (TFD), atomes dans une molécule « AIM », approximation relativiste d'ordre zéro (AROZ).

[Traduit par la Rédaction]

Introduction

The acid–base adduct between bis(cyclopentadienyl)dihydridotungsten (Cp_2WH_2) and BF_3 was firstly communicated by Shriver[1] in 1963. It represented one of the first (and representative) examples of Lewis base behaviour of a transition-metal centre. The adduct formation was reported as a fast process in toluene and benzene solutions in an inert atmosphere. The resulting solid was insoluble in common solvents, limiting its characterization to nujol dispersion IR spectroscopy. The substantial invariance of the W–H stretching frequency in comparison to the free complex was used as proof of the direct interaction of the BF_3 moiety with the central metal without assistance from the hydride ligands.

A more complete successive investigation extended the study to BCl_3 and B_2H_6 as acid compounds and Cp_2MoH_2 (other than Cp_2ReH and cyclopentadielylmetal carbonyl complexes) as Lewis basic metal centres in addition to Cp_2WH_2.[2] BF_3 was reported to form adducts with both W and Mo complexes, whereas BCl_3 only reacted with the W complex. The reported adducts were prepared in an inert atmosphere and temperatures lower than 0 °C when the reaction was performed in solution. In all the cases, insoluble solids are quickly produced and IR analyses substantially confirmed the little effect of the acid–base interaction on the M–H stretching band (particularly in the case of BF_3). This observation seemed to confirm the direct metal–boron interaction, which has been paralleled in the protonated forms, $[Cp_2MH_3]^+$, and often proposed in inorganic chemistry text books as an example of Lewis acidity of transition metals.[3]

The ability of Cp_2MoH_2 and Cp_2WH_2 to bind group-13 acids was confirmed by Storr and Thomas[4] who clearly demonstrated the adduct formation with $AlMe_3$ in solution by NMR analysis. Interestingly, these adducts were evidenced as precursors of chemical reactions with the evolution of methane and production of metal clusters with bridging aluminium atoms.[5] On the other hand, the existence of a direct metal–aluminum bond was not corroborated by

Received 11 March 2009. Accepted 7 April 2009. Published on the NRC Research Press Web site at canjchem.nrc.ca on 29 September 2009.

This article is part of a Special Issue dedicated to Professor T. Ziegler.

M. Amati and F. Lelj.[1] Univesità degli Studi della Basilicata, Dipartimento di Chimica, Via N. Sauro, 85, IT-85100 Potenza, Italy.

[1]Corresponding author (e-mail: francesco.lelj@unibas.it).

the X-ray analysis.[6] The Cp_2WH_2–$AlMe_3$ Lewis adduct structure was compared with the free Cp_2MoH_2 neutron diffraction structure.[7] From this study, the acid–base interaction led to a reduction of the H–W–H angle and (possibly) loss of symmetry in the two W–H bond distances. Furthermore, the metal–aluminum distance was considered too long for a direct donation from the transition metal. On this basis, hydride ligands were considered as bridging donors in a $Cp_2W(\mu\text{–}H)_2AlMe_3$ dinuclear complex. A different conclusion was proposed for the adduct between $Cp^*(PMe_3)IrH_2$ ($Cp^* = \eta^5$-pentametylcyclopentadienyl) and $AlPh_3$.[8] In this case, the H–Ir–H angle widened in comparison to the free complex and the Ir–Al distance was reported as much shorter than the W–Al one (2.68 vs. 3.11 Å, respectively). As for Cp_2WH_2, the Lewis adduct is the starting step for further (rather slow) reactions leading to metal clusters.

More recently, the existence of the Cp_2WH_2–BF_3 adduct has been excluded on the basis of the work of Braunschweig and Wagner.[9] The ionic solid $[Cp_2WH_3][BF_4]$ has been recognised by NMR analysis as the reaction product rather than the insoluble compound described by Shriver[1] and Johnson and Shriver.[2] In these same papers, a similar conclusion has been claimed for the reaction between Cp_2WH_2 and BCl_3 (the salt $[Cp_2WH_3][BCl_4]$). The scarce likelihood of the Lewis adducts proposed by Shriver[1,2] was successively stressed by Braunschweig[10] and Braunschweig and Colling[11] in review works and, to our knowledge, has never been more deeply investigated to date.

A comparison of the works of Shriver[1] and co-worker[2] and Braunschweig and co-workers[9–11] pushes us to think that different products have been obtained by these two authors. Shriver[1] and co-worker[2] reported that their compounds were insoluble in common solvents, so that no NMR analysis was possible. This fact does not agree with Braunschweig and his co-workers'[9–11] observations, whose compounds were soluble. Johnson and Shriver[2] reported a dark-yellow adduct, Cp_2WH_2–BF_3, and a yellow adduct, Cp_2WH_2–BCl_3. Braunschweig and co-workers[9–11] reported colourless solids. Charge-transfer bands in the visible region are indicative of adduct formation between Cp_2MH_2 (M = W and Mo) and several olefins.[12] Furthermore, Shriver[1] and co-worker[2] excluded the formation of $[Cp_2MH_3]^+$ ions on the basis of their supposed different IR behaviour. Braunschweig and co-workers[9–11] reported a Cp_2WH_2–BF_3 W–H stretching frequency, which is blue-shifted by more than 30 cm^{-1} in comparison to the one by Shriver[1] and co-worker.[2] These facts would suggest that Shriver[1] and co-worker[2] were able to quench the reaction at the stage of the Lewis adduct, whereas Braunschweig and co-workers[9–11] reported what evolved from this initial stage.

In this paper, we present a comparative study on Lewis adducts between Cp_2MH_2 (M = Mo, W) and group 13 acids BX_3 (X = F and Cl) and $AlMe_3$. Computational techniques have been primarily tested on the well-characterized Cp_2WH_2–$AlMe_3$ adduct[4,6] with the further aim to verify the stability of the adducts with boron halogenides. Furthermore, a computational description of the bond between complex and acid fragments has been directed to quantify the direct metal–aluminium or metal–boron interactions. IR spectrum has been computed to verify if the M–H stretching band can be considered a valuable tool for identifying bridging hydrides. An attempt to reconcile Shriver[1] and co-worker's[2] and Braunschweig and co-workers'[9–11] reports is proposed.

Methods

Density functional theory (DFT) calculations have been performed with the ADF2007[13] and Gaussian03[14] packages. The fragment-oriented approach of the ADF2007[13] program was particularly useful in this work. Furthermore, the ADF2007[13] program allowed us to consider relativistic effects by means of the ZORA (zero order regular approximation) approach.[15] This variationally stable scheme is based on a regular-potential expansion and produces a Hamiltonian that in zeroth order reproduces all important relativistic effects including the spin–orbit interaction.

A valence triple-zeta STO (Slater-type orbital) basis set with one polarization function (ZORA/TZP (triple-ζ plus polarization) without frozen cores) has been used for the relativistic calculations. Gradient-corrected exchange-correlation (XC) functionals have been used: the 1988 Becke[16] functional for the exchange and the 1986 Perdew[17] functional for the correlation. The local part of the XC functionals has been the default VWN (Vosko, Wilk, and Nusair[18]). The integrals accuracy has been increased to 10^{-8} (keyword "INTEGRATION 8.0") and the self-consistent field (SCF) convergence criterium has been set to 10^{-9} (keyword "SCF", subkey "converge 1e–9"). The structures have been optimized without using symmetry constraints and applying default convergence criteria apart from the maximum gradient, which has been set to 1.0×10^{-4} hartree/bohr. Delocalized coordinates have been used ("delocal" option). Similar levels of approximation have been shown to be reliable in analogue computations performed for 15th and 16th group complexes with ICF_3.[19]

Analytical computation of the Hessian (the matrix containing the energy second-derivatives with respect to the cartesian coordinates) has been performed to confirm the nature of minima of the found stationary points.

The interaction between the acid and base fragments have been analyzed by using the fragment analysis proposed by Ziegler and Rauk,[20] as better detailed in the Acid–base interaction section.

The Gaussian03[14] computations have been performed by using the hybrid XC functional of Adamo and Barone[21] known as MPW1PW91. Geometry optimizations were performed by applying the Stuttgart–Dresden ECP (effective core potentials) and basis set[22] ("SDD" keyword) on Mo and W atoms, and the 6-31G(d,p) basis set[23] on C, B, Al, F, and H atoms. Default gradient and displacement thresholds were used for the geometry optimization convergence criteria. All the reported geometries are relative minima of the potential energy surface (electronic energy in the Born–Oppenheimer approximation), as confirmed by the analytical computation of the Hessian matrix at the same level of approximation.

In the rest of the paper, "ADF computations" refers to the ZORA-based methods detailed above, whereas "Gaussian computations" refers to the MPW1PW91-based computations.

The AIM (atoms in molecules)-based study (see the AIM analysis section) has been performed on the electron density produced by ADF computations. The Xaim[24] program

Table 1. Some structural parameters from the computations in this paper and literature data (when present). See Fig. 1 for atomic labels.

Parameter	ADF[a]	Gaussian[a]	Experimental[a]
Cp_2WH_2			
W—H	1.707	1.700	1.703(2)[b]
H–W–H	78.3	77.0	78.0(12)[b]
Cp_2WH_2–$Al(CH_3)_3$			
W—H1	1.727	1.718	1.70(5)[c]
W—H2	1.706	1.700	1.22(17)[c]
Al—H1	1.975	2.017	1.96(5)[c]
Al—H2	2.584	2.525	2.08(16)[c]
W—Al	3.230	3.239	3.110(3)[c]
H1–W–H2	84.3	83.1	60(7)[c]
Cp_2WH_2–BF_3			
W—H1	1.779	1.742	No data
W—H2	1.699	1.694	No data
B—H1	1.470	1.520	No data
B—H2	3.528	3.591	No data
H1–W–H2	77.9	77.2	No data
Cp_2WH_2–BCl_3			
W—H1	1.852	1.816	No data
W—H2	1.694	1.687	No data
B—H1	1.364	1.358	No data
B—H2	3.329	3.188	No data
H1–W–H2	77.0	76.9	No data
Cp_2MoH_2			
Mo—H	1.697	1.674	1.685(3)[d]
H–Mo–H	76.3	74.8	75.5(3)[d]
Cp_2MoH_2–$Al(CH_3)_3$			
Mo—H1	1.724	1.695	No data
Mo—H2	1.697	1.677	No data
Al—H1	1.948	2.008	No data
Al—H2	2.562	2.489	No data
Mo—Al	3.230	3.232	No data
H1–Mo–H2	82.3	81.4	No data
Cp_2MoH_2–BF_3			
Mo—H1	1.783	1.720	No data
Mo—H2	1.684	1.668	No data
B—H1	1.401	1.513	No data
B—H2	3.313	3.501	No data
H1–Mo–H2	78.0	77.3	No data
Cp_2MoH_2–BCl_3			
Mo—H1	1.852	1.805	No data
Mo—H2	1.679	1.658	No data
B—H1	1.341	1.341	No data
B—H2	3.315	3.189	No data
H1–Mo–H2	75.9	75.6	No data

[a]Bond distances and angles are in angstrom and degrees, respectively. Computations performed as detailed in the Methods section.

[b]Microwave spectroscopy, ref. 27.

[c]X-ray diffraction, ref. 6.

[d]Neutron diffraction, ref. 7.

Fig. 1. The computed adducts (*a*) Cp_2WH_2–$Al(CH_3)_3$ and (*b*) $Cp_2WH_2BF_3$.

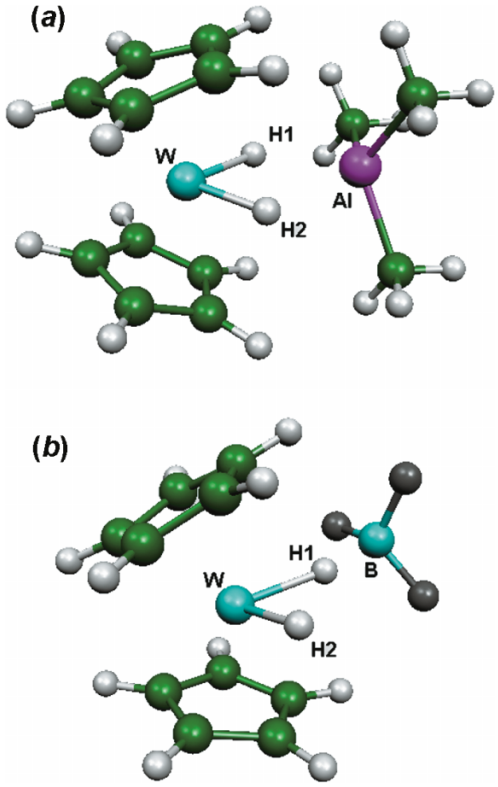

(developed by José Carlos Oritz Alba and Carles Bo Jané) has been used.

The proposed figures have been produced by the Molekel4.3[25] and ADF-GUI[26] software.

Results and discussion

Structures

Table 1 lists the acid–base adducts of this paper and relative relevant geometric parameters resulting from geometry optimizations and literature experimental works.

All the computed adducts show an asymmetric disposition of the acid moiety relative to the MH_2 fragment. As shown in Fig. 1, this asymmetry is particularly evident for the boron halogenide adducts, where the boron atom clearly points toward one hydride and is external to the WH_2 group.

In Cp_2WH_2–$Al(CH_3)_3$, the aluminium centre is closer to one of the hydride atoms, but now it is internal to the WH_2 group and appears not too far from the second hydride atom to exclude some interaction with it (see the following paragraph for details). This description is in line with the reported X-ray structure,[6] whose parameters are listed in Table 1. Because of the asymmetric disposition of the aluminium atom, the two W–H distances are different. As expected, the H1 hydride (the one closer to the acid centre shown in Fig. 1) is farther from the central transition metal, possibly due to higher charge donation toward the acid. As a consequence, the second hydride ligand slightly approaches the central transition metal. A comparison of computed and experimental hydride–aluminium distances would suggest that the computations overestimate the asymmetric character

of the hydride–aluminium interactions. However, the use of W–H distances would lead to the opposite conclusion. Furthermore, the experimental W–H2 distance of 1.22(17) Å, although subject to a higher measure error, appears particularly poorly reproduced by the computations, especially if we consider that the computed W–H1 and Al–H1 distances are in the experimental error and that the W–Al distance inaccuracy amounts to less than 4%. Indeed, the possibility to apply X-ray analysis to accurately determine the hydride positions in this class of complexes has been questioned.[7] The fact that the more reliable neutron diffraction data are in good agreement with the computations (Cp_2MoH_2 as a free complex in Table 1) seems to suggest that the reported position of H2 (the closest to the central metal) in Cp_2WH_2–$Al(CH_3)_3$ is not accurate. As a consequence, the H–W–H angle also appears neatly overestimated by our computations in this compound, but not in the W and Mo free complexes obtained by gas-phase microwave spectroscopy[27] and neutron diffraction data,[7] respectively.

The possible error on the experimental measure of the H–W–H angle could have important implications. In fact, as said above, the presence of a direct metal–acid interaction has been excluded for Cp_2WH_2–$Al(CH_3)_3$ on the basis of H–W–H angle reduction induced by adduct formation.[6] In truth, the authors compared the reported H–Mo–H angle of the free Cp_2MoH_2 complex with the H–W–H angle in the adduct (both in Table 1) because no experimental structures of free Cp_2WH_2 have been previously reported. Contrarily, our computations describe a 6.0° angle opening from ADF computations and 6.1° from Gaussian computations on passing from the free Cp_2WH_2 to the acid–base adduct. An identical change is predicted for the Mo complex with $Al(CH_3)_3$ in the case of ADF computations (6.6° from Gaussian computations). In all the adducts with BF_3 and BCl_3, we noted lower changes in the H–M–H angle in comparison to the free complexes (both Mo and W complexes). Furthermore, the angle closes in all the cases, apart from Cp_2MoH_2–BF_3 where it opens slightly (1.7° from ADF computations). From above, if we base our study only on a structural analysis, we would conclude that in the case of $Al(CH_3)_3$ a certain metal–acid direct interaction is present, which induces the Al centre to lay internally to the MH_2 group. BF_3 and BCl_3, in contrast, do not seem to be able to significantly interact with the transition metal. In the following paragraph we will deeply discuss this point.

A final point to be discussed is the computational evaluation of the energy barrier associated with the acid fragment jump from one hydride atom to the other one. It has been computed that such a barrier amounts to 3.1 kcal/mol in Cp_2WH_2–BF_3 and 2.7 kcal/mol in Cp_2WH_2–$Al(CH_3)_3$ (Gaussian computations). Such values suggest a very fast exchange of the acid fragment between the two hydride atoms. Proton NMR spectra of Cp_2WH_2–$Al(CH_3)_3$ shows a single peak associated with the WH_2 group[4] possibly for this reason. We think that a similar behaviour is to be expected for boron halogenide adducts in solution at room temperature.

Acid–base interaction

Table 2 collects computed data about the complex–acid interaction. The whole energy variation from free relaxed fragments to the adduct (ΔE_{TOT} or formation energy) has been decomposed as

$$\Delta E_{TOT} = \Delta E_{def} + \Delta E_{bond}$$

where ΔE_{def} is the energy change from relaxed (free) fragments to fragments in the distorted structure assumed in the acid–base adduct. This term is always positive and it is reported for both the acid and base fragments in Table 2. The ΔE_{bond} is the negative energy term due to both steric interaction of the fragments in the adduct, which includes electrostatic interaction, and the charge transfer from one fragment to the other one (covalence). In the case of ADF computations, the two contributions are computed according to the Ziegler–Rauk's decomposition scheme[20] and have been written as

$$\Delta E_{bond} = \Delta E_s + \Delta E_o$$

where ΔE_S and ΔE_o are the steric term (sum of Pauli repulsion and electrostatic interaction) and the orbital term (charge donation from the base to the acid), respectively.

From Table 2, it is possible to note that none of the adducts seem particularly stable in comparison to its free fragments, although all the adduct formation energies are negative. In all the reported syntheses of the studied adducts,[2,4] a solid separation from solution has been used to obtain the compound. On this basis, we can suggest that a relevant part of the favourable Gibbs reaction energy could be associated with the crystallization process. However, returning to the computational study, we can note that the most stable adducts have been obtained with boron halogenides rather than $Al(CH_3)_3$. This fact is mainly due to lower charge donation, as evidenced by the lower ΔE_o term and the consequently lower ΔE_{bond} (Table 2). On the other hand, the neatly more stabilizing ΔE_o terms in boron halogenides are counterbalanced by higher steric repulsions, which reduce the adduct stability gap with $Al(CH_3)_3$ adducts.

Table 2. Interaction energies from ADF computations. The deformation energy of $Al(CH_3)_3$ is computed on relaxed dimeric $Al_2(CH_3)_6$.

Compound	ΔE_{def} [a]	ΔE_{bond} [a]	ΔE_{TOT} [a]
Cp_2WH_2–$Al(CH_3)_3$	$Al(CH_3)_3$: 14.9	ΔE_S = +10.7	–2.4
	Cp_2WH_2: 1.0	ΔE_o = –29.0	–2.4
	Total: 15.9	ΔE_{bond} = –18.3	–2.4
Cp_2WH_2–BF_3	BF_3: 17.4	ΔE_S = +30.1	–4.2
	Cp_2WH_2: 1.6	ΔE_o = –53.3	–4.2
	Total: 19.0	ΔE_{bond} = –23.3	–4.2
Cp_2WH_2–BCl_3	BCl_3: 20.9	ΔE_S = +58.4	–2.6
	Cp_2WH_2: 4.4	ΔE_o = –86.4	–2.6
	Total: 25.4	ΔE_{bond} = –28.0	–2.6
Cp_2MoH_2–$Al(CH_3)_3$	$Al(CH_3)_3$: 15.0	ΔE_S = +11.7	–2.2
	Cp_2MoH_2: 1.2	ΔE_o = –30.1	–2.2
	Total: 16.2	ΔE_{bond} = –18.4	–2.2
Cp_2MoH_2–BF_{3l}	BF_3: 21.6	ΔE_S = +36.8	–4.2
	Cp_2MoH_2: 2.2	ΔEo = –64.9	–4.2
	Total: 23.8	ΔE_{bond} = –28.1	–4.2
Cp_2MoH_2–BCl_3	BCl_3: 22.0	ΔE_S = +61.4	–4.3
	Cp_2MoH_2: 5.2	ΔE_o = –92.9	–4.3
	Total: 27.2	ΔE_{bond} = –31.5	–4.3

[a]Electronic energy in the Born–Oppenheimer approximation (kcal/mol).

Table 3. Computed Hirshfeld[28] charges of the acid fragment in each studied compound.

Compound	Charge (e)[a]
Cp_2WH_2–$Al(CH_3)_3$	–0.140
Cp_2WH_2–BF_3	–0.204
Cp_2WH_2–BCl_3	–0.321
Cp_2MoH_2–$Al(CH_3)_3$	–0.138
Cp_2MoH_2–BF_3	–0.231
Cp_2MoH_2–BCl_3	–0.337

[a]ADF computations.

The lower charge donation in $Al(CH_3)_3$ adducts is evidenced by the more positive fragment charge computed on the basis of Hirshfeld's method[28] and listed in Table 3. In Cp_2WH_2–$Al(CH_3)_3$ and Cp_2MoH_2–$Al(CH_3)_3$ the acid fragment charge is clearly more positive in comparison to BF_3 and BCl_3 adducts. BCl_3 is able to accept more electronic charge than BF_3.

In all the studied compounds, the acid fragment is able to receive electronic charge by using its LUMO (lowest-in-energy unoccupied molecular orbital). Figure 2 shows the $Al(CH_3)_3$ fragment LUMO in Cp_2MoH_2–$Al(CH_3)_3$. It is labelled as 21 (because 20 orbitals are doubly occupied in the free fragment), and, not surprisingly, it is an empty sp^3-like orbital (according to ADF computations, p-type orbitals contribute a 69.5% weight with s-type orbitals for the remaining part). Its gross population in the adduct amounts to 0.23 e (e = electron charge) and no other virtual orbitals seem to be interested by charge donation (gross population lower than 0.01 e). Interestingly, the acceptor orbital mainly receives charge from three Cp_2WH_2 fragment orbitals (Fig. 2*a*). Orbital 73 is the HOMO (highest occupied molecular orbital) in the free complex. In agreement with previous computational studies about bent metallocenes,[29] it is a metal localized d-type orbital whose gross population is reduced to 1.95 e due to adduct formation. Orbitals 71 and 70 are mainly localized on the hydride ligands. They are more effective in donating charge toward the acid fragment. Orbital 71 is localized on the hydride atom, which is closer to the aluminium centre (H1 in Fig. 1). Its gross population in the adduct is 1.87 e, lower than orbital 70 (1.94 e), which is mostly localized on the farther hydride atom (H2). We can conclude that the base behaviour of Cp_2WH_2 is mainly due to the hydride ligands, particularly the hydride atom closer to the aluminium centre. However, the central metal is able to donate charge. This fact can be associated with the previously discussed H–W–H angle opening (Table 1) in comparison to the free complex.

In Cp_2MoH_2–BF_3, we find again that the LUMO fragment orbital on BF_3 is the principal acceptor orbital of the charge transfer process. It is similar, in terms of shape, to orbital 23 of Fig. 2. In this case, the stronger covalent interaction is reflected by a higher gross population of this orbital, which now amounts to 0.43 e. In spite of this fact, however, in this adduct only the hydride ligands are able to donate. The complex fragment orbital 73 (still the HOMO in the free complex) now maintains the 2.00 e gross population in the adduct and no other metal-localized orbitals are involved in charge donation. Thus, the central metal Lewis behaviour is not present in this complex. This implies that the H–W–H angle is less affected by adduct formation in comparison to Cp_2MoH_2–$Al(CH_3)_3$. Hydride-localized orbitals (very similar to orbitals 70 and 71 in Fig. 2*a*) are the main ones responsible for charge donation.

Fig. 2. Relevant fragment orbitals in the charge donation process of Cp_2WH_2–$Al(CH_3)_3$. (*a*) The most important Cp_2WH_2 donor orbitals and (*b*) the main $Al(CH_3)_3$ acceptor orbital are reported.

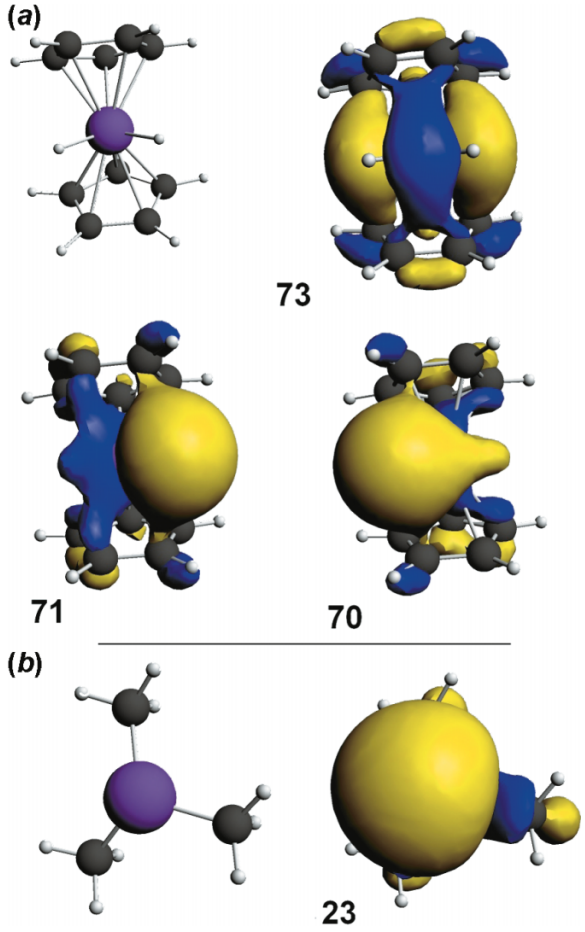

The same conclusions can be applied to Cp_2WH_2–BCl_3. In this case, however, we evidence a higher charge donation toward the sp^3-like acid fragment LUMO (0.63 e gross population). This is in line with the more negative Hirshfeld charge of BCl_3 in the acid–base adduct (Table 3) and higher ΔE_o in Table 2. Donation from the central metal can also be excluded in this case.

In the case of Mo complexes, we have substantially comparable results. Boron halogenide adducts are characterized by somewhat higher charge donations as evidenced in Table 2 (more negative ΔE_o) and Table 3 (more negative charges). The $Al(CH_3)_3$ adduct characteristics are in line with the W complex. In this case, a direct donation from the central metal is present. The Cp_2MoH_2 fragment HOMO donates a 0.04 e charge and the H–Mo–H angle opens by 6° (ADF computations) by virtue of adduct formation as in Cp_2WH_2.

AIM analysis

According to the AIM (atoms in molecules) model, it is possible to define an atom inside a molecule and recognize connections between them (bond paths) from the analysis of

Fig. 3. Bond critical points (BCPs) describing the metal–hydride and hydride–acid interactions and cut plane level curves of the electron density in (*a*) Cp_2WH_2–$Al(CH_3)_3$ and (*b*) Cp_2WH_2–BF_3. The plane is defined by the WH_2 group. A logarithmic scale has been used.

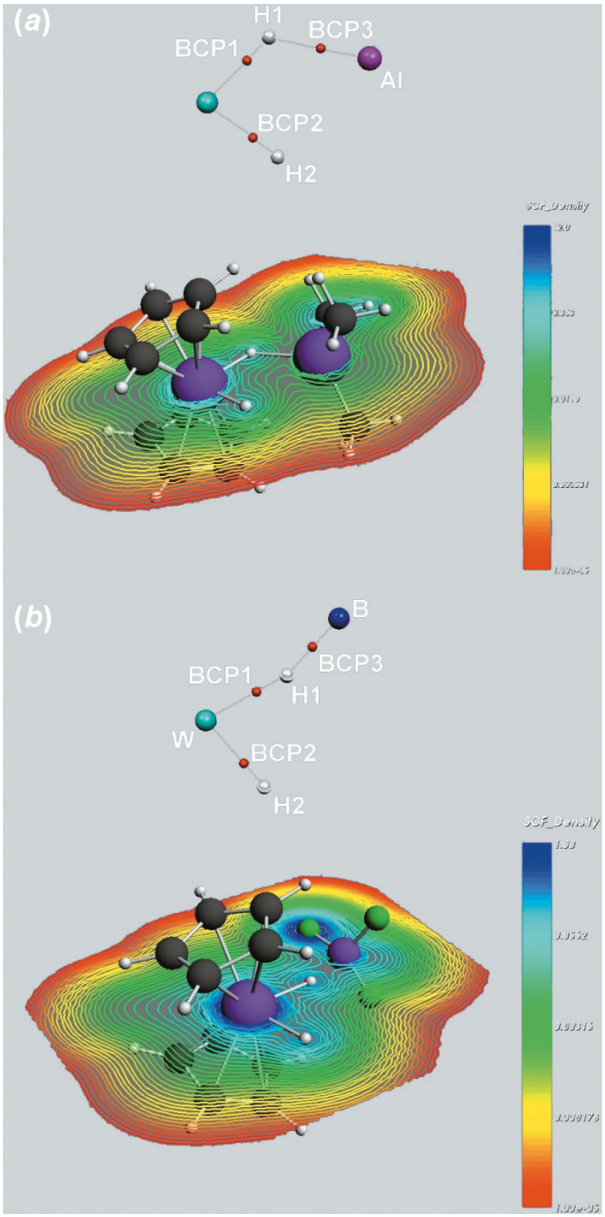

the electron density (ρ) and its gradient field (▽ρ).[30] From the detection of bond critical points (BCPs) as the points where ▽ρ vanishes, and from the determination of the eigenvalues of the electron density Hessian (second derivatives matrix of ρ) in the BCPs, it is possible to recover the bond patterns within a system of interacting particles defined, according to this view, as atoms in a molecule.

This approach has given interesting results in molecules and in the description of supramolecular systems generated by low intensity interactions as in the case of van der Walls and hydrogen bonds[31] and in the case of halogen bonds.[32]

Organometallic compounds, in particular π-acid–metal complexes, frequently show unusual interaction schemes that are difficult to describe in terms of elementary bond theories. We believe that the AIM approach can also be a useful tool in discussing the bond pattern in the case we are examining and can help to shed some light on what the bond pattern is in the case of these molecules.

Table 4. Characterization of the bond critical points (BCPs) from the AIM study. See Fig. 3 for the definition of the three BCPs. The electron density (ρ) has bee computed by the ADF program (see the Methods section).

BCP	ρ^a	$\nabla^2\rho^b$	$\lambda_1{}^c$	$\lambda_2{}^c$	$\lambda_3{}^c$	ε^d
Cp_2WH_2–$Al(CH_3)_3$						
BCP1	0.115	0.215	–0.176	–0.133	0.523	0.328
BCP2	0.126	0.196	–0.196	–0.157	0.529	0.252
BCP3	0.031	0.0513	–0.030	–0.017	0.099	0.786
Cp_2WH_2–BF_3						
BCP1	0.094	0.294	–0.133	–0.097	0.525	0.370
BCP2	0.129	0.147	–0.210	–0.167	0.523	0.258
BCP3	0.083	–0.102	–0.117	–0.115	0.129	0.019
Cp_2WH_2–BCl_3						
BCP1	0.075	0.278	–0.097	–0.065	0.440	0.490
BCP2	0.131	0.155	–0.213	–0.172	0.540	0.240
BCP3	0.109	–0.196	–0.162	–0.162	0.127	0.001
Cp_2MoH_2–$Al(CH_3)_3$						
BCP1	0.109	0.105	–0.181	–0.141	0.426	0.284
BCP2	0.110	0.060	–0.208	–0.170	0.438	0.221
BCP3	0.033	0.0627	–0.033	–0.019	0.115	0.699
Cp_2MoH_2–BF_3						
BCP1	0.084	0.160	–0.129	–0.098	0.387	0.316
BCP2	0.125	0.040	–0.221	–0.184	0.445	0.201
BCP3	0.096	–0.146	–0.142	–0.141	0.137	0.007
Cp_2MoH_2–BCl_3						
BCP1	0.069	0.154	–0.097	–0.071	0.322	0.367
BCP2	0.126	0.037	–0.255	–0.189	0.450	0.196
BCP3	0.115	–0.205	–0.175	–0.174	0.145	0.005

[a]Electron density.
[b]Lapacian of the electron density.
[c]Eigenvalues of the electron density Hessian matrix.
[d]Ellipticity.

The cut plane plots of the Cp_2WH_2–$Al(CH_3)_3$ and Cp_2WH_2–BF_3 ρ are reported in Fig. 3 (the cut plane contains the WH_2 group). Figure 3 also shows a plot of the same molecules where (3, –1) critical points (two negative eigenvalues of the electron density Hessian) are indicated by red dots (BCP in Fig. 3). Table 4 collects information about the found BCPs. No (3, –1) critical points are present between Al (or B) and W atoms, a fact that seems to exclude direct transition-metal – acid interaction. Furthermore, no (3, –1) BCPs can be located between H2 (the farther atom) and acid centre. Similar results have been found in the case of BCl_3 complexes (both W and Mo ones).

This suggests that the studied acid–base adducts can be seen as μ-hydrido complexes and not as μ-dihydrogen ones. This view is further supported by the absence of (3, +1) ring critical points (two positive eigenvalues of the electron density Hessian) inside the W–H1–Al–H2 ring (and in the cases of a boron acid centre) as required by the Poincaré–Hopf's relation.[33]

IR spectra

IR spectra represented the principal tool used by Johnson and Shriver[2] to demonstrate that boron halogenides accept charge directly from the transition metal without relevant contributions from the hydride ligands. A similar approach with similar conclusions has been used for Cp_2MH_2–AlR_3 adducts,[4] but successive X-ray investigations demonstrated that, in the last adduct, the aluminium centre mostly interacts with the hydride ligands,[7] as confirmed by our computational work.

The IR suggestion was based on the substantial invariance of the W–H stretching band frequency passing from the free complex to the acid–base adducts.

Table 5 contains experimental data about the W–H stretching frequencies collected in different environments and the computational results from our work. The reported computed frequencies have not been scaled. We can note a much better agreement between ADF computations and experimental data in Cp_2MoH_2 and Cp_2WH_2 free complexes. From our computations, two bands with similar intensity are predicted, which are the asymmetric and symmetric stretching modes. The lowest frequency is always associated with the asymmetric stretching. In all the experimental works, a single band is reported, allowing us to think that the two computed bands merge or that the computed intensities are not reliable.

When the acid–base adducts are considered, our computations predict relatively low influences on the W–H stretching frequency due to adduct formation with $Al(CH_3)_2$. This seems particularly evident in the case of the Mo complex, where the computed most intense band shifts of 10 cm^{-1}, in agreement with the reported, scarce change due to adduct formation.[4] Also, BF_3 is described to have a low influence on the stretching frequency in the case of the W complex, in agreement with the data reported by Johnson and Shriver.[2] In contrast, when Mo complexes are considered, BF_3 is computed to induce a very strong shift, which does not seem to be justified by experimental data. A relatively large error is associated with the BCl_3 adduct with Cp_2WH_2.

The fact that the free complexes are much better described than the acid–base adducts can be explained on the basis of the scarce directionality of the acid–base interaction. As said above, the acid fragment is predicted to easily jump from the hydride ligand to the other one. In truth, the energy surface associated with the movement of the acid fragment appears flat. In our study, we have noted that small changes in the acid fragment position can lead to significant changes in the W–H stretching frequency. As an example, a relative minimum in Cp_2WH_2–BF_3 is 0.5 kcal/mol higher in energy with respect to the absolute minimum that has been described in this paper (Fig. 1*b* and Fig. 3*b*). It only differs for the BF_3 group position, that is slightly internal to the WH_2 group rather than being slightly external. This small structural change leads to a blue shift of the W–H stretching frequency of more than 20 cm^{-1}. A flat energy surface means great changes in the molecular structure induced by the environment that cannot be easily modelled by computational studies and that can lead to relatively poor predictions.

However, from the above results and an analysis of the experimental data, it is hard to claim that the W–H stretching frequency is a reliable tool for distinguishing between direct metal donation and hydride donation.

Table 5. Computed M–H stretching frequencies (cm^{-1}) and intensities (in parenthesis; km/mol) of the studied complexes.

Compound	ADF	Gaussian	Experimental
Cp_2WH_2	1917 (47); 1929 (77)	1982 (40); 1998 (68)	1922;[a] 1890;[b] 1900;[c] 1896[d]
Cp_2WH_2–$Al(CH_3)_3$	1871 (40); 1943 (48)	1950 (42); 2014 (44)	—[e]
Cp_2WH_2–BF_3	1941 (794); 1957 (144)	2012 (56); 2050 (676)	1917;[a] 1956[f]
Cp_2WH_2–BCl_3	1896 (2031); 1977 (47)	2034 (574); 2055 (1772)	1967;[a] 1956[g]
Cp_2MoH_2	1848 (35); 1865 (58)	1938 (33); 1959 (59)	1853;[a] 1823[b]; 1833;[c] 1847[d]
Cp_2MoH_2–$Al(CH_3)_3$	1804 (27); 1875 (40)	1912 (36); 1973 (46)	—[e]
Cp_2MoH_2–BF_3	1899 (25); 2025 (1095)	1974 (47); 2033 (739)	1853[a]
Cp_2MoH_2–BCl_3	1915 (38); 1958 (1914)	2009 (51); 2064 (2328)	No data

[a]Solid state, ref. 2.

[b]THF (tetrahydrofuran) solution, ref. 34.

[c]Argon matrix, ref. 34.

[d]CS_2 solutions, ref. 35.

[e]In ref. 4, no mention is made of the vibration frequency. It is only reported that "no noteworthy changes due to complex formation" have been observed in benzene solution.

[f]Ref. 9; the supposed structure is the $[Cp_2WH_3][BF_4]$ salt.

[g]Ref. 9; the supposed structure is the $[Cp_2WH_3][BCl_4]$ salt.

Conclusions

According to our computations, Cp_2WH_2 and Cp_2MoH_2 can act as Lewis bases mainly by virtue of their hydride ligands. BX_3 acids show a stronger preference for the coordination with a single hydride ligand, a fact that excludes direct metal donation toward the acid centre. In this light, the supposed direct metal–boron interaction does not seem to be likely. In the case of $Al(CH_3)_3$ adducts, the central metal shows a significant ability to donate charge to the aluminum centre. This fact leads to a more central, although still asymmetric, disposition of the aluminium atom with respect to the WH_2 group.

Two criteria have been suggested to evaluate the entity of the charge donation from the central transition metal. The first one is the H–M–H angle, which should widen when such a charge donation occurs. The second one is the W–H stretching frequencies, which should be unaffected by adduct formation when the central metal is the only one responsible for the Lewis behaviour.

The first criterion is confirmed by our computations. The relatively low metal charge donation in Cp_2MH_2–$Al(CH_3)_3$ adducts induces an angle opening of about 6°, which has not been observed in the case of the BX_3 acid fragments.

The second criterion seems less reliable and does not seem to be confirmed by our computations. A possible explanation could be the relatively high dependence of the W–H stretching frequency on the position assumed by the acid fragment and the relatively flat energy surface associated with the acid fragment movement in proximity to the WH_2 group.

According to our computations, the adducts with BX_3 are stronger than the $Al(CH_3)_3$ ones. In this light, since the last ones have been isolated and characterized, we cannot exclude the existence of Cp_2MH_2–BX_3 adducts, at least as precursors of successive reactions. The fact that Braunschweig and co-workers[9–11] excluded the presence of these adducts could be induced by slight changes in the reaction conditions in comparison to the Shriver[1] and co-worker's[2] experiments. These could lead to further reactions. For instance, the presence of water could catalyze further reactions toward the $[Cp_2WH_3][BX_4]$ ionic solid obtained by Braunschweig and co-workers.[9–11] According to us, further experimental investigations could be fruitfully addressed in this field, with the aim to confirm or confute the existence of the Shriver[1] and co-worker's[2] adducts.

Acknowledgement

This work has been supported by the Italian Ministero dell'Istruzione, dell'Università e della Ricerca (MiUR) through a PRIN 2005 200503527 grant.

References

(1) Shriver, D. F. *J. Am. Chem. Soc.* **1963**, *85* (21), 3509–3510. doi:10.1021/ja00904a052.

(2) Johnson, M. P.; Shriver, D. F. *J. Am. Chem. Soc.* **1966**, *88* (2), 301–304. doi:10.1021/ja00954a022.

(3) Purcell, K. F.; Kotz, J. C. *Inorganic Chemistry;* Holt-Saunders International Editions: Philadelphia, 1976; p 889.

(4) Storr, A.; Thomas, B. S. *Can. J. Chem.* **1971**, *49* (15), 2504–2507. doi:10.1139/v71-413.

(5) Green, M. L. H.; MacKenzie, R. E.; Poland, J. S. *J. Chem. Soc., Dalton Trans.* **1976**, 1993. doi:10.1039/dt9760001993.

(6) Bruno, J. W.; Huffman, J. C.; Caulton, K. G. *J. Am. Chem. Soc.* **1984**, *106* (2), 444–445. doi:10.1021/ja00314a044.

(7) Schultz, A. J.; Stearley, K. L.; Williams, J. M.; Mink, R.; Stucky, G. D. *Inorg. Chem.* **1977**, *16* (12), 3303–3306. doi:10.1021/ic50178a063.

(8) Golden, J. T.; Peterson, T. H.; Holland, P. L.; Bergman, R. G.; Andersen, R. A. *J. Am. Chem. Soc.* **1998**, *120* (1), 223–224. doi:10.1021/ja973230v.

(9) Braunschweig, H.; Wagner, T. *Z. Naturforsch.* **1996**, *51b*, 1618–1620.

(10) Braunschweig, H. *Angew. Chem. Int. Ed.* **1998**, *37* (13–14), 1786–1801. doi:10.1002/(SICI)1521-3773(19980803)37:13/14<1786::AID-ANIE1786>3.0.CO;2-C.

(11) Braunschweig, H.; Colling, M. *Coord. Chem. Rev.* **2001**, *223* (1), 1–51. doi:10.1016/S0010-8545(01)00378-2.

(12) Ko, J. J.; Bockman, T. M.; Kochi, J. K. *Organometallics* **1990**, *9* (6), 1833–1842. doi:10.1021/om00156a024.

(13) (a) *ADF2007.01;* SCM, Theoretical Chemistry, Vrije Universiteit, Amsterdam, The Netherlands. Available from http://www.scm.com; (b) te Velde, G.; Bickelhaupt, F. M.; van Gisbergen, S. J. A.; Fonseca Guerra, C.; Baerends, E. J.; Snijders, J. G.; Ziegler, T. *J. Comput. Chem.* **2001**, *22* (9), 931–967. doi:10.1002/jcc.1056.; (c) Fonseca Guerra, C.; Snijders, J. G.; te Velde, G.; Baerends, E. J. *Theor. Chem. Acc.* **1998**, *99* (6), 391–403. doi:10.1007/s002140050021.

(14) Frisch, M. J.; Trucks, G. W.; Schlegel, H. B.; Scuseria, G. E.; Robb, M. A.; Cheeseman, J. R.; Montgomery, J. A., Jr.; Vreven, T.; Kudin, K. N.; Burant, J. C.; Millam, J. M.; Iyengar, S. S.; Tomasi, J.; Barone, V.; Mennucci, B.; Cossi, M.; Scalmani, G.; Rega, N.; Petersson, G. A.; Nakatsuji, H.; Hada, M.; Ehara, M.; Toyota, K.; Fukuda, R.; Hasegawa, J.; Ishida, M.; Nakajima, T.; Honda, Y.; Kitao, O.; Nakai, H.; Klene, M.; Li, X.; Knox, J. E.; Hratchian, H. P.; Cross, J. B.; Bakken, V.; Adamo, C.; Jaramillo, J.; Gomperts, R.; Stratmann, R. E.; Yazyev, O.; Austin, A. J.; Cammi, R.; Pomelli, C.; Ochterski, J. W.; Ayala, P. Y.; Morokuma, K.; Voth, G. A.; Salvador, P.; Dannenberg, J. J.; Zakrzewski, V. G.; Dapprich, S.; Daniels, A. D.; Strain, M. C.; Farkas, O.; Malick, D. K.; Rabuck, A. D.; Raghavachari, K.; Foresman, J. B.; Ortiz, J. V.; Cui, Q.; Baboul, A. G.; Clifford, S.; Cioslowski, J.; Stefanov, B. B.; Liu, G.; Liashenko, A.; Piskorz, P.; Komaromi, I.; Martin, R. L.; Fox, D. J.; Keith, T.; Al-Laham, M. A.; Peng, C. Y.; Nanayakkara, A.; Challacombe, M.; Gill, P. M. W.; Johnson, B.; Chen, W.; Wong, M. W.; Gonzalez, C.; Pople, J. A. *Gaussian03,* revision D.02; Gaussian, Inc.: Wallingford CT, 2004.

(15) (a) van Lenthe, E.; Ehlers, A. E.; Baerends, E. J. J. *Chem. Phys.* **1999**, *110* (18), 8943–8953;(b) van Lenthe, E.; Baerends, E. J.; Snijders, J. G. *J. Chem. Phys.* **1993**, *99* (6), 4597–4610. doi:10.1063/1.466059.; (c) van Lenthe, E.; Baerends, E. J.; Snijders, J. G. *J. Chem. Phys.* **1994**, *101* (11), 9783–9792. doi:10.1063/1.467943.; (d) van Lenthe, E.; van Leeuwen, R.; Baerends, E. J.; Snijders, J. G. *Int. J. Quantum Chem.* **1996**, *57* (3), 281–293. doi:10.1002/(SICI)1097-461X(1996)57:3<281::AID-QUA2>3.0.CO;2-U.

(16) Becke, A. D. *Phys. Rev. A* **1988**, *38* (6), 3098–3100. doi:10.1103/PhysRevA.38.3098. PMID:9900728.

(17) Perdew, J. P. *Phys. Rev. B* **1986**, *33* (12), 8822–8824. doi:10.1103/PhysRevB.33.8822.

(18) Vosko, S. H.; Wilk, L.; Nusair, M. *Can. J. Phys.* **1980**, *58* (8), 1200–1211.

(19) Romaniello, P.; Lelj, F. *J. Phys. Chem. A* **2002**, *106* (39), 9114–9119. doi:10.1021/jp0255334.

(20) (a) Ziegler, T.; Rauk, A. *Theor. Chim. Acta* **1977**, *46*, 1–10; (b) Ziegler, T.; Rauk, A. *Inorg. Chem.* **1979**, *18* (6), 1558–1565. doi:10.1021/ic50196a034.

(21) Adamo, C.; Barone, V. *J. Chem. Phys.* **1998**, *108* (2), 664–675. doi:10.1063/1.475428.

(22) Nicklass, A.; Dolg, M.; Stoll, H.; Preuss, H. *J. Chem. Phys.* **1995**, *102* (22), 8942–8952, and references cited therein. doi:10.1063/1.468948.

(23) (a) Binkley, J. S.; Pople, J. A.; Hehre, W. J. *J. Am. Chem. Soc.* **1980**, *102* (3), 939–947. doi:10.1021/ja00523a008.; (b) Gordon, M. S.; Binkley, J. S.; Pople, J. A.; Pietro, W. J.; Hehre, W. J. *J. Am. Chem. Soc.* **1982**, *104* (10), 2797–2803. doi:10.1021/ja00374a017.

(24) Ortiz Alba, J. C.; Jané, C. B. *Xaim;* Departament de Quimica Fisica i Inorganica, Universitat Rovira i Virgili: Tarragona, Spain. Available from http://www.quimica.urv.es/XAIM.

(25) (a) Fluckiger, P.; Luthi, H. P.; Portmann, S.; Weber, J. *Molekel4.3;* Swiss Center for Scientific Computing: Manno, Switzerland, 2000–2002.; (b) Portmann, S.; Luthi, H. P. *Chimia (Aarau)* **2000**, *54*, 766.

(26) *ADF-GUI 2008.01;* SCM: Amsterdam, The Netherlands, 2008. Available from www.scm.com.

(27) Tackett, B. S.; Karunatilaka, C.; Daly, A. M.; Kukolich, S. G. *Organometallics* **2007**, *26* (8), 2070–2076. doi:10.1021/om061027f.

(28) (a) Hirshfeld, F. L. *Theor. Chim. Acta* **1977**, *44* (2), 129–138. doi:10.1007/BF00549096.; (b) Wiberg, K. B.; Rablen, P. R. *Comput. Chem.* **1993**, *14* (12), 1504–1518. doi:10.1002/jcc.540141213.

(29) Green, J. C. *Chem. Soc. Rev.* **1998**, *27*, 263. doi:10.1039/a827263z.
(30) Bader, R. F. W. *Atoms in Molecules: A Quantum Theory;* Oxford University Press: Oxford, 1990.
(31) Carrol, M. T.; Bader, R. F. W. *Mol. Phys.* **1988**, *63* (3), 387–405. doi:10.1080/00268978800100281.
(32) Wang, W.; Wong, N.; Zheng, W.; Tian, A. *J. Phys. Chem. A* **2004**, *108* (10), 1799–1805. doi:10.1021/jp036769q.
(33) Collard, K.; Hall, G. G. *Int. J. Quantum Chem.* **1977**, *12* (4), 623–637. doi:10.1002/qua.560120404.
(34) Girling, R. B.; Grebenik, P.; Perutz, R. *Inorg. Chem.* **1986**, *25* (1), 31–36. doi:10.1021/ic00221a010.
(35) Green, M. L. H.; McCleverty, J. A.; Pratt, L.; Wilkinson, G. *J. Chem. Soc.* **1961**, 4854–4858. doi:10.1039/jr9610004854.

Theoretical prediction of O–H, Si–H, and Si–C σ-bond activation reactions by titanium(IV)–imido complex

Noriaki Ochi, Yoshihide Nakao, Hirofumi Sato, and Shigeyoshi Sakaki

Abstract: The O–H σ-bond activation of methanol, the Si–H σ-bond activation of silane, and the Si–C σ-bond activation of methylsilane by titanium(IV)–imido complex $(Me_3SiO)_2Ti(NSiMe_3)$ were theoretically investigated with DFT and MP2 to MP4(SDQ) methods. The O–H σ-bond activation of methanol occurs with small activation barrier (E_a) of 7.1 (14.6) kcal/mol and large exothermicity (E_{exo}) of 65.8 (61.4) kcal/mol to afford $(Me_3SiO)_2Ti(OCH_3)[NH(SiMe_3)]$, indicating that the O–H σ-bond activation occurs easier than the C–H σ-bond activation (E_a = 14.6 (21.5) kcal/mol and E_{exo} = 22.7 (16.5) kcal/mol), where DFT- and MP4(SDQ)-calculated values are presented without and in parenthesis hereafter. Though the OCH_3 group becomes anionic and the H atom becomes proton-like in this activation reaction, population changes more moderately occur than those of the C–H σ-bond activation. This is because the H–OCH_3 bond is already polarized in methanol. In the Si–H σ-bond activation, two reaction courses were investigated; in one course, the product is $(Me_3SiO)_2Ti(SiH_3)[NH(SiMe_3)]$ in which the H atom and the SiH_3 group are bound to the N atom and the Ti center, respectively, while in the other course the product is $(Me_3SiO)_2Ti(H)[N(SiH_3)(SiMe_3)]$ in which the H atom and the SiH_3 group are bound to the Ti center and the imido N atom, respectively. Though the former reaction occurs with small E_a value and large exothermicity, the latter reaction occurs easier with further smaller E_a value of 2.6 (4.3) kcal/mol and larger E_{exo} value of 32.5 (34.1) kcal/mol than those of the former reaction. This is because the Ti–H bond energy is much larger than the Ti–SiH_3 one. The Si–C σ-bond activation occurs with moderate activation barrier of 19.1 (18.6) kcal/mol and considerably large exothermicity of 33.9 (37.7) kcal/mol. Based on these results, we wish to propose the theoretical prediction that the titanium(IV)–imido complex is useful for O–H, Si–H, and Si–C σ-bond activation reactions.

Key words: σ-bond activation, titanium(IV)–imido complex, heterolytic σ-bond activation, density functional theory (DFT), bond energy.

Résumé : Faisant appel aux méthode de la théorie de la fonctionnelle de la densité (TFD) et aux méthodes MP2 et MP4(SDQ), on a étudié d'une façon théorique l'activation de la liaison σ du O–H du méthanol, lactivation de la liaison σ du Si–H du silane et l'activation de la liaison σ Si–C du méthylsilane par le complexe titane(IV)–imido $(Me_3Si)_2Ti(NSiMe_3)$. L'activation de la liaison σ du OH du méthanol donne lieu à une faible barrière d'activation (E_a) de 7,1 (14,6) kcal/mol et une grande exothermicité (E_{exo}) de 65,8 (61,4) kcal/mol qui conduit à la formation de $(Me_3Si)_2Ti(OCH_3)[NH(SiMe_3)]$ indiquant que l'activation de la liaison σ du O–H se produit plus facilement que celle de la liaison σ C–H [(E_a) de 14,6 (21,5) kcal/mol et (E_{exo}) de 22,7 (16,5) kcal/mol] dans lesquelles les valeurs obtenues par la méthode TFD sont rapportées sans parenthèses alors que celles calculées par la méthode MP4(SDQ) sont rapportées entre parenthèses. Même si le groupe OCH_3 devient ionique et que l'atome H prend une forme semblable à celle d'un proton dans cette réaction d'activation, les changements de population sont plus modérés que ceux observés lors de l'activation σ de la liaison C–H. Ceci résulte du fait que la liaison H–OCH_3 est déjà polarisée dans le méthanol. Dans la réaction d'activation σ de la liaison Si–H, on a étudié deux voies réactionnelles; dans l'une, le produit est $(Me_3Si)_2Ti(SiH_3)[NH(SiMe_3)]$ dans lequel l'atome H et le groupe SiH_3 sont liés respectivement à l'atome N et au centre Ti alors que dans l'autre voie réactionnelle le produit est $(Me_3Si)_2Ti(H)[NH(SiCH_3)(SiMe_3)]$ dans lequel l'atome H et le groupe SiH_3 sont liés respectivement au centre Ti et à l'atome N imido. Même si la première réaction se produit avec une valeur de E_a faible et une grande exothermicité, la dernière réaction se produit plus facilement avec une valeur de E_a encore plus faible 2,6 (4,3) kcal/mol et une valeur de E_{exo} plus élevée de 32,5 (34,1) kcal/mol que celle de la réaction précédente. Ceci résulte du fait que l'énergie de liaison du Ti–H est beaucoup plus élevée que celle de la liaison Ti–SiH_3. L'activation σ de la liaison Si–C se produit avec une barrière d'activation modérée de 19,1 (18,6) kcal/mol et une exothermicité beaucoup plus élevée de 33,9 (37,7) kcal/mol. Sur la base de ces résultats, on désire proposer une prédiction théorique que le complexe titane(IV)–imido $(Me_3Si)_2Ti(NSiMe_3)$ s'avérera utile pour l'activation des liaisons σ O–H, Si–H et Si–C.

Received 13 February 2009. Accepted 11 June 2009. Published on the NRC Research Press Web site at canjchem.nrc.ca on 30 September 2009.

This article is part of a Special Issue dedicated to Professor T. Ziegler.

N. Ochi, Y. Nakao, H. Sato, and S. Sakaki.[1,2] Department of Molecular Engineering, Graduate School of Engineering, Kyoto University, Nishikyo-ku, Kyoto 615-8510, Japan.

[1]Corresponding author (e-mail: sakaki@moleng.kyoto-u.ac.jp).
[2]Present address: Fukui Institute for Fundamental Chemistry, Nishihiraki-cho, Takano, Sakyo-ku 610-8103, Japan.

Mots-clés : activation dune liaison σ, complexe titane(IV)–imido, activation d'une liaison σ hétérocyclique, théorie de la fonctionnelle de la densité (TFD), énergie de liaison.

[Traduit par la Rédaction]

Introduction

The σ-bond activation of a saturated molecule by a transition-metal complex is one of the important reactions in organometallic chemistry, inorganic chemistry, and catalytic chemistry, because active species is produced by this reaction in many cases.[1] There are several categories of σ-bond activation: (*i*) The first is the σ-bond activation via oxidative addition reaction by late transition-metal complexes. This reaction has been theoretically investigated well by many groups.[2–15] (*ii*) The second is the σ-bond activation via metathesis by lanthanide and actinide complexes, which was theoretically investigated by Eisenstein and her coworkers.[16] (*iii*) The third is the σ-bond activation by metal–ligand single bond such as the platinum(II)–chloride, palladium(II)–acetate, and iridium(III)–acetate bonds,[17–19] which were theoretically investigated by Siegbahn et al.,[20] Sakaki et al.,[21] Ziegler et al.,[22] Goddard et al.,[23] and Schwarz et al.[24] (*iv*) The last is the σ-bond activation via addition of C–H σ-bond across M=N multiple bond by early to middle transition-metal complexes.[25] This σ-bond activation was theoretically investigated by Cundari and his collaborators in the last decade.[26] Recently, the C–H σ-bond activation of benzene by the titanium(IV)–alkylidyne complex was experimentally succeeded and theoretically investigated with the DFT method by Mindiola group.[27] We also theoretically investigated the C–H σ-bond activation of methane by the titanium(IV)–imido complex recently, and clearly showed that not only the charge transfer (CT) from the Ti=N moiety to the σ*-anti-bonding orbital but also the reverse CT from the C–H σ-bonding orbital to the Ti empty d orbital plays important role in this σ-bond activation.[28]

In our previous work,[28] we presented theoretical prediction that N–H σ-bond activation of ammonia can be achieved by the titatnium(IV)–imido and titanium(IV)–alkylidyne complexes. Though one successful N–H σ-bond activation of ammonia has been reported recently,[29] it is still difficult. Considering that the titanium(IV)–imido complex is useful for the C–H and N–H σ-bond activations, one can expect that this complex can be also applied to other σ-bond activations of O–H, Si–H, and Si–C bonds. Because the O–H bond is strong like the N–H bond, its activation is interesting. Also, the Si–H σ-bond activation is important because it is involved in many catalytic reactions producing organosilicon compounds. The Si–C σ-bond activation is challenging, because it is difficult as well-known.

In this theoretical work, we investigated the O–H σ-bond activation of methanol, the Si–H σ-bond activation of silane, and the Si–C σ-bond activation of methylsilane with titanium(IV)–imido complex, $(Me_3SiO)_2Ti(NSiMe_3)$, by DFT and MP2 to MP4(SDQ) methods. This complex was used for many experimental works by Wolczanski group.[25] Our purposes here are to show the differences of the O–H, Si–H, and Si–C σ-bond activations from the C–H σ-bond activation, to present theoretical prediction if the titanium(IV)–imido complex can be utilized for these σ-bond activations, and to clarify what factor is important in these σ-bond activations.

Computational details

Geometries were optimized by the DFT method with the B3LYP functional.[30–32] We ascertained that each equilibrium geometry has no imaginary frequency and each transition state has only one imaginary frequency. Two kinds of basis set systems were used. The smaller system (BS1) was used for geometry optimization. In this BS1, core electrons of Ti (up to 2p) were replaced with effective core potentials (ECPs),[33] and their valence electrons were represented with (311111/2111/411/1) basis set.[33] For H, C, N, O, and Si, 6–31G* basis sets[34] were employed, where a p-polarization function[35] was added to the active H atom that reacts with the Ti complex to form either Ti–H or N–H bond. The better basis set system (BS2) was used for evaluation of energy changes. In this BS2, (311111/2111/411/11) basis set was employed for Ti,[33,36] where the same ECPs as those of BS1 were employed for core electrons. For H, C, N, O, and Si, the 6–311G* basis sets were employed,[37–39] where a p-polarization function was added to the active H atom and a diffuse function was added to the imido N atom. Zero-point energy was evaluated with the DFT/BS1 method under assumption of harmonic oscillator. The energy changes are presented here after correction of zero-point energy.

The Gaussian 03 program package[40] was used for all calculations. Population analysis was carried out with the method of Weinhold and co-workers.[41] Molecular orbitals were drawn with the MOLEKEL program package.[42]

Results and discussion

Geometry and energy changes in the O–H σ-bond activation of methanol by titanium(IV)–imido complex, $[(Me_3SiO)_2Ti(NSiMe_3)]$ (R)

The O–H σ-bond activation of methanol by $(Me_3SiO)_2Ti(NSiMe_3)$ **R** occurs through precursor complex (**PC1**) and transition state (**TS1**) to afford product complex (**PRD1**), as shown in Fig. 1. The optimized geometry of **R** agrees well with the experimental one[43,44] except for the moderate discrepancies in the Ti–N and N–Si bond distances, as reported previously.[26,28] We stop to discuss the moderate discrepancies here because we presented the discussion in our recent work.[28] In **PC1**, the O atom of methanol approaches the Ti center, where the Ti–O distance is 2.109 Å, but the H atom is considerably distant from the N atom. The O–H bond little lengthens in **PC1**, which is different from the moderately elongated C–H bond in the precursor complex of the C–H σ-bond activation of methane. This difference will be discussed below in more detail. In **TS1**, the Ti–O distance becomes shorter to 2.034 Å, which is moderately longer than that of **PRD1**. The O–H distance is moderately elongated to

Fig. 1. Geometry changes in O–H σ-bond activation of methanol by $(Me_3SiO)_2Ti(NSiMe_3)$ **R**. Bond lengths are in angstroms, and bond angles are in degrees. In parenthesis is relative energy calculated by DFT(B3LYP)/BS2 method.

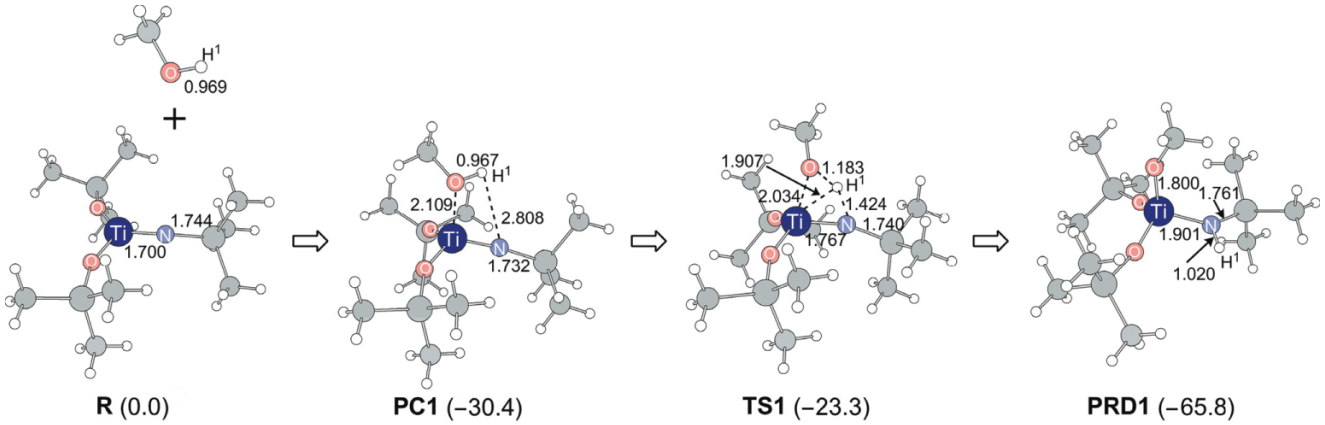

Table 1. Binding energy (BE), activation barrier (E_a), and reaction energy (ΔE) of the Si–H σ-bond activation of silane, O–H σ-bond activation of methanol, and C–Si σ-bond activation of methylsilane by $(Me_3SiO)_2Ti(NSiMe_3)$ **R** (in kcal/mol unit).

	CH_3O–H			H–SiH_3						CH_3–SiH_3			H–CH_3[d]		
				Path A			Path B								
	BE[a]	E_a[b]	ΔE[c]	BE[a]	E_a[b]	ΔE[c]	BE[a]	E_a[b]	ΔE[c]	BE[a]	E_a[b]	ΔE[c]	BE[a]	E_a[b]	ΔE[c]
DFT(B3LYP)	–30.4	7.1	–65.8	–6.0	9.7	–27.7	–6.8	2.6	–32.5	–8.1	19.1	–33.9	–4.5	14.6	–22.7
MP2	–36.6	12.4	–59.7	–13.7	11.0	–24.3	–14.9	4.0	–32.7	–17.2	16.5	–38.0	–9.8	17.6	–16.5
MP3	–36.3	9.0	–74.2	–11.2	10.6	–42.2	–13.0	0.5	–50.6	–14.7	13.1	–54.9	–7.1	12.7	–36.5
MP4(DQ)	–35.5	13.4	–65.4	–12.3	13.4	–32.4	–13.5	3.4	–40.9	–15.7	17.6	–44.4	–7.8	18.0	–25.3
MP4(SDQ)	–36.6	14.6	–61.4	–13.9	15.0	–26.4	–15.2	4.3	–34.1	–17.5	18.6	–37.7	–9.4	21.5	–16.5

[a]BE = E(precursor complex) – E(sum of reactants).
[b]E_a = E(transition state) – E(precursor complex).
[c]ΔE = E(product) – E(sum of reactants).
[d]Reference 28.

1.183 Å, and the N–H distance (1.424 Å) is still considerably long. The moderate elongation of the O–H distance in **TS1** is in contrast to the considerable elongation of the C–H bond in the transition state of the C–H σ-bond activation of methane.[28] The product **PRD1** takes pseudo-tetrahedral structure, as expected from the d^0 electron configuration of Ti(IV).

Binding energy (BE), activation barrier (E_a), and reaction energy (ΔE) are defined as the energy differences between **PC1** and the sum of reactants, between **PC1** and **TS1**, and between **PRD1** and the sum of reactants, respectively. Negative ΔE value means that the σ-bond activation is exothermic, and vice versa. The BE value is –30.4 (–36.6) kcal/mol, as shown in Table 1, where DFT- and MP4(SDQ)-calculated values are presented without and in parenthesis hereafter, respectively. This large BE value indicates that methanol strongly coordinates with the Ti center to afford **PC1** unlike the methane complex.[28] This difference is interpreted as follows: Because methanol has the lone-pair orbital on the O atom, the charge-transfer (CT) occurs from the lone-pair orbital to the Ti empty d orbital. Also, the O atom forms considerably strong electrostatic interaction with the positively charged Ti(IV) center, because the O atom is much negatively charged. In the precursor complex of methane, the CT occurs from the C–H bonding orbital to the Ti empty d orbital like agostic interaction,[28] but the CT is weak because the C–H bonding-orbital energy is much lower than the O lone pair of CH_3OH. Because the CT occurs from the O lone pair to the Ti empty d orbital in **PC1**, the O–H σ-bonding orbital little participates in the CT, which induces little elongation of the O–H bond; remember that the C–H bond is moderately elongated in the precursor complex of the C–H σ-bond activation, because the CT occurs from the C–H bonding orbital to the Ti empty d orbital.[28] It is also noted that the DFT-calculated BE value is similar to the MP4(SDQ)-calculated one here, though the MP4(SDQ)-calculated BE value is much larger than the DFT-calculated one in the C–H σ-bond activation of methane (see Table 1). This difference would arise from the fact that van der Waals interaction, as well as the CT, also participates in the weak interaction between the C–H bond and the metal center.

In the O–H σ-bond activation, the E_a value is 7.1 (14.6) kcal/mol, which is much smaller than that of the C–H σ-bond activation of methane, as shown in Table 1. The ΔE value is much more negative than in the C–H σ-bond activation of methane. These results suggest that the titanium(IV)–imido complex can be utilized for the O–H σ-bond activation of alcohol.

Geometry and energy changes in the Si–H σ-bond activation of silane SiH_4 by titanium(IV)–imido complex, $[(Me_3SiO)_2Ti(NSiMe_3)]$ (R)

In the reaction, we need to consider two possibilities; in one reaction course (course A), the H atom and the SiH_3 group are bound to the N atom and the Ti center, respectively,

Fig. 2. Geometry changes in Si–H σ-bond activation of silane by $(Me_3SiO)_2Ti(NSiMe_3)$ **R** (reaction course A). In this reaction course, Ti–SiH_3 and N–H bonds were formed. Bond lengths are in angstroms, and bond angles are in degrees. In parenthesis is relative energy calculated by DFT(B3LYP)/BS2 method.

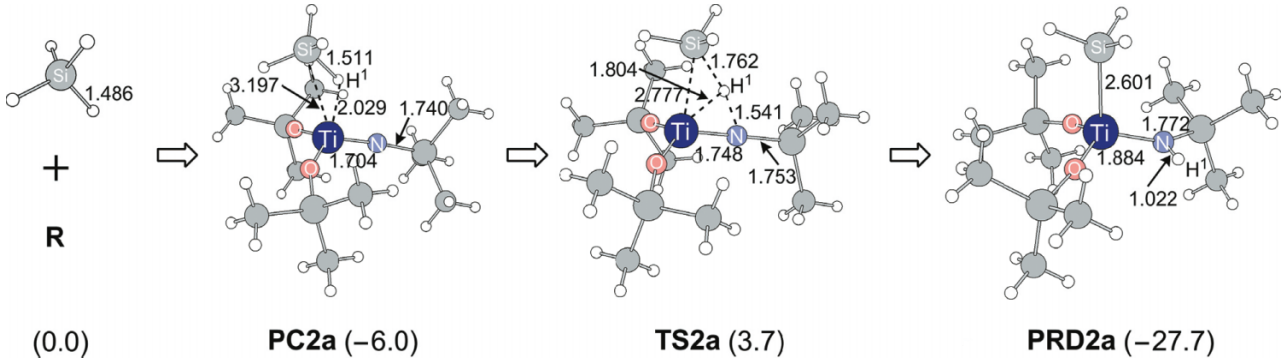

Fig. 3. Geometry changes in Si–H σ-bond activation of silane by $(Me_3SiO)_2Ti(NSiMe_3)$ **R** (reaction course B). In this reaction course, Ti–H and N–SiH_3 bonds were formed. Bond lengths are in angstroms, and bond angles are in degrees. In parenthesis is relative energy calculated by DFT(B3LYP)/BS2 method.

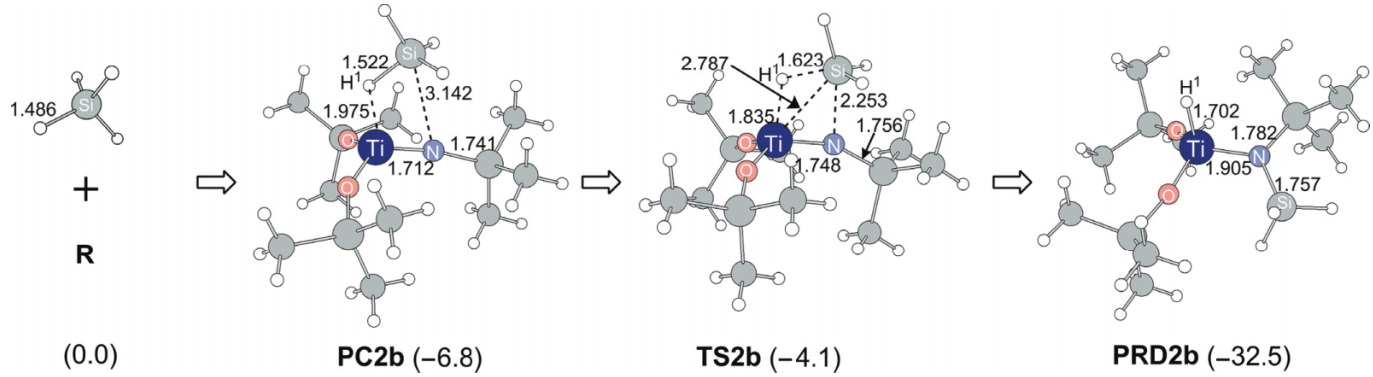

in the product like the C–H σ-bond activation, while in the other course (course B) the H atom and the SiH_3 group are bound to the Ti center and the N atom, respectively, in the product unlike the C–H σ-bond activation. The former reaction occurs through precursor complex **PC2a** and transition state **TS2a** to afford product $(Me_3SiO)_2Ti(SiH_3)[NH(SiMe_3)]$ **PRD2a**, as shown in Fig. 2. In **PC2a**, the Ti–H distance is 2.029 Å, which is shorter than that of the precursor complex in the C–H σ-bond activation of methane. Also, the Si–H distance is moderately elongated to 1.511 Å. These results indicate that the agostic interaction of the Si–H σ-bond with the Ti center more contributes to the stabilization of **PC2a** than does the C–H σ-bond. This is because the Si–H σ-bonding orbital exists at higher energy than the C–H σ-bonding orbital. In **TS2a**, the Si–H bond is moderately elongated to 1.762 Å, and the Ti–Si distance becomes shorter to 2.777 Å, which is slightly longer than that of **PRD2a**. But, the N–H distance is still long. These geometrical features indicate that **TS2a** is more reactant-like than the transition state of the C–H σ-bond activation. **PRD2a** is four-coordinate pseudo-tetrahedral titanium(IV)–alkyl amino complex, as expected.

In the course B, the precursor complex **PC2b** is formed. As shown in Fig. 3, its Si–H distance is moderately elongated to 1.522 Å like that of **PC2a**. The Ti–H distance is 1.975 Å and the Si–N distance is very long. In the transition state **TS2b**, the Si–H distance is moderately elongated to 1.623 Å, and the Ti–H and N–Si distances become shorter to 1.835 Å and 2.253 Å, respectively. The Ti–H distance is somewhat and the N–Si distance is considerably longer than those of the product $(Me_3SiO)_2Ti(H)[N(SiH_3)(SiMe_3)]$ **PRD2b**, indicating that **TS2b** is reactant-like, too. **PRD2b** is a four-coordinate titanium(IV)–hydride disilylamino complex, the geometry of which is pseudo-tetrahedral.

In the reaction course A, the BE value is –6.0 (–13.9) kcal/mol, which is somewhat larger than that of the precursor complex of the C–H σ-bond activation. This is because the CT from the Si–H σ-bonding orbital to the Ti empty d orbital is stronger than that from the C–H σ-bonding orbital to the Ti empty d orbital; remember that the Si–H σ-bonding orbital exists at higher energy than the C–H σ-bonding orbital. The E_a value is 9.7 (15.0) kcal/mol and the ΔE value is –27.7 (–26.4) kcal/mol. This E_a value is much smaller than that of the C–H σ-bond activation, but moderately larger than that of the O–H σ-bond activation. In the reaction course B, the BE value is similar to that of the course A. However, the E_a value (2.7 (4.3) kcal/mol) is much smaller and the ΔE value (–32.5 (–34.1) kcal/mol) is much more negative than those of the course A. These results clearly show that the course B is easier than the course A and the titanium(IV)–hydride disilylamino complex $(Me_3SiO)_2Ti(H)[N(SiH_3)(SiMe_3)]$ **PRD2b** is a product of the Si–H σ-bond activation. It is noted that the E_a value is much smaller than those of the C–H and O–H σ-bond activations, and that the ΔE value is much more negative than that of the C–H σ-bond activation but much less negative than that of the O–H σ-bond activation. The reasons will be discussed below in detail.

Fig. 4. Geometry changes in Si–C σ-bond activation of methylsilane by $(Me_3SiO)_2Ti(NSiMe_3)$ **R**. Bond lengths are in angstroms, and bond angles are in degrees. In parenthesis is relative energy calculated by DFT(B3LYP)/BS2 method.

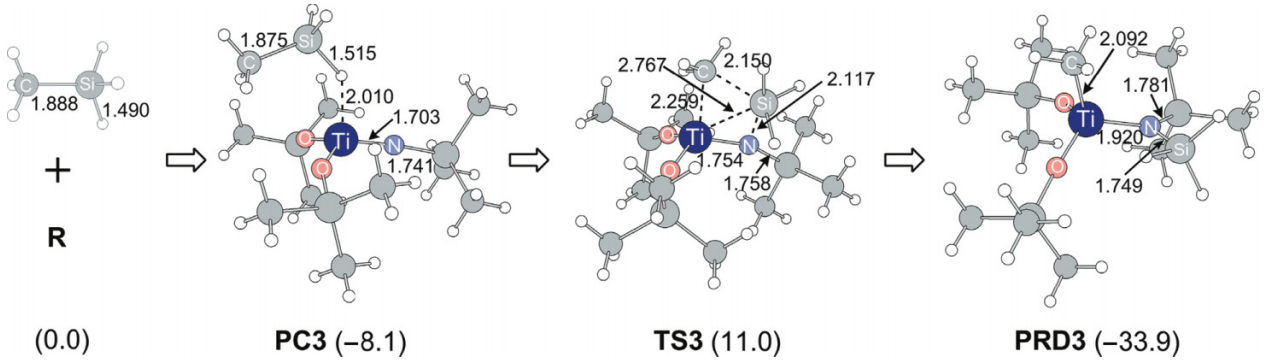

Geometry and energy changes in the Si–C σ-bond activation of methylsilane SiH_3–CH_3 by titanium(IV)–imido complex, $[(Me_3SiO)_2Ti(NSiMe_3)]$ (R)

The precursor complex **PC3** is formed by the CT interaction of the Si–H σ-bond with the Ti empty d orbital like **PC2b**, as shown in Fig. 4. In the transition sate **TS3**, the Ti–C distance is 2.259 Å and the N–Si distance is 2.117 Å, which are not very much longer than those of the product **PRD3**. Also, the Si–C distance is moderately elongated to 2.150 Å. These geometrical features suggest that **TS3** is understood to be more product-like than **TS1** and **TS2b** but more reactant-like than the transition state of the C–H σ-bond activation. The product **PRD3** is a titanium(IV)–methyl disilylamino complex $(Me_3SiO)_2Ti(CH_3)[N(SiH_3)(SiMe_3)]$, the geometry of which is pseudo-tetrahedral, as expected.

The BE value is similar to that of **PC2b**. The E_a value is 19.1 (18.6) kcal/mol and the ΔE value is –33.9 (–37.7) kcal/mol. The E_a value is similar to and the ΔE value is much larger than those of the C–H σ-bond activation reaction. Considering that the C–H σ-bond activation by the titanium(IV)–imido complex was reported experimentally,[25] these E_a and ΔE values suggest that the Si–C σ-bond activation can be achieved by the titanium(IV)–imido complex.

Comparisons of the population changes among O–H, Si–H, and Si–C σ-bond activations

In the O–H σ-bond activation, the H atomic population little decreases and the electron population of the OCH_3 group little increases in the reaction, as shown in Fig. 5. On the other hand, the Ti atomic population increases in **PC1** because of the CT from the O lone pair to the Ti empty d orbital, while it moderately decreases upon going from **PC1** to **PRD1**. These population changes are quite different from those of the C–H σ-bond activation, in which the H atomic population considerably decreases and the electron population of the CH_3 moiety considerably increases. The moderate population changes by the O–H σ-bond activation are easily interpreted in terms of the highly polarized O–H bond of CH_3OH; actually, the positive charge of the H atom and the negative charge of the OCH_3 group are considerably large in CH_3OH. In the product, the H atom is bound to the N atom, the electronegativity of which is not different very much from that of the O atom. The OCH_3 group is anionic in the product because it is bound to the Ti center. Because the OCH_3 group is sufficiently anionic in CH_3OH,

Fig. 5. Population changes in (A) O–H σ-bond activation of methanol, (B) Si–H σ-bond activation of silane (course B), and (C) Si–C σ-bond activation of methylsilane by $(Me_3SiO)_2Ti(NSiMe_3)$ **R**. The positive value represents the increase in electron population, and vice versa. The DFT(B3LYP)/BS2 method was employed.

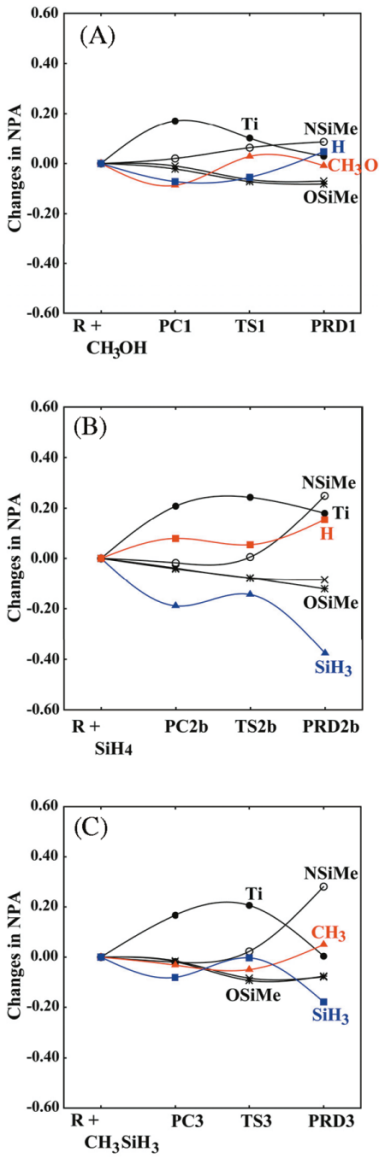

as discussed above, the electron redistribution does not considerably occur in the O–H σ-bond activation.

In the Si–H σ-bond activation via the course B, the total electron population of H–SiH_3 moderately decreases by 0.113 e and the electron population of the Ti–imido complex moderately increases by 0.113 e upon going to **PC2b** from **R**. Also, the Ti atomic population increases. These population changes arise from the fact that the net CT occurs from the Si–H bond to the Ti empty d orbital in **PC2b**, as discussed above. Interestingly, the H atomic population increases and the electron population of SiH_3 decreases upon going to **PC2b** from **R**, as shown in Fig. 5B. The increase in the H atomic population and the decrease in the SiH_3 electron population are interpreted in terms of the polarization, as follows: Because the H atom and the SiH_3 moiety approach the positively charged Ti center and the negatively charged N atom, respectively, in **PC2b**, the polarization occurs so as to increase the H atomic population and decrease the electron population of the SiH_3 moiety. Little population change occurs upon going from **PC2b** to **TS2b**, because **TS2b** is reactant-like; remember that the Si–H distance is elongated by only 0.1 Å upon going to **TS2b** from **PC2b**. However, the populations considerably change upon going to **PRD2b** from **TS2b**, in which the H atomic population considerably increases and the electron population of SiH_3 considerably decreases. These population changes indicate that the Si–H σ-bond cleavage occurs via heterolytic σ-bond activation. It is noted that the increase in the H atomic population and the decrease in the SiH_3 electron population contrast with those of the C–H σ-bond activation of methane in which the H atomic population considerably decreases but the CH_3 electron population considerably increases. The reason is easily interpreted in terms of the polarized Si–H bond; because of the very small electronegativity of the Si element, the H atom is negatively charged and the Si atom is positively charged in SiH_4. As a result, the H atomic population does not need to increase but rather decreases and the SiH_3 electron population does not need to decrease but rather increases.

In the Si–C σ-bond activation, the populations moderately change too, as shown in Fig. 5C. The reason is the same as those of the O–H and Si–H σ-bond activations, as follows: Because the SiH_3 group is bound to the N atom and the CH_3 group is bound to the Ti center in **PRD3**, the SiH_3 group is positively charged and the CH_3 group is negatively charged in **PRD3**. In CH_3–SiH_3, the CH_3 group is negatively charged and the SiH_3 group is positively charged, due to the electronegativity difference between C and Si atoms. As a result, the large population changes do not necessarily occur in the reaction too.

Comparisons of the reactivity among O–H, Si–H, Si–C, and C–H σ-bond activations

First, we wish to discuss the reason why the course B is easier than the course A in the Si–H σ-bond activation. In the course A, the Ti–SiH_3 and N–H bonds are formed, while the Ti–H and N–SiH_3 bonds are formed in the course B. We evaluated these bond energies, considering assumed reactions shown in Scheme 1. Though the DFT-computed bond energies are moderately smaller than the CCSD(T)-computed values, as shown in Table 2, the trends are the same

Scheme 1.

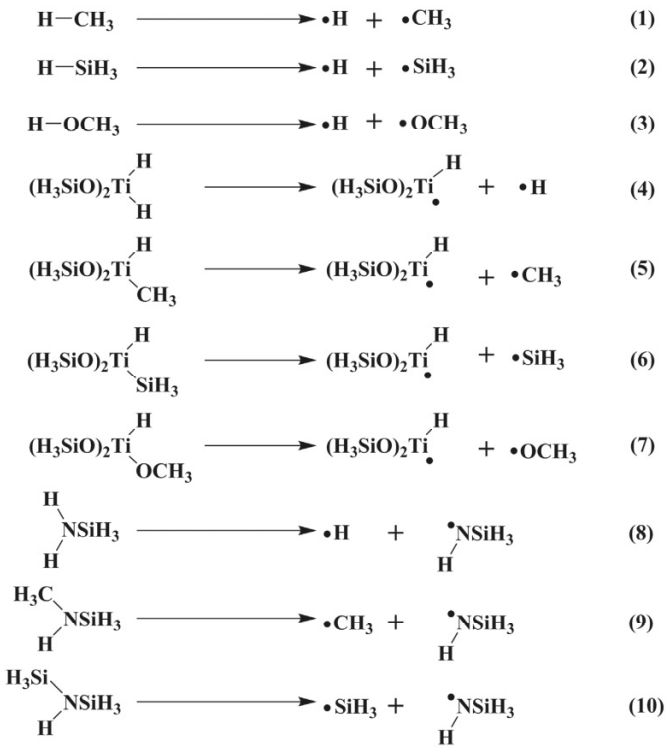

in both computational values. Apparently, the N–H bond energy is moderately larger than the N–SiH_3 bond energy by 11.3 kcal/mol at the DFT level and by 6.1 kcal/mol at the CCSD(T) level. However, the Ti–H bond is much stronger than the Ti–SiH_3 bond by 19.5 kcal/mol and 13.3 kcal/mol at the DFT and CCSD(T) levels, respectively. As a result, the course B is easier than the course A.

The O–H σ-bond activation is more exothermic than the Si–H σ-bond activation. In the O–H σ-bond activation, the Ti–OCH_3 and N–H bonds are formed. Though the O–H bond is much stronger than the Si–H bond, the difference (12.4 kcal/mol) is much smaller than the difference between the sum of Ti–OCH_3 and N–H bond energies and that of the Ti–H and N–SiH_3 bond energies, because the Ti–OCH_3 bond is much stronger than the Ti–H bond. This is the reason why the H–OCH_3 σ-bond activation is more exothermic than the Si–H σ-bond activation. However, the O–H σ-bond activation needs larger E_a value than the Si–H σ-bond activation unexpectedly from the above-described exothermicity. One of the important factors to determine the E_a value is the strength of the σ-bond to be broken. The O–H bond is considerably stronger than the Si–H bond. In the transition state, the O–H bond should be cleaved, while the Ti–OCH_3 bond is not completely formed yet. Actually, the elongation of the O–H bond to 1.183 Å gives rise to larger destabilization energy than that of the Si–H bond to 1.623 Å, as shown in Table 3; remember the O–H distance is 1.183 Å and the Si–H distance is 1.623 Å in the transition state. The difference in the destabilization energy between CH_3OH and SiH_4 is similar to the difference in E_a value. Thus, it is concluded that the O–H σ-bond activation needs larger E_a value than the Si–H σ-bond activation because the strong O–H bond should be broken.

Table 2. Bond energies calculated with DFT(B3LYP), MP2-MP4(SDQ), and CCSD(T)/BS2 methods (in kcal/mol unit).

	DFT(B3LYP)	MP2	MP3	MP4(DQ)	MP4(SDQ)	CCSD(T)
Ti–H	65.4	69.9	62.0	64.4	70.1	67.5
Ti–SiH_3	45.9	59.4	47.4	49.0	55.9	54.2
Ti–OCH_3	108.7	130.5	105.6	109.5	119.5	116.8
Ti–CH_3	68.4	83.0	69.0	69.3	75.2	74.5
N–H	115.9	116.9	114.0	114.2	114.2	114.5
N–SiH_3	104.6	114.4	107.9	107.5	107.8	108.4
N–CH_3	100.3	108.4	101.0	100.4	100.8	102.1
C–H	118.4	114.5	115.0	114.9	115.1	115.5
Si–H	94.8	90.6	92.9	93.2	93.3	93.4
O–H	107.2	111.0	106.5	107.1	107.0	107.3
Si–C	96.1	99.0	96.7	95.6	95.9	96.5

Table 3. Distortion energies of CH_3OH and SiH_4 in **TS1** and **TS2b**, respectively (in kcal/mol unit).

	CH_3OH	SiH_4
DFT(B3LYP)	21.3	16.6
MP2	23.2	18.8
MP3	24.2	18.5
MP4(DQ)	23.6	18.4
MP4(SDQ)	23.3	18.3
CCSD(T)	22.6	17.9

Then, we will compare the O–H σ-bond activation with the C–H σ-bond activation. In the C–H σ-bond activation, the Ti–CH_3 and N–H bonds are formed. Though the C–H bond is moderately stronger than the O–H bond, the Ti–CH_3 bond is much weaker than the Ti–OCH_3 bond. Thus, the O–H σ-bond activation occurs much easier than the C–H σ-bond activation.

The difference between the Si–H and C–H σ-bond activations is easily interpreted in terms of bond energy too, as follows: In the Si–H σ-bond activation, the Ti–H and N–SiH_3 bonds are formed. Though the N–SiH_3 bond is somewhat weaker than the N–H bond and the Ti–H bond is as strong as the Ti–CH_3 bond, the Si–H bond is much weaker than the C–H bond. As a result, the Si–H σ-bond activation occurs easier than the C–H σ-bond activation.

It is worth investigating the reason why the C–H σ-bond activation occurs via the course A, which leads to the formation of the Ti–CH_3 and N–H bonds,[28] but the Si–H σ-bond activation occurs via the course B, leading to the formation of the Ti–H and N–SiH_3 bonds. One of the reasons is that the N–SiH_3 bond is stronger than the N–CH_3 bond. Another reason is that the Ti–SiH_3 bond is much weaker than the Ti–CH_3 bond. This is because the electropositive Si element tends to form a strong bond with the electronegative N atom but a weak bond with the electropositive Ti atom. Also, the electronegative C element tends to form a strong bond with the electropositive Ti center. Because of the formation of this strong N–SiH_3 bond and the weak Ti–SiH_3 bond, the Si–H σ-bond activation occurs via the course B. On the other hand, because the Ti–CH_3 and N–H bonds are stronger than the Ti–H and N–CH_3 bonds, respectively, the C–H σ-bond activation occurs via the course A.

Scheme 2.

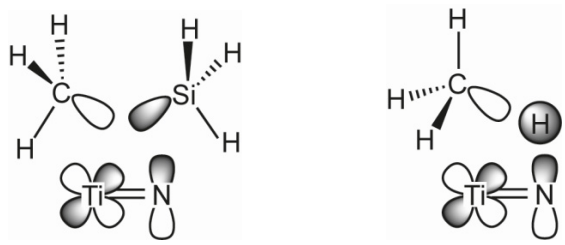

(A) Si–C σ-bond activation (B) C–H σ-bond activation

In the Si–C σ-bond activation, the MP4(SDQ)-calculated E_a value is similar to and the DFT-calculated value is moderately larger than those of the C–H σ-bond activation, while the former reaction is more exothermic than the latter one. In the Si–C σ-bond activation, not the bond energy but another factor plays an important role to determine the E_a value. This is the same as the difference between the C–H and C–C σ-bond activations.[8a] In general, the C–C σ-bond activation of ethane is much more difficult than the C–H σ-bond activation, though the exothermicity is similar between them. The difference between the C–H and C–C σ-bond activations was interpreted in terms of the distortion of valence orbital.[4,5a,45] The difference here is interpreted in the same way, as follows: In the Si–C σ-bond activation, the CH_3 and SiH_3 groups must change their directions toward the Ti center and the N atom, respectively, to form Ti–CH_3 and N–SiH_3 bonds, as shown in Scheme 2, because the valence orbitals of CH_3 and SiH_3 are sp^3-like. Such direction changes give rise to considerably large distortion energy. On the other hand, the C–H σ-bond activation, only the CH_3 group must change its direction toward the Ti center but the H atom can interact with both CH_3 and imido groups because of the spherical 1s orbital. As a result, the Si–C σ-bond activation needs larger E_a value than the C–H σ-bond activation.

Reasons why bond energy increases in the order $Ti–SiH_3 < Ti–H < Ti–CH_3 < Ti–OCH_3$

Because these bond energies are important factor to determine the reactivity of the σ-bond activation, it is worthy investigating the reason why bond energy increases in the

Table 4. Orbital energies of $^{\bullet}TiH(OSiH_3)_2$, $^{\bullet}CH_3$, $^{\bullet}SiH_3$, $^{\bullet}OCH_3$, $^{\bullet}NH(SiH_3)$, and $^{\bullet}H$ calculated with DFT(B3LYP)/BS2 and HF/BS2 (in eV).

	$^{\bullet}TiH(OSiH_3)_2$	$^{\bullet}CH_3$	$^{\bullet}SiH_3$	$^{\bullet}OCH_3$	$^{\bullet}NH(SiH_3)$	$^{\bullet}H$
SOMO (Kohn–Sham)	–5.56	–7.23	–6.24	–9.33	–9.18	–8.75
SOMO (Hartree–Fock)	–10.68	–11.63	–9.29	–14.38	–12.93	–13.60

above order. The covalent bond energy ΔE_{cov} is approximately represented by eq. [1],[46] as follows:

If the $|\varepsilon_A - \varepsilon_B|$ value is much larger than the $|\beta_{AB}|$ value, eq. [1] can be further simplified to eq. [2]. In the above equations, ε_A and ε_B are valence orbital energies of A and B, respectively, and β_{AB} is resonance integral between valence orbitals of A and B. As shown in Table 4, the valence orbital energy of $^{\bullet}TiH(OSiH_3)_2$ is calculated to be –5.56 eV, where we employ Kohn–Sham orbital energy. This is much higher than those of $^{\bullet}CH_3$, $^{\bullet}SiH_3$, and $^{\bullet}OCH_3$. Because the valence orbital energy becomes lower in the order $^{\bullet}SiH_3 > {}^{\bullet}CH_3 > {}^{\bullet}OCH_3$, as expected from their electronegativities, the $|\varepsilon_A - \varepsilon_B|$ value increases in the order $^{\bullet}SiH_3 < {}^{\bullet}CH_3 < {}^{\bullet}OCH_3$. Thus, the Ti–$SiH_3$ bond is the weakest and the Ti–OCH_3 is the strongest in these three bonds.[47] In other words, the electronegative group forms strong bond with the Ti center. Also, the Ti–H bond is much stronger than the Ti–SiH_3 bond, because the H 1s orbital is at lower energy (–8.75 eV) than the $^{\bullet}SiH_3$ valence orbital and the $|\varepsilon_A - \varepsilon_B|$ value for the H 1s orbital is considerably larger than that for the $^{\bullet}SiH_3$ valence orbital. Though the H 1s orbital energy is lower than the $^{\bullet}CH_3$ valence orbital, the Ti–H bond is moderately weaker than the Ti–CH_3 bond. This is probably because the $|\beta_{AB}|$ value is larger for the Ti–CH_3 pair than that for the Ti–H pair. It is likely that the CH_3 sp^3 orbital more expands toward the Ti center than the H 1s orbital to provide the larger $|\beta_{AB}|$ value for the Ti–CH_3 pair. Though Hatree–Fock orbital energies are much different from Kohn–Sham orbital energies, the trend is the same between them (see Table 4).

$$[1] \qquad \Delta E_{cov} = \sqrt{(\varepsilon_A - \varepsilon_B)^2 + 4\beta_{AB}^2}$$

$$[2] \qquad \Delta E_{cov} \approx |\varepsilon_A - \varepsilon_B| + \frac{2\beta_{AB}^2}{|\varepsilon_A - \varepsilon_B|}$$

The same explanation can be presented on the N–X bond energy except for the N–H bond energy. The valence orbital energy of $^{\bullet}NH(SiH_3)$ is calculated at –9.18 eV, which is lower than the valence orbital of $^{\bullet}H$, $^{\bullet}CH_3$, and $^{\bullet}SiH_3$. Because the difference in orbital energy between $^{\bullet}CH_3$ and $^{\bullet}NH(SiH_3)$ is the smallest, the N–CH_3 bond is the weakest in these three bonds, as seen in Table 2. Because the energy difference between valence orbitals of $^{\bullet}NH(SiH_3)$ and $^{\bullet}SiH_3$ is the largest, the N–SiH_3 bond is strongest. Though the valence orbitals of $^{\bullet}SiH_3$ and $^{\bullet}CH_3$ are higher than that of the H atom, the N–H bond is stronger than the N–SiH_3 and N–CH_3 bonds. It is likely that this result arises from the larger $|\beta_{AB}|$ value for the N–H pair because the N–H distance is much shorter than the N–C and N–Si distances due to the small size of H atom.

From these results, we wish to present theoretical prediction that the X–H σ-bond activation by the titanium(IV)–imido complex becomes easier as the X group becomes electronegative, when the X and H are bound to the Ti and N atoms, respectively, in the product. However, the X–H σ-bond activation becomes easier as the X group becomes electropositive, when the X and H are bound to the N and Ti atoms, respectively, in the product.

Conclusions

The O–H σ-bond activation of methanol, the Si–H σ-bond activation of silane, and the Si–C σ-bond activation of methysilane by $(Me_3SiO)_2Ti(NSiMe_3)$ **R** were theoretically investigated with the DFT and MP2 to MP4(SDQ) methods. The σ-bond activations of methanol and silane (course B) occur much easier than the C–H σ-bond activation to afford the products $(Me_3SiO)_2Ti(OCH_3)[NH(SiMe_3)]$ and $(Me_3SiO)_2Ti(H)[N(SiH_3)(SiMe_3)]$, respectively. Their activation barriers (E_a) are 7.1 (14.6) kcal/mol and 2.7 (4.3) kcal/mol, respectively, and their exothermicities are 65.8 (61.4) kcal/mol and 32.5 (34.1) kcal/mol. The very large exothermicity and moderate E_a value of the O–H σ-bond activation arise from the formation of the very strong Ti–OCH_3 bond. The very small E_a value and the considerably large exothermicity of the Si–H σ-bond activation arise from the weak Si–H bond.

The Si–C σ-bond activation, which is in general considered to be difficult, occurs with moderate activation barrier and considerably large exothermicity. These results arise from the formations of considerably strong Ti–CH_3 and N–SiH_3 bonds.

In the Si–H σ-bond activation, the other reaction course (course A) leading to the formation of $(Me_3SiO)_2Ti(SiH_3)[NH(SiMe_3)]$ was also investigated. However, the activation barrier is larger and the exothermicity is smaller than those of the course B leading to $(Me_3SiO)_2Ti(H)[N(SiH_3)(SiMe_3)]$. This result is understood in terms of the bond energy; the Ti–SiH_3 bond is considerably weaker than the Ti–H bond, while the N–SiH_3 bond is moderately stronger than the N–H bond. These results of the weak Ti–SiH_3 bond and the strong N–SiH_3 bond arise from the fact that the Si element is considerably electropositive.

From these results, we wish to theoretically propose that the titanium(IV)–imido complex can be utilized for the O–H, Si–H, and Si–C σ-bond activation reactions. In the X–H σ-bond activation (X = CH_3, OCH_3, and so forth), the reaction becomes easier as the electronegativity of X increases, when the X and H are bound to the Ti center and the N atom, respectively, in the product. However, the X–H σ-bond activation becomes easier as the X becomes electropositive, when the X and H are bound to the N atom and the Ti center, respectively, in the product. Considering these results, one can construct the reaction system leading to the formation of the Ti–X species through the σ-bond activation of H–X.

Acknowledgement

This work was financially supported by Grant-in-Aids on basic research (No. 15350012), Priority Areas for "Molecular Theory for Real Systems" (No. 461), and National Research Grid Initiative (NAREGI) project from the Ministry of Education, Science, Sports, and Culture. One of the authors (N. Ochi) thanks the Grant-in-Aid for Japan Society for the Promotion of Science (JSPS) Fellows. Some of theoretical calculations were performed with SGI Altix4700 workstations of Institute for Molecular Science (Okazaki, Japan), and some of them were carried out with PC cluster computers of our laboratory.

References

(1) (a) Recent reviews: Arndtsen, B. A.; Bergman, R. G.; Mobley, T. A.; Peterson, T. H. *Acc. Chem. Res.* **1995**, *28* (3), 154–162. doi:10.1021/ar00051a009.; (b) Shilov, A. E.; Shul'pin, G. B. *Chem. Rev.* **1997**, *97* (8), 2879–2932. doi:10.1021/cr9411886. PMID:11851481.; (c) Jones, W. D. *Top. Organomet. Chem.* **1999**, *3*, 9–46. doi:10.1007/3-540-68525-1_2.; (d) Sen, A. *Top. Organomet. Chem.* **1999**, *3*, 81–95. doi:10.1007/3-540-68525-1_4.; (e) Crabtree, R. H. J. Chem. Soc. Dalton Trans. 2001, 2437; (f) Labinger, J. A.; Bercaw, J. E. *Nature* **2002**, *417* (6888), 507–514. doi:10.1038/417507a. PMID:12037558.; (g) Sakaki, S.; Ochi, N.; Ohnishi, Y.-y. In *Computational Modeling for Homogeneous and Enzymatic Catalysis: A Knowledge-base for Designing Efficient Catalysts;* Morokuma, K. and Musaev, D. G., Eds.; Wiley-VCH: Weinheim, 2008; p. 265.

(2) Saillard, J.-Y.; Hoffmann, R. *J. Am. Chem. Soc.* **1984**, *106* (7), 2006–2026. doi:10.1021/ja00319a020.

(3) (a) Obara, S.; Kitaura, K.; Morokuma, K. *J. Am. Chem. Soc.* **1984**, *106* (24), 7482–7492. doi:10.1021/ja00336a030.; (b) Koga, N.; Morokuma, K. *J. Phys. Chem.* **1990**, *94* (14), 5454–5462. doi:10.1021/j100377a007.; (c) Koga, N.; Morokuma, K. *J. Am. Chem. Soc.* **1993**, *115* (15), 6883–6892. doi:10.1021/ja00068a053.; (d) Matsubara, T.; Koga, N.; Musaev, D. G.; Morokuma, K. *J. Am. Chem. Soc.* **1998**, *120* (48), 12692–12693. doi:10.1021/ja9816943.

(4) (a) Low, J. J.; Goddard, W. A., III. *J. Am. Chem. Soc.* **1986**, *108* (20), 6115–6128. doi:10.1021/ja00280a003.; (b) Low, J. J.; Goddard, W. A., III. *Organometallics* **1986**, *5* (4), 609–622. doi:10.1021/om00135a001.

(5) (a) Blomberg, M. R. A.; Siegbahn, P. E. M.; Nagashima, U.; Wennerberg, J. *J. Am. Chem. Soc.* **1991**, *113* (2), 424–433. doi:10.1021/ja00002a007.; (b) Svensson, M.; Blomberg, M. R. A.; Siegbahn, P. E. M. *J. Am. Chem. Soc.* **1991**, *113* (18), 7076–7077. doi:10.1021/ja00018a077.; (c) Blomberg, M. R. A.; Siegbahn, P. E. M.; Svensson, M. *J. Am. Chem. Soc.* **1992**, *114* (15), 6095–6102. doi:10.1021/ja00041a030.; (d) Siegbahn, P. E. M.; Blomberg, M. R. A.; Svensson, M. *J. Am. Chem. Soc.* **1993**, *115* (10), 4191–4200. doi:10.1021/ja00063a042.; (e) Blomberg, M. R. A.; Siegbahn, P. E. M.; Svensson, M. *J. Phys. Chem.* **1994**, *98* (8), 2062–2071. doi:10.1021/j100059a014.; (f) Siegbahn, P. E. M.; Blomberg, M. R. A. *Organometallics* **1994**, *13* (1), 354–363. doi:10.1021/om00013a052.; (g) Siegbahn, P. E. M. *Organometallics* **1994**, *13* (7), 2833–2842. doi:10.1021/om00019a045.; (h) Siegbahn, P. E. M.; Svensson, M. *J. Am. Chem. Soc.* **1994**, *116* (22), 10124–10128. doi:10.1021/ja00101a034.; (i) Siegbahn, P. E. M. *J. Am. Chem. Soc.* **1996**, *118* (6), 1487–1496. doi:10.1021/ja952338c.; (j) Siegbahn, P. E. M.; Crabtree, R. H. *J. Am. Chem. Soc.* **1996**, *118* (18), 4442–4450. doi:10.1021/ja9541894.

(6) (a) Ziegler, T.; Tschinke, V.; Fan, L.; Becke, A. D. *J. Am. Chem. Soc.* **1989**, *111* (26), 9177–9185. doi:10.1021/ja00208a007.; (b) Bickelhaupt, F. M.; Ziegler, T. *Organometallics* **1995**, *14* (5), 2288–2296. doi:10.1021/om00005a030.

(7) (a) Song, J.; Hall, M. B. *Organometallics* **1993**, *12* (8), 3118–3126. doi:10.1021/om00032a039.; (b) Jiménez–Cataño, R.; Hall, M. B. *Organometallics* **1996**, *15* (7), 1889–1897. doi:10.1021/om950416z.; (c) Niu, S.-Q.; Hall, M. B. *J. Am. Chem. Soc.* **1998**, *120* (24), 6169–6170. doi:10.1021/ja980297p.

(8) (a) Sakaki, S.; Ieki, M. *J. Am. Chem. Soc.* **1993**, *115* (6), 2373–2381. doi:10.1021/ja00059a036.; (b) Sakaki, S.; Biswas, B.; Sugimoto, M. *J. Chem. Soc., Dalton Trans.* **1997**, (5): 803–810. doi:10.1039/a605720i.; (c) Sakaki, S.; Biswas, B.; Sugimoto, M. *Organometallics* **1998**, *17* (7), 1278–1289. doi:10.1021/om970705i.; (d) Sakaki, S.; Mizoe, M.; Musashi, Y.; Biswas, B.; Sugimoto, M. *J. Phys. Chem. A* **1998**, *102* (41), 8027–8036. doi:10.1021/jp981899y.; (e) Biswas, B.; Sugimoto, M.; Sakaki, S. *Organometallics* **2000**, *19* (19), 3895–3908. doi:10.1021/om000002s.; (f) Sakaki, S. *Top. Organomet. Chem.* **2005**, *12*, 31.

(9) Hinderling, C.; Feichtinger, D.; Plattner, D. A.; Chen, P. *J. Am. Chem. Soc.* **1997**, *119* (44), 10793–10804. doi:10.1021/ja970995u.

(10) Su, M.-D.; Chu, S.-Y. *J. Am. Chem. Soc.* **1997**, *119* (23), 5373–5383. doi:10.1021/ja961847r.

(11) Espinosa-García, J.; Corchado, J. C.; Truhlar, D. G. *J. Am. Chem. Soc.* **1997**, *119* (41), 9891–9896. doi:10.1021/ja972209r.

(12) Hill, G. S.; Puddephatt, R. J. *Organometallics* **1998**, *17* (8), 1478–1486. doi:10.1021/om9709291.

(13) (a) Heiberg, H.; Swang, O.; Ryan, O. B.; Gropen, O. *J. Phys. Chem. A* **1999**, *103* (48), 10004–10008. doi:10.1021/jp992484v.; (b) Heiberg, H.; Johansson, L.; Gropen, O.; Ryan, O. B.; Swang, O.; Tilset, M. *J. Am. Chem. Soc.* **2000**, *122* (44), 10831–10845. doi:10.1021/ja0019171.

(14) Ustynyuk, Y. A.; Ustynyuk, L. Y.; Laikov, D. N.; Lunin, V. V. *J. Organomet. Chem.* **2000**, *597* (1-2), 182–189. doi:10.1016/S0022-328X(99)00686-5.

(15) Bartlett, K. L.; Goldberg, K. I.; Borden, W. T. *Organometallics* **2001**, *20* (13), 2669–2678. doi:10.1021/om010072e.

(16) (a) Maron, L.; Eisenstein, O. *J. Am. Chem. Soc.* **2001**, *123* (6), 1036–1039. doi:10.1021/ja0033483. PMID:11456656.; (b) Maron, L.; Perrin, L.; Eisenstein, O. *J. Chem. Soc., Dalton Trans.* **2002**, (4): 534–539. doi:10.1039/b107698c.; (c) Perrin, L.; Maron, L.; Eisenstein, O. *Inorg. Chem.* **2002**, *41* (17), 4355–4362. doi:10.1021/ic011275y. PMID:12184751.; (d) Barros, N., Eisenstein, O.; Maron, L. *J. Chem. Soc., Dalton Trans.* **2006**, 3052.

(17) (a) Moritani, I.; Fujiwara, Y. *Tetrahedron Lett.* **1967**, *8* (12), 1119–1122. doi:10.1016/S0040-4039(00)90648-8.; (b) Fujiwara, Y.; Takaki, K.; Taniguchi, Y. *Synlett* **1996**, *1996* (07), 591–599; and reference therein. doi:10.1055/s-1996-5541.

(18) (a) Periana, R. A.; Taube, D. J.; Evitt, E. R.; Löffler, D. G.; Wentrcek, P. R.; Voss, G.; Masuda, T. *Science* **1993**, *259* (5093), 340–343. doi:10.1126/science.259.5093.340. PMID:17832346.; (b) Periana, R. A.; Taube, D. J.; Gamble, S.; Taube, H.; Satoh, T.; Fujii, H. *Science* **1998**, *280* (5363), 560–564. doi:10.1126/science.280.5363.560. PMID:9554841.

(19) Matsumoto, T.; Taube, D. J.; Periana, R. A.; Taube, H.; Yoshida, H. *J. Am. Chem. Soc.* **2000**, *122* (30), 7414–7415. doi:10.1021/ja0009830.

(20) Siegbahn, P. E. M.; Crabtree, R. H. *J. Am. Chem. Soc.* **1996**, *118* (18), 4442–4450. doi:10.1021/ja9541894.
(21) Biswas, B.; Sugimoto, M.; Sakaki, S. *Organometallics* **2000**, *19* (19), 3895–3908. doi:10.1021/om000002s.
(22) (a) Ziegler, T.; Li, J. *Organometallics* **1995**, *14* (1), 214–223. doi:10.1021/om00001a033.; (b) Gilbert, T. M.; Hristov, I.; Ziegler, T. *Organometallics* **2001**, *20* (6), 1183–1189. doi:10.1021/om0007264.
(23) (a) Kua, J.; Xu, X.; Periana, R. A.; Goddard, W. A., III. *Organometallics* **2002**, *21* (3), 511–525. doi:10.1021/om0101691.; (b) Xu, X.; Kua, J.; Periana, R. A.; Goddard, W. A., III. *Organometallics* **2003**, *22* (10), 2057–2068. doi:10.1021/om0202165.
(24) (a) Böhme, D. K.; Schwarz, H. *Angew. Chem. Int. Ed.* **2005**, *44*, 2336 doi:10.1002/anie.200461698.; (b) Schlangen, M.; Schwarz, H. 2007, 46, 5614.; (c) Paul, A.; Musgrave, C. B. *Organometallics* **2007**, *26* (4), 793–809. doi:10.1021/om060465j.
(25) (a) Bennett, J. L.; Wolczanski, P. T. *J. Am. Chem. Soc.* **1994**, *116* (5), 2179–2180. doi:10.1021/ja00084a082.; (b) Bailey, B. C.; Fan, H.; Baum, E. W.; Huffman, J. C.; Baik, M.–H.; Mindiola, D. J. *J. Am. Chem. Soc.* **2005**, *127* (46), 16016–16017. doi:10.1021/ja0556934. PMID:16287275.
(26) (a) Cundari, T. R. *J. Am. Chem. Soc.* **1992**, *114* (26), 10557–10563. doi:10.1021/ja00052a060.; (b) Cundari, T. R. *Organometallics* **1993**, *12* (6), 1998–2000. doi:10.1021/om00030a003.; (c) Cundari, T. R. *Organometallics* **1993**, *12* (12), 4971–4978. doi:10.1021/om00036a042.; (d) Cundari, T. R. *J. Am. Chem. Soc.* **1994**, *116* (1), 340–347. doi:10.1021/ja00080a039.; (e) Benson, M. T.; Cundari, T. R.; Moody, E. W. *J. Organomet. Chem.* **1995**, *504* (1-2), 1–13. doi:10.1016/0022-328X(95)05566-8.; (f) Cundari, T. R.; Matsunaga, N.; Moody, E. W. *J. Phys. Chem.* **1996**, *100* (16), 6475–6483. doi:10.1021/jp952678k.; (g) Cundari, T. R.; Klinckman, T. R.; Wolczanski, P. T. *J. Am. Chem. Soc.* **2002**, *124* (7), 1481–1487. doi:10.1021/ja016248l. PMID:11841318.
(27) Bailey, B. C.; Fan, H.; Baum, E. W.; Huffman, J. C.; Baik, M.–H.; Mindiola, D. J. *J. Am. Chem. Soc.* **2005**, *127* (46), 16016–16017. doi:10.1021/ja0556934. PMID:16287275.
(28) Ochi, N.; Nakao, Y.; Sato, H.; Sakaki, S. *J. Am. Chem. Soc.* **2007**, *129* (27), 8615–8624. doi:10.1021/ja071825c. PMID:17579411.
(29) (a) Zhao, J.; Goldman, A. S.; Hartwig, J. F. *Science* **2005**, *307* (5712), 1080–1082. doi:10.1126/science.1109389. PMID:15718464.; (b) Kanzelberger, M.; Zhang, X.; Emge, T. J.; Goldman, A. S.; Zhao, J.; Incarvito, C.; Hartwig, J. F. *J. Am. Chem. Soc.* **2003**, *125* (45), 13644–13645. doi:10.1021/ja037363u. PMID:14599186.
(30) Becke, A. D. *Phys. Rev.* A **1988**, *38*, 3098.
(31) Becke, A. D. *J. Chem. Phys.* **1993**, *98* (7), 5648. doi:10.1063/1.464913.
(32) Lee, C.; Yang, W.; Parr, R. G. *Phys. Rev.* B **1988**, *37*, 785.
(33) Couty, M.; Hall, M. B. *J. Comput. Chem.* **1996**, *17* (11), 1359–1370. doi:10.1002/(SICI)1096-987X(199608)17:11<1359::AID-JCC9>3.0.CO;2-L.
(34) (a) Hariharan, P. C.; Pople, J. A. *Theor. Chim. Acta* **1973**, *28* (3), 213–222. doi:10.1007/BF00533485.; (b) Hariharan, P. C.; Pople, J. A. *Mol. Phys.* **1974**, *27* (1), 209–214. doi:10.1080/00268977400100171.
(35) Hehre, W. J.; Ditchfield, R.; Pople, J. A. *J. Chem. Phys.* **1972**, *56* (5), 2257. doi:10.1063/1.1677527.
(36) Martin, J. M. L.; Sundermann, A. *J. Chem. Phys.* **2001**, *114* (8), 3408. doi:10.1063/1.1337864.
(37) Krishnan, R.; Binkley, J. S.; Seeger, R.; Pople, J. A. *J. Chem. Phys.* **1980**, *72* (1), 650. doi:10.1063/1.438955.
(38) McLean, A. D.; Chandler, G. S. *J. Chem. Phys.* **1980**, *72* (10), 5639. doi:10.1063/1.438980.
(39) Blaudeau, J.-P.; McGrath, M. P.; Curtiss, L. A.; Radom, L. *J. Chem. Phys.* **1997**, *107* (13), 5016. doi:10.1063/1.474865.
(40) Frisch, M. J.; Trucks, G. W.; Schlegel, H. B.; Scuseria, G. E.; Robb, M. A.; Cheeseman, J. R.; Montgomery, J. A., Jr.; Vreven, T.; Kudin, K. N.; Burant, J. C.; Millam, J. M.; Iyengar, S. S.; Tomasi, J.; Barone, V.; Mennucci, B.; Cossi, M.; Scalmani, G.; Rega, N.; Petersson, G. A.; Nakatsuji, H.; Hada, M.; Ehara, M.; Toyota, K.; Fukuda, R.; Hasegawa, J.; Ishida, M.; Nakajima, T.; Honda, Y.; Kitao, O.; Nakai, H.; Klene, M.; Li, X.; Knox, J. E.; Hratchian, H. P.; Cross, J. B.; Bakken, V.; Adamo, C.; Jaramillo, J.; Gomperts, R.; Stratmann, R. E.; Yazyev, O.; Austin, A. J.; Cammi, R.; Pomelli, C.; Ochterski, J. W.; Ayala, P. Y.; Morokuma, K.; Voth, G. A.; Salvador, P.; Dannenberg, J. J.; Zakrzewski, V. G.; Dapprich, S.; Daniels, A. D.; Strain, M. C.; Farkas, O.; Malick, D. K.; Rabuck, A. D.; Raghavachari, K.; Foresman, J. B.; Ortiz, J. V.; Cui, Q.; Baboul, A. G.; Clifford, S.; Cioslowski, J.; Stefanov, B. B.; Liu, G.; Liashenko, A.; Piskorz, P.; Komaromi, I.; Martin, R. L.; Fox, D. J.; Keith, T.; Al-Laham, M. A.; Peng, C. Y.; Nanayakkara, A.; Challacombe, M.; Gill, P. M. W.; Johnson, B.; Chen, W.; Wong, M. W.; Gonzalez, C.; Pople, J. A. *Gaussina 03,* revision C.02; Gaussian, Inc.: Wallingford, CT, 2004.
(41) Reed, A. E.; Curtiss, L. A.; Weinhold, F. *Chem. Rev.* **1988**, *88* (6), 899–926. doi:10.1021/cr00088a005.
(42) (a) Flükiger, P.; Lüthi, H. P.; Portann, S.; Weber, J. *MOLEKEL,* v.4.3; Scientific Computing: Manno, Switzerland, 2002; (b) Portman, S.; Lüthi, H. P. *Chimia (Aarau)* **2000**, *54*, 766.
(43) (a) Haymore, B. L.; Maatta, E. A.; Wentworth, R. D. *J. Am. Chem. Soc.* **1979**, *101* (8), 2063–2068. doi:10.1021/ja00502a021.; (b) Parkin, G.; van Asselt, A.; Leahy, D. J.; Whinnery, L.; Hua, N. G.; Quan, R. W.; Henling, L. M.; Schaefer, W. P.; Santarsiero, B. D.; Bercaw, J. E. *Inorg. Chem.* **1992**, *31* (1), 82–85. doi:10.1021/ic00027a016.
(44) Bennett, J. L.; Wolczanski, P. T. *J. Am. Chem. Soc.* **1997**, *119* (44), 10696–10719. doi:10.1021/ja9707419.
(45) Blomberg, M. R. A.; Brandemark, U.; Siegbahn, P. E. M. *J. Am. Chem. Soc.* **1983**, *105* (17), 5557–5563. doi:10.1021/ja00355a005.
(46) Sakaki, S.; Kai, S.; Sugimoto, M. *Organometallics* **1999**, *18* (23), 4825–4837. doi:10.1021/om990461x.
(47) Overlap integral also decreases in the order Ti–O ≈ Ti–C >> Ti–Si.

The flattening phase transition in systems of trapped ions

Taunia L. L. Closson and Marc R. Roussel

Abstract: When the anisotropy of a harmonic ion trap is increased, the ions eventually collapse into a two-dimensional structure consisting of concentric shells of ions. This collapse generally behaves like a second-order phase transition. A graph of the critical value of the anisotropy parameter vs. the number of ions displays substructure closely related to the inner-shell configurations of the clusters. The critical exponent for the order parameter of this phase transition (maximum extent in the z direction) was found computationally to have the value $\beta = 1/2$. A second critical exponent related to displacements perpendicular to the z axis was found to have the value $\delta = 1$. Using these estimates of the critical exponents, we derive an equation that relates the amplitudes of the displacements of the ions parallel to the x–y plane to the amplitudes along the z axis during the flattening process.

Key words: ion trap, flattening, phase transition, critical exponent.

Résumé : Quand on augmente l'anisotropie d'un piège ionique, les ions adoptent tôt ou tard une structure aplatie formée de couches concentriques d'ions. Cet aplatissement se comporte comme une transition de phase du deuxième ordre. Un graphe de l'anisotropie critique contre le nombre d'ions démontre une organisation reliée à la configuration de la couche interne de l'amas. Nos calculs numériques démontrent que l'exposant critique associé au paramètre d'ordre de cette transition de phase (l'étendue maximale le long de l'axe z) a la valeur $\beta = 1/2$. Un deuxième exposant critique associé aux déplacements des ions perpendiculairement à l'axe z a la valeur $\delta = 1$. Ces estimations numériques des exposants critiques nous permettent d'obtenir une équation qui relie les amplitudes des déplacements des ions parallèles au plan x–y aux déplacements parallèles à l'axe z durant l'aplatissement.

Mots-clés : piège ionique, aplatissement, transition de phase, exposant critique.

Introduction

The potential energy of a system of N identically charged ions in a harmonic trap, expressed in dimensionless form, is[1,2]

$$[1] \qquad u = \sum_{i=1}^{N-1} \sum_{j=i+1}^{N} \frac{1}{r_{ij}} + \frac{1}{2} \sum_{i=1}^{N} [x_i^2 + y_i^2 + \alpha z_i^2]$$

where r_{ij} is the distance between ions i and j, (x_i,y_i,z_i) is the position of particle i, and α is the anisotropy parameter of the trap. Ion traps have a number of applications in chemistry, notably in mass spectroscopy, chemical dynamics, and high-resolution spectroscopy.[3] The ions can be cooled to temperatures down to the milliKelvin range, leading to Wigner crystallization.[4–6]

The anisotropy is experimentally controllable in many ion trap designs. At sufficiently low temperatures and large anisotropies, the ions undergo a structural phase transition, collapsing onto the x–y plane.[1,2] Dahm and Vinen have argued that the study of two-dimensional systems enhances our understanding of surfaces, interfaces, and anisotropic solids.[7] We concur, and point out that because of the flattening phase transition, ion traps afford us the possibility of studying two-dimensional "crystals" involving from two to several thousand ions. Ion traps specifically designed to study two-dimensional clusters have been devised, particularly for the closely related dusty plasma problem.[8–10] There has also been considerable interest in the confinement of charged particles in two dimensions in condensed matter physics for a number of reasons. First, these systems may give us some insight into the poorly understood phenomenon of superconductivity in two-dimensional electron systems at low temperatures.[11] Second, they may be used as models of contact phenomena at semiconductor boundaries,[12] of electron dimples on liquid helium,[13] or of quantum dots.[14] Third, there has been a suggestion that ions trapped in a two-dimensional geometry could be used in quantum computing.[15,16] And finally, problems of this class are of historical interest since Thomson's "plum pudding" model of the atom led him to study the closely related problem of stabilization by rotation of planar arrangements of point charges in a neutralizing background.[17] Given the importance of two-dimensional systems, understanding the conditions under which a three-dimensional system can be flattened is clearly of interest.

Received 12 December 2008. Accepted 26 June 2009. Published on the NRC Research Press Web site at canjchem.nrc.ca on 30 September 2009.

This article is part of a Special Issue dedicated to Professor T. Ziegler.

T.L.L. Closson and M.R. Roussel.[1] Department of Chemistry and Biochemistry, University of Lethbridge, Lethbridge, AB T1K 3M4, Canada.

[1]Corresponding author (e-mail: roussel@uleth.ca).

There have been a number of studies of structural phase transitions in trapped-ion clusters.[1,2,18–20] Early studies of the flattening phase transition in particular have focused on the large-N regime.[1,2] Cornellissens and co-workers have studied the sequence of phase transitions that occur in both small and large clusters as the anisotropy of the trap is increased, the flattening transition being the final phase transition in this sequence.[18] Calvo and Yurtsever have obtained a phase diagram showing the regions in the (N,α) parameter plane where one-, two-, and three-dimensional structures can be observed.[19] Here, we focus specifically on the final collapse to a two-dimensional structure in smaller clusters, which we show to be a second-order structural phase transition. We characterize both the critical anisotropy and a pair of critical exponents of the collapse process. The computed values of the critical exponents then allow us to derive a very interesting connection between the displacements of the ions along the z axis and perpendicular to this axis during the flattening process.

Computing methods

We study structural phase transitions of cold clusters as α is varied, i.e., qualitative changes in the equilibrium structures. Our approach is closely related to that described by Schweigert and Peeters[21] and since applied by the Peeters group to structural phase transitions in trapped-ion clusters.[18,20] Specifically, we use a gradient optimizer to locate minimum energy structures, as described elsewhere.[22] As pointed out by Schweigert and Peeters, this greatly speeds convergence, and typically avoids locking into saddle points on the potential energy surface (PES) when combined with a method to explore the local vicinity of a critical point.[21] Our program takes a previously discovered equilibrium structure, adds or deletes particles or changes the value of α, and reminimizes the potential energy (eq. [1]) using a fast gradient optimizer. The program allows other operations used to probe the stability and accuracy of determined structures, including "jiggling" (adding small random numbers to all coordinates prior to energy minimization as a probe of stability), and "squashing" (replacing all z coordinates by small random numbers). The latter operation was particularly useful near the flattening phase transition to test whether a given flattened structure was higher or lower in energy than the corresponding completely flat structure. To avoid trapping in unstable states, Schweigert and Peeters used molecular dynamics steps.[21] Our jiggling operation, implemented by adding uniformly distributed random numbers in the range [–0.005,0.005] to each of the x, y, and z coordinates of the ions, plays the same role. To put the random amplitudes of the jiggling operation in perspective, note that in our scaling, the equilibrium coordinates for the small clusters studied here are of unit magnitude. Moreover, for the small values of α studied in this paper, jiggling typically results in a relative increase of the energy of the order of one part in 10^5. Empirically, we find that the small random displacements used here are not generally sufficient to displace a stable equilibrium structure out of its potential well when two equilibria coexist, although they are often sufficient to avoid trapping at saddle points. Additionally, note that the isotropic displacements in space used here are not isotropic in potential energy due to the anisotropy of the trapping potential.

As in our previous work,[22] we used the balancing condition between the Coulomb and trapping contributions to the energy[23] to estimate the errors in the computed energies. We thus determined that the energies computed by our programs are always accurate to at least six decimal places.

We also computed some key global minima, particularly the global minima of the two-dimensional problem corresponding to the large-α limit of the potential, eq. [1], using simulated annealing.[24]

Our main computations involved repeated gradient optimizations after small changes in α, sometimes in combination with other operations such as jiggling or squashing. These calculations are roughly equivalent to an experiment where the trap anisotropy is changed very slowly while maintaining the laser cooling so that at any time, the cluster is in quasi-equilibrium at the instantaneous value of α. In cases where there were questions about the nature of the critical points computed (which mainly occurred when jiggling was not used), we calculated the eigenvalues of the Hessian matrix of u (the matrix of second partial derivatives of u with respect to the $3N$ particle coordinates) to eliminate structures that are saddle points on the potential energy surface.

To study the dependence of the equilibrium geometries on α, we used two different sampling strategies. In one strategy, we scanned the value of α using a large number of small steps (often in steps of 0.01, but verifying results in key regions with smaller step sizes), either with or without jiggling. Jiggling generally had little effect on the results, except very near the phase transition, although it typically resulted in slightly more accurate energies. In this variation, we used the statistics (energies, coordinates, etc.) from a single scan in further analyses (e.g., determination of critical parameters). In the second strategy, we computed an ensemble of minima for each value of α starting from a variety of different initial configurations (e.g., structures obtained at nearby values of α) and using different program options (jiggling, squashing, etc.), with the difference in α values between adjacent points adapted to study the region of the phase transition particularly finely. When we used this procedure, we typically extracted statistics only from the best structure in an ensemble at a given value of α for further analysis. The best structure was taken to be the one that simultaneously had the lowest energy and smallest error in the energy as determined by the balancing criterion. Occasionally, several structures had identical energies and errors. In these cases, the median structural statistics from this set of structures were used. Both strategies produced estimates of the parameters studied that are within error of each other.

The critical parameters (β and α_c from eqs. [2] and [3] below) were obtained using the Marquardt–Levenberg non-linear least-squares algorithm[25] as implemented in OCTAVE 2.9.9.[26] Error bars were calculated by a simple Monte Carlo method based on the analysis of ensembles of structures generated for each value of α. This generated a range of values of ζ (maximum absolute value of z) for each α. The fitting procedure was repeated 1000 times, each time choosing random values of ζ uniformly within the range identified from the ensemble of structures. The standard deviations of β and α_c obtained from these fits are the uncertainties in our

estimates of these parameters. Note that the average values of β and α_c from the Monte Carlo procedure were always within error of the values obtained from the best structures.

Results and discussion

Computational results

When $\alpha \rightarrow \infty$, minimizing the potential (eq. [1]) becomes equivalent to finding minimum-energy structures of the two-dimensional problem where all particles have a z coordinate of zero. We computed the global minima of this two-dimensional problem by simulated annealing. These calculations were useful to determine the global minimum-energy structure for each value of N. Our results agree with previously published global minima[27,28] and are thus not reproduced here. Note that these authors found minimum-energy structures that improve on those presented earlier by Bedanov and Peeters[29] for $N = 29$, 39, and 49, as did our own calculations. Also note that both of these groups use a somewhat different scaling of the energy than we do: Energies in our scaling can be converted to theirs by multiplying by $2^{1/3}$.

Our main calculations follow the fate of particular local minima on the PES as α is varied. As we increase α, we observe qualitative changes in the cluster structures. These changes are associated with discontinuities in the derivatives of u with respect to α, i.e., to structural phase transitions, which are classified according by the order of the discontinuity in the derivatives of the energy.

In most cases, the last phase transition observed as we increase α is a second-order flattening phase transition, i.e., a phase transition in which the second derivative of u with respect to α is discontinuous at the critical value of this parameter, α_c. Figure 1 illustrates the behavior of the energy and of its first and second derivatives in a typical example of the flattening phase transition. Since u is constant above the critical anisotropy and the first derivative is continuous, the first derivative must converge to zero as α approaches α_c, as observed in Fig. 1. Moreover, the second derivative of u with respect to α must be negative below the phase transition since the energy increases with increasing anisotropy, but the rate of change of the energy must decrease to zero as $\alpha \rightarrow \alpha_c$ from below. Again, our numerical results are consistent with this argument. Interestingly, $d^2u/d\alpha^2$ appears to be constant, and $du/d\alpha$ decreases linearly with α near the phase transition, implying that the linear coefficient of a Taylor series of $u(\alpha)$ expanded about $\alpha = \alpha_c$ for $\alpha < \alpha_c$ is identically zero, a fact that will feature prominently in our later analysis of this phase transition.

It is useful to define an order parameter for the flattening phase transition, i.e., a quantity that decreases to zero at the critical value of α.[30] We chose the maximum absolute value of z of the configuration, a quantity we will denote by ζ. Near the flattening phase transition, an order parameter should behave as

$$[2] \qquad \zeta(\varepsilon) \sim (-\varepsilon)^{\beta}$$

where

$$[3] \qquad \varepsilon = \frac{\alpha - \alpha_c}{\alpha_c}$$

Fig. 1. Second-order flattening phase transition for $N = 18$. The energy of the fully flattened structure, $u_{flat} = 104.408\ 542\ 872\ 30 \pm 0.000\ 000\ 000\ 15$, is subtracted from the energy of the minimum-energy structure for each value of α in panel (*a*). While the result is shown as a continuous curve, this graph is in fact the result of a set of calculations in which the value of α was increased in steps of 0.001 and the energy reminimized at each step. In panels (*b*) and (*c*), we see a kink in $du/d\alpha$ and a corresponding jump discontinuity in $d^2u/d\alpha^2$ near $\alpha = 4.926$, characteristic of a second-order phase transition. The derivatives in these panels were calculated by finite differences of adjacent points and the computed points are shown, along with the trend lines in each region.

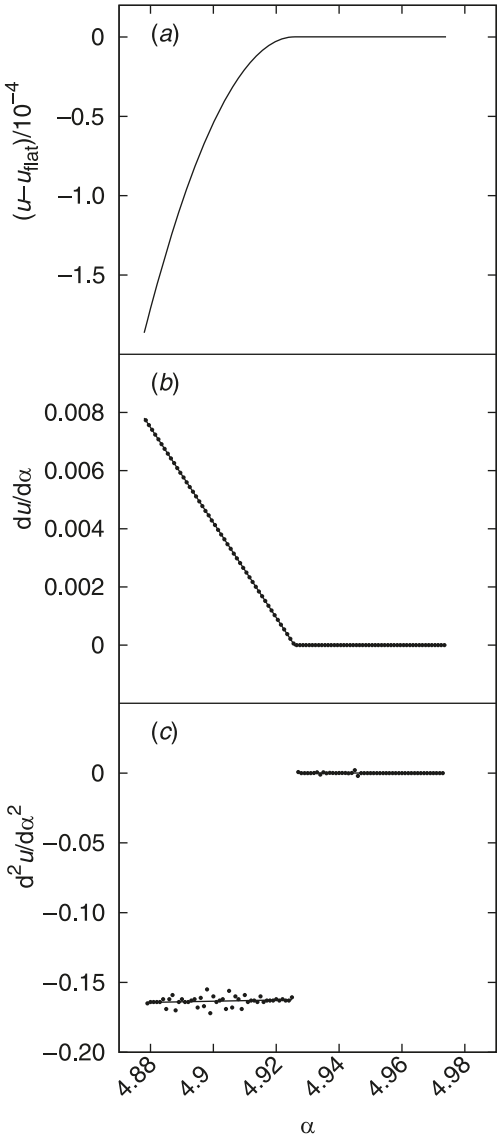

Figure 2 shows the behavior of the order parameter near the critical point for $N = 18$. The inset confirms that the behavior is consistent with eq. [2] over several orders of magnitude in −ε. Note the larger error bars near the critical point. During flattening, deformation of the cluster follows the two "softest" eigenmodes of the Hessian matrix, i.e., the two modes with the smallest eigenvalues, not counting the trivial zero eigenvalue associated with rigid rotation of the whole cluster around the z axis. The first of these ei-

Fig. 2. Behavior of the order parameter ζ near the critical value of α for $N = 18$. For this structure, $\alpha_c = 4.925\,800 \pm 0.000\,009$ and the critical exponent $\beta = 0.5000 \pm 0.0022$. The error bars show the spread of values obtained by computing the minimum-energy structure at a given value of α from several different initial configurations. Configurations in which the Hessian matrix has a negative eigenvalue, i.e., those that are not stable equilibria, were discarded from each of these sets. The spread of values is only significant for points near the critical α. The inset shows that the analytic form eq. [2] is a good fit to the data (The error bars are not shown in the inset for clarity).

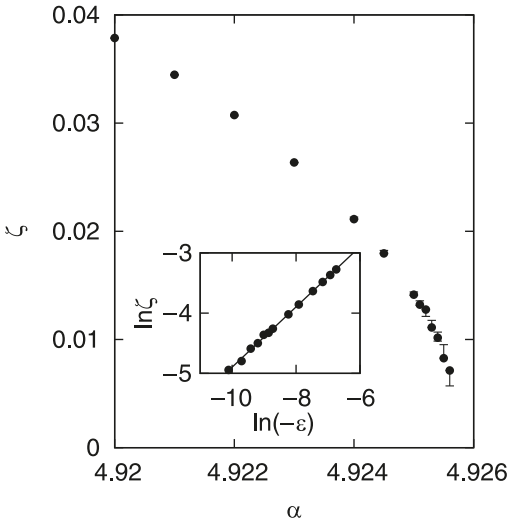

Fig. 3. Second nontrivial eigenvalue of the Hessian matrix (λ_2) vs. α near the critical anisotropy for $N = 18$. In this case, the eigenvalues were recovered from a succession of structures obtained by scanning α with jiggling. The first nontrivial eigenvalue is associated with deformation of the structure parallel to the *x*–*y* plane during flattening. The eigenvalue plotted here is associated with deformation along the *z* axis during flattening. Note the decrease in λ_2 by a factor of more than 20 over this range of α.

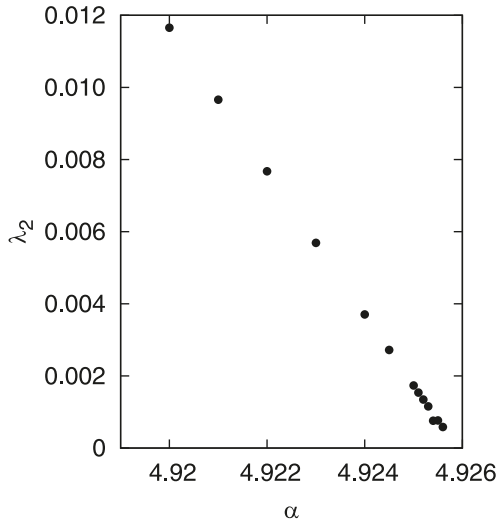

genmodes corresponds to the deformation of the structure parallel to the *x*–*y* plane. The second eigenmode largely involves deformation along the *z* axis. The eigenvalue corresponding to the latter mode (λ_2) decreases significantly as we approach the phase transition (Fig. 3), indicating an effective softening of the potential in this direction. The eigenvalue for the first eigenmode varies much less dramatically (it increases by about 11% over the same range of α), and the other eigenvalues hardly vary at all with α. Accordingly, it becomes harder for numerical methods to converge to the minimum along the second eigenvector, and we typically find a wider dispersion in values of ζ near $\alpha = \alpha_c$. This complicates the computation of critical data for this phase transition, which is why we generally found it necessary to retain only the lowest energy structure at a given value of α for high-resolution studies of the vicinity of the critical point.

As a rule, the minimum-energy structures in both the two-dimensional and three-dimensional versions of this and related problems can be thought of as having ions organized in shells.[6,17,22,23,29,31–38] Each ion within a shell is at a similar distance from the centre of the trap as other ions in the same shell, and the distance between shells is much larger than the variability of the distance from centre within a shell. It is convenient to have a shorthand notation for the shell structure of a cluster. We denote a configuration by a set of indices (*n*,*m*,...), where *n* is the number of ions in the outermost shell, *m* is the number of ions in the next shell, and so on, all the way to the centre.

The description of the phase transitions in this system is complicated by the coexistence of multiple equilibria. For example, for $N = 5$ and $1 < \alpha < 1.76412$, the global minimum-energy structure is a square pyramid. (The base of the pyramid becomes nonplanar for values of α approaching 1 from above, the overall structure converging on a trigonal bipyramid as α tends to 1.) Above $\alpha = 1.76412$, a planar pentagon is the global minimum-energy structure. The planar pentagon results from the flattening of a nonplanar ring (with all atoms roughly equidistant from the centre of the trap) at $\alpha_c = 1.76394$, while the pyramid becomes a centered square at $\alpha_c = 2.55482$. Thus, it is not only the number of particles that matters in determining the critical value of α, but also the geometry of the structure being flattened. We did not attempt to build an exhaustive catalog of metastable two-dimensional structures. Rather, we started from our set of $\alpha = 1$ three-dimensional structures[22] and studied how these structures flatten. In many cases, different initial structures flattened to the same two-dimensional structure. Nevertheless, when the opportunity presented itself, we did study the flattening transition for multiple structures for a given *N*. Additional data points could be added to this study using the catalog of metastable states of the two-dimensional problem compiled by Kong, Partoens, and Peeters.[27]

In other cases, a region of bistability and hysteresis is observed, complicating the observation of the flattening phase transition. We use hysteresis here in the sense it is used in dynamical systems theory, namely that a different equilibrium is followed when we vary a parameter forward and backward through a region sufficiently slowly (equivalently, using sufficiently small steps in the parameter scanned). This is the case, for example, for $N = 8$, where, in addition to the sequence of first- and second-order phase transitions reported by Cornelissens and co-workers,[18] two different examples of hysteresis are observed. Our results for this value of *N* are summarized in Fig. 4. The red curve in this figure

Fig. 4. Cluster energy vs. α during forward and reverse scans of the anisotropy for $N = 8$. Red curve: forward scan; green curve: reverse scan; diamonds: first-order phase transitions; squares: second-order phase transitions. Typical structures at various points along the $u(\alpha)$ curve are shown. Each structure is illustrated from a perspective looking down the z axis; where a second image is shown, the illustration on the right shows a perpendicular view of the same cluster. The "bonds" connecting the ions have no particular interpretation and are only there to guide the eye. Due to the order in which the curves were plotted, the green (reverse) curve overlies the red (forward) curve for $\alpha > 3.4$ and $\alpha < 2.28$. Note the discontinuous jumps due to sudden loss of stability of, respectively, the (6,2) structure above $\alpha = 3.4$ and the (7,1) structure below $\alpha = 2.28$, and the consequent region of hysteresis.

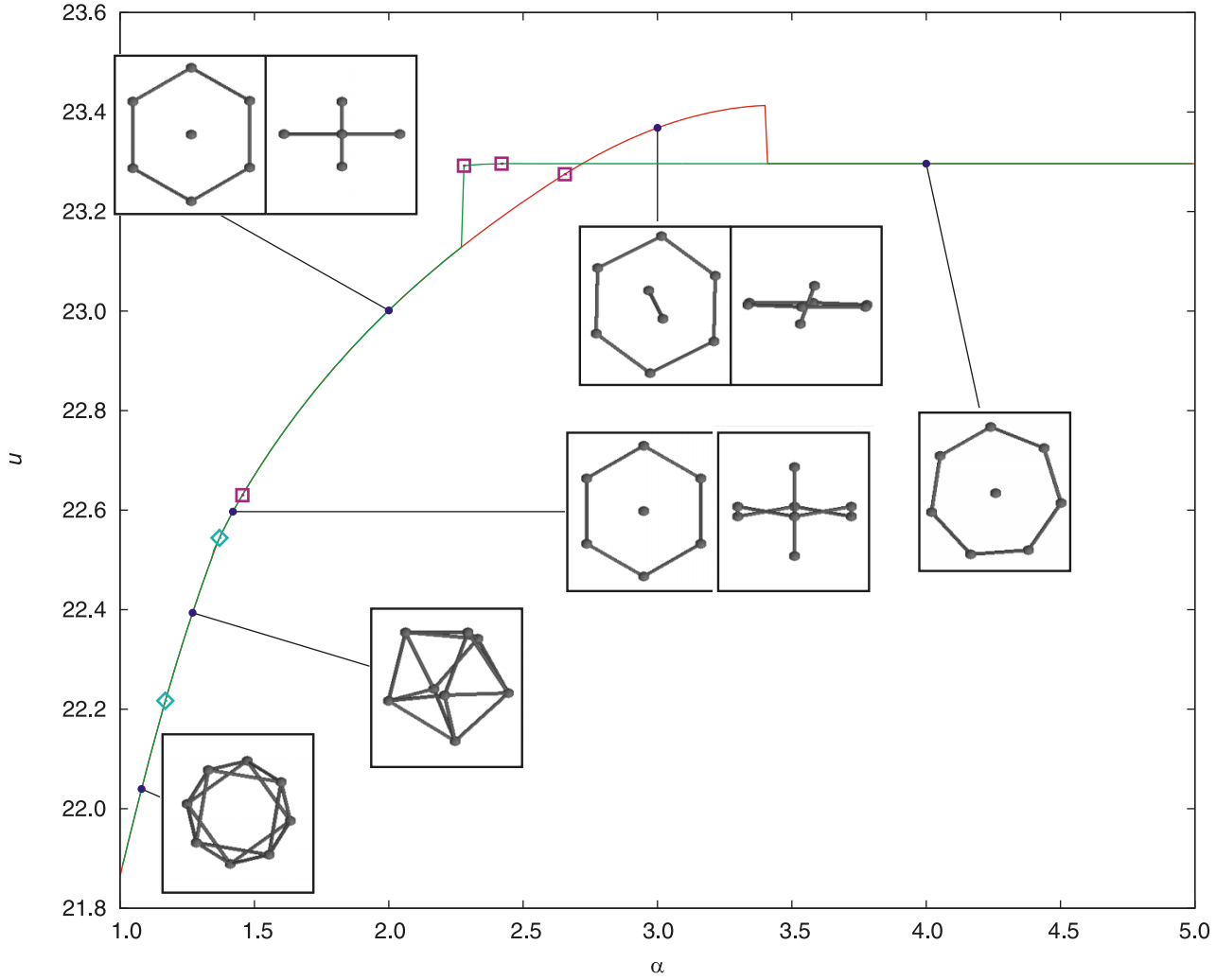

was obtained by increasing α in steps of 0.01, adding small random increments to all the coordinates (jiggling), and re-minimizing. The same procedure was followed along the reverse path (green curve). Phase transitions were located by numerical differentiation of the energy and identification of discontinuities in the derivatives. In some regions, scans were carried out at higher resolution to confirm the existence and location of a phase transition. The jiggling amplitudes used (see Computing methods) are only large enough to avoid converging to a saddle point, but are not usually large enough to jump out of a local minimum well on the PES. This empirical observation of course depends on the height of the barrier between the structures. These barriers decrease in magnitude along the upper branch of a hysteresis loop. It is the eventual vanishing of the barrier, leaving a downhill path to the lower-energy structure, that is responsible for the loss of stability of the upper branch of a hysteresis loop. Near the jump points, we therefore cannot be sure that jiggling, even at very low amplitudes, will not displace a structure out of its well on the PES. To verify whether this was a problem, we scanned through the regions where the jumps occur using very small increments in α without jiggling. One of two situations was always observed: either a branch of equilibria in a high-resolution scan ended between the two endpoints of the jump identified in the lower resolution calculations, or the high-resolution scan followed an unstable branch of equilibria, as verified by computing the eigenvalues of the Hessian matrix. In the latter case, the first value of α at which the equilibrium became unstable was always between the two endpoints identified in the lower resolution scan with jiggling. We therefore have a high degree of confidence that, at least to the resolution of Fig. 4, we have fully mapped out each branch of equilibria.

For $N = 8$ at $\alpha = 1$, the equilibrium structure can be described as a pair of squares rotated 45° with respect to each other (Fig. 4). For α just slightly larger than 1, the square

faces are orthogonal to the z axis. The structure compresses smoothly in the z direction as α increases until approximately $\alpha = 1.17$ where a first-order phase transition occurs in which the structure reorients with respect to the z axis, with some distortion of the structure as the ions are no longer in symmetry-equivalent positions with respect to the trapping field. At $\alpha = 1.37$, another first-order phase transition occurs, yielding a (6,2) structure consisting of a six-membered ring in a chair conformation (a hexagon with one vertex tipped up out of the plane and the directly opposite vertex tipped down) and a pair of ions lying along the z axis. If we decrease α through this region, we find that the phase transition is slightly delayed, to $\alpha = 1.35$. This is a true example of hysteresis as the relevant structures are both stable in the region indicated, as determined by computing the eigenvalues of the Hessian matrix. As we continue to increase α, we pass through two second-order phase transitions, the first of which flattens the ring while the second results in the central pair of ions tilting away from the z axis. This latter structure suddenly loses stability (i.e., the PES undergoes a catastrophe[39]) above $\alpha = 3.4$ (approximately). The lone stable structure at higher values of α is the planar (7,1) structure. If we now decrease α starting from the planar (7,1) structure, we do not retrace our steps. Rather, there is a region of coexistence of the (7,1) and (6,2) structures, i.e., hysteresis is again observed. The planar (7,1) structure is stable down to $\alpha_c = 2.421$. A second-order phase transition then occurs which is associated with a displacement of the central ion along the z axis, with some slight displacements of the ring ions along this coordinate axis as well. This is of course the reverse process of a flattening phase transition. If we start a forward scan from this branch with α between 2.28 and 2.421, we do observe a normal flattening transition. Another second-order phase transition occurs near $\alpha = 2.28$ where the central ion starts to slide away from the z axis, i.e., it acquires nonzero x and y components, with corresponding deformation of the outer ring. (These last two structures, which are easily imagined, are not shown in Fig. 4, both due to space constraints and to the relatively subtle nature of the deformations.) Then, near $\alpha = 2.273$, the (7,1) structure suddenly loses stability and the (6,2) hexagon+vertical-stick structure reappears. Thereafter, the sequence of phase transitions described for the forward scan is followed in reverse, give or take the narrow region of hysteresis already noted for the first-order phase transition near $\alpha = 1.37$. Whether we would observe the two examples of hysteresis seen here either in molecular dynamics simulations or in experiments would depend a great deal on the barriers between the two conformations and on the temperature of the simulation. Since we deliberately avoided saddle points, for the moment we can say nothing with certainty about this subject, although the significant structural differences between the planar (7,1) structure and the (6,2) structure are at least suggestive of a significant activation barrier.

Figure 5 shows how the structure deforms during some selected flattening sequences, using color coding for the z displacements and arrows to show the x–y displacements of the ions. These displacements were computed directly from our structure optimizations at different values of α, although they could also have been recovered from the eigenvectors of the Hessian, as described above. We can make several observations: First, the outer-shell ions typically approach the x–y plane earlier in the flattening sequence than the inner-shell ions as we increase α, no doubt because the latter have more neighbors and are closer to each other on average. Flattening thus often occurs in distinct phases corresponding to the progressive flattening of shells, starting from the outside. The one exception to this trend in Fig. 5 is the $N = 21$ (12,8,1) cluster where the middle-shell ions approach the x–y plane later than the central ion. Second, as one might expect, the increased Coulomb repulsion as ions are pushed into the x–y plane causes the cluster to expand radially (on average). However, there is an energetic cost to this expansion because of the trapping field. As a result, the outer-shell ions typically have smaller displacement amplitudes parallel to the x–y plane than ions in inner shells.

Figure 6 shows the critical value of α as a function of N. The observations here are compatible with those we made of the displacements of the ions in the last paragraph. Typically, the critical anisotropy changes little for clusters that have the same number of ions in their inner shells, with the notable exception of the $N = 16$ and $N = 21$ (n,m,1) configurations. In other words, the force required to push the ions down into a plane is relatively insensitive to the number of ions in the outer shell(s) because the flattening phase transition typically involves only modest displacements of the outer-shell ions. On the other hand, going from 1 to 2 ions in the inner shell, or from 3 to 4 ions, tends to cause the critical anisotropy to increase significantly. Contrast in particular the large differences in α_c between configurations with the same number of ions but different inner-shell configurations for $N = 12$, 21, and 26 to the very small difference in α_c for the (8,2) and (7,3) configurations for $N = 10$, or the (12,6,1) and (11,7,1) configurations for $N = 19$. Again, this occurs because inner-shell ions have more neighbors, so that the increase in the Coulomb repulsion energy is larger when one of these is pushed down into the x–y plane than when an outer-shell ion undergoes a similar displacement. When there is more than one ion in the inner shell, this effect will be particularly large. The largest exception to these trends, the large jump in α_c between the $N = 20$ and 21 (n,m,1) configurations, is related to the peculiar flattening sequence of the $N = 21$ (12,8,1) cluster where the central ion collapses onto the x–y plane earlier than the eight middle-shell ions (Fig. 5). The reason for the other major exception, the anomalously large value of α_c for the $N = 16$ (10,5,1) cluster, is the high symmetry of this configuration which requires an outward displacement of middle-shell ions directly towards outer-shell ions as the central ion is pushed down (Fig. 5). Note that the critical anisotropies for the $N = 16$ (10,5,1) and $N = 19$ (12,6,1) clusters, both of which have the same symmetry-induced restraint of the middle-shell by the outer-shell ions (Fig. 5), are similar ($\alpha_c = 5.078\ 125 \pm 0.000\ 026$ for the former and $4.995\ 054 \pm 0.000\ 018$ for the latter). Finally, we can understand why there is essentially no difference in α_c for clusters with either two or three inner-shell ions by considering the example of the $N = 25$ (13,9,3) cluster: One of the inner-shell ions of a three-ion inner shell approaches the x–y plane much earlier than the other two as α increases, so that the final flattening process in these cases is not very different from the case of a two-ion inner shell.

Fig. 5. Structural deformations during some flattening sequences. The number of ions and shell structures of the clusters are indicated in the top left-hand corner of each panel. The value of the critical anisotropy, α_c, and the value of the normalized distance from the phase transition at which these snapshots were taken, ε, is given in the top right corner. The arrows indicate the displacements of the ions parallel to the x–y plane. These displacements are greatly exaggerated, these clusters all being close to their final fully flattened configurations. Note also that the arrows are scaled independently in each of the panels for ease of visualization. Only the relative sizes of the arrows within a panel are significant. The colors of the ions indicate their positions relative to the x–y plane, and thus the direction of change of their z coordinates during the flattening process: Red indicates an ion above the x–y plane for which $dz/d\varepsilon < 0$, and blue indicates an ion situated below the plane for which $dz/d\varepsilon > 0$. The intensity of the color is proportional to the distance of the ion from the plane, again with each panel scaled independently. The relative sizes of the z displacements and of the displacements parallel to the x–y plane are maintained throughout the final stages of the flattening process, i.e., they do not depend on the value of ε provided this value is not too large.

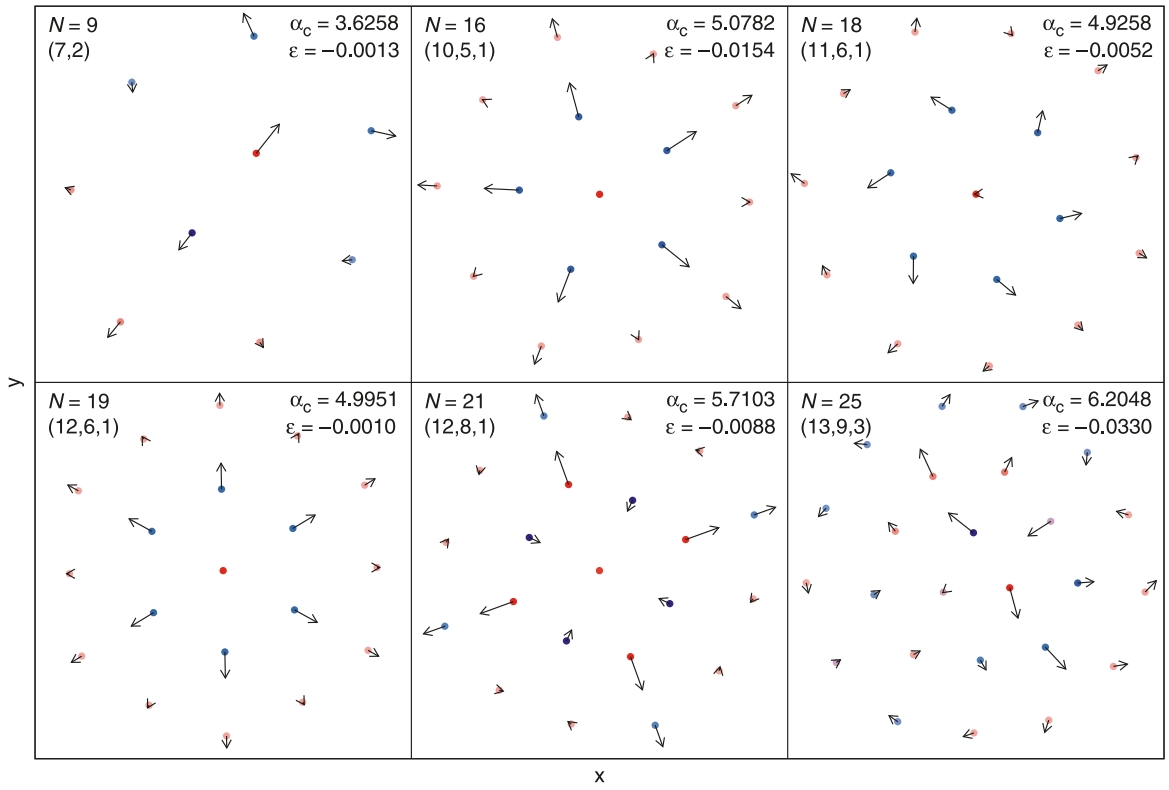

Fig. 6. Critical value of α vs. N. The line segments connect configurations with a common inner-shell configuration. In the three-shell configurations, n and m are both variable. The isolated points are the $N = 15$ (10,5) and $N = 30$ (15,10,5) clusters. Error bars are negligible on this scale and are not plotted.

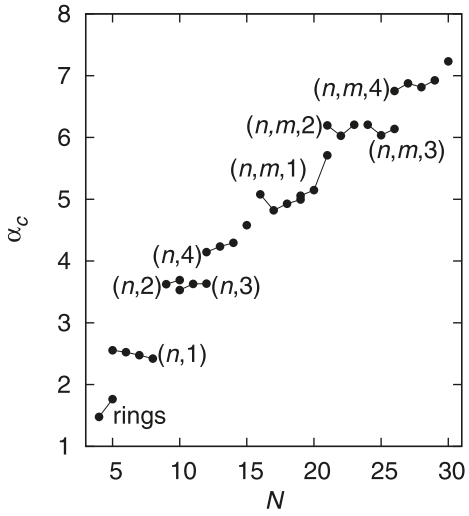

Figure 6 may be compared to Fig. 8 in Calvo and Yurtsever .[19] The latter reports the critical anisotropy as a function of N on a log–log plot, for N between 10 and 1000. This presentation disguises a great deal of the substructure identified here. In fact, the roughly $N^{1/2}$ scaling originally predicted by Dubin[2] and confirmed by Calvo and Yurtsever does not seem to set in until larger values of N are reached than those studied here, where we find a scaling exponent significantly greater than 1/2 (results not shown).

Figure 7 shows the values of the critical exponent β calculated for each of the flattening phase transitions observed in this study. In each case, the estimated value of β is within error of 1/2.

Of course, we expect that all the z coordinates, and not just the largest one, will follow a law similar to eq. [2]. Specifically, we can write

$$[4] \qquad z_i = c_i(-\varepsilon)^{\beta}$$

Figure 8 shows a typical set of z coordinates as we approach the phase transition. Most of the z coordinates behave as shown, with a value of β within error of 1/2. Occasionally, one finds an ion that sits at a small finite distance from the x–y plane for all values of α near (but below)

Fig. 7. Critical exponent β vs. *N*. The error bars are statistical fitting errors, i.e., standard deviations of the parameter estimates, reported only for some typical cases to avoid visual clutter. Where two points are seen for a given value of *N*, the flattening of two different structures was studied.

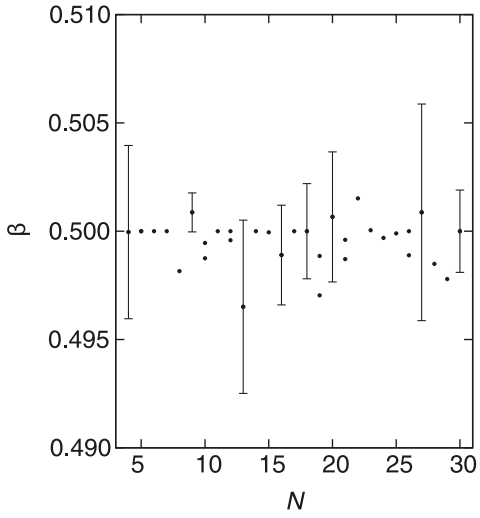

Fig. 8. Fits to eq. [4] of some representative *z* coordinates for the flattening transition of the nine-ion cluster. ε was calculated using eq. [3] and the estimate of α_c obtained from the nonlinear fit of the ζ(α) data (procedure of Fig. 2 with results in Fig. 6). In each case, a critical exponent of approximately 1/2 is obtained.

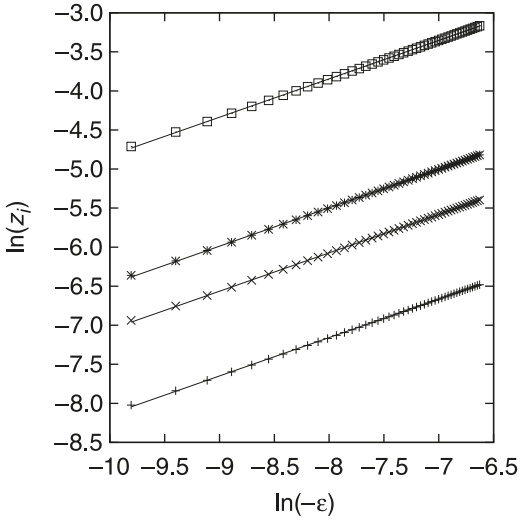

α_c, and whose approach to $z_i = 0$ does not fit eq. [4] particularly well. It is likely that the poor fits in these cases are due to the limited numerical precision of our calculations. Even if this is not the case, the low displacement amplitudes of these ions in the *z* direction makes the precise functional form of their approach to $z_i = 0$ relatively unimportant.

We now analyze the deformation of the structure parallel to the *x*–*y* plane. We can study the changes in the *x* and *y* coordinates individually, but because there is no constraint keeping the cluster from rotating around the *z* axis, energy minimization sometimes results in an incidental twisting component which somewhat obscures the true behavior. Rather, we define the radial coordinate

Fig. 9. Behavior of χ_i near the flattening phase transition for several representative ions for the same process as in Fig. 8. The critical exponent for this coordinate is found to be approximately δ = 1.

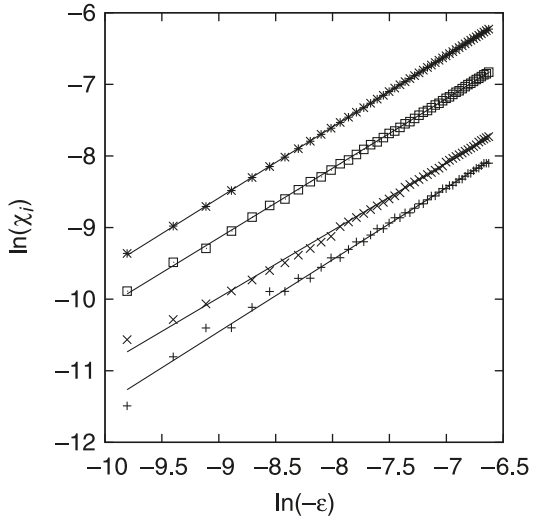

$$[5] \qquad \rho_i = \sqrt{x_i^2 + y_i^2}$$

which is invariant with respect to rotations around the *z* axis. Let ρ_i^∞ be the value of ρ_i beyond the phase transition, i.e., in the fully flattened cluster. Define also

$$[6] \qquad \chi_i = |\rho_i - \rho_i^\infty|$$

Clearly, $\chi_i \to 0$ as $\varepsilon \to 0^-$. We assume that, below the phase transition,

$$[7] \qquad \chi_i \sim (-\varepsilon)^\delta$$

Again, with the exception of ions with very small displacement amplitudes parallel to the *x*–*y* plane during the phase transition, we find that eq. [7] is generally a good fit to the displacements (Fig. 9). Moreover, we find that the exponent δ is generally within error of 1.

Coupling of expansion and flattening

We can use our computational results to motivate a theoretical treatment that will determine the coupling of the radial expansion (parallel to the *x*–y plane) to the flattening in the *z* direction. We begin by assuming that eq. [4] holds and that the behavior found for χ_i also holds for x_i and y_i. With the caveats mentioned above regarding the rotational freedom around the *z* axis, this appears to be true except perhaps for ions whose displacement amplitudes parallel to the *x*–*y* plane are vanishingly small. Thus we write

$$[8] \qquad x_i = x_i^\infty - a_i(-\varepsilon)^\delta$$

and

$$[9] \qquad y_i = y_i^\infty - b_i(-\varepsilon)^\delta$$

In these equations, x_i^∞ and y_i^∞ are the coordinates of the ion in the fully flattened structure. The geometric interpretation of the vector (a_i,b_i) is that it points in the direction of displacement for an ion parallel to the *x*–*y* plane as the ion approaches its final coordinates (x_i^∞, y_i^∞). Note that

eqs. [4], [8], and [9] define the trajectory of an individual ion in three-dimensional space during the flattening process. If we substitute these equations into the potential (eq. [1]) and use eq. [3] to eliminate α, we obtain an equation for the variation of u with ε as we approach the phase transition, i.e., as $\varepsilon \to 0^-$. In this region, both $(-\varepsilon)^\beta$ and $(-\varepsilon)^\delta$ are small quantities. We can expand the potential in powers of these small quantities, a tedious but straightforward process. To lowest order, and assuming that $1 + 2\beta > \delta$, we get

$$[10] \quad u(\varepsilon) \approx u(0) + \sum_{i=1}^{N-1}\sum_{j=i+1}^{N}[p_{ij}(-\varepsilon)^\delta - q_{ij}(-\varepsilon)^{2\beta}] + \frac{1}{2}\sum_{i=1}^{N}[-2(a_i x_i^\infty + b_i y_i^\infty)(-\varepsilon)^\delta + \alpha_c c_i^2(-\varepsilon)^{2\beta}]$$

where

$$[11] \quad p_{ij} = \frac{(x_i^\infty - x_j^\infty)(a_i - a_j) + (y_i^\infty - y_j^\infty)(b_i - b_j)}{(r_{ij}^\infty)^3}$$

$$[12] \quad q_{ij} = \frac{(c_i - c_j)^2}{2(r_{ij}^\infty)^3}$$

r_{ij}^∞ is the distance between ions i and j in the fully flattened structure, and $u(0)$ is the corresponding energy (a well-defined quantity due to the continuity of the energy in a second-order phase transition). Note that we can immediately rule out cases where either δ or 2β is less than one since, for a second-order phase transition, the first derivative is continuous through the phase transition, whereas, according to eq. [10], it diverges for $\delta < 1$ or $2\beta < 1$. We can also rule out the possibility that both δ and 2β are greater than 2 since, in this case, both $u'(\varepsilon)$ and $u''(\varepsilon)$ would tend to zero as $\varepsilon \to 0^-$. As we saw earlier (Fig. 1 and associated discussion), this is the correct behavior for $u'(\varepsilon)$ but not for $u''(\varepsilon)$, which must be negative for $\varepsilon < 0$. We can go a little further, and state that the leading coefficient cannot have an exponent between 1 and 2, or $u''(\varepsilon)$ would diverge as $\varepsilon \to 0^-$, which is not observed in our numerical results (Fig. 1). Accordingly, we can conclude that $\delta \geq 1$, $2\beta \geq 1$, and min $(\delta, 2\beta) \in \{1,2\}$.

Our computational results support the values $\delta = 2\beta = 1$ for the critical exponents. Assume that this is the case. Then we have

$$[13] \quad u'(\varepsilon) \approx -\sum_{i=1}^{N-1}\sum_{j=i+1}^{N}[p_{ij} - q_{ij}] - \frac{1}{2}\sum_{i=1}^{N}[-2(a_i x_i^\infty + b_i y_i^\infty) + \alpha_c c_i^2]$$

where again this result is valid only for $\varepsilon < 0$. As noted above, we must have $u'(\varepsilon) \to 0$ as $\varepsilon \to 0^-$. Thus, the constant expression given in eq. [13] must be identically zero. The first nonzero term in the expansion of $u(\varepsilon)$ would therefore be the quadratic term, which is consistent with our computational results, as discussed earlier.

We also know that at every critical point, $u_{\text{Coulomb}} = 2u_{\text{trap}}$, where u_{Coulomb} is the Coulomb repulsion energy, and u_{trap} is the energy due to the harmonic trapping potential.[23] If we separate eq. [10] into Coulomb and trapping terms and apply the balancing relationship, the corresponding terms of $u(0)$ automatically satisfy the balancing relationship since they are critical points of the large-α problem. This leaves

$$[14] \quad \sum_{i=1}^{N-1}\sum_{j=i+1}^{N}[p_{ij} - q_{ij}] = \sum_{i=1}^{N}[-2(a_i x_i^\infty + b_i y_i^\infty) + \alpha_c c_i^2]$$

If we now set eq. [13] to zero and use eq. [14] to eliminate the double sum, we conclude that each of the two contributions to $u'(\varepsilon)$ must individually be equal to zero. In particular,

$$[15] \quad 2\sum_{i=1}^{N}(a_i x_i^\infty + b_i y_i^\infty) \approx \alpha_c \sum_{i=1}^{N} c_i^2$$

Numerically, we find that eq. [15] is approximately obeyed, typically to a few parts in 10^3, and always within 2%. The small deviations observed are due to a number of factors: the precision of the estimate of α_c, which also affects our estimates of the vectors (a_i,b_i) and of the amplitudes c_i through eqs. [3], [4], [8], and [9]; the loss of precision in the subtraction necessary to obtain the vectors (a_i,b_i) using eqs. [8] and [9]; the possibility of slight rotations of the whole cluster during optimization; and of course the fact that we derived eq. [15] through a theory that only examines the lowest-order terms.

We can obtain a great deal of qualitative insight from eq. [15]. For instance, since the right-hand side of this equation is strictly positive, the sum of dot products on the left must also be a positive quantity. This confirms the intuition that, on average, displacements of the ions must be directed outward during flattening. Moreover, since the left-hand side involves the dot product of the vectors (a_i,b_i) and (x_i^∞, y_i^∞), we would typically expect that ions in the outer shells would have smaller displacements during flattening, which is again confirmed by our numerical results (Fig. 5).

Given the numerical confirmation of eq. [15], which implies that the double sum on the left-hand side of eq. [14] is also zero, we can then ask whether these equalities impose any further conditions on the critical exponents. Suppose that $\delta = 2\beta = 2$. Then the limit as $\varepsilon \to 0^-$ of $u'(\varepsilon)$ is automatically zero. However, $u''(\varepsilon)$ is then also identically zero for $\varepsilon < 0$, which is contrary both to our data (Fig. 1) and to the argument presented above that the second derivative of u should be negative. Thus, if we take both [14] and [15] as premises along with our earlier reasoning about the critical exponents, we conclude that at least one of δ or 2β must have the value 1.

Conclusions

We have studied the flattening phase transition in systems of ions held in a harmonic trap. The critical exponent corresponding to the order parameter ζ was found by computational experiment to have the value 1/2. The critical value of the trap anisotropy, α_c, was shown to display jumps where the inner-shell configuration changes. A second critical exponent related to the amplitude of displacements parallel to the x–y plane was found to have the value $\delta = 1$. Using these estimates of the critical exponents, we derived

eq. [15], which gives an explicit coupling between the amplitudes of displacements toward the *x*–*y* plane and the radial expansion of the cluster during the flattening process. Using a combination of numerical results and analysis, we were also able to place some constraints on the values of the critical exponents, specifically that $\delta \geq 1$, $2\beta \geq 1$, and $\min(\delta,2\beta) = 1$. It would be gratifying to prove from first principles that β and δ must have the values obtained in our computations. Notwithstanding, our analysis does provide a useful consistency check on our computational results.

There are several ways in which this study could be extended. One of the more interesting variations would be to examine what happens if either the interatomic potential or the trapping potential were different in form. For the interatomic potential, the shielded Coulomb potential would be particularly interesting since it describes, among other systems, dusty plasmas.[9,40] Are the critical exponents found here universal exponents for flattening processes, or are they particular to the interatomic and trapping potentials in eq. [1]? We have focused here on the final flattening, which is the easiest phase transition to define and the only one that occurs for almost every flattening sequence. Since we often find phase transitions associated with the flattening of parts of the structure (e.g., the flattening of the outer ring for $N = 8$ illustrated in Fig. 4), it would also be of some interest to study the behavior of a suitably constructed order parameter for these transitions. Does the corresponding critical exponent have a value of 1/2 as for the final flattening?

Complementary information could also be gathered using other techniques. We have focused here on the equilibrium structures on the PES and the manner in which they change as α is varied. We have not attempted to search for saddle points (i.e., transition states) connecting coexisting equilibria found, for instance, in the $N = 8$ system. These could be found using constrained optimization methods, and would yield valuable information on the expected rate of transitions between coexisting structures. Information on the transition rates could also be obtained from molecular dynamics (MD) simulations. MD simulations of these systems would yield a wealth of additional information, notably on the response of these systems to fluctuations in the trap parameters, especially in the vicinity of phase transitions or in regions displaying hysteresis.

Acknowledgments

Messrs Richard Beekman and Peter Wilson contributed some of the code used in these simulations. This work was funded by the Natural Sciences and Engineering Research Council of Canada (NSERC).

References

(1) Schiffer, J. P. *Phys. Rev. Lett.* **1993**, *70* (6), 818–821. doi:10.1103/PhysRevLett.70.818. PMID:10054211.
(2) Dubin, D. H. E. *Phys. Rev. Lett.* **1993**, *71* (17), 2753–2756. doi:10.1103/PhysRevLett.71.2753. PMID:10054767.
(3) Willitsch, S.; Bell, M. T.; Gingell, A. D.; Softley, T. P. *Phys. Chem. Chem. Phys.* **2008**, *10* (48), 7200–7210. doi:10.1039/b813408c. PMID:19060963.
(4) Wigner, E. *Phys. Rev.* **1934**, *46* (11), 1002–1011. doi:10.1103/PhysRev.46.1002.
(5) Wineland, D. J.; Bergquist, J. C.; Itano, W. M.; Bollinger, J. J.; Manney, C. H. *Phys. Rev. Lett.* **1987**, *59* (26), 2935–2938. doi:10.1103/PhysRevLett.59.2935. PMID:10035691.
(6) Rafac, R.; Schiffer, J. P.; Hangst, J. S.; Dubin, D. H. E.; Wales, D. J. *Proc. Natl. Acad. Sci. U.S.A.* **1991**, *88* (2), 483–486. doi:10.1073/pnas.88.2.483. PMID:11607146.
(7) Dahm, A. J.; Vinen, W. F. *Phys. Today* **1987**, *40* (2), 43–50. doi:10.1063/1.881098.
(8) Melzer, A.; Homann, A.; Piel, A. *Phys. Rev. E Stat. Phys. Plasmas Fluids Relat. Interdiscip. Topics* **1996**, *53* (3), 2757–2766. PMID:9964566.
(9) Juan, W.-T.; Hsu, J.-W.; Huang, Z.-H.; Lai, Y.-J.; Lin I. *Chin. J. Phys.* **1999**, *37* (2), 184–195.
(10) Sheridan, T. E. *Phys. Rev. E Stat. Nonlin. Soft Matter Phys.* **2005**, *72* (2 Pt 2),o. 026405. PMID:16196716.
(11) Phillips, P.; Wan, Y.; Martin, I.; Knysh, S.; Dalidovich, D. *Nature* **1998**, *395* (6699), 253–257. doi:10.1038/26179.
(12) Lozovik, Y. E. *Sov. Phys. Usp.* **1987**, *30* (10), 912–913. doi:10.1070/PU1987v030n10ABEH002971.
(13) Leiderer, P.; Ebner, W.; Shikin, V. B. *Surf. Sci.* **1982**, *113* (1-3), 405–411. doi:10.1016/0039-6028(82)90623-9.
(14) Bolton, F.; Rössler, U. *Superlattices Microstruct.* **1993**, *13* (2), 139–145. doi:10.1006/spmi.1993.1026.
(15) Mitchell, T. B.; Bollinger, J. J.; Huang, X.-P.; Itano, W. M.; Dubin, D. H. E. *Phys. Plasmas* **1999**, *6* (5), 1751–1758. doi:10.1063/1.873433.
(16) Porras, D.; Cirac, J. I. *Phys. Rev. Lett.* **2006**, *96* (25),o. 250501. doi:10.1103/PhysRevLett.96.250501. PMID:16907291.
(17) Thomson, J. J. *Philos. Mag.* **1904**, *7* (39), 237–265.
(18) Cornelissens, Y. G.; Partoens, B.; Peeters, F. M. *Physica E* **2000**, *8* (4), 314–322. doi:10.1016/S1386-9477(00)00163-6.
(19) Calvo, F.; Yurtsever, E. *Eur. Phys. J. D* **2007**, *44* (1), 81–91. doi:10.1140/epjd/e2007-00137-2.
(20) Apolinario, S. W. S.; Partoens, B.; Peeters, F. M. *Phys. Rev. B* **2008**, *77* (3),o. 035321. doi:10.1103/PhysRevB.77.035321.
(21) Schweigert, V. A.; Peeters, F. M. *Phys. Rev. B* **1995**, *51* (12), 7700–7713. doi:10.1103/PhysRevB.51.7700.
(22) Beekman, R. A.; Roussel, M. R.; Wilson, P. J. *Phys. Rev. A* **1999**, *59* (1), 503–511. doi:10.1103/PhysRevA.59.503.
(23) Lozovik, Y. E.; Mandelshtam, V. A. *Phys. Lett. A* **1990**, *145* (5), 269–271. doi:10.1016/0375-9601(90)90362-R.
(24) Corana, A.; Marchesi, M.; Martini, C.; Ridella, S. *ACM Trans. Math. Softw.* **1987**, *13* (3), 262–280. doi:10.1145/29380.29864.
(25) Marquardt, D. W. *J. Soc. Ind. Appl. Math.* **1963**, *11* (2), 431–441. doi:10.1137/0111030.
(26) Eaton, J. W. *Octave 2.9.9* [computer program]; University of Wisconsin: Madison, WI, 2006.
(27) Kong, M.; Partoens, B.; Peeters, F. M. *Phys. Rev. E Stat. Nonlin. Soft Matter Phys.* **2002**, *65* (4 Pt 2B),o. 046602. PMID:12006042.
(28) de Moraes, S. S.; Coimbra, D.; de Sousa, J. R.; da Frota, H. O. *Braz. J. Phys.* **2004**, *34* (2A), 408–413.
(29) Bedanov, V. M.; Peeters, F. M. *Phys. Rev. B* **1994**, *49* (4), 2667–2676. doi:10.1103/PhysRevB.49.2667.
(30) Stanley, H. E. *Introduction to Phase Transitions and Critical Phenomena*; Oxford: New York, 1971.
(31) Berezin, A. A. *Chem. Phys. Lett.* **1986**, *123* (1-2), 62–64. doi:10.1016/0009-2614(86)87015-4.
(32) Rahman, A.; Schiffer, J. P. *Phys. Rev. Lett.* **1986**, *57* (9), 1133–1136. doi:10.1103/PhysRevLett.57.1133. PMID:10034256.
(33) Dubin, D. H. E.; O'Neil, T. M. *Phys. Rev. Lett.* **1988**, *60* (6), 511–514. doi:10.1103/PhysRevLett.60.511. PMID:10038569.
(34) Gilbert, S. L.; Bollinger, J. J.; Wineland, D. J. *Phys. Rev.*

Lett. **1988**, *60* (20), 2022–2025. doi:10.1103/PhysRevLett.60.2022. PMID:10038237.
(35) Schiffer, J. P. *Phys. Rev. Lett.* **1988**, *61* (16), 1843–1846. doi:10.1103/PhysRevLett.61.1843. PMID:10038912.
(36) Lozovik, Y. E.; Pomirchy, L. M. *Phys. Status Solidi B* **1990**, *161* (1), K11–K13. doi:10.1002/pssb.2221610147.
(37) Hasse, R. W.; Avilov, V. V. *Phys. Rev. A* **1991**, *44* (7), 4506–4515. doi:10.1103/PhysRevA.44.4506. PMID:9906491.
(38) Birkl, G.; Kassner, S.; Walther, H. *Nature* **1992**, *357* (6376), 310–313. doi:10.1038/357310a0.
(39) Berezin, A. A. *Phys. Scr.* **1991**, *43* (1), 111–115. doi:10.1088/0031-8949/43/1/019.
(40) Lee, H. C.; Chen, D. Y.; Rosenstein, B. *Phys. Rev. E Stat. Phys. Plasmas Fluids Relat. Interdiscip. Topics* **1997**, *56* (4), 4596–4607. doi:10.1103/PhysRevE.56.4596.

Neptunium(VII) in high-ionic-strength alkaline solutions — $[NpO_2(OH)_4]^{1-}$ or $[NpO_4(OH)_2]^{3-}$?

John E. C. Wren and Georg Schreckenbach

Abstract: Relativistic density functional theory (ZORA-PBE, COSMO solvation) is used to address the title question, based on comparison with recent experimental data (1). Structural data (bond lengths), vibrational frequencies, and ^{17}O NMR chemical shifts are used to prove that $[NpO_4(OH)_2]^{3-}$ is the predominant species in high-ionic-strength alkaline solutions of Np^{VII}. Neptunium(VII) complexes have stronger bonds than their formally isoelectronic uranium(VI) analogues. The experimentally observed 300 ppm shift in ^{17}O chemical shifts between the known $[UO_2(OH)_4]^{2-}$ and Np^{VII} solution is shown to be partly a function of the central metal (Np^{VII} vs. U^{VI}) and not of the coordination environment (tetraoxo vs. dioxo). Comparing, for a given An (U^{VI} or Np^{VII}), actinyl complexes $[AnO_2X_4]^{2-/1-}$, X = Cl, F, OH, a decreasing strength of the axial actinyl bond is observed that is traced to electronic factors (equatorial π-competition).

Key words: neptunium, density functional theory, relativity, NMR chemical shifts, alkaline solution.

Résumé : En se basant sur une comparaison avec des données expérimentales récentes (1), on a utilisé la théorie de la fonctionnelle de la densité relativiste « ZORA-PBE, solvatation COSMO » pour étudier la question mentionnée dans le titre. On a utilisé les données de structure (longueurs de liaison), les fréquences de vibration et les déplacements chimiques en RMN du ^{17}O pour prouver que le cation $[NpO_4(OH)_2]^{3-}$ est l'espèce prédominante dans les solutions alcalines de force ionique élevée du Np^{VII}. Les complexes du Np^{VII} possèdent des liaisons plus fortes que leurs analogues formellement isoélectroniques de l'uranium(VI). On a démontré que les déplacements chimiques de 300 ppm observés expérimentalement pour les ^{17}O du cation connu $[UO_2(OH)_4]^{2-}$ et de la solution de Np^{VII} sont partiellement fonction de l'atome métallique central [Np^{VII} vs. U^{VI}] et non pas de l'environnement de coordination (tétraoxo vs. dioxo). Pour un actinyle, An, donné, lorsqu'on compare des complexes d'actinyle d'uranium(VI) et de neptunium(VII) de formule générale $[AnO_2X_4]^{2-/1-}$ dans lesquels X = Cl, F, OH, on observe une diminution de la force de la liaison axiale de l'actinyle qui peut être attribuée à des facteurs électroniques (compétition équatoriale/π).

Mots-clés : neptunium, théorie de la fonctionnelle de la densité, relativité, déplacements chimiques en RMN, solution alcaline.

[Traduit par la Rédaction]

Introduction

The purpose of this paper is to provide a definite answer to the title question: Is neptunium(VII) in high-ionic-strength alkaline solution present as $[NpO_2(OH)_4]^{1-}$ or as $[NpO_4(OH)_2]^{3-}$? We address this question by applying the tools of computational quantum chemistry to calculate a variety of spectroscopic properties that can be compared directly to the available experiment, particularly the new data from Clark and co-workers published in 2004.[1]

Neptunium is the first transuranic element, and the lowest of the artificially produced actinides in the periodic table. Because of its relatively long half-life of 2.1×10^6 years, the isotope ^{237}Np, when part of high-level nuclear wastes, is of great environmental concern.[2] Hence, besides fundamental interest, there is immediate practical interest in understanding the aqueous chemistry of the element.

The identity of neptunium(VII) in alkaline solutions has been discussed controversially in the literature.[1,3–7] Although originally the dominant ion was thought to be $[NpO_2(OH)_4]^{1-}$, i.e., a neptunyl structure similar to that of most early actinides in high oxidation states (including the isoelectronic uranyl(VI) hydroxide, $[UO_2(OH)_4]^{2-}$[8,9]), in recent years, this has been contested. Appelman et al.[3] proposed a coordination environment of four oxo ligands, i.e., the $[NpO_4(OH)_2]^{3-}$ version of the molecule. This has been disputed by Clark and co-workers[4] who interpreted their solution X-ray data (XAFS) as pointing towards the neptunyl species, $[NpO_2(OH)_4]^{1-}$. Williams et al.,[5] however, confirmed the original tetraoxo proposal of Appelman et al., based on solution X-ray measurements (XANES, EXAFS). Simple gas-phase density functional theory (DFT) calculations were also performed, though they suffer from imaginary frequencies.

Bolvin and co-workers[6,7] picked up the discussion using both DFT calculations with small-core effective core poten-

Received 19 December 2008. Accepted 21 May 2009. Published on the NRC Research Press Web site at canjchem.nrc.ca on 30 September 2009.

This article is part of a Special Issue dedicated to Professor T. Ziegler (on the occasion of his 65th birthday).

J.E.C. Wren and G. Schreckenbach.[1] Department of Chemistry, University of Manitoba, Winnipeg, MB R3T 2N2, Canada.

[1]Corresponding author (e-mail: schrecke@cc.umanitoba.ca).

tials (SCECP) and X-ray measurements (EXAFS). They, too, interpret their data as pointing toward the tetraoxo species. This conclusion is chiefly based on comparing experimental EXAFS results (mostly bond lengths) and DFT calculations with and without continuum solvation (CPCM). Bolvin et al. also provide a discussion of the bonding modes in tetraoxo actinide complexes.

The most recent experimental paper came again from the Clark group.[1] In this paper, the authors revise their earlier conclusion and find strong support for the tetraoxo species, $[NpO_4(OH)_2]^{3-}$. This new work clearly goes beyond any of the earlier studies that had relied on bond-length information, both on the experimental (various solution X-ray techniques, with their associated need for fitting the data and resulting uncertainties) and theoretical sides. Indeed, Clark et al. provide evidence from ^{17}O NMR shifts of the oxo ligands (viz. a shift of some 300 ppm as compared with the known uranyl(VI) hydroxide complexes in basic solution). Furthermore, additional evidence comes from Raman spectroscopy (where we note, however, that the expected B_{1g} Raman frequency was not present in their analysis of the structure, although the expected A_{1g} frequency was), as well as from solution X-ray studies.

In light of this new data, we feel that it is timely to computationally reexamine the nature of neptunium(VII) in basic solutions, and to include *all* of the available spectroscopic data (i.e., ^{17}O NMR chemical shifts and vibrational spectroscopy, in addition to the bond-length data of the previous studies). Specifically, we make use of the ability of theory to examine hypothetical species such as, for example, a hypothetical $[UO_4(OH)_2]^{4-}$, and to differentiate between the various effects. Likewise, while Clark et al.[1] had to *assume* that the observed 300 ppm difference in ^{17}O chemical shifts is a function of the ligand environment (tetraoxo vs. dioxo) and not the central metal (Np^{VII} vs. the isoelectronic U^{VI}), we can address that question directly.

For this study, we undertook calculations on eight different actinide complexes, namely $[UO_2(OH)_4]^{2-}$, $[NpO_2(OH)_4]^{1-}$, $[UO_4(OH)_2]^{4-}$, $[NpO_4(OH)_2]^{3-}$, $[UO_2Cl_4]^{2-}$, $[NpO_2Cl_4]^{1-}$, $[UO_2F_4]^{2-}$, and $[NpO_2F_4]^{1-}$. All species were chosen to be in either the U^{VI} or Np^{VII} oxidation state, creating essentially isoelectric species. Although not all of these species have been found experimentally, the three uranyl(VI) complexes have been well-explored computationally.[10] These species were therefore used as a guide along which the neptunyl(VII) ions could be compared, providing confirmation of the correct methodology, particularly for the NMR calculations.

Computational details

Currently, density functional theory (DFT)[11–13] is the almost sole practical method for calculations on actinide molecules.[14–17] This is due to the size of typical molecules, combined with the central importance of electron correlation effects that are included in DFT in an approximate and efficient manner. In this study, we have applied DFT with the PBE exchange-correlation functional.[18] Generalized gradient approximation (GGA) functionals such as PBE have been shown to provide reasonably accurate geometries and vibrational frequencies for actinide molecules.[19–22] All calculations were performed with the ADF program.[23–25]

Relativistic effects are essential for even a qualitative description of heavy-element chemistry.[26] Relativity has been included by applying the zeroth order regular approximation (ZORA) for relativistic effects.[27–32] ZORA has been shown to give accurate results that are comparable to other modern relativistic methods such as, for instance, all-electron four-component calculations.[19–22] Spin-orbit effects have been neglected for the computation of structures and frequencies. This is a generally thought to be a good approximation, particularly since the molecules at hand are formally closed-shell, f^0 species. For NMR calculations, however, spin-orbit cannot be neglected.[10,33–35]

The ADF code uses accurate numerical integration for all integrals.[25,36] A numerical integration parameter of ACCINT = 5.5 was applied. All structures were optimized either in the gas phase or in continuum solvation (see below) without any symmetry constraints, using standard convergence criteria as implemented in ADF. The optimized structures of $[NpO_4(OH)_2]^{3-}$ and $[NpO_2(OH)_4]^{1-}$ are shown in Fig. 1. Frequency calculations were then performed to verify that true minima had been achieved. In the gas phase, the hypothetical $[UO_4(OH)_2]^{4-}$ complex did not converge to a true minimum state with real frequencies, despite numerous attempts. This is likely related to the significant charge of this ion that leads to the molecule being unstable without the stabilizing effect of a polarizable solvent (as, e.g., in the COSMO model).

Following our earlier work on NMR shielding (chemical shift) calculations in diamagnetic (f^0) compounds of actinide elements,[10,33,34,37] we applied the GIAO-NMR methods as implemented in ADF.[38–42]

All-electron Slater-type basis sets of triple- and quadruple-ζ polarized quality (ZORA-TZ2P, ZORA-QZ4P) were used, since NMR chemical shifts tend to place higher requirements on basis set convergence than, for instance, geometries. For reduced computational cost, quadruple-ζ basis sets were reserved solely for the metal centers, while the ligands were calculated using the triple-ζ basis sets.

Solvation effects might be crucial for the electronic structure (and consequently for the spectroscopic observables) of the highly charged molecules of interest. In our previous studies on NMR parameters of actinide molecules,[10,33,34,37] we had not been able to include such effects, since, at the time, no code had both, relativistic NMR and a continuum solvation model implemented. This has changed since, and we have modeled bulk solvation with the COSMO model[43] as implemented in ADF.[44] ADF requires that radii be assigned to the individual atoms to set up the COSMO surfaces. These radii were taken from Klamt's paper on the COSMO surfaces (see ref. 45), where parameters are provided for all of the necessary elements.[45,46] Test calculations with a different set of atomic radii (having smaller values) resulted in minor changes of the spectroscopic observables only. Although Klamt did not publish radii for the actinide elements, it has been shown that, due to their central position in the complex, the central atom is essentially solvated by the overlap of the ligands; therefore, the actinide radius was set to a relatively small value of 1.70 Å. The effects of central-metal-atom radii for COSMO surfaces has

Fig. 1. Optimized structures of $[NpO_4(OH)_2]^{3-}$ and $[NpO_2(OH)_4]^{1-}$.

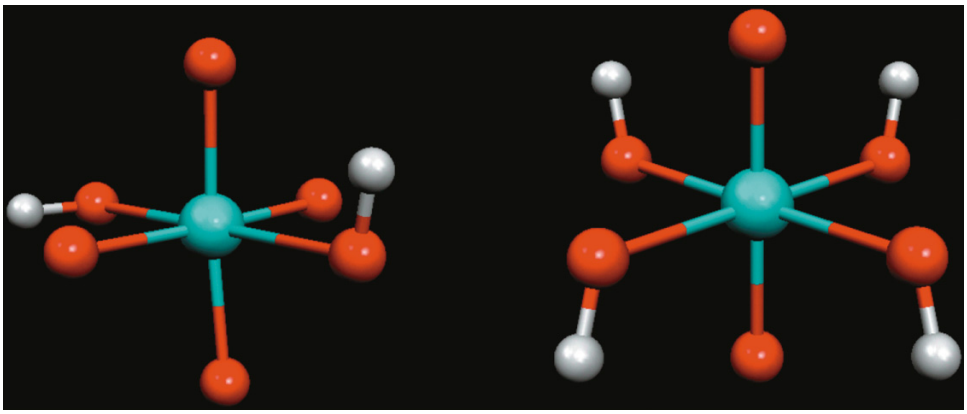

Table 1. Calculated and observed ^{17}O absolute NMR shieldings for the oxo ligands of diamagnetic actinide complexes (ppm).

					Gas phase			
Np^{VII} complexes	Gas phase	COSMO	Experimental	U^{VI} complexes	Reference 10	This work	COSMO	Experimental
$[NpO_2F_4]^-$	–997. 5	–991.1		$[UO_2F_4]^{2-}$	–768.0	–815.6	–891.3	
$[NpO_2Cl_4]^-$	–918.4	–918.2		$[UO_2Cl_4]^{2-}$	–747.5	–792.5	–817.7	
$[NpO_2(OH)_4]^-$	–910.9	–978.7		$[UO_2(OH)_4]^{2-}$	–737.1	–767.9	–736.7	–826[b]
$[NpO_4(OH)_2]^{3-}$	–1041.1	–1022.1	–1179.1±8[a]	$[UO_4(OH)_2]^{4-}$		Dissociative	–1005.2	

Note: These values represent the average of all formally equivalent oxo ligands within the complex. The experimental values have been converted to absolute shieldings.

[a]Reference 1; assigned to $[NpO_4(OH)_2]^{3-}$ (see the text).

[b]Reference 8; cited as absolute shielding as per ref. 10. It is likely that this particular experimental value refers to the pentahydroxide, $[UO_2(OH)_5]^{3-}$, or a mixture of $[UO_2(OH)_4]^{2-}$ and $[UO_2(OH)_5]^{3-}$; see the discussion in our earlier paper.[10]

been shown to have little effect on results, noting that the central atom is indeed mostly buried. Hence, the current choice of metal radius is considered reasonable.[47,48]

Results

^{17}O NMR shieldings (chemical shifts) in U^{VI} and Np^{VII} complexes

As discussed in the introduction, Clark et al.[1] have taken their new ^{17}O NMR data as the strongest evidence for the tetraoxo complex to be the dominant species in highly alkaline solutions of neptunium(VII). Hence, we have calculated ^{17}O NMR shieldings for the pertinent Np^{VII} complexes, the analogous isoelectronic U^{VI} complexes, as well as four other diamagnetic (f^0) actinyl compounds. This series of compounds allows us to verify our computational protocol and to distinguish between effects of the central metal and the ligand environment.

In our earlier paper,[10] we had studied ^{17}O NMR shieldings for a few uranyl(VI) complexes. Comparison with the available experimental data (converted to absolute shieldings) yielded modest agreement between theory and experiment. Importantly, though, the qualitative experimental trend within a series of three compounds was reproduced correctly. Since our current computational protocol differs from the earlier one (basis sets, the particular choice of GGA functional, and, perhaps most importantly, the inclusion of COSMO solvation), we have reexamined some of these compounds, specifically $[UO_2Cl_4]^{2-}$, $[UO_2F_4]^{2-}$, and $[UO_2(OH)_4]^{2-}$, Table 1. This was done to verify the current computational protocol and to provide reference data for the formally isoelectronic Np^{VII} compounds that are the target of our study. We have also included the hypothetical uranium(VI) complex $[UO_4(OH)_2]^{4-}$, as well as the corresponding neptunium(VII) complexes.

Comparing first our gas-phase calculations on uranium(VI) complexes to the older results from ref. 10, we note that there is reasonable agreement between the two sets of data, giving confidence in the current protocol. Most importantly, the relative chemical shift between the three compounds is similar between the two methods, and the current calculations are slightly (though not dramatically) closer to the experimental value for the uranyl hydroxide. The overall agreement with experiment is modest, similar in quality to our earlier studies. However, it is sufficient to draw conclusions regarding the neptunium(VII) complexes, see below.

Bulk solvation effects (COSMO), not covered in the earlier studies, are seen to have a modest, relatively constant influence on the shieldings in the uranium(VI) complexes, Table 1 (solvation shifts of –53 to –74 ppm). The solvation influence on the isoelectronic neptunium(VII) species is generally much smaller. This can be understood from the smaller charge in the neptunium case, noting that the free energy of solvation is to first order proportional to the charge squared. The only exception to this statement is the (hypothetical) $[NpO_2(OH)_4]^{1-}$ complex where the solvation shift is –68 ppm. This is larger than for the other Np species, though still modest. The reason for this difference is not clear. We note that trends in calculated shieldings (chemical shifts) depend on a variety of factors that can all

be influenced by continuum solvation, particularly structural parameters, molecular orbital (MO) compositions (polarization of the electronic structure), and MO energies.

The data in Table 1 allow for a direct comparison between the two actinide metals U^{VI} and Np^{VII}, as well as between different ligand environments. Inspection of the data demonstrates that the effect of the central metal atom within each of the studied complexes on the absolute shift of the oxo ligands is variable. In the fluorine complexes, we note a shift of about 100 ppm between the neptunium(VII) species and the corresponding uranium(VI) species, while in the less electronegative chlorine complexes, the shift is only in the order of 60 ppm (for COSMO solvated species).

The neptunium(VII) data allow for a comparison between the two target species of this paper, viz. $[NpO_2(OH)_4]^-$ and $[NpO_4(OH)_2]^{3-}$. It is noteworthy that the difference in the shift between the tetraoxo and and dioxo hydroxide species is only a meager 43 ppm for neptunium(VII) (solvated complexes; the gas-phase difference is still relatively small at 130 ppm), but in uranium(VI), the shift is a significant ~270 ppm. While we do reproduce the experimentally observed shift of some 300 ppm between $[NpO_4(OH)_2]^{3-}$ and $[UO_2(OH)_4]^{2-}$, a large part of that difference appears to be a function of the central metal and *not* the ligand environment. Below, we will further discuss this data in comparison with the available experiment.

Vibrational frequencies

Vibrational frequencies (Raman) provide another set of data to help assign the coordination environment of neptunium(VII). Calculated vibrational frequencies for the symmetric and antisymmetric actinyl stretches in Np^{VII} and U^{VI} complexes are collected in Table 2. From the data in Table 2, we can see that of the standard actinyl ($[AnO_2L_4]^n$) species the stretching frequencies are strongest for the chlorine complexes, and weakest for the hydroxide species. This can be related to the equatorial bonding mode in these complexes, with the hydroxide complexes having the strongest equatorial bond that contains partial π-character. The ensuing π-competition weakens the axial bond, as is directly evident from the frequencies, see also below.[15]

For the tetraoxo complexes, there are four stretching modes in total. They can either be classified by symmetry labels within the approximate D_{4h} point group of the $[AnO_4]^{-/2-}$ ion or they can be viewed as linear combinations of the two sets of AnO_2 stretches along the x and y axes, respectively. We have chosen the latter classification, since the optimized structures have no symmetry. Moreover, this approach allows for a direct comparison with the dioxo complexes (Table 2).

When the tetraoxo species are compared with the others, it is notable that the stretching modes incorporate all four ligands moving together in unison. The frequencies are lower than those in the dioxo complexes, which is indicative of much weaker bonds.[6,7] Whereas, for the various actinyl complexes, the range in frequencies did not exceed 100 cm^{-1}, the tetraoxo species have stretching frequencies that are ~200 cm^{-1} lower then those of the other complexes. As mentioned, in the tetraoxo complexes, the antisymmetric stretches occur over two frequencies, each involving a different pair of oxo ligands. Also, the trend seen in the other complexes is for the symmetric stretch of the oxo ligands to be at lower frequency over the antisymmetric stretch, but in the tetraoxo species, the two symmetric stretches bracket the antisymmetric ones, with the totally symmetric four-oxo-ligand stretch being at higher frequency as compared with the two antisymmetric stretches.

It is also instructive to compare the calculated frequencies for corresponding isoelectronic complexes of uranium(VI) and neptunium(VII). We note that, in each case, the latter metal has stronger bonds, evident from higher stretching frequencies. The difference is particularly pronounced for the antisymmetric stretches but is consistently present in the symmetric stretches also. This is in contrast to periodic trends when the actinide metal oxidation state stays the same along the series, e.g., comparing U^{VI} with Np^{VI} and Pu^{VI}. In these cases, we generally see weaker bonds as we go along the series.[19,49] Along the series, the 5f orbitals gradually decrease in size and energy, leading to this trend. However, the higher positive charge of Np^{VII} as compared with Np^{VI} offsets the trend.

Geometries

Calculated metal–oxo-ligand bond distances have been collected in Table 3. The data show a strong indication that as the electronegativity increases in the equatorial ligands, the bond distances grow shorter for the actinide–oxygen double bond. This can be related to the differing degree of equatorial π-competition, as discussed above.

Neptunium(VII) bond lengths are significantly shorter than the corresponding uranium(VI) bond lengths. We relate this to the stronger bonds in the former case (see the frequency discussion above), as well as to the actinide contraction, which results in 5f orbitals that become more contracted and lower in energy towards the right of the actinide series. This can be compared to trends for compounds in the same oxidation state. In these cases, the bonds are generally getting shorter *and* weaker along the series, which has been traced solely to the actinide contraction.[19,49]

Regarding the title question of the paper, we note that the AnO_4 species have a much greater average bond length than the corresponding AnO_2 species. This suggests much weaker overall bond strengths and a more diffuse electronic structure, similar to what was already suggested in the discussion of the frequencies. A further comparison of some of the neptunium(VII) bond lengths with experiment will be provided below.

Discussion

Within their 2004 paper,[1] Clark et al. make three specific arguments for the preferential state of Np^{VII} in high-ionic-strength alkaline solutions. One argument is based on geometry, a second one on vibrational frequencies, and finally a third argument on the observed ^{17}O NMR chemical shift. From our results, we are able to add further insight into these arguments.

Geometries / bond lengths

Table 4 contains a comparison between Clark's 2004 solution XAFS data,[1] Bolvin's 2001 EXAFS, and computational results (both gas phase and CPCM solvated[6,7]), and

Table 2. Vibrational frequencies for oxo-ligand symmetric and antisymmetric stretches in Np^{VII} and U^{VI} complexes (cm^{-1}).

	$[NpO_2(OH)_4]^-$		$[UO_2(OH)_4]^{2-}$		$[NpO_4(OH)_2]^{3-}$		$[UO_4(OH)_2]^{4-}$	
Complex	Gas phase	COSMO	Gas phase	COSMO	Gas phase	COSMO	Gas phase	COSMO
Symmetric stretch	767.0	758.7	726.9	722.4	493.3	478.9	Dissociative	412.3
					686.9	693.6		661.6
Antisymmetric stretch	873.4	838.5	801.3	760.3	667.5	636.1		544.3
					676.7	636.6		545.5
Expected range/experiment [a]	850–780				735, 716			
Complex	$[NpO_2Cl_4]^-$		$[UO_2Cl_4]^{2-}$		$[NpO_2F_4]^-$		$[UO_2F_4]^{2-}$	
Symmetric stretch	824.1	811.9	806.3	786.3	799.6	797.1	750.6	750.4
Antisymmetric stretch	939.6	910.0	893.1	850.8	901.6	879.0	813.4	780.6

[a]Cited from Clark et al., ref. 1. The numbers cited for $[NpO_2(OH)_4]^-$ correspond to an *expected* range for neptunyl(VII) in general, based on literature data, whereas those listed under $[NpO_4(OH)_2]^{3-}$ are the actually *observed* Raman frequencies. In this case, the two numbers refer to alkaline solution and crystal structure, respectively.

Table 3. Calculated metal–oxo-ligand bond distances for Np^{VII} and U^{VI} complexes (average; Å).

Complex	Gas phase	COSMO
Np^{VII} complexes		
$[NpO_2F_4]^-$	1.792	1.789
$[NpO_2Cl_4]^-$	1.769	1.768
$[NpO_2(OH)_4]^-$	1.813	1.812
$[NpO_4(OH)_2]^{3-}$	1.930	1.922
U^{VI} complexes		
$[UO_2F_4]^{2-}$	1.855	1.845
$[UO_2Cl_4]^{2-}$	1.809	1.808
$[UO_2(OH)_4]^{2-}$	1.875	1.865
$[UO_4(OH)_2]^{4-}$	Dissociative	2.006

our own computational data in both gas-phase and solvated COSMO models. Our results agree reasonably well with those of Bolvin et al., particularly if we keep in mind that the B3LYP hybrid DFT functional used by these authors has a tendency for overbinding in actinide complexes, i.e., bond lengths that are too short and frequencies that are too high[20] (even in cases where the best choice of DFT functional might not be as clear cut that the designation of "overbinding" would be justified, one can still confidently state that B3LYP bond lengths are shorter than those from GGA functionals, which tend to be too long as compared with experiment; all of this is borne out clearly in the data in Table 4).

As mentioned already, the bond lengths for the actinide-to-oxygen bonds in the $[AnO_2(OH)_4]^{-/2-}$ species (where they are partial triple bonds) are always in the order of 10–15 pm shorter than for the corresponding $[AnO_4(OH)_2]^{3-/4-}$ species. This would confirm that the long oxo-ligand bond lengths observed by Clark et al.[1] within their Np^{VII} solution sample (XAFS) are likely those of $[NpO_4(OH)_2]^{3-}$. This conclusion is further strengthened with the comparison between their observed neptunium–hydroxide bond lengths and our calculated bond lengths, which are within the experimental error of the crystal X-ray data for $[NpO_4(OH)_2]^{3-}$, with the solution data leaning heavily towards the tetraoxo Np^{VII} species (particularly when keeping in mind that GGA bond lengths would be expected to be slightly too long, as mentioned above).[20] We note in passing the strong influence of solvation on the Np–O(H) distance. This is consistent with earlier results.[19]

Vibrational frequencies

The next argument of Clark et al.[1] was based on the observation of the Raman spectra of both crystal and solutions of Np^{VII} complexes. Specifically, they note that the expected symmetric and antisymmetric oxo-ligand stretching modes should be observed with, respectively, A_{1g} and B_{1g} symmetry. Although they were unable to observe the antisymmetric stretch for some unknown reason, they were able to observe a symmetric stretch with a frequency of 716 cm^{-1} in the crystal and 735 cm^{-1} in 2.2 mol/L LiOH solution.

Table 2 provides a comparison of these data with our calculated data for the two neptunium(VII) structures. From a qualitative view point, we can say that in both Clark's experimental and our calculated data, we observe a strong decrease in frequency between the dioxo and tetraoxo complexes. This reduction in frequency provides further confirmation that, within Clark's sample, there appears to be a tendency towards the formation of the tetraoxo neptunium complex over the dioxo complex. We should also note that GGA functionals tend to yield frequencies that are slightly too low (in accordance with the mentioned overestimation of bond lengths). Hence, it is logical to assign the observed frequency to a calculated value that is lower (as in the tetraoxide) rather than higher (in the dioxo complex).

^{17}O NMR

Finally, the Np^{VII} complexes were investigated by ^{17}O NMR, both by Clark et al. through experimentation and by us using relativistic density functional theory. Clark's team was able to observe an ^{17}O NMR chemical shift of 1470 ppm for Np^{VII} in a high-ionic-strength alkaline solution, which, if referenced against water at 290.9 ppm, gives an absolute shielding of –1179.1 ppm, Table 1. It is their reasoning that since the commonly observed ^{17}O chemical shift for UO_2^{2+} is only about 1125 ppm, or –834.1 ppm in absolute shieldings, the greater NMR shift for Np^{VII} must indicate a greater electron density on the oxygen atoms and therefore implies a weaker bond, which would coincide with the expected electronic structure of the $[NpO_4(OH)_2]^{3-}$ complex over the dioxo species.

In our calculations, we notice an error within this argument; it essentially ignores the contributions of the central metal to the NMR shifts of the oxo ligands, which appears to be more significant than expected. By calculating the NMR shifts for both the dioxo and tetraoxo complexes for both

Table 4. Calculated and experimental actinide-to-ligand bond distances (average; Å).

	Reference	$[NpO_2(OH)_4]^{-}$	$[UO_2(OH)_4]^{2-}$	$[NpO_4(OH)_2]^{3-}$	$[UO_4(OH)_2]^{4-}$
An=O distance					
Calculated; gas phase	This work	1.813	1.875	1.930	Dissociative
Calculated; solution (COSMO)	This work	1.812	1.865	1.922	2.006
XAFS; solution	Clark[1]	(1.75)[a]		1.88(1)	
X-ray diffraction; crystal	Clark[1]			1.878(5)	
EXAFS Np^{VII}; solution[b]	Bolvin[6,7]	1.89[b]		1.89[b]	
Calculated B3LYP; gas phase	Bolvin[6,7]	1.79		Dissociative	
Calculated; solution (CPCM)	Bolvin[6,7]	1.79		1.90	
An–O(H) distance					
Calculated; gas phase	This work	2.192	2.308	2.587	Dissociative
Calculated; solution (COSMO)	This work	2.181	2.274	2.377	2.446
XAFS; solution	Clark[1]			2.30(1)	
X-ray diffraction; crystal	Clark[1]			2.238(4)	
Calculated; gas phase	Bolvin[6,7]	2.18		Dissociative	
Calculated; solution (CPCM)	Bolvin[6,7]	2.17		2.33	

[a]Clark et al. reference various known dioxo-Np^{VII} species as having average oxo-ligand bond lengths of 1.75 Å.

[b]The discussion in the paper of Bolvin et al. left the identity of the Np^{VII} species within solution as an unknown; therefore, their EXAFS results could be applied to either. However, in light of the current discussion, it appears as though they were likely observing $[NpO_4(OH)_2]^{3-}$.

neptunium and uranium, we can see that the metal has a large influence on the shift behavior, Table 1. It is noteworthy that there appears to be a difference between the literature values and the calculated values of about 90–150 ppm, depending on whether the COSMO data are considered over the gas-phase calculations and whether the comparison is between the experimental values for the dioxo uranyl or the tetraoxo neptunyl complexes and their respective calculated shifts. It could also be argued that the COSMO model is not entirely accurate for this system, since it was optimized for representing a solvent shell of water, not a high-ionic-strength alkaline solution such as the one Clark's samples are in. However, it was established in our practice that the COSMO surfaces allowed for easier convergence for the highly charged species such as the tetraoxo uranium complex.

Looking at the data collected in Table 1, we observe that the differences between the di- and tetra-oxo species is seen to be fairly significant between the two uranyl species, with a difference in the order of 274 ppm. Meanwhile, the difference between the Np^{VII} dioxo and tetraoxo species is only in the order of 43 ppm, much less significant than that of uranium(VI). This observation dictates that these NMR shifts are not solely a factor of the conformation of the ligands or their bonding structure but also depend on the nature of the central contributing metal. Still, the comparison of computed and experimental shieldings allows again for an unequivocal assignment of the observed complex to be $[NpO_4(OH)_2]^{3-}$, Table 1.

Axial and equatorial bond strengths in actinyl complexes

In addition to addressing the title question, the data (particularly the data in Tables 2 and 3) allow for a comparitive discussion of actinyl complexes $[UO_2X_4]^{2-}$ and $[NpO_2X_4]^{1-}$ along the series of ligands X = Cl, F, and OH,. Along the series, we notice a clear trend of increasing axial (actinyl) bond lengths and decreasing bond strengths, the latter inferred from the calculated vibrational frequencies, Table 2. We had found the same trend in our earlier study of the uranyl complexes, at the time using inferior relativistic methods.[15] It is reassuring, then, that these trends are confirmed by the current, more accurate calculations.

The three complexes in each series have the same charge (2– and 1–, respectively, for U^{VI} and Np^{VII}) and the same coordination environment, octahedral coordination of two axial oxo ligands and four equatorial X^{-} ligands. Moreover, none of the ligands is sterically demanding. The trend in axial actinyl bond strengths must therefore be traced to electronic factors. Earlier, we had argued that partial π-bonding of the equatorial bonds in the hydroxy and, to a lesser degree, fluoride complexes is responsible for weakening the corresponding axial bonds.[15]

Conclusion

Quantum-chemical methods (relativistic DFT) have been used to investigate and answer the title question, i.e., the identity of neptunium(VII) in high-ionic-strength alkaline solutions. Based on various spectroscopic observables, we conclude that the most likely candidate for the dominant ion is the $[NpO_4(OH)_2]^{3-}$ complex, at least in the kind of high-ionic strength, highly-alkaline environment that was used in the experiments. This conclusion is in agreement with the majority of the literature studies, particularly the more recent ones.[1,3,5–7] However, we feel that the combination of modern computational chemistry and three qualitatively different types of data (structural data, vibrational frequencies, and ^{17}O NMR) makes this conclusion stronger then before. Indeed, any single one of the previous experimental techniques could be critiqued in one way or another: First, solution X-ray experiments such as EXAFS depend heavily on fitting, and therefore, on some structural model that the fitting procedure is based upon from the outset. As a consequence, coordination numbers are notoriously difficult to obtain accurately.[50] Second, Clark's vibrational Raman data is not fully conclusive by and of itself, since

the expected B_{1g} Raman frequency was not observed.[1] Third, as mentioned in the introduction, Clark et al.[1] *assumed* that the observed 300 ppm shift in the oxo-ligand ^{17}O NMR between U^{VI} and Np^{VII} should be assigned to the difference in ligand environment (di- vs. tetra-oxo), but had no direct proof for this assumption. Indeed, as discussed above, our calculations show clearly that this argument is not entirely correct.

In discussing each of these points and combing the computational and experimental data, we can confidently assign the identity of neptunium(VII) in high-ionic-strengths alkaline solutions as being $[NpO_4(OH)_2]^{3-}$.

A number of other, secondary conclusions are as follows:

Regarding NMR, the identity of the central metal has a strong influence on the (ligand) ^{17}O NMR shieldings and chemical shifts. This can be understood by noting that the paramagnetic parts of the calculated shieldings are inversely proportional to the gap between occupied and virtual molecular orbitals with significant f contributions,[10] and this gap is expected to be smaller for neptunium than for uranium. Therefore, conclusions that are solely based on comparisons between formally isoelectronic uranium(VI) and neptunium(VII) complexes are not necessarily fully conclusive.

Comparing oxo-ligand stretching frequencies for U^{VI} and Np^{VII}, we find that the latter are consistently higher than the former, indicating stronger bonds. This is also borne out by shorter bond lengths but is on contrast with series of compounds that have the same metal oxidation state along the actinide series.

Comparing, for a given metal (An = U^{VI} or Np^{VII}), the respective actinyl complexes $[AnO_2X_4]^{2-/1-}$ with X = Cl, F, OH, we observe a decreasing strength of the axial actinyl bond. This must be traced to electronic factors, and should be due to increasing amounts of π-competition from the equatorial ligands.[15]

Acknowledgements

We gratefully acknowledge financial support from the Natural Sciences and Engineering Research Council of Canada (NSERC). GS would like to thank Tom Ziegler for giving him the opportunity to come to Canada almost twenty years ago, for his example and insight in scientific matters and elsewhere, and, most importantly, for his ongoing support over all those years.

References

(1) Clark, D. L.; Palmer, P. D.; Tait, C. D.; Keogh, D. W. *Actinide Research Quarterly* **2004**, First Quarter.

(2) Yoshida, Z.; Johnson, S. G.; Kimura, T.; Krsul, J. R. In *The Chemistry of the Actinide and Transactinide Elements;* Morss, L. R., Edelstein, N. M., Fuger, J., and Katz, J. J., Eds.; Springer: Dordrecht, The Netherlands, 2006; p. 699.

(3) Appelman, E. H.; Kostka, A. G.; Sullivan, J. C. *Inorg. Chem.* **1988**, *27* (11), 2002–2005. doi:10.1021/ic00284a034.

(4) Clark, D. L.; Conradson, S. D.; Neu, M. P.; Palmer, P. D.; Runde, W.; Tait, C. D. *J. Am. Chem. Soc.* **1997**, *119* (22), 5259–5260. doi:10.1021/ja964053l.

(5) Williams, C. W.; Blaudeau, J. P.; Sullivan, J. C.; Antonio, M. R.; Bursten, B.; Soderholm, L. *J. Am. Chem. Soc.* **2001**, *123* (18), 4346–4347. doi:10.1021/ja005640g. PMID: 11457206.

(6) Bolvin, H.; Wahlgren, U.; Gropen, O.; Marsden, C. *J. Phys. Chem. A* **2001**, *105* (46), 10570–10576. doi:10.1021/jp011240j.

(7) Bolvin, H.; Wahlgren, U.; Moll, H.; Reich, T.; Geipel, G.; Fanghanel, T.; Grenthe, I. *J. Phys. Chem. A* **2001**, *105* (51), 11441–11445. doi:10.1021/jp0114283.

(8) Clark, D. L.; Conradson, S. D.; Donohoe, R. J.; Keogh, D. W.; Morris, D. E.; Palmer, P. D.; Rogers, R. D.; Tait, C. D. *Inorg. Chem.* **1999**, *38* (7), 1456–1466. doi:10.1021/ic981137h.

(9) Schreckenbach, G.; Hay, P. J.; Martin, R. L. *Inorg. Chem.* **1998**, *37* (17), 4442–4451. doi:10.1021/ic980057a. PMID: 11670581.

(10) Schreckenbach, G. *Inorg. Chem.* **2002**, *41* (25), 6560–6572. doi:10.1021/ic020370j. PMID:12470051.

(11) Koch, W.; Holthausen, M. C. *A. Chemist's Guide to Density Functional Theory;* Wiley Verlag Chemie: New York, 2000.

(12) Ziegler, T. *Chem. Rev.* **1991**, *91* (5), 651–667. doi:10.1021/cr00005a001.

(13) Ziegler, T. *Can. J. Chem.* **1995**, *73* (6), 743–761. doi:10.1139/v95-095.

(14) Pepper, M.; Bursten, B. E. *Chem. Rev.* **1991**, *91* (5), 719–741. doi:10.1021/cr00005a005.

(15) Schreckenbach, G.; Hay, P. J.; Martin, R. L. *J. Comput. Chem.* **1999**, *20* (1), 70–90. doi:10.1002/(SICI)1096-987X(19990115)20:1<70::AID-JCC9>3.0.CO;2-F.

(16) Kaltsoyannis, N. *Chem. Soc. Rev.* **2003**, *32* (1), 9–16. doi:10.1039/b204253n. PMID:12596541.

(17) Kaltsoyannis, N.; Hay, P. J.; Li, J.; Blaudeau, J. P.; Bursten, B. E. In *The Chemistry of the Actinide and Transactinide Elements;* Morss, L. R., Edelstein, N. M., Fuger, J., and Katz, J. J., Eds.; Springer: Dordrecht, The Netherlands, 2006; p. 1893.

(18) Perdew, J. P.; Burke, K.; Ernzerhof, M. *Phys. Rev. Lett.* **1996**, *77* (18), 3865–3868. doi:10.1103/PhysRevLett.77.3865. PMID:10062328.

(19) (a) Shamov, G. A.; Schreckenbach, G. *J. Phys. Chem. A* **2005**, *109* (48), 10961–10974. doi:10.1021/jp053522f. PMID:16331940.; (b) Shamov, G. A.; Schreckenbach, G. *J. Phys. Chem. A* **2006**, *110* (43), 12072. doi:10.1021/jp0662855.

(20) Shamov, G. A.; Schreckenbach, G.; Vo, T. *Chem. Eur. J.* **2007**, *13* (17), 4932–4947. doi:10.1002/chem.200601244.

(21) Shamov, G. A.; Schreckenbach, G. *J. Phys. Chem. A* **2006**, *110* (30), 9486–9499. doi:10.1021/jp063060l. PMID: 16869700.

(22) Shamov, G. A.; Schreckenbach, G.; Martin, R. L.; Hay, P. J. *Inorg. Chem.* **2008**, *47* (5), 1465–1475. doi:10.1021/ic7015403. PMID:18225857.

(23) Fonseca Guerra, C.; Snijders, J. G.; Te Velde, G.; Baerends, E. J. *Theor. Chem. Acc.* **1998**, *99* (6), 391. doi:10.1007/s002140050021.

(24) Fonseca Guerra, C.; Visser, O.; Snijders, J. G.; Te Velde, G.; Baerends, E. J. In *Methods and Techniques in Computational Chemistry METECC-95;* Clementi, E. and Corongiu, C., Eds.; STEF: Cagliari, Italy, 1995; p. 305.

(25) te Velde, G.; Bickelhaupt, F. M.; Baerends, E. J.; Fonseca Guerra, C.; Van Gisbergen, S. J. A.; Snijders, J. G.; Ziegler, T. *J. Comput. Chem.* **2001**, *22* (9), 931–967. doi:10.1002/jcc.1056.

(26) Pyykkö, P. *Chem. Rev.* **1988**, *88* (3), 563–594. doi:10.1021/cr00085a006.

(27) van Lenthe, E.; Baerends, E. J.; Snijders, J. G. *J. Chem. Phys.* **1993**, *99* (6), 4597. doi:10.1063/1.466059.
(28) van Lenthe, E.; Baerends, E. J.; Snijders, J. G. *J. Chem. Phys.* **1994**, *101* (11), 9783. doi:10.1063/1.467943.
(29) van Lenthe, E.; Ehlers, A.; Baerends, E. J. *J. Chem. Phys.* **1999**, *110* (18), 8943. doi:10.1063/1.478813.
(30) van Lenthe, E.; Snijders, J. G.; Baerends, E. J. *J. Chem. Phys.* **1996**, *105* (15), 6505. doi:10.1063/1.472460.
(31) van Lenthe, E.; Van Leeuwen, R.; Baerends, E. J.; Snijders, J. G. *Int. J. Quantum Chem.* **1996**, *57* (3), 281–293. doi:10.1002/(SICI)1097-461X(1996)57:3<281::AID-QUA2>3.0.CO;2-U.
(32) Van Lenthe, E.; Wormer, P. E. S.; Van Der Avoird, A. *J. Chem. Phys.* **1997**, *107* (7), 2488. doi:10.1063/1.474590.
(33) Schreckenbach, G.; Wolff, S. K.; Ziegler, T. *J. Phys. Chem. A* **2000**, *104* (35), 8244–8255. doi:10.1021/jp001143a.
(34) Schreckenbach, G.; Wolff, S. K.; Ziegler, T. In *Modelling NMR Chemical Shifts: Gaining Insight into Structure and Environment;* Facelli, J. C. and de Dios, A., Eds.; ACS Symposium Series 732; American Chemical Society: WA, 1999; p. 101.
(35) Kaupp, M.; Malkina, O. L.; Malkin, V. G.; Pyykkö, P. *Chem. Eur. J.* **1998**, *4* (1), 118–126. doi:10.1002/(SICI)1521-3765(199801)4:1<118::AID-CHEM118>3.0.CO;2-6.
(36) Te Velde, G.; Baerends, E. J. *J. Comput. Phys.* **1992**, *99* (1), 84–98. doi:10.1016/0021-9991(92)90277-6.
(37) Schreckenbach, G. *Int. J. Quantum Chem.* **2005**, *101* (4), 372–380. doi:10.1002/qua.20350.
(38) Schreckenbach, G.; Ziegler, T. *J. Phys. Chem.* **1995**, *99* (2), 606–611. doi:10.1021/j100002a024.
(39) Schreckenbach, G.; Ziegler, T. *Int. J. Quantum Chem.* **1997**, *61* (6), 899–918. doi:10.1002/(SICI)1097-461X(1997)61:6<899::AID-QUA3>3.0.CO;2-R.
(40) Schreckenbach, G.; Ziegler, T. *Theor. Chem. Acc.* **1998**, *99*, 71–82. doi:10.1007/s002140050306.
(41) Wolff, S. K.; Ziegler, T. *J. Chem. Phys.* **1998**, *109* (3), 895. doi:10.1063/1.476630.
(42) Wolff, S. K.; Ziegler, T.; Van Lenthe, E.; Baerends, E. J. *J. Chem. Phys.* **1999**, *110* (16), 7689. doi:10.1063/1.478680.
(43) Klamt, A.; Schüürmann, G. *J. Chem. Soc. Perkin Trans.* **1993**, *2*, 799.
(44) Pye, C. C.; Ziegler, T. *Theor. Chem. Acc.* **1999**, *101*, 396.
(45) Klamt, A.; Eckert, F. *Fluid Phase Equilib.* **2000**, *172* (1), 43–72. doi:10.1016/S0378-3812(00)00357-5.
(46) Klamt, A.; Jonas, V.; Bürger, T.; Lohrenz, J. C. W. *J. Phys. Chem. A* **1998**, *102* (26), 5074–5085. doi:10.1021/jp980017s.
(47) Autschbach, J.; Le Guennic, B. *Chem. Eur. J.* **2004**, *10* (10), 2581–2589. doi:10.1002/chem.200305513.
(48) Autschbach, J.; Le Guennic, B. *J. Am. Chem. Soc.* **2003**, *125* (44), 13585–13593. doi:10.1021/ja0368047. PMID: 14583056.
(49) Denning, R. G. *J. Phys. Chem. A* **2007**, *111* (20), 4125–4143. doi:10.1021/jp071061n. PMID:17461564.
(50) Den Auwer, C.; Simoni, E.; Conradson, S.; Madic, C. *Eur. J. Inorg. Chem.* **2003**, *2003* (21), 3843–3859. doi:10.1002/ejic.200300093.

Charge density reconstitution from approximate exchange-correlation holes

Paola Gori-Giorgi, János G. Ángyán, and Andreas Savin

Abstract: The electronic charge density and the expectation of any monoelectronic operator can be reconstructed by a density-weighted integral of the exchange-correlation hole. This property can be used to test and improve approximate holes that are not spherically averaged. As an example, we test the Becke–Roussel exhange-hole model in its nonspherical formulation on small atoms, finding that it accurately reproduces the density in the core region, while missing some of the features of the valence and core-valence regions. The same test on the local-density approximation shows poor results, as expected.

Key words: electronic structure theory, density functional theory, electronic correlations, exchange-correlation functionals, pair-correlation functions.

Résumé : On peut reconstruire la densité de charge électronique et la valeur moyenne des opérateurs monoélectroniques sous forme d'une intégrale du trou d'échange-corrélation pondérée par la densité. Cette propriété peut être utilisée pour tester et améliorer les trous approximatifs qui ne sont pas moyennés selon les directions dans l'espace. Comme exemple, opérant sur de petits atomes, on peut tester le modèle d'échange de trou de Becke–Roussel dans sa formulation non sphérique et on trouve qu'elle reproduit d'une façon precise la densité dans la région de coeur même si l'accord est moins bon dans les régions de valence et de coeur-valence. Tel que prévu, le même test effectué en utilisant l'approximation de densité locale produit des résultats assez médiocres.

Mots-clés : théorie de la structure électronique, théorie de la fonctionnelle de la densité, corrélations électroniques, fonctionnelles d'échange-corrélation, fonctions de corrélation de paires.

Introduction

Density functional theory (DFT)[1,2] in its Kohn–Sham (KS)[3] formulation is nowadays a widely used method in quantum chemistry and solid-state physics, thanks to its unique combination of low computational cost and reasonable accuracy.[4] In the Kohn–Sham formalism, the total energy of a many-electron system in the external electron-nuclei potential, $\widehat{V}_{\rm ne} = \sum_i v_{\rm ne}(\mathbf{r}_i)$, is rewritten as a functional of the one-electron density, $\rho(\mathbf{r})$,

$$[1] \qquad E[\rho] = T_{\rm s}[\rho] + U[\rho] + E_{\rm xc}[\rho] + \int {\rm d}\mathbf{r}\, v_{\rm ne}(\mathbf{r})\, \rho(\mathbf{r})$$

In eq. [1], $T_{\rm s}[\rho]$ is the kinetic energy of a non-interacting system of fermions (usually called the KS system) having the same one-electron density, ρ, of the physical, interacting system. The Hartree energy, $U[\rho]$, is the classical repulsion energy, $U[\rho] = \frac{1}{2}\int {\rm d}\mathbf{r} \int {\rm d}\mathbf{r}' \rho(\mathbf{r})\rho(\mathbf{r}')|\mathbf{r} - \mathbf{r}'|^{-1}$, and the exchange-correlation functional, $E_{\rm xc}[\rho]$, must be approximated.

Despite its success, to which can be ascribed the description of a variety of systems, from bulk materials to proteins, KS DFT is still plagued by several unsolved problems. For example, approximate KS DFT has well known problems in handling near-degeneracy effects (rearrangement of electrons within partially filled shells) and in the description of long-range dispersion forces. The quest for better approximations for the exchange-correlation functional, $E_{\rm xc}[\rho]$, is thus a very active research field (for recent reviews see, e.g., refs. 5–9).

The exchange-correlation (xc) hole has always played a special role in this quest, as a powerful tool to understand[10–18] and build (see, e.g., refs. 19–27) approximations. In particular, the exact properties of the xc hole have been extensively used to construct nonempirical $E_{\rm xc}[\rho]$. As we shall review later, to compute the exchange-correlation energy one only needs knowledge of the system- and spheri-

Received 6 March 2009. Accepted 22 May 2009. Published on the NRC Research Press Web site at canjchem.nrc.ca on 1 October 2009.

This article is part of a Special Issue dedicated to Professor T. Ziegler. It is a pleasure to dedicate this paper to Tom Ziegler who was among the first to recognize the importance of the exchange-correlation hole in the understanding of the density functional theory.

P. Gori-Giorgi[1] and A. Savin. Laboratoire de Chimie Théorique, CNRS UMR 7616, Université Pierre et Marie Curie, 4 Place Jussieu, F-75252 Paris, France.
J.G. Ángyán. Équipe Modélisation Quantique et Cristallographique, CRM2, UMR 7036, Institut Jean Barriol, Nancy-University - CNRS, B.P. 239, F-54506 Vandœuvre-lès-Nancy, France.

[1]Corresponding author (e-mail: gori@lct.jussieu.fr).

cally averaged xc hole. Usually, most of the approximations try to construct a model for the spherically averaged hole in each point of space, neglecting those exact properties that do not affect the final system-averaged result (i.e., the final integration over all space). In real systems of nonuniform density, the xc hole can be highly nonspherical (an elegant discussion based on the shape of localized orbitals was given in ref. 11), and one can expect that somehow taking into account this anisotropy would improve the resulting $E_{xc}[\rho]$ and other properties that can be calculated from the xc hole. For example, an interesting recent model for describing van der Waals interactions is precisely based on the anisotropy of the exchange hole.[28–32]

In this paper, we focus on an exact property (the "charge density reconstitution") of the (nonspherically averaged) xc hole that is often overlooked (since it does not affect system- and spherically averaged models), by testing some approximate holes on small atoms. After giving the basic definitions in the next section, we analyze the charge density reconstitution in the "charge reconstitution" section, discussing its generalization to one-electron properties. In the "Becke–Roussel exchange hole before spherical average" and "local density approximation" sections, we give two examples of charge density reconstitution for small atoms from the Becke–Roussel[23] exchange hole and the local-density approximation (LDA) xc hole, respectively.

Definitions

Although KS DFT was first formulated as a method "without wavefunction", writing an expression for the xc functional, $E_{xc}[\rho]$, in terms of wave functions is a useful step to define the xc hole. This can be done via the adiabatic connection formalism.[10,33–36] In its simplest version,[10,33,34] the electron–electron repulsion operator, $\widehat{W}_{ee} = \sum_{i=1}^{N}\sum_{j=i+1}^{N} 1/|\mathbf{r}_i - \mathbf{r}_j|$, in the N-electron hamiltonian is multiplied by a real parameter, λ, which varies between 0 and 1. At the same time, the physical external potential, $v_{ne}(\mathbf{r})$, is replaced by another local potential, $v^{\lambda}(\mathbf{r})$, determined by the condition that the one-electron density, $\rho(\mathbf{r})$, does not change with λ. If Ψ^{λ} denotes the ground state of these λ-dependent hamiltonians, we have the exact formula[10,34]

$$[2] \qquad E_{xc}[\rho] = \int_0^1 \langle \Psi^{\lambda} | \widehat{W}_{ee} | \Psi^{\lambda} \rangle \mathrm{d}\lambda - U[\rho]$$

This decomposition of $E_{xc}[\rho]$ is by no means unique: for example, one can consider different ways of turning on the electron-electron interaction[35,36] or a formula that only involves the expectation of the kinetic energy.[37,38] The simple adiabatic connection that leads to eq. [2] is by far the most used to build approximations.

Introducing the spin-summed pair density, $P_2(\mathbf{r}, \mathbf{r}')$, associated with a given N-electron wave function, Ψ,

$$[3] \qquad P_2(\mathbf{r}, \mathbf{r}') = N(N-1) \times \sum_{\sigma_1,\ldots,\sigma_N} \int |\Psi(\mathbf{r}\sigma_1, \mathbf{r}'\sigma_2, \mathbf{r}_3\sigma_3, \ldots, \mathbf{r}_N\sigma_N)|^2 \mathrm{d}\mathbf{r}_3, \ldots, \mathrm{d}\mathbf{r}_N$$

we can rewrite eq. [2] as

$$[4] \qquad E_{xc}[\rho] = \frac{1}{2} \int \mathrm{d}\mathbf{r} \int \mathrm{d}\mathbf{r}' \frac{\bar{P}_2(\mathbf{r}, \mathbf{r}') - \rho(\mathbf{r})\rho(\mathbf{r}')}{|\mathbf{r} - \mathbf{r}'|}$$

where

$$[5] \qquad \bar{P}_2(\mathbf{r}, \mathbf{r}') = \int_0^1 \mathrm{d}\lambda \, P_2^{\lambda}(\mathbf{r}, \mathbf{r}')$$

is the coupling-constant-averaged pair density, and P_2^{λ} is obtained by putting Ψ^{λ} in eq. [3]. The interaction-averaged xc hole, $h_{xc}(\mathbf{r}, \mathbf{r}')$, is then usually defined as

$$[6] \qquad h_{xc}(\mathbf{r}, \mathbf{r}') = \frac{\bar{P}_2(\mathbf{r}, \mathbf{r}')}{\rho(\mathbf{r})} - \rho(\mathbf{r}')$$

so that

$$[7] \qquad E_{xc}[\rho] = \frac{1}{2} \int \mathrm{d}\mathbf{r} \, \rho(\mathbf{r}) \int \mathrm{d}\mathbf{r}' \frac{h_{xc}(\mathbf{r}, \mathbf{r}')}{|\mathbf{r} - \mathbf{r}'|}$$

Since the xc hole is simply related to the pair density, all its properties come from exact conditions satisfied by the pair density itself.[39] The xc hole is often divided into exchange (x) and correlation (c),

$$[8] \qquad h_x(\mathbf{r}, \mathbf{r}') = \frac{P_2^{KS}(\mathbf{r}, \mathbf{r}')}{\rho(\mathbf{r})} - \rho(\mathbf{r}')$$

$$[9] \qquad h_c(\mathbf{r}, \mathbf{r}') = h_{xc}(\mathbf{r}, \mathbf{r}') - h_x(\mathbf{r}, \mathbf{r}')$$

where $P_2^{KS}(\mathbf{r}, \mathbf{r}')$ is the pair density of the Kohn–Sham system, obtained by putting the Kohn–Sham Slater determinant (i.e., $\Psi^{\lambda=0}$) into eq. [3]. Notice that, because of its definition (eq. [6]), the xc hole is not symmetric in its variables, $h_{xc}(\mathbf{r}, \mathbf{r}') \neq h_{xc}(\mathbf{r}', \mathbf{r})$, but satisfies $\rho(\mathbf{r})h_{xc}(\mathbf{r}, \mathbf{r}') = \rho(\mathbf{r}')h_{xc}(\mathbf{r}', \mathbf{r})$.

Because the Coulomb interaction, $1/|\mathbf{r} - \mathbf{r}'|$, only depends on the electron–electron distance, to compute $E_{xc}[\rho]$ of eq. [7] we only need the spherical average, $h^s_{xc}(\mathbf{r}, u)$, of the xc hole with respect to the direction of $\mathbf{u} = \mathbf{r} - \mathbf{r}'$,

$$[10] \qquad h^s_{xc}(\mathbf{r}, u) = \int h_{xc}(\mathbf{r}, \mathbf{r} + \mathbf{u}) \frac{d\Omega_{\mathbf{u}}}{4\pi}$$

so that

$$[11] \qquad E_{xc}[\rho] = \frac{1}{2} \int d\mathbf{r}\, \rho(\mathbf{r}) \int_0^\infty du\, 4\pi u^2 \frac{h^s_{xc}(\mathbf{r}, u)}{u}$$

We can go one step further, and realize that to compute $E_{xc}[\rho]$ we actually only need the system- and spherically averaged hole,

$$[12] \qquad \langle h^s_{xc}(u) \rangle = \int d\mathbf{r}\, \rho(\mathbf{r}) h^s_{xc}(\mathbf{r}, u)$$

$$[13] \qquad E_{xc}[\rho] = \frac{1}{2} \int_0^\infty du\, 4\pi u^2 \frac{\langle h^s_{xc}(u) \rangle}{u}$$

The most common practice when constructing approximations in DFT is somehow in between eqs. [10] and [12]: most models prefer to build $h^s_{xc}(\mathbf{r}, u)$ (e.g., refs. 23, 26, 40–44), but with the idea in mind that only $\langle h^s_{xc}(u) \rangle$ matters for the exchange-correlation energy, so that exact properties of $h^s_{xc}(\mathbf{r}, u)$ that do not affect $\langle h^s_{xc}(u) \rangle$ can be neglected. One of the reasons to follow this practice is that an approximation defined locally is believed to be automatically size consistent, even if this might not be true in the case of systems with a degenerate ground state.[45,46]

As we integrate information out, passing from $h_{xc}(\mathbf{r}, \mathbf{r}')$ to $h^s_{xc}(\mathbf{r}, u)$ and then to $\langle h^s_{xc}(u) \rangle$, there are exact properties that do not hold anymore (i.e., they can either be hidden in a very complicated way in the integrated quantities, or may just not be important anymore). For instance, the symmetry property, $\rho(\mathbf{r}) h_{xc}(\mathbf{r}, \mathbf{r}') = \rho(\mathbf{r}') h_{xc}(\mathbf{r}', \mathbf{r})$, does not translate into a simple condition for the spherically averaged hole, $h^s_{xc}(\mathbf{r}, u = |\mathbf{r}' - \mathbf{r}|)$, so that, in general, even for the exact hole we have $\rho(\mathbf{r}) h^s_{xc}(\mathbf{r}, |\mathbf{r}' - \mathbf{r}|) \neq \rho(\mathbf{r}') h^s_{xc}(\mathbf{r}', |\mathbf{r} - \mathbf{r}'|)$. When targeting only the spherically and system-averaged hole, $\langle h^s_{xc}(u) \rangle$, the original symmetry in $\mathbf{r}$, $\mathbf{r}'$ does not play a role anyhow: even if we start from a model hole that does not respect it, the integration over all space cancels the contribution from its antisymmetric part.

Besides the possibility of constructing $E_{xc}[\rho]$, the xc holes, $h_{xc}(\mathbf{r}, \mathbf{r}')$ and $h^s_{xc}(\mathbf{r}, u)$, are interesting quantities per se: they contain chemical information, they can be used to estimate the expectation of two-electron properties, and they define a gauge for the exchange-correlation energy density, $\epsilon_{xc}(\mathbf{r})$,

$$[14] \qquad \epsilon_{xc}(\mathbf{r}) = \frac{1}{2} \int_0^\infty du\, 4\pi u^2 \frac{h^s_{xc}(\mathbf{r}, u)}{u}$$

$$[15] \qquad E_{xc}[\rho] = \int d\mathbf{r}\, \rho(\mathbf{r})\, \epsilon_{xc}(\mathbf{r})$$

The exchange-correlation energy density, $\epsilon_{xc}(\mathbf{r})$, is often used as a starting point to refine approximations.

Charge reconstitution

From the definition of the exchange-correlation hole (eq. [6]) and of the one-electron density,

$$\rho(\mathbf{r}) = \frac{1}{N-1} \int d\mathbf{r}' P_2(\mathbf{r}, \mathbf{r}')$$

one obtains the two sum rules

$$[16] \qquad \int d\mathbf{r}'\, h_{xc}(\mathbf{r}, \mathbf{r}') = -1$$

$$[17] \qquad \int d\mathbf{r}\, \rho(\mathbf{r})\, h_{xc}(\mathbf{r}, \mathbf{r}') = -\rho(\mathbf{r}')$$

Equation [16] is the usual xc hole sum rule, satisfied by almost all models. It leads to a corresponding sum rule for the spherically averaged hole,

$$[18] \qquad \int_0^\infty 4\pi u^2\, h^s_{xc}(\mathbf{r}, u)\, du = -1$$

The second sum rule, eq. [17], is a simple consequence of the symmetry property, $\rho(\mathbf{r}) h_{xc}(\mathbf{r}, \mathbf{r}') = \rho(\mathbf{r}') h_{xc}(\mathbf{r}', \mathbf{r})$, and shows that the electronic charge density can be reconstructed by a density-weighted integral of the exchange-correlation hole (charge reconstitution). Like the symmetry property from which it is derived, this second sum rule does not translate into a simple condition for the spherically averaged hole, because its information is partially averaged out in the integration over the direction of $\mathbf{u} = \mathbf{r}' - \mathbf{r}$ in eq. [10]. Since most of the approximate holes only try to model $h^s_{xc}(\mathbf{r}, u)$, eq. [17] is often neglected in the literature. Notice that if we consider exchange and correlation separately, we obtain

$$[19] \qquad \int d\mathbf{r}\, \rho(\mathbf{r})\, h_x(\mathbf{r}, \mathbf{r}') = -\rho(\mathbf{r}')$$

$$[20] \qquad \int d\mathbf{r}\, \rho(\mathbf{r})\, h_c(\mathbf{r}, \mathbf{r}') = 0$$

We can define, for any monoelectronic local operator, $\hat{O} = \sum_i o(\mathbf{r}_i)$, an associated exchange-correlation hole projected property

$$[21] \qquad o_{xc}(\mathbf{r}) = -\int d\mathbf{r}'\, o(\mathbf{r}')\, h_{xc}(\mathbf{r}, \mathbf{r}')$$

By the virtue of eq. [17], the exchange-correlation hole projected property, $o_{xc}(\mathbf{r})$, weighted by the charge density, $\rho(\mathbf{r})$, leads to the same value as the expectation value of the operator, $\hat{O}$,

$$[22] \qquad \langle \Psi | \hat{O} | \Psi \rangle = \int d\mathbf{r}\, \rho(\mathbf{r})\, o(\mathbf{r}) = \int d\mathbf{r}\, \rho(\mathbf{r})\, o_{xc}(\mathbf{r})$$

Another way to look at it is that, for any local monoelectronic operator, $\hat{O}$, there exist an associated "exchange-correlation-hole weighted" operator, $\hat{O}_{xc} = \sum_i o_{xc}(\mathbf{r}_i)$, with $o_{xc}(\mathbf{r})$, given by eq. [21], with the same ground-state expectation value.

For instance, $o(\mathbf{r})$ can be a multipole moment function. In the case of the monopole, i.e., $o(\mathbf{r}) = 1$, one obtains the total number of electrons. For the first order moment, $o(\mathbf{r}) = r_\alpha$, where α denotes a cartesian component, x, y, or z, one has

$$[23] \qquad \mu_\alpha = -\int d\mathbf{r}\rho(\mathbf{r}) \int d\mathbf{r}' h_{xc}(\mathbf{r},\mathbf{r}') r'_\alpha$$

where μ_α denotes a cartesian component of the electronic dipole moment. The corresponding characteristic exchange-correlation weighted function, $D_\alpha(\mathbf{r})$,

$$[24] \qquad D_\alpha(\mathbf{r}) = -\int d\mathbf{r}' h_{xc}(\mathbf{r},\mathbf{r}') r'_\alpha$$

provides the coordinates of the xc hole barycenter (center of charge) belonging to the point $\mathbf{r}$.[30] Thus, eq. [23] tells us that the total electronic dipole moment can be obtained as the weighted sum of the xc hole barycenters. This result can be regarded as a generalization of the Wannier-center decomposition of the polarization,[47] widely used in the solid-state physics community: the Wannier-center, which is a Dirac-like distribution placed in the barycenters of the localized orbitals, is replaced by a fuzzy distribution of xc hole barycenters.[48] Similar analysis can be carried out for higher-order multipole moments. Notice that if we consider exchange and correlation separately, we see that eqs. [19]–[20] imply that eqs. [21]–[22] hold as well for the exchange hole alone.

Becke and Johnson[28,31] have constructed a heuristic model to take into account van der Waals interactions between two subsystems using the square, $d_x^2(\mathbf{r}) = \mathbf{d}_x(\mathbf{r}) \cdot \mathbf{d}_x(\mathbf{r})$, of the dipole moment of the exchange hole plus its reference electron on each subsystem,

$$[25] \qquad \mathbf{d}_x(\mathbf{r}) = -\int d\mathbf{r}' h_x(\mathbf{r},\mathbf{r}')\mathbf{r}' - \mathbf{r} = \mathbf{D}(\mathbf{r}) - \mathbf{r}$$

where here the subscript x stands for exchange hole.

Because of the charge density reconstitution sum rule of eq. [17], the exact $\mathbf{d}_x(\mathbf{r})$ has zero expectation,[30]

$$[26] \qquad \int \rho(\mathbf{r})\, \mathbf{d}_x(\mathbf{r})\, d\mathbf{r} = 0$$

A density functional approximation for $d_x^2(\mathbf{r})$ has been constructed by Becke and Johnson[29] using the Becke–Roussel (BR)[23] exchange-hole model. As briefly reviewed in the next section, the BR exchange-hole model is based on the spherical average of an anisotropic hole. Thus, even if its final outcome is a spherically averaged hole, it is based on the idea that the real hole is nonspherical, and for this reason it can be used to estimate the exchange-hole dipole moment. In this context, it is interesting to check how well the BR model before spherical average satisfies eq. [19]. This is the object of the next section.

The Becke–Roussel exchange hole before spherical average

The BR exchange-hole model[23] is inspired by the exact exchange hole of the hydrogen atom: it places a normalized exponential at a distance $b(\mathbf{r})$ from the position $\mathbf{r}$ of the σ-spin reference electron (the total exchange hole considered in the previous sections is the sum over the two σ-spin holes, $h_x = h_{x,\uparrow} + h_{x,\downarrow}$),

$$[27] \qquad h_{x,\sigma}^{BR}(\mathbf{r},\mathbf{r}') = -\frac{a^3(\mathbf{r})}{8\pi} e^{-a(\mathbf{r})|\mathbf{r}'-\mathbf{r}+\mathbf{b}(\mathbf{r})|}$$

The dipole moment of this hole plus its reference electron, evaluated with eq. [25], is simply $\mathbf{b}(\mathbf{r})$.

The final form of the BR model is obtained by taking the spherically averaged with respect to the direction of $\mathbf{u} = \mathbf{r}' - \mathbf{r}$ of eq. [27]. This way, the BR spherically averaged hole only depends on the magnitude $b(\mathbf{r})$ of $\mathbf{b}(\mathbf{r})$. The two parameters $a(\mathbf{r})$ and $b(\mathbf{r})$ are fixed by imposing the exact on-top ($\mathbf{r} \to \mathbf{r}'$ or $u \to 0$) depth and curvature,

$$[28] \qquad h_{x,\sigma}(\mathbf{r}, u) = -\rho_\sigma + \frac{u^2}{6}\left(2\tau_\sigma - \frac{|\nabla\rho_\sigma|^2}{2} - \nabla^2\rho_\sigma\right) + O(u^4)$$

where $\rho_\sigma(\mathbf{r})$ is the density of spin-σ electrons and $\tau_\sigma = \sum_i |\nabla\phi_{i,\sigma}|^2$ ($\phi_{i,\sigma}$ are the Kohn–Sham orbitals). The model, thus, provides the magnitude of $\mathbf{b}(\mathbf{r})$ but not its direction, since it is not needed either in the spherically averaged hole or in the Becke–Johnson dispersion model,[29] which only uses $b^2(r)$.

In an atom, however, with the BR ingredients, the only possible choice is having $\mathbf{b}(\mathbf{r})$ pointing towards the nucleus. In this case we can thus test without ambiguity how well the BR hole model *before* spherical average satisfies eq. [19]. In a spherical atom, the charge density reconstitution of eq. [19] from the BR hole would read

$$[29] \qquad \int d\mathbf{r}\ \rho(r)\ \frac{a^3(r)}{8\pi} e^{-a(r)|(b(r)/r-1)\mathbf{r}+\mathbf{r}'|} = \rho(r')$$

where we now have to check how well this equality is actually satisfied. In the left-hand side of eq. [29], the integration over the angular part of $\mathbf{r}$ is analytical, so that we are left with a one-dimensional integral, which is evaluated numerically on a grid.

In Figs. 1–3, we show our results for the He, Be, and Ne atoms, respectively, using highly accurate input ingredients to avoid any bias (using almost "exact" input quantities allows us to focus on the results of the model, without introducing any other source of error). For the He atom we have used the density coming from the variational wave function of ref. 49, while for Be and Ne we have used the density and the Kohn–Sham orbitals from the accurate Kohn–Sham potentials of refs. 50 and 51. We see that eq. [29] is almost satisfied for the He atom, and for the core region of Be and Ne, which are dominated by 1s-type orbitals qualitatively similar to eq. [27]. The valence region of Be, instead, is poorly reproduced, with the BR hole yielding results of similar quality to the LDA (see the next section). Some of the features of the core-valence region of the Ne atom are also missed by the BR hole.

Local density approximation

The local density approximation (LDA) to the exchange-correlation hole consists in taking the xc hole of a uniform

Fig. 1. Charge density reconstitution from approximate holes for the He atom. We tested the Becke–Roussel (BR) exchange hole before spherical average, and the LDA exchange and exchange-correlation hole at full coupling strength.

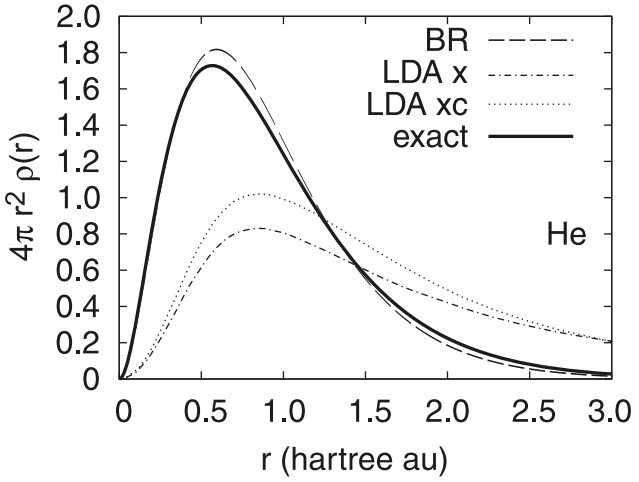

Fig. 2. Charge density reconstitution from approximate holes for the Be atom. We tested the Becke–Roussel (BR) exchange hole before spherical average, and the LDA exchange and exchange-correlation hole at full coupling strength.

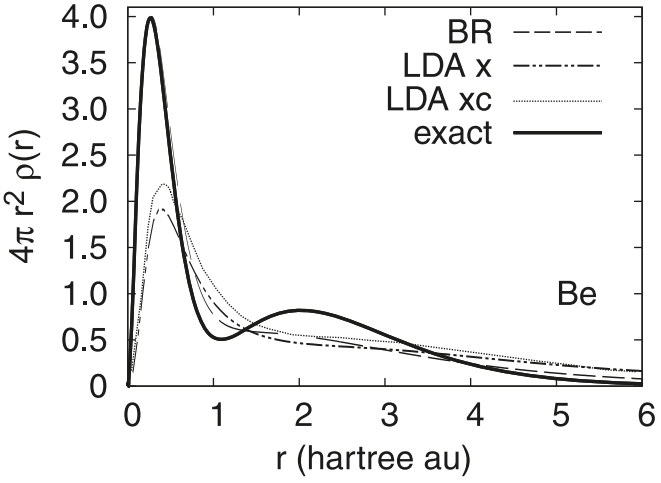

electron gas with density $\rho(\mathbf{r})$ from around the reference electron at position $\mathbf{r}$,

$$[30] \qquad h_{xc}^{LDA}(\mathbf{r},\mathbf{r}') = \rho(\mathbf{r}) g_{xc}^{UEG}(|\mathbf{r}' - \mathbf{r}|; \rho(\mathbf{r}))$$

where $g_{xc}^{UEG}(u;\rho)$ is the exchange-correlation pair-distribution function (see, e.g., ref. 52). Being that the uniform electron gas is an isotropic system, the LDA xc hole is spherical, and it has been shown to be a surprisingly good approximation for the short-range part (small $u = |\mathbf{r}' - \mathbf{r}|$) of the spherically averaged xc hole of systems of nonuniform density.[13–15]

As explained in the charge reconstitution section, the sum rule of eq. [17] does not translate into a simple condition on the spherically averaged hole. Thus, if we want to consider LDA as a good approximation for the spherically averaged hole, there is no space for checking eq. [17]. However, since the LDA hole is intrinsically spherical, we can also consider eq. [30] as an approximation for the nonspherically averaged hole. In this case, the charge density reconstitution of eq. [17] for spherical atoms reduces to the condition

$$[31] \qquad \rho(r') = 2\pi \int_0^\infty \mathrm{d}r\, r^2\, \rho^2(r) \times \int_{-1}^{1} \mathrm{d}y\, g_{xc}^{UEG}\left(\sqrt{r^2 + r'^2 - 2rr'y}; \rho(r)\right)$$

where again the point is to check whether this equality is actually satisfied. Notice also that other widely used models such as PBE[40,41] and TPSS[42] only approximate the spherically averaged hole, so that we cannot carry out similar tests for those models.

Using the same densities of the previous section, we have numerically evaluated the right-hand side of eq. [31] for He, Be, and Ne. We have considered the case of the exchange-only hole and of the exchange-correlation hole at full coupling strength (i.e., with $P_2^{\lambda=1}$ in eq. [6] instead of the coupling-constant averaged $\bar{P}_2$), using the parametrization of $g_{xc}^{UEG}(u;\rho)$ of ref. 52. We see from Figs. 1–3 that, as expected, LDA does not satisfy eq. [31], which should actually be fulfilled at the exchange-only level, meaning that adding the correlation part should not change the result. Notice that the curve corresponding to the coupling-constant-averaged xc hole will always lie between the exchange-only result and the full-coupling strength xc result.

Fig. 3. Charge density reconstitution from approximate holes for the Ne atom. We tested the Becke–Roussel (BR) exchange hole before spherical average, and the LDA exchange and exchange-correlation hole at full coupling strength.

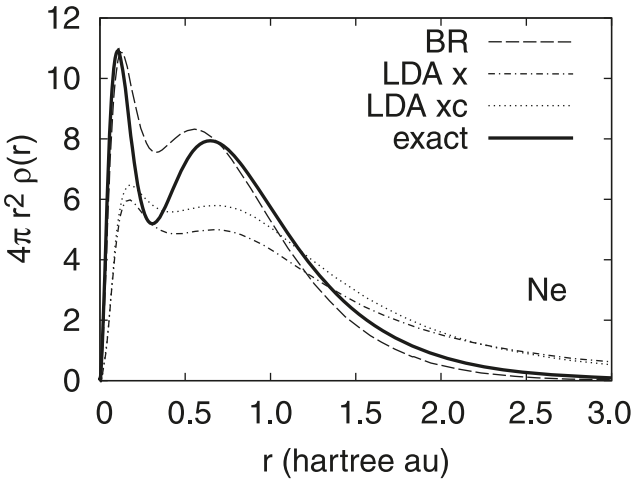

This failure of LDA to fulfill eq. [17] should not be considered as a flaw of the model, if we regard LDA as an approximation to the spherically averaged hole, $h_{xc}^{s}(\mathbf{r}, u)$. As said, the exact spherically averaged hole, $h_{xc}^{s}(\mathbf{r}, u = |\mathbf{r}' - \mathbf{r}|)$, in fact, is not supposed to satisfy eq. [17] (only the nonspherically averaged hole does). So, if LDA is a reasonable approximation (even if only at short range) for the spherically averaged hole, it should not fulfill eq. [17]. This point is somehow philosophical, since the LDA hole model is exactly the same for the nonspherically averaged $h_{xc}(\mathbf{r}, \mathbf{r}')$ and the spherically averaged $h_{xc}(\mathbf{r}, u)$.

Conclusions and perspectives

We have discussed a sum rule concerning the (nonspherically averaged) exchange-correlation hole, in which different monoelectronic local operators can be used. Even if, eventually, only the system- and spherically averaged hole is needed to obtain the exchange-correlation energy, a given model for the spherically averaged hole (which is interesting by itself to compute different properties and to define energy densities) could be improved by taking into account, in some approximate way, the sum rule of eq. [17]. If the whole eq. [17] may be too hard to impose, a selection of local operators $o(\mathbf{r})$ in eq. [22] might be simpler to handle. For example, the Becke–Roussel[23] hole could be improved by adding some parameters that are adjusted to fulfill, at least approximately, eq. [22] for the case of the dipole moment. This may give a more accurate estimate of the exchange-hole dipole moment needed in the Becke–Johnson model[29] for dispersion forces.

Another important point to consider is the following. When dealing with open systems or with systems with strong nondynamical correlation, a better local model for the exchange hole can be obtained by relaxing[18,27] the sum rule of eq. [16], and thus also, by symmetry, the sum rule of eq. [17] considered here. Again, taking this symmetry into account in some approximate way before the spherical average could also improve a given model for nondynamical correlation.

Acknowledgments

This work was supported by Agence Nationale de la Recherche (ANR)(07-BLAN-0272).

References

(1) Hohenberg, P.; Kohn, W. *Phys. Rev.* **1964**, *136* (3B), B864–B871. doi:10.1103/PhysRev.136.B864.
(2) Kohn, W. *Rev. Mod. Phys.* **1999**, *71* (5), 1253–1266. doi:10.1103/RevModPhys.71.1253.
(3) Kohn, W.; Sham, L. J. *Phys. Rev.* **1965**, *140* (4A), A1133–A1138. doi:10.1103/PhysRev.140.A1133.
(4) Ziegler, T.; Autschbach, J. *Chem. Rev.* **2005**, *105* (6), 2695–2722. doi:10.1021/cr0307188. PMID:15941226.
(5) Mattsson, A. E. *Science* **2002**, *298* (5594), 759–760. doi:10.1126/science.1077710. PMID:12399569.
(6) Perdew, J. P.; Ruzsinszky, A.; Tao, J.; Staroverov, V. N.; Scuseria, G. E.; Csonka, G. I. *J. Chem. Phys.* **2005**, *123* (6), 062201. doi:10.1063/1.1904565.
(7) Becke, A. D.; Johnson, E. R. *J. Chem. Phys.* **2007**, *127* (12), 124108. doi:10.1063/1.2768530. PMID:17902894.
(8) Zhao, Y.; Schultz, N. E.; Truhlar, D. G. *J. Chem. Theory Comput.* **2006**, *2* (2), 364–382. doi:10.1021/ct0502763.
(9) Kümmel, S.; Kronik, L. *Rev. Mod. Phys.* **2008**, *80* (1), 3–60. doi:10.1103/RevModPhys.80.3.
(10) Gunnarsson, O.; Lundqvist, B. I. *Phys. Rev. B* **1976**, *13* (10), 4274–4298. doi:10.1103/PhysRevB.13.4274.
(11) Tschinke, V.; Ziegler, T. *Can. J. Chem.* **1989**, *67* (3), 460–472. doi:10.1139/v89-073.
(12) Tschinke, V.; Ziegler, T. *J. Chem. Phys.* **1990**, *93* (11), 8051–8060. doi:10.1063/1.459335.
(13) Burke, K.; Perdew, J. P.; Ernzerhof, M. *J. Chem. Phys.* **1998**, *109* (10), 3760–3771. doi:10.1063/1.476976.
(14) Burke, K.; Perdew, J. P. *Int. J. Quantum Chem.* **1995**, *56* (4), 199–210. doi:10.1002/qua.560560403.
(15) Becke, A. D.; Savin, A.; Stoll, H. *Theor. Chim. Acta* **1995**, *91* (3–4), 147–156.
(16) Perdew, J. P.; Savin, A.; Burke, K. *Phys. Rev. A* **1995**, *51* (6), 4531–4541. doi:10.1103/PhysRevA.51.4531. PMID:9912142.
(17) Baerends, E. J. *Phys. Rev. Lett.* **2001**, *87* (13), 133004. doi:10.1103/PhysRevLett.87.133004. PMID:11580585.
(18) Perdew, J. P.; Ruzsinszky, A.; Csonka, G. I.; Vydrov, O. A.; Scuseria, G. E.; Staroverov, V. N.; Tao, J. *Phys. Rev. A* **2007**, *76* (4), 040501. doi:10.1103/PhysRevA.76.040501.
(19) Langreth, D. C.; Perdew, J. P. *Phys. Rev. B* **1980**, *21* (12), 5469–5493. doi:10.1103/PhysRevB.21.5469.
(20) Becke, A. D. *Int. J. Quantum Chem.* **1983**, *23* (6), 1915–1922. doi:10.1002/qua.560230605.
(21) Becke, A. D. *J. Chem. Phys.* **1986**, *85* (12), 7184–7187. doi:10.1063/1.451353.
(22) Perdew, J. P.; Wang, Y. *Phys. Rev. B* **1986**, *33* (12), 8800–8802. doi:10.1103/PhysRevB.33.8800.
(23) Becke, A. D.; Roussel, M. R. *Phys. Rev. A* **1989**, *39* (8), 3761–3767. doi:10.1103/PhysRevA.39.3761. PMID:9901696.
(24) Perdew, J. P. In *Electronic Structure of Solids '91;* Ziesche, P., Eschrig, H., Ed.; Akademie Verlag: Berlin, 1991.
(25) Heyd, J.; Scuseria, G. E.; Ernzerhof, M. *J. Chem. Phys.* **2003**, *118* (18), 8207–8215. doi:10.1063/1.1564060.
(26) Gritsenko, O.; Cordero, N.; Rubio, A.; Alonso, J. *J. Mol. Struct.* **2000**, *501*, 153.
(27) Becke, A. D. *J. Chem. Phys.* **2003**, *119* (6), 2972–2977. doi:10.1063/1.1589733.
(28) Becke, A. D.; Johnson, E. R. *J. Chem. Phys.* **2005**, *122* (15), 154104. doi:10.1063/1.1884601. PMID:15945622.
(29) Becke, A. D.; Johnson, E. R. *J. Chem. Phys.* **2005**, *123* (15), 154101. doi:10.1063/1.2065267. PMID:16252936.
(30) Ángyán, J. G. *J. Chem. Phys.* **2007**, *127* (2), 024108. doi:10.1063/1.2749512. PMID:17640120.
(31) Becke, A. D.; Johnson, E. R. *J. Chem. Phys.* **2007**, *127* (15), 154108. doi:10.1063/1.2795701. PMID:17949133.
(32) Ayers, P. W. *J. Math. Chem.* **2009**, *46* (1), 86–96. doi:10.1007/s10910-008-9451-y.
(33) Harris, J.; Jones, R. *J. Phys. F* **1974**, *4* (8), 1170–1186. doi:10.1088/0305-4608/4/8/013.
(34) Langreth, D. C.; Perdew, J. P. *Solid State Commun.* **1975**, *17* (11), 1425–1429. doi:10.1016/0038-1098(75)90618-3.
(35) Yang, W. *J. Chem. Phys.* **1998**, *109* (23), 10107–10110. doi:10.1063/1.477701.
(36) Savin, A.; Colonna, F.; Pollet, R. *Int. J. Quantum Chem.* **2003**, *93* (3), 166–190. doi:10.1002/qua.10551.
(37) Savin, A. *Phys. Rev. A* **1995**, *52* (3), R1805–R1807. doi:10.1103/PhysRevA.52.R1805.
(38) Levy, M.; Görling, A. *Phys. Rev. A* **1995**, *52* (3), R1808–R1810. doi:10.1103/PhysRevA.52.R1808.
(39) Ayers, P. W. *J. Math. Chem.* **2009**; in press.
(40) Perdew, J. P.; Burke, K.; Wang, Y. *Phys. Rev. B* **1996**, *54* (23), 16533–16539. doi:10.1103/PhysRevB.54.16533.
(41) Ernzerhof, M.; Perdew, J. P. *J. Chem. Phys.* **1998**, *109* (9), 3313–3320. doi:10.1063/1.476928.
(42) Constantin, L. A.; Perdew, J. P.; Tao, J. *Phys. Rev. B* **2006**, *73* (20), 205104. doi:10.1103/PhysRevB.73.205104.
(43) Bahmann, H.; Ernzerhof, M. *J. Chem. Phys.* **2008**, *128* (23), 234104. doi:10.1063/1.2937447. PMID:18570488.
(44) Henderson, T. M.; Janesko, B. G.; Scuseria, G. E. *J. Chem. Phys.* **2008**, *128* (19), 194105. doi:10.1063/1.2921797. PMID:18500854.

(45) Gori-Giorgi, P.; Savin, A. *J. Phys.: Conf. Ser.* **2008**, *117*, 012017. doi:10.1088/1742-6596/117/1/012017.
(46) Savin, A. *Chem. Phys.* **2009**, *356* (1–3), 91–97. doi:10.1016/j.chemphys.2008.10.023.
(47) Marzari, N.; Vanderbilt, D. *Phys. Rev. B* **1997**, *56* (20), 12847–12865. doi:10.1103/PhysRevB.56.12847.
(48) Ángyán, J. G. Unpublished results.
(49) Freund, D. E.; Huxtable, B. D.; Morgan, J. D. *Phys. Rev. A* **1984**, *29* (2), 980–982. doi:10.1103/PhysRevA.29.980.
(50) Umrigar, C. J.; Gonze, X. In *High Performance Computing and its Application to the Physical Sciences,* Proceedings of the Mardi Gras 93 Conference; Browne, D. A. et al., Eds.; World Scientific: Singapore, 1993.
(51) Filippi, C.; Gonze, X.; Umrigar, C. J. In *Recent Developments and Applications in Modern DFT;* Seminario, J. M., Ed.; Elsevier: Amsterdam, 1996.
(52) Gori-Giorgi, P.; Perdew, J. P. *Phys. Rev. B* **2002**, *66* (16), 165118. doi:10.1103/PhysRevB.66.165118.

Density functional theory analyses of bis(bipyridine)ruthenium noninnocent quinonoid and thiolosulfinato complexes containing ligands formally in the semiquinone oxidation state

A.B.P. Lever

Abstract: Density functional theory and the polarized continuum model are used to derive the electronic structures of some open-shell, bis(bipyridine)ruthenium complexes bound to noninnocent quinonoid or thiolosulfinato ligands formally in the semiquinone oxidation state. The noninnocent properties of the *o*-thiolosulfinato ligand are explored and compared with those of the more conventional *o*-semiquinones with nitrogen, oxygen, and sulfur donor atoms. Spin densities are shown to be fairly localized in the metallocycle ring. It is demonstrated that oxidation of the parent $[Ru^{II}(bpy)_2$ (1,2-(S,SO_2)–$C_6H_4]$ species occurs primarily in the metallocycle ring and is localized in the Ru–S^0 bond.

Key words: ruthenium, sulfenate, sulfinate, thiol, optical spectrum, density functional theory (DFT), infrared, noninnocent ligand.

Résumé : On a fait appel à la théorie de la fonctionnelle de densité et du modèle du continuum polarisé pour dériver les structures électroniques de quelques complexes à couches ouvertes du bis(bipyridine)ruthénium lié à des ligands quinonoïdes ou thiolosulfinato non innocents formellement dans l'état d'oxydation semiquinone. On a étudié les propriétés non innocentes du ligand *o*-thiolosulfinato et on les a comparées avec celles de *o*-semiquinones plus conventionnelles portant des atomes d'azote, d'oxygène et de soufre donneurs. On a montré que les densités de spin sont assez localisées dans le noyau métallocyclique. On démontre que l'oxydation de l'espèce parente $[Ru^{II}(bpy)_2(1,2\text{-}(S,SO_2)\text{–}C_6H_4)]$ se produit principalement dans le noyau métallocyclique et qu'elle est localisée dans la liaison Ru–S^0.

Mots-clés : ruthénium, sulfénate, sulfinate, thiol, spectre optique, théorie de la fonctionnelle de la densité (TFD), infrarouge, ligand non innocent.

[Traduit par la Rédaction]

Introduction

We have recently reported[1] the physical properties and electronic structures of bis(bipyridine)ruthenium complexes of *o*-thiolosulfinatobenzene **1** $[Ru(bpy)_2(1,2\text{-}(S,SO_2)\text{–}C_6H_4)]$ and *o*-disulfinatobenzene **2** $[Ru(bpy)_2(1,2\text{-}(SO_2,SO_2)\text{–}C_6H_4)]$, which are of interest, in part, because of the biological involvement of ligating systems of this type in nitrile hydratase.[2–5] Species **1** contains sulfur in oxidation states S^0 and S^{IV}, while in species **2**, both S are S^{IV}. A detailed analysis of the binding of these ligands was presented[1] revealing extensive metal–ligand covalency. In the isolated complexes, these sulfinato ligands were doubly negatively charged and attached to a ruthenium(II) center. Species **1** is henceforth written as $[Ru(bpy)_2(S,SO_2)]$ where (S,SO_2) in the following text will signify the 1,2-(S,SO_2)–C_6H_4 ligand.

Electrochemically, in acetonitrile, these species show reduction of the bipyridine ligands and an oxidation process, in the commonly explored potential range. In complexes of the general class $Ru(bpy)_2(X,Y)$, the first reduction potential at bipyridine spans a considerable range[6,7] depending on the donor and acceptor properties of the ligands X,Y. In general, the more negative the first reduction potential, the less positive is the $Ru^{III/II}$ oxidation potential and indeed, there is a linear relationship[7] between these two potentials involving the electrochemical parameter values (E_L(L))[8] of ligands X,Y. Based upon this relationship, the observed first oxidation potential of species **2** lay at a potential reasonably expected for oxidation of Ru^{II} to Ru^{III} but in species **1** the first oxidation potential was insufficiently positive to be simply associated with the $Ru^{III/II}$ process. This suggests that oxidation of the sulfinato^{2-} ligand may be occurring and hence that this ligand, like the quinonoid ligands, is also noninnocent.[9–12] In this paper, we explore the electronic properties of this oxidized species, $\mathbf{1}^+$, and use this as an opportunity to compare the properties of a series of complexes, $[Ru(bpy)_2(o\text{-}X,Y\text{–}C_6H_4)]^+$, formally in the semiquinone oxidation state, for comparative purposes, and hitherto not studied computationally in great detail.

Received 20 January 2009. Accepted 19 March 2009. Published on the NRC Research Press Web site at canjchem.nrc.ca on 1 October 2009.

This article is part of a Special Issue dedicated to Professor T. Ziegler.

A.B.P. Lever. Department of Chemistry, CB124, York University, 4700 Keele St, Toronto, ON M3J 1P3, Canada. (e-mail: blever@yorku.ca).

Experimental

Synthesis

The synthesis of complex **1** was carried out according to the literature.[1] Spectroelectrochemical oxidation was carried out in acetonitrile using a gold foil working electrode and

silver/silver chloride quasi-reference electrode. Optical data were collected using an Ocean Optics HR4000 high-resolution, fibre-optic spectrometer.

Calculations

Density functional theory (DFT) calculations were performed using the Gaussian 03 (Revision C.02) program.[13] Optimized geometries were calculated using the B3LYP exchange-correlation functional[14] with the TZVP basis set[15,16] for all elements except ruthenium for which the DGDZVP basis set[17,18] was used. Tight self-consistent field (SCF) convergence criteria (10^{-8} au) were used for all calculations. Vibrational frequency calculations were performed to ensure that the stationary points were minima. Wave functions were checked for stability.

Molecular orbital (MO) compositions and the overlap populations between molecular fragments were calculated using the AOMix-CDA program[19,20] using the Mulliken scheme.[21–24] Atomic charges were calculated using the Mulliken[21–24] and natural population analysis[25] methods (MPA and NPA, respectively) as implemented in Gaussian 03.[13] The analysis of the MO compositions, and the charge decomposition analysis was performed using AOMix-CDA.[20,26] The PCM model[27,28] was used to model solvation assuming acetonitrile as the solvent.

Time-dependent DFT (TDDFT)[29–32] was used to calculate the energies and intensities of the 60 lowest-energy electronic transitions of complex $\mathbf{1}^+$. These were converted with the SWizard program[33] into simulated spectra as described before,[34] using Gaussian functions.

Results and discussion

Experimental characterization of species $\mathbf{1}^+$

Species **1** displays the first $E_{1/2}$[bpy/bpy$^-$] potential at –1.58 V versus a saturated calomel electrode (SCE) and an oxidation potential at 0.18 V versus SCE.[1] Using the correlation[7]

$$[1] \qquad E_{1/2}[Ru^{III}/Ru^{II}] = 4.5[E_{1/2}(bpy/bpy^-) + 1.69] \quad (V, \text{ vs. SCE})$$

then $E_{1/2}$[Ru^{III}/Ru^{II}] should lie at ~ +0.5 V rather than +0.18 V versus SCE. The correlation (eq. [1]) was rather scattered, i.e., the statistics are imprecise, but the discrepancy between observed and predicted potential, especially the experimental value being observed as significantly negative of that predicted, is sufficiently large to give one cause to argue that oxidation does not occur primarily at ruthenium.

Although species $\mathbf{1}^+$ was not isolated, its visible region optical spectrum was obtained using spectroelectrochemical oxidation of species **1** in acetonitrile (Fig. 1).

The two visible region bands in the electronic spectrum of **1** are replaced in $\mathbf{1}^+$ by one stronger band at a lower energy with at least two weaker transitions, in the visible region, to the blue of the strong band, as shown in Fig. 1 (see legend for energy values). To assign the spectrum, a molecular orbital analysis was carried out using density functional theory. Good agreement between the observed and DFT predicted UV–vis and IR spectra of the precursor species **1** was obtained[1] using the popular B3LYP functional[14] and the triple zeta basis set, TZVP, for all atoms except ruthenium (for which the TZVP bases are not yet available); thus, a double zeta DGDZVP was used for ruthenium, in a spin unrestricted calculation. The solvent was included, using the polarizable continuum model (PCM).[27,35] We therefore use the same procedure here.

Fig. 1. Spectroelectrochemical oxidation of $Ru^{II}(bpy)_2(S,SO_2)$ (**1**) to species $\mathbf{1}^+$ in acetonitrile/tetrabutylammonium hexafluorophosphate, at ~0.3 V vs. SCE. Initial species **1**: bold black line, and subsequent timed spectra (bold lines) changing to species $\mathbf{1}^+$: bold hatched line. Experimental band maximum at 14 600 cm^{-1} (ε = 2900 L mol^{-1} cm^{-1}) with weak shoulders at ~16 200 and 21 000 cm^{-1}. The time dependent DFT predicted spectrum is shown as a long hatched line. Transitions are shown as vertical lines scaled to their oscillator strengths.

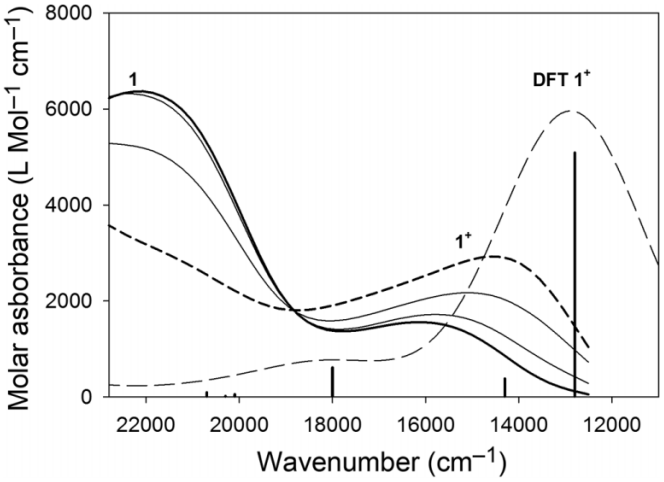

Table 1 shows the percent contributions of (S,SO_2) ligand; Ru s, p, and d; bipyridine; individual S^0 and S^{IV} orbital; and the contribution of the C_2S_2Ru metallocycle ring to the frontier molecular orbitals of species $\mathbf{1}^+$. The two visible region bands shown in Fig. 1 for species **1** are assigned as ligand to ligand charge transfer (LLCT) transitions from the S^0 ligator to π^*-bpy.[1] Based on the calculation, the new, strong, red-shifted band in the spectrum of $\mathbf{1}^+$ (exptl. 14 600 cm^{-1}, predicted 12 900 cm^{-1}) is primarily 146β,147β → 148β, which comprises an internal π–π* type of transition largely associated with the metallocycle ring with some d–d component since the d orbitals involved in these three orbitals are not all the same. There are two weaker transitions predicted in the visible region that may be associated with the two shoulders. The weak predicted band at 14 300 cm^{-1} (exptl. ~16 200 cm^{-1}) is mainly 144β → 148β, which is also metallocycle localized. The transition at 18 000 cm^{-1} (exptl. ~21 000 cm^{-1}) is mainly 143β → 148β, which is best described as a π–π* from the benzenoid fragment of the sulfinato ligand to the metallocycle but with a ligand to metal charge transfer (LMCT) component to the β-hole on ruthenium (see Table 1).

The unpaired (α) electron resides in #148H and is localized primarily in the metallocycle ring and with significant involvement of the ruthenium atom and the S^0 ligand but not the S^{IV} ligand. It mainly involves the overlap of highest occupied MO (HOMO; #45α) (see Fig. 2) of the sulfinato-ligand fragment (formal 1– oxidation state) with several

Table 1. Percent composition of frontier orbitals in species $\mathbf{1}^+$ using DFT (see text for details).

#Index	Energy (eV)	%(S,SO$_2$)[a]	%Ru s,p	%Ru 4d	%bpy	%S^0 [b]	%S^{IV}[c]	Mcycle[d]
Alpha spin molecular orbitals								
151	–1.92	0.9	0.1	0.6	98.4	0.2	0	1.0
150	–2.70	0.2	0.6	2.4	96.8	0	0	3.1
149L	–2.72	0.3	0.3	1.8	97.6	0	0.1	2.4
Occupied–unoccupied orbital gap (3.71 eV)								
148H	–6.43	76.3	0.2	20.5	3.0	41.1	0.1	74.1
147	–7.00	54.3	3.8	28.3	13.6	3.0	8.5	47.8
146	–7.19	25.3	0.8	56.0	17.9	2.7	2.4	67.0
145	–7.24	28.3	1.3	56.2	14.2	3.6	2.1	67.4
144	–7.39	89.4	0.1	4.4	6.1	0.9	0.5	20.9
143	–7.47	5.3	0.1	1.5	93.1	0.1	0	2.2
142	–7.54	6.3	0.0	3.2	90.4	0.5	0	5.6
Beta spin molecular orbitals								
151	–1.91	0.8	0.1	0.6	98.5	0.1	0	0.9
150	–2.69	0.4	0.5	2.4	96.7	0.1	0	3.1
149	–2.70	0.4	0.3	3.1	96.1	0.1	0.1	3.8
148L	–4.31	54.0	0.1	40.0	5.9	38.7	0.1	83.8
Occupied–unoccupied orbital gap (2.52 eV)								
147H	–6.84	45.4	2.6	41.8	10.2	11.1	3.1	66.9
146	–6.95	36.0	1.8	49.6	12.5	8.9	0.8	71.6
145	–7.03	15.3	0.2	71.6	12.8	0.2	0.8	73.9
144	–7.13	62.3	3.7	23.5	10.5	3.5	9.0	50.5
143	–7.34	94.7	0.3	1.4	3.6	0.8	0.3	16.1
142	–7.48	1.2	0.0	0.6	98.2	0.1	0	1.0

Note: The very low symmetry of these species does not allow these orbitals to be defined uniquely as σ or π.

[a]1,2-(S,SO$_2$)–C$_6$H$_4$ ligand contribution.

[b]Percent S^0 atom contribution.

[c]Percent S^{IV} atom contribution.

[d]Percent atom contribution from metallocycle C$_2$S$_2$Ru; Note that since this number includes %Ru, it may exceed the percentage shown in column 3.

Fig. 2. Left: Spin density on species $\mathbf{1}^+$. Middle: Kohn–Sham HOMO (#148α) of the species $\mathbf{1}^+$. Right: Kohn–Sham HOMO (#45α) of the sulfinato ligand in the 1– oxidation state. DFT/PCM: see text for details. The orientation of the molecule is such that the S^{IV}(O$_2$) group lies to the lower left (note two small red oxygen atoms) and the S^0 to the lower right of the (S,SO$_2$) ligand.

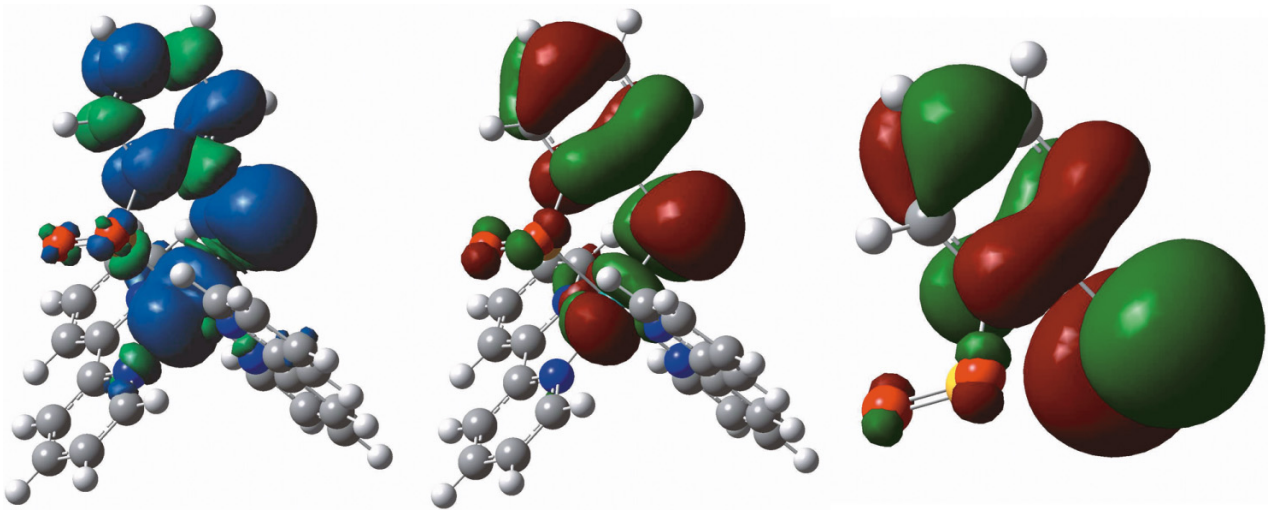

MOs of the $[Ru(bpy)_2]^{2+}$ fragment. The spin density within the oxidized sulfinato ligand is very heavily localized on the S^0 atom; thus, of the 55% on the ligand overall, 44% of the total spin density resides on S^0, none on S^{IV}, and the remaining 11% is localized on the other atoms of the sulfinato ligand (see Fig. 2) (Table 2).

Before discussing how this species should be understood electronically, we digress to looking at relevant computa-

Table 2. Charge, population, and spin density data for $[Ru(bpy)_2(X,Y)]^+$, $Ru(acac)_2(NH,NH)]^-$ and species $\mathbf{1}^+$ and **1**.

X,Y	NBO charge[a] X,Y ligand	CDA charge[b] X,Y ligand	NBO charge[a] Ru (population)	Total spin density[c] X,Y ligand	Total spin density[c] Ru	Spin density[d] (charge) X	Spin density[d] (charge) Y
NH,NH	–0.53	–0.44	0.98 (6.99)	0.88	0.12	0.30(–0.68)	0.30(–0.68)
O,O	–0.73	–0.54	1.07 (6.90)	0.86	0.16	0.22(–0.61)	0.22(–0.61)
O,NH	–0.64	–0.47	1.03 (6.94)	0.84	0.17	0.13(–0.67)	0.43(–0.62)
S,NH	–0.49	–0.22	0.86 (7.11)	0.78	0.22	0.18(–0.15)	0.39(–0.61)
(acac)NH,NH	–0.8	–0.65	1.18 (6.80)	0.63	0.35	0.24(–0.69)	0.24(–0.69)
S,SO_2	–0.46	–0.08	0.65 (7.30)	0.55	0.44	0.45(+0.14)	0(+1.69)
S,SO_2 **1**[e]	–1.14	–0.75	0.58(7.37)	NR	NR	NR	NR

Note: NR = not relevant.

[a]Natural bond orbital charge and NBO 4d population for ruthenium in brackets.

[b]Mulliken charge.

[c]Mulliken spin density on X,Y ligand and on ruthenium.

[d]Mulliken spin density on coordinating X,Y atoms with NBO charge in parenthesis. There is no significant net spin on bipyridine or acetylacetonate ligands.

[e]Data for the parent Ru^{II} species **1**. The NBO charges on the sulfur donors of species **1** are: S^0 (–0.28), S^{IV} (+1.67). Charges are expressed using the elementary charge 'e'.

tional data for a series of related derivatives formally in the semiquinone oxidation state and described as $[Ru(bpy)_2(1,2\text{-}X,Y\text{–}C_6H_4)]^+$ with (X,Y) = (O,O), (O,NH), (S,NH), and (NH,NH). Since the oxidation of species **1** reveals that the (S,SO_2) ligand is noninnocent, then the sulfinato-ligand complexes might be described as members of this series, with X = S and Y = SO_2. It is of interest to explore whether this is the case, and if not, just how they differ.

We also include $[Ru(acac)_2(1,2\text{-}NH,NH\text{–}C_6H_4)]^-$ (acac = 2,4-pentanedionate) because of our earlier work with this species[36] and to provide a direct connection with the work of Remenyi and Kaupp.[37] For ease of discussion, we henceforth abbreviate these species as $[Ru(bpy)_2(X,Y)]^+$ and $[Ru(acac)_2(NH,NH)]^-$.

Remenyi and Kaupp[37] have discussed in great depth the electronic and geometric structures of several $[Ru(acac)_2(1,2\text{-}X,Y\text{–}C_6H_4)]^-$ species. Although we use a different basis set from that study, the bond distances in our optimized geometry of $[Ru(acac)_2(NH,NH)]^-$ (see selected distances in Table 3) are essentially identical to theirs. Our discussion of the $[Ru(bpy)_2(X,Y)]^-$ species follows similar arguments to those presented by Remenyi and Kaupp[37] and is therefore kept rather brief. The fully reduced species, $[Ru^{II}(bpy)_2\ (X,Y)]^0$, are regarded as ruthenium(II) complexes of the doubly reduced quinone, i.e., generically called a catecholate, which we write as $[Ru^{II}(bpy)_2(cat.X,Y)]^0$. The ambiguity arises when an electron is removed by oxidation. Is the product now a ruthenium(III) catecholate^{2-}, i.e., $[Ru^{III}(bpy)_2(cat.X,Y)]^+$, or a ruthenium(II) semiquinonate^{1-}, $[Ru^{II}(bpy)_2(sq.X,Y)]^+$? The general conclusion reached by Remenyi and Kaupp[37] for the acetylacetonate series was that they were best represented by a resonance hybrid between the Ru^{II} and Ru^{III} representations. Clearly, individual species may be closer to the Ru^{II} or to the Ru^{III} formulations.

We have recently reported[36] that the $[Ru^{II}(acac)_2(q.X,Y)]^0$ formally quinone oxidation state complexes reveal extensive π-back donation into the Ru–X,Y metallocycle ring. The very covalent Ru–X,Y interaction confers aromatic properties on this metallocycle ring.[38–40] Thus, another way to view the 'semiquinone' species is to regard it as being formed by the oxidation of the $[Ru^{II}(bpy)_2(cat.X,Y)]$ complex by the removal of an electron from this metallocycle.

Based on this background, we can now discuss the electronic and geometric properties of all of these semiquinone X,Y species, leaving aside for now the (S,SO_2) species, which we defer for later comparison below. Figure 3 (left) shows the bond distances in the DFT optimized $[Ru(bpy)_2((O,NH)\text{–}C_6H_4)]^+$ structure, which is typical (Table 3). The benzene ring C–C distances alternate in length (Table 3) but to a much smaller degree than observed experimentally in quinone complexes and to a similar degree to those observed in semiquinone species. Bond alternation in these quinonoid species has been discussed elsewhere.[11,41]

The bond order data in Table 4 provide greater insight. The Ru–NH and Ru–O bond orders in $[Ru(bpy)_2(NH,NH)]^+$ and analogous (O,NH) and (O,O) species have rather similar values. Those of $[Ru(acac)_2(NH,NH)]^-$ are substantially larger. The (S,NH) species displays a very strong Ru–S bond, evidently highly covalent. This covalency extends to the Ru–NH bond whose bond order is significantly higher than the Ru–NH bonds of the previous complexes. The metallocycle C=N and C=O bond orders do not change a great deal in this series except that the values for $[Ru(acac)_2(NH,NH)]^-$ are larger. Table 4 also provides the Mayer bond orders[42,43] between the $[RuL_2]$ and [X,Y] fragments for the α- and β-electrons. There is one more α-electron than β, and it resides in an orbital (148α) that is antibonding between these fragments explaining why the α-bond order is always less than the β-bond order. Not unexpectedly, the β-bond orders are again substantially larger for the (S,NH) and acac(NH,NH) species.

In Table 2, we report natural bond orbital[25,44] charges, and Mulliken charge decomposition analysis (CDA) charges[20,26,45–47] in an extended method, ECDA, developed by Gorelsky and co-workers[45,48] on the fragments and on the donor atoms. Spin densities are also provided. The natural bond orbital (NBO) and CDA charges differ somewhat

Fig. 3. Left: DFT calculated bond distances in $[Ru(bpy)_2(O,NH)]^+$ (Å). Right: MPA spin density distribution in $[Ru(bpy)_2(O,NH)]^+$ (au).

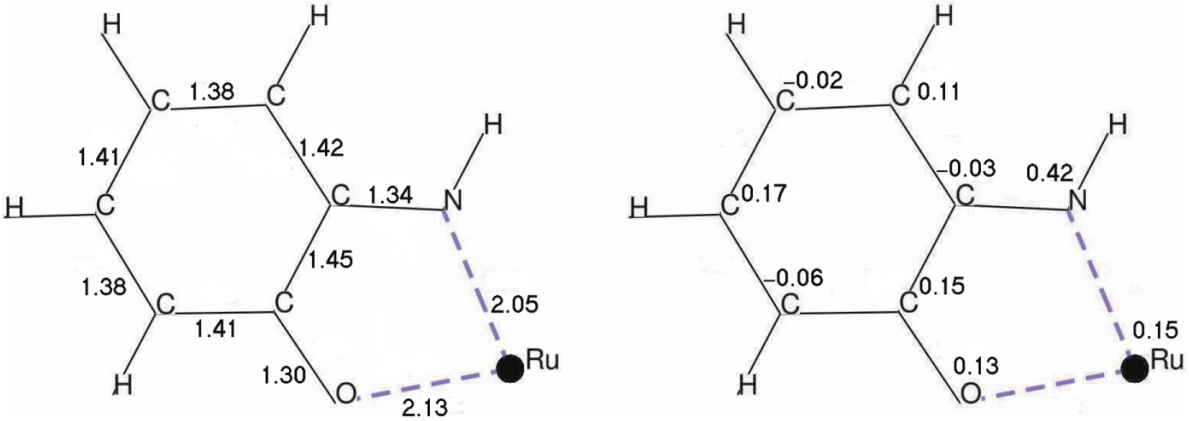

Table 3. Selected DFT/PCM optimized bond distances (Å).

(X,Y)	Ru—X	Ru—Y	C=X	C=Y	C=C (Mtc)[a]	C=C(Bz)[b]	Ru—N(bpy)
NH,NH	2.08	2.08	1.34	1.34	1.45	1.37–1.42	2.11–2.13
O,NH	2.13	2.05	1.30	1.34	1.45	1.38–1.42	2.10–2.13
S,NH	2.42	2.04	1.75	1.35	1.43	1.37–1.42	2.11–2.14
O,O	2.11	2.11	1.30	1.30	1.45	1.37–1.42	2.10–2.11
(acac)NH,NH	2.05	2.05	1.35	1.35	1.45	1.39–1.41	2.11–2.14[c]
S,SO_2	2.30	2.37	1.78	1.84	1.40	1.39–1.40	2.14–2.17

[a]Within the metallocycle ring.
[b]The range of C—C in the benzenoid ring.
[c]Ru—O(acac).

Table 4. Bond orders for $[Ru(bpy)_2(X,Y)]^+$, $Ru(acac)_2(NH,NH)]^-$, species **1** and $\mathbf{1}^+$ (DFT, PCM).

X,Y	Ru–X	Ru–Y	C=X	C=Y	C=C[a]	Ru–N(bpy)[a]	Mayer-α[b]	Mayer-β[b]
O,O	0.48	0.48	1.18	1.18	1.46	0.3	0.50	0.79
NH,NH	0.52	0.52	1.31	1.31	1.47	0.24	0.60	0.87
O,NH	0.59	0.48	1.27	1.18	1.43	0.28	0.58	0.87
(acac)NH,NH	0.67	0.67	1.39	1.39	1.41	NA	0.58	1.07
S,NH	0.89	0.96	1.26	1.11	1.47	0.26	0.83	1.19
S,SO_2 $\mathbf{1}^+$	1.31	0.83	0.99	0.72	1.40	0.29	1.10	1.57
S,SO_2 **1**	0.86	0.84	0.98	0.72	1.42	0.26	2.16	2.16

Note: See the text for details. The table is ordered with respect to Mayer-β bond order. NA = not available.
[a]Average values.
[b]Bond order between fragments (see text).

but have the same relative values. An ionic semiquinone would obviously carry a net unit negative charge. All these species have charges less than –1 but are generally more negative than those reported previously[36] for the quinone oxidation state species. The net charge on the (X,Y) ligand decreases to small negative values in the sequence acac(NH,NH) > (O,O) > (O,NH) > (NH,NH) > (NH.S). Predictably, the net positive charge on ruthenium decreases in the same sequence.

The spin density on the ruthenium atom in the (NH,NH), (O,NH), and (O,O) species is small (Table 2), while that on the (X,Y) ligand is greater than 0.8. They also all have roughly the same net negative charge on the (X,Y) ligand (and net positive charge on Ru). Thus, these three derivatives are most reasonably defined as $[Ru^{II}(bpy)_2(sq.X,Y)]^+$. The (S,NH) derivative has a somewhat larger positive charge on Ru and a larger spin density on Ru; thus, one may argue for a greater $[Ru^{III}(bpy)_2(cat.X,Y)]^+$ contribution than for the aforementioned three derivatives. Clearly, the bond orders cited in Table 4 convey arguments for much stronger covalent bonds in this complex.

The $[Ru(acac)_2(NH,NH)]^-$ species is evidently quite different from $[Ru^{II}(bpy)_2(NH,NH)]^+$ with a substantially larger Mayer β-electron bond order (Table 4), significantly larger net negative charge on the (NH,NH) ligand, and a larger positive charge on Ru, and the C–C benzene ring bond distances are similar to those of a catecholate (Table 3). It also has a significantly larger spin density on Ru and a smaller spin density on (NH,NH) (data are similar to those reported by Remenyi and Kaupp[37]). It therefore appears to have a significantly greater degree of Ru^{III}(cat.NH,NH) character than the bipyridine analog.

It is of interest to explore in more depth why replacing the neutral bipyridine with the mono-anionic acetylacetonate

Table 5. Net σ donation and net back donation in selected species as a function of spin. (CDA analysis; au).

	α-Electrons		β-Electrons		
	σ Donation[a]	Back donation[b]	σ Donation[a]	Back donation[b]	Net charge on bpy/acac
$[Ru(bpy)_2(NH,NH)]^+$	0.40	0.06	0.43	0.17	+0.55
$[Ru(acac)_2(NH,NH)]^-$	0.38	0.03	0.41	0.40	–1.38
$[Ru(bpy)_2(S,SO_2)]^+$	0.73	0.07	0.75	0.50	+0.81

[a]σ Donation to fragment A $[RuL_2]^{n+}$ (L = bpy, n = 2; $acac^{1-}$, n = 0).

[b]π Back donation to fragment B $(1,2\text{-}(NH,NH)\text{–}C_6H_4)^{1-}$ or $(1,2\text{-}(S,SO_2)\text{–}C_6H_4)^{1-}$.

has such an effect. Net charge transfer between $[RuL_2]^{n+}$ (L = bpy, n = 2; L = $acac^{1-}$, n = 0) (fragment A) and $(1,2(NH,NH)\text{–}C_6H_4{}^{1-})$ (fragment B) depends on the net contribution of the empty orbitals of each fragment to the filled orbitals of the final complex, which are subject to changes in polarization (ECDA method[26,36,45]). Using the CDA method, one can factor the charge σ donated from fragment B to fragment A and the charge returned by back donation from fragment A to fragment B.

The major difference between the first two species in Table 5 is clearly the much greater β-electron back donation in the acac species; otherwise, the electron distributions are rather similar. This back donation arises through mixing of the lowest unoccupied MO (LUMO) and some higher virtual orbitals of fragment B into filled orbitals of the acac complex. The dominant contribution, by far, is mixing of the β-LUMO (#29, fragment B) into the HOMO-2 of the complex. Obviously, a major factor is the dinegative charge of the acac ligands, which softens the metal atom and makes it a stronger π donor. Nevertheless, the net positive charge on Ru is larger for the acac ligand than for the bpy ligand complex reflecting an increased resonance contribution of Ru^{III}(cat.NH,NH). Evidently, negative charge is transferred from acac to (NH,NH) (rendering it the most negative (X,Y) ligand of our comparative group), and 'bypassing' the ruthenium center!

Electronic structure of $[Ru(bpy)_2(S,SO_2)]^-$

We are now in a position to discuss the electronic structure of this species. We note previous studies on the structures of sulfinato species by Grapperhaus et al.[49,50] while Wieghardt and co-workers,[11,51–55] and other groups,[56–58] have extensively studied thiolato species in comparison with other noninnocent ligands. These studies provide a theoretical background but do mostly deal with first row transition metal ions, which offer a rather different perspective than does ruthenium. However, a mixed thiolato-sulfinato ruthenium(II) species, which can be oxidized to its Ru^{III} oxidation product, is relevant to this study.[50]

Clearly (Table 4), there is a much stronger interaction of ruthenium with this ligand than for any of the other species discussed, with substantially larger Ru–S and Mayer fragment bond orders. The C=S bond order is substantially smaller than the corresponding value for the (S,NH) species (Table 4) and the NBO charges on Ru and on the (S,SO_2) ligand are the smallest of the group (Table 2). The C–C bond distances (Table 3) in the benzenoid ring are similar to those found in the catecholate oxidation state.

Table 2 is displayed in order of spin density on ruthenium, and it is seen that the largest spin density on ruthenium is observed with this (S,SO_2) complex; indeed, the spin densities on Ru and the (S,SO_2) ligand are similar and approach 50:50. Clearly, the complex is very covalent as indicated by the large (Ru,X,Y) bond orders and by the fact that the charge separation between Ru and (S,SO_2) ligand is

Fig. 4. Upper: Spin density diagram in the $Ru(S,SO_2)$ fragment. Lower: Kohn–Sham HOMO (#45α) of the free oxidation state^{1-} ligand $(S,SO_2)^-$. THe ligand is in the same relative orientation. The β-LUMO, #45β, has almost an identical appearance to #45α.

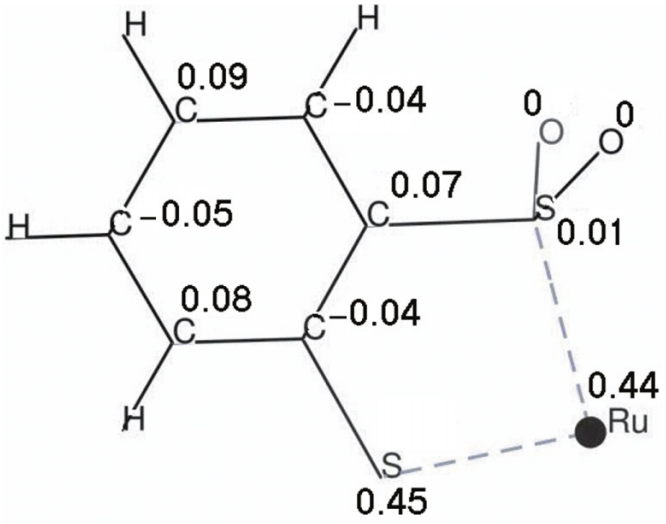

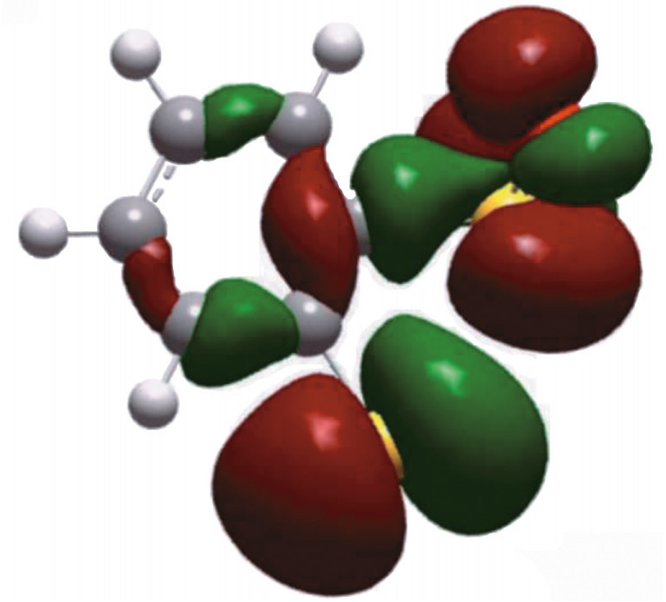

Fig. 5. Left: C—S, C—S(O_2), and S—O bond distances in the free ligands $(S,SO_2)^{n-}$ cited from top to bottom n = 2–, 1–, 0. (DFT optimized (not PCM), see text). Right: C—S, Ru—S, and S—O DFT computed bond distances in species $\mathbf{1}^+$. The benzene C—C distances are all about 1.39 Å in the complex and in the ligand, independent of the oxidation state.

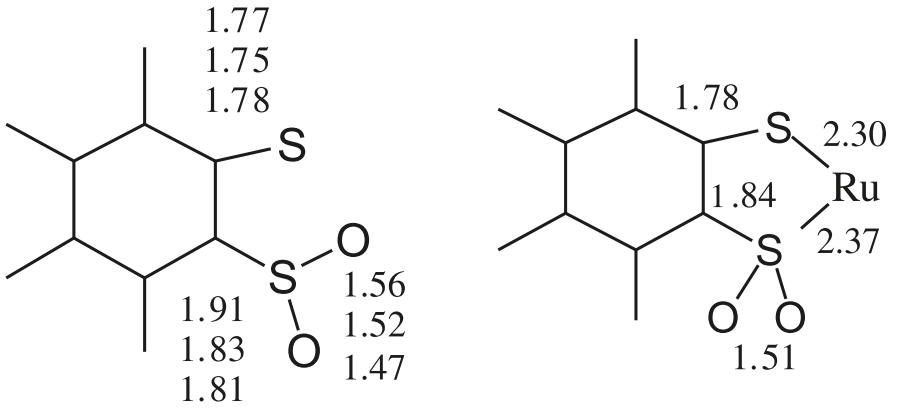

mitigated, i.e., charges are smaller on both fragments than is the case with the other species.

As noted above, many of these species in the quinonoid oxidation contain an aromatic metallocycle ring and, at least for the Ru(acac)$_2$ group, back donation occurs primarily into this ring rather than to the ligand overall.[36] It was suggested above that the current group of semiquinone species might arise through removal of an electron from this ring (from the 2– oxidation state), rather than from the ligand overall. Indeed, based on the spin density distribution (Fig. 3, Table 2) much of the spin density does lie inside the metallocycle with relatively little in the phenyl ring. This distribution would clearly have an influence on the reactivity of the species.

The spin distribution for the (O,NH) derivative is shown in Fig. 3. By considering the data in Table 2, comparing total spin on the X,Y ligand with those on X and Y alone, it is clear that the spin does tend to lie mostly in the metallocycle ring, for all the species, and this is most obvious for the (S,NH) and especially (S,SO_2) species (Fig. 4). In the asymmetric species, (O,NH) and (S,NH), the spin density is predominantly on the NH ligator because the HOMO of the complex has very little Ru–O(S) character (e.g., see Fig. 3).

Clearly, in the case of the (S,SO_2) species where the HOMO very definitively involves the Ru–S^0 and has little contribution from the Ru–S^{IV} bond (Fig. 2), the spin resides mostly within the Ru–S^0 bond. Indeed, the HOMO of the free ligand (S,SO_2) in the 1– oxidation state shows electron density primarily on the S ligators and not in the benzene ring (Fig. 4 (lower)).

Figure 5 reveals the variation in free ligand sulfur related bond distances as a function of the net oxidation state of the free ligand. The C–C (benzene) and C–S^0 bond lengths are essentially independent of oxidation state but the C–S^{IV} and S–O distances are fairly sensitive to the oxidation state. Thus, changing the oxidation state alters the electron density in what will become the metallocycle ring but has little influence on the benzene ring. Comparison with the bond distances in the [Ru(bpy)$_2$(S,SO_2)]$^+$ complex (Fig. 5 (right)) shows reasonable agreement with the 1– ligand oxidation state. The Ru–S^0 and Ru–S^{IV} bond distances have been reported (X-ray) for a so-called Ru^{III} species[50] containing Ru–S^0 (2.14 Å), Ru–S^{IV} (2.30–2.35 Å), and Ru–P bonds. Our calculated Ru–S^0 is substantially shorter in agreement with the strong covalent interaction, while our Ru–S^{IV} is slightly longer.

Given the spin density on both the ruthenium atom and S^0 atoms, then the best description is $[Ru^{II0.5}(bpy)_2(S,SO_2)^{I0.5-}]^+$. Thus, it is evident that the actual oxidation process from species **1** is best described neither as ruthenium oxidation nor as ligand oxidation, but as oxidation of the metallocycle ring. Over 90% of the spin density lies inside this ring (Fig. 4). The electron that is 'removed' is in an antibonding orbital largely localized along the Ru–S^0 vector and we note, indeed, that the Ru–S^0 bond order jumps from 0.86 in species **1** to 1.31 in species $\mathbf{1}^+$ (Table 4), which is a dramatic increase.

The net negative charge on the (S,SO_2) fragment is the smallest of the group and it is evident from the data in Table 5 that this is because the sulfinato ligand is a much stronger donor than the other quinonoid ligands. Nevertheless, there is a quite significant back donation contribution from the β-electrons from fragment A to the sulfinato^{1-} ligand. How does this occur? Several β-virtual orbitals of the (S,SO_2) ligand (fragment B) contribute to filled orbitals of the complex, but by far the dominant contributor is the β-LUMO (#45β). This is the counterpart to the HOMO (#45α) and indeed appears almost identical to it (Fig. 4). It is localized within the S,SO_2 groups (Fig. 4). In effect, therefore, β back donation involves back donation primarily to the metallocycle ring (and hence reduces the C=S^0 bond order), and very little back donated charge reaches the phenyl ring. One needs to be cautious in describing this situation. We might have chosen the fragments to be $[Ru^{III}(bpy)_2\ ]^{3+}$ and $(1,2(S,SO_2)–C_6H_4)^{2-}$ in which case there is an extra electron on the (S,SO_2) ligand and ligand orbital #45β is now occupied. The overall description of the complex, of course, remains the same.

Referring to Table 2, as one passes from species **1** to species $\mathbf{1}^+$ the net charge on the (S,SO_2) ligand decreases, the net positive charge on Ru increases, the charge on the S^0 donor becomes positive but that of S^{IV} remains unchanged (positive). The dramatic change in the charge on S^0 from a negative to positive value is consistent with the removal of an electron from the Ru–S^0 bond.

Thus, in summary, oxidation of species **1** to $\mathbf{1}^+$ involves loss of an electron from the metallocycle ring

generating a highly covalent species best represented as $[Ru^{II0.5}(bpy)_2(S,SO_2)^{I0.5-}]^+$. There is very little change in the geometry and electronic structure of the phenyl ring component of the (S,SO_2) ligand in species **1** and $\mathbf{1}^+$.

The $[Ru(bpy)_2(S,NH)]^+$ species is significantly more covalently bound than the other nonsulfur species. Both sulfur species have a larger 4d Ru population (Table 2) than the other complexes, due to this covalency.

The other formally Ru^{II} semiquinone species described here are similar species with a spin density largely associated with the metallocycle ring but with a greater relative contribution from the (X,Y) benzenoid ring. As noted by Remenyi and Kaupp:[37] "The anionic (acac) complexes turn out to be approximately halfway between a d^6-Ru^{II}/semiquinone and a d^5-Ru^{III}/catecholate formulation, ..." but the important involvement of the metallocycle ring makes such labels rather incomplete.

Acknowledgements

We thank the Natural Sciences and Engineering Research Council of Canada (NSERC, Ottawa) for funding, the Johnson Matthey Company for the loan of ruthenium trichloride and Rowshan Ara Begum for the spectroelectrochemistry. This work was made possible by the facilities of the Shared Hierarchical Academic Research Computing Network (SHARCNET: www.sharcnet.ca).

References

(1) Begum, R. A.; Farah, A. A.; Hunter, H. N.; Lever, A. B. P. *Inorg. Chem.* **2009**, *48* (5), 2018–2027. doi:10.1021/ic801898t.

(2) Nagashima, S.; Nakasako, M.; Dohmae, N.; Tsujimura, M.; Takio, K.; Odaka, M.; Yohda, M.; Kamiya, N.; Endo, I. *Nat. Struct. Biol.* **1998**, *5* (5), 347–351. doi:10.1038/nsb0598-347. PMID:9586994.

(3) Bourles, E.; Alves de Sousa, R.; Galardon, E.; Giorgi, M.; Artaud, I. *Angew. Chem.* **2005**, *117* (38), 6318–6321. doi:10.1002/ange.200500814.

(4) Kung, I.; Schweitzer, D.; Shearer, J.; Taylor, W. D.; Jackson, H. L.; Kovacs, J. A. *J. Am. Chem. Soc.* **2000**, *122* (34), 8299–8300. doi:10.1021/ja0017561.

(5) Lee, C.-M.; Chen, C.-H.; Chen, H.-W.; Hsu, J.-L.; Lee, G.-H.; Liaw, W.-F. *Inorg. Chem.* **2005**, *44* (19), 6670–6679. doi:10.1021/ic0501081.

(6) Juris, A.; Balzani, V.; Barigelletti, F.; Campagna, S.; Belser, P.; von Zelewsky, A. *Coord. Chem. Rev.* **1988**, *84* (1), 85–277. doi:10.1016/0010-8545(88)80032-8.

(7) Dodsworth, E. S.; Lever, A. B. P. *Chem. Phys. Lett.* **1986**, *124* (2), 152–158. doi:10.1016/0009-2614(86)85135-1.

(8) Lever, A. B. P. *Inorg. Chem.* **1990**, *29* (6), 1271–1285. doi:10.1021/ic00331a030.

(9) Jorgensen, C. K. *Oxidation Numbers and Oxidation States;* Springer-Verlag: New York, 1969.

(10) Ward, M. D.; McCleverty, J. A. *J. Chem. Soc., Dalton Trans.* **2002**, 275–288. doi:10.1039/b110131p.

(11) Ray, K.; Petrenko, T.; Wieghardt, K.; Neese, F. *J. Chem. Soc., Dalton Trans.* **2007**, 1552–1566. doi:10.1039/b700096k.

(12) Lever, A. B. P.; Gorelsky, S. I. *Struct. Bond.* **2004**, *107*, 77–114. doi:10.1007/b83927.

(13) Frisch, M. J.; Trucks, G. W.; Schlegel, H. B.; Scuseria, G. E.; Robb, M. A.; Cheeseman, J. R.; Montgomery, A., Jr.; Vreven, T.; Kudin, K. N.; Burant, J. C.; Millam, J. M.; Iyengar, S. S.; Tomasi, J.; Barone, V.; Mennucci, B.; Cossi, M.; Scalmani, G.; Rega, N.; Petersson, G. A.; Nakatsuji, H.; Hada, M.; Ehara, M.; Toyota, K.; Fukuda, R.; Hasegawa, J.; Ishida, M.; Nakajima, T.; Honda, Y.; Kitao, O.; Nakai, H.; Klene, M.; Li, X.; Knox, J. E.; Hratchian, H. P.; Cross, J. B.; Bakken, V.; Adamo, C.; Jaramillo, J.; Gomperts, R.; Stratmann, R. E.; Yazyev, O.; Austin, A. J.; Cammi, R.; Pomelli, C.; Ochterski, J. W.; Ayala, P. Y.; Morokuma, K.; Voth, G. A.; Salvador, P.; Dannenberg, J. J.; Zakrzewski, V. G.; Dapprich, S.; Daniels, A. D.; Strain, M. C.; Farkas, O.; Malick, D. K.; Rabuck, A. D.; Raghavachari, K.; Foresman, J. B.; Ortiz, J. V.; Cui, Q.; Baboul, A. G.; Clifford, S.; Cioslowski, J.; Stefanov, B. B.; Liu, G.; Liashenko, A.; Piskorz, P.; Komaromi, I.; Martin, R. L.; Fox, D. J.; Keith, T.; Al-Laham, M. A.; Peng, C. Y.; Nanayakkara, A.; Challacombe, M.; Gill, P. M. W.; Johnson, B.; Chen, W.; Wong, M. W.; Gonzalez, C.; Pople, J. A. *Gaussian 03,* revision C.02; Gaussian, Inc.: Wallingford, CT, 2004.

(14) Lee, C.; Yang, W.; Parr, R. G. *Phys. Rev. B* **1988**, *37* (2), 785–789. doi:10.1103/PhysRevB.37.785.

(15) Schäfer, A.; Horn, H.; Ahlrichs, R. *J. Chem. Phys.* **1992**, *97* (4), 2571–2577. doi:10.1063/1.463096.

(16) Schäfer, A.; Huber, C.; Ahlrichs, R. *J. Chem. Phys.* **1994**, *100* (8), 5829–5835. doi:10.1063/1.467146.

(17) Godbout, N.; Salahub, D. R.; Andzelm, J.; Wimmer, E. *Can. J. Chem.* **1992**, *70* (2), 560–571. doi:10.1139/v92-079.

(18) Sosa, C.; Andzelm, J.; Elkin, B. C.; Wimmer, E.; Dobbs, K. D.; Dixon, D. A. *J. Phys. Chem.* **1992**, *96* (16), 6630–6636. doi:10.1021/j100195a022.

(19) Gorelsky, S. I.; Lever, A. B. P. *J. Organomet. Chem.* **2001**, *635* (1–2), 187–196. doi:10.1016/S0022-328X(01)01079-8.

(20) Gorelsky, S. I. *AOMix-CDA Program;*Centre for Catalysis Research and Innovation (CCRI), University of Ottawa: Ottawa, ON, 2005. Available from http://www.sg-chem.net.

(21) Mulliken, R. S. *J. Chem. Phys.* **1955**, *23* (12), 2338–2342. doi:10.1063/1.1741876.

(22) Mulliken, R. S. *J. Chem. Phys.* **1955**, *23* (10), 1833–1840. doi:10.1063/1.1740588.

(23) Mulliken, R. S. *J. Chem. Phys.* **1955**, *23* (12), 2343–2346. doi:10.1063/1.1741877.

(24) Mulliken, R. S. *J. Chem. Phys.* **1955**, *23* (10), 1841–1846. doi:10.1063/1.1740589.

(25) Reed, A. E.; Curtiss, L. A.; Weinhold, F. *Chem. Rev.* **1988**, *88* (6), 899–926. doi:10.1021/cr00088a005.

(26) Gorelsky, S. I.; Ghosh, S.; Solomon, E. I. *J. Am. Chem. Soc.* **2006**, *128* (1), 278–290. doi:10.1021/ja055856o. PMID:16390158.

(27) Noodleman, L.; Lovell, T.; Han, W. G.; Liu, T.; Torres, R. A. In *Comprehensive Coordination Chemistry II: From Biology to Nanotechnology;* Elsevier: Oxford, 2004; pp 491–510.

(28) Bickelhaupt, F. M.; Baerends, E. J. In *Reviews in Computational Chemistry;* Lipkowitz, K. B., Boyd, D. R. E., Eds.; Wiley: New York, 2000; Vol. 15; pp 1–86.

(29) Stratmann, R. E.; Scuseria, G. E.; Frisch, M. J. *J. Chem. Phys.* **1998**, *109* (19), 8218–8224. doi:10.1063/1.477483.

(30) Bauernschmitt, R.; Ahlrichs, R. *Chem. Phys. Lett.* **1996**, *256* (4–5), 454–464. doi:10.1016/0009-2614(96)00440-X.

(31) Casida, M. E.; Jamorski, C.; Casida, K. C.; Salahub, D. R. *J. Chem. Phys.* **1998**, *108* (11), 4439–4449. doi:10.1063/1.475855.

(32) Neese, F. *Coord. Chem. Rev.* **2009**, *253* (5–6), 526–563. doi:10.1016/j.ccr.2008.05.014.

(33) Gorelsky, S. I. *SWizard;* CCRI, University of Ottawa: Ottawa, ON, 2008. Available from http://www.sg-chem.net.
(34) Gorelsky, S. I. In *Comprehensive Coordination Chemistry-II;* Elsevier Science Publishers: San Diego, CA, 2004; Vol. 2 ; Chap. 2.51; pp 651–660.
(35) Cossi, M.; Barone, V.; Mennucci, B.; Tomasi, J. *Chem. Phys. Lett.* **1998**, *286* (3–4), 253–260. doi:10.1016/S0009-2614(98)00106-7.
(36) Kalinina, D.; Dares, C.; Kaluarachchi, H.; Potvin, P. G.; Lever, A. B. P. *Inorg. Chem.* **2008**, *47* (21), 10110–10126. doi:10.1021/ic8014496. PMID:18844345.
(37) Remenyi, C.; Kaupp, M. *J. Am. Chem. Soc.* **2005**, *127* (32), 11399–11413. doi:10.1021/ja051811b. PMID:16089469.
(38) Masui, H. *Coord. Chem. Rev.* **2001**, *219–221*, 957–992. doi:10.1016/S0010-8545(01)00389-7.
(39) Milčić, M. K.; Ostojić, B. D.; Zarić, S. D. *Inorg. Chem.* **2007**, *46* (17), 7109–7114. doi:10.1021/ic062292w. PMID:17655219.
(40) Beaulac, R.; Lever, A. B. P.; Reber, C. *Eur. J. Inorg. Chem.* **2007**, *2007* (1), 48–52. doi:10.1002/ejic.200600925.
(41) Bhattacharya, S.; Gupta, P.; Basuli, F.; Pierpont, C. G. *Inorg. Chem.* **2002**, *41* (22), 5810–5816. doi:10.1021/ic025766+. PMID:12401087.
(42) Cavigliasso, G.; Ireland, L. R.; Rothery, J. *J. Chem. Soc., Dalton Trans.* **2001**, 2095–2108. doi:10.1039/b102094n.
(43) Mayer, I. *Chem. Phys. Lett.* **1983**, *97* (3), 270–274. doi:10.1016/0009-2614(83)80005-0.
(44) Foster, J. P.; Weinhold, F. *J. Am. Chem. Soc.* **1980**, *102* (24), 7211–7218. doi:10.1021/ja00544a007.
(45) (a) Gorelsky, S. I.; Solomon, E. I. *Theor. Chem. Acc.* **2008**, *119* (1–3), 57–65. doi:10.1007/s00214-007-0270-1.; (b) Gorelsky, S. I.; Solomon, E. I. *Theor. Chem. Acc.* **2008**, *119* (1–3), 67. doi:10.1007/s00214-007-0289-3.
(46) Frenking, G.; Fröhlich, N. *Chem. Rev.* **2000**, *100* (2), 717–774. doi:10.1021/cr980401l. PMID:11749249.
(47) Solomon, E. I.; Hedman, B.; Hodgson, K. O.; Dey, A.; Szilagyi, R. K. *Coord. Chem. Rev.* **2005**, *249* (1–2), 97–129. doi:10.1016/j.ccr.2004.03.020.
(48) Gorelsky, S. I.; Basumallick, L.; Vura-Weis, J.; Sarangi, R.; Hodgson, K. O.; Hedman, B.; Fujisawa, K.; Solomon, E. I. *Inorg. Chem.* **2005**, *44* (14), 4947–4960. doi:10.1021/ic050371m. PMID:15998022.
(49) Grapperhaus, C. A.; Kozlowski, P. M.; Kumar, D.; Frye, H. N.; Venna, K. B.; Poturovic, S. *Angew. Chem. Int. Ed.* **2007**, *46* (22), 4085–4088. doi:10.1002/anie.200700297.
(50) Grapperhaus, C. A.; Poturovic, S.; Mashuta, M. S. *Inorg. Chem.* **2005**, *44* (23), 8185–8187. doi:10.1021/ic051211d. PMID:16270951.
(51) Herebian, D.; Bothe, E.; Bill, E.; Weyhermüller, T.; Wieghardt, K. *J. Am. Chem. Soc.* **2001**, *123* (41), 10012–10023. doi:10.1021/ja011155p. PMID:11592879.
(52) Roy, N.; Sproules, S.; Bill, E.; Weyhermüller, T.; Wieghardt, K. *Inorg. Chem.* **2008**, *47* (23), 10911–10920. doi:10.1021/ic801109n. PMID:18989920.
(53) Ray, K.; Bill, E.; Weyhermüller, T.; Wieghardt, K. *J. Am. Chem. Soc.* **2005**, *127* (15), 5641–5654. doi:10.1021/ja040237l. PMID:15826204.
(54) Ghosh, P.; Begum, A.; Bill, E.; Weyhermüller, T.; Wieghardt, K. *Inorg. Chem.* **2003**, *42* (10), 3208–3215. doi:10.1021/ic020617c. PMID:12739961.
(55) Ray, K.; Weyhermüller, T.; Goossens, A.; Crajé, M. W. J.; Wieghardt, K. *Inorg. Chem.* **2003**, *42* (13), 4082–4087. doi:10.1021/ic0207092. PMID:12817965.
(56) Periyasamy, G.; Burton, N. A.; Hillier, I. H.; Vincent, M. A.; Disley, H.; McMaster, J.; Garner, C. D. *Faraday Discuss.* **2007**, *135*, 469–488. doi:10.1039/b607144a. PMID:17328443.–Discussion. *Faraday Discuss.* **2007**, *135*, 489–502. doi:10.1039/b615645m.
(57) O'Toole, M. G.; Kreso, M.; Kozlowski, P. M.; Mashuta, M. S.; Grapperhaus, C. A. *J. Biol. Inorg. Chem.* **2008**, *13* (8), 1219–1230. doi:10.1007/s00775-008-0405-4. PMID:18633652.
(58) Jacobsen, H.; Donahue, J. P. *Inorg. Chem.* **2008**, *47* (21), 10037–10045. doi:10.1021/ic801277r. PMID:18823113.

Carbon–hydrogen vs. carbon–halogen oxidative addition of chlorobenzene to a cationic iridium(I) system — A density functional theory study

Hong Wu and Michael B. Hall

Abstract: Density functional theory (DFT) is used to explore the competitive C–H and C–Cl oxidative additions (OA) of chlorobenzene to the cationic Ir(I) complex: $[(PNP^*)Ir^I]^+$ [PNP* = 2,6-bis((dimethylphosphino)methyl)pyridine]. Consistent with experimental results, the calculated activation barrier for C–H OA ($\Delta G^{\ddagger}$ = 10.7 kcal mol^{-1}) is lower than that for C–Cl OA ($\Delta G^{\ddagger}$ = 19.7 kcal mol^{-1}). However, the C–Cl OA product is calculated to be thermodynamically preferred as its ΔG^{o} is 14.3 kcal mol^{-1} below that for the most stable C–H OA product.

Key words: iridium, catalysis, density functional, bond activation, oxidative addition, reaction mechanism, thermochemistry.

Résumé : On a utilisé la théorie de la fonctionnelle de la densité (TFD) pour étudier les réactions d'additions oxydantes (AO) C–H et C–Cl du chlorobenzène sur le complexe cationique de l'iridium(I), $[(PNP^*)Ir^I]^+$ [PNP* = 2,6-bis{(diméthylphosphino)méthyl}pyridine]. En accord avec les résultats expérimentaux, la barrière d'activation calculée pour la réaction d'addition oxydante du C–H ($\Delta G^{\ddagger}$ = 10,7 kcal·mol^{-1}) est inférieure à celle pour la réaction d'addition oxydante du C–Cl ($\Delta G^{\ddagger}$ = 19,7 kcal·mol^{-1}). Toutefois, on a calculé que le produit de la réaction d'addition oxydante du C–Cl est thermodynamiquement privilégié puisque son ΔG^{o} est 14,3 kcal·mol^{-1} inférieur au produit le plus stable de l'addition oxydante d'un C–H.

Mots-clés : iridium, catalyse, fonctionnelle de la densité, activation d'une liaison, addition oxydante, mécanisme réactionnel, thermochimie.

[Traduit par la Rédaction]

Introduction

Carbon–hydrogen bond activation by transition-metal complexes, an extremely important process because of its widespread use in functionalizing arenes, alkanes, and other organic molecules, has been studied extensively by experimental and theoretical investigations[1] since the pioneering studies of Crabtree,[2] Chatt and co-workers,[3] Shilov,[4] Bergman and co-workers,[5] Jones and co-workers,[6] and Graham and co-workers.[7] Group-9 metal complexes[8] have played a central role in the expansion of this challenging field, especially those of iridium.[9]

The ability to selectively and catalytically activate C–H bonds has tremendous utility in organic synthesis. Because of their strength, C–X bonds in haloarenes, commonly used organic substrates,[10] are expected to be less likely to undergo oxidative additions (OA) to transition-metal species than the C–H bonds. However, because of their higher polarity, C–X bonds may have stronger initial binding tendencies compared with C–H bonds in forming σ-complexes, precursors to OA reactions. Due to steric effects, C–H bond activation in haloarenes usually takes place at less hindered positions, forming predominantly mixtures of meta- and para-activated complexes. In a recent work, Milstein and co-workers described an unprecedented ortho C–H activation preference (at ≤60 °C) in chloro- and bromo-benzene via oxidative addition to the cationic $[(PNP^*)Ir^I]^+$ [PNP* = 2,6-bis((di-*tert*-butylphosphino)methyl)pyridine] where the halogen apparently acts as a directing group (Scheme 1).[11] No C–X activation products were observed in this study. On the other hand, Ozerov and co-workers reported that $(PNP)Ir(H)_2$ [PNP = bis(2-(diisopropylphosphino)-4-methylphenyl)amino] activates the ortho C–H bond at 70 °C but forms C–X OA products above 100 °C.[12] Further, the PNP Rh system exclusively activates the C–X bond.[13] Clearly, the strongly electron-donating and bulky tridentate PNP ligands generate a variety of unusual transition-metal chemistry.[14] All studies suggest that the OA reactions proceed via a 14-electron three-coordinated intermediates, such as $[(PNP^*)Ir^I]^+$.

Although there have been extensive theoretical studies of C–H bond addition in group-9 metals, there has been only one recent report of the thermodynamic vs. kinetic preference of C–X bonds vs. C–H bonds, respectively, and that was for a simple $Ir(PH_3)_2(H)$ model compound.[15] Here, we report a theoretical study to explore the kinetic and thermodynamic parameters in OA reactions of aromatic C–H and C–X bonds for the $[(PNP)(Me)Ir^I]^+$ system (Scheme 2).

Received 6 January 2009. Accepted 19 March 2009. Published on the NRC Research Press Web site at canjchem.nrc.ca on 5 October 2009.

This article is part of a Special Issue dedicated to Professor T. Ziegler.

H. Wu and M.B. Hall.[1] Department of Chemistry, Texas A&M University, College Station, TX 77843-3255, USA.

[1]Corresponding author (e-mail: mbh@mail.chem.tamu.edu).

Scheme 1.

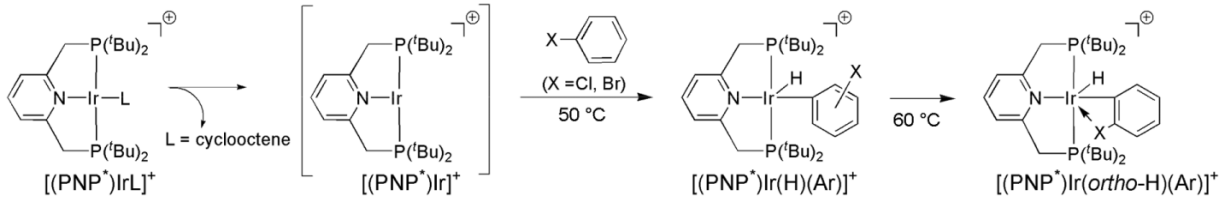

Scheme 2.

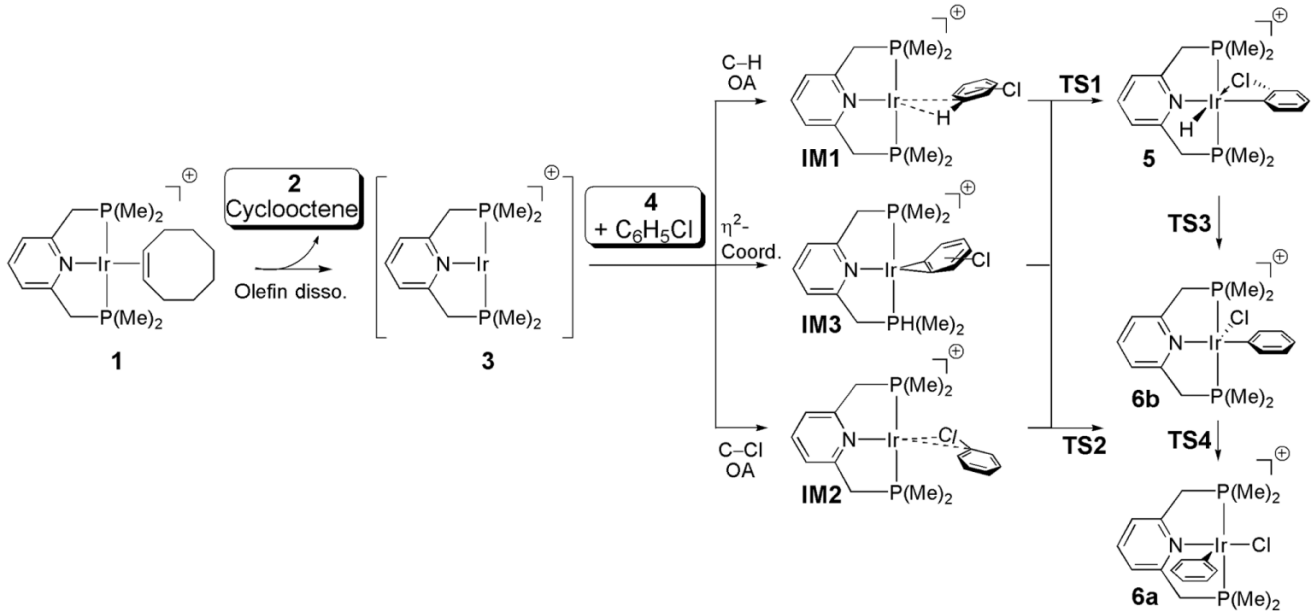

Computational details

All geometry optimizations and frequency determinations were carried out with the Gaussian 03 package of programs[16] at the B3LYP computational level.[17] Transition states were located with the use of synchronous transit-guided quasi-Newton method.[18] The basis set used for Ir is the extended valence double-zeta LANL2DZ[19] basis in which the 6s and 6p functions are replaced by the functions reoptimized by Couty and Hall,[20] and sets of diffuse f functions (exponent = 0.938(Ir)) were added.[21] The LANL2DZdp basis sets were employed for phosphorus and chlorine.[22] The 6–31G(d′) basis sets were used for all carbon, nitrogen, and hydrogen atoms.[23] Our computational models have methyl groups attached to the phosphorus atoms (i.e., $P(CH_3)_2$), a compromise between the use of hydrogen atoms and the bulky ^{t}Bu groups actually employed in the experiment.[11]

All computed structural data are documented in the Supplementary data, and we show models only of the most relevant conformations of the reactants, intermediates, and products and of the transition-state structures between them. Total electronic energies E, zero-point energies ZPE, E_0, ΔH, and ΔG, are reported as part of the Supplementary data (Table S1). Here, we report and discuss ΔH and ΔG data unless noted otherwise.

No basis set superposition error corrections were made for ligand-dissociation or substrate-association energy, since we are mainly interested in C–Cl vs. C–H OA in the current study. Following a reviewer's suggestion, we would like to note that the B3LYP functional sometimes predicts absolute dissociation energies that are too small, but this problem should not affect our main results, which depend on the relative energies. Solvent effects were considered only for dissociation-energy calculations with single-point calculations based on gas-phase geometries using the polarizable conductor calculation model (CPCM).[24] Chlorobenzene was the chosen solvent as employed in the experiments.

Scheme 3.

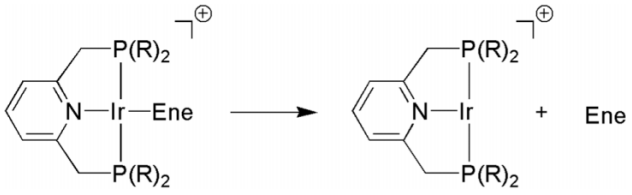

Throughout this paper, bond lengths are given in Ångstroms, bond angles in degrees, and relative reaction energies in kcal mol^{-1}.

Results and discussion

Complex **1** is used to model the reactant [(PNP*)Ir^{I}(cyclooctene)]$^+$ of the related experimental study.[11] In the solvent chlorobenzene (**4**), the unsaturated 14-electron [(PNP*)Ir^{I}]$^+$ species **3** is generated via the release of cyclooctene (**2**) from **1,** and species **3** undergoes either C–H OA to **5** or C–Cl OA to **6** (Scheme 2). Fourteen-electron ML_2L' fragments, like species **3** could have T- or Y-shaped struc-

Table 1. Dissociation energies and structural parameters.

R	Ene	ΔH_{gas}	ΔG_{gas}	$\Delta G_{solvent}$	Ir–C_1	Ir–C_2	C_1–Ir–C_2	P_1–Ir–C_1	P_2–Ir–C_2
Methyl	*Z*-2-butene	42.14	27.89	24.84	2.168	2.174	38.2	100.0	94.0
Methyl	Cyclooctene	35.93	22.68	16.90	2.161	2.180	38.1	98.6	92.2
^{t}Butyl	*Z*-2-butene	21.71	6.22	2.42	2.188	2.195	37.7	102.1	90.2
^{t}Butyl	Cyclooctene	17.54	2.80	–6.08	2.171	2.190	37.9	99.7	90.1

Fig. 1. Superimposed optimized geometries for the two olefins, Ene = *Z*-2-butene (orange) and Ene = cyclooctene (blue), when R = methyl (left) and R = ^{t}butyl (right).

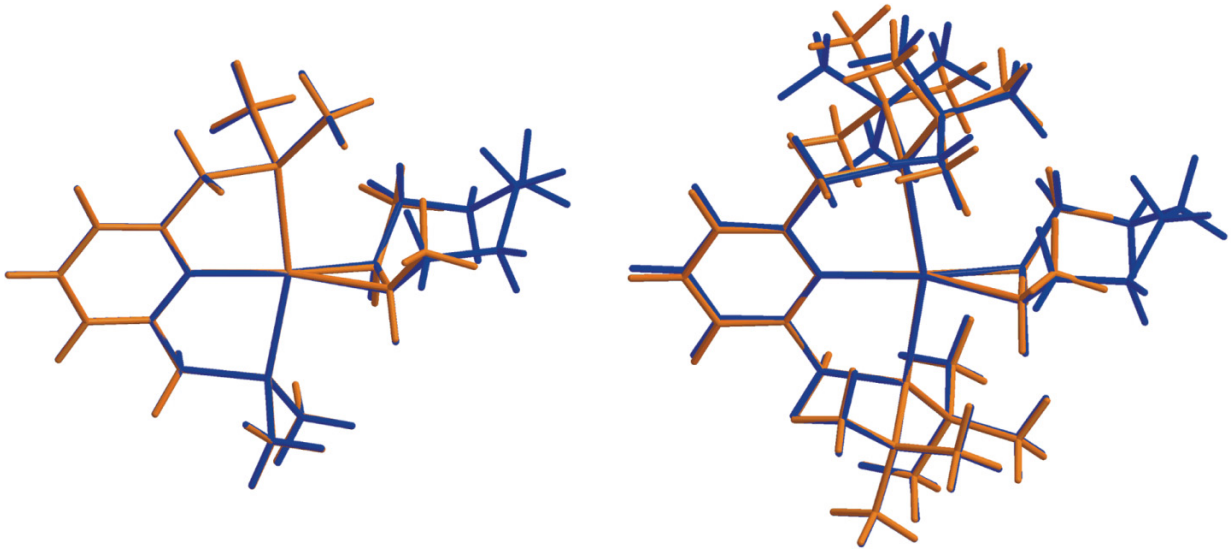

tures,[25] but the tridentate PNP* ligand enforces a T-shaped structure on $[(PNP^*)Ir^I]^+$, **3**, with Ir, P, P, and N approximately lying in a plane.

Loss of Ene

The steric and electronic effects in the olefin dissociation process (Scheme 3) are explored by the comparison of different R groups (methyl and ^{t}butyl) on P and different Enes (*Z*-2-butene and cyclooctene) on Ir.

The predominance of steric over electronic effects is seen in the dissociation energies when R and Ene groups are varied. Replacing the *Z*-2-butene with cyclooctene only reduces the gas-phase endoergicity of the dissociation process by 5.2 and 3.4 kcal mol^{-1}, respectively, but replacing the methyl groups attached to the phosphorus atoms with ^{t}butyl groups reduces this endoergicity by 21.6 and 19.8 kcal mol^{-1}, respectively. Thus, in the experimental system, R = ^{t}butyl and Ene = cyclooctene, the endoergicity of the dissociation process reduces dramatically in the gas phase to 2.8 kcal mol^{-1}, and the process is even exoergonic ($\Delta G_{solvent}$ = –6.1 kcal mol^{-1}) when the solvent effects are included (Table 1). Therefore, consistent with the experimental observation, the cyclooctene dissociation is facile, and the formation of the 14 e$^-$ $[(PNP^*)Ir]^+$ intermediate is energetically favored.

Examination of the structural difference for these four systems reveals the origin of the larger energy difference. There are strong structural similarities for the two olefins (*Z*-2-butene or cyclooctene) bonding to the $[(PNP^*)Ir^I]^+$ center in both cases of R = methyl (left) and R = ^{t}butyl (right) (Fig. 1). When R = methyl (left), except for the additional atoms in cyclooctene, the two geometries perfectly match each other, while there is some deviation on the $[(PNP^*)Ir^I]^+$ part when R = ^{t}butyl (right). The steric effects are more apparent when different R groups are structurally compared (Fig. 2). Unlike Fig. 1, in which structures overlay to each other fairly well, when the R group is changed from methyl to ^{t}butyl, there are strong deviations for the olefin functionality and also some for PR_2 group. Hence, the steric effect dominates the favorable loss of cyclooctene from $[(PNP^*)IrL]^+$.

Attachment of C_6H_5Cl to $[(PNP^*)Ir^I]^+$, 3

Transition-metal complexes with three-coordinate d^8 configurations are typically highly active.[26] Oxidative addition (OA) of chlorobenzene, **4**, to the unsaturated 14-electron $[(PNP^*)Ir^I]^+$ complex **3** leads to the formation of 16-electron five-coordinate adducts from C–H OA, $[(PNP^*)Ir^{III}(H)(C_6H_4Cl)]^+$ (**5**) or from C–Cl OA, $[(PNP^*)Ir^{III}(Cl)(C_6H_5)]^+$ (**6**). Initially, Ir binds weakly to the chlorobenzene forming either a σ-adduct, through a C–H (agostic), or a C–Cl bond, or a π-arene adduct. These three intermediates may be in rapid equilibria with the 14 e$^-$ complex (**3**) and solvent (**4**). We discuss the results of these initial adducts next.

(*i*) "Agostic" C–H σ-adducts, IM1-a – IM1-e

Prior to C–H OA, **3** reacts with **4** to form the C–H σ-adducts as intermediates **IM1**. With respect to the positions between the activated C–H bond and the Cl atom, five inter-

Fig. 2. Superimposed optimized geometries for the two R groups, R = methyl (orange) and R = ^{t}butyl (blue) when Ene = *Z*-2-butene (left) and Ene = cyclooctene (right).

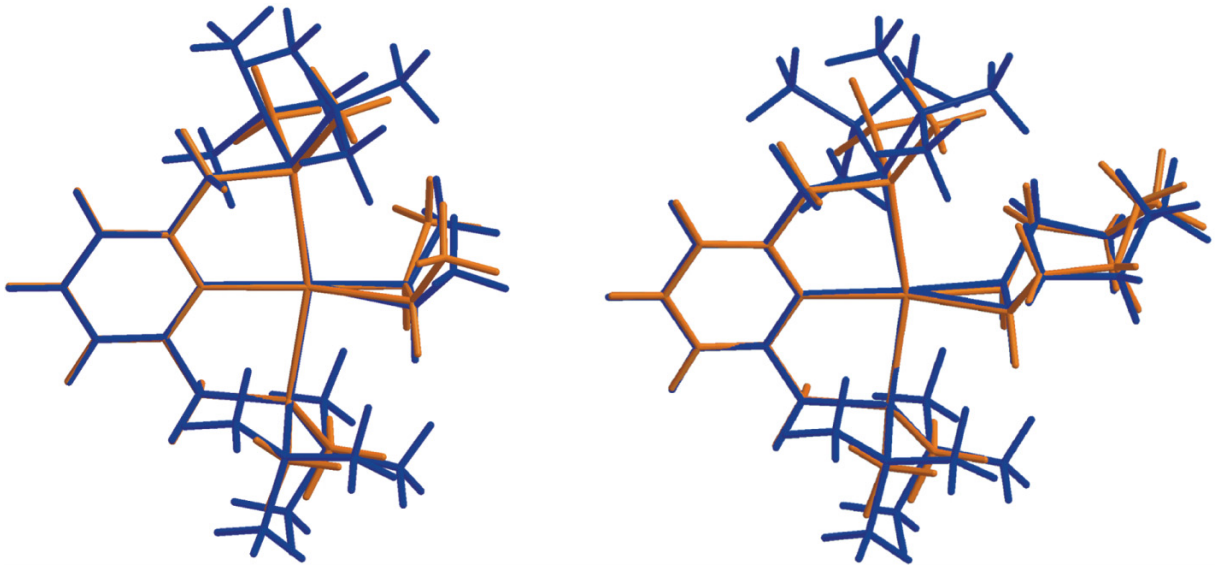

mediates are found: **IM1-a** and **IM1-b** are two intermediates for the ortho C–H OA, **IM1-c** and **IM1-d** are the two for the meta C–H OA, and **IM1-e** is the one for the para C–H OA (Fig. 3). In all structures, the H atom is closer to the Ir, but each one also has a close contact to the corresponding C atom.

All of the calculated energetic quantities are given in the Supplementary data (Table S2). We will discuss the most important quantities in the text. The attachment of chlorobenzene to $[(PNP^*)Ir^I]^+$ in C–H bond is strongly exothermic (ΔH = –15.2, –17.1, –16.7, –16.9, and –16.5 kcal mol^{-1}) and slightly exergonic (ΔG = –3.4, –4.6, –5.0, –5.1, and –4.9 kcal mol^{-1}) for all five pathways, respectively.

(*ii*) C–Cl σ-adduct, IM2

Prior to the C–Cl OA reaction, $[(PNP^*)Ir^I]^+$ binds **4** via the adduct Ir···Cl–C **IM2**. The optimized geometry of intermediate **IM2** is shown in Fig. 3. The attachment of chlorobenzene to $[(PNP^*)Ir^I]^+$ (**IM2**) is strongly exothermic (ΔH = –20.7 kcal mol^{-1}) and exergonic (ΔG = –10.5 kcal mol^{-1}).

(*iii*) η^2-Arene adduct, (PNP*)Ir(η^2-C_6H_5Cl), IM3

Six isomers of the η^2-C_6H_5Cl, complex with the C=C double bond perpendicular to the pyridine plane (Fig. 4) are also considered, since this partial coordination of arene to transition metals has often been suggested as a step prior to oxidative additions.[27] Because the PNP ligand is not completely planar, the six isomers correspond to two orientations of the three different C–C arene bonds. The pairs of isomers with respect to the twist of the PNP ligand are denoted as unprimed and primed isomers (Fig. 4). The energetic differences between the unprimed and primed relatives are less than 0.5 kcal mol^{-1} (Table S2), and we focus on the unprimed **IM3** isomers. When incoming chlorobenzene binds in an η^2 fashion, the 2,3-position (site **a**) is the most preferred site for η^2-coordination to **3** because the double bond character is highest between C(2) and C(3) (high population in π and low population in π*) as a result of the conjugation with the π donor Cl. The Cl-substituted double bond (site **c**) is the least favored site by 2.7 (unprimed) and 4.2 (primed) kcal mol^{-1} due to the decreased olefinic character at the C=C bonds carrying Cl. Furthermore, the dislocation at the two coordinated C atoms will disfavor the Cl substitution from being on one of these C atoms. Because of its similar electronic structure, coordination to 3,4-position (site **b**) is only 0.9 kcal mol^{-1} less stable than site **a**. In spite of some loss in resonance energy in the aromatic ring induced by the η^2-coordination of C_6H_5Cl to **3**,[28] the addition of chlorobenzene to $[(PNP^*)Ir^I]^+$ to the most stable η^2-intermediate, **IM3-a**, is strongly exothermic (ΔH = –25.8 kcal mol^{-1}) and exergonic (ΔG = –13.2 kcal mol^{-1}). **IM3-a** is 9.8 and 2.8 kcal mol^{-1} lower in free energy than **IM1-a** and **IM2**, respectively.

C–H and C–X oxidative addition products

Before discussing the transition states and reaction paths, we will discuss the structures and energetics of the OA products. Addition of chlorobenzene, **4**, to the unsaturated 14-electron $[(PNP^*)Ir^I]^+$ complex **3** leads to the C–H OA product, $[(PNP^*)Ir^{III}(H)(C_6H_4Cl)]^+$ (**5**), or C–Cl OA product, $[(PNP^*)Ir^{III}(Cl)(C_6H_5)]^+$ (**6**). For the C–H OA reaction, five isomers of product **5** (Fig. 5) have been calculated: ortho C–H bond activation produces isomers **5a** and **5b**, meta C–H bond activation produces isomers **5c** and **5d**, and para C–H bond activation produces isomer **5e**. The isomer **5a** is the most stable one by ~10 kcal mol^{-1}, as the chlorophenyl ring is oriented such that the Cl is weakly bound to the sixth coordination site, anti to the H. (Fig. 5) For isomers **5b**–**5e**, the Ir(III) metal center has a five-coordinate square-pyramidal geometry where the hydride occupies the apical site.

For the (**5a**, **5b**) and (**5c**, **5d**) rotamer pairs, transition states **TS(5a, 5b)** and **TS(5c, 5d)** for rotation about the Ir–C bond show that the Ir(III) center maintains the square-pyramidal geometry and the TSs have the chlorophenyl ring nearly coplanar with the pyridine. Our calculations also show much higher rotational barrier required for ortho-sub-

Fig. 3. Optimized geometries of agostic C–H σ-adducts, **IM1-a** – **IM1-e**, and the C–Cl adduct, **IM2**.

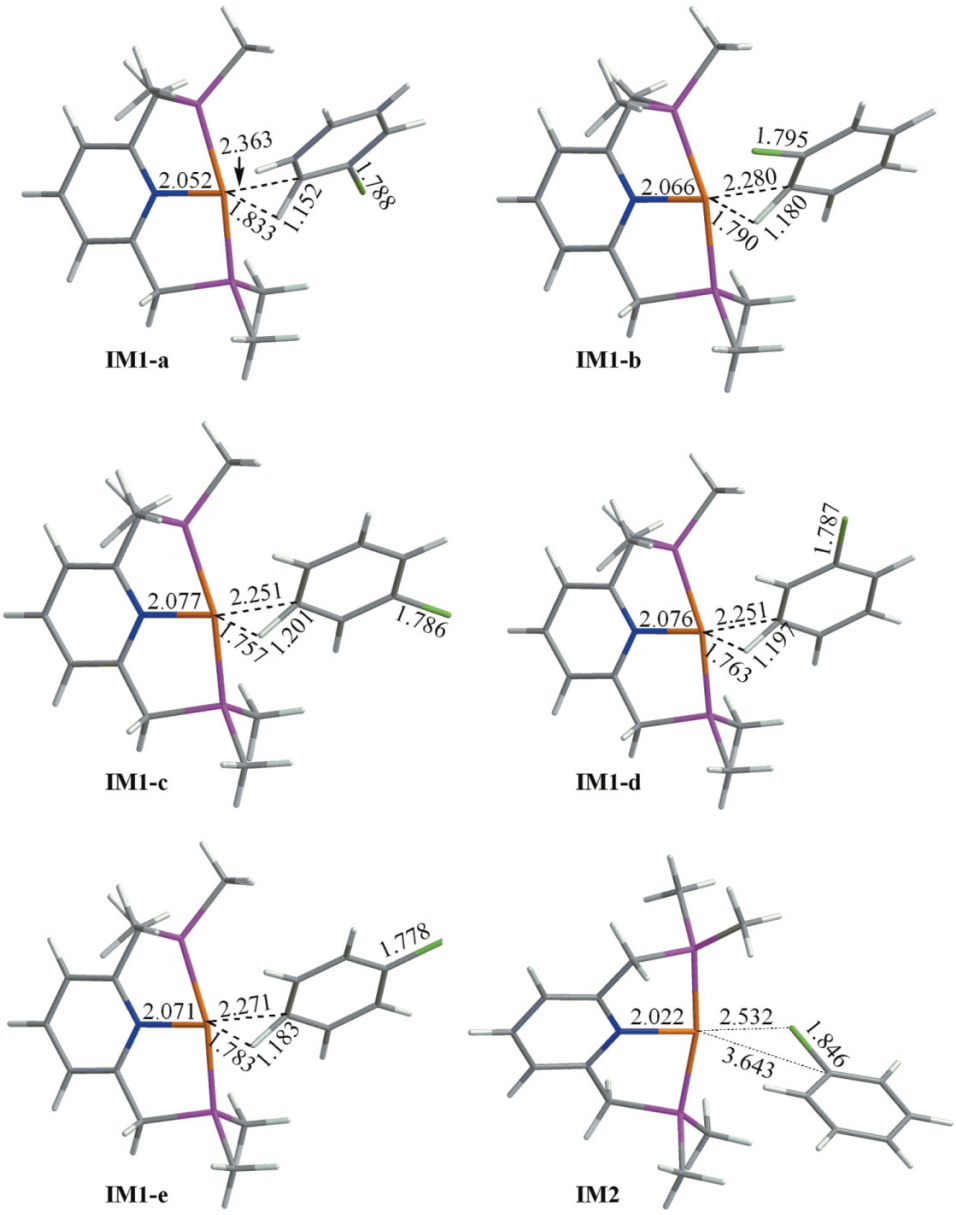

stituted **5a** → **5b** ($\Delta H^{\ddagger}$ = 23.8 kcal mol^{-1}) than for meta-substituted **5c** → **5d** ($\Delta H^{\ddagger}$ = 4.1 kcal mol^{-1}) (Table S2). **5c** and **5d** are nearly isoenergetic and interconvert too fast to be detected separately by NMR. Hence, only one meta-C–H activated complex will be detected. However, the rotation between **5a** and **5b** is relatively slow on the NMR time scale, and thus both **5a** and **5b** will be observed easily. Experimental observations show that, for (PNP)Ir(aryl)(H) system, the rotation about the Ir–C bond is restricted only for the ortho-substituted aryls.[29] The para-C–H activated complex **5e** is the fourth isomer that will be observed. The higher thermodynamic stability of **5a** than **5b**–**5e** can be explained by its additional intramolecular coordination of Cl to the Ir center (Cl → Ir donation).

For the C–Cl OA reaction, two approximately square-pyramidal isomers of product **6** were optimized (Fig. 6). Only isomer **6a**, which has the phenyl group occupying the apical site, was observed in the related experimental study, and no isomerization of **6a** was detected.[12] Consistent with this observation, our calculations show that **6b** is 18 kcal mol^{-1} higher in energy than **6a**.

Among the various isomeric stationary points (intermediates and products) for C–H and C–X activations, the C–Cl OA product **6a** is the global minimum. The lowest energy C–H OA product **5a** is 14.3 kcal mol^{-1} higher in enthalpy than the C–Cl OA product, **6a**. Hence, under equilibrium conditions we would expect to see the formation of C–Cl OA product, but the authors did not observe any in their experiments[11] at 60 °C.

Transition states for C–H OA reaction

Since both the η^2-C_6H_5Cl and the agostic Ir···H–C adducts are possible precursors/intermediates prior to C–H OA, we searched for C–H OA transition states starting from both ad-

Fig. 4. Optimized geometries of isomers of η^2-C_6H_5Cl complexes, **IM3-a – IM3-c′.**

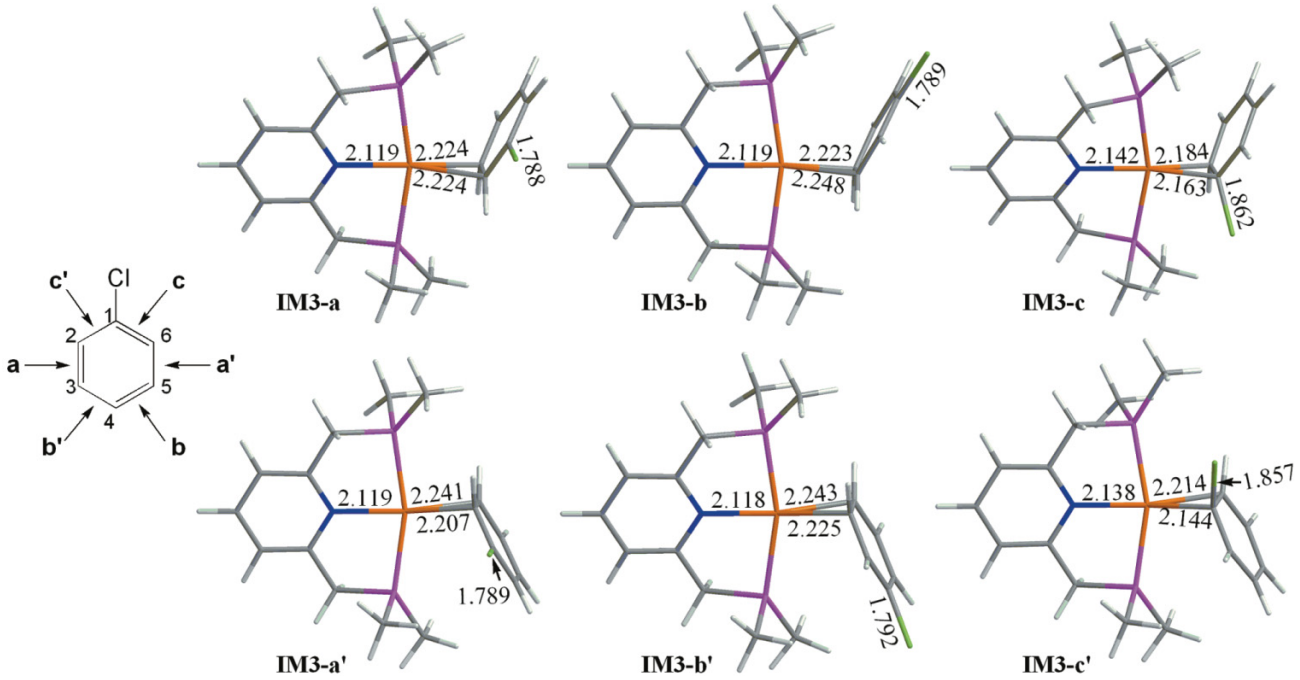

ducts. The same transition states, **TS1-a** – **TS1-e** (Fig. 6), were obtained from both starting points. In all these TS, the Ir–H and Ir–C bonds are nearly formed as indicated by their short distances. Overall, the geometries of the transition states correspond to a highly distorted trigonal-bipyrimidal metal center (Y-shaped) with relatively small H–Ir–C angles.

The η^2-C_6H_5Cl adducts are more stable than the agostic Ir···H–C adducts (i.e., **IM3-a** is 9.8 kcal mol^{-1} lower in free energy than **IM1-a**); hence, **IM3-a** is taken as the intermediate for the formation of **5a**–**5d**, and **IM3-b** is taken as the one for the formation of **5e**. The five C–H OA reactions are all exothermic and exergonic. The activation barriers ($\Delta G^{\ddagger}$) for all reaction pathways are fairly small ($\Delta G^{\ddagger}$ = 10.6 (**a**), 8.4 (**b**), 8.0 (**c**), 7.9 (**d**), and 7.1 (**e**) kcal mol^{-1}). The calculations, therefore, predict that the C–H bond activation by [(PNP*)Ir^{I}]$^{+}$ upon the addition of chlorobenzene is quite facile. The formation of the thermodynamically most stable C–H OA product **5a** requires a somewhat higher barrier (~2.2–3.5 kcal mol^{-1}) than the formation of other products. Therefore, **5a** is observed together with other isomers by experiments at 50 °C and becomes the dominant C–H OA product at higher temperatures due to its thermodynamic stability.

Transition state for C–Cl OA reaction

Similarly, since both the η^2-C_6H_5Cl and C–Cl σ-adducts are possible precursors/intermediates prior to C–Cl OA, we searched for C–Cl OA transition states starting from both adducts. The same transition state, **TS2** (Fig. 6), was found in both attempts.

Again, since the η^2-C_6H_5Cl complex **IM3-a** is more stable than the **IM2** by 2.7 kcal mol^{-1}, **IM3-a** is taken as the intermediate for the formation of **6a**. In contrast to the C–H OA reactions, which require fairly small activation barriers, C–Cl bond activation requires an activation free energy of 19.7 kcal mol^{-1}. Because of the large kinetic preference for C–H OA, those products are not observed[11] in spite of the thermodynamic preference for product **6a**, which is the global minimum.

Isomerization of 5a to 6a

Although Milstein and co-workers did not observe any C–Cl OA product,[11] other experimental work[12] shows that the yield of the C–X (X = F, Cl, and Br) activation product increases at higher temperature as the kinetically favored C–H activation products undergo isomerization to the thermodynamically favored C–Cl OA product. Hence, it is critical to understand the isomerization path from the most stable C–H OA product **5a** to the most stable C–Cl OA product **6a**. The calculations show a low-energy route involving simultaneous cleavage of Ir–H and C–Cl bonds in **5a** and formation of C–H and Ir–Cl bonds via **TS3.** The product is intermediate **6b**, an isomer of the most stable C–Cl OA product, **6a**, with Cl occupying the apical site of Ir center, which then undergoes isomerization to **6a** via transition state **TS4** (Scheme 2). The optimized geometries of the two transition states involved in this isomerization, **TS3** and **TS4**, are shown in Fig. 7.

The activation free energy ($\Delta G^{\ddagger}$) for **5a** → **6b** is 16.7 kcal mol^{-1}, which is lower than that for **5a** → **5b** ($\Delta G^{\ddagger}$ = 25.6 kcal mol^{-1}) and for **5a** → **IM3-a** ($\Delta G^{\ddagger}$ = 27.1 kcal mol^{-1}). Thus, a direct route will be preferred over routes leading back to the reactants. Therefore, after formation of **5a**, increasing the reaction temperature converts **5a** directly to **6b** through **TS3** and then through **TS4** to the thermodynamically favored product **6a**. The activation barrier ($\Delta G^{\ddagger}$) for the latter step **6b** → **6a** is only 6.0 kcal mol^{-1}, while that for its reverse reaction (**6a** → **6b**) is 23.9 kcal mol^{-1}. Thus, the entire process of **5a** → **6a** is likely to proceed irreversibly.

Fig. 5. Optimized geometries of **5a**-**5e**, **TS(5a, 5b)**, **TS(5c, 5d)**, **6a**, and **6b**.

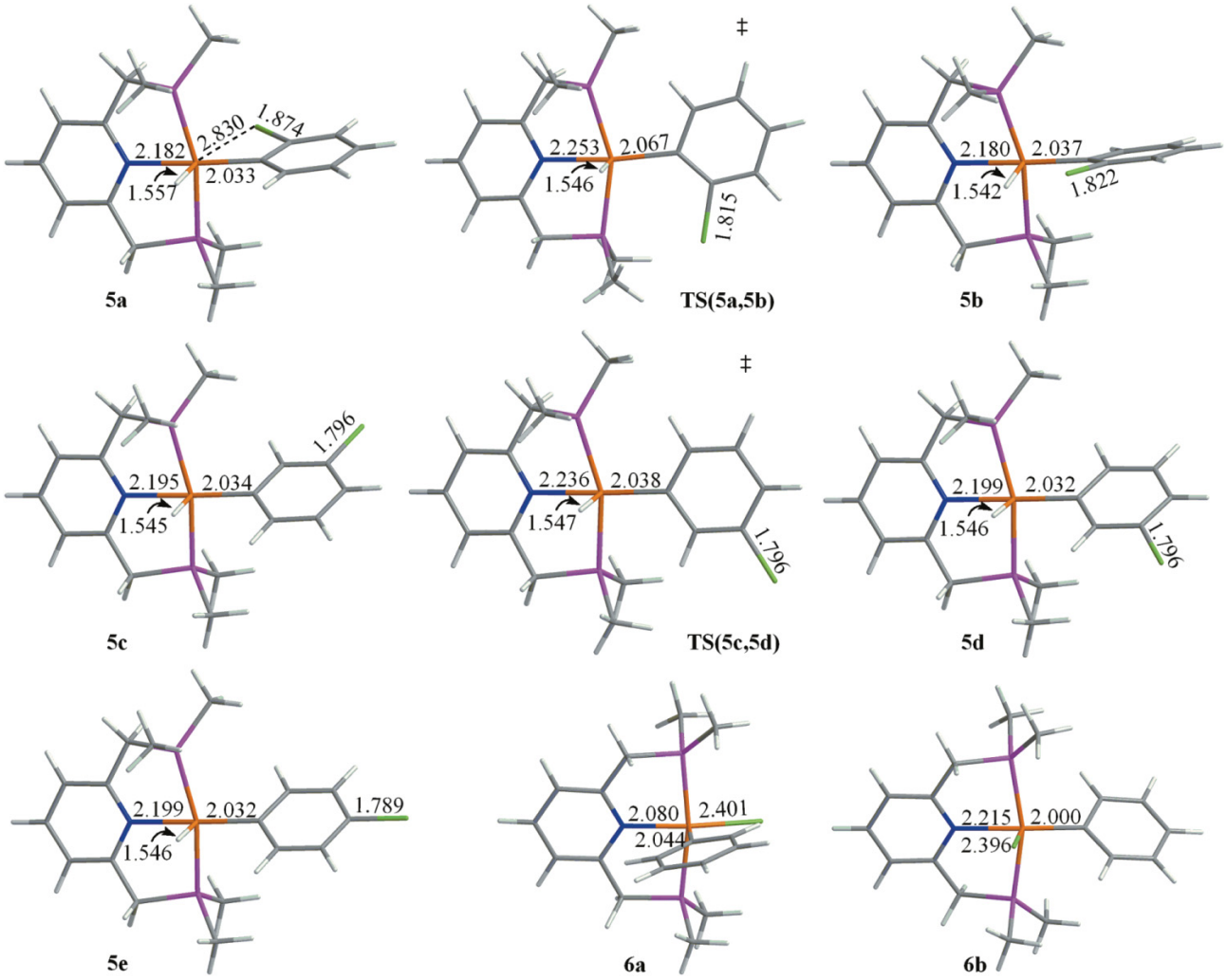

Conclusions

The energetic data for the reaction of the 14 e$^-$ intermediate [(PNP*)Ir^I]$^+$ (**3**) with chlorobenzene (**4**) are summarized by the ΔG potential-energy surface diagram (Fig. 8). All the energies are relative to the starting materials. Both C–H OA and C–Cl OA reactions are exothermic and exoergonic. Although **5a** is the most stable C–H OA product, it and the other C–H OA products (**5b**–**5e**) are formed through their own TS such as **TS1-a** (**TS1-b** – **TS1-e**). Additionally, some C–H OA products may be formed from the common intermediate **IM3-a**, but the interconvertion of these isomers (**5a**–**5e**) occurs only as higher temperatures are reached. The C–Cl OA product **6a** is the globe minimum; it is likely formed by the irreversible conversion from **5a** via intermediate **6b**; the higher energy direct C–Cl activation is a less likely route.

C–H activations are more competitive kinetically. The formation of the most stable C–H OA product, **5a,** only requires 10.6 kcal mol^{-1} activation free energy from **IM3-a** and much less from **IM1-a**, but the formation of C–Cl OA product, **6a**, requires 19.6 kcal mol^{-1} activation free energy for the direct C–Cl OA. In all cases, C–H OA is kinetically favored over C–Cl OA by at least 9.0 kcal mol^{-1}; therefore, only C–H OA reactions proceed at lower temperatures. This prediction is consistent with the experimental results that show no C–Cl OA product even at 60 °C.[11] However, as the temperature increases, **5a** becomes the only C–H OA product, and it isomerizes to **6b** and finally to **6a**. **6a** is thermodynamically much more stable than any of the intermediates or other products and its formation from the isomerization of **5a** requires 16.7 kcal mol^{-1} of activation energy, which is much less than that needed for **5a** converting back to either **5b** (25.6 kcal mol^{-1}) or **IM3-a** (27.1 kcal mol^{-1}). Hence, the isomerization of **5a** to **6a** is the exclusive pathway for the formation of **6a**, the thermodynamically most favored product. Even though the experimental workers did not report the results at temperatures higher than 60 °C,[11] we would expect that the C–Cl OA product, **6a**, be observed at higher temperatures.

In summary, the density functional calculations of the OA reactions of chlorobenzene with the cationic Ir^I complex [(PNP*)Ir^I]$^+$ (**3**) [PNP* = 2,6-bis((dimethylphosphino)methyl)pyridine] show that the PNP*-based Ir^I system exhibits high kinetic selectivity for the aromatic C–H activations. Lower-energy transition states in C–H activation and lower-energy products in C–Cl activation support the conclusion that C–H activation is more competitive kinetically, whereas

Fig. 6. Optimized geometries of transition states, **TS1-a** – **TS1-e** and **TS2**.

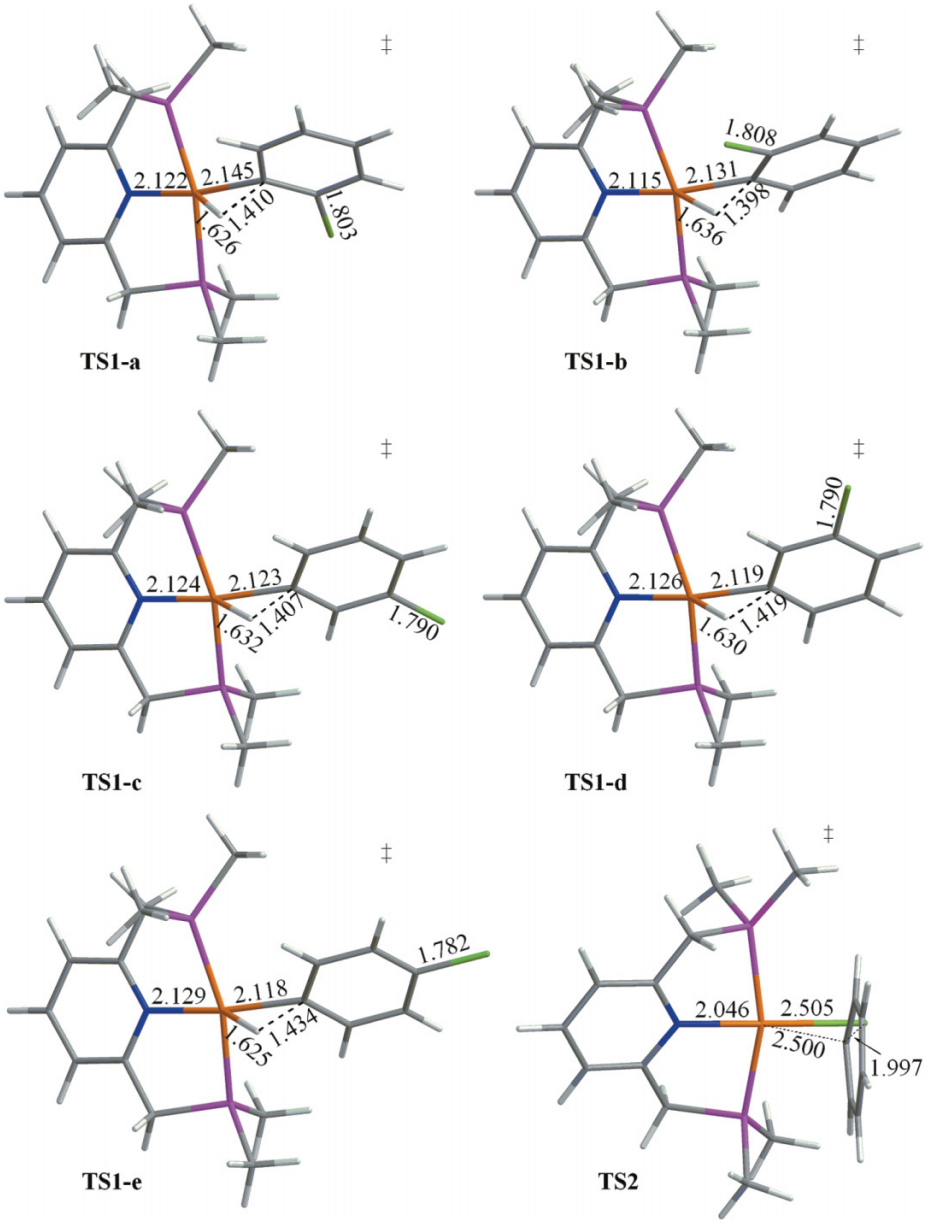

Fig. 7. Optimized geometries of transition states **TS3** and **TS4**.

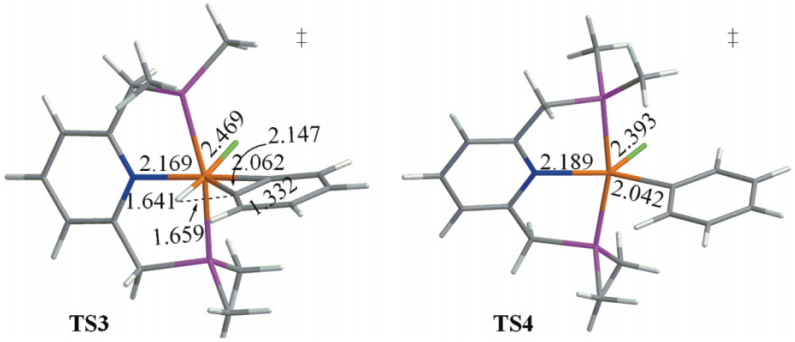

Fig. 8. Free-energy (ΔG) diagram for reactions of $[(PNP^*)Ir^I]^+$ (**3**) with chlorobenzene (**4**).

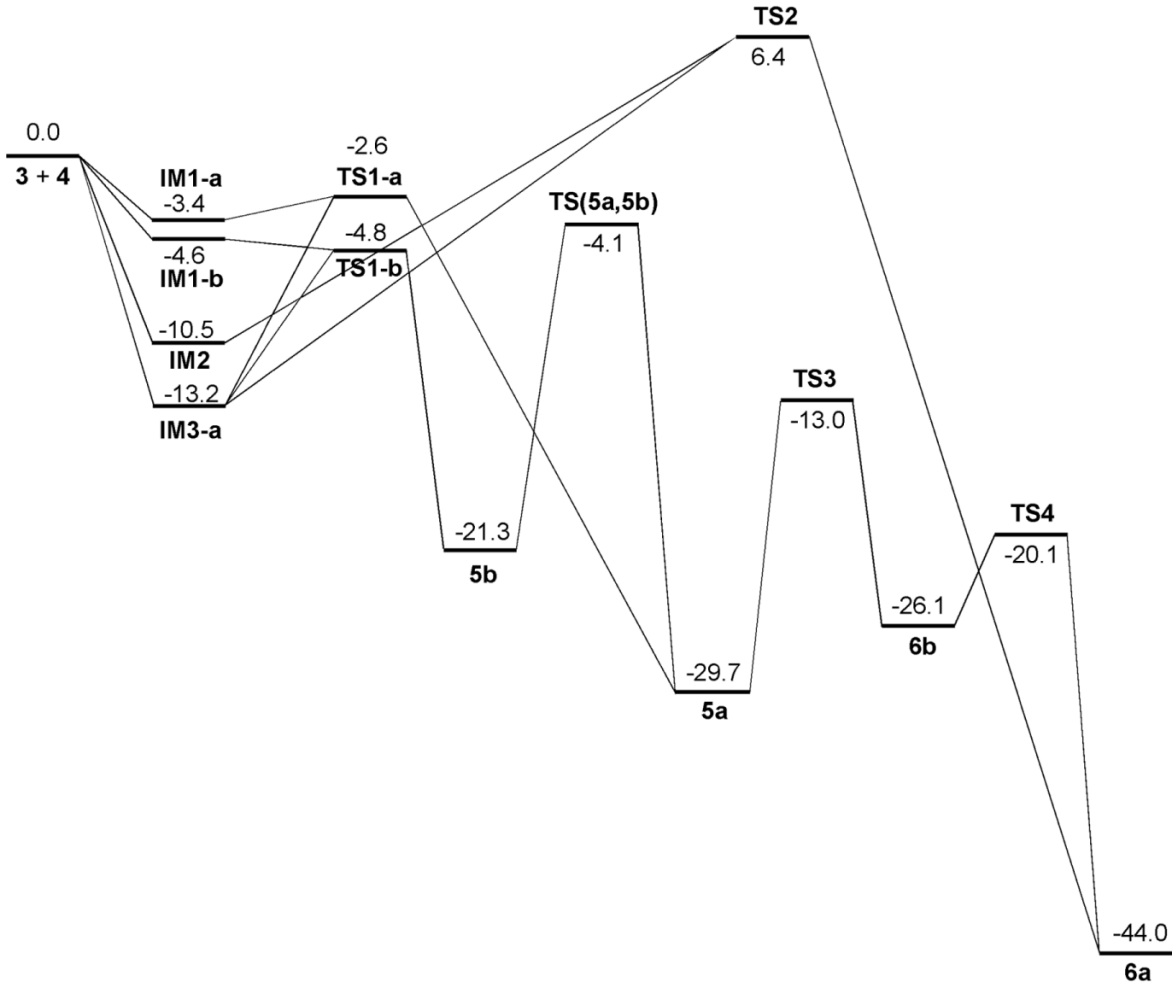

C–Cl activation is more favorable thermodynamically. We expect that a similar energetic scenario may appear to other transition-metal systems that are capable of OA reactions upon the addition of haloarenes (X = Cl, Br, and I).[30]

Supplementary data

Supplementary data for this article (a table with total energies and thermochemical data) are available on the journal Web site (canjchem.nrc.ca) or may be purchased from the Depository of Unpublished Data, Document Delivery, CISTI, National Research Council Canada, Ottawa, ON K1A 0R6, Canada. DUD 5272. For more information on obtaining material, refer to cisti-icist.nrc-cnrc.gc.ca/cms/unpub_e.shtml.

Acknowledgment

We acknowledge the Robert A. Welch Foundation (Grant No. A-0648) for financial support.

References

(1) (a) Arndtsten, B. A.; Bergman, R. G.; Mobley, T. A.; Peterson, T. H. *Acc. Chem. Res.* **1995**, *28* (3), 154–162. doi:10.1021/ar00051a009.; (b) Shilov, A. E.; Shul'pin, G. B. *Chem. Rev.* **1997**, *97* (8), 2879–2932. doi:10.1021/cr9411886. PMID:11851481.; (c) Niu, S.; Hall, M. B. *Chem. Rev.* **2000**, *100* (2), 353–406. doi:10.1021/cr980404y. PMID:11749240.; (d) Ritleng, V.; Sirlin, C.; Pfeffer, M. *Chem. Rev.* **2002**, *102* (5), 1731–1770. doi:10.1021/cr0104330. PMID:11996548.; (e) Bergman, R. G. *Nature* **2007**, *446* (7134), 391–393. doi:10.1038/446391a. PMID:17377575.

(2) Crabtree, R. H. In *The Organometallic Chemistry of the Transition Metals,* 3rd ed.; Wiley-Interscience: New York, 2001; p. 149.

(3) Chatt, J.; Davidson, J. M. *J. Chem. Soc.* **1965**, 843. doi:10.1039/jr9650000843.

(4) Shilov, A. E. *Pure Appl. Chem.* **1978**, *50* (8), 725–733. doi:10.1351/pac197850080725.

(5) (a) Janowicz, A. H.; Bergman, R. G. *J. Am. Chem. Soc.* **1982**, *104* (1), 352–354. doi:10.1021/ja00365a091.; (b) Walsh, P. J.; Hollander, F. J.; Bergman, R. G. *J. Am. Chem. Soc.* **1988**, *110* (26), 8729–8731. doi:10.1021/ja00234a043.

(6) (a) Jones, W. D.; Feher, F. J. *Organometallics* **1983**, *2* (4), 562–563. doi:10.1021/om00076a020.; (b) Jones, W. D.; Feher, F. J. *Acc. Chem. Soc.* **1989**, *22* (3), 91–100. doi:10.1021/ar00159a002.

(7) (a) Hoyano, J. K.; McMaster, A. D.; Graham, W. A. G. *J. Am. Chem. Soc.* **1983**, *105* (24), 7190–7191. doi:10.1021/ja00362a039.; (b) Sweet, J. R.; Graham, W. A. G. *Organometallics* **1983**, *2* (1), 135–140. doi:10.1021/om00073a025.

(8) (a) Cotton, S. A. In *Chemistry of Precious Metals;* Chapman and Hall: London, 1997; p. 78.(b) Dickson, R. S. In *Organo-*

metallic Chemistry of Rodium and Iridium; Academic Press: New York, 1983.

(9) (a) Niu, S.; Hall, M. B. *J. Am. Chem. Soc.* **1999**, *121* (16), 3992–3999. doi:10.1021/ja981314d.; (b) Fan, Y.; Cui, X.; Burgess, K.; Hall, M. B. *J. Am. Chem. Soc.* **2004**, *126* (51), 16688–16689. doi:10.1021/ja044240g. PMID:15612683.; (c) Zhang, X.; Kanzelberger, M.; Emge, T. J.; Goldman, A. S. *J. Am. Chem. Soc.* **2004**, *126* (41), 13192–13193. doi:10.1021/ja046476q. PMID:15479051.; (d) Davies, D. L.; Donald, S. M. A.; Al-Duaij, O.; Macgregor, S. A.; Pölleth, M. *J. Am. Chem. Soc.* **2006**, *128* (13), 4210–4211. doi:10.1021/ja060173+. PMID:16568979.

(10) Mureinik, R. J.; Weitzberg, M.; Blum, J. *Inorg. Chem.* **1979**, *18* (4), 915–918. doi:10.1021/ic50194a003.

(11) Ben-Ari, E.; Gandelman, M.; Rozenberg, H.; Shimon, L. J. W.; Milstein, D. *J. Am. Chem. Soc.* **2003**, *125* (16), 4714–4715. doi:10.1021/ja028362p. PMID:12696882.

(12) Fan, L.; Parkin, S.; Ozerov, O. V. *J. Am. Chem. Soc.* **2005**, *127* (48), 16772–16773. doi:10.1021/ja0557637. PMID:16316208.

(13) Gatard, S.; Celenligil–Cetin, R.; Guo, C.; Foxman, B. M.; Ozerov, O. V. *J. Am. Chem. Soc.* **2006**, *128* (9), 2808–2809. doi:10.1021/ja057948j. PMID:16506753.

(14) Hermann, D.; Gandelman, M.; Rozenberg, H.; Shimon, L. J. W.; Milstein, D. *Organometallics* **2002**, *21* (5), 812–818. doi:10.1021/om010719v.

(15) Cundari, T. R.; Vaddadi, S. *Inorg. Chim. Acta* **2004**, *357* (10), 2863–2869. doi:10.1016/j.ica.2004.05.034.

(16) Frisch, M. J.; Trucks, G. W.; Schlegel, H. B.; Scuseria, G. E.; Robb, M. A.; Cheeseman, J. R.; Montgomery, J. A., Jr.; Vreven, T.; Kudin, K. N.; Burant, J. C.; Millam, J. M.; Iyengar, S. S.; Tomasi, J.; Barone, V.; Mennucci, B.; Cossi, M.; Scalmani, G.; Rega, N.; Petersson, G. A.; Nakatsuji, H.; Hada, M.; Ehara, M.; Toyota, K.; Fukuda, R.; Hasegawa, J.; Ishida, M.; Nakajima, T.; Honda, Y.; Kitao, O.; Nakai, H.; Klene, M.; Li, X.; Knox, J. E.; Hratchian, H. P.; Cross, J. B.; Adamo, C.; Jaramillo, J.; Gomperts, R.; Stratmann, R. E.; Yazyev, O.; Austin, A. J.; Cammi, R.; Pomelli, C.; Ochterski, J. W.; Ayala, P. Y.; Morokuma, K.; Voth, G. A.; Salvador, P.; Dannenberg, J. J.; Zakrzewski, V. G.; Dapprich, S.; Daniels, A. D.; Strain, M. C.; Farkas, O.; Malick, D. K.; Rabuck, A. D.; Raghavachari, K.; Foresman, J. B.; Ortiz, J. V.; Cui, Q.; Baboul, A. G.; Clifford, S.; Cioslowski, J.; Stefanov, B. B.; Liu, G.; Liashenko, A.; Piskorz, P.; Komaromi, I.; Martin, R. L.; Fox, D. J.; Keith, T.; Al-Laham, M. A.; Peng, C. Y.; Nanayakkara, A.; Challacombe, M.; Gill, P. M. W.; Johnson, B.; Chen, W.; Wong, M. W.; Gonzalez, C.; Pople, J. A. *Gaussian 03,* revision B.4; Gaussian, Inc.: Pittsburgh, PA, 2003.

(17) (a) Stephens, P. J.; Devlin, F. J.; Chabalowski, C. F.; Frisch, M. *J. Phys. Chem.* **1994**, *98* (45), 11623–11627. doi:10.1021/j100096a001.; (b) Becke, A. D. *J. Chem. Phys.* **1993**, *98* (7), 5648. doi:10.1063/1.464913.; (c) Lee, C.; Yang, W.; Parr, R. G. *Phys. Rev. B* **1988**, *37* (2), 785–789. doi:10.1103/PhysRevB.37.785.

(18) Peng, C.; Ayala, P. Y.; Schlegel, H. B.; Frisch, M. J. *J. Comput. Chem.* **1996**, *17* (1), 49–56. doi:10.1002/(SICI)1096-987X(19960115)17:1<49::AID-JCC5>3.0.CO;2-0.

(19) Hay, P. J.; Wadt, W. R. *J. Chem. Phys.* **1985**, *82* (1), 299. doi:10.1063/1.448975.

(20) Couty, M.; Hall, M. B. *J. Comput. Chem.* **1996**, *17* (11), 1359–1370. doi:10.1002/(SICI)1096-987X(199608)17:11<1359::AID-JCC9>3.0.CO;2-L.

(21) Ehlers, A. W.; Böhme, M.; Dapprich, S.; Gobbi, A.; Höllwarth, A.; Jonas, V.; Köhler, K. F.; Stegmann, R.; Veldkamp, A.; Frenking, G. *Chem. Phys. Lett.* **1993**, *208* (1-2), 111–114. doi:10.1016/0009-2614(93)80086-5.

(22) Check, C. E.; Faust, T. O.; Bailey, J. M.; Wright, B. J.; Gilbert, T. M.; Sunderlin, L. S. *J. Phys. Chem. A* **2001**, *105* (34), 8111–8116. doi:10.1021/jp011945l.

(23) (a) Petersson, G. A.; Al-Laham, M. A. *J. Chem. Phys.* **1991**, *94* (9), 6081. doi:10.1063/1.460447.; (b) Petersson, G. A.; Bennett, A.; Tensfeldt, T. G.; Al-Laham, M. A.; Shirley, W. A.; Mantzaris, J. *J. Chem. Phys.* **1988**, *89* (4), 2193. doi:10.1063/1.455064.; (c) Foresman, J. B.; Frisch, Æ. The 6–31G(d') basis set has the d polarization functions for C, N, O, and F taken from the 6–311G basis set, instead of the original arbitrarily assigned value of 0.8 used in the 6–31G basis set. In *Exploring Chemistry with Electronic Structure Methods,* 2nd ed.; Gaussian, Inc.: Pittsburgh, PA, 1996; p. 110.

(24) (a) Barone, V.; Cossi, M. *J. Phys. Chem. A* **1998**, *102* (11), 1995–2001. doi:10.1021/jp9716997.; (b) Cossi, M.; Rega, N.; Scalmani, G.; Barone, V. *J. Comput. Chem.* **2003**, *24* (6), 669–681. doi:10.1002/jcc.10189. PMID:12666158.

(25) Albright, T. A.; Burdett, J. K.; Whangbo, M. In *Orbital Interactions in Chemistry;* John Wiley & Sons: New York, 1985; p. 78.

(26) (a) Crumpton, D. M.; Goldberg, K. I. *J. Am. Chem. Soc.* **2000**, *122* (5), 962–963. doi:10.1021/ja9912123.; (b) Harper, T. G. P.; Desrosiers, P. J.; Flood, T. C. *Organometallic* **1990**, *9* (9), 2523–2528. doi:10.1021/om00159a022.

(27) (a) Parshall, G. W. *Acc. Chem. Res.* **1970**, *3* (4), 139–144. doi:10.1021/ar50028a004.; (b) Belt, S. T.; Helliwell, M.; Jones, W. D.; Partridge, M. G.; Perutz, R. N. *J. Am. Chem. Soc.* **1993**, *115* (4), 1429–1440. doi:10.1021/ja00057a028.

(28) Schilling, B. E. R.; Hoffmann, R.; Lichtenberger, D. L. *J. Am. Chem. Soc.* **1979**, *101* (3), 585–591. doi:10.1021/ja00497a017.

(29) Renkema, K. B.; Bosque, R.; Streib, W. E.; Maseras, F.; Eisenstein, O.; Caulton, K. G. *J. Am. Chem. Soc.* **1999**, *121* (47), 10895–10907. doi:10.1021/ja990523a.

(30) (a) Wu, H.; Hall, M. B. *Dalton Trans.*in press; (b) Wu, H.; Hall, M. B. *J. Phys. Chem. A*, in press.

The Dewar–Chatt–Duncanson model reversed — Bonding analysis of group-10 complexes $[(PMe_3)_2M–EX_3]$ (M = Ni, Pd, Pt; E = B, Al, Ga, In, Tl; X = H, F, Cl, Br, I)

Catharina Goedecke, Pierre Hillebrecht, Till Uhlemann, Robin Haunschild, and Gernot Frenking

Abstract: Quantum chemical calculations using BP86 with TZ2P basis sets were carried out to elucidate the structures and the bond–bond dissociation energies of the donor–acceptor complexes $[(PMe_3)_2M–EX_3]$ with X = H, F, Cl, Br, I; E = B, Al, Ga, In, Tl; and M = Ni, Pd, Pt. The nature of the metal–ligand bond was investigated with an energy decomposition analysis. The geometry optimizations gave for most compounds T-shaped structures with nearly linear P–M–P angles where the EX_3 ligand has either a staggered or eclipsed conformation with respect to the PMP plane. The energy differences between the conformations are very small which means that there is nearly free rotation about the M–EX_3 axis. The equilibrium structures of eight nickel compounds have a distorted geometry where one E–X bond is engaged in attractive interactions with the metal atom which yields a distorted square-planar arrangement of the metal atom. The complex $[(PMe_3)_2Ni–TlI_3]$ exhibits two attractive interactions between Tl–I bonds and the metal which features a five-coordinated metal atom. The calculated bond dissociation energies show that the boron complexes exhibit a different trend for the D_e values than the heavier group-13 homologues. The results for the Pd and Pt complexes suggest that the $[(PMe_3)_2M–BX_3]$ bond strength increases with F < Cl < Br < I < H which means that the BH_3 ligands are the most strongly bonded Lewis acids and BF_3 is the most weakly bonded species . The trend for the heavier group-13 complexes $[(PMe_3)_2M–EX_3]$ where E = Al, Ga, In, Tl follows the opposite order F > Cl > Br > I > H. The energy decomposition analysis of the M–EX_3 bonds indicates a substantial π contribution of between 12.7% and 30.3% to the total orbital interactions. There is no direct correlation between the strength of the orbital interactions or any of the other energy terms ΔE_{elstat} or ΔE_{Pauli} which correlates with the total interaction energy. The bond dissociation energy of the EX_3 ligands after breaking the M–EX_3 bonds is quite large. It is shown that the intrinsic strength of the M–EX_3 bonds is much larger than the BDEs and that the trends of ΔE_{int} and D_e are not always the same. The EX_3 ligands in $[(PMe_3)_2M–BX_3]$ always carry a large negative charge.

Key words: density functional calculations, bonding analysis, Lewis acids, transition metal complexes, reversed DCD model.

Résumé : On a effectué des calculs de mécanique quantique BP86 à l'aide d'ensembles de base TZ2P dans le but d'élucider les structures et les énergies de dissociation de liaison des complexes donneur–accepteur $[(PMe_3)_2M–EX_3]$ dans lesquels X = H, F, Cl, Br, et I; E = B, Al, et Ga, In, Tl; et M = Ni, Pd, et Pt. On a étudié la nature de la liaison métal–ligand par le biais d'une analyse de l'énergie de décomposition. Les optimisations de la géométrie conduisent, pour la plupart des composés, à des structures en forme de T avec des angles P–M–P pratiquement linéaires, dans lesquels le ligand EX_3 se trouve dans une conformation décalée ou éclipsée par rapport au plan PMP. Les différences d'énergie entre les conformations sont très faibles, ce qui implique qu'il existe une rotation pratiquement libre autour de l'axe M–EX_3. Les structures à l'équilibre dans les neuf composés du nickel comportent toutes une géométrie déformée dans laquelle une liaison E–X est engagée dans des interactions attractives avec l'atome métallique ce qui conduit à un arrangement plan carré déformé de l'atome métallique. Le complexe $[(PMe_3)_2Ni–TlI_3]$ présente même deux interactions attractives entre les liaisons Tl–I et le métal qui comporte un atome de métal pentacoordonné. Les énergies de dissociation de liaison calculées montrent que les complexes de bore présentent une tendance différente pour les valeurs D_e que les homologues plus lourds du groupe 13. Les résultats pour les complexes du Pd et du Pt suggèrent que la force de la liaison $[(PMe_3)_2M–EX_3]$ augmente avec F < Cl < Br < I < H, ce qui signifie que les ligands BH_3 sont les acides de Lewis les plus fortement liés et que les espèces BF_3 participent aux liaisons les plus faibles. La tendance pour les complexes plus lourds du groupe 13 $[(PMe_3)_2M–EX_3]$ dans lesquels E = Al, Ga, In et Tl conduit à l'ordre inverse F > Cl > Br > I > H. L'analyse de l'énergie de décomposition des liaisons M–EX_3 met en évidence la présence d'une contribution π importante, allant de 12,7 % à 30,3 % des interactions or-

Received 17 February 2009. Accepted 10 June 2009. Published on the NRC Research Press Web site at canjchem.nrc.ca on 6 October 2009.

This article is part of a Special Issue dedicated to Professor T. Ziegler.

C. Goedecke, P. Hillebrecht, T. Uhlemann, R. Haunschild, and G. Frenking.[1] Fachbereich Chemie der Universität Marburg, Hans-Meerwein-Strasse, D-35043 Marburg, Germany.

[1]Corresponding author (e-mail: frenking@chemie.uni-marburg.de).

bitalaires totales. Il n'existe aucune corrélation directe entre la force des interactions orbitalaires ou l'un des autres termes d'énergie, tel ΔE_{elstat} ou ΔE_{Pauli} et l'énergie totale d'interaction. L'énergie de dissociation de la liaison des ligands EX_3 après le bris des liaisons M–EX_3 est très élevée. On a démontré que la force intrinsèque des liaisons M–EX_3 est beaucoup plus élevée que les BDE et que les tendances des ΔE_{int} et D_e ne sont pas toujours les mêmes. Les ligands EX_3 dans les complexes [$(PMe_3)_2$M–EX_3] portent toujours une forte charge négative.

Mots-clés : calculs de la fonctionnellle de la densité, analyse de liaison, acides de Lewis, complexes de métaux de transition, modèle DCD inversé.

[Traduit par la Rédaction]

Introduction

The chemical bonds in donor–acceptor complexes of transition metals with main-group ligands are usually described using the Dewar–Chatt–Duncanson (DCD) model[1] where the ligand, being a Lewis base, serves as a σ-donor and π-acceptor and the metal, being a Lewis acid, is a σ-acceptor and π-donor (Scheme 1*a*). Quantum chemical investigations using charge and energy decomposition analyses have shown that the DCD model is a very useful description of the metal–ligand interactions.[2] It is conceivable that electron deficient ligands which are Lewis acids bind to electron rich (late) transition metals in a reversed fashion where the metal, which behaves as a Lewis base, becomes a σ-donor whereas the Lewis acidic ligand is a σ-acceptor (Scheme 1*b*). This could be possible when a group-13 Lewis acid EX_3 (E = B, Al, Ga, In, Tl) is bonded to a d^{10} metal fragment. Note that the main difference between the DCD model shown in Fig. 1 (A) and the reverse DCD model shown in Fig. 1 (B) lies in the direction of the σ donation. The M–L π interaction between a Lewis base ligand and a metal may also take place through donation from occupied π orbitals of L to empty d(π) orbitals of the metal. This was recently suggested for *N*-heterocyclic carbenes which may serve not only as (weak) π acceptors but also as (weak) π donors.[3] Ligands which serve as σ donors *and* as π donors are carbodiphosphoranes $C(PR_3)_2$[4] because the divalent carbon(0) atom has two electron lone pairs with σ and π symmetry.[5] In the present case it is conceivable that the π interaction between the metal and the EX_3 ligands takes place not only via back–donation from the ligand to the metal but also through donation from the occupied d(π) orbitals to the vacant (antibonding) E–X orbitals which have π symmetry. This question is discussed below.

There have been early reports on the synthesis of donor–acceptor complexes of BF_3, BCl_3, $AlBr_3$, and $AlMe_3$ with group 6–8 transition metals[6] but none of the compounds was structurally characterized. Recent work by Braunschweig[7] and co-workers question the alleged syntheses of complexes [M]–EX_3. Several borane complexes of transition metals have been synthesized in recent years but the bonding of the BR_3 ligand was only made possible with the use of chelating ligands.[8] A qualitative description of the possible bonding modes in transition metal borane complexes was given recently.[9] The first neutral donor–acceptor complex with a non-chelating EX_3 ligand of a group-13 element E which was identified by X-ray structure analysis was only reported in 2005 by R.A. Fischer and co-workers.[10] The authors succeeded in isolating the complex [$Cp^*Rh(GaCp^*)_2(GaCl_3)$]. Later Braunschweig reported the syntheses and X-ray analyses of [$(Cy_3P)_2Pt$–$AlCl_3$][11a] and [$(Cy_3P)_2Pt$–$GaCl_3$].[11b] A review on the coordination chemistry of aluminum, gallium, and indium with transition metals shows that it is very difficult to prepare neutral complexes [M]–EX_3 which have a non-chelating group-13 ligand EX_3.[12]

Scheme 1. Schematic representation of (*a*) the Dewar–Chatt–Duncanson model and (*b*) the reversed Dewar–Chatt–Duncanson model.

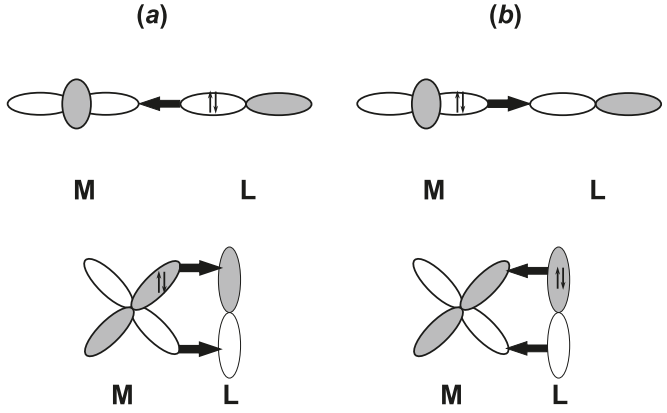

To the best of our knowledge there is no publication which reports a theoretical analysis of the metal–ligand interactions in transition metal complexes with "reversed" DCD bonding using modern quantum chemical methods. In this work we describe a charge and energy decomposition analysis of the metal–ligand bonding in the complexes [$(Me_3P)_2$M–X_3] for M = Ni, Pd, Pt; E = B through Tl; X = H, F through I. We also give the equilibrium structures and bond dissociation energies which should be helpful as a guideline in the search for further examples of stable complexes with EX_3 ligands.

Computational methods

The presented structures have been preoptimized with C_S symmetry constraints in Gaussian 03.[13] For the energy, gradient and frequency calculations, gradient-corrected density functional theory was employed using the gradient-corrected density functional BP86[14] with the resolution of the identity (RI) approximation[15] as implemented in TURBOMOLE[16] in conjunction with the def2-SVP basis sets by Weigend and Ahlrichs.[17] The analytically calculated harmonic vibrational frequencies showed that all but two complexes ([$(PMe_3)_2Pt$–$InCl_3$] and ([$(PMe_3)_2Pt$–$TlCl_3$] are local minima. The latter compounds each exhibit an imaginary mode whose magnitude is smaller than 10 cm^{-1}, which can

Fig. 1. Conformations A (left) and B (right) of the equilibrium geometries.

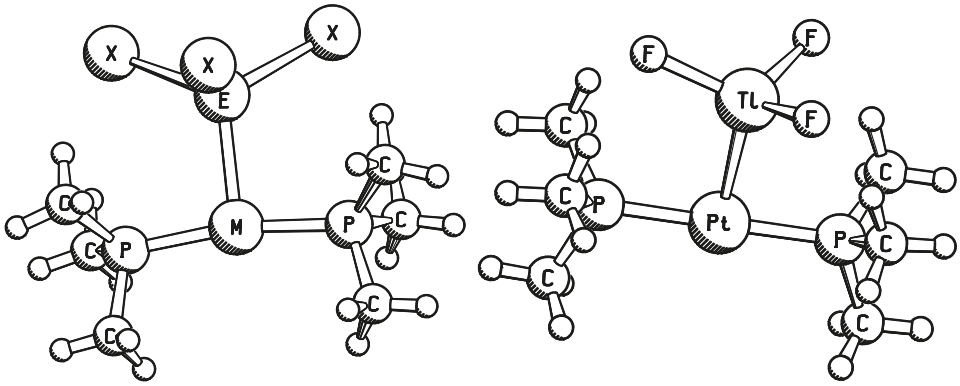

Fig. 2. Optimized structures of the compound where only bridged isomers were found. Selected atomic distances (in Å) are given at RI-BP86/def2-SVP level of theory.

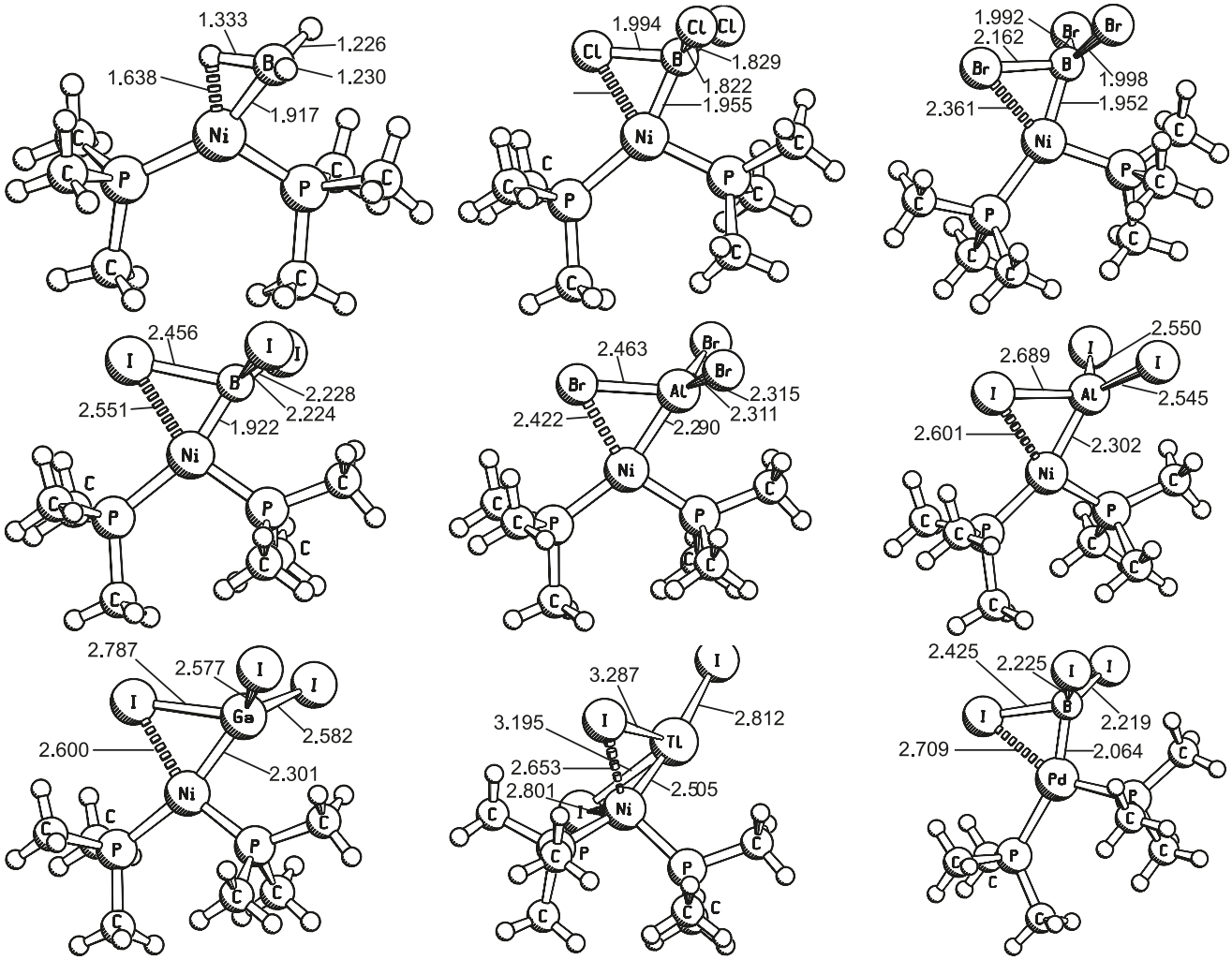

be neglected because they refer to the rotation of the methyl groups. The atomic partial charges have been estimated by the NBO method of Weinhold and co-workers.[18]

The analysis of the chemical bond between the ER_3 and the $M(PMe_3)_2$ closed-shell fragments was carried out using the program ADF 2006.01[19] employing the energy decomposition analysis (EDA) suggested by Morokuma[20] and Ziegler.[21] For the EDA calculations the geometries were optimized under C_S symmetry constraints at the BP86 level of theory using triple-*zeta* valence basis sets consisting of uncontracted Slater-type orbitals (TZ2P)[22] as implemented in ADF 2006.01 with the notation "TZ2P+" for nickel and "TZ2P" for all other elements used in this study. The differences in the RI-BP86/def2-SVP and BP86/TZ2P geometries

Table 1. Dissociation energies (in kcal/mol) and M–E bond lengths in parentheses (given in Å) of the $[(Me_3P)_2MEX_3]$ componds for M = Ni, Pt, Pd; E = B, Al, Ga, In, Tl; and X = H, F, Cl, Br, I at the RI-BP86/TZ2P level of theory.

	E				
X	B	Al	Ga	In	Tl
Ni					
H	—[b]	26.5 (2.412)	22.9 (2.457)	21.6 (2.655)	17.3 (2.744)
F	11.9 (2.125)	35.6 (2.375)	44.4 (2.330)	47.5 (2.514)	51.2 (2.541)
Cl	—[b]	33.2 (2.357)	35.4 (2.341)	39.1 (2.533)	40.2 (2.569)
Br	—[b]	—[b]	34.2 (2.341)	36.4 (2.540)	36.9 (2.583)
I	—[b]	—[b]	—[b]	33.6 (2.536)	—[b]
Pd					
H	23.4 (2.102)	26.0 (2.515)	21.5 (2.582)	20.7 (2.756)	16.0 (2.865)
F	10.2 (2.250)	35.8 (2.453)	42.7 (2.427)	44.0 (2.603)	50.2 (2.645)
Cl	12.9 (2.159)	32.4 (2.442)	32.7 (2.446)	36.8 (2.627)	36.0 (2.679)
Br	16.7 (2.123)	31.9 (2.438)	30.9 (2.450)	33.9 (2.638)	32.4 (2.696)
I	—[b]	31.5 (2.424)	28.5 (2.449)	30.5 (2.641)	28.1 (2.707)
Pt					
H	26.9 (2.215)	30.2 (2.507)	24.4 (2.585)	23.1 (2.771)	17.5 (2.884)
F	14.7 (2.227)	41.1 (2.451)	46.7 (2.439)	48.3 (2.624)	47.9 (2.671)[a]
Cl	17.5 (2.152)	37.9 (2.439)	36.8 (2.456)	39.4 (2.645)	36.6 (2.701)
Br	21.7 (2.119)	37.3 (2.435)	34.9 (2.459)	36.4 (2.654)	33.1 (2.716)
I	24.5 (2.089)	36.9 (2.422)	32.4 (2.458)	33.1 (2.656)	29.0 (2.726)

[a]Structure type B.

[b]Not calculated because the energy minimum has a bridged geometry.

are very small. Relativistic effects were considered by the zeroth-order regular approximation (ZORA).[23] The density fitting procedure has been used to represent coulomb and exchange potentials accurately in each SCF cycle.[24] Additional information to the ADF calculations are given in the Supplementary data.

The focus of the bonding analysis is the instantaneous interaction energy, ΔE_{int}, of the bond, which is the energy difference between the molecule and the fragments in the electronic reference state and frozen geometry of the compound. The interaction energy can be divided into three main components:

$$[1] \qquad \Delta E_{int} = \Delta E_{elstat} + \Delta E_{Pauli} + \Delta E_{orb}$$

ΔE_{elstat} gives the electrostatic interaction energy between the fragments, which are calculated using the frozen electron density distribution of the fragments in the geometry of the complex. It can be considered as an estimate of the *electrostatic contribution* of the bonding interaction. The second term in eq. [1] ΔE_{Pauli} refers to the repulsive interactions between the fragments, which are caused by the fact that two electrons with the same spin cannot occupy the same region in space. ΔE_{Pauli} is calculated by enforcing the Kohn–Sham determinant on the superimposed fragments to obey the Pauli principle by antisymmetrization and renormalization. The stabilizing orbital interaction term, ΔE_{orb}, is calculated in the final step of the energy decomposition analysis when the Kohn–Sham orbitals relax to their optimal form. The ΔE_{orb} term can be considered as the *covalent contribution* to the bonding interaction. Thus, the ratio $\Delta E_{orb}/\Delta E_{elstat}$ indicates the *covalent/electrostatic* character of the investigated bond. The orbital interaction can be further partitioned into contributions by the orbitals belonging to different irreducible representations of the point group of the interacting system. The EDA calculations of the present molecules have been carried out using C_S symmetry which means that the irreducible representation a′ contains σ and π contributions. Assuming that both orthogonal π interactions are equally strong, the following partitioning scheme is possible:

$$[2] \qquad \Delta E_{orb} + \Delta E_{\sigma} + \Delta E_{\pi} = \Delta E_{a'} - \Delta E_{a''} + 2\Delta E_{a''}$$

where $\Delta E_{\sigma} = \Delta E_{a'} - \Delta E_{a''}$ and $\Delta E_{\pi} = 2\ \Delta E_{a''}$. Finally, the negative value of the bond dissociation energy ($-D_e = \Delta E$) is given by the sum of the interaction energy and the preparation energy:

$$[3] \qquad \Delta E = \Delta E_{int} + \Delta E_{prep}$$

The latter term is the energy necessary to promote the fragments from their equilibrium geometry and electronic ground state to the geometry and electronic state they have in the optimized structure of the complex. Technical details about the EDA method can be found in the literature.[19e,19f] The performance of the EDA for analyzing donor–acceptor bonds has been published in recent reviews.[24]

Results and discussion

The geometry optimizations of the complexes $[(PMe_3)_2M–EX_3]$ gave for most compounds T-shaped structures with nearly linear P–M–P angles where the EX_3 ligand has a staggered conformation (structure type A; Fig. 1) For one molecule $[(PMe_3)_2Pt–TlF_3]$, an eclipsed conformation

Table 2. EDA results of the $[(Me_3P)_2MEH_3]$ compounds for E = Al, Ga, In, Tl, M = Ni, Pd, Pt at BP86/TZ2P. Energy values are given in kcal/mol.

Compound	$(Me_3P)_2NiBH_3$	$(Me_3P)_2NiAlH_3$	$(Me_3P)_2NiGaH_3$	$(Me_3P)_2NiInH_3$	$(Me_3P)_2NiTlH_3$
ΔE_{int}	—[a]	–35.5	–30.0	–27.9	–21.8
ΔE_{Pauli}	—[a]	62.0	67.9	61.8	60.3
ΔE_{elstat}[b]	—[a]	–49.5 (50.8%)	–53.1 (54.3%)	–53.2 (59.3%)	–49.8 (60.6%)
ΔE_{orb}[b]	—[a]	–48.0 (49.2%)	–44.7 (45.7%)	–36.6 (40.7%)	–32.3 (39.4%)
ΔE_{σ}[c]	—[a]	–35.4 (73.8%)	–36.6 (81.8%)	–28.8 (78.8%)	–26.3 (81.4%)
ΔE_{π}[d]	—[a]	–12.6 (26.2%)	–8.1 (18.2%)	–7.8 (21.2%)	–6.0 (18.6%)
ΔE_{prep} $(Me_3P)_2Ni$	—[a]	1.4	1.1	1.3	1.0
ΔE_{prep} EH_3	—[a]	7.6	6.0	5.1	3.5
$\Delta E_{prep,total}$	—[a]	9.0	7.1	6.4	4.5
ΔE (= $-D_e$)	—[a]	–26.5	–22.9	–21.6	–17.3
Compound	$(Me_3P)_2PdBH_3$	$(Me_3P)_2PdAlH_3$	$(Me_3P)_2PdGaH_3$	$(Me_3P)_2PdInH_3$	$(Me_3P)_2PdTlH_3$
ΔE_{int}	–32.1	–34.9	–28.0	–26.4	–19.6
ΔE_{Pauli}	72.3	58.9	61.1	59.2	55.8
ΔE_{elstat}[b]	–41.7 (39.1%)	–48.6 (51.8%)	–48.9 (54.9%)	–51.6 (60.2%)	–46.4 (61.6%)
ΔE_{orb}[b]	–62.7 (60.1%)	–45.2 (48.2%)	–40.2 (45.1%)	–34.0 (39.8%)	–29.0 (38.4%)
ΔE_{σ}[c]	–54.8 (87.3%)	–33.2 (73.4%)	–32.3 (80.2%)	–26.2 (76.9%)	–22.9 (78.9%)
ΔE_{π}[d]	–7.9 (12.7%)	–12.0 (26.6%)	–8.0 (19.8%)	–7.9 (23.1%)	–6.1 (21.1%)
ΔE_{prep} $(Me_3P)_2Pd$	0.6	1.0	0.7	0.8	0.6
ΔE_{prep} EH_3	8.2	7.9	5.8	4.9	3.0
$\Delta E_{prep,total}$	8.7	8.9	6.5	5.7	3.6
ΔE (= $-D_e$)	–23.4	–26.0	–21.5	–20.7	–16.0
Compound	$(Me_3P)_2PtBH_3$	$(Me_3P)_2PtAlH_3$	$(Me_3P)_2PtGaH_3$	$(Me_3P)_2PtInH_3$	$(Me_3P)_2PtTlH_3$
ΔE_{int}	–38.3	–40.1	–31.8	–29.1	–21.4
ΔE_{Pauli}	87.1	68.3	69.5	64.4	60.1
ΔE_{elstat}[b]	–51.9 (41.4%)	–58.4 (53.9%)	–57.2 (56.4%)	–57.5 (61.5%)	–50.7 (62.3%)
ΔE_{orb}[b]	–73.5 (58.6%)	–49.9 (46.1%)	–44.1 (43.6%)	–36.0 (38.5%)	–30.7 (37.7%)
ΔE_{σ}[c]	–64.0 (87.0%)	–36.4 (73.0%)	–35.2 (79.8%)	–27.5 (76.4%)	–24.2 (78.5%)
ΔE_{π}[d]	–9.5 (13.0%)	–13.5 (27.0%)	–8.9 (20.2%)	–8.5 (23.6%)	–6.6 (21.5%)
ΔE_{prep} $(Me_3P)_2Pt$	0.8	1.2	0.9	1.0	0.8
ΔE_{prep} EH_3	10.6	8.7	6.5	5.0	3.1
$\Delta E_{prep,total}$	11.4	9.9	7.4	6.0	3.9
ΔE (= $-D_e$)	–26.9	–30.2	–24.4	–23.1	–17.5

[a]Not calculated because the energy minimum has a bridged geometry.

[b]The values in parentheses give the percentage contribution to the total attractive interactions $\Delta E_{elstat} + \Delta E_{orb}$.

[c]The values in parentheses give the percentage contribution of the σ-type orbital interaction to the total orbital interactions. The σ-type orbital interaction was calculated by $\Delta E_{\sigma} = \Delta E_{a'} - \Delta E_{a''}$.

[d]The values in parentheses give the percentage contribution of the π-type orbital interaction to the total orbital interactions. The π-type orbital interaction was calculated by $\Delta E_{\pi} = 2\Delta E_{a''}$.

with respect to the PMP plane (structure type B) was found as the equilibrium structure. The energy differences between the conformations A and B which have C_s symmetry are very small (<0.5 kcal/mol for all compounds) which means that there is nearly free rotation about the M–EX_3 axis. The equilibrium structures of eight nickel compounds $[(PMe_3)_2Ni–EX_3]$ have a distorted geometry where one E–X bond is engaged in bonding interactions with the metal atom which yields a distorted square-planar arrangement of the metal atom (Fig. 2). The P–Ni–P angle in the latter complexes is significantly smaller than 180°. The complex $[(PMe_3)_2Ni–TlI_3]$ exhibits two attractive interactions between Tl–I bonds and the metal which features a five-coordinated metal atom.

Table 1 gives the calculated M–EX_3 bond lengths and bond dissociation energies D_e for the structure types A and B of $[(PMe_3)_2M–EX_3]$. There are only a few experimental geometries and no experimentally derived BDE which may be used for comparison with the calculated values. The calculated bond length for $[(PMe_3)_2Pt–GaCl_3]$ (2.456 Å) is in good agreement with the experimental value for $[(PCyc_3)_2Pt–GaCl_3]$ (2.402 Å)[11b] and the theoretical value for the aluminum homologue $[(PMe_3)_2Pt–AlCl_3]$ (2.439 Å) concurs with the experimental result for $[(PCyc_3)_2Pt–AlCl_3]$ (2.386 Å).[11a] Please note that the experimental values for the bond lengths come from X-ray analyses of the compounds in the solid states which are always shorter than for the free molecules.[25]

The theoretically predicted bond dissociation energies show (Table 1) that the boron complexes exhibit a different trend for the D_e values than the heavier group-13 homologues. The results for the Pd and Pt complexes suggest that the $[(PMe_3)_2M–BX_3]$ bond strength increases with F < Cl < Br < I < H which means that the BH_3 ligands are the most strongly bonded Lewis acids and BF_3 is the most weakly bonded species . The trend for the heavier group-13 complexes $[(PMe_3)_2M–EX_3]$ where E = Al, Ga, In, Tl follows

Table 3. EDA results of the $[(Me_3P)_2MEF_3]$ compounds for E = B, Al, Ga, In, Tl, M = Ni, Pd, Pt at BP86/TZ2P. Energy values are given in kcal/mol.

Compound	$(Me_3P)_2NiBF_3$	$(Me_3P)_2NiAlF_3$	$(Me_3P)_2NiGaF_3$	$(Me_3P)_2NiInF_3$	$(Me_3P)_2NiTlF_3$
ΔE_{int}	–39.7	–55.3	–67.8	–65.3	–71.1
ΔE_{Pauli}	80.1	59.5	89.2	84.8	102.3
ΔE_{elstat}[b]	–54.6 (45.4%)	–57.4 (50.0%)	–81.0 (51.6%)	–83.0 (55.3%)	–92.4 (53.3%)
ΔE_{orb}[b]	–65.2 (54.6%)	–57.4 (50.0%)	–76.0 (48.4%)	–67.0 (44.7%)	–81.0 (46.7%)
ΔE_{σ}[c]	–54.9 (84.2%)	–40.3 (70.2%)	–58.2 (76.6%)	–49.8 (74.4%)	–65.6 (80.4%)
ΔE_{π}[d]	–10.3 (15.8%)	–17.1 (29.8%)	–17.8 (23.4%)	–17.2 (25.6%)	–15.9 (19.6%)
ΔE_{prep} $(Me_3P)_2Ni$	1.4	2.3	3.1	3.6	4.6
ΔE_{prep} EF_3	26.4	17.4	20.3	14.2	15.4
$\Delta E_{prep,total}$	27.3	19.7	23.4	17.8	20.0
ΔE (= $-D_e$)	–11.9	–35.6	–44.4	–47.5	–51.2
Compound	$(Me_3P)_2PdBF_3$	$(Me_3P)_2PdAlF_3$	$(Me_3P)_2PdGaF_3$	$(Me_3P)_2PdInF_3$	$(Me_3P)_2PdTlF_3$
ΔE_{int}	–35.0	–54.6	–64.2	–62.4	–65.2
ΔE_{Pauli}	75.3	59.1	87.1	84.5	99.3
ΔE_{elstat}[b]	–53.0 (48.0%)	–58.4 (51.4%)	–80.0 (52.9%)	–83.3 (56.7%)	–89.9 (54.6%)
ΔE_{orb}[b]	–57.3 (52.0%)	–55.2 (48.6%)	–71.3 (47.1%)	–63.6 (43.3%)	–74.7 (45.4%)
ΔE_{σ}[c]	–48.0 (83.7%)	–39.2 (71.0%)	–54.9 (76.9%)	–47.4 (75.4%)	–59.6 (79.8%)
ΔE_{π}[d]	–9.4 (16.3%)	–16.0 (29.0%)	–16.5 (23.1%)	–16.2 (25.5%)	–15.1 (20.2%)
ΔE_{prep} $(Me_3P)_2Pd$	1.0	1.8	2.3	4.7	0.7
ΔE_{prep} EF_3	23.8	17.0	19.2	13.7	14.4
$\Delta E_{prep,total}$	24.8	18.7	21.6	18.4	15.0
ΔE (= $-D_e$)	–10.2	–35.8	–42.6	–44.0	–50.2
Compound	$(Me_3P)_2PtBF_3$	$(Me_3P)_2PtAlF_3$	$(Me_3P)_2PtGaF_3$	$(Me_3P)_2PtInF_3$	$(Me_3P)_2PtTlF_3$[a]
ΔE_{int}	–44.4	–60.6	–67.7	–63.8	–64.6
ΔE_{Pauli}	95.2	66.8	96.6	90.2	106.9
ΔE_{elstat}[b]	–67.6 (48.4%)	–68.1 (53.5%)	–90.5 (55.1%)	–90.6 (58.8%)	–97.3 (56.7%)
ΔE_{orb}[b]	–72.0 (51.6%)	–59.3 (46.5%)	–73.8 (44.9%)	–63.4 (41.2%)	–74.2 (43.3%)
ΔE_{σ}[c]	–60.1 (83.5%)	–41.7 (70.4%)	–56.3 (76.2%)	–46.7 (73.7%)	–61.3 (82.6%)
ΔE_{π}[d]	–11.9 (16.5%)	–17.5 (29.6%)	–17.5 (23.8%)	–16.7 (26.3%)	–12.9 (17.4%)
ΔE_{prep} $(Me_3P)_2Pt$	1.3	2.0	2.4	2.7	3.2
ΔE_{prep} EF_3	28.4	17.4	18.6	12.8	13.5
$\Delta E_{prep,total}$	29.7	19.4	21.0	15.5	16.7
ΔE (= $-D_e$)	–14.7	–41.1	–46.7	–48.3	–47.9

[a]Structure type B.

[b]The values in parentheses give the percentage contribution to the total attractive interactions $\Delta E_{elstat} + \Delta E_{orb}$.

[c]The values in parentheses give the percentage contribution of the σ-type orbital interaction to the total orbital interactions. The σ-type orbital interaction was calculated by $\Delta E_{\sigma} = \Delta E_{a'} - \Delta E_{a''}$.

[d]The values in parentheses give the percentage contribution of the π-type orbital interaction to the total orbital interactions. The π-type orbital interaction was calculated by $\Delta E_{\pi} = 2\Delta E_{a''}$.

the opposite order F > Cl > Br > I > H. It is interesting to note that, in the latter complexes, EF_3 is the strongest bonded ligand while EH_3 is the most weakly bonded moiety. We considered only the C_s symmetric structures A and B to compare the intrinsic strength of the M–EX_3 bonds. The trend for the bond strength of $[(PMe_3)_2M–EX_3]$ for the elements E depends somewhat on the nature of X and also on the metal M. The strongest bonds for the trifluorides and trichlorides are calculated for the indium and thallium complexes while the EI_3 complexes show a maximum for E = Al. The BX_3 ligands are always significantly more weakly bonded than the heavier group-13 homologues except for X = H. The calculated values should be helpful for future experimental studies aimed at isolating further examples of the rare $[(PMe_3)_2M–EX_3]$ species.

Table 2 presents the results of the energy decomposition analysis of the $[(PMe_3)_2M–EH_3]$ complexes. Tables 3 and 4 show the EDA values for the compounds $[(PMe_3)_2M–EX_3]$ for X = F, Cl. The EDA results for X = Br, I give no further insight into the bonding situation of the molecules. Therefore, they are given in the Tables SI-1 and SI-2 in the Supplementary data and are not discussed in the text.

The calculated data for the interaction energies ΔE_{int} give the intrinsic strength of the metal–ligand bonding in $[(PMe_3)_2M–EX_3]$, while the ΔE_{prep} values give the relaxation of the fragments after breaking the bonds. The results in Tables 2–4 show that ΔE_{prep} values are are not negligible and that they become quite large for the complexes with EF_3 and ECl_3 ligands particularly for E = B. The data show that the rather low bond dissociation energies D_e of the BF_3 and BCl_3 ligands do not come from the weak metal–boron attraction but from the large energy differences between the planar equilibrium geometries of BX_3 and the pyramidal structures of the ligands in the complex. The intrinsic bond strength of the halogenide ligands EF_3 and ECl_3 in $[(PMe_3)_2M–EX_3]$ which is given by the ΔE_{int} values is sig-

Table 4. EDA results of $[(Me_3P)_2MEX_3]$ for E = Al, Ga, In, Tl, M = Ni, Pd, Pt at BP86/TZ2P. Energy values are given in kcal/mol.

Compound	$(Me_3P)_2NiBCl_3$	$(Me_3P)_2NiAlCl_3$	$(Me_3P)_2NiGaCl_3$	$(Me_3P)_2NiInCl_3$	$(Me_3P)_2NiTlCl_3$
ΔE_{int}	—[a]	–55.1	–59.2	–57.5	–58.4
ΔE_{Pauli}	—[a]	77.3	98.1	86.9	98.5
ΔE_{elstat}[b]	—[a]	–64.0 (48.3%)	–78.9 (50.2%)	–77.5 (53.7%)	–83.2 (53.0%)
ΔE_{orb}[b]	—[a]	–68.5 (51.7%)	–78.4 (49.8%)	–66.9 (46.3%)	–73.7 (47.0%)
ΔE_{σ}[c]	—[a]	–48.7 (71.0%)	–61.8 (78.8%)	–51.8 (77.4%)	–61.2 (83.0%)
ΔE_{π}[d]	—[a]	–19.8 (29.0%)	–16.6 (21.2%)	–15.1 (22.6%)	–12.5 (17.0%)
ΔE_{prep} $(Me_3P)_2Ni$	—[a]	3.2	3.6	3.6	4.1
ΔE_{prep} ECl_3	—[a]	18.8	20.3	14.8	14.2
$\Delta E_{prep,total}$	—[a]	22.0	23.9	18.4	18.3
ΔE (= $-D_e$)	—[a]	–33.2	–35.4	–39.1	–40.2
Compound	$(Me_3P)_2PdBCl_3$	$(Me_3P)_2PdAlCl_3$	$(Me_3P)_2PdGaCl_3$	$(Me_3P)_2PdInCl_3$	$(Me_3P)_2PdTlCl_3$
ΔE_{int}	–40.4	–53.7	–54.8	–54.0	–52.9
ΔE_{Pauli}	122.1	78.9	96.0	87.3	95.5
ΔE_{elstat}[b]	–79.1 (48.7%)	–67.4 (50.8%)	–78.6 (52.1%)	–78.5 (55.5%)	–81.0 (54.6%)
ΔE_{orb}[b]	–83.4 (51.3%)	–65.3 (49.2%)	–72.3 (47.9%)	–62.8 (44.5%)	–67.4 (45.4%)
ΔE_{σ}[c]	–68.1 (81.7%)	–46.0 (70.5%)	–56.1 (77.7%)	–47.9 (76.3%)	–54.6 (81.0%)
ΔE_{π}[d]	–15.3 (18.3%)	–19.2 (29.5%)	–16.1 (22.3%)	–14.9 (23.7%)	–12.8 (19.0%)
ΔE_{prep} $(Me_3P)_2Pd$	2.8	2.5	2.7	2.7	3.0
ΔE_{prep} ECl_3	24.7	18.8	19.5	14.5	13.9
$\Delta E_{prep,total}$	27.5	21.3	22.2	17.3	16.9
ΔE (= $-D_e$)	–12.9	–32.4	–32.7	–36.8	–36.0
Compound	$(Me_3P)_2PtBCl_3$	$(Me_3P)_2PtAlCl_3$	$(Me_3P)_2PtGaCl_3$	$(Me_3P)_2PtInCl_3$	$(Me_3P)_2PtTlCl_3$
ΔE_{int}	–50.7	–60.0	–58.7	–55.9	–52.3
ΔE_{Pauli}	153.4	91.7	108.9	95.0	102.3
ΔE_{elstat}[b]	–99.4 (48.7%)	–80.0 (52.8%)	–90.4 (53.9%)	–86.7 (57.5%)	–87.5 (56.6%)
ΔE_{orb}[b]	–104.8 (51.3%)	–71.6 (47.2%)	–77.2 (46.1%)	–64.2 (42.5%)	–67.1 (43.4%)
ΔE_{σ}[c]	–85.4 (81.5%)	–49.9 (69.7%)	–59.2 (67.7%)	–48.2 (75.0%)	–53.4 (79.6%)
ΔE_{π}[d]	–19.4 (18.5%)	–21.7 (30.3%)	–18.0 (23.3%)	–16.0 (25.0%)	–13.7 (20.4%)
ΔE_{prep} $(Me_3P)_2Pt$	3.2	3.0	3.0	3.0	3.0
ΔE_{prep} ECl_3	30.0	19.1	18.9	13.5	12.6
$\Delta E_{prep,total}$	33.2	22.1	21.9	16.5	15.6
ΔE (= $-D_e$)	–17.5	–37.9	–36.8	–39.4	–36.6

[a]Not calculated because the energy minimum has a bridged geometry.

[b]The values in parentheses give the percentage contribution to the total attractive interactions $\Delta E_{elstat} + \Delta E_{orb}$.

[c]The values in parentheses give the percentage contribution of the σ -type orbital interaction to the total orbital interactions. The σ-type orbital interaction was calculated by $\Delta E_{\sigma} = \Delta E_{a'} - \Delta E_{a''}$.

[d]The values in parentheses give the percentage contribution of the π-type orbital interaction to the total orbital interactions. The π-type orbital interaction was calculated by $\Delta E_{\pi} = 2\Delta E_{a''}$.

nificantly higher than that of $[(PMe_3)_2M–EH_3]$. The differences between the D_e values of the two classes of compounds are smaller because of the larger ΔE_{prep} values of the former species. The results show that bond dissociation energies may not be faithful probes for the intrinsic strength of a chemical bond.

The breakdown of the ΔE_{int} values into the attractive components ΔE_{elstat} and ΔE_{orb} shows that the two terms contribute nearly equally to the chemical bonds in most $[(PMe_3)_2M–EX_3]$ compounds. The electrostatic attraction is somewhat larger than the orbital term in some complexes (up to 62.3% of the total attraction in $[(PMe_3)_2Pt–TlH_3]$) while it is smaller in others (down to 39.1% in $[(PMe_3)_2Pd–BH_3]$). The most interesting EDA result concerns the breakdown of the orbital interactions into σ and π type bonding. The ΔE_{π} term gives the strength of the intrinsic π orbital interactions of the M–EX_3 bonds. Tables 2–4 show that the π orbital interactions contribute between 12.7% $[(PMe_3)_2Pd–BH_3]$) and 29.8% ($[(PMe_3)_2Ni–AlF_3]$). The π orbital interactions of the trifluoride and trichloride ligands are in most cases slightly larger than the π bonding of the BH_3 ligands but the differences are not very large.

The calculated values for the π orbital interactions may come from M←EX_3 π-back-donation as shown in the reversed DCD model (Scheme 1) but they may also come from M→EX_3 π-donation because the group-10 metals have a d^{10} electron configuration. To distinguish between the two types of π orbital interactions we carried out EDA calculations on some complexes where the a″ orbitals of EX_3 or the $(PMe_3)_2M$ fragments are deleted. The results showed that both components contribute with comparable strength when $EX_3 = BH_3$, BF_3, AlH_3, and AlF_3. For the fluorides, the M→EX_3 π-donation is a little stronger than the M←EX_3 π-back-donation while the reversed trend is found for the hydrides, a result which could be expected.

Does the trend of the interaction energies ΔE_{int} correlate

Table 5. NBO partial charges of the EX_3 fragments and the metal atoms M in parentheses of the $(Me_3P)_2MEX_3$ compounds for M = Ni, Pd, Pt; E = B, Al, Ga, In, Tl; and X = H, F, Cl, Br, I at the RI-BP86/def2-SVP level of theory.

	E				
X	B	Al	Ga	In	Tl
Ni					
H	—[b]	–0.51 (+0.24)	–0.52 (+0.26)	–0.49 (+0.24)	–0.47 (+0.25)
F	–0.46 (+0.23)	–0.42 (+0.14)	–0.54 (+0.22)	–0.55 (+0.25)	–0.67 (+0.33)
Cl	—[b]	–0.57 (+0.21)	–0.64 (+0.28)	–0.64 (+0.29)	–0.72 (+0.36)
Br	—[b]	—[b]	–0.68 (+0.30)	–0.70 (+0.30)	–0.74 (+0.37)
I	—[b]	—[b]	—[b]	–0.69 (+0.33)	—[b]
Pd					
H	–0.47 (–0.13)	–0.37 (–0.26)	–0.38 (–0.24)	–0.35 (–0.25)	–0.32 (–0.26)
F	–0.31 (–0.25)	–0.29 (–0.33)	–0.39 (–0.26)	–0.40 (–0.24)	–0.51 (–0.10)
Cl	–0.46 (–0.08)	–0.39 (–0.27)	–0.47 (–0.20)	–0.47 (–0.20)	–0.89 (+0.05)
Br	–0.51 (–0.04)	–0.43 (–0.24)	–0.50 (–0.18)	–0.50 (–0.18)	–0.58 (–0.12)
I	—[b]	–0.47 (–0.21)	–0.53 (–0.16)	–0.52 (–0.17)	–0.58 (–0.12)
Pt					
H	–0.50 (–0.23)	–0.36 (–0.39)	–0.37 (–0.36)	–0.33 (–0.39)	–0.30 (–0.40)
F	–0.35 (–0.35)	–0.27 (–0.47)	–0.35 (–0.40)	–0.34 (–0.39)	–0.42 (–0.31)[a]
Cl	–0.52 (–0.18)	–0.37 (–0.40)	–0.44 (–0.33)	–0.42 (–0.35)	–0.48 (–0.29)
Br	–0.57 (–0.14)	–0.41 (–0.37)	–0.47 (–0.31)	–0.45 (–0.33)	–0.49 (–0.28)
I	–0.60 (–0.11)	–0.44 (–0.34)	–0.49 (–0.29)	–0.46 (–0.32)	–0.49 (–0.28)

[a]Structure type B.
[b]Bridged equilibrium structure.

with any of the contributing terms which could be singled out as a crucial factor for determining the change in the metal–ligand interactions? Table 2 shows that AlH_3 has the largest ΔE_{int} value in the $[(PMe_3)_2M–EH_3]$) complexes of all EH_3 ligands. Inspection of the attractive terms ΔE_{elstat} and ΔE_{orb} shows that neither term has a maximum value for AlH_3 but also that the repulsive term ΔE_{Pauli} of the latter ligand exhibits a minimum value. It is the combination of the three terms which makes AlH_3 the strongest bonded EH_3 ligand. Note that BH_3 has a much stronger orbital attraction than AlH_3 but the weaker electrostatic attraction and the significantly stronger Pauli repulsion makes BH_3 more weakly bonded than AlH_3. This is a warning against the ubiquitious use of orbital interactions as a sole indicator for the trend in bonding interactions. A pertinent example has been reported before.[26] A similar situation is found for the trend of the bond strength of the trifluorides and trichlorides in $[(PMe_3)_2M–EX_3]$ (Tables 3, 4). None of the terms ΔE_{elstat}, ΔE_{orb}, or ΔE_{Pauli} corelates with the trend of ΔE_{int}.

The NBO partial charges given in Table 5 provide further details about the electronic structure of the complexes. The partial charge of EX_3 is always negative which means that the donation from the metal fragment to the Lewis acid dominates the metal–ligand interactions which agrees with the relative contributions of the σ and π interactions to the ΔE_{orb} term of the EDA. Note that the PMe_3 ligands carry always a positive partial charge which is clearly smaller in the nickel compounds than in the Pd and Pt homologues, whereas the negative partial charges of EX_3 in the latter species are smaller than in the former. The NBO charges thus predict that Ni carries positive partial charge while Pd and Pt are negatively charged in $[(PMe_3)_2M–EX_3]$ except $[(PMe_3)_2Pd–TlCl_3]$ where Pd is predicted to have a small positive partial charge.

Summary

The geometry optimizations of $[(PMe_3)_2M–EX_3]$ for most compounds gave T-shaped structures with nearly linear P–M–P angles where the EX_3 ligand has either a staggered or eclipsed conformation with respect to the PMP plane. The energy differences between the conformations are very small which means that there is nearly free rotation about the M–EX_3 axis. The equilibrium structures of eight nickel compounds have a distorted geometry where one E–X bond is engaged in attractive interactions with the metal atom which yields a distorted square-planar arrangement of the metal atom. The complex $[(PMe_3)_2Ni–TlI_3]$ even exhibits two attractive interactions between Tl–I bonds and the metal which features a five-coordinated metal atom. The calculated bond dissociation energies show that the boron complexes exhibit a different trend for the D_e values than the heavier group-13 homologues. The results for the Pd and Pt complexes suggest that the $[(PMe_3)_2M–BX_3]$ bond strength increases with F < Cl < Br < I < H which means that the BH_3 ligands are the most strongly bonded Lewis acids and BF_3 is the most weakly bonded species . The trend for the heavier group-13 complexes $[(PMe_3)_2M–EX_3]$ where E = Al, Ga, In, Tl follows the opposite order F > Cl > Br > I > H. The energy decomposition analysis of the M–EX_3 bonds indicates a substantial π contribution of between 12.7% and 30.3% to the total orbital interactions. There is no direct correlation between the strength of the orbital interactions or any of the other energy terms ΔE_{elstat} or ΔE_{Pauli}

and the total interaction energy. The bond dissociation energy of the EX_3 ligands after breaking the M–EX_3 bonds is quite large. It is shown that the intinsic strength of the M–EX_3 bonds are much larger than the BDEs and that the trends of ΔE_{int} and D_e are not always the same. The EX_3 ligands in $[(PMe_3)_2M–BX_3]$ carry always a large negative charge.

Supplementary data

Table SI-1 gives the EDA results for the $[(Me_3P)_2MEBr_3]$ compounds. Table SI-2 gives the EDA results for the $[(Me_3P)_2MEI_3]$ compounds. Table SI-3 gives the Cartesian coordinates of the optimized geometries at the RI-BP86/def2-SVP level of theory. Supplementary data for this article are available on the journal Web site (canjchem.nrc.ca) or may be purchased from the Depository of Unpublished Data, Document Delivery, CISTI, National Research Council Canada, Ottawa, ON K1A 0R6, Canada. DUD 5274. For more information on obtaining material, refer to cisti-icist.nrc-cnrc.gc.ca/cms/unpub_e.shtml.

Acknowledgement

This work was supported by the Deutsche Forschungsgemeinschaft. The generous allotment of computer time by the HRZ Marburg, the CSC Frankfurt, and the HHLR Darmstadt, as well as their excellent service, are gratefully acknowledged.

References

(1) (a) Dewar, M. *Bull. Soc. Chim. Fr.* **1951**, *18*, C79; (b) Chatt, J.; Duncanson, L. A. *J. Chem. Soc.* **1953**, 2939. doi:10.1039/JR9530002939.

(2) (a) Frenking, G. *J. Organomet. Chem.* **2001**, *635* (1-2), 9–23. doi:10.1016/S0022-328X(01)01154-8.; (b) Frenking, G. In *Modern Coordination Chemistry: The Legacy of Joseph Chatt*. Leigh, G. J., Winterton, N., Eds.; The Royal Society: London, 2002; p. 111.

(3) (a) Jacobsen, J. *J. Organomet. Chem.* **2005**, *690* (24-25), 6068–6078. doi:10.1016/j.jorganchem.2005.07.112.; (b) Jacobsen, J.; Correa, E.; Costabile, C.; Cavallo, L. *J. Organomet. Chem.* **2006**, *691* (21), 4350–4358. doi:10.1016/j.jorganchem.2006.01.026.

(4) (a) Petz, W.; Kutschera, C.; Heitbaum, M.; Frenking, G.; Tonner, R.; Neumüller, B. *Inorg. Chem.* **2005**, *44* (5), 1263–1274. doi:10.1021/ic048397l. PMID:15732966.; (b) Tonner, R.; Öxler, F.; Neumüller, B.; Petz, W.; Frenking, G. *Angew. Chem. Int. Ed. Engl.* **2006**, *118* (47), 8206–8211. doi:10.1002/ange.200602552.; (c) Tonner, R.; Öxler, F.; Neumüller, B.; Petz, W.; Frenking, G. *Angew. Chem. Int. Ed. Engl.* **2006**, *45* (47), 8038–8042. doi:10.1002/anie.200602552. PMID:17075933.

(5) (a) Tonner, R.; Frenking, G. *Chem. Eur. J.* **2008**, *14* (11), 3260–3272. doi:10.1002/chem.200701390.; (b) Tonner, R.; Frenking, G. *Chem. Eur. J.* **2008**, *14* (11), 3273–3289. doi:10.1002/chem.200701392.; (c) Frenking, G.; Tonner, R. *Pure Appl. Chem.* **2009**, *81* (4), 597–614. doi:10.1351/PAC-CON-08-11-03.

(6) Johnson, M. P.; Shriver, D. F. *J. Am. Chem. Soc.* **1966**, *88* (2), 301–304. doi:10.1021/ja00954a022.

(7) (a) Braunschweig, H.; Wagner, T. *Chem. Ber.* **1994**, *127* (9), 1613–1614. doi:10.1002/cber.19941270910.; (b) Braunschweig, H.; Wagner, T. *Z. Naturforsch. B* **1996**, *51*, 1618; (c) Braunschweig, H.; Kollann, C. *Z. Naturforsch. B* **1999**, *54*, 839.

(8) (a) Hill, A. F.; Owen, G. R.; White, A. J. P.; Williams, D. J. *Angew. Chem. Int. Ed.* **1999**, *38* (18), 2759. doi:10.1002/(SICI)1521-3773(19990917)38:18<2759::AID-ANIE2759>3.0.CO;2-P.; (b) Bontemps, S.; Gornitzka, H.; Bouhadir, G.; Miqueu, K.; Bourissou, D. *Angew. Chem. Int. Ed.* **2006**, *45* (10), 1611–1614. doi:10.1002/anie.200503649.; (c) Landry, V. K.; Melnick, J. G.; Buccella, D.; Pang, K.; Ulichny, J. C.; Parkin, G. *Inorg. Chem.* **2006**, *45* (6), 2588–2597. doi:10.1021/ic051975t. PMID:16529480.

(9) Parkin, G. *Organometallics* **2006**, *25* (20), 4744–4747. doi:10.1021/om060580u.

(10) Steinke, T.; Gemel, C.; Cokoja, M.; Winter, M.; Fischer, R. A. *Dalton Trans.* **2005**, (1): 55–62. doi:10.1039/b408632e. PMID:15605147.

(11) (a) Braunschweig, H.; Gruss, K.; Radacki, K. *Angew. Chem.* **2007**, *119* (41), 7929–7931. doi:10.1002/ange.200702726.; (b) Braunschweig, H.; Gruss, K.; Radacki, K. *Inorg. Chem.* **2008**, *47* (19), 8595–8597. doi:10.1021/ic801293e. PMID:18785731.

(12) Fischer, R. A.; Weiss, J. *Angew. Chem. Int. Ed.* **1999**, *38*, 2831.

(13) Frisch, M. J.; Trucks, G. W.; Schlegel, H. B.; Scuseria, G. E.; Robb, M. A.; Cheeseman, J. R.; Montgomery, J. A., Jr.; Vreven, T.; Kudin, K. N.; Burant, J. C.; Millam, J. M.; Iyengar, S. S.; Tomasi, J.; Barone, V.; Mennucci, B.; Cossi, M.; Scalmani, G.; Rega, N.; Petersson, G. A.; Nakatsuji, H.; Hada, M.; Ehara, M.; Toyota, K.; Fukuda, R.; Hasegawa, J.; Ishida, M.; Nakajima, T.; Honda, Y.; Kitao, O.; Nakai, H.; Klene, M.; Li, X.; Knox, J. E.; Hratchian, H. P.; Cross, J. B.; Bakken, V.; Adamo, C.; Jaramillo, J.; Gomperts, R.; Stratmann, R. E.; Yazyev, O.; Austin, A. J.; Cammi, R.; Pomelli, C.; Ochterski, J. W.; Ayala, P. Y.; Morokuma, K.; Voth, G. A.; Salvador, P.; Dannenberg, J. J.; Zakrzewski, V. G.; Dapprich, S.; Daniels, A. D.; Strain, M. C.; Farkas, O.; Malick, D. K.; Rabuck, A. D.; Raghavachari, K.; Foresman, J. B.; Ortiz, J. V.; Cui, Q.; Baboul, A. G.; Clifford, S.; Cioslowski, J.; Stefanov, B. B.; Liu, G.; Liashenko, A.; Piskorz, P.; Komaromi, I.; Martin, R. L.; Fox, D. J.; Keith, T.; Al-Laham, M. A.; Peng, C. Y.; Nanayakkara, A.; Challacombe, M.; Gill, P. M. W.; Johnson, B.; Chen, W.; Wong, M. W.; Gonzalez, C.; Pople, J. A. *Gaussian 03,* Revision D.01; Gaussian, Inc.: Wallingford CT, 2004.

(14) (a) Becke, A. D. *Phys. Rev. A* **1988**, *38* (6), 3098–3100. doi:10.1103/PhysRevA.38.3098. PMID:9900728.; (b) Perdew, J. P. *Phys. Rev. B* **1986**, *33* (12), 8822–8824. doi:10.1103/PhysRevB.33.8822.

(15) Ahlrichs, R. *Phys. Chem. Chem. Phys.* **2004**, *6* (22), 5119. doi:10.1039/b413539c.

(16) Häser, M.; Horn, H.; Kölmel, C. *Chem. Phys. Lett.* **1989**, *162* (3), 165–169. doi:10.1016/0009-2614(89)85118-8.

(17) (a) Weigend, F.; Ahlrichs, R. *Phys. Chem. Chem. Phys.* **2005**, *7* (18), 3297–3305. doi:10.1039/b508541a. PMID:16240044.; (b) Weigend, F. *Phys. Chem. Chem. Phys.* **2006**, *8* (9), 1057–1065. doi:10.1039/b515623h. PMID:16633586.; (c) [For Pd, Pt, In, Tl and I, relativistic effective core potentials (ECP) from the Stuttgart/Köln group were employed:] Andrae, D.; Häußermann, U.; Dolg, M.; Stoll, H.; Preuß, H. *Theor. Chim. Acta* **1990**, *77*, 123 doi:10.1007/BF01114537.; (d) Peterson, K. A.; Figgen, D.; Goll, E.; Stoll, H.; Dolg, M. *J. Chem. Phys.* **2003**, *119* (21), 11113. doi:10.1063/1.1622924.; (e) Metz, B.; Schweizer, M.; Stoll, H.; Dolg, M.;

Liu, W. *Theor. Chem. Acc.* **2000**, *104*, 22; doi:10.1007/s002149900101.(f) Metz, B.; Stoll, H.; Dolg, M. *J. Chem. Phys.* **2000**, *113* (7), 2563. doi:10.1063/1.1305880.

(18) Reed, A.; Curtiss, L. A.; Weinhold, F. *Chem. Rev.* **1988**, *88* (6), 899–926. doi:10.1021/cr00088a005.

(19) (a) Baerends, E. J.; Ellis, D. E.; Ros, P. *Chem. Phys.* **1973**, *2* (1), 41–51. doi:10.1016/0301-0104(73)80059-X.; (b) Versluis, L.; Ziegler, T. *J. Chem. Phys.* **1988**, *322*, 88; (c) te Velde, G.; Baerends, E. J. *J. Comput. Phys.* **1992**, *99* (1), 84–98. doi:10.1016/0021-9991(92)90277-6.; (d) Fonseca Guerra, C.; Snijders, J. G.; te Velde, G.; Barends, E. J. *Theor. Chim. Acta* **1998**, *99* (6), 391. doi:10.1007/s002140050021.; (e) Bickelhaupt, F. M.; Baerends, E. J. In *Reviews of Computational Chemistry*. Lipkowitz, K. B., Boyd, D. B., Eds.; Wiley-VCH: New York, 2000; Vol. **15**, p. 1; (f) te Velde, G.; Bickelhaupt, F. M.; Baerends, E. J.; van Gisbergen, S. J. A.; Fonseca Guerra, C.; Snijders, J. G.; Ziegler, T. *J. Comput. Chem.* **2001**, *22* (9), 931–967. doi:10.1002/jcc.1056.

(20) (a) Morokuma, K. *J. Chem. Phys.* **1971**, *55* (3), 1236. doi:10.1063/1.1676210.; (b) Ziegler, T.; Rauk, A. *Theor. Chim. Acta* **1977**, *46*, 1.

(21) Van Lenthe, E.; Baerends, E. J. *J. Comput. Chem.* **2003**, *24* (9), 1142–1156. doi:10.1002/jcc.10255. PMID:12759913.

(22) (a) Chang, C.; Pelissier, M.; Durand, Ph. *Phys. Scr.* **1986**, *34* (5), 394–404. doi:10.1088/0031-8949/34/5/007.; (b) Heully, J.-L.; Lindgren, I.; Lindroth, E.; Lundquist, S.; Martensson-Pendrill, A.-M. *J. Phys. B* **1986**, *19* (18), 2799–2815. doi:10.1088/0022-3700/19/18/011.; (c) van Lenthe, E.; Baerends, E. J.; Snijders, J. G. *J. Chem. Phys.* **1993**, *99* (6), 4597. doi:10.1063/1.466059.; (d) van Lenthe, E.; Baerends, E. J.; Snijders, J. G. *J. Chem. Phys.* **1996**, *105* (15), 6505. doi:10.1063/1.472460.; (e) van Lenthe, E.; van Leeuwen, R.; Baerends, E. J.; Snijders, J. G. *Int. J. Quantum Chem.* **1996**, *57* (3), 281–293. doi:10.1002/(SICI)1097-461X(1996)57:3<281::AID-QUA2>3.0.CO;2-U.

(23) Krijn, J.; Baerends, E. J. *Fit Functions in the HFS-Method, Internal Report;* Vrije Universiteit Amsterdam: The Netherlands, 1984 (In Dutch).

(24) (a) Frenking, G.; Wichmann, K.; Fröhlich, N.; Loschen, C.; Lein, M.; Frunzke, J.; Rayón, V. M. *Coord. Chem. Rev.* **2003**, *238–239*, 55–82. doi:10.1016/S0010-8545(02)00285-0.; (b) Dykstra, C. E.; Frenking, G.; Kim, K. S.; Scuseria, G. E. In *Theory and Applications of Computational Chemistry: The First 40 Years*. Dykstra, C. E., Frenking, G., Kim, K. S., Scuseria. G. E., Eds.; Elsevier: Amsterdam, 2005.

(25) (a) Jonas, V.; Frenking, G.; Reetz, M. T. *J. Am. Chem. Soc.* **1994**, *116* (19), 8741–8753. doi:10.1021/ja00098a037.; (b) Bühl, M.; Steinke, T.; von Ragué Schleyer, P.; Boese, R. *Angew. Chem.* **1991**, *103* (9), 1179–1181. doi:10.1002/ange.19911030931.; (c) Bühl, M.; Steinke, T.; von Ragué Schleyer, P.; Boese, R. *Angew. Chem. Int. Ed. Engl.* **1991**, *30* (9), 1160–1161. doi:10.1002/anie.199111601.; (d) Merino, G.; Bakhmutov, V.; Vela, A. *J. Phys. Chem. A* **2002**, *106* (37), 8491–8494. doi:10.1021/jp026087n.; (e) Burns, W. R.; Leopold, K. A. *J. Am. Chem. Soc.* **1993**, *115* (24), 11622–11623. doi:10.1021/ja00077a081.

(26) Frenking, G.; Wichmann, K.; Fröhlich, N.; Grobe, J.; Golla, W.; Le Van, D.; Krebs, B.; Läge, M. *Organometallics* **2002**, *21* (14), 2921–2930. doi:10.1021/om020311d.

A quantum mechanical approach to ligand binding — Calculation of ligand–protein binding affinities for stromelysin-1 (MMP-3) inhibitors

Jian Li and Charles. H. Reynolds

Abstract: Linear-scaling quantum mechanical method was applied to calculate binding affinities of six stromelysin-1 (MMP-3) inhibitors with two different zinc binding groups (ZBGs). The entire protein and ligand–protein complexes were calculated using PM5 Hamiltonian, which enables the treatment of metal ion coordination, bond forming/breaking, and proton/charge transfers associated with the ligand binding process by the self-consistent field method. The calculated binding energies reproduce the binding-affinity trend observed experimentally.

Key words: ligand–protein binding affinities, stromelysin-1 inhibitors, matrix metalloproteinase, linear-scaling quantum calculation.

Résumé : On a appliqué la méthode de mécanique quantique de mise l'échelle pour calculer les affinités de fixation de six inhibiteurs de la stromélysine-1 (MMP-3) avec deux groupes différents fixés au zinc (GFZ). On a effectué des calculs pour la protéine complète et pour les complexes ligand-protéine à l'aide de l'hamiltonien PM5 qui permet de traiter la coordination de l'ion métallique, la formation et le bris d'une liaison et les transferts de proton et de charge associés au processus de fixation de ligand par la méthode du champ autocohérent. Les énergies de fixation calculées permettent de reproduire la tendance dans les affinités de fixation observées expérimentalement.

Mots-clés : affinités de fixation ligand–protéine, inhibiteurs de la stromélysine-1, matrice de métalloprotéinase, calcul de mécanique quantique de mise l'échelle.

[Traduit par la Rédaction]

Introduction

Accurate prediction of ligand–protein binding affinity is of fundamental importance to all aspects of structure-based drug design and virtual screening. Many computational approaches have been developed to tackle this problem. These methods include thermodynamic integration (TI), free-energy perturbation (FEP), linear interaction energy (LIE), and molecular mechanics/Possion–Boltzmann surface area (MM/PBSA).[1] Although many aspects of these methods vary, they all rely on classical force-field energies.[2] This is severely limiting in cases where the ligand binding process involves bond breaking/forming, proton/charge transfer, or metal ion coordination. In these cases, a quantum mechanical (QM) description of the system becomes indispensable.

Traditionally, QM calculations have been limited to relatively small molecules due to their scaling of N^3 with respect to the number of basis functions even for semi-empirical methods. Any QM calculation for a protein was impractical even with the fastest computers. This has changed with the introduction of linear-scaling quantum mechanical methods. Divide-and-conquer (D&C)[3] and localized molecular orbital methods[4] allow for QM calculations that scale linearly with respect to size rather than exponentially. This makes calculations for very large systems, even proteins, practical. Linear-scaling QM calculations have been used to study hydration effects,[5] charge transfer,[6] reaction mechanisms,[7] and enzyme dynamics.[8] Recently, a quantum-mechanics-based scoring function was reported, along with specific applications to zinc-ion-mediated carbonic anhydrases and carboxypeptidases.[9]

Matrix metalloproteinases (MMPs) are a family of zinc-containing endoproteinases that mediate degradation and remodeling of the extracellular matrix. The Zn ion in the active site of MMPs plays a central role in the catalytic function of these enzymes and inhibitor binding. Therefore, almost all MMP inhibitors contain some type of zinc binding group (ZBG) such as hydroxamate or carboxylate.[10] The zinc center presents a long-standing challenge to efforts to model the binding affinity of zinc-containing proteins. Using classical methods, one must assume either a bonded or non-bonded structure for the zinc ion (i.e., either the ZBG has a valence bond to Zn or it does not).[11] The calculation results are strongly affected by this ad hoc assumption, and it is virtually impossible to compare results for inhibitors containing different ZBGs. In addition, the protonation states of some acidic residues in the active site also change upon ligand

Received 22 June 2009. Accepted 3 August 2009. Published on the NRC Research Press Web site at canjchem.nrc.ca on 6 October 2009.

This article is part of a Special Issue dedicated to Professor T. Ziegler.

J. Li[1,2] and C.H. Reynolds. Computer-Aided Drug Discovery, Johnson & Johnson Pharmaceutical Research and Development L.L.C., Welsh and McKean Roads, Spring House, PA 19477-0776, USA.

[1]Corresponding author (e-mail: jian_li@wuxiapptec.com).
[2]Present address: WuXi AppTec Co. Ltd., 288 Fute Zhong Road, Shanghai 200131, China.

Chart 1. Six stromelysin-1 inhibitors with binding affinities.

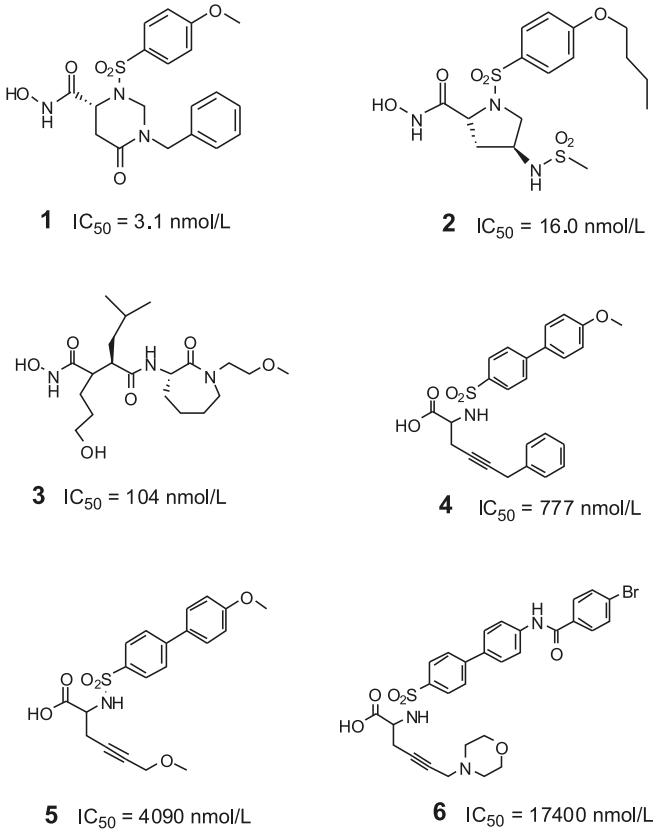

binding. This further complicates selection of the relevant classical representation. These complications can be readily addressed by QM methods.

We have used linear-scaling quantum calculations to study the binding affinities of six inhibitors for stromelysin-1 (MMP-3). The entire protein and ligand–protein complexes were treated quantum-mechanically. This allowed the binding characteristics of the zinc center and the protonation states to be determined automatically by the QM wave function.

Computational method

All calculations were carried out using MOZYME as implemented in MOPAC2002/BioMedCACHe 6.0.[12] The PM5 Hamiltonian[13] was employed for all atoms including Zn^{2+} and Ca^{2+}. Protein backbone atoms were fixed, but all side chain atoms and the inhibitors were optimized. Following gas-phase geometry optimization, the solvation energy was calculated by a continuum COSMO model using the water dielectric constant of 78.[14] The non-polar contribution to the solvation term was calculated by using the solvent accessible surface area (SASA) as 0.00542 × SASA + 0.92 kcal/mol. The entropic contribution was omitted in the calculation.

The binding affinity in this calculation is defined as the energy difference between the ligand–protein complex and the free protein plus free ligand. The total ΔE_{ba} then can be divided into QM and solvation contributions, ΔE_{qm} and ΔE_{sol}, respectively .

Fig. 1. Structure of inhibitor **3** and stromelysin-1 complex. The magenta balls are Zn^{2+} ions and blue balls are Ca^{2+} ions.

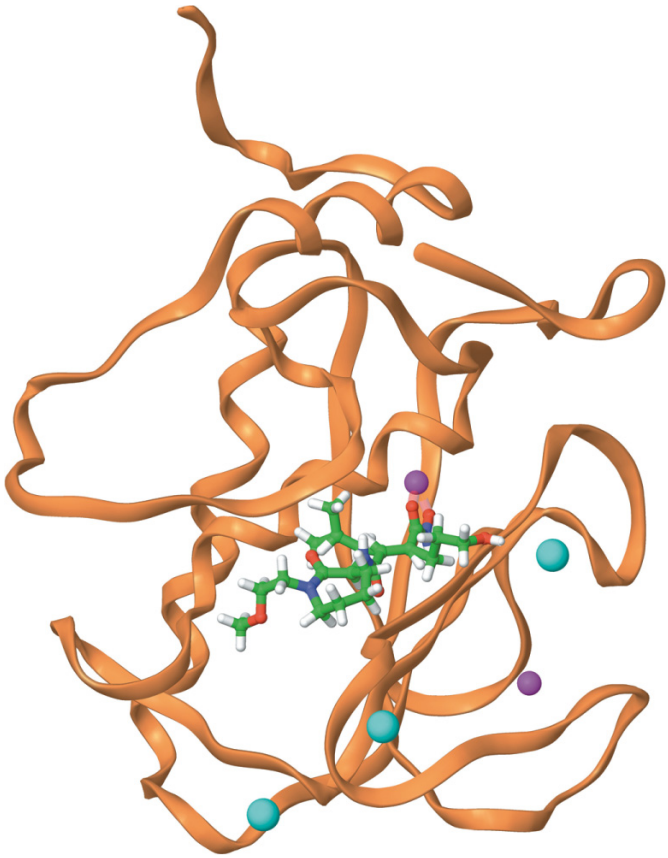

$$\begin{aligned}\Delta E_{ba} &= E(\text{complex}) - E(\text{protein}) \\ &= E_{qm}(\text{complex}) + E_{sol}(\text{complex}) - E_{qm}(\text{protein}) \\ &\quad - E_{sol}(\text{protein}) - E_{qm}(\text{ligand}) - E_{sol}(\text{ligand}) \\ &= \Delta E_{qm} + \Delta E_{sol}\end{aligned} \quad [1]$$

Results and discussion

Chart 1 shows six stromelysin-1 (MMP-3) inhibitors with hydroxamate and carboxylate ZBGs.[12] The potencies of these compounds span a wide range from IC_{50} = 3 nmol/L to 17 μmol/L.[15] The crystal structures of four inhibitors (**1**, **2**, **3**, and **4**) bound to truncated stromelysin-1 (MMP-3) were downloaded from Protein Data Bank (PDB codes: 1G05, 1G49, 1BIW, and 1HY7, respectively).[15] The calculations were carried out for the MMP-3 monomer, which consists of 172 residues and 2686 atoms. All crystalline waters were removed except three within the Ca^{2+} coordination spheres. Protonation states were assigned and hydrogen atoms were added using the Schrödinger/Maestro protein-preparation procedure.[16] Figure 1 demonstrates the structure of compound **3** complexed in stromelysin-1 (PDB code: 1BIW). The binding modes of inhibitors **5** and **6** were assigned by docking the ligands to 1HY7, using inhibitor **4** as a reference template. The docking calculation was done using Schrödinger/Glide package.[17] The free protein was obtained by removing the ligand from 1BIW structure, and no zinc-bound water was added. This approximation will not affect the calculation of relative binding energies.

Table 1. Calculated and experimental energies (kcal/mol).

Inhibitor	ΔE_{qm}	ΔE_{sol}	ΔE_{ba}	pIC_{50}	ΔG^a	$\Delta G_{pred}{}^b$
1	–24.2	30.0	3.1	8.5	–12.1	–11.0
2	–27.2	31.4	1.2	7.8	–11.1	–11.3
3	–37.6	47.6	6.4	7.0	–9.9	–10.7
4	–39.3	67.1	23.6	6.1	–8.7	–8.6
5	–30.9	61.4	27.4	5.4	–7.7	–8.2
6	–38.9	85.7	42.3	4.8	–6.8	–6.5

[a]Experimental binding energies are estimated according to $\Delta G \approx -2.303RT\ pIC_{50}$.
[b]Calculated according to $\Delta G_{pred} = 0.117\Delta E_{ba} - 11.414$, see Fig. 2.

Fig. 2. Plot of calculated vs. experimental relative binding energies for six stromelysin-1 inhibitors.

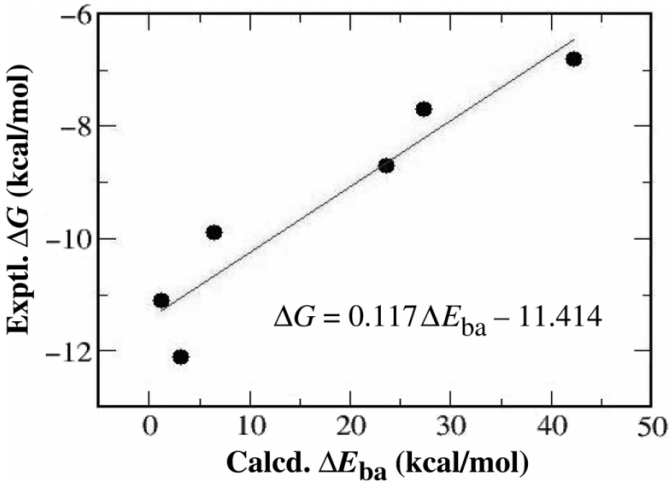

The experimental binding free energies ΔG and computed energy terms are summarized in Table 1. The ΔG values were estimated based on pIC_{50} ($-\log IC_{50}$) and therefore are relative binding free energies. For all six inhibitors, the QM terms ΔE_{qm} are negative, indicating a stabilizing interaction between the ligand and the protein in the gas phase. The positive ΔE_{sol} terms correspond to a large desolvation penalty to the formation of the ligand–protein complex. Due to underestimation of the van der Waals interaction by semi-empirical QM methods, the overall calculated ΔE_{ba} terms are positive. However, they show an excellent correlation to experimental binding energies ($r^2 = 0.95$). Figure 2 shows the correlation between the relative experimental binding energies and the calculated binding energies for six inhibitors. While a relatively small set of inhibitors, this correlation is remarkable given that two different ZBGs are involved. The calculated $\Delta\Delta E_{ba}$ correctly predict that inhibitors with hydroxamate ZBG bind more tightly to stromelysin-1 than those with carboxylate ZBG. Except for the two most potent binders, **1** and **2**, the model ranks the inhibitor affinities correctly.

The gas-phase geometry optimization of the protein–ligand complexes starts with the protonated state where the ligand is neutral and Glu-202 is deprotonated. During the course of geometry optimization, the ligand spontaneously donates a proton to Glu-202 and binds to zinc as a bidentate ligand (Fig. 3). This would be impossible with a classical force-field representation. This indicates that binding to the zinc ion decreases the pK_a of the ligand's ZBG, a result that

Fig. 3. Proton transfer from hydroxamate group in inhibitor **1** to Glu-202 in stromelysin-1: (A) before the gas-phase geometry optimization; (B) after the gas-phase geometry optimization.

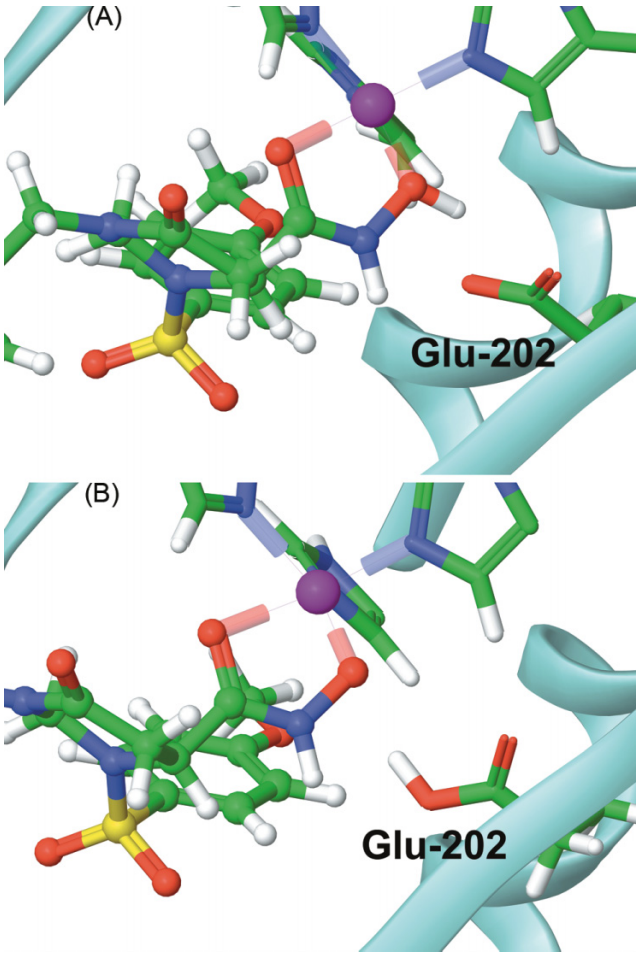

is consistent with experimental evidence that zinc-bound water exhibits a lower pK_a value.[18] Meanwhile, the electrostatic and hydrogen-bonding environment of Glu-202 causes it to be mostly protonated at physiological pH.[19]

Mulliken charge analysis on the free and bound inhibitors reveal a non-negligible charge transfer accompanying ligand binding. As shown in Table 2, the net charges for Zn in free protein and in the complex are +0.88 and +0.83, respectively. This is significantly lower than the formal +2 charge commonly assigned to Zn ion in force-field-based calculations. The most dramatic change in charge is on the oxygen atoms of the ZBG hydroxyl group. The charge changes

Table 2. Mulliken atomic charges.

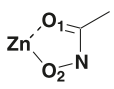

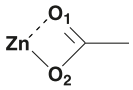

		Free form			Complex		
Inhibitor	Δ|e|[a]	Zn	O_1	O_2	Zn	O_1	O_2
1	–0.21	+0.88	–0.40	–0.31	+0.83	–0.48	–0.59
2	–0.11	+0.88	–0.43	–0.31	+0.83	–0.48	–0.56
3	–0.20	+0.88	–0.43	–0.31	+0.82	–0.50	–0.62
4	–0.27	+0.88	–0.43	–0.38	+0.83	–0.53	–0.58
5	–0.25	+0.88	–0.37	–0.38	+0.82	–0.51	–0.57
6	–0.27	+0.88	–0.42	–0.38	+0.83	–0.52	–0.59

[a]Charge transferred from protein to ligand.

from –0.3 to –0.6 and from –0.4 to –0.6 in carboxylate and hydroxamate, respectively. Overall, the protein transfers 0.2|e| to the hydroxamate ligand and 0.3|e| to the carboxylate ligand.

Conclusion

In summary, these calculations show that QM methods can be applied to the ligand–protein binding problem, even when metals are involved. Although dynamic and entropy contributions were not considered, the calculated binding energies reproduce the experimental trend in binding potency. This is true even though two very different ZBGs were modeled together, i.e., hydroxamate and carboxylate. This methodology can treat metal ions such as Zn, bond forming and breaking processes, proton transfer, and charge transfer in a consistent way that cannot be achieved by classical forcefield approaches.

Acknowledgement

We thank Drs. Brett Tounge and Ramkumar Rajamani for many useful discussions, and Ms. Heidi Klein (CACheGroup) for her assistance on many occasions.

References

(1) (a) Kollman, P. A. *Chem. Rev.* **1993**, *93* (7), 2395–2417. doi:10.1021/cr00023a004.; (b) Aqvist, J.; Luzhkov, V. B.; Brandsdal, B. O. *Acc. Chem. Res.* **2002**, *35* (6), 358–365. doi:10.1021/ar010014p. PMID:12069620.; (c) Simonson, T.; Archontis, G.; Karplus, M. *Acc. Chem. Res.* **2002**, *35* (6), 430–437. doi:10.1021/ar010030m. PMID:12069628.

(2) Ponder, J. W.; Case, D. A. *Adv. Protein Chem.* **2003**, *66*, 27–85. doi:10.1016/S0065-3233(03)66002-X. PMID:14631816.

(3) (a) Yang, W. *Phys. Rev. Lett.* **1991**, *66* (11), 1438–1441. doi:10.1103/PhysRevLett.66.1438. PMID:10043209.; (b) Yang, W.; Lee, T.-S. *J. Chem. Phys.* **1995**, *103* (13), 5674. doi:10.1063/1.470549.; (c) Dixon, S. L.; Merz, K. M., Jr. *J. Chem. Phys.* **1996**, *104* (17), 6643. doi:10.1063/1.471382.

(4) (a) Stewart, J. J. P. *Int. J. Quantum Chem.* **1996**, *58* (2), 133–146. doi:10.1002/(SICI)1097-461X(1996)58:2<133::AID-QUA2>3.0.CO;2-Z.; (b) Stewart, J. J. P. *J. Mol. Struct. THEOCHEM* **1997**, *401* (3), 195–205. doi:10.1016/S0166-1280(97)00050-X.

(5) (a) York, D. M.; Lee, T.-S.; Yang, W. *J. Am. Chem. Soc.* **1996**, *118* (44), 10940–10941. doi:10.1021/ja961937w.; (b) Ohno, K.; Kamiya, N.; Asakawa, N.; Inoue, Y.; Sakurai, M. *J. Am. Chem. Soc.* **2001**, *123* (33), 8161–8162. doi:10.1021/ja015589w. PMID:11506591.

(6) van der Vaart, A.; Merz, K. M., Jr. *J. Am. Chem. Soc.* **1999**, *121* (39), 9182–9190. doi:10.1021/ja9912325.

(7) Titmuss, S. J.; Cummins, P. L.; Rendell, A. P.; Bliznyuk, A. A.; Gready, J. E. *J. Comput. Chem.* **2002**, *23* (14), 1314–1322. doi:10.1002/jcc.10122. PMID:12214314.

(8) Liu, H.; Elstner, M.; Kaxiras, E.; Frauenheim, T.; Hermans, J.; Yang, W. *Proteins* **2001**, *44* (4), 484–489. doi:10.1002/prot.1114. PMID:11484226.

(9) Raha, K.; Merz, K. M., Jr. *J. Am. Chem. Soc.* **2004**, *126* (4), 1020–1021. doi:10.1021/ja038496i. PMID:14746460.

(10) Whittaker, M.; Floyd, C. D.; Brown, P.; Gearing, A. J. H. *Chem. Rev.* **1999**, *99* (9), 2735–2776. doi:10.1021/cr9804543. PMID:11749499.

(11) (a) Donini, O. A.; Kollman, P. A. *J. Med. Chem.* **2000**, *43* (22), 4180–4188. doi:10.1021/jm000040d. PMID:11063614.; (b) Hou, T. J.; Zhang, W.; Xu, X. J. *J. Phys. Chem. B* **2001**, *105* (22), 5304–5315. doi:10.1021/jp0044476.; (c) Hou, T. J.; Guo, S.; Xu, X. J. *J. Phys. Chem. B* **2002**, *106* (21), 5527–5535. doi:10.1021/jp015516z.; (d) Rizzo, R. C.; Toba, S.; Kuntz, I. D. *J. Med. Chem.* **2004**, *47* (12), 3065–3074. doi:10.1021/jm030570k. PMID:15163188.

(12) CAche Group. *BioMedCAChe 6.0;* CAche Group: Portland, OR, 2003.

(13) Stewart, J. J. P. *J. Mol. Model.* **2004**, *10* (1), 6–12. doi:10.1007/s00894-003-0157-6.

(14) Klamt, A.; Schuurmann, G. *J. Chem. Soc. Perkin. Trans. 2* **1993**, 799.

(15) (a) Natchus, M. G.; Cheng, M.; Wahl, C. T.; Pikul, S.; Almstead, N. G.; Bradley, R. S.; Taiwo, Y. O.; Mieling, G. E.; Dunaway, C. M.; Snider, C. E.; McIver, J. M.; Barnett, B. L.; McPhail, S. J.; Anastasio, M. B.; De, B. *Bioorg. Med. Chem. Lett.* **1998**, *8* (16), 2077–2080. doi:10.1016/S0960-894X(98)00370-9. PMID:9873489.; (b) Natchus, M. G.; Bookland, R. G.; De, B.; Almstead, N. G.; Pikul, S.; Janusz, M. J.; Heitmeyer, S. A.; Hookfin, E. B.; Hsieh, L. C.; Dowty, M. E.; Dietsch, C. R.; Patel, V. S.; Garver, S. M.; Gu, F.; Pokross, M. E.; Mieling, G. E.; Baker, T. R.; Foltz, D. J.; Peng, S. X.; Bornes, D. M.; Strojnowski, M. J.; Taiwo, Y. O. *J. Med. Chem.* **2000**, *43* (26), 4948–4963. doi:10.1021/jm000246e. PMID:11150165.; (c) Pikul, S.; Dunham, K. M.; Almstead, N. G.; De, B.; Natchus, M. G.; Taiwo, Y. O.; Williams, L. E.; Hynd, B. A.; Hsieh, L. C.; Janusz, M. J.; Gu, F.; Mieling, G. E. *Bioorg. Med. Chem. Lett.* **2001**, *11* (8), 1009–1013. doi:10.1016/S0960-894X(01)00137-8. PMID:

11327577.; (d) Natchus, M. G.; Bookland, R. G.; Laufersweiler, M. J.; Pikul, S.; Almstead, N. G.; De, B.; Janusz, M. J.; Hsieh, L. C.; Gu, F.; Pokross, M. E.; Patel, V. S.; Garver, S. M.; Peng, S. X.; Branch, T. M.; King, S. L.; Baker, T. R.; Foltz, D. J.; Mieling, G. E. *J. Med. Chem.* **2001**, *44* (7), 1060–1071. doi:10.1021/jm000477l. PMID:11297453.

(16) SCHRÖDINGER. *Maestro 5.0;* Schrödinger, L.L.C.: Portland, OR, 2003.

(17) SCHRÖDINGER. *Glide 2.0;* Schrödinger, L.L.C.: Portland, OR, 2003.

(18) Lipscomb, W. N.; Sträter, N. *Chem. Rev.* **1996**, *96* (7), 2375–2434. doi:10.1021/cr950042j. PMID:11848831.

(19) Cross, J. B.; Duca, J. S.; Kaminski, J. J.; Madison, V. S. *J. Am. Chem. Soc.* **2002**, *124* (37), 11004–11007. doi:10.1021/ja0201810. PMID:12224947.

Non-empirical derivation of the parameter in the B88 exchange functional

Peter Elliott and Kieron Burke

Abstract: The B88 exchange energy density functional (created by Becke in 1988) is a crucial part of the most popular density functional in use today, B3LYP. B88 contains one empirical parameter which was fitted to Hartree–Fock exchange energies for the noble gas atoms. We show how local approximations to exchange become relatively exact under a very specific approach to the limit of large numbers, but the usual gradient expansion does not. The leading corrections can be captured by generalized gradient approximations, producing a non-empirical derivation of the parameter in B88.

Key words: density functional theory (DFT), exchange functional, B88, potential scaling.

Résumé : La fonctionnelle de la densité d'énergie d'échange B88 (développée par Becke en 1988) est une partie cruciale de la fonctionnelle de densité B3LYP, la plus populaire parmi les bases en usage aujourd'hui. La fonction B88 comprend un paramètre empirique qui a été ajusté aux énergies d'échange d'Hartree–Fock des atomes des gaz rares. On démontre comment des approximations locales des échanges deviennent relativement exactes dans une approche très spécifique à la limite des grands nombres, ce que l'expansion habituelle des gradients ne permet pas. Les corrections principales peuvent être capturées par les approximations de gradients généralisées et produire une dérivation non empirique du paramètre dans la fonction B88.

Mots-clés : théorie de la fonctionnelle de densité (TFD), fonctionnelle d'échange, B88, mise à l'échelle du potentiel.

[Traduit par la Rédaction]

I. Introduction

Density functional theory (DFT) has become the method of choice for many electronic structure calculations in quantum chemistry.[1] It balances the demands of accuracy and computation time, making it advantageous to other available methods. Although DFT is a formally rigorous theory, in practice, it requires an approximation to the exchange-correlation (XC) energy, E_{xc}, as a functional of the density. In the late 1980s and early 1990s, approximations, such as B88, were developed which proved accurate enough for their application in many areas of both chemistry and physics. The explosion in the use of DFT, driven by newly available computational power, could not have succeeded without the development of such functionals.

Modern DFT began with the Hohenberg–Kohn theorem of 1964[2] and the Kohn–Sham scheme of 1965.[3] The first approximation to the XC energy was the local density approximation (LDA), which uses only the density at a given point to determine the energy density at that point. This is exact for a uniform gas, since it is the known energy density of the uniform gas that is used to define LDA. The natural successor to LDA is a semi-local (or gradient-corrected) approximation which adds information about the derivative of the density at that point. In fact, in the same paper in which LDA is introduced, so too is the gradient expansion approximation (GEA) for XC. The coefficients of the GEA are determined by the energy of a slowly varying gas.[4–6] However, it was found that the GEA often worsened LDA results, and two decades passed before substantial improvements were made.

Generalized gradient approximations (GGAs) effectively resum the gradient expansion, but using only $|\nabla n|$. The B88 functional[7] is the most used GGA for exchange overall (as part of B3LYP[8,9]), but the most popular GGA in solid-state applications is PBE.[10] Neither reduces to the GEA in the limit of small gradients. In this paper, we explain the reason why this must be the case. Asymptotic expressions for the energy components as functionals of N, the number of electrons, display "unreasonable accuracy"[11] even for low N. To give good energies for finite systems, any approximate XC functional must have accurate coefficients in its large-N expansion. LDA gives the dominant contribution, but the GEA does not yield an accurate leading correction for atoms. Popular GGAs such as B88 and PBE do get this correction right.

In ref. 12, the underlying ideas behind this work were developed; however, the reasoning was based upon scaling the density and not on the potential scaling discussed below. We refine these ideas and explicitly show how they can be used for functional development, and in particular, we show how the parameter in B88 may be derived in a non-empirical manner.

Received 10 February 2009. Accepted 12 May 2009. Published on the NRC Research Press Web site at canjchem.nrc.ca on 6 October 2009.

This article is part of a Special Issue dedicated to Professor T. Ziegler.

P. Elliott.[1] Department of Physics and Astronomy, University of California, Irvine, CA 92697, USA.
K. Burke. Department of Chemistry, University of California, Irvine, CA 92697, USA.

[1]Corresponding author (e-mail: pelliott@uci.edu).

II. Background theory

In this section, we review the theory behind asymptotic expansions of the energy, including the expression for the exchange energy. A demonstration of the usefulness of this asymptotic expansion for exchange is also given, where the constant in LDA is found without referring to the electron gas. We also show the form of the gradient correction to LDA exchange, as well as discussing the form of the GGAs, B88, and PBE.

A. Asymptotic expansion in *N*

Begin with any system (atom, molecule, cluster, or solid) containing N electrons. We then imagine changing the number of electrons to N'. Since we usually begin from a neutral system, usually we consider only $N' > N$. Thus, we define a scaling parameter $\zeta = N'/N > 1$. As we change the particle number, we simultaneously change the one-body potential $v_{\text{ext}}(\mathbf{r})$ in such a way as to retain overall charge neutrality, which means

$$[1] \qquad v_{\text{ext}}^{\zeta}(\mathbf{r}) = \zeta^{4/3} v_{\text{ext}}(\zeta^{1/3}\mathbf{r}), \qquad N \to \zeta N$$

We refer to this as charge–neutral (CN) scaling. For an isolated atom, $Z \to \zeta Z$ under this scaling, so it remains neutral as the electron number grows. For molecules with nuclear positions R_α and charges Z_α, $Z_\alpha \to \zeta Z_\alpha$, and $R_\alpha \to \zeta^{-1/3} R_\alpha$. In the special case of neutral atoms, the resulting series for the energy is well-known:

$$[2] \qquad E = -a_0 N^{7/3} - a_1 N^2 - a_2 N^{5/3} - \ldots$$

where $a_0 = 0.768745$, $a_1 = -1/2$, and $a_2 = 0.269900$.[11,13] We say an approximation is large-N *asymptotically exact* to the pth degree (AEp) if it recovers exactly the first $p + 1$ coefficients for a given quantity under the potential scaling of eq. [1]. Lieb and Simon[14,15] showed that Thomas–Fermi (TF) theory becomes *exact* in the limit $\zeta \to \infty$ for *all* systems. TF is exact in a statistical sense, in that TF gives the correct first term of eq. [2], but not the other terms. We say TF is AE0 for the total energy.

A similar expression exists for the exchange component of the energy alone

$$[3] \qquad E_{\text{x}} = -c_0 N^{5/3} - c_1 N - \ldots$$

where $c_0 = 0.2208 = 9a_2/11$, and c_1 will be the main topic of this paper. In a similar fashion, Schwinger demonstrated that the local approximation for exchange is AE0, and this coefficient is given exactly by local exchange evaluated on the TF density.[11,13,16] However, to give atomic exchange energies needed for chemical accuracy, any exchange approximation should be at least AE1.

Now, suppose we want to make a local approximation for E_{x} but know nothing about the uniform gas. Dimensional analysis (coordinate scaling[17]) tells us that it must be of the form:

$$[4] \qquad E_{\text{x}}^{\text{LDA}}[n] = A_{\text{x}} I, \quad I = \int \mathrm{d}^3 r n^{4/3}(\mathbf{r})$$

Requiring that this gives the leading contribution to eq. [3] then fixes the value of the constant A_{x}. Using any (all-electron) Hartree–Fock atomic code, such as were already available in the 1960s,[18] one calculates I for densities running down a particular column of the periodic table and then deduces its dependence on $Z^{5/3}$. A modern alternative is to use the fully numerical OPMKS code[19] using the OEP exact exchange functional to find densities for neutral atoms from $Z = 1$ to $Z = 88$. By fitting, one finds $I = 0.2965 Z^{5/3}$ and hence $A_{\text{x}} = -0.7446$. This is remarkably close to the derived result of

$$[5] \qquad A_{\text{x}} = -\frac{3}{4}\left[\frac{3}{\pi}\right]^{1/3} = -0.7386$$

Thus, without any recourse to the uniform electron gas, we have derived the correct local approximation to $E_{\text{x}}[n]$. This demonstrates that, via asymptotic exactness, the local approximation to exchange is a universal feature of all systems as $N \to \infty$, when scaled appropriately. (In fact, Schwinger only proved this for atoms,[11] we know of no proof for arbitrary systems).

B. Gradient expansions

The next step up the ladder of increasingly sophisticated density-functional approximations[20] is a semi-local approximation for $E_{\text{x}}[n]$, i.e., one which includes information about the gradient of the density. We introduce the dimensionless measure of the gradient:

$$[6] \qquad s(\mathbf{r}) = \frac{|\nabla n(\mathbf{r})|}{2k_{\text{F}}(\mathbf{r}) n(\mathbf{r})}$$

where $k_{\text{F}}(\mathbf{r}) = (3\pi^2 n(\mathbf{r}))^{1/3}$ is the local Fermi wave vector. This is often written in terms of $x = |\nabla n|/n^{4/3}$, which is simply proportional to s. Assuming smoothness in s and no preferred spatial direction, we know any sensible approximation depends only on s^2. The gradient expansion is defined as the expansion of the energy as a functional of the density around the uniform limit. The leading correction for exchange is

$$[7] \qquad E_{\text{x}}^{(2)}[n] = \mu \int \mathrm{d}^3 r s^2(\mathbf{r}) \epsilon_{\text{x}}^{\text{LDA}}(n(\mathbf{r}))$$

where $\varepsilon_{\text{x}} = A_{\text{x}} n^{4/3}$ and μ is a constant. Alternatively, we may write

$$[8] \qquad E_{\text{x}}^{(2)}[n] = -\beta \int \mathrm{d}^3 r n^{4/3}(\mathbf{r}) x^2$$

with

$$[9] \qquad \beta = \frac{3}{16\pi}\left[\frac{1}{3\pi^2}\right]^{1/3} \mu$$

In a very slowly-varying electron gas, the gradient is very small, and the exchange energy will be accurately given by $E_{\text{x}}^{\text{LDA}} + E_{\text{x}}^{(2)}$. For such systems, the constant $\mu = 10/81$,[4] so that $\beta \approx 0.0024$.

The gradient expansion approximation (GEA) means applying this form to a finite system, using the value of μ from the slowly-varying gas. The GEA for exchange typically reduces the LDA error by about 50%. However, it's counterpart for correlation worsens the LDA error, as its en-

ergy density is not even always negative. In many cases, GEA strongly overcorrects LDA leading to positive correlation energies and giving poor total energies.[5]

A generalized gradient approximation (GGA) seeks to include the information contained in $s(\mathbf{r})$ while improving on the success of LDA. The B88 exchange functional was designed to reduce to the GEA form when s is small, but also recover the correct $-n(r)/2r$ decay of the exchange energy density for large r in atoms. Thus, it interpolates between two known limits, and has the form:

$$[10] \qquad \Delta E_{\mathrm{x}}^{\mathrm{B88}}[n] = -\beta^{\mathrm{B88}} \int \mathrm{d}^3 r n^{4/3}(\mathbf{r}) \frac{x^2}{1 + 6x\beta^{\mathrm{B88}} \sinh^{-1}[2^{1/3}x]}$$

where ΔE_{x} denotes the correction to LDA. Thus, the B88 functional[7] contains one unknown parameter, β^{B88}. In 1988, Becke found this parameter by fitting to the Hartree–Fock exchange energies of the noble gases, finding a value of 0.0053. In fact, Becke notes that this value is consistent with the observation of a high-Z asymptote for β. In ref. 21, B86, Becke calculates what value of β in eq. [8] is required to give the HF exchange energy for each atom in the first two rows of the periodic table along with the noble gas atoms. Thus, β is treated as a function of Z, and he observes that it converges for high-Z. Thanks to the previous section on asymptotic series, we can now understand why this convergence occurs. Although the B88 form reduces to that of the gradient expansion for small gradients, the value for β is about twice as large as that predicted from the slowly varying gas.

Another common GGA for exchange is the Perdew–Burke–Ernzerhof (PBE) approximation,[10] usually written in terms of an enhancement factor, $F_{\mathrm{x}}(s)$, to the LDA exchange energy density

$$[11] \qquad E_{\mathrm{x}}^{\mathrm{PBE}}[n] = \int \mathrm{d}^3 r F_{\mathrm{x}}^{\mathrm{PBE}}(s) \epsilon_{\mathrm{x}}^{\mathrm{LDA}}[n]$$

where

$$[12] \qquad F_{\mathrm{x}}^{\mathrm{PBE}}(s) = 1 + \kappa - \frac{\kappa}{1 + \mu s^2/\kappa'}$$

and $\mu = 0.2195$ and $\kappa = 0.8040$. This form for the enhancement factor is chosen so that it reduces to LDA for $s = 0$ and again recovers the form of the gradient expansion for small s. For large s, it becomes a constant determined by the parameter κ. Both κ and μ are determined via satisfaction of various exact conditions. The value of μ was chosen to preserve the good linear response of LDA for the uniform electron gas under a weak perturbation,[22,23] while κ is set by the Lieb–Oxford bound[24] on the exchange-correlation energy. (That condition is obviously violated by B88, while PBE does not accurately recover the X energy density in the tails of Coulombic systems).

III. Theory

LDA yields the dominant term in *either* the asymptotic charge–neutral expansion ($\zeta \to \infty$) *or* the gradient expansion for the slowly varying electron gas, $s \to 0$. We next show that, contrary to popular myth, the important expansion is the charge–neutral expansion, *not* the gradient expansion.

The charge–neutral expansion can be applied to any type of matter, be it molecule or extended solid. For any finite system, the density decays exponentially far from the nuclei. This is a key distinction between finite systems and bulk matter, treated with periodic boundary conditions. Bulk matter has no such regions.

But, for slowly varying gases, or more generally when there are no classical turning points at the Fermi surface, the charge–neutral scaling and the gradient expansion become identical, i.e., the gradient expansion for the slowly varying gas is simply a *special case* of charge–neutral scaling. To see that this is so, consider just the kinetic energy as a density-functional. Here, the gradient expansion is known out to 6th order,[25] and eventually, the integrated quantity itself diverges for atomic densities due to the evanescent tail. But no such divergence occurs for extended systems with finite density everywhere.[25,26]

Thus, CN scaling applies to all systems, but only becomes identical to the gradient expansion for slowly varying bulk systems. For the dominant contribution, effectively the local Fermi wavelength becomes short on the length scale on which the density is changing, so that the local approximation applies and yields the exact answer for this term. Hence, LDA reproduces the AE0 terms, but GEA does *not* produce the leading corrections. All this has been amply demonstrated for simple 1D model systems[16] and for the Kohn–Sham kinetic energy for atoms.[27]

Here, we apply the same reasoning for exchange. The local approximation becomes relatively exact as $\zeta \to \infty$, but the gradient expansion does not reproduce the leading correction in the CN expansion. Below, we use the simple reasoning of ref. 12 to recover this leading correction. We perform a much more extensive calculation of the asymptotic behavior, using methods developed in ref. 27. We find, in agreement with ref. 12, that the leading correction for atoms is about double that given by the gradient expansion, matching quite closely that of B88 and of PBE. Reversing this logic for B88, we show that B88 may be more or less derived non-empirically via the constraint that the approximation be AE1. If we enforce AE1 exactly, we find a slightly different value for β, and discuss the properties of the resulting functional, excogitated B88.

IV. Extracting asymptotic coefficients

Under the potential scaling of eq. [1], any approximation for the exchange energy that reduces to LDA in the uniform limit has an expansion in N like eq. [3], with the same value for c_0. However, the coefficient c_1 depends on the particular approximation. Below, we explain the procedure used to extract these coefficients.

As mentioned in the previous section, the OPMKS[19] electronic structure code is a fully numerical electronic structure code that has the ability to perform optimized effective potential (OEP) calculations. We evaluate the various approximations using atomic densities found with the OEP exact exchange (EXX) method. The densities found using this method will be extremely close to the exact densities despite the fact that correlation is missing. Moreover, the effect of correlation will contribute at higher orders in the asymptotic expansions of the energy than those we are interested in.

Fig. 1. The OEP exact exchange energies E_x for neutral atoms from $Z = 1$ to 88, divided by $Z^{5/3}$ to pick out the leading term in its asymptotic series. The leading corrections are proportional to powers of $Z^{-1/3}$. The values for the noble gas atoms are given as the circle symbols.

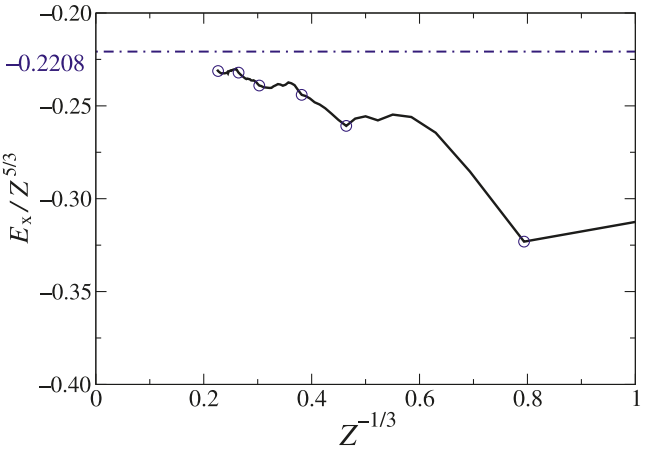

Fig. 2. We add to Fig. 1 the results for the LDA functional evaluated on the OEP densities (dashed-line) keeping the EXX values (solid line). As in Fig. 1, the noble gas atoms are highlighted with circle and square symbols for EXX and LDA, respectively.

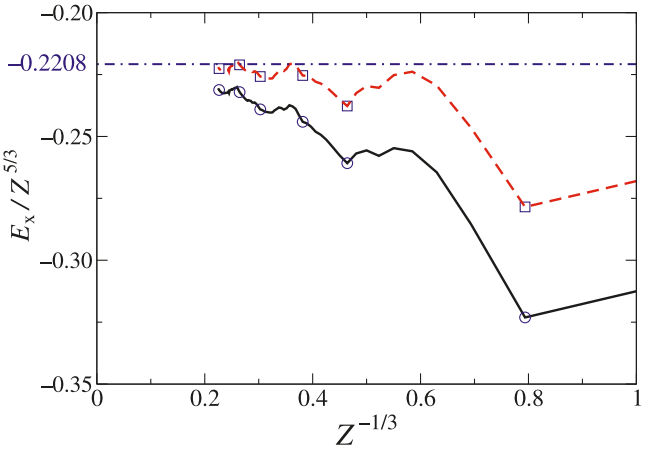

Thus, EXX calculations are in principle sufficient for extracting the coefficient we seek.

In Fig. 1, we plot $E_x/Z^{5/3}$ vs. $Z^{-1/3}$ where E_x is the exchange energy from the exact exchange calculation. Since the leading term in the asymptotic expansion of eq. [3] is $Z^{5/3}$, this procedure picks out the c_0 coefficient as a constant while all other terms are functions of $Z^{-1/3}$. One can see that the curve in Fig. 1 is heading towards the exact value of $c_0 = -0.2208$, but it is difficult to extract higher coefficients due to oscillation of the curve due to the shell structure.

To overcome this difficulty, in Fig. 2, we add the LDA curve to Fig. 1. It can be seen that it too recovers the exact c_0 coefficient, but also clearly differs in higher orders in the asymptotic expansion. More usefully, we see that the LDA curve mimics the oscillations shown by exact exchange, so subtracting LDA from EXX will minimize this effect and make the extraction of asymptotic coefficients more accurate.

In Fig. 3, we plot $(E_x - E_x^{LDA})/Z$ vs. $Z^{-1/3}$ and find that it behaves close to linearly. There appears to be no $Z^{4/3}$ term

Fig. 3. We now find the next coefficient in the exchange asymptotic series. To minimize the error due to shell structure oscillations, the LDA exchange energy is subtracted from the exact exchange for each atom. As both give the leading correction, their difference will then have ΔcZ, $\Delta c = c_1 - c_1^{LDA}$, as the leading term in its asymptotic expansion. The dashed line is the result of fitting to the noble gas atoms (circle symbols).

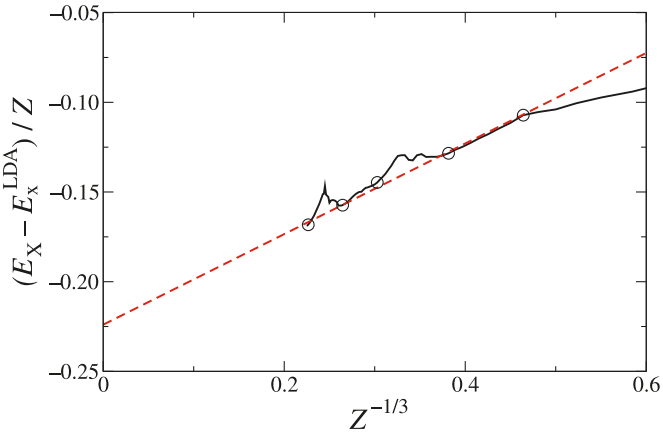

in E_x. Such a contribution was argued not to exist in ref. 12, but this was based on CN scaling of the density and studying the behavior of the terms in the gradient expansion. That reasoning is insufficient, as the expansion should be performed in terms of the potential, as described in section II. But since the Scott correction (the Z^2 contribution to the total energy) comes from the core region, there is no reason to expect an analogous contribution for exchange. To show this and also to precisely determine the c_1 coefficient, one should use the techniques developed by Schwinger for deriving the Scott correction to the total energy,[11] but apply them to exchange.

To further reduce the remaining uncertainty due to shell structure oscillations, we choose simply to use the noble gas atoms (excluding helium) for our fit. The strongest deviations from linearity come from the transition metals and lanthanides and actinides. We fit the difference $(E_x - E_x^{LDA})/Z$ with a straight line in $Z^{-1/3}$, and extrapolate to $Z \to \infty$, finding $\Delta c = -0.2240$, where $\Delta c = c_1 - c_1^{LDA}$, and

$$[13] \qquad E_x \approx E_x^{LDA} - 0.2240\,Z + 0.2467\,Z^{2/3}$$

The coefficient of the last term is given by the slope of the dashed line in Fig. 3, although the meaning of this term is unclear in the presence of such strong oscillating contributions.

If instead we used the alkaline earth atoms (excluding beryllium), we find an almost identical value, $\Delta c = -0.2236$. If we use all elements with $Z > 10$, we find a similar value, $\Delta c = -0.2164$. If all elements from $Z = 1$ to 88 are used, we find $\Delta c = -0.1982$. In ref. 12, Δc was found using noble gas atoms, except with the helium value included, and that method gave a value of $\Delta c = -0.1978$. In our analysis, atoms with $Z < 10$ are not used as they are not necessarily dominated by the asymptotic series.

Since LDA displays the shell oscillations that prevented us from fitting EXX directly, the value of the LDA c_1 coefficient cannot be found exactly. But we estimate

Fig. 4. To see that LDA does not significantly contribute to the higher orders of the exchange asymptotic series, we plot the difference between LDA and the leading term $c_0 Z^{5/3}$ (dashed line), as a function of Z. The exact exchange value is also shown (solid line).

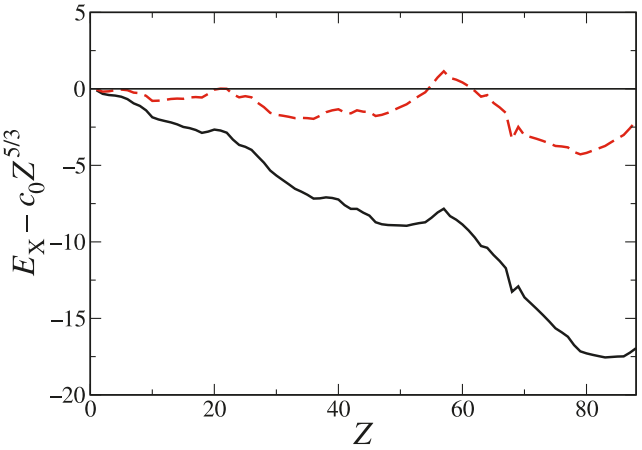

$0 \geq c_1^{\mathrm{LDA}} \geq -0.04$, i.e., at least five times smaller in magnitude than Δc. In Fig. 4, we show $E_x - c_0 Z^{5/3}$ as a function of Z for both the exact values and within LDA, demonstrating that the linear contribution comes almost entirely from the beyond-LDA terms.

Finally, we determine Δc for GEA. In Fig. 5, we plot $(E_x^{\mathrm{GEA}} - E_x^{\mathrm{LDA}})/Z$ vs. $Z^{-1/3}$ to find $\Delta c = c_1^{\mathrm{GEA}} - c_1^{\mathrm{LDA}}$, finding $\Delta c = -0.1062$. This plot is much closer to linear than the previous one. The leading corrections to LDA in the asymptotic expansion produce corrections to the shell structure *beyond* those captured by LDA evaluated on the exact density.[16,27] Although the smooth contribution can be partially captured by GEA, there is almost no correction to the shell structure. Just as for the kinetic energy,[27] GEA yields a correction to the smooth part that is about half of the accurate value.

To understand the power of these asymptotic expansions, we add the corrections of eq. [13] to the LDA energies, and in Fig. 6, plot the percentage error relative to exact exchange, as a function of Z. For all but the second row of the periodic table, the resulting error is below 0.5% in magnitude, and typically of the order 0.2%.

V. Generalized gradient approximations

Generalized gradient expansions were designed to improve energetics over LDA for electron systems of interest and relevance. Early versions, such as PW91,[28,29] were tortured into reducing to the gradient expansion when the density is slowly varying. But this was later given up, in both B88 and PBE exchange, which both reduce to the gradient expansion form for slow variations, but with coefficients much larger than that of the gradient expansion.

Our analysis explains why this must be so. Regardless of its derivation, any modern GGA for exchange is tested against the neutral atoms. Any approximation that cannot recover the right c_1 will be generally inaccurate for these energies, and so discarded. Thus, any that become popular have already passed this test.

In Table 1, we give the results for Δc for several different functionals. The same methodology was used in all extractions. Both popular GGAs recover (at least approximately) the accurate value. B88, designed specifically for molecular systems, is very close to the accurate value. PBE exchange is less so, but is also designed to bridge molecular and solid-state systems. The PBE value is between that of GEA and B88, but much closer to the latter than the former. Taking advantage of this insight, a new variation on PBE, called PBEsol,[30] restores the original gradient expansion, thereby worsening atomization energies (total energy differences), but improving many lattice constants of solids over PBE and LDA.

Fig. 5. We use the same procedure as in Fig. 3 to find the Δc coefficient for the gradient correction to LDA, $E_x^{(2)}[n]$, as defined in eq. [7]. The dashed line was fitted to the noble gas atoms (circle symbols).

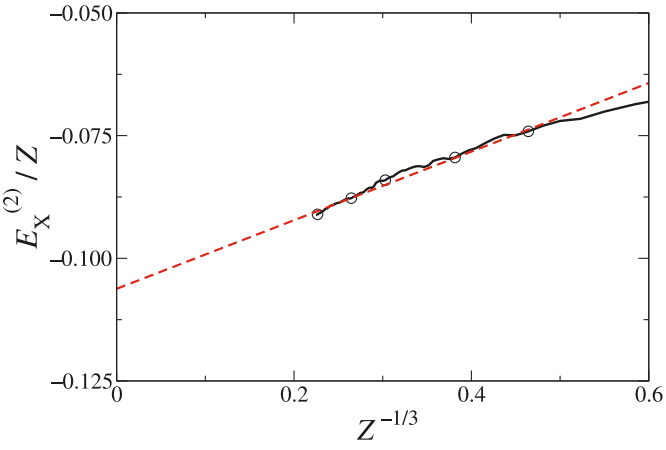

Fig. 6. The percentage error of the approximate asymptotic series given in eq. [13] is plotted as a function of Z. The error is remarkably low and demonstrates the power of these asymptotic series.

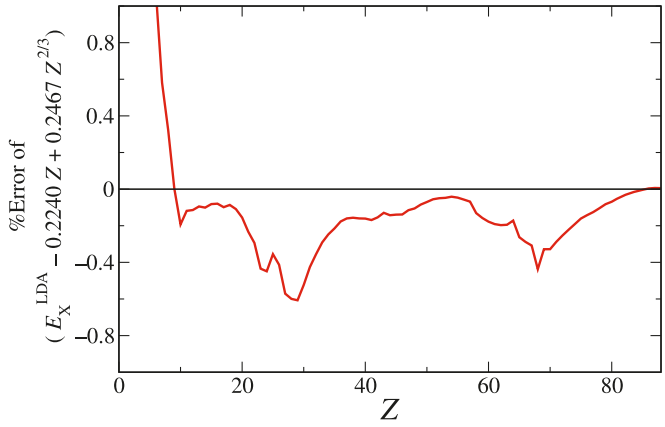

Deriving the β in B88

When designing a good GGA, one first chooses the functional form in terms of the dimensionless gradient s. This is usually based upon satisfying various constraints that the designer feels are important, e.g., reduce to LDA for $s = 0$, give correct asymptotic behavior for large r, prevent divergence for large s, and so forth. This is the most important step, and we do not discuss it in this paper, although work is ongoing in this direction.[16] After picking a functional form, there is usually still some freedom to choose any pa-

Table 1. $\Delta c = c_1 - c_1^{LDA}$ values for several different functionals.

	E_x	LDA	GEA	B88	PBE
Δc	–0.2240	—	–0.1062	–0.2216	–0.1946

Fig. 7. The percentage error for LDA, GEA and the modified GEA (MGEA) exchange functionals for $Z > 10$. The coefficient of $E_X^{(2)}$ is multiplied by 2.109 to make the MGEA AE1 asymptotically exact.

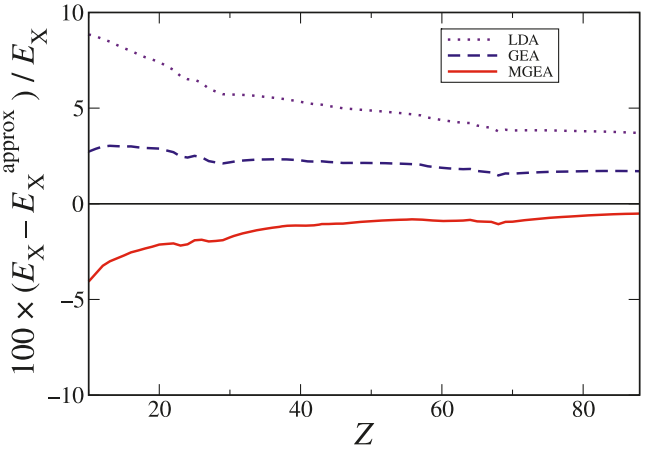

Fig. 8. We add to Fig. 7 the results for B88, PBE, and the excogitated B88 functional, all evaluated on the OEP exact exchange densities.

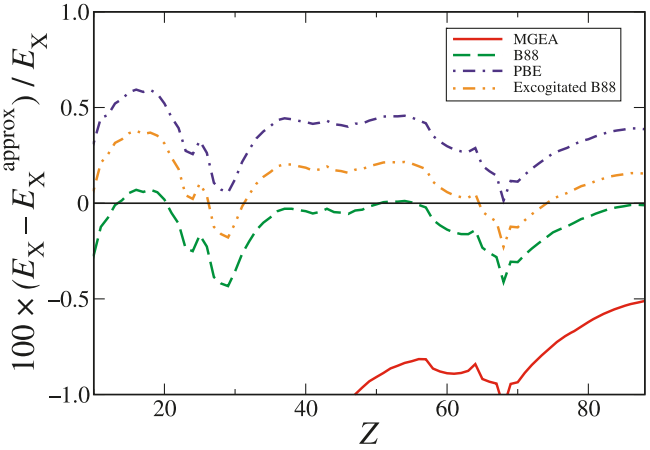

rameters (hopefully a small number) that may be left. These can be fixed by satisfying different exact constraints or by fitting to a set of experimental or computational data. The former is considered more favorable by some,[31] as it makes a functional more trustworthy for application to many different classes of systems, while the latter generally gives better properties for systems close to the fitting set. In the case of B88, we now show that the previously empirical parameter can be derived by requiring the exact condition that it be AE1. This explains why B88 was so successful when applied to different types of system.

The exchange energies found using GGAs such as B88 or PBE are generally dominated by their gradient expansion components for most chemically relevant densities (see Table 2 in ref. 12). Thus, to make B88 AE1, it is sufficient to impose this exact condition on just the $E_x^{(2)}[n]$ functional form. Since both B88 and the GEA are built on top of LDA, we can simply look at the Δc values calculated above. If we set $\mu = 2.109\mu_{AK}$ in eq. [7], we multiply the c_1 coefficient of GEA by a factor of 2.109, making it AE1. In Fig. 7, we name this functional MGEA for modified GEA and plot its percentage errors. The values for LDA and GEA are also shown. It can be seen that modifying GEA to be AE1 has greatly reduced the error.

We now require that the B88 functional form, eq. [10], reduce to this MGEA for small values of x. Using eq. [9], this corresponds to using a value of $\beta = 0.0050$. Thus, we have derived an excogitated B88 that is free of any empirical parameters. The actual value used in B88 is $\beta^{B88} = 0.0053$ (for spin-polarized systems, this becomes 0.0042, which is the value given in ref. 7), so the values are very close. This is not surprising as fitting to Hartree–Fock exchange energies is an approximate way of demanding asymptotic exactness. Interestingly, the value quoted as the high-Z asymptote in ref. 7 and found using ref. 21 is essentially the same as our value, but was evidently rejected in favor of a better fit. In Fig. 8, we plot the percentage errors for B88, PBE, and the excogitated B88. As is typical for empirically fitted functionals, B88 performs very well for systems close to the data set used in the fitted procedure. Although the error for PBE is higher than both B88 and the excogitated B88, it is systematic in its overestimation. As noted, PBE was designed to perform reasonably well for a wide range of systems, so again, its behavior is not surprising. On this data set, the excogitated B88 was never going to do better than B88, although it remains to be seen how it performs for more complicated systems.

VI. Conclusion

We have carefully and systematically extracted the leading large-Z correction to the exchange energy of atoms. Our results differ slightly from those of ref. 12 but yield the same qualitative conclusion, i.e., that the gradient expansion yields an error of a factor of 2 or more for this coefficient. We have clarified some of the reasoning, and applied it more generally to any atom, molecule, or cluster. By looking in detail at the exchange energy asymptotic series for neutral atoms, we have demonstrated the power of using such series for functional development. Requiring that the small gradient expansion of B88 capture the two leading coefficients of the asymptotic expansion is a method by which the unknown coefficient β can be found. This gives a coefficient very close to the one actually used in B88, and thus is an *ex post facto* "derivation" of B88. Inserting our most accurate estimate for β into the B88 form yields an excogitated B88.

Acknowledgements

We thank Eberhard Engel for the use of his atomic OPMKS code, and National Science Foundation (NSF) CHE-0809859.

References

(1) Fiolhais, C.; Nogueira, F.; Marques, M., Eds.; *A Primer in Density Functional Theory;* Springer-Verlag: New York, 2003.

(2) Hohenberg, P.; Kohn, W. *Phys. Rev.* **1964**, *136* (3B), B864–B871. doi:10.1103/PhysRev.136.B864.
(3) Kohn, W.; Sham, L. J. *Phys. Rev.* **1965**, *140* (4A), A1133–A1138. doi:10.1103/PhysRev.140.A1133.
(4) Antoniewicz, P. R.; Kleinman, L. *Phys. Rev. B* **1985**, *31* (10), 6779–6781. doi:10.1103/PhysRevB.31.6779.
(5) Ma, S.-K.; Brueckner, K. A. *Phys. Rev.* **1968**, *165* (1), 18–31. doi:10.1103/PhysRev.165.18.
(6) Rasolt, M.; Geldart, D. J. W. *Phys. Rev. B* **1986**, *34* (2), 1325–1328. doi:10.1103/PhysRevB.34.1325.
(7) Becke, A. D. *Phys. Rev. A* **1988**, *38* (6), 3098–3100. doi:10.1103/PhysRevA.38.3098. PMID:9900728.
(8) Lee, C.; Yang, W.; Parr, R. G. *Phys. Rev. B* **1988**, *37* (2), 785–789. doi:10.1103/PhysRevB.37.785.
(9) Becke, A. D. *J. Chem. Phys.* **1993**, *98* (7), 5648. doi:10.1063/1.464913.
(10) (a) Perdew, J. P.; Burke, K.; Ernzerhof, M. *Phys. Rev. Lett.* **1996**, *77* (18), 3865–3868. doi:10.1103/PhysRevLett.77.3865. PMID:10062328.; (b) Perdew, J. P.; Burke, K.; Ernzerhof, M. *Phys. Rev. Lett.* **1997**, *78* (7), 1396. doi:10.1103/PhysRevLett.78.1396.
(11) (a) Schwinger, J. *Phys. Rev. A* **1980**, *22* (5), 1827–1832. doi:10.1103/PhysRevA.22.1827.; (b) Schwinger, J. *Phys. Rev. A* **1981**, *24* (5), 2353–2361. doi:10.1103/PhysRevA.24.2353.
(12) Perdew, J. P.; Constantin, L. A.; Sagvolden, E.; Burke, K. *Phys. Rev. Lett.* **2006**, *97* (22),o. 223002. doi:10.1103/PhysRevLett.97.223002. PMID:17155798.
(13) Englert, B.-G.; Schwinger, J. *Phys. Rev. A* **1985**, *32* (1), 26–35. doi:10.1103/PhysRevA.32.26. PMID:9896023.
(14) Lieb, E. H. *Rev. Mod. Phys.* **1981**, *53* (4), 603–641. doi:10.1103/RevModPhys.53.603.
(15) Lieb, E. H.; Simon, B. *Phys. Rev. Lett.* **1973**, *31* (11), 681–683. doi:10.1103/PhysRevLett.31.681.
(16) Elliott, P.; Lee, D.; Cangi, A.; Burke, K. *Phys. Rev. Lett.* **2008**, *100* (25),o. 256406. doi:10.1103/PhysRevLett.100.256406. PMID:18643686.
(17) Levy, M.; Perdew, J. P. *Phys. Rev. A* **1985**, *32* (4), 2010–2021. doi:10.1103/PhysRevA.32.2010. PMID:9896312.
(18) Froese-Fischer, C. *The Hartree–Fock method for atoms: A numerical approach;* Wiley: New York, 1977.
(19) Engel, E. *OPMKS, atomic DFT program;* University of Frankfurt: Germany.
(20) Perdew, J. P.; Schmidt, K. In *Density Functional Theory and Its Applications to Materials;* van Doren, V. E., van Alsenoy, K., and Geerlings, P., Eds.; American Institute of Physics: Melville, NY, 2001.
(21) Becke, A. D. *J. Chem. Phys.* **1986**, *84* (8), 4524. doi:10.1063/1.450025.
(22) Bowen, C.; Sugiyama, G.; Alder, B. J. *Phys. Rev. B* **1994**, *50* (20), 14838–14848. doi:10.1103/PhysRevB.50.14838.
(23) Moroni, S.; Ceperley, D. M.; Senatore, G. *Phys. Rev. Lett.* **1995**, *75* (4), 689–692. doi:10.1103/PhysRevLett.75.689. PMID:10060089.
(24) Lieb, E. H.; Oxford, S. *Int. J. Quantum Chem.* **1981**, *19* (3), 427–439. doi:10.1002/qua.560190306.
(25) Murphy, D. R. *Phys. Rev. A* **1981**, *24* (4), 1682–1688. doi:10.1103/PhysRevA.24.1682.
(26) Yan, Z. D.; Perdew, J. P.; Korhonen, T.; Ziesche, P. *Phys. Rev. A* **1997**, *55* (6), 4601–4604. doi:10.1103/PhysRevA.55.4601.
(27) Lee, D.; Constantin, L. A.; Perdew, J. P.; Burke, K. *J. Chem. Phys.* **2009**, *130* (3),o. 034107. doi:10.1063/1.3059783. PMID:19173510.
(28) Perdew, J. P. In *Electronic Structure of Solids '91;* Ziesche, P. and Eschrig, H., Eds.; Akademie Verlag: Berlin, 1991, p. 11.
(29) Burke, K.; Perdew, J. P.; Wang, Y. In *Electronic Density Functional Theory: Recent Progress and New Directions;* Dobson, J. F., Vignale, G., and Das, M. P., Eds.; Plenum, NY, 1998; p. 81.
(30) Perdew, J. P.; Ruzsinszky, A.; Csonka, G. I.; Vydrov, O. A.; Scuseria, G. E.; Constantin, L. A.; Zhou, X.; Burke, K. *Phys. Rev. Lett.* **2008**, *100* (13),o. 136406. doi:10.1103/PhysRevLett.100.136406. PMID:18517979.
(31) Perdew, J. P.; Ruzsinszky, A.; Constantin, L. A.; Sun, J.; Csonka, G. I. *J. Chem. Theory Comput.* **2009**, *5* (4), 902–908. doi:10.1021/ct800531s.

DFT studies of complexes between ethylenediamine tetraacetate and alkali and alkaline earth cations

Melissa Gajewski and Mariusz Klobukowski

Abstract: Density functional theory (DFT) calculations for M–($C_{10}H_{12}N_2O_8^{4-}$) and M–($(H_2O)_6$, where M = Na^+, K^+, Rb^+, Mg^{2+}, Ca^{2+}, and Sr^{2+}, and ($C_{10}H_{12}N_2O_8^{4-}$) = $EDTA^{4-}$, were carried out at both all-electron and pseudopotential levels. Results from these four methods were compared, and it was found that the ions bind to $EDTA^{4-}$ with selectivity of $Mg^{2+} > Ca^{2+} > Sr^{2+} > Na^+ > K^+ > Rb^+$.

Key words: ethylenediamine tetraacetic acid (EDTA), alkali metal ions, alkaline earth metal ions, binding affinity.

Résumé : Faisant appel à la théorie de la fonctionnelle de la densité et opérant aux niveaux de tous les électrons ainsi que du pseudopotentiel, on a effectué des calculs sur les cations M–($C_{10}H_{12}N_2O_8^{4-}$) et M–($(H_2O)_6$ dans lesquels M = Na^+, K^+, Rb^+, Mg^{2+}, Ca^{2+}, et Sr^{2+} et $C_{10}H_{12}N_2O_8^{4-} = EDTA^{4-}$. Les résultats obtenus avec ces méthodes ont été comparés entre eux et on a trouvé que les ions se lient avec $EDTA^{4-}$ avec la sélectivité suivante : $Mg^{2+} > Ca^{2+} > Sr^{2+} > Na^+ > K^+ > Rb^+$.

Mots-clés : acide éthylènediaminetétraacétique, ions de métaux alcalins, ions de métaux alcalinoterreux, affinité de fixation.

[Traduit par la Rédaction]

Introduction

Ethylenediamine tetraacetic acid (H_4EDTA) is a polyprotic acid that has been widely used, together with its associated anion ethylenediamine tetraacetate ($EDTA^{4-}$), since the pioneering work on H_4EDTA was done by Schwarzenbach in the 1940s.[1] One of the most useful properties of $EDTA^{4-}$ is its ability to form exceptionally strong complexes with Mn^{2+}, Cu^{2+}, Fe^{3+}, and Co^{3+};[2] $EDTA^{4-}$ will also form complexes with many other cations. For this reason, $EDTA^{4-}$ can be used in sequestering heavy metal ions, buffering solutions, and many forms of titration.[3] Also, some of the properties of $EDTA^{4-}$ allow it to be used in the pulp and paper industry,[4] and as an industrial cleaner,[2] as a food preservative,[5] as a drug,[6] and as a detergent to complex with Ca^{2+} and Mg^{2+} to reduce the hardness of water.[7]

H_4EDTA is a polyprotic acid with $pK_{a1} = 1.99$, $pK_{a2} = 2.67$, $pK_{a3} = 6.16$, and $pK_{a4} = 10.26$.[8] This can allow for different ion selectivity based on the pH of the solution; one can adjust the pH of the solution and influence the order in which the ions forms complexes with H_nEDTA^{n-4} (n = 0, 1, 2, 3, 4). Crystal structures of $EDTA^{4-}$ complexed with Na^+, Mg^{2+}, and Ca^{2+} are available[9–11] and may be used to compare with calculated geometries.

One computational approach that can be taken to establish the order with which cations bind to $EDTA^{4-}$ is to calculate the energy difference between reactants and products. Based on this energy difference (ΔE_{rxn}), the binding affinities of cations to $EDTA^{4-}$ could be determined by comparing the energy of complexation. Equation [1] illustrates the calculation of ΔE_{rxn}, or the stabilization energy (SE), for cation–$EDTA^{4-}$ and the cation–$(H_2O)_6$ complexes:

$$[1] \qquad \begin{aligned} EDTA^{4-} + M^{n+} &\rightleftharpoons [MEDTA]^{n-4} \\ 6H_2O + M^{n+} &\rightleftharpoons [M(H_2O)_6]^{n+} \end{aligned}$$

where M $\in$ {Na^+, K^+, Rb^+, Mg^{2+}, Ca^{2+}, Sr^{2+}}.

Density functional theory (DFT) calculations that were performed in the present work were carried out for the gas phase; in such a case, eq. [1] introduces errors because solvation effects have not been taken into account. Thompson et. al.[12] and Glendening et. al.[13] suggested that an alternative approach may be used to assess the binding affinity of cations to a ligand in aqueous solution. Their method is shown in eq. [2] and depicted in Fig. 1,

$$[2] \qquad [M_1EDTA]^{n_1-4} + [M_2(H_2O)_6]^{n_2+} \rightleftharpoons [M_2EDTA]^{n_2-4} + [M_1(H_2O)_6]^{n_1+}$$

where $M_1 \neq M_2$, and $M_i \in$ {Na^+, K^+, Rb^+, Mg^{2+}, Ca^{2+}, Sr^{2+}}. This method is based on an exchange reaction of two cations, which are enclosed in six water molecules, and the host ligand, in the present case the $EDTA^{4-}$ anion.

Glendening et al.[13] demonstrated that this approach will mimic some of the solvation effect that influence the binding affinity of cations to ligands. Their work on crown-ether complexes[13] showed that using eq. [2] changed the ordering

Received 19 February 2009. Published on the NRC Research Press Web site at canjchem.nrc.ca on 6 October 2009.

This article is part of a Special Issue dedicated to Professor T. Ziegler.

M. Gajewski and M. Klobukowski.[1] Department of Chemistry, University of Alberta, Edmonton, AB T6G 2G2, Canada.

[1]Corresponding author (e-mail: mariusz.klobukowski@ualberta.ca).

Fig. 1. Pictorial representation of the exchange reaction used to calculate $\Delta\Delta E_{rxn}$.

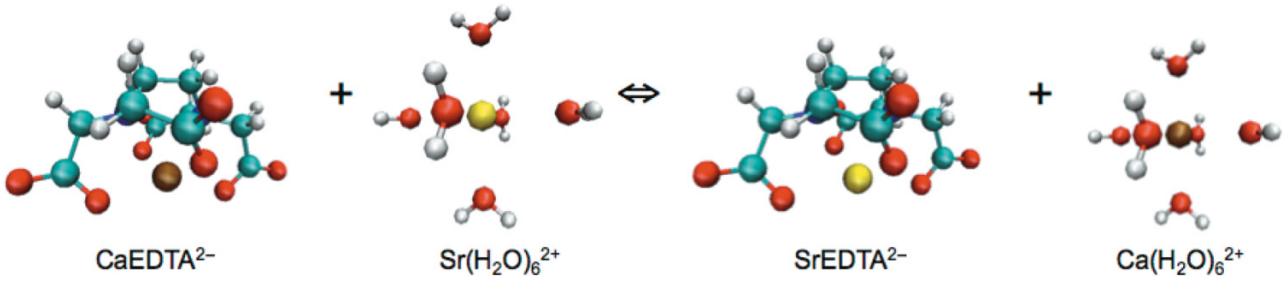

Fig. 2. Structures of water complexes with alkali and alkaline earth cations: S_6 symmetry (left), C_{2v} symmetry (centre), T_h symmetry (right).

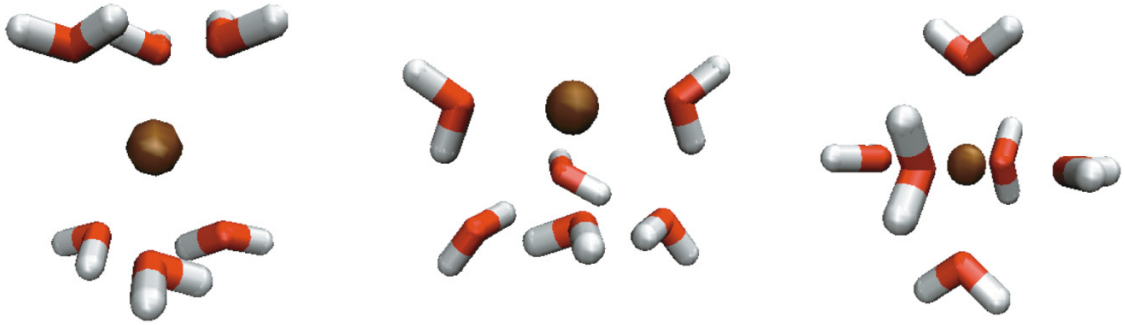

Fig. 3. Structures of free EDTA^{4-} (left) and complexes [Na–EDTA]$^{3-}$ (centre) and [Ca–EDTA]$^{2-}$ (right).

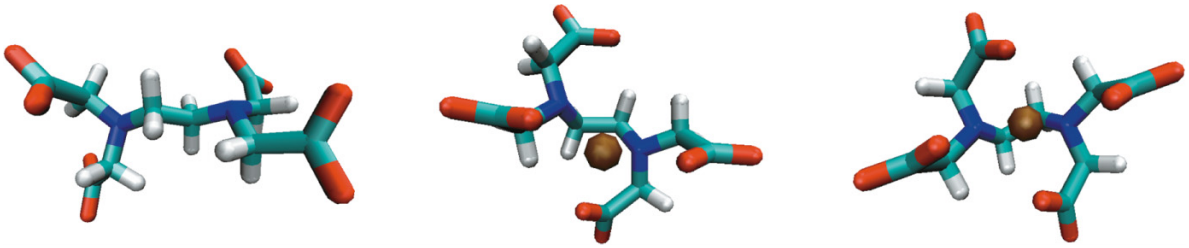

of the gas phase calculations on the binding affinity of cations to 18-crown-6 to match experimental results obtained in aqueous solution. Using eq. [2] may also lead to a reduction in errors which are due to inadequate basis set representation because it may be expected that these errors would be approximately equivalent on both sides of eq. [2]. In the present work, corrections for basis set superposition errors (BSSE) were calculated and it was found that these BSSE corrections were approximately equal for all the cation–EDTA^{4-} complexes. Therefore the BSSE corrections need not be included as they cancel out when using eq. [2]. It is for these reasons that eq. [2] was used to determine the order of selectivity of selected alkali and alkaline earth cations.

Glendening et. al.[14,15] carried out extensive studies to determine the lowest energy structure for different configurations of water clusters with various cations. The different structures of water complexes are shown in Fig. 2. Alkali cations have lower energies for the first two geometries depicted in Fig. 2, with the first structure possessing S_6 symmetry (left image) and the second C_{2v} symmetry (centre image). The results from the calculations show that the energy difference between these two water complex conformations either is negligible or slightly favors the C_{2v} geometry. Therefore the C_{2v} geometry was chosen for all of the alkali cations. Alkaline earth cations all prefer the T_h geometry that is shown in the right image of Fig. 2. As seen in Fig. 2, the lowest energy structures of the alkali cations are very different from the lowest-energy structures of the alkaline earth cations.

The structures of free EDTA^{4-} and the cation–EDTA^{4-} complexes are quite different and are shown in Fig. 3. The free EDTA^{4-} has all four carboxylate groups pointing away from the central N–C–C–N dihedral angle, as shown in the left image of Fig. 3. As the cations are sequestered, three or four oxygen atoms envelope the cation (one oxygen atom from each of the carboxylate groups). The case of three oxygen atoms from three carboxylate groups sequestering a cation is shown in the centre image of Fig. 3 and the case of four oxygen atoms from four carboxylate groups sequestering a cation is shown in the right image of Fig. 3. It is interesting to note that the carboxylate groups do not lose their resonance structure upon complexation with a cation: all of the carbon–oxygen bond lengths are approximately 1.26 ± 0.03 Å in all of the calculated geometries and the crystal structure geometries.[9–11] There is little change (±0.02 Å) in the carbon–oxygen bond lengths between the free EDTA^{4-} and the cation–EDTA^{4-} complex.

Method of calculations

DFT with two different functionals was used to calculate the cation–EDTA^{4-} and the cation–$(H_2O)_6$ complexes. The

DFT calculations in the first set were carried out using Gill 1996 exchange[16] and Perdew 1986 correlation functional[17] (GP86) while in the second set the commonly used B3LYP functional[18,19] was employed. Furthermore, two different methods were used to describe electron distribution: the all-electron (AE) and a pseudopotential method, more specifically the model core potential (MCP). For all the studied systems, geometry optimization was performed, followed by a Hessian calculation and harmonic vibrational analysis. The Hessian calculation was done to ensure that the stationary points found in the geometry optimization were minima rather than saddle points.

For the AE calculations, the following composite basis set was used: 6–31G* basis set on carbon, magnesium, calcium, sodium, potassium;[20,21] 6–31+G* on oxygen, nitrogen, hydrogen;[20,21] and a split-valence all-electron basis set (SVPall) on rubidium and strontium;[22] the SVPall basis is roughly equivalent to 6–31G*.[23] The AE DFT calculations are denoted by B3LYP/AE and GP86/AE.

To reduce computational effort as well as to calibrate the pseudopotential method, the MCP method[24] and basis sets were used in the second set of DFT calculations. The MCP method approximates the core electrons by a potential and explicitly treats only the valence electrons and thus offers an effective manner of reducing the basis set size, leading to reduction of CPU time. The recently prepared MCP-DZP parameters and basis sets[25] were used. The MCP DFT calculations are referred to as B3LYP/MCP and GP86/MCP.

All of the computations for the complexes were done for systems in gas phase. Computer programs GAMESS-US[26] and Gaussian03[27] were used, running concurrently on computer clusters at the University of Alberta. The GP86 DFT functional is implemented equivalently in both GAMESS and Gaussian03 for the AE calculations, which allowed for both GAMESS and Gaussian03 to be used for the AE/GP86 calculations. Visualization of molecular structures, vibrational modes, and molecular orbitals were done using Molden[28] and MacMolPlt.[29]

Results, discussion, and conclusions

The two functionals, GP86 and B3LYP, were employed to ensure that the results were independent of the DFT functional used. In the present calculations, the cations were surrounded by six water molecules to mimic some of the solvent effects[12,14] and reduce the significance of the errors that may be introduced due to inadequate basis set representation.

Glendening et al.,[14] who carried out calculations on the 18-crown-6 molecule and calculated the binding affinities to the alkali cations, showed that by using an equation equivalent to eq. [1] the ordering of binding affinities matched experimental results that were obtained using a kinetics method in a collision-induced dissociation, liquid secondary ion mass spectrometry study of mixed crown ether – alkali halide complexes which was done by Maleknia and Brodbelt.[30] The calculations that best describe this type of experimental measurement are gas phase calculations. The gas phase calculations done by Glendening et al. and the experimental results given by Maleknia et al. both gave the same order of binding affinities for the crown ether – alkali cation complexes.

As mentioned earlier, in order to calculate the binding affinities with some of the solvation effects being represented in the calculations, eq. [2] can be used, as demonstrated by Glendening et al.[14] It is for this reason that eq. [2] was used in the present work to determine the binding affinities that selected alkali and alkaline earth cations have with $EDTA^{4-}$, since $EDTA^{4-}$ is typically used in the aqueous phase. Equations below show how the $\Delta\Delta E$ is derived using the equations for the stabilization energies of individual complexes:

$$[\Delta E_1] \qquad EDTA^{4-} + M_1{}^{n+} \rightleftharpoons [M_1EDTA]^{n-4}$$

$$[\Delta E_2] \qquad EDTA^{4-} + M_2{}^{n+} \rightleftharpoons [M_2EDTA]^{n-4}$$

$$[\Delta E_3] \qquad 6H_2O + M_1{}^{n+} \rightleftharpoons [M_1(H_2O)_6]^{n_2+}$$

$$[\Delta E_4] \qquad 6H_2O + M_2{}^{n+} \rightleftharpoons [M_2(H_2O)_6]^{n_2+}$$

Suitable combination of these equations cancels out $EDTA^{4-}$ and six H_2O molecules, leaving only cation–$EDTA^{4-}$ or cation–$(H_2O)_6$ complexes, with the energy change given by

$$[3] \qquad \Delta\Delta E_{rxn} = (\Delta E_2 + \Delta E_3) - (\Delta E_1 + \Delta E_4)$$

for the reaction

$$[M_1EDTA]^{n_1-4} + [M_2(H_2O)_6]^{n_2+} \rightleftharpoons [M_2EDTA]^{n_2-4} + [M_1(H_2O)_6]^{n_1+}$$

that is equivalent to eq. [2]. Thus, the specific equation that was used to calculate the binding affinities of the cation to $EDTA^{4-}$ is based on eq. [2]:

$$[4] \qquad \Delta\Delta E_{rxn} = \left(E_{[M_2EDTA]^{n_2-4}} + E_{[M_1(H_2O)_6]^{n_1+}}\right) - \left(E_{[M_1EDTA]^{n_1-4}} + E_{[M_2(H_2O)_6]^{n_2+}}\right)$$

A negative value of $\Delta\Delta E$ indicates that M_2 binds with greater affinity to $EDTA^{4-}$ than M_1. The results for the calculated order of selectivity for some of the alkali and alkaline earth cations are summarized in Tables 1 and 2.

The data shown in Tables 1 and 2 show that the relative difference between the $\Delta\Delta E$ for the two different functionals is smaller when using the AE DFT method. More importantly, it is apparent from these tables that the same selectivity of cations to $EDTA^{4-}$ was obtained for all four methods used, B3LYP/AE, GP86/AE, B3LYP/MCP, and GP86/MCP, namely, $Mg^{2+} > Ca^{2+} > Sr^{2+} > Na^{+} > K^{+} > Rb^{+}$, which matches experimental results except for the reverse ordering of Ca^{2+} and Mg^{2+}.[31] To understand this discrepancy, it must be noticed that at the high *p*H required for the existence of $EDTA^{4-}$ in aqueous solution, Mg^{2+} would have precipitated out of solution forming $Mg(OH)_2$. The magnesium cation would more likely bind to $HEDTA^{3-}$ according to the reaction

$$[5] \qquad HEDTA^{3-} + Mg^{2+} \rightleftharpoons Mg[HEDTA]^{-}$$

unlike the calcium cation which reacts with $EDTA^{4-}$ as shown in the generic $EDTA^{4-}$ reaction in eq. [1]. To address the inconsistency in the binding order, the stabilization en-

Table 1. Binding affinity (in kcal/mol) for cation–$EDTA^{4-}$ complexes results from B3LYP/AE calculations (GP86/AE values in parentheses); PCM values in italics.

	M_2					
M_1	Na^+	K^+	Rb^+	Mg^{2+}	Ca^{2+}	Sr^{2+}
Na^+	—	6.8(7.5)	10.6(11.7)	–333.1(–335.3)	–315.1(–315.9)	–301.8(–299.8)
	—	*2.9*	*6.0*	*–63.3*	*–32.1*	*–15.0*
K^+	–6.8(–7.5)	—	3.7(4.2)	–339.9(–342.9)	–322.0(–323.4)	–308.6(–307.3)
	–2.9	—	*3.2*	*–66.1*	*–35.0*	*–17.9*
Rb^+	–10.6(–11.7)	–3.7(–4.2)	—	–343.6(–347.0)	–325.7(–327.6)	–312.3(–311.5)
	–6.0	*–3.2*	—	*–69.3*	*–38.2*	*–21.0*
Mg^{2+}	333.1(335.3)	339.9(342.9)	343.6(347.0)	—	17.9(19.4)	31.3(35.6)
	63.3	*66.1*	*69.3*	—	*31.1*	*48.2*
Ca^{2+}	315.1(315.9)	322.0(323.4)	325.7(327.6)	–17.9(–19.4)	—	13.4(16.1)
	32.1	*35.0*	*38.2*	*–31.1*	—	*17.1*
Sr^{2+}	301.8(299.8)	308.6(307.3)	312.3(311.5)	–31.3(–35.6)	–13.4(–16.1)	—
	15.0	*17.9*	*21.0*	*–48.2*	*–17.1*	—

Table 2. Binding affinity (in kcal/mol) for cation–$EDTA^{4-}$ complexes: results from B3LYP/MCP calculations (GP86/MCP values in parentheses).

	M_2					
M_1	Na^+	K^+	Rb^+	Mg^{2+}	Ca^{2+}	Sr^{2+}
Na^+	—	8.7(11.1)	9.7(17.8)	–340.3(–342.7)	–320.3(–319.9)	–310.2(–306.6)
K^+	–8.7(–11.1)	—	1.0(6.7)	–349.0(–353.8)	–329.0(–331.0)	–318.9(–317.7)
Rb^+	–9.7(–17.8)	–1.0(–6.7)	—	–350.0(–360.5)	–330.0(–337.7)	–319.9(–324.4)
Mg^{2+}	340.3(342.7)	349.0(353.8)	350.0(360.5)	—	20.0(22.9)	30.1(36.1)
Ca^{2+}	320.3(319.9)	329.0(331.0)	330.0(337.7)	–20.0(–22.9)	—	10.1(13.2)
Sr^{2+}	310.2(306.6)	318.9(317.7)	319.9(324.4)	–30.1(–36.1)	–10.1(–13.2)	—

Table 3. Experimental and B3LYP/AE PCM (in parentheses) values of ΔG values for cation-*EDTA*$^{4-}$ complexes (in kcal/mol).

	M_2				
M_1	Na^+	K^+	Mg^{2+}	Ca^{2+}	Sr^{2+}
Na^+	—	1.17(3.83)	–9.72(–6.36)	–12.3(–25.8)	–9.64(–7.06)
K^+	–1.17(–3.83)	—	–10.9(–63.6)	–13.5(–29.6)	–10.8(–10.9)
Mg^{2+}	9.72(6.36)	10.9(63.6)	—	–2.59(3.40)	0.082(52.7)
Ca^{2+}	12.3(25.8)	13.5(29.6)	2.59(–3.40)	—	2.67(18.7)
Sr^{2+}	9.64(7.06)	10.8(10.9)	–0.082(–52.7)	–2.67(–18.7)	—

ergy for the $Mg[HEDTA]^-$ complex in eq. [5] was calculated and compared to the stabilization energy from the $Ca[EDTA]^{2-}$ complex using the B3LYP/MCP method. It was found that the stabilization energy of the calcium–EDTA complex was approximately 18 kcal/mol lower than that of the magnesium–HEDTA complex. It may be assumed that if analogous calculations were performed with the replacement of $EDTA^{4-}$ with $HEDTA^{3-}$, the reversal of the Mg^{2+} and Ca^{2+} binding affinities for the complexes would remain consistent across all of the DFT calculations and a correct matching of calculated binding affinities to experimental results would be obtained.

To assess whether the same trend in the binding affinities would be seen in the presence of implicit solvent, single point calculations were done using the polarizable continuum model (PCM)[32] in GAMESS.[26] The previously described B3LYP/AE DFT method was employed at the geometry optimized in B3LYP/AE calculations. The uncorrected energies from the PCM calculations were corrected using the ZPE (zero-point energy) energy corrections from the B3LYP/AE calculations and the results were analyzed using eq. [4] to determine the binding affinity for the cation–$EDTA^{4-}$ complexes. The same trend, $Mg^{2+} > Ca^{2+} > Sr^{2+} > Na^+ > K^+ > Rb^+$, was observed for the PCM results as for the gas-phase ones. It can be conjectured that, if similar calculations were performed using the other DFT methods described in this paper, the same binding affinity order would be obtained. It should be noted that compared to gas-phase results, all PCM calculations led to more stable, lower energy metal–ligand systems. The alkali cation – $EDTA^{4-}$ complexes are all more stable by approximately 330 kcal/mol, whereas the alkaline earth cation – $EDTA^{4-}$ complexes are all more stable by approximately 190 kcal/mol. A similar trend is seen for the cation–$(H_2O)_6$ complexes with the increase in stability of 60 kcal/mol and 190 kcal/mol for the alkali and alkaline earth cation complexes, respectively.

Table 4. All-electron stabilization energies of $EDTA^{4-}$ and $(H_2O)_6$ complexes (in kcal/mol).

	B3LYP			GP86		
Ion–complex	ΔE_0	ΔZPE	ΔE_{corr}	ΔE_0	ΔZPE	ΔE_{corr}
$[Na(EDTA)]^{3-}$	–333.2	2.4	–330.8	–322.5	2.3	–320.2
$[K(EDTA)]^{3-}$	–305.5	1.9	–303.6	–297.6	1.6	–296.0
$[Rb(EDTA)]^{3-}$	–296.5	1.3	–295.2	–288.7	1.3	–287.4
$[Mg(EDTA)]^{2-}$	–881.4	5.1	–876.3	–866.2	5.2	–861.0
$[Ca(EDTA)]^{2-}$	–786.0	4.1	–781.9	–775.9	4.2	–771.7
$[Sr(EDTA)]^{2-}$	–733.1	3.4	–729.7	–723.0	3.5	–719.5
$[Na(H_2O)_6]^{+}$	–117.0	15.2	–101.8	–94.3	14.7	–79.6
$[K(H_2O)_6]^{+}$	–96.2	14.7	–81.5	–76.9	13.9	–63.0
$[Rb(H_2O)_6]^{+}$	–91.3	14.6	–76.7	–72.5	14.0	–58.5
$[Mg(H_2O)_6]^{2+}$	–329.1	14.9	–314.2	–299.6	14.5	–285.1
$[Ca(H_2O)_6]^{2+}$	–250.5	12.7	–237.8	–227.9	12.7	–215.2
$[Sr(H_2O)_6]^{2+}$	–210.6	11.7	–198.9	–191.0	11.7	–179.3

Table 5. MCP stabilization energies of $EDTA^{4-}$ and $(H_2O)_6$ complexes (in kcal/mol).

	B3LYP			GP86		
Ion–complex	ΔE_0	ΔZPE	ΔE_{corr}	ΔE_0	ΔZPE	ΔE_{corr}
$[Na(EDTA)]^{3-}$	–351.0	2.3	–348.7	–338.1	2.2	–335.9
$[K(EDTA)]^{3-}$	–319.5	1.7	–317.8	–305.2	1.6	–303.6
$[Rb(EDTA)]^{3-}$	–318.8	1.2	–317.6	–293.3	0.9	–292.4
$[Mg(EDTA)]^{2-}$	–913.3	5.2	–908.1	–896.0	5.3	–890.8
$[Ca(EDTA)]^{2-}$	–799.9	4.4	–795.5	–785.7	4.4	–781.3
$[Sr(EDTA)]^{2-}$	–756.0	3.3	–752.7	–738.2	3.3	–734.9
$[Na(H_2O)_6]^{+}$	–123.4	14.3	–109.1	–97.6	13.8	–83.8
$[K(H_2O)_6]^{+}$	–100.8	14.0	–86.8	–75.8	13.3	–62.5
$[Rb(H_2O)_6]^{+}$	–101.3	13.6	–87.7	–71.3	13.2	–58.1
$[Mg(H_2O)_6]^{2+}$	–342.8	14.7	–328.1	–310.2	14.2	–296.0
$[Ca(H_2O)_6]^{2+}$	–248.0	12.4	–235.6	–221.5	12.3	–209.2
$[Sr(H_2O)_6]^{2+}$	–214.1	11.3	–202.8	–187.2	11.1	–176.1

Experimental data for cation–$EDTA^{4-}$ complexes are available for all of the cation–$EDTA^{4-}$ complexes that were studied in this paper except for Rb^+.[31] The experimental results show that on the basis of the logarithms of the stability constants (log K), the binding affinities for the cation–$EDTA^{4-}$ complexes is $Ca^{2+} > Mg^{2+} > Sr^{2+} > Na^+ > K^+$. The log K values are 1.7, 0.8, 8.8, 10.7, and 8.7 for the reaction:

$$EDTA^{4-} + M^{n+} \rightleftharpoons [MEDTA]^{n-4}$$

for Na^+, K^+, Mg^{2+}, Ca^{2+}, and Sr^{2+}, respectively. Using these values of log K, the stability constant for the exchange reaction were calculated using the following equations (in aqueous solution),

$$[K_1] \qquad EDTA^{4-} + M_1{}^{n+} + \rightleftharpoons [M_1EDTA]^{n-4}$$

$$[K_2] \qquad EDTA^{4-} + M_2{}^{n+} \rightleftharpoons [M_2EDTA]^{n-4}$$

$$[K_3] \qquad [M_2EDTA]^{n-4} + M_1{}^{n+} \rightleftharpoons [M_1EDTA]^{n-4} + M_2{}^{n+}$$

where $K_3 = K_1/K_2$. These values of K_3 inserted into the formula for Gibbs free energy, $\Delta G = -RT \ln K$, allowed for the experimental ΔG_{rxn} values to be calculated for the reaction shown in eq. [2], with the exception of Rb^+. These values are summarized in Table 3 along with the values of ΔG obtained from the PCM calculations. The calculated values for ΔG_{rxn} were obtained from the PCM results by using the uncorrected energies ($E_{o(PCM)}$) from the AE B3LYP PCM single-point calculations and adding the thermodynamic Gibbs

Fig. 4. Stabilization energies (in kcal/mol).

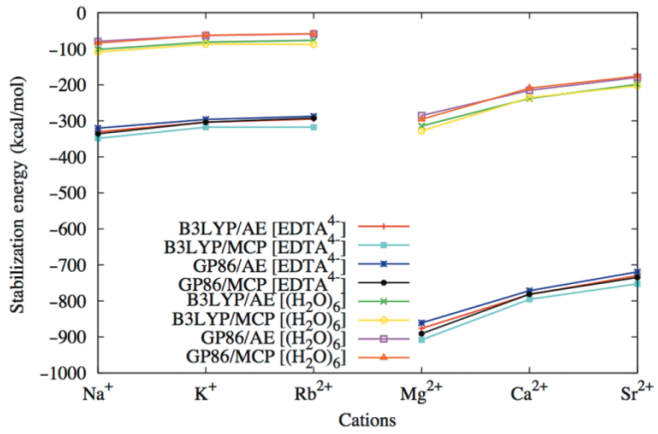

Table 6. Selected bond distances (Å) and C–N–N–C dihedral angle (°) in $EDTA^{4-}$ complexes for AE and MCP basis sets. X-ray experimental results shown in parentheses.

	B3LYP			GP86		
	O–M	N–M	C–N–N–C	O–M	N–M	C–N–N–C
Cation	AE/MCP	AE/MCP	AE/MCP	AE/MCP	AE/MCP	AE/MCP
Na^+	2.373/2.285 (2.464)	2.578/2.612 (2.534)	69.276/68.908 (57.50)	2.428/2.330	2.559/2.575	71.142/70.421
K^+	2.894/2.779	2.791/2.746	72.897/71.357	2.951/2.834	2.772/2.731	75.514/73.578
Rb^+	3.017/2.934	2.909/2.859	76.462/74.262	3.057/3.041	2.883/2.921	78.915/79.055
Mg^{2+}	2.085/2.031 (2.182)	2.318/2.280 (2.396)	59.027/57.736 (57.39)	2.105/2.050	2.301/2.255	59.584/57.977
Ca^{2+}	2.364/2.344 (2.408)	2.559/2.538 (2.67)	63.045/62.115 (57.83)	2.331/2.356	2.536/2.519	63.383/62.683
Sr^{2+}	2.554/2.521	2.727/2.691	66.384/65.054	2.562/2.540	2.700/2.675	67.243/66.046

Table 7. NBA charges on metal cations.

Ligand and method	Cation					
	Na^+	K^+	Rb^+	Mg^{2+}	Ca^{2+}	Sr^{2+}
$EDTA^{4-}$						
B3LYP/AE	0.911	0.928	0.950	1.792	1.851	1.901
GP86/AE	0.918	0.935	0.934	1.778	1.843	1.900
B3LYP/MCP	0.866	0.903	0.873	1.741	1.809	1.816
GP86/MCP	0.872	0.909	0.935	1.723	1.801	1.833
$(H_2O)_6$						
B3LYP/AE	0.958	0.986	0.996	1.826	1.890	1.936
GP86/AE	0.950	0.971	0.989	1.815	1.881	1.933
B3LYP/MCP	0.922	0.964	0.947	1.772	1.867	1.894
GP86/MCP	0.932	0.974	0.988	1.760	1.866	1.916

free energy correction ($G_{corr(GAS)}$) from the Hessian calculations of AE B3LYP.

$$G_{[M_nEDTA]^{n_2-4}} = E_{o(PCM)} + G_{corr(GAS)}$$
$$G_{[M_n(H_2O)_6]^{n_1+}} = E_{o(PCM)} + G_{corr(GAS)}$$

The values of the ΔG_{rxn} that were obtained for the PCM calculations using eq. [6],

$$[6] \qquad \Delta G_{rxn} = \left(G_{[M_2EDTA]^{n_2-4}} + G_{[M_1(H_2O)_6]^{n_1+}}\right) - \left(G_{[M_1EDTA]^{n_1-4}} + G_{[M_2(H_2O)_6]^{n_2+}}\right)$$

are summarized in Table 3. It is apparent from Table 3 that the calculated and experimental trends of ΔG_{rxn} match except for Mg^{2+}. This is again due to the discrepancy between these calculated binding affinities and the experimental binding affinities, i.e., the reversal of the Mg^{2+} and Ca^{2+} ordering, which was discussed earlier.

The ZPE-corrected energies are shown in Tables 4 and 5. In these tables ΔE_0 denotes the stabilization energy, calculated using eq. [1]. The energies were taken at the optimized geometry (minimum, as confirmed by Hessian calculation). ΔZPE is the ZPE correction which, when added to ΔE_0, gives the ZPE-corrected energy ΔE_{corr}. It is interesting to note that the magnitude of the ΔZPE correction is much larger for the water complexes than it is for the $EDTA^{4-}$ complexes. This difference is due to the way ZPE was evaluated: the ZPE correction is calculated by summing over all normal modes (3N-6 for non-linear molecules). In the cation–water complexation reaction, there is an increase of 33 normal modes when going from reactants to products, while there is an increase of only 3 normal modes in the cation–$EDTA^{4-}$ complexation reaction. This 11-fold increase in the number of normal modes between the two different reactions is the reason that the cation–$(H_2O)_6$ complexation reaction has a much greater ΔZPE correction. The ΔZPE is fairly consistent across the two functionals (B3LYP and GP86) and the basis sets (AE and MCP).

The two different DFT functionals (B3LYP and GP86) provide similar results for the AE and MCP calculations. The corrected stabilization energies (ΔE_{corr}) that are shown in Table 4 for B3LYP/AE and GP86/AE and in Table 5 for B3LYP/MCP and GP86/MCP, are summarized in Fig. 4. In addition to revealing that the four methods give the same trend in the corrected stabilization energies, this figure also shows that the MCP calculations for the cation-$(H_2O)_6$ and cation-$EDTA^{4-}$ complexes give a lower stabilization energy.

Selected bond lengths and the C–N–N–C dihedral angle for the optimized structures of ligands and complexes for the four sets of calculations are shown in Table 6. The calculated B3LYP/AE, GP86/AE, B3LYP/MCP, and GP86/MCP geometries exhibit great similarity. The bond lengths and dihedral angles are also given for the crystal structures that were available. However, it is difficult to compare the calculated gas phase structural parameters to the crystal structure data, because in all crystal structures there are other cations, water molecules, or other complexes present. The presence of these extra atoms and molecules as well as the crystal packing effects will affect not only the dihedral angle but also the bond lengths. However, Durand et al.[33] showed in molecular dynamics simulations that the cation–oxygen and cation–nitrogen bond distances are comparable with calculated geometries in the present work. Specifically, Durand et al. found that the cation–oxygen distances are 2.3 Å and 2.5 Å for Ca^{2+} and Sr^{2+}, respectively, and the cation–nitrogen distances are 2.5 Å and 2.6 Å for Ca^{2+} and Sr^{2+}, respectively, which is within 0.1 Å of the calculated values in the present work, which are shown in Table 6.

The natural bond orbital analysis (NBO)[34,35] was carried out for both cation–$(H_2O)_6$ and cation–$EDTA^{4-}$ complexes, and the obtained atomic charges are summarized in Table 7. It may be noticed that cationic charge was reduced by approximately 10% for all cations in both cation–$(H_2O)_6$ and cation–$EDTA^{4-}$ complexes. This indicates that there is little transfer of charge between the ligand and the cation and thus the bonding is mainly electrostatic.

Acknowledgments

This research was funded in part by Natural Sciences and Engineering Research Council (NSERC) research grant to MK. Results presented in this work were obtained using computing resources of the Department of Academic Information and Communication Technologies of University of Alberta as well as two Beowulf clusters maintained by the Department of Chemistry, University of Alberta.

References

(1) Wheelwright, E. J.; Spedding, F. H.; Schwarzenbach, G. *J. Am. Chem. Soc.* **1953**, *75* (17), 4196–4201. doi:10.1021/ja01113a020.
(2) Chalmers, L. *Manuf. Chem. Aerosol News* **1978**, *49* (3), 79.
(3) Flaschka, H. A. *EDTA titrations: An Introduction to Theory and Practice*; Pergamon Press: New York, 2nd ed.,1964.
(4) Yang, Z.; D'Entremont, M.; Ni, Y.; Heiningen, A. R. P. *Pulp. Pap. Can.* **1997**, *11*, T408.
(5) Whalley, G. *Manufacturing Chemist* **1991**, *62* (9), 22.
(6) *A Textbook on EDTA Chelation Therapy; Cranton, E. M., Ed.;*.Hampton Roads Publishing Company: Charlottesville, VA, 2nd ed., 2001.
(7) Verissimo, M.; Oliveira, J.; Gomes, M. *Sens. Actuators* **2007**, *127* (1), 102–106. doi:10.1016/j.snb.2007.07.006.
(8) *Handbook of Organic Analytical Reagents*; Cheng, K. L., Ueno, K., Imamura, T., Eds;. CRC Press Inc., 1982.
(9) Font-Bardia, M.; Solans, X.; Font-Altaba, M. *Acta Crystallogr.* **1993**, *C49*, 1452. doi:10.1107/S0108270193001350.
(10) Passer, E.; White, J.; Cheng, K. *Inorg. Chim. Acta* **1977**, *24* (2), 13–23. doi:10.1016/S0020-1693(00)93844-1.
(11) Barnett, B.; Uchtman, V. *Inorg. Chem.* **1979**, *18* (10), 2674–2678. doi:10.1021/ic50200a007.
(12) Thompson, M. A.; Glendening, E. D.; Feller, D. *J. Phys. Chem.* **1994**, *98* (41), 10465–10476. doi:10.1021/j100092a015.
(13) Glendening, E. D.; Feller, D.; Thompson, M. A. *J. Am. Chem. Soc.* **1994**, *116* (23), 10657–10669. doi:10.1021/ja00102a035.
(14) Glendening, E.; Feller, D. *J. Phys. Chem.* **1996**, *100* (12), 4790–4797. doi:10.1021/jp952546r.
(15) Glendening, E. D.; Feller, D. *J. Phys. Chem.* **1995**, *99* (10), 3060–3067. doi:10.1021/j100010a015.
(16) Gill, P. M. W. *Mol. Phys.* **1996**, *89* (2), 433–445. doi:10.1080/002689796173813.
(17) Perdew, J. P. *Phys. Rev. B* **1986**, *33* (12), 8822–8824. doi:10.1103/PhysRevB.33.8822.
(18) Becke, A. *J. Chem. Phys.* **1993**, *98* (7), 5648. doi:10.1063/1.464913.
(19) Lee, C.; Yang, W.; Parr, R. *Phys. Rev. B* **1988**, *37*, 785. doi:10.1103/PhysRevB.37.785.
(20) Feller, D. *J. Comput. Chem.* **1996**, *17*, 1571. doi:10.1002/jcc.9.
(21) Schuchardt, K.; Didier, B.; Elsethagen, T.; Sun, L.; Gurumoorthi, V.; Chase, J.; Li, J.; Windus, T. *J. Chem. Inf. Model.* **2007**, *47* (3), 1045–1052. doi:10.1021/ci600510j.
(22) Ahlrichs, R.; May, K. *Phys. Chem. Chem. Phys.* **2000**, *2* (5), 943–945. doi:10.1039/a908859h.
(23) Ahlrichs, R.; Armbruster, M. K.; Bär, M.; Baron, H.-P.; Bauernschmitt, R.; Böcker, S.; Crawford, N.; Deglmann, P.; Ehrig, M., et al. Turbomole version 5.10. Available from http://www.cosmologic.de/data/DOK.pdf (accessed 15 September 2009).
(24) Klobukowski, M.; Sakai, M.; Huzinaga, S. In *Computational Chemistry: Reviews of Current Trends*; Leszczynski, J., Ed.;.World Scientific: Singapore, 1999; Vol. 3.
(25) Miyoshi, E.; Mori, H.; Hirayama, R.; Osanai, Y.; Noro, T.; Hondo, H.; Klobukowski, M. *J. Chem. Phys.* **2005**, *122* (7), 074104. doi:10.1063/1.1845392.
(26) Schmidt, M.; Baldridge, K.; Boatz, J.; Elbert, S.; Gordon, M.; Jensen, J.; Koseki, S.; Matsunaga, N.; Nguyen, K.; Su, S.; Windus, T.; Dupuis, M.; Mongomery, J. *J. Comput. Chem.* **1993**, *14* (11), 1347–1363. doi:10.1002/jcc.540141112.
(27) Frisch, M. J.; Trucks, G. W.; Schlegel, H. B.; Scuseria, G. E.; Robb, M. A.; Cheeseman, J. R.; Montgomery, J. A., Jr.; Vreven, T.; Kudin, K. N.; Burant, J. C.; Millam, J. M.; Iyengar, S. S.; Tomasi, J.; Barone, V.; Mennucci, B.; Cossi, M.; Scalmani, G.; Rega, N.; Petersson, G. A.; Nakatsuji, H.; Hada, M.; Ehara, M.; Toyota, K.; Fukuda, R.; Hasegawa, J.; Ishida, M.; Nakajima, T.; Honda, Y.; Kitao, O.; Nakai, H.; Klene, M.; Li, X.; Knox, J. E.; Hratchian, H. P.; Cross, J. B.; Bakken, V.; Adamo, C.; Jaramillo, J.; Gomperts, R.; Stratmann, R. E.; Yazyev, O.; Austin, A. J.; Cammi, R.; Pomelli, C.; Ochterski, J. W.; Ayala, P. Y.; Morokuma, K.; Voth, G. A.; Salvador, P.; Dannenberg, J. J.; Zakrzewski, V. G.; Dapprich, S.; Daniels, A. D.; Strain, M. C.; Farkas, O.; Malick, D. K.; Rabuck, A. D.; Raghavachari, K.; Foresman, J. B.; Ortiz, J. V.; Cui, Q.; Baboul, A. G.; Clifford, S.; Cioslowski, J.; Stefanov, B. B.; Liu, G.; Liashenko, A.; Piskorz, P.; Komaromi, I.; Martin, R. L.; Fox, D. J.; Keith, T.; Al-Laham, M. A.; Peng, C. Y.; Nanayakkara, A.; Challacombe, M.; Gill, P. M. W.; Johnson, B.; Chen, W.; Wong, M. W.; Gonzalez, C.; Pople, J. A. *Gaussian 03*, revision c.02; Wallingford: CT, 2004.
(28) Schaftenaar, G.; Noordik, J. H. *J. Comput. Aided Mol. Des.* **2000**, *14* (2), 123–134. doi:10.1023/A:1008193805436. PMID:10721501.
(29) Bode, B. M.; Gordon, M. S. *J. Mol. Graph. Model.* **1998**, *16* (3), 133–138, 164. doi:10.1016/S1093-3263(99)00002-9. PMID:10434252.
(30) Maleknia, S.; Brodbelt, J. *J. Am. Chem. Soc.* **1992**, *114* (11), 4295–4298. doi:10.1021/ja00037a038.
(31) *Critical Stability Constants*; Martell, A. E., Smith, R. M., Eds.; Plenum Press: New York, London, 1974; Vol. 1.
(32) Miertus, S.; Scrocco, E.; Tomasi, J. *Chem. Phys.* **1981**, *55* (1), 117–129. doi:10.1016/0301-0104(81)85090-2.
(33) Durand, S.; Dognon, J.-P.; Guilbaud, P.; Rabbe, C.; Wipff, G. *J. Chem. Soc., Perkin Trans. 2* **2000**, *2*, 705. doi:10.1039/a908879b.
(34) Foster, J. P.; Weinhold, F. *J. Am. Chem. Soc.* **1980**, *102* (24), 7211–7218. doi:10.1021/ja00544a007.
(35) Reed, A. E.; Curtiss, L. A.; Weinhold, F. *Chem. Rev.* **1988**, *88* (6), 899–926. doi:10.1021/cr00088a005.

Explorations of many-body relativistic wave equations within a one-dimensional model

Marcel Nooijen

Abstract: A one-dimensional analog that reflects many of the features of the many-body Dirac equation is considered. The model can be solved numerically using a convenient finite basis discrete variable representation. Both an (unbound) harmonic oscillator potential and a (bound) inverse Gaussian one-particle potential are discussed for interacting particles. In a second thread in the paper, the mass term is neglected in the model many-body Dirac equation, and it is shown that the original equation, which has 2^N coupled components for N particles can then be reduced to 2^N decoupled one-component equations, which can be solved "analytically" for arbitrary many particles interacting through central two-body potentials.

Key words: many-body, Dirac equation, relativity, one-dimensional model, exact solutions, massless neutrino.

Résumé : On étudie un analogue unidimensionnel de l'équation de Dirac à plusieurs composants qui est un reflet de plusieurs caractéristiques de cette équation. Le modèle peut être résolu numériquement en utilisant une représentation variable commode avec base finie individuelle. Pour les particules qui interagissent, on discute d'un potentiel d'oscillateur harmonique non lié ainsi que d'un potentiel gaussien inverse et non lié à une particule. Dans la seconde partie de ce travail, on néglige le terme de masse dans le modèle de l'équation de Dirac à plusieurs composants et on montre que l'équation originale qui comporte 2^N composants couplés pour N particules peut être réduite à 2^N équations découplées à un composant et qu'elle peut être résolue d'une façon analytique pour plusieurs particules arbitraires interagissant par le biais de potentiels à deux composants centraux.

Mots-clés : plusieurs composants, équation de Dirac, relativité, modèle unidimensionnel, solutions exactes, neutrino sans masse.

[Traduit par la Rédaction]

I. Introduction

The Dirac equation[1] is the basis for relativistic quantum chemistry, and results from accurate computations based on the Dirac equation in general agree well with experiment, e.g., refs. 2 and 3. However, there are significant difficulties with the theoretical framework.[4–11] In particular, the many-body Dirac–Coulomb equation is not Lorentz-covariant,[5] while in addition, the no-pair approximation[6–8] is typically invoked to obtain a discrete low-energy spectrum[4] for many-body problems. Some of these fundamental difficulties disappear if the techniques of quantum field theory, e.g., ref. 12, are invoked, but in practice, bound-state quantum field theoretical calculations, e.g., refs. 13–15, are cumbersome, and there are few prospects that methods rooted in such methodologies can become routinely applicable. Even within a quantum field theoretical conception, it is not entirely clear if Lorentz covariance can be strictly maintained.[16,17]

To discuss the difficulties with solving the Dirac equation for many-particle systems, let us first recall the standard no-pair Dirac–Coulomb procedure, e.g., ref. 7. The first step consists of solving the four-component Dirac–Fock one-particle problem, in which the Dirac–Fock operator is given by

$$[1] \qquad \widehat{f} = \begin{pmatrix} (\widehat{U} + mc^2)\mathbf{1}_2 & c\sigma \cdot \mathbf{p} \\ c\sigma \cdot \mathbf{p} & (\widehat{U} - mc^2)\mathbf{1}_2 \end{pmatrix}$$

in which each entry in $\widehat{f}$ is a 2×2 matrix operator, in particular σ_i, $i = x, y, z$ denote the Pauli spin matrices. The effective potential operator $\hat{U}$ contains a nuclear attraction Coulomb potential $\widehat{V}_{\mathrm{Ne}}$ in addition to a mean field Coulomb-exchange repulsion, which is calculated self-consistently. To define the no-pair many-body problem, the one-particle Dirac–Fock equation is solved and the many-particle no-pair Dirac–Hamiltonian operator is expressed in second quantization, where only matrix elements over positive energy orbitals are included, i.e.,

Received 13 December 2008. Accepted 10 June 2009. Published on the NRC Research Press Web site at canjchem.nrc.ca on 7 October 2009.

This article is part of a Special Issue dedicated to Professor T. Ziegler. It is my pleasure to contribute this paper to the Festschrift honoring Tom Ziegler. Over the years, I have enjoyed many discussions with Tom ever since he spent a sabbatical year in Amsterdam in the mid 1980s, when I was a starting graduate student. I have always felt it was easy to discuss things with Tom, even as the volume might rise during our (sometimes) passionate arguments, as it was always clear this did not affect feelings of mutual appreciation and respect. For some reason, many of our discussions have touched upon fundamental aspects of our science, and the topic of this paper reflects this common interest.

M. Nooijen. Department of Chemistry, University of Waterloo, Waterloo, ON, Canada. (e-mail: nooijen@scienide.uwaterloo.ca).

$$[2] \qquad \hat{H} = \sum_{i,j} \langle i|\hat{f} + \hat{V}_{\mathrm{Ne}} - \hat{U}|j\rangle \hat{a}_i^{\dagger}\hat{a}_{\mathrm{j}} + \frac{1}{4}\sum_{i,j,k,l} \langle ij|\frac{1}{r_{12}}|kl\rangle \hat{a}_i^{\dagger}\hat{a}_j^{\dagger}\hat{a}_l\hat{a}_k$$

This Hamiltonian is mathematically similar to the usual non-relativistic Hamiltonian, and can be solved using more or less conventional techniques. The main issue is the different spin-symmetry, as the Hamiltonian explicitly includes spin-orbit coupling, while in addition, the matrix elements are complex. The Coulomb–Breit interaction, e.g., ref. 18, is sometimes used rather than the Coulomb interaction to include additional relativistic effects. However, irrespective of the potential used, the resulting approach is not Lorentz covariant. Moreover, the projection on positive energy solutions is not unique. In principle, one could use different potentials in the one-particle Dirac–Fock operator, e.g., including electron-correlation using a DFT approach, or solving the one-particle problem for inividual atoms first and using the positive energy solutions to create a molecular Hamiltonian, as advocated by Liu et al.[19,20] It hence transpires that the no-pair Dirac–Coulomb problem has some intrinsic arbitrariness, and it is disconcerting that the most accurate, still practical, formulation in relativistic quantum chemistry is not rigorously defined. Other groups, e.g., refs. 9, 10, argue that the no-pair approximation is not needed, but then the (low-energy) spectrum for a many-body system will consist of discrete energies embedded in a continuum. The physical meaning of this continuum is not clear, in particular one might ask if this continuum should then be included in the calculation of properties using statistical mechanics.

This paper is just a small step in a wider ranging investigation, and it may be good to try to put it in perspective. On the long term, we are pursuing a strictly Lorentz-covariant many-body quantum mechanics in which each particle would be described by four spacetime coordinates and the many-body wave function in addition depends on a universal time-evolution parameter denoted u. In prior work, a suitable Lorentz-covariant framework is developed for a many-body classical relativistic mechanics, in which each particle is described by its own spacetime coordinates,[21–24] and which appears to be a suitable candidate for quantization.[25–30] Not surprisingly, interpretation is easier for quantities defined in a computer simulation than interpreting, e.g., spacetime coordinates and a universal time in the real world. Partly for this reason, we have become interested in what we call "physics for a computable universe".[23] This also might become the basis for simulations of a virtual reality, and the requirements are primarily ease of computation and a semblance of the (perhaps very complicated) computed virtual reality with real world phenomena. To illustrate further what I have in mind, the "physics for a computable universe" might be the theoretical foundation for sophisticated 3D computer games. Obviously, there is no reason to insist on quantitative agreement with real world phenomena, but efficient computation would have very high priority. In the context of this paper, an intriguing possibility arises because momentum occurs linearly in the Dirac equation, and for this reason, it may be possible to find exact analytical solutions to the many-body problem, at least after some modification of the equation. Even if such an exactly solvable wave equation does not describe physical reality, it may provide new insights, for example, regarding the somewhat troublesome relation between quantum mechanics and statistical mechanics, and it might be useful in simulations of virtual reality, or perhaps even in classical renditions of a quantum computer. On the one hand, this type of consideration entails the danger of taking us far a field. On the other hand, this point of view allows us to explore possibilities freely, constrained by the requirement of mathematical consistency, but less by the harness of physical reality. Of course, there is always the (perhaps remote) possibility that we might arrive at an improved description of physical reality that avoids the mathematical problems of the many-particle Dirac equation.

To make some progress and to guide the thoughts, I will analyze here a simple model for a many-particle wave equation in one spatial dimension. In Section II, the model is described in detail, as well as the techniques used to find solutions to the many-body problem. In Section III, numerical solutions are presented for a small number of selected model Hamiltonians. In particular, it will be shown that numerically stable solutions exist that correspond to positive energy components, but in case of the many-body problem, these stable solutions are embedded in what is likely a continuum of solutions. There is substantial literature on the treatment of relativistic Dirac-like problems in one dimension, e.g., refs. 31–34. Our results, obtained for both a harmonic oscillator and an inverted Gaussian potential, confirm the phenomena reported in the literature, and qualitatively agree with results for the two-body Dirac–Coulomb problem, see e.g., ref. 11. I will not attempt to be complete or systematic in the simulations, but merely discuss selected examples. Neither is a more sophisticated mathematical analysis pursued, e.g., based on complex scaling to investigate the precise nature of the continuum, see e.g., ref. 11. The model captures the somewhat strange features of the many-body Dirac equation (if the no-pair approximation is *not* invoked), and in this respect, the model serves its purpose. The simplicity of the model allows easy access, I think, to understanding these issues.

When I started this investigation, the idea was to use the computer program to investigate whether solutions to the many-particle Dirac equation could be constructed directly from numerical solutions to the two-body problem. This amounted to a construction of exact many-body wave functions from two-body geminals, which superficially seemed possible due to the occurrence of linear momentum in the Dirac Hamiltonian. On closer examination, the many-component form of the Dirac solution poses a problem, and the original purpose of the program was to understand this aspect better by pursuing numerical simulations. While the idea of using geminals for this purpose did not come to fruition, pondering the problem led me into another direction, towards a quest for an exactly solvable quantum many-body problem. This is discussed in Section IV where we switch gears and discuss a modification of the 1D problem that allows an analytical solution for the eigenfunctions of the many-body problem for arbitrarily many interacting particles, for essentially arbitrary two-body central potentials in one dimension. The spectrum of solutions is found to be

continuous, and the linearity of the momentum operator is crucial. However, let me mention immediately here that the modification is not innocent, and the physical relevance of the resulting equation is not at all clear. Nonetheless, future work is planned to find suitable generalizations to design a solvable many-body relativistic wave equation in three and possibly four (spacetime) dimensions. While it is doubtful perhaps that such equations would have an immediate relevance to problems in chemistry, they may have applications in other fields like mathematics or computer science, and they may potentially serve as a starting point for creating the physics underlying a virtual reality that can be rapidly computed and trivially propagated in time. At this point in time, we can only speculate.

II. Description of the one-dimensional model

The basic model contains a one-particle Hamiltonian

$$[3]\qquad \widehat{h} = \begin{pmatrix} U(x)+mc^2 & -ic\widehat{p} \\ ic\widehat{p} & U(x)-mc^2 \end{pmatrix} = \begin{pmatrix} U(x)+mc^2 & -c\dfrac{\mathrm{d}}{\mathrm{d}x} \\ c\dfrac{\mathrm{d}}{\mathrm{d}x} & U(x)-mc^2 \end{pmatrix}$$

in which the choice is made to use

$$[4]\qquad \sigma_y\widehat{p} = \begin{pmatrix} 0 & -i \\ i & 0 \end{pmatrix}\left(-i\frac{\mathrm{d}}{\mathrm{d}x}\right) = \begin{pmatrix} 0 & -\dfrac{\mathrm{d}}{\mathrm{d}x} \\ \dfrac{\mathrm{d}}{\mathrm{d}x} & 0 \end{pmatrix}$$

to represent the kinetic energy operator. Alternatively, one could use $\sigma_x\widehat{p}$ leading to identical energy spectra, but the actual operator, using σ_y has the advantage that all matrix elements are real. For the one-particle potential operator, we choose a harmonic potential $U(x) = \frac{1}{2}x^2$, although later on, an inverted Gaussian potential will be considered also. To describe the many-particle system, a repulsive two-particle interaction is introduced of the form $G(x_{12}) = qe^{-\mu(x_1-x_2)^2}$, in which q and μ are parameters, which we take to be q = 0.1and μ = 1.0. This potential has the advantage that it provides a smooth interaction without singularities and is easy to use in our employed numerical procedure, discussed next.

To numerically diagonalize the resulting one- or many-body Hamiltonian, a non-relativistic harmonic oscillator basis is used in a discrete variable representation (DVR), e.g., ref. 35. Specifically, the momentum operator and position operator can be expressed in second quantization

$$[5]\qquad \begin{aligned} \widehat{x} &= \frac{1}{\sqrt{2}}(\widehat{a}^\dagger + \widehat{a}) \\ -i\widehat{p} &= \frac{1}{\sqrt{2}}(\widehat{a}^\dagger - \widehat{a}) \end{aligned}$$

such that matrix elements over these operators are easily evaluated over the basis

$$[6]\qquad |n\rangle = \frac{1}{\sqrt{n!}}(a^\dagger)^n|0\rangle$$

The orthonormal DVR basis is defined by diagonalizing the operator $\widehat{x}$ in a finite Harmonic oscillator basis of dimension M (maximum degree M – 1). This provides the DVR basis $|\lambda_i\rangle$, which satisfies

$$[7]\qquad \begin{aligned} \langle\lambda_i|\widehat{x}|\lambda_j\rangle &= \lambda_j\delta_{ij} \\ \langle\lambda_i|\widehat{U}|\lambda_j\rangle &= U(\lambda_j)\delta_{ij} \end{aligned}$$

for any one-particle potential $U(x)$. Hence, the DVR basis allows us to conveniently evaluate matrix elements of arbitrary potentials. Even more conveniently, the evaluation of two-particle matrix elements is straightforward, and importantly, the two-particle integrals are diagonal in the DVR basis:

$$[8]\qquad \begin{aligned} \langle\lambda_k\lambda_l|\mathrm{G}(\mathrm{x}_{12})|\lambda_\mathrm{i}\lambda_\mathrm{j}\rangle &= G(|\lambda_\mathrm{i}-\lambda_\mathrm{j}|)\delta_{ik}\delta_{jl} \\ &= \delta_{ik}\delta_{jl}q\mathrm{e}^{-\mu(\lambda_i-\lambda_j)^2} \end{aligned}$$

The numerical diagonalization procedure converges smoothly with the size M of the one-particle basis set, provided fairly smooth potentials are chosen, such that the integrations are accurate using the DVR "grid" points λ_i. The described procedure is not accurate for rapidly varying potentials, e.g., of the Coulombic type. In that case, one would need to explicitly evaluate the Coulombic two-particle integrals analytically, and this would destroy the sparsity of the integrals. For this reason, we simplify things and use the Gaussian repulsion potential. The DVR procedure was tested first for non-relativistic problems in which there is no issue with continuum states. In that case, the operator $\widehat{p}^2 = -\frac{\mathrm{d}^2}{\mathrm{d}x^2}$ is required also. The exact harmonic oscillator energies $(n+\frac{1}{2})\omega$ are obtained in the non-relativistic DVR calculation, provided that the matrix elements of $\widehat{p}^2$ are obtained from a resolution of the identity $\langle n|\widehat{p}^2|m\rangle \approx -\sum_{k=0}^{M-1}\langle n|\frac{\mathrm{d}}{\mathrm{d}x}|k\rangle\langle k|\frac{\mathrm{d}}{\mathrm{d}x}|m\rangle$.

For a relativistic one-particle system, one would need to diagonalize a matrix of dimension $2M$, if we assume equal basis set dimensions for the two components of the wave function. In electronic structure calculations, one often invokes kinetic balance for the basis set. In the present case, this would mean that one uses one more basis function for the second component. For the current model, this does not seem very important (judging from our simulations), and we restrict ourselves here to discussing results using equal basis expansions for the first and second components.

For a two-particle system, a multi-component product basis of the form $|\lambda_i, \lambda_j, a\rangle$ is used in which the index a, a = $\{(s_1,s_2)\}$ = {(1,1), (1,2), (2,1), (2,2)}, refers to one of the possible four components of the two-body wave function. The two-body Hamiltonian can be represented as

$$[9]\qquad \widehat{H}_2 = \begin{pmatrix} V+2mc^2 & -ic\widehat{p}_2 & -ic\widehat{p}_1 & 0 \\ ic\widehat{p}_2 & V & 0 & -ic\widehat{p}_1 \\ ic\widehat{p}_1 & 0 & V & -ic\widehat{p}_2 \\ 0 & ic\widehat{p}_1 & ic\widehat{p}_2 & V-2mc^2 \end{pmatrix}$$

The momentum operators are assigned based on the component labels (s_1,s_2) of the columns and row in the matrix. The mass term only enters on the diagonal and is the sum

of $\pm mc^2$ contributions for each particle. The plus sign applies for the first component, and the minus sign for the second component. The second and third diagonal elements hence have no mass dependence as they consist of mixed entries, and the sum of the mass terms vanishes for the two-body hamiltonian. The total potential V for two particles is given by

$$[10] \qquad V = U(x_1) + U(x_2) + G(x_{12})$$
$$\langle \lambda_k \lambda_l b|V|\lambda_i \lambda_j a\rangle = \delta_{ab}\delta_{ij}\delta_{kl}(U(\lambda_i) + U(\lambda_j) + G(|\lambda_i - \lambda_j|)$$

and is completely diagonal due to the choice of DVR basis. The momentum operators are also readily evaluated, e.g.,

$$[11] \qquad \langle \lambda_k \lambda_l 1| - ic\hat{p}_2|\lambda_i \lambda_j 2\rangle = -c\delta_{ik}\left\langle \lambda_l \left| \frac{\mathrm{d}}{\mathrm{d}x} \right| \lambda_j \right\rangle$$

The structure of the Hamiltonian is quite similar to a vibronic Hamiltonian, in which the various components are analogous to electronic states, while the one-particle basis states are analogous to quanta along the vibrational normal modes. We use a Davidson type of diagonalization procedure to obtain eigenstates of the many-particle Hamiltonian, and we built the current relativistic code from modified subroutines in VIBRON, our Waterloo package for vibronic simulations.[36] The procedure of multiplying H by an arbitrary vector was checked against explicit construction of one- and two-particle Hamiltonians. It is easily seen that using M basis functions for n particles, the full dimension of the diagonalization problem is $2Mn$. To reach convergence, a typical size of the one-particle basis set is around 20. Hence, for two-particle problems, 1600 basis functions would be used; for three particles, one would already require 64 000 many-body basis functions; and for four particles, 2 560 000. It is readily seen that the dimension of the problem grows very rapidly, and even for this simple one-dimensional problem, a direct diagonalization technique is required beyond two-particle problems. The direct diagonalization procedure used here has some special features to calculate high lying (i.e., positive energy) states, which may be embedded in a continuum. In particular, after some initial iterations using the shifted Hamiltonian ($H - n\ mc^2$), (for n particles), which allows us to converge the energy to, say, 10^{-3}, we switch to diagonalizing the operator $(H - n\ mc^2)^2$, (applying the finite basis operator twice), and calculate the final energy as the square root of the eigenvalue from this operator. The squared operator has the advantage that the sought for eigenvalues are the lowest eigenvalues of the operator, and the energies satisfy a variational lower bound. As a result, the energies in the direct diagonalization procedure steadily decrease, and this improves the convergence behavior. In addition, we do not use an energy denominator to find the next iteration vector, which would be usual in the Davidson procedure used in electronic structure theory. The relativistic many-body problem may require a large number of iterations (in the order of 100s for difficult cases), which is in stark contrast to the non-relativistic case, for which the analogous many-body problem is solved using typically 10s of iterations. This reflects the additional complication of the presence of close-lying pseudo-continuum states. Two types of solutions to the many-body problem are considered. In what I refer to as the fermion problem, the wave function is taken to by fully antisymmetric upon permutation of one-particle basis states, while in the boson problem the states are fully symmetric. In three dimensions, the Dirac equation describes spin-1/2 particles, which is reflected by the full angular momentum symmetry, which has both orbital and spin contributions. For spin-0 particles, the Klein–Gordon equation would be appropriate, e.g., ref. 12. This, however, does not imply by itself that many-body wave functions describing spin-1/2 particles are antisymmetric. The notion of fermions and bosons refers to statistics, or equivalently the symmetry of the many-body wave function. The argument that spin-1/2 particles are fermions and particles with integer spin are bosons and the spin-statistics theorem are rooted in quantum field theory.[37,38] From a mathematical perspective, there is no problem to impose either antisymmetry or symmetry on the many-body wave function, even for the Dirac Hamiltonian. Likewise, there are solutions with yet different permutational symmetries, transforming to yet different irreducible representations of the permutation group. Here, I will consider both antisymmetric solutions (denoted as fermionic) and symmetric solutions (denoted as bosonic). It is found to be advantageous to explicitly (anti)symmetrize every state in the iterative diagonalization procedure, as numerical noise can easily destroy the symmetry, further exacerbating convergence issues. In the next section, we will investigate the behavior of the numerical solutions as we vary the speed of light in the problem and the nature of the one-particle potential.

III. Numerical results

(*a*) The one-particle relativistic harmonic oscillator

The one-particle one-dimensional Dirac harmonic oscillator is a classic problem in relativity theory. It was first studied in the 1930s,[31,32] and it continues to be a topic of research even today. [39] The spectrum consists of (very) sharp resonances in the continuum, and formally there are no square integrable eigenfunctions. This is different from the Hydrogenic 3D Dirac–Coulomb problem, for which bound square integrable eigenstates do exist. From a numerical point of view, it is still possible to study the 1D Dirac harmonic oscillator using a finite non-relativistic square integrable harmonic oscillator basis set, and in this way, the convergence of the eigenvalues representing the sharp resonances can be examined. Undoubtedly, the use of finite basis sets is a very convenient way to obtain approximate solutions in quantum chemistry, in particular for many-body problems, and here, we will elucidate some of the subtleties involved for the Dirac equation, without striving for rigor.

In the first set of test cases, we use a harmonic one-particle potential, $U(x_i) = \frac{1}{2}x_i^2$, the speed of light is set to 10.0 au, rather than the physical value of 137 au to enhance relativistic effects. In Table 1, the lowest positive energy eigenvalues, shifted by $-mc^2$, are listed. The largest basis set used has 30 one-particle basis functions, and in the Table also, the energy difference is reported between the largest ($M = 30$) results and the results for calculations with $M = 10$ and $M = 20$ basis functions. The results in Table 1 suggest that the diagonalization problem is well-behaved. Convergence of the positive energy levels with the size of the

Table 1. Relativistic one-particle energies: c = 10, Harmonic oscillator potential, total energies for 30 basis functions. Energy differences between 30 and 10 and 20 basis functions.

E (au) for 30 basis functions	$E(30) - E(10)$	$E(30) - E(20)$
0.500313878932	0.00E+00	0.00E+00
1.496593282866	0.00E+00	0.00E+00
2.489201958117	7.10E–11	0.00E+00
3.478191241057	–4.95E–10	0.00E+00
4.463611245061	5.08E–10	0.00E+00
5.445510901342	–7.14E–08	0.00E+00
6.423937998043	2.56E–04	0.00E+00
7.398939217668	–2.23E–04	0.00E+00
8.370560172953	6.61E–01	3.00E–12
9.338845441240	9.58E–01	–1.60E–11

basis set is smooth, and there is no indication of so-called Brown–Ravenhall disease, meaning the presence of positive energy continuum solutions. This does not mean these do not exist however, as the basis set is simply not large enough to show their presence. This will be discussed below.

Despite the seemingly smooth convergence, it is illuminating to monitor the one-particle spectrum for the harmonic oscillator potential. In Fig. 1, the resulting energies are drawn for the M = 30 calculations. The x-axis labels the energies, while the y-axis indicates the fraction of the first component: $f_1(\lambda) = \sum_{i \in S_1} |c_{i\lambda}|^2$ for an overall normalized state. For the negative energy states, this fraction would become very small, and instead, we use $f_2(\lambda) = -(1 - f_1(\lambda))$. It follows that positive fractions indicate states dominated by the first component, while negative fractions indicate states dominated by the second component. In all figures below, we shift to the negative fraction representation when $f_1(\lambda) <$ 0.25. There is no physical significance to this convention. It is simply used to clarify the pictures. In Fig. 2, we focus on the positive energy solutions, and it is seen that they more or less follow the equidistant spectrum of the non-relativistic harmonic oscillator. The doubling of the level near 23 au in Fig. 2 occurs because of the lack of kinetic balance in the calculations.

In Fig. 1, obtained for M = 30, it is seen that there are many negative energy states that fall in the gap between $-2mc^2 = -200$ and 0. As the size of the basis set increases, the number of such states and their energies keeps growing, and there is no reason for them not to become larger than 0, such that the states with large second components have similar energies as the "true" positive energy states, having large first components.

Rather than through an increase of the basis set, this issue can be investigated by reducing the speed of light. In Fig. 3, the one-particle spectrum is shown for the case c = 3 au and 40 basis functions. It is seen that indeed positive energy levels with large first components are interspersed with positive energy levels that are dominated by the second component of the wave functions (having negative fractions in the figure). Moreover, in numerical experiments, we were not able to converge the eigenvalues with respect to the basis set for these positive energy second-component states (using up to 300 basis states). These levels therefore are the finite basis

Fig. 1. One-particle energies for harmonic oscillator potential, c = 10, 30 basis functions included. Negative fractions of first components equal $-(1 - f_1)$, for small f_1. They indicate states dominated by the second component.

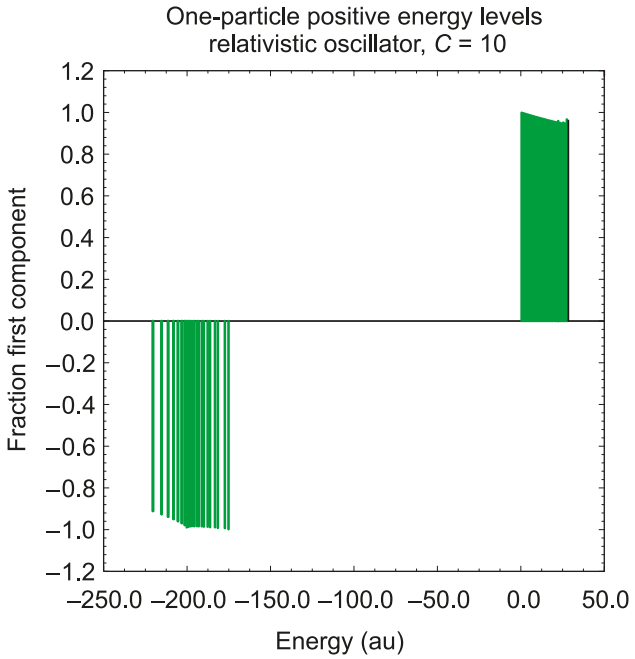

Fig. 2. One-particle energies for harmonic oscillator potential, c = 10, 30 basis functions included. Focus on positive energy spectrum. Energy levels are essentially equidistant, except for relativistic corrections. The double energy level around 23 au reflects a lack of kinetic balance in the basis.

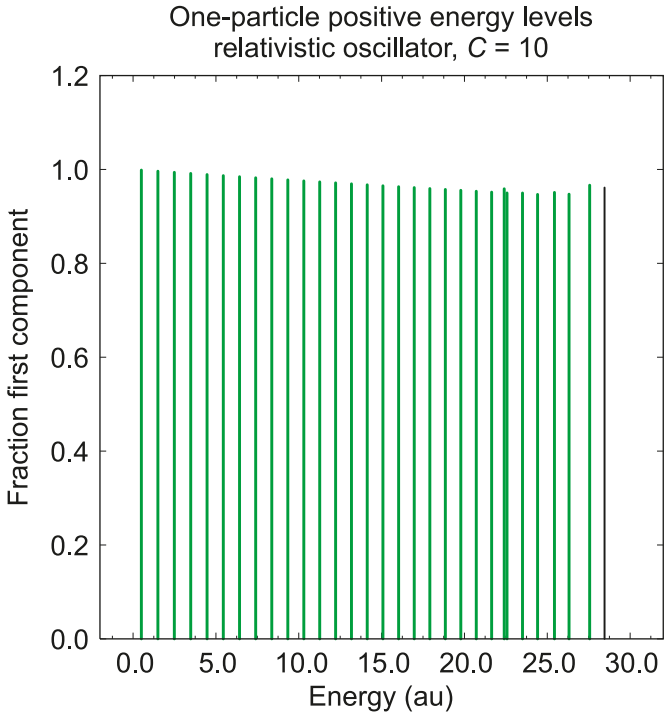

representation of a continuum using the harmonic oscillator potential that extends from $-2mc^2$ upwards. It is intriguing that the first-component positive energy levels converge rea-

sonably well with the size of the basis. These states can be interpreted therefore as sharp resonances embedded in a continuum, in accordance with the discussion of results in the literature for the harmonic oscillator.[31,32] This is also in accord with the two-body Dirac–Coulomb problem, when negative energy one-particle states are included.[11]

While we will use basis set convergence studies below to study many-particle problems in one dimension, it is clear that this is a somewhat crude vehicle to understand the subtle issue of sharp resonances in a continuum. For the one-dimensional Harmonic oscillator, we can pursue another analysis and calculate the energy dispersion in the approximate energy state $|\Psi_\lambda\rangle$

$$[12] \qquad \Delta H_\lambda = \langle\Psi_\lambda|(\widehat{H} - E_\lambda)^2|\Psi_\lambda\rangle = \langle\widehat{H}^2\rangle_\lambda - \langle\widehat{H}\rangle_\lambda^2$$

For the one-body Dirac equation, the square of the Hamiltonian operator is given by

$$[13] \qquad \widehat{H}^2 = \begin{pmatrix} (V+mc^2)^2 - c^2\dfrac{\mathrm{d}^2}{\mathrm{d}x^2} & -c\left(V\dfrac{\mathrm{d}}{\mathrm{d}x} + \dfrac{\mathrm{d}}{\mathrm{d}x}V\right) \\ c\left(V\dfrac{\mathrm{d}}{\mathrm{d}x} + \dfrac{\mathrm{d}}{\mathrm{d}x}V\right) & (V-mc^2)^2 - c^2\dfrac{\mathrm{d}^2}{\mathrm{d}x^2} \end{pmatrix}$$

For the case that $V = \frac{1}{2}kx^2$, $\widehat{H}^2$ is easily expressed in second quantization, and hence, we can evaluate the dispersion explicitly for any state expressed in a finite harmonic oscillator basis. Let me note that the full integral representation of the operators is used here (or equivalently the second quantized matrix elements), *not* the DVR diagonal basis to evaluate the potential, which was discussed in the previous section. The DVR representation will continue to be used for the many-body problems discussed below, but never to calculate ΔH. In Fig. 4, $\log(\Delta H_\lambda)$ is plotted vs. the energy E_λ for the case $c = 3$, $M = 40$. Sharp resonances in Fig. 4 are characterized by relatively small dispersions ($< 10^{-4}$ say), or negative values for $\log(\Delta H_\lambda)$. The values of the energies can be improved for these states with increasing size of the basis set (up to a limit, see below). In contrast, states with negative energies all have large dispersion ($\log(\Delta H_\lambda) > 0$). They represent continuum states and they do not converge at all with the basis set. In addition, positive energy states occur with large values for the dispersion, which also represent continuum states, and whose energies show no convergence with the basis set. In Table 2, we list positive energies for the cases $c = 3$, $M = 100$, and the energy difference with calculations using $M = 20$, 30, 40, and 60. Table 2 also includes the dispersion at $M = 40$ and $M = 100$. The identification of the sharp resonances using the dispersion criterion or alternatively the convergence of their energies with respect to the basis set is unambiguous. However, Table 2 also suggests that the sharp resonances do not strictly correspond to square integrable wave functions. The dispersion is often lower for $M = 40$ than for $M = 100$, which would be unexpected for true bound states. Moreover the energies are not strictly variational, as revealed by negative errors, e.g., certain entries in the $E(30) - E(100)$ column in Table 2. Interestingly, for the $M = 40$ case, the level around 2.39 au is poorly converged, and this can be attributed to the presence of a close lying

Fig. 3. One-particle energies for harmonic oscillator potential, $c = 3$, 40 basis functions. For this value of c, the "continuum" part of the levels dominated by the second-component overlaps the positive energy first-component levels.

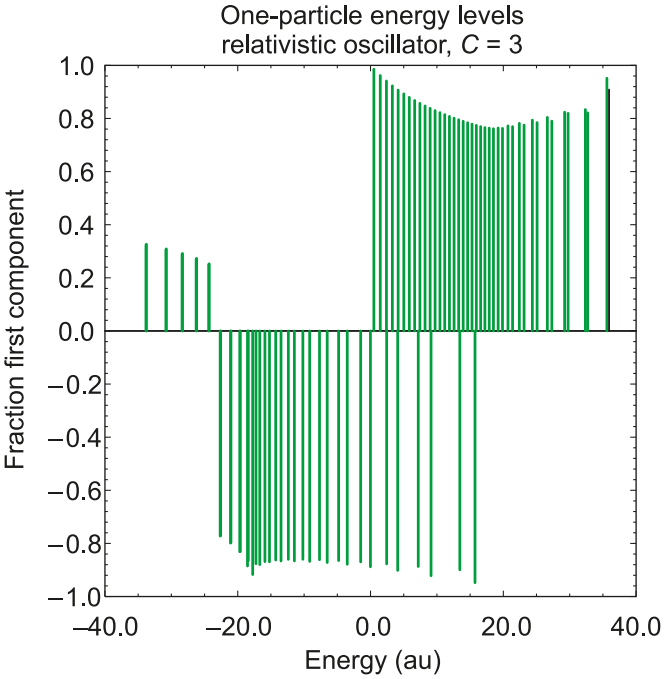

Fig. 4. Dispersion vs. energy for one-particle harmonic oscillator using 40 basis functions and $c = 3$.

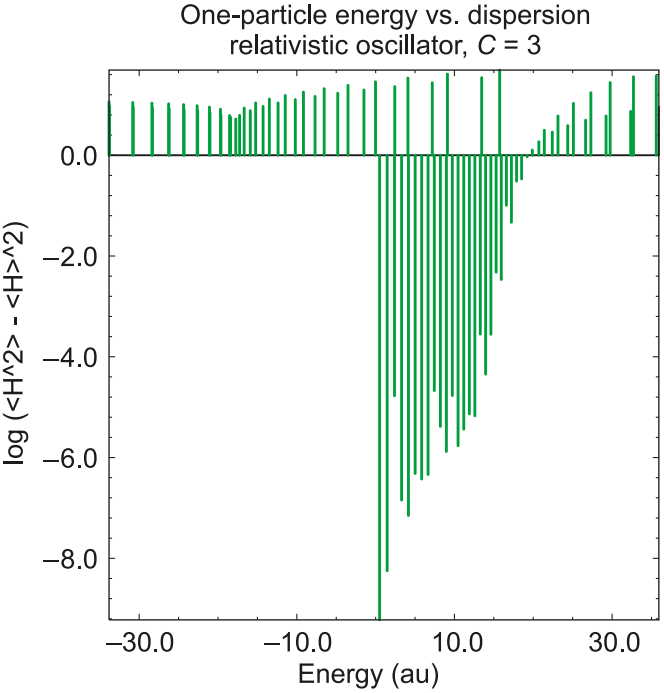

continuum level for this basis set, around 2.43 au. A similar conclusion can be drawn from calculations with different values for the speed of light. From numerical results (not shown) the dispersion for $c = 10$ is typically 10^{-10}, while for $c = 3$, one obtains values around 10^{-8} for "converged" levels. These numbers do not improve with an increasing size

Table 2. Relativistic one-particle energies: $c = 3$, Harmonic oscillator potential, total energies for 100 basis functions, and energy differences between nominally converged $E(100)$ and calculations with 60 and 40 and 30 and 20 basis functions for the bound states. Absolute energies are given for the continuum states. In addition, log(dispersion) is tabulated for $M = 100$ and $M = 40$.

E (au) for 100 basis functions	$\log(\Delta H)$ (100 basis functions)	$E(40) - E(100)$	$E(60) - E(100)$	$\mathrm{Log}(\Delta H)$ (40 basis functions)	$E(30) - E(100)$	$E(20) - E(100)$
Bound levels						
0.5036596644	–7.80	2E–10	1E–10	–9.222	1.E–10	1E–10
1.4653101823	–7.06	1E–09	7E–10	–8.248	1.E–09	6E–10
2.3934582530	–7.23	–3E–10	–3E–08	–4.7756	4.E–10	–9E–11
3.2921991289	–6.92	3E–10	–1E–09	–6.8441	2.E–09	5E–10
4.1648346295	–6.85	2E–09	2E–09	–7.151	–2.E–08	–1E–08
5.0140748058	–6.53	8E–09	9E–09	–6.3172	–8.E–09	–4E–09
5.8421778948	–6.03	–4E–08	–2E–08	–6.4269	6.E–09	–5E–08
6.6510502034	–5.30	–6E–08	–5E–08	–6.3369	–1.E–06	5E–08
Continuum levels (absolute energies)						
0.7009	1.40	1.2160	2.4294	1.40	0.6664	—
1.6853	1.46	2.9693	4.0961	1.53	4.5108	
2.9134	1.43	4.3076			6.6951	
3.9460	1.49	6.2676				
5.2457	1.46					
6.3285	1.51					

of the basis set. If the speed of light is lowered even further to $c = 1$ (not shown), all states are found to have rather high values for $\log(\Delta H_\lambda)$, and none of the energies converge well with the basis set size. For this value of c then, the resonances have lost most of their sharpness, and the finite basis set approach very clearly shows its deficiencies. The behavior clearly seen for $c = 1$, in principle is present for all values of c. The exact eigenstates are not square integrable, but have continuum tails that may have a very small relative magnitude (or ratio) compared with the bound part of the wave function. For most values of the speed of light, the finite basis set approach can be expected to yield very good approximations to the energy of the sharp resonance and to the wave function in the bound state region. The continuum part of the wave function extends to infinity, however, and for very large basis sets, the continuum region would dominate the matrix elements, and the finite basis approach would break down. I think that it is justified to conclude from this (brief) investigation that one can meaningfully diagonalize finite basis Hamiltonians for the harmonic Dirac problem in basis sets that are not too large. One can monitor convergence with the size of the basis set, and the results agree with results based on monitoring the dispersion, which can be done using a single basis set. It should be kept in mind, however, that rigorous convergence is not possible. Very large basis sets would introduce the problem with continuum states. Below, we will use the convergence with basis set criterion to study many-body problems.

(*b*) Many-body relativistic problems in one dimension in harmonic confinement

In a first set of many-body test cases, we use a harmonic one-particle potential as above, the speed of light is set to 10.0 au, while for all models, the two-body potential is the Gaussian form discussed in section II. In Tables 3 and 4, the lowest positive energy solutions (from diagonalizing $(H - n{\cdot}mc^2)$, where n indicates the number of particles) are listed for the two- and three-particle problems. The largest basis set used has 30 one-particle basis functions, and in Tables 3 and 4, the energy difference is reported between the largest ($M = 30$) results and the results for calculations with $M = 10$ and $M = 20$ basis functions.

I also attempted to converge the two-particle and three-particle problems for the $c = 3$ harmonic model with Gaussian interparticle interactions, using direct diagonalization techniques. The current implementation is not powerful enough to extract converged eigenvalues for this problem, however. For the two-body problem, the size of the matrix is small enough to resort to an in-core diagonalization procedure. The spectrum then has similar features as the one-particle problem (not shown). Solutions dominated by the first-component ($s_1 = s_2 = 1$) appear stable with respect to variations in the basis set, and they are embedded in a continuum of solutions, which have smaller first components, and which do not show a semblance of convergence with respect to the size of the one-particle basis set.

(*c*) Results for an inverted Gaussian potential

The harmonic oscillator potential is somewhat pathological perhaps. It is unusual to see a continuum positive energy contribution for a one-particle problem arising from wave functions dominated by the second component. This does not happen in the one-electron Dirac–Coulomb problem. As another example, we therefore consider a potential that is bound both from above and from below, namely, an inverted Gaussian of the form $V(x) = B(1 - \mathrm{e}^{-\lambda x^2})$, $B = 5.0$, $\lambda = 0.1$, in which the parameters are chosen such that near the minimum, the potential has the harmonic oscillator form $\frac{1}{2}x^2$, indicating that the usual harmonic oscillator basis functions are a suitable expansion set. The non-relativistic Hamiltonian supports a number of bound levels below $E = B$, and has a continuous spectrum above the asymptote of the potential, B. In Fig. 5, the relativistic one-particle spectrum is shown, for $c = 3$, and it can be seen that the spectrum is

Table 3. Relativistic two-particle energies for bound states, $c = 10$, harmonic oscillator one-particle potential, Gaussian interparticle repulsion. Both Fermionic and Bosonic states are included.

Primary orbital population		Total energy for 30 basis functions	$E(30) - E(10)$	$E(30) - E(20)$
Fermion				
1	0	2.016173229129	4.86E–08	8.47E–10
2	0	3.008850552908	1.25E–08	1.15E–09
3	0	3.996294179779	7.53E–06	1.43E–09
2	1	4.002527415102	5.73E–06	9.30E–11
4	0	4.980912755004	–2.72E–05	1.08E–08
3	1	4.992418551495	–3.15E–05	–2.53E–09
Boson				
0	0	1.057887676847	7.35E–08	2.00E–11
1	0	2.054237060402	3.69E–07	5.80E–11
2	0	3.010797141473	–1.28E–07	3.51E–10
1	1	3.048830970675	–8.48E–07	2.87E–10

Table 4. Relativistic three-particle energies for bound levels, $c = 10$, harmonic oscillator one-particle potential, Gaussian interparticle repulsion. Both Fermionic and Bosonic states are included.

Primary orbital population			Total energy for 30 basis functions	$E(30) - E(10)$	$E(30) - E(20)$
Fermions					
2	1	0	4.540853824022	3.65E–06	8.25E–09
3	1	0	5.529961769085	–1.18E–05	1.18E–08
4	1	0	6.512998447428	8.92E–05	7.73E–09
3	2	0	6.520161020721	8.98E–05	8.43E–09
Bosons					
0	0	0	1.672133347610	2.31E–07	1.90E–11
1	0	0	2.668551250315	2.63E–07	9.30E–11
2	0	0	3.606851596391	3.87E–07	6.72E–10
1	1	0	3.663790277695	3.81E–06	4.83E–10

qualitatively different from the harmonic oscillator case. There are a few stable negative energy states with energy above $E = -2mc^2$ (analogous to the positive energy states), and then there is a continuum extending to $-\infty$. There are no energy levels in the gap between the highest discrete negative energy state (at about –12.2 au in Fig. 5) and $E = 0$, and we assume this continues to hold for any size of the one-particle basis set (up to 300 basis functions were used to check). However, the two-particle spectrum is qualitatively similar to the case discussed before. There are continuum states of mixed component character that increase in energy with an increase of the basis set.

The above calculations illustrate the delicate nature of the solutions of the many-particle Dirac equation, even for simple problems like interacting particles in one dimension. From a numerical point of view, it is not easy to demonstrate convergence. Nevertheless, our calculations seem to indicate that the many-body solutions consist of isolated sharp resonances, well-described in a square integrable basis set, embedded in a continuum that is represented by energy levels that do not converge with the size of the basis set. This lack of convergence for the continuum states is analogous to diagonalizing the operator x, which we use to define the DVR basis set. The eigenvalues of the operator x (or DVR points) are different for every finite basis, and do not show convergence.

I also conclude it is not trivial to converge the relativistic many-body problem using direct diagonalization techniques, and moreover, the presence of the continuum seems to be in conflict with physical reality. The same phenomena occur for the two-particle Dirac–Coulomb problem, e.g., for Helium, as discussed for example in ref. 11. It is not clear what the presence of the low-energy continuum solutions would imply for the specific heat of Helium. It certainly seems less controversial to restrict the many-particle basis set to determinants built from one-particle positive energy solutions, as advocated for example by Sucher,[7] as then the continuum disappears. However, as mentioned in the introduction, the choice of (effective) one-particle operator used to define the manifold of positive energy one-particle states is ambiguous, and we are left with the undesirable situation that the most accurate model in quantum chemistry is mathematically not well-defined. It is not clear to me to what extent the problem is resolved in quantum field theory for bound-state systems, as these calculations are so difficult and invariably have their basis in perturbation theory.

IV. Alternative approaches: an analytically solvable many-body problem

Let us first discuss some alternate forms of the one-particle Hamiltonian, which would provide exactly the same eigenvalues as presented in section III. Previously, the kinetic energy part of the Hamiltonian was represented as

$$[14] \qquad \widehat{T} = mc^2\sigma_z + c\sigma_y\widehat{p}$$

Let us note that we used $\sigma_y\widehat{p}$ to create a suitable momentum operator, but we could as well have used $\sigma_x\widehat{p}$. The reason to use $\sigma_y\widehat{p}$ was that all matrix-elements and diagonalization steps then can use real numbers. However, there are more substantially different representations. One might equally well use

$$[15] \qquad \widehat{T} = mc^2\sigma_x + c\sigma_y\widehat{p} = \begin{pmatrix} 0 & mc^2 - c\dfrac{\mathrm{d}}{\mathrm{d}x} \\ mc^2 + c\dfrac{\mathrm{d}}{\mathrm{d}x} & 0 \end{pmatrix}$$

where the mass is transferred to the off-diagonal, which in the literature (for the 3D case) is known as the Weyl representation.[12] If one follows the reasoning by Dirac in his derivation of the Dirac eq. [1], the essential element is to find a representation of the classical relativistic square-root kinetic energy operator

$$[16] \qquad T = \sqrt{c^2p^2 + m^2c^4}$$

Using $\widehat{T} = mc^2\sigma_i + cp\sigma_j$ for any two of the Pauli matrices, which satisfy the Clifford algebra relation $\sigma_i\sigma_j + \sigma_j\sigma_i = 2\delta_{ij}\mathbf{1}$, then satisfies the fundamental relation $\widehat{T}^2 = (m^2c^4 + c^2p^2)\mathbf{1}$. Additional freedom arises as the Pauli matrices might be subject to an overall similarity transformation which preserves the Clifford algebra relations. A convenient proof that the above forms of Hamiltonian are equivalent is to demonstrate that they are related by simple similarity transformations. Let us simply demonstrate by some examples, without striving for full generality.

Fig. 5. One-particle energy levels for inverse Gaussian potential, c = 3, 30 basis functions. The negative energy states dominated by the second component do not overlap with the positive energy first-component solutions.

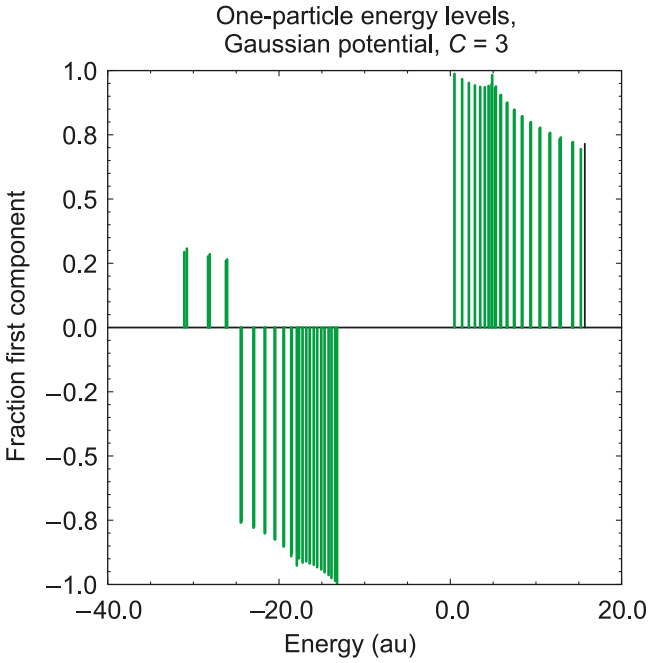

$$[17] \qquad \frac{1}{2}\begin{pmatrix} 1 & 1 \\ 1 & -1 \end{pmatrix}\begin{pmatrix} V+m & p \\ p & V-m \end{pmatrix}\begin{pmatrix} 1 & 1 \\ 1 & -1 \end{pmatrix} = \begin{pmatrix} V+p & m \\ m & V-p \end{pmatrix}$$

where we have set the speed of light to unity for notational convenience. Alternatively,

$$[18] \qquad \frac{1}{2}\begin{pmatrix} 1 & -i \\ -i & 1 \end{pmatrix}\begin{pmatrix} V & m-ip \\ m+ip & V \end{pmatrix}\begin{pmatrix} 1 & i \\ i & 1 \end{pmatrix} = \begin{pmatrix} V+p & m \\ m & V-p \end{pmatrix}$$

Any similarity transformation of the Hamiltonian preserves the eigenvalues, while the eigenvectors would be related by a corresponding transformation. In this fashion, we can essentially use any two of the Pauli matrices to represent the mass and momentum terms. It was verified numerically that the real forms

$$[19] \qquad \begin{pmatrix} V+mc^2 & -icp \\ icp & V-mc^2 \end{pmatrix}, \begin{pmatrix} V & mc^2-icp \\ mc^2+icp & V \end{pmatrix}$$

yield indeed identical eigenvalues, both for the single particle and the many-particle (i.e., two- and three-body) problems.

For the sequel, the representation in which

$$[20] \qquad \widehat{h} = V\mathbf{1} + mc^2\sigma_x + c\sigma_z\widehat{p} = \begin{pmatrix} V+c\widehat{p} & mc^2 \\ mc^2 & V-c\widehat{p} \end{pmatrix} = \begin{pmatrix} V - ic\dfrac{\mathrm{d}}{\mathrm{d}x} & mc^2 \\ mc^2 & V + ic\dfrac{\mathrm{d}}{\mathrm{d}x} \end{pmatrix}$$

is most convenient to use. The two-particle Hamiltonian in this representation reads

$$[21]\qquad \widehat{H}_2 = \begin{pmatrix} V + c\widehat{p}_1 + c\widehat{p}_2 & m_2c^2 & m_1c^2 & 0 \\ m_2c^2 & V + c\widehat{p}_1 - c\widehat{p}_2 & 0 & m_1c^2 \\ m_1c^2 & 0 & V - c\widehat{p}_1 + c\widehat{p}_2 & m_2c^2 \\ 0 & m_1c^2 & m_2c^2 & V - c\widehat{p}_1 - c\widehat{p}_2 \end{pmatrix}$$

and likewise for higher-particle Hamiltonians.

An interesting observation can be made if the mass terms of the particles are neglected. This is of course not a small modification, and it greatly changes the physics of the problem. In the literature, this model (in the 3D case) is known as the two-component model for the neutrino,[12] although as far as I am aware, it is not often used with many-body interations. Let us however treat this as a mathematical exercise and first consider the 1D one-body problem without mass and a harmonic potential. It is easily confirmed that the analytical solutions to the corresponding equation are given by

$$[22]\qquad \begin{pmatrix} e^{ik_1x+if(x)} \\ 0 \end{pmatrix}, \begin{pmatrix} 0 \\ e^{-ik_1x-if(x)} \end{pmatrix}$$

where the function $f(x)$ satisfies $\frac{1}{2}kx^2 + c\frac{\mathrm{d}f}{\mathrm{d}x} = 0 \rightarrow f(x) = -\frac{k}{6c}x^3$, and the energy eigenvalues are continuous and are given by $E = ck_1 = c\hbar k_1$, in units in which $\hbar = 1$. Also, the two-body problem can be solved, and the solutions would be one-component functions (if the mass term is neglected). Solutions corresponding to the first component read

$$\Psi_1(x_1, x_2) = \exp\left(i\left[k_1x_1 + k_2x_2 - \frac{k}{6c}(x_1^3 + x_2^3) - \frac{1}{2c}(x_1 + x_2)v(x_{12})\right]\right)$$

$$[23]\qquad \left[V - ic\left(\frac{\partial}{\partial x_1} + \frac{\partial}{\partial x_2}\right)\right]\Psi_1(x_1, x_2) = \left[V + c(k_1 + k_2) - \frac{1}{2}kx_1^2 - \frac{1}{2}kx_2^2 - v(x_{12})\right]\Psi_1(x_1, x_2)$$
$$= c(k_1 + k_2)\Psi_1(x_1, x_2)$$

where it is used that for central potentials

$$[24]\qquad \left(\frac{\partial}{\partial x_1} + \frac{\partial}{\partial x_2}\right)v(|x_1 - x_2|) = \frac{\partial v}{\partial x_{12}}\left(\frac{\partial x_{12}}{\partial x_1} + \frac{\partial x_{12}}{\partial x_2}\right) = 0$$

Following these simple examples, it is straightforward to obtain the general analytical solution to the one-component many-body problem defined by the Hamiltonian

$$[25]\qquad \widehat{H} = \sum_\alpha S_\alpha cp_\alpha + \sum_\alpha U(r_\alpha) + \frac{1}{2}\sum_{\alpha\neq\beta} v(r_{\alpha\beta})$$

where the signs $S_\alpha = \pm 1$. The general solution has the form

$$[26]\qquad \Psi = \exp\left[i\sum_\mu S_\mu x_\mu(k_\mu + f(r_\mu)) + \frac{1}{2}i\sum_{\mu\neq\nu}(S_\mu x_\mu + S_\nu x_\nu)g_{\mu\nu}(r_{\mu\nu})\right]$$

with energy $c\sum_\mu k_\mu$, provided the functions f,g satisfy the radial first-order differential equations

$$[27]\qquad f(r) + r\frac{\mathrm{d}f}{\mathrm{d}r} = -\frac{U(r)}{c}$$

and

$$[28]\qquad g_{\mu\nu}(r) = -\frac{v}{2c},\ (S_\mu = S_\nu)$$
$$g_{\mu\nu}(r) + r\frac{\mathrm{d}g_{\mu\nu}}{\mathrm{d}r} = -\frac{v(r)}{2c},\ (S_\mu = -S_\nu)$$

The geminal function $g_{\mu\nu}$ hence depends on the relative signs of the momentum operators. The verification that the above function satisfies the differential equation is elementary and is given in the appendix. Also, the solution of the inhomogenous differential equations for the radial functions f and g for essentially arbitrary potentials is straightforward, and a series expansion of the solution is given in the appendix. In a very simple way, we hence obtain exact, analytical, continuum solutions to the one-dimensional mass-less Dirac equation for arbitrary many particles and (essentially) arbitrary central force potentials.

The solution is particularly simple if the diagonal representation for the momentum operators is used, but if a one-particle Hamiltonian is related by a similarity transformation to the diagonal representation, one can construct continuum multicomponent eigenfunctions using an overall similarity transformation. It may be instructive to discuss this by example. If a mass-less two-body Hamiltonian would be given by

$$[29]\qquad \widehat{H}_2 = \begin{pmatrix} V & c\widehat{p}_2 & c\widehat{p}_1 & 0 \\ c\widehat{p}_2 & V & 0 & c\widehat{p}_1 \\ c\widehat{p}_1 & 0 & V & c\widehat{p}_2 \\ 0 & c\widehat{p}_1 & c\widehat{p}_2 & V \end{pmatrix}$$

then the corresponding *one-body* problem can be transformed into a diagonal form by the transformation $\frac{1}{\sqrt{2}}\begin{bmatrix} 1 & 1 \\ 1 & -1 \end{bmatrix}$. The corresponding transformation for the two-body problem would be given by the direct product of the transformation matrices, denoted symbolically as

$$[30]\qquad \frac{1}{2}\begin{bmatrix}1 & 1\\ 1 & -1\end{bmatrix}\otimes\begin{bmatrix}1 & 1\\ 1 & -1\end{bmatrix}=\frac{1}{2}\begin{bmatrix}1 & 1 & 1 & 1\\ 1 & -1 & 1 & -1\\ 1 & 1 & -1 & -1\\ 1 & -1 & -1 & 1\end{bmatrix}=U=U^{\dagger}$$

Transforming the Hamiltonian, $U^{\dagger}HU$ then brings the Hamiltonian to diagonal form, with the momentum operator in the (s_1,s_2)-sectors given by the linear combination $S_1p_1 + S_2p_2$. This example shows more clearly that in the absence of a mass term, the 2^N coupled differential equation can be reduced to 2^N uncoupled differential equations, of the form shown in relation to eq. [25].

Let me discuss one more intriguing perspective. Let us focus on a particular component for the block-diagonal Dirac problem $H = c\sum_{\alpha} S_{\alpha}p_{\alpha} + V(\{\mathbf{x}\})$. The solutions to this mass-less one-component Dirac problem are plane waves $e^{\mathbf{ik}\cdot\mathbf{x}}$ times a solution to the zero energy problem, which might be written $\Psi_0 = \mathrm{e}^{ig(\mathbf{x})}$, and which satisfies $\widehat{H}\Psi_0 = 0$. The function $\Psi_0(\{\mathbf{x}\})$ can be associated with a transformation $\hat{U}$, such that the transformed Hamiltonian $\widehat{G} = \widehat{U}^{\dagger}\widehat{H}\widehat{U} = \widehat{T}$ is reduced to purely the momentum operators, and the potential is eliminated. The solutions of the transformed Hamiltonian are plane waves. From the above considerations, it follows that for the mass-less Dirac equation it is easy to find what amounts to a gauge transformation, *analytically*, that eliminates the potential completely, and reduces the problem of interacting particles to a free-particle problem under a suitable transformation. It then follows that solutions to the time-dependent mass-less Dirac equation are wave packets propagating analogously to plane waves, times an overall (time-independent) gauge factor. If one considers the full multi-component block diagonal Hamiltonian, each many-body component would consist of a wave packet of the form $\Psi_0(\{\mathbf{x}\})\int \mathrm{d}\mathbf{k}\mathrm{e}^{i(\mathbf{k}\cdot\mathbf{x}-E_{\mathbf{k}}t)}a(\mathbf{k})$. The function $\Psi_0 = \mathrm{e}^{ig(\mathbf{x})}$, and the coefficients $a(\mathbf{k})$ would be different for each component of the wave function.

I find this a fascinatingly simple picture for the many-body problem, but let me emphasize it only works if we first remove the mass from the equation. To make this aspect explicit, let us transform the simplest one-particle Hamiltonian, including masses

$$[31]\qquad \begin{bmatrix}e^{-ig(x)} & 0\\ 0 & e^{ig(x)}\end{bmatrix}\begin{bmatrix}V+cp & mc^2\\ mc^2 & V-cp\end{bmatrix}\begin{bmatrix}e^{ig(x)} & 0\\ 0 & e^{-ig(x)}\end{bmatrix}=\begin{bmatrix}cp & 0\\ 0 & -cp\end{bmatrix}+mc^2\begin{bmatrix}e^{-ig(x)} & 0\\ 0 & e^{ig(x)}\end{bmatrix}\begin{bmatrix}0 & e^{-ig(x)}\\ e^{ig(x)} & 0\end{bmatrix}$$
$$=\begin{bmatrix}cp & mc^2e^{-2ig(x)}\\ mc^2e^{2ig(x)} & -cp\end{bmatrix}$$

It is seen that this leads to a complicated transformed Hamiltonian, as the phase factor in the mass term can be a rapidly oscillating function. I conclude there is a simplifying feature to the one-dimensional many-body Dirac problem only if the mass term is discarded. Similar simplifications are expected to be possible for the mass-less many-body problem in three and perhaps four dimensions. These issues will be discussed in future work.

V. Concluding remarks

In this paper, a one-dimensional relativistic Hamiltonian is considered, and it was found useful to illustrate some of the pathological behavior of the many-body Dirac equation. The model employs a finite basis set, but all of the necessary integrals are conveniently obtained using second quantization techniques that are familiar from the harmonic oscillator and a DVR representation for the potentials. In particular, we find very sharp resonances that can be described quite well using finite basis set expansions, even if one can argue that such solutions are formally not correct.

The use of the dispersion relation $\Delta H = \langle H^2\rangle - \langle H\rangle^2$ in combination with finite basis sets seems to provide a powerful tool for analysis of this kind of problem. This requires evaluating $\langle H^2\rangle$ analytically over a finite basis set, and in particular for many-body problems, this leads to elaborate integrals. The DVR idea is not applicable to calculate the dispersion, e.g., for the one-body harmonic problem, the use of the DVR such that $\mathbf{V}^2 = \mathbf{V}$ for the matrices yields 0 dispersion for all states, and does not provide useful information regarding the continuum nature of the solutions, or the sharpness of the resonances.

The second part of the paper (section IV), in which we discuss analytical solutions to the many-body problem, is perhaps most interesting. We took the drastic measure to discard the mass from the equations, and this will clearly affect the physics. However, a number of observations are likely more generally applicable. For example, the reduction of the (mass-less) many-body Dirac equation in three dimensions from 4^N to a two- or four-component form. Moreover, there might be possibilities to identify mass with the time component of momentum in a spacetime formulation, and in this way, retain the analyticity of the solutions for problems that effectively include mass. The analytical solution discussed above can be essentially viewed as a gauge transformation that eliminates the potential and transforms the (mass-less) Dirac equation to a free-particle problem. This may be an interesting viewpoint to discuss dynamical equations between interacting particles. The ideas presented in section IV are clearly still in their infancy and require further development.

Acknowledgement

This work is supported by the Natural Science and Engineering Research Council of Canada (NSERC).

References

(1) Dirac, P. A. M. *Proc. R. Soc. Lond., A Contain. Pap. Math. Phys. Character* **1928**, *117* (778), 610–624. doi:10.1098/rspa.1928.0023.
(2) Hirao, K.; Ishikawa, Y., Eds. *Recent Advances in Relativistic Molecular Theory;* World Scientific: Singapore, 2004.
(3) Wilson, S.; Grant, I. P.; Gyorffy, B. L., Eds. *The Effects of Relativity in Atoms, Molecules, and the Solid State;* Plenum Press: New York, 1991.
(4) Brown, G. E.; Ravenhall, D. G. *Proc. R. Soc. Lond. A Math. Phys. Sci.* **1951**, *208* (1095), 552–559. doi:10.1098/rspa.1951.0181.
(5) Bethe, H. A.; Salpeter, E. E. *Quantum Mechanics of One- and Two Electron Atoms;* Springer-Verlag: Berlin, 1957.
(6) Sucher, J. *Phys. Rev. A* **1980**, *22*, 348.
(7) Sucher, J. *Int. J. Quantum Chem.* **1984**, *25* (1), 3–21. doi:10.1002/qua.560250103.
(8) Sucher, J. *Phys. Scr.* **1987**, *36* (2), 271–281. doi:10.1088/0031-8949/36/2/015.
(9) Grant, I. P. *Phys. Rev. A* **1982**, *25* (2), 1230–1232. doi:10.1103/PhysRevA.25.1230.
(10) Grant, I. P.; Quiney, H. M. *Phys. Rev. A* **2000**, *62* (2),o. 022508. doi:10.1103/PhysRevA.62.022508.
(11) Pestka, G.; Bylicki, M.; Karwowski, J.; Wilson, S.; Grout, P. J.; Maruani, J.; Delgado-Barrio, G.; Piecuch, P., Eds. *Frontiers in Quantum Systems in Chemistry and Physics;* Springer: Netherlands, 2008.
(12) Gross, F. *Relativistic Quantum Mechanics and Field Theory;* John Wiley and Sons: Toronto, ON, 1993.
(13) Blundell, S. A.; Johnson, W. R.; Liu, Z. W.; Sapirstein, J. *Phys. Rev. A* **1989**, *39* (8), 3768–3775. doi:10.1103/PhysRevA.39.3768. PMID:9901697.
(14) Sapirstein, J. *Int. J. Quantum Chem.* **2006**, *106* (15), 3178–3185. doi:10.1002/qua.21066.
(15) Sapirstein, J.; Cheng, K. T. *Can. J. Phys.* **2008**, *86* (1), 25–31. doi:10.1139/P07-098.
(16) Lindgren, I.; Salomonson, S.; Hedendahl, D. *Phys. Rev. A* **2006**, *73* (6),o. 062502. doi:10.1103/PhysRevA.73.062502.
(17) Lindgren, I.; Salomonson, S.; Hedendahl, D. *Int. J. Quantum Chem.* **2008**, *108* (12), 2272–2279. doi:10.1002/qua.21748.
(18) Eliav, E.; Kaldor, U.; Ishikawa, Y. *Chem. Phys. Lett.* **1994**, *222*, 82. doi:10.1016/0009-2614(94)00317-3.
(19) Liu, W.; Peng, D. *J. Chem. Phys.* **2006**, *125*,o. 044102.
(20) Peng, D.; Liu, W.; Xiao, Y.; Cheng, L. J. *Chem. Phys.* **2007**, *127*,o. 104106.
(21) Cook, J. L. *Aust. J. Phys.* **1972**, *25*, 117.
(22) Trump, M. A.; Schieve, W. C. *Classical Relativistic Many-Body Dynamics;* Kluwer Academic: Dordrecht, 1999.
(23) Nooijen, M.; Upadhyay, D. *Int. J. Quantum Chem.* **2009**, *109* (8), 1684–1698. doi:10.1002/qua.22114.
(24) Hsu, J.-P.; Hsu, L. *A Broader View of Relativity;* World Scientific: Singapore, 2006.
(25) Cook, J. L. *Aust. J. Phys.* **1972**, *25*, 141.
(26) Horwitz, L. P.; Piron, C. *Helv. Phys. Acta* **1973**, *46*, 316.
(27) Arshansky, R. I.; Horwitz, L. P. *Found. Phys.* **1985**, *15* (6), 701–715. doi:10.1007/BF00738298.
(28) Arshansky, R. I.; Horwitz, L. P. *J. Math. Phys.* **1989**, *30* (1), 1. doi:10.1063/1.528571.
(29) Fanchi, J. R. *Parameterized Relativistic Quantum Theory;* Kluwer Academic: Dordrecht, 1993.
(30) Huntington, L. M.; Nooijen, M. *Int. J. Quantum Chem.* **2009**, *109* (13), 2885–2896. doi:10.1002/qua.22206..
(31) Nikolsky, K. *Z. Phys.* **1930**, *62* (9-10), 677–681. doi:10.1007/BF01843485.
(32) Popestka, I. *Acta Physiol. Pol.* **1935**, *4*, 269.
(33) Domínguez-Adame, F.; Rodríguez, A. *Phys. Lett. A* **1995**, *198* (4), 275–278. doi:10.1016/0375-9601(95)00064-A.
(34) Long, C.; Qin, S. *Chin. Phys.* **2007**, *16* (4), 897–900. doi:10.1088/1009-1963/16/4/004.
(35) Light, J.; Carrington, T., Jr. *Adv. Chem. Phys.* **2000**, *114*, 263–310. doi:10.1002/9780470141731.ch4.
(36) Nooijen, M.; Hazra, A. *VIBRON — A Program for Vibronic Coupling and Franck–Condon Calculations,* With contributions from J. F. Stanton and K. Sattelmeyer; University of Waterloo; 2003.
(37) Fierz, M. *Helv. Phys. Acta* **1939**, *12* (1), 3–18. doi:10.1002/hlca.19390220102.
(38) Pauli, W. *Phys. Rev.* **1940**, *58* (8), 716–722. doi:10.1103/PhysRev.58.716.
(39) Karwowski, J.; Pestka, G. *Theor. Chem. Acc.* **2007**, *118* (3), 519–525. doi:10.1007/s00214-007-0362-y.

Appendix: Form of exact many-body wave function for one-component Hamiltonian

Consider the many-body Hamiltonian in one dimension

$$[A.1] \qquad \widehat{H} = \sum_{\alpha} S_\alpha c p_\alpha + \sum_{\alpha} U(r_\alpha) + \frac{1}{2}\sum_{\alpha\neq\beta} v(r_{\alpha\beta})$$

Then, if we assume a wave function of the following form:

$$[A.2] \qquad \Psi = \exp[i\sum_{\mu} S_\mu x_\mu (f(r_\mu) + k_\mu) + \frac{1}{2} i \sum_{\mu\neq\nu} (S_\mu x_\mu + S_\nu x_\nu) g_{\mu\nu}(r_{\mu\nu})]$$

we can find differential equations for the functions $f(r_\mu)$, $g_{\mu\nu}(r_{\mu\nu})$

$$[A.3] \qquad E = \frac{1}{\Psi} H\Psi = \sum_{\alpha} [c S_\alpha^2 (k_\alpha + f(r_\alpha)) + \sum_{\mu} S_\alpha S_\mu x_\mu \frac{\partial f}{\partial r_\mu}\frac{\partial r_\mu}{\partial x_\alpha} + U(r_\alpha)] + \frac{1}{2}\sum_{\alpha,\mu\neq\nu} (c S_\alpha S_\mu \delta_{\alpha\mu} + c S_\alpha S_\nu \delta_{\alpha\nu}) g_{\mu\nu}(r_{\mu\nu})$$
$$+ \frac{1}{2}\sum_{\mu\neq\nu} v(r_{\mu\nu}) + \frac{1}{2}\sum_{\alpha,\mu\neq\nu} (c S_\alpha (S_\mu x_\mu + S_\nu x_\nu) \frac{\partial g_{\mu\nu}(r_{\mu\nu})}{\partial r_{\mu\nu}}\frac{\partial r_{\mu\nu}}{\partial x_\alpha}$$

Using

$$[A.4]\qquad \frac{\partial r_\mu}{\partial x_\alpha} = \frac{\partial}{\partial x_\alpha}(x_\mu^2)^{1/2} = \frac{x_\alpha}{r_\alpha}\delta_{\alpha\mu}$$
$$\frac{\partial r_{\mu\nu}}{\partial x_\alpha} = \frac{\partial}{\partial x_\alpha}[(x_\mu - x_\nu)^2]^{1/2} = \frac{(x_\mu - x_\nu)(\delta_{\alpha\mu} - \delta_{\alpha\nu})}{r_{\mu\nu}}$$

such that

$$[A.5]\qquad \begin{aligned}\frac{1}{2}\sum_\alpha (cS_\alpha(S_\mu x_\mu + S_\nu x_\nu)\frac{\partial g_{\mu\nu}(r_{\mu\nu})}{\partial r_{\mu\nu}}\frac{(x_\mu - x_\nu)(\delta_{\alpha\mu} - \delta_{\alpha\nu})}{r_{\mu\nu}} &= \frac{c}{2r_{\mu\nu}}\frac{\partial g_{\mu\nu}(r_{\mu\nu})}{\partial r_{\mu\nu}}(S_\mu x_\mu + S_\nu x_\nu)(x_\mu - x_\nu)(S_\mu - S_\nu)\\ &= \begin{cases} 0, S_\nu = +S_\mu \\ \dfrac{c}{2r_{\mu\nu}}\dfrac{\partial g_{\mu\nu}(r_{\mu\nu})}{\partial r_{\mu\nu}}(x_\mu - x_\nu)^2(2S_\mu^2), & S_\nu = -S_\mu \end{cases}\\ &= \begin{cases} 0, S_\mu = S_\nu \\ cr_{\mu\nu}\dfrac{\partial g_{\mu\nu}(r_{\mu\nu})}{\partial r_{\mu\nu}}, S_\nu = -S_\mu \end{cases}\end{aligned}$$

Equation [A.3] simplifies to

$$[[A.6]]\qquad E = \frac{1}{\Psi}H\Psi = c\sum_\alpha k_\alpha + \sum_\alpha [cf(r_\alpha) + cr_\alpha\frac{\partial f}{\partial r_\alpha} + U(r_\alpha)] + \frac{1}{2}\sum_{\mu\neq\nu}[2cg_{\mu\nu}(r_{\mu\nu}) + v(r_{\mu\nu}) + 2cr_{\mu\nu}\frac{\partial g_{\mu\nu}(r_{\mu\nu})}{\partial r_{\mu\nu}}\delta(S_\mu, -S_\nu)]$$

If we equate the above equation to a constant, $E = c\sum_\alpha k_\alpha$, we obtain differential equations for the functions f, g

$$[A.7]\qquad \begin{aligned} f(r) + r\frac{\mathrm{d}f}{\mathrm{d}r} &= -\frac{U(r)}{c}\\ g_{\mu\nu}(r) + r\frac{\mathrm{d}g_{\mu\nu}}{\mathrm{d}r} &= -\frac{v(r)}{2c}, (S_\mu = -S_\nu)\\ g_{\mu\nu}(r) &= -\frac{v(r)}{2c}, (S_\mu = S_\nu)\end{aligned}$$

It is seen that the one- and the "opposite S" two-body differential equations are essentially the same. It is easily verified that a particular solution of the differential equation

$$[A.8]\qquad f(r) + r\frac{\mathrm{d}f}{\mathrm{d}r} = y(r) \equiv \sum_{k=-\infty}^{k=+\infty} a_k r^k$$

is given by

$$[A.9]\qquad f(r) = a_{-1}\frac{\ln r}{r} + \sum_{k\neq -1}\frac{1}{(1+k)}a_k r^k$$

The verification is elementary. For the series in eq. [A.9],

$$[A.10]\qquad \begin{aligned} f(r) + r\frac{\mathrm{d}f}{\mathrm{d}r} &= a_{-1}\frac{\ln r}{r} + ra_{-1}\frac{1}{r^2} - ra_{-1}\frac{\ln r}{r^2}\\ &+ \sum_{k\neq -1}\frac{a_k r^k + ka_k r r^{k-1}}{(1+k)} = a_{-1}\frac{1}{r} + \sum_{k\neq -1} a_k r^k = y(r)\end{aligned}$$

The solution to the homogenous differential equation

$$[A.11]\qquad f(r) + r\frac{\mathrm{d}f}{\mathrm{d}r} = 0$$

is given by $f(r) = \frac{\lambda}{r}$, and this solution can be added to the particular solution in eq. [A.9]. The effect of including this arbitrary term amounts to a phase factor in the overall wave function: $\lambda x\alpha/r\alpha = \pm\lambda$ for f, and $\lambda(x_\mu - x_\nu)/r_{\mu\nu} = \pm\lambda$ for g. The phase factor would change sign discontinuously for each coincidence of the particles, and this pathological behavior does not seem desirable. For this reason, it seems best to take $\lambda = 0$, as was assumed in eq. [26] in the body of the text.

In conclusion, for any potential expressed as a power series expansion, it is easy to obtain the exact solution of the one-component many-body differential equation.

Catalyzed β scission of a carbenium ion III — Scission observed in ab initio molecular dynamics simulations

Greg M. Berner and Allan L. L. East

Abstract: The β scission (cracking) of branched carbenium ions have been observed in molecular dynamics simulations, possibly for the first time. Simulations were performed with molecular dynamics based on PW91 density functional theory, and which included three-dimensional periodic boundary replication of the unit cell to mimic long-range bulk effects. A rising-temperature algorithm was used to encourage reaction within the narrow time windows ($\sim$10 ps) of the simulations. Twenty-eight simulations were performed, featuring alkyl ions in three different catalytic systems: the ionic liquid, $[(C_5H_5NH^+)_5(Al_2Cl_7^-)_6]^-$, the chabazite zeolite, $[AlSi_{23}O_{48}]^-$, and the chabazite zeolite, $[Al_4Si_{20}O_{45}(OH)_3]^-$. Twenty-four runs began with unbranched *sec-n*-alkyl ions, but only one exhibited β scission, and only after branching to a tertiary ion and under extreme heating. In contrast, the four simulations that began with branched alkyl ions were all successful in demonstrating β scission at lower temperatures: 2,4,4-trimethyl-2-pentyl ion and 2,4-dimethyl-2-hexyl ion in each of the first two catalysts. The lifetimes of desorbed alkyl ions in the chabazite models were < 5 ps at 1000–1500 K. The β scission results support the classical Weitkamp et al. (*Appl. Catal.* **1983,** *8,* 123) mechanism over the nonclassical Sie (*Ind. Eng. Chem. Res.* **1992,** *31,* 1881) and the chemisorping Kazansky et al. (*J. Catal.* **1989,** *119,* 108) mechanisms.

Key words: C–C bond fission, cationic β scission, carbenium ions, alkyl ions, protonated cyclopropane (PCP^+), catalysis, chloroaluminate, catalytic cracking mechanism.

Résumé : On a observé, peut être pour la première fois, une scission β (craquage) d'ions carbénium ramifiés dans des simulations de dynamique moléculaire. Les simulations ont été effectuées à l'aide de la dynamique moléculaire basée sur la théorie de la fonctionnelle de densité PW91 qui inclut une réplication tridimensionnelle de la frontière périodique de la cellule unitaire pour représenter les effets globaux à long terme. On a utilisé un algorithme avec température croissante pour encourager la réaction vers des fenêtres étroites de temps ($\sim$10 ps) des simulations. On a effectué vingt-huit simulations mettant en évidence des ions alkyles dans trois systèmes catalytiques différents, un liquide ionique, $[C_5H_5NH^+)_5(Al_2Cl_7^-)_6]^-$, la chabazite zéolithe, $[AlSi_{23}O_{48}]^-$ et la zéolithe chabazite, $[Al_4Si_{20}O_{45}(OH)_3]^-$. Vingt-quatre de ces simulations commençaient avec des ions linéaires alkyles secondaires, mais seulement un a présenté une scission β et uniquement après avoir ramifié la chaîne vers un ion tertiaire, avec un chauffage intense. Par ailleurs, les quatre simulations lancées avec des ions ramifiés ont toutes conduit à des scissions β, à des températures plus basses, dont l'ion 2,4,4-triméthylpent-2-yle et l'ion 2,4-diméthylhex-2-yle dans chacun des deux premiers catalyseurs. Les temps de vie des ions alkyles désorbés dans les modèles de la chabazite sont de < 5 ps à 1000–1500 K. Les résultats de scission β sont en accord avec le mécanisme classique de Weitkamp et al. (*Appl. Catal.* **1983,** *8,* 123) concernant le mécanisme non classique de Sie (*Ind. Eng. Chem. Res.* **1992,** *31,* 1881) et celui de chimisorption de Kazansky et al. (*J. Catal.* **1989,** *119,* 108).

Mots-clés : fission d'une liaison C–C, scission cationique β, ions carbénium, ions alkyles, PCP^+, catalyse, chloroaluminate, mécanisme de craquage catalytique.

[Traduit par la Rédaction]

Introduction

In petroleum cracking of aliphatic hydrocarbon feedstock, the dominant C–C-bond scission step is β scission of carbocations (carbenium ions). The 1949 mechanisms of Thomas[1] and Greensfelder et al.[2] assumed classical alkyl ions with a three-coordinate charged carbon atom and viewed primary carbocations as acceptable primary products of the scission. In the ensuing 60 years, primary carbocations have proven to be impossibly recalcitrant to observation, and in response to this "primary carbocation dilemma", several modern versions of the β scission mechanism have been proposed. Review articles in 2001[3] and 2007[4] have expressed chagrin that the proper mechanism has still not been resolved. In this paper, we address this problem by reporting the results of ab initio molecular dynamics simulations, which shed light on which of these proposals is most likely to be correct.

In 1983, Weitkamp, Jacobs, and Martens (WJM)[5] proposed a mechanism variation (Fig. 1, top) that kept the concept of classical carbocations, but avoided the formation of

Received 21 February 2009. Accepted 18 June 2009. Published on the NRC Research Press Web site at canjchem.nrc.ca on 8 October 2009.

This article is part of a Special Issue dedicated to Professor T. Ziegler.

G.M. Berner and A.L.L. East.[1] Department of Chemistry and Biochemistry, University of Regina, Regina, SK S4S 0A2, Canada.

[1]Corresponding author (e-mail: Allan.East@uregina.ca).

Fig. 1. Three commonly cited mechanisms for catalytic β scission. Upper: Weitkamp, Jacobs, and Martens classical mechanism,[5] where *m* is the minimum number of carbons needed in the alkyl ion. Middle: Sie PCP$^+$ mechanism.[6] Lower: Li and East's version[14] of Kazansky and Senchenya[10] and van Santen and co-workers[11] chemisorption mechanism, where A, B, and C are the electron rearrangement steps, which could be stepwise or concerted. The extra final step of hydride transfer in the Sie mechanism,[6] presumably from another alkane in a chain reaction, would be common to all three mechanisms.

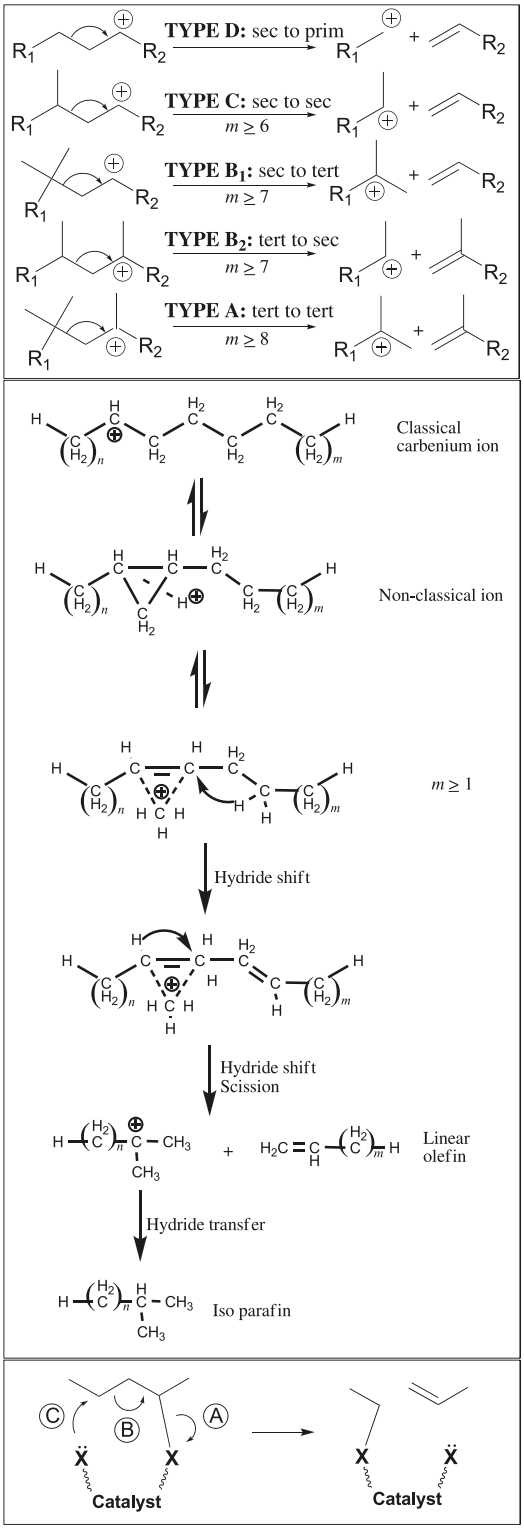

primary carbocations by requiring *n*-alkyl ions to undergo skeletal branching first, so that β scission could begin with secondary or tertiary ions and lead directly to secondary or tertiary ions. Their scheme categorized the reactions by ion type, and helped to explain the absence of two-carbon fragments in cracking experiments. Although the classical mechanism for skeletal branching was also at odds with the primary carbocation dilemma, by 1983 there was a newer branching mechanism proposed by others that involved a nonclassical protonated cyclopropane (PCP$^+$) structure (see the Discussion section).

In 1992–1993, Sie published a series of three papers,[6–8] which criticized the WJM[5] classical scheme, suggesting that if PCP$^+$ structures exist for the branching step, then they should exist for the β scission step as well. The mechanism of the 1992 Sie paper[6] is the most detailed (Fig. 1, middle), with hydrogen–atom rearrangement steps, and features the product double bond forming outside of the PCP$^+$ structure. Far less steps are presented in the 1993 papers.[7,8] The Sie[6–8] mechanism has been quoted often.[3,4,9]

The third prominent variation has been the chemisorption hypothesis, put forward by Kazansky and Senchenya[10] and popularized by van Santen and co-workers.[11] In this hypothesis, the carbocations are thought to exist not as classical or nonclassical ions, but as alkyl substituents chemisorbed to the catalyst (typically an oxygen atom in an aluminosilicate zeolite). Such alkoxide or silyl-ether structures are the only forms of nonresonant alkyl ions observed in in situ NMR experiments.[12] This variation can avoid the primary carbocation dilemma because, shortly after desorption, β scission can proceed as an S_N2 reaction (Fig. 1, bottom): instead of β scission resulting in a primary alkyl fragment containing the gamma carbon atom, a nucleophilic site on the catalyst attacks the gamma carbon first, causing the β scission while preventing the formation of a primary alkyl fragment.

In the first two papers of this series,[13,14] we examined this third variation, because we recognized that all previous computational studies[15] were adversely affected by the computational expense required to calculate transition states correctly, and hence made unfortunate compromises. Our work entailed computational geometry-optimization studies of secondary carbenium ions ($C_5H_{11}^+$, $C_6H_{13}^+$) on aluminum-containing molecular fragments of varying sizes, thoroughly exploring the potential energy surfaces and using accurate transition-state algorithms. One of the major conclusions was that the mechanism tended to be two-step, with the initial step being desorption and the rate-limiting second step being S_N2 β scission. This conclusion opens the possibility that desorption might lead to the Sie[6–8] or WJM[5] mechanisms, instead of the S_N2 second step of the chemisorption mechanism.

Faced with multiple possibilities, we have switched tactics and turned to rising-temperature molecular dynamics (MD) simulations[16] based on PW91 density functional theory. The simulation should, in principle, reveal which of the three β-scission variations is most likely to occur. Use of ab initio MD simulation to explore mechanisms was promoted by Dupuis and co-workers.[17] The rising-temperature technique is a means of increasing the probability of observing a chemical "rare event" in the narrow molecular times of the simulation (typically 10 ps from a week of simulation).

Fig. 2. Octyl ions studied.

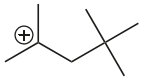

2,4,4-trimethylpent-2-yl cation

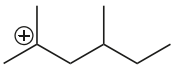

2,4-dimethylhex-2-yl cation

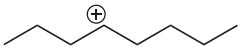

oct-4-yl cation

Although the simulated temperatures did get artificially high (sometimes over 2000 K), potentially opening up alternative high-barrier reaction possibilities, the processes with lower barriers remain orders of magnitude more probable. Furthermore, our simulations are incapable of producing homolytic C–C bond cleavage, because all electrons are required to be paired and hence unable to create radical products.

In this paper, we report the results of several simulations: five of *sec*-*n*-nonyl in the ionic liquid, $[(C_5H_5NH^+)_5(Al_2Cl_7^-)_6]^-$,[18] fifteen of *sec*-*n*-heptyl in chabazite, $[AlSi_{23}O_{48}]^-$,[19] two of *sec*-*n*-heptyl in chabazite, $[Al_4Si_{20}O_{45}(OH)_3]^-$, and a set of six from combining each of three octyl ion isomers (Fig. 2) with each of the first two catalysts. This final set of six include branched isomers to better test the WJM[5] mechanism. The ionic liquid simulations were motivated by the experiments of Johnson and co-workers,[18] who demonstrated that this particular liquid could crack nonane.

Methods

The ab initio molecular dynamics (AIMD) simulations were performed with the Vienna ab initio simulation package (VASP).[20] The level of theory was PW91, a gradient-corrected density functional theory (GGA DFT).[21] The calculations used Blöchl's[22] projector augmented wave technique,[23] applied to pseudopotentials appropriate for GGA DFT,[24,25] and a plane-wave basis set with various choices of the energy cutoff parameter ENMAX (350–500 eV). Simulations were performed with the NVT (canonical) ensemble, using a Nosé[26] thermostat set for a thermal oscillation every 40 timesteps (SMASS = 0), and a Verlet velocity algorithm[27] with a timestep of 1 fs. These condensed-phase calculations employed periodic replication of a unit cell, and calculations were restricted to the gamma point. The unit cell contained catalysts of an overall –1 charge, to counterbalance the positive charge of the alkyl ion. Each atom had an isotope-averaged mass (e.g., 35.453 amu for Cl), except for H (mass 1.000 amu).

Simulations were performed of various C_7–C_9 alkyl ions in three different condensed-phase catalytic environments (Fig. 3). System IL was an ionic liquid, consisting of five pyridinium cations ($C_5H_5NH^+$) and six $Al_2Cl_7^-$ ions. Sys-

Fig. 3. Snapshot of parent geometries (within the replicated cell) used for simulations. Atom colour scheme: C atoms of alkyl ion, light blue; C atoms of pyridinium ions, light grey; N atoms of pyridinium ions, dark blue; Cl atoms, green; H atoms, white; O atoms, red; Si atoms, dark grey; Al atoms, pink.

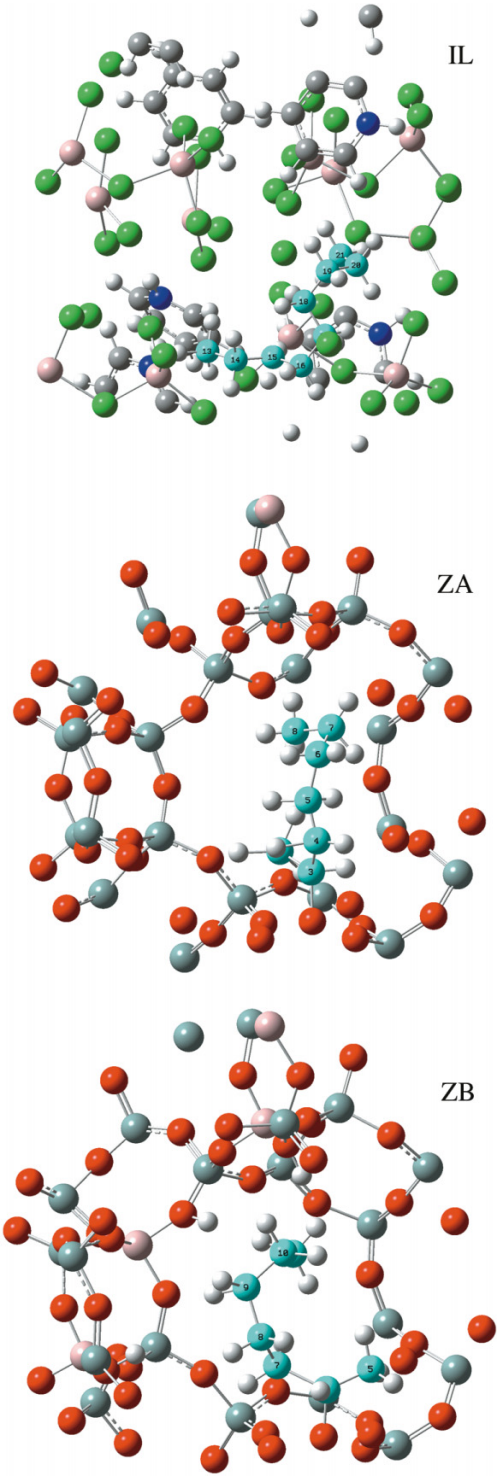

tems ZA and ZB were based on chabazite zeolite; our unit cell contains $Si_{24}O_{48}$ (twice the true unit cell of chabazite). System ZA had an Al^- substituted in the place of one Si atom. System ZB was derived from system ZA by the sub-

Fig. 4. Energy (upper plot) and temperature (lower plot) vs. time for the 50 K quench run of trimethylpentyl ion on chabazite ZA. E_0: potential energy for nuclear motion. $E_0 + E_K$: total internal energy. Regular nuclear speeds (temperature plot) are achieved after ~50 fs.

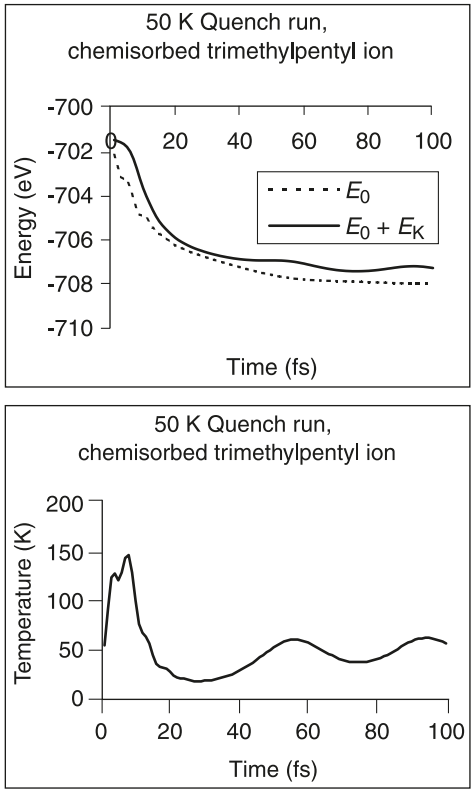

stitution of three Si–O diatom units with Al–O–H units. The purpose of system ZB was to increase the number of Brønsted acid sites, because simulations with system ZA tended to quickly result in deactivation of the carbocation to an alkene, thereby requiring reactivation by a Brønsted site. Details on the initial structures can be found in Appendices A–C.

Results

Preparatory runs

Equilibration runs were performed as described in Appendices A–C. For the zeolite simulations, attempts at equilibrating chemisorbed alkyl ions normally resulted in immediate desorption. We present some results from our preparatory runs to reassure the reader that we did ensure that immediate desorption was not the result of poor initial geometries.

For the tertiary 2,4,4-trimethylpent-2-yl ion, in system ZA, a quick quench run was performed at 50 K for only 100 fs. The choice of initial chemisorbed structure did not produce unreasonable velocities at the start (Fig. 4), but desorption began regardless, after only one C–O vibrational period (Fig. 5). Hence, one cannot equilibrate tertiary carbocations chemisorbed to chabazite with PW91-based simulations.

For *n*-alkyl secondary ions, which should bind more strongly than tertiary ions, we could maintain chemisorption at temperatures below ~1000 K, but above 1000 K desorption would occur within 1 ps. For instance, when our simulation of *n*-4-octyl chemisorbed on system ZA showed rapid desorption upon simulation above 1000 K, we tried a 4000 fs chemisorption-maintaining pseudo-equilibration run, rising in temperature from 200 to 600 K, before relaunching the production run from 1000 K. This relaunched production run produced desorption at t = 50 fs, earlier than in the original, nonequilibrated run (Fig. 5).

Fig. 5. Plot of chemisorption bond lengths to chabazite ZA vs. time: an equilibrated run (dashed line), a pre-equilibrated run (thick line), and the 50 K quench run for the tertiary trimethylpentyl ion (black line), demonstrating rapid desorption in each case.

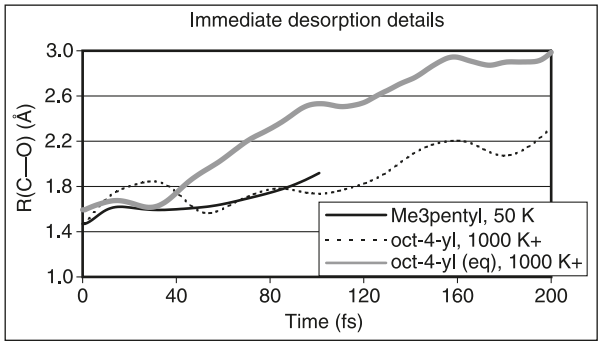

Production runs: unbranched alkyl ions

Twenty four of our 28 production runs began with *sec-n*-alkyl ions: six with desorbed ions in ionic liquid (IL) (Table 1, run 1, and Table 2) and 18 with chemisorbed ions on chabazite systems ZA and ZB (Tables 3 and 4, and Table 1, run 2). Of these 24 runs, β scission was observed in only the very first one: the ion branched first[17] and then, after taken to a very high temperature, performed a very rare tertiary-to-primary β scission. Although the other 23 runs did not produce β scission, there is useful information to be gleaned from them. One general observation from these other 23 runs was that the ultimate fate of the ions was deactivation: the loss of H^+ back to the catalyst to generate an alkene. On longer timescales, these C_7–C_9 alkenes could be reactivated by the Brønsted catalyst, but such a reactivation was not observed in the small (10^{-11} s) timescales of the simulations, even in system ZB, presumably because reactivation is a neutral–neutral bimolecular reaction requiring a specific low-probability collision.

Of the six runs in system IL, three resulted in branching before deactivation occurred. Several 1,2-H-shifts were observed, as were episodes of short-lived (~100 fs) PCP^+ structures, particularly at temperatures above 1000 K. Secondary carbocations tended to live for 1–4 ps in these rising-temperature simulations, until temperatures reached 1800–2000 K. Branching occurred between 1300 and 2000 K, after which the tertiary carbocations tended to live another 1–4 ps, until temperatures reached ~2500 K. The stability of these ions in system IL at constant temperatures was not tested: at experimental temperatures (~373 K) these ions would be expected to live longer, although not indefinitely, as carbocations would undergo oligomerization and cracking cycles until they either reach their most stable form (*t*-butyl ions) or become deactivated hydrocarbons that would settle into an organic layer.

Table 1. The results of simulations of various octyl ions.

Run	Baseline temperature (K)	Time (fs)	Event description
1. Oct-4-yl cation, system IL	1000 + 0.25/fs (to 2000)	1225	1,2-Propyl-shift, sec → prim
		1250	1,3-H-shift, prim → sec
		1695	1,2-Methyl-shift, sec → sec
		3590	1,2-H-shift, sec → prim
		3650	1,2-Hexyl-shift, prim → prim
		3730	1,6 H-shift (ene + pentavalent C)
		3830	Loss of H_2 (3-methylhept-6-en-2-yl)
		4010	Deactivation
2. Oct-4-yl cation, system ZA	1000 + 0.25/fs (to 2000)	135	Desorption
		3045	Deactivation
3. 2,4-Dimethylhex-2-yl cation, system IL	1000 + 0.25/fs (to 2000)	2250	1,2-H-shift, tert → sec
		2380	1,2-H-shift, sec → tert
		2790	1,2-H-shift, tert → sec
		2850	1,2-Ethyl-shift, sec → sec
		3468	***β Scission, sec → sec***
		3858	Deactivation
4. 2,4-Dimethylhex-2-yl cation, system ZA	1000 + 0.25/fs (to 2000)	20	Desorption
		365–546	Attempted β scission
		875–1005	Attempted β scission
		1905	***β Scission, tert → sec***
		3735	H transfer, sec → tert
5. 2,4,4-Trimethylpent-2-yl cation, system IL	600 + 0.2/fs (to 2200)	6880	***β Scission, tert → tert***
		7060	Deactivation
6. 2,4,4-Trimethylpent-2-yl cation, system ZA	300 + 0.25/fs (to 1300)	1	Desorption
		2317	***β Scission, tert → tert***
		3000	H transfer, tert → tert

Note: In each run, ENMAX = 350 eV. Deactivation refers to the loss of H^+ to the catalyst. H transfer refers to the transfer between hydrocarbon fragments. The numerous 1,2-H-shifts that did not result in a change of ion type were not reported.

Table 2. The results of simulations of non-3-yl ion in system IL (ionic liquid).

Run	Baseline temperature (K)	Time (fs)	Event description[a]
1	973 + 0.2/fs	5000	Branched, sec → tert
		7705	***β Scission, tert → prim***
		7775	Deactivated
2	973 + 0.2/fs	4248	Deactivated
3	1773 + 0.1/fs	145	Branched, sec → tert
		5583	Deactivated
4	1773 + 0.2/fs	1630	Deactivated
5	1773 + 0.2/fs	1380	Deactivated

Note: Each run was continued until deactivation occurred, and ENMAX = 400 eV except for runs 1 and 5 (500 eV).

[a]At these elevated temperatures, H-shifts were too numerous to report.

The 18 runs with the model zeolite systems, ZA and ZB, were begun with the alkyl ions in the chemisorbed state, to test the chemisorption hypothesis (Fig. 1), but the ion either stayed chemisorbed (three runs) or desorbed without performing the S_N2 β scission step (15 runs). Deactivation generally occurred at lower temperatures (1000–1800 K) than with the ionic liquid catalyst (>1700 K), because the zeolite is a stronger conjugate base than the ionic liquid, and this early deactivation is likely why neither cracking nor branching was observed in any of these 18 runs. In Table 3, several constant-temperature runs were performed to lengthen times before deactivation, but these longer times were not long enough to witness any branching or β scission events. The longest lifetime observed for a desorbed alkyl ion inside chabazite was 4.7 ps (Table 3, runs 3e and 4a).

Production runs: branched alkyl ions

In contrast to the 24 *sec-n*-alkyl runs, all four of the branched-alkyl runs succeeded in performing β scission, and are reported as the last four runs of Table 1. We make some minor remarks first. In Table 1, run 3, the starting tertiary ion spent some time as a secondary ion, during which an ethyl shift occurred before the β scission event. In Table 1, run 4 there were two unsuccessful attempts at β scission before the successful one occurred; this is demonstrated in Fig. 6 as a plot of the β C–C bond distance vs. time. In Table 1, runs 4 and 6, there were hydrogen transfers between the two product fragments, after β scission, the probability of which was likely enhanced by the solid pore structure of the zeolite, which kept the two fragments in close proximity.

Most importantly, in all four cases, the β scission mechanisms observed were classical WJM[5] ones from desorbed ions. No attempts at chemisorption-style S_N2 β scission were observed. Although occasional PCP^+ structures were observed for secondary alkyl ions during the simulations, none existed during the β scission events: in Fig. 7 we plot the critical C–C–C angle during the C–C bond scission events in these four runs, and the angle is never near the $\sim 80^\circ$ expected for a PCP^+ structure. The observed β-scission reactions are summarized in Table 5.

Table 3. The results of simulations of chemisorbed hept-2-yl ion in system ZA (zeolite).

Run	Baseline temperature (K)	Event description
Set I		
1	298	Stayed chemisorbed
2	300 + 0.2/fs (to 1100)	Stayed chemisorbed
3 (from 2)	1100 + 0.2/fs	Desorbed 770 fs, 3,2-H-shift 1600 fs, deactivated 1990 fs
3b (from 2)	1100 + 0.2/fs	Desorbed 50 fs, deactivated 500 fs
3c (from 2)	1000	Stayed chemisorbed
Set II (from 3c)		
3d[a]	1000	Desorbed 535 fs, deactivated 1670 fs
3f[a]	1100	Desorbed 500 fs, 3,2-H-shift 2035 fs, 2,3-H-shift 2065 fs, deactivated 2790 fs, reactivated 2920 fs, 3,2-H-shift 2935 fs, re-chemisorbed 3320 fs
3g[a]	1200	Desorbed 510 fs, 3,2-H-shift 1110 fs, 4,3-H-shift 1375 fs, deactivated 1465 fs
3e[a]	1300	Desorbed 500 fs, 3,2-H-shift 1220 fs, 5,3-H-shift 2340 fs, 6,5-H-shift 3440 fs
Set III (from 3c)		
4d[b]	1000	Desorbed 3150 fs, deactivated 3340 fs
4f[b]	1100	Desorbed 1200 fs, deactivated 1630 fs
4g[b]	1200	Desorbed 2080 fs, deactivated 2200 fs
4e[b]	1300	Desorbed 430 fs, deactivated 660 fs
Set IV (from 3e)		
4a[c]	1300	Deactivated 1250 fs
4b[d]	1300	Deactivated 2170 fs

Note: In each run, ENMAX = 350 eV and the length of the runs were 4000 fs.
[a]Set II runs began with the last positions and velocities of run 3c.
[b]Set III runs began with the last positions of run 3c, but with fresh Boltzmann velocities each run.
[c]Run 4a began with the last positions and velocities of run 3e.
[d]Run 4b began with the last positions of run 3e, but with fresh Boltzmann velocities.

Table 4. Results of simulations of chemisorbed hept-2-yl ion in system ZB (zeolite).

Run	Baseline temperature (K)	Length of simulation (fs)	Event description
1	1500	12000	Desorbed 140 fs, 3,2-H-shift 510 fs, deactivated 520 fs
1b	1900	4000	Desorbed 120 fs, 1,2-H-shift 250 fs, deactivated 267 fs, reactivated 285 fs, deactivated 380 fs

Note: In each run, ENMAX = 350 eV.

Fig. 6. A plot of the rupturing C–C bond distance vs. time, Table 1, run 4 (dimethylhexyl ion, chabazite catalyst).

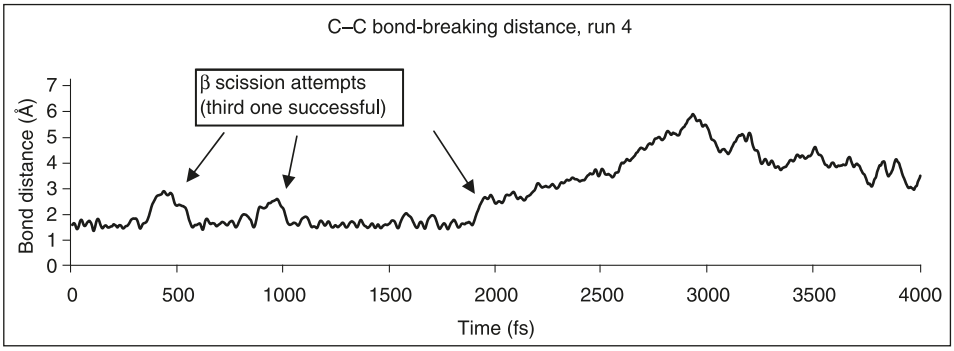

The use of artificially high temperatures does not bias the simulations against producing PCP^+ structures and Sie's[6–8] nonclassical mechanism; in fact, it produces more of these high-energy structures, but no β scissions resulted from them. The use of artificially high temperatures may bias the simulations against the chemisorption hypothesis, if it promotes desorption over S_N2 reaction, but our previous potential-energy-surface work[13,14] has already indicated that partial desorption is a commonly required step even at 0 K. Indeed, all the simulations are in accord with the WJM[5] scheme, in which desorbed and branched classical carbocations are the ones that undergo β scission.

Discussion

PCP^+ as an intermediate in *isomerizations* was proposed long ago, perhaps first by Nevell, de Salas, and Wilson,[28] who in 1939 described the possibility of an intermediate

Fig. 7. $C^+–C_\alpha–C_\beta$ bond angles during the four β scission events of Table 1. An expected angle for a β scission from a PCP^+ intermediate would be 80°, which was not observed.

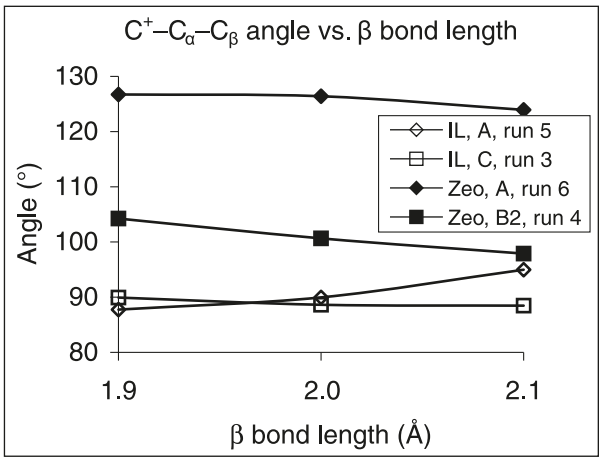

"mesomeric" between the two classical carbocation intermediates that Meerwein and van Emster[29] had postulated for the Wagner–Meerwein rearrangement. In the Wagner–Meerwein rearrangement, the PCP^+ ring has four alkyl substituents (2,1,1 distribution). In 1943, in a general article on organic reaction rates, Eyring, Hulbert, and Harman[30] speculated that "triangular configurations" for carbocations should have low enough energies to explain 1,2-alkyl rearrangements, quoting the early calculations on H_3^+ by Hirschfelder,[31] which revealed a triangular minimum-energy structure. These two suggestions, plus knowledge of triangular Ag^+-bridged alkenes,[32] led Winstein and Trifan[33] in 1949 to draw a symmetric "alkyl-bridged" norbornyl carbocation intermediate to account for racemization of its substituted exo enantiomers. In this racemization, the PCP^+ ring has only three substituents (1,1,1 distribution). Brown[34] would later famously contest the symmetric PCP^+ structure in Winstein and Trifan's[33] case, arguing that it is a transition state but not an intermediate. However, quantum chemistry calculations since 1983[35,36] have demonstrated that the bare ion does indeed have the (symmetric) PCP^+ structure, and not a classical one as Meerwein[29] would have thought.

In the Wagner–Meerwein and norbornyl rearrangements, the three participating carbons in the PCP^+ ring are tethered in a tricyclic structure. In 1952, Stevenson et al.[37] extended the PCP^+ idea for acyclic alkyl ions, proposing such structures as intermediates for alkyl shifts that change the amount of branching in the ion. This required a 1,2-H-shift to take place "concomitantly" with the PCP^+ branching mechanism. McCaulay,[38] in 1959, published a rate study demonstrating much slower rates of rearrangements for those that change the extent of branching, and explained this with PCP^+ arguments, arguing that PCP^+ allows partial, but not complete, avoidance of primary carbenium ion structures in the branching cases. The role of the hydrogens during branching was correctly postulated by Edwards and Lesage[39] in 1963, with the mechanism determined to be two-step in 1996 calculations by Corma and co-workers[40] and verified in recent simulations.[17] A seminal demonstration of the importance of PCP^+ structures for nontethered alkyl ions was provided by the thorough ab initio study of $C_4H_9^+$ conformers by Sieber et al.[41]

Table 5. Summary of β-scission events observed in our simulations.

Type	Reaction	Catalyst system
tert→tert (A)	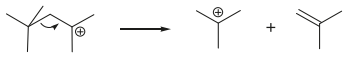	Ionic liquid Zeolite
tert→sec (B_2)	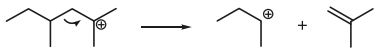	Zeolite
sec→sec (C)	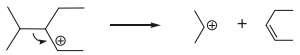	Ionic liquid
tert→prim	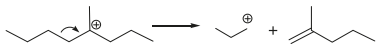	Ionic liquid

In contrast, there is no such long history of PCP^+ as an intermediate in *β scission*. Sie[6] proposed this mechanism in 1992. We could not find any significant challenges to this proposal in the literature, but there are in fact three criticisms that can be made. First, the Sie[6–8] mechanism is faulty on theoretical grounds because, in the last structure leading to β scission (Fig. 1, middle panel, fourth structure down), there are two carbon atoms each sharing 10 electrons (third and fourth carbons from the right), a disastrous violation of the octet rule. Second, this mechanism describes not β scission, but γ scission, and is thus clearly contrary to experimental evidence. Third, Sie[6–8] had originally criticized the WJM[5] mechanism because it implied that cracking rates should be independent of the original extent of branching (WJM[5] assumed that branching occurs before cracking), in contrast to experiments such as those by Nace,[42] which appeared to show otherwise. However, the Nace[42] experiments that Sie[6–8] quoted were two-minute experiments on alkanes with a zeolite catalyst, and can be explained (as Nace[42] himself did) by realizing that the overall cracking rate is determined by the initiation step, not the branching or cracking steps. The two probable reasons why Nace's[42] heptamethylnonane cracked more slowly than *n*-hexadecane are that (*i*) each heptamethylnonane molecule had only seven attackable hydrogens (six secondary and one tertiary), while each *n*-hexadecane has 28 (all secondary), and (*ii*) the heptamethylnonane possessed three quaternary carbon atoms, giving the molecule sufficient bulk that it may have had difficulty fitting into the zeolite pores.

Since the current study demonstrates that simulations biased towards PCP^+ structures (due to elevated temperatures) do not use PCP^+ structures during β scission, it would seem appropriate to retire the Sie[6–8] mechanism altogether. Since the WJM[5] mechanism only applies to hexyl ions and larger, there may be a role for PCP^+ structures in the extreme high-temperature monomolecular cracking of pentyl and butyl ions, but certainly not with 10-valence-electron carbon atoms as Sie[6] had envisaged.

The chemisorption hypothesis, while unimportant for ionic liquids, cannot yet be ruled out for zeolites. The simulations employed here used elevated temperatures, which are biased toward desorption. There might also be possible bias against the chemisorption hypothesis due to the PW91 DFT approximation, which might underestimate desorption ener-

gies and overestimate S_N2-scission barriers due to omission of dispersion interactions; future research should test these possibilities. However, since computed activation enthalpy barriers[13,14] for the chemisorption mechanism are not much lower than those for full desorption, since entropy would favour desorption, and since our simulations gave four instances of unimolecular scission and none of bimolecular-S_N2 scission, it would seem to us that the S_N2-chemisorbed mechanism in Fig. 1 is on shakier ground than unimolecular WJM[5] mechanisms. We are now inclined to think that the chemisorbed state is a storage state for alkyl ions, but that β scission likely occurs in the desorbed state. Although in situ NMR experiments have failed to identify desorbed carbocations inside zeolites, the simulations offer the explanation that the desorbed alkyl ions simply have short (10^{-9} to 10^{-12} s) lifetimes relative to deactivation to alkenes (or chemisorption), and that cracking must occur during these brief but periodic lifetimes.

Conclusions

In 28 simulations of branched and unbranched alkyl (carbenium) carbocations in the presence of catalysts, only the branched alkyl ions performed β scission within simulation timescales, and all five performed straightforward bond breaking without involving chemisorbed or PCP^+ structures. Formation of a primary carbocation, which would have been produced by β scission of *sec-n*-alkyl ions, is simply not energetically favourable, and only occurred in one simulation at a very high temperature (>2500 K). Desorption was common to all simulations that began in the chemisorbed state, and the lifetimes of desorbed carbocations (relative to deprotonation by the zeolite) was <5 ps at 1000–2000 K. These new simulations give support for the WJM[5] classical mechanism, and not for the Sie[6–8] PCP^+ mechanism, which has several theoretical problems. The S_N2-chemisorbed and alternative PCP^+ mechanisms cannot yet be ruled out, but they should be considered targets for further scrutiny.

Acknowledgements

Grants were made available by the Natural Sciences and Engineering Research Council of Canada (NSERC) and the Canada Foundation for Innovation (CFI). All simulations were performed on a Parallel Quantum Solutions computer (56 processors) housed in the Laboratory of Computational Discovery at the University of Regina. J. Hafner and T. Bučko (University of Vienna) are thanked for for valuable advice, and T. Bučko for providing the chabazite input deck.

References

(1) Thomas, C. L. *Ind. Eng. Chem.* **1949**, *41* (11), 2564–2573. doi:10.1021/ie50479a042.

(2) Greensfelder, B. S.; Voge, H. H.; Good, G. M. *Ind. Eng. Chem.* **1949**, *41* (11), 2573–2584. doi:10.1021/ie50479a043.

(3) Kissin, Y. V. *Catal. Rev.* **2001**, *43* (1–2), 85–146. doi:10.1081/CR-100104387.

(4) Akhmedov, V. M.; Al-Khowaiter, S. H. *Catal. Rev.* **2007**, *49* (1), 33–139. doi:10.1080/01614940601128427.

(5) Weitkamp, J.; Jacobs, P.; Martens, J. A. *Appl. Catal.* **1983**, *8* (1), 123–141. doi:10.1016/0166-9834(83)80058-X.

(6) Sie, S. T. *Ind. Eng. Chem. Res.* **1992**, *31* (8), 1881–1889. doi:10.1021/ie00008a008.

(7) Sie, S. T. *Ind. Eng. Chem. Res.* **1993**, *32* (3), 397–402. doi:10.1021/ie00015a001.

(8) Sie, S. T. *Ind. Eng. Chem. Res.* **1993**, *32* (3), 403–408. doi:10.1021/ie00015a002.

(9) (a) Jentoft, F. C.; Gates, B. C. *Top. Catal.* **1997**, *4* (1/2), 1–13. doi:10.1023/A:1019184004885.; (b) Ono, Y. *Catal. Today* **2003**, *81* (1), 3–16. doi:10.1016/S0920-5861(03)00097-X.; (c) Leckel, D. *Energy Fuels* **2007**, *21* (3), 1425–1431. doi:10.1021/ef060601x.; (d) Bhan, A.; Gounder, R.; Macht, J.; Iglesia, E. *J. Catal.* **2008**, *253* (1), 221–224. doi:10.1016/j.jcat.2007.11.003.

(10) Kazansky, V. B.; Senchenya, I. N. *J. Catal.* **1989**, *119* (1), 108–120. doi:10.1016/0021-9517(89)90139-5.

(11) (a) Bates, S. P.; van Santen, R. A. *Adv. Catal.* **1998**, *42*, 1–114. doi:10.1016/S0360-0564(08)60627-6.; (b) Frash, M. V.; van Santen, R. A. *Top. Catal.* **1999**, *9* (3/4), 191–205. doi:10.1023/A:1019183110705.

(12) (a) Nicholas, J. B.; Haw, J. F. *J. Am. Chem. Soc.* **1998**, *120* (45), 11804–11805. doi:10.1021/ja982012e.; (b) Haw, J. F. *Phys. Chem. Chem. Phys.* **2002**, *4* (22), 5431–5441. doi:10.1039/b206483a.

(13) Li, Q.; East, A. L. L. *Can. J. Chem.* **2005**, *83* (8), 1146–1157. doi:10.1139/v05-135.

(14) Li, Q.; East, A. L. L. *Can. J. Chem.* **2006**, *84* (9), 1159–1166. doi:10.1139/V06-143.

(15) (a) Frash, M. V.; Kazansky, V. B.; Rigby, A. M.; van Santen, R. A. *J. Phys. Chem. B* **1998**, *102* (12), 2232–2238. doi:10.1021/jp973203r.; (b) Hay, P. J.; Redondo, A.; Guo, Y. *Catal. Today* **1999**, *50* (3–4), 517–523. doi:10.1016/S0920-5861(98)00486-6.; (c) Svelle, S.; Kolboe, S.; Swang, O. *J. Phys. Chem. B* **2004**, *108* (9), 2953–2962. doi:10.1021/jp0371985.; (d) Demuth, T.; Rozanska, X.; Benco, L.; Hafner, J.; van Santen, R. A.; Toulhoat, H. *J. Catal.* **2003**, *214* (1), 68–77. doi:10.1016/S0021-9517(02)00074-X.

(16) (a) Sørensen, M. R.; Voter, A. F. *J. Chem. Phys.* **2000**, *112* (21), 9599–9606 doi:10.1063/1.481576.; (b) East, A. L. L.; Bučko, T.; Hafner, J. *J. Phys. Chem. A* **2007**, *111* (27), 5945–5947. doi:10.1021/jp072327t. PMID:17559202.

(17) Ammal, S. C.; Yamataka, H.; Aida, M.; Dupuis, M. *Science* **2003**, *299* (5612), 1555–1557. doi:10.1126/science.1079491. PMID:12624261.

(18) Xiao, L.; Johnson, K. E.; Treble, R. G. *J. Mol. Catal. A* **2004**, *214* (1), 121–127. doi:10.1016/j.molcata.2003.12.030.

(19) Bučko, T.; Benco, L.; Hafner, J.; Ángyán, J. G. *J. Catal.* **2007**, *250* (1), 171–183. doi:10.1016/j.jcat.2007.05.025.

(20) Kresse, G.; Furthmüller, J. *J. Phys. Rev. B* **1996**, *54* (16), 11169–11186. doi:10.1103/PhysRevB.54.11169.

(21) Perdew, J. P.; Chevary, J. A.; Vosko, S. H.; Jackson, K. A.; Pederson, M. R.; Singh, D. J.; Fiolhais, C. *Phys. Rev. B* **1992**, *46* (11), 6671–6687. doi:10.1103/PhysRevB.46.6671.

(22) Blöchl, P. E. *Phys. Rev. B* **1994**, *50* (24), 17953–17979. doi:10.1103/PhysRevB.50.17953.

(23) Kresse, G.; Joubert, D. *Phys. Rev. B* **1999**, *59* (3), 1758–1775. doi:10.1103/PhysRevB.59.1758.

(24) Vanderbilt, D. *Phys. Rev. B* **1990**, *41* (11), 7892–7895. doi:10.1103/PhysRevB.41.7892.

(25) Kresse, G.; Hafner, J. *J. Phys. Condens. Matter* **1994**, *6* (40), 8245–8257. doi:10.1088/0953-8984/6/40/015.

(26) Nosé, S. *J. Chem. Phys.* **1984**, *81* (1), 511–519. doi:10.1063/1.447334.

(27) Allen, M. P.; Tildesley, D. J. *Computer Simulations of Liquids;* Clarendon: Oxford, UK, 1987.

(28) Nevell, T. P.; de Salas, E.; Wilson, C. L. *J. Chem. Soc.* **1939**, 1188. doi:10.1039/jr9390001188.
(29) Meerwein, H.; van Emster, K. *Chem. Ber.* **1922**, *55*, 2500–2528.
(30) Eyring, H.; Hulburt, H. M.; Harman, R. A. *Ind. Eng. Chem.* **1943**, *35* (5), 511–521. doi:10.1021/ie50401a003.
(31) Hirschfelder, J. O. *J. Chem. Phys.* **1938**, *6* (12), 795–806. doi:10.1063/1.1750173.
(32) Winstein, S.; Lucas, H. J. *J. Am. Chem. Soc.* **1938**, *60* (4), 836–847. doi:10.1021/ja01271a021.
(33) Winstein, S.; Trifan, D. S. *J. Am. Chem. Soc.* **1949**, *71* (8), 2953. doi:10.1021/ja01176a536.
(34) Brown, H. C. *The Nonclassical Ion Problem;* Plenum Press: New York, 1977.
(35) Raghavachari, K.; Haddon, R. C.; Schleyer, P. R.; Schaefer, H. F., III. *J. Am. Chem. Soc.* **1983**, *105* (18), 5915–5917. doi:10.1021/ja00356a034.
(36) Yoshimine, M.; McLean, A. D.; Liu, B.; DeFrees, D. J.; Binkley, J. S. *J. Am. Chem. Soc.* **1983**, *105* (19), 6185–6186. doi:10.1021/ja00357a055.
(37) Stevenson, D. P.; Wagner, C. D.; Beeck, O.; Otvos, J. W. *J. Am. Chem. Soc.* **1952**, *74* (13), 3269–3282. doi:10.1021/ja01133a017.
(38) McCaulay, D. A. *J. Am. Chem. Soc.* **1959**, *81* (24), 6437–6443. doi:10.1021/ja01533a026.
(39) Edwards, O. E.; Lesage, M. *Can. J. Chem.* **1963**, *41* (6), 1592–1605. doi:10.1139/v63-218.
(40) Boronat, M.; Viruela, P.; Corma, A. *J. Phys. Chem.* **1996**, *100* (41), 16514–16521. doi:10.1021/jp961179w.
(41) Sieber, S.; Buzek, P.; Schleyer, P. R.; Koch, W.; Carneiro, J. W. M. *J. Am. Chem. Soc.* **1993**, *115* (1), 259–270. doi:10.1021/ja00054a037.
(42) Nace, D. M. *Ind. Eng. Chem. Prod. Res. Dev.* **1969**, *8* (1), 31–38. doi:10.1021/i360029a005.

Appendix A. Starting geometries: system IL

An ionic liquid starting geometry was meticulously built by hand, with six $[C_5H_5NH]^+$ ions and six $[Al_2Cl_7]^-$ ions, in a cubic unit cell of width 13.72 Å to match the experimental density of 1.476 g/mL.[18] This was equilibrated at 373 K with a Nosé[26] thermostat for 1004 fs. Initially, the temperature rose to 1700 K due to the initial forces caused by the artificial geometry, but the thermostat quenched this within 50 fs, and the cell energy was steady from 200 fs onward. The velocities of all 126 atoms were plotted vs. time to ensure that no lingering "hot modes" existed after 1004 fs.

Table 2 runs: the structure from the first equilibration was taken, the cell width was expanded from 13.72 to 13.90 Å (a 4% volume expansion), and one $C_5H_5NH^+$ was replaced with a non-3-yl ion (Fig. 3, top). This corresponds to a nonyl ion concentration of 5% by weight; although the experiment of interest[18] used 25% nonane by weight, the nonane is insoluble in an ionic liquid until it is ionized, so that 5% nonyl ion concentration may be a reasonable estimate of reality. Four copies of this geometry file were made. The first copy was further equilibrated, for 3000 fs at 773 K followed by another 3000 fs at 973 K, and then split into two copies for trials 1 and 2, each starting at 973 K. Trials 3, 4, and 5 ignored the further 6 ps of equilibration and began from the three other original copies.

Table 1 runs: the structure from the first equilibration was taken, the cell width was expanded from 13.72 to 13.90 Å (a 4% volume expansion), one $C_5H_5NH^+$ was replaced with a 2,6-H-bridged $C_9H_{19}^+$ ion (originally intended for a different study), and this mixture was further equilibrated at 300 K for another 1000 fs (the $C_9H_{19}^+$ ion began and ended with the 2,6-H-bridge). The resulting structure was split into three copies, and in each the $C_9H_{19}^+$ ion was replaced with one of the three starting $C_8H_{17}^+$ ions of the current study. No further equilibration was performed, as the liquid quickly adjusted to the new ion in the first $\sim$100 fs of each of the rising-temperature runs in this study.

Appendix B. Starting geometries: system ZA

The chabazite structure, $[AlSi_{23}O_{48}]^-$, contains two unit cells of chabazite, with an Al atom substituted for a Si one, as described previously.[19] We received a pre-equilibrated one (containing a desorbed $C_4H_{11}^+$ ion) from Tomas Bučko (Vienna).

Table 3 runs: the desorbed $C_4H_{11}^+$ ion was replaced with a hept-2-yl ion chemisorbed to an oxygen atom neighbouring an Al atom of a replicated cell (Fig. 3, centre). The first run reported in Table 3 served as the equilibration run, but it possessed a continually rotating methyl group, so the second run was begun from the first but with velocities removed to reset the methyl rotation. All remaining runs in Table 3 are descendants of this second run.

Table 1 runs: the desorbed $C_4H_{11}^+$ ion was replaced with one of the three $C_8H_{17}^+$ ions of this study, chemisorbed to the same oxygen atom. Attempts at equilibrating the chemisorbed *sec*- and *tert*-alkyl ions failed to prevent immediate desorption (see text), so the rising-temperature production runs were run from the structures built.

Appendix C. Starting geometries: system ZB

Table 4 runs: the final heptyl ion/chabazite chemisorbed complex from run 3c of Table 3 was copied to a new input file, three Si atoms were replaced with Al atoms, and three H atoms were then added to O atoms bonded to these new Al atoms, creating three Brønsted AlOH sites within the same pore as the alkyl ion (Fig. 3, bottom). This structure was used as the starting structure for both runs in Table 4.

Validation of broken-symmetry density functional methods for the calculation of electron paramagnetic resonance parameters of dinuclear mixed-valence $Mn^{IV}Mn^{III}$ complexes

Sandra Schinzel and Martin Kaupp

Abstract: . The EPR parameters of a series of dinuclear manganese(III,IV) complexes with mono(μ-oxo), bis(μ-oxo), (μ-oxo)(μ-carboxylato), bis(μ-oxo)(μ-carboxylato), and (μ-oxo)bis(μ-carboxylato) bridges were studied by broken-symmetry density functional (DFT) methods. The influence of the exchange-correlation functional on the agreement with experiment has been evaluated systematically for **g** tensors; ^{55}Mn, ^{14}N, and ^{1}H hyperfine coupling tensors; and Heisenberg exchange couplings. ^{14}N and ^{1}H hyperfine couplings, ^{55}Mn hyperfine anisotropies, **g** tensors, and exchange couplings are well described by hybrid functionals with moderate exact-exchange admixtures such as B3LYP. The isotropic ^{55}Mn hyperfine couplings require larger exact-exchange admixtures. However, the errors of the B3LYP calculations are systematic and may be corrected by a constant scaling factor, providing good predictive power for a wide range of EPR parameters with broken-symmetry DFT and standard functionals. The influence of terminal and bridging ligands on structure, spin-density distributions, and EPR parameters are evaluated systematically. Computed hyperfine and **g** tensors are not covariant to each other. This may have consequences for spectra simulations. The nature of the broken-symmetry state and the origin of its spin contamination were analyzed by an expansion into restricted determinants, based on paired orbitals.

Key words: broken-symmetry density functional theory, electron paramagnetic resonance, **g** tensor, Heisenberg exchange coupling constant, hyperfine tensor, dinuclear manganese complex, paired orbital analysis.

Résumé : Faisant appel aux méthodes de la théorie de la fonctionnelle de la densité (TFD) à symétrie brisée, on a étudié les paramètres de résonance paramagnétique électronique (RPE) d'une série de complexes dinucléaires du manganèse(III,IV) comportant des ponts mono(μ-oxo), bis(μ-oxo), (μ-oxo)(μ-carboxylato), bis(μ-oxo)(μ-carboxylato) et (μ-oxo)bis(μ-carboxylato). On a évalué d'une façon systématique l'influence de la fonctionnelle d'échange de corrélation sur l'accord entre les valeurs expérimentales et calculées des tenseurs-**g**, des tenseurs de couplage hyperfin du ^{55}Mn, du ^{14}N, et du ^{1}H ainsi que des couplages d'échange d'Heisenberg. Les couplages hyperfins du ^{14}N et du ^{1}H hyperfine, les anisotropies hyperfines du ^{55}Mn, les tenseurs-**g** et les couplages d'échange sont bien décrits par les fonctionnelles hybrides avec un mélange d'échange exact modéré du type B3LYP. Les couplages hyperfins isotrope du ^{55}Mn nécessitent des mélanges d'échange exact plus importants. Toutefois les erreurs découlant d'une utilisation de calculs B3LYP sont systématiques et peuvent être corrigées par un facteur d'échelle constant, ce qui permet de profiter de bons pouvoirs de prédiction pour une grande variété de paramètres RPE avec la TFD à symétrie brisées et des fonctionnelles standard. On a évalué d'une façon systématique l'influence des ligands terminaux et ceux agissant comme pont sur la structure, les distributions de la densité de spin et les paramètres RPE. Les valeurs calculées pour les tenseurs-**g** et les propriétés hyperfines ne sont pas covariantes l'une par rapport à l'autre. Cette situation peut avoir des conséquences pour les simulations de spectres. On a analysé la nature de l'état de la symétrie brisée et l'origine de sa contamination du spin par une expansion dans des déterminants restreints, basée sur des orbitales en paires.

Mots-clés : théorie de la fonctionnelle de densité à symétrie brisée, résonance paramagnétique électronique, tenseur-**g**, constante de couplage d'échange d'Heisenberg, tenseur hyperfin, complexe dinucléaire du manganese, analyse d'orbitales par paires.

[Traduit par la Rédaction]

Received 13 February 2009. Accepted 2 April 2009. Published on the NRC Research Press Web site at canjchem.nrc.ca on 9 October 2009.

This article is part of a Special Issue dedicated to Professor T. Ziegler.

S. Schinzel and M. Kaupp.[1] Institut für Anorganische Chemie, Universität Würzburg, Am Hubland D-97074, Würzburg, Germany.

[1]Corresponding author (e-mail: kaupp@mail.uni-wuerzburg.de).

Introduction

The structure and electronic properties of multinuclear manganese complexes are of substantial importance in such diverse fields as molecular magnetism[1] and bioinorganic chemistry. Prominent examples for the latter area are the active sites of metalloenzymes,[2] in particular, the oxygen-evolving complex (OEC) of photosystem II.[3,4] The oxidation of two water molecules to provide the molecular oxygen of Earth's atmosphere is driven by sunlight and catalyzed by a tetranuclear manganese complex. Structure, protein environment, and function of the OEC have been at the focus of a

tremendous amount of research over the past 25 years. The methodology applied ranges from biochemical studies via X-ray diffraction,[5–7] X-ray absorption spectroscopies,[8,9] and IR and optical spectroscopies[10,11] to electron paramagnetic resonance (EPR) spectroscopy.[12,13] Significant progress has been made, yet many questions remain open, e.g., the precise position of the manganese atoms, the ligand sphere, or the nature of the bridging ligands. For many steps along the catalytic cycle of the OEC (and for dinuclear enzyme sites like catalase), EPR provides important information. Optimal use of EPR for structure elucidation should benefit greatly from the quantum chemical computation of EPR parameters for the evaluation of the validity of proposed molecular models. The development of suitable methodology applicable to such multinuclear mixed-valence manganese sites is thus highly desirable.

A main challenge for spin-coupled multinuclear transition metal systems is their energetically close-lying electronic levels. To correctly describe the antiferromagnetic couplings present in ground and excited statess would require a multideterminant based treatment for very accurate calculations. For the systems of interest, their size typically prohibits such a multideterminantal treatment at present. This holds in particular for the OEC. A cost-efficient approximate alternative in widespread use is broken-symmetry density functional theory (BS-DFT)[14,15] technique, where single-determinantal unrestricted Kohn–Sham (KS) wave functions are appropriately spin-projected[16,17] to simulate energy levels and spin-density distributions of the true antiferromagnetically coupled states. The main area of application of BS-DFT has been in the computation of Heisenberg exchange coupling constants that describe the spin couplings of the system. Yet, EPR parameters like hyperfine coupling constants (HFCs) or electronic **g** tensors also have been the focus of interest early on[18] (also see ref. 19).[19] Recently, Sinnecker et al.[20,21] have carried out BS-DFT based EPR parameter calculations (for **g** tensors and ^{55}Mn, ^{14}N, and ^{1}H HFCs) for the dinuclear Mn^{III}–Mn^{IV} complexes $[(dtne)Mn(\mu\text{-}O)_2(\mu\text{-}OAc)Mn]^{2+}$ and for a model of the superoxidized state of dimanganese catalase (**Mn-cat**). Here, we extend these important studies to a larger set of mixed-valence dinuclear Mn^{IV}–Mn^{III} complexes with different bridging and terminal ligand sets and to a wider selection of functionals, with the aim of validating the BS-DFT approaches for application to the OEC. In particular, we are interested in examining the effect of an exact-exchange (EXX) admixture in hybrid exchange-correlation functionals. This point has not yet been addressed in detail for BS-DFT calculations of EPR parameters, but it is deemed crucial for accurate predictions. Calculations on mononuclear Mn complexes suggest, for example,[22] that Mn HFCs and certain ligand HFCs require substantially larger EXX admixtures than provided by standard hybrid functionals like B3LYP. As we will also provide results for Heisenberg exchange coupling constants, we note in passing, in addition to the above-mentioned work of Sinnecker et al., the BS-DFT studies on the exchange couplings of dinuclear Mn^{III}–Mn^{IV} [23] and Mn^{IV}–Mn^{IV}[24] complexes (the vast literature on BS-DFT calculations of exchange couplings of di- and multi-nuclear transition metal complexes in general is outside the scope of this Introduction; some references will be given later in the paper). We compare different functionals and different spin-projection schemes[15,25] in this context and we also study the influence of bridging and terminal ligand sets.

Theoretical formalism and computational details

The theoretical background of EPR parameters and spin-projection techniques for simulations of spectra of multinuclear complexes are covered in detail in various text books.[17,26–31] Here, we summarize only the most relevant points.

g-Tensor calculations

The **g** tensor is provided as a correction to the free-electron value g_e (in ppt, i.e., in units of 1×10^{-3})

$$[1] \qquad \mathbf{g} = g_e 1 + \Delta g$$

with $g_e = 2.002\,319$. Up to the level of second-order perturbation theory based on the Breit–Pauli Hamiltonian, the g-shift Δg consists of three terms:

$$[2] \qquad \Delta g = \Delta g^{SO/OZ} + \Delta g^{RMC} + \Delta g^{GC}$$

of which the "paramagnetic" second-order spin-orbit/orbital Zeeman cross term, $\Delta g^{SO/OZ}$, dominates (except for extremely small Δg values).[31] The relativistic mass correction term Δg^{RMC} and the one-electron part of the gauge correction term Δg^{GC} are also included in our implementation[32,33] (also see refs. 34 and 35 for related implementations).

Hyperfine tensor calculations

In the usual nonrelativistic first-order approximation, isotropic hyperfine splittings $\mathbf{A}_{iso}(N)$ correspond to the Fermi-contact term $\mathbf{A}^{FC}$:

$$[3] \qquad \mathbf{A}_{iso}(N) = \mathbf{A}^{FC} = \frac{4\pi}{3}\beta_e\beta_N g_e g_N \langle S_Z\rangle^{-1} \sum_{\mu,\nu} P^{\alpha-\beta}_{\mu,\nu} \langle \varphi_\mu | \delta(\mathbf{R}_N) | \varphi_\nu \rangle$$

β_e is the Bohr magneton, β_N the nuclear magneton, g_N is the g value of nucleus N, $\langle S_Z\rangle$ is the expectation value of the z component of the total electronic spin, $P^{\alpha-\beta}_{\mu,\nu}$ is the spin density matrix, φ_μ and φ_ν are basis functions, $\mathbf{R}_N$ is the position vector of nucleus N, and the summation runs over all occupied molecular orbitals. The components $\mathbf{A}^{dip}_{ij}$ of the anisotropic tensor are given by

$$[4] \qquad \mathbf{A}^{dip}_{ij}(N) = \frac{1}{2}\beta_e\beta_N g_e g_N \langle S_Z\rangle^{-1} \times \sum_{\mu,\nu} P^{\alpha-\beta}_{\mu,\nu} \langle \varphi_\mu | \mathbf{r}_N^{-5} (\mathbf{r}_N^2 \delta_{ij} - 3\mathbf{r}_{N,i}\mathbf{r}_{N,j}) | \varphi_\nu \rangle$$

where $\mathbf{r}_N = r - \mathbf{R}_N$. In the rest of this section, we will refer to the metal hyperfine interaction and omit subscript N. The second-order perturbation treatment of refs. 36 and 37[36,37] is used to compute spin-orbit (SO) corrections to the hyperfine tensor (in this work, the corrections are only relevant for the metal HFC). At the coupled-perturbed KS level, the dominant SO correction term arises as a second-order cross term between the one- and two-electron SO Hamiltonian $\mathscr{H}^{SO}$ and the perturbed Fock operator F'

$$[5]\qquad \mathbf{A}^{\mathrm{SO}-I}_{K,uv} = \frac{1}{2}\alpha^4 g_e \gamma_K \frac{1}{2\langle S_Z\rangle}\left[\sum_k^{\mathrm{occ}(\alpha)}\sum_a^{\mathrm{virt}(\alpha)} \frac{\langle\psi_k^\alpha|h_u^{\mathrm{SO}}|\psi_a^\alpha\rangle\langle\psi_a^\alpha|F_v'|\psi_k^\alpha\rangle}{\varepsilon_k^\alpha - \varepsilon_a^\alpha} - \sum_k^{\mathrm{occ}(\beta)}\sum_a^{\mathrm{virt}(\beta)} \frac{\langle\psi_k^\beta|h_u^{\mathrm{SO}}|\psi_a^\beta\rangle\langle\psi_a^\beta|F_v'|\psi_k^\beta\rangle}{\varepsilon_k^\beta - \varepsilon_a^\beta}\right]$$

where α is the fine-structure constant; γ_K is the gyromagnetic ratio of the nucleus; h_u^{SO} are matrix elements of the spatial part of the spin-orbit Hamiltonian; $F_v' = (\ell_v/r^3) - \frac{2}{\alpha}a_0\sum_{k=1}^{n/2} K_v'$, where (ℓ_v/r^3) is the paramagnetic nuclear-spin electron-orbit (PSO) operator, K_v' is a component of the response exchange operator, and a_0 is the weight of HF exchange depending on the specific hybrid functional used (see ref. 38 for a related simultaneous CPKS implementation and also refs. 36 and 37 for references to earlier work); ψ^σ and ε^σ are spin-polarized KS orbitals and orbital energies, respectively. GGA or LDA functionals lead to an uncoupled DFT (UDFT) treatment for this second-order term ($a_0 = 0$).

Spin-projection techniques

The Heisenberg exchange coupling constant J describes the magnetic coupling between localized spins in the Heisenberg Hamiltonian

$$[6]\qquad \widehat{H}_{HDvV} = -2J\boldsymbol{S}_A\boldsymbol{S}_B$$

where $\boldsymbol{S}_A$ and $\boldsymbol{S}_B$ are spins localized on centers A and B, respectively.

Next, we compare two different spin-projection schemes: Noodleman's[15] broken-symmetry expression for weakly coupled centers provides J as

$$[7]\qquad J = -\frac{E_{hs} - E_{bs}}{4S_AS_B}$$

where E_{hs} and E_{bS} are the energies of the high-spin and broken-symmetry spin states, respectively, and S_A and S_B are the individual spins. Yamaguchi and co-workers[25] suggested using

$$[8]\qquad J = -\frac{E_{hs} - E_{bs}}{\langle\widehat{S}^2\rangle_{hs} - \langle\widehat{S}^2\rangle_{bs}}$$

where $\langle\widehat{S}^2\rangle_{hs}$ and $\langle\widehat{S}^2\rangle_{bs}$ are the computed total spin angular momentum expectation values for the high-spin and broken-symmetry spin states, respectively. This scheme is supposed to be independent of the bonding situation and hence usable for any coupling strength.

For the evaluation of the **g** tensor, two separate DFT calculations were carried out, from which the **g** tensors of the high-spin state ($\mathbf{g}_{hs}$) and of the broken-symmetry doublet configuration ($\mathbf{g}_{bs}$) are obtained. Spin-projection schemes give access to the **g** tensor site values ($\mathbf{g}_i$) of the exchange-coupled Mn^{III}–Mn^{IV} complex ($M_S^{hs} = S_A + S_B$, $M_S^{bs} = S_A - S_B$)[17]

$$[9]\qquad \mathbf{g}_1 = \frac{1}{2S_1}(\mathbf{g}_{hs}M_S^{hs} + \mathbf{g}_{bs}M_S^{bs})$$

and

$$[10]\qquad \mathbf{g}_2 = \frac{1}{2S_2}(\mathbf{g}_{hs}M_S^{hs} + \mathbf{g}_{bs}M_S^{bs})$$

Following this approach, the effective **g** is given by[39]

$$[11]\qquad \mathbf{g} = c_1\mathbf{g}_1 + c_2\mathbf{g}_2 \frac{c_1c_2}{5J}(\mathbf{g}_1 - \mathbf{g}_2)[(3c_1+1)\cdot\mathbf{D}_1 - (3c_2+1)\cdot\mathbf{D}_2]$$

where c_i is the spin projection coefficient, $\mathbf{D}_1$ and $\mathbf{D}_2$ are site zero-field splitting tensors.

In eq. [11] the spin projection coefficient is

$$[12]\qquad c_i = \frac{S(S+1) + S_i(S_i+1) - S_j(S_j+1)}{2S(S+1)}$$

For dinuclear Mn^{III}–Mn^{IV} complexes this gives $c_1 = 2$ (Mn^{III}, d^4) and $c_2 = -1$ (Mn^{IV}, d^3). In view of the large exchange coupling ($J > 100$ cm^{-1}) and relatively small zero-field splitting (<5 cm^{-1}),[39,40], the ZFS contributions may be neglected,[20] and eq. [11] then reduces to

$$[13]\qquad \mathbf{g} = c_1\mathbf{g}_1 + c_2\mathbf{g}_2$$

The hyperfine site values A_i^{eff} for a dinuclear Mn^{III}–Mn^{IV} complex are given as[39]

$$[14]\qquad A_1^{\mathrm{eff}} = c_1\mathbf{a}_1 - \frac{\mathbf{a}_1}{5J}c_1c_2[(3c_1+1)\cdot\mathbf{D}_1 - (3c_2+1)\cdot\mathbf{D}_2]$$

$$[15]\qquad A_2^{\mathrm{eff}} = c_2\mathbf{a}_2 - \frac{\mathbf{a}_2}{5J}c_1c_2[(3c_1+1)\cdot\mathbf{D}_1 - (3c_2+1)\cdot\mathbf{D}_2]$$

where $\boldsymbol{a}_i$ are intrinsic hyperfine tensors (site tensors).

Again, neglecting the ZFS contributions, eqs. [14] and [15] can be simplified to

$$[16]\qquad A_1^{\mathrm{eff}} = c_1\mathbf{a}_1$$

and

$$[17]\qquad A_2^{\mathrm{eff}} = c_2\mathbf{a}_2$$

In our analysis, we have not considered double-exchange interactions within the effective spin Hamiltonian. While these can, in principle, affect the EPR parameters of mixed-valence complexes mainly via vibronic coupling,[41,42] the necessary computations are outside the scope of the present work (see ref. 43 for a computational study of double exchange for energies of a smaller Mn^{III}–Mn^{IV} model system). In the analyses of the experimental EPR spectra for the present type of Mn^{III}–Mn^{IV} systems, double exchange has also generally been neglected. This is justified by the rather large antiferromagnetic couplings, which suggest relatively large energy differences between the lowest excited states and the ground state.[44]

Paired-orbital analysis of the BS-state KS wave functions

Based on the paired-orbital (PO) transformation,[45] it is possible to analyze the nature of the BS-KS wave function more closely. The magnetically active orbitals may already

be identified by computing the natural orbitals (NOs) of the system. These orthogonal NOs may be subsequently transformed to POs, where corresponding magnetic pairs are identified by their small finite (non-integer) overlap. In particular, the origin of the spin contamination may be traced back to a limited number of PO pairs, following an expansion of the unrestricted wave function ψ^{U} into quasi-restricted determinants in the PO basis:[46,47]

$$[18] \qquad \Psi^{U} = C^0 D^0 + \sum_{i=1}^{k} C_i^1 D_i^1 + \sum_{i<j}^{k} C_{ij}^2 D_{ij}^2 + \ldots + C^k D^k$$

where C_i is the expansion coefficient, k is the number of corresponding orbitals, and D is the set of restricted determinants obtained by substitutions of "occupied" by "virtual" POs.[46]

Computational details

Structure optimizations and KS wave function computations were done with the Turbomole code (revisions 5.8 and 5.9.1, the latter locally modified to allow the use of custom-made hybrid functionals).[48] For catalase, initial coordinates were taken from crystallographic studies of ref. 49. To construct the model **Mn-cat**,[21] histidine residues were substituted by methyl imidazole and glutamates by acetate. Structure optimizations were done at the B3LYP/SVP level,[50–52] using unrestricted KS wave functions. Structures of both BS and HS solutions have been fully optimized.

Subsequent unrestricted KS single-point calculations used a 9s7p4d all-electron manganese basis set (designed for hyperfine calculations[50,52–54]) and flexible IGLO-II[55,56] basis sets for the ligand atoms. Different exchange-correlation functionals were compared (*i*) the BLYP[50,51] GGA functional; the hybrid functionals (*ii*) B3LYP[50,51] with 20% exact exchange and (*iii*) BHLYP[50,57] with 50% exact exchange; as well as the custom-made hybrid functionals (*iv*) B-XXLYP with XX = 60%, 70%, 80%, or 90% exact exchange (100% – XX% E_X^{Slater}, 100% – XX% ΔE_x^{B88}, and E_c^{LYP}). Mulliken spin densities were used to characterize the broken-symmetry and high-spin states.

The unrestricted KS orbitals were transferred to the MAG-Respect property package[58] by suitable interface routines. The atomic mean-field approximation (AMFI)[59,60] was used to compute the matrix elements of the Breit–Pauli SO operator for **g** tensors and SO corrections to the Mn hyperfine tensors.

The PO analyses were done with the UHF decomposition code of Zilberberg and Ruzankin[46] and Zilberberg et al.[47] based on a Gaussian03[61] single-point calculation at the B3LYP[50,51] DFT level with the extended basis set described earlier.

Figure 1 shows the labels of the core atoms (Mn, O) of the investigated model systems $[LMn(\mu\text{-}O)MnL]^{3+}$ (**1-(μ-O)**, L = *N*,*N*-bis(2-pyridylmethyl)-*N*′-salicyliden-1,2-diaminoethane); $[(bipy)_2Mn(\mu\text{-}O)_2Mn(bipy)_2]^{3+}$ (**2-(μ-O)$_2$**, bipy = 2,2′-bipyridine); $[(phen)_2Mn(\mu\text{-}O)_2Mn(phen)_2]^{3+}$ (**3-(μ-O)$_2$**, phen = 1,10-phenanthroline); $[(dtne)Mn(\mu\text{-}O)_2(\mu\text{-}OAc)Mn]^{2+}$ (**4-(μ-O)$_2$(μ-OAc)**, dtne = 1,2-bis(1,4,7-triazacyclonon-1-yl)ethane); $[(tacn)Mn_2(\mu\text{-}O)_2(\mu\text{-}OAc)(tacn)]^{2+}$ (**5-(μ-O)$_2$(μ-OAc)**, tacn = 1,4,7-triazacyclononane); $[(tacn)Mn(\mu\text{-}O)(\mu\text{-}OAc)_2Mn(tacn)]^{3+}$ (**6-(μ-O)(μ-OAc)$_2$**); and **Mn-cat** (a previously studied model[21] for the superoxidized state of dimanganese catalase). The two systems **4-(μ-O)$_2$(μ-OAc)**[20] and **Mn-cat**[21] are those investigated in previous computational studies by Sinnecker, Neese, and co-workers.

Results and discussion

For all seven dinuclear Mn^{IV}–Mn^{III} complexes (Fig. 1), we compare the results of structure optimization in the HS and BS states. For each parameter (Heisenberg exchange coupling, **g** tensors, and ^{55}Mn, ^{14}N, and ^{1}H HFC constants) the dependence on an exact-exchange admixture are discussed. The influence of terminal ligand size and of the bridging ligand sets are studied for Heisenberg exchange couplings and for the ^{55}Mn HFC constants.

Structures

For the OEC, one usually assumes[62–65] that the differences between the optimization in the HS and the BS states are rather small (but cf. refs. 20 and 21).[20,21] The comparison of central distances of the optimized HS and BS states with experimental data in Table 1 (**Mn-cat** was not analyzed, as no experimental data for the superoxidized state was available), indicates first of all the distinctly different coordination environment of the two Mn centers in all cases, consistent with localized ("trapped") mixed-valent complexes. Generally, the distorted octahedral Mn^{III} ion exhibits larger distances to the ligand atoms than the Mn^{IV} center.

The optimized BS structure (S = 1/2) exhibits generally better agreement with the experimental X-ray data than the optimized HS structure (S = 7/2). The largest differences between BS and HS structure (Table 1) by far are found for **1-(μ-O)**, where the single (μ-O) bridge provides relatively high flexibility of the core region. Here, the HS calculation gives significantly larger Mn–Mn and Mn^{III}–O1 distances than the BS optimization. In the other cases, the differences tend to be <0.03 Å. The deviations of the BS results from experimental are <0.05 Å for Mn–Mn distances and <0.07 Å for Mn–O distances. The largest discrepancy is again found for **1-(μ-O)**. Comparison with the experimental for **5-(μ-O)$_2$(μ-OAc)** should be made only after averaging the two sides in the computations, as the reported experimental C_2 symmetry is due to statistical disorder.[70] This is a common problem in the structural characterization of such trapped mixed-valence systems.[70]

Based on the BS optimizations, we note the following points: clearly different Mn–Mn distances occur for the different cores. The largest Mn–Mn distance is obtained for the mono-μ-oxo bridged core owing to its almost linear arrangement. The di-μ-oxo bridged complexes **2-(μ-O)$_2$** and **3-(μ-O)$_2$** exhibit Mn–Mn distances of 2.76 Å with very similar planar central units. That is, bipy and phen ligands provide very similar frameworks for the central bridge. Even smaller model complexes $[(dab)_2Mn(\mu\text{-}O)_2Mn(dab)_2]^{3+}$ and $[(NH_3)_4Mn(\mu\text{-}O)_2Mn(NH_3)_4]^{3+}$ differ in the core region by <0.02 Å from the larger systems (see Supplementary data). The di-μ-oxo-mono-μ-acetato bridged complexes **4-**

Fig. 1. Structures and atom labels of model systems **1**–**6** and **Mn-cat**.

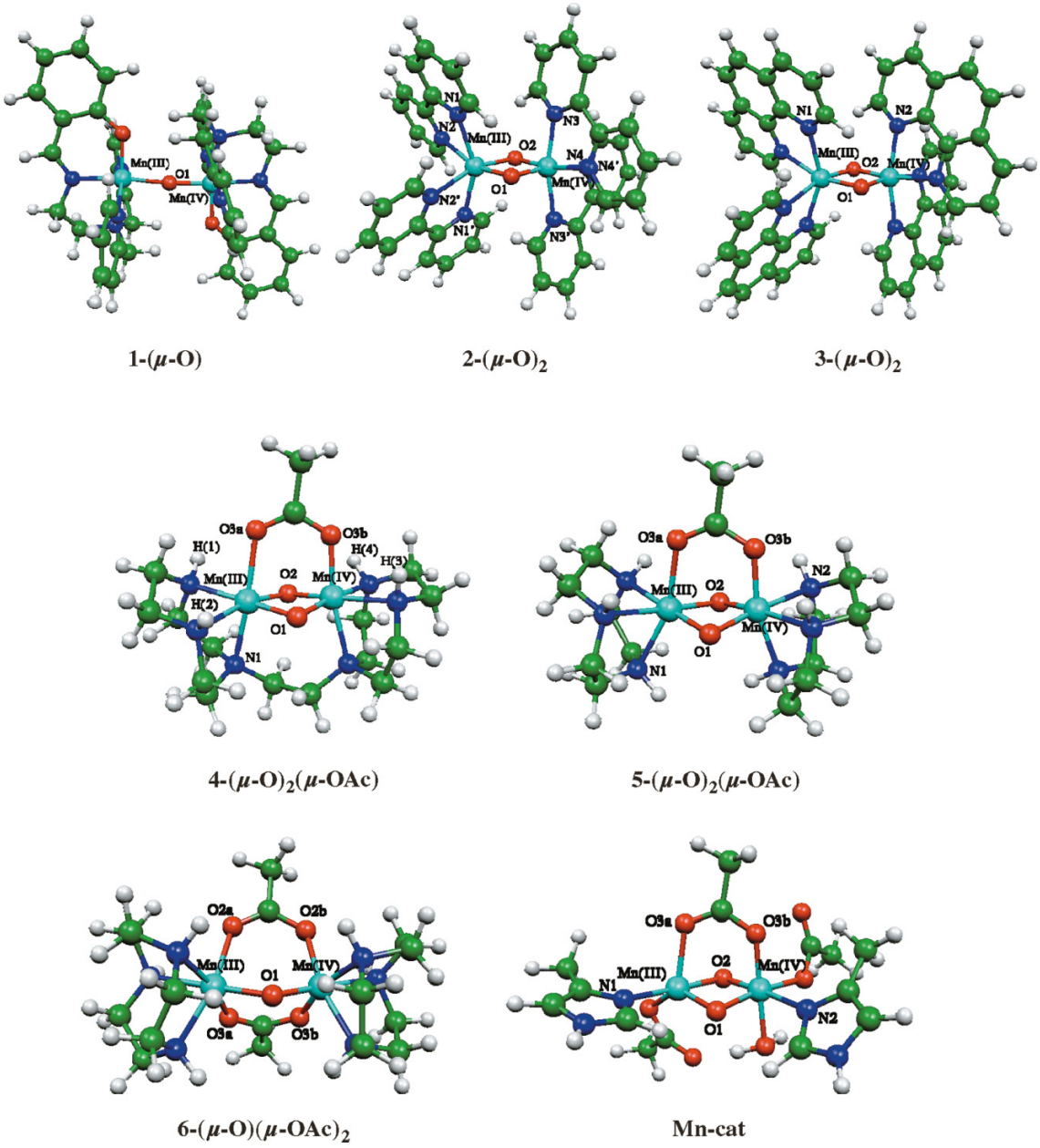

(μ-O)$_2$(μ-OAc) and **5-(μ-O)$_2$(μ-OAc)** have even lower Mn–Mn distances (Table 1). In contrast, a significantly larger distance is obtained for the mono-μ-oxo-di-μ-acetato bridged complex **6-(μ-O)(μ-OAc)$_2$**.

Table 2 provides the BS-optimized core distances for Mn^{III}–Mn^{IV} complexes with similar terminal ligand sets (one tacn and sometimes additionally one water ligand) but with different bridges. For the modified model systems, similar trends are found as for the experimentally studied complexes, indicating the importance of the bridging ligands and the limited influence of the terminal ligands.

Mulliken spin densities

Mulliken atomic spin densities (Table 3) provide a simple check of the unrestricted KS wave function obtained, regarding both the oxidation states of the individual Mn centers and the spin-coupling pattern. For all systems, the HS state is well represented by a ferromagnetic coupling between a Mn^{III} and a Mn^{IV} center. The BS state exhibits the expected antiferromagnetic coupling. The S^2 expectation values of the HS solutions are close to the nominal value for an $S = 7/2$ state, whereas the broken-symmetry nature of the BS solution is apparent from the fact that values around 3.7–4.0 are found (at the given computational level) instead of the 0.75 expected for a pure $S = 1/2$ state (see the PO analysis section). The spin densities on the Mn^{III} center are close to the ideal d^4 configuration (the somewhat lower value for the HS state in **1-(μ-O)** reflects the larger delocalization across the linear bridge in this case). More notable deviations from the ideal d^3 configuration for the Mn^{IV} center are seen for the BS states of the first three complexes (and again for the HS state of **1-(μ-O)**). Interestingly, the spin density on the Mn^{IV}

Table 1. Comparison of optimized interatomic distances (in Å) for HS and BS states with experimental data.

		Bond distance (Å)						
Complex	State	Mn–Mn	Mn^{III}–O1	Mn^{III}–O2a	Mn^{III}–O3a	Mn^{IV}–O1	Mn^{IV}–O2b	Mn^{IV}–O3b
1-(μ-O)	HS	3.668	1.929	—	—	1.743	—	—
	BS	3.569	1.861	—	—	1.739	—	—
	Exp.*	3.524	1.797	—	—	1.727	—	—
2-(μ-O)$_2$	HS	2.761	1.898	1.899	—	1.779	1.779	—
	BS	2.761	1.883	1.894	—	1.772	1.767	—
	Exp.†	2.716	1.853	1.856	—	1.784	1.784	—
3-(μ-O)$_2$	HS	2.754	1.897	1.897	—	1.777	1.777	—
	BS	2.755	1.886	1.885	—	1.767	1.767	—
	Exp.‡	2.748	1.802	1.802	—	1.798	1.798	—
4-(μ-O)$_2$(μ-OAc)	HS	2.639	1.867	1.88	2.191	1.783	1.772	1.919
	BS	2.611	1.859	1.862	2.192	1.778	1.768	1.923
	Exp.§	2.55	1.83	1.83	2.14	1.78	1.78	1.97
5-(μ-O)$_2$(μ-OAc)	HS	2.663	1.883	1.878	2.224	1.784	1.785	1.92
	BS	2.645	1.873	1.866	2.224	1.778	1.779	1.922
	Exp.‖	2.588	1.817	1.808	2.079	1.817	1.808	2.079
6-(μ-O)(μ-OAc)$_2$	HS	3.198	1.867	2.111	2.058	1.772	1.906	1.915
	BS	3.210	1.843	2.116	2.061	1.759	1.908	1.917
	Exp.¶	3.230	1.826	1.999	1.948	1.814	1.951	2.000

Note: B3LYP/SVP optimized structures. See Fig. 1 for the different complexes and labels.
*X-ray data taken from ref. 66.
†X-ray data taken from ref. 67.
‡X-ray data taken from ref. 68.
§X-ray data taken from ref. 39.
‖X-ray data taken from ref. 69. The C_2 symmetrical structure is due to statistical disorder.
¶X-ray data taken from ref. 70.

Table 2. Influence of the bridge on interatomic distances (in Å) in tacn model complexes.

		Bond distance (Å)						
Model complex	State	Mn–Mn	Mn^{III}–O1a	Mn^{III}–O2a	Mn^{III}–O3a	Mn^{IV}–O1b	Mn^{IV}–O2b	Mn^{IV}–O3b
[(tacn)(H_2O)Mn(μ-O)Mn(H_2O)(tacn)]$^{5+}$	BS	3.835	2.113	—	—	1.730	—	—
[(tacn)(H_2O)Mn(μ-O)$_2$Mn(tacn)]$^{3+}$	BS	2.713	1.872	1.866	—	1.778	1.778	—
[(tacn)Mn(μ-O)(μ-OOAc)Mn(tacn)]$^{4+}$	BS	3.422	1.958	1.934	—	1.709	1.908	—
[(tacn)Mn$_2$(μ-O)$_2$(μ-OAc)(tacn)]$^{2+}$	BS	2.645	1.873	1.866	2.224	1.778	1.779	1.922
(5-(μ-O)$_2$(μ-OAc))	Exp.*	2.588	1.817	1.808	2.079	1.817	1.808	2.079
[(tacn)Mn(μ-O)(μ-OAc)$_2$Mn(tacn)]$^{3+}$	BS	3.210	1.843	2.116	2.061	1.759	1.908	1.917
(6-(μ-O)(μ-OAc)$_2$)	Exp.†	3.230	1.826	1.999	1.948	1.814	1.951	2.000

*X-ray data were taken from ref. 69. Comparison with the experiment is difficult because of statistical disorder and effective C_2 symmetry (see above).
†X-ray data were taken from ref. 70.

center depends notably on the bridging ligand, reflecting the more pronounced covalency of the Mn^{IV}–O bonds and an associated larger spin polarization. Acetate bridges tend to diminish this effect and provide somewhat larger absolute spin densities on the Mn^{IV} centers. In the BS states, spin polarization of the bridge oxygen atoms is particularly pronounced for the single bridge in **1-(μ-O)** but is also large for the di-μ-oxo bridges and still notable for the other oxo bridges. Slightly positive spin density on the bridging acetate oxygen atoms points more to spin delocalization than to spin polarization. Interestingly, the HS state of **1-(μ-O)** exhibits large positive spin density on the bridging oxygen, in accordance with substantial spin delocalization (this is made possible by the parallel orientation of the unpaired spins). Smaller positive spin densities are visible on the other oxo bridges in the HS states. Curiously, in the HS states small negative spin densities are found on bridging acetate oxygen atoms.

The influence of the exact-exchange admixture on the atomic spin densities of the BS state of **2-(μ-O)$_2$** is studied in Table 4. As also found for mononuclear complexes,[53,54,71] a larger exact-exchange admixture enhances the spin density on the Mn centers, because of the more ionic metal-ligand bonding and partly because of increased spin polarization. GGA functionals tend to overestimate metal–ligand covalency, and this is compensated for by some exact exchange. However, for very large admixtures (>50%), a counteracting effect is visible, which leads to a slight decrease of the spin density on the Mn^{III} center, likely because of the effects of spin polarization. The spin densities on the bridging oxygen atoms depend in a striking manner on the functional: starting from appreciably negative values at the GGA level, they go through 0 between a 50% and 60% exact exchange

Table 3. Mulliken atomic spin densities and $\langle S^2 \rangle$ expectation values of HS and BS states.

Complex	State	Mn^{III}	Mn^{IV}	O1	O2a	O3a	O2b	O3b	$\langle S^2 \rangle$
1-(μ-O)	HS	3.58	2.34	0.46	—	—	—	—	15.75
	BS	3.82	–2.55	–0.29	—	—	—	—	3.72
2-(μ-O)$_2$	HS	3.95	2.89	0.09	—	—	—	—	15.86
	BS	3.95	–2.69	–0.21	–0.21	—	—	—	3.77
3-(μ-O)$_2$	HS	3.96	2.89	0.09	0.09	—	—	—	15.88
	BS	3.95	–2.69	–0.21	–0.21	—	—	—	3.77
4-(μ-O)$_2$(μ-OAc)	HS	3.88	2.88	0.13	0.16	0.06	—	–0.03	15.85
	BS	3.86	–2.71	–0.15	–0.16	0.02	—	0.05	3.74
5-(μ-O)$_2$(μ-OAc)	HS	3.92	2.88	0.14	0.12	0.06	—	–0.03	15.85
	BS	3.88	–2.74	–0.16	–0.14	0.02	—	0.04	3.76
6-(μ-O)(μ-OAc)$_2$	HS	4.00	3.05	0.13	0.03	0.02	–0.02	–0.02	15.88
	BS	3.93	–2.94	–0.18	0.01	–0.01	0.03	0.03	3.81
Mn-cat	HS	3.87	2.93	0.16	0.03	0.05	—	–0.03	15.85
	BS	3.89	–2.78	–0.09	–0.13	0.02	—	0.05	3.77

Note: B3LYP single-point calculation with a 9s7p4d basis for Mn and a IGLO-II basis for the ligand atoms.

and then turn significantly positive at a 70%–80% exact exchange. As enhanced spin polarization with more exact exchange would be expected to lead to more negative values overall, apparently, the more ionic Mn–O bonding at a larger exact exchange counteracts this effect. At 90% exact exchange, pronounced symmetry breaking renders the two oxygen atoms strongly nonequivalent, indicating this KS wave function to be unphysical.

Paired-orbital analysis of spin contamination in the BS state

The S^2 expectation value tends to be near 3.75 for all systems at the B3LYP level (cf. Table 3), lower at the GGA level, and higher at larger exact-exchange admixtures (Table 4). The value may be analyzed within the formalism of an expansion of the BS determinant into quasi-restricted determinants in the basis of the POs (see the Theory section).[45–47] The magnetic NOs for **2-(μ-O)$_2$** obtained at the B3LYP level are shown in Fig. 2 and also look similar to other functionals (data not shown). The occupation numbers of the NOs (see Table 5 for **2-(μ-O)$_2$**) generally give the expected picture of seven magnetic orbitals: this includes the "true" SOMO of the $S = 1/2$ system (occupation 1.00) and three pairs of corresponding orbitals, indicated by complementary deviations of the NO occupation numbers from 1.0. These deviations may be translated[45–47] into overlaps of the corresponding POs, also shown in Table 5 (numbers in parentheses). As has been discussed in refs. 45–47,[45–47] all spin contamination (i.e., deviation of $\langle S^2 \rangle$ from the nominal value of 0.75 for $S = 1/2$) may be traced back to those active pairs. Indeed, three magnetic pairs with small overlap should give rise to an increase of $\langle S^2 \rangle$ by three units.[46,47] This situation is almost ideally represented by the B3LYP results (cf. Tables 3 and 4). The BLYP GGA calculations are known to overestimate delocalization. This may be seen from the larger overlaps of ca. 0.4 for the three corresponding magnetic POs (or from the larger deviations of the NO occupation numbers from 1.0; Table 5). The B3LYP PO overlaps are close to 0.2 and the BHLYP ones are close to 0.1. Whereas the larger overlap for BLYP decreases the spin contamination compared with the B3LYP results, the small overlap for BHLYP enhances it. Moreover, the spin

Table 4. Dependence of Mulliken atomic spin densities and $\langle S^2 \rangle$ expectation values of the BS state of **2-(μ-O)$_2$** on the amount of exact-exchange admixture.

	Mn^{III}	Mn^{IV}	O1	O2	$<S^2>$
BLYP	3.60	–2.36	–0.195	–0.204	3.39
B3LYP	3.95	–2.69	–0.208	–0.213	3.77
BHLYP	4.09	–3.17	–0.047	–0.043	4.00
B60LYP	4.07	–3.40	0.071	0.083	4.11
B70LYP	4.03	–3.63	0.207	0.234	4.25
B80LYP	3.98	–3.79	0.303	0.373	4.39
B90LYP	4.00	–3.81	0.006	0.710	4.58

polarization of formally inactive NOs and (or) POs increases with increasing exact-exchange admixture. This is visible in Table 5 from the deviations of formally doubly occupied NOs 190, 191, and 192 from 2.0 (and from the non-zero occupations of the corresponding NOs 200, 201, and 202). Further analyses based on the PO-based expansion into quasi-restricted determinants in eq. [18][46,47] are provided in Table S5 in the Supplementary data. The spin contamination of the BS–KS determinant arises from single, double, and triple substitutions of the leading restricted determinant of the expansion (some contributions arise also from the spin polarization of the formally doubly occupied set — POs 190, 191, and 192).

Exchange coupling constants

As knowledge of spin-coupling patterns in multinuclear systems is essential for an understanding of the spectroscopic properties, we have also computed the Heisenberg exchange couplings, using the above-mentioned spin projection schemes of Noodleman et al. and Yamaguchi et al. The vast literature[72–82] on broken-symmetry DFT calculations of exchange couplings for multinuclear transition metal complexes cannot be described here in detail. The small energy differences involved, the intrinsically multideterminantal nature of the lower spin states, and the necessity of mapping the electronic structure onto the Heisenberg spin Hamiltonian make this a challenge for quantum chemistry. BS-DFT with standard hybrid functionals like B3LYP tends to work surprisingly well when spin projection is used.[24] This is con-

Fig. 2. Active (magnetic) natural orbitals (NOs) for **2-(μ-O)$_2$** (B3LYP results; ±0.05 au isosurfaces). Orbital number ([a]); NO occupation ([b]).

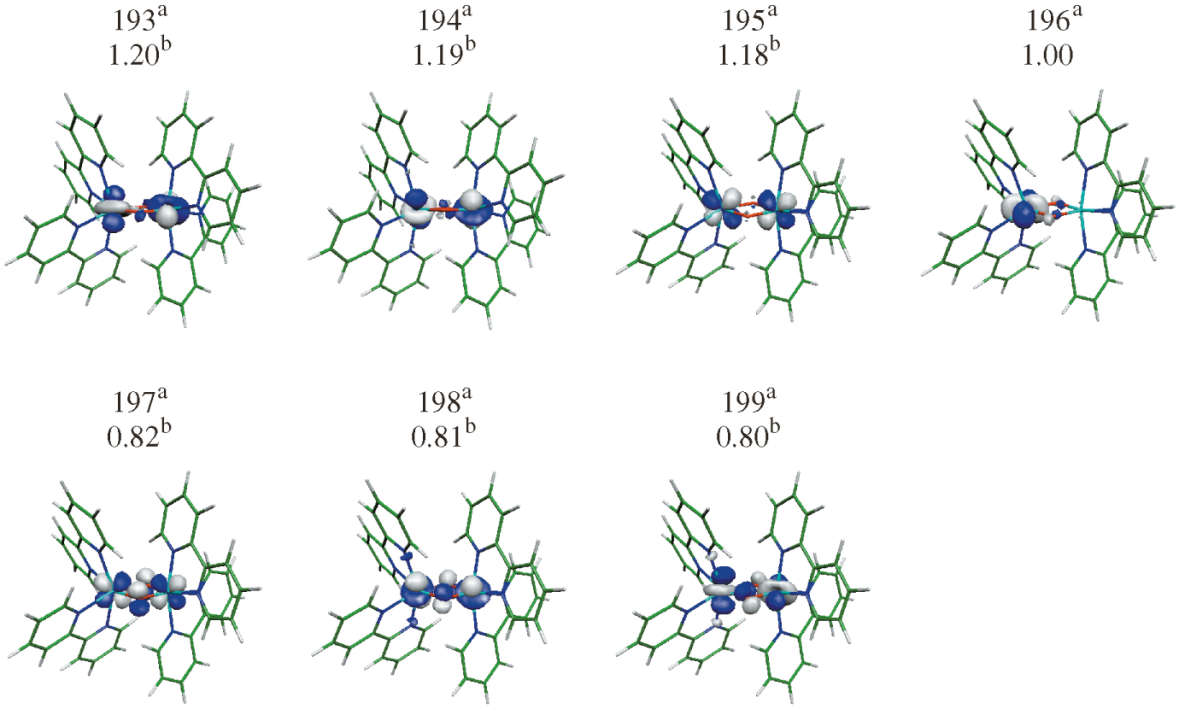

Table 5. Dependence of natural orbital (NO) occupation numbers and paired orbital (PO) overlaps for **2-(μ-O)$_2$** on the functional.

NO No.	BLYP	B3LYP	BHLYP
190	2.000 00	2.000 00	1.988 21 (0.988 21)
191	2.000 00	1.987 05 (0.987 05)	1.980 57 (0.980 57)
192	1.983 57 (0.983 57)	1.951 15 (0.951 15)	1.965 95 (0.965 95)
193	1.465 88 (0.465 88)	1.203 03 (0.203 03)	1.118 33 (0.118 33)
194	1.409 30 (0.409 30)	1.192 58 (0.192 58)	1.106 17 (0.106 17)
195	1.343 38 (0.343 38)	1.180 20 (0.180 20)	1.104 83 (0.104 83)
196	1.000 00 (SOMO)	1.000 00 (SOMO)	1.000 00 (SOMO)
197	0.656 62 (0.343 38)	0.819 80 (0.180 20)	0.895 17 (0.104 83)
198	0.590 70 (0.409 30)	0.807 42 (0.192 58)	0.893 83 (0.106 17)
199	0.534 12 (0.465 88)	0.796 97 (0.203 03)	0.881 67 (0.118 33)
200	0.016 43 (0.983 57)	0.038 85 (0.951 15)	0.034 05 (0.965 95)
201	0.000 00	0.012 95 (0.987 05)	0.019 43 (0.980 57)
202	0.000 00	0.000 00	0.011 79 (0.988 21)

Note: See Fig. 2 for the seven magnetic NOs 193–199.

firmed for the present title systems. Figure 3 illustrates the example of **2-(μ-O)$_2$**, the large dependence of J on the exact-exchange admixture in the functional, and the good performance of B3LYP (likely related to the physically well-defined structure of the BS–KS determinant at this level, see the above). The Noodleman[15] and the Yamaguchi[25] mapping schemes perform similarly, confirming the weak interaction between the spins for the complexes studied here. The pure GGA BLYP functional exhibits larger spin delocalization[83] and thus more negative J values. In contrast, the larger exact-exchange admixture overcorrects and gives absolute values for J that are too low. The unprojected BS-DFT formula of Ruiz et al.[73,75,84] gives generally lower values (see Table S6 in the Supplementary data) and provides poorer agreement with the experimental when used with B3LYP (but reasonable agreement with BLYP).

Fig. 3. Dependence of the Heisenberg exchange coupling constant J on the amount of the exact-exchange admixture for **2-(μ-O)$_2$**. The experimental J value is taken from Pavlov et al..[64]

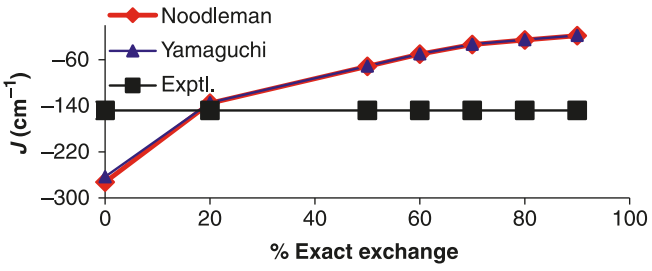

Table 6. Heisenberg exchange coupling constants J (in cm^{-1}).

	Noodleman*		Yamaguchi†		
Complex	SVP	9s7p4d/II	SVP	9s7p4d/II	Exp.
1-(μ-O)	–138	–135	–136	–134	–353‡
2-(μ-O)$_2$	–141	–136	–140	–134	–148§
3-(μ-O)$_2$	–142	–136	–141	–135	–148§
4-(μ-O)$_2$(μ-OAc)	–127	–120	–125	–119	–110‖
5-(μ-O)$_2$(μ-OAc)	–117	–109	–117	–108	–110¶
6-(μ-O)(μ-OAc)$_2$	–15	–12	–15	–12	–40**
Mn-cat	–79	–73	–78	–72	††

Note: B3LYP results with either a SVP basis for all atoms or with a 9s7p4d basis for Mn and IGLO-II for N, O, H, and C.

*Values taken from Noodleman.[15]

†Values taken from Soda et al.[25]

‡Experimental value taken from Horner et al.[66]

§Experimental value taken from Stebler et al.[68]

‖Experimental value taken from Schafer et al.[39]

¶Experimental value taken from Wieghardt et al.[69]

**Experimental value taken from Wieghardt et al.[70]

††A lower bound of –175 cm^{-1} has been estimated.[86]

B3LYP results for the entire series of complexes are provided in Table 6. Differences between data obtained with the moderate-basis SVP and data obtained with extended basis sets are very small. Obviously, the energy differences between HS and BS states are not very basis-set dependent.[24] In all cases, the Noodleman (eq. [7] and Yamaguchi (eq. [8] projection schemes provide very similar results. For complexes with di-μ-oxo or di-μ-oxo-μ-carboxylato cores, agreement with the experimental is excellent (for **Mn-cat** no truly reliable estimate is available). For the remaining two compounds **1-(μ-O)** and **6-(μ-O)(μ-OAc)$_2$**, the calculations underestimate the experimental absolute values by factors of 3–4. Presumably,[24] OAc bridges give rise to some spin delocalization between the centers in the HS state, thus partly invalidating the basis for the spin projection. In the case of **1-(μ-O)**, the question of the accuracy of the structure optimization may come into play (cf. Table 1). The calculated distances are, especially for the HS state, much larger than distances derived from X-ray experiments (Mn–Mn: HS, 3.67 Å; X-ray[66], 3.52 Å). Computation of J for the X-ray structure of **1-(μ-O)**[66] gives –185 cm^{-1}, i.e., a value closer to the experimental.

The di-μ-oxo bridged complexes exhibit larger antiferromagnetic coupling than the di-μ-oxo-μ-carboxylato bridged ones, in spite of the longer Mn–Mn distances. The magnetic interactions are more efficient in the planar di-μ-oxo structures than in a tilted Mn_2O_2 core,[78] as present in the (μ-O)$_2$(μ-OAc) bridged systems. In general, O^{2-} is a strong donor, leading to strong Mn – oxo π interactions, which are responsible for the strong, super exchange-mediated[79,85] antiferromagnetic interactions.

To evaluate the influence of the terminal ligand sets, we computed J for smaller models of **3-(μ-O)$_2$**, where the phen ligands were replaced by simpler ligands. Even for the simplest model $[(NH_3)_4Mn(\mu\text{-}O)_2Mn(NH_3)_4]^{3+}$ (–132 cm^{-1}) are obtained (Noodleman projection, SVP basis), in good agreement with the experimental (see Table S7 in the Supplementary data).

In the opposite type of computational experiment, we kept the terminal ligand framework similar (tacn and H_2O; see also the above) and changed the bridges. As expected,[78] this had a larger effect on J (see Table 6). The influence of the bridge depends on the various super exchange pathways provided by the bridging oxo and acetato ligands.[20,21] Overall, smaller Mn–Mn distances and a planar Mn_2O_2 core give rise to larger antiferromagnetic couplings. These effects work into opposite directions for $[(tacn)(H_2O)Mn(\mu\text{-}O)_2Mn(tacn)]^{3+}$ and $[(tacn)Mn(\mu\text{-}O)_2(\mu\text{-}OAc)Mn(tacn)]^{2+}$, leading to rather similar couplings. Complexes with a di-μ-oxo bridge have J couplings in the range of –110 to –150 cm^{-1} (Tables 6 and 7). A similar range is covered by di-μ-oxo-μ-carboxylato bridged complexes (–108 to –127 cm^{-1}). A small antiferromagnetic coupling was computed for **6-(μ-O)(μ-OAc)$_2$**. A small ferromagnetic coupling was obtained for $[(tacn)Mn(\mu\text{-}O)(\mu\text{-}OAc)Mn(tacn)]^{4+}$ (Table 7). Because of the OAc bridge, a delocalization of the unpaired electrons in the high-spin state occured,[24] reducing the antiferromagnetic coupling. This effect was also be observed in complexes $[(tacn)Mn(\mu\text{-}O)_2(\mu\text{-}OAc)Mn(tacn)]^{2+}$ and $[(tacn)Mn(\mu\text{-}O)(\mu\text{-}OAc)_2Mn(tacn)]^{3+}$. The more μ-carboxylato bridges, the lower the antiferromagnetic coupling. The spin-density distributions of these complexes are given in Fig. 4.

g Tensors

Computed effective **g** tensors (eq. [13]) tend to agree reasonably well with the experimental (Table 8). The **g** anisotropy is generally small for all title complexes, and the isotropic **g** value is close to the free-electron value. Dependence on the functional is small, and for **2-(μ-O)$_2$** even the BLYP GGA functional provides reasonable results for $\mathbf{g}_{iso}$. At very large exact-exchange admixtures, agreement with the experimental values may be improved further (also see the results for **Mn-cat** in Fig. S1 in the Supplementary data). Comparing our B3LYP results with those of Sinnecker et al. for **4-(μ-O)$_2$(μ-OAc)**[20] and **Mn-cat**,[21] we see

Table 7. Dependence of J (in cm^{-1}) on the bridging ligand set.

Complex	Noodleman*	Yamaguchi†	Exp.
$[(tacn)(H_2O)Mn(\mu\text{-}O)Mn(H_2O)(tacn)]^{5+}$	–23	–23	—
$[(tacn)(H_2O)Mn(\mu\text{-}O)_2Mn(tacn)]^{3+}$	–106	–105	—
$[(tacn)Mn(\mu\text{-}O)(\mu\text{-}OAc)Mn(tacn)]^{4+}$	44	43	—
$[(tacn)Mn(\mu\text{-}O)_2(\mu\text{-}OAc)Mn(tacn)]^{2+}$	–109	–108	–110‡
$[(tacn)Mn(\mu\text{-}O)(\mu\text{-}OAc)_2Mn(tacn)]^{3+}$	–12	–12	–40§

Note: B3LYP calculations with a 9s7p4d basis for Mn and IGLO-II for N, O, H, and C.
*Values taken from Noodleman.[15]
†Values taken from Soda et al.[25]
‡Experimental value taken from Wieghardt et al.[69]
§Experimental value taken from Wieghardt et al.[70]

Fig. 4. Spin-density isosurfaces (±0.005 au) for tacn complexes with different bridging ligands.

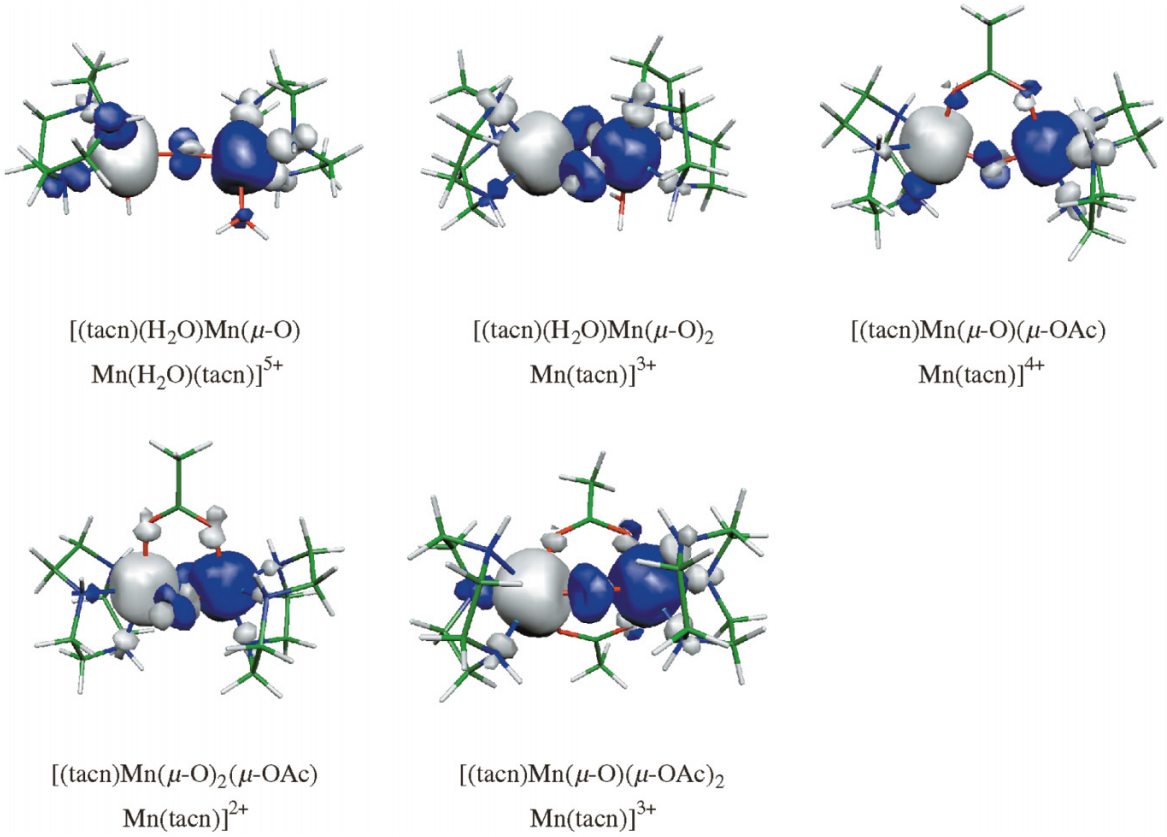

some moderate discrepancies (data not shown) in that their overall effective g-shift components are all somewhat below g_e, whereas in our calculations, $\boldsymbol{g}_{22}$ and $\boldsymbol{g}_{33}$ are above g_e and $\boldsymbol{g}_{11}$ is below (Table 8). This brings their data closer to the experiment value for **4-(μ-O)$_2$(μ-OAc)**[20] (in fact, most of the complexes in Table 8), whereas our positive $\boldsymbol{g}_{22}$ and $\boldsymbol{g}_{33}$ values agree better for **Mn-cat**. Differences between the two sets of calculations could arise from (*i*) different spin-orbit operators (atomic-meanfield operators in this work vs. semi-empirical operators in refs. 20 and 21), (*ii*) different structures (we used optimized structures individually for HS and BS states, whereas Sinnecker and Neese and co-workers used the HS structures for both calculations), (*iii*) general differences between the optimized structures and basis sets used, or (*iv*) the gauge origin of the magnetic vector potential (placed at the center of charge density in our calculations). Yet, our evaluations of all of these points did not reveal the origin: Our use of the same semi-empirical spin-orbit operators used by Sinnecker et al. actually increased $\boldsymbol{g}_{22}$ and $\boldsymbol{g}_{33}$ further in all cases, and the dependencies on structures, basis sets, or gauge origin turned out to be too small to account for the differences. Therefore, we do not have a good explanation for the (moderate) discrepancies in the computed effective **g** tensors, but hyperfine couplings computed from the same Kohn–Sham wave functions agree very well.

Overall, the **g** tensors for different systems tend in to be too similar to have much diagnostic value for structural details. **g** Tensor orientations will be discussed further in the following section together with those of the ^{55}Mn hyperfine tensors.

Table 8. **g**-Shift components (in ppt) and absolute **g** values.

	Δg_{iso}	Δg_{11}	Δg_{22}	Δg_{33}
1-(μ-O)				
B3LYP	–1.7 (2.001)	–14.7 (1.988)	0.5 (2.003)	9.1 (2.011)
Exp.*	7.3 (1.995)	20.3 (1.982)	5.3 (1.997)	–3.7 (2.006)
2-(μ-O)$_2$				
B3LYP	3.2 (1.9991)	14.5 (1.9878)	–1.7 (2.0040)	–3.2 (2.0055)
Exp.†	11.0 (1.9913)	20.6 (1.9817)	9.1 (1.9932)	3.3 (1.9990)
3-(μ-O)$_2$				
B3LYP	2.9 (1.9994)	14.2 (1.9881)	–2.2 (2.0045)	–3.3 (2.0056)
Exp.‡	11 (1.992)	20 (1.982)	8 (1.994)	3 (1.999)
4-(μ-O)$_2$(μ-OAc)				
B3LYP	1.0 (2.0013)	11.5 (1.9908)	–3.4 (2.0057)	–5.2 (2.0075)
Exp.†	8.1 (1.9942)	18.5 (1.9838)	4.9 (1.9974)	1.0 (2.0013)
5-(μ-O)$_2$(μ-OAc)				
B3LYP	0.9 (2.0014)	11.0 (1.9913)	–3.2 (2.0055)	–5.1 (2.0074)
Exp.†	6.3 (1.9960)	17.2 (1.9851)	1.8 (2.0005)	–0.2 (2.0025)
Mn-cat				
B3LYP	–1.0 (2.0033)	10.0 (1.9923)	–3.5 (2.0058)	–9.6 (2.0119)
Exp.†	3.5 (1.9988)	14.7 (1.9876)	–1.7 (2.0040)	–2.5 (2.0048)
6-(μ-O)(μ-OAc)$_2$				
B3LYP	1.3 (2.0010)	5.4 (1.9969)	1.7 (2.0006)	–3.1 (2.0054)

Note: Absolute **g** value refers to the effective **g** tensor. Absolute **g** values are in parentheses. EPR, electron paramagnetic resonance.

*X-band EPR studies from Horner et al.[66]

†High-field EPR studies from Teutloff et al.[87]

‡Mulitfrequency EPR studies from Schaefer et al.[88]

^{55}Mn hyperfine coupling tensors

The ^{55}Mn hyperfine couplings exhibit much more sensitivity to bonding and structural details. Isotropic HFCs of transition metal nuclei are known to also depend sensitively on the exchange-correlation functional employed.[53] This includes manganese HFCs and has recently been confirmed for the mononuclear manganese binding site of concanavalin A.[22] Table 9 evaluates the ^{55}Mn tensors for **2-(μ-O)$_2$** with different functionals. Tensors after spin projection (eqs. [16] and [17])) and isotropic site values are provided.

Because of the distorted coordination of high-spin d^4, Mn^{III} exhibits appreciable HFC anisotropy (and a nearly axial tensor). An almost isotropic HFC is found for the high-spin d^3 Mn^{IV} center. The dependence on the functional is as found before,[22] for both Mn centers: The isotropic Fermi-contact term A_{FC} becomes more negative with increasing EXX admixture because of the enhancement of (overall negative) core-shell spin polarization contributions to the spin density at the nucleus.[53,54,71] Agreement with experimental values is thus improved even up to rather large admixtures of exact exchange. SO contributions are on the order of about 5%–10% of the nonrelativistic values. This value is less than the values for some complexes of other 3d transition metals,[36,38,89] yet not negligible.[20,21] The HFC anisotropy of the Mn^{III} ions depends less on the functional. It is already reproduced reasonably well at the B3LYP level and tends to be overshot somewhat at higher EXX admixtures. Notably, at EXX admixtures >60%, the HFC anisotropies of the Mn^{IV} centers start to increase notably. This is likely an unphysical artefact of the increased spin contamination[53,54] (cf. S^2 expectation values in Table 4 and the PO analysis section). Another observation in this context is the faster increase of the a_{iso} site values with exact exchange for the Mn^{IV} compared with the Mn^{III} centers (Table 9). We note, in passing, that the differences between the BLYP GGA functional and the B3LYP hybrid functional are clear-cut and consistent with the above-mentioned dependence on EXX admixture. Somewhat more similar results obtained by Sinnecker et al.[20] with BP86 vs. B3LYP functionals may be attributed to the compensating effects of exchange and correlation contributions to the functional (see Munarová and Kaupp[53]).

In the long run, improved exchange-correlation functionals will be needed that will allow optimum agreement with the experimental values for a wide range of spectroscopic parameters with one given functional. A possible route towards this goal are local hybrid functionals with position-dependent EXX admixtures[90–94] (as self interaction errors may be particularly relevant for mixed-valence systems, functionals that effectively decrease self interaction yet still provide a good simulation of static correlation are of interest). For the moment, we are content with more approximate short-term solutions. As the exchange couplings (see above) and several ligand HFCs (see the following) are reproduced well with B3LYP, it would be desirable to be able to scale the computed A_{iso} at this level, as suggested recently,[20] to provide essentially quantitative predictions for the entire tensor. This requires that the errors owing to the incorrect description of the core-shell spin polarization are systematic and apply similarly to both Mn^{III} and Mn^{IV} centers, as well as to different coordination environments. The latter is

Table 9. Dependence of ^{55}Mn hyperfine tensors (in MHz) for **2-(μ-O)$_2$** on the exchange-correlation functional.

	Mn^{III}							Mn^{IV}						
	a_{iso}, (site)	A_{iso}	T_1, T_2, T_3	A_{FC}	$\mathbf{A}_1^{dip,2}$, $\mathbf{A}_2^{dip,2}$, $\mathbf{A}_3^{dip,2}$	A_{PC}	$\mathbf{A}_1^{dip,2}$, $\mathbf{A}_2^{dip,2}$, $\mathbf{A}_3^{dip,2}$	a_{iso} (site)	A_{iso}	T_1, T_2, T_3	A_{FC}	$\mathbf{A}_1^{dip,2}$, $\mathbf{A}_2^{dip,2}$, $\mathbf{A}_3^{dip,2}$	A_{PC}	$\mathbf{A}_1^{dip,2}$, $\mathbf{A}_2^{dip,2}$, $\mathbf{A}_3^{dip,2}$
BLYP	–133	–265	–48, –37, 85	–251	–50, –39, 89	–14	3, 1, –4	–122	122	–2, 1, 1	114	–1, 1, 0	8	–1, –1, 2
B3LYP	–158	–316	–53, –45, 98	–302	–57, –48, 105	–14	4, 3, –7	–150	150	–6, 0, 5	139	–7, 0, 7	11	1, 0, –2
BHLYP	–181	–361	–55, –47, 102	–346	–60, –51, 111	–15	5, 4, –10	–174	174	–6, –1, 7	160	–8, –2, 10	14	2, 1, –3
B60LYP	–188	–376	–57, –48, 105	–360	–63, –53, 117	–16	6, 5, –11	–179	179	–7, –4, 11	165	–10, –5, 15	14	3, 1, –4
B70LYP	–198	–395	–61, –51, 111	–377	–68, –57, 124	–18	7, 5, –13	–183	183	–10, –7, 17	170	–14, –9, 22	13	4, 2, –6
B80LYP	–209	–417	–65, –52, 117	–398	–73, –59, 132	–19	8, 7, –15	–190	190	–15, –8, 23	177	–19, –1, 29	13	5, 5, –7
B90LYP	–220	–440	–88, –26, 114	–421	–98, –30, 129	–19	11, 4, –15	–252	252	–41, 14, 27	239	–51, 19, 31	13	10, –5, –4
Exp.*	–227	–454	–25, –48, 78					–218	218	–8, –3, 14				

Note: Site values were obtained with an extended basis set (see Computational details). a_{iso} (site) is the intrinsic site isotropic hyperfine coupling constant. A_{iso} is the total isotropic value, T_i represents the traceless part of the full **A** tensor, A_{FC} and A_{PC} denote the isotropic first-order Fermi-contact and second-order pseudo-contact (spin-orbit) contributions to the full total **A** tensor, respectively. $\mathbf{A}_i^{dip}$ and $\mathbf{A}_i^{dip,2}$ denote, respectively, the first-order nonrelativistic and second-order spin-orbit anisotropic tensors. EPR, electron paramagnetic resonance.

*HF-EPR studies from ref. 87.

clearly the case, as the B3LYP results for A_{iso} in **2-(μ-O)$_2$** have to be scaled by 1.44 for Mn^{III} and by 1.45 for Mn^{IV} (Table 9) to agree with the experimental values.

The validity of the former condition for a range of the present dinuclear systems is explored in Table 10. Spin-projected B3LYP results are compared with ^{55}Mn HFC tensors from several EPR studies.[39,66,87] The behavior is as previously delineated for **2-(μ-O)$_2$**: significant anisotropy for Mn^{III} centers and essentially isotropic HFCs for Mn^{IV} centers. Scaling the total computed A_{iso} by a factor of ca. 1.45 provides excellent agreement with the experimental value (A_{iso}*, Table 10), independent of terminal and bridging ligand sets. Similar scaling factors were found from a somewhat more limited set of complexes by Sinnecker et al.[20,21] The anisotropies of the Mn^{III} centers are generally reproduced more or less reasonably without scaling. The small anisotropies of the Mn^{IV} centers are less well reproduced.

Turning our magnifying glass on the a_{iso} site values (Table 10), we see that the relative magnitudes for the Mn^{III} vs. Mn^{IV} centers are, in most cases, reproduced, but not always; for **1-(μ-O)** and **4-(μ-O)$_2$(μ-OAc)**, the experimental values would suggest slightly larger absolute values for the Mn^{III} center, whereas the calculations give the opposite behavior (but the differences are tiny). The switch from larger absolute a_{iso} site values for Mn^{III} in **2-(μ-O)$_2$** and **3-(μ-O)$_2$** to larger values for Mn^{IV} in **5-(μ-O)$_2$(μ-OAc)** and **Mn-cat** is well reproduced. The latter two cases are the most clear-cut ones. These results show that, overall, the intrinsic isotropic site values for Mn^{III} and Mn^{IV} are surprisingly similar and translate into rather different projected A_{iso} values owing to the factor two in the Mn^{III} projection. This will have to be kept in mind in studies on, e.g., the OEC.

In Table 11, the ^{55}Mn HFC tensors are provided for **3-(μ-O)$_2$** and for models in which the phen ligands have been replaced by smaller units. Even for the smallest model system, $[(NH_3)_4Mn(\mu\text{-}O)_2Mn(NH_3)_4]^{3+}$, the isotropic ^{55}Mn HFC of the Mn^{IV} center is essentially the same as for the full system with phen ligands. In the case of NH_3 or dab ligands, the value for the Mn^{III} center is 7% too small in absolute value compared with the phen complex (note the switch in relative magnitude of the Mn^{III} and Mn^{IV} a_{iso} site values). Slight structural differences for the dab complex and the bipy and phen complexes might explain this deviation (see Table S1 in the Supplementary data). For NH_3, its nonaromatic nature and different donor character come into play. The bipy complex is an almost perfect model of phen in this context. These findings suggest that similar simplifications of the terminal ligand sets may be cautiously applied to models of the OEC, where full modelling of the protein and co-factor environment is computationally demanding.

Table 12 keeps the terminal ligand set more or less constant (tacn and possibly terminal H_2O) and varies the bridges. Surprisingly, at first sight $[(tacn)(H_2O)Mn(\mu\text{-}O)Mn(H_2O)(tacn)]^{5+}$ and $[(tacn)Mn(\mu\text{-}O)(\mu\text{-}OAc)\ Mn(tacn)]^{4+}$ exhibit unusually small A_{iso} valuesfor the Mn^{IV} center. This can be traced back clearly to a five coordination at this center, suggesting a diagnostic value of the Mn HFC in this context. This is interesting for the OEC, as the coordination number of the different centers is currently far from settled. The other variations of the Mn^{IV} HFC are much smaller, with the $(\mu\text{-}O)(\mu\text{-}OAc)_2$-bridged system having the lowest

Table 10. ^{55}Mn hyperfine coupling tensors (in MHz).

	Mn^{III}						Mn^{IV}					
	a_{iso} (site)	A_{iso}	A_{iso}*	T_1, T_2, T_3	A_{FC}	A_{PC}	a_{iso} (site)	A_{iso}	A_{iso}*	T_1, T_2, T_3	A_{FC}	A_{PC}
1-(μ-O)												
Calcd.	–114	–228	–331	–83, –21, 104	–214	–14	–125	125	181	–13, 0, 12	113	12
Exp.*	|191|	|381|		|99|, |9|, |108|			|183|	|183|		|3|, |3|, |6|		
2-(μ-O)$_2$												
Calcd.	–158	–316	–458	–53, –45, 98	–302	–14	–150	150	218	–6, 0, 5	139	11
Exp.†	–227	–454		–25, –48, 78			–218	218		–3, –8, 14		
3-(μ-O)$_2$												
Calcd.	–156	–311	–451	–52, –46, 98	–297	–14	–150	150	218	–7, 0, 7	138	12
Exp.‡	–226	–451		–28, –50, 78			–221	221		–8, –6, 11		
4-(μ-O)$_2$(μ-OAc)												
Calcd.	–137	–274	–397	–54, –52, 106	–261	–13	–149	149	216	–6, –2, 7	138	11
Exp.†	–195	–389		–17, –81, 92			–207	207		–14, 6, 14		
5-(μ-O)$_2$(μ-OAc)												
Calcd.	–133	–266	–386	–52, –51, 104	–253	–13	–150	150	218	–6, 0, 6	139	11
Exp.†	–193	–386		–25, –73, 92			–213	213		–14, 8, 11		
Mn-cat												
Calcd.	–134	–267	–387	–92, 0, 91	–254	–13	–160	160	232	–5, 0, 6	148	12
Exp.†	–189	–378		–34, –48, 78			–238	238		–6, –14, 17		
6-(μ-O)(μ-OAc)$_2$												
Calcd.	–141	–282	–410	–112, 25, 86	–268	–14	–133	133	193	–10, –5, 15	122	11

Note: B3LYP results. See the Note for Table 9. A_{iso}* is obtained after scaling A_{iso} by 1.45. EPR, electron paramagnetic resonance.
*X-band EPR data taken from Horner et al.[66]
†HF-EPR data taken from Teutloff et al.[87]
‡Mulitfrequency EPR data taken from Schaefer et al.[88]

A_{iso}. Stronger ligation appears to lead to larger HFCs. This agrees with results for mononuclear complexes. For example, at the same computational level we obtain an A_{iso} value of –147.8 MHz for $[Mn(H_2O)_6]^{4+}$, a value of –227.6 MHz for $[Mn(H_2O)_5(OH)]^{3+}$, and a value of –303.3 MHz for $[Mn(H_2O)_5(O)]^{2+}$. On the Mn^{III} side, the observed variations in Table 12 are smaller but suggest the largest A_{iso} for the triply bridged systems and the lowest value for the (μ-O)$_2$-bridged system. The mono-μ-O and (μ-O)(μ-OAc) bridged systems feature fivefold coordination for the Mn^{III} center and are therefore more difficult to compare. Interestingly, however, the Mn^{III} HFCs appear to be changed less when going from six- to five-fold coordination. Insight from mononuclear complexes would suggest a similar trend as for Mn^{IV}, namely increasing A_{iso} with stronger coordination: a $[Mn(H_2O)_6]^{3+}$ value of –171.4 MHz compared with a $[Mn(H_2O)_5(OH)]^{2+}$ value of –226.4 MHz, as well as a $[Mn(H_2O)_5]^{3+}$ value of –135.6 MHz compared with a $[Mn(H_2O)_4(OH)]^{2+}$ value of –158.0 MHz.

Orientation of g and ^{55}Mn hyperfine tensors

The orientation of the **g** and hyperfine tensors with respect to the molecular framework and, in particular, with respect to each other, is crucial in the simulation of the EPR spectra. Often assumptions about co-axiality or of axial symmetry of tensors are made to reduce the degrees of freedom in a simulation. The known ability of modern DFT methods to typically provide the tensor orientations reliably is thus of interest to validate or invalidate these assumptions. The orientations of the computed HS, BS, and site **g** tensors and of the **A** tensors relative to the effective **g** tensor have been thus evaluated (see Table 13 for two of the complexes). Figure 5 shows the orientations for **2-(μ-O)$_2$** (orientations for **4-(μ-O)$_2$(μ-OAc)** are given in Fig. S3 in the Supplementary data). The computed **g**tensor orientation for **2-(μ-O)$_2$** agrees with the experimental assignment.[39] The $\mathbf{g}_{11}$ vector lies perpendicular to the Mn_2O_2 plane. The $\mathbf{g}_{22}$ axis is parallel to the Mn–Mn connection line, and the $\mathbf{g}_{33}$ axis is parallel to the connection between the bridging oxygen atoms. The Euler angles between the principal axes of the HS and BS **g** tensors are small, between 11.7° and 17.8°, as expected for a planar Mn_2O_2 core. Spin-projection results in an effective **g** tensor orientation intermediate between those of $\mathbf{g}_{HS}$ and $\mathbf{g}_{BS}$ (slightly closer to $\mathbf{g}_{HS}$ owing to the larger mass of the HS tensor after spin projection; eqs. [9]–[13]). As expected, the orientation of the site **g** tensor of the distorted Mn^{III} center ($\mathbf{g}_1$) dominates the effective **g** tensor orientation, as indicated by the smaller absolute values of the Euler angles relative to the effective **g** tensor.

The often assumed covariance between HFC and **g** tensors is clearly not fulfilled for **2-(μ-O)$_2$** (Fig. 5 and Table 13); whereas $\mathbf{A}_3$ of the Mn^{III} HFC tensors coincides with $\mathbf{g}_{11}$, the $\mathbf{A}_2$ and $\mathbf{A}_1$ orientations are rotated significantly relative to $\mathbf{g}_{22}$ and $\mathbf{g}_{33}$, respectively. The HFC tensor orientation of the Mn^{IV} center is also not covariant to **g** or the Mn^{III} HFC tensor ($\mathbf{A}_2$ is covariant with $\mathbf{g}_{22}$). But this is of lesser importance owing to the small HFC anisotropy on this center (see above).

Table 11. Dependence of ^{55}Mn hyperfine tensors (in MHz) of $(\mu\text{-O})_2$-bridged complexes on the terminal ligand set.

	Mn^{III}						Mn^{IV}					
Complex	a_{iso} (site)	A_{iso}	A_{iso}^*	T_1, T_2, T_3	A_{FC}	A_{PC}	a_{iso} (site)	A_{iso}	A_{iso}^*	T_1, T_2, T_3	A_{FC}	A_{PC}
$[(NH_3)_4Mn(\mu\text{-O})_2\ Mn(NH_3)_4]^{3+}$	–144	–288	–417	–54, –46, 99	–275	–13	–153	153	222	–5, 0, 4	142	11
$[(dab)_2Mn(\mu\text{-O})_2\ Mn(dab)_2]^{3+}$	–145	–290	–421	–54, –46, 100	–277	–13	–153	153	222	–4, –3, 7	141	12
$[(bipy)_2Mn(\mu\text{-O})_2\ Mnbipy)_2]^{3+}$	–158	–316	–454	–53, –45, 98	–302	–14	–150	150	218	–6, 0, 5	139	11
$[(phen)_2Mn(\mu\text{-O})_2\ Mn(phen)_2]^{3+}$	–156	–311	–450	–52, –46, 98	–297	–14	–150	150	218	–7, 0, 7	139	11
Exp.*	–226	–451		–28, –50, 78			–221	221		–8, –6, 11		

Note: B3LYP results. See the Note for Table 9. EPR, electron paramagnetic resonance.
*Mulitfrequency EPR data of $[(phen)_2Mn(\mu\text{-O})_2Mn(phen)_2]^{3+}$ taken from Schaefer et al.[88]

Table 12. Dependence of ^{55}Mn hyperfine tensors (in MHz) of tacn-based complexes on the bridging ligand set.

	Mn^{III}						Mn^{IV}					
Complex	a_{iso} (site)	A_{iso}	A_{iso}^*	T_1, T_2, T_3	A_{FC}	A_{PC}	a_{iso} (site)	A_{iso}	A_{iso}^*	T_1, T_2, T_3	A_{FC}	A_{PC}
$[(tacn)(H_2O)Mn(\mu\text{-O})\ Mn(H_2O)(tacn)]^{5+}$	–110	–219	–318	–66, –6, 72	–207	–12	–45	45	65	–35, –11, 45	29	16
$[(tacn)(H_2O)Mn^{III}(\mu\text{-O})_2\ Mn^{IV}(tacn)]^{3+}$	–99	–198	–287	–56, –47, 102	–185	–13	–145	145	210	–9, –4, 14	133	11
$[(tacn)Mn(\mu\text{-O})(\mu\text{-OAc})\ Mn(tacn)]^{4+}$	–104	–208	–302	–86, –2, 88	–195	–13	–40	40	58	–29, –17, 46	24	16
$[(tacn)Mn(\mu\text{-O})_2(\mu\text{-OAc})\ Mn(tacn)]^{2+}$	–133	–266	–386	–52, –51, 104	–253	–13	–150	150	218	–6, 0, 6	139	11
$[(tacn)Mn(\mu\text{-O})(\mu\text{-OAc})_2\ Mn(tacn)]^{3+}$	–141	–282	–409	–112, 25, 86	–268	–14	–133	133	193	–10, –5, 15	122	11

Note: B3LYP results. See the Note for Table 9.

Table 13. Euler angles (°) relative to the effective **g**-tensor principal axis system.

Complex	**g**	$\mathbf{g}_{11}$		$\mathbf{g}_{22}$		$\mathbf{g}_{33}$	
2-(μ-O)$_2$	$\mathbf{g}_{HS}$	$\mathbf{g}_{11}$	4.8	$\mathbf{g}_{22}$	5.6	$\mathbf{g}_{33}$	7.4
	$\mathbf{g}_{BS}$	$\mathbf{g}_{11}$	–5.7	$\mathbf{g}_{22}$	–5.7	$\mathbf{g}_{33}$	–10.4
	$\mathbf{g}_1$ [Mn^{III}]	$\mathbf{g}_{11}$	3.4	$\mathbf{g}_{22}$	3.9	$\mathbf{g}_{33}$	5.2
	$\mathbf{g}_2$ [Mn^{IV}]	$\mathbf{g}_{11}$	–5.8	$\mathbf{g}_{22}$	–7.9	$\mathbf{g}_{33}$	–10.3
	A [Mn^{III}]	$\mathbf{A}_3$	–0.7	$\mathbf{A}_1$	–35.5	$\mathbf{A}_2$	35.6
	A [Mn^{IV}]	$\mathbf{A}_3$	32.8	$\mathbf{A}_2$	–7.0	$\mathbf{A}_1$	33.7
4-(μ-O)$_2$(μ-OAc)	$\mathbf{g}_{HS}$	$\mathbf{g}_{11}$	6.1	$\mathbf{g}_{22}$	12.0	$\mathbf{g}_{33}$	12.0
	$\mathbf{g}_{BS}$	$\mathbf{g}_{11}$	–8.6	$\mathbf{g}_{22}$	–16.9	$\mathbf{g}_{33}$	–16.9
	$\mathbf{g}_1$ [Mn^{III}]	$\mathbf{g}_{11}$	4.3	$\mathbf{g}_{22}$	8.5	$\mathbf{g}_{33}$	8.5
	$\mathbf{g}_2$ [Mn^{IV}]	$\mathbf{g}_{11}$	–8.6	$\mathbf{g}_{22}$	–16.5	$\mathbf{g}_{33}$	–16.5
	A [Mn^{III}]	$\mathbf{A}_1$	41.9	$\mathbf{A}_3$	–8.2	$\mathbf{A}_2$	40.1
	A [Mn^{IV}]	$\mathbf{A}_3$	4.2	$\mathbf{A}_2$	–1.2	$\mathbf{A}_1$	–1.9

Fig. 5. Orientation of **g** tensor and manganese hyperfine tensors for **2-(μ-O)$_2$** (B3LYP results).

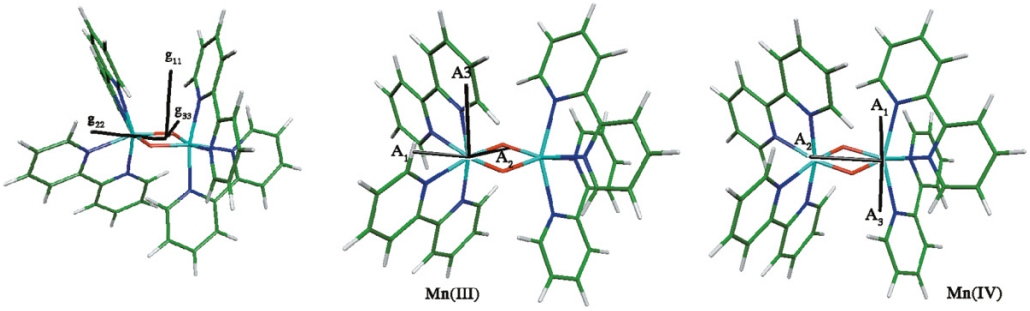

For the di-μ-oxo-μ-carboxylato bridged complex **4-(μ-O)$_2$(μ-OAc)** with its nonplanar core, **g** tensor orientations are similar as for **2-(μ-O)$_2$**: $\mathbf{g}_{22}$ is again parallel to the Mn–Mn connection line, $\mathbf{g}_{33}$ is parallel to the O–O connection line, and $\mathbf{g}_{11}$ is perpendicular to the $\mathbf{g}_{22}$–$\mathbf{g}_{33}$ plane, which does not contain all four atoms of the core. Yet, the differences between the orientations of $\mathbf{g}_{HS}$ and $\mathbf{g}_{BS}$ are more pronounced (Table 13). Again, $\mathbf{g}_1$ dominates the effective **g** tensor orientation. As for **2-(μ-O)$_2$**, we find the Mn^{III} **A** tensor not to be covariant with the **g** tensor, as shown by the large Euler angles for $\mathbf{A}_1$ than for $\mathbf{g}_{11}$ and for $\mathbf{A}_2$ than for $\mathbf{g}_{33}$. The Mn^{IV} HFC tensor orientation is close to that of the **g** tensor but again likely to be less important for spectra simulations.

Table 14. Dependence of nitrogen hyperfine coupling constants (HFCs) and nuclear quadrupole coupling tensors (in MHz) on the exact-exchange admixture.

	N(1)–Mn^{III}								N(2)–Mn^{IV}							
	a_{iso} (site)	A_{iso}	T_1	T_2	T_3	$\lvert e^2qQ\rvert$	$\lvert\eta\rvert$	$\rho^{\alpha-\beta}$	a_{iso} (site)	A_{iso}	T_1	T_2	T_3	$\lvert e^2qQ\rvert$	$\lvert\eta\rvert$	$\rho^{\alpha-\beta}$
BLYP	–2.3	–4.5	–0.7	–0.5	1.2	2.55	0.56	–0.036	–2.8	2.8	–0.4	0.1	0.2	2.59	0.53	0.031
B3LYP	–2.4	–4.7	–0.8	–0.5	1.3	2.63	0.53	–0.038	–2.7	2.7	–0.5	0.2	0.3	2.64	0.51	0.032
BHLYP	–2.4	–4.7	–0.9	–0.5	1.4	2.75	0.52	–0.037	–1.1	1.1	–0.7	0.3	0.5	2.79	0.48	0.027
B60LYP	–2.6	–5.2	–0.9	–0.5	1.4	2.74	0.53	–0.038	0.2	–0.2	–0.9	0.4	0.5	2.90	0.46	0.022
B70LYP	–3.1	–6.1	–0.9	–0.4	1.4	2.70	0.56	–0.039	2.7	–2.7	–1.3	0.6	0.7	3.09	0.42	0.011
B80LYP	–3.6	–7.2	–0.9	–0.4	1.3	2.63	0.61	–0.041	6.8	–6.8	–1.8	0.8	0.9	3.37	0.36	–0.007
B90LYP	–3.9	–7.7	–0.9	–0.4	1.3	2.59	0.65	–0.042	8.6	–8.6	–2.0	0.9	1.1	3.52	0.34	–0.017
Exp.*									|2.45|	|2.45|				2.34	0.51	

Note: HFC data are spin-projected. $\lvert e^2QC\rvert$ denotes the electric quadrupole coupling and $\lvert\eta\rvert$ the asymmetry parameter. $\rho^{\alpha-\beta}$ is the Mulliken spin density at nitrogen.

*Electron spin echo envelope modulation (ESEEM) data for catalase are from Ivancich et al.[97]

^{14}N Hyperfine coupling and nuclear quadrupole coupling tensors

Nitrogen donor ligands are present in several of the model systems studied, including catalase, and also in the OEC. In catalase, histidine imidazole nitrogens are coordinated to the two manganese centers (cf. Fig. 1), and in the OEC, a histidine is known to coordinate to one of the manganese centers.[95,96] Nitrogen HFCs and (given the quadrupolar nature of the ^{14}N nucleus) nuclear quadrupole coupling tensors are thus spectroscopic parameters with potential value for structure elucidation. Table 14 evaluates the dependence of the parameters for the two distinguishable ligand nitrogen atoms for **Mn-cat** on the exchange-correlation functional. Increased EXX admixture makes the isotropic ^{14}N HFC of N1 (bound to the Mn^{III} center) more negative. For the N2 atom bound to the Mn^{IV} center, the BLYP GGA functional gives a positive value, whereas increasing EXX admixture moves A_{iso} first towards small positive values (e.g., BHLYP or B60LYP) before turning it increasingly negative. No sign information is available from the experimental, but the good agreement of the B3LYP results with both the absolute value of A_{iso} and with the nuclear quadrupole coupling and asymmetry (Table 14) suggests this level (and the positive sign of A_{iso}) to be more reliable than large EXX admixtures >60%. Only one nitrogen atom was seen[97] in the ESEEM experiment, and its assignment[98] to N2–Mn^{IV} is consistent with our calculations and with those of Sinnecker et al.[21] The larger ^{14}N HFC of N1 is outside the range detectable by ESEEM, but it might be detected by ENDOR spectroscopy. For both N1 and N2, the calculations suggest small hyperfine anisotropy, with a somewhat larger dependence on the functional on the Mn^{IV} side (N2). For both nuclei, the nuclear quadrupole couplings increase with EXX admixture. Already, BLYP and B3LYP perform almost identically compared with the experimental. The asymmetry parameter behaves differently on the two nuclei. Again, the B3LYP results agree well with the experimental.

The second dinuclear system, for which the ^{14}N HFCs have previously been computed, is **4-(μ-O)$_2$(μ-OAc)**[20] (cf. Table 15). Our results for N1 (ligand to Mn^{III} along the Jahn–Teller axis) agree well with those of Sinnecker and Neese and co-workers and with the experimental. In the closely related **5-(μ-O)$_2$(μ-OAc)**, ESEEM has provided a second, smaller splitting assigned to N2 (equatorial ligand to Mn^{IV}; cf. Fig. 1 for atom labels). This relatively small splitting is underestimated somewhat by the computations. Notably, however, the smaller nuclear quadrupole coupling on N2 is better reproduced than the larger one on N1, which is overestimated. The asymmetry parameter is too low. Possible error sources are inaccuracies in the computed Mn–N distances along the Jahn–Teller axes of the Mn^{III} centers. The hyperfine tensors of these nitrogen nuclei at the Mn^{III} centers have nearly axial symmetry and are highly anisotropic, which is rather difficult to observe with either ESEEM or ENDOR.[98]

Table 15 shows only results for those nitrogen atoms for which an experimental assignment is available (see Table S9 in the Supplementary data for the remaining nitrogen nuclei). In addition to **Mn-cat**, **4-(μ-O)$_2$(μ-OAc)**, and **5-(μ-O)$_2$(μ-OAc)** discussed previously, experimental data are also available for **2-(μ-O)$_2$** and **3-(μ-O)$_2$**. Agreement with experimental values is similar as for the other complexes. Taking **2-(μ-O)$_2$** as an example, all ligating nitrogen atoms may be differentiated, based on the computed nitrogen HFCs and nuclear quadrupole tensors. The nitrogen atoms on the Jahn–Teller axes of the Mn^{III} center (N1, N1′) exhibit particularly large A_{iso}, whereas the equatorial N2 and N2′ have small values (0.6 MHz). The four nitrogen atoms bonded to Mn^{IV} exhibit similar, intermediate values (N3, N3′, 2.5 MHz; N4, N4', 1.9 MHz). These results suggest that similar evaluations may help in structure elucidation in more complex cases, provided nitrogen parameters are available from ESEEM and (or) ENDOR.

^{1}H hyperfine coupling tensors

Finally, we evaluate the dependence of the ligand proton HFCs on the functional. For this, we have chosen **4-(μ-O)$_2$(μ-OAc)**, which was studied previously by Sinnecker and Neese and co-workers at the BP86 and B3LYP levels.[20] Only the hydrogen atoms directly attached to the nitrogen nuclei in the first coordination sphere of the manganese atoms were experimentally accessible.[39] Moreover, H(1) vs. H(2) and H(3) vs. H(4) are in a too similar environment (cf. Fig. 1) and could not be distinguished experimentally. They

Table 15. ^{14}N hyperfine and nuclear quadrupole couplings (in MHz).

		a_{iso} (site)	A_{iso}	T_1	T_2	T_3	$\lvert e^2qQ\rvert$	$\lvert\eta\rvert$	$\rho^{\alpha-\beta}$
2-(μ-O)$_2$									
Mn^{III}	N1	7.3	14.6	–2.0	–1.7	3.7	3.83	0.07	0.027
Exp.*		6.8	13.5						
Exp.†		4.8	9.5				2.9		
Mn^{IV}	N2	–2.5	2.5	–0.5	0.0	0.5	2.28	0.30	0.044
Exp.‡		–2.8	2.8				2.3		
3-(μ-O)$_2$									
Mn^{III}	N1	6.4	12.8	–1.9	–1.7	3.6	3.81	0.07	0.026
Exp.†		4.9	9.7				3.0		
4-(μ-O)$_2$ (μ-OAc)									
Mn^{III}	N1	5.4	10.8	–2.4	–2.2	4.5	5.45	0.09	0.041
Exp.†		4.9	9.7				3.0		
5-(μ-O)$_2$ μ-OAc)									
Mn^{III}	N1	5.9	11.7	–2.2	–2.1	4.4	4.89	0.15	0.044
Exp.†		4.8	9.6				2.20		
Mn^{IV}	N2	–1.7	1.7	–0.1	0.0	0.1	2.36	0.27	0.039
Exp.§		–2.9	2.9				2.5	0.6	
Catalase									
Mn^{IV}	N2	–2.7	2.7	–0.5	0.2	0.3	–2.64	0.51	0.032
Exp.‖			(|2.88|)				(2.29)	(0.58)	

Note: B3LYP results. Cf. the Note for Table 14. ENDOR, electron–nuclear double resonance; ESEEM, electron spin echo envelope modulation.

*ENDOR data taken from Usov et al.[99]

†ENDOR data taken from Schafer et al.[39]

‡ENDOR data taken from Britt.[100]

§ESEEM data taken from Schafer et al.[39]

‖ESEEM data taken from Stemmler et al.[98]

Table 16. Dependence of hydrogen hyperfine coupling constant (HFC) tensors (in MHz) on the exact-exchange admixture for **4-(μ-O)$_2$(μ-OAc)**.

	H(1/H(2))–Mn^{III}						H(3)/H(4)–Mn^{IV}					
Method	a_{iso} (site)	A_{iso}	T_1	T_2	T_3	$\rho^{\alpha-\beta}$	a_{iso} (site)	A_{iso}	T_1	T_2	T_3	$\rho^{\alpha-\beta}$
BLYP	2.8	5.3	–7.5	–6.2	13.5	0.005	3.0	–3.0	–6.1	2.6	3.6	–0.005
B3LYP	2.5	4.4	–8.4	–6.8	14.8	0.005	2.9	–2.9	–7.1	3.0	4.1	–0.005
BHLYP	2.4	4.6	–8.6	–6.9	15.5	0.005	2.8	–2.8	–8.2	3.5	4.7	–0.005
B60LYP	2.3	4.5	–8.6	–7.0	15.6	0.005	2.7	–2.7	–8.6	3.7	4.9	–0.005
B70LYP	2.3	4.5	–8.7	–7.0	15.7	0.005	2.5	–2.5	–8.9	3.9	5.1	–0.004
B80LYP	2.3	4.5	–8.7	–7.0	15.7	0.005	2.0	–2.0	–9.5	4.2	5.4	–0.004
B90LYP	2.3	4.4	–8.8	–7.0	15.8	0.005	1.5	–1.5	–9.9	4.3	5.6	–0.002
Sinnecker*	2.6	5.1	–8.1	–6.4	14.5		2.9	–2.9	–6.9	2.9	4.0	
Exp.†	2.6	+3.1	–8.7	–8.0	+16.7		1.5	–1.5	–7.2	+2.8	+4.4	

Note: HFC data are spin-projected. $\rho^{\alpha-\beta}$ is the Mulliken spin density at hydrogen.

*DFT study using ORCA (B3LYP//B3LYP) from Sinnecker et al.[20]

†Experimental data for [MnMn(μ-O)$_2$(μ-OAc)(CH$_3$)$_4$DTNE](BPh)$_4$.[39]

have been averaged computationally. Our B3LYP results (Table 16) are similar to those of Sinnecker et al.,[20] small differences likely arising from the different basis sets employed. As found already for mononuclear Mn complexes like the divalent site in concanavalin A or simple aqua complexes,[22] the isotropic HFC decreases somewhat with increasing EXX admixture. Yet, even at very high admixtures, the absolute value at the Mn^{III} site is still overestimated compared with the experimental value. In the case of the Mn^{IV} site, the values for H3 and H4 start to diverge for large EXX admixtures, suggesting artificial symmetry breaking because of unphysical spin contamination (see above). The HFC anisotropies are already reproduced well at B3LYP level (somewhat better than with BLYP) and cannot be improved significantly by enhanced EXX admixture.

Conclusions

The detailed interpretation of EPR spectra for di- and multi-nuclear manganese complexes, such as the oxygen-

evolving complex of photosystem II, could be improved considerably if we could assist the experimentalists by providing reliable quantum chemical calculations and analyses. Building on important recent computational work by Sinnecker et al. on a synthetically available dinuclear model complex and on a model for dimanganese catalase, we provide a systematic study of various EPR parameters of a wider set of dinuclear $Mn^{III}Mn^{IV}$ complexes, using broken-symmetry DFT approaches. A main focus has been the evaluation of the influence of exact-exchange admixture in hybrid functionals on the computed spin-density distributions and spectroscopic parameters.

Spin-projected **g** tensors are generally almost isotropic and exhibit only relatively small deviations from the free-electron value. Whereas the **g** tensors are reproduced well by the standard B3LYP functional, their diagnostic value remains low at this point. Computations on the ^{55}Mn hyperfine tensors confirm that (*i*) the isotropic hyperfine couplings are underestimated by standard functionals, but (*ii*) this systematic error may be remedied to a good approximation by an empirical scaling factor (~1.45 at B3LYP level). The hyperfine anisotropies are already well reproduced by standard functionals. The same holds for the ligand ^{14}N and ^{1}H hyperfine tensors. Ongoing work in our lab concentrates on also finding suitable spin-projection schemes for bridging ligand sets. We find the Mn^{III} hyperfine tensors not to be generally covariant to the **g** tensors. This information is of importance for spectra simulations and will possibly affect simulation results for the OEC.

The spin contamination of the BS–KS determinants has been analyzed using NO occupations, PO overlaps, and an expansion into quasi-restricted determinants in the PO basis. It turns out that the S^2 expectation values near 3.75 obtained at B3LYP level are well in line with the expected seven active orbitals, which include the truly unpaired "SOMO" and three pairs of corresponding magnetic orbitals. The lower $\langle S^2 \rangle$ for the BLYP functional arises from a larger overlap between the POs, in line with an overestimation of delocalization by GGA functionals. The increased $\langle S^2 \rangle$ at higher exact-exchange admixtures arises partly from an increased active PO space, related to the spin polarization of nominally double-occupied orbitals. This additional spin contamination and the partly deteriorated results for other quantities somewhat restrict the amount of exact exchange one may use to improve the isotropic ^{55}Mn HFCs. Fortunately, the insufficiently negative intrinsic isotropic Mn HFCs at the B3LYP level may be easily corrected by scaling (see above). Standard hybdrid functionals such as B3LYP with ~20% exact exchange thus may be used with predictive power also for more complicated systems such as the oxygen-evolving complex of photosystem II. In the long run, improved generations of functionals are desirable, which will allow a well-balanced description of core- and valence-shell spin polarization. Work along these lines is in progress in our laboratory.

Supplementary data

Supplementary data for this article are available on the journal Web site (canjchem.nrc.ca) or may be purchased from the Depository of Unpublished Data, Document Delivery, CISTI, National Research Council Canada, Ottawa, ON K1A 0R6, Canada. DUD 5258. For more information on obtaining material, refer to cisti-icist.nrc-cnrc.gc.ca/cms/unpub_e.shtml.

Acknowledgments

We are grateful to R. Reviakine and to H. Bahmann for technical assistance and to I. Zilberberg for providing his code for the PO analyses. S.S. thanks Fonds der Chemischen Industrie for a doctoral scholarship. This work has been supported by Deutsche Forschungsgemeinschaft within priority program SPP1137 "Molecular Magnetism".

References

(1) Gatteschi, D.; Barra, A. L.; Caneschi, A.; Cornia, A.; Sessoli, R.; Sorace, L. *Coord. Chem. Rev.* **2006**, *250* (11–12), 1514–1529. doi:10.1016/j.ccr.2006.02.006.

(2) Dismukes, G. C. *Chem. Rev.* **1996**, *96* (7), 2909–2926. doi:10.1021/cr950053c. PMID:11848845.

(3) McEvoy, J. P.; Brudvig, G. W. *Chem. Rev.* **2006**, *106* (11), 4455–4483. doi:10.1021/cr0204294. PMID:17091926.

(4) Mukhopadhyay, S.; Mandal, S. K.; Bhaduri, S.; Armstrong, W. H. *Chem. Rev.* **2004**, *104* (9), 3981–4026. doi:10.1021/cr0206014. PMID:15352784.

(5) Barber, J.; Murray, J. W. *Coord. Chem. Rev.* **2008**, *252* (3-4), 233–243. doi:10.1016/j.ccr.2007.08.013.

(6) Ferreira, K. N.; Iverson, T. M.; Maghlaoui, K.; Barber, J.; Iwata, S. *Science* **2004**, *303* (5665), 1831–1838. doi:10.1126/science.1093087. PMID:14764885.

(7) Loll, B.; Kern, J.; Saenger, W.; Zouni, A.; Biesiadka, J. *Nature* **2005**, *438* (7070), 1040–1044. doi:10.1038/nature04224. PMID:16355230.

(8) Dau, H.; Haumann, M. *Coord. Chem. Rev.* **2008**, *252* (3-4), 273–295. doi:10.1016/j.ccr.2007.09.001.

(9) Yano, J.; Yachandra, V. K. *Photosynth. Res.* **2007**, *92* (3), 289–303. doi:10.1007/s11120-007-9153-5. PMID:17429751.

(10) Noguchi, T. *Coord. Chem. Rev.* **2008**, *252* (3–4), 336–346. doi:10.1016/j.ccr.2007.05.001.

(11) Taguchi, Y.; Noguchi, T. *Biochim. Biophys. Acta* **2007**, *1767* (6), 535–540. doi:10.1016/j.bbabio.2006.11.002. PMID:17184726.

(12) Britt, R. D.; Campbell, K. A.; Peloquin, J. M.; Gilchrist, M. L.; Aznar, C. P.; Dicus, M. M.; Robblee, J.; Messinger, J. *Biochim. Biophys. Acta* **2004**, *1655* (1-3), 158–171. PMID:15100028.

(13) Haddy, A. *Photosynth. Res.* **2007**, *92* (3), 357–368. doi:10.1007/s11120-007-9194-9. PMID:17551843.

(14) Noodleman, L.; Peng, C.; Case, D.; Mouesca, J. *Coord. Chem. Rev.* **1995**, *144*, 199–244. doi:10.1016/0010-8545(95)07011-L.

(15) Noodleman, L. J. *Chem. Phys.* **1981**, *74*, 5737.

(16) Blondin, G.; Girerd, J. J. *Chem. Rev.* **1990**, *90* (8), 1359–1376. doi:10.1021/cr00106a001.

(17) Bencini, A.; Gatteschi, D. *In* EPR of exchange coupled systems. Springer. 1990.

(18) Noodleman, L.; Baerends, E. J. *J. Am. Chem. Soc.* **1984**, *106* (8), 2316–2327. doi:10.1021/ja00320a017.

(19) Mouesca, J. M.; Noodleman, L.; Case, D. A.; Lamotte, B. *Inorg. Chem.* **1995**, *34* (17), 4347–4359. doi:10.1021/ic00121a013.

(20) Sinnecker, S.; Neese, F.; Noodleman, L.; Lubitz, W. *J. Am. Chem. Soc.* **2004**, *126* (8), 2613–2622. doi:10.1021/ja0390202. PMID:14982471.

(21) Sinnecker, S.; Neese, F.; Lubitz, W. *J. Biol. Inorg. Chem.* **2005**, *10* (3), 231–238. doi:10.1007/s00775-005-0633-9. PMID:15830216.
(22) Schinzel, S.; Müller, R.; Kaupp, M. *Theor. Chem. Acc.* **2008**, *120* (4-6), 437–445. doi:10.1007/s00214-008-0420-0.
(23) Sproviero, E. M.; Gascon, J. A.; McEvoy, J. P.; Brudvig, G. W.; Batista, V. S. *J. Inorg. Biochem.* **2006**, *100* (4), 786–800. doi:10.1016/j.jinorgbio.2006.01.017. PMID:16510187.
(24) Rudberg, E.; Salek, P.; Rinkevicius, Z.; Aagren, H. *J. Chem. Theory Comput.* **2006**, *2* (4), 981–989. doi:10.1021/ct050325b.
(25) Soda, T.; Kitagawa, Y.; Onishi, T.; Takano, Y.; Shigeta, Y.; Nagao, H.; Yoshioka, Y.; Yamaguchi, K. *Chem. Phys. Lett.* **2000**, *319* (3-4), 223. doi:10.1016/S0009-2614(00)00166-4.
(26) Atherton, N. M. *Principles of electron spin resonance*; Prentice Hall, New York. 1993.
(27) McGarvey, B. R. *Trans. Metal Chem.* **1966**, *3*, 89.
(28) Mabbs, F. E.; Collison, D. *Electron Paramagnetic Resonance of d Transition Metal Compounds*; Elsevier: Amsterdam, 1992.
(29) Abragam, A.; Bleaney, B. *Electron Paramagnetic Resonance of Transition Ions*; Clarendon Press: Oxford. 1970.
(30) Weil, J. A.; Bolton, J. R.; Wertz, J. E. *Electron Paramagnetic Resonance: Elementary Theory and Practical Applications*; Wiley & Sons: New York, 1994.
(31) Harriman, J. E. *Theoretical Foundations of Electron Spin Resonance*; Academic Press: New York, 1978.
(32) Kaupp, M.; Reviakine, R.; Malkina, O. L.; Arbuznikov, A.; Schimmelpfennig, B.; Malkin, V. G. *J. Comput. Chem.* **2002**, *23* (8), 794–803. doi:10.1002/jcc.10049. PMID:12012356.
(33) Malkina, O. L.; Vaara, J.; Schimmelpfennig, B.; Munzarová, M.; Malkin, V. G.; Kaupp, M. *J. Am. Chem. Soc.* **2000**, *122* (38), 9206–9218. doi:10.1021/ja000984s.
(34) Neese, F. *J. Chem. Phys.* **2001**, *115* (24), 11080. doi:10.1063/1.1419058.
(35) Schreckenbach, G.; Ziegler, T. *J. Phys. Chem. A* **1997**, *101* (18), 3388–3399. doi:10.1021/jp963060t.
(36) Remenyi, C.; Reviakine, R.; Arbuznikov, A. V.; Vaara, J.; Kaupp, M. *J. Phys. Chem. A* **2004**, *108* (23), 5026–5033. doi:10.1021/jp049395p.
(37) Arbuznikov, A. V.; Vaara, J.; Kaupp, M. *J. Chem. Phys.* **2004**, *120* (5), 2127–2139. doi:10.1063/1.1636720. PMID:15268351.
(38) Neese, F. *J. Chem. Phys.* **2003**, *118* (9), 3939. doi:10.1063/1.1540619.
(39) Schäfer, K.-O.; Bittl, R.; Zweygart, W.; Lendzian, F.; Haselhorst, G.; Weyhermuller, T.; Wieghardt, K.; Lubitz, W. *J. Am. Chem. Soc.* **1998**, *120* (50), 13104–13120. doi:10.1021/ja9827548.
(40) Zheng, M.; Khangulov, S. V.; Dismukes, G. C.; Barynin, V. V. *Inorg. Chem.* **1994**, *33* (2), 382–387. doi:10.1021/ic00080a030.
(41) Palii, A. V.; Belinsky, M. I.; Tsukerblat, B. S. *Chem. Phys.* **2000**, *255* (1), 51–57. doi:10.1016/S0301-0104(00)00060-4.
(42) Borrás-Almenar, J. J.; Coronado, E.; Ostrovsky, S. M.; Palii, A. V.; Tsukerblat, B. S. *Chem. Phys.* **1999**, *240* (1–2), 149–161. doi:10.1016/S0301-0104(98)00375-9.
(43) Barone, V.; Bencini, A.; Gatteschi, D.; Totti, F. *Chem. Eur. J.* **2002**, *8* (21), 5019–5027. doi:10.1002/1521-3765(20021104)8:21<5019::AID-CHEM5019>3.0.CO;2-Y.
(44) Randall, D. W.; Chan, M. K.; Armstrong, W. H.; Britt, R. D. *Mol. Phys.* **1998**, *95* (6), 1283–1294. doi:10.1080/002689798166297.
(45) Amos, A. T.; Hall, G. G. *Proc. R. Soc. Lond. A Math. Phys. Sci.* **1961**, *263* (1315), 483–493. doi:10.1098/rspa.1961.0175.
(46) Zilberberg, I.; Ruzankin, S. P. *Chem. Phys. Lett.* **2004**, *394* (1–3), 165–170. doi:10.1016/j.cplett.2004.06.126.
(47) Zilberberg, I.; Ruzankin, S. P.; Malykhin, S.; Zhidomirov, G. M. *Chem. Phys. Lett.* **2004**, *394* (4-6), 392–396. doi:10.1016/j.cplett.2004.06.144.
(48) Ahlrichs, R.; Bär, M.; Häser, M.; Horn, H.; Kölmel, C. *Chem. Phys. Lett.* **1989**, *162* (3), 165–169. doi:10.1016/0009-2614(89)85118-8.
(49) Barynin, V. V.; Whittaker, M. M.; Antonyuk, S. V.; Lamzin, V. S.; Harrison, P. M.; Artymiuk, P. J.; Whittaker, J. W. *Structure* **2001**, *9* (8), 725–738. doi:10.1016/S0969-2126(01)00628-1. PMID:11587647.
(50) Becke, A. D. *J. Chem. Phys.* **1993**, *98* (7), 5648. doi:10.1063/1.464913.
(51) Stephens, P. J.; Devlin, F. J.; Chabalowski, C. F.; Frisch, M. J. *J. Phys. Chem.* **1994**, *98* (45), 11623–11627. doi:10.1021/j100096a001.
(52) Schäfer, A.; Horn, H.; Ahlrichs, R. *J. Chem. Phys.* **1992**, *97* (4), 2571. doi:10.1063/1.463096.
(53) Munzarová, M.; Kaupp, M. *J. Phys. Chem. A* **1999**, *103* (48), 9966–9983. doi:10.1021/jp992303p.
(54) Munzarová, M.; Kubácek, P.; Kaupp, M. *J. Am. Chem. Soc.* **2000**, *122* (48), 11900–11913. doi:10.1021/ja002062v.
(55) Kutzelnigg, W.; Fleischer, U.; Schindler, M. In *NMR Basis Principles and Progress*; Diehl, P., Ed.; Springer-Verlag: Berlin/Heidelberg, 1990; Vol. 23, pp 165–262.
(56) Huzinaga, S. Ph.D. thesis, University of Alberta, Edmonton, AB. 1971.
(57) Lee, C.; Yang, W.; Parr, R. G. *Phys. Rev. B* **1988**, *37* (2), 785–789. doi:10.1103/PhysRevB.37.785.
(58) Malkin, V. G.; Malkina, O. L.; Reviakine, R.; Arbouznikov, A. V.; Kaupp, M.; Schimmelpfennig, B.; Malkin, I.; Helgaker, T.; Ruud, K. *MAG-ReSpect*, version 1.2; MAG-ReSpect. 2003.
(59) Hess, B. A.; Marian, C. M.; Wahlgren, U.; Gropen, O. *Chem. Phys. Lett.* **1996**, *251* (5–6), 365–371. doi:10.1016/0009-2614(96)00119-4.
(60) Schimmelpfennig, B. Ph.D. thesis, University of Stockholm, Stockholm, Sweden, 1996.
(61) Frisch, M. J.; Trucks, G. W.; Schlegel, H. B.; Scuseria, G. E.; Robb, M. A.; Cheeseman, J. R.; Montgomery, J. A., Jr.; Vreven, T.; Kudin, K. N.; Burant, J. C.; Millam, J. M.; Iyengar, S. S.; Tomasi, J.; Barone, V.; Mennucci, B.; Cossi, M.; Scalmani, G.; Rega, N.; Petersson, G. A.; Nakatsuji, H.; Hada, M.; Ehara, M.; Toyota, K.; Fukuda, R.; Hasegawa, J.; Ishida, M.; Nakajima, T.; Honda, Y.; Kitao, O.; Nakai, H.; Klene, M.; Li, X.; Knox, J. E.; Hratchian, H. P.; Cross, J. B.; Bakken, V.; Adamo, C.; Jaramillo, J.; Gomperts, R.; Stratmann, R. E.; Yazyev, O.; Austin, A. J.; Cammi, R.; Pomelli, C.; Ochterski, J. W.; Ayala, P. Y.; Morokuma, K.; Voth, G. A.; Salvador, P.; Dannenberg, J. J.; Zakrzewski, V. G.; Dapprich, S.; Daniels, A. D.; Strain, M. C.; Farkas, O.; Malick, D. K.; Rabuck, A. D.; Raghavachari, K.; Foresman, J. B.; Ortiz, J. V.; Cui, Q.; Baboul, A. G.; Clifford, S.; Cioslowski, J.; Stefanov, B. B.; Liu, G.; Liashenko, A.; Piskorz, P.; Komaromi, I.; Martin, R. L.; Fox, D. J.; Keith, T.; Al-Laham, M. A.; Peng, C. Y.; Nanayakkara, A.; Challacombe, M.; Gill, P. M. W.; Johnson, B.; Chen, W.; Wong, M. W.; Gonzalez, C.; Pople, J. A.

Gaussian 03, revision C.02; Gaussian Inc., Wallington, CT, 2004.
(62) Siegbahn, P. E. M. *Curr. Opin. Chem. Biol.* **2002**, *6* (2), 227–235. doi:10.1016/S1367-5931(02)00312-5. PMID: 12039009.
(63) Siegbahn, P. E. M.; Westerberg, J.; Svensson, M.; Crabtree, R. H. *J. Phys. Chem. B* **1998**, *102* (9), 1615–1623. doi:10.1021/jp972207t.
(64) Pavlov, M.; Blomberg, M. R. A.; Siegbahn, P. E. M. *Int. J. Quantum Chem.* **1999**, *73* (2), 197–207. doi:10.1002/(SICI)1097-461X(1999)73:2<197::AID-QUA13>3.0.CO;2-R.
(65) Sigfridsson, E.; Olsson, M. H. M.; Ryde, U. *Inorg. Chem.* **2001**, *40* (11), 2509–2519. doi:10.1021/ic000752u. PMID: 11350228.
(66) Horner, O.; Anxolabéhère-Mallart, E.; Charlot, M.-F.; Tchertanov, L.; Guilhem, J.; Mattioli, T. A.; Boussac, A.; Girerd, J.-J. *Inorg. Chem.* **1999**, *38* (6), 1222–1232. doi:10.1021/ic980832m. PMID:11670906.
(67) Plaksin, P. M.; Stoufer, R. C.; Mathew, M.; Palenik, G. J. *J. Am. Chem. Soc.* **1972**, *94* (6), 2121–2122. doi:10.1021/ja00761a059.
(68) Stebler, M.; Ludi, A.; Buergi, H. B. *Inorg. Chem.* **1986**, *25* (26), 4743–4750. doi:10.1021/ic00246a032.
(69) Wieghardt, K.; Bossek, U.; Zsolnai, L.; Huttner, G.; Blondin, G.; Girerd, J.-J.; Babonneau, F. *J. Chem. Soc. Chem. Commun.* **1987**, (9): 651. doi:10.1039/c39870000651.
(70) Wieghardt, K.; Bossek, U.; Bonvoisin, J.; Beauvillain, P.; Girerd, J.-J.; Nuber, B.; Weiss, J.; Heinze, J. *Angew. Chem.* **1986**, *98* (11), 1026–1027. doi:10.1002/ange.19860981128.
(71) Patchkovskii, S.; Ziegler, T. *J. Chem. Phys.* **1999**, *111* (13), 5730. doi:10.1063/1.479869.
(72) Rudra, I.; Wu, Q.; Van Voorhis, T. *Inorg. Chem.* **2007**, *46* (25), 10539–10548. doi:10.1021/ic700871f. PMID:17999488.
(73) Ruiz, E.; Cano, J.; Alvarez, S.; Alemany, P. *J. Am. Chem. Soc.* **1998**, *120* (43), 11122–11129. doi:10.1021/ja981661n.
(74) Ruiz, E.; Cano, J.; Alvarez, S.; Alemany, P. *J. Comput. Chem.* **1999**, *20* (13), 1391–1400. doi:10.1002/(SICI)1096-987X(199910)20:13<1391::AID-JCC6>3.0.CO;2-J.
(75) Ruiz, E.; Rodríguez-Fortea, A.; Cano, J.; Alvarez, S.; Alemany, P. *J. Comput. Chem.* **2003**, *24* (8), 982–989. doi:10.1002/jcc.10257. PMID:12720319.
(76) Ruiz, E. *Chem. Phys. Lett.* **2008**, *460* (1-3), 336–338. doi:10.1016/j.cplett.2008.05.073.
(77) Ruiz, E.; Rodríguez-Fortea, A.; Tercero, J.; Cauchy, T.; Massobrio, C. *J. Chem. Phys.* **2005**, *123* (7),o. 074102. doi:10.1063/1.1999631. PMID:16229554.
(78) Delfs, C. D.; Stranger, R. *Inorg. Chem.* **2001**, *40* (13), 3061–3076. doi:10.1021/ic0008767. PMID:11399174.
(79) McGrady, J. E.; Stranger, R. *J. Am. Chem. Soc.* **1997**, *119* (36), 8512–8522. doi:10.1021/ja964360r.
(80) Petrie, S.; Mukhopadhyay, S.; Armstrong, W. H.; Stranger, R. *Phys. Chem. Chem. Phys.* **2004**, *6* (20), 4871. doi:10.1039/b407512a.
(81) Soda, T.; Kitagawa, Y.; Onishi, T.; Takano, Y.; Shigeta, Y.; Nagao, H.; Yoshioka, Y.; Yamaguchi, K. *Chem. Phys. Lett.* **2000**, *319* (3-4), 223–230. doi:10.1016/S0009-2614(00)00166-4.
(82) Caballol, R.; Castell, O.; Illas, F.; de Pinho Ribeiro Moreira, I.; Malrieu, J. P. *J. Phys. Chem. A* **1997**, *101*, 7860. doi:10.1021/jp9711757.
(83) Ruiz, E.; Cirera, J.; Alvarez, S. *Coord. Chem. Rev.* **2005**, *249* (23), 2649–2660. doi:10.1016/j.ccr.2005.04.010.
(84) Ruiz, E.. *Struct. Bond.* **2004**, *113*, 71–102.
(85) Delfs, C. D.; Stranger, R. *Inorg. Chem.* **2000**, *39* (3), 491–495. doi:10.1021/ic990790h. PMID:11229568.
(86) Michaud-Soret, I.; Jacquamet, L.; Debaecker-Petit, N.; Le Pape, L.; Barynin, V. V.; Latour, J.-M. *Inorg. Chem.* **1998**, *37* (15), 3874–3876. doi:10.1021/ic9712176. PMID: 11670494.
(87) Teutloff, C.; Schäfer, K. O.; Sinnecker, S.; Barynin, V.; Bittl, R.; Wieghardt, K.; Lendzian, F.; Lubitz, W. *Magn. Reson. Chem.* **2005**, *43* (S1)(Spec no), S51–S64. doi:10.1002/mrc.1685. PMID:16235205.
(88) Schäfer, K.-O.; Bittl, R.; Lendzian, F.; Barynin, V.; Weyhermüller, T.; Wieghardt, K.; Lubitz, W. *J. Phys. Chem. B.* **2003**, *107* (5), 1242–1250. doi:10.1021/jp0259768.
(89) Remenyi, C.; Reviakine, R.; Kaupp, M. *J. Phys. Chem. B.* **2007**, *111* (28), 8290–8304. doi:10.1021/jp071745v. PMID:17592871.
(90) Kaupp, M.; Bahmann, H.; Arbuznikov, A. V. *J. Chem. Phys.* **2007**, *127* (19),o. 194102. doi:10.1063/1.2795700. PMID:18035874.
(91) Bahmann, H.; Rodenberg, A.; Arbuznikov, A. V.; Kaupp, M. *J. Chem. Phys.* **2007**, *126* (1),o. 011103. doi:10.1063/1.2429058. PMID:17212482.
(92) Arbuznikov, A. V.; Kaupp, M. *Chem. Phys. Lett.* **2007**, *440* (1–3), 160–168. doi:10.1016/j.cplett.2007.04.020.
(93) Arbuznikov, A. V.; Kaupp, M. *Chem. Phys. Lett.* **2007**, *442* (4–6), 496–503. doi:10.1016/j.cplett.2007.06.015.
(94) Arbuznikov, A. V.; Kaupp, M.; Bahmann, H. *J. Chem. Phys.* **2006**, *124* (20),o. 204102. doi:10.1063/1.2196883. PMID:16774314.
(95) Yeagle, G. J.; Gilchrist, M. L., Jr.; Walker, L. M.; Debus, R. J.; Britt, R. D. *Philos. Trans. R. Soc. Lond. B Biol. Sci.* **2008**, *363* (1494), 1157–1166, discussion 1166. doi:10.1098/rstb.2007.2211. PMID:17954435.
(96) Yeagle, G. J.; Gilchrist, M. L.; McCarrick, R. M.; Britt, R. D. *Inorg. Chem.* **2008**, *47* (6), 1803–1814. doi:10.1021/ic701680c. PMID:18330971.
(97) Ivancich, A.; Barynin, V. V.; Zimmermann, J.-L. *Biochemistry* **1995**, *34* (20), 6628–6639. doi:10.1021/bi00020a008. PMID:7756295.
(98) Stemmler, T. L.; Sturgeon, B. E.; Randall, D. W.; Britt, R. D.; Penner-Hahn, J. E. *J. Am. Chem. Soc.* **1997**, *119* (39), 9215–9225. doi:10.1021/ja9704040.
(99) Usov, O. M.; Grigoryants, V. M.; Tagore, R.; Brudvig, G. W.; Scholes, C. P. *J. Am. Chem. Soc.* **2007**, *129* (39), 11886–11887. doi:10.1021/ja073179n. PMID:17850079.
(100) Britt, R. D. Ph.D. thesis, Lawrence Berkeley Laboratory. 1988.

Out of one, many — Using moment expansions of the virial relation to deduce universal density functionals from a single system

Paul W. Ayers and Juan I. Rodriguez

Abstract: Moment expansions for density functionals are revisited. This allows for a simple proof of the equivalence between the integrodifferential virial relation and the coordinate-scaling equation. The virial relation is then used to show how, starting from an exact and explicit form of a functional for one system, one may deduce the exact functional for other systems with the same number of electrons.

Key words: density functional theory, coordinate scaling, electron density moments.

Résumé : On a réexaminé les expansions de moments pour les fonctionnelles de densité. Cet exercice permet de présenter une preuve simple de l'équivalence entre la relation virielle intégrodifférentielle et l'équation d'ajustement des coordonnées. On utilise ensuite la relation virielle pour montrer comment, en partant d'une forme exacte et explicite d'une fonctionnelle pour un système, on peut déduire une fonctionnelle exacte pour d'autres systèmes avec le même nombre d'électrons.

Mots-clés : théorie de la fonctionnelle de la densité, ajustement des coordonnées, moments de la densité électronique.

[Traduit par la Rédaction]

I. Introduction

When the present authors began working with density functional theory (DFT) in the mid-1990s, it was clear that the rich vein of "generalized gradient approximation" functionals (GGAs) was essentially depleted:[1] it seemed impossible to build GGAs that were significantly better than the old standbys.[2–9] Reasoning that the next generation of density functionals would be nonlocal, some researchers explored the idea of building functionals from the moments of the electron density,[10–16] e.g., the Cartesian moments

$$[1] \qquad m_{ijk}[\rho] = \int x^i y^j z^k \rho(\mathbf{r}) \mathrm{d}\mathbf{r}$$

(however, for reasons that will soon be clear, most of this work used different sets of moments). The moments are manifestly nonlocal functionals of the electron density and have a clear physical interpretation in terms of multipoles, but, in retrospect, this idea failed. For example, it is difficult to design moment functionals that are size-consistent[17] and invariant to rotations and translations of the density. While moment functionals may not be useful computationally, we believe that moments are useful as a *theoretical* tool. In particular, it is sometimes useful to express *functionals* of the electron density as *functions* of the density moments,

$$[2] \qquad Q[\rho] \leftrightarrow Q(\{m_{ijk}\})$$

if only because most theoreticians find functions easier to manipulate and understand than functionals.

Equation [1] presumes that for a given set of moments, there is only one and only one electron density. This is not always true, and discovering sufficient conditions for a set of moments to uniquely specify a probability distribution function (p.d.f.) is called the "problem of moments." For one-dimensional systems, the problem of moments is well-characterized[18–20] and Stieltjes's sufficient condition establishes that any p.d.f. that decays asymptotically faster than $r^{\beta}\mathrm{e}^{-\alpha r^{\lambda}}$ for some $\alpha,\beta > 0$ and some $\lambda \geq 1/2$ is uniquely determined by its moments.[21] For spherically symmetric systems with positive ionization potentials, $\rho(r) \sim \mathrm{e}^{-r\sqrt{8IP}}$,[22–26] and so the set of moments $\left\{\int_0^{\infty} r^k \rho(\mathbf{r})\mathrm{d}\mathbf{r}\right\}_{k=0}^{\infty}$ is complete. By contrast, the multi-dimensional moment problem is related to Hilbert's 17th problem, and is still being studied by mathematicians.[27] The extension of the Stieltjes condition to the multi-dimensional case,[28] however, establishes that the electron density is uniquely determined by the set of Cartesian moments,[1] as long as it decays exponentially fast. So, the densities of finite electronic systems with positive ionization potentials are determined by their moments. Additional infor-

Received 26 December 2008. Accepted 29 April 2009. Published on the NRC Research Press Web site at canjchem.nrc.ca on 9 October 2009.

This article is part of a Special Issue dedicated to Professor T. Ziegler. PWA recalls meeting Prof. Tom Ziegler for the first time in 2003, at breakfast in the Hotel Melia at the 10th International Conference on the Applications of Density Functional Theory in Chemistry and Physics (in Brussels, Belgium). Starting then, and to the present time, he has admired Prof. Zieglers ability to balance openness and skepticism, utility and rigor, humility and confidence, courtesy and candor.

P.W. Ayers[1] and J.I. Rodriguez. Department of Chemistry, McMaster University, Hamilton, ON L8S 4M1, Canada.

[1]Corresponding author (e-mail: ayers@mcmaster.ca).

mation about sufficient sets of moments can be found in ref. 13.

Not all electron densities are determined by their moments. In particular, one cannot represent an infinite system (like the uniform electron gas) in terms of its moments. In fact, only a tiny fraction of the p.d.f.s in the commonly considered spaces of electron densities, $\mathbb{L}^1 \cap \mathbb{L}^3$ or $\mathbb{L}^1 \cap \mathbb{L}^\infty$,[29,30] are determined by their moments.[31] However, for realistic systems of chemical and physical interest, the electron density is determined by its moments. In this way, mathematical arguments based on moments sacrifice universality for convenience. This is similar to current work on studying functionals that are "subuniversal" but still exact for molecules.[32–34] The mathematics of subuniversal density functional theories is complicated because functional derivatives on restricted sets of densities are sometimes ill-defined.[35–38] Because the set of densities that are determined by their moments is a dense subset of the full space of densities, the functionals and functional derivatives used in the following are well-defined, and equal to their values in conventional density functional theory.

In this paper, we will present two results that follow from the method of moments. In Section II, we will show how moments provide a short and lucid proof for the equivalence between the coordinate-scaling condition of a functional,[39–42]

$$[3] \qquad Q[\rho_\alpha] = \alpha^k Q[\rho]$$

$$[4] \qquad \rho_\alpha(x, y, z) = \alpha^3 \rho(\alpha x, \alpha y, \alpha z)$$

and its virial relation,[40,43–45]

$$[5] \qquad Q[\rho] = \frac{-1}{k} \int \rho(\mathbf{r}) \mathbf{r} \cdot \nabla \frac{\delta Q[\rho]}{\delta \rho(\mathbf{r})} \mathrm{d}\mathbf{r}$$

Generalizing and extending the argument in ref. 13, in Section III, we will show how, given the exact and explicit form of a density functional for a single reference system, one may obtain the exact functional for any other density that is determined by its moments and has the same number of electrons as the reference system.

II. Equivalence between scaling and the virial relation

The coordinate-scaling conditions for density functionals and the relationship between coordinate scaling and the adiabatic connection were first established by Levy and Perdew in their classic 1985 paper.[40] Almost all of the coordinate-scaling conditions of interest here are either contained in that paper[40] or easily derived from equations contained therein.[46,47] The general coordinate-scaling equalities in density functional theory can be summarized in a single formula,

$$[6] \qquad Q[\rho_\alpha; \alpha\lambda] = \alpha^n Q[\rho; \lambda]$$

Here, $\alpha = 1$ for potential-like quantities (Coulomb energy, J; exchange energy, E_x; correlation energy, E_c; exchange-correlation energy, $E_{xc} = E_x + E_c$; correlation potential energy, V_c; electron–electron repulsion energy, $V_{ee} = J + E_x + V_c$) and $\alpha = 2$ for kinetic-like quantities (noninteracting kinetic energy, T_s; correlation-kinetic energy, T_c; total kinetic energy, $T = T_s + T_c$). For functionals that do not change over the adiabatic connection path (J, E_x, and T_s), the λ index is superfluous, and the generalized coordinate-scaling conditions reduce to the simpler form in eq. [3]. Notice that even though the exchange-correlation energy and the correlation energy have both kinetic-energy and potential-energy components, they satisfy the potential-like coordinate-scaling relation because they can be computed as the integral of a potential-like quantity over the adiabatic connection path.

The first people to write coordinate-scaling relations in this general form were Levy, Yang, and Parr, who wrote down the special cases of eq. [6] appropriate to the kinetic energy and the electron–electron repulsion energy in this form.[42] More inclusive forms of this equation play an important role in Wang's work on coordinate scaling.[41]

To derive virial equations that are equivalent to eq. [6], it is helpful to use a set of moments with uniform coordinate scaling. For atoms, such a set was proposed by Nagy, Liu, and Parr[11]; generalizing their result to arbitrary systems gives

$$[7] \qquad m_{ijk}^{(NLP)}[\rho] = (m_{ijk}[\rho])^{\left(\frac{-1}{i+j+k}\right)} = \left(\int x^i y^j z^k \rho(\mathbf{r}) \mathrm{d}\mathbf{r}\right)^{\left(\frac{-1}{i+j+k}\right)} \quad \begin{matrix} i,j,k \geq 0 \\ \\ \\ i+j+k > 0 \end{matrix}$$

The Nagy–Liu–Parr moments are homogeneous of degree one with respect to coordinate scaling,

$$[8] \qquad m_{ijk}^{(NLP)}[\rho_\alpha] = \left(\iiint \left[\frac{(\alpha x)^i (\alpha y)^j (\alpha z)^k}{\alpha^{(i+j+k)}} \rho(\alpha x, \alpha y, \alpha z) \mathrm{d}(\alpha x) \mathrm{d}(\alpha y) \mathrm{d}(\alpha z) \right] \right)^{\left(\frac{-1}{i+j+k}\right)} = \alpha m_{ijk}^{(NLP)}[\rho]$$

Notice that the zeroth Nagy–Liu–Parr moment is undefined; for this reason, all of our subsequent arguments assume that the number of electrons does not change. This is clearly true in this context, because the normalization of the density is not changed upon coordinate scaling.

Consider the Euler equation,

$$[9] \qquad nQ[\{m_{ijk}^{(NLP)}\}, \lambda] = \lambda \frac{\partial Q}{\partial \lambda} + \sum_{\substack{i+j+k>0 \\ i,j,k \geq 0}}^{\infty} m_{ijk}^{(NLP)} \frac{\partial Q}{\partial m_{ijk}^{(NLP)}}$$

If this equation is valid, then the function Q is homogeneous of degree n with respect to scaling of its variables:[48]

$$[10] \qquad Q\left(\{\alpha m_{ijk}^{(NLP)}[\rho]\}, \alpha\lambda\right) = \alpha^n Q\left(\{m_{ijk}^{(NLP)}[\rho]\}, \lambda\right)$$

From the scaling of the Nagy–Liu–Parr moments (cf. Equation [8]), we have

$$[11] \qquad Q\left(\{m_{ijk}^{(NLP)}[\rho_\alpha]\}, \alpha\lambda\right) = \alpha^n Q[\{m_{ijk}^{(NLP)}[\rho]\}, \lambda]$$

which is equivalent to eq. [6].

So, eq. [9] is equivalent to the coordinate-scaling condition, eq. [6]. Now, it follows from the chain rule for functional derivatives,

$$[12] \qquad \int \rho(\mathbf{r})\mathbf{r}\cdot\nabla\left(\frac{\delta Q[\rho]}{\delta\rho(\mathbf{r})}\right)d\mathbf{r} = \int \rho(\mathbf{r})\mathbf{r}\cdot\nabla \sum_{\substack{i,j,k=0\\ i+j+k>0}}^{\infty}\left(\frac{\partial Q[\{m_{ijk}^{(NLP)}\}]}{\partial m_{ijk}^{(NLP)}}\frac{\delta m_{ijk}^{(NLP)}}{\delta\rho(\mathbf{r})}\right)d\mathbf{r}$$

$$= \sum_{\substack{i,j,k=0\\ i+j+k>0}}^{\infty}\left(\frac{\partial Q[\{m_{ijk}^{(NLP)}\}]}{\partial m_{ijk}^{(NLP)}}\left[\frac{-\left[\int x^i y^j z^k \rho(\mathbf{r}')d\mathbf{r}'\right]^{\left(\frac{-1}{i+j+k}-1\right)}}{i+j+k}\right]\int \rho(\mathbf{r})\mathbf{r}\cdot\nabla(x^i y^j z^k)d\mathbf{r}\right)$$

that

$$[13] \qquad \sum_{i,j,k=0}^{\infty} m_{ijk}^{(NLP)}\frac{\partial Q}{\partial m_{ijk}^{(NLP)}} = -\int \rho(\mathbf{r})\mathbf{r}\cdot\nabla\left(\frac{\delta Q[\rho]}{\delta\rho(\mathbf{r})}\right)d\mathbf{r}$$

Inserting eq. [13] into eq. [9] allows us to rewrite the coordinate-scaling condition, eq. [6], in its virial form,

$$[14] \qquad nQ[\rho;\lambda] = \lambda\frac{\partial Q[\rho;\lambda]}{\partial\lambda} - \int \rho(\mathbf{r})\mathbf{r}\cdot\nabla\left(\frac{\delta Q[\rho;\lambda]}{\delta\rho(\mathbf{r})}\right)d\mathbf{r}$$

Many special cases of eq. [14] are known in the literature.[40,49] When Q does not depend on λ, the first term on the right-hand-side of eq. [14] vanishes and eq. [5] is obtained.

The original derivation of eq. [5] from eq. [3] requires that $\rho(\mathbf{r})\delta Q[\rho]/\delta\rho(\mathbf{r})$ decay faster that r^{-3} as $r \to \infty$.[43] The present derivation clarifies the situation by showing that the DFT virial theorem is equivalent to the Eulerian virial theorem for simple functions. The moment-based derivation requires only that the moments determine the density, which imposes a different condition, albeit one that is often more stringent than the restriction on the asymptotic decay of $\rho(\mathbf{r})\delta Q[\rho]/\delta\rho(\mathbf{r})$. However, given the recent realization that the asymptotic decay of $\delta T_s/\delta\rho(\mathbf{r})$, $\delta E_x/\delta\rho(\mathbf{r})$, and $\delta E_{xc}/\delta\rho(\mathbf{r})$ is nonuniform,[50–53] there is merit in a derivation that does not depend in any way on the asymptotic decay of the functional derivative.

III. Deducing "universal" functionals from a single system

Equation [9] is a first-order partial differential equation that can be solved by the method of characteristics.[13] Suppose, then, that the *exact and explicit* expression for $Q\left(\{m_{ijk}^{(NLP)}\}, \lambda\right)$ is known for a specific N-electron system. Notice that we are not merely assuming that the value of the functional is known; we require that the exact *functional form* is known. The values of λ and the moments for this system are the initial values from which the differential equation will be solved. To simplify the notation, it is helpful to introduce a new set of coordinates, $\{x_p\}$, where $x_0 = \lambda$ and $x_{p>0}$ denote the various Nagy–Liu–Parr moments. The values of these variables for the known system are denoted $\{x_p^{(0)}\}$ and, in terms of these coordinates, eq. [9] (equivalently, eq. [14]) has the form

$$[15] \qquad nQ(\{x_p\}) = \sum_{p=0}^{\infty} x_p\frac{\partial Q}{\partial x_p}$$

We define a variable, τ, that parameterizes the characteristics through the equations

$$[16] \qquad \frac{dQ}{d\tau} = nQ \qquad \frac{dx_p}{d\tau} = x_p$$

Note that inserting these formulae into eq. [15] yields the identity

$$[17] \qquad \frac{\partial Q}{\partial\tau} = \sum_{p=0}^{\infty}\frac{\partial x_p}{\partial\tau}\frac{\partial Q}{\partial x_p}$$

Equation [16] can be solved by inspection, giving

$$[18] \qquad Q = C_Q e^{n\tau} \qquad x_p = C_p e^{\tau}$$

The Cs are constants of integration and can be determined based on the functional form of the known system

$$[19]\qquad \begin{aligned} C_Q &= Q\left(\{x_p^{(0)}\}\right)\mathrm{e}^{-n\tau^{(0)}} \\ C_p &= x_p^{(0)}\mathrm{e}^{-\tau^{(0)}} \end{aligned}$$

Substituting back into eq. [18] gives

$$[20]\qquad \begin{aligned} Q &= Q\left(\{x_p^{(0)}\}\right)\mathrm{e}^{n\left(\tau-\tau^{(0)}\right)} \\ x_p &= x_p^{(0)}\mathrm{e}^{\tau-\tau^{(0)}} \end{aligned}$$

To eliminate most of the explicit dependence on the initial conditions, we will express all of the other variables in terms of a specific variable, q,

$$[21]\qquad \mathrm{e}^{\tau-\tau^{(0)}} = \frac{x_q}{x_q^{(0)}}$$

$$[22]\qquad x_p^{(0)} = \frac{x_{p\neq q}x_q^{(0)}}{x_p}$$

giving the "final" form

$$[23]\qquad \begin{aligned} Q(\{x_p\}_{p=0}^{\infty}) = &\left(\frac{x_q}{x_q^{(0)}}\right)^n \\ &\times Q\left(\frac{x_0x_q^{(0)}}{x_q}, \frac{x_1x_q^{(0)}}{x_q}, \ldots, \frac{x_{q-1}x_q^{(0)}}{x_q}, x_q^0, \frac{x_{q+1}x_q^{(0)}}{x_q}, \ldots\right) \end{aligned}$$

This functional can be used for any system with the same number of electrons as the reference system, so long as both that system and the reference system are determined by their moments. The key to using this formula, however, and the reason this formula is not computationally facile, is that it requires that one know the *exact* functional form of $Q(\{x_p\}) = Q[\rho;\lambda]$. If the exact functional form were known for some $\{\rho_0(\mathbf{r}),\lambda_0\}$, however, then all of the derivatives of Q would also be known, and one could evaluate $Q[\rho;\lambda]$ from perturbation theory or, somewhat more elegantly, through the Parr–Liu–Kugler–Nagy expansion.[54,55] So, the reader should not be too surprised that full knowledge of a functional for a single system is generally sufficient to determine it for other systems also. For example, the work of Ludeña and his colleagues on local scaling transformations is also based on using extending functionals from a single known system to the general case.[56–61] Equation [23] is still important, however, as a constraint on the functional form of exact functionals.

IV. Specific cases and extensions

If the exact functional is known for an intermediate point on the adiabatic connection path, $0 < \lambda_0 < \infty$, then the exact functional can be determined at any other value of λ. Recalling that $x_0 = \lambda$, eq. [23] becomes

$$[24]\qquad \begin{aligned} Q(\lambda, \{x_p\}_{p=1}^{\infty}) &= \left(\frac{\lambda}{\lambda_0}\right)^n Q\left(\lambda_0, \frac{x_1\lambda_0}{\lambda}, \frac{x_2\lambda_0}{\lambda}, \ldots\right) \\ Q[\rho;\lambda] &= \left(\frac{\lambda}{\lambda_0}\right)^n Q\left[\rho_{\lambda_0/\lambda};\lambda_0\right] \end{aligned}$$

The scaling of the Nagy–Liu–Parr moments was used to derive the second line. This equation is obviously equivalent to eq. [6] with $\alpha = \frac{\lambda_0}{\lambda}$. Levy has presented several specific cases of eq. [24], including the electron–electron repulsion potential case. He has also described the "out of one, many" nature of this formula, by which knowledge of a functional at a specific point on the adiabatic connection curve suffices to determine that functional at all other points.[62]

The analysis in Sections II and III can be extended to other sets of density functionals that fully specify the electron density and scale homogeneously, $g_{ijk}[\rho_\alpha] = \alpha g_{ijk}[\rho]$. For any such functional, eq. [5] implies that

$$[25]\qquad g_{ijk}[\rho] = -\int \rho(\mathbf{r})\mathbf{r}\cdot\nabla\frac{\delta g_{ijk}[\rho]}{\delta\rho(\mathbf{r})}\mathrm{d}\mathbf{r}$$

so there is an analogue to eq. [13], namely

$$[26]\qquad \begin{aligned} g_{ijk}\frac{\partial Q}{\partial g_{ijk}} &= -\int \rho(\mathbf{r})\mathbf{r}\cdot\nabla\frac{\partial Q}{\partial g_{ijk}}\frac{\delta g_{ijk}}{\delta\rho(\mathbf{r})}\mathrm{d}\mathbf{r} \\ \sum_{i,j,k} g_{ijk}\frac{\partial Q}{\partial g_{ijk}} &= -\sum_{i,j,k}\int \rho(\mathbf{r})\mathbf{r}\cdot\nabla\frac{\partial Q}{\partial g_{ijk}}\frac{\delta g_{ijk}}{\delta\rho(\mathbf{r})}\mathrm{d}\mathbf{r} \\ &= \int \rho(\mathbf{r})\mathbf{r}\cdot\nabla\frac{\delta Q}{\delta\rho(\mathbf{r})}\mathrm{d}\mathbf{r} \end{aligned}$$

Then, from the generalized scaling relation, eq. [6],

$$[27]\qquad nQ[\{g_{ijk}\},\lambda] = \lambda\frac{\partial Q}{\partial\lambda} + \sum_{\substack{i+j+k>0 \\ i,j,k\geq 0}}^{\infty} g_{ijk}\frac{\partial Q}{\partial g_{ijk}}$$

From this equation and eq. [26], the generalized virial relation (eq. [14]) follows. Equation [27] can be solved by the method of characteristics to obtain a solution in the form of eq. [23]. This means that were the exact functional form known for *any value* of *any* homogeneously scaling functional, $g_{ijk}[\rho] = g_{ijk}^{(0)}$, then a "universal" functional for other systems with the same numbers of electrons could be written using eq. [23]. This suggests considering alternative sets of homogeneous functionals, e.g.,

$$[28]\qquad g_k[\rho] = \left(\int (\rho(\mathbf{r}))^{1+\frac{k}{3}}\mathrm{d}\mathbf{r}\right)^{\frac{1}{k}},\quad k = 1, 2, \ldots$$

$$[29]\qquad g_{ijk}[\rho] = \left(\int \frac{\partial^{i+j+k}\rho(\mathbf{r})}{\partial x^i\partial y^j\partial z^k}\mathrm{d}\mathbf{r}\right)^{\frac{1}{i+j+k}}$$

The former set of functionals may be argued to be (over)-complete,[13] but the latter set of functionals is probably incomplete.

V. Summary

The purpose of this paper is to demonstrate that using the moments of the electron density, instead of the electron density itself, in density functional theory is a useful theoretical trick. Part of this is because the mathematical tools for working with functions of moments are more familiar than the tools for working with functionals of the density. Part of this is because moment-based density functionals are subu-

niversal in useful ways. Most notably, the moment-based techniques are not necessarily applicable to systems with "strange" nonexponentially decaying electron densities. Second, the convenient Nagy–Liu–Parr set of moments excludes the number of electrons; using a different moment functional for each number of electrons avoids difficulties associated with the derivative discontinuity,[63–65] though it introduces size-consistency problems.

To demonstrate the power of moment-based reasoning, we first derived the equivalence of the the generalized coordinate-scaling condition (eq. [6]) and its virial form (eq. [14]). One advantage of this derivation is that it clarifies the link between density scaling in DFT and variable scaling in real analysis. In fact, the DFT virial equation is exactly equivalent to the Euler differential equation for functions that scale homogeneously with respect to their coordinates, eq. [9]. The Euler differential equation can then be solved, provided a suitable initial condition is known. This means that for any quantity (e.g., the kinetic energy, the electron–electron repulsion energy, or the exchange-correlation energy) that satisfies a generalized coordinate-scaling condition, if one knows the exact functional (not just its value, but its functional form) for *one N*-electron density, then one can determine the value of the functional for all other *N*-electron densities that are determined uniquely by their moments. We hope that results of this type may guide the use of special cases (e.g., the strongly interacting limit[66–70]) in the development of density functionals.

Acknowledgments

PWA would like to thank the Natural Sciences and Engineering Research Council of Canada (NSERC), the Canada Research Chairs, and the Alfred P. Sloan foundation for funding.

References

(1) Chan, G. K. L.; Handy, N. C. *J. Chem. Phys.* **2000**, *112* (13), 5639. doi:10.1063/1.481139.
(2) Becke, A. D. *Phys. Rev. A* **1988**, *38* (6), 3098–3100. doi:10.1103/PhysRevA.38.3098. PMID:9900728.
(3) Perdew, J. P.; Burke, K.; Ernzerhof, M. *Phys. Rev. Lett.* **1996**, *77* (18), 3865–3868. doi:10.1103/PhysRevLett.77.3865. PMID:10062328.
(4) Perdew, J. P.; Burke, K.; Ernzerhof, M. *Phys. Rev. Lett.* **1998**, *80* (4), 891. doi:10.1103/PhysRevLett.80.891.
(5) Zhang, Y.; Yang, W. *Phys. Rev. Lett.* **1998**, *80* (4), 890. doi:10.1103/PhysRevLett.80.890.
(6) Lee, C.; Yang, W.; Parr, R. G. *Phys. Rev. B* **1988**, *37* (2), 785–789. doi:10.1103/PhysRevB.37.785.
(7) Perdew, J. P. *Phys. Rev. B* **1986**, *33* (12), 8822–8824. doi:10.1103/PhysRevB.33.8822.
(8) Cohen, A. J.; Handy, N. C. *Mol. Phys.* **2001**, *99*, 607. doi:10.1080/00268970010023435.
(9) Handy, N. C.; Cohen, A. J. *Mol. Phys.* **2001**, *99*, 403. doi:10.1080/00268970010018431.
(10) Liu, S.; Nagy, A.; Parr, R. G. *Phys. Rev. A* **1999**, *59* (2), 1131–1134. doi:10.1103/PhysRevA.59.1131.
(11) Nagy, A.; Liu, S. B.; Parr, R. G. *Phys. Rev. A* **1999**, *59* (5), 3349–3354. doi:10.1103/PhysRevA.59.3349.
(12) Bene, E.; Nagy, A. *Chem. Phys. Lett.* **2000**, *324* (5–6), 475–481. doi:10.1016/S0009-2614(00)00674-6.
(13) Ayers, P. W.; Lucks, J. B.; Parr, R. G. *Acta Chim. Phys. Debricina* **2002**, *34–35*, 223.
(14) Ayers, P. W. *Phys. Rev. A* **2005**, *71* (6),o. 062506. doi:10.1103/PhysRevA.71.062506.
(15) Ayers, P. W.; De Proft, F.; Geerlings, P. *Phys. Rev. A* **2007**, *75* (1),o. 012508. doi:10.1103/PhysRevA.75.012508.
(16) Ayers, P. W. *Proc. Natl. Acad. Sci. U.S.A.* **2000**, *97* (5), 1959–1964. doi:10.1073/pnas.040539297. PMID:10688883.
(17) Notice, for example, that the zeroth moment is just the number of electrons. No functional with a nonlinear dependence on the number of electrons can be size consistent.
(18) Shohat, J. A.; Tamarkin, J. D. *The problem of moments;* AMS: New York, 1943.
(19) Achieser, N. I. In *Theory of Approximation;* Dover: New York, 1992.
(20) Stuart, A.; Ord, J. K. In *Kendall's Advanced Theory of Statistics;* Vol. 1: Distribution Theory; Halsted: New York, 1994.
(21) Hardy, G. H. *Messenger of Mathematics* **1917**, *46*, 175.
(22) Katriel, J.; Davidson, E. R. *Proc. Natl. Acad. Sci. U.S.A.* **1980**, *77* (8), 4403–4406. doi:10.1073/pnas.77.8.4403. PMID:16592857.
(23) Morrell, M. M.; Parr, R. G.; Levy, M. *J. Chem. Phys.* **1975**, *62* (2), 549. doi:10.1063/1.430509.
(24) Levy, M.; Perdew, J. P.; Sahni, V. *Phys. Rev. A* **1984**, *30* (5), 2745–2748. doi:10.1103/PhysRevA.30.2745.
(25) Hoffmann-Ostenhof, M.; Hoffmann-Ostenhof, T.; Morgan, J. D., III. *Phys. Rev. A* **1981**, *23* (1), 21. doi:10.1103/PhysRevA.23.21.
(26) Almbladh, C. O.; Von Barth, U. *Phys. Rev. B* **1985**, *31* (6), 3231–3244. doi:10.1103/PhysRevB.31.3231.
(27) Hilbert, D. *Bull. Am. Math. Soc.* **2000**, *37* (4), 407–437. doi:10.1090/S0273-0979-00-00881-8.
(28) Cramer, H.; Wold, H. *J. London Math.* **1936**, *11* (4), 290–294. doi:10.1112/jlms/s1-11.4.290.
(29) Lieb, E. H. *Int. J. Quantum Chem.* **1983**, *24* (3), 243–277. doi:10.1002/qua.560240302.
(30) Ayers, P. W. *Phys. Rev. A* **2006**, *73* (1),o. 012513. doi:10.1103/PhysRevA.73.012513.
(31) Ayers, P. W.; Yang, W. T. *J. Chem. Phys.* **2006**, *124* (22),o. 224108. This paper shows that it is possible, albeit rather cumbersome, to define the space of densities so that the moments exist. doi:10.1063/1.2200884. PMID:16784264.
(32) Ayers, P. W.; Golden, S.; Levy, M. *J. Chem. Phys.* **2006**, *124* (5),o. 054101. doi:10.1063/1.2006087. PMID:16468845.
(33) Ayers, P. W.; Nagy, A. *J. Chem. Phys.* **2007**, *126* (14),o. 144108. doi:10.1063/1.2718950. PMID:17444702.
(34) Ludena, E. V.; Illas, F.; Ramirez-Solis, A. *Int. J. Mod. Phys. B* **2008**, *22* (25 & 26), 4642. doi:10.1142/S0217979208050395.
(35) Parr, R. G.; Bartolotti, L. J. *J. Phys. Chem.* **1983**, *87* (15), 2810–2815. doi:10.1021/j100238a023.
(36) Gál, T. *J. Math. Chem.* **2007**, *42* (3), 661–676. doi:10.1007/s10910-006-9216-4.
(37) Gál, T. *J. Phys. A* **2002**, *35*, 5899. doi:10.1088/0305-4470/35/28/309.
(38) Gal, T. *Phys. Rev. A* **2001**, *6302* (2).
(39) Levy, M. *Phys. Rev. A* **1982**, *26* (3), 1200–1208. doi:10.1103/PhysRevA.26.1200.
(40) Levy, M.; Perdew, J. P. *Phys. Rev. A* **1985**, *32* (4), 2010–2021. doi:10.1103/PhysRevA.32.2010. PMID:9896312.
(41) Wang, Y. A. *Phys. Rev. A* **1997**, *56* (2), 1646–1649. doi:10.1103/PhysRevA.56.1646.
(42) Levy, M.; Yang, W.; Parr, R. G. J. *J. Chem. Phys.* **1985**, *83* (5), 2334. doi:10.1063/1.449326.

(43) Ghosh, S. K.; Parr, R. G. *J. Chem. Phys.* **1985**, *82* (7), 3307. doi:10.1063/1.448229.
(44) Ou-Yang, H.; Levy, M. *Phys. Rev. Lett.* **1990**, *65* (8), 1036–1039. doi:10.1103/PhysRevLett.65.1036. PMID:10043089.
(45) Ou-Yang, H.; Levy, M. *Phys. Rev. A* **1991**, *44* (1), 54–58. doi:10.1103/PhysRevA.44.54. PMID:9905653.
(46) Görling, A.; Levy, M. *Phys. Rev. B* **1993**, *47* (20), 13105–13113. doi:10.1103/PhysRevB.47.13105.
(47) Levy, M. In *Single Particle Density in Chemistry and Physics;* March, N. H., and Deb, B. M., Eds.; Academic: London, 1987.
(48) Levine, I. N. In *Quantum Chemistry;* Prentice Hall: Englewood Cliffs, NJ, 1999.
(49) Wang, Y. A.; Liu, S. B.; Parr, R. G. *Chem. Phys. Lett.* **1997**, *267* (1–2), 14–22. doi:10.1016/S0009-2614(97)00074-2.
(50) Della Sala, F.; Görling, A. *Phys. Rev. Lett.* **2002**, *89* (3),o. 033003. doi:10.1103/PhysRevLett.89.033003. PMID: 12144389.
(51) Della Sala, F.; Gorling, A. *J. Chem. Phys.* **2002**, *116* (13), 5374. doi:10.1063/1.1453958.
(52) Vitale, V.; Della Sala, F.; Görling, A. *J. Chem. Phys.* **2005**, *122* (24),o. 244102. doi:10.1063/1.1938868. PMID: 16035741.
(53) Wu, Q.; Ayers, P. W.; Yang, W. T. *J. Chem. Phys.* **2003**, *119* (6), 2978. doi:10.1063/1.1590631.
(54) Parr, R. G.; Liu, S. B.; Kugler, A. A.; Nagy, A. *Phys. Rev. A* **1995**, *52* (2), 969–976. doi:10.1103/PhysRevA.52.969. PMID:9912336.
(55) Liu, S. B.; Parr, R. G. *J. Chem. Phys.* **1997**, *106* (13), 5578. doi:10.1063/1.473580.
(56) Ludeña, E. V.; Lopez-Boada, R.; Maldonado, J. E.; Valderrama, E.; Kryachko, E. S.; Koga, T.; Hinze, J. *Int. J. Quantum Chem.* **1995**, *56*, 285. doi:10.1002/qua.560560413.
(57) Ludeña, E. V.; Lopez-Boada, R. *Density Functional Theory I* **1996**, *180*, 169.
(58) Ludeña, E. V.; Lopezboada, R.; Pino, R. *Can. J. Chem.* **1996**, *74* (6), 1097–1105. doi:10.1139/v96-123.
(59) Valderrama, E.; Ludena, E. V.; Hinze, J. *J. Chem. Phys.* **1997**, *106* (22), 9227. doi:10.1063/1.474024.
(60) López-Boada, R.; Ludeña, E. V.; Karasiev, V.; Colle, R. *Int. J. Quantum Chem.* **1998**, *69*, 439. doi:10.1002/(SICI)1097-461X(1998)69:4<439::AID-QUA1>3.0.CO;2-W.
(61) Karasiev, V. V.; Ludena, E. V.; Artemyev, A. N. *Phys. Rev. A* **2000**, *62* (6),o. 062510. doi:10.1103/PhysRevA.62.062510.
(62) Levy, M. *Phys. Rev. A* **1991**, *43* (9), 4637–4646. doi:10.1103/PhysRevA.43.4637. PMID:9905580.
(63) Perdew, J. P.; Parr, R. G.; Levy, M.; Balduz, J. L., Jr. *Phys. Rev. Lett.* **1982**, *49* (23), 1691–1694. doi:10.1103/PhysRevLett.49.1691.
(64) Yang, W. T.; Zhang, Y. K.; Ayers, P. W. *Phys. Rev. Lett.* **2000**, *84* (22), 5172–5175. doi:10.1103/PhysRevLett.84.5172. PMID:10990895.
(65) Zhang, Y. K.; Yang, W. T. *Theor. Chem. Acc.* **2000**, *103*, 346.
(66) Seidl, M. *Int. J. Quantum Chem.* **2003**, *91* (2), 145–150. doi:10.1002/qua.10431.
(67) Seidl, M.; Gori-Giorgi, P.; Savin, A. *Phys. Rev. A* **2007**, *75* (4),o. 042511. doi:10.1103/PhysRevA.75.042511.
(68) Seidl, M.; Perdew, J. P.; Kurth, S. *Phys. Rev. A* **2000**, *62* (1),o. 012502. doi:10.1103/PhysRevA.62.012502.
(69) Gori-Giorgi, P.; Seidl, M.; Savin, A. *Phys. Chem. Chem. Phys.* **2008**, *10* (23), 3440–3446. doi:10.1039/b803709b. PMID:18535727.
(70) Seidl, M.; Perdew, J. P.; Levy, M. *Phys. Rev. A* **1999**, *59* (1), 51–54. doi:10.1103/PhysRevA.59.51.

Experimental and theoretical investigations of selenium nuclear magnetic shielding tensors in Se–N heterocycles

Andre Sutrisno, Andy Y.H. Lo, Joel A. Tang, Jason L. Dutton, Gregg J. Farrar, Paul J. Ragogna, Shaohui Zheng, Jochen Autschbach, and Robert W. Schurko

Abstract: A preliminary study involving solid-state ^{77}Se NMR spectroscopy and first principles calculations of ^{77}Se NMR parameters in Se–N heterocycles is reported. ^{77}Se CP/MAS NMR spectra of the ring systems reveal expansive selenium chemical shift (CS) tensors, which are extremely sensitive to molecular geometry, symmetry, ligand substitution, and intermolecular contacts. For systems with known crystal structures, hybrid density functional theory (DFT) calculations of selenium nuclear magnetic shielding (NMS) tensors were carried out, and tensor orientations in the molecular frames examined. Additional DFT calculations of selenium NMS tensors are presented, along with a detailed analysis of pairs of occupied and virtual molecular orbitals that give rise to the Se NMS tensors. A new naturalized local molecular orbital (NLMO) analysis under the same DFT framework is also discussed. Collectively, the NMR data and first principles calculations provide understanding of the influences of electronic structure, bonding, and intermolecular interactions on the selenium NMS tensors, allowing for (*i*) prediction of unknown molecular structures and (*ii*) insight into the positions of the stereochemically active selenium lone pairs.

Key words: solid-state NMR, ^{77}Se NMR, ab initio calculations, chemical shielding, main-group inorganic chemistry, heterocycles, DFT calculations, MO analysis, Gaussian 03, ADF.

Résumé : On rapporte les résultats d'une étude préliminaire de spectroscopie RMN du ^{77}Se à l'état solide et de calculs à partir de principes fondamentaux des paramètres RMN du ^{77}Se dans des hétérocycles Se–N. Les spectres RMN des systèmes cycliques par la technique de la rotation à l'angle magique avec polarisation croisée (RAMPC) mettent en évidence l'existence d'un large éventail de tenseurs du déplacement chimique (DC) du sélénium qui sont extrêmement sensibles à la géométrie moléculaire, à la substitution par des ligands et aux contacts intermoléculaires. Pour les systèmes dont on connaît les structures cristallines, on a effectué des calculs des tenseurs de blindage magnétique nucléaire (BMN) du sélénium avec la théorie de la fonctionnelle de la densité (TFD) hybride et on a examiné les orientations des tenseurs dans des cadres moléculaires. On rapporte les résultats de calculs effectués sur la base de la TFD des tenseurs de blindage magnétique nucléaire ainsi qu'une analyse détaillée des paires d'orbitales moléculaires occupées et virtuelles qui donnent lieu aux tenseurs de blindage magnétique nucléaire du sélénium. On discute aussi d'une nouvelle analyse de l'orbitale moléculaire naturalisée (OMLN) dans le même cadre de la TFD. Pris collectivement, les données de la RMN et les calculs à partir de principes fondamentaux permettent de comprendre les influences de la structure électronique, des liaisons et des interactions intermoléculaires sur les tenseurs de BMN et aussi (*i*) de faire des prédictions pour 15 structures moléculaires inconnues et (*ii*) de se faire une idée sur les positions des paires d'électrons libres du sélénium qui sont actives d'un point de vue stéréochimique.

Mots-clés : RMN à l'état solide, RMN du ^{77}Se, calculs ab initio, blindage chimique, chimie inorganique du groupe principal, hétérocycles, calculs TFD, analyse des OM, gaussienne 03, fonctionnelle de la densité d'Amsterdam (FDA).

[Traduit par la Rédaction]

Received 4 March 2009. Accepted 22 April 2009. Published on the NRC Research Press Web site at canjchem.nrc.ca on 9 October 2009.

This article is part of a Special Issue dedicated to Professor T. Ziegler.

A. Sutrisno, A.Y. Lo, J.A. Tang, and R.W. Schurko.[1] Department of Chemistry and Biochemistry, University of Windsor, Windsor, ON N9B 3P4, Canada.
J.L. Dutton, G.J. Farrar, and P.J. Ragogna. Department of Chemistry, The University of Western Ontario, London, ON N6A 5B7, Canada.
S. Zheng and J. Autschbach. Department of Chemistry, The State University of New York, Buffalo, NY 14260-3000, USA.

[1]Corresponding author (e-mail: rschurko@uwindsor.ca).

Introduction

Carbenes are known to be important reaction intermediates, and there is an enormous amount of literature reporting their syntheses, structures, and reactivities.[1–7] Since the first report of the synthesis of stable crystalline *N*-heterocyclic carbenes by Arduengo,[8] there have been a substantial number of papers discussing the isovalent p-block analogues known as the *N*-heterocyclic carbenoids.[4,5,9–11] In these carbenoids, the main-group element is bi-coordinate and bears a lone pair. *N*-heterocyclic carbenoids have been successfully synthesized and characterized for group 13 (B^-, Al^-, Ga^-, In^-, Tl^-), group 14 (Si, Ge, Sn), group 15 (N^+, P^+, As^+, Sb^+), and group 16 (S^{2+}), with main-group elements being formally understood as anionic, neutral, cationic, and dicationic, respectively.[12–20] The recent synthesis of dicationic

Chart 1. Schematic drawings of selenium carbenoid compounds **1–9**.

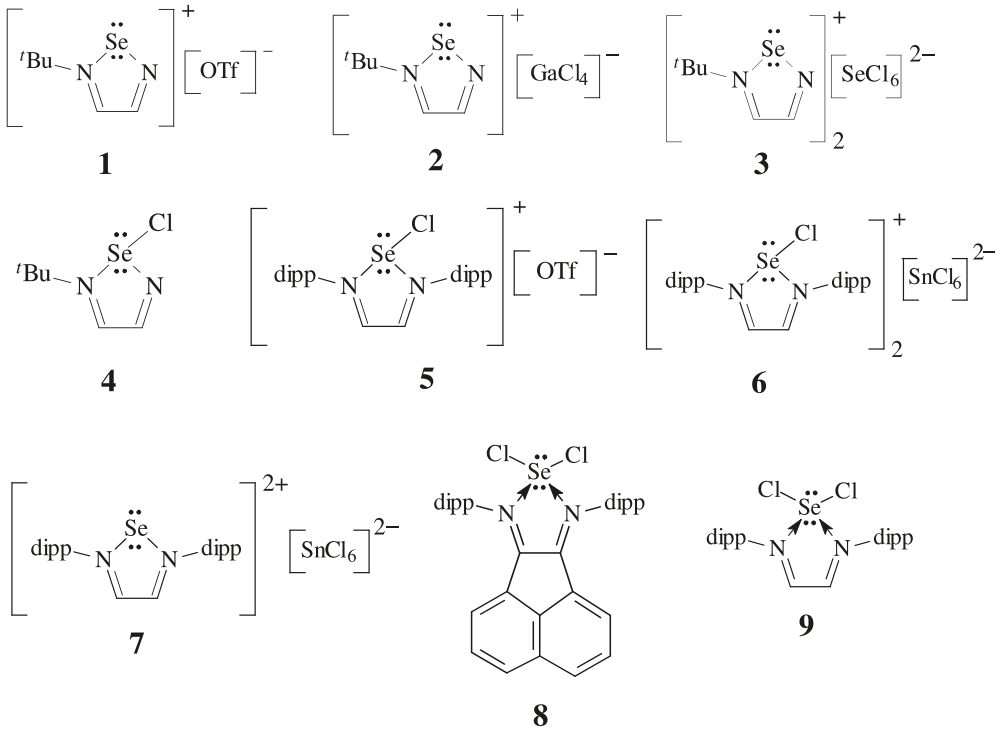

N-heterocyclic selenium carbenoids has extended the series into group 16, and the distinct formal charge at the Se atom (+2) has a significant impact on the reactivity of these carbenoids.[21–23]

^{77}Se solid-state NMR (SSNMR) spectroscopy should prove to be valuable for the study of molecular structure and reactivity for a wide array of organometallic selenium heterocycles,[13,24,25] including the *N*-heterocyclic selenium carbenoids and derivative structures. Selenium has only one NMR-active isotope, ^{77}Se, which has a spin quantum number $I = 1/2$, 7.58% natural abundance, and a gyromagnetic ratio of 5.1214×10^7 rad T^{-1} s^{-1} (relative receptivity of 2.9 in comparison to ^{13}C). Selenium chemical shifts (CS or δ) are very sensitive to the local electronic environment of the selenium atom and are presently known to span a range of about 5800 ppm,[26–43] with the extreme isotropic chemical shifts, δ_{iso}, being marked by values of 3691 and 4531 ppm for Se sites in Mo_6Se_8,[44] to –1274 ppm for Se^{2-} sites in Ag_7PSe_6.[45,46] Solution ^{77}Se NMR and ab initio calculations have been applied to many selenium containing compounds;[34,35,38,39,42,43,47–55] however, there have been fewer reports of ^{77}Se SSNMR experiments,[26–30,40,41,56,57] despite the significant number of selenium-containing solid materials that could benefit from such characterization. There have also been a number of recent studies detailing ab initio calculations of selenium shielding tensors and their relationships to molecular electronic structure for systems such as aryl selenides,[58] square-planar metal complexes of the diselenoimidodiphosphinate anion,[59] and a variety of organic, inorganic and organometallic selenium containing compounds.[30] In particular, the careful examination of which molecular orbitals make dominant contributions to nuclear magnetic shielding (NMS) tensors, and the effects of alteration of molecular structure, have been studied in great detail.[58]

Herein, a preliminary ^{77}Se SSNMR study of selenium heterocyclic compounds is reported. The aims of this study are to experimentally measure the selenium CS tensors in these heterocycles (Chart 1) using ^{77}Se SSNMR spectroscopy, and to investigate the relationships between the selenium NMS tensor parameters and the molecular structure, bonding, and symmetry in these systems using first-principles calculations. Density functional theory (DFT) calculations using the Amsterdam density functional (ADF) software package[60] are applied to a series of model systems to examine the origin of the selenium NMS tensors from the perspective of contributions of single and pairs of molecular orbitals (MOs), under the formalism developed by Ziegler and coworkers.[52,61–63] A natural localized molecular orbital (NLMO)[64] analysis of MOs contributing to selenium shielding is also presented,[65,66] which classifies these MOs according to "chemically intuitive" orbitals, such as bonding, core, and lone pairs. By applying this methodology and developing an understanding of relationships between shielding tensors and molecular structure for a series of well-characterized Se heterocycles, we will demonstrate that ^{77}Se NMR is useful for (*i*) predicting unknown heterocyclic structures for which crystal structure data are not available and (*ii*) confirming the orientation and nature of the selenium lone pairs, which will be of great importance for understanding the reactivity and stability of these systems.

Experimental methods

Sample preparation

Samples of 1,2,5-selenadiazolium trifluoromethane sulfonate ([*t*-Bu-N_2C_2Se][OTf]) (**1**), 1,2,5-selenadiazolium gallium(III) tetrachloride ([*t*-Bu-N_2C_2Se][$GaCl_4$]) (**2**), bis(1,2,5-selenadiazolium) selenium(IV) hexachloride ([*t*-Bu-N_2C_2Se]$_2$[$SeCl_6$]) (**3**), 1,2,5-selenadiazolium chlorine ([*t*-Bu-N_2C_2Se–Cl]) (**4**),

2-chloro-1,2,5-selenadiazole trifluoromethane sulfonate ($[SeN_2C_{26}H_{36}Cl][OTf]$) (**5**), 2-chloro-1,2,5-selenadiazole tin(IV) hexachloride ($[SeN_2C_{26}H_{36}Cl]_2[SnCl_6]$) (**6**), selenium "carbenoid" 1,2,5-selenadiazole tin(IV) hexachloride ($[SeN_2C_{26}H_{36}]_2[SnCl_6]$) (**7**), $SeCl_2$-BIAN (bis(imino)acenapthene) ($[SeN_2C_{36}H_{40}Cl_2]$) (**8**), and selenium carbene analogue $SeCl_2$-dipp ($[SeN_2C_{26}H_{36}Cl_2]$) (**9**) were synthesized using previously reported procedures,[21,22] with some modifications which will be discussed in a forthcoming publication.

Sample purity

^{13}C CP/MAS NMR and powder X-ray diffraction experiments were performed to confirm sample purity (Table S1 and Figs. S1–S12 in Supplementary data).

Solid-state NMR spectroscopy

Solid-state NMR experiments were conducted on a Varian Infinity Plus spectrometer with an Oxford 9.4 T (ν_0 (^1H) = 400 MHz) wide-bore magnet, operating at resonance frequencies of ν_0 (^{77}Se) = 76.28 MHz and ν_0 (^{13}C) = 100.52 MHz. A Varian/Chemagnetics 4 mm double resonance HX magic-angle spinning (MAS) probe was used for all experiments. All samples were finely ground and packed into 4 mm o.d. zirconia rotors and sealed with airtight caps under a dry N_2 atmosphere. Selenium chemical shifts were referenced to a solution of Me_2Se in $CDCl_3$ (60% *v/v*) at 0.0 ppm, using solid $(NH_4)_2SeO_4$ as a secondary standard (δ_{iso} = 1040.2 ppm).[31] Carbon chemical shifts were referenced to tetramethylsilane (TMS) at 0.0 ppm, by using the high-frequency peak of solid adamantane as a secondary standard (δ_{iso} = 38.57 ppm).[67]

^{77}Se VACP/MAS NMR

Proton-decoupled ^{77}Se variable-amplitude cross-polarization magic-angle spinning (VACP/MAS)[68,69] NMR spectra were acquired with spinning speeds ranging from 4.5 to 12.0 kHz (a minimum of two spinning speeds were utilized to isolate peaks corresponding to isotropic shifts). Calibrated recycle delays from 1.0 to 5.0 s were used. The ^{77}Se radio-frequency (rf) frequencies, $\nu_1(^{77}Se)$, were calibrated at various power levels using a solution of 1.0 mol/L $(NH_4)_2SeO_4$. The Hartmann–Hahn matching condition was optimized using a sample of solid $(NH_4)_2SeO_4$. The proton $\pi/2$ pulse widths were between 1.6 and 4.0 μs, and optimized contact times of 15 to 17 ms were used, with spectral widths of 200 to 300 kHz (see Table S2 for detailed experimental parameters). TPPM ^1H decoupling[70] was used in all experiments, with decoupling fields of 62.5 kHz or greater.

Spectral simulations

Selenium chemical shift tensor parameters, δ_{iso}, Ω, and κ (see tables for definitions) were extracted using Herzfeld–Berger (HB)[71] analysis and analytical simulations of ^{77}Se SSNMR spectra were performed using the WSOLIDS package.[72]

Theoretical Methods: G03 and ADF

Hybrid DFT and Hartree–Fock calculations were conducted using Gaussian 03[73] running on a dual-2.8 GHz Xenon Dell Precision 650 workstation or a dual-3.6 GHz Xenon Dell Precision 670n workstation, as well as quad-2.2 and 2.4 GHz Opteron HP workstations on SHARCNET. Selenium nuclear magnetic shielding tensors were calculated using the GIAO method[74,75] with the B3LYP (Becke's three-parameter hybrid density functional[76] with the Lee, Yang, and Parr correlation functional[77,78]) and RHF (Restricted Hartree–Fock) techniques. The 6–31G**, 6–311G**, and 6–311++G** basis sets were used on the Se atoms, as well as the 13s10p4d, 14s10p5d, 17s13p6d, and 24s20p10d all-electron Huzinaga basis sets.[79] Basis sets for the lighter atoms are listed in the Supplementary data. Selenium chemical shifts were referenced to Me_2Se by comparing calculated shielding values to the absolute shielding value of Me_2Se.[31,52] The ADF software package[61] was applied to several model systems; contributions from individual MO pairs to the NMS tensors were analyzed using the NMR–EPR module.[63] The BLYP[77,78] and VWN-BP (Vosko–Wilk–Nusair[80] local density approximation with the Becke–Perdew[76,77] generalized gradient approximation) exchange-correlation functionals were applied for non-relativistic (NR) calculations, and all-electron gauge including atomic orbitals (GIAO)[74,75] double-ζ (DZ) or triple-ζ doubly polarized (TZ2P) basis sets were used on all atoms. Full sets of crystal structure coordinates with optimized proton positions were used for Gaussian 03 calculations, while symmetry-constrained geometry-optimized structures were used for ADF calculations.

NLMO analyses

For the natural bond orbital (NBO) / natural localized molecular orbital (NLMO) analysis of the Se shielding, a locally modified version of the ADF package was used. The modifications include an interface program "adfnbo" integrating the DFT computations with a generic version of the NBO 5.0 version by Glendening et al.[64] Details of the NBO/NLMO analysis of shielding constants are published elsewhere.[65,66] The approach taken is a relativistic generalization of the NBO shielding analysis of Bohmann et al.[81] The zeroth-order regular approximation (ZORA)[82] in its spin-free (scalar relativistic) form was applied to treat relativistic effects. The triple-ζ doubly polarized (TZ2P) all-electron Slater-type basis sets from the ADF basis set library was used for the shielding calculation and the accompanying NBO/NLMO analyses. The calculations employed the VWN-BP functional.

Results and discussion

Prior to the detailed discussion of our results, it is important to differentiate between the chemical shift (CS) and nuclear magnetic shielding (NMS). Nuclear magnetic shielding, σ, describes the degree of magnetic shielding of a nucleus in an atom or molecule with respect to a bare nucleus. The nuclear magnetic shielding is related to the chemical shift, δ, which is measured experimentally with respect to a reference compound, via the equation:

$$[1] \qquad \delta = \frac{\sigma_{ref} - \sigma}{1 - \sigma_{ref}} \approx \sigma_{ref} - \sigma$$

where σ_{ref} is the nuclear magnetic shielding of the reference compound. The approximation in eq. [1] generally holds for most nuclei with small to moderate chemical shift ranges

Table 1. Summary of observed ^{77}Se CS tensor parameters for compounds **1**–**9**.

Compound	δ_{11} (ppm)[a]	δ_{22} (ppm)	δ_{33} (ppm)	δ_{iso} (ppm)[b]	Ω (ppm)[c]	κ[d]
1 (site 1)	2005	1520	1275	1600 (10)[e]	730 (10)	–0.33 (3)
1 (site 2)	1997	1504	1277	1593 (5)	720 (10)	–0.37 (2)
2	1959	1489	1247	1565 (15)	712 (10)	–0.32 (2)
3 (site 1)	1861	1384	1322	1522 (10)	539 (20)	–0.77 (4)
3 (site 2)	1849	1382	1290	1507 (10)	559 (20)	–0.67 (3)
4	1789	1316	1252	1452 (5)	537 (10)	–0.76 (4)
5	1970	1818	754	1514 (5)	1216 (15)	0.75 (4)
6	2030	1789	761	1527 (5)	1269 (15)	0.62 (3)
7	2115	1692	772	1526 (50)	1343 (70)	0.37 (9)
8	2362	2008	976	1782 (15)	1386 (25)	0.49 (3)
9	1983	1896	831	1570 (15)	1152 (20)	0.85 (6)

[a]The chemical shift tensor is described by three principal components, ordered such that $\delta_{11} \geq \delta_{22} \geq \delta_{33}$.
[b]Isotropic chemical shift: $\delta_{iso} = (\delta_{11} + \delta_{22} + \delta_{33})/3$. δ_{iso} is given relative to Me_2Se [$\delta_{iso}(^{77}Se) = 0.0$ ppm].
[c]Span: $\Omega = \delta_{11} - \delta_{33}$.
[d]Skew: $\kappa = 3(\delta_{22} - \delta_{iso})/\Omega$.
[e]The uncertainty in the last digit of each value is denoted in brackets.

Table 2. Calculated ^{77}Se NMR parameters using Gaussian 03 showing best agreement with experimental results.

Compound[a]	Method	Basis set	σ_{11}[b]	σ_{22}	σ_{33}	σ_{iso}[c]	δ_{iso} (ppm)[d]	Ω (ppm)[e]	κ[f]
2	**exp.**						**1565** (15)	**712** (10)	**-0.32 (2)**
	B3LYP	14s10p5d	121.6	475.2	739.7	445.5	1327.9	618	–0.14
		17s13p6d[g]	30.7	406.3	627.2	354.7	1352.6	596.4	–0.26
3	**exp.**	**site 1**					**1522 (10)**	**539 (20)**	**-0.77 (4)**
		site 2					**1507 (10)**	**559 (20)**	**–0.67 (3)**
	B3LYP	13s10p4d	276.4	716.3	867.2	620.0	1371.4	590.9	–0.49
		14s10p5d[g]	–71.9	398.9	552.4	293.2	1480.2	624.3	–0.51
4	**exp.**						**1452 (5)**	**537 (10)**	**-0.76 (4)**
	B3LYP	6–311++G**[g]	–319.3	317.2	439.8	145.9	1490.4	759.1	–0.68
	RHF	14s10p5d	111.6	675.8	1060.3	615.9	1440.9	948.7	–0.19
5	**exp.**						**1514 (5)**	**1216 (15)**	**0.75 (4)**
	B3LYP	14s10p5d[g]	–505.5	543.5	981.2	339.7	1433.6	1486.7	–0.41
		17s13p6d	–684.1	376.4	845.5	179.3	1528	1529.6	–0.39
6	**exp.**						**1527 (5)**	**1269 (15)**	**0.62 (3)**
	B3LYP	17s13p6d[g]	–576.5	515.9	660.3	199.9	1507.4	1236.8	–0.77
	RHF	17s13p6d	–402.1	708.1	1185.2	497	1500.3	1587.3	–0.4
7	**exp.**						**1526 (10)**	**1343 (25)**	**0.37 (2)**
	RHF	14s10p5d[g]	–385.8	239	1362.5	405.2	1651.6	1748.4	0.29
		17s13p6d	–509	83.6	1298	290.8	1706.5	1807	0.34
8	**exp.**						**1782 (15)**	**1386 (25)**	**0.49 (3)**
	RHF	14s10p5d	–60.7	269.8	1085.8	431.6	1625.2	1146.6	0.42
		17s13p6d[g]	–176.3	175.3	1049	349.3	1648	1225.3	0.43

[a]No calculations are done on compounds **1** and **9** due to the unavailability of the single crystal X-ray structures.
[b]The chemical shielding tensor is described by three principal components, ordered such that $\sigma_{11} \leq \sigma_{22} \leq \sigma_{33}$.
[c]$\sigma_{iso} = (\sigma_{11} + \sigma_{22} + \sigma_{33})/3$.
[d]The chemical shift values were referenced to Me_2Se by comparing the calculated shielding values of all compounds to the absolute shielding value of Me_2Se (see eq. [1] in main text).
[e]$\Omega = \sigma_{33} - \sigma_{11}$.
[f]$\kappa = 3(\sigma_{iso} - \sigma_{22})/\Omega$.
[g]These particular methods and basis sets were used to generate the CS tensor orientations in Fig. 4.

(exceptions include nuclei with enormous chemical shift ranges like ^{59}Co, ^{195}Pt, ^{207}Pb, etc.). Hence, theoretically calculated shielding parameters can be easily compared to experimentally measured chemical shifts by calculating the absolute shielding for both the system under investigation and the reference system or compound. In this work, CS tensors will refer to experimentally measured data, and NMS tensors (or shielding tensors) will refer to theoretically calculated data. The two can easily be compared via eq. [1]. Definitions of the CS and NMS tensor parameters are found in Tables 1 and 2, respectively. More details on the relations between chemical shifts and nuclear magnetic shielding, as well as conventions utilized for describing these parameters, can be found elsewhere.[83,84]

Fig. 1. Experimental ^{77}Se VACP/MAS and simulated spectra for (A) **1**, (B) **2**, (C) **3,** and (D) **4** at 9.4 T. (A) Inset: the deconvolution of the isotropic peak. (C) Note: # denotes the isotropic shift for the $SeCl_6^{2-}$ anion, and * denotes impurities in the sample.

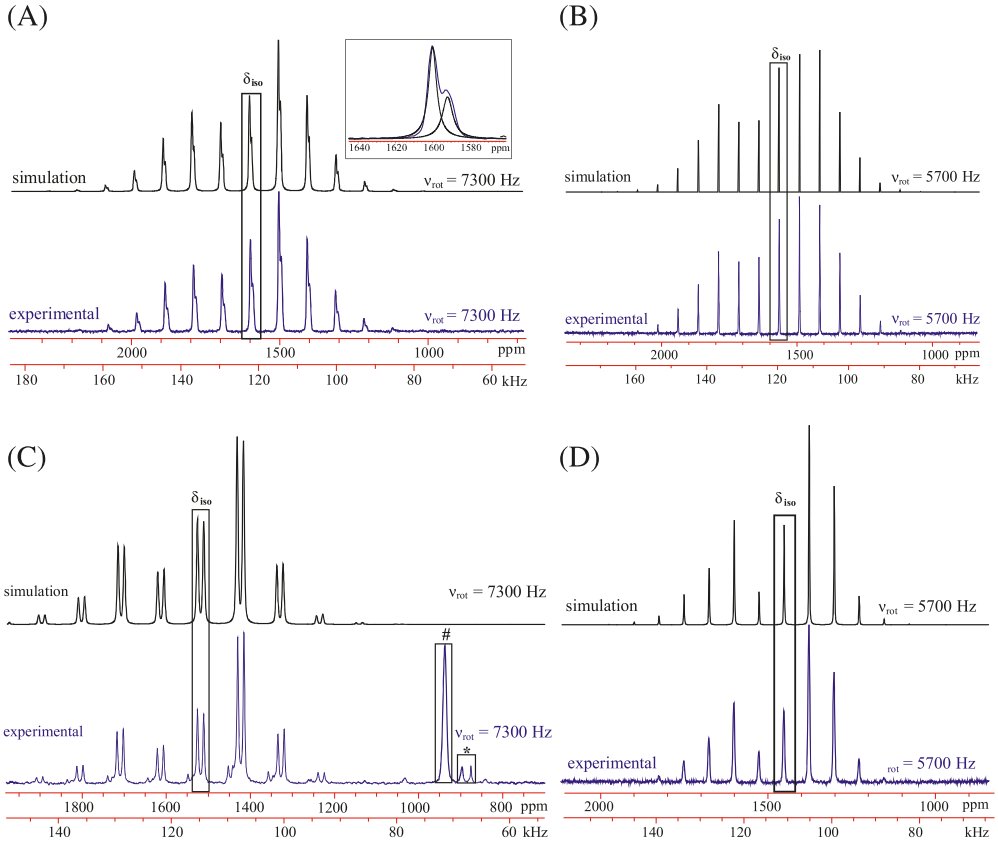

In the first part of this section, the acquisition and interpretation of solid-state ^{77}Se VACP/MAS NMR spectra of all of the heterocycles are discussed (the compounds are grouped according to common structural features in Chart 1). Second, a discussion of hybrid DFT and Hartree–Fock calculations of selenium NMS tensors is presented. Finally, we examine the application of DFT calculations to model systems to ascertain which molecular orbitals (MOs) are key in determining the nature of the selenium NMS tensor. A summary of the experimentally observed ^{77}Se NMR parameters is shown in Table 1.

[*t*-Bu–N_2C_2Se][OTf] (1) and [*t*-Bu–N_2C_2Se][$GaCl_4$] (2)

Complexes **1** and **2** are isostructural 1,2,5-selenadiazolium heterocyclic cations which are singly substituted by a *t*-butyl group at one nitrogen position. Furthermore, atoms in the counteranions of these species are not expected to make any distant contacts or formal bonds with the Se atoms. The crystal structure has been determined for **2**,[21] revealing a dimeric structure featuring an inversion centre at the heart of a four-membered Se_2N_2 ring and inter-ring Se···N contacts of 2.605 Å. The ^{77}Se VACP/MAS NMR spectra of **1** and **2** (Figs. 1A and 1B) are very similar in appearance, except for the two separate resonances in the spectrum of **1**. There are two isotropic chemical shifts observed for **1** at 1600 and 1593 ppm, corresponding to two magnetically distinct sites. The NMS tensor parameters for these sites are almost identical, and the total powder patterns have equal integrated intensities, indicating that there are two crystallographically distinct Se sites whose environments differ only slightly. For **2**, there is only one isotropic chemical shift observed at 1565 ppm, which is consistent with the unique crystallographic Se site.

Although the crystal structure is unknown for **1**, the similarity of the NMR parameters suggest that the local Se environment is very similar to that of **2**; however, the crystallographic space group must be different, because of the appearance of two distinct peaks in the spectrum of **1**. The low frequency peak is broader than the high frequency peak, with full-widths at half-height (FWHH) of 550 and 400 Hz, respectively (Fig. 1A, inset). The differential broadening might be caused by distinct dipolar or *J*-coupling interactions, likely resulting from distinct Se–N bond distances, though no effects of residual dipolar coupling are observed. The large spans and non-axial skews are not surprising given the planar structure of these molecules.[30] In both cases, the skew is negative, indicating that δ_{11} is the distinct component of the NMS tensor. Since these types of molecules are known to have significant aromatic character, and a π-system delocalized over the five-membered ring, the δ_{33} component is likely directed perpendicular to the plane of the heterocycle. NMS tensor orientations will be further discussed in the theoretical section below.

[*t*-Bu–N_2C_2Se]$_2$[$SeCl_6$] (3) and [*t*-Bu–N_2C_2Se–Cl] (4)

Complexes **3** and **4** have the same heterocyclic structures as **1** and **2**; however, the counteranions are positioned such

Fig. 2. Experimental ^{77}Se VACP/MAS and simulated spectra for (A) **5**, (B) **6**, (C) **7**, (D) **8** and (E) **9** at 9.4 T.

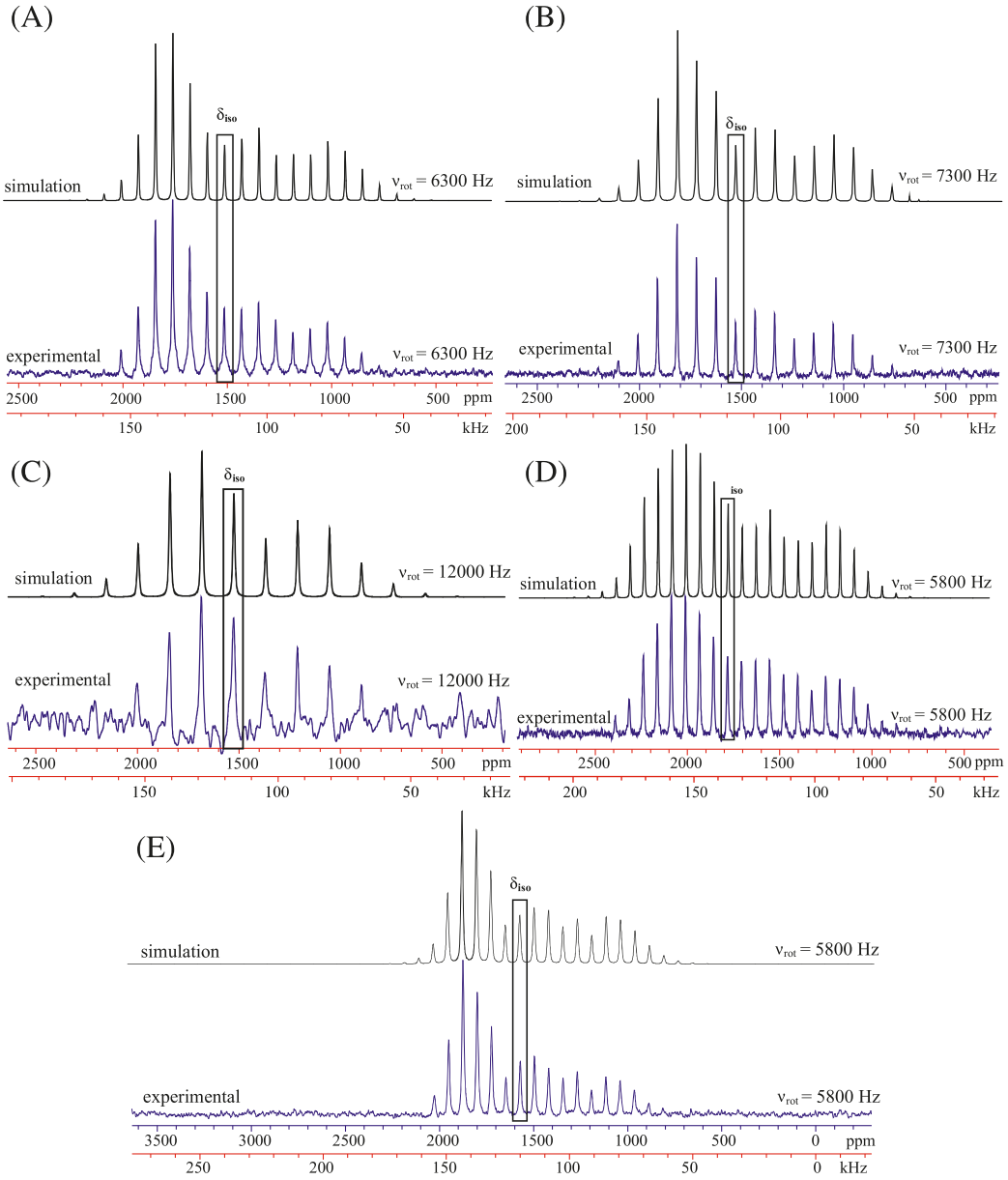

that one chlorine atom makes a distant contact with the Se atom (we define a "distant contact" as a weak bonding interaction with energy significantly less than a formal covalent bond). Formal Se–Cl bonds are best described in the range of 2.2 to 2.5 Å, while distant Se···Cl contacts fall in the range of 2.6 to 2.9 Å. The distances between Se and Cl (2.850 Å for **3** and 2.605 Å for **4**)[21] are significantly shorter than that in **2** (3.510 Å). Solid-state structures of **3** and **4** also reveal different types of N–Se–N bonding arrangements: **3** has a much longer Se···N inter-ring contact (4.147 Å) than **2**, which falls outside of the sum of the van der Waals radii for Se and N (3.54 Å). However, for **4**, the presence of the Cl atom on Se prevents the creation of a four-membered Se_2N_2 ring, as observed for **2**.

^{77}Se VACP/MAS NMR spectra of **3** and **4** are presented in Figs. 1C and 1D, respectively. Three isotropic chemical shifts were observed in the spectrum of **3**, two of which are assigned to the two [*t*-Bu-N_2C_2Se]$^+$ cations (1522 and 1507 ppm), and one to the $SeCl_6^{2-}$ anion (935 ppm). The former two isotropic chemical shifts correspond to the two distinct crystallographic cations, which are structurally similar enough that the Se NMS tensor parameters are comparable. For **4**, there is only one isotropic chemical shift observed at 1452 ppm, consistent with a single crystallographic site. Compared to **1** and **2**, the spans of **3** and **4** are reduced by about 200 ppm, and the skews are more negative (i.e., δ_{11} is increasingly distinct), suggesting that the Cl atoms play a role in reducing the span and moving the isotropic chemical shift to lower frequency (δ_{iso} becomes more negative). The ^{77}Se nuclei are more shielded with respect to **1** and **2**; since the Cl is in the plane of the heterocycles, it is likely that changes in δ_{11} and δ_{22} are influencing the overall value of δ_{iso}, consistent with δ_{33} being oriented perpendicular to the ring plane; further comments are made in the theoretical section.

Fig. 3. Summary of the observed ^{77}Se NMR parameters for selected structural motifs: A (**1**, **2**), B (**3**, **4**), C (**5**, **6**), D (**7**, **8**), and E (**9**). The shaded region indicates the range of isotropic chemical shifts, δ_{iso}.

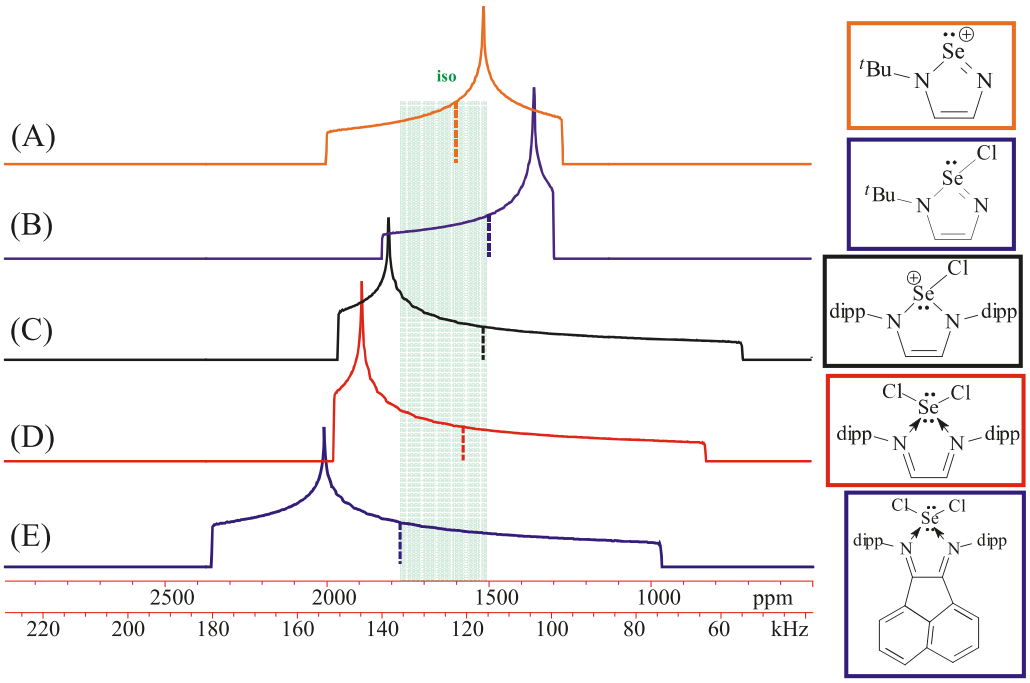

$[SeN_2C_{26}H_{36}Cl][OTf]$ (5) and $[SeN_2C_{26}H_{36}Cl]_2[SnCl_6]$ (6)

Complexes **5** and **6** are planar 2-chloro-1,2,5-selenadiazolium heterocyclic cations which are substituted by dipp (2,6-di(isopropyl)phenyl) groups at each nitrogen position, and have formal Se–Cl bonds of 2.323 and 2.458 Å, respectively. The N–Se–Cl bond angles are 92.3° and 93.1° for **5** (owing to the presence of a disorder with an occupancy of 80:20), while it is approximately 92.8° for **6**. ^{77}Se VACP/MAS NMR spectra of **5** and **6** (Figs. 2A and 2B) reveal isotropic shifts of 1514 and 1527 ppm, respectively, which are similar to those of **1** through **4**. However, the anisotropic selenium NMS tensors are quite different from those of earlier complexes: first, the spans of **5** and **6** are more than double those of **3** and **4**, and secondly, the skews are positive, meaning that the δ_{33}s are now the distinct components (the change in κ is especially noticeable, since the discontinuous portion of the pattern corresponding to δ_{22} is now located to high frequency of δ_{iso}). Clearly, the addition of a ligand to the second nitrogen position alters the selenium NMS tensor, although it does not necessarily mean that the selenium nucleus becomes more or less shielded. The second nitrogen substituent undoubtedly results in a significant change in the electronic environment at the Se atom, serving to increase the magnetic shielding along the direction of δ_{33}.

$[SeN_2C_{26}H_{36}]_2[SnCl_6]$ (7), $[SeN_2C_{36}H_{40}Cl_2]$ (8), and $[SeN_2C_{26}H_{36}Cl_2]$ (9)

Complexes **7**, **8**, and **9** are 2,2-dichloro-1,2,5-selenadiazolium complexes with a dipp group at each of the nitrogen positions. The crystal structure of **7** reveals short Se···Cl contacts from the counteranion which are approximately in the same range as that in **3** (~ 2.74 Å), while in **8**, the Se–Cl bond distances are similar to those in **5** and **6** (~ 2.29 to 2.32 Å). A comparison of ^{77}Se VACP/MAS NMR spectra of **7**, **8**, and **9** (Figs. 2C, 2D, and 2E, respectively) reveals values of δ_{iso} ranging from 1526 to 1782 ppm, along with large spans and positive skews (Table 1). Unfortunately, the VACP/MAS spectra of **7** have very poor S/N, increasing the errors associated with the selenium NMS tensor parameters for this sample. A large reduction in CP efficiency was observed for this sample, the reason for which is unknown at this time; however, it is recognized that the poor spectral quality does not arise from sample size, quality, or crystallinity (see Figure S7 for ^{13}C solid-state NMR spectra).

For **7** and **8**, the spans are increased and the skews are less positive than those of **5** and **6**, undoubtedly due to the additional Se···Cl contacts in the former. It is also interesting to note that the δ_{iso} for **8** is significantly higher than for all other species, perhaps suggesting that the presence of an extended aromatic system plays a role in deshielding the ^{77}Se nucleus. The structure of **9** is unknown; however, ^{77}Se NMR spectra are useful in helping to elucidate the structures of these systems: a comparison of the NMS tensor parameters of **9** with those of **5** through **8** suggest that the structure of **9** is akin to that of **5** and **6**, which have single Se···Cl contacts.

Summary of the observed ^{77}Se NMR parameters

^{77}Se SSNMR spectra are very sensitive to the local bonding environment of the selenium atom and serve as a powerful probe of changes in molecular structure as well as intermolecular interactions.[28,29] Several trends in the selenium NMS tensors for this series of the *N*-heterocyclic compounds (**1** to **9**) are observed (Table 1, Fig. 3). First, a single Se···Cl contact results in a reduction of the span (compare **1** and **2** vs. **3** and **4**), whereas two Se···Cl contacts increase the span and reduce the axial symmetry of the tensor (**5** and **6** vs. **7** and **8**). Second, the addition of a substituent to the second N atom of the ring (compare **5**–**9** vs. **1**–**4**), increases the span of the NMS tensor significantly and changes the sign

Fig. 4. Selenium NMS tensor orientations obtained by the B3LYP functional. σ_{33} is directed $\perp$ to the page for all molecules.

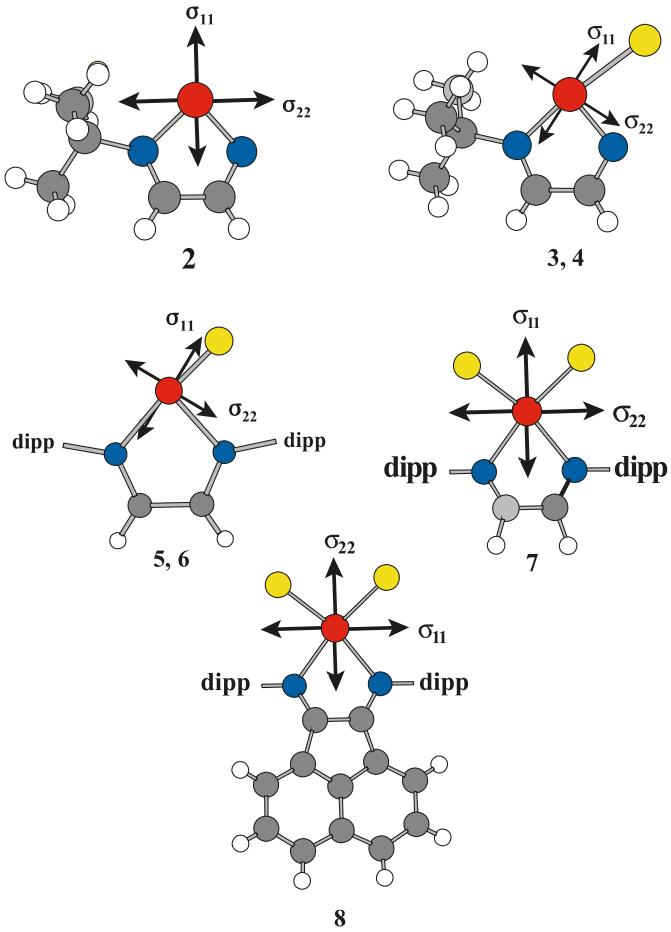

Fig. 5. Model systems and Se NMS tensor orientations from VWN-BP calculations. Note that **B** is the analogue of **1** and **2**, **B′** for **3** and **4**, **A′** for **5** and **6**, and **A″** for **7**, **8**, and **9**. NMS tensor orientations for all model systems generated from ADF calculations.

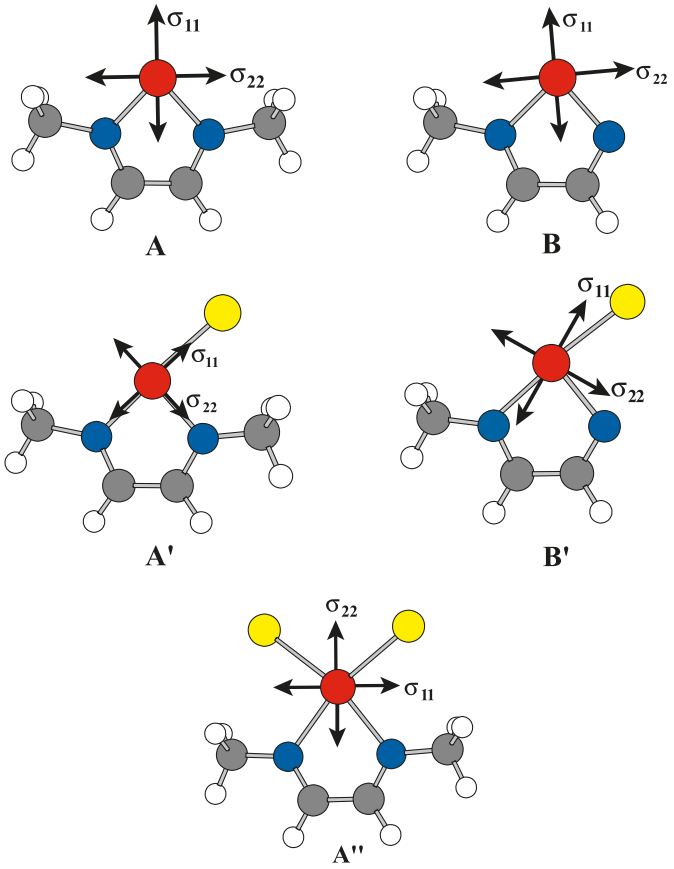

of the skew from negative to positive, mainly via a large increase in shielding along the direction of δ_{33}. Finally, interactions between the cation and anion (e.g., **3** and **7**) and the relative Se–Cl bond distances have a significant influence on the NMR parameters.

Theoretical selenium nuclear magnetic shielding tensors

A subset of the density functional calculations of selenium NMS tensor parameters and their orientations in the molecular frames were performed with the Gaussian 03 software package with the aim of correlating molecular structure, symmetry, and the experimental NMR parameters. Calculated NMS tensor parameters having the best agreement with the experimental results are presented in Table 2 (See Tables S3–S9 for a summary of all of the calculations). Since there are no solid-state structures for **1** and **9**, calculations are not reported for these molecules.

Selenium NMS tensors calculated with the B3LYP functional were generally superior to those from RHF calculations, with the former resulting in NMS tensor parameters that are reasonably close to the experimental values (about 5 to 15% error), and the latter not correctly predicting NMS tensor parameters in most cases (except for **7** and **8**). In general, Huzinaga's basis set (14s10p5d and 17s13p6d) seems to be the most appropriate for predicting selenium NMS tensor parameters. For **3** and **7**, intermolecular interactions between the cation and the anion have a large influence on the magnitudes of the NMR parameters. Calculations that were performed without the $SeCl_6^{2-}$ and $SnCl_6^{2-}$ anions overestimate the magnitudes of the spans, while those performed with the anions yielded a better agreement with the experimental results (e.g., refer to Table S4 for **3**). For the doubly-substituted compounds (**5**–**8**), the calculations do predict larger spans, as observed experimentally. The only major discrepancy is observed from calculations on **5** and **6**, where negative skews are consistently predicted, regardless of the chosen structural model (vide infra).

For all of the systems, DFT calculations predict that σ_{33}, the most shielded component, is directed perpendicular to the plane of the heterocyclic ring, along the direction of a presumed Se lone pair. The orientation of σ_{33} is the same as those predicted for the analogous ^{13}C NMS tensors in carbenes; however, in carbenes, the lone pair is in the plane of the ring along the direction of σ_{22}.[85,86] The σ_{11} and σ_{22} components of the Se NMS tensor are always in the plane of the heterocycle, and vary in magnitude and position depending on the presence of intermolecular Se···Cl contacts and the nature of the N-substituents (Fig. 4). For **2**, it is predicted that σ_{11}, the most deshielded component of the NMS tensor, is oriented towards the centroid of the five-membered ring. Similar tensor orientations are observed for **7** and **8**, which have local, two-fold symmetry at the Se atom; however, for

Table 3. Non-relativistic (NR) ADF calculations of ^{77}Se CS tensor parameters.

System	Method	Basis set	σ_{11}[a]	σ_{22}	σ_{33}	σ_{iso}[b]	δ_{iso}[c]	Ω[d]	κ[e]
A	BLYP	DZ[f]	–2015.4	–632.5	441.9	–735.3	2128.0	2457.2	–0.13
		TZ2P[f]	–1338.7	–111.6	530.4	–306.6	1789.9	1869.2	–0.31
	VWN-BP	DZ[g]	–1935.7	–594.3	462.8	–689.1	2216.9	2398.6	–0.12
		TZ2P	–1240.2	–57.6	555.4	–247.5	1858.6	1795.7	–0.32
B	BLYP	DZ	–1139.8	–517.9	–489.6	–715.7	2108.4	650.2	–0.91
		TZ2P	–706.3	32.3	183.3	–163.5	1646.8	889.6	–0.66
	VWN-BP	DZ[g]	–1353.3	–478.6	–197.2	–676.4	2204.2	1156.1	–0.51
		TZ2P	–486.9	5.1	158.6	–107.7	1718.9	645.5	–0.52
A′	BLYP	DZ	–1513.5	–542.4	–199.4	–751.7	2144.4	1314.1	–0.48
		TZ2P	–915.4	–13.6	296.4	–210.9	1694.1	1211.9	–0.49
	VWN-BP	DZ	–1437.3	–480.1	–139.4	–685.6	2213.4	1297.9	–0.48
		TZ2P[g]	–825.3	58.5	346.2	–140.2	1751.4	1171.6	–0.51
B′	BLYP	DZ	–380.2	328.2	397.9	115.3	1277.4	778.1	–0.82
		TZ2P	–293.4	270.9	410.6	129.4	1353.9	704.1	–0.6
	VWN-BP	DZ	–332.3	375.6	423.6	155.7	1372.2	755.8	–0.87
		TZ2P[g]	–231.8	331.3	438	179.1	1432.0	669.8	–0.68
A″	BLYP	DZ	–1291.8	–777.7	–339.6	–803	2195.7	952.1	–0.08
		TZ2P	–873.6	–307.1	123.6	–352.4	1835.6	997.2	–0.14
	VWN-BP	DZ	–1212.3	–693.4	–259.6	–721.8	2249.6	952.8	–0.09
		TZ2P[g]	–780.5	–214	191.8	–267.6	1878.8	972.3	–0.17

[a]The chemical shielding tensor is described by three principal components, ordered such that $\sigma_{11} \leq \sigma_{22} \leq \sigma_{33}$.

[b]$\sigma_{iso} = (\sigma_{11} + \sigma_{22} + \sigma_{33})/3$.

[c]The chemical shift values were referenced to Me_2Se by comparing the calculated shielding values of all compounds to the absolute shielding value of Me_2Se (see eq. [1] in main text).

[d]$\Omega = \sigma_{33} - \sigma_{11}$.

[e]$\kappa = 3(\sigma_{iso} - \sigma_{22})/\Omega$.

[f]DZ is double-ζ and TZ2P is triple-ζ doubly polarized.

[g]These particular methods and basis sets were used to generate the occupied and virtual MOs in Figs. 6, 7, and S13–S16.

8, σ_{22} is oriented towards the ring centroid rather than σ_{11}. In **3** and **4**, the Se···Cl contact results in σ_{11} being oriented away from the ring centroid and closer to the direction of the Se–Cl bond. For **5** and **6**, despite the disagreement between experiment and theory, the tensor orientations resemble those in **3** and **4**, with σ_{11} oriented nearly along the direction of the Se–Cl bond. Some of the resonance structures of the Se carbenoids are often drawn with two lone pairs at the Se atom; however, there is no implicit suggestion from the NMR data of a second lone pair localized on the Se atom (vide infra).

Calculations on model systems

To analyze the influences of electronic structure and bonding on the Se NMS tensors, we have conducted calculations using ADF on several model systems (Fig. 5), including detailed analyses of contributing molecular orbitals (vide infra). A summary of NR ADF calculations of ^{77}Se NMS tensor parameters is shown in Table 3. Given that these are geometry-optimized model systems, the agreement between these calculations and the experimental data is poor relative to the benchmarks of the previous section; however, selenium NMS tensor orientations from the NR calculations are almost identical to the Gaussian 03 results (Fig. 5).

Nuclear magnetic shielding at a nucleus, or *nuclear shielding*, is arbitrarily decomposed into two components according to the formalism of Ramsey,[87–89] which are known as the diamagnetic and paramagnetic contributions, such that $\boldsymbol{\sigma}_{tot} = \boldsymbol{\sigma}_d + \boldsymbol{\sigma}_p$. This division of contributions persists in modern descriptions of the origins of nuclear shielding.[74,75,90–93] The diamagnetic shielding arises from the field-induced electron circulation in the ground electronic state which creates a local field anti-parallel to the applied field; hence, it is responsible for shielding the nucleus and gives rise to a negative frequency shift (neglecting the sign of the Larmor frequency). The paramagnetic shielding arises from symmetry-allowed magnetic-field induced mixing of MOs, which in most cases gives rise to a local field that is parallel to the applied magnetic field, thereby deshielding the nucleus and causing a positive frequency shift. The DFT–GIAO formalism developed by Ziegler and co-workers describes diamagnetic and paramagnetic shielding contributions in a manner distinct from that of Ramsey, in the sense that the basis set incompleteness is taken into account.[62,63] As a consequence, the paramagnetic shielding contribution is further partitioned into contributions arising from the mixing of occupied MOs ($\boldsymbol{\sigma}_P^{occ-occ}$) and mixing of the occupied (occ) and virtual (vir) MOs ($\boldsymbol{\sigma}_P^{occ-vir}$). The NMR–EPR module of the ADF program outputs paramagnetic shielding contributions associated with each MO pair (Table 4). Despite the fact that the NR calculations are not in good quantitative agreement with the experimental results, they are still useful in understanding the origin of selenium nuclear magnetic shielding in these systems.

Model complex **A** (Fig. 5) has been chosen as the focus of discussion for this section, due to its high symmetry (C_{2v}). Paramagnetic shielding contributions account for approximately 90% of the total isotropic shielding and occ-

Table 4. ADF calculations: contributions to paramagnetic shielding from mixing of occ-vir MOs in model compounds.

	Occupied MO		Virtual MO*[a]		σ_{iso} contrib.[b]	σ_{11}	σ_{22}	σ_{33}
System	MO	Symm. label	MO	Symm. label	(ppm)	(ppm)	(ppm)	(ppm)
A (***C*****$_{2v}$**)[c]	32	$2A_2$	40*	$7B_1'$ (LUMO)	–207.8	–623.5		
	34	$17A_1$	40*	$7B_1^*$	–245.4		–736.3	
	34	$17A_1$	41*	$13B_2^*$	–636.8			**–1910.4**[d]
	36	$18A_1$	42*	$19A_1^*$	–159.2			–477.5
	39	$6B_1$ (HOMO)	41*	$13B_2^*$	–1245.3	**–3735.8**		
	39	$6B_1$	42*	$19A_1^*$	–710.1		**–2130.4**	
B (***C*****$_s$**)	30	25A′	37*	28A′*	–201			–603.1
	32	26A′	36*	9A″* (LUMO)	–324	–240.7	–731.5	
	32	26A’	37*	28A′*	–216.7			–650.0
	34	27A′	37*	28A′*	–437.8			**–1313.4**
	35	8A″ (HOMO)	37*	28A′*	–1068.6	**–3193.3**	–12.6	
	35	8A″	38*	29A′*	–464.4	–0.8	**–1392.5**	
A′ (***C*****$_s$**)	45	10A″	50*	12A″*	–260.3	–534.6	–246.2	
	45	10A″	51*	38A′*	–400.3	–136.1	**–1064.8**	
	46	36A′	51*	38A′*	–95.6			**–286.7**
	48	11A″ (HOMO)	50*	12A″*	–484.2	**–1462.4**	9.8	
	48	11A"	51*	38A′*	–197.7	–226.7	–366.2	
B′ (***C*****$_s$**)	36	30A′	45*	11A″* (LUMO)	–131.5	–400.6	6.1	
	38	31A′	45*	11A″*	–416.3	–26.4	**–1222.4**	
	38	31A′	46*	35A′*	–184.9			**–554.8**
	40	32A′	45*	11A′*	–121.6	–476.7	112.0	
	40	32A′	46*	35A′*	–135.2			–405.7
	41	9A″	46*	35A′*	–332.9	**–801.4**	–197.3	
	41	9A″	49*	37A′*	–268.1	–10.9	–793.4	
	42	33A′ (HOMO-2)	45*	11A″*	–198.8	–565.7	–30.6	
A″ (***C*****$_{2v}$**)	47	$23A_1$	58*	$9B_1^*$ (LUMO)	–311.1	–933.3		
	47	$23A_1$	59*	$20B_2^*$	–353.6			**–1060.7**
	49	$17B_2$	58*	$9B_1^*$	–226.4		–679.1	
	49	$17B_2$	60*	$26A_1^*$	–282.7			–848.0
	51	$18B_2$	60*	$26A_1^*$	–109.6			–328.7
	52	$7B_1$	59*	$20B_2^*$	–436.1		**–1308.3**	
	52	$7B_1$	60*	$26A_1^*$	–397.9	–1193.6		
	57	$8B_1$ (HOMO)	59*	$20B_2^*$	–322.7		–968.1	
	57	$8B_1$	60*	$26A_1^*$	–510.8	**–1532.4**		

[a]The asterisk (*) sign indicates a virtual MO.

[b]Signifies the total contribution to the isotropic chemical shielding.

[c]The point group of the molecule is given in parentheses. All systems are pictured in Fig. 5.

[d]All shielding values in bold correspond to the highest contribution for each tensor component. Blank spaces indicate no contribution to these tensor components.

vir MO mixing is the dominant contribution to the anisotropy of the NMS tensor; therefore, occ-occ mixing will not be considered here. Due to the large number of MO pairs, only those that contribute to greater than 5% (~200 ppm) of the total isotropic shielding arising from occ-vir MO mixing (–3909.8 ppm) are listed. This focuses the analysis on a few crucial MOs that are near the HOMO and (or) involved in the bonding.

In **A,** the occupied-virtual MO pairs 34–41*, 39–41*, and 39–42* make the largest contributions to deshielding along the directions of σ_{33}, σ_{11}, and σ_{22}, respectively (Fig. 6, Table 4). The mixing of the occupied MO 34 (HOMO–5) with virtual MO 41* (LUMO+1) results in deshielding along the direction of σ_{33} and contributes –636.8 ppm to the total paramagnetic shielding ($\boldsymbol{\sigma}_p$) of –3721.2 ppm; however, the mixing of the HOMO, MO 39, with energetically proximate MOs 41* and 42*, causes even greater deshielding along the directions of σ_{11} and σ_{22}, respectively. We also note that the LUMO, MO 40*, plays a role in creating additional deshielding along σ_{11} and σ_{22}.

The analysis of contributions of individual MOs to paramagnetic shielding combined with the calculation of gross AO populations of each MO (Table 5) can provide some insights into the origin of nuclear magnetic shielding at a nucleus. The HOMO, MO 39, has a relatively high Se $4p_x$-orbital character (71.0%) and smaller contributions from the C1 and C2 $2p_x$-orbitals (12.9% each) on the aromatic rings. The stereochemically active lone pair of selenium is best described by MO 39, and is oriented along the direction of the σ_{33} component (perpendicular to the plane of the ring). The

Fig. 6. The occupied and virtual MOs of **A** that make significant contributions to the paramagnetic shielding term. A partial MO diagram indicating the magnetic-dipole allowed transition between the occupied and virtual MOs shown above. An isosurface of ±0.04 is used for the diagrams above.

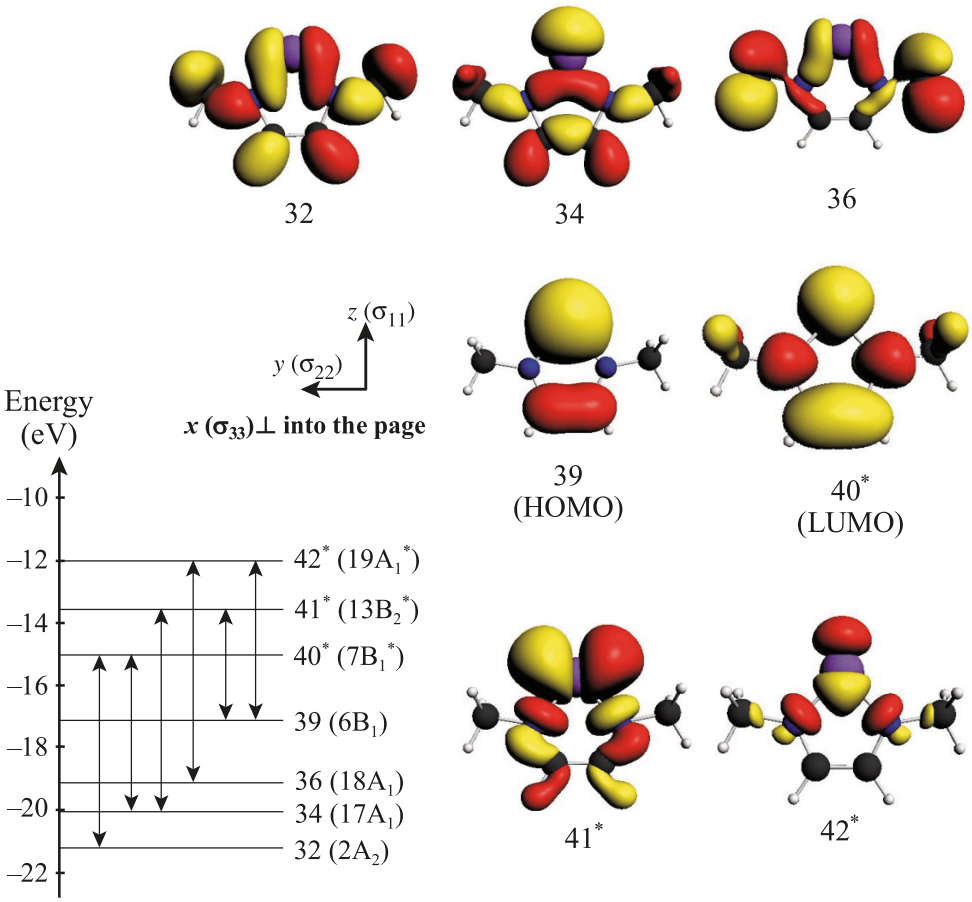

LUMO, MO 40*, is largely delocalized over the heterocyclic ring, while MOs 41* and 42* have high Se $4p_y$ (75.0%) and $4p_z$ (58.9%) orbital characters, respectively, oriented for convenient mixing with the HOMO.

To qualitatively understand why these particular MO pairs make important contributions to the selenium nuclear magnetic shielding tensor, it is useful to consider the point group symmetry representations for both the MOs and the angular momentum operators (i.e., from Ramsey's equations).[94] Ramsey's equations and various modern modifications feature three-centre integrands which can describe the magnetically-induced mixing of MOs[95]

$$[2] \qquad \langle \psi_m | \hat{L}_i | \psi_n \rangle$$

where ψ_m and ψ_n are the occupied and virtual MOs, respectively, and $\hat{L}_i$ (i = x,y,z) is an angular momentum operator. The integrand above is only nonzero if the direct product of the irreducible representations (IRs) of the MOs and angular momentum operators (which have the same IRs as the rotational operators, $\hat{R}_i$, listed in the point group tables) is equal to or contains the totally symmetric representation of the point group (for this case of C_{2v}, it is A_1):

$$[3] \qquad \Gamma(\psi_n) \otimes \Gamma(\hat{R}_i) \otimes \Gamma(\psi_m) \supseteq A_1$$

The symmetry representations of the rotational operators $\hat{R}_x$, $\hat{R}_y$, and $\hat{R}_z$ are B_2, B_1, and A_2, respectively. Hence, the 34–41*, 39–41*, and 39–42* MO pairs, which contribute to paramagnetic shielding along σ_{33}, σ_{11}, and σ_{22}, respectively, are all nonzero,

$$[4] \qquad \Gamma(\psi_n) \otimes \Gamma(\hat{R}_x) \otimes \Gamma(\psi_m) = B_2 \otimes B_2 \otimes A_1 = A_1$$

$$[5] \qquad \Gamma(\psi_n) \otimes \Gamma(\hat{R}_z) \otimes \Gamma(\psi_m) = B_2 \otimes A_2 \otimes B_1 = A_1$$

$$[6] \qquad \Gamma(\psi_n) \otimes \Gamma(\hat{R}_y) \otimes \Gamma(\psi_m) = A_1 \otimes B_1 \otimes B_1 = A_1$$

and make symmetry-allowed contributions to the selenium NMS tensor.

Simple visualization, often referred to as "charge rotation",[63,66,96,97] can also be used to understand how MO pairs make paramagnetic shielding contributions. MOs which contribute to the shielding along the direction of a particular principal component must be relatively close in energy and have the correct symmetry to overlap or mix with one another when rotated about the direction of the tensor component. An arbitrary convention of a right-handed ninety degree rotation of the virtual MOs about their nuclear origins (i.e., rotating the contributing AOs about their own origins) is utilized. The three MO pairs which make the largest contributions to the three different NMS tensor components are

Table 5. ADF calculations: composition of the MOs in **A** from NR calculations (see Supplementary data for other model compounds).

System	MO	Energy (eV)	Occ. of MO[a]	Composition of MO	SFO[b] (first member)	Occ. of SFO	Fragment
A	32	–21.297	2	12.80%	$2p_y$	1	N1
				12.80%	$2p_y$	1	N2
				10.37%	$4p_y$	1.33	Se
				5.24%	$2p_z$	0.67	C1
				5.24%	$2p_z$	0.67	C2
	34	–20.101	2	21.64%	$4p_z$	1.33	Se
				8.98%	$2p_y$	1	N1
				8.98%	$2p_y$	1	N2
				8.63%	$2p_y$	0.67	C1
				8.63%	$2p_y$	0.67	C2
	36	–19.162	2	25.22%	$2p_z$	0.67	C1
				25.22%	$2p_z$	0.67	C2
				9.06%	1s	1	H3
				9.06%	1s	1	H7
				5.19%	$4p_y$	1.33	Se
	39[c]	–17.094	2	71.04%	$4p_x$	1.33	Se
				12.90%	$2p_x$	0.67	C2
				12.90%	$2p_x$	0.67	C1
	40*	–14.093	0	21.95%	$2p_x$	1	N1
				21.95%	$2p_x$	1	N2
				19.65%	$4p_x$	1.33	Se
				16.81%	$2p_x$	0.67	C2
				16.81%	$2p_x$	0.67	C1
	41*	–13.699	0	75.01%	$4p_y$	1.33	Se
				5.92%	$2p_z$	1	N2
				5.92%	$2p_z$	1	N1
				4.17%	$2p_y$	1	N2
				4.17%	$2p_y$	1	N1
	42*	–12.071	0	58.95%	$4p_z$	1.33	Se
				8.05%	$2p_z$	1	N1
				8.05%	$2p_z$	1	N2

[a]Occ stands for occupancy.

[b]SFO stands for symmetrized fragment orbitals.

[c]MO 39 is the best representation of the Se "lone pair" MO, and is the HOMO in this case. All MOs following with asterisks are virtual (unoccupied).

discussed (Figs. 7A–7C): 34–41* for σ_{33}, 39–41* for σ_{11}, and 39–42* for σ_{22}. A right-handed 90° rotation of MO 41* about σ_{33} (out of the page), which is coincident to the *x*-axis, gives a constructive overlap (i.e., lobes of the same phase overlap) with MO 34. Similarly, a right-handed rotation of MO 41* about σ_{11} (pointing away from the direction of the centroid of the five-membered ring) results in a large constructive orbital overlap with MO 39, accounting for the largest deshielding contribution. Finally, a right-handed rotation of MO 42* about σ_{22} (pointing to the direction of the methyl group) leads to a constructive overlap with MO 39 as well, but to a lesser extent. All of the other paramagnetic contributions can be visualized in this manner as well (see Table 4 and Fig. 6 for the MO pairs). Such visualizations, of course, do not provide any sort of formally quantitative measure of nuclear magnetic shielding (this is left to the calculations).

An understanding of how individual MOs play roles in determining the selenium NMS tensor characteristics can be extended to describe experimentally observed variations in NMS tensors. Of all of the NR ADF calculations that we performed, the VWN-BP/DZ method best reproduces some of the experimental trends (Table 3): specifically, (1) a single Se···Cl contact reduces the span and (2) an extra substituent at a heterocyclic nitrogen position increases the span.

First, let us consider how Se···Cl interactions reduce the span of the Se NMS tensor by comparing **A** and **B** with their chlorinated analogs **A′** and **B′**. For both **A′** and **B′**, calculations indicate that the HOMO is no longer associated with the lone pair on Se, but rather, is described by an MO which is largely localized on the Cl atom (Table S10). For example, in **B′**, the HOMO, MO 44, is largely comprised of the $3p_x$ AO (96.7%) of the Cl atom, whereas the HOMO-3, MO 41, describes the Se lone pair (major contribution from the $4p_z$ AO of Se atom (59.7%)), which is oriented perpendicular to the plane of the ring. Similar changes in relative MO energies are observed when comparing **A** and **A′**. The effects of the Se···Cl interactions of the selenium NMS tensor are seen by comparing **B** and **B′** (Table 4, Figs. S13, S15): in the former, the 35–37*, 35–38*, and 34–37* MO pairs

Fig. 7. A representation of (A) 34–41* MO pair, in which their mixing contributes to paramagnetic deshielding along σ_{33}, (B) 39–41* MO pair (σ_{11}), and (C) 39–42* MO pair (σ_{22}).

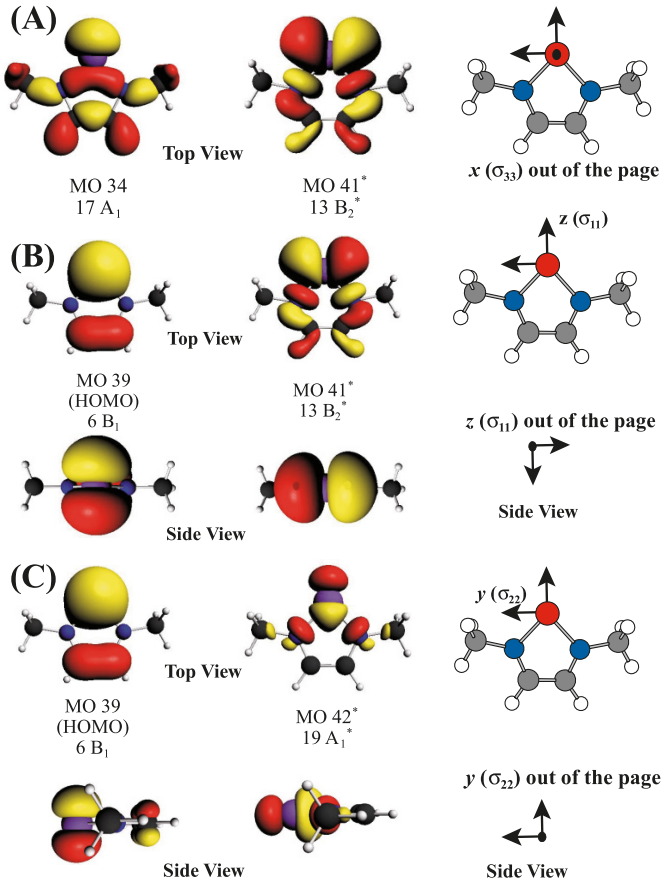

are responsible for the largest contributions to deshielding along σ_{11}, σ_{22}, and σ_{33}, respectively; however, in the latter, the analogous 41–46*, 41–49*, and 40–46* pairs make significantly smaller contributions. This is largely due to both the increased energy spacings and decreased induced MO overlaps in **B**′. With very few exceptions, almost all of the valence MOs in **B** have analogues in **B**′, featuring similar AO compositions and energies (e.g., there is an additional MO 42 in **B**′ because of the Cl atom). The difference in the composition of MO 37* in **B** (57.7% of $4p_y$ and 16.5% of $4p_x$ of Se atom) compared to MO 46* in **B**′ (27.6% of $4p_x$ and 19.6% of $4p_y$ of Se atom) has a major influence on shielding along the σ_{11} and σ_{33} directions, serving to reduce the span in the latter.

Now, let us consider how the selenium NMS tensor is affected by the presence of a second substituent at a heterocyclic nitrogen position. In accordance with experimental observations, comparison of theoretical Se NMS tensors of **A** and **B** reveal an increased span and an increasingly positive skew in the former (Table 3). This is the result of reduced shielding along σ_{11} and increased shielding along σ_{33} in **A**. The source of the reduced shielding in **A** is the 39–41* MO pair (Table 4), which serves to deshield the ^{77}Se nucleus by a significantly higher degree than the corresponding 35–37* MO pair in **B** (Table 6). The second substituent serves to increase the symmetry of the molecule, thereby increasing the MO mixing in **A**, and resulting in greater deshielding. Deshielding along σ_{33} is similarly described by the 34–41* MO pair for **A** and the 34–37* MO pair for **B**. However, MO 37* in **B** also mixes efficiently with MOs 30 and 32, which serves to increase deshielding along σ_{33} in general.

It is important to note that there is a general difficulty with both sets of DFT calculations in the prediction of positive skews for heterocycles with two substituents and a single chlorine contact (e.g., complexes **5** and **6** and model system **A**′); though, in every case an increasingly positive skew is calculated with respect to systems with a single substituent (e.g., complexes **3** and **4** and model system **B**′). Gaussian 03 calculations were performed on the isolated monomeric cations, the combined cations and anions, and the full dimeric structures for both **5** and **6**; however, in all cases, negative skews are predicted. ADF calculations on model complex **A**′ involved calculations on heterocyclic rings with methyl, *t*-butyl, and dipp substituents, all of which yielded negative skews. The reason for this disagreement between experiment and theory in these particular systems is unknown at this time.

NLMO analysis of nuclear magnetic shielding contributions

The classical resonance structures for these Se–N heterocycles are often drawn with two lone pairs at the Se atom, and previous NBO calculations on a variety of main-group heterocycles analogous to those discussed herein indicated that there are indeed two lone pairs[98] (see below for analysis of this situation). However, the MO analysis of the nuclear shielding tensor contributions reveals only one MO which might be considered as describing a lone pair, along with other significant MOs which are difficult to describe as traditional, "chemically intuitive," Lewis-type orbitals. A more intuitive understanding of the contributions of individual MOs can be accomplished via a natural localized molecular orbital (NLMO) analysis; hence, we have employed a set of NLMOs to analyze the shielding tensor in terms of these orbitals. In this section, we describe the results of such analyses for model systems **A** and **A**′. In the NBO algorithm, each NLMO is constructed from a strongly localized "parent" NBO and a delocalization tail that may or may not be large, depending upon how delocalized the molecule really is. The parent NBOs are classified as "chemically intuitive" orbital types, such as bonding, core, or lone pair orbitals. Besides the delocalization tail of the NLMOs, another useful criterion revealing information about delocalization or other non-Lewis type behavior is the NBO occupancy number: values less than 2.0 indicate a departure from Lewis structure descriptions. In the data tables, we report the type and occupancy of the parent NBO for each NLMO of interest, as well as the composition of the NLMOs in terms of the weighted coefficients of the atomic orbitals (AOs). Finally, the contributions of each NLMO to the isotropic nuclear magnetic shielding are presented, in terms of its main localized part ("Lewis" contribution, from the parent NBO) and from its delocalization tail (the "non-Lewis" contribution).

Characteristics and compositions for various key NLMOs, with most contributing more than ~ ±200 ppm to the isotropic nuclear magnetic shielding, are summarized for **A** and **A**′ in Tables 6 and 7, respectively (full listings of NLMO

Table 6. Analysis of major NLMO Contributions to isotropic chemical shift for model compound **A**.

System	Calcd. σ_{iso} (ppm)	NLMO Number[a]	Orbital Type[b]	Occ.[c]	NLMO composition[d]	Lewis σ_{iso} (ppm)	non-Lewis σ_{iso} (ppm)	Total σ_{iso} (ppm)
A	–316.80	1	BD (Se–N2)	1.969	32.48 Se (8.89 4s, 90.48 4p) 66.12 N2 (23.74 2s, 76.11 2p)	–446.558	–2.103	–448.661
		2	BD (Se–N3)	1.969	32.48 Se (8.89 4s, 90.48 4p), 66.12 N3 (23.74 2s, 78.45 2p)	–446.558	–2.103	–448.661
		3–17[e]	BD			–55.048	–244.838	–299.884
					Sum of bonding orbital contributions	–948.164	–249.044	–1197.206
		18	core	2.000	100 Se (1s)	712.092	–0.001	712.091
		19	core	2.000	100 Se (2s)	740.339	0.028	740.367
		21	core	2.000	100 Se ($2p_x$)	264.243	0.008	264.251
		23	core	2.000	100 Se ($2p_y$)	257.771	–0.269	257.502
		25	core	2.000	100 Se ($2p_z$)	239.079	–0.730	238.349
		9 others[e]	core			236.511	–0.964	235.547
					Sum of core orbital contributions	2450.035	–1.928	2448.107
		38	LP(1) Se	1.983	99.15 Se (84.78 4s, 15.20 4p)	–194.919	4.190	–190.729
		39	LP(2) Se	1.546	75.11 Se (99.85 4p) 4.02% N2 (98.90 2p) 4.03% N3 (98.91 2p) 8.38% C4 (99.96 2p) 8.42% C5 (99.96 2p)	–1407.759	32.311	–1375.448
					Sum of lone pair orbital contributions	–1602.678	36.501	–1566.177
					Sum of all NLMO contributions	–100.804	–214.47	–315.274

[a]This is the index number assigned by the NBO program.

[b]This is the label assigned by the NBO program. BD denotes a bonding electron pair, core to a non-bonding pair in the sub-shell below the valence shell, and LP to a lone pair.

[c]Occ refers to the occupancy of the parent NBO of the NLMO, the analysis data is for the NLMO itself. Occupancies less than 2 indicate deviation away from an ideal Lewis structure.

[d]The number before the atom symbol indicates the percentage composition of each NLMO in terms of atomic orbitals from the given atom(s). The contribution of each atom is then broken down by percentage orbital type (e.g., s, p, *d*).

[e]A full listing for all of the contributing NLMOs is provided in the Supplementary data.

contributions are in the Supplementary data). In system **A**, two major deshielding contributions come from MOs 1 and 2, which are well localized, and describe bonding (BD) between the Se and neighbouring N atoms (Fig. 8). Interestingly, there is also a significant non-Lewis deshielding contribution from the remaining bonding MOs,[3–17] with some of the key contributors describing the C–H bonds in the five-membered ring. The majority of the core MOs on Se are responsible for shielding the ^{77}Se nucleus; notably, the NLMOs that describe the core 1s, 2s, and 2p Se AOs. Finally, there are two key NLMOs which were also identified as important in the MO analysis in the previous section. NLMOs 38 and 39 are classified as being Se lone pairs (LP) which make significant deshielding contributions. The former is a typical Lewis-type LP with a small deshielding contribution, while the latter departs significantly from such an LP classification. The Se π-lone pair NLMO 39 is strongly delocalized over the five-membered ring, and makes the most significant deshielding contribution of all of the NLMOs.

In system **A**′, the presence of the weakly coordinated Cl atom breaks the molecular symmetry and influences the Se shielding characteristics. Two major deshielding contributions from bonding NLMOs now arise from Se–N and Se–Cl bonds instead of two Se–N bonds; however, their net contribution is similar to that of system **A**. Similarly, the contributions from the core orbitals are very close in magnitude and character for **A** and **A**′. The difference between the isotropic shielding for **A** and **A**′ seems to arise in this analysis from the NLMOs which are formally classified as Se LPs. Indeed, NLMOs 43 and 44 are very similar to their counterparts in **A** (NLMOs 38 and 39) in both their composition and contributions to the nuclear shielding (though the former pair makes a smaller net deshielding contribution). NLMO 45, which is unique to **A**′, is classified as a LP, is largely localized on the N3 atom (the side opposite to the Se–Cl bond), and forms a weak σ-type bond with Se. NLMO 45 does not make a large Lewis contribution to shielding; rather, it makes a non-Lewis contribution of ~ –192 ppm, which is comparable to the net non-Lewis contribution from all of the other bonding NLMOs. This, in combination with additional non-Lewis shielding from the three Cl LPs, results in a net deshielding at the ^{77}Se nucleus in **A**′ with respect to that in **A**, inferring that the presence of a single Cl atom in these species should decrease the isotropic selenium chemical shift, or at least dramatically impact the character of the Se NMS tensor.

To test whether the delocalization of the Se π lone pair orbital is to some extent created by the specific nature of the NLMO localization method, we have additionally carried out the Boys localization[99] of the occupied orbitals. Unlike the occupation-driven localization by the NBO algorithm, the Boys method minimizes directly the spatial extent of the orbitals around their center of gravity, i.e., it minimizes

$$[7] \qquad \sum_i (\Delta r)_i^2 = \sum_i \langle \psi_i | r^2 | \psi_i \rangle - \langle \psi_i | \mathbf{r} | \psi_i \rangle^2$$

for the set of orbitals $\{\psi_i\}$. The Boys criterion tends to yield "banana bond" orbitals for double bonds instead of the

Table 7. Analysis of major NLMO Contributions to isotropic chemical shift for model compound **A′**.

System	Calcd. σ_{iso} (ppm)	NLMO number[a]	Orbital type[b]	Occ.[c]	NLMO composition[d]	Lewis σ_{iso} (ppm)	Non-Lewis σ_{iso} (ppm)	Total σ_{iso} (ppm)
A′	–227.671	1	BD (Se–N2)	1.968	30.81% Se (8.91 4s, 90.35 4p) 67.74% N2 (25.5 2s 74.45 2p)	–396.697	7.369	–389.328
		2	BD (Se–Cl)	1.983	33.58% Se (1.05 4s, 97.93 4p) 65.78% Cl (6.65 2*s,* 93.01 2p)	–538.066	12.059	–526.008
		3–17[e]	BD			–12.477	–221.664	–234.140
					Sum of bonding orbital contributions	–947.240	–202.236	–1149.476
		18	core	2.000	100% Se (1s)	706.461	0.000	712.091
		19	core	2.000	100% Se (2s)	748.086	0.026	740.367
		21	core	2.000	100% Se ($2p_x$)	243.523	–0.514	264.251
		23	core	2.000	100% Se ($2p_y$)	262.565	–0.145	257.502
		25	core	2.000	100% Se ($2p_z$)	267.034	0.007	238.349
		9 others[e]	core			248.631	–0.535	248.096
					Sum of all core orbital contributions	2476.300	–1.161	2475.136
		43	LP(1) Se	1.984	99.2% Se (91.43 4s, 8.55 4p)	–85.891	3.207	–82.684
		44	LP(2) Se	1.594	77.27% Se (99.81 4p) 4.44% N2 (99.22 2p) 3.44% N3 (99.81 2p) 9.05% C4 (99.96 2p) 5.64% C5 (99.89 2p)	–1256.230	12.533	–1243.700
		45	LP(1) N3	1.635	10.89% Se (95.41 4p) 81.34% N3 (35.79 2s, 64.19 2p) 4.40% Cl (7.31 2s, 92.65 2p)	35.803	–191.978	–156.175
		46–48	LP(1–3) Cl			–10.044	–59.449	–69.491
					Sum of lone pair orbital contributions	–1316.36	–235.687	–1552.050
					Sum of listed NLMO contributions	212.698	–439.084	–226.390

[a]This is the index number assigned by the NBO program.

[b]This is the label assigned by the NBO program. BD denotes a bonding electron pair, core to a non-bonding pair in the sub-shell below the valence shell, and LP to a lone pair.

[c]Occ refers to the occupancy of the parent NBO of the NLMO, the analysis data is for the NLMO itself. Occupancies less than 2 indicate deviation away from an ideal Lewis structure.

[d]The number before the atom symbol indicates the percentage composition of each NLMO in terms of atomic orbitals from the given atom(s). The contribution of each atom is then broken down by percentage orbital type (e.g., s, p, *d*).

[e]A full listing for all of the contributing NLMOs is provided in the Supplementary data.

more commonly chosen set of orbitals with local σ and π symmetry. This is easily remedied, however, by taking positive and negative linear combinations of pairs of such banana bond orbitals. Figure 9 shows the Boys localized orbital corresponding to the Se π lone pair alongside the corresponding NLMO, using the same plot plane roughly 1 a.u. above the ring. It is apparent that the high degree of delocalization is very similar in both cases; hence, the delocalized nature of the Se π lone pair orbital is not a matter of which orbital localization method is chosen.

To investigate the nature of the Se lone pairs further, we performed a search for resonance structures for model system **A** using the "natural resonance theory" (NRT) algorithm implemented in the NBO 5 code.[100–102] This method decomposes the density matrix of the molecule into contributions from idealized resonance structures utilizing a given NBO set. Five types of main natural resonance structures, along with the weights they contribute to the overall electron density matrix according to the NRT procedure, are shown in Fig. 10. The resonance structure with two lone pairs has the greatest overall weight of about 1/3. The following two pairs of resonance structures with combined weights of 19% and 14% both involve delocalization of the Se π lone pair over the five-membered ring. This analysis agrees with the strong delocalization seen for the Se π lone pair NLMO, and with the rather strong delocalization of the corresponding Boys localized orbital.

Conclusions

^{77}Se VACP/MAS NMR spectra of selenium-containing heterocycles reveal expansive Se chemical shift tensors which are extremely sensitive to molecular geometry, symmetry, and ligand substitution. A single Se···Cl contact results in a reduction of the CSA, whereas a second substituent at the N atom in the heterocycles increases the span of the CS tensor significantly, and changes the sign of the skew from negative to positive. Cation–anion interactions and variation in Se–Cl bond distances both have significant influence on the NMR parameters. The experimental measurement of selenium CS tensors via SSNMR is especially useful for series of complexes like these, since solution NMR would only yield isotropic shifts over a very narrow shift range that may only provide ambiguous identification of structural variation; this is clearly not the case for the data obtained from SSNMR.

Hybrid DFT is capable of reproducing experimental Se NMS tensors in most cases, as well as predicting their orientations with respect to the molecular frames. The σ_{33} component, which is oriented perpendicular to the heterocycle

Fig. 8. NLMOs with major contributions to the Se nuclear magnetic shielding for model systems **A** (top, isosurfaces) and **A′** (bottom, contour plots). **A**: NLMO 1 (and 2, not shown) are bonding MOs with large deshielding contributions. NLMO 38 describes a lone pair localized at Se, while 39 describes delocalization of the MO into the ring system. Both make deshielding contributions. **A′**: NLMOs 1, 43 and 44 in **A′** are counterparts to 1, 38 and 39 in **A**. NLMO 45, which is largely localized on N3, makes a major contribution to the selenium shielding.

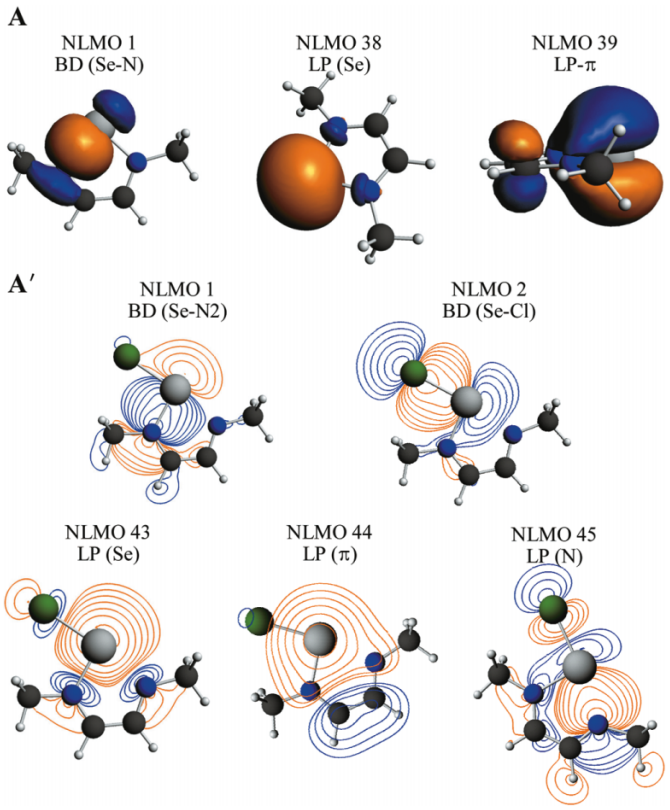

Fig. 9. *Left*: Se π "lone pair" orbital of model system **A** from a Boys localization (after generating the σ–π linear combination from two σ–π mixed Boys orbitals). *Right*: The corresponding Se π "lone pair" NLMO 39. Contour values: ±0.01, ±0.02, ±0.04,...

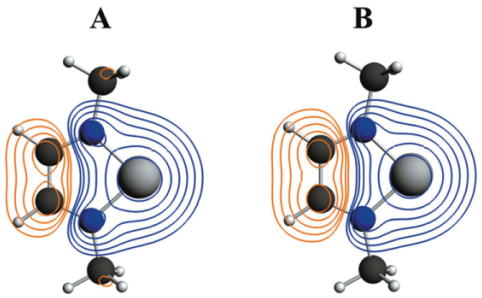

plane, is a good indicator of the direction of the lone pair localized on the Se atom. DFT calculations on model systems explain the origin of the selenium NMS tensors from the perspective of paramagnetic shielding arising from induced mixing of occupied and virtual MOs, and confirm the presumed orientation of the stereochemically active lone pair of selenium. Se···Cl interactions are predicted to shift the MO describing the Se lone pair to a lower energy, which

Fig. 10. Most important resonance structures contributing to the electronic structure of model system A, as calculated using the natural resonance theory (NRT) module in the NBO 5.0 code, with resonance structure weights in percent. A large number of resonance structures with small weights are not shown.

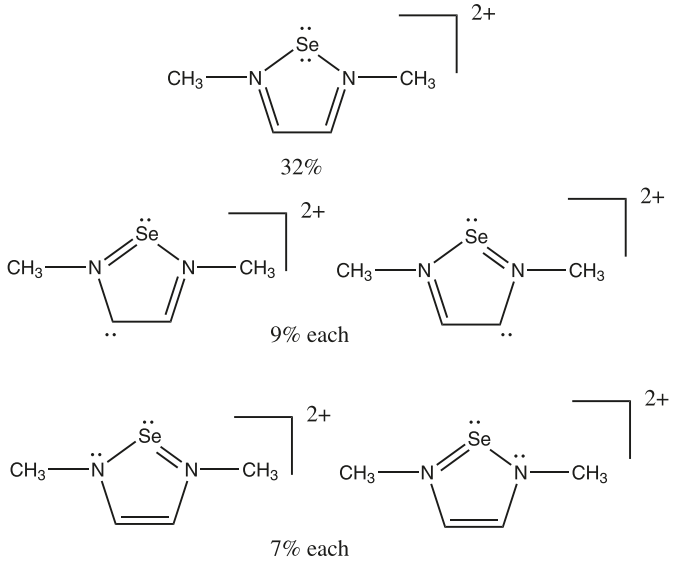

results in both increased energy spacings and decreased induced MO overlaps, leading to a reduction in the span of the Se NMS tensor. The second substituent at nitrogen increases the symmetry of the molecule, thereby increasing MO overlap, and producing greater deshielding along σ_{11}. The NLMO analysis of two of the model systems demonstrates how the presence of the weakly coordinated Cl atom results in increased nuclear shielding. As well, these analyses confirm that there are two lone pairs on the Se atom, one localized and one delocalized, and both of which play an important role in determining the nuclear shielding characteristics.

A precise understanding of the origins of the variations in Se NMS tensors with subtle structural changes should lead to a deeper understanding of the electronic structure of these systems, and possibly even further rational design of heterocycles with specific reactivities, stabilities, and other properties.

Supplementary data

Supplementary data for this article (sample preparation, ^{77}Se CP/MAS NMR experimental parameters, ^{13}C solid-state NMR data, ^{13}C CP/MAS NMR experimental parameters, powder X-ray diffraction patterns, ab initio calculations, and ADF calculations) are available on the journal Web site (canjchem.nrc.ca) or may be purchased from the Depository of Unpublished Data, Document Delivery, CISTI, National Research Council Canada, Ottawa, ON K1A 0R6, Canada. DUD 5264. For more information on obtaining material, refer to cisti-icist.nrc-cnrc.gc.ca/cms/unpub_e.shtml.

Acknowledgments

RWS gratefully acknowledges the Natural Sciences and Engineering Research Council of Canada (NSERC), the Canadian Foundation for Innovation (CFI), and the Ontario

Innovation Trust (OIT) for financial support. RWS and AS also acknowledge the Centre for Catalysis and Materials Research (CCMR) at the University of Windsor for funding. Mr. Cory M. Widdifield and Mr. Aaron J. Rossini are thanked for the assistance with ADF calculations. PJR and JLD thank NSERC, CFI, and the University of Western Ontario for their generous financial support. RWS and PJR acknowledge the Ontario Ministry of Research and Innovation for Early Research Awards. JA and SZ acknowledge financial support from the National Science Foundation (CHE-0447321). This work was made possible in part by the facilities of the Shared Hierarchical Academic Research Computing Network (SHARCNET: http://www.sharcnet.ca).

References

(1) Bethell, D. *Adv. Phys. Org. Chem.* **1969**, *7*, 153–209. doi:10.1016/S0065-3160(08)60265-8.

(2) Gaspar, P.; Hammond, G. S. In *Carbenes*; Moss, R. A., Jones, M. Jr., Eds.; Wiley-Interscience: New York, 1975; Vol. II, pp 207-362.

(3) Atkinson, R. S. *Aromatic and Heteroaromatic Chemistry* **1978**, *6*, 223–238. doi:10.1039/9781847555748-00223.

(4) Arduengo, A. J., III. *Acc. Chem. Res.* **1999**, *32* (11), 913–921. doi:10.1021/ar980126p.

(5) Bourissou, D.; Guerret, O.; Gabbaï, F. P.; Bertrand, G. *Chem. Rev.* **2000**, *100* (1), 39–92. doi:10.1021/cr940472u. PMID:11749234.

(6) Cardin, D. J.; Cetinkaya, B.; Lappert, M. F. *Chem. Rev.* **1972**, *72* (5), 545–574. doi:10.1021/cr60279a006.

(7) Moss, R. A. *Chem. Eng. News* **1969**, *47*, 60–68.

(8) Arduengo, A. J., III; Harlow, R. L.; Kline, M. *J. Am. Chem. Soc.* **1991**, *113* (1), 361–363. doi:10.1021/ja00001a054.

(9) Ellis, B. D.; Dyker, C. A.; Decken, A.; Macdonald, C. L. B. *Chem. Commun. (Camb.)* **2005**, (15): 1965–1967. doi:10.1039/b500692a. PMID:15834473.

(10) Gade, L. H.; Bellemin-Laponnaz, S. *Top. Organomet. Chem.* **2007**, *21*, 117–157. doi:10.1007/3418_028.

(11) Rogers, M. M.; Stahl, S. S. *Top. Organomet. Chem.* **2007**, *21*, 21–46. doi:10.1007/978-3-540-36930-1_2.

(12) Reeske, G.; Hoberg, C. R.; Hill, N. J.; Cowley, A. H. *J. Am. Chem. Soc.* **2006**, *128* (9), 2800–2801. doi:10.1021/ja058459m. PMID:16506749.

(13) Jones, C.; Junk, P. C.; Platts, J. A.; Stasch, A. *J. Am. Chem. Soc.* **2006**, *128* (7), 2206–2207. doi:10.1021/ja057967t. PMID:16478162.

(14) Jones, C.; Junk, P. C.; Platts, J. A.; Rathmann, D.; Stasch, A. *Dalton Trans.* **2005**, (15): 2497–2499. doi:10.1039/b507242e. PMID:16025168.

(15) Hill, M. S.; Hitchcock, P. B. *Chem. Commun. (Camb.)* **2004**, (16): 1818–1819. doi:10.1039/b406017b. PMID: 15306899.

(16) Baker, R. J.; Farley, R. D.; Jones, C.; Kloth, M.; Murphy, D. M. *J. Chem. Soc., Dalton Trans.* **2002**, (20): 3844–3850. doi:10.1039/b206605j.

(17) Gans-Eichler, T.; Gudat, D.; Nieger, M. *Angew. Chem. Int. Ed.* **2002**, *41* (11), 1888–1891. doi:10.1002/1521-3773(20020603)41:11<1888::AID-ANIE1888>3.0.CO;2-O.

(18) Segawa, Y.; Yamashita, M.; Nozaki, K. *Science* **2006**, *314* (5796), 113–115. doi:10.1126/science.1131914. PMID: 17023656.

(19) Boche, G.; Andrews, P.; Harms, K.; Marsch, M.; Rangappa, K. S.; Schimeczek, M.; Willeke, C. *J. Am. Chem. Soc.* **1996**, *118* (21), 4925–4930. doi:10.1021/ja9536274.

(20) Martin, C. D.; Jennings, M. C.; Ferguson, M. J.; Ragogna, P. J. *Angew. Chem. Int. Ed. Engl.* **2009**, *48* (12), 2210–2213. doi:10.1002/anie.200805198. PMID:19137516.

(21) (a) Dutton, J. L.; Tindale, J. J.; Jennings, M. C.; Ragogna, P. J. *Chem. Commun. (Camb.)* **2006**, (23), 2474–2476. doi:10.1039/b603777a. PMID:16758020.; (b) Dutton, J. L.; Farrar, G. J.; Sgro, M. J.; Battista, T. L.; Ragogna, P. J. *Chem. Eur. J.* **2009**, early view (online). doi:10.1002/chem.200901000.

(22) Dutton, J. L.; Tuononen, H. M.; Jennings, M. C.; Ragogna, P. J. *J. Am. Chem. Soc.* **2006**, *128* (39), 12624–12625. doi:10.1021/ja064381d. PMID:17002337.

(23) Dutton, J. L.; Sutrisno, A.; Schurko, R. W.; Ragogna, P. J. *Dalton Trans.* **2008**, (26): 3470–3477. doi:10.1039/b719779a. PMID:18580984.

(24) Gray, I. P.; Woollins, J. D. *Main Group Chem.* **2005**, *4* (1), 69–88. doi:10.1080/10241220500045754.

(25) Chivers, T.; Doxsee, D. D. *Comments Inorg. Chem.* **1993**, *15* (2), 109–135. doi:10.1080/02603599308035839.

(26) Demko, B. A.; Wasylishen, R. E. *Prog. Nucl. Magn. Reson.* **2009**, *54* (3-4), 208–238. doi:10.1016/j.pnmrs.2008.10.002.

(27) Duddeck, H.; Hotopp, T. *Magn. Reson. Chem.* **1995**, *33* (6), 490–492. doi:10.1002/mrc.1260330614.

(28) Duddeck, H. *Ann. Rep. NMR Spectrosc.* **2004**, *52*, 105–166. doi:10.1016/S0066-4103(04)52003-3.

(29) Duddeck, H. *Prog. Nucl. Magn. Reson. Spectrosc.* **1995**, *27* (1-3), 1–323. doi:10.1016/0079-6565(94)00005-F.

(30) Demko, B. A.; Eichele, K.; Wasylishen, R. E. *J. Phys. Chem. A* **2006**, *110* (50), 13537–13550. doi:10.1021/jp064543s. PMID:17165881.

(31) Collins, M. J. R.; Ratcliffe, C. I.; Ripmeester, J. A. *J. Magn. Reson.* **1986**, *68*, 172–179.

(32) Yu, K.; Zaman, B.; Ripmeester, J. A. *J. Nanosci. Nanotechnol.* **2005**, *5* (4), 669–681. doi:10.1166/jnn.2005.123. PMID:16004136.

(33) Yu, K.; Zaman, B.; Singh, S.; Dashan, W.; Ripmeester, J. A. *J. Nanosci. Nanotechnol.* **2005**, *5* (4), 659–668. doi:10.1166/jnn.2005.122. PMID:16004135.

(34) Baiwir, M. In *Proceedings of the 4th International Conference on the Organic Chemistry of Selenium and Tellurium;* Birmingham: England, 1983; pp 406–467.

(35) Bayse, C. A. *J. Chem. Theory Comput.* **2005**, *1* (6), 1119–1127. doi:10.1021/ct050136t.

(36) Grossmann, G.; Potrzebowski, M. J.; Fleischer, U.; Krüger, K.; Malkina, O. L.; Ciesielski, W. *Solid State Nucl. Magn. Reson.* **1998**, *13* (1-2), 71–85. doi:10.1016/S0926-2040(98)00077-0. PMID:9875605.

(37) Maaninen, T.; Tuononen, H. M.; Kosunen, K.; Oilunkaniemi, R.; Hiitola, J.; Laitinen, R.; Chivers, T. *Z. Anorg. Allg. Chem.* **2004**, *630* (12), 1947–1954. doi:10.1002/zaac.200400286.

(38) Johannsen, I.; Eggert, H. *J. Am. Chem. Soc.* **1984**, *106* (5), 1240–1243. doi:10.1021/ja00317a012.

(39) Eggert, H.; Nielsen, O.; Henriksen, L. *J. Am. Chem. Soc.* **1986**, *108* (8), 1725–1730. doi:10.1021/ja00268a001.

(40) Balzer, G.; Duddeck, H.; Fleischer, U.; Rohr, F. *Fresenius J. Anal. Chem.* **1997**, *357*, 473–476. doi:10.1007/s002160050194.

(41) Barrie, P. J.; Clark, R. J. H.; Withnall, R.; Chung, D.-Y.; Kim, K.-W.; Kanatzidis, M. G. *Inorg. Chem.* **1994**, *33* (6), 1212–1216. doi:10.1021/ic00084a040.

(42) Duddeck, H.; Wagner, P.; Mueller, D.; Jaszberenyi, J. C. *Magn. Reson. Chem.* **1990**, *28* (6), 549–552. doi:10.1002/mrc.1260280614.
(43) Koch, W.; Lutz, O.; Nolle, A. *Z. Physica A* **1978**, *289* (1), 17–20. doi:10.1007/BF01408490.
(44) Hamard, C.; Auffret, V.; Peña, O.; Le Floch, M.; Nowak, B.; Wojakowski, A. *Phys. B* **2000**, *291* (3-4), 339–349. doi:10.1016/S0921-4526(99)02286-3.
(45) Maxwell, R.; Lathrop, D.; Franke, D.; Eckert, H. *Angew. Chem. Int. Ed. Engl.* **1990**, *29* (8), 882–884. doi:10.1002/anie.199008821.
(46) Gaudin, E.; Boucher, F.; Evain, M.; Taulelle, F. *Chem. Mater.* **2000**, *12* (6), 1715–1720. doi:10.1021/cm001011u.
(47) Johannsen, I.; Henriksen, L.; Eggert, H. *J. Org. Chem.* **1986**, *51* (10), 1657–1663. doi:10.1021/jo00360a005.
(48) Tossell, J. A.; Lazzeretti, P. *J. Magn. Reson.* **1988**, *80*, 39–44.
(49) House, K. L.; Dunlap, R. B.; Odom, J. D.; Wu, Z. P.; Hilvert, D. *J. Am. Chem. Soc.* **1992**, *114* (22), 8573–8579. doi:10.1021/ja00048a033.
(50) Bühl, M.; Gauss, J.; Stanton, J. F. *Chem. Phys. Lett.* **1995**, *241* (3), 248–252. doi:10.1016/0009-2614(95)00635-H.
(51) Buehl, M.; Thiel, W.; Fleischer, U.; Kutzelnigg, W. *J. Phys. Chem.* **1995**, *99* (12), 4000–4007. doi:10.1021/j100012a021.
(52) Schreckenbach, G.; Ruiz-Morales, Y.; Ziegler, T. *J. Chem. Phys.* **1996**, *104* (21), 8605–8612. doi:10.1063/1.471549.
(53) Block, E.; Dikarev, E. V.; Jin, J.; Li, B.; Petrukhina, M. A.; Zhang, S.-Z. *Pure Appl. Chem.* **2005**, *77* (12), 2029–2032. doi:10.1351/pac200577122029.
(54) Rautiainen, J. M.; Way, T.; Schatte, G.; Passmore, J.; Laitinen, R. S.; Suontamo, R. J.; Valkonen, J. *Inorg. Chem.* **2005**, *44* (6), 1904–1913. doi:10.1021/ic048310w. PMID: 15762716.
(55) Facey, G.; Wasylishen, R. E.; Collins, M. J.; Ratcliffe, C. I.; Ripmeester, J. A. *J. Phys. Chem.* **1986**, *90* (10), 2047–2052. doi:10.1021/j100401a015.
(56) Keal, T. W.; Tozer, D. J. *Mol. Phys.* **2005**, *103* (6), 1007–1011. doi:10.1080/00268970412331332989.
(57) Demko, B. A.; Wasylishen, R. E. *Dalton Trans.* **2008**, (4): 481–490. doi:10.1039/b712011g. PMID:18185864.
(58) Nakanishi, N.; Hayashi, S.; Shimizu, D.; Hada, M. *Chem. Eur. J.* **2006**, *12* (14), 3829–3846. doi:10.1002/chem.200500927.
(59) Demko, B. A.; Wasylishen, R. E. *Inorg. Chem.* **2008**, *47* (7), 2786–2797. doi:10.1021/ic7019999. PMID:18269237.
(60) SCM. *ADF2005.01: Theoretical Chemistry;* Vrije Universiteit: Amsterdam, 2005.
(61) te Velde, G.; Bickelhaupt, F. M.; Baerends, E. J.; Fonseca Guerra, C.; Van Gisbergen, S. J. A.; Snijders, J. G.; Ziegler, T. *J. Comput. Chem.* **2001**, *22* (9), 931–967. doi:10.1002/jcc.1056.
(62) Schreckenbach, G.; Ziegler, T. *Int. J. Quantum Chem.* **1997**, *61* (6), 899–918. doi:10.1002/(SICI)1097-461X(1997)61:6<899::AID-QUA3>3.0.CO;2-R.
(63) Schreckenbach, G.; Ziegler, T. *J. Phys. Chem.* **1995**, *99* (2), 606–611. doi:10.1021/j100002a024.
(64) Glendening, E. D.; Badenhoop, J. K.; Reed, A. E.; Carpenter, J. E.; Bohmann, J. A.; Morales, C. M.; Weinhold, F. NBO, Version 5.0. Theoretical chemistry institute: University of Wisconsin: Madison, WI. 2001.
(65) Autschbach, J. *J. Chem. Phys.* **2008**, *128* (16), 164112–164123.
(66) Autschbach, J.; Zheng, S. *Magn. Reson. Chem.* **2008**, *46* (Suppl 1), S45–S55. PMID:18855339.
(67) Harris, R. K. *Nuclear Magnetic Resonance Spectroscopy;* Longman: London, 1986.
(68) Peersen, O. B.; Wu, X. L.; Kustanovich, I.; Smith, S. O. *J. Magn. Reson. Ser A* **1993**, *104* (3), 334–339. doi:10.1006/jmra.1993.1231.
(69) Peersen, O. B.; Wu, X.; Smith, S. O. *J. Magn. Reson. Ser A* **1994**, *106* (1), 127–131. doi:10.1006/jmra.1994.1014.
(70) Bennett, A. E.; Rienstra, C. M.; Auger, M.; Lakshmi, K. V.; Griffin, R. G. *J. Chem. Phys.* **1995**, *103* (16), 6951–6958. doi:10.1063/1.470372.
(71) Herzfeld, J.; Berger, A. E. *J. Chem. Phys.* **1980**, *73* (12), 6021–6030. doi:10.1063/1.440136.
(72) Eichele, K.; Wasylishen, R. E. In *Solids1: Solid-State NMR Spectrum Simulation*. 2001.
(73) Frisch, M. J.; Trucks, G. W.; Schlegel, H. B.; Scuseria, G. E.; Robb, M. A.; Cheeseman, J. R.; Montgomery, J. A., Jr.; Vreven, T.; Kudin, K. N.; Burant, J. C.; Millam, J. M.; Iyengar, S. S.; Tomasi, J.; Barone, V.; Mennucci, B.; Cossi, M.; Scalmani, G.; Rega, N.; Petersson, G. A.; Nakatsuji, H.; Hada, M.; Ehara, M.; Toyota, K.; Fukuda, R.; Hasegawa, J.; Ishida, M.; Nakajima, T.; Honda, Y.; Kitao, O.; Nakai, H.; Klene, M.; Li, X.; Knox, J. E.; Hratchian, H. P.; Cross, J. B.; Bakken, V.; Adamo, C.; Jaramillo, J.; Gomperts, R.; Stratmann, R. E.; Yazyev, O.; Austin, A. J.; Cammi, R.; Pomelli, C.; Ochterski, J. W.; Ayala, P. Y.; Morokuma, K.; Voth, G. A.; Salvador, P.; Dannenberg, J. J.; Zakrzewski, V. G.; Dapprich, S.; Daniels, A. D.; Strain, M. C.; Farkas, O.; Malick, D. K.; Rabuck, A. D.; Raghavachari, K.; Foresman, J. B.; Ortiz, J. V.; Cui, Q.; Baboul, A. G.; Clifford, S.; Cioslowski, J.; Stefanov, B. B.; Liu, G.; Liashenko, A.; Piskorz, P.; Komaromi, I.; Martin, R. L.; Fox, D. J.; Keith, T.; Al-Laham, M. A.; Peng, C. Y.; Nanayakkara, A.; Challacombe, M.; Gill, P. M. W.; Johnson, B.; Chen, W.; Wong, M. W.; Gonzalez, C.; Pople, J. A. *Gaussian 03.* Gaussian, Inc.: Pittsburgh, 2003.
(74) Ditchfield, R. *Mol. Phys.* **1974**, *27* (4), 789–807. doi:10.1080/00268977400100711.
(75) Wolinski, K.; Hinton, J. F.; Pulay, P. *J. Am. Chem. Soc.* **1990**, *112* (23), 8251–8260. doi:10.1021/ja00179a005.
(76) Becke, A. D. *Phys. Rev. A* **1988**, *38* (6), 3098–3100. doi:10.1103/PhysRevA.38.3098. PMID:9900728.
(77) Lee, C.; Yang, W.; Parr, R. G. *Phys. Rev. B* **1988**, *37* (2), 785–789. doi:10.1103/PhysRevB.37.785.
(78) Perdew, J. P. *Phys. Rev. B* **1986**, *34* (10), 7406. doi:10.1103/PhysRevB.34.7406.
(79) Huzinaga, S.; Andzelm, J. *Gaussian Basis Sets for Molecular Calculations*. Elsevier: New York, 1984; Vol. 16.
(80) Vosko, S. H.; Wilk, L.; Nusair, M. *Can. J. Phys.* **1980**, *58*, 1200–1211. doi:10.1139/p80-159.
(81) Bohmann, J. A.; Weinhold, F.; Farrar, T. C. *J. Chem. Phys.* **1997**, *107* (4), 1173–1184. doi:10.1063/1.474464.
(82) van Lenthe, E.; Baerends, E. J.; Snijders, J. G. *J. Chem. Phys.* **1993**, *99* (6), 4597–4610. doi:10.1063/1.466059.
(83) Widdifield, C. M.; Schurko, R. W. *Concepts Magn. Reson.* **2009**, *34A* (2), 91–123. doi:10.1002/cmr.a.20136.
(84) Harris, R. K.; Becker, E. D.; De Menezes, S. M. C.; Granger, P.; Hoffman, R. E.; Zilm, K. W.; International Union of Pure and Applied Chemistry Physical and Biophysical Chemistry Division. *Magn. Reson. Chem.* **2008**, *46* (6), 582–598. doi:10.1002/mrc.2225. PMID:18407566.
(85) Arduengo, A. J., III; Dixon, D. A.; Kumashiro, K. K.; Lee,

C.; Power, W. P.; Zilm, K. W. *J. Am. Chem. Soc.* **1994**, *116* (14), 6361–6367. doi:10.1021/ja00093a041.
(86) Wiberg, K. B.; Hammer, J. D.; Keith, T. A.; Zilm, K. *J. Phys. Chem. A* **1999**, *103* (1), 21–27. doi:10.1021/jp983282m.
(87) Ramsey, N. F. *Phys. Rev.* **1950**, *78* (6), 699–703. doi:10.1103/PhysRev.78.699.
(88) Ramsey, N. F. *Phys. Rev.* **1951**, *83* (3), 540–541. doi:10.1103/PhysRev.83.540.
(89) Ramsey, N. F. *Phys. Rev.* **1952**, *86* (2), 243–246. doi:10.1103/PhysRev.86.243.
(90) Schindler, M.; Kutzelnigg, W. *J. Chem. Phys.* **1982**, *76* (4), 1919–1933. doi:10.1063/1.443165.
(91) Keith, T. A.; Bader, R. F. W. *Chem. Phys. Lett.* **1993**, *210* (1-3), 223–231. doi:10.1016/0009-2614(93)89127-4.
(92) de Dios, A. C. *Prog. Nucl. Magn. Reson. Spectrosc.* **1996**, *29* (3-4), 229–278. doi:10.1016/S0079-6565(96)01029-1.
(93) Facelli, J. C. *Concepts Magn. Reson. Part A* **2004**, *20A* (1), 42–69. doi:10.1002/cmr.a.10096.
(94) Jameson, C. J.; Gutowsky, H. S. *J. Chem. Phys.* **1964**, *40* (6), 1714–1724. doi:10.1063/1.1725387.
(95) Fowler, P. W.; Steiner, E.; Havenith, R. W. A.; Jennekens, L. W. *Magn. Reson. Chem.* **2004**, *42* (S1)(Spec no), S68–S78. doi:10.1002/mrc.1445. PMID:15366043.
(96) Wiberg, K. B.; Hammer, J. D.; Zilm, K. W.; Cheeseman, J. R.; Keith, T. A. *J. Phys. Chem. A* **1998**, *102* (45), 8766–8773. doi:10.1021/jp982214x.
(97) Wiberg, K. B.; Hammer, J. D.; Zilm, K. W.; Cheeseman, J. R. *J. Org. Chem.* **1999**, *64* (17), 6394–6400. doi:10.1021/jo990423n.
(98) Tuononen, H. M.; Roesler, R.; Dutton, J. L.; Ragogna, P. J. *Inorg. Chem.* **2007**, *46* (25), 10693–10706. doi:10.1021/ic701350e. PMID:17997547.
(99) Boys, S. F. *Rev. Mod. Phys.* **1960**, *32* (2), 296–299. doi:10.1103/RevModPhys.32.296.
(100) Glendening, E. D.; Weinhold, F. *J. Comput. Chem.* **1998**, *19* (6), 593–609. doi:10.1002/(SICI)1096-987X(19980430)19:6<593::AID-JCC3>3.0.CO;2-M.
(101) Glendening, E. D.; Weinhold, F. *J. Comput. Chem.* **1998**, *19* (6), 610–627. doi:10.1002/(SICI)1096-987X(19980430)19:6<610::AID-JCC4>3.0.CO;2-U.
(102) Glendening, E. D.; Weinhold, F. *J. Comput. Chem.* **1998**, *19* (6), 628–646. doi:10.1002/(SICI)1096-987X(19980430)19:6<628::AID-JCC5>3.0.CO;2-T.

REVIEW / SYNTHÈSE

Naturally occurring and synthetic polyyne glycosides

Yanqing Pan, Todd L. Lowary, and Rik R. Tykwinski

Abstract: Polyyne glycosides are a class of natural products that have been found in terrestrial plants, fungi, and marine algae. Many display interesting and potentially useful biological activities, which in some cases has initiated synthetic efforts toward their formation. This review provides a comprehensive report of polyyne glycosides isolated from natural sources, as well as the synthesis of these molecules and their analogues.

Key words: polyynes, polyacetylenes, carbohydrates, natural products.

Résumé : Les glycosides de polyyne correspondent à une classe de produits naturels qu'on retrouve dans les plantes terrestres, les champignons et les algues marines. Plusieurs présentent des activités biologiques intéressantes et potentiellement utiles qui, dans certains cas, ont conduit à l'initiation d'efforts de synthèse orientés vers leur formation. Cette revue fournit un rapport approfondi sur les glycosides de polyyne isolés de sources naturelles et sur les efforts de synthèse de ces molécules et de leurs analogues.

Mots-clés : polyynes, polyacétylènes, hydrates de carbone, produits naturels.

[Traduit par la Rédaction]

Introduction

Polyynes[1] have long been known to exist in natural sources, and thousands have been isolated in the past century from a wide range of terrestrial plant species, fungi, sponges, corals, and bacteria. Many of these compounds have interesting biological activities, such as antibacterial, antimicrobial, anticancer, anti-HIV, antifeedant, and pesticidal properties.[2] Despite their widespread distribution in nature, the number of polyynes pales in comparison to the diversity of carbohydrates, one of the most abundant families of natural products. Carbohydrates are involved in a wide range of biological processes, including energy storage and transport, modulation of protein function, cell–cell adhesion, and signal transduction.[3–5] Consequently, carbohydrate-containing molecules have attracted attention as novel pharmaceuticals; indeed, many drugs in common use (e.g., erythromycin, doxorubicin) are functionalized with sugars. Over the past few years we have developed an interest in molecules that posses both a polyyne and a carbohydrate moiety. Polyyne glycosides, which consist of a carbohydrate group attached to a polyyne alcohol via an acetal linkage, are one such class of molecules.

In 1959, the first natural polyyne glycoside was found in the metabolites of the wood destroying fungus Basidiomycete B-841.[6] Since then, about fifty polyyne glycosides have been isolated from natural sources. Similar to polyynes lacking a carbohydrate group, several polyyne glycoside natural products display biological properties, including antibacterial activity,[7] the ability to inhibit nitric oxide production,[8] and the capacity to modulate blood glucose levels.[9] The majority of polyyne glycosides have been isolated from plants, and they are particularly common in species such as *Panax* and *Bidens*, which have been used for centuries as traditional medicines in many countries. Although biological testing has often not been reported in conjunction with their isolation, in those studies in which this work has been performed, interesting bioactivity profiles have been obtained. It is therefore likely that most (if not all) polyyne glycosides possess useful biological activities.

Synthetic analogues of polyyne glycosides might also have significant biological activity, yet virtually no efforts in this direction have been undertaken.[10,11] The isolation, biological activity, and synthesis of polyyne glycosides are the subject of this review. The first section offers a compilation of polyyne glycosides that have been isolated from plants,

Received 28 April 2009. Accepted 30 June 2009. Published on the NRC Research Press Web site at canjchem.nrc.ca on 28 October 2009.

Y. Pan, T.L. Lowary,[1] and R.R. Tykwinski.[2,3] Department of Chemistry, University of Alberta, Edmonton, AB T6G 2G2, Canada.

[1]Corresponding author (e-mail: todd.lowary@ualberta.ca).
[2]Corresponding author (e-mail: rik.tykwinski@chemie.uni-erlangen.de).
[3]Present address: Institut für Organische Chemie, Friedrich-Alexander-Universität Erlangen-Nürnberg, Henkestrasse 42, 91054 Erlangen, Germany.

Fig. 1. Polyyne glycosides from the genus *Panax*.

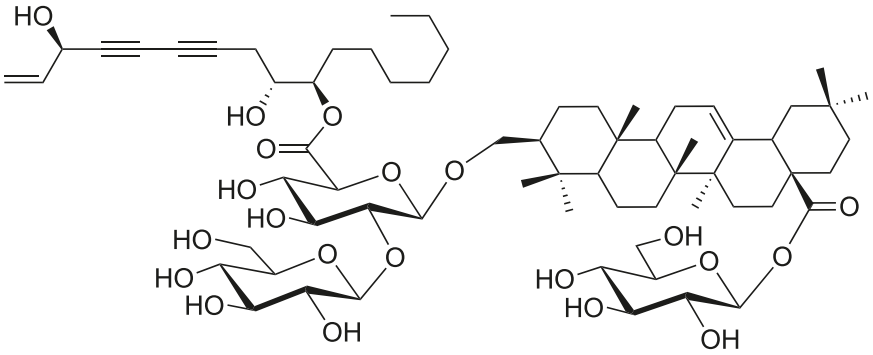

1 *ginsenoside-Ro*

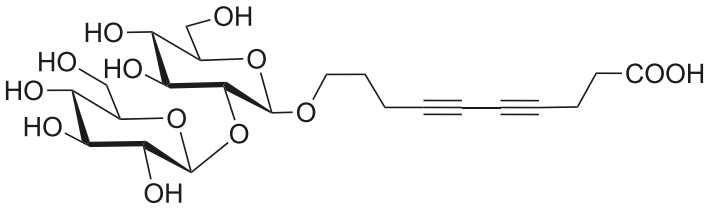

2 *notoginsenic acid* β*-sophoroside*

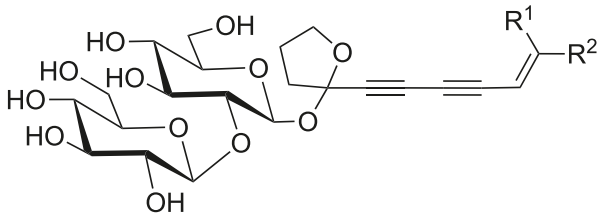

3a R^1 = H, R^2 = Me *panaxfurayne A*
3b R^1 = Me, R^2 = H *panaxfurayne B*

fungi and algae; where possible, information on the biological activity of these compounds is provided. The second section documents syntheses of naturally occurring polyyne glycosides, natural products analogues, and several molecules that, while strictly speaking are not polyyne glycosides, are composed of polyyne and carbohydrate moieties.

Polyyne glycosides isolated from plants

Family Araliaceae — Ginseng family

Red ginseng, the steamed and dried root of *P. ginseng* C. A. Meyer, has been used extensively in Asian traditional medicine.[12] From this plant and other ginseng species,[13,14] a host of polyynes have been identified, and this class of compounds has received substantial synthetic attention.[2] To date, however, only two polyyne glycosides have been isolated from *P. ginseng*, as well as one related species, the oleanolic acid-derived saponin ginsenoside-Ro, **1** (Fig. 1). Studies on the natural product **1** showed that it inhibited the replication of human immunodeficiency virus type 1 (HIV-1) with an IC_{50} value of 13.4 μg/mL (11.1 μmol/L).[15] It should be mentioned that the carbohydrate ester functionality of **1** contains the natural polyyne panaxytriol, one of the most studied of all known naturally occurring polyynes.[2]

More recently, guided by the hepatoprotecting activity of fractions extracted from the dried root of *P. notoginseng*, Yoshikawa et al.[16] isolated and characterized notoginsenic acid β-sophoroside (**2**, Fig. 1) as fine, colorless crystals. Unfortunately, nothing further has been reported on the bioactivity of this compound.

Finally, two structurally intriguing polyyne glycosides have been identified from *P. ginseng*, the trans and cis isomers panaxfurayne A and B, **3a** and **3b** (Fig. 1), respectively.[17] To date, no studies of biological activity have been reported for these tetrahyrofuranic[18] derivatives.

Family Asteraceae — Aster family

Polyynes are widely distributed in the plant family Asteraceae,[19–23] and they are particularly prevalent in the species of the genus *Bidens*, commonly referred to as beggarticks in North America.[24] Species of the genus *Bidens* have long been used as traditional medicinal plants in numerous countries, and many of them have afforded polyyne natural products.[25–27] In 1970, Romussi and Pagani[28] isolated a polyyne

Fig. 2. Polyyne glycoside from the species *Bidens frondosa* (devil's beggarticks).

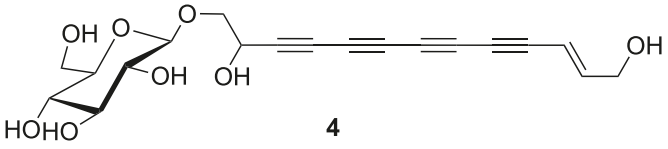

Fig. 3. Polyyne glycosides from the species *Bidens campylotheca* (viper beggarticks).

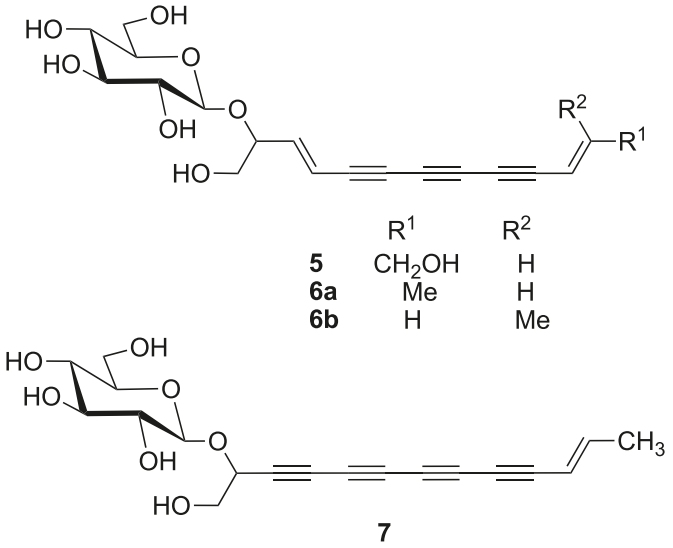

glycoside from the species devil's beggarticks, *B. frondosa*, and the structure was initially determined to be a D-glycoside of trideca-4,6,8,10-tetrayn-2-en-1,12,13-triol, although neither the attachment point of the sugar moiety, nor the stereochemistry of the glycosidic linkage was established (the aglycone was also isolated). In subsequent papers, the authors reported their efforts to confirm the structure of this natural product as **4** (Fig. 2), but they did not provide any information about its biological activity.[29,30]

More than two decades later, in 1992, Davis and co-workers[31] reported the isolation of four polyyne glucosides, **5**–**7**, from polar extracts of the dried aerial parts of viper beggarticks, *B. campylotheca* (Fig. 3). This herb is found only on the Hawaiian islands and has been used in traditional Hawaiian folk medicine as an appetite stimulant, as well as a treatment of general debility, throat and stomach afflictions, and severe cases of asthma.[32] There was no reported study of the bioactivity of **5**–**7** at the time of isolation. It was suggested, however, that glycosylation of the polyyne may facilitate the transportation of the typically lipophilic polyynes that are commonly isolated from the many members of this genus.[33] Subsequently, safynol, the aglycone of **6a**, was isolated from the same species, and this compound showed a weak inhibitory affect on prostaglandin biosynthesis.[34] In 1999, de Moraes and co-workers[35] reported that tetrayne **7** was also present in the methanolic extract of hairy beggarticks (*B. pilosa*) and also examined its bioactivity. Their investigations showed that both the methanolic extract and polyyne glycoside **7** suppressed human lymphocyte proliferation, with the pure compound **7** being 10-fold more potent than the crude extract.

Fig. 4. Polyyne glycosides from *Bidens pilosa* (hairy beggarticks).

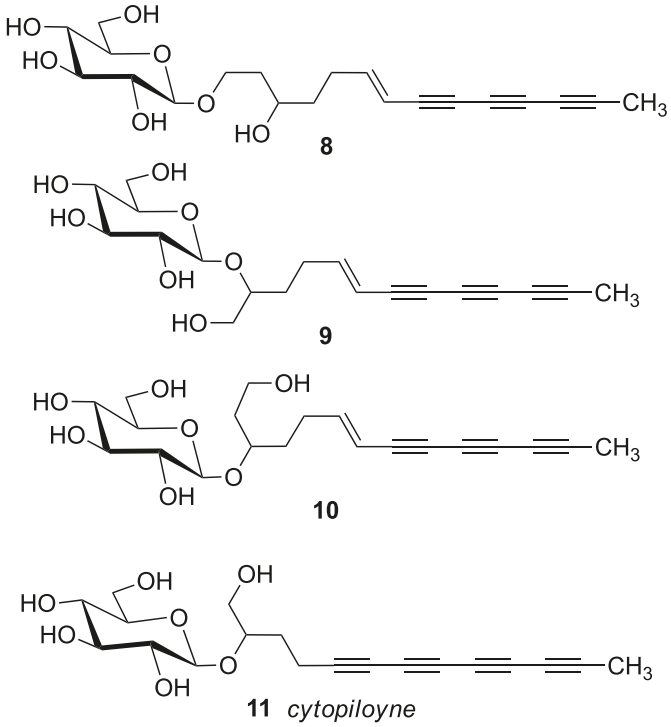

Bidens pilosa is a widely distributed weed in tropical and subtropical regions, and its leaves and flowers are commonly used as a traditional medicine. In Cuba, for example, it is used for treating renal and respiratory problems, as well as inflammation,[26] while it is used in China to treat inflammation,[36] in South Africa for diarrhea,[37] and in Brazil to combat malaria.[38] Alvarez et al.[39] have isolated triyne glucoside, **8**, from the methanolic extract of the whole plants of *B. pilosa* in 1996 (Fig. 4). Although **8** did not show activity against a range of bacterial and fungal species including *Staphylococcus aureus*, *Salmonella typhimurium*, *Escherichia coli*, *Pseudomonas aeruginosa*, *Microspoum gypseum*, and *Candida albicans*, it did have moderate activity against *Trichophyton mentagrophytes* (MIC = 100 μg/mL), a fungus that causes scalp infections in children.[40] The cytotoxicity of **8**, and the parent polyyne, were also evaluated against several cancer cell lines, including HCT-15 (colon carcinoma), UISO (uterine–cervix cancer), KB (nasopharyngeal carcinoma), and W138 (lung embryonic fibroblasts), and in all cases the ED_{50} was greater than 4 μg/mL, indicating moderate potency. Interestingly, however, was that **8** enhanced the growth of cells, particularly the W138 cells. It was suggested that this proliferative activity might be related to cocarcinogenic action found for dried leaves of *B. pilosa* for esophageal tumors induced in rats.[41]

Two polyyne glucosides, **9** and **10**, were isolated from the African shrub *Microglossa pyrifolia* by Rücker et al.[7a] in 1992. The same compounds were obtained as a 3:2 mixture from *B. pilosa* in 2000 by Fort and co-workers[9] (Fig. 4), but the individual compounds (**9** and **10**) were neither separated nor tested individually because of their instability during purification. When administered as a mixture (250 mg/kg, twice daily) to genetically altered obese diabetic mice, a significant drop in blood glucose levels was observed on the

second day, along with a noticeable reduction in food intake. In another investigation, Chang et al.[42] have explored the bioactivity of **9** and **10** and found that both prevent diabetes development in nonobese diabetic mice.

Tetrayne **11** (cytopiloyne, Fig. 4) was recently isolated from the methanolic extract of *B. pilosa*, together with the known triyne glucosides **9** and **10**.[43,44] Similar to the triyne glucosides **8**–**10**, it was found that cytopiloyne was able to control or prevent type I diabetes in nonobese diabetic mice. More detailed investigations on cytopiloyne revealed that it was capable of inducing the selective differentiation of T helper (Th0) cells into type II T helper (Th2) cells, over type I T helper (Th1) cells. Cytopiloyne also suppressed IFN-γ expression and promoted IL-4 expression. These studies, therefore, demonstrated that cytopiloyne is a T cell modulator, and this function may explain, in part, why *B. pilosa* extracts prevent diabetes. Very recently, cytopiloyne was also found to suppress the maturation of human dendritic cells.[45] The corresponding triyne glycosides were not, however, evaluated in this study and thus the immunomodulatory potential of these compounds is unknown.

In addition to *B. frondosa*, *B. campylotheca*, and *B. pilosa*, two other *Bidens* species have afforded polyyne glucosides, *B. parviflora* and *B. bipinnata*. Both species have been used in traditional Chinese medicine for treatment of, for example, inflammation and rheumatism.[46] In 2001, polyyne glucosides **12**–**16** (Fig. 5), the bidensyneosides, were isolated from *B. parviflora*. These molecules were characterized as part of a study designed to identify antiallergic agents,[8] and all five were shown to inhibit both histamine release and nitric oxide production. Subsequently, in 2004, Okuyama and co-workers[47] reported the isolation of bidensyneoside C (**15**) from *B. bipinnata* (Spanish needles), as well as a new polyyne glycoside, bidenoside D (**17**), through extraction of the aerial parts with hot ethanol. To date, the biological activity of **17** remains unexplored.

The isolation of polyyne glycosides from other genera of the Asteraceae family, such as *M. pyrifolia*, has also been reported. Parts of this shrub are used as a traditional medicine in Ghana for treating fever and impotence,[25] while hunters in the Ivory Coast have used the leaf extract as an arrow poison.[48] In 1992, Rücker et al.[7a] reported the isolation of acetylenic glucosides from the leaves of this species, including triynes **9** and **10** (Fig. 4), as well as a tetrayne **18** and, remarkably, the pentayne **19** (Fig. 6). All of these molecules are β-glucopyranosides and were characterized spectroscopically through comparisons to their aglycones, which were generated via enzymatic hydrolysis. These four polyyne glycosides were then evaluated for their antimicrobial properties against five bacterial stains, and it was determined that only pentayne **19** possessed any substantial activity, in particular against *P. aeruginosa* and *S. aureus*.[7a] Pentayne **19** and its aglycone have most recently been isolated from *B. pilosa*.[7b] It was suggested by the authors that the successful isolation of these unstable pentaynes was a result of following the Fijian tradition of using the fresh plant for extraction rather than using the dried root, as prescribed by Asian tradition. The aglycone of **19** showed highly potent antimalarial and antibacterial properties in vitro. Furthermore, the aglycone also showed significant antimalarial activity in vivo, based on intravenous injection of the drug in mice infected with the *Plasmodium berghei* NK-65 strain.[7b]

Fig. 5. Polyyne glycosides from *Bidens parviflora* and *B. bipinnata*.

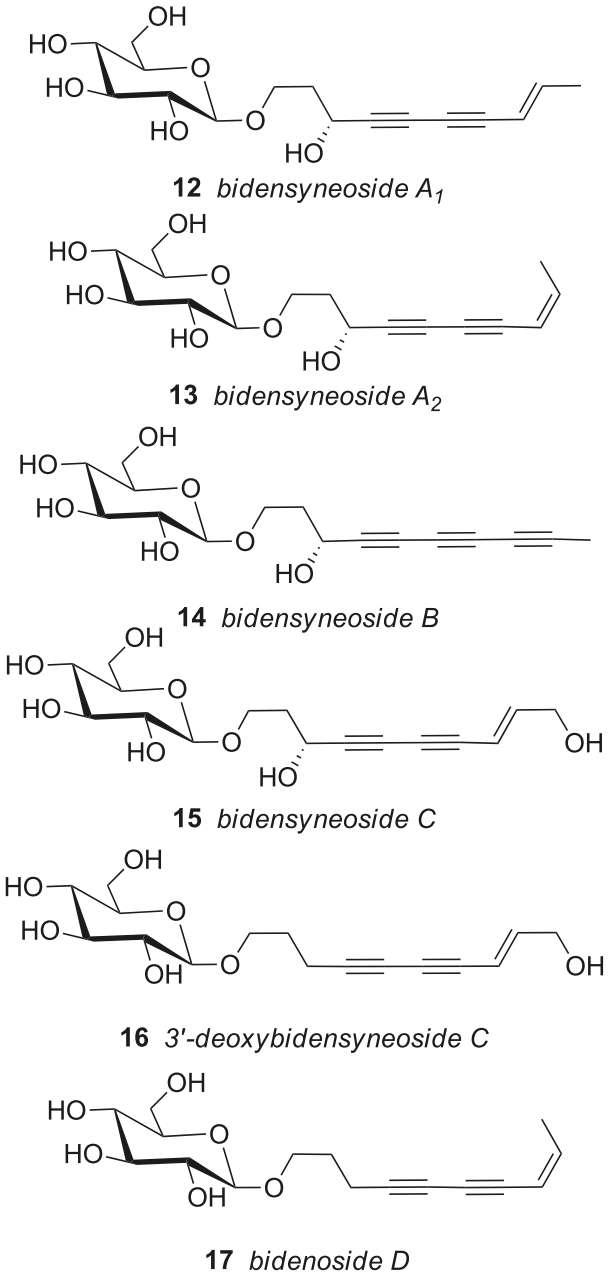

In 1993, Yoshihara, and co-workers[49] isolated two new methyl β-D-glucopyranosyl helianthenates, **20** and **21**, from the ethyl acetate soluble portion of the 70% aqueous ethanol extract of the leaves of Jerusalem artichoke (*Helianthus tuberosus*), which, despite its name, is a species of sunflower (Fig. 7).[22] Both **20** and **21** showed tuber-forming activity in potatoes. This same group has reported four additional methyl β-D-glucopyranosyl helianthenates, **22**–**25**, which were isolated from the same plant species.[50] It is worth noting that the helianthenates A–E share a similar substructure with falcarinol and falcarindiol, two of the most widely studied, naturally occurring polyynes.[2,13,51]

Members of the *Aster* genus have been used in traditional

Fig. 6. Polyyne glycosides from *Microglossa pyrifolia*.

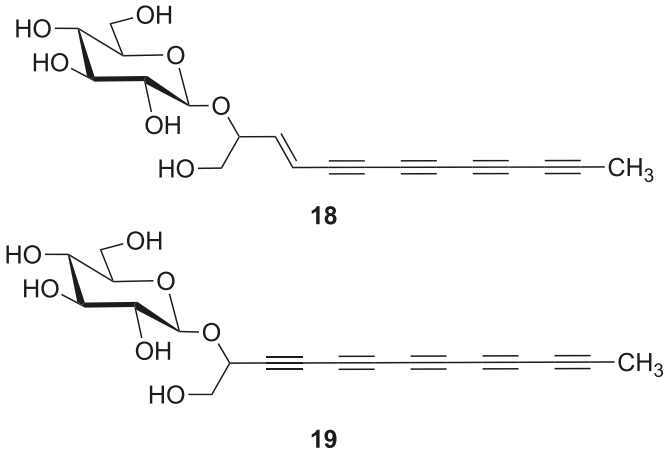

medicine for the treatment of, for example, fever, colds, snakebites, and bee stings.[52] As part of their study of *Aster* species as sources of bioactive compounds, Zhou and co-workers[53] have isolated asteryunnanoside I, **26** (Fig. 8) from the *n*-butanol soluble portion of a 70% ethanol extract of *A. yunnanensis* roots.

In a similar investigation, Wang and Yu[54] isolated four glycosidic constituents, **27**–**30**, from the 70% ethanol extract of the roots of the species *A. auriculatus*. Compounds **27** and **28** are both disaccharides that possess the same aglycone, but differ in the structure of the carbohydrate moiety. In contrast, compounds **29** and **30** are both β-D-glucopyranosides, but differ in the position of the double bond in their aglycone. Compound **29** resembles bidensyneoside D (**17**, Fig. 5), which was isolated by Okuyama and co-workers[47] from *B. bipinnata*, except that the configuration of the olefin at the distal end of the aglycone is *E*, rather than *Z*.

Another member of the aster family recently studied is *Gymnaster koraiensis*, a common Korean plant. From this species, a series of polyyne natural products was recently isolated, including gymnasterkoreaynes A–G (not shown).[55,56] Because gymnasterkoreaynes A–G showed significant cytotoxicity against L1210 tumor cells (ED values of 0.12–3.3 μg/mL),[55] Bae and co-workers[57] continued their work toward identifying pharmacologically active constituents from this species. This ultimately led to the isolation of two polyyne glycosides, gymnasterkoreasides A (**12**, Fig. 5) and B (**31**, Fig. 9) from the root extracts (butanol soluble fraction). Compound **12** had been previously isolated from *B. parviflora* by Wang et al.,[8] who christened it bidensyneoside A_1, while compound **31** (which like **28** (Fig. 8) possesses a β-D-apiofuranosyl-(1→6)-β-D-glucopyranosyl moiety) represented a new polyyne disaccharide.

The rhizomes of another genus of the aster family, *Atractylodes*, have long been used in Japanese traditional medicine.[58] A number of polyyne natural products have been discovered in this genus, including glucoside derivative **32** (Fig. 10) identified from *A. lancea* by Kitajima et al.[59] It is worth noting that the aglycone of **32** has also been isolated from the aerial parts of the ornamental knapweed (*Centaurea ruthenica*) by Bohlmann and co-workers.[60] From a related species, *A. ovata*, the same group isolated and identified the polyyne glycoside **33**.[61] While there are no reports

Fig. 7. Polyyne glycosides **20**–**25** from *Helianthus tuberosus*.

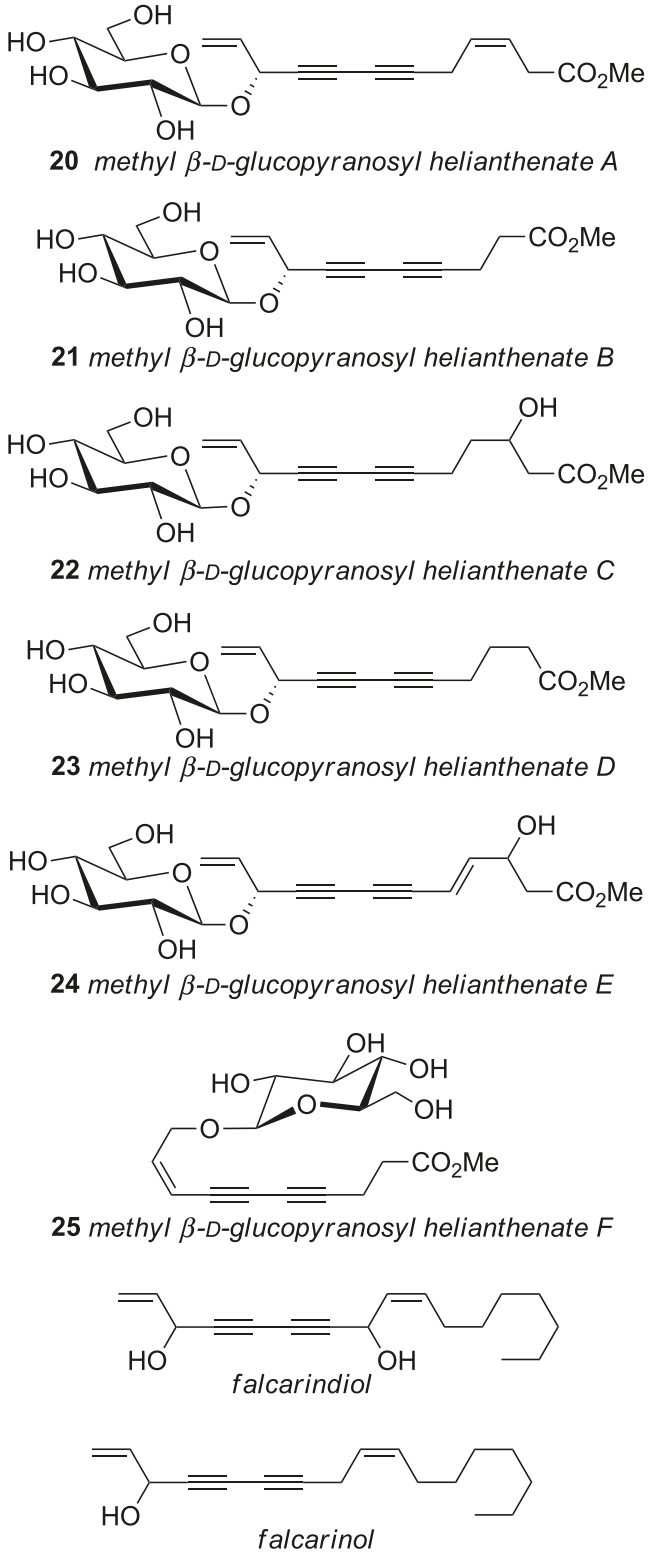

on the biological activity of either **32** or **33** to date, it is interesting to note the structural similarity of these two compounds to 3′-deoxybidensyneoside C and bidensyneoside C (**16** and **15**, respectively, Fig. 5), respectively, both of which inhibit histamine release and nitric oxide production.[8]

The aster family species *Artemisia monosperma* is a des-

Fig. 8. Polyyne glycosides from *Aster yunnanensis* and *A. auriculatus*.

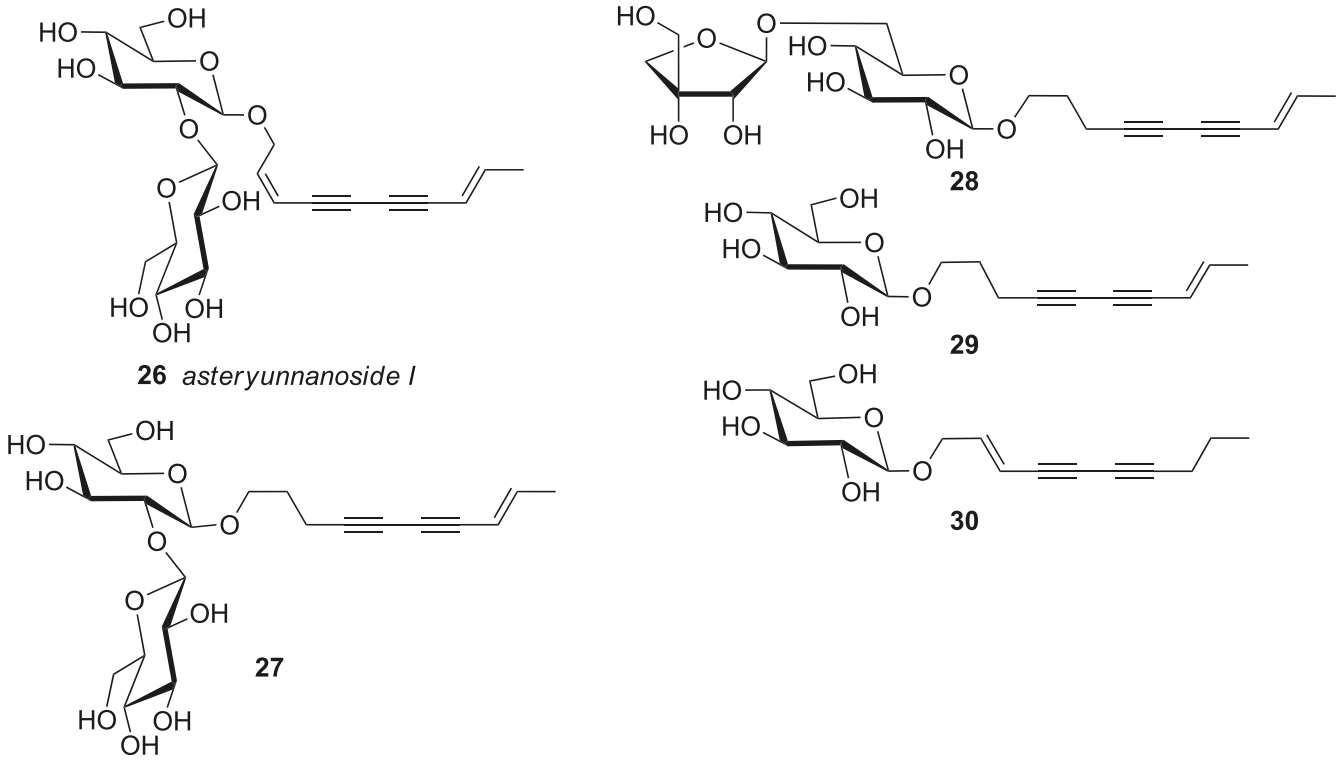

Fig. 9. Polyyne glycoside from *Gymnaster koraiensis*.

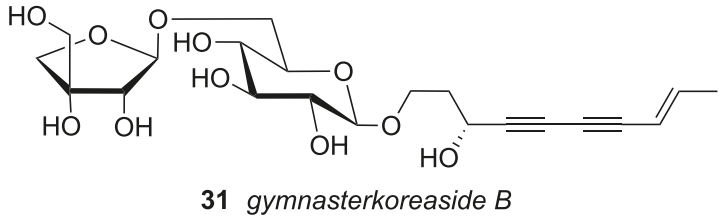

Fig. 10. Polyyne glycosides from *Atractylodes lancea* and *A. ovata*.

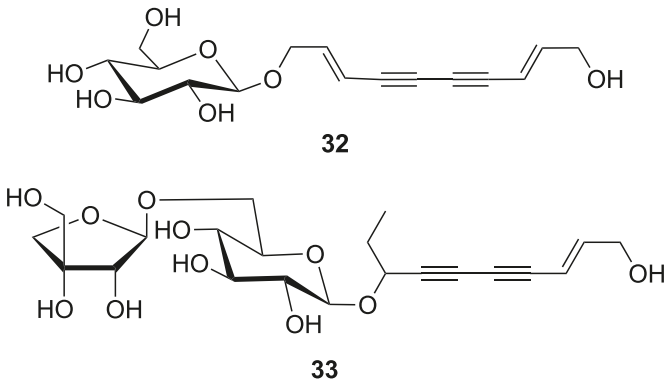

ert shrub native to a number of countries in the Middle East, for example, Egypt, Libya, Israel, Jordan, and Lebanon. Phytochemical studies on this species have resulted in the isolation of polyyne, sesquiterpene, and acetophenone natural products.[62,63] In 2005, Gibbons and co-workers[64] reported the isolation of additional bioactive constituents from *A. monosperma*, including a new polyyne glucoside **34a** and its aglycone **34b** (Fig. 11). Diol **34b** had been isolated previously from the same plant[62] and it was proposed, but not established, that the stereochemistry of the aglycone of **34a** was the same. These two compounds were tested for their ability to inhibit the enzyme 12-lipoxygenase, and both exhibited moderate activity against the enzyme at 30 μg/mL.

In addition to cultivation for its seed oil, the dried flower petals of the safflower plant (*Carthamus tinctorius*) are widely used in traditional Chinese medicine to, for example, promote blood circulation.[65] Two new compounds, carthamoside A_1 (**35**) and A_2 (**36**, Fig. 12), were isolated from *C. tinctorius*, as well as **17** (bidenoside D, Fig. 5).[66] It should be noted that compound carthamoside A_2 has an unusual 4,6-*O*-isoproylidene glucopyranosyl moiety, a rare structural motif in a natural product. Similar to bidenoside D, whose biological activity has not been reported, the ability of neither **35** nor **36** to modulate biological processes has seemingly been investigated.

Pluchea indica (Indian fleabane or Indian camphorweed) is a native plant of India, South China, Malaysia, and Australia, and recently it has been classified as an invasive species in the Hawaiian Islands.[67] The species has been used traditionally to remedy a variety of ailments; for example, in

Fig. 11. Polyyne glycoside from *Artemisia monosperma* and the aglycone **34b**.

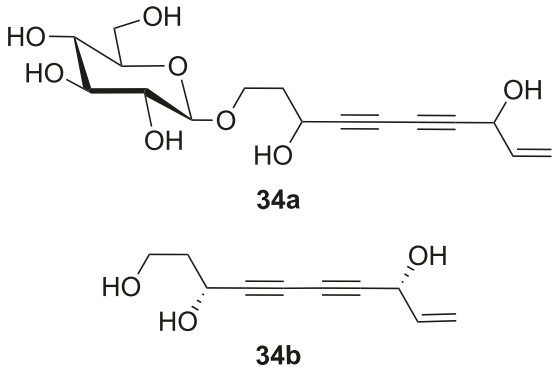

Thailand and Java the chopped stem bark is smoked as cigarettes to relieve the pain of sinusitis.[68] From the aerial parts of this plant, the thiophene based polyyne glycoside **37** has been isolated, together with several other polyynes including the aglycone (Fig. 13).[69] The antimicrobial properties of these derivatives have been explored, and, using a standard disk diffusion assay, it was shown that **37** was active against *S. aureus* and *Bacillus subtilis*. By way of comparison, the aglycone of **37** was active against not only *S. aureus* and *B. subtilis*, but also *Saccharomyces cerevisiae*. Neither was active against *E. coli* or *B. thuringiensis*. The aglycone of **37** has been previously identified from several sources, including *Pterocaulon allopecuroides* (blackroot),[70] *Onoseris alata*,[71] and *P. suaveolens* (wingstem camphorweed).[72]

Family Campanulaceae — Bellflower family

Of the known polyyne glycosides from the bellflower family of plants, two have been particularly well-studied: lobetyolin (**38**) and lobetyolinin (**39**, Fig. 14). The aglycone of both glycosides, lobetyol (**40**), has also been included in these investigations. In 1990, Tanaka and co-workers[73] first identified lobetyolin (**38**), along with a number of other glucosides, from the herb *Codonopsis tangshen*, a very common drug plant in China (known as dangshen) whose root is widely used as a substitute for ginseng.[74] In 1994, Nörr and Wagner[75] also reported the isolation of lobetyolin from *C. pilosula*, a related species that is sometimes called "poor man's ginseng".

In 1991, Ishimaru et al.[76] isolated lobetyolin (**38**) and lobetyol (**40**) from *Lobelia inflata*, a common North American plant, typically called Indian tobacco or puke weed. In the following year, lobetyolinin (**39**), was isolated from this same species.[77] Ishimaru and co-workers also isolated lobetyol, lobetyolin, and lobetyolinin from hairy root cultures of *L. sessilifolia*, *L. chinensis*, and *L. cardinalis*.[78–80] More recently, Bálványos et al.[81] analyzed these three compounds in hairy root cultures of *L. inflata* cultivated in a bioreactor by direct infection of the sterile plants with *rhizogenes* strain R1601.

In 1995, Ishimaru and co-workers[82] infected the cultured hairy roots of *Platycodon grandiflorum* with *A. rhizogenes* to produce lobetyol, lobetyolin, and lobetyolinin. Over the next few years, this group reported the use of the same method to culture hairy roots of *P. grandiflorum* (Korean balloon flower) and *Trachelium caeruleum* with the goal of

Fig. 12. Polyyne glycosides from *Carthamus tinctorius*.

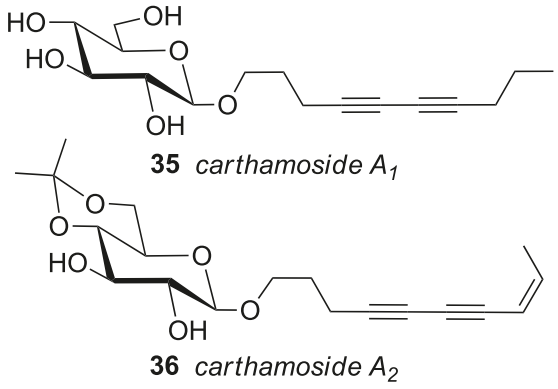

Fig. 13. Polyyne glycoside from *Pluchea indica*.

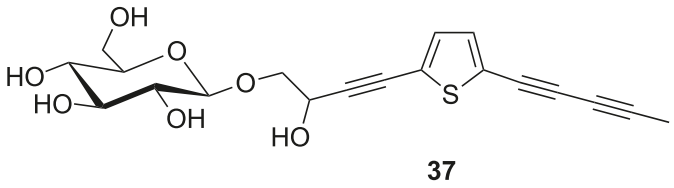

obtaining larger amounts of the polyyne glycosides.[83,84] The isolation of **38**–**40** from hairy root cultures of *Campanula medium*,[85] *C. glomerata*,[86] *Wahlenbergia marginata*,[87,88] and *Dialypetalum floribundum*[89] has also been reported.

Interestingly, despite the significant amount of work directed at producing and isolating lobetyolin, lobetyolinin, or lobetyol from various sources, in none of these studies has their biological activity been reported. Indeed, the only report on the biological activity of these compounds comes from Dumlu et al.[90] who isolated five known compounds, including lobetyol and lobetyolin, from the methanolic extract of the ivory bellflower (*C. alliariifolia*) and studied their antioxidant (free radical scavenging) activity. These investigations revealed that lobetyolin (**38**) and lobetyol (**40**) showed similar antioxidant activity.

In 2008, another plant species used in Chinese herbal remedies, *C. cordifolioidea*, was shown to produce three polyyne glycosides, cordifolioidynes A–C (**41**–**43**, Fig. 15), as well as lobetyolin (**38**).[91] Using the agar dilution method, the antibacterial activity of these compounds was assessed against eight microbial strains, and none exhibited antibacterial effects at concentrations up to 100 μg/mL.[91]

Pratia nummularia is a perennial plant found at high altitudes in China, India, Malaysia, Thailand, Myanmar, Australia, and South America. The whole plant has been commonly used as a traditional medicine for the treatment of contusions, cough, and inflammation.[92] From the hairy root cultures of *P. nummularia*, Ishimaru et al.[93] isolated two unique glycosides (Fig. 16), pratialin-A (**44**) and pratialin-B (**45**), as well as lobetyolin and lobetyolinin. Their report did not include any biological testing of these complex glycolipids.

Polyyne glycosides isolated from fungi

While polyynes are rather commonly found in fungi,[94–96] only two reports describe polyyne glycosides isolated from

Fig. 14. Polyyne glycosides lobetyolin (**38**), lobetyolinin (**39**), and lobetyol (**40**).

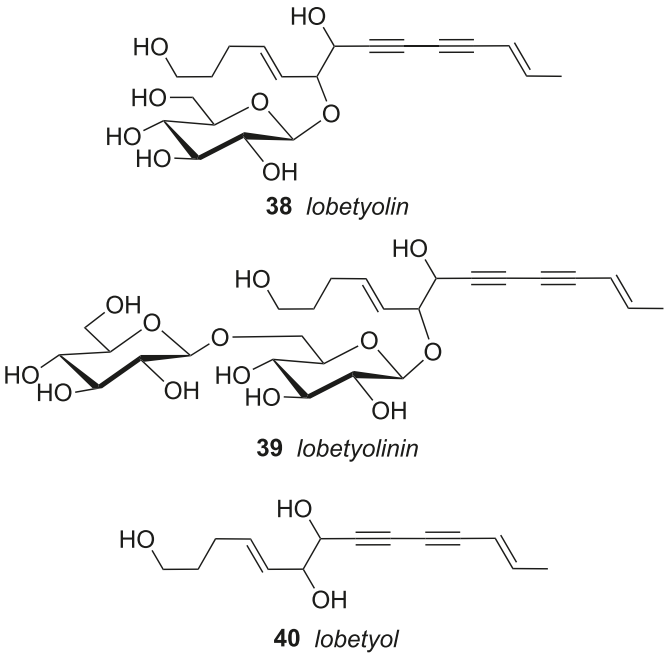

Fig. 15. Polyyne glycosides from *Codonopsis cordifolioidea*.

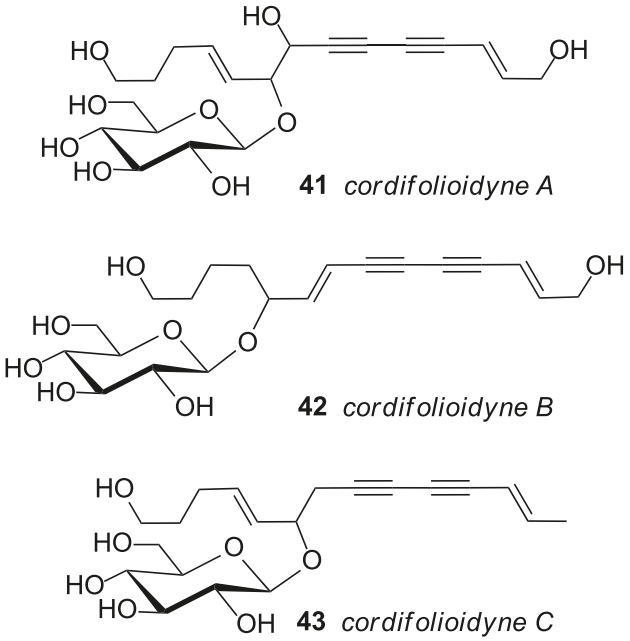

this class of organisms. The first comes from species of the fungus *Fistulina*, which are known to produce polyynes both in mycelia cultures[97] and in fruiting bodies in the field.[98] In 1974, it was demonstrated that extracts from the culture fluids of the pale beefsteak fungus (*F. pallida*) grown in surface cultures produced small amounts of several triyne products, including a polyyne glucoside and the corresponding aglycone. Unfortunately, this glucoside could not be isolated in a pure state, but on the basis of their analyses on the impure materials, the compound was determined to be one of two isomeric structures, triyne **46** or **47** (Fig. 17).[99] No biological activity of these compounds was reported.

In 1950, research at the New York Botanical Gardens identified the isolation and characterization of two highly unsaturated molecules in extracts of the fungi *Poria cortical* and *P. tenuis*, as well as in an unidentified Basidiomycete.[100] It was noted that the liquid cultures of these compounds showed antibiotic activity against a number of microorganisms, including *Mycobacterium tuberculosis*.[101] Spectral evidence suggested that the new molecules, christened nemotinic acid and nemotin, contained a polyyne framework. It was not until 1955, however, that the structures were elucidated as the allene-diynes **48a** and **48b** (Fig. 18), respectively, by Bu'Lock, Jones, and Leeming,[102] using cultures of Basidiomycete B-841.[103] In their subsequent investigation of the polyyne metabolites from Basidiomycete B-841, the β-D-xylopyranoside of nemotinic acid (**49**) was identified (Fig. 18).[6,104] While the configuration of the allene group remains unknown, the identification of **48** and **49** is very impressive given that structural assignment was achieved prior to 1960 through chemical analysis and degradation, rather than NMR spectroscopic analysis.

These early studies of **48** and **49** also provide some of the only experimental insight into the mechanism of polyyne glycoside biosynthesis.[6,104] When [1-^{14}C]-acetate (15%–20%) is added to Basidiomycete B-841, under conditions in which glucose is the only nutrient, the label is efficiently incorporated into the polyyne, but not the monosaccharide. This result suggests that, under these conditions, the source of the carbohydrate moiety is glucose, not acetate. Basidiomycete B-841 will also grow using ethanol as only nutrient and when 15%–20% of [1-^{14}C]-acetate is added under these conditions, both the polyyne and sugar segments of **48** are labeled. From these results it was concluded that in the ethanol cultures, where all metabolic intermediates are synthesized from two-carbon units, the xylose moiety is produced by a pathway similar to glucose.

Polyyne glycosides isolated from algae

The unicellular alga *Prymnesium parvum* is one of the most damaging red tide species,[105,106] and its bloom has been responsible for devastating fish kills.[107] It has been known for over three decades that the organism produces a potent ichthyotoxin named prymnesin, although the structure of this toxin was unknown at the time this discovery was made.[108] In 1996, 10 mg of prymnesin-1 (**50**) and 15 mg of prymnesin-2 (**51**, Fig. 19) were isolated by Yasumoto and co-workers from 400 L of *P. parvum* cultures.[109] Initially, only the structure of the major component, prymnesin-2, was reported, albeit without the stereochemistry established; the structure of prymnesin-1 remained unknown.[109] However, in 1999, Yasumoto and co-workers[110] reported, on the basis of extensive NMR spectroscopic analyses, the structural elucidation of both prymnesins, including stereochemical assignments. The relative configuration of two stereogenic centers of these initial structures (at the E/F ring junction) have subsequently been reassigned.[111] The toxicity of both molecules is quite impressive: both are toxic to fish at concentrations less than 10 nmol/L, and they also lead to complete lysis of mouse cells at a concentration of 3 nmol/L.[112]

Fig. 16. Polyyne glycosides from *Pratia nummularia*.

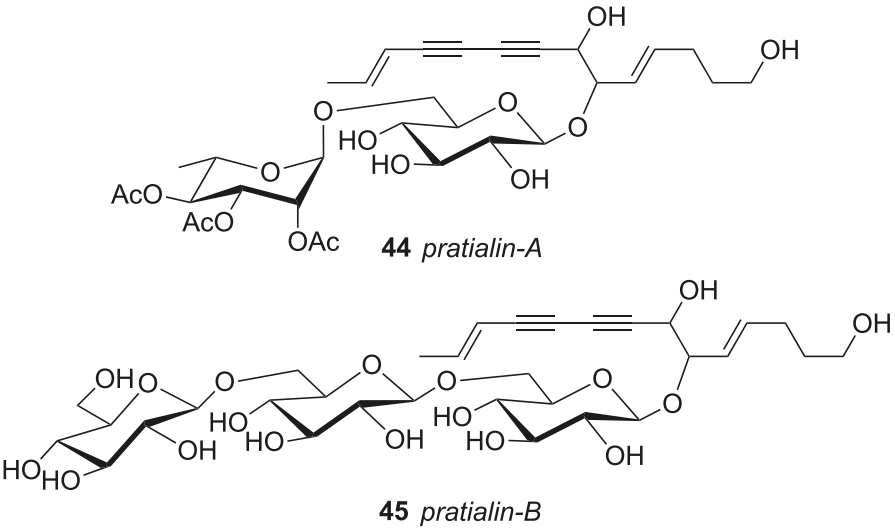

Fig. 17. Polyyne glycosides from *Fistulina pallida*

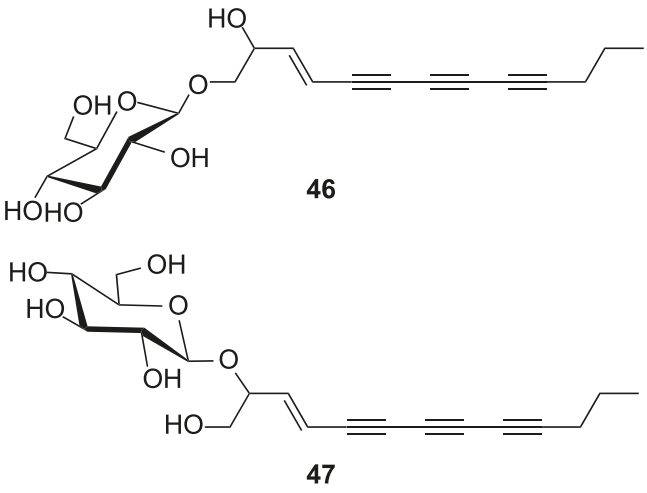

Fig. 18. Polyynes and polyyne glycosides from Basidiomycete B-841.

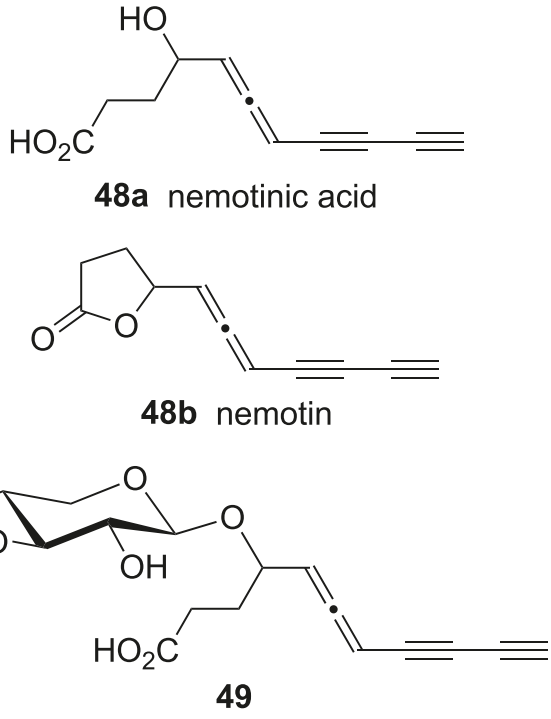

Synthesis of polyyne glycosides

Synthesis of natural products

Although many polyyne glycosides have been isolated from natural sources, and some of them have been shown to possess a range of biological activities, there has been surprisingly little interest in their synthesis.[11] To date, only two studies have described the synthesis of naturally occurring polyyne glycosides. Gung and co-workers[113,114] have reported the syntheses of bidensyneosides A_1, A_2, B, and C (**12**–**15**, respectively), and an analogue bidensyneoside C (**16**, Scheme 1). Although the protecting group strategy employed for the sugar moiety varied among the individual syntheses, the general approach for construction of the polyyne segment remained constant. In each case, the di- or triyne segment of the bidensyneoside was completed with a Cadiot–Chodkiewicz coupling between a glycosyl bromoacetylene derivative and a mono- or diyne. Depending on the coupling partners, yields between 31% and 91% were realized. Global deprotection, in one or two steps, then afforded the desired products. It should be mentioned that the synthesis of these glycosides also allowed for the confirmation of the stereochemistry at C3 of the aglycone of **12**–**15**, which had not yet been established.

Synthesis of natural product analogues

As is the case described above for naturally occurring polyyne glycosides, there has also been surprisingly little effort amongst synthetic chemists toward the assembly of natural product analogues. The synthesis of polyyne glycosides, particularly derivatives with a tri-, tetra-, or pentayne skeleton can be challenging, in part due to the inherently unstable nature of these longer polyynes.[2] Presumably this instability,

Fig. 19. Polyyne glycosides prymnesin-1 (**50**) and prymnesin-2 (**51**) from alga *Prymnesium parvum.*

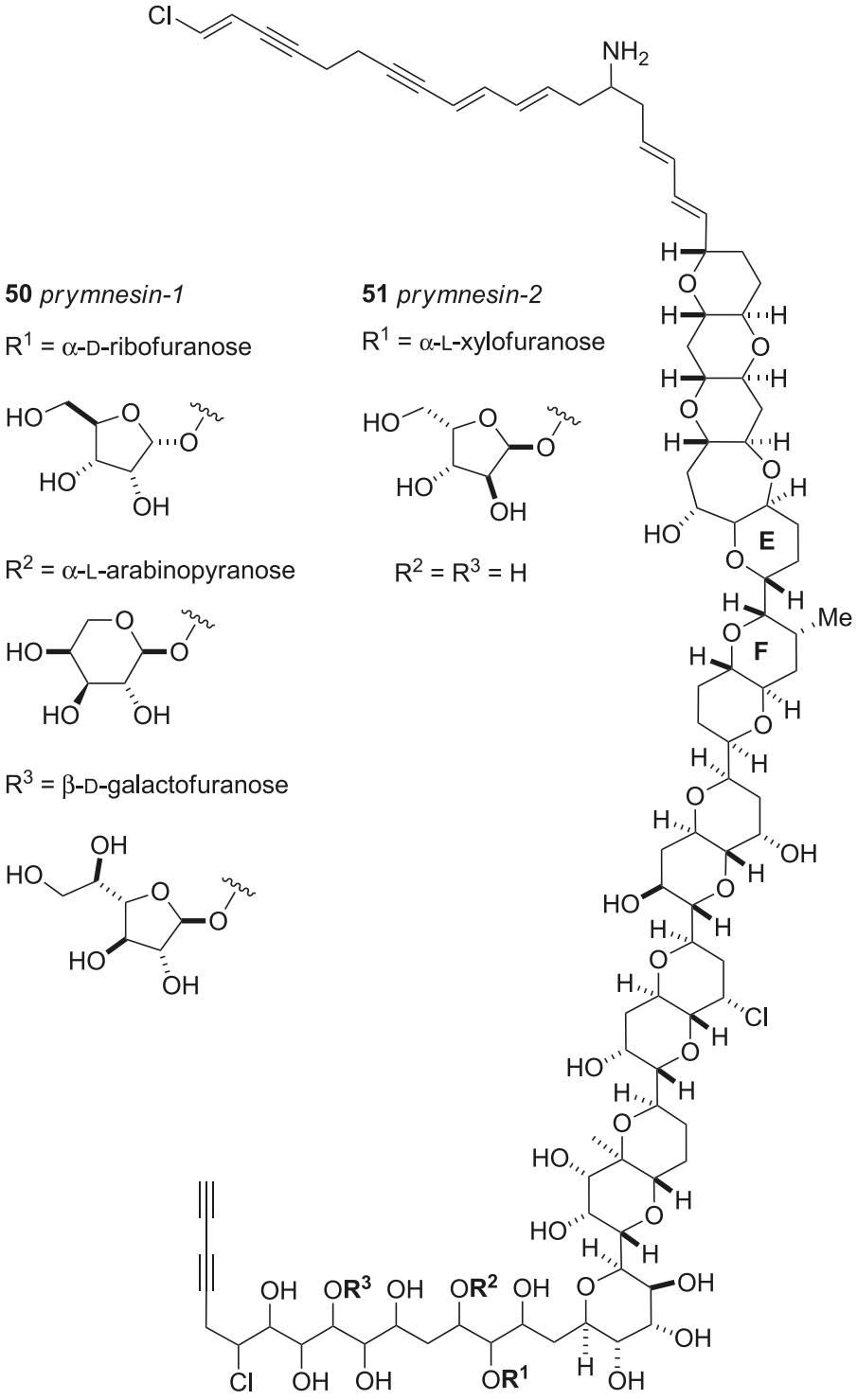

and the dearth of effective methods for making polyynes, are factors that have limited synthesis of compounds in this class of molecules. To date, there has been a single report that has specifically targeted the synthesis of natural product analogues of polyyne glycosides.

In 2005, Tykwinski and co-workers[115] described the first syntheses of triyne glycosides using triynol **52** that, together with its acetate derivative **53** (Scheme 2), has been isolated from several species of *Bidens* (beggarticks), including *B. pilosa* and *B. leucanthus*.[116] The synthesis of **52** and **53** started from 1,4-butynediol.[115] Monoprotection of this diol as *tert*-butyldiphenylsilyl (TBDPS) ether followed by oxidation gave the corresponding aldehyde, which was then reacted with lithium phenylacetylide to provide alcohol **54**. A sequence of oxidation, dibromoolefination, and Fritsch–Buttenberg–Wiechell rearrangement gave the triyne core **55**. Fi-

Scheme 1. Bidensyneoside syntheses from Gung and co-workers.[113,114] (a) CuCl, Et_2NH, $NH_2OH{\cdot}HCl$, MeOH, H_2O, 0 °C, 91% (**12**), 86% (**13**), 46% (**14**), 56% (**15**), 31% (**16**); (b) (*i*) HF–pyr, THF, 0 °C; (*ii*) MeOH, K_2CO_3, RT, 87% (**12**), 85% (**13**), 53% (**14**), 50% (**15**) over the two steps; (c) HF–pyr, THF, 0 °C, 51%.

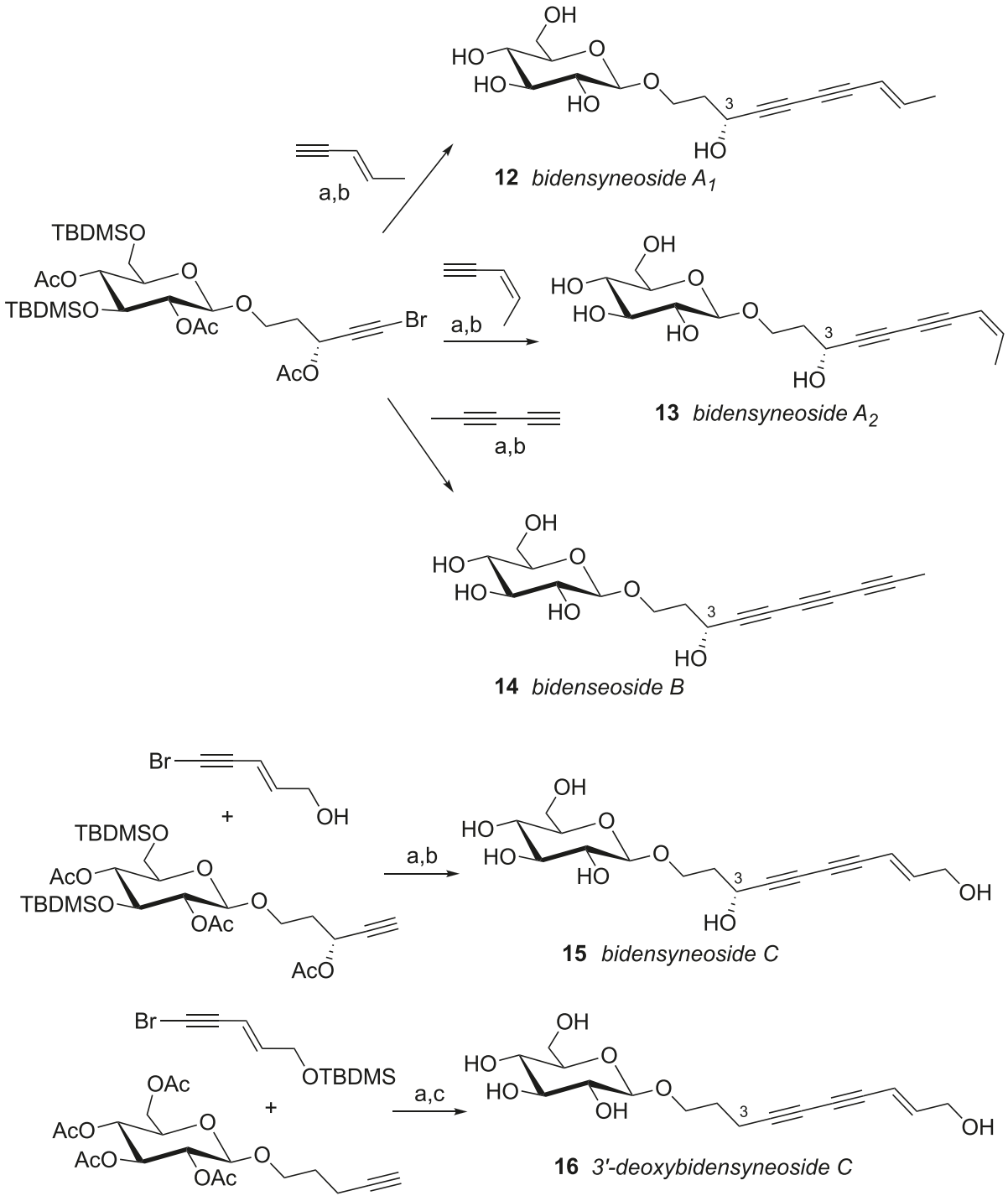

nally, liberation of the alcohol with TBAF gave a 90% yield of triynol **52**, which was then acetylated affording an 81% yield of **53**.

In theory, coupling triynol **52** to different sugar moieties could be achieved through the use of a number of different glycosylation protocols. In this study, three standard methods, each employing a different class of glycosylating agent (glycosyl acetates, glycosyl halides, and glycosyl imidates) were investigated. The reaction rate and yields were both low when glycosyl bromides were used as donors, while the coupling reactions using trichloroacetimidates as donors led to multiple products. In contrast, using glycosyl acetates as donors gave the desired products **56**–**58** in modest to good (61%–78%) yields. Deacetylation of the protected sugars afforded the triynol glycosides **59**–**61** (Scheme 3).[115]

In addition to the natural product analogues just described,

Scheme 2. Synthesis of triynol (**52**) by Luu et al.[115] (a) TBDPsCl, THF, Et_3N, DMAP, RT, 84%; (b) $BaMnO_4$, CH_2Cl_2, RT, 58%; (c) PhC≡CLi, THF, –78 °C, 85%; (d) $BaMnO_4$, CH_2Cl_2, RT, 89%; (e) CBr_4, PPh_3, CH_2Cl_2, Et_3N, 0 °C, 53%; (f) *n*-BuLi, hexanes, –78 °C to 10 °C, 90%; (g) TBAF, THF, RT, 96%; (h) Ac_2O, DMAP, CH_2Cl_2, Et_3N, RT, 81%.

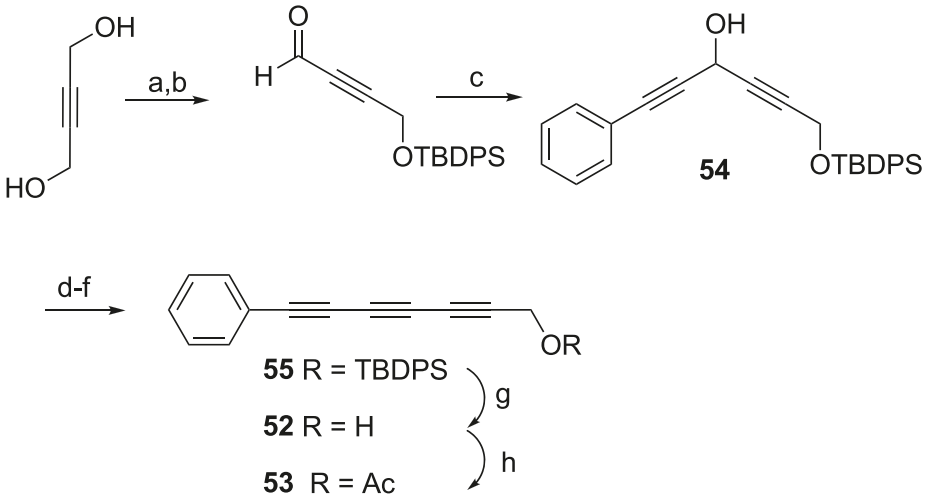

Scheme 3. Synthesis of triynol glycosides by Luu et al.[115] (a) **52**, $BF_3{\cdot}OEt_2$, 4 Å MS, CH_2Cl_2, RT; (b) K_2CO_3, CH_3OH, –78 °C to RT.

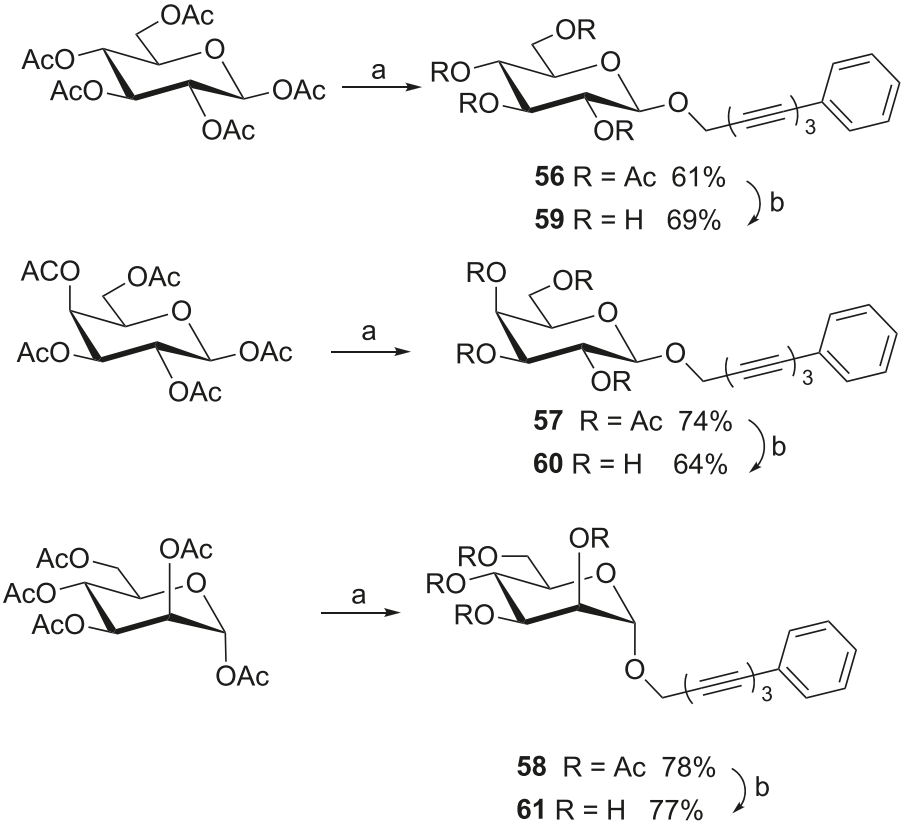

there have been several forays into combining the conjugated framework of a polyyne with that of a carbohydrate. Although these studies have not always targeted natural products or their analogues (indeed most are not, strictly speaking, polyyne glycosides) several are mentioned here to show the broad and evolving scope of this area of chemistry.[10]

Vasella and co-workers[117] have explored a number of potential mimics of cellulose, such as **62**, which possesses two cellooctaosyl chains with a C-glycosidic mono- or diyne linkage between the "reducing" end of the oligosaccharide and an anthraquinone core (Fig. 20). The anthraquinone template was used to ensure a parallel orientation of the oligosaccharide chains, and the distance between the two chains was designed to correspond to that determined crystallographically for the two independent chains of cellulose I. The ethynyl and butadiynyl linker units enforced an appropriate phase shift between the two chains. Key steps in the synthesis of these compounds involved the formation of a carbon-linked

Fig. 20. Polyyne glycoside oligomers synthesized by Vasella and co-workers.[118–126]

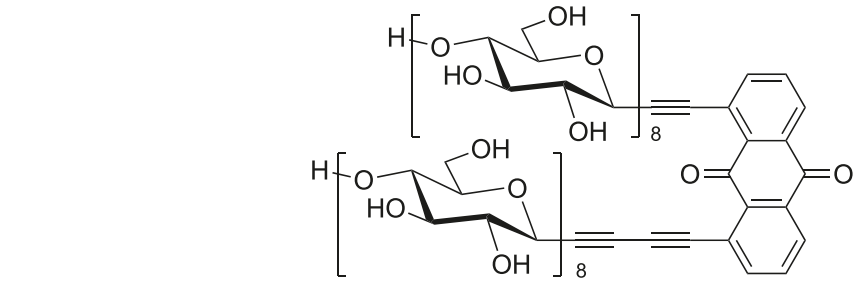

62

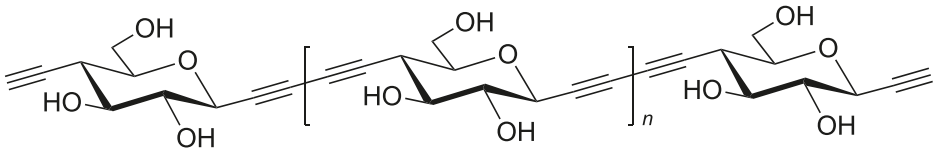

63 n = 0, 2, 6, 14

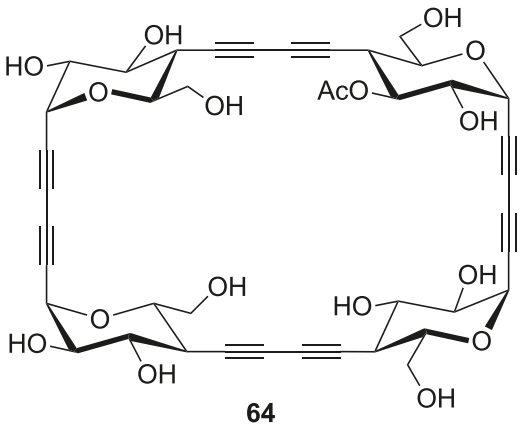

64

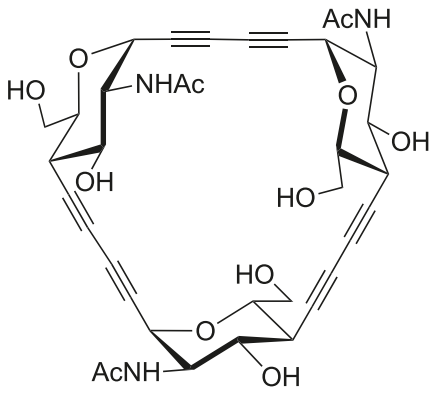

65

glycosyl acetylene or diacetylene derivative, which was then coupled via a Sonagashira coupling to anthraquinone triflates. The use of a selective protection–deprotection sequence on 1,8-dihydroxyanthraquinone facilitated the introduction of two different carbohydrate substitutents. The Vasella group has also used butadiyne-linked saccharide oligomers as cellulose analogues in which intrachain–interresidue hydrogen bonding can be avoided. This has led to the development of efficient methodology for the formation of monodisperse oligomers such as **63**, which relies on palladium-catalyzed coupling of carbohydrate building blocks functionalized at C1 and C4 (or C4′) with ethynyl fragments to form the diyne linkers.[118–123]

4-Ethynyl-α-D-glucopyranosylacetylenes have also been used by the Vasella group[124–126] for the preparation of cyclodextrin analogues free of inter-residue hydrogen bonds (**64**, **65**). In the synthesis of these compounds, a series of sequential Cadiot–Chodkiewicz cross-couplings was used to form

Fig. 21. Glycoside dimers by Roy et al.[129]

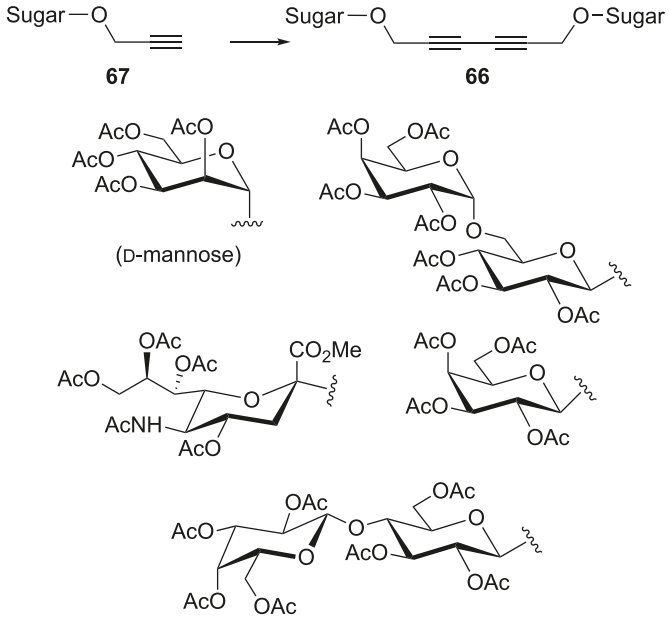

linear oligomers, which were then cyclized via an intramolecular Cadiot–Chodkiewicz or Glaser coupling to provide tri-, tetra-, penta-, and hexamers.[124–126] In other cases, oxidative homocoupling has been used to assemble the cyclic acetylenosaccharides.[127] One example involves the formation of **65** via reaction of a 4-ethynyl-α-D-pyranosylacetylene monomer under Eglinton conditions.[128] In addition to their synthesis, the host-guest properties of these cyclic structures were investigated and they have indeed been shown to act as hosts for small molecules. For example, the D2-symmetric tetramer **64** forms complexes of approximately the same strength with D- or L-adenosine in D_2O, albeit with rather low affinity (K_a = 40 mol/L^{-1}).[124,125]

Roy et al.[129] have explored the use of butadiyne moieties to connect carbohydrate residues. Their procedure is based on a mild Pd-catalyzed homocoupling method for the formation of conjugated carbohydrate diynes **66** based from the corresponding monomer **67** (Fig. 21). Five derivatives were reported, with yields ranging from 65%–85%. The mannose terminated dimer was subsequently deacylated and its ability to cross-link the tetrameric plant lectin concanavalin (Con A) was examined.

Conjugates of carbohydrates and polyynes have also been synthesized as potential biological sensors. An example are diynes **68** and **69**, which were synthesized and then incorporated into self-assembled monolayer of polydiacetylenes by Charych et al.[130] (Fig. 22). The sialic acid component of **68** acts as a ligand for molecular recognition for the influenza virus, while the photochromic conjugated polymer backbone serves to signal the binding event, which is visible to the naked eye as a blue to red color change. The lactose analogue **69** was also prepared and used to test for nonspecific binding.

In work related to that of Charych et al.,[130] Nie and Wang[131] have synthesized a series of 24 diacetylene-containing sugar lipids, **70**, that incorporated a range of different chain lengths, substituents, as well as varied positioning of diyne moiety (Fig. 23). The self-assembling properties of these diynes were then explored in several solvents including hexane, ethanol, and ethanol–water mixtures. Many of these derivatives exhibited excellent gelation properties in ethanol or ethanol–water mixtures, and this behavior was dependent both on the position of the diyne on the carbohydrate and the chain length. The production of new materials, via diacetylene polymerization of the resulting gels, was also explored.

Most recently, Hoheisel and Frauenrath,[132] have expanded on the concept of polyyne tethered saccharides through the construction of two derivatives, a hexayne and octayne (**71**, Fig. 24). The formation of these extended molecules relied on a newly devised cross-coupling method using the combination of a zinc acetylide and a bromoacetylene in the presence of $Pd(Cl_2)$dppf. Despite their highly unsaturated polyyne skeleton, both molecules were stable for days under ambient conditions.[133]

Conclusion

Polyyne glycosides are a structurally interesting class of compounds with important biological activities including antibacterial and anti-inflammatory properties, as well as the ability to modulate blood glucose levels. To date, about fifty polyyne glycoside natural products have been isolated. Although biological data exists for some of these compounds, it is absent for many others and a systematic study of their biological activity will require multimilligram amounts of these glycoconjugates. Such quantities are most realistically available by chemical synthesis. However, with the exception of the seminal work of Gung and co-workers,[11,113,114] the synthesis of naturally occurring polyyne glycosides has not received significant attention, although analogs of these compounds have been prepared.[115] This is clearly an area that is ripe for further investigation and future studies in this area should include both methodological investigations as well as total synthesis followed by the measurement of biological activity.

One significant and currently unanswered question is the role that the carbohydrate residue plays on the bioactivity of these molecules. It should be noted that in those species isolated from plants, the sugar moiety directly attached to the polyyne is always glucopyranose. Occasionally, this carbohydrate residue is further glycosylated, and most often the identity of the additional sugar residues is another glucopyranose moiety (e.g., lobetyolinin, **39**, Fig. 14). Less commonly, apiofuranose (gymnasterkoreaside B, **31**, Fig. 9) or rhamnopyranose (pratialin-A, **44**, Fig. 16) moieties are found attached to the core glucopyranose residue. Polyyne glycosides isolated from fungi incorporate a broader range of carbohydrate residues including xylopyranose, xylofuranose, arabinopyranose, galactofuranose, and ribofuranose (see Figs. 18 and 19).

The relative lack of diversity of sugars present in these compounds may suggest that the carbohydrate serves either to solubilize the typically hydrophobic polyyne, or facilitates the delivery of these molecules to certain cell types (e.g., through binding to a glucose transporter that tolerates substitutions at the anomeric carbon).[33] It is also possible that the

Fig. 22. Glycoside diynes from Charych et al.[130]

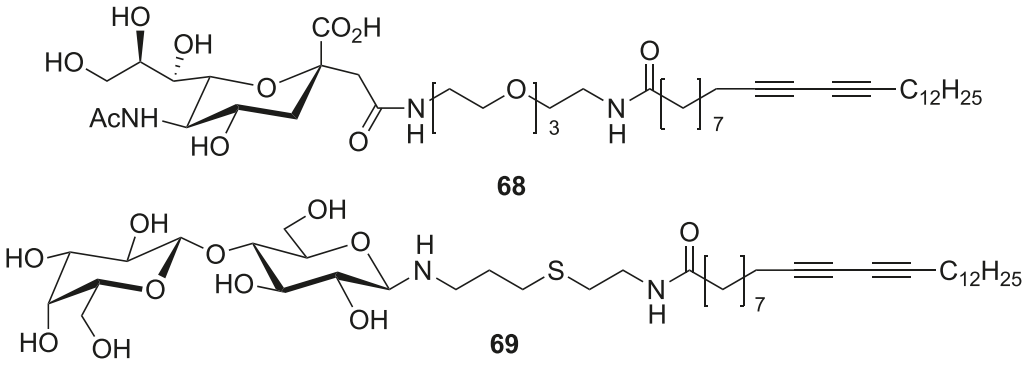

Fig. 23. Glycoside dimers synthesized by Nie and Wang.[131]

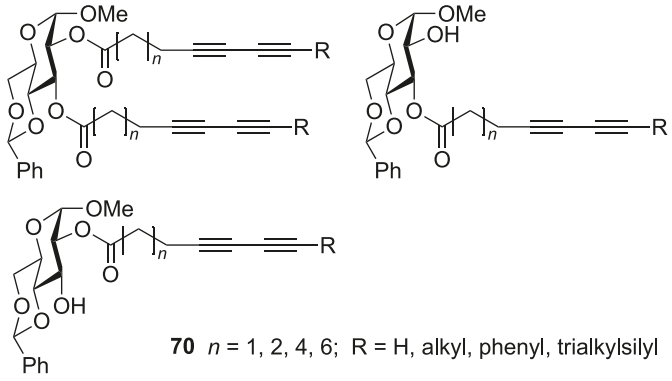

Fig. 24. Glycoside polyynes prepared by Hoheisel and Frauenrath.[132,133]

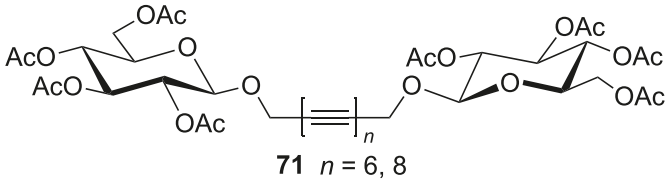

carbohydrate plays a "protecting" role in either stabilizing the polyyne moiety, or in masking its biological activity until cleavage of the carbohydrate moiety by a glycosidase. The latter mechanism is intriguing, and is a strategy used by some plants as protection against herbivores.[134] However, given the lack of detailed structure activity relationships on polyyne glycosides, proposals of this type must at this point be regarded only as speculation. Without question, developing a deeper understanding of the bioactivity of these fascinating molecules justifies more intense future study, from both a chemical and biological perspective.

Acknowledgements

This work has been supported by the Natural Sciences and Engineering Research Council of Canada (NSERC), the Alberta Ingenuity Centre for Carbohydrate Science, and the University of Alberta. We thank Ms. Annie Tykwinski for her original artwork and design of the cover illustration for this issue.

References

(1) The term polyyne is meant to denote compounds with a structural sequence of two or more consecutive (conjugated) acetylene units. The term polyacetylene has often been used in this context as well, but can be ambiguous because of its more common use in reference to polymerized acetylene, –[CH=CH]*n*–.

(2) Shi Shun, A. L. K.; Tykwinski, R. R. *Angew. Chem. Int. Ed.* **2006**, *45* (7), 1034–1057. doi:10.1002/anie.200502071.

(3) Varki, A. *Glycobiology* **1993**, *3* (2), 97–130. doi:10.1093/glycob/3.2.97. PMID:8490246.

(4) Dwek, R. A. *Chem. Rev.* **1996**, *96* (2), 683–720. doi:10.1021/cr940283b. PMID:11848770.

(5) Lowe, J. B.; Marth, J. D. *Annu. Rev. Biochem.* **2003**, *72* (1), 643–691. doi:10.1146/annurev.biochem.72.121801.161809. PMID:12676797.

(6) Bu'Lock, J. D.; Gregory, H. *Experientia* **1959**, *15* (11), 420–421. doi:10.1007/BF02157688. PMID:13805490.

(7) (a) Rücker, G.; Kehrbaum, S.; Sakulas, H.; Lawong, B.; Goeltenboth, F. *Planta Med.* **1992**, *58* (3), 266–269. doi:10.1055/s-2006-961450. PMID:1409982.; (b) Tobinaga, S.; Sharma, M. K.; Aalbersberg, W. G. L.; Watanabe, K.; Iguchi, K.; Narui, K.; Sasatsu, M.; Waki, S. *Planta Med.* **2009**, *75* (6), 624–628. doi:10.1055/s-0029-1185377. PMID:19263339.

(8) Wang, N.; Yao, X.; Ishii, R.; Kitanaka, S. *Chem. Pharm. Bull. (Tokyo)* **2001**, *49* (8), 938–942. doi:10.1248/cpb.49.938. PMID:11515581.

(9) Ubillas, R. P.; Mendez, C. D.; Jolad, S. D.; Luo, J.; King, S. R.; Carlson, T. J.; Fort, D. M. *Planta Med.* **2000**, *66* (1), 82–83. PMID:10705745.

(10) Bernet, B.; Vasella, A. In *Acetylene Chemistry: Chemistry, Biology, and Material Science;* Diederich, F., Stang, P. J., Tykwinski, R. R., Eds.; Wiley-VCH: Weinheim, Germany, 2005; Chapter 5.

(11) Gung, B. *C. R. Chim.* **2009**, *12* (3–4), 489–505.

(12) Saita, T.; Matsunaga, H.; Yamamoto, H.; Nagumo, F.; Fujito, H.; Mori, M.; Katano, M. *Biol. Pharm. Bull.* **1994**, *17* (6), 798–802. PMID:7951141.

(13) Hansen, L.; Boll, P. M. *Phytochemistry* **1986**, *25* (2), 285–293. doi:10.1016/S0031-9422(00)85468-0.

(14) Tang, W.; Eisenbrand, G. *Chinese Drugs of Plant Origin;* Springer-Verlag: Berlin, 1992; pp 711–751.

(15) Zhang, H.; Lu, Z.; Tan, G. T.; Qiu, S.; Farnsworth, N. R.; Pezzuto, J. M.; Fong, H. H. S. *Tetrahedron Lett.* **2002**, *43* (6), 973–977. doi:10.1016/S0040-4039(01)02310-3.

(16) Yoshikawa, M.; Murakami, T.; Ueno, T.; Yashiro, K.; Hir-

okawa, N.; Murakami, N.; Yamahara, J.; Matsuda, H.; Saijoh, R.; Tanaka, O. *Chem. Pharm. Bull. (Tokyo)* **1997**, *45* (6), 1039–1045. PMID:9214709.

(17) Lee, S. M.; Bae, K. H.; Sohn, H. J. *Tetrahedron Lett.* **2009**, *50* (4), 416–418. doi:10.1016/j.tetlet.2008.11.020.

(18) Bezuidenhoudt, B. C. B.; Russell, M. A. *J. Am. Chem. Soc.* **1989**, *111* (4), 1392–1396. doi:10.1021/ja00186a037.

(19) Bohlmann, F.; Burkhardt, H.; Zdero, C. *Naturally Occuring Acetylenes;* Academic Press: New York, 1973.

(20) Christensen, L. P.; Lam, J. *Phytochemistry* **1990**, *29* (9), 2753–2785. doi:10.1016/0031-9422(90)87075-6.

(21) Christensen, L. P.; Lam, J. *Phytochemistry* **1991**, *30* (8), 2453–2476. doi:10.1016/0031-9422(91)85085-E.

(22) Christensen, L. P.; Lam, J. *Phytochemistry* **1991**, *30* (1), 11–49. doi:10.1016/0031-9422(91)84096-B.

(23) Christensen, L. P. *Phytochemistry* **1992**, *31* (1), 7–49. doi:10.1016/0031-9422(91)83002-3.

(24) Taxonomy and common names were assigned on the basis of primary literature as well as the following sources: Plants: the USDA PLANTS Classification Report available at http://plants.usda.gov.

(25) Abbiw, D. *Useful Plants of Ghana;* Intermediate Technology Publications and the Royal Botanical Gardens, Kew: London, 1990.

(26) Cano, J. H.; Volpato, G. *J. Ethnopharmacol.* **2004**, *90* (2–3), 293–316. doi:10.1016/j.jep.2003.10.012. PMID: 15013195.

(27) Christensen, L. P.; Lam, J. *Phytochemistry* **1991**, *30* (1), 11–49. doi:10.1016/0031-9422(91)84096-B.

(28) Romussi, G.; Pagani, F. *Boll. Chim. Farm.* **1970**, *109* (8), 467–475. PMID:5505160.

(29) Pagani, F.; Romussi, G. *Phytochemistry* **1971**, *10* (9), 2233. doi:10.1016/S0031-9422(00)97231-5.

(30) Pagani, F.; Romussi, G.; Bohlmann, F. *Chem. Ber.* **1972**, *105* (9), 3126–3127. doi:10.1002/cber.19721050938.

(31) Bauer, R.; Redl, K.; Davis, B. *Phytochemistry* **1992**, *31* (6), 2035–2037. doi:10.1016/0031-9422(92)80357-K.

(32) Kaaiakamanu, D. M.; Akina, J. K. *Hawaiian Herbs of Medicinal Value;* Pacific Book House: Honolulu, 1992.

(33) Marchant, Y. Y.; Ganders, F. R.; Wat, C.-K.; Towers, G. H. N. *Biochem. Syst. Ecol.* **1984**, *12* (2), 167–178. doi:10.1016/0305-1978(84)90030-9.

(34) Redl, K.; Breu, W.; Davis, B.; Bauer, R. *Planta Med.* **1994**, *60* (1), 58–62. doi:10.1055/s-2006-959409. PMID: 8134419.

(35) Pereira, R. L. C.; Ibrahim, T.; Lucchetti, L.; da Silva, A. J. R.; Gonçalves de Moraes, V. L. *Immunopharmacology* **1999**, *43* (1), 31–37. doi:10.1016/S0162-3109(99)00039-9. PMID:10437654.

(36) Chih, H.-W.; Lin, C. C.; Tang, K.-S. *Am. J. Chin. Med.* **1995**, *23* (3–4), 273–278. PMID:8571923.

(37) Rabe, T.; van Staden, J. *J. Ethnopharmacol.* **1997**, *56* (1), 81–87. doi:10.1016/S0378-8741(96)01515-2. PMID: 9147258.

(38) Brandão, M. G. L.; Krettli, A. U.; Soares, L. S. R.; Nery, C. G. C.; Marinuzzi, H. C. *J. Ethnopharmacol.* **1997**, *57* (2), 131–138. doi:10.1016/S0378-8741(97)00060-3. PMID: 9254115.

(39) Alvarez, L.; Marquina, S.; Villarreal, M. L.; Alonso, D.; Aranda, E.; Delgado, G. *Planta Med.* **1996**, *62* (4), 355–357. doi:10.1055/s-2006-957902. PMID:8792670.

(40) Chan, Y.-C.; Friedlander, S. F. *Curr. Opin. Infect. Dis.* **2004**, *17* (2), 97–103. doi:10.1097/00001432-200404000-00005. PMID:15021047.

(41) Mirvish, S. S.; Salmasi, S.; Lawson, T. A.; Pour, P.; Sutherland, D. *J. Natl. Cancer Inst.* **1985**, *74* (6), 1283–1290. PMID:3858597.

(42) Chang, S.-L.; Chang, C. L.-T.; Chiang, Y.-M.; Hsieh, R.-H.; Tzeng, C.-R.; Wu, T.-K.; Sytwu, H.-K.; Shyur, L.-F.; Yang, W.-C. *Planta Med.* **2004**, *70* (11), 1045–1051. doi:10.1055/s-2004-832645. PMID:15549660.

(43) Chiang, Y.-M.; Chang, C. L.-T.; Chang, S.-L.; Yang, W.-C.; Shyur, L.-F. *J. Ethnopharmacol.* **2007**, *110* (3), 532–538. doi:10.1016/j.jep.2006.10.007. PMID:17101254.

(44) Chang, C. L.-T.; Chang, S.-L.; Lee, Y.-M.; Chiang, Y.-M.; Chuang, D.-Y.; Kuo, H.-K.; Yang, W.-C. *J. Immunol.* **2007**, *178* (11), 6984–6993. PMID:17513748.

(45) Wei, W. C.; Staniforth, V.; Yang, W. C.; Sheu, J. H.; Shyur, L. F.; Yang, N. S. *Planta Med.* **2008**, *74* (09), 940–940. doi:10.1055/s-0028-1084006.

(46) Xia, G.; Zhang, J.; Chen, X.; Ma, L. *Chin. Tradit. Herbal Drugs* **1985**, *16*, 37–40.

(47) Li, S.; Kuang, H.-X.; Okada, Y.; Okuyama, T. *Chem. Pharm. Bull. (Tokyo)* **2004**, *52* (4), 439–440. doi:10.1248/cpb.52.439. PMID:15056959.

(48) Neuwinger, H. D. *African Ethnobotany: Poisons and Drugs;* Chapman & Hall: New York, 1996; p 366.

(49) Matsuura, H.; Yoshihara, T.; Ichihara, A.; Kikuta, Y.; Koda, Y. *Biosci. Biotechnol. Biochem.* **1993**, *57* (8), 1253–1256.

(50) Matsuura, H.; Yoshihara, T.; Ichihara, A. *Biosci. Biotechnol. Biochem.* **1993**, *57* (9), 1492–1498.

(51) Christensen, L. P.; Brandt, K. *J. Pharm. Biomed. Anal.* **2006**, *41* (3), 683–693. doi:10.1016/j.jpba.2006.01.057. PMID:16520011.

(52) Shao, Y.; Zhou, B.-N.; Lin, L.-Z.; Cordell, G. A. *Phytochemistry* **1995**, *38* (6), 1487–1492. doi:10.1016/0031-9422(94)00794-T. PMID:7786479.

(53) Shao, Y.; Zhou, B.-N.; Gao, J.-H.; Lin, L.-Z.; Cordell, G.-A. *Phytochemistry* **1995**, *38* (3), 675–680. doi:10.1016/0031-9422(94)00716-7. PMID:7766163.

(54) Wang, C. Z.; Yu, D. Q. *Phytochemistry* **1998**, *48* (4), 711–717. doi:10.1016/S0031-9422(98)00019-3.

(55) Jung, H.-J.; Min, B.-S.; Park, J.-Y.; Kim, Y.-H.; Lee, H.-K.; Bae, K.-H. *J. Nat. Prod.* **2002**, *65* (6), 897–901. doi:10.1021/np0104018. PMID:12088435.

(56) Dat, N.-T.; Cai, X.-F.; Shen, Q.; Lee, I.-S.; Lee, E.-J.; Park, Y.-K.; Bae, K.-H.; Kim, Y.-H. *Chem. Pharm. Bull. (Tokyo)* **2005**, *53* (9), 1194–1196. doi:10.1248/cpb.53.1194. PMID:16141596.

(57) Park, J.-Y.; Min, B.-S.; Jung, H.-J.; Kim, Y.-H.; Lee, H.-K.; Bae, K.-H. *Chem. Pharm. Bull. (Tokyo)* **2002**, *50* (5), 685–687. doi:10.1248/cpb.50.685. PMID:12036032.

(58) Tang, W.; Eisenbrand, G. *Chinese Drugs of Plant Origin: Chemistry, Pharmacology, and Use in Traditional and Modern Medicine;* Springer-Verlag: Berlin, 1992; pp 199–201.

(59) Kitajima, J.; Kamoshita, A.; Ishikawa, T.; Takano, A.; Fukuda, T.; Isoda, S.; Ida, Y. *Chem. Pharm. Bull. (Tokyo)* **2003**, *51* (6), 673–678. doi:10.1248/cpb.51.673. PMID: 12808245.

(60) Jente, R.; Bohlmann, F.; Schöneweiss, S. *Phytochemistry* **1979**, *18* (5), 829–837. doi:10.1016/0031-9422(79)80023-0.

(61) Kitajima, J.; Kamoshita, A.; Ishikawa, T.; Takano, A.; Fukuda, T.; Isoda, S.; Ida, Y. *Chem. Pharm. Bull. (Tokyo)* **2003**, *51* (9), 1106–1108. doi:10.1248/cpb.51.1106. PMID: 12951459.

(62) Stavri, M.; Mathew, K. T.; Gibson, T.; Williamson, R. T.; Gibbons, S. *J. Nat. Prod.* **2004**, *67* (5), 892–894. doi:10.1021/np030558v. PMID:15165159.
(63) Bohlmann, F.; Ehlers, D. *Phytochemistry* **1977**, *16* (9), 1450–1451. doi:10.1016/S0031-9422(00)88807-X.
(64) Stavri, M.; Ford, C. H. J.; Bucar, F.; Streit, B.; Hall, M. L.; Williamson, R. T.; Mathew, K. T.; Gibbons, S. *Phytochemistry* **2005**, *66* (2), 233–239. doi:10.1016/j.phytochem.2004.11.010. PMID:15652580.
(65) College, J. N. M. *A Dictionary of the Traditional Chinese Medicines;* Shanghai People's Publishing House: Shanghai, 1986.
(66) Zhou, Y.-Z.; Ma, H.-Y.; Chen, H.; Qiao, L.; Yao, Y.; Cao, J.-Q.; Pei, Y.-H. *Chem. Pharm. Bull. (Tokyo)* **2006**, *54* (10), 1455–1456. doi:10.1248/cpb.54.1455. PMID:17015990.
(67) Wagner, W. L.; Herbst, D. R.; Sohmer, S. H. In *Manual of the Flowering Plants of Hawaii, Revised ed.;* University of Hawaii Press/Bishop Museum Press: Honolulu, 1999; p 351.
(68) Mukhopadhyay, S.; Cordell, G. A.; Ruangrungsi, N.; Rodkird, S.; Tantivatana, P.; Hylands, P. J. *J. Nat. Prod.* **1983**, *46* (5), 671–674. doi:10.1021/np50029a014.
(69) Qiu, Y.-Q.; Qi, S.-H.; Zhang, S.; Tian, X.-P.; Xiao, Z.-H.; Li, M.-Y.; Li, Q.-X. *Heterocycles* **2008**, *75* (7), 1757–1764. doi:10.3987/COM-08-11345.
(70) Magalhaes, A. F.; Magalhaes, E. G.; Junior, V. N.; Leitao Filho, H. F. *Phytochemistry* **1989**, *28* (9), 2497–2499. doi:10.1016/S0031-9422(00)98013-0.
(71) Sigstad, E. E.; Cuenca, M. D.; Catalan, C. A. N.; Gedris, T. E.; Herz, W. *Phytochemistry* **1999**, *50* (5), 835–838. doi:10.1016/S0031-9422(98)00462-2.
(72) Bohlmann, F.; Ziesche, J.; King, R. M.; Robinson, H. *Phytochemistry* **1980**, *19* (5), 969–970. doi:10.1016/0031-9422(80)85152-1.
(73) Yuda, M.; Ohtani, K.; Mizutani, K.; Kasai, R.; Tanaka, O.; Jia, M.-R.; Ling, Y.-R.; Pu, X.-F.; Saruwatari, Y.-I. *Phytochemistry* **1990**, *29* (6), 1989–1993. doi:10.1016/0031-9422(90)85053-I.
(74) Wang, Z.-T.; Ma, G.-Y.; Tu, P.-F.; Xu, G.-J.; Ng, T.-B. *Biochem. Syst. Ecol.* **1995**, *23* (7-8), 809–812. doi:10.1016/0305-1978(95)00082-8.
(75) Nörr, H.; Wagner, H. *Planta Med.* **1994**, *60* (5), 494–495. doi:10.1055/s-2006-959552. PMID:17236076.
(76) Ishimaru, K.; Yonemitsu, H.; Shimomura, K. *Phytochemistry* **1991**, *30* (7), 2255–2257. doi:10.1016/0031-9422(91)83624-T.
(77) Ishimaru, K.; Sadoshima, S.; Neera, S.; Koyama, K.; Takahashi, K.; Shimomura, K. *Phytochemistry* **1992**, *31* (5), 1577–1579. doi:10.1016/0031-9422(92)83110-K.
(78) Ishimaru, K.; Arakawa, H.; Yamanaka, M.; Shimomura, K. *Phytochemistry* **1994**, *35* (2), 365–369. doi:10.1016/S0031-9422(00)94765-4.
(79) Yamanaka, M.; Ishibashi, K.; Shimomura, K.; Ishimaru, K. *Phytochemistry* **1996**, *41* (1), 183–185. doi:10.1016/0031-9422(95)00606-0.
(80) Tada, H.; Shimomura, K.; Ishimaru, K. *J. Plant Physiol.* **1995**, *146*, 199–202.
(81) Bálványos, I.; Kursinszki, L.; Bányai, P.; Szöke, E. *Chromatographia* **2004**, *60*, S235–S238. doi:10.1365/s10337-004-0188-x.
(82) Tada, H.; Shimomura, K.; Ishimaru, K. *J. Plant Physiol.* **1995**, *145*, 7–10.
(83) Ahn, J. C.; Hwang, B.; Tada, H.; Ishimaru, K.; Sasaki, K.; Shimomura, K. *Phytochemistry* **1996**, *42* (1), 69–72. doi:10.1016/0031-9422(95)00849-7.
(84) Murakami, Y.; Shimomura, K.; Yoshihira, K.; Ishimaru, K. *J. Plant Physiol.* **1998**, *152*, 574–576.
(85) Tada, H.; Nakashima, T.; Kunitake, H.; Mori, K.; Tanaka, M.; Ishimaru, K. *J. Plant Physiol.* **1996**, *147*, 617–619.
(86) Tanaka, N.; Matsuura, E.; Terahara, N.; Ishimaru, K. *J. Plant Physiol.* **1999**, *155*, 251–254.
(87) Ando, M.; Shimomura, K.; Yamakawa, T.; Ishimaru, K. *J. Plant Physiol.* **1997**, *151*, 759–762.
(88) Ma, W. G.; Tan, R. X.; Fuzzati, N.; Li, Q. S.; Wolfender, J.-L.; Hostettmann, K. *Phytochemistry* **1997**, *45* (2), 411–415. doi:10.1016/S0031-9422(96)00849-7.
(89) Krebs, H. C.; Ramiarantsoa, H. *Phytochemistry* **1998**, *48* (5), 911–913. doi:10.1016/S0031-9422(97)00929-1.
(90) Dumlu, M. U.; Gurkan, E.; Tuzlaci, E. *Nat. Prod. Res.* **2008**, *22* (6), 477–482. doi:10.1080/14786410701640429. PMID:18415853.
(91) Mei, R.-Q.; Lu, Q.; Hu, Y.-F.; Liu, H.-Y.; Bao, F.-K.; Zhang, Y.; Cheng, Y.-X. *Helv. Chim. Acta* **2008**, *91* (1), 90–96. doi:10.1002/hlca.200890018.
(92) Chiu, N.-Y. *Alpine Medicine Plants of Taiwan;* SMC Publishing Inc.: Taipei, 1987; p 152.
(93) Ishimaru, K.; Osabe, M.; Yan, L.; Fujioka, T.; Mihashi, K.; Tanaka, N. *Phytochemistry* **2003**, *62* (4), 643–646. doi:10.1016/S0031-9422(02)00669-6. PMID:12560040.
(94) Jones, E. R. H.; Thaller, V. In *The Chemistry of the Carbon-Carbon Triple Bond, Part 2;* Patai, S., Ed.; Wiley: New York, 1978; pp 621–633.
(95) Jones, E. R. H. *Proc. Chem. Soc. Lond.* **1960**, 199–210.
(96) Bu'Lock, J. D. *Prog. Org. Chem.* **1964**, *6*, 86–134.
(97) Jones, E. R. H.; Lowe, G.; Shannon, P. V. R. *J. Chem. Soc. (C)* **1966**, 139–144. doi:10.1039/J39660000139.
(98) Farrell, I. W.; Keeping, J. W.; Pellatt, M. G.; Thaller, V. *J Chem Soc Perkin 1* **1973**, *22*, 2642–2643. doi:10.1039/p19730002642. PMID:4799454.
(99) Ahmed, M.; Barley, G. C.; Hearn, M. T. W.; Jones, E. R. H.; Thaller, V.; Yates, J. A. J. *Chem. Soc. Perkin Trans. 1* **1974**, 1981–1987. doi:10.1039/p19740001981.
(100) Anchel, M.; Polatnick, J.; Kavanagh, F. *Arch. Biochem.* **1950**, *25* (1), 208–220. PMID:15401231.
(101) Kavanagh, F.; Hervey, A.; Robbins, W. J. *Proc. Natl. Acad. Sci. U.S.A.* **1950**, *36* (1), 1–7. doi:10.1073/pnas.36.1.1. PMID:16588939.
(102) Bu'Lock, J. D.; Jones, E. R. H.; Leeming, P. R. *J. Chem. Soc.* **1955**, 4270–4276. doi:10.1039/jr9550004270.
(103) Bu'Lock, J. D.; Leadbeater, E. F. *Biochem. J.* **1956**, *62* (3), 476–480. PMID:13304001.
(104) Bu'Lock, J. D.; Gregory, H. *J. Chem. Soc.* **1960**, 2280–2285. doi:10.1039/jr9600002280.
(105) Yasumoto, T. *Chem. Rec.* **2001**, *1* (3), 228–242. doi:10.1002/tcr.1010. PMID:11895121.
(106) Murata, M.; Yasumoto, T. *Nat. Prod. Rep.* **2000**, *17* (3), 293–314. doi:10.1039/a901979k. PMID:10888014.
(107) Eikrem, W.; Throndsen, J. In *Toxic Phytoplankton Blooms in the Sea;* Smayde, T. J., Shimizu, Y., Eds.; Elsevier: Amsterdam, 1993; pp 687–692.
(108) Yariv, J.; Hestrin, S. *J. Gen. Microbiol.* **1961**, *24*, 165–175. PMID:13787241.
(109) Igarashi, T.; Satake, M.; Yasumoto, T. *J. Am. Chem. Soc.* **1996**, *118* (2), 479–480. doi:10.1021/ja9534112.
(110) Igarashi, T.; Satake, M.; Yasumoto, T. *J. Am. Chem. Soc.* **1999**, *121* (37), 8499–8511. doi:10.1021/ja991740e.
(111) Sasaki, M.; Ebine, M.; Takagi, H.; Takakura, H.; Shida,

T.; Satake, M.; Oshima, Y.; Igarashi, T.; Yasumoto, T. *Org. Lett.* **2004**, *6* (9), 1501–1504. doi:10.1021/ol049569l. PMID:15101777.
(112) Igarashi, T.; Aritake, S.; Yasumoto, T. *Nat. Toxins* **1998**, *6* (1), 35–41. doi:10.1002/(SICI)1522-7189(199802)6:1<35::AID-NT7>3.0.CO;2-7. PMID:9851510.
(113) Gung, B. W.; Fox, R. M. *Tetrahedron* **2004**, *60* (42), 9405–9415. doi:10.1016/j.tet.2004.08.012.
(114) Gung, B. W.; Fox, R. M.; Falconer, R.; Shissler, D. *Tetrahedron Asymmetry* **2006**, *17* (1), 40–46. doi:10.1016/j.tetasy.2005.10.027.
(115) Luu, T.; Shi, W.; Lowary, T. L.; Tykwinski, R. R. *Synthesis* **2005**, 3167–3178.
(116) Bohlmann, F.; Arndt, C.; Kleine, K.-M.; Wotschokowsky, M. *Chem. Ber.* **1965**, *98* (4), 1228–1232. doi:10.1002/cber.19650980432.
(117) Murty, K. V. S. N.; Xie, T.; Bernet, B.; Vasella, A. *Helv. Chim. Acta* **2006**, *89* (4), 675–730. doi:10.1002/hlca.200690068.
(118) Cai, C.; Vasella, A. *Helv. Chim. Acta* **1995**, *78* (8), 2053–2064. doi:10.1002/hlca.19950780814.
(119) Cai, C.; Vasella, A. *Helv. Chim. Acta* **1995**, *78* (3), 732–757. doi:10.1002/hlca.19950780319.
(120) Alzeer, J.; Vasella, A. *Helv. Chim. Acta* **1995**, *78* (5), 1219–1237. doi:10.1002/hlca.19950780515.
(121) Alzeer, J.; Cai, C.; Vasella, A. *Helv. Chim. Acta* **1995**, *78* (1), 242–264. doi:10.1002/hlca.19950780122.
(122) Alzeer, J.; Vasella, A. *Helv. Chim. Acta* **1995**, *78* (1), 177–193. doi:10.1002/hlca.19950780117.
(123) Cai, C.; Vasella, A. *Helv. Chim. Acta* **1996**, *79* (1), 255–268. doi:10.1002/hlca.19960790126.
(124) Bürli, R.; Vasella, A. *Helv. Chim. Acta* **1997**, *80*, 2215–2237. doi:10.1002/hlca.19970800720.
(125) Bürli, R.; Vasella, A. *Angew. Chem. Int. Ed. Engl.* **1997**, *36* (17), 1852–1853. doi:10.1002/anie.199718521.
(126) Bürli, R.; Vasella, A. *Helv. Chim. Acta* **1997**, *80*, 1027–1052. doi:10.1002/hlca.19970800403.
(127) Stichler-Bonaparte, A.; Bernet, B.; Vasella, A. *Helv. Chim. Acta* **2002**, *85* (8), 2235–2257. doi:10.1002/1522-2675(200208)85:8<2235::AID-HLCA2235>3.0.CO;2-I.
(128) Siemsen, P.; Livingston, R. C.; Diederich, F. *Angew. Chem. Int. Ed.* **2000**, *39* (15), 2632–2657. doi:10.1002/1521-3773(20000804)39:15<2632::AID-ANIE2632>3.0.CO;2-F.
(129) Roy, R.; Das, S. K.; Hernandex-Mateo, F.; Santoyo-Gonzalez, F.; Gan, Z. H. *Synthesis* **2001**, 1049–1052.
(130) Charych, D. H.; Nagy, J. O.; Spevak, W.; Bednarski, M. D. *Science* **1993**, *261* (5121), 585–588. doi:10.1126/science.8342021. PMID:8342021.
(131) Nie, X.; Wang, G. *J. Org. Chem.* **2006**, *71* (13), 4734–4741. doi:10.1021/jo052317t. PMID:16776497.
(132) Hoheisel, T. N.; Frauenrath, H. *Org. Lett.* **2008**, *10* (20), 4525–4528. doi:10.1021/ol801807a. PMID:18811175.
(133) For a discussion of extended polyynes, see: Chalifoux, W. A.; Tykwinski, R. R. *C. R. Chimie* **2009**, *12*, 341–358.
(134) Felton, G. W.; Tumlinson, J. H. *Curr. Opin. Plant Biol.* **2008**, *11* (4), 457–463. doi:10.1016/j.pbi.2008.07.001. PMID:18657469.

Energy additivity in branched and cyclic hydrocarbons

Hongwei Gao, Richard F. W. Bader, and Fernando Cortés-Guzmán

Abstract: This paper considers the degree to which branched hydrocarbons obey a group additivity scheme for energy and population, extending the study of the known experimental and theoretical transferability of the methyl and methylene groups of the linear hydrocarbons. The chemical groups are defined and their properties are determined using the quantum theory of atoms in molecules (QTAIM). The calculations are carried out with a large basis set at the restricted Hartree–Fock and MP2(full) levels of theory. The deviations from additivity, noted for small ring hydrocarbons leading to the definition of strain energy, are also investigated, showing that the QTAIM energies recover the experimental values. The particular delocalization of the electron density over the surface of the cyclopropane ring, responsible for its "homoaromatic" properties, is discussed in some detail. The calculations reported here satisfy the virial theorem as required for the atomic definition of energy. The problems associated with the use of DFT theory arising from its failure to satisfy the virial theorem are discussed with reference to the study of group transferability.

Key words: atoms in molecules, group additivity, transferability, strain energy.

Résumé : Dans ce travail, on considère le degré auquel des hydrocarbures ramifiés obéissent à un schéma d'additivité de groupe pour l'énergie et la population, étendant ainsi l'étude de la transférabilité expérimentale et théorique connue des groupes méthyle et méthylène des hydrocarbures linéaires. Les groupes chimiques sont définis et leurs propriétés sont déterminées en faisant appel à la théorie quantique des atomes dans les molécules (TQADM). Les calculs sont effectués avec un grand ensemble de base aux niveaux de Hartree–Fock et MP2(complet) de la théorie. On a aussi examiné les déviations par rapport à l'additivité notés pour les petits cycles hydrocarbonés, ce qui a conduit à la définition de l'énergie de tension et qui a permis de montrer que les énergies de la TQADM récupèrent les valeurs expérimentales. On discute en détail de la délocalisation particulière de la densité électronique sur la surface du noyau cyclopropane, responsable de ses propriétés homoaromatiques. Les calculs rapportés ici satisfont le théorème du viriel, tel que requis pour la définition atomique de l'énergie. En référence avec l'étude sur la transférabilité de groupe, on discute aussi des problèmes associés avec l'utilisation de la théorie de la fonctionnelle de la densité découlent de son incapacité à satisfaire le théorème du viriel.

Mots-clés : atomes dans les molécules, additivité de groupe, transférabilité, énergie de tension.

[Traduit par la Rédaction]

Experimental additivity schemes

It is nearly 80 years since Rossini and co-workers demonstrated that the heats of formation of the homologous series of linear saturated hydrocarbons obey a group additivity relationship of the form indicated in eq. [1]

$$[1] \qquad E(C_nH_{2n+2}) = 2E^o(CH_3) + (n-2)E^o(CH_2)$$

where $E^o(CH_3)$ is the standard additive energy for the methyl group and $E^o(CH_2)$ is the same for the methylene group.[1–3] The compilations of the additive group contributions to thermodynamic properties by Benson and co-workers demonstrate the remarkable degree to which the heat of formation may be equated to a sum of group contributions, those for the methyl and methylene groups exhibiting an average deviation of less than 0.1 kcal/mol for data up to and including $n = 12$ for the homologous series of linear hydrocarbons.[4]

The relationship in eq. [1] has been shown to apply not only to the measured heats under standard conditions, but also to the energies referenced to the vibrationless states at 0 K, energies that can be estimated in theoretical calculations.[5] In 1987, it was shown that the RHF (the acronym used here for single determinant SCF calculation) obeyed the same linear relationship using basis sets ranging from 6–31G* to 6–311++G(2d,2p), with the linear regression analyses yielding $R^2 = 1.00000$.[6] The same goodness of fit is obtained at the MP2(full) level of theory determined by a linear scaling of the methylene group.[7]

This paper considers the degree to which branched hydrocarbons obey a group additivity scheme for energy and populations, using the quantum theory of atoms in molecules (QTAIM) to define the properties of the groups.[8] Previous studies have demonstrated that the QTAIM group properties recover the experimentally determined values for the linear hydrocarbons.[6,7,9] A closely related property is "ring strain",

Received 25 April 2009. Accepted 2 July 2009. Published on the NRC Research Press Web site at canjchem.nrc.ca on 9 September 2009.

H. Gao[1] and R.F.W. Bader.[2] Department of Chemistry, McMaster University, Hamilton, ON L7L 2T1, Canada.
F. Cortés-Guzmán. Departamento de Fisicoquimica, Instituto de Química, Universidad Nacional Autónoma de México, Ciudad Universitaria, México DF 04510, México.

[1]Present address: Institute of Watershed Science and Environmental Ecology, Wenzhou Medical College, Zheijiang 325035, China.
[2]Corresponding author (e-mail: bader@mcmaster.ca).

defined as the difference in the calculated or measured energy of cyclic hydrocarbon $(CH_2)_n$ with that predicted by n times the energy of the standard methylene group as defined in eq. [1], $E^o(CH_2)$.[10] While measured ring strain has also been shown to be recovered by QTAIM,[6] the present paper presents the first study of this property using the group energies of QTAIM determined in MP2(full) calculations from wave functions that satisfy the virial theorem.

The recently proposed theorem,[11] stating that the electron density of an atom or functional grouping of atoms in a molecule determines its contributions to the properties of the total system, had its origin in studies that focused on the degree of retention of an atom's properties during its transfer between molecules. The atoms of QTAIM are "proper open systems" whose properties are defined by quantum mechanics. They have been shown to recover all measurable atomic and group properties, including second-order field-induced response properties along with those resulting from exposure to electromagnetic radiation and atomic charges and moments measured in the atomic polar tensors governing infrared intensities.[12,13] Someone unfamiliar with the mathematics necessary to follow the derivation of the physics of an open system from Schwinger's principle of stationary action[14,15] may derive QATIM heuristically. This requires only knowledge of Schrödinger's equation together with rudimentary mathematics using Gauss' theorem to relate the volume integral of the divergence of a vector to a surface integral of its flux, coupled with an appeal to experiment to demonstrate the validity of the "zero-flux" boundary condition.[16]

The physics of an open system demonstrates that transferability of an atom's energy and density is paralleled by the transferability in its virial field, the total potential-energy density, a transferability that can be maintained in spite of gross changes in its external potential, the quantity that according to the theorem of Hohenberg and Kohn, determines a molecule's electron density.[17] There is no conflict here, as the theorem of Hohenberg and Kohn refers to a closed isolated molecule, while chemical transferability is concerned with the physics of an open system that governs the transfer of groups between different molecules. Figure 1 shows the 0.001 au density envelope of the *iso*-butane molecule. The methyl groups and the H at the top of the CH group are clearly defined by the intersections of the zero-flux interatomic surfaces with the density envelope. The properties of these groups determine the properties of the molecule, their properties being determined by their charge distributions.[11] The extent to which that the density of a methyl group in this molecule differs from the density of a methyl group in a linear hydrocarbon determines the extent to which its properties differ from those of the standard transferable methyl group. The methyl group in *iso*-butane is found to be 14 kcal/mol more stable than the standard group, though they may come from molecules that differ in many thousands of kcal/mol in their external potentials.

A recent study extended these observations to determine the atomic transferability encountered in chemical change through a study of the changes in an atom's virial, energy, and population engendered by the formation of the hydrogen-bonded interactions that underlie DNA base-pairing.[18] The present paper provides further examples of how the transferability of a group's energy mirrors the changes in its density.

Fig. 1. The 0.001 au isodensity surface of the *iso*-butane molecule that contains over 99% of the total electron density. The methyl groups and the hydrogen atom of the interior CH group are clearly defined by the intersections of the ClC zero-flux interatomic surfaces with the density envelope. The contributions of each group to the total properties of the molecule are determined by its electron density distribution.

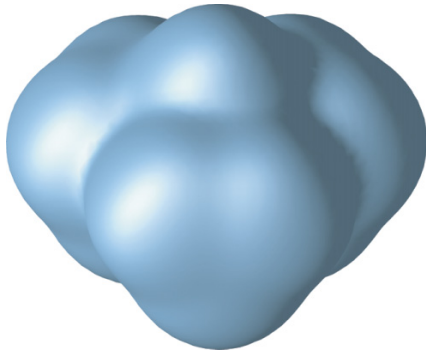

Perfect and compensatory transferability of group properties

The linear additivity scheme observed for the hydrocarbon heats of formation was the first experimental property demonstrated to result from functional group contributions defined by QTAIM.[6] Later studies demonstrated that the molecular values for the electric polarizability[19] and magnetic susceptibility[20] of the hydrocarbons are also recovered in terms of the additive methyl and methylene group contributions defined by QTAIM, with the physics of an open system equating all measurable molecular properties to the sum of their atomic contributions. While all properties are additive, groups and their properties are in general not completely transferable between molecules, as would seem to be required for an experimental additivity scheme, as represented by eq. [1].

While QTAIM does indeed predict the occurrence of such essentially "perfect transferability" of groups and their properties, this is not the sole mechanism underlying the observation of experimental additivity schemes. The extensive tabulations of thermodynamic properties by Benson et al. demonstrate that group additivity must in many cases be only apparent, as it is found in cases where a group is unavoidably perturbed by a change in its environment.[4] The additivity scheme in these cases is a result of compensatory transferability, with the change in all properties experienced by one group being equal and opposite to those experienced by the second group. Charge is of course, necessarily conserved, but to have the energy and all other properties conserved as well is nothing short of remarkable and is a phenomenon neither predicted nor understood and found to apply even in complex systems. Thus, Benson et al. proposed a rule of the arithmetic mean to account for the observation that many examples can be found wherein the energy of AGGB is the mean of the energies of AGGA and BGGB. As an example where the rule of the mean applies to molecules with delocalized charge distributions, one finds that the experimental heat of formation of pyridine is the mean of the energies of benzene and pyrazine to within 0.1 kcal/mol.[9]

Table 1. Total energies in atomic units and energy related quantities for branched hydrocarbons.

Molecule	Method	Molecular energy	$\gamma = -V/T$	$\Sigma N(\Omega) - N$	$\Sigma E(\Omega) - E_n$
$CH(CH_3)_3$	RHF/SCVS	–157.35069	1.9999994	–0.0029	0.5
C_{3v}	MP2/SCVS	–158.09749	2.0000000	–0.0032	0.4
$CH(CH_2CH_3)_3$	RHF/SCVS	–274.47790	1.9999989	–0.0017	–0.4
C_s	MP2/SCVS	–275.77390	1.9999999	0.0003	0.0
$CH(CH_2CH_2CH_3)_3$	RHF/SCVS	–391.62023	1.9999999	0.0022	0.2
C_s	MP2/SCVS	–393.45964	2.0000000	–0.0068	1.2
$C(CH_3)_4$	RHF/SCVS	–196.39690	1.9999995	–0.0033	0.6
T_d	MP2/SCVS	–197.33071	1.9999985	0.0000	0.0
$C(CH_2CH_3)_4$	RHF/SCVS	–352.56508	1.9999995	–0.00692	1.4
D_{2d}	MP2/SCVS	–354.23811	1.9999865	0.00035	–0.2

The observed additivity in the linear hydrocarbons is the result of both perfect and compensatory transferabilities. The standard methyl group energy $E^o(CH_3)$ necessarily equals one-half of the molecular energy for ethane, but the methyl group in the succeeding members of the series must differ from this, as they are bonded to a methylene group from which they withdraw electronic charge with $\Delta N(CH_3)$ = +0.016 e and undergo a corresponding energy decrease with $\Delta E(CH_3)$ = –9 kcal/mol, referring to RHF/SCVS values. These values remain unchanged as n increases, and this perturbed methyl group exhibits perfect transferability in all members past ethane to within computational accuracy. The methylene groups bonded to methyl groups undergo compensating changes in N and E from the values for the standard group: zero net charge and an energy equal to $E^o(CH_2)$. The group bonded to two methyls in propane exhibits twice the changes for methyl with ΔN = –0.32 e and ΔE = +19 kcal/mol. Those bonded to a single methyl have ΔN and ΔE values equal and opposite to those for the bonded methyl group. This is the transferable methylene group bonded to a single methyl. The remaining methylene groups must necessarily exhibit perfect transferability with an energy equal to the standard energy $E^o(CH_2)$ and a zero net charge. For example, the six innermost "standard" methylene groups in n = 12 have energy and population changes relative to the standard values within computational accuracy, with $\Delta N(CH_2)$ = 0.2 e and $\Delta E(CH_2)$ = 0.001 kcal/mol. Once removed from methyl, the population of a methylene group is slightly perturbed relative to the standard methylene group with an average $\Delta N(CH_2)$ value of –0.001 e.

The same pattern of perfect and compensatory transferability applies to the polysilanes Si_nH_{2n+2}.[9] Mosquera et al. have demonstrated linear fittings of the RHF energies for a wide range of molecules of the form $X(CH_2)_nCH_3$ for X = F, for aldehydes and ketones, for nitriles and alkanols, all for extended chains of up to 30 carbon atoms.[21–23] The contribution of the methylene group, $E^o(CH_2)$, is the same for all X and equal to the energy of the repeating $|CH_2|$ group of QTAIM, the vertical bars denoting its defining zero-flux interatomic surfaces. Their results for X = F have been repeated using both RHF and MP2 in SCVS calculations to demonstrate that their findings of apparent deviations in the transferability of group energies are artefacts arising from the failure of their calculations to satisfy the virial theorem.[7]

Transferability of group properties in branched hydrocarbons

Total molecular energies

All calculations were done using the 6–311++(2d,2p) basis in RHF/SCVS and MP2(full)/SCVS calculations, where SCVS denotes a self-consistent scaling of the electronic coordinates so that the virial theorem is satisfied.[24] Table 1 lists the RHF and MP2 total energies of the branched hydrocarbons studied in this paper along with the virial ratio $\gamma = -V/T$, which should equal 2 for satisfaction of the virial theorem, which is seen to be the case to computational accuracy. The symmetries of the molecules are also given and are in agreement with those previously reported for *neo*-pentane[25] and for *iso*-butane.[26,27] The errors in the summation of the integrated atomic populations $N(\Omega)$ and energies $E(\Omega)$ are all acceptably small, the magnitudes of the largest differences being 0.007 e for N and 1.4 kcal/mole for E. The total energies are denoted by E_n, where n denotes the number of carbon atoms. The iso- molecules, *iso*-butane, *iso*-heptane, and *iso*-dodecane are given first, followed by the neo- forms of pentane and nonane.

Table 2 lists the difference Δ between the calculated energy and that predicted by the linear relationship given in eq. [1], $\Delta = E_n - E_n^o$, where $E_n^o = E(C_nH_{2n+2})$ for the same level of theory, with the RHF results given in bold. It should be noted that the energies of the corresponding linear molecules agree with the predictions of eq. [1] to within 0.02 kcal/mol or less for both levels of theory. In two cases, C4 and C5, the difference Δ is of smallest magnitude for the RHF result and so close to zero as to fall within the limits of the integration error. In the remaining three cases, C7, C10, and C9, the RHF result exhibits Δ values lying between 7 and 11 kcal/mol.

The MP2 energies predict the branched hydrocarbons to be more stable than their linear isomers by 1 to 5 kcal/mol with the exception of C10 where the difference is approaching computational uncertainties. The differences fluctuate in a manner that does not appear to be related to the degree of branching. The differences in the experimental heats of formation between the linear and branched molecule are available for butane/*iso*-butane and pentane/*neo*-pentane pairs[28] and are listed in Table 2 and are in excellent agreement with the MP2 results.

The results do indicate that the inclusion of electron correlation beyond the Fermi correlation of RHF causes the

Table 2. Difference in energy of branched hydrocarbons and that predicted for the corresponding linear isomers.

Molecule	Method	$\Delta = E_n - E_n^o$ (kcal/mol)	H_f^o (298.15 g)
$CH(CH_3)_3$	RHF/SCVS	**–0.4**	
C4	MP2/SCVS	–1.9	–1.9
$CH(CH_2CH_3)_3$	RHF/SCVS	**+7.1**	
C7	MP2/SCVS	–0.8	
$CH(CH_2CH_2CH_3)_3$	RHF/SCVS	**+5.0**	
C10	MP2/SCVS	+0.5	
$C(CH_3)_4$	RHF/SCVS	**–0.3**	
C5	MP2/SCVS	–5.4	–4.5
$C(CH_2CH_3)_4$	RHF/SCVS	**+10.5**	
C9	MP2/SCVS	–3.4	

Table 3. Methyl group contributions to N and E for branched hydrocarbons,.

Methods	Molecule	$N(CH_3)$	$E(CH_3)$ au	$\Delta N(CH_3)$	$\Delta E(CH_3)$ kcal/mole
RHF/SCVS	$C(CH_3)_4$	9.0318	–39.67108	0.032	–26.6
	$CH(CH_3)_3$	9.0262	–39.65812	0.026	–18.4
	$C(CH_2CH_3)_4$	9.0210	–39.65270	0.021	–15.0
	$CH(CH_2CH_3)_3$	9.0193	–39.64963	0.019	–13.1
	$CH(CH_2CH_2CH_3)_3$	9.0178	–39.64273	0.018	–8.9
MP2/SCVS	$C(CH_3)_4$	9.0216	–39.84968	0.022	–18.9
	$CH(CH_3)_3$	9.0192	–39.84123	0.019	–13.6
	$C(CH_2CH_3)_4$	9.0133	–39.83164	0.013	–7.6
	$CH(CH_2CH_3)_3$	9.0126	–39.83253	0.013	–8.1
	$CH(CH_2CH_2CH_3)_3$	9.0107	–39.82582	0.011	–3.9

Note: RHF/SCVS: $E^o(CH_3)$ = –39.62873 au. MP2/SCVS: $E^o(CH_3)$ = –39.81955 au.

branched isomer to be more stable than its linear isomer, a result that might have its origin in an increased electron delocalization among the neighboring groups, which is possible in the branched molecules. This is something that can be determined by a comparison of the RHF and MP2 delocalization indices, which have been shown to be accurate indicators of the effective range of the stabilizing contributions from the exchange energy.[11] Rafat and Popelier give more direct confirmation of this correspondence by demonstrating that the delocalization index between atoms A and B is proportional to the negative of the exchange energy multiplied by their internuclear separation if the expansion of the exchange energy is restricted to the harmonics $L = 1$.[29] Overall, the percentage delocalization is greater for linear octane than for branched C7, $CH(CH_2CH_3)_3$, at both RHF and MP2, and greater at RHF than at MP2. However, the delocalization indices between the hydrogen atoms of different methyl and methylene groups in C7 at MP2 exceed those at RHF, and it is these interactions that specifically contribute to a lowering of the energy as a result of the "crowding" in the branched hydrocarbons.

Group contributions

Although there is no a priori reason to expect the energies of the branched molecules to follow those predicted by the relationship for their linear isomers, it is instructive to compare the methyl and methylene group contributions with those determined by the linear relationship. This comparison is given in Tables 3 and 4. It should be recalled that the transferable methyl group in a linear hydrocarbon is found for all cases with $n > 2$, wherein the group is bonded to a methylene from which it withdraws electrons, giving it a $\Delta N(CH_3)$ = +0.016 e and a $\Delta E(CH_3)$ = –9 kcal/mol at RHF and $\Delta N(CH_3)$ = +0.011 e and $\Delta E(CH_3)$ = –5.0 kcal/mol at MP2. The deviations of the energies of the methyl groups from the standard value $E^o(CH_3)$ are given in Table 3 in order of decreasing magnitude.

Considering first the RHF results, the increase in stability of the methyl group, measured by $\Delta E(CH_3)$, parallels the increase in its population $\Delta N(CH_3)$, with the methyl group withdrawing an increasing number of electrons as the number of hydrogens on the group it is bonded to decreases. Thus, it is most stable and withdraws the most electrons from the C group, next most from CH and least from CH_2, determining the order of electron withdrawing ability as $CH_3 > CH_2 > CH > C$. The extent of electron withdrawal and the accompanying decrease in energy approach the deviations found for the transferable methyl group in the linear hydrocarbons: +0.016 e and –9 kcal/mol observed for a methyl bonded in the extended chain $CH_2CH_2CH_3$ found in C10. The MP2 results parallel those for RHF, with the values of $\Delta N(CH_3)$ being slightly reduced, and the values of $\Delta E(CH_3)$ slightly less negative. As for the RHF results, one finds that the values for the methyl group bonded to the extended chain in C10 approach the values found for the transferable methyl group, with $\Delta N(CH_3)$ = 0.011 e and $\Delta E(CH_3)$ = –4 kcal/mol.

Table 4 lists the deviations of the populations and energies of the methylene groups in the branched hydrocarbons from their standard values in the linear molecules. A meth-

Table 4. Methylene group contributions to branched hydrocarbons

Methods	Molecule	$N(CH_2)$	$E(CH_2)$	$\Delta N(CH_2)$	$\Delta E(CH_2)$
RHF/SCVS	$C(CH_2CH_3)_4$	7.9997	–39.06049	0.000	–8.9
	$CH(CH_2CH_3)_3$	7.9924	–39.04377	–0.008	1.6
	$CH(CH_2CH_2CH_3)_3$[a]	7.9852	–39.03688	–0.015	5.9
	$CH(CH_2CH_2CH_3)_3$[b]	8.0073	–39.06191	0.007	–9.8
MP2/SCVS	$C(CH_2CH_3)_4$	8.0004	–39.24060	0.000	–8.1
	$CH(CH_2CH_3)_3$	7.9954	–39.22656	–0.005	0.7
	$CH(CH_2CH_2CH_3)_3$	7.9895	–39.22263	–0.011	3.2
	$CH(CH_2CH_2CH_3)_3$	8.0056	–39.23779	0.006	–6.4

Note: RHF/SCVS: $E^o(CH_2)$ = –39.04634 au. MP2/SCVS: $E^o(CH_2)$ = –39.22766 au.

[a] CH_2 bonded to CH_3.

[b] CH_2 bonded to CH.

Table 5. CH group contributions to branched hydrocarbons.

Methods	Molecule	N(CH)	E(CH)	ΔN(CH)	ΔE(CH)
RHF/SCVS	$CH(CH_3)_3$	6.9184	–38.37721	0.000	0.0
	$CH(CH_2CH_3)_3$	6.9592	–38.39403	0.041	–10.6
	$CH(CH_2CH_2CH_3)_3$	6.9586	–38.39606	0.040	–11.8
MP2/SCVS	$CH(CH_3)_3$	6.9393	–38.57447	0.000	0.0
	$CH(CH_2CH_3)_3$	6.9751	–38.59335	0.036	–11.8
	$CH(CH_2CH_2CH_3)_3$	6.9727	–38.59502	0.033	–12.9

Note: Differences relative to CH group in $CH(CH_3)_3$.

Table 6. Contributions of C group to branched hydrocarbons.

Methods	Molecule	N(CH)	E(CH)	ΔN(CH)	ΔE(CH)
RHF/SCVS	$C(CH_3)_4$	5.8694	–37.71355	0.0333	–6.2
	$C(CH_2CH_3)_4$	5.9100	–37.71455	0.0739	–6.9
MP2/SCVS	$C(CH_3)_4$	5.9138	–37.93191	0.0026	–3.8
	$C(CH_2CH_3)_4$	5.9450	–37.94877	0.0343	–14.4

ylene group bonded to the transferable methyl in a linear molecule transfers density equal to the amount the methyl groups gain, $\Delta N(CH_2)$ = –0.16 e, and is destabilized by an amount opposite to the stabilization of the methyl group, $\Delta E(CH_2)$ = +9 kcal/mol. Only in the case of the methylene bonded to a methyl in the extended chain found in C10 are these values approached. The groups bonded to either a C or a CH group have population changes close to zero and are either stabilized, as in C9 and C10, or only slightly destabilized as in C7. Again, the same pattern in population and energy changes is found for the MP2 results. While there is no significant transfer of charge from either C or CH to a bonded methylene, the methylene gains in stability unless it is sandwiched between a methyl group and the end group in question, when it is slightly destabilized.

The CH group contributions are listed in Table 5, where they are referenced to the CH group in *iso*-butane, C4. To put the results on an absolute scale, the energies of the C and H atoms of the CH group in $CH(CH_3)_3$ are compared with the energies of the C and the H atoms in the standard methyl group, $E^o(CH_3)$, i.e., the energy of methyl group in ethane. Both atoms gain in electronic charge and decrease in energy compared with the corresponding atoms in the standard methyl group; the C atom gains 0.020 e and undergoes a decrease of 20 kcal/mol, while the H atom gains 0.028 e and undergoes a decease in energy of 13 kcal/mol at the RHF level, which is illustrative of MP2 as well. Thus, the atoms of the CH group of $CH(CH_3)_3$ are more stable than their counterparts in standard methyl, and these stabilities increase with increasing length of the linear group at MP2.

The contributions of the C atom to C5 and C9 are listed in Table 6, again referenced to the C atom in the CH group of C4, $CH(CH_3)_3$. The C atom is more stable than the C atom in the CH group in C4, and the results determine the relative stabilities of the energies of the C atoms in the acyclic hydrocarbons: the stability of C increases as the number of bonded hydrogens decreases. Thus, E(C) in the group C < E(C) in CH < E(C) in CH_2 < E(C) in CH_3. The populations of the C atoms decrease in the same order from 5.87 e in the group C to 5.82 e in methyl, and it is the transfer of density from C to H that results in a decrease in the stability of C.

Summary

The energies of the branched hydrocarbons do not differ significantly from those predicted by the linear relationship, eq. [1], with the differences decreasing with the inclusion of electron correlation. This is found in spite of deviations in the methyl and methylene group energies from their standard transferable values. The deviations parallel the increasing transfer of electron density from C to H, a transfer that results in an increasing stability of the group. Thus, the order of electron withdrawing ability $CH_3 > CH_2 > CH > C$ parallels the increasing stability of the methyl group. Start-

ing from the other end of hydrogen substitution, the most stable carbon atom is the one not bonded to any hydrogens, resulting in the energy order: E(C) in the group C < E(C) in CH < E(C) in CH_2 < E(C) in CH_3. Thus, the methylene group is least stable when bonded to either methyl as in $CH(CH_2CH_2CH_3)_3$ or to a C group as in $C(CH_2CH_3)_4$. Thus, the direction of charge transfer appears to be the dominating feature in determining the relative group energies.

Dependence of results on theoretical method

This summary brings into question a possible dependence of the direction of charge transfer of the group properties on q(H) and thus with the method of calculation. DFT calculations can predict a transfer of density from C to H in saturated hydrocarbons, but this direction is reversed with the inclusion of diffuse functions on the hydrogen atoms. Thus, q(H) = +0.0094 e in ethane for a B3PW91/6–311+G(2d,p) DFT calculation, a value that decreases to –0.0149 e for the same calculation with an extra diffuse function on H, that is with G(2d,2p). The direction of negative-charge transfer is C → H in RHF and all post-HF calculations, and this direction is maintained in all DFT calculations that employ a basis set with a diffuse function on H, results that are made clear in Fig. 2. The energies of the H atoms parallel the populations with the most negative energies associated with the diffuse basis set that gives the largest H populations, Fig. 2. An investigation of the changes in populations and energies of the linear hydrocarbons at B3PW91/6–311+G(2d,2p) DFT shows a transfer of electronic charge from methyl to its bonded methylene, with the charge transfer being reduced to zero for the interior methylene groups in pentane and octane. These results are in agreement with those found in the SCF calculations. The group energies only partially emulate the SCF results, with methyl being stabilized in comparison with its standard value in the linear molecules, but by a decreasing amount with increasing n, one that is not balanced by an energy increase of the bonded methylene group. In addition, the changes in energies of the interior methylene groups referenced to their standard linear values do not reduce to zero, the change for a central methylene in octane for example equalling –2.7 kcal/mol. These results are, however, anticipated, as a DFT calculation is incapable of satisfying the virial theorem, unlike the SCVS results reported here for the RHF and MP2 calculations. The kinetic energy used in a DFT calculation in the determination of the atomic energies is T_s, the kinetic energy of a set of non-interacting electrons and is in error by the omission of T_c, the "correlation" kinetic energy. This problem is discussed at some length in an appendix to the paper by Mata et al.[30] and treated in more detail in a forthcoming paper by Rodríguez et al.[31]

Cyclic hydrocarbons and strain energy

Total molecular energies

Table 7 gives the RHF and MP2 total energies of the cyclic hydrocarbons $(CH_2)_n$ with n = 3, 4,5, and 6, along with the virial ratio $\gamma = -V/T$, which should equal 2 for satisfaction of the virial theorem. The symmetries of the molecules are also indicated. The errors in the summation of the integrated atomic populations $N(\Omega)$ and energies $E(\Omega)$ are all acceptably small, with the magnitudes of the largest differences being 0.008 e for N and 1.6 kcal/mole for E.

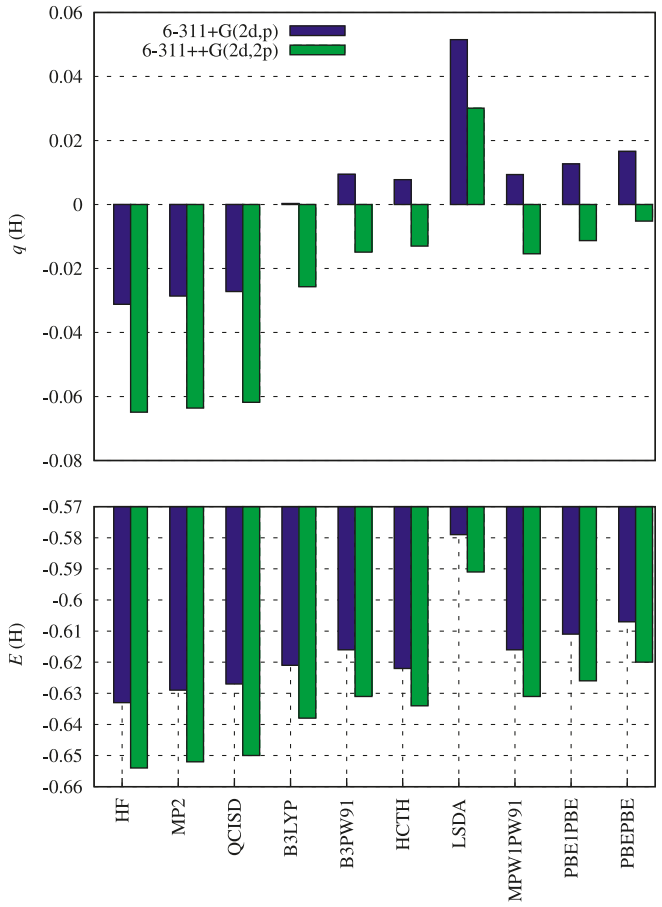

Fig. 2. Bar graphs of the atomic charges q(H) and energies E(H) of a hydrogen atom in ethane, showing their variation with the mode of calculation and basis-set dependence. The first three are RHF and post HF, and the remaining seven are DFT results for differing functionals.

Table 8 gives the integrated populations and energies of a methylene group in each molecule and the difference between the group energy and that of the standard methylene group, $E^o(CH_2)$ of eq. [1]. The strain energy is given by n times this difference in the column entitled "Strain energy". The "experimental" value for the strain energy is given as a bracketed value in the same column. The experimental value is from a recent compilation of the known heats of formation of alkanes and cycloalkanes by Cohen and Benson,[10] values that are almost unchanged from the Franklin equivalents[32] used in the first determination of strain energies using QTAIM.[6] As anticipated, the value of $\Delta E(CH_2)$ decreases as n increases, giving a zero value for the strain energy in cyclohexane, in essential agreement with experiment.

Overall, the agreement with experiment is seen to be better at RHF than at the correlated level MP2, although MP2 does recover the small observed ring strain in cyclohexane. In fact, RHF frequently does better than MP2 at reproducing experimental energies for the saturated hydrocarbons, a consequence of the C and H atoms possessing almost equal electronegativities and thus possessing similar density-based

Table 7. Total energies in atomic units and related energy quantities for cyclic hydrocarbons.

Molecule	Method	Molecular energy	$\gamma = -V/T$	$\Sigma N(\Omega) - N$	$\Sigma E(\Omega) - E_n$
Cyclopropane	RHF/SCVS	–117.09541	2.0000001	0.0001	–0.1
D_{3h}	MP2/SCVS	–117.63228	2.0000002	–0.0009	0.0
Cyclobutane	RHF/SCVS	–156.14387	1.9999998	–0.0002	0.2
D_{2d}	MP2/SCVS	–156.86288	2.0000002	–0.0011	0.1
Cyclopentane	RHF/SCVS	–195.22173	1.9999999	–0.0006	0.1
C_2	MP2/SCVS	–196.12277	2.0009401	–0.0002	0.1
Cyclohexane	RHF/SCVS	–234.27747	2.0000000	–0.0042	0.0
D_{3d}	MP2/SCVS	–235.36282	1.9999999	–0.0090	1.6

Table 8. Populations and energies of CH_2 groups and their differences from the standard energy E^o(CH2) defining the strain energy for cyclic hydrocarbons.

Method	Molecule	$N(CH_2)$	$E(CH_2)$	$\Delta E(CH_2)$	Strain energy (experimental)
RHF/SCVS	Cyclopropane	8.000	–39.03172	9.2	27.6 (27.7)
	Cyclobutane	8.000	–39.03605	6.5	26.0 (26.8)
	Cyclopentane[a]	8.000	–39.04417	1.3	6.3 (7.1)
	Cyclohexane	7.999	–39.04644	0.0	0.0(0.7)
MP2/SCVS	Cyclopropane	8.000	–39.21077	10.6	31.8 (27.7)
	Cyclobutane	8.000	–39.21576	7.5	30.0 (26.8)
	Cyclopentane	8.002	–39.22457	1.9	9.7 (7.1)
	Cyclohexane	7.999	–39.22750	0.1	0.6 (0.7)

Note: RHF/SCVS: $E^o(CH_2)$ = –39.04634 au. MP2/SCVS: $E^o(CH_2)$ = –39.22766 au.

[a]These are average values for N, E, and ΔE. At RHF, the unique CH_2 has N and E values of 8.003 e and –39.03659 au, methylenes bonded to it have $N(CH_2)$ = 8.000 e and $E(CH_2)$ = –39 04282 au, and the remaining methylenes have $N(CH_2)$ = 7.998 e and $E(CH_2)$ = –39.04982 au. At MP2, the corresponding sets of values are 8.003 e, –39.21672 au; 8.001 e, –39.22315 au; 7.998 e, –3922992 au.

energy contributions. In density functional theory, the correlation energy is expressed as a functional of the density. Thus, when the density remains unchanged for a given group in different molecules, the group's contribution to the correlation energy should also remain unchanged. If transferability is maintained with the addition of correlation, as it appears to be since transferability is an observed property, this should result in contributions to the correlation energy that parallel the uncorrelated results. This is borne out by calculation of the correlation energy of the methyl and methylene groups at RHF in 6–31G**/6–31G* calculations[33] using the functional of Langreth et al.[34] As anticipated, the correlation energies for the transferable methyl and methylene groups from propane to hexane were separately conserved to 1 to 2 kcal/mol.

The introduction of limited electron correlation as done in MP2 appears to upset this balance in some properties.Thus, RHF using the smaller basis set 6–31G** recovers the experimental strain energies to an almost equal extent to that found here with the larger basis set; 28.7, 26.8, 7.1, and 0.6 kcal/mol for n = 3, 4, 5, and 6, respectively.[6] It has also been demonstrated that the strain energies in branched and bicyclic hydrocarbons, such as the propellanes, are also recovered at this level of theory.[6,35] In any event, the agreement with experiment leaves no doubt that QTAIM recovers the essential features of strain energy, approaching quantitative agreement at the RHF level of theory, a conclusion borne out by the following discussion of QTAIM's accounting for the origin of strain energy.

The unique ability of RHF with relatively simple basis sets to recover experimental heats of formation of hydrocarbons has been amply illustrated by Herndon[28] wherein he demonstrated that a multilinear regression analysis using the calculated HF 6–31G*//STO-3G energies enabled the fitting of the measured heats of formation of hydrocarbons with only two parameters (the number of carbon atoms and the number of hydrogen atoms) for structures ranging from acyclic to planar and nonplanar polycyclic aromatics, alkyl substituted benzenes, and highly strained alkenes, alkanes, and alkynes, with a mean deviation in ΔH_f^o (g) of 1.1 kcal/mol and with a correlation coefficient of 0.9998.

Origin of strain energy in cyclic hydrocarbons

Within the orbital model, the angle strain in a 3-MR causes an increase in the p character of the C–C bonds, thereby increasing the s character of the bonds to H and increasing the electronegativity of C relative to H, which results in the carbon atoms approaching ethylenic carbons in electronegativity. Coulson and Moffitt emphasize this point in their classic study of strain in cyclopropane by noting that the bond lengths and bond angles of the methylene group in cyclopropane resemble those for ethylene.[36] The limit of sp hybridization of C in ethyne results in H possessing a net positive charge in this molecule, thus accounting for this molecule's acidic properties. The effective sp^2 hybridization in cyclopropane increases the stability of its carbons relative to their unstrained analogue, and ring strain is not a result of a "repulsive" destabilization of the carbon atoms. Rather, it is a result of the destabilization of the bonded hydrogens following their loss of electron density to the carbons. Thus, the atomic populations and energies of the methylene group in cyclopropane are similar to those for the CH_2 group of ethene, with the group being 3 kcal/mol more stable than in ethene. The transfer of density

Table 9. Bond and ring critical-point data for C|C bonded interactions in cyclic hydrocarbons.

Molecule	Method	C—C bond length in au	$\rho_{b(rc)}$ (in au)	$\rho_{r(rc)}$ (in au)	Ellipticity (ε)
Cyclopropane	HF/SCVS	2.827	0.2467	0.1984	0.445
	MP2/SCVS	2.842	0.2339	0.1903	0.442
Cyclobutane	HF/SCVS	2.916	0.2438	0.0891	0.011
	MP2/SCVS	2.920	0.2311	0.0897	0.010
Cyclopentane	HF/SCVS	2.905	0.2473	0.0416	0.004
	MP2/SCVS	2.901	0.2363	0.0432	0.004
Cyclohexane	HF/SCVS	2.888	0.2521	0.0193	0.003
	MP2/SCVS	2.880	0.2413	0.0211	0.003

from H to C results in a decrease in energy of the C atom in the amount of 18.8 kcal/mol while the energies of the two H atoms increase by a greater amount, equal to 28.0 kcal/mol (relative to their value in the standard transferable methylene group) and the CH_2 group of cyclopropane is less stable than the standard methylene group of saturated hydrocarbons by 9.2 kcal/mol, thus reproducing the strain energy of 27.5 kcal/mol. This transfer of density from H to C decreases with the size of the ring and vanishes for cyclohexane, which is consequently predicted to have zero strain energy, in agreement with experiment. The hybridization model is simple and powerful; s electrons are bound more tightly than p electrons, and hybridization is determined primarily by bond angles. Thus, with the increasing bond angles (RHF), from 60.0 in cyclopropane to 88.5, to 103.3, and to 111.5 in cyclohexane, there is a decreasing extent of transfer of density from the hydrogens to the carbon atom; the amount deceasing from 0.047 e in cyclopropane to 0.013 e for $n = 4$, to 0.01 e for $n = 5$, and to zero for cyclohexane. Correspondingly, the energies of the H atoms, in excess of the energy of a H atom in the standard transferable methylene group, decrease in the same order from +14 in $n = 3$ to +5 in $n = 4$, to +2 in $n = 5$, and to zero in cyclohexane, with the energy of the C atom undergoing corresponding increases to yield the tabulated strain energies.

It is important to note that QTAIM energies are in complete accord with the hybridization model.[35,37,38] The carbon atom energies in ethane, ethene, and ethyne for example, yield a near linear relationship with respect to their atomic populations at B3PW91/6–311+G(2d,p) with a regression coefficient of 0.996.[38] The resulting "linear charge/energy relationship" enables one to determine the extent to which a carbon atom is stabilized in a system with electron delocalization. A carbon atom in benzene for example, with a population intermediate between that in ethane and ethene, is more stable than that predicted by the linear charge/energy relationship by 17 kcal/ mol. A comparison of the energy of a |CH group in benzene with that of the corresponding non-conjugated group in cyclohexane, yields a "resonance" energy of 40 kcal/mol in agreement with the generally accepted values.

One should note that this definition of strain energy is not determined by symmetry, that is, determined by the fact that the energy of an *n*-cyclic hydrocarbon is 1/*n* that of the total. The strain energy is instead determined by comparing 1/*n*th of the cyclic energy with the energy of the standard methylene group defined by the linear regression analysis of the energies of the linear hydrocarbons, the quantity $E^o(CH_2)$ of eq. [1]. This energy is determined theoretically by integration of the electronic kinetic energy density over a region of space bounded by the two C|C zero-flux surfaces bounding the $|CH_2|$ group in a linear hydrocarbon, using the virial theorem of an open system. The finding that this energy is given precisely by the slope $E^o(CH_2)$ (to within 0.2 kcal/mol) assigned to the methylenic energy in a linear-regression analysis of the hydrocarbon energies is a striking proof of the physical relevance of the zero-flux surface and of the energies defined by QTAIM.[39]

The physics underlying Winstein's "homoaromaticity"

To account for enhanced solvolysis rates in systems containing a three-membered ring, Winstein postulated that cyclopropane may enter into conjugation with an unsaturated system when the ring surface is properly aligned, giving rise to homoconjugated or homoaromatic interactions.[40] An example of the former is cyclopropyl carbinyl cation $C_4H_7^+$, wherein the ring surface is conjugated with an empty p orbital on a CH_2 group. A recent paper describes in detail examples of homoaromatic behaviour and of how it is accounted for in terms of QTAIM.[38] The paper demonstrates that homoaromaticity is a direct consequence of the unique delocalization of the electron density found over the surface of a three-membered ring of carbon atoms and illustrates the consequences of this delocalization in accounting for the Cope rearrangement in semibullvalene.

The chemistry of cyclopropane emulates that of an unsaturated system. This is accounted for in MO theory by Walsh orbitals, which ascribe π character to orbitals lying in the plane of the ring.[41,42] QTAIM gives physical substance to this model by determining that the C|C bond paths exhibit significant ellipticities whose major axes lie in the ring surface. This is a topological consequence of the proximity of the ring and bond critical points unique to a three-membered ring (3-MR).

The electron density of "bonds", which in an orbital model possesses "π" character, is elliptically disposed about the bond path with the density being preferentially accumulated in a plane that, in ethene for example, is perpendicular to the plane of the nuclei, the plane determined by the major axis of the ellipse. Thus, the presence of π bonding should lead to a measurable distortion of the density from circular symmetry about the bond axis.

This distortion is measured by the bond's "ellipticity". The ellipticity is defined in terms of the two negative eigen-

values of the Hessian of the density at the bond critical point that determine the curvatures of the density perpendicular to the bond path. The ellipticity ε is defined as $\lambda_1/\lambda_2 - 1$, where λ_1 and λ_2 are the negative eigenvalues of the Hessian of the electron density at the bond critical point.[8]

These are the curvatures perpendicular to the bond path with $|\lambda_1| > |\lambda_2|$ whose associated eigenvectors determine the interatomic surface. Thus, λ_2 is the curvature along the major axis of the ellipse, that is, the direction of the "soft" curvature.[43] The ellipticities of the C–C bonds in ethane, benzene, and ethylene are 0.0, 0.18, and 0.30, respectively. What is important is that the ellipticity provides a measure of the distortion of the density away from cylindrical symmetry that is independent of any model, orbital, or otherwise thereby enabling one to determine "π" character in any situation independent of the nominal order of the bond.[38] Thus, in molecules exhibiting homoaromaticity, significant ellipticities are found for bonds with orders less than unity. Because of the accumulation of density within the interior of a three-membered ring, the value of the density at the ring critical point in cyclopropane approaches to within 0.05 au of its value at the C|C bond critical points. The result is a delocalization of the density over the surface of the ring, resulting in the density exhibiting a distinct elliptical distortion relative to the cylindrical distribution found in an isolated C|C bond with the major axis of the ellipticity lying in the ring surface. Table 9 shows that the ellipticity of a C–C bond in cyclopropane is actually greater than that found in ethene. In cyclopropane, the major axes of the C|C ellipticities are perpendicular to the ring axis, the axis associated with the unique positive eigenvalue of the (3,+1) critical points, just the opposite behaviour to that found in an aromatic system such as benzene where the C|C bond ellipticities, as anticipated for bonds with π character, are aligned with the ring axis, perpendicular to the plane of the molecule.

Table 9 also gives the values of the density at the bond and ring critical points in the cyclic hydrocarbons. The data demonstrate that the surface delocalization of the density is unique to a three-membered ring in hydrocarbon chemistry. On the other hand, the stabilities of boranes and carboranes have been shown to be accounted for by the significant delocalization of the density over the surfaces of both three- and four-membered rings.[44] Not only does the ellipticity decrease significantly with increase in ring size in the cyclic hydrocarbons, the soft axis does not lie in the ring surface as found for the delocalization of the density over the surface of cyclopropane. In cyclobutane, the soft curvature is directed 28° above the ring surface, and in cyclohexane, it is parallel to the ring axis, the reverse of the situation found in cyclopropane.

Acknowledgement

Dr. Cortés-Guzmán would like to express his thanks to Universidad Nacional Autónoma de México-Dirección General de Servicios de Cómputo Académico (UNAM-DGSCA) for their generous support in supplying the necessary computer time. Dr. Gao thanks the National Research Council of Canada for financial support. This work was supported by Zhejiang Provincial Natural Science Foundation (Y5080043) and the Scientific Research Foundation of Wenzhou Medical College (QTJ07014).

References

(1) Rossini, F. D. *J. Res. Natl. Bur. Stand. (US)* **1931**, *6*, 37.
(2) Rossini, F. D. *J. Res. Natl. Bur. Stand. (US)* **1931**, *7*, 329.
(3) Rossini, F. D. *J. Res. Natl. Bur. Stand. (US)* **1934**, *13*, 21.
(4) Benson, S. W.; Cruickshank, F. R.; Golden, D. M.; Haugen, G. R.; O'Neal, H. E.; Rodgers, A. S.; Shaw, R.; Walsh, R. *Chem. Rev.* **1969**, *69* (3), 279–324. doi:10.1021/cr60259a002.
(5) Fliszar, S. *Charge Distributions and Chemical Effects;* Springer-Verlag: Berlin, 1983.
(6) Wiberg, K. B.; Bader, R. F. W.; Lau, C. D. H. *J. Am. Chem. Soc.* **1987**, *109* (4), 1001–1012. doi:10.1021/ja00238a005.
(7) Cortés-Guzmán, F.; Bader, R. F. W. *Chem. Phys. Lett.* **2003**, *379* (1-2), 183–192. doi:10.1016/j.cplett.2003.07.021.
(8) Bader, R. F. W. *Atoms in Molecules: A Quantum Theory;* Oxford University Press: Oxford, UK, 1990.
(9) Bader, R. F. W.; Bayles, D. *J. Phys. Chem. A* **2000**, *104* (23), 5579–5589. doi:10.1021/jp9943631.
(10) (a) Benson, S. W. The Thermochemistry of Alkanes and Cycloalkanes. In *The Chemistry of Alkanes and Cycloalkanes: Series; The Chemistry of Functional Groups edition;* Patai, S., Rappoport, Z., Eds.; John Wiley and Sons: New York, 1992; Chap. 6, pp 215–287.
(11) Bader, R. F. W. *J. Phys. Chem. A* **2008**, *112* (51), 13717–13728. doi:10.1021/jp806282j. PMID:19032142.
(12) Bader, R. F. W.; Matta, C. F. *J. Phys. Chem. A* **2004**, *108* (40), 8385–8394. doi:10.1021/jp0482666.
(13) Matta, C. F.; Bader, R. F. W. *J. Phys. Chem. A* **2006**, *110* (19), 6365–6371. doi:10.1021/jp060761+. PMID:16686473.
(14) Schwinger, J. *Phys. Rev.* **1951**, *82* (6), 914–927. doi:10.1103/PhysRev.82.914.
(15) Bader, R. F. W. *Phys. Rev. B* **1994**, *49* (19), 13348–13356. doi:10.1103/PhysRevB.49.13348.
(16) Bader, R. F. W. *J. Phys. Chem. A* **2007**, *111* (32), 7966–7972. doi:10.1021/jp073213k. PMID:17629258.
(17) Hohenberg, P.; Kohn, W. *Phys. Rev. B* **1964**, *136* (3B), B864. doi:10.1103/PhysRev.136.B864.
(18) Bader, R. F. W.; Cortés-Guzmán, F. *The Virial Field and Transferability in DNA Base-Pairing;* Quantum Biochemistry edition; Matta, C. F., Ed.; Wiley-VCH: Weinheim, Germany, 2009.
(19) Bader, R. F. W.; Gough, K. M.; Laidig, K. E.; Keith, T. A. *Mol. Phys.* **1992**, *75* (5), 1167–1189. doi:10.1080/00268979200100901.
(20) Bader, R. F. W.; Keith, T. A. *J. Chem. Phys.* **1993**, *99* (5), 3683. doi:10.1063/1.466166.
(21) Graña, A. M.; Mosquera, R. A. *J. Chem. Phys.* **2000**, *113* (4), 1492. doi:10.1063/1.481966.
(22) Quiñónez, B.; Vila, A.; Graña, A. M.; Mosquera, R. A. *Chem. Phys.* **2003**, *287* (1-2), 227–236. doi:10.1016/S0301-0104(02)00993-X.
(23) Mandado, M.; Vila, A.; Graña, A. M.; Mosquera, R. A.; Cioslowski, J. *Chem. Phys. Lett.* **2003**, *371* (5-6), 739–743. doi:10.1016/S0009-2614(03)00357-9.
(24) Keith, T.A. *AIMALL,* Beta Version 09.08.26; 2007. aim.tkgristmill.com
(25) Cheng, M.-F.; Li, W.-K. *J. Phys. Chem. A* **2003**, *107* (28), 5492–5498. doi:10.1021/jp034879r.
(26) Lopes, A. R.; Bettega, M. H. F.; Lima, M. A. P.; Ferreira, L. G. *J. Phys. At. Mol. Opt. Phys.* **2004**, *37* (5), 997–1012. doi:10.1088/0953-4075/37/5/004.
(27) Bürger, H.; Pawelke, G. *Spectrochimica Acta A Mol. Spect.* **1979**, *35* (6), 559–564. doi:10.1016/0584-8539(79)80109-9.
(28) Herndon, W. C. *Chem. Phys. Lett.* **1995**, *234* (1-3), 82–86. doi:10.1016/0009-2614(95)00015-V.

(29) Rafat, M.; Popelier, P. L. A. Topological Atom–Atom Partitioning of Molecular Exchange Energy And Its Multipolar Convergence. In *The Quantum Theory of Atoms In Molecules: From Solid State to Drug Design edition;* Matta, C. F., Boyd, R. J., Eds.; Wiley-VCH: Weiheim Germany, 2007; Chap. 5, pp 121–140.
(30) Matta, C. F.; Arabi, A. A.; Keith, T. A. *J. Phys. Chem. A* **2007**, *111* (36), 8864–8872. doi:10.1021/jp0735280. PMID: 17713891.
(31) Rodríguez, J. I.; Ayers, P. W.; Götz, A. W.; Castillo-Alvarado, F. L. *J. Chem. Phys.* **2009**, *131* (2),o. 021101. doi:10.1063/1.3160670. PMID:19603962.
(32) Franklin, J. L. *Ind. Eng. Chem.* **1949**, *41* (5), 1070–1076. doi:10.1021/ie50473a041.
(33) Bader, R. F. W.; Larouche, A.; Gatti, C.; Carroll, M. T.; MacDougall, P. J.; Wiberg, K. B. *J. Chem. Phys.* **1987**, *87* (2), 1142. doi:10.1063/1.453294.
(34) Langreth, D. C.; Mehl, M. J. *Phys. Rev. B* **1983**, *28* (4), 1809–1834. doi:10.1103/PhysRevB.28.1809.
(35) Bader, R. F. W. Atomic and group properties in the alkanes. In *The Chemistry of Alkanes and Cycloalkanes: Series; The Chemistry of Functional Groups edition;* Patai, S., Rappoport, Z., Eds.; John Wiley and Sons: New York, 1992; Chap. 1, pp 1–77.
(36) Coulson, C. A.; Moffitt, W. E. *Philos. Mag.* **1949**, *40*, 1.
(37) Bader, R. F. W.; Cheeseman, J. R.; Laidig, K. E.; Breneman, C.; Wiberg, K. B. *J. Am. Chem. Soc.* **1990**, *112* (18), 6530–6536. doi:10.1021/ja00174a012.
(38) Brown, E. C.; Bader, R. F. W.; Werstiuk, N. H. *J. Chem. Phys. A* **2009**, *113* (13), 3254–3265. doi:10.1021/jp8109385.
(39) Cortés-Guzmán, F.; Bader, R. F. W. *J. Phys. Org. Chem.* **2004**, *17* (2), 95–99. doi:10.1002/poc.702.
(40) Winstein, S. Q. *Rev. Chem. Soc.* **1969**, *23* (2), 141. doi:10.1039/qr9692300141.
(41) Walsh, A. D. *Nature* **1947**, *159* (4047), 712–713. doi:10.1038/159712a0.
(42) Walsh, A. D. *Trans. Faraday Soc.* **1949**, *45*, 179. doi:10.1039/tf9494500179.
(43) Bader, R. F. W.; Slee, T. S.; Cremer, D.; Kraka, E. *J. Am. Chem. Soc.* **1983**, *105* (15), 5061–5068. doi:10.1021/ja00353a035.
(44) Bader, R. F. W.; Legare, D. A. *Can. J. Chem.* **1992**, *70* (2), 657–676. doi:10.1139/v92-089.

QSPR studies on normal boiling points and molar refractivities of organic compounds by correlation-ranking-based PCR and PC–ANN analyses of new topological indices

Raouf Ghavami, Amir Najafi, and Bahram Hemmateenejad

Abstract: The new topological indices (Sh indices) based on the distance sum and connectivity of a molecular graph, previously developed by our team, were extended to predict the two physicochemical properties, including normal boiling point (NBP) and molar refractivity (MR), of a large set of organic compounds consisting of alkanes, alkenes, ethers, amines, alcohols, alkylbenzenes, and alkylhalides. The sets of molecular descriptors were derived directly from the two-dimensional molecular structure of the compounds based on graph theory. Both linear and nonlinear modelings were implemented by using principal component regression (PCR) and principal component – artificial neural network (PC–ANN) with back-propagation learning algorithm, respectively. Eigenvalue and correlation-ranking procedures were used to rank the principal components and entered them into the models. Principal component analysis of Sh data matrix showed that the respective six and seven PCs could explain 97.49% and 99.22% of variances in the Sh indices. PCR analysis of the NBP and MR data demonstrated that the proposed Sh indices could explain about 97.52% and 99.52% of variations, while the variations explained by the PC–ANN modeling were more than 99.00% and 99.82%, respectively. The predictive ability of the models were evaluated using an external test set for NBP and MR of the molecules with the respective root-mean-square errors lower than 9.69 K and 0.660 cm^3 mol^{-1} for the linear model and 6.17 K and 0.416 cm^3 mol^{-1} for the nonlinear model.

Key words: topological Sh indices, eigenvalue ranking, correlation ranking, normal boiling point, molar refractivity, principal component analysis, principal component regression (PCR), principal component – artificial neural network (PC–ANN).

Résumé : Les nouveaux indices topologiques (indices Sh) basés sur la somme de la distance et la connectivité d'un graphe moléculaire et développés antérieurement par notre équipe ont été étendus afin de pouvoir prédire deux propriétés physico-chimiques, dont le point d'ébullition normal (PEN) et la réfractivité molaire (RM) d'un large ensemble de composés organiques formés d'alcanes, d'alcènes, d'amines, d'alkylbenzènes et d'halogénures d'alkyle. Les ensembles de descripteurs moléculaires ont été dérivés directement de la structure moléculaire bidimensionnelle des composés basée sur la théorie des graphes. On a développé des modèles linéaires et non linéaires en utilisant l'algorithme d'apprentissage en rétropropagation respectivement avec une régression du composant principal (RCP) et avec le réseau neural artificiel du composant principal (RNA–CP). On a fait appel aux méthodes de la valeur de eigen et du classement des corrélations pour classer les composants principaux qui ont ensuite été introduits dans les modèles. L'analyse du composant principal d'une matrice de données Sh a permis de montrer que respectivement six ou sept composants principaux (CP) peuvent expliquer 97,49 % et 99,22 % des variances dans les indices Sh. L'analyse de la RCP des données relatives aux PEN et aux RM a permis de démontrer que les indices Sh peuvent expliquer environ 97,52 % et 99,52 % des variations alors que les variations expliquées par me modèle RNA–CP expliquent respectivement 99,00 % et 99,82 % des variations. On a évalué l'habilité des modèles à faire des prédictions relatives aux PEN et aux RM des molécules en utilisant un ensemble externe et les erreurs quadratiques moyennes respectives étaient inférieures réseau neural artificiel du composant principal (RNA–CP) à 9,69 K et 0,660 cm^3 m^{-1} pour le modèle linéaire et de 6,17 K et 0,416 cm^3 m^{-1} pour le modèle non linéaire.

Mots-clés : indices SH topologiques, classement de valeurs de eigen, classement de corrélation, point d'ébullition normal (PEN), réfractivité moléculaire (RM), analyse du composant principal, régression du composant principal (RCP), réseau neural artificiel du composant principal (RNA–CP).

[Traduit par la Rédaction]

Received 11 February 2009. Accepted 14 May 2009. Published on the NRC Research Press Web site at canjchem.nrc.ca on 16 September 2009.

R. Ghavami[1] and A. Najafi. Department of Chemistry, Faculty of Science, University of Kurdistan, P. O. Box 416, Sanandaj, Iran.
B. Hemmateenejad.[2] Department of Chemistry, Shiraz University, Shiraz 71454, Iran.

[1]Corresponding author (e-mail: rghavami@uok.ac.ir).
[2]Present address: Medicinal & Natural Products Chemistry Research Center, Shiraz University of Medical Sciences, Shiraz, Iran.

Introduction

One of the most fundamental ideas of chemistry is that the physicochemical properties, for instance, normal boiling point and molar refractivity, for chemical and chemical engineering substances are determined on the basis of their molecular structures (the term "structure" taken here in its broadest sense to include both geometric and electronic aspects).[1–6] It is necessary to describe the chemical structure of the examined compound as one or more parameters such as various topological indices in developing a quantitative structure–property relationship (QSPR) model. The normal boiling points (NBPs) of liquids reflect the strength of the intermolecular forces that hold them together. The stronger the intermolecular forces, the more tightly atoms will be held together; therefore, it causes higher normal boiling point. However, the boiling points are not always available in tables or other reference materials, while molar refractivity (MR) is a constitutive–additive property. Alternative definitions of MR have been proposed by Lorentz and Lorentz[7,8] (see eq. [1]), Gladston and Dale[9] (see eq. [2]), and Vogel[10] (see eq. [3]).

$$[1] \qquad MR_{LL} = (n^2 - 1)/(n^2 + 1)(M/\rho)$$

$$[2] \qquad MR_{GD} = (n - 1)(M/\rho)$$

$$[3] \qquad MR_{V} = nM$$

where n is the refractive index, M is the molecular mass, and ρ is the density of a molecule. MR is dependent on volume and polarizability. MR can be used for the substituted or for the whole molecule. Although molecular volume aspect of MR is of some interest to chemists and biologists, its relationship to polarizability is also of special interest to drug-design workers. Electronic polarization or molecular polarizability α_E and molar refractivity are related as ($MR = 4/3\pi\alpha_E$). The polarizability α_E of a molecule related to the intermolecular forces is important in drug and receptor reactions. Significantly, the α_E term is a dominant term in the expression for dispersion energy of interactions. The uses of α_E and MR have recently become significant in correlating physical properties with biological actions of drug molecule series.[11] Its ability to predict molar refractivity from a simple chemical graph has significant consequences in gaining insight into the SAR of biological molecules as well as the study of their physical properties such as boiling point. As a result, methods of estimation have increasingly become important and useful for procedures and consumers of many organic chemical compounds.

Quantitative structure–property relationships (QSPR) are mathematical equations relating the chemical structure to a wide variety of physical, chemical, biological, and technological properties.[12–14] The established QSPR models could be used to predict the properties of compounds that have not been measured or even have been unknown. Thus, QSPR approach saves resources and expedites the process of development of new molecules.[15] Because getting the physicochemical parameters for each considerable compound is not always possible, development of capable nonempirical structural representation to give a satisfactory correlation with the studied property would be useful. Several topological, geometric, electronic, and quantum chemical indices have been already used in quantitative structure–property relationship researches.[16,17] Topological indices (TIs) consider the molecule as a mathematical graph; a number of these descriptors simply are various graph invariants or other functions of the molecular graph. TIs are able to provide a more detailed description of molecular shape features such as branching and crowdedness. In this regard, TIs can be easily designed and calculated; however, the correlation of them to present the normal boiling point and molar refractivity properties is in a good way, and their applications in QSPR studies instead of more complicated geometric, electronic, and quantum chemical descriptors are preferred. More than 100 topological indices such as the Wiener index, Hosoya index, Balaban index, and Randic indices were developed, and these structural descriptors have been widely applied in QSPR studies.[18–22] Many investigators have reported a good correlation of both the normal boiling point and molar refractivity with structural characteristics of molecules by using different topological indices as structural descriptors.[6,23–25]

The development of QSPR studies is required for the suitable mathematical technique to make the models. In this regard, there are many available classical multivariate calibration techniques that could be used. These include multivariate linear regression (MLR), principal components regression (PCR), and partial least-squares regression (PLS).[26–28]

As an alternative to the fitting of data to an equation and reporting the coefficients derived from there, a neural net or artificial neural network (ANN) is designed to process input information and generate a hidden model of the relationships. One advantage of neural nets is that they are naturally capable of modeling nonlinear systems.[29] Disadvantages include a tendency to overfit the data, and a significant level of difficulty in ascertaining which descriptors are most significant in the resulting model (a consequence of the interconnected character of a multilayered neural network [30]). Recently, the ANN modeling technique has attracted an increasing interest as a very promising method for classification and multivariate calibration problems.[31–33] The flexibility of ANN enables it to discover more complex relationships in experimental data when it is compared with the traditional statistical models. Hence, the ANNs provide proper analytical alternatives to conventional techniques and interesting approaches to the QSAR/QSPR studies.[34–36] The principal component – artificial neural network (PC–ANN) is another version of the PCR, which models the nonlinear relationships between the PCs and dependent variables, and it was proposed by Gemperline et al. to improve the training speed and decrease the overall calibration error.[37]

The relationship between molar refraction and normal boiling point has been found the literature. Gonzales et al.[38] proposed the use of corrlation weighing of atomic orbitals with extended connectivity of zero- and first-order graphs of atomic orbitals to estimate normal boiling points for a set of 200 organic molecules through the application of QSPR theory. Jäntschi et al. reported the relationship of molecular descriptor familiy to predict the normal boiling points and molar refraction values for 33 504 alkanes and 10 cyclic organophosphorous compounds, respectively.[39,40]

Qian et al.[41] have proposed the use of 3–6–1 back-propagation neural network technique to link the relation between molecular structures and boiling points. The data sets were composed of 73 saturated aliphatic aldehydes and alkanones, with experimental boiling points ranging from 253.7 K to 631.2 K, and the number of carbon atoms ranging from 1 to 20. Balaban et al.[42] predicted 200 carbonyl compounds contained 127 mono- and di-aldehydes and ketones and 73 esters using five topological indices. Toropov and Toropova[43] obtained one-variable models of the normal boiling points of carbonyl compounds by the nearest-neighboring code (NNC). Toropov and co-workers[44] have used simplified molecular input line entry system (SMILES) to model normal boiling points of acyclic carbonyl compounds.

In our previous paper, some new topological indices (Sh_1–Sh_{10} indices) based on the molecular connectivity[22] and Balaban-distance-sum[20,21] approaches were proposed.[45–48] The aim of the present investigation was to extend our previously developed model with an enlarged data set for QSPR characterization of normal boiling points and molar refractivities of a set of 394 diverse organic compounds using the new topological Sh indices. Obviously, these topological indices have been selected for the representation of molecular structure to obtain a prediction model as simple as possible. Besides the PCR model, a three-layered feed-forward PC–ANN has also been employed, as a statistical method, for building the prediction model.

Materials and methods

Dataset

The QSPR treatment started with the assembly of the data set. A collection of diverse organic compounds containing 394 compounds having C, H, O, N, and halogen atoms, and moreover, the two physicochemical properties of normal boiling point and their molar refractivity, which were realized experimentally along with the various number of carbon atoms from 2 to 9, which are taken from the scientific resources, have been investigated.[23,25,49,50] The normal boiling points of these compounds range from 266.25 to 545.95 K and their molar refractivities are from 12.9267 to 63.3751 cm^3 mol^{-1}, respectively. The mentioned organic compounds include 52 alcohols, 22 amines, 69 alkanes, 156 monoalkenes, 9 ethers, 69 alkylbenzenes, and 17 alkylhalides. The histogram presenting the experimental values related to the normal boiling points and molar refractivities' distribution for all data collected is depicted in Figs. 1A and 1B), respectively. As it is shown, the average values of NBP and MR belonging to all mentioned compounds are 395.80 and 37.69 along with the standard deviation (SD) of 45.92 and 7.55, respectively. A complete list of the compounds in the data set and their corresponding experimental normal boiling points and molar refractivities has been categorized in Table S1 of the Supplementary data. The range of the molecular masses of the compounds is also extensive and located in the range of 24 to 266 g mol^{-1} for ethanol and 1-iodoheptane, respectively.

Sh and Randic connectivity topological descriptors

Initially, the structure related to the computer design of each of the 394 diverse organic compounds, then for any

Fig. 1. Histogram of the distribution of the experimental NBPs (A) and MRs (B) for the total data set of 394 organic compounds used in this study. The solid curve is the fitting of the NBP and MR data to the normal distribution.

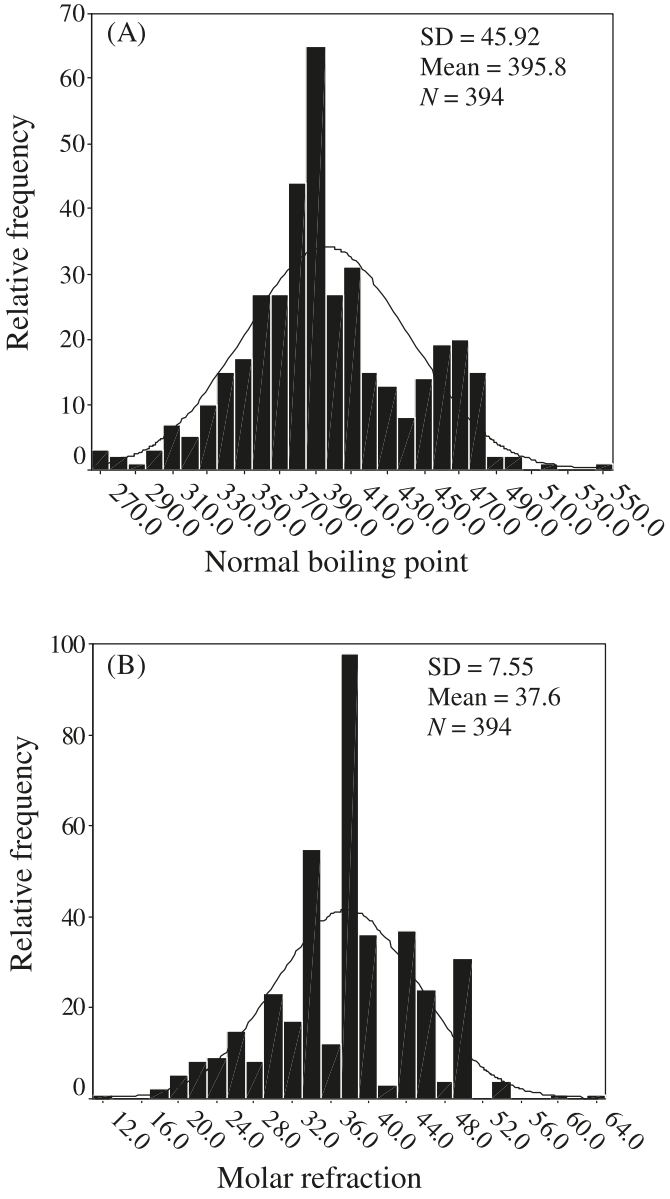

composition, the 10 Sh and Randic connectivity index (χ) topological molecular-structure descriptors were calculated from the combination of connectivity vectors and distance matrices, which were expressed by their computational style in our previous studies.[45–48] These indices were calculated by a home-made program (written in MATLAB environment), then the values of 10 Sh indices were placed inside the matrix with dimensions of 394 × 10. So, any chemical compound was placed inside as a point in the 10-dimensional space, X^{10}. The results are demonstrated in Table S2 (see Supplementary data).

Linear modeling: principal component regression

The $\boldsymbol{b}$ vector of the model equation $\boldsymbol{y} = \mathbf{X}\boldsymbol{b} + e$ was calculated by singular value decomposition (SVD)[51] according to

Table 1. Linear multivariate regression models and statistical parameters of compounds properties using PC indices. *N* denotes of the number of organic molecules.

Subset	Equation	R^{2a}	SE[a]	RMS[a]	REP[a]	F^a	R^2_{LOO} [a]	RMS_{LOO} [a]	*N*
Alcohol	NBP = 424.797 + 39.571 PC_1 – 6.952 PC_2 – 3.588 PC_4 – 3.318 PC_5 + 3.824 PC_7	0.9772	6.54	6.12	1.45	394	0.9652	7.60	52
	MR = 34.772 + 9.913 PC_1 + 1.316 PC_2 – 1.088 PC_3 – 0.772 PC_4	0.9936	0.84	0.81	2.30	1830	0.9911	0.95	
Amine	NBP = 377.882 + 34.603 PC_1 – 4.951 PC_2 + 7.709 PC_3 – 6.040 PC_4 + 5.396 PC_5	0.9568	9.17	8.01	2.07	71	0.9355	9.59	22
	MR = 32.866 + 7.322 PC_1 + 1.539 PC_2 – 0.858 PC_4 + 0.451 PC_5	0.9966	0.49	0.44	1.31	1242	0.9945	0.55	
Alkane	NBP = 387.636 + 29.800 PC_1 + 7.278 PC_2 + 4.182 PC_3 – 1.764 PC_4 + 1.413 PC_7 + 1.211 PC_9	0.9928	2.77	2.65	0.68	1424	0.9905	3.02	69
	MR = 39.486 + 4.986 PC_1 + 1.554 PC_2 + 0.310 PC_4 – 0.359 PC_5	0.9976	0.26	0.26	0.65	6648	0.9970	0.28	
Alkene	NBP = 369.224 + 27.030 PC_1 + 4.626 PC_2 + 2.051 PC_3 + 1.914 PC_4 + 1.213 PC_9	0.9781	4.20	4.13	1.12	1337	0.9756	4.34	156
	MR = 35.777 + 4.302 PC_1 + 0.968 PC_2 + 0.595 PC_3 – 0.377 PC_4 – 0.300 PC_5 + 0.211 PC_6	0.9914	0.42	0.42	1.16	2874	0.9887	0.48	
Ether	NBP = 352.545 + 31.779 PC_1 – 4264.188 PC_9	0.9630	7.40	6.46	1.73	77	0.8005	14.45	9
	MR = 30.604 + 6.038 PC_1 + 0.419 PC_2	0.9955	0.47	0.47	1.25	663	0.9878	0.65	
Alkylbenzene	NBP = 457.100 + 22.262 PC_1 + 5.961 PC_2 – 1.833 PC_6 + 4.210 PC_8 + 1.957 PC_9	0.9672	4.51	4.34	0.94	371	0.9590	4.81	69
	MR = 46.166 + 5.234 PC_1 + 0.948 PC_2 + 0.209 PC_3 + 0.519 PC_4 – 0.164 PC_5	0.9977	0.27	0.26	0.55	5484	0.9970	0.29	
Alkylhalide	NBP = 381.203 + 40.680 PC_1 + 17.429 PC_2 + 2.167 PC_3 – 1.709 PC_4	0.9987	1.86	1.61	0.41	2263	0.9964	2.65	17
	MR = 31.347 + 6.852 PC_1 + 2.849 PC_2 + 1.602 PC_3 – 0.490 PC_4 – 0.423 PC_7	0.9984	0.36	0.30	0.93	1379	0.9952	0.51	

[a] R^2: correlation coefficient; SE: standard error of estimation; RMS: root-mean-square error; REP: root-mean-square error prediction; *F*: Fisher's criterion at the 95% probability level; R^2_{LOO}: square of the leave-one-out cross-validation correlation coefficient; RMS_{LOO}: leave-one-out cross-validation root-mean-square error.

the procedure of Sutter and Kalivas.[52] The $\mathbf{X}(m \times n)$ matrix, where m and n are the number of molecules and descriptors, respectively, was decomposed by SVD to give three matrices $\mathbf{U}(m \times n)$, $\mathbf{S}(n \times n)$, and $\mathbf{V}(n \times n)$ such that $\mathbf{X} = \mathbf{USV}^{\mathrm{T}}$, where $\mathbf{U}$ and $\mathbf{V}$ are the orthonormal matrices spanning the respective row and column spaces of the data matrix ($\mathbf{X}$) and $\mathbf{S}$ is a diagonal matrix whose diagonal elements are the square roots of the corresponding eigenvalues of the $\mathbf{U}$ and $\mathbf{V}$ eigenvectors. The eigenvalues are denoted by λ_i. The superscript T denotes the matrix transpose. As presented by Sutter and Kalivas,[52] the $\boldsymbol{b}$ vector in PCR can be obtained as

$$[4] \qquad \boldsymbol{b} = \sum_{i \in M} \frac{1}{\lambda_i} \boldsymbol{\upsilon}_i \boldsymbol{\upsilon}_i^{\mathrm{T}} \mathbf{X}^{\mathrm{T}} \boldsymbol{y}$$

where M contains k elements that are a subset of $\{1, 2, \ldots, w\}$ and w is the largest number such that $\lambda_w > 0$. By using this equation, it is possible to select a subset of PCs for building the PCR model. A column vector ($\boldsymbol{y}$) was made by the physicochemical property or activity data. The PCs of the validation ($\mathbf{X}_{\mathrm{v}}$) and test ($\mathbf{X}_{\mathrm{t}}$) sets were calculated by the following equation:

$$[5] \qquad \mathbf{U}_{\mathrm{v/t}} = \mathbf{X}_{\mathrm{v/t}} \mathbf{S}_{\mathrm{c}}^{-1} \mathbf{V}_{\mathrm{c}}$$

Application of the PCA on the Sh indices data matrix resulted in 10 principal components or factors (PC_1–PC_{10}). A linear regression model was built between the NBP and MR with the resulted factors. The best set of PCs was selected by the eigenvalue ranking (EV) and correlation ranking (CR) procedures.[53,54] In the EV–PCR procedure, the PCs were entered to the PCR model consecutively based on their decreasing eigenvalue. Once each new PC was entered to the model, the model performances were evaluated by the leave-one-out cross validation (LOO-CV), twofold out cross validation (2FO-CV), and external validation. In the external validation procedure, we used the method suggested by Hawkins and co-workers.[55,56] So, first, the data were arranged based on the $\boldsymbol{y}$ increase (the physical properties were including NBP and MR), then they were classified into two data sets as odd and even, which makes the same distribution for $\boldsymbol{y}$ values of the two sets. The separate QSPR model was made, for odd and even data sets, and then each of them was used to predict the data belonging to the other method. To compare the estimation abilities of the models, two statistical parameters, RMS error prediction (RMSEP) and R^2, were calculated. These parameters were determined for the same data set (the "calibration set") that was used to fit the models (resubstitution parameters, i.e., $\mathrm{RMSEP_{RS}}$ and R^2_{RS}) and for the other data set that was not involved in the fitting (holdout parameters, i.e., $\mathrm{RMSEP_{HO}}$ and R^2_{HO}). The resubstitution statistical parameters base their predictions on the regression fitted to that sample, and holdout statistical parameters base their prediction on the regression fitted to the other samples. In the CR–PCR, the correlation of each one of the extracted PCs with the NBP and MR data was determined first. The stepwise entrance of the PCs to the PCR model was based on their decreasing correlation with the NBP or MR. Some statistical parameters such as the square of the correlation coefficient (R^2), square of the leave-one-out and twofold out cross-validation correlation coefficient (R^2_{LOO}, R^2_{2FO}), the standard error of estimation (SE), the root-mean-square error (RMS), the leave-one-out and twofold out cross-validation root-mean-square error ($\mathrm{RMS_{LOO}}$, $\mathrm{RMS_{2FO}}$), and the Fisher's criterion at the 95% probability level were calculated to estimate the quality of the resulted models.

Nonlinear modeling: neural networks

The extracted PCs by CR–PCR and EV–PCR were used as the predictor variables (input) for the neural network model.[46,47,53,54] A three-layered feed-forward ANN with back-propagation of an error algorithm was constructed to model the structure–property relationship.[57–60] The 394 compounds were randomly divided to 300 calibration (or training) samples, 54 validation samples, and 40 test samples. The validation set is a subset of compounds used to help find an optimal set of weights and biases during ANN calibrating, and it is also used to avoid overtraining of the ANN. The number of neurons in the input layer is equal to the number of PCs selected for the model. The transformed values are then passed to the hidden layer. The input value of a hidden-layer neuron is the summation of the products of the weights (neuron connections) times the corresponding outputs of the previous input layer plus a bias term. The ANN model is confined to a single hidden layer, because the network with more than one hidden layer would be harder to train. The neuron parameters and architectures were optimized to obtain better performances. The summation is put through a nonlinear transfer function, and then the resulting values are passed to the output layer, which contains a single neuron, which represents the predicted NBP and MR values. The training and validation data sets were used to optimize the network performance. To ensure that the overfitting and underfitting of the ANN models did not occur, for each configuration, the fitness function (η), calculated from both the root-mean-square errors of calibration and validation (RMSEC and RMSEV, respectively), was used to evaluate the performance of each neuron for both physical properties. This fitness function, recently proposed by Depczynski et al.[61] was used in this paper.

$$[6] \qquad \eta = \{[(m_{\mathrm{c}} - n - 1)\mathrm{RMSEC}^2 + m_{\mathrm{v}}\,\mathrm{RMSEV}^2]/(m_{\mathrm{c}} + m_{\mathrm{v}} - n - 1)\}^{1/2}$$

where m_{c} and m_{v} are the number of compounds in the calibration and validation sets, respectively, and n represents the number of selected PCs. The training of each network was stopped after observing no improvement in η for both properties.

Software

Calculations were performed by a Pentium IV (CPU at 2.8 GHz) personal computer equipped with Windows$^{\mathrm{xp}}$ operating system. Calculation of Sh indices, cross validation, and other mathematical operations, such as error calculations, were performed by homemade programs in MATLAB environments (Mathwork Inc., version 7, MA, USA). The PLS toolbox (Eigenvector Research, Inc., 1991–1998) was used for PLS and PCR regressions. The other necessary programs were written in our laboratory. The ANN processing was performed by a homemade program written in MATLAB environment, where all necessary codes were provided by our laboratory.

Table 2. Statistical parameters of the over-fitting and predictive ability of the models.

Physical property	Odd samples				Even samples			
	$RMSEP_{RS}$ [a]	R^2_{RS} [a]	$RMSEP_{HO}$ [b]	R^2_{HO} [b]	$RMSEP_{RS}$ [a]	R^2_{RS} [a]	$RMSEP_{HO}$ [b]	R^2_{HO} [b]
NBP	2.43	0.9559	2.58	0.9503	2.65	0.948	2.80	0.9424
MR	2.41	0.9857	2.52	0.9848	2.52	0.984	2.59	0.9834

[a]Root-mean-square error prediction and square of the regression coefficient for resubstitution.
[b]Root-mean-square error prediction and square of the regression coefficient for hold out.

Results and discussion

Correlation of NBP and MR with Sh and χ indices

At first, the correlation of the Sh indices along with the NBP and MR properties of compounds has been studied. It has been characterized that some of the indices, such as Sh1, revealed good correlation with the mentioned properties of compounds. To control the physicochemical properties for any chemical compounds through molecular mass more than molecular topology, we combined the number of carbon atoms belonging to any organic compounds (as a measure of molecular mass) with some of Sh indices and produced a novel topological index with high correlation ability presented in eq. [7] as

$$[7] \qquad Sh = n + n^{0.5}Sh1$$

To demonstrate the mentioned ability, the correlation of the combinational index of Sh with NBP and MR properties for organic compounds has been studied, and also the linear relationships between them have been computed as the following:

$$[8] \quad \begin{array}{ll} NBP = 253.576(\pm 5.023) + 9.419(\pm 0.321)Sh & R^2 = 0.6866,\ SE = 25.74,\ F = 859 \\ MR = 9.891(\pm 0.273) + 1.838(\pm 0.017)Sh & R^2 = 0.9659,\ SE = 1.40,\ F = 11098 \end{array}$$

Furthermore, for comparison, the correlation of Randic connectivity index (χ) has been validated with these properties, and the obtained relations are the following:

$$[9] \quad \begin{array}{ll} NBP = 233.463(\pm 4.925) + 44.484(\pm 1.311)\chi & R^2 = 0.7459,\ SE = 23.176,\ F = 1150 \\ MR = 7.676(\pm 0.397) + 8.211(\pm 0.106)\chi & R^2 = 0.9391,\ SE = 1.867,\ F = 6042 \end{array}$$

Clearly, the topological index of Sh rather than the topological index of χ presents the best model and statistical parameters for predictiing the MR of organic compounds ($SE_{Sh} = 1.40 < SE_\chi = 1.87$, $R^2_{Sh} = 0.9659 > R^2_\chi = 0.9391$, and $F_{Sh} = 11098 > F_\chi = 6042$), while the Randic index produces the better model and statistical parameters to predict the NBPs ($SE_{Sh} = 1.25.74 < SE_\chi = 23.17$, $R^2_{Sh} = 0.6866 < R^2_\chi = 0.7459$, and $F_{Sh} = 859 < F_\chi = 1150$). Also, the best correlation coefficients and statistical parameters to predict the MR against NBP would be obtained by using both mentioned topological molecular descriptors.

PCR modeling

At first, the eigenvalue ranking procedure was employed to build the PCR-based QSPR model equations of the different types of organic compounds independently, but this procedure did not produce satisfactory results for NBP and MR properties. Using the correlation ranking procedure produced more suitable models, for which the QSPR related to the whole sets of molecules, and their subsets from the correlation ranking procedure are listed in Table 1. Furthermore, a number of statistical parameters, such as R^2, SE, RMS, the relative error of prediction (REP), and F statistics are also shown in Table 1. The obtained QSPR models to predict the MR values have the best results in all cases (i.e., $R^2 > 0.99\%$ and $REP < 2.40\%$) while they only have the high statistical quality to predict the NBPs of alkanes and alkyl halides (i.e., $R^2 > 0.95\%$ and $REP < 2.00\%$). Also, as it is shown in Table 1, for the QSPR produced models for any subset of compounds, the number and type of selected PCs against the correlation ranking procedure vary from two PCs for ethers to six PCs for alkane compounds.

At the next stage, we applied the PCR method, based on the correlation ranking procedure for making the model of NBP and MR properties, to a complete set containing 394 compounds. Two CR–PCR models were obtained as follows

$$[10] \quad \begin{array}{l} NBP = 395.798 + 39188PC_1 + 12.947PC_6 - 11.674PC_4 - 8.522PC_7 + 7.729PC_2 + 4.471PC_3 + 3.532PC_{10} \\ R^2 = 0.9505;\ SE = 10.31;\ REP = 2.58;\ F = 1059;\ R^2_{LOO} = 0.9454;\ RMS_{LOO} = 10.72;\ R^2_{2FO} = 0.9450;\ \text{and}\ RMS_{2FO} = 10.76 \end{array}$$

$$[11] \quad \begin{array}{l} MR = 37.642 + 7.509PC_1 + 1.791PC_3 + 1.017PC_2 + 1.009PC_7 + 0.858PC_{10} - 0.608PC_8 \\ R^2 = 0.9846;\ SE = 0.94;\ REP = 2.49;\ F = 4122;\ R^2_{LOO} = 0.9833;\ RMS_{LOO} = 0.98;\ R^2_{2FO} = 0.9829;\ \text{and}\ RMS_{2FO} = 0.99 \end{array}$$

As it is clear from these equations, to make the NBP model of a complete set of compounds, we used seven PCs, and for the MR modeling of them, six PCs were used. The trend of PCs to decrease their correlation with NBP is PC1 > PC6 > PC4 > PC7 > PC2 > PC3 > PC10, and also for their correlation with MR, the trend is PC1 > PC3 > PC2 > PC7 > PC10 > PC8, which is not parallel to decreasing their eigenvalues ranking, so we avoid showing the results of the modeling based on the eigenvalues ranking. The study of obtained results showed that the mentioned models

Fig. 2. Plot of the predicted properties: NBP (A) and MR (B) by twofold cross-validation CR–PCR for the total data set of 394 organic compounds used in this study against the experimental values. The dashed lines are the ideal fits to the straight lines.

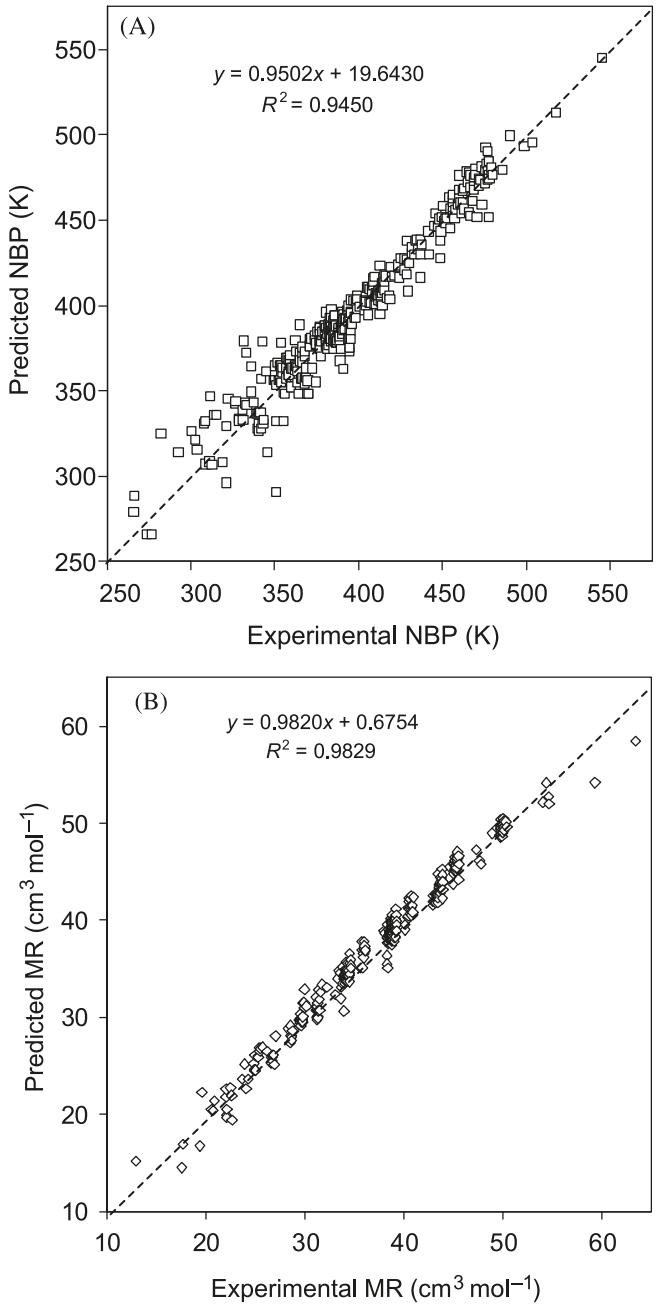

Fig. 3. Plots of the properties predicted: NBP (A) and MR (B) for the odd-number (■) and even-number (□) samples by holdout model against the corresponding experimental values. The dashed lines are the ideal fits to the straight lines.

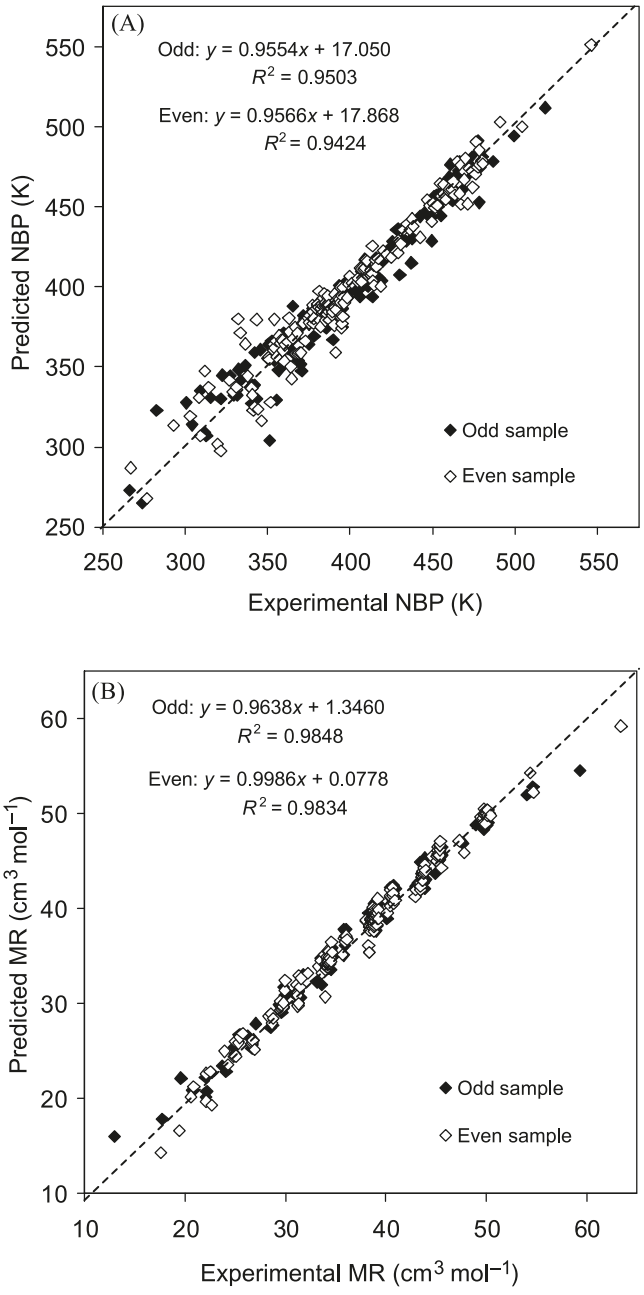

explain more than 97% and 99% variance in the experimental values of NBP and MR with a root-mean-square error of 10.21 K and 0.94 cm^3 mol^{-1}, respectively.

To demonstrate the ability of the obtained models to estimate the properties related to NBP and MR of these organic compounds during this study, the prediction ability was examined for external samples, in which the leave-one-out and twofold cross validation and external validation (EV) have been used for this investigation. The cross-validation results showed R^2 values, for LOO and twofold cross-validation values, greater than 0.94% for NBP and MR in both models. For more investigation, the predicting ability of the models, the EV can also be applied. The NBP and MR properties predicted by the best model against the corresponding experimental values by twofold CV procedure are plotted in Fig. 2 (A and B), respectively. For more checking of the prediction ability of the QSPR models, the external validation was also applied. The results are listed in Table 2. In odd- and even-number samples, the resubstitution and holdout RMS and REP are very similar, which shows that the same-sample and out-of-sample predictions were equally precise. This indicated that the resulting QSPR models had high prediction

Table 3. Statistics of principal component regression and artificial neural network models with one hidden-layer neuron for the calculation of normal boiling points and molar refractivities.

Physical property	Statistical parameters	CR–PCR		EV–PC–ANN			CR–PC–ANN		
		CS[a]	VS[a]	CS[a]	VS[a]	TS[a]	CS[a]	VS[a]	TS[a]
N	340	54	300	54	40	300	54	40	
NBP	SE	10.33	9.82	5.65	6.13	7.73	5.18	6.25	6.72
	RMS	10.30	9.69	5.72	6.10	8.00	5.17	6.17	7.08
	REP	2.61	2.43	1.44	1.53	2.04	1.31	1.55	1.81
	R^2	0.9503	0.9510	0.9847	0.9809	0.9785	0.9871	0.9802	0.9837
	RE% range	(–10.05)–(14.73)	(–4.97)–(11.31)	(–3.75)–(7.21)	(–3.91)–(4.07)	(–3.07)–(8.49)	(–5.97)–(8.25)	(–4.85)–(3.63)	(–2.28)–(7.87)
MR	SE	0.9765	06600	0.6181	0.7533	0.9339	0.3890	0.3992	0.6100
	RMS	0.9736	0.6600	0.6236	0.7663	0.9457	0.3879	0.4163	0.6002
	REP	2.5940	1.7225	1.6605	2.0000	2.5311	1.0328	1.0864	1.6064
	R^2	0.9839	0.9905	0.9933	0.9877	0.9894	0.9973	0.9965	0.9955
	RE% range	(–19.09)-–(12.03)	(–8.81)–(5.17)	(–5.17)–(10.83)	(–4.23)–(8.76)	(–6.93)–(3.13)	(–3.47)–(3.13)	(–1.87)–(3.76)	(–6.09)–(5.91)

[a]CS: calibration set; VS: validation set; TS: test set.

Fig. 4. Plots of the predicted properties: NBP (A) and MR (B) by CR–PCR for the calibration set (□) and the validation set (■) against the experimental values. The dashed lines are the ideal fits to the straight lines.

ability with low overfitting. The plots of the properties estimated by odd- and even-number QSPR models (holdout prediction) vs. the properties observed experimentally are given in Fig. 3 (A and B) for the NBP and MR, respectively. As seen, the plots show the distribution of the data around a straight line with very low scattering, which confirms that there was good agreement between the predicted and experimental values. Comparison of the results of CV and EV indicated that the resulting QSPR models not only had high CV statistical qualities but there was also a good agreement between the results of the two validation methods. The cross-validation test indicates that the Sh indices can model-ize the properties of NBP and MR of all types of organic

Table 4. The results of application of artificial neural network architectures with different configurations.

					Root-mean-square error (RMS error)							
					Normal boiling point				Molar refractivity			
Run no.	n_H[a]	TF_H[a]	Mom[a]	LR[a]	CS[b]	VS[b]	TS[b]	η[a]	CS[b]	VS[b]	TS[b]	η[a]
1	2	Tansig	0.15	0.98	8.65	8.99	8.53	37.88	0.6632	0.5631	0.8264	0.2104
2	2	Logsig	0.27	0.88	8.41	7.87	9.09	34.68	0.7871	0.5459	0.7608	0.2847
3	2	Purelin	0.19	0.75	10.51	9.70	8.67	53.95	0.9492	0.6555	1.1697	0.4138
4	3	Tansig	0.26	0.88	8.58	8.83	8.84	37.15	0.5283	0.5389	0.8384	0.1404
5	3	Logsig	0.17	0.97	9.69	9.99	9.25	47.41	0.7082	0.5212	0.7369	0.2329
6	3	Purelin	0.29	0.72	10.51	9.67	8.65	53.91	0.9715	0.6532	1.1547	0.4317
7	**4**	**Tansig**	**0.22**	**0.74**	10.51	9.67	8.65	53.91	**0.3879**	**0.4163**	**0.6002**	**0.0770**
8	4	Logsig	0.27	0.85	7.22	9.34	10.33	28.80	0.5658	0.5597	0.8006	0.1595
9	4	Purelin	0.14	0.99	10.51	9.70	8.67	53.95	0.9492	0.6555	1.1697	0.4138
10	5	Tansig	0.25	0.69	9.78	9.92	8.42	48.04	0.4028	0.4736	1.2585	0.0860
11	5	Logsig	0.31	0.77	8.42	7.97	8.60	34.87	0.7582	0.6452	0.7827	0.2751
12	5	Purelin	0.21	0.97	10.51	9.70	8.67	53.95	0.9493	0.6531	1.1687	0.4137
13	**6**	**Tansig**	**0.26**	**0.84**	**5.17**	**6.17**	**7.08**	**14.25**	0.5926	0.5320	0.7866	0.1703
14	6	Logsig	0.15	0.94	5.64	7.91	10.08	18.31	0.5328	0.4862	0.6403	0.1382
15	6	Purelin	0.25	0.89	10.51	9.70	8.67	53.95	0.9492	0.6555	1.1697	0.4138
16	7	Tansig	0.16	0.77	7.49	7.67	9.80	28.26				
17	7	Logsig	0.21	0.85	6.67	7.12	9.63	22.73				
18	7	Purelin	0.24	0.96	10.51	9.70	8.67	53.95				

[a] n_H: number of presented nodes; TF_H: transfer function in the hiden layer; Mom: momentum; LR: learning rate; η: fitness function.
[b] CS: calibration set; VS: validation set; TS: test set.

compounds used during these studies perfectly. Other cross-validation parameters also support these results.

On the basis of the obtained results, the QSPR model to MR property has less PC numbers and better statistical results for the MR linear property, while the QSPR model to NBP has more PC numbers, so we can find the nonlinear behavior for NBP property. The latter attempts to test the quality of obtained models produced by dividing the data set into calibration (340 molecules) and validation sets (54 molecules). Also, to produce the CR–PCR model of the calibration set, the same PCs, which were obtained for the complete set of compounds, have been used. In Table 3, the statistical parameters have been presented for the best fitted models related to the NBP and MR. The results show that seven and six selected PCs by correlation ranking method could at least explain 97.52% and 99.66% variances in NBP and MR values for external data, respectively. The graphs of the predicted values against their corresponding experimental values are depicted in Fig. 4 (A and B).

PC–ANN modeling

In another attempt to improve the overall RMS error of the linear models obtained by PCR, we focused on demonstrating if prediction results could be improved by the use of nonlinear artificial neural network modeling methods. A fully connected, three-layered feed-forward ANN model with back-propagation learning algorithm is developed for nonlinear modeling between the selected PCs by the EV–PCR and CR–PCR models.[47,53,54] In this step, the selected PCs of seven and six numbers, respectively, for NBP and MR data were gathered in a new data matrix. To evaluate the network architecture effect on the performance of the PC–ANN models, many networks have been selected with various parameters for all types of properties. In Table 4, the results obtained from different network configurations are presented. Also in Table 4, the network parameters containing the number of presented nodes (n_H) and type of transfer function in the hidden layer (denotes by TF_H), also momentum (Mom) and learning rate (LR), have been demonstrated. In addition, the fitness function (η), based on EMSEC and RMSEV, was calculated for any PC–ANN model and shown for any property. The convergence criterion is the least fitness function according to eq. [6]. The number of iterations for convergence was between 15 000 and 20 000. As it is obvious from the data shown in Table 4, for NBP property, the performance of ANN model to execute architecture run number 13 is better than the others. Moreover, the fitness function of the ANN model configuration number 13 is equal to 14.25. This model has acceptable quality with six nodes in hidden layer, tansig transfer function, learning rate of 0.84, and momentum of 0.26 and is also able to predict the NBP of organic compounds in the test set with low error scale. The optimized PC–ANN model was used for predicting the NBP values of the compounds that have not been used in any step of the ANN modeling procedure (test set). In Table S1, the predicted NBP values using optimized models of EV–PC–ANN and CR–PC–ANN have been demonstrated, and they have also been depicted the against their experimentally determined values in Figs. 5A and 5B. Also, the statistical parameters to take the best-fitted model for EV–PC–ANN and CR–PC–ANN are shown in Table 3.

In the next step, the ANN models were built to predict the molar refraction. To take these models, the same calibration, validation, and test sets of compounds were employed. As it was realized before, the model containing six PCs has the effective performance to predict the MR of these compounds. Table 4 shows that the performance of ANN model having architecture number 7 is better than the other models

Fig. 5. Plots of the predicted NBP by (A) PC–EV–ANN and (B) PC–CR–ANN against the experimental values. The dashed lines are the ideal fits to the straight lines.

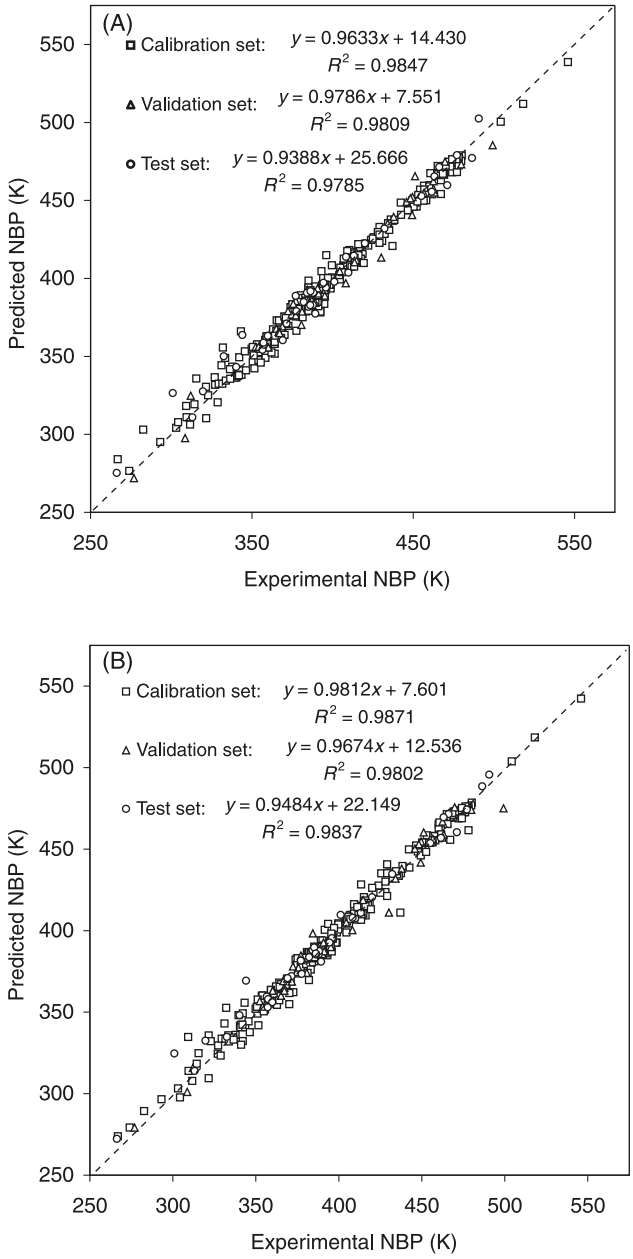

Fig. 6. Plots of the predicted MR by (A) PC–EV–ANN and (B) PC–CR–ANN against the experimental values. The dashed lines are the ideal fits to the straight lines.

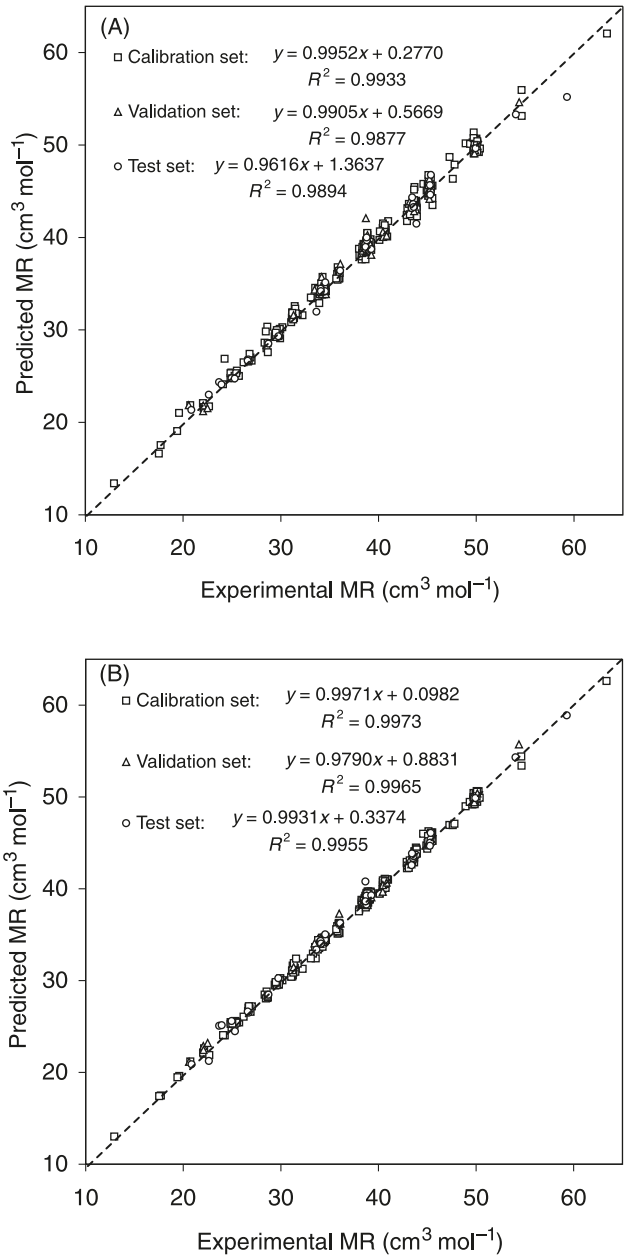

with the fitness function equal to 0.0770. This model with four nodes in the hidden layer, a tansig transfer function, learning rate of 0.74, and momentum of 0.22 has acceptable quality and can predict the MR of the organic compounds of the test set with less error scales, while the optimized PC–ANN model used to predict the MR related compounds that were not utilized in any step of ANN modeling (test set). In Table S1, the values of the predicted MRs were depicted for optimized EV–PC–ANN and CR–PC–ANN models, respectively, and in Figs. 6A and 6B, against their corresponding experimental values have been demonstrated. Also, the statistical parameters to take the best corresponding models are summarized in Table 4.

As it can be observed from Table 3, the obtained models from PC–ANN, compared with PCR models, have relative higher quality for both physical properties. It means that between the suggested topological Sh indices and the studied NBP values of organic compounds during this research, there are nonlinear relationships, while the ANN could not extent the linear models obtained from the linear method studies for MR values of those compounds. Furthermore, the comparison of the results obtained from PC–ANN modeling, according to the eigenvalue ranking and correlation ranking, revealed that the CR–PC–ANN produced more accurate results, which is in accordance with our previous finding.[47,53,54,62]

Conclusion

In this study, it was shown that accurate QSPR models can be developed to predict the normal boiling point and molar refractivity of structurally diverse set of organic compounds having C, H, O, N, and halogen atoms, including some alkanes, alkenes, ethers, amines, alcohols, alkylbenzenes, and alkylhalides, using some newly proposed topological indices (Sh indices) by using principal component regression and principal component – artificial neural network modeling methods. In addition, the performances of two different principal components selection procedures, including eigenvalue ranking and correlation ranking, were evaluated. The PCs were entered to the models based on their decreasing eigenvalue and correlation-ranking coefficients. The obtained results showed that the frequent extraction of PCs based on decreasing the correlation ranking with NBP and MR physical properties presents the better results. These results demonstrated that normal boiling points and molar refractivities for a wide range of organic compounds could be predicted easily and accurately based solely on molecular structure, with no corrective factor for physical state or use of other additional data.

Supplementary data

Supplementary data for this article are available on the journal Web site (canjchem.nrc.ca) or may be purchased from the Depository of Unpublished Data, Document Delivery, CISTI, National Research Council Canada, Ottawa, ON K1A 0R6, Canada. DUD 3993. For more information on obtaining material, refer to cisti-icist.nrc-cnrc.gc.ca/cms/unpub_e.shtml.

References

(1) Herndon, W. C.; Nowak, P. C.; Connor, D. A.; Lin, P. *J. Am. Chem. Soc.* **1992**, *114* (1), 41–47. doi:10.1021/ja00027a005.

(2) Hall, L. H.; Kier, L. B. *J. Chem. Inf. Comput. Sci.* **1995**, *35*, 1039.

(3) Cash, G. G. *J. Chem. Inf. Comput. Sci.* **1995**, *35*, 815.

(4) Estrada, E. *J. Chem. Inf. Comput. Sci.* **1995**, *35*, 31.

(5) Yuan, H.; Cao, C. *J. Chem. Inf. Comput. Sci.* **2003**, *43* (2), 501–512. PMID:12653514.

(6) Ren, B. *J. Mol. Struct. THEOCHEM* **2002**, *586* (1-3), 137–148. doi:10.1016/S0166-1280(02)00080-5.

(7) Lorentz, H. A. *Wied. Ann. Phys.* **1880**, *9*, 641.

(8) Lorentz, L. V. *Wied. Ann. Phys.* **1880**, *11*, 70.

(9) Gladstone, J. H.; Dale, T. P. *Philos. Trans. R. Soc. Lond. A* **1858**, *148* (-1), 887–894. doi:10.1098/rstl.1858.0036.

(10) Vogel, A. *J. Chem. Soc.* **1948**, 1833. doi:10.1039/jr9480001833.

(11) Norrington, F. E.; Hyde, R. M.; Williams, S. G.; Wooten, R. J. *Med. Chem.* **1975**, *18* (6), 604–607. doi:10.1021/jm00240a016.

(12) Ravi, M.; Hopfinger, A. J.; Hormann, R. E.; Dinan, L. *J. Chem. Inf. Comput. Sci.* **2001**, *41* (6), 1587–1604. PMID:11749586.

(13) Luke, B. T. *J. Mol. Struct. THEOCHEM* **1999**, *468* (1-2), 13–20. doi:10.1016/S0166-1280(98)00492-8.

(14) Bruneau, P. *J. Chem. Inf. Comput. Sci.* **2001**, *41* (6), 1605–1616. PMID:11749587.

(15) Katritzky, A. R.; Petrukhin, R.; Tatham, D.; Basak, S.; Benfenati, E.; Karelson, M.; Maran, U. *J. Chem. Inf. Comput. Sci.* **2001**, *41* (3), 679–685. PMID:11410046.

(16) Katritzky, A. R.; Gordeeva, E. V. *J. Chem. Inf. Comput. Sci.* **1993**, *33* (6), 835–857. PMID:8113335.

(17) Karelson, M.; Lobanov, V. S.; Katritzky, A. R. *Chem. Rev.* **1996**, *96* (3), 1027–1044. doi:10.1021/cr950202r. PMID:11848779.

(18) Wiener, H. *J. Am. Chem. Soc.* **1947**, *69* (1), 17–20. doi:10.1021/ja01193a005.

(19) Hosoya, H. *Bull. Chem. Soc. Jpn.* **1971**, *44* (9), 2332–2339. doi:10.1246/bcsj.44.2332.

(20) Balaban, A. T. *Chem. Phys. Lett.* **1982**, *89* (5), 399–404. doi:10.1016/0009-2614(82)80009-2.

(21) Balaban, A. T. *Pure Appl. Chem.* **1983**, *55* (2), 199–206. doi:10.1351/pac198855020199.

(22) Randić, M. *J. Math. Chem.* **1991**, *7* (1), 155–168. doi:10.1007/BF01200821.

(23) Nelson, S. D.; Seybold, P. G. *J. Mol. Graph. Model.* **2001**, *20* (1), 36–53. doi:10.1016/S1093-3263(01)00099-7.

(24) Liu, S.; Liu, H.; Xia, Z.; Cao, C.; Li, Z. *J. Chem. Inf. Comput. Sci.* **1999**, *39*, 951.

(25) Liu, S.; Cai, S.; Cao, C.; Li, Z. *J. Chem. Inf. Comput. Sci.* **2001**, *40*, 1337.

(26) Haaland, D. In *Computer-Enhanced Analytical Spectroscopy;* Jurs, P. C., Ed.; Plenum Press: New York, 1992; Vol. 3.

(27) Wold, S.; Sjostrom, M.; Eriksson, L. *Chemom. Intell. Lab. Syst.* **2001**, *58* (2), 109–130. doi:10.1016/S0169-7439(01)00155-1.

(28) Tang, T.; Li, T. *Chemom. Intell. Lab. Syst.* **2002**, *64* (1), 55–64. doi:10.1016/S0169-7439(02)00050-3.

(29) Liu, S.; Zhang, R.; Liu, M.; Hu, Z. *J. Chem. Inf. Comput. Sci.* **1997**, *37*, 1146.

(30) Walczak, B. *Anal. Chim. Acta* **1996**, *322* (1-2), 21–29. doi:10.1016/0003-2670(95)00552-8.

(31) Shamsipur, M.; Hemmateenejad, B.; Akhond, M. *J. AOAC Int.* **2002**, *85* (3), 555–562. PMID:12083247.

(32) Kim, B.; Park, S. *Chemom. Intell. Lab. Syst.* **2002**, *56* (1), 39–50. doi:10.1016/S0169-7439(01)00107-1.

(33) Tomás-Vert, F.; Perez-Gimenez, F.; Salvador, M. T.; Garcia-March, F. J.; Jaen-Oltra, J. *J. Mol. Struct. THEOCHEM* **2000**, *504* (1-3), 249–259. doi:10.1016/S0166-1280(00)00366-3.

(34) Peterson, K. L. *J. Chem. Inf. Comput. Sci.* **1995**, *35* (5), 896–904. PMID:7593373.

(35) Shamsipur, M.; Hemmateenejad, B.; Akhond, M. *Anal. Chim. Acta* **2002**, *461* (1), 147–153. doi:10.1016/S0003-2670(02)00236-2.

(36) Agatonovic-Kustrin, S.; Zecevic, M.; Zivanovic, L.; Tucker, I. G. *J. Pharm. Biomed. Anal.* **1998**, *17* (1), 69–76. doi:10.1016/S0731-7085(97)00170-2. PMID:9608428.

(37) Gemperline, P. J.; Long, J. R.; Gregoriou, V. G. *Anal. Chem.* **1991**, *63* (20), 2313–2323. doi:10.1021/ac00020a022.

(38) González, M. P.; Toropov, A. A.; Duchowicz, P. R.; Castro, E. A. *Molecules* **2004**, *9* (12), 1019–1033. doi:10.3390/91201019. PMID:18007502.

(39) Jäntschi, L.; Bolboacă, S.-D. *Int. J. Mol. Sci.* **2007**, *8* (3), 189–203. doi:10.3390/i8030189.

(40) Jäntschi, L.; Bolboac, S.-D. *Leonardo Electronic Journal of Practices and Technologies* **2005**, *7*, 55.

(41) Qian, C.; Hongyi, Z. *Chem. J. Internet* **2006**, *8* (9), 58.

(42) Balaban, A. T.; Mills, D.; Basak, S. C. *J. Chem. Inf. Comput. Sci.* **1999**, *39*, 758.

(43) Toropov, A. A.; Toropova, A. P. *J. Mol. Struct. THEO-*

CHEM **2002**, *581* (1-3), 11–15. doi:10.1016/S0166-1280(01)00733-3.
(44) Mukhamedzhanova, D. V.; Gutman, I. *Indian J. Chem. A* **2005**, *44*, 1545.
(45) Shamsipur, M.; Hemmateenejad, B.; Akhond, M. *Bull. Korean Chem. Soc.* **2004**, *25*, 253.
(46) Shamsipur, M.; Ghavami, R.; Hemmateenejad, B.; Sharghi, H. *QSAR Comb. Sci.* **2004**, *23* (9), 734–753. doi:10.1002/qsar.200430894.
(47) Shamsipur, M.; Ghavami, R.; Hemmateenejad, B.; Sharghi, H. *Internet Electron. J. Mol. Des.* **2005**, *4*, 882.
(48) Shamsipur, M.; Hemmateenejad, B.; Ghavami, R.; Sharghi, H. *Pol. J. Chem.* **2007**, *81*, 269.
(49) Kier, L. B.; Hall, L. H. In *Molecular Connectivity in Chemistry and Drug Research;* Academic Press: New York, 1976.
(50) David, R. L., Ed. CRC Handbook of Chemistry and Physics, 81st ed.; CRC Press, 2000–2001.
(51) Malinowski, E. R. In *Factor Analysis in Chemistry;* Wiley: New York, 2002; pp 224–225.
(52) Sutter, J. M.; Kalivas, J. H.; Lang, P. M. *J. Chemometr.* **1992**, *6* (4), 217–225. doi:10.1002/cem.1180060406.
(53) Hemmateenejad, B. *J. Chemometr.* **2004**, *18* (11), 475–485. doi:10.1002/cem.891.
(54) Hemmateenejad, B. *Chemom. Intell. Lab. Syst.* **2005**, *75* (2), 231–245. doi:10.1016/j.chemolab.2004.09.005.
(55) Hawkins, D. M.; Basak, S. C.; Mills, D. *J. Chem. Inf. Comput. Sci.* **2003**, *43* (2), 579–586. PMID:12653524.
(56) Hawkins, D. M. *J. Chem. Inf. Comput. Sci.* **2004**, *44* (1), 1–12. PMID:14741005.
(57) Rumelhart, D. E.; Hinton, G. E.; Williams, R. J. *Nature* **1986**, *323* (6088), 533–536. doi:10.1038/323533a0.
(58) Svozil, D.; Kvasnicka, V.; Pospichal, J. *Chemom. Intell. Lab. Syst.* **1997**, *39* (1), 43–62. doi:10.1016/S0169-7439(97)00061-0.
(59) Devillers, J.; Domine, D.; Guillon, C. *Eur. J. Med. Chem.* **1998**, *33* (7-8), 659–664. doi:10.1016/S0223-5234(98)80024-X.
(60) Taskinen, J.; Yliruusi, J. *Adv. Drug Deliv. Rev.* **2003**, *55* (9), 1163–1183. doi:10.1016/S0169-409X(03)00117-0. PMID:12954197.
(61) Depczynski, U.; Frost, V. J.; Molt, K. *Anal. Chim. Acta* **2000**, *420* (2), 217–227. doi:10.1016/S0003-2670(00)00893-X.
(62) Shamsipur, M.; Ghavami, R.; Sharghi, H.; Hemmateenejad, B. *J. Mol. Graph. Model.* **2008**, *27* (4), 506–511. doi:10.1016/j.jmgm.2008.09.005.

Water-promoted regioselective hydrothiolation of alkynes

Sukalyan Bhadra and Brindaban C. Ranu

Abstract: Water promotes hydrothiolation of unactivated alkynes efficiently without any catalyst or additive. The reaction at room temperature furnishes vinyl sulfides with high regioselectivity via anti-Markovnikov addition. The terminal alkynes provide dithiolanes at 80 °C by bis-addition. The reactions are very clean and high yielding.

Key words: alkynes, hydrothiolation, vinyl sulfides, regioselectivity, water.

Résumé : L'eau favorise l'hydrothiolation des alcynes non activés d'une façon efficace, sans catalyseur ou additif. À la température ambiante, la réaction conduit à la formation de sulfures de vinyle, avec une régiosélectivité par le biais d'une addition anti-Markovnikov. Les additions à 80 °C sur des alcynes terminaux conduisent à des dithiolanes résultant d'une bis-addition. Les réactions sont très propres et les rendements sont élevés.

Mots-clés : alcynes, hydrothiolation, sulfures de vinyle, régiosélectivité, eau.

[Traduit par la Rédaction]

Introduction

The hydrothiolation of alkynes by thiols is a very interesting and challenging reaction being associated with mono- and bis-condensation, Markovnikov and (or) anti-Markovnikov addition, and stereoselectivity. This reaction is also of great importance as it provides an attractive method for the formation of vinyl sulfides, which are valuable synthetic intermediates in total synthesis[1] and serve as precursors to a wide range of functionalized molecules.[2] The conventional procedures for hydrothiolation of alkynes involves transition metal catalysts[3] or a base[4] in organic solvents. Recently, a few procedures using catalytic phenylselenyl bromide,[5a] Al_2O_3–KF,[5b] nickel[5c] under solvent-free conditions, β-cyclodextrin in water–acetone,[5d] and $NaBH_4$–alumina under solvent-free conditions[5e,5f] have been reported.

According to the basic principles of Green Chemistry the use of organic solvents should be avoided wherever possible and use of alternative green solvents such as water are encouraged.[6a] Thus, the reaction in water has attracted considerable interest in the context of Green Chemistry.[6] In addition, water often exhibits unique reactivity and selectivity that cannot be attained in conventional organic solvents.[7] Thus, development of an efficient procedure for an organic reaction using water as a promoter as well as reaction medium has received intense attention in the design of a chemical process. Here, we report an efficient hydrothiolation of alkynes in water without any catalysts or additives, imparting good control on regioselectivity (Scheme 1).

Received 2 March 2009. Accepted 24 July 2009. Published on the NRC Research Press Web site at canjchem.nrc.ca on 27 October 2009.

S. Bhadra and B.C. Ranu.[1] Department of Organic Chemistry, Indian Association for the Cultivation of Science, Jadavpur, Kolkata 700 032, India.

[1]Corresponding author (e-mail: ocbcr@iacs.res.in).

Scheme 1. Reaction of alkynes with thiols in water.

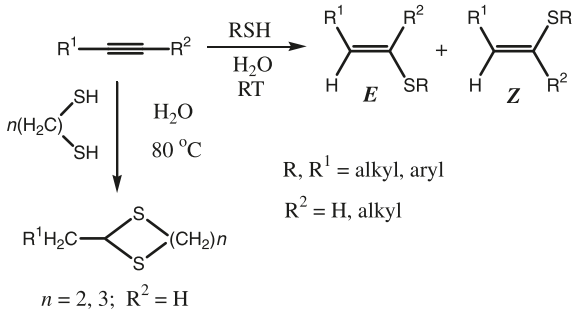

Results and discussion

The experimental procedure is very simple. A mixture of alkyne and thiol in water was stirred at room temperature (or at 80 °C) for a required period of time (TLC). Standard work-up provided the product.

A variety of terminal and internal alkynes underwent hydrothiolation with thiophenol and alkane thiols at room temperature by this procedure to provide the corresponding vinyl sulfides. The results are summarized in Table 1. Aryl- as well as alkyl-substituted alkynes and both aromatic and aliphatic thiols participated in this reaction uniformly. All reactions proceeded through anti-Markovnikov additions. Regarding the stereochemistry of the products, the reaction of terminal alkynes and thiophenols (entries 1–3, 6–8, 10, and 11 in Table 1) provided low to high selectivity with respect to *E*-isomers, whereas alkane thiols (entries 13, 14, 16, and 17 in Table 1) produced *Z*-isomers predominantly. The internal alkynes (entries 5 and 9 in Table 1) provided *Z*-isomers selectively. However, dimethyl acetylene dicarboxylate (entries 4, 12, 15, and 18 in Table 1) furnished *Z*-isomers as the sole product. As a whole, the stereoselectivity is excellent in a few of the reactions, although, in some reactions, no selectivity was observed. The steric distribution of prod-

Table 1. Hydrothiolation of alkynes.

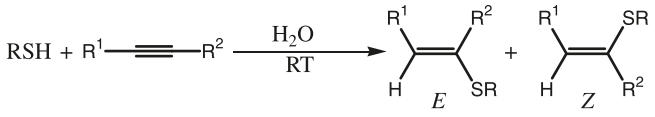

Entry	R	R^1	R^2	*Z*:*E*[a]	Time (h)	Yield (%)[b]	Reference
1	Ph	Ph	H	38:62	3	96	5d
2	Ph	C_4H_9	H	47:53	3	87	4b
3	Ph	C_6H_{13}	H	47:53	3.2	88	3c
4	Ph	CO_2Me	CO_2Me	100:0	3	94	8
5	Ph	C_2H_5	C_2H_5	75:25	3	86	9
6	Ph	*p*-ClC_6H_4	H	42:58	2.5	89	5d
7	*p*-MeC_6H_4	*p*-ClC_6H_4	H	0:100	2.5	95	10
8	*p*-ClC_6H_4	Ph	H	33:67	2.7	94	5d
9	*p*-MeC_6H_4	C_2H_5	C_2H_5	83:17	2.5	84	11
10	*p*-MeC_6H_4	*p*-MeC_6H_4	H	23:77	2	92	12
11	*p*-ClC_6H_4	*p*-$ClCC_6H_4$	H	12:88	2.8	90	13
12	$C_6H_4CH_2$	CO_2Me	CO_2Me	100:0	2	90	14
13	$C_6H_4CH_2$	Ph	H	69:31	2.5	89	3a
14	C_4H_9	Ph	H	70:30	3	93	15
15	$C_{12}H_{25}$	CO_2Me	CO_2Me	100:0	2	90	—
16	$C_{12}H_{25}$	Ph	H	85:15	3.4	85	4b
17	C_4H_9	*p*-ClC_6H_4	H	70:30	3	87	—
18	C_4H_9	CO_2Me	CO_2Me	100:0	2	86	16
19	HSC_2H_4	Ph	H	89:11	3.2	87	—

[a]*E*:*Z* ratio is based on NMR.
[b]Isolated yields.

Table 2. Bis-hydrothiolation of alkyne.

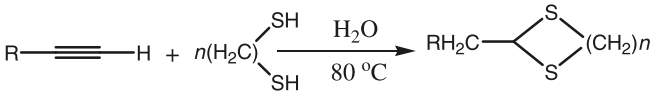

Sample No.	R	*n*	Time (h)	Yield (%)[a]	Reference
1	C_4H_9	2	4	72	11
2	C_6H_{13}	2	8	67	17a
3	Ph	2	4	81	17a
4	*p*-$MeOC_6H_4$	2	5	76	—
5	*p*-ClC_6H_4	2	5	73	—
6	*p*-ClC_6H_4	3	5	74	—
7	Ph	3	4.5	80	18

[a]Isolated yields.

ucts is probably controlled by the steric compulsion of the bulky substituents.

The terminal alkynes produced dithiolanes or dithianes when treated with dithiols at 80 °C, based on the use of ethane or propane dithiol. It has already been mentioned that a similar reaction at room temperature produced only vinyl sulfide (entry 19 in Table 1). The results are summarized in Table 2. However, the use of 2 equiv. of monothiols in the reaction of phenyl acetylene under identical conditions produced only vinyl sulfides and no dithioacetal was obtained. On the other hand, reaction of 0.5 equiv. of ethane dithiol and phenyl acetylene at room temperature produced the corresponding vinyl sulfide associated with the starting material, whereas reaction at 80 °C provided the corresponding dithiolane together with unreacted phenyl acetylene.

The dithianes and dithiolanes are very useful compounds.[19] The standard methods[17] employ aldehydes for dithiolane–dithiane formation using an acid catalyst, whereas this procedure provides an attractive and novel alternative using alkynes through a simple operation in mild and neutral conditions.

Water plays a very significant role in this reaction. Without water the reaction in neat is very slow and low yielding. Possibly, water promotes the reaction through hydrogen bond formation with the sulfhydryl hydrogen of the thiol and thus enhances the nucleophilicity of the thiolate ion to add to the alkyne at the less-hindered carbon atom, giving anti-Markovinkov product. Although we do not have any concrete evidence regarding the exact mechanism, it may be speculated that addition of thiolate anion to the C≡C bond

Scheme 2. Speculative reaction pathway.

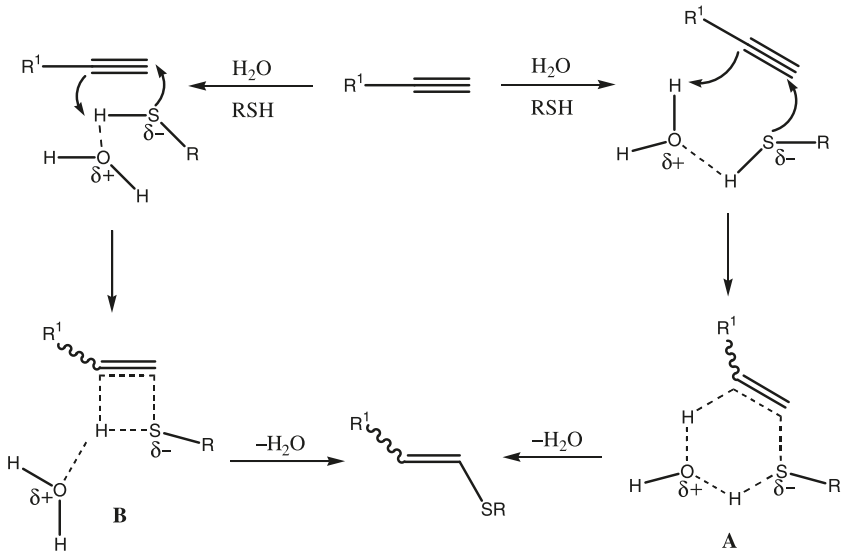

takes place either through a six- (**A**) or four-membered (**B**) transition state,[3f] with steric factors controlling the regioselectivity (Scheme 2).

It was found that, with the progress of reaction the product, vinyl sulfide isomerizes to the thermodynamically more stable isomer over time. For example, during the reaction of phenyl acetylene and thiophenol, the 32:68 *E*/*Z* mixture of product after 45 min of reaction ultimately gave rise to a 68:32 *E*/*Z* mixture at the end of the reaction after 3 h. This ratio for this mixture did not change even when the reaction was allowed to proceed past the 3 h time point. To check for the possibility of a radical process, the reaction was carried out in the dark. The progress of the reaction remained undisturbed. It should be mentioned that all the reactions were carried out in water that contained dissolved oxygen without an interference. Thus, a radical pathway is unlikely.

In general, the reactions were very clean. The hydrothiolations were accomplished in water at room temperature much faster (2–3.5 h) and in higher yields (84%–96%) when compared with many of the existing procedures.[3–5] All the products were obtained in high purities. The ratio of stereoisomers was determined by integration of the corresponding peaks in ^{1}H NMR spectra. Although a report[5d] using β-cyclodextrin in water stated that no reaction was observed in the absence of β-cyclodextrin, very interestingly, all the reactions listed in Tables 1 and 2 proceeded in water without any difficulty in the absence of additive. In addition, our water-mediated procedure is more general. The cyclodextrin–water mediated procedure[5d] failed to initiate reactions with alkane thiol, terminal alkyl alkynes, and internal alkynes, whereas our procedure was very successful for all these substrates. However, the stereoselectivity is better in cyclodextrin–water than in water alone by the present procedure. The reason for all these differences is not very clear to us. In general, the transition metal catalyzed reactions led to predominantly Markovnikov products,[3a,3b,3d,3e] whereas nonmetal-catalyzed reactions, including the present procedure, proceeded through anti-Markovnikov addition.[3f,4,5a,5b,5d,5e,5f] Excellent stereoselectivity was observed producing *E*-isomers in all the reactions using β-cyclodextrin,[5d] whereas attainment of high stereoselectivities providing a single isomer is not uniform in reactions using other reagents.[3,4,5a,5b,5c,5e,5f]

In conclusion, we have developed a very simple and efficient methodology for the addition of thiols to unactivated alkynes in water, producing vinyl sulfides and dithiolanes at room temperature and 80 °C, respectively. The additions exhibited high regioselectivity (exclusive anti-Markovnikov addition) and excellent stereoselectivity in several reactions (products obtained as one stereoisomer). Other significant advantages are simple operation, mild conditions (room temperature and neutral reaction media), general applicability to a variety of substituted alkynes and aromatic as well as aliphatic thiols, no catalyst or additive is required, high yields of isolated products, environment-friendly experimental conditions, and cost effectiveness. We believe, being endowed with so many attractive features, that this procedure will make an important addition to the existing methods of hydrothiolation.

Experimental

IR spectra were recorded on a Shimadzu 8300 FT IR spectrometer in neat. ^{1}H NMR and ^{13}C NMR spectra were run on a Bruker DPX-300 instrument at 300 and 75 MHz, respectively. HR-MS were taken on a Microtek Qt of a Micro YA263 spectrometer. All commercial reagents were distilled before use.

General experimental procedure for the synthesis of vinyl sulfides

Representative procedure for the reaction of phenyl acetylene with thiophenol (Table 1, entry 1)

A mixture of phenyl acetylene (102 mg, 1 mmol) and thiophenol (121 mg, 1.1 mmol) was stirred in H_2O (2 mL) at room temperature (30 °C) for 3 h (TLC). The reaction mixture was extracted with Et_2O (3 × 15 mL). The ether extract was washed with H_2O, NaOH (5%) solution, and brine and then dried over Na_2SO_4. Evaporation of solvent gave a crude product that was purified by column chromatography over silica gel (hexane) to provide (*E*)- and (*Z*)-phenyl styryl sulfane (204 mg, 96%) as a colourless liquid (*E*:*Z* = 62:38). IR (neat, cm^{-1}) ν: 3057, 3022, 1598, 1581, 1477, 1438, 1024,

945, 738, 688. ^{1}H NMR (300 MHz, $CDCl_3$) δ: 6.61 (d, 1H, J = 10.8 Hz), 6.70 (d, 1H, J = 10.8 Hz), 6.85 (d, 1H, J = 15.4 Hz), 6.99 (d, 1H, J = 15.4 Hz), 7.34–7.54 (m, 20H). ^{13}C NMR (75 MHz, $CDCl_3$) δ: 123.4, 126.0 (2C), 126.9, 127.2, 127.6, 128.3, 128.7 (2C), 128.8, 129.2 (2C), 129.8 (2C), 130.1, 131.8, 135.3, 136.2, 136.5 (2C). These data are in good agreement with those reported.[5d] This procedure was followed for all the reactions listed in Table 1. The known compounds were identified by comparison of their spectral data with those reported earlier (see refs. in Table 1). The unknown compounds were characterized properly by their spectroscopic data (IR, ^{1}H NMR, ^{13}C NMR, and HRMS), which are reported as follows.

2-Dodecylsulfanyl-but-2-enedioic acid dimethyl ester (Table 1, entry 15)

Pale yellow oil. IR (neat, cm^{-1}) ν: 2925, 2854, 1741, 1716, 1585, 1434, 1338, 1247, 1164, 1035, 723. ^{1}H NMR (300 MHz, $CDCl_3$) δ: 0.87 (t, 3H, J = 6.02 Hz), 1.25–1.39 (m, 17H), 1.61–1.69 (m, 3H), 2.79 (t, 2H J = 7.34 Hz), 3.69 (s, 3H), 3.87 (s, 3H), 5.70 (s, 1H). ^{13}C NMR (75 MHz, $CDCl_3$) δ: 14.2, 22.8, 28.1, 28.9, 29.1, 29.4 (2C), 29.5, 29.6, 29.7, 31.9, 32.0, 51.9, 53.2, 112.4, 150.9, 164.2, 166.2. HRMS *m/z* [M + Na]$^+$ calcd. for $C_{18}H_{32}O_4SNa$: 367.1919; found: 367.1915.

1-(2-Butylsulfanyl-vinyl)-4-chloro-benzene (Table 1, entry 17; Z:E = 70:30)

Colourless oil. IR (neat, cm^{-1}) ν: 2957, 2928, 2871, 1558, 1520, 1489, 1397, 1091. ^{1}H NMR (300 MHz, $CDCl_3$) δ: 0.69–0.76 (m, 6H), 1,17–1.29 (m, 4H), 1.41–1.50 (m, 4H), 2.55–2.60 (m, 4H), 6.06 (d, 1H, J = 10.9 Hz), 6.13–6.19 (m, 2H), 6.50 (d, 1H, J = 15.6 Hz), 6.96–7.04 (m, 2H), 7.09 (d, 2H, J = 8.5 Hz), 7.20 (d, 2H, J = 8.5 Hz). ^{13}C NMR (75 MHz, $CDCl_3$) δ: 13.7 (2C), 21.7 (2C), 32.3 (2C), 35.7 (2C), 124.0 (2C), 125.1, 126.6, 128.6, 128.7, 128.8, 128.9, 129.8 (2C), 130.1 (2C), 132.0 (2C), 135.6 (2C). HRMS *m/z* [M + Na]$^+$ calcd. for $C_{12}H_{15}ClSNa$: 249.0481; found: 249.1879.

2-Styrylsulfanyl-ethanethiol (Table 1, entry 19; Z:E = 89:11)

Colorless oil. IR (neat, cm^{-1}) ν: 2980, 2930, 2865, 2223, 1487, 1462, 1272, 730. ^{1}H NMR (300 MHz, $CDCl_3$) δ: 2.93–3.00 (m, 4H), 3.04–3.14 (m, 4H), 6.19 (d, 1H, J = 10.8 Hz), 6.48 (d, 1H, J = 10.8 Hz), 6.55 (d, 1H, J = 15.1 Hz), 6.67 (d, 1H, J = 15.1 Hz), 7.19–7.25 (m, 2H), 7.28–7.37 (m, 4H), 7.45 (d, 4H, J = 7.6 Hz). ^{13}C NMR (75 MHz, $CDCl_3$) δ: 35.4 (2C), 39.3 (2C), 126.3 (2C), 127.2 (2C), 127.3 (2C), 128.7 (4C), 129.0 (4C), 137.0 (2C). Anal. calcd. for $C_{10}H_{12}S_2$: C 61.18, H 6.16; found: C 61.57, H 6.28.

General procedure for the synthesis of dithiolanes–dithianes

Representative procedure for the reaction of phenyl acetylene and 1,2-ethane dithiol (Table 2, entry 2)

A mixture of phenyl acetylene (102 mg, 1 mmol) and 1,2-ethane dithiol (103 mg, 1.1 mmol) in water (2 mL) was heated at 80 °C for a required period of time (4 h) (TLC). Then the mixture was extracted with Et_2O (3 × 15 mL). The ether extract was washed with brine, dried (Na_2SO_4), and evaporated to get the crude product, which was purified by column chromatography over silica gel (hexane–ether, 95:5) to provide 2-benzyl-[1,3]-dithiolane (159 mg, 81%) as a colorless oil. IR (neat, cm^{-1}) 3060, 3026, 2930, 2894, 1604, 1498, 1453, 1427, 1270, 1240, 1172, 743, 688. ^{1}H NMR (300 MHz, $CDCl_3$) δ: 3.10 (d, 2H, J = 7.08 Hz), 3.17–3.24 (m, 4H), 4.72 (t, 1H, J = 7.08 Hz), 7.20–7.32 (m, 5H). ^{13}C NMR (75 MHz, $CDCl_3$) δ: 38.5 (2C), 45.2, 54.8, 126.7, 127.9 (2C), 129.0 (2C), 139.0. These data are in good agreement with those reported.[17a] This procedure was followed for all the reactions listed in Table 2. The known compounds were identified by comparison of their spectral data with those reported earlier (see refs. in Table 2). The unknown compounds were characterized properly by their spectroscopic data (IR, ^{1}H NMR, ^{13}C NMR, and HRMS), which are reported as follows.

2-(3-Methoxy-benzyl)-[1,3]-dithiolane (Table 2, entry 4)

Yellowish oil. IR (neat, cm^{-1}) ν: 2999, 2922, 2833, 1598, 1583, 1488, 1454, 1434, 1259, 1153, 1049, 769, 694. ^{1}H NMR (300 MHz, $CDCl_3$) δ: 3.09 (d, 2H, J = 7.2 Hz,), 3.12–3.22 (m, 4H), 3.79 (s, 3H), 4.72 (t, 1H, J = 7.2 Hz), 6.73–6.87 (m, 3H), 7.21 (t, 1H, J = 7.68 Hz). ^{13}C NMR (75 MHz, $CDCl_3$) δ: 28.0 (2C), 45.1, 54.6, 55.0, 112.0, 114.6, 121.2, 129.2, 140.5, 159.4. HRMS *m/z* [M + Na]$^+$ calcd. for $C_{11}H_{14}OS_2Na$: 249.0384; found: 249.0412.

2-(4-Chloro-benzyl)-[1,3]-dithiolane (Table 2, entry 5)

Colourless oil. IR (neat, cm^{-1}) ν: 2923, 2250, 1712, 1490, 1397, 1222, 909, 732. ^{1}H NMR (300 MHz, $CDCl_3$) δ: 2.84–2.93 (m, 4H), 2.97–3.04 (m, 2H), 4.59 (t, 1H, J = 6.9 Hz), 7.12–7.29 (m, 4H). ^{13}C NMR (75 MHz, $CDCl_3$) δ: 5.0, 38.2, 38.9, 54.6, 129.2 (2C), 129.9 (2C), 132.8, 135.1. HRMS *m/z* [M + H]$^+$ calcd. for $C_{10}H_{11}ClS_2H$: 231.0069; found: 231.1078.

2-(4-Chloro-benzyl)-[1,3]-dithiane (Table 2, Entry 6)

Yellowish oil. IR (neat, cm^{-1}) ν: 3060, 3026, 2898, 2825, 1602, 1494, 1452, 1421, 1274, 1242, 1178, 906, 740, 698, 663. ^{1}H NMR (300 MHz, $CDCl_3$) δ: 1.98–2.06 (m, 2H), 2.70–2.81 (m, 4H), 2.91 (d, 2H, J = 7.3 Hz), 4.13 (t, 1H, J = 7.3 Hz), 7.08 (d, 2H, J = 7.4 Hz), 7.20 (d, 2H, J = 7.4 Hz). ^{13}C NMR (75 MHz, $CDCl_3$) δ: 25.5, 30.4 (2C), 40.9, 48.3, 128.3 (2C), 130.5 (2C), 130.8, 135.6. HRMS calcd. for [M+Na]$^+$ $C_{11}H_{13}ClS_2Na$: 267.0045; found: 267.010.

Acknowledgements

We are pleased to acknowledge the financial support from Department of Science and Technology (DST), New Delhi (Grant No. SR/S5/GC-02/2006). S.B. is thankful to Council of Scientific and Industrial Research (CSIR) for a fellowship.

References

(1) (a) Pearson, W. H.; Lee, I. Y.; Mi, Y.; Stoy, P. *J. Org. Chem.* **2004**, *69* (26), 9109–9122. doi:10.1021/jo048917u. PMID:15609944.; (b) Mizuno, H.; Domon, K.; Masuya, K.; Tanino, K.; Kuwajima, I. *J. Org. Chem.* **1999**, *64* (8), 2648–2656. doi:10.1021/jo981478c. PMID:11674332.

(2) (a) Aucagne, V.; Lorin, C.; Tatibouët, A.; Rollin, P. *Tetrahedron Lett.* **2005**, *46* (25), 4349–4352. doi:10.1016/j.tetlet.

2005.04.112.; (b) Muraoka, N.; Mineno, M.; Itami, K.; Yoshida, J.-I. *J. Org. Chem.* **2005**, *70* (17), 6933–6936. doi:10.1021/jo0510437. PMID:16095319.; (c) Woodland, C. A.; Crawley, G. C.; Hartley, R. C. *Tetrahedron Lett.* **2004**, *45* (6), 1227–1231. doi:10.1016/j.tetlet.2003.11.132.; (d) McReynolds, M. D.; Dougherty, J. M.; Hanson, P. R. *Chem. Rev.* **2004**, *104* (5), 2239–2258. doi:10.1021/cr020109k. PMID:15137790.

(3) (a) Shoai, S.; Bichler, P.; Kang, B.; Buckley, H.; Love, J. A. *Organometallics* **2007**, *26* (24), 5778–5781. doi:10.1021/om700811e.; (b) Cao, C.; Fraser, L. R.; Love, J. A. *J. Am. Chem. Soc.* **2005**, *127* (50), 17614–17615. doi:10.1021/ja055096h. PMID:16351085.; (c) Ogawa, A.; Ikeda, T.; Kimura, K.; Hirao, T. *J. Am. Chem. Soc.* **1999**, *121* (22), 5108–5114. doi:10.1021/ja983949i.; (d) Field, L. D.; Messerle, B. A.; Vuong, K. Q.; Turner, P. *Dalton Trans.* **2009**, (18): 3599–3614. doi:10.1039/b821188d. PMID:19381423.; (e) Kuniyasu, H.; Ogawa, A.; Sato, K.-I.; Ryu, I.; Kambe, N.; Sonoda, N. *J. Am. Chem. Soc.* **1992**, *114* (14), 5902–5903. doi:10.1021/ja00040a087.; (f) Banerjee, S.; Das, J.; Santra, S. *Tetrahedron Lett.* **2009**, *50* (1), 124–127. doi:10.1016/j.tetlet.2008.10.110.

(4) (a) Schneider, C. C.; Godoi, B.; Prigol, M.; Nogueira, C. W.; Zeni, G. *Organometallics* **2007**, *26* (17), 4252–4256. doi:10.1021/om070229o.; (b) Kondoh, A.; Takami, K.; Yorimitsu, H.; Oshima, K. *J. Org. Chem.* **2005**, *70* (16), 6468–6473. doi:10.1021/jo050931z. PMID:16050711.

(5) (a) Manarin, F.; Roehrs, J. A.; Prigol, M.; Alves, D.; Nogueira, C. W.; Zeni, G. *Tetrahedron Lett.* **2007**, *48* (28), 4805–4808. doi:10.1016/j.tetlet.2007.05.076.; (b) Silva, M. S.; Lara, R. G.; Marczewski, J. M.; Jacob, R. G.; Lenardao, E. J.; Perin, G. *Tetrahedron Lett.* **2008**, *49* (12), 1927–1930. doi:10.1016/j.tetlet.2008.01.093.; (c) Ananikov, V. P.; Orlov, N. V.; Beletskaya, I. P. *Organometallics* **2006**, *25* (8), 1970–1977. doi:10.1021/om051105j.; (d) Sridhar, R.; Surendra, K.; Krishnaveni, N. S.; Srinivas, B.; Rao, K. R. *Synlett* **2006**, 3495; (e) Perin, G.; Jacob, R. G.; de Azambuja, F.; Botteselle, G. V.; Siqueira, G. M.; Freitag, R. A.; Lenardão, E. J. *Tetrahedron Lett.* **2005**, *46* (10), 1679–1682. doi:10.1016/j.tetlet.2005.01.060.; (f) Lenardão, E. J.; Silva, M. S.; Mendes, S. R.; Azambuja, F.; Jacob, R. G.; Santos, P. C. S.; Perin, G. *J. Braz. Chem. Soc.* **2007**, *18* (5), 943. doi:10.1590/S0103-50532007000500011.

(6) (a) Anastas, P. T.; Warner, J. *Green Chemistry: Theory and Practice;* Oxford University Press: Oxford, 1998; (b) Li, C.-J.; Chang, T. H. In *Organic Reactions in Aqueous Media;* Wiley: New York, 1997; (c) Grieco, P. A., Ed. *Organic Synthesis in Water;* Blackie Academic and Professional: London, 1998; (d) Lindström, U. M. *Chem. Rev.* **2002**, *102* (8), 2751–2772. doi:10.1021/cr010122p. PMID:12175267.; (e) Li, C.-J. *Chem. Rev.* **2005**, *105* (8), 3095–3165. doi:10.1021/cr030009u. PMID:16092827.

(7) (a) Azizi, N.; Saidi, M. R. *Org. Lett.* **2005**, *7* (17), 3649–3651. doi:10.1021/ol051220q. PMID:16092841.; (b) Azizi, N.; Aryanasab, F.; Torkiyan, L.; Ziyaei, A.; Saidi, M. R. *J. Org. Chem.* **2006**, *71* (9), 3634–3635. doi:10.1021/jo060048g. PMID:16626155.; (c) Khatik, G. L.; Kumar, R.; Chakraborti, A. K. *Org. Lett.* **2006**, *8* (11), 2433–2436. doi:10.1021/ol060846t. PMID:16706544.; (d) Ranu, B. C.; Banerjee, S. *Tetrahedron Lett.* **2007**, *48* (1), 141–143. doi:10.1016/j.tetlet.2006.10.142.; (e) Ranu, B. C.; Mandal, T. *Synlett* **2007**, *2007* (6), 0925. doi:10.1055/s-2007-973877.; (f) Ranu, B. C.; Dey, R.; Chattopadhyay, K. *Tetrahedron Lett.* **2008**, *49* (21), 3430–3432. doi:10.1016/j.tetlet.2008.03.121.

(8) Benati, L.; Montevecchi, P. C.; Spagnolo, P. *J. Chem. Soc., Perkin Trans. 1* **1991**, (9): 2103. doi:10.1039/p19910002103.

(9) Truce, W. E.; Breiter, J. J. *J. Am. Chem. Soc.* **1962**, *84* (9), 1623–1624. doi:10.1021/ja00868a022.

(10) Karunakaran, K. *Oxidation Commun.* **1998**, *21*, 519.

(11) De, S. K. *Adv. Synth. Catal.* **2005**, *347* (5), 673–676. doi:10.1002/adsc.200404323.

(12) Zheng, Y.; Du, X.; Bao, W. *Tetrahedron Lett.* **2006**, *47* (7), 1217–1220. doi:10.1016/j.tetlet.2005.11.164.

(13) Mukaiyama, T.; Fukuyama, S.; Kumamoto, T. *Tetrahedron Lett.* **1968**, *9* (34), 3787–3790. doi:10.1016/S0040-4039(00)75541-9.

(14) Meindertsma, A. F.; Pollard, M. M.; Feringa, B. L.; de Vries, J. G.; Minnaard, A. J. *Tetrahedron Asymmetry* **2007**, *18* (24), 2849–2858. doi:10.1016/j.tetasy.2007.11.020.

(15) Kaydos, J. A.; Smith, D. L. *J. Org. Chem.* **1983**, *48* (7), 1096–1099. doi:10.1021/jo00155a033.

(16) Andres, D. F.; Dietrich, U.; Laurent, E. G.; Marquet, B. S. *Tetrahedron* **1997**, *53* (2), 647–658. doi:10.1016/S0040-4020(96)00997-0.

(17) (a) Besra, R. C.; Rudrawar, S.; Chakraborti, A. K. *Tetrahedron Lett.* **2005**, *46* (37), 6213–6217. doi:10.1016/j.tetlet.2005.07.059.; (b) Aoyama, T.; Takido, T.; Kodomari, M. *Synlett* **2004**, (13): 2307–2310. doi:10.1055/s-2004-832812.; (c) Garlaschelli, L.; Vidari, G. *Tetrahedron Lett.* **1990**, *31* (40), 5815–5816. doi:10.1016/S0040-4039(00)97967-X.

(18) Firouzabadi, H.; Iranpoor, N.; Hazarkhani, H. *J. Org. Chem.* **2001**, *66* (22), 7527–7529. doi:10.1021/jo015798z. PMID:11681974.

(19) (a) Green, T. W.; Wuts, P. G. M. *Protective Groups in Organic Synthesis,* 3rd ed.; John Wiley and Sons: New York,1999; p. 329; (b) Seebach, D. *Angew. Chem. Int. Ed. Engl.* **1979**, *18* (4), 239–258. doi:10.1002/anie.197902393.

A theoretical model study on the cyclic reaction of 4-hydroxybutanal catalyzed by Brønsted acid

Qingyong Meng, Chenggen Zhang, and Ming-Bao Huang

Abstract: For a theoretical model study on the cyclic reaction of 4-hydroxybutanal (4-OH-BL), we have examined five assumed reaction pathways (I–V) by performing the B3LYP calculations in the gas phase and self-consistent isodensity polarized continuum model (SCIPCM)-B3LYP calculations in aqueous solution. Pathways II (4-OH-BL + H^+), III (4-OH-BL + H_3O^+), and IV (4-OH-BL + H_3O^+ + H_2O) represent three models for the cyclic reaction catalyzed by Brønsted acids. The present study leads to the following conclusions concerning the five pathways (mainly on the basis of the calculation results in the solution). The high barrier along pathway I (with no catalyst) implies that the reaction does not occur without a catalyst, and the extremely large stabilization energy of the intermediate implies that pathway II is not a realistic model for the reaction catalyzed by Brønsted acid. Along pathway III, there are two intermediates and a transition state in between, and they are 10–16 kcal/mol lower in energy than the reactants (4-OH-BL + H_3O^+). Along pathway IV, there is only one intermediate, and it is 20.6 kcal/mol lower in energy than the reactants (4-OH-BL + H_3O^+ + H_2O). Pathways III and IV are predicted to be feasible. Energetically, pathway IV is more favourable than pathway III and it is considered as a rational model for the cyclic reaction of 4-OH-BL catalyzed by Brønsted acid. Our calculations for pathway V (catalyzed by H_2O) indicate that the water molecule may also serve as a catalyst for the cyclic reaction. The transition state along pathway V is 20.0 kcal/mol higher in energy than the reactants (4-OH-BL + H_2O), and one can clearly see the "proton wire" in its structure. Our calculations show strong solvent effects on energetics of the charged intermediates along pathways II, III, and IV.

Key words: cyclic reaction of 4-hydroxybutanal, catalyzed by Brønsted acid, B3LYP, self-consistent isodensity polarized continuum model (SCIPCM), model study.

Résumé : Comme modèle théorique pour une étude de la réaction cyclique du 4-hydroxybutanal (4-OH-BL), on a étudié cinq présumées voies réactionnelles (I–V) en effectuant des calculs B3LYP en phase gazeuse et des calculs SCIPCM-B3LYP en solution et les voies réactionnelles II (4-OH-BL + H^+), III (4-OH-BL + H_3O^+) et IV (4-OH-BL + H_3O^+ + H_2O) représentent trois modèles pour la réaction cyclique catalysée par les acides de Brønsted. La présente étude conduit aux conclusions suivantes concernant les cinq voies réactionnelles (principalement sur la base des résultats de calculs en solution). La barrière élevée le long de la voie I (sans catalyseur) implique que la réaction ne se produit pas sans catalyseur et l'énergie de stabilisation extrêmement grande de l'intermédiaire implique que la voie réactionnelle II n'est pas un modèle réaliste pour la réaction catalysée par un acide de Brønsted. Le long de la voie III, on rencontre deux intermédiaires et un état de transition entre les deux et leurs énergies sont de 10 à 16 kcal/mol inférieures à celles des réactifs (4-OH-BL + H_3O^+). Le long de la voie IV, il n'existe qu'un intermédiaire et son énergie est de 20,6 kcal/mol inférieure à l'énergie des réactifs (4-OH-BL + H_3O^+ + H_2O). Les voies réactionnelles III et IV sont donc toutes les deux possibles. D'un point de vue énergétique, la voie IV est plus favorable que la voie III et on la considère comme un modèle rationnel pour la réaction du 4-OH-BL catalysée par un acide de Brønsted. Les calculs pour la voie V (catalysée par l'eau) indiquent que la molécule d'eau peut aussi servir de catalyseur pour la réaction cyclique. L'énergie de transition de l'état de transition le long de la voie V est de 20,0 kcal/mol plus élevée que celles des réactifs (4-OH-BL + H_2O) et on peut voir le « treillis de proton » dans sa structure. Les calculs montrent l'existence d'importants effets de solvant sur les énergies des intermédiaires chargés le long des voies réactionnelles II, III et IV.

Mots-clés : réaction cyclique du 4-hydroxybutanal, catalyse par un acide de Brønsted, B3LYP, SCIPCM, étude modèle.

[Traduit par la Rédaction]

Introduction

Nucleophilic reactions are very important reactions in organic chemistry.[1] There are numerous theoretical studies[2–9] on nucleophilic substitution reactions (S_N2 reactions), but less theoretical studies on nucleophilic addition reactions. The cyclic reaction of 4-hydroxybutanal (4-OH-BL) to form 2-hydroxytetrahydrofuran (2-OH-THF), catalyzed by Brønsted acid, is a simple nucleophilic addition reaction, which generates the ring framework of an α- or β-furanose.

Received 7 May 2009. Accepted 17 July 2009. Published on the NRC Research Press Web site at canjchem.nrc.ca on 22 October 2009.

Q. Meng, C. Zhang, and M. Huang.[1] College of Chemistry and Chemical Engineering, Graduate University of Chinese Academy of Sciences, P.O. Box 4588, Beijing 100049, P. R. China.

[1]Corresponding author (e-mail: mbhuang1@gucas.ac.cn).

Following the experimentally suggested mechanism,[10–12] we performed theoretical calculations for a model reaction system of (4-OH-BL + H^+) (the H^+ ion being a prototype of Brønsted acid), and the calculations predicted an intermediate with a stabilization energy of around 200 kcal/mol along the path of the cyclic reaction (see the Results and discussion section). The extremely large stabilization energy, which must be the proton affinity energy of 4-OH-BL, indicates that the model reaction system was too simple to lead to a realistic description of the reaction. The experimentally reported cyclic reaction of 4-OH-BL catalyzed by Brønsted acid occurs in aqueous solution.[1,10–12] We realized that the reaction system might include the H_3O^+ ion (a prototype of Brønsted acid) and the H_2O molecule (as catalyst).

For the cyclic reaction of 4-OH-BL, we have assumed five reaction pathways, I, II, III, IV, and V, which correspond to the model reaction systems of (4-OH-BL), (4-OH-BL + H^+), (4-OH-BL + H_3O^+), (4-OH-BL + H_3O^+ + H_2O), and (4-OH-BL + H_2O), respectively. The species, besides 4-OH-BL, in these reaction systems are considered as catalyst(s). Pathways II, III, and IV represent three models for the cyclic reaction of 4-OH-BL catalyzed by Brønsted acids and pathway V represents a model for the cyclic reaction catalyzed by an H_2O molecule. The five reaction pathways were first studied in the gas phase using the density functional theory (DFT) B3LYP (the Becke's three-parameter hybrid function with the nonlocal correlation of Lee–Yang–Parr)[13,14] method. The theoretical study on a ground-state reaction in the gas phase is a kind of routine work: geometry optimization and frequency analysis calculations for stationary points (intermediates and transition states), followed by intrinsic reaction coordinate (IRC) calculations. The gas-B3LYP calculations can give us general pictures (sequences of stationary points) of the five pathways in the gas phase.

Considering that the experimentally reported cyclic reaction occurs in aqueous solution,[1,10–12] we should study the five assumed reaction pathways in aqueous solution. There are several models of the SCRF (self-consistent reaction field) theory to simulate solution effects, and we used the SCIPCM (self-consistent isodensity polarizable continuum model),[15] which is the latest model in the SCRF theory. In our SCIPCM-B3LYP calculations, water is considered as solvent and for some of the assumed pathways the water molecule is also considered as catalyst, which should be included in the model reaction systems. We performed geometry optimization calculations for the stationary points in aqueous solution and obtained the SCIPCM-B3LYP energetic and geometric results, which are quite different from the B3LYP results in the gas phase (see the Results and discussion section). We assume that each of the five pathways has the same sequence of the stationary points in the gas phase and in aqueous solution.

In the present paper, we will report and discuss the B3LYP (in the gas phase) and SCIPCM-B3LYP (in aqueous solution) calculation results for the five pathways. The present study is a model study and it is different from theoretical studies on reactions for which the reaction systems are explicitly known. The main purpose of the present study is to suggest a rational model for the experimentally reported cyclic reaction of 4-OH-BL catalyzed by Brønsted acid in aqueous solution on the basis of the SCIPCM-B3LYP results. We will also discuss the calculation results for pathway V (catalyzed by H_2O). In the present paper, we will show that the results (relative energies and geometries) in the solution, based on the SCIPCM-B3LYP geometry optimization calculations, are quite different from those in the gas phase obtained in the gas-B3LYP calculations, and we will discuss the difficulties in using the SCIPCM model.

Computational details

All the calculations were carried out with the Gaussian 03W suite of programs.[16]

As mentioned above, the five assumed reaction pathways, I, II, III, IV, and V, correspond to the model reaction systems (including catalyst molecules and (or) ions) of (4-OH-BL), (4-OH-BL + H^+), (4-OH-BL + H_3O^+), (4-OH-BL + H_3O^+ + H_2O), and (4-OH-BL + H_2O), respectively, and the calculations were performed on these five reaction systems. In the gas phase, the geometry optimization calculations were performed for the reactants, transition states (TSs), intermediates (IMs), and products along the pathways at the B3LYP/6-31G(d), B3LYP/6-311G(d,p), and B3LYP/6-311++G(d,p) levels. Frequency analysis calculations at the same levels were then performed for all the species to ensure the absence of imaginary frequencies for the intermediates, the presence of the unique imaginary frequencies for the transition states, and the frequency calculations produce the zero-point energies (ZPEs). All the reaction steps along the pathways were checked at the B3LYP/6-31G(d) level: (1) the reaction steps having transition states were checked by the intrinsic reaction coordinate (IRC) calculations[17–19] and (2) the reaction steps having no transition states were checked by partial geometry optimization calculations along "reaction coordinates".

In aqueous solution, the geometry (re)optimization calculations were performed for the reactants, TSs, IMs, and products along the pathways at the SCIPCM-B3LYP/6-311++G(d,p) level, and the calculations predicted the geometries and energies of those species in aqueous solution. In the SCIPCM we used an isodensity value of 0.0004, which was recommended by Wiberg and Rablen.[20] Since the SCIPCM-B3LYP geometry optimization calculations for one IM and one TS along pathway III were not successful (see below), we performed the PCM-B3LYP/6-311++G(d,p) geometry optimization calculations for the stationary species along pathway III (PCM (polarizable continuum model)[21–24] being another model of the SCRF theory) and calculated the SCIPCM-B3LYP/6-311++G(d,p)//PCM-B3LYP/6-311++G(d,p) relative energies.

In the following discussion on the reaction pathways in the gas phase, we use the B3LYP/6-311++G(d,p) geometries ("geometries in the gas phase") and B3LYP/6-311++G(d,p) relative energies corrected with the gas-B3LYP/6-311++G(d,p) ZPEs ("relative energies in the gas phase"). In the following discussion on the reaction pathways in aqueous solution, we use the SCIPCM-B3LYP/6-311++G(d,p) geometries ("geometries in aqueous solution") and SCIPCM-B3LYP/6-311++G(d,p) relative energies corrected with the gas-B3LYP/6-311++G(d,p) ZPEs ("relative energies in aqueous solution"), unless otherwise noted. The reported (Mulliken) charge values on atoms (with hydrogens

summed into the heave atoms) in some of the TSs and IMs are the results of the gas-B3LYP/6-311++G(d,p) calculations.

Results and discussion

Figures 1a and 1b are schematic diagrams of the calculated potential energy curves for pathways I–V in the gas phase and in aqueous solution, respectively. In Fig. 1a, the relative energies in the gas phase for the TSs and IMs to the respective reactants along the pathways are given in parentheses, and in Fig. 1b, the relative energies in aqueous solution for the TSs and IMs to the respective reactants along the pathways are given in parentheses (for the TS and IMs along pathway III, the ZPE-corrected SCIPCM-B3LYP//PCM-B3LYP relative energies are given). Given in Table 1 are the relative energies, without and with the ZPE corrections, of the TSs and IMs along the pathways. Before we describe and discuss the results for the five reaction pathways, we will first report our results for the reactant (4-OH-BL) and product (2-OH-THF).

Reactant and product

The 4-OH-BL molecule has many conformations. In our calculations we located 17 conformations, which have very similar energies. For convenience, we take the conformation (R) shown in Fig. 2a as the reactant of the cyclic reaction, which is less stable than the most stable conformation by only 0.91 and 0.61 kcal/mol in the gas phase and in aqueous solution, respectively. The 2-OH-THF molecule has six conformations.[25–27] In our calculations we located all the conformations. We take the most stable conformation (P) shown in Fig. 2b as the product of the cyclic reaction. Our calculations predict that in the gas phase 2-OH-THF (P) is only 2.0 kcal/mol more stable than 4-OH-BL (R), while in aqueous solution 2-OH-THF (P) is only 0.8 kcal/mol less stable than 4-OH-BL (R). Therefore, the cyclic reaction can thermodynamically occur.

The geometries of R and P (in the gas phase and in aqueous solution) are shown in Figs. 2a and 2b, respectively, and we give only the bond length values in the heavy-atom frameworks. The geometries of R or P in the gas phase and in aqueous solution are very similar. In the geometries of R, the O(10), C(7), C(1), and C(12) atoms are almost in one plane, and the C(4) atom is out of the plane. In the geometries of P, the O(10), C(7), C(4), and C(12) atoms are almost in one plane, and the C(1) atom is out of the plane. The O(10)–C(12) bond length [r(10–12)] values are 2.824 and 2.829 Å in the geometries of R in the gas phase and in aqueous solution and 1.413 and 1.419 Å in the geometries of P in the gas phase and in aqueous solution, respectively. The C(12)–O(14) bond length [r(12–14)] values are 1.207 and 1.213 Å in the geometries of R in the gas phase and in aqueous solution and 1.420 and 1.421 Å in the geometries of P in the gas phase and in aqueous solution, respectively.

Reaction pathway I (R → P)

The assumed pathway I represents a cyclic reaction of 4-OH-BL leading to 2-OH-THF with no catalyst. Our gas-B3LYP calculations indicate that pathway I has only one reaction step and a transition state (denoted as TS1) that is the unique stationary point along the potential energy curve (see Fig. 1). The structure of TS1 is shown in Fig. 3a. Important parameters in the geometries of TS1 in the gas phase and in aqueous solution are given in Table 2. The r(10–12) value (1.653 Å) in aqueous solution is somewhat smaller than the value (1.716 Å) in the gas phase. The r(10–12) values in TS1 are much smaller than those in R and larger than those in P. The r(10–11) and r(11–14) values in TS1 indicate that the H(11) atom is migrating from the hydroxyl oxygen (O(10)) to the carbonyl oxygen (O(14)).

The barrier values (the relative energies of TS1 to R) for pathway I are predicted to be 38.0 and 38.8 kcal/mol in the gas phase and in aqueous solution, respectively. The high barrier along pathway I indicates that the cyclic reaction does not occur without a catalyst.

Fig. 1. Schematic diagrams of the potential energy curves for the five assumed pathways (I–V) of the cyclic reaction of 4-hydroxybutanal in (a) the gas phase and (b) aqueous solution. In part (a), the ZPE-corrected B3LYP/6-311++G(d,p) relative energies (in kcal/mol) for transition states (TSs) and intermediates (IMs) to the respective reactants are given in parentheses. In part (b), the ZPE-corrected SCIPCM-B3LYP/6-311++G(d,p) relative energies for the TSs and IMs are given in parentheses (for the TS and IMs along pathway III the ZPE-corrected SCIPCM-B3LYP/6-311++G(d,p)//PCM-B3LYP/6-311++G(d,p) relative energies are given).

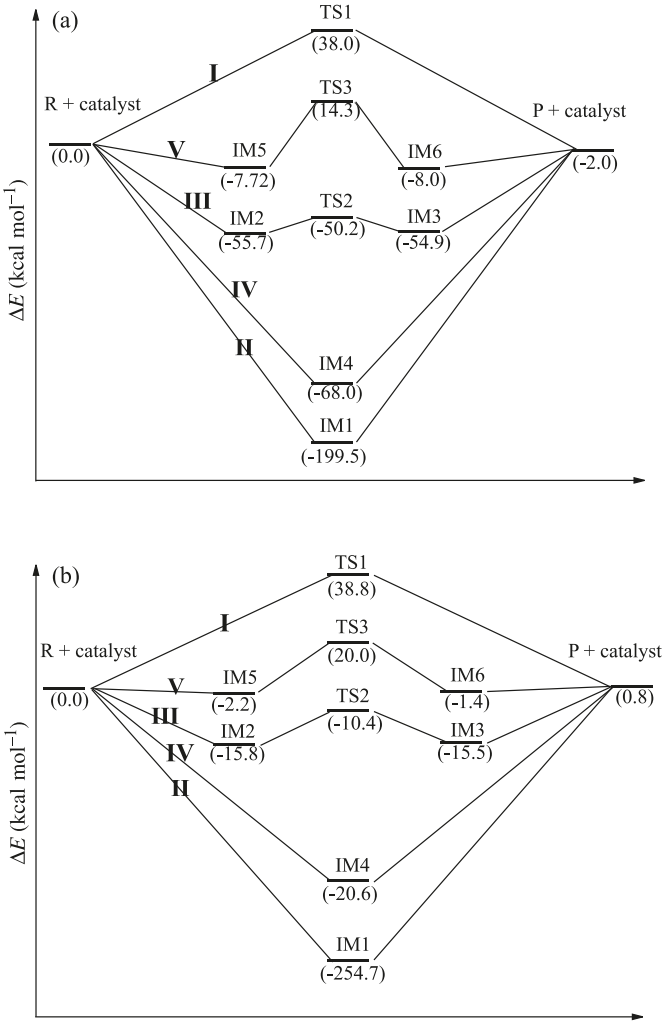

Table 1. B3LYP/6-311++G(d,p) and SCIPCM-B3LYP/6-311++G(d,p) relative energies (to the respective reactants, in kcal/mol) of transition states (TSs) and intermediates (IMs) along the five assumed reaction pathways (I–V) for the cyclic reaction of 4-hydroxybutanal, and values in parentheses are the relative energies corrected with the B3LYP/6-311++G(d,p) zero-point energies.

	B3LYP/6-311++G(d,p)	SCIPCM-B3LYP/6-311++G(d,p)[a]
Reactant	0.0 (0.0)	0.0 (0.0)
Product	–4.2 (–2.0)	–1.4 (0.8)
I. 4-OH-BL → 2-OH-THF		
TS1	39.7 (38.0)	40.5 (38.8)
II. 4-OH-BL + H^+ → 2-OH-THF + H^+		
IM1	–209.0 (–199.5)	–264.2 (–254.7)
III. 4-OH-BL + H_3O^+ → 2-OH-THF + H_3O^+		
IM2	–58.2 (–55.7)	–18.3 (–15.8)
TS2	–53.8 (–50.2)	–14.0 (–10.4)
IM3	–58.5 (–54.9)	–19.1 (–15.5)
IV. 4-OH-BL + H_2O + H_3O^+ → 2-OH-THF + H_2O + H_3O^+		
IM4	–73.6 (–68.0)	–26.3 (–20.6)
V. 4-OH-BL + H_2O → 2-OH-THF + H_2O		
IM5	–10.4 (–7.7)	–4.86 (–2.2)
TS3	14.0 (14.3)	19.7 (20.0)
IM6	–12.6 (–8.0)	–5.97 (–1.4)

[a]For IM2, TS2, and IM3 along pathway III, the relative energies were calculated at the SCIPCM-B3LYP/6-311++G(d,p)//PCM-B3LYP/6-311++G(d,p) level and the values in parentheses are the relative energies corrected with the B3LYP/6-311++G(d,p) zero-point energies.

Fig. 2. Bond length values (in Å) in the B3LYP/6-311++G(d,p) (the upper values) and SCIPCM-B3LYP/6-311++G(d,p) (the lower values) geometries of ((a) R) 4-OH-BL and ((b) P) 2-OH-THF.

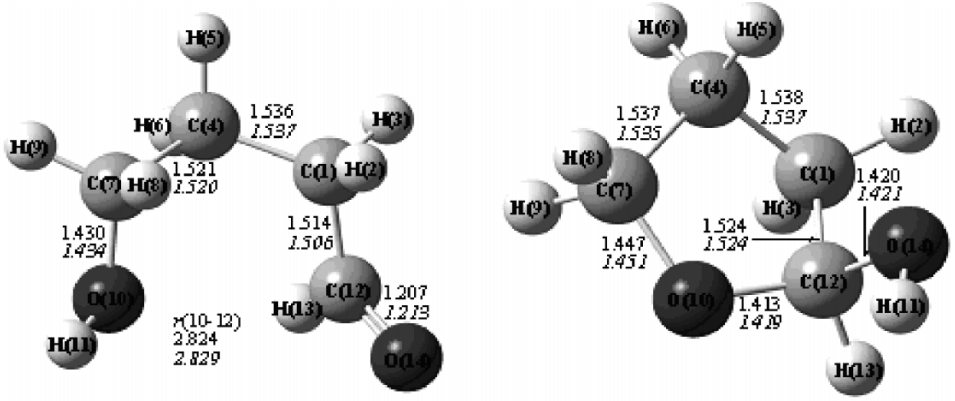

(a) R (b) P

Reaction pathway II (R + H^+ → P + H^+)

The assumed pathway II represents a cyclic reaction of 4-OH-BL leading to 2-OH-THF with a proton as catalyst (the reactants being (R + H^+)), and it is the simplest model for the reaction catalyzed by Brønsted acid. Our gas-B3LYP calculations indicate that there is only one stationary point along the potential energy curve (see Fig. 1), which is an intermediate (denoted as IM1). The structure of IM1 (H(15) being the catalyst "proton") is shown in Fig. 3b. Important parameters in the geometries of IM1 in the gas phase and in aqueous solution are given in Table 2. The *r*(10–12) value (1.682 Å) in aqueous solution is considerably smaller than the value (1.844 Å) in the gas phase, and the *r*(12–14) value in aqueous solution is larger than the value in the gas phase. The *r*(10–12) values in IM1 are much smaller than those in R and significantly larger than those in P. The *r*(10–11) and *r*(14–15) values of around 0.97 Å indicate that the O(10)–H(11) and O(14)–H(15) bonds in IM1 are two normal O–H bonds, and the calculated charges on the two hydroxyl groups are +0.161 and +0.246 e, respectively. The experimentally suggested mechanism[10–12] for the cyclic reaction catalyzed by Brønsted acid implies that there be two inter-

Fig. 3. Structures of (a) TS1 along pathway I and (b) IM1 along pathway II (important geometric parameters are given in Table 2).

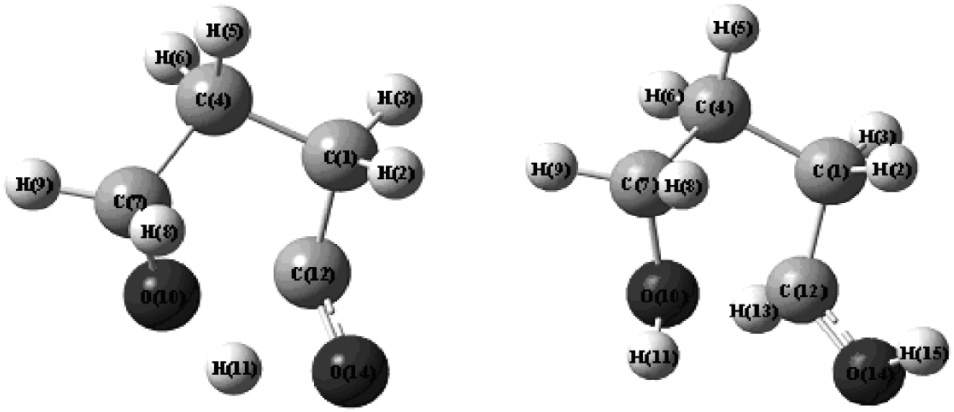

(a) TS1 (b) IM1

Table 2. Important parameters in the B3LYP/6-311++G(d,p) (the upper values) and SCIPCM-B3LYP/6-311++G(d,p) (the lower values in parentheses) geometries of the transition states (TSs) and intermediates (IMs) along pathways I, II, and III for the cyclic reaction of 4-hydroxybutanal (the bond length values are given in Å; for notations, see Figs. 3 and 4).

	TS1	IM1	IM2	TS2	IM3
r(10–11)	1.193 (1.176)	0.970 (0.974)		0.972 (0.976)	1.028 (1.044)
r(10–12)	1.716 (1.653)	1.844 (1.682)	2.277 (2.258)	1.867 (1.807)	1.581 (1.565)
r(11–14)	1.305 (1.332)				
r(11–16)				2.430 (2.298)	1.516 (1.460)
r(12–14)	1.313 (1.333)	1.308 (1.332)	1.264 (1.265)	1.300 (1.309)	1.355 (1.359)
r(14–15)		0.971 (0.970)	1.018 (1.031)	0.983 (0.985)	
r(15–16)			1.564 (1.508)	1.892 (1.852)	

Note: For IM2, TS2, and IM3 along pathway III, the lower values in parentheses are the parameters in the PCM-B3LYP/6-311++G(d,p) geometries.

mediate species along the reaction path, while our calculations indicate that there is only one intermediate species along pathway II.

The relative energies of IM1 to the reactants (R + H^+) in the gas phase and in aqueous solution are –199.5 and –254.7 kcal/mol, respectively (see Fig. 1). Actually, the value of 199.5 kcal/mol (8.65 eV) is the value of the proton affinity energy[28] for the 4-OH-BL molecule. There are no experimental indications for such extremely large stabilization energies. The assumed reaction pathway II is not a realistic model for the cyclic reaction catalyzed by Brønsted acid.

Reaction pathway III (R + H_3O^+ → P + H_3O^+)

The assumed pathway III represents a cyclic reaction of 4-OH-BL leading to 2-OH-THF with an H_3O^+ ion as catalyst (the reactants being (R + H_3O^+)), and it is a second model for the reaction catalyzed by Brønsted acid.

We will first consider pathway III in the gas phase. Our gas-B3LYP calculations indicate that along the potential energy curve (see Fig. 1a) in the gas phase there are two intermediates and a transition state (denoted as TS2) between the two intermediates. The intermediate between the reactants and TS2 is denoted as IM2 and the intermediate between TS2 and the products is denoted as IM3. The structures of IM2 (the H(15)–O(16)–H(17)–H(18) moiety representing the catalyst "H_3O^+"), TS2, and IM3 are shown in Figs. 4a, 4b, and 4c, respectively, and important geometric parameters are given in Table 2. The *r*(14–15) value of 1.018 Å and the *r*(15–16) value of 1.564 Å in IM2 indicate that there is an H-bond between O(14) and O(16) (with the H-atom close to O(14)). The *r*(10–11) value of 1.028 Å and the *r*(11–16) value of 1.516 Å in IM3 indicate that there is an H-bond between O(10) and O(16) (with the H-atom close to O(10)). In the structure of TS2 the *r*(15–16) and *r*(11–16) values are very large and the sum of the calculated charge values on the H(17)–O(16)–H(18) moiety ("the migrating group") is close to zero (0.0315 e). The *r*(10–12) and *r*(12–14) values are 2.277 and 1.264 Å in IM2, 1.867 and 1.300 Å in TS2, and 1.581 and 1.355 Å in IM3, respectively. The relative energies of IM2, TS2, and IM3 to the reactants (R + H_3O^+) in the gas phase are –55.7, –50.2, and –54.9 kcal/mol, respectively (see Fig. 1a). Therefore, the assumed pathway III is feasible in the gas phase.

In aqueous solution the SCIPCM-B3LYP/6-311++G(d,p) geometry optimization calculations were not successful for IM2 and TS2 (successful only for IM3). We performed the PCM-B3LYP/6-311++G(d,p) geometry optimization calculations for the reactants, IM2, TS2, IM3, and products along pathway III and then calculated the SCIPCM-B3LYP/6-311++G(d,p)//PCM-B3LYP/6-311++G(d,p) relative energies of IM2, TS2, IM3, and the products to the reactants. Important parameters in the PCM-B3LYP geometries of IM2, TS2, and IM3 are given in Table 2. The PCM-B3LYP val-

Fig. 4. Structures of (a) IM2, (b) TS2, and (c) IM3 along pathway III (important geometric parameters are given in Table 2).

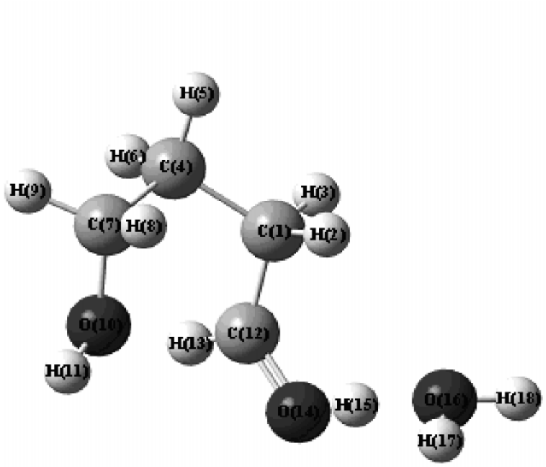

(a) IM2

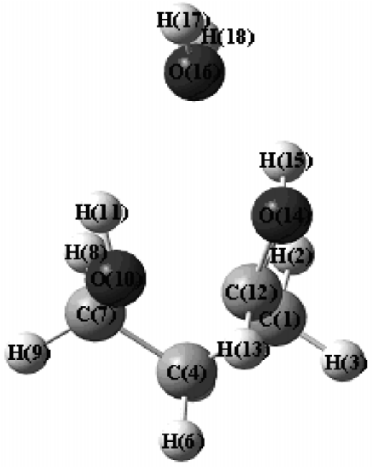

(b) TS2

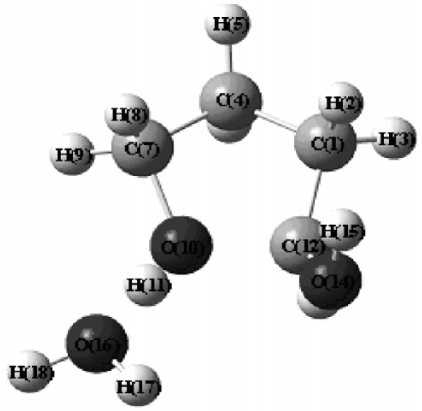

(c) IM3

ues for important geometric parameters in IM3 are similar to the respective SCIPCM-B3LYP values. As shown in Table2, the PCM-B3LYP *r*(10–12) values in IM2, TS2, and IM3 are smaller than the respective gas-B3LYP values, but the PCM-B3LYP *r*(12–14) values in IM2, TS2, and IM3 are very close to the respective gas-B3LYP values. The PCM-B3LYP values for the O(16)–H(15) long distance in IM2 and TS2 and for the O(16)–H(11) long distance in TS2 and IM3 are smaller than the respective gas-B3LYP values. The (ZPE-corrected) SCIPCM-B3LYP//PCM-B3LYP relative energies of IM2, TS2, IM3, and the products to the reactants along pathway III are –15.8, –10.4, –15.5, and 0.8 kcal/mol, respectively (see Fig. 1b). Therefore, the assumed pathway III is feasible in aqueous solution.

Reaction pathway IV ($R + H_2O + H_3O^+ \rightarrow P + H_2O + H_3O^+$)

The assumed pathway IV represents a cyclic reaction of 4-OH-BL leading to 2-OH-THF with H_2O and H_3O^+ as catalysts (the reactants being ($R + H_2O + H_3O^+$)), and it is a third model for the reaction catalyzed by Brønsted acid. Our gas-B3LYP calculations indicate that there is only one stationary point along the potential energy curve (see Fig. 1), which is an intermediate (denoted as IM4). The reaction paths from ($R + H_2O + H_3O^+$) to IM4 and from IM4 to ($P + H_2O + H_3O^+$) were checked by partial geometry optimization calculations at the B3LYP/6-31G(d) level, and no other stationary points were found. The structure of IM4 (the H(15)–O(16)–H(17)–H(18) moiety representing the catalyst H_3O^+ and the H(20)–O(19)–H(21) moiety representing the catalyst "H_2O") is given in Fig. 5a. The geometries of IM4 in the gas phase and in aqueous solution are quite similar, and important geometric parameters are given in Table 3. As in the case of IM1, the *r*(10–12) values in IM4 are much smaller than those in R and significantly larger than those in P. The *r*(10–11) and *r*(11–19) values in IM4 indicate that there is an H-bond between O(10) and O(19) (with the H(11) atom close to the hydroxyl oxygen). The *r*(14–15) and *r*(15–16) values in IM4 indicate that there is another H-bond between O(14) and O(16) (with the H(15) atom close to the carbonyl oxygen).

The relative energies of IM4 to the reactants ($R + H_2O + H_3O^+$) in the gas phase and in aqueous solution are –68.0 and –20.6 kcal/mol, respectively (see Fig. 1). The assumed pathway IV is feasible in the gas phase and in aqueous solution. The relative energy value of –20.6 kcal/mol in aqueous solution is rational.

We also performed the PCM-B3LYP/6-311++G(d,p) geometry optimization calculations for the reactants and IM4

Fig. 5. The structure of (a) IM4 along pathway IV and structures of (b) IM5, (c) TS3, and (d) IM6 along pathway V (important geometric parameters are given in Table 3).

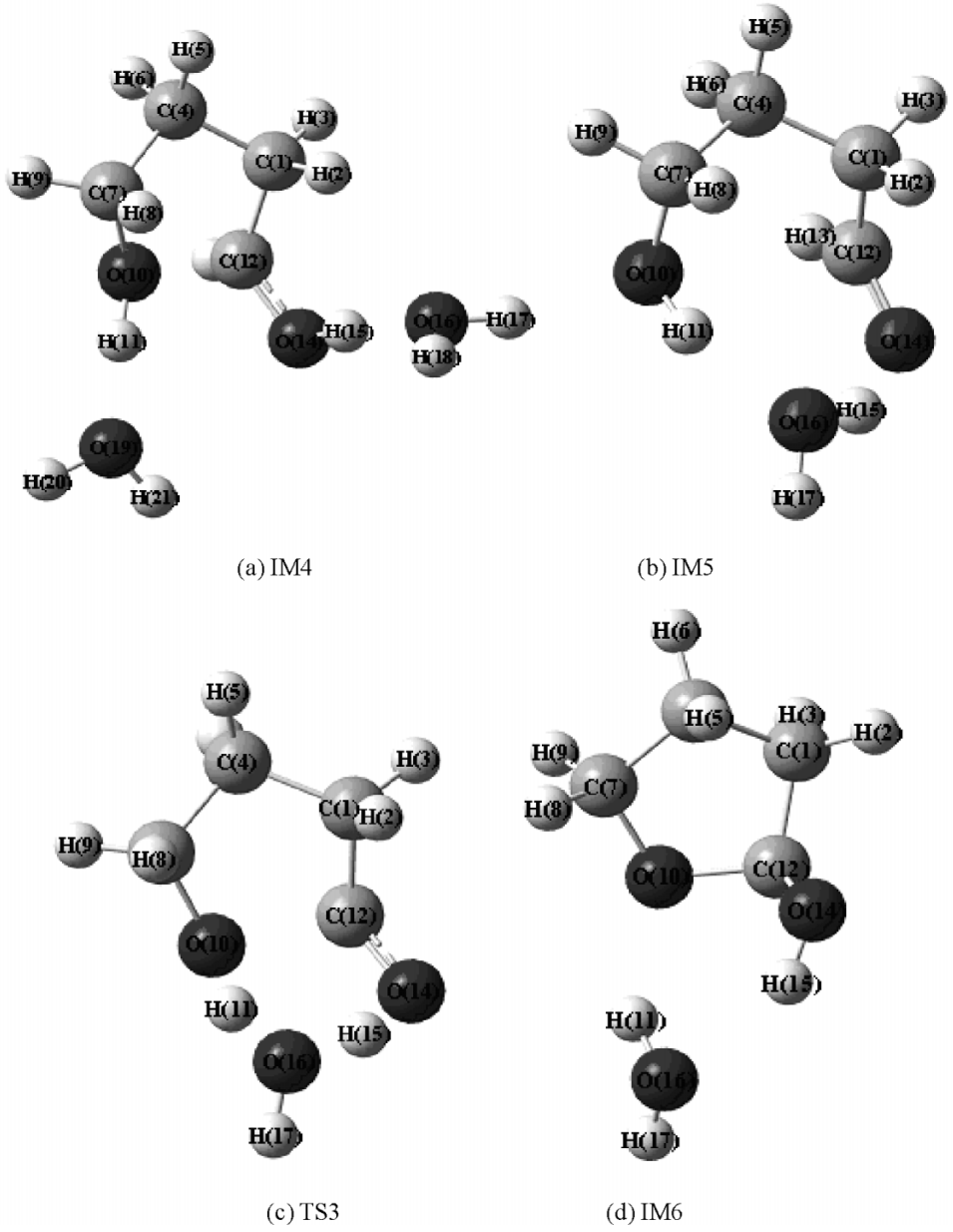

Table 3. Important parameters in the B3LYP/6-311++G(d,p) (the upper values) and SCIPCM-B3LYP/6-311++G(d,p) (the lower values in parentheses) geometries of the transition states (TSs) and intermediates (IMs) along pathways IV and V for the cyclic reaction of 4-hydroxybutanal (the bond length values are given in Å; for notations, see Fig. 5).

	IM4	IM5	TS3	IM6
r(10–11)	1.014 (1.011)	0.972 (0.975)	1.192 (1.197)	1.919 (1.938)
r(10–12)	1.650 (1.681)	2.842 (2.979)	1.771 (1.708)	1.438 (1.434)
r(11–16)		1.893 (1.860)	1.223 (1.219)	0.974 (0.974)
r(11–19)	1.573 (1.615)			
r(12–14)	1.333 (1.327)	1.214 (1.217)	1.296 (1.312)	1.403 (1.413)
r(14–15)	0.988 (0.997)	1.933 (1.968)	1.230 (1.272)	0.972 (0.973)
r(15–16)	1.731 (1.675)	0.973 (0.972)	1.190 (1.155)	2.018 (2.004)

along pathway IV and calculated the SCIPCM-B3LYP/6-311++G(d,p)//PCM-B3LYP/6-311++G(d,p) relative energy of IM4 to the reactants. The (ZPE-corrected) SCIPCM-B3LYP//PCM-B3LYP relative energy of IM4 to the reactants is –20.7 kcal/mol (we will mention this value in the Conclusion section).

Reaction pathway V ($R + H_2O \rightarrow P + H_2O$)

Experimental and theoretical studies[29] suggest that glycolaldehyde in the chain conformation can form complexes with the water molecule by H-bonds. The 4-OH-BL (R) molecule is similar to glycolaldehyde, which also has one hydroxyl and one aldehyde groups, in the chain conformation. Thus, we have considered the role of the water molecule (without the proton) in the cyclic reaction of 4-OH-BL.

The assumed pathway V represents a cyclic reaction of 4-OH-BL leading to 2-OH-THF with a water molecule as catalyst (the reactants being ($R + H_2O$)). Our gas-B3LYP calculations indicate that along the potential energy curve (see Fig. 1) there are two intermediates and a transition state (denoted as TS3) between the two intermediates. The intermediate between the reactants and TS3 is denoted as IM5 and the intermediate between TS3 and the products is denoted as IM6. The structures of IM5 (the H(15)–O(16)–H(17) moiety representing the catalyst H_2O), TS3, and IM6 are shown in Figs. 5b, 5c, and 5d, respectively. Important parameters in the geometries of IM5, TS3, and IM6 in the gas phase and in aqueous solution are given in Table 3, and the geometries in the gas phase and in the solution are similar. IM5 has one H-bond between O(10) and O(16) (with the H(11) atom close to O(10)) and another H-bond between O(14) and O(16) (with the H(15) atom close to O(16)) in its structure, and IM5 is an analogue to the glycolaldehyde–water complex "CC-W-1" or "CC-W-2" shown in Fig. 1 of ref. 29. By checking the bond distance values (see Table 3) in the O(10)–H(11)–O(16) part of IM5, TS3, and IM6, we note that the H(11) atom is migrating from O(10) to O(16). By checking the bond distance values (see Table 3) in the O(16)–H(15)–O(14) part of IM5, TS3, and IM6, we note that the H(15) atom is migrating from O(16) to O(14). Along the O(10)–H(11)–O(16)–H(15)–O(14) chain in TS3, the bond distance values range from 1.15 to 1.28 Å, and this O–H–O–H–O chain serves as a "proton wire".[30]

IM5 and IM6 are predicted to be slightly more stable than the reactants ($R + H_2O$) in the gas phase and in aqueous solution (see Fig. 1). The relative energies of TS3 to the reactants are 14.3 and 20.0 kcal/mol in the gas phase and in aqueous solution, respectively (see Fig. 1), and the barriers in the gas phase and in aqueous solution are not very high. Therefore, the assumed pathway V represents a possible mechanism for the cyclic reaction (catalyzed by H_2O).

The so-called proton wire was discussed by Eigen[31] as a cyclic (cooperative) mechanism in proton transfer processes as early as in 1965. Wolfe and co-workers[32–39] have extensively studied the cooperative mechanism in hydrolysis reactions. In their theoretical study on hydration of a carbonyl group, Wolfe et al.[32] confirmed that the reaction proceeds via a cyclic transition state containing two water molecules. In the structures of their transition state ($(TS)_2$), reactant ($(RC)_2$), and product ($(PC)_2$), one can see an O–H–O–H–O–C ring (the two H's in the ring being the transferring protons). In the structure of TS3 (see Fig. 5c) one can see the O(10)–H(11)–O(16)–H(15)–O(14)–C(12) ring (the O(10)–H(11)–O(16)–H(15)–O(14) part was called a proton wire, see above). One can also see the O–H–O–H–O–C ring in the structures of IM5 and IM6 (see Figs. 5b and 5d). IM5, TS3, and IM6 along pathway V are similar to $(RC)_2$, $(TS)_2$, and $(PC)_2$ (in ref. 32), respectively, if the "H(11)–O(10)–C(7)-" part of IM5, TS3, and IM6 was viewed as the second water molecule. The barrier value for the $(RC)_2 \rightarrow (TS)_2 \rightarrow (PC)_2$ process in aqueous solution was calculated to be 24.6 kcal/mol[32] (at the Onsager-MP2/6-31G(d)//3-21G level), and it is quite close to the relative energy value (20.0 kcal/mol) of TS3 to the reactants (pathway V) in aqueous solution (at the SCIPCM-B3LYP/6-311++G(d,p) level). Pathway V (with one water molecule as catalyst) has a "cooperative mechanism" as the hydrolysis reactions of the carbonyl group.[32]

Conclusions

Since the experimentally reported cyclic reaction of 4-OH-BL occurs in aqueous solution,[1,10–12] discussions leading to conclusions on the reaction mechanisms will be on the basis of the energetic and geometric results calculated in aqueous solution for the five assumed reaction pathways, and the energetic data are given in Fig. 1b and in parentheses in the last column of Table 1.

The high barrier along pathway I (with no catalyst) indicates that the cyclic reaction does not occur without catalyst. Pathways II, III, and IV represent three models for the cyclic reaction catalyzed by Brønsted acids. The extremely large stabilization energy of the intermediate along pathway II (catalyzed by H^+) implies that pathway II is not a realistic model for the cyclic reaction catalyzed by Brønsted acid.

Along pathway III (catalyzed by H_3O^+), there are two intermediates (IM2 and IM3) and one transition state (TS2) between IM2 and IM3. The (ZPE-corrected) SCIPCM-B3LYP//PCM-B3LYP relative energies of IM2, TS2, and IM3 to the reactants ($R + H_3O^+$) are –15.8, –10.4, and –15.5 kcal/mol, respectively. Along pathway IV (catalyzed by H_3O^+ and H_2O) there is only one intermediate (IM4), and the (ZPE-corrected SCIPCM-B3LYP) relative energy of IM4 to the reactants ($R + H_2O + H_3O^+$) is –20.6 kcal/mol. The negative relative energy values indicate that pathways III and IV are both feasible in aqueous solution. For comparison purposes, we calculated the (ZPE-corrected) SCIPCM-B3LYP//PCM-B3LYP relative energy of IM4 to the reactants ($R + H_2O + H_3O^+$) and obtained a value of –20.7 kcal/mol (see the last section), which is lower than the relative energy values of IM2, TS2, and IM3 to the reactants ($R + H_3O^+$) calculated at the same level. Therefore, pathway IV is considered to be more (energetically) favourable than pathway III, and we conclude that pathway IV is a rational model for the cyclic reaction of 4-OH-BL catalyzed by Brønsted acid.

By checking the structures of IM2, TS2, and IM3, we can consider that the process of pathway III consists of three steps: (*i*) the H_3O^+ ion (catalyst) attacks 4-OH-BL at the carbonyl oxygen (see the structure of IM2), and it leaves a proton (H^+) at the carbonyl oxygen and becomes an H_2O moiety; (*ii*) the H_2O moiety (the charge on the moiety being

almost zero, see the last section) migrates from the carbonyl oxygen side of 4-OH-BL to the hydroxyl group side (see the structure of TS2); and (*iii*) the H_2O moiety takes a proton (H^+) from the hydroxyl group and leaves the system (becoming 2-OH-THF) as an H_3O^+ ion. However, steps (*ii*) and (*iii*) are not quite realistic in aqueous solution. One H_2O molecule in the solvent around the hydroxyl group can complete step (*iii*) and the H_2O moiety at the carbonyl oxygen side can leave the system as a H_2O molecule (the migration step, step (*ii*), is not needed). The H_2O molecule in the solvent is a second catalyst, and this realistic process is just that of pathway IV (see the structure of IM4). We do believe that pathway IV is a rational model for the cyclic reaction of 4-OH-BL catalyzed by Brønsted acid.

Our calculations for pathway V indicate that the H_2O molecule may also serve as a catalyst for the cyclic reaction of 4-OH-BL, though the transition state along the pathway is 20.0 kcal/mol higher in energy than the reactants ($R + H_2O$). In the structure of the transition state one can clearly see the proton wire. The H_2O molecule can be considered as a weak Brønsted acid.

We note that, for the neutral reaction systems (pathways I and V), the relative energy values of IMs and TSs in aqueous solution are similar to the values in the gas phase (see the data in Figs. 1a and 1b). However, the situations for the charged reaction systems (pathways II, III, and IV) are different. The stabilization energy values (the negatives of the relative energy values) for IMs along pathways III (IM2 and IM3) and IV (IM4) in aqueous solution are much smaller than those in the gas phase, which can be explained by considering the fact that the positive charges in IMs are more delocalized than in the reactants (($R + H_3O^+$) and ($R + H_2O + H_3O^+$)). The positive charges are mainly located on the O(10), O(14), C(1), and C(7) atoms in IM2, IM3, and IM4. The stabilization energy value for IM1 along pathway II in aqueous solution is much larger than the value (already very large) in the gas phase, for which we have no explanations.

Supplementary data

Supplementary data for this article are available on the journal Web site (canjchem.nrc.ca) or may be purchased from the Depository of Unpublished Data, Document Delivery, CISTI, National Research Council Canada, Ottawa, ON K1A 0R6, Canada. DUD 5286. For more information on obtaining material, refer to cisti-icist.nrc-cnrc.gc.ca/cms/unpub_e.shtml.

Acknowledgement

We appreciate the financial support of this work that was provided by the National Natural Science Foundation of China through Contract No. 20773161.

References

(1) Smith, M. B.; March, J. *March's Advanced Organic Chemistry: Reactions, Mechanisms, and Structure;* Wiley: New York, 2007.

(2) Bento, A. P.; Bickelhaupt, F. M. *J. Org. Chem.* **2008**, *73* (18), 7290–7299. doi:10.1021/jo801215z. PMID:18690745.

(3) van Bochove, M. A.; Bickelhaupt, F. M. *Eur. J. Org. Chem.* **2008**, *2008* (4), 649–654. doi:10.1002/ejoc.200700953.

(4) Chabinyc, M. L.; Craig, S. L.; Regan, C. K.; Brauman, J. I. *Science* **1998**, *279* (5358), 1882–1886. doi:10.1126/science.279.5358.1882. PMID:9506930.

(5) Hase, W. L. *Science* **1994**, *266* (5187), 998–1002. doi:10.1126/science.266.5187.998. PMID:17779941.

(6) Laerdahl, J. K.; Uggerud, E. *Int. J. Mass Spectrom.* **2002**, *214* (3), 277–314. doi:10.1016/S1387-3806(01)00575-9.

(7) Mikosch, J.; Trippel, S.; Eichhorn, C.; Otto, R.; Lourderaj, U.; Zhang, J. X.; Hase, W. L.; Weidemüller, M.; Wester, R. *Science* **2008**, *319* (5860), 183–186. doi:10.1126/science.1150238. PMID:18187650.

(8) Schmatz, S. *ChemPhysChem* **2004**, *5* (5), 600–617. doi:10.1002/cphc.200301043. PMID:15179712.

(9) Sun, L.; Song, K.; Hase, W. L. *Science* **2002**, *296* (5569), 875–878. doi:10.1126/science.1068053. PMID:11988565.

(10) Carey, F. A.; Sundberg, R. J. *Advanced Organic Chemistry, Part A: Structure and Mechanisms,* 5 ed.; Springer: New York, 2007.

(11) Cordes, E. E. H.; Bull, H. G. *Chem. Rev.* **1974**, *74* (5), 581–603. doi:10.1021/cr60291a004.

(12) Fife, T. H. *Acc. Chem. Res.* **1972**, *5* (8), 264–272. doi:10.1021/ar50056a002.

(13) Becke, A. D. *J. Chem. Phys.* **1993**, *98* (7), 5648–5653. doi:10.1063/1.464913.

(14) Lee, C.; Yang, W.; Parr, R. G. *Phys. Rev. B* **1988**, *37* (2), 785–789. doi:10.1103/PhysRevB.37.785.

(15) Foresman, J. B.; Keith, T. A.; Wiberg, K. B.; Snoonian, J.; Frisch, M. J. *J. Phys. Chem.* **1996**, *100* (40), 16098–16104. doi:10.1021/jp960488j.

(16) Frisch, M. J.; Trucks, G. W.; Schlegel, H. B.; Scuseria, G. E.; Robb, M. A.; Cheeseman, J. R.; Montgomery, J. A. J.; Vreven, T.; Kudin, K. N.; Burant, J. C.; Millam, J. M.; Iyengar, S. S.; Tomasi, J.; Barone, V.; Mennucci, B.; Cossi, M.; Scalmani, G.; Rega, N.; Petersson, G. A.; Nakatsuji, H.; Hada, M.; Ehara, M.; Toyota, K.; Fukuda, R.; Hasegaw, J.; Ishida, M.; Nakajima, T.; Honda, Y.; Kitao, O.; Nakai, H.; Klene, M.; Li, X.; Knox, J. E.; Hratchian, H. P.; Cross, J. B.; Adamo, C.; Jaramillo, J.; Gomperts, R.; Stratmann, R. E.; Yazyev, O.; Austin, A. J.; Cammi, R.; Pomelli, C.; Ochterski, J. W.; Ayala, P. Y.; Morokuma, K.; Voth, G. A.; Salvador, P.; Dannenberg, J. J.; Zakrzewski, V. G.; Dapprich, S.; Daniels, A. D.; Strain, M. C.; Farkas, O.; Malick, D. K.; Rabuck, A. D.; Raghavachari, K.; Foresman, J. B.; Ortiz, J. V.; Cui, Q.; Baboul, A. G.; Clifford, S.; Cioslowski, J.; Stefanov, B. B.; Liu, G.; Liashenko, A.; Piskorz, P.; Komaromi, I.; Martin, R. L.; Fox, D. J.; Keith, T.; Al-Laham, M. A.; Peng, C. Y.; Nanayakkara, A.; Challacombe, M.; Gill, P. M. W.; Johnson, B.; Chen, W.; Wong, M. W.; Gonzalez, C.; Pople, J. A. *Gaussian 03W;* Gaussian, Inc.: Pittsburgh, PA, 2003.

(17) Fukui, K.; Kato, S.; Fujimoto, H. *J. Am. Chem. Soc.* **1975**, *97* (1), 1–7. doi:10.1021/ja00834a001.

(18) Gonzalez, C.; Schlegel, H. B. *J. Chem. Phys.* **1989**, *90* (4), 2154–2161. doi:10.1063/1.456010.

(19) Gonzalez, C.; Schlegel, H. B. *J. Phys. Chem.* **1990**, *94* (14), 5523–5527. doi:10.1021/j100377a021.

(20) Wiberg, K. B.; Rablen, P. R. *J. Comput. Chem.* **1993**, *14* (12), 1504–1518. doi:10.1002/jcc.540141213.

(21) Cancès, E.; Mennucci, B.; Tomasi, J. *J. Chem. Phys.* **1997**, *107* (8), 3032–3041. doi:10.1063/1.474659.

(22) Cossi, M.; Barone, V.; Cammi, R.; Tomasi, J. *Chem. Phys.*

Lett. **1996**, *255* (4–6), 327–335. doi:10.1016/0009-2614(96)00349-1.
(23) Miertus, S.; Tomasi, J. *Chem. Phys.* **1982**, *65* (2), 239–245. doi:10.1016/0301-0104(82)85072-6.
(24) Mierts, S.; Scrocco, E.; Tomasi, J. *Chem. Phys.* **1981**, *55* (1), 117–129. doi:10.1016/0301-0104(81)85090-2.
(25) Chung-Phillips, A.; Chen, Y. Y. *J. Phys. Chem. A* **1999**, *103* (7), 953–964. doi:10.1021/jp9846126.
(26) Gordon, M. T.; Lowary, T. L.; Hadad, C. M. *J. Org. Chem.* **2000**, *65* (16), 4954–4963. doi:10.1021/jo000426w. PMID: 10956478.
(27) Legon, A. C. *Chem. Rev.* **1980**, *80* (3), 231–262. doi:10.1021/cr60325a002.
(28) Blackwell Scientific Publications. *IUPAC Compendium of Chemical Terminology (the "Gold Book");* Blackwell Scientific Publications: Oxford, 1997.
(29) Aviles-Moreno, J.-R.; Demaison, J.; Huet, T. R. *J. Am. Chem. Soc.* **2006**, *128* (32), 10467–10473. doi:10.1021/ja062312t. PMID:16895412.
(30) Nagle, J. F.; Morowitz, H. J. *Proc. Natl. Acad. Sci. U.S.A.* **1978**, *75* (1), 298–302. doi:10.1073/pnas.75.1.298. PMID: 272644.
(31) Eigen, M. *Discuss. Faraday Soc.* **1965**, *39*, 7–15. doi:10.1039/df9653900007.
(32) Wolfe, S.; Kim, C.-K.; Yang, K.; Weinberg, N.; Shi, Z. *J. Am. Chem. Soc.* **1995**, *117* (15), 4240–4260. doi:10.1021/ja00120a005.
(33) Rauk, A.; Wolfe, S.; Csizmadia, I. G. *Can. J. Chem.* **1969**, *47* (1), 113–135. doi:10.1139/v69-014.
(34) Hsieh, Y.-H.; Weinberg, N.; Wolfe, S. *Can. J. Chem.* **2008**, *86* (2), 81–90. doi:10.1139/V07-074.
(35) Wolfe, S.; Shi, Z.; Yang, K.; Ro, S.; Weinberg, N.; Kim, C.-K. *Can. J. Chem.* **1998**, *76* (1), 114–124. doi:10.1139/cjc-76-1-114.
(36) Hsieh, Y.-H.; Weinberg, N.; Yang, K.; Kim, C.-K.; Shi, Z.; Wolfe, S. *Can. J. Chem.* **2005**, *83* (6–7), 769–785. doi:10.1139/v05-027.
(37) Hsieh, Y.-H.; Weinberg, N.; Wolfe, S. *Can. J. Chem.* **2009**, *87* (4), 539–543. doi:10.1139/V09-003.
(38) Shi, Z.; Hsieh, Y.-H.; Weinberg, N.; Wolfe, S. *Can. J. Chem.* **2009**, *87* (4), 544–555. doi:10.1139/V09-011.
(39) Wolfe, S.; Weinberg, N.; Hsieh, Y.-H. *Theor. Chem. Acc.* **2007**, *118* (1), 265–269. doi:10.1007/s00214-007-0321-7.

Copolymerization of sterically demanding phosphine-olefins and 1-hexene

Jenny S.J. McCahill and Douglas W. Stephan

Abstract: The copolymerization of 1-hexene with *t*-$Bu_2P(CH_2)_3CH{=}CH_2$ **(1)** or *t*-$Bu_2P(CH_2)_9CH{=}CH_2$ **(2)** has been achieved using $CpMe_2Ti(NPt\text{-}Bu_3)$ as the precatalyst and $B(C_6F_5)_3$, $[Ph_3C][B(C_6F_5)_4]$, or $[PhNMe_2H][B(C_6F_5)_4]$ as the activator. The resulting polymers are shown to incorporate up to 9% of the phosphine comonomer, albeit with reduced catalyst activity and polymer molecular mass. The cause of the catalyst inhibition is also considered in the light of phosphine–activator interactions.

Key words: titanium phosphinimide, copolymerization, phosphine-containing polymers, phosphine–activator interactions.

Résumé : On a effectué la copolymérisation du hex-1-ène avec le *t*-$Bu_2P(CH_2)_3CH{=}CH_2$ (**1**) ou le *t*-$Bu_2P(CH_2)_9CH{=}CH_2$ (**2**) en utilisant le $CpMe_2Ti(NPt\text{-}Bu_3)$ comme précatalyseur et le $B(C_6F_5)_3$, $[Ph_3C][B(C_6F_5)_4]$, ou $[PhNMe_2H][B(C_6F_5)_4]$ comme activateurs. On a montré que les polymères qui en résultent incorporent jusqu'à 9 % du comonomère phosphine, avec une réduction de l'activité du catalyseur et du poids moléculaire du polymère. On considère la cause de cette inhibition du catalyseur en fonction des interactions entre la phosphine et l'activateur.

Mots-clés : phosphinimide de titane, copolymérisation, polymères contenant une phosphine, interaction entre une phosphine et un activateur.

[Traduit par la Rédaction]

Introduction

The development of single-site catalysts for the polymerization of ethylene and other α-olefins has been a major area of research for the past quarter of a century. The specific tuning of defined metal complexes allows strict control over the microstructure of polyolefins produced.[1,2] This rational catalyst development, although extensively studied, continues to be a motivating objective in numerous research endeavors. A driving force behind some of these investigations is the expansion of these systems to incorporate functional moieties into the polymer, to enhance or change the polymer properties and range of applications.

There are two main approaches to the synthesis of functional polyolefins: chain-end functionalization and in-chain functionalization.[3–5] Chain-end functionalization is achieved through reactivity on unsaturated chain-ends or via functionalization of polymer terminae. In-chain functionalization is typically achieved through post-polymerization reactivity, the use of groups to protect the functionality during the polymerization, or via direct polymerization. Of these methods of in-chain functionalization, direct polymerization is preferred, since it requires no post-polymerization modification. Therefore, numerous studies have been carried out to incorporate the functional moieties directly during the polymerization process. Furthermore, it is desirable to add these moieties in a controlled manner without compensation of any desirable properties.

The direct polymerization of functionalized monomers using group-IV transition-metal catalysts has been limited, as many polar monomers poison the catalyst by coordination to the electrophilic metal center. Nonetheless, functionalized monomers containing Si,[6,7] halogens,[8] and N[7,9] have been directly polymerized using group-IV catalysts as such groups afford weak donor interactions.

Previous efforts in our group have shown that activation of $CpMe_2Ti(NPt\text{-}Bu_3)$ with borane and borate activators affords highly active catalysts for olefin polymerization. Moreover, the catalytically active cation can be intercepted with phosphine donors affording species of the form $[CpMeTi(NPt\text{-}Bu_3)(PR_3)]^+$. However, with sterically bulky phosphines (R = Cy, *t*-Bu, and *o*-tolyl) there was no evidence of phosphine binding to Ti and the free phosphine was observed in solution by NMR methods.[10,11] In this paper, we exploit this absence of interaction of bulky phosphines to probe the viability of copolymerization of olefins with olefins containing pendant bulky phosphine fragments.

Experimental section

General considerations

All preparations were performed under an atmosphere of dry O_2-free N_2 employing either Schlenk-line techniques or a Vacuum Atmospheres inert atmosphere glovebox. Solvents were purified employing Grubbs-type column systems man-

Received 28 April 2009. Accepted 13 July 2009. Published on the NRC Research Press Web site at canjchem.nrc.ca on 27 October 2009.

J.S. McCahill and D.W. Stephan.[1,2] Department of Chemistry & Biochemistry, University of Windsor, Windsor, ON N9B 3P4, Canada.

[1]Corresponding author (e-mail: dstephan@chem.utoronto.ca).
[2]Present address: Department of Chemistry, University of Toronto, 80 St. George St., Toronto, ON M5S 3H6, Canada.

ufactured by Innovative Technologies. Uninhibited THF purchased from EDM and deuterated benzene, toluene, and methylenechloride purchased from Cambridge Isotopes Laboratories, were dried, distilled, and freeze-pump-thaw degassed (three times) prior to use. ^{1}H and ^{13}C NMR spectra were recorded on Bruker Avance 300 and 500 spectrometers. Trace amounts of protonated solvents were used as references, and ^{1}H and ^{13}C{^{1}H} NMR chemical shifts are reported relative to $SiMe_4$. ^{31}P{^{1}H}, ^{11}B{^{1}H}, and ^{19}F NMR spectra were referenced to external 85% H_3PO_4, $BF_3{\cdot}Et_2O$, and $CFCl_3$, respectively. Combustion analyses were performed at the University of Windsor Chemical Laboratories employing a PerkinElmer CHN Analyzer. Molecular mass determinations were performed using a Waters Breeze system GPC using THF as eluent. The detector used was a Waters model 410 refractive index detector at 35 °C, and molecular masses were calibrated using narrow polystyrene standards (Polymer Laboratories Inc.). High-temperature GPC data were provided by the technical staff at NOVA Chemicals Corporation.

HP*t*-Bu_2, $Br(CH_2)_3CHCH_2$, $Br(CH_2)_4CH_3$, $Br(CH_2)_9CH_3$, and anhydrous MeOH were purchased from Sigma-Aldrich Chemical Company, and $[Me_2PhNH][B(C_6F_5)_4]$ was purchased from Strem Chemical Inc.; all were used as received. 1-Hexene was purchased from Sigma-Aldrich Chemical Company and distilled from Na/benzophenone. $B(C_6F_5)_3$, and $[Ph_3C][B(C_6F_5)_4]$ were generously donated by NOVA Chemicals Corp. $CpTiMe_2(NPt\text{-}Bu_3)$ was prepared via literature methods.[12]

Synthesis of *t*-$Bu_2P(CH_2)_3CH{=}CH_2$ (1), *t*-$Bu_2P(CH_2)_9CH{=}CH_2$ (2), *t*-$Bu_2P(CH_2)_4CH_3$ (3)

These compounds were prepared in a similar fashion, and thus only one preparation is detailed. A solution of $Br(CH_2)_3CH{=}CH_2$ (4.829 g 32.40 mmol) in THF (5 mL) was added to a solution of *t*-Bu_2PLi (4.392g, 28.87 mmol) in THF (50 mL) cooled to 0 °C. The solution was stirred and warmed to room temperature for 12 h. The solvent was removed in vacuo, and hexanes were added to precipitate LiBr. The solution was filtered through Celite and vacuum-distilled (58–62 °C) to yield a clear liquid.

(1): Yield: 4.89 g (79%). ^{1}H NMR (C_6D_6) δ: 5.71–5.85 (m, 1H, C*H*=CH_2), 4.97–5.08 (m, 2H, CH=CH_2), 2.13 (q, 2H, $^3J_{H-H}$ = 7 Hz, CH_2CHCH_2), 1.65 (sextet, 2H, $^2J_{H-H}$ = 7 Hz, $CH_2CH_2CH_2$), 1.22–1.33 (m, 2H, PCH_2CH_2), 1.07 (d, 18H, $^3J_{H-P}$ = 10 Hz, *t*-Bu). ^{13}C{^{1}H} NMR (C_6D_6) δ: 139.20 (s, *C*H=CH_2), 115.39 (s, CH=*C*H_2), 36.06 (d, $^3J_{C-P}$ = 13 Hz, CH_2CH_2CH), 31.66 (d, $^1J_{C-P}$ = 23 Hz, *t*-Bu), 30.65 (s, PCH_2CH_2), 30.25 (d, $^2J_{C-P}$ = 15 Hz, *t*-Bu), 21.46 (d, $^1J_{C-P}$ = 22 Hz, P*C*H_2). ^{31}P{^{1}H} NMR (C_6D_6) δ: 27.82 (s). Anal. calcd. for $C_{13}H_{27}P$: C 72.85, H 12.70; found: C 72.73, H 12.43.

(2): Yield: 2.70 g (66%) ^{1}H NMR (C_6D_6) δ: 5.73–5.87 (m, 1H, C*H*=CH_2), 4.98–5.09 (m, CH=CH_2), 1.99 (q, 2H, CH_2CH=CH_2), 1.29–1.66 (m, 14H, CH_2), 1.16 (d, 18H, $^3J_{H-P}$ = 11 Hz, *t*-Bu). ^{13}C{^{1}H} NMR (C_6D_6) partial δ: 139.59 (s, *C*H=CH_2), 114.86 (s, CH=*C*H_2), 34.57 (s, CH_2), 32.27 (d, $^2J_{C-P}$ = 13 Hz, CH_2), 31.58 (d, $^1J_{C-P}$ = 23 Hz, *t*-Bu), 31.56 (s, *C*H_2), 22.13 (d, $^1J_{C-P}$ = 23 Hz, *t*-Bu). ^{31}P{^{1}H} NMR (C_6D_6) δ:27.82 (s). Anal. calcd. for $C_{19}H_{39}P$: C 76.45, H 13.17; found: C 76.25, H 13.00.

(3): Yield: 0.71 g (51%). ^{1}H NMR (C_6D_6) δ: 1.27–1.54 (m, 8H, CH_2), 1.11 (d, 18H, $^3J_{H-P}$ = 11 Hz, *t*-Bu), 0.97 (t, 3H, $^3J_{H-H}$= 7 Hz, CH_3). ^{13}C{^{1}H} NMR (C_6D_6) δ: 34.41 (d, $^3J_{C-P}$ = 12 Hz, $CH_2CH_2CH_2$), 31.56 (d, $^1J_{C-P}$ = 23 Hz, *t*-Bu), 31.02 (d, $^2J_{C-P}$ = 12 Hz, PCH_2CH_2), 30.19 (d, $^2J_{C-P}$ = 14 Hz, *t*-Bu), 23.26 (s, $CH_2CH_2CH_3$) 22.03 (d, $^1J_{C-P}$ = 22 Hz, P*C*H_2), 14.68 (s, *C*H_3). ^{31}P{^{1}H} NMR (C_6D_6) δ: 27.84 (s). Anal calcd. for $C_{14}H_{39}P$: C 76.45, H 13.17; found: C 76.13, H 13.13.

Synthesis of *t*-$Bu_2P((CH_2)_9CHCH_2)C_6F_4BF(C_6F_5)_2$ (5)

To a solution of $B(C_6F_5)_3$ (0.254 g, 0.50 mmol) in CH_2Cl_2 (10 mL) **2** (0.156 g, 0.52 mmol) was added. The solution was stirred overnight, and the solvent was removed in vacuo. The residue was dissolved in 3 mL of CH_2Cl_2 and hexanes were added to precipitate an off-white solid. The solid was filtered and washed with pentanes several times to give a white solid. Yield: 0.198 g (50%). ^{1}H NMR (CD_2Cl_2) δ: 5.74–5.88 (m, 1H, C*H*=CH_2), 4.89–5.01 (m, 2H, CH=CH_2), 2.51–2.63 (br m, 2H, CH_2), 1.99–2.08 (br m, 2H, CH_2), 1.62–1.79 (br, m, 2H, CH_2), 1.51 (d, 18H, $^3J_{H-P}$ = 13 Hz, *t*-Bu_2), 1.25–1.36 (br, 12H, CH_2). ^{11}B{^{1}H} NMR (CD_2Cl_2) δ: –0.16 (br). ^{13}C{^{1}H} NMR (CD_2Cl_2) partial δ: 148.41 (dm, $^1J_{C-F}$ = 238 Hz, *C*F), 139.77 (s, *C*H=CH_2), 139.53 (dm, $^1J_{C-F}$ = 244 Hz, *C*F), 137.15 (dm, $^1J_{C-F}$ = 244 Hz, *C*F), 114.39 (s, CH=*C*H_2), 38.37 (d, $^1J_{C-P}$ = 32 Hz, *t*-Bu), 34.27 (s, CH=*C*H_2), 32.12 (s, *C*H_2), 31.94 (s, *C*H_2), 29.91 (s, *C*H_2), 29.53 (s, *C*H_2), 29.42 (s, *C*H_2), 29.27 (s, *C*H_2), 27.92 (s, *t*-Bu_2), 20.00 (dd, $^1J_{C-P}$ = 40 Hz, $^3J_{C-F}$ = 13 Hz, *C*H_2). ^{19}F NMR (CD_2Cl_2) δ: –119.93 to –119.73 (m, 1F, C_6F_4), –125.24 (s, 1F, C_6F_4), –125.82 (s, 1F, C_6F_4), –130.28 to –130.06 (m, 1F, C_6F_4), –132.54 (t, 4F, $^3J_{F-F}$ = 12 Hz, *o*-C_6F_5), –158.28 (t, 2F, $^3J_{F-F}$ = 20 Hz , *p*-C_6F_5), –163.78 to –163.22 (m, 4F, *m*-C_6F_5), –190.87 (br s, BF). ^{31}P{^{1}H} NMR (CD_2Cl_2) δ: 54.98 (s). Anal. calcd. for $C_{37}H_{39}BP$: C 54.83, H 4.85; found: C 54.72, H 4.65.

Generation of [*t*-$Bu_2PH((CH_2)_3CH{=}CH_2)][B(C_6F_5)_4]$ (6)

A solution of **1** (0.021 g, 0.100 mmol) in C_6D_5Br (0.5 mL) was added to a solution of $[Me_2PhNH][B(C_6F_5)_4]$ (0.079 g, 0.100 mmol) in C_6D_5Br. Quantitative product formation was observed by NMR. ^{1}H NMR (C_6D_5Br) δ: 7.22 (t, $^3J_{H-H}$ = 7 Hz, 2H, Ph), 6.75 (t, $^3J_{H-H}$ = 7 Hz, 1H, Ph), 6.65 (d, $^3J_{H-H}$ = 8 Hz, 2H, Ph), 5.50–5.54 (m, 1H, C*H*=CH_2), 4.96–5.08 (m, 2H, CH=CH_2), 4.22 (d, $^1J_{H-P}$ = 444 Hz, P*H*), 2.69 (s, 6H, Me_2), 1.93–1.95 (m, 2H, CH_2), 1.29–1.61 (m, 4H, CH_2), 0.87 (d, $^3J_{H-P}$ = 17 Hz, 18H, *t*-Bu). ^{11}B NMR (C_6D_5Br) δ: –16.70 (s). ^{19}F NMR (C_6D_5Br) δ: –132.37 (s, 8F, *o*-C_6F_5), –162.76 (t, 4F, $^3J_{F-F}$ = 19 Hz, *p*-C_6F_5), –166.46 (t, 8F, $^3J_{F-F}$ = 18 Hz, *m*-C_6F_5). ^{31}P NMR (C_6D_5Br) δ: 53.26 (d, $^1J_{P-H}$ = 438 Hz).

Polymerization procedures

A 20 mL vial with a propylene top closure with TFE–silicone septa was equipped with a magnetic stir bar. 0.673 g of 1-hexene (8 mmol), 0.015 g of $CpMe_2Ti(NPt\text{-}Bu_3)$ (0.04 mmol) and 6 mL of toluene were added to the vial. The vial was then immersed in a bath of desired temperature and stirred for 5 min at the polymerization temperature. A syringe containing 0.020 g of $B(C_6F_5)_3$ (0.04 mmol) dissolved in 4 mL of toluene was then brought out of the glovebox,

and its contents were injected into the vial. After a desired time interval, polymerizations were quenched by injection of 1 mL of MeOH. Volatiles were removed in vacuo. 1 mL of toluene was added and 5 mL MeOH was added to precipitate the polymer. Polymer was washed two times with 5 mL MeOH and dried in vacuo.

The % P incorporation is based on the relative integrals of the ^{13}C resonances attributable to methyl groups from the *t*-Bu groups on P and methyl groups of the hexene side chains. While differences in the T_1 relaxation times are expected to be small, a 10 s relaxation delay was employed to record these spectra. This delay was selected based on previously determined T_1 experiments on polyhexene.[13]

Results and discussion

In designing an appropriate phosphine-containing monomer for the polymerization with the $CpTiMe_2(NPt\text{-}Bu_3)$/$B(C_6F_5)_3$ system, we noted the previous studies by Waymouth and co-workers in which polymerization incorporated amine-functionalized olefin.[7,14] It was shown that the steric bulk of amine substituents correlated with the resulting activity of the catalyst. Similar results were also observed by Hakala et al. for the copolymerization of oxygen-functionalized olefins.[15] In addition to the influence of the steric properties of the functional group, the length of the spacer between the functional group and the olefinic residue was also seen to have a profound impact on polymerization. For example, reducing the spacer to two carbons from three carbons to the 4-amino-1-butene, resulted in a decreased polymerization activity.[14] Gianni et al.[16] also observed this trend for the polymerization of amino-functionalized olefins using Ziegler catalysts. Lofgren and co-workers have also reported the increased incorporation of oxygen-functionalized monomers into the polyethylene chain with the increase of the spacer group.[17]

In our efforts to incorporate phosphine residues into polyolefins, these earlier results prompted us to target a sterically encumbered phosphine with the pendant olefinic substituent, $t\text{-}Bu_2P(CH_2)_3CH{=}CH_2$ (**1**). This species was readily prepared via treatment of the corresponding halide derivative with lithium phosphide (Scheme 1). Employing the same methodology, the species $t\text{-}Bu_2P(CH_2)_9CH{=}CH_2$ (**2**) and $t\text{-}Bu_2P(CH_2)_4CH_3$ (**3**) were also prepared.

Initial attempts to effect the homopolymerizations of the phosphine-functionalized monomer were unsuccessful as no polymer was formed. However, copolymerization using 1, 5, and 10 mol% of (**1**) with 1-hexene did yield isolable polymeric products. In the cases where 5 and 10 mol% of the phosphine-functionalized monomer were used (Table 1), this resulted in a marked suppression of yield and molecular mass of the resulting polymers. The PDI of these polymers were typical of the single-site phosphinimide catalyst[12] used, ranging between 1.0 and 4.2. The degree of comonomer incorporation was determined by analysis of the $^{13}C\{^1H\}$ NMR spectra of the polymers. Specifically, the ratio of the integrals of signal attributable to the terminal methyl group of the hexyl residue was compared with that ascribed to the *tert*-butyl fragment (Fig. 1). The level of comonomer incorporation ranges between 3% and 5% with use of 5–10 mol% of comonomer **1**. While these values vary

Table 1. Copolymerizations of 1-hexene and **1**–**2** using the catalyst precursor $CpMe_2Ti(NPt\text{-}Bu_3)$.

% 1-Hexene	Co-monomer	Catalyst (mmol)	Activator	Time (h)	Temperature (°C)	Yield (%)	MM (M_n)	PDI	% Incorporation
100		0.16	$B(C_6F_5)_3$	16	0	94	7980	1.28	
100		0.04	$B(C_6F_5)_3$	5	30	98	3230	1.82	
99	**1**	0.16	$B(C_6F_5)_3$	16	0	93	7740	1.37	n/a
95	**1**	0.16	$B(C_6F_5)_3$	16	0	21	1140	1.02	4
95	**1**	0.04	$B(C_6F_5)_3$	5	30	23	1065	3.18	3
95	**1**	0.04	$[Ph_3C][B(C_6F_5)_4]$	5	30	19	1125	3.65	4
95	**1**	0.04	$[Me_2PhNH][B(C_6F_5)_4]$	5	30	18	916	4.21	4
95	**1**	0.04	$B(C_6F_5)_3$	5	30	59	1480	3.30	3
90	**1**	0.16	$B(C_6F_5)_3$	16	0	21	2650	1.40	5
90	**1**	0.04	$B(C_6F_5)_3$	5	30	44	1590	n/a	4
90	**2**	0.04	$B(C_6F_5)_3$	5	30	51	n/a[a]		9
75	**1**	0.04	$B(C_6F_5)_3$	5	30	36	1800	2.91	n/a

[a]n/a: Not applicable.

Fig. 1. ^{13}C NMR spectrum of copolymer of 1-hexene–(**1**).

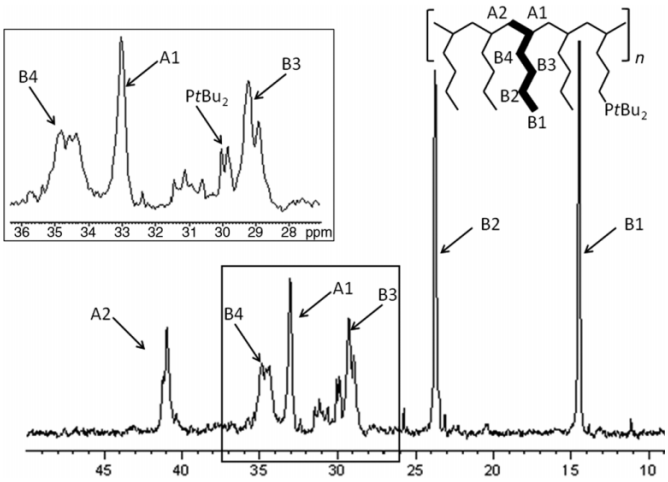

Scheme 1. Synthesis of **1**–**3**.

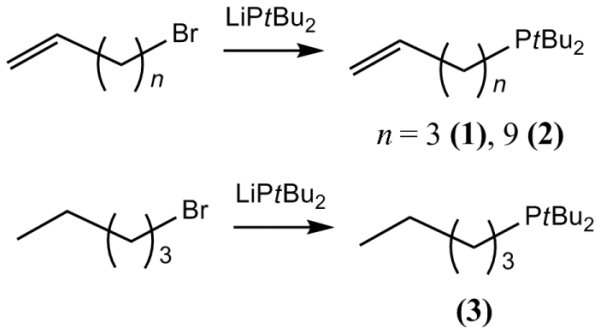

slightly with co-catalyst used, in general the level of incorporation of comonomer into the polymer increase with increased comonomer concentration. Use of 5 mol% comonomer results in less than 5 mol% incorporation, reflecting the differing steric demands of comonomer and hexene. In the case where 10 mol% of **2** is employed, incorporation rises to 9%, reflecting the decreased steric influence of the P*t*-Bu_2 fragment with the increase chain length in **2**. This result is consistent with observations made for N- and O-containing functional monomers where longer spacers between the heteroatom and the olefinic fragment were used.[18]

Competitive reactions

The reduced catalyst activity observed in the presence of the phosphine-olefin comonomers could be attributed to competitive and independent interactions of these species with the activators. For example, the independent reaction of **1** with $B(C_6F_5)_3$ has been previously reported to effect addition of P and B to the olefinic fragment to give the cyclic phosphonium borate *t*-$Bu_2P((CH_2)_4CHCH_2B(C_6F_5)_3$ (**4**). This yields a cyclic phosphonium borate (Scheme 2). In contrast, as a result of the longer chain in **2**, it is unlikely to undergo such cyclization. However, reaction of $B(C_6F_5)_3$ with **2** does proceed to give a new species **5** in 50% isolated yield. This species exhibits a $^{31}P\{^1H\}$ NMR signal at 54.98 ppm. Perhaps most diagnostic, however, is the ^{19}F NMR data. Here signals at –119.8, –125.24, –125.82, and –130.1 ppm are

Scheme 2. Reactions of olefinic phosphines with activators.

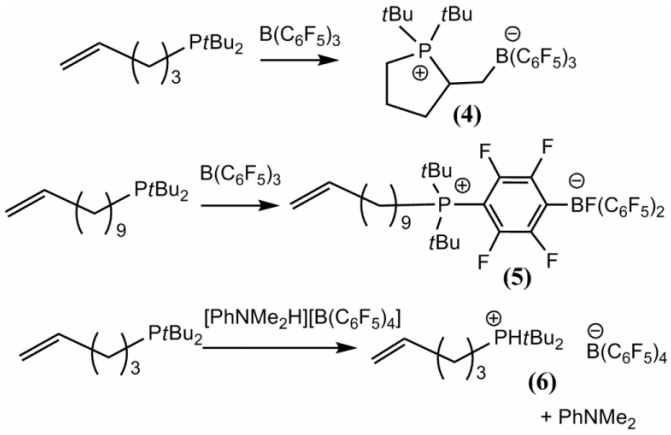

consistent with the presence of a C_6F_4 fragment in addition to signals attributable to C_6F_5 rings. As well, the signal at –190.87 ppm is attributable to a B–F residue. These data together with the ^1H and ^{13}C data confirm the formulation of **5** as *t*-$Bu_2P((CH_2)_9CH{=}CH_2)C_6F_4BF(C_6F_5)_2$ (Scheme 2). This species forms by para-attack on a C_6F_5 ring by the sterically encumbered P center. We have previously documented such reactivity of bulky phosphines with $B(C_6F_5)_3$.[19,20]

Such reactions of comonomer with the activator could compete with the precatalyst and thus account for the lesser activity observed. Similarly, in the case of the activator $[Ph_3C][B(C_6F_5)_4]$, interactions of phosphines are known to form traditional acid–base adducts affording the corresponding phosphonium salts. Alternatively, bulky phosphines are also known to effect nucleophilic aromatic substitution of a ring of $[Ph_3C]^+$ yielding cations of the form $[R_3PC_6H_4CH(C_6H_5)_2]^+$.[21] In the case of the activator $[Me_2PhNH]$ $[B(C_6F_5)_4]$, it is operative via protonation of the Ti–Me fragment. Clearly, the basicity of the phosphine centers in **1** or **2** could compete for this proton, affording the corresponding phosphonium salt. Indeed, independent reaction of **1** with $[Me_2PhNH][B(C_6F_5)_4]$ generated [*t*-$Bu_2P(H)((CH_2)_3CH{=}CH_2)][B(C_6F_5)_4]$ (**6**) (Scheme 2) and free amine Me_2PhN as evidenced by the NMR data, and in particular, the ^{31}P NMR signal at 52.5 ppm which exhibits P–H coupling of 438 Hz. Such phosphonium salts have been shown ineffective activators. Thus, such competitive side reactions could also slow catalyst generation.

The yields of polymerizations conducted in the presence of **1** or **3** were also compared. The yield of polymer generated, under otherwise identical conditions was significantly reduced when **1** was employed. This suggests the possibility that an intramolecular interaction of inserted comonomer could inhibit catalyst activity. This proposition is consistent with observations made by Waymouth and co-workers,[18] where the aminopentene, *i*$Pr_2N(CH_2)_3CHCH_2$, was found to be a more potent inhibitor than the amine, *i*$Pr_2N(CH_2)_4CH_3$, which lacks an olefinic group.[18] Nonetheless, the yield was also seen to decrease with increasing concentration of **3**, albeit to a lesser extent, suggesting that intermolecular coordination of the phosphine to the Ti cation could also diminish polymerization to some extent.

Conclusions

Copolymerization of 1-hexene and phosphine functionalized monomers is possible, although the catalyst activity is diminished. The cause of this diminished reactivity could be competitive reactions of the comonomer with the activator or the Ti catalyst. This issue can be mitigated to some extent by increasing the separation of the functional group from the double bond. Presumably, increased steric bulk at the heteroatom and decreased nucleophilicity would also facilitate comonomer incorporation.

Acknowledgements

Financial support from the Natural Sciences and Engineering Research Council of Canada (NSERC) and NOVA Chemicals Corporation is gratefully acknowledged. DWS is grateful for the award of a Canada Research Chair.

References

(1) Coates, G. W. *Chem. Rev.* **2000**, *100* (4), 1223–1252. doi:10.1021/cr990286u. PMID:11749265.
(2) Gibson, V. C.; Spitzmesser, S. K. *Chem. Rev.* **2003**, *103* (1), 283–316. doi:10.1021/cr980461r. PMID:12517186.
(3) Yanjarappa, M. J.; Sivaram, S. *Prog. Polym. Sci.* **2002**, *27* (7), 1347–1398. doi:10.1016/S0079-6700(02)00011-4.
(4) Boffa, L. S.; Novak, B. M. *Chem. Rev.* **2000**, *100* (4), 1479–1494. doi:10.1021/cr990251u. PMID:11749273.
(5) Dong, J. Y.; Hu, Y. L. *Coord. Chem. Rev.* **2006**, *250* (1-2), 47–65. doi:10.1016/j.ccr.2005.05.008.
(6) Tsuchida, A.; Bolln, C.; Sernetz, F. G.; Frey, H.; Mulhaupt, R. *Macromolecules* **1997**, *30* (10), 2818–2824. doi:10.1021/ma960846g.
(7) Kesti, M. R.; Coates, G. W.; Waymouth, R. M. *J. Am. Chem. Soc.* **1992**, *114* (24), 9679–9680. doi:10.1021/ja00050a069.
(8) Bruzaud, S.; Cramail, H.; Duvignac, L.; Deffieux, A. *Macromol. Chem. Phys.* **1997**, *198* (2), 291–303. doi:10.1002/macp.1997.021980206.
(9) Schneider, M. J.; Schafer, R.; Mulhaupt, R. *Polymer (Guildf.)* **1997**, *38* (10), 2455–2459. doi:10.1016/S0032-3861(96)00785-9.
(10) Cabrera, L. M. Sc. Thesis, University of Windsor, 2004.
(11) Cabrera, L.; Hollink, E.; Stewart, J. C.; Wei, P. R.; Stephan, D. W. *Organometallics* **2005**, *24* (6), 1091–1098. doi:10.1021/om0492202.
(12) Stephan, D. W.; Stewart, J. C.; Guerin, F.; Courtenay, S.; Kickham, J.; Hollink, E.; Beddie, C.; Hoskin, A.; Graham, T.; Wei, P. R.; Spence, R. E. V.; Xu, W.; Koch, L.; Gao, X. L.; Harrison, D. G. *Organometallics* **2003**, *22* (9), 1937–1947. doi:10.1021/om020954t.
(13) Clemens, S. M. M. Sc. Thesis, University of Windsor, 2003.
(14) Stehling, U. M.; Stein, K. M.; Kesti, M. R.; Waymouth, R. M. *Macromolecules* **1998**, *31* (7), 2019–2027. doi:10.1021/ma971053c.
(15) Hakala, K.; Lofgren, B.; Helaja, T. *Eur. Polym. J.* **1998**, *34* (8), 1093–1097. doi:10.1016/S0014-3057(97)00227-9.
(16) Giannini, U.; Bruckner, G.; Pellino, E.; Cassata, A. *J. Polym. Sci. Pol. Sym.* **1968**, *22*, 157. doi:10.1002/polc.5070220112.
(17) Seppala, J.; Lofgren, B.; Hakala, K.; Lipponen, S.; Helaja, T.; Anttila, U. *Abstracts Am. Chem. Soc* **2001**, *221*, U380.
(18) Stehling, U. M.; Stein, K. M.; Fischer, D.; Waymouth, R. M. *Macromolecules* **1999**, *32* (1), 14–20. doi:10.1021/ma980856c.
(19) Welch, G. C.; Cabrera, L.; Chase, P. A.; Hollink, E.; Masuda, J. D.; Wei, P. R.; Stephan, D. W. *Dalton Trans.* **2007**, (31): 3407–3414. doi:10.1039/b704417h. PMID:17664977.
(20) Welch, G. C.; San Juan, R. R.; Masuda, J. D.; Stephan, D. W. *Science* **2006**, *314* (5802), 1124–1126. doi:10.1126/science.1134230. PMID:17110572.
(21) Cabrera, L.; Welch, G. C.; Masuda, J. D.; Wei, P.; Stephan, D. W. *Inorg. Chim. Acta* **2006**, *359* (9), 3066–3071. doi:10.1016/j.ica.2006.02.006.

Emitting-state properties of square-planar dithiocarbamate complexes of palladium(II) and platinum(II) probed by pressure-dependent luminescence spectroscopy

Caroline Genre, Geneviève Levasseur-Thériault, and Christian Reber

Abstract: Temperature- and pressure-dependent Raman and luminescence spectra of four crystalline complexes of palladium(II) and platinum(II) with chelating diethyldithiocarbamate (EDTC) and pyrrolidine-*N*-dithiocarbamate (PDTC) ligands are reported. The crystal structure of $[Pd(PDTC)_2]$ was resolved at 120 K. Luminescence band maxima are observed at approximately 14 500 cm^{-1} and 16 000 cm^{-1} for the palladium(II) and platinum(II) complexes, respectively. Pressure leads to blue shifts of the band maxima by +9 and +13 cm^{-1}/kbar for $[Pd(EDTC)_2]$ and $[Pd(PDTC)_2]$, and +15 cm^{-1}/kbar for $[Pt(EDTC)_2]$. These spin-forbidden d–d luminescence transitions have lifetimes of approximately 600 μs at temperatures below 20 K. Luminescence intensities at room temperature are low, but they increase significantly with external pressure. The experimental results show that strong increases of luminescence intensities caused by pressure are not limited to complexes with monodentate ligands, a result providing insight on the coordinates with emitting-state distortions responsible for this effect.

Key words: palladium(II) complexes, platinum(II) complexes, high-pressure luminescence spectroscopy, high-pressure Raman spectroscopy.

Résumé : Cet article porte sur les propriétés spectroscopiques d'une série de quatre composés du palladium(II) et du platine(II) avec les ligands chélatants diéthyldithiocarbamate (EDTC) et pyrrolidine-*N*-dithiocarbamate (PDTC). La structure cristalline du complexe $[Pd(PDTC)_2]$ à 120 K a en outre été résolue. Les spectres Raman et de luminescence à température et pression variable ont été mesurés pour les quatre composés. Les maxima des bandes de luminescence se trouvent à environ 14 500 cm^{-1} et 16 000 cm^{-1} pour les complexes de palladium(II) et platine(II). La pression induit un décalage vers le bleu des maxima de luminescence de +9 cm^{-1}/kbar pour $[Pd(EDTC)_2]$, de +13 cm^{-1}/kbar pour $[Pd(PDTC)_2]$ et de +15 cm^{-1}/kbar pour $[Pt(EDTC)_2]$. Ces transitions d–d interdites de spin ont des durées de vie de l'ordre de 600 μs à basse température. Les bandes de luminescence ont une faible intensité à température ambiante, mais celle-ci augmente de manière importante avec la pression. Les résultats expérimentaux montrent que l'augmentation de l'intensité de luminescence à haute pression n'est pas limitée aux complexes avec ligands monodentates.

Mots-clés : complexes du palladium(II), complexes du platine(II), spectroscopie de luminescence à basse température et à haute pression, spectroscopie Raman à haute pression.

Introduction

Square-planar complexes of d^8-configured metal ions such as platinum(II) and palladium(II) have a rich variety of electronic excited states, which has made them attractive systems for studies of electronic structure. They show intriguing and widely variable luminescence properties. Applications as luminescent sensors or organometallic light-emitting devices have been proposed.[1,2]

One recent focus of attention are luminescence properties that show drastic variations as a consequence of small structural changes, such as mechanical grinding, reported recently for a platinum(II) terdentate polypyridyl complex.[3] While the observed variations of spectroscopic properties such as the energies of band maxima are significant, more controlled and preferably reversible structural changes are desirable, as they lead to additional and detailed insight through clear trends. External pressure is one experimental approach to obtain such variations. Recent advances in high-sensitivity detection using CCD cameras for both structural and spectroscopic studies have led to renewed interest in pressure as an attractive probe.[4–7] In addition, theoretical modeling of such effects has also obtained recent attention.[8]

In this study, we present new d–d luminescence spectra for a series of complexes of palladium(II) and platinum(II) with the chelating diethyldithiocarbamate (EDTC) and pyrrolidine-*N*-dithiocarbamate (PDTC) ligands. The temperature-dependent luminescence spectra and lifetimes support the d–d assignment for these transitions. Temperature- and pressure-dependent spectra show quantitative variations that are compared to those

Received 11 May 2009. Accepted 31 July 2009. Published on the NRC Research Press Web site at canjchem.nrc.ca on 27 October 2009.

C. Genre, G. Levasseur-Thériault, and C. Reber.[1]
Département de chimie, Université de Montréal, Montréal QC H3C 3J7, Canada.

[1]Corresponding author (e-mail: christian.reber@umontreal.ca).

reported for monodentate ligands such as thiocyanate.[5–7] Luminescence intensities increase with pressure for all complexes presented here, but to a lesser extent than for compounds with monodentate ligands, most likely due to the chelating ligands that block excited-state distortions along ligator atom – metal ion – ligator atom bending normal coordinates. Raman spectra show continuous changes of frequencies as a function of pressure, indicative of the absence of structural phase transitions in the pressure range studied. The spectra allow us to identify trends and to characterize differences between structurally very similar compounds.

Experimental

All reagents and solvents were purchased from Sigma-Aldrich and used without further purification.

Synthesis of [Pd(EDTC)$_2$] and [Pt(EDTC)$_2$]

Hydrated $PdCl_2$ was dissolved in a minimum of DMSO. Two equivalents of Na(EDTC) in an ethanol solution were then added, and a pale yellow powder immediately precipitated. It was filtered and washed with diethyl ether. Single crystals were obtained by slow evaporation of an acetone solution of the complex. Elemental analysis calculated for $C_{10}H_{20}N_2S_4Pd$ (402.96): C 29.81, H 5.00, N 6.95, S 31.83; found: C 29.97, H 5.02, N 6.86, S 28.51.

[Pt(EDTC)$_2$] was prepared in an analogous fashion from hydrated $PtCl_2$, orange crystals were obtained. Elemental analysis calculated for $C_{10}H_{20}N_2S_4Pt$ (491.62): C 24.43, H 4.10, N 5.70, S 26.09; found: C 24.54, H 4.07, N 5.63, S 25.89.

Synthesis of [Pd(PDTC)$_2$] and [Pt(PDTC)$_2$]

[Pd(PDTC)$_2$] was prepared from hydrated $PdCl_2$ and NH_4(PDTC) as described above. Pale yellow crystals were grown from an acetone solution of the complex. Elemental analysis calculated for $C_{10}H_{16}N_2S_4Pd$ (398.93): C 30.11, H 4.04, N 7.02, S 32.15; found: C 29.97, H 5.02, N 6.86, S 28.51.

Powdered [Pt(PDTC)$_2$] was prepared with the same method, and orange crystals were grown by slow evaporation of a dichloromethane solution of the complex. Elemental analysis calculated for $C_{10}H_{16}N_2S_4Pt$ (487.57): C 24.63, H 3.31, N 5.75, S 26.31; found: C 24.66, H 3.06, N 5.77, S 25.84.

Single crystal X-ray diffraction

X-ray crystallographic data for [Pd(PDTC)$_2$] were collected from a single crystal sample, which was mounted on a loop fiber. Data were collected using a Bruker Platform diffractometer, equipped with a Bruker SMART 2K Charged-Coupled Device (CCD) Area Detector using the program SMART and normal focus sealed-tube source graphite monochromated Cu K_α radiation. The crystal-to-detector distance was 4.908 cm, and the data collection was carried out in 512×512 pixel mode, utilizing 4×4 pixel binning. The initial unit cell parameters were determined by a least-squares fit of the angular setting of strong reflections, collected by a 9.0° scan in 30 frames over four different parts of the reciprocal space (120 frames total). One complete sphere of data was collected, to better than 0.8 Å resolution. Upon completion of the data collection, the first 101 frames were recollected to improve the decay correction analysis.

Table 1. Crystallographic data for [Pd(PDTC)$_2$].

Compound	[Pd(PDTC)$_2$]
Empirical formula	$C_{10}H_{16}N_2S_4Pd$
M	398.89
System	Triclinic
Space group	$P\bar{1}$
a (Å)	6.383(2)
b (Å)	7.573(2)
c (Å)	7.842(2)
α (°)	72.424(4)
β (°)	89.515(5)
γ (°)	85.997(4)
V (Å^3)	360.4(2)
Z	1
λ (Å)	1.54178
μ (Cu K_α, mm^{-1})	15.627
F (000)	200
θ range (°)	42.10–65.15
Independent reflections	1076
Independent reflections with $I > 2\sigma$ (I)	1070
R [$F^2 > 2\sigma$ $(F)^2$]	0.099
wR_2 (F^2)	0.241

Note: Estimated standard deviations on the least-significant digits are given in parentheses.

All non-H atoms were refined by full-matrix least-squares with anisotropic displacement parameters. The H atoms were generated geometrically (C–H 0.97 Å and N–H 0.86 Å) and were included in the refinement in the riding model approximation; their temperature factors were set to 1.2 times those of the equivalent isotropic temperature factors of the parent site. A final verification of possible voids was performed using the VOID routine of the PLATON program.[9]

Spectroscopic measurements

The solution absorption spectra of the complexes were recorded with a double-beam Varian Cary 5E spectrophotometer. The luminescence and Raman spectra of the crystalline samples were measured using a Renishaw 3000 imaging microscope system equipped with a CCD camera. The excitation sources were the 488 and 514.5 nm lines of argon ion lasers for the luminescence experiments and the 785 nm line of a diode laser for the Raman experiments. All spectra are unpolarized and corrected for spectrometer response. Pressure was applied to the solid samples by loading crystals into a gasketed diamond-anvil cell (DAC, High-Pressure Diamond Optics) with paraffin oil as the pressure-transmitting medium. The ruby (R_1) method was used to calibrate the pressure.[10] All pressure effects reported here are reversible: upon gradual release of external pressure, all quantities return to their normal values at ambient pressure. For the temperature-dependent measurements, the samples were cooled in a gas-flow microcryostat system (Janis ST-500) with liquid nitrogen or liquid helium.

Luminescence lifetimes were measured using the 532 nm line of a pulsed Nd:YAG laser, a 0.5 m single monochromator (Spex 500M, 600 lines/mm grating) and a Hamamatsu R928 photomultiplier.[11,12]

Fig. 1. View of a molecule of $[Pd(PDTC)_2]$ showing the labelling scheme. The hydrogen atoms are omitted for clarity.

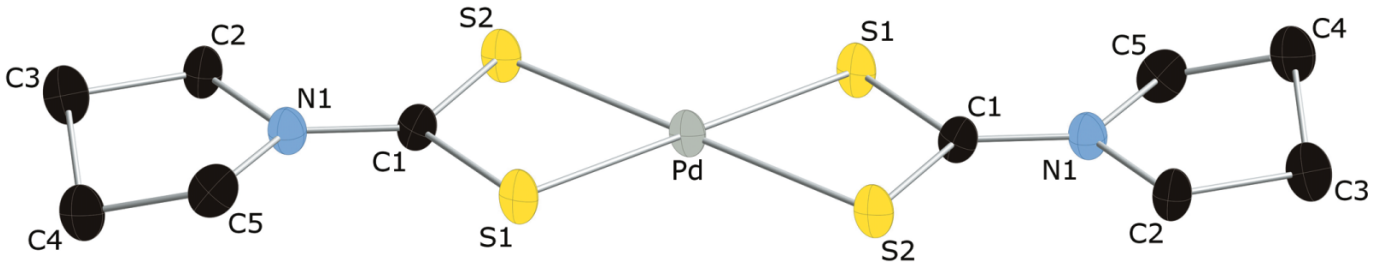

Results

Crystal structure of $[Pd(PDTC)_2]$

The single crystal structure of $[Pd(PDTC)_2]$ was determined by X-ray diffraction at 120 K. The compound crystallizes in the $P\bar{1}$ space group, with $Z = 1$. The palladium atom lies at the inversion center of the cell. Table 1 provides further information about the unit cell.

The complex molecule displays a square-planar coordination for palladium(II), with the metal ion situated exactly in the plane of the four S donor atoms, as illustrated in Fig. 1. The Pd–S distances are 2.343(2) and 2.352(2) Å, typical for this kind of complex.[13,14] The S(1)–Pd–S(2) angle is 75.69(8)°, the distortion from a perfect square geometry being imposed by the chelating PDTC ligand, as summarized in Table 2. The C1 and N atoms lie fairly close to the coordination plane, consistent with the double-bond character of the C1–N bond. The complex molecules globally have planar structures, and are packed in parallel sheets, as illustrated in Fig. 2. The shortest intermolecular metal–metal distance is 6.38 Å, indicating that there is no Pd–Pd interaction. The C3 atom of each molecule is situated at a nearly axial position above the Pd atom of the molecule translated by a (0,0,1) vector, the distance between these two atoms being 3.85 Å. The Pd–C3 bond forms a 75.4° angle with the metal-coordination plane.

Although numerous palladium(II) and platinum(II) bis-dithiocarbamato complexes are known, only a few have been structurally characterized.[13–25] All of them have a planar centrosymmetric [MS4] core unit. Due to the shape of the dithiocarbamate ligands, the S–M–S angles are not exactly 90° but have values of approximately 75° for both platinum(II) and palladium(II) complexes. The M–S distances are within a 2.31–2.33 Å range for both metals. Structures for palladium(II) and platinum(II) complexes with identical ligands are isomorphous. None of the structurally characterized palladium(II) or platinum(II) dithiocarbamate complexes report any significant metal–metal interactions. The structural data presented here are in perfect agreement with structures reported for other dithiocarbamate complexes.

It is interesting to note that the complexes with EDTC ligands are packed orthogonally to one another, whereas the structures of the PDTC complexes consist of parallel sheets of molecular units.

Table 2. Selected bond lengths (Å) and angles (°) for $[Pd(PDTC)_2]$.

$[Pd(PDTC)_2]$	
Pd—S1	2.352(2)
Pd—S2	2.343(2)
S1—C1	1.742(9)
S2—C1	1.726(9)
C1—N	1.35(2)
N—C2	1.47(2)
N—C5	1.49(2)
S1–Pd–S2	75.69(8)
S1–Pd–S1[a]	180
S1–Pd–S1[a]	180
S1–C1–S2	112.3(6)

Note: Estimated standard deviations in the least-significant digits are given in parentheses.

[a]Symmetry operation: $-x, -y, -z$.

Absorption spectroscopy

The absorption spectra of the title complexes in solution have been recorded and are given as Supplementary data. In the region of the lowest-energy absorption bands, the spin-allowed d–d $^1A_{1g} \rightarrow {}^1E_g$ transition is higher in energy than the spin-forbidden $^1A_{1g} \rightarrow {}^3E_g$ band. For $[Pd(SCN)_4](n\text{-}Bu_4N)_2$,[11] the energy of the spin-forbidden transition is 16 450 cm^{-1} with a molar absorptivity ε of 10 $mol/L^{-1}cm^{-1}$, while the singlet–singlet transition occurs at 18 590 cm^{-1} and has a molar absorptivity ε of approximately 100 $mol/L^{-1}cm^{-1}$. The lowest-energy metal–ligand charge-transfer band has an energy of 29 000 cm^{-1}, significantly higher in energy than the d–d bands. For the platinum(II) complexes, the spin-forbidden $^1A_{1g} \rightarrow {}^3E_g$ transition is not observed due to its weak intensity and possible overlap with the onset of the spin-allowed d–d band. For $[Pt(SCN)_4](n\text{-}Bu_4N)_2$, this transition has an energy of 19 460 cm^{-1} and a molar absorptivity of less than 10 $mol/L^{-1}cm^{-1}$.[11] The spin-allowed d–d band of this complex has a maximum at 21 960 cm^{-1} ($\varepsilon > 100$ $mol/L^{-1}cm^{-1}$), similar to the $^1A_{1g} \rightarrow {}^1E_g$ transitions of both platinum(II) dithiocarbamate complexes. The absorption spectra of the title complexes are very similar to those of other square-planar d^8 complexes with sulfur ligator atoms.

Temperature-dependent luminescence and Raman spectroscopy

The luminescence spectra of crystals of the title compounds are broad, spanning up to 4500 cm^{-1}. The band maxima are at approximately 14 500 cm^{-1} for the palladium(II) complexes and 16 000 cm^{-1} for the platinum(II) complexes, values comparable to those reported in the literature for other square-planar complexes of these two metals.[11,12,26–30] It is commonly observed that the luminescence energies of square-planar platinum(II) complexes are higher than those of their palladium(II) analogs.[11,27]

Fig. 2. View of the crystal packing of $[Pd(PDTC)_2]$. The hydrogen atoms are omitted for clarity.

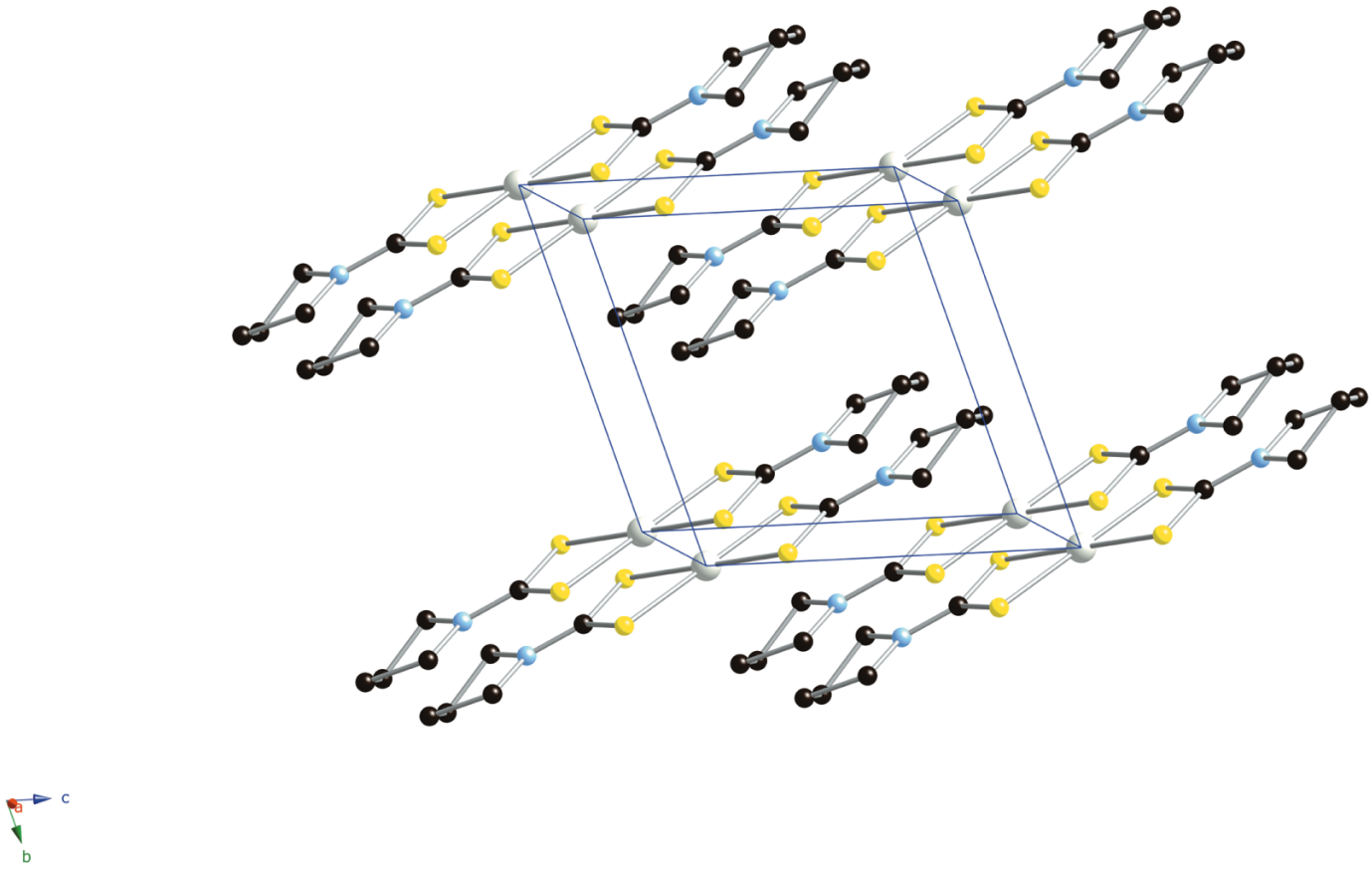

Figures 3 and 4 display representative temperature-dependent luminescence spectra of the four complexes on identical wavenumber scales. Their luminescence intensities clearly increase as temperature is lowered due to a lower rate of non-radiative relaxation at low temperature. The luminescence lifetimes of $[Pd(PDTC)_2]$ at three wavelengths have been measured at different temperatures as shown in Fig. 5. The luminescence lifetime of $[Pd(PDTC)_2]$ at 8 K is 650 μs, similar to the value of 947 μs observed for $[Pd(SCN)_4](n\text{-}Bu_4N)_2$ at 5 K.[11,12] This indicates that the nature of the luminescence transition is similar, confirming our d–d assignment. Much shorter lifetimes are observed at higher temperature. At 150 K, the lifetime is 0.1 μs for $[Pd(PDTC)_2]$, even shorter than the value of 19 μs for $[Pd(SCN)_4](n\text{-}Bu_4N)_2$ observed at this temperature,[11] a consequence of efficient non-radiative relaxation processes.

The temperature-dependent luminescence spectra of $[Pd(EDTC)_2]$ have been recorded between 20 K and 140 K. In this temperature range, the emission maximum is located at approximately 12 800 cm^{-1}. This is quite different from the value of 14 500 cm^{-1} observed at room temperature. The band at 12 800 cm^{-1} is only observed at low temperature, while another band emerges when the sample is heated above approximately 70 K, as illustrated in Fig. 3*b*, where the onset of the higher energy band is clearly visible in the spectrum measured at 70 K. A possible explanation for this could be the occurrence of a structural phase transition. The luminescence band maximum for $[Pd(PDTC)_2]$ is at approximately 14 100 cm^{-1}. The spectra of both palladium(II) complexes show a decrease in energy of the luminescence band maxima when the sample is heated from 70 K to room temperature, with a similar red shift of about -4 cm^{-1}/K.

Figure 4 displays the temperature-dependent luminescence spectra of $[Pt(EDTC)_2]$ and $[Pt(PDTC)_2]$. The luminescence intensity of those compounds also decreases with temperature. The temperature-dependent emission lifetimes of $[Pt(PDTC)_2]$ have been recorded at 16 667 cm^{-1}, close to the luminescence band maximum. They decrease with increasing temperature, from 700 μs at 77 K to 145 μs at 200 K. These lifetimes are somewhat longer than those for $[Pt(SCN)_4](n\text{-}Bu_4N)_2$, where values of 320 μs at 5 K and 0.3 μs at 200 K have been reported.[11] In contrast to the palladium(II) complexes, the platinum(II) complexes studied here show a blue shift of their luminescence band maxima with increasing temperature. The energy of the band maximum for $[Pt(EDTC)_2]$ changes from approximately 16 300 cm^{-1} at 15 K to approximately 16 600 cm^{-1} at 200 K, a blue shift of $+2.5$ cm^{-1}/K. A similar blue shift of $+3.3$ cm^{-1}/K is observed for $[Pt(PDTC)_2]$, with its emission maxima shifting from 15 800 cm^{-1} at 15 K to 16 500 cm^{-1} at 250 K.

Temperature-dependent Raman spectra of all four complexes have been recorded between 80 K and room temperature, given as Supplementary data. There are no major modifications in the shape of the spectra or major shifts of the Raman peaks for any of the compounds, suggesting that none of them undergoes a phase transition in this temperature range.

Fig. 3. Representative temperature-dependent luminescence spectra of (*a*) [Pd(PDTC)$_2$] at 15, 26, 42, and 70 K (top to bottom) and (*b*) [Pd(EDTC)$_2$] at 20, 50, 70, and 140 K (top to bottom).

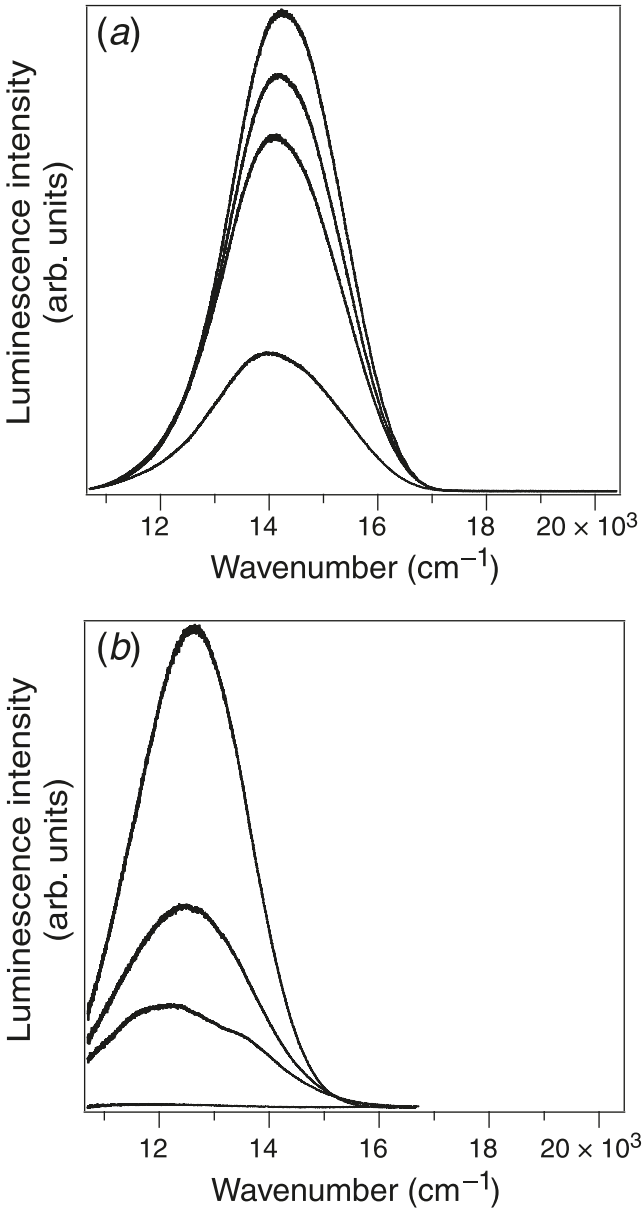

Fig. 4. Representative temperature-dependent luminescence spectra of (*a*) [Pt(PDTC)$_2$] at 78, 125, 200, and 250 K (top to bottom) and (*b*) [Pt(EDTC)$_2$] at 60, 150, and 200 K (top to bottom).

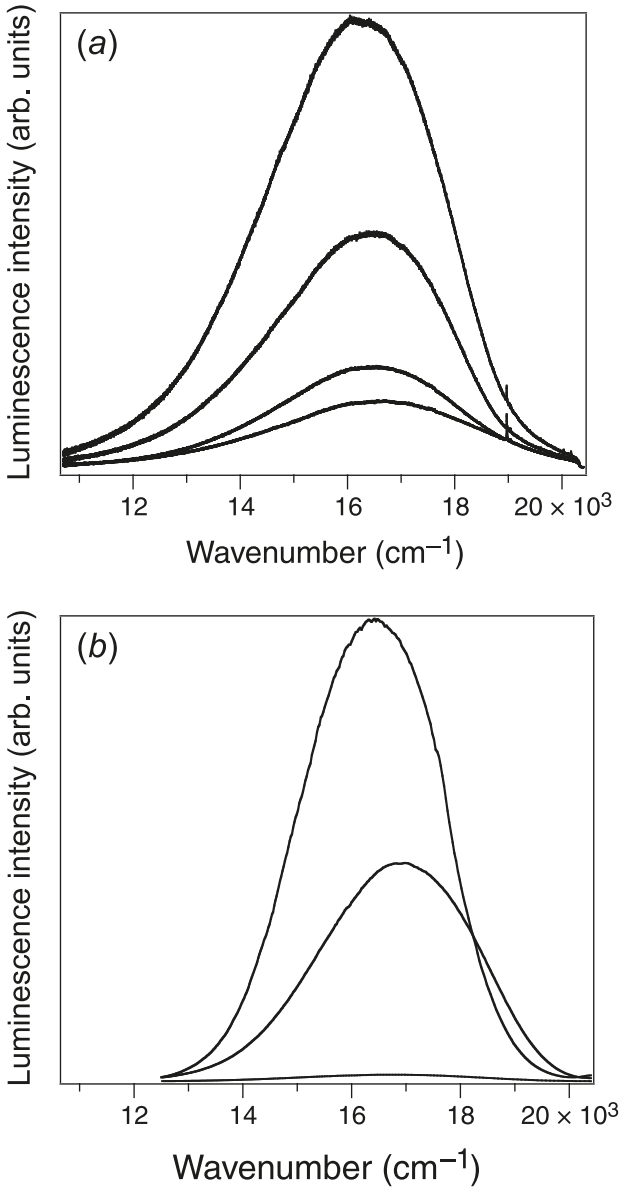

Pressure-dependent luminescence and Raman spectroscopy

Figures 6 and 7 show representative pressure-dependent luminescence spectra of the title compounds. The luminescence intensities show a fast and continuous increase with pressure, followed by a decrease above a threshold pressure. For the palladium(II) complexes, this effect is accompanied by a blue shift of the luminescence band maxima by +9 cm^{-1}/kbar for [Pd(EDTC)$_2$] and +13 cm^{-1}/kbar for [Pd(PDTC)$_2$]. This blue shift is easily seen by comparing the spectra of [Pd(PDTC)$_2$] at 21 kbar and 42 kbar in Fig. 6*a*. The luminescence of [Pt(EDTC)$_2$] displays a blue shift of +15 cm^{-1}/kbar. Although several attempts were made, it was not possible to establish a clear trend for the pressure-induced shift of the emission maximum for [Pt(PDTC)$_2$]. All luminescence maxima and shifts are summarized in Table 3. These blue shifts are comparable to those observed for palladium(II) and platinum(II) tetrathiocyanate and tetraselenocyanate complexes.[11,31] They are clearly different from the red shifts observed for the well-studied tetracyanoplatinate(II) complexes where the metal–metal interaction between the stacked [Pt(CN)$_4$]$^{2-}$ chromophores[32,33] is enhanced by pressure, leading to strong red shifts of the luminescence maxima. No such interactions are present in the dithiocarbamate complexes, as shown by the pressure effects reported here.

Pressure-dependent Raman spectra of the four title complexes are shown in Figs. 8 and 9. The 100–600 cm^{-1} region contains the vibrational modes involving the metal ions and ligator atoms. The ambient-pressure Raman spectra of [Pd(EDTC)$_2$] and [Pt(EDTC)$_2$] and those of [Pd(PDTC)$_2$] and [Pt(PDTC)$_2$] are similar in shape and number of peaks.

Fig. 5. Temperature-dependent luminescence lifetimes for $[Pd(PDTC)_2]$ measured at different wavelengths across the emission spectrum. The excitation wavelength is 532 nm.

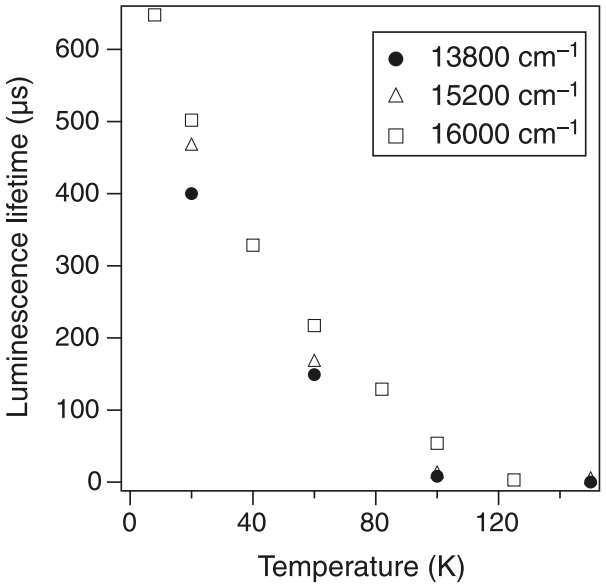

Changes of the band shapes and Raman shifts occur as pressure is increased on the crystalline samples. A precise study of the evolution of each Raman band shows that most of them are shifted towards higher energies as pressure is increased, indicative of shorter and stronger chemical bonds at high pressure. The Raman band maxima of all four complexes show linear shifts with pressure. The shape of the peaks is also influenced by pressure. It is interesting to note that the complexes with the two different ligands show a different behavior. The bands at 160–175 cm^{-1} and at 400 cm^{-1} are split and enlarged at high pressure for both EDTC complexes, but not for the PDTC complexes. This difference could indicate a possible structural phase transition in the EDTC complexes, most likely involving slight changes in packing. The pressure-dependent luminescence spectra of the EDTC complexes in Figs. 6*b* and 7*b* do not show evidence for a structural phase transition, as the bands are likely too large to be influenced by small changes in the packing of the chromophores. In general, it appears that the EDTC complexes are more susceptible to structural phase transitions, as illustrated by the pressure-dependent Raman spectra and the temperature-dependent luminescence spectra in Fig. 3*b*.

Discussion

Assignment of the luminescence transitions

The absorption spectra of the title complexes all show bands with molar absorptivities of 2000 $mol/L^{-1}cm^{-1}$ or less, which can be attributed to d–d transitions. $[Pd(EDTC)_2]$ in particular has a very weak band at 16 050 cm^{-1}, corresponding to the symmetry and spin-forbidden $^1A_{1g} \rightarrow {}^3E_g$ transition. This is a strong indication that the observed luminescence bands also are of a d–d nature. The oscillator strength of the corresponding absorption bands in thiocyanate and halide complexes with better resolved bands than observed for the title complexes increases with temperature, again typical for forbidden d–d transitions gaining vibronic intensity.[26,27,34] The comparison of the luminescence spectra of the dithiocarbamate complexes with those of $[Pd(SCN)_4](n\text{-}Bu_4N)_2$ and $[Pt(SCN)_4](n\text{-}Bu_4N)_2$, which also show d–d transitions,[11,26,31] supports this assignment. The observed luminescence lifetimes at low temperatures for the dithiocarbamate complexes are between 300 μs and

Fig. 6. Representative pressure-dependent luminescence spectra of (*a*) $[Pd(PDTC)_2]$ at 28, 32, 21, 42, and 16 kbar (top to bottom) and (*b*) $[Pd(EDTC)_2]$ at 39, 37, 48, 33, and 15 kbar (top to bottom). The square and asterisk markers denote the ruby luminescence used for pressure calibration and the Raman peak of the diamond anvils, respectively.

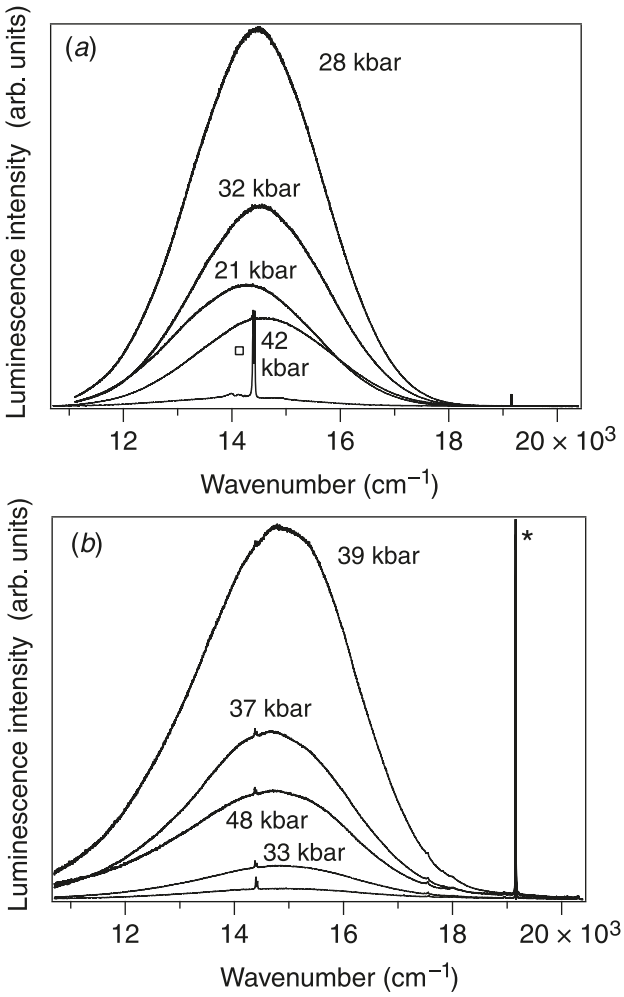

Table 3. Luminescence band maxima E_{max} at ambient pressure and pressure-induced shifts of the luminescence maxima $\Delta E_{max}/\Delta p$.

Compound	E_{max} (cm^{-1})	$\Delta E_{max}/\Delta p$ (cm^{-1}/kbar)
$[Pd(EDTC)_2]$[a]	14400	+9
$[Pd(PDTC)_2]$[a]	14300	+13
$[Pt(EDTC)_2]$[a]	16000	+15
$[Pt(PDTC)_2]$[a]	15800	Not measurable
$[Pd(SCN)_4](n\text{-}Bu_4N)_2$[b]	12390	+29
$[Pt(SCN)_4](n\text{-}Bu_4N)_2$[b]	14440	+24

[a]This work.
[b]Reference 11.

Fig. 7. Representative pressure-dependent luminescence spectra of (*a*) [Pt(PDTC)$_2$] at 19, 24, 27, and 12 kbar (top to bottom) and (*b*) [Pt(EDTC)$_2$] at 21, 28, 12, and 4 kbar (top to bottom).

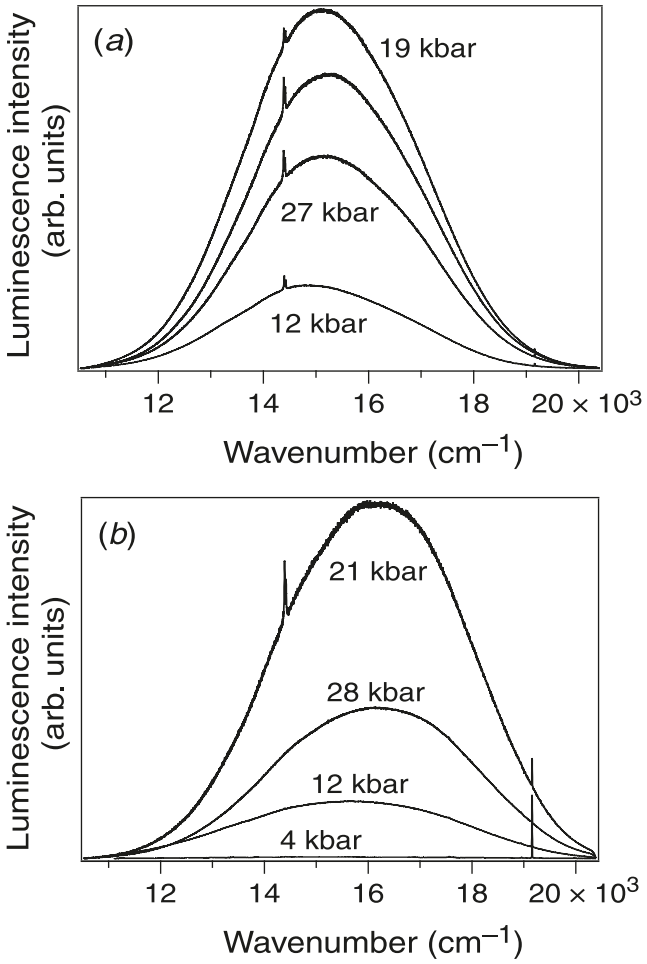

Fig. 8. Representative pressure-dependent Raman spectra of (*a*) [Pd(PDTC)$_2$] at 44, 42, 38, 32, 20, 16, and 12 kbar and 1 bar (top to bottom) and (*b*) [Pd(EDTC)$_2$] at 32, 29, 23, 17, 11, and 2 kbar and 1 bar (top to bottom).

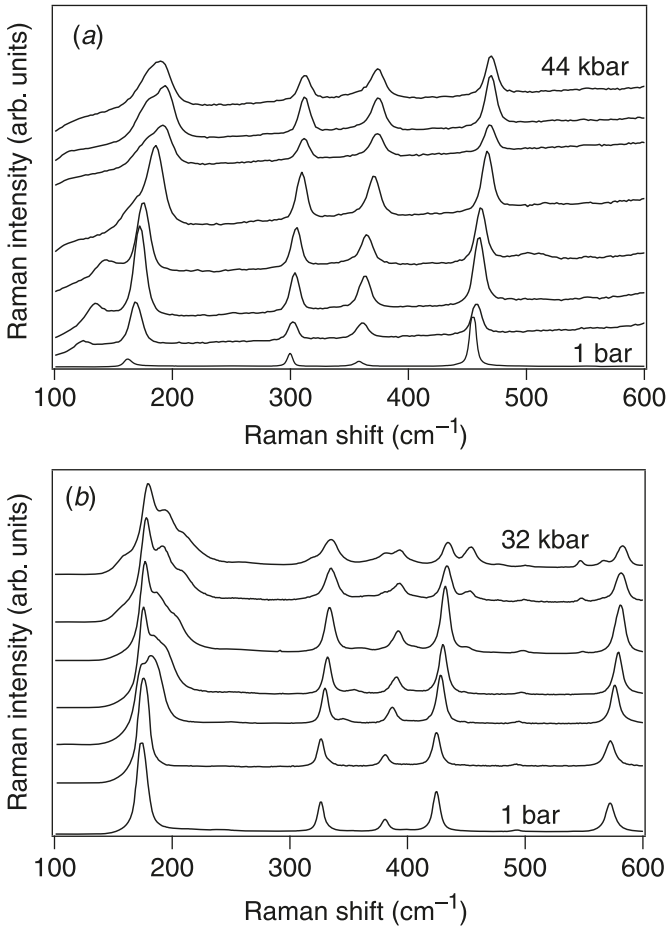

1000 μs, similar to those reported for the thiocyanate complexes.[11] The luminescence maxima of both kinds of complexes can also be compared. They are observed between 14 200 cm^{-1} and 14 800 cm^{-1} for all platinum(II) complexes and between 12 400 cm^{-1} and 12 800 cm^{-1} for palladium(II) tetrathiocyanate and tetraselenocyanate complexes, close to the band maxima of the title complexes summarized in Table 3. The width at half height of the luminescence bands of the dithiocarbamate complexes is between 2500 cm^{-1} and 4000 cm^{-1}, again similar to the thiocyanate compounds.

Vibronic structure in low-temperature luminescence spectra

The low-temperature luminescence spectra of [Pd(EDTC)$_2$] and [Pd(PDTC)$_2$] display vibronic progressions. The intensity distributions provide insight on the structural changes which the complex molecules undergo when emitting a photon. The simplest model to analyze vibronic progressions is based on harmonic potential energy curves along a single configurational coordinate with identical vibrational frequencies for the ground and emitting states. The theoretical equations used to calculate spectra have been published and discussed in detail before.[35–37] The energy of the electronic origin of the luminescence band maximum E_{00} and the dimensionless normal coordinate offset Δ are the only adjustable parameters. Vibrational frequencies are known from the Raman spectra, and the width of the vibronic lines Γ is set to a value somewhat lower than observed to better illustrate the progression. The 7 K luminescence spectrum of [Pd(EDTC)$_2$] is displayed in Fig. 10*a*, along with a series of calculated spectra. The average interval between the members of the progression in the experimental spectrum is 390 cm^{-1}, close but not identical to the observed frequency of 381 cm^{-1}, corresponding to the range of the M–S_4 stretching vibrations. This discrepancy is possibly a manifestation of a missing mode effect.[29,37] The consequence of a variation of the offset Δ by ±10% is shown by the dotted calculated spectra in Fig. 10*a*. It is obvious that these spectra do not reproduce the band width and intensities within the progression as well as the best calculated spectrum shown as a solid line. The low value for Δ leads to a calculated spectrum narrower than the experimental spectrum; the high value results in a calculated band larger than the experimental spectrum, indicating that offsets are defined to within better than 10% by the simple model used here. The comparison of the luminescence spectrum of [Pd(PDTC)$_2$] measured at 6 K and a calculated spectrum is shown in Fig. 10*b*. The parameter values obtained for the palladium(II) dithio-

Fig. 9. Representative pressure-dependent Raman spectra of (*a*) [Pt(PDTC)$_2$] at 28, 20, 18, 13, 9, and 3 kbar (top to bottom) and (*b*) [Pt(EDTC)$_2$] at 30, 28, 23, 21, and 4 kbar (top to bottom).

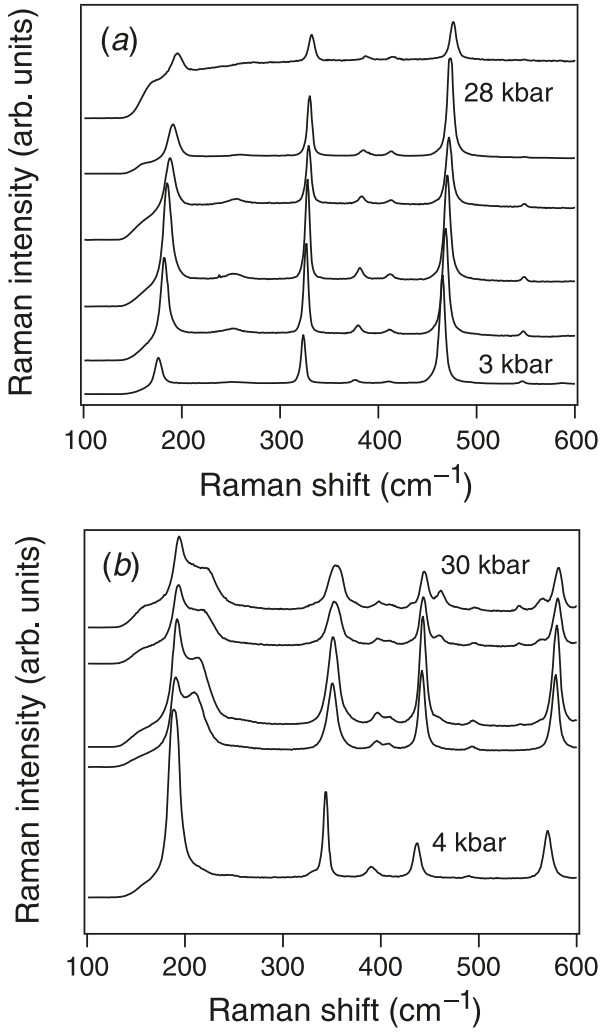

Fig. 10. Comparison of experimental and calculated luminescence spectra. (*a*) [Pd(EDTC)$_2$] at 7 K with calculated spectrum given as a solid line. The dotted and dash–dotted calculated spectra were obtained by changing the Δ value in Table 4 by ±10%. (*b*) [Pd(PDTC)$_2$] at 6 K with calculated spectrum shown as a solid line.

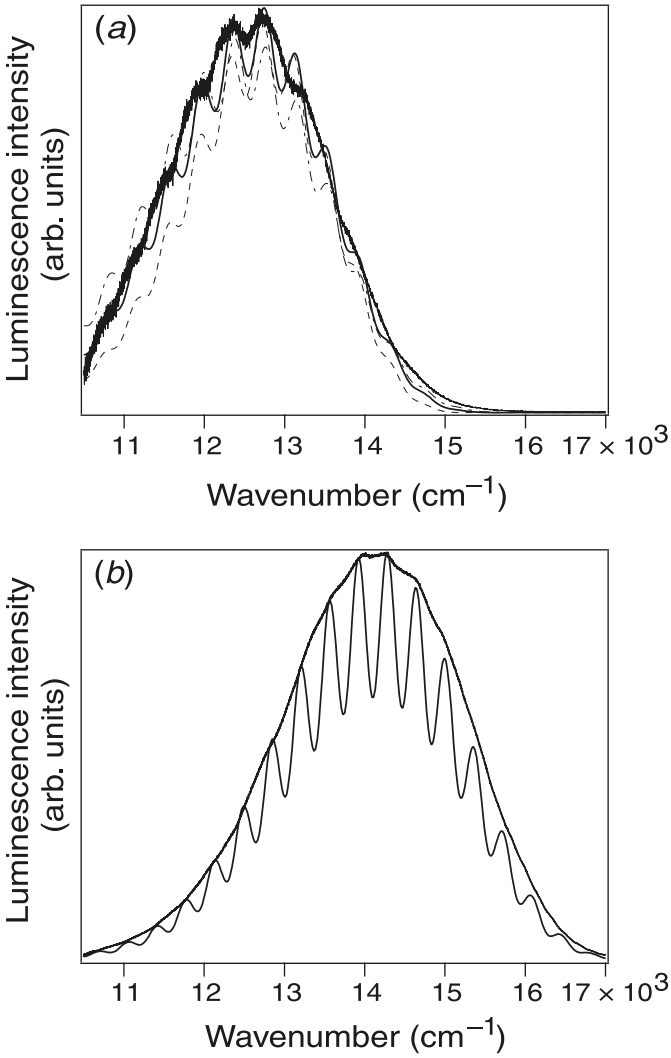

carbamate complexes are summarized in Table 4 and compared to literature values for [Pd(SCN)$_4$](*n*-Bu$_4$N)$_2$.[11] The low-temperature spectrum of [Pd(SCN)$_4$](*n*-Bu$_4$N)$_2$ displays better resolved vibronic structure than the spectra in Fig. 10. Four different vibrational modes contribute to the observed progressions. The normal coordinate offset Δ for the totally symmetric (a_{1g}) mode is lower for [Pd(SCN)$_4$](*n*-Bu$_4$N)$_2$ than for the two palladium(II) dithiocarbamate complexes. This is due to the fact that other vibrational modes are identified in the vibronic structure of [Pd(SCN)$_4$](*n*-Bu$_4$N)$_2$, allowing the emitting-state distortion of the molecule to be distributed on several normal coordinates. In contrast, the low-temperature spectra of the dithiocarbamate complexes in Fig. 10 are not sufficiently resolved to determine multiple offsets, and only a single coordinate is used in our analysis, leading to the results in Table 4.

Pressure effects on luminescence and Raman spectra

A detailed study of the pressure-dependent Raman spectra of the four title complexes shows that a vast majority of the frequencies increase when pressure is imposed on the samples. This is an indication that submitting the crystals to a higher pressure reduces most interatomic distances, as is intuitively expected. The frequencies of the Raman bands vary linearly with pressure, and there is no sign of an abrupt change that would indicate a phase transition in the studied pressure range.

The luminescence spectra of the palladium(II) and platinum(II) dithiocarbamate complexes also show a pressure-dependence. Their luminescence energies are shifted towards higher values with pressure, as is the case for [Pd(SCN)$_4$](*n*-Bu$_4$N)$_2$ and [Pt(SCN)$_4$](*n*-Bu$_4$N)$_2$[11,12] with numerical values given in Table 3. These blue shifts are linear with pressure, and the width of the luminescence bands does not vary significantly over the studied pressure range. The sign of the shift is due to the σ-antibonding $d_{x_2-y_2}$ LUMO whose energy increases sharply with decreasing metal–S distances. The HOMO is π-antibonding, and its energy increases to a lesser extent as bond lengths de-

Table 4. Parameters used to calculate the luminescence spectra of $[Pd(EDTC)_2]$, $[Pd(PDTC)_2]$, and $[Pd(SCN)_4](n\text{-}Bu_4N)_2$.

Parameter	$[Pd(EDTC)_2]$[a]	$[Pd(PDTC)_2]$[a]	$[Pd(SCN)_4](n\text{-}Bu_4N)_2$[b]
Vibrational frequency (cm^{-1})	390	358	274 (a_{1g})
Δ (dimensionless)	3.85	4.61	3.55
E_{00} (cm^{-1})	15050	17500	14343
Γ (cm^{-1})	110	85	6

[a]This work.
[b]Reference 11.

Fig. 11. One-dimensional harmonic potential energy curves of the ground and excited states at atmospheric pressure (solid lines) and high pressure (dotted lines). ΔE_{act} represents the activation energy barrier for non-radiative relaxation in a qualitative model view.

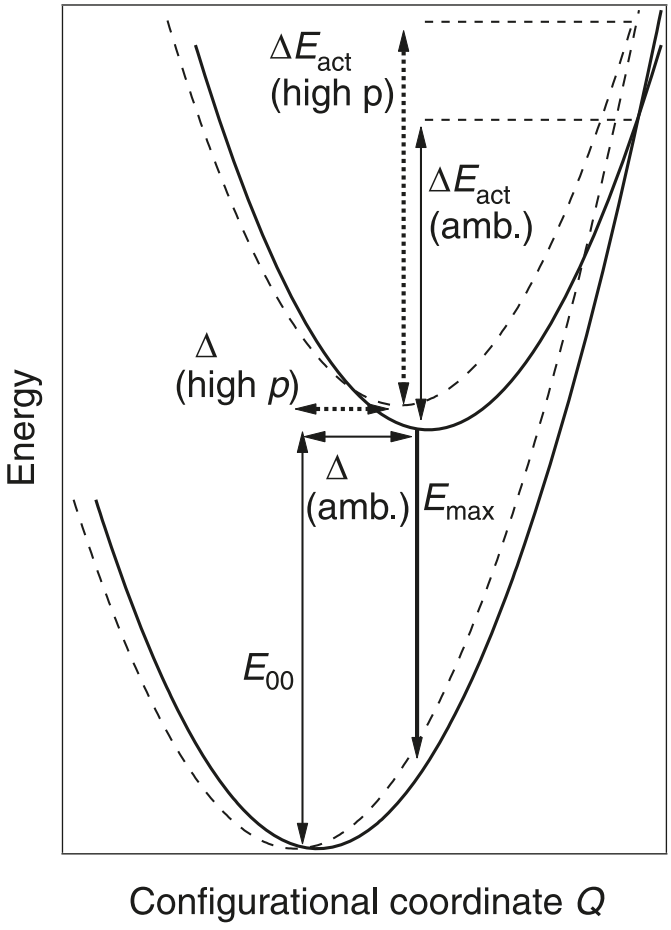

crease. These blue shifts again support the d–d assignment for the luminescence transitions.

At room temperature and ambient pressure, the luminescence of the title complexes is fairly weak, but all four compounds exhibit a pressure-induced enhancement of their luminescence intensities. The same phenomenon takes place, albeit in a more dramatic fashion, with the $[M(SCN)_4](n\text{-}Bu_4N)_2$ (M = Pd(II), Pt(II)) complexes, whose luminescence intensities increase by two to three orders of magnitude between ambient pressure and 30 kbar.[11,12] The enhancement of the luminescence intensity is due to less efficient non-radiative processes at high pressure, as documented by lifetimes for thiocyanate complexes.[11,12] This effect can be qualitatively rationalized with the model shown in Fig. 11, based on the same potential energy curves used for the calculations in Fig. 10. The main effect of high pressure is a decrease of the offset Δ along the coordinate Q, leading to a higher activation energy barrier for non-radiative relaxation, as illustrated by the dotted potential energy curves denoting the ground and emitting states at high pressure. While this model rationalizes the observed luminescence intensity increase, it cannot account quantitatively for the observed behavior, as many factors, such as the different influence of several normal coordinates with nonzero offsets Δ, the change of the potential energy curves with increasing pressure, and all energy-transfer processes are neglected. The effects of multiple modes can be analyzed from the well-resolved luminescence transition of $[M(SCN)_4](n\text{-}Bu_4N)_2$ (M = Pd, Pt),[11] and the offset along some of these modes could be blocked by the rigidity of the chelate ligand, thus not allowing a shift of the wells along this coordinate for the title compounds. Pressure appears to have a smaller effect on the chelate compounds and causes a smaller enhancement of their luminescence intensities. This reasoning is further supported by the values of the luminescence energy shifts of the dithiocarbamate compounds, which are also lower than for the thiocyanate complexes.

The pressure-dependent Raman spectra support this analysis, since the frequency of the totally symmetric metal–ligand stretching mode shifts less in the dithiocarbamate than in the tetrathiocyanate compounds. The precise values of the pressure-induced shifts are +0.17 cm^{-1}/kbar and +0.49 cm^{-1}/kbar for $[Pd(EDTC)_2]$ and $[Pd(PDTC)_2]$, respectively, lower than the value of +0.68 cm^{-1}/kbar for $[Pd(SCN)_4](n\text{-}Bu_4N)_2$.[11,12] For the platinum(II) complexes, the values are +0.29 cm^{-1}/kbar for $[Pt(EDTC)_2]$ and +0.47 cm^{-1}/kbar for $[Pt(PDTC)_2]$, again lower than the value of +0.60 cm^{-1}/kbar for $[Pt(SCN)_4](n\text{-}Bu_4N)_2$.[11] It is interesting to note the different evolution of the Raman spectra of the EDTC and the PDTC complexes of both metal ions with pressure. Both EDTC complexes exhibit a splitting of their 160–175 cm^{-1} band, corresponding to the metal–sulfur bending mode. A band at approximately 400 cm^{-1} also shows a pressure-induced splitting. The frequency of the bending mode shifts by +0.19 cm^{-1}/kbar and +0.17 cm^{-1}/kbar for palladium(II) and platinum(II), respectively, less than in the thiocyanate complexes, where shifts of +0.72 cm^{-1}/kbar and +0.78 cm^{-1}/kbar are observed. In the PDTC complexes, this frequency shifts by +0.83 cm^{-1}/kbar for palladium(II) and by +0.80 cm^{-1}/kbar for platinum(II), closer to the values observed for complexes with monodentate ligands. It can be assumed that the metal–sulfur bending mode is more affected by pressure in the EDTC compounds than in their PDTC

analogues or in $[M(SCN)_4](n\text{-}Bu_4N)_2$ (M = Pd, Pt). The orthogonal structure of the EDTC complexes seems more easily perturbed by pressure than the parallel sheet structure of their PDTC counterparts. The alkyl substituents are also more prone to be disordered than the pyrrolidine cycle. When pressure is increased on the crystal, there is a higher probability of them arranging differently, thus provoking the broadening and splits of certain Raman bands observed for the EDTC compounds.

The spectroscopic comparison of d^8 complexes, with different substituents on otherwise identical chelating ligands shows that even groups located far from the metal core of the complex can have a bearing on the spectroscopic features of the complexes. Pressure-dependent spectroscopic methods as those illustrated here can therefore be valuable tools to probe detailed effects in solid molecular materials.

Supplementary data

Supplementary data for this article are available on the journal Web site (canjchem.nrc.ca) or may be purchased from the Depository of Unpublished Data, Document Delivery, CISTI, National Research Council Canada, Ottawa, ON K1A 0R6, Canada. DUD 5278. For more information on obtaining material, refer to cisti-icist.nrc-cnrc.gc.ca/cms/unpub_e.shtml. CCDC 730045 contains the X-ray data in CIF format for seven complexes for this manuscript. These data can be obtained, free of charge, via www.ccdc.cam.ac.uk/conts/retrieving.html (Or from the Cambridge Crystallographic Data Centre, 12 Union Road, Cambridge CB2 1EZ, UK; fax +44 1223 336033; or deposit@ccdc.cam.ac.uk).

Acknowledgements

The authors thank Francine Bélanger-Gariépy for help with the crystal structure determination and Kari A. Frantzen for preliminary measurements. Financial support from the Natural Sciences and Engineering Research Council of Canada (NSERC) is gratefully acknowledged.

References

(1) Williams, J. A. G.; Develay, S.; Rochester, D. L.; Murphy, L. *Coord. Chem. Rev.* **2008**, *252* (23-24), 2596–2611. doi:10.1016/j.ccr.2008.03.014.

(2) Hissler, M.; McGarrah, J. E.; Connick, W. B.; Geiger, D. K.; Cummings, S. D.; Eisenberg, R. *Coord. Chem. Rev.* **2000**, *208* (1), 115–137. doi:10.1016/S0010-8545(00)00254-X.

(3) Abe, T.; Itakura, T.; Ikeda, N.; Shinozaki, K. *Dalton Trans.* **2009**, (4): 711–715. doi:10.1039/b811107c. PMID:19378564.

(4) Bray, K. L. *Top. Curr. Chem.* **2001**, *213*, 1–94. doi:10.1007/3-540-44447-5_1.

(5) Reber, C.; Grey, J. K.; Lanthier, E.; Frantzen, K. A. *Comments Inorg. Chem.* **2005**, *26* (5-6), 233–254. doi:10.1080/02603590500403909.

(6) Levasseur-Thériault, G.; Reber, C.; Aronica, C.; Luneau, D. *Inorg. Chem.* **2006**, *45* (6), 2379–2381. doi:10.1021/ic051836b. PMID:16529450.

(7) Allan, D. R.; Blake, A. J.; Huang, D.; Prior, T. J.; Schröder, M. *Chem. Commun.* **2006**, 4081. doi:10.1039/b606736k.

(8) Grochala, W.; Hoffmann, R.; Feng, J.; Ashcroft, N. W. *Angew. Chem. Int. Ed.* **2007**, *46* (20), 3620–3642. doi:10.1002/anie.200602485.

(9) Spek, A. L. *Platon,* 2000 version; University of Utrecht: Utrecht, The Netherlands, 2000.

(10) Piermarini, G. J.; Block, S.; Barnett, J. D.; Forman, R. A. *J. Appl. Phys. (Berl.)* **1975**, *46* (6), 2774. doi:10.1063/1.321957.

(11) Grey, J. K.; Butler, I. S.; Reber, C. *Inorg. Chem.* **2003**, *42* (20), 6503–6518. doi:10.1021/ic0342503. PMID:14514328.

(12) Grey, J. K.; Butler, I. S.; Reber, C. *J. Am. Chem. Soc.* **2002**, *124* (32), 9384–9385. doi:10.1021/ja026629e.

(13) Beurskens, P. T.; Cras, J. A.; Hummelink, Th. W.; Noordik, J. H. *J. Cryst. Mol. Struct.* **1971**, *1* (3), 253–257. doi:10.1007/BF01198537.

(14) Riekkola, M.-L.; Pakkanen, T.; Niinistö, L.; Seip, R.; Watt, C. I. F. *Acta Chem. Scand. A* **1983**, *37a*, 807–816. doi:10.3891/acta.chem.scand.37a-0807.

(15) Amanov, A. Z.; Kukina, G. A.; Porai-Koshits, M. A. *Zh. Strukt. Khim.* **1967**, *8*, 174.

(16) Amim, R. S.; Oliveira, M. R.; Perpétuo, G. J.; Janczak, J.; Miranda, L. D.; Rubinger, M. M. *Polyhedron* **2008**, *27* (7), 1891–1897. doi:10.1016/j.poly.2008.02.030.

(17) Baker, A. T.; Emett, M. T. *Aust. J. Chem.* **1992**, *45* (2), 429. doi:10.1071/CH9920429.

(18) Jian, F.; Bei, F.; Zhao, P.; Wang, X.; Fun, H.; Chinnakali, K. *J. Coord. Chem.* **2002**, *55* (4), 429–437. doi:10.1080/00958970211907.

(19) Oliveira, M. R. L.; Rubinger, M. M. M.; Guilardi, S.; de Faria Franca, E.; Ellena, J.; De Bellis, V. M. *Polyhedron* **2004**, *23* (7), 1153–1158. doi:10.1016/j.poly.2004.01.021.

(20) Shaheen, F.; Badshah, A.; Gielen, M.; Dusek, M.; Fejfarova, K.; de Vos, D.; Mirza, B. *J. Organomet. Chem.* **2007**, *692* (14), 3019–3026. doi:10.1016/j.jorganchem.2007.03.019.

(21) Shahzadi, S.; Ali, S.; Badshah, A.; Shaheen, F.; Ahmed, F.; Fettouhi, M. *J. Chem. Crystallogr.* **2006**, *36* (9), 567–570. doi:10.1007/s10870-006-9101-9.

(22) Tian, Y.-P.; Duan, C.-Y.; Lu, Z.-L.; You, X.-Z.; Fun, H.-K.; Yip, B.-C. *Polyhedron* **1996**, *15* (9), 1495–1502. doi:10.1016/0277-5387(95)00397-5.

(23) Konarev, D. V.; Kovalevsky, A. Y.; Otsuka, A.; Saito, G.; Lyubovskaya, R. N. *Inorg. Chem.* **2005**, *44* (25), 9547–9553. doi:10.1021/ic051261i. PMID:16323943.

(24) Burchell, C. J.; Aucott, S. M.; Milton, H. L.; Slawin, A. M. Z.; Derek Woollins, J. *Dalton Trans.* **2004**, (3): 369–374. doi:10.1039/b314949h. PMID:15252541.

(25) Maekawa, M.; Munakata, M.; Kuroda-Sowa, T.; Motokawa, M. *Anal. Sci.* **1994**, *10* (6), 977–978. doi:10.2116/analsci.10.977.

(26) Pelletier, Y.; Reber, C. *Inorg. Chem.* **2000**, *39* (20), 4535–4541. doi:10.1021/ic000133l.

(27) Pelletier, Y.; Reber, C. *Inorg. Chem.* **1997**, *36* (4), 721–728. doi:10.1021/ic960388s.

(28) Basch, H.; Gray, H. B. *Inorg. Chem.* **1967**, *6* (2), 365–369. doi:10.1021/ic50048a038.

(29) Preston, D. M.; Guentner, W.; Lechner, A.; Gliemann, G.; Zink, J. I. *J. Am. Chem. Soc.* **1988**, *110* (17), 5628–5633. doi:10.1021/ja00225a007.

(30) Guentner, W.; Gliemann, G.; Kunkely, H.; Reber, C.; Zink, J. I. *Inorg. Chem.* **1990**, *29* (26), 5238–5241. doi:10.1021/ic00351a020.

(31) Hidvegi, L.; Tuszynski, W.; Gliemann, G. *Chem. Phys. Lett.* **1981**, *77* (3), 517–519. doi:10.1016/0009-2614(81)85198-6.

(32) Gliemann, G.; Yersin, H. *Struct. Bond.* **1985**, *62*, 87–153. doi:10.1007/BFb0009186.

(33) Lechner, A.; Gliemann, G. *J. Am. Chem. Soc.* **1989**, *111* (19), 7469–7475. doi:10.1021/ja00201a030.

(34) Tuszynski, W.; Gliemann, G. *Z. Naturforsch.* **1979**, *34a*, 211.
(35) Davis, M. J.; Reber, C. *Inorg. Chem.* **1995**, *34* (18), 4585–4590. doi:10.1021/ic00122a014.
(36) Heller, E. J. *Acc. Chem. Res.* **1981**, *14* (12), 368–375. doi:10.1021/ar00072a002.
(37) Larson, L. J.; Zink, J. I. *Inorg. Chem.* **1989**, *28* (18), 3519–3523. doi:10.1021/ic00317a025.

Cowaxanthone F, a new tetraoxygenated xanthone, and other anti-inflammatory and antioxidant compounds from *Garcinia cowa*

Kanda Panthong, Nongporn Hutadilok-Towatana, and Ampai Panthong

Abstract: A new tetraoxygenated xanthone, cowaxanthone F (**1**), as well as four known compounds, morelloflavone (**2**), volkensiflavone (**3**), morelloflavone-7″-*O*-glucoside (fukugiside, **4**), and 1,6-dihydroxyxanthone (**5**), were isolated from the crude acetone extract of the twigs of *Garcinia cowa* (Guttiferae). All compounds (**1**–**5**) were tested for antioxidant activity against DPPH (diphenylpicrylhydrazyl), hydroxyl, and superoxide radicals; only morelloflavone (**2**) and morelloflavone-7″-*O*-glucoside (**4**) exhibited high potency. Eight tetraoxygenated xanthones from the fruits of *G. cowa*, cowaxanthones A–D (**6**–**9**), cowanin (**15**), α-mangostin (**16**), mangostanin (**17**), and cowanol (**18**), were also investigated for anti-inflammatory activity using ethyl phenylpropiolate (EPP)-induced ear edema. Assessment at 30, 60, and 120 min revealed that cowaxanthones B–D (**7**–**9**), cowanin (**15**), and α-mangostin (**16**) exhibited significant anti-inflammatory activity when compared to phenylbutazone, while cowaxanthone A (**6**), mangostanin (**17**), and cowanol (**18**) showed less activity.

Key words: Guttiferae, *Garcinia cowa*, cowaxanthone F, anti-inflammatory activity, antioxidant activity.

Résumé : On a isolé une nouvelle xanthone tétraoxygénée, la cowaxanthone F (**1**) ainsi que quatre composés connus : morelloflavone (**2**), volkensiflavone (**3**), morellosflavone-7″-*O*-glucoside (fukugiside, **4**), et la 1,6-dihydroxyxanthone (**5**) à partir de l'extrait brut à l'acétone des rameaux de *Garcinia cowa* (Guttiferae). On a testé tous les produits pour leurs propriétés antioxydantes contre les radicaux DPPH, hydroxyles et superoxydes et seuls la morelloflavone (**2**) et le morellosflavone-7″-*O*-glucoside présentent des potentiels élevés. On a aussi examiné huit xanthones tétraoxygénées extraites des fruits de *G. cowa* : cowaxanthones (A–D) (**6**–**9**), cowanine (**15**), α-mangostine (**16**), mangostanine (**17**) et cowanol (**18**) pour déterminer leur activité anti-inflammatoire à l'aide de l'œdème de l'oreille induite par EPP. L'évaluation à 30, 60 et 120 minutes révèle que, par comparaison avec la phénylbutazone, les cowaxanthones (B–D) (**7**–**9**), cowanine (**15**) et α-mangostine (**16**) présentent une activité anti-inflammatoire significative alors que la cowaxanthones (A) (**6**), la mangostanine (**17**) et le cowanol (**18**) en possède moins.

Mots-clés : Guttiferae, *Garcinia cowa*, cowaxanthone F, activité anti-inflammatoire, activité antioxydante.

[Traduit par la Rédaction]

Introduction

Garcinia cowa Roxb. (Guttiferae, Clusiaceae), commonly known as "Cha-muang", is a small to medium sized tree found widely distributed in Thailand. The fruits and leaves are used for the improvement of blood circulation, as an expectorant for the treatment of coughs and indigestion, and as a laxative, while the root is used for fever relief.[1] The bark of *G. cowa* has been used in Thai folk medicine as an antipyretic agent.[2] Xanthones and flavanone glucosides were isolated from *G. cowa* by other groups.[2–7] Our previous phytochemical study of its fruits has led us to the isolation of five new tetraoxygenated xanthones (cowaxanthones A–E, **6**–**10**), and 10 known tetraoxygenated xanthones.[8] In this continuing investigation on its twigs, one new xanthone was identified. We describe herein the isolation and structural elucidation of the new tetraoxygenated xanthone (**1**), named cowaxanthone F, as well as four other known compounds. In a search for bioactive substances from this plant, we also evaluated the antioxidant activity of all compounds isolated from the twigs as well as the anti-inflammatory activity of eight tetraoxygenated xanthones from the fruits.

Received 2 April 2009. Accepted 15 June 2009. Published on the NRC Research Press Web site at canjchem.nrc.ca on 28 October 2009.

K. Panthong.[1] Department of Chemistry, Center for Innovation in Chemistry, and Natural Products Research Center, Faculty of Science, Prince of Songkla University, Hat Yai 90112, Thailand.
N. Hutadilok-Towatana. Department of Biochemistry, and Natural Products Research Center, Faculty of Science, Prince of Songkla University, Hat Yai 90112, Thailand.
A. Panthong. Department of Pharmacology, Faculty of Medicine, Chiang Mai University, Chiang Mai 50200, Thailand.

[1]Corresponding author (e-mail: kanda.p@psu.ac.th).

Results and discussion

The acetone extract of the dried twigs of *G. cowa* was subjected to chromatographic purification to yield one new tetraoxygenated xanthone (cowaxanthone F, **1**), together with four known compounds: morelloflavone (**2**),[9–11] volkensiflavone (**3**),[12,13] morelloflavone-7″-*O*-glucoside (fukugiside, **4**),[14,15] and 1,6-dihydroxyxanthone (**5**).[16] The structures of all compounds were elucidated by analysis of 1D and 2D NMR spectroscopic data. The ^{1}H and (or) ^{13}C spectroscopic data of known compounds (see Fig. 1) were also compared with those reported in the literature.

Fig. 1. Structures of isolated compounds.

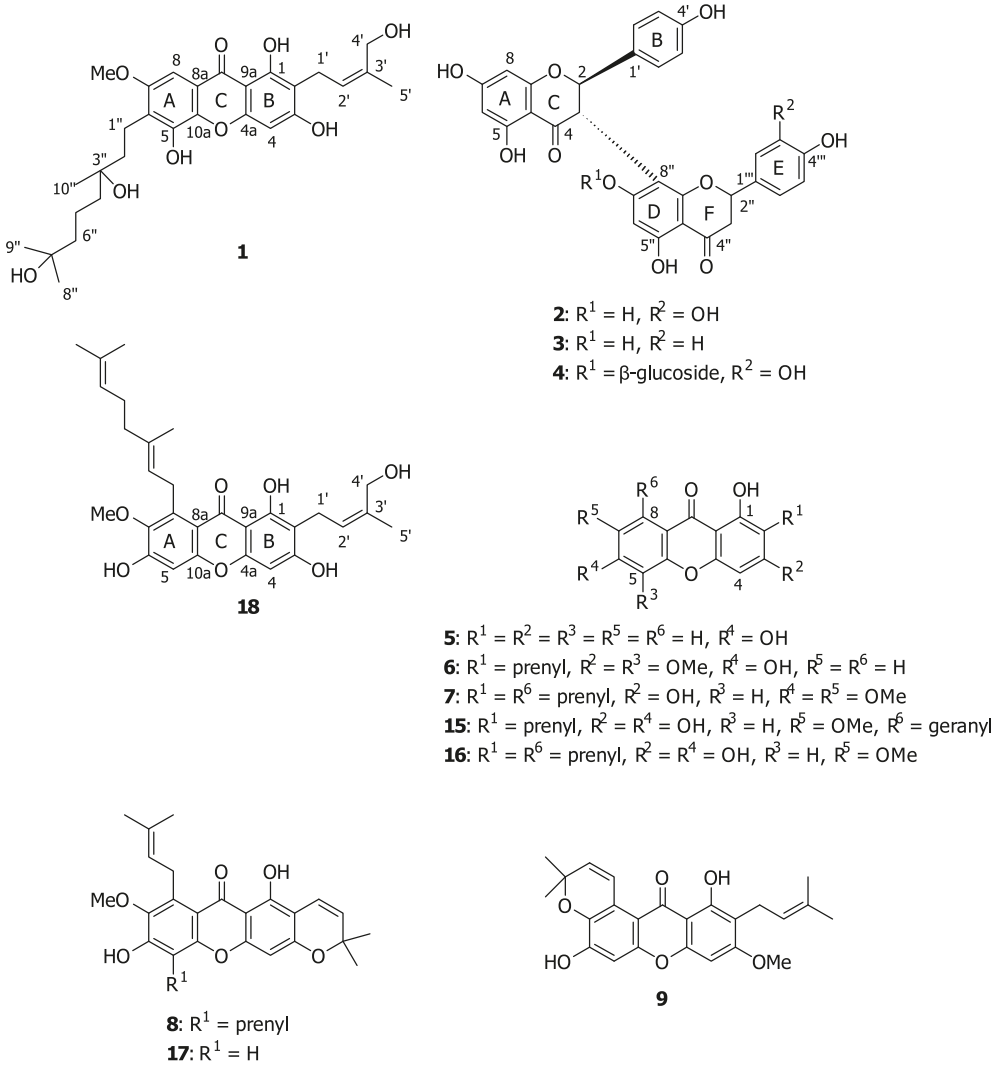

Cowaxanthone F (**1**) was obtained as a pale yellow solid. Its molecular formula was determined as $C_{29}H_{38}O_9$ by HRTOFMS (atmospheric pressure chemical ionization (APCI) positive) measurement for $C_{29}H_{38}O_9Na$ at *m/z* 553.2366 (calcd. 553.2414). The IR spectrum of compound **1** suggested hydroxyl (3436 cm^{-1}) and carbonyl absorptions (1639 cm^{-1} (conjugated aryl ketone)). The UV spectrum showed absorptions at 243, 257, and 316 nm, which is typical of the xanthone chromophore.[17] The ^1H NMR spectrum (Table 1) was comparable to that of cowanol (**18**).[2,8] The differences were found at position 5, 6, and 8 of ring A. An aromatic proton (δ 6.72, s)[2,8] at position 5 of **18** was replaced, in **1**, by a hydroxyl proton (δ 9.95, br s). The hydroxyl group (not observed)[2, 8] at position 6 of **18** was replaced, in **1**, by a dihydroxy geranyl group (δ 3.44 (2H, m, H-1″), 1.77 (2H, m, H-6″), 1.57 (4H, m, H-2″ and H-5″), 1.30 (6H, s, H-8″ and H-9″), and 1.20 (3H, s, H-10″)). In the HMBC spectrum (Table 1), the methylene protons (δ 3.44, H-1″) of the dihydroxy geranyl unit showed cross peaks with C-5 (δ 160.7), C-6 (δ 139.4), and C-7 (δ 143.6), indicating the attachment of the dihydroxy geranyl side chain at C-6. The geranyl group (δ 5.24 (1H, br t, *J* = 6.0 Hz), 5.01 (1H, br t, *J* = 6.6 Hz), 4.03 (2H, d, *J* = 6.0 Hz), 2.02 (4H, m), 1.83 (3H, s), 1.58 (3H, s), and 1.53 (3H, s)) at position 8 of **18** was replaced, in **1**, by an aromatic proton (δ 6.84, s) whose assignment was confirmed by its HMBC cross peaks with C-7 (δ 143.6), C-8a (δ 110.7), C-9 (δ 181.9), and C-10a (δ 155.5). In addition, the substituents on ring B were located at the same position as those of **18**, indicated by HMBC correlations and comparison of the NMR data of **1** and **18**. Thus, cowaxanthone F was identified as 1,3,5-trihydroxy-7-methoxy-2-(3-methyl-4-hydroxy-2-butenyl)-6-(3,7-dihydroxy-3,7-dimethyloctyl)xanthone (**1**).

When compounds **1** (cowaxanthone F), **2** (morelloflavone), **3** (volkensiflavone), **4** (morelloflavone-7″-*O*-glucoside), and **5** (1,6-dihydroxyxanthone), isolated from the twigs of *G. cowa*, were evaluated for their free radical scavenging activities, only **2** and **4** were effective in the DPPH (diphenylpicrylhydrazyl) assay.[18] Both compounds showed equal potency with an IC_{50} value of 18 μmol/L, whereas the butylated hydroxytoluene (BHT) control had an IC_{50} of 136 μmol/L. These results implied that the crucial parts responsible for the radical scavenging activity should be the ortho dihydroxy of ring E.[19–21] Compounds **2** and **4** also exerted their inhibitory effects on the hydroxyl radical with IC_{50} values of 0.56 and 0.74 mmol/L, respectively, which are rather weaker than

Table 1. ^{1}H, ^{13}C, and major HMBC correlations for cowaxanthone F (**1**) in acetone-d_6.

Position	δ_H (mult, *J* in Hz)	δ_C	HMBC
1		160.7	
1-OH	13.89, s		C-1, C-2, C-9a
2		109.2	
3		162.2	C-2, C-3, C-4a, C-9a
3-OH	9.95, br s		
4	6.40, s	92.6	
4a		154.9	
5		160.7	
5-OH	9.95, br s		
6		139.4	
7		143.6	
7-OMe	3.87, s	60.6	C-7
8	6.84, s	101.6	C-7, C-8a, C-9, C-10a
8a		110.7	
9		181.9	
9a		102.7	
10a		155.5	
1′	3.42, dd, 13.5, 8.1	22.0	C-1, C-2, C2′, C-3′
2′	5.36, br t, 8.1	124.7	
3′		134.8	
4′	4.30, s	60.8	C-2′, C-3′
5′	1.74, s	21.0	C-2′, C-3′, C-4′
1″	3.44, m	20.7	C-5, C-6, C-7, C-2″
2″	1.57, m	42.4	C-4″
3″		69.4	
4″	1.50, m	44.8	
5″	1.57, m	18.6	C-4″
6″	1.77, m	42.7	C-7″
7″		71.8	
8″	1.30, s	26.6	C-6″, C-7″
9″	1.30, s	29.7	C-6″, C-7″
10″	1.20, s	29.4	C-3″, C-4″

tannin (IC_{50} 0.12 mmol/L). Thus, a substitution of a hydroxyl group at C-7″ of morelloflavone (**2**) by a sugar moiety as in **4** seems to diminish the hydroxyl radical scavenging activity. In the superoxide anion assay, compound **4** (IC_{50} 0.89 mmol/L) was less effective than compound **2** (IC_{50} 0.27 mmol/L), however, both compounds showed better activity than the standard trolox (IC_{50} 1.36 mmol/L). Taken together with the above results, it is likely that a sugar moiety at the C-7″ position of ring D would not only diminish the superoxide dismutase-like activity but also attenuate the potency to scavenge the most reactive hydroxyl radical (comparison of **2** and **4**).

Eight compounds, cowaxanthones A–D (**6**–**9**), cowanin (**15**), α-mangostin (**16**), mangostanin (**17**), and cowanol (**18**), previously isolated from the fruits of *G. cowa*, were investigated for anti-inflammatory activity in a rat ear edema model (Table 2).[22] At 15 min after ethyl phenylpropiolate (EPP) application, cowaxanthones B (**7**) and C (**8**) exhibited the strongest anti-inflammatory activity while cowaxanthone D (**9**), cowanin (**15**), and α-mangostin (**16**) showed moderate activity and the others exhibited less activity. However, at 30, 60, and 120 min after administration of EPP, it was found that most compounds showed similar intensity of anti-inflammatory effect as those of phenylbutazone. Only cowanol (**18**) showed less activity. The results suggested the inhibitory effect of the compounds on synthesis and (or) release of inflammatory mediators involved in this model, especially histamine, kinins, and prostaglandins.

Experimental

General

Melting points were determined on an Electrothermal 9100 melting point apparatus and are uncorrected. IR spectra were obtained using a FTS 165 FTIR spectrometer (PerkinElmer 783). UV spectra were recorded using a UV-160A spectrophotometer (SHIMADZU). ^{1}H and ^{13}C NMR spectra were recorded on a Bruker FTNMR Ultra Shield™ 300 MHz and 500 MHz spectrometer using a $CDCl_3$ solution unless otherwise stated with TMS (tetramethylsilane) as the internal standard. EIMS were measured on a Thermo Finnigan Polaris Q mass spectrometer at 70 eV (probe). The HRMS were recorded on a Micromass model VQ-TOF-2 spectrometer. Optical rotations were measured on a JASCO DIP-370 digital polarimeter by using a 50 mm microcell (1 mL). TLC (thickness 200 μm) and precoated TLC (thickness 250 μm) were performed on silica gel 60 F_{254} (Merck). Quick column chromatography (QCC) and column chromatography (CC) were performed on silica gel (Merck) types 60H and 100 (70–230 mesh ASTM), respectively.

Plant material

The twigs of *G. cowa* Roxb. were collected from Sathingmoo District, Amphur Singhanakhon, Songkhla Province, in the southern part of Thailand, in June 2003. A voucher specimen (WIPAPAN 01) has been deposited at the Herbarium of the Department of Biology, Faculty of Science, Prince of Songkla University, Thailand.

Extraction and isolation

The dried and chopped twigs of *G. cowa* (2 kg) were extracted with acetone (5 L) for 7 d at room temperature three times. Filtration and subsequent evaporation of the combined acetone extracts to dryness in vacuo afforded a dark brown gum (40.48 g). The crude acetone extract (22.56 g) was subjected to QCC, eluting with CH_2Cl_2 and MeOH in a polarity-gradient manner to afford seven fractions.[1–7] Fraction 3 (2.26 g, eluted with 10%–20% MeOH–CH_2Cl_2) was further purified by CC on silica gel and eluted with a gradient of CH_2Cl_2–MeOH to afford **5** (12.0 mg). Fraction 4 (674.7 mg, eluted with 20%–30% MeOH–CH_2Cl_2) was further separated by CC using a gradient of CH_2Cl_2–MeOH to afford **3** (18.04 mg) and **4** (25.6 mg). Fraction 5 (8.10 g, eluted with 30%–50% MeOH–CH_2Cl_2) was fractionated further by QCC using a gradient system (CH_2Cl_2–MeOH) to yield four subfractions (A1–A4). Subfraction A2 (3.26 g, eluted with 5%–8% MeOH–CH_2Cl_2) was further subjected to QCC using CH_2Cl_2–MeOH to yield 8 fractions (B1–B8). Further chromatography of fraction B7 (650 mg) on CC and preparative TLC using 8% MeOH–CH_2Cl_2 as a mobile phase (4 elutions) gave **2** (379.6 mg) and **3** (23.0 mg) as a yellow solid. Subfraction A3 (663.6 mg, eluted with 4%–10% MeOH–CH_2Cl_2) was further subjected to CC using CH_2Cl_2–MeOH as an eluent to give five subfractions (C1–

Table 2. Inhibitory effects of the isolated compounds **6–9**, **15**, **16**, **17**, and **18** from the fruits of *G. cowa* on EPP-induced rat ear edema.

		Edema thickness (μm)				Edema inhibition (%)			
Compound	Dose (mg/kg)	15 min	30 min	1 h	2 h	15 min	30 min	1 h	2 h
Control	—	120±5	230±7	333±11	303±15	—	—	—	—
Phenylbutazone	1	3±3***	80±7***	163±6***	153±8***	98	65	51	50
6	1	50±5***	107±4***	157±6***	153±8***	58	54	53	50
7	1	23±3***	113±4***	147±4***	107±4***	81	51	56	65
8	1	47±4***	113±8***	133±4***	107±4***	88	51	60	65
9	1	43±3***	80±7***	120±7***	130±11***	64	65	64	57
15	1	40±5***	83±6***	120±13***	123±15***	67	64	64	59
16	1	43±6***	87±8***	110±5***	100±0***	64	62	67	67
17	1	50±5***	140±5***	157±8***	127±10***	58	39	53	58
18	1	80±7***	163±6***	197±3***	173±4***	33	29	41	43

Note: The values are mean ± SEM (n = 6). Statistically significant from the control group: *P < 0.05, **P < 0.01, ***P < 0.001.

C5). Further chromatography of subfraction C2 (181.4 mg) on CC and preparative TLC using 10% MeOH–CH_2Cl_2 as a mobile phase (3 elutions) yielded a yellow solid of **1** (5.1 mg) and a yellow solid of **2** (100.9 mg). Subfraction C3 (253.6 mg) was further subjected to CC, followed by preparative TLC using 14% MeOH–CH_2Cl_2 as a mobile phase (4 elutions) to give a yellow solid of **3** (17.3 mg) and a yellow solid of **4** (147.2 mg). Subfraction A4 (1.54 g, eluted with 10%–15% MeOH–CH_2Cl_2) was further purified by CC, followed by preparative TLC using 12% MeOH–CH_2Cl_2 as a mobile phase (7 elutions) to yield a yellow solid of **4** (117.6 mg).

1,3,5-Trihydroxy-7-methoxy-2-(3-methyl-4-hydroxy-2-butenyl)-6-(3,7-dihydroxy-3,7-dimethyloctyl)xanthone (cowaxanthone F, 1)

Pale yellow solid (CH_2Cl_2); mp 163.8–164.7 °C (decomposed). $[\alpha]_D^{28}$ + 57.1 (*c* 0.065, acetone). UV (EtOH) λ_{max} (log ε, nm): 243 (4.61), 257 (4.54), 316 (4.47). IR (neat, cm^{-1}) ν_{max}: 3436, 1639, 1607. ^1H (300 MHz, acetone-d_6) and ^{13}C NMR (75 MHz, acetone-d_6) data: see Table 1. EI-MS *m/z*: 530 $[M]^+$ (1), 279 (3), 167 (22), 149 (100), 121 (10), 77 (8), 67 (9). HRTOFMS (APCI positive) *m/z*: 553.2366 [M+ + Na] (calcd. for $C_{29}H_{38}O_9Na$: 553.2414).

Animals

Male Sprague-Dawley rats weighing 40–60 g were purchased from the National Laboratory Animal Center, Nakorn Pathom. The animals had free access to water and food and were acclimatized at least one week before starting the experiments. The animal experiment was performed according to the Ethical Principles and Guidelines for the Use of Animals prepared by the National Research Council of Thailand.

Anti-inflammatory activity

The method described by Brattsand et al.,[22] ethyl phenylpropiolate (EPP)-induced ear edema in rat, was performed. Male rats weighing 40–60 g were used. Ear edema was induced by topical application of EPP, dissolved in acetone, at a dose of 1 mg/20 μL per ear to the inner and outer surfaces of both ears by means of an automatic microliter pipet. Each test compound, also dissolved in acetone, was applied topically in a volume of 20 μL just before the EPP. The control group received acetone only. Before and at 15, 30, 60, and 120 min after edema induction, the thickness of each ear was measured by the digital vernier calipers. The percent inhibition of the edema formation of test substances was calculated.

Free radical scavenging activity

In this study, three assays were carried out, as previously described by Hutadilok-Towatana et al.,[18] as follows.

DPPH assay

To different concentrations of a sample in methanol (0.5 mL each) was added 1 mL of a methanolic solution of 0.2 mmol/L DPPH. After mixing thoroughly, the mixture was allowed to stand in the dark for 30 min and the absorbance at 523 nm was measured using methanol for the baseline correction. The results were then compared with that of the control, which was prepared as above but without a test sample. Radical scavenging activity was expressed as a percentage and was calculated using the following formula: %Scavenging = $[(A_{control} - A_{sample}) / A_{control}] \times 100$. For each sample, the result was presented as an IC_{50} (the sample concentration that produced 50% scavenging of the DPPH radical). BHT (butylated hydroxytoluene) was used as a positive control.

Hydroxyl radical scavenging assay

Various amounts of test sample were mixed with 134 μL of 30 mmol/L KH_2PO_4–KOH buffer (pH 7.4), 67 μL of 17 mmol/L deoxyribose, 33 μL of 34 mmol/L H_2O_2, 33 μL of 1.2 mmol/L EDTA (ethylenediaminetetraacetic acid), 67 μL of 300 μmol/L $FeCl_3$, and 67 μL of 600 μmol/L ascorbic acid was then added to start the reaction. After incubation at 37 °C for 1 h, the products of the hydroxyl radical attack on deoxyribose were determined by adding 333 μL of 1% (*w/v*) TBA (thiobarbituric acid) in 50 mmol/L NaOH, followed by 333 μL of 2.8% (*w/v*) TCA (trichloroacetic acid). After further incubation at 80 °C for 20 min, the reaction mixtures were centrifuged. The clear supernatants were then measured for their absorption at 532 nm. A parallel assay omitting the test sample was used as a control whereas that without the addition of deoxyribose was used as a sample blank. The results were expressed as percent inhibition of the deoxyribose attack using the following formula: %In-

hibition = $[(A_{control} - (A_{sample} - A_{sample\ blank}) / A_{control}] \times 100$. For each sample, the result was presented as an IC_{50} (the sample concentration that produced 50% inhibition of hydroxyl radical). Tannin was used as a positive control.

Superoxide anion scavenging assay

Test samples were prepared in methanol and 20 μL of each was added to 1 mL of the reagent composed of 9.9 mmol/L L-methionine, 1.72 mmol/L NBT (nitroblue tetrazolium), 1% (*w*/*v*) Triton X-100, and 117 μmol/L riboflavin in 50 mmol/L K_2HPO_4, with a pH 7.8. After mixing, the reaction mixture was illuminated under a 40 W fluorescent light for 7 min. A control tube in which the test sample was replaced by methanol and a sample blank, which contained no riboflavin, were also run in parallel. The absorbance at 560 nm was then measured. The results were expressed as percent scavenging of the superoxide radical using the following formula: %Scavenging = $[(A_{control} - (A_{sample} - A_{sample\ blank}) / A_{control}] \times 100$. For each sample, the result was presented as an IC_{50} (the sample concentration that produced 50% inhibition of superoxide radical). Trolox was used as a positive control.

Acknowledgements

K.P. would like to thank the Prince of Songkla University for a research grant. The authors are grateful to Associate Professor Dr. Kitichate Sridith from the Herbarium of the Department of Biology, Faculty of Science, Prince of Songkla University for the identification of the plant. We are also grateful to the Commission on Higher Education (CHE-RES-RG), the Center for Innovation in Chemistry (PERCH-CIC), and the Royal Thai Government for their partial support of this work.

References

(1) Poomipamorn, S.; Kumkong, A. *Edible Multipurpose Tree Species* (in Thai); FaungFa Printing: Bangkok, 1997; p 486.
(2) na Pattalung, P.; Thongtheeraparp, W.; Wiriyachitra, P.; Taylor, W. C. *Planta Med.* **1994**, *60* (4), 365–368. doi:10.1055/s-2006-959502. PMID:7938273.
(3) Likhitwitayawuid, K.; Ruchirawat, S. *Phytochemistry* **1997**, *45* (6), 1299–1301. doi:10.1016/S0031-9422(97)00125-8.
(4) Likhitwitayawuid, K.; Phadungcharoen, T.; Krungkrai, J. *Planta Med.* **1998**, *64* (1), 70–72. doi:10.1055/s-2006-957370. PMID:9491769.
(5) Mahabusarakam, W.; Chairerk, P.; Taylor, W. C. *Phytochemistry* **2005**, *66* (10), 1148–1153. doi:10.1016/j.phytochem.2005.02.025. PMID:15924919.
(6) Shen, J.; Yang, J. S. *Chem. Pharm. Bull. (Tokyo)* **2006**, *54* (1), 126–128. doi:10.1248/cpb.54.126. PMID:16394566.
(7) Shen, J.; Tian, Z.; Yang, J. S. *Pharmazie* **2007**, *62* (7), 549–551. PMID:17718199.
(8) Panthong, K.; Pongcharoen, W.; Phongpaichit, S.; Taylor, W. C. *Phytochemistry* **2006**, *67* (10), 999–1004. doi:10.1016/j.phytochem.2006.02.027. PMID:16678870.
(9) Karanjgaokar, C. G.; Radhakrishnan, P. V.; Venkataraman, K. *Tetrahedron Lett.* **1967**, *8* (33), 3195–3198. doi:10.1016/S0040-4039(01)89897-X.
(10) Pelter, A.; Warren, R.; Chexal, K. K.; Handa, B. K.; Rahman, W. *Tetrahedron* **1971**, *27* (8), 1625–1634. doi:10.1016/S0040-4020(01)98028-7.
(11) Li, X.-C.; Joshi, A. S.; Tan, B.; ElSohly, H. N.; Walker, L. A.; Zjawiony, J. K.; Ferreira, D. *Tetrahedron* **2002**, *58* (43), 8709–8717. doi:10.1016/S0040-4020(02)01096-7.
(12) Joshi, B. S.; Kamat, V. N.; Viswanathan, N. *Phytochemistry* **1970**, *9* (4), 881–888. doi:10.1016/S0031-9422(00)85197-3.
(13) Konoshima, M.; Ikeshiro, Y.; Miyahara, S. *Tetrahedron Lett.* **1970**, *11* (48), 4203–4206. doi:10.1016/S0040-4039(01)98703-9.
(14) Chen, F. C.; Lin, Y. M.; Hung, J. G. *Phytochemistry* **1975**, *14* (3), 818–820. doi:10.1016/0031-9422(75)83048-2.
(15) Lin, Y.-M.; Anderson, H.; Flavin, M. T.; Pai, Y.-H. S.; Mata-Greenwood, E.; Pengsuparp, T.; Pezzuto, J. M.; Schinazi, R. F.; Hughes, S. H.; Chen, F. C. *J. Nat. Prod.* **1997**, *60* (9), 884–888. doi:10.1021/np9700275. PMID:9322359.
(16) Noro, T.; Ueno, A.; Mizutani, M.; Hashimoto, T.; Miyase, T.; Kuroyanagi, M.; Fukushima, S. *Chem. Pharm. Bull. (Tokyo)* **1984**, *32* (11), 4455–4459. PMID:6549438.
(17) Ito, C.; Itoigawa, M.; Takakura, T.; Ruangrungsi, N.; Enjo, F.; Tokuda, H.; Nishino, H.; Furukawa, H. *J. Nat. Prod.* **2003**, *66* (2), 200–205. doi:10.1021/np020290s. PMID:12608849.
(18) Hutadilok-Towatana, N.; Chaiyamutti, P.; Panthong, K.; Mahabusarakam, W.; Rukachaisirikul, V. *Pharm. Biol.* **2006**, *44* (3), 221–228. doi:10.1080/13880200600685592.
(19) Rice-Evans, C. A.; Miller, N. J.; Paganga, G. *Free Radic. Biol. Med.* **1996**, *20* (7), 933–956. doi:10.1016/0891-5849(95)02227-9. PMID:8743980.
(20) Chen, Z. Y.; Chan, P. T.; Ho, K. Y.; Fung, K. P.; Wang, J. *Chem. Phys. Lipids* **1996**, *79* (2), 157–163. doi:10.1016/0009-3084(96)02523-6. PMID:8640902.
(21) Arora, A.; Nair, M. G.; Strasburg, G. M. *Free Radic. Biol. Med.* **1998**, *24* (9), 1355–1363. doi:10.1016/S0891-5849(97)00458-9. PMID:9641252.
(22) Brattsand, R.; Thalén, A.; Roempke, K.; Källström, L.; Gruvstad, E. *J. Steroid Biochem.* **1982**, *16* (6), 779–786. doi:10.1016/0022-4731(82)90035-8. PMID:7109581.

Structural control of Au and Au–Pd nanoparticles by selecting capping ligands with varied electronic and steric effects

Patrick B. Murphy, Feng Liu, Stephen C. Cook, Nusrat Jahan, D. Gerrard Marangoni, T. Bruce Grindley, and Peng Zhang

Abstract: Weakly interacting ligands including three Gemini surfactants, didodecyldimethylammonium bromide (DDAB), and amines (RNH_2, R_2NH, and R_3N) were used to prepare Au nanoparticles (NPs). Aqueous Au NPs capped with DDAB and Gemini surfactants showed similar sizes (3–4 nm), whereas toluene-based NPs stabilized with DDAB, amines, and their mixtures range from 2.5 to 9.3 nm. Ligand effect on Au–Pd NP structure was also studied with EXAFS. These findings were consistently accounted for by considering the ligand's electronic/steric effects and mixed ligands coadsorption, and suggest useful ways to control NP structure by manipulating the two effects and using mixed capping ligands.

Key words: metal nanoparticles, capping ligands, electronic effect, steric effect, EXAFS.

Résumé : On a utilisé des ligands interagissant faiblement, dont trois agents de surface Gemini, le bromure de didodécyldiméthylammonium (BDDA) et des amines (RNH_2), R_2NH et R_3N) pour préparer des nanoparticules (NP) d'or (Au). Les tailles des nanoparticules d'or aqueuses, fermées avec du BDDA ou des agents de surfaces Gemini sont assez semblables (3–4 nm) alors que celles des nanoparticules à base de toluène et stabilisées par du BDDA, des amines ou leurs mélanges varient de 2,5 à 9,3 nm. On a aussi examiné l'effet de ligand sur la structure des nanoparticules Au–Pd par la technique de structure fine d'absorption des rayons-X étendue (SFAXE). Les observations peuvent être expliquées d'une façon cohérente en considérant les effets stérique/électronique du ligand et la coadsorption des ligands mixtes et ceci suggère des façons utiles de contrôler la structure des nanoparticules en manipulant les deux effets et en utilisant des ligands mixtes pour les fermer.

Mots-clés : nanoparticules métalliques, ligands de fermeture, effet électronique, effet stérique, structure fine d'absorption des rayons X étendue (SFAXE).

[Traduit par la Rédaction]

Introduction

Selection of capping ligands for the synthesis of metal nanoparticles (NPs) is of fundamental and technological importance.[1–6] Capping the NP surface with alkanethiols and their derivatives has become a widely used method in the past decade.[1] The availability of a large variety of commercial thiol derivatives and the advancement in thiol ligand-exchange reactions for the NPs have made such an approach particularly attractive.[7–9] However, the primary limitation of using thiol derivatives to functionalize NP surface is that the metal–ligand interaction is too strong and this hinders some applications such as catalysis. An alternative route to control the NP surface structure is to use weakly interacting molecules (relative to thiols) such as tetraalkylammonium surfactants. A noteworthy advantage of using weakly binding ligands is that the catalytic activity of NPs can be dramatically improved relative to those of their thiol-stabilized counterparts.[4,10] More significantly, the use of weakly interacting ligands can offer excellent control of NP structures, making possible the synthesis of NPs with flexibly controlled size and shape (e.g., nanorods and nanowires).[3,11] In addition, weakly interacting ligands are easily replaceable/exchangeable if strongly binding ligands are desired to surface-functionalize the NP surface.

Tetraalkylammonium surfactants are among the most widely studied weakly interacting ligands in recent years. Numerous syntheses of NPs have been reported using tetraalkylammonium ligands, such as tetraoctylammonium bromide (TOAB),[12] didodecyldimethylammonium bromide (DDAB),[13] and cetyltrimethylammonium bromide (CTAB).[11] Remarkably, significant progress has also been made in understanding the binding/stabilization mechanism of NP capping ligands, which plays a critically important role in the development of more efficient NP synthetic routes.[2,4,14] However, most of the in-depth studies on the stabilization mechanisms of weakly interacting ligands are based on ionic

Received 22 May 2009. Accepted 20 July 2009. Published on the NRC Research Press Web site at canjchem.nrc.ca on 28 October 2009.

P.B. Murphy, F. Liu, S.C. Cook, N. Jahan, T.B. Grindley, and P. Zhang.[1] Department of Chemistry and Institute for Research in Materials, Dalhousie University, Halifax, NS B3H 4J3, Canada.
D.G. Marangoni. Department of Chemistry, St. Francis Xavier University, Antigonish, NS B2G 2W5, Canada.

[1]Corresponding author (e-mail: peng.zhang@dal.ca).

Scheme 1. Molecular structures of three Gemini surfactants, three fatty amines, and DDAB.

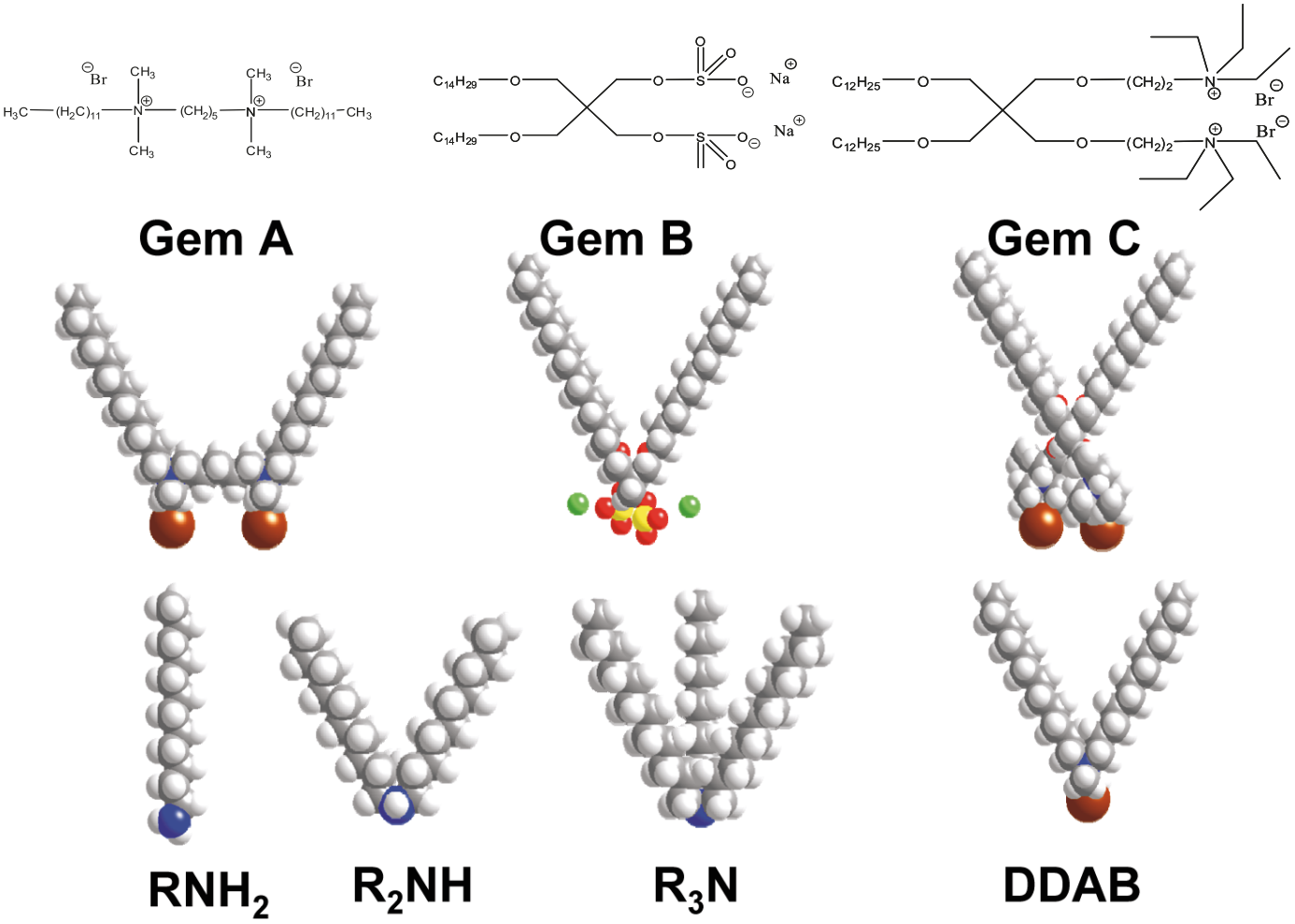

ligands.[4] For instance, one of the widely accepted ligand-stabilization mechanisms used for NP catalysis, proposed by Ott and Finke, mainly consider two effects of the ligands, i.e., the so-called electronic effect (also known as charge or DLVO effect) and the steric effect.[4] Such a mechanism has been found to provide good interpretation of the structural and catalytic properties of high-charge ionic ligands such as $(Bu_4N^+)_9$ $(P_2W_{15}Nb_3O_{62})^{9-}$. In contrast, detailed stabilization mechanisms of other types of ligands, such as neutral weakly interacting ligands, has remained largely under-explored. Such studies are particularly desirable in light of the recent remarkable findings on amine-based nanoelectronic devices.[15–17] Herein, we report the synthesis of Au NPs with a variety of weakly interacting ligands (Scheme 1), including some novel Gemini surfactants, didodecyldimethylammonium bromide (DDAB), dodecylamine, didecylamine, tridodecylamine, and nine mixtures of DDAB/amines (DDAB mixed with three amine ligands, each with three different molar ratios). The purposes of the present work are threefold: (*i*) exploring how Finke's models on ligand's electronic and steric effects can be used/extended to understand the stabilization of Au/Au–Pd NPs with the above-mentioned ligands (particularly the neutral amine ligands); (*ii*) seeking possible ways to controllably synthesize Au NPs by selecting ligands with varied electronic/steric effects or using a mixed capping method, and (*iii*) investigating how the capping ligands influence the local structure (i.e., the bimetal mixing pattern) of Au–Pd NPs.

Experimental section

All the chemicals were obtained commercially from Alfa Aesar or Aldrich except for ligands Gem A, Gem B, and Gem C (Scheme 1). Synthetic details for the preparations of Gemini surfactants will be published elsewhere[18] and can also be found in the Supplementary data. Au nanoparticles (Au NPs) were prepared by reducing $HAuCl_4$ in aqueous solution or $AuCl_3$ in toluene with sodium borohydride. Three amine capping ligands were used singularly or in combination with DDAB. For combination systems, the ratios of amine to DDAB used were 1:4, 1:1, and 4:1. In a typical procedure, 0.03 mmol gold(III) chloride and 0.45 mmol of capping ligands (gold:ligand = 1:15 molar ratio) were dispersed in 30 mL of toluene by sonication. Then, the gold(III) was reduced with sodium borohydride (0.3 mmol) in 20 μL of water, and stirred under argon for 2 h at room temperature. The as-prepared Au NP liquid suspensions were then stored in darkness in a refrigerator without further purification. UV–vis experiments were conducted

Scheme 2. A schematic demonstration of the electronic and steric effect of ionic (DDAB) and neutral (R_2NH) ligands.

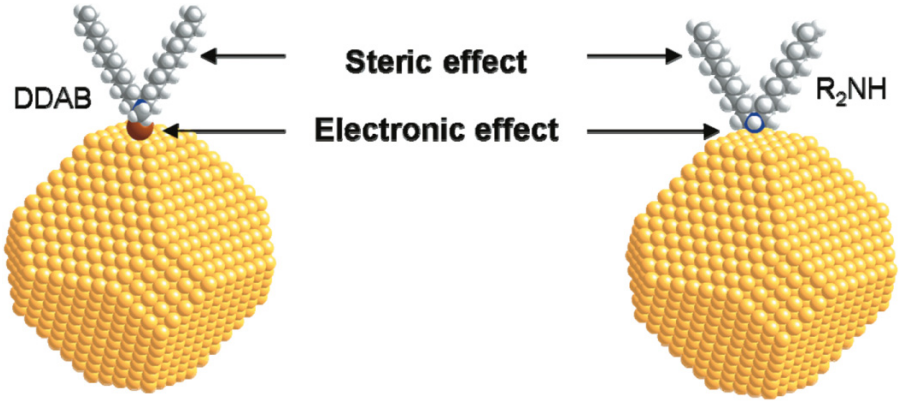

right after the NP synthesis, and TEM measurements were done within three days. Although only as-prepared samples (ideally purified samples are preferred) were measured in the present work, the reported TEM and UV–vis results were proved to be valid by time-dependent UV–vis measurements. Indeed, the as-prepared Au NPs were found to be stable for at least one month, as shown by comparing the UV–vis spectra of fresh and one month old samples. The bimetallic Au–Pd NPs capped with DDAB/RNH_2 (80% RNH_2) were synthesized using the same conditions as those reported recently for TOPB/RNH_2–capped Au–Pd NPs.[19] It was assumed that the initial Au-to-Pd molar ratio in the starting materials was maintained after the Au–Pd NPs were formed, which was supported by the XPS composition analysis result reported for similar Au–Pd NPs in our recent publication.[19]

The morphology of the nanoparticles was characterized with a Technai 12 or JEOL 123 transmission electron microscope (TEM), both equipped with a CCD camera and operated at a voltage of 80 keV. One or two drops of the nanoparticle solutions were cast to carbon or formvar-coated Cu grids for the TEM measurements. The particle size information was obtained using a size-measuring program from the TEM by counting at least 100 particles. The Au–Pd NPs were purified using the centrifuge method described in our recent publication[19] to obtain high-quality EXAFS data. The Au L_3-edge EXAFS measurements were conducted at the HXMA beamline at the Canadian Light Source (CLS) operated at 2.9 GeV. Purified Au–Pd NPs were cast onto a Mylar tape to form a uniform film, and the samples were measured at room temperature using a transmission mode. The EXAFS data were normalized and fitted with theoretical phase-shift and amplitude generated from FEFF 8 program[20] using a WinXAS program, following the procedure described in our recent papers.[19,21] The best-fit FT-EXAFS was provided in the Supplementary data.

Results and discussion

The mechanism of nanoparticle stabilization by ligands

Finke and co-workers have recently reviewed the stabilization modes of catalytic NPs with a particular emphasis on metal NPs capped with anionic ligands.[2,4] Electronic and steric effects are proposed as the main factors influencing ligand stabilization. These two effects are schematically illustrated in Scheme 2 by inspecting the interaction between DDAB and Au NP. The electronic effect in Finke's model can be described as the Coulombic repulsive interaction between NPs due to the binding of Br^- onto Au NP surface, resulting in negatively charged NPs. That is why the electronic effect for these ionic ligands is also called the charge effect. The steric effect, on the other hand, originates from the relatively bulky ammonium groups that stay near the negatively charged NPs as counter cations. For DDAB used In the present work, the two 12-carbon alkyl chains sterically hinder direct contact between Au NPs.

When non-ionic ligands interact with Au NPs, the charge-induced Coulombic effect used for ionic ligands does not directly apply. However, the steric effect alone is not sufficient to account for the stabilities of NPs. For instance, Au NPs stabilized with dodecylamine and dodecylthiol ligands should experience very similar steric effects, but these two types of NPs have significantly different stabilities (amine–Au < thiol–Au). A second important stabilizing effect is apparently related to the metal–ligand electronic bonding (e.g., Au–SR and Au–amine), which can be considered as another type of electronic effect. Such an electronic effect for non-ionic ligands can also play an important role in the stabilization of NPs. In a later section, it will be shown that the electronic and steric effects for non-ionic ligands, which are considered as a simple extension of the models for ionic ligands, can be used to understand the ligand-dependent NP size when Au samples were capped with primary, secondary, tertiary amines, and with amine/DDAB mixtures.

Au NPs in aqueous vs. toluene phase

Recently, it has been reported that Gemini surfactants form a unique category of capping ligands for the preparation of metal nanoparticles in the aqueous phase.[22,23] In addition, the molecular structures of the Gemini surfactants can be altered to a much greater degree than those of the monomers, which may offer new opportunities to control the size and stability of NPs. Herein, two novel Gemini surfactants (Gem B and Gem C) together with a standard Gemini surfactant (Gem A) were used for the synthesis of Au NPs in aqueous solutions. The molecular structures of these Gemini surfactants are displayed in Scheme 1. In addition, DDAB was also used as a reference, since it has been found that DDAB can form a bilayer capping structure similar to those of the Gemini capping ligands.[13] Figure 1 shows the

Fig. 1. TEM images of aqueous Au NPs capped with (a) DDAB, (b) Gem A, (c) Gem B, and (d) Gem C. The average size and standard deviation are also presented in the figure.

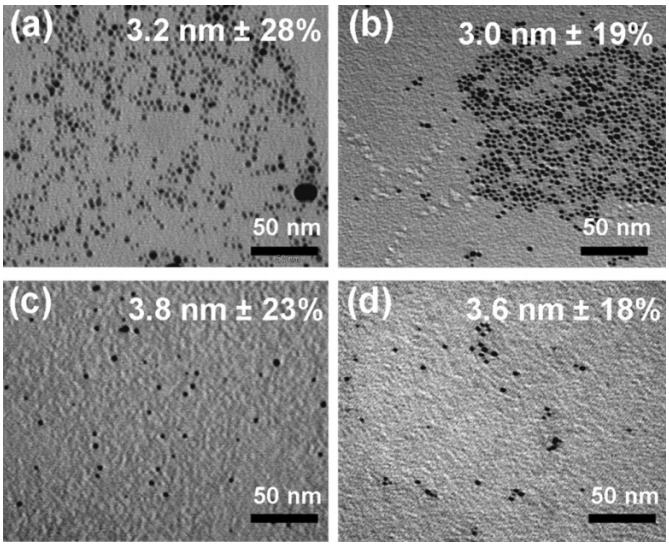

TEM images of four Au NP samples prepared with the four ligands in water. It can be seen that all four capping ligands lead to Au NPs of similar sizes (average diameter ranging from 3.0 nm to 3.8 nm), although their molecular structures, including both the binding groups and the steric non-binding moiety, vary. It has been proposed that the double-chained structure of surfactants facilitates the formation of vesicles.[13,23–25] The inner polar heads of the vesicles bind to the metal surface and the outer ones are exposed to the aqueous environment. The hydrophobic alkyl chains exist inside bilayers with quite dense packing through chain–chain interaction. Formation of such densely packed bilayers should significantly enhance the role of the steric effect in the stabilization of NPs and thus make it dominant in controlling the NP size. The dominant role of the steric effect can be more clearly revealed by the identical size of Au NPs capped with Gem B and Gem C (3.8 nm vs. 3.6 nm), whose binding head-groups are different (bromide vs. sulfate, respectively) but have similar steric moieties.

Next, we turn to toluene-phase Au NPs prepared with DDAB and three fatty amines (primary, secondary, and tertiary) under identical synthetic conditions. The use of amines with systematically varied structures in the synthesis of NPs is particularly interesting in light of the recent remarkable findings in amine-based single-molecule circuits. Venkataraman and co-workers reported that amines bind selectively to undercoordinated Au atoms with sufficient angular flexibility for easy junction formation but well-defined electronic coupling of the N lone pair to the Au.[16] It was also found that the variability of observed conductance for diamine–Au junctions is much less than that for dithiol–Au junctions.[16] Therefore, amines can be considered as promising molecules for the construction of single-molecule junctions and circuits. According to recent results from theoretical studies, methyl-substituted primary, secondary, and tertiary amines almost have the same adsorption energy when binding to undercoordinated Au structures such as an adatom.[26] These results suggest that when the three amines stay at the same distance from Au (e.g., amines with small-sized subsituents), the electronic effects are identical. On the other hand, ionic DDAB ligand should have different electronic effects from the neutral amine ligands.

Fig. 2. TEM images of toluene-phase Au NPs capped with (a) RNH_2, (b) R_2NH, (c) R_3N, and (d) DDAB.

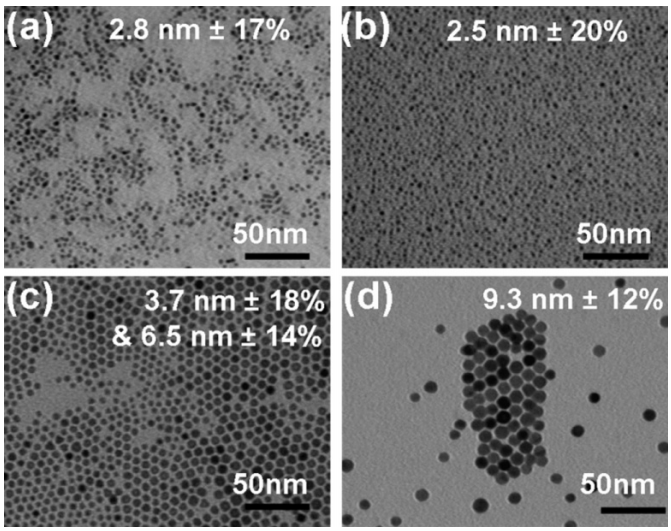

Figure 2 shows the TEM results of Au NPs prepared using DDAB and three amines. The sizes of RNH_2-capped (2.8 nm) and R_2NH-capped (2.5 nm) NPs are very close to each other. Based on the model illustrated in Scheme 2, this observation can be easily understood. For RNH_2- and R_2NH-capped NPs, the electronic effect is dominant; thus, the two NP samples have very similar sizes due to their identical metal–ligand bonding. On the other hand, the steric effect should play a less significant role when going from a primary to a secondary amine.

Interestingly, the sizes of R_3N-capped NPs are considerably different from those of primary- and secondary-amine-capped samples. Indeed, as seen in Fig. 2c, there exist two groups of particles for R_3N-capped NPs, one group being 3.7 nm in diameter and the other is 6.5 nm. Similar phenomena were observed from other spots on the same TEM grid. The steric effect for the bulky R_3N ligand should be more significant than the other two amines, favouring the formation of smaller NPs. However, it has been shown that due to steric hindrance, the electronic bonding between Au and amine is significantly weakened for bulky tertiary amines.[15] As a result, the electronic effect for R_3N ligands should be weaker than that for RNH_2 and R_2NH ligands. Indeed, the overall low monodispersity of R_3N-capped NPs also supports the suggestion of a weaker electronic effect for the tertiary ligands.

The DDAB-capped sample has very different particle size (9.3 nm) from those capped with amines, which can be easily attributed to the pronounced difference of its stabilization mechanism from that of the neutral amine ligands. Indeed, it has been reported that amines preferentially bind to low-coordination Au sites (e.g., adatoms and corner atoms), whereas those bound to terrace-type surface atoms are not stable.[15,26] In contrast, tetraalkylammonium bromide molecules were found to be mainly adsorbed to the terrace atoms on Au surface, although the Br^- alone, being separated from the ammo-

Scheme 3. An illustrative presentation of the surface-capping structure of Au NPs in aqueous (a) and toluene phase (b).

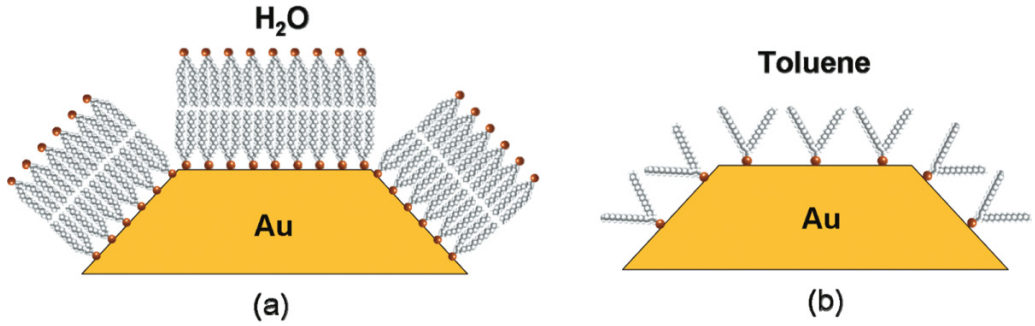

nium counterions, can strongly bind to low-coordination Au sites.[27] Therefore, the considerable NP size increase when going from amines to DDAB can be accounted for by considering their different ligand-binding mechanisms. The use of amines resulted in much smaller NPs which contain higher percentage of low-coordination surface atoms (i.e., adatoms, corner, and edge atoms) that can be bound by the ligands; the use of DDAB produced bigger NPs where the terrace-type surface atoms are more abundant.

One may also consider the possibility that the size difference among amine- and DDAB-capped NPs observed in Fig. 2 might be caused by different reduction rates of gold compound in toluene phase by aqueous $NaBH_4$. Since DDAB is a phase-transfer agent, the absence of DDAB in the three amine-capped samples may cause a slower reduction rate. However, the fact that Au NPs capped with 100% RNH_2 and those capped with a mixture of 80% RNH_2 and 20% DDAB (see next section) have very similar sizes (2.8 nm vs. 2.4 nm) suggests that such a possibility can be ruled out. Note that the presence of Cl^- anions from $AuCl_3$ starting materials can also bind to the NP surface. However, the possibility that the chloride anions play an important role in determining the NP size can be ruled out in this work. This argument is supported by the following two facts. First, it is well-known that bromide (from DDAB) can bind to gold surface more strongly than chloride. Therefore, in the presence of DDAB, the anion adsorption effect associated with Br^- should be more significant. Second, even in the absence of bromide, the above argument seems still true as the Au NP size was found to be largely determined by the molecular structure of amines (Fig. 2). It is also noted that different sizes for DDAB-capped Au NPs have been reported in the literature.[28] This could be attributed to differences between the synthetic procedures. Indeed, the stability of weakly bound NPs is largely kinetic in nature, thus causing the NP size to vary in different reports.[29] In the present work, it is still valid to make a comparison between the amine- and DDAB-capped NPs, as they were prepared under identical conditions.

Overall, a comparison of the syntheses of Au NPs in aqueous and toluene phases highlights the very different roles that the steric and electronic effects of the ligands play, which is schematically illustrated in Scheme 3 using DDAB as an example. Due to the existence of densely packed bilayer capping structure in aqueous solutions, the steric effect is dominant, whereas in toluene, the electronic effect is more important than the steric effect.

Au NPs with mixed ligands

To further study the interplay between the electronic and steric effects of the ligands as well as to explore the possibility of manipulating the two effects to control NP size, we next used a combination of amine and DDAB to synthesize Au NPs. Nine NP samples (3×3) were prepared using mixed ligands of RNH_2, R_2NH, or R_3N with DDAB, each series having 20%, 50%, and 80% amines, respectively. Figure 3 shows the TEM images of these nine NP samples. UV–vis results of the three series of Au NPs (i.e., NPs capped with DDAB/RNH_2, DDAB/R_2NH, and DDAB/R_3N) with systematically varied concentration of amines (0%, 20%, 50%, 80%, and 100%) are also displayed in the figure. A few interesting observations are noted. Firstly, the three samples capped with mixed DDAB and RNH_2, shown in Figs. 3a–3c, all have similar sizes (2.4 nm to 2.8 nm in diameter) to that of pure RNH_2-capped NPs (2.8 nm), which are considerably different from that of DDAB-capped samples (9.3 nm). The UV–vis spectra in Fig. 3j show that all the amine-capped NPs exhibit diminishing surface plasmon resonance band, indicating the small sizes for these NPs and consistently supporting the TEM data. Secondly, the DDAB/R_2NH-capped NPs displayed in Figs. 3d–3f exhibit nearly the same particle size (6.8 nm to 7.1 nm in diameter), which are very different from pure R_2NH-capped Au sample (2.5 nm), consistent with the UV–vis results in Fig. 3k. Thirdly, the size of DDAB/R_3N-capped NPs increase gradually with the concentration of DDAB, from 5.7 nm (80% R_3N) to 6.7 nm (50% R_3N) and then to 7.6 nm (20% R_3N). The UV–vis spectra of NPs in this series in Fig. 3l all exhibit fairly intense surface plasmon resonance bands. A close inspection of Fig. 3l reveals that the surface plasmon resonance band of Au shows a noticeable blue shift when DDAB is present, even if the concentration of DDAB is low (20%).

The use of cosurfactants adsorbing onto Au 2D surfaces has been reported.[30] Generally, the existence of a cosurfactant can either reduce the adsorption of the primary surfactant due to a competitive adsorbing mechanism or enhance the adsorption caused by a collaborative adsorption of the two surfactants. The results of DDAB/RNH_2-capped NPs in Figs. 3a–3c suggest a competitive adsorbing process between DDAB and RNH_2 ligands and indicate that stabilization of Au NPs by the latter is dominant. A plausible reason is that RNH_2 is much smaller in size than DDAB, making the former more competitive in the coadsorption process. This is consistent with the reported results in the literature

Fig. 3. TEM images of Au NPs (in toluene) prepared using mixed amines and DDAB: (a) 80% RNH_2, (b) 50% RNH_2, (c) 20% RNH_2, (d) 80% R_2NH, (e) 50% R_2NH, (f) 20% R_2NH, (g) 80% R_3N, (h) 50% R_3N, and (i) 20% R_3N. (j)–(l) are UV–vis spectra of RNH_2 series (j), R_2NH series (k), and R_3N series (l).

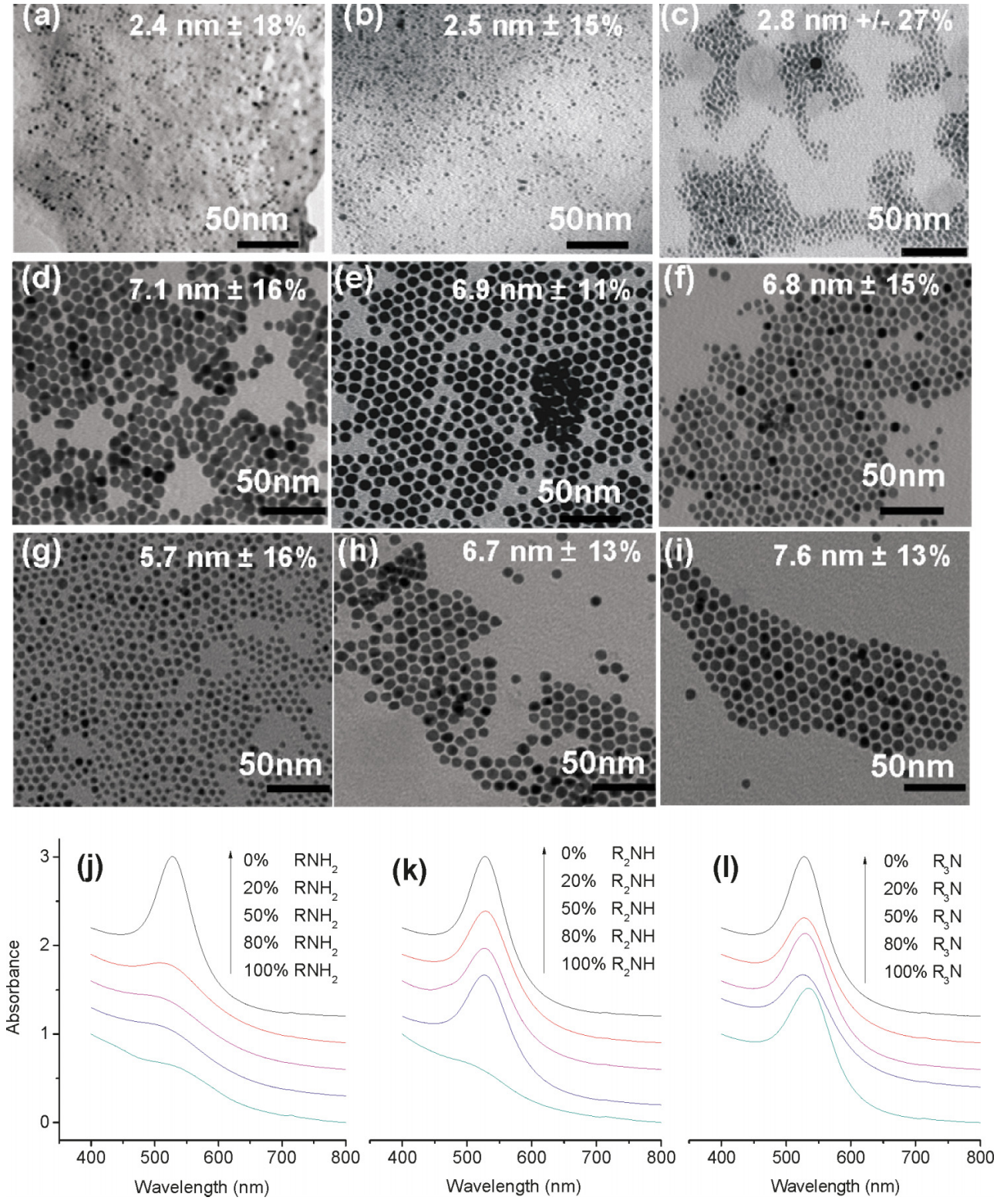

on Au 2D surface where cosurfactants of smaller sizes even at low concentration (e.g., 1%–2%) greatly reduced the amount of adsorbed primary surfactants.[30] The results of DDAB/R_2NH-capped NPs, however, seem to be very different from the case of primary amine. The sizes of the three NP samples (~7 nm) shown in Figs. 3d–3f are close to that of pure DDAB-capped NPs (9.3 nm), but quite different from that of pure R_2NH-stabilized sample (2.5 nm). Interest-

Fig. 4. TEM images of (a) $Au_{0.25}Pd_{0.75}$ NPs, (b) $Au_{0.50}Pd_{0.50}$ NPs, and (c) $Au_{0.75}Pd_{0.25}$ NPs. Au L_3-edge FT-EXAFS is presented in (d) using *k*-space EXAFS data of 3–13 $Å^{-1}$. Idealized local structure models of the three NPs are also shown in (d).

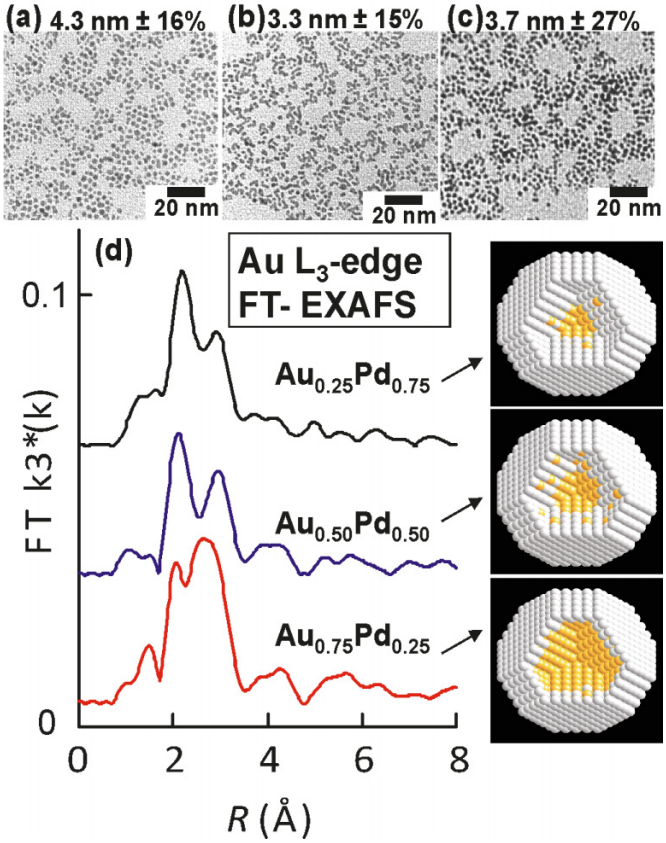

ingly, the size of the three DDAB/R_2NH-capped NPs, which are all slightly smaller than that of DDAB-capped ones, does not change as the concentration of DDAB increases. A possible explanation will be discussed in conjunction with the discussion of DDAB/R_3N-capped NPs. The results of DDAB/R_3N-capped NPs clearly indicate that both DDAB and R_3N ligands play an important role in the NP synthesis. As a result, when more DDAB ligands were used, the NP size was closer to that of pure DDAB-capped NPs. As was discussed in a previous section, R_3N has the weakest electronic effect among the three amine ligands. Therefore, it is understandable that the adsorption of DDAB is significant even at low concentration (20%). Supporting evidence is provided by the UV–vis results presented in Fig. 3l. However, the secondary amine (R_2NH), whose electronic effect is stronger than the tertiary amine, seems to be less competitive than R_3N in the coadsorption process with DDAB. Considering their very similar molecular structure (see Scheme 1), we propose that R_2NH and DDAB were collaboratively adsorbed onto the NP surface.[30] Since the NP surfaces mainly consist of terrace atoms, it can be easily understood that DDAB ligands are the ones that mainly determine the NP size, as amines cannot form stable bonds with the terrace Au atoms.[26] This notion can also explain why the particle size of DDAB/R_2NH-capped samples (~7 nm) is close to that of pure DDAB-capped NPs (9.3 nm) and remained almost unchanged when the concentration of DDAB was increased from 20% to 80%.

In summary, the particle-size data of Au NPs capped with mixed amines and DDAB ligands indicate that the coadsorption mechanism of ligands determines the NP size. RNH_2 is more competitive than DDAB in the coadsorption process; thus, the NPs capped with 20%–80% RNH_2 are all very small (<3 nm), similar to that of pure RNH_2-capped NPs. R_2NH may be coadsorbed onto Au in a collaborative way with DDAB, making the NP size close to that of pure DDAB-capped ones. R_3N and DDAB, whose competitive abilities in the coadsorption process are comparable, are similarly important in determining the NP size. Consequently, the NP size increases with the concentration of DDAB. Overall, these results suggest that by selecting ligands with desired molecular structure (and thus the electronic and steric effect), one can possibly control Au NP size with this mixed-capping method. Although further experimentation is needed to rigorously evaluate the effectiveness of this mixed-capping method, the results presented in Fig. 3 do show some promise of more flexible control of NP size than using a single type of ligands.

Au–Pd NPs with mixed ligands

We have recently reported the use of this mixed-capping method to prepare Ag–Pd and Au–Pd NPs.[19,21] Herein, we present results on bimetallic Au–Pd NPs capped with mixed DDAB (20%) and RNH_2 (80%) ligands. These results can be considered as an extension of the work on Au monometallic NPs presented in the above sections. Moreover, the effect of weakly binding ligands on the structure of bimetallic NPs is even more interesting, as not only the particle size but also the bimetal mixing pattern can possibly be influenced by selecting the ligands. We have recently reported EXAFS results on the local structure of Au–Pd NPs capped with a mixture of 20% tetraoctylphosphonium bromide (TOPB) and 80% *n*-dodecylamine, which show alloying-structure-dependent physical and chemical properties.[19] In the present work, we intend to compare the local structure of Au–Pd NPs capped with 20% DDAB and 80% *n*-dodecylamine (RNH_2) with the previous results with an attempt to study the effect of different type of bromide ligands (DDAB vs. TOPB) on the bimetal mixing pattern of Au–Pd NPs.

Figures 4a–4c depict the TEM images of Au–Pd NPs with varied concentrations of Au. The average sizes for $Au_{0.75}Pd_{0.25}$, $Au_{0.50}Pd_{0.50}$, and $Au_{0.25}Pd_{0.75}$ are 4.3 ± 0.7 nm, 3.3 ± 0.5 nm, and 3.7 ± 1.0 nm, respectively. The fact that these NPs are all bigger than their pure Au counterpart (2.4 nm) implies that the metal–ligand binding differed after Pd was introduced. To investigate the ligand effect on the mixing patterns of Au–Pd NPs, Au L_3-edge EXAFS measurements were performed. The FT-EXAFS and fitting results were presented in Fig. 4d and Table 1, respectively. A comparison of the experimental EXAFS data and first-shell best fit is provided in the Supplementary data. The information about Au–Pd mixing pattern can be obtained by analyzing the coordination numbers ($N_{Au–Au}$, $N_{Au–Pd}$, and N_{total}) in the table. It has been established[19,31–33] that if $N_{Au–Au}/N_{Au–Pd}$ is equal to Au/Pd molar ratio, a homogeneous alloy was resulted. If $N_{Au–Au}/N_{Au–Pd}$ is considerably greater than Au/Pd

Table 1. Au L_3-edge EXAFS fitting results for three Au–Pd NP samples.

Sample (% Au)	M–M bond	N^a	N_{total}	R (Å)^b	$\Delta\delta^2$	ΔE (eV)
25	Au–Au	7.4	11.8	2.830	0.0088	0.88
	Au–Pd	4.4		2.804	0.0082	2.28
50	Au–Au	7.8	11.8	2.827	0.0090	–1.14
	Au–Pd	4.0		2.797	0.0093	0.63
75	Au–Au	10.4	12.4	2.810	0.0088	–3.29
	Au–Pd	2.0		2.793	0.0079	3.28

Note: The uncertainty is ~20% for N and ~0.02 Å for R.

[a]Nearest-neighbor coordination number.

[b]First-shell metal–metal bond distance.

molar ratio, then Au-core Pd-shell NPs were formed. Moreover, N_{total} is useful to obtain the information about the location of Au atoms. If N_{total} is 12, which is the first-shell coordination number for a bulk fcc metal, Au atoms cannot be found on the NP surface (i.e., all the neighboring sites for Au are occupied). If N_{total} is less than 12, some Au atoms should be located on the surface, as the surface atoms of a metal with fcc crystalline structure have a coordination number less than 12. The results of $N_{Au–Au}$ and $N_{Au–Pd}$ in Table 1 indicate that all the three Au–Pd NPs have core-shell structures. In addition, all the three N_{total} values are nearly 12, indicating that the particle surfaces are essentially all covered by Pd atoms. Based on the above analysis, the structural models for the three Au–Pd NPs are schematically illustrated in Fig. 4. The core-shell structural models are consistent with the TEM results, which show that Au–Pd NPs are all bigger than pure Au NPs, since the surface metal–ligand bonding in the Au-core Pd-shell NPs is different from that of pure Au NPs. It is interesting to note that the present structural results of Au–Pd NPs capped with DDAB/RNH_2 (80% RNH_2) differ from those capped with TOPB/RNH_2 (80% RNH_2) we recently reported.[19] For the TOPB/RNH_2-capped NPs, core-shell structures were found only for the $Au_{0.50}Pd_{0.50}$ and $Au_{0.75}Pd_{0.25}$ NPs, whereas the $Au_{0.25}Pd_{0.75}$ NPs showed a cluster-on-cluster structure. Therefore, a comparison of the bimetal mixing patterns of these two series of samples indicates that the Au–Pd bimetallic mixing pattern can be modified by varying the type of ligands used in this mixed-capping method. We are in the process of systematically investigating the correlation between the Au–Pd mixing pattern and the structure/concentration of the two types of ligands (e.g., TOPB, DDAB, amines, and so forth) used in the mixed-capping synthesis.

Conclusion

To conclude, we have reported results of Au NP synthesis using a variety of weakly interacting ligands. Aqueous Au NPs capped with DDAB and three Gemini surfactants were found to have very similar sizes (average diameter of 3–4 nm), whereas in toluene, the use of DDAB, amines, and their mixtures as capping ligands led to Au NPs with average sizes ranging from 2.5 nm to 9.3 nm. The ligand effect on the bimetal mixing patterns of Au–Pd NPs was also studied with EXAFS. These results can be accounted for by considering the electronic and steric effects of capping ligands and the ligand coadsorption mechanism when mixed ligands (cosurfactants) were used. The experimental findings presented in this work suggest that manipulation of the electronic and steric effects of weakly interacting ligands and the use of mixed capping ligands can offer useful routes to control NP size and bimetal mixing patterns.

Supplementary data

Supplementary data for this article are available on the journal Web site (canjchem.nrc.ca) or may be purchased from the Depository of Unpublished Data, Document Delivery, CISTI, National Research Council Canada, Ottawa, ON K1A 0R6, Canada. DUD 5287. For more information on obtaining material, refer to cisti-icist.nrc-cnrc.gc.ca/cms/unpub_e.shtml.

Acknowledgements

We thank the financial support for this work by Dalhousie University, the Natural Sciences and Engineering Research Council of Canada (NSERC), the Atlantic Innovation Fund, and Canada Foundation for Innovation (CFI). The CLS is funded by NSERC, the Canadian Institutes of Health Research (CIHR), the National Research Council Canada (NRC), and the University of Saskatchewan. The EXAFS technical support from CLS staff scientist, Dr. Ning Chen, is also acknowledged.

References

(1) Templeton, A. C.; Wuelfing, W. P.; Murray, R. W. *Acc. Chem. Res.* **2000**, *33* (1), 27–36. doi:10.1021/ar9602664. PMID:10639073.

(2) Finke, R. G.; Ozkar, S. *Coord. Chem. Rev.* **2004**, *248* (1-2), 135–146. doi:10.1016/j.cct.2003.08.003.

(3) Daniel, M. C.; Astruc, D. *Chem. Rev.* **2004**, *104* (1), 293–346. doi:10.1021/cr030698+. PMID:14719978.

(4) Ott, L. S.; Finke, R. G. *Coord. Chem. Rev.* **2007**, *251* (9-10), 1075–1100. doi:10.1016/j.ccr.2006.08.016.

(5) Sperling, R. A.; Rivera Gil, P.; Zhang, F.; Zanella, M.; Parak, W. J. *Chem. Soc. Rev.* **2008**, *37* (9), 1896–1908. doi:10.1039/b712170a. PMID:18762838.

(6) Brust, M.; Fink, J.; Bethell, D.; Schiffrin, D. J.; Kiely, C. *J. Chem. Soc. Chem. Commun.* **1995**, *10* (16), 1655. doi:10.1039/c39950001655.

(7) Hostetler, M. J.; Templeton, A. C.; Murray, R. W. *Langmuir* **1999**, *15* (11), 3782–3789. doi:10.1021/la981598f.

(8) Song, Y.; Murray, R. W. *J. Am. Chem. Soc.* **2002**, *124* (24), 7096–7102. doi:10.1021/ja0174985. PMID:12059234.

(9) Song, Y.; Huang, T.; Murray, R. W. *J. Am. Chem. Soc.* **2003**, *125* (38), 11694–11701. doi:10.1021/ja0355731. PMID:13129374.
(10) Roucoux, A.; Schulz, J.; Patin, H. *Chem. Rev.* **2002**, *102* (10), 3757–3778. doi:10.1021/cr010350j. PMID:12371901.
(11) Murphy, C. J.; Sau, T. K.; Gole, A. M.; Orendorff, C. J.; Gao, J. X.; Gou, L.; Hunyadi, S. E.; Li, T. *J. Phys. Chem. B* **2005**, *109* (29), 13857–13870. doi:10.1021/jp0516846. PMID:16852739.
(12) Fink, J.; Kiely, C. J.; Bethell, D.; Schiffrin, D. J. *Chem. Mater.* **1998**, *10* (3), 922–926. doi:10.1021/cm970702w.
(13) Zhang, L. X.; Sun, X. P.; Song, Y. H.; Jiang, X.; Dong, S. J.; Wang, E. A. *Langmuir* **2006**, *22* (6), 2838–2843. doi:10.1021/la052822l. PMID:16519492.
(14) Grubbs, R. B. *Pol. Rev.* **2007**, *47* (2), 197–215. doi:10.1080/15583720701271245.
(15) Venkataraman, L.; Klare, J. E.; Nuckolls, C.; Hybertsen, M. S.; Steigerwald, M. L. *Nature* **2006**, *442* (7105), 904–907. doi:10.1038/nature05037. PMID:16929295.
(16) Venkataraman, L.; Klare, J. E.; Tam, I. W.; Nuckolls, C.; Hybertsen, M. S.; Steigerwald, M. L. *Nano Lett.* **2006**, *6* (3), 458–462. doi:10.1021/nl052373+. PMID:16522042.
(17) Quek, S. Y.; Venkataraman, L.; Choi, H. J.; Louie, S. G.; Hybertsen, M. S.; Neaton, J. B. *Nano Lett.* **2007**, *7* (11), 3477–3482. doi:10.1021/nl072058i. PMID:17900162.
(18) (a) Jahan, N.; Paul, N.; Petropolis, C. J.; Marangoni, D. G.; Grindley, T. B. *J. Org. Chem.*, **2009**, *74* (20), 7762–7773. doi:10.1021/jo9018107.; (b) Tran, T.; Jahan, N.; Marangoni, D. G.; Grindley, T. B. Manuscript in preparation.
(19) Liu, F.; Wechsler, D.; Zhang, P. *Chem. Phys. Lett.* **2008**, *461* (4-6), 254–259. doi:10.1016/j.cplett.2008.07.029.
(20) Ankudinov, A. L.; Ravel, B.; Rehr, J. J.; Conradson, S. D. *Phys. Rev. B* **1998**, *58* (12), 7565–7576. doi:10.1103/PhysRevB.58.7565.
(21) Cook, S. C.; Padmos, J. D.; Zhang, P. *J. Chem. Phys.* **2008**, *128* (15),o. 154705. doi:10.1063/1.2901034. PMID:18433256.
(22) Liu, Q.; Guo, M. L.; Nie, Z.; Yuan, J. B.; Tan, J.; Yao, S. Z. *Langmuir* **2008**, *24* (5), 1595–1599. doi:10.1021/la702978z. PMID:18237211.
(23) Zhong, L.; Jiao, T.; Liu, M. H. *Langmuir* **2008**, *24* (20), 11677–11683. doi:10.1021/la802338f. PMID:18823092.
(24) Zana, R.; Talmon, Y. *Nature* **1993**, *362* (6417), 228–230. doi:10.1038/362228a0.
(25) Danino, D.; Talmon, Y.; Zana, R. *Langmuir* **1995**, *11* (5), 1448–1456. doi:10.1021/la00005a008.
(26) Hoft, R. C.; Ford, M. J.; McDonagh, A. M.; Cortie, M. B. *J. Phys. Chem. C* **2007**, *111* (37), 13886–13891. doi:10.1021/jp072494t.
(27) Király, Z.; Findenegg, G. H.; Mastalir, A. *Langmuir* **2006**, *22* (7), 3207–3213. doi:10.1021/la053184+. PMID:16548579.
(28) Lin, X. M.; Sorensen, C. M.; Klabunde, K. J. *Chem. Mater.* **1999**, *11* (2), 198–202. doi:10.1021/cm980665o.
(29) Leff, D. V.; Brandt, L.; Heath, J. R. *Langmuir* **1996**, *12* (20), 4723–4730. doi:10.1021/la960445u.
(30) Knag, M.; Sjoblom, J.; Gulbrandsen, E. *J. Disper. Sci. Tech. (Paris)* **2005**, *26* (2), 207–215. doi:10.1081/DIS-200045595.
(31) Frenkel, A. I.; Hills, C. W.; Nuzzo, R. G. *J. Phys. Chem. B* **2001**, *105* (51), 12689–12703. doi:10.1021/jp012769j.
(32) Davis, R. J.; Boudart, M. *J. Phys. Chem.* **1994**, *98* (21), 5471–5477. doi:10.1021/j100072a012.
(33) Harada, M.; Asakura, K.; Toshima, N. *J. Phys. Chem.* **1993**, *97* (19), 5103–5114. doi:10.1021/j100121a042.

Synthesis and properties of ionic liquids based on 1-methyl-3-(2-phenethyl)imidazolium

Hossein Fakhraian and Azam Gorgi-douze

Abstract: The synthesis and properties of three ionic liquids based on 1-methyl-3-(2-phenethyl)imidazolium cation ([MPIm]) and the chloride, tetrafluoroborate, and hexafluorophosphate anions have been investigated. The proposed quaternization and anion exchange processes afforded quantitative amounts of the three ionic liquids, and very pure [MPIm][BF_4] and [MPIm][PF_6] were obtained after recrystallization from ethanol. [MPIm][BF_4] showed low melting point and high electrical conductivity. These ionic liquids (immiscible with diethyl ether but miscible with water and DMSO) absorb air moisture, increasing their mass and decreasing their viscosity. The results of NMR spectroscopy (^{1}H, ^{13}C, and ^{19}F) and X-ray structure determination confirm the possibility of ion-pair and hydrogen-bond formation in [MPIm][BF_4].

Key words: ionic liquid, 1-methyl-3-(2-phenethylimidazolium), X-ray diffraction, tetrafluoroborate, hexafluorophosphate.

Résumé : La synthèse et les propriétés de trois liquide ioniques basés sur le cation de 1-méthyl-3-(2-phénéthyl)imidazolium ([MPIm]) et des anions comme chlorude, tétrafluoroborate et hexafluorophosphate ont été investigués. Le processus proposé pour les réactions de quaternization et d'échange d'anion a offert les trois liquide ioniques de façon quantitative et très pure [MPIm][BF_4] et [MPIm][PF_6] ont été obtenus après la cristallisation dans l'éthanol. [MPIm][BF_4] a montré le point de fusion bas et la conductivité électrique élevée. Ces liquide ioniques (immiscibles dans l'éther mais miscibles dans l'eau et le DMSO) absorbent l'humidité de l'air qui augmente leur poids et diminue leur viscosité. Les résultats de spectroscopie RMN (^{1}H, ^{13}C et ^{19}F) et la détermination de structure par rayon-X confirment la possibilité de la formation d'une paire d'ion et de la bande hydrogène dans [MPIm][BF_4].

Mots-clés : liquide ionique, 1-méthyl-3-(2-phénéthyl)imidazolium, Diffraction du rayon X, tetrafluoroborate, hexafluorophosphate.

Introduction

Intense research activity in the field of ionic liquids is currently in progress. Because the properties of ionic liquids (miscibility with water and other solvents, solvation ability, polarity, viscosity, density, and so forth) can be adjusted by an appropriate choice of the anion and cation, ionic liquids are often considered designer solvents.[1–5] Some of the applications of ionic liquids include their use as solvents for extraction processes and as electrolytes for batteries, fuel cells, and dye-sensitized solar cells.[6–8]

Functionalized imidazolium salts have applications, such as catalyst recycling, support for organic synthesis, and separation of specific metal ions from aqueous solution.[9–11] Bulky imidazolium cations such as 1-benzyl-3-methylimidazolium have been considered as a new class of stationary phase for gas chromatography.[12] The three ionic liquids 1-benzyl-3-methylimidazolium chloride, tetrafluoroborate, and hexafluorophosphate are commercially available (Sigma-Aldrich) and have mp of 70, 77, and 136 °C, respectively.[13] Asymmetric synthesis of the chiral 1-phenethyl analogue of methylimidazole has attracted attention due to the applications of these liquids in electrochemistry (capillary electrophoresis) and in asymmetric phase transfer catalysis.[14,15]

The formation of hydrogen bonds (CH···F) between the counterions imidazolium cation and $[BF_4]^-$ has been identified by analysis of the ^{13}C dipole–dipole relaxation rate.[16] Hydrogen bonding was found in BMImX (BMIm = butylmethylimidazolium) with X = BF_4 and PF_6, and the latter was recognized as a better hydrogen bond acceptor.[17] On the other hand, [BMIm][BF_4] was found to have dual (ionic polymer – ionic pair) behaviour.[18]

In this study, we have investigated the synthesis of three ionic liquids based on 1-methyl-3-(2-phenethyl)imidazolium cation ([MPIm]) and the chloride, tetrafluoroborate. and hexafluorophosphate anions and have studied their properties such as melting point, solvent miscibility, electrical conductivity (in aqueous solution), water uptake from air, NMR spectra characteristics, and X-ray structure.

Results and discussion

Previous reports on the quaternization of pyridine with 2-phenethylchloride have indicated that it does not take place under reflux conditions and microwave irradiation at normal pressure, but when the reaction is carried out in a closed vessel in a microwave digester (for 1 h at 200 °C and 56 psi), excellent yield of the product can be obtained.[19] This result is therefore extrapolated to apply to 1-methylimidazole without explicit experimental confirmation.

Received 20 April 2009. Accepted 6 July 2009. Published on the NRC Research Press Web site at canjchem.nrc.ca on 28 October 2009.

H. Fakhraian[1] and A. Gorgi-douze. Department of Chemistry, Imam Hossein University, Tehran, Iran.

[1]Corresponding author (e-mail: fakhraian@yahoo.com).

Scheme 1. Reaction conditions for the preparation of [MPIm][X] with X=BF_4 and PF_6.

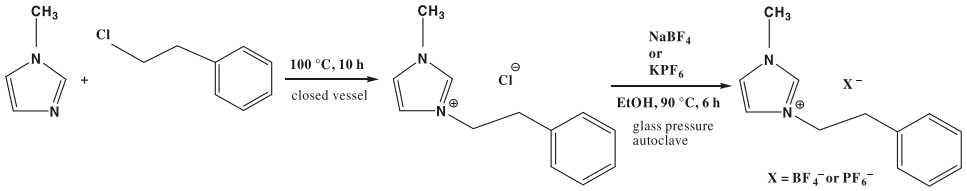

We have prepared 1-methyl-3-(2-phenethyl)imidazolium chloride ([MPIm][Cl], **1**) quantitatively via a solventless quaternization reaction between equimolar amounts of 1-methyl imidazol and 2-phenethyl chloride in a closed vessel at a temperature of 100 °C for 10 h (Scheme 1).

Anion exchanges of salt **1** with $NaBF_4$ and KPF_6 were performed successfully under soft conditions in ethanol (in a glass pressure autoclave at temperatures of 95 and 85 °C, respectively, for 6 h) and produced pure crystals of 1-methyl-3-(2-phenethyl)imidazolium tetrafluoroborate ([MPIm][BF_4], **2**) and 1-methyl-3-(2-phenethyl)imidazolium hexafluorophosphate ([MPIm][PF_6], **3**) after recrystallization from EtOH (Scheme 1). The purification of ionic liquids (especially the imidazolium salt of BF_4^-) formed by anion exchange presents its own set of problems, but in the cases of salts **2** and **3**, we have found EtOH to be an appropriate solvent for both their preparation and their purification.

The melting points, water uptake from the air, and electrical conductivities of these three ionic liquids are outlined in Table 1, and their solubilities in different solvents are presented in Table 2. [MPIm] contains an aromatic system in which the phenyl ring shows a high electron density including electron donor potential. The main lipophilic parts within this molecule are the methyl group and the phenyl structural element, but some lipophilicity also resides in the aromatic imidazolium ring. Salts **1**, **2**, and **3** are miscible with DMSO but immiscible with ether and $CHCl_3$ (Table 2). Salts **1** and **2** are miscible with water, but salt **3** is immiscible with water, consistent with other ionic liquids based on $[PF_6]^-$ as anion.

The most common impurities in ionic liquids are halide anions or unwanted cations inefficiently separated from the final product. The presence of impurities such as halide anions after anion exchange can be extremely detrimental to the performance of ionic liquids. This problem occurs more frequently in water-soluble ionic liquids. The first requirement for the preparation of colourless ionic liquids is that all starting materials used for the preparation of the cation should be distilled prior to use. Due to the non-volatile nature of ionic liquids, they cannot be purified by distillation. Purification is therefore usually carried out by dissolving the ionic liquid in acetonitrile or tetrahydrofuran (THF), treating it with activated charcoal for at least 24 h, and finally removing the solvent in vacuo.[7]

The miscibility difference of salt **1** with salts **2** and **3** in ethanol, along with the fact that salts **2** and **3** are immiscible with cold EtOH and miscible with hot EtOH, led us to the production of pure crystals of salts **2** and **3** with melting points of 61 and 112 °C, respectively.

Salts **1** and **2** were water miscible, and their aqueous solution showed interesting electrical conductivity compared to an aqueous solution of NaCl (Table 1) and other neat ionic liquids.[1] The lower electrical conductivity of salt **2** compared to salt **1** is consistent with the size of the anion in the two ionic liquids.

Table 1. Melting point, mass gain (Δw), and electrical conductivity of ionic liquids based on 1-methyl-3-(2-phenethyl)imidazolium.

Ionic liquid	Mp (°C)	Δw (%)[a]	Conductivity[b] ms/cm
[MPIm][Cl]	92	21	1.090
[MPIm][BF_4]	61	45	0.783
[MPIm][PF_6]	112	30	Immiscible

[a]Mass gain due to water uptake from air after 24 h.

[b]Electrical conductivities were measured in 0.2 mol/L aqueous solution at 25 °C. Electrical conductivities of distilled H_2O and 0.2 mol/L aqueous solution of NaCl in the same conditions were 0.04 and 1.994 ms/cm, respectively.

The other impurity likely to be present in the largest concentration in most ionic liquids is water. It has been stated that even a water-immiscible ionic liquid based on $[PF_6]^-$ as the anion can absorb up to 2 wt% water on equilibration with the air.[1] Water uptake from air, causing liquefaction and decreasing the viscosity of an ionic liquid at RT, was greater for salt **2** (Table 1). The order of increasing hydrophilicity with respect to the anion is $[BF_4]^- > [PF_6]^- > [Cl]^-$. The hydrophilicity of salt **3** (immiscible with water) is consistent with previous observations.[1]

Elemental analysis of salts **2** and **3** is consistent with calculated values for these salts (see the Experimental section). For salt **1**, elemental analysis is compatible with hydrated salt **1** (calculated for $C_{12}H_{15}N_2Cl$: C 64.72, H 6.74, N 12.58; calculated for $C_{12}H_{15}N_2Cl$ (H_2O): C 59.87, H, 7.07, N 11.64; found: C 59.84, H 7.73, N 11.73). Water uptake from air by salt **1** was so fast that liquefaction was nearly instantaneous (in a few minutes), and we were unable to send salt **1** for elemental analysis before water absorption.

The chemical shifts in both ^1H and ^{13}C NMR spectra of 1-methyl-3-(2-phenethyl)imidazolium salts containing $[Cl]^-$, $[BF_4]^-$ and $[PF_6]^-$ are presented in Tables 3 and 4. Anion exchange of salt **1** by $[BF_4]^-$ and $[PF_6]^-$ decreased the chemical shifts of H_a, H_b, and H_c but this effect is stronger for H_a and H_b. It seems that the interaction of the H_a atom with the relatively small and basic Cl^- is closer than its interaction with the larger and less basic $[BF_4]^-$ and $[PF_6]^-$. This is consistent with the idea of hydrogen bonding between H_a and these anions (as has been previously reported).[17]

The same observations have been made in ^{13}C NMR spectra of salts **1**, **2**, and **3**, in which all chemical shifts are fairly similar except for C_4 and C_9 in salt **2**, which showed $\Delta\delta$ of 0.5 and 0.9 ppm, respectively. The ^{19}F NMR spectra of salt **2** showed two peaks at –148.91 and –148.96 ppm with relative integrals of 20% and 80%, respectively. This situation persists in a threefold diluted solution of salt **2**, and the same multiplicity is observed for $NaBF_4$ in DMSO-d_6 and D_2O. The peak downshifted by 0.05 ppm is due to

Table 2. Miscibility of ionic liquids based on 1-methyl-3-(2-phenethyl)imidazolium in different solvents.

Ionic liquid	H_2O	DMSO	$CHCl_3$	Me_2CO	EtOAc	EtOH	Et_2O
[MPIm][Cl]	+	+	–	–	–	+	–
[MPIm][BF_4]	+	+	–	+	+	–	–
[MPIm][PF_6]	–	+	–	+	–	–	–

Table 3. Chemical shifts of protons in ^{1}H NMR spectrum of ionic liquids based on 1-methyl-3-(2-phenethyl)imidazolium.

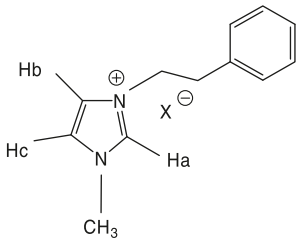

X	CH_3	Ha	Hb	Hc	Phenethyl
$[Cl]^-$	3.86	9.49	7.88	7.79	3.17 (t, J_{H-H} = 7.5 Hz, CH_2), 4.50 (t, J_{H-H}= 7.5 Hz CH_2), 7.23–7.34 (m, C_6H_5)
$[BF_4]^-$	3.87	9.05	7.55	7.71	3.18 (t, J_{H-H} = 7.5 Hz, CH2), 4.47 (t, J_{H-H} = 7.5 Hz CH_2), 7.25–7.38 (m, C_6H_5)
$[PF_6]^-$	3.82	9.01	7.70	7.65	3.14 (t, J_{H-H} = 7.5 Hz CH2), 4.44 (t, J_{H-H} = 7.5 Hz CH_2), 7.21–7.35 (m, C_6H_5)

Table 4. Chemical shifts of carbons in ^{13}C NMR spectrum of ionic liquids based on 1-methyl-3-(2-phenethyl)imidazolium.

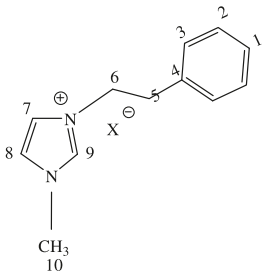

X	1	2	3	4	5	6	7	8	9*	10
$[Cl]^-$	127.2	129.3	128.9	137.1	35.9	50.1	123.8	122.8	137.3	36.2
$[BF_4]^-$	127.4	129.4	129.1	137.6	36.1	50.3	124.0	122.9	138.2	36.2
$[PF_6]^-$	127.5	129.3	129.3	137.1	36.0	50.4	124.1	122.9	137.5	36.3

fluorine on boron-10 (with isotopic abundance of 20%), as was previously reported.[20] The chemical shift of fluorine is consistent with the shifts reported for other ionic liquids with $[BF_4]^-$ as anion.[21]

The structure of the crystalline salt **2** was determined by X-ray single diffraction (Table 5, Fig. 1–3). The structural characteristics and ORTEP diagram of salt **2** (Fig. 1) were consistent with those of other imidazolium-based salts containing fluoroanions.[22] It crystallized in the monoclinic space group $P2_1$. Cross-sections of crystal packing (projection along *a* crystal axis) show that C–H···F bonded anion–cation layers are formed (Fig. 2 and 3). The shortened C–H···F contacts for salt **2** are C(2)–H(2)···F(4) (2.47 Å), C(4)–H(4)···F(1) (2.28 Å), C(5)–H(5)···F(2) (2.45 Å),and C(6)–H(6)···F(3) (2.40 Å) with C–H–F angles of 121°, 162°, 140°, and 162°, respectively. Thus it appears that the more acidic proton (H(4)) is engaged in a hydrogen bond with the $[BF_4]^-$ anion. This is also consistent with the ion pair formation model previously suggested for this type of ionic liquid in solution.[18]

Conclusion

In summary, the synthesis and properties of three ionic liquids based on 1-methyl-3-(2-phenethyl)imidazolium cation ($[MPIm]^+$) and chloride ($[Cl]^-$), tetrafluoroborate ($[BF_4]^-$) and hexafluorophosphate ($[PF_6]^-$) anions have been investigated. The neat (solventless) equimolar mixture of 1-methyl imidazole and phenethyl chloride was used for the quaternization reaction at a temperature of 100 °C for 10 h in a glass pressure autoclave, and quantitative amounts of [MPIm][Cl] were obtained. Afterward, anion exchange with $NaBF_4$ and KPF_6

Table 5. Crystal data and structure refinement for [MPIm][BF_4]

Empirical formula	$C_{12}H_{15}BF_4N_2$
Formula mass	274.07
Temperature (K)	100(2)
Wavelength (Å)	0.71073
Crystal system, space group	Monoclinic, $P2_1$
a (Å)	8.6560(4)
b (Å)	9.3496(5)
c (Å)	8.6566(4)
α, β, γ (°)	90.000, 112.211, 90.000
Volume (Å^3)	648.60(5)
Z, calculated density (g/cm^3)	2, 1.403
Absorption coefficient (mm^{-1})	0.123
F (000)	284
Crystal size (mm^3)	0.46×0.27×0.12
θ range for data collection (°)	2.54 to 30.00
Limiting indices	–12<h<12
	–13<k<13
	–12<l<12
Measured reflections	1996
Independent reflections	1917
Refinement method	Full matrix least-squares on F^2
Goodness-of-fit on F^2	1.062
Final R indices	R_1 = 0.0285, wR_2 = 0.0788
R indices (all data)	R_1 = 0.0301, wR_2 = 0.0799

Fig. 1. ORTEP diagram of [MPIm][BF_4].

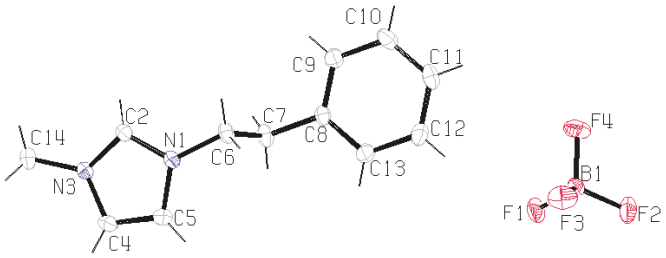

Fig. 2. Projection along a crystal axis of the crystal packing of salt **2**.

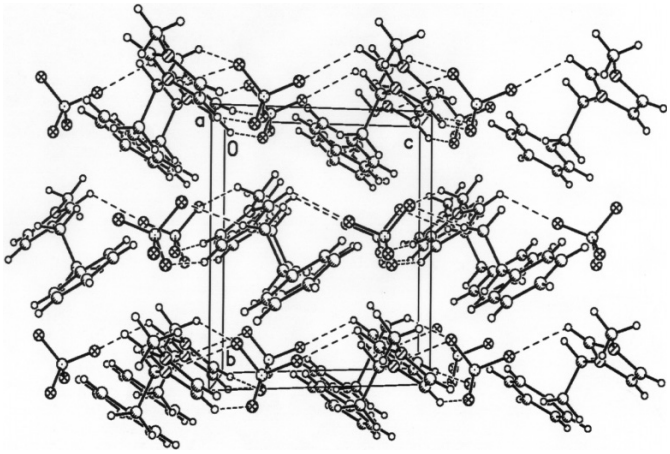

and finally recrystallization from ethanol produced very pure crystals of [MPIm][BF_4] and [MPIm][PF_6]. [MPIm][BF_4] showed a melting point of 60 °C and an electrical conductivity of 0783 ms/cm. These ionic liquids (immiscible with diethyl ether but miscible with water and DMSO) absorb air moisture, increasing their mass and decreasing their viscosity. Crystallographic analysis of [MPIm][BF_4] permitted us to identify the relative positions of the [BF_4]$^-$ anion and the CH–F bonded anion–cation layer in the crystal cell.

Experimental

General

NMR spectra were recorded on a Bruker DPX-250 instrument (250 MHz for ^{1}H, 62.5 MHz for ^{13}C, 100 MHz for ^{31}P, and 235 MHz for ^{19}F); DMSO-d_6 and D_2O were used as solvents; chemical shifts were reported in δ (ppm). Melting points were obtained on a Mettler FP61 apparatus. Conductivities of aqueous solutions of ionic liquids were measured by a Jenway 4060 apparatus at room temperature.

X-ray analysis

X-ray single diffraction analysis was performed on a colorless crystal of salt **2**. It was carried out on a Bruker SMART APEX II CCD area detector diffractometer (Mo-K_α radiation, graphite monochromator, λ = 0.71073) at 100.0(2) K. The structure was solved by a direct method using SHELXTL, V. 6.12.[23] The ORTEP diagram of salt **2** represents the atoms by thermal ellipsoids drawn at 50% probability level. See Supplementary data section for crystallographic data (excluding structure factors) for the structure of salt **2**.

Preparation of 1-methyl-3-(2-phenyl ethyl) imidazolium chloride([MPIm][Cl] (salt 1))

Quantities of 1-methyl imidazole (8.2 g, 8 mL, 0.1 mol) and 2-phenyl ethyl chloride (14.1 g, 13 mL, 0.1 mol) were placed in a 50 mL closed glass vessel equipped with a magnetic stir bar. The mixture was stirred at 100 °C for 10 h. The yellow solid formed was washed with ether (2 × 50 mL) at 100 °C in a glass autoclave to afford pure [MPIm][Cl]; mp 91–92 °C. ^{1}H NMR (DMSO) δ: 3.17 (t, $J_{H–H}$ = 7.5 Hz, CH_2), 3.86 (s, 3H, CH_3), 4.50 (t, $J_{H–H}$ = 7.5 Hz, CH_2), 7.23–7.34 (m, C_6H_5), 7.79 (s, 1H), 7.88 (s, 1H), 9.49 (s, 1H). ^{13}C NMR (DMSO) δ: 35.9, 36.2, 50.1, 122.8, 123.8, 127.2, 128.9, 129.3, 137.1, 137.3.

Preparation of 1-methyl-3-(2-phenyl ethyl) imidazolium tetrafluoroborate ([MPIm][BF_4] (salt 2))

[MPIm][Cl] (22.2 g, 0.1 mol), $NaBF_4$ (10.9 g, 0.1 mol), and ethanol (50 mL) were placed in a 150 mL glass pressure autoclave equipped with a magnetic stirrer. The solution was stirred at 95 °C for 6 h. Hot solution with suspended NaCl was filtered. Cooling the filtrate to RT caused precipitation of [MPIm][BF_4] which was recrystallized from ethanol to afford white crystals; mp 61–62 °C. ^{1}H NMR (DMSO-d_6) δ: 3.18 (t, $J_{H–H}$ = 7.5 Hz, CH_2), 3.87 (s, 3H, CH_3), 4.48 (t, $J_{H–H}$ = 7.5 Hz, CH_2), 7.25–7.38 (m, C_6H_5), 7.55 (s, 1H), 7.71 (s, 1H), 9.05 (s, 1H). ^{13}C NMR (DMSO-d_6) δ: 36.1, 36.2, 50.3, 122.9, 124.0, 127.4, 129.1, 129.4, 137.6, 138.2. ^{19}F NMR (DMSO-d_6) δ: –148.91 (20%, ^{19}F–^{10}B), –148.96 (80%, ^{19}F–^{11}B); (D_2O) δ: –150.74 (20%, ^{19}F–^{10}B), –150.79 (80%, ^{19}F–^{11}B). Anal. calcd. for $C_{12}H_{15}N_2BF_4$: C 52.55, H 5.47, N 10.22; found: C 52.28, H 5.83, N 9.85.

Fig. 3. Crystal packing diagrams of [MPIm][BF_4].

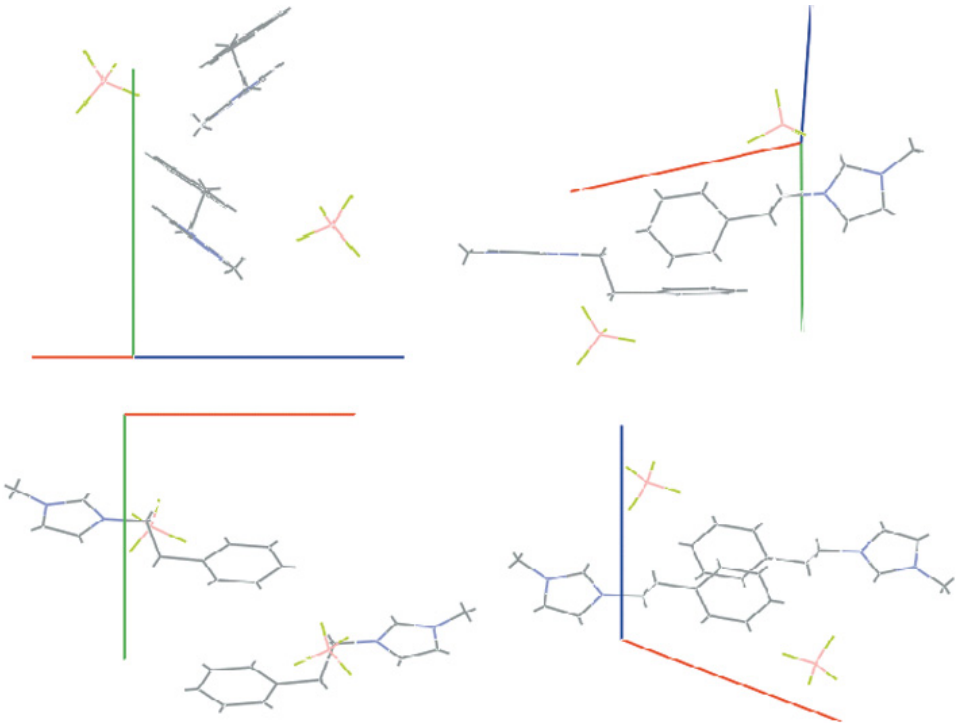

Preparation of 1-methyl-3-(2-phenyl ethyl) imidazolium hexafluorophosphate ([MPIm][PF_6] (salt 3))

[MPIm][Cl] (22.2 g, 0.1 mol), KPF_6 (18.4 g, 0.1 mol), and ethanol (50 mL) were placed in a 150 mL glass pressure autoclave equipped with a magnetic stirrer. The solution was stirred at 85 °C for 6 h. Hot solution with suspended NaCl was filtered. Cooling the filtrate to RT caused precipitation of [MPIm][PF_6] which was recrystallized from ethanol to afford white crystals; mp 112–113 °C. ^{1}H NMR (DMSO-d_6) δ: 3.14 (t, $J_{H–H}$ = 7.5 Hz, CH_2), 3.87 (s, 3H, CH_3), 4.44 (t, $J_{H–H}$ = 7.5 Hz, CH_2), 7.21–7.35(m, C_6H_5), 7.65 (s, 1H), 7.70 (s, 1H), 9.01 (s, 1H). ^{13}C NMR (DMSO-d_6) δ: 36.0, 36.3, 50.4, 122.9, 124.1, 127.5, 129.3, 129.3, 137.1, 137.5. ^{19}F NMR (DMSO-d_6) δ –70.58 (d, $J_{F–P}$ = 710 Hz). ^{31}P NMR (DMSO-d_6) δ: –143.70 (septet, $J_{F–P}$ = 710 Hz). Anal. calcd. for $C_{12}H_{15}N_2PF_6$: C 43.37, H 4.52, N 8.43; found: C 43.07, H 4.46, N 7.69.

Supplementary data

Supplementary data for this article are available on the journal Web site (canjchem.nrc.ca) or may be purchased from the Depository of Unpublished Data, Document Delivery, CISTI, National Research Council Canada, Ottawa, ON K1A 0R6, Canada. DUD 5316. For more information on obtaining material, refer to cisti-icist.nrc-cnrc.gc.ca/cms/unpub_e.shtml. CCDC 653740 contains the X-ray data in CIF format (crystallographic data (excluding structure factors) for the structure of salt **2**) for this manuscript. These data can be obtained, free of charge, via www.ccdc.cam.ac.uk/conts/retrieving.html (Or from the Cambridge Crystallographic Data Centre, 12 Union Road, Cambridge CB2 1EZ, UK; fax +44 1223 336033; or deposit@ccdc.cam.ac.uk).

References

(1) Wasserscheid, P.; Welton, T. *Ionic liquids in synthesis;* Wiley-VCH: Weinheim, 2002.

(2) Binnemans, K. *Chem. Rev.* **2005**, *105* (11), 4148–4204. doi:10.1021/cr0400919. PMID:16277373.

(3) Fredlake, C. P.; Crosthwaite, J. M.; Hert, D. G.; Aki, S. N. V. K.; Brennecke, J. F. J. *J. Chem. Eng. Data* **2004**, *49* (4), 954–964. doi:10.1021/je034261a.

(4) Papaiconomou, N.; Yakelis, N.; Salminen, J.; Bergman, R.; Prausnitz, J. M. J. *J. Chem. Eng. Data* **2006**, *51* (4), 1389–1393. doi:10.1021/je060096y.

(5) Wishart, J. F.; Lall-Ramnarine, S. I.; Raju, R.; Scumpia, A.; Bellvue, S.; Ragbir, R.; Engel, R. *Radiat. Phys. Chem.* **2005**, *72* (2-3), 99–104. doi:10.1016/j.radphyschem.2004.09.005.

(6) Galinski, M.; Lewandowski, A.; Stepniak, I. *Electrochim. Acta* **2006**, *51* (26), 5567–5580. doi:10.1016/j.electacta.2006.03.016.

(7) Jain, N.; Kumar, A.; Chauhan, S.; Chauhan, S. M. S. *Tetrahedron* **2005**, *61* (5), 1015–1060. doi:10.1016/j.tet.2004.10.070.

(8) Yanes, E. G.; Gratz, S. R.; Baldwin, M. J.; Robison, S. E.; Stalcup, A. M. *Anal. Chem.* **2001**, *73* (16), 3838–3844. doi:10.1021/ac010263r. PMID:11534705.

(9) Sang-gi, L. *Chem. Commun.* **2006**, 1049. doi:10.1039/b514140k.

(10) Angell, C. A.; Xu, W.; Bellieres, J. P.; Yoshizawa, M. US patent 2007/0026295. 2007.

(11) Fields, M.; Huston, G. V.; Seddon, K. R.; Gordon, C. M. US patent 6,379,634. 2002.

(12) Anderson, J. L.; Armstrong, D. W. *Anal. Chem.* **2003**, *75* (18), 4851–4858. doi:10.1021/ac0345749. PMID:14674463.

(13) Sigma-Aldrich. Chemfiles Enabling Technologies Ionic Liquids. Vol. 5, No. 6, p. 18. Available from www.sigma-aldrich.com/ionicliquids (accessed 2 October 2009).

(14) Yathavakilla, S. Ph.D. thesis, University of Cincinnati. 2004.
(15) Lauth-de Viguerie, N.; Gorrichon, L. *Tetrahedron Asymmetry* **2005**, *16* (5), 1017–1023. doi:10.1016/j.tetasy.2005.01.014.
(16) Huang, J. F.; Chen, P. Y.; Sun, I. W.; Wang, S. P. *Inorg. Chim. Acta* **2001**, *320* (1-2), 7–11. doi:10.1016/S0020-1693(01)00477-7.
(17) Suarez, P. A. Z.; Einloft, S.; Dullius, J. E. L.; Souz, R. F.; Dupont, J. J. *J. Chim. Phys.* **1998**, *95* (7), 1626–1639. doi:10.1051/jcp:1998103.
(18) Katsuta, S.; Ogawa, R.; Yamaguchi, N.; Ishitani, T.; Takeda, Y. J. *J. Chem. Eng. Data* **2007**, *52* (1), 248–251. doi:10.1021/je060369p.
(19) Khadilkar, B. M.; Rebeiro, G. L. *Org. Process Res. Dev.* **2002**, *6* (6), 826–828. doi:10.1021/op025551j.
(20) Gillespie, R. J.; Hartman, J. S.; Parekh, M. *Can. J. Chem.* **1968**, *46* (10), 1601–1610. doi:10.1139/v68-268.
(21) Plakhotnyk, V. N.; Schmutzler, R.; Ernst, L.; Kovtun, Y. V.; Plakhotnyk, A. V. *J. Fluor. Chem.* **2002**, *116* (1), 41–44. doi:10.1016/S0022-1139(02)00072-6.
(22) Matsumoto, K.; Hagiwara, R. *J. Fluor. Chem.* **2007**, *128* (4), 317–331. doi:10.1016/j.jfluchem.2006.10.016.
(23) Sheldrick, G. M. *SHELXTL,* v. 6.12; Bruker AXS: Madison, WI, 2001.

AWARD LECTURE / CONFÉRENCE D'HONNEUR

Design and synthesis of some biologically interesting natural and unnatural products based on organosulfur and selenium chemistry

Thomas G. Back

Abstract: Organosulfur and selenium chemistry has provided fertile ground for the discovery of novel synthetic methodology and for the design of bioactive molecules with potential therapeutic applications. Thus, acetylenic sulfones have been employed in novel strategies for the synthesis of nitrogen heterocycles, including several biologically active alkaloids. The conjugate addition of nitrogen nucleophiles containing ester or chloroalkyl substituents to acetylenic sulfones was followed by base-mediated intramolecular alkylation or acylation to afford variously substituted piperidines, pyrrolizidines, indolizidines, quinolizidines, decahydroquinolines, and 4-quinolones. The products include the dendrobatid alkaloids (–)-pumiliotoxin C, indolizidines (–)-167B, 207A, 209B, and 209D, as well as (–)-(*ent*)-julifloridine, (–)-lasubine II, myrtine, and two recently discovered alkaloids from the medicinal plant *Ruta chalepensis*, which had not been previously synthesized. Acetylenic sulfones were also incorporated on solid supports and employed in the types of cyclizations mentioned above, as well as for Diels–Alder reactions and a large variety of 1,3-dipolar cycloadditions. Conjugate additions of tertiary cyclic α-vinyl amines to acetylenic sulfones generated zwitterions that underwent exceptionally facile formal aza-Cope rearrangements to afford ring-expanded macrocyclic amines. An iterative version was developed and used in the synthesis of motuporamine A and B. With respect to organoselenium chemistry, two classes of compounds are described that function as novel mimetics of the selenoenzyme glutathione peroxidase (GPx), which protects cells from oxidative stress caused by the formation of peroxides during aerobic metabolism. They include cyclic seleninates and spirodioxyselenuranes, both of which efficiently catalyze the reduction of peroxides with thiols and are of potential value in the mitigation of oxidative stress. Their aromatic derivatives are generally less effective catalysts, but substituent effects can be used to modulate their activities. The mechanism of their catalytic cycles has been elucidated and Hammett plots indicate that the oxidation of Se(II) to Se(IV) is the rate-determining step for both classes. A methoxy-substituted aromatic spirodioxyselenurane provided the fastest rate for a small-molecule selenium compound that we have observed to date for the reduction of hydrogen peroxide with benzyl thiol.

Key words: acetylenic sulfones, conjugate addition, intramolecular alkylation and acylation, alkaloid synthesis, aza-Cope reaction, solid-phase organic synthesis, glutathione peroxide mimetics, cyclic seleninates, spirodioxyselenuranes.

Résumé : La chimie des composés organiques du soufre et du sélénium a fourni un champ fertile pour la découverte d'une nouvelle méthodologie de synthèse et de développement de molécules bioactives possédant des applications thérapeutiques potentielles. Ainsi, les sulfones acétyléniques ont été utilisés dans de nouvelles stratégies pour la synthèse d'hétérocycles azotés, dont plusieurs alcaloïdes biologiquement actifs. L'addition conjuguée de nucléophiles azotés comportant des substituants esters ou chloroalkyles sur des sulfones acétyléniques a été suivie par des alkylations ou des acylations intramoléculaires catalysées par des bases qui ont conduit à la formation des diverses pipéridines, pyrrolizidines, indolizidines, quinolizidines, décahydroquinoléines et 4-quinolones. Les produits incluent les alcaloïdes dendrobatides (–)-pumiliotoxine C, indolizidines (–)-176B, 207A, 209B et 209D, ainsi que la (–)-(*ent*)-julifloridine, la (–)-lasubine II, la myrtine et deux alcaloïdes découverts récemment à partir de la plante médicinale *Ruta chalepensis* et qui n'avaient pas été synthétisés antérieurement. Les sulfones acétyléniques ont aussi été incorporées sur des supports solides et utilisés dans les réactions de cyclisations mentionnées plus haut ainsi que dans des réactions de Diels-Alder et une grande variété de réactions de cycloadditions 1,3-dipolaires. Les additions conjuguées d'amines α-vinyliques cycliques tertiaires à des sulfones acétyléniques conduisent à des zwitterions qui subissent des réarrangements formels azo-Cope exceptionnellement faciles qui fournissent des amines macrocycliques avec expansion de cycle. Une version itérative a été développée et utilisée dans la synthèse des motuporamines A et B. Pour ce

Received 20 April 2009. Accepted 20 July 2009. Published on the NRC Research Press Web site at canjchem.nrc.ca on 20 November 2009.

Based on the Alfred Bader Award Lecture presented at the 91st Canadian Society for Chemistry Conference, Edmonton, Alberta, May 27, 2008.

T.G. Back. Department of Chemistry, University of Calgary, Calgary, AB T2N 1N4, Canada (e-mail: tgback@ucalgary.ca).

qui est de la chimie des composés organiques du sélénium, on décrit deux classes de composés qui fonctionnent comme de nouveaux mimétiques du sélénoenzyme peroxydaze du glutathion « GPx » qui protège les cellules contre la tension oxydante causée par la formation de peroxydes durant le métabolisme aérobie. Elles comprennent les séléninates et les spirodioxysélénuranes cycliques qui catalysent tous les deux la réduction des peroxydes avec des thiols et qui ont une valeur potentielle dans la mitigation de la tension oxydante. Leurs dérivés aromatiques sont généralement moins efficaces comme catalyseurs, mais les effets de substituant peuvent être utilisés pour moduler leurs activités. On a élucidé le mécanisme de leurs cycles catalytiques et les courbes de Hammett indiquent que, pour chacune des deux classes, l'oxydation du Se(II) au Se(IV) correspond à l'étape cinétiquement limitante. Pour la réaction de réduction du peroxyde d'hydrogène à l'aide de benzylthiol, de tous les composés à base de petites molécules contenant du sélénium, la vitesse la plus rapide a été obtenue avec un spirodioxysélénurane aromatique portant un substituant méthoxy.

Mots-clés : sulfones acétyléniques, addition conjuguée, alkylation et acylation intramoléculaire, synthèse d'alcaloïdes, réaction aza-Cope, synthèse organique en phase solide, mimétiques du peroxyde de glutathion, séléninates cycliques, spirodioxysélénuranes.

[Traduit par la Rédaction]

Introduction

Organosulfur and selenium chemistry has played a prominent role in our laboratory, both in the development of new synthetic methodology and in the design of biologically interesting compounds containing these elements. The first part of this article describes several novel protocols based on acetylenic sulfones for the synthesis of a broad range of nitrogen heterocycles. These include various types of alkaloids, some of which display potentially useful medicinal properties. In the latter section, the design and synthesis of several types of small-molecule selenium compounds that emulate the selenoenzyme glutathione peroxidase are described. This enzyme plays a crucial role as a biological antioxidant, which protects cells of living organisms against oxidative stress by catalyzing the reduction of harmful peroxides with the tripeptide glutathione.

Organosulfur chemistry: synthesis of nitrogen heterocycles using acetylenic sulfones

The electron-withdrawing sulfonyl group in acetylenic sulfones **1**,[1,2] as well as in other types of unsaturated sulfones,[3,4] renders these compounds excellent dienophiles and dipolarophiles. It also promotes the conjugate additions of various types of nucleophiles to the β-position and stabilizes anions at the α-position. In this way, unsaturated sulfones behave in a comparable manner to that of unsaturated carbonyl compounds. However, unlike the latter species, where the presence of the carbonyl moiety is generally desired in the product, the sulfonyl group is typically cleaved at the end of such transformations by a variety of reductive, oxidative, or cross-coupling procedures.[5] The sequence of conjugate addition, α-alkylation or acylation, and desulfonylation therefore renders the acetylenic sulfone the synthetic equivalent of the hypothetical dipole species **2** (Scheme 1). The possibility of performing the conjugate addition in tandem with an intramolecular alkylation or acylation step suggests a variety of novel cyclization protocols.

First, however, one requires a reliable source of acetylenic sulfones for such studies and, fortunately, several versatile methods for preparing these compounds are available.[2] We have found the procedure shown in Scheme 2, which we named "selenosulfonation",[6] to be particularly convenient for this purpose. The dropwise addition of a readily available sulfonhydrazide **3** in methanol solution to a stirred methanolic solution of commercially available benzeneseleninic acid (**4**) at 0 °C results in the evolution of nitrogen and the crystallization in high yield of the corresponding selenosulfonate **5** directly from the reaction mixture as an odourless, yellow solid.[7] When the selenosulfonate is heated with an acetylene in the presence of a radical initiator, or subjected to photoinitiation, a highly regio- and stereo-selective 1,2-addition is observed. Homolytic cleavage of the S–Se bond of **5** takes place, followed by addition of the sulfonyl radical to the terminus of the acetylene. The intermediate vinyl radical **6** then undergoes rapid chain transfer with additional **5**, resulting in an overall anti addition to produce **7**, with accompanying generation of a new sulfonyl radical to propagate the chain. The addition product, in which the vinylic hydrogen and the phenylseleno group are cis-oriented, is then subjected to oxidation with MCPBA or hydrogen peroxide, followed by a selenoxide syn-elimination to afford the desired product **1**.[8] There is a strong preference for the formation of the acetylene, instead of the corresponding allene, even when the substituent R is an alkyl group containing available hydrogens for syn-elimination.

Several typical cyclizations via the conjugate addition–intramolecular alkylation/acylation pathway of acetylenic sulfones are shown in Scheme 3. For example, when a primary amine containing a chloroalkyl substituent is employed as the nucleophile, the adduct **8** is obtained in generally excellent yield in a variety of solvents. The product **8** in THF is then typically cooled to –78 °C and excess LDA in THF is added to generate a sulfone-stabilized enamide anion by abstraction of the acidic N–H proton. After ~15–30 min, the reaction is quenched with water to afford the corresponding dehydropiperidine **9**.[9,10] The use of THF in both the conjugate addition and cyclization steps results in a particularly convenient one-pot procedure for obtaining **9**, as the solution of **8** is simply cooled to –78 °C prior to the addition of LDA. The chloroalkylamines can be stored indefinitely, as their hydrochloride salts and the free bases are liberated prior to use. Similarly, amino esters can be cyclized via intramolecular acylation of addition products **10** to produce enaminones **11**. In the case of cyclic secondary amines, the

Scheme 1.

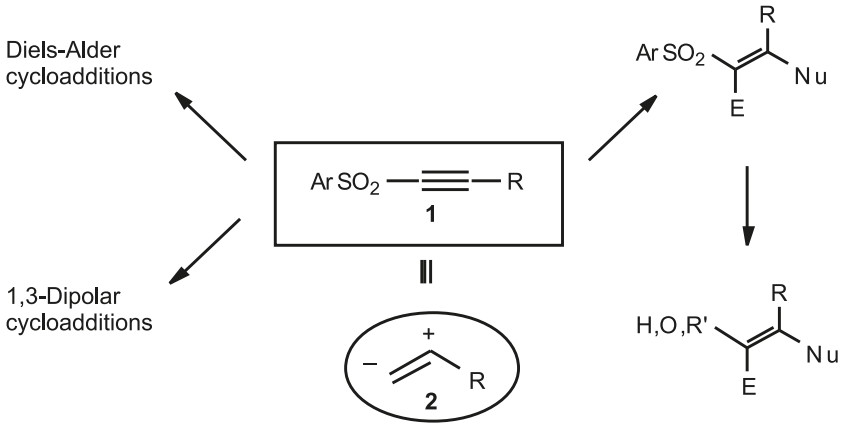

Scheme 2.

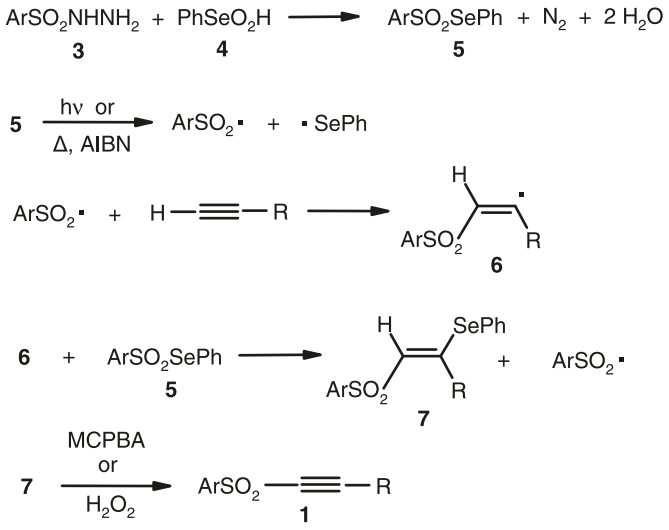

addition products **12** lack the acidic N–H proton present in **8** and **10**. However, providing that the substituent R contains a hydrogen atom in the γ-position (relative to the sulfonyl substituent), then cyclization can be effected via the corresponding sulfone-stabilized allyl anion, which reacts with high regioselectivity at its α-position. The ring sizes of the bicyclic products **13** are determined by the size of ring in the starting amine and by the length of the pendant chloroalkyl substituent. To date, we have only investigated *n*, *m* = 1 or 2, but it is entirely possible that other ring sizes could also be prepared in this manner. Intramolecular acylation can be effected similarly, starting with cyclic amines containing ester substituents. It is also worth noting that the precursor amines are typically prepared from amino acids and the stereocenters in the latter are incorporated intact into the cyclized products, where they may be used to control the configurations of new stereocenters developed in subsequent steps. In this way, we have prepared series of pyrrolizidines **14** (*n*, *m* = 1),[9] indolizidines **15** or **16** (*n* = 1, *m* = 2 or *n* = 2, *m* = 1),[9] and quinolizidines **17** (*n*, *m* = 2),[9] as well as decahydroquinolines **18**[11] and 4-quinolones **19**[12] by minor variations of the protocol. These core structures are shown in Fig. 1, after appropriate desulfonylation and reduction, with the part originating from the acetylenic sulfone indicated in bold. Several illustrative examples of the syntheses of natural products containing these ring systems follow.

The dendrobatid alkaloids are found in the toxic skin secretions of certain species of neotropical frogs that are found principally in the rain forests of Central and South America.[13] These compounds serve as a chemical defense against predators, and the skin secretions are employed by indigenous tribes as coatings for blowgun darts and arrows to enhance their effectiveness in hunting. Over 800 dendrobatid alkaloids have been identified,[14] largely through the lifelong efforts of the late John Daly, and many contain the types of ring systems that we envisaged as possible products via Scheme 3. When used individually, and at appropriate doses, some dendrobatid alkaloids display potentially useful pharmacological properties, including cardiotonic, analgesic, and neuroregulatory activity. They are therefore of interest as leads in drug discovery and as biochemical tools. Moreover, many dendrobatid alkaloids occur naturally in but trace amounts, and their structures have only been tentatively identified, often based solely on GC–MS data. Thus, their synthesis has attracted considerable attention because of possible medicinal applications and to verify their assigned structures.

(–)-Pumiliotoxin C (**27**) was first isolated from the frog *Dendrobates pumilio* by Daly et al.[15] Although it is one of the most abundant dendrobatid alkaloids, only 80 mg of **27** were isolated from 2540 frogs collected in Panama,[16] and this compound has therefore been the subject of numerous synthetic efforts.[17] Our approach to pumiliotoxin C is illustrated in Scheme 4. The amino ester **20** is available as a single enantiomer.[11b,18] Conjugate addition of **20** to acetylenic sulfone **21** was effected in the usual manner, and cyclization of **22** by intramolecular acylation occurred without epimerization of the ester substituent via its enolate. Conversion of the product enaminone **23** to the intermediate enol triflate **24** was followed, without isolation of the latter, by stereoselective hydrogenation from the exo face and simultaneous hydrogenolysis of the C–O bond. The major diastereomer, in the form of the easier-to-handle Cbz derivative **26**, was then desulfonylated with sodium amalgam and deprotected to afford (–)-pumiliotoxin C (**27**) as a pure enantiomer.[11b] This

Scheme 3.

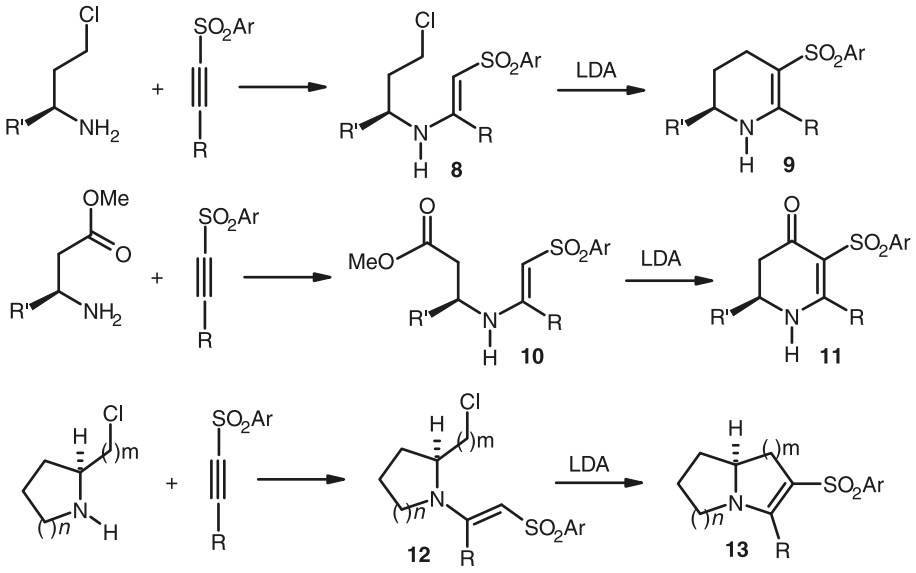

Fig. 1. Bicyclic nitrogen heterocycles produced from acetylenic sulfones.

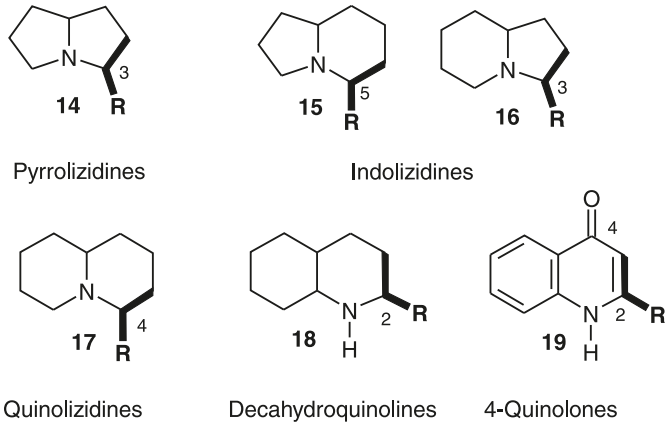

provided a concise and relatively efficient synthesis of the alkaloid from the key intermediates **20** and **21**.

The dendrobatid alkaloid family also includes numerous examples of substituted indolizidines,[14,19] several of which proved amenable to synthesis via cyclizations of acetylenic sulfones. Thus, indolizidines (–)-167B (**33**) and (–)-209D (**34**) were easily prepared from 2-(2-chloroethyl)pyrrolidine (**29**), which was in turn obtained from L-proline (Scheme 5).[9] Thus, conjugate addition of **29** to acetylenic sulfones **21** and **30**, followed by treatment with LDA to effect intramolecular alkylation, afforded dehydroindolizidines **31** and **32**, respectively. Stereoselective reduction of the enamine double bond via the corresponding iminium ion, followed by reductive desulfonylation under Birch conditions, provided the two alkaloids **33** and **34** as pure enantiomers in high overall yield. Similarly, the homologated proline derivative **35** was prepared by the method of Lhommet et al.[20] and converted into chloroalkylamine **36**. The latter compound was then used to obtain the 5,8-disubstituted indolizidines (–)-209B (**39**) and (–)-207A (**43**) via a similar sequence of steps, as shown in Scheme 6.[9]

The synthesis of the quinolizidine alkaloid (–)-lasubine II (**50**) from the homologated pipecolic acid derivative **44** and the acetylenic sulfone **45** by this protocol (Scheme 7) posed an additional challenge. As seen earlier, the base-mediated cyclization step proceeds via a sulfone-stabilized enamide anion formed by abstraction of the remaining N–H proton when a primary amine is used (as in **22** in Scheme 4), or via a sulfone-stabilized allyl anion formed by deprotonation of the γ-position of the sulfone in cases where a secondary amine is employed (as in the preparation of the indolizidine products in Schemes 5 and 6). Since amine **44** is secondary and the acetylenic sulfone contains an aromatic substituent, the conjugate addition product **46** lacks both N–H and γ-protons. Cyclization is therefore contingent upon the formation of the corresponding sulfone-stabilized vinyl anion preferentially to that of the ester enolate of **46**, upon treatment with LDA. Fortunately, it appears that the acidity of the vinyl sulfone is at least comparable to that of the ester and the desired cyclization to **47** was achieved, albeit in somewhat lower yield than usual. We hoped that the reduction of the enamine double bond in **47** could be performed simultaneously with stereoselective reduction of the ketone function to the axial alcohol. However, a variety of reducing agents that were investigated failed to provide the desired outcome. The enamine and ketone were therefore reduced with sodium borohydride, which afforded the product as a mixture of inseparable alcohol epimers. These were reoxidized back to the ketone and a more hindered reducing agent, L-selectride, with a stronger preference for equatorial approach, then afforded the axial alcohol required in the final product **50** with high stereoselectivity.[21] A similar approach to the quinolizidine alkaloid myrtine was also successful.[21b]

We next explored the possibility of using anthranilic esters to produce 4-quinolones by conjugate additions to acetylenic sulfones, followed by intramolecular acylation. The 4-quinolone structure comprises the core of numerous compounds that display a remarkable variety of biological activities.[22,23] Perhaps, the best known is the antibacterial agent ciprofloxacin, which inhibits bacterial topoisomerase and is

Scheme 4.

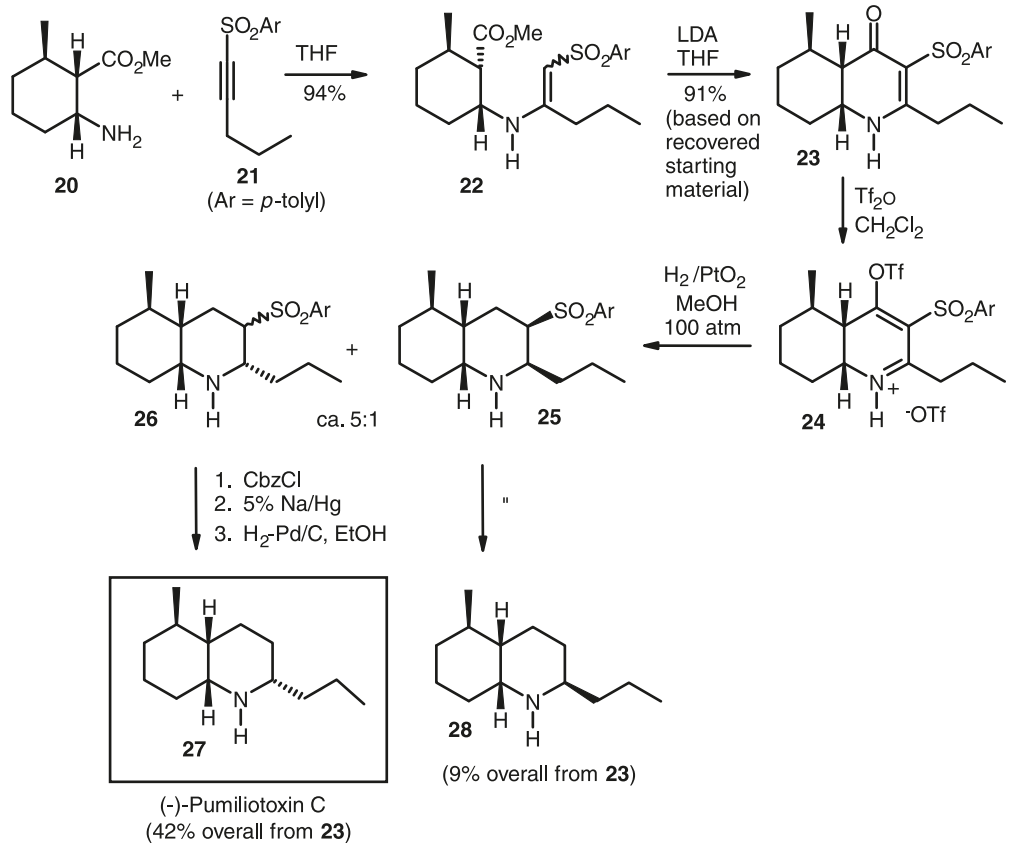

Scheme 5.

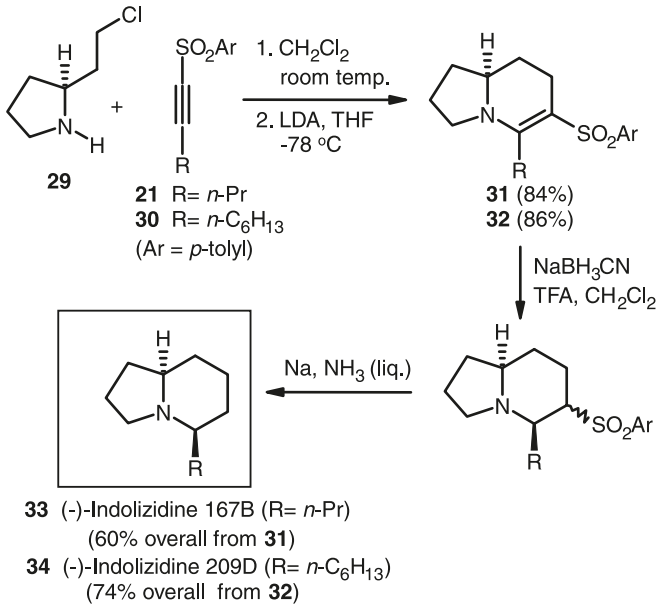

Scheme 6.

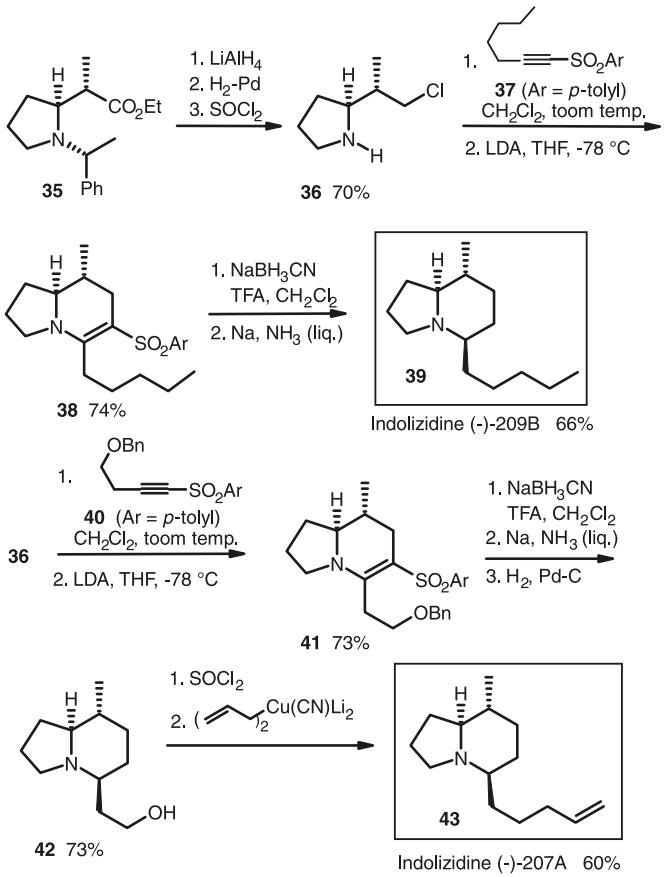

currently among the most widely prescribed antibiotics. A few other representative 4-quinolones and their principal bioactivities are shown in Fig. 2.[24–26] The principal difficulty in our approach to these target molecules lies in the doubly deactivated aniline amino group, where the lone pair is delocalized not only by the aromatic ring, but also by the ester substituent required for the cyclization step. After considerable effort at optimization, it was found that the conjugate

Fig. 2. Examples of bioactive 4-quinolones.

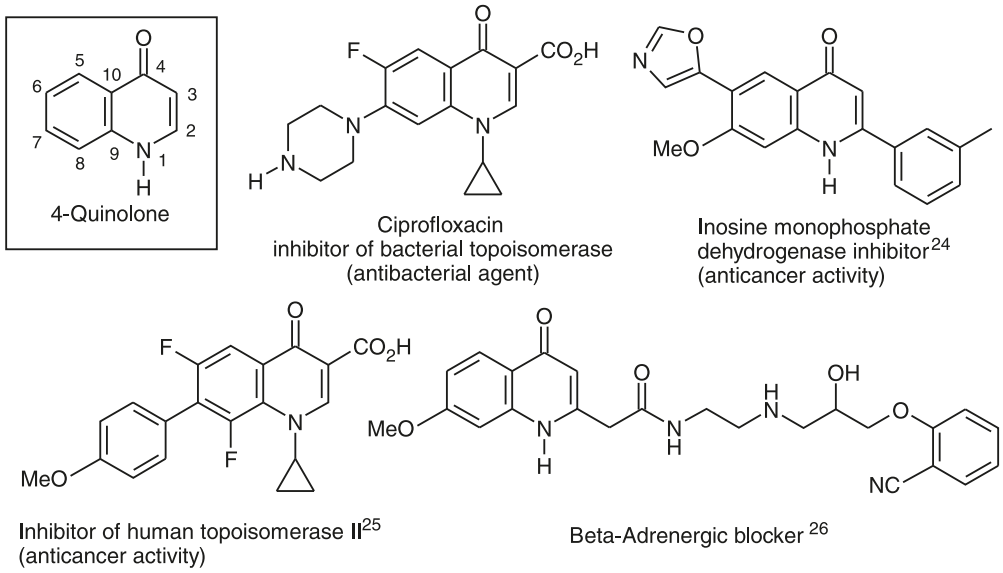

Scheme 7.

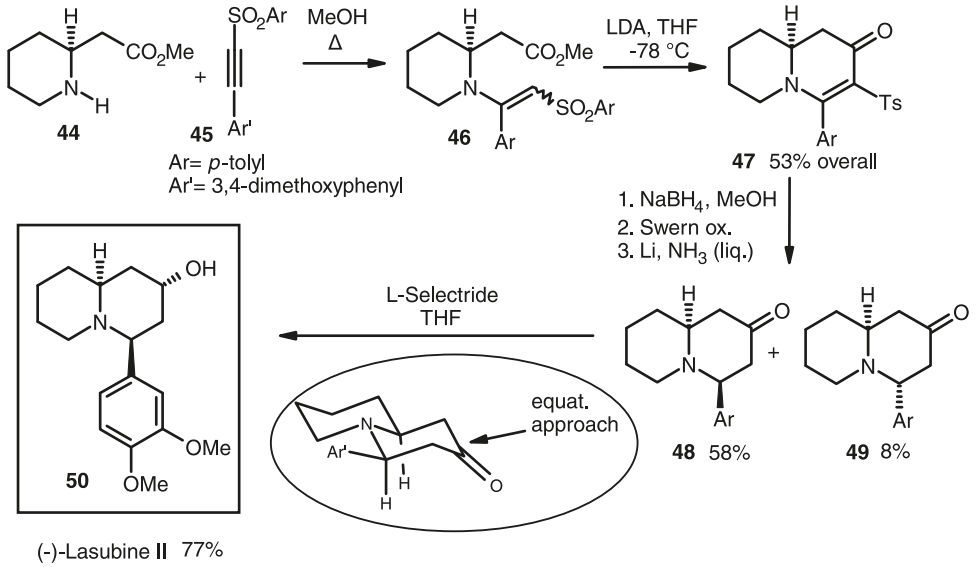

base of the *N*-formyl anthranilate **51** could be added to acetylenic sulfone **37** under the conditions indicated in Scheme 8.[12b] However, the sluggish reaction rate and competing polymerization of the acetylenic sulfone necessitated the use of excess **37**. Furthermore, the presence of DMAP was required, and even under precisely optimized conditions, the best yield of the addition product **52** was only 57%. It was therefore evident that the process in this form would not be of general synthetic utility. Finally, it was also noted that product **52** contained an allyl sulfone moiety instead of being formed as the typically observed vinyl sulfone isomer, which was present in only trace amounts.

While it was tempting to assume that the allyl sulfone **52** was produced by prototropic isomerization of the initially formed, but thermodynamically less stable vinyl sulfone, further investigation revealed that this was not the case.[12b] An authentic sample of the vinyl sulfone **53** was subjected to the same conditions under which **52** had been obtained, and it was observed that the isomerization was too slow to account for the formation of **52** as the main product in Scheme 8. Furthermore, a control experiment with acetylenic sulfone **37** in the absence of amine **51** showed that it isomerized readily to its allenic counterpart **54** under the basic conditions of Scheme 8, followed by further isomerization to the propargylic isomer **55** (Scheme 9). Finally, it was observed that authentic allene **54** reacted with amine **51** considerably faster than did acetylene **37**. Thus, the pathway for the reaction of the poorly nucleophilic aniline derivative **51** with acetylenic sulfone **37** proceeds via the prior isomerization of **37** to its allenic isomer **54**, followed by conjugate addition of **51** to the latter and not by the initial conjugate addition of amine **51** to acetylene **37**, with subsequent isomerization of the vinyl adduct **53** to the observed allyl product **52**. The propargylic sulfone **55** is inert toward conjugate addition, but can slowly regenerate the more reactive allenic sulfone through further equilibration, as shown in Scheme 9.

Scheme 8.

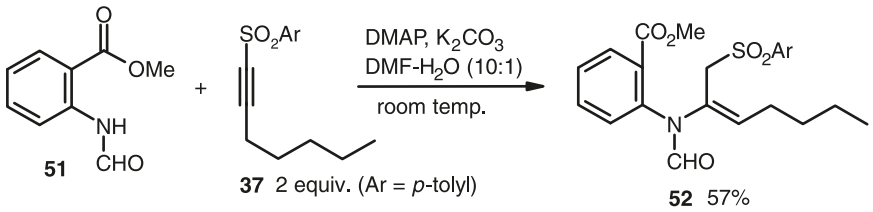

Scheme 9.

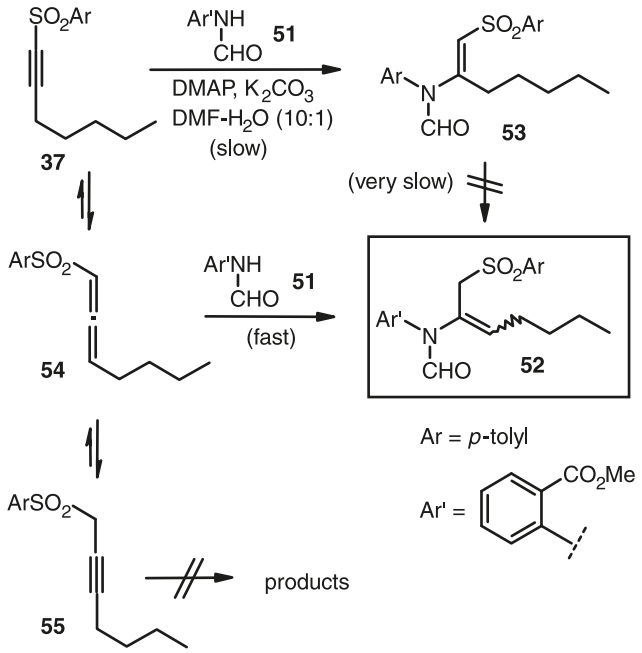

Scheme 10.

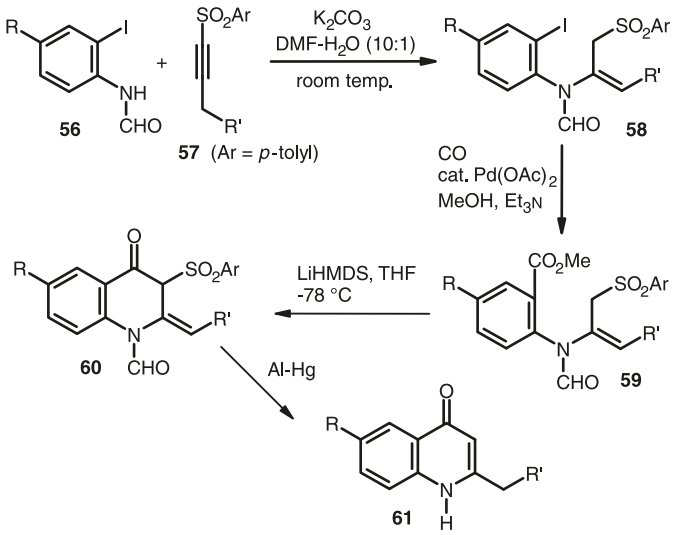

The complexity and limitations of the above method prompted us to develop an improved procedure, based on the enhanced nucleophilicity of the conjugate bases of *N*-formyl-*o*-iodoanilines compared with those of the corresponding anthranilate esters such as **51** in Scheme 8.[12b] For example, iodoaniline **56** (R = H) added smoothly to equimolar amounts of acetylenic sulfone **57** (R = *n*-pentyl), without the need for DMAP, affording the corresponding **58** in the improved yield of 81%. Similar conjugate additions of substituted *o*-iodoanilines **56** with other acetylenic sulfones **57** proved equally effective. The ester moiety required for the subsequent cyclization step was then introduced into **58** by a palladium-catalyzed carbonylation reaction.[27] Cyclization of the latter products **59** to **60** was effected with LiHMDS, while simultaneous desulfonylation, deformylation, and isomerization of the double bond into conjugation with the carbonyl group was carried out in one step with aluminum amalgam. This procedure proved widely applicable to variously substituted *o*-iodoanilines, including one already containing an ester moiety (i.e., **56**, R = CO_2Me), leading to an efficient and concise route to 4-quinolones **61** (Scheme 10). Of special note is the preparation of **61** with R = H and R′ = *n*-Bu from iodoaniline **56** (R = H) and acetylenic sulfone **37** in 40% overall yield.[12b] This compound had been isolated from a marine pseudomonad by Andersen and co-workers[28] and exhibits antibiotic and other bioactivities.[28,29] An X-ray crystal structure confirmed the presence of the 4-quinolone tautomer, as opposed to the corresponding pyridinol.[12b]

In 2000, quinolone **64** and quinoline **65** were isolated from the medicinal plant *Ruta chalepensis* by El-Sayed et al.[30] Extracts of this plant are used in the Middle East as antispasmodic and antirheumatic agents. The synthesis of these natural products was easily completed via the general protocol shown in Scheme 10. Thus, *N*-formyl-*o*-iodoaniline (**56**, R = H) and acetylenic sulfone **62** were converted to **63** in 71% overall yield via the usual three-step sequence of conjugate addition, palladium-catalyzed carbonylation, and base-mediated cyclization. Treatment of **63** with aluminum amalgam then afforded the 4-quinolone alkaloid **64** and O-alkylation produced the corresponding methoxyquinoline **65** in yields of 68% and 75%, respectively (Scheme 11). This represents the first synthesis of these two alkaloids.[12]

The success of the above cyclizations prompted us to explore ways in which acetylenic sulfones could be immobilized on polymer supports, since solid-phase variations of these processes might lend themselves to the production of small libraries of nitrogen heterocycles (Scheme 12).

Commercially available Merrifield resin was first converted to the polymer-supported carboxylic acid **66** by a literature method.[31a] The benzylic bromide **67** was then prepared by selenosulfonation (see Scheme 2) of the corresponding acetylene and coupled to the polymer by esterification with the cesium carboxylate of **66**.[31b] Selenoxide syn-elimination was performed on the support rather than prior to the coupling step to avoid competing conjugate addition of the carboxylate to the fully developed acetylenic sulfone. Several representative solid-supported acetylenic sulfones **68** were thus prepared (Scheme 13) and comprise the first such species to be reported.[32]

Scheme 11.

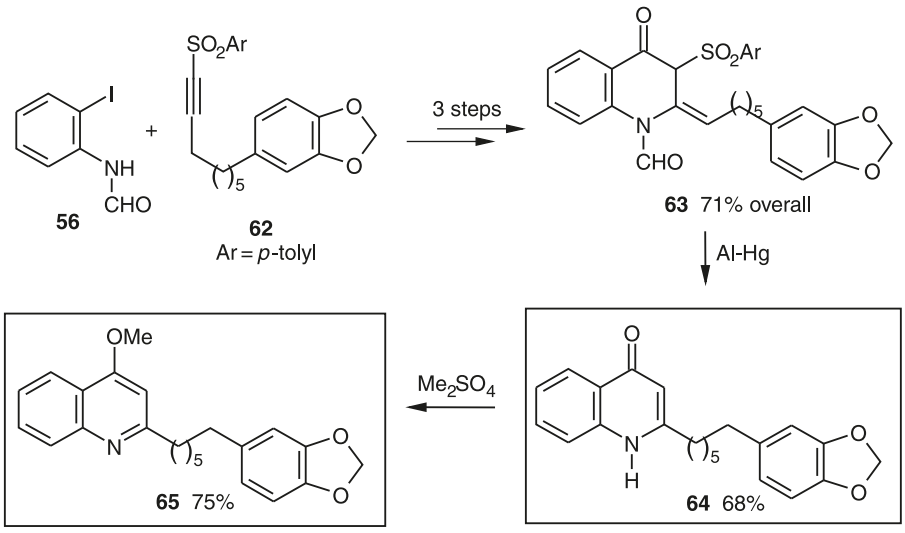

Ruta chalepensis alkaloids

Scheme 12.

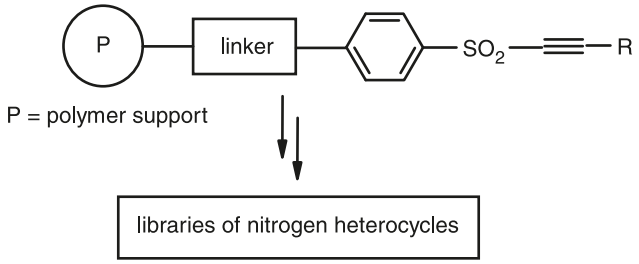

We were delighted to discover that a variety of cyclizations with various chloroalkylamines could be effected with solid-supported acetylenic sulfones **68** under similar conditions as in solution phase. Furthermore, various Diels–Alder and 1,3-dipolar cycloadditions could also be performed with **68**. The products were cleaved from the supports in either of two ways. First, hydrolysis of the ester linker afforded cyclized products containing the 4-(hydroxymethyl)phenylsulfonyl moiety intact. Alternatively, if products devoid of the sulfonyl group were desired, cleavage by reductive desulfonylation with sodium amalgam was also feasible. Scheme 14 illustrates a few representative examples.[32]

A more extensive investigation of 1,3-dipolar cycloadditions of acetylenic sulfones ensued, both on solid supports and in solution phase.[33] Successful cycloadditions were observed with azides, diazo compounds, nitrile oxides, nitrile imines, nitrile ylides, nitrones, azomethine imines, azomethine ylides, munchnones, and sydnones.

The final applications of acetylenic sulfones that will be described here involve the reactions of acetylenic sulfone **70** with tertiary cyclic amines containing α-vinyl substituents, such as **69**. The expectation was that the usual conjugate addition would occur, producing a zwitterion intermediate **71** that would undergo a formal aza-Cope rearrangement to **72** (Scheme 15).[34] Aza-Cope reactions are generally characterized by high activation energies and so require strongly elevated temperatures. However, it has been reported that quaternization of the nitrogen atom by protonation or complexation with a Lewis acid lowers the activation energy and accelerates the rearrangement considerably.[35] In the case of a dipolar intermediate such as **71**, one might expect an even more facile rearrangement because of the cancellation of charge during the course of the transformation. The overall process would result in the ring expansion of the original starting amine **69** by four carbon atoms and would provide a potentially useful approach to the synthesis of medium- and large-ring cyclic amines such as **72**.

The results of this study are illustrated in Scheme 16.[36] We observed that, as expected, the rearrangement took place under remarkably mild conditions, typically in dichloromethane at temperatures ranging from –78 °C to reflux. In some cases, other solvents, including methanol, acetonitrile, ether, DMF, and THF, were also employed successfully. The products contained from nine- to 17-membered rings and the method tolerated other heteroatoms, as well as substituents at either position of the vinyl group. Selective reduction of either the enamine or isolated double bonds could be effected with sodium borohydride or cyanoborohydride, or by hydrogenation, respectively. Desulfonylation was accomplished with sodium amalgam or under Birch conditions.

While the precise mechanism of the rearrangement is not fully understood, a kinetic investigation indicated that the process is bimolecular (first-order in each reactant) and that it is accelerated by the presence of electron-withdrawing substituents at the para position of the aryl group in the acetylenic sulfones. This supports the formation of the zwitterion **71** as the rate-determining step, as a more strongly electron-withdrawing arylsulfonyl substituent better stabilizes the vinyl anion moiety of **71** and lowers the activation energy leading to its formation.[36a] The rearrangement step may, however, be different from a classical Cope or hetero-Cope reaction, where the new sigma bond is produced from the interaction of p orbitals at the terminal positions of a 1,5-diene or heterodiene system. In the present case, this step could alternatively be envisaged as an intramolecular allylic substitution (S_N') of the quaternary nitrogen atom by a sulfone-stabilized vinyl anion.

Scheme 13.

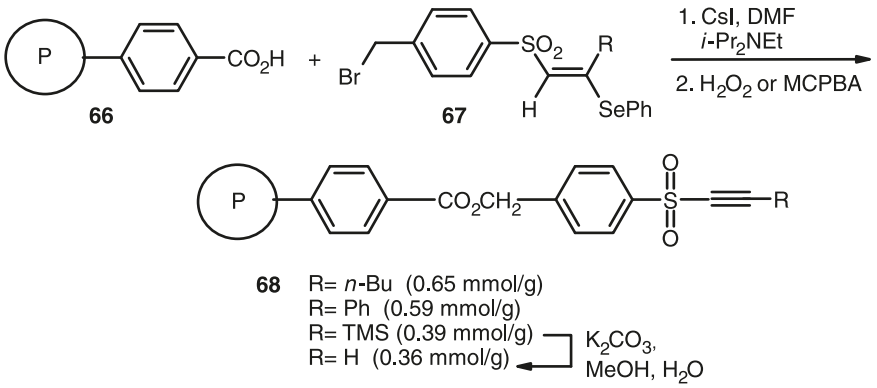

Scheme 14.

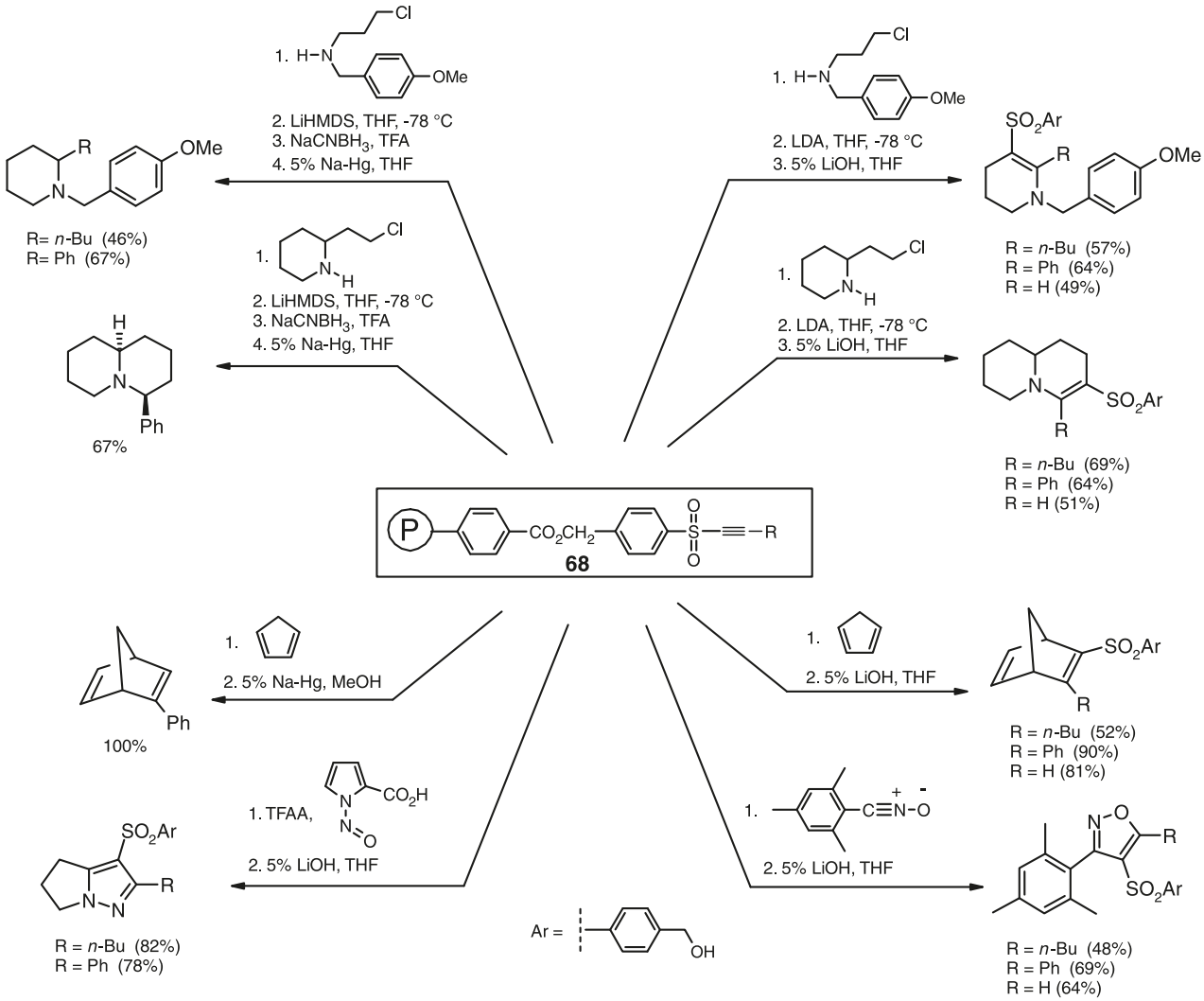

An iterative version of the aza-Cope reaction was also achieved by introducing a new α-vinyl substituent into the sulfonyl-substituted enamine moiety of the initial ring-expanded products **73** and **74**. This was accomplished by treatment of the latter with triflic acid and vinylmagnesium bromide, resulting in incorporation of the desired vinyl group via the corresponding iminium ion. In general, some starting material was also recovered because of competing deprotonation of the iminium intermediate by the Grignard reagent. The iterative ring-expansion was successfully applied to the synthesis of motuporamine A and B (**75** and **76**, respectively; Scheme 17).[36a,37] These compounds are marine natural products that were discovered by the Andersen group.[38a] They exhibit powerful anti-invasive and anti-angiogenic activity which makes them potentially useful as anticancer agents.[38]

Scheme 15.

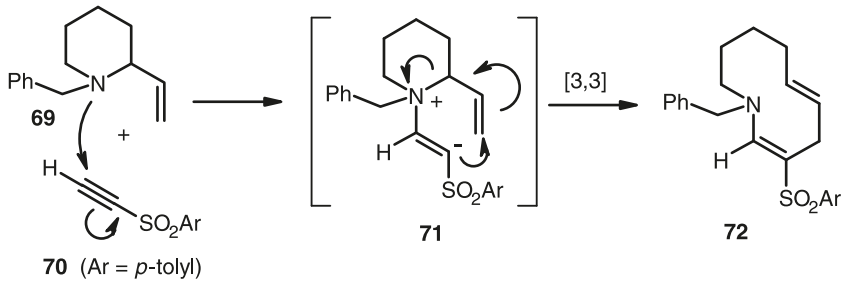

Scheme 16.

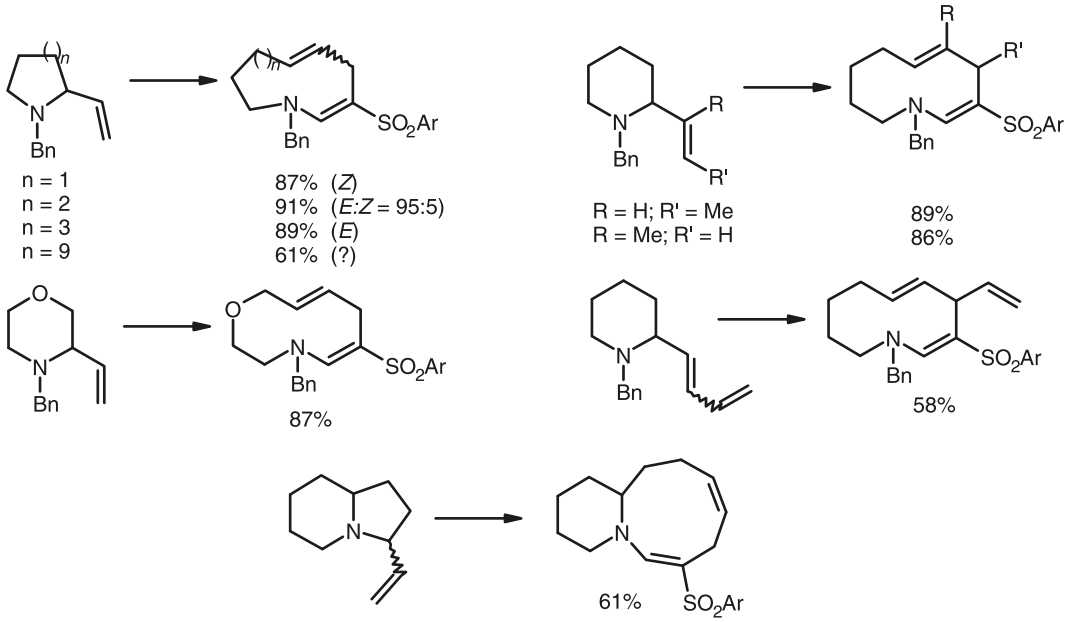

All reactions were performed in CH_2Cl_2 (-78 °C to reflux); Ar = *p*-tolyl

The preceding results indicate that acetylenic sulfones are a very useful and, to date, somewhat overlooked class of compounds in organic synthesis. Among other applications, they readily undergo conjugate additions by primary, secondary, and even tertiary amines, followed by intramolecular alkylations, acylations, or formal aza-Cope rearrangements to afford a variety of nitrogen heterocycles. These include the dendrobatid alkaloids (–)-pumiliotoxin C and indolizidines (–)-167B, (–)-207A, (–)-209B, and (–)-209D, as well as the piperidine alkaloid (–)-*ent*-julifloridine and the quinolizidines (–)-lasubine II and myrtine. Anilines provide access to 4-quinolones, as in the first syntheses of two alkaloids from the medicinal plant *R. chalepensis*, while cyclic tertiary α-vinylamines afford macrocyclic amines such as the motuporamines.

Organoselenium chemistry: design and synthesis of glutathione peroxidase mimetics

The preceding section described some of our studies of organosulfur chemistry during the past 10 years that enabled us to develop new synthetic routes to a host of biologically interesting natural products. During this period, we also investigated applications of selenium in the design and synthesis of unnatural products that would mimic the antioxidant properties of the selenoenzyme glutathione peroxidase (GPx). Harmful peroxides and other reactive oxygen species are produced during normal aerobic metabolism and contribute to a condition generally referred to as oxidative stress.[39] This in turn can lead to a variety of degenerative conditions and disease states, including inflammation, cancer and mutagenesis, cardiovascular and neurological disease, and possibly the aging process. Fortunately, protection from oxidative stress is available from both exogenous and endogenous sources. The former include natural antioxidants present in a variety of foods and beverages,[39b,39c] while several enzymes (e.g., superoxide dismutase, catalase, and a series of peroxidases) afford endogenous protection. In particular, the selenoenzyme GPx catalyzes the destruction of peroxides with the sacrificial reductant glutathione, which is a ubiquitous tripeptide thiol that occurs in high concentration in the cells of higher organisms. X-ray crystallography has established that GPx has a tetrameric structure, in which each subunit contains a selenocysteine residue bearing a redox-active selenol function at its active site.[40] The catalytic cycle of GPx[41] is shown in Scheme 18, where the selenol (EnzSeH) reduces a peroxide molecule to the corresponding

Scheme 17.

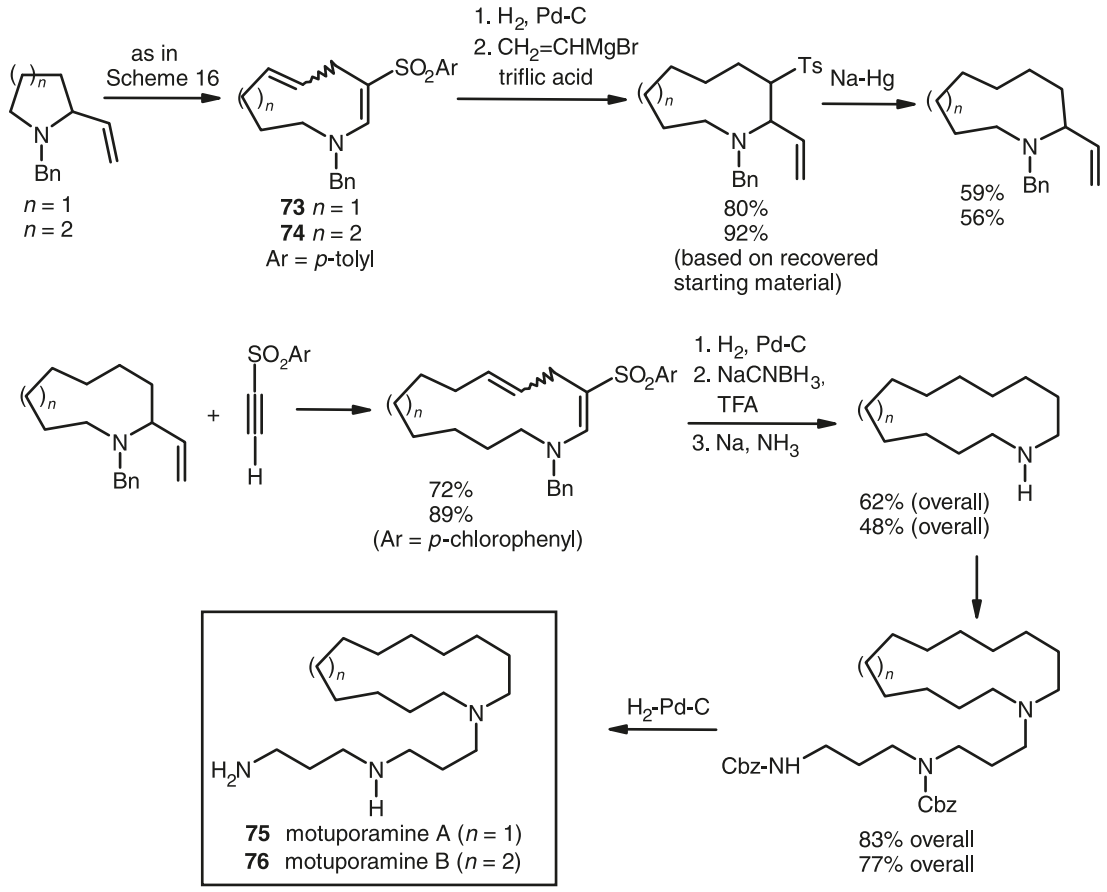

alcohol (or water in the case of hydrogen peroxide) and is in turn oxidized to the selenenic acid EnzSeOH. This reacts successively with two molecules of glutathione (GSH), first producing an intermediate selenenyl sulfide (EnzSeSG), followed by regeneration of the original selenol moiety and oxidation of GSH to its disulfide (GSSG).

Although a diet rich in antioxidants, together with endogenous enzymes such as GPx, help to mitigate the deleterious effects of oxidative stress, there are conditions where such effects overwhelm one's natural defenses. For example, heart attack and stroke patients suffer increased levels of oxidative stress during ischemic reperfusion, resulting in cardiovascular and neurological damage. Consequently, several groups have devised small-molecule selenium compounds designed to emulate the catalytic activity of GPx that could be administered as additional protective measures to such patients.[42] Figure 3 shows a few examples of such compounds that have been reported in the literature.[43–51] Many contain a nitrogen atom that is covalently bonded to selenium, or that can coordinate with it at appropriate stages in the catalytic cycle, which appears to modulate the redox properties of the selenium center. Several tellurium compounds have also been investigated in this context. Two compounds, SYI 2074[52] and ebselen,[53,54] are currently in Phase I and Phase III clinical trials being conducted by Synvista Therapeutics Inc. and Daiichi Sankyo Inc., respectively.

During an investigation of camphor-based chiral auxiliaries for asymmetric electrophilic selenium reactions, we had

Scheme 18.

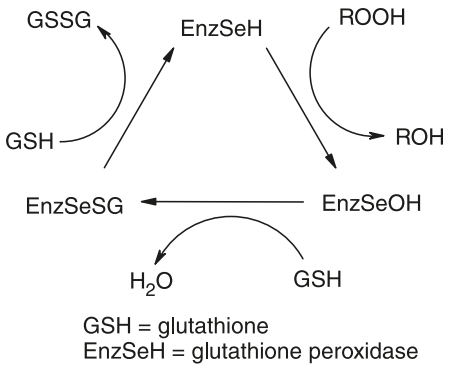

occasion to prepare cyclic selenenamide **77** (Scheme 19).[55] Since this compound bears a superficial similarity to some of the existing Se–N-containing GPx mimetics in Fig. 4, it seemed opportune to test the compound for GPx-like behaviour in an assay that we developed for this purpose. The assay employed *t*-butyl hydroperoxide as a model peroxide and benzyl thiol as a surrogate for glutathione, which permitted the reaction to be monitored conveniently by HPLC or NMR methods. The catalytic activity of various selenium compounds could then be compared according to the time

Fig. 3. Examples of small-molecule mimetics of GPx.

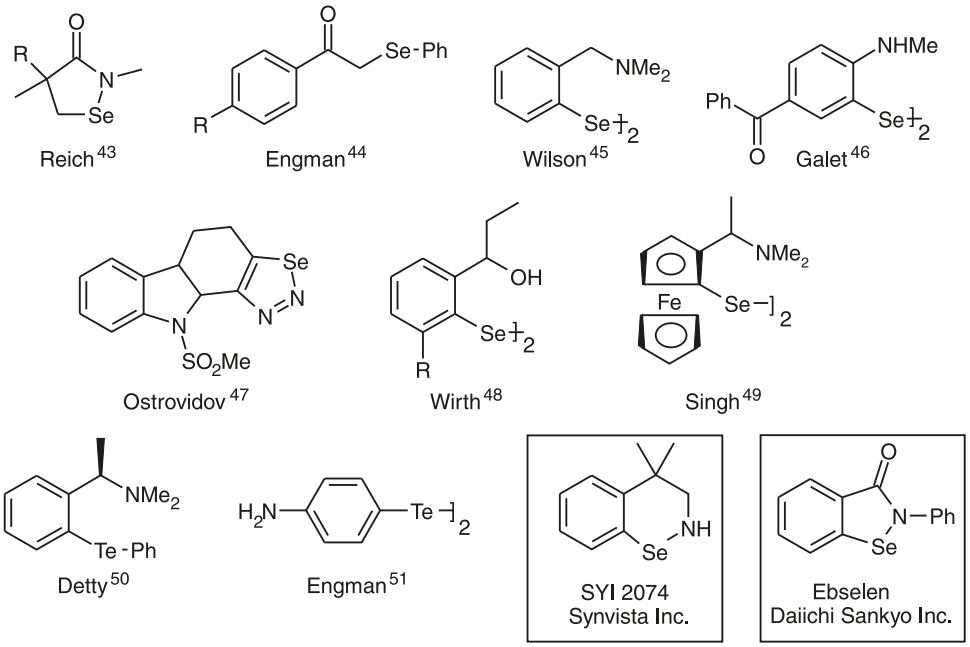

Scheme 19.

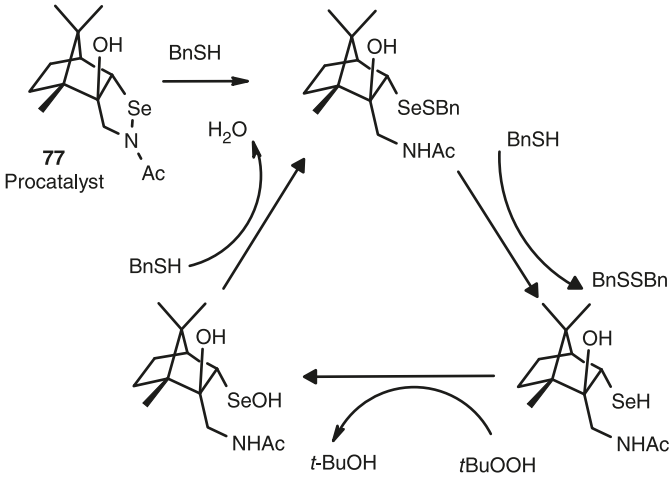

Fig. 4. ORTEP diagram for the X-ray structure of spirodioxyselenurane **88**.

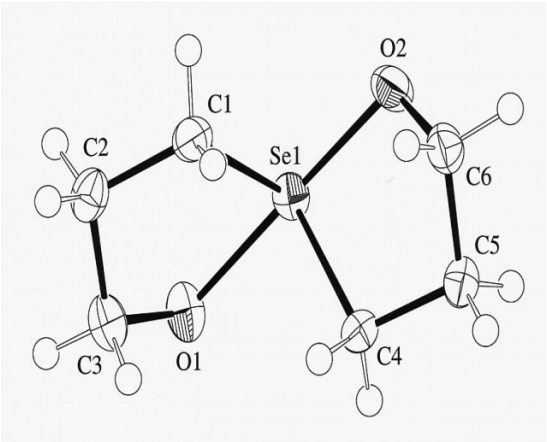

Scheme 20.

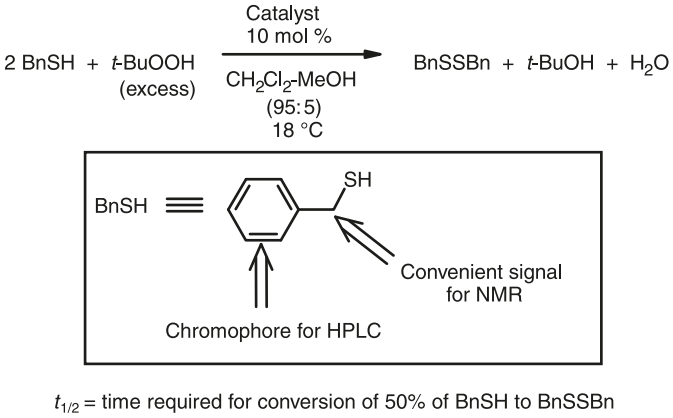

($t_{1/2}$) required for the consumption of 50% of the thiol under the conditions indicated in Scheme 20. When **77** was thus tested, it produced a $t_{1/2}$ of 18 h, compared with 42 h for ebselen and >300 h for a control reaction with no catalyst.[55,56] A study of the mechanism revealed that **77** was merely a procatalyst that reacted with the thiol in the initial step to generate a selenenyl sulfide analogous to EnzSeSG in Scheme 18. From there, the catalytic cycle mimicked that of GPx, proceeding via a putative selenol and selenenic acid.[55]

These encouraging results prompted us to investigate many other types of organoselenium compounds for GPx activity in the ensuing years, of which two classes stood out. In the first, we examined a series of allyl ω-hydroxyalkyl selenides (e.g., **78**), reasoning that oxidation with a peroxide would produce the corresponding selenoxide **79**, which would undergo a very rapid [2,3]sigmatropic rearrangement, affording the selenenate ester **80**. This was expected to provide entry into a catalytic cycle similar to those shown in Schemes 18 and 19, where a related selenenic acid is generated and reacts with a thiol to afford the selenenyl sulfide in one of the three key

Scheme 21.

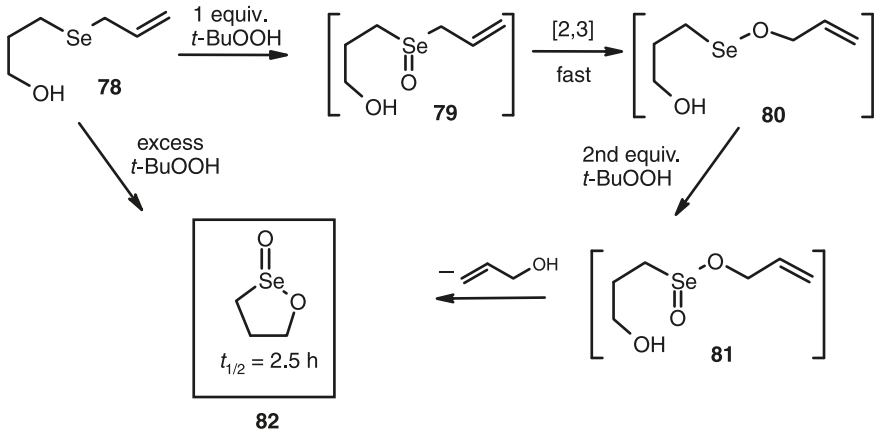

steps. When a control reaction was performed in the absence of thiol, the expected selenenate ester **80** proved unstable, but could be tentatively identified by NMR when only one equivalent of hydroperoxide was added. However, oxidation of selenide **78** with excess hydroperoxide cleanly afforded the cyclic seleninate **82**, presumably via the mechanism shown in Scheme 21.[56] To our surprise, despite its simple structure, **82** proved to be a novel compound, with remarkable catalytic activity ($t_{1/2}$ = 2.5 h; 17 times faster than with ebselen). Moreover, it was a stable, odourless solid that could be conveniently handled and stored. A comparison of selenide **78** with 2-hydroxyethyl and 4-hydroxybutyl analogues indicated that the 3-hydroxypropyl derivative and the corresponding five-membered cyclic seleninate **82** were optimum for catalytic activity. Moreover, a variety of other functionalities (carboxylic acids, amines, amides, and so forth) in place of the hydroxyl group in allyl alkyl selenides also proved inferior.[57] Therefore, it appears that compounds containing Se–O bonds, which have been much less studied than Se–N systems,[58] can also function as highly effective GPx mimetics.

Further studies revealed that **82** reacted very rapidly with benzyl thiol, presumably via intermediates **83** and **84**, which could not be detected. In the presence of excess hydroperoxide, cyclic seleninate **82** was regenerated, as shown in Scheme 22. However, varying amounts of another product, identified as the selenenyl sulfide **85**, were also observed when both thiol and hydroperoxide were present, with increasing amounts formed when the thiol:hydroperoxide ratio was increased. When the reaction was conducted with excess thiol in the absence of the hydroperoxide, **85** was obtained quantitatively. Since selenenyl sulfides were key intermediates in the catalytic cycles of GPx and **77** (Schemes 18 and 19, respectively), selenenyl sulfide **85** was isolated, characterized, and tested for GPx activity independently. We were surprised to discover that although **85** is slowly converted back to the cyclic seleninate **82** by *t*-butyl hydroperoxide, its $t_{1/2}$ in our standard assay was 35 h, which precludes it from playing an active role in the catalytic cycle of **82**, with $t_{1/2}$ = 2.5 h. Thus, in contrast to the key roles of selenenyl sulfides in Schemes 18 and 19, we conclude that the formation of **85** in Scheme 22 actually comprises a deactivation pathway.[57]

The discovery of a second class of GPx mimetics stemmed from an alternative attempt to generate cyclic sele-

Scheme 22.

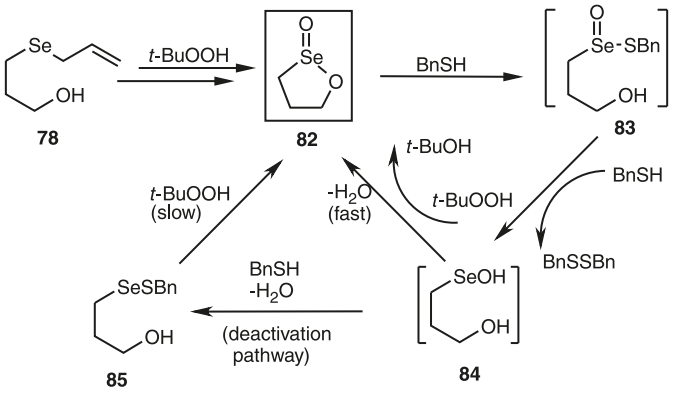

ninate **82** by oxidation and selenoxide elimination of bis(3-hydroxypropyl) selenide **86** (Scheme 23). Instead, the selenoxide **87** underwent an intramolecular condensation to produce the spirodioxyselenurane **88** in essentially quantitative yield.[59] While various other substituted and fused-ring spiroselenuranes have been reported previously, it was again surprising to discover that the parent structure **88** was novel. It was subjected to our standard assay and was also found to possess high catalytic activity, with $t_{1/2}$ = 2.9 h. Like the cyclic seleninate **82**, it too is an odourless, stable, crystalline solid. An X-ray crystal structure was obtained and is shown in Fig. 4.[59] As expected, the geometry of **88** is that of a distorted trigonal bipyramid in which the oxygen atoms occupy apical positions, while the carbon substituents on the central selenium, as well as the lone pair (not shown) define the equatorial plane. The bond angles O(1)–Se(1)–O(2) and C(1)–Se(1)–C(4) were found to be 172.99° and 102.95°, respectively.

The proposed mechanism for the catalytic activity of **88** is shown in Scheme 24. The selenide **86** is inert to benzyl thiol, but is readily oxidized to selenoxide **87**, which, as described previously, cyclizes spontaneously to the spiro compound **88**. The latter undergoes substitution with one mole of the thiol to form **89** and then, presumably, a reductive elimination with a second mole, regenerating the selenide **86** and producing dibenzyl disulfide as a byproduct.[59]

The discovery of two novel structures, **82** and **88**, that act as GPx mimetics by catalyzing the reduction of a model hy-

Scheme 23.

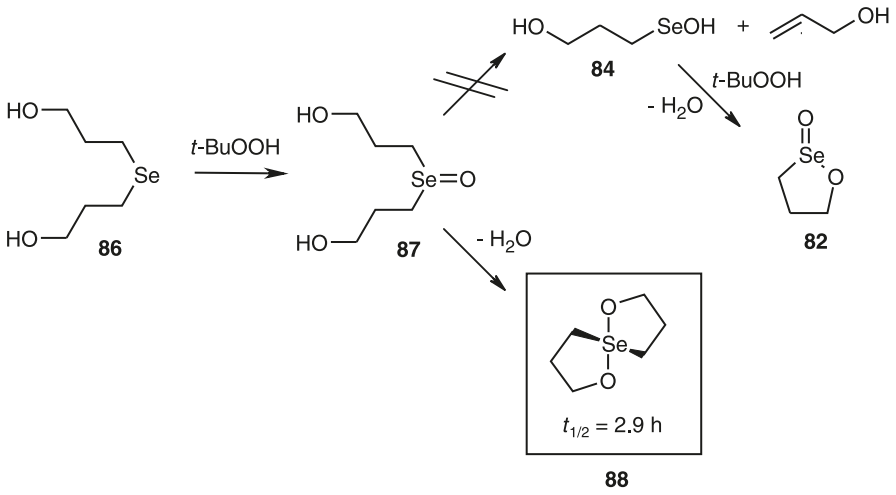

Scheme 24.

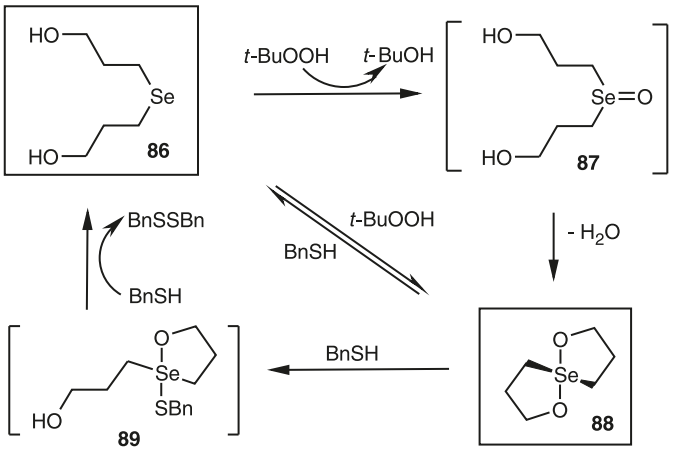

droperoxide with a thiol by mechanisms distinct from that of the enzyme itself was encouraging. However, aliphatic organoselenium compounds tend to be more toxic than aromatic ones,[42b,60] possibly a reflection of their weaker C–Se bonds and greater ease of metabolic degradation. We therefore turned our attention to aromatic analogues of **82** and **88** to determine if they too would exhibit desirable catalytic properties. Compounds **90**–**92** were synthesized and tested, but their catalytic activity was greatly diminished compared with that of their aliphatic counterparts for the reduction of *t*-butyl hydroperoxide, while only the spiro compound **92** provided a satisfactory $t_{1/2}$ of 2.9 h when hydrogen peroxide was used as the model peroxide (Fig. 5).[61,62] Attempts to prepare spirodiazaselenuranes afforded unsymmetrical selenonium species that proved relatively ineffective as GPx mimetics.[63] On the other hand, the tellurium analogues of **82** and **88** showed extremely high catalytic activity, with $t_{1/2}$ of ~5 min.[61] A related study of some similar compounds was reported by Singh and co-workers.[64]

Since the reactivity of aromatic systems is often strongly affected by electron-donating or -withdrawing groups, a series of aromatic derivatives of cyclic seleninate **90** and of the spiro compound **92** were prepared with substituents attached para to the selenium atom. These analogues were subjected

Fig. 5. Aromatic derivatives of GPx mimetics.

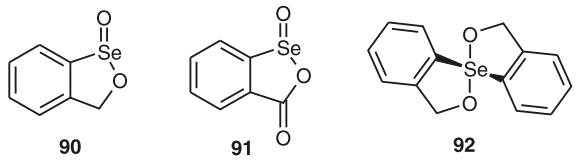

t-BuOOH: $t_{1/2}$ = 162 h (61) $t_{1/2}$ = 252 h (61) $t_{1/2}$ = 62 h (61)

H_2O_2: $t_{1/2}$ = 50 h (62) $t_{1/2}$ = 73 h (61) $t_{1/2}$ = 2.9 h (62)

Table 1. Catalytic activities of substituted aromatic derivatives of **90** and **92**.

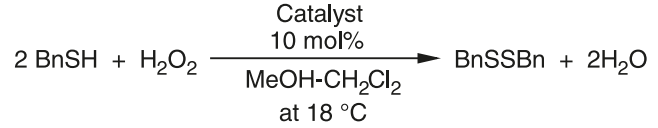

Catalyst	$t_{1/2}$ (h)
Ebselen	21
R = H	50
R = F	72
R = Cl	69
R = Br	62
R = Me	48
R = Ph	57
R = OMe	38

Catalyst	$t_{1/2}$ (h)
R = H	2.9
R = F	22
R = Cl	25
R = Br	31
R = Me	3.6
R = OMe	0.5

to the assay with hydrogen peroxide as the oxidant, and the results are shown in Table 1, where it is clear that electron-donating substituents enhance catalytic activity, while electron-withdrawing groups suppress it. Indeed, the methoxy-substituted spirodioxyselenurane displayed $t_{1/2}$ = 0.5 h, which is the shortest time observed with any of the selenium compounds we have tested to date in this regard.[62]

Fig. 6. Hammett plot for the reduction of hydrogen peroxide with benzyl thiol in the presence of substituted derivatives of **90**.

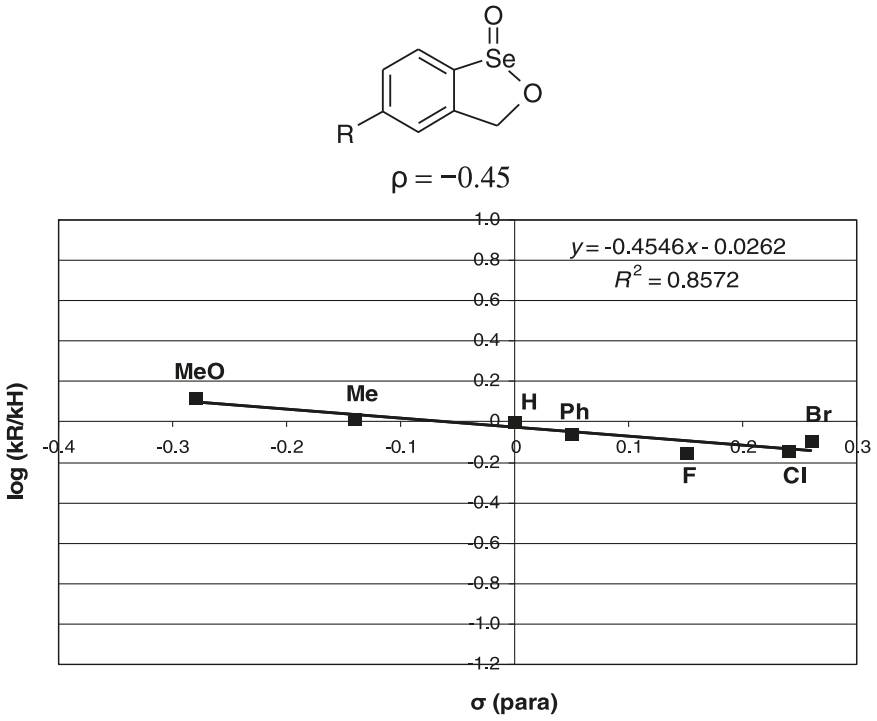

Fig. 7. Hammett plot for the reduction of hydrogen peroxide with benzyl thiol in the presence of substituted derivatives of **92**.

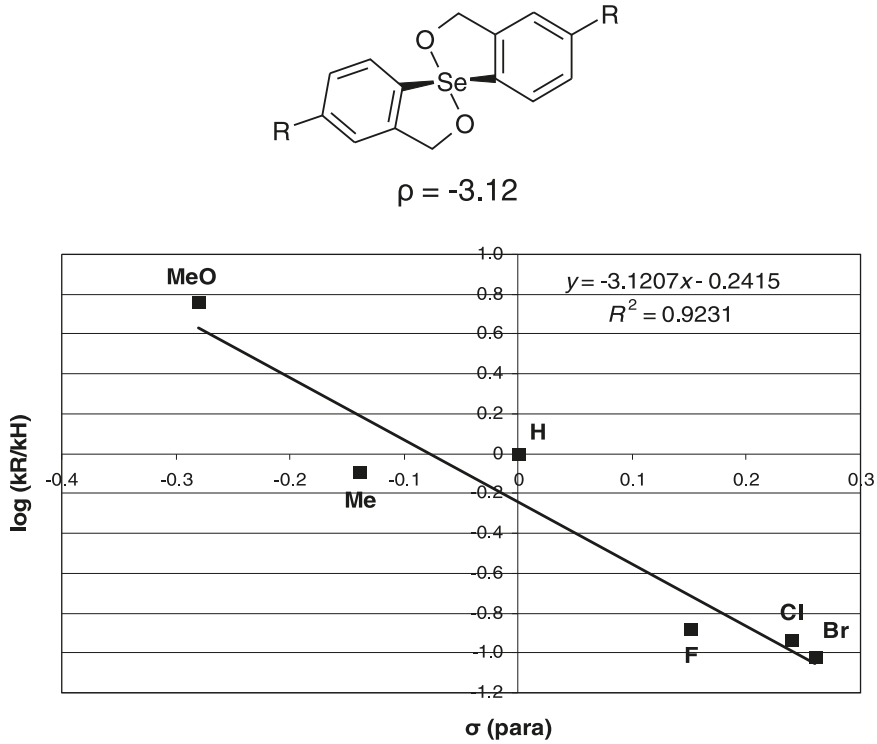

A more detailed kinetic study of the compounds in Table 1 revealed that the reactions are zero-order in thiol, suggesting that the steps in their catalytic cycles that involve oxidation of selenium(II) to selenium(IV) are rate-determining. This was confirmed by means of the corresponding Hammett plots, shown in Figs. 6 and 7. In both the cyclic seleninates and the spirodioxyselenuranes, the Hammett plots show negative slopes, indicating that the transition states of the rate-determining steps are stabilized by electron donation, consistent with an increase in the oxidation state of the selenium. It was also noted that the reaction constant had a considerably greater magnitude in the case of the spiroselenuranes (ρ = –3.12) compared with the corresponding seleninates (ρ = –0.45), indicating that the overall rate of the reaction

was significantly more susceptible to substituent effects in the former series than in the latter.[62] Moreover, the kinetic plots of the assays of the spirodioxyselenuranes showed positive *y*-intercepts, indicating anomalously high rates of formation in the early stages of the reaction. This is consistent with the rapid consumption of the catalyst (10 mol%) and simultaneous conversion of benzyl thiol to its disulfide in the first two steps in Scheme 24, prior to the rate-determining oxidation of Se(II) to Se(IV), and eventual regeneration of the catalyst.

A final point concerns the ability of some GPx mimetics that employ selenol or selenolate intermediates in their catalytic cycles to reduce dioxygen to reactive oxygen species that can then, paradoxically, contribute to oxidative stress instead of suppressing it.[65] Both the cyclic seleninates and spirodioxyselenuranes described above operate through catalytic cycles that do not rely on selenol intermediates. This precludes the possibility of undesired concomitant generation of harmful reduced oxygen species.

In conclusion, various mechanisms for GPx-like activity are possible, not just the one that was established for the enzyme itself. Both the cyclic seleninates and the spirodioxyselenuranes exhibit mechanisms that are different from that of GPx and from each other. Moreover, selenenyl sulfides are not essential intermediates. In fact, in Scheme 22, selenenyl sulfide **85** is part of a deactivation pathway instead of the primary catalytic cycle. As noted earlier, most of the GPx mimetics studied to date focused on the modulation of catalytic activity by means of appropriate amine substituents bonded to or capable of coordinating with the selenium atom. The above work indicates that oxygen substituents can serve equally well in this regard, and the novel aliphatic cyclic seleninate **82** and spirodioxyselenurane **88** proved remarkably effective catalysts in our assay. Aromatic derivatives are expected to be less toxic than the above aliphatic compounds, but they generally display poorer catalytic activity. Fortunately, kinetic studies revealed that oxidation of Se(II) to Se(IV) is the rate-determining step of the process and that catalytic activity can be significantly improved by the inclusion of electron-donating substituents para to the selenium atom. With these insights, it may be possible to devise an improved second generation of GPx mimetics with enhanced catalytic activity and improved therapeutic properties, and such work is ongoing in our laboratory. Indeed, the *p*-methoxy-substituted spirodioxyselenurane compound in Table 1 is a promising candidate for further in vivo studies of antioxidant activity[66] because of its exceptional catalytic activity and absence of selenol or selenolate intermediates in the catalytic cycle.

Acknowledgement

I am honoured and most grateful to the Alfred Bader Award Selection Committee for choosing me as the 2008 recipient of the award. The results described here were obtained through the determination and hard work of numerous talented undergraduate and graduate students, postdoctoral fellows, and colleagues, whose names are listed in the cited references. We also acknowledge the generous financial support for the work described here from the Natural Sciences and Engineering Research Council of Canada (NSERC) and Merck Frosst (Canada) Inc.

References

(1) (a) For general reviews of sulfone chemistry, see: Patai, S.; Rappoport, Z.; Stirling, C., Eds. *The Chemistry of Sulphones and Sulphoxides;* Wiley: Chichester, 1988; (b) Simpkins, N. S. *Sulphones in Organic Synthesis;* Pergamon Press: Oxford, 1993; (c) Trost, B. M. *Bull. Chem. Soc. Jpn.* **1988**, *61* (1), 107. doi:10.1246/bcsj.61.107.

(2) For a review of acetylenic and allenic sulfones, see: Back, T. G. *Tetrahedron* **2001**, *57* (25), 5263. doi:10.1016/S0040-4020(01)00299-X.

(3) (a) For reviews of vinyl sulfones, see: Simpkins, N. S. *Tetrahedron* **1990**, *46* (20), 6951. doi:10.1016/S0040-4020(01)87882-0.; (b) Nenajdenko, V. G.; Krasovskiy, A. L.; Balenkova, E. S. *Tetrahedron* **2007**, *63* (51), 12481. doi:10.1016/j.tet.2007.10.018.

(4) For a review of dienyl sulfones, see: Bäckvall, J.-E.; Chinchilla, R.; Nájera, C.; Yus, M. *Chem. Rev.* **1998**, *98* (6), 2291. doi:10.1021/cr970326z. PMID:11848964.

(5) Nájera, C.; Yus, M. *Tetrahedron* **1999**, *55* (35), 10547. doi:10.1016/S0040-4020(99)00600-6.

(6) For a review of selenosulfonation, see: Back, T. G., Ed. In *Organoselenium Chemistry — A Practical Approach;* Oxford University Press: Oxford, 1999; pp 175–178.

(7) Back, T. G.; Collins, S.; Krishna, M. V. *Can. J. Chem.* **1987**, *65* (1), 38. doi:10.1139/v87-009.

(8) (a) Back, T. G.; Collins, S. *Tetrahedron Lett.* **1981**, *22* (51), 5111. doi:10.1016/S0040-4039(01)92433-5.; (b) Back, T. G.; Collins, S.; Kerr, R. G. *J. Org. Chem.* **1983**, *48* (18), 3077. doi:10.1021/jo00166a030.; (c) Miura, T.; Kobayashi, M. *J. Chem. Soc. Chem. Commun.* **1982**, (8): 438. doi:10.1039/c39820000438.

(9) (a) Back, T. G.; Nakajima, K. *Org. Lett.* **1999**, *1* (2), 261. doi:10.1021/ol990592u.; (b) Back, T. G.; Nakajima, K. *J. Org. Chem.* **2000**, *65* (15), 4543. doi:10.1021/jo000080p. PMID:10959857.

(10) For a recent application of this cyclization method to the synthesis of the piperidine alkaloid (–)-*ent*-julifloridine from L-alanine, see: Zhai, H.; Parvez, M.; Back, T. G. *J. Org. Chem.* **2007**, *72* (10), 3853. doi:10.1021/jo0703101. PMID:17439181.

(11) (a) Back, T. G.; Nakajima, K. *Tetrahedron Lett.* **1997**, *38* (6), 989. doi:10.1016/S0040-4039(96)02506-3.; (b) Back, T. G.; Nakajima, K. *J. Org. Chem.* **1998**, *63* (19), 6566. doi:10.1021/jo980647q.

(12) (a) Back, T. G.; Wulff, J. E. *Chem. Commun.* **2002**, *10*, 1710. doi:10.1039/b205408f.; (b) Back, T. G.; Parvez, M.; Wulff, J. E. *J. Org. Chem.* **2003**, *68* (6), 2223. doi:10.1021/jo026595t. PMID:12636385.

(13) (a) For selected reviews, see: Daly, J. W.; Garraffo, H. M.; Spande, T. F. In *Alkaloids: Chemical and Biological Perspectives;* Pelletier, S. W., Ed.; Pergamon: New York, 1999; Vol. 13, Chapter 1;(b) Witkop, B.; Gössinger, E. In *The Alkaloids — Chemistry and Pharmacology.* Brossi, A., Ed.; Academic Press: New York, 1983; Vol. 21, Chapter 5;(c) Daly, J. W.; Brown, G. B.; Mensah-Dwumah, M.; Myers, C. W. *Toxicon* **1978**, *16* (2), 163. doi:10.1016/0041-0101(78)90036-3. PMID:635931.; (d) Daly, J. W.; Myers, C. W.; Whittaker, N. *Toxicon* **1987**, *25* (10), 1023. doi:10.1016/0041-0101(87)90265-0. PMID:3321567.

(14) Daly, J. W.; Spande, T. F.; Garraffo, H. M. *J. Nat. Prod.* **2005**, *68* (10), 1556. doi:10.1021/np0580560. PMID:16252926.

(15) Daly, J. W.; Tokuyama, T.; Habermehl, G.; Karle, I. L.; Witkop, B. *Liebigs Ann. Chem.* **1968**, *729*, 198.

(16) Tokuyama, T.; Nishimori, N.; Shimada, A.; Edwards, M. W.; Daly, J. W. *Tetrahedron* **1987**, *43* (3), 643. doi:10.1016/S0040-4020(01)89998-1.

(17) For a review of syntheses of pumiliotoxin C and related compounds, see: Sklenicka, H. M.; Hsung, R. P. *Chemtracts* **2002**, *15*, 391.

(18) Davies, S. G.; Bhalay, G. *Tetrahedron Asymmetry* **1996**, *7* (6), 1595. doi:10.1016/0957-4166(96)00190-5.

(19) For reviews of indolizidine and quinolizidine alkaloids, see: Michael, J. P. *Nat. Prod. Rep.* **2008**, *25* (1), 139; and previous reviews by this author cited therein. doi:10.1039/b612166g. PMID:18250900.

(20) Bardou, A.; Célérier, J.-P.; Lhommet, G. *Tetrahedron Lett.* **1998**, *39* (29), 5189. doi:10.1016/S0040-4039(98)01040-5.

(21) (a) Back, T. G.; Hamilton, M. D. *Org. Lett.* **2002**, *4* (10), 1779. doi:10.1021/ol0258482. PMID:12000297.; (b) Back, T. G.; Hamilton, M. D.; Lim, V. J. J.; Parvez, M. *J. Org. Chem.* **2005**, *70* (3), 967. doi:10.1021/jo048284j. PMID:15675856.

(22) For an overview of drugs based on the 4-quinolone motif, see: Wulff, J. E. *A Novel Route to 4-Quinolones and an Enantioselective Total Synthesis of Virantmycin;* Ph.D. thesis, University of Calgary, 2004.

(23) Hooper, D. C.; Rubinstein, E., Eds. *Quinolone Antimicrobial Agents,* 3rd ed.; ASM Press: WA, 2003.

(24) Watterson, S. H.; Carlsen, M.; Dhar, T. G. M.; Shen, Z.; Pitts, W. J.; Guo, J.; Gu, H. H.; Norris, D.; Chorba, J.; Chen, P.; Cheney, D.; Witmer, M.; Fleener, C. A.; Rouleau, K.; Townsend, R.; Hollenbaugh, D. L.; Iwanowicz, E. J. *Bioorg. Med. Chem. Lett.* **2003**, *13* (3), 543. doi:10.1016/S0960-894X(02)00944-7. PMID:12565968.

(25) Wentland, M. P.; Lesher, G. Y.; Reuman, M.; Gruett, M. D.; Singh, B.; Aldous, S. C.; Dorff, P. H.; Rake, J. B.; Coughlin, S. A. *J. Med. Chem.* **1993**, *36* (19), 2801. doi:10.1021/jm00071a010. PMID:8410993.

(26) Large, M. S.; Smith, L. H. *J. Med. Chem.* **1982**, *25* (12), 1417. doi:10.1021/jm00354a005. PMID:6130155.

(27) Tsuji, J. *Palladium Reagents and Catalysts;* Wiley: Chichester, 1995; pp 188–209.

(28) Wratten, S. J.; Wolfe, M. S.; Andersen, R. J.; Faulkner, D. J. *Antimicrob. Agents Chemother.* **1977**, *11* (3), 411. PMID:324390.

(29) (a) Reil, E.; Höfle, G.; Draber, W.; Oettmeier, W. *Biochim. Biophys. Acta* **1997**, *1318* (1-2), 291. doi:10.1016/S0005-2728(96)00150-8. PMID:9030270.; (b) Reil, E.; Höfle, G.; Draber, W.; Oettmeier, W. *Biochim. Biophys. Acta* **2001**, *1506* (2), 127. doi:10.1016/S0005-2728(01)00189-X. PMID:11522254.

(30) El Sayed, K.; Al-Said, M. S.; El-Feraly, F. S.; Ross, S. A. *J. Nat. Prod.* **2000**, *63* (7), 995. doi:10.1021/np000012y. PMID:10924184.

(31) (a) Beebe, X.; Schore, N. E.; Kurth, M. J. *J. Org. Chem.* **1995**, *60* (13), 4196. doi:10.1021/jo00118a041.; (b) The esterification of the polymer-supported carboxylic acid was performed by the general method of the following ref.: Morales, G. A.; Corbett, J. W.; DeGrado, W. F. *J. Org. Chem.* **1998**, *63* (4), 1172. doi:10.1021/jo971688+.

(32) Back, T. G.; Zhai, H. *Chem. Commun. (Camb.)* **2006**, (3): 326. doi:10.1039/b512016k. PMID:16391749.

(33) Gao, D.; Zhai, H.; Parvez, M.; Back, T. G. *J. Org. Chem.* **2008**, *73* (20), 8057. doi:10.1021/jo801621d. PMID:18798677.

(34) (a) For reviews of aza-Cope and related rearrangements, see: Nubbemeyer, U. *Top. Curr. Chem.* **2005**, *244*, 149; (b) Enders, D.; Knopp, M.; Schiffers, R. *Tetrahedron Asymmetry* **1996**, *7* (7), 1847. doi:10.1016/0957-4166(96)00220-0.; (c) Blechert, S. *Synthesis* **1989**, *1989* (02), 71. doi:10.1055/s-1989-27158.; (d) Przheval'skii, N. M.; Grandberg, I. I. *Russ. Chem. Rev.* **1987**, *56* (5), 477. doi:10.1070/RC1987v056n05ABEH003284.; (e) Lutz, R. P. *Chem. Rev.* **1984**, *84* (3), 205. doi:10.1021/cr00061a001.; (f) For earlier related studies of formal aza-Cope reactions that proceed via dipolar intermediates produced from tertiary allyl amines and acetylenic esters, see: Vedejs, E.; Gingras, M. *J. Am. Chem. Soc.* **1994**, *116* (2), 579. doi:10.1021/ja00081a019.; (g) Baxter, E. W.; Labaree, D.; Ammon, H. L.; Mariano, P. S. *J. Am. Chem. Soc.* **1990**, *112* (21), 7682. doi:10.1021/ja00177a032.; (h) Schwan, A. L.; Warkentin, J. *Can. J. Chem.* **1988**, *66* (7), 1686. doi:10.1139/v88-273.; (i) Kandeel, K. A.; Vernon, J. M. *J. Chem. Soc., Perkin Trans. 1* **1987**, 2023. doi:10.1039/p19870002023.; (j) Hassner, A.; D'Costa, R.; McPhail, A. T.; Butler, W. *Tetrahedron Lett.* **1981**, *22* (38), 3691. doi:10.1016/S0040-4039(01)81995-X.; (k) Hassner, A.; Chau, W.; D'Costa, R. *Isr. J. Chem.* **1982**, *22*, 76.

(35) For example, ab initio calculations by Walters revealed that the activation energy for the [3,3]sigmatropic rearrangement of allyl vinyl amine is 34.6 kcal/mol, while that for its protonated counterpart is only 21.4 kcal/mol, see: Walters, M. A. *J. Org. Chem.* **1996**, *61* (3), 978; for early examples of the beneficial effects of quaternization or Lewis acid catalysis, see references cited therein. doi:10.1021/jo951131z.

(36) (a) Weston, M. H.; Nakajima, K.; Back, T. G. *J. Org. Chem.* **2008**, *73* (12), 4630. doi:10.1021/jo800600a. PMID:18498198.; (b) Weston, M. H.; Nakajima, K.; Parvez, M.; Back, T. G. *Chem. Commun. (Camb.)* **2006**, (37): 3903. doi:10.1039/b607713g. PMID:17268665.

(37) The side chain was introduced by the method of Baldwin, see: Baldwin, J. E.; Vollmer, H. R.; Lee, V. *Tetrahedron Lett.* **1999**, *40* (29), 5401. doi:10.1016/S0040-4039(99)01016-3.

(38) (a) Williams, D. E.; Lassota, P.; Andersen, R. J. *J. Org. Chem.* **1998**, *63* (14), 4838. doi:10.1021/jo980355p.; (b) Williams, D. E.; Craig, K. S.; Patrick, B.; McHardy, L. M.; van Soest, R.; Roberge, M.; Andersen, R. J. *J. Org. Chem.* **2002**, *67* (1), 245. doi:10.1021/jo016101c. PMID:11777468.; (c) Roskelley, C. D.; Williams, D. E.; McHardy, L. M.; Leong, K. G.; Troussard, A.; Karsan, A.; Andersen, R. J.; Dedhar, S.; Roberge, M. *Cancer Res.* **2001**, *61* (18), 6788. PMID:11559552.; (d) McHardy, L. M.; Sinotte, R.; Troussard, A.; Sheldon, C.; Church, J.; Williams, D. E.; Andersen, R. J.; Dedhar, S.; Roberge, M.; Roskelley, C. D. *Cancer Res.* **2004**, *64* (4), 1468. doi:10.1158/0008-5472.CAN-03-2733. PMID:14973060.; (e) To, K. C. W.; Loh, K. T.; Roskelley, C. D.; Andersen, R. J.; O'Connor, T. P. *Neuroscience* **2006**, *139* (4), 1263. doi:10.1016/j.neuroscience.2006.01.065. PMID:16564636.; (f) Kaur, N.; Delcros, J.-G.; Martin, B.; Phanstiel, O., 4th. *J. Med. Chem.* **2005**, *48* (11), 3832. doi:10.1021/jm0491288. PMID:15916435.

(39) (a) Sies, H., Ed. *Oxidative Stress*; Academic Press: London, 1985; (b) Rice-Evans, C.; Halliwell, B.; Lunt, G. G., Eds. *Free Radicals and Oxidative Stress: Environment, Drugs and Food Additives;* Portland Press: London, 1995; (c) Paoletti, R.; Samuelsson, B.; Catapano, A. L.; Poli, A.; Rinetti, M., Eds. *Oxidative Processes and Antioxidants;* Raven Press: New York, 1994.

(40) Epp, O.; Ladenstein, R.; Wendel, A. *Eur. J. Biochem.* **1983**, *133* (1), 51. doi:10.1111/j.1432-1033.1983.tb07429.x. PMID:6852035.

(41) (a) Ganther, H. E. *Chem. Scr.* **1975**, *8a*, 79; (b) Ganther, H. E.; Kraus, R. J. In *Methods in Enzymology;*Colowick, S. P.; Kaplan, N. O., Eds.; Academic Press: New York, 1984; Vol. 107, pp 593–602;(c) Stadtman, T. C. *J. Biol. Chem.* **1991**, *266* (25), 16257. PMID:1832153.; (d) Tappel, A. L. *Curr. Top. Cell. Regul.* **1984**, *24*, 87. PMID:6238814.; (e) Flohé, L. *Curr. Top. Cell. Regul.* **1985**, *27*, 473. PMID: 4092495.

(42) (a) For reviews, see: Mugesh, G.; du Mont, W.-W.; Sies, H. *Chem. Rev.* **2001**, *101* (7), 2125. doi:10.1021/cr000426w. PMID:11710243.; (b) Mugesh, G.; Singh, H. B. *Chem. Soc. Rev.* **2000**, *29* (5), 347. doi:10.1039/a908114c.; (c) Mugesh, G.; du Mont, W.-W. *Chem. Eur. J.* **2001**, *7* (7), 1365. doi:10.1002/1521-3765(20010401)7:7<1365::AID-CHEM1365>3.0.CO;2-Y.; (d) Sarma, B. K.; Mugesh, G. *Org. Biomol. Chem.* **2008**, *6* (6), 965. doi:10.1039/b716239a. PMID:18327317.

(43) Reich, H. J.; Jasperse, C. P. *J. Am. Chem. Soc.* **1987**, *109* (18), 5549. doi:10.1021/ja00252a055.

(44) Engman, L.; Andersson, C.; Morgenstern, R.; Cotgreave, I. A.; Andersson, C. M.; Hallberg, A. *Tetrahedron* **1994**, *50* (9), 2929. doi:10.1016/S0040-4020(01)87004-6.

(45) Wilson, S. R.; Zucker, P. A.; Huang, R.-R. C.; Spector, A. *J. Am. Chem. Soc.* **1989**, *111* (15), 5936. doi:10.1021/ja00197a065.

(46) Galet, V.; Bernier, J.-L.; Henichart, J.-P.; Lesieur, D.; Abadie, C.; Rochette, L.; Lindenbaum, A.; Chalas, J.; Renaud de la Faverie, J.-F.; Pfeiffer, B.; Renard, P. *Med. Chem.* **1994**, *37* (18), 2903. doi:10.1021/jm00044a011.

(47) Ostrovidov, S.; Franck, P.; Joseph, D.; Martarello, L.; Kirsch, G.; Belleville, F.; Nabet, P.; Dousset, B. *J. Med. Chem.* **2000**, *43* (9), 1762. doi:10.1021/jm991019j. PMID: 10794693.

(48) Wirth, T. *Molecules* **1998**, *3* (7), 164. doi:10.3390/30700164.

(49) (a) Mugesh, G.; Panda, A.; Singh, H. B.; Punekar, N. S.; Butcher, R. J. *J. Chem. Soc. Chem. Commun.* **1998**, 2227; (b) Kumar, S.; Tripathi, S. K.; Singh, H. B.; Wolmershäuser, G. *J. Organomet. Chem.* **2004**, *689* (19), 3046. doi:10.1016/j.jorganchem.2004.06.054.

(50) You, Y.; Ahsan, K.; Detty, M. R. *J. Am. Chem. Soc.* **2003**, *125* (16), 4918. doi:10.1021/ja029590m. PMID:12696911.

(51) Engman, L.; Stern, D.; Cotgreave, I. A.; Andersson, C. M. *J. Am. Chem. Soc.* **1992**, *114* (25), 9737. doi:10.1021/ja00051a002.

(52) (a) SYI 2074 was formerly known as BXT 51072. For lead references, see: Moutet, M.; d'Alessio, P.; Malette, P.; Devaux, V.; Chaudière, J. *Free Radic. Biol. Med.* **1998**, *25* (3), 270. doi:10.1016/S0891-5849(98)00038-0. PMID:9680172.; (b) Erdelmeier, I.; Tailhan-Lomont, C.; Yadan, J.-C. *J. Org. Chem.* **2000**, *65* (24), 8152. doi:10.1021/jo000418f. PMID: 11101367.; (c) Jacquemin, P. V.; Christiaens, L. E.; Renson, M. J.; Evers, M. J.; Dereu, N. *Tetrahedron Lett.* **1992**, *33* (27), 3863. doi:10.1016/S0040-4039(00)74805-2.

(53) (a) Müller, A.; Cadenas, E.; Graf, P.; Sies, H. *Biochem. Pharmacol.* **1984**, *33* (20), 3235. doi:10.1016/0006-2952(84)90083-2. PMID:6487370.; (b) Wendel, A.; Fausel, M.; Safayhi, H.; Tiegs, G.; Otter, R. *Biochem. Pharmacol.* **1984**, *33* (20), 3241. doi:10.1016/0006-2952(84)90084-4. PMID: 6487371.; (c) Parnham, M. J.; Kindt, S. *Biochem. Pharmacol.* **1984**, *33* (20), 3247. doi:10.1016/0006-2952(84)90085-6. PMID:6593071.; (d) Müller, A.; Gabriel, H.; Sies, H. *Biochem. Pharmacol.* **1985**, *34* (8), 1185. doi:10.1016/0006-2952(85)90493-9. PMID:3994741.; (e) Safayhi, H.; Tiegs, G.; Wendel, A. *Biochem. Pharmacol.* **1985**, *34* (15), 2691. doi:10.1016/0006-2952(85)90569-6. PMID:2990494.; (f) Wendel, A.; Tiegs, G. *Biochem. Pharmacol.* **1986**, *35* (13), 2115. doi:10.1016/0006-2952(86)90578-2. PMID:3729968.; (g) Fischer, H.; Dereu, N. *Bull. Soc. Chim. Belg.* **1987**, *96*, 757; (h) Haenen, G. R. M. M.; De Rooij, B. M.; Vermeulen, N. P. E.; Bast, A. *Mol. Pharmacol.* **1990**, *37* (3), 412. PMID: 2107391.; (i) Glass, R. S.; Farooqui, F.; Sabahi, M.; Ehler, K. W. *J. Org. Chem.* **1989**, *54* (5), 1092. doi:10.1021/jo00266a018.

(54) For a list of potential medicinal applications of ebselen, see: Fong, M. C.; Schiesser, C. H. *Tetrahedron Lett.* **1995**, *36* (40), 7329. doi:10.1016/0040-4039(95)01511-F.

(55) Back, T. G.; Dyck, B. P. *J. Am. Chem. Soc.* **1997**, *119* (9), 2079. doi:10.1021/ja963602k.

(56) Back, T. G.; Moussa, Z. *J. Am. Chem. Soc.* **2002**, *124* (41), 12104. doi:10.1021/ja028030k. PMID:12371844.

(57) Back, T. G.; Moussa, Z. *J. Am. Chem. Soc.* **2003**, *125* (44), 13455. doi:10.1021/ja0357588. PMID:14583041.

(58) Wirth and colleagues also demonstrated that compounds with pendant alcohol groups (e.g., see Fig. 3) that are capable of coordinating to selenium can function as GPx mimetics; see ref. 48.

(59) Back, T. G.; Moussa, Z.; Parvez, M. *Angew. Chem. Int. Ed.* **2004**, *43* (10), 1268. doi:10.1002/anie.200353128.

(60) Nogueira, C. W.; Zeni, G.; Rocha, J. B. T. *Chem. Rev.* **2004**, *104* (12), 6255. doi:10.1021/cr0406559. PMID:15584701.

(61) Back, T. G.; Kuzma, D.; Parvez, M. *J. Org. Chem.* **2005**, *70* (23), 9230. doi:10.1021/jo0512711. PMID:16268595.

(62) Press, D. J.; Mercier, E. A.; Kuzma, D.; Back, T. G. *J. Org. Chem.* **2008**, *73* (11), 4252. doi:10.1021/jo800381s. PMID: 18433177.

(63) Kuzma, D.; Parvez, M.; Back, T. G. *Org. Biomol. Chem.* **2007**, *5* (19), 3213. doi:10.1039/b710685h. PMID:17878981.

(64) Tripathi, S. K.; Patel, U.; Roy, D.; Sunoj, R. B.; Singh, H. B.; Wolmershäuser, G.; Butcher, R. J. *J. Org. Chem.* **2005**, *70* (23), 9237. doi:10.1021/jo051309+. PMID:16268596.

(65) For example, see: Chaudiere, J.; Courtin, O.; Leclaire, J. *Arch. Biochem. Biophys.* **1992**, *296* (1), 328. doi:10.1016/0003-9861(92)90580-P. PMID:1605642.

(66) The cyclic seleninates and spirodioxyselenuranes described here were licensed to Synvista Therapeutics Inc. for further investigation as GPx mimetics.

Direct halogenation of organic compounds with halides using oxone in water — A green protocol

H. Firouzabadi, N. Iranpoor, and S. Kazemi

Abstract: Direct bromination and iodination of various aromatic compounds with NaBr and NaI using oxone ($2KHSO_5 \cdot KHSO_4 \cdot K_2SO_4$) in water was accomplished successfully in high-to-excellent yields. The main benefit of this protocol is the performance of the reactions in water in the presence of a harmless oxidant without the use of any organic co-solvents. Using NaBr and NaI as the safe sources of halogens is another advantage of the protocol. This method is easily applicable to the large-scale operations. We have also applied this method successfully for the iodocyclization of an unsaturated alcohol and an unsaturated carboxylic acid.

Key words: iodination, bromination, oxone, water.

Résumé : On a effectué avec succès la bromation et l'iodation directe de divers composés aromatiques avec du NaBr et du NaI à l'aide d'oxone ($2KHSO_5 \cdot KHSO_4 \cdot K_2SO_4$) dans l'eau; les rendements vont d'élevés à excellents. Le bénéfice principal de ce protocole réside dans le fait que les réactions sont effectuées dans l'eau, en présence d'un oxydant inoffensif, sans nécessité de solvant organique. L'utilisation de NaBr et de NaI comme source sécuritaire d'halogène est un autre avantage de cette méthode qui peut facilement être appliquée à des opérations d'envergure. On a aussi appliqué avec succès cette méthode à l'iodocyclisation d'un alcool et d'un acide carboxylique insaturés.

Mots-clés : iodation, bromation, oxone, eau.

[Traduit par la Rédaction]

Introduction

Waste prevention rather than its treatment is of great concern for the industry and academia. For this aim, the use of less toxic materials as solvents and reagents is encouraged.[1] However, disposing organic solvents in pharmaceutical industries is their current major problem, as these solvents compose ~80% of their waste.[2,3] Replacement of toxic, flammable, non-recyclable, expensive, and organic solvents with water in organic reactions is a great challenge for academia and chemical industries.[4,5]

Using water is beneficial from different aspects. Water is a cheap, abundant, nontoxic, nonflammable, and green solvent. On the other hand, water with its chemical and physical properties imposes selectivity and reactivity in reactions, which cannot be achieved using organic solvents.[6] In addition, organic compounds are insoluble in water; therefore, phase separation is easier and they can be easily isolated from aqueous media.

Recently, we have paid attention towards using water as a reaction medium. Along this line, Michael addition of amines and thiols to α,β-unsaturated ketones,[7] regioselective iodination of aromatic compounds,[7b] ring opening of epoxides with varieties of nucleophiles,[7c] oxidation of sulfides to their sulfoxides with H_2O_2,[7d] Michael addition of indoles and pyrroles to α,β-unsaturated electron-deficient compounds,[7e] conversion of epoxides to thiiranes and amino alcohols,[7f] C–S bond formation via odorless thia-Michael addition,[7g] C–C bond formation via Heck–Mizoroki reactions in water,[7h] and highly efficient halogenation of organic compounds with halides catalyzed by $CeCl_3 \cdot 7H_2O$ using H_2O_2 as the terminal oxidant in H_2O[7i] are reported.

The aromatic halogenation reaction is an important electrophilic substitution reaction, and haloarenes are useful synthetic intermediates in the pharmaceuticals, pesticides, and agrochemical industries.[8] In addition, haloarenes are useful and important substrates for the preparation of organometallic compounds. The other important uses of haloarenes are in Heck, Stille, Sozuki, and Sonogashira reactions.[9] Halogenation of organic substrates requires using chlorine, bromine, or iodine. This reaction is associated with serious environmental hazards with respect to handling, transportation, and storage of chlorine, bromine, and iodine.[10]

Handling of halide salts is safer and easier than their molecular halogens. They are oxidized to the corresponding positive halogens or hypohalous acids by a variety of oxidants, including peroxo compounds.[8] However, the articles describing the application of peroxo compounds for the oxidative halogenation of arenes include $Ce(OH)_3OH$/SDS-H_2O,[7b] KI/benzyltriphenylphosphoniumperoxo mono-sulfate/MeCN,[11] KI/H_2O_2(30%)/H_2SO_4/MeOH,[12] KI or I_2/PVP-supported $H_2O_2/H_3PW_{12}O_{40}$ in CH_2Cl_2,[13] I_2 or KI /($Na_2CO_3 \cdot 3H_2O_2$),[14] $I_2/[(Bu_4N)_4(S_2O_8)]$/MeCN or CH_2Cl_2,[15] $I_2/[(MePPh_3)_2(S_2O_8)]$/MeCN,[16] I_2/NaS_2O_8/MeCN,[17] and NaI/H_2O_2/organotelluride cat. at pH-6 buffer in Et_2O/H_2O,[18] KBr/benzyltriphenylphosphonium peroxodisulfate/ MeCN,[19] Br_2 or LiBr/tetrabutylammonium peroxydizulfate/MeCN or CH_2Cl_2,[20] I_2/

Received 3 March 2009. Accepted 6 July 2009. Published on the NRC Research Press Web site at canjchem.nrc.ca on 6 November 2009.

H. Firouzabadi,[1] N. Iranpoor,[2] and S. Kazemi. Department of Chemistry, College of Sciences, Shiraz University, Shiraz 71454, Iran.

[1]Corresponding author (e-mail: firouzabadi@chem.susc.ac.ir).
[2]Corresponding author (e-mail: iranpoor@chem.susc.ac.ir).

poly(4-vinylpyridine)-supported peroxodisulfate/MeCN,[21] and NaI/Oxone/CH_3OH.[22] The other methods using hydrogen peroxide include the use of NH_4I/H_2O_2/HOAc,[23] NH_4Br/H_2O_2/HOAc,[24] HX/ $H_2O_2/C_2H_4Cl_2$/MW,[25] H_2O_2/I_2,[26] and NaBr/ H_2O_2/ H_2SO_4/ $CHCl_3$.[27]

Oxone is a ternary composite of $2KHSO_5$, $KHSO_4$, and K_2SO_4 that is a stable peroxo inorganic compound. Oxone has a low order of toxicity when taken internally, based on animal studies. The approximate lethal dose (ALD) for rats is 2250 mg/kg.[28] Iodination of arenes with NH_4I in MeOH in the presence of oxone is recently reported.[29] This procedure encounters limitations such as the following: (*i*) it is applicable to electron-rich aryl compounds, (*ii*) usually long reaction times are required (8–48 h), and (*iii*) moderately deactivated aryl compounds such as bromobenzene remain intact even after 24 h.

In this article, we report a green method for the iodination and bromination of structurally different arenes by NaI and NaBr with oxone in H_2O in the absence of any organic co-solvents with high regioselectivity. In addition, halocyclization of unsaturated alcohols and a carboxylic acid with NaI/oxone system in water is also reported.

Results and discussion

In this study, we report a green procedure for the halogenation of structurally diverse arenes using NaBr and NaI salts as safe sources of halogens and oxone as a safe solid oxidant in water in the absence of any organic co-solvents. For optimization of the reaction conditions, we studied the reaction of anisole with NaI in the presence of oxone in water at room temperature. We found that the optimized molar ratio of anisole/NaI/Oxone was 1:1:0.5 mmol in 2 mL of water. The reaction proceeded well with excellent para selectivity, and after 8 h (GC or TLC), the *p*-iodoanisole was isolated in 90% yield. The structure of the isolated compound was confirmed by ^1H and ^{13}C NMR and compared with an authentic sample. The reaction was also investigated under reflux conditions. The reaction proceeded to completion faster, and after 30 min (GC or TLC), the para isomer was isolated with excellent selectivity in 93% yield (Scheme 1).

To show the general application of the method, the optimized conditions were applied to structurally different arenes. The results of this investigation are tabulated in Table 1. As it is evident from the results, this protocol is applicable to a broad spectrum of arenes, such as electron-rich aromatic compounds, toluene, benzene, bromo-, and chlorobenzenes. As shown in Table 1, electron-poor compounds like acetophenone and benzonitrile were also subjected to iodination reaction. The reaction of acetophenone proceeded very slowly, and after 48 h, the meta product was isolated in 40% yield. Benzonitrile was isolated intact from the reaction mixture after 48 h.

Bromination of arenes was also investigated by this protocol. For this purpose, we first optimized the reaction conditions for the bromination of anisole with NaBr in the presence of oxone in water as a model reaction. The optimized molar ratio of anisole/NaBr/oxone was 1:1:0.5 mmol in 2 mL of water at room temperature. In contrast to the iodination reaction, bromination proceeded well to completion after 10 min at room temperature, and the *para*-bromo compound was isolated in 93% yield as the sole product. Then, we applied these conditions to electron-rich aromatic compounds, e.g., benzene, toluene, naphthalene, and chlorobenzene. The reactions proceeded well in high isolated yields. All the reactions were performed with high selectivity and only one product was isolated from the reaction mixtures. The structures of the products were also confirmed by ^1H and ^{13}C NMR and were compared with authentic samples. The results are tabulated in Table 2.

Scheme 1.

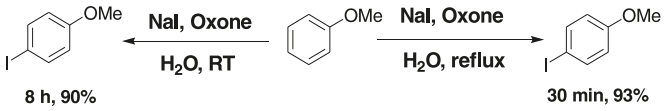

Scheme 2.

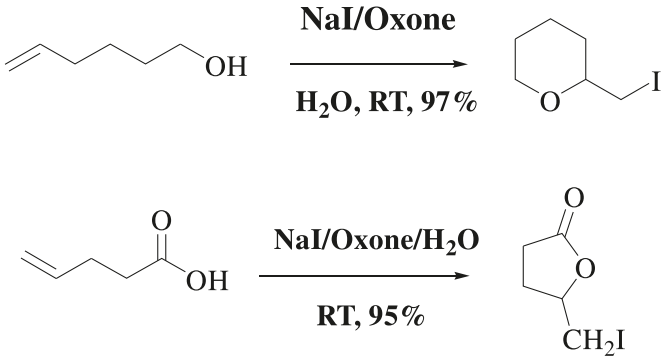

We also easily scaled up the bromination reaction of anisole, xylene, and naphthalene to 20 mmol. All the reactions proceeded well within the reaction times indicated in Table 2, and the mono-brominated compounds were isolated with the same yields as indicated in the table.

To show the advantage of using water as the reaction medium, we compared the results of the iodination of arenes with some of the reactions that proceeded in methanol,[29] as presented in Table 3.

Iodoetherification and iodolactonization are important and crucial reactions in organic synthesis and also for the structural elucidation of organic molecules.[30,31] Examples include Corey's prostaglandin synthesis,[32] total synthesis of tumor inhibitors, e.g., vernolepin and vernomenin,[33] and in vitamin D_2 and D_3 syntheses.[34]

We were also interested in investigating halocyclization reactions, such as iodoetherification and iodolactonization, by this system. For this purpose, a similar molar ratio to the ratio used for the iodination of arenes was applied to the reaction of 5-hexene-1-ol and 4-pentene-1-oic acid as model compounds. Our preliminary studies show that iodination – ring-closure reaction proceeded immediately, and the corresponding iodocyclic ethers and the iodolactone were isolated in excellent yields as shown in Scheme 2.

Most of the products are known compounds, and their spectral data and physical constants along with their references are given in the Experimental section. The data of the known compounds have been found to be identical with those reported. For the unknown compounds, spectral data along with their elemental analyses are also given in the Experimental section.

Table 1. Mono-iodination of aromatic compounds using NaI/oxone/H_2O under reflux conditions.

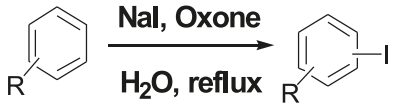

Entry	Substrate	product	Time	GC conversion (%)	Isolated yield (%)
1	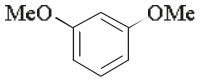	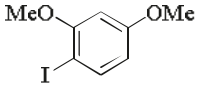	15 min	100	98
2	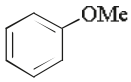	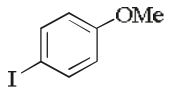	30 min	100	93
3	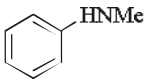	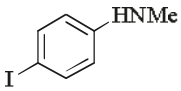	10 min	100	85
4	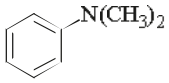	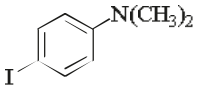	15 min	100	89
5	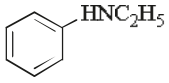	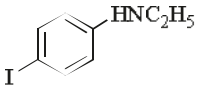	15 min	100	90
6	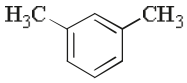	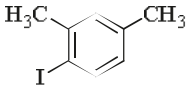	3 h	100	90
7	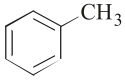	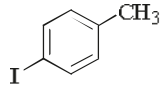	3.5 h	100	87
8			6 h	100	88
9	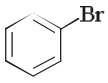	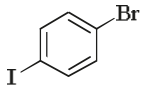	12 h	100	85
10	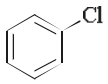	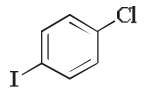	12 h	100	83
11	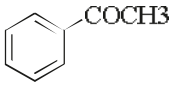	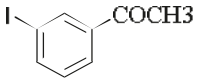	48 h	45[a]	40
12	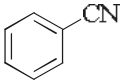	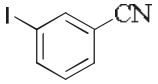	48 h	–	–

[a] *n*-Ocatane was used as an internal standard.

Conclusions

In conclusion, in this article, we have presented a green protocol for the halogenation of organic compounds using NaI or NaBr/oxone/H_2O system. We have modified the previously reported protocol using NaI/oxone system in MeOH for the iodination of activated aromatic compounds with NaI/oxone system in H_2O as a green solvent. As we have shown, similar iodination reactions proceeded more efficiently in H_2O than in MeOH. NaI/oxone/H_2O system

Table 2. Bromination of aromatic compounds using NaBr/Oxone/H_2O at room temperature.

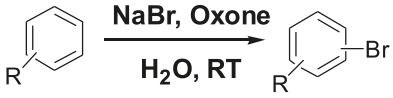

Entry	Substrate	product	Time (min)	GC conversion (%)	Isolated yield (%)
1	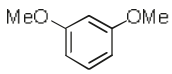	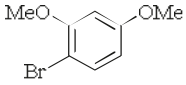	5	100	95
2	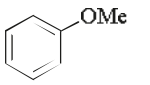	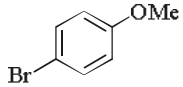	10	100	93
3	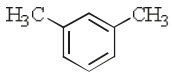	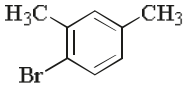	20	100	87
4	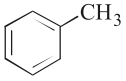	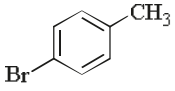	25	100	85
5	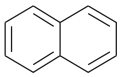	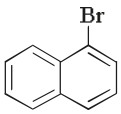	7	100	80
6		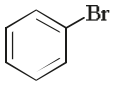	1.5 h	100	88
7	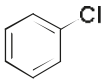	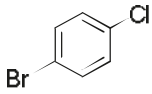	3 h	100	90
8	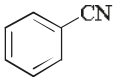	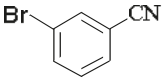	12 h	–	–

Table 3. A comparison between two procedures using NaI/oxone/MeOH[29] and NaI/oxone/ H_2O for the iodination of different aromatic compounds.

	NaI/Oxone/MeOH		NaI/Oxone/H_2O	
Substrate	Time (h)	Conversion	Time (h)	Conversion
Bromobenzene	24	NR	12	85%
m-Xylene	24	99%	3	90%
Anisole	8	99%	0.5	93%

has been successfully applied to highly efficient and regioselective iodination and bromination of structurally different aromatic compounds. In addition, we have also successfully applied the protocol to highly efficient one-pot iodination/cyclization of unsaturated alcohols and iodination/lactonization of an unsaturated carboxylic acid. The method is also applicable to the large-scale reactions without any difficulties.

Experimental section

Typical procedure for the mono-iodination of 1,3-dimetoxybenzene with NaI/oxone system in H_2O

To a stirring mixture of 1,3-dimetoxybenzene (0.138 g, 1 mmol) and NaI (0.149 g, 1 mmol) in water (3 mL), oxone (0.307 g, 0.5 mmol) was added, and the mixture was refluxed for 15 min. The progress of the reaction was monitored by GC or TLC. The resulting reaction mixture was treated with $Na_2S_2O_4$ solution (10 mol%, 10 mL) and extracted with diethyl ether (2 × 10 mL). The ethereal solution was dried over anhydrous Na_2SO_4 and filtered. Evaporation of the solvent resulted in the desired crude product, which was further purified by plate chromatography technique to produce the pure compound in 98% (Table 1, entry 1).

Typical procedure for the mono-bromination of 1,3-dimetoxybenzene with NaBr/oxone system in H_2O

To a stirring mixture of 1,3-dimetoxybenzene (0.138 g,

1 mmol) and NaBr (0.102 g, 1 mmol) in water (3 mL), oxone (0.307 g, 0.5 mmol) was added. The reaction was completed within 5 min (GC or TLC). The resulting reaction mixture was treated with $Na_2S_2O_4$ solution (5 mol%, 30 mL) and extracted with diethyl ether. The organic layer was separated and dried over anhydrous Na_2SO_4, and after filtration and evaporation of the solvent, the desired mono-brominated crude product was obtained. Further purification was performed by plate chromatography technique to give the pure compound in 95% yield (Table 2, entry 1).

Typical procedure for the iodoetherification of 5-hexene-1-ol with NaI/oxone system in H_2O

To a stirring mixture of 5-hexene-1-ol (0.1 g, 1 mmol) and NaI (0.149 g, 1 mmol) in water (3 mL) was added oxone (0.307 g, 0.5 mmol). An immediate reaction occurred (GC or TLC). To the resulting reaction mixture, $Na_2S_2O_4$ solution (5 mol%, 30 mL) was added, and the mixture was extracted with diethyl ether. The organic layer was separated and dried over anhydrous Na_2SO_4. After filtration and evaporation of the solvent, the resulting crude product was further purified by plate chromatography technique to give the desired iodocyclic ether in 97% yield (Scheme 2). The structure of the product was identified by ^1H and ^{13}C NMR.

Typical procedure for the iodolactonization of 4-pentene-1-oic acid with NaI/oxone system in H_2O

To a stirring mixture of 4-pentene-1-oic acid (0.1 g, 1 mmol) and NaI (0.149 g, 1 mmol) in water (3 mL) was added oxone (0.307 g, 0.5 mmol). An immediate reaction occurred (GC or TLC). To the resulting reaction mixture, $Na_2S_2O_4$ solution (5 mol%, 30 mL) was added, and the mixture was extracted with diethyl ether. The organic layer was separated and dried over anhydrous Na_2SO_4. After filtration and evaporation of the solvent, the resulting crude product was further purified by plate chromatography technique to give the desired iodolactone in 95% yield (Scheme 2). The structure of the product was identified by ^1H and ^{13}C NMR.

Physical constants of known compounds

4-Iodo-1,3-dimethoxy benzene
Mp 39–41 °C (lit.[41] mp 37–41 °C).

4-Iodoanisole
Mp 52–53 °C (lit.[35] mp 48–55 °C).

4-Iodo*-N-*methylaniline
Mp 30–32 °C (lit.[36] mp 31.5).

4-Iodo*-N,N-*dimethylaniline
Mp 75–76 °C (lit.[37] mp 77 °C).

4-Iodo-1,3-dimethylbenzene
Bp 229–230 °C (lit.[35] mp 229 °C).

4-Iodotoluene
Mp (petroleum ether) 33–35 °C (lit.[38] mp 34 °C).

Iodobenzene
Bbp 187–189 °C (lit.[41] mp 188 °C).

4-Bromo-1-iodobenzene
Mp (petroleum ether) 91–93 °C (lit.[39] mp 95–97 °C).

4-Chloro-1-iodobenzene
Mp (diethyl ether) 55–57 °C (lit.[39] mp 54–56 °C).

4-Bromo-1,3-dimethoxy benzene
Mp (petroleum ether) 24–26 °C (lit.[41] mp 25–26 °C).

4-Bromoanisole
Bp 222–224 °C (lit.[41] mp 223 °C).

4-Bromo-1,3-dimethylbenzene
Bp 212–213 °C (lit.[41] mp 214 °C).

4-Bromotoluene
Mp (petroleum ether) 24–26 °C (lit.[40] mp 25–26 °C).

1-Bromonaphthalene
Bp 280–282 °C (lit.[42] mp 279–281 °C).

Bromobenzene
Bp 153–155 °C (lit.[41] mp 156 °C).

4-Chloro-1-bromobenzene
Mp (diethyl ether) 66–68 °C (lit.[40] mp 65–66 °C).

Spectral data and elemental analysis for the unknown compounds

4-Iodo*-N-*ethylaniline
Mp($CHCl_3$/diethyl ether) 79–81 °C. ^1H NMR ($CDCl_3$, 250 MHz) δ (ppm): 1.11 (t, 3 H, J = 7.1 Hz), 2.97 (q, 2 H, J = 7.1 Hz), 3.37 (m, 1 H), 6.27 (d, 1 H, J = 4.9 Hz), 7.30 (d, 1 H, J = 4.8 Hz). ^{13}C NMR ($CDCl_3$, 62.9 MHz) δ (ppm): 13.65, 37.26, 76.55, 113.89, 136.66, 146.84. Anal. calcd.: C, 38.88; H, 4.05; N, 5.67. Found: C, 38.69; H, 4.00; N, 5.38.

5-(Iodomethyl)dihydrofuran-2-one
Liquid. ^{13}C NMR ($CDCl_3$, 62.9 MHz) δ (ppm): 7.39, 27.01, 27.89, 77.42, 175.38. Anal. calcd.: C, 31.85; H, 4.86. Found: C, 31.70; H, 4.07.

2-Iodomethyltetrahydropyran
Liquid. ^1H NMR ($CDCl_3$, 250 MHz) δ (ppm): 1.18–1.80(m, 6 H), 3.10 (d, 2 H, J = 3.5), 3.21–3.40 (m, 1 H), 3.93–4.12 (m, 2 H). ^{13}C NMR ($CDCl_3$, 62.9 MHz) δ (ppm): 9.10, 22.14, 24.56, 30.69, 67.77, 76.61. Anal. calcd.: C, 26.54; H, 3.09. Found: C, 26.22; H, 3.00.

Acknowledgements

We are grateful to TWAS Chapter of Iran based at ISMO and Shiraz University Research Council for the support of this work. We also acknowledge help and technical assistance of Arash Ghaderi.

References

(1) Anastas, P. T.; Kirchhoff, M. M. *Acc. Chem. Res.* **2002**, *35* (9), 686–694. doi:10.1021/ar010065m. PMID:12234198.
(2) Sheldon, R. A. *Chemtech* **1994**, *24*, 38.
(3) Jiménez-González, C.; Curzons, A. D.; Constable, D. J. C.;

Cunningham, V. *Int. J. LCA* **2004**, *9* (2), 114–121. doi:10.1007/BF02978570.

(4) Anastas, P. T.; Warner, J. C. *Green Chemistry: Theory and Practice;* Oxford University Press: Oxford, 1998.

(5) Tundo, P.; Anastas, P.; Black, D. StC.; Breen, J.; Collins, T.; Memoli, S.; Miamoto, J.; Polyakoff, M.; Tumas, W. *Pure Appl. Chem.* **2000**, *72* (7), 1207–1228. doi:10.1351/pac200072071207.

(6) (a) Grieco, P. A., Ed.; *Organic Synthesis in Water;* Blacky Academic and Professional: London, 1998; (b) Li, C.-J.; Chan, T.-H. *Organic Reactions in Aqueous Media;* John Wiley & Sons: New York, 1997; (c) Cornils, B.; Hermann, W. A. *Aqueous-Phase Organometallic Chemistry: Concepts and Applications;* Wiley-VCH:Weiheim, 1998; (d) Rideout, D. C.; Breslow, R. *J. Am. Chem. Soc.* **1980**, *102* (26), 7816–7817. doi:10.1021/ja00546a048.; (e) Breslow, R. *Acc. Chem. Res.* **1991**, *24* (6), 159–164. doi:10.1021/ar00006a001.; (f) Li, C.-J. *Chem. Rev.* **2005**, *105* (8), 3095–3165. doi:10.1021/cr030009u. PMID:16092827.

(7) (a) Firouzabadi, H.; Iranpoor, N.; Jafari, A. A. *Adv. Synth. Catal.* **2005**, *347* (5), 655–661. doi:10.1002/adsc.200404348.; (b) Firouzabadi, H.; Iranpoor, N.; Garzan, A. *Adv. Synth. Catal.* **2005**, *347* (15), 1925–1928. doi:10.1002/adsc.200505222.; (c) Iranpoor, N.; Firouzabadi, H.; Shekarize, M. *Org. Biomol. Chem.* **2003**, *1* (4), 724–727. doi:10.1039/b211697a. PMID:12929461.; (d) Firouzabadi, H.; Iranpoor, N.; Jafari, A. A.; Riazymontazer, E. *Adv. Synth. Catal.* **2006**, *348* (4-5), 434. doi:10.1002/adsc.200505312.; (e) Firouzabadi, H.; Iranpoor, N.; Nowrouzi, F. *Chem. Commun. (Camb.)* **2005**, *6* (6), 789–791. doi:10.1039/b412653j. PMID:15685339.; (f) Firouzabadi, H.; Iranpoor, N.; Khoshnood, A. *J. Mol. Catal. Chem.* **2007**, *274* (1-2), 109–115. doi:10.1016/j.molcata.2007.04.035.; (g) Firouzabadi, H.; Iranpoor, N.; Abbassi, M. *Adv. Synth. Catal.* **2009**, *351* (5), 755–766. doi:10.1002/adsc.200800690.; (h) Robertson, L.; Hartley, R. C. *Tetrahedron* **2009**, *65* (27), 5284–5292. doi:10.1016/j.tet.2009.04.083. PMID:19693262.; (i) Firouzabadi, H.; Iranpoor, N.; Kazemi, S.; Ghaderi, A.; Garzan, A. *Adv. Synth. Catal.* **2009**, *351* (11-12), 1925–1932. doi:10.1002/adsc.200900124.

(8) (a) Stavber, S.; Jereb, M.; Zupan, M. *Synthesis* **2008**, *2008* (10), 1487–1513. doi:10.1055/s-2008-1067037.; (b) Miyaura, N.; Suzuki, A. *Chem. Rev.* **1995**, *95* (7), 2457–2483. doi:10.1021/cr00039a007.; (c) Merkushev, E. B. *Synthesis* **1988**, *1988* (12), 923–937. doi:10.1055/s-1988-27758.

(9) (a) Beletskaya, I. P.; Cheprakov, A. V. *Chem. Rev.* **2000**, *100* (8), 3009–3066. doi:10.1021/cr9903048. PMID:11749313.; (b) Yin, L.; Liebscher, J. *Chem. Rev.* **2007**, *107* (1), 133–173. doi:10.1021/cr0505674. PMID:17212474.; (c) Chinchilla, R.; Najera, C. *Chem. Rev.* **2007**, *107* (3), 874. doi:10.1021/cr050992x.; (d) Felpin, F. X.; Ayad, T.; Mitra, S. *Eur. J. Chem.* **2006**, 2679.; (e) Merkushev, E. B. *Synthesis* **1988**, *1988* (12), 923–937. doi:10.1055/s-1988-27758.; (f) Miyaura, N.; Suzuki, A. *Chem. Rev.* **1995**, *95* (7), 2457–2483. doi:10.1021/cr00039a007.

(10) Clark, J. H.; Ross, J. C.; Macquarrie, D. J.; Barlow, S. J.; Bastock, T. W. *Chem. Commun. (Camb.)* **1997**, (13): 1203–1204. doi:10.1039/a702399e.

(11) Hajipour, A. R.; Adibi, H. *J. Chem. Res. Synop.* **2004**, 294.

(12) Iskra, J.; Stavber, S.; Zupan, M. *Synthesis* **2004**, *2004* (11), 1869–1873. doi:10.1055/s-2004-829136.

(13) Pourali, A. R.; Ghanei, M. *Chin. J. Chem.* **2006**, *24* (8), 1077–1079. doi:10.1002/cjoc.200690201.

(14) Zielinska, A.; Skulski, L. *Molecules* **2005**, *10* (10), 1307–1317. doi:10.3390/10101307. PMID:18007524.

(15) Yang, S. G.; Kim, Y. H. *Tetrahedron Lett.* **1999**, *40* (33), 6051–6054. doi:10.1016/S0040-4039(99)01236-8.

(16) Hajipour, A. R.; Ruoho, A. E. *Org. Prep. Proced. Int.* **2005**, *180*, 1235.

(17) Barton, O. G.; Mattay, J. *Synthesis* **2008**, 110.

(18) Higgs, D. E.; Nelen, M. I.; Detty, M. R. *Org. Lett.* **2001**, *3* (3), 349–352. doi:10.1021/ol0068142. PMID:11428011.

(19) Tajik, H.; Mohammadpoor-Baltork, I.; Albadi, J. *Synth. Commun.* **2007**, *37* (2), 323–328. doi:10.1080/00397910601033906.

(20) Park, M. Y.; Yang, S. G.; Jadhav, V.; Kim, Y. H. *Tetrahedron Lett.* **2004**, *45* (25), 4887–4890. doi:10.1016/j.tetlet.2004.04.112.

(21) Tajik, H.; Mohammadpoor-Baltork, I.; Rasht-Abadi, H. R. *Synth. Commun.* **2004**, *34* (19), 3579–3585. doi:10.1081/SCC-200031032.

(22) (a) Krishna Mohan, K. V. V.; Narender, N.; Kulkarni, S. J. *Tetrahedron Lett.* **2004**, *45* (43), 8015–8018. doi:10.1016/j.tetlet.2004.09.010.; (b) Narender, N.; Srinivasu, P.; Kulkarni, S. J.; Raghavan, K. *Synth. Commun.* **2002**, *32* (15), 2319–2324. doi:10.1081/SCC-120006002.

(23) Narender, N.; Reddy, K. S. K.; Krishna Mohan, K. V. V.; Kulkarni, S. J. *Tetrahedron Lett.* **2007**, *48* (35), 6124–6128. doi:10.1016/j.tetlet.2007.06.138.

(24) Krishna Mohan, K. V. V.; Narender, N.; Srinivasu, P.; Kulkarni, S. J.; Raghavan, K. V. *Synth. Commun.* **2004**, *34* (12), 2143–2152. doi:10.1081/SCC-120038491.

(25) Bogdal, D.; Lukasiewicz, M.; Pielichowski, J. *Green Chem.* **2004**, *6* (2), 110. doi:10.1039/b312706k.

(26) Kim, M. M.; Ruck, R. T.; Zhao, D.; Huffman, M. A. *Tetrahedron Lett.* **2008**, *49* (25), 4026–4028. doi:10.1016/j.tetlet.2008.04.082.

(27) Mestres, R.; Palenzuela, J. *Green Chem.* **2002**, *4* (4), 314–316. doi:10.1039/b203055a.

(28) Dupont. *DuPont™ Oxone® monopersulfate compound;* Available from www.dupont.com/oxone, 2009.

(29) (a) Krishna Mohan, K. V. V.; Narender, N.; Kulkarni, S. J. *Tetrahedron Lett.* **2004**, *45* (43), 8015–8018. doi:10.1016/j.tetlet.2004.09.010.; (b) Narender, N.; Srinivasu, P.; Kulkarni, S. J.; Raghavan, K. *Synth. Commun.* **2002**, *32* (15), 2319–2324. doi:10.1081/SCC-120006002.

(30) Chavan, S. P.; Sharma, A. K. *Tetrahedron Lett.* **2001**, *42* (29), 4923–4924. doi:10.1016/S0040-4039(01)00876-0.

(31) Ranganathan, S.; Muraleedharan, K. M.; Vaish, N. K.; Jayaraman, N. *Tetrahedron* **2004**, *60* (25), 5273–5308. doi:10.1016/j.tet.2004.04.014.

(32) Corey, E. J.; Noyori, R. *Tetrahedron Lett.* **1970**, *11* (45), 311–313. doi:10.1016/S0040-4039(00)61816-6.

(33) Danishefsky, S.; Schuda, P. F.; Kitahara, T.; Etheredge, S. J. *J. Am. Chem. Soc.* **1977**, *99* (18), 6066–6075. doi:10.1021/ja00460a038.

(34) Lythgoe, B.; Nanbudiry, M. E.; Tideswell, J. *Tetrahedron Lett.* **1977**, *18* (41), 3685–3688. doi:10.1016/S0040-4039(01)83327-X.

(35) Ghorbani-Vaghei, R. *Tetrahedron Lett.* **2003**, *44* (40), 7529–7532. doi:10.1016/j.tetlet.2003.08.019.

(36) Kajigaeshi, S.; Kakinami, T.; Yamasaki, H.; Fujisaki, S.; Okamoto, T. *Bull. Chem. Soc. Jpn.* **1988**, *61* (2), 600–602. doi:10.1246/bcsj.61.600.

(37) Illuminati, G.; Marino, G. *J. Am. Chem. Soc.* **1956**, *78* (19), 4975–4980. doi:10.1021/ja01600a047.

(38) Mulholland, G. K.; Zheng, Q.-H. *Synth. Commun.* **2001**, *31* (20), 3059–3068. doi:10.1081/SCC-100105877.

(39) Krassowska-Swiebocka, B.; Prokopienko, G.; Skulski, L.

Molecules **2005**, *10* (2), 394–400. doi:10.3390/10020394. PMID:18007310.
(40) Özkan, H.; Dis li,A.; Yıldırır, Y.; Türker, L. *Molecules* **2007**, *12* (11), 2478–2483. doi:10.3390/12112478. PMID:18065952.
(41) ChemicalBook. www.chemicalbook.com.
(42) chemBlink. www.chemblink.com.

Chemo- and regio-selective functionalization of Morita–Baylis–Hillman bromides with anthranilic acid

Yusuf Zulykama, Ulagamani Uma, Palanisamy Chitra Devi, and Paramasivan T. Perumal

Abstract: Nucleophilic substitution products of Morita–Baylis–Hillman adducts and their derivatives are valuable synthons. In an attempt to ameliorate the functionality of these functionalized motifs, we report the regio- and chemo-selective functionalization of Morita–Baylis–Hillman bromides with anthranilic acid.

Key words: Morita–Baylis–Hillman reaction, Morita–Baylis–Hillman bromides, nucleophilic substitution, anthranilic acid.

Résumé : Les produits de substitution nucléophile des adduits de Morita–Baylis–Hillman et de leurs dérivés sont des synthons très utiles. Afin d'améliorer la fonctionnalité de ces motifs fonctionnalisés, on a réalisé la fonctionnalisation régio- et chimio-sélective des bromures de Morita–Baylis–Hillman avec l'acide anthranilique.

Mots-clés : réaction de Morita–Baylis–Hillman, bromures de Morita–Baylis–Hillman, substitution nucléophile, acide anthranilique.

[Traduit par la Rédaction]

Introduction

The Morita–Baylis–Hillman reaction[1–4] (MBH), a powerful C–C bond forming reaction, has earned overwhelming popularity in recent years. The MBH adduct comprise of a contiguous assembly of three different functionalities and a chiral center. The versatility of the functionality of MBH adducts have made them valuable synthetic intermediates. Efforts of various research groups contributing to the widening of the substrate scope[1] of the MBH reaction have further diversified the functionality of MBH adducts (Fig. 1).

Functionalization of MBH adducts and their derivatives is an active area of research, as it provides valuable synthetic intermediates, which have been successfully translated into various useful synthetic targets, including substituted alkenes,[5] carbocycles,[6] heterocycles,[7] and several biologically relevant molecules.[1e,1g] The repertoire of nucleophiles added to MBH adducts includes carbon,[8] hydrogen,[9] heteroatomic nucleophiles,[10] aromatics,[11] and heteroaromatics.[12] In addition to newer nucleophiles[13] being added to MBH acetates/bromides, the synthetic potential of previously reported nucleophilic substitution products is illustrated by newer applications.[14]

Nucleophilic substitution of MBH adducts and their derivatives with monofunctional aromatics and their further elaboration to several synthetic targets have been extensively studied.[15] Basavaiah et al.[16] synthesized chromones from phenol[16b–16d] substitution products and successfully applied the same strategy to the synthesis of antifungal agents.

Fig. 1. The Morita–Baylis–Hillman adduct.

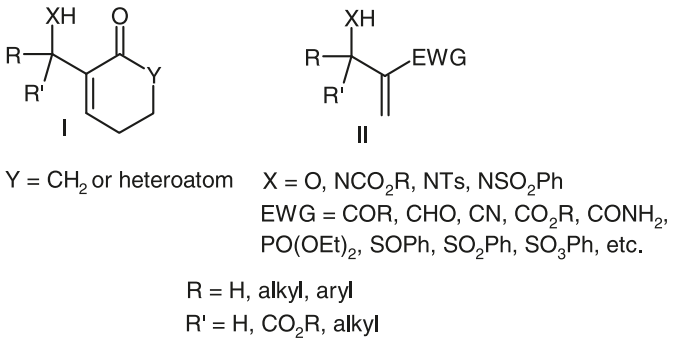

Aniline substitution products have been elaborated to synthesize indenoquinolinones,[17a] polysubstituted quinolines,[17b] quinolones, quinolinols, indanones and indenoindenones,[17c] and β-lactam.[17d,17e] The fascinating post modifications of nucleophilic substitution products of monofunctional aromatics made the nucleophilic substitution of bifunctional aromatics intriguing. However, literature scanning reveals only a few reports of nucleophilic substitution of MBH derivatives with bifunctional aromatics.[18] Kim et al.[18a] added *o*-phenylenediamine on Baylis–Hillman acetates and subsequently converted to benzodiazepinones and benzoimidazoles. Basavaiah and Satyanarayana[18b] reported one-pot transformation of the Baylis–Hillman acetates to fused pyrimidones via a reaction with 2-aminopyridine in aqueous media. The synthetic utility of dinaphthol substitution products were illustrated in the synthesis of bis-chromones.[18c] In this context, we were prompted to explore this avenue of MBH chemistry, and herein, we wish to report the results of our

Received 12 May 2009. Accepted 24 July 2009. Published on the NRC Research Press Web site at canjchem.nrc.ca on 6 November 2009.

Y. Zulykama, U. Uma, P.C. Devi, and P.T. Perumal.[1] Organic Chemistry Division, Central Leather Research Institute, Adyar, Chennai-20, India.

[1]Corresponding author (e-mail: ptperumal@gmail.com).

Scheme 1.

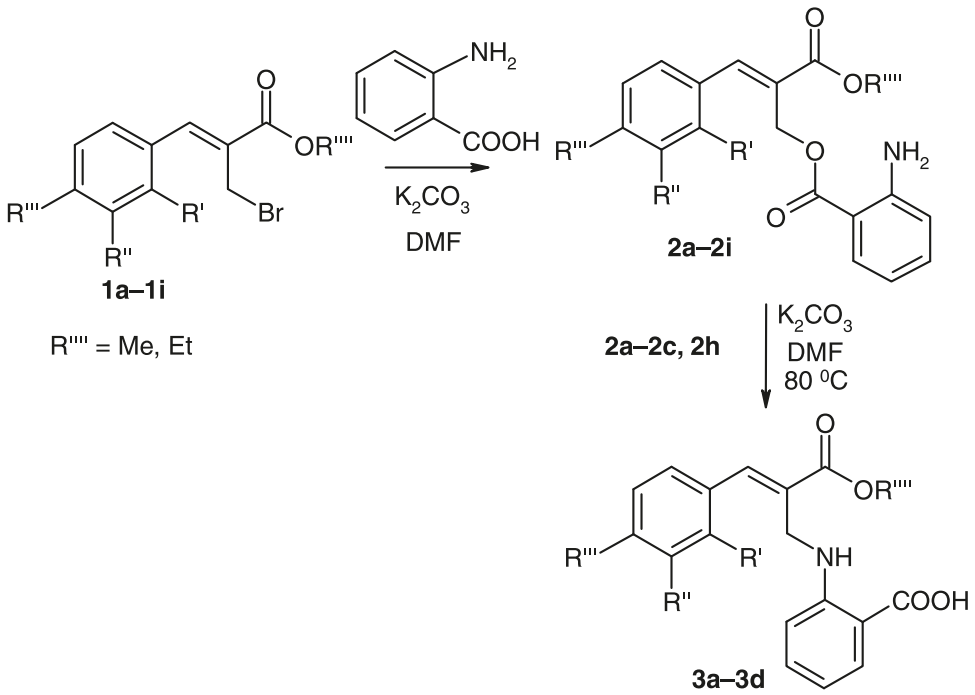

investigation of the chemo- and regio-selectivity of nucleophilic substitution of MBH bromides with anthranilic acid.

Results and discussion

Recently, we have reported the functionalization of MBH bromides with symmetric and asymmetric bifunctional aromatics,[19] and in continuation of our interest in this avenue of MBH chemistry, we intended to study the functionalization of MBH bromides with anthranilic acid. Accordingly, a solution of MBH bromide (**1a**) in DMF was treated with anthranilic acid in the presence of potassium carbonate to furnish **2a** in 61% isolated yield (Scheme 1).

The presence of two stretching absorptions in the IR spectrum of **2a** (3266 and 3468 cm^{-1}) indicated that the N-terminal of the anthranilic acid moiety is free. Moreover, the downfield appearance of the allylic protons (δ 5.15 ppm) confirmed the formation of O-linked products. The reaction was then extended to other MBH bromides (**1b**–**1i**), and the results are assembled in Table 1.

The stereochemistry of the products **2a**–**2i** was settled on the basis of difference nuclear Overhauser effect (NOE) experiments on **2f**. Irradiation of the methylene protons at δ 5.0 ppm led to the enhancement of the aromatic signal at δ 7.33 by 5.25%. However, there was comparatively less enhancement in the olefinic signal (0.69%) implying they are spatially far, and thus confirming *E* stereochemistry (Fig. 2). Further irradiation of the ester methyl proton resulted in the enhancement of the olefinic peak, confirming their spatial proximity.

To study the regio- and chemo-selective outcome of the reaction, we further treated MBH bromide with anthranilic acid in the presence of K_2CO_3 in DMF at 80 °C. TLC monitoring revealed the formation of a new minor product in addition to O-linked product. Prolonging the heating did not improve the yield of the minor product. The new product was characterized by IR, NMR, and Mass studies. The IR spectrum of the product exhibited only one stretching absorption, suggesting secondary amine functionality. The allylic protons were observed at δ 4.26 ppm (as compared with the O-linked allylic protons at δ 4.92–5.15 ppm), confirming the formation of N-linked product **3a**. Small coupling was observed in the allylic proton signal due to the NH proton further confirming the formation of N-linked products. However, the carboxyl proton was not detected in the ^1H NMR spectrum, and the presence of the carboxyl group in the product was confirmed through IR and ^{13}C spectral analysis.

Interestingly, on heating O-linked anthranilic acid, substitution products **2a** in DMF with K_2CO_3 at 80 °C, N-linked S_N2 products **3a** was obtained in comparatively good yields (Scheme 1).[20] The generality of the reaction was demonstrated by the successful conversion of O-linked products **2b**, **2c**, and **2h** to **3b**, **3c**, and **3d**, respectively (Table 2).

With the O-linked anthranilic acid products in our hands, we intended to further derivatize these substitution products by treatment with trifluoroacetic anhydride (Scheme 2). Consequently, **2a** was stirred in trifluoroacetic anhydride at ice temperature under nitrogen atmosphere, and we observed solidification of the reaction mixture immediately. TLC profile of the reaction mixture showed two new spots. The major product was assigned the structure **4a** and the minor product was found to be **5a**.[20]

The formation of **5a** can be explained as the result of the reaction of **4a** with **2a**. In the ^1H NMR spectrum of **5a**, the signal for the BH moiety was observed in duplicate, indicating that the bisfunctionalisation[21] of anthranilic moiety with the MBH bromides at both the N- and O-terminal had occurred.

The diastereotropic methylenic protons were observed as four doublets at δ 4.46, 5.02, 5.11, and 5.36 ppm. Further

Table 1. S_N2 substitution of Morita–Baylis–Hillman bromides with anthranilic acid.

Entry	O-linked S_N2 substitution product	Yield (%)[a]
1	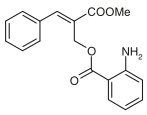 **2a**	61
2	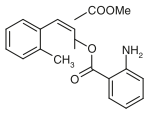 **2b**	81
3	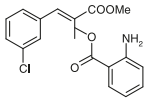 **2c**	68
4	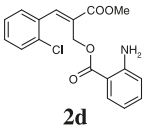 **2d**	63
5	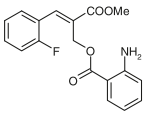 **2e**	83
6	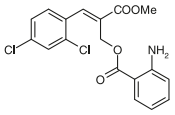 **2f**	75
7	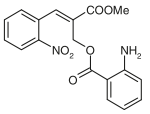 **2g**	59
8	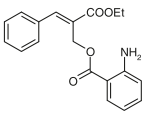 **2h**	60
9	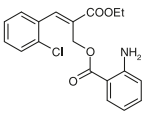 **2i**	70

[a] Isolated yield.

Fig. 2. Difference NOE studies of **2f**.

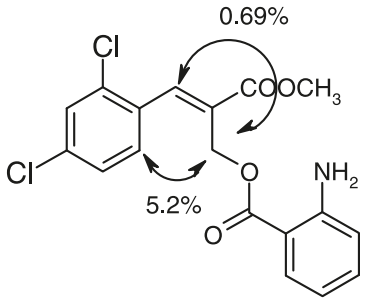

Table 2. Syntheses of S_N2 N-linked anthranilic acid substitution products.

Entry	*O*-linked S_N2 product	*N*-linked S_N2 product	Yield(%)[a]
1	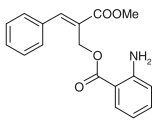 **2a**	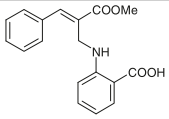 **3a**	57
2	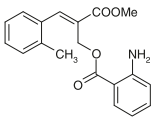 **2b**	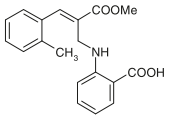 **3b**	55
3	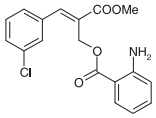 **2c**	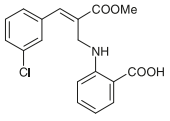 **3c**	59
4	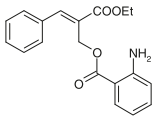 **2h**	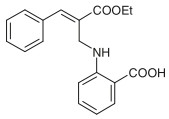 **3d**	54

[a] Isolated yield.

mass spectral analysis [604 (M^+ + Na)] confirmed the formation of the product. Next, it was our interest to obtain S_N2' anthranilic acid substitution products adopting DABCO-salt strategy.[22] In accordance, the MBH bromide (**1a**) was stirred with an equivalent of DABCO in acetone for 30 min at ambient temperature. After the salt formation as indicated by the TLC, anthranilic acid and potassium carbonate were added and stirring continued for an hour to afford **6a** (Scheme 3).

In the ^{1}H NMR of **6a**, two singlets were obtained for the olefinic protons and were observed at δ 5.63 and 6.39 ppm, confirming the formation of S_N2' products. The signal due to the benzylic proton at δ 5.87 ppm was split into a doublet by the NH proton (J = 6.1 Hz), and also the signal for the NH proton was observed as a doublet at δ 8.11 ppm (J = 6.1 Hz), confirming that the S_N2' product was N-linked. For **6a**–**6h**, the carboxyl proton was not detected in ^{1}H NMR spectra. However, the presence of the carboxyl group in the product was confirmed through IR and ^{13}C spectral analyses. Table 3 reveals the results of S_N2' substitution of MBH bro-

Scheme 2.

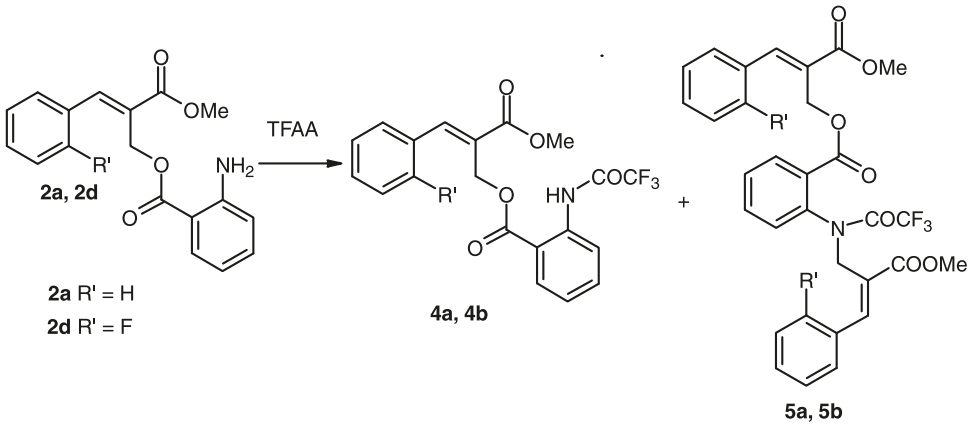

Scheme 3.

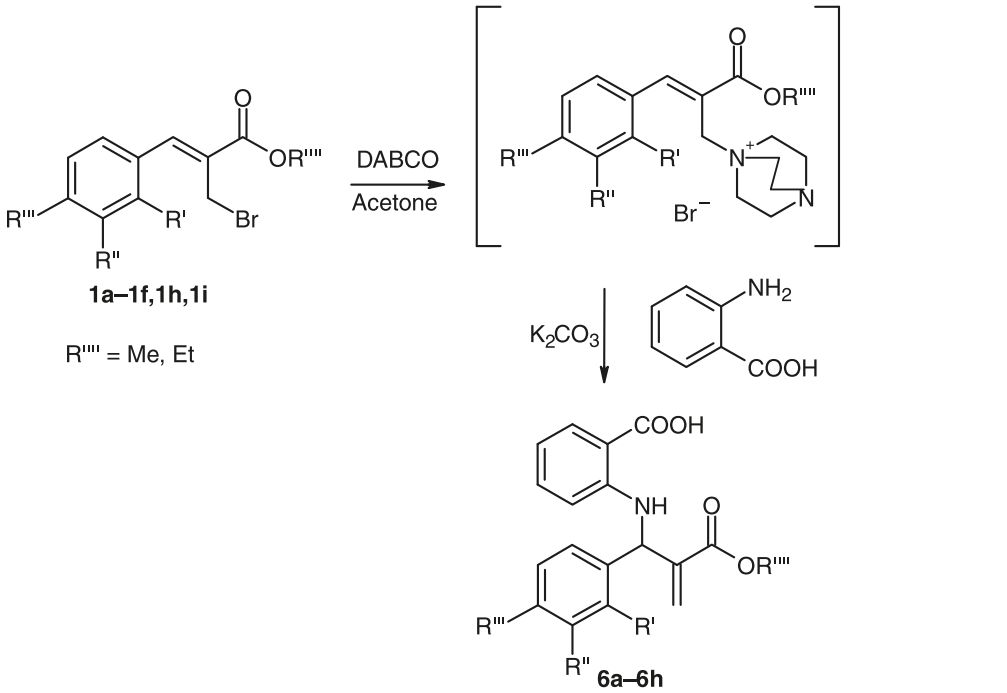

mides with anthranilic acid. Salt formation of anthranilic acid with DABCO explains the formation of N-linked S_N2' product and not the O-linked S_N2' product.

Conclusion

In conclusion, we have demonstrated a simple and practical methodology for the chemo- and regio-selective functionalization of MBH bromides with anthranilic acid. Extension of the same methodology to other bifunctional nucleophiles and their chemical transformation to synthetically important scaffolds are underway.

Experimental section

Melting points were determined in open capillary tubes and are uncorrected. IR measurements were carried out using KBr pellets in PerkinElmer Spectrometer RXI FTIR. Nuclear magnetic resonance spectra were recorded on a Bruker spectrometer or a JEOL spectrometer. ^{1}H NMR spectra were recorded at 300 MHz or 500 MHz in $CDCl_3$ or DMSO-d_6 combination with tetramethylsilane as internal standard. ^{13}C NMR spectra were recorded at 75 MHz or 125 MHz spectrometer in $CDCl_3$ or DMSO-d_6 combination with the same internal standard. The chemical shifts are given in δ in ppm scale. Mass spectra were recorded on a varian VG 70–70H mass spectrometer or on a Thermo Finnigan LCQ Advantage MAX 6000 ESI spectrometer. TLC was performed on silica gel alumina plates. Column chromatography was carried out using 100–200 mesh silica gel.

General procedure for the syntheses of 2a–2i

To a stirred solution of Baylis–Hillman bromide (0.3 g, 1.18 mmol) in DMF (5 mL) was added anthranilic acid (0.16 g, 1.18 mmol) and K_2CO_3 (0.19 g, 1.18 mmol). The reaction mixture was stirred at room temperature. After the disappearance of the starting compound (TLC), reaction mixture was poured into water and extracted with ethyl ace-

Table 3. S_N2' substitution of BH bromides with anthranilic acid.

Entry	BH bromide	N-linked S_N2' substitution product	Yield (%)[a]
1	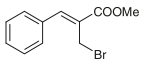 **1a**	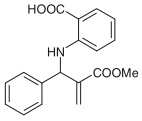 **6a**	60
2	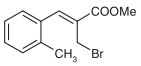 **1b**	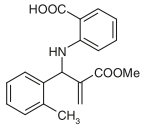 **6b**	55
3	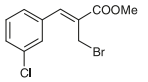 **1c**	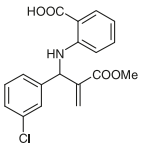 **6c**	59
4	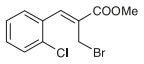 **1d**	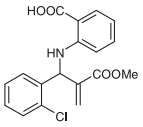 **6d**	65
5	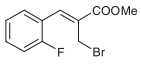 **1e**	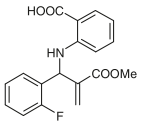 **6e**	67
6	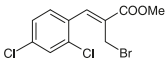 **1f**	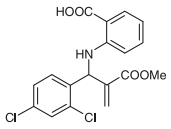 **6f**	63
7	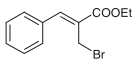 **1h**	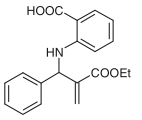 **6g**	61
8	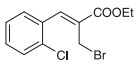 **1i**	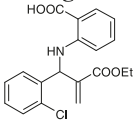 **6h**	65

[a] Isolated yield.

tate (3 × 30 mL). The organic layer was dried over Na_2SO_4 and evaporated under reduced pressure. Column purification (15% ethyl acetate in hexane) furnished the products.

Methyl 2-(2-aminophenylcarbonyloxymethyl)-3-phenyl prop-2-enoate (2a)

Yellow solid; mp 68 °C. IR (KBr) ν: 1617, 1692, 2952, 3366, 3468 cm^{-1}. ^1H NMR (500 MHz, $CDCl_3$) δ: 3.83 (s, 3H), 5.15 (s, 2H), 5.79 (br s, 2H), 6.60 (d, *J* = 9.15 Hz, 1H), 6.63 (t, *J* = 9.15 Hz, 1H), 7.38–7.44 (m, 6H), 7.82 (t, *J* = 8.05 Hz, 1H), 8.04 (s, 1H). ^{13}C NMR (125 MHz, $CDCl_3$) δ: 52.49, 59.34, 110.58, 111.66, 116.34, 116.79, 126.82, 128.91, 129.67, 129.75, 131.47, 134.34, 145.92, 150.75, 167.6, 167.88. MS *m*/*z*: 311 (M^+). Anal. calcd. for $C_{18}H_{17}NO_4$: C, 69.44; H, 5.50; N, 4.50. Found: C, 69.20; H, 5.49; N, 4.52.

Methyl 2-(2-aminophenylcarbonyloxymethyl)-3-(2-methylphenyl) prop-2-enoate (2b)

Brown solid; mp 60 °C. IR (KBr) ν: 1616, 1692, 2944, 3373, 3483 cm^{-1}. ^1H NMR (500 MHz, $CDCl_3$) δ: 2.33 (s, 3H), 3.84 (s, 3H), 5.03 (s, 2H), 5.73 (br s, 2H), 6.61 (d, *J* = 7.65 Hz, 1H), 6.64 (d, *J* = 8.4 Hz, 1H), 7.18–7.28 (m, 5H), 7.81 (d, *J* = 7.65 Hz, 1H), 8.13 (s, 1H). ^{13}C NMR (125 MHz, $CDCl_3$) δ: 20.12, 52.45, 59.46, 110.71, 116.36, 116.73, 126.05, 127.63, 128.86, 129.49, 130.33, 131.46, 133.68, 134.28, 137.21, 145.04, 150.62, 167.37, 167.75. MS *m*/*z*: 325 (M^+). Anal. calcd. for $C_{19}H_{19}NO_4$: C, 70.14; H, 5.90; N, 4.30. Found: C, 70.25; H, 5.92; N, 4.29.

Methyl 2-(2-aminophenylcarbonyloxymethyl)-3-(3-chlorophenyl) prop-2-enoate (2c)

Pale yellow solid; mp 130 °C. IR (KBr) ν: 1050, 1630, 1684, 2928, 3372, 3480 cm^{-1}. ^1H NMR (500 MHz, $CDCl_3$) δ: 3.83 (s, 3H), 5.11 (s, 2H), 5.75 (br s, 2H), 6.59 (t, *J* = 8.4 Hz, 1H), 6.64 (d, *J* = 8.4 Hz, 1H), 7.23 (t, *J* = 6.85 Hz, 1H), 7.29–7.36 (m, 3H), 7.43 (s, 1H), 7.79 (d, *J* = 7.65 Hz, 1H), 7.95 (s, 1H). ^{13}C NMR (125 MHz, $CDCl_3$) δ: 52.60, 58.93, 110.39, 111.6, 115.3, 116.35, 116.78, 127.47, 128.33, 129.58, 129.63, 130.16, 131.37, 144.0, 150.77, 167.17, 167.66. MS *m*/*z*: 346 (M^+), 348 ($M^+ + 2$). Anal. calcd. for $C_{18}H_{16}ClNO_4$: C, 62.52; H, 4.66; N, 4.05. Found: C,62.41; H, 4.65; N, 4.04.

Methyl 2-(2-aminophenylcarbonyloxymethyl)-3-(2-chlorophenyl) prop-2-enoate (2d)

Yellow solid; mp 84 °C. IR (KBr) ν: 1052, 1629, 1685, 2926, 3475, 3482 cm^{-1}. ^1H NMR (500 MHz, $CDCl_3$) δ: 3.86 (s, 3H), 5.03 (s, 2H), 5.73 (br s, 2H), 6.60 (t, *J* = 8.4 Hz, 1H), 6.64 (d, *J* = 8.4 Hz, 1H), 7.24 (t, *J* = 7.65 Hz, 2H), 7.29 (t, *J* = 7.65 Hz, 1H), 7.39 (d, *J* = 7.65 Hz, 1H), 7.41 (d, *J* = 7.65 Hz, 1H), 7.78 (d, *J* = 8.4 Hz, 1H), 8.13 (s, 1H). ^{13}C NMR (125 MHz, $CDCl_3$) δ: 52.58, 59.35, 110.50, 116.35, 116.75, 127.07, 128.82, 129.83, 129.98, 130.38, 130.68, 131.41, 133.05, 134.36, 142.51, 150.68, 166.94, 167.63. MS *m*/*z*: 345 (M^+), 347 ($M^+ + 2$). Anal. calcd. for $C_{18}H_{16}ClNO_4$: C, 62.52; H, 4.66; N, 4.05. Found: C, 62.42; H, 4.64; N, 4.06.

Methyl 2-(2-aminophenylcarbonyloxymethyl)-3-(2-fluorophenyl) prop-2-enoate (2e)

Yellow solid; mp 54 °C. IR (KBr) ν: 1239, 1616, 1717, 2951, 3373, 3480 cm^{-1}. ^1H NMR (500 MHz, $CDCl_3$) δ: 3.85 (s, 3H), 5.11 (s, 2H), 5.79 (br s, 2H), 6.58 (t, *J* = 7.45 Hz, 1H), 6.63 (d, *J* = 8.6 Hz, 1H), 7.07 (d, *J* = 8.6 Hz, 1H), 7.11 (t, *J* = 8 Hz, 1H), 7.21 (t, *J* = 8 Hz, 1H), 7.32 (q, *J* = 7.45 Hz, 1H), 7.41 (t, *J* = 8 Hz, 1H), 7.76 (d, *J* = 8.6 Hz, 1H), 8.08 (s, 1H). ^{13}C NMR (125 MHz, $CDCl_3$) δ: 52.55, 59.43, 110.37, 115.54, 115.97(d, *J* = 38.1 Hz), 116.78, 122.37 (d, *J* = 13.1 Hz), 124.51, 128.97, 130.44, 131.37, 131.62 (d, *J* = 8.35 Hz), 131.92, 134.37, 138.07,

150.81, 166.99, 167.72. MS *m/z*: 329 (M^+). Anal. calcd. for $C_{18}H_{16}FNO_4$: C, 65.65; H, 4.90; N, 4.25. Found: C, 65.72; H, 4.89; N, 4.26.

Methyl 2-(2-aminophenylcarbonyloxymethyl)-3-(2,4-dichlorophenyl) prop-2-enoate (2f)

Yellow solid; mp 144 °C. IR (KBr) ν: 1049, 1621, 1680, 2926, 3370, 3484 cm^{-1}. ^1H NMR (500 MHz, $CDCl_3$): 3.86 (s, 3H), 5.0 (s, 2H), 5.75 (br s, 2H), 6.60 (t, *J* = 6.9 Hz, 1H), 6.64 (d, *J* = 7.65 Hz, 1H), 7.24–7.27 (m, 2H), 7.33 (d, *J* = 8.4 Hz, 1H), 7.44 (s, 1H), 7.74 (d, *J* = 8.4 Hz, 1H), 8.03 (s, 1H). ^{13}C NMR (125 MHz, $CDCl_3$) δ: 52.68, 59.19, 110.29, 116.37, 116.79, 127.49, 129.36, 129.77, 131.10, 131.31, 131.59, 134.47, 135.13, 136.05, 141.20, 150.71, 166.73, 167.54. MS *m/z*: 382 (M^+), 384 (M^+ + 2), 386 (M^+ + 4). Anal. calcd. for $C_{18}H_{15}Cl_2NO_4$: C, 56.86; H, 3.98; N, 3.68. Found: C, 56.80; H, 3.97; N, 3.67.

Methyl 2-(2-aminophenylcarbonyloxymethyl)-3-(2-nitrophenyl) prop-2-enoate (2g)

Yellow oil. IR (neat) ν: 1351, 1524, 1620, 1721, 2955, 3374, 3482 cm^{-1}. ^1H NMR (500 MHz, $CDCl_3$) δ: 3.85 (s, 3H), 4.92 (s, 2H), 5.72 (br s, 2H), 6.58 (t, *J* = 6.9 Hz, 1H), 6.60 (d, *J* = 8.4 Hz, 1H), 7.21 (t, *J* = 8.4 Hz, 1H), 7.40 (d, *J* = 7.65 Hz, 1H), 7.49 (t, *J* = 7.65 Hz, 1H), 7.60 (t, *J* = 7.65 Hz, 1H), 7.68 (d, *J* = 7.65 Hz, 1H), 8.15 (d, *J* = 8.4 Hz, 1H), 8.26 (s, 1H). ^{13}C NMR (125 MHz, $CDCl_3$) δ: 52.64, 59.06, 110.18, 116.26, 116.73, 125.19, 128.32, 130.01, 130.77, 131.03, 131.27, 134.0, 134.40, 142.40, 147.37, 150.71, 166.49, 167.42. MS *m/z*: 356 (M^+). Anal. calcd. for $C_{18}H_{16}N_2O_6$: C, 60.67; H, 4.53; N, 7.86. Found: C, 60.78; H, 4.52; N, 7.89.

Ethyl 2-(2-aminophenylcarbonyloxymethyl)-3-phenyl prop-2-enoate (2h)

Orange solid; mp 80 °C. IR (KBr) ν: 1625, 1689, 2949, 3357, 3466 cm^{-1}. ^1H NMR (500 MHz, $CDCl_3$) δ: 1.30 (t, *J* = 6.9 Hz, 3H), 4.28 (q, *J* = 6.9 Hz, 2H), 5.15 (s, 2H), 5.73 (br s, 2H), 6.60 (t, *J* = 8.4 Hz, 1H), 6.65 (d, *J* = 8.4 Hz, 1H), 7.24 (t, *J* = 6.9 Hz, 1H), 7.36 (q, *J* = 7.6 Hz, 4H), 7.44 (d, *J* = 6.9 Hz, 2H), 7.83 (d, *J* = 8.4 Hz, 1H). ^{13}C NMR (125 MHz, $CDCl_3$) δ: 14.35, 59.29, 61.32, 110.73, 116.63, 116.73, 127.26, 128.77, 128.85, 129.60, 131.48, 134.28, 134.45, 145.42, 150.65, 167.05, 167.86. MS *m/z*: 325 (M^+). Anal. calcd. for $C_{19}H_{19}NO_4$: C, 70.14; H, 5.89; N, 4.31. Found: C, 70.26; H, 5.91; N, 4.30.

Ethyl 2-(2-aminophenylcarbonyloxymethyl)-3-(2-chlorophenyl) prop-2-enoate (2i)

Brown oil. IR (neat) ν: 1620, 1690, 2952, 3365, 3472 cm^{-1}. ^1H NMR (500 MHz, $CDCl_3$) δ: 1.31 (t, *J* = 7.65 Hz, 3H), 4.30 (q, *J* = 6.9 Hz, 2H), 5.05 (s, 2H), 5.83 (br s, 2H), 6.60 (t, *J* = 8.4 Hz, 1H), 6.64 (d, *J* = 8.4 Hz, 1H), 7.23 (d, *J* = 8.4 Hz, 2H), 7.27 (t, *J* = 7.65 Hz, 1H), 7.39 (t, *J* = 7.65 Hz, 2H), 7.78 (d, *J* = 7.65 Hz, 1H), 8.11 (s, 1H). ^{13}C NMR (125 MHz, $CDCl_3$) δ: 14.33, 59.35, 61.30, 110.50, 116.35, 116.75, 127.07, 128.82, 129.83, 129.98, 130.38, 130.68, 131.41, 133.05, 134.36, 142.51, 150.68, 166.94, 167.63. MS *m/z*: 360 (M^+), 362 (M^+ + 2). Anal. calcd. for $C_{19}H_{18}ClNO_4$: C, 63.42; H, 5.04; N, 3.89. Found: C, 63.50; H, 5.06; N, 3.90.

General procedure for the syntheses of 3a–3d

To a solution of **2a** (0.3 g, 0.96 mmol) in DMF (5 mL) was added K_2CO_3 (0.133 g, 0.96 mmol). The reaction mixture was heated at 80 °C. After the completion of the reaction as indicated by TLC, the reaction mixture was poured into water and extracted with ethyl acetate. The excess solvent was removed, and column purification (10% ethyl acetate in hexane) furnished the products.

Methyl 2-(2-carboxyphenylaminomethyl)-3-phenyl prop-2-enoate (3a)

Yellow solid; mp 110 °C. IR (KBr) ν: 1655, 1717, 2956, 3370 cm^{-1}. ^1H NMR (500 MHz, $CDCl_3$) δ: 3.86 (s, 3H), 4.26 (br s, 2H), 6.44 (d, *J* = 8.4 Hz, 1H), 6.60 (t, *J* = 8.4 Hz, 1H), 7.27 (t, *J* = 8.4 Hz, 2H), 7.37–7.41 (m, 5H), 7.95 (s, 1H), 7.97 (t, *J* = 6.1 Hz, 1H). ^{13}C NMR (125 MHz, $CDCl_3$) δ: 39.70, 52.32, 109.50, 111.77, 115.16, 116.46, 116.83, 129.29, 130.24, 132.14, 134.71, 135.49, 143.24, 151.08, 167.93, 173.62. MS *m/z*: 311 (M^+). Anal. calcd. for $C_{18}H_{17}NO_4$: C, 69.44; H, 5.50; N, 4.50. Found: C, 6955; H, 5.48; N, 4.51.

Methyl 2-(2-carboxyphenylaminomethyl)-3-(2-methylphenyl)prop-2-enoate (3b)

Pale yellow solid; mp 125 °C. IR (KBr) ν: 1660, 1725, 2953, 3355 cm^{-1}. ^1H NMR (500 MHz, $CDCl_3$) δ: 2.24 (s, 3H), 3.86 (s, 3H), 4.20 (br s, 2H), 6.22 ((d, *J* = 8.4 Hz, 1H), 6.55 (t, *J* = 7.65 Hz, 1H), 7.18–7.27 (m, 5H), 7.93 (d, *J* = 7.65 Hz, 1H), 7.93 (t, *J* = 6.1 Hz, 1H), 7.96 (s, 1H). MS *m/z*: 325 (M^+). Anal. calcd. for $C_{19}H_{19}NO_4$: C, 70.14; H, 5.89; N, 4.31. Found: C, 70.06; H, 5.88; N, 4.30.

Methyl 2-(2-carboxyphenylaminomethyl)-3-(3-chlorophenyl)prop-2-enoate (3c)

Pale yellow solid; mp 130 °C. IR (KBr) ν: 1037, 1657, 1719, 2950, 3360 cm^{-1}. ^1H NMR (500 MHz, $CDCl_3$) δ: 3.85 (s, 3H), 4.25 (br s, 2H), 6.44 (d, *J* = 8.4 Hz, 1H), 6.60 (t, *J* = 7.65 Hz, 1H), 7.28 (t, *J* = 6.9 Hz, 1H), 7.37–7.41 (m, 5H), 7.94 (s, 1H), 7.95 (t, *J* = 6.1 Hz, 1H). ^{13}C NMR (125 MHz, $CDCl_3$) δ: 39.76, 52.40, 109.53, 111.83, 115.22, 128.25, 128.84, 129.01, 129.36, 129.47, 132.78, 134.45, 134.78, 135.56, 143.32, 151.14, 167.98, 173.70. MS *m/z*: 346 (M^+), 348 (M^+ + 2). Anal. calcd. for $C_{18}H_{16}ClNO_4$: C, 62.52; H, 4.66; N, 4.05. Found: C,62.60; H, 4.68; N, 4.04.

Ethyl 2-(2-carboxyphenylaminomethyl)-3-phenyl prop-2-enoate (3d)

Brown oil. IR (neat) ν: 1655, 1720, 2985, 3360 cm^{-1}.^1H NMR (500 MHz, $CDCl_3$) δ: 1.34 (t, *J* = 6.9 Hz, 3H), 4.26 (s, 2H), 4.29 (q, *J* = 6.9 Hz, 2H), 6.42 (d, *J* = 8.4 Hz, 1H), 6.59 (t, *J* = 7.65 Hz, 1H), 7.26–7.30 (m, 2H), 7.37–7.41 (m, 5H), 7.93 (s, 1H), 7.95 (t, *J* = 6.1 Hz, 1H). MS *m/z*: 325 (M^+). Anal. calcd. for $C_{19}H_{19}NO_4$: C, 70.14; H, 5.89; N, 4.31. Found: C, 70.01; H, 5.87; N, 4.32.

General procedure for the syntheses of 4 and 5

2a (0.5 g, 1.6 mmol) was taken in a 50 mL RB flask, and 1 mL of TFAA was added under ice temperature in N_2 atmosphere. The reaction mixture solidified and was extracted with ethyl acetate. The excess solvent was removed and col-

umn purified (25% ethyl acetate in hexane) to obtain **4a** (63%) and **5a** (11%).

Methyl2-(2-trifluoroacetamidophenylcarbonyloxymethyl)-3-phenyl prop-2-enoate (4a)

White solid; mp 108 °C. IR (KBr) ν: 1616, 1635, 1685, 2955, 3332 cm^{-1}. ^1H NMR (500 MHz, $CDCl_3$) δ: 3.86 (s, 3H), 5.24 (s, 2H), 7.21 (t, *J* = 7.65 Hz, 1H), 7.39–7.41 (m, 5H), 7.61 (t, *J* = 8.45 Hz, 1H), 8.06 (d, *J* = 8.45 Hz, 1H), 8.11 (s, 1H), 8.65 (d, *J* = 7.65 Hz, 1H), 12.24 (s, 1H). ^{13}C NMR (125 MHz, $CDCl_3$) δ: 52.57, 60.84, 114.63 (q, *J* = 287 Hz), 116.15, 116.93, 120.80, 124.85, 125.81, 128.99, 129.47, 129.97, 131.36, 134.07, 135.20, 139.10, 146.70, 154.92 (q, *J* = 36.9 Hz), 167.14, 167.96. MS *m/z*: 407 (M^+). Anal. calcd. for $C_{20}H_{16}F_3NO_5$: C, 58.97; H, 3.96; N, 3.44. Found: C, 58.85; H, 3.96; N, 3.45.

Methyl2-(2-trifluoroacetamidophenylcarbonyloxymethyl)-3-(2-fluoro-phenyl) prop-2-enoate (4b)

White solid; mp 120 °C. IR (KBr) ν: 1230, 1618, 1620, 1642, 1680, 2958 cm^{-1}. ^1H NMR (500 MHz, $CDCl_3$) δ: 3.86 (s, 3H), 5.18 (s, 2H), 7.10 (t, *J* = 7.65 Hz, 1H), 7.14 (t, *J* = 7.65 Hz, 1H), 7.19 (t, *J* = 7.65 Hz, 1H), 7.32 (t, *J* = 7.65 Hz, 1H), 7.37 (t, *J* = 7.65 Hz, 1H), 7.60 (t, *J* = 8.4 Hz, 1H), 7.98 (d, *J* = 7.65 Hz, 1H), 8.09 (s, 1H), 8.63 (d, *J* = 8.4 Hz, 1H), 12.19 (s, 1H). ^{13}C NMR (125 MHz, $CDCl_3$) δ: 52.64, 60.91, 114.63 (q, *J* = 288.5 Hz), 116.02 (d, *J* = 22.7 Hz), 120.78, 122.12 (d, *J* = 11.9 Hz), 122.23, 124.50, 124.81, 128.09, 130.21, 131.30, 131.79 (d, *J* = 7.2 Hz), 131.85, 135.20, 139.03, 139.06, 154.93 (q, *J* = 39.3 Hz), 166.54, 167.80. MS *m/z*: 425 (M^+). Anal. calcd. for $C_{20}H_{15}F_4NO_5$: C, 56.48; H, 3.55; N, 3.29. Found: C, 56.39; H, 3.56; N, 3.30.

2-(Methoxycarbonyl)-3-phenyl-2-propenyl-2-[2-(methoxy carbonyl)-3-phenylpropenyl]trifluoroacetamidobenzene carboxylate (5a)

Yellow oil. IR (neat) ν: 1617, 1620, 1637, 2945, 3340 cm^{-1}. ^1H NMR (500 MHz, $CDCl_3$) δ: 3.61 (s, 3H), 3.80 (s, 3H), 4.46 (d, *J* = 14.5 Hz, 1H), 5.02 (d, *J* = 11.45 Hz, 1H), 5.11 (d, *J* = 11.45 Hz, 1H), 5.36 (d, *J* = 14.5 Hz, 1H), 6.96–6.98 (m, 3H), 7.22–7.23 (m, 3H), 7.32–7.34 (m, 5H), 7.38 (t, *J* = 7.65 Hz, 1H), 7.43 (t, *J* = 7.65 Hz, 1H), 7.76 (s, 1H), 7.94 (d, *J* = 8.4 Hz, 1H), 8.03 (s, 1H). ^{13}C NMR (125 MHz, $CDCl_3$) δ: 44.78, 52.23, 52.42, 60.61 115.6 (q, *J* = 282 Hz), 115.30, 117.60, 125.87, 125.98, 128.71, 128.84, 129.0, 129.39, 129.50, 129.66, 129.77, 132.08, 132.12, 132.98, 133.88, 134.10, 136.93, 145.88, 146.25, 155.84 (q, *J* = 34.6 Hz), 167.14, 167.46. MS *m/z*: 604 (M^+ + Na). Anal. calcd. for $C_{31}H_{26}F_3NO_7$: C, 64.03; H, 4.51; N, 2.43. Found: C, 64.14; H, 4.53; N, 2.44.

2-(Methoxycarbonyl)-3-(2-fluorophenyl)-2-propenyl-2-[2-(methoxycarbonyl)-3-(2-fluorophenyl)propenyl] trifluoroacetamidobenzene carboxylate (5b)

Yellow oil. IR (neat) ν: 1225, 1619, 1640, 1689 cm^{-1}. ^1H NMR (500 MHz, $CDCl_3$) δ: 3.68 (s, 3H), 3.85 (s, 3H), 4.34 (d, *J* = 13.75 Hz, 1H), 4.93 (d, *J* = 12.25 Hz, 1H), 5.03 (d, *J* = 11.45 Hz, 1H), 5.35 (d, *J* = 14.5 Hz, 1H), 6.86 (t, *J* = 7.65 Hz, 1H), 6.92 (t, *J* = 9.2 Hz, 1H), 6.98 (t, *J* = 7.65 Hz, 1H), 7.02 (d, *J* = 8.4 Hz, 1H), 7.07–7.11 (m, 2H), 7.23 (t, *J* = 8.4 Hz, 2H), 7.32–7.35 (m, 1H), 7.39 (t, *J* = 7.65 Hz, 1H), 7.48 (t, *J* = 7.65 Hz, 1H), 7.76 (s, 1H), 7.89 ((d, *J* = 6.9 Hz, 1H), 8.05 (s, 1H). ^{13}C NMR (125 MHz, $CDCl_3$) δ: 52.38, 52.53, 58.28, 60.65, 115.2 (q, *J* = 291.4 Hz), 115.66 (d, *J* = 21.4 Hz), 115.83 (d, *J* = 29.7 Hz), 121.86 (d, *J* = 13.1 Hz), 122.12 (d, *J* = 14.3 Hz), 128.1, 128.45, 129.62, 129.75, 130.30, 131.14, 131.20, 131.67, 131.74, 132.03, 132.13, 133.09, 135.12, 137.07, 138.66 (d, *J* = 15.5 Hz), 145.59, 156.02 (q, *J* = 35.7 Hz), 163.9, 166.60, 166.97. MS *m/z*: 617 (M^+). Anal. calcd. for $C_{31}H_{24}F_5NO_7$: C, 60.29; H, 3.92; N, 2.27. Found: C, 60.20; H, 3.93; N, 2.28.

General procedure for the syntheses of 6a–6h

To a stirred solution of Baylis–Hillman bromide (0.3 g, 1.18 mmol) in acetone (5 mL), DABCO (0.132 g, 1.18 mmol) was added. The reaction mixture was stirred for 30 min. The salt formation was confirmed by TLC. After the salt formation, anthranilic acid (0.16 g, 1.18 mmol) and K_2CO_3 (0.163 g, 1.18 mmol) were added. The reaction mixture was stirred at room temperature. After the formation of the product, as indicated by TLC, the reaction mixture was poured into water and extracted with ethyl acetate (3 × 30 mL). The organic layers were dried over Na_2SO_4 and evaporated under reduced pressure. Column purification (20% ethyl acetate in hexane) furnished the products.

Methyl 3-(2-carboxylphenylamino)-2-methylene-3-phenyl propanoate (6a)

Yellow solid; mp 150 °C. IR (KBr) ν: 1664, 1716, 2951, 3365 cm^{-1}. ^1H NMR (500 MHz, $CDCl_3$) δ: 3.74 (s, 3H), 5.63 (s, 1H), 5.87 (d, *J* = 6.1 Hz, 1H), 6.39 (s, 1H), 6.60 (d, *J* = 8.5 Hz, 1H), 6.63 (t, *J* = 7.7 Hz, 1H), 7.30 (d, *J* = 7.7 Hz, 1H), 7.34–7.37 (m, 3H), 7.39 (d, *J* = 6.9 Hz, 2H), 7.98 (d, *J* = 7.7 Hz, 1H), 8.11 (d, *J* = 6.1 Hz, 1H). ^{13}C NMR (125 MHz, $CDCl_3$) δ: 52.18, 57.61, 109.55, 112.68, 115.70, 126.24, 127.48, 127.96, 128.96, 132.72, 135.72, 140.06, 140.47, 150.19, 166.67, 173.89. MS *m/z*: 311 (M^+). Anal. calcd. for $C_{18}H_{17}NO_4$: C, 69.44; H, 5.50; N, 4.50. Found: C, 69.37; H, 5.51; N, 4.49.

Methyl 3-(2-carboxylphenylamino)-2-methylene-3-(2-methylphenyl) propanoate (6b)

White solid; mp 158 °C. IR (KBr) ν: 1667, 1724, 2955, 3354 cm^{-1}. ^1H NMR (500 MHz, DMSO-d_6) δ: 2.28 (s, 3H), 3.62 (s, 3H), 5.66 (d, *J* = 6.9 Hz, 1H), 5.88 (s, 1H), 6.31 (s, 1H), 6.53 (d, *J* = 8.4 Hz, 1H), 6.58 (t, *J* = 7.65 Hz, 1H), 7.14–7.20 (m, 4H), 7.30 (t, *J* = 8.4 Hz, 1H), 7.79 (d, *J* = 7.65 Hz, 1H), 8.08 (d, *J* = 6.9 Hz, 1H). ^{13}C NMR (125 MHz, DMSO-d_6) δ: 19.15, 52.59, 53.76, 111.28, 112.43, 115.90, 126.44, 126.82, 126.91, 128.31, 131.29, 132.28, 135.18, 136.65, 138.42, 140.06, 149.86, 166.53, 170.52. MS *m/z*: 325 (M^+). Anal. calcd. for $C_{19}H_{19}NO_4$: C, 70.14; H, 5.89; N, 4.31. Found: C, 70.06; H, 5.91; N, 4.32.

Methyl 3-(2-carboxylphenylamino)-2-methylene-3-(3-chlorophenyl) propanoate (6c)

Pale yellow solid; mp 162 °C. IR (KBr) ν: 1035, 1660, 1720, 2955, 3362 cm^{-1}. ^1H NMR (500 MHz, $CDCl_3$) δ: 3.75 (s, 3H), 5.58 (d, *J* = 5.35 Hz, 1H), 5.87 (s, 1H), 6.42 (s, 1H), 6.55 (d, *J* = 8.4 Hz, 1H), 6.65 (t, *J* = 7.6 Hz, 1H), 7.28–7.29 (m, 3H), 7.33 (t, *J* = 7.6 Hz, 1H), 7.37 (s, 1H),

7.99 (d, J = 6.9 Hz, 1H), 8.11 (d, J = 6.15 Hz, 1H). ^{13}C NMR (125 MHz, $CDCl_3$) δ: 52.31, 57.17, 109.73, 112.54, 116.02, 125.62, 127.03, 127.68, 128.22, 130.25, 132.78, 134.75, 135.77, 139.97, 142.25, 149.97, 166.38, 173.74. MS *m*/*z*: 346 (M^+), 348 (M^+ + 2). Anal. calcd. for $C_{18}H_{16}ClNO_4$: C, 62.52; H, 4.66; N, 4.05. Found: C, 62.46; H, 4.65; N, 4.04.

Methyl 3-(2-carboxylphenylamino)-2-methylene-3-(2-chlorophenyl) propanoate (6d)

Yellow solid; mp IR (KBr) ν: 1037, 1656, 1723, 2944, 3352 cm^{-1}. ^{1}H NMR (500 MHz, $CDCl_3$) δ: 3.76 (s, 3H), 5.70 (s, 1H), 6.04 (d, J = 6.1 Hz, 1H), 6.44 (s, 1H), 6.56 (d, J = 8.4 Hz, 1H), 6.63 (t, J = 8.4 Hz, 1H), 7.23–7.25 (m, 2H), 7.32 (t, J = 6.9 Hz, 1H), 7.40–7.42 (m, 2H), 7.97 (d, J = 6.9 Hz,1H), 8.01 (d, J = 6.1 Hz, 1H). ^{13}C NMR (125 MHz, $CDCl_3$) δ: 52.37, 54.25, 109.67, 112.57, 115.96, 127.34, 128.03, 128.40, 129.24, 130.13, 132.66, 133.97, 135.85, 137.38, 139.50, 150.20, 166.45, 173.91. MS *m*/*z*: 346 (M^+), 348 (M^+ + 2). Anal. calcd. for $C_{18}H_{16}ClNO_4$: C, 62.52; H, 4.66; N, 4.05. Found: C, 62.63; H, 4.67; N, 4.04.

Methyl 3-(2-carboxylphenylamino)-2-methylene-3-(2-fluorophenyl) propanoate (6e)

White solid; mp 130 °C. IR (KBr) ν: 1222, 1672, 1720, 3011, 3357 cm^{-1}. ^{1}H NMR (500 MHz, $CDCl_3$) δ: 3.75 (s, 3H), 5.85 (s, 1H), 5.94 (d, J = 6.1 Hz, 1H), 6.42 (s, 1H), 6.63–6.65 (m, 2H), 7.06–7.10 (m, 1H), 7.11 (t, J = 7.65 Hz, 1H), 7.26–7.29 (m, 1H), 7.34 (q, J = 8.4 Hz, 2H), 7.98 (d, J = 8.4 Hz, 1H), 8.14 (d, J = 6.1 Hz, 1H). ^{13}C NMR (125 MHz, $CDCl_3$) δ: 51.20, 52.26, 109.64, 112.46, 115.82 (d, J = 38.15 Hz), 127.03 (d, J = 13.1 Hz), 127.13, 128.67, 129.66 (d, J = 8.35 Hz), 129.73, 132.72, 135.82, 139.39, 150.07, 159.65, 161.61, 166.36, 173.88. MS *m*/*z*: 329 (M^+). Anal. calcd. for $C_{18}H_{16}FNO_4$: C, 65.65; H, 4.90; N, 4.25. Found: C, 65.58; H, 4.88; N, 4.26.

Methyl 3-(2-carboxylphenylamino)-2-methylene-3-(2,4-dichlorophenyl) propanoate (6f)

Brown solid; mp 114 °C. IR (KBr) ν: 1043, 1656, 1722, 2948, 3355 cm^{-1}. ^{1}H NMR (500 MHz, $CDCl_3$) δ: 3.76 (s, 3H), 5.71 (s, 1H), 5.95 (d, J = 5.35 Hz, 1H), 6.45 (s, 1H), 6.51 (d, J = 8.4 Hz, 1H), 6.65 (t, J = 7.65 Hz, 1H), 7.21 (t, J = 8.4 Hz, 1H), 7.34 (t, J = 8.4 Hz, 2H), 7.43 (s, 1H), 7.98 (d, J = 7.65 Hz, 2H). ^{13}C NMR (125 MHz, $CDCl_3$) δ: 52.41, 54.02, 109.76, 112.45, 116.23, 127.64, 128.23, 129.35, 129.98, 132.74, 134.37, 134.69, 135.91, 136.14, 139.08, 149.96, 166.22, 173.75. MS *m*/*z*: 380 (M^+), 382 (M^+ + 2), 384 (M^+ + 4). Anal. calcd. for $C_{18}H_{15}Cl_2NO_4$: C, 56.86; H, 3.98; N, 3.68. Found: C, 56.92; H, 3.99; N, 3.69.

Ethyl 3-(2-carboxylphenylamino)-2-methylene-3-phenyl propanoate (6g)

White solid; mp 124 °C. IR (KBr) ν: 1650, 1719, 2982, 3359 cm^{-1}. ^{1}H NMR (500 MHz, DMSO-d_6) δ: 1.08 (d, J = 7.65 Hz, 3H), 4.04 (m, 2H), 5.58 (d, J = 7.6 Hz, 1H), 5.81 (s, 1H), 6.24 (s, 1H), 6.57 (d, J = 7.6 Hz, 1H), 6.59 (d, J = 8.4 Hz,1H), 7.30–7.34 (m, 5H), 7.79 (d, J = 7.65 Hz, 2H), 8.44 (d, J = 7.65 Hz, 1H). ^{13}C NMR (125 MHz, DMSO-d_6) δ: 14.34, 57.42, 61.14, 111.33, 112.69, 115.73, 126.47, 127.66, 128.13, 129.19, 132.25, 135.01, 140.76, 140.91, 149.81, 165.79, 170.54. MS *m*/*z*: 325 (M^+). Anal. calcd. for $C_{19}H_{19}NO_4$: C, 70.14; H, 5.89; N, 4.31. Found: C, 70.0; H, 5.91; N, 4.30.

Ethyl 3-(2-carboxylphenylamino)-2-methylene-3-(2-chlorophenyl) propanoate (6h)

Brown solid; mp 110 °C. IR (KBr) ν: 1038, 1656, 1715, 2984, 3356 cm^{-1}. ^{1}H NMR (500 MHz, $CDCl_3$) δ: 1.21 (t, J = 6.9 Hz, 3H), 4.19 (m, 2H), 5.68 (s, 1H), 6.02 (d, J = 4.6 Hz, 1H), 6.43 (s, 1H), 6.57 (d, J = 8.4 Hz, 1H), 6.63 (t, J = 7.65 Hz, 1H), 7.23–7.25 (m, 2H), 7.32 (t, J = 7.65 Hz, 1H), 7.39–7.42 (m, 2H), 7.96 (d, J = 7.65 Hz, 2H). ^{13}C NMR (125 MHz, $CDCl_3$) δ: 14.13, 54.34, 61.25, 109.59, 112.54, 115.90, 127.31, 127.63, 128.44, 129.19, 130.05, 132.64, 133.97, 135.83, 137.50, 139.74, 150.25, 165.95, 173.75. MS *m*/*z*: 360 (M^+), 362 (M^+ + 2). Anal. calcd. for $C_{19}H_{18}ClNO_4$: C, 63.42; H, 5.04; N, 3.89. Found: C, 63.50; H, 5.05; N, 3.88.

Acknowledgement

YZ thanks the Council of Scientific and Industrial Research (CSIR), India for the financial support.

References

(1) (a) For reviews see: Drewes, S. E.; Roos, G. H. P. *Tetrahedron* **1988**, *44* (15), 4653–4670. doi:10.1016/S0040-4020(01)86168-8.; (b) Basavaiah, D.; Rao, P. D.; Hyma, R. S. *Tetrahedron* **1996**, *52* (24), 8001–8062. doi:10.1016/0040-4020(96)00154-8.; (c) Ciganek, E. In *Organic Reactions;* John Wiley: New York, 1997; Vol. 51, Chapter 2, p. 201; (d) Almeida, W. P.; Coelho, F. *Quim. Nova* **2000**, *23*, 98; *Chem. Abstr.* **2000**, *132*, 236532e.; (e) Basavaiah, D.; Rao, A. J.; Satyanarayana, T. *Chem. Rev.* **2003**, *103* (3), 811–892. doi:10.1021/cr010043d. PMID:12630854.; (f) Kim, J. N.; Lee, K. Y. *Curr. Org. Chem.* **2002**, *6* (7), 627–645. doi:10.2174/1385272023374094.; (g) Lee, K. Y.; Gowrisankar, S.; Kim, J. N. *Bull. Korean Chem. Soc.* **2005**, *26*, 1481; (g) Basavaiah, D.; Venkateswara Rao, K.; Jannapu Reddy, R. *Chem. Soc. Rev.* **2007**, *36* (10), 1581–1588. doi:10.1039/b613741p. PMID:17721583.; (h) Singh, V.; Batra, S. *Tetrahedron* **2008**, *64* (20), 4511–4574. doi:10.1016/j.tet.2008.02.087.

(2) (a) For the mechanism of Baylis–Hillman reaction see: Bode, M. L.; Kaye, P. T. *Tetrahedron Lett.* **1991**, *32* (40), 5611–5614. doi:10.1016/0040-4039(91)80098-Q.; (b) Drewes, S. E.; Emslie, N. D.; Field, J. S.; Khan, A. A.; Ramesar, N. S. *Tetrahedron Lett.* **1993**, *34* (7), 1205–1208. doi:10.1016/S0040-4039(00)77529-0.; (c) Santos, L. S.; Pavam, C. H.; Almeida, W. P.; Coelho, F.; Eberlin, M. N. *Angew. Chem. Int. Ed.* **2004**, *43* (33), 4330–4333. doi:10.1002/anie.200460059.; (d) Price, K. E.; Broadwater, S. J.; Jung, H. M.; McQuade, D. T. *Org. Lett.* **2005**, *7* (1), 147–150. doi:10.1021/ol047739o. PMID:15624999.; (e) Price, K. E.; Broadwater, S. J.; Walker, B. J.; McQuade, D. T. *J. Org. Chem.* **2005**, *70* (10), 3980–3987. doi:10.1021/jo050202j. PMID:15876086.; (f) Aggarwal, V. K.; Fulford, S. Y.; Lloyd-Jones, G. C. *Angew. Chem. Int. Ed.* **2005**, *44* (11), 1706–1708. doi:10.1002/anie.200462462.

(3) (a) For a review on Aza Baylis–Hillman reaction see: Shi, Y.-L.; Shi, M. *Eur. J. Org. Chem.* **2007**, *2007* (18), 2905–2916. doi:10.1002/ejoc.200700030.; (b) Declerck, V.; Martinez, J.; Lamaty, F. *Chem. Rev.* **2009**, *109* (1), 1–48. doi:10.1021/cr068057c. PMID:19140772.

(4) (a) For review on Asymmetric Baylis–Hillman reaction see: Langer, P. *Angew. Chem. Int. Ed.* **2000**, *39* (17), 3049–3052. doi:10.1002/1521-3773(20000901)39:17<3049::AID-ANIE3049>3.0.CO;2-5.; (b) Masson, G.; Housseman, C.; Zhu, J. *Angew. Chem. Int. Ed.* **2007**, *46* (25), 4614–4628. doi:10.1002/anie.200604366.

(5) (a) Basavaiah, D.; Sarma, P. K. S.; Bhavani, A. K. D. *Chem. Commun.* **1994**, 1091; (b) Kabalka, G. W.; Venkataiah, B.; Dong, G. *Org. Lett.* **2003**, *5* (21), 3803–3805. doi:10.1021/ol0351798. PMID:14535714.; (c) Navarre, L.; Darses, S.; Genet, J.-P. *Adv. Synth. Catal.* **2006**, *348* (3), 317–322. doi:10.1002/adsc.200505336.; (d) Kabalka, G. W.; Dong, G.; Venkataiah, B.; Chen, C. *J. Org. Chem.* **2005**, *70* (23), 9207–9210. doi:10.1021/jo051177k. PMID:16268591.; (e) Das, B.; Banerjee, J.; Mahender, G.; Majhi, A. *Org. Lett.* **2004**, *6* (19), 3349–3352. doi:10.1021/ol048721g. PMID:15355049.; (f) Ranu, B. C.; Chattopadhyay, K.; Jana, R. *Tetrahedron Lett.* **2007**, *48* (22), 3847–3850. doi:10.1016/j.tetlet.2007.03.154.

(6) (a) Park, D. Y.; Gowrisankar, S.; Kim, J. N. *Tetrahedron Lett.* **2006**, *47*, 6645; (b) Park, D. Y.; Kim, S. J.; Kim, T. H.; Kim, J. N. *Tetrahedron Lett.* **2006**, *47* (35), 6315–6319. doi:10.1016/j.tetlet.2006.06.147.; (c) Kim, J. N.; Im, Y. J.; Gong, J. H.; Lee, K. Y. *Tetrahedron Lett.* **2001**, *42* (25), 4195–4197. doi:10.1016/S0040-4039(01)00687-6.

(7) (a) Chandrasekhar, S.; Basu, D.; Rambabu, Ch. *Tetrahedron Lett.* **2006**, *47* (18), 3059–3063. doi:10.1016/j.tetlet.2006.03.037.; (b) Yi, H.-W.; Park, H. W.; Song, Y. S.; Lee, K.-J. *Synthesis* **2006**, 1953.; (c) Basavaiah, D.; Aravindu, K. *Org. Lett.* **2007**, *9* (13), 2453–2456. doi:10.1021/ol070380u. PMID:17536808.; (d) Singh, V.; Batra, S. *Eur. J. Org. Chem.* **2007**, *2007* (18), 2970–2976. doi:10.1002/ejoc.200700175.; (e) Song, Y. S.; Lee, K.-J. *J. Heterocycl. Chem.* **2006**, *43* (6), 1721–1724. doi:10.1002/jhet.5570430647.

(8) (a) Chung, Y. M.; Gong, J. H.; Kim, T. H.; Kim, J. N. *Tetrahedron Lett.* **2001**, *42* (51), 9023–9026. doi:10.1016/S0040-4039(01)01971-2.; (b) Kabalka, G. W.; Venkataiah, B.; Dong, G. *Org. Lett.* **2003**, *5* (21), 3803–3805. doi:10.1021/ol0351798. PMID:14535714.; (c) Das, B.; Banerjee, J.; Mahender, G.; Majhi, A. *Org. Lett.* **2004**, *6* (19), 3349–3352. doi:10.1021/ol048721g. PMID:15355049.; (d) Ballini, R.; Barboni, L.; Bosica, G.; Fiorini, D.; Mignini, E.; Palmieri, A. *Tetrahedron* **2004**, *60* (23), 4995–4999. doi:10.1016/j.tet.2004.04.030.; (e) GowriSankar, S.; Lee, K. Y.; Lee, C. G.; Kim, J. N. *Tetrahedron Lett.* **2004**, *45* (32), 6141–6146. doi:10.1016/j.tetlet.2004.06.057.

(9) (a) Basavaiah, D.; Krishnamacharyulu, M.; Hyma, R. S.; Sarma, P. K. S.; Kumaragurubaran, N. *J. Org. Chem.* **1999**, *64* (4), 1197–1200. doi:10.1021/jo981761b.; (b) Basavaiah, D.; Kumaragurubaran, N. *Tetrahedron* **2001**, *42* (3), 477–479. doi:10.1016/S0040-4039(00)01967-5.

(10) (a) Sá, M. M.; Fernandes, L.; Ferreira, M.; Bortoluzzi, A. J. *Tetrahedron Lett.* **2008**, *49* (7), 1228–1232. doi:10.1016/j.tetlet.2007.12.029.; (b) Singh, V.; Pathak, R.; Batra, S. *Catal. Commun.* **2007**, *8* (12), 2048–2052. doi:10.1016/j.catcom.2007.03.032.; (c) Sá, M. M.; Ramos, M. D.; Fernandes, L. *Tetrahedron* **2006**, *62* (50), 11652–11656. doi:10.1016/j.tet.2006.09.059.; (d) Das, B.; Majhi, A.; Banerjee, J.; Chowdhury, N. *J. Mol. Cat. A* **2006**, *260* (1-2), 32–34. doi:10.1016/j.molcata.2006.06.051.

(11) (a) Lee, H. J.; Seong, M. R.; Kim, J. N. *Tetrahedron Lett.* **1998**, *39* (34), 6223–6226. doi:10.1016/S0040-4039(98)01280-5.; (b) Basavaiah, D.; Reddy, R. M. *Tetrahedron Lett.* **2001**, *42* (16), 3025–3027. doi:10.1016/S0040-4039(01)00354-9.

(12) (a) Yadav, J. S.; Subba Reddy, B. V.; Basak, A. K.; Narsaiah, A. V.; Prabhakar, A.; Jagadeesh, B. *Tetrahedron Lett.* **2005**, *46* (4), 639–641. doi:10.1016/j.tetlet.2004.11.139.; (b) Li, J.; Wang, X.; Zhang, Y. *Tetrahedron Lett.* **2005**, *46* (31), 5233–5237. doi:10.1016/j.tetlet.2005.05.107.

(13) (a) Srihari, P.; Singh, A. P.; Jain, R.; Yadav, J. S. *Synthesis* **2006**, *2006* (16), 2772–2776. doi:10.1055/s-2006-942479.; (b) Kim, J. M.; Kim, S. H.; Kim, J. N. *Bull. Korean Chem. Soc.* **2007**, *28*, 2505; (c) Sá, M. M.; Fernandes, L.; Ferreira, M.; Bortoluzzi, A. J. *Tetrahedron Lett.* **2008**, *49* (7), 1228–1232. doi:10.1016/j.tetlet.2007.12.029.; (d) Wolfe, J. P.; Xu, X. S.; Zheng, H.; Xu, D. Q.; Xu, Z. Y.; Zhang, Y. M. *Synlett* **2006**, *2007* (4), 571–582. PMID:19183704.

(14) (a) Singh, V.; Yadav, G. P.; Maulik, P. R.; Batra, S. *Tetrahedron* **2006**, *62* (37), 8731–8739. doi:10.1016/j.tet.2006.06.099.; (b) Lee, M. J.; Park, D. Y.; Lee, K. Y.; Kim, J. N. *Tetrahedron Lett.* **2006**, *47* (11), 1833–1837. doi:10.1016/j.tetlet.2005.12.134.; (c) Shanmugam, P.; Rajasingh, P. *Tetrahedron Lett.* **2005**, *46* (19), 3369–3372. doi:10.1016/j.tetlet.2005.03.086.; (d) Kim, S. C.; Lee, K. Y.; Lee, H. S.; Kim, J. N. *Tetrahedron* **2008**, *64* (1), 103–109. doi:10.1016/j.tet.2007.10.068.

(15) (a) Charette, A. B.; Côté, B. *Tetrahedron Lett.* **1993**, *34* (43), 6833–6836. doi:10.1016/S0040-4039(00)91807-0.; (b) Ciclosi, M.; Fava, C.; Galeazzi, R.; Orena, M.; Sepulveda-Arques, J. *Tetrahedron Lett.* **2002**, *43* (12), 2199–2202. doi:10.1016/S0040-4039(02)00233-2.; (c) Paira, M.; Mandal, S. K.; Roy, S. C. *Tetrahedron Lett.* **2008**, *49* (15), 2432–2434. doi:10.1016/j.tetlet.2008.02.054.; (d) Rajesh, S.; Banerji, B.; Iqbal, J. *J. Org. Chem.* **2002**, *67* (22), 7852–7857. doi:10.1021/jo010981d. PMID:12398513.

(16) (a) Basavaiah, D.; Bakthadoss, M.; Pandiaraju, S. *Chem. Commun. (Camb.)* **1998**, (16): 1639–1640. doi:10.1039/a804796k.; (b) Trost, B. M.; Tsui, H.-C.; Toste, F. D. *J. Am. Chem. Soc.* **2000**, *122* (14), 3534–3535. doi:10.1021/ja994326n.; (c) Basavaiah, D.; Kumaragurubaram, N.; Sharada, D. S.; Reddy, R. M. *Tetrahedron* **2001**, *57* (38), 8167–8172. doi:10.1016/S0040-4020(01)00786-4.; (d) Roy, O.; Riahi, A.; Henin, F.; Muzart, J. *Tetrahedron* **2000**, *56* (41), 8133–8140. doi:10.1016/S0040-4020(00)00727-4.

(17) (a) Lee, C. G.; Lee, K. Y.; Gowrisankar, S.; Kim, J. N. *Tetrahedron Lett.* **2004**, *45* (40), 7409–7413. doi:10.1016/j.tetlet.2004.08.075.; (b) Kim, S. C.; Gowrisankar, S.; Kim, J. N. *Bull. Korean Chem. Soc.* **2005**, *26*, 1001; (c) Lee, C. G.; Lee, K. Y.; Lee, S.; Kim, J. N. *Tetrahedron* **2005**, *61* (6), 1493–1499. doi:10.1016/j.tet.2004.11.082.; (d) Buchholz, R.; Hoffmann, H. M. R. *Helv. Chim. Acta* **1991**, *74* (6), 1213–1220. doi:10.1002/hlca.19910740608.; (e) Chen, H.-Y.; Patkar, L. N.; Ueng, S.-H.; Lin, C.-C.; Lee, A. S.-Y. *Synlett* **2005**, 2035.

(18) (a) Kim, J. M.; Lee, K. Y.; Kim, J. N. *Bull. Korean Chem. Soc.* **2002**, *23*, 1055; (b) Basavaiah, D.; Satyanarayana, T. *Tetrahedron Lett.* **2002**, *43* (24), 4301–4303. doi:10.1016/S0040-4039(02)00802-X.; (c) Rajan, Y. C.; Kanakam, C. C.; Selvam, S. P.; Murugesan, K. *Tetrahedron Lett.* **2007**, *48* (48), 8562–8565. doi:10.1016/j.tetlet.2007.09.097.

(19) Zulykama, Y.; Perumal, P. T. *Aust. J. Chem.* **2007**, *60* (3), 205. doi:10.1071/CH06342.

(20) (a) It is well-documented in the literature that β vinylic proton cis to ester appear downfield when compared to trans β vinylic proton; see for example: Jackman, L. M.; Sternhell, S. *Applications of nuclear magnetic resonance spectroscopy*

in organic chemistry, 2nd ed; Pergamon: Oxford, 1969; Vol. 5;(b) It is reported that β vinylic proton cis and trans to ester resonate at ~ δ 7.5 and δ 6.5, respectively. The β vinylic protons of compounds **3a**–**3d**, **4a**, **4b**, **5a**, and **5b** were observed at δ 7.76–8.11 ppm. Thus, *E* stereochemistry was assigned to these compounds: Tobey, S. W. *J. Org. Chem.* **1969**, *34* (5), 1281–1298. doi:10.1021/jo01257a019.

(21) Kim, J. N.; Chung, Y. M.; Im, Y. J. *Tetrahedron Lett.* **2002**, *43* (35), 6209–6211. doi:10.1016/S0040-4039(02)01314-X.

(22) Chung, Y. M.; Gong, J. H.; Kim, T. H.; Kim, J. N. *Tetrahedron Lett.* **2001**, *42* (51), 9023–9026. doi:10.1016/S0040-4039(01)01971-2.

Benzimidazole quinoline derivatives — An effective green fluorescent dye for bacterial imaging

Mahalingam Malathi, Palathurai Subramaniam Mohan, Raymond J. Butcher, and Chidambaram Kulandaisamy Venil

Abstract: A one-pot synthesis of benzimidazoles by condensing naphthyl or quinoline aldehyde with benzene-1,2-diamine has been reported. IR, ^{1}H and ^{13}C NMR, mass spectral, and CHN analyses were used to elucidate the structures of the products. The molecular structural correlation in the optical properties of the quinoline and naphthalene benzimidazoles was explored. The fluorescence quantum yield (ϕ_f) and time-resolved fluorescent lifetime of the quinoline benzimidazoles derivatives were estimated. The influence of solvent polarity and pH on the optical property of quinoline derivatives was illustrated. To explore the bioanalytical applicability, the thermal stability by TG–DTA analysis and the cytogenetic analysis of 3-(1*H*-benzoimidazol-2-yl)-2-chloro-8-methyl-quinoline (**1b**) compound were carried out. The fluorescent staining ability of **1b** was analyzed and also compared with the normal Gram staining in the bacterium.

Key words: benzimidazole quinolines, optical property, fluorescence quantum yield, cytogenetic analysis, fluorescence staining.

Résumé : On a réalisé une synthèse monotope de benzimidazoles par condensation de naphtyl- et de quinoléinealdéhydes avec de la benzène-1,2-diamine. On a fait appel aux analyses CHN et aux spectroscopies IR, RMN ^{1}H et ^{13}C et de masse pour élucider la structure des produits. On a exploré la corrélation de la structure moléculaire dans les propriétés optiques des benzimidazolylquinoléines et des benzimidazolylnaphtalènes. On a évalué le rendement quantique de fluorescence (ϕ_f) et le temps de vie fluorescent résolu en fonction du temps des dérivés benzimidazolylquinoléines. On a aussi illustré l'influence de la polarité du solvant et du pH sur les propriétés optiques de ces dérivés de la quinoléine. Afin de pouvoir évaluer les possibilités de l'utiliser dans le domaine des analyses biologiques, on a aussi effectué une analyse cytogénétique et on a évalué la stabilité thermique de la 3-(1*H*-benzimidazol-2-yl)-2-chloro-8-méthylquinoléine (**1b**) par analyse thermogravimétrique (TG) et analyse thermique différentielle (ATD). On a analysé la capacité du composé 1b à agir comme colorant fluorescent et on a comparé ses propriétés à celles de la coloration Gram normale dans les bactéries.

Mots-clés : benzimidazolylquinoléines, propriété optique, rendement quantique de fluorescence, analyse cytogénétique, coloration de fluorescence.

[Traduit par la Rédaction]

Introduction

Rapid advances in optical technologies have recently led to significant progress in medical diagnostics, drug discovery, and (bio)chemical analysis, in particular for methods that use fluorescence detection in microscopy, for microarrays or single-molecule tracking.[1] These developments have fueled the search for novel fluorophore (stains, labels, and indicators)[2] with high brightness that can be excited and which could emit well within the visible or near-infrared (NIR) region of the spectrum.[3] This is a part of continual shift away from the use of radioactive tracers in the bioanalytical study. Particularly, it eliminates the dangers of handling carcinogenic dyes, radioactive materials, and the cost of their proper disposal such as crystal violet, ethidium bromide, and ^{32}P in DNA staining analysis.

Accordingly, much research has been done to develop one-photon fluorescent (OPF) probes because they are useful tools for know how the functions in biological systems. One of the major drawbacks of such probes is that the excitation wavelengths are in the range of 350–560 nm, which may cause damage to the substrates specifically in the living

Received 23 March 2009. Accepted 27 August 2009. Published on the NRC Research Press Web site at canjchem.nrc.ca on 6 November 2009.

Abbreviations: OPF: one-photon fluorescent. TPF: two-photon fluorescent. FTIR: fourier transform infrared. UV–vis: ultraviolet–visible. NMR: nuclear magnetic resonance. XRD: X-ray diffraction. TG–DTA: thermogravimetric and differential thermal analysis. EtOAc: ethyl acetate. EtOH: ethanol.

M. Malathi and P.S. Mohan.[1] Department of Chemistry, Bharathiar University, Coimbatore 641 046, India.
R.J. Butcher. Department of Chemistry, Howard University, WA, USA.
C.K. Venil. Department of Environmental Science, Division of Microbiology, Bharathiar University, Coimbatore 641 046, India.

[1]Corresponding author (e-mail: ps_mohan_in@yahoo.com).

cells.[5] A fluorescent probe having higher excitation wavelength[6] overcomes these shortcomings in two ways: (*i*) using lower energy photon can cause less damage to the cells or tissues and (*ii*) lower energy photon has longer wavelength that can penetrate deep inside the tissue. Many applications of such materials have become reality, some of which include optical power limiting,[7] two-photon (TP) upconversion lasing,[8] TP fluorescence excitation microscopy,[9] three-dimensional optical-data storage,[10] and photodynamic therapy.[11] An important addition to such applications would be the development of TP probes for bioanalytical applications. As a result, the design and synthesis of fluorescent probes with higher excitation wavelength have attained the central position of the current research.[12]

A detailed search of structural correlation in the fluorescent probes reveals that the benzimidazole derivatives could act as an effective fluorescent probe.[13] In addition to the biological activity,[14] many of benzimidazole derivatives are studied as luminescent singling sensors for anions.[15] Recently, Zang et al.[16] have reported a Y-shaped TP-active material based on the imidazole core. Consecutively, Iyer et al.[17] have reported that the benzimidazole ring in a heteroaromatic system could exhibit efficient fluorescence-light-emitting property. All the reports reveal that the benzimidazole and its derivatives have different fluorescence efficiencies, depending on the molecular structure. Consequently, the molecular-structure-based designing is one of the convenient tools for the innovation of the new efficient fluorescent probes.

In this connection, quinoline system gains importance due to its recent revolution in optical chemistry.[18] Basically, quinoline derivatives have been synthesized and widely utilized as drugs for antimalarial, anticancer, and also as DNA intercalators.[19] In contrary, there has been a paucity of imperative papers account that the quinoline derivatives could be used as selective fluorescence chemosensors for biologically important metal ions, as fluorescent dopent in OLEDs and electrochemiluminescence,[20] and so forth. This kindles interest to study the optical property of the benzimidazole-substituted quinoline derivatives. Consecutively, the synthesis of benzimidazole naphthalene derivatives also intended to study the role of quinoline system in the optical property of the synthesized quinoline benzimidazole derivatives.[4]

On par with our objective, we propose a conventional synthetic methodology for the synthesis of quinoline and naphthalene benzimidazole derivatives (BIQ, BIN) in high yield (see Scheme 1 for structures). The optical properties of the synthesized compounds were analyzed by using absorption and emission spectral studies. Based on the fluorescence property, the applicability of the compounds in the bioanalytical studies is focused.

Experimental section

Materials and physical measurements

All reagents and chemicals were purchased from Ranchem chemicals. All the solvents were HPLC-grade. Thin-layer chromatography (TLC) was performed using glass plates coated with silica gel-G containing 13% calcium sulphate as binder. Melting points were determined using a Raga melting point apparatus and are uncorrected. The starting quinoline carbaldehyde compounds were synthesized according to the reported procedure.[21] The naphthalene carbaldehyde starting material was purchased from Sigma-Aldrich chemicals and used without further purification. FTIR spectra (4000–400 cm^{-1}) of compounds were recorded as KBr pellets with a Nicolet Avatar Model FTIR spectrophotometer. ^1H and ^{13}C NMR spectra were recorded on a Bruker Avance 400 (400 MHz) spectrometer in $CDCl_3$ as a solvent and tetramethylsilane (TMS) as an internal standard. Mass spectra were recorded on a Trace DSQ mass spectrograph. Microanalyses (C, H, and N) were performed on a Vario EL-III Elementar elemental analyzer. UV–vis absorption spectra (200–800 nm) were recorded using a Shimadzu UV/2501PC spectrophotometer. The fluorescence spectra were recorded using JASCO FP-6600 spectrofluorometer (Xenon lamp). The fluorescence microscopy analysis was done by using Nikon fluorescence microscopes.

Scheme 1. Quinoline and naphthalene benzimidazoles.

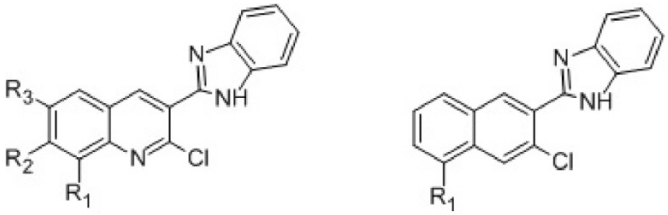

1a R_1, R_2, and $R_3 = H$
1b $R_1 = CH_3$, R_2, and $R_3 = H$
1c R_1, $R_3 = H$, $R_2 = CH_3$
1d R_1, $R_2 = H$, $R_3 = CH_3$

2a $R_1 = H$
2b $R_1 = CH_3$

Synthesis of benzimidazole compounds

Scheme 2 outlines the general procedure for the synthesis of quinoline and naphthalene benzimidazole derivatives. The aldehyde compound (**3** or **4**) in chloroform was stirred with two drops of glacial acetic acid. To this, benzene-1,2-diamine (**5**) was added, and the stirring was continued for about 15 min. The formation of product was confirmed by TLC. Excess $CHCl_3$ was evaporated, and the resulting crude was washed with water. The dried crude was adsorbed for column chromatography using petroleum ether and EtOAc mixture as eluent. The benzimidazole product was isolated in petroleum ether/EtOAc (9:1) medium. The obtained product was characterized by IR, ^1H and ^{13}C NMR, mass, and elemental analyses.

Synthesis of 3-(1H-benzoimidazol-2-yl)-2-chloro-quinoline (1a)

The compound was prepared as described above by the reaction of 2-chloro-quinoline-3-carbaldehyde (10 mmol, 1.73 g) and benzene-1,2-diamine (5 mmol, 0.541 g). Off-white solid (yield: 1.25 g, 89.33%); mp 202 °C. IR (KBr): 3424, 1607, 1405, 1034, 741. ^1H NMR (400 MHz, $CDCl_3$) δ: 7.27 to 7.38 (m, 2H, C6–quinoline–Q–H, C3′–benzo–BE–H), 7.60–7.64 (m, 2H, C2′ and C5′ of BE–H), 7.79–7.83 (m, 2H, C7–Q–H and C4′–BE–H), 7.92–7.94 (d, 1H, J = 8 Hz, C5–Q–H), 8.03–8.05 (d, 1H, J = 8 Hz, C8–Q–H), 9.26 (s, 1H, C4–Q–H), 10.59 (bs, NH–imidazole–IMD–H). ^{13}C NMR δ: 120.22, 122.66, 123.84, 126.31, 127.10, 127.45, 127.81, 130.59, 131.30, 131.80, 136.21, 140.83, 141.11,

Scheme 2. Preparation of quinoline and naphthalene benzimidazole derivatives.

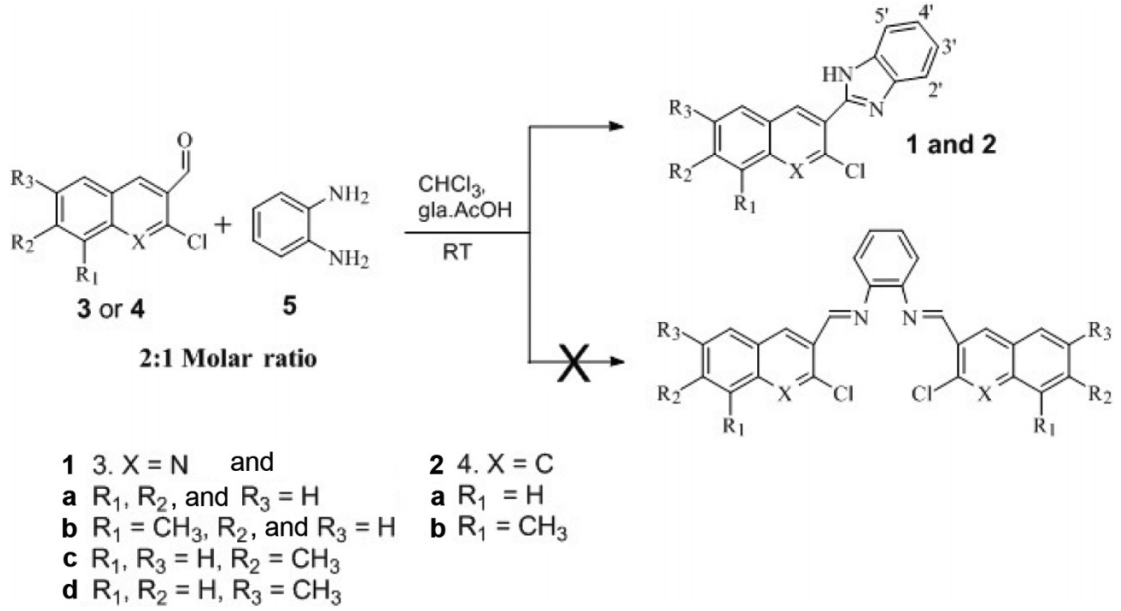

146.68, 147.03, 147.38. EI-MS: m/z = [M$^+$] 279, [M + 2]$^+$ 281. Anal. calcd. for $C_{16}H_{10}N_3Cl$: C, 68.70; H, 3.60; N, 15.02. Found: C, 68.55; H, 3.48; N, 14.78.

*Synthesis of 3-(1*H*-benzoimidazol-2-yl)-2-chloro-8-methyl-quinoline (1b)*

The compound was prepared as described above by the reaction of 2-chloro-8-methyl-quinoline-3-carbaldehyde (9 mmol, 1.85 g) and benzene-1,2-diamine (4.5 mmol, 0.4866 g). Off-white solid (yield: 1.4 g, 89.82%); mp 215 °C. IR (KBr): 3432, 1604, 1330, 1024, 760. ^{1}H NMR (400 MHz, $CDCl_3$) δ: 2.78 (s, 3H, C8–Q–CH_3–H), 7.34–7.38 (m, 2H, C3′ and C4′ BE–H), 7.48–7.52 (t, 1H, C6–Q–H, J = 8 Hz), 7.62–7.64 (d, 1H, C7–Q–H, J = 8 Hz), 7.74–7.76 (d, 3H, C5–Q–H, C2′ and C5′ BE–H, J = 8 Hz), 9.22 (s, 1H, C4–Q–H), 10.40 (bs, NH–IMD–H). ^{13}C NMR δ: 22.05, 120.31, 122.26, 123.42, 126.27, 126.99, 127.52, 127.82, 130.59, 131.34, 131.81, 136.22, 140.84, 141.11, 146.69, 147.12, 147.38. EI-MS: m/z = [M$^+$] 293, [M + 2]$^+$ 295. Anal. calcd. for $C_{17}H_{12}N_3Cl$: C, 69.51; H, 4.12; N, 14.31. Found: C, 69.43; H, 3.98; N, 14.18.

*Synthesis of 3-(1*H*-benzoimidazol-2-yl)-2-chloro-7-methyl-quinoline (1c)*

The compound was prepared as described above by the reaction of 2-chloro-7-methyl-quinoline-3-carbaldehyde (9 mmol, 1.85 g) and benzene-1,2-diamine (4.5 mmol, 0.4866 g). Off-white solid (yield: 1.305 g, 88.80%); mp 220 °C. IR (KBr): 3435, 1606, 1370, 1044, 752. ^{1}H NMR (400 MHz, $CDCl_3$) δ: 2.57 (s, 3H, C7–Q–CH_3–H), 7.33 to 7.38 (m, 3H, C6–Q–H, C3′ and C4′–BE–H), 7.48–7.45 (dd, 1H, J_1 = 8 Hz, J_2 = 4 Hz, C5–Q–H), 7.83–7.86 (m, 3H, C8–Q–H, C2′ and C5′–BE–H), 9.25 (s, 1H, C4–Q–H), 10.42 (bs, NH–IMD–H). ^{13}C NMR δ: 22.03, 120.25, 121.92, 123.39, 126.32, 124.82, 127.15, 127.78, 130.13, 131.32, 131.81, 136.21, 140.82, 142.75, 145.80, 147.39, 147.66. EI-MS: m/z = [M$^+$] 293, [M + 2]$^+$ 295. Anal. calcd. for $C_{17}H_{12}N_3Cl$: C, 69.51; H, 4.12; N, 14.31. Found: C, 69.42; H, 3.97; N, 14.12.

*Synthesis of 3-(1*H*-benzoimidazol-2-yl)-2-chloro-6-methyl-quinoline (1d)*

The compound was prepared as described above by the reaction of 2-chloro-6-methyl-quinoline-3-carbaldehyde (9 mmol, 1.85 g) and benzene-1,2-diamine (4.5 mmol, 0.4866 g). Off-white solid (yield: 1.305 g, 88.80%); mp 220 °C. IR (KBr): 3443, 1605, 1334, 1024, 762. ^{1}H NMR (400 MHz, $CDCl_3$) δ: 2.64 (s, 3H, C6–Q–CH_3–H), 7.34–7.38 (m, 2H, C3′ and C4′–BH–H), 7.48–7.52 (m, 2H, C5 and C7–Q–H), 7.76–7.81 (d, 3H, C8–Q–H, C2′ and C5′–BH–H, J = 8 Hz), 9.25 (s, 1H, C4–Q–H), 10.42 (bs, NH–IMD–H). ^{13}C NMR δ: 22.03, 120.25, 122.67, 123.02, 126.32, 127.11, 127.45, 127.81, 130.59, 131.32, 131.81, 136.21, 140.83, 141.11, 146.69, 147.03, 147.40. EI-MS: m/z = [M$^+$] 293, [M + 2]$^+$ 295. Anal. calcd. for $C_{17}H_{12}N_3Cl$: C, 69.51; H, 4.12; N, 14.31. Found: C, 69.32; H, 3.89; N, 14.14.

*Synthesis of 2-(3-chloro-naphthalen-2-yl)-1*H*-benzoimidazole (2a)*

The compound was prepared as described above by the reaction of 3-chloro-naphthalene-2-carbaldehyde (9 mmol, 1.72 g) and benzene-1,2-diamine (4.5 mmol, 0.4866 g). Yellowish orange solid (yield: 1.125 g, 89.70%); mp 210 °C. IR (KBr): 3470, 1614, 1321, 744. ^{1}H NMR (400 MHz, $CDCl_3$) δ: 7.25–7.34 (m, 4H, C6 and C7–naphthalene–NA, C3′ and C4′–BH–H), 7.65–7.67 (d, 2H, C5 and C8–NA, J = 8 Hz), 7.69–7.75 (m, 3H, C4–NA, C2′ and C5′–BE–H), 7.84 (s, 1H, C1–NA–H), 9.5 (bs, NH–IMD–H). ^{13}C NMR δ: 115.4, 115.5, 122.9, 123.0, 126.1, 126.9, 127.0, 127.1, 127.8, 128.0, 130.1, 132.2, 134.3, 134.7, 137.9, 138.0, 141.5. EI-MS: m/z = [M$^+$] 278, [M + 2]$^+$ 280. Anal. calcd. for $C_{17}H_{11}N_2Cl$: C, 73.26; H, 3.98; N, 10.05. Found: C, 73.15; H, 3.79; N, 9.85.

*Synthesis of 2-(3-chloro-5-methyl-naphthalen-2-yl)-1*H*-benzoimidazole (2b)*

The compound was prepared as described above by the

reaction of 3-chloro-5-methyl-naphthalene-2-carbaldehyde (9 mmol, 1.84 g) and benzene-1,2-diamine (4.5 mmol, 0.4866 g). Yellowish orange solid (yield: 1.132 g, 85.65%); mp 225 °C. IR (KBr): 3456, 1607, 1332, 756. ^{1}H NMR (400 MHz, $CDCl_3$) δ: 2.61 (s, 3H, C6–Q–CH_3–H), 7.20–7.29 (m, 4H, C6 and C7–NA–H, C3′ and C4′–BE–H), 7.59–7.63 (d, 2H, C5 and C8–NA–H, J = 8 Hz), 7.65–7.72 (m, 3H, C4–NA–H, C2′ and C5′–BE–H), 7.82 (s, 1H, C1–NA–H), 9.2 (bs, 1H, NH–IMD–H). ^{13}C NMR δ: 20.63, 114.2, 114.5, 121.9, 122.0, 125.1, 125.9, 127.2, 127.5, 127.9, 128.0, 130.2, 132.2, 134.2, 134.5, 137.5, 138.2, 140.5. EI-MS: m/z = [M$^+$] 292, [M + 2]$^+$ 294. Anal. calcd. for $C_{17}H_{11}N_2Cl$: C, 73.85; H, 4.48; N, 9.57. Found: C, 73.65; H, 4.34; N, 9.47.

Optical measurements

For the absorption analysis, stock solution was prepared by dissolving 10 mg of BIQ derivatives in 100 mL ethanol. The solution was diluted to 10^{-5} mol/L concentration for the absorption and 10^{-7} mol/L for the emission analysis. But in the case of solvent polarity study of **1b**, the compounds in the specified solvent medium were only used for both absorption and emission analysis. The fluorescence intensity vs. pH titration was carried out using 10% aqueous alcoholic solution of the BIQ-**1b** compound. 0.1 mol/L HCL and 0.1 mol/L NaOH were used to adjust the pH of the medium.

Fluorescence decays were recorded using TCSPC method using the following setup. A diode-pumped millena CW laser (Spectra Physics) 532 nm was used to pump the Ti:sapphire rod in Tsunami picosecond mode locked laser system (Spectra Physics). The 750 (80 MHz) was taken from the Ti:sapphire laser and passed through pulse picker (Spectra Physics, 3980 2S) to generate 4 MHz pulses. The seond harmonic output (375 nm) was generated by a flexible harmonic generator (Spectra Physics, GWU 23PS). The vertically polarized 375 nm laser was used to excite the sample. The fluorescence emission at magic angle (54.7°) was dispersed in a monochromator (f/3 aperture), counted by a MCP PMT (Hamamatsu R 3809), and processed through CFD, TAC, and MCA. The instrument response function for this system is ~52 ps. The fluorescence decay was analyzed by using the software provided by IBH (DAS-6) and PTI global analysis software.[22]

Cytogenetic analysis

Cytogenetic analysis was performed for compound **1b** in human peripheral blood lymphocyte culture (PBLC). They were obtained from peripheral blood set-up following the method of Hungerford.[23] Two experiments were carried out using four smoking and non-smoking healthy male donors, aged 23, 24, and 28 years. The testing compound was dissolved in 1% methanol. Its four different concentrations of 0.02, 0.2, 2, and 20 μg mL^{-1} were added to the culture medium (0.1 mL solution of compound **1b** per 8 mL of the medium) after 48 h culture initiation. Duplicate cultures for each dose were maintained for the study of chromosomal aberrations. Then, cultures were incubated at 37 °C for a period of 24 (total 72 h) h. Methanol (1%) was applied to control I and II, respectively.

The cultures were shaken periodically up to three times a day. During the two hours before the culture harvest, the dividing cells were arrested in the metaphase by adding 0.05 mL of colchicine solution (w = 0.01%). The contents in the vial were centrifuged at 1200 rpm for 5 min at the end of the colchicine treatment. The supernatant was discarded, and 5 mL of pre-warmed hypotonic solution (0.075 mol L^{-1} KCl) was added to the cell button. The cells were incubated for 20 min, sedimented after centrifugation at 1200 rpm for 10 min, and then fixed in a freshly prepared fixative (methanol/glacial acetic acid, 3:1, v/v). Two or three changes of the fixative were applied. Slides were prepared by placing a drop of the cell suspension on a clean chilled slide and dried immediately at 40 °C for a few seconds. The slides were routinely stained in a 2% buffered solution of Giemsa.[23] Three-hundred-and-fifty well-banded metaphases were analyzed for each treatment under an oil immersion lens.

Staining analysis in the bacterial microbe

Potent strains of bacteria were isolated from the gut of sulfur butterfly (*Kricogonialyside*). The isolation and culturing experimental procedures of the bacteria were carried out using the reported methods.[24] The confirmed *Serratia marcescens* SB08 was used in the staining process. Initially, the bacterium was heat-fixed in the clean glass slide. Two or three drops of 10% ethanolic solution of **1b** (10^{-9} mol/L) was added to the heat-fixed bacterial smear and allowed to bind for 15–60 s. After that, the slide was rinsed with distilled water and air-dried. Then, the slide was examined under the fluorescence microscopy.

Results and discussion

Synthesis of benzimidazole derivatives

Recent exploration of pyrene- and benzimidazole-based compounds as long-wavelength fluorophores[25] raise our interest to synthesize quinoline and naphthalene derivatives containing benzimidazole unit and study their structural correlation in the optical property. To achieve our objective, the work is started by synthesizing benzimidazole compounds from the derivatives of quinoline and naphthalene aldehydes with 1,2-diaminobenzene (Scheme 2). Such quinoline benzimidazole derivative was first prepared by Bhanumathi et al.[26] in two-stage approach. Their synthetic method was low-yielding, time-consuming, and did not seem amenable for the synthesis of benzimidazole compounds as demanded by the need of their application. Additionally, Kidwai et al.[27] reported a bisquinoline formation in the condensation reaction of quinoline aldehyde with benzene-1,2-diamine. Their reaction conditions and medium are similar to the Bhanumathi et al. synthetic methodology. Recently, Chen reported a one-pot synthetic methodology for the synthesis of 2-benzimidazolyl quinoline by the direct condensation of diamine with quinoline acid.[28] In this sequence, the exploration of reaction conditions and temperature for the synthesis of benzimidazole derivatives from the diamine and aldehydes could be significant. It may give a valuable outlook for the synthesis of complex benzimidazole derivatives.

Initially, the reaction was carried out with the 1:1 molar ratio of reactants in chloroform with catalytic amount of glacial acetic acid. This reaction conditions resulted in the formation of a mixture of products. However, 2:1 molar ratio

Table 1. Yields, NH ^{1}H NMR, ν_{NH} IR, and absorption λ_{max} values of quinoline, naphthalene benzoimidazoles **1a**–**1d** and **2a**, **2b**.

Serial No.	Compound	Yield (%)	δ_H [a] (ppm)	IR $\nu_{(NH)}$ (cm^{-1})	λ_{max} in nm[b] ($\varepsilon \times 10^5$ M^{-1} cm^{-1})
1	**1a**	89.33	10.59	3424	346 (1.89)
2	**1b**	89.82	10.40	3432	354 (1.94)
3	**1c**	88.80	10.42	3435	351 (1.92)
4	**1d**	88.80	10.42	3443	352 (1.93)
5	**2a**	89.70	9.5	3470	317 (2.55)
6	**2b**	85.65	9.2	3456	332 (2.62)

[a]NH proton of the benzimidazole ring in the BIQ and BIN (400 MHz, $CDCl_3$).
[b]The 30 μmol/L ethanolic solution of BIQ and BIN compounds were used in the UV–vis absorption analysis.

of the reactants, i.e., aldehyde and diamine, respectively, produced a single product in the same reaction medium after 15 min. The purification of the products from the crude mixture was done by column chromatography using petroleum ether:ethyl acetate (9:1) mixture as eluent. The structure of the products was confirmed by IR, NMR, mass, and elemental analyses. The single-crystal structure of one of the quinoline benzimidazole derivatives (**1b**) was solved by X-ray crystallographic technique and was reported.[29] The characterization analysis supports the formation of benzimidazole derivatives using the 2:1 molar ratio of reactants. The same reaction was carried out smoothly in a beaker without changing the environmental condition, such as the high temperature, inert atmosphere, and expensive catalysts. It is believed that the presence of excess aldehydes might help to stop the backward reaction.

In the characterization analysis, a broad spectral correlation could be observed specifically in the benzimidazole N–H functional group of BIQ and BIN derivatives (Table 1). The IR spectrum of the BIQ and BIN derivatives shows ν_{NH} band in the region of 3420–3445 and 3455–3470 cm^{-1}, respectively. The lower ν_{NH} wavelength for BIQ compounds illustrates the existence of strong hydrogen bonding (Imida–N–H···Cl–Q) in their molecular structure. In addition, the ^{1}H NMR spectra of BIQ and BIN derivatives show a pronounced deshielding effects in the δ value of BIQ–N–H functional group (δ 10.40–10.59 and 8.52–8.55, respectively), which further confirms the existence of strong hydrogen bonding (Imida–N–H···Cl–Q) in the BIQ derivatives. It is concluded that the nitrogen lone-pair electrons in the quinoline ring could facilitate the existence of strong hydrogen bonding in the BIQ derivatives. This specific molecular structural conformation will play a vital role in the optical behavior of BIQ compounds compared with BIN compounds.

Absorption and emission spectral studies

The optical analyses of BIQ and BIN compounds were recorded in ethanol. Figure 1 shows the absorption spectra of compounds **1b** and **2b**. In general, UV–vis absorption spectra of BIQ and BIN ethanolic solutions exhibit peaks with λ_{max} in the range of 340 to 355 nm (Table 1). λ_{max} values of the respective compounds was used to excite the corresponding compound in the spectrofluorimetric analysis. The resulting fluorescence spectra of BIQ and BIN compounds prove the existence of fluorescence property only in BIQ compounds.

The absorption λ_{max} of **1b** is 354 nm in ethanol. This solution, on excitation in the range of λ_{max} 350–355 nm (single excitation), exhibits two fluorescence peaks around λ_{max} 432 and 851 nm (Fig. 2*a*). But the intensity of the first fluorescence peak is 10 times higher compared with the following peak (10:1). The same solution, on excitation in the range of λ_{max} 700–710 nm (double excitation), exhibits a fluorescence peak and a hump (Fig. 2*b*) around λ_{max} 433 and 849 nm, respectively. In this double excitation, the intensity ratio of the fluorescence peak and hump is also found to be 10:1. However, the fluorescence peak intensity in the single excitation (350–355 nm) is five times higher than the doubly excited (700–710 nm) fluorescence peak. This shows the sensitivity of the double excitation process. All the spectrofluorimetric experiments of **1b** were repeated in different solvents, i.e., in CH_2Cl_2, $CHCl_3$, DMF, DMSO, and EtOH. The combined spectral data expose the double-excitation property of **1b** in the above mentioned solvent. Additionally, it illustrates that the intensity of the fluorescent λ_{max} is higher in polar solvents than in non-polar solvents.

All the observed results propose that the BIQ derivatives should have intramolecular charge transfer (ICT) interaction in the solution form. ICT occurs between the quinoline and imidazole ring systems during electronic excitation. It restricts the internal rotation of imidazole unit within the molecule, which creates a self-organized supramolecular architecture. This molecular conformational arrangement of

Fig. 1. The UV–vis absorption spectra of the BIQ and BIN compounds in 30 μmol/L concentration: (*i*) absorption spectra of BIQ-**1b** with λ_{max} = 336 and 354; (*ii*) absorption spectra of BIN-**2b** with λ_{max} = 332 and 350 nm.

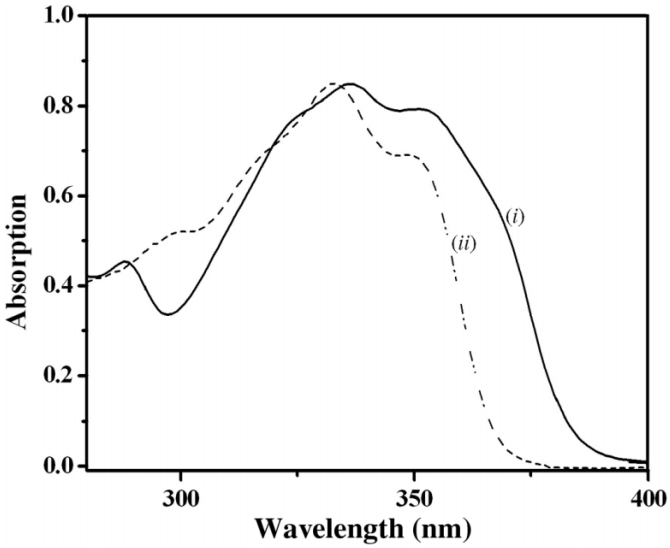

Fig. 2. Fluorescence spectra of ethanolic solution of BIQ-**1b** in 0.3 μmol/L concentration: (*a*) Solid line: emission spectra of **1b** in the excitation wavelength λ_{exc} 354 nm and the resulting emission λ_{emi} = 434 and 852 nm; dashed line: emission spectra of **1b** in the excitation wavelength λ_{exc} = 708 nm and the resulting emission λ_{emi} = 447 nm. (*b*) Expansion form of fluorescence spectra of **2a** from 750 to 1000 nm.

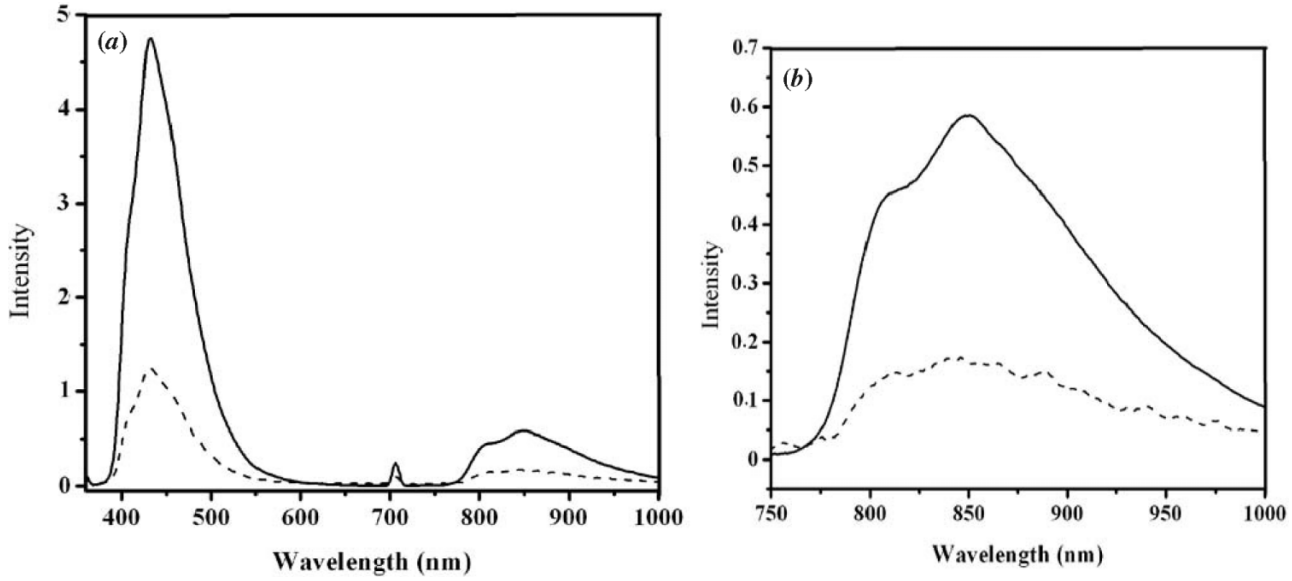

excited molecules can facilitate radiative decay during the electronic relaxation process, while in the case of naphthalene bearing imidazole moiety, the absence of ICT can sustain the internal rotation, thereby the electronic relaxation frequently takes place as non-radiative decay process.[30] Spectrofluorimetric analysis of other derivatives of BIQ (**1a**, **1c**, and **1d**) also exhibits the higher wavelength excitation and fluorescence emission property in solution.

Fluorescence quantum-yield measurement

Fluorescence quantum yield (ϕ_f) of the BIQ derivatives (x) in ethanol was determined using 2-amino pyridine as a standard (std), since both compounds have excitation wavelength in the range of 340–450 nm. 0.1 mol/L H_2SO_4 solution was used in the preparation of 2-amino pyridine solution in different concentrations. For quantum-yield measurement, the absorption and fluorescence spectra of 2-amino pyridine solution were recorded in the following concentrations: 0 (blank), 0.2, 0.4, 0.6, 0.8, and 1 μmol/L. The spectral experimental procedures were repeated in the ethanolic solution of BIQ derivatives in the same concentrations. The integrated fluorescence intensity vs. absorbance was plotted (Fig. 3), and the slope was calculated. The quantum yields of the benzimidazolyl quinoline compounds were calculated by applying the observed experimental data in the following equation:

$$[1] \qquad \phi_x = \phi_{std}\left(\frac{Grad_{std}}{Grad_x}\right)\left(\frac{\eta_x^2}{\eta_{std}^2}\right)$$

Here, ϕ_x and ϕ_{std} denote the fluorescence quantum yields of unknown (BIQ derivatives) and standard (2-amino pyridine) compounds, respectively. The "Grad" and η denote the gradient (slop) of the graph and refractive index of the respective solvent, respectively. The ϕ_{std} of the 2-amino pyridine in 0.1 mol/L H_2SO_4 solution is 0.6. The refractive index of the 0.1 mol/L H_2SO_4 and ethanol is 1.36 and 1.003, respectively. By doing the calculation, the fluorescence quantum yields (ϕ_f) of the BIQ derivatives are determined, and the values are tabulated (Table 2).

Fig. 3. Fluorescence quantum-yield measurement of **1b** (μmol/L concentration range). (*i*) Fluorescent vs. absorption intensities of 2-aminopyridine in 0.1 mol/L H_2SO_4 solution, λ_{exc} = 335 nm and λ_{emi} = 370 nm. (*ii*) Fluorescent vs. absorption intensities of BIQ-**1b** in ethanol, λ_{exc} = 354 nm and λ_{emi} = 434 nm.

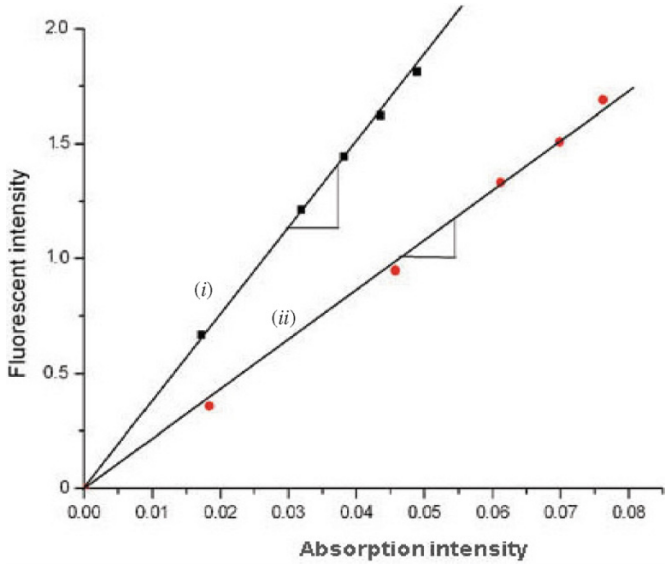

Fluorescence lifetime measurement

Time-dependent measurements of receptors have been performed using time-correlated single-photon counting (TCSPC) technique (Fig. 4). The fluorescecent lifetime of

Table 2. UV–vis, fluorescence spectra, quantum yield, and lifetime measurement data of compounds **1a–1d** in selected solvents.

	DMF			Ethanol			Water[b]				
Compounds[a]	$\lambda_{max\ ab}$	$\lambda_{max\ fl}$ [c]	$\lambda_{max\ fl}$ [d]	$\lambda_{max\ ab}$	$\lambda_{max\ fl}$ [c]	$\lambda_{max\ fl}$ [d]	$\lambda_{max\ ab}$	$\lambda_{max\ fl}$ [c]	$\lambda_{max\ fl}$ [d]	ϕ_f [e]	τ[e]
1a	317 332	415 805	410	322 346	424 824	430	348 365	432 861	432	0.501	2.12
1b	326 342	425 838	421	337 354	434 852	447	354 375	442 875	456	0.629	3.03
1c	322 339	424 839	423	331 351	433 851	445	350 372	441 874	455	0.617	3.09
1d	327 341	423 838	424	334 352	432 853	448	352 376	440 875	454	0.622	3.03

[a]30 and 0.3 μmol/L concentration of BIQ compounds were used to measure the absorption and emission spectra, respectively.
[b]10% ethanolic medium was used.
[c]Single-photon excitation.
[d]Double-photon excitation.
[e]The fluorescence quantum-yield measurements were done in ethanol using 2-aminopyridine as a standard.

Fig. 4. Fluorescence decay and residual curves profiles of BIQ-**1b** in ethanol, λ_{exc} = 354 nm and λ_{emi} = 432 nm. The solid lines represent the best fit to the data.

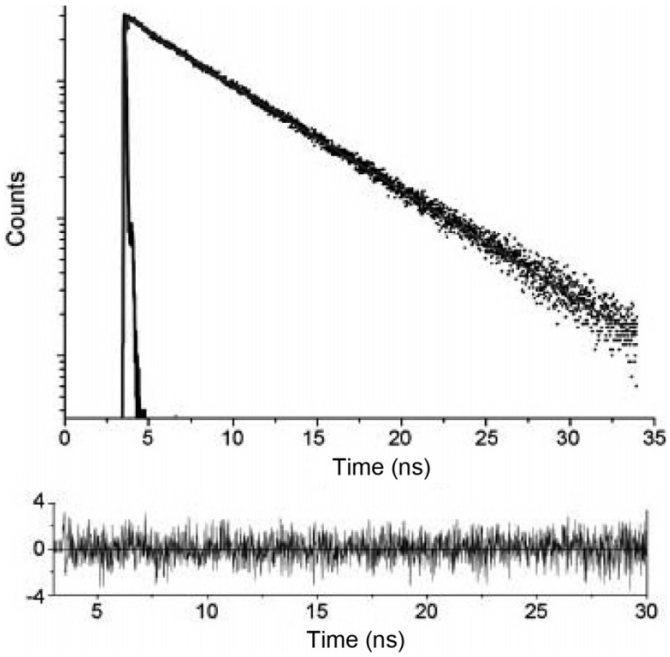

each BIQ derivative was measured in ethanol using the corresponding solution absorption λ_{max} wavelength as the excitation wavelength. The fluorescence lifetimes (τ_f) of the compounds are found to be in the range of 2–3 ns (Table 2).

Fluorescence efficiency

To optimize the fluorescence efficiency of BIQ derivatives, the influence of solvent polarity and pH of the medium on the optical property of **1b** was studied. In this fluorescence-optimizing spectrofluorimetric analysis, the single excitation of **1b** (428–435 nm) is mainly accounted.

Solvent-polarity study

The absorption and emission of **1b** were studied in different solvents with increasing polarity (toluene, CH_2Cl_2, $CHCl_3$, DMSO, DMF, EtOH, and 10% EtOH). Absorption spectra of the quinoline benzimidazole derivatives showed a gradual red shift with the increase in solvent polarity. This shift is much pronounced in the last three solvents in the following order: DMF < EtOH < H_2O (10% ethanol) (Fig. 5). Absorption λ_{max} values of **1b** in different solvents were used to record fluorescence spectra of the corresponding solutions. The recorded fluorescence spectrum shows red shift with the increase in solvent polarity. This illustrates the utility of this compound as a polar fluorescent probe (Fig. 6).[31] The experiment was repeated with double-excitation wavelength λ_{max}. The resulting spectra in the combined form were shown in Fig. 7. Absorbance and fluorescence wavelength λ_{max} of all other BIQ derivatives (**1a**, **1c**, and **1d**) in DMF, EtOH, and water (10% ethanol) were measured and tabulated (Table 2).

Figures 5, 6, and 7 point out that **1b** in the excited state is more polar than in the ground state. For the increase of the polarity of the solvent, the energy level which corresponds to a more polar molecular conformation will be more inten-

Fig. 5. UV–vis absorption spectra of BIQ-**1b** in (*i*) toluene, λ_{max} = 312 nm; (*ii*) DMF, λ_{max} = 326 and 342 nm; (*iii*) EtOH, λ_{max} = 330 and 354 nm; (*iv*) 10% aqueous ethanol, λ_{max} = 354 and 375 nm.

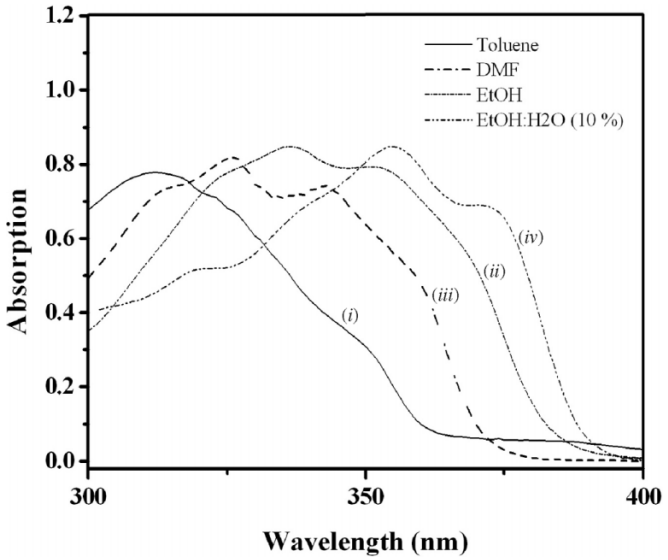

Fig. 6. Emission spectra of **1b** (single excitation) in (*i*) toluene, λ_{exc} = 312 nm and λ_{emi} = 370 nm; (*ii*) DMF, λ_{exc} = 342 and λ_{emi} = 425 nm; (*iii*) EtOH, λ_{exc} = 354 nm and λ_{emi} = 434 nm; (*iv*) 10% aqueous ethanol, λ_{exc} = 375 nm and λ_{emi} = 442 nm.

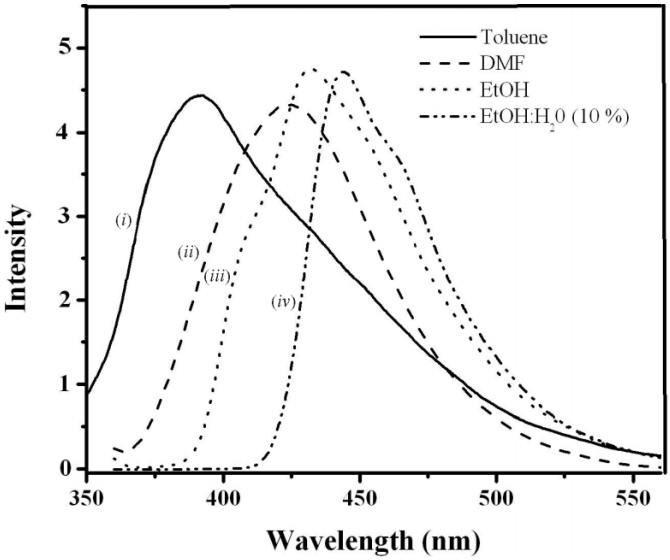

sively lowered.[32] Hence, a red shift of the wavelength is observed in the absorption and emission spectra of **1b** with the increase in solvent polarity.

In addition to the red shift of wavelength, Figs. 6 and 7 illustrate marked difference in the λ_{max} of the solution during double excitation compared with the single excitation. This further confirms the sensitivity of the double-excitation processes. This type of shifting also suggests that the excited geometrical conformation of **1b** may be suitable for the model of twisted intramolecular charge transfer (TICT).[32]

Fluorescence pH titration

Quantitative pH titration was performed to find the fluorescent efficiencies of BIQ compounds in the wide range of pH. In this analysis, the intensity of first fluorescence peak during the single excitation of **1b** (λ_{exc} = 354 nm and λ_{emi} = 432 nm) was accounted. The fluorescence spectrum of the 3 μmol/L aqueous ethanol solution of **1b** was recorded in the pH range of 2 to 14, and a plot was drawn between the fluorescence intensity and pH. Figure 8 shows the fluorescent intensity vs. pH titration plot of **1b**. From the graph, it is observed that the fluorescent intensity is higher in the lower pH range and continuously decreases in higher pH range, owing to the deprotonation of the N atoms in the basic medium. However, it should be noted that the difference in the fluorescent intensity is very little when the pH is greater than 6.5. The fluorescent stability of **1b** in this pH range might be helpful to avoid the interference of possible pH change induced by biological stimulation.

Bioanalytical study of 1b

Cytogenetic analysis

The observed results in the optical measurements support the suitability of BIQ derivatives as efficient polar fluorescent probes for bioanalytical study. But in the case of in vivo analysis, the cytotoxicity of the compound is the main factor which determines the suitability of the compound in cell-line analysis. With this necessity, the cytogenetic analysis was performed by using one of the BIQ compounds **1b** to scale up the utility of the derivatives in living-cells analysis. The preparation of the metaphase plates is detailed in the Experimental section.

Fig. 7. Emission spectra of **1b** (double excitation) in (*i*) toluene, λ_{exc} = 624 nm and λ_{emi} = 385 nm; (*ii*) DMF, λ_{exc} = 684 nm and λ_{emi} = 421 nm; (*iii*) EtOH, λ_{exc} = 708 nm and λ_{emi} = 447 nm; (*iv*) 10% aqueous ethanol, λ_{exc} = 750 nm and λ_{emi} = 456 nm.

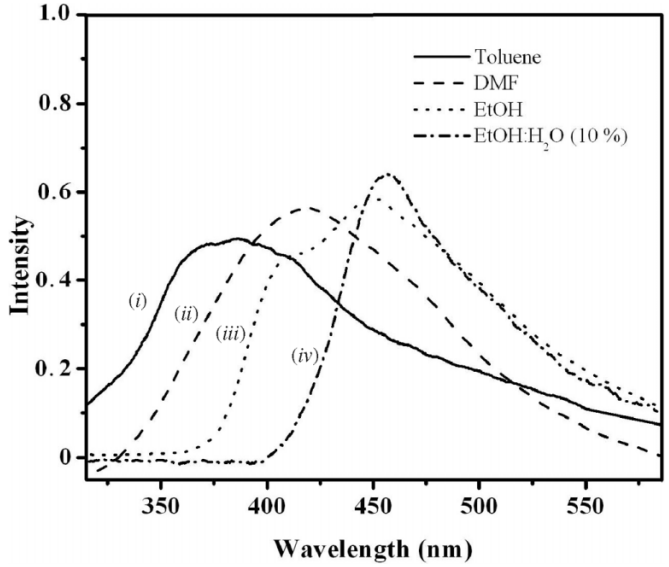

All the prepared slides in well metaphase plates were screened for chromosomal aberrations (Table 3). The aberration includes endoreduplication, fragments, chromatid breaks, and chromatid gaps. The clastogenic properties of the compound were studied by investigating the effects of the compounds on human chromosomes through in vitro

Fig. 8. Fluorescence pH titration of BIQ-**1b** (3 μmol/L of 10% aqueous ethanolic solution) with λ_{exc} = 354 nm and λ_{emi} = 432 nm. The pH of the solution was adjusted by using 0.1 mol/L HCl and 0.1 mol/L NaOH to get acidic and basic pH, respectively.

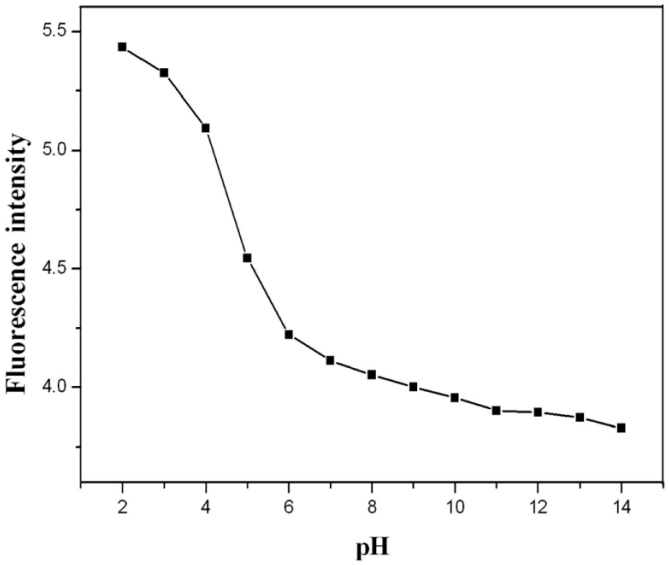

analysis in the lymphocyte cultures. The data of the compound are pooled and shown in Table 3. It was noted that the increase in the chromosomal aberrations is dose-dependent. Chromosomal aberrations like chromatid gaps and chromatid breaks were also observed. Polyploid cells were absent in all examined slides. From Table 3, it is inferred that the compound did not show any aberration up to 10^{-4} mol/L concentration, which is essential for cell-lines in vitro studies.

Thermal analysis

BIQ compounds are remarkably stable towards air. It can be kept under air for a long time without any noticeable decomposition. Figure 9 shows the TG–DTA curves of **1b**. Compound **1b** exhibits two steps of decomposition in TG. The endothermic peak at 200 °C corresponds to the melting point of the compound. The first exothermic peak at 275 °C corresponds to the loss of chlorine. Then, a complete exothermic decomposition of the molecule occurs between 500 and 800 °C. During the decomposition, the masses of the compound, intermediate, and final product are those which best fit with observed mass loss in TG curve. The TG results are in good agreement with the DTA data. From this study, it is inferred that the compound is highly stable up to 250 °C.

Staining study

All the photophysical, cytotoxicity, and thermal analyses of BIQ derivatives support its applicability for bioanalytical studies. This creates an intention to carry out the staining analysis using BIQ compounds as staining dye. The appreciable fluorescence efficiency (high ϕ_f, water solubility, and thermal stability analysis) of **1b** makes it attractive for the staining analysis. For the initial staining analysis, we prefer small microorganism selectively bacteria because they are one of the primary microbes used in the drug discovery. Apart from the pathogenic activity of bacteria, they have significant applications in the industrial biotech processes, such as biocatalysis,[33] bioremediation[34], and so forth, in such a way that leads to the implementation of green chemistry in various industrial processes. Additionally, the enzyme-producing bacteria have promising medicinal activity.[35] In this regard, many enzyme-producing bacteria are analyzed in anticancer studies.[36]

In this margin, *S. marcescens* a Gram-negative bacterium produces L-asparaginase enzyme that has anti-proliferative and anti-tumor activities.[37] Accordingly, its identification, proliferation, and its structural analysis become significant in the bacterial research. Recently, Venil et al.[24] discussed the factors affecting the production of enzyme L-asparaginase from the bacterium *S. marcescens* SB and optimized an effective medium for its production. In this progress, the fluorescence imaging of the bacteria should have significant value. The surface morphological study will reveal many fundamental features of this organism and produce novel tools to study previously inaccessible problems. Additionally, this staining analysis can give a fundamental idea about the affinity of the BIQ compounds in the cell wall and also decides its applicability for further bioanalytical studies, such as optical imaging of living systems, detection of intracellular free metal ions, and so forth. With this intension preliminarily, we concentrate the staining analysis in the Gram-negative bacterium *S. marcescens* SB08.

Bacterial staining analysis

The fluorescent microscopic view shows that **1b** is an excellent green-fluorescence light-emitting material (Fig. 10*a*). The details of the slide preparation are explained in the Experimental section. In addition to the fluorescence staining, normal Gram staining of the bacterium were also done. The normal Gram-stained bacterial smear in the slide was viewed in the microscope (Fig. 10*b*), whereas the BIQ-stained one was viewed in the fluorescence microscope. The clean rod-shape image (Fig. 10*c*) of the bacterium confirms the binding of **1b** to the surface of the bacterium.

Conclusion

A specific molar ratio is implemented for the synthesis of BIQ and BIN compounds at room temperature. This short-reaction-time method offers high yield with reference to the reported procedures. All the synthesized compounds are characterized by various spectral and analytical techniques (IR, ^{1}H, ^{13}C NMR, mass, and CHN analyses).

The preliminary optical analysis confirms the fluorescence property of the BIQ derivatives and also reveals that such property is silent in the BIN derivatives. This optical behavior of BIQ derivatives can be attributed to the quinoline moiety facilitating a strong charge-transfer interaction with the imidazole group during the electronic relaxation. Due to that, its derivatives alone show intense absorption and fluorescence bands with ϕ_f approximately close to 1. In addition to the fluorescence property, the spectrofluorimetric analysis of BIQ derivatives exhibits a higher excitation wavelength (λ_{exc} = 708 nm) and emission property (λ = 434 and 850 nm) in different solvents, since it is also an essential parameter for the recognition of TP fluorescence probes. This low energy excitation and emission photophys-

Table 3. Cytogenetic analysis of the BIQ compound **1b**.

	Control		**1b** (24 h)[a]			
Mean number of aberrations	0 h	24 h	0.02 μg mL^{-1}	0.2 μg mL^{-1}	2 μg mL^{-1}	20 μg mL^{-1}
Average No. of metaphases (n = 8)	400	400	400	400	400	400
Endoreduplication	—	0.57±0.20	0.59±0.23	0.60±0.25	0.62±0.27	1.69±0.24
Fragments	—	0.32±0.35	0.34±0.30	0.37±0.22	0.45±0.28	1.49±0.52
Chromatid breaks	—	0.89±0.318	0.94±0.20	0.97±0.19	1.02±0.15	1.34±0.47
Chromatid gaps	—	0.02±0.17	0.05±0.10	0.07±0.10	0.09±0.14	0.69±0.29

[a]Chromosomal aberrations after 24 h incubation of 48 h initiated human peripheral blood lymphocyte culture with compound **1b**.

Fig. 9. TG–DTA of BIQ-**1b**: (*i*) TG of BIQ-**1b**; (*ii*) DTA of BIQ-**1b**.

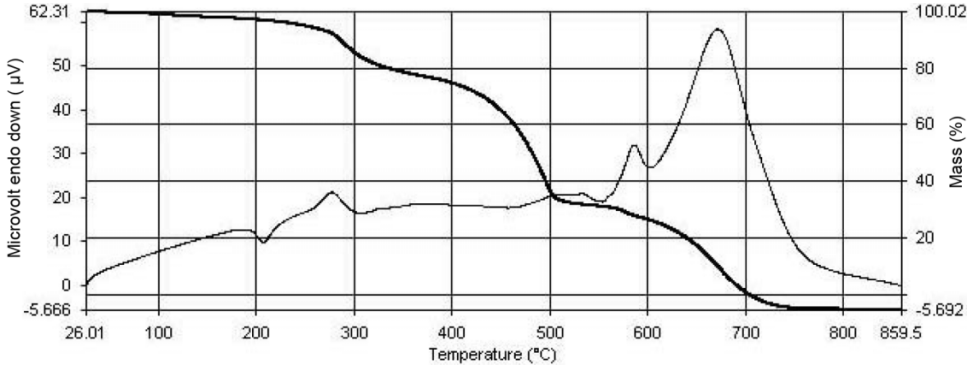

Fig. 10. Staining analysis of BIQ-**1b**: (*a*) fluorescent green-light-emitting view of BIQ-**1b**; (*b*) Gram-stained microscopic view of the *S. marcescens* SB; (*c*) BIQ-**1b**-stained fluorescence microscopic view of the *S. marcescens* SB.

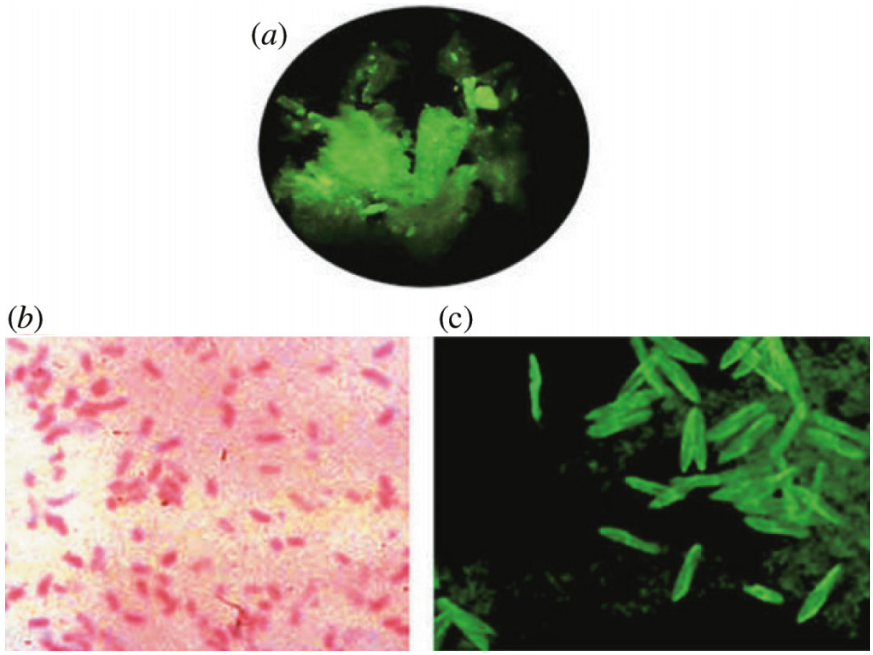

ical property of BIQ compounds is significantly economic in the preliminary bioanalytical study of the living systems.

The fluorescence quantum yield (ϕ_f) and time-resolved fluorescent lifetime (T_f) of the BIQ derivatives were measured to evaluate its fluorescence efficiency. The optical analysis with increasing solvent polarity exposed the polar fluorescent probe nature of the BIQ derivatives. The fluorescence pH-titration measurement confirms the applicability of the BIQ derivatives in a wide range of pH.

In general, the combined optical spectral data of the BIQ and BIN derivatives conclude that the methyl derivatives have better photophysical properties in comparison with the unsubstituted derivatives. In addition to the optical property, a vast difference also exists in the IR and NMR spectral data of the substituted and unsubstituted benzimidazole derivatives. This is mainly due to the extension of conjugation (hyperconjugation)[38] facilitated by the methyl protons.

Based on the optical properties, one of the BIQ deriva-

tives (**1b**) was completely examined to evaluate its applicability in the bioanalytical studies. The TG–DTA analysis of **1b** exhibits that it is stable around the 250 °C and can withstand up to 500 °C with the loss of chlorine atom. The cytogenetic analysis exposed that up to the 10^{-4} mol/L concentration of **1b** can be used in living cells, which is expected to be sufficient for the in vitro analysis.

From the optimization, the bacterial staining applicability of **1b** was attempted. The **1b**-stained bacterial view in the fluorescence microscopy explores its staining ability. It reveals that BIQ derivatives could be good alternative for green beads in fluorescence-imaging studies. Solvent polarity and pH-sensitivity analyses illustrate the promising platform to design TP biomarkers from the BIQ derivatives. The low energy excitation and emission property of the BIQ derivatives in the solid form and its TP analysis are underway.

Supplementary data

Supplementary data for this article are available on the journal Web site (canjchem.nrc.ca) or may be purchased from the Depository of Unpublished Data, Document Delivery, CISTI, National Research Council Canada, Ottawa, ON K1A 0R6, Canada. DUD 5304. For more information on obtaining material, refer to cisti-icist.nrc-cnrc.gc.ca/cms/unpub_e.shtml.

Acknowledgement

One of the authors (MM) thanks the Council of Science and Industrial Research (CSIR), New Delhi, for the award of Senior Research Fellowship (SRF). Authors are thankful to the analytical instrumentation support from the NMR research center, IISc., Bangalore, India, and National Centre for Ultrafast Processes, University of Madras, Taramani Campus, India.

References

(1) (a) Cornish, P. V.; Ha, T. *ACS Chem. Biol.* **2007**, *2* (1), 53. doi:10.1021/cb600342a. PMID:17243783.; (b) Fricker, M.; Runions, J.; Moore, I. *Annu. Rev. Plant Biol.* **2006**, *57* (1), 79. doi:10.1146/annurev.arplant.57.032905.105239. PMID:16669756.; (c) Nagl, S.; Schaferling, M.; Wolfbeis, O. S. *Mikrochim. Acta* **2005**, *151*, 1.

(2) (a) Johnsson, N.; Johnsson, K. *ACS Chem. Biol.* **2007**, *2* (1), 31. doi:10.1021/cb6003977. PMID:17243781.; (b) Carol, P.; Sreejith, S.; Ajayaghosh, A. *Chem. Asian J.* **2007**, *2* (3), 338. doi:10.1002/asia.200600370. PMID:17441169.; (c) Wang, F.; Tan, W. B.; Zhang, Y.; Fan, X.; Wang, M. *Nanotechnology* **2006**, *17* (1), R1. doi:10.1088/0957-4484/17/1/R01.

(3) (a) Ghoroghchian, P. P.; Frail, P. R.; Susumu, K.; Park, T.-H.; Wu, S. P.; Uyeda, H. T.; Hammer, D. A.; Therien, M. J. *J. Am. Chem. Soc.* **2005**, *127* (44), 15388. doi:10.1021/ja055571b. PMID:16262400.; (b) Achilefu, S. *Technol. Cancer Res. Treat.* **2004**, *3* (4), 393. PMID:15270591.

(4) (a) Au, W.; Pathak, S.; Collie, C. J.; Hsu, T. C. *Mutat. Res.* **1978**, *58* (2-3), 269. doi:10.1016/0165-1218(78)90019-8. PMID:745616.; (b) Mohanty, K.; Naidu, J. T.; Meikap, B. C.; Biswas, M. N. *Ind. Eng. Chem. Res.* **2006**, *45* (14), 5165. doi:10.1021/ie060257r.; (c) Downing, T. W.; Garner, D. L.; Ericsson, S. A.; Redelman, D. *J. Histochem. Cytochem.* **1991**, *39* (4), 485. PMID:1900872.

(5) Haugland, R. P., Ed. *The Handbooks — A Guide to fluorescent Probes and Labeling Technologies,* 10th ed.; Molecular Probes: Eugene, OR, 2005.

(6) (a) Badugu, R.; Lakowicz, J. R.; Geddes, C. D. *Anal. Chem.* **2004**, *327* (1), 82; (b) Woodroofe, C. C.; Won, A. C.; Lippard, S. J. *Inorg. Chem.* **2005**, *44* (9), 3112. doi:10.1021/ic048789s. PMID:15847416.

(7) (a) Fleitz, P. A.; Brant, M. C.; Sutherland, R. L.; Strohkendl, F. P.; Larson, J. R.; Dalton, L. R. *SPIE Proc.* **1998**, *91*, 3472; (b) He, G. S.; Bhawalkar, J. D.; Zhao, C. F.; Prasad, P. N. *Appl. Phys. Lett.* **1995**, *67* (17), 2433. doi:10.1063/1.114598.; (c) Ehrlich, J. E.; Wu, X. L.; Lee, I.-Y. S.; Hu, Z.-Y.; Röckel, H.; Marder, S. R.; Perry, J. W. *J. Opt. Lett.* **1997**, *22* (24), 1843. doi:10.1364/OL.22.001843.

(8) (a) Bhawalkar, J. D.; He, G. S.; Prasad, P. N. *Rep. Prog. Phys.* **1996**, *59* (9), 1041. doi:10.1088/0034-4885/59/9/001.; (b) He, G. S.; Zhao, C. F.; Bhawalkar, J. D.; Prasad, P. N. *Appl. Phys. Lett.* **1995**, *67* (25), 3703. doi:10.1063/1.115355.; (c) Zhao, C. F.; He, G. S.; Bhawalkar, J. D.; Park, C. K.; Prasad, P. N. *Chem. Mater.* **1995**, *7* (10), 1979. doi:10.1021/cm00058a032.

(9) (a) Denk, W.; Strickler, J. H.; Webb, W. W. *Science* **1990**, *248* (4951), 73. doi:10.1126/science.2321027. PMID:2321027.; (b) Mertz, J.; Xu, C.; Webb, W. W. *Opt. Lett.* **1995**, *20* (24), 2532. doi:10.1364/OL.20.002532.; (c) Denk, W.; Svoboda, K. *Neuron* **1997**, *18* (3), 351. doi:10.1016/S0896-6273(00)81237-4. PMID:9115730.; (d) Köhler, R. H.; Cao, J.; Zipfel, W. R.; Webb, W. W.; Hanson, M. R. *Science* **1997**, *276* (5321), 2039. doi:10.1126/science.276.5321.2039. PMID:9197266.; (e) Xu, C.; Zipfel, W. R.; Shear, J. B.; Williams, R. M.; Webb, W. W. *Proc. Natl. Acad. Sci. U.S.A.* **1996**, *93* (20), 10763. doi:10.1073/pnas.93.20.10763. PMID:8855254.; (f) Denk, W. *Proc. Natl. Acad. Sci. U.S.A.* **1994**, *91* (14), 6629. doi:10.1073/pnas.91.14.6629. PMID:7517555.

(10) (a) Parthenopoulos, D. A.; Rentzepis, P. M. *Science* **1989**, *245* (4920), 843. doi:10.1126/science.245.4920.843. PMID:17773360.; (b) Dvornikov, A. S.; Rentzepis, P. M. W. *Opt. Commun.* **1995**, *119* (3-4), 341. doi:10.1016/0030-4018(95)00338-9.; (c) Cumpston, B. H.; Ananthavel, S. P.; Barlow, S.; Dyer, D. L.; Ehrlich, J. E.; Erskine, L. L.; Heikal, A. A.; Kuebler, S. M.; Lee, I.-Y. S.; McCord-Maughon, D.; Qin, J.; Röckel, H.; Rumi, M.; Wu, X.-L.; Marder, S. R.; Perry, J. W. *Nature* **1999**, *398* (6722), 51. doi:10.1038/17989.

(11) Bhawalkar, J. D.; Kumar, N. D.; Zhao, C. F.; Prasad, P. N. *J. Clin. Laser Med. Surg.* **1997**, *15* (5), 201. PMID:9612170.

(12) (a) Gómez-Hens, A.; Aguilar-Caballos, M. P. *Trends Analyt. Chem.* **2004**, *23* (2), 127. doi:10.1016/S0165-9936(04)00305-X.; (b) Lord, S. J.; Lu, Z.; Wang, H.; Willets, K. A.; Schuck, P. J.; Lee, H.-L. D.; Nishimura, S. Y.; Twieg, R. J.; Moerner, W. E. *J. Phys. Chem. A* **2007**, *111* (37), 8934. doi:10.1021/jp0712598. PMID:17718454.; (c) Aslan, K.; Zhang, Y.; Geddes, C. D. *Anal. Chem.* **2009**, *81* (10), 3801. doi:10.1021/ac9001673. PMID:19354285.; (d) Cuppoletti, A.; Cho, Y.; Park, J.-S.; Strässler, C.; Kool, E. T. *Bioconjug. Chem.* **2005**, *16* (3), 528. doi:10.1021/bc0497766. PMID:15898718.

(13) (a) Jung, H. J.; Singh, N.; Jang, D. O. *Tetrahedron Lett.* **2008**, *49* (18), 2960. doi:10.1016/j.tetlet.2008.03.002.; (b) Joo, T. Y.; Singh, N.; Lee, G. W.; Jang, D. O. *Tetrahedron Lett.* **2007**, *48* (50), 8846. doi:10.1016/j.tetlet.2007.10.060.; (c) Krishnamoorthy, G.; Dogra, S. K. *J. Photochem. Photobiol. Chem.* **1999**, *123* (1–3), 109. doi:10.1016/S1010-6030(99)00030-1.

(14) (a) Reed, J. E.; Arnal, A. A.; Neidle, S.; Vilar, R. *J. Am. Chem. Soc.* **2006**, *128* (18), 5992. doi:10.1021/ja058509n.

PMID:16669641.; (b) Mandal, S. S.; Varshney, U.; Bhattacharya, S. *Bioconjug. Chem.* **1997**, *8* (6), 798. doi:10.1021/bc970121x. PMID:9404652.; (c) Chaudhuri, P.; Majumder, H. K.; Bhattacharya, S. *J. Med. Chem.* **2007**, *50* (10), 2536. doi:10.1021/jm0610604. PMID:17444624.; (d) Bhattacharya, S.; Chaudhuri, P. *Curr. Med. Chem.* **2008**, *15* (18), 1762. doi:10.2174/092986708785133013. PMID:18691037.

(15) (a) Tobey, S. L.; Anslyn, E. V. *Org. Lett.* **2003**, *5* (12), 2029. doi:10.1021/ol034427x. PMID:12790520.; (b) Kang, J.; Kim, H. S.; Jang, D. O. *Tetrahedron Lett.* **2005**, *46* (36), 6079. doi:10.1016/j.tetlet.2005.07.002.

(16) Zhang, M.; Li, M.; Zhao, Q.; Li, F.; Zhang, D.; Zhang, J.; Yi, T.; Huang, C. *Tetrahedron Lett.* **2007**, *48* (13), 2329. doi:10.1016/j.tetlet.2007.01.158.

(17) (a) Chetia, B.; Iyer, P. K. *Tetrahedron Lett.* **2008**, *49* (1), 94. doi:10.1016/j.tetlet.2007.11.011.; (b) Chetia, B.; Iyer, P. K. *Tetrahedron Lett.* **2007**, *48* (1), 47. doi:10.1016/j.tetlet.2006.11.022.; (c) Chetia, B.; Iyer, P. K. *Tetrahedron Lett.* **2006**, *47* (46), 8115. doi:10.1016/j.tetlet.2006.09.042.

(18) (a) Liu, Y.; Zhang, N.; Chen, Y.; Wang, L.-H. *Org. Lett.* **2007**, *9* (2), 315. doi:10.1021/ol062816w. PMID:17217293.; (b) Gross, E. M.; Anderson, J. D.; Slaterbeck, A. F.; Thayumanavan, S.; Barlow, S.; Zhang, Y.; Marder, S. R.; Hall, H. K.; Flore Nabor, M.; Wang, J.-F.; Mash, E. A.; Armstrong, N. R.; Wightman, R. M. *J. Am. Chem. Soc.* **2000**, *122* (20), 4972. doi:10.1021/ja0005993.

(19) Bonjean, K.; De Pauw-Gillet, M. C.; Defresne, M. P.; Colson, P.; Houssier, C.; Dassonneville, L.; Bailly, C.; Greimers, R.; Wright, C.; Quetin-Leclercq, J.; Tits, M.; Angenot, L. *Biochemistry* **1998**, *37* (15), 5136. doi:10.1021/bi972927q. PMID:9548744.

(20) (a) Bronson, R. T.; Montalti, M.; Prodi, L.; Zaccheroni, N.; Lamb, R. D.; Dalley, N. K.; Izatt, R. M.; Bradshaw, J. S.; Savage, P. B. *Tetrahedron* **2004**, *60* (49), 11139. doi:10.1016/j.tet.2004.08.062.; (b) Bronson, R. T.; Bradshaw, J. S.; Savage, P. B.; Fuangswasdi, S.; Lee, S. C.; Krakowiak, K. E.; Izatt, R. M. *J. Org. Chem.* **2001**, *66* (14), 4752. doi:10.1021/jo0017584. PMID:11442399.; (c) Kulkarni, P.; Tonzola, C. J.; Babel, A.; Jenekhe, S. A. *Chem. Mater.* **2004**, *16* (23), 4556. doi:10.1021/cm049473l.

(21) Ali, M. M.; Rajanna, K. C.; Prakash, P. K. S. *Synlett* **2001**, *2*, 251.

(22) Thiagarajan, V.; Ramamurthy, P. *J. Lumin.* **2007**, *126* (2), 886. doi:10.1016/j.jlumin.2007.01.003.

(23) Jude, A. L. C.; Sasikala, K.; Ashok Kumar, R.; Sudha, S.; Raichel, J. *Int. J. Hum. Genet.* **2002**, *2*, 95.

(24) (a) Venil, C. K.; Nanthakumar, K.; Karthikeyan, K.; Lakshmanaperumalsamy, P. *Iranian J. Biotechnol.* **2009**, *7* (1), 10; (b) Venil, C. K.; Lakshmanaperumalsamy, P. *Pak. J. Sci. Ind. Res.* **2008**, *51* (6), 333.

(25) (a) Penedo, J. C.; Pérez Lustres, J. L.; Lema, I. G.; Rodriguez, M. C. R.; Mosquera, M.; Rodríguez-Prieto, F. *J. Phys. Chem. A* **2004**, *108* (29), 6117. doi:10.1021/jp049056w.; (b) Dogra, S. K. *J. Lumin.* **2006**, *118* (1), 45. doi:10.1016/j.jlumin.2005.06.008.

(26) Bhanumathi, N.; Rao, K. R.; Sattur, P. B. *Heterocycles* **1986**, *24* (6), 1683. doi:10.3987/R-1986-06-1683.

(27) Kidwai, M.; Negi, N. *Monatsh. Chem.* **1997**, *128* (1), 85. doi:10.1007/BF00807642.

(28) Chen, T. R. *Mater. Lett.* **2005**, *59* (8-9), 1050. doi:10.1016/j.matlet.2004.12.002.

(29) Rominger, F.; Malathi, M.; Mohan, P. S.; Dondeti, T. R.; Hashmi, A. S. K. *Acta Crystallogr.* **2009**, *E65*, o400.

(30) Jlakowicz, J. R. *Principles of Fluorescence Spectroscopy,* 2nd ed.; Kluwer Academic/Plenum Publishers: New York, 2006.

(31) Kim, H. M.; Choo, H. J.; Jung, S. Y.; Ko, Y. G.; Park, W. H.; Jeon, S. J.; Kim, C. H.; Joo, T.; Cho, B. R. *ChemBioChem* **2007**, *8* (5), 553. doi:10.1002/cbic.200700003. PMID:17300111.

(32) Liu, Z. Q.; Fang, Q.; Yu, W. T.; Xue, G.; Cao, D. X.; Wang, D.; Xia, G. M.; Jiang, M. H. *Chin. Chem. Lett.* **2002**, *13* (10), 997.

(33) (a) Leresche, J. E.; Meyer, H.-P. *Org. Process Res. Dev.* **2006**, *10* (3), 572. doi:10.1021/op0600308.; (b) Kafarski, P.; Lejczak, B. *J. Mol. Catal., B Enzym.* **2004**, *29* (1-6), 99. doi:10.1016/j.molcatb.2003.12.013.

(34) (a) Chaerun, S. K.; Tazaki, K.; Asada, R.; Kogure, K. *Environ. Int.* **2004**, *30* (7), 911. doi:10.1016/j.envint.2004.02.007. PMID:15196839.; (b) Zahoor, A.; Rehman, A. *J. Environ. Sci. (China)* **2009**, *21* (6), 814. PMID:19803088.; (c) Frische, T.; Höper, H. *Chemosphere* **2003**, *50* (3), 415. doi:10.1016/S0045-6535(02)00603-3. PMID:12656263.

(35) (a) Azuma, T.; Watanabe, N.; Yagisawa, H.; Hirata, H.; Iwamura, M.; Kobayashi, Y. *Immunopharmacology* **2000**, *46* (1), 29. doi:10.1016/S0162-3109(99)00153-8. PMID:10665777.; (b) Bennett, J. W.; Bentley, R. *Adv. Appl. Microbiol.* **2000**, *47*, 1. doi:10.1016/S0065-2164(00)47000-0. PMID:12876793.

(36) (a) Ryan, R. M.; Green, J.; Lewis, C. E. *BioEssay* **2006**, *28* (1), 84. doi:10.1002/bies.20336.; (b) Senter, P. D.; Springer, C. J. *Adv. Drug Deliv. Rev.* **2001**, *53* (3), 247. doi:10.1016/S0169-409X(01)00206-X. PMID:11744170.

(37) (a) Deorukhkar, A. A.; Chander, R.; Ghosh, S. B.; Sainis, K. B. *Res. Microbiol.* **2007**, *158* (5), 399. doi:10.1016/j.resmic.2007.02.010. PMID:17467243.; (b) Grabley, S.; Thiericke, R. *Adv. Biochem. Eng. Biotechnol.* **1999**, *64*, 101. PMID:9933977.

(38) (a) Testa, A. C.; Wild, U. P. *J. Phys. Chem.* **1979**, *83* (23), 3044. doi:10.1021/j100486a023.; (b) Pan, J. H.; Chou, Y. M.; Chiu, H. L.; Wang, B. C. *Tamkang J. Sci. Eng.* **2005**, *8* (20), 175; (c) Srividya, N.; Ramamurthy, P.; Ramakrishnan, V. T. *Spectrochimica Acta Part A* **1998**, *54* (2), 245. doi:10.1016/S1386-1425(97)00211-4.

Multi-component supramolecular synthesis of spirooxindoles catalyzed by β-cyclodextrin in water

Regati Sridhar, Boga Srinivas, Bandaru Madhav, Vutukuri Prakash Reddy, Yadavalli Venkata Durga Nageswar, and Kakulapati Rama Rao

Abstract: A neutral and efficient one-pot three-component aqueous-phase synthesis is developed for various spirooxindole derivatives from isatin, malononitrile, and 1,3-dicarbonyl compounds in high yields by supramolecular catalysis involving β-cyclodextrin. The β-cyclodextrin can be recovered and reused a number of times without any loss of activity.

Key words: spirooxindole, isatin, dimedone, 4-hydroxy coumarin, barbituric acid, biomimetic synthesis, β-cyclodextrin, water.

Résumé : On a mis au point une synthèse monotope neutre et efficace, à trois composants et en milieu neutre qui permet d'obtenir avec des rendements élevés des dérivés spirooxindoles de l'isatine à partir du malononitrile et de composés 1,3-dicarbonylés et faisant appel à une supracatalyse impliquant la β-cyclodextrine. La β-cyclodextrine peut être récupérée et réutilisée un certain nombre de fois sans aucune perte d'activité.

Mots-clés : spirooxindole, isatine, dimédone, 4-hydroxycoumarine, acide barbiturique, synthèse biomimétique, β-cyclodextrine, eau.

[Traduit par la Rédaction]

Introduction

The spirooxindole is an important structure present in a number of natural bioactive compounds, such as coerulescine, elacomine, horsfiline, welwitindolinone A, spirotryprostatin A, alstonisine, and surugatoxin.[1] They display potent cytotoxic activity and are also known as h5-HT6 serotonin receptors, estrogen-receptor modulators, antiproliferative agents, and oxytocin antagonists.[2] In view of their significance, various methodologies have been developed for the construction of spirooxindole frameworks.[2] However, our interest in the synthesis of heterocyclic compounds involving supramolecular chemistry[3] and the growing focus on environment-friendly processes prompted us to revisit the synthesis of spiroxindoles.

It is highly desirable to develop a chemical system that can mimic the action of enzymes and effect organic reactions in water with excellent efficiency and selectivity. Water is a safe, inexpensive, and environment-friendly solvent, which makes its use favorable in both academic laboratories and industry. The pioneering studies of organic reactions in water by Breslow[4] in the early 1980s triggered a more widespread interest in the use of water as a medium for organic synthesis, not only because these reactions eliminate the necessity for vigorously drying solvents and substrates, but also because of the unique reactivity and selectivity often observed in aqueous reactions. However, the synthesis of spirooxindoles described so far by the three-component reaction of isatin, malononitrile or methyl cyanoacetate, and 1,3-dicarbonyl compounds have limited scope because of the use of transition-metal catalysts, microwave irradiation, surfactants, acidic or basic conditions, and hazardous solvents.[5] As a consequence, the development of environmentally benign practical synthetic routes under neutral conditions using a recyclable catalyst in water for accessing these spirooxindole derivatives still remains a major goal.

These aqueous reactions can be made more sophisticated if they can be performed under supramolecular catalysis, such as β-cyclodextrin, overcoming many of the drawbacks observed in the previous methodologies. Cyclodextrins (CDs) are cyclic oligosaccharides possessing hydrophobic cavities which bind substrates and catalyze chemical reactions with high selectivity. They catalyze reactions by supramolecular catalysis involving reversible formation of host-guest complexes by non-covalent bonding as seen in enzymes.

In continuation of our interest in the β-cyclodextrin catalyzed biomimetic synthesis of heterocyclic compounds in aqueous phase,[3] we have explored the aqueous-phase synthesis of spiooxindole derivatives by the three-component reaction of isatin, malononitrile, and dimedone under neutral conditions catalyzed by β-cyclodextrin (Scheme 1).

Results and discussion

In general, the reactions were carried out by forming an in situ β-CD complex of the isatin in water, followed by the

Received 5 April 2009. Accepted 5 August 2009. Published on the NRC Research Press Web site at canjchem.nrc.ca on 13 November 2009.

R. Sridhar, B. Srinivas, B. Madhav, V.P. Reddy, Y.V.D. Nageswar, and K.R. Rao.[1] Organic Chemistry Division-I, Indian Institute of Chemical Technology, Uppal Road, Hyderabad 500-007, India.

[1]Corresponding author (e-mail: kakulapatirama@gmail.com).

Scheme 1.

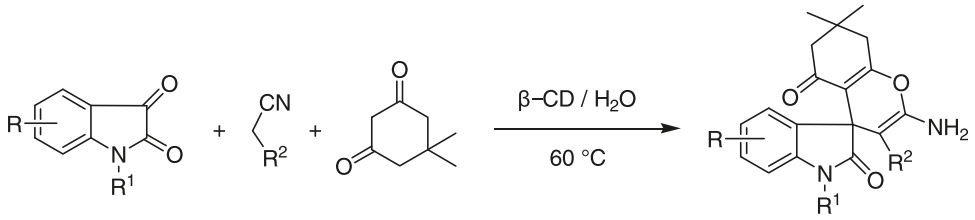

R = H, 4-Br, 6-Br, 5-CH_3, 5-NO_2
R^1= CH_3, CH_2Ph, Ph
R^2= CN, COOMe

Table 1. β-CD-catalyzed multi-component synthesis of spirooxindoles **1**–**10**.

Entry	R	R^1	R^2	Time (h)	Yield (%)
1	H	H	CN	5	90
2	4-Br	H	CN	5	89
3	6-Br	H	CN	5	85
4	5-CH_3	H	CN	5	88
5	5-NO_2	H	CN	6	84
6	H	CH_3	CN	4	91
7	H	CH_2Ph	CN	4	90
8	H	Ph	CN	4	89
9	H	H	COOMe	6	85
10	6-Br	H	COOMe	5	87

Scheme 2.

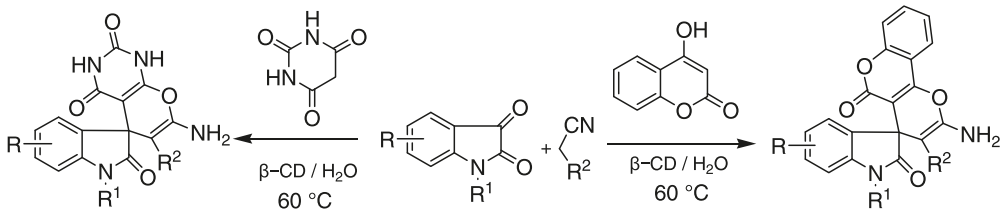

14-16

R = H, Br
R^1= H, CH_3
R^2= CN, COOMe

11-13

Table 2. β-CD-catalyzed multi-component synthesis of spirooxindoles **11**–**16**.

Entry	R	R^1	R^2	Time (h)	Yield (%)
11	H	H	CN	8	88
12	4-Br	H	CN	7	88
13	H	CH_3	COOMe	8	85
14	H	H	CN	8	86
15	H	CH_3	CN	7	85
16	H	H	COOMe	8	84

addition of malononitrile and dimedone, and stirring at 60 °C. The corresponding spirooxindole compounds were obtained in impressive yields (84%–91%) after 4–6 h by simple filtration. This methodology is compatible with various substituted isatins having different functionalities such as bromo, methyl, nitro, phenyl, and benzyl groups (Table 1, entries 1–8). It was found that methyl cyanoacetate also underwent condensation with isatin and dimedone to give the desired product in impressive yields (Table 1, entries 9–10, 85%–87%) under similar conditions. These reactions proceeded efficiently under neutral conditions. No byproduct formation was observed. β-Cyclodextrin can be easily recovered and reused.

Further applications of this methodology involve the reactions of 4-hydroxy coumarin and barbituric acid under the above optimized conditions (Scheme 2) to produce spirooxindole derivatives (Table 2, entries 11–16) efficiently in yields ranging from 84–88%.

The complexation of isatin with β-CD was confirmed by the isolation of the β-CD–isatin complex and the study of its ^{1}H NMR spectrum, which shows an upfield shift of H3 and H5 of β-CD as observed by us earlier.[3a] The ^{1}H NMR spectra (D_2O) of β-CD, the β-CD–isatin complex, and the freeze-dried reaction mixture of the β-CD–isatin complex after the addition of malononitrile and dimedone were studied. It was observed from Fig. 1 that there was an upfield shift of H3 (0.02 ppm) and H5 (0.02 ppm) protons of cyclodextrin in the β-CD–isatin complex as compared to β-CD, indicating the formation of an inclusion complex of isa-

Fig. 1. [1]H NMR spectra of (a) β-CD; (b) β-CD–isatin complex; and (c) reaction mixture after 2 h. The spectra were recorded in D_2O at 25 °C.

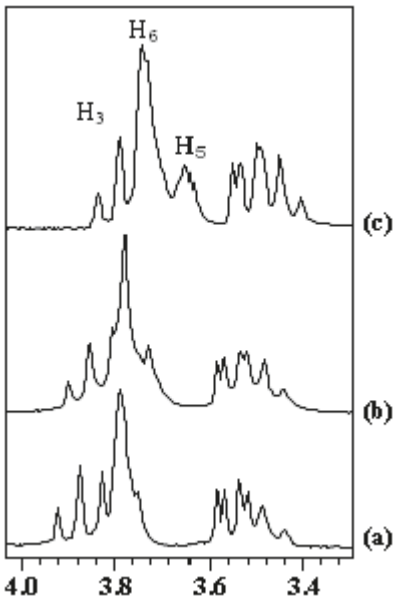

tin with β-CD from the secondary side of cyclodextrin.[6] In the spectra of the reaction mixture of the β-CD–isatin complex after the addition of malononitrile and dimedone after 2 h, an upfield shift of the CD H6 proton by 0.048 ppm was also observed. This indicated that the reaction proceeded by complexation of malononitrile and dimedone from the primary side of cyclodextrin (Fig. 1). This clearly demonstrates that the isatin is ideally located for the condensation with malononitrile and dimedone in the hydrophobic environment of the β-cyclodextrin cavity.

The catalytic activity of cyclodextrins for these reactions is established by the fact that in the absence of cyclodextrin, the reaction was observed to proceed in very poor yields (20%) even after long reaction times (24 h). The complexation of isatin with β-CD increases the reactivity of the keto group due to intermolecular hydrogen bonding with the CD-hydroxyl groups[7] facilitating the Knoevenagel condensation with malononitrile to form an isatylidene malononitrile derivative. It then undergoes the established sequence of reactions such as Michael addition of dimedone followed by the cycloaddition of hydroxyl group to the cyano moiety to form the spiro compound.[5] Here, β-CD not only forms the inclusion complex with isatin but is also involved in the intermolecular hydrogen bonding with the guest to promote the condensation and cycloaddition of the hydroxyl group to the cyano moiety.

In summary, we have developed a neutral aqueous-phase synthesis of various spirooxindole derivatives by the one-pot three-component reaction of the corresponding isatin, activated methylene reagent, and 1,3-dicarbonyl compounds under biomimetic conditions in the presence of β-cyclodextrin. These cyclodextrin mediated water solvent reactions are very useful from both economical and environmental points of view. β-Cyclodextrin, apart from being nontoxic, is also considered as metabolically safe. This straightforward, environmentally benign methodology may find widespread applications in organic and medicinal chemistry.

Experimental

General

Melting points were recorded on a Buchi R-535 apparatus and are uncorrected. IR spectra were recorded on a PerkinElmer FT-IR 240-c spectrometer using KBr optics. [1]H NMR spectra were recorded on Gemini-200/Avance-300/Inova-400 spectrometer in DMSO or $CDCl_3$ using TMS as internal standard. Mass spectra were recorded on an Agilent 1200 spectrometer. Starting materials were obtained commercially from Sigma-Aldrich or Lancaster and were used without purification.

General procedure for the synthesis of spirooxindole

β-CD (1 mmol) was dissolved in water (15 mL) by warming to 60 °C until a clear solution was formed. Then, isatin (1 mmol) dissolved in methanol (0.5 mL) was added dropwise followed by malononitrile (1.2 mmol) and dimedone (1 mmol), and the mixture was stirred at 60 °C until the reaction was complete (as monitored by TLC) (Table 1). The mixture was cooled to 40 °C and the solid was filtered off, washed with water (10 mL), and recrystallized from EtOH to yield colorless crystals. The filtrate of the reaction mixture was cooled to 5 °C to recover β-CD.

Characterization data

*2-Amino-5-oxo-7,7-dimethyl-spiro[(4**H**)-5,6,7,8-tetrahydrochromene-4,3′-(3′**H**)-indol]-(1′**H**)-2′-one-3-carbonitrile (1)*

Colorless solid; mp 287–289 °C. IR (cm^{-1}) : 3380, 3308, 3142, 2195, 1723, 1659, 1608, 1466, 1350, 1219, 1059, 908, 748. [1]H NMR (DMSO-d_6, 300 MHz) δ: 10.41 (s, 1H, NH), 7.22 (br s, 2H, NH_2), 7.11 (t, 1H, J = 10.0 Hz, ArH), 7.01–6.73 (m, 3H, ArH), 2.56 (s, 2H, CH_2), 2.23–2.03 (m, 2H, CH_2), 1.03 (s, 3H, CH_3), 1.00 (s, 3H, CH_3). EIMS *m/z*: 335 [M^+]. Anal. calcd. for $C_{19}H_{17}N_3O_3$: C 68.05, H 5.11, N 12.53; found: C 68.24, H 5.22, N 12.61.

*2-Amino-5-oxo-7,7-dimethyl-spiro[(4**H**)-5,6,7,8-tetrahydrochromene-4,3′-(3′**H**)-4′-bromo-indol]-(1′**H**)-2′-one-3-carbonitrile (2*

Colorless solid; mp 312–315 °C. IR (cm^{-1}): 3363, 3310, 3152, 2962, 2199, 1724, 1659, 1605, 1497, 1350, 1219, 1048, 928. [1]H NMR (DMSO-d_6, 300 MHz) δ: 10.41 (s, 1H, NH), 7.28 (br s, 2H, NH_2), 7.14 (t, 1H, J = 7.6 Hz, ArH), 6.98 (d, 1H, J = 7.2 Hz, ArH), 6.78 (d, 1H, J = 7.6 Hz, ArH), 2.56 (d, 2H, J = 7.6 Hz, CH_2), 2.17 (d, 1H, J = 15.6 Hz, CH), 2.08 (d, 1H, J = 16.0 Hz, CH), 1.03 (s, 3H, CH_3), 1.00 (s, 3H, CH_3). Anal. calcd. for $C_{19}H_{16}BrN_3O_3$: C 55.09, H 3.89, N 10.14; found: C 55.19, H 3.97, N 10.19.

*Methyl 2-amino-5-oxo-7,7-dimethyl-spiro[(4**H**)-5,6,7,8-tetrahydrochromene-4,3′-(3′**H**)-indol]-(1′**H**)-2′-one-3-carboxylate (9)*

Colorless solid; mp 255–256 °C. IR (cm^{-1}): 3366, 3241, 3187, 2955, 1690, 1614, 1520, 1471, 1304, 1225, 1167, 1054, 928, 746. [1]H NMR ($CDCl_3$, 400 MHz) δ: 10.22 (s, 1H, NH), 7.88 (br s, 2H, NH_2), 7.05–7.11 (m, 1H, ArH),

6.90 (d, 1H, *J* = 6.0 Hz, ArH), 6.82 (t, 1H, *J* = 7.8 Hz, ArH), 6.76 (d, 1H, *J* = 6.9 Hz, ArH), 3.32 (s, 3H, CH_3), 2.66 (d, 1H, *J* = 17.4 Hz, CH), 2.55 (d, 1H, *J* = 17.4 Hz, CH), 2.23 (d, 1H, *J* = 15.66 Hz, CH), 2.07 (d, 1H, *J* = 15.66 Hz, CH), 1.10 (s, 3H, CH_3), 1.01 (s, 3H, CH_3). EIMS *m*/*z*: 368 [M^+]. Anal. calcd. for $C_{20}H_{20}N_2O_5$: C 65.21, H 5.47, N 7.60; found: C 65.47, H 5.35, N 7.68.

2-Amino-5,7-dioxo-spiro[(3′H)-indol-3′,4,4(H)-5,6,7,8-tetrahydropyrano(2,3-d)pyrimidine]-(1′H)-2′-one-3-carbonitrile (11)

Colorless solid; mp 273–274 °C. IR (cm^{-1}): 3448, 3280, 3142, 3033, 2204, 1697, 1643, 1511, 1443, 1396, 1242, 1114, 1003, 846, 663. ^{1}H NMR (DMSO-d_6, 300 MHz) δ: 12.40 (br s, 1H, NH), 12.02 (br s, 1H, NH), 10.52 (br s, 1H, NH), 7.41 (br s, 2H, NH_2), 7.17 (t, 2H, *J* = 8.0 Hz, ArH), 6.91 (t, 1H, *J* = 7.6 Hz, ArH), 6.79 (d, 1H, *J* = 7.6 Hz, ArH). EIMS *m*/*z*: 323 [M^+]. Anal. calcd. for $C_{15}H_9N_5O_4$: C 55.73, H 2.81, N 21.66; found: C 55.40, H 2.89, N 21.68.

2-Amino-5-oxo-spiro[(3′H)-indol-3′,4-4(H)-pyrano(3,2-c)chromen]-(1′H)-2′-one-3-carbonitrile (14)

Colorless solid; mp 290–292 °C. IR (cm^{-1}): 3350, 3300, 3195, 2954, 2199, 1720, 1667, 1613, 1522, 1474, 1364, 1224, 1132, 1072, 972, 748. ^{1}H NMR (DMSO-d_6, 300 MHz) δ: 10.64 (s, 1H, NH), 7.95 (d, 1H, *J* = 8.0 Hz, ArH), 7.77 (t, 1H, *J* = 7.6 Hz, ArH), 7.67 (br s, 2H, NH_2), 7.57 (t, 1H, *J* = 7.6 Hz, ArH), 7.50 (d, 1H, *J* = 8.4 Hz, ArH), 7.22 (t, 2H, *J* = 7.6 Hz, ArH), 6.93 (t, 1H, *J* = 7.6 Hz, ArH), 6.85 (d, 1H, *J* = 8.0 Hz, ArH). EIMS *m*/*z*: 357 [M^+]. Anal. calcd. for $C_{20}H_{11}N_3O_4$: C 67.23, H 3.10, N 11.76; found: C 67.49, H 3.02, N 11.86.

Supplementary data

Supplementary data for this article are available on the journal Web site (canjchem.nrc.ca) or may be purchased from the Depository of Unpublished Data, Document Delivery, CISTI, National Research Council Canada, Ottawa, ON K1A 0R6, Canada. DUD 5305. For more information on obtaining material, refer to cisti-icist.nrc-cnrc.gc.ca/cms/unpub_e.shtml.

Acknowledgement

We thank the Council for Scientific and Industrial Research (CSIR), New Delhi, India, for fellowships to RS, BS, BM, and VPR.

References

(1) (a) Baran, P. S.; Richter, J. M. *J. Am. Chem. Soc.* **2005**, *127* (44), 15394. doi:10.1021/ja056171r. PMID:16262402.; (b) Chang, M.-Y.; Pai, C.-L.; Kung, Y. H. *Tetrahedron Lett.* **2005**, *46* (49), 8463. doi:10.1016/j.tetlet.2005.10.015.; (c) Hilton, S. T.; Ho, T. C.; Pljevaljcic, G.; Jones, K. *Org. Lett.* **2000**, *2* (17), 2639. doi:10.1021/ol0061642. PMID:10990416.; (d) Kosuge, T.; Tsuji, K.; Hirai, K.; Yamaguchi, K.; Okamoto, T.; Iitaka, Y. *Tetrahedron Lett.* **1981**, *22* (35), 3417. doi:10.1016/S0040-4039(01)81920-1.

(2) (a) Edmondson, S. E.; Danishefsky, S. J.; Sepp-Lorenzino, L.; Rosen, N. *J. Am. Chem. Soc.* **1999**, *121* (10), 2147. doi:10.1021/ja983788i.; (b) Zaveri, N. T.; Jiang, F.; Olsen, C. M.; Deschamps, J. R.; Parrish, D.; Polgar, W.; Toll, L. *J. Med. Chem.* **2004**, *47* (12), 2973. doi:10.1021/jm034249d. PMID:15163178.; (c) Tokunaga, T.; Hume, W. E.; Umezome, T.; Okazaki, K.; Ueki, Y.; Kumagai, K.; Hourai, S.; Nagamine, J.; Seki, H.; Taiji, M.; Noguchi, H.; Nagata, R. *J. Med. Chem.* **2001**, *44* (26), 4641. doi:10.1021/jm0103763. PMID:11741481.; (d) Gallagher, G., Jr.; Lavanchy, P. G.; Webster, C. A.; Wilson, J. W.; Hieble, J. P.; DeMarinis, R. M. *J. Med. Chem.* **1985**, *28* (10), 1533. doi:10.1021/jm00148a028. PMID:4045928.

(3) (a) Sridhar, R.; Srinivas, B.; Kumar, V. P.; Reddy, V. P.; Kumar, A. V.; Rao, K. R. *Adv. Synth. Catal.* **2008**, *350* (10), 1489. doi:10.1002/adsc.200800121.; (b) Narender, M.; Reddy, M. S.; Kumar, V. P.; Reddy, V. P.; Nageswar, Y. V. D.; Rao, K. R. *J. Org. Chem.* **2007**, *72* (5), 1849. doi:10.1021/jo062421q. PMID:17266376.; (c) Narender, M.; Reddy, M. S.; Pavan Kumar, V.; Srinivas, B.; Sridhar, R.; Rama Rao, K. *Synthesis* **2007**, *22*, 3469; doi:10.1055/s-2007-990849;.(d) Narender, M.; Reddy, M. S.; Sridhar, R.; Nageswar, Y. V. D.; Rama Rao, K. *Tetrahedron Lett.* **2005**, *46* (35), 5953. doi:10.1016/j.tetlet.2005.06.130.

(4) (a) Rideout, D. C.; Breslow, R. *J. Am. Chem. Soc.* **1980**, *102* (26), 7816. doi:10.1021/ja00546a048.; (b) Breslow, R. *Acc. Chem. Res.* **1991**, *24* (6), 159. doi:10.1021/ar00006a001.; (c) Breslow, R. *Acc. Chem. Res.* **2004**, *37* (7), 471. doi:10.1021/ar040001m. PMID:15260509.

(5) (a) Gao, S.; Tsai, C. H.; Tseng, C.; Yao, C.-F. *Tetrahedron* **2008**, *64* (38), 9143. doi:10.1016/j.tet.2008.06.061.; (b) Zhu, S.-L.; Jia, S.-J.; Zhanga, Y. *Tetrahedron* **2007**, *63* (38), 9365. doi:10.1016/j.tet.2007.06.113.; (c) Joshi, K. C.; Dandia, A.; Baweja, S.; Joshi, A. *J. Heterocycl. Chem.* **1989**, *26* (4), 1097. doi:10.1002/jhet.5570260435.; (d) Joshi, K. C.; Jain, R.; Nishith, S. *J. Indian Chem. Soc.* **1990**, *67*, 490; (e) Abdel-Latif, F. F.; Mashaly, M. M.; El-Gawish, E. H. *J. Chem. Res. Miniprint* **1995**, *5*, 1220; (f) Dandia, A.; Singh, R.; Sarawgi, P.; Khaturia, S. *Chin. J. Chem.* **2006**, *24* (7), 950. doi:10.1002/cjoc.200690180.; (g) Shanthi, G.; Subbulakshmi, G.; Perumal, P. T. *Tetrahedron* **2007**, *63* (9), 2057. doi:10.1016/j.tet.2006.12.042.

(6) (a) Jia, S.-Y.; Hao, Y.-Q.; Li, L.-N.; Chen, K.; Wu, Y.; Liu, J.; Wu, L.; Ding, Y.-H. *Chem. Lett.* **2005**, *34* (9), 1248. doi:10.1246/cl.2005.1248.; (b) Schneider, H. J.; Hacket, F.; Rüdiger, V.; Ikeda, H. *Chem. Rev.* **1998**, *98* (5), 1755. doi:10.1021/cr970019t. PMID:11848948.; (c) Demarco, P. V.; Thakkar, A. L. *J. Chem. Soc. D, Chem. Commun.* **1970**, *2*, 2; doi:10.1039/C29700000002;.(d) Krishnaveni, N. S.; Surendra, K.; Rao, K. R. *Chem. Commun. (Camb.)* **2005**, (5): 669. doi:10.1039/b411736k. PMID:15672172.; (e) Surendra, K.; Krishnaveni, N. S.; Reddy, M. A.; Nageswar, Y. V. D.; Rao, K. R. *J. Org. Chem.* **2003**, *68* (5), 2058. doi:10.1021/jo026751w. PMID:12608839.

(7) Netto-Ferreira, J. C.; Ilharco, L. M.; Gracia, A. R.; Vieira Ferreira, L. F. *Langmuir* **2000**, *16* (26), 10392. doi:10.1021/la001041b.

Remarkable high-yielding chemical modification of gold nanoparticles using uncatalyzed click-type 1,3-dipolar cycloaddition chemistry and hyperbaric conditions

Hossein Ismaili, Abdolhamid Alizadeh, Kristen E. Snell, and Mark S. Workentin

Abstract: Azide-terminated alkyl thiolate monolayer-protected gold nanoparticles (**1**-C_{12}MPN) with a core size of 1.8 ± 0.2 nm were prepared. **1**-C_{12}MPN was modified in high yields via an uncatalyzed 1,3-dipolar cycloaddition (click-type reaction) with a variety of terminal acyl–alkynes under hyperbaric conditions at 11 000 atm. The resulting 1,2,3-triazole modified MPNs (**2**-C_{12}MPN) were characterized using ^{1}H NMR spectroscopy and were verified by comparison of the spectra to those obtained for the products of the model reactions of 1-azidododecane with the same alkynes. TEM analysis showed that the high-pressure conditions did not affect the size of the gold core, suggesting that the only effect is to facilitate the chemical reaction on the particles.

Key words: nanoparticles, hyperbaric chemistry, 1,3-dipolar cycloaddition, monolayers.

Résumé : On a préparé des nanoparticules d'or protégées par une monocouche d'alkylthiol (**1**-C_{12}MPN) portant une fonction azide en position terminale et dont le diamètre principal est égal à 1,8 ± 0,2 nm. Le produit **1**-C_{12}MPN a été modifié avec des rendements élevés par le biais d'une cycloaddition 1,3-dipolaire non catalysée (réaction de type par un clic) avec une variété d'acyl–alcynes terminales, dans des conditions hyperbariques, à 11,000 atmosphères. Les nanoparticules d'or modifiées, protégées par une monocouche d'alkylthiol (**2**-C_{12}MPN) et portant un cycle 1,2,3-triazole ont été caractérisées par spectroscopie RMN du ^{1}H et ont été vérifiées par comparaison avec les spectres obtenus pour les produits des réactions modèles du 1-azidodécane avec les mêmes alcynes. Une analyse par microscopie électronique à transmission (MET) a permis de montrer que les conditions de haute pression n'ont pas affecté la taille du diamètre principal de l'or suggérant que le seul effet est de faciliter la réaction chimique sur les particules.

Mots-clés : nanoparticules, chimie hyperbarique, cycloaddition 1,3-dipolaire, monocouches.

[Traduit par la Rédaction]

Introduction

The Cu(I)-catalyzed Huisgen 1,3-dipolar cycloaddition of azides to terminal alkynes to produce a triazole ring, the "click" reaction, is a popular and powerful tool in organic synthesis and combinatorial chemistry.[1] This reaction is also being exploited in material science applications for the modification of metal and silica surfaces,[2] dendrimers,[3] and polymers.[4] Recently, the reaction was extended to monolayer-protected CdSe,[5] iron oxide,[6] and monolayer-protected gold nanoparticles (MPN).[7–12] Because the 1,3-dipolar cycloaddition reaction of an alkyne and azide is slow, this type of reaction is typically done in the presence of a Cu(I) catalyst because it facilitates the rapid, high reaction conversions with little or no byproducts under mild conditions. The later is of key importance for the functionalization of Au-MPN. While the catalyzed reaction is effective for the modification of the CdSe and iron oxide nanoparticles, this approach is not considered as feasible with gold nanoparticles. Gold MPNs (now simply referred to as MPNs) in the presence of the Cu catalyst have been suggested to be unstable, and lead to aggregation or decomposition likely due to the reaction of the Cu catalyst with the gold surface. In another case, Brennan et al. reported using the Cu-catalyzed route to modifiy azide-functionalized 12 nm MPNs with alkyne-appended lipases but a million-fold excess of Cu was required and the yield was less than 1% conversion.[7] More recently, and while this work was in progress, Astruc and co-workers reported specific reaction conditions to circumvent the difficulties of the Cu(I) click reaction on azide-terminated MPNs.[13]

Williams and co-workers reported a thorough study showing that the Huisgen dipolar cycloaddition reaction can be used to modify azide-terminated MPNs with a variety of activated alkynes without a catalyst.[8] However, the yields (extent of conversion of the azide groups) were extremely low (13% and less after 60 h in dioxane, depending on the alkyne) and could only be marginally improved by altering the solvent. In a latter study where they reported on the kinetics of this reaction on the MPN, they stated that these

Received 28 April 2009. Accepted 9 July 2009. Published on the NRC Research Press Web site at canjchem.nrc.ca on 21 November 2009.

H. Ismaili, A. Alizadeh,[1] K.E. Snell, and M.S. Workentin.[2] Department of Chemistry, The University of Western Ontario, London, ON N6A 5B7.

[1]Present address: Chemistry Department and Nanoscience and Nanotechnology Research Center (NNRC), Razi University, Kermanshah 67149, Iran.

[2]Corresponding author (e-mail: mworkent@uwo.ca).

yields were slightly underestimated because of the method used to follow reaction conversion.[9] However, the yields were still relatively low (22%, or 54% in one specific case) and did not allow the product MPNs to be completely characterized by NMR spectroscopy. Because of the potential of this type of reaction as a general approach to surface modification and to allow the introduction of a variety of functionalities from common starting MPNs, an important goal is to improve the efficiency of this type of reaction on MPN. To this end, and while this work was in progress, Sommer and Weck reported on the microwave-assisted catalyzed 1,3-dipolar cycloaddition of azide-terminated MPNs.[10] The method proved successful and allowed a large variety of terminal alkynes to form triazole-functionalized MPN with near-quantitative yields, but still required very careful control of the microwave conditions because excess heating of the MPN lead to nanoparticle decomposition ascribed to particle aggregation.

Recently, we reported that the inefficient modification of a maleimide-modified MPN by the Diels–Alder reaction at ambient conditions with a series of dienes was improved remarkably using hyperbaric conditions without affecting the particle core.[14] The hyberbaric method for modification of gold MPNs was more general and was further used to accelerate the 1,3-cycloaddition of a large variety of nitrones to the maleimide-modified MPN in quantitative yields.[15] In both these studies, we showed that the reactions carried out on the MPNs at ambient temperature and pressure were significantly slower than the corresponding reactions on model compounds under the same conditions. We attributed this difference in reactivity to the unique steric effects of the environment at the interfacial site of reactivity on the MPN. In the present report, we extend this methodology to study the Huisgen 1,3-dipolar cycloaddition of azide-terminated MPN to terminal alkynes to improve the efficiency of this reaction and to expand the scope of reactions that can be utilized for modification of nanoparticles using hyperbaric conditions. The Huisgen 1,3-dipolar cycloaddition of azides to terminal alkynes is also subject to rate acceleration at elevated pressure, although as far as we are aware, this has only been the subject of one report.[16] Specifically, we report herein that azide-terminated, 1.8 nm core size MPNs prepared to be essentially identical to the original report of Williams and co-workers,[8] will react with activated acyl–alkynes efficiently under high-pressure conditions at ambient temperature to form the 1,2,3-triazoles essentially quantitatively in the absence of a Cu catalyst. This approach eliminates the complications due to the presence of catalysts or higher temperatures.

Experimental

Commercial solvents and reagents used

The compounds dodecanethiol, hydrogen tetrachloroaurate (III), tetraoctylammonium bromide, 1,12-dibromododecane, 11-bromo-1-undecene, azobis(isobutyronitrile) (AIBN), 1-bromododecane, sodium azide, ethynyl magnesium bromide, 1-octyn-3-ol, and ethyl propionate were all purchased from Aldrich and used as received. Deuterated benzene (C_6D_6), deuterated chloroform ($CDCl_3$), and deuterated dichloromethane (CD_2Cl_2) (Cambridge Isotope Laboratories) were also used as received.

General instrumentation

High-pressure reactions were carried out utilizing a LECO Tempres High-Pressure chemical reactor, which operates at 11 000 atm. ^1H and ^{13}C NMR spectra were recorded, as indicated, on either a Varian Inova 600 (^1H: 600 MHz, ^{13}C: 150 MHz) or 400 (^1H: 400 MHz, ^{13}C: 100 MHz) spectrometers and were referenced to the residual protons in the solvent relative to $(CH_3)_4Si$ (δ (ppm): chloroform-*d*, 7.26; dichloromethane-d_2, 5.32; or benzene-d_6, 7.15). Mass spectra and exact mass were recorded on a MAT 8200 Finnigan High resolution Mass Spectrometer. Infrared spectra were recorded on a Bruker Vector 33 FTIR spectrometer and are reported in wavenumbers (cm^{-1}). Melting points were measured using the Electrothermal 9100 melting-point instrument and are uncorrected. High resolution transmission electron microscopy (HRTEM) images were collected on a JEOL 2010F HRTEM.

Synthetic details

Dodecanethiolate MPN (C_{12}MPN)

Following the procedures of Brust–Shiffrin and Murray,[17,18] hydrogen tetrachloroaurate (III) trihydrate (0.30 g, 0.77 mmol) was dissolved in 28 mL distilled water (resulting in a bright yellow solution) and then mixed with tetraoctylammonium bromide (2.30 g, 4.2 mmol) in 70 mL toluene. The contents were stirred for 30 min at room temperature to facilitate the phase transfer of the hydrogen tetrachloroaurate (III) trihydrate into the toluene layer, which resulted in the organic layer turning to a dark orange colour and the aqueous layer becoming clear and colourless. After phase transfer, the aqueous layer was removed and the organic layer was cooled to 0 °C in ice bath. Dodecanethiol (0.468 g, 0.57 mL, 2.31 mmol) was added to the solution via a volumetric pipette and allowed to stir for 10 min. The addition of dodecanethiol resulted in a colour change from brownish-orange to clear and colourless. A fresh solution of sodium borohydride (0.33 g, 8.7 mmol) in 28 mL water was then added to the rapidly stirring toluene solution over 5 s. The solution darkened instantly, eventually becoming dark brown. The mixture was allowed to stir overnight (~18 h) as it warmed to room temperature, after which time, the aqueous layer was removed and the toluene layer was washed with 3 × 20 mL distilled water and dried over $MgSO_4$. The toluene layer was then isolated by gravity filtration and evaporated to dryness. The resulting mixture of C_{12}MPN and tetraoctylammonium bromide was suspended in 200 mL of 95% ethanol and placed in the freezer overnight during which time the C_{12}MPN precipitated from solution. When the MPN had precipitated, the supernatant was decanted and the precipitate was dissolved in benzene and concentrated, resulting in the formation of a film in the round-bottom flask. This film was washed repeatedly with 10 × 15 mL of 95% ethanol, resulting in pure C_{12}MPN as judged by ^1H NMR spectroscopy, which showed no signs of free dodecanethiol, dodecyldisulfide, or tetraoctylammonium bromide. The resulting C_{12}MPN was dark brown.

Synthesis of bromo-terminated C_{12}MPN

Approximately 200 mg of C_{12}MPN was dissolved in 60 mL of benzene and degassed with nitrogen. 290 mg

(1.54 mmol) of 11-bromo-1-undecanethiol was added to the solution and stirred for 2 days at room temperature. The mixture was then concentrated and the resulting film was washed with 95% ethanol and dried. The ^{1}H NMR spectrum of this MPN is shown in Fig. S1. ^{1}H NMR (600 MHz, CD_2Cl_2) δ: 3.4, 1.9, 1.8–1.0, 0.9. The integrated areas of methylene protons alpha to the bromide and terminal methyl group of dodecanethiolate in the ^{1}H NMR spectra reveals that the ratio of ligands on the bromoundecane-thiolate-modified C_{12}MPN was 1:1.2, terminal bromide to terminal methyl.

The required 11-bromo-1-undecanethiol was synthesized by the reported method.[19] 11-Bromo-1-undecene (1.5 g, 6.43 mmol), AIBN (0.6 g, 3.65 mmol), and thioacetic acid (3 mL) were dissolved in toluene and refluxed for 2 h. The reaction mixture was washed with water and then concentrated. The crude product was purified by column chromatography (eluting with 5:1 hexanes/ethyl acetate) to separate. A solution of 11-bromo-1-undecanethioacetate in dry methanol was cooled in an ice bath, then 3 mL acetyl chloride was added dropwise, and the solution was stirred for 6 h at room temperature. The reaction was quenched by adding water and extracted with CH_2Cl_2, and then combined extracts were washed with water. The organic layer was dried over $MgSO_4$ and evaporated to get the pure product: Yellow oil. ^{1}H NMR (600 MHz, $CDCl_3$) δ: 3.40 (t, J = 6.8 Hz, 2H), 2.51 (q, J = 7.3 Hz, 2H), 1.84 (m, 2H), 1.60 (m, 2H), 1.44–1.27 (m, 15H).

Synthesis of azide-terminated MPN: (1-C_{12}MPN)

1-C_{12}MPN was prepared according to the procedure of Fleming et al.[8] A 60 mL solution of 0.25 mol/L NaN_3 in DMSO was added to the mixture of the bromo-terminated MPN (prepared as above) in benzene (~200 mg of bromo-terminated C_{12}MPN in 60 mL of benzene) and the mixture was stirred for 48 h. After which time, the reaction was quenched with water and organic layer was separated and washed with water three times, dried over $MgSO_4$, and then concentrated. The resulting film was rinsed with 95% ethanol and dried. ^{1}H NMR (600 MHz, CD_2Cl_2) δ: 3.4, 3.25, 1.9, 1.85–1.0, 0.9. The ^{1}H NMR spectrum of this **1**-C_{12}MPN is shown in Fig. 1*a*. The integrated areas of the three types of ligands, determined by decomposition of 10 mg of **1**-C_{12}MPN with ~2 mg of iodine, showed that the ratio of terminal azide/bromide/methyl was 3.5:1:5. Additionally, **1**-C_{12}MPN was characterized using IR spectroscopy and TEM. IR (cm^{-1}): 2959, 2921, 2853, 2096, 1467, 1366, 1282, 1089, 1040, 801. The average particle size was determined by analysis of TEM images of numerous samples: 1.8 ± 0.2 nm

Synthesis of 1-azidododecane (3)

A solution of 1-bromododecane (2 g, 8 mmol) and NaN_3 (0.57 g, 8.8 mmol) in DMSO (30 mL) was stirred overnight at room temperature. The reaction mixture was diluted with diethyl ether and washed with water five times to remove DMSO. The ethereal layer was dried over $MgSO_4$ and concentrated. The spectral data are in accord with the literature.[20] Colourless oil. ^{1}H NMR (400 MHz, $CDCl_3$) δ: 3.25 (t, J = 6.9 Hz, 2H), 1.59 (m, 2H), 1.37–1.26 (broad, 18H), 0.88 (t, J = 6.8 Hz, 3H). ^{13}C NMR (100 MHz, $CDCl_3$) δ: 51.7, 32.1, 29.8, 29.77, 29.71, 29.5, 29.4, 29.0, 26.9, 22.9, 14.3. IR (cm^{-1}): 2955, 2924, 2854, 2095, 1467, 1366, 1258.

Synthesis of alkynes (4a–4i)

Compounds 1-pyren-1-yl-propyn-1-one (**4a**), 1-anthracen-9-yl-propyn-1-one (**4c**), propynoic acid phenylamide (**4h**),[8] 1-ferrocenyl-2-propyn-1-one (**4b**),[21] and 1-(4-nitrophenyl)-2-propyn-1-one (**4e**)[22] were prepared by their literature method, and their ^{1}H NMR spectra are in accord with those reported. Compounds 1-phenyl-2-propyn-1-one (**4f**), 1-(4-biphenyl)-2-propyn-1-one (**4d**), and 1-octyn-3-one (**4i**),[23] as well as 1-(2-methylphenyl)-2-propyn-1-one (**4g**),[24] were synthesized by the following procedure (except for **4i** where commercial alcohol was oxidized by magnesium(IV) oxide), and their ^{1}H NMR spectra are in accord with those reported: 5 mmol of the corresponding aldehyde was dissolve in 10 mL of THF and cooled in an ice bath. 10 mL of ethynyl magnesium bromide (0.5 mol/L in THF) was added dropwise in 15 min. The mixture was allowed to stir for 3 h as it warmed to room temperature, after which time, the reaction was quenched with saturated NH_4Cl and extracted with ether. Organic layer was dried over $MgSO_4$ and then concentrated. The crude product was purified by column chromatography (eluting with 3:1 hexanes/ethyl acetate).The corresponding alcohol was dissolved in 10 mL CH_2Cl_2 and 5.2 g (60 mmol) of magnesium(IV) oxide was added and the mixture was stirred at room temperature for 1 h. The oxidized reagent was removed by filtration through Celite, the organic layer was washed with water (three times), and the solvent was evaporated.

General procedures for azide–alkyne Huisgen 1,3-dipolar cycloaddition reactions at high-pressure conditions

Preparation of 2-C_{12}MPN

Approximately 10 mg of **1**-C_{12}MPN was dissolved in ~2.0 mL of CH_2Cl_2 then mixed with 15–20 equiv. of the appropriate activated acyl–alkynes (**4a**–**4j**). The mixture was transferred into a brass-clamp-sealed PTFE tube and placed in the LECO Tempres High-Pressure reactor at 11 000 atm for 15–24 h. The product **2a**–**2j**-C_{12}MPNs were purified by washing with 95% ethanol and then CH_3CN to remove any unreacted alkyne. IR and ^{1}H NMR spectroscopy were used to check the completion of the reaction, as described below, and purity of the resulting **2a**–**2j**-C_{12}MPNs. The NMR spectra obtained were compared to those of the products of the model reaction, **5a**–**5j**. These are provided, along with IR spectra in the Supporting information.

2a-C_{12}MPN: ^{1}H NMR (600 MHz, CD_2Cl_2) δ: 8.63–7.73, 4.28, 3.40. IR (cm^{-1}, dropcast on NaCl): 2921, 2851, 1643, 1467, 1225, 923, 849, 805, 716.

2b-C_{12}MPN: ^{1}H NMR (600 MHz, CD_2Cl_2) δ: 8.23, 5.49, 4.95, 4.63, 4.42, 4.14, 3.66, 3.41, 3.25, 1.9–0.88. IR (cm^{-1}, dropcast on NaCl): 2925, 2853, 2096, 1631, 1530, 1453, 1260, 1039, 825, 721.

2c-C_{12}MPN: ^{1}H NMR (600 MHz, CD_2Cl_2) δ: 8.58, 8.04, 7.73, 7.39, 4.16, 3.40, 1.70–0.86 IR (cm^{-1}, dropcast on NaCl): 2962, 2921, 2851, 1678, 1467, 1261, 1095, 1019, 805.

2d-C_{12}MPN: ^{1}H NMR (600 MHz, CD_2Cl_2) δ: 8.45–8.30, 7.67–7.42, 4.41, 3.40, 1.94–0.87. IR (cm^{-1}, dropcast on

NaCl): 2961, 2922, 2851, 1652, 1603, 1458, 1261, 1092, 1056, 906, 801, 749.

2e-C_{12}MPN: ^{1}H NMR (600 MHz, CD_2Cl_2) δ: 8.58, 8.33, 4.45, 3.40, 1.97–0.87. IR (cm^{-1}, dropcast on NaCl): 2960, 2920, 2851, 1653, 1525, 1343, 1261, 1093, 1041, 848, 798.

2f-C_{12}MPN: ^{1}H NMR (600 MHz, CD_2Cl_2) δ: 8.34, 7.59–7.46, 4.40, 3.40, 1.90–0.87. IR (cm^{-1}, dropcast on NaCl): 2964, 2924, 2854, 1653, 1603, 1457, 1261, 1115, 1019, 904, 815, 698.

2g-C_{12}MPN: ^{1}H NMR (600 MHz, CD_2Cl_2) δ: 8.18, 7.67, 7.38–7.26, 4.36, 3.38, 2.38, 1.89–0.87. IR (cm^{-1}, dropcast on NaCl): 2918, 2849, 2075, 1657, 1524, 1457, 1228, 1015, 904, 798, 742.

2h-C_{12}MPN: ^{1}H NMR (600 MHz, CD_2Cl_2) δ: 9.09, 8.24, 7.71, 7.33, 7.13, 4.36, 3.41, 1.86–0.87. IR (cm^{-1}, dropcast on NaCl): 2961, 2921, 2851, 2094, 1678, 1599, 1467, 1260, 1087, 1036, 797.

2i-C_{12}MPN: ^{1}H NMR (600 MHz, CD_2Cl_2) δ: 8.18, 4.33, 3.37, 1.87–0.87. IR (cm^{-1}, dropcast on NaCl): 2955, 2921, 2852, 1739, 1437, 1260, 1224, 1199, 1108, 1039, 800, 721.

2j-C_{12}MPN: ^{1}H NMR (600 MHz, CD_2Cl_2) δ: 8.15, 4.39, 3.40, 3.25, 3.06, 1.92–0.89. IR (cm^{-1}, dropcast on NaCl): 2922, 2852, 2091, 1691, 1468, 1261, 1224, 798, 723.

Preparation of 5a–5j

Alkynes (**4a**–**4j**) (0.15 mmol) and 1-azidododecane (**3**) (0.16 mmol) were dissolved in ~2 mL of CH_2Cl_2 then transferred into a brass-clamp-sealed PTFE tube and placed in the LECO Tempres High-Pressure reactor at 11 000 atm and room temperature for 10 h. The product was removed from unreacted alkyne by preparative TLC plate (3:1 hexanes/ethyl acetate). The resulting products, **5a**–**5j**, were characterized as summarized below.

5a: Yellow solid, mp 81–84 °C. ^{1}H NMR (600 MHz, $CDCl_3$) δ: 8.61 (d, *J* = 9.3 Hz, 1H), 8.32–8.30 (m, 2H), 8.25–8.20 (m, 4H), 8.15–8.10 (m, 2H), 7.81 (s, 1H), 4.93 (t, *J* = 7.4 Hz, 2H), 2.10–2.04 (m, 2H), 1.49–1.37 (m, 4H), 1.32–1.25 (broad, 14 H), 0.87 (t, *J* = 7.0, 3H). ^{13}C NMR ($CDCl_3$) δ: 14.1, 22.7, 26.6, 29.1, 29.3, 29.4, 29.5, 29.6, 30.5, 31.9, 50.9, 123.8, 123.9, 124.1, 124.8, 126.5, 126.6, 126.7, 126.9, 127.1, 127.2, 127.3, 130.0, 130.2, 130.9, 131.1, 132.1, 134.3, 140.4, 186.0. IR (cm^{-1}, dropcast on NaCl): 3240, 2923, 2853, 1650, 1510, 1221, 999, 926, 849, 708. MS (EI): Exact mass ($C_{31}H_{35}N_3O$) calcd.: 465.2780, found: 465.2777.

5b: Maroon oil. ^{1}H NMR (400 MHz, $CDCl_3$) δ: 8.16 (s, 1H), 5.52–5.51 (m, 2H), 4.65–4.64 (m, 2H), 4.42 (t, *J* = 7.2 Hz, 2H), 4.17 (s, 5H), 2.00–1.93 (m, 2H), 1.35–1.25 (broad, 18H), 0.87 (t, *J* = 6.7 Hz, 3H). ^{13}C NMR (100 MHz, $CDCl_3$) δ: 14.1, 22.7, 26.4, 28.9, 29.3, 29.4, 29.5, 29.6, 30.1, 31.9, 50.5, 70.2, 71.6, 73.0, 126.3, 149.1, 189.2. IR (cm^{-1}, dropcast on NaCl): 3117, 2925, 2853, 1629, 1528, 1444, 1377, 1260, 1107, 1041, 826, 771. MS (EI): Exact mass ($C_{25}H_{35}N_3FeO$) calcd.: 449.2129, found: 449.2139.

5c: Yellow solid, mp 84–86 °C. ^{1}H NMR (600 MHz, $CDCl_3$) δ: 8.57 (s, 1H), 8.05 (d, *J* = 8.2 Hz, 2H), 7.97 (s, 1H), 7.80 (d, *J* = 8.6 Hz, 2H), 7.47 (t, 2H), 7.42 (t, 2H), 4.35(t, *J* = 7.3 Hz, 2H), 1.92–1.87 (m, 2H), 1.31–1.24 (broad, 18H), 0.88 (t, *J* = 7.0 Hz, 3H). ^{13}C NMR (150 MHz, $CDCl_3$) δ: 14.1, 22.7, 26.4, 28.9, 29.3, 29.4, 29.5, 29.6, 30.1, 31.9, 50.7, 125.0, 125.4.3, 126.6, 127.4, 128.5, 128.7, 129.1, 131.1, 133.4, 149.0, 192.0. IR (cm^{-1}, dropcast on NaCl): 3132, 3056, 2920, 2852, 1653, 1525, 1470, 1180, 884, 841, 729. MS (EI): Exact mass ($C_{29}H_{35}N_3O$) calcd.: 441.2780, found: 441.2783.

5d: Yellow solid, mp 94–98 °C. ^{1}H NMR (600 MHz, $CDCl_3$) δ: 8.55 (d, *J* = 8.2 Hz, 2H), 8.27 (s, 1H), 7.75 (d, *J* = 8.2 Hz, 2H), 7.66 (d, *J* = 7.4 Hz, 2H), 7.48 (t, 2H), 7.40 (t, *J* = 7.3 Hz, 1H), 4.45(t, *J* = 7.2 Hz, 2H), 2.00–1.95 (m, 2H), 1.37–1.25 (broad, 18H), 0.88 (t, *J* = 6.9 Hz, 3H). ^{13}C NMR (150 MHz, $CDCl_3$) δ: 14.1, 22.6, 26.4, 28.9, 29.2, 29.3, 29.4, 29.5, 30.1, 31.9, 50.8, 127.0, 127.3, 128.1, 128.2, 128.9, 131.2, 135.3, 140.0, 145.8, 148.2, 185.2. IR (cm^{-1}, dropcast on NaCl): 3126, 2918, 2848, 1633, 1602, 1523, 1467, 1344, 1255, 909, 876, 851, 746, 692. MS (EI): Exact mass ($C_{27}H_{35}N_3O$) calcd.: 417.2780, found: 417.2787.

5e: Yellow solid, mp 74–76 °C. ^{1}H NMR (400 MHz, $CDCl_3$) δ: 8.64 (d, *J* = 9.0 Hz, 2H), 8.35 (d, *J* = 9.0 Hz, 2H), 8.32 (s, 1H), 4.46 (t, *J* = 7.2 Hz, 2H), 2.01–1.94 (m, 2H), 1.35–1.24 (broad, 18H), 0.86 (t, *J* = 6.8 Hz, 3H). ^{13}C NMR (100 MHz, $CDCl_3$) δ: 14.0, 22.6, 26.4, 28.9, 29.2, 29.3, 29.4, 29.5, 30.1, 31.8, 50.8, 123.4, 128.5, 131.6, 141.2, 147.4, 150.3, 183.8. IR (cm^{-1}, dropcast on NaCl): 3129, 2915, 2849, 1643, 1599, 1518, 1331, 1237, 1047, 1016, 911, 881, 847, 785, 725, 694. MS (EI): Exact mass ($C_{21}H_{30}N_4O_3$) calcd.: 386.2317; found: 386.2320.

5f: Yellow solid, mp 49–51 °C. ^{1}H NMR (400 MHz, $CDCl_3$) δ: 8.43 (d, *J* = 8.7 Hz, 2H), 8.25(s, 1H), 7.61 (t, 1H), 7.51 (t, 2H), 4.44 (t, *J* = 7.2 Hz, 2H), 1.99–1.92 (m, 2H), 1.34–1.24 (broad, 18H), 0.86 (t, *J* = 6.8 Hz, 3H). ^{13}C NMR (100 MHz, $CDCl_3$) δ: 14.0, 22.6, 26.4, 28.9, 29.2, 29.3, 29.4, 29.5, 30.1, 31.8, 50.6, 128.1, 128.4, 130.6, 133.2, 136.5, 148.0, 185.7. IR (cm^{-1}, dropcast on NaCl): 3137, 2957, 2853, 1653, 1577, 1260, 1234, 1181, 1045, 1018, 904, 798, 725, 696. MS (EI): Exact mass ($C_{21}H_{31}N_3O$) calcd.: 341.2467; found: 341.2477.

5g: Yellow oil. ^{1}H NMR (400 MHz, $CDCl_3$) δ: 8.15 (s, 1H), 7.77 (d, *J* = 7.7 Hz, 1H), 7.41 (t, *J* = 7.5 Hz, 1H), 7.31–7.28 (m, 2H), 4.42 (t, *J* = 7.2 Hz, 2H), 2.45(s, 3H), 1.98–1.91 (m, 2H), 1.33–1.25 (broad, 18H), 0.87 (t, *J* = 6.8 Hz, 3H). ^{13}C NMR (100 MHz, $CDCl_3$) δ: 14.1, 20.3, 22.6, 26.4, 28.9, 29.2, 29.3, 29.4, 29.5, 30.1, 31.8, 50.6, 125.2, 127.5, 130.1, 131.2, 131.3, 137.1, 137.9, 148.3, 189.5. IR (cm^{-1}, dropcast on NaCl): 3135, 2925, 2855, 1658, 1524, 1460, 1440, 1233, 1042, 905, 742 MS (EI): Exact mass ($C_{22}H_{33}N_3O$) calcd.: 355.2623, found: 355.2614.

5h: Yellow solid, mp 128–130 °C. ^{1}H NMR (400 MHz, $CDCl_3$) δ: 8.94 (s, 1H), 8.13 (s, 1H), 7.69 (*J* = 7.6 Hz, 2H), 7.38 (t, 2H), 7.15 (t, *J* = 7.4 Hz, 1H), 4.42 (t, *J* = 7.2 Hz, 2H), 1.98–1.92 (m, 2H), 1.33–1.25 (broad, 18H), 0.87 (t, *J* = 6.9 Hz, 3H). ^{13}C NMR (100 MHz, $CDCl_3$) δ: 14.1, 22.7, 26.4, 28.9, 29.3, 29.34, 29.5, 29.6, 30.1, 31.9, 50.9, 119.8, 124.5, 125.5, 129.1, 137.5, 143.4, 163.9. IR (cm^{-1}, dropcast on NaCl): 3317, 3139, 2920, 2851, 1664, 1558, 1437, 1047, 800, 749, 689. MS (EI): Exact mass ($C_{21}H_{32}N_4O$) calcd.: 356.2576, found: 356.2589.

5i: Colourless solid, mp 80–82 °C. ^{1}H NMR (400 MHz, $CDCl_3$) δ: 8.02 (s, 1H), 4.39 (t, *J* = 7.2 Hz, 2H), 3.11 (t, *J* = 7.5 Hz, 2H), 1.95–1.88 (m, 2H), 1.78–1.71 (m 2H), 1.40–1.24(broad, 22H), 0.92–0.86 (m, 6H). ^{13}C NMR (100 MHz, $CDCl_3$) δ: 13.9, 14.1 22.5, 22.7, 23.7, 26.4, 28.9, 29.31, 29.33, 29.5, 29.6, 30.1, 31.5, 31.9, 39.5, 50.6, 125.1, 148.1,

195.7. IR (cm^{-1}, dropcast on NaCl): 3102, 2915, 2847, 1687, 1469, 1241, 1159, 1055, 970, 887, 719. MS (EI): Exact mass ($C_{20}H_{37}N_3O$) calcd.: 335.2936, found: 335.3001.

5j: Colourless oil. ^1H NMR (400 MHz, $CDCl_3$) δ: 8.11 (s, 1H), 4.70 (t, J = 7.4 Hz, 2H), 4.38 (q, J = 7.1 Hz, 2H), 1.94–1.84 (m, 2H), 1.39 (t, J = 7.1 Hz, 2H), 1.31–1.24 (broad, 18H), 0.87 (t, J = 6.5 Hz, 3H). ^{13}C NMR (100 MHz, $CDCl_3$) δ: 14.1, 14. 14, 22.7, 26.4, 29.0, 29.3, 29.4, 29.5, 29.6, 30.3, 31.9, 50.4, 61.7, 127.7, 137.9, 158.5. IR (cm^{-1}, dropcast on NaCl): 2956, 2855, 1731, 1528, 1457, 1311, 1255, 1092, 772. MS (EI): Exact mass ($C_{17}H_{32}N_3O_2$) ($M+H^+$) calcd.: 310.2494, found: 310.2482.

Results and discussion

The azide-terminated MPNs were prepared according to the method recently reported.[8] Starting with 1.8 ± 0.2 nm dodecanethiol-stabilized MPN (C_{12}-MPN), 11-bromoundecanethiol was introduced onto the MPN using the place-exchange method to yield a mixed monolayer containing Br-terminated undecanethiol ligands. Reaction of this MPN with NaN_3 in DMSO introduced the azide functionality onto the MPN. The ratio of terminal azide/bromide/methyl in the newly made mixed MPN was estimated to be roughly 3.5:1:5 by ^1H NMR spectroscopy of I_2-reduced MPNs. This mixed monolayer particle (**1**-C_{12}MPN) was further characterized by IR and UV–vis spectroscopy and TEM. Figure 1*a* shows the ^1H NMR spectrum of **1**-C_{12}MPN. The key diagnostic signals are the characteristically broad signals due to the methylene protons alpha to the azide and bromide functionality at 3.24 and 3.41 ppm, respectively. The IR spectrum of **1**-C_{12}-MPN also shows a strong absorbance at 2096 cm^{-1} due to the antisymmetric –N=N=N stretch in addition to the CH_2/CH_3 stretches at 2959, 2921, and 2852 cm^{-1}.

Compound **1**-C_{12}MPN (~10 mg) was then mixed with each of the activated acyl–alkynes **4a**–**4j**, shown in Scheme 1, in a ratio of 1:15–20 in 2 mL of CH_2Cl_2 and placed in a high-pressure reactor at 11 000 atm at ambient temperature. Model reactions of 1-azidododecane (**3**) with each alkyne were also performed under high-pressure conditions to aid in monitoring the extent of reaction and to provide analogous 1,2,3-triazole products (**5a**–**5j**) to allow for characterization of the reactions on **1**-C_{12}MPN (Scheme 2). The extent of reaction of **1**-C_{12}MPN was followed by ^1H NMR and IR spectroscopy. The reaction was considered complete when there was no evidence of the protons alpha to the azide in the ^1H NMR spectrum and by the disappearance of the azide peak in the IR spectrum. For most cases, this occurred after 15–24 h, depending on the alkyne (Table 1). We note that high temperatures cannot be employed to decrease reaction times for **1**-C_{12}MPN because MPNs are not thermally stable for extended periods. The reaction of **1**-C_{12}MPNs with alkynes **4a**, **4c**, **4d**, **4e**, and **4f**, resulting in the corresponding **2**-C_{12}MPNs, was quantitative after 15 h (perhaps less). Alkynes **4b**, **4g**, **4h**, **4i**, and **4j** had slightly lower 1,3-dipolar cycloaddition reactivity, and their reactions with **1**-C_{12}MPNs was carried out for 24 h. After which time, the azide peak in the IR spectra was completely absent for mixtures containing **4g**, **4h**, and **4j**, indicating near-complete conversion, but only around 80% conversion was observed for the reaction of the **1**-C_{12}MPNs with **4b** and **4i** (Table 1). Presumably, extending the reaction times further would lead to more complete conversion for these two less activated alkynes.

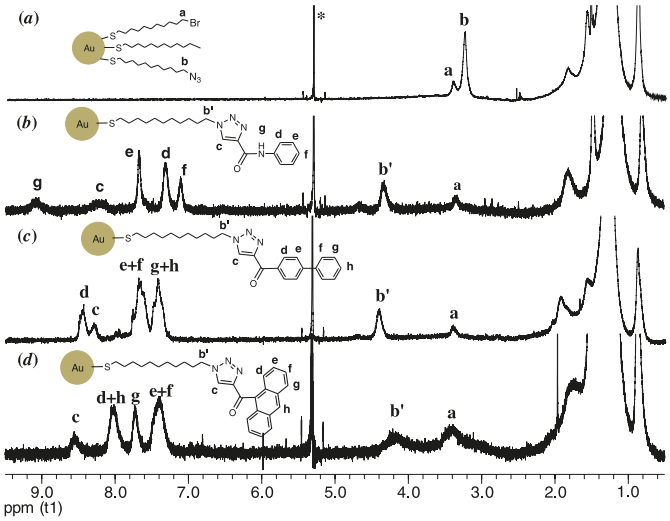

Fig. 1. ^1H NMR spectra of **1**-C_{12}MPN (*a*) and representative product 1,2,3-triazoles **2**-C_{12}MPN formed in click reactions of **1**-C_{12}MPN with acyl alkynes **4h**, **4d**, and **4c**: (*b*) **2h**-C_{12}MPN, (*c*) **2d**-C_{12}MPN, and (*d*) **2c**-C_{12}MPN. Solvent: CD_2Cl_2, residual proton signal is indicated by *.

After completion of the reaction and removal of the reaction mixture from the high-pressure reactor, the mixtures were washed several times to remove excess alkyne from the MPN and a ^1H NMR spectrum was recorded. These spectra show that **1**-C_{12}MPN had reacted to form the corresponding 1,2,3-triazole product **2**-C_{12}MPN. Figures 1*b*–1*d* show representative ^1H NMR spectra of the product **2**-C_{12}MPN formed by reaction of **1**-C_{12}MPN with alkynes **4h**, **4d**, and **4c**, respectively. Evidence for the reaction includes the downfield chemical shift of the protons alpha to the nitrogen atom from 3.24 ppm in the azide (labeled b) to ~4.2 ppm (labeled b′), alpha to the triazole ring (Fig. 1). The disappearance of the signal at 3.24 ppm on the **1**-C_{12}MPNs was considered as a sign of complete conversion of the azide. IR spectra of **2a**–**2j**-C_{12}MPN also show loss of the –N=N=N stretch at 2096 cm^{-1}, verifying completion of the reaction, and a new stretch at ~ 1639–1670 cm^{-1} due to the C=O (1734 cm^{-1} for ester **2j**-C_{12}MPN). Common to all spectra is the absence of the signal at 3.24 due to the CH_2 alpha to the azide, and a new signal appears between 7.8–8.6 ppm (chemical shift varies slightly with structure) due to the triazole C–H proton (labeled c in the spectra). Of course, other signals in the NMR spectra due to the functionality introduced with the cycloaddition with the alkyne are assignable easily by comparison to the spectra of the products of the model reactions, **5a**–**5j**. These are provided in the Supporting information. For example, The ^1H NMR spectra of **2h**-C_{12}MPNs (Fig. 1*b*) shows new peaks in the aromatic region attributed to the aromatic ring as well as the triazole C–H proton at 8.25 ppm and the amide proton at 9.15 ppm, verifying the formation of the triazole ring. It is noticeable that the ^1H NMR of the **2a**- and **2c**-C_{12}MPN with a relatively bulky R group (pyrene and anthracene) shows broad-

Scheme 1. The 1,3-dipolar cycloaddition of **1**-C_{12}MPN with a variety of terminal acyl-alkynes (**4a**–**4j**) at 11 000 atm.

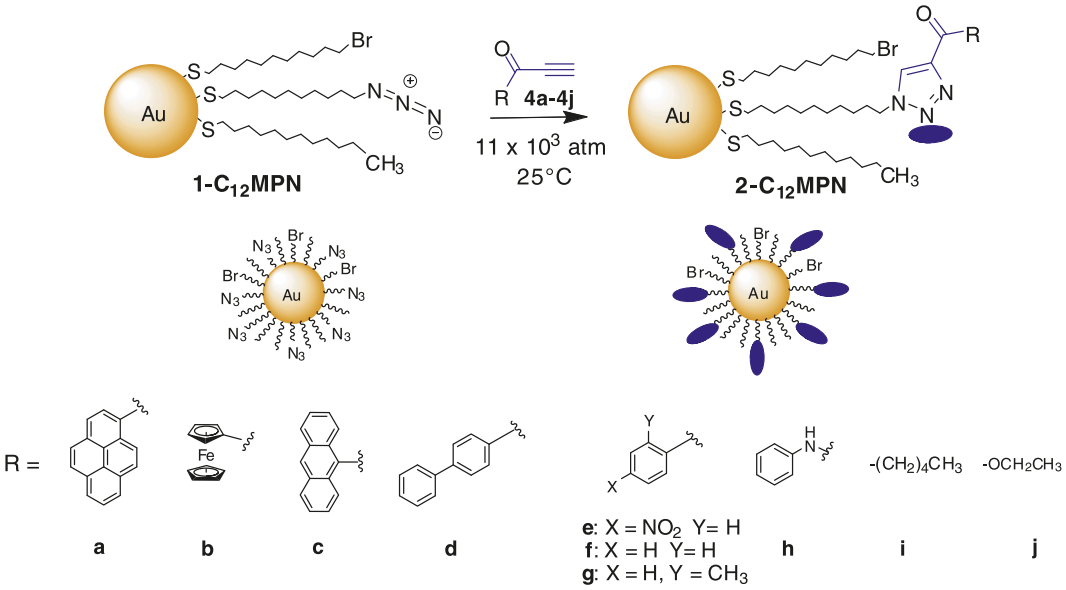

Scheme 2. Model reaction of 1-azidododecane (**3**) with alkenes (**4a**–**4j**) to yield 1,2,3-triazoles (**5a**–**5j**).

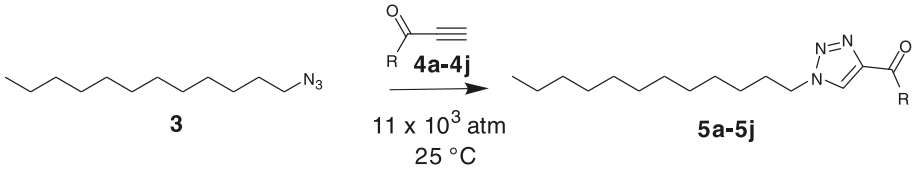

Table 1. Extent of reaction of **1**-C_{12}MPN with alkynes (**4a**–**4j**) via uncatalyzed 1,3-dipolar cycloaddition reaction at atmospheric and hyperbaric pressure conditions.

Alkyne	% Conversion (atmospheric pressure)[a]	% Conversion (11 000 atm)
4a	13	>95[c]
4b	12	>80[d]
4c	6	>95[c]
4d	6	>95[c]
4e	6	>95[c]
4f	NR[b]	>95[c]
4g	NR	>95[d]
4h	NR	>95[d]
4i	NR	>80[d]
4j	NR	>95[d]

[a]60 h in dioxane; see ref. 8.
[b]NR: Not reported.
[c]As determined by NMR after 15 h.
[d]As determined by NMR after 24 h.

ened peaks, especially for the peak assigned to the methylene group (b′) adjacent to the triazole ring, in comparison with the **2**-C_{12}MPNs with less-bulky R groups. This broadness suggests that the bulky group limits the mobility of these groups on the MPNs more than that of the less-bulky R groups. UV–vis spectra and TEM of the particles after reaction verify that there is no measureable change to the Au core size and that the only effect of the high-pressure conditions is the acceleration of the 1,3-dipolar cycloaddition. Although these reactions were only carried out at relatively small scale, they are easily scalable to the gram scale (or more) making the use of the hyperbaric reactor practical for synthetic preparations on MPNs. As mentioned above, to facilitate the assignment of the protons of the ^{1}H NMR spectra of **2**-C_{12}MPNs, the reactions were also carried out using the solution-phase reaction of 1-azidododecane with the same alkynes at high-pressure conditions as a model reaction to yield compounds **5a**–**5j** (Scheme 2). Compounds **5a**–**5j** could be characterized more completely via ^{1}H NMR, ^{13}C NMR, and IR spectroscopy, as well as mass spectrometry (see Experimental). Because the ^{1}H NMR spectra of **5a**–**5j** are not as broad as those of **2**-C_{12}MPN, they are more easily assignable, and hence they provide the confidence in the assignments of the spectra for **2**-C_{12}MPN. For example, Fig. 2 shows the ^{1}H NMR spectra of **2g**-C_{12}MPN and the model compound **5g**, respectively. The signals at 4.4 ppm (b′), alpha to the triazole ring, and 8.18 ppm (c), attributed to the C–H proton of triazole ring, verify the formation of the cycloaddition product on the MPN. The other signals observed for **2g**-C_{12}MPN are also readily assignable because the intensity and chemical shift are comparable to **5g** except the expected broadening of the ^{1}H NMR signals on the MPN. The labeled ^{1}H NMR spectra of **2a**–**2j**-C_{12}MPN and the corresponding model compounds **5a**–**5j** are provided in the Supporting information. In general, the reaction of the 1-azidododecane with the less-electron-deficient dipolarophiles (**4d**, **4f**, and **4h**) provided a higher yield in the same reaction time compared with the more-electron-deficient (**4e** and **4j**) and the sterically hindered (**4a**–**4c**)

Fig. 2. ^{1}H NMR spectra of (*a*) **2g**-C_{12}MPN in CD_2Cl_2* and (*b*) compound **5g** in $CDCl_3$.

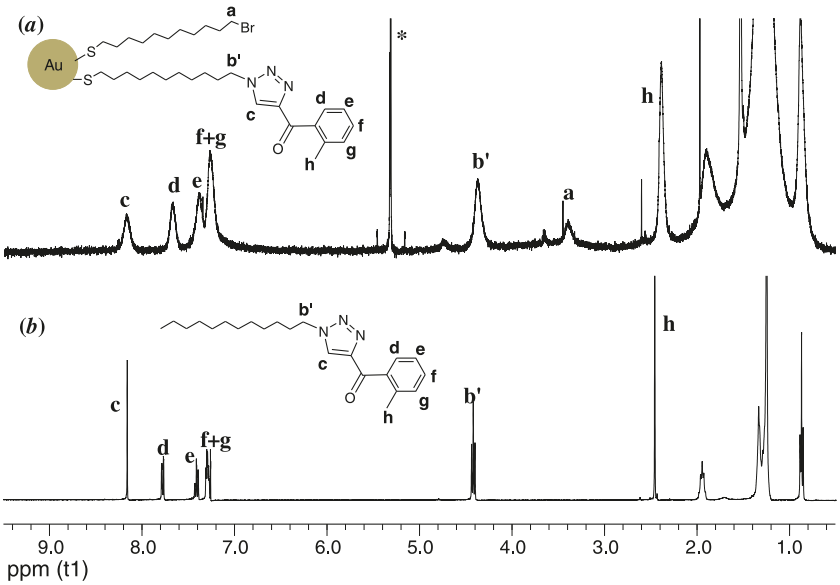

alkynes; a result mirrored in the reactivity of **1**-C_{12}MPN with the same alkynes (Table 1).

The Huisgen uncatalyzed 1,3-dipolar cycloaddition of an azide with an alkyne can lead to two possible regioisomers: the 1,4- (anti) and 1,5- (syn) isomers. Only the 1,4 isomer is shown as a product in Schemes 1 and 2. In cases where the alkyne is electron-defficient[25] or when a sterically bulky azide[26] is used, the 1,4-isomer is usually the major product (e.g., 1,3-dipolar cycloadditions of 1-azidoadamantane with ethyl propionates form only 1,4 isomers). The formation and ratio of the 1,4- and 1,5-isomers can be determined by ^{1}H NMR spectroscopy because the C–H triazole protons of the 1,4- and1,5-isomers are different, the latter usually downfield of the former. In this study, the ^{1}H NMR spectra of **2a**–**2j**-C_{12}MPNs show only one peak that can be assigned as a C–H proton of the triazole ring; this indicates that there is one major isomer formed. Because the alkynes used in this study are electron-deficient and the environment around the azide moiety in **1**-C_{12}MPN is sterically hindered, the formation of 1,4-isomer is the regioisomer that is most likely preferred.

The NMR and IR data together indicate the essentially quantitative conversion of the azide-terminated ligand **1**-C_{12}MPN to the corresponding 1,2,3-triazole **2a**–**2j**-C_{12}MPN under hyperbaric conditions. This can be compared to those of the reaction of the similarly azide-terminated MPN with a number of the same alkynes in the absence of a catalyst in dioxane for 60 h: **a** (13%), **b** (12%), **c** (6%), **e** (6%), and **h** (6%).[8] The use of high pressure leads to efficient and high-yielding chemical modification of monolayer-protected gold nanoparticles for this reaction system. We believe that the hyperbaric reaction method described here is general for performing this reaction with activated alkynes in the absence of catalyst. As such, it can be used as a preparative tool in performing these azide–alkyne 1,2-dipolar cycloadditions for the preparation of novel materials where high chemical conversion is desirable, where the use of the copper-based catalysts is problematic, or in applications where the toxicity of the Cu complicates purification.

Supplementary data

Supplementary data (^{1}H NMR spectra of the bromine-terminated-MPN, **1**-C_{12}MPN, ^{1}H NMR and IR spectra **2a**–**2j**-C_{12}MPN, and ^{1}H NMR spectra of **5a**–**5j**) for this article are available on the journal Web site (canjchem.nrc.ca) or may be purchased from the Depository of Unpublished Data, Document Delivery, CISTI, National Research Council Canada, Ottawa, ON K1A 0R6, Canada. DUD 5301. For more information on obtaining material, refer to cisti-icist.nrc-cnrc.gc.ca/cms/unpub_e.shtml.

Acknowledgements

This work was supported by the Natural Sciences and Engineering Research Council of Canada (NSERC Discovery and RTI for the hyberbaric reactor). Doug Hairsine is thanked for technical assistance with mass spectrometry measurements. M. A. Kerr is thanked for use of the high-pressure apparatus.

References

(1) (a) Lewis, W. G.; Green, L. G.; Grynszpan, F.; Radic, Z.; Carlier, P. R.; Taylor, P.; Finn, M. G.; Sharpless, K. B. *Angew. Chem. Int. Ed.* **2002**, *41*, 1053; (b) Moses, J. E.; Moorhouse, A. D. *Chem. Soc. Rev.* **2007**, *36* (8), 1249. doi:10.1039/b613014n. PMID:17619685.

(2) (a) [See as examples:] Ciampi, S.; Böcking, T.; Kilian, K. A.; James, M.; Harper, J. B.; Gooding, J. J. *Langmuir* **2007**, *23* (18), 9320. doi:10.1021/la701035g. PMID:17655337.; (b) Lummerstorfer, T.; Hoffmann, H. *J. Phys. Chem. B* **2004**, *108* (13), 3963. doi:10.1021/jp049601t.; (c) Collman, J. P.; Devaraj, N. K.; Chidsey, C. E. D. *Langmuir* **2004**, *20* (4), 1051; and references therein. doi:10.1021/la0362977. PMID:15803676.

(3) Whittaker, M. R.; Urbani, C. N.; Monteiro, M. J. *J. Am. Chem. Soc.* **2006**, *128* (35), 11360; and references therein. doi:10.1021/ja0645990. PMID:16939252.

(4) Lutz, J.-F. *Angew. Chem. Int. Ed.* **2007**, *46* (7), 1018; and references therein. doi:10.1002/anie.200604050.

(5) Binder, W. H.; Sachsenhofer, R.; Straif, C. J.; Zirbs, R. *J. Mater. Chem.* **2007**, *17* (20), 2125. doi:10.1039/b618510j.
(6) White, M. A.; Johnson, J. A.; Koberstein, J. T.; Turro, N. J. *J. Am. Chem. Soc.* **2006**, *128* (35), 11356. doi:10.1021/ja064041s. PMID:16939250.
(7) Brennan, J. L.; Hatzakis, N. S.; Tshikhudo, T. R.; Dirvianskyte, N.; Razumas, V.; Patkar, S.; Vind, J.; Svendsen, A.; Nolte, R. J.; Rowan, A. E.; Brust, M. *Bioconjug. Chem.* **2006**, *17* (6), 1373. doi:10.1021/bc0601018. PMID:17105213.
(8) Fleming, D. A.; Thode, C. J.; Williams, M. E. *Chem. Mater.* **2006**, *18* (9), 2327. doi:10.1021/cm060157b.
(9) Thode, C. J.; Williams, M. E. *J. Colloid Interface Sci.* **2008**, *320* (1), 346. doi:10.1016/j.jcis.2007.12.027. PMID: 18191872.
(10) Sommer, W. J.; Weck, M. *Langmuir* **2007**, *23* (24), 11991. doi:10.1021/la7018742. PMID:17944499.
(11) Limapichat, W.; Basu, A. *J. Colloid Interface Sci.* **2008**, *318* (1), 140. doi:10.1016/j.jcis.2007.09.054. PMID:17936777.
(12) Zhou, Y.; Wang, S.; Zhang, K.; Jiang, X. *Angew. Chem. Int. Ed.* **2008**, *47* (39), 7454. doi:10.1002/anie.200802317.
(13) Boisselier, E.; Salmon, L.; Ruiz, J.; Astruc, D. *Chem. Commun.* **2008**, (44), 5788. doi:10.1039/b812249k. PMID: 19009082.
(14) Zhu, J.; Ganton, M. D.; Kerr, M. A.; Workentin, M. S. *J. Am. Chem. Soc.* **2007**, *129* (16), 4904. doi:10.1021/ja070828m. PMID:17397169.
(15) Zhu, J.; Lines, B. M.; Ganton, M. D.; Kerr, M. A.; Workentin, M. S. *J. Org. Chem.* **2008**, *73* (3), 1099. doi:10.1021/jo702398r. PMID:18181644.
(16) Melai, V.; Brillante, A.; Zanirato, P. *J. Chem. Soc., Perkin Trans. 2* **1998**, (11): 2447. doi:10.1039/a804681f.
(17) Brust, M.; Walker, M.; Bethell, D.; Schiffrin, D. J.; Whyman, R. J. J. *Chem. Soc. Chem. Commun.* **1994**, (7): 801. doi:10.1039/c39940000801.
(18) Hostetler, M. H.; Wingate, J. E.; Zhong, C. J.; Harris, J. E.; Vachet, R. W.; Clark, M. R.; Londono, J. D.; Green, S. J.; Stokes, J. J.; Wignall, G. D.; Glish, G. L.; Porter, M. D.; Evans, N. D.; Murray, R. W. *Langmuir* **1998**, *14* (1), 17. doi:10.1021/la970588w.
(19) Rothrock, A. R.; Donkers, R. L.; Schoenfisch, M. H. *J. Am. Chem. Soc.* **2005**, *127* (26), 9362. doi:10.1021/ja052027u. PMID:15984851.
(20) Hays, D. S.; Fu, G. C. *J. Org. Chem.* **1998**, *63* (9), 2796. doi:10.1021/jo9721958.
(21) Barriga, S.; Marcos, C. F.; Riant, O.; Torroba, T. *Tetrahedron* **2002**, *58* (49), 9785. doi:10.1016/S0040-4020(02)01295-4.
(22) Pigge, F. C.; Ghasedi, F.; Zheng, Z.; Rath, N. P.; Nichols, G.; Chickos, J. S. *J. Chem. Soc., Perkin Trans. 2* **2000**, (12): 2458. doi:10.1039/b005702i.
(23) Kumar, N.; Kiuchi, M.; Tallarico, J. A.; Schreiber, S. L. *Org. Lett.* **2005**, *7* (13), 2535. doi:10.1021/ol0504345. PMID:15957884.
(24) Maeda, Y.; Washitake, Y.; Nishimura, T.; Iwai, K.; Yamauchi, T.; Uemuraa, S. *Tetrahedron* **2004**, *60* (41), 9031. doi:10.1016/j.tet.2004.08.004.
(25) Houk, K. N.; Sims, J.; Watts, C. R.; Luskus, L. J. *J. Am. Chem. Soc.* **1973**, *95* (22), 7301. doi:10.1021/ja00803a018.
(26) Sasaki, T.; Eguchi, S.; Yamaguchi, M.; Esaki, T. *J. Org. Chem.* **1981**, *46*, 1800. doi:10.1021/jo00322a009.

Theoretical investigation of the oxidation pathways of HO•-initiated reactions of acrolein, methacrolein, and *trans*-crotonaldehyde

Sabry El-Taher

Abstract: Ab initio molecular-orbital calculations have been performed to investigate the reaction mechanisms of the HO•-initiated reactions of the α,β-unsaturated aldehydes: acrolein (ACR), methacrolein (MACR), and *trans*-crotonaldehyde (CROT). All geometries were fully optimized at the MP2(Full)/6–31G(d,p) level. The correlation energy corrections were introduced by carrying out single-point calculations using both spin-projected second-order Møller–Plesset perturbation theory (PMP2) and coupled-cluster theory (CCSD(T)) using basis sets of different sizes. All reaction pathways studied proceed via a barrierless formation of a loosely bound pre-reactive complex in the entrance channel. The transition-state structures of the HO• additions to the terminal (β) and to the central (α) carbon atoms of the C=C double bond are found to be reactant-like structures. The lowest-energy barrier pathways are found to be the aldehydic H-atom abstraction. The β-addition pathways are found to be energetically more favored than the α-addition pathways. The HO• addition and aldehydic H-atom abstraction pathways are found to be highly exoergic, with the H-atom abstraction pathway being more exoergic than the addition pathways. Although the methyl substitution at the C=C double bond of methacrolein and crotonaldehyde lowers the energies of the transition-state structures of both α- and β-addition pathways, it destabilizes the energies of the transition-state structures of the corresponding aldehydic H-atom abstraction pathways, compared with that of acrolein.

Key words: ab initio, transition-state structures, acrolein, methacrolein, crotonaldehyde.

Résumé : On a effectué des calculs théoriques d'orbitales moléculaires ab initio afin d'étudier les mécanismes de réactions initiées par le radical HO• d'aldéhydes α,β-insaturées, tel l'acroléine (ACR), la méthacroléine (MACR) et le *trans*-crotonaldéhyde (CROT). Toutes les géométries ont été complètement optimisées au niveau MP2(full)/6–31G(d,p). Des corrections d'énergie de corrélation ont été introduites en effectuant des calculs ponctuels à l'aide de la théorie des perturbations de Møller–Plesset du deuxième ordre en projection de spin (PMP2) ainsi que la théorie des agrégats couplés [CCSD(T)], en faisant appel à des ensembles de bases de diverses tailles. Toutes les voies réactionnelles étudiées procèdent, à l'entrée du tunnel, par la formation sans barrière réactionnelle d'un complexe préréactif à interactions faibles. On a trouvé que les structures des états de transition résultant de l'addition du HO• aux atomes de carbone terminal (β) et central (α) de la double liaison C=C possèdent des structures qui ressemblent aux réactifs. On a trouvé que les voies réactionnelles impliquant la barrière d'énergie la plus faible correspondent à l'enlèvement de l'atome d'hydrogène aldéhydique. On a trouvé que les voies réactionnelles correspondant à l'addition du radical HO•et à l'enlèvement de l'atome d'hydrogène sont fortement exoergiques; la voie impliquant l'enlèvement de l'atome d'hydrogène est plus exoergique que les voies réactionnelles conduisant à une addition α. Même si elle diminue les énergies des structures de transition de chacune des deux voies réactionnelles des additions en α et en β, par comparaison avec celle de l'acroléine, la présence de substituants méthyles sur la double liaison C=C de la méthacroléine et du crotonaldéhyde déstabilise les énergies des structures de l'état de transition des voies réactionnelles correspondantes d'enlèvement de l'atome d'hydrogène aldéhydique.

Mots-clés : ab initio, structure de l'état de transition, acroléine, méthacroléine, crotonaldéhyde.

[Traduit par la Rédaction]

Introduction

Aldehydes play an important role in the chemistry of the polluted troposphere. They may be emitted as primary pollutants from partial oxidation of hydrocarbon fuels, industrial uses, and from biogenic sources. They may also arise as secondary pollutants from atmospheric oxidation of volatile organic compounds (VOCs).[1–4] The principal unsaturated compounds of atmospheric interest are the α,β-unsaturated carbonyls: acrolein (ACR), methacrolein (MACR), and *trans*-crotonaldehyde (CROT). Acrolein and *trans*-crotonaldehyde are both emitted into the atmosphere through different sources, such as combustion and chemical industries.[5] Acrolein is also generated as a byproduct of the atmospheric oxidation of buta-1,3-diene[6,7] On the other hand, methacrolein has a central importance as a major product in the atmospheric degradation of isoprene.[8]

It is well-established that the main atmospheric degradation processes of α,β-unsaturated carbonyl compounds are controlled by photolysis, reaction with HO•, NO_3, radicals,

Received 22 May 2009. Accepted 14 September 2009. Published on the NRC Research Press Web site at canjchem.nrc.ca on 21 November 2009.

S. El-Taher. Department of Chemistry, Faculty of Science, Cairo University, Giza, Egypt. (e-mail: sabry_ea@yahoo.com).

Table 1. Calculated classical energy barriers ($\Delta U^{\ddagger}$), activation energies at 0 K ($\Delta E^{\ddagger}$), enthalpies of activation ($\Delta H^{\ddagger}$), and Gibbs free energies of activation ($\Delta G^{\ddagger}$) at 298.15 K for methacrolein + HO• reaction at different levels of theory.

	$\Delta U^{\ddagger}$			$\Delta E^{\ddagger}$ (ZPE)			$\Delta H^{\ddagger}$ (298 K)			$\Delta G^{\ddagger}$ (298 K)		
Levels of calculation	(*abst*)	(*ad-t*)	(*ad-c*)	(*abst*)	(*ad-t*)	(*ad-c*)	(*abst*)	(*ad-t*)	(*ad-c*)	(*abst*)	(*ad-t*)	(*ad-c*)
UMP2(Full)/6–31G(d,p)	4.61	9.61	9.04	3.48	12.89	11.98	2.90	12.04	11.09	11.01	21.00	20.44
PMP2(Full)/6–31G(d,p)	3.03	–0.45	0.01	1.90	2.83	2.90	1.26	1.98	2.06	9.48	11.00	11.41
PMP2/6–311+G(d,p) //MP2/6–31G(d,p)	2.44	–0.79	–0.38	1.31	2.49	2.51	0.73	1.64	1.67	8.95	10.66	11.02
PMP4(SDTQ)/6–311+G(d,p)//MP2/6–31G(d,p)	1.19	–0.96	–0.58	0.06	2.32	1.31	–0.52	1.47	1.47	7.70	10.49	10.82
PMP2/6–311++G(d,p) //MP2/6–31G(d,p)	2.46	–0.85	–0.40	1.33	2.43	2.49	0.75	1.58	1.65	8.95	10.60	11.00
PMP4(SDTQ)/6–311++G(d,p)//MP2/6–31G(d,p)	1.19	–1.03	–0.60	0.06	2.25	2.29	–0.52	1.40	1.45	7.70	10.42	10.80
PMP2/aug-cc-pVTZ//MP2/6–31G(d,p)	1.17	–2.76	–1.91	0.04	0.52	0.98	–0.54	–0.33	0.14	7.69	8.69	9.49
CCSD(T)/6–31G(d,p)//MP2/6–31G(d,p)	0.95	1.66	2.49	–0.14	4.94	6.38	–0.76	4.09	4.54	7.46	13.11	13.89
CCSD(T)/cc-pVDZ//MP2/6–31G(d,p)	–0.59	2.09	2.60	–1.68	5.37	5.49	–2.31	4.52	4.65	5.92	13.54	14.00
CCSD(T)/cc-pVTZ(Q)//MPW1K/6–31+G(d,p)[a]				–1.70	–0.60	–0.20						
MPWB1K/6–311++G(d,p)[b]							–1.96	–0.67	–0.87	5.28	7.98	8.76
M05–2X/6–311++G(d,p)[b]							–2.23	–1.87	–1.35	6.13	7.23	8.43
Experiment[c]										5.85	5.77	5.77

[a]Reference 21.
[b]Reference 23.
[c]Reference 20.

and O_3. However, the dominant tropospheric removal pathway for these species is via reactions with HO• radicals during the daytime. The atmospheric lifetimes during the day for acrolein (*trans*-crotonaldehyde) for the reactions with OH, NO_3, and O_3 are estimated to be 7 h (4 h), 14 months (83 days), and 36 days (5 days), respectively.[9] For methacrolein, the atmospheric lifetime for the reaction with HO• during the day is found to be $\approx$ 2–3 h.[10]

The HO•-initiated oxidation reactions of methacrolein have been the subject of numerous experimental studies.[8,11–15] It has been shown[11,12] that about 50%–55% of those reactions occur via electrophilic addition of HO• to the C=C double bond (eqs. [1] and [2]), while about 45%–50% occur via abstraction of the aldehydic hydrogen (eq. [3]).

[1] $CH_2{=}C(CH_3)CHO + HO^{\bullet} \rightarrow CH_2(OH)^{\bullet}C(CH_3)CHO$

[2] $CH_2C(CH_3)CHO + HO^{\bullet} \rightarrow CH_2C(OH)(CH_3)CHO$

[3] $CH_2{=}C(CH_3)CHO + HO^{\bullet} \rightarrow CH_2{=}C(CH_3)^{\bullet}CO + H_2O$

[4] $CH_2{=}CHCHO + HO^{\bullet} \rightarrow CH_2(OH)^{\bullet}CHCHO$

[5] $CH_2{=}CHCHO + HO^{\bullet} \rightarrow CH_2C(OH)HCHO$

[6] $CH_2{=}CHCHO + HO^{\bullet} \rightarrow CH_2{=}CH^{\bullet}CO + H_2O$

[7] $CH(CH_3){=}CHCHO + HO^{\bullet} \rightarrow CH(CH_3)(OH)CHCHO$

[8] $CH(CH_3){=}CHCHO + HO^{\bullet} \rightarrow CH(CH_3)^{\bullet}CH(OH)CHO$

[9] $CH(CH_3){=}CHCHO + HO^{\bullet} \rightarrow CH(CH_3){=}CH^{\bullet}CO + H_2O$

While the kinetics of the reactions of HO• with both acrolein (eqs. [4]–[6]) and crotonaldehyde (eqs. [7]–[9]) are well-established,[16–19] only two recent studies have been reported[9,20] on the corresponding reaction mechanisms. It has been suggested that 20%–25% (56%)[9] and 32% (50%)[20] of the HO• reactions with acrolein (crotonaldehyde) proceed via addition to the double bond (eqs. [4], [5], [7], and [8]), with the remainder occurring via abstraction of the aldehydic hydrogen (eqs. [6] and [9]). For the addition reaction, there is an unresolved question concerning the actual site of the HO• addition. It has been estimated that at least 80% of the addition occurs at the β-carbon (the furthest double-bonded carbon from the carbonyl group) for both acrolein and methacrolein.[20] On the other hand, the experimental data provide a situation which is less clear concerning the favorable site of the HO• addition in the case of crotonaldehyde.[20]

It seems that there is an actual need for a theoretical study to analyze the different pathways in the HO• reactions with ACR, MACR, and CROT. To accomplish this goal, herein, a systematic investigation for the different pathways of HO•-

initiated reactions of acrolein, methacrolein, and *trans*-crotonaldehyde is performed using high levels of ab initio calculations. The results are expected to shed light on the reactivity of HO• radical toward the studied compounds by providing a quantitative estimation of the preferability of the suggested pathways, based on accurate calculations of the electronic energies, enthalpies, and Gibbs free energies of activation of parts of the corresponding energy surfaces. The results will be compared with the available experimental findings[20] as well as with theoretical calculations recently reported during the course of carrying out[21,22] and publishing[23] this work.

Computational methods

All ab initio molecular-orbital calculations were performed using Gaussian 98W series of programs.[24] Unrestricted ab initio methods were used for all open-shell radical species. All geometries were fully optimized at the MP2(Full)/6–31G(d,p) level. The nature of each stationary point was confirmed by calculating the corresponding vibrational frequencies at the same level (scaled by using a factor of 0.9608). Zero-point vibrational energy and thermal corrections at the MP2(Full)/6–31G(d,p) level were used in the estimation of the electronic energies, enthalpies, and Gibbs free energies of activation. The correlation energy corrections were introduced by carrying out single-point calculations using both Møller–Plesset perturbation theory up to second order (MP2)[25] and CCSD(T) coupled cluster method[26] using basis sets of different sizes. Furthermore, intrinsic reaction coordinate (IRC) calculations[27] were performed to confirm the connections of the transition-state structures between the corresponding minima.

For methacrolein + HO• reaction, single-point calculations at different levels of theory were performed (MP2, MP4(SDTQ), and CCSD(T)) using large basis sets up to the aug-cc-pVTZ, which is Dunning's correlation-consistent triple-ζ basis set,[28] augmented with diffuse functions.

Results and discussion

The internal rotation around the C–C single bond joining the vinyl and the aldehydic moieties of ACR, MACR, and CROT results in two conformers. The more stable conformer is calculated to have an antiperiplanar (ap) conformation for the C=C–C=O chain of atoms, whereas the less stable one has a synperiplanar (sp) conformation for this chain. The MP2(full)/6–31G(d,p)-optimized structures of the two conformers are depicted in Fig. S1 (Supplementary data) for ACR, and those of conformer (ap) for each of MACR and CROT. At the MP2(full)/6–31G(d,p) level, the ap conformer turns out to be 1.41, 2.67, and 1.30 kcal/mol more stable than the sp conformer in terms of Gibbs free energy at 298.15 K for ACR, MACR, and CROT, respectively. These results provide equilibrium constants of 0.092, 0.011, and 0.111, which give ap:sp population ratios of 91.6:8.4, 98.9:1.1, and 90:10 for ACR, MACR, and CROT, respectively. The results show that the ap conformers of the studied aldehydes have significant weights in their reactivity at room temperature, which are in good agreement with available experimental results (97.5:2.5) for MACR.[29] As a result, only the reactions of HO• with the ap conformers of the studied molecules will be considered in this study.

The MP2, MP4(SDTQ), and CCSD(T) methods were used to calculate the energies of the reactants and transition states for the HO•-initiated addition and aldehydic hydrogen abstraction reactions of MACR using different basis sets. The zero-point vibrational energy and thermal corrections to enthalpy and Gibbs free energy were calculated at the MP2/6–31G(d,p) level. Table 1 shows the classical energy barriers ($\Delta U^{\ddagger}$), the ZPE-corrected activation energies at 0 K ($\Delta E^{\ddagger}$(0 K)), the Gibbs free energies ($\Delta G^{\ddagger}$(298 K)), and enthalpies ($\Delta H^{\ddagger}$(298 K)) of activation for the studied reactions calculated at PMP2, PMP4(SDTQ), and CCSD(T) levels of theory. In addition, Fig. 1 displays the free-energy surfaces along the reaction coordinate that connect the reactants, the pre-reactive complexes, the transition states, and the final products for the reaction of HO• with MACR in which the relative free energies are calculated at the PMP2/aug-cc-pVTZ level of theory. Inspection of the results in Table 1 and the free-energy surfaces in Fig. 1 reveals the following: (*i*) The spin-projected MP2 $\Delta E^{\ddagger}$(0 K), $\Delta H^{\ddagger}$(298 K), and $\Delta G^{\ddagger}$(298 K) are considerably lower by about 10 kcal/mol as compared with the UMP2 values for addition reactions, whereas they are lower by only 1.5 kcal/mol for the abstraction reaction (Table 1). This may be due to severe spin contamination in the UMP2 method. (*ii*) The increase of the basis set size decreases the deviation of the calculated Gibbs free energies of activation, from those ($\Delta G^{\ddagger}(298\ \mathrm{K})_{\mathrm{abs}}$ = 5.81 kcal/mol and $\Delta G^{\ddagger}(298\ \mathrm{K})_{\mathrm{add}}$ = 5.77 kcal/mol) estimated from experimental rate coefficients ($k_{\mathrm{abs}} = 1.4 \times 10^{-11}$ cm^3 molecule^{-1} s^{-1} and $k_{\mathrm{add}} = 1.5 \times 10^{-11}$ cm^3 molecule^{-1} s^{-1}, respectively)[20] using the transition-state theory (TST) equation.[30] (*iii*) The use of the large aug-cc-pVTZ basis set gives the best PMP2 energy barriers for the HO• additions to the terminal ($\Delta U^{\ddagger}$(*ad-t*) = –2.76 kcal/mol) and the central ($\Delta U^{\ddagger}$(*ad-c*) = –1.91 kcal/mol) carbons of the C=C double bond, respectively. This result agrees well with the slopes of the experimental Arrhenius plots for MACR + OH system (E_a/R = –(1050/R ± 120) K at 5 torr and 300–420 K),[14] in which the negative activation energy is reported to be due to the negative value of the energy barriers of the corresponding reactions, particularly the addition pathways. On the other hand, the single-point calculations at the CCSD(T)/cc-pDVZ level give $\Delta U^{\ddagger}$(*ad-t*) = 2.09 kcal/mol and $\Delta U^{\ddagger}$(*ad-c*) = 2.6 kcal/mol. Inclusion of ZPE corrections leads to $\Delta E^{\ddagger}$(0 K)(*ad-t*) and $\Delta E^{\ddagger}$(0 K)(*ad-c*) of 5.37 and 5.49 kcal/mol, respectively. In fact, these findings are in agreement with previously reported results,[31] showing that single-point calculations at the PMP2/aug-cc-pVTZ level give the best agreement between theoretical and experimental activation energies for HO• addition reactions, whereas the single-point coupled-cluster method does not give satisfactory results, probably due to the fact that the geometry is not optimized at this level, and hence, spin contamination is not effectively eliminated.[31] (*iv*) Another important reason may be the use of the relatively small cc-pVDZ basis set; it is worth noting that the use of Møller–Plesset perturbation methods (MP2 and MP4(SDTQ)) does not contribute significantly to lowering the activation energy of the hydrogen-atom abstraction reaction even with

Fig. 1. Schematic free-energy profiles for the HO•-initiated addition and aldehydic H-atom abstraction reactions of methacrolein. Relative free energies are calculated at the PMP2/aug-cc-pVTZ level of theory.

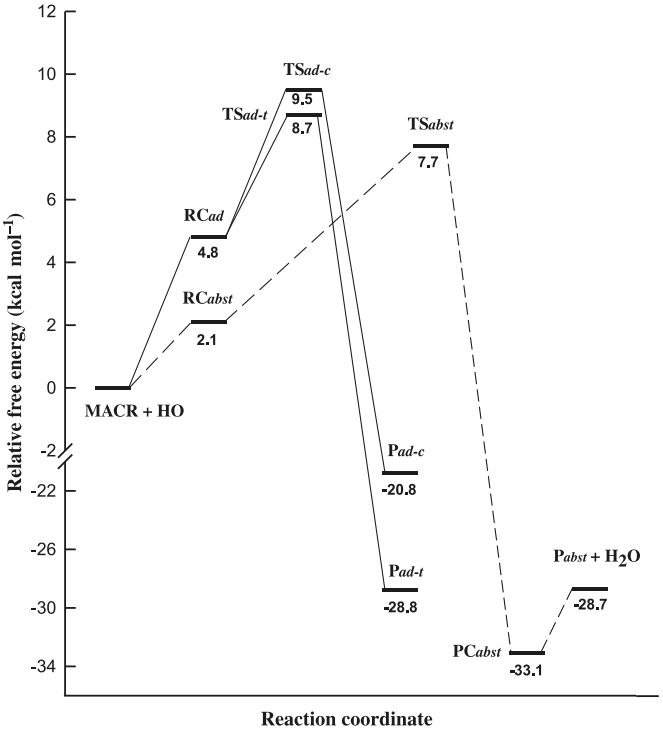

large basis sets (aug-cc-pVTZ and 6–311++G(d,p)). This means that the transition-state structure of the H-atom abstraction reaction should be optimized using highly correlated ab initio method, where the electron correlation provided by the MP2 method is insufficient for quantitative results for these open-shell systems as observed previously.[32] However, the single-point coupled-cluster calculation at the CCSD(T)/cc-pVDZ level, though the basis set cc-pVDZ is relatively small, significantly lowers the energy barrier of the H-atom abstraction reaction, giving activation energy of –1.68 kcal/mol, which is identical to the reported value (–1.70 kcal/mol) at CCSD(T)/cc-pVTZ(Q)//MPW1K/6–31+G(d,p) level.[21] Moreover, the corresponding value of $\Delta G^{\ddagger}$(298 K) at CCSD(T)/cc-pVDZ level is found to be 5.92 kcal/mol, which is in excellent agreement with the experimentally estimated one (5.85 kcal/mol). Considering what was mentioned above, one concludes that the appropriate single-point calculation methods to be adopted in this study for the HO•-initiated addition reactions are the spin-projected MP2 method using the large aug-cc-pVTZ basis set, while for H-atom abstraction reactions, the coupled-cluster CCSD(T) method using the cc-pVDZ basis set may be more appropriate. These methods may be a proper choice for the study of HO•-initiated reactions of relatively large α,β-unsaturated carbonyl compounds in which using large basis sets will be computationally demanding.

HO•-initiated addition reactions

The electrophilic additions of HO• to both terminal (β-addition) and central (α-addition) carbon atoms of ACR, MACR, and CROT proceed via the formation of a barrierless pre-reactive complex (RC*ad*). The MP2(Full)/6–31G(d,p)-optimized structures of RC*ad* are characterized as true local minima on the corresponding potential-energy surfaces (PES) and are depicted in Fig. 2 together with enthalpies and Gibbs free energies, relative to the corresponding reactants. These complexes are in agreement with the ones obtained in recently reported work.[22,23] They may be considered as van der Waals complexes, not hydrogen-bonded ones. The distances between the HO• and the C=C double-bond carbons are very long; they range from 2.875 to 3.042 Å. This is in accord with the distance range calculated at RQCISD(T)/aug-cc-pVTZ level[21] for the acrolein + HO• system (2.830–2.934 Å). On the other hand, the distances between the HO• and ACR (2.612 Å), MACR (2.566 Å), and CROT (2.520 Å) calculated at M05–2X/6–311++G(d,p) level of DFT theory[23] are relatively small as compared with the ones calculated in this work. Starting from the pre-reactive complex RC*ad*, the reaction proceeds via two different pathways. The corresponding transition-state structures for the additions of the HO• to the terminal (TS*ad-t*) and the central (TS*ad-c*) carbon atoms of the C=C double bond are depicted in Fig. 3 for ACR, MACR, and CROT. In general, the C=C double-bond character is almost unperturbed as compared to that of the corresponding reactants, preserving the planarity of the C=C π system. In addition, the distance between the carbon and oxygen atoms (C···O) is rather long and ranges from 2.03 to 2.04 Å. It is slightly longer in TS*ad-c* by 0.004, 0.003, and 0.01 Å in ACR, CROT, and MACR, respectively, than that in TS*ad-t*. These structures are in agreement with the ones obtained in recently reported work,[22,23] except for the C···O distances, which are rather longer by ≈ 0.16 Å than the ones obtained in this work. Therefore, both TS*ad-t* and TS*ad-c* are reactant-like transition structures. The angle of attack, O–C=C, in TS*ad-t* (93.4°) of ACR is smaller by 8° than that in TS*ad-c* (101.3°). This difference is reduced to 3° in MACR and increased to 12° in CROT due to the steric hindrance caused by the methyl group attached to the central (MACR) and the terminal (CROT) carbon atoms of the C=C double bond, respectively.

The MP2(Full)/6–31G(d,p)-optimized structures of the corresponding adducts, P*ad-t* and P*ad-c*, are shown in Fig. S2 (Supplementary data) for ARC, MACR, and CROT. In an attempt to obtain the most stable adduct structures, rotations of the torsion angle, φ(HOCC), were performed. It represents the torsion angle of the HO• hydrogen atom, where the reference carbon atom is the central carbon of the C=C double bond and the aldehydic carbon for P*ad-t* and P*ad-c*, respectively. In the case of P*ad-c*, another torsion angle, φ(OCCO), has been rotated in addition to the φ(HOCC) angle, which describes the rotation of the aldehydic CHO group. The P*ad-c* structures chosen are found to be the most stable conformers due to the hydrogen bonding between the HO• hydrogen and the carbonyl oxygen, where φ(HCCO) = 2.8°, 1.3°, and 2.7° for ACR, MACR, and CROT, respectively. The H···O hydrogen-bonded distances in P*ad-c* adducts of ACR, MACR, and CROT are found to be 2.018, 1.999, and 2.016 Å, respectively. Those P*ad-c* conformers have not been detected in the previously reported work.[21,22] The most stable conformers of P*ad-t* ad-

Fig. 2. Optimized structures of the pre-reactive complexes located in the entrance channels of the HO•-initiated additions (RC*ad*) and aldehydic H-atom abstraction (RC*ad*) reactions of acrolein (ACR), methacrolein (MACR), and crotonaldehyde (CROT) calculated at MP2(Full)/6–31G(d,p) level. Relative enthalpies, Gibbs free energies (kcal/mol), and distances (Å) between HO• and aldehydes are given.

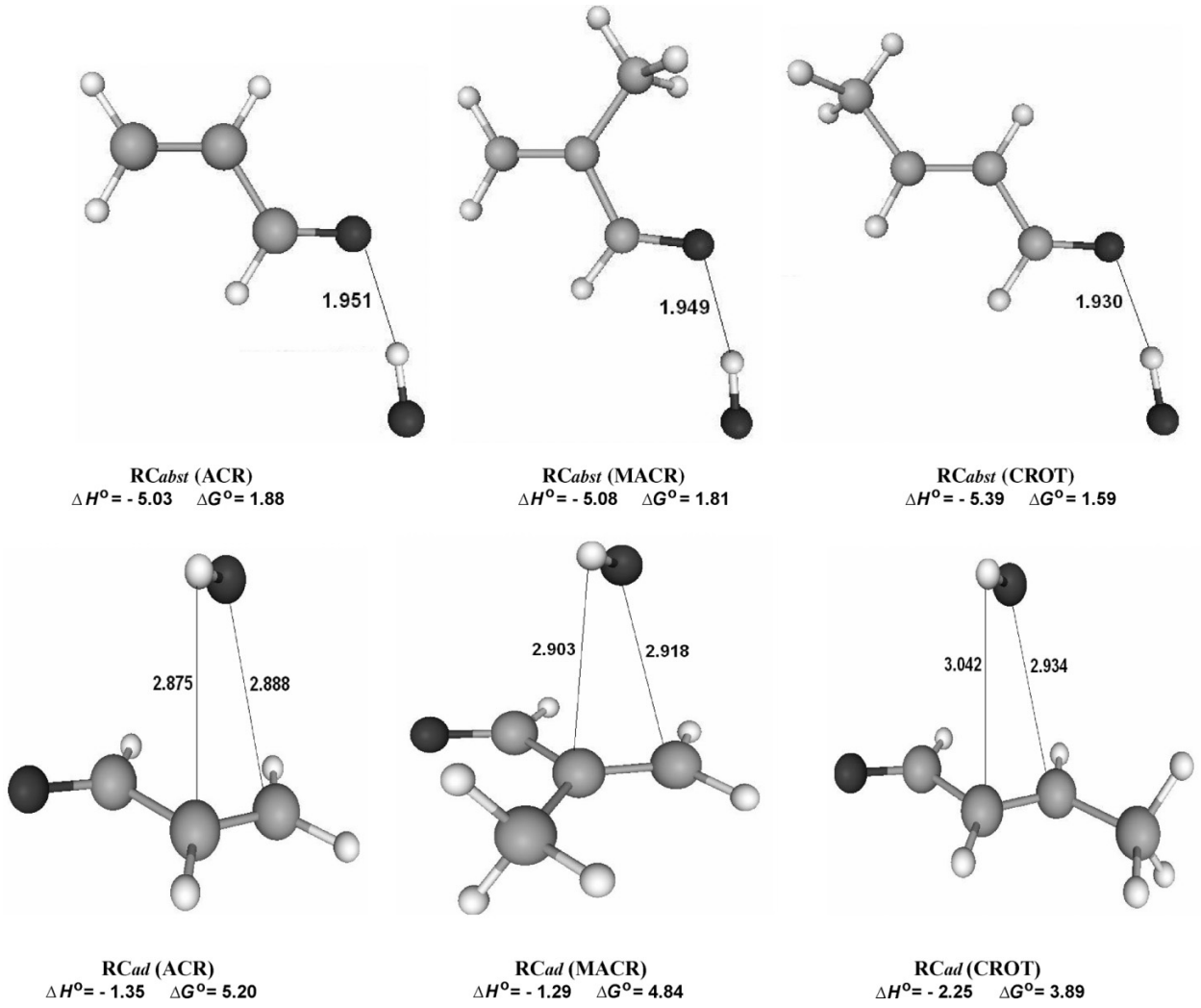

ducts in ACR, MACR, and CROT are found to be the ones that have the angles φ(HOCC) equal to –62.3°, –64.8°, and –59.7°, respectively.

The total electronic energies as well as the corresponding ZPEs, thermal corrections to enthalpy, and Gibbs free energy computed at different levels of theory are collected in Table S1 for reactants, transition-state structures, and products, and in Table S2 for the corresponding pre-reactive (RC*ad* and RC*abst*) and post-reactive (PC*abst*) complexes for all studied reaction pathways. Figure 4 shows schematic energy profiles obtained for the HO• addition pathways of the studied aldehydes using (ZPE-uncorrected) relative energies calculated at PMP2/aug-cc-pVTZ level of theory. Figure 4 shows that the RC*ad* structures lie 2.44, 2.36, and 3.43 kcal/mol below the energies of the isolated reactants for ARC, MACR, and CROT, respectively. This is in accord with a reported value of –2.7 kcal/mol for HO• + ACR system.[22] The corresponding ΔG^{o}(298 K) values are 5.20, 4.84, and 3.89 kcal/mol (see Fig. 1) for the pre-reactive complexes of HO• with ACR, MACR, and CROT, respectively. These ΔG^{o}(298 K) values are in agreement with the reported ones of 4.23, 4.43, and 3.33 kcal/mol, respectively. However, this finding disagrees with the reported results for HO• + MACR reaction[21] that only one pre-reactive complex, in which the hydrogen atom of the HO• moiety is hydrogen-bonded to the aldehydic oxygen atom, is formed in the entrance channel of the HO• addition as well as the H-atom abstraction reactions.

TS*ad-t* (TS*ad-c*) structures of ACR, MACR, and CROT lie 2.5 (1.1), 2.8 (1.9), and 4.4 (2.2) kcal/mol below the energies of the corresponding reactants (Fig. 4). Inclusion of ZPE corrections to energy leads to $\Delta E^{\ddagger}$(0 K) values for the HO• addition to the terminal (central) carbon atom of the C=C double bond of 0.93 (2.03), 0.52 (0.98), and –0.96 (0.88) for ACR, MACR, and CROT, respectively. Inspection of these results reveals that the addition of HO• to the terminal carbon atom of the C=C double bond is energetically more favorable than the addition to the central carbon atom, which may be due to the delocalization of the unpaired electron into the π-bond of the adjacent carbonyl group. This is in agreement with a calculated branching ratio of 95.1:4.9 recently reported for the HO• + ACR[22] and with experimen-

Fig. 3. Optimized structures of the transition states of the HO•-initiated addition (TS*ad-t* and TS*ad-c*) and aldehydic H-atom abstraction (TS*abst*) reactions of ACR, MACR, and CROT calculated at MP2(Full)/6–31G(d,p) level. The Symbol φ refers to dihedral angles.

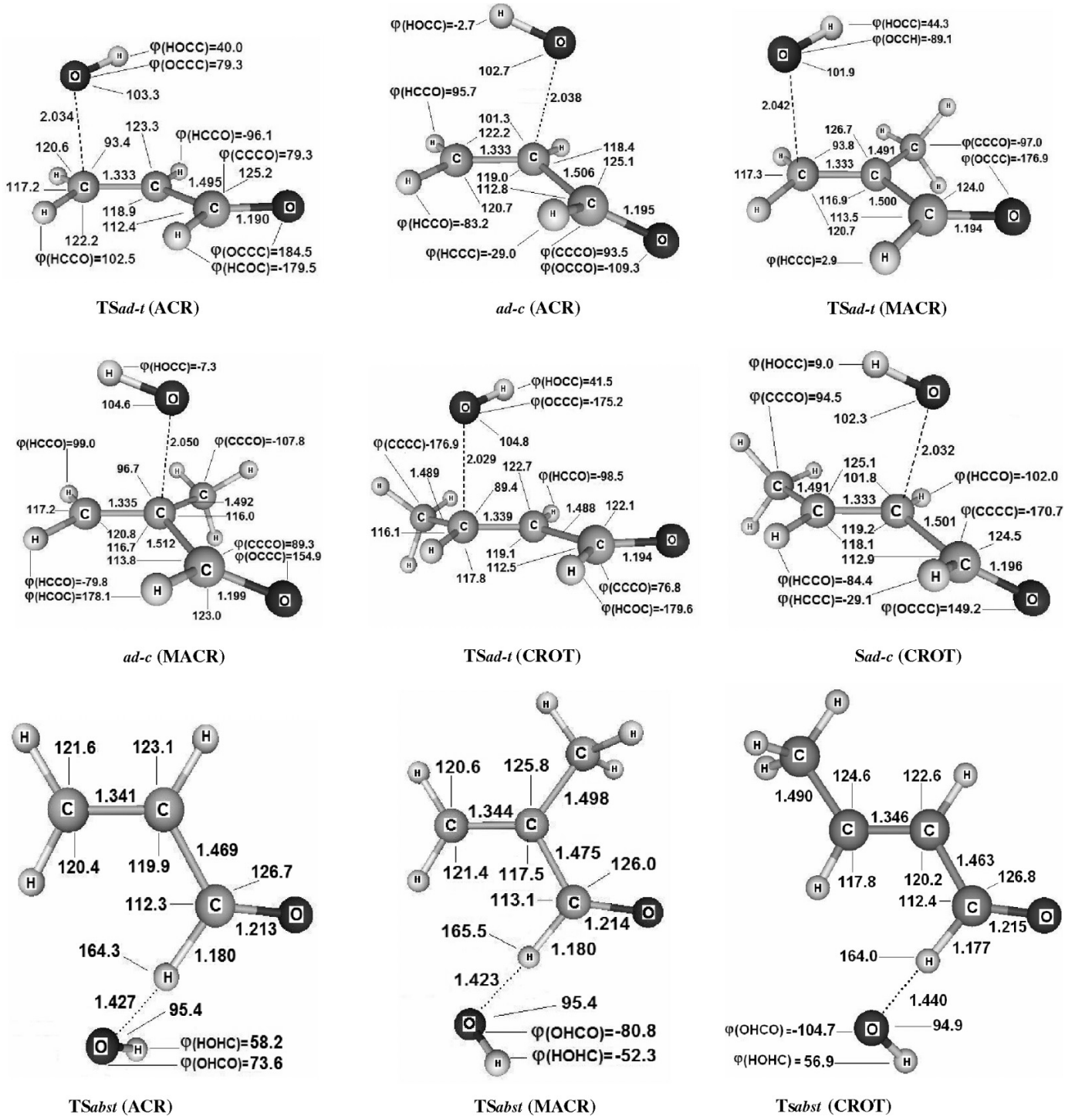

tal data indicating that at least 80% of the HO• additions to ACR and MACR take place on the terminal carbon atom.[20] Furthermore, the $\Delta G^{\ddagger}$(298 K) values for the HO• addition to the terminal (central) carbon atom are found to be 9.0 (10.2), 8.7 (9.5), and 7.5 (9.1) for ACR, MACR, and CROT, respectively (Tables 1 and 2). The values of $\Delta G^{\ddagger}$(298 K) for the terminal additions are relatively smaller than those of the central ones. This trend is in agreement with recently reported values of $\Delta G^{\ddagger}$(298 K) of 6.04 (8.72), 7.98 (8.76), and 6.09 (8.24) for ACR, MACR, and CROT, respectively.[23] On the other hand, the value of $\Delta E^{\ddagger}$(0 K) decreases by 0.41 (1.05) and 1.89 (1.15) kcal/mol on going from ACR to MACR and CROT, respectively. The presence of the methyl group attached to the double bond may increase the stabilization energy of RC*ad*, resulting in a subsequent lowering in the energies of TS*ad-t* and TS*ad-c* as a

Fig. 4. Schematic energy profiles for the HO• additions to ACR, MACR, and CROT. Relative energies (kcal/mol) are calculated at the PMP2/aug-cc-pVTZ level of theory (ZPE-uncorrected).

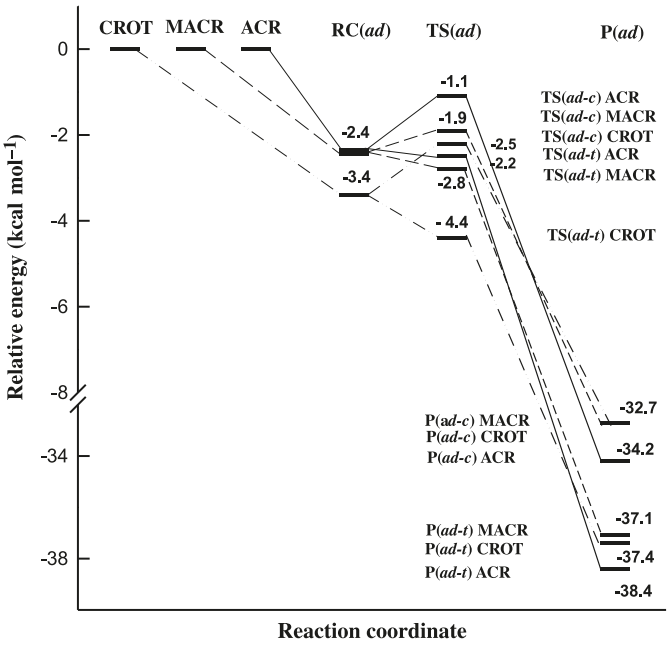

result of the inductive and the dipole–dipole effects. This is in agreement with a reported increase in the rate coefficients for the HO• addition to the methyl-substituted species: MACR (1.5×10^{-11} cm^3 molecule^{-1} s^{-1}) and CROT (1.7×10^{-11} cm^3 molecule^{-1} s^{-1}), compared with that of ACR (6×10^{-11} cm^3 molecule^{-1} s^{-1}).[20]

The imaginary frequencies of TS*ad-t* (TS*ad-c*) are found to be 557*i* (530*i* cm^{-1}), 566*i* (521*i* cm^{-1}), and 568*i* (544*i* cm^{-1}) for ACR, MACR, and CROT, respectively. This means that these frequencies decrease when going from ACR to CROT, and thus the curvatures of the calculated energy barriers and their heights are reduced as well. Figure 4 shows that HO• additions to the terminal and central carbons are highly exoergic, where the P*ad-t* (P*ad-c*) structures of ACR, MACR, and CROT are –38.4 (–34.2), 37.1 (32.7), and –37.4 (–32.7) kcal/mol lower in energy than the isolated reactants, respectively. The exoergicity of the HO• addition to the terminal carbon is found to be 4.2, 4.4, and 4.7 kcal/mol, respectively, larger than that to the central carbon. This may be due to the delocalization of the unpaired electron into the π-system of the adjacent carbonyl group.

HO•-initiated H-atom abstraction reactions

The aldehydic H-atom abstraction from ACR, MACR, or CROT by HO• proceeds via a barrierless pre-reactive complex, RC*abst*, in the entrance channel. Figure 5 shows schematic potential-energy profiles obtained for the HO•-initiated aldehydic H-atom abstraction pathways of the studied aldehydes using ZPE-uncorrected CCSD(T)/cc-pVDZ//MP2/6–31G(d,p) relative energies (ΔU). The formation of a stable pre-reactive complex RC*abst* in the entrance channel followed by a transition-state structure TS*abst* whose energy is lower than the energy of the isolated reactants is clearly observed. The MP2(Full)/6–31G(d,p)-optimized structures of these complexes (Fig. 2) are characterized as true local minima on the potential-energy surface. These complexes have been identified as hydrogen-bonded ones[21–23] in which a hydrogen-bonding interaction occurs between the hydrogen atom of HO• and the carbonyl oxygen atom. In addition, the data given in Fig. 2 show that the H···O distance decreases and the stabilization energy (ΔH^o(298 K)) increases from ACR to CROT. This is in good agreement with previously reported trends.[23] Inspection of Fig. 5 reveals that RC*abst* structures are found to be 6.46, 6.50, and 6.83 kcal/mol lower in energy than the isolated reactants, respectively. After the formation of RC*abst*, the aldehydic hydrogen atom is transferred to the HO• moiety through the transition-state structure TS*abst* and then to a product complex, PC*abst*, in which the pre-formed water is loosely bound to the unsaturated aldehydic fragment. Finally, PC*abst* dissociates into the isolated products.

The MP2(Full)/6–31G(d,p)-optimized structures of PC*abst* are given in Fig. S3 (Supplementary data) for ACR, MACR, and CROT. The H···C distance is equal to 2.402, 2.369, and 2.370 Å, respectively. The PC*abst* structures are stabilized by a hydrogen-bonding interaction between the oxygen atom of the pre-formed water molecule and the nearest hydrogen of the methylene group in the unsaturated aldehydic fragment, where the distances between them are 2.339, 2.395, and 2.354 Å, respectively. The PC*abst* structures of ACR, MACR, and CROT lie, respectively, 26.1 (22.5), 25.3 (21.7), and 27.5 (24.0) kcal/mol lower in energy (ZPE-corrected energy) than the isolated reactants, and 3.5 (0.6), 3.5 (0.9), and 4.5 (4.1) kcal/mol lower in energy (ZPE-corrected energy) than the separated products, P*abst* and H_2O (Fig. 5). This means that the aldehydic H-atom abstractions from ACR, MACR, and CROT by HO• are predicted to be exoergic due to the O–H bond strength of water. In addition, the dissociation of PC*abst* to the separated products has insignificant energy barrier, especially in the case of ACR and MACR, and hence it is expected to irreversibly occur as soon as the PC*abst* is formed.

The MP2(full)/6–31G(d,p)-optimized geometries of TS*abst* are shown in Fig. 3 for ACR, MACR, and CROT. The H···C distance slightly increases from ACR (1.181 Å) to CROT (1.177 Å), while the H···O distance slightly decreases from ACR (1.427 Å) to CROT (1.440 Å) . This means that larger energy barrier has to be overcome. This trend is consistent with the increase in $\Delta E^{\ddagger}$(0 K) on going from ACR to CROT, where the results in Tables 1 and 2 show that $\Delta E^{\ddagger}$(0 K) of the H-atom abstraction reactions for ACR, MACR, and CROT has values of –1.82, –1.68, and –0.34 kcal/mol at the CCSD(T)/cc-pVDZ level, respectively. In contrast to the HO• additions, the substitution of the methyl group at the C=C double bond destabilizes the transition-state structures of the aldehydic H-atom abstraction pathways of the HO• reactions with MACR and CROT by 0.14 and 1.48 kcal/mol, respectively, as compared with that of ACR. On the other hand, the results in Table 1 show that the activation energy, $\Delta E^{\ddagger}$(0 K), of the H-atom abstraction reaction of HO• with MACR is 0.04 kcal/mol at the PMP2/aug-cc-pVTZ level, which is lower by 0.48 and 0.94 kcal/mol than that of the terminal and the central additions, respectively. This trend is found to be in agreement with previously reported data for HO• + MACR in which $\Delta E^{\ddagger}$(0 K) of H-abstraction reaction is lower by 1.1 and 1.5 kcal/mol in energy than that of the terminal and central additions at

Table 2. Calculated classical energy barriers ($\Delta U^{\ddagger}$), activation energies at 0 K ($\Delta E^{\ddagger}$), enthalpies of activation ($\Delta H^{\ddagger}$), and Gibbs free energies of activation ($\Delta G^{\ddagger}$) at 298.15 K for acrolein + HO$^{\bullet}$ and crotonaldehyde + HO$^{\bullet}$ reactions.

	$\Delta U^{\ddagger}$			$\Delta E^{\ddagger}$ (0 K)			$\Delta H^{\ddagger}$ (298 K)			$\Delta G^{\ddagger}$ (298 K)		
Levels of calculation	(*abst*)	(*ad-t*)	(*ad-c*)	(*abst*)	(*ad-t*)	(*ad-c*)	(*abst*)	(*ad-t*)	(*ad-c*)	(*abst*)	(*ad-t*)	(*ad-c*)
Acrolein + OH$^{\bullet}$												
PMP2(Full)/6–31G(d,p)	2.97	–0.18	1.08	1.87	3.26	4.20	1.28	2.28	3.28	9.59	11.29	12.41
CCSD(T)/cc-pVDZ//MP2/6–31G(d,p)	–0.72			–1.82			–2.41			5.91		
PMP2/aug-cc-pVTZ//MP2/6–31G(d,p)	0.92	–2.45	–1.09	–0.09	0.93	2.03	–0.78	0.01	1.10	7.55	9.02	10.23
RQCISD(T)/aug-cc-pVTZ//UQCISD/aug-cc-pVDZ[a]				–1.10	–0.70	0.80	–1.80	–1.50	0.00	6.30	7.10	8.80
MPWB1K/6–311++G(d,p)[b]							–2.06	–1.94	0.27	5.63	6.04	8.72
M05–2X/6–311++G(d,p)[b]							–2.53	–1.94	–1.26	5.83	5.84	7.83
Experiment[c]										5.81	6.31	
Crotonaldehyde + OH$^{\bullet}$												
PMP2(Full)/6–31G(d,p)	2.54	–1.14	1.17	1.68	2.26	4.24	1.05	1.22	3.37	9.34	10.76	12.48
CCSD(T)/cc-pVDZ//MP2/6–31G(d,p)	0.52			–0.34			–2.73			5.56		
PMP2/aug-cc-pVTZ//MP2/6–31G(d,p)	–0.45	–4.36	–2.18	–1.24	–0.96	0.88	–1.94	–2.00	0.01	6.35	7.54	9.13
MPWB1K/6–311++G(d,p)[b]							–1.55	–2.55	–0.01	5.25	6.09	8.24
M05–2X/6–311++G(d,p)[b]							–2.76	–3.56	–1.16	5.59	5.41	7.27
Experiment[c]										5.69	5.69	

[a]Reference 22.
[b]Reference 23.
[c]Reference 20.

CCSD(T)/cc-pVTZ(Q)//MPW1K/6–31+G(d,p) level, respectively.[21] However, the branching ratio for the HO• addition vs. the H-atom abstraction reaction has been determined to be 50:50[11] and 55:45,[12] respectively. The H-atom abstraction channel for the HO• + MACR reaction has been suggested to dominate the overall rate constant at higher temperatures as the contribution of the pressure-dependent HO• addition channel decreases leading to a weak pressure-dependence of the overall rate constant.[14] For HO• + ACR reaction, the results in Table 2 show that the value of $\Delta E^{\ddagger}$(0 K) for the H-atom abstraction reaction is –0.09 kcal/mol at the PMP2/aug-cc-pVTZ level, which is lower by 1.02 and 2.12 kcal/mol than that of the terminal and the central additions, respectively. This trend is in agreement with recently reported data in which the value of $\Delta E^{\ddagger}$(0 K) for H-abstraction reaction is lower by 1.1 and 1.5 kcal/mol in energy than that of the terminal and central additions at RQCISD(T)/aug-cc-pVTZ//UQCISD/aug-cc-pVDZ level, respectively.[22] In addition, the calculated rate coefficients at 298 K for the three reaction pathways are found to lead to a branching ratio of about 75:4:1,[22] which is in good agreement with the experimental data, which showed that about 68% of the HO• reaction with acrolein proceeds via aldehydic H-atom abstraction.[20] For HO• + CROT reaction, the value of $\Delta E^{\ddagger}$(0 K) for the H-atom abstraction reaction is –1.24 kcal/mol at the PMP2/aug-cc-pVTZ level, which is lower by 0.28 and 2.12 kcal/mol than that of the terminal and the central additions, respectively. This means that the H-atom abstraction pathway is slightly more important than the HO•-addition one, which is inconsistent with the experimental data, which reported that 56% of the reaction proceeds via the HO•-addition pathway, while 46% proceeds via the H-atom abstraction pathway.[9] However, another reported experimental data showed that 50 ± 15% of the reaction proceeds via HO•-addition pathway.[20] On the other hand, inspection of the values of $\Delta G^{\ddagger}$(298 K) calculated at CCSD(T)/cc-pVDZ level (Tables 1 and 2) reveals that, for HO• + MACR, the $\Delta G^{\ddagger}$(298 K) is found to be 5.92 kcal/mol, which is in excellent agreement with the experimentally estimated one (5.85 kcal/mol). Moreover, the values of $\Delta G^{\ddagger}$(298 K) for the hydrogen-atom abstraction reaction of HO• + ACR and HO• + CROT at CCSD(T)/cc-pVDZ level are found to be 5.91 and 5.56 kcal/mol, respectively. These values are in agreement with recently reported values of 5.83 and 5.59 kcal/mol[23] and with values of 5.81 and 5.69 kcal/mol estimated from experimental rate coefficients using the TST eq. [20].

Conclusions

High-level ab initio molecular-orbital calculations have been performed to study the mechanisms of the HO•-initiated reactions of acrolein, methacrolein, and *trans*-crotonaldehyde. The exploration of the corresponding potential-energy surfaces shows the existence of different reaction pathways, with multiple stationary points, which have been located, verified, and connected. From the above discussion, one concludes the following:

The spin-projected MP2 method using the large aug-cc-pVTZ basis set and the coupled-cluster CCSD(T) method using the relatively small cc-pVDZ basis set are found to be appropriate single-point calculation methods for the studied HO•-initiated addition and aldehydic hydrogen-atom abstraction reactions, respectively. These methods may be a proper choice for relatively large α,β-unsaturated carbonyl compounds in which using large basis sets will be computationally demanding.

All reaction pathways studied proceed via the barrierless formation of a van der Waals loosely bound pre-reactive complex in the entrance channel of the HO•-addition pathways and a hydrogen-bonded pre-reactive complex in the entrance of the aldehydic H-atom abstraction pathway.

The lowest-energy barrier pathways (ZPE-corrected) at 0 K are found to be the aldehydic H-atom abstraction pathway via a transition-state structure lying 1.82, 1.68, and 0.34 kcal/mol below the energy of the reactants for acrolein, methacrolein, and *trans*-crotonaldehyde, respectively, at the CCSD(T)/cc-pVDZ level.

The transition-state structures of the additions of HO• to the terminal (β) and the central (α) carbon atoms of the C=C double bond are found to be reactant-like structures.

The lowest-energy barrier pathway at 0 K for the HO• addition is found to be the β-addition one, which proceeds via a transition-state structure lying 0.93 and 0.52 kcal/mol above the energy of the reactants for acrolein and methacrolein, respectively, and 0.96 below the energy of the reactants for *trans*-crotonaldehyde.

Fig. 5. Schematic energy profiles for the HO•-initiated aldehydic H-atom abstraction reactions of ACR, MACR, and CROT. Relative energies (kcal/mol) are calculated at the CCSD(T)/cc-pVDZ level of theory (ZPE-uncorrected).

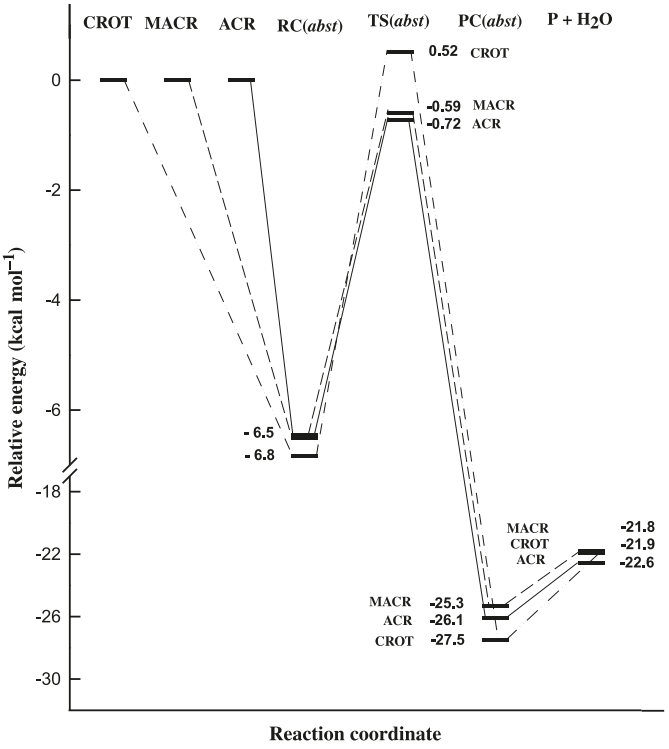

The α-addition pathway proceeds via a transition-state structure lying 2.03, 0.98, and 0.88 kcal/mol above the energy of previously mentioned reactants, respectively, at the PMP2/aug-cc-pVTZ level. This is in agreement with experimental rate coefficients at 298 K, calculated for these HO•-addition reactions, which lead to a branching ratio of about 80:20 for both acrolein and methacrolein and 60:40 for crotonaldehyde.[20]

Both the HO•-initiated additions and aldehydic H-atom abstraction pathways are found to be highly exoergic. The H-atom abstraction pathways are found to be more exoergic than the addition pathways (see Fig. 1 for methacrolein).

The presence of the methyl group attached to the double bond increases the stabilization energy of the pre-reactive complex, resulting in a subsequent lowering in the energies of the transition-state structures of both α- and β-addition pathways, which may be due to an inductive and dipole–dipole effects. This is in agreement with an experimentally reported increase in the rate coefficients for the HO• addition to the methyl-substituted species (methacrolein and crotonaldehyde) as compared with that of acrolein.[20] On the other hand, the methyl substitution destabilizes the transition-state structures of the corresponding aldehydic H-atom abstraction pathways of both methacrolein and crotonaldehyde, compared with that of acrolein.

Supplementary data

Supplementary data for this article are available on the journal Web site (canjchem.nrc.ca) or may be purchased from the Depository of Unpublished Data, Document Delivery, CISTI, National Research Council Canada, Ottawa, ON K1A 0R6, Canada. DUD 5293. For more information on obtaining material, refer to cisti-icist.nrc-cnrc.gc.ca/cms/unpub_e.shtml.

Acknowledgements

The author would like to thank Dr. J. Raúl Alvarez-Idaboy for helpful discussion and two anonymous reviewers for their constructive comments on the manuscript.

References

(1) Nondek, L.; Rodler, D. R.; Birks, J. W. *Environ. Sci. Technol.* **1992**, *26* (6), 1174. doi:10.1021/es50002a605.

(2) Benning, L.; Wahner, A. *J. Atmos. Chem.* **1998**, *31* (1/2), 105. doi:10.1023/A:1005884116406.

(3) Grosjean, D. J. *Air Waste Manag. Assoc.* **1990**, *40*, 1664.

(4) Grosjean, E.; Grosjean, D.; Fraser, M. P.; Cass, G. R. *Environ. Sci. Technol.* **1996**, *30* (9), 2687. doi:10.1021/es950758w.

(5) Graedel, T. E.; Hawkins, D. T.; Claxton, L. D. *Atmospheric Chemical Compounds: Sources, Occurance and Bioassay;* Academic Press: Orlando, FL, 1986.

(6) Lui, X.; Jeffries, H. E.; Sexton, K. G. *Atmos. Environ.* **1999**, *33* (18), 3005. doi:10.1016/S1352-2310(99)00078-3.

(7) Tuazon, E. C.; Alvarado, A.; Aschmann, S. M.; Atkinson, R.; Arey, J. *Environ. Sci. Technol.* **1999**, *33* (20), 3586. doi:10.1021/es990193u.

(8) Tuazon, E. C.; Atkinson, R. *Int. J. Chem. Kinet.* **1990**, *22* (12), 1221. doi:10.1002/kin.550221202.

(9) Magneron, I.; Thévenet, R.; Mellouki, A.; Le Bras, G.; Moortgat, G. K.; Wirtz, K. *J. Phys. Chem. A* **2002**, *106* (11), 2526. doi:10.1021/jp013413a.

(10) Gierczak, T.; Burkholder, J. B.; Talukdar, R. K.; Mellouki, A.; Barone, S. B.; Ravishankara, A. R. *J. Photochem. Photobiol. A* **1997**, *110* (1), 1. doi:10.1016/S1010-6030(97)00159-7.

(11) Tuazon, E. C.; Atkinson, R. *Int. J. Chem. Kinet.* **1990**, *22* (6), 591. doi:10.1002/kin.550220604.

(12) Orlando, J. J.; Tyndall, G. S.; Paulson, S. E. *Geophys. Res. Lett.* **1999**, *26* (14), 2191. doi:10.1029/1999GL900453.

(13) Canosa-Mas, C. E.; Carr, S.; King, M. D.; Shallcross, D. E.; Thompson, K. C.; Wayne, R. P. *Phys. Chem. Chem. Phys.* **1999**, *1* (18), 4195. doi:10.1039/a904613e.

(14) Chuong, B.; Stevens, P. S. *J. Phys. Chem. A* **2003**, *107* (13), 2185. doi:10.1021/jp026036q.

(15) Chuong, B.; Stevens, P. S. *Int. J. Chem. Kinet.* **2004**, *36* (1), 12. doi:10.1002/kin.10167.

(16) Maldotti, A.; Chiorboli, C.; Bignozzi, C. A.; Bartocci, C.; Carassiti, V. *Int. J. Chem. Kinet.* **1980**, *12* (12), 905. doi:10.1002/kin.550121202.

(17) Kerr, J. A.; Sheppard, D. W. *Environ. Sci. Technol.* **1981**, *15* (8), 960. doi:10.1021/es00090a012.

(18) Atkinson, R.; Aschmann, S. M.; Winer, A. M.; Pitts, J. N., Jr. *Int. J. Chem. Kinet.* **1981**, *13* (11), 1133. doi:10.1002/kin.550131104.

(19) Edney, E. O.; Kleindienst, T. E.; Corse, E. W. *Int. J. Chem. Kinet.* **1986**, *18* (12), 1355. doi:10.1002/kin.550181207.

(20) Orlando, J. J.; Tyndall, G. S. *J. Phys. Chem. A* **2002**, *106* (51), 12252. doi:10.1021/jp021530f.

(21) Ochando-Pardo, M.; Nebot-Gil, I.; González-Lafont, Á.; Lluch, J. M. *Chem. Eur. J.* **2007**, *13* (4), 1180. doi:10.1002/chem.200600529.

(22) Olivella, S.; Sole, A. *J. Chem. Theory Comput.* **2008**, *4* (6), 941. doi:10.1021/ct8000798.

(23) Vega-Rodriguez, A.; Alvarez-Idaboy, J. R. *Phys. Chem. Chem. Phys.* **2009**, *11* (35), 7649. doi:10.1039/b906692f.

(24) Frisch, M. J.; Trucks, G. W.; Schlegel, H. B.; Scuseria, G. E.; Robb, M. A.; Cheeseman, J. R.; Zakrzewski, V. G.; Montgomery, J. A.; Stratmann, R. E.; Burant, J. C.; Dapprich, S.; Millam, J. M.; Daniels, A. D.; Kudin, K. N.; Strain, M. C.; Farkas, O.; Tomasi, J.; Barone, V.; Cossi, M.; Cammi, R.; Mennucci, B.; Pomelli, C.; Adamo, C.; Clifford, S.; Ochterski, J.; Petersson, G. A.; Ayala, P. Y.; Cui, Q.; Morokuma, K.; Malick, D. K.; Rabuck, A. D.; Raghavachari, K.; Foresman, J. B.; Cioslowski, J.; Ortiz, J. V.; Stefanov, B. B.; Liu, G.; Liashenko, A.; Piskorz, P.; Komaromi, I.; Gomperts, R.; Martin, R. L.; Fox, D. J.; Keith, T.; Al-Laham, M. A.; Peng, C. Y.; Nanayakkara, A.; Gonzalez, C.; Challacombe, M.; Gill, P. M. W.; Johnson, B. G.; Chen, W.; Wong, M. W.; Andres, J. L.; Head-Gordon, M.; Replogle, E. S.; Pople, J. A. *Gaussian 98W*, Revision 5.1; Gaussian: Pittsburgh, PA, 1998.

(25) Hehre, W. J.; Radom, L.; Schleyer, P. v. R.; Pople, J. A. *Ab initio Molecular Orbital Theory;* Wiley: New York, 1986.

(26) Pople, J. A.; Head-Gordon, M.; Raghavachari, K. *J. Chem. Phys.* **1987**, *87* (10), 5968. doi:10.1063/1.453520.

(27) (a) Fukui, K. *Acc. Chem. Res.* **1981**, *14* (12), 363. doi:10.1021/ar00072a001.; (b) Ishida, K.; Morokuma, K.; Komornicki, A. *J. Chem. Phys.* **1977**, *66* (5), 2153. doi:10.1063/1.434152.

(28) Kendall, R. A.; Dunning, T. H.; Harrison, R. J. *J. Chem. Phys.* **1992**, *96* (9), 6796. doi:10.1063/1.462569.

(29) Durig, J. R.; Qiu, J.; Dehoff, B.; Little, T. S. *Spectrochim. Acta [A]* **1986**, *42*, 89.

(30) Eyring, H. *J. Chem. Phys.* **1935**, *3* (2), 107. doi:10.1063/1.1749604.
(31) Sekušak, S.; Liedl, K. R.; Sabljić, A. *J. Phys. Chem. A* **1998**, *102* (9), 1583. doi:10.1021/jp972449t.
(32) Chuang, Y.-Y.; Coitino, E. L.; Truhlar, D. G. *J. Phys. Chem. A* **2000**, *104* (3), 446. doi:10.1021/jp993661v.

Development of additive isotropic site potential for exchange-repulsion energy, based on intermolecular perturbation theory

Daisuke Yokogawa, Hirofumi Sato, Sergey Gusarov, and Andriy Kovalenko

Abstract: We have developed an additive spherical site potential for exchange-repulsion energy by applying the local density approximation in Hilbert space, the local-site approximation, and the s-type auxiliary basis set to the equation derived from intermolecular perturbation theory. The method efficiently addresses the decomposition of molecular interactions derived from quantum chemistry into additive spherical site potentials, required as force field input in a statistical-mechanical, reference interaction site model (RISM and 3D-RISM), molecular theory of solvation. The present method reproduces the exchange-repulsion energy between simple molecules obtained from quantum chemical calculations.

Key words: exchange-repulsive potential, intermolecular perturbation theory, quantum chemical calculation, force field, reference interaction site model.

Résumé : On a développé un nouveau potentiel de site sphérique et additif pour l'énergie de répulsion d'échange qui est obtenu en appliquant l'approximation de densité locale de l'espace de Hilbert, l'approximation de site local, ainsi que l'ensemble de base auxiliaire de type s à l'équation dérivée de la théorie de la perturbation intermoléculaire. La méthode tient compte exactement de la décomposition des interactions moléculaires dérivées de la chimie quantique en potentiels de site sphériques additifs requis comme donnée du champ de force en mécanique statistique, le modèle de site d'interaction de référence (MSIR et MSIR-3D), théorie moléculaire de solvatation. La présente méthode reproduit l'énergie de répulsion d'échange entre les molécules simples obtenues à l'aide de calculs de la chimie quantique.

Mots-clés : potentiel de répulsion d'échange, théorie de la perturbation intermoléculaire, calcul de chimie quantique, champ de force, modèle du site d'interaction de référence.

[Traduit par la Rédaction]

Introduction

A large number of studies to develop force fields for predicting the interactions between molecules have been performed over the last three decades.[1] In a standard force field, interactions are split up into terms classified, for example, as electrostatic interaction, dispersion interaction, and exchange interaction. Expressions for these interactions are constructed under the assumption that they can be treated as a sum of additive spherical potentials dependent on the distance R between the constituent atoms or interaction sites but not on the molecular orientations. This type of force field makes it possible to study a large system such as a biosystem by molecular simulation with reasonable computational cost. Nowadays, many parameter sets have been proposed.[2–4]

The most important term in the force field at long range is the electrostatic interaction when a molecule is polarized. This interaction has been widely studied for a long time. Fortunately, this interaction is sufficiently well-approximated with point charges assigned on each atom (point charge model) and described as a sum of additive isotropic, Coulomb potentials $1/R$. Nowadays, atomic charges are easily assessed from quantum chemical calculations.[5,6]

At short range, the exchange interaction becomes important. In a standard force field, this interaction is modelled with additive isotropic potentials as well, such as $1/R^{12}$.

Received 9 July 2009. Accepted 21 August 2009. Published on the NRC Research Press Web site at canjchem.nrc.ca on 28 November 2009.

We dedicate this paper to Professor Tom Ziegler, our dear collaborator, with compliments and best wishes of health, prosperity, and scientific joy and further achievements.

D. Yokogawa and H. Sato. Department of Molecular Engineering, Graduate School of Engineering, Kyoto University, Nishikyo-ku, Kyoto 615-8510, Japan.
S. Gusarov. National Institute for Nanotechnology, National Research Council of Canada, 11421 Saskatchewan Drive, Edmonton, AB T6G 2M9, Canada.
A. Kovalenko.[1] National Institute for Nanotechnology, National Research Council of Canada, 11421 Saskatchewan Drive, Edmonton, AB T6G 2M9, Canada; Department of Mechanical Engineering, University of Alberta, 4-9 Mechanical Engineering Building, Edmonton, AB T6G 2G8, Canada.

[1]Corresponding author (e-mail: andriy.kovalenko@nrc-cnrc.gc.ca).

However, determination of its parameters is much more involved than for the electrostatics. One reason is that the interaction originates from the Pauli exclusion principle, which requires an accurate nonlocal, multideterminant representation of the wave function and thus makes it very difficult to derive an additive isotropic potential directly from quantum mechanics. Therefore, parameter sets for exchange interaction are usually empirically adjusted to fit some chemical properties. Although this approach works well for many systems, it is not easy to improve a force field systematically. Theoretical methods to evaluate the exchange potential based on ab initio calculations have also been proposed.[7–11] One of the well established theories is intermolecular perturbation theory (IMPT).[1,7,8] The resulting method can evaluate the energy very accurately.[9,10] However, this is computationally expensive because of the necessity to compute two-electron integrals of the total system.

There have been some approaches to derive the exchange-repulsive potential in a less empirical way, based on ab initio treatment.[12–16] In the effective fragment potential (EFP) method, a very simple equation was derived based on IMPT.[17,18] The potential between molecules is composed of fundamental intermolecular interactions, similar to the SIBFA (sum of interactions between fragments ab initio computed) method.[19] The parameter of each interaction term is generated in a single ab initio calculation; therefore, the integrals required in the calculation are greatly simplified, compared to those in IMPT.

In this work, we derived a simple exchange-repulsion energy potential based on IMPT. This method has the advantage of being fully ab initio, without any semiempirical parameters. The derivation focuses on the following three goals: (1) construct the total potential from additive atomic interaction potentials; (2) have the atomic potentials spherically symmetric; (3) tabulate the site potentials on a spatial grid directly from the matrix elements of the operators projected onto the augmented spherical basis set, rather than calculate the site contributions by brute-force orientational averaging of the six-dimensional intermolecular potential obtained from symmetry-adapted perturbation theory or its derivatives. Such site potentials are typically required in a self-consistent field coupling of quantum chemical methods with statistical-mechanical, molecular theory of solvation,[20] such as KS-DFT/3D-RISM-KH[21,22] and CASSCF/3D-RISM-KH.[23] As classical force fields typically use terms constructed along the lines of requirements (1) and (2), the present strategy will be helpful to systematically improve the classical force field, based on ab initio calculations.

Fig. 1. Exchange-repulsion energy of the model system, calculated at levels E_{S2}^{exch}, $E_{S2}^{exch} + E_{S4,P4}^{exch}$, and E^{XR}. The exponent of ABS is 2.0.

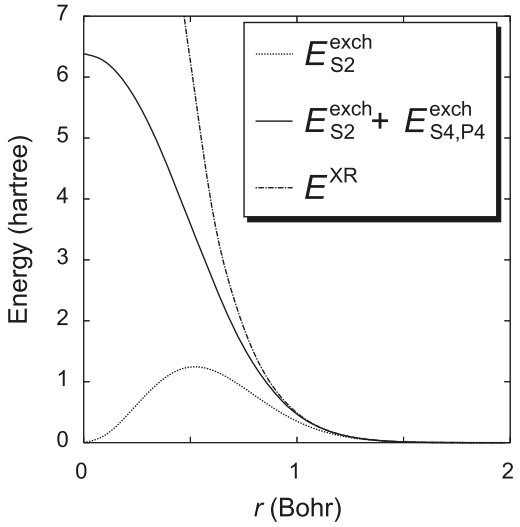

Method

Under the condition of orthogonality of the orbitals inside the isolated molecules A and B, exchange-repulsion energy between the molecules can be expressed with intermolecular overlap integrals of atomic orbitals (AOs),[7,8,18]

$$
\begin{aligned}
E^{\mathrm{exch}} = & -\frac{1}{2}\sum_{\mu\delta}\sum_{\nu\gamma} P^A_{\mu\delta} P^B_{\nu\gamma} \langle \mu\nu|\delta\gamma\rangle - \frac{1}{2}\sum_{\mu\delta}\sum_{\nu\gamma} P^A_{\mu\delta} P^B_{\nu\gamma} \langle \mu|\nu\rangle \left[V^A_{\delta\gamma} + G^A_{\delta\gamma} + V^B_{\delta\gamma} + G^B_{\delta\gamma} \right] \\
& + \frac{1}{4}\sum_{\mu\eta}\sum_{\nu\gamma} P^A_{\mu\eta} P^B_{\nu\gamma} \langle \mu|\nu\rangle \left[\sum_{\delta\theta} P^A_{\delta\theta} \langle \delta|\gamma\rangle (V^B_{\eta\theta} + J^B_{\eta\theta}) + \sum_{\delta\theta} P^B_{\delta\theta} \langle \eta|\delta\rangle (V^A_{\theta\gamma} + J^A_{\theta\gamma}) \right] \\
& - \frac{1}{8}\sum_{\mu\eta}\sum_{\nu\gamma}\sum_{\delta\theta}\sum_{\varepsilon\omega} P^A_{\mu\eta} P^B_{\nu\gamma} P^A_{\delta\theta} P^B_{\varepsilon\omega} \langle \mu|\nu\rangle \langle \delta|\varepsilon\rangle \langle \eta\theta|\omega\gamma\rangle \\
& - \frac{1}{8}\sum_{\mu\delta}\sum_{\gamma\eta} P^A_{\mu\delta} P^B_{\gamma\eta} \langle \delta|\gamma\rangle \left[\sum_{\nu\theta} P^A_{\nu\theta} \langle \eta|\theta\rangle K^B_{\mu\nu} + \sum_{\nu\theta} P^B_{\nu\theta} \langle \mu|\theta\rangle K^A_{\eta\nu} \right] \\
& + \frac{1}{2}\sum_{\mu\eta}\sum_{\nu\theta}\sum_{\gamma\omega}\sum_{\delta\varepsilon} P^A_{\mu\eta} P^B_{\nu\theta} P^A_{\gamma\omega} P^B_{\delta\varepsilon} \langle \eta|\theta\rangle \langle \omega|\varepsilon\rangle \langle \mu\nu|\gamma\delta\rangle \\
= & \; E^{\mathrm{exch}}_{S2} + E^{\mathrm{exch}}_{S4,P4}
\end{aligned}
\qquad [1]
$$

Fig. 2. Exchange-repulsion energies between H_2O and molecule X (X = H_2O, NH_3, CH_4, Cl^-, and Na^+) calculated by the present method (solid line), EFP (dashed line), KM (dotted line), and LJ (dash-dotted line). (*a*) water oxygen site approaching molecule X (approach I); (*b*) water hydrogen sites approaching molecule X (approach II).

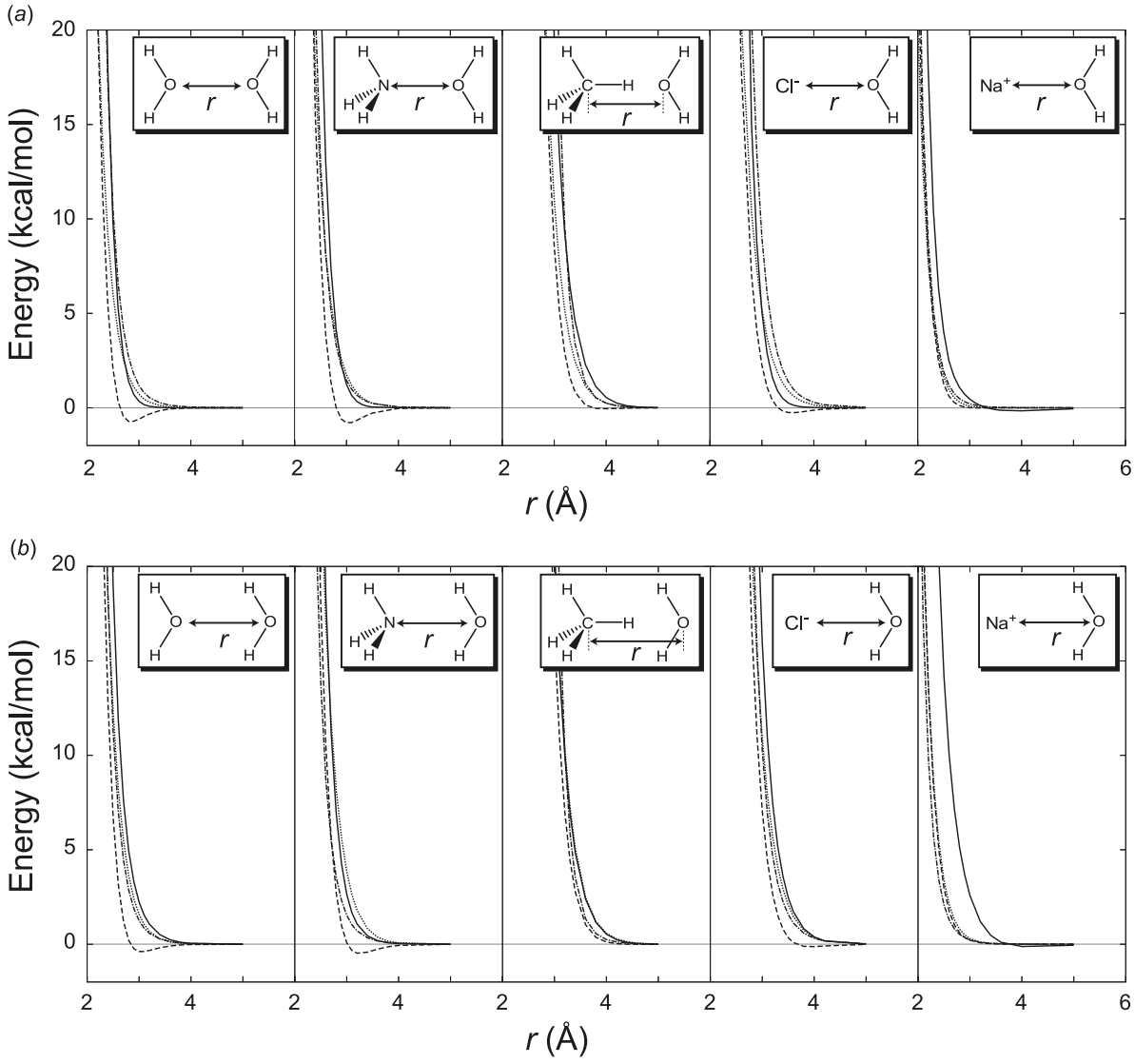

where $\mathbf{P}^X$ is the density matrix for molecule X (X = *A* or *B*), $<\mu|\nu>$ is the overlap matrix, $V^X_{\mu\nu}$ is the nucleus attraction integral in the field of molecule X, and $<\mu\nu|\delta\gamma>$ is the electron repulsion integral. $\mathbf{J}^X$ and $\mathbf{K}^X$ are the Coulomb and exchange matrices and $\mathbf{G}^X$ is defined as

$$[2] \qquad G^X_{\mu\nu} = J^X_{\mu\nu} - \frac{1}{2}K^X_{\mu\nu}$$

The exchange-repulsion energy $E^{\text{exch}}_{\text{S2}}$ to the second order of $<\mu|\nu>$ has a familiar form obtained in previous work.[7] $E^{\text{exch}}_{\text{S4,P4}}$ is the exchange-repulsion energy to the fourth order of $<\mu|\nu>$ and to the fourth order of $\mathbf{P}^X$.

Equation [1] can be simplified by density fitting. The electron density is expressed with AOs as follows:

$$[3] \qquad \rho^X(\mathbf{r}) = \sum_{\mu\nu} P^X_{\mu\nu}\phi_\mu(\mathbf{r})\phi_\nu(\mathbf{r})$$

This value is fitted by the auxiliary basis set $\tilde{\phi}$ with coefficients *d*,

$$[4] \qquad \tilde{\rho}^X(\mathbf{r}) = \sum_{\nu} d^X_\nu \tilde{\phi}_\nu(\mathbf{r})\tilde{\phi}_\nu(\mathbf{r})$$

Fitting $\rho(\mathbf{r})$ with $\tilde{\rho}(\mathbf{r})$ using proper auxiliary basis set (ABS) $\tilde{\phi}$ can reproduce the effect of considerable off-diagonal elements of the density matrix. The use of *d* and $\tilde{\phi}$ leads to the following equation:

$$
\begin{aligned}
E^{\mathrm{exch}} = & -\frac{1}{2}\sum_{\mu}\sum_{\nu} d_{\mu}^{A} d_{\nu}^{B} \langle \tilde{\mu}\,\tilde{\nu} \,|\tilde{\mu}\,\tilde{\nu}\rangle - \frac{1}{2}\sum_{\mu}\sum_{\nu} d_{\mu}^{A} d_{\nu}^{B} \langle \tilde{\mu}\,|\tilde{\nu}\rangle \left[V_{\mu\nu}^{A} + \widehat{G}_{\mu\nu}^{A} + V_{\mu\nu}^{B} + \widehat{G}_{\mu\nu}^{B} \right] \\
& + \frac{1}{4}\sum_{\mu}\sum_{\nu} d_{\mu}^{A} d_{\nu}^{B} \langle \tilde{\mu}\,|\tilde{\nu}\rangle \left[\sum_{\delta} d_{\delta}^{A} \langle \tilde{\delta}\,|\tilde{\nu}\rangle (V_{\mu\delta}^{B} + \widehat{J}_{\mu\delta}^{B}) + \sum_{\delta} d_{\delta}^{B} \langle \tilde{\mu}\,|\tilde{\delta}\rangle (V_{\delta\nu}^{A} + \widehat{J}_{\delta\nu}^{A}) \right] \\
& - \frac{1}{8}\sum_{\mu}\sum_{\nu}\sum_{\delta}\sum_{\varepsilon} d_{\mu}^{A} d_{\nu}^{B} d_{\delta}^{A} d_{\varepsilon}^{B} \langle \tilde{\mu}\,|\tilde{\nu}\rangle \langle \tilde{\delta}\,|\tilde{\varepsilon}\rangle \langle \tilde{\mu}\,\tilde{\delta}\,|\tilde{\varepsilon}\,\tilde{\nu}\rangle \\
& - \frac{1}{8}\sum_{\mu}\sum_{\gamma} d_{\mu}^{A} d_{\gamma}^{B} \langle \tilde{\mu}\,|\tilde{\gamma}\rangle \left[\sum_{\nu} d_{\nu}^{A} \langle \tilde{\gamma}\,|\tilde{\nu}\rangle \widehat{K}_{\mu\nu}^{B} + \sum_{\nu} d_{\nu}^{B} \langle \tilde{\mu}\,|\tilde{\nu}\rangle \widehat{K}_{\gamma\nu}^{A} \right] \\
& + \frac{1}{2}\sum_{\mu}\sum_{\nu}\sum_{\gamma}\sum_{\delta} d_{\mu}^{A} d_{\nu}^{B} d_{\gamma}^{A} d_{\delta}^{B} \langle \tilde{\mu}\,|\tilde{\nu}\rangle \langle \tilde{\gamma}\,|\tilde{\delta}\rangle \langle \tilde{\mu}\,\tilde{\nu}\,|\tilde{\gamma}\,\tilde{\delta}\rangle
\end{aligned} \tag{5}
$$

The matrices $\widehat{\mathbf{G}}^{X}$, $\widehat{\mathbf{J}}^{X}$, and $\widehat{\mathbf{K}}^{X}$ are given by

$$\widehat{G}_{\mu\nu}^{X} = \widehat{J}_{\mu\nu}^{X} - \frac{1}{2}\widehat{K}_{\mu\nu}^{X} \tag{6}$$

$$\widehat{J}_{\mu\nu}^{X} = \sum_{\gamma} d_{\gamma}^{X} \langle \tilde{\mu}\,\tilde{\nu}\,|\tilde{\gamma}\,\tilde{\gamma}\rangle \tag{7}$$

$$\widehat{K}_{\mu\nu}^{X} = \sum_{\gamma} d_{\gamma}^{X} \langle \tilde{\mu}\,\tilde{\gamma}\,|\tilde{\gamma}\,\tilde{\nu}\rangle \tag{8}$$

Our first goal is to derive the equation for the decomposition of the exchange-repulsion energy

$$E^{\mathrm{exch}} = \sum_{I\in A}\sum_{J\in B} E_{IJ}^{\mathrm{exch}} \tag{9}$$

where **I** and **J** refer to atoms belonging to molecules *A* and *B*, respectively. Based on eq. [5], the component E_{IJ}^{exch} is defined as

$$
\begin{aligned}
E_{IJ}^{\mathrm{exch}} \equiv & -\frac{1}{2}\sum_{\mu\in I}\sum_{\nu\in J} d_{\mu}^{A} d_{\nu}^{B} \langle \mu\nu|\mu\nu\rangle - \frac{1}{2}\sum_{\mu\in I}\sum_{\nu\in J} d_{\mu}^{A} d_{\nu}^{B} \langle \mu|\nu\rangle \left[V_{\mu\nu}^{(\mu)} + G_{\mu\nu}^{(\mu)} + V_{\mu\nu}^{(\nu)} + G_{\mu\nu}^{(\nu)} \right] \\
& + \frac{1}{4}\sum_{\mu\in I}\sum_{\nu\in J} d_{\mu}^{A} d_{\nu}^{B} \langle \mu|\nu\rangle \left[\sum_{\delta\in I} d_{\delta}^{A} \langle \delta|\nu\rangle (V_{\mu\delta}^{(\nu)} + J_{\mu\delta}^{(\nu)}) + \sum_{\delta\in I} d_{\delta}^{B} \langle \mu|\delta\rangle \left(V_{\delta\nu}^{(\mu)} + J_{\delta\nu}^{(\mu)} \right) \right] \\
& - \frac{1}{8}\sum_{\mu\in I}\sum_{\nu\in J}\sum_{\delta\in I}\sum_{\varepsilon\in J} d_{\mu}^{A} d_{\nu}^{B} d_{\delta}^{A} d_{\varepsilon}^{B} \langle \mu|\nu\rangle \langle \delta|\varepsilon\rangle \langle \mu\delta|\varepsilon\nu\rangle - \frac{1}{8}\sum_{\mu\in I}\sum_{\gamma\in J} d_{\mu}^{A} d_{\gamma}^{B} \langle \mu|\gamma\rangle \left[\sum_{\nu\in I} d_{\nu}^{A} \langle \gamma|\nu\rangle K_{\mu\nu}^{(\gamma)} + \sum_{\nu\in J} d_{\nu}^{B} \langle \mu|\nu\rangle K_{\gamma\nu}^{(\mu)} \right] \\
& + \frac{1}{2}\sum_{\mu\in I}\sum_{\nu\in J}\sum_{\gamma\in I}\sum_{\delta\in J} d_{\mu}^{A} d_{\nu}^{B} d_{\gamma}^{A} d_{\delta}^{B} \langle \mu|\nu\rangle \langle \gamma|\delta\rangle \langle \mu\nu|\gamma\delta\rangle
\end{aligned} \tag{10}
$$

The matrix elements $V_{\mu\gamma}^{(\nu)}$, $G_{\mu\gamma}^{(\nu)}$, $J_{\mu\gamma}^{(\nu)}$, and $K_{\mu\gamma}^{(\nu)}$ are given by

$$V_{\mu\gamma}^{(\nu)} = -Z_{I_\nu} \left\langle \mu \left| \frac{1}{|\mathbf{r} - \mathbf{R}_{I_\nu}|} \right| \nu \right\rangle \tag{11}$$

$$G_{\mu\gamma}^{(\nu)} = J_{\mu\gamma}^{(\nu)} - \frac{1}{2}K_{\mu\gamma}^{(\nu)} \tag{12}$$

$$J_{\mu\gamma}^{(\nu)} = \sum_{\eta} d_{\eta}^{I_\nu} \langle \mu\gamma|\eta\eta\rangle \tag{13}$$

$$K_{\mu\gamma}^{(\nu)} = \sum_{\eta} d_{\eta}^{I_\nu} \langle \mu\eta|\eta\gamma\rangle \tag{14}$$

where $\mathbf{I}_\nu$ is the atom to which AO χ_ν belongs, Z_I is the atomic number of atom **I**, and $\{d_\eta^{I_\nu}\}$ is the density coefficient which is assigned to atom $\mathbf{I}_\nu$.

To achieve our second goal, E_{IJ}^{exch} defined in eq. [10] has to be evaluated only in terms of the distance between atoms **I** and **J**. Applying s-type ABS makes each component in E_{IJ}^{exch} very simple. For example, the two-electron integral $\langle \mu\nu|\gamma\delta\rangle$ in the last term of eq. [10] is expressed as

$$
\begin{aligned}
\langle \mu\nu|\gamma\delta\rangle = & \left[\frac{\sqrt{\alpha_\mu \alpha_\nu}}{\alpha_\mu + \alpha_\nu} \right]^{\frac{3}{2}} \left[\frac{\sqrt{\alpha_\gamma \alpha_\delta}}{\alpha_\gamma + \alpha_\delta} \right]^{\frac{3}{2}} \\
& \times \frac{8}{R_{AB}} \mathrm{erf}\left[\sqrt{\frac{(\alpha_\mu + \alpha_\nu)(\alpha_\gamma + \alpha_\delta)}{\alpha_\mu + \alpha_\nu + \alpha_\gamma + \alpha_\delta}} \right]
\end{aligned} \tag{15}
$$

Fig. 3. Basis set dependence of the exchange-repulsion energy between water molecules in approach II, evaluated by the present method. Also shown are the values of the energy at $r = 2.6$ Å evaluated by MK with cc-pVDZ, cc-pVTZ, and aug-cc-pVTZ, from bottom to top, respectively. The reaction coordinate is the same as in Fig. 2*b* for water molecules.

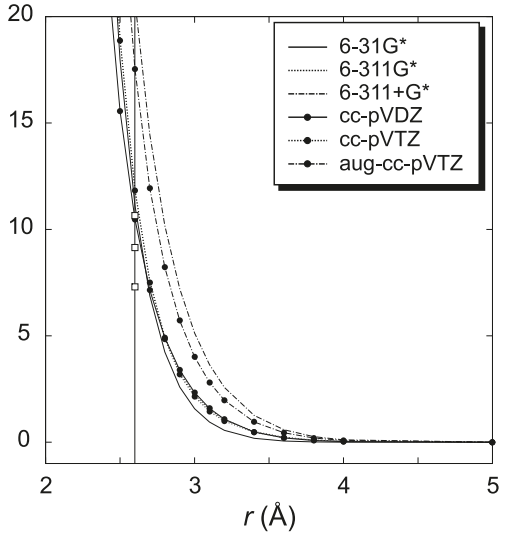

where orbitals ϕ_ν and ϕ_μ are assigned to atom **I**, ϕ_γ and ϕ_δ to atom **J**, and α_χ ($\chi = \nu$, μ, γ, and δ) is the index of the exponent of ϕ_χ. The strategy for preparing such an ABS and determining the d coefficients was described in detail in the previous work.[24,25]

In statistical-mechanical studies of classical systems, many kinds of empirical potentials for exchange-repulsion energy are employed. Interestingly, even a hard-sphere potential, infinite if atom cores overlap and zero otherwise, can account for some chemical properties of liquid systems.[1,26] This means that the atomic radius (the position where the potential becomes very large) is a very important point in the exchange-repulsion energy. In the following discussion, we focus on the shape and radius evaluated by the present method rather than on the numerical values, and compare them with those obtained from ab initio calculations and empirical potentials.

Application to water and simple molecules and ions

Before applying eq. [9] to the molecular system, the exchange-repulsive potential in a model system is evaluated. In this system, two atoms with $Z = 2$ are prepared and then one Gaussian AO is employed for each atom,

$$[16] \qquad \phi(\mathbf{r}) = \left(\frac{2\alpha}{\pi}\right)^{\frac{3}{4}} \exp(-\alpha(\mathbf{r}-\mathbf{R})^2)$$

where **R** is the position of each atom. The number of electrons for each atom is two (each atom is neutral). With the basis set, eqs. [1] and [9] reduce to the same equation. Figure 1 presents the exchange-repulsive potentials for the component E_{S2}^{exch} and $E_{S2}^{exch} + E_{S4,P4}^{exch}$ versus the interatomic distance r for $\alpha = 2.0$. For comparison, the exchange-repulsion energies without the truncation of the AO overlap (E^{XR}, eq. [13] in [18]) are also calculated and shown in Fig. 1. The exchange-repulsion energy calculated as E_{S2}^{exch} becomes zero at $r = 0$. Because the higher term, larger than the second order of AO overlap, is truncated in E_{S2}^{exch}, it gets far from E^{XR} in the region where the AO overlap is large. However, the component $E_{S4,P4}^{exch}$ improves the potential in that region.

The exchange-repulsion energies between H_2O and molecules H_2O, NH_3, CH_4, Cl^-, and Na^+ were calculated from eq. [9]. The geometry optimization of H_2O, NH_3, and CH_4, and calculation of the exchange-repulsion energy were performed at the HF/6–311G* level. For comparison, the exchange-repulsion energy was also evaluated by using the Kitaura–Morokuma (KM) analysis,[27] the EFP,[12] and the Lennard-Jones potential. The KM analysis is one of the methods used in decomposing the total intermolecular interaction energy into specific energy components. Because the KM analysis is widely employed to analyze intermolecular interactions and its definition is very clear, we took the KM exchange-repulsion energy as a reference. It should be noted that the surfaces evaluated by EFP show some areas of negative values in the panels of water–water and water–NH_3 in Fig. 2. This effect is probably due to the fact that the equation employed in EFP is constructed from many interaction terms,[18] and the values of the exchange-repulsion potential come from a cancellation of the large positive and negative terms. The reasonable balance might have been lost in the regions where the value evaluated by the EFP implementation we used is negative. The repulsive part of the Lennard-Jones potential was calculated using the SPC-like potential,[28] with a correction concerning the Lennard-Jones parameters of the hydrogen sites ($\sigma = 1.0$ Å, $\varepsilon = 0.056$ kcal/mol) for H_2O, and the OPLS-AA all-atom models[29] for NH_3, CH_4, Cl^-, and Na^+. All calculations were performed by using our in-house code implemented in the GAMESS software package.[30]

The exchange-repulsion energy surfaces were calculated for H_2O approaching molecule X in two directions: the oxygen site approaching molecule X (approach I), and the hydrogen site approaching molecule X (approach II). Figures 2*a* and 2*b* present the corresponding energy surfaces; the reaction coordinates for approaches I and II are also depicted in the right upper panel of each figure. Except for $Na^+ \cdot H_2O$ in approach II, the shapes calculated by the present method are close to those evaluated by using quantum chemical calculation and standard classical potentials. The strategy of MK analysis is summarized well by Mo et al.[31] This also shows that the atomic radii evaluated with these methods are almost the same. Although the present method somewhat overestimates the repulsion for $Na^+ \cdot H_2O$ in approach II, this does not lead to severe problems, because the electrostatic interaction between Na^+ and the positively charged H site of H_2O is dominant, compared to the exchange-repulsion energy.

To check the dependence of the results of the present method on the basis set, we calculated the exchange-repulsion energy between water molecules in approach II at the HF/(6–31G*, 6–311+G*, cc-pVDZ, cc-pVTZ, and aug-cc-pVTZ) levels. The resulting energy surfaces are shown in Fig. 3, including the energy at $r = 2.6$ Å evaluated by the

KM analysis with cc-pVDZ, cc-pVTZ, and aug-cc-pVTZ. The calculation using the basis sets without diffuse functions (6–31G*, 6–311G*, cc-pVDZ, and cc-pVTZ) gave almost the same shape for the energy surface. The energies, which become very large (r = 2.6 Å), are very close to those calculated by MK with aug-cc-pVTZ. On the other hand, the energy surfaces evaluated with 6–311+G* and aug-cc-pVTZ are somewhat repulsive. This is because the electron distribution determined by the present density-fitting approach is broad, so the overlap of electrons between two waters becomes large.

Conclusions

We have proposed an ab initio IMPT-based scheme to derive the exchange-repulsive intermolecular energy, broken down into additive spherical-site potentials. This strategy is capable of becoming an important bridge in a multiscale scheme that will produce classical force fields for molecular modeling with high accuracy from ab initio calculations.

Acknowledgments

We gratefully acknowledge the financial support from the Grant-in Aid for "Molecular Theory for Real Systems" (461), from the Global COE Program "International Center for Integrated Research and Advanced Education in Materials Science" (No. B-09), and from the Ministry of Education, Culture, Sports, Science and Technology (MEXT) in Japan. D.Y. acknowledges the Grant-in Aid for JSPS Fellows, and thanks the National Institute for Nanotechnology (NINT), Alberta, Canada, for the hospitality during his visit there. S.G. and A.K. are supported by the National Research Council (NRC) of Canada.

References

(1) Stone, A. J. *The Theory of Intermolecular Forces*; Clarendon Press: Oxford, 2000.
(2) Cornell, W. D.; Cieplak, C. I.; Bayly, I. R.; Gould, K. M.; Merz, K. M., Jr.; Ferguson, D. M.; Kollman, P. A. *J. Am. Chem. Soc.* **1995**, *117* (3), 5179. doi:10.1021/ja00108a006.
(3) Neria, E.; Fischer, S.; Karplus, M. *J. Chem. Phys.* **1996**, *105* (5), 1902. doi:10.1063/1.472061.
(4) Weiner, S. J.; Kollman, P. A.; Case, D. A.; Singh, U. C.; Ghio, C.; Alagona, G.; Profeta, S., Jr.; Weiner, P. *J. Am. Chem. Soc.* **1984**, *106* (3), 765–784. doi:10.1021/ja00315a051.
(5) Besler, B. H.; Merz, K. M., Jr.; Kollman, P. A. *J. Comput. Chem.* **1990**, *11* (4), 431–439. doi:10.1002/jcc.540110404.
(6) Bayly, C. I.; Cieplak, P.; Cornell, W. D.; Kollman, P. A. *J. Phys. Chem.* **1993**, *97* (40), 10269–10280. doi:10.1021/j100142a004.
(7) Murrell, J. N.; Shaw, G. *J. Chem. Phys.* **1967**, *46* (5), 1768. doi:10.1063/1.1840933.
(8) Jeziorski, B.; Bulski, M.; Piela, L. *Int. J. Quantum Chem.* **1976**, *10* (2), 281–297. doi:10.1002/qua.560100208.
(9) Jeziorski, B.; Moszynski, R.; Szalewicz, K. *Chem. Rev.* **1994**, *94* (7), 1887–1930. doi:10.1021/cr00031a008.
(10) Heßelmann, A.; Jansen, G.; Schütz, M. *J. Chem. Phys.* **2005**, *122* (1), 014103. doi:10.1063/1.1824898.
(11) Liu, S. *J. Chem. Phys.* **2007**, *126* (24),o. 244103. doi:10.1063/1.2747247. PMID:17614533.
(12) Gordon, M. S.; Freitag, M. A.; Bandyopadhyay, P.; Jensen, J. H.; Kairys, V.; Stevens, W. J. *J. Phys. Chem. A* **2001**, *105* (2), 293–307. doi:10.1021/jp002747h.
(13) Brdarski, S.; Karlström, G. *J. Phys. Chem. A* **1998**, *102* (42), 8182–8192. doi:10.1021/jp9819893.
(14) Söderhjelm, P.; Karlström, G.; Ryde, U. *J. Chem. Phys.* **2006**, *124* (24),o. 244101. doi:10.1063/1.2206182. PMID:16821967.
(15) Katsuki, S. *J. Chem. Phys.* **1993**, *98* (1), 496. doi:10.1063/1.464644.
(16) Yamazaki, T.; Sato, H.; Hirata, F. *J. Chem. Phys.* **2003**, *119* (13), 6663. doi:10.1063/1.1604381.
(17) Jensen, J. H.; Gordon, M. S. *Mol. Phys.* **1996**, *89* (5), 1313–1325. doi:10.1080/00268979609482543.
(18) Jensen, J. H. *J. Chem. Phys.* **2001**, *114* (20), 8775. doi:10.1063/1.1356017.
(19) Gresh, N.; Claverie, P.; Pullman, A. *Theor. Chim. Acta* **1984**, *66* (1), 1–20. doi:10.1007/BF00577135.
(20) *Molecular Theory of Solvation*; Hirata, F., Ed.;Understanding Chemical Reactivity;Kluwer Academic Publishers: Dordrecht, 2003, Vol. 24.
(21) Kovalenko, A.; Hirata, F. *J. Chem. Phys.* **1999**, *110* (20), 10095. doi:10.1063/1.478883.
(22) Gusarov, S.; Ziegler, T.; Kovalenko, A. *J. Phys. Chem. A* **2006**, *110* (18), 6083–6090. doi:10.1021/jp054344t. PMID:16671679.
(23) Sato, H.; Kovalenko, A.; Hirata, F. *J. Chem. Phys.* **2000**, *112* (21), 9463. doi:10.1063/1.481564.
(24) Gill, P. M. W.; Johnson, B. G.; Pople, J. A.; Taylor, S. W. *J. Chem. Phys.* **1992**, *96* (9), 7178. doi:10.1063/1.462530.
(25) Yokogawa, D.; Sato, H.; Sakaki, S. *J. Chem. Phys.* **2007**, *126* (24),o. 244504. doi:10.1063/1.2742380. PMID:17614561.
(26) Hansen, J. P.; McDonald, I. R. *Theory of Simple Liquids*; Academic: London, 1986; 2nd ed.
(27) Kitaura, K.; Morokuma, K. *Int. J. Quantum Chem.* **1976**, *10* (2), 325–340. doi:10.1002/qua.560100211.
(28) Berendsen, H. J. C.; Postma, J. P. M.; van Gunsteren, W. F.; Hermans, J. In *Intermolecular Forces,* Proceedings of the 14th Jerusalem Symposium on Quantum Chemistry and Biochemistry; Jerusalem, Israel, April 13–16, 1981; Pullman, R., Ed.; Reidel: Dordrecht, 1981; p. 331.
(29) Jorgensen, W. L.; Maxwell, D. S.; Tirado-Rives, J. *J. Am. Chem. Soc.* **1996**, *118* (45), 11225–11236. doi:10.1021/ja9621760.
(30) Schmidt, M. W.; Baldridge, K. K.; Boatz, J. A.; Elbert, S. T.; Gordon, M. S.; Jensen, J. H.; Koseki, S.; Matsunaga, N.; Nguyen, K. A.; Su, S.; Windus, T. L.; Dupuis, M.; Montgomery, J. A. *J. Comput. Chem.* **1993**, *14* (11), 1347–1363. doi:10.1002/jcc.540141112.
(31) Mo, Y.; Gao, J.; Peyerimhoff, S. D. *J. Chem. Phys.* **2000**, *112* (13), 5530. doi:10.1063/1.481185.

A facile method for the preparation of sugar orthoesters promoted by anhydrous sodium bicarbonate

Shanqiao Wei, Jinzhong Zhao, and Huawu Shao

Abstract: A facile and eco-friendly method for the preparation of sugar orthoesters by using anhydrous sodium bicarbonate is described. Various sugar orthoesers, including sugar–sugar orthoesters, were synthesized in good-to-excellent yields by the reaction of a protected glycosyl bromide with an alcohol or sugar.

Key words: sugar orthoesters, anhydrous sodium bicarbonate, protected glycosyl bromide.

Résumé : On a développé une méthode facile et écologique de préparation d'orthoesters de sucres utilisant le bicarbonate de sodium anhydre. On a réalisé la synthèse de divers orthoesters de sucres, y compris des orthoesters de sucre-sucre, avec des rendements allant de bons à excellents en procédant à la réaction d'un bromure de glycosyle protégé avec un alcool ou un sucre.

Mots-clés : orthoesters de sucres, bicarbonate de sodium anhydre, bromure de glycosyle protégé.

[Traduit par la Rédaction]

Introduction

Sugar 1,2-orthoesters are some of the most important intermediates in organic synthesis,[1,2] especially in the oligosaccharide synthesis.[3–7] Sugar 1,2-orthoesters are classic glycosyl donors and can be efficiently converted to the corresponding 1,2-*trans*-glycosides by the action of protonic or Lewis acids, such as TMSOTf,[8] $BF_3{\cdot}Et_2O$,[9a] and TfOH.[9b] Sugar 1,2-orthoesters are also extremely practical for the selective protection of a pyranose ring while the other acetyl groups on the 3, 4, and 6 positions are converted to benzyl groups, and so forth. At present, there are several methods in the literature for the preparation of carbohydrate 1,2-orthoesters.[10,11] The well-known method involves the treatment of peracetylated or perbenzoylated glycosyl bromides with alcohols in the presence of a quaternary ammonium salt[12] or silver triflate[5,13] and an organic base, usually *syn*-collidine or 2,6-lutidine.[14] It is necessary to utilize two kinds of reagents, quaternary ammonium salt and bulky amine compound, for the reaction to occur.[11a,15] Although the method has been extensively used, there is one large disadvantage: the use of a smelly, toxic, and eco-unfriendly organic base. Knowing the broad spectrum of the significant applications of sugar orthoesters, we have focused our interest on improving the synthesis of sugar orthoesters. Herein, a facile, less toxic, and efficient procedure for the synthesis of 1,2-orthoesters, including sugar–sugar orthoesters, by using anhydrous sodium bicarbonate instead of an organic base is reported.[15,16]

Received 21 May 2009. Accepted 4 September 2009. Published on the NRC Research Press Web site at canjchem.nrc.ca on 28 November 2009.

S. Wei, J. Zhao, and H. Shao.[1] Natural Products Research Centre, Chengdu Institute of Biology, Chinese Academy of Sciences, Chengdu 610041, China.

[1]Corresponding author (e-mail: shaohw@cib.ac.cn).

Result and discussion

Our studies started with the reaction of peracetylated glucopyranosyl bromide with methanol in the presence of tetrabutylammonium bromide, anhydrous sodium bicarbonate, and a 4 Å molecular sieve in dry acetonitrile solvent (Scheme 1). The reaction was carried out at room temperature for 4 h, affording the glucopyranosyl methyl orthoester in an 86% yield (Table 1, entry 1). To optimize the method, we used toluene, 1,2-dichlorethane, *N*,*N*-dimethylformamide (DMF), and tetrahydrofuran (THF), respectively, as the solvent, and afforded the target product **2** in various yields (Table 1, entries 2–5).

To establish the feasibility of this reaction as a general method for the preparation of 1,2-orthoesters (Scheme 2), we carried out the synthesis of 3,4,6-tri-*O*-acetyl mannose, 3,4,6-tri-*O*-acetyl galactose, 3,4-di-*O*-acetyl rhamnose orthoesters, and 3,4,6-tri-*O*-benzoyl mannose orthoester in good to excellent yields, and the results are shown in Table 2 (entries 1–4). Since 6-*O*-tosyl and 6-*O*-mesyl of these orthoesters can be easily substituted by other groups, the library of sugar orthoesters is greatly expanded. However, the synthesis of 6-*O*-tosyl and 6-*O*-mesyl orthoesters has not been reported in the literature. Herein, with the suitable protocol in hand, 6-*O*-mesyl and 6-*O*-tosyl mannopyranosyl bromide were treated by using various alcohols such as methanol, isopropyl alcohol, and allyl alcohol, and the corresponding orthoesters (Table 2, entries 5–10). 6-*O*-Mesyl orthosters **13** and **14** (Table 2, entries 5 and 6) and 6-*O*-tosyl orthoster **19** (Table 2, entry 11) were obtained in good yields. Whereas 6-*O*-mesyl orthoesters **15–18** (Table 2, entries 7–10) and 6-*O*-tosyl orthoesters **20** and **21** (Table 2, entries 12 and 13) were obtained in modest yields. The

Scheme 1. The synthesis of glucopyranosyl methyl orthoester.

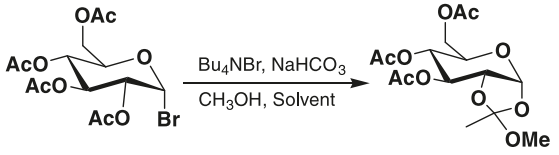

1 2

Table 1. Optimization of the synthesis of glucopyranosyl methyl orthoester.

Entry	Slovent	Time (h)	Yield (%)
1	MeCN	3	86
2	Toluene	6	69
3	$ClCH_2CH_2Cl$	6	71
4	DMF	4	60
5	THF	8	75

sugar–sugar orthoesters are extremely important intermediates for oligosaccharide synthesis. Comparing simple sugar orthoesters, the reaction pathways of sugar–sugar orthoesters are relatively simplified for oligosaccharide preparation; the consideration is mainly focused on intra- and inter-molecular rearrangement of the alkoxide.[8a] Sugar–sugar orthoesters are usually synthesized by the reaction of a glycosyl bromide donor with a glycosyl acceptor with only one free hydroxyl group in dichloromethane in the presence of silver triflate and 2,4-lutidine.[8a] Although this method is efficient, both silver triflate and 2,4-lutidine are toxic and expensive. We hoped that our newly developed method could be applied to the synthesis of sugar–sugar orthoesters. Hence, **3** and **22** were treated in the presence of tetrabutylammonium bromide and anhydrous sodium bicarbonate, the reaction was completed at room temperature for 12 h, and readily afforded the sugar–sugar orthoester **24** in an excellent yield (90%). Encouraged by the success in synthesizing **24**, we subsequently prepared sugar–sugar orthoesters **25**–**28** in good yields (Table 2, entries 15–18).

In summary, we developed a facile and effective protocol for the synthesis of various sugar 1,2-orthoesters and sugar–sugar orthoesters by using anhydrous sodium bicarbonate as an inexpensive and environmentally friendly base. The approach, in terms of low toxicity of reagents, simplicity, economy, and efficiency, will be a general, useful, and attractive strategy for the synthesis of sugar 1,2-orthoesters.

Scheme 2. The synthesis of glucopyranosyl various orthoester.

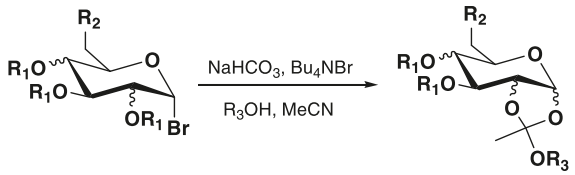

Experimental

Reactions were monitored by thin layer chromatography (TLC) using silica gel HSGF254 plates. Flash chromatography was performed using silica gel HG/T2354–92. ^1H and ^{13}C NMR (600 and 150 MHz, respectively) spectra

Table 2. Preparation for various orthoesters using anhydrous sodium bicarbonate.

Entry	Glycosyl bromide	ROH	Product	Yield (%)
1	3	methanol	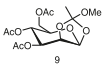 9	84
2	4	methanol	10	80
3	5	methanol	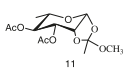 11	66
4	6	methanol	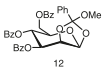 12	91
5	7	methanol	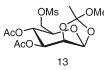 13	88
6	7	ethanol	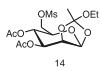 14	83
7	7	allyl alcohol	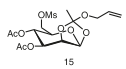 15	77
8	7	propynol	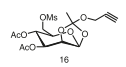 16	70
9	7	isopropyl alcohol	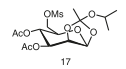 17	60
10	7	benzylalcohol	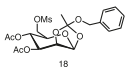 18	69
11	8	methanol	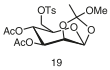 19	80
12	8	ethanol	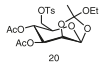 20	78
13	8	propynol	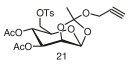 21	71
14	3	22	24	90
15	5	22	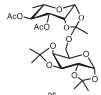 25	76
16	1	22	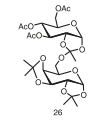 26	78
17	4	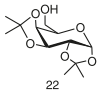 22	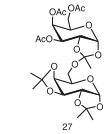 27	78
18	3	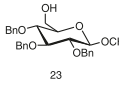 23	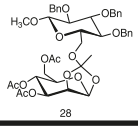 28	80

were recorded in $CDCl_3$. ^1H NMR chemical shifts are reported in ppm (δ) relative to tetramethylsilane (TMS) with the solvent resonance employed as the internal standard ($CDCl_3$, δ 7.26 ppm). Data are reported as follows: chemical shift, multiplicity (s = singlet, d = doublet, t = triplet, m = multiplet), integration, and coupling constants (Hz). ^{13}C NMR chemical shifts are reported in ppm from tetramethylsilane (TMS) with the solvent resonance as the internal standard ($CDCl_3$, δ 77.0 ppm). HR-MS (ESI) spectra were recorded on BioTOF Q. Optical rotations were acquired on a PerkinElmer M341 Digital Polarimeter.

General procedure for the synthesis of 1,2-orthoesters 2, 9–21

The acetobromo glycoside (1 mmol) was dissolved in dry acetonitrile (4 mL), then alcohol (10 mmol), tetrabutylammonium bromide (0.7 mmol), anhydrous sodium bicarbonate (2 mmol), and molecular sieves 4 Å; (400 mg) were added. The reaction mixture was vigorously stirred for 3–7 h at room temperature. TLC indicated when the reaction was complete. The solvent was evaporated to dryness and the residue was purified by silica gel column chromatrography.

General procedure for the synthesis of sugar–sugar orthoesters 24–28

The glycosyl acceptor (1 mmol) and acetobromo glycoside (2 mmol) were dissolved in dry acetonitrile (10 mL), then tetrabutylammonium bromide (1 mmol), anhydrous sodium bicarbonate (4 mmol), and molecular sieves 4 Å; (600 mg) were added. The reaction mixture was vigorously stirred at room temperature for 12–15 h. TLC indicated when the reaction was complete. The solvent was evaporated to dryness and the residue was purified by silica gel column chromatrography.

Characterization data

Compound 2

Yield: 86%. Syrup. $[\alpha]_D^{25}$ +31 (*c* 0.8, EtOAc). ^1H NMR ($CDCl_3$) δ: 5.72 (d, 1H, *J* = 5.1 Hz), 5.19 (dd, 1H, *J* = 2.8, 3.0), 4.90 (dd, 1H, *J* = 2.8, 9.6), 4.32 (m, 1H), 4.20 (m, 2H), 3.95 (m, 1H), 3.29 (s, 3H), 2.11 (s, 3H), 2.10 (s, 3H,), 2.09 (s, 3H), 1.71 (s, 3H).

Compound 9

Yield: 84%. White needle, mp 107–108 °C. $[\alpha]_D^{25}$ –24 (*c* 0.2, EtOAc). ^1H NMR ($CDCl_3$) δ: 5.49 (d, 1H, *J* = 2.5), 5.30 (dd, 1H, *J* = 9.7, 9.8), 5.15 (dd, 1H, *J* = 4.0, 10.0), 4.61 (dd, 1H, *J* = 2.9, 3.5), 4.24 (dd, 1H, *J* = 5.0, 12.2), 4.14 (dd, 1H, *J* = 1.9, 11.7), 3.68 (m, 1H), 3.28 (s, 3H), 2.12 (s, 3H), 2.07 (s, 3H), 2.05 (s, 3H), 1.74 (s, 3H).

Compound 10

Yield: 80%. Syrup. $[\alpha]_D^{25}$ +80 (*c* 0.2, EtOAc). ^1H NMR [$(CD_3)_2CO$] δ: 5.87 (d, 1H, *J* = 4.6), 5.40 (dd, 1H, *J* = 2.9, 3.1), 5.06 (dd, 1H, *J* = 3.4, 6.5), 4.42–4.40 (m, 2H), 4.17 (dd, 1H, *J* = 7.0, 11.3), 4.10 (dd, 1H, *J* = 5.8, 11.3), 3.23 (s, 3H), 2.08 (s, 3H), 2.01 (s, 3H), 2.00 (s, 3H), 1.60 (s, 3H).

Compound 11

Yield: 66%. $[\alpha]_D^{25}$ +20 (*c* 0.4, EtOAc). ^1H NMR ($CDCl_3$) δ: 5.41 (d, 1H, *J* = 2.3), 5.06 (m, 2H), 4.59 (dd, 1H, *J* = 2.3, 3.9), 3.51 (m, 1H), 3.27 (s, 3H), 2.12 (s, 3H), 2.06 (s, 3H), 1.73 (s, 3H), 1.23 (d, 3H, *J* = 6.2).

Compound 12

Yield: 91%. White solid, mp 150–152 °C. $[\alpha]_D^{25}$ –129 (*c* 0.7, EtOAc). ^1H NMR ($CDCl_3$) δ: 8.01 (d, 2H, *J* = 7.6), 7.90–7.89 (m, 4H), 7.71–7.69 (m, 2H), 7.53–7.47 (m, 3H), 7.42–7.32 (m, 6H), 7.30–7.26 (m, 3H), 5.88 (dd, 1H, *J* = 9.5, 9.6), 5.80 (d, 1H, *J* = 2.9), 5.66 (dd, 1H, *J* = 4.1, 10.0), 5.08 (dd, 1H, *J* = 3.3, 3.7), 4.51 (dd, 1H, *J* = 3.1, 11.9), 4.35 (dd, 1H, *J* = 4.7, 12.1), 4.14–4.09 (m, 1H), 3.23 (s, 3H).

Compound 13

Yield: 88%. White solid, mp 128–129 °C. $[\alpha]_D^{25}$ –2.5 (*c* 0.2, EtOAc). ^1H NMR ($CDCl_3$) δ: 5.51 (d, 1H, *J* = 2.5), 5.25 (dd, 1H, *J* = 9.4, 9.8), 5.17 (dd, 1H, *J* = 3.8, 10.0), 4.63 (dd, 1H, *J* = 3.1, 3.1), 4.3 (dd, 1H, *J* = 5.5, 11.1), 4.28 (dd, 1H, *J* = 2.7, 11.1), 3.79 (m, 1H), 3.28 (s, 3H), 3.05 (s, 3H), 2.12 (s, 3H), 2.08 (s, 3H), 1.73 (s, 3H). ^{13}C NMR ($CDCl_3$) δ: 170.3, 169.6, 124.3, 97.5, 76.2, 71.6, 70.2, 67.2, 65.5, 50.1, 37.7, 24.0, 20.7, 20.6. HR-MS (ESI) anal. calcd. for $C_{14}H_{22}NaO_{11}S$ [M + Na]: 421.0775; found: 421.0772.

Compound 14

Yield: 83%. White solid, mp 145–146 °C. $[\alpha]_D^{25}$ –1 (*c* 0.2, EtOAc). ^1H NMR ($CDCl_3$) δ: 5.49 (d, 1H, *J* = 2.5), 5.25 (dd, 1H, *J* = 9.5, 9.7), 5.17 (dd, 1H, *J* = 3.9, 9.9), 4.61 (dd, 1H, *J* = 3.1, 3.5), 4.33 (dd, 1H, *J* = 5.5, 11.1), 4.28 (dd, 1H, *J* = 2.7, 11.0), 3.78 (m, 1H), 3.59–3.50 (m, 2H), 3.05 (s, 3H), 2.12 (s, 3H), 2.08 (s, 3H), 1.73 (s, 3H), 1.18 (t, 3H, *J* = 7.0). ^{13}C NMR ($CDCl_3$) δ: 170.3, 169.6, 124.0, 97.5, 76.0, 71.6, 70.2, 67.3, 65.6, 58.4, 37.7, 24.3, 20.7, 20.6, 15.1. HR-MS (ESI) anal. calcd. for $C_{15}H_{24}NaO_{11}S$ [M + Na]: 435.0932; found: 435.0936.

Compound 15

Yield: 77%. White solid, mp 127–129 °C. $[\alpha]_D^{25}$ +11 (*c* 0.1, EtOAc). ^1H NMR ($CDCl_3$) δ: 5.87 (m, 1H), 5.51 (d, 1H, *J* = 2.8), 5.27–5.24 (m, 2H), 5.18–5.14 (m, 2H), 4.62 (dd, 1H, *J* = 3.1, 3.8), 4.33 (dd, 1H, *J* = 5.6, 11.3), 4.28 (dd, 1H, *J* = 3.0, 11.3), 4.06–4.00 (m, 2H), 3.79 (m, 1H), 3.05 (s, 3H), 2.12 (s, 3H), 2.08 (s, 3H), 1.75 (s, 3H). ^{13}C NMR ($CDCl_3$) δ: 170.2, 169.6, 133.9, 124.1, 116.8, 97.6, 76.0, 71.7, 70.1, 67.3, 65.5, 64.0, 37.7, 24.4, 20.7, 20.6. HR-MS (ESI) anal. calcd. for $C_{16}H_{24}NaO_{11}S$ [M + Na]: 447.0932; found: 447.0925.

Compound 16

Yield: 70%. White solid, mp 130-132 °C. $[\alpha]_D^{25}$ +1 (*c* 0.2, EtOAc). ^1H NMR ($CDCl_3$) δ: 5.53 (d, 1H, *J* = 2.9), 5.25 (dd, 1H, *J* = 9.4, 9.7), 5.18 (dd, 1H, *J* = 4.0, 10.0), 4.68 (dd, 1H, *J* = 3.2, 3.2), 4.33 (dd, 1H, *J* = 5.6, 11.5), 4.29 (dd, 1H, *J* = 2.8, 11.2), 4.18 (d, 2H, *J* = 2.1), 3.80 (m, 1H), 3.05 (s, 3H), 2.38 (t, 1H, *J* = 1.9), 2.12 (s, 3H), 2.08 (s, 3H), 1.77 (s, 3H). ^{13}C NMR ($CDCl_3$) δ: 170.2, 169.6, 123.9, 97.6, 79.4, 76.0, 73.7, 71.8, 69.9, 67.2, 65.4, 51.1, 37.7, 24.0, 20.7. HR-MS (ESI) anal. calcd. for $C_{16}H_{22}NaO_{11}S$ [M + Na]: 445.0775; found: 445.0783.

Compound 17

Yield: 60%. White solid, mp 109–111 °C. $[\alpha]_D^{25}$ +1 (*c* 0.4,

EtOAc). ^{1}H NMR ($CDCl_3$) δ: 5.48 (d, 1H, *J* = 2.7), 5.25 (dd, 1H, *J* = 9.5, 9.5), 5.17 (dd, 1H, *J* = 4.1, 9.9), 4.62 (dd, 1H, *J* = 2.9, 3.7), 4.33 (dd, 1H, *J* = 5.8, 11.3), 4.28 (dd, 1H, *J* = 2.9, 11.2), 3.95 (m, 1H), 3.79 (m, 1H), 3.05 (s, 3H), 2.11 (s, 3H), 2.08 (s, 3H), 1.73 (s, 3H), 1.15 (d, 3H, *J* = 6.2), 1.14 (d, 3H, *J* = 9.1). ^{13}C NMR ($CDCl_3$) δ: 170.2, 169.6, 124.1, 97.4, 75.5, 71.7, 70.1, 67.4, 66.6, 65.6, 37.7, 24.4, 23.7, 20.7. HR-MS (ESI) anal. calcd. for $C_{16}H_{26}NaO_{11}S$ [M + Na]: 449.1088; found: 449.1011.

Compound 18

Yield: 68%. White solid, mp 141–142 °C. $[\alpha]_D^{25}$ +10 (*c* 0.2, EtOAc). ^{1}H NMR ($CDCl_3$) δ: 7.37–7.26 (m, 5H), 5.52 (d, 1H, *J* = 2.7), 5.26 (dd, 1H, *J* = 9.5, 9.7), 5.16 (dd, 1H, *J* = 3.9, 9.9), 4.64–4.54 (m, 3H), 4.35–4.28 (m, 2H), 3.80 (m, 1H), 3.05 (s, 3H), 2.10 (s, 3H), 2.08 (s, 3H), 1.81 (s, 3H). ^{13}C NMR ($CDCl_3$) δ: 170.2, 169.6, 137.4, 128.6, 128.4, 127.7, 127.5, 127.0, 124.2, 97.6, 76.0, 71.7, 70.0, 67.3, 65.5, 65.0, 37.7, 24.4, 20.7; HR-MS (ESI) anal. calcd for $C_{20}H_{26}NaO_{11}S$ [M + Na]: 497.1088; found: 497.1079.

Compound 19

Yield: 80%. Syrup. $[\alpha]_D^{25}$ +30.5 (*c* 0.2, EtOAc). ^{1}H NMR ($CDCl_3$) δ: 7.78 (d, 2H, *J* = 8.3), 7.34 (d, 2H, *J* = 7.9), 5.41 (d, 1H, *J* = 2.7), 5.16 (dd, 1H, *J* = 9.2, 9.6), 5.11 (dd, 1H, *J* = 3.8, 9.8), 4.56 (dd, 1H, *J* = 2.9, 3.7), 4.11 (m, 2H), 3.72 (m, 1H), 3.24 (s, 3H), 2.45 (s, 3H), 2.10 (s, 3H), 2.03 (s, 3H), 1.59 (s, 3H). ^{13}C NMR ($CDCl_3$) δ: 170.3, 169.5, 145.0, 132.5, 129.8, 128.1, 124.3, 97.4, 76.3, 71.3, 70.2, 67.9, 65.9, 50.0, 24.0, 21.6, 20.7, 20.6; HR-MS (ESI) anal. calcd for $C_{20}H_{26}NaO_{11}S$ [M + Na]: 497.1088; found: 497.1081.

Compound 20

Yield: 78%. Syrup. $[\alpha]_D^{25}$ +19.7 (*c* 0.6, EtOAc). ^{1}H NMR ($CDCl_3$) δ: 7.78 (d, 2H, *J* = 7.3), 7.34 (d, 2H, *J* = 7.7), 5.40 (m, 1H), 5.27–5.11 (m, 2H), 4.55 (m, 1H), 4.13–4.07 (m, 2H), 3.72 (m, 1H), 3.51 (m, 2H), 2.44 (s, 3H), 2.10 (s, 3H), 2.02 (s, 3H), 1.60 (s, 3H), 1.16 (t, 3H, *J* = 6.72). ^{13}C NMR ($CDCl_3$) δ: 170.3, 169.5, 145.0, 132.5, 129.8, 128.1, 124.0, 97.4, 76.1, 71.3, 70.2, 68.0, 65.9, 58.2, 24.3, 21.6, 20.7, 20.6, 15.0 HR-MS (ESI) anal. calcd for $C_{21}H_{28}NaO_{11}S$ [M + Na]: 511.1245; found: 511.1268.

Compound 21

Yield: 71%. Syrup. $[\alpha]_D^{25}$ +23 (*c* 0.2, EtOAc). ^{1}H NMR ($CDCl_3$) δ: 7.78 (d, 2H, *J* = 8.2), 7.34 (d, 2H, *J* = 8.0), 5.43 (d, 1H, *J* = 2.8), 5.18–5.11 (m, 2H), 4.62 (dd, 1H, *J* = 3.2, 3.3), 4.15 (d, 2H, *J* = 1.8), 4.15–4.07 (m, 4H), 3.76 (m, 1H), 2.45 (s, 3H), 2.37 (t, 1H, *J* = 2.3), 2.10 (s, 3H), 2.03 (s, 3H), 1.63 (s, 3H). ^{13}C NMR ($CDCl_3$) δ: 170.2, 169.5, 145.1, 132.5, 130.0, 129.8, 128.1, 123.9, 97.5, 79.4, 76.0, 73.7, 71.6, 69.9, 68.0, 65.7, 51.0, 24.0, 21.6, 20.7, 20.6, 14.2; HR-MS (ESI) anal. calcd for $C_{22}H_{26}NaO_{11}S$ [M + Na]: 521.1088; found: 521.1065.

Compound 24

Yield: 90%. White solid, mp 121–123 °C. $[\alpha]_D^{25}$ –27.7 (*c* 0.3, EtOAc). ^{1}H NMR ($CDCl_3$) δ: 5.50 (m, 2H), 5.28 (dd, 1H, *J* = 9.4, 9.8), 5.18 (dd, 1H, *J* = 4.1, 10.0), 4.62 (dd, 1H, *J* = 3.1, 3.5), 4.58 (dd, 1H, *J* = 2.4, 7.9), 4.29 (dd, 1H, *J* = 2.4, 5.1), 4.24–4.22 (m, 2H), 4.15 (dd, 1H, *J* = 2.8, 11.9), 3.91 (dd, 1H, *J* = 5.5, 6.1), 3.74–3.69 (m, 2H), 3.60 (dd, 1H, *J* = 6.2, 9.2), 2.11 (s, 3H), 2.06 (s, 3H), 2.04 (s, 3H), 1.76 (s, 3H), 1.53 (s, 3H), 1.42 (s, 3H), 1.33 (s, 3H), 1.32 (s, 3H).

Compound 25

Yield: 76%. Syrup. $[\alpha]_D^{25}$ –34.3 (*c* 0.3, EtOAc). ^{1}H NMR [$(CD_3)_2CO$)] δ: 5.61 (d, 1H, *J* = 2.2), 5.44 (d, 1H, *J* = 5.0), 5.20 (dd, 1H, *J* = 4.0, 10.0), 4.97 (dd, 1H, *J* = 9.7, 9.8), 4.65 (dd, 1H, *J* = 2.4, 4.0), 4.60 (dd, 1H, *J* = 2.0, 7.9), 4.32 (dd, 1H, *J* = 2.2, 4.9), 4.23 (dd, 1H, *J* = 1.4, 7.9), 3.91 (m, 1H), 3.69 (m, 1H), 3.64 (dd, 1H, *J* = 5.6, 10.1), 3.56 (dd, 1H, *J* = 6.7, 9.8), 2.03 (s, 6H), 1.66 (s, 3H), 1.47 (s, 3H), 1.36 (s, 3H), 1.31 (s, 3H), 1.30 (s, 3H), 1.16 (d, 3H, *J* = 6.2). ^{13}C NMR ($CDCl_3$) δ: 169.6, 169.5, 123.8, 108.7, 108.1, 97.3, 96.3, 77.3, 71.0, 70.7, 70.5, 66.9, 61.4, 25.5, 24.8, 24.3, 23.8, 19.8, 16.9. HR-MS (ESI) anal. calcd. for $C_{24}H_{36}NaO_{13}$ [M + Na]: 555.2048; found: 555.2037.

Compound 26

Yield: 78%. Syrup. $[\alpha]_D^{25}$ –18.5 (*c* 0.2, EtOAc). ^{1}H NMR [$(CD_3)_2CO$] δ: 5.72 (d, 1H, *J* = 5.3), 5.44 (d, 1H, *J* = 4.9), 5.13 (dd, 1H, *J* = 2.8, 2.8), 4.86 (dd, 1H, *J* = 2.0, 9.5), 4.60 (dd, 1H, *J* = 2.4, 7.9), 4.45 (m, 1H), 4.32 (dd, 1H, *J* = 2.4, 5.2), 4.25 (dd, 1H, *J* = 1.8, 7.9), 4.15 (d, 2H, *J* = 4.4), 3.99 (m, 1H), 3.87 (m, 1H), 3.67 (dd, 1H, *J* = 6.3, 9.7), 3.52 (dd, 1H, *J* = 6.5, 9.7), 2.05 (s, 6H), 2.01 (s, 3H), 1.67 (s, 3H, CH_3), 1.45 (s, 3H), 1.37 (s, 3H), 1.31 (s, 3H), 1.30 (s, 3H).

Compound 27

Yield: 78%. Syrup. $[\alpha]_D^{25}$ +9.5 (*c* 0.2, EtOAc). ^{1}H NMR [$(CD_3)_2CO$] δ: 5.87 (d, 1H, *J* = 4.9), 5.45 (dd, 1H, *J* = 4.9), 5.40 (dd, 1H, *J* = 2.5, 2.9), 5.07 (dd, 1H, *J* = 3.5, 6.4), 4.61 (dd, 1H, *J* = 2.2, 7.8), 4.43–4.40 (m, 2H), 4.27 (m, 1H), 4.18 (dd, 1H, *J* = 7.2, 11.5), 4.10 (dd, 1H, *J* = 5.5, 11.3), 4.04 (dd, 1H, *J* = 7.2, 14.1), 3.90 (dd, 1H, *J* = 4.9, 6.7), 3.68 (m, 1H), 3.55 (m, 1H), 2.13–2.01 (m, 9H), 1.63 (s, 3H), 1.46 (s, 3H), 1.37 (s, 3H), 1.31 (s, 3H), 1.30 (s, 3H).

Compound 28

Yield: 80%. Syrup. $[\alpha]_D^{25}$ +10 (*c* 0.3, EtOAc). ^{1}H NMR ($CDCl_3$) δ: 7.34–7.26 (m, 15H), 5.39 (d, 1H, *J* = 2.5), 5.27 (dd, 1H, *J* = 9.6, 9.6), 5.12 (dd, 1H, *J* = 3.9, 9.8), 4.90 (dd, 2H, *J* = 7.8, 10.9), 4.82 (d, 1H, *J* = 11.0), 4.77 (d, 1H, *J* = 11.0), 4.69 (d, 1H, *J* = 11.0), 4.62 (d, 1H, *J* = 10.9), 4.48 (dd, 1H, *J* = 2.9, 3.3), 4.28 (d, 1H, *J* = 7.8), 4.23 (dd, 1H, *J* = 5.1, 12.3), 4.14 (dd, 1H, *J* = 2.6, 12.2), 3.75 (d, 1H, *J* = 8.8), 3.68–3.60 (m, 3H), 3.55 (s, 3H), 3.51 (d, 1H, *J* = 9.2), 3.41 (m, 2H), 2.07 (s, 3H), 2.04 (s, 3H), 2.00 (s, 3H), 1.74 (s, 3H). ^{13}C NMR ($CDCl_3$) δ: 170.6, 170.3, 169.4, 138.6, 138.5, 138.3, 128.5, 128.4, 128.1, 128.0, 127.9, 127.8, 127.7, 127.6, 124.2, 104.6, 97.4, 84.6, 82.3, 77.7, 76.4, 75.6, 74.9, 74.7, 73.8, 71.5, 70.3, 65.7, 62.5, 61.8, 57.0, 24.4, 20.7, 20.6. HR-MS (ESI) anal. calcd. for $C_{42}H_{50}NaO_{15}$ [M + Na]: 817.3042; found: 817.3018.

Supplementary data

Supplementary data for this article are available on the journal Web site (canjchem.nrc.ca) or may be purchased from the Depository of Unpublished Data, Document Delivery, CISTI, National Research Council Canada, Ottawa, ON K1A 0R6, Canada. DUD 5297. For more information on ob-

taining material, refer to cisti-icist.nrc-cnrc.gc.ca/cms/unpub_e.shtml.

Acknowledgment

We are grateful for financial support from the Chinese Academy of Sciences (Hundreds of Talents Program).

References

(1) (a) Jayaprakash, K. N.; Lu, J.; Fraser-Reid, B. *Angew. Chem. Int. Ed.* **2005**, *44* (36), 5894. doi:10.1002/anie.200500505.; (b) Jayaprakash, K. N.; Chaudhuri, S. R.; Murty, C. V.; Fraser-Reid, B. *J. Org. Chem.* **2007**, *72* (15), 5534. doi:10.1021/jo070018t. PMID:17595135.; (c) Katano, K.; Chang, P.-I.; Millar, A.; Pozsgay, V.; Minster, D. K.; Ohgi, T.; Hecht, S. M. *J. Org. Chem.* **1985**, *50* (26), 5807. doi:10.1021/jo00350a073.; (d) Mukhopadhyay, B.; Field, R. A.; Woo, C. H.; Kariuki, B. M.; Cox, L. R. *Carbohydr. Res.* **2003**, *338* (20), 2149. doi:10.1016/S0008-6215(03)00349-5. PMID:14505883.; (e) Beignet, J.; Tiernan, J.; Woo, C. H.; Kariuki, B. M.; Cox, L. R. *J. Org. Chem.* **2004**, *69* (19), 6341. doi:10.1021/jo049061w. PMID:15357594.

(2) (a) Nukada, T.; Berces, A.; Zgierski, M. Z.; Whitfield, D. M. *J. Am. Chem. Soc.* **1998**, *120* (51), 13291. doi:10.1021/ja981041m.; (b) Mari, S.; Posteri, H.; Marcou, G.; Potenza, D.; Micheli, F.; Cañada, F.; Jimenez-Barbero, J.; Bernardi, A. *Eur. J. Org. Chem.* **2004**, 5119 doi:10.1002/ejoc.200400520.; (c) Prosperi, D.; Ronchi, S.; Lay, L.; Rencurosi, A.; Russo, G. *Eur. J. Org. Chem.* **2004**, 395. doi:10.1002/ejoc.200300483.; (d) Dong, L.; Roosenberg, J. M., II; Miller, M. J. *J. Am. Chem. Soc.* **2002**, *124* (50), 15001. doi:10.1021/ja028386w. PMID:12475343.

(3) (a) Mach, M.; Schlueter, U.; Mathew, F.; Fraser-Reid, B.; Hazen, K. C. *Tetrahedron* **2002**, *58* (36), 7345. doi:10.1016/S0040-4020(02)00671-3.; (b) Sureshkumar, G.; Hotha, S. *Tetrahedron Lett.* **2007**, *48* (37), 6564. doi:10.1016/j.tetlet.2007.07.015.; (c) Roberts, C.; Madsen, R.; Fraser-Reid, B. *J. Am. Chem. Soc.* **1995**, *117* (5), 1546. doi:10.1021/ja00110a010.; (d) Jayaprakash, K. N.; Radhakrishnan, K. V.; Fraser-Reid, B. *Tetrahedron Lett.* **2002**, *43* (39), 6953. doi:10.1016/S0040-4039(02)01590-3.; (e) Zhu, Y.; Kong, F. *Synlett* **2000**, 1783. doi:10.1055/s-2000-8704.

(4) (a) Wang, W.; Kong, F. *J. Org. Chem.* **1998**, *63* (17), 5744. doi:10.1021/jo981135e. PMID:11672169.; (b) Yamago, S.; Yamada, T.; Hara, O.; Ito, H.; Mino, Y.; Yoshida, J. I. *Org. Lett.* **2001**, *3* (24), 3867. doi:10.1021/ol016713j. PMID:11720556.

(5) (a) Wang, W.; Kong, F. *J. Org. Chem.* **1999**, *64* (14), 5091. doi:10.1021/jo982508e.; (b) Wang, W.; Kong, F. *Angew. Chem. Int. Ed.* **1999**, *38* (9), 1247. doi:10.1002/(SICI)1521-3773(19990503)38:9<1247::AID-ANIE1247>3.0.CO;2-J.

(6) (a) Allen, J. G.; Fraser-Reid, B. J. *J. Am. Chem. Soc.* **1999**, *121* (2), 468. doi:10.1021/ja9832358.; (b) Fraser-Reid, B.; Lu, J.; Jayaprakash, K. N.; Lopez, J. C. *Tetrahedron Asymmetry* **2006**, *17* (17), 2449. doi:10.1016/j.tetasy.2006.09.008.

(7) (a) Xue, J.; Shao, N.; Guo, Z. *J. Org. Chem.* **2003**, *68* (10), 4020. doi:10.1021/jo034213t. PMID:12737586.; (b) Duynstee, H. I.; de Koning, M. C.; Ovaa, H.; van der Marel, G. A.; van Boom, J. H. *Eur. J. Org. Chem.* **1999**, 2623. doi:10.1002/(SICI)1099-0690(199910)1999:10<2623::AID-EJOC2623>3.0.CO;2-K.

(8) (a) Kong, F. *Carbohydr. Res.* **2007**, *342* (3–4), 345. doi:10.1016/j.carres.2006.09.025. PMID:17109835.; (b) Yang, Z.; Lin, W.; Yu, B. *Carbohydr. Res.* **2000**, *329* (4), 879. doi:10.1016/S0008-6215(00)00242-1. PMID:11125831.; (c) Zeng, Y.; Ning, J.; Kong, F. *Tetrahedron Lett.* **2002**, *43* (20), 3729. doi:10.1016/S0040-4039(02)00584-1.; (d) Fraser-Reid, B.; Grimme, S.; Piacenza, M.; Mach, M.; Schlueter, U. *Chem. Eur. J.* **2003**, *9* (19), 4687. doi:10.1002/chem.200304856.

(9) (a) Lam, S. N.; Gervay-Hague, J. *J. Org. Chem.* **2005**, *70* (22), 8772. doi:10.1021/jo051360d. PMID:16238308.; (b) Millar, A.; Kim, K. H.; Minster, D. K.; Ohgi, T.; Hecht, S. M. *J. Org. Chem.* **1986**, *51* (2), 189. doi:10.1021/jo00352a012.

(10) (a) Sznaidman, M. L.; Johnson, S. C.; Crasto, C.; Hecht, S. M. *J. Org. Chem.* **1995**, *60* (13), 3942. doi:10.1021/jo00118a006.; (b) Betaneli, V.; Ovchinnikov, M. V.; Backinowsky, L. V.; Kochetkov, N. K. *Carbohydr. Res.* **1979**, *68* (1), C11. doi:10.1016/S0008-6215(00)84072-0.; (c) Banoub, J.; Boullanger, P.; Potier, M.; Descotes, G. *Tetrahedron Lett.* **1986**, *27* (35), 4145. doi:10.1016/S0040-4039(00)84932-1.; (d) Lichtenthaler, F. W.; Schneider-Adams, T. *J. Org. Chem.* **1994**, *59* (22), 6728. doi:10.1021/jo00101a035.; (e) Adinolfi, M.; Iadonisi, A.; Ravida, A.; Schiattarella, M. *Tetrahedron Lett.* **2003**, *44* (43), 7863. doi:10.1016/j.tetlet.2003.09.022.

(11) (a) Shoda, S.-i.; Moteki, M.; Izumi, R.; Noguchi, M. *Tetrahedron Lett.* **2004**, *45* (48), 8847. doi:10.1016/j.tetlet.2004.09.175.; (b) Radhakrishnan, K. V.; Sajisha, V. S.; Chacko, J. S. *Synlett* **2005**, *6* (6), 0997. doi:10.1055/s-2005-864818.; (c) Anas, S.; Sajisha, V. S.; Rajan, R.; Kumaran, T. R.; Radhakrishnan, K. V. *Bull. Chem. Soc. Jpn.* **2007**, *80* (3), 553. doi:10.1246/bcsj.80.553.; (d) Gama, Y.; Sasaki, M.; Yasumoto, M.; Ishigami, Y. *Chem. Lett.* **1990**, *19* (11), 2099. doi:10.1246/cl.1990.2099.; (e) Rukhman, I.; Yudovich, L.; Nisnevich, G.; Gutman, A. L. *Tetrahedron* **2001**, *57* (6), 1083. doi:10.1016/S0040-4020(00)01080-2.

(12) (a) Baeschlin, D. K.; Green, L. G.; Hahn, M. G.; Hinzen, B.; Ince, S. J.; Ley, S. V. *Tetrahedron Asymmetry* **2000**, *11* (1), 173. doi:10.1016/S0957-4166(99)00519-4.; (b) Vogel, C.; Torres, G. M.; Reinke, H.; Michalik, D.; Voss, A. *Carbohydr. Res.* **2007**, *342* (3–4), 520. doi:10.1016/j.carres.2006.09.015. PMID:17056018.; (c) Adinolfi, M.; Iadonisi, A.; Ravidà, A.; Schiattarella, M. *J. Org. Chem.* **2005**, *70* (13), 5316. doi:10.1021/jo050301x. PMID:15960539.; (d) Plé, K.; Chwalek, M.; Voutquenne-Nazabadioko, L. *Tetrahedron* **2005**, *61* (18), 4347. doi:10.1016/j.tet.2005.03.003.

(13) Mohal, N.; Bernet, B.; Vasella, A. *Helv. Chim. Acta* **2005**, *88* (12), 3232. doi:10.1002/hlca.200590260.

(14) (a) Mootoo, D. R.; Konradsson, P.; Fraser-Reid, B. *J. Am. Chem. Soc.* **1989**, *111* (22), 8540. doi:10.1021/ja00204a049.; (b) Hölemann, A.; Stocker, B. L.; Seeberger, P. H. *J. Org. Chem.* **2006**, *71* (21), 8071. doi:10.1021/jo061233x. PMID:17025296.; (c) Beignet, J.; Tiernan, J.; Woo, C. H.; Kariuki, B. M.; Cox, L. R. *J. Org. Chem.* **2004**, *69* (19), 6341. doi:10.1021/jo049061w. PMID:15357594.

(15) Shoda, S.; Izumi, R.; Suenaga, M.; Saito, K.; Fujita, M. *Chem. Lett.* **2002**, *2* (2), 150. doi:10.1246/cl.2002.150.

(16) Lemieux, R. U.; Driguez, H. *J. Am. Chem. Soc.* **1975**, *97* (14), 4063. doi:10.1021/ja00847a033.

Molecular dynamics simulations of *N*-methylacetamide (NMA) in water by the ABEEM/MM model

Ping Qian, Li-Nan Lu, and Zhong-Zhi Yang

Abstract: The *N*-methylacetamide (NMA) is a very interesting kind of compound and often serves as a model of the peptide bond. The interaction between NMA and water provides a convenient prototype for the solvation of peptides in aqueous solutions. We have carried out molecular dynamics (MD) simulations of a NMA molecule in water under 1 atm and 298 K. The simulations make use of the newly developed NMA–water fluctuating charge ABEEM/MM potential model (Yang, Z. Z.; Qian, P. *J. Chem. Phys.* **2006,** *125,* 064311), which is based on the combination of the atom-bond electronegativity equalization method (ABEEM) and molecular mechanics (MM). This model has been successfully applied to NMA–water gas clusters, $NMA(H_2O)_n$ (n = 1–6), and accurately reproduced many static properties. For the NMA–water ABEEM/MM potential model, two characters must be emphasized in the simulations. Firstly, the model allows the charges in system to fluctuate, responding to the ambient environment. Secondly, for two major types of intermolecular hydrogen bonds, which are the hydrogen bond forming between the lone-pair electron on amide oxygen and the water hydrogen, and the one forming between the lone-pair electron on water oxygen and the amide hydrogen, we take special treatments in describing the electrostatic interaction by the use of the parameters $k_{lpO=,H}$ and $k_{lpO-,HN-}$, respectively, which explicitly describe the short-range interaction of hydrogen bonds in the hydrogen bond interaction region. All sorts of properties have been studied in detail, such as, radial distribution function, energy distribution, ABEEM charge distribution and dipole moment, and so on. These simulation results show that the ABEEM/MM-based NMA–water potential model appears to be robust, giving the solution properties in excellent agreement with other dynamics simulations on similar systems.

Key words: ABEEM/MM model, atom-bond electronegativity equalization method (ABEEM), molecular mechanics (MM), *N*-methylacetamide (NMA) aqueous solution, hydrogen bond.

Résumé : Le *N*-méthylacétamide (NMA) est un type de composé très intéressant qui est souvent utilisé comme modèle pour la liaison peptidique. L'interaction entre le NMA et l'eau fournit un prototype approprié pour la solvatation des peptides en milieu aqueux. On a effectué des simulations à l'aide de calculs de dynamique moléculaire (DM) pour une molécule de NMA dans l'eau sous une atmosphère et à 298 K. Les simulations ont été faites en utilisant le modèle de potentiel MEELA/MM de charge fluctuante développée récemment pour les complexes NMA–eau (Yang, Z. Z.; Qian, P. *J. Chem. Phys.* **2006,** *125,* 064311), qui est basé sur la combinaison de la méthode d'égalisation de l'électronégativité de la liaison atomique (MEELA) et de la mécanique moléculaire (MM). Cette méthode a été appliquée avec succès pour des agrégats gazeux d'eau et de NMA, $NMA(H_2O)_n$ (n = 1–6) et elle a permis de reproduire correctement plusieurs propriétés statiques. Pour le modèle de potentiel MEELA/MM de l'eau et du NMA, on dont tenir particulièrement compte de deux caractères dans les simulations. Premièrement, le modèle permet de faire fluctuer les charges du système afin de correspondre à l'environnement ambiant. Deuxièmement, pour deux types importants de liaisons hydrogènes intermoléculaires, soit la liaison hydrogène reliant la paire d'électrons libre de l'oxygène de l'amide et l'hydrogène de l'eau et celle entre la paire d'électron libre de l'atome d'oxygène de l'eau et l'hydrogène de l'amide, des traitements spéciaux sont appliqués pour décrire l'interaction électrostatique à l'aide, respectivement, des paramètres $k_{lpO=,H}$ et $k_{lpO-,HN-}$, qui décrivent explicitement l'interaction à faible distance de l'atome d'hydrogène dans la région d'interaction de la liaison hydrogène. On a étudié un grand nombre de propriétés en détail, telle la fonction de distribution radiale, la distribution d'énergie la distribution de charge MEELA, le moment dipolaire et autres. Ces résultats de simulation montrent que le modèle de potentiel de l'eau et du NMA à base de MEELA/MM semble approprié pour prédire des propriétés de solutions en excellent accord avec d'autres simulations dynamiques de systèmes semblables.

Received 4 June 2009. Accepted 17 August 2009. Published on the NRC Research Press Web site at canjchem.nrc.ca on 27 November 2009.

P. Qian.[1] College of Chemistry and Material Science, Shandong Agricultural University, Tai'an 271018, P.R.China.
L.-N. Lu and Z.-Z. Yang.[2] Chemistry and Chemical Engineering Falculty, Liaoning Normal University, Dalian 116029, P.R.China.

[1]Corresponding author (e-mail: qianp@sdau.edu.cn).
[2]Corresponding author (e-mail: zzyang@lnnu.edu.cn).

Mots-clés : méthode d'égalisation de l'électronégativité de la liaison atomique (MEELA), mécanique moléculaire (MM), MEELA/MM, solution aqueuse de *N*-méthylacétamide (NMA), liaison hydrogène.

[Traduit par la Rédaction]

Introduction

The nature of the amide functional group has long been of fundamental interest because of its presence as a repeat unit in proteins and peptides. For understanding the structural properties and biological functions of proteins, it is important to know how they interact with an aqueous environment through hydrogen bonds. *N*-Methylacetamide (NMA), one of the simplest representative models for the main chain of proteins, has been extensively studied in this aspect. So far, a substantial number of experimental investigations[1–8] on the important structural information of NMA have been obtained, such as gas-phase electron diffraction,[1] and X-ray diffraction[2] in a crystal, and so forth.

To the best of our knowledge, the two major types of intermolecular hydrogen bonds[9–11] that occur in amide–water complexes are C=O···H–O–H and N–H···OH_2, respectively. The former forms between the amide oxygen in the NMA molecule and the water hydrogen, the latter forms between the amide hydrogen and the water oxygen. Both are the key to the stabilities of the secondary and tertiary structures of proteins in aqueous phase. These special types of nonbonded interactions have been studied by ab initio[12–20] and molecular mechanics methods.[20–35] Ab initio calculations at different levels and methods have been carried out to investigate the intermolecular interaction of the NMA–water system, and yield theoretical structures and other static properties. Dobbs and co-workers[14] investigated the strengths of the hydrogen bonds between a water molecule and model amide NMA by using ab initio molecule orbital theory, and performed the extensive calculations at the MP2 level with correlation consistent basis sets. Han and Suhai[15] studied the conformations, the hydrogen-bonding effects, and the stabilities of different methyl group orientations of isolated *trans*- and *cis*-NMA and of NMA$(H_2O)_n$ (n = 1–3) complexes, using all kinds of density functional theory (DFT) methods, such as B3LYP, BLYP, and 6-311++G(d,p) basis set. Recently, to fit the hydrogen bonding parameters for the molecular mechanics force field MM4, Langley and Allinger[20] performed the calculations for the amide–water and formamide dimer systems at the MP2/6-311++G(2d,2p) level. Currently, the majority of potential functions for studying amide–water systems employ rigid potential models.[20–30] Studies of combining quantum mechanical and molecular mechanical (QM/MM) simulations of *N*-methylacetamide in aqueous solution have been carried out to investigate the charge polarization of the solute and to explore the feasibility of hybrid QM/MM calculations using ab initio methods by Gao and Freindorf.[31] In addition, the fluctuating charge models in combination with molecular mechanics have been widely developed in the past few years. For example, Rick et al.[32,33] have developed the dynamical fluctuating charge (FQ) force field to study the aqueous solution of amides, and Patel et al.[34,35] have developed the CHARMM fluctuating charge (FQ) force field to research the protein simulations. Lately, based on the atom-bond electronegativity equalization method (ABEEM)[36–42] fused into molecular mechanics (MM), Yang and co-workers[43–50] have reported the ABEEM/MM fluctuating charge model, which has been successfully applied to water clusters,[43] ion–water clusters,[45] and their molecular dynamics simulations,[44,46,47] and have also been engaged in the research on conformations of organic molecules and peptides,[48–50] and so forth.

The purpose of this paper is to carry out a systematic investigation of molecular dynamics simulations on the NMA molecule in liquid water using the previously constructed NMA–water ABEEM/MM potential model. The correlating properties characterizing the NMA–water solution include radial distribution functions, coordination numbers, hydrogen bonds, energy distribution, ABEEM charges, and dipole moments, and so on, and the results are comparable with those obtained from other molecular dynamics simulations.

Theoretical method

The ABEEM/MM model for NMA–water system

Based on the combination of ABEEM and MM, the potential energy, $E_{\mathrm{ABEEM/MM}}$, of an amide–water system is expressed as

$$[1] \qquad E_{\mathrm{ABEEM/MM}} = \sum_{\text{bonds}} E_{\mathrm{b}} + \sum_{\text{angles}} E_{\theta} + \sum_{\text{torsions}} E_{\mathrm{tors}} + \sum_{\text{imptors}} E_{\mathrm{imptors}} + \sum_{\text{nonbonded}} (E_{\mathrm{vdw}} + E_{\mathrm{elec}})$$

where E_{b}, E_{θ}, E_{tors}, E_{imptors}, E_{vdw}, and E_{elec} stand for the energies of individual bond stretching, angle bending, dihedral angle torsion, improper torsion, van der Waals, and electrostatic interaction, respectively. This moment, the cross-terms, like stretch-bend coupling, stretch-torsion coupling, and so forth, are omitted in eq. [1]. The above equation can be concretely expressed as follows:

$$
\begin{aligned}
[2]\quad E = & \sum_{\text{bonds}\in\text{NMA}} k_r (r - r_{eq})^2 + \sum_{\text{bonds}\in \text{H}_2\text{O}} D[e^{-2\alpha(r-r_{eq})} - 2e^{-\alpha(r-r_{eq})}] + \sum_{\text{angles}} f_\theta (\theta - \theta_{eq})^2 \\
& + \frac{1}{2}\sum_{\text{torsions}} \left[v_1(1+\cos\phi) + v_2(1-\cos 2\phi) + v_3(1+\cos 3\phi)\right] + \sum_{\text{improper torsions}} v(1-\cos 2\phi) \\
& + \left[\sum_{\substack{a\\a,b\in\text{NMA}}}\sum_{b} \varepsilon_{a,b}\left[\left(\frac{r_{\min_{a,b}}}{r_{a,b}}\right)^{12} - 2\times\left(\frac{r_{\min_{a,b}}}{r_{a,b}}\right)^{6}\right] f_{a,b} + \sum_{c}\sum_{\substack{d\geq c+6\\c,d\in\text{NMA}}} k\frac{q_c q_d}{R_{c,d}}\right] \\
& + \sum_{i=1}^{N_{mol}}\sum_{j=1(\neq i)}^{N_{mol}}\left\{\sum_a\sum_b \varepsilon_{ia,jb}\left[\left(\frac{r_{\min_{ia,jb}}}{r_{ia,jb}}\right)^{12} - 2\times\left(\frac{r_{\min_{ia,jb}}}{r_{ia,jb}}\right)^{6}\right] + \sum_{H\in i}\sum_{\substack{lp\in j\\H,lp\text{inHBIR}}} k_{H,lp}(R_{iH,j(lp)})\frac{q_{iH}q_{j(lp)}}{R_{iH,j(lp)}}\right. \\
& + k\left(\frac{1}{2}\sum_a\sum_b\frac{q_{ia}q_{jb}}{R_{ia,jb}} + \frac{1}{2}\sum_m\sum_k\frac{q_{im}q_{jk}}{R_{im,jk}} + \frac{1}{2}\sum_{a-b}\sum_{g-h}\frac{q_{i(a-b)}q_{j(g-h)}}{R_{i(a-b),j(g-h)}} + \frac{1}{2}\sum_{\sigma m=n}\sum_{\sigma k=l}\frac{q_{i(\sigma m=n)}q_{j(\sigma k=1)}}{R_{i(\sigma m=n),j(\sigma k=1)}}\right. \\
& + \frac{1}{2}\sum\sum_{\pi m=n\,\pi k=l}\frac{q_{i(\pi m=n)}q_{j(\pi k=1)}}{R_{i(\pi m=n),j(\pi k=1)}} + \frac{1}{2}\sum_{lp}\sum_{lp'}\frac{q_{i(lp)}q_{j(lp')}}{R_{i(lp),j(lp')}} + \sum_a\sum_{g-h}\frac{q_{ia}q_{j(g-h)}}{R_{ia,j(g-h)}} + \sum_a\sum_m\frac{q_{ia}q_{jm}}{R_{ia,jm}} + \sum_a\sum_{\sigma m=n}\frac{q_{ia}q_{j(\sigma m=n)}}{R_{ia,j(\sigma m=n)}} \\
& + \sum_a\sum_{\pi m=n}\frac{q_{ia}q_{j(\pi m=n)}}{R_{ia,j(\pi m=n)}} + \sum_a\sum_{\substack{lp\\(a\neq H,\,H\text{ in HBIR}\\\text{and }lp\text{ not in HBIR})}}\frac{q_{ia}q_{j(lp)}}{R_{ia,j(lp)}} + \sum_m\sum_{a-b}\frac{q_{im}q_{j(a-b)}}{R_{im,j(a-b)}} + \sum_m\sum_{\sigma k=l}\frac{q_{im}q_{j(\sigma k=1)}}{R_{im,j(\sigma k=1)}} + \sum_m\sum_{\pi k=l}\frac{q_{im}q_{j(\pi k=1)}}{R_{im,j(\pi k=1)}} \\
& + \sum_m\sum_{lp}\frac{q_{im}q_{j(lp)}}{R_{im,j(lp)}} + \sum_{a-b}\sum_{\sigma m=n}\frac{q_{i(a-b)}q_{j(\sigma m=n)}}{R_{i(a-b),j(\sigma m=n)}} + \sum_{a-b}\sum_{\pi m=n}\frac{q_{i(a-b)}q_{j(\pi m=n)}}{R_{i(a-b),j(\pi m=n)}} + \sum_{a-b}\sum_{lp}\frac{q_{i(a-b)}q_{j(lp)}}{R_{i(a-b),j(lp)}} \\
& \left.\left. + \sum_{\sigma m=n}\sum_{\pi k=l}\frac{q_{i(\sigma m=n)}q_{j(\pi k=1)}}{R_{i(\sigma m=n),j(\pi k=1)}} + \sum_{\sigma m=n}\sum_{lp}\frac{q_{i(\sigma m=n)}q_{j(lp)}}{R_{i(\sigma m=n),j(lp)}} + \sum_{\pi m=n}\sum_{lp}\frac{q_{i(\pi m=n)}q_{j(lp)}}{R_{i(\pi m=n),j(lp)}}\right)\right\}
\end{aligned}
$$

In eq. [2], the Harmonic and Morse potentials are used to represent the bond stretching energies, E_b, of the NMA molecule and water molecule, respectively, where k_r is the force constant of bond stretching of the NMA molecule, the O–H bond dissociation energy, D, of the water molecule is 529.6 kcal/mol and α is related to the bond force constant ($\alpha = \sqrt{f_b/2D}$, f_b is the bond force constant), and r_{eq} is the equilibrium bond length. The harmonic potential is employed to represent the angle bending, E_θ, where f_θ is the angle force constant and θ_{eq} is the equilibrium bond angle. E_{tors} is almost always expressed as a cosine series expansion, and the energy term $E_{imptors}$ of improper torsion is also applied in this potential model, where v_1, v_2, v_3, and v represent the force constants of the dihedral angle torsion and improper torsion, respectively. r, θ, and ϕ stand for the actual values of bond lengths, bond angles, and dihedral angles.

The nonbonded interactions existing in the amide molecule are represented by a sum of the Lennard–Jones and Coulomb terms, where standard combining rules are used: $\varepsilon_{a,b} = (\varepsilon_{aa}\varepsilon_{bb})^{1/2}$, $r_{\min\,a,b} = \frac{1}{2}(r_{\min\,a-a} + r_{\min\,b-b})$. $\varepsilon_{a,b}$ and $r_{\min\,a,b}$ are the Lennard–Jones well-depth and minimum energy distance for the interaction between atoms a and b belonging to the NMA molecule. Furthermore, among all pairs of atoms ($a < b$) separated by three or more bonds, $f_{a,b}$ = 1.0, except for the intramolecular 1,4 interactions for which $f_{a,b}$ = 0.5. For the intramolecular electrostatic interactions in the NMA molecule, as far as all the site points of the system are concerned, we consider interactions of the site points that have greater than or equal to 1,6 bonding relationships. Then, in eq. [2], q_c and q_d are point charges, which have the above mentioned bonding relationship. $R_{c,d}$ is the distance between the site points c and d in the NMA molecule, k = 0.57, which is an overall optimized correction coefficient.

For the amide–water and water–water intermolecular interactions, the electrostatic interaction is taken from the last term of eq. [A1] in ref. 50, in which the outline of the ABEEM for describing NMA in water are detailed. This is the essence of the ABEEM fused into MM, which is to take the ABEEM charges of all atoms, bonds, and lone-pair electrons in the system to the intermolecular electrostatic interactions term of MM. In eq. [2], q is the charge on every site point of the system and R is the distance between sites. $R_{iH,j(lp)}$ is the distance between the hydrogen atom belonging to molecule i and the lone-pair electron belonging to molecule j in the hydrogen bond interaction region (HBIR), accordingly, the parameter $k_{H,lp}(R_{iH,j(lp)})$ is used to describe the electrostatic interaction between the hydrogen atom and the lone-pair electron in the HBIR. First of all, we use the ABEEM method to compute the charges of all atoms, bonds,

and lone-pair electrons, and then we use eq. [2] to compute the total energy of the system. It is worth noting that the last term of eq. [2] denotes the solute–solvent interaction energy when molecule *i* belongs to NMA and molecule *j* doesn't belong to NMA.

When there is a change of bond length, bond angle, or dihedral angle, or a change of the relative position between the NMA and water molecules, we recalculate the charges by using the ABEEM method from time to time, and then recalculate the total potential energy by eq. [2]. Therefore, the combination of ABEEM and molecular mechanics (MM) cannot only truly reflect the electrostatic polarization by way of the fluctuating charges, but also well-describes the NMA–water interaction explicitly. The detailed information concerning the ABEEM/MM-7P water and ABEEM/MM NMA–water potential models can be found in refs. 43 and 50. The above parameters all derive from the previous studies[43,50] on small water clusters and NMA–water clusters, and are directly transferred to this work without any modification to simulate the correlated dynamics properties of NMA aqueous solution, and further test the reasonableness of this potential model and the correctness and transferability of parameters.

Computational details

All our molecular dynamics (MD) simulation runs were performed on the SGI-3700 Server by using the modified Tinker program in the canonical (constant temperature and volume, NVT) ensemble with Berendsen thermostats and the velocity Verlet integrator. The SETTLE algorithm was used to constrain the water geometry, and the SHAKE algorithm was applied to constrain the bond length of NMA. All the runs used the cubic periodic boundary conditions, one *trans*-NMA molecule and 208 water molecules in a cubic box of size 18.409 Å, and a time step of 1 fs. The density of solvent was set to the experimental value for the temperature 298 K by adjusting the volume of the box. The way to deal with the nonbonded interactions was to use a nonbonded cutoff and to apply the minimum image convention. The cutoff distance was 9.0 Å for all different liquid structures, and the nonbonded interactions were truncated using the force shifting where the calculated forces and energies were smoothly shifted to zero at the cutoff distance. The fact that charges are or are not allowed to transfer between different molecules or just between charged site points on the same molecule makes some difference for the two ABEEM/MM-7P water models.[43] For the computed properties of gas-phase small water clusters, the ABEEM/MM-7P-2 model, which constrains the charge neutrality and electronegativity equalization on each water molecule, gives better results, to some degree, than those by the ABEEM/MM-7P-1 model, which constrains the charge neutrality and electronegativity equalization on the entire water system, especially for the computation of the dimer dipole moment. Therefore, in the present applications, we only considered a charge neutrality constraint on each molecule and there is no charge transfer between molecules and the effective chemical potential of each single bond atom, each double bond atom, each single bond, each σ bond region of double bond, each π bond region of double bond, and each lone-pair electron are to be equal only within a molecule. Rather than solve for the charges exactly at each time step, we recalculated the charges of each site point every picosecond, in consideration of the expensive computational time. Equilibration was performed over 400 ps followed by the evaluation of 600 ps for averaging.

Results and discussions

Radial distribution function

The solute–solvent structures can be well-characterized through radial distribution functions (rdfs) and energy distribution in the following sections.

All rdfs $g_{xy}(r)$ give the probability of finding an atom of type *y* at a distance *r* from an atom of type *x*. Figures 1–4 show the rdfs between water and NMA molecules, indicating the nature of the solvent structure around the amide. These are quite similar to those computed by Rick and Berne[32] using the rigid molecule model with constant intramolecular shielded interactions based on the atom-centered Slater orbital overlaps. The carbonyl oxygen – water oxygen (OO) and carbonyl oxygen – water hydrogen (OH) rdfs are shown in Fig. 1 for the aqueous solution of NMA. The OH rdf has well-defined peaks at 2.2 and 3.4 Å, while the first peak for the OO rdf is at 2.9 Å. This pattern is as expected for hydrogen bonding to the carbonyl oxygen with water molecules acting as the hydrogen bond donors. The hydrogen bonds are not bifurcated in that the two peaks of the OH rdf show that the near and far hydrogens are roughly separated by the H–H distance in a water monomer. The first peaks of OO and OH rdfs can be integrated to obtain estimates of the number of nearest neighbors for the carbonyl oxygen. Integration to the first minima for OO and OH rdfs at 3.8 and 2.7 Å yields 2.1 water neighbors for NMA. On the basis of the shorter O–H distance and further analyses below, the two water molecules may be assigned as hydrogen bonded to the carbonyl oxygen. Of course, this is a very reasonable result.[51,52] Moreover, the OO rdf also has the second peak between 4.0 and 6.4 Å. The water molecules in the second shell around the carbonyl oxygen contribute to this peak as well as the first shell waters near other groups. In particular, the peak near 5.5 Å for the OO rdf corresponds to the expected position for a water molecule hydrogen bonded to the trans NH group.

The hydrogen bonding at the amino end is most clearly represented in amide hydrogen (H_N) – water oxygen and H_N – water hydrogen rdfs (Figs. 2a and 2b). The first peak positions show that the oxygen is closer to the H_N than the hydrogen, so the water molecule is the hydrogen bond acceptor. Integrating the first peak in the HO rdf to the minimum at 3.0 Å reveals 0.9 water oxygen that is in the hydrogen bonding range of the H_N in NMA.

The rdfs involving the carbonyl carbon and the nitrogen in the NMA molecule have less interesting structure and provide little additional insight. Thus, they are not shown here. Rdfs involving the methyl groups in NMA are shown in Figs. 3–4. For NMA, the C_NO and C_CO rdfs are all typical for terminal methyl groups with adjacent secondary atoms as found for *n*-alkanes in water.[53] Integrations to the first minima for the C_NO and C_CO rdfs at 5.0 Å yield 14 and 13 neighboring water molecules, respectively. The difference in solvent structures around hydrophilic and hydrophobic groups is well-contrasted by comparing Figs. 1–2

Fig. 1. Carbonyl oxygen – water oxygen (a) and carbonyl oxygen – water hydrogen (b) rdfs computed for NMA in water using the ABEEM/MM model.

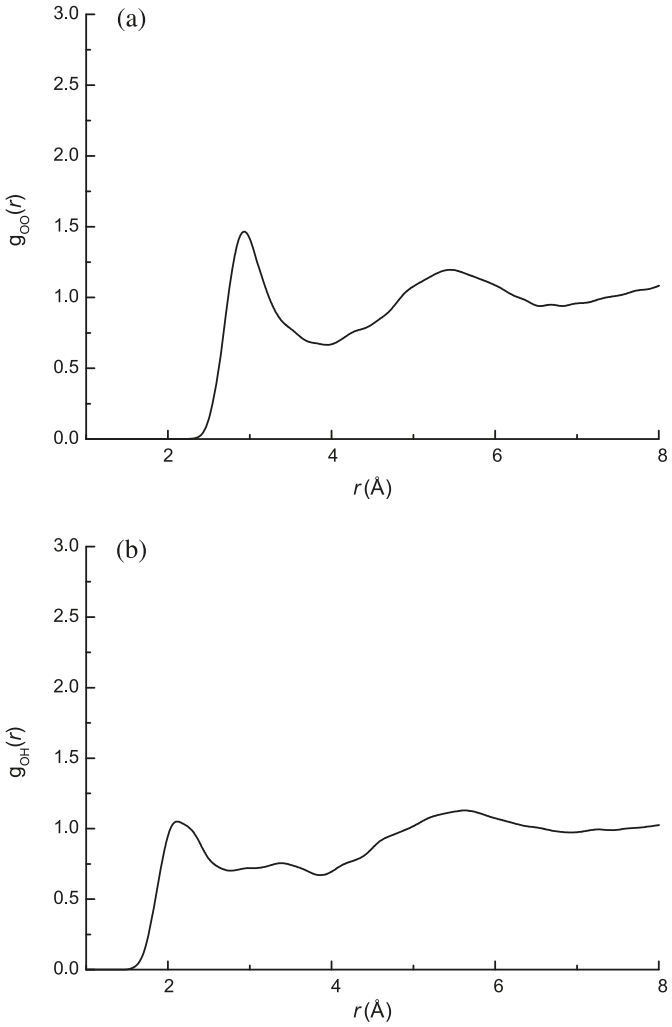

Fig. 2. Rdfs involving the hydrogen on nitrogen and oxygen (a) and hydrogen of water (b) computed for NMA in water using the ABEEM/MM model.

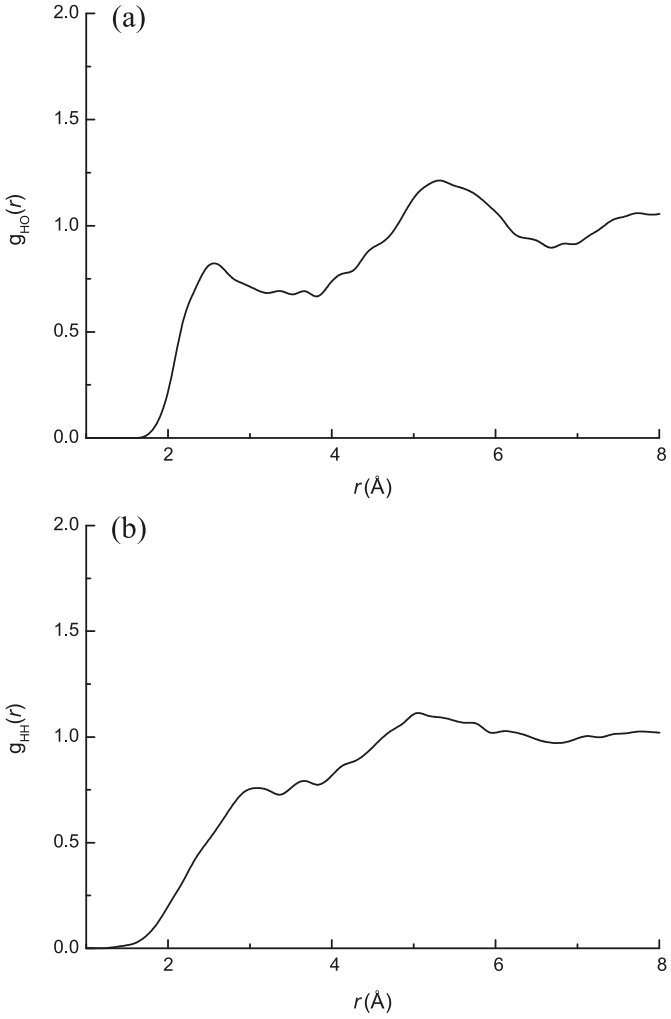

with Figs. 3–4. The sharp peaks of Figs. 1–2 at short range with small areas characterize the geometrical restrictions accompanying hydrogen bonds, while the broad peaks of Figs. 3–4 centered near 3.5 Å with large areas reflect the caging of water molecules around hydrophobic groups.

Energy distribution

Some detail of the solute–solvent energy is revealed in the distribution for total solute–solvent interaction energy (Fig. 5). It can be seen that the solute experiences a continuum of energetic environments covering the range of about –21 kcal/mol. Thus, the instantaneous number of hydrogen bonds to the solute undoubtedly shows substantial variation in the solution at 298 K. At the same time, the result of –21 kcal/mol is larger than the value of –25 kcal/mol from the Monte Carlo simulation by Jorgensen and Swenson.[27]

ABEEM charge distribution and dipole moment

The polarization effects in aqueous solution can be described by the changes of dipole moments of NMA and its neighboring water molecules. The computed average dipole moment for NMA in solution state is 5.49 D (1 D = 1×10^{-18} statC cm), higher than the 3.62 D in gas state[50] with the ABEEM/MM model. This prediction is a little higher than the values obtained from electronic structure calculations using the continuum dielectric model and from an ab initio study using explicit TIP3P water, the former giving 5.33 D[19] and the latter giving 5.18 D,[54] but more reasonable than 7.2 D[35] calculated from the CHARMM fluctuating charge model.

Compared with other potentials, the ABEEM/MM model can fully consider the changes of charge distributions of all atoms, bonds, and lone-pair electrons upon the different ambient environments, and explicitly give the quantitative charges. The average charge distributions of each site point for the NMA molecule in MD simulation are listed in Table 1. At the same time, the table presents a comparison between the gas and aqueous results. The agreement for both the gas-phase and the aqueous charges is very good. The first largest difference takes place in the hydrogen bond interaction regions. For example, the lone-pair electrons (q_{lpO2} and $q_{lp'O2}$) on carbonyl oxygen and water hydrogens can form the hydrogen bonds, which make the charges of lone-pair electrons on the carbonyl oxygen obviously polarized. Therefore, two

Fig. 3. Rdfs involving the methyl on carbon and oxygen (a) and hydrogen of water (b) computed for NMA in water using the ABEEM/MM model.

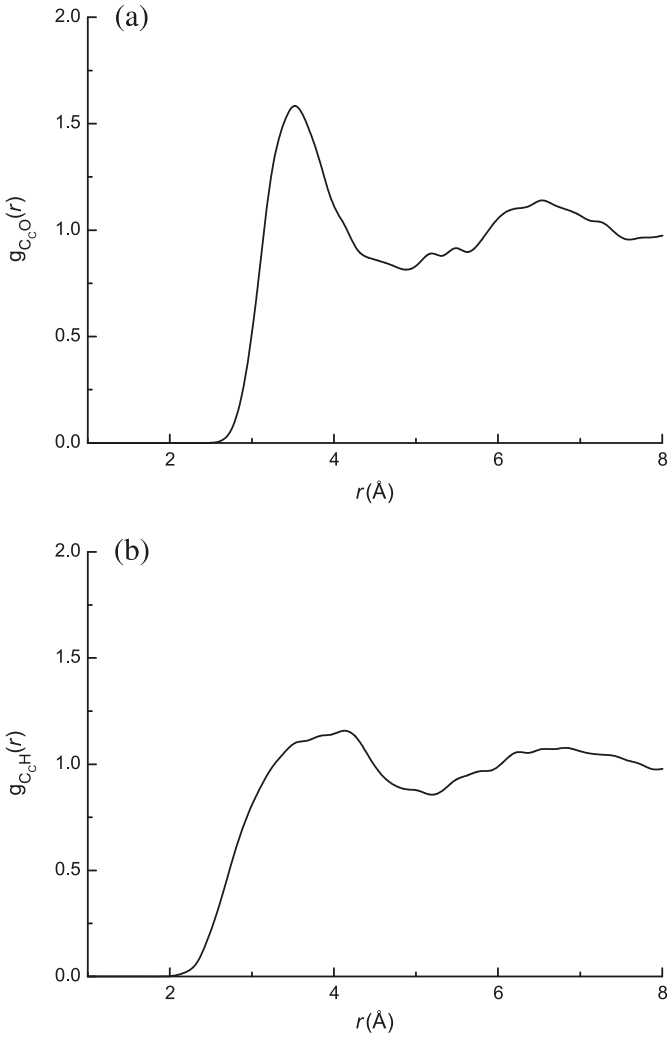

Fig. 4. Rdfs involving the methyl on nitrogen and oxygen (a) and hydrogen of water (b) computed for NMA in water using the ABEEM/MM model.

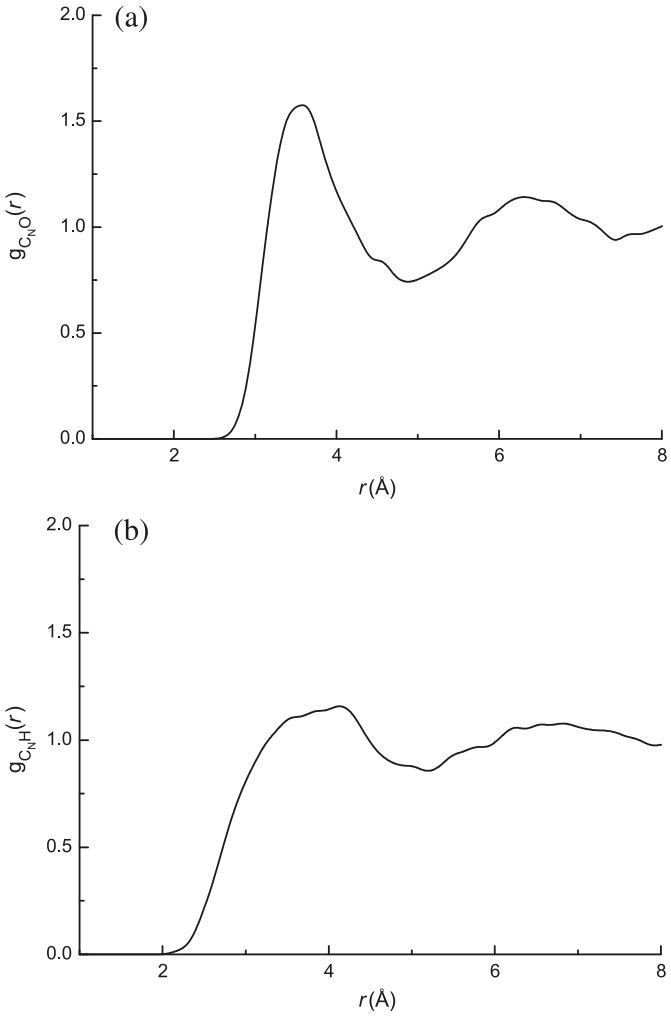

lone-pair electrons ($q_{lp\mathrm{O2}}$ is –0.2075 and $q_{lp'\mathrm{O2}}$ is –0.2053) of the O atom exhibit relatively larger absolute charges than the corresponding values (–0.1704 and –0.1647) of the monomer in the gas phase. Similarly, the amide hydrogen and the lone-pair electron on the water oxygen can also form the hydrogen bond, which also makes the charge of the amide hydrogen obviously polarized. Moreover, the second largest difference is for the charges on the methyl groups. In both the gas phase and aqueous phase, the charges on the methyl hydrogens (q_{H7} and q_{H11}) are about 0.03 $\sim$ 0.04 e larger than the gas results, which indicates that two methyl groups in the NMA molecule are found to have different capabilities in forming weak C–H···O contacts in aqueous solution.[55] In contrast, the fixed-charge models use fixed charges. Thus, the charges used in the simulations based on fixed-charge models must reflect the average or mean field charge values for the particular phase and are not transferable to different thermodynamic states or heterogeneous environments. The aforementioned results show that the ABEEM/MM fluctuating charge model can accurately describe aqueous phase properties, and also correctly reflect the charge redistribution with the changed

Fig. 5. The distribution of total solute–solvent interaction energy (kcal/mol) for NMA in water computed by the ABEEM/MM model. Units for the ordinate are mole fraction per kcal/mol.

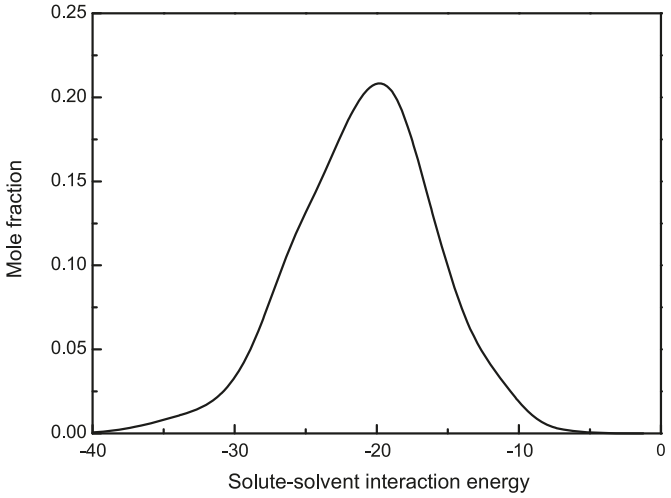

Table 1. Charges of every site point for the NMA molecule in the gas phase and in aqueous phase using the ABEEM/MM model, in units of electronic charge, e.

	Gas phase	Aqueous
q_{C1}	0.6653	0.6308
q_{O2}	*-0.0597*	*-0.1067*
q_{N3}	0.4111	0.4164
q_{H4}	*0.5937*	*0.6324*
q_{C5}	0.4076	0.4009
q_{H6}	0.2143	0.2266
q_{H7}	*0.1818*	*0.2201*
q_{H8}	0.2143	0.2234
q_{C9}	0.3750	0.3703
q_{H10}	0.2306	0.2334
q_{H11}	*0.2058*	*0.2314*
q_{H12}	0.2306	0.2392
$q_{\sigma C1=O2}$	–0.1439	–0.1154
$q_{\sigma C1\sim N3}$	–0.1682	–0.1664
q_{C1-C5}	–0.2316	–0.2331
q_{C1-N3}	–0.1464	–0.1461
q_{H4-N3}	–0.8020	–0.8091
q_{H6-C5}	–0.2891	–0.2898
q_{H7-C5}	–0.2981	–0.2906
q_{H8-C5}	–0.2891	–0.2904
q_{H10-C9}	–0.2863	–0.2858
q_{H11-C9}	–0.2899	–0.2859
q_{H12-C9}	–0.2863	–0.2868
q_{lpO2}	*-0.1704*	*-0.2075*
$q_{lp'O2}$	*-0.1647*	*-0.2053*
$q_{\pi C1=}$	–0.0105	–0.0114
$q_{\pi' C1=}$	–0.0105	–0.0118
$q_{\pi O2=}$	–0.0104	–0.0119
$q_{\pi' O2=}$	–0.0104	–0.0120
$q_{\pi N3\sim}$	–0.0313	–0.0294
$q_{\pi' N3\sim}$	–0.0313	–0.0294

Note: q_{C1}, q_{O2}, q_{N3}, and q_{H4} are the charges on the sites of carbonyl C, carbonyl O, amide N, and amide H of the peptide bond, q_{C5}, q_{H6}, q_{H7}, and q_{H8} are the charges of the atoms on (C)CH_3, q_{C9}, q_{H10}, q_{H11}, and q_{H12} are charges of the atoms on (N)CH_3, $q_{\sigma C=O}$, $q_{\sigma C-N}$, q_{C-C}, q_{C-N}, and q_{H-C} are the bond charges on the sites of the ratio of covalent atomic radii of the directly bonded atoms, q_{lpO} is the charge on the site 0.74 Å from the amide O, $q_{\pi C=}$, $q_{\pi O=}$, and $q_{\pi N\sim}$ are the charges of the π bond region of the double bond atoms C, O, and amide N.

ambient environment and make a compensation for the shortages of the fixed-charge models.

Of particular interest in the application of the polarizable model to peptide simulation is the polarization of the solvent in the vicinity of the solute. That structural and dynamics properties of vicinal water are different from those of the bulk is well-documented. Here, we show the polarization responses for vicinal and bulk water molecules. Figure 6 shows the average dipole moment distributions of water molecules in a shell between 1.0 and 2.9 Å from the center of mass of the solute and in the bulk, respectively. As one would anticipate, the average dipole moment of 2.35 D for water molecules nearest to the carbonyl oxygen is higher than the bulk water value of 2.30 D. By comparison, Rick and Berne[32] reported a higher average dipole moment of 2.72 D for water molecules nearest to the carbonyl oxygen

Fig. 6. Average dipole moment distributions of water molecules using the ABEEM/MM model. The solid curve represents the distribution for molecules near the solute, and the broken curve represents that for the bulk-like water.

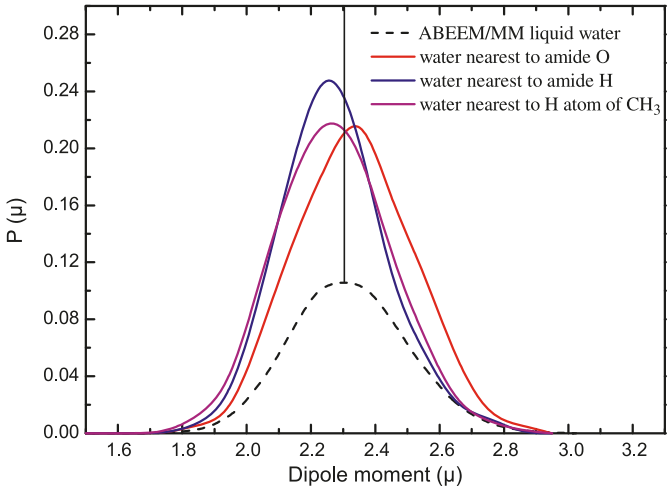

relative to the bulk value of 2.62 D, and a shift is higher in magnitude than that observed in the present simulations. It is this mutual enhancement of the dipole moment that leads to the strong amide–water interaction as testified in the relevant radial distribution functions (Fig. 1). Water forms stronger hydrogen bonds with the carbonyl oxygen atom of the solute than it does with other atoms of the solute. In particular, the average dipole moments of water molecules neighboring the other solute atoms are all about 2.27 D, less than the bulk value, indicating that these electrostatic interactions are weak.

Conclusions

This contribution presents the results of our current efforts towards developing and implementing a fluctuating charge ABEEM/MM model for use. The fluctuating charge approach has been applied widely, and is no longer a novelty in some respects. In the present work, several key details of dynamics properties of the NMA molecule in liquid water have been studied by classical MD simulation in terms of the ABEEM/MM-based NMA–water potential model. Based on the ABEEM/MM model, the NMA–water interaction potential and the ABEEM-7P water model parameterized by NMA–water clusters and gas-phase water clusters are tested in the aqueous NMA solution simulations. The simulations have been performed at 298 K with the SETTLE algorithm. Although this investigation is far from being complete, the obtained, systematically simulated results display a few important observations. Simulation results with our own potential model, particularly for the liquid structure and the numbers of hydrogen bonds, are in good agreement with those obtained in other molecular simulations. The computed solute–solvent interaction energy is about –21 kcal/mol. The present model also captures the condensed phase polarization, as testified by the shift in average dipole moment distributions of Fig. 6, although the accuracy of such predicted shifts is difficult to assess at this time. The above results are very important, and could provide the important reference

for studies modeling other biomacromolecular systems based on the ABEEM/MM fluctuating charge model, and also provide the reliable evidence for testing the reasonableness of this model and the correctness and transferability of parameters.

Acknowledgement

This research has been aided by the National Natural Science Foundation of China (No. 20903063) and the grant from the Youth Science and Technology Innovation Foundation of the Shandong Agricultural University in China (No. 23480).

References

(1) Kitano, M.; Fukuyama, T.; Kuchitsu, K. *Bull. Chem. Soc. Jpn.* **1973**, *46* (2), 384. doi:10.1246/bcsj.46.384.
(2) Katz, J. L.; Post, B. *Acta Crystallogr.* **1960**, *13* (8), 624. doi:10.1107/S0365110X60001485.
(3) Itoh, K.; Shimanouchi, T. *Biopolymers* **1967**, *5* (10), 921. doi:10.1002/bip.1967.360051006. PMID:6078880.
(4) Fillaux, F.; Baron, M. H. *Chem. Phys.* **1981**, *62* (3), 275. doi:10.1016/0301-0104(81)85124-5.
(5) Fillaux, F.; De Loze, C. *Chem. Phys. Lett.* **1976**, *39* (3), 547. doi:10.1016/0009-2614(76)80326-0.
(6) Allen, F. H.; Bellard, S.; Brice, M. D.; Cartwright, B. A.; Doubleday, A.; Higgs, H.; Hummelink, T.; Hummelink-Peters, B. G.; Kennard, O.; Motherwell, W. D. S.; Rodgers, J. R.; Watson, D. G. *Acta Crystallogr. B* **1979**, *35* (10), 2331. doi:10.1107/S0567740879009249.
(7) *CRC Handbook of Chemistry and Physics;* Weast, R. C., Ed.; CRC Press: Boca Raton, FL, 1985–1986.
(8) Drakenberg, T.; Forsén, S. *J. Chem. Soc. Chem. Commun.* **1971**, 1404. doi:10.1039/C29710001404.
(9) Hagler, A. T.; Huler, E.; Lifson, S. *J. Am. Chem. Soc.* **1974**, *96* (17), 5319. doi:10.1021/ja00824a004.
(10) Brooks, B. R.; Bruccoleri, R. E.; Olafson, B. D.; States, D. J.; Swaminathan, S.; Karplus, M. *J. Comput. Chem.* **1983**, *4* (2), 187. doi:10.1002/jcc.540040211.
(11) Lii, J.-H.; Allinger, N. L. *J. Comput. Chem.* **1998**, *19* (9), 1001. doi:10.1002/(SICI)1096-987X(19980715)19:9<1001::AID-JCC2>3.0.CO;2-U.
(12) Guo, H.; Karplus, M. *J. Phys. Chem.* **1992**, *96* (18), 7273. doi:10.1021/j100197a027.
(13) Guo, H.; Karplus, M. *J. Phys. Chem.* **1994**, *98* (29), 7104. doi:10.1021/j100080a002.
(14) Dixon, D. A.; Dobbs, K. D.; Valentini, J. J. *J. Phys. Chem.* **1994**, *98* (51), 13435. doi:10.1021/j100102a001.
(15) Han, W.-G.; Suhai, S. *J. Phys. Chem.* **1996**, *100* (10), 3942. doi:10.1021/jp952250l.
(16) Mirkin, N. G.; Krimm, S. *J. Am. Chem. Soc.* **1991**, *113* (26), 9742. doi:10.1021/ja00026a005.
(17) Radzicka, A.; Pedersen, L.; Wolfenden, R. *Biochemistry* **1988**, *27* (12), 4538. doi:10.1021/bi00412a047. PMID: 3166998.
(18) Radom, L.; Riggs, N. V. *Aust. J. Chem.* **1982**, *35* (6), 1071. doi:10.1071/CH9821071.
(19) Tannor, D. J.; Marten, B.; Murphy, R.; Friesner, R. A.; Sitkoff, D.; Nicholls, A.; Honig, B.; Ringnalda, M.; Goddard, W. A. *J. Am. Chem. Soc.* **1994**, *116* (26), 11875. doi:10.1021/ja00105a030.
(20) Langley, C. H.; Allinger, N. L. *J. Phys. Chem. A* **2003**, *107* (26), 5208. doi:10.1021/jp021764z.
(21) Jorgensen, W. L.; Gao, J. *J. Am. Chem. Soc.* **1988**, *110* (13), 4212. doi:10.1021/ja00221a020.
(22) Baudry, J.; Smith, J. C. *J. Mol. Struct. THEOCHEM* **1994**, *308*, 103. doi:10.1016/0166-1280(94)80096-0.
(23) MacKerell, A. D.; Bashford, D.; Bellott.; Dunbrack, R. L.; Evanseck, J. D.; Field, M. J.; Fischer, S.; Gao, J.; Guo, H.; Ha, S.; Joseph-McCarthy, D.; Kuchnir, L.; Kuczera, K.; Lau, F. T. K.; Mattos, C.; Michnick, S.; Ngo, T.; Nguyen, D. T.; Prodhom, B.; Reiher, W. E.; Roux, B.; Schlenkrich, M.; Smith, J. C.; Stote, R.; Straub, J.; Watanabe, M.; Wiórkiewicz-Kuczera, J.; Yin, D.; Karplus, M. *J. Phys. Chem. B* **1998**, *102* (18), 3586. doi:10.1021/jp973084f.
(24) Vargas, R.; Garza, J.; Friesner, R. A.; Stern, H.; Hay, B. P.; Dixon, D. A. *J. Phys. Chem. A* **2001**, *105* (20), 4963. doi:10.1021/jp003888m.
(25) Kang, Y. K. *J. Phys. Chem. B* **2000**, *104* (34), 8321. doi:10.1021/jp000772h.
(26) Buck, M.; Karplus, M. *J. Phys. Chem. B* **2001**, *105* (44), 11000. doi:10.1021/jp011042s.
(27) Jorgensen, W. L.; Swenson, C. J. *J. Am. Chem. Soc.* **1985**, *107* (6), 1489. doi:10.1021/ja00292a007.
(28) Yu, H. A.; Karplus, M.; Pettitt, B. M. *J. Am. Chem. Soc.* **1991**, *113* (7), 2425. doi:10.1021/ja00007a012.
(29) Morgantini, P.-Y.; Kollman, P. A. *J. Am. Chem. Soc.* **1995**, *117* (22), 6057. doi:10.1021/ja00127a019.
(30) Ding, Y.; Bernardo, D. N.; Krogh-Jespersen, K.; Levy, R. M. *J. Phys. Chem.* **1995**, *99* (29), 11575. doi:10.1021/j100029a040.
(31) Gao, J.; Freindorf, M. *J. Phys. Chem. A* **1997**, *101* (17), 3182. doi:10.1021/jp970041q.
(32) Rick, S. W.; Berne, B. J. *J. Am. Chem. Soc.* **1996**, *118* (3), 672. doi:10.1021/ja952535b.
(33) Rick, S. W.; Stuart, S. J.; Berne, B. J. *J. Chem. Phys.* **1994**, *101* (7), 6141. doi:10.1063/1.468398.
(34) Patel, S.; Mackerell, A. D., Jr.; Brooks, C. L., III. *J. Comput. Chem.* **2004**, *25* (12), 1504. doi:10.1002/jcc.20077. PMID: 15224394.
(35) Patel, S.; Brooks, C. L., III. *J. Comput. Chem.* **2004**, *25* (1), 1. doi:10.1002/jcc.10355. PMID:14634989.
(36) Yang, Z. Z.; Shen, E. Z.; Wang, L. H.. *J. Mol. Struct. THEOCHEM* **1994**, *312* (2), 167. doi:10.1016/S0166-1280(09)80029-8.
(37) Yang, Z. Z.; Wang, C. S. *J. Phys. Chem. A* **1997**, *101* (35), 6315. doi:10.1021/jp9711048.
(38) Wang, C. S.; Li, S. M.; Yang, Z. Z. *J. Mol. Struct. THEOCHEM* **1998**, *430* (1–3), 191. doi:10.1016/S0166-1280(98)90239-1.
(39) Wang, C. S.; Yang, Z. Z. *J. Chem. Phys.* **1999**, *110* (13), 6189. doi:10.1063/1.478524.
(40) Cong, Y.; Yang, Z. Z. *Chem. Phys. Lett.* **2000**, *316* (3–4), 324. doi:10.1016/S0009-2614(99)01289-0.
(41) Cong, Y.; Yang, Z. Z.; Wang, C. S.; Liu, X. C.; Bao, X. H. *Chem. Phys. Lett.* **2002**, *357* (1–2), 59. doi:10.1016/S0009-2614(02)00439-6.
(42) Yang, Z. Z.; Wang, C. S. *J. Theor. Comput. Chem.* **2003**, *2* (2), 273. doi:10.1142/S0219633603000434.
(43) (a) Yang, Z. Z.; Wu, Y.; Zhao, D. X. *J. Chem. Phys.* **2004**, *120* (6), 2541. doi:10.1063/1.1640345. PMID:15268398.; (b) Qian, P.; Yang, Z. Z. *Sci. China Ser. B* **2007**, *50* (2), 190. doi:10.1007/s11426-007-0003-2.; (c) Qian, P.; Lu, L. N.; Song, W.; Yang, Z. Z. *Theor. Chem. Acc.* **2009**, *123* (5-6), 487. doi:10.1007/s00214-009-0569-1.
(44) Wu, Y.; Yang, Z. Z. *J. Phys. Chem. A* **2004**, *108* (37), 7563. doi:10.1021/jp0493881.

(45) Li, X.; Yang, Z. Z. *J. Phys. Chem. A* **2005**, *109* (18), 4102. doi:10.1021/jp0458093. PMID:16833733.
(46) Yang, Z. Z.; Li, X. *J. Phys. Chem. A* **2005**, *109* (16), 3517. doi:10.1021/jp051106p. PMID:16839014.
(47) Li, X.; Yang, Z. Z. *J. Chem. Phys.* **2005**, *122* (8), 084514. doi:10.1063/1.1853372.
(48) Zhang, Q.; Yang, Z. Z. *Chem. Phys. Lett.* **2005**, *403* (4–6), 242. doi:10.1016/j.cplett.2005.01.011.
(49) Yang, Z. Z.; Zhang, Q. *J. Comput. Chem.* **2006**, *27* (1), 1. doi:10.1002/jcc.20317. PMID:16235260.
(50) Yang, Z. Z.; Qian, P. *J. Chem. Phys.* **2006**, *125* (6), 064311. doi:10.1063/1.2210940.
(51) Pullman, A.; Alagona, G.; Tomasi, J. *Theor. Chim. Acta* **1974**, *33* (1), 87. doi:10.1007/BF00527628.
(52) Spencer, J. N.; Berger, S. K.; Powell, C. R.; Henning, B. D.; Furman, G. S.; Loffredo, W. M.; Rydberg, E. M.; Neubert, R. A.; Shoop, C. E.; Blauch, D. N. *J. Phys. Chem.* **1981**, *85* (9), 1236. doi:10.1021/j150609a028.
(53) Jorgensen, W. L. *J. Chem. Phys.* **1982**, *77* (11), 5757. doi:10.1063/1.443732.
(54) Gao, J.; Xia, X. *Science* **1992**, *258* (5082), 631. doi:10.1126/science.1411573. PMID:1411573.
(55) Zhang, R.; Li, H. R.; Lei, Y.; Han, S. J. *J. Phys. Chem. B* **2004**, *108* (33), 12596. doi:10.1021/jp049623f.

A spectral displacement study of cyclodextrin/naphthenic acids inclusion complexes

Mohamed H. Mohamed, Lee D. Wilson, John V. Headley, and Kerry M. Peru

Abstract: The spectral displacement technique has been used to obtain 1:1 β-cyclodextrin (β-CD)/carboxylate anion equilibrium binding constants (K_2) for some complex mixtures of naphthenic acids (NAs) and some examples of single-component NAs in aqueous solution. Three specific examples of single-component NAs were chosen with variable Z values as follows: 2-hexyldecanoic acid ($Z = 0$; S1), *trans*-4-pentylcyclohexanecarboxylic acid ($Z = -2$; S2), and dicyclohexylacetic acid ($Z = -4$; S3). The estimated K_2 values for S1, S2, and S3 are as follows: 1.42×10^3 M^{-1}, 52.2×10^4 M^{-1}, and 13.1×10^4 M^{-1}, respectively. The corresponding K_2 values are 2.34×10^4 M^{-1} and 1.27×10^4 M^{-1} for commercial (Fluka) and industrial (Syncrude) sourced NAs, respectively. The magnitude of K_2 for 1:1 complexes formed between β-CD and S1, S2, or S3 did not correlate with the degree of hydrogen deficiency (Z-series) but there was a correlation with the size of the guest molecules (n) examined in this study. The correlation between complex stability and the relative size of the lipophilic fragments of the guest molecule are related to the importance of the hydrophobic effect for inclusion of such carboxylic acid guest molecules within β-CD.

Key words: spectral displacement, cyclodextrin, carboxylic acids, naphthenic acids, binding constant, hydrophobic hydration, lipophilic surface area.

Résumé : On a fait appel à la technique du déplacement spectral pour déterminer les constantes d'équilibre de fixation (K_2) du complexe 1 :1 β-cyclodextrine/anion carboxylate pour quelques mélanges complexes d'acides naphténiques (AN) et pour quelques exemples d'acides naphténiques particuliers en solution aqueuse. On a choisi trois exemples spécifiques d'acide naphténique possédant des valeurs de Z variables : acide 2-hexyldécanoïque ($Z = 0$; S1), l'acide *trans*-4-pentylcyclohexanecarboxylique ($Z = -2$; S2) et l'acide dicyclohexylacétique ($Z = -4$; S3). Les valeurs de K_2 évaluées pour les composés S1, S2 et S3 sont respectivement égales à $1{,}42 \times 10^3$ M^{-1}, $52{,}2 \times 10^4$ M^{-1} et $13{,}1 \times 10^4$ M^{-1}. Les valeurs correspondantes de K_2 pour les acides naphténiques de source commerciale (Fluka) et produit industrielle (Syncrude) sont respectivement de $2{,}34 \times 10^4$ M^{-1} et $1{,}27 \times 10^4$ M^{-1}. L'amplitude de la valeur K_2 pour les complexes 1 :1 formées entre la β-cyclodextrine et les produits S1, S2 et S3 ne présentent aucune corrélation avec le degré de déficience en hydrogène (série Z), mais il existe une corrélation entre la taille des molécules hôtes (n) examinées dans cette étude. La corrélation entre la stabilité du complexe et la taille relative de chacun des fragments lipophiles des molécules hôtes est liée à l'importance de l'effet hydrophobe pour l'inclusion de tels acides carboxyliques comme molécules hôtes dans la β-CD.

Mots-clés : déplacement spectral, cyclodextrine, acides carboxyliques, acides naphténiques, constante de fixation, hydration hydrophobe, aire de la surface lipophile.

[Traduit par la Rédaction]

Introduction

Naphthenic acids (NAs) are predominantly complex mixtures of saturated alicyclic and aliphatic carboxylic acids with the general formula $C_nH_{2n+Z}O_2$, where n is the number of carbon atoms and $(2n + Z)$ is the number of hydrogen atoms where Z is the hydrogen deficiency; hydrogen loss due to ring structure. Generally, the carboxyl group is attached to a cyclopentane or cylcohexane ring through a methylene group or an alkyl chain containing five or more methylene groups as shown in Fig. 1. The molecular structure, composition, and concentration of NAs are dependent on the source of crude oil.[1–5]

NAs are non-volatile, chemically stable, and possess surface activity. The acid dissociation constants range between 10^{-5} and 10^{-6} M^{-1} and are comparable to typical carboxylic acids (acetic acid = $10^{-4.8}$ M, propionic acid = $10^{-4.9}$ M, and palmitic acid $10^{-4.9}$ M).[5–7] The presence of NAs in petroleum has led to environmental, health, and industrial concerns. NAs are known to be toxic to aquatic organisms, algae, and mammals.[5–8] NAs are suspected endocrine-disrupting substances; however, the toxicological implications of the various types of NAs are not well-understood. Thus, there is a great need to develop improved methods to sequester NAs leachates from aquatic environments, such as

Received 11 June 2009. Accepted 17 August 2009. Published on the NRC Research Press Web site at canjchem.nrc.ca on 27 November 2009.

M.H. Mohamed and L.D. Wilson.[1] Department of Chemistry, Thorvaldson Building, University of Saskatchewan, 110 Science Place, Saskatoon, SK S7N 5C9, Canada.
J.V. Headley and K.M. Peru. Water Science and Technology Directorate, Environment Canada, 11 Innovation Boulevard, Saskatoon, SK S7N 3H5, Canada.

[1]Corresponding author (e-mail: lee.wilson@usask.ca).

Fig. 1. Generalized molecular structures of NAs for the $Z = 0$, –2, –4, and –6 series with both five and six carbon rings present $n \geq 5$ for $Z = 0$ while $n \geq 1$ for $Z = -2$, –4, and –6.

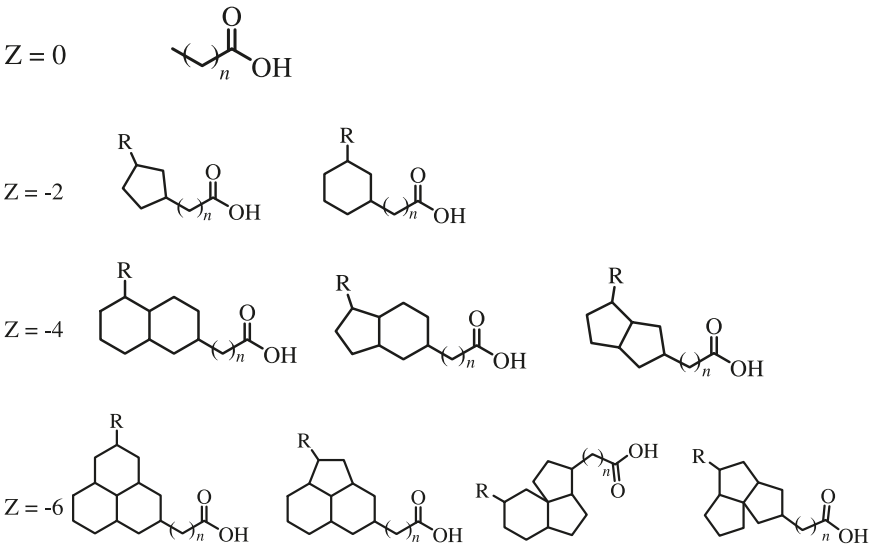

Scheme 1. The formation of a host–guest complex is shown for a β-CD (toroid) and a chromophore guest molecule (rectangle) according to an equilibrium process where K_1 is the equilibrium binding constant. Addition of a non-chromophore guest molecule (oval): the chromophore is replaced and the guest molecule is included into the β-CD according to an equilibrium constant, K_2.

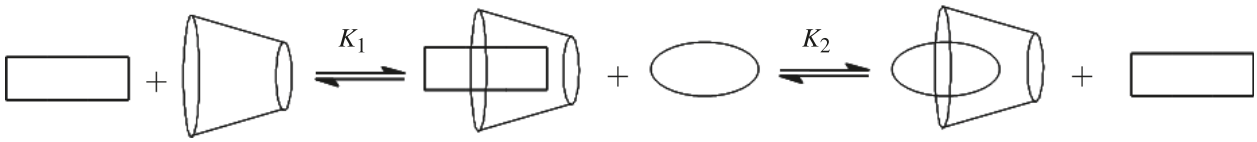

oil-sands tailings ponds, and to alleviate concerns of their deleterious health and environmental effects.

Cylodextrins (CDs) are of interest, in part, because of their ability to form inclusion complexes in aqueous solution. In particular, they are well-known to form relatively stable inclusion complexes with aliphatic and alicyclic carboxylic acids.[9–12] For the latter reason, CDs may display strong binding affinity to NA molecules.

Recently, cyclodextrin-based polymeric materials were used to adsorb NAs from aqueous solutions with considerable success.[13] However, a detailed understanding of the sorption mechanism for polymeric materials requires an understanding of the types of inclusion complexes formed and the magnitude of the binding constants. Thus, this study outlines the use of the spectral displacement technique to study the interaction of β-cyclodextrin (β-CD) with NAs and single-component examples of NAs in aqueous solution, respectively.

Various instrumental methods have been used to examine the nature of the CD/inclusate complexes formed between β-CD and carboxylic acid guest compounds. Among these techniques are ^{1}H NMR,[14] sound velocity,[15] conductivity,[16] surface tension,[17] electrochemical measurements,[18] UV–vis spectrophotometry,[19] and fluorescence measurements.[20] The latter three methods involve direct measurement of bound or free concentrations of inclusates, whereas the other methods involve the measurement of a bulk solution property (time-averaged property consisting of two or more states) that is proportional to some aspect of the complexation process. The apparent discrepancies in the literature between the values of binding constants obtained from different techniques have been attributed to the relative accuracy of the measured variables. However, methods involving the measurement of free or bound inclusate concentration are expected to yield a more accurate estimate of the binding constant.[21]

The spectral displacement technique[22–32] enables determination of the binding constants of spectroscopically transparent compounds, such as NAs, to β-CD. The determination of the binding constants for such complexes involves the measurement of the absorbance changes of a suitable chromophore in the presence of CD and a competing non-chromophoric inclusate. Some examples of the chromophores employed include phenolphthalein (phth),[22–30] methyl orange,[31] and *p*-nitrophenol.[32] Scheme 1 illustrates the two competitive equilibria involved in the spectral displacement technique.

This technique involves certain assumptions and provides good accuracy for the determination of a CD/inclusate binding constant (K_2) values when the relative change in the absorbance of phth between bound and unbound states is large and is directly related to the amount of unbound inclusate. Non-spectroscopic techniques are sometimes susceptible to large errors when K_2 is large ($>10^4$ M^{-1}) because the fraction of unbound species is generally low for this condition and techniques which involve the measurement of macroscopic changes for a total solution property and do not reflect this contribution accurately. Consequently, there are greater uncertainties for the value of K_2 derived from such methods. A further complication arises because of implicit statistical bias in the analysis of the primary data using linearization methods; for example, the inherent assumptions in

Fig. 2. Molecular structures of specific examples of single-component NAs with variable *Z*-values (*Z* = 0, –2, and –4, respectively): (*a*) 2-hexyldecanoic acid (S1), (*b*) *trans*-4-pentylcyclohexanecarboxylic acid (S2), and (*c*) dicyclohexylacetic acid (S3).

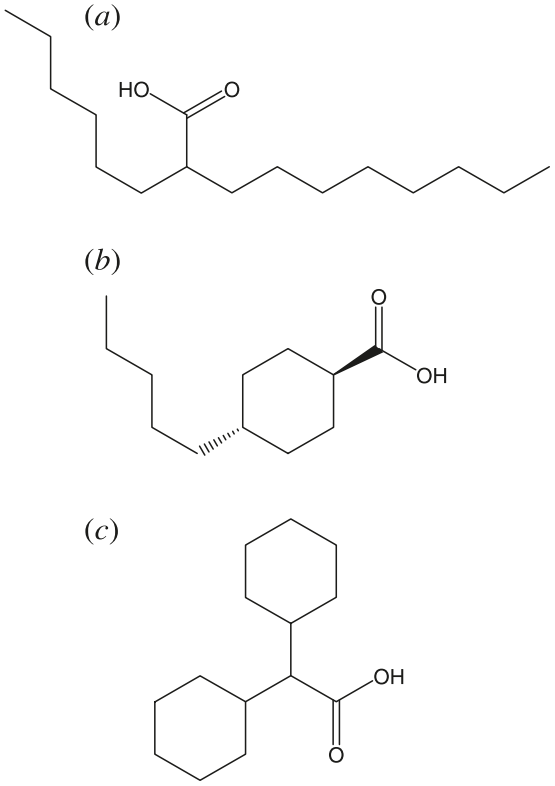

the Benesi–Hildebrand plots are generally not met for strongly bound host–guest systems.[22,33]

This paper presents the results of a determination of the binding constants between β-CD and different types of NAs and some single-component examples of NAs in aqueous solutions at room temperature. The three components chosen to represent examples of NAs with variable *Z* values are 2-hexyldecanoic acid (*Z* = 0; S1), *trans*-4-pentylcyclohexanecarboxylic acid (*Z* = –2; S2), and dicyclohexylacetic acid (*Z* = –4; S3), respectively, as shown in Fig. 2.

Experimental

Absorption measurements were obtained with a double-beam spectrophotometer (Varian CARY 100) at room temperature (295 ± 0.5 K). All solutions were prepared by volume in a 0.1 mol/L sodium hydrogen carbonate buffer adjusted to pH 10.5 with 6 mol/L sodium hydroxide. The concentration of phth (C_{phth}) was maintained at ~ 2×10^{-5} mol/L in all experiments. For the determination of the CD/inclusate binding constants, K_2, the concentration of β-CD ($C_{\beta\text{-CD}}$) was held constant at ~ 3×10^{-4} mol/L, and the concentrations of NAs or single-component NAs (S1, S2, or S3) were varied to exceed the 1:1 molar ratio of the CD/inclusate. A stock solution of phth in ethanol was made and aliquots were utilized to prepare aqueous solutions of phth in buffer. The ethanol/water (0.04%, *v*/*v*)[28] solution was used to increase the solubility of phth. All aqueous solutions were freshly prepared and run within 1.5 h to ensure that the absorbance changes due to any instability of phth at pH 10.5 did not contribute to experimental artefacts. The respective compositions of Fluka and Syncrude NAs were determined using electrospray ionization mass spectrometry (ESI-MS) measurements with a Quattro Ultima mass spectrometer (Micromass, UK) equipped with an electrospray interface operating in the negative-ion mode configuration, as described previously.[13]

Scheme 2. Lipophilic fragments of the guest molecules that are included in β-CD. LSA values are derived from these included fragments. These molecular structures are; β-CD (I), β-CD/S1 (II), β-CD/S2 (III), and β-CD/S3 (IV) complexes, respectively. Note: The relative size of the β-CD torus and the carboxylic acid are not drawn to scale.

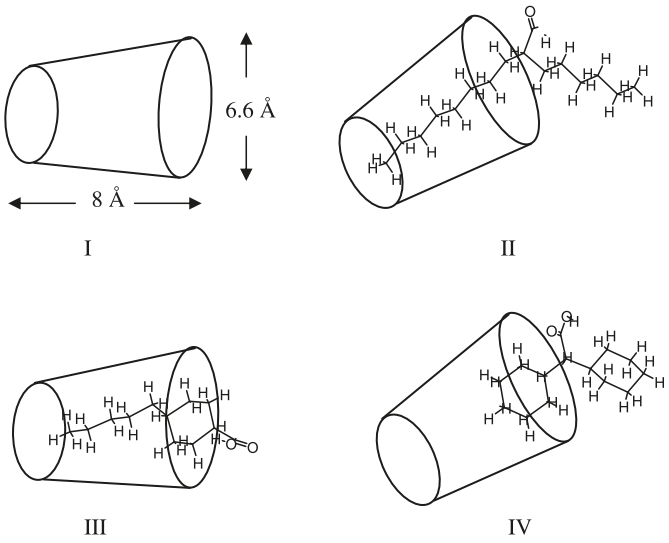

β-CD (VWR) was used as received, and the water content was determined using a thermogravimetric analyzer (Q5000, TA Instruments). The water contents were accounted for in the determination of $C_{\beta\text{-CD}}$ where the hydrate content varied from 10.98% to 11.53% (±0.3)% for different samples of β-CD hydrate. 2-Hexyldecanoic acid (S1), *trans*-4-pentylcyclohexanecarboxylic acid (S2), dicyclohexylacetic acid (S3), and Fluka NAs were obtained from Sigma-Aldrich. Syncrude NAs were extracted in bulk from an Athabasca oil-sands tailings pond using a published procedure.[34] Phenolphthalein (phth) (Aldrich) was used as received, since there was no difference in molar absorptivity between the purified and unpurified materials.[28]

A previously described[22] non-linear least-squares (NLLS) fitting procedure was used to determine the 1:1 binding constants, K_1 and K_2, between β-CD and phth and the inclusate, respectively. The method utilizes the Beer–Lambert law and the assumption that the molar absorptivity of the β-CD/phth complex is zero.[24] The following equilibrium and mass-balance relations apply to the competitive equilibrium, as outlined in Scheme 2.

$$[1] \qquad [S]_o = [S] + [CD{-}S] = [S](1 + K_2[CD])$$

$$[2] \qquad [phth]_o = [phth] + [CD{-}phth] = [phth](1 + K_1[CD])$$

$$[3] \qquad [CD]_o = [CD] + [CD{-}S] + [CD{-}phth]$$

The terms $[S]_o$, [S], and [CD–S] refer to the total, unbound, and 1:1 complexed forms of the inclusate, respectively. [CD–S] and [CD–phth] are related to $[S]_o$, $[phth]_o$, K_2, and K_1 as follows:

$$[4] \qquad [CD{-}S] = [S]_o\left(1 + \frac{1}{K_2[CD]}\right)^{-1}$$

$$[5] \qquad [CD{-}phth] = [phth]_o\left(1 + \frac{1}{K_1[CD]}\right)^{-1}$$

Upon substitution into eq. [3] and rearrangement, the following cubic expression in terms of unbound β-CD ([CD]) is obtained in eq. [6].

$$[6] \qquad [CD]^3 + [CD]^2\left(\frac{K_2 + K_1}{K_2K_1} + [phth]_o + [S]_o - [CD]_o\right) + [CD]\left(\frac{1}{K_2K_1} + \frac{[S]_o}{K_1} + \frac{[phth]_o}{K_2} - \frac{[CD]_o}{K_1} - \frac{[CD]_o}{K_2}\right) - \left(\frac{[CD]_o}{K_2K_1}\right) = 0$$

The real solution to the cubic root of eq. [6] was obtained by application of the Newton–Raphson method[35,36] using appropriate boundary values of $[S]_o$, $[phth]_o$, K_2, and K_1. Values for [CD–S], [CD–phth], and [phth] were obtained using Beer–Lambert law for phth and eqs. [1]–[3]. The criterion utilized for the best fit in the NLLS procedure was the minimization of the sums of the squares of the residuals (SSR) according to the relation: $\text{SSR} = \sum_i [(A_{calc})_i - (A_{expt})_i]^2$, where A_{calc} and A_{expt} are the calculated and experimental absorbance values, respectively.

The lipophilic surface area (LSA) of the apolar molecular fragments of the guest molecule included by β-CD was calculated using Spartan 06. The calculations were based on an equilibrium geometry optimization in the ground state with Hartree–Fock 3–21G in vacuum to obtain the minimized molecular structures.

Results and discussion

The low ethanol composition (0.04%, *v*/*v*) was chosen to eliminate possible interferences due to competitive binding by ethanol and undue solvent effects.[28,37–39] A pH of 10.5 was chosen to optimize ε_{phth}, to provide greater sensitivity for absorption measurements, and to minimize the potential for deprotonation of the hydroxyl groups of β-CD (pK_a ~ 12). All absorption measurements were carried out at λ = 552 nm, and no change in the shape of the visible absorption band with $C_{β\text{-CD}}$ was observed at this wavelength.

To obtain valid estimates of the 1:1 binding constant, the following conditions must be met when using the spectral displacement technique: (*i*) competing inclusate must not absorb in the wavelength region of interest or interact with the chromophore and (*ii*) inclusates must bind exclusively in a 1:1 stoichiometry. The first condition has been verified experimentally by measuring the absorbance change as a function of added NAs and the single-component NAs (S1, S2, or S3). *trans*-4-Pentylcyclohexanecarboxylic acid and Fluka NAs showed a small increase in absorbance due to an increased background absorbance, which is attributed to weak interactions between unbound carboxylic anion guests and phth. Appropriate corrections were applied to absorbance data for these conditions. The formation of 1:1 inclusion complexes has been independently verified in these systems from a recent ESI-MS study of the same host–guest systems.[40] A further requirement is that the competing inclusate must fully displace the chromophore from the β-CD cavity and form a well-defined inclusion complex; not as a ternary outersphere complex, since the latter is known to affect the magnitude of K_2.[39] An additional practical consideration is the value of K_1 for β-CD/phth be greater than or equal to the value of K_2 for β-CD/inclusate ($K_1 \geq K_2$).[22] Under these circumstances, it is possible to displace the phth over a suitable concentration range to obtain adequate absorbance changes.

Fig. 3. Absorbance (abs; λ = 552 nm) vs. concentration of β-CD ($C_{β\text{-CD}}$) in 0.1 mol/L $NaHCO_3$ at pH 10.5, [phth] = 2×10^{-5} mol/L and T = 295 K.

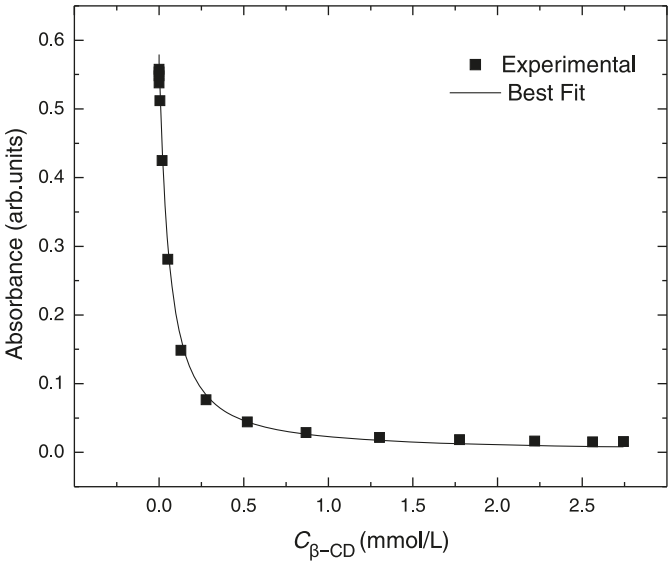

Figure 3 illustrates a typical plot of absorbance vs. $C_{β\text{-CD}}$ at a fixed concentration of phth. The line through the data points represents the calculated absorbance values obtained from the NLLS fitting procedure. The sharp falloff of absorbance as $C_{β\text{-CD}}$ increases represents the formation of the β-CD/phth complex, since the molar absorptivity of the β-CD/phth complex is regarded as zero. Benesi–Hildebrand[41] plots were not utilized to determine values of K_1, since the assumption that the concentration of the complex is lower than the total concentration of β-CD is not usually valid for strongly bound inclusates. As well, such classical double reciprocal plots (1/abs vs. $1/C_{β\text{-CD}}$) improperly weigh the data at lower values of absorbance and higher values of $C_{β\text{-CD}}$. Consequently, an NLLS fitting procedure was employed to obtain values of K_1 and K_2. An average value of the 1:1 β-CD/phth binding constant (K_1 = $2.6 \pm 0.3 \times 10^4$ M^{-1}) was estimated with good agreement with independent literature values.[23–25,27] The conditions employed in this study utilized a relatively low ethanol composi-

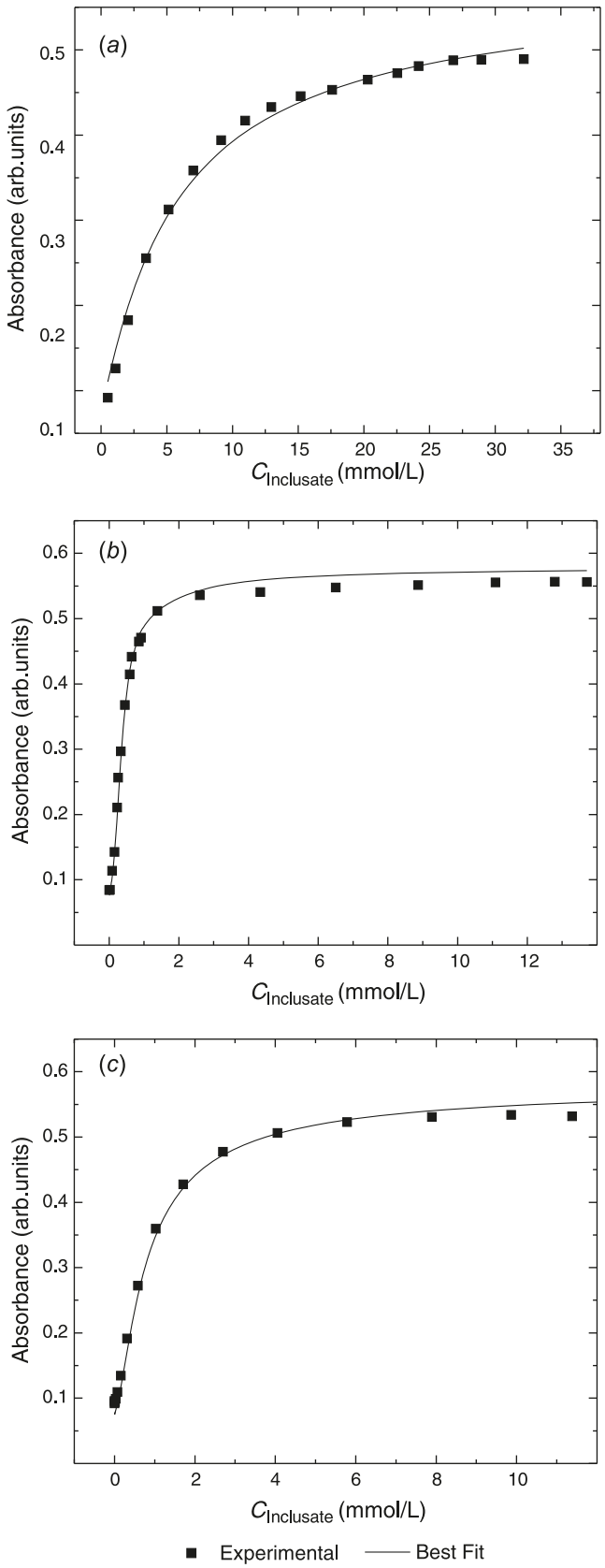

Fig. 4. Absorbance (abs; λ = 552 nm) vs. concentration of specific examples of single-component NAs in 0.1 mol/L $NaHCO_3$ at pH 10.5, [β-CD] = 2 × 10^{-4} mol/L, [phth] = 2 *x* 10^{-5} mol/L, and *T* = 295 K: (*a*) 2-hexyldecanoic acid (S1), (*b*) *trans*-4-pentylcyclohexanecarboxylic acid (S2), and (*c*) dicyclohexylacetic acid (S3).

tion (0.04%, *v*/*v*) as compared with Selvidge and Eftink,[22] and the corresponding value of K_1 obtained is greater.

Figures 4*a*–4*c* are representative plots of the absorbance vs. $C_{Inclusate}$ for the single-component NAs (i.e., S1, S2 and S3). The absorbance values exhibit a smooth monotonic increase with increasing $C_{Inclusate}$, which corresponds to the displacement of phth from the β-CD cavity upon inclusion binding of the single-component molecules. Figure 4*b* represents an example of a strongly bound β-CD/inclusate system where the absorbance changes sharply for S2, the shape of the isotherm becomes increasingly sigmoidal, and the displacement of phth occurs over a narrower range of concentration of guest. S1 displays the weakest binding (cf. Fig. 4*a*) amongst the three examples of single-component NAs examined in Fig. 4. Phenolphthalein (phth) is displaced when $[S1]_o$ reaches ~25 mmol/L, whereas S2 and S3 reach saturation binding ~4 mmol/L and 8 mmol/L, respectively. In Fig. 4*c*, S3 displays a prominent sigmoidal shape as concentration increases but the absorbance changes are more gradual, as compared with S2. These observations indicate that there are differences in the binding affinity of β-CD/inclusate systems as follows: K_2 (S2) > K_2 (S3) > K_2 (S1). Table 1 lists the values of K_2 and ΔG^o for the formation of 1:1 complexes and estimates of lipophilic surface area (LSA) for the single-component NAs. The values of K_2 range between 10^3 and 10^4 M^{-1}, and Gibbs energy change values are negative, indicating the complexation process of β-CD with the inclusates are favourable. There are several factors that govern the formation of CD inclusion complexes.[42] The hydrophobic effect is concluded as very important and is corroborated by the positive correlation between K_2 values and the LSA[43,44] values for the carboxylic acid guest molecules included in the β-CD cavity, as shown in Table 1. β-CD has an approximate cavity length[45] of 8 Å and a diameter of 6.6 Å; thus, β-CD can include ~53 $Å^2$ of an inclusate's LSA. An illustration of the latter is shown for the three single-component NAs as outlined in Scheme 2. Moreover, the cavity volume of β-CD is ~262 $Å^3$ and may include relatively large apolar groups, such as dodecyl alkyl chains,[28] whereas it has been shown that α-CD (less in diameter than β-CD) can include octyl chains.[44,46] Although the LSA of the inclusates were calculated as gas-phase-optimized structures while the experiment was done in aqueous solution, the approach offers a semiquantitative method of relating complex stability to the LSA parameter.[47] The use of LSA values is further corroborated by Connors [45] in his study of CDs with substituted carboxylic acids (cf. Table 1). The binding constants increase as the LSA value increases for a series of cyclohexane carboxylic acids. These results support the important role of the thermodynamics for hydration and dehydration of apolar compounds during complex formation between β-CD and carboxylic acids guests.[28,48–50] The rearrangement of hydrate water includes desolvation of β-CD, dehydration

Table 1. 1:1 Binding constants and Gibbs free energy of complex formation for 1:1 CD/inclusate complexes using the spectral displacement method in 0.1 mol/L $NaHCO_3$ buffer at pH 10.5 and T = 295 K.

Inclusate	K_2 (M^{-1})	χ^2 [a]	SEE[b]	ΔG (kJ/mol)[c]	LSA ($Å^2$)[d]
S1	1.42(0.164) × 10^3	0.0103	0.0232	–17.9	17.2
S2	52.2(6.02) × 10^4	0.0140	0.0279	–26.8	45.4
S3	13.1(1.51) × 10^4	0.0319	0.0316	–23.3	21.3
Fluka NAs	23.4(2.70) × 10^4[e]	0.00326	0.0117	–24.8	NR[f]
Syncrude NAs	12.7(1.46) × 10^4[e]	0.0113	0.0232	–23.3	NR[f]

[a] χ^2 = chi-square.

[b] SEE = standard error of estimate.

[c] $\Delta G = -RT\ln K_2$ (K_2 is the 1:1 equilibrium binding constant).

[d] Refer to Fig. 2 for molecular structures. Due to their distribution of variable molecular structures, the LSA values were not calculated for NAs and LSA values (S1, S2, and S3) were estimated using Spartan 06.

[e] Based on average molecular mass values; Fluka NAs (230 g mol^{-1}) and Syncrude NAs (362 g mol^{-1}), respectively.

[f] NR = Not reported.

of inclusates, and reformation of a hydration shell for the complex. This is outlined by the following contributions to the overall Gibbs energy change of complexation (ΔG°) for a typical 1:1 CD/inclusate complex.[51]

$$[7] \qquad \Delta G^\circ = \Delta G^\circ_{H/W} + \Delta G^\circ_{I/W} + \Delta G^\circ_{H/I/W} + \Delta G^\circ_{W/W}$$

where I, H, and W are inclusate, host, and solvent (water), respectively. The LSA has a large effect on the magnitude of solvent rearrangement, as anticipated for apolar guest compounds and associative processes governed by the hydrophobic effect.

Figures 5*a*–5*b* are representative plots of absorbance vs. $C_{Inclusate}$ for the binding of β-CD/inclusate for Fluka and Syncrude NAs, respectively. Fluka NAs are more strongly bound than Syncrude NAs, as shown by the sigmoidal appearance of the absorbance profile in Fig. 5*a*, as compared with Fig. 5*b*. The former is the more pronounced of the two curves, particularly the change in absorbance at the lower inclusate concentrations. The values of K_2 are shown in Table 1, and the observed differences may be related to the structural variability of the NAs according to the Z value and the carbon number of the respective samples. Fluka NAs have a narrower size distribution and lower average molecular mass, as shown in Figs. 6*a*–6*b* and 7*a*–7*b*. The K_2 values represent an average binding constant, since the NAs studied are mixtures of compounds with similar Z values and carbon number. The molecular mass used in estimates of K_2 utilized the average molecular mass of NAs, since it is not known which specific cogeners are included by β-CD. It is assumed that a random statistical distribution of the NA components are included; however, it is anticipated that high molecular mass components of NAs possessing greater LSA values will be bound more strongly than the lower molecular mass components. The average molecular mass may not represent the fraction of bound species but it is reasonable to report that the K_2 values reported herein reflect the average binding constant for 1:1 complexes of β-CD/NAs. Recent developments in mass spectrometry have also indicated that the Athabasca oil-sands acids may contain co-extractants containing S and N heteratoms along with aromatic and dicarboxylic acids.[52] The interactions of these species with β-CD are indirectly detected in the spectral displacement technique. However, the binding constants reported are representative of the oil-sands acids in the

Fig. 5. Absorbance (abs; λ = 552 nm) vs. concentration of inclusate (Fluka NAs) in 0.1 mol/L $NaHCO_3$ at pH 10.5, [β-CD] = 2 × 10^{-4} mol/L, [phth] = 2 × 10^{-5} mol/L, and T = 295 K: (*a*) Fluka NAs and (*b*) Syncrude NAs.

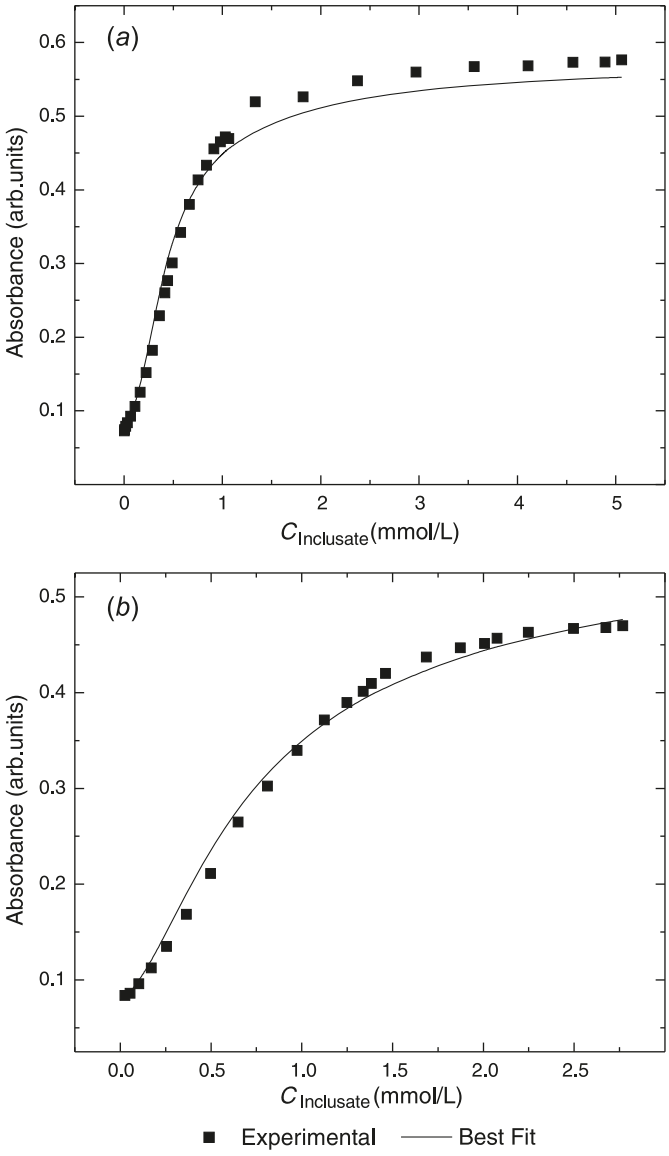

Fig. 6. (*a*) ESI-MS spectrum of a 94.4 ppm sample of NAs (Fluka) at pH 6.3, illustrating the distribution of cogeners according to molecular mass, and (*b*) 3D plot of ESI-MS data representing percentage abundance of NAs with variable carbon number (*n*) and *Z* family series for a 94.4 ppm sample of NAs (Fluka) at pH 6.3.

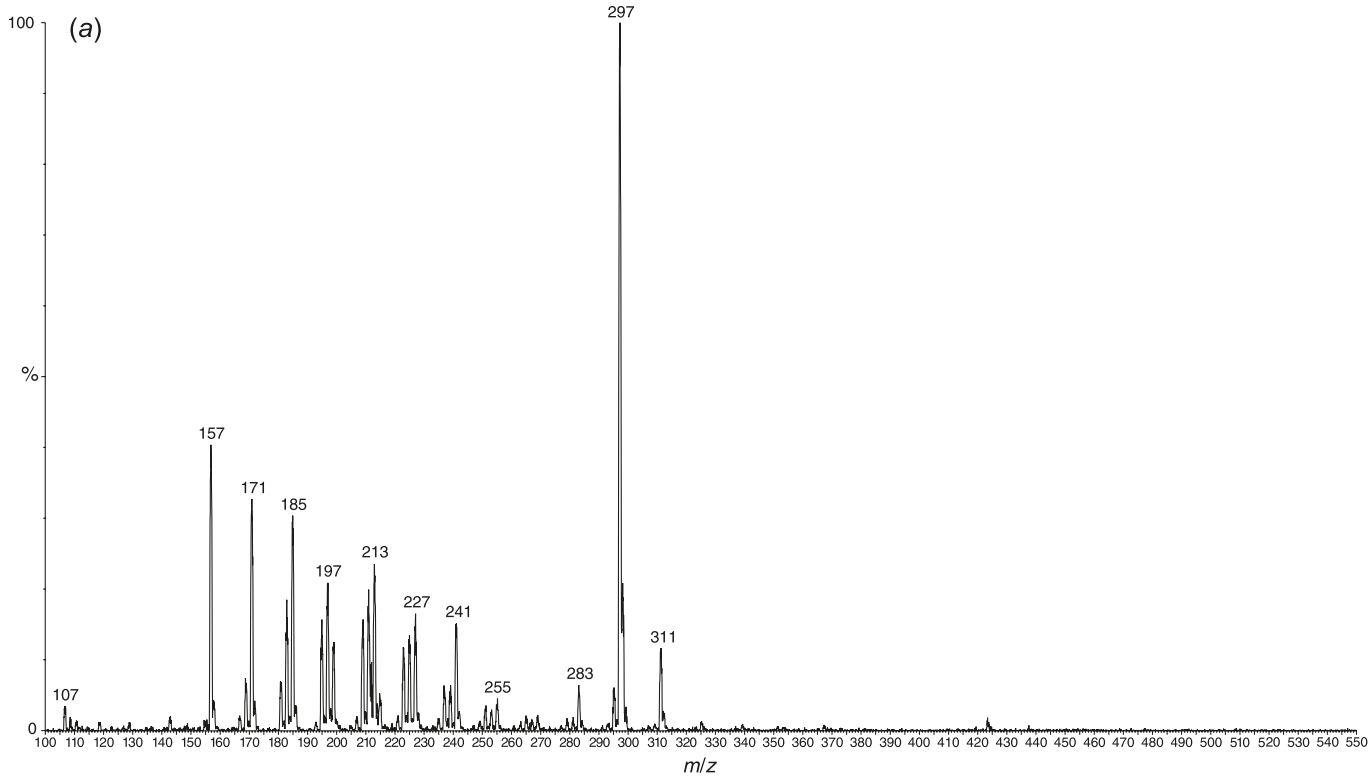

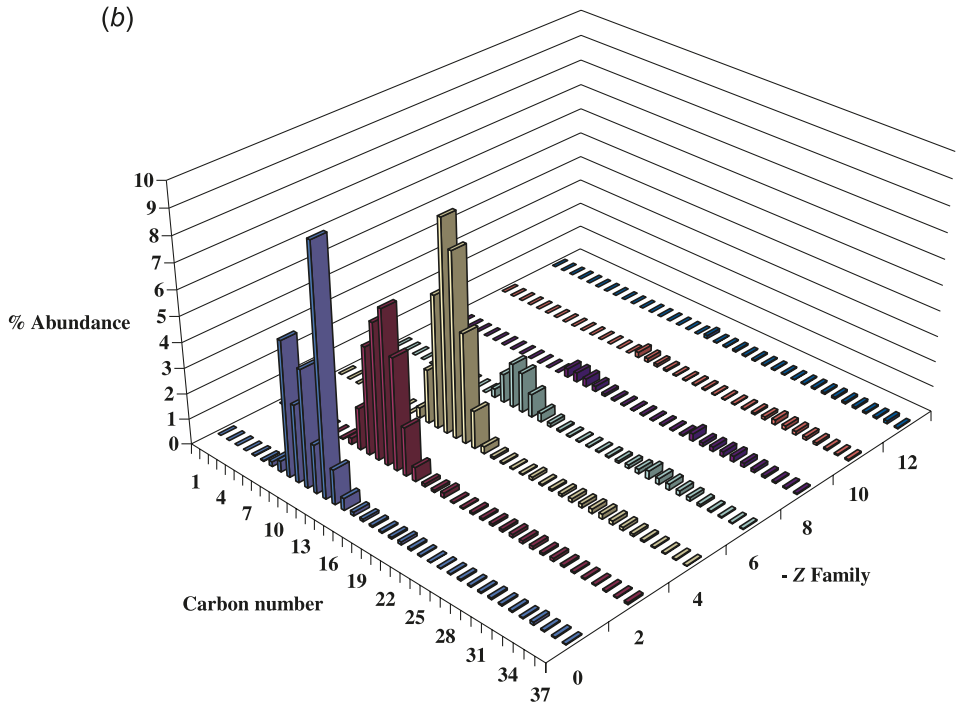

Fig. 7. (*a*) ESI-MS spectrum of a 95.8 ppm sample of NAs (Syncrude) at pH 9.0, illustrating the distribution of cogeners according to molecular mass, and (*b*) 3D plot of ESI-MS data representing percentage abundance of NAs with variable carbon number (*n*) and *Z* family series for a 95.8 ppm sample of NAs (Syncrude) at pH 9.0.

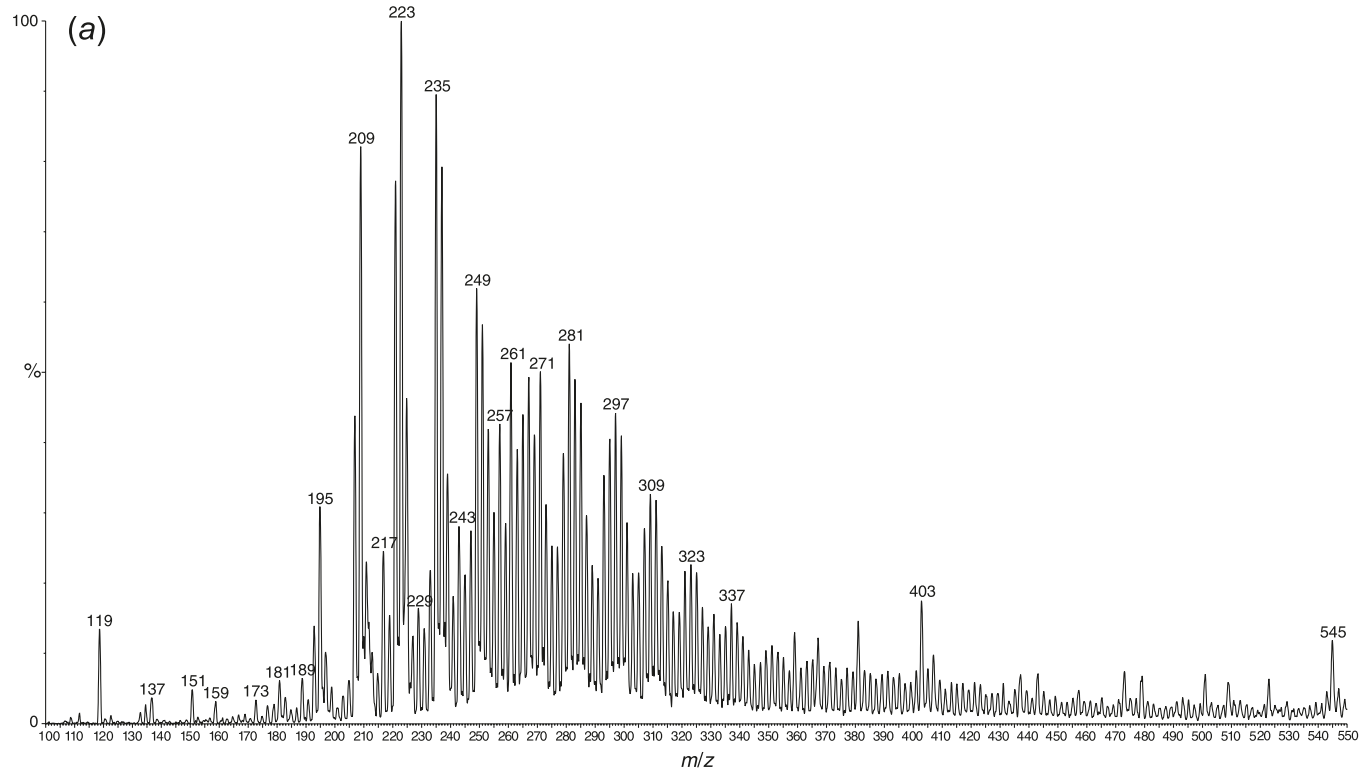

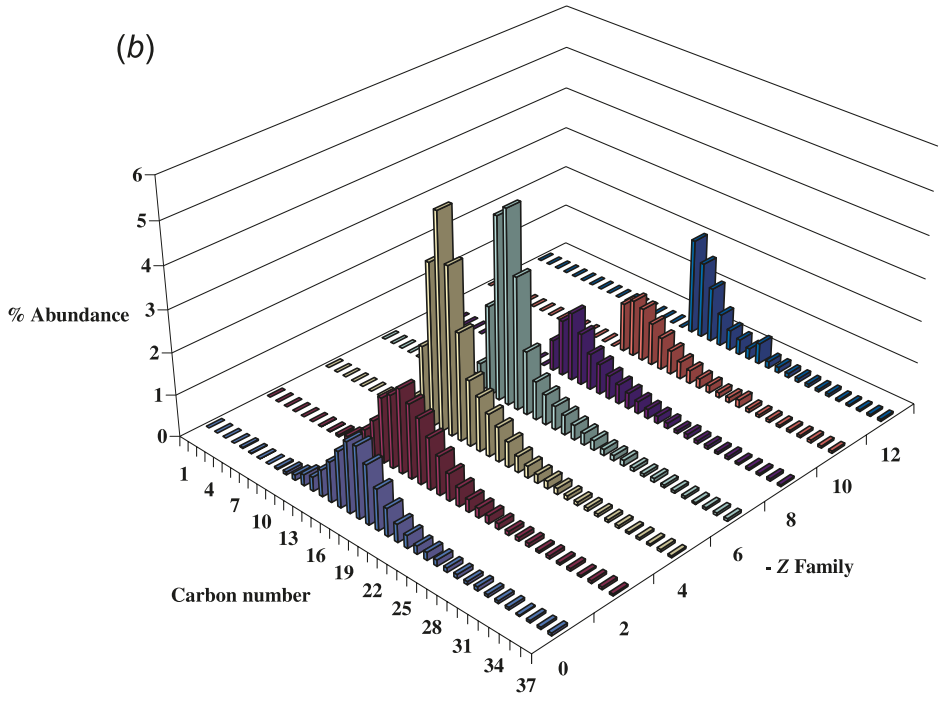

wider context and not limited to the classical structures (cf. Scheme 1) of naphthenic acids.

Conclusion

The spectral displacement technique provides accurate estimates of the 1:1 binding constants (K_2) for a series of NAs and three examples of single-component NAs (S1, S2, and S3). The values of K_2 for single components ranged from 10^3 to 10^4 M^{-1}, and the NAs (i.e., Fluka and Syncrude) had K_2 values ~10^4 M^{-1}. The K_2 values increased in accordance to their respective LSA values. Fluka NAs have greater K_2

values than Syncrude NAs, and the differences were attributed to the binding of corresponding greater molecular mass components in Fluka NAs vs. Syncrude coextracted oil-sands acids. Although the average molecular mass of Syncrude NAs is higher than Fluka, the former contain impurities which do not appear to bind strongly to the β-CD.

The spectral displacement technique is a versatile method for obtaining accurate estimates of K_2 for carboxylate anions that possess strong binding affinities to β-CD and allows the indirect determination of the concentrations of inclusates in solution. To our knowledge, this is the first quantitative study of the binding constants between NAs and β-CD reported to date. Further thermodynamic studies of complex formation are underway and should provide useful information regarding temperature effects on the stability of these CD/inclusate complexes. The results of this study will contribute toward a further understanding of the sorption mechanism between β-CD-based polymeric materials and carboxylate ions in aqueous solution.

Acknowledgements

Financial assistance was provided by the Natural Sciences and Engineering Research Council of Canada (NSERC) and the Program of Energy Research and Development. M.H.M. acknowledges the University of Saskatchewan for the award of a Graduate Teaching Fellowship and Environment Canada for the Science Horizons Program award.

References

(1) Jolly, S. E. *Kirk-Othmer Encycl. Chem. Technol.* **1967**, *13* (2), 727.
(2) Lo, C. C.; Brownlee, B. G.; Bunce, N. J. *Anal. Chem.* **2003**, *75* (23), 6394. doi:10.1021/ac030093d. PMID:16465694.
(3) Headley, J. V.; McMartin, D. W. *J. Env. Sci. Health* **2004**, *39* (8), 1989. doi:10.1081/ESE-120039370.
(4) McMartin, D. W.; Headley, J. V.; Friesen, D. A.; Peru, K. M.; Gillies, J. A. *J. Env. Sci. Health* **2004**, *39* (6), 1361. doi:10.1081/ESE-120037839.
(5) Clemente, J. S.; Fedorak, P. M. *Chemosphere* **2005**, *60* (5), 585. doi:10.1016/j.chemosphere.2005.02.065. PMID: 15963797.
(6) Brient, J. A.; Wessner, P. J.; Doly, M. N. Naphthenic acids. In *Kirk–Othmer Encyclopedia of Chemical Technology,* 4th ed.; Kroschwitz, J. I., Ed.; John Wiley & Sons, Inc., 1995; Vol. 16, pp 1017–1029.
(7) Kanicky, J. R.; Poniatowski, A. F.; Mehta, N. R.; Shah, D. O. *Langmuir* **2000**, *16* (1), 172. doi:10.1021/la990719o.
(8) Quagraine, E. K.; Peterson, H. G.; Headley, J. V. *J. Env. Sci. Health* **2005**, *40* (3), 685.
(9) Buvári, A.; Szejtli, J.; Barcza, L. *J. Incl. Phenom.* **1983**, *1* (2), 151. doi:10.1007/BF00656817.
(10) Eftink, M. R.; Andy, M. L.; Bystrom, K.; Perlmutter, H. D.; Kristol, D. S. *J. Am. Chem. Soc.* **1989**, *111* (17), 6765. doi:10.1021/ja00199a041.
(11) Gadre, A.; Rüdiger, V.; Schneider, H. J.; Connors, K. A. *J. Pharm. Sci.* **1997**, *86* (2), 236. doi:10.1021/js960202m. PMID:9040102.
(12) Gadre, A.; Connors, K. A. *J. Pharm. Sci.* **1997**, *86* (11), 1210. doi:10.1021/js9702527. PMID:9383727.
(13) Mohamed, M. H.; Wilson, L. D.; Headley, J. V.; Peru, K. M. *Process Saf. Environ. Prot.* **2008**, *86* (4), 237. doi:10.1016/j.psep.2008.04.001.
(14) Wood, D. J.; Hruska, F. E.; Saenger, W. *J. Am. Chem. Soc.* **1977**, *17*, 694.
(15) Junquera, E.; Tardajos, G.; Aicart, E. *Langmuir* **1993**, *9* (5), 1213. doi:10.1021/la00029a011.
(16) Saint Aman, E.; Serve, D. *J. Colloid Interface Sci.* **1990**, *138* (2), 365. doi:10.1016/0021-9797(90)90219-E.
(17) Dharmawardana, U. R.; Christian, S. D.; Tucker, E. E.; Taylor, R. W.; Scamehorn, J. F. *Langmuir* **1993**, *9* (9), 2258. doi:10.1021/la00033a003.
(18) Wan Yunus, W. M. Z.; Taylor, J.; Bloor, D. M.; Hall, D. G.; Wyn-Jones, E. *J. Phys. Chem.* **1992**, *96* (22), 8979. doi:10.1021/j100201a052.
(19) Gelb, R. I.; Schwartz, L. M.; Cardelino, B.; Laufer, D. A. *Anal. Biochem.* **1980**, *103* (2), 362. doi:10.1016/0003-2697(80)90624-7. PMID:7386867.
(20) Fourmentin, S.; Surpateanu, G. G.; Blach, P.; Landy, D.; Decock, P.; Surpateanu, G. *J. Incl. Phenom. Macrocycl. Chem.* **2006**, *55* (3–4), 263. doi:10.1007/s10847-006-9045-x.
(21) Mwakibete, H.; Cristiantino, R.; Bloor, D. M.; Wyn-Jones, E.; Holzwarth, J. F. *Langmuir* **1995**, *11* (1), 57. doi:10.1021/la00001a013.
(22) Selvidge, L. A.; Eftink, M. R. *Anal. Biochem.* **1986**, *154* (2), 400. doi:10.1016/0003-2697(86)90005-9. PMID:3755301.
(23) Buvári, Á.; Szeijtli, J.; Barcza, L. *J. Inclusion Phenom.* **1983**, *1*, 151. doi:10.1007/BF00656817.
(24) Buvári, Á.; Barcza, L.; Kajtár, M. *J. Chem. Soc. Perkin Trans. 2* **1988**, 1627.
(25) Sasaki, K. J.; Christian, S. D.; Tucker, E. E. *Fluid Phase Equilib.* **1989**, *49* (1-2), 281. doi:10.1016/0378-3812(89)80022-6.
(26) Buvári, Á.; Barcza, L. *Inorg. Chim. Acta* **1979**, *33* (2), L179. doi:10.1016/S0020-1693(00)89441-4.
(27) Gray, J. E.; MacLean, S. A.; Reinsborough, V. C. *Aust. J. Chem.* **1995**, *48* (3), 551. doi:10.1071/CH9950551.
(28) Wilson, L. D.; Siddall, S. R.; Verrall, R. E. *Can. J. Chem.* **1997**, *75* (7), 927. doi:10.1139/v97-111.
(29) Meier, M. M.; Bordignon Luiz, M. T.; Farmer, P. J.; Szpoganicz, B. *J. Incl. Phenom. Macrocycl. Chem.* **2001**, *40* (4), 291. doi:10.1023/A:1012705301448.
(30) Tutaj, B.; Kasprzyk, A.; Czapkiewicz, J. *J. Incl. Phenom. Macrocycl. Chem.* **2003**, *47* (3/4), 133. doi:10.1023/B:JIPH.0000011783.40427.56.
(31) Landy, D.; Fourmentin, S.; Salome, M.; Surpateanu, G. *J. Incl. Phenom. Macrocycl. Chem.* **2000**, *38* (1/4), 187. doi:10.1023/A:1008156110999.
(32) Suzuki, I.; Yamauchi, A. *J. Incl. Phenom. Macrocycl. Chem.* **2006**, *54* (3-4), 193. doi:10.1007/s10847-005-7367-8.
(33) Funasaki, N.; Yodo, H.; Hada, S.; Neya, S. *Bull. Chem. Soc. Jpn.* **1992**, *65* (5), 1323. doi:10.1246/bcsj.65.1323.
(34) Rogers, V. V.; Liber, K.; MacKinnon, M. D. *Chemosphere* **2002**, *48* (5), 519. doi:10.1016/S0045-6535(02)00133-9. PMID:12146630.
(35) Mortimer, R. G. In *Mathematics for Physical Chemistry;* Macmillan: New York, 1981.
(36) Parker, O. J.; Breneman, G. L. In *Spreadsheet Chemistry;* Prentice Hall: NJ, 1991; pp 274–277.
(37) Donzé, C.; Chatjigakis, A.; Coleman, A. W. *J. Inclusion Phenom. Mol. Recog. Chem.* **1992**, *13*, 155. doi:10.1007/BF01053639.
(38) Schuette, J. M.; Warner, I. M. *Anal. Lett.* **1994**, *27* (6), 1175.
(39) Warner, I. M.; Schuette, J. M. *Adv. Mult. Lum.* **1993**, *2*, 61.
(40) Mohamed, M. H.; Wilson, L. D.; Headley, J. V.; Peru, K. M. *Rapid Commun. Mass Spectrom.* In press.

(41) Benesi, H.; Hildebrand, H. *J. Am. Chem. Soc.* **1949**, *71* (8), 2703. doi:10.1021/ja01176a030.
(42) Liu, L.; Guo, A.-X. *J. Incl. Phenom. Macrocycl. Chem.* **2002**, *42* (1/2), 1. doi:10.1023/A:1014520830813.
(43) Cserhati, T. *Anal. Lett.* **1993**, *26* (12), 2687.
(44) Ishikawa, S.; Hada, S.; Neya, S.; Funasaki, N. *J. Phys. Chem. B* **1999**, *103* (8), 1208. doi:10.1021/jp983217c.
(45) Connors, K. A. *Chem. Rev.* **1997**, *97* (5), 1325. doi:10.1021/cr960371r. PMID:11851454.
(46) Funasaki, N.; Yamauchi, J.; Ishikawa, S.; Hirota, S. *Bull. Chem. Soc. Jpn.* **2004**, *77* (12), 2165. doi:10.1246/bcsj.77.2165.
(47) Rodriguez, C.; Bugay, D. E. *J. Pharm. Sci.* **1997**, *86* (2), 263. doi:10.1021/js960286z. PMID:9040107.
(48) Merino, C.; Junquera, E.; Jiménez-Barbero, J.; Aicart, E. *Langmuir* **2000**, *16* (4), 1557. doi:10.1021/la9905766.
(49) Castronuovo, G.; Niccoli, M. *J. Incl. Phenom. Macrocycl. Chem.* **2005**, *53* (1-2), 69. doi:10.1007/s10847-005-0995-1.
(50) Todorova, N. A.; Schwarz, F. P. *J. Chem. Thermodyn.* **2007**, *39* (7), 1038. doi:10.1016/j.jct.2006.12.019.
(51) Wilson, L. D. Binding Studies of Cyclodextrin-Surfactant Complexes. Ph.D. thesis, University Of Saskatchewan, 1998.
(52) Headley, J. V.; Peru, K. M.; Barrow, M. P. *Mass Spectrom. Rev.* **2009**, *28* (1), 121. doi:10.1002/mas.20185.

Canadian Journal of Chemistry

Author Index
Volume 87, 2009

Revue canadienne de chimie

Index des auteurs
Volume 87, 2009

Accardi, S.J., 448
Acosta-Silva, C., 1074
Aguado, J.E., 341
Ahmad, I, 714
Alhazmi, A.M., 453
Alhomaidan, O., 1163
Ali, D., 433
Alizadeh, A., 1708
Alo, B.I., 745
Amati, M., 1406
Amini, S.K., 563
Anderson, C.M., 80
Ángyán, J.G., 1444
Ansary, I., 472
Araujo, M.H., 361
Arias, K., 440
Arion, V.B., 146
Arora, R., 422
Au, R.H.W., 904
Augugliaro, V., 673
Autschbach, J., 927, 1546
Ávalos, J.B., 1296
Ayers, P.W., 1540
Babu, K.S., 393
Babu, S.S., 393
Back, T.G., 1657
Bacsa, J., 171
Bader, R.F.W., 1583
Baerends, E.J., 1383
Bai, G., 1163
Bain, A.D., 563
Baines, K.M., 307
Bakavoli, M., 724
Baker, A.E., 738
Balakrishnan, V.K., 662
Bandrauk, A.D., 1081
Barry, S.D., 942
Bassalah, L., 706
Baumgartner, T., 1222
Bearpark, M.J., 872
Beaupré, S., 1201
Becke, A.D., 1369
Ben Amor, N., 1006
Bendix, J., 1302
Berar, S., 422
Berar, U., 422
Bercaw, J.E., 264
Berner, G.M., 1512
Bérubé, M., 1180
Beyzavi, M.H., 416
Bhadra, S., 1605
Bhanage, B.M., 401
Bhandari, P., 1230
Bickelhaupt, F.M., 806
Blight, B.A., 205
Bo, C., 1296
Boden, B.N., 314
Boehme, R., 738
Boeré, R.T., 103, 738
Boland, P.G., 448
Bolton, T.M., 197
Borges de Castro, L., 678
Bosdet, M.J.D., 8
Bourgeois, C.J., 151
Bowmaker, G.A., 161
Boyd, R.J., 974
Brevet, D., 103
Branchadell, V, 1074
Breidung, J., 1322
Brigas, A., 171
Britten, J.F., 1055
Britton, R., 430
Brown, A., 1022
Brown, R.S., 640
Bryce, D.L., 927, 1338
Brzezinski, J., 386
Budzelaar, P.H.M., 832
Bühl, M., 818
Buncel, E., 433, 1127
Burke, K., 1485
Bussarawit, S., 612
Butcher, R.J., 1692
Cai, Z., 684
Campagna, S., 254
Cardoso Filho, J.E.P., 1135
Carosi, L., 650
Carrington, T., 864
Cavallo, L., 1362
Chaichit, N., 161
Chanthathamrongsiri, N., 612
Chattopadhyay B., 472
Chawla, H.M., 523
Cheah, S.-M., 151
Chen, F., 1090
Chen, L., 47
Chen, M., 502
Chen, Y., 280
Chen, Z., 30
Chikwana, E., 689
Chisholm, M.H., 88
Chivers, T., 39, 461
Chong, D.P., 1148
Choudhury, J., 183
Chu, A. Y-C., 335
Ciriminna, R., 673
Closson, T.L.L., 1425
Corrigan, J.F., 380
Cortés, J., 571
Cortés-Guzmán, F., 1583
Cox, R.A., 1127
Cook, S.C., 1641
Crespo, M., 80
Crisp , M.G., 212
Cugnet, C., 103
Cundari, T.R., 775
Dahl, J.P., 784
Dalgarno, S.J., 361
Daniel, C., 1006
Davis, B., 689
De Crisci, A.G., 95
de Jong, G.T., 806
de Sousa, A.L.F., 1135
Deacon, G.B., 121
Decken, A., 139, 368
Dedieu, A., 838
Deiseroth, H.-J., 619
Demko, B.A., 348

Derrick, S.D., 738
Deshmukh, K.M., 401
Desper, J., 224
Detellier, C., 272
Devi, P.C., 1682
Di Vitta, C., 1135
Dibble, P.W., 738
Ding, Z., 386
Djukic, B., 533
Dodd, D.W., 321
Donald, S.M.A., 1273
dos Santos, E.N., 361
Douglas, C.D., 729
Duarte Silva, J.A., 361
Dube, P.A., 533
Dussault, È.B., 662
Dutton, J.L., 1546
East, A.L.L., 1512
Eisler, D.J., 39
Elbokl, T.A., 272
Elder, P.J.W., 1055
Elgersma, W., 121
Eliav, E., 802
Elliott, P., 1485
El-Sherbiny, A., 1313
El-Taher, S., 1716
Esbata, A., 433
Eshghi, H., 724
Fakhraian H., 1650
Farrar, G.J., 1546
Feixas, F., 1063
Fekl, U., 95
Fernàndez, L.E., 507
Findlay-Shirras, L.J., 904
Firouzabadi, H., 1675
Fleischer, A., 146
Fogg, D.E., 361, 738
Fournier, R., 1013
Fowe, E.P., 1081
Fox, M.A., 63
Frenking, G., 1470
Gajewski, M., 1492
Ganguly, B., 514
Gao, H., 1583
Gao, J.-M., 397
Genre, C., 1625
Ghavami, R., 1593
Ghorbani-Choghamarani, A., 1144
Ghorbel, A, 706
Gimeno, M.C., 341
Goedecke, C., 1470
Gong, X., 502
Gonzàlez-Blanco, Ò, 1074
Gorelsky, S.I., 361
Gorgi-douze, A., 1650
Gori-Giorgi, P., 1444
Gorman, J.S.T., 328
Gossage, R.A., 368
Goudarziafshar, H., 1144
Goursot, A., 1261
Goward, G.R., 563
Green, J.R., 745
Gries, G., 430
Grindley, T.B., 974, 1641
Gritsenko, O., 1383
Gu, Q.-Q., 486
Gupta, S.C., 422
Gusarov, S., 1727
Guthrie, J.P., 1154
Halcovitch, N.R., 139
Hall, D.G., 650
Hall, M.B., 1460
Hanan, G.S., 254
Haras, A., 33
Harika, R., 121
Harrington, L.E., 232
Harris, K.J., 1338
Harvey, P.D., 103
Hasaninejad, A., 416
Haunschild, R., 1470
Headley, J.V., 1747
Hemmateenejad, B., 1593
Herdtweck, E., 1173
Hill, R.H., 217
Hillebrecht, P., 1470
Hirano, M., 176
Hongsui, S., 1248
Hosseini-Sarvari, M., 1122
Hsieh, Y.-H., 539, 544
Hu Q.Y., 134
Huang, H., 151
Huang, M.-B., 1610
Hudson, R.H.E., 321
Hughes, R.P., 151
Hurubeanu, N.R., 151
Hutadilok-Towatana, N., 1636
Ihmels, H., 619
Iranpoor, N., 1675
Ishiwata, T., 176
Ismaili, H., 1708
Itoh, K., 760
Ivanova, L., 478
Jacobsen, H., 965, 1362
Jahan, N., 1641
James, B.R., 582, 1248
Jansen, A.P.J., 824
Jechow, J., 496
Jenkins, H.A., 563
Jennings, M.C., 205, 321, 904
Jia, G., 134
Jiang, C., 502
Jiang, W. 502
Jiao, D., 406
Johnson, E.R., 1369
Jones, N.D., 321
Jones, P.G., 341
Jones, S., 1109
Junk, P.C., 121
Jürgensen, A., 601
Kaldor, U., 802
Kamboj, R.C., 422
Kamnaing, P., 397
Kapral, R., 880
Kasahara, J.-y., 176
Kasem, K.K., 1109
Kästner, J., 1322
Kaupp, M., 1521
Kaur, I., 1230
Kazemi, S., 1675
Keppler, B.K., 146
Keum, S.-R., 1127
Khalafi-Nezhad, A., 416
Khaskin, G., 430
Khorshidi, A., 1213
Khungar, B., 714
Khusnutdinova, J.R., 110
Kirtman, B., 984
Kishimoto, S., 760
Klassen, S.A., 738
Kleingardner, J., 95
Klobukowski, M., 1492
Ko, J.Y.P., 1255
Komine, N., 176
Komiya, S., 176
Konishi, Y., 397
Konu, J., 461
Koo, I.S., 433
Kovalenko, A., 1727
Krishnamurty, S., 1261
Kumar, A., 714
Kumar, N., 1230
Labinger, J.A., 264
Laguna, A., 341

Larkin, S.M., 872
Larsen, A., 95
Leclerc, M., 1201
Lee, S.-T., 335
Lelj, F., 1406
Lemaire, M.T., 533
Lemmen, P., 1173
Levasseur-Thériault, G., 1625
Lever, A.B.P., 1451
Levy, C.J., 224
Li, J., 1480
Li, J.-J., 490
Li, X., 917
Li, X.-H., 1218
Liimatainen, H., 954
Lin, B.-L., 264
Lin, Z.-J., 486
Linder, T., 1222
Liu, C., 640
Liu, C.T., 640
Liu, F., 1641
Liu, H., 47
Liu, Z., 1235
Lo, A.Y.H., 1546
Lobacheva, O., 1255
Loiseau, F., 254
Lough, A.J., 95
Louwen, J.N., 790
Lowary, T.L., 1565
Lu, C., 1, 30
Lu, L.-N., 1738
Lu, N., 1103
Lu, X., 684
Lucas, D., 103
Luo, J., 619
Lynch, V., 328
MacInnis, T.D., 368
MacLachlan, M.J., 314
MacLean, B.J., 729
Madhav, B., 1704
Mahmoodi, N., 1213
Mahmoudkhani, A.H., 247
Maity, A.K., 183
Majewski, M., 745
Majumdar, K.C., 472
Malathi, M., 1692
Mamaghani, M., 1213
Manguro, L.O.A., 1173
Manzhos, S., 864
Marangoni, D.G., 1641
Marcazzan, P., 582, 1248
Marder, T.B., 63
Margl, P., 891
Martins, N., 171
Marzorati, L., 1135
Maseras, F., 1273
Matsumoto, E., 176
Mayer, P.M., 453
McCahill, J.S.J., 1620
McDonald, R., 328
McGlinchey, M.J., 232
Medlycott, E.A., 254
Mehrabi, H., 1117
Melnychuk, S.A., 640
Meng, Q. 1610
Menges, S., 1109
Michalak, A., 1039
Millen, A.L., 850
Milnes, K.K., 307
Mineva, T., 1261
Miró, P., 1296
Mitoraj, M., 1039
Mohamed, M.H., 1747
Mohan, P.S., 1692
Mohr, F., 146
Moiseev, D.V., 582
Molin, S.D., 103
Monfette, S., 361
Moock, K., 738
Moosavi-Zare, A.R., 416
Morakinyo, M.K., 689
Morokuma, K., 872
Morra, N.A., 328
Morris, R.H., 54
Mota, A.J., 838
Mukhopadhyay, I., 514
Mugnier, Y., 103
Murphy, M.W., 1255
Murphy, P.B., 1641
Nageswar, Y.V.D., 1704
Najafi, A., 1593
Najari, A., 1201
Nakao, Y., 1415
Nandurkar, N.S., 401
Nassimi, A., 880
Nastasi, F., 254
Neverov, A.A., 640
Nie, J., 30
Nikoorazm, M., 1144
Nolan, S.P., 1362
Nooijen, M., 1499
Ochi, N., 1415
Ogini, F.O., 1055
Oh, S.-W, 1090
Omary, M.A., 775
Opiyo, S.A., 1173
Ortin, Y., 232
O'Sullivan, T.J., 533
Pagenkopf, B.L., 328
Pagliaro, M., 673
Pakawatchai, C., 161
Paldus, J., 917
Palmisano, G., 673
Pan, Y. 1565
Panthong, A., 1636
Panthong, K., 1636
Parhami, A., 416
Park, Y., 433
Patmore, N.J., 88
Patrick, B.O., 1248
Pedras, M.S.C., 556
Pennanen, T.O., 954
Peppe, C., 678
Perdew, J.P., 1268
Peru, K.M., 1747
Perumal, P.T., 698, 1682
Piers, W.G., 8
Pietrangelo, A., 314
Plubrukarn, A., 612
Poblet, J.M., 1296
Poirier, D., 1180
Poirier, R.A., 1313
Pordel, M., 724
Povar, I., 1154
Pratihar, S., 183
Puddephatt, R.J., 904
Pushie, M.J., 942
Pye, C.C., 790
Pyykkö, P., 798
Qi, H.-Y., 1218
Qian, P., 1738
Quail, J.W., 368
Qureshi, Z.S., 401
Rabaâ, H., 775
Radecka-Paryzek, W., 1
Ragogna, P.J., 1546
Rahimizadeh, M., 724
Rajagopal, S., 1127
Rakotondradany, F., 627
Ranu, B.C., 1605
Rao, J.M., 393
Rao, K.R., 1704
Rao, M.S., 714

Rao, R.R., 393
Rao, V.R.S., 393
Rauk, A., 942
Reber, C., 1625
Reddy, V.P., 1704
Reginato, N., 232
Reichwein, J.F., 328
Ren, Y., 1222
Renaud, J., 453
Rendina, L.M., 212
Reynolds, C.H., 1480
Rezaeian, S., 724
Rheingold, A.L., 151
Ricciardi, G., 994
Rickard, G.A., 942
Rizzo, A., 1352
Robertson, S.D., 39
Rodriguez, J.I., 1540
Roller, A., 146
Rosa, A., 994
Ross, B., 188
Roussel, M.R., 1425
Rowley, C.N., 1030
Roy, P.-N., 1022
Roy, S., 183
Ruiz-Morales, Y., 1280
Ruud, K., 1352
Sagi, K., 760
Sagvolden, E., 1268
Sahu, N.S., 523
Saidi, O., 171
Sakaki, S., 1415
Salahub, D.R., 1261
Santoni, M.-P., 254
Sarkadi-Pribóczki, E., 478
Sato, H., 1415, 1727
Savin, A., 1444
Schäffer, C.E., 1302
Schinzel, S., 1521
Schlosser, M., 619
Schreckenbach, G., 1436
Schurko, R.W., 1546
Selvam, N.P. 698
Selvamani, T., 514
Senn, H.M., 1322
Sham, T.-K., 335, 1255
Shanmugam, P., 591
Shao, H., 1733
Shcherbin, D., 1352
Shetty, S., 824
Shi, Y.-P., 1218
Shi, Z., 544
Shimizu, G.K.H., 247
Shrivastava, R., 523
Sibley, P.K., 662
Siegel, J.S., 440
Simoyi, R.H., 689
Singh, A., 514
Singh, B., 1230
Skelton, B.W., 121, 161
Sleiman, H., 627
Snell, K.E., 1708
Snieckus, V., 745
Snow, C.A., 448
Solà, M, 1063
Solomon, K.R., 662
Song, Y., 1235
Song, Z., 1374
Springborg, M., 984
Srebro, M., 1039
Sridhar, R., 1704
Srinivas, B.,1704
Stephan, D.W., 1163, 1620
Sterenberg, B.T., 197
Sterner, O., 397
Stradiotto, M., 72
Strych, S., 824
Sun, H., 1248
Sun, X., 684
Sun, Y., 188
Sutrisno, A., 1546
Suwanborirux, K., 612
Swart, M., 1063
Tabatabaeian, K., 1213
Tafazzoli, M., 563
Taher, D., 380
Tang, J.A., 1546
Tang, Y., 406
Tanski, J.M., 80
Taylor, N.J., 380
Templeton, J.L., 288
Thakur, M., 422
Thiel, W., 1322
Thurbide, K.B., 490
Tobisch, S., 1392
Toews, H.E., 321
Tuononen, H.M., 461
Trevail, M.J., 321
Trudel, S., 217
Tse, J.S., 1374
Tsoncheva, T., 478
Tsopmo, A., 397
Tsui, J.A., 197
Tykwinski, R.R., 1565
Uhlemann, T., 1470
Uma, U., 1682
Vaara, J., 954
Vaidhyanathan, R., 247
Vaithiyanathan, V., 591
Valencia, E., 571
van Lenthe, E., 790
vanLoon, G.W., 433
van Santen, R.A., 824
Varetti, E.L., 507
Vargas-Baca, I., 1055
Vedernikov, A.N., 110
Venil, C.K., 1692
Vidal-Ferran, A., 1273
Vinci, D., 171
Vogels, C.M., 139
Vreven, T., 872
Wagner, B.D., 448
Walker, D.T., 729
Wang, H., 406, 1209
Wang, J., 328
Wang, J., 47
Wang, R.-Y., 188
Wang, S., 188
Wang, Xi., 47
Wang, Xu., 297
Wasylishen, R.E., 348, 1090, 1338
Watchueng, J., 397
Wattanapiromsakul, C., 612
Watson, I.D.G., 54
Wechsler, D., 72
Wei, H.-J., 486
Wei, S., 1733
Weinberg, N., 539, 544
Welch, G.C., 1163
Wesemann, L., 63
West, N.W., 288
Westcott. S.A., 139
Wetmore, S.D., 850
White, A.H., 121, 161
Whitehead, M.A., 627
Whittleton, S.R., 974
Wilson, L.D., 1747
Wisner, J.A., 205
Wiznycia, A.V., 224
Wladislaw, B., 1135
Wolf, M.O., 314
Wolfe, S., 539, 544
Wong, S.Y.Y, 1022

Woo, T.K., 1030
Woody, N.M., 904
Workentin, M.S., 1708
Wren, J.E.C., 1436
Wu, H., 1460
Xia, W.W., 1103
Xiao, J., 171
Xie, S., 1235
Xuan, S., 502
Yadav, P.N., 368
Yakobi, H., 802
Yang, D.-S., 297
Yang, G., 30
Yang, J.J., 1374
Yang, K., 47
Yang, K., 433
Yang, Z.-Z., 1738
Yao, L., 1103
Yao, Y., 335
Yokogawa, D., 1727
Yousefi, S., 1144
Yu, B., 720
Yu, X.-Y., 1248
Yu, Y., 556
Yuan, J., 151
Yudin, A.K., 54
Yue, H., 684
Yuenyongsawad, S., 612
Zaleski-Ejgierd, P., 798
Zamiruddin, S., 1013
Zare, A., 416
Zargarian, D., 280
Zavalij, P.Y., 110
Zeng, J., 1209
Zhang, C., 1610
Zhang, G.-J., 486
Zhang, M., 1013
Zhang, P., 335, 1641
Zhang, W.-J., 1218
Zhang, Y., 406
Zhang, Z., 502
Zhao, G. 720
Zhao, H., 328
Zhao, J., 1733
Zheng, S., 1546
Zhong, H., 1103
Zhou, J., 386
Zhu, J., 386
Zhu, T.-J., 486
Ziegler, T., 33, 496, 790
Zimmer De Iuliis, M., 54
Zina, M.S., 706
Zulykama, Y., 1682
Zysman-Colman, E., 440

Canadian Journal of Chemistry

Contents
Volume 87, 2009

Revue canadienne de chimie

Sommaire
Volume 87, 2009

January / Janvier

This issue is dedicated to Professor R.J. Puddephatt on the occasion of his 65th birthday and to honour his outstanding contributions to Canadian chemistry.
Le présent numéro est dédié à Professor R.J. Puddephatt à l'occasion de son 65e anniversaire de naissance et en reconnaissance de ses contributions exceptionelles à la chimie au Canada.

MINI-REVIEW / MINI-SYNTHÈSE

Wanda Radecka-Paryzek Self-assembly in Schiff base lanthanide complexes — From supramolecular dimers to coordination polymers **1**

REVIEW / SYNTHÈSE

Michael J.D. Bosdet and Warren E. Piers B–N as a C–C substitute in aromatic systems **8**

ARTICLES / ARTICLES

Cuifen Lu, Junqi Nie, Guichun Yang, and Zuxing Chen An improved synthesis of sitophilure **30**

Alicja Haras and Tom Ziegler DFT mechanistic studies on the epoxidation of cyclohexene by non-heme tetraaza manganese complexes **33**

Dana J. Eisler, Stuart D. Robertson, and Tristram Chivers Gold complexes of ditelluridoimidodiphosphinate ligands — Reversible oxidation of Au(I) to Au(III) via insertion of gold into a phosphorus–tellurium bond **39**

Long Chen, Haitao Liu, Keli Yang, Jiankang Wang, and Xiaolai Wang Catalytic synthesis of carbon nanotubes from the decomposition of methane over a Ni–Co/La_2O_3 catalyst **47**

Marco Zimmer De Iuliis, Iain D.G. Watson, Andrei K. Yudin, and Robert H. Morris A DFT investigation into the origin of regioselectivity in palladium-catalyzed allylic amination **54**

Mark A. Fox, Todd B. Marder, and Lars Wesemann DFT studies of the σ-donor/π-acceptor properties of $[SnCB_{10}H_{11}]^-$ and its relationship to $[SnCl_3]^-$, CO, PF_3, $[SnB_{11}H_{11}]^{2-}$, $SnC_2B_9H_{11}$, and related $SnC_2B_nH_{n+2}$ compounds **63**

Dominik Wechsler and Mark Stradiotto Exploring the utility of a new chiral phosphoramidite *P*,*N*-ligand derived from (*R*)-BINOL and 7-azaindole in asymmetric catalysis **72**

Margarita Crespo, Craig M. Anderson, and Joseph M. Tanski Synthesis of platinum(II) cyclometallated compounds derived from imines containing pyridyl or pyrimidyl groups **80**

Malcolm H. Chisholm and Nathan J. Patmore Oxalate bridged heteronuclear compounds containing MM quadruple bonds (M = Mo and W) and their radical cations **88**

Antonio G. De Crisci, Jesse Kleingardner, Alan J. Lough, Anna Larsen, and Ulrich Fekl A weakly coordinating anion as a tripodal "Br_3"-ligand for platinum(IV) — Structure of [(*closo*-$CB_{11}H_6Br_6$)$PtMe_3$] **95**

Cyril Cugnet, Sophie Dal Molin, David Brevet, Dominique Lucas, Yves Mugnier, Pierre D. Harvey, and René T. Boeré Alkyne adducts of paramagnetic and diamagnetic tripalladium clusters supported by dppm ligands **103**

Julia R. Khusnutdinova, Peter Y. Zavalij, and Andrei N. Vedernikov Study of aerobic oxidation of phenyl Pt^{II} complexes (dpms)Pt^{II}Ph(L) (dpms = di(2-pyridyl)methanesulfonate; L = water, methanol, or aniline) **110**

Glen B. Deacon, Winfried Elgersma, Rita Harika, Peter C. Junk, Brian W. Skelton, and Allan H. White The synthesis and X-ray crystal structures of rare earth(III) perfluoroadipate complexes — Novel coordination polymers **121**

Quan Yuan Hu and Guochen Jia Synthesis and electrochemical properties of bimetallic η^5-indenyl ruthenium complexes **134**

Nathan R. Halcovitch, Christopher M. Vogels, Andreas Decken, and Stephen A. Westcott Synthesis, characterization, and reactivity of a novel thallium arylspiroboronate ester **139**

Angela Fleischer, Alexander Roller, Vladimir B. Arion, Bernhard K. Keppler, and Fabian Mohr Synthesis and structures of palladium(II) and platinum(II) complexes containing heterocyclic thiolate ligands formed by cycloaddition reactions of coordinated azides **146**

Hui Huang, N. Raluca Hurubeanu, Cheryl J. Bourgeois, Sue-Mei Cheah, Jian Yuan, Arnold L. Rheingold, and Russell P. Hughes Octahedral perfluoroalkyl complexes of Ir(III) formed by oxidative addition of perfluoroalkyl iodides to $Ir(acac)(CO)_2$ **151**

Graham A. Bowmaker, Narongsak Chaichit, Chaveng Pakawatchai, Brian W. Skelton, and Allan H. White Structural and spectroscopic studies of some adducts of silver(I) salts with ethylenethiourea **161**

Daniele Vinci, Nelson Martins, Ourida Saidi, John Bacsa, Amadeu Brigas, and Jianliang Xiao Ferrocenyl phosphine–oxazaphospholidine oxide ligands for the Suzuki–Miyaura coupling of hindered aryl bromides and chlorides **171**

Nobuyuki Komine, Tomoko Ishiwata, Jun-ya Kasahara, Erino Matsumoto, Masafumi Hirano, and Sanshiro Komiya Synthesis and organic group transfer of organodiplatinum complex with a 1,2-bis(diphenylphosphino)ethane ligand **176**

Joyanta Choudhury, Sanjay Pratihar, Arnab Kumar Maity, and Sujit Roy Reactivity of $IrCl(PPh_3)_3$ with diphenylacetylene — A direct route to 1-iridaindene **183**

Yi Sun, Bryan Ross, Rui-Yao Wang, and Suning Wang $Pt(2,2'\text{-bpy})(O_2CCF_3)_2$ as a terminator for $[Ag(O_2CCF_3)]_n$ aggregates — Syntheses and structures of heterobimetallic $Pt^{II}Ag^{I}$ complexes **188**

Jordan A. Tsui, Timothy M. Bolton, and Brian T. Sterenberg Tungsten coordination chemistry of 1,4-bisdiphenylphosphinobutadiyne — Synthesis of coordination macrocycles and factors controlling diyne cycloaddition **197**

Barry A. Blight, James A. Wisner, and Michael C. Jennings Formation of a [2]rotaxane and [2]catenane based on $PdBr_2L_2$ as a template **205**

Michael G. Crisp and Louis M. Rendina Dinuclear organoplatinum(II) complexes containing *N*-methylbenzamide **212**

Simon Trudel and Ross H. Hill Top-down meets bottom-up — Electron-beam induced metalorganic deposition of amorphous iron oxide nanostructures **217**

Alexander V. Wiznycia, John Desper, and Christopher J. Levy Zinc and iron complexes of a helix-directing (1*R*,2*R*)-cyclohexyl salen ligand with phenanthryl sidearms **224**

Nada Reginato, Laura E. Harrington, Yannick Ortin, and Michael J. McGlinchey Unexpectedly different reactions of $[(arene)Mn(CO)_3]^+$ cations (arene = trindane, indane, tetralin, or dibenzosuberane) with potassium *t*-butoxide — C-H insertions, haptotropic shifts, dimerization, or elimination **232**

Ramanathan Vaidhyanathan, Amir H. Mahmoudkhani, and George K.H. Shimizu A microporous alkaline-earth phosphonate sustained by one-dimensional inorganic and organic units **247**

Francesco Nastasi, Frédérique Loiseau, Sebastiano Campagna, Elaine A. Medlycott, Marie-Pierre Santoni, and Garry S. Hanan Synthesis and photophysical properties of naphthyl-, phenanthryl-, and pyrenyl-appended bis(pyridyl)triazine ligands and their Zn(II) and Ru(II) complexes **254**

Bo-Lin Lin, Jay A. Labinger, and John E. Bercaw Mechanistic investigations of bipyrimidine-promoted palladium-catalyzed allylic acetoxylation of olefins **264**

Tamer A. Elbokl and Christian Detellier Kaolinite–poly(methacrylamide) intercalated nanocomposite via in situ polymerization **272**

Yaofeng Chen and Davit Zargarian Phenylsilane dehydrocoupling and addition to styrene catalyzed by (R-indenyl)Ni(phosphine)(methyl) complexes **280**

Nathan M. West and Joseph L. Templeton Approaches to alkane functionalization with Tp′Pt and (nacnac)Pt reagents **288**

Xu Wang and Dong-Sheng Yang Bonding and structures of copper-aminopyridine complexes — High-resolution electron spectroscopy and ab initio calculations **297**

Kaarina K. Milnes and Kim M. Baines A mechanistic study of the addition of alkynes to Brook silenes **307**

A. Pietrangelo, B.N. Boden, M.J. MacLachlan, and M.O. Wolf Synthesis and electrochemistry of new thienyl – Schiff base complexes **314**

David W. Dodd, Heather E. Toews, Michael J. Trevail, Michael C. Jennings, Robert H.E. Hudson, and Nathan D. Jones Synthesis and evaluation of the in vitro DNA-binding properties of chiral *cis*-dichloro (pyridyloxazoline)platinum(II) complexes **321**

Jian Wang, Nicholas A. Morra, Hongda Zhao, Jeffrey S.T. Gorman, Vincent Lynch, Robert McDonald, John F. Reichwein, and Brian L. Pagenkopf Synthesis and first X-ray structures of cobalt(II) and cobalt(III) complexes bearing 2,4-dioxo-alkanoic acid dialkylamide ligands **328**

Peng Zhang, Andy Yuan-Chi Chu, Tsun-Kong Sham, Yun Yao, and Shuit-Tong Lee Chemical synthesis and structural studies of thiol-capped gold nanoparticles **335**

Javier E. Aguado, M. Concepción Gimeno, Peter G. Jones, and Antonio Laguna Unusual coordination behaviour of the ferrocenyl-terpyridine ligand with group 11 complexes **341**

Bryan A. Demko and Roderick E. Wasylishen Probing solid iminobis(diorganophosphine chalcogenide) systems with multinuclear magnetic resonance **348**

Sebastien Monfette, João A. Duarte Silva, Serge I. Gorelsky, Scott J. Dalgarno, Eduardo N. dos Santos, Maria H. Araujo, and Deryn E. Fogg Dissecting out the effect of Ru-OAr bonding in a five-coordinate complex of ruthenium (II) **361**

Robert A. Gossage, Paras N. Yadav, Timothy D. MacInnis, J. Wilson Quail, and Andreas Decken Zinc halide oxazoline complexes — The quest for structural diversity **368**

Deeb Taher, Nicholas J. Taylor, and John F. Corrigan Phenylene-1,4- and biphenylene-4,4′-diselenolate bridged complexes of gold(I) **380**

Jigang Zhou, Jun Zhu, Jack Brzezinski, and Zhifeng Ding Tunable electrogenerated chemiluminescence from CdSe nanocrystals **386**

Author Index / Index des auteurs **AI-1**

February / Février

ARTICLES / ARTICLES

Kothamasu Suresh Babu, Vidadala Rama Subba Rao, Ravu Ranga Rao, Sakhamuri Sivaram Babu, and Janaswami Madhusudana Rao A mild and efficient chemoselective *N*-benzyloxycarbonylation of amines using TBAB as a catalyst under solvent-free conditions **393**

Apollinaire Tsopmo, Pierre Kamnaing, Jean Watchueng, Jin-Ming Gao, Yasuo Konishi, and Olov Sterner Chemical constituents from the bark of *Anisopus mannii* **397**

Krishna M. Deshmukh, Ziyauddin S. Qureshi, Nitin S. Nandurkar, and Bhalchandra M. Bhanage One-pot synthesis of β-amido ketones using Brønsted acidic ionic liquid as an efficient and reusable catalyst **401**

Dongsheng Jiao, Hongyan Wang, Yanlan Zhang, and Yu Tang A DFT study of thymine and its tautomers **406**

Abdolkarim Zare, Abolfath Parhami, Ahmad Reza Moosavi-Zare, Alireza Hasaninejad, Ali Khalafi-Nezhad, and Mohammad Hassan Beyzavi A catalyst-free protocol for the green and efficient condensation of indoles with aldehydes in ionic liquids **416**

Ramesh C. Kamboj, Urmila Berar, Surinder Berar, Mandeep Thakur, Rita Arora, and Satish C. Gupta Photochemistry of 3-alkoxychromones I — Photocyclisation of 6-chloro-3-alkoxy-2-(furan-3-yl)-4*H*-chromen-4-ones **422**

Robert Britton, Grigori Khaskin, and Gerhard Gries A chromatography-free synthesis of (2*S*,12*Z*)-2-acetoxy-12-heptadecene — The major sex pheromone component of the pistachio twig borer moth (*Kermania pistaciella*) **430**

In Sun Koo, Dildar Ali, Kiyull Yang, Yong Park, Abdelhamid Esbata, Gary W. vanLoon, and Erwin Buncel ^{31}P NMR and ESI-MS studies of metal ion-phosphoruspesticide residue complexes **433**

Eli Zysman-Colman, Karla Arias, and Jay S. Siegel Synthesis of arylbromides from arenes and *N*-bromosuccinimide (NBS) in acetonitrile — A convenient method for aromatic bromination **440**

Patricia G. Boland, Sara J. Accardi, Carrie A. Snow, and Brian D. Wagner Investigations of the supramolecular host properties of a fluorescent bistren cage compound **448**

Justin Renaud, Abdulhrahman M. Alhazmi, and Paul M. Mayer Comparing the fragmentation chemistry of gas-phase adducts of poly(dimethylsiloxane) oligomers with metal and organic ions **453**

Author Index / Index des auteurs **AI-1**

March / Mars

ARTICLES / ARTICLES

Jari Konu, Heikki M. Tuononen, and Tristram Chivers Syntheses, X-ray structures, and redox behaviour of the group 14 bis-boraamidinates M[PhB(μ-*N*-*t*-Bu)$_2$]$_2$ (M = Ge, Sn) and Li$_2$M[PhB(μ-*N*-*t*-Bu)$_2$]$_2$ (M = Sn, Pb) **461**

Krishna C. Majumdar, Buddhadeb Chattopadhyay, and Inul Ansary Concise strategy for the synthesis of eleven-membered and ansa-bridged thirteen-membered lactone macrolides by ring-closing metathesis reaction **472**

Eva Sarkadi-Pribóczki, Tanya Tsoncheva, and Ljubomira Ivanova Radioisotopic study of ^{11}C-labelling methanol decomposition on iron oxide modified mesoporous MCM-41 silica **478**

Zhen-Jian Lin, Tian-Jiao Zhu, Guo-Jian Zhang, Hong-Juan Wei, and Qian-Qun Gu Deoxy-cytochalasins from a marine-derived fungus *Spicaria elegans* **486**

Jian Jun Li and Kevin B. Thurbide Novel pressure control in supercritical fluid chromatography using a resistively heated restrictor **490**

Jason Jechow and Tom Ziegler On the relationship between free energy difference calculations by thermodynamic integration and harmonic frequency analysis **496**

Cuifeng Jiang, Mingwei Chen, Shouhu Xuan, Wanquan Jiang, Xinglong Gong, and Zhong Zhang Magnetic separable PSA@Fe_3O_4/Ag composites — Fabrication and catalytic properties **502**

L.E. Fernández and E.L. Varetti Scaled quantum mechanical force fields for trifluoromethyl selenium derivatives. II. The $(CF_3)_2Se$ and $(CF_3Se)_2$ molecules. **507**

Ajeet Singh, T. Selvamani, Indrajit Mukhopadhyay, and Bishwajit Ganguly Morphology of potassium chloride in aqueous and in formamide solution — An experimental and computational investigation **514**

Har Mohindra Chawla, Satya Narayan Sahu, and Rahul Shrivastava Synthesis and binding characteristics of novel calix[4]arene(amidocrown) diquinones **523**

Author Index / Index des auteurs **AI-1**

April / Avril

ARTICLES / ARTICLES

Thomas J. O'Sullivan, Brandon Djukic, Paul A. Dube, and Martin T. Lemaire Preparation and properties of thienyl and 2,2′- bithienyl substituted cobalt-bis(semiquinone) valence tautomers **533**

Yih-Huang Hsieh, Noham Weinberg, and Saul Wolfe The neutral hydrolysis of methyl acetate — Part 1. Kinetic experiments **539**

Zheng Shi, Yih-huang Hsieh, Noham Weinberg, and Saul Wolfe The neutral hydrolysis of methyl acetate — Part 2. Is there a tetrahedral intermediate? **544**

M. Soledade C. Pedras and Yang Yu Mapping the sirodesmin PL biosynthetic pathway — A remarkable intrinsic steric deuterium isotope effect on a ^{1}H NMR chemical shift determines β-proton exchange in tyrosine **556**

Saeed K. Amini, Mohsen Tafazzoli, Hilary A. Jenkins, Gillian R. Goward, and Alex D. Bain Measurement and calculation of ^{13}C and ^{15}N NMR chemical-shift tensors of a push–pull ethylene **563**

Joaquín Cortés and Eliana Valencia Effect of surface heterogeneity steps-terraces in a mean field model for the catalytic CO-NO reaction **571**

Dmitry V. Moiseev, Paolo Marcazzan, and Brian R. James Reversible decomposition of mono(α-hydroxy)-phosphines and their reaction with α,β-unsaturated aldehydes **582**

Ponnusamy Shanmugam and Vadivel Vaithiyanathan Activation of the *N*C–H bond of Morita–Baylis–Hillman adducts of N-substituted isatins with cerium ammonium nitrate (CAN) and alcohol (ROH) **591**

Author Index / Index des auteurs **AI-1**

May / Mai

ARTICLES / ARTICLES

Astrid Jürgensen X-ray absorption spectroscopy of aqueous solutions in the X-ray energy region from 1800 to 3700 eV **601**

Chatchai Wattanapiromsakul, Naphatson Chanthathamrongsiri, Somchai Bussarawit, Supreeya Yuenyongsawad, Anuchit Plubrukarn, and Khanit Suwanborirux 8-Isocyanoamphilecta-11(20),15-diene, a new antimalarial isonitrile diterpene from the sponge *Ciocalapata* sp. **612**

Jia Luo, Heiko Ihmels, Hans-Jörg Deiseroth, and Marc Schlosser Controlling the regioselectivity of the di-π-methane rearrangements of 1,2-naphtho-annelated barrelene derivatives — Solution versus solid-state photochemistry **619**

Felaniaina Rakotondradany, Hanadi Sleiman, and M.A. Whitehead Hydrogen-bond self-assembly of DNA-base analogues — Experimental results **627**

C. Tony Liu, Stephanie A. Melnychuk, Chaomin Liu, Alexei A. Neverov, and R. Stan Brown Cleavage of models for RNA mediated by a diZn(II) complex of bis[1,4-N_1,N_1'(1,5,9-triazacyclododecanyl)]butane in methanol and ethanol **640**

Lisa Carosi and Dennis G. Hall Chiral α-substituted allylboronates in a one-pot three-component asymmetric allylic alkylation/carbonyl allylation reaction sequence — Applications to the syntheses of (+)-(3*R*,5*R*)-3-hydroxy-5-decanolide and (–)-massoialactone **650**

Ève B. Dussault, Vimal K. Balakrishnan, Keith R. Solomon, and Paul K. Sibley Matrix effects on mass spectrometric determinations of four pharmaceuticals and personal care products in water, sediments, and biota **662**

Giovanni Palmisano, Vincenzo Augugliaro, Rosaria Ciriminna, and Mario Pagliaro NanoMORALs — Metal nanoparticles doped with organic molecules **673**

Clovis Peppe and Liérson Borges de Castro On the reactivity of indium(III) benzenechalcogenolates (chalcogen = sulfur and selenium) towards organyl halides for the synthesis of organyl phenyl chalcogenides **678**

Hong Yue, Xi Lu, Zhengting Cai, and Xiaomin Sun Theoretical study on the scattering resonance state and isotope effect of the F + HD(H_2) → HF + D(H) reactive system **684**

Author Index / Index des auteurs **AI-1**

June /Juin

ARTICLES / ARTICLES

Edward Chikwana, Bradley Davis, Moshood K. Morakinyo, and Reuben H. Simoyi Oxyhalogen–sulfur chemistry — Kinetics and mechanism of oxidation of methionine by aqueous iodine and acidified iodate **689**

Nagarajan Panneer Selvamand Paramasivan T. Perumal Cerium(IV) sulfate catalyzed one-pot three-component diastereo selective synthesis of 4-amidotetrahydropyrans **698**

Mongia Saïd Zina, Lobna Bassalahet Abdelhamid Ghorbel Effet des cations extra-réseau de la zéolithe Y sur l'activité catalytique du palladium dans la réaction de combustion du méthane **706**

Anil Kumar, M. Sudershan Rao, Israr Ahmad, and Bharti Khungar A simple and facile synthesis of amidoalkyl naphthols catalyzed by $Yb(OTf)_3$ in ionic liquids **714**

Guangping Zhao and Bingjie Yu Chemical-bond properties and hardness of nonlinear optical crystals LiB_3O_5 and β-BaB_2O_4 **720**

Mohammad Rahimizadeh, Mehdi Pordel, Mehdi Bakavoli, Shima Rezaeian, and Hossein Eshghi Synthesis of a new heterocyclic system — Fluoreno[1,2-*d*]imidazol-10-one **724**

D.T. Walker, C.D. Douglas, and B.J. MacLean Synthesis, characterization, and surface studies of conjugated polymers possessing 2,2′-biimidazole moieties **729**

Sheri A. Klassen, Richard Boehme, Sean D. Derrick, Klaus Moock, A. Elizabeth Baker, Deryn E. Fogg, René T. Boeré, and Peter W. Dibble Stable phenylene- and biphenylene-bis(isobenzofuran)s related to diphenylisobenzofuran **738**

James R. Green, Babajide I. Alo, Marek Majewski, and Victor Snieckus γ-Silylated α,β-unsaturated amides — Preparation by [1,5]-sigmatropic rearrangement and use as masked dienolate equivalents in carbonyl condensations **745**

Kuniaki Itoh, Shigehisa Kishimoto, and Kazuo Sagi Novel formation of isoxazoline *N*-oxide in addition to Michael adduct from the reaction of β-nitrostyrenes with 2-methoxyfuran — Experimental and theoretical studies **760**

Author Index / Index des auteurs **AI-1**

July / Juillet

This issue is dedicated to Professor Tom Ziegler to honour his outstanding contributions to Canadian chemistry.
Ce numéro spécial est dédié au Professeur Tom Ziegler en reconnaissance de ses contributions exceptionnelles à la chimie au Canada.

ARTICLES / ARTICLES

Hassan Rabaâ , Thomas R. Cundari,and Mohammad A. Omary Combined tight-binding/DFT investigation of the electronic structure of triimine-platinum(II)/TCNQ extended stacks **775**

Jens Peder Dahl Moshinsky atom and density functional theory — A phase space view **784**

Cory C. Pye, Tom Ziegler, Erik van Lenthe,and Jaap N. Louwen An implementation of the conductor-like screening model of solvation within the Amsterdam density functional package — Part II. COSMO for real solvents **790**

Patryk Zaleski-Ejgierd and Pekka Pyykkö Bonding analysis for sterically uncongested simple aurocarbons C_nAu_m **798**

Hana Yakobi, Ephraim Eliav, and Uzi Kaldor The nuclear quadrupole moment of ^{69}Ga and ^{115}In **802**

G. Theodoor de Jong and F. Matthias Bickelhaupt Bond activation by group-11 transition-metal cations **806**

Michael Bühl Structure and stability of aquotetrafluorouranyl(VI) in the solid state — Density functional study of $[UO_2F_4(H_2O)][NMe_4]_2{\cdot}2H_2O$ **818**

Sharan Shetty, Sebastian Strych, A.P.J. Jansen, and Rutger A. van Santen Theoretical investigation of CO adsorption on Rh_n (n = 3–13) clusters **824**

Peter H.M. Budzelaar Ethene trimerization at Cr^{I}/Cr^{III} — A density functional theory (DFT) study **832**

Alain Dedieu and Antonio J. Mota Pd/X group interchange in the $[Pd(Br)(PH_3)(C_6H_5)(C_6H_5X)]$ system — Theoretical insights from the isolobal analogy perspective **838**

Andrea L. Millen and Stacey D. Wetmore Glycosidic bond cleavage in deoxynucleotides — A density functional study **850**

Sergei Manzhos and Tucker Carrington, Jr. An improved neural network method for solving the Schrödinger equation **864**

Susan M. Larkin, Thom Vreven, Michael J. Bearpark, and Keiji Morokuma The application of the ONIOM hybrid method to the cycloaddition reactions of bromo-substituted 2(*H*)-pyran-2-ones **872**

Ali Nassimi and Raymond Kapral Mapping approach for quantum-classical time correlation functions **880**

Peter Margl Mechanisms for anionic butadiene polymerization with alkyl lithium species **891**

Richard H.W. Au, Lisa J. Findlay-Shirras, Neil M. Woody, Michael C. Jennings, and Richard J. Puddephatt Organoplatinum(IV) complexes with functional alkyl groups and their use in supramolecular chemistry **904**

Xiangzhu Li and Josef Paldus Energetics of naphthynes — Performance of reduced multi-reference coupled-cluster methods for diradicals **917**

David L. Bryce and Jochen Autschbach Relativistic hybrid density functional calculations of indirect nuclear spin–spin coupling tensors — Comparison with experiment for diatomic alkali metal halides **927**

Stephen D. Barry, Gail A. Rickard, M. Jake Pushie, and Arvi Rauk The affinity of HGGG, GHGG, GGHG, and GGGH peptides for copper(II) and the structures of their complexes — An ab initio study **942**

Helmi Liimatainen, Teemu O. Pennanen, and Juha Vaara ^{1}H chemical shifts in nonaxial, paramagnetic chromium(III) complexes — Application of novel pNMR shift theory **954**

Heiko Jacobsen Localized-orbital locator (LOL) profiles of transition-metal hydride and dihydrogen complexes **965**

Sarah R. Whittleton, Russell J. Boyd, and T. Bruce Grindley Homolytic bond-dissociation enthalpies of tin bonds and tin–ligand bond strengths — A computational study **974**

Michael Springborg and Bernard Kirtman The response of extended systems to electrostatic fields **984**

Angela Rosa and Giampaolo Ricciardi A time-dependent density functional theory (TDDFT) interpretation of the optical spectra of zinc phthalocyanine π-cation and π-anion radicals **994**

N. Ben Amor and C. Daniel Spin–orbit ab initio investigation of the UV photoinduced bond cleavage in iodotrimethylstannane **1006**

René Fournier, Shaima Zamiruddin, and Min Zhang Competition between mixing and segregation in bimetallic Ag_nRb_n clusters (n = 2–10) **1013**

Stephanie Y.Y. Wong, Pierre-Nicholas Roy, and Alex Brown Ab initio electronic structure and direct dynamics simulations of CH_3OCl **1022**

Christopher N. Rowley and Tom K. Woo Computational design of ruthenium hydride olefin-hydrogenation catalysts containing hemilabile ligands **1030**

Monika Srebro, Mariusz Mitoraj, and Artur Michalak Binding of polar monomers in the complexes with organometallic ethylene polymerization catalysts — Natural orbitals for chemical valence and energy decomposition analysis **1039**

Francis O. Ogini, Philip J.W. Elder, James F. Britten, and Ignacio Vargas-Baca An investigation of $(C_5H_5)Fe(C_5H_4–C(OBF_3)–CH_3)$ **1055**

Ferran Feixas, Miquel Solà, and Marcel Swart Chemical bonding and aromaticity in metalloporphyrins **1063**

Carles Acosta-Silva, Òscar González-Blanco, and Vicenç Branchadell Hetero-Diels–Alder reactions involving $Fe(CO)_3$-coordinated dienal and formyltrimethylenemethane catalyzed by Lewis acids — A theoretical study **1074**

Emmanuel Penka Fowe and André Dieter Bandrauk Nonlinear time-dependent density functional theory studies of the ionization of CO_2 by ultrashort intense laser pulses **1081**

Fu Chen, Se-Woung Oh, and Roderick E. Wasylishen A solid-state ^{31}P NMR study of 1:1 silver–triphenylphosphine complexes — Interpretation of $^{1}J(^{107,109}Ag,^{31}P)$ values **1090**

Author Index / Index des auteurs **AI-1**

August /Août

ARTICLES / ARTICLES

Wen Wen Xia, Ning Lu, Haiyang Zhong, and Li Yao Quasi-classical trajectory calculation of the Ba + HBr chemical reaction **1103**

Kasem K. Kasem, Sara Menges, and Stephenie Jones Photoelectrochemical studies on poly[1-(2-aminophenyl)pyrrole] — Creation of a photoactive inorganic–organic semiconductor interface (IOI) **1109**

Hossein Mehrabi Synthesis of both isomers of aziridine derived from the mixture of *cis*- and trans-limonene oxide **1117**

Mona Hosseini-Sarvari Commercial ZrO_2 as a new, efficient, and reusable catalyst for the one-step synthesis of quinolines in solvent-free conditions **1122**

Erwin Buncel, Sam-Rok Keum, Srinivasan Rajagopal, and Robin A. Cox Rearrangement mechanisms for azoxypyridines and azoxypyridine N-oxides in the 100% H_2SO_4 region — The Wallach rearrangement story comes full circle **1127**

Andrea L.F. de Sousa, José E.P. Cardoso Filho, Blanka Wladislaw, Liliana Marzorati, and Claudio Di Vitta Studies on chemo- and diastereo-selectivity of the Diels–Alder reactions of sulfinyltoluquinones with cyclopentadiene **1135**

Arash Ghorbani-Choghamarani, Hamid Goudarziafshar, Mohsen Nikoorazm, and Somaieh Yousefi Aluminum nitrate and silica sulfuric acid as efficient nitrating media for the mononitration of phenols under mild and heterogeneous conditions **1144**

Delano P. Chong Theoretical study of the electronic spectra of *s*-triazine vapour **1148**

J. Peter Guthrie and Igor Povar A test of various computational solvation models on a set of ''difficult'' organic compounds **1154**

Osamah Alhomaidan, Gregory C. Welch, Guangcai Bai, and Douglas W. Stephan Hafnium–phosphinimide complexes **1163**

Lawrence Onyango Arot Manguro, Sylvia Awino Opiyo, Eberhardt Herdtweck, and Peter Lemmen Triterpenes of *Commiphora holtziana* oleo-gum resin **1173**

Marie Bérubé and Donald Poirier Design, chemical synthesis, and in vitro biological evaluation of simplified estradiol–adenosine hybrids as inhibitors of 17β-hydroxysteroid dehydrogenase type 1 **1180**

Author Index / Index des auteurs **AI-1**

September / Septembre

AWARD LECTURE / CONFÉRENCE D'HONNEUR

Mario Leclerc, Ahmed Najari, and Serge Beaupré 2008 Macromolecular Science and Engineering Division Award Lecture — Conjugated polymers: From microelectronics to genomics **1201**

ARTICLES / ARTICLES

Hongshe Wang and June Zeng Iodine-catalyzed efficient synthesis of chalcones by grinding under solvent-free conditions **1209**

Khalil Tabatabaeian, Manouchehr Mamaghani, Nosratollah Mahmoodi, and Alireza Khorshidi Ruthenium-catalyzed efficient routes to oxindole derivatives **1213**

Xue-Hu Li, Wen-Juan Zhang, Huan-Yang Qi, and Yan-Ping Shi Phenolic constituents of *Phellodendron chinense* bark **1218**

Yi Ren, Thomas Linder, and Thomas Baumgartner Synthesis and properties of ladder-type 1,4-dihydro-1,4-phosphasilins **1222**

Pamita Bhandari, Neeraj Kumar, Bikram Singh, and Inderjeet Kaur Dammarane triterpenoid saponins from *Bacopa monnieri* **1230**

Shuntai Xie, Yang Song, and Zhenxian Liu In situ high-pressure study of ammonia borane by Raman and IR spectroscopy **1235**

Hongsui Sun, Xiao-Yan Yu, Paolo Marcazzan, Brian O. Patrick, and Brian R. James Rhodium(I) – (*N*-heterocyclic carbene) – diphosphine complexes **1248**

Olga Lobacheva, Michael W. Murphy, Jun Young Peter Ko, and Tsun-Kong Sham Morphology-dependent luminescence from ZnO nanostructures — An X-ray excited optical luminescence study at the Zn K-edge **1255**

Author Index / Index des auteurs **AI-1**

October / Octobre

This issue is dedicated to Professor Tom Ziegler to honour his outstanding contributions to Canadian chemistry.
Ce numéro spécial est dédié au Professeur Tom Ziegler en reconnaissance de ses contributions exceptionnelles à la chimie au Canada.

ATICLES / ARTICLES

Annick Goursot, Tzonka Mineva, Sailaja Krishnamurty, and Dennis R. Salahub Structural analysis of phosphatidyl choline lipids and glycerol precursors **1261**

John P. Perdew and Espen Sagvolden Exact exchange-correlation potentials in spin-density functional theory and their discontinuities at unit electron number **1268**

Steven M.A. Donald, Anton Vidal-Ferran, and Feliu Maseras A DFT/MM analysis of the effect of ligand substituents on asymmetric hydrogenation catalyzed by rhodium complexes with phosphine–phosphinite ligands **1273**

Yosadara Ruiz-Morales Aromaticity in pericondensed cyclopent a-fused polycyclic aromatic hydrocarbons determined by density functional theory nucleus-independent chemical shifts and the Y-rule — Implications in oil asphaltene stability **1280**

Pere Miró, Josep M. Poblet, Josep Bonet Ávalos, and Carles Bo Towards a computational treatment of polyoxometalates in solution using QM methods and explicit solvent molecules **1296**

Claus E. Schäffer and Jesper Bendix Kohn–Sh am DFT and ligand-field theory — Is there a synergy? **1302**

Aisha El-Sherbiny and Raymond A. Poirier Comprehensive study of some well-known molecular numerical integration methods **1313**

Hans Martin Senn, Johannes Kästner, Jürgen Breidung, and Walter Thiel Finite-temperature effects in enzymatic reactions —Insights from QM/MM free-energy simulations **1322**

Kristopher J. Harris, David L. Bryce, and Roderick E. Wasylishen NMR line shapes from AB spin systems in solids — The role of antisymmetric spin–spin coupling **1338**

Antonio Rizzo, Dmitry Shcherbin, and Kenneth Ruud Jones and magnetoelectric birefringence of pure substances — A computational study **1352**

Luigi Cavallo, Steven P. Nolan, and Heiko Jacobsen Mechanism of dihydride formation and hydrogen/deuterium exchange in a cationic iridium(III) complex **1362**

Erin R. Johnson and Axel D. Becke Tests of an exact-exchange-based density-functional theory on transition-metal complexes **1369**

Z. Song, J.J. Yang, and J.S. Tse A comparative study on the LDA + *U* and hybrid functional methods on the description of the electronic structure of $YTiO_3$ under high pressure **1374**

Oleg Gritsenko and Evert Jan Baerends The analog of Koopmans' theorem for virtual Kohn–Sham orbital energies **1383**

Sven Tobisch Mechanistic insight into the selective trans-1,4-polymerization of butadiene by terpyridine–iron(II) complexes — A computational study **1392**

Mario Amati and Francesco Lelj Bis(cyclopentadienyl)dihydrido Mo and W complexes as Lewis bases — A computational study about their adducts with BX_3 (X = F, Cl) and $Al(CH_3)_3$ **1406**

Noriaki Ochi, Yoshihide Nakao, Hirofumi Sato, and Shigeyoshi Sakaki Theoretical prediction of O–H, Si–H, and Si–C S-bond activation reactions by titanium(IV)–imido complex **1415**

Taunia L.L. Closson and Marc R. Roussel The flattening phase transition in systems of trapped ions **1425**

John E.C. Wren and Georg Schreckenbach Neptunium(VII) in high-ionic-strength alkaline solutions — $[NpO_2(OH)_4]^{1-}$ or $[NpO_4(OH)_2]^{3-}$? **1436**

Paola Gori-Giorgi, János G. Ángyán, and Andreas Savin Charge density reconstitution from approximate exchange-correlation holes **1444**

A.B.P. Lever Density functional theory analyses of bis(bipyridine)ruthenium noninnocent quinonoid and thiolosulfinato complexes containing ligands formally in the semiquinone oxidation state **1451**

Hong Wu and Michael B. Hall Carbon–hydrogen vs. carbon–halogen oxidative addition of chlorobenzene to a cationic iridium(I) system — A density functional theory study **1460**

Catharina Goedecke, Pierre Hillebrecht, Till Uhlemann, Robin Haunschild, and Gernot Frenking The Dewar–Chatt–Duncanson model reversed — Bonding analysis of group-10 complexes $[(PMe_3)_2M–EX_3]$ (M = Ni, Pd, Pt; E = B, Al, Ga, In, Tl; X = H, F, Cl, Br, I) **1470**

Jian Li and Charles. H. Reynolds A quantum mechanical approach to ligand binding — Calculation of ligand–protein binding affinities for stromelysin-1 (MMP-3) inhibitors **1480**

Peter Elliott and Kieron Burke Non-empirical derivation of the parameter in the B88 exchange functional **1485**

Melissa Gajewski and Mariusz Klobukowski DFT studies of complexes between ethylenediamine tetraacetate and alkali and alkaline earth cations **1492**

Marcel Nooijen Explorations of many-body relativistic wave equations within a one-dimensional model **1499**

Greg M. Berner and Allan L.L. East Catalyzed β scission of a carbenium ion III — Scission observed in ab initio molecular dynamics simulations **1512**

Sandra Schinzel and Martin Kaupp Validation of broken-symmetry density functional methods for the calculation of electron paramagnetic resonance parameters of dinuclear mixed-valence $Mn^{IV}Mn^{III}$ complexes **1521**

Paul W. Ayers and Juan I. Rodriguez Out of one, many — Using moment expansions of the virial relation to deduce universal density functionals from a single system **1540**

Andre Sutrisno, Andy Y.H. Lo, Joel A. Tang, Jason L. Dutton, Gregg J. Farrar, Paul J. Ragogna, Shaohui Zheng, Jochen Autschbach, and Robert W. Schurko Experimental and theoretical investigations of selenium nuclear magnetic shielding tensors in Se–N heterocycles **1546**

Author Index / Index des auteurs **AI-1**

November / Novembre

REVIEW / SYNTHÈSE

Yanqing Pan, Todd L. Lowary, and Rik R. Tykwinski Naturally occurring and synthetic polyyne glycosides **1565**

ARTICLES / ARTICLES

Hongwei Gao, Richard F.W. Bader, and Fernando Cortés-Guzmán Energy additivity in branched and cyclic hydrocarbons **1583**

Raouf Ghavami, Amir Najafi, and Bahram Hemmateenejad QSPR studies on normal boiling points and molar refractivities of organic compounds by correlation-rankingbased PCR and PC–ANN analyses of new topological indices **1593**

Sukalyan Bhadra and Brindaban C. Ranu Water-promoted regioselective hydrothiolation of alkynes **1605**

Qingyong Meng, Chenggen Zhang, and Ming-Bao Huang A theoretical model study on the cyclic reaction of 4-hydroxybutanal catalyzed by Brønsted acid **1610**

Jenny S.J. McCahill and Douglas W. Stephan Copolymerization of sterically demanding phosphineolefins and 1-hexene **1620**

Caroline Genre, Geneviève Levasseur-Thériault, and Christian Reber Emitting-state properties of square-planar dithiocarbamate complexes of palladium(II) and platinum(II) probed by pressure-dependent luminescence spectroscopy **1625**

Kanda Panthong, Nongporn Hutadilok-Towatana, and Ampai Panthong Cowaxanthone F, a new tetraoxygenated xanthone, and other anti-inflammatory and antioxidant compounds from *Garcinia cowa* **1636**

Patrick B. Murphy, Feng Liu, Stephen C. Cook, Nusrat Jahan, D. Gerrard Marangoni, T. Bruce Grindley, and Peng Zhang Structural control of Au and Au–Pd nanoparticles by selecting capping ligands with varied electronic and steric effects **1641**

Hossein Fakhraian and Azam Gorgi-douze Synthesis and properties of ionic liquids based on 1-methyl- 3-(2-phenethyl)imidazolium **1650**

Author Index / Index des auteurs **AI-1**

December / Décembre

AWARD LECTURE / CONFÉRENCE D'HONNEUR

Thomas G. Back Design and synthesis of some biologically interesting natural and unnatural products based on organosulfur and selenium chemistry **1657**

ARTICLES / ARTICLES

H. Firouzabadi, N. Iranpoor, and S. Kazemi Direct halogenation of organic compounds with halides using oxone in water — A green protocol **1675**

Yusuf Zulykama, Ulagamani Uma, Palanisamy Chitra Devi, and Paramasivan T. Perumal Chemo- and regio-selective functionalization of Morita–Baylis–Hillman bromides with anthranilic acid **1682**

Mahalingam Malathi, Palathurai Subramaniam Mohan, Raymond J. Butcher, and Chidambaram Kulandaisamy Venil Benzimidazole quinoline derivatives — An effective green fluorescent dye for bacterial imaging **1692**

Regati Sridhar, Boga Srinivas, Bandaru Madhav, Vutukuri Prakash Reddy, Yadavalli Venkata Durga Nageswar, and Kakulapati Rama Rao Multi-component supramolecular synthesis of spirooxindoles catalyzed by β-cyclodextrin in water **1704**

Hossein Ismaili, Abdolhamid Alizadeh, Kristen E. Snell, and Mark S. Workentin Remarkable high-yielding chemical modification of gold nanoparticles using uncatalyzed click-type 1,3-dipolar cycloaddition chemistry and hyperbaric conditions **1708**

Sabry El-Taher Theoretical investigation of the oxidation pathways of $HO^{\bullet}$-initiated reactions of acrolein, methacrolein, and *trans*-crotonaldehyde **1716**

Daisuke Yokogawa, Hirofumi Sato, Sergey Gusarov, and Andriy Kovalenko Development of additive isotropic site potential for exchange-repulsion energy, based on intermolecular perturbation theory **1727**

Shanqiao Wei, Jinzhong Zhao, and Huawu Shao A facile method for the preparation of sugar orthoesters promoted by anhydrous sodium bicarbonate **1733**

Ping Qian, Li-Nan Lu, and Zhong-Zhi Yang Molecular dynamics simulations of *N*-methylacetamide (NMA) in water by the ABEEM/MM model **1738**

Mohamed H. Mohamed, Lee D. Wilson, John V. Headley, and Kerry M. Peru A spectral displacement study of cyclodextrin/naphthenic acids inclusion complexes **1747**

Author Index / Index des auteurs **AI-1**

Contents for Volume 87 / Sommaire pour volume 87 **C-1**

NOTE OF APPRECIATION / NOTE DE RECONNAISSANCE

The editors of the *Canadian Journal of Chemistry* thank the reviewers listed below for their valuable efforts in the 2009 edition of the journal.

Les rédacteurs en chef de la *Revue canadienne de chimie* tiennent à remercier les examinateurs énumérés ci-dessous des efforts qu'ils ont consacrés à l'édition 2009 de la Revue.

Adam, A.
Amsden, B.
Andersen, R.
Arnason, J.
Arndtsen, B.
Ashby, M.
Ata, A.
Autschbach, J.
Auzanneau, F.-I.
Ayers, P.
Back, T.
Baer, T.
Baik, M.
Bain, A.
Baker, R.T.
Banerjee, R.
Barluenga, J.
Barra, M.
Bartlett, R.
Basavaiah, D.
Batra, S.
Bazuin, G.
Beccalli, E.
Bengu, E.
Bentley, T.
Bergens, S.
Bertagnolli, H.
Bhanage, B.
Bhattacharya, S.
Bickelhaupt, F.M.
Bitsanis, I.A.
Bodwell, G.
Boeré, R.
Bohne, C.
Bolboaca, S.D.
Bonchev, D.
Bonella, S.
Bowmaker, G.A.
Boyd, R.
Boyle, R.
Branda, N.
Breau, L.
Breslow, R.
Britton, R.
Broggini, G.
Brook, M.
Brookhart, M.
Brown, A.
Brown, P.
Brown, S.
Bryce, D.
Budzelaar, P.
Bühlmann, P.
Buist, P.
Burnell, D.J.
Cai, X.
Cai, Z.
Campbell, R.
Canuto, S.
Cardenas, A.E.
Casavecchia, P.
Case, D.
Castellano, R.
Cavaleiro, A.
Cavallo, L.
Champagne, B.
Chang, C.-W.
Chattopadhyaya, J.
Chen, K.
Chenevert, R.
Choi, D.H.
Chong, D.
Chong, M.
Ciufolini, M.
Clark, A.J.
Clennan, E.
Clive, D.
Clyburne, J.
Coelho, F.
Consonni, V.
Consta, S.
Crich, D.
Crudden, C.
Csámpai, A.
Custodio, R.
Daiguebonne, C.
Dake, G.
Damha, M.
Dannenberg, J.
de Bruin, T.
De Jong, W.
de la Hoz, A.
de la Pradilla, R.
Deb, B.M.
Debowska, L.
Deeth, R.
Delmau, L.
Deng, L.
Deng, X.
Detty, M.
Dey, G.R.
Dickman, R.
Ding, Z.
Dong, V.
Doorn, J.
Dorta, R.
Doyle, M.
Drueckhammer, D.
Dudding, T.
Dudley, T.
Duhamel, J.
Dust, J.
Duthaler, R.
Dybowski, C.
Eisenstein, O.
Enders, M.
Engelzos, P.
Ercag, A.
Ercolani, C.
Ernzerhof, M.
Ervin, K.
Evangelista, F.A.
Evans, C.
Ferraccioli, R.
Fillion, E.
Findlay, J.
Fokas, D.
Forgione, P.
Fournier, R.
Fraceto, L.
Francis, R.
Fraser-Reid, B.
Freitas, M.P.
Frenking, G.
Gagliardi, L.
Gal, T.
Gao, J.
Garson, M.
Gates, D.
Gauthier, M.
Gibson, H.
Gilson, D.
Glaser, R.
Glass, R.
Glinski, M.
Gmehling, J.
Goddard, J.
Goekjian, P.
Gordon, H.
Grapperhaus, C.A.
Gree, R.
Green, J.
Grindley, B.
Gudat, D.
Gunduz, G.
Guo, Y.
Guthrie, P.
Ha, D.-C.
Hailes, H.
Hall, D.
Hanan, G.
Hanrahan, J.
Harnly, J.
Harrison, P.
Hart, D.
Heard, G.
Hearn, M.
Heilmann, J.
Hemscheidt, T.
Herberich, B.
Hicks, R.
Hitchcock, A.
Holdcroft, S.
Houk, K.
Huang, J.
Hudlicky, T.
Hudson, R.
Hughes, R.
Ikeda, H.
Ishida, T.
Islami, M.R.
Itami, K.
Ito, M.
Jackson, G.
Jackson, S.
Jacobsen, H.
Jacquemin, D.
Jha, A.
Johnson, D.
Johnston, R.
Jones, K.
Jones, N.
Jones, S.
Juaristi, E.
Kalinin, V.
Kallos, M.
Kanazirev, V.
Kappe, O.
Karanassios, V.
Karwowski, J.
Katsuta, S.
Kaupp, M.
Kawashima, T.
Keay, B.
Keillor, J.
Keller, B.
Kellogg, R.
Kerr, R.
Kidwai, M.
Kinghorn, A.D.
Kirk, K.
Kita, Y.
Kloo, L.
Kluger, R.
Klumpp, D.
Knight, D.
Konermann, L.
Kotsuki, H.
Kovacs, A.
Kowalewski, J.
Krogh-Jespersen, K.
Krukowski, S.
Kruse, A.
Kruse, P.

Krygowski, T.M.
Kubicki, J.
Kuckling, D.
Kurita, K.
Kurth, M.
Kustowski, P.
Kuwata, K.
Ladmiral, V.
Lagaris, I.E.
Lai, P.-S.
Langer, P.
Larachi, F.
Larock, R.
Latosinska, J.
Lavoie, G.
Lee, M.
Lehmler, H.-J.
Lenardão, E.
Lever, A.B.P.
Levy, M.
Leznoff, C.
Li, C.-J.
Li, S.-M.
Li, X.
Lin, Y.
Lindgren, I.
Lindsey, J.
Liu, G.J.
Liu, S.-T.
Lo, K.K.-W.
Loh, T.
Love, J.
Lowary, T.
Lukeman, M.
Luo, M.
Lyon, L.A.
Ma, D.
Macartney, D.
Macfie, S.
Macias, R.
MacKinnon, C.
MacLachlan, M.
Magee, D.
Maitra, N.
Makosza, M.
Manderville, R.
Marban, G.
Marcantoni, E.
Marshall, P.
Martell, J.
Martens, C.
Martinho, J.M.G
Masciadri, R.
Maseras, F.
Matovic, Z.D.
McBreen, P.
McCubbin, A.
McDonald, R.
McGlinchey, M.
McNulty, J.
Mehandjiev, D.
Meli, V.
Merino, G.
Michalak, A.
Milioto, S.
Miller, B.
Miller, S.A.
Moloney, M.
Montaut, S.
Monteiro, M.
Mora-Diez, N.
More O'Ferrall, R.
Mori, A.
Morris, R.
Müllen, K.
Mueller, L.
Mueller-Herold, U.
Mullins, O.
Murphy, S.
Murzin, D.
Nagasawa, H.
Nagle, J.
Nair, V.
Nakanishi, W.
Nath, M.
Navarrete-Vázquez, G.
Nelsen, S.
Nelson, D.
Nemykin, V.
Nguyen, M.T.
Nitz, M.
Norman, P.
Norrby, P.-O.
Nyokong, T.
Ollevier, T.
Olojo, R.
Pakkanen, T.
Pan, Q.
Pankiewicz, K.
Pansare, S.
Paquet, C.
Pasini, D.
Pauwels, E.
Peeters, F.
Pellerin, C.
Pelton, R.
Penner, G.
Perdew, J.
Peters, D.
Peterson, K.
Pittner, J.
Ple, N.
Plettner, E.
Plourde, G.
Poirier, R.
Popescu, I.
Pottie, I.
Prud'homme, R.E.
Purisima, E.
Pye, C.
Queguiner, G.
Quemener, D.
Quemener, G.
Raeppel, S.
Ragogna, P.
Ranu, Br.
Rao, M.
Rebeiro, G.
Reber, C.
Reimer, K.
Ren, Y.
Richard, J.
Richeson, D.
Rinke, P.
Rochefort, D.
Rodriguez, J.
Roesler, R.
Rohrdanz, M.A.
Rumi, M.
Russo, N.
Ryde, U.
Salahub, D.
Salin, E.
Sambria, L.
Sammartano, S.
Sartori, G.
Sauers, R.R.
Savin, A.
Sayari, A.
Schaefer, H.F.
Schafer, L.
Schaper, F.
Scherer, W.
Schiffer, J.
Schlaf, M.
Schlangen, M.
Schreckenbach, G.
Schreiner, P.
Schwan, A.
Schweizer, F.
Scott, J.
Scott, L.
Scuseria, G.
Shan, Z.
She, Y.
Shi, X.M.
Shipp, D.
Siddik, I.
Singer, R.
Singh, U.P.
Sithole, B.
Skene, W.
Slomkowski, S.
Sobot, P.
Solà, M.
Solovyev, I.
Somsook, E.
Sorensen, T.
Sovago, I.
Spillane, W.
Spino, C.
Springborg, M.
Stadlbauer, W.
St-Amant, A.
Staroverov, V.
Steer, R.
Stillman, M.
Storr, T.
Stradiotto, M.
Strassner, T.
Stubbs, K.
Su, Z.
Suárez, A.
Sugawara, M.
Sum, A.
Sumerlin, B.
Suzuki, I.
Swihart, M.
Tachikawa, H.
Tajmir-Riahi, H.
Takacs, J.
Takaguchi, Y.
Takeuchi, E.
Tala, S.
Tam, W.
Taniguchi, N.
Taylor, S.
Telfer, S.
Tennyson, J.
Tesler, J.
Thakkar, A.
Thomas, N.
Tinto, W.
Totti, F.
Trofimov, A.
Tsushima, S.
Tundo, P.
Turculet, L.
Turnbull, J.
Turner, C.H.
Turner, R.
Tuzar, Z.
Ugalde, J.
Valiente, R.
Valliant, J.
Vargas-Baca, I.
Veinot, J.
Verkade, J.
Villemure, G.
Vlcek, A.
Wagner, B.
Walsby, C.
Wang, J.
Wang, S.
Wang, X.-S.
Wang, Xi.
Wang, Y.X.
Warwicker, J.
Werstiuk, N.
Wettig, S.
White, R.
White, R.
Whittaker, A.
Wiberg, K.
Williams, I.
Williams, S.
Williams, V.
Wilson, P.
Wirth, T.
Wolf, M.
Wolfe, S.
Woo, T.
Workentin, M.
Wright, T.
Wu, G.
Wu, H.
Wulff, J.
Wuts, P.
Xue, D.
Yamanaka, S.
Yamazaki, S.
Yan, H.
Yenamandra, V.
Yoshizawa, K.
Young, R.
Yu, H.-Z.
Zargarian, D.
Zechel, D.

Zeinalipour-Yazdi, C.
Zhang, L.
Zhang, P.
Zhang, X.
Zhao, C.-G.
Zhao, W.
Zhao, Y.
Zhao, Z.
Zhichkin, P.
Ziff, R.
Zolfigol, M.
Zou, S.L.
Zugenmaier, P.